MINIREVIEW / MINISYNTHÈSE

Recent development in functionalized ionic liquids as reaction media and promoters

Wing-Leung Wong and Kwok-Yin Wong

Abstract: The recent development in the use of functionalized ionic liquids as both reaction media and promoters is reviewed. Ionic liquids designed with special functionality can enhance the reaction rate, selectivity, and productivity in various chemical reactions. In this context, some important chemical reactions involving C–C, C–O, C–N, and C–S bond formation in functionalized ionic liquids are discussed. These functionalized ionic liquids were found to provide distinct advantages over conventional organic solvents in these catalytic reactions.

Key words: ionic liquids, homogeneous catalysis, organocatalysis, green chemistry.

Résumé : On passe en revue les développements récents dans le domaine de l'utilisation des liquides ioniques fonctionnalisés tant comme milieux réactionnels que comme catalyseurs. Les liquides ioniques préparés avec des fonctionnalités spéciales peuvent augmenter la vitesse de réaction, la sélectivité et la productivité dans diverses réactions chimiques. Dans ce contexte, on discute de quelques réactions chimiques importantes impliquant la formation de liaisons C–C, C–O, C–N et C–S dans des liquides ioniques fonctionnalisés. On a trouvé que, dans ces réactions catalytiques, ces liquides ioniques fonctionnalisés présentent des avantages distincts par rapport aux solvants organiques conventionnels.

Mots-clés : liquides ioniques, catalyse homogène, catalyse organique, chimie écologique.

[Traduit par la Rédaction]

Can. J. Chem. Downloaded from www.nrcresearchpress.com by Renmin University of China on 09/02/12
For personal use only.

Introduction

Research into ionic liquids has experienced tremendous growth during the past 10 years. There were over 10 000 research articles published with ionic liquid as the keyword in this period. The most important driving force of the booming research on ionic liquids is their potential in substituting for volatile organic solvents in chemical synthesis because they are generally nonvolatile.[1–4] The use of ionic liquids to replace conventional solvents as the medium for industrial chemical processes could partially eliminate the emission of volatile organic compounds, which are a major source of environmental pollution, although the concept of using ionic liquids as "greener" replacements may need to be further validated because organic solvents are often used in the synthesis of ionic liquids. For the production of high-value chemicals, such as fine chemicals and pharmaceuticals, the replacement of a conventional process by a process based on ionic liquid is still attractive if the ionic liquid permits a high degree of reusability, high yields, and easy separation of products. In recent years, scientists have realized that not all ionic liquids are intrinsically green solvents as some are extremely toxic.[4,5] However, there is no doubt that chemists are able to tune the properties of ionic liquids via molecular design, and ionic liquids, if used properly, can contribute to the sustainability of our Earth.

The importance of ionic liquids can be deduced from their applications in a wide range of areas, which include organic synthesis and catalysis,[6–11] separations,[12,13] lubrication,[14] and materials science.[15,16] Ionic liquids are readily synthesized from a number of classes of cations, typically including those based on imidazolium, pyrrolidinium, ammonium, phosphonium, guanidinium, and pyridinium. An immense number of ionic liquids can be made by combining these cations with a variety of anions. Nowadays, ionic liquids are not only utilized as solvents but integrated with functionalities for specific purposes. During the past decade, reviews on the use of functionalized ionic liquids in specific applications rather than simply as solvents have appeared. The latest developments for ionic liquids, for example, in inorganic material synthesis (ionic liquids as templates and precursors),[17] supported ionic liquid-phase catalysis (ionic liquids as supports or ionic tags for immobilization of molecular catalysts),[18–22] asymmetric organocatalysis,[23] and biocatalytic transformations,[24–26]

Received 20 March 2011. Accepted 8 July 2011. Published at www.nrcresearchpress.com/cjc on 29 September 2011.

W.-L. Wong and K.-Y. Wong. Department of Applied Biology and Chemical Technology and The State Key Laboratory of Chirosciences, The Hong Kong Polytechnic University, Hung Hom, Kowloon, Hong Kong SAR, China.

Corresponding author: Kwok-Yin Wong (e-mail: bckywong@polyu.edu.hk).

This article is part of a Special Issue dedicated to Professor Tak-Hang Chan.

have been reviewed. In this review, only recent (2000–2011) and special contributions of functional ionic liquids that serve as both promoters and reaction media will be discussed. Other systems in which the ionic liquids were used just as alternative solvents and (or) media for chemical reactions are not included as they are outside the scope of this review.

Applications in C–C bond formation reactions

Knoevenagel condensation

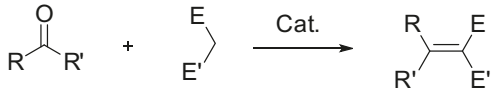
The Knoevenagel condensation reaction is one of the most useful reactions for carbon–carbon bond formation in organic syntheses. It involves the nucleophilic addition of an active methylene compound to a carbonyl group (aldehyde or ketone) to give electrophilic alkenes with a base or an acid as the catalyst (Scheme 1). More recently, a zeolite imidazolate framework[27] (ZIF-8) has been demonstrated to be an efficient heterogeneous catalyst for Knoevenagel reaction.

A simple ionic liquid system for Knoevenagel condensation, in which ethylammonium nitrate (an ionic liquid) was used as both solvent and promoter for the condensation of 4-oxo-(4*H*)-1-benzopyran-3-carbaldehydes with 3-methyl-1-phenylpyrazolin-5-(4*H*)-one at room temperature and was reported by Shingare and co-workers.[28] In this ionic liquid system, the water produced during the reaction was absorbed by the ionic liquid and thus the reaction was able to proceed well. The reaction gave high yields (70%–92%) in a very short reaction time (20–30 min) compared with conventional methods in organic solvents.

A cyclic guanidinium lactate ionic liquid (**IL1**) reported by Lin and co-workers[29] was also investigated in the Knoevenagel condensation (Scheme 2). It was found that the aromatic aldehydes were able to react with a number of active methylene compounds in **IL1** at room temperature and a high yield of products (over 90%) were obtained in just 1–7 min. The work-up procedure for the ionic liquid system was very simple and the products did not need to be purified further. The ionic liquid could be reused six times without a loss in catalytic activity. Another alkylammonium-based ionic liquid (**IL2**, 2-hydroxyethylammonium formate) reported by Alizadeh et al.[30,31] is able to act as a task-specific ionic liquid for promoting Knoevenagel condensation reactions. Nitroalkanes were reacted with various aldehydes in **IL2** at room temperature to produce β-nitrostyrenes in high yields. This reaction does not involve any hazardous organic solvent or toxic catalyst. **IL2** is also recoverable and recyclable by simple separation procedures. A mechanism involving the ambiphilic dual activation by **IL2**, which bears a hydroxyl group, an ammonium acidic moiety, and a formate anion, was proposed.[30]

The imidazolium-based ionic liquids such as **IL3** and **IL4** were also investigated for the Knoevenagel condensation. **IL3** as reported by Ranu and Jana[32] is able to catalyze a wide range of aliphatic and aromatic aldehydes and ketones to undergo condensations with a variety of active methylene compounds including diethyl malonate, ethyl cyanoacetate, malononitrile, malonic acid, and ethyl acetoacetate. **IL3** was found to promote the reaction of aliphatic aldehydes with diethyl malonate effectively. When its OH^- counteranion was replaced by BF_4^- or Br^-, however, the reaction did not proceed. The results indicated that the hydroxyl counterion played a vital role in the condensation reaction. **IL4** with

Scheme 1. A typical Knoevenagel condensation reaction.



R, R' = aryl, alkyl, H

E, E' = electron withdrawing groups

PF_6^- as the counteranion was demonstrated by Valizadeh and Gholipour[33] to be a reusable reaction promoter and a solvent for the synthesis of *E*-acrylates via the Knoevenagel condensation reaction. The success of **IL4** in the catalysis may arise from its phosphinite-functionalized pendant, which shows weak Lewis base characters.

Michael addition

Michael addition is the nucleophilic addition of a carbanion or another nucleophile to an α,β-unsaturated carbonyl compound (Scheme 3). It is one of the most frequently used C–C bond formation reactions in organic synthesis. The reaction is catalyzed by various basic catalysts. For example, NaOH and KOH salts are commonly used in Michael addition reactions.

The use of basic ionic liquids as reaction promoters and media in Michael addition reactions has been demonstrated by a number of research groups in recent years. Ranu et al. reported a task-specific ionic liquid (**IL3**) system for the reaction.[34,35] Interestingly, **IL3** always drives the reaction of nitriles and 1,3-dicarbonyl compounds with α,β-unsaturated esters to produce bis-adducts exclusively in a one-pot process. These results are difficult to achieve by one-step preparation via conventional methods, which demonstrates the dramatic influence of ionic liquids in Michael additions.

The Michael addition of malonodinitrile to chalcone was also found to proceed well in some ionic liquids (**IL5**–**IL8**) without the addition of other catalysts (Scheme 4). Mečiarová and Toma[36] explicated the effects of ionic liquids on the proton dissociation constants of the C–H bond of some active methylene compounds such as malonodinitrile ($CH_2(CN)_2$). In addition, they concluded that ionic liquids exert special effects on the Michael addition of malonodinitrile to chalcone because the nucleophility of the malonodinitrile anion after the dissociation of a C–H acid is significantly enhanced in the ionic liquid medium.

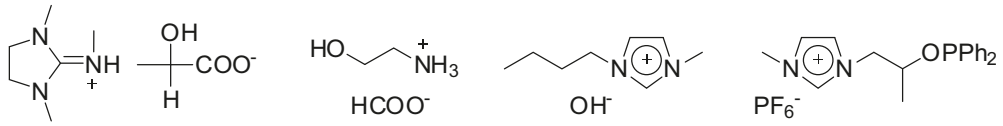
A chiral pool of functionalized ammonium-, imidazolium-, and pyridinium-based ionic liquids, which are derived from (–)-ephedrine, were developed by Truong and Vo-Thanh[37] (Scheme 5). These chiral ionic liquids (**IL9**–**IL11**) were used as both chiral reaction media and promoters (with 6 mol% of KOH as a co-catalyst) for the asymmetric Michael addition of diethyl acetylaminomalonate to chalcone derivatives. Moderate to good yields (up to 80%) and enantioselectivities (up to 70% ee) were obtained under microwave activation conditions. The ionic liquids could be recycled and reused three times. Similar activity and stereoselectivity were maintained in the recycling. However, loss of activity was observed in the fourth cycle.

Diels–Alder reaction

The Diels–Alder reaction is a very important tool for carbon–carbon bond formation reactions in organic synthesis. It is an

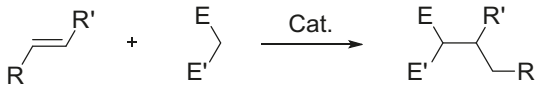
Can. J. Chem. Downloaded from www.nrcresearchpress.com by Renmin University of China on 09/02/12
For personal use only.

Scheme 2. Some ionic liquids for Knoevenagel condensation reactions.



IL1 **IL2** **IL3** **IL4**

Scheme 3. A typical Michael addition reaction.



E, E' = electron-withdrawing groups

addition reaction of a conjugated diene to a dienophile (usually an alkene) to produce a six-membered carbocycle in one concerted step (Scheme 6). Many investigations have been devoted to both the mechanisms and reaction rates of this reaction. In addition, there are a number of reports on Diels–Alder reactions using various ionic liquids as reaction media.[38–45] The efficiency and selectivity of the reaction are also known to be influenced by the acidity of the ionic liquid medium.[46]

The use of functionalized ionic liquids as solvents and promoters for the Diels–Alder reaction is rarely reported in the literature. Some protic imidazolium ionic liquids (**IL12**–**IL13**) developed by Pernak and co-workers[47] were demonstrated to be effective reaction media and promoters in Diels–Alder reactions (Scheme 7). In the reaction of cyclopentadiene with two dienophiles (dimethyl maleate and methyl acrylate), good conversions and endo/exo selectivities were achieved. It is believed that the dienophile was activated by the formation of hydrogen bonds with protic imidazolium ionic liquids. In addition, the ionic liquids could be recycled and no alterations in both yield and selectivity of the process were observed after 10 reaction cycles.

Friedel–Crafts reaction

The Friedel–Crafts reaction is an attractive synthetic approach for C–C bond formation in aromatic rings. The reaction usually involves the alkylation of an aromatic ring with an alkyl halide using a strong Lewis acid as the catalyst. Diphenylmethane and its derivatives, for example, are important pharmaceutical intermediates and are produced industrially via the Friedel–Crafts reaction of benzene with benzyl chloride using acid catalysts such as $AlCl_3$, $FeCl_3$, or H_2SO_4 (Scheme 8). It is also known that organochloroaluminate ionic liquids, which are prepared by a mixture of a quaternary ammonium chloride salts (typically 1,3-dialkylimidazolium chloride) with aluminum chloride, are effective catalysts for this reaction.[48–51]

Friedel–Crafts alkylation of nitrogen heterocycles, such as indoles and pyrroles, can be carried out in ionic liquids under mild conditions. A study using **IL14a**–**IL14d** as the reaction media for the alkylation of various indoles with styrene oxide under ambient conditions was reported by Kantam et al.[52] The investigation indicated that **IL14a** gave better catalytic reactivity than other ionic liquids (**IL14b**–**IL14d**), whereas **IL14d** did not catalyze the alkylation reaction. When the reaction was carried out in CH_2Cl_2 instead of ionic liquid, no product was formed even after a prolonged reaction time. The strong Lewis acid character of **IL14a** may account for its high reactivity in the reaction (Scheme 9).

The pyrrolidinium-based ionic liquid (**IL15**) with fluorine-containing anions developed by Xiao and co-workers[53] is a highly fluidic liquid even below room temperature. **IL15** was used as a recyclable solvent and an efficient Brønsted acid promoter for Friedel–Crafts alkylations of indoles with nitroalkenes. The reaction may proceed via an ionic liquid – nitroalkene complex that involves the formation of intermolecular double hydrogen bonds between the protons on the nitrogen of the cation and the oxygens of the nitro group. However, when **IL15** was replaced by DMSO for the addition of indole to *trans*-β-nitrostyrene, no product was formed even when the reaction was allowed to proceed for 2 days. This ionic liquid was also recyclable after extraction and drying under vacuum. The recycled **IL15** was directly reused in the catalysis and showed no significant decrease in catalytic performance.

Pyridinium-based ionic liquids **IL16a**–**IL16b** reported by Xiao and Malhotra[54] were also investigated in the Friedel–Crafts acylations of some aromatic compounds with acetic anhydride. It was found that a significant amount of products (51%–81% conversion) was obtained simply using the ionic liquid as the reaction medium (without any metal catalyst) under relatively mild conditions (at 50–75 °C for 4 h). The ionic liquids could be recycled and reused in Friedel–Crafts acylations. In addition, an excellent solvent–catalyst system for the reaction was obtained by adding $FeCl_3$ as a co-catalyst in **IL16b**. High conversions were achieved at a relatively low temperature (50 °C). As compared with **IL16a**, ionic liquid **IL16b** exhibited better performance in the acylation reaction with $FeCl_3$ as the co-catalyst.

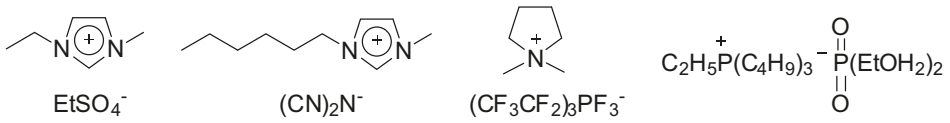
Prins reaction

The Prins reaction is an important C–C bond forming reaction and is a powerful synthetic route for the construction of six-membered tetrahydropyran derivatives, which are commonly found in a number of natural products, for example, avermectins, aplysiatoxins, oscillatoxins, latrunculins, talaromycins, and acutiphycins. The typical Prins reaction usually involves the use of strong Brønsted acids, for example, sulfuric acid, hydrochloric acid, and *p*-toluenesulfonic acid, as the catalyst to catalyze the reaction of olefins with aldehydes to produce tetrahydropyran derivatives (Scheme 10).

Some Brønsted acid ionic liquids have been utilized as effective and recyclable promoters for Prins reactions (Scheme 11) in recent years.[55,56] However, reports on investigations with ionic liquids as both promoters and solvents for Prins reactions are relatively rare. The use of ionic liquid **IL17** (1-*n*-butyl-3-methylimidazolium chloroaluminate) in Prins cyclizations to produce 4-chlorotetrahydropyran derivatives was reported by Yadav et al.[57] The reaction took place in **IL17**,

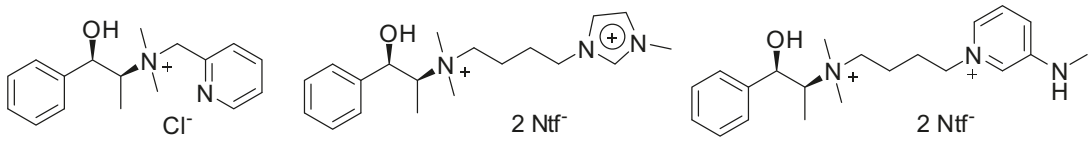
Can. J. Chem. Downloaded from www.nrcresearchpress.com by Renmin University of China on 09/02/12
For personal use only.

Scheme 4. Some ionic liquids for Michael addition reactions.



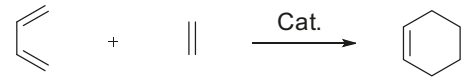
IL5 **IL6** **IL7** **IL8**

Scheme 5. Some chiral ionic liquids used in asymmetric Michael addition.



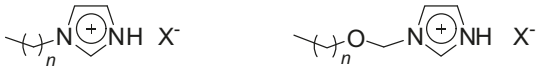
IL9 **IL10** **IL11**

Scheme 6. A typical Diels–Alder reaction.



diene dienophile cyclohexene

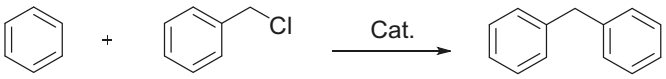
Scheme 7. Protic imidazolium-based ionic liquids for Diels–Alder reaction (Ntf_2^- = bis(trifluromethane)sulfonamide).



IL12a: X^- = lactate
IL12b: X^- = salicylate
IL12c: X^- = BF_4^-
IL12d: X^- = Ntf_2^-

IL13a: X^- = lactate
IL13b: X^- = salicylate
IL13c: X^- = BF_4^-
IL13d: X^- = Ntf_2^-

Scheme 8. Friedel–Crafts reaction of benzene with benzyl chloride to produce diphenylmethane.



which played a dual role as a promoter and a solvent, to give excellent yields of chlorotetrahydropyrans in short reaction times (5–15 min) at room temperature. The Lewis acid species in this ionic liquid system was recognized to be $Al_2Cl_7^-$, and its concentration in the 1-*n*-butyl-3-methylimidazolium chloride ionic liquid depended on the amount of $AlCl_3$ present. The reaction rate was enhanced by increasing the molar fraction of $AlCl_3$ in the ionic liquid. However, no reaction was observed under both basic and neutral conditions.

The cyclization of homoallylic alcohols with various aldehydes was investigated by Fuchigami and co-workers[58] in some ionic liquids. The alkylammonium ionic liquids containing hydrogen fluoride played roles as reaction medium, promoter, and the fluorine source simultaneously in the Prins reaction. Whereas $Et_3N{\cdot}3HF$ (molar ratio = 1:3) and $Et_3N{\cdot}4HF$ did not promote the cyclization reaction, the reaction in **IL18**·5HF afforded the corresponding 4-fluorinated tetrahydropyrans in excellent yields with very high stereoselectivity (cis isomers exclusively). For benzaldehydes with an electron-donating group (OCH_3 or OH) at the para position, no stereoselectivity was observed (a mixture of cis and trans isomers was obtained in an almost 1:1 ratio).

Applications in C–O bond formation reactions

Esterification

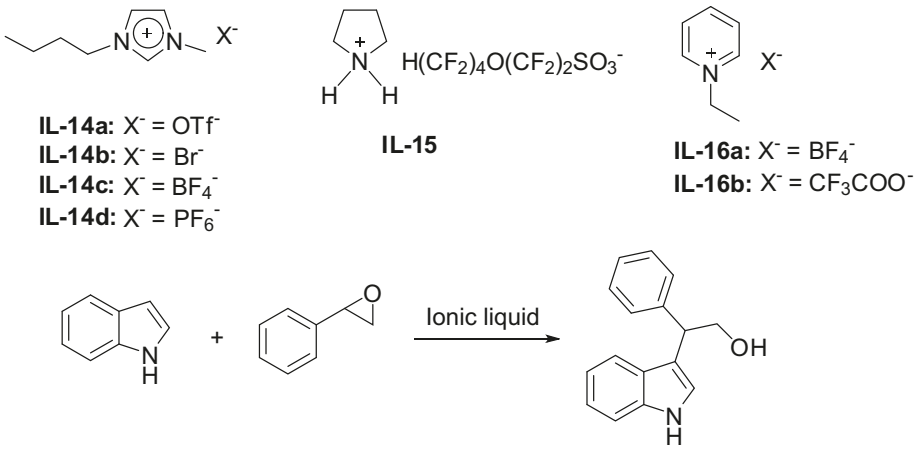
Organic esters, including aliphatic, arylic, and heterocyclic esters, are valuable intermediates in both chemical and pharmaceutical industries. The typical methodology employs Brønsted acids as the catalysts for esterification of carboxylic acids and alcohols. The main difficulty usually encountered in acid-catalyzed esterification arises from its reversible reactions (Scheme 12). To shift the equilibrium to favor ester production, it is necessary that one of the reactants is in excess and (or) the produced ester or water is removed constantly during the reaction.

In the past 10 years, Lewis acid or base ionic liquids have been synthesized and used as both reaction media and promoters in the esterification process. 1-Butylpyridinium chloroaluminate ionic liquid (**IL19**) developed by Deng et al.[59] was able to promote the esterifiation of acetic acid with equal equivalents of alcohols (isopropyl, isopentyl, isooctanol, benzyl alcohol, and glycerol) at 30–110 °C for 2 h. The study demonstrated that the aluminium chloride-based ionic liquid is stable enough to resist degradation by water if the molar ratio of aluminium chloride – butylpyridine chloride is 1:2. Comparison studies on the catalytic performance between **IL19** and concentrated sulfuric acid indicated that the ionic liquid gave better results under the same reaction conditions because the esters produced were not soluble in the reaction medium (ionic liquid). **IL19** was recycled three times and comparable yields and selectivity of esters were obtained in the reactions.

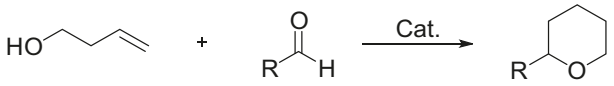
Another ionic liquid system prepared by choline chloride and $ZnCl_2$ was reported by Prasad and co-workers.[60] The Lewis acid ionic liquid (**IL20**) was used in the synthesis of wax esters using equal molar quantities of long-chain carboxylic acids and long-chain alcohols at 110 °C for 4–24 h. This liquid–liquid biphasic method shows several advantages in wax ester preparation. **IL20** is water insensitive, so there is no need to remove the water produced during the reaction. It can be reused for at least six cycles without pretreatment or significant loss of activity, and the liquid esters being a separate phase can be readily decanted from the ionic liquid phase after reaction. Thus, the use of volatile organic solvents for extraction can be avoided (Scheme 13).

Can. J. Chem. Downloaded from www.nrcresearchpress.com by Renmin University of China on 09/02/12
For personal use only.

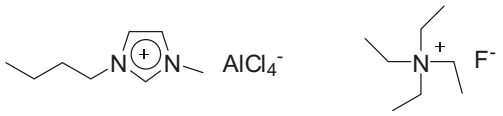
Scheme 9. Some ionic liquids for Friedel–Crafts reactions (Otf^- = trifluoromethanesulfonate) and an example of alkylation of indole with styrene oxide.



Scheme 10. A typical Prins reaction.



Scheme 11. Some ionic liquids used in Prins reactions.



The strong Brønsted acid ionic liquids (**IL21**–**IL22**), which bear an appended sulfonic acid group (SO_3H), were reported by Forbes and co-workers[61,62] (Scheme 14). **IL21a** showed no observable loss of triflic acid (CF_3SO_3H, bp = 162 °C at 760 torr; 1 torr = 133.3224 Pa) even under vacuum (10 torr) at 150 °C. For **IL22**, no free *p*-toluene sulfonic acid was found in the extracts after washing with toluene or diethyl ether. The application of these ionic liquids as dual solvent catalysts was demonstrated in the Fisher esterification. With an equal mole ratio of acetic acid and ethanol, both **IL21a** and **IL22** were able to promote the formation of ethylacetate in 82%–96% yields at 22–175 °C for 0.75–48 h. **IL22** was also successfully reused for five cycles in the esterification. Other acid-promoted organic reactions such as alcohol dehydrodimerization and pinacol–benzopinacole rearrangement were also explored for **IL22**.

A number of other sulfonic acid-functionalized imidazolium ionic liquids, which are analogues of **IL21a** with different *n*-alkyl chain lengths, were reported by Deng and co-workers.[63] The addition reactions of aliphatic acids and olefins to give the corresponding esters were also investigated. The esters were simply isolated by decantation, and the ionic liquids were reused continuously after drying in a vacuum (5–12 mm Hg; 1 mm Hg = 122.3224 Pa) at 80 °C.

More recently, Fradet and co-workers[64] developed a new method for the synthesis of polyesters using a Brønsted acid ionic liquid. It was found that the polyesterification of 12-hydroxydodecanoic acid in **IL21b** yielded high molar mass poly(12-hydroxydodecanoic acid) at low to moderate temperatures (90–130 °C) in short reaction times (30–60 min) under atmospheric pressure. Another similar ionic liquid reported by Dai and co-workers[65] was also employed as a promoter and medium in the alcoholysis of acetonitrile to ester. The results showed that the Brønsted acid ionic liquid bearing an appended sulfonic acid group and with HSO_4^- as a counteranion gave better catalytic performance than other counteranions such as BF_4^- and $H_2PO_4^-$. However, the ionic liquid system encounters a solubility problem for the cyclic or long-chained alcohols because these substrates are relatively nonpolar. The highest yield of 85% was achieved for *n*-butyl alcohol. *n*-Octyl alcohol is almost insoluble in the ionic liquid medium and a poor yield of octyl acetate was obtained.

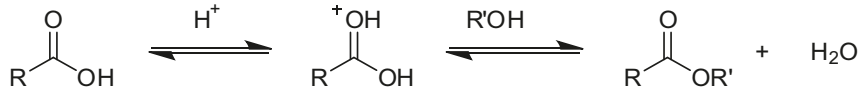
The pyridinium- and tetraalkylammonium-based ionic liquids functionalized with an appended sulfonic acid group were also investigated for ester synthesis. The Brønsted acids **IL23** and **IL24** with hydrogen sulfate as counterions were reported by Sun and co-workers[66] (Scheme 15). It was found that the esterification of ethanol and acetic acid (in 1:1 molar ratio) in these ionic liquid media gave both good conversion and high selectivity. Moreover, the liquid esters formed a separate phase that was readily decanted from the ionic liquid after reaction. The ionic liquids could be reused after removal of water under vacuum.

Li and co-workers[67] also reported a pyridinium-based ionic liquid that is similar to **IL23** (with a shorter alkyl chain) and demonstrated its activity in esterification of salicylic acid with a number of alcohols under microwave irradiation conditions. The results indicated that the sulfonic acid-functionalized ionic liquid with HSO_4^- as the counteranoin exhibited high catalytic activity and the esters were obtained in 92%–94% yield. The ionic liquid can be readily used after the separation of esters by decantation. The activity of the ionic liquids in esterification reactions is generally dependent on their Brønsted acidity.

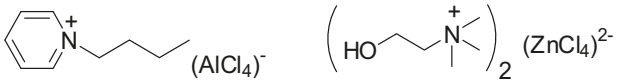
Some other sulfonic acid-functionalized ionic liquids based on the tetraalkylammonium cation (structurally similar to **IL24** with either HSO_4^- or $H_2PO_4^-$ as the counteranions) were developed by Yu and co-workers.[68] In the investigation of the esterification of α-pinene and acetic acid, the ionic liquids functionalized with an alkyl sulfonic acid showed much better catalytic activity than those simply using H_2SO_4

Can. J. Chem. Downloaded from www.nrcresearchpress.com by Renmin University of China on 09/02/12
For personal use only.

Scheme 12. Reversible reactions in acid-catalyzed esterification.

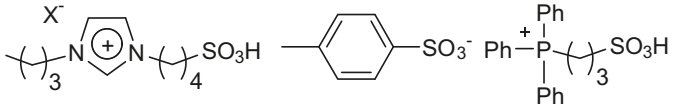


Scheme 13. Lewis acidic ionic liquids.



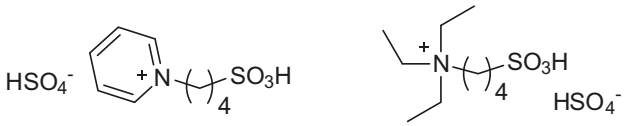
IL19 **IL20**

Scheme 14. Ionic liquids bearing an appended sulfonic acid group.



IL21a: $X^- = CF_3SO_3^-$
IL21b: $X^- = HSO_4^-$ **IL22**

Scheme 15. Pyridinium- and tetraalkylammonium-based ionic liquids functionalized with an appended sulfonic acid group.



IL23 **IL24**

or H_3PO_4 as the catalyst in organic solvents. Moreover, the ionic liquid with HSO_4^- as the counteranion exhibited better catalytic performance (in terms of conversion and selectivity of esters) than the one with the $H_2PO_4^-$ anion. The difference in the selectivity of esters was attributed to the HSO_4^- anion, which possessed better stabilization ability than $H_2PO_4^-$ for the unstable carbonium intermediate during the esterification reaction.

Ionic liquids with acidic counteranions were also developed for esterification. For example, **IL25a**–**IL25b**, **IL26**, and **IL27** reported by Bazureau and co-workers[69,70] were used as the recyclable task-specific ionic liquids in the synthesis of lipophilic esters (Scheme 16). Experimental results showed that the increase of Brønsted acidity of the counteranion (**IL25a** and **IL25b**) could increase the reaction rate in the esterification reactions. In addition, the performance of an ionic liquid in the reaction is dependent on the character of the side chain of the cation (low lipophilic character of **IL25a** and high polarity of **IL26**). The immiscibility of the produced esters with the ionic liquid medium also facilitates the reaction equilibrium to shift to the product side. Along with the four ionic liquids examined in the esterification, **IL27** gave the best performance because of its low lipophilic characters. **IL25c** with dicyanamide as the couteranion was reported by Biswas et al.[71] This ionic liquid showed high solubility for maltodextrin and was demonstrated to be a good promoter and (or) medium for the reaction between maltodextrin and vinyl stearate or stearic acid at 75 °C.

Some simple alkylammonium salts including triethylammonium hydrogen sulfate, triethylammonium dihydrogen phosphate, and triethylammonium tetrafluoroborate were reported by Ganeshpure et al.[72,73] for the esterification of carboxylic acids with primary alcohols. The ionic liquids **IL28a**–**IL28d** utilized as the Brønsted acid promoter and reaction media in esterifications were prepared directly by the reaction of tertiary alkylamines with inorganic acids (Scheme 17). Among the various anions used, HSO_4^- gave the best activity because it provided strong Brønsted acidity for the catalysis. The ionic liquids with p-$CH_3C_6H_4SO_3^-$, $H_2PO_4^-$, or BF_4^- anions are relatively weaker acids and thus they show lower activity in the esterification reactions. For a given anion, however, the yield of esters was found to increase as the size of the ionic liquid cation became smaller. The better solvation of water by the smaller cations is probably responsible for their high activity. The ionic liquids also show phase separation properties in the esterification process. When the reaction was complete, the ester product did not dissolve in and readily separated from the ionic liquid medium. The separation and recycling process are therefore simple and convenient.

Ionic liquid **IL29** was synthesized by the reaction of *N*-alkylimidazoles with inorganic acids such as tetrafluoroboric acid. Tang and He and co-workers[74] reported the use of **IL29** in the esterification of a variety of carboxylic acids with some common alcohols (methanol, ethanol, 1-butanol, and 1-octanol) at 110 °C. The esters produced were easily separated as they are immiscible with the ionic liquid medium. No volatile organic solvent is required in the work up and recycling processes for the ester synthesis in **IL29**. Continuous removal of water or using an excess of reactant was also not necessary.

Later on, a similar ionic liquid system based on **IL29** for the esterification of alcohols with acetic acids was reported by Halligudi and co-workers.[75] A comparison study of **IL29** and **IL25d** on the catalytic activity for the esterification was also conducted. **IL29** was found to exhibit superior performance in the reaction, probably because of its stronger Brønsted acidity than that of **IL25d**.

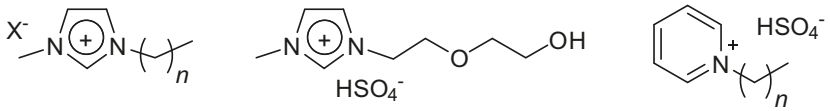
Paal–Knorr furan synthesis

The Paal–Knorr synthesis is an important reaction in organic chemistry because it is the most widely used approach to generate furans, pyrroles, or thiophenes from 1,4-diketones. The substituted furans and pyrroles are the common structural components of many pharmaceutical and natural products. The reaction can proceed under neutral or slightly acidic conditions (Scheme 18). In general, the addition of a weak acid such as acetic acid accelerates the cyclization reaction. The use of amine or ammonium hydrochloride salts as the catalyst or by controlling the reaction pH at <3 lead to furans as the main products.

In recent years, many methods have been developed for the conversion of 1,4-dicarbonyl compounds to furan derivatives via acid-mediated dehydrative cyclization. The use of ionic liquids in the Paal–Knorr furan synthesis is relatively unexplored. There are only a few reports in the literature. A

Can. J. Chem. Downloaded from www.nrcresearchpress.com by Renmin University of China on 09/02/12
For personal use only.

Scheme 16. Ionic liquids with acidic/neutral counteranions.



IL25a: $X^- = HSO_4^-$
IL25b: $X^- = H_2PO_4^-$
IL25c: $X^- = (CN)_2N^-$
IL25d: $X^- = BF_4^-$

IL26 **IL27**

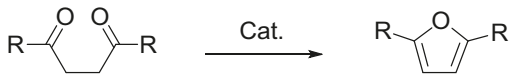
Scheme 17. Ionic liquids prepared from tertiary amines and acids.



IL28a: $X^- = HSO_4^-$
IL28b: $X^- = H_2PO_4^-$
IL28c: $X^- = BF_4^-$
IL28d: $X^- = p\text{-}CH_3C_6H_4SO_3^-$

IL29

Scheme 18. Paal–Knorr furan synthesis.

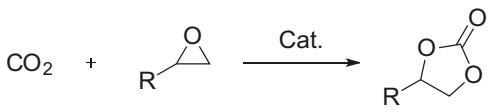


Scheme 19. Ionic liquid used in Paal–Knorr furan synthesis.



IL30

Scheme 20. The reaction of CO_2 with oxiranes to produce cyclic carbonates.



Brønsted acid ionic liquid (**IL30**) was reported independently by two research groups for furan synthesis (Scheme 19).[76,77] Wang and co-workers[77] demonstrated that **IL30** was able to promote the synthesis of 9-aryl-3,4,5,6,7,9-hexahydro-1*H*-xanthene-1,8-(2*H*)-dione. In the reaction, **IL30** offered remarkable improvement over existing methods with organic solvents. Excellent yields (85%–94%) of products were achieved in the ionic liquid system. The ionic liquid was recycled and reused without showing loss of activity. In addition, the nature of the anion and cation of ionic liquids showed strong influence on the catalytic performance in the Paal–Knorr reaction.

The Paal–Knorr reaction of the ester-substituted 1,4-diketones in **IL30** was first reported by He and co-workers.[76] In this ionic liquid system, a wide range of aliphatic and aromatic 1,4-diketones were able to undergo cyclization to form furan derivatives in high yields. A mechanism for the conversion of 1,4-diketones into furans in ionic liquid was also proposed. It was suggested that **IL30** acted as a Brønsted acidic promoter and provided protons to catalyze the reaction.

Chemical fixation of carbon dioxide

The reaction of CO_2 with oxiranes to form organic cyclic carbonates is readily catalyzed by a number of onium halide salts such as tetraethyl ammonium bromide (Scheme 20). The reaction also proceeds in the presence of a wide range of catalysts, including metal halides or transition-metal complexes in ionic liquid medium.[78–80] The utilization of ionic liquids as both reaction promoters and media in the transformation of CO_2 to cyclic carbonate under metal-free conditions has attracted increasing attention in recent years. Among the developed ionic liquid systems based on imidazolium, pyrridinium, and quaternary ammonium salts, halides such as Br^- and I^- are commonly used as the counteranions. It is probably because halides, particularly Br^- and I^- anions, are able to assist the ring-opening process of terminal epoxides.[81]

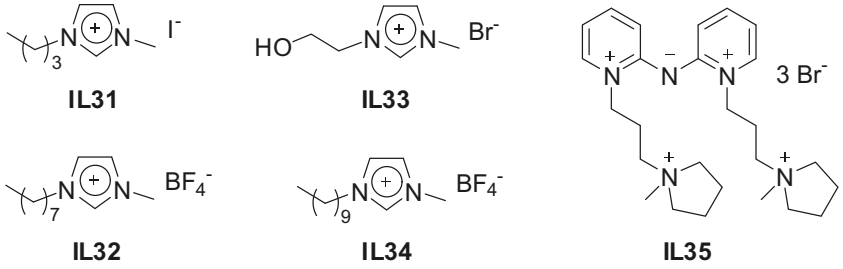
Tetrabutylammonium halides, such as bromide or iodide salts, have been reported to serve as solvents and promoters in cyclic carbonate synthesis from CO_2 and various epoxides. Caló et al.[82] reported that epoxides dissolved in tetrabutylammonium bromide (TBAB) reacted with CO_2 at atmospheric pressure to give good yields of cyclic carbonates. The cyclic carbonate was then isolated by vacuum distillation or by extraction with ethyl acetate. This procedure allowed the recycling of tetrabutylammonium salts. The possible role exerted by different cations such as imidazolium and pyridinium on the CO_2 fixation reaction was also investigated. It was found that the halide salts of imidazolium and pyridinium were unstable and readily decomposed under the high reaction temperature conditions. The stability of ionic liquids observed in this study is in accordance with a recent report.[83]

Another example of using TBAB in cyclic carbonate synthesis was demonstrated by Arai and co-workers.[84] In this system, two sequential reactions of epoxidation and cycloaddition were coupled into a one-pot process. Styrene carbonate was synthesized in ionic liquid medium by a direct oxidative carboxylation of styrene with *tert*-butyl hydroperoxide as the oxidant. It was found that both the structure of ionic liquids and the nucleophilicity of anions (nucleophilic tendency decreases in the order: $I^- > Br^- > Cl^-$) strongly affected the production of styrene carbonate. TBAB was identified to be the most effective promoter in the reaction.

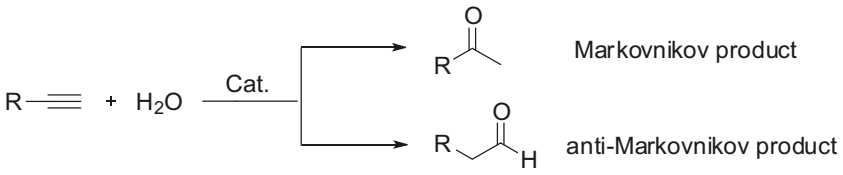
IL31 reported by Kim and Cheong[85] is also an efficient promoter and reaction medium in the coupling reaction of CO_2 with propylene oxide (Scheme 21). Under mild reaction conditions (50 °C, 1 h), propylene carbonates were obtained in 87% yields. When ZnI_2 was added as a co-catalyst in the ionic liquid system, significant improvements on both yield and reaction rate were observed. Interestingly, when DMF was used as the solvent for the reaction, less than 4% yields

Can. J. Chem. Downloaded from www.nrcresearchpress.com by Renmin University of China on 09/02/12
For personal use only.

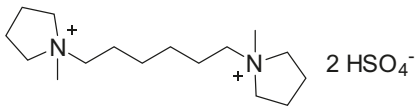
Scheme 21. Some ionic liquids used in cyclic carbonate synthesis from CO_2 and oxiranes.



Scheme 22. Hydration of terminal alkynes.



Scheme 23. An ionic liquid for hydration of terminal alkynes.



of carbonates were obtained even when using ZnI_2 as the catalyst in the reaction.

A rapid and effective ionic liquid – supercritical CO_2 system for the synthesis of propylene carbonate was developed by Kawanami et al.[86] The reactions conducted in **IL32** (1-octyl-3-methylimidazolium tetrafluoroborate) were able to achieve 99% yield and 100% selectivity of propylene carbonate within 5 min at 100 °C under supercritical conditions (operation pressure at 14 MPa). The TOF value (516 h^{-1}) achieved in the study was 77 times larger than another system (operation pressure at 4 MPa, at 110 °C, TOF = 6.7 h^{-1}) that employed a similar ionic liquid (1-*n*-butyl-3-methylimidazolium tetrafluoroborate, **IL14c**) for the reaction.[87] This may be due to the increase in the solubility of both CO_2 and propylene oxide in **IL32** as its *n*-alkyl chain is lengthened. Under supercritical conditions, the effects of counterions (NO_3^-, $CF_3SO_3^-$, BF_4^-, and PF_6^-) of the 1-ethyl-3-methylimidazolium ionic liquid were also investigated. BF_4^- was found to be most effective for promoting the chemical fixation of CO_2.

The hydroxyl-functionalized ionic liquid (**IL33**) developed by Zhang and co-workers[88] was also an effective medium for the synthesis of cyclic carbonate in the absence of co-catalyst and co-solvents. The OH group of **IL33** was demonstrated to be essential for the reaction to proceed smoothly because it facilitates in the ring opening of epoxides. The reaction of propylene oxide and CO_2 in **IL33** under 125 °C and 2.0 MPa for 1 h gave 99% conversion of propylene oxide and 99.8% selectivity of propylene carbonates. More recently, a similar system in which the ionic liquid was functionalized with one or more carboxylic acid groups (COOH) was reported as an efficient acid–base bifunctional catalyst for the fixation of CO_2 with epoxides under metal and solvent-free conditions.[89]

IL34 reported by Deng and co-workers[90] was also an effective promoter and reaction medium for the carbonylation of amines with propargylic alcohol using CO_2 as the carbonyl source to yield N-substituted 4-methylene-2-oxazolidinones under mild conditions. Comparison studies using dimethyl sulfoxide and toluene as solvents without additional catalysts under the same reaction conditions indicated that the CO_2 fixation reaction between cyclohexyl amine and 2-methyl-3-butyn-2-ol did not proceed readily. It was thus suggested that the ionic liquid took some crucial effects in the reaction. In addition, the nature of the cation and anion of **IL34** exhibited a strong influence on the formation of N-substituted 4-methylene-2-oxazolidinone derivatives.

A robust ionic liquid (**IL35**) that integrated with both pyrrolidinium and pyridinium moieties was developed by Wong et al.[91] for chemical fixation of CO_2. **IL35** designed with polycationic sites was demonstrated to be an efficient promoter and reaction medium in the synthesis of cyclic carbonates from CO_2 and epoxides. The ionic liquid system without other metal salts as co-catalysts showed excellent reactivity and selectivity of cyclic carbonates under the conditions of mild reaction temperature (80 °C) and low operation pressure (0.5 MPa). Also, the ionic liquid could be recycled and reused without significant loss in its catalytic activity. However, **IL35**, similar to many ionic liquid-based catalytic systems reported in literature, encountered difficulties for nonpolar epoxides. For the long-chain aliphatic epoxides such as 2-butyloxirane, the yield of isolated product was found to be 58% under relatively harsh reaction conditions (80 °C, 3 MPa, 3 h). The reduced productivity in the reaction was presumably caused by the lower solubility of the long-chain aliphatic epoxides in the highly polar ionic liquid medium.

Hydration of alkynes to ketones

Hydration of alkynes to carbonyl compounds is one of the most important and fundamental functional group transformations. The addition of water to alkynes requires a strong acid, usually sulfuric acid, and is facilitated by mercuric sulfate (Scheme 22). In general, the addition of water to alkynes gives ketones as the product (except for acetylene, which yields acetaldehyde) in the mercuric–sulfuric acid system. In recent years, alternative transition-metal complexes have also been successfully developed for hydration of alkynes. Some

Can. J. Chem. Downloaded from www.nrcresearchpress.com by Renmin University of China on 09/02/12
For personal use only.

Can. J. Chem. Downloaded from www.nrcresearchpress.com by Renmin University of China on 09/02/12
For personal use only.

of these metal-catalyzed systems are able to produce aldehydes selectively (anti-Markovnikov product) from terminal alkynes.[92]

The use of functionalized ionic liquids for the transformation of alkynes to ketones or aldehydes is relatively unexplored. In addition, most methodologies reported in the literature for this chemical process are usually carried out in organic solvents. Recently, a nonmetallic protocol based on **IL36** with a small amount of sulfuric acid for rapid conversion of alkynes to ketones has been reported by Wong et al.[93] In the ionic liquid system, various alkynes were efficiently converted to ketones under mild conditions (40 °C, 0.5 h). Moreover, the system exhibited excellent reactivity and stability over multiple cycles. The good efficiency of the system is attributed to the high chemical activity of protons in the ionic liquid medium. A larger scale hydration of phenylacetylene (up to 70 mmol) was also demonstrated with good yield and selectivity. The product could be isolated in high yields by vacuum distillation. Both the ionic liquid medium and H_2SO_4 can be constantly recycled and promoted the transformation of terminal alkynes to ketones without losing its catalytic reactivity (Scheme 23).

Applications in C–N bond formation reactions

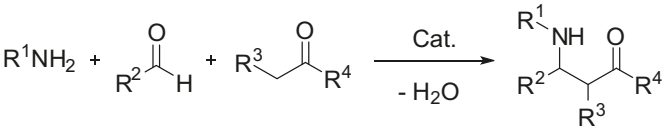
Mannich reaction

The Mannich reaction is a one-pot three-component reaction, which consists of an amino alkylation of an α-methylene carbonyl compound (an acidic proton placed next to a carbonyl functional group) with an aldehyde and ammonia or any primary and (or) secondary amine (Scheme 24). The final product is a β-aminocarbonyl compound, which is also known as Mannich base. The β-aminocarbonyl compounds are the key intermediates for the synthesis of natural products and pharmaceutically valuable compounds. During the past decade, Lewis acids or bases, Brønsted acids, and rare earth metal salts have been used as active catalysts in Mannich-type reactions.

In recent years, the use of ionic liquid for Mannich reactions has attracted considerable attention. Brønsted acid ionic liquids, including l-butyl-3-methylimidazolium hydrogen sulfate, l-butyl-3-methylimidazolium dihydrogen phosphate, 1-methylimidazolium *p*-toluenesulfonic acid and 1-methylimidazolium trifluoroacetic acid developed by Jiang and co-workers,[94] were demonstrated to be effective solvents and promoters for the three-component Mannich reaction of aldehdyes, amines, and ketones at 25 °C. **IL37** was able to catalyze the reaction efficiently and exhibited the highest catalytic activity among the ionic liquids examined in the investigation. Increasing the amount of **IL37** in the reaction could also improve the Mannich base formation. In addition, as indicated by the results of control experiments, Mannich reactions taking place in ionic liquids could in general produce higher yields than traditional systems conducted in organic solvents such as ethanol.

A Lewis acid ionic liquid **IL38** (1-ethyl-3-methylimidazolium triflate) was reported by Akiyama et al.[95] to effectively promote the Mannich-type reaction of silyl enolates with aldimines. The reaction simply employed **IL38** as the solvent without the addition of extra activator, and excellent yields of β-aminocarbonyl compounds were obtained under room-temperature conditions. The ionic liquid could be recycled as least 5 times before a significant decrease in the yield was observed. Another imidazolium-based ionic liquid (**IL39**) was developed by Xu and co-workers[96] for the synthesis of 2,2-dimethyl-6-substituted 4-piperidones via the Mannich reaction. When compared with the results in organic solvents such as ethanol or ethylene glycol, the Mannich reactions taking place in **IL39** usually gave a better performance in chemoselectivity (up to 78%). It was speculated that **IL39** might favor the formation of imine and, consequently, resulted in a preferential occurrence of Mannich reaction over aldol reaction. The different chemoselectivities obtained in various ionic liquid media may be attributed to the different viscosity of the ionic liquids or ammonia solubility. However, the addition of L-proline (20 mol%) as the co-catalyst in **IL37** resulted in a chemoselectivity up to 93% (Scheme 25).

Scheme 24. A typical Mannich reaction.



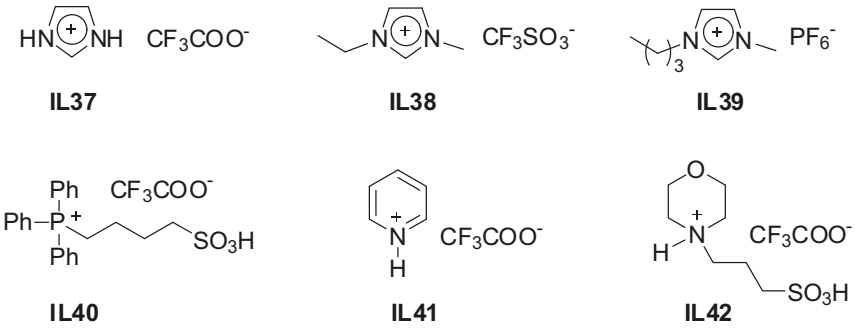
The ionic liquid **IL40** reported by Joseph and co-workers[97] was Brønsted acidic and was able to catalyze the Mannich reaction smoothly to afford β-aminocarbonyl compounds in excellent yields with short reaction times at 25 °C. In the reaction, benzaldehyde, aniline, and acetophenone were in equal molar ratios. It was found that the system suffered from poor miscibility and therefore a low yield of products was obtained. However, simply adding a small amount of water into the ionic liquid medium could improve the productivity effectively. The ionic liquid could be separated by water extraction from the reaction mixture and was recycled 4 times without any loss in activity. The structure of the ionic liquid was confirmed by NMR and remained unchanged after recycling.

An acidic pyridinium trifluoroacetate (**IL41**) synthesized by Yue et al.[98] was also investigated in the Mannich reaction of various aromatic aldehydes, aromatic ketones, and aromatic amines. The corresponding β-aminocarbonyl compounds were obtained in reasonable yields (50%–90%) at room temperature. As the molar ratio of benzaldehyde, acetophenone, and aniline was 1:1:1, the yield of product was increased with an increasing amount of **IL41** (130 mol% of a reactant). **IL41** was believed to provide protons to catalyze the Mannich reaction. The ionic liquid was reused 4 times without significant loss of activity. The morpholinium-based ionic liquid **IL42**, which is functionalized with an alkane sulfonic acid group, was utilized for the Mannich reactions with a number of aromatic aldehydes, acetophenone, and aromatic amines under mild reaction conditions.[99] In this ionic liquid system, the addition of a small amount of water could also improve the yield of Mannich products. However, in the case of using HSO_4^- as the counteranion, no Mannich product was obtained under the same reaction conditions because the strong acidic ionic liquid readily reacted with aniline.

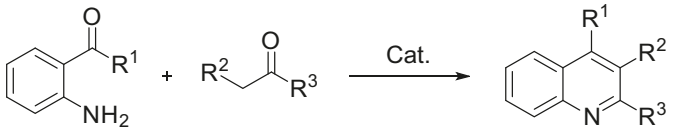
Friedländer synthesis

The Friedländer synthesis is a convenient method for the preparation of quinoline derivatives. This class of compounds

Scheme 25. Some ionic liquids developed for the Mannich reaction.



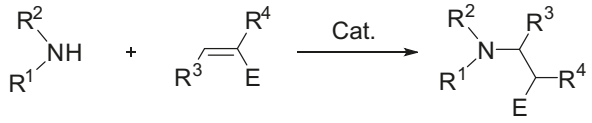
Scheme 26. A typical reaction of Friedländer synthesis.



Scheme 27. Some ionic liquids for the Friedländer reaction.

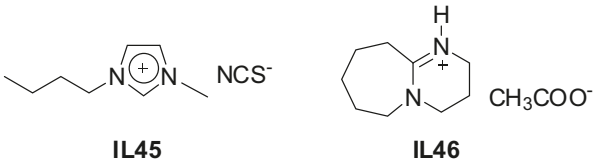


Scheme 28. A typical aza-Michael addition reaction.



E = electron-withdrawing groups

Scheme 29. Some ionic liquids for aza-Michael addition reactions.



shows a broad range of biological activities such as antibacterial and antihypersensitive activities. The synthesis typically involves the condensation reaction of a 2-aminoaryl ketone and a carbonyl compound with a reactive α-methylene group and is usually catalyzed by strong acids or bases (Scheme 26).

Recently, Friedländer reactions have also been investigated in ionic liquids.[100,101] Some simple acidic ionic liquids, for example, the Lewis acidic choline chloride – $ZnCl_2$,[102] 1-butyl-3-methylimidazolium chloride – $ZnCl_2$,[103] and ethyl-ammonium nitrate[104], were recognized as excellent solvents and promoters for green synthesis of quinolines via Friedländer reactions under mild conditions.

Srinivasan and co-workers[105,106] evaluated a number of 1-butylimidazolium ionic liquids with varying anions in the preparation of substituted quinolines and fused polycyclic quinolines through Friedländer heteroannulation reactions (Scheme 27). **IL43** was found to be the best ionic liquid for this synthesis. The efficiency of the ionic liquid for promoting the heterocyclization reaction increased progressively with the increase of Brønsted acidity of ionic liquids in the reaction. This correlation became more obvious in a comparison study that used **IL44** (less acidic than **IL43**) as the reaction medium under similar conditions. However, the ionic liquid system based on **IL43** suffered some drawbacks from its reaction conditions. For example, the reaction of *o*-aminoacetophenone with cyclopentanone in **IL43** at 90 °C for 24 h only gave a conversion of less than 30%. On other hand, when the temperature was increased to 130 °C, **IL43** decomposed during the reaction.

aza-Michael addition

The aza-Michael addition is an important reaction for the synthesis of C–N heterocyclic compounds with a β-aminocarbonyl functional moiety (Scheme 28). This class of compound serves as essential intermediates in the synthesis of a number of biologically active compounds, such as β-amino ketones, β-amino acids, and β-lactam antibiotics. The aza-Michael reactions are generally promoted by harsh bases or strong acids.

Recently, some room-temperature ionic liquids such as 1-butyl-3-methylimidazolium salts (with BF_4^- or PF_6^- as counterions) have been found to be efficient promoters for the conjugate addition reaction of azides to α,β-unsaturated carbonyl compounds. The use of azides as the Michael donor is a new synthetic procedure in aza-Michael addition reactions.[107] A basic ionic liquid (1-butyl-3-methylimidazolium hydroxide) developed by Lin and co-workers,[108–110] was used as both promoter and reaction medium in aza-Michael addition reactions for various amines and α,β-unsaturated carbonyl compounds. Control experiments in the addition reaction of piperidine and methyl acrylate, taking place in organic solvents such as THF and DMSO without adding 1-butyl-3-methylimidazolium hydroxide, gave yields of only less than 30% after 48 h reaction. These results indicated the ionic liquid played the role of promoter while serving as the reaction medium.

1-Butyl-3-methylimidazolium thiocyanate ionic liquid (**IL45**) developed by Yadav et al.[111] was also investigated in the aza-Michael addition of diethyl *N*-arylphosphoramidates to chalcones. The excellent reactivity and high diastereoselectivity achieved in **IL45** was probably induced by the NCS^- anions of the ionic liquid. Adding KSCN salt to 1-butyl-3-methylimidazolium tetrafluoroborate ionic liquid instead of using **IL45**, however, gave a significantly lower yield of product. This indicates that the nucleophilicity of NCS^- anion was considerably higher in **IL45** compared with that of KSCN (Scheme 29).

Can. J. Chem. Downloaded from www.nrcresearchpress.com by Renmin University of China on 09/02/12
For personal use only.

Can. J. Chem. Downloaded from www.nrcresearchpress.com by Renmin University of China on 09/02/12
For personal use only.

The use of a DBU-derived ionic liquid as a promoter in aza-Michael addition was reported by Chen and co-workers.[112] The basic ionic liquid **IL46** was found suitable for the conjugate addition of various aliphatic or aromatic amines to various electron-deficient alkenes under room-temperature conditions. It was demonstrated that the protocol could be scaled up to 100 mmol. **IL46** was recovered by drying under vacuum at 60 °C for 5 h after the reaction and was reused for 6 times without significant loss of catalytic activity.

Applications in C–S bond formation reactions

Thia-Michael addition

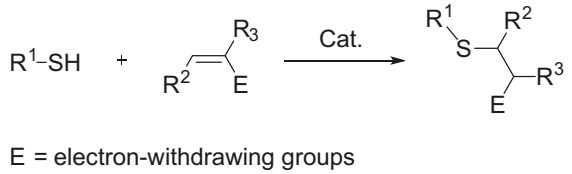
The conjugate addition of thiols to α,β-unsaturated carbonyl or nitrile compounds by Michael reaction to form carbon–sulfur bond constituents is an important reaction in both biosynthetic processes and organic synthesis. A large number of methods have been developed for the 1,4-addition of thiols to electron-deficient olefins through the activation of thiols (sulfur nucleophiles as the Michael donors) by using bases or acids as catalysts (Scheme 30).

α,β-Unsaturated ketones undergo rapid conjugate addition with thiols in a hydrophobic ionic liquid, such as 1-butyl-3-methylimidazolium hexafluorophosphate (with water as a co-solvent), without the use of any acid catalyst to afford the corresponding Michael adducts in high to quantitative yields. This ionic liquid system developed by Yadav et al.[113] exhibits excellent 1,4-selectivity under mild and neutral conditions. The ionic liquid plays the dual role of solvent and promoter in the Michael addition reactions. The reactivity of enones can be enhanced in ionic liquid medium and thus the reaction time was reduced and the yield was improved. The recovered ionic liquid was reused 4–5 times with consistent activity. In addition, Ranu and Dey[114] reported the use of 1-pentyl-3-methylimidazolium bromide in the Michael addition of aliphatic and aromatic thiols with a variety of acyclic- and cyclic-conjugated alkenes at room temperature. The role of the ionic liquid in the catalytic system was also investigated. It was postulated that the bromide ion forms a hydrogen bond to the thiol and then increases the nucleophilicity of the sulfur atom. The thiolate anion is thus a better Michael donor for the addition reaction of conjugated alkenes.

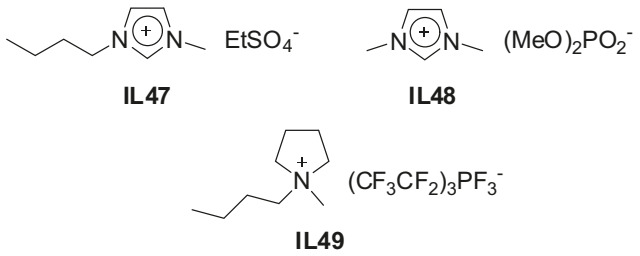
Sharma and Degani[115] reported the use of 2-hydroxyethylammonium formate as a cost-effective ionic liquid for the thia-Michael addition reaction. This ionic liquid system was effective in the addition of various aromatic sulfur nucleophiles to the activated olefins and could be recycled without significant loss in activity. The activity of this ionic liquid was comparable to ethyl-tri-*n*-butylphosphonium tosylate ionic liquid,[116] but showed better catalytic activity than 1-pentyl-3-methylimidazolium bromide.

The use of a phosphonium-based ionic liquid such as tetradecyl-trihexylphosphonium chloride in the thia-Michael addition of aromatic thiols to chalcones was reported by Pawar and co-workers.[117] This ionic liquid was highly basic and thermally more stable than ammonium salts. However, it exhibited higher viscosities than the ammonium ionic liquids at room temperature. The viscosity can be reduced by raising the temperature to 70–100 °C. In addition, tetraalkylphosphonium ionic liquid is chemically more stable compared with the imidazolium cations because it does not have acidic protons or aromatic rings.

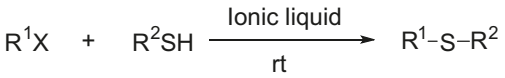
Scheme 30. A typical C–S bond formation via Michael addition.



Scheme 31. Some ionic liquids used in thia-Michael addition reactions.



Scheme 32. The conversion of thiols to thioether in ionic liquid.



Organocatalyzed addition of thiophenols to chalcones in ionic liquids was also reported by Toma and co-workers.[118] The reactions carried out in ionic liquids **IL47**–**IL49** without any additional catalysts gave excellent yields. Comparison studies showed that the addition reactions conducted in ionic liquid media generally proceeded faster than those in organic solvents. Also, the reaction rate was strongly dependent on the structure of the ionic liquids. **IL48** showed a much higher reaction rate (2 min, 94%) than **IL47** (15 min, 94%) and **IL49** (3 h, 91%) under the same conditions. A possible explanation for the high reactivity of thiophenol in ionic liquids, particularly in **IL48**, could be that the dissociation constant of thiophenol is higher in ionic liquids than in organic solvents. Furthermore, **IL48** is slightly basic in nature, whereas **IL47** and **IL49** are neutral. It thus facilitates the formation of PhS^- anions from PhSH. Consequently, the reaction rate was effectively enhanced in **IL48** (Scheme 31).

Thioether and thioester synthesis

Thioethers and thioesters are very useful building blocks for the preparation of various organosulfur compounds. A number of synthetic methods have been reported in the literature. The convenient and direct conversion of thiols to thioethers or thioesters usually involves the reaction of thiolate anions with organic halides. A room-temperature ionic liquid (1-pentyl-3-methylimidazolium bromide) used for this chemical process was reported by Ranu and Jana.[119] The ionic liquid was able to promote the reaction of alkyl halides or acyl halides with thiols to give thioethers or thioesters in high yields at room temperature (Scheme 32). This ionic liquid system was also extended for the synthesis of dithianes and *trans*-thioetherification. The products were isolated by direct distillation from the reaction mixture under reduced

Can. J. Chem. Downloaded from www.nrcresearchpress.com by Renmin University of China on 09/02/12
For personal use only.

pressure and therefore the ionic liquid could be readily recovered and recycled.

Applications in other chemical reactions

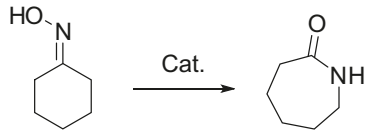
Beckmann rearrangement

The Beckmann rearrangement is an important synthetic method for the preparation of various N-substituted amides, which are valuable intermediates for the synthesis of various natural products and medicinal drugs and materials, through the conversion of ketoximes to amides. ε-Caprolactam, for example, has been synthesized industrially through the Beckmann rearrangement of cyclohexanone oxime (Scheme 33). The reaction is usually conducted with stoichiometic or excess amounts of strong Brønsted or Lewis acids under high-temperature (130 °C) conditions. Over the past years, ionic liquid systems with catalytic amounts of acidic catalysts, such as PCl_5,[120,121] P_2O_5,[122] H_2SO_4,[123] metaboric acid,[124] cyanuric chloride,[125] and $ZnCl_2$[126] have been developed for this chemical process.

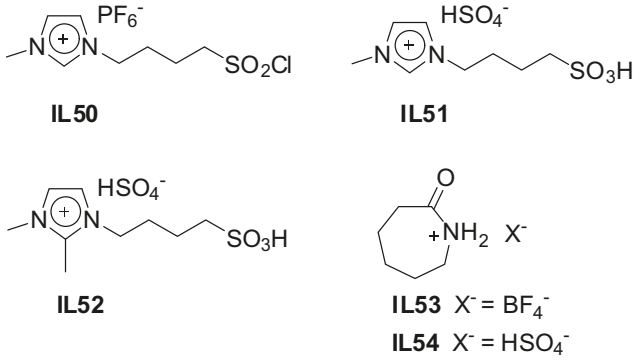
An imidazolium-based ionic liquid functionalized with a sulfonyl chloride group was developed by Sun and co-workers[127] and was demonstrated to be a stable and highly active reaction medium for Beckmann rearrangement of ketoximes under mild conditions. **IL50** was found particularly effective for the conversion of cyclohexanone oxime to ε-caprolactam (Scheme 34). For a reaction taking place at 80 °C for 2 h, 98% conversion and 98% selectivity of ε-caprolactam were achieved. The ionic liquid is immiscible with water, whereas ε-caprolactam has good solubility. The products were easily separated from **IL50** by water extraction. **IL51** and **IL52** (both functionalized with a sulfonic acid group) also showed good performance for the preparation of ε-caprolactam via the Beckmann rearrangement. Lévêque and co-workers[128] revealed that the good activity of these ionic liquid systems was essentially a result of the acidity of the sulfonic acid group on the ionic liquid. However, the ionic liquids also suffered from their high viscosity when they were used as a reaction medium. The drawbacks could be overcome at higher reaction temperatures. Moreover, it was concluded that a combination of the hydrogen sulfate anion and the sulfonic acid group of an ionic liquid was needed to obtain the rearrangement product rapidly under mild conditions.

Caprolactam-based Brønsted acidic ionic liquids were also developed as effective promoters and (or) media for the Beckmann rearrangement of cyclohexanone oxime to afford caprolactam. **IL53** reported by Deng and co-workers[129] was able to achieve high conversion (93%) and good selectivity (89%) at 100 °C. The occurrence of the Beckmann rearrangement of cyclohexanone oxime in **IL53** was confirmed by in situ FT-Raman spectroscopy. Later on, Horváth and co-workers[130] also reported the use of **IL54** for this reaction. The mechanism for the conversion of cyclohexanone oxime into caprolactam in **IL54** was established using NMR spectroscopy. The results indicated that the cyclohexanone oxime was first protonated (either on the oxygen or the nitrogen atom), followed by the elimination of water to form a cationic species, which was identified as a key intermediate in the Beckmann rearrangement. The study also pointed out that the mixture (or oleum) of caprolactam and sulfuric acid should be considered as an ionic liquid. In addition, the mixture (**IL54**) was able to hold SO_3 very strongly up to 140 °C and therefore provided a safe environment for a very exothermic reaction.

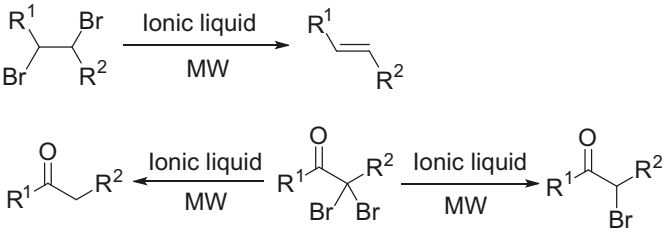
Scheme 33. A typical Beckmann rearrangement reaction of cyclohexanone oxime.



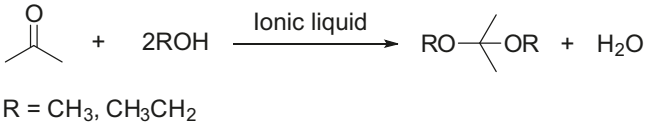
Scheme 34. Some ionic liquids developed for Beckmann rearrangement reactions.



Scheme 35. Debromination reactions in ionic liquid.



Scheme 36. The preparation of dialkoxypropanes in ionic liquid.



R = CH_3, CH_3CH_2

Debromination reaction

A debromination reaction is usually carried out in organic solvents under refluxing conditions with a reactive metal, such as Sm, In, Mg, and Zn, as the reducing agent. Ranu and Jana[131] developed a simple ionic liquid system for this process without using metals. The investigation demonstrated that the stereoselective debromination of a variety of structurally diverse vicinal-dibromides to the corresponding *E*-alkenes could be achieved in ionic liquid medium (1-methyl-3-pentylimidazolium fluoroborate) under microwave irradiation for 2–5 min (Scheme 35). The reaction did not occur without the ionic liquid and did not proceed effectively in 1-methyl-3-pentylimidazolium bromide under similar reaction conditions. It was therefore proposed that the BF_4^- anion of the ionic liquid plays a vital role in the debromination process under microwave irradiation conditions. The ionic liquid also promoted the selective debromination of α-bromoketones

Can. J. Chem. Downloaded from www.nrcresearchpress.com by Renmin University of China on 09/02/12
For personal use only.

under microwave irradiation.[132] *gem*-α-Dibromoketones were selectively debrominated to either monobromoketone or debromoketones as the final product by controlling the reaction time of the process.

Dialkoxypropane synthesis

Dialkoxypropanes are a class of valuable fine chemicals widely used in polymer preparation, surfactants, and natural product extraction. They are also important intermediates in pharmaceutical and medicinal industry for the synthesis of clarithromycin, β-ionone, vitamin A, and vitamin E. The formation of dialkoxypropanes from ketones and alcohols with acid catalysts is one of the most practical methods.

Li and co-workers[133] reported the use of some simple ammonium ionic liquids as reaction promoters and media for the preparation of a dialkoxypropane (2,2-dimerthoxypropane) from acetone and methanol or ethanol (Scheme 36). These air- and water-stable ammonium ionic liquids were easily synthesized from the reaction of acids and various alkylamines, such as diethylamine, ethylamine, triethylamine, *n*-tripropylamine, isopropylamine, *n*-tributylamine, and *n*-butylamine. The study demonstrated that the catalytic activity of the ionic liquids was strongly influenced by their anions. The best results were obtained using ionic liquids with hydrogen sulfate counteranions, for example, $[Et_3NH]^+[HSO_4]^-$, probably because of their high acidity. The ammonium cations showed only a small influence on catalytic performance. Nonetheless, the immiscibility of the dialkoxypropanes produced with the ionic liquid medium shifted the reaction equilibrium in favor of dialkoxypropane formation.

Conclusions and outlook

This review summarizes some successful examples of using functionalized ionic liquids as both reaction media and promoters in a number of important chemical reactions including C–C, C–O, C–N, and C–S bond formation. Ionic liquids designed with special functionality are generally found to enhance the reaction rate, selectivity, and productivity in various chemical reactions.

The recent developments of ionic liquids in catalysis as well as in other research fields indicates that ionic liquids are no longer just "green solvents" for the replacement of organic solvents. Numerous excellent papers published in recent years also demonstrate the novel applications of ionic liquids with specific functionalities in chemical reactions, catalysis, separation, and material science.

There is no doubt that ionic liquids can provide advantages over conventional solvents in the development of green technologies through molecular design and synthesis of new ionic liquids with different functionalities. Nevertheless, with respect to the literature reviewed in this article, imidazolium-based ionic liquids are still dominant in ionic liquid design over other analogues such as pyrrolidinium and alkylammonium, although the later two classes of cations are chemically more stable. As a matter of fact, ionic liquids used as solvents or catalysts in organic synthesis are not totally inert under the reaction conditions. In some cases, they provide unexpected reactivity and are advantageous to the reaction, whereas in others they may lead to problems. It is thus imperative that properly selecting or preparing an ionic liquid for a particular application is essential, and more attention should be paid to its compatibility with the reaction conditions. However, only a few reports addressed the stability issues of ionic liquids in organic reactions and catalysis.[82,83,105,106]

It can be foreseen that new utilizations of ionic liquids will appear over time. Large-scale applications of ionic liquid however remain a challenge which is of great importance for industrial processes. We expect that more and more exciting discoveries and news will emerge in the coming decade.

Acknowledgements

We acknowledge the support from The Hong Kong Polytechnic University and the Research Grants Council (PolyU 5015/07P).

References

(1) Wasserscheid, P.; Keim, W. *Angew. Chem. Int. Ed.* **2000**, *39*, 3772. doi:10.1002/1521-3773(20001103)39:21<3772::AID-ANIE3772>3.0.CO;2-5.
(2) Earle, M. J.; Seddon, K. R. *Pure Appl. Chem.* **2000**, *72* (7), 1391. doi:10.1351/pac200072071391.
(3) Welton, T. *Chem. Rev.* **1999**, *99* (8), 2071. doi:10.1021/cr980032t.
(4) Rogers, R. D.; Seddon, K. R. *Science* **2003**, *302* (5646), 792. doi:10.1126/science.1090313.
(5) Pretti, C.; Chiappe, C.; Pieraccini, D.; Gregori, M.; Abramo, F.; Monni, G.; Intorre, L. *Green Chem.* **2006**, *8* (3), 238. doi:10.1039/b511554j.
(6) Gordon, C. M. *Appl. Catal. A Gen.* **2001**, *222* (1–2), 101. doi:10.1016/S0926-860X(01)00834-1.
(7) Olivier-Bourbigou, H.; Magna, L. *J. Mol. Catal. Chem.* **2002**, *182–183* (1–2), 419. doi:10.1016/S1381-1169(01)00465-4.
(8) Welton, T. *Coord. Chem. Rev.* **2004**, *248* (21–24), 2459. doi:10.1016/j.ccr.2004.04.015.
(9) Chowdhury, S.; Mohan, R. S.; Scott, J. L. *Tetrahedron* **2007**, *63* (11), 2363. doi:10.1016/j.tet.2006.11.001.
(10) Greaves, T. L.; Drummond, C. J. *Chem. Rev.* **2008**, *108* (1), 206. doi:10.1021/cr068040u.
(11) Jiang, T.; Han, B. X. *Curr. Org. Chem.* **2009**, *13* (13), 1278. doi:10.2174/138527209789055117.
(12) Yao, C.; Anderson, J. L. *J. Chromatogr. A* **2009**, *1216* (10), 1658. doi:10.1016/j.chroma.2008.12.001.
(13) Han, D.; Row, K. H. *Molecules* **2010**, *15* (4), 2405. doi:10.3390/molecules15042405.
(14) Zhou, F.; Liang, Y.; Liu, W. *Chem. Soc. Rev.* **2009**, *38* (9), 2590. doi:10.1039/b817899m.
(15) Zakeeruddin, S. M.; Grätzel, M. *Adv. Funct. Mater.* **2009**, *19* (14), 2187. doi:10.1002/adfm.200900390.
(16) Armand, M.; Endres, F.; MacFarlane, D. R.; Ohno, H.; Scrosati, B. *Nat. Mater.* **2009**, *8* (8), 621. doi:10.1038/nmat2448.
(17) Ma, Z.; Yu, J.; Dai, S. *Adv. Mater. (Deerfield Beach Fla.)* **2010**, *22* 261. doi:10.1002/adma.200900603.
(18) Van Doorslaer, C.; Wahlen, J.; Mertens, P.; Binnemans, K.; De Vos, D. *Dalton Trans.* **2010**, *39* (36), 8377. doi:10.1039/c001285h.
(19) Ni, B.; Headley, A. D. *Chemistry* **2010**, *16* (15), 4426. doi:10.1002/chem.200902747.
(20) Miao, W.; Chan, T. H. *Acc. Chem. Res.* **2006**, *39* (12), 897. doi:10.1021/ar030252f.

Can. J. Chem. Downloaded from www.nrcresearchpress.com by Renmin University of China on 09/02/12
For personal use only.

(21) Snelders, D. J. M.; van Koten, G.; Klein Gebbink, R. J. M. *Chemistry* **2011**, *17* (1), 42. doi:10.1002/chem.201002508.
(22) Lombardo, M.; Trombini, C. *ChemCatChem* **2010**, *2* (2), 135. doi:10.1002/cctc.200900256.
(23) Luo, S.; Zhang, L.; Cheng, J.-P. *Chem. Asian J.* **2009**, *4* (8), 1184. doi:10.1002/asia.200900080.
(24) Sheldon, R. A.; Lau, R. M.; Sorgedrager, M. J.; van Rantwijk, F.; Seddon, K. R. *Green Chem.* **2002**, *4* (2), 147. doi:10.1039/b110008b.
(25) Sureshkumar, M.; Lee, C.-K. *J. Mol. Catal., B Enzym.* **2009**, *60* (1–2), 1. doi:10.1016/j.molcatb.2009.03.008.
(26) Domínguez de María, P. *Angew. Chem. Int. Ed.* **2008**, *47* (37), 6960. doi:10.1002/anie.200703305.
(27) Tran, U. P. N.; Le, K. K. A.; Phan, N. T. S. *ACS Catal.* **2011**, *1* (2), 120. doi:10.1021/cs1000625.
(28) Hangarge, R. V.; Jarikote, D. V.; Shingare, M. S. *Green Chem.* **2002**, *4* (3), 266. doi:10.1039/b111634g.
(29) Xin, X.; Guo, X.; Duan, H.; Lin, Y.; Sun, H. *Catal. Commun.* **2007**, *8* (2), 115. doi:10.1016/j.catcom.2006.05.034.
(30) Alizadeh, A.; Khodaei, M. M.; Eshghi, A. *J. Org. Chem.* **2010**, *75* (23), 8295. doi:10.1021/jo101696z.
(31) Alizadeh, A.; Khodaei, M. M.; Eshghi, A. *Can. J. Chem.* **2010**, *88* (6), 514. doi:10.1139/V10-011.
(32) Ranu, B. C.; Jana, R. *Eur. J. Org. Chem.* **2006**, *2006* (16), 3767. doi:10.1002/ejoc.200600335.
(33) Valizadeh, H.; Gholipour, H. *Synth. Commun.* **2010**, *40* (10), 1477. doi:10.1080/00397910903097310.
(34) Ranu, B. C.; Banerjee, S. *Org. Lett.* **2005**, *7* (14), 3049. doi:10.1021/ol051004h.
(35) Ranu, B. C.; Banerjee, S.; Jana, R. *Tetrahedron* **2007**, *63* (3), 776. doi:10.1016/j.tet.2006.10.077.
(36) Mečiarová, M.; Toma, Š. *Chemistry* **2007**, *13* (4), 1268. doi:10.1002/chem.200600870.
(37) Truong, T.-K.-T.; Vo-Thanh, G. *Tetrahedron* **2010**, *66* (27–28), 5277. doi:10.1016/j.tet.2010.03.101.
(38) Fischer, T.; Sethi, A.; Welton, T.; Woolf, J. *Tetrahedron Lett.* **1999**, *40* (4), 793. doi:10.1016/S0040-4039(98)02415-0.
(39) Earle, M. J.; McCormac, P. B.; Seddon, K. R. *Green Chem.* **1999**, *1* (1), 23. doi:10.1039/a808052f.
(40) Song, C. E.; Roh, E. J.; Lee, S.-g.; Shim, W. H.; Chol, J. H. *Chem. Commun. (Camb.)* **2001**, (12): 1122. doi:10.1039/b101140p.
(41) Ludley, P.; Karodia, N. *Tetrahedron Lett.* **2001**, *42* (10), 2011. doi:10.1016/S0040-4039(01)00064-8.
(42) Xiao, Y.; Malhotra, S. V. *Tetrahedron Lett.* **2004**, *45* (45), 8339. doi:10.1016/j.tetlet.2004.09.070.
(43) Han, X.; Armstrong, D. W. *Org. Lett.* **2005**, *7* (19), 4205. doi:10.1021/ol051637w.
(44) Yanai, H.; Ogura, H.; Taguchi, T. *Org. Biomol. Chem.* **2009**, *7* (18), 3657. doi:10.1039/b910488g.
(45) Harjani, J. R.; Singer, R. D.; Garcia, M. T.; Scammells, P. J. *Green Chem.* **2009**, *11* (1), 83. doi:10.1039/b811814k.
(46) Cui, X.; Zhang, S.; Shi, F.; Zhang, Q.; Ma, X.; Lu, L.; Deng, Y. *ChemSusChem* **2010**, *3* (9), 1043. doi:10.1002/cssc.201000075.
(47) Janus, E.; Goc-Maciejewska, I.; Łożyński, M.; Pernak, J. *Tetrahedron Lett.* **2006**, *47* (24), 4079. doi:10.1016/j.tetlet.2006.03.172.
(48) Boon, J. A.; Levisky, J. A.; Pflug, J. L.; Wilkes, J. S. *J. Org. Chem.* **1986**, *51* (4), 480. doi:10.1021/jo00354a013.
(49) Qiao, K.; Deng, Y. *J. Mol. Catal. Chem.* **2001**, *171* (1–2), 81. doi:10.1016/S1381-1169(01)00107-8.
(50) Naik, P. U.; Nara, S. J.; Harjani, J. R.; Salunkhe, M. M. *Can. J. Chem.* **2003**, *81* (10), 1057. doi:10.1139/v03-152.
(51) Cui, S.; Lu, B.; Cai, Q.; Cai, X.; Li, X.; Xiao, X.; Hou, L.; Han, Y. *Ind. Eng. Chem. Res.* **2006**, *45* (5), 1571. doi:10.1021/ie0510268.
(52) Kantam, M. L.; Chakravarti, R.; Sreedhar, B.; Bhargava, S. *Synlett* **2008** (10), 1449. doi:10.1055/s-2008-1078423.
(53) Lin, J.-H.; Zhang, C.-P.; Zhu, Z.-Q.; Chen, Q.-Y.; Xiao, J.-C. *J. Fluor. Chem.* **2009**, *130* (4), 394. doi:10.1016/j.jfluchem.2009.01.004.
(54) Xiao, Y.; Malhotra, S. V. *J. Organomet. Chem.* **2005**, *690* (15), 3609. doi:10.1016/j.jorganchem.2005.04.047.
(55) Wang, W.; Shao, L.; Cheng, W.; Yang, J.; He, M. *Catal. Commun.* **2008**, *9* (3), 337. doi:10.1016/j.catcom.2007.07.006.
(56) Keh, C. C. K.; Namboodiri, V. V.; Varma, R. S.; Li, C.-J. *Tetrahedron Lett.* **2002**, *43* (28), 4993. doi:10.1016/S0040-4039(02)00889-4.
(57) Yadav, J. S.; Reddy, B. V. S.; Reddy, M. S.; Niranjan, N.; Prasad, A. R. *Eur. J. Org. Chem.* **2003**, *2003* (9), 1779. doi:10.1002/ejoc.200210638.
(58) Kishi, Y.; Inagi, S.; Fuchigami, T. *Eur. J. Org. Chem.* **2009** (1), 103. doi:10.1002/ejoc.200800872.
(59) Deng, Y.; Shi, F.; Beng, J.; Qiao, K. *J. Mol. Catal. Chem.* **2001**, *165* (1–2), 33. doi:10.1016/S1381-1169(00)00422-2.
(60) Sunitha, S.; Kanjilal, S.; Reddy, P. S.; Prasad, R. B. N. *Tetrahedron Lett.* **2007**, *48* (39), 6962. doi:10.1016/j.tetlet.2007.07.159.
(61) Cole, A. C.; Jensen, J. L.; Ntai, I.; Tran, K. L. T.; Weaver, K. J.; Forbes, D. C.; Davis, J. H. *J. Am. Chem. Soc.* **2002**, *124* (21), 5962. doi:10.1021/ja026290w.
(62) Forbes, D. C.; Weaver, K. J. *J. Mol. Catal. Chem.* **2004**, *214* (1), 129. doi:10.1016/j.molcata.2003.09.035.
(63) Gu, Y.; Shi, F.; Deng, Y. *J. Mol. Catal. Chem.* **2004**, *212* (1–2), 71. doi:10.1016/j.molcata.2003.10.039.
(64) Dukuzeyezu, E.-M.; Lefebvre, H.; Tessier, M.; Fradet, A. *Polymer (Guildf.)* **2010**, *51* (6), 1218. doi:10.1016/j.polymer.2010.01.053.
(65) Jiang, D.; Wang, Y. Y.; Tu, M.; Dai, L. Y. *Chin. Chem. Lett.* **2008**, *19* (8), 889. doi:10.1016/j.cclet.2008.04.035.
(66) Gui, J.; Cong, X.; Liu, D.; Zhang, X.; Hu, Z.; Sun, Z. *Catal. Commun.* **2004**, *5* (9), 473. doi:10.1016/j.catcom.2004.06.004.
(67) Shi, H.; Zhu, W.; Li, H.; Liu, H.; Zhang, M.; Yan, Y.; Wang, Z. *Catal. Commun.* **2010**, *11* (7), 588. doi:10.1016/j.catcom.2009.12.025.
(68) Liu, S.; Xie, C.; Yu, S.; Liu, F.; Ji, K. *Catal. Commun.* **2008**, *9* (7), 1634. doi:10.1016/j.catcom.2008.01.017.
(69) Fraga-Dubreuil, J.; Bourahla, K.; Rahmouni, M.; Bazureau, J. P.; Hamelin, J. *Catal. Commun.* **2002**, *3* (5), 185. doi:10.1016/S1566-7367(02)00087-0.
(70) Arfan, A.; Bazureau, J. P. *Org. Process Res. Dev.* **2005**, *9* (6), 743. doi:10.1021/op058002x.
(71) Biswas, A.; Shogren, R. L.; Willett, J. L. *Ind. Crops Prod.* **2009**, *30* (1), 172. doi:10.1016/j.indcrop.2009.02.003.
(72) Ganeshpure, P. A.; George, G.; Das, J. *ARKIVOC* **2007** (viii), 273.
(73) Ganeshpure, P. A.; George, G.; Das, J. *J. Mol. Catal. Chem.* **2008**, *279* (2), 182. doi:10.1016/j.molcata.2007.06.025.
(74) Zhu, H.-P.; Yang, F.; Tang, J.; He, M.-Y. *Green Chem.* **2003**, *5* (1), 38. doi:10.1039/b209248b.
(75) Joseph, T.; Sahoo, S.; Halligudi, S. B. *J. Mol. Catal. Chem.* **2005**, *234* (1–2), 107. doi:10.1016/j.molcata.2005.03.005.
(76) Wang, G.; Guan, Z.; Tang, R.; He, Y. *Synth. Commun.* **2010**, *40* (3), 370. doi:10.1080/00397910902978049.

Can. J. Chem. Downloaded from www.nrcresearchpress.com by Renmin University of China on 09/02/12
For personal use only.

(77) Ma, J.; Zhou, X.; Zang, X.; Wang, C.; Wang, Z.; Li, J.; Li, Q. *Aust. J. Chem.* **2007**, *60* (2), 146. doi:10.1071/CH06225.
(78) Zhang, S.; Chen, Y.; Li, F.; Lu, X.; Dai, W.; Mori, R. *Catal. Today* **2006**, *115* (1–4), 61. doi:10.1016/j.cattod.2006.02.021.
(79) Sakakura, T.; Kohno, K. *Chem. Commun. (Camb.)* **2009**, (11), 1312. doi:10.1039/b819997c.
(80) Wong, W. L.; Cheung, K. C.; Chan, P. H.; Zhou, Z. Y.; Lee, K. H.; Wong, K. Y. *Chem. Commun. (Camb.)* **2007**, (21), 2175. doi:10.1039/b618423e.
(81) Sakakura, T.; Choi, J.-C.; Yasuda, H. *Chem. Rev.* **2007**, *107* (6), 2365. doi:10.1021/cr068357u.
(82) Caló, V.; Nacci, A.; Monopoli, A.; Fanizzi, A. *Org. Lett.* **2002**, *4* (15), 2561. doi:10.1021/ol026189w.
(83) Ho, K.-P.; Wong, W.-L.; Lee, L. Y. S.; Lam, K.-M.; Chan, T. H.; Wong, K.-Y. *Chem. Asian J.* **2010**, *5* (9), 1970. doi:10.1002/asia.201000109.
(84) Sun, J.; Fujita, S.-I.; Bhanage, B. M.; Arai, M. *Catal. Commun.* **2004**, *5* (2), 83. doi:10.1016/j.catcom.2003.11.016.
(85) Kim, Y.-J.; Cheong, M. *Bull. Korean Chem. Soc.* **2002**, *23* (7), 1027. doi:10.5012/bkcs.2002.23.7.1027.
(86) Kawanami, H.; Sasaki, A.; Matsui, K.; Ikushima, Y. *Chem. Commun. (Camb.)* **2003**, (7), 896. doi:10.1039/b212823c.
(87) Peng, J.; Deng, Y. *N. J. Chem.* **2001**, *25* (4), 639. doi:10.1039/b008923k.
(88) Sun, J.; Zhang, S.; Cheng, W.; Ren, J. *Tetrahedron Lett.* **2008**, *49* (22), 3588. doi:10.1016/j.tetlet.2008.04.022.
(89) Sun, J.; Han, L.; Cheng, W.; Wang, J.; Zhang, X.; Zhang, S. *ChemSusChem* **2011**, *4* (4), 502. doi:10.1002/cssc.201000305.
(90) Zhang, Q.; Shi, F.; Gu, Y.; Yang, J.; Deng, Y. *Tetrahedron Lett.* **2005**, *46* (35), 5907. doi:10.1016/j.tetlet.2005.06.116.
(91) Wong, W.-L.; Chan, P.-H.; Zhou, Z.-Y.; Lee, K.-H.; Cheung, K.-C.; Wong, K.-Y. *ChemSusChem* **2008**, *1* (1–2), 67. doi:10.1002/cssc.200700097.
(92) Hintermann, L.; Labonne, A. *Synthesis* **2007**, *2007* (8), 1121. doi:10.1055/s-2007-966002.
(93) Wong, W.-L.; Ho, K.-P.; Lee, L. Y. S.; Lam, K.-M.; Zhou, Z.-Y.; Chan, T. H.; Wong, K.-Y. *ACS Catal.* **2011**, *1* (2), 116. doi:10.1021/cs100016h.
(94) Zhao, G.; Jiang, T.; Gao, H.; Han, B.; Huang, J.; Sun, D. *Green Chem.* **2004**, *6* (2), 75. doi:10.1039/b309700p.
(95) Akiyama, T.; Suzuki, A.; Fuchibe, K. *Synlett* **2005**, *6* (6), 1024. doi:10.1055/s-2005-864816.
(96) Feng, L.-C.; Sun, Y.-W.; Tang, W.-J.; Xu, L.-J.; Lam, K.-L.; Zhou, Z.-Y.; Chan, A. S. C. *Green Chem.* **2010**, *12* (6), 949. doi:10.1039/b926498a.
(97) Sahoo, S.; Joseph, T.; Halligudi, S. B. *J. Mol. Catal. Chem.* **2006**, *244* (1–2), 179. doi:10.1016/j.molcata.2005.09.012.
(98) Yue, C. B.; Yi, T. F.; Zhu, C. B.; Liu, G. *J. Ind. Eng. Chem.* **2009**, *15* 653. doi:10.1016/j.jiec.2009.09.038.
(99) Yue, C. *Synth. Commun.* **2010**, *40* (24), 3640. doi:10.1080/00397910903470509.
(100) Wang, J.; Fan, X.; Zhang, X.; Han, L. *Can. J. Chem.* **2004**, *82* (7), 1192. doi:10.1139/v04-066.
(101) Zhang, X. Y.; Fan, X. S.; Wang, J. J.; Li, Y. Z. *Chin. Chem. Lett.* **2004** *15*, 1170.
(102) Wang, H.-M.; Hou, R.-S.; Cheng, H.-T.; Chen, L.-C. *Heterocycles* **2009**, *78* (2), 487. doi:10.3987/COM-08-11516.
(103) Karthikeyan, G.; Perumal, P. T. *J. Heterocycl. Chem.* **2004**, *41* (6), 1039. doi:10.1002/jhet.5570410632.
(104) Zhou, T.; Lin, J.-L.; Chen, Z.-C. *Lett. Org. Chem.* **2008**, *5* (1), 47. doi:10.2174/157017808783330261.
(105) Palimkar, S. S.; Siddiqui, S. A.; Daniel, T.; Lahoti, R. J.; Srinivasan, K. V. *J. Org. Chem.* **2003**, *68* (24), 9371. doi:10.1021/jo035153u.
(106) Potewar, T. M.; Nadaf, R. N.; Daniel, T.; Lahoti, R. J.; Srinivasan, K. V. *Synth. Commun.* **2005**, *35* (2), 231. doi:10.1081/SCC-200048433.
(107) Xu, L.-W.; Li, L.; Xia, C.-G.; Zhou, S.-L.; Li, J.-W. *Tetrahedron Lett.* **2004**, *45* (6), 1219. doi:10.1016/j.tetlet.2003.11.129.
(108) Xu, J.-M.; Wu, Q.; Zhang, Q.-Y.; Zhang, F.; Lin, X.-F. *Eur. J. Org. Chem.* **2007**, *2007* (11), 1798. doi:10.1002/ejoc.200600999.
(109) Xu, J.-M.; Qian, C.; Liu, B.-K.; Wu, Q.; Lin, X.-F. *Tetrahedron* **2007**, *63* (4), 986. doi:10.1016/j.tet.2006.11.013.
(110) Xu, J.-M.; Liu, B.-K.; Wu, W.-B.; Qian, C.; Wu, Q.; Lin, X.-F. *J. Org. Chem.* **2006**, *71* (10), 3991. doi:10.1021/jo0600914.
(111) Yadav, L. D. S.; Patel, R.; Srivastava, V. P. *Synlett* **2008**, *4* 583. doi:10.1055/s-2008-1042757.
(112) Ying, A.-G.; Liu, L.; Wu, G.-F.; Chen, G.; Chen, X.-Z.; Ye, W.-D. *Tetrahedron Lett.* **2009**, *50* (14), 1653. doi:10.1016/j.tetlet.2009.01.123.
(113) Yadav, J. S.; Reddy, B. V. S.; Baishya, G. *J. Org. Chem.* **2003**, *68* (18), 7098. doi:10.1021/jo034335l.
(114) Ranu, B. C.; Dey, S. S. *Tetrahedron* **2004**, *60* (19), 4183. doi:10.1016/j.tet.2004.03.052.
(115) Sharma, Y. O.; Degani, M. S. *J. Mol. Catal. Chem.* **2007**, *277* (1–2), 215. doi:10.1016/j.molcata.2007.07.053.
(116) Karodia, N.; Liu, X.; Ludley, P.; Pletsas, D.; Stevenson, G. *Tetrahedron* **2006**, *62* (48), 11039. doi:10.1016/j.tet.2006.09.052.
(117) Sarda, S. R.; Jadhav, W. N.; Shete, A. S.; Dhopte, K. B.; Sadawarte, S. M.; Gadge, P. J.; Pawar, R. P. *Synth. Commun.* **2010**, *40* (14), 2178. doi:10.1080/00397910903221050.
(118) Mečiarová, M.; Toma, Š.; Kotrusz, P. *Org. Biomol. Chem.* **2006**, *4* (7), 1420. doi:10.1039/b516289k.
(119) Ranu, B. C.; Jana, R. *Adv. Synth. Catal.* **2005**, *347* (14), 1811. doi:10.1002/adsc.200505122.
(120) Peng, J.; Deng, Y. *Tetrahedron Lett.* **2001**, *42* (3), 403. doi:10.1016/S0040-4039(00)01974-2.
(121) Elango, K.; Srirambalaji, R.; Anantharaman, G. *Tetrahedron Lett.* **2007**, *48* (51), 9059. doi:10.1016/j.tetlet.2007.10.051.
(122) Ren, R. X.; Zueva, L. D.; Ou, W. *Tetrahedron Lett.* **2001**, *42* (48), 8441. doi:10.1016/S0040-4039(01)01850-0.
(123) Lee, J. K.; Kim, D.-C.; Song, C. E.; Lee, S.-G. *Synth. Commun.* **2003**, *33* (13), 2301. doi:10.1081/SCC-120021511.
(124) Guo, S.; Deng, Y. *Catal. Commun.* **2005**, *6* (3), 225. doi:10.1016/j.catcom.2005.01.003.
(125) Betti, C.; Landini, D.; Maia, A.; Pasi, M. *Synlett* **2008**, *6* 908. doi:10.1055/s-2008-1042804.
(126) Liu, X.; Xiao, L.; Wu, H.; Li, Z.; Chen, J.; Xia, C. *Catal. Commun.* **2009**, *10* (5), 424. doi:10.1016/j.catcom.2008.09.007.
(127) Gui, J.; Deng, Y.; Hu, Z.; Sun, Z. *Tetrahedron Lett.* **2004**, *45* (12), 2681. doi:10.1016/j.tetlet.2004.01.131.
(128) Turgis, R.; Estager, J.; Draye, M.; Ragaini, V.; Bonrath, W.; Lévêque, J.-M. *ChemSusChem* **2010**, *3* (12), 1403. doi:10.1002/cssc.201000203.
(129) Guo, S.; Du, Z.; Zhang, S.; Li, D.; Li, Z.; Deng, Y. *Green Chem.* **2006**, *8* (3), 296. doi:10.1039/b513139a.

(130) Fábos, V.; Lantos, D.; Bodor, A.; Bálint, A.-M.; Mika, L. T.; Sielcken, O. E.; Cuiper, A.; Horváth, I. T. *ChemSusChem* **2008**, *1* (3), 189. doi:10.1002/cssc.200700135.
(131) Ranu, B. C.; Jana, R. *J. Org. Chem.* **2005**, *70* (21), 8621. doi:10.1021/jo051373r.
(132) Ranu, B. C.; Chattopadhyay, K.; Jana, R. *Tetrahedron* **2007**, *63* (1), 155. doi:10.1016/j.tet.2006.10.035.
(133) Jiang, H.; Wang, C.; Li, H.; Wang, Y. *Green Chem.* **2006**, *8* (12), 1076. doi:10.1039/b608249a.

Can. J. Chem. Downloaded from www.nrcresearchpress.com by Renmin University of China on 09/02/12
For personal use only.

REVIEW / SYNTHÈSE

Discovery of green tea polyphenol-based proteasome inhibitors — A successful collaboration with Tak-Hang (Bill) Chan

Kristin Landis-Piwowar, Saeed Bazzi, and Q. Ping Dou

Abstract: This article is written to commemorate the contributions of Professor Tak-Hang (Bill) Chan to the field of chemistry and his collaborative efforts that have lead to insights pertaining to cancer cell biology and the development of potential cancer therapeutic agents. This article reviews the chronological scientific findings that evolved from a partnership between Bill Chan and Q. Ping Dou, spanning more than 10 years. While many compounds have been chemically synthesized by the Chan group and biologically scrutinized by the Dou group, the outcomes presented here will focus on green tea polyphenols as tumor proteasome inhibitors and anticancer agents. Furthermore, the biochemical alterations that increase or decrease the therapeutic potential of the polyphenol compounds in human cancer cells will also be discussed.

Key words: proteasome, anticancer agents, (–)-epigallocatechin-3-gallate (EGCG), structure–activity relationships.

Résumé : Cet article a été rédigé pour commémorer les contributions du professeur Tak-Hang (Bill) Chan au domaine de la chimie et les efforts de collaboration qui ont conduit à une meilleure compréhension de la biologie cellulaire du cancer et au développement d'agents thérapeutiques potentiels pour le cancer. Cet article présente une revue chronologique des découvertes scientifiques découlant des travaux effectués en partenariat entre Bill Chan et Q. Ping Dou sur une période s'étalant sur plus de 10 ans. Même si plusieurs composés ont été obtenus par synthèse chimique par le groupe de Chan et que ceux-ci ont été étudiés d'un point de vue biologique par le groupe de Dou, les résultats présentés ici sont focalisés sur les possibilités d'utiliser les polyphénols du thé vert comme inhibiteurs de protéasome de tumeurs et comme agents anticancéreux. Des plus, on discute aussi des modifications biochimiques qui augmentent ou qui diminuent le potentiel thérapeutique des composés polyphénols dans les cancéreuses humaines.

Mots-clés : protéasome, agents anticancéreux, gallate d'épigallocatéchine (GEGC), relations structure activité.

[Traduit par la Rédaction]

Introduction

This year is the 10th anniversary of our collaboration with Professor Tak-Hang (Bill) Chan. Our collaboration has focused on discovering novel green tea polyphenol-based proteasome inhibitors for cancer treatment and prevention. Chan's contributions, both intellectually and chemically, have been vital to the success of understanding the manner in which green tea polyphenols inhibit proteasome activity in cancer cells. Chan's group has been instrumental in conceptualizing and generating compounds that impart proteasome inhibition and ultimately anticancer effects in numerous cell culture and animal models. The compounds developed by his group have proven to be potentially used as alternatives to some of the more traditional cancer therapeutics.

The proteasome is the heart of ubiquitin-mediated protein degradation and is responsible for the vast majority of regulated proteolysis in eukaryotic cells. Proteasome function is crucial for biological homeostasis and the regulation of numerous cellular processes in both normal and cancer cells. For this reason, understanding the anticancer effects of molecules that inhibit proteasome activity persists. While it may seem disastrous to alter the activity of this crucial protein degradation system, proteasome inhibition has been well established as a rational strategy for multiple myeloma,[1,2] non-Hodgkin lymphoma,[3] and some solid tumors.[4]

Received 25 March 2011. Accepted 14 June 2011. Published at www.nrcresearchpress.com/cjc on 19 October 2011.

K. Landis-Piwowar. Biomedical Diagnostic and Therapeutic Sciences, School of Health Sciences, Oakland University, Rochester, MI 48309, USA.
S. Bazzi and Q.P. Dou. The Developmental Therapeutics Program, Barbara Ann Karmanos Cancer Institute, and Departments of Oncology, Pharmacology, and Pathology, School of Medicine, Wayne State University, Detroit, MI 48201, USA.

Corresponding authors: Kristin Landis-Piwowar (e-mail: landispi@oakland.edu) and Q. Ping Dou (e-mail: doup@karmanos.org).

This article is part of a Special Issue dedicated to Professor Tak-Hang Chan.

Can. J. Chem. Downloaded from www.nrcresearchpress.com by Renmin University of China on 09/02/12
For personal use only.

Can. J. Chem. Downloaded from www.nrcresearchpress.com by Renmin University of China on 09/02/12
For personal use only.

Bortezomib (Velcade, PS-341) was the first proteasome inhibitor to receive approval from the US Food and Drug Administration for the treatment of multiple myeloma and mantle cell lymphoma. Clinical trials have indicated that bortezomib has remarkable efficacy against hematological malignancies, in both single and combination regimens. However, bortezomib has failed to show significant efficacy for the treatment of solid tumors. The toxicity of bortezomib was also observed in clinical trials, which warrants continued examination of new compounds that exhibit safe, nontoxic proteasome inhibition. Bill Chan has been pivotal in chemically synthesizing numerous compounds, such as green tea polyphenol derivatives, as reviewed in this article, that have been investigated for their proteasome-inhibitory activities. Significantly, green tea polyphenols, as well as several other flavonoids (e.g., curcumin, genistein, and resveratrol), have been shown to not only act as anticancer agents alone, but have also demonstrated chemosensitizing properties in prostate, breast, hepatic, and lung tumors.[5]

Because proteasome inhibition was well established as a mechanism to induce tumor cell growth arrest or cell death and because consumption of green tea has been associated with cancer prevention, our group began investigating the green tea compound (–)-epigallocatechin-3-gallate or EGCG (Fig. 1) for its potential as a proteasome inhibitor. Our group first described that ester bond-containing tea polyphenols, such as EGCG, potently and specifically inhibited the chymotrypsin-like (CT-like) activity of the proteasome, but not trypsin-like activity, in vitro (IC_{50} = 86–194 nmol/L) and in vivo (1–10 μmol/L), at the concentrations found in the serum of green tea drinkers. Among the tea polyphenols examined, EGCG showed the strongest inhibitory activity against purified 20S proteasome, 26S proteasome of tumor cell extracts, and 26S proteasome in intact tumor cells. Atomic orbital energy analyses and high performance liquid chromatography (HPLC) indicated that the carbonyl carbon of EGCG is essential for proteasome inhibition and resulted in accumulation of the natural proteasome substrates, p27 and IκB-α. Furthermore, normal human fibroblasts were found to be resistant to EGCG-mediated proteasome inhibition compared with a simian virus-transformed fibroblast counterpart. These early studies suggested that the proteasome is a cancer-related molecular target of tea polyphenols and its inhibition by ester bond-containing polyphenols may contribute to the cancer-preventative effect of tea.[6]

While our group investigated the biological effects of EGCG, Chan's group began the enantioselective synthesis of EGCG. Their work was critical for subsequent studies that required a pure compound without the laborious extraction of EGCG from the leaves of the *Camillia sinensis* plant. Until then, green tea polyphenols had been extracted or purified from green tea leaves for preclinical and clinical studies. At the time, EGCG was isolated from green tea extract, and the yield was highly dependent upon the processing and source of the tea. With the advancement of EGCG chemical synthesis, mechanistic studies for the cellular action of EGCG could be evaluated. A synthetic approach for the generation of EGCG and its analogs was thus developed to provide sufficient quantities of the biochemicals for examination as anticancer agents.[7]

In 2001, while working at the Moffitt Cancer Institute, Tampa, Florida, Dr. Dou read Chan's aforementioned paper and was impressed by his novel synthetic route for EGCG. Dr. Dou then approached him by e-mail to ask if he was willing to do a collaboration to study the effect of his synthetic EGCG analogs on tumor proteasomes. Dr. Chan was pleased to accept this invitation after reading our manuscript.[6] Our 10-year collaboration started from there. While the collaboration continued, in 2003, Dr. Dou moved to his current position (Karmanos Cancer Institute, Wayne State University, Detroit, Michigan), which is much closer to McGill University in Montreal, Quebec, and the proximity brought us several fruitful visits.

Chemical and biological analysis of natural product synthetic analogs

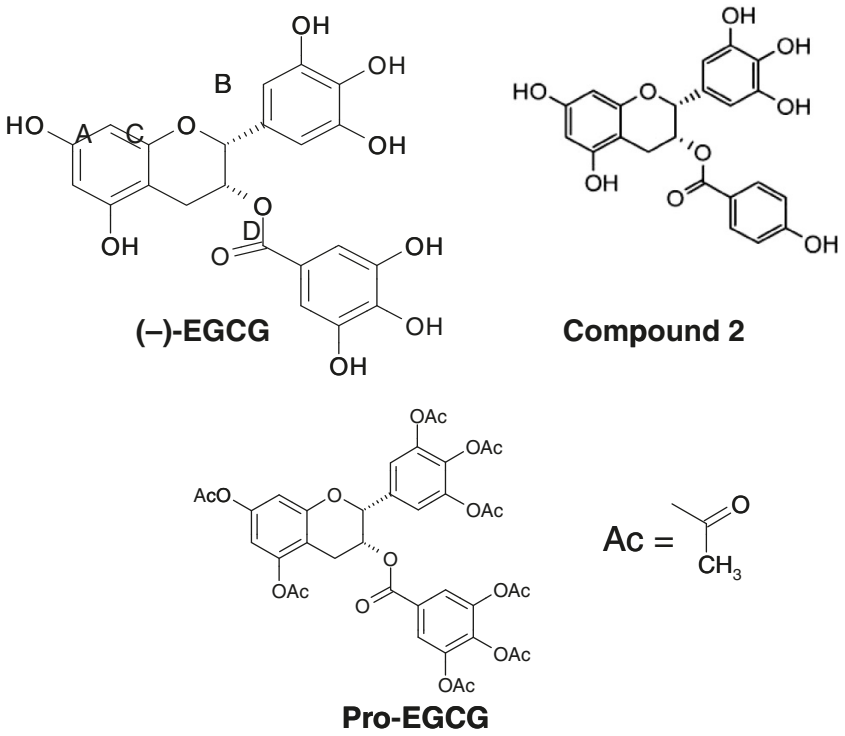
The novel synthesis of green tea polyphenols as proteasome inhibitors

Over the last 10 years, we have studied proteasome activity and apoptosis induction in cells that have been exposed to naturally occurring and chemically synthesized derivatives of green tea. We identified that ester bond-containing tea polyphenols, such as EGCG, inhibited CT-like proteasome activity in vitro and in vivo. However, EGCG had also been shown to be relatively unstable under neutral or alkaline conditions and could be rapidly degraded via deprotonation of hydroxyl (–OH) groups on the phenol rings.[8] Furthermore, these –OH groups could be modified through major biotransformation reactions, including methylation, glucuronidation, and sulfonation, resulting in reduced biological activities of EGCG in vivo.[9–11]

In a joint *Molecular Medicine* paper published in 2002,[12] our collaborative efforts resulted in the first description of enantioselective synthesis of EGCG analogs, followed by validation with multiple biological assays. This landmark publication detailed findings that novel synthetic tea chemicals could be developed as unique proteasome inhibitors. The paper described the biological evaluation of synthetic green tea polyphenols and showed that these compounds exhibited proteasome-inhibitory activity in vitro and in vivo. Chan's group generated a benzyl-protected compound (Bn-EGCG), which lacked –OH groups for hydrogen binding and showed no proteasome-inhibitory activity, serving as one of the first clues to the great importance of hydroxylated EGCG. Not surprisingly, the hydroxylated synthetic green tea polyphenols acted as anticancer agents by inhibiting cell proliferation, inducing apoptosis, and suppressing the transforming activity of human cancer cells. The findings suggested that hydrogen bonding to some or all of the –OH groups surrounding EGCG are vital for proteasome inhibition.[12]

The previous study established that naturally occurring ester bond-containing green tea polyphenols (EGCG, GCG, and ECG) possess proteasome-inhibitory activity in vitro and in vivo and that green tea polyphenols without the gallate ester (EGC, GC, and EC) were not proteasome inhibitors. To validate the model, the syntheses of the natural (+)-CG and (–)-ECG as well as their enantiomers were conducted and the compounds were examined for biological proteasome inhibition. The green tea polyphenol catechin-3-gallate (CG) and epicatechin-3-gallate (ECG) were synthesized enantioselectively via a

Fig. 1. The natural (–)-epigallocatechin-3-gallate (EGCG) and synthetic (compound **2** and protected EGCG (pro-EGCG)) green tea polyphenols are depicted.



Can. J. Chem. Downloaded from www.nrcresearchpress.com by Renmin University of China on 09/02/12
For personal use only.

Sharpless hydroxylation reaction followed by a diastereoselective cyclization. Their abilities to inhibit proteasome activity were measured. The unnatural enantiomers were found to be as equally potent as the natural compounds.[13]

The novel synthesis of EGCG analogs as proteasome inhibitors

Structure–activity relationships (SARs) of synthetically derived green tea polyphenols

In the earliest studies, the molecular mechanisms of proteasome inhibition by tea polyphenols were not well understood. To elucidate the interaction of green tea polyphenols and proteasome active site interaction, our group considered the importance of acylation of the proteasome β5-subunit's catalytic N-terminal threonine (Thr 1). In silico docking experiments were used to aid in the understanding of the binding of EGCG to induce proteasome inhibition. On the basis of these docking experiments, we proposed that EGCG could bind the CT site in an orientation and conformation suitable for a nucleophilic attack by Thr 1. In fact, the distance from the electrophilic carbonyl carbon of EGCG to the hydroxyl group of Thr 1 was measured as 3.18 Å. Furthermore, the A ring of EGCG (Fig. 1) was found to act as a tyrosine mimic, binding to the hydrophobic S1 pocket of the β5 subunit and the EGCG scissile bond appeared to become strained, lowering the activation energy for attack by the hydroxyl group of Thr 1. The model was validated by comparison of predicted and actual activities of several EGCG analogs, either naturally occurring or previously synthesized by Chan's group.[14]

EGCG analogs of the A and C rings

Analysis of various EGCG analogs continued to dominate our search for the most effective proteasome inhibitors and anticancer agents. EGCG amides and five simple analogs were prepared by enantioselective synthesis. Proteasome inhibition, in vitro, was measured by fluorogenic substrate assay and in vivo by accumulation of proteasome target proteins (p27, IκB-α, and Bax). Inhibition of tumor cell proliferation and (or) induction of cell death were determined by G_1 arrest, DNA fragmentation, and colony formation inhibition. EGCG analogs with modifications in the A ring, C ring, or ester bond were found to inhibit the CT-like activity of a purified 20S proteasome with altered potencies, while they were able to potently inhibit proteasome activity in tumor cells. Furthermore, colony formation of prostate cancer LNCaP cells was suppressed and some compounds induced G_1 arrest and DNA fragmentation in leukemia Jurkat T cells. However, these EGCG analogs caused no or little proteasome inhibition in normal or nontransformed cells. From these studies, it was well established that the A ring and gallate ester and amide bond are essential for the proteasome-inhibitory function of (–)-EGCG.[15]

EGCG analogs of the A and B rings

In the next set of studies, the SAR of EGCG analogs possessing changes to the A and B rings (Fig. 1) were examined. An analysis of the importance of the various –OH groups in the B ring (Fig. 1) as well as the effect of a hydrophobic substituent in the A ring was conducted in regard to biological activity against the proteasome. Four unnatural green tea catechin analogs and two benzyl compounds were prepared and their biological activities were compared with compounds from previous studies. It was found that a decrease in the number of –OH groups in the B ring led to a decreased potency, whereas the introduction of a hydrophobic benzyl

Can. J. Chem. Downloaded from www.nrcresearchpress.com by Renmin University of China on 09/02/12
For personal use only.

group into the A ring did not significantly affect the proteasome-inhibitory potency.[16]

Peracetate-protected EGCG analogs as prodrugs of proteasome inhibitors

EGCG analogs of the B and D rings and peracetate protection

In an effort to discover still more stable polyphenol proteasome inhibitors, Chan's group next synthesized several novel EGCG analogs with –OH groups eliminated from the B and (or) D rings. In an attempt to increase the stability of green tea catechins in vivo, a group of putative prodrugs with –OH groups protected by peracetate were also synthesized. These prodrugs can be converted to an active form by removal of the peracetate groups by cellular cytosolic esterases. The SAR of the unprotected and protected compounds was examined for their proteasome-inhibitory potentials. It was determined that decreasing –OH groups from either the B or D ring led to diminished proteasome-inhibitory activity in vitro. However, in cultured tumor cells only the protected analogs were capable of potently inhibiting the proteasome activity. Furthermore, these protected analogs induced apoptotic cell death in a tumor cell-specific manner. The superior efficacy of the protected (–)-EGCG analogs indicated the formation of an entirely new compound(s) in intact tumor cells and that peracetate protection could be developed into novel anticancer and cancer-preventive agents.[17]

Because the –OH groups of the EGCG D ring were found to form hydrogen bonds with Gly47 or Ser131 of the proteasome by in silico analysis, a D-ring analog, compound **2** (Fig. 1) (peracetate protected and unprotected) was synthesized by Chan's group and examined for its proteasome-inhibitory activity. Compound **2** contains only one *p*-hydroxyl group on the D ring and was found to be a much weaker proteasome inhibitor than EGCG, confirming the importance of D-ring –OH groups. Since an amino group is capable of forming hydrogen bonds both as a donor and an acceptor, Chan's group also synthesized a compound that replaced the hydroxyl group in the D ring with an amino group in an attempt to increase the potency of compound **2**. The *para*-amino substituent on the D ring of compound **2** exhibited proteasome-inhibitory activity with a potency similar to that of EGCG. Furthermore, the *O*-acetylated amino – green tea polyphenol analogs appeared to behave as prodrugs and the mechanism of action involves targeting the proteasome in tumor cells, thereby inducing cell death. The presence of the *para*-amino substituent could increase the bioavailability of these compounds by limiting biotransformation reactions to the hydroxyls, such as glucuronidation, sulfonation, and methylation. Since the *p*-aminobenzoic acid moiety is a normal constituent of folic acid and generally presumed to be innocuous, the study of these *para*-amino substituted green tea polyphenols may offer the possibility of discovering novel anticancer drugs.[18]

Peracetate protection of EGCG and EGCG analogs

We began to more heavily investigate the effect of peracetate protection on green tea catechins and especially on EGCG to enhance its in vivo stability. Chan's group synthesized fully protected EGCG (later named pro-EGCG, Fig. 1). HPLC analysis revealed that the protected EGCG analog was six times more stable than natural, unprotected EGCG under slightly alkaline conditions. A series of bioassays showed that protected EGCG was not inhibitory against a purified 20S proteasome in vitro, but exhibited increased proteasome-inhibitory activity in intact leukemic cells over natural (–)-EGCG, indicating an intercellular conversion. Furthermore, inhibition of cellular proteasome activity by protected EGCG was associated with the induction of cell death. Therefore, our results indicated that the protected EGCG analog functioned as a prodrug of the proteasome inhibitor, EGCG.[19]

Chan's group next synthesized several (–)-EGCG analogs with peracetate protection on the –OH groups. The acetylated synthetic tea analogs inhibited proteasome activity in cultured tumor cells more potently than natural EGCG and exhibited higher potency to inhibit proliferation and transforming activity and to induce apoptosis in human leukemic, prostate, breast, and simian virus 40-transformed cells. Additionally, the protected analogs were relatively benign to normal and nontransformed human cells.[20]

We next assessed the activity of fully protected EGCG (pro-EGCG) in breast cancer culture and animal models. It became clear that when cultured human breast cancer MDA-MB-231 cells were treated with pro-EGCG, EGCG was not only converted but also accumulated in those cells, accompanied by enhanced levels of proteasome inhibition, growth suppression, and apoptosis induction, compared with cells treated with natural EGCG. In fact, HPLC analysis confirmed conversion of pro-EGCG to EGCG in cultured human leukemic Jurkat T cells.[21] We investigated the potential use of pro-EGCG as a novel prodrug that converts to a cellular proteasome inhibitor and anticancer agent in vivo by inducing MDA-MB-231 tumors in nude mice, followed by treatment with pro-EGCG or EGCG for 31 days. A significant inhibition of breast tumor growth by pro-EGCG (greater than that of EGCG) was associated with increased proteasome inhibition and apoptosis induction in tumor tissues. Pro-EGCG was confirmed to increase the bioavailability, stability, and proteasome-inhibitory and anticancer activities of EGCG in human breast cancer cells and tumors, more strongly suggesting its potential use for cancer prevention and treatment.[22]

Methylation as a biotransforming event on EGCG

SARs of methylated EGCG analogs

Biological and in silico docking experiments revealed that EGCG binds the CT site in an orientation and conformation that is suitable for a nucleophilic attack by Thr 1 of the proteasomal β5 subunit. In addition, our in silico docking study suggested that a particular pose of EGCG could lead to potential covalent modification of Thr 1. Because biotransformation reactions, such as methylation, could result in reduced biological activity of EGCG in vivo, we hypothesized that methylation reduces binding of EGCG to the β5 subunit of the proteasome and, therefore, decreases its proteasomal chymotrypsin-like-inhibitory potency. We examined the potential effects of methylated EGCG analogs in an in silico model and determined that methylation had no effect on nucleophilic susceptibility of EGCG and ECG. However, it appeared to disrupt the ability of these polyphenols to

Can. J. Chem. Downloaded from www.nrcresearchpress.com by Renmin University of China on 09/02/12
For personal use only.

interact with Thr 1 of the proteasome β5 subunit by moving the ester carbon away from, or entirely blocking, Thr 1. Additionally, methylation impaired the ability of EGCG and ECG to dock in a consistent low energy pose. We determined that methylation disrupts the ability of EGCG and ECG to bind to the proteasome β5 subunit, which was likely responsible for their diminished proteasomal inhibitory and, therefore, other biological activities.[23]

Biological activities and HPLC analysis of methylated EGCG analogs

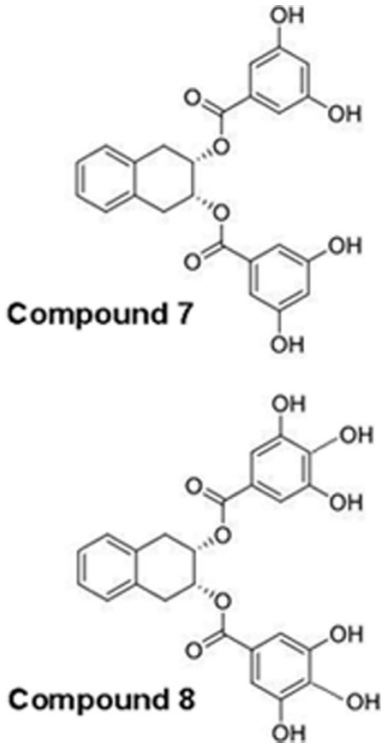
We next tested whether methylated green tea polyphenols (GTPs) decreased proteasome-inhibitory abilities in cultured cells. Methylated EGCG and ECG analogs, which are known to be found in vivo, were synthesized and studied for their SARs using a purified 20S proteasome. The addition of a single methyl group on EGCG or ECG led to decreased proteasome inhibition and as the number of methyl groups increased, the inhibitory potencies further decreased. Furthermore, peracetate-protected forms of methylated GTPs were added to intact Jurkat T cells to observe the intracellular effects of methylation. Peracetate-protected, monomethylated EGCG induced greater cellular proteasome inhibition and apoptosis than did peracetate-protected, trimethylated EGCG, which is consistent with the potencies of the parent methylated analogs against a purified 20S proteasome. Therefore, methylation on GTPs, under physiological conditions, could decrease their proteasome-inhibitory activity, contributing to decreased cancer-preventive effects of tea consumption.[21]

Catechol-O-methyltransferase activity in human breast cancer cells

Because EGCG was known to be unstable under physiological conditions and methylation of EGCG by catechol-*O*-methyltransferase (COMT) reduces the biological activity of EGCG, we hypothesized that COMT suppression in human breast cancer cells could increase the proteasome-inhibitory potency of EGCG and, therefore, enhance its tumor cell growth-inhibitory activity. We determined the COMT genotype and basal levels of COMT activity in various human breast cancer cell lines. When breast cancer MDA-MB-231 cells containing high COMT activity were tested, the diminished COMT activity appeared to increase the effectiveness of EGCG via augmented proteasome inhibition and apoptosis induction. The findings supplemented our previous conclusions that methylated EGCG is less bioactive and supported the notion that COMT inhibition may increase the anticancer properties of tea polyphenols. Furthermore, the combination of COMT inhibition and EGCG administration may serve as a novel approach or supplemental treatment for breast cancer chemotherapy.[24]

Toward the goal of targeting the problem of EGCG biological methylation in vivo, a novel EGCG analog devoid of the *O*-catechol structure (compound **7**, Fig. 2) that should not be a substrate of COMT was examined. While the proteasome-inhibitory activity of this EGCG analog (**7**) was not affected by the addition of the COMT inhibitor dinitrocatechol (DNC), proteasome inhibition by compound **8** (Fig. 2), as well as EGCG, was enhanced. Similarly, the addition of DNC potently enhanced the antiproliferative activities of acetate protected EGCG, but not the acetate-protected form of this novel synthetic compound (**7**) in MDA-MB-231 breast cancer cells expressing high COMT activity.[25]

Fig. 2. The synthetic compounds **7** and **8** are shown. Compound **7** is resistant to methylation by the enzyme catechol-*O*-methyltransferase.



Although compound **7**, presumably resistant to COMT-mediated methylation and inactivation in cells, was able to inhibit the activity of purified 20S proteasome and cellular 26S proteasome, the involved molecular mechanism is unknown. Most recently, we applied a computational solution to understand the possible interaction between compound **7** and the proteasome β5 subunit. We found that the ester carbonyls at the C2 and C3 atoms may be targets for nucleophilic attack in both compounds **7** and **8**. The metadiol structure in presumably COMT-resistant compound **7** gives a more stable conformation and lower docked free energy than other EGCG analogs.[26] These studies suggest that COMT is a critical factor in mediating the antiproliferative activities of EGCG and EGCG analogs, especially in cells expressing high COMT activity, such as MDA-MB-231 breast cancer cells.

Conclusion

Throughout the 10 years of collaborative efforts with Bill Chan and members of his laboratory, we have developed numerous green tea polyphenol-based proteasome inhibitors as potential anticancer drugs and chemosensitizers for cancer treatment and prevention. Of these compounds, EGCG and EGCG derivates have proven to be most effect in both in vitro and in vivo models. From conception to generation, the Chan group have provided the insight to generate innocuous compounds that impart proteasome inhibition and ultimately anticancer effects in various cell culture and animal systems. These compounds should have great potential to be used as preventive agents and even as cancer therapeutics. Our

biological findings would not have been possible without Bill's invaluable contributions.

Acknowledgements

Because of space limitation and the special focus of this review article, we mainly cited our joint publications with Chan's group and we therefore sincerely apologize to those colleagues whose work has not been cited in this succinct review article. We would like to extend a special thanks to Elizabeth DeWitt for critical reading of this manuscript. Her attention to detail and thoughtful analysis of this work was invaluable to its completion.

References

(1) Richardson, P. G.; Mitsiades, C.; Hideshima, T.; Anderson, K. C. *Cell Cycle* **2005**, *4* (2), 289. doi:10.4161/cc.4.2.1414.
(2) Catley, L.; Tai, Y.-T.; Chauhan, D.; Anderson, K. C. *Drug Resist. Update* **2005**, *8* (4), 205. doi:10.1016/j.drup.2005.06.001.
(3) Goy, A.; Younes, A.; McLaughlin, P.; Pro, B.; Romaguera, J. E.; Hagemeister, F.; Fayad, L.; Dang, N. H.; Samaniego, F.; Wang, M.; Broglio, K.; Samuels, B.; Gilles, F.; Sarris, A. H.; Hart, S.; Trehu, E.; Schenkein, D.; Cabanillas, F.; Rodriguez, A. M. *J. Clin. Oncol.* **2005**, *23* (4), 667. doi:10.1200/JCO.2005.03.108.
(4) Dou, Q. P.; Goldfarb, R. H. *IDrugs* **2002**, *5* (8), 828. PMID: 12802699.
(5) Landis-Piwowar, K. R.; Milacic, V.; Chen, D.; Yang, H.; Zhao, Y.; Chan, T. H.; Yan, B.; Dou, Q. P. *Drug Resist. Update* **2006**, *9* (6), 263. doi:10.1016/j.drup.2006.11.001.
(6) Nam, S.; Smith, D. M.; Dou, Q. P. *J. Biol. Chem.* **2001**, *276* (16), 13322. doi:10.1074/jbc.M004209200.
(7) Li, L.; Chan, T. H. *Org. Lett.* **2001**, *3* (5), 739. doi:10.1021/ol000394z.
(8) Chen, Z.-Y.; Zhu, Q. Y.; Tsang, D.; Huang, Y. *J. Agric. Food Chem.* **2001**, *49* (1), 477. doi:10.1021/jf000877h.
(9) Zhu, Q. Y.; Zhang, A.; Tsang, D.; Huang, Y.; Chen, Z.-Y. *J. Agric. Food Chem.* **1997**, *45* (12), 4624. doi:10.1021/jf9706080.
(10) Okushio, K.; Suzuki, M.; Matsumoto, N.; Nanjo, F.; Hara, Y. *Biosci. Biotechnol. Biochem.* **1999**, *63* (2), 430. doi:10.1271/bbb.63.430.
(11) Lu, H.; Meng, X.; Yang, C. S. *Drug Metab. Dispos.* **2003**, *31* (5), 572. doi:10.1124/dmd.31.5.572.
(12) Smith, D. M.; Wang, Z.; Kazi, A.; Li, L.-h.; Chan, T.-H.; Dou, Q. P. *Mol. Med.* **2002**, *8* (7), 382.
(13) Wan, S. B.; Chen, D.; Dou, Q. P.; Chan, T. H. *Bioorg. Med. Chem.* **2004**, *12* (13), 3521. doi:10.1016/j.bmc.2004.04.033.
(14) Smith, D. M.; Daniel, K. G.; Wang, Z.; Guida, W. C.; Chan, T.-H.; Dou, Q. P. *Proteins* **2004**, *54* (1), 58. doi:10.1002/prot.10504.
(15) Kazi, A.; Wang, Z.; Kumar, N.; Falsetti, S. C.; Chan, T.-H.; Dou, Q. P. *Anticancer Res.* **2004**, *24* (2B), 943.
(16) Wan, S. B.; Landis-Piwowar, K. R.; Kuhn, D. J.; Chen, D.; Dou, Q. P.; Chan, T. H. *Bioorg. Med. Chem.* **2005**, *13* (6), 2177. doi:10.1016/j.bmc.2004.12.056.
(17) Landis-Piwowar, K. R.; Kuhn, D. J.; Wan, S. B.; Chen, D.; Chan, T. H.; Dou, Q. P. *Int. J. Mol. Med.* **2005**, *15* (4), 735.
(18) Osanai, K.; Landis-Piwowar, K. R.; Dou, Q. P.; Chan, T. H. *Bioorg. Med. Chem.* **2007**, *15* (15), 5076. doi:10.1016/j.bmc.2007.05.041.
(19) Lam, W. H.; Kazi, A.; Kuhn, D. J.; Chow, L. M. C.; Chan, A. S. C.; Dou, Q. P.; Chan, T. H. *Bioorg. Med. Chem.* **2004**, *12* (21), 5587. doi:10.1016/j.bmc.2004.08.002.
(20) Kuhn, D. J.; Lam, W. H.; Kazi, A.; Daniel, K. G.; Song, S.; Chow, L. M. C.; Chan, T. H.; Dou, Q. P. *Front. Biosci.* **2005**, *10* (2), 1010. doi:10.2741/1595.
(21) Landis-Piwowar, K. R.; Wan, S. B.; Wiegand, R. A.; Kuhn, D. J.; Chan, T. H.; Dou, Q. P. *J. Cell. Physiol.* **2007**, *213* (1), 252. doi:10.1002/jcp.21124.
(22) Landis-Piwowar, K. R.; Huo, C.; Chen, D.; Milacic, V.; Shi, G.; Chan, T. H.; Dou, Q. P. *Cancer Res.* **2007**, *67* (9), 4303. doi:10.1158/0008-5472.CAN-06-4699.
(23) Daniel, K. G.; Landis-Piwowar, K. R.; Chen, D.; Wan, S. B.; Chan, T.-H.; Dou, Q. P. *Int. J. Mol. Med.* **2006**, *18* (4), 625.
(24) Landis-Piwowar, K.; Chen, D.; Chan, T. H.; Dou, Q. P. *Oncol. Rep.* **2010**, *24* (2), 563.
(25) Huo, C.; Yang, H.; Cui, Q. C.; Dou, Q. P.; Chan, T. H. *Bioorg. Med. Chem.* **2010**, *18* (3), 1252. doi:10.1016/j.bmc.2009.12.034.
(26) Kanwar, J.; Mohammad, I.; Yang, H.; Huo, C.; Chan, T. H.; Dou, Q. P. *Int. J. Mol. Med.* **2010**, *26* (2), 209.

Can. J. Chem. Downloaded from www.nrcresearchpress.com by Renmin University of China on 09/02/12
For personal use only.

Synthesis of polyhydroxylated flavonoids bearing a lipophilic decyl tail as potential therapeutic antioxidants

Stuart T. Caldwell, Donald B. McPhail, Garry G. Duthie, and Richard C. Hartley

Can. J. Chem. Downloaded from www.nrcresearchpress.com by Renmin University of China on 09/02/12
For personal use only.

Abstract: Antioxidants have potential for the treatment of stroke and neurodegeneration, and chimeric compounds that combine a flavon-3-ol head group related to myricetin and a lipophilic decyl tail are known to protect membranes from oxidative damage at least as well as vitamin E. New flavon-3-ols that are highly hydroxylated in the B ring in ways not found in natural flavon-3-ols and bearing a lipophilic decyl tail have been prepared from trimethoxy- and tetramethoxybenzoic acids accessed by lithiation–carboxylation reactions. Direct enolate acylation was preferred over Baker–Venkataraman rearrangement when there were methoxy groups at both the 2- and the 6-position of the benzoic acid derivatives.

Key words: flavonol, antioxidant, synthesis, polyphenols, tocopherol.

Résumé : Les antioxydants pourraient potentiellement être utilisés dans le traitement des défaillances cardiovasculaires et des processus neurodégénératifs et il est connu que des produis chimériques qui combinent un groupe de tête flavon-3-ol apparenté à la myricétine et un groupe de queue lipophile décyle protègent les membranes des dommages oxydants, au moins aussi bien que la vitamine E. Utilisant comme produits de départs des acides triméthoxy- et tétraméthoxybenzoïques obtenus par des réactions de lithiation/carboxylation, on a préparé de nouveaux flavon-3-ols hautement hydroxylés dans le noyau B, qui diffèrent ainsi des flavon-3-ols naturels et qui portent un groupe de queue lipophile décyle. Dans les cas où on retrouve des groupes méthoxy à la fois dans les positions 2- et 6- des dérivés de l'acide benzoïque, on a préféré l'acylation directe de l'énolate par rapport au réarrangement de Baker–Venkataramn.

Mots-clés : flavonol, antioxydant, synthèse, polyphénols, tocophérol.

[Traduit par la Rédaction]

Introduction

Flavonoids (Fig. 1) are polyphenolic compounds produced as secondary metabolites by plants. They have attracted a great deal of attention over the years because they are found in a range of fruit, vegetables, and beverages, including wine, chocolate and green tea, and so are a common component of the human diet.[1] The consumption of foods rich in these compounds has been associated with a plethora of health benefits. Although feeding studies[2–5] using isotopically labelled flavonoids[6,7] have shown that such compounds are highly metabolized and the dietary benefits are probably due to smaller phenolic compounds,[1] the original interest has led to flavonols being tested in a wide range of assays. These tests have revealed that flavonols have promising properties including as antioxidants, antivirals, antibacterials, and anticancer agents.[8] Indeed, flavopiridol (Alvocidib), a flavonoid analogue of the natural product rohitukine, is a powerful inhibitor of cyclin-dependent kinases and is undergoing clinical trails for the treatment of hematologic malignancies.[9] Different flavonoids have been shown to have different modes of action even when the same therapeutic effect is sought, and inhibition of the proteasome has been investigated as a mode for the anticancer activity for the flavonoids in green tea and their analogues.[10–12] Consequently, the chromone core of flavonoids has been regarded as a scaffold for the construction of potential drug candidates,[13,14] and is considered a privileged substructure for drug discovery.[15]

We were interested in the potential of flavon-3-ols as therapeutic antioxidants, in particular for the treatment of stroke[16] and neurodegeneration.[17,18] Flavon-3-ols that are capable of forming orthoquinones or extended paraquinones[19] have been shown to react very rapidly with oxygen-centred radicals.[20] Myricetin **1** in particular was found to react nearly 28 times as fast as vitamin E with galvinoxyl radicals and to destroy twice as many radicals, and this is believed to be related to its ability to form orthoquinone **2** and extended paraquinone **3** (Scheme 1).[20] However, myricetin itself does not protect membranes well from oxidative assault because of its poor solubility in lipids.[21,22] We prepared chimeric compounds[23,24] with a head based on myricetin **1** and a tail

Received 4 May 2011. Accepted 14 June 2011. Published at www.nrcresearchpress.com/cjc on 6 October 2011.

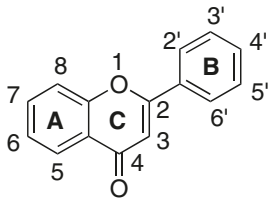
S.T. Caldwell and R.C. Hartley. WestCHEM School of Chemistry, University of Glasgow, Glasgow, G12 8QQ Scotland, UK.
D.B. McPhail. Antoxis Limited, 5:16 Institute of Medical Sciences, Foresterhill, Aberdeen, AB25 2ZD Scotland, UK.
G.G. Duthie. Rowett Institute of Nutrition and Health, University of Aberdeen, Aberdeen AB21 9SB Scotland, UK.

Corresponding author: Richard C. Hartley (e-mail: Richard.Hartley@glasgow.ac.uk).

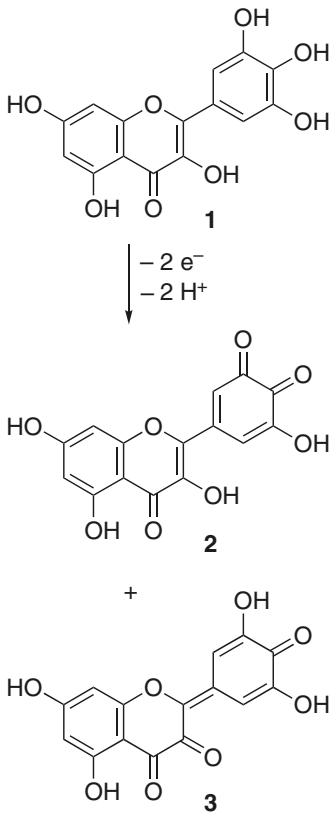
This article is part of a Special Issue dedicated to Professor Tak-Hang Chan.

Can. J. Chem. Downloaded from www.nrcresearchpress.com by Renmin University of China on 09/02/12
For personal use only.

Fig. 1. Flavone core of flavonoids with ring labelling and numbering.



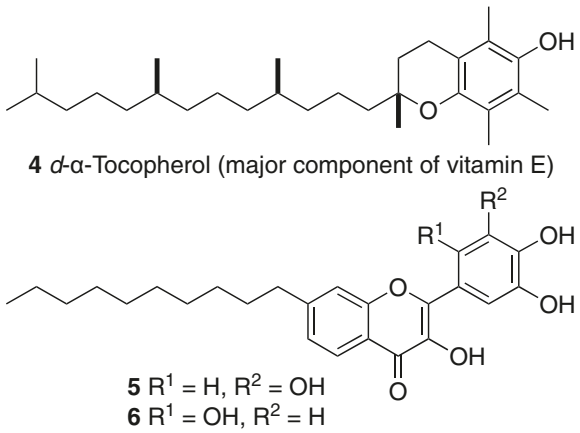
Scheme 1. Oxidation of myricetin **2** to an orthoquinone **2** and an extended paraquinone **3**.



similar to that of *d*-α-tocopherol **4** (the main component of vitamin E,[25] Fig. 2). Varying the tail length and position indicated that the chain length and orientation were of primary importance and compounds **5** and **6**, which matched the overall length of *d*-α-tocopherol best, protected vitamin E-deficient microsomes from oxidation most effectively. Optimal alkyl chain lengths rather than simple relationships to lipophilicity have been observed for other polar antioxidants bearing lipophilic tails and appear to be associated with location of the antioxidant at the water–lipid interface.[26] Chimeric molecules based on flavones have also been reported for other medicinal applications.[27,28]

We have now investigated the preparation of analogues **7a**–**7g** (Fig. 3) of compounds **5** and **6**. These fall into two categories: those with a trihydroxylated B ring (**7a**–**7c**) but different substitution patterns and those with a tetrahydroxylated B ring (**7d**–**7g**). Flavon-3-ols bearing hydroxyl groups in these substitution patterns on the B ring are not naturally occurring, although there are synthetic examples with the 2′,3′,4′-trihydroxy and 2′,3′,4′,5′-tetrahydroxy substi-

Fig. 2. Comparison of *d*-α-tocopherol **4** and chimeric antioxidants **5** and **6**.



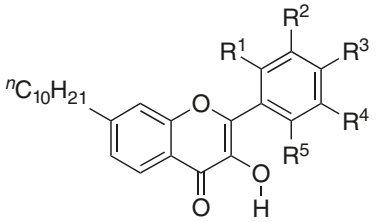
tution patterns.[29–31] The decyl chain was chosen because it was the optimum chain length in the related compounds **5** and **6**, and for the flavonoids trihydroxylated on the B ring (**7a**–**7c**), the hydrophilicity–lipophilicity balance[26] would be very similar. The routes demonstrated could, in theory, be applied to a wide range of chain lengths.

Results and discussion

We previously prepared 7-decyl-flavonoid **6** from the B-ring fragment, 2,4,5-trimethoxybenzoic acid, by a sequence involving esterification, Baker–Venkataraman rearrangement, cyclization, and deprotection. Benzoic acid derivatives **8a**–**8g** (Fig. 4) were required to follow the same route. Carboxylic acids **8a** and **8d** were commercially available, whereas the remaining carboxylic acids were synthesized by combining various literature methods. Following the method of Dorn et al.[32] (later used by Cortez et al.[33]) vanillin **9** was brominated, and Dakin oxidation of the resulting aldehyde **10** then gave phenol **11** (Scheme 2). Methylation using methyl iodide (rather than dimethyl sulfate[32,33]) gave aryl bromide **12**. Lithiation–carboxylation of aryl bromide **12** then gave carboxylic acid **8b**.[33,34] Ortholithiation–carboxylation of trimethyl ether **13** gave carboxylic acid **8c** in low yield (Scheme 3).[35,36] Acid **8e** was prepared by bromination of carboxylic acid **14** followed by substitution with methoxide according to the method of Meyers et al.[37] (Scheme 4). Carboxylic acid **8f** was prepared in a similar way to acid **8b**, Baeyer–Villiger oxidation of aldehyde **15** and saponification of the resulting formate ester gave phenol **16** (Scheme 5).[38] Methylation of phenol **16** yielded ether **17**[39] and ortholithiation–carboxylation gave acid **8f**.[40] Reduction of quinone **18** followed by methylation of the resulting tetra-ol by modification of the method of Keegstra et al.[41] gave tetramethyl ether **19** (Scheme 6). In our hands palladium on carbon proved to be superior to platinum oxide. Alternatively, tetramethyl ether **19** was accessed by Baeyer–Villiger oxidation of aldehyde **20** followed by hydroylsis to give phenol **21** and then methylation gave **19** in 51% yield over two steps.[42] Although acid **8g** has been accessed directly from tetramethyl ether **19** by ortholithiation–carboxylation,[43] in our hands only the diacid was obtained. Fortunately, formylation by the method of Poigny et al.[44]

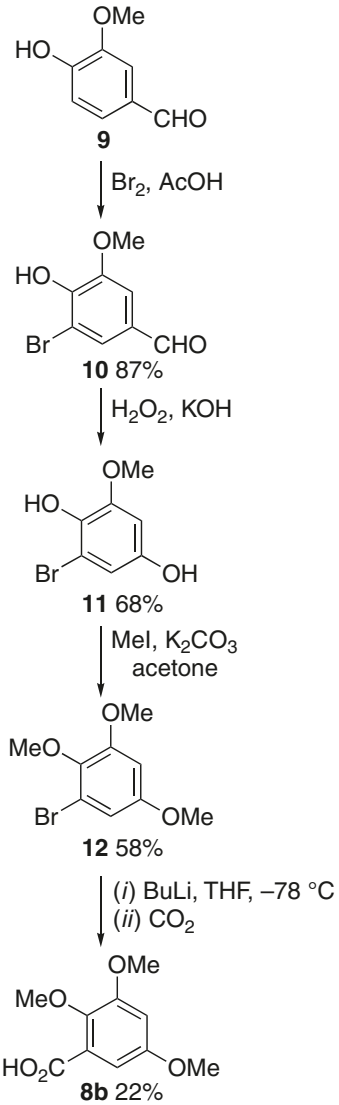
Can. J. Chem. Downloaded from www.nrcresearchpress.com by Renmin University of China on 09/02/12
For personal use only.

Fig. 3. Target polyhydroxylated 7-decyl-flavonoids **7**.



7a $R^1 = R^2 = R^3 = OH$, $R^4 = R^5 = H$
b $R^1 = R^2 = R^4 = OH$, $R^3 = R^5 = H$
c $R^1 = R^2 = R^5 = OH$, $R^3 = R^4 = H$
d $R^1 = R^3 = R^5 = OH$, $R^2 = R^4 = H$
e $R^1 = R^2 = R^3 = R^4 = OH$, $R^5 = H$
f $R^1 = R^2 = R^3 = R^5 = OH$, $R^4 = H$
g $R^1 = R^2 = R^4 = R^5 = OH$, $R^3 = H$

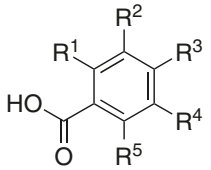
Scheme 2. Synthesis of 2,3,5-trimethoxybenzoic acid **8b**.



followed by oxidation[45] of the aldehyde **22** proved more successful.

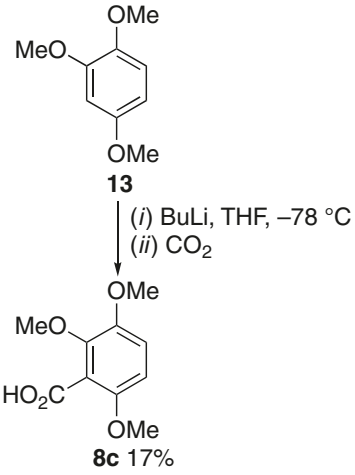
Phenol **23** was prepared as we described previously,[23] and was esterified by reaction with carboxylic acids **8a**, **8b**, **8d**, and **8e** using the water-soluble coupling reagent *N*-(3-dimethylaminopropyl)-*N*′-ethylcarbodiimide hydrochloride (EDCI) to give esters **24a**, **24b**, **24d**, and **24e**, respectively, in poor to good yield (Scheme 7). The esterification typically proceeded smoothly with the exception of the reaction using acid **8d**, which failed to couple completely even after extended reaction times, presumably because of steric hindrance by the 2- and 6-methoxy groups, whereas ester **24b** appeared to be unstable to column chromatography on silica gel. Baker–Venkataraman rearrangement of esters **24a**, **24b**, **24d**, and **24e** to give diketones **25a**, **25b**, **25d**, and **25e** was then achieved using lithium bis(trimethylsilyl)amide

Fig. 4. Trimethoxy- and tetramethoxy-benzoic acids **8**.

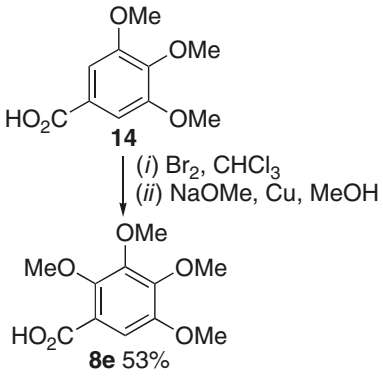


8a $R^1 = R^2 = R^3 = OMe$, $R^4 = R^5 = H$
b $R^1 = R^2 = R^4 = OMe$, $R^3 = R^5 = H$
c $R^1 = R^2 = R^5 = OMe$, $R^3 = R^4 = H$
d $R^1 = R^3 = R^5 = OMe$, $R^2 = R^4 = H$
e $R^1 = R^2 = R^3 = R^4 = OMe$, $R^5 = H$
f $R^1 = R^2 = R^3 = R^5 = OMe$, $R^4 = H$
g $R^1 = R^2 = R^4 = R^5 = OMe$, $R^3 = H$

Scheme 3. Synthesis of 2,3,6-trimethoxybenzoic acid **8c**.

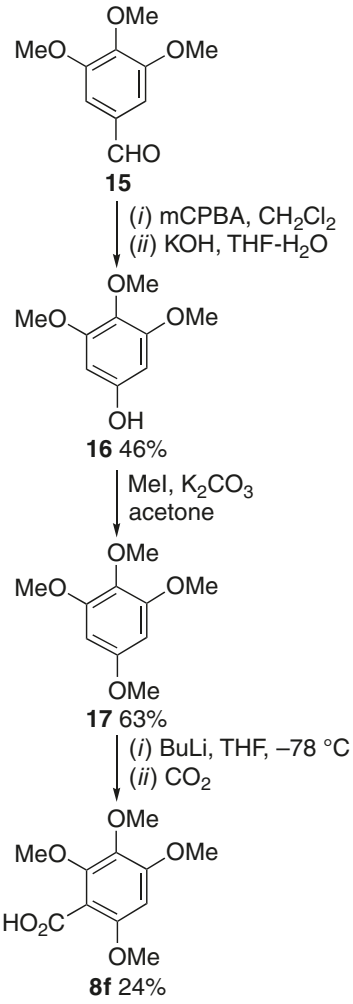


Scheme 4. Synthesis of 2,3,4,5-tetramethoxybenzoic acid **8e**.



Can. J. Chem. Downloaded from www.nrcresearchpress.com by Renmin University of China on 09/02/12
For personal use only.

Scheme 5. Synthesis of 2,3,4,6-tetramethoxybenzoic acid **8f**.



(LiHMDS) in THF at low temperature. To overcome the problem of poor esterification owing to steric hindrance when there are methoxy groups at both the 2 and 6 position of the benzoic acid derivative, carboxylic acids **8c**, **8f**, and **8g** were converted into the corresponding acid chlorides **26c**, **26f**, and **26g** by reaction with thionyl chloride and then reacted with the enolate generated by double deprotonation of phenol–ketone **23** (Scheme 8). This direct C acylation of the acetophenone **23** was more successful and diketones **25c** and **25g** were obtained in good yield, although the yield of diketone **25f** remained rather poor. Cyclisation of the diketones **25a**–**25g** using trimethylsilyl triflate gave protected flavonols **27a**–**27g** in moderate to excellent yield. Interestingly, a highly methoxylated flavone from *Struthiola argentea* is a potent antiparasitic lead compound for livestock health.[46] Boron tribromide deprotection of the methoxy protecting groups gave flavonols **7a**–**7e** again in excellent yield (Scheme 9). Unfortuantely, although demethylation appeared to be successful, it was not possible to obtain pure samples of flavonols **7f** and **7g**, presumably because of oxidative processes.

In summary, we report the preparation of five new chimeric compounds that combine flavon-3-ol head groups having B rings that are more highly hydroxylated or differently substituted from natural flavonols with the lipophilic decyl tail. The new head groups are potentially potent antioxidants having arrangements that would allow the formation of quinones and (or) extended quinones,[19,20,47] whereas the lipophilic tail has been shown previously to be optimal for the membrane protective properties of myricetin analogues.[23,24]

Experimental

The synthesis of carboxylic acids **8a**–**8g** were carried out by the methods described in the papers cited in the text.[32–45] Reactions carried out under argon used oven-dried or flame-dried glassware. Solutions were added via syringe. Reagents and solvents were obtained from commercial suppliers and used without further purification. Where dry solvents were used, THF was freshly distilled from sodium–benzophenone and dichloromethane (DCM) was distilled from CaH_2. Purification by column chromatography was carried out using silica gel (mesh size 35–70 μm) as the stationary phase. Melting points are uncorrected. IR spectra were obtained on a Nicolet Impact 410 FTIR, JASCO FTIR, or Shimadzu FTIR-8400S spectrometer. In some cases an attachment that allows attenuated total reflectance (ATR) was used so that the IR spectrum of the compound (solid or liquid) could be directly detected (thin layer) without any sample preparation. NMR spectra were recorded using a Bruker DPX-400. All NMR *J* values are given in Hz. DEPT was used to assign the signals in the ^{13}C NMR spectra as C, CH, CH_2, or CH_3. Mass spectra were recorded on a JEOL JMS700 spectrometer.

General procedure 1 — Esterification

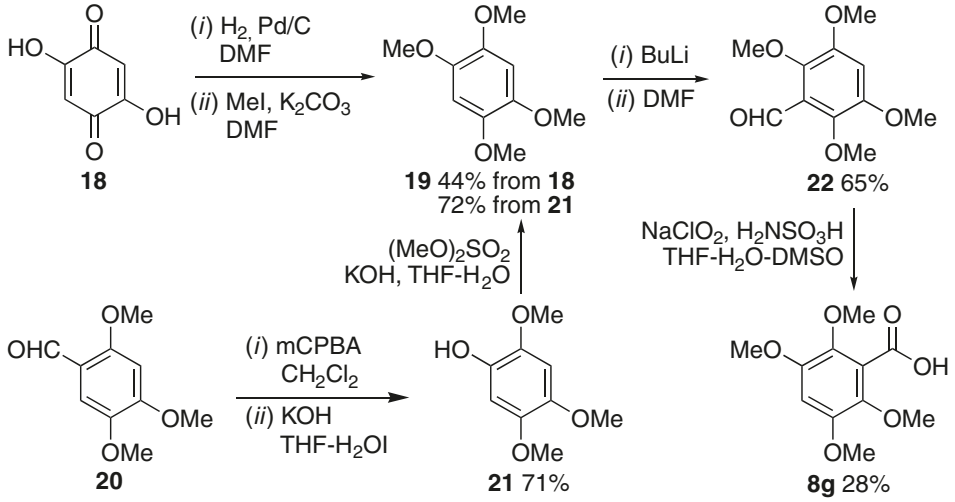
A solution of phenol **23** (0.3 mol/L), benzoic acid **8a**, **8b**, **8d**, or **8e** (1.0 equiv), EDCI (1.5 equiv), and DMAP (0.1 equiv) in dry DCM was stirred at room temperature (RT) under argon for 24 h. The solution was then diluted with DCM and washed with water. The aqueous washings were re-extracted with DCM. The combined organics were washed with brine, dried over magnesium sulfate, and concentrated under vacuum to give the ester, which was purified as described in the following.

4′-Decyl-2-methoxy-2′-(2″,3″,4″-trimethoxybenzoyloxy) acetophenone (24a)

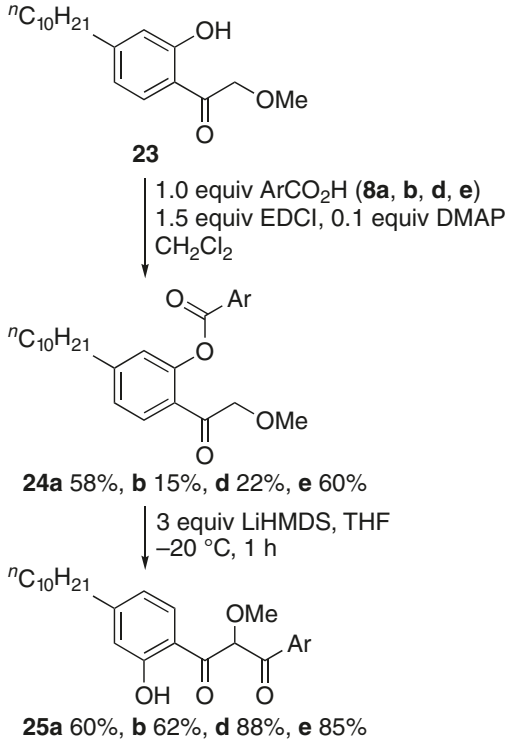
Ester **24a** (927 mg, 58%) was obtained as an oil following general procedure 1 on a 3.18 mmol scale, followed by column chromatography (SiO_2, EtOAc–hexane (1:1)). R_f (SiO_2, EtOAc–hexane (1:1)) 0.30. IR υ_{max} (thin film, cm^{-1}): 2927 (CH_2), 1743 (C=O), 1702 (C=O). δ_H (400 MHz, $CDCl_3$): 0.88 (3H, t, J 6.8 Hz, CH_2CH_3), 1.25–1.31 (14H, m, 7 × CH_2), 1.60–1.68 (2H, m, $ArCH_2CH_2$), 2.67 (2H, t, J = 7.6 Hz, $ArCH_2CH_2$), 3.39 (3H, s, OCH_3), 3.91 (3H, s, OCH_3), 3.95 (3H, s, OCH_3), 3.98 (3H, s, OCH_3), 4.55 (2H, s, OCH_2), 6.78 (1H, d, J = 8.8 Hz, H-5″), 7.07 (1H, d, J = 1.2 Hz, H-3′), 7.16 (1H, dd, J = 1.2 and 8.0 Hz, H-5′), 7.77 (1H, d, J = 8.0 Hz, H-6′), 7.88 (1H, d, J = 8.8 Hz, H-6″). δ_C (100 MHz, $CDCl_3$): 14.03 (CH_3), 22.59 (CH_2), 29.18 (CH_2), 29.23 (CH_2), 29.34 (CH_2), 29.45 (CH_2), 29.50 (CH_2), 30.70 (CH_2), 31.81 (CH_2), 35.70 (CH_2), 56.10 (CH_3), 59.17 (CH_3), 60.98 (CH_3), 61.84 (CH_3), 76.87 (CH_2), 107.06 (CH), 116.46 (C), 123.76 (CH), 126.03 (CH), 126.39 (C), 127.83 (CH), 129.62 (CH), 143.06 (C), 149.61 (C), 149.92 (C), 155.50 (C), 158.00 (C), 163.25 (C), 196.00 (C). *m/z* (EI): 500 (M^+, 5%),

Can. J. Chem. Downloaded from www.nrcresearchpress.com by Renmin University of China on 09/02/12
For personal use only.

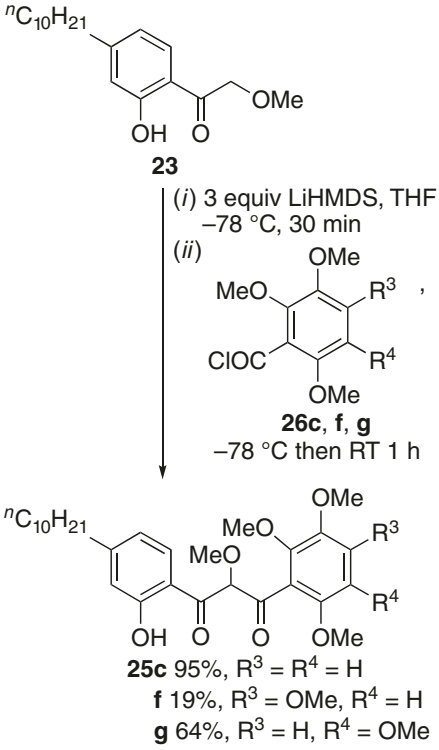
Scheme 6. Synthesis of 2,3,5,6-tetramethoxybenzoic acid **8g**.



Scheme 7. Synthesis of diketones **25a**, **25b**, **25d**, and **25e** by Baker–Venkataraman rearrangement.



Scheme 8. Synthesis of diketones **25c**, **25f**, and **25g** by enolate acylation.



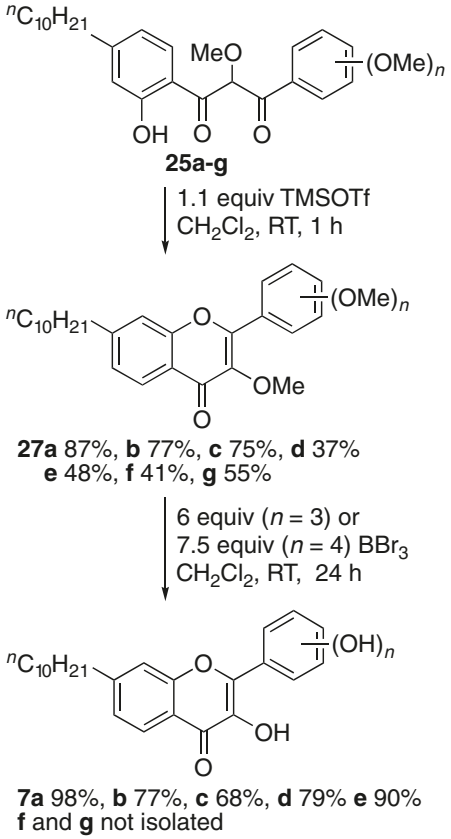
261 (15), 195 (100). HRMS calcd for $C_{29}H_{40}O_7$: (M^+) 500.2774; found: 500.2772.

4′-Decyl-2-methoxy-2′-(2″,3″,5″-trimethoxybenzoyloxy) acetophenone (24b)

Ester **24b** (257 mg, 15%) was obtained as a pale yellow oil following general procedure 1 on a 3.39 mmol scale, followed by column chromatography (SiO_2, EtOAc–hexane (1:2)). R_f (SiO_2, EtOAc–hexane (1:2)) 0.26. IR υ_{max} (ATR, cm^{-1}): 2927 (CH_2), 1751 (C=O), 1702 (C=O). δ_H (400 MHz, $CDCl_3$): 0.88 (3H, t, J = 6.6 Hz, CH_2CH_3), 1.24–1.32 (14H, m, 7 × CH_2), 1.59–1.68 (2H, m, $ArCH_2CH_2$), 2.67 (2H, t, J = 7.6 Hz, $ArCH_2CH_2$), 3.39 (3H, s, OCH_3), 3.86 (3H, s, OCH_3), 3.88 (6H, s, 2 × OCH_3), 4.55 (2H, s, OCH_2), 6.73 (1H, d, J = 2.9 Hz, H-4″), 7.08 (1H, d, J = 2.9 Hz, H-6″), 7.09 (1H, d, J = 1.4 Hz, H-3′), 7.17 (1H, dd, J = 1.4 and 8.0 Hz, H-5′), 7.77 (1H, d, J = 8.0 Hz, H-6′). δ_C (100 MHz, $CDCl_3$): 14.02 (CH_3), 22.59 (CH_2), 29.17 (CH_2), 29.23 (CH_2), 29.34 (CH_2), 29.45 (CH_2), 29.50 (CH_2), 30.70 (CH_2), 31.80 (CH_2), 35.69 (CH_2), 55.69 (CH_3), 56.03 (CH_3), 59.18 (CH_3), 61.65 (CH_3), 76.82 (CH_2), 104.58 (CH), 105.24 (CH), 123.62 (CH), 124.28 (C), 126.19 (CH), 126.32 (C), 129.64 (CH), 144.21 (C), 149.43 (C), 150.00 (C), 154.37 (C), 155.71 (C), 164.00 (C), 196.08 (C). *m/z* (EI): 500 (M^+, 2%), 306 (10), 261 (100), 195 (25). HRMS calcd for $C_{29}H_{40}O_7$: (M^+) 500.2774; found: 500.2773.

Can. J. Chem. Downloaded from www.nrcresearchpress.com by Renmin University of China on 09/02/12
For personal use only.

Scheme 9. Completion of the synthesis of 7-decyl-flavonoids.



4′-Decyl-2-methoxy-2′-(2″,4″,6″-trimethoxybenzoyloxy) acetophenone (24d)

Ester **24d** (295 mg, 22%) was obtained as a pale yellow oil following general procedure 1 on a 2.70 mmol scale except the reaction time was extended to 3 days, followed by column chromatography (SiO_2, EtOAc–hexane (1:1)). R_f (SiO_2, EtOAc–hexane (1:1)) 0.38. IR υ_{max} (thin film, cm^{-1}): 2913 (CH_2), 1751 (C=O), 1695 (C=O). δ_H (400 MHz, $CDCl_3$): 0.88 (3H, t, J = 6.8 Hz, CH_2CH_3), 1.26–1.31 (14H, m, 7 × CH_2), 1.60–1.67 (2H, m, $ArCH_2CH_2$), 2.66 (2H, t, J = 7.6 Hz, $ArCH_2CH_2$), 3.42 (3H, s, OCH_3), 3.85 (3H, s, OCH_3), 3.87 (6H, s, 2 × OCH_3), 4.65 (2H, s, OCH_2), 6.15 (2H, s, H-3″ + H-5″), 7.12–7.15 (2H, m, H-3′ + H-5′), 7.85 (1H, d, J = 8.0 Hz, H-6′). δ_C (100 MHz, $CDCl_3$): 14.04 (CH_3), 22.61 (CH_2), 29.15 (CH_2), 29.24 (CH_2), 29.38 (CH_2), 29.48 (CH_2), 29.53 (CH_2), 30.71 (CH_2), 31.82 (CH_2), 35.68 (CH_2), 55.49 (CH_3), 55.96 (CH_3), 59.17 (CH_3), 77.93 (CH_2), 90.52 (CH), 104.58 (C), 123.08 (CH), 126.22 (CH), 126.66 (C), 129.94 (CH), 149.67 (C), 150.08 (C), 158.94 (C), 163.30 (C), 164.51 (C), 196.22 (C). *m/z* (CI): 501 [$(M + H)^+$, 5%], 471 (10), 307 (100), 195 (100). HRMS calcd for $C_{29}H_{41}O_7$: $(M + H)^+$ 501.2853; found: 501.2851.

4′-Decyl-2-methoxy-2′-(2″,3″,4″,5″-tetramethoxybenzoyloxy) acetophenone (24e)

Ester **24e** (896 mg, 60%) was obtained as a pale yellow oil following general procedure 1 on a 2.82 mmol scale, followed by column chromatography (SiO_2, EtOAc–hexane (1:2)). R_f (SiO_2, EtOAc–hexane (1:2)) 0.30. IR υ_{max} (thin film, cm^{-1}): 2927 (CH_2), 1749 (C=O), 1698 (C=O). δ_H (400 MHz, $CDCl_3$): 0.88 (3H, t, J = 6.8 Hz, CH_2CH_3), 1.19–1.31 (14H, m, 7 × CH_2), 1.60–1.68 (2H, m, $ArCH_2CH_2$), 2.67 (2H, t, J = 7.6 Hz, $ArCH_2CH_2$), 3.40 (3H, s, OCH_3), 3.91 (3H, s, OCH_3), 3.92 (3H, s, OCH_3), 3.94 (3H, s, OCH_3), 4.00 (3H, s, OCH_3), 4.56 (2H, s, OCH_2), 7.08 (1H, d, J = 1.4 Hz, H-3′), 7.16 (1H, dd, J = 1.5 and 8.0 Hz, H-5′), 7.38 (1H, s, H-6″), 7.76 (1H, d, J 8.0 Hz, H-6′). δ_C (100 MHz, $CDCl_3$): 14.07 (CH_3), 22.63 (CH_2), 29.22 (CH_2), 29.27 (CH_2), 29.38 (CH_2), 29.49 (CH_2), 29.55 (CH_2), 30.74 (CH_2), 31.85 (CH_2), 35.75 (CH_2), 56.25 (CH_3), 59.24 (CH_3), 61.23 (CH_3), 61.37 (CH_3), 62.04 (CH_3), 77.72 (CH_2), 108.94 (CH), 117.81 (C), 123.78 (CH), 126.16 (CH), 126.26 (C), 129.62 (CH), 147.75 (C), 147.78 (C), 149.10 (C), 149.52 (C), 149.89 (C), 150.09 (C), 163.52, (C), 196.06 (C). *m/z* (EI): 530 (M^+, 15%), 261 (10), 225 (100). HRMS calcd for $C_{30}H_{42}O_8$: (M^+) 530.2879; found: 530.2880.

General procedure 2 — The Baker–Venkataraman rearrangement

LiHMDS (3.0 equiv, 1.0 mol/L solution in THF) was added to a stirred solution of ester **24a**, **24b**, **24d**, or **24e** (0.3 mol/L) in dry THF at –20 °C under argon. After 1 h the reaction was quenched with aqueous HCl (1 mol/L) and the mixture extracted with EtOAc (2×). The combined organics where washed with water and brine and then dried over magnesium sulfate. The diketones **25** were purified as described in the following.

1-(4′-Decyl-2′-hydroxyphenyl)-2-methoxy-3-(2″,3″,4″-trimethoxyphenyl)propan-1,3-dione (25a)

Diketone **25a** (387 mg, 60%) was obtained as a bright yellow solid following general procedure 2 on a 1.28 mmol scale, followed by column chromatography (SiO_2, EtOAc–hexane (1:2)). R_f (SiO_2, EtOAc–hexane (1:2)) 0.29; mp 60–62 °C. IR υ_{max} (thin film, cm^{-1}): 3409 (OH), 2927 (CH_2), 1685 (C=O), 1637 (C=O). δ_H (400 MHz, $CDCl_3$): 0.88 (3H, t, J = 6.8 Hz, CH_2CH_3), 1.26–1.31 (14H, m, 7 × CH_2), 1.58–1.63 (2H, m, $ArCH_2CH_2$), 2.60 (2H, t, J = 7.5 Hz, $ArCH_2CH_2$), 3.57 (3H, s, OCH_3), 3.79 (3H, s, OCH_3), 3.80 (3H, s, OCH_3), 3.91 (3H, s, OCH_3), 5.78 (1H, s, H-2), 6.73 (1H, d, J = 8.8 Hz, H-5″), 6.76 (1H, dd, J = 1.6 and 8.4 Hz, H-5′), 6.80 (1H, d, J = 1.6 Hz, H-3′), 7.66 (1H, d, J = 8.8 Hz, H-6″), 7.81 (1H, d, J = 8.4 Hz, H-6′), 11.72 (1H, s, OH). δ_C (100 MHz, $CDCl_3$): 14.08 (CH_3), 22.65 (CH_2), 29.24 (CH_2), 29.29 (CH_2), 29.41 (CH_2), 29.51 (CH_2), 29.56 (CH_2), 30.50 (CH_2), 31.86 (CH_2), 36.28 (CH_2), 56.13 (CH_3), 58.77 (CH_3), 60.80 (CH_3), 61.01 (CH_3), 88.19 (CH), 107.14 (CH), 116.20 (C), 117.76 (CH), 119.90 (CH), 123.04 (C), 126.21 (CH), 130.79 (CH), 141.29 (C), 153.59 (C), 153.66 (C), 158.36 (C), 163.28 (C), 193.54 (C), 198.84 (C). *m/z* (EI): 500 (M^+, 1%), 261 (5), 195 (100). HRMS calcd for $C_{29}H_{40}O_7$: (M^+) 500.2774; found: 500.2773.

1-(4′-Decyl-2′-hydroxyphenyl)-2-methoxy-3-(2″,3″,5″-trimethoxyphenyl)propan-1,3-dione (25b)

Diketone **25b** was obtained as a yellow oil (144 mg, 62%) and as a complex mixture with cyclic diastereomers and keto–enol forms following general procedure 2 on a 0.46 mmol scale and then column chromatography (SiO_2, EtOAc–hexane (1:2)). The mixture was used in the next step without further purification.

Can. J. Chem. Downloaded from www.nrcresearchpress.com by Renmin University of China on 09/02/12
For personal use only.

1-(4′-Decyl-2′-hydroxyphenyl)-2-methoxy-3-(2″,4″,6″-trimethoxyphenyl)propan-1,3-dione (25d)

Diketone **25d** (222 mg, 88%) was obtained as a yellow oil following general procedure 2 on a 0.50 mmol scale, followed by column chromatography (SiO_2, EtOAc–hexane (1:1)). R_f (SiO_2, EtOAc–hexane (1:1)) 0.43.IR υ_{max} (thin film, cm^{-1}): 3469 (OH), 2925 (CH_2), 1725 (C=O), 1589 (Ar) δ_H (400 MHz, $CDCl_3$): 0.88 (3H, t, J = 6.6 Hz, CH_2CH_3), 1.26–1.30 (14H, m, 7 × CH_2), 1.56–1.60 (2H, m, $ArCH_2CH_2$), 2.56 (2H, t, J 7.5 Hz, $ArCH_2CH_2$), 3.52 (3H, s, OCH_3), 3.61 (6H, s, 2 × OCH_3), 3.79 (3H, s, OCH_3), 5.26 (1H, s, H-2), 6.01 (2H, s, H-3″ and -5″), 6.66 (1H, dd, J = 1.6 and 8.3 Hz, H-5′), 6.74 (1H, d, J = 1.4 Hz, H-3′), 7.94 (1H, d, J = 8.3 Hz, H-6′), 11.81 (1H, s, OH). δ_C (100 MHz, $CDCl_3$): 14.07 (CH_3), 22.64 (CH_2), 29.21 (CH_2), 29.27 (CH_2), 29.40 (CH_2), 29.51 (CH_2), 29.56 (CH_2), 30.56 (CH_2), 31.85 (CH_2), 36.25 (CH_2), 55.36 (CH_3), 56.51 (CH_3), 58.77 (CH_3), 90.48 (CH), 93.84 (CH), 109.51 (C), 116.21 (C), 117.09 (CH), 119.43 (CH), 132.03 (CH), 153.27 (C), 158.73 (C), 163.05 (C), 163.38 (C), 196.33 (C), 198.82 (C). *m/z* (EI): 500 (M^+, 1%), 261 (8), 195 (100). HRMS calcd for $C_{29}H_{40}O_7$: (M^+) 500.2774; found: 500.2773.

1-(4′-Decyl-2′-hydroxyphenyl)-2-methoxy-3-(2″,3″,4″,5″-tetramethoxyphenyl)propan-1,3-dione (25e)

Diketone **25e** (737 mg, 85%) was obtained as an orange oil following general procedure 2 on a 1.63 mmol scale, without further purification. R_f (SiO_2, EtOAc–hexane (1:1)) 0.45. IR υ_{max} (thin film, cm^{-1}): 3401 (OH), 2921 (CH_2), 1689 (C=O), 1638 (C=O). δ_H (400 MHz, $CDCl_3$): 0.88 (3H, t, J = 6.6 Hz, CH_2CH_3), 1.26–1.32 (14H, m, 7 × CH_2), 1.59–1.64 (2H, m, $ArCH_2CH_2$), 2.56 (2H, t, J = 7.5 Hz, $ArCH_2CH_2$), 3.60 (3H, s, OCH_3), 3.72 (3H, s, OCH_3), 3.84 (3H, s, OCH_3), 3.87 (3H, s, OCH_3), 3.93 (3H, s, OCH_3), 5.84 (1H, s, H-2), 6.78 (1H, dd, J = 1.6 and 8.2 Hz, H-5′), 6.81 (1H, d, J = 1.6 Hz, H-3′), 7.20 (1H, s, H-6″), 7.80 (1H, d, J 8.3 Hz, H-6′), 11.60 (1H, s, OH). δ_C (100 MHz, $CDCl_3$): 14.04 (CH_3), 22.61 (CH_2), 29.21 (CH_2), 29.25 (CH_2), 29.38 (CH_2), 29.47 (CH_2), 29.53 (CH_2), 30.47 (CH_2), 31.83 (CH_2), 36.25 (CH_2), 56.08 (CH_3), 58.75 (CH_3), 61.03 (CH_3), 61.06 (CH_3), 61.12 (CH_3) 87.73 (CH), 106.72 (CH), 116.19 (C), 117.78 (CH), 119.90 (CH), 123.59 (C), 130.66 (CH), 148.30 (C), 148.21 (C), 149.28 (C), 153.62 (C), 163.27 (C), 196.68 (C), 198.66 (C). *m/z* (EI): 530 (M^+, 10%), 270 (12), 225 (100), 195 (25). HRMS calcd for $C_{30}H_{42}O_8$: (M^+); 530.2880; found: 530.2879.

General procedure 3 — C-acylation

Thionyl chloride was added to benzoic acid **8c**, **8f**, or **8g** under argon to give a 1.0 mol/L solution and the mixture was then heated under reflux for 2 h. After cooling, the excess thionyl chloride was removed under vacuum to give acid chloride **26c**, **26f**, or **26g**, which was then used in the next reaction without further purification. LiHMDS (3.0 equiv, 1.0 mol/L solution in THF) was added to a stirred solution of phenol **23** in dry THF (0.3 mol/L solution) at –78 °C under an atmosphere of argon. The solution was stirred at –78 °C for 30 min. After this time a solution of the freshly prepared acid chloride in THF was added. After stirring at –78 °C for a further 5 min, the solution was immediately warmed to RT and stirred for 1 h. The reaction mixture was then quenched with aqueous HCl (1 mol/L) and extracted with EtOAc (2×). The combined organics were washed with water, then brine, and then were dried over magnesium sulfate and concentrated under vacuum. The diketones **25** were purified as described in the following.

1-(4′-Decyl-2′-hydroxyphenyl)-2-methoxy-3-(2″,3″,6″-trimethoxyphenyl)propan-1,3-dione (25c)

Diketone **25c** (536 mg, 95%) was obtained as a golden yellow oil and as a complex mixture of cyclic diastereomers, diketone, and keto–enol forms following general procedure 3 on a 1.13 mmol scale and was used in the next step without further purification. Using general procedure 3, diketone **25c** was synthesized on a 1.13 mmol scale. The diketone, obtained as a golden yellow oil, was used without further purification in the next step.

1-(4′-Decyl-2′-hydroxyphenyl)-2-methoxy-3-(2″,3″,4″,6″-tetramethoxyphenyl)propan-1,3-dione (25f)

Diketone **25f** (148 mg, 19%) was obtained as a golden yellow oil following general procedure 3 on a 1.48 mmol scale, followed by column chromatography (SiO_2, EtOAc–hexane (1:2)). R_f (SiO_2, EtOAc–hexane (1:2)) 0.22. In $CDCl_3$ the product existed as a 6:1 ratio of diketone and keto–enol forms. NMR data given is for the diketone form **25f**. IR υ_{max} (thin film, cm^{-1}): 3488 (OH), 2927 (CH_2), 1722 (C=O), 1633 (C=O). δ_H (400 MHz, $CDCl_3$): 0.88 (3H, t, J = 6.6 Hz, CH_2CH_3), 1.24–1.30 (14H, m, 7 × CH_2), 1.57–1.61 (2H, m, $ArCH_2CH_2$), 2.56 (2H, t, J = 7.8 Hz, $ArCH_2CH_2$), 3.61 (3H, s, OCH_3), 3.68 (3H, s, OCH_3), 3.77 (3H, s, OCH_3), 3.78 (3H, s, OCH_3), 3.86 (3H, s, OCH_3), 5.31 (1H, s, H-2), 6.17 (1H, s, H-5″), 6.68 (1H, dd, J = 1.6 and 8.3 Hz, H-5′), 6.75 (1H, d, J = 1.6 Hz, H-3″), 7.95 (1H, d, J = 8.3 Hz, H-6″), 11.81 (1H, s, OH). δ_C (100 MHz, $CDCl_3$): 14.00 (CH_3), 22.57 (CH_2), 29.14 (CH_2), 29.20 (CH_2), 29.33 (CH_2), 29.43 (CH_2), 29.48 (CH_2), 30.47 (CH_2), 31.77 (CH_2), 36.18 (CH_2), 56.66 (CH_3), 55.98 (CH_3), 58.66 (CH_3), 60.88 (CH_3), 61.49 (CH_3), 91.67 (CH), 93.45 (CH), 113.93 (C), 116.20 (C), 117.14 (CH), 119.47 (CH), 131.80 (CH), 135.63 (C), 151.55 (C), 153.01 (C), 153.33 (C), 155.96 (C), 163.03 (C), 195.90 (C), 198.52 (C). *m/z* (EI): 530 (M^+, 1%), 499.3 (1), 225.1 (100), 195 (6). HRMS calcd for $C_{30}H_{42}O_8$: (M^+) 530.2880; found: 530.2882.

1-(4′-Decyl-2′-hydroxyphenyl)-2-methoxy-3-(2″,3″,5″,6″-tetramethoxyphenyl)propan-1,3-dione (25g)

Diketone **25g** (538 mg, 64%) was obtained as a golden yellow oil following general procedure 3 on a 1.82 mmol scale, followed by column chromatography (SiO_2, EtOAc–hexane (1:2)). R_f (SiO_2, EtOAc–hexane (1:2)) 0.25. In $CDCl_3$ the product existed as a 4:1 ratio of diketone and keto–enol forms. NMR data given is for the diketone form **25g**. υ_{max} (thin film, cm^{-1}): 3469 (OH), 2927 (CH_2), 1720 (C=O), 1633 (C=O). δ_H (400 MHz, $CDCl_3$): 0.88 (3H, t, J = 6.6 Hz, CH_2CH_3), 1.24–1.30 (14H, m, 7 × CH_2), 1.57–1.61 (2H, m, $ArCH_2CH_2$), 2.56 (2H, t, J = 7.8 Hz, $ArCH_2CH_2$), 3.50 (3H, s, OCH_3), 3.66 (6H, s, 2 × OCH_3), 3.83 (6H, s, 2 × OCH_3), 5.27 (1H, s, H-2), 6.58 (1H, s, H-4″), 6.69 (1H, dd, J = 1.6 and 8.2 Hz, H-5′), 6.76 (1H, d, J = 1.6 Hz, H-3″), 7.98 (1H, d, J = 8.3 Hz, H-6′), 11.78 (1H, s, OH). δ_C (100 MHz, $CDCl_3$): 13.98 (CH_3), 22.55

Can. J. Chem. Downloaded from www.nrcresearchpress.com by Renmin University of China on 09/02/12
For personal use only.

(CH_2), 29.11 (CH_2), 29.19 (CH_2), 29.32 (CH_2), 29.42 (CH_2), 29.47 (CH_2), 30.39 (CH_2), 31.76 (CH_2), 36.17 (CH_2), 56.41 (CH_3), 58.78 (CH_3), 61.58 (CH_3), 93.38 (CH), 101.28 (CH), 116.20 (C), 117.22 (CH), 119.46 (CH), 127.67 (C), 131.79 (CH), 138.88 (C), 148.55 (C), 153.39 (C), 163.10 (C), 197.16 (C), 198.18 (C). *m/z* (EI): 530 (M^+, 15%), 499 (10), 261 (20), 225 (100), 195 (15). HRMScalcd for $C_{30}H_{42}O_8$: (M^+) 530.2879; found: 530.2878.

General procedure 4 — Cyclization

TMSOTf (1.1 equiv) was added to a stirred solution of the diketone **25a**–**25g** (0.3 mol/L) in dry DCM at RT under argon. After stirring at RT for 1 h, the reaction mixture was diluted with DCM and quenched with saturated aqueous $NaHCO_3$. The layers were separated and the aqueous layer extracted with DCM. The combined organics were washed with brine, dried over magnesium sulfate, and concentrated under vacuum. The flavone derivatives **27** were purified further where necessary as described in the following.

7-Decyl-3,2′,3′,4′-tetramethoxyflavone (27a)

Flavone **27a** (251 mg, 87%) was obtained as a viscous yellow oil following general procedure 4 on a 0.59 mmol scale. IR υ_{max} (thin film, cm^{-1}): 2929 (CH_2), 1621 (C=O). δ_H (400 MHz, $CDCl_3$): 0.88 (3H, t, J = 6.8 Hz, CH_2CH_3), 1.26–1.31 (14H, m, 7 × CH_2), 1.62–1.70 (2H, m, $ArCH_2CH_2$), 2.72 (2H, t, J = 7.5 Hz, $ArCH_2CH_2$), 3.80 (3H, s, OCH_3), 3.93 (3H, s, OCH_3), 3.94 (3H, s, OCH_3), 3.95 (3H, s, OCH_3), 6.78 (1H, d, J = 8.7 Hz, H-5′), 7.19–7.25 (3H, m, H-6, 8 and 6′), 8.18 (1H, d, J = 8.2 Hz, H-5). δ_C (100 MHz, $CDCl_3$): 14.06 (CH_3), 22.63 (CH_2), 29.15 (CH_2), 29.39 (CH_2), 29.49 (CH_2), 29.54 (CH_2), 29.54 (CH_2), 30.89 (CH_2), 31.84 (CH_2), 35.99 (CH_2), 56.07 (CH_3), 60.40 (CH_3), 60.88 (CH_3), 61.48 (CH_3), 107.00 (CH), 117.03 (CH), 118.04 (C), 122.47 (C), 125.40 (CH), 125.46 (CH), 125.60 (CH), 141.69 (C), 142.37 (C), 149.55 (C), 152.36 (C), 155.61 (C), 155.75 (C), 155.78 (C), 174.76 (C). *m/z* (EI): 482 (M^+, 60%), 467 (75), 451 (100). HRMS calcd for $C_{29}H_{38}O_6$: (M^+) 482.2669; found: 482.2666.

7-Decyl-3,2′,3′,5′-tetramethoxyflavone (27b)

Flavone **27b** (102 mg, 77%) was obtained as a viscous yellow oil following general procedure 4 on a 0.27 mmol scale. IR υ_{max} (thin film, cm^{-1}): 2925 (CH_2), 1619 (C=O). δ_H (400 MHz, $CDCl_3$): 0.88 (3H, t, J = 6.8 Hz, CH_2CH_3), 1.24–1.32 (14H, m, 7 × CH_2), 1.62–1.70 (2H, m, $ArCH_2CH_2$), 2.72 (2H, t, J = 7.5 Hz, $ArCH_2CH_2$), 3.81 (6H, s, 2 × OCH_3), 3.82 (3H, s, OCH_3), 3.91 (3H, s, OCH_3), 6.65 (1H, d, J = 2.9 Hz, H-4′), 6.66 (1H, d, J = 2.9 Hz, H-6′), 7.22–7.25 (2H, m, H-6 and H-8), 8.19 (1H, d, J = 8.1 Hz, H-5). δ_C (100 MHz, $CDCl_3$): 14.08 (CH_3), 22.64 (CH_2), 29.16 (CH_2), 29.27 (CH_2), 29.40 (CH_2), 29.50 (CH_2), 29.55 (CH_2), 30.87 (CH_2), 31.85 (CH_2), 36.01 (CH_2), 55.72 (CH_3), 55.90 (CH_3), 60.56 (CH_3), 61.50 (CH_3), 102.68 (CH), 104.60 (CH), 117.08 (CH), 125.38 (C), 125.60 (CH), 125.65 (CH), 141.60 (C), 141.72 (C), 149.74 (C), 153.69 (C), 155.79 (C), 174.75 (C). *m/z* (EI): 482 (M^+, 55%), 467 (70), 451 (100). HRMS calcd for $C_{29}H_{38}O_6$: (M^+) 482.2669; found: 482.2666.

7-Decyl-3,2′,3′,6′-tetramethoxyflavone (27c)

Flavone **27c** (77 mg, 75%) was obtained as a viscous yellow oil following general procedure 4 on a 0.23 mmol scale, followed by column chromatography (SiO_2, EtOAc–hexane (1:2)). R_f (SiO_2, EtOAc–hexane (1:2)) 0.21. IR υ_{max} (thin film, cm^{-1}): 2927 (CH_2), 1623 (C=O). δ_H (400 MHz, $CDCl_3$): 0.87 (3H, t, J = 6.8 Hz, CH_2CH_3), 1.22–1.31 (14H, m, 7 × CH_2), 1.62–1.69 (2H, m, $ArCH_2CH_2$), 2.71 (2H, t, J = 7.5 Hz, $ArCH_2CH_2$), 3.75 (3H, s, OCH_3), 3.81 (3H, s, OCH_3), 3.83 (3H, s, OCH_3), 3.86 (3H, s, OCH_3), 6.69 (1H, d, J = 9.1 Hz, H-4′), 7.02 (1H, d, J = 9.1 Hz, H-3′), 7.21–7.24 (2H, m, H-6 and H-8), 8.21 (1H, d, J = 8.1 Hz, H-5). δ_C (100 MHz, $CDCl_3$): 14.06 (CH_3), 22.63 (CH_2), 29.17 (CH_2), 29.26 (CH_2), 29.39 (CH_2), 29.48 (CH_2), 29.53 (CH_2), 30.84 (CH_2), 31.83 (CH_2), 35.98 (CH_2), 56.08 (CH_3), 56.47 (CH_3), 60.21 (CH_3), 61.29 (CH_3), 105.91 (CH), 115.09 (CH), 115.57 (C), 117.208 (CH), 122.61 (C), 125.41 (CH), 125.58 (CH), 142.65 (C), 146.65 (C), 148.41 (C), 149.40 (C), 151.70 (C), 153.09 (C), 156.19 (C), 174.68 (C). *m/z* (EI): 482 (M^+, 15%), 451 (100). HRMS calcd for $C_{29}H_{38}O_6$: (M^+) 482.2669; found: 482.2668.

7-Decyl-3,2′,4′,6′-tetramethoxyflavone (27d)

Flavone **27d** (77 mg, 37%) was obtained as a viscous oil following general procedure 4 on a 0.43 mmol scale, followed by column chromatography (SiO_2, EtOAc–hexane (1:2)). R_f (SiO_2, EtOAc–hexane (1:2)) 0.15. δ_H (400 MHz, $CDCl_3$): 0.87 (3H, t, J = 6.7 Hz, CH_2CH_3), 1.26–1.31 (14H, m, 7 × CH_2), 1.61–1.69 (2H, m, $ArCH_2CH_2$), 2.70 (2H, t, J = 7.5 Hz, $ArCH_2CH_2$), 3.76 (6H, s, 2 × OCH_3), 3.79 (3H, s, OCH_3), 3.87 (3H, s, OCH_3), 6.21 (2H, s, H-3′and H-5′), 7.19 (1H, dd, J = 1.4 and 8.2 Hz, H-6), 7.24 (1H, s, H-8), 8.18 (1H, d, J = 8.2 Hz, H-5). δ_C (100 MHz, $CDCl_3$): 14.02 (CH_3), 22.58 (CH_2), 29.13 (CH_2), 29.22 (CH_2), 29.35 (CH_2), 29.44 (CH_2), 29.49 (CH_2), 30.80 (CH_2), 31.79 (CH_2), 35.91 (CH_2), 55.37 (CH_3), 55.77 (CH_3), 60.01 (CH_3), 90.58 (CH), 102.19 (C), 117.22 (CH), 122.65 (C), 125.08 (CH), 125.45 (CH), 142.98 (C), 148.98 (C), 153.42 (C), 156.29 (C), 159.31 (C), 163.20 (C), 174.68 (C). *m/z* (EI): 482 (M^+, 10%), 451 (100). HRMS calcd for $C_{29}H_{38}O_6$: (M^+) 482.2669; found: 482.2666.

7-Decyl-3,2′,3′,4′,5′-pentamethoxyflavone (27e)

Flavone **27e** (305 mg, 48%) was obtained as a viscous yellow oil following general procedure 4 on a 1.23 mmol scale, followed by column chromatography (SiO_2, EtOAc–hexane (1:2)). R_f (SiO_2, EtOAc–hexane (1:2)) 0.24. IR υ_{max} (thin film, cm^{-1}): 2927 (CH_2), 1646 (C=O). δ_H (400 MHz, $CDCl_3$): 0.88 (3H, t, J = 6.8 Hz, CH_2CH_3), 1.24–1.32 (14H, m, 7 × CH_2), 1.63–1.71 (2H, m, $ArCH_2CH_2$), 2.73 (2H, t, J = 7.6 Hz, $ArCH_2CH_2$), 3.84 (3H, s, OCH_3), 3.86 (3H, s, OCH_3), 3.89 (3H, s, OCH_3), 3.99 (6H, s, 2 × OCH_3), 6.77 (1H, s, H-6′), 7.23 (1H, dd, J = 1.3 and 8.2 Hz, H-6), 7.26 (1H, s, H-8), 8.19 (1H, d, J = 8.2 Hz, H-5). δ_C (100 MHz, $CDCl_3$): 14.01 (CH_3), 22.58 (CH_2), 29.10 (CH_2), 29.20 (CH_2), 29.33 (CH_2), 29.44 (CH_2), 29.48 (CH_2), 30.82 (CH_2), 31.78 (CH_2), 35.94 (CH_2), 56.23 (CH_3), 60.42 (CH_3), 61.14 (2 × CH_3), 61.65 (CH_3), 107.86 (CH), 116.98 (CH), 119.33 (C), 122.40 (C), 125.51 (CH), 125.57 (CH), 141.59 (C), 144.97 (C), 146.25 (C), 147.24 (C), 149.18 (C), 149.62 (C), 155.37 (C), 155.69 (C), 174.66 (C). *m/z* (EI): 512 (M^+, 50%), 497 (80), 481 (100), 280 (70), 91 (55). HRMS calcd for $C_{30}H_{40}O_7$: (M^+) 512.2774; found: 512.2772.

Can. J. Chem. Downloaded from www.nrcresearchpress.com by Renmin University of China on 09/02/12
For personal use only.

7-Decyl-3,2′,3′,4′,6′-pentamethoxyflavone (27f)

Flavone **27f** (40 mg, 41%) was obtained as a yellow oil following general procedure 4 on a 0.19 mmol scale, followed by column chromatography (SiO_2, EtOAc–hexane (1:2)). R_f (SiO_2, EtOAc–hexane (1:2)) 0.13. IR υ_{max} (thin film, cm^{-1}): 2927 (CH_2), 1625 (C=O). δ_H (400 MHz, $CDCl_3$): 0.87 (3H, t, J = 6.8 Hz, CH_2CH_3), 1.24–1.31 (14H, m, 7 × CH_2), 1.62–1.69 (2H, m, $ArCH_2CH_2$), 2.71 (2H, t, J = 7.6 Hz, $ArCH_2CH_2$), 3.77 (3H, s, OCH_3), 3.83 (3H, s, OCH_3), 3.85 (3H, s, OCH_3), 3.88 (3H, s, OCH_3), 3.95 (3H, s, OCH_3), 6.37 (1H, s, H-5′), 7.21 (1H, dd, J = 1.3 and 8.2 Hz, H-6), 7.24 (1H, s, H-8), 8.20 (1H, d, J = 8.2 Hz, H-5). δ_C (100 MHz, $CDCl_3$): 14.15 (CH_3), 22.63 (CH_2), 29.18 (CH_2), 29.26 (CH_2), 29.39 (CH_2), 29.49 (CH_2), 29.54 (CH_2), 30.86 (CH_2), 31.84 (CH_2), 35.98 (CH_2), 56.07 (CH_3), 56.11 (CH_3), 60.14 (CH_3), 61.04 (CH_3), 61.48 (CH_3), 92.10 (CH), 107.14 (C), 117.18 (CH), 122.67 (C), 125.29 (CH), 125.57 (CH), 136.10 (C), 142.91 (C), 149.24 (C), 152.75 (C), 152.95 (C), 153.93(C), 155.74 (C), 156.17 (C), 174.69 (C). m/z (EI): 512 (M^+, 25%), 481 (100). HRMS calcd for $C_{30}H_{40}O_7$: (M^+) 512.2774; found: 512.2773.

7-Decyl-3,2′,3′,5′,6′-pentamethoxyflavone (27g)

Flavone **27g** (244 mg, 44%) was obtained as a yellow solid following general procedure 4 on a 1.09 mmol scale, followed by column chromatography (SiO_2, EtOAc–hexane (1:1)). R_f (SiO_2, EtOAc–hexane (1:1)) 0.31; mp 93–96 °C. IR υ_{max} (ATR, cm^{-1}): 2921 (CH_2), 1619 (C=O). δ_H (400 MHz, $CDCl_3$): 0.87 (3H, t, J = 6.8 Hz, CH_2CH_3), 1.21–1.31 (14H, m, 7 × CH_2), 1.62–1.70 (2H, m, $ArCH_2CH_2$), 2.71 (2H, t, J = 7.5 Hz, $ArCH_2CH_2$), 3.76 (6H, s, 2 × OCH_3), 3.83 (3H, s, OCH_3), 3.93 (6H, s, 2 × OCH_3), 6.72 (1H, s, H-4′), 7.23–7.25 (2H, m, H-6 and H-8), 8.21 (1H, d, J = 8.6 Hz, H-5). δ_C (100 MHz, $CDCl_3$): 14.06 (CH_3), 22.63 (CH_2), 29.18 (CH_2), 29.26 (CH_2), 29.38 (CH_2), 29.48 (CH_2), 29.54 (CH_2), 30.84 (CH_2), 31.84 (CH_2), 35.98 (CH_2), 56.56 (CH_3), 60.34 (CH_3), 61.48 (CH_3), 101.53 (CH), 117.09 (CH), 120.89 (C), 122.68 (C), 125.48 (CH), 125.64 (CH), 140.78 (C), 142.57 (C), 148.91 (C), 149.48 (C), 152.76 (C), 156.02 (C), 174.61 (C). m/z (EI): 512 (M^+, 55%), 481 (100). HRMS calcd for $C_{30}H_{40}O_7$: (M^+) 512.2774; found: 512.2772.

General procedure 5 — Deprotection

Boron tribromide (1.0 mol/L in DCM, 1.25 equiv per OMe to be removed) was added to a stirred solution of the flavone **27** in DCM (0.3 mol/L) at RT under argon. The solution was stirred overnight at RT. After this time MeOH was added slowly (0.5 mL per 1.0 mL of BBr_3 solution used). Once gas evolution had ceased, the reaction mixture was heated under reflux for 30 min and then concentrated under vacuum. Water (5.0 mL per mmol of starting material) was added and the resulting suspension placed in a sonic bath for 15 min. The solid was filtered off, washed with water, and then dried under vacuum over P_2O_5 to give the flavonol **7**.

7-Decyl-3,2′,3′,4′-tetrahydroxyflavone (7a)

Flavonol **7a** was obtained as a greeny brown amorphous solid (188 mg, 98%) following general procedure 5 on a 0.45 mmol scale. mp decomp >90 °C. IR υ_{max} (ATR, cm^{-1}): 3203 (OH), 2915 (CH_2), 1594 (C=O). δ_H (400 MHz, D_6-DMSO): 0.84 (3H, t, J = 6.8 Hz, CH_2CH_3), 1.22–1.28 (14H, m, 7 × CH_2), 1.60–1.74 (2H, m, $ArCH_2CH_2$), 2.72 (2H, t, J = 7.4 Hz, $ArCH_2CH_2$), 6.44 (1H, d, J = 8.5 Hz, H-5′), 6.81 (1H, d, J = 8.5 Hz, H-6′), 7.28 (1H, d, J = 8.2 Hz, H-6), 7.39 (1H, s, H-8), 8.01 (1H, d, J 8.2 Hz, H-5). δ_C (100 MHz, D_6-DMSO): 14.28 (CH_3), 22.43 (CH_2), 28.91 (CH_2), 29.02 (CH_2), 29.14 (CH_2), 29.29 (CH_2), 29.30 (CH_2), 30.70 (CH_2), 31.62 (CH_2), 35.37 (CH_2), 107.53 (CH), 111.00 (C), 117.50 (CH), 120.26 (C), 120.69 (CH), 124.95 (CH), 125.39 (CH), 133.84 (C), 138.27 (C), 145.32 (C), 148.14 (C), 148.31 (C), 149.06 (C), 155.50 (C), 172.66 (C). m/z (FAB): 427 [$(M + H)^+$, 100%]. HRMS calcd for $C_{25}H_{31}O_6$: [$(M + H)^+$] 427.2120; found: 427.2121.

7-Decyl-3,2′,3′,5′-tetrahydroxyflavone (7b)

Flavonol **7b** was obtained as a red-brown amorphous solid (64 mg, 77%) following general procedure 5 on a 0.20 mmol scale. mp decomp >90 °C. IR υ_{max} (ATR, cm^{-1}): 3210 (OH), 2919 (CH_2), 1589 (C=O). δ_H (400 MHz, D_6-DMSO): 0.83 (3H, m, CH_2CH_3), 1.22–1.28 (14H, m, 7 × CH_2), 1.60–1.64 (2H, m, $ArCH_2CH_2$), 2.72 (2H, t, J = 7.5 Hz, $ArCH_2CH_2$), 6.31 (1H, d, J = 2.5 Hz, H-4′), 6.43 (1H, d, J = 2.5 Hz, H-6′), 7.28 (1H, d, J = 7.9 Hz, H-6), 7.41 (1H, s, H-8), 8.00 (1H, d, J = 8.2 Hz, H-5). δ_C (100 MHz, D_6-DMSO): 14.30 (CH_3), 22.44 (CH_2), 28.92 (CH_2), 29.02 (CH_2), 29.14 (CH_2), 29.30 (CH_2), 29.31 (CH_2), 30.71 (CH_2), 31.63 (CH_2), 35.38 (CH_2), 105.56 (CH), 106.15 (CH), 117.53 (CH), 119.35 (C), 120.26 (C), 124.99 (CH), 125.51 (CH), 136.67 (C), 138.62 (C), 147.08 (C), 147.64 (C), 149.27 (C), 150.01 (C), 155.52 (C), 172.84 (C). m/z (FAB): 427 [$(M + H)^+$, 75%], 261 (80), 86 (100). HRMS calcd for $C_{25}H_{31}O_6$: [$(M + H)^+$] 427.2120; found: 427.2120.

7-Decyl-3,2′,3′,6′-tetrahydroxyflavone (7c)

Flavonol **7c** was obtained as a red-brown amorphous solid (136 mg, 68%) following general procedure 5 on a 0.46 mmol scale. mp decomp >90 °C. IR υ_{max} (ATR, cm^{-1}): 3355 (OH), 2919 (CH_2), 1589 (C=O). δ_H (400 MHz, D_6-DMSO): 0.85 (3H, t, J 6.8 Hz, CH_2CH_3), 1.22–1.28 (14H, m, 7 × CH_2), 1.61–63 (2H, m, $ArCH_2CH_2$), 2.72 (2H, t, J = 7.2 Hz, $ArCH_2CH_2$), 6.21 (1H, d, J = 8.8 Hz, H-5′), 6.71 (1H, d, J = 8.4 Hz, H-4′), 7.29 (1H, d, J = 8.2 Hz, H-6), 7.40 (1H, s, H-8), 8.03 (1H, d, J = 8.2 Hz, H-5), 8.53 (1H, s, OH), 8.57 (1H, s, OH), 8.69 (1H, s, OH), 8.85 (1H, s, OH). δ_C (100 MHz, D_6-DMSO): 13.93 (CH_3), 22.07 (CH_2), 28.58 (CH_2), 28.66 (CH_2), 28.80 (CH_2), 28.95 (CH_2), 28.96 (CH_2), 30.41 (CH_2), 31.25 (CH_2), 35.00 (CH_2), 104.86 (CH), 107.65 (C), 117.10 (CH), 117.18 (CH), 120.11 (C), 124.61 (CH), 124.90 (CH), 137.38 (C), 139.95 (C), 144.60 (C), 145.10 (C), 148.51 (C), 148.75 (C), 155.53 (C), 172.54 (C). m/z (FAB): 427 [$(M + H)^+$, 25%], 261 (15), 169 (20), 86 (100). HRMS calcd for $C_{25}H_{31}O_6$: [$(M + H)^+$] 427.2121; found: 427.2120.

7-Decyl-3,2′,4′,6′-tetrahydroxyflavone (7d)

Flavonol **7d** was obtained as a pale green amorphous solid (45 mg, 79%) following general procedure 5 on a 0.13 mmol scale. mp decomp >90 °C. IR υ_{max} (ATR, cm^{-1}): 3207 (OH), 2917 (CH_2), 1614 (C=O). δ_H (400 MHz, D_6-DMSO): 0.85 (3H, t, J = 6.7 Hz, CH_2CH_3), 1.22–1.28 (14H, m, 7 × CH_2), 1.60–1.64 (2H, m, $ArCH_2CH_2$), 2.71 (2H, t, J = 7.7 Hz,

Can. J. Chem. Downloaded from www.nrcresearchpress.com by Renmin University of China on 09/02/12
For personal use only.

ArCH_2CH$_2$), 5.89 (2H, s, H-3′ and H-5′), 7.26 (1H, dd, J = 1.2 and 8.4 Hz, H-6), 7.37 (1H, s, H-8), 8.00 (1H, d, J = 8.4 Hz, H-5), 8.32 (1H, broad s, OH), 9.29 (2H, s, OH), 9.38 (1H, s, OH). δ_C (100 MHz, D_6-DMSO): 14.29 (CH_3), 22.43 (CH_2), 28.93 (CH_2), 29.01 (CH_2), 29.13 (CH_2), 29.30 (CH_2), 29.32 (CH_2), 30.76 (CH_2), 31.62 (CH_2), 35.36 (CH_2), 94.38 (CH), 98.91 (C), 117.54 (CH), 120.43 (C), 124.93 (CH), 125.14 (CH), 140.46 (C), 146.09 (C), 148.73 (C), 155.90 (C), 157.79 (C), 160.47 (C), 172.79 (C). *m/z* (FAB): 427 [(M + H)$^+$, 25%], 169 (45), 86 (100). HRMS calcd for $C_{25}H_{31}O_6$: [(M + H)$^+$] 427.2121; found: 427.2118.

7-Decyl-3,2′,3′,4′,5′-pentahydroxyflavone (7e)

Flavonol **7e** was obtained as a red-brown amorphous solid (229 mg, 90%) following general procedure 5 on a 0.57 mmol scale. mp decomp >90 °C. IR υ_{max} (ATR, cm^{-1}): 3453 (OH), 3234 (OH), 2954 (CH_2), 1578 (C=O). δ_H (400 MHz, D_6-DMSO): 0.85 (3H, t, J = 6.6 Hz, CH_2CH_3), 1.23–1.29 (14H, m, 7 × CH_2), 1.60–1.64 (2H, m, ArCH$_2$CH_2), 2.72 (2H, t, J = 7.4 Hz, ArCH_2CH$_2$), 6.48 (1H, s, H-6′), 7.30 (1H, d, J = 8.2 Hz, H-6), 7.40 (1H, s, H-8), 8.01 (1H, d, J = 8.2 Hz, H-5), 8.18 (1H, broad s, OH), 8.51 (1H, broad s, OH), 8.67 (1H, broad s, OH), 8.73 (1H, s, OH). δ_C (100 MHz, D_6-DMSO): 14.28 (CH_3), 22.43 (CH_2), 28.91 (CH_2), 29.01 (CH_2), 29.14 (CH_2), 29.29 (CH_2), 29.30 (CH_2), 30.70 (CH_2), 31.62 (CH_2), 35.38 (CH_2), 106.16 (CH), 109.08 (C), 117.45 (CH), 120.24 (C), 124.95 (CH), 125.42 (CH), 135.31 (C), 137.25 (C), 137.80 (C), 138.01 (C), 138.10 (C), 139.19 (C), 148.24 (C), 149.11 (C), 155.58 (C), 172.51 (C). *m/z* (FAB): 443 [(M + H)$^+$, 100%], 261 (10), 169 (20), 86 (65). HRMS calcd for $C_{25}H_{31}O_7$: [(M + H)$^+$] 443.2070; found: 443.2075.

Acknowledgements

The authors thank Scottish Enterprise and the University of Glasgow for funding.

References

(1) Review:Crozier, A.; Jaganath, I. B.; Clifford, M. N. *Nat. Prod. Rep.* **2009**, *26* (8), 1001. doi:10.1039/b802662a.

(2) Mullen, W.; Rouanet, J.-M.; Auger, C.; Teissèdre, P. L.; Caldwell, S.; Hartley, R. C.; Lean, M. E. J.; Edwards, C. A.; Crozier, A. *J. Agric. Food Chem.* **2008**, *56* (24), 12127. doi:10.1021/jf802754s.

(3) Graf, B. A.; Mullen, W.; Caldwell, S. T.; Hartley, R. C.; Duthie, G. G.; Lean, M. E. J.; Crozier, A.; Edwards, C. A. *Drug Metab. Dispos.* **2005**, *33* (7), 1036. doi:10.1124/dmd.104.002691.

(4) Mullen, W.; Hartley, R. C.; Crozier, A. *J. Chromatogr. A* **2003**, *1007* (1–2), 21. doi:10.1016/S0021-9673(03)00882-3.

(5) Mullen, W.; Graf, B. A.; Caldwell, S. T.; Hartley, R. C.; Duthie, G. G.; Edwards, C. A.; Lean, M. E. J.; Crozier, A. *J. Agric. Food Chem.* **2002**, *50* (23), 6902. doi:10.1021/jf020598p.

(6) Caldwell, S. T.; Petersson, H. M.; Farrugia, L. J.; Mullen, W.; Crozier, A.; Hartley, R. C. *Tetrahedron* **2006**, *62* (31), 7257. doi:10.1016/j.tet.2006.05.046.

(7) Caldwell, S. T.; Crozier, A.; Hartley, R. C. *Tetrahedron* **2000**, *56* (24), 4101. doi:10.1016/S0040-4020(00)00325-2.

(8) Review: Verma, A. K.; Pratap, R. *Nat. Prod. Rep.* **2010**, *27* (11), 1571. doi:10.1039/c004698c.

(9) Karp, J. E.; Smith, B. D.; Resar, L. S.; Greer, J. M.; Blackford, A.; Zhao, M.; Moton-Nelson, D.; Alino, K.; Levis, M. J.; Gore, S. D.; Joseph, B.; Carraway, H.; McDevitt, M. A.; Bagain, L.; Mackey, K.; Briel, J.; Doyle, L. A.; Wright, J. J.; Rudek, M. A. *Blood* **2011**, *117* (12), 3302. doi:10.1182/blood-2010-09-310862.

(10) Huo, C.; Yang, H.; Cui, Q. C.; Dou, Q. P.; Chan, T. H. *Bioorg. Med. Chem.* **2010**, *18* (3), 1252. doi:10.1016/j.bmc.2009.12.034.

(11) Huo, C.; Shi, G.; Lam, W. H.; Chen, D.; Cui, Q. C.; Dou, Q. P.; Chan, T. H. *Can. J. Chem.* **2008**, *86* (6), 495. doi:10.1139/v07-141.

(12) Osanai, K.; Huo, C.; Landis-Piwowar, K. R.; Dou, Q. P.; Chan, T. H. *Tetrahedron* **2007**, *63* (32), 7565. doi:10.1016/j.tet.2007.05.043.

(13) Yao, N.; Song, A.; Wang, X.; Dixon, S.; Lam, K. S. *J. Comb. Chem.* **2007**, *9* (4), 668. doi:10.1021/cc070009y.

(14) Dahlén, K.; Wallén, E. A. A.; Grøtli, M.; Luthman, K. *J. Org. Chem.* **2006**, *71* (18), 6863. doi:10.1021/jo061008f.

(15) Review: Horton, D. A.; Bourne, G. T.; Smythe, M. L. *Chem. Rev.* **2003**, *103* (3), 893. doi:10.1021/cr020033s.

(16) Review: Chen, H.; Yoshioka, H.; Kim, G. S.; Jung, J. E.; Okami, N.; Sakata, H.; Maier, C. M.; Narasimhan, P.; Goeders, C. E.; Chan, P. H. *Antioxid. Redox Signal.* **2011**, *14* (8), 1505. doi:10.1089/ars.2010.3576.

(17) Review: Roberts, R. A.; Smith, R. A.; Safe, S.; Szabo, C.; Tjalkens, R. B.; Robertson, F. M. *Toxicology* **2010**, *276* (2), 85. doi:10.1016/j.tox.2010.07.009.

(18) Review: van Horssen, J.; Witte, M. E.; Schreibelt, G.; de Vrie, H. E. *Biochim. Biophys. Acta* **2011**, *1812*, 141.

(19) Dangles, O.; Fargeix, G.; Dufour, C. *J. Chem. Soc., Perkin Trans. 2* **1999**, (7): 1387. doi:10.1039/a901460h.

(20) McPhail, D. B.; Hartley, R. C.; Gardner, P. T.; Duthie, G. G. *J. Agric. Food Chem.* **2003**, *51* (6), 1684. doi:10.1021/jf025922v.

(21) Mitchell, J. H.; Gardner, P. T.; McPhail, D. B.; Morrice, P. C.; Collins, A. R.; Duthie, G. G. *Arch. Biochem. Biophys.* **1998**, *360* (1), 142. doi:10.1006/abbi.1998.0951.

(22) Tutorial review of lipid oxidation: Shahidi, F.; Zhong, Y. *Chem. Soc. Rev.* **2010**, *39* (11), 4067. doi:10.1039/b922183m.

(23) Bennett, C. J.; Caldwell, S. T.; McPhail, D. B.; Morrice, P. C.; Duthie, G. G.; Hartley, R. C. *Bioorg. Med. Chem.* **2004**, *12* (9), 2079. doi:10.1016/j.bmc.2004.02.031.

(24) Caldwell, S. T.; Bennett, C. J.; Hartley, R. C.; McPhail, D. B.; Duthie, G. G. International Patent No. WO 2004/007475, 2004.

(25) A recent example of modifying tocopherol: Wang, Y.; Panagabko, C.; Atkinson, J. *Bioorg. Med. Chem.* **2010**, *18* (2), 777. doi:10.1016/j.bmc.2009.11.051.

(26) Shahidi, F.; Zhong, Y. *J. Agric. Food Chem.* **2011**, *59* (8), 3499. doi:10.1021/jf104750m.

(27) Basabe, P.; de Román, M.; Marcos, I. S.; Diez, D.; Blanco, A.; Bodero, O.; Mollinedo, F.; Sierra, B. G.; Urones, J. G. *Eur. J. Med. Chem.* **2010**, *45* (9), 4258. doi:10.1016/j.ejmech.2010.06.025.

(28) Mays, J. R.; Hill, S. A.; Moyers, J. T.; Blagg, B. S. J. *Bioorg. Med. Chem.* **2010**, *18* (1), 249. doi:10.1016/j.bmc.2009.10.061.

(29) Balakrishna, K. J.; Rao, N. P.; Seshadri, T. R. *Proc. Ind. Acad. Sci., Sect. A* **1951**, *33*, 151.

(30) Ahluwalia, V. K.; Krishnaswami, N. R.; Mukerjee, S. K.; Murti, V. V. S.; Seshadri, T. R.; Venkataramani, C. *Proc. Ind. Acad. Sci., Sect. A* **1958**, *47*, 230.

(31) Hong, C.-Y.; Lee, J.-H.; Park, T.-S.; Kim, J.-H.; Choi, S.-H.; Yoon, S.-K.; Chung, H.-H.; Son, H.-S.; Kim, E. E.-K.; Ro, S.-G.; Jeong, S.-W.; Kim, D.-M. US Patent US2003/125356.

(32) Dorn, H. W.; Warren, W. H.; Bullock, J. L. *J. Am. Chem. Soc.* **1939**, *61* (1), 144. doi:10.1021/ja01870a047.
(33) Cortez, F. J.; Sarpong, R. *Org. Lett.* **2010**, *12* (7), 1428. doi:10.1021/ol902959v.
(34) Kreuchunas, A. *J. Org. Chem.* **1956**, *21* (8), 910. doi:10.1021/jo01114a023.
(35) Zaitsu, K.; Katagi, M.; Kamata, H.; Kamata, T.; Shima, N.; Miki, A.; Iwamura, T.; Tsuchihashi, H. *J. Mass Spectrom.* **2008**, *43* (4), 528. doi:10.1002/jms.1347.
(36) Sengupta, S.; Drew, M. G. B.; Mukhopadhyay, R.; Achari, B.; Banerjee, A. K. *J. Org. Chem.* **2005**, *70* (19), 7694. doi:10.1021/jo051082i.
(37) Meyers, A. I.; Flisak, J. R.; Aitken, R. A. *J. Am. Chem. Soc.* **1987**, *109* (18), 5446. doi:10.1021/ja00252a022.
(38) Narsaiah, A. V.; Nagaiah, B. *Synthesis* **2010**, *2010* (16), 2705. doi:10.1055/s-0030-1258173.
(39) Deodhar, M.; Black, D. StC.; Kumar, N. *Tetrahedron* **2007**, *63* (24), 5227. doi:10.1016/j.tet.2007.03.173.
(40) Mathison, I. W.; Gueldner, R. C.; Carroll, D. M. *J. Pharm. Sci.* **1968**, *57* (10), 1820. doi:10.1002/jps.2600571050.
(41) Keegstra, E. M. D.; Huisman, B.-H.; Paardekooper, E. M.; Hoogesteger, F. J.; Zwikker, J. W.; Jenneskens, L. W.; Kooijman, H.; Schouten, A.; Veldman, N.; Spek, A. L. *J. Chem. Soc., Perkin Trans. 2* **1996**, (2): 229. doi:10.1039/p29960000229.
(42) Poigny, S.; Guyot, M.; Samadi, M. *Tetrahedron* **1998**, *54* (49), 14791. doi:10.1016/S0040-4020(98)00927-2.
(43) Schäfer, W.; Leute, R. *Chem. Ber.* **1966**, *99* (5), 1632. doi:10.1002/cber.19660990530.
(44) Poigny, S.; Guyot, M.; Samadi, M. *J. Org. Chem.* **1998**, *63* (17), 5890. doi:10.1021/jo9805192.
(45) Garbaccio, R. M.; Stachel, S. J.; Baeschlin, D. K.; Danishefsky, S. J. *J. Am. Chem. Soc.* **2001**, *123* (44), 10903. doi:10.1021/ja011364+.
(46) Ayers, S.; Zink, D. L.; Mohn, K.; Powell, J. S.; Brown, C. M.; Murphy, T.; Brand, R.; Pretorius, S.; Stevenson, D.; Thompson, D.; Singh, S. B. *Phytochemistry* **2008**, *69* (2), 541. doi:10.1016/j.phytochem.2007.08.003.
(47) It is also possible that toxicity may arise from such structures. Lambert, J. D.; Sang, S.; Yang, C. S. *Chem. Res. Toxicol.* **2007**, *20* (4), 583. doi:10.1021/tx7000515.

Can. J. Chem. Downloaded from www.nrcresearchpress.com by Renmin University of China on 09/02/12
For personal use only.

Formation and recognition of G-quadruplex relevant for pilin antigenic variation in *Neisseria gonorrhoeae*

Zhenjiang Zhang, Xiangwei He, and Gu Yuan

Can. J. Chem. Downloaded from www.nrcresearchpress.com by Renmin University of China on 09/02/12
For personal use only.

Abstract: In this research, NMR, ESI-MS, and circular dichroism (CD) spectroscopies were used to investigate the formation and recognition of G-quadruplex by a G-rich sequence that has been demonstrated to be relevant for pilin variation in *Neisseria gonorrhoeae*. The NMR spectra provided strong evidence that the G-quadruplex structure was formed from this G-rich sequence, and this result was confirmed by CD spectroscopy. In addition, two small-molecule natural products (jatrorrhizine hydrochloride (**J**) and dehydrocorydaline (**D**)) were found to bind to this G-quadruplex over the corresponding duplex DNA with high selectivity by ESI-MS.

Key words: formation, recognition, G-quadruplex, pilin antigenic variation, *Neisseria gonorrhoeae*.

Résumé : Dans ce travail, on a fait appel à la résonance magnétique nucléaire (RMN), la spectrométrie de masse avec ionisation par électronébulisation (SM-IEN) et le dichroïsme circulaire (DC) pour étudier la formation et la reconnaissance d'un quadruplex G par une séquence riche en G qui serait pertinente pour la variation antigénique de la piline dans *Neisseria gonorrhoeae*. Les spectres RMN ont fourni de solides résultats qui permettent d'affirmer que la structure du quadruplex G se forme à partir de la séquence riche en G et cette conclusion a été confirmée par la spectroscopie de DC. De plus, faisant appel à la SM-IEN, on a trouvé que deux petites molécules de produits naturels, le chlorhydrate de jatrorrhizine (**J**) et la déhydrocorydaline (**D**) se lient avec une grande sélectivité à ce quadruplex G sur le duplexe d'ADN correspondant.

Mots-clés : formation, reconnaissance, quadruplex G, variation antigénique de la piline, *Neisseria gonorrhoeae*.

[Traduit par la Rédaction]

Introduction

G-quadruplex is a specific secondary structure of DNA that consists of π-stacked G-quartets, where four guanines are linked by eight hydrogen bonds.[1,2] G-quadruplex structures have been found to be formed in the regions of human telomeres, oncogene promoters, and other regions of the human genome.[1–4] Their biological significance has been demonstrated by numerous in vitro and in vivo studies.[3–8]

Gonorrhea is an infectious disease caused by *Neisseria gonorrhoeae*, which can use DNA recombination to prompt pilin antigenic variation (Av) to avoid immune surveillance[9] and this has impeded vaccine development. Recently, Cahoon and Seifert[10] found that a G-rich sequence is required for the pilin antigenic variation and this G-rich sequence can form a G-quadruplex structure. Therefore, the selective recognition and binding of the G-quadruplex is important for suppressing the pilin antigenic variation using small molecules.

ESI-MS, NMR, and circular dichroism (CD) spectroscopies have been used widely to analyze G-quadruplex structure and its interactions with small molecules. In this research, NMR and CD spectroscopies were used to investigate the formation of the pilin G-quadruplex and the recognition selectivity and stoichiometry of small-molecule natural products to the pilin G-quadruplex were probed by electrospray ionization mass spectrometry (ESI-MS). It was found that two small molecule natural products (jatrorrhizine hydrochloride and dehydrocorydaline) recognize and bind to the pilin G-quadruplex over the corresponding duplex DNA with high selectivity.

Results and discussion

The wild-type G-rich sequence relevant to the pilin antigenic variation contains three GGG tracts and one GGGG tract (Fig. 1A). According to the typical G-quadruplex topology reported in the literature,[11,12] the four G-tracts will form four separate strands of G-quadruplex and all the guanines in the three GGG tracts will be involved in G-tetrad formation. However, there are two options for the four guanines in the GGGG tract to be involved in G-tetrad formation: G15 to G17 or, alternatively, G16 to G18. In this research, a single G was mutated into T at G15 (15T mutant) and G18 (18T

Received 18 April 2011. Accepted 13 June 2011. Published at www.nrcresearchpress.com/cjc on 7 October 2011.

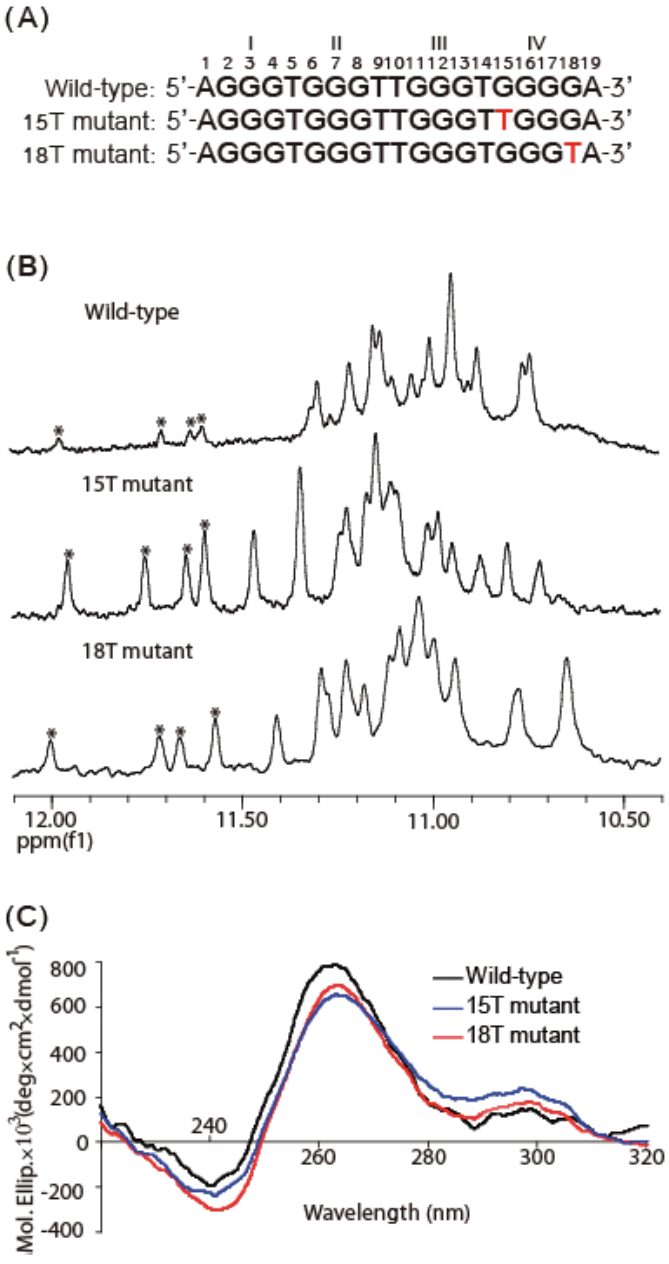
Z. Zhang, X. He, and G. Yuan. Beijing National Laboratory for Molecular Sciences, Key Laboratory of Bioorganic Chemistry and Molecular Engineering of Ministry of Education, Department of Chemical Biology, College of Chemistry and Molecular Engineering, Peking University, Beijing 100871, P.R. China.

Corresponding author: G. Yuan (e-mail: guyuan@pku.edu.cn).

This article is part of a Special Issue dedicated to Professor Tak-Hang Chan.

Can. J. Chem. Downloaded from www.nrcresearchpress.com by Renmin University of China on 09/02/12
For personal use only.

Fig. 1. (A) DNA sequences. (B) Imino region of 1D ^{1}H NMR. (C) Circular dichroism (CD) spectra of the three DNA sequences in potassium solution. DNA concentration for NMR and CD are 0.2 mmol/L and 10 μmol/L, respectively, in a solution of 25 mmol/L K-PO_4 and 70 mmol/L KCl at pH 7.0.



mutant), respectively (Fig. 1A) to help characterize the G-quadruplex structure formed by the wild-type sequence.

G-quadruplex formation by a wild-type pilin Av sequence and two mutants

The formation of G-quadruplex structures of the wild-type pilin Av sequence and the two mutants in potassium solution were probed by ^{1}H NMR spectroscopy. The ^{1}H NMR spectra in Fig. 1B show that there is a cluster of imino H peaks at 10.50–12.10 ppm. These are the characteristic peaks of the G-quadruplex structure. The intense cluster peak corresponding to 12 protons indicated the formation of a dominant G-quadruplex, whereas the small peaks labeled with a star in the downfield region suggested the presence of a minor G-quadruplex in the solution. In the case of the two mutants, four peaks at the same downfield region can also be detected. This suggests that they form a similar structure to the wild-type minor G-quadruplex.

G-quadruplex formation by the three sequences is confirmed by their CD spectra. The three G-rich sequences shown similar profiles in potassium ion solution with a major positive peak at 265 nm, a negative peak at 245 nm, and a minor positive peak at 295 nm (Fig. 1C). These peaks are consistent with the character of a typical G-quadruplex reported in the literature.[13,14] The results from the CD spectra indicate that the three G-rich sequences adopt relatively similar conformations in G-quadruplex formation because their CD spectra almost overlap.

Small molecule recognition of the G-quadruplex

Small molecules that can selectively recognize pilin G-quadruplex might have the potential to inhibit pilin Av. Here, the interaction of small molecule natural products and the pilin G-quadruplex were studied by ESI-MS. It was found that three natural small molecules (Fig. 2), jatrorrhizine hydrochloride (**J**), dehydrocorydaline (**D**), and nitidine chloride (**N**), have good binding properties to the G-quadruplex. Figure 3 shows the mass spectra of the G-quadruplex and small molecules in molar ratios of 1:1 and 1:2 ([G] denotes G-quadruplex ion, [G + nP] denotes a 1:n complex ion of G-quadruplex (G) and a small molecule (P) (P = **J**, **N**, or **D**)). After an equal amount of **J** was added, the complex ion ($[G + \mathbf{J}]^{4-}$) at *m/z* 1605.5 became the base peak (100%), while the abundance of the G-quadruplex peak ($[G]^{4-}$) at *m/z* 1521.4 decreased to about 70% (Fig. 3A). When the concentration ratio of **J** to DNA was increased to 2.0, the abundance of complex ion ($[G + 2\mathbf{J}]^{4-}$) at *m/z* 1689.1 was 100%, whereas the peak of the G-quadruplex almost disappeared (Fig. 3B). The complex ion at *m/z* 1689.1 ($[G + 2\mathbf{J}]^{4-}$) suggested that two small molecules (**J**) stack on the two ends of the G-tetrad. For **D**, the ESI mass spectra show that the complex ions of $[G + \mathbf{D}]^{4-}$ at *m/z* 1612 were also the base peak (100%) at G:**D** = 1:1 and 1:2 (Figs. 3C and 3D). As for **N** in Fig. 3F, the relative abundance of the 1:1 complex ion ($[G + \mathbf{N}]^{4-}$) at *m/z* 1608.0 was 100% at G:**N** = 1:2. These results indicate that the three small molecules bind strongly to the G-quadruplex.

Here, a parameter (BA, binding affinity) was used to compare the binding affinity of the three small molecules with the pilin G-quadruplex.[15,16] The BAs are shown in Table 1 and the maximum value of BA is 1. If the BA value is greater, the BA of the small molecule to the pilin G-quadruplex is greater. From the data in Table 1, the order of the BAs is **J** > **D** > **N**.

Small molecules selectively binding to G-quadruplex over duplex DNA

To evaluate selective recognition for the G-quadruplex, the mixed solutions of the pilin G-quadruplex, the corresponding duplex DNA, and the small molecules were analyzed by ESI-MS (Fig. 4). For **J** and **D**, 1:1 complex ions with G-quadruplex at *m/z* 1607 and 1614 were base peaks (100%), respectively, and no complex ion of the small molecule with the duplex

Fig. 2. Structures of the three small molecules.

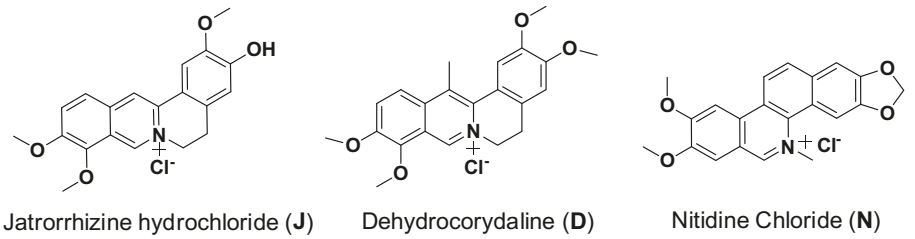
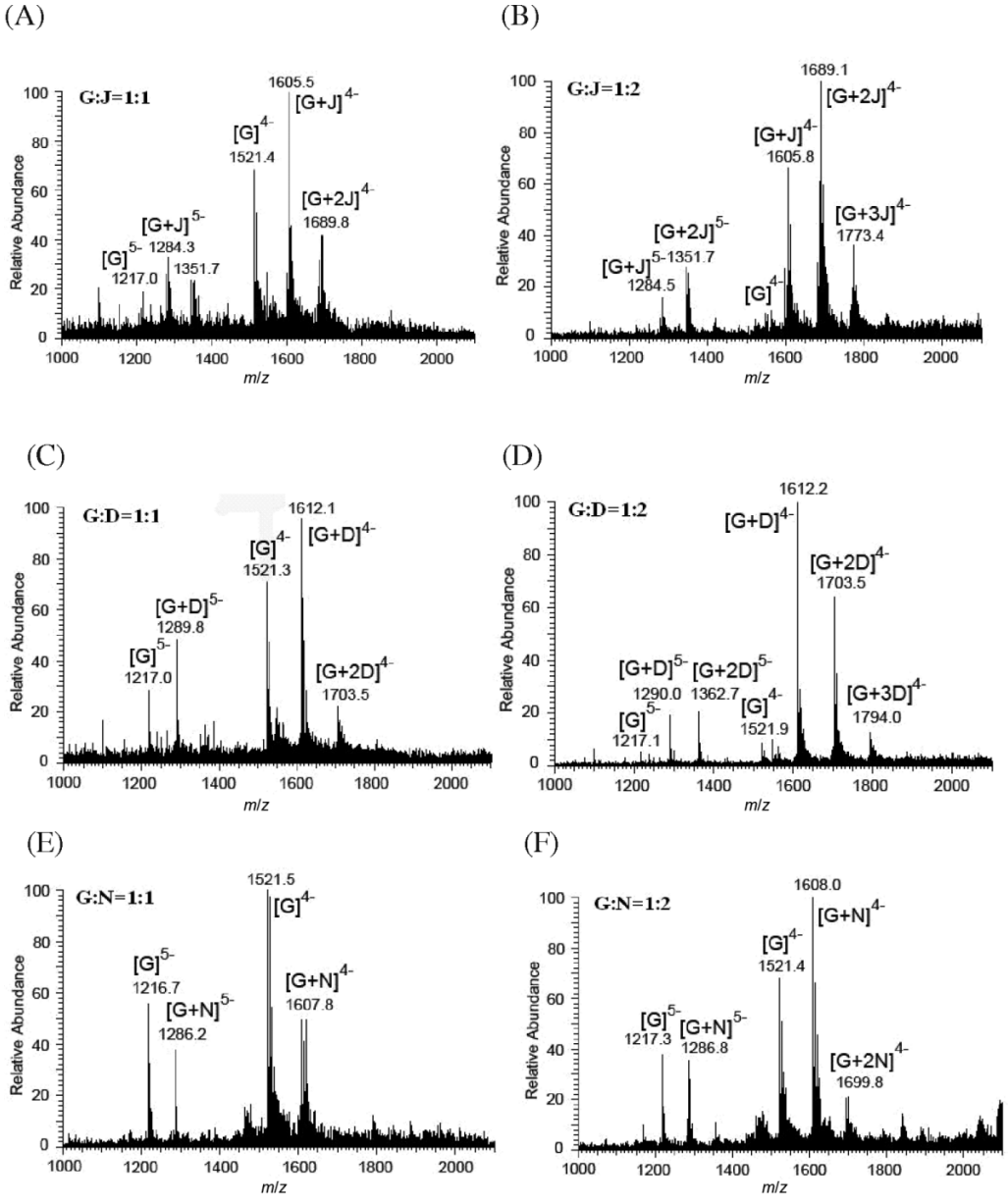


Fig. 3. Mass spectra of the complexes of the G-quadruplex with small molecules. (A) G:**J** = 1:1, (B) G:**J** = 1:2, (C) G:**D** = 1:1, (D) G:**D** = 1:2, (E) G:**N** = 1:1, and (F) G:**N** = 1:2. **J**, jatrorrhizine hydrochloride, **D**, dehydrocorydaline, and **N**, nitidine chloride.



DNA was observed (Figs. 4A and 4B). **N** showed a lower binding capacity (Fig. 4C) with the G-quadruplex DNA than **J** or **D**. These results indicate that **J** and **D** have very high binding selectivities to the G-quadruplex over the duplex DNA.

Conclusion

G-quadruplex formation by a G-rich sequence that is relevant for the pilin Av in *Neisseria gonorrhoeae* was demonstrated using NMR and CD spectroscopy. Two small molecule natural

Can. J. Chem. Downloaded from www.nrcresearchpress.com by Renmin University of China on 09/02/12
For personal use only.

Can. J. Chem. Downloaded from www.nrcresearchpress.com by Renmin University of China on 09/02/12
For personal use only.

Fig. 4. ESI-MS spectra of mixed solutions of G-quadruplex – duplex – small molecules = 1:1:2. $[G + 2NH_4^+ - 7H^+]^{5-}$ and $[G + 2NH_4^+ - 6H^+]^{4-}$ are denoted as $[G]^{5-}$ and $[G]^{4-}$, respectively. Duplex DNA is denoted as "D". The concentration of the G-quadruplex or the duplex DNA is 5 μmol/L in 50 mmol/L NH_4Ac solution.

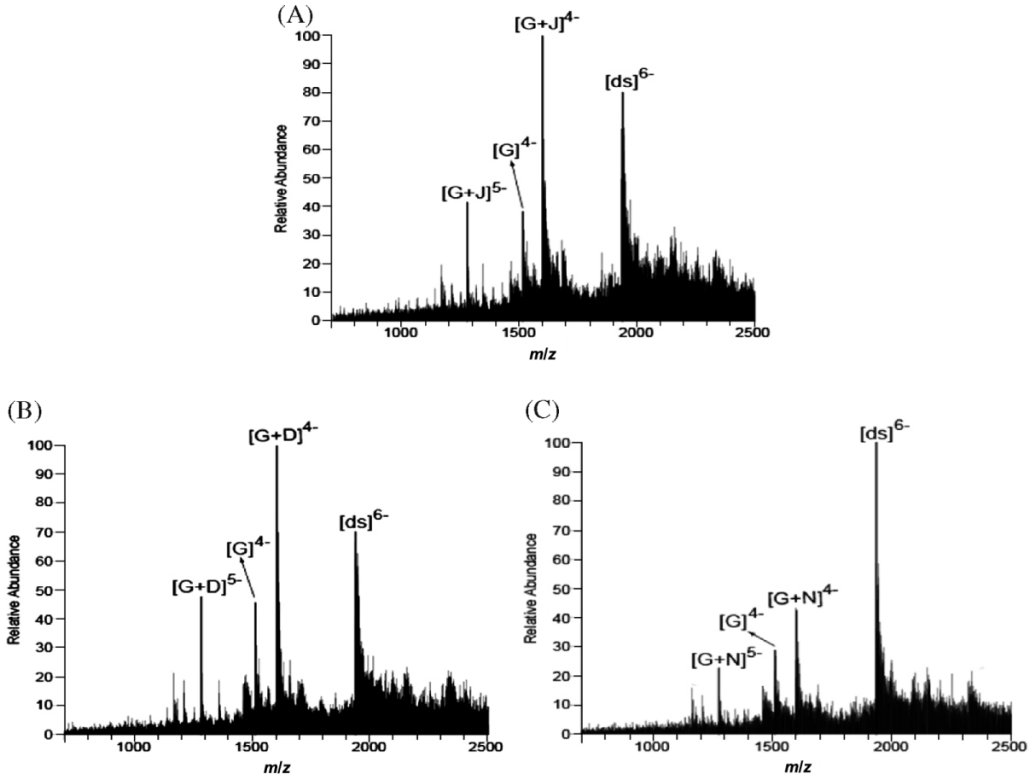


Table 1. The binding affinities (BAs) of the small molecules.

	BA	
	Concentration ratio	
Small molecule	1:1	1:2
Jatrorrhizine hydrochloride	0.68	0.97
Dehydrocorydaline	0.63	0.93
Nitidine chloride	0.35	0.60

products (dehydrocorydaline and jatrorrhizine hydrochloride) were found to bind preferably to the pilin G-quadruplex over the corresponding duplex DNA by ESI-MS. Jatrorrhizine hydrochloride and dehydrocorydaline can be used to probe the biological function of the G-quadruplex in vivo.

Materials and methods

Oligonucleotides

The wild-type G-rich sequence relevant to pilin Av and two single G to T mutants were purchased from Sangon Biotech Co., Ltd., Shanghai (Fig. 1A). The oligonucleotides were dissolved in ultra-purified water at a concentration of 1 mmol/L as a stock. Samples for NMR were prepared by dilution to a solution of 90%:10% H_2O:D_2O. The final NMR samples contained 0.2 mmol/L oligonucleotides in a buffer of 25 mmol/L K-PO_4 and 70 mmol/L KCl at pH 7.0. Samples for CD measurement were prepared with 25 mmol/L K-PO_4 and 70 mmol/L KCl solution to a DNA concentration of 10 μmol/L. Samples for ESI-MS were prepared by dilution with an ammonium acetate buffer (100 mmol/L) to a DNA concentration of 5–10 μmol/L.

Small molecules

Small molecules for ESI-MS screening were obtained from the Chinese National Institute for the Control of Pharmaceutical and Biological Products, Beijing. A 10 mmol/L stock solution in distilled water was prepared and stored at –20 °C.

NMR analysis

NMR experiments were performed on a 600 MHz Bruker spectrometer equipped with a 5 mm Penta probe. The *Jump and Return* program was used for solvent signal suppression with maximum sensitivity.

CD spectrometry

CD spectra of the oligonucleotides were recorded on a Jasco J-810 spectropolarimeter (Jasco, Japan). A 1 mm quartz cell was used with a scanning speed of 100 nm/min between 200 and 400 nm at room temperature. Spectra were baseline-corrected and the signal contributions of the buffer were subtracted.

Mass spectrometry

ESI-MS spectra were obtained using a Finnigan LCQ Deca XP Plus mass spectrometer (San Jose, California). The direct infusion flow rate was 2.0 μL/min, the electrospray voltage was 2.7 kV, and the capillary temperature was 120 °C.

Acknowledgment

This project supported by the National Natural Science Foundation of China (Nos. 20872008 and 90913004).

References

(1) Neidle, S.; Read, M. A. *Biopolymers* **2000**, *56* (3), 195. doi:10.1002/1097-0282(2000)56:3<195::AID-BIP10009>3.0.CO;2-5.
(2) Brooks, T. A.; Kendrick, S.; Hurley, L. *FEBS J.* **2010**, *277* (17), 3459. doi:10.1111/j.1742-4658.2010.07759.x.
(3) Keniry, M. A. *Biopolymers* **2000**, *56* (3), 123. doi:10.1002/1097-0282(2000/2001)56:3<123::AID-BIP10010>3.0.CO;2-3.
(4) Hurley, L. H.; Wheelhouse, R. T.; Sun, D.; Kerwin, S. M.; Salazar, M.; Fedoroff, O. Y.; Han, F. X.; Han, H.; Izbicka, E.; Von Hoff, D. D. *Pharmacol. Ther.* **2000**, *85* (3), 141. doi:10.1016/S0163-7258(99)00068-6.
(5) Neidle, S.; Parkinson, G. *Nat. Rev. Drug Discov.* **2002**, *1* (5), 383. doi:10.1038/nrd793.
(6) Siddiqui-Jain, A.; Grand, C. L.; Bearss, D. J.; Hurley, L. H. *Proc. Natl. Acad. Sci. U.S.A.* **2002**, *99* (18), 11593. doi:10.1073/pnas.182256799.
(7) Schaffitzel, C.; Berger, I.; Postberg, J.; Hanes, J.; Lipps, H. J.; Plückthun, A. *Proc. Natl. Acad. Sci. U.S.A.* **2001**, *98* (15), 8572. doi:10.1073/pnas.141229498.
(8) Neidle, S. *FEBS J.* **2010**, *277* (5), 1118. doi:10.1111/j.1742-4658.2009.07463.x.
(9) Kline, K. A.; Sechman, E. V.; Skaar, E. P.; Seifert, H. S. *Mol. Microbiol.* **2003**, *50* (1), 3. doi:10.1046/j.1365-2958.2003.03679.x.
(10) Cahoon, L. A.; Seifert, H. S. *Science* **2009**, *325* (5941), 764. doi:10.1126/science.1175653.
(11) Yang, D.; Hurley, L. H. *Nucleosides Nucleotides Nucleic Acids* **2006**, *25* (8), 951. doi:10.1080/15257770600809913.
(12) Rezler, E. M.; Seenisamy, J.; Bashyam, S.; Kim, M. Y.; White, E.; Wilson, W. D.; Hurley, L. H. *J. Am. Chem. Soc.* **2005**, *127* (26), 9439. doi:10.1021/ja0505088.
(13) Dapić, V.; Abdomerović, V.; Marrington, R.; Peberdy, J.; Rodger, A.; Trent, J. O.; Bates, P. *J. Nucleic Acids Res.* **2003**, *31* (8), 2097. doi:10.1093/nar/gkg316.
(14) Zhang, Z.; Dai, J.; Veliath, E.; Jones, R. A.; Yang, D. *Nucleic Acids Res.* **2010**, *38* (3), 1009. doi:10.1093/nar/gkp1029.
(15) Li, H. H.; Yuan, G.; Du, D. M. *J. Am. Soc. Mass Spectrom.* **2008**, *19* (4), 550. doi:10.1016/j.jasms.2008.01.012.
(16) Li, H. H.; Liu, Y. Q.; Lin, S.; Yuan, G. *Chemistry* **2009**, *15* (10), 2445. doi:10.1002/chem.200801922.

Can. J. Chem. Downloaded from www.nrcresearchpress.com by Renmin University of China on 09/02/12
For personal use only.

Cyclohexylamine oxidase as a useful biocatalyst for the kinetic resolution and dereacemization of amines

Hannes Leisch, Stephan Grosse, Hiroaki Iwaki, Yoshie Hasegawa, and Peter C.K. Lau

Can. J. Chem. Downloaded from www.nrcresearchpress.com by Renmin University of China on 09/02/12
For personal use only.

Abstract: The biocatalytic performance of a cloned cyclohexylamine oxidase derived from *Brevibacterium oxydans* IH-35A towards structurally different amines was investigated. Cycloalkyl primary amines, alkyl aryl amines, and α-carbon-substituted aliphatic amines were identified as suitable substrates for the biocatalyst based on an activity assay. Kinetic resolutions of several amines by either recombinant whole cells or crude enzyme extracts prepared therefrom gave enantiomerically pure (*R*)-amines besides the corresponding ketones. When cyclohexylamine oxidase in combination with a borane–ammonia complex as reducing agent was applied to the deracemization of several substrates, excellent enantiomeric ratios (>99:1) and good isolated yields (62%–75%) of the corresponding (*R*)-amines were obtained.

Key words: biocatalysis, cyclohexylamine oxidase, chiral amines, kinetic resolution, deracemization.

Résumé : On a étudié la performance biocatalytique d'un clone de l'oxydase de la cyclohexylamine dérivé du *Brevibacterium oxydans* IH-35A vis-à-vis des amines de structures diverses. Sur la base d'un essai d'activité, il a été possible d'identifier les cycloalkylamines primaires, les alkylarylamines primaires et les amines aliphatiques portant un substituant sur le carbone en α comme des substrats appropriés pour le biocatalyseur. Les résolutions cinétiques de plusieurs amines par des cellules recombinantes complètes ou des extraits bruts d'enzyme préparés à partir de celles-ci conduisent à des amines (*R*) énantiomériquement pures aux côtés des cétones correspondantes. On a utilisé l'oxydase de la cyclohexylamine en combinaison avec un complexe de borane–ammoniac comme agent réducteur pour effectuer la déracémisation de plusieurs substrats, avec d'excellents rapports énantiomériques (>99/1) et de bons rendements en produits isolés (72 % à 75 %) des amines (*R*) correspondantes.

Mots-clés : biocatalyseur, oxydase de la cyclohexylamine, amines chirales, résolution cinétique, déracémisation.

[Traduit par la Rédaction]

Introduction

The importance of enantiomerically pure amines as starting materials for pharmaceuticals and agrochemicals, as chiral auxiliaries, and as resolving agents is beyond question.[1] Despite the wide applications of chiral amines in chemistry, medicine, and biology, their synthesis remains challenging. Chemical protocols include the resolution of racemic amines as their diasteriomeric salts, enantioselective enamide and imine reduction, reductive amination, olefin hydroamination, and enantioselective carbanion addition to imines.[2] Alternative to the chemical method biocatalytic routes have been developed as promising strategies.[3] Most notably are the applicatons of ω-transaminases, which can be either used for the kinetic resolution of racemic amines and amino acids or for the asymmetric synthesis of amines from ketones.[4]

In addition, the ability of flavoproteins to oxidize amines to imines has been exploited for the synthesis of chiral amines (Scheme 1).[5] Initial experiments by Hafner and Weller[6] using D-amino acid oxidase in combination with sodium borohydride led to the preparation of L-amino acids from the corresponding *R*-enantiomers. Applying the same concept, Soda and co-workers[7] demonstrated the deracemization of racemic amino acids. Synthetically useful protocols, which allowed for the synthesis of enantiopure amino acids

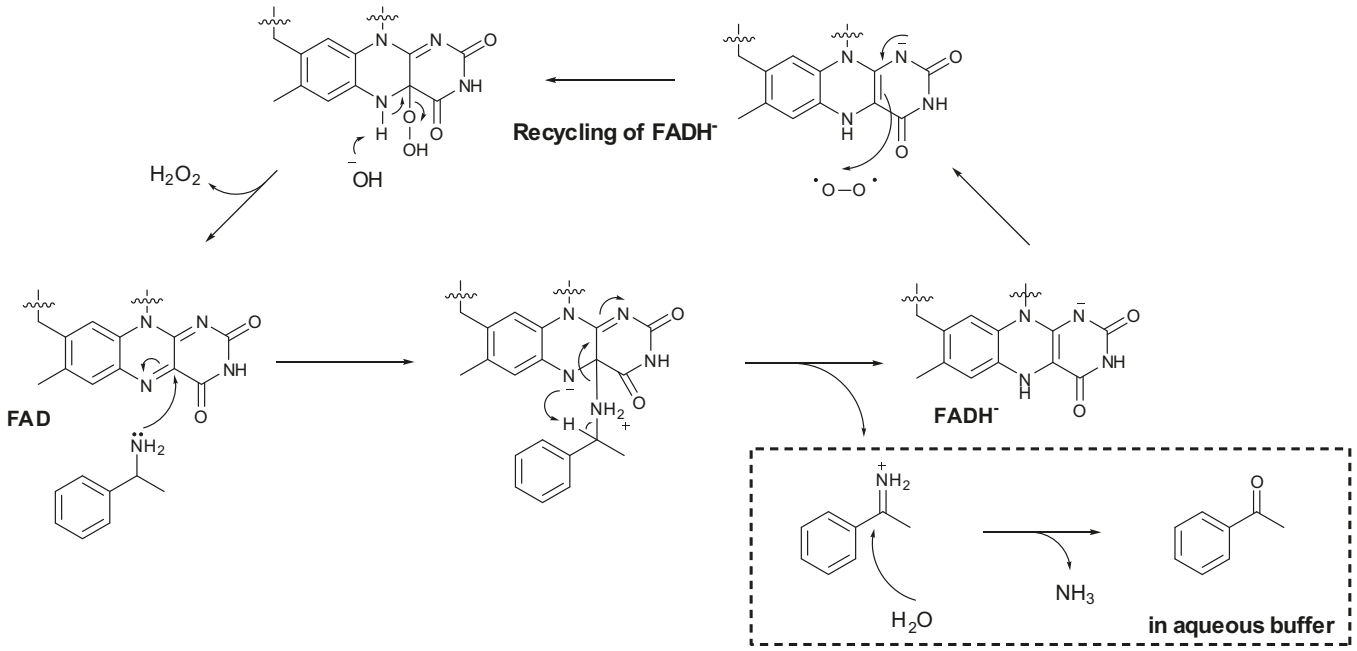
Received 11 April 2011. Accepted 26 June 2011. Published at www.nrcresearchpress.com/cjc on 19 October 2011.

H. Leisch and S. Grosse. Biotechnology Research Institute, National Research Council Canada, 6100 Royalmount Avenue, Montreal, QC H4P 2R2, Canada.
H. Iwaki and Y. Hasegawa. Department of Life Science and Biotechnology and ORDIST, Kansai University, Suita, Osaka 564-8680, Japan.
P.C.K. Lau. Biotechnology Research Institute, National Research Council Canada, 6100 Royalmount Avenue, Montreal, QC H4P 2R2, Canada; McGill University, Department of Chemistry and Department of Microbiology and Immunology, 3775 University Street, Montreal, QC H3A 2B4, Canada; FQRNT Centre in Green Chemistry and Catalysis, Montreal, QC, Canada.

Corresponding author: Peter C.K. Lau (e-mail: peter.lau@cnrc-nrc.gc.ca).

This article is part of a Special Issue dedicated to Professor Tak-Hang Chan in recognition and admiration of his long-standing contributions to green catalysis and synthesis.

Scheme 1. Proposed mechanism for the oxidation of amines with flavoproteins by nucleophilic attack of the heteroatam at C-4 of the flavoprotein.[5]



Can. J. Chem. Downloaded from www.nrcresearchpress.com by Renmin University of China on 09/02/12
For personal use only.

in excellent yields from racemic starting materials, were developed by Turner and co-workers[8] using porcine D-amino acid oxidase. Subsequently, the application of recombinant monoamine oxidase from *Aspergillus niger*[9] and mutants obtained by directed evolution led to the development of biocatalytic protocols for the deracemization of primary,[10] secondary,[11] and tertiary amines,[12] desymmetrization of substituted pyrrolidines,[13] enantioselective oxidation of hydroxylamines,[14] and the design of tandem biocatalysis multicomponent reactions.[15]

Prompted by the wide-ranging applications and excellent enantioselectivity of monoamine oxidase and its mutants from *A. niger*, we were interested in the exploitation of a bacterial amine oxidase as an alternative or complementary biocatalyst. As a result, cyclohexylamine oxidase (CHAO), a 50 kDa flavoprotein responsible for the oxidation of cyclohexylamine to cyclohexanone in *Brevibacterium oxydans* IH-35A,[16] was investigated and this new biocatalytic potential is reported herein.

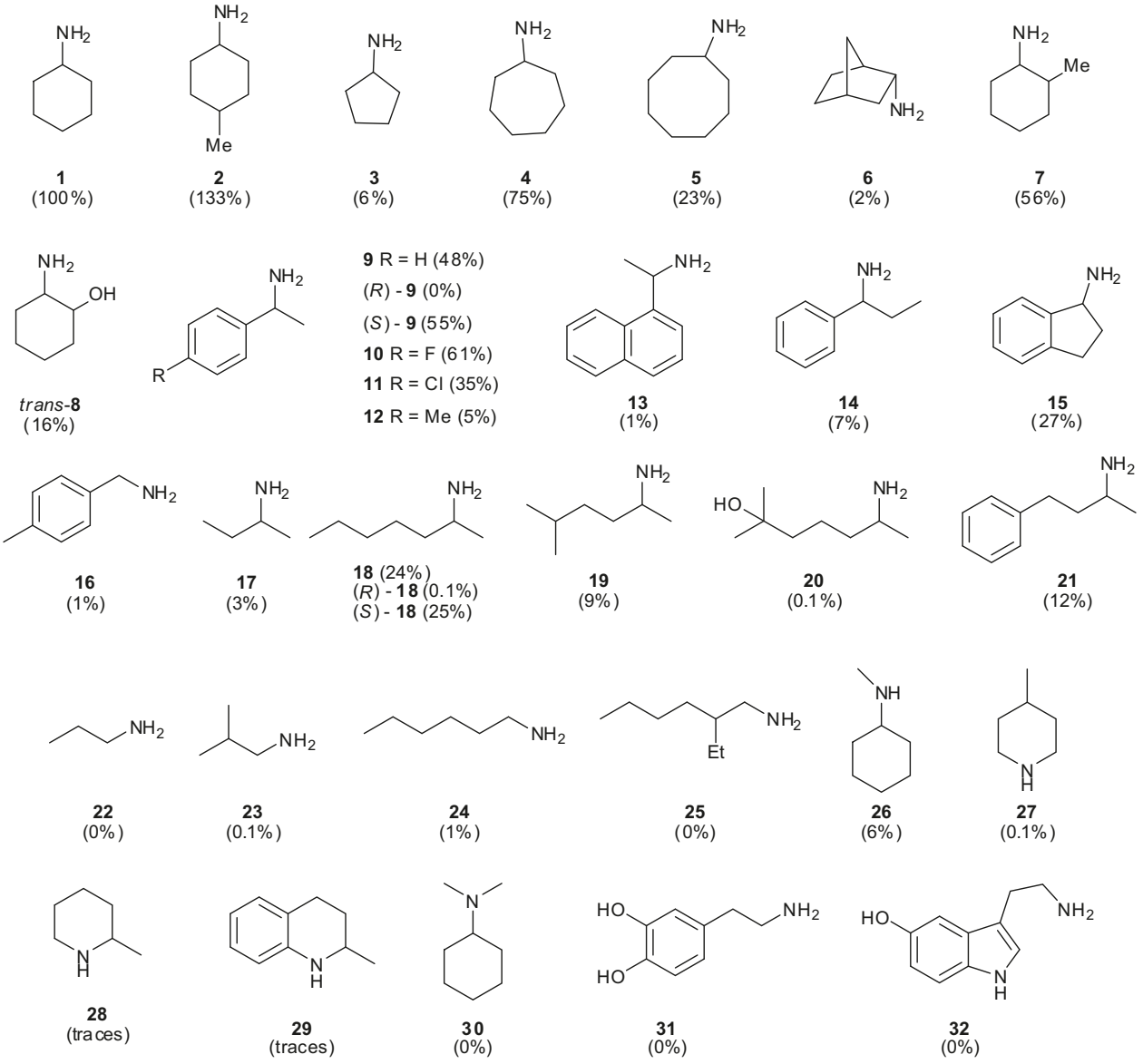
Results and discussion

To gain access to sufficient amounts of CHAO, the CHAO-encoding gene was cloned in a conventional isopropyl-β-D-thiogalactopyranoside (IPTG)-inducible expression vector (pSD80), and the recombinant plasmid was produced in *Escherichia coli* strain BL 21.[17] Crude cell extracts, prepared from a Luria Bertani medium grown and with IPTG-induced cells, were assayed for their rate of oxidation of structurally diverse amines (Fig. 1). CHAO was found to exhibit activity towards a wide range of amines with cycloalkyl primary amine derivatives **1**–**8** showing the highest activity. The specific activity for cyclohexylamine was determined to be 10.7 U per mg crude enzyme preparation. Given the fact that a nonoptimized 1 L Terrific Broth medium fermentation experiment produced 650 mg of crude CHAO enzyme preparation (6955 U/L), this amount of biocatalyst produced would be capable of transforming 40 g of cyclohexylamine per h. Interestingly, 4-methyl cyclohexylamine (**2**) was oxidized 1.3 times faster than cyclohexylamine (**1**). Additionally, α-alkyl aryl derivatives **9**–**15** and α-carbon-substituted aliphatic amines **17**–**21** were acceptable substrates, whereas compounds of the structure R–CH_2–NH_2 (**22**–**25**) and straight-chain and cyclic secondary and tertiary amines showed very limited activity. Amino acids and monoamine neurotransmitters such as dopamine (**31**) or serotonin (**32**) were not oxidized by CHAO. With respect to enantioselectivity of CHAO we tested the oxidation rates of enantiomerically pure (*R*)- and (*S*)-α-methyl benzylamine (**9**) and 2-heptylamine (**18**). In both cases, CHAO displayed virtually no detectable activity for the (*S*)-enantiomers, indicating a highly enantioselective biocatalyst.

To demonstrate the practicality of CHAO in the syntheses of chiral amines, we tested either whole cells overexpressing CHAO or crude enzyme extracts for the kinetic resolution of racemic amines (Table 1). α-Alkyl aryl derivatives **9**–**12**, **14**, and **15** were resolved in excellent enantioselectivities and CHAO selectively oxidized the (*S*)-enantiomer of the aryl amine derivative to the corresponding ketone, whrereas the (*R*)-enantiomer remained unreacted even after complete consumption of the (*S*)-enantiomer. Preparative scale experiments led to the isolation of enantiopure (*R*)-α-methyl benzylamine (**9**) with recombinant whole cells in 38% and with crude enzyme extracts in 42% isolated yield after simple acid–base extraction. In contrast, the kinetic resolution of 2-heptylamine (**18**) had to be stopped after approximately 50% conversion, since after complete consumption of the (*S*)-enantiomer the less reactive (*R*)-enantiomer (Fig. 1) was oxidized by CHAO at a considerable rate. Interestingly, CHAO oxidized both enantiomers of 2-phenylbutylamine (**21**) at the same rate and only racemic **21** was detected by GC analysis.

Since the kinetic resolution of a racemate only produced a maximum yield of 50% of enantiopure amine, we examined

Fig. 1. Relative rates of the oxidation of amines using crude enzyme extracts of cyclohexylamine oxidase (CHAO). Activities are relative to the oxidation of cyclohexylamine (**1**).



CHAO for the deracemization of amines. Based on the existing deracemization protocols developed by Turner and co-workers,[8,10–12] we investigated the deracemization of α-methyl benzylamine (**9**) under varying reaction conditions (Table 2). Initial experiments using 20 equiv of borane–ammonia complex as the reducing reagent led to the formation of (*R*)-**9** in 79% as determined by GC, confirming the concept of deracemization.

In addition, we observed the formation of 21% phenylethanol, most likely derived from hydrolyzed imine, which was further reduced. The use of sodium cyanoborohydride or sodium borohydride as alternative and more reactive reducing agents led to either decreased yields of amines or insufficient reaction rates. The use of increased equivalents of borane–ammonia complex led to the formation of higher amounts of amine and (*R*)-**9** was isolated in 69% yield after workup. The use of whole cells gave a slightly lower yield. In addition, CHAO in combination with borane–ammonia complex was applied successfully to the deracemization of phenylpropan-1-amine (**14**) and 1-indanamine (**15**).

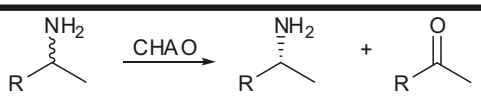
The great potential of CHAO as a biocatalyst for the deracemization of amines is reflected by the fact that both phenylpropan-1-amine (**14**) and 1-indanamine (**15**) were isolated in higher yield than α-methylbenzylamine (**9**), although the relative activities toward both compounds were much lower than that of compound **9**. This underscores the fact that even compounds with relatively low activity can be used for this powerful biocatalytic application.

Although relative oxidation rates of secondary amines were very low as determined by colorimetric assay, we applied the same protocol to the deracemization of 2-methylpiperidine (**28**) and tetrahydroquinaldine (**29**). As expected, we observed only a slight enrichment of one enantiomer of tetrahydroquinaldine, and 2-methylpiperidine was recovered in racemic form.

Can. J. Chem. Downloaded from www.nrcresearchpress.com by Renmin University of China on 09/02/12
For personal use only.

Can. J. Chem. Downloaded from www.nrcresearchpress.com by Renmin University of China on 09/02/12
For personal use only.

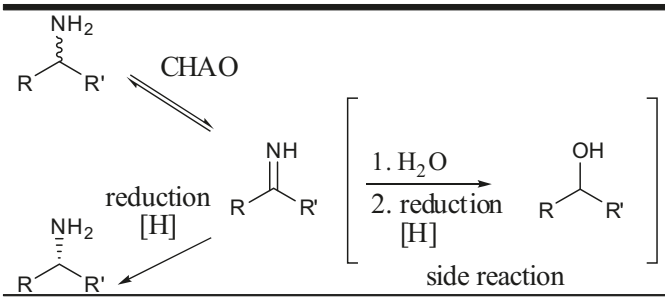
Table 1. Kinetic resolution of amines with cyclohexylamine oxidase (CHAO).



Amine	Biocatalyst	Conversion (%)[a]	R:S[b]
9	Whole cells[c]	50 (38)	>99:1 (*R*)
9	Crude enzyme[d]	50 (42)	>99:1 (*R*)
10	Whole cells	50	>99:1 (*R*)
11	Whole cells	50	>99:1 (*R*)
12	Whole cells	50	>99:1 (*R*)
14	Whole cells	50	>99:1 (*R*)
15	Whole cells	50	>99:1 (*R*)
18	Whole cells[e]	65	>99:1 (*R*)
18	Crude enzyme[e]	47	94:6 (*R*)
21	Whole cells[e]	85	1:1
21	Crude enzyme[e]	60	1:1

[a]Determined by GC; isolated yields are in parentheses.
[b]Determined by GC after acetamide formation.
[c]Resuspended cells OD_{600} 5.
[d]CHAO 1.2 U/mL.
[e]Reaction was stopped after 2 h.

Table 2. Deracemization of amines with CHAO.



Starting material	Biocatalyst	Reducing agent[a]	Recovered amine (%)[b]	R:S[c]	Alcohol (%)[b]
9	Crude enzyme[d]	$NH_3{\cdot}BH_3$	79	>99:1 (*R*)	21
9	Crude enzyme	$NaBH_4$	96	67:33 (*R*)	4
9	Crude enzyme	$NaCNBH_4$	56	>99:1 (*R*)	44
9	Crude enzyme	$NH_3{\cdot}BH_3$ (30 equiv)	86 (69)	>99:1 (*R*)	14
9	Whole cells[e]	$NH_3{\cdot}BH_3$	75 (62)	>99:1 (*R*)	25
14	Crude enzyme	$NH_3{\cdot}BH_3$	84 (75)	>99:1 (*R*)	16
15	Crude enzyme	$NH_3{\cdot}BH_3$	80 (69)	>99:1 (*R*)	20
28	Crude enzyme	$NH_3{\cdot}BH_3$	100	50:50	—
29	Crude enzyme	$NH_3{\cdot}BH_3$	100	57:43	—
29	Whole cells	$NH_3{\cdot}BH_3$	100	52:48	—

[a]Twenty equivalents of reducing agent were used unless otherwise stated.
[b]Determined by GC; isolated yield in parentheses.
[c]Enantiomeric ratio determined by GC after acetamide formation.
[d]CHAO 1.2 U/mL.
[e]Resuspended cells OD_{600} 5.

Conclusion

We demonstrated for the first time the application of a bacterial amine oxidase to the synthesis of chiral amines. Recombinant CHAO from *B. oxydans* IH-35A displays high activity towards a wide range of structurally different amines, a substrate spectrum that is different from that of the fungal monoamine oxidase.[13] In addition, we demonstrated that CHAO can be applied to the synthesis of primary (*R*)-amines by either kinetic resolution or deracemization protocols. Currently, we are working on the preparation of CHAO mutants with increased activities towards secondary and tertiary amines and their application to biocatalysis.

Can. J. Chem. Downloaded from www.nrcresearchpress.com by Renmin University of China on 09/02/12
For personal use only.

Experimental

All chemicals and reagents, including amines **1**–**30**, chiral amines (*R*)-**9**–**12**, (*R*)-**14**, (*R*)-**15**, and (*R*)-**18**, (*S*)-**9**, (*S*)-**18**, and the corresponding ketones derived from **9**–**12**, **14**, **15**, and **18** were purchased from Sigma-Aldrich (Mississauga, Ontario), Alfar Aesar (USA), TCI America (USA), and Thermo Fisher Scientific (USA) and were used without further purification.

For the determination of the conversion of amines by GC, appropriate calibration curves and response factors for product/substrate mixtures were prepared.[18] The enantiomeric ratio of α-methylbenzylamine (**9**) was determined after reaction with propionyl chloride (4 equiv) in the presence of triethylamine (8 equiv) in DCM; for all other amines (**10**–**12**, **14**, **15**, **18**, and **28**) acetamides were prepared using acetylchloride (4 equiv) and triethylamine (8 equiv) in DCM. Enantiomers of **29** were separated by chiral GC without derivatization. Co-injection with samples of acetamides prepared from commercial (chiral) standards allowed for the determination of the absolute configuration. The structure of acetamides were confirmed by GC–MS analysis, and the structures of isolated amines were confirmed by ^{1}H nuclear magnetic resonance (NMR) analysis performed on a Bruker (500 MHz) spectrometer.

GC analysis of products and reaction mixtures

GC analysis of reaction mixtures, acetamides, and racemic and chiral standards was carried out on a Hewlett-Packard 6890 Series gas chromatograph with a Hewlett-Packard 6890 Series autosampler equipped with a flame ionization detector. One microlitre was injected under pulse split (1:5) conditions on a Varian Chirasil-Dex CB column (25 m × 0.25 mm × 0.25 μm) with 8 mL/min helium flow. The following temperature program was used: 75 °C for 5 min; 2.5 °C/min to 175 °C, 10 min at 175 °C, 10 °C/min to 200 °C, 2.5 min at 200 °C. Table 3 illustrates retention times for the ketones and acetamides.

GC–MS analysis of acetamides

Analysis of acetamides derived from compounds **10**, **11**, **12**, **14**, and **15** was performed on an Agilent Technologies 7890A GC coupled to a 5975C quadrupole MS and a CTC Analytics Combipal autosampler. One microlitre was injected under pulse split (1:10) conditions on a 30 m × 0.25 mm × 0.25 μm HP-5MS capillary column (Agilent). The temperature program was as follows: 70 °C for 1.5 min; 65 °C/min to 135 °C, 5 °C/min to 280 °C, and 15 min at 280 °C. Helium was used as the carrier gas. The injector and the detector were adjusted to 250 and 280 °C, respectively. The MSD detector was run in the EI (70 eV) scan mode between 45 and 500 amu.

Analysis of propionate amide derived from **9** and acetamide from **18** was performed on a Hewlett-Packard 6890 GC coupled to a 5973 quadrupole MS and a 7683 autosampler. One microlitre was injected under pulse splitless conditions on a 50 m × 0.2 mm × 0.25 μm HP-5MS capillary column (Agilent). The temperature program was as follows: 70 °C for 1.5 min; 65 °C/min to 135 °C, 5 °C/min to 280 °C, and 15 min at 280 °C. Helium was used as the carrier gas. The injector and the detector were adjusted to 250 and 280 °C, respectively. The MSD detector was run in the EI (70 eV) scan mode between 45 and 500 amu.

Preparation of bacterial cells and the crude enzyme extract of CHAO

Escherichia coli BL21 harboring the CHAO-containing plasmid was maintained on LB medium containing glycerol (50%, v/v) at –80 °C. For biotransformation experiments, a fresh LB agar plate (1.5% agar) containing ampicillin (100 μg/mL) was prepared from the stock culture, and one colony was transferred to a preculture (10 mL) containing LB medium supplemented with ampicillin (100 μg/mL) and grown at 30 °C at 200 rpm on an orbital shaker overnight. In a 2 L DASGIP bioreactor system (Germany) an aliquot of the suspension (10 mL) was used to inoculate 1 L of TB medium. The temperature was set to 30 °C and the pH was controlled at 7.0 by the addition of concentrated ammonium hydroxide. The cell broth was aerated at 1.0 vvm and stirred at 400–1000 rpm to maintain 30% dissolved oxygen. If necessary, the airflow was supplemented with oxygen. At an OD_{600} of 10 (~7 h), protein expression was induced by the addition of IPTG (final concentration 1 mmol/L) and glucose (33% w/w aqueous solution) was fed at an initial rate of 3 mL/h and gradually increased to 7 mL/h. The cells were harvested by centrifugation (6300*g*, 4 °C, 20 min) 16 h after induction and washed with 20 mmol/L sodium phosphate buffer (pH 7), followed by centrifugation. Whole cells (could be stored at 4 °C up to 3 days without loss of activity) were resuspended in the appropriate amount of 100 mmol/L phosphate buffer (pH 7) to give a final OD_{600} of 5 and used for the biotransformations.

Alternatively, the centrifuged and washed cells were resuspended in 20 mmol/L sodium phosphate buffer (OD_{600} ~ 70) and broken using a French press cell operating at 20 000 psi (1 psi = 6.894757 kPa). The crude extract was obtained by centrifugation (20 000*g*, 45 min), followed by sterile filtration using a 0.22 μm membrane. Protein concentration was determined by Bradford assay[19] and the activity was determined as described below. A 1 L fermentation yielded ~650 mg of crude CHAO.

Activity assay

Cyclohexylamine oxidase activity was determined by a modified procedure of Braun et al.[20]

The formation of a dye (ε = 29.4 mmol/L^{-1} cm^{-1}) produced by the action of horseradish peroxidase with liberated hydrogen peroxide from the reaction of the amine (5 mmol/L) and CHAO, 4-aminoantipyrine, and 2,4,6-tribromo-3-hydroxybenzoic acid was monitored at 510 nm using a Beckman spectrophotometer (model DU 640). The standard assay mixture (1 mL total volume) contained: 965 μL of 50 mmol/L phosphate buffer (pH 7), 10 μL of a 2,4,6-tribromo-3-hydroxybenzoic acid stock solution (20 mg/ mL in DMSO), 0.15 mg of 4-aminoantipyrine, 5 μL of an amine stock solution (1 mol/L in DMSO), and 10 μL of a horse radish peroxidase stock solution (5 mg/mL). The reaction (1 mL) was started by the addition of 10 μL of an appropriate amount of enzyme at room temperature. Enzymatic assays were performed in triplicate with the appropriate control experiments. One enzyme unit (U) was defined as the amount of enzyme that produced 1 μmol of hydrogen peroxide from

Table 3. Retention times of ketones and alcohols and response factors for amines and ketones.

Compound	Retention time (min) (*R*)-Enantiomer acetamide	(*S*)-Enantiomer acetamide	Ketone	Alcohol[a]	Amine:ketone response factor
9[b]	38.97	38.66	18.69	25.59 and 26.32	1:1.48
10	38.22	37.54	18.59	na	1:1.51
11	45.41	45.95	27.54	na	1:1.63
12	40.69	40.13	23.50	na	1.02:1[c]
14	38.84	38.29	22.47	29.56 and 29.94	1:1.68
15	45.14	44.52	29.06	32.18 and 32.39	1:1.81
18	44.27	43.88	26.83	na	1:1.25
21	28.70	27.65	8.76	na	1:2.57
28	29.66	29.26	na	na	na
29[e]	32.34	32.73	na	na	na

Note: na, not applicable.

[a]Two enantiomers.

[b]Propionate amides were prepared.

[d]Response factor based on acetamide and ketone.

[e]Absolute configuration was not determined; (*R*)- and (*S*)- based on enrichment by CHAO.

Can. J. Chem. Downloaded from www.nrcresearchpress.com by Renmin University of China on 09/02/12
For personal use only.

cyclohexylamine (**1**) per min. Relative activities (%) were calculated by dividing the activity of the amine tested by the activity of cyclohexylamine (**1**).

Kinetic resolution of racemic amines using either whole cells or crude enzyme extract

Screening scale

The amine (0.2 mmol) dissolved in DMSO (0.2 mL) was added to either a solution of CHAO (final concentration 1.2 U/mL) in 100 mmol/L phosphate buffer (pH 7, 20 mL) or a suspension of whole cells overexpressing CHAO (OD_{600} 5) resuspended in 100 mmol/L phosphate buffer (pH 7, 20 mL). The mixture was shaken at 200 rpm at 30 °C on an orbital shaker for 18 h, before the pH of the reaction mixture was adjusted to 2 with 2 mol/L HCl. The suspension was centrifuged (6300*g*, 20 min) and the supernatant was basified to pH 9 with 5 mol/L NaOH. The aqueous layer was extracted 3 times with DCM and the organic layers were combined, washed with brine, dried over anhydrous sodium sulphate, and filtered. An aliquot (1 mL) was analyzed for the conversion of amine to ketone. For determination of the enantiomeric ratio the organic solvent was concentrated to 1 mL, cooled to 0 °C, and triethylamine (81 mg, 0.8 mmol) was added followed by the dropwise addition of acetylchloride (31 mg, 0.4 mmol). Then the reaction mixture was allowed to react at room temperature for 1 h. An aliquot of the reaction mixture (20 µL) was added to a mixture of DCM–MeOH, 8:2 (1 mL) and analyzed by chiral GC and GC–MS.

Preparative scale

α-Methylbenzylamine (**9**) (121 mg, 1 mmol) dissolved in DMSO (0.5 mL) was added to either a solution of CHAO (final concentration 1.2 U/mL) in 100 mmol/L phosphate buffer (pH 7, 100 mL) or a suspension of whole cells overexpressing CHAO (OD_{600} 5) resuspended in 100 mmol/L phosphate buffer (pH 7, 100 mL). The mixture was shaken at 200 rpm at 30 °C on an orbital shaker for 18 h, before the pH of the reaction mixture was adjusted to 2 with 2 mol/L HCl. The suspension was centrifuged (6300*g*, 20 min) and the supernatant was basified to pH 9 with 5 mol/L NaOH. For the crude enzyme extracts the centrifugation step could be omitted. The aqueous layer was extracted 3 times with DCM and the organic layers were combined. An aliquot (1 mL) was analyzed for the conversion by GC analysis. The organic solvent was concentrated (25 mL) and extracted 3 times with 1 mol/L HCl. The aqueous layers were combined, basified to pH 9 with 5 mol/L NaOH, and extracted 3 times with DCM. The organic layers were combined, washed with brine, dried over anhydrous sodium sulphate, and filtered. Evaporation of the solvent gave enantiopure (*R*)-α-methylbenzylamine (**9**) in 38% yield (46 mg) with whole cell transformations and in 42% yield (51 mg) with the crude enzyme extract experiment. The enantiomeric ratio of the obtained products was determined as described before.

Deracemization of racemic amines using either whole cells or crude enzyme extract

Screening scale

The amine (0.2 mmol) dissolved in DMSO (0.2 mL) was either added to a solution of CHAO (final concentration 1.2 U/mL) and borane–ammonia complex (123 mg, 4.0 mmol) in 100 mmol/L phosphate buffer (pH 7, 20 mL) or to a suspension of whole cells overexpressing CHAO (OD_{600} 5) resuspended in 100 mmol/L phosphate buffer (pH 7, 20 mL) and borane–ammonia complex (123 mg, 4.0 mmol). The mixture was shaken at 200 rpm at 30 °C on an orbital shaker for 18 h, before the pH of the reaction mixture was carefully adjusted to 2 with 2 mol/L HCl. The suspension was centrifuged (6300*g*, 20 min) and the supernatant was basified to pH 9 with 5 mol/L NaOH. The aqueous layer was extracted 3 times with DCM and the organic layers were combined, washed with brine, dried over anhydrous sodium sulphate, and filtered. An aliquot (1 mL) was analyzed for the content of amine, the corresponding ketone, and alcohol derivatives. For determination of the enantiomeric ratio the organic solvent was concentrated to 1 mL, treated with acetylchloride, and analyzed by chiral GC as described before.

Can. J. Chem. Downloaded from www.nrcresearchpress.com by Renmin University of China on 09/02/12
For personal use only.

Preparative scale

The amine (1 mmol) dissolved in DMSO (0.5 mL) was either added to a solution of CHAO (final concentration 1.2 U/mL) and borane–ammonia complex (617 mg, 20.0 mmol; for the deracemization of **9**, 926 mg, 30 mmol) in 100 mmol/L phosphate buffer (pH 7, 20 mL) or to a suspension of whole cells overexpressing CHAO (OD_{600} 5) resuspended in 100 mmol/L phosphate buffer (pH 7, 20 mL) and borane–ammonia complex (617 mg, 20.0 mmol). The mixture was shaken at 200 rpm at 30 °C on an orbital shaker for 18 h, before the pH of the reaction mixture was carefully adjusted to 2 with 2 mol/L HCl. The suspension was centrifuged (6300*g*, 20 min) and the supernatant was basified to pH 9 with 5 mol/L NaOH. The aqueous layer was extracted 3 times with DCM, the organic layers were combined, and an aliquot (1 mL) was analyzed for the content of amine and the corresponding ketone and alcohol. The organic solvent was concentrated (25 mL) and extracted 3 times with 1 mol/L HCl. The aqueous layers were combined, basified to pH 9 with 5 mol/L NaOH, and extracted 3 times with DCM. The organic layers were combined, washed with brine, dried over anhydrous sodium sulphate, and filtered.

Evaporation of the solvent gave 83 mg (69% yield) of (*R*)-**9** using crude enzyme extracts, 75 mg (62% yield) of (*R*)-**9** using whole cells, 101 mg (75% yield) of (*R*)-**14** using crude enzyme extracts, and 92 mg (69% yield) of (*R*)-**14** using crude enzyme extracts. The enantiomeric ratio of the obtained products was determined after derivatization of an aliquot of the product as described before.

Acknowledgements

We thank A. Corriveau, S. Deschamps, and C. Beaulieu for their expert help in various analytical analyses, and K. Morley for suggestions and comments on the manuscript.

References

(1) (a) Farina, V.; Reeves, J. T.; Senanayake, C. H.; Song, J. J. *Chem. Rev.* **2006**, *106* (7), 2734. doi:10.1021/cr040700c; (b) Breuer, M.; Ditrich, K.; Habicher, T.; Hauer, B.; Keßeler, M.; Stürmer, R.; Zelinski, T. *Angew. Chem. Int. Ed.* **2004**, *43* (7), 788. doi:10.1002/anie.200300599.

(2) (a) For recent reviews on the chemical synthesis of chiral amines see Nugent, T. C.; El-Shazly, M. *Adv. Synth. Catal.* **2010**, *352* (5), 753; (b) Müller, T. E.; Hultzsch, K. C.; Yus, M.; Foubelo, F.; Tada, M. *Chem. Rev.* **2008**, *108* (9), 3795. doi:10.1021/cr0306788; (c) Kizirian, J.-C. *Chem. Rev.* **2008**, *108* (1), 140. doi:10.1021/cr040107v; (d) Friestad, G. K.; Mathies, A. K. *Tetrahedron* **2007**, *63* (12), 2541. doi:10.1016/j.tet.2006.11.076.

(3) Höhne, M.; Bornscheuer, U. T. *ChemCatChem* **2009**, *1* (1), 42. doi:10.1002/cctc.200900110.

(4) (a) For recent examples of ω-transaminases in chiral amine synthesis see Shin, J.-S.; Kim, B.-G.; Liese, A.; Wandrey, C. *Biotechnol. Bioeng.* **2001**, *73* (3), 179. doi:10.1002/bit.1050; (b) Koszelewski, D.; Lavandera, I.; Clay, D.; Guebitz, G. M.; Rozzell, D.; Kroutil, W. *Angew. Chem. Int. Ed.* **2008**, *47* (48), 9337. doi:10.1002/anie.200803763; (c) Koszelewski, D.; Lavandera, I.; Clay, D.; Rozzell, D.; Kroutil, W. *Adv. Synth. Catal.* **2008**, *350* (17), 2761. doi:10.1002/adsc.200800496; (d) Höhne, M.; Robins, K.; Bornscheuer, U. T. *Adv. Synth. Catal.* **2008**, *350* (6), 807. doi:10.1002/adsc.200800030; (e) Truppo, M. D.; Turner, N. J.; Rozzell, J. D. *Chem. Commun. (Camb.)* **2009**, (16), 2127. doi:10.1039/b902995h; (f) Savile, C. K.; Janey, J. M.; Mundorff, E. C.; Moore, J. C.; Tam, S.; Jarvis, W. R.; Colbeck, J. C.; Krebber, A.; Fleitz, F. J.; Brands, J.; Devine, P. N.; Huisman, G. W.; Hughes, G. J. *Science* **2010**, *329* (5989), 305. doi:10.1126/science.1188934; (g) For a review see Koszelewski, D.; Tauber, K.; Faber, K.; Kroutil, W. *Trends Biotechnol.* **2010**, *28* (6), 324. doi:10.1016/j.tibtech.2010.03.003.

(5) Fitzpatrick, P. F. *Arch. Biochem. Biophys.* **2010**, *493* (1), 13. doi:10.1016/j.abb.2009.07.019.

(6) Hafner, E. W.; Wellner, D. *Proc. Natl. Acad. Sci. U.S.A.* **1971**, *68* (5), 987. doi:10.1073/pnas.68.5.987.

(7) (a) Huh, J. W.; Yokoigawa, K.; Esaki, N.; Soda, K. *J. Ferment. Bioeng.* **1992**, *74* (3), 189. doi:10.1016/0922-338X(92)90082-6; (b) Huh, J. W.; Yokoigawa, K.; Esaki, N.; Soda, K. *Biosci. Biotechnol. Biochem.* **1992**, *56* (12), 2081. doi:10.1271/bbb.56.2081.

(8) (a) Beard, T. M.; Turner, N. J. *Chem. Commun. (Camb.)* **2002**, (3), 246. doi:10.1039/b107580m; (b) Alexandre, F.-R.; Pantaleone, D. P.; Taylor, P. P.; Fotheringham, I. G.; Ager, D. J.; Turner, N. J. *Tetrahedron Lett.* **2002**, *43* (4), 707. doi:10.1016/S0040-4039(01)02233-X.

(9) (a) For cloning and characterization of monoamine oxidase from *A. niger* see Schilling, B.; Lerch, K. *Biochim. Biophys. Acta* **1995**, *1243* (3), 529; (b) Schilling, B.; Lerch, K. *Mol. Gen. Genet.* **1995**, *247* (4), 430. doi:10.1007/BF00293144.

(10) (a) Alexeeva, M.; Enright, A.; Dawson, M. J.; Mahmoudian, M.; Turner, N. J. *Angew. Chem. Int. Ed.* **2002**, *41* (17), 3177. doi:10.1002/1521-3773(20020902)41:17<3177::AID-ANIE3177>3.0.CO;2-P; (b) Carr, R.; Alexeeva, M.; Enright, A.; Eve, T. S. C.; Dawson, M. J.; Turner, N. J. *Angew. Chem. Int. Ed.* **2003**, *42* (39), 4807. doi:10.1002/anie.200352100.

(11) Carr, R.; Alexeeva, M.; Dawson, M. J.; Gotor-Fernández, V.; Humphrey, C. E.; Turner, N. J. *ChemBioChem* **2005**, *6* (4), 637. doi:10.1002/cbic.200400329.

(12) (a) Dunsmore, C. J.; Carr, R.; Fleming, T.; Turner, N. J. *J. Am. Chem. Soc.* **2006**, *128* (7), 2224. doi:10.1021/ja058536d; (b) Bailey, K. R.; Ellis, A. J.; Reiss, R.; Snape, T. J.; Turner, N. J. *Chem. Commun. (Camb.)* **2007**, (35), 3640. doi:10.1039/b710456a.

(13) Köhler, V.; Bailey, K. R.; Znabet, A.; Raftery, J.; Helliwell, M.; Turner, N. J. *Angew. Chem. Int. Ed.* **2010**, *49* (12), 2182. doi:10.1002/anie.200906655.

(14) Eve, T. S. C.; Wells, A.; Turner, N. J. *Chem. Commun. (Camb.)* **2007**, (15), 1530. doi:10.1039/b617537f.

(15) (a) Znabet, A.; Zonneveld, J.; Janssen, E.; De Kanter, F. J. J.; Helliwell, M.; Turner, N. J.; Ruijter, E.; Orru, R. V. A. *Chem. Commun. (Camb.)* **2010**, *46* (41), 7706. doi:10.1039/c0cc02938f; (b) Znabet, A.; Ruijter, E.; De Kanter, F. J. J.; Köhler, V.; Helliwell, M.; Turner, N. J.; Orru, R. V. A. *Angew. Chem. Int. Ed.* **2010**, *49* (31), 5289. doi:10.1002/anie.201001592.

(16) (a) Iwaki, H.; Shimizu, M.; Tokuyama, T.; Hasegawa, Y. *Appl. Environ. Microbiol.* **1999**, *65* (5), 2232; (b) Iwaki, H.; Shimizu, M.; Tokuyama, T.; Hasegawa, Y. *J. Biosci. Bioeng.* **1999**, *88* (3), 264. doi:10.1016/S1389-1723(00)80007-9.

(17) Iwaki, H.; Hasegawa, Y.; Lau, P. C. K. Unpublished data.

(18) Wernerova, M.; Hudlicky, T. *Synlett* **2010**, (18), 2701.

(19) Bradford, M. M. *Anal. Biochem.* **1976**, *72* (1–2), 248. doi:10.1016/0003-2697(76)90527-3.

(20) Braun, M.; Kim, J. M.; Schmid, R. D. *Appl. Microbiol. Biotechnol.* **1992**, *37* (5), 594. doi:10.1007/BF00240732.

The role of solvent in organometallic chemistry — Oxidative addition with dichloromethane or chloroform

Anwar Abo-Amer, Matthew S. McCready, Fenbao Zhang, and Richard J. Puddephatt

Can. J. Chem. Downloaded from www.nrcresearchpress.com by Renmin University of China on 09/02/12
For personal use only.

Abstract: Dimethylplatinum(II) complexes [$PtMe_2$(NN)], with NN = diimine ligand, can react with dichloromethane or chloroform solvent to give the corresponding organoplatinum(IV) complexes [$PtClMe_2(CH_2Cl)$(NN)] or [$PtClMe_2(CHCl_2)$(NN)], respectively. The products can exist in isomeric forms, corresponding to products of cis or trans oxidative addition. The structures of three dichloromethane adducts and one chloroform adduct are reported.

Key words: platinum, dichloromethane, chloroform, oxidative addition.

Résumé : Les complexes du diméthylplatine(II) [$PtMe_2$(NN)] dans lesquels NN correspond à un ligand diimine peuvent réagir avec les solvants dichlorométhane et chloroforme pour conduire respectivement aux complexes organoplatine(IV) correspondants [$PtClMe_2(CH_2Cl)$(NN)] ou [$PtClMe_2(CHCl_2)$(NN)]. Les produits peuvent exister sous des formes isomères qui correspondent à des produits d'addition oxydante cis ou trans. On a déterminé et on rapporte les caractéristiques des structures de trois adduits du dichlorométhane et d'un adduit du chloroforme.

Mots-clés : platine, dichlorométhane, chloroforme, addition oxydante.

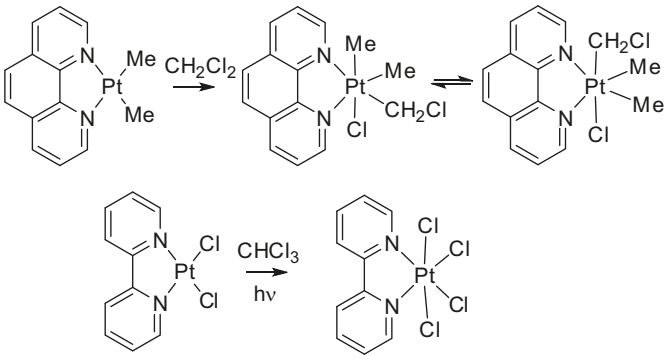
[Traduit par la Rédaction]

Introduction

One of the challenges in the application of organometallic compounds is that there are limits on the range of solvents that can be used. For example, the development of organometallic chemistry in "greener" solvents, such as water or ionic liquids, has presented unusual challenges and opportunities.[1,2] Metal–alkyl bonds are often cleaved by protic solvents, whereas halogen-containing solvents can react to form metal halides.[1,2] Chlorinated solvents such as dichloromethane and chloroform may react with transition-metal complexes in low oxidation states by oxidative addition of one or more of the C–Cl bonds, and examples are known with several late-transition metals including rhenium,[3,4] ruthenium,[5] cobalt,[6,7] rhodium,[8–22] iridium,[23] palladium,[24–27] platinum,[28–37] and gold.[38] In previous studies of electron-rich dimethylplatinum(II) complexes, it has been noted that reactions with chlorinated solvents can occur to give oxidative addition of a C–Cl bond or to give chlorine atom abstraction or a mixture of these reactions (Scheme 1).[31–37,39,40]

This paper describes new examples of these reactions including the first examples with unsymmetrical supporting ligands, leading to a greater range of isomeric organoplatinum(IV) products, and the first structure determinations on

Scheme 1. Oxidative addition and chlorine abstraction reactions.[33,40]



chloromethyl and dichloromethyl derivatives of platinum(IV). This allows a comparison of the structures of the platinum(IV) complexes with known platinum(II) complexes, which have been prepared either by oxidative addition to Pt(0) or by methylene insertion reactions.[27,28,41–43]

Results

The complex [$PtMe_2$(2,2′-bipyridine)] is already known to react with dichloromethane by oxidative addition of a C–Cl

Received 22 March 2011. Accepted 31 May 2011. Published at www.nrcresearchpress.com/cjc on 24 October 2011.

A. Abo-Amer. Department of Chemistry, Al al-Bayt University, Al-Mafraq, Jordan.
M.S. McCready, F. Zhang, and R.J. Puddephatt. Department of Chemistry, The University of Western Ontario, London, ON N6A 5B7, Canada.

Corresponding author: Richard J. Puddephatt (e-mail: pudd@uwo.ca).

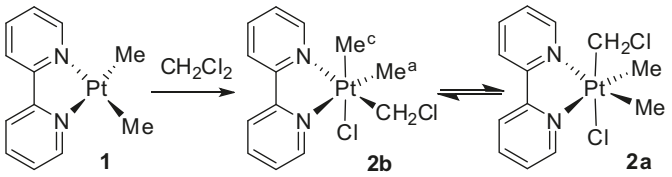
This article is part of a Special Issue dedicated to Professor Tak-Hang Chan for his pioneering research on organometallic chemistry in nontraditional solvents.

Can. J. Chem. Downloaded from www.nrcresearchpress.com by Renmin University of China on 09/02/12
For personal use only.

Table 1. Selected NMR data (δ in ppm, *J* in Hz) for the dichloromethane adducts (see Schemes 2 and 3 for labelling system).

Complex	δ(Me[a])	*J*(PtH)	δ(Me[b])	*J*(PtH)	δ(Me[c])	*J*(PtH)	δ(CH_2Cl)	*J*(PtH)
2a	1.29	69					3.55	52
2b	1.39	69			0.65	74	4.34	46
							4.67	88
4a	1.26	70	1.41	70			3.53	48
							3.54	58
4b	1.44	70			0.61	74	4.72	78
							4.89	86
4c			1.55	70	0.66	74	4.26	44
							4.74	92
6a	1.46	74	1.60	74			3.62	44
							3.83	57
6b	1.45	73			0.92	73	4.27	43
							4.84	89
6c			1.69	73	0.93	73	4.22	43
							4.89	91

Scheme 2. Complexes with 2,2′-bipyridine.

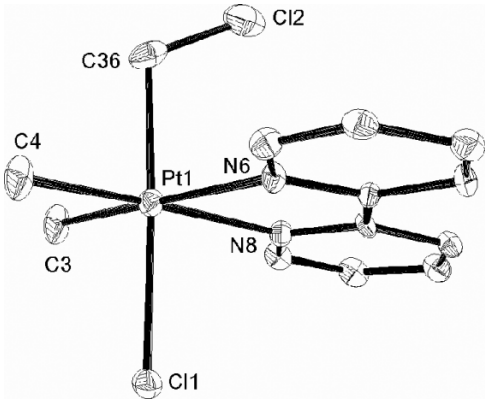


bond (Scheme 2).[32,37] The thermodynamically more stable product is **2a**, but the kinetic product is mostly **2b**, formed by cis-oxidative addition. At equilibrium, the ratio of isomers **2a**:**2b** in roughly 5:2. Complexes **2a** and **2b** have effective C_s and C_1 symmetry, respectively, so, in the ^{1}H NMR spectrum, **2a** gives a single methylplatinum resonance and a single $PtCH_2Cl$ resonance, whereas **2b** gives two methylplatinum resonances and two resonances for the $PtCH^aH^bCl$ protons (Table 1). The equatorial and axial PtMe and $PtCH_2Cl$ groups (defined with respect to the Pt–bipy plane) are readily identified by the characteristic differences in chemical shifts (Table 1). For example, in **2b** the equatorial $PtMe^a$ and $PtMe^c$ resonances occur at δ(^{1}H) = 1.39 and 0.65, respectively, and the equatorial and axial $PtCH_2Cl$ resonances in **2b** and **2a**, respectively, occur at δ(^{1}H) = 4.34 and 4.67 and at δ(^{1}H) = 3.33 (Table 1).

Recrystallization of the mixture of isomeric compounds **2a** and **2b** gave single crystals of **2a**, but crystals of **2b** could not be obtained. The structure of complex **2a** is shown in Fig. 1. It confirms that the chloromethyl group and chloride ligand are mutually trans in the octahedral platinum(IV) complex. The chloromethyl group is oriented such that the chlorine atom lies towards one of the pyridyl nitrogen atoms of the 2,2′-bipyridine ligand, with the torsion angle N(8)–Pt(1)–C(36)–Cl(2) = –3.5°. The angle Pt(1)–C(36)–Cl(2) of 115.2(7)° is larger than the tetrahedral angle, perhaps to reduce steric interactions. There is minor unresolved disorder in the position of the chloromethyl group.

The reactions of dichloromethane solvent with two unsymmetrical dimethylplatinum(II) complexes were studied, as shown in Scheme 3. In these cases, there are three possible isomeric products of oxidative addition and all three were observed. In the slow reaction of the dimethylplatinum(II) complex **3**, with the 3,6-di-2-pyridylpyridazine derivative (dppd) as the supporting ligand,[44,45] the reaction with CD_2Cl_2 gave a mixture of **4a**:**4b**:**4c** in the ratio 3:2:1 after 2 h reaction, but 5:1:1 after 24 or 48 h, as determined by monitoring using ^{1}H NMR. In this case, the oxidative addition was slow and was only about 20% complete after 2 h, but complete after 24 h, and it seems that the rate of isomerization is competitive with the rate of oxidative addition. Complex **4b** is formed in a higher proportion early in the reaction, so it can be considered as the kinetically preferred product, but the selectivity cannot be determined accurately. The reaction of dimethylplatinum(II) complex **5** with the 2,5-di-2-pyridyl-1,3,4-oxadiazole supporting ligand dpox[46,47] occurred in a similar way to give **6a**:**6b**:**6c** in a final ratio of 9:1:1.

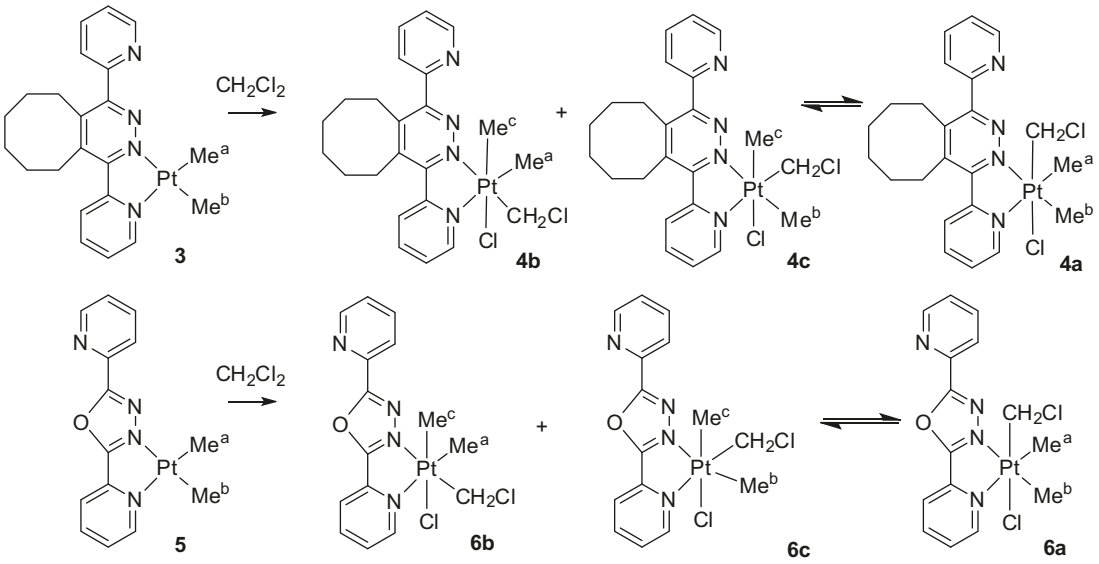
Fig. 1. A view of the structure of complex **2a**. Selected dimensions: Pt(1)–C(3) 2.079(12) Å, Pt(1)–C(4) 2.115(16) Å, Pt(1)–C(36) 2.076(14) Å, Pt(1)–N(6) 2.167(8) Å, Pt(1)–N(8) 2.177(10) Å, Pt(1)–Cl(1) 2.435(3) Å, Cl(2)–C(36) 1.74(2) Å; Pt(1)–C(36)–Cl(2) 115.2(7)°.



The isomers were identified by their ^{1}H NMR spectra, as illustrated here for the mixture **4a**, **4b**, and **4c**. The major isomer **4a** was readily identified by the presence of two equatorial methylplatinum chemical shifts and the typical chemical shift values for an axial $PtCH_2Cl$ group (Table 1, compare with **2a** and **2b**). Distinguishing between the isomers **4b** and

Can. J. Chem. Downloaded from www.nrcresearchpress.com by Renmin University of China on 09/02/12
For personal use only.

Scheme 3. The unsymmetrical dichloromethane adducts.



4c was more difficult and relied on information from COSY and NOESY NMR spectra to identify whether the methyl or CH_2Cl group was adjacent to the *ortho*-pyridyl proton for a given isomer. It can be seen from the data in Table 1 that the equatorial methylplatinum group $PtMe^b$ consistently had a higher chemical shift than for the other equatorial methylplatinum group $PtMe^a$.[48,49] The isomers **6a**, **6b**, and **6c** were identified in a similar way.

The structure of complex **4a** is shown in Fig. 2. The structure is similar to that of **2a**. In **4a** the chlorine atom of the chloromethyl group lies above the nitrogen atom of the coordinated pyridyl group, with a torsion angle of N(4)–Pt(1)–C(21)–Cl(1) = 5° and with the angle Pt(1)–C(21)–Cl(1) = 116.2(4)°. The presence of the cyclooctene ring in **4a** causes steric hindrance, and the pyridyl and pyridazine rings are skewed by 17° to reduce the steric congestion. In contrast, the two pyridyl rings in **2a** are skewed by only 1°. The uncoordinated pyridyl group is skewed with respect to the pyridazine ring by 49°; this distortion is presumably again to reduce steric hindrance, since potential conjugation would favour the planar structure.

The structure of complex **6a**·H_2O is shown in Fig. 3. There are similarities and some differences when compared with the structures of **2a** and **4a**. In **6a**, as observed in **4a**, the chlorine atom of the chloromethyl group lies roughly above the nitrogen atom of the coordinated pyridyl group, with a torsion angle N(1)–Pt(1)–C(2)–Cl(1) = –15° and with the angle Pt(1)–C(21)–Cl(1) = 116.2(4)°. In contrast to **4a**, the coordinated pyridyl and oxadiazole rings are skewed by only 2°, and the free pyridyl ring and the oxadiazole ring are skewed by only 3°. These differences clearly arise as a result of the much lower steric hindrance in **6a** compared with **4a**. The nitrogen atom of the free pyridyl group and the oxygen atom of the oxadiazole group are mutually syn, and they are involved in hydrogen bonding to one hydrogen atom of a water solvate molecule (Fig. 3, O(1)···O(2B) = 2.98 Å and N(5)···O(2B) = 3.03 Å). The second hydrogen atom of the water molecule hydrogen bonds to the PtCl chlorine atom of a neighbouring molecule, and this hydrogen bonding forms racemic dimer units in which the two

Fig. 2. A view of the structure of complex **4a**. Selected parameters: Pt(1)–C(21) 2.027(8) Å, Pt(1)–C(22) 2.046(7) Å, Pt(1)–C(23) 2.052 (8) Å, Pt(1)–N(4) 2.133(6) Å, Pt(1)–N(1) 2.136(5) Å, Pt(1)–Cl(2) 2.4371(18) Å Cl(1)–C(21) 1.767(9) Å, Cl(1)–C(21)–Pt(1) 116.2(4)°.

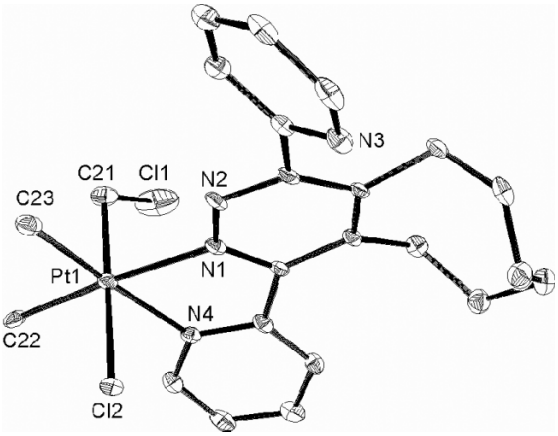
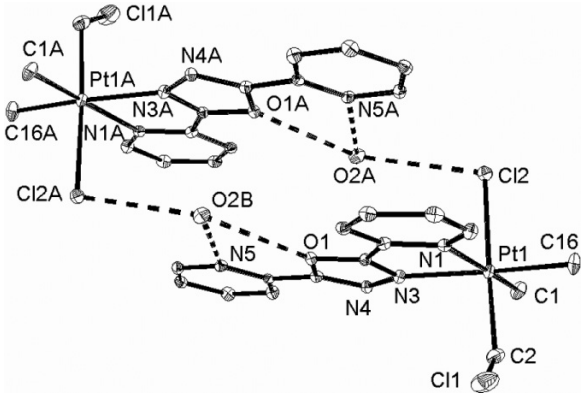
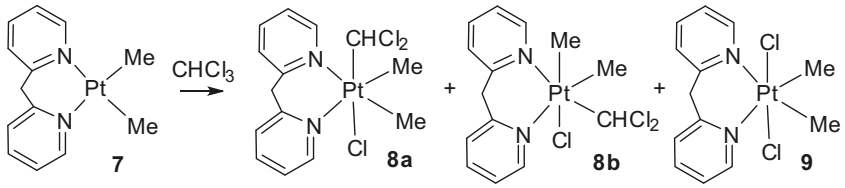


Fig. 3. The structure of complex **6a**. Selected parameters: Pt(1)–C(1) 2.057(5) Å, Pt(1)–C(2) 2.013(7) Å, Pt(1)–C(16) 2.032(6) Å, Pt(1)–N(1) 2.223(4) Å, Pt(1)–N(3) 2.169(5) Å, Pt(1)–Cl(2) 2.449(1) Å, Cl(1)–C(2) 1.773(7) Å; Pt(1)–C(2)–C(11) 116.2(4)°.



Scheme 4. Oxidative addition of chloroform.

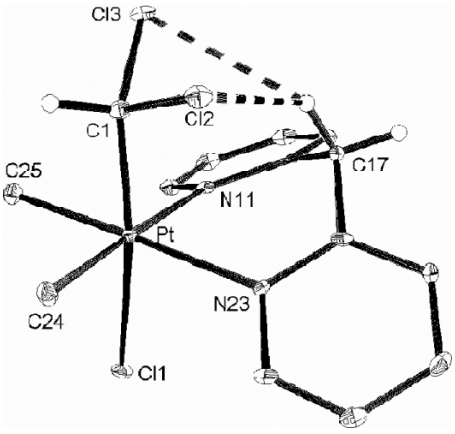


chiral molecules of **6a** are related by an inversion centre (Fig. 3; Cl(2)···O(2A) = 3.23 Å).

The oxidative addition of chloroform to dimethylplatinum (II) complexes often gives intractable mixtures of products,[32,35] but the reaction with [$PtMe_2$(dpm)] (dpm = di-2-pyridylmethane)[48] occurred to give complex **8a** as the major product according to Scheme 4. The complex **8b** was not confidently detected, but there was evidence for formation of complex **9**, the product of chlorine atom abstraction, when the reaction was monitored in $CDCl_3$.[35,39]

The structure of complex **8a** is shown in Fig. 4 and confirms the trans orientation of the $CHCl_2$ and Cl groups. The dichloromethyl group adopts a conformation with the chlorine atoms roughly above each coordinated nitrogen atom of the dpm ligand, with torsion angles N(11)–PtC(1)–Cl(3) = 20.3° and N(23)–PtC(1)–Cl(2) = –18°. The dpm ligand adopts a bowed conformation (angle between the planes of the pyridyl groups = 47°) with the CH_2 group oriented towards the dichloromethyl group. In this conformation, one of the hydrogens is in a position to form a weak CH···Cl hydrogen bond to both of the $CHCl_2$ chlorine atoms with C(17)···Cl(2) = 3.43 Å and C(17)···Cl(3) = 3.49 Å (Fig. 4).

Fig. 4. A view of the structure of complex **8a**. Selected bond parameters: Pt–C(1) 2.040(7) Å, Pt–C(25) 2.051(7) Å, Pt–C(24) 2.062(7) Å, Pt–N(23) 2.163(5) Å, Pt–N(11) 2.171(5)Å, Pt–Cl(1) 2.406(2) Å, C(1)–Cl(2) 1.796(7) Å, C(1)–-Cl(3) 1.806(7) Å; selected angle parameters: Cl(2)–C(1)–Cl(3) 108.2(4)°, Cl(2)–C(1)–Pt 114.7(4)°, Cl(3)–C(1)–Pt 114.2(3)°.



Discussion

The structure determination of both chloromethyl (**2a**, **4a**, and **6a**) and dichloromethyl (**8a**) complexes of platinum(IV) allows a comparison of the bond parameters, and selected data are given in Table 2.[50,51] The Pt–Cl distance is slightly shorter in **8a** than in the chloromethyl complexes, indicating that the more electronegative dichloromethyl group in **8a** has a slightly lower trans influence than the chloromethyl group. The Pt–Cl distances are all in the range expected for a Pt–Cl bond trans to an alkyl group, but the data indicate the trans-influence series $CH_3 > CH_2Cl > CHCl_2$.[52–54]

In the parent chlorocarbons, the C–Cl distance decreases slightly in the sequence $CH_3Cl > CH_2Cl_2 > CHCl_3$ (Table 2),[50] but the limited data suggest that the trend is reversed in the platinum complexes with *d*(C–Cl) for **8a** > **6a**. This could be interpreted in terms of carbene character from resonance forms $[Pt{=}CHCl]^+Cl^-$, but the other bond parameters, such as the value of *d*(Pt–C) = 2.040(7) Å, do not support this interpretation. Instead the parameters suggest a more polar group $Pt^{\delta+}$–$CHCl_2^{\delta-}$, but without significant carbene character. We note that the differences in C–Cl distances (excluding the disordered **2a**) are just statistically significant, so further comment is not warranted.

A second feature of interest is the kinetic preference for cis-oxidative addition in the reactions of dichloromethane to form **2**, **4**, and **6** (Schemes 2 and 3), and this will be considered in terms of the simplest example with the 2,2′-bipyridine ligand. Three possible mechanisms are shown in Scheme 5. Dichloromethane can undergo nucleophilic substitution,[51] and this could lead to oxidative addition by the polar mechanism involving an initial intermediate $[PtMe_2(CH_2Cl)(bipy)]^+Cl^-$ (***A***), which would need to isomerize to a second intermediate ***B*** before coordination of chloride occurs to form the cis product **2b** (Scheme 5).[55–57] Subsequent isomerization of **2b** to **2a** would require reversal of this step, to proceed through intermediates ***B*** and ***A*** (Scheme 5). There is evidence that the reactions with dichloromethane can be accelerated by photolysis or by radical initiators and retarded by radical scavengers, indicating that at least part of the oxidative addition occurs through a radical chain mechanism.[33,34,58,59] The initial radical, formed by attack of the chain-carrying radical $CH_2Cl\cdot$ would be ***C*** and this would need to isomerize to ***D*** prior to chlorine-atom abstraction from solvent to form **2b** as the kinetic product (Scheme 5). The subsequent isomerization of **2b** to **2a** would occur through intermediates ***B*** and ***A***, as in the polar mechanism (Scheme 5).[55–57] A third mechanism might involve a free radical nonchain mechanism, involving a radical pair formed by chlorine-atom abstraction to give ***E***, but there is no easy way to form isomer **2b** in this case, since isomerization of ***E*** to ***F*** followed by recombination would give the unobserved isomer ***G*** (Scheme 5). Therefore, this mechanism can probably be eliminated. The activation energy for the chlorine-atom abstraction step to give $[PtClMe_2(bipy)]\cdot + CH_2Cl\cdot$ is calculated to be 193 kJ mol^{-1} and this represents the initiation step for the free radical chain reaction. The chain reaction is expected to be fast (Fig. 5), but thermal initiation is slow.

Some further insight into the mechanism was obtained by carrying out DFT calculations. First, it was calculated that **2a** is more stable than **2b** by only 2 kJ mol^{-1}, consistent with the

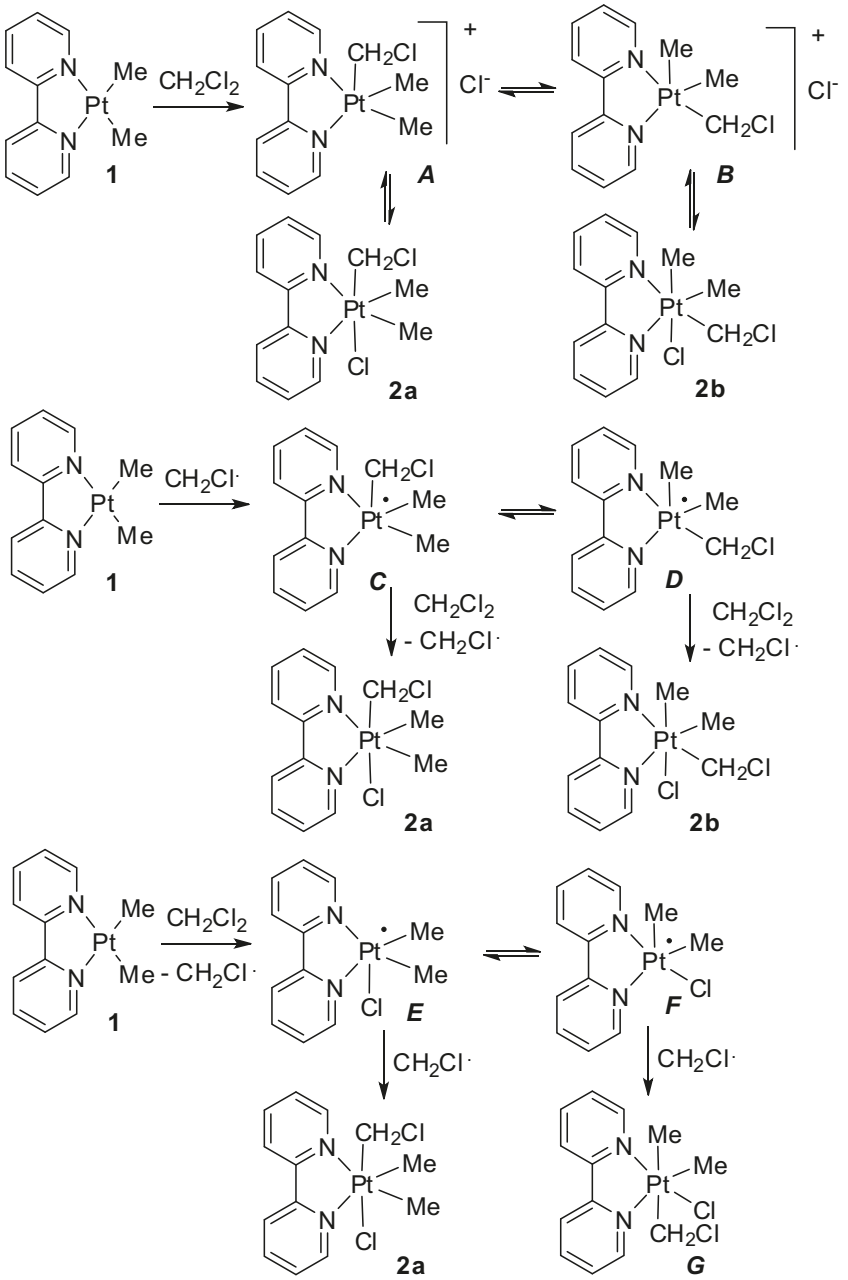
Can. J. Chem. Downloaded from www.nrcresearchpress.com by Renmin University of China on 09/02/12
For personal use only.

Can. J. Chem. Downloaded from www.nrcresearchpress.com by Renmin University of China on 09/02/12
For personal use only.

Table 2. A comparison of selected bond parameters (distance (*d*) in Å, π in °) for the platinum complexes with those of the parent chlorocarbons, determined by electron diffraction.[50]

Compound	*d*(Pt–Cl)	*d*(Pt–C)	*d*(C–Cl)	π(Pt–C–Cl)	π(Cl–C–Cl)
CH_3Cl			1.777		
CH_2Cl_2			1.764		112.2
$CHCl_3$			1.760		110.7
2a	2.435(3)	2.08(1)	1.74(2)	115.2(7)	
4a	2.437(2)	2.027(8)	1.767(9)	116.2(4)	
6a	2.449(1)	2.013(7)	1.773(7)	116.2(4)	
8a	2.406(2)	2.040(7)	1.796(7), 1.806(7)	114.7(4), 114.2(3)	108.2(4)

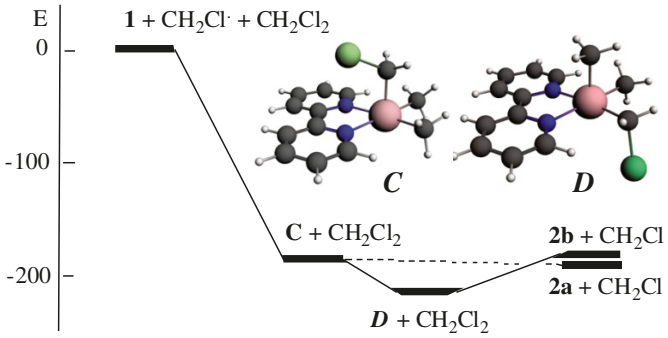
Scheme 5. Three possible mechanisms of reaction.



observed equilibrium constant K = [**2a**]/[**2b**] = 2.5, corresponding to ΔG(293K) = –2.2 kJ mol^{-1}. However, for the radical intermediates (Fig. 5), it was calculated that ***D*** is more stable than ***C*** by 37 kJ mol^{-1}, so the required isomerization step in Scheme 5 should be favoured. Chlorine-atom abstraction by ***D*** would then give **2b** as the kinetic isomer.

Can. J. Chem. Downloaded from www.nrcresearchpress.com by Renmin University of China on 09/02/12
For personal use only.

Fig. 5. Calculated energies (kJ mol^{-1}) and structures of intermediates ***C*** and ***D*** in the radical chain mechanism of oxidative addition of dichloromethane.



There are two factors that appear to favour the isomerization of ***C*** to ***D***. First, there is a steric factor because the chloromethyl group in ***D*** can adopt a conformation with the larger chlorine atom towards the open coordination site (Fig. 5) and so it is favourable to have the bulkier alkyl group in an equatorial position in the 5-coordinate compound, whereas in the octahedral complex, it is favourable to have the chloromethyl group in the axial position in **2a**, where the chlorine substituent can lie above the flat 2,2′-bipyridine ligand (Fig. 1). Second, there is an electronic effect because the methyl group has a slightly greater trans influence than the chloromethyl group and the vacant site tends to be in the position across from the ligand with highest trans influence, and perhaps also because of more favourable delocalization of the radical onto the chloromethyl group (Fig. 6). The angle Pt–C–Cl is calculated to be 107°, compared with 117° in **2b**, but the associated distance Pt···Cl = 3.28 Å is still too long for there to be a significant bonding interaction. Figure 6 indicates that the radical is also delocalized over the π-system of the bipy ligand. A similar trend in relative energies is calculated for the possible cationic intermediates, with ***B*** calculated to be more stable than ***A*** by 20 kJ mol^{-1}. Hence, the stereochemistry of the oxidative addition reaction can be rationalized in terms of either the polar S_N2 mechanism or the free radical chain mechanism, but not by the free radical nonchain mechanism (Scheme 5). The experimental data indicate that the free radical chain reaction is the dominant mechanism.

For oxidative addition of chloroform, the S_N2 mechanism is precluded because of steric effects in the transition state and so the free radical chain mechanism is most likely. The DFT calculations indicate a greater overall driving force for oxidative addition (–239 vs –197 kJ mol^{-1} for the reaction of **1** with chloroform vs dichloromethane; Figs. 5 and 7). There is less preference (25 vs 37 kJ mol^{-1}) for the radical *cis*-[$PtMe_2(CHCl_2)$(bipy]· (***H***) over the isomer *trans*-[$PtMe_2(CHCl_2)$(bipy]· (***I***), but higher preference (25 vs 2 kJ mol^{-1}) for the product *trans*-[$PtClMe_2(CHCl_2)$(bipy] (***J***) over *cis*-[$PtMe_2(CHCl_2)$(bipy] (***K***), when compared with the dichloromethane reaction. The formation of only isomer **8a** in the reaction of **7** with chloroform is therefore not surprising.

Experimental section

^{1}H NMR spectra were recorded using a Varian Mercury 400 or a Varian Inova 400 NMR spectrometer. The ligands

Fig. 6. The singly occupied molecular orbital in the radicals (*a*) ***C*** and (*b*) ***D***, and the LUMO in the cationic complexes (*c*) ***A*** and (*d*) ***B***.

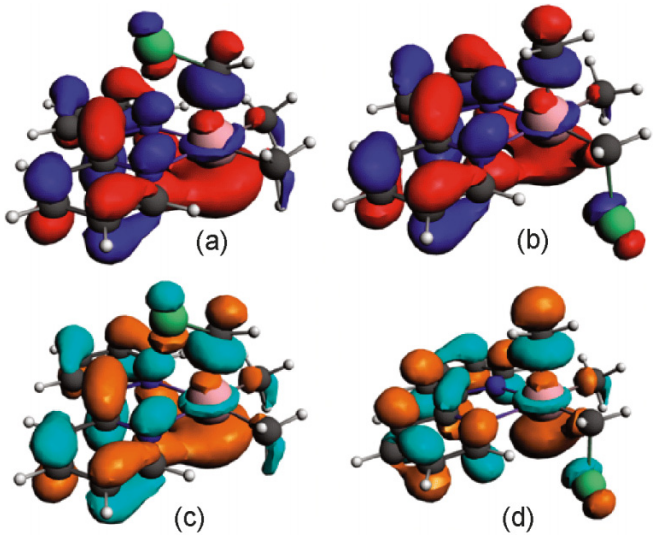
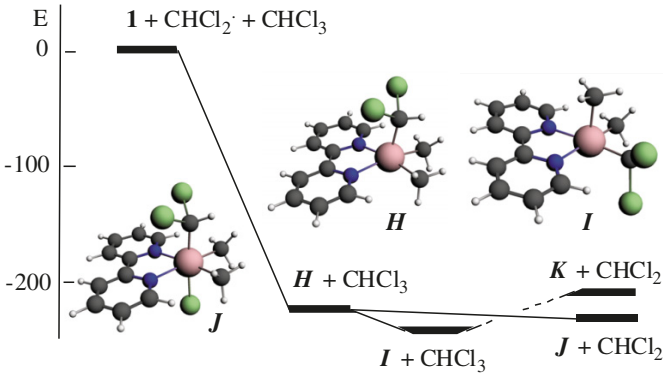


Fig. 7. Calculated energies (kJ mol^{-1}) and structures of intermediates ***H*** and ***I*** and product ***J*** in the radical chain mechanism of the oxidative addition of chloroform.



and the complexes [$PtMe_2$(NN)] (NN = bipy, **1**; dppn, **3**; dpox, **5**; dpm, **7**) were prepared using the literature methods.[45,46,48,49,60,61] The DFT calculations were carried out by DFT calculations, using the Amsterdam Density Functional program based on the Becke–Perdew functional, with first-order scalar relativistic corrections.[62] Data for the X-ray structure determinations were collected using a Bruker diffractometer. The frames were integrated with the Bruker SAINT software package using a narrow-frame algorithm. Data were corrected for absorption effects using the multi-scan method (SADABS). The structures were solved by direct methods and refined using the Bruker SHELXTL software package. Details are given in Table 3. For complex **6a**, the hydrogen atoms of the water molecule could not be located or positions calculated using the riding atom procedure, so the water molecule was treated as an oxygen atom only. For **2a**, there was evidence for minor disorder of the chloromethyl group, but the disorder could not be resolved; the positions of the CH_2Cl atoms are therefore poorly defined.

Can. J. Chem. Downloaded from www.nrcresearchpress.com by Renmin University of China on 09/02/12
For personal use only.

Table 3. Crystal and refinement data.

Complex	**2a**	**4a**	**6a**·H_2O	**8a**
Formula	$C_{13}H_{16}Cl_2N_2Pt$	$C_{23}H_{28}Cl_2N_4Pt$	$C_{15}H_{16}Cl_2N_4O_2Pt$	$C_{14}H_{17}Cl_3N_2Pt$
fw	466.27	626.48	550.31	514.74
T (K)	150	150	150	150
λ (Å)	0.710 73	0.710 73	0.710 73	0.710 73
Crystal system	Monoclinic	Monoclinic	Monoclinic	Triclinic
Space group	$P2_1$	$P2_1/n$	$P2_1/c$	P–1
a (Å)	6.8129(14)	8.0978(6)	15.4082(7)	8.9056(4)
b (Å)	15.090(3)	20.7047(16)	7.1709(3)	8.9863(5)
c (Å)	7.2117(14)	13.9170(11)	16.3878(7)	10.9278(6)
α (°)	90	90	90	92.181(2)
β (°)	102.73(3)	98.960(2)	99.655(2)	91.032(3)
γ (°)	90	90	90	114.427(3)
V (Å^3)	723.2(2)	2304.9(3)	1785.05(13)	795.13(7)
Z	2	4	4	2
d(calcd)	2.14	1.80	2.05	2.15
μ (mm^{-1})	10.05	6.34	8.17	9.32
Data/restraints/parameters	3224/1/160	5095/0/273	4425/0/219	2762/0/182
R_1, $I > 2\sigma(I)$	0.045	0.045	0.033	0.031
wR_2, $I > 2\sigma(I)$	0.117	0.080	0.083	0.079

Note: Further information for these structures can be found in the Supplementary data.

[PtClMe$_2$(CH$_2$Cl)(bipy)] (2a and 2b)

A solution of [PtMe$_2$(bipy)] (60 mg, 0.16 mmol) in CH_2Cl_2 (15 mL) was stirred at room temperature for 24 h. The red solution became pale yellow. The solvent was removed under vacuum and the resulting pale yellow solid was washed with diethyl ether. Crystals of **2a** were grown from CH_2Cl_2/pentane by slow diffusion. Yield: 90%, as isomeric mixture. NMR in CD_2Cl_2 **2a**: δ(^{1}H) = 1.29 (s, 6H, ^2J(PtH) = 69 Hz, PtMe), 3.55 (s, 2H, ^2J(PtH) = 52 Hz, PtCH_2Cl), 7.64 (m, 2H, bipy), 8.10 (m, 2H, bipy), 8.26 (m, 2H, bipy), 8.84 (m, 2H, bipy); **2b**: δ(^{1}H) = 0.65 (s, 3H, ^2J(PtH) = 74 Hz, PtMe^c *trans* to Cl), 1.39 (s, 3H, ^2J(PtH) = 69 Hz, PtMe^a *trans* to N), 4.34 (m, 1H, ^2J(HH) = 8 Hz, ^2J(PtH) = 46 Hz, PtCH_2Cl), 4.67 (m, 1H, ^2J(HH) = 8 Hz, ^2J(PtH) = 88 Hz, PtCH_2Cl); bipy resonances partly obscured in the range δ(^{1}H) = 7.6 – 9.3. Anal. calcd for $C_{13}H_{16}C_{l2}N_2Pt$ (%): C 33.49, H 3.46, N 6.01; found: C 33.02, H 3.11, N 5.95.

[PtClMe$_2$(CH$_2$Cl)(dppn)] (4a–4c)

A solution of [PtMe$_2$(6-dppn)] (25 mg) in CH_2Cl_2 (5 mL) was allowed to stand overnight. The solvent was then removed under vacuum and the product was washed with pentane (2 × 5 mL). The resultant yellow solid was recrystallized from acetone/pentane. The crystal of **4a** was obtained from acetone/pentane by slow diffusion. Yield: 84% as isomeric mixture. NMR in acetone-d^6) **4a**: δ(^{1}H) = 1.26 (s, 3H, ^2J(PtH) = 70 Hz, Pt–Me^a trans to N), 1.41 (s, 3H, ^2J(PtH) = 70 Hz, Pt–Me^b trans to N), 1.54–1.75 (m, 4H, 2 × ring CH_2), 2.01 (m, 2H, ring CH_2), 2.13 (m, 2H, ring CH_2), 3.25 (m, 2H, ring CH_2), 3.49 (m, 2H, ring CH_2), 3.53 (d, 1H, ^2J(H^{a}H^b) = 7 Hz, ^2J(PtH^b) = 48 Hz, Pt–CH^a*H^b*Cl), 3.54 (d, 1H, ^2J(H^{a}H^b) = 7 Hz, ^2J(PtH^a) = 58 Hz, Pt–C*H^a*H^{b}Cl), 7.61 (m, 1H, $H_5{}^1$), 7.95 (t, 1H, H_5), 8.11 (m, 2H, $H_3{}^2$/$H_4{}^2$), 8.41 (t, 1H, $H_4{}^1$), 8.60 (d, 1H, $H_3{}^1$), 8.79 (d, 1H, $H_6{}^1$), 9.06 (d, 1H, H_6, ^3J(PtH) = 19 Hz); **4b**: δ(^{1}H) = 0.61 (s, 3H, ^2J(PtH) = 74 Hz, Pt–Me^c trans to Cl), 1.44 (s, 3H, ^2J(PtH) = 70 Hz, Pt–Me^a trans to N), 1.55–3.50 (12H, 6 × ring CH_2), 4.72 (d, 1H, ^2J(H^a*H^b*) = 6 Hz, ^2J(PtH) = 78 Hz, PtCH_2Cl), 4.89 (d, 1H, ^2J(*H^a*H^b) = 6 Hz, ^2J(PtH) = 86 Hz, PtCH_2Cl), 7.55–9.55 (8H, pyridyl); **4c**: δ(^{1}H) = 0.66 (s, 3H, ^2J(PtH) = 74 Hz, Pt–Me^c trans to Cl), 1.55 (s, 3H, ^2J(PtH) = 70 Hz, Pt–Me^b trans to N), 1.55–3.50 (12H, 6 × ring CH_2), 4.26 (d, 1H, ^2J(H^a*H^b*) = 8 Hz, ^2J(PtH) = 44 Hz, PtCH_2Cl), 4.74 (d, 1H, ^2J(*H^a*H^b) = 8 Hz, ^2J(PtH) = 92 Hz, PtCH_2Cl), 7.55–9.55 (8H, 8 × py CH). Anal. calcd for $C_{23}H_{28}Cl_2N_4Pt$ (%): C 44.10, H 4.50, N 8.94; found: C 43.83, H 4.58, N 8.67.

[PtMe$_2$Cl(CH$_2$Cl)(dpox)] (6a–6c)

A solution of [PtMe$_2$(dpox)] (**5**, 20 mg) in dichloromethane (5 mL) was stirred at room temperature for 24 h. The red solution turned pale yellow. The solvent was removed under vacuum and the resulting pale yellow solid was washed with diethyl ether. The crystal of **6a** was obtained from CH_2Cl_2/pentane by slow diffusion. Yield: 80%. ^{1}H NMR in CD_2Cl_2 **6a**: δ(^{1}H) = 1.46 (s, 3H, ^2J(PtH) = 74 Hz, PtMe^a), 1.60 (s, 3H, ^2J(PtH) = 74 Hz, PtMe^b), 3.62 (d, 1H, ^2J(HH) = 7 Hz, ^2J(PtH) = 44 Hz, PtCH_2Cl), 3.83 (d, 1H, ^2J(HH) = 7 Hz, ^2J(PtH) = 57 Hz, PtCH_2Cl), 7.63 (m, 1H, py), 7.88 (m, 1H), 8.04 (m, 1H), 8.27 (m, 1H), 8.37 (m, 1H), 8.43 (m, 1H), 8.86 (m, 1H), 8.94 (m, 1H); **6b**: δ(^{1}H) = 0.92 (s, 3H, ^2J(PtH) = 73 Hz, PtMe^c), 1.45 (s, 3H, ^2J(PtH) = 73 Hz, PtMe^a), 4.27 (d, 1H, ^2J(HH) = 7 Hz, ^2J(PtH) = 43 Hz, PtCH_2Cl), 4.84 (d, 1H, ^2J(HH) = 7 Hz, ^2J(PtH) = 89 Hz, PtCH_2Cl; aromatic peaks partly obscured in region δ(^{1}H) = 7.5–9.6; **6c**: δ(^{1}H) = 0.93 (s, 3H, ^2J(PtH) = 73 Hz, PtMe^c), 1.69 (s, 3H, ^2J(PtH) = 73 Hz, PtMe^b), 4.22 (d, 1H, ^2J(HH) = 7 Hz, ^2J(PtH) = 43 Hz, PtCH_2Cl), 4.89 (d, 1H, ^2J(HH) = 7 Hz, ^2J(PtH) = 91 Hz, PtCH_2Cl); aromatic peaks partly obscured in region δ(^{1}H) = 7.5–9.6.

[PtClMe$_2$(CHCl$_2$)(dpm)] (8a)

A solution of [PtMe$_2$(dpm)] (0.10 g) in $CHCl_3$ (2 mL) was allowed to stand at room temperature for 1 day. The pale

yellow crystals that precipitated were separated by filtration, washed with ether, and dried under vacuum. Yield: 87%. NMR in $CDCl_3$: $\delta(^1H)$ = 1.50 (s, 6H, ^2J(PtH) = 67 Hz, PtMe), 4.24, 5.49 (each d, 1H, ^2J(HH) = 16 Hz, CH_2), 5.83 (s, 1H, ^2J(PtH) = 45 Hz, $PtCHCl_2$), 7.34 (t, 2H, ^3J(HH) = 7 Hz, py H^5), 7.52 (d, 2H, ^3J(HH) = 7 Hz, py H^3), 7.81 (t, 2H, ^3J(HH) = 7 Hz, py H^4), 8.81 (d, 2H, ^3J(HH) = 7 Hz, ^3J(PtH) = 13 Hz, py H^6). Anal. calcd for $C_{14}H_{17}Cl_3N_2Pt$ (%): C 32.67, H 3.33, N 5.44; found: C 32.48, H 3.47, N 5.39.

Supplementary data

Supplementary data are available with the article through the journal Web site (http://nrcresearchpress.com/doi/suppl/10.1139/v11-096). CCDC 818474–818477 contain the X-ray data in CIF format for this manuscript. These data can be obtained, free of charge, via http://www.ccdc.cam.ac.uk/cgi-bin/catreq.cgi (Or from the Cambridge Crystallographic Data Centre, 12 Union Road, Cambridge CB2 1Ez, UK; fax +44 1223 336033; or deposit@ccdc.cam.ac.uk).

Acknowledgments

We thank the Natural Sciences and Engineering Research Council of Canada (NSERC) for financial support and Dr. G. Popov for assistance with the structure determinations.

References

(1) Chan, T. H.; Li, C. J.; Lee, M. C.; Wei, Z. Y. *Can. J. Chem.* **1994**, *72* (5), 1181. doi:10.1139/v94-151.
(2) Miao, W. S.; Chan, T. H. *Acc. Chem. Res.* **2006**, *39* (12), 897. doi:10.1021/ar030252f.
(3) Winter, C. H.; Gladysz, J. A. *J. Organomet. Chem.* **1988**, *354* (3), C33. doi:10.1016/0022-328X(88)80664-8.
(4) Peng, T. S.; Winter, C. H.; Gladysz, J. A. *Inorg. Chem.* **1994**, *33* (12), 2534. doi:10.1021/ic00090a011.
(5) Oliván, M.; Caulton, K. G. *Chem. Commun. (Camb.)* **1997** (18), 1733. doi:10.1039/a703097e.
(6) Olson, W. L.; Nagaki, D. A.; Dahl, L. F. *Organometallics* **1986**, *5* (4), 630. doi:10.1021/om00135a003.
(7) Pattacini, R.; Jie, S.; Braunstein, P. *Chem. Commun. (Camb.)* **2009** (8), 890. doi:10.1039/b817728g.
(8) Ho, H.-A.; Dunne, J. F.; Ellern, A.; Sadow, A. D. *Organometallics* **2010**, *29* (18), 4105. doi:10.1021/om100515u.
(9) Vetter, A. J.; Rieth, R. D.; Brennessel, W. W.; Jones, W. D. *J. Am. Chem. Soc.* **2009**, *131* (30), 10742. doi:10.1021/ja9002316.
(10) Blank, B.; Glatz, G.; Kempe, R. *Chem. Asian J.* **2009**, *4* (2), 321. doi:10.1002/asia.200800359.
(11) Tejel, C.; Ciriano, M. A.; Lopez, J. A.; Jimenez, S.; Bordonaba, M.; Oro, L. A. *Chem. Eur. J.* **2007**, *13* (7), 2044. doi:10.1002/chem.200600971.
(12) Tejel, C.; Ciriano, M. A.; Oro, L. A.; Tiripicchio, A.; Ugozzoli, F. *Organometallics* **2001**, *20* (8), 1676. doi:10.1021/om000946h.
(13) Zeng, J. Y.; Hsieh, M. H.; Lee, H. M. *J. Organomet. Chem.* **2005**, *690* (24–25), 5662. doi:10.1016/j.jorganchem.2005.07.025.
(14) Chan, K. T. K.; Spencer, L. P.; Masuda, J. D.; McCahill, J. S. J.; Wei, P.; Stephan, D. W. *Organometallics* **2004**, *23* (3), 381. doi:10.1021/om030539g.
(15) Dorta, R.; Shimon, L. J. W.; Rozenberg, H.; Milstein, D. *Eur. J. Inorg. Chem.* **2002**, *2002* (7), 1827. doi:10.1002/1099-0682(200207)2002:7<1827::AID-EJIC1827>3.0.CO;2-Q.
(16) Haarman, H. F.; Ernsting, J. M.; Kranenburg, M.; Kooijman, H.; Veldman, N.; Spek, A. L.; van Leeuwen, P. W. N. M.; Vrieze, K. *Organometallics* **1997**, *16* (5), 887. doi:10.1021/om9607614.
(17) Nishiyama, H.; Horihata, M.; Hirai, T.; Wakamatsu, S.; Itoh, K. *Organometallics* **1991**, *10* (8), 2706. doi:10.1021/om00054a036.
(18) Ball, G. E.; Cullen, W. R.; Fryzuk, M. D.; James, B. R.; Rettig, S. J. *Organometallics* **1991**, *10* (10), 3767. doi:10.1021/om00056a058.
(19) Brunet, J. J.; Couillens, X.; Daran, J. C.; Diallo, O.; Lepetit, C.; Neibecker, D. *Eur. J. Inorg. Chem.* **1998** *1998* (3), 349. doi:10.1002/(SICI)1099-0682(199803)1998:3<349::AID-EJIC349>3.0.CO;2-5.
(20) Kashiwabara, K.; Morikawa, A.; Suzuki, T.; Isobe, K.; Tatsumi, K. *J. Chem. Soc. Dalton* **1997** (6), 1075. doi:10.1039/a606730a.
(21) Burns, E. G.; Chu, S. S. C.; Demeester, P.; Lattman, M. *Organometallics* **1986**, *5* (11), 2383. doi:10.1021/om00142a037.
(22) Bradd, K. J.; Heaton, B. T.; Jacob, C.; Sampanthar, J. T.; Steiner, A. *J. Chem. Soc. Dalton Trans.* **1999**, 1109. doi:10.1039/A809652J.
(23) López, J. A.; Mereiter, K.; Paneque, M.; Poveda, M. L.; Serrano, O.; Trofimenko, S.; Carmona, E. *Chem. Commun. (Camb.)* **2006**, 3921. doi:10.1039/b608293a.
(24) Herrmann, W. A.; Thiel, W. R.; Brossmer, C.; Ofele, K.; Priermeier, T.; Scherer, W. *J. Organomet. Chem.* **1993**, *461* (1–2), 51. doi:10.1016/0022-328X(93)83273-X.
(25) Leoni, P. *Organometallics* **1993**, *12* (7), 2432. doi:10.1021/om00031a012.
(26) Balch, A. L.; Hunt, C. T.; Lee, C. L.; Olmstead, M. M.; Farr, J. P. *J. Am. Chem. Soc.* **1981**, *103* (13), 3764. doi:10.1021/ja00403a025.
(27) Ghilardi, C. A.; Midollini, S.; Moneti, S.; Orlandini, A.; Ramirez, J. A. *J. Chem. Soc., Chem. Commun.* **1989** (5), 304. doi:10.1039/C39890000306.
(28) Scherer, O. J.; Jungmann, H. *J. Organomet. Chem.* **1981**, *208* (2), 153. doi:10.1016/S0022-328X(00)82670-4.
(29) Puddephatt, R. J. *Polyhedron* **1988**, *7* (10–11), 767. doi:10.1016/S0277-5387(00)86301-9.
(30) Friedrich, H. B.; Moss, J. R. *Adv. Organomet. Chem.* **1991**, *33*, 235. doi:10.1016/S0065-3055(08)60697-8.
(31) Rendina, L. M.; Puddephatt, R. J. *Chem. Rev.* **1997**, *97* (6), 1735. doi:10.1021/cr9704671.
(32) Kuyper, J. *Inorg. Chem.* **1978**, *17* (1), 77. doi:10.1021/ic50179a017.
(33) Monaghan, P. K.; Puddephatt, R. J. *Organometallics* **1985**, *4* (8), 1406. doi:10.1021/om00127a017.
(34) Monaghan, P. K.; Puddephatt, R. J. *J. Chem. Soc. Dalton Trans.* **1988** (3), 595. doi:10.1039/dt9880000595.
(35) Stöhr, F.; Sturmayr, D.; Kickelbick, G.; Schubert, U. *Eur. J. Inorg. Chem.* **2002** (9), 2305. doi:10.1002/1099-0682(200209)2002:9<2305::AID-EJIC2305>3.0.CO;2-P.
(36) (a) Chassot, L.; von Zelewsky, A.; Sandrini, D.; Maestri, M.; Balzani, V. *J. Am. Chem. Soc.* **1986**, *108* (19), 6084. doi:10.1021/ja00279a092; (b) von Zelewsky, A.; Suckling, A. P.; Stoeckli-Evans, H. *Inorg. Chem.* **1993**, *32* (21), 4585. doi:10.1021/ic00073a020.
(37) Momeni, B. Z.; Moradi, Z.; Rashidi, M.; Rominger, F. *Polyhedron* **2009**, *28* (2), 381. doi:10.1016/j.poly.2008.11.008.

Can. J. Chem. Downloaded from www.nrcresearchpress.com by Renmin University of China on 09/02/12
For personal use only.

(38) Jandik, P.; Schubert, U.; Schmidbaur, H. *Angew. Chem. Int. Ed. Engl.* **1982**, *21* (1), 73. doi:10.1002/anie.198200731.
(39) Song, D.; Sliwowski, K.; Pang, J.; Wang, S. *Organometallics* **2002**, *21* (23), 4978. doi:10.1021/om020641y.
(40) Vogler, A.; Kunkely, H. *Angew. Chem. Int. Ed. Engl.* **1982**, *21* (3), 209. doi:10.1002/anie.198202091.
(41) Alcock, N. W.; Pringle, P. G.; Bergamini, P.; Sostero, S.; Traverso, O. *J. Chem. Soc. Dalton* **1990** (5), 1553. doi:10.1039/dt9900001553.
(42) Ferguson, G.; Li, Y. W.; McAlees, A. J.; McCrindle, R.; Zang, E. L. *J. Organomet. Chem.* **2001**, *617–618*, 671. doi:10.1016/S0022-328X(00)00732-4.
(43) McCrindle, R.; Ferguson, G.; McAlees, A. J.; Arsenault, G. J.; Gupta, A.; Jennings, M. C. *Organometallics* **1995**, *14* (6), 2741. doi:10.1021/om00006a021.
(44) Ghedini, M.; Neve, F.; Longeri, M.; Bruno, M. C. *Inorg. Chim. Acta* **1988**, *149* (1), 131. doi:10.1016/S0020-1693(00)90579-6.
(45) Sauer, J.; Heldmann, D. K.; Hetzenegger, J.; Krauthan, J.; Sichert, H.; Schuster, J. *Eur. J. Org. Chem.* **1998** (12), 2885. doi:10.1002/(SICI)1099-0690(199812)1998:12<2885::AID-EJOC2885>3.0.CO;2-L.
(46) Bentiss, F.; Lagrenee, M. *J. Heterocycl. Chem.* **1999**, *36* (4), 1029. doi:10.1002/jhet.5570360433.
(47) Gueddi, A.; Mernari, B.; Giorgi, M.; Pierrot, M. *Acta Crystallogr. C* **2000**, *C56*, e426.
(48) Zhang, F.; Kirby, C.; Hairsine, D.; Jennings, M. C.; Puddephatt, R. J. *J. Am. Chem. Soc.* **2005**, *127* (41), 14196. doi:10.1021/ja055436z.
(49) Scott, J. D.; Puddephatt, R. J. *Organometallics* **1983**, *2* (11), 1643. doi:10.1021/om50005a028.
(50) Colmont, J.-M.; Priem, D.; Drean, P.; Demaison, J.; Boggs, J. E. *J. Mol. Spectrosc.* **1998**, *191* (1), 158. doi:10.1006/jmsp.1998.7623.
(51) Rudine, A. B.; Walter, M. G.; Wamser, C. C. *J. Org. Chem.* **2010**, *75* (12), 4292. doi:10.1021/jo100276m.
(52) Cooper, S. J.; Brown, M. P.; Puddephatt, R. J. *Inorg. Chem.* **1981**, *20* (5), 1374. doi:10.1021/ic50219a008.
(53) Au, R. H. W.; Jennings, M. C.; Puddephatt, R. J. *Organometallics* **2009**, *28* (13), 3734. doi:10.1021/om9001878.
(54) Brown, M. P.; Keith, A. N.; Manojlovic-Muir, Lj.; Muir, K. W.; Puddephatt, R. J.; Seddon, K. R. *Inorg. Chim. Acta* **1979**, *34* (1), L223. doi:10.1016/S0020-1693(00)94642-5.
(55) Scott, J. D.; Puddephatt, R. J. *Organometallics* **1986**, *5*, 1538. doi:10.1021/om00139a005.
(56) Puddephatt, R. J. *Angew. Chem. Int. Ed.* **2002**, *41* (2), 261. doi:10.1002/1521-3773(20020118)41:2<261::AID-ANIE261>3.0.CO;2-5.
(57) Goldberg, K. I.; Yan, J. Y.; Breitung, E. M. *J. Am. Chem. Soc.* **1995**, *117* (26), 6889. doi:10.1021/ja00131a010.
(58) Hill, R. H.; Puddephatt, R. J. *J. Am. Chem. Soc.* **1985**, *107* (5), 1218. doi:10.1021/ja00291a022.
(59) Nabavizadeh, S. M.; Habibzadeh, S.; Rashidi, M.; Puddephatt, R. J. *Organometallics* **2010**, *29* (23), 6359. doi:10.1021/om100810t.
(60) Monaghan, P. K.; Puddephatt, R. J. *Organometallics* **1984**, *3* (3), 444. doi:10.1021/om00081a019.
(61) Scott, J. D.; Puddephatt, R. J. *Organometallics* **1986**, *5* (12), 2522. doi:10.1021/om00143a021.
(62) te Velde, G.; Bickelhaupt, F. M.; Baerends, E. J.; Fonseca Guerra, C.; van Gisbergen, S. J. A. ; Snijders, J. G.; Ziegler, T. *J. Comput. Chem.* **2001**, *22* (9), 931. doi:10.1002/jcc.1056.

Can. J. Chem. Downloaded from www.nrcresearchpress.com by Renmin University of China on 09/02/12
For personal use only.

Selective recognition of G-quadruplex in the vascular endothelial growth factor gene with small-molecule natural products by electrospray ionization (ESI) mass spectrometry and circular dichroism (CD) spectrometry

Xiangwei He, Zhenjiang Zhang, Qiang Zhang, and Gu Yuan

Can. J. Chem. Downloaded from www.nrcresearchpress.com by Renmin University of China on 09/02/12
For personal use only.

Abstract: In this study, electrospray ionization mass spectrometry (ESI-MS) and circular dichroism (CD) spectroscopy were used to investigate selective recognition of G-quadruplex in the vascular endothelial growth factor (*VEGF*) gene with 12 small-molecule natural products. We found that kaempferol, a natural flavonol, shows the highest binding affinity among the 12 natural molecules. The results from ESI-MS and CD spectra indicated that kaempferol could enhance the thermal stability of the *VEGF*–G-quadruplex and showed selective recognition for the G-quadruplex in a solution consisting of the G-quadruplex and the corresponding duplex DNA.

Key words: VEGF gene, natural products, DNA recognition, ESI mass spectrometry, CD spectroscopy.

Résumé : Dans ce travail, on a utilisé la spectrométrie de masse avec ionisation par électronébulisation (SM-IEN) et la spectroscopie de dichroïsme circulaire (DC) pour étudier la reconnaissance sélective d'un quadruplex G dans le gène du facteur de croissance endothélial vasculaire (*FCEV*) par 12 petites molécules de produits naturels. On a trouvé que le kaempférol, un flavonol naturel, possède l'affinité de fixation la plus élevée parmi ces 12 molécules naturelles. Les résultats des spectres de SM-IEN et de DC indiquent que le kaempférol pourrait augmenter la stabilité thermique du *FCEV*–quadruplex G et qu'il présente une reconnaissance sélective pour le quadruplex G dans une solution formée du quadruplex G et du duplex correspondant de l'ADN.

Mots-clés : gène du facteur de croissance endothélial vasculaire (*FCEV*), produits naturels, reconnaissance de l'ADN, spectrométrie de masse avec ionisation par électronébulisation (IEN), spectroscopie de dichroïsme circulaire (DC).

[Traduit par la Rédaction]

Introduction

Targeting G-guadruplex with chemical small molecules is a useful strategy for gene therapy of cancers.[1–4] Thus, the development of novel small-molecule ligands has attracted the interest of many scientists.[5–7]

The human vascular endothelial growth factor (*VEGF*) gene has an important function in the spread of cancers, and the overexpression of *VEGF* is found in some human tumors.[8,9] The d(GGGGCGGGCCGGGGGCGGGG) sequence located at –85 to –66 bp upstream of the *VEGF* promoter can form the G-quadruplex structure, which is essential for the regulation of *VEGF* expression in cancer cells.[10–13] In our previous study,[11] a synthetic molecule, perylene derivative, showed good binding affinity to the G-quadruplex. Because of the structural diversity of natural products and their lower toxicity compared with synthetic compounds,[14,15] 12 small-molecule natural products were selected to study the selective recognition for the human *VEGF*–G-quadruplex structure (Fig. 1).

Electrospray ionization mass spectrometry (ESI-MS) with high sensitivity and rapid speed is a powerful tool for investigation of noncovalent interactions between small molecules and DNA[16–19] and it is easy to get the information about the stoichiometry of the complexes and the binding affinities. Circular dichroism (CD) spectroscopy can obtain the DNA conformation information and is also widely used to study interactions of DNA and small molecules.[7,20–22] In this research, ESI-MS coupled with CD spectroscopy was used to probe the selective recognition of small-molecule natural products to *VEGF*–G-quadruplex. The results indicate that

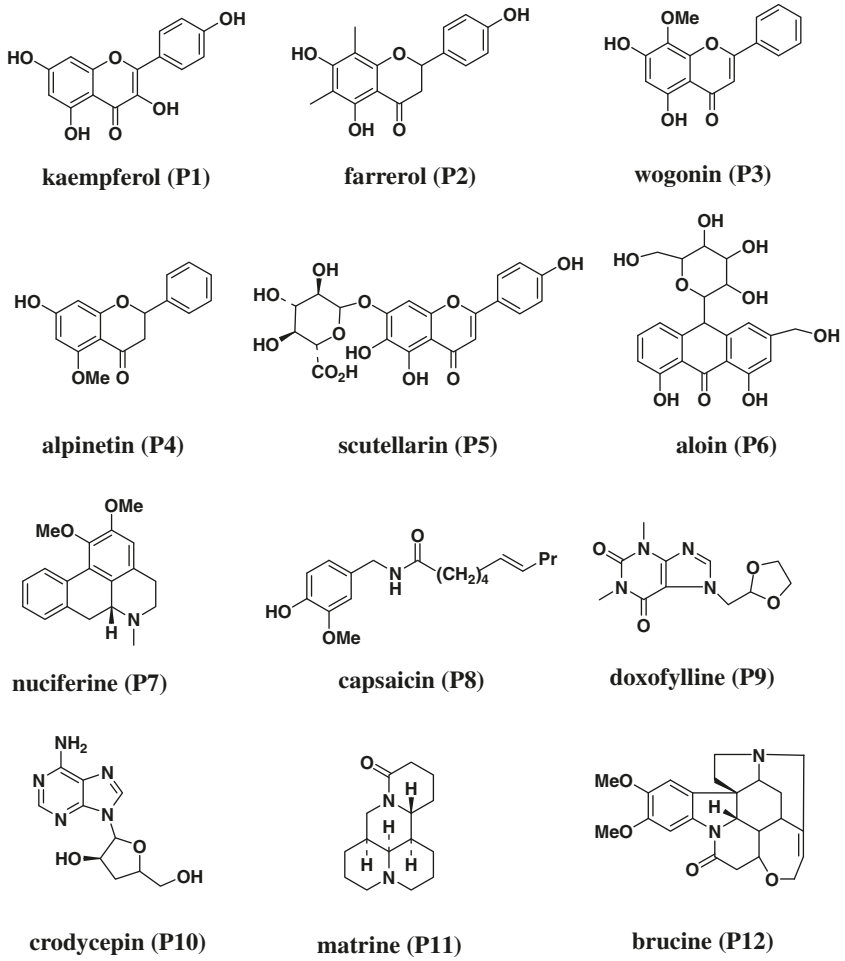
Received 12 April 2011. Accepted 18 June 2011. Published at www.nrcresearchpress.com/cjc on 19 October 2011.

X. He, Z. Zhang, Q. Zhang, and G. Yuan. Beijing National Laboratory for Molecular Sciences, Key Laboratory of Bioorganic Chemistry and Molecular Engineering of the Ministry of Education, Department of Chemical Biology, College of Chemistry, Peking University, Beijing 100871, P. R. China.

Corresponding author: Gu Yuan (e-mail: guyuan@pku.edu.cn).

This article is part of a Special Issue dedicated to Professor Tak-Hang Chan.

Fig. 1. Structures of the 12 natural-product molecules studied.



Can. J. Chem. Downloaded from www.nrcresearchpress.com by Renmin University of China on 09/02/12
For personal use only.

kaempferol, a natural flavonol isolated from tea, is a potential G-quadruplex binding agent with selective recognition.

Results and discussion

Noncovalent interactions between small molecules and *VEGF*–G-quadruplex

It has been confirmed that NH_4Ac can induce the *VEGF* G-rich sequence (S1) to adopt intramolecular parallel/antiparallel G-quadruplex structure.[11] In this study, 12 natural-product molecules were selected to probe the noncovalent interactions with human *VEGF*–G-quadruplex by ESI-MS. The mass spectra of *VEGF*–G-quadruplex and four small-molecule natural products in a molar ratio of 1:4 as examples are shown in Fig. 2. In the ESI mass spectra,[11] $[G]^{5-}$ and $[G]^{4-}$ denote the G-quadruplex ions with –5 and –4 charge, respectively, $[G + nP]^{5-}$ and $[G + nP]^{4-}$ denote the 1:*n* complex ion of G-quadruplex and a small molecule with –5 and –4 charge, respectively. The mass spectrum (Fig. 2A) shows that the 1:1 complex ion ($[G + P]^{5-}$ at *m*/*z* 1335.3) of the G-quadruplex (G) with kaempferol (P1) was the base peak (100%) and the 1:2 complex ion ($[G + 2P]^{5-}$ at *m*/*z* 1392.4) was nearly 50%, whereas the intensity of the G-quadruplex peak ($[G]^{5-}$ at *m*/*z* 1278.0) was only 70%. The results from ESI-MS indicate that kaempferol is a good binding molecule to the *VEGF*–G-quadruplex. For the other molecules, such as P6, the intensity of the 1:1 complex ion ($[G + P]^{5-}$ at *m*/*z* 1361.6) was about 80%, but the G-quadruplex peak ($[G]^{5-}$ at *m*/*z* 1278.0) remained the base peak (Fig. 2B). And the ESI mass spectra of P7 and P12 with the *VEGF*–G-quadruplex also exhibited the stronger peaks of the complex ions (Figs. 2C and 2D), respectively.

To estimate the binding properties of small molecules, the parameter IR, is introduced to compare the binding affinities of different small molecule natural products with the *VEGF*–G-quadruplex.[11] IR[G + P] and IR[G + 2P] denote the ability of G-quadruplex to bind with one or two small molecules, respectively, IRa is a ratio of the total intensity of the complex ion to the total intensity of the G-quadruplex ion and denotes the relative binding affinity of the small molecule to the G-quadruplex.

$$[1] \qquad \mathrm{IR}[\mathrm{G}+n\mathrm{P}] = \frac{\sum I_r(\mathrm{G}+n\mathrm{P})}{\sum I_r(\mathrm{G})} \qquad (n = 1 \text{ or } 2)$$

$$[2] \qquad \mathrm{IRa} = \frac{\sum I_r(\mathrm{G}+\mathrm{P}) + \sum I_r(\mathrm{G}+2\mathrm{P})}{\sum I_r(\mathrm{G})}$$

where $\sum I_r$ (G) and $\sum I_r$ (G + *n*P) (*n* = 1 or 2) are the total intensities of the G-quadruplexes and the 1:1 and 1:2

Can. J. Chem. Downloaded from www.nrcresearchpress.com by Renmin University of China on 09/02/12
For personal use only.

Fig. 2. Electrospray ionization (ESI) mass spectra of 5 μmol/L G-quadruplex DNA (G) with 20 μmol/L small molecules (P). (A) P1, (B) P6, (C) P7, and (D) P12.

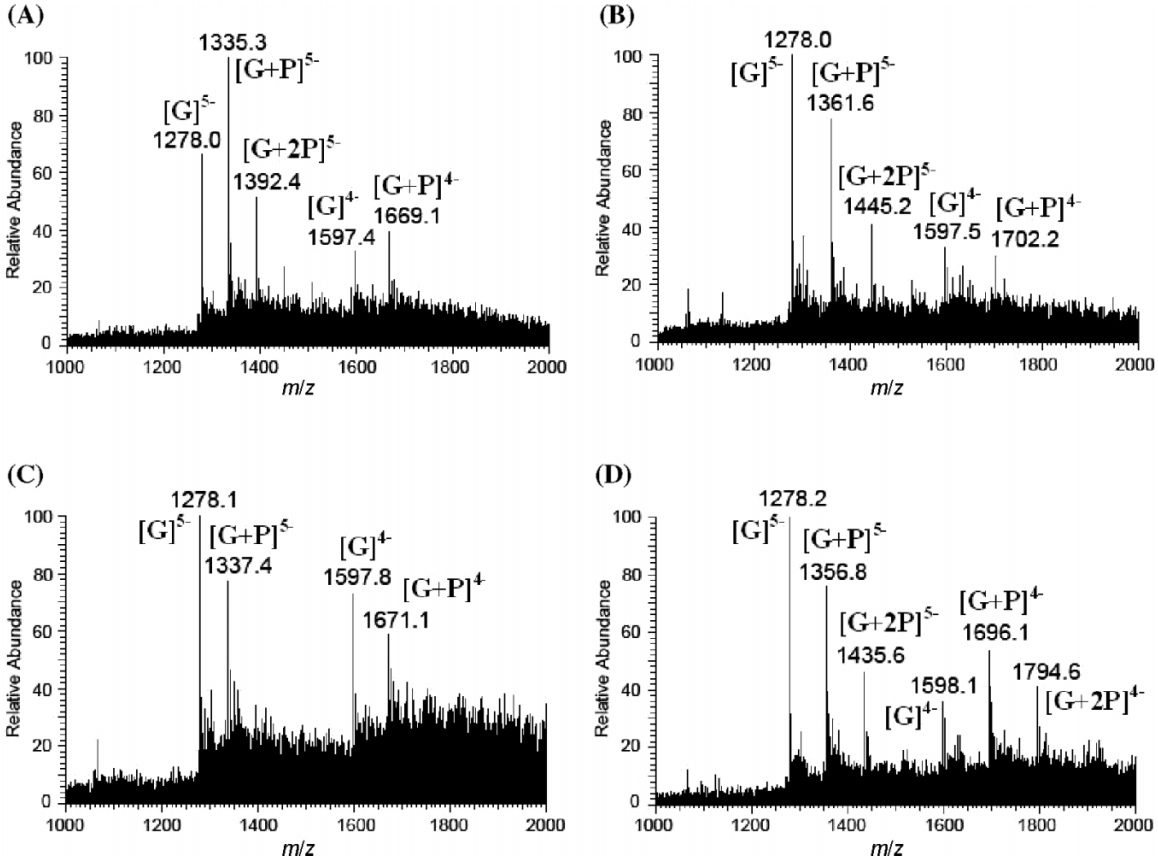
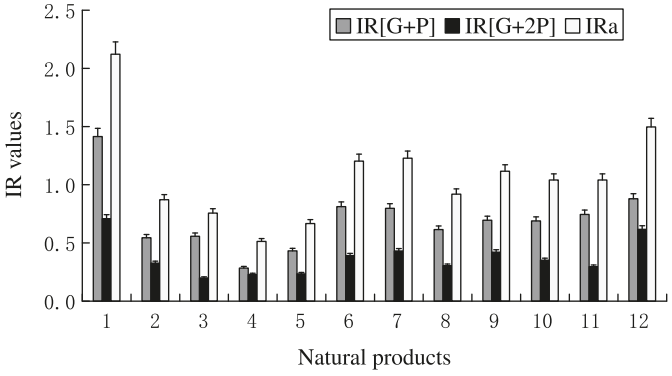


Fig. 3. IR values of 12 small molecules with *VEGF*–G-quadruplex. The error bar is the standard deviation of three independent measurements.



complex ions, respectively, and P represents the small-molecule natural product.

All the IR values of the 12 small molecules with *VEGF*–G-quadruplex were calculated by this formula and are shown in Fig. 3. If the IRa value of the small molecule to the G-quadruplex is greater, the binding affinity of the small molecule is also greater. It obviously shows that P1 has the best binding affinity among the 12 small-molecule natural products and the relative binding affinity order is P1 > P12 > P7 > P6 > P9 > P10~P11 > P8 > P2 > P3 > P5 > P4. Furthermore, P1–P4 are all flavonols with similar structure, but they show different binding affinities to *VEGF*–G-quadruplex. Comparing the structures of P1–P4, the aromaticity and the phenolic hydroxyl group were important for G-quadruplex recognition.

Selective recognition of *VEGF*–G-quadruplex by P1

Besides the binding affinity of the ligands, the selectivity of the recognition is also important. So the selective recognition of P1 to the G-quadruplex structures and corresponding duplex DNA was probed in a solution consisting of the duplex DNA and the G-quadruplex. The mass spectrum of the *VEGF* duplex and the G-quadruplex solution is shown in Fig. 4A. The $[G]^{5-}$ peak at *m/z* 1278.0 was the base peak because of a better ESI efficiency of the G-quadruplex and the intensity of the duplex peak ($[ds]^{6-}$) at *m/z* 2041.8 was nearly 70%. After P1 was added to the duplex DNA / G-quadruplex solution, the ESI mass spectrum showed that the intensity of the complex ion of P1 and the *VEGF*–G-quadruplex ($[G + P]^{5-}$ at *m/z* 1335.3) was 80%, whereas the complex ion of P1 and the duplex DNA is not observed (Fig. 4B). It shows that P1 could bind selectively with *VEGF*–G-quadruplex in a solution consisting of the G-quadruplex and the corresponding duplex DNA.

P1-enhanced *VEGF*–G-quadruplex thermal stability

The *VEGF* G-rich sequence (S1) (Fig. 5A) showed a positive peak at 264 nm and a shoulder peak at 290 nm that are the characteristics of the parallel/antiparallel G-quadruplex structure. After P1 was added to this DNA solution, the CD spectrum still showed the 264 nm positive peak and the

Fig. 4. Mass spectra of (A) 5 μmol/L vascular endothelial growth factor (*VEGF*) – G-quadruplex and duplex DNA solution and (B) the DNA solution adding 20 μmol/L kaempferol.

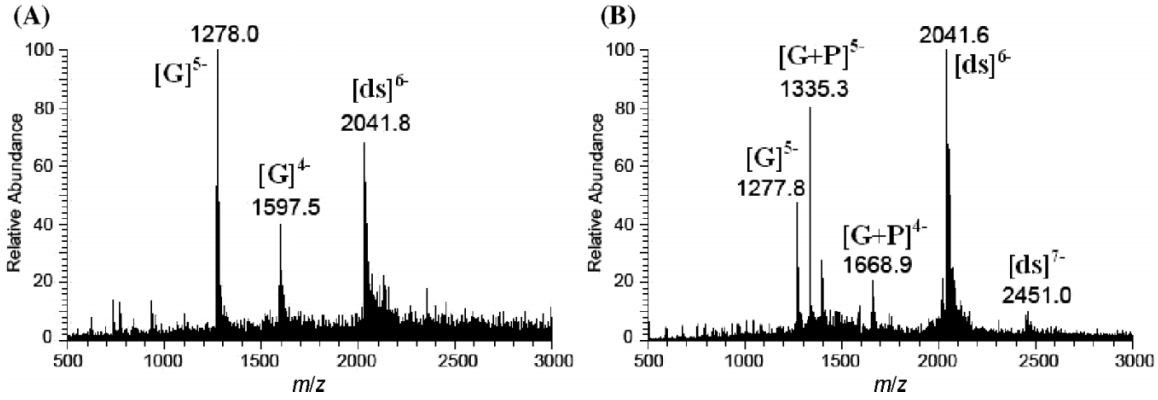
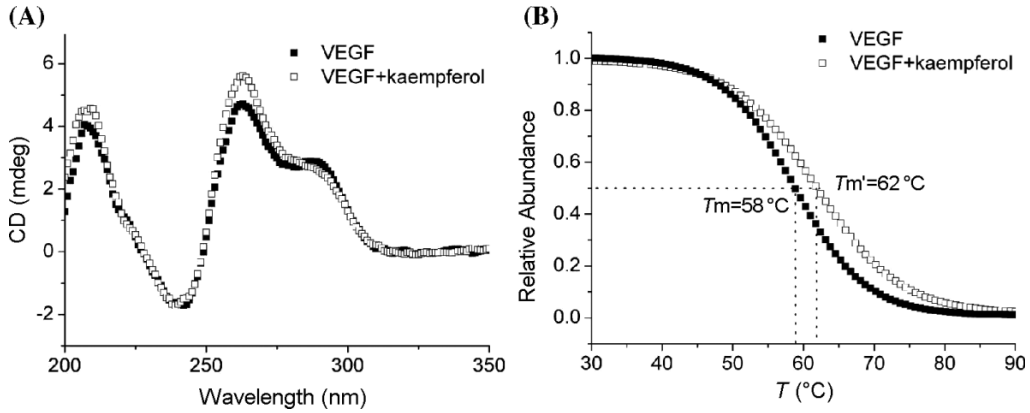


Fig. 5. (A) Circular dichroism (CD) spectra and (B) CD melting curves of 10 μmol/L vascular endothelial growth factor (*VEGF*) – G-quadruplex in the absence or presence of 40 μmol/L kaempferol (P1).



shoulder peak at 290 nm. These results indicated that the structure of the G-quadruplex was maintained after binding with P1. The thermal stability of the *VEGF*–G-quadruplex and the complex was evaluated using CD spectroscopy by the melting experiment. The CD melting experiment revealed that the *T*m (melting temperature) value of the *VEGF*–G-quadruplex was 58 °C and the *T*m value of the complex of *VEGF*–G-quadruplex with P1 was increased to 62 °C. These results indicate that P1 can stabilize the *VEGF*–G-quadruplex.

In this work, the selective recognitions of 12 small-molecule natural products with human *VEGF*–G-quadruplex were studied. P1 was found to have the highest binding affinity among these molecules. More importantly, P1 was then proven to bind *VEGF*–G-quadruplex selectively compared with *VEGF* – duplex DNA. And the results of the CD experiments revealed that P1 could enhance the thermal stability of *VEGF*–G-quadruplex. In conclusion, P1 selectively recognizes the *VEGF*–G-quadruplex and could be a potential *VEGF*–G-quadruplex binding agent.

Experimental

Chemicals

Single-strand oligonucleotides (S1 = d (GGGGCGGGC-CGGGGGCGGGG), *m/z* 6359.1; S2 = d (CCCCGCCCC-CGGCCCGCCCC), *m/z* 5879.0) were purchased from the Sangon Company (Shanghai, China). The obtained oligonucleotides were dissolved in deionized water and the concentrations were determined by a Nanodrop 2000 spectrophotometer (Thermo Scientific). For duplex DNA (S1/S2), two complementary single-strand oligonucleotides were mixed with equal molar quantities in buffers, then annealed at 90 °C for 10 min and then slowly cooled to room temperature (over 4 h) . The duplex and G-quadruplex mixed solution for ESI study was obtained by mixing the same molar of ds DNA and G-quadruplex DNA.

The natural product molecules used in this study were purchased from the China National Institute for the Control of Pharmaceutical and Biological Products (NICPBP), Beijing, P. R. China.

Mass spectrometry

ESI-MS spectra were obtained with a Finnigan LCQ Deca XP Plus ion trap mass spectrometer (Thermo Finnigan, San Jose, California), and all the experiments were carried out in the negative-ion mode. The DNA solution was directly injected into the mass spectrometer at a flow rate of 2 μL/min. The ESI conditions were optimized to observe the noncovalent complexes. The electrospray source conditions were 2.7 kV spray voltage and 120 °C capillary temperature.

Circular dichroism

The CD spectra were obtained using a JASCO J-815 spectropolarimeter equipped with a Peltier junction temperature-

Can. J. Chem. Downloaded from www.nrcresearchpress.com by Renmin University of China on 09/02/12
For personal use only.

controlled cell holder. CD experiments were carried out on samples at a concentration of 10 μmol/L DNA (10 mmol/L Tris–HCl and 50 mmol/L NH_4Ac, pH 7.40). Melting experiments were measured at 290 nm, and the *T*m values were calculated from the normalized CD melting curves according to the methods described previously.[23,24]

Acknowledgments

This project was supported by the National Natural Science Foundation of China (Grant Nos. 20872008 and 90913004) and the Natural Science Foundation of Beijing (Grant No. 2092015). We thank L. Li for his contribution to the writing of this paper.

References

(1) Cogoi, S.; Paramasivam, M.; Filichev, V.; Geci, I.; Pedersen, E. B.; Xodo, L. E. *J. Med. Chem.* **2009**, *52* (2), 564. doi:10.1021/jm800874t.

(2) Doherty, K. M.; Sharma, S.; Gupta, R.; Brosh, R. M., Jr. *Recent Patents Anticancer. Drug Discov.* **2006**, *1* (2), 185. doi:10.2174/157489206777442232.

(3) Gunaratnam, M.; Swank, S.; Haider, S. M.; Galesa, K.; Reszka, A. P.; Beltran, M.; Cuenca, F.; Fletcher, J. A.; Neidle, S. *J. Med. Chem.* **2009**, *52* (12), 3774. doi:10.1021/jm900424a.

(4) Zimmermann, S.; Martens, U. M. *Cell. Mol. Life Sci.* **2007**, *64* (7–8), 906. doi:10.1007/s00018-007-6481-8.

(5) Arola, A.; Vilar, R. *Curr. Top. Med. Chem.* **2008**, *8* (15), 1405. doi:10.2174/156802608786141106.

(6) Luedtke, N. W. *Chimia (Aarau)* **2009**, *63* (3), 134. doi:10.2533/chimia.2009.134.

(7) Zhou, J. A.; Yuan, G. *Chem. Eur. J.* **2007**, *13* (17), 5018. doi:10.1002/chem.200601605.

(8) Plate, K. H.; Breier, G.; Weich, H. A.; Risau, W. *Nature* **1992**, *359* (6398), 845. doi:10.1038/359845a0.

(9) Boocock, C. A.; Charnockjones, D. S.; Sharkey, A. M.; McLaren, J.; Barker, P. J.; Wright, K. A.; Twentyman, P. R.; Smith, S. K. *J. Natl. Cancer Inst.* **1995**, *87* (7), 506. doi:10.1093/jnci/87.7.506.

(10) Guo, K.; Gokhale, V.; Hurley, L. H.; Sun, D. *Nucleic Acids Res.* **2008**, *36* (14), 4598. doi:10.1093/nar/gkn380.

(11) Li, H. H.; Yuan, G. *Rapid Commun. Mass Spectrom.* **2010**, *24* (14), 2030. doi:10.1002/rcm.4613.

(12) Sun, D.; Liu, W. J.; Guo, K. X.; Rusche, J. J.; Ebbinghaus, S.; Gokhale, V.; Hurley, L. H. *Mol. Cancer Ther.* **2008**, *7* (4), 880. doi:10.1158/1535-7163.MCT-07-2119.

(13) Sun, D. Y.; Guo, K. X.; Rusche, J. J.; Hurley, L. H. *Nucleic Acids Res.* **2005**, *33* (18), 6070. doi:10.1093/nar/gki917.

(14) Brassart, B.; Gomez, D.; De Cian, A.; Paterski, R.; Montagnac, A.; Qui, K.-H.; Temime-Smaali, N.; Trentesaux, C.; Mergny, J.-L.; Gueritte, F.; Riou, J.-F. *Mol. Pharmacol.* **2007**, *72* (3), 631. doi:10.1124/mol.107.036574.

(15) Lee, H. M.; Chan, D. S. H.; Yang, F.; Lam, H. Y.; Yan, S. C.; Che, C. M.; Ma, D. L.; Leung, C. H. *Chem. Commun. (Camb.)* **2010**, *46* (26), 4680. doi:10.1039/b926359d.

(16) Casagrande, V.; Alvino, A.; Bianco, A.; Ortaggi, G.; Franceschin, M. *J. Mass Spectrom.* **2009**, *44* (4), 530. doi:10.1002/jms.1529.

(17) Rosu, F.; De Pauw, E.; Guittat, L.; Alberti, P.; Lacroix, L.; Mailliet, P.; Riou, J. F.; Mergny, J. L. *Biochemistry* **2003**, *42* (35), 10361. doi:10.1021/bi034531m.

(18) Baker, E. S.; Lee, J. T.; Sessler, J. L.; Bowers, M. T. *J. Am. Chem. Soc.* **2006**, *128* (8), 2641. doi:10.1021/ja0564968.

(19) Zhang, J. L.; Fu, Y.; Zheng, L.; Li, W.; Li, H.; Sun, Q.; Xiao, Y.; Geng, F. *Nucleic Acids Res.* **2009**, *37* (8), 2471. doi:10.1093/nar/gkp055.

(20) Garbett, N. C.; Ragazzon, P. A.; Chaires, J. B. *Nat. Protoc.* **2007**, *2* (12), 3166. doi:10.1038/nprot.2007.475.

(21) Kypr, J.; Kejnovska, I.; Renciuk, D.; Vorlickova, M. *Nucleic Acids Res.* **2009**, *37* (6), 1713. doi:10.1093/nar/gkp026.

(22) He, X. W.; Li, S. F.; Xu, M.; Lin, S.; Zhou, J.; Yuan, G. *Rapid Commun. Mass Spectrom.* **2011**, *25* (7), 993. doi:10.1002/rcm.4953.

(23) Joachimi, A.; Benz, A.; Hartig, J. S. *Bioorg. Med. Chem.* **2009**, *17* (19), 6811. doi:10.1016/j.bmc.2009.08.043.

(24) Garner, T. P.; Williams, H. E. L.; Gluszyk, K. I.; Roe, S.; Oldham, N. J.; Stevens, M. F. G.; Moses, J. E.; Searle, M. S. *Org. Biomol. Chem.* **2009**, *7* (20), 4194. doi:10.1039/b910505k.

Can. J. Chem. Downloaded from www.nrcresearchpress.com by Renmin University of China on 09/02/12
For personal use only.

Synthesis and application of Co(salen) complexes containing proximal imidazolium ionic liquid cores

Swapnil Sonar, Kenson Ambrose, Arthur D. Hendsbee, Jason D. Masuda, and Robert D. Singer

Can. J. Chem. Downloaded from www.nrcresearchpress.com by Renmin University of China on 09/02/12
For personal use only.

Abstract: Ionic ligands derived from a salen ligand containing two proximal 1,3-disubstituted imidazolium ionic liquid cores form cobalt(III) complexes capable of selectively oxidizing veratryl alcohol, a lignin model compound, to veratraldehyde using air as the source of oxygen. These complexes are easy to prepare, inexpensive, water stable, and soluble in ionic liquids, making them viable candidates for use as oxidation catalysts.

Key words: task-specific ionic liquid (TSIL), oxidation, IL–salen–Co complex, catalysis, veratryl alcohol.

Résumé : Les ligands ioniques dérivés d'un ligand salène comportant deux noyaux proximaux de liquides ioniques d'imidazolium 1,3-disubstitué forment des complexes avec le cobalt(III) qui peuvent oxyder d'une façon sélective le vératrol, un composé modèle de la lignine, en vératraldéhyde en utilisant de l'air comme source d'oxygène. Ces complexes, qui peuvent être préparés facilement et qui ne sont pas coûteux, sont stables dans l'eau et sont solubles dans les liquides ioniques ce qui en fait des candidats intéressants comme catalyseurs de réactions d'oxydation.

Mots-clés : liquide ionique (ILTS) à tâche spécifique, oxydation, complexe IL–salène–Co, catalyse, vératrol.

[Traduit par la Rédaction]

Introduction

As one of the 12 principles of green chemistry,[1] the use of alternative solvents in chemical applications has become an increasingly important and highly studied area of interest over the last decade. The advent of green chemistry in the 1990s was due in no small part to the earlier work of chemists such as Trost who coined the term, "Atom Economy",[2] and Chan who reported pioneering work in which organometallic reagents were used in aqueous systems.[3] Although water is the most obvious solvent of choice in terms of its environmental friendliness and its ubiquitous nature and acceptance as the "universal solvent" as described in many undergraduate textbooks, there are a number of other potential alternative solvents that warrant investigation. Hence, the work of Chan has provided inspiration for the study of a number of materials that have emerged as viable alternatives to conventional solvents. These include supercritical fluids, polymeric liquids, fluorous solvents, and ionic liquids (ILs).

ILs are now well-established in the chemical literature and are now enjoying growing utility in industrial applications. Among the current industrial applications are ILs for acid scavenging in the BASIL process developed by BASF, performance additives in paints developed by Degussa, cleaning fluids by Iolotec–Wandres, as well as a number of other processes at the pilot scale.[4] Hence, it is obvious that these liquids are now being investigated for their utility in several applications in addition to being used merely as reaction media. These include applications such as lubricants,[5] extractants,[6] electrolytes,[7] surfactants,[8] and biomass processing.[9] These applications arose because of the unique set of properties attributed to ILs that make them interesting not only from a green chemistry point of view but also from a more purely chemical point of view. Such properties include a general lack of volatility and flammability, polarity and (or) ionic nature, and the ability to dissolve a wide array of organic and inorganic materials. Pertinent to this report is the ability to tune these properties through careful manipulation of the structural features of the IL under investigation. The coordinating ability, viscosity, thermal stability, and biodegradability can all be easily tuned by adopting a modular approach to the synthesis of ILs. Simple variation of the cationic core, the counterion, and substituents on either, or both, of these can have profound effects on these properties. The incorporation of functionality into an IL to control its properties and to impart the ability to perform a predetermined function gives rise to task-specific ionic liquids (TSILs).[10]

We recently reported the preparation of TSILs **1a**–**1d**, capable of forming octahedral complexes with copper, cobalt, and nickel (Scheme 1).[11] Replacement of a methyl group on these complexes with an *n*-decyl group imparted sufficient hydrophobicity on the complex to enable it to spontaneously separate from aqueous solution upon its formation. These TSILs were shown to be useful in the removal of copper

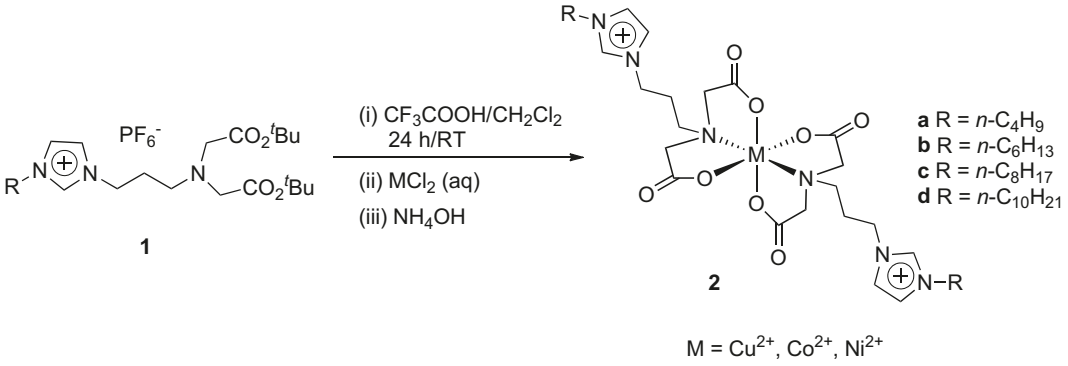
Received 18 April 2011. Accepted 28 June 2011. Published at www.nrcresearchpress.com/cjc on 24 October 2011.

S. Sonar, K. Ambrose, A.D. Hendsbee, J.D. Masuda, and R.D. Singer. Maritimes Centre for Green Chemistry, Department of Chemistry, Saint Mary's University, Halifax, NS B3H 3C3, Canada.

Corresponding author: Robert D. Singer (e-mail: Robert.Singer@SMU.ca).

This article is part of a Special Issue dedicated to Professor Tak-Hang Chan.

Scheme 1. Copper chelation using a task-specific ionic liquid (TSIL).[11]



from an aqueous solution indicating potential use in hydrometallurgical applications.

A subsequent study reported by our research group demonstrated the modular approach to preparing TSILs capable of metal chelation. Incorporation of a salicylaldehyde moiety into an imidazolium-based IL allowed the chelating moiety in the resulting TSILs to be easily altered (Scheme 2).[12] A common precursor to a series of TSILs is easily prepared through the chloromethylation of salicylaldehyde followed by quaternization of 1-methylimidazole to afford compound **3a** after metathesis of the chloride salt to the hexafluorophosphate analogue. Reaction of compound **3a** with hydroxylamine hydrochloride resulted in the formation of an imidazolium salt containing a salicylaldoxime moiety, **4**. The salicylaldoxime moiety is a well-established chelator of copper and this TSIL, not surprisingly, easily formed an isolable complex with copper (**5**). The same precursor (**3a**) was also reacted with copper(II) acetate and 1,2-diaminoethane in situ to afford an IL–salen–Cu^{II} complex (**6**). Incorporation of a manganese(III) atom into a complex using this same ligand resulted in a complex capable of catalyzing the epoxidation of alkenes. Hence, this study demonstrated the ability of such TSILs to be used both in metal separations and in the preparation of ionic complexes for use in catalysis.

It has been demonstrated that catalytic species derived from TSILs, or ion-tagged ligands, provide the ability to more efficiently entrain the resulting catalytic ionic complex in an IL of similar structure.[13] If the IL used to entrain the TSIL-derived catalyst is water immiscible then the IL/catalyst phase may be more easily separated from aqueous- or organic-phase reaction mixtures containing substrates and products. Hence, not only is product isolation facilitated but catalyst recycling becomes possible. Furthermore, the advantages of both a heterogeneous catalyst and a homogenous catalyst may be exploited.

The catalytic abilities of a number of salen–Co complexes have been reported in the literature.[14] Among these are the Co–salen complexes (**7a** and **7b**, Scheme 3), which have been reported to catalyze the oxidation of benzylic alcohols to aldehydes without over oxidation to the corresponding carboxylic acids. These reactions have been reported to proceed via a superoxo- or a bridging μ-peroxo complex formed from the Co–salen complex reacting with dioxygen.[15] The nature of the actual catalytic species present in solution has been shown to be dependent upon reaction conditions such as temperature, pH, the nature of added base, and the reaction time.[14] Of particular significance is the Co–salen-catalyzed oxidation of veratryl alcohol (3,4-dimethoxybenzyl alcohol) a lignin model compound, to veratraldehyde (3,4-dimethoxybenzaldehyde). The ability to selectively perform such a reaction without further oxidation to the carboxylic acid (3,4-dimethoxybenzoic acid) provides a potential commercially viable route to value-added products based on lignin degradation products such as veratryl alcohol.

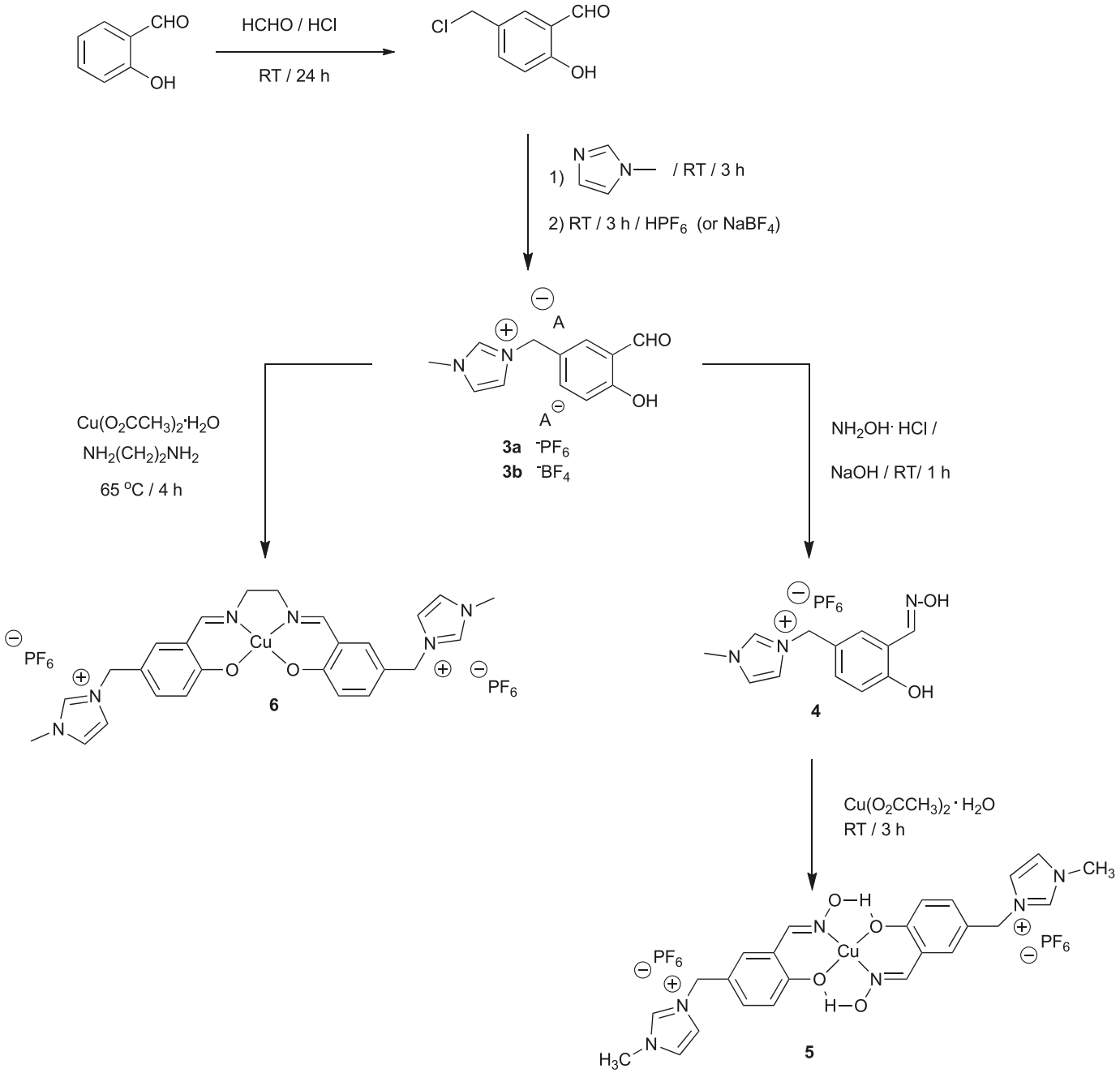
It became clear that if the ligand contained in the IL–salen–Cu^{II} (**6**) complex could be isolated in the absence of a chelated metal, the opportunity to coordinate it to a wider variety of metals would be presented. The catalytic ability of such IL–salen–metal complexes and the ability to entrain them in other ILs could then be investigated. Hence, we report herein our investigations in which the IL–salen ligand used in **6** was prepared and characterized. We also report the chelation of cobalt(III) using this ligand to afford an octahedral complex containing two axial ammine ligands as well as the catalytic activity of this complex in the oxidation of veratryl alcohol using air as the source of oxygen.

Results and discussion

The key precursors to the imidazolium-tagged ligands containing the salen-chelating ligand were prepared according to a previous procedure used in our laboratory starting with the reaction of salicylaldehyde with formaldehyde in the presence of HCl at room temperature over 1 day to afford 5-chloromethyl-2-hydroxybenzaldehyde.[12] Quaternization of 1-methylmidazole using this chloromethylated salicylaldehyde as an alkylating agent afforded the chloride salt, which was then metathesized to either the hexafluorophosphate salt (**3a**) or the tetrafluoroborate salt (**3b**) using aqueous hexafluorophosphoric acid (HPF_6(aq)) or sodium tetrafluoroborate as appropriate. The salicylaldehyde-functionalized imidazolium salts **3a** and **3b** could then be reacted with ethylene diamine to afford the IL–salen ligands **8a** and **8b** (Scheme 4 and Fig. 1). Recrystallization of **8a** from the slow evaporation of an acetone solution afforded a 64% yield of crystals appropriate for X-ray diffraction. This salen ligand is a dication owing to the presence of two proximal 1,3-disubstituted imidazolium substituents at either end of the salen moiety. Two poorly coordinating hexafluorophosphate ions act as the counterions as demonstrated by their remote locations relative to any positive charges or lone pairs of electrons on the complex as seen in its crystal structure (Fig. 1).

Can. J. Chem. Downloaded from www.nrcresearchpress.com by Renmin University of China on 09/02/12
For personal use only.

Scheme 2. Synthesis of ionic liquid (IL) – salen – Cu (**6**) and bis(salicylaldoxime)Cu (**5**) complexes from task-specific ionic liquids (TSILs).[12]



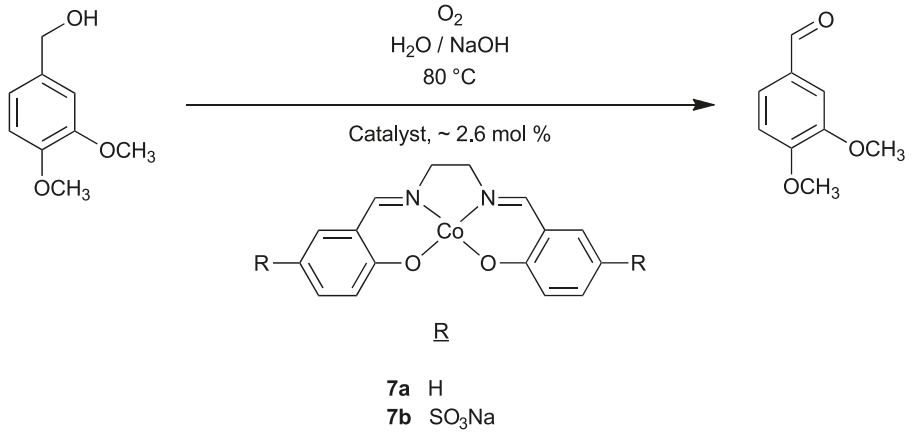
The cobalt chelate complex **9a** was easily prepared through reaction of the ligand **8a** and cobalt(II) acetate under basic conditions and reflux for 10 h, after which the complex precipitated out of solution. Recrystallization from a 9:1 *v*/*v* mixture of acetone and methanol afforded a 58% yield of crystals appropriate for X-ray diffraction.

The structure of **9a** shows an octahedral geometry about the cobalt atom with two axial ammine ligands. These ligands originate from the ammonium hydroxide solution used to basify the solution to ensure the phenoxide oxygen atoms were deprotonated and hence be available for coordination to the metal centre. Interestingly, the structure shows the presence of three hexafluophosphate ions in the asymmetric unit indicating a cobalt(III) metal centre. It appears the cobalt(II) metal centre contained in the cobalt(II) acetate reactant was oxidized under the aerobic conditions under which complex formation occurred. Hence, three hexafluorophosphate ions are required to balance the charge on the ionic complex. The stoichiometry of the reaction, in which ligand **8a** is the limiting reactant, then dictates that one-third of the IL–salen ligand will be uncomplexed and is removed during the ethanol wash of the product or during recrystallization. The two tethered, proximal 3-methylimidazolium cores of this complex provide for the potential exploitation of enhanced solubility in typical ILs such as 1-butyl-3-methylimidazolium hexafluorophosphate ([bmim]PF_6). The use of such enhanced solubility is a topic of a subsequent paper focusing on the use of entrained catalysts of this type in ILs. The present study

Can. J. Chem. Downloaded from www.nrcresearchpress.com by Renmin University of China on 09/02/12
For personal use only.

Can. J. Chem. Downloaded from www.nrcresearchpress.com by Renmin University of China on 09/02/12
For personal use only.

Scheme 3. Oxidation of veratryl alcohol with salen–Co catalysts.[14]



Scheme 4. Synthesis of ionic liquid (IL) – salen ligands **8a** and **8b**.

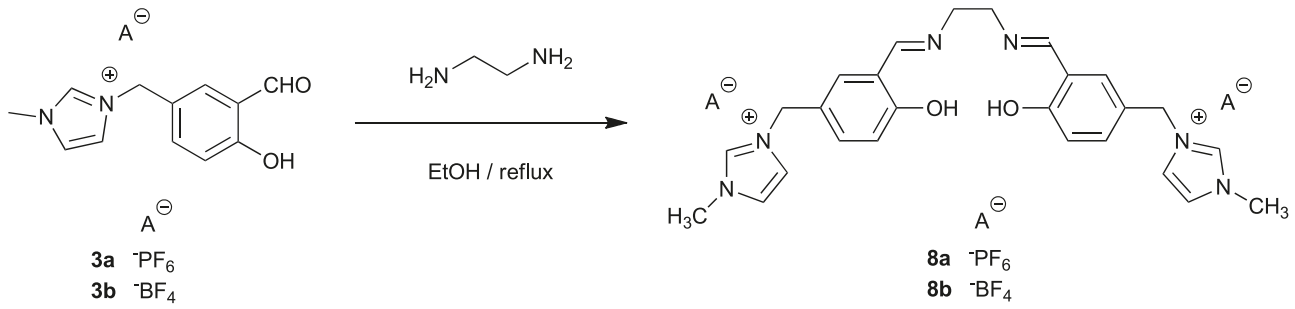
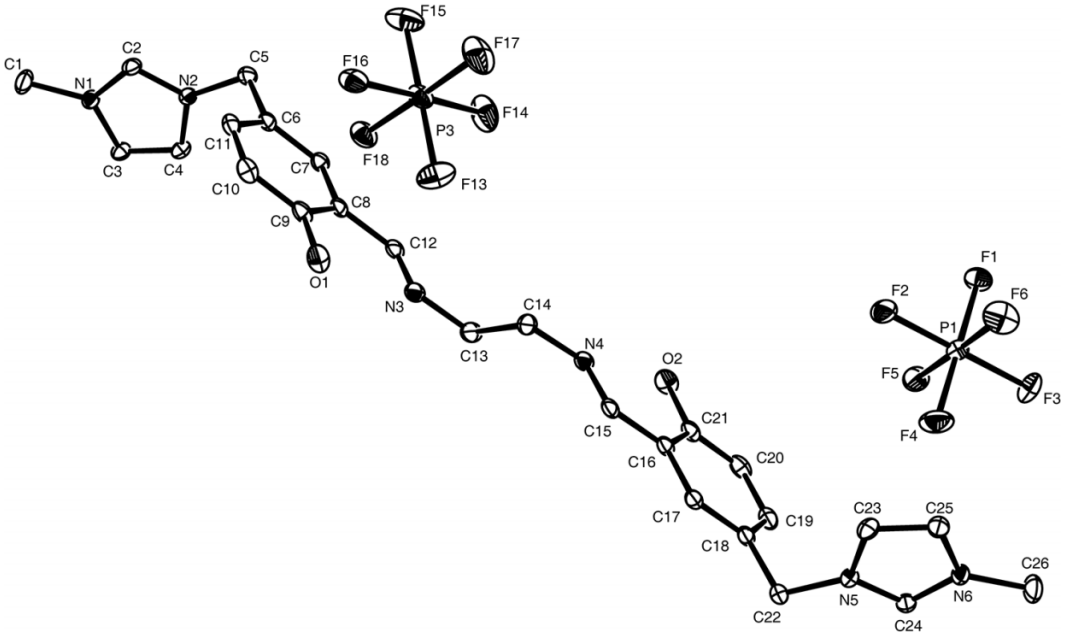


Fig. 1. Crystal structure of ionic liquid (IL) – salen task-specific ionic liquid (TSIL) **8a**. Thermal ellipsoids are drawn at 30% probability.



has focused on establishing the presence of any catalytic activity of this complex in oxidations in aqueous systems.

An isostructural tetrafluoroborate complex (**9b**) was isolated in an identical fashion through the reaction of the IL–salen ligand **8b**, again under basic conditions using NH_4OH (aq) as the base. The octahedral cobalt centre in this case also displays two axial ammine ligands and three tetrafluoroborate counterions. Once again there is a cobalt(III) metal centre required to account for the overall neutral charge on the complex and the presence of three tetrafluoroborate anions in the asymmetric unit.

With the IL–salen–Co complexes **9a** and **9b** in hand, we sought to determine whether they possessed any catalytic activity in the oxidation of veratryl alcohol to veratraldehyde. Veratryl alcohol was chosen as the substrate for this study, since, as alluded to above, it is a typical lignin model

Can. J. Chem. Downloaded from www.nrcresearchpress.com by Renmin University of China on 09/02/12
For personal use only.

compound and is often used in studies of enzymatic lignin degradation.[16] It had been shown in a previous study by Repo and co-workers[14] that the optimum pH for these reactions was ca. pH 12.5 and that the optimum temperature was above 60 °C. These reported reactions were typically run at 80 °C; hence, we used these reaction conditions to conduct our oxidation reactions of veratryl alcohol catalyzed by IL–salen–Co complexes **9a** and **9b**.

Initial reactions in which IL–salen–Co complex **9a** was used as the catalyst utilized pure oxygen as the oxidant. Whereas these reactions generally gave very high yields of veratraldehyde, as determined by gas chromatographic analysis and were consistent with other catalysts that have been used using oxygen as the oxidant, we opted to use air as our source of oxygen. We regarded this as a much safer, cheaper, and therefore a green advantage of our approach.

A series of reactions using IL–salen–Co complex **9a** as the catalyst in which the base used to adjust the pH to ca. 12.5 was varied, gave moderate yields of veratraldehyde. Essentially no difference in the yield of the aldehyde product was observed when the base was changed from potassium hydroxide to sodium hydroxide (Table 1, entries 1 and 2). A noticeable decrease in yield occurred when NH_4OH(aq) was used. However, use of sodium carbonate resulted in an increase in yield even in the absence of pyridine (Table 1, entries 3–5). Switching the catalyst to IL–salen–Co complex **9b** with a tetrafluoroborate counterion gave slightly lower yield of the aldehyde product (Table 1, entry 7). IL–salen–Co complex **9a** could be dissolved in the water immiscible IL [bmim]PF_6, giving a biphasic catalytic system when used with water. Using air as the source of oxygen, this system afforded a comparable, yet moderate, yield of veratraldehyde (Table 1, entry 6). This biphasic system facilitated separation of the catalytic layer from the product and unreacted starting material. Further investigation into the utility of this, and other similar biphasic systems in which catalysts are entrained in IL phases, are the topics of current studies ongoing in our laboratory.

Noteworthy is the experiment in which no IL–salen–Co catalysts **9a** or **9b** were added. Not surprisingly, only a trace amount of aldehyde product was detected in this reaction where all other reaction conditions were maintained except for the exclusion of the catalytic complex (Table 1, entry 8). This confirms the role of the cobalt complexes **9a** and **9b** as active catalysts for the selective oxidation of veratryl alcohol to veratraldehyde.

Conclusions

The synthesis and isolation of two new IL–salen ligands (**8a** and **8b**) containing proximal 1,3-disubstituted imidazolium IL moieties, from cheap and readily available starting materials, further demonstrates the effectiveness of the modular approach we have developed for the preparation of TSILs capable of chelating metals. Theses complexes are easy to prepare, water stable, and soluble in ILs. The potential of the ionic metal complexes described herein as catalysts has been established through the selective oxidation of veratryl alcohol, using air as the source of oxygen, to afford moderate yields of veratraldehyde. No evidence of further oxidation to the carboxylic acid was detected. Although yields using air as the oxygen source are generally lower than those when pure oxygen is used, the method does offer a safer and less expensive methodology. Future studies in which these and other related catalysts useful for the oxidation of lignin model compounds are entrained in other ILs are ongoing and will be the topic of future publications. Such immobilization of the catalysts in these systems may enable ready recycling of the catalyst while also facilitating product isolation and yield, hence enhancing the overall greenness of this methodology.

Experimental

General procedures

Veratryl alcohol (96%) and all other commercial reagents were purchased from Sigma-Aldrich and used without further purification. Thin layer chromatography (TLC) was performed on silica gel plates and visualization was done by UV light. Column chromatography was performed using 230–400 mesh silica gel. IR spectra were acquired on a Bruker Vertex-70 IR using a KBr disc. ^{1}H, ^{13}C, and ^{31}P NMR spectra were acquired on a Bruker AV Sspectrometer (^{1}H, 500 MHz; ^{13}C, 126 MHz; and ^{31}P, 202 MHz) or on a Bruker/Tecmag AC spectrometer (^{1}H, 250 MHz; ^{13}C, 62 MHz); ^{19}F NMR spectra (235 MHz) were also acquired using the Bruker/Tecmag spectrometer. When DMSO-d_6 was used as a solvent, the chemical shifts are reported in ppm relative to TMS as an internal standard (0.00 ppm for ^{1}H and ^{13}C) or DMSO-d_6 (2.50 ppm for ^{1}H and 39.52 ppm for ^{13}C). The chemical shifts in ^{31}P NMR spectra are reported in ppm with respect to aq 85% H_3PO_3 as the external standard (0.00 ppm for ^{31}P) and in ^{19}F NMR spectra with respect to 0.5% $CF_3C_6H_5$ in $CDCl_3$ as the external standard (63.72 ppm for ^{19}F). Multiplicities are indicated by singlet (s), doublet (d), and triplet (t). Coupling constants (*J*) are reported in Hz. ESI-MS data were acquired in positive and negative modes on an Agilent 1100 LC equipped with an MSD trap. High-resolution mass spectra were acquired in positive mode on a Bruker microTof Focus orthogonal ESI-TOF.

Single crystals were placed in Paratone-N oil, mounted in a nylon loop, and cooled to 150 K (**8a**), to 100 K (**9a**), or to 130 K (**9b**) using an Oxford Cryostream cooling system. The data were collected using the Bruker APEX2 software package[17,18] on a Siemens diffractometer equipped with an APEXII CCD detector, a graphite monochromator, and Mo Kα radiation (λ = 0.71073 Å). A hemisphere of data was collected in 1664 frames. Data processing and absorption corrections were applied using the APEX2 software package.[17,18] The structure was solved (direct methods) and all non-H atoms were refined anisotropically. Hydrogen atoms were placed in calculated positions using an appropriate riding model and coupled isotropic temperature factors. ORTEP-3[19] renderings are provided in Figs. 1–3. Selected crystallographic data are included in Tables 2–4 and are also included in the Supplementary data for this manuscript.

All spectra of known compounds agreed with those reported in the literature. For new compounds (i.e., **8a** and **8b** and **9a** and **9b**), the ^{1}H and ^{13}C NMR of the purified compounds and the HRMS (in addition to other spectral data) are provided in lieu of combustion analysis, since these compounds are characteristically resistant to combustion.

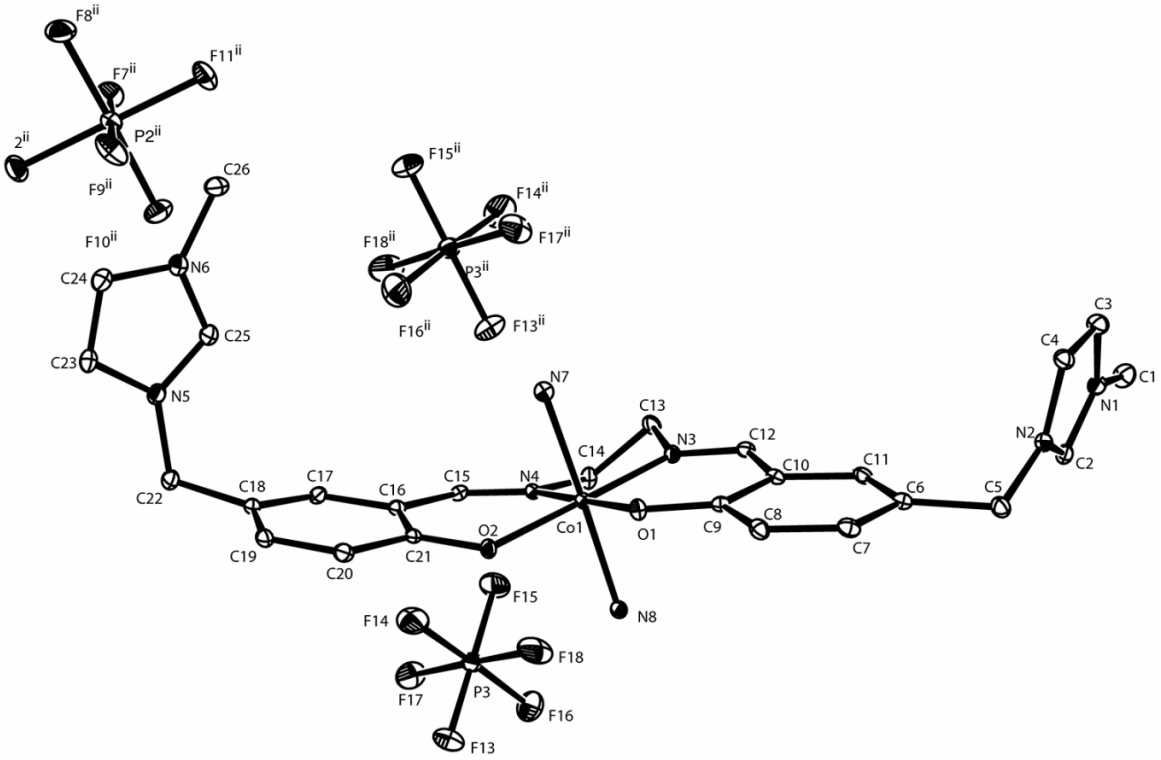
Can. J. Chem. Downloaded from www.nrcresearchpress.com by Renmin University of China on 09/02/12
For personal use only.

Table 1. Oxidations of veratryl alcohol catalyzed by ionic liquid (IL) – salen – Co complexes **9a** and **9b**.

Entry	Catalyst	Base	Solvent	Yield (%)[a]
1	**9a**	NaOH(aq)	H_2O	40
2	**9a**	KOH(aq)	H_2O	38
3	**9a**	NH_4OH(aq)	H_2O	24
4	**9a**	K_2CO_3	H_2O	56
5	**9a**	K_2CO_3	H_2O	52[b]
6	**9a**	K_2CO_3	H_2O, [bmim]PF_6	41
7	**9b**	K_2CO_3	H_2O	46
8	None	K_2CO_3	H_2O	Trace

[a]Isolated yield after chromatography.
[b]No pyridine, as axial ligand, added.

Fig. 2. Crystal structure of ionic liquid (IL) – salen – Co PF_6 complex **9a.** Thermal ellipsoids are drawn at 30% probability.



Preparation of 5-chloromethyl-2-hydroxybenzaldehyde

To a well stirred mixture of concd hydrochloric acid (150 mL) and formaldehyde (10.8 mL; 37 wt% in H_2O) was added salicylaldehyde (15.0 mL, 141.4 mmol). The reaction was stirred at room temperature for 24 h. The solid that separated out was filtered, dissolved in diethyl ether, and reisolated through evaporation of the solvent. Recrystallization from *n*-hexane afforded a white solid. Yield: 51.5%; mp 84–85 °C. ^{1}H NMR (250 MHz, DMSO-d_6) δ: 4.74 (s, 2H, Cl–CH_2), 7.00 (d, 1H, J = 8.5 Hz, Ar–H), 7.57 (dd, 1H, J = 2.3, 6.3 Hz, Ar–H), 7.70 (d, 1H, J = 2 Hz, Ar–H), 10.26 (s, 1H, CHO), 10.92 (s, 1H, OH). ^{13}C NMR (62 MHz, DMSO-d_6) δ: 45.71, 117.73, 122.15, 128.78, 129.08, 136.97, 160.74, 190.66.

Preparation of 1-(3-formyl-4-hydroxybenzyl)-3-methylimidazolium chloride

To a solution of 1-methylimidazole (14.0 mL, 140.3 mmol) in toluene (30 mL) at room temperature was added 5-chloromethyl-2-hydroxybenzaldehyde (20.0 g, 117 mmol) under a nitrogen atmosphere. The resulting solution was stirred at room temperature for 3 h. The solid that separated out was washed with ether (3 × 20 mL) and dried to give a pale yellow solid. Yield: 97.0%; mp 185–187 °C. IR (KBr, cm^{-1}): 1562 (C=C), 1611 (C=N), 1675 (C=O), 3459 (O–H). ^{1}H NMR (500 MHz, DMSO-d_6) δ: 3.86 (s, 3H, N–CH_3), 5.39 (s, 2H, $^+$N–CH_2), 7.21 (d, 1H, J = 8.5 Hz, Ar–H), 7.63 (dd, 1H, J = 2.5, 6.0 Hz, Ar–H), 7.73 (t, 1H, J = 1.5, 2.0 Hz, Ar–H), 7.76 (d, 1H, J = 2.5 Hz, Ar–H), 7.83 (t, 1H, J = 1.5 Hz, Ar–H), 9.33 (s, 1H, Ar–H), 10.31 (s, 1H, CHO), 11.31 (s, 1H, OH). ^{13}C NMR (126 MHz, DMSO-d_6) δ: 35.85, 51.03, 118.20, 122.14, 122.54, 123.96, 125.59, 128.47, 136.50, 136.53, 161.43, 190.06. MS ESI(+): 217.1, 135.0, 120.8, 99.4, 83.1.

Fig. 3. Crystal structure of ionic liquid (IL) – salen – Co BF_4 complex **9b.** Thermal ellipsoids are drawn at 30% probability.

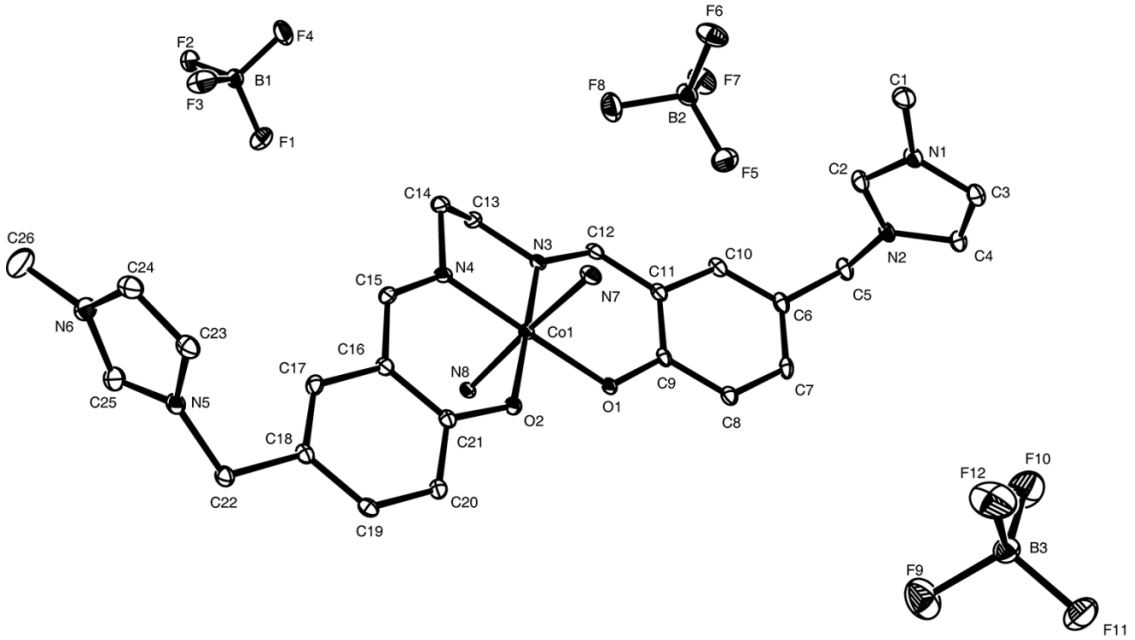


Table 2. Crystal data and structure refinement for task-specific ionic liquid (TSIL) **8a**.

Parameter	Crystal data
Empirical formula	$C_{26}H_{30}F_{12}N_6O_2P_2$
Formula mass	748.50
Temperature (K)	150(2)
Wavelength (Å)	0.71073
Crystal system	Triclinic
Space group	*P*-1
Unit cell dimensions	a = 9.851(5) Å, b = 16.967(8) Å, c = 20.443(9) Å α = 69.197(5)°, β = 81.843(5)°, γ = 89.738(5)°
Volume (Å^3)	3158(2)
Z	4
Density (calculated, Mg/m^3)	1.574
Absorption coefficient (mm^{-1})	0.246
F(000)	1528
Crystal dimensions	0.387×0.139×0.101 mm^3
θ range for data collection (°)	1.95–25.00
Index ranges	$-11 \leq h \leq 11$, $-20 \leq k \leq 20$, $-24 \leq l \leq 24$
Reflections collected	31 304
Independent reflections	11 107 (R(int) = 0.0395)
Completeness to θ = 25.00° (%)	99.7
Refinement method	Full-matrix least-squares on F^2
Data/restraints/parameters	11 107 / 2 / 873
Goodness-of-fit on F^2	1.033
Final R indices ($I > 2\sigma(I)$)	$R1$ = 0.0526, $wR2$ = 0.1278
R indices (all data)	$R1$ = 0.0910, $wR2$ = 0.1496
Largest diff. peak and hole (e Å^{-3})	0.529 and –0.424

1-(3-Formyl-4-hydroxybenzyl)-3-methylimidazolium hexafluorophosphate (3a)

To a solution of 1-(3-formyl-4-hydroxybenzyl)-3-methylimidazolium chloride (14.80 g, 58.70 mmol) in water (100 mL) at room temperature was added an aqueous solution of hexafluorophosphate (12.8 mL, 88.1 mmol) while cooling in an ice bath over 1 h. The resulting solution was stirred at room temperature for 3 h. The solid that separated out was washed with water and then with diethyl ether (3 × 20 mL) and dried to give a solid white product. Yield:

Can. J. Chem. Downloaded from www.nrcresearchpress.com by Renmin University of China on 09/02/12
For personal use only.

Can. J. Chem. Downloaded from www.nrcresearchpress.com by Renmin University of China on 09/02/12
For personal use only.

Table 3. Crystal data and structure refinement for ionic liquid (IL) – salen – Co complex **9a**.

Parameter	Crystal data
Empirical formula	$C_{28}H_{39}CoF_{18}N_9O_2P_3$
Formula weight	1027.52
Temperature (K)	100(2)
Wavelength (Å)	0.71073
Crystal system	Monoclinic
Space group	*P*2(1)/*c*
Unit cell dimensions	a = 18.028(3) Å, b = 13.648(2) Å, c = 17.958(3) Å α = 90°, β = 115.856(2)°, γ = 90°
Volume (Å^3)	3976.1(10)
Z	4
Density (calculated, Mg/m^3)	1.716
Absorption coefficient (mm^{-1})	0.680
F(000)	2080
Crystal dimensions (mm^3)	0.3021×0.2128×0.1126
θ range for data collection (°)	1.95–25.00
Index ranges	$-21 \le h \le 21$, $-16 \le k \le 16$, $-21 \le l \le 21$
Reflections collected	38 333
Independent reflections	6996 (R(int) = 0.0748)
Completeness to θ = 25.00° (%)	100.0
Absorption correction	Semiempirical from equivalents
Max and min transmission	0.7457 and 0.6957
Refinement method	Full-matrix least-squares on F^2
Data/restraints/parameters	6996/3/527
Goodness-of-fit on F^2	1.050
Final R indices ($I > 2\sigma(I)$)	$R1$ = 0.0480, $wR2$ = 0.1106
R indices (all data)	$R1$ = 0.0757, $wR2$ = 0.1200
Largest diff. peak and hole (e Å^{-3})	0.693 and –0.581

97.7%; mp 132–134 °C. IR (KBr, cm^{-1}): 1573 (C=C), 1627 (C=N), 1663 (C=O), 3443 (O–H). ^{1}H NMR (500 MHz, DMSO-d_6) δ: 3.85 (s, 3H, N–CH_3), 5.36 (s, 2H, $^+$N–CH_2), 7.05 (d, 1H, J = 8.5 Hz, Ar–H), 7.60 (dd, 1H, J = 2.5, 6.0 Hz, Ar–H), 7.69 (t, 1H, J = 1.5, 2.0 Hz, Ar–H), 7.77 (t, 2H, J = 2.0 Hz, Ar–H), 9.16 (s, 1H, Ar–H), 10.30 (s, 1H, CHO), 10.98 (s, 1H, OH). ^{13}C NMR (126 MHz, DMSO-d_6) δ: 35.86, 51.11, 118.06, 122.18, 122.50, 124.02, 125.74, 128.93, 136.50, 136.62, 161.13, 190.39. ^{19}F NMR (235 MHz, DMSO-d_6) δ: –66.3 (d, J = 705 Hz). ^{31}P NMR (202 MHz, DMSO-d_6) δ: –44.19 (septet, J = 709.4 Hz). MS ESI(+) *m*/*z*: 217.0; ESI(–) *m*/*z*: 144.7.

Preparation of 1-(3-formyl-4-hydroxybenzyl)-3-methylimidazolium tetrafluoroborate (3b)

To a stirred solution of 3-(3-formyl-4-hydroxybenzyl)-3-methylimidazolium chloride (10.00 g, 39.57 mmol) in water (100 mL) at room temperature was added sodium tetrafluoroborate (5.21 g, 47.49 mmol). The resulting solution was stirred at room temperature for 3 h. The solution was concentrated in vacuo and filtered off to obtain a light pink solid product. This was washed with water to remove NaCl and unreacted sodium tetrafluoroborate. Pink solid. Yield: 95.30%; mp 102–104 °C. IR (KBr, cm^{-1}): 1575 (C=C), 1622 (C=N), 1660 (C=O). ^{1}H NMR (500 MHz, DMSO-d_6) δ: 3.85 (s, 3H, N–CH_3), 5.36 (s, 2H, $^+$N–CH_2), 7.05 (d, 1H, J = 8.5 Hz, Ar–H), 7.12 (dd, 1H, J = 2.5, 6.0 Hz, Ar–H), 7.68 (t, 1H, J = 1.5 Hz, Ar–H), 7.76–7.78 (m, 2H, Ar–H), 9.14 (s, 1H, Ar–H), 10.29 (s, 1H, CHO), 10.97 (s, 1H, OH). ^{13}C NMR (126MHz, DMSO-d_6) δ: 35.88, 51.14, 118.09, 122.18, 122.50, 124.04, 125.77, 129.06, 136.51, 136.67, 161.14, 190.53. ^{19}F NMR (235 MHz, DMSO-d_6) δ: –144.2. MS ESI(+) *m*/*z*: 217.1.

Preparation of 1–4-hydroxy-3-[(2-[((*E*)-1–2-hydroxy-5-[(3-methyl-1*H*-imidazol-3-ium-1-yl)methyl]phenylmethylidene)amino]ethylimino)methyl]phenyl-3-methyl-1*H*-imidazol-3-ium hexafluorophosphate (8a)

To a solution of 1-(3-formyl-4-hydroxybenzyl)-3-methylimidazolium hexafluorophosphate (5.00 g, 13.80 mmol, **3a**) in dry ethanol (40 mL) was added ethylenediamine (1.12 mL, 6.86 mmol) slowly at room temperature. The resulting solution was stirred at reflux temperature for 6 h. The solution was allowed to cool to room temperature after which a solid separated out. The solid was washed with ethanol (3 × 5 mL) and dried in vacuo to give a yellow solid. Yield: 64.7%; mp 167–169 °C. IR (KBr, cm^{-1}): 1593 (C=C), 1637 (C=N), 3459 (O–H). ^{1}H NMR (500 MHz, acetone-d_6) δ: 4.0 (s, 10H, 2 × N–CH_3, 2 × =N–CH_2), 5.51 (s, 4H, 2 × $^+$N–CH_2), 6.94 (d, 2H, J = 8.5 Hz, Ar–H), 7.51 (dd, 2H, J = 2.5, 6.0 Hz, Ar–H), 7.62 (d, 2H, J = 2.0 Hz, Ar–H), 7.70 (t, 2H, J = 1.5, 2.0 Hz, Ar–H), 7.73 (t, 2H, J = 2.0 Hz, Ar–H), 8.59 (s, 2H, N=C–H), 9.01 (s, 2H, Ar–H), 13.50 (s, 2H, OH). ^{13}C NMR (126 MHz, acetone-d_6) δ: 36.76, 53.15, 60.38, 118.35, 120.03, 123.26, 125.13, 125.23, 133.53, 133.86, 137.38, 162.33, 167.39. ^{19}F NMR

Can. J. Chem. Downloaded from www.nrcresearchpress.com by Renmin University of China on 09/02/12
For personal use only.

Table 4. Crystal data and structure refinement for ionic liquid (IL) – salen – Co complex **9b**.

Parameter	Crystal data
Empirical formula	$C_{26}H_{35.2}B_3CoF_{12}N_8O_{2.6}$
Formula weight	820.76
Temperature (K)	130(2)
Wavelength (Å)	0.71073
Crystal system	Monoclinic
Space group	*P*2(1)/*c*
Unit cell dimensions	a = 16.944(3) Å, b = 13.424(2) Å, c = 16.654(3) Å $\alpha = 90°$, $\beta = 113.072(2)°$, $\gamma = 90°$
Volume (Å^3)	3485.0(10)
Z	4
Density (calculated, Mg/m^3)	1.426
Absorption coefficient (mm^{-1})	0.587
F(000)	1457
Crystal dimensions (mm^3)	0.239×0.177×0.121
θ range for data collection (°)	2.0225.00
Index ranges	$-20 \le h \le 20$, $-15 \le k \le 15$, $-19 \le l \le 19$
Reflections collected	33 387
Independent reflections	6126 (R(int) = 0.0704)
Completeness to $\theta = 25.00°$ (%)	100.0
Refinement method	Full-matrix least-squares on F^2
Data/restraints/parameters	6126/332/526
Goodness-of-fit on F^2	1.065
Final R indices ($I > 2\sigma(I)$)	$R1$ = 0.0417, $wR2$ = 0.1171
R indices (all data)	$R1$ = 0.0601, $wR2$ = 0.1252
Largest diff. peak and hole (e Å^{-3})	0.691 and –0.374

(235 MHz, acetone-d_6) δ: –68.0 (d, J = 705 Hz). ^{31}P NMR (202 MHz, acetone-d_6) δ: –144.2 (septet, J = 707.0 Hz). MS (ESI+) *m/z*: 603.2; ESI(–) *m/z*: 144.6. HRMS (ESI) ESI$^+$ calcd for $C_{26}H_{30}F_6N_6O_2P^+$: 603.2067; found: 603.2064.

Preparation of 1–4-hydroxy-3-[(2-[((*E*)-1–2-hydroxy-5-[(3-methyl-1*H*-imidazol-3-ium-1-yl)methyl] phenylmethylidene)amino]ethylimino)methyl]phenyl-3-methyl-1*H*-imidazol-3-ium tetrafluoroborate (8b)

To a stirred solution of 1-(3-formyl-4-hydroxybenzyl)-3-methylimidazolium tetrafluoroborate (5.00 g, 16.44 mmol, **3b**) in dry ethanol (40 mL) was added ethylenediamine (0.55 mL, 8.15 mmol). The resulting solution was refluxed for 6 h with constant stirring. The solution was allowed to cool to room temperature after which a solid separated out. The solid was washed with ethanol (3 × 5 mL) and dried in vacuo to give a yellow solid product. Yield: 47.33%; mp 162–164 °C. IR (KBr, cm^{-1}): 1580 (C=C), 1636 (C=N), 3405 (O–H). ^{1}H NMR (500 MHz, DMSO-d_6) δ: 3.84 (s, 6H, 2 × N–CH_3), 3.96 (s, 4H, 2 × =N–CH_2), 5.34 (s, 4H, 2 × $^+$N–CH_2), 6.92 (d, 2H, J = 8.5 Hz, Ar–H), 7.42 (dd, 2H, J = 2.0, 6.5 Hz, Ar–H), 7.54 (d, 2H, J = 2.5 Hz, Ar–H), 7.69 (d, 2H, J = 1.5 Hz, Ar–H), 7.73 (t, 2H, J = 1.5 Hz, Ar–H), 8.59 (s, 2H, N=C–H), 9.13 (s, 2H, Ar–H), 13.59 (s, 2H, OH). ^{13}C NMR (126 MHz, DMSO-d_6) δ: 35.84, 51.30, 58.54, 117.40, 118.44, 123.13, 123.96, 124.66, 132.03, 132.93, 136.42, 161.26, 166.33. ^{19}F NMR (235 MHz, DMSO-d_6) δ: –144.2. MS (ESI+) *m/z*: 545.0; ESI(–) *m/z*: 87.0. HRMS (ESI) ESI$^+$ calcd for $C_{26}H_{30}BF_4N_6O_2^+$: 545.2454; found: 545.2455.

Preparation of IL–salen–Co hexafluorophosphate complex (9a)

To a solution of hexafluorophosphate ligand (3.30 g, 4.41 mmol, **8a**) in dry ethanol (30 mL) was added ammonium hydroxide to bring the pH to 8–9. This solution was stirred for 15 min after which cobalt(II) acetate (1.21 g, 4.85 mmol) was added at room temperature. The resulting solution was stirred at reflux temperature for 10 h after which a solid separated out. This solid was washed with ethanol (3 × 5 mL) and dried to give a brown solid product. The product was recrystallized from an acetone–methanol mixture (9:1 *v/v*) to give crystals suitable for X-ray crystallographic analysis. Yield: 2.53 g (58% based upon the ligand **8a**). IR (KBr, cm^{-1}): 1574 (C=C), 1620 (C=N), 3595 (N–H). ^{1}H NMR (500 MHz, acetone-d_6) δ: 2.88 (s, 6H, 2 × NH_3), 4.06 (s, 6H, 2 × N–CH_3), 4.20 (s, 4H, 2 × =N–CH_2), 5.45 (s, 4H, 2 × $^+$N–CH_2), 7.07 (d, 2H, J = 9.0 Hz, Ar–H), 7.37 (dd, 2H, J = 2.5, 6.5 Hz, Ar–H), 7.55 (d, 2H, J = 2.0 Hz, Ar–H), 7.70 (d, 2H, J = 1.5 Hz, Ar–H), 7.72 (d, 2H, J = 1.5 Hz, Ar–H), 8.22 (s, 2H, N=C–H), 9.00 (s, 2H, Ar–H), (s, 2H, OH). ^{13}C NMR (126 MHz, acetone-d_6) δ: 36.78, 53.17, 59.40, 119.35, 120.86, 123.11, 124.61, 125.24, 135.82, 136.46, 137.15, 167.75, 169.46. ^{19}F NMR (235 MHz, acetone-d_6) δ: –68.0 (d, J = 705 Hz). ^{31}P NMR (202 MHz, acetone-d_6) δ: –144.2 (septet, J = 707.0 Hz). MS (ESI+) *m/z*: 804.9; ESI(–) *m/z*: 144.6. HRMS (ESI) ESI$^+$ calcd for $C_{26}H_{34}CoF_{12}N_8O_2P_2^+$: 839.1420; found: 839.1438.

Can. J. Chem. Downloaded from www.nrcresearchpress.com by Renmin University of China on 09/02/12
For personal use only.

Preparation of IL–salen–Co tetrafluoroborate complex (9b)

To a solution of tetrafluoroborate ligand (3.00 g, 4.75 mmol, **8b**) in dry ethanol (30 mL) was added ammonium hydroxide to bring the pH to 8–9. This solution was stirred for 15 min after which cobalt(II) acetate (1.30 g, 5.22 mmol) was added at room temperature. The resulting solution was stirred at reflux temperature for 10 hafter which a solid separated out. This solid was washed with ethanol (3 × 5 mL) and dried to give a brown solid product. The product was recrystallized from an acetone–methanol mixture (9:1 *v*/*v*) to give crystals suitable for X-ray crystallographic analysis. Yield: 2.58 g (67% based upon the ligand, **8b**). IR (KBr, cm^{-1}): 1573 (C=C), 1646 (C=N), 3618 (N–H). ^{1}H NMR (500 MHz, DMSO-d_6) δ: 2.76 (s, 6H, 2 × N–CH_3), 3.86 (s, 6H, 2 × N–CH_3), 3.88 (s, 4H, 2 × =N–CH_2), 5.27 (s, 4H, 2 × $^+$N–CH_2), 7.02 (d, 2H, J = 9.0 Hz, Ar–H), 7.33 (dd, 2H, J = 2.0, 6.5 Hz, Ar–H), 7.41 (d, 2H, J = 2.0 Hz, Ar–H), 7.69 (d, 2H, J = 1.5 Hz, Ar–H), 7.73 (d, 2H, J = 1.5 Hz, Ar–H), 8.08 (s, 2H, N=C–H), 9.20 (s, 2H, Ar–H). ^{13}C NMR (126 MHz, DMSO-d_6) δ: 35.87, 51.35, 57.86, 118.35, 119.94, 121.98, 122.80, 124.04, 134.23, 134.88, 136.19, 166.08, 167.61. ^{19}F NMR (235 MHz, DMSO-d_6) δ: –144.3. MS (ESI+) *m*/*z*: 723.0; ESI(–) *m*/*z*: 86.9. HRMS (ESI) ESI^+ calcd for $C_{26}H_{34}B_2CoF_8N_8O_2^+$: 723.2195; found: 723.2176.

Typical procedure for the oxidation of veratryl alcohol using IL–salen–Co catalysts 9a and **9b**

In a 50 mL two-necked flask IL–salen–Co complex (**9a** or **9b**, 10 mol%) and pyridine (10 mol%) were added to 10 mL of distilled water and stirred for about 15 min. Base, as indicated in Table 1, was then added to adjust the pH to about 12.5, followed by the slow addition of veratryl alcohol. At this point, the pH of the solution was monitored to ensure a basic pH. The reaction mixture was heated at 80 °C with constant air bubbling. The reaction was allowed to proceed for the desired time. The reaction was stopped by cooling to room temperature. The pH of the reaction mixture was adjusted to 6–7 with 2 mol/L HCl. The product (veratraldehyde) was extracted by dichloromethane, and the combined organic extracts were dried over magnesium sulfate followed by solvent removal in vacuo to afford a white solid; mp 41–43 °C. ^{1}H NMR (250 MHz, DMSO-d_6) δ: 3.8 (s, 3H, O–CH_3), 3.9 (s, 3H, O–CH_3), 7.1 (dd, 1H, Ar–H), 7.2 (s, 1H, Ar–H), 7.5 (d, 1H, Ar–H), 9.8 (s, 1H, CHO). ^{13}C NMR (62 MHz, DMSO-d_6) δ: 55.4, 55.8, 109.3, 111.2, 126.1, 129.6, 149.2, 154.2, 191.4. MS *m*/*z*: 166.

Supplementary data

Supplementary data are available with the article through the journal Web site (http://nrcresearchpress.com/doi/suppl/10.1139/v11-106). CCDC 822063–822065 contain the X-ray data in CIF format (for compounds **8a**, **9a**, and **9b**) for this manuscript. These data can be obtained, free of charge, via http://www.ccdc.cam.ac.uk/cgi-bin/catreq.cgi (Or from the Cambridge Crystallographic Data Centre, 12 Union Road, Cambridge CB2 1Ez, UK; fax +44 1223 336033; or deposit @ccdc.cam.ac.uk).

Acknowledgements

We are thankful to the Natural Sciences and Engineering Research Council of Canada (NSERC, Discovery and LIGNOWORKS, The NSERC Biomaterials and Chemicals Network) and Saint Mary's University (SMU–FGSR) for funding this research. J.D.M. wishes to thank the Canadian Foundation for Innovation and the Nova Scotia Research and Innovation Trust for upgrades to the X-ray diffractometer.

References

(1) Anastas, P.; Warner, J. *Green Chemistry: Theory and Practice;* Oxford University Press: Oxford, UK, 1998.

(2) Trost, B. M. *Angew. Chem. Int. Ed. Engl.* **1995**, *34* (3), 259. doi:10.1002/anie.199502591.

(3) Li, C. J.; Chan, T.-H. *Comprehensive Organic Reactions in Aqueous Media;* 2nd ed.; Wiley Interscience: New York, 2007, and references cited therein.

(4) Wasserscheid, P.; Welton, T., Eds. *Ionic Liquids in Synthesis;* 2nd ed.; Wiley-VCH Verlag GmbH & Co. KGaA: Weinheim, 2008.

(5) (a) Jiménez, A.-E.; Bermúdez, M.-D. *Tribol. Lett.* **2007**, *26* (1), 53. doi:10.1007/s11249-006-9182-9; (b) Mu, Z.; Liu, W.; Zhang, S.; Zhou, F. *Chem. Lett.* **2004**, *33* (5), 524. doi:10.1246/cl.2004.524.

(6) (a) Mathur, J. N.; Murali, M. S.; Nash, K. L. *Solvent Extr. Ion Exch.* **2001**, *19* (3), 357. doi:10.1081/SEI-100103276; (b) Shimojo, K.; Goto, M. *Anal. Chem.* **2004**, *76* (17), 5039. doi:10.1021/ac049549x; (c) Visser, A. E.; Swatloski, R. P.; Reichert, W. M.; Griffin, S. T.; Rogers, R. D. *Ind. Eng. Chem. Res.* **2000**, *39* (10), 3596. doi:10.1021/ie000426m; (d) Dietz, M. L. *Sep. Sci. Technol.* **2006**, *41* (10), 2047. doi:10.1080/01496390600743144; (e) Dietz, M. L.; Jakab, S.; Yamato, K.; Bartsch, R. A. *Green Chem.* **2008**, *10* (2), 174. doi:10.1039/b713750h; (f) Dietz, M. L.; Stepinski, D. C. *Talanta* **2008**, *75* (2), 598. doi:10.1016/j.talanta.2007.11.051; (g) Visser, A. E.; Swatloski, R. P.; Reichert, W. M.; Mayton, R.; Sheff, S.; Wierzbicki, A.; Davis, J. H., Jr; Rogers, R. D. *Chem. Commun. (Camb.)* **2001** (1), 135. doi:10.1039/b008041l; (h) Fraga-Dubreuil, J.; Famelart, M.-H.; Bazureau, J. P. *Org. Process Res. Dev.* **2002**, *6* (4), 374. doi:10.1021/op020027y; (i) Liu, H.; Wang, H.-Z.; Tao, G.-H.; Kou, Y. *Chem. Lett.* **2005**, *34* (8), 1184. doi:10.1246/cl.2005.1184; (j) Ouadi, A.; Gadenne, B.; Hesemann, P.; Moreau, J. J. E.; Billard, I.; Gaillard, C.; Mekki, S.; Moutiers, G. *Chemistry* **2006**, *12* (11), 3074. doi:10.1002/chem.200500741.

(7) Caja, J.; Dunstan, T. D. J.; Ryan, D. M.; Katovic, V. In *Molten Salts XII*, Proceedings of the 196th Electrochemical Society Meeting, Honolulu, Hawaii, 1999; Trulove, P. C., De Long, H. C., Stafford, G. R., Deki, S., Eds.; The Electrochemical Society: Pennington, NJ, 2000; Vol. 99-41, p 150; (b) Matsumoto, H.; Sakaebe, H.; Tatsumi, K.; Kikuta, M.; Ishiko, E.; Kono, M. *J. Power Sources* **2006**, *160* (2), 1308. doi:10.1016/j.jpowsour.2006.02.018; (c) Ishikawa, M.; Sugimoto, T.; Kikuta, M.; Ishiko, E.; Kono, M. *J. Power Sources* **2006**, *162* (1), 658. doi:10.1016/j.jpowsour.2006.02.077; (d) Garcia, B.; Lavall'ee, S.; Perron, G.; Michot, C.; Armand, M. *Electrochim. Acta* **2004**, *49* (26), 4583. doi:10.1016/j.electacta.2004.04.041.

(8) (a) Singh, K.; Marangoni, D. G.; Quinn, J. G.; Singer, R. D. *J. Colloid Interface Sci.* **2009**, *335* (1), 105. doi:10.1016/j.jcis.2009.03.075; (b) Bowers, J.; Butts, C. P.; Martin, P. J.; Vergara-Gutierrez, M. C.; Heenan, R. K. *Langmuir* **2004**, *20* (6), 2191. doi:10.1021/la035940m; (c) Inoue, T.; Ebina, H.;

Dong, B.; Zheng, L. *J. Colloid Interface Sci.* **2007**, *314* (1), 236. doi:10.1016/j.jcis.2007.05.052.

(9) (a) Zhu, S.; Wu, Y.; Chen, Q.; Yu, Z.; Wang, C.; Jin, S.; Ding, Y.; Wu, G. *Green Chem.* **2006**, *8* (4), 325. doi:10.1039/b601395c; (b) Swatloski, R. P.; Spear, S. K.; Holbrey, J. D.; Rogers, R. D. *J. Am. Chem. Soc.* **2002**, *124* (18), 4974. doi:10.1021/ja025790m.

(10) (a) Davis, J. H., Jr. *Chem. Lett.* **2004**, *33* (9), 1072. doi:10.1246/cl.2004.1072; (b) Lee, S.-G. *Chem. Commun. (Camb.)* **2006** (10), 1049. doi:10.1039/b514140k.

(11) (a) Harjani, J. R.; Friscic, T.; MacGillivray, L. R.; Singer, R. D. *Inorg. Chem.* **2006**, *45* (25), 10025. doi:10.1021/ic061479k; (b) Harjani, J. R.; Friscić, T.; MacGillivray, L. R.; Singer, R. D. *Dalton Trans.* **2008** (34), 4595. doi:10.1039/b806369a.

(12) Naik, P. U.; McManus, G. J.; Zaworotko, M. J.; Singer, R. D. *Dalton Trans.* **2008** (36), 4834. doi:10.1039/b811232k.

(13) (a) Pârvulescu, V. I.; Hardacre, C. *Chem. Rev.* **2007**, *107* (6), 2615. doi:10.1021/cr050948h; (b) Jiménez, A.-E.; Bermúdez, M.-D. *Tribol. Lett.* **2007**, *26* (1), 53. doi:10.1007/s11249-006-9182-9; (c) Mu, Z.; Liu, W.; Zhang, S.; Zhou, F. *Chem. Lett.* **2004**, *33* (5), 524. doi:10.1246/cl.2004.524; (d) Welton, T. *Chem. Rev.* **1999**, *99* (8), 2071. doi:10.1021/cr980032t; (e) Wasserscheid, P.; Keim, W. *Angew. Chem.* **2000**, *39* (21), 3772. doi:10.1002/1521-3773(20001103)39:21<3772::AID-ANIE3772>3.0.CO;2-5; (f) Earle, M. J.; Seddon, K. R. *Pure Appl. Chem.* **2000**, *72* (7), 1391. doi:10.1351/pac200072071391; (g) Sheldon, R. *Chem. Commun. (Camb.)* **2001** (23), 2399. doi:10.1039/b107270f; (h) Wilkes, J. S. *Green Chem.* **2002**, *4* (2), 73. doi:10.1039/b110838g; (i) Hemeon, I.; Singer, R. D. *J. Mol. Catal. Chem.* **2004**, *214* (1), 33. doi:10.1016/j.molcata.2003.09.032; (j) Hemeon, I.; Singer, R. D. *Chem. Commun. (Camb.)* **2002** (17), 1884. doi:10.1039/b205999a.

(14) (a) Kervinen, K.; Korpi, H.; Leskelä, M.; Repo, T. *J. Mol. Catal. Chem.* **2003**, *203* (1–2), 9. doi:10.1016/S1381-1169(03)00156-0; (b) Kervinen, K.; Lahtinen, P.; Repo, T.; Svahn, M.; Leskelä, M. *Catal. Today* **2002**, *75* (1–4), 183. doi:10.1016/S0920-5861(02)00064-0.

(15) (a) Martell, A., Sawyer, D., Eds. *Oxygen Complexes and Oxygen Activation by Transition Metals;* Plenum Press: New York, 1987; pp 87–107; (b) Drago, R. S.; Corden, B. B. *Acc. Chem. Res.* **1980**, *13* (10), 353. doi:10.1021/ar50154a003; (c) Bozell, J. J.; Hames, B. R.; Dimmel, D. R. *J. Org. Chem.* **1995**, *60* (8), 2398. doi:10.1021/jo00113a020; (d) Motekaitis, R. J.; Martell, A. E. *Inorg. Chem.* **1988**, *27* (15), 2718. doi:10.1021/ic00288a031.

(16) (a) Balakshin, M. Y.; Chen, C. L.; Gratzl, J. S.; Kirkman, A. G.; Jakob, H. *Holzforschung* **2000**, *54* (2), 171. doi:10.1515/HF.2000.029; (b) ten Have, R.; Teunissen, P. J. M. *Chem. Rev.* **2001**, *101* (11), 3397. doi:10.1021/cr000115l; (c) Sollewijn Gelpke, M. D.; Lee, J.; Gold, M. H. *Biochemistry* **2002**, *41* (10), 3498. doi:10.1021/bi011930d.

(17) *APEX2,* Version 2008.5; Bruker AXS, Inc.: Madison, WI, 2008.

(18) Sheldrick, G. M. *Acta Crystallogr.* **2008**, *A64*, 112.

(19) Farrugia, L. J. *J. Appl. Crystallogr.* **1997**, *30* (5), 565. doi:10.1107/S0021889897003117.

Can. J. Chem. Downloaded from www.nrcresearchpress.com by Renmin University of China on 09/02/12
For personal use only.

Increments for ^{1}H and ^{13}C NMR chemical shifts in pinacol arylboronates

Di Qiu, Zhitong Zheng, Fanyang Mo, Yan Zhang, and Jianbo Wang

Can. J. Chem. Downloaded from www.nrcresearchpress.com by Renmin University of China on 09/02/12
For personal use only.

Abstract: Arylboronates are important compounds widely used in cross-coupling reactions. By analyzing the NMR spectra data of a variety of pinacol arylboronates, we have determined the increments for ^{1}H and ^{13}C NMR chemical shifts caused by a pinacol boronate substituent in the benzene ring. These data can be used in the estimation of chemical shifts of aromatic pinacol boronates.

Key words: ^{1}H NMR, ^{13}C NMR, pinacol boronates, chemical shift increments.

Résumé : Les esters arylboronates sont des composés importants fréquemment utilisés dans des réactions de couplages croisés. Sur la base d'une analyse de données spectrales de RMN pour une variétés d'arylboronates du pinacol, il a été possible de déterminer les incréments dans les déplacements chimiques de RMN du ^{1}H et du ^{13}C provoqués par un substituant présent dans le noyau aromatique d'un boronate du pinacol. Ces données peuvent être utilisées pour évaluer les déplacements chimiques de boronates aromatiques du pinacol.

Mots-clés : RMN du ^{1}H, RMN du ^{13}C, boronates du pinacol, incréments dans les déplacements chimiques.

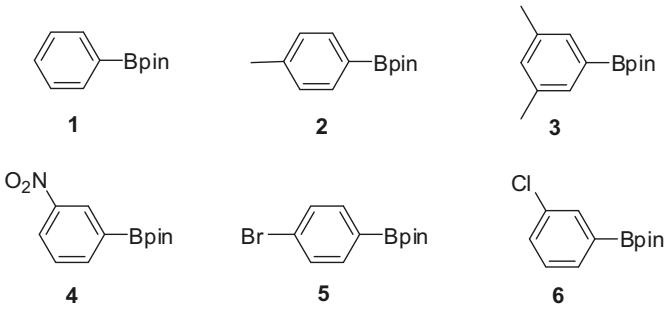
[Traduit par la Rédaction]

Introduction

Functionalized arylboronic acid and arylboronates have attracted much attention in the organic chemistry community in recent years because of their extensive applications in organic synthesis as well as in other fields.[1,2] Particularly, the Pd-catalyzed reaction of aromatic boron compounds, namely Suzuki–Miyaura cross-coupling reactions, have proved to be powerful tools for the construction of Csp^2–Csp^2 bond formations. The widespread use of aromatic boron compounds has stimulated the development of methods for the synthesis of these valuable chemicals. Pinacol boronic esters can be easily prepared from the corresponding boronic acids. They can also be synthesized by using Pd-catalyzed coupling of bis(pinacolato)diboron with aromatic halides (Miyaura borylation) or by rhodium- or iridium-catalyzed direct C–H bond activation.[1f,3] Because of the importance of aromatic boron compounds, it is highly desirable to develop methods that can conveniently and rapidly determine the structure of aromatic boronates.[4] In this context, Voss and co-workers[5] developed a formula to show the increments for ^{1}H and ^{13}C NMR chemical shifts of arylboronic acids. Since pinacol arylboronates are also widely used in organic synthesis, it would be helpful to develop methods that can be used for rapid structure elucidation. To the best of our knowledge, the corresponding NMR chemical-shift increments for pinacol arylboronates have not been reported in the literature. As a continuation of our recent interest in the chemistry of aromatic pinacol esters,[6] we have investigated the increments for ^{1}H and ^{13}C NMR chemical shifts caused by the pinacol boronate group in the benzene rings.

Results and discussion

We used the pinacol arylboronates **1**–**6** shown below as the reference compounds to calculate the NMR increments. $CDCl_3$ is used as the NMR solvent and the spectra were all measured with a Bruker 400 MHz NMR spectrometer.



Increments I^{H}_{B} for the ^{1}H chemical-shift differences caused by the pinacol boronate group (Bpin) are calculated from the $\delta(^{1}H)$ of the pinacol arylboronates **1**–**6** by using eq. [1] (7.34 is the ^{1}H NMR chemical shift of benzene in $CDCl_3$). The results are summarized in Table 1. The increments for I^{H}s are taken from the literature (for methyl, meta = –0.12 and para = –0.22; for nitro, meta = 0.26; for bromo, para = –0.04; and for chloro, meta = –0.02).[7]

Received 21 April 2011. Accepted 28 June 2011. Published at www.nrcresearchpress.com/cjc on 26 October 2011.

D. Qiu, Z. Zheng, F. Mo, Y. Zhang, and J. Wang. Beijing National Laboratory of Molecular Sciences (BNLMS) and Key Laboratory of Bioorganic Chemistry and Molecular Engineering of the Ministry of Education, College of Chemistry, Peking University, Beijing 100871, China.

Corresponding author: Jianbo Wang (e-mail: wangjb@pku.edu.cn).

This article is part of a Special Issue dedicated to Professor Tak-Hang Chan.

Table 1. ^{1}H chemical shifts (δ, ppm) and increments for the ^{1}H chemical-shift differences (I^H_B) caused by the pinacol boronate group for the pinacol arylboronates.

	Pinacol arylboronate											
	1		**2**		**3**		**4**		**5**		**6**	
Position	δ	I^H_B	δ	I^H_B	δ	I^H_B	δ	I^H_B	δ	I^H_B	δ	I^H_B
ortho-H	7.81	0.47	7.70	0.48	7.44	0.49	8.64	0.42	7.66	0.46	7.78	0.41
	7.81	0.47	7.70	0.48	7.44	0.49	8.10	0.39	7.66	0.46	7.66	0.37
meta-H	7.36	0.02	7.18	0.04	—	—	7.54	–0.01	7.50	0.03	7.30	0.01
	7.36	0.02	7.18	0.04	—	—	—	—	7.50	0.03	—	—
para-H	7.45	0.11	—	—	7.10	0.14	8.30	0.08	—	—	7.42	0.05

[1] $$I^H_B = \delta(^1H) - (7.34 + \Sigma I^H s)$$

From the results shown in Table 1, the mean I^H_Bs and the standard deviation can be calculated as follows:

$$I^H_B(\text{ortho}) = 0.44 \pm 0.04$$
$$I^H_B(\text{meta}) = 0.02 \pm 0.02$$
$$I^H_B(\text{para}) = 0.10 \pm 0.04$$

Compared with the chemical-shift increments caused by the boronic acid group (I^H_B(ortho) = 1.02 ± 0.03, I^H_B(meta) = 0.25 ± 0.04, I^H_B(para) = 0.34 ± 0.04),[5] I^H_B values for the pinacol boronate substituent clearly indicate that it is less electron withdrawing when compared with boronic acid.[8] They are comparable to the values of a cyano or a trifluoromethyl substituent, whereas the corresponding values for the boronic acid substituent are comparable to those of a nitro substituent. However, the factors that are related to the NMR chemical shift of boronic acids are more complicated because of reversible anhydride formation and possible dimerization through hydrogen bonding.

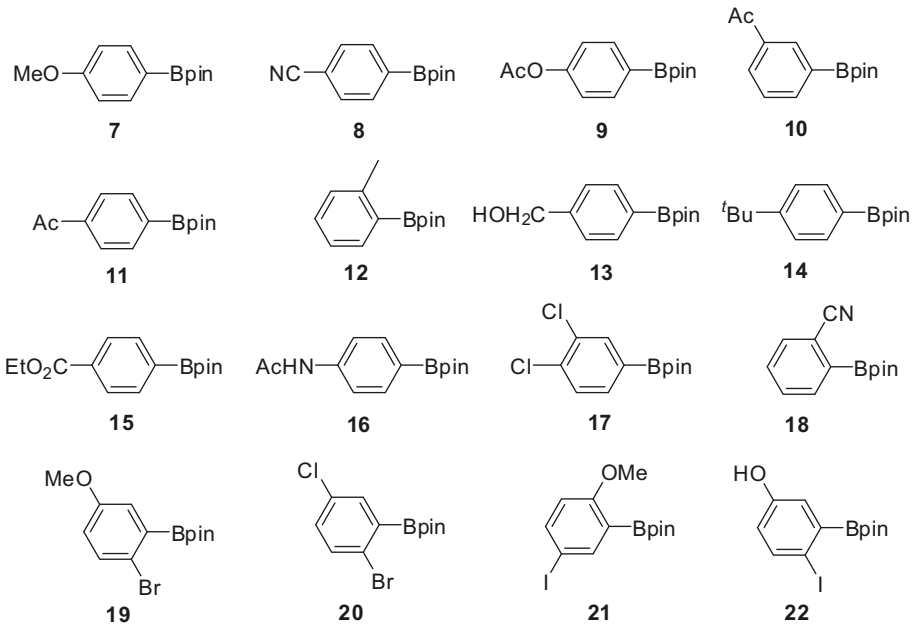
Similarly, the corresponding ^{13}C chemical-shift increments (I^C_B) caused by the pinacol boronate substituent can be calculated from the δ(^{13}C) of the pinacol arylboronates **1**–**6** by using eq. [2] (128.32 is the ^{13}C NMR chemical shift of benzene in $CDCl_3$). The results are summarized in Table 2. The increments for I^Cs are taken from the literature for methyl, ipso = 9.3, ortho = 0.6, meta = 0.0, and para = –3.1; for nitro, ipso = 19.6, ortho = –5.3, meta = 0.8, and para = 6.0; for bromo, ipso = –5.4, ortho = 3.3, meta = 2.2, and para = –1.0).[7]

[2] $$I^C_B = \delta(^{13}C) - (128.32 + \Sigma I^C s)$$

From the results shown in Table 2, the average increments and the standard deviation can be calculated as follows:

$$I^C_B(\text{ortho}) = 6.2 \pm 0.2$$
$$I^C_B(\text{meta}) = -0.5 \pm 0.2$$
$$I^C_B(\text{para}) = 3.1 \pm 0.5$$

With the I^H_B and the I^C_B data in hand, we subsequently verified the efficacy of these data in the estimation of chemical shifts of aromatic pinacol boronates by using the compounds **7**–**22**.



Can. J. Chem. Downloaded from www.nrcresearchpress.com by Renmin University of China on 09/02/12
For personal use only.

Table 2. ^{13}C chemical shifts (δ, ppm) and increments for the ^{13}C chemical-shift differences (I^{C}_{B}) caused by the pinacol boronate group for the pinacol arylboronates.

	Pinacol arylboronate											
	1		**2**		**3**		**4**		**5**		**6**	
Position	δ	I^{C}_{B}	δ	I^{C}_{B}	δ	I^{C}_{B}	δ	I^{C}_{B}	δ	I^{C}_{B}	δ	I^{C}_{B}
C-2	134.72	6.40	134.79	6.58	132.37	6.35	129.37	6.01	136.29	6.30	134.54	5.97
C-6	134.72	6.40	134.79	6.58	132.37	6.35	140.61	6.07	136.29	6.30	132.62	6.23
C-3	127.69	–0.63	128.49	–0.52	137.12	–0.62	147.82	–0.23	130.93	–0.55	134.01	–0.20
C-5	127.69	–0.63	128.49	–0.52	137.12	–0.62	128.70	–0.53	130.93	–0.55	129.16	–0.52
C-4	131.23	2.91	141.35	3.56	132.96	3.07	125.82	2.46	126.20	3.73	131.24	2.67

Table 3. Comparison of calculated and experimental ^{1}H NMR chemical shifts (δ, ppm) of the pinacol arylboronates.

	Position					
	ortho-H		*meta*-H		*para*-H	
	δ (ppm)					
Compound	Calculated	Measured	Calculated	Measured	Calculated	Measured
7	7.69	7.75	6.88	6.89	—	—
8	7.96	7.88	7.54	7.64	—	—
9	7.81	7.83	7.11	7.09	—	—
10	8.40	8.37	7.50	7.47	8.06	8.00
	7.99	8.06				
11	7.92	7.94~7.88	7.98	7.94~7.88	—	—
12	7.66	7.76	7.16	7.16	7.32	7.31
			7.14	7.16		
13	7.71	7.79	7.29	7.34	—	—
14	7.70	7.76	7.38	7.41	—	—
15	7.85	7.87	8.06	8.02	—	—
16	7.71	7.76	7.48	7.52	—	—
17	7.83	7.86	7.41	7.43	—	—
	7.58	7.60				
18	7.96	7.89	7.72	7.70	7.55	7.55
			7.64	7.55		
19	7.22	7.13	7.45	7.41	6.88	6.80
20	7.73	7.58	7.48	7.45	7.39	7.20
21	8.08	7.92	6.67	6.63	7.74	7.65
22	7.01	7.02	7.63	7.64	6.67	6.60

The calculated ^{1}H and ^{13}C chemical shifts of pinacol arylboronates found by using eqs. [1] and [2] and the corresponding measured chemical shifts are summarized in Tables 3 and 4 (see the Supplementary data for more information). The measured data were all recorded by a Bruker-400 NMR spectrometer. The increments of other functional groups are taken from the literature.[7]

From the data collected in Tables 3 and 4, the standard deviations for the estimated and measured chemical shifts were obtained.

$$d^{H}_{B}(\text{ortho}) = 0.06 \pm 0.04$$
$$d^{H}_{B}(\text{meta}) = 0.02 \pm 0.02$$
$$d^{H}_{B}(\text{para}) = 0.07 \pm 0.06$$

$$d^{C}_{B}(\text{ortho}) = 0.9 \pm 1.3$$
$$d^{C}_{B}(\text{meta}) = 0.8 \pm 0.9$$
$$d^{C}_{B}(\text{para}) = 0.8 \pm 0.5$$

The data compiled in Tables 3 and 4 demonstrate satisfactory agreement of the calculated and measured ^{1}H and ^{13}C NMR chemical shifts. However, when there are multiple substituents in the aromatic ring, relatively larger deviations of the ^{13}C chemical shifts are observed, as shown by compounds **19–22**.

Conclusion

In conclusion, we have obtained the increments for ^{1}H and ^{13}C NMR chemical shifts caused by the existence of a pinacol boronate substituent in the aromatic rings. These data could be widely used in the estimation of the NMR chemical shifts of aromatic pinacol boronates.[9]

Supplementary data

Supplementary data are available for this article through the journal Web site at http://nrcresearchpress.com/doi/suppl/10.1139/v11-099.

Can. J. Chem. Downloaded from www.nrcresearchpress.com by Renmin University of China on 09/02/12
For personal use only.

Table 4. Comparison of calculated and measured ^{13}C NMR chemical shifts (δ, ppm) of the pinacol arylboronates.

	Position					
	C-2,6		C-3,5		C-4	
	δ (ppm)					
Compound	Calculated	Measured	Calculated	Measured	Calculated	Measured
7	135.4	136.48	113.1	113.29	161.6	162.13
8	135.2	135.06	131.3	131.10	115.4	114.51
9	135.8	136.16	121.4	120.91	154.4	153.16
10	134.7	134.76	137.1	136.47	131.6	130.72
	138.7	139.35	128.0	127.99		
11	134.7	134.86	128.0	127.24	140.7	138.94
12	144.0	144.81	128.6	129.75	131.3	130.75
	135.2	135.83	124.8	124.68		
13	134.5	134.96	126.4	126.00	144.4	144.00
14	134.1	134.67	124.4	124.68	153.5	154.47
15	134.3	134.59	128.9	128.52	133.5	132.65
16	135.0	135.78	119.9	118.51	141.3	140.55
17	136.6	136.52	131.9	132.21	135.5	135.45
	133.8	133.73	129.9	129.98		
18	118.5	118.91	131.3	131.03	132.1	133.37
	135.2	135.80	132.1	131.51		
19	122.0	121.09	157.0	158.05	118.9	118.31
	121.0	118.04	132.0	133.47		
20	136.9	136.04	133.2	132.77	133.8	133.90
	127.1	125.68	132.1	131.74		
21	164.3	163.84	115.7	112.94	142.2	140.89
	145.3	144.83	87.4	83.76		
22	124.4	123.17	154.3	154.88	121.3	119.51
	94.9	88.65	139.1	140.48		

Can. J. Chem. Downloaded from www.nrcresearchpress.com by Renmin University of China on 09/02/12
For personal use only.

Acknowledgements

Financial support from the National Natural Science Foundation of China (Grant Nos. 20902005, 20832002, 210722009, and 20821062) and the 973 Program (No. 2009CB825300) is gratefully acknowledged.

References

(1) (a) For selected reviews see Miyaura, N.; Suzuki, A. *Chem. Rev.* **1995**, *95* (7), 2457. doi:10.1021/cr00039a007; (b) Suzuki, A. *Acc. Chem. Res.* **1982**, *15* (6), 178. doi:10.1021/ar00078a003; (c) Miyaura, N. *J. Organomet. Chem.* **2002**, *653* (1–2), 54. doi:10.1016/S0022-328X(02)01264-0; (d) Miyaura, N. *Bull. Chem. Soc. Jpn.* **2008**, *81* (12), 1535. doi:10.1246/bcsj.81.1535; (e) Merino, P.; Tejero, T. *Angew. Chem. Int. Ed.* **2010**, *49* (40), 7164. doi:10.1002/anie.201003191; (f) Miyaura, N. *Top. Curr. Chem.* **2002**, *219*, 11. doi:10.1007/3-540-45313-X_2.

(2) Hall, D. G. *Boronic Acids;* Wiley-VCH: Weinheim, 2005.

(3) (a) Mkhalid, I. A. I.; Barnard, J. H.; Marder, T. B.; Murphy, J. M.; Hartwig, J. F. *Chem. Rev.* **2010**, *110* (2), 890. doi:10.1021/cr900206p; (b) Ishiyama, T.; Murata, M.; Miyaura, N. *J. Org. Chem.* **1995**, *60* (23), 7508. doi:10.1021/jo00128a024.

(4) (a) Wrackmeyer, B. *Prog. Nucl. Magn. Reson. Spectrosc.* **1979**, *12* (4), 227. doi:10.1016/0079-6565(79)80003-5; (b) Gragg, B. R.; Layton, W. J.; Niedenzu, K. *J. Organomet. Chem.* **1977**, *132* (1), 29. doi:10.1016/S0022-328X(00)92511-7; (c) Niedenzu, K.; Müller, K.-D.; Layton, M. S.; Komorowsky, L. *Z. Anorg. Allg. Chem.* **1978**, *439*, 112. doi:10.1002/zaac.19784390113.

(5) Bruns, S.; Sinnwell, V.; Voss, J. *Magn. Reson. Chem.* **2003**, *41* (4), 269. doi:10.1002/mrc.1163.

(6) (a) Mo, F.; Jiang, Y.; Qiu, D.; Zhang, Y.; Wang, J. *Angew. Chem. Int. Ed.* **2010**, *49* (10), 1846. doi:10.1002/anie.200905824; (b) Qiu, D.; Mo, F.; Zheng, Z.; Zhang, Y.; Wang, J. *Org. Lett.* **2010**, *12* (23), 5474. doi:10.1021/ol102350v.

(7) Williams, D. H.; Fleming, I. *Spectroscopic Methods in Organic Chemistry;* 5th ed.; McGraw-Hill: Berkshire, 1995.

(8) Entwistle, C. D.; Marder, T. B. *Chem. Mater.* **2004**, *16* (23), 4574. doi:10.1021/cm0495717.

(9) The validity of these data has been further verified by comparison of the estimated NMR chemical shifts with those reported in the literature; see the Supplementary data.

Synthesis of (±)-14-*epi*-hydroxydolasta-1(15),7,9-triene and (±)-7-*epi*-acetoxy-14-*epi*-hydroxydolasta-1(15),8-diene*

George Majetich and Jianhua Yu

Can. J. Chem. Downloaded from www.nrcresearchpress.com by Renmin University of China on 09/02/12
For personal use only.

Abstract: 1,3-Dimethyl-2-nitrobenzene was converted to the key intramolecular Friedel–Crafts intermediate **24** in ten steps. Treatment of **24** with $TiCl_4$ produced tricyclic enone **25** in 61%–75% yield, having the requisite trans relationship of the two angular methyl groups and many of the salient features of the dolastane diterpenes. The structure of enone **25** was verified by X-ray crystallography analysis. Cyclization product **25** permitted the facile synthesis of (±)-14-*epi*-hydroxydolasta-1(15),7,9-triene and (±)-7-*epi*-acetoxy-14-*epi*-hydroxydolasta-1(15),8-diene, which are detailed in this article.

Key words: dolastanes, cyclialkylation, intramolecular Friedel–Crafts reactions, conformational biasing, regiospecific reductions.

Résumé : On a effectué la transformation en dix étapes du 1,3-diméthyl-3-nitrobenzène en composé **24**, l'intermédiaire clé d'une réaction de Friedel–Crafts intramoléculaire. Le traitement du produit **24** par du $TiCl_4$ à conduit avec un rendement de 61 à 75 % à formation de l'énone tricyclique **25** comportant la relation trans requise entre les deux groupes méthyles angulaires ainsi que plusieurs des caractéristiques principales des diterpènes du dolastane. La structure de l'énone **25** par diffraction des rayons-X. La cyclisation du produit **25** a permis de réaliser facilement la synthèse du (±)-14-*épi*-hydroxydolasta-1(15),7,9-triène et du (±)-7-*épi*-acétoxy-14-*épi*-hydroxydolasta-1(15),8-diène. Veuillez noter la cyclialkylation dans le texte.

Mots-clés : dolastanes, cycloalkylation, réactions de Friedel–Crafts intramoléculaires, biais conformationnel, réductions régiospécifiques.

[Traduit par la Rédaction]

Introduction

Fifty years ago, the diterpenoids were rare components of the marine environment. However, there are now more than 1900 diterpenoids known,[1] including twenty-five dolastanes. Dolatriol (**1**), the first dolastane isolated, was obtained from extracts of the digestive gland of the poisonous Indian Ocean sea hare *Dolabella auricularia* (Scheme 1)[2–5] and was very cytotoxic. Further work, however, established that dolatriol was actually produced by a brown algae genus *Dictyota* and only concentrated by *Dolabella auricularia* through its diet. All dolastanes have a distinctive 5,7,6-linear fused tricyclic framework. Their structural diversity rests on the following features: (*i*) the number and the position(s) of the hydroxyl group and double bond(s) (cf. **3**); (*ii*) the trans configuration of the two angular methyl groups at C-5 and C-12; (*iii*) the BC-ring system is usually trans fused; and (*iv*) many of the relative stereochemical configurations have been assigned based on X-ray crystal structure analysis or NMR studies. Finally, isoamijiol (**2**) has antimicrobial activity against *Mucor mucedo* and *Staphylococcus aureus*, and several dolastanes exhibit promising biological activity.[6]

The research groups of Pattenden,[7] Piers,[8] Mehta,[9] Paquette,[10] Williams,[11] and Majetich[12] have completed total syntheses of various dolastanes. The first dolastane synthesized was (±)-amijiol (**2**) by Pattenden and co-workers in 1986.[7] Their strategy for introducing the trans angular methyl groups is shown in Chart 1. The alkylation of hydroazulenone **5**, produced in seven steps from cyclopentanone, gave exclusively the α–epimer **6** because of the steric influence of the C-16 angular methyl group. The C-ring was formed with the requisite C-14 stereochemistry, using an intramolecular reductive coupling of ketone **6** with the alkyne; an allylic oxidation of alkene **7** introduced the C-2 hydroxyl group, albeit in low yield. In their synthesis of **3** from ketone **8**, Piers and Friesen used a similar alkylation strategy to introduce the C-12 and C-5 chirality (cf. **9** → **10**).[8] Vinylstannane **10** was converted into a Grignard reagent, which added to the C-14 carbonyl group to complete the synthesis. In 1987 Mehta and Krishnamurthy used a similar A+B→AB+C→ABC strategy to prepare **10**, using Pattenden's strategy, to install the C–14 hydroxyl group and create the C-ring.[9] The synthesis of the non-natural (±)-4aβ,10β-doladiol acetate (**4**) was achieved by Paquette et. al.[10] Instead of using the C-12

Received 2 May 2011. Accepted 10 July 2011. Published at www.nrcresearchpress.com/cjc on 1 November 2011.

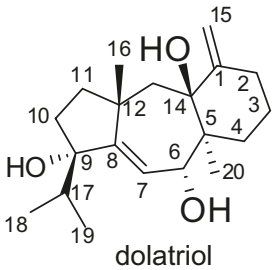
G. Majetich and J. Yu. Department of Chemistry, University of Georgia, Athens, Georgia, 30602, USA.

Corresponding author: George Majetich (e-mail: Majetich@uga.edu).

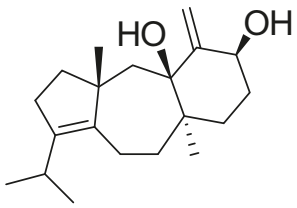
This article is part of a Special Issue dedicated to Professor Tak-Hang Chan.

*Taken in part from the Ph.D. dissertation of Jianhua Yu, University of Georgia, Athens, Georgia, USA, 2009.

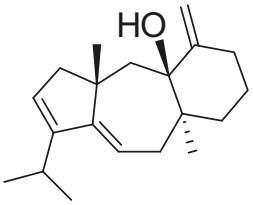
Scheme 1.



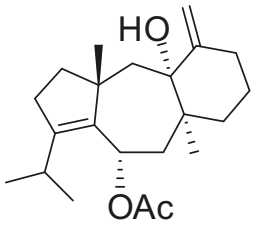
dolatriol (**1**)[2]



isoamijiol (**2**)[3]



14-hydroxydolasta-1(15),7,9-triene (**3**)[4]



7-*epi*-acetoxy-14-*epi*-hydroxydolasta-1(15),8-diene (**4**)[5]

methyl group to create the C-5 stereocenter, the alkylation of decalenone **11** produced alkylated product **12**, using the C-5 angular methyl group to create the C-12 stereochemistry. This synthesis featured a photochemical rearrangement to isomerize the 6,6,6-tricyclic α,β-epoxy ketone **13** into a 5,7,6-tricyclic dolastane skeleton. Six additional steps were needed to convert enone **14** into the 7,14-epimers of natural dolastane **4**. Williams and co-workers synthesized (–)-clavulara-1(15),17-dien-3,4-diol (**18**) from (+)-9,10-dibromocamphor **15**, which fragmented to form acid **16** upon exposure to NaOH.[11] Thirty-four transformations were required to transform **16** into macrocyclic epoxide **17**. An acid-catalyzed transannular epoxide opening of **17** created the C-ring with the required C-5 stereogenic center in 38% yield. In contrast to these strategies, Majetich and co-workers used an A +C→AC→ABC strategy to synthesize natural (±)-1(15),8-dolastadien-2-ol (±)-**23** (also called 14-deoxyisoamijiol).[12] In this synthesis, a functionalized A-ring (cf. **19**) was coupled with a C-ring containing an allylsilane (cf. **20**), followed by the addition of vinyllithium to the C-8 carbonyl group to produce dienone **21**. An intramolecular 1,6-addition of the allylsilane to the dienone **21** produced the dolastane skeleton with the trans relationship of the C-5 and C-12 angular methyl groups (cf. **22**). Nine steps were needed to introduce the C-1,C-15 double bond and the β-oriented C-2 hydroxyl group of **23**.

We have found that intramolecular Friedel–Crafts reactions, or cyclialkylations,[13] of conjugated dienones represent a powerful strategy to assemble various tricyclic frameworks.[14] We speculated that conformational biasing prior to ring formation would also create stereogenic centers (Scheme 2). However, the examination of a Dreiding model of **24** suggests that steric interactions between the C-16 and C-20 methyl groups in conformer **i**, and the steric interactions between the C-16 and C-15 methyl groups in conformer **ii** are comparable. We have observed that when the ortho and para positions are both substituted with identical groups (H, CH_3, or Cl), cyclization occurs at the para position relative to the electron donating substitutent (cf. **ii**). Thus, ring closure via conformer **ii** would produce the central cyclohexane ring and a trans relationship between the C-12 and C-5 angular methyl groups. If so, the functionality present in the A- and C-rings of enone **25** makes it an attractive precursor for the synthesis of several dolastanes. Herein, we report the synthesis of tricyclic enone **25** and its conversion into (±)-14-*epi*-hydroxydolasta-1(15),7,9-triene (**3**) and (±)-7-*epi*-acetoxy-14-*epi*-hydroxydolasta-1(15),8-diene (**4**).

Our study began with the preparation of the A- and C-rings. The A-ring was synthesized from 4-methylpentan-2-one (**26**), using our published procedure (Scheme 3);[12] commercially available 1,3-dimethyl-2-nitrobenzene (**29**) was our starting material for the C-ring synthesis (Scheme 4).

Monobromination of **29** followed by nucleophilic aromatic substitution gave anisole derivative **30** in 83% yield.[15] Zinc metal reduction of the nitro group provided aniline compound **31**.[16] The next step, a Sandmeyer reaction,[17] gave an inseparable mixture of mono- and di-bromination products **32** and **35**, respectively. Fortunately, the reaction of the organolithium reagents derived from **32** and **35** with DMF produced aldehyde **33** and dialdehyde **36**, which were easily separated. Reduction of aldehyde **33** to an alcohol with LAH was followed by the conversion of the benzylic alcohol to the corresponding benzyl bromide **34** by treatment with PBr_3.

With the A- and C-rings in hand, we set out to prepare dienone **24**, the key cyclization precursor. Coupling of **19** with **34** gave adduct **37** in excellent yield (Scheme 5). Addition of vinyllithium to ketone **37**, followed by acidic work-up, gave dienone **24** in high yield. There are two facial-selective products possible from the cyclization of dienone **24** (cf. **25** and **25a**) and two possible regioisomers (cf. **25b** and **25c**). In each case, cyclialkylation would produce a C-ring dienone, since the newly created quaternary carbon center (either at C-5 or at C-1) precludes re-aromatization. In a related cyclialkylation,[18] we found that under Lewis acid catalysis, dienone **38** produces tricycle **39** having an angularly fused quaternary carbon center (Scheme 6). We were pleased to find that treatment of dienone **24** with $TiCl_4$ at –60 °C for 30 min produced only enone **25**, albeit the isolated yield varied between 61% and 75%. An X-ray crystal structure analysis of **25** verified the trans configuration of the two angular methyl groups.

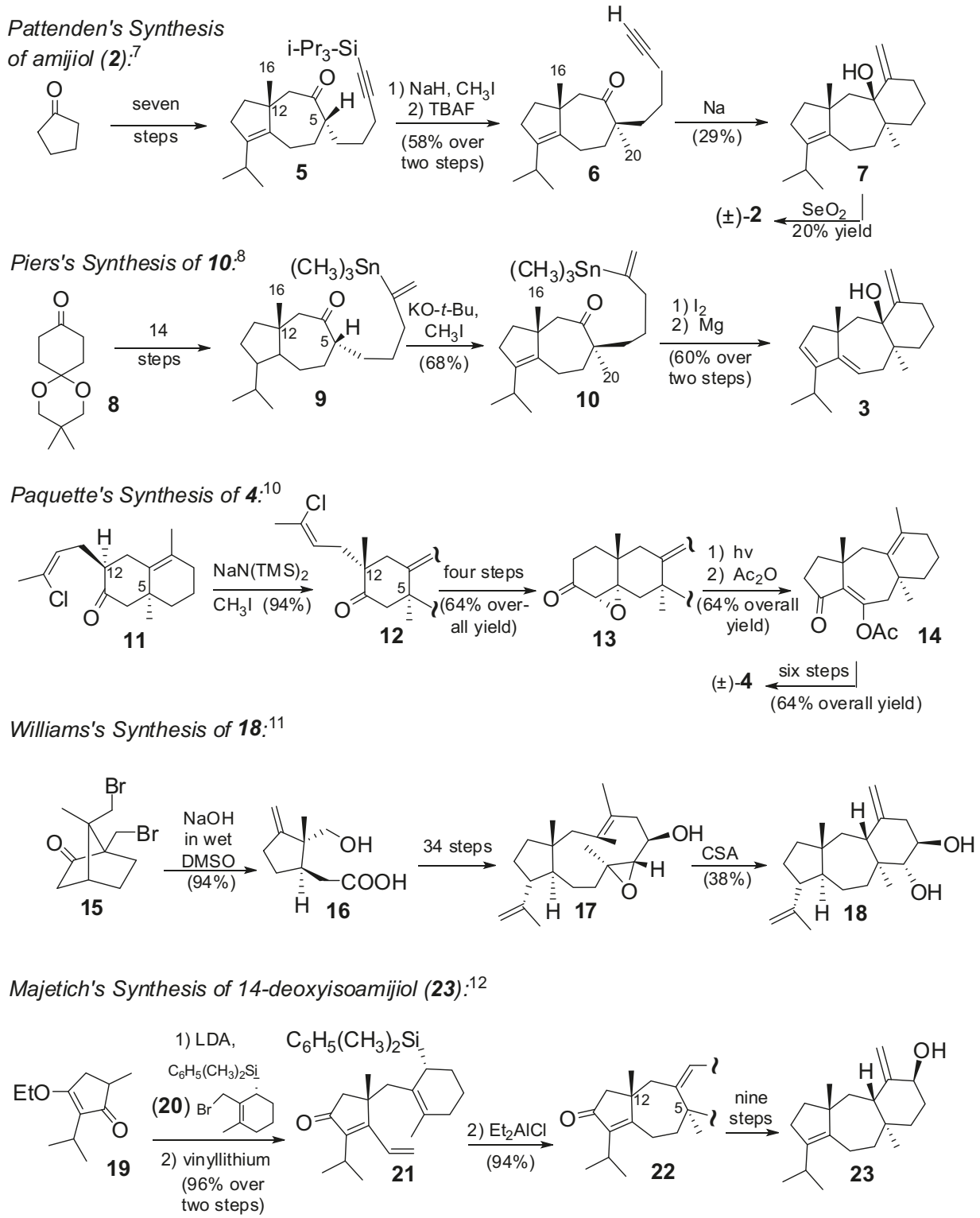
Several of the dolastanes have a β-hydroxyl group at C-2 and a C-1, C-15 exocyclic double bond, or a C-14 β-hydroxyl group, or a hydroxyl group or an acetate at C-4 (Scheme 7). To achieve a synthesis of (±)-7,14-*epi*-1(15),8-dolastadiene-7,14-diol 7-acetate (**4**), we needed to selectively reduce the C-2 and C-10 carbonyl groups and the C-3,C-4 double bond of enone **25**, as well as selectively introduce an acetate at C-7 and an α-oriented hydroxyl group at C-14 (cf. **4**). We were confident that the A-ring enone moiety would permit the introduction of the C-7,C-9 diene (cf. **40**) thereby facilitating a synthesis of **10**.

The C-2 carbonyl group, which is conjugated to two double bonds, has more resonance contributors with a negative charge on oxygen, thereby making it less reactive than the C-10 carbonyl group (Scheme 8). Indeed, treatment of enone

Can. J. Chem. Downloaded from www.nrcresearchpress.com by Renmin University of China on 09/02/12
For personal use only.

Can. J. Chem. Downloaded from www.nrcresearchpress.com by Renmin University of China on 09/02/12
For personal use only.

Chart 1.

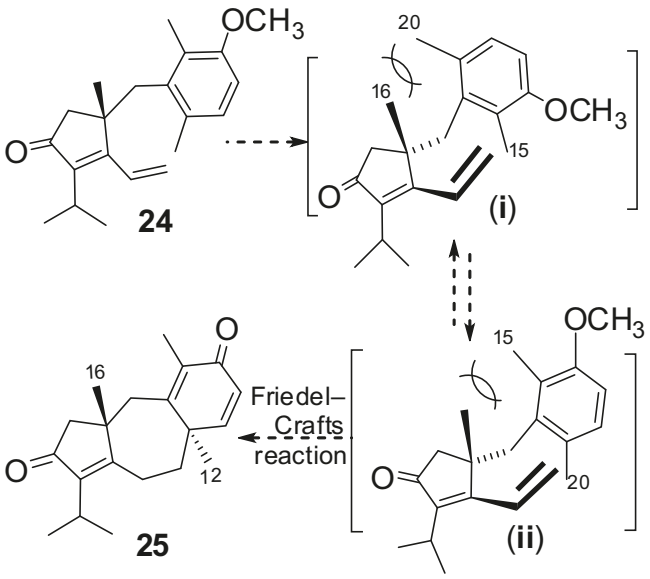


25 with sodium borohydride in the presence of TFA in dichloromethane selectivity reduced the C-10 carbonyl group to a methylene unit.[19] If, however, we first reduced the C-3, C-4 double bond (cf. **42**), the C-2 carbonyl group was found to be more reactive, presumably a result of the steric hindrance by the isopropyl group. Note that under the reaction conditions, enone **43** is rapidly reduced to produce diene **44**.

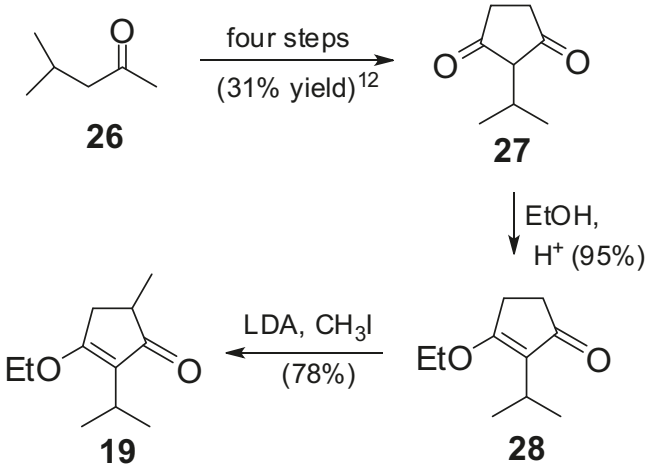
In their synthesis of **4**, Paquette et al. found that singlet oxygen migrated the C-1,C-14 double bond to the C-1,C-15 position and introduced an α-oriented alcohol at C-14.[10a] Reaction of enone **43** with singlet oxygen, followed by reduction of the intermediate allylic peroxide, introduced an alcohol from the α-face because of the steric effect of the C-16 methyl, which added in Michael fashion to the A-ring enone

Can. J. Chem. Downloaded from www.nrcresearchpress.com by Renmin University of China on 09/02/12
For personal use only.

Scheme 2.



Scheme 3.

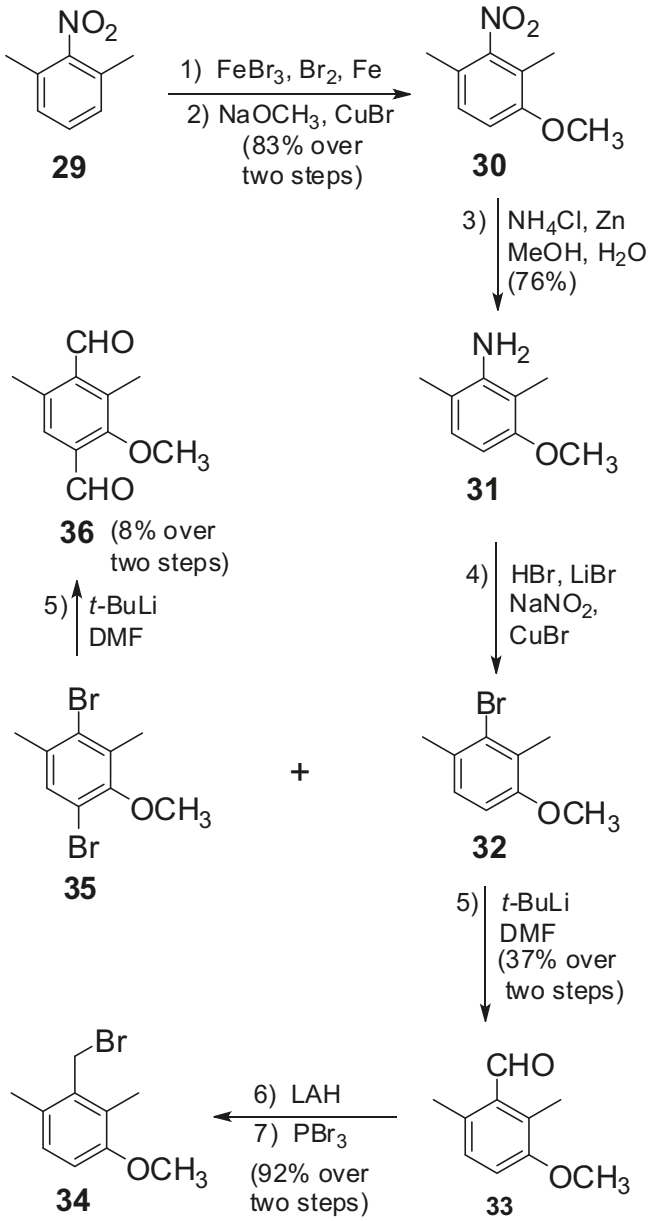


to form tetrahydrofuran **45** in 92% yield. This result indicated that the C-10 carbonyl group had to be removed, or protected, before the C-14 α-hydroxyl group is introduced.

Another way to introduce the C-14 α-allylic alcohol was by opening a C-1,C-14 α-epoxide. However, because of the steric influence of the C-16 methyl group, the epoxidation of **43** gave only epoxide **46** (Scheme 9). The reduction of the C-10 carbonyl group with LAH gave an allylic alcohol, which rapidly dehydrated to form diene **47**. Treatment of **47** with LDA at 50 °C overnight gave alcohol **48** in 93% yield; this compound is epimeric at C-14 to natural dolastane **10**. A traditional way to prepare an epimeric epoxide is to make the bromohydrin from the alkene and then treat it with base. Since the C-16 methyl blocks the β-face of the C-1,C-14 double bond, bromonium ion formation must occur from the α-face so that the addition of water to the bromonium ion generated in situ must add from the β-face to provide the β-epoxide. However, when **43** was treated with NBS in wet acetone, allylic oxidation at C-2 produced dienone **42** in 71% yield.

Scheme 10 presents a formal synthesis of **4** from diene **44**. Longer reaction time in the reduction of enone **42** produced

Scheme 4.

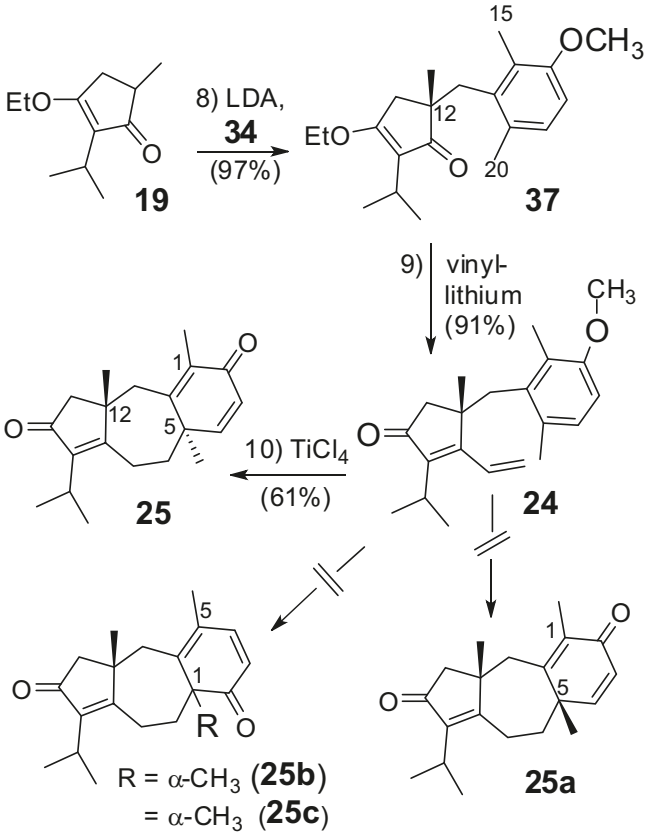


diene **44** in 73% yield. The reaction of diene **44** with selenium dioxide and *t*-butylhydroperoxide produced alcohol **49** in 45% yield and triene **50** in 40% yield; all efforts to prevent the in situ dehydration of **49** failed. Allylic alcohol **49** was oxidized using freshly activated MnO_2 to enone **51**, which Paquette and co-workers converted to **4** using the three transformations shown in 64% overall yield.[10c]

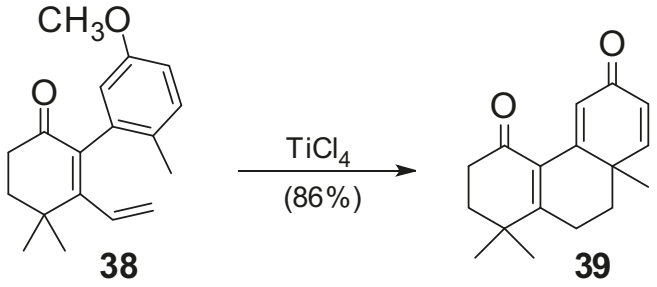
In summary, 1,3-dimethyl-2-nitrobenzene was converted in ten steps into tricyclic dienone **25.** In the key reaction, diene **24** was cyclized to produce the central seven-membered ring and created the required stereochemistry of the C-5 and C-12 quaternary carbon atoms. Changing the oxidation states at C-3, C-4, C-10, C-14, and C-15 required six transformations and produced (±)-14-*epi*-hydroxydolasta-1(15),7,9-triene (**48**), which is epimeric at C-14 to the natural dolastane. Diene **44**, at first an unwanted side product in the reduction of dienone **42**, was optimized and then converted in two steps into enone **51**, an intermediate in Paquette's synthesis of

Can. J. Chem. Downloaded from www.nrcresearchpress.com by Renmin University of China on 09/02/12
For personal use only.

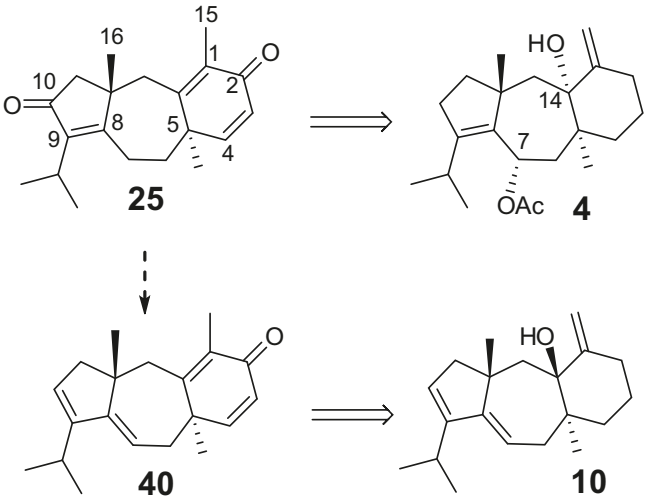
Scheme 5.



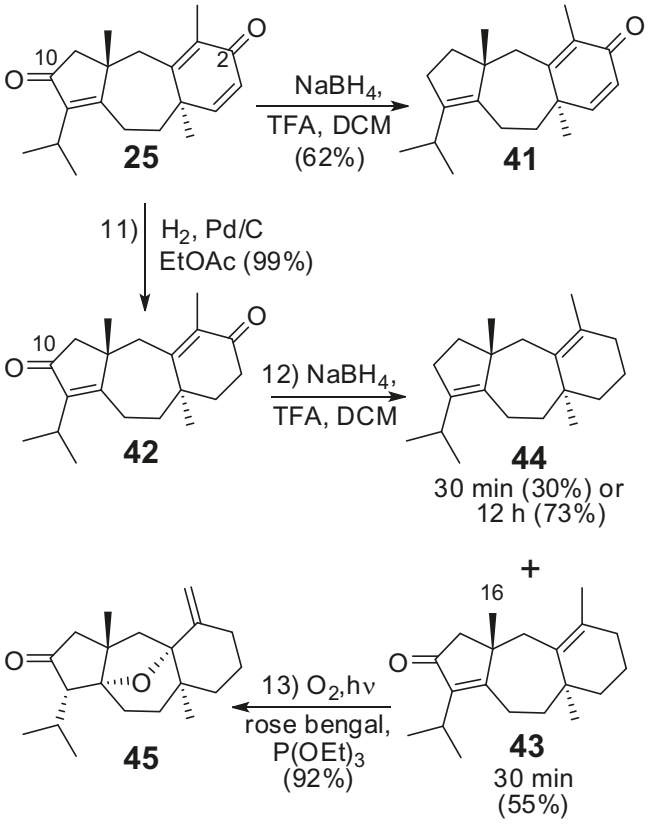
Scheme 6.



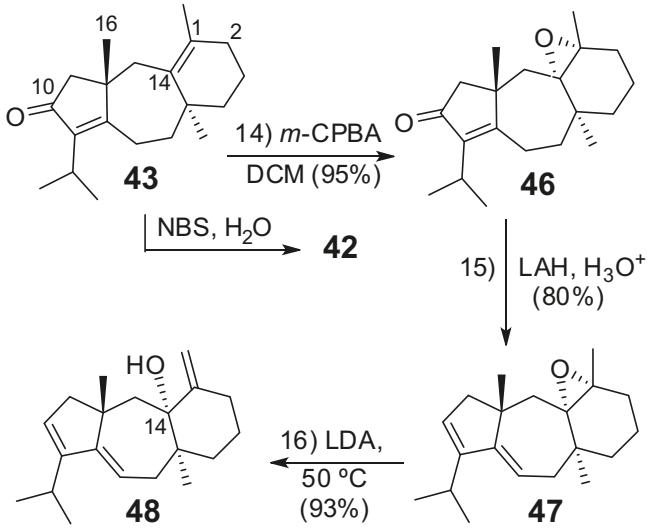
Scheme 7.



Scheme 8.



Scheme 9.



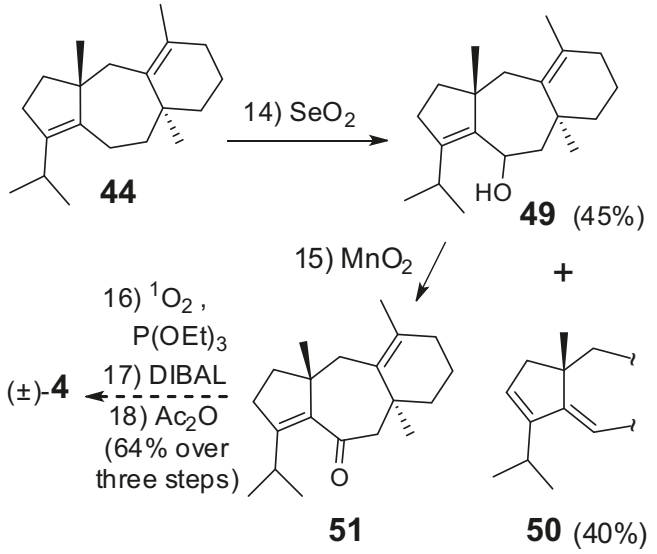
(±)-7-*epi*-acetoxy-14-*epi*-hydroxydolasta-1(15),8-diene (**4**). We are confident that dienone **25,**, or a derivative thereof, will permit the efficient synthesis of the more oxygenated naturally occurring dolastanes.

Experimental section

General procedures

All reactions were run under a nitrogen atmosphere and monitored by TLC analysis. Unless otherwise indicated, all ethereal work-ups consisted of the following procedure. The

Scheme 10.



reaction was quenched at RT (RT) with water. The organic solvent was removed under reduced pressure on a rotary evaporator, and the residue was extracted with diethyl ether twice. The combined organic layer was washed with water, brine, and dried over anhydrous magnesium sulfate. Filtration, followed by concentration at reduced pressure on a rotary evaporator and at 1 torr (1 torr = 133.322 4 Pa) to constant weight, afforded a crude residue that was purified by flash chromatography using silica gel 60 (230–400 mesh ASTM) eluted with distilled reagent grade petroleum ether and diethyl ether. Melting points were recorded on a Laboratory Devices Mel–Temp 3.0. ^{1}H and ^{13}C NMR spectra were recorded on Bruker AVB–400 and DRX–500 MHz spectrometers with ^{13}C operating frequencies of 100 and 125 MHz, respectively. ^{1}H NMR spectra were obtained in $CDCl_3$ and were calibrated using trace $CHCl_3$ present (δ 7.27) as an internal reference. ^{13}C NMR spectra were obtained in $CDCl_3$ and were calibrated using trace $CHCl_3$ present (δ 77.23) as an internal reference. The IR spectra were obtained using an Avatar 360FT-IR spectrophotometer and are reported in frequency of absorption (cm^{-1}). Only selected IR absorbances are reported. High-resolution MS spectra were taken using a LCT Premier mass spectrometer from Waters.

1-Methoxy-2,4-dimethyl-3-nitrobenzene (30)

To a solution of 1,3-dimethyl-2-nitrobenzene (**29**) (50.0 g, 331 mmol) in freshly distilled DCM (150 mL) was added $FeBr_3$ (2.0 g, 6.8 mmol) and Fe (5.0 g, 89 mmol). Molecular bromine (18.6 mL, 361 mmol) was added dropwise, and 100 mL of DCM was added to the mixture. The reaction mixture was refluxed for 8 h. The reaction mixture was cooled to RT, followed by standard ethereal work-up. The organic layer was dried over anhydrous $MgSO_4$, filtered, and then concentrated under vacuum using rotary evaporator to give 74.3 g (98.0%) of the bromide as a crude red oil. IR (film): λ_{max}: 2927, 1517, 1370, 815 cm^{-1}. ^{1}H (400 MHz) δ: 7.55 (d, J = 4.8 Hz, 1H), 7.02 (d, J = 4.8 Hz, 1H), 2.35 (s, 3H), 2.26 (s, 3H). ^{13}C NMR (100 MHz) δ: 134.0 (d), 129.9 (d), 129.6 (s), 128.7 (s), 123.2 (s), 18.3 (q), 17.3 (q) ppm. HR-MS: $[M]^+_{obs}$ = 228.9738, $[M]^+_{calcd}$ = 228.9738. This crude bromide was used in the next reaction without purification.

A solution of sodium methoxide was prepared by adding small pieces of sodium metal (21.0 g, 0.913 mol) to anhydrous methanol (300 mL). After the complete consumption of the sodium, a solution of the above bromide (70.0 g, 304 mmol) in anhydrous DMF (300 mL) was added, followed by the addition of CuBr (4.0, 28.0 mmol). The reaction mixture was heated at 110 °C for 12 h, then cooled to RT, and water (100 mL) was added dropwise to quench the reaction. Standard ethereal work-up gave 46.8 g (85%) of nitrobenzene **30** as a crude red solid, which was recrystallized (benzene) to give white crystals. Mp 48.7–49.0 °C. IR (film) λ_{max}: 2930, 1524, 1263, 810 cm^{-1}. ^{1}H (400 MHz) δ: 7.06 (d, J = 8.8 Hz, 1H), 6.84 (d, J = 8.8 Hz, 1H), 3.85 (s, 3H), 2.23 (s, 3H), 2.14 (s, 3H). ^{13}C NMR (100 MHz) δ: 181.1 (s), 156.4 (s), 128.9 (d), 120.6 (s), 118.7 (s), 111.8 (d), 56.2 (q), 16.7 (q), 10.9 (q) ppm. HR-MS: $[M]^+_{obs}$ = 181.0741, $[M]^+_{calcd}$ = 181.0739.

3-Methoxy-2,6-dimethylaniline (31)

To a solution of anisole **30** (30.0 g, 166 mmol) in MeOH (270 mL) and H_2O (30 mL) was added NH_4Cl (26.0 g, 486 mmol), followed by Zn powder (110 g, 1.68 mol) in small portions. The reaction mixture was stirred at RT for 2 h, followed by standard ethereal work-up, to give 19.0 g (76.0%) of aniline **31** as a crude red oil which was used in the next step without purification. IR (film) λ_{max}: 3393, 2910, 1626, 1496, 1262, 791 cm^{-1}. ^{1}H (400 MHz) δ: 6.89 (d, J = 8.4 Hz, 1H), 6.32 (d, J = 8.4 Hz, 1H), 3.80 (s, 3H), 2.15 (s, 3H), 2.09 (s, 3H). ^{13}C NMR (100 MHz) δ: 156.7 (s), 143.8 (s), 127.6 (d), 115.1 (s), 110.9 (s), 101.0 (d), 55.9 (q), 17.4 (q), 9.4 (q) ppm. HR-MS: $[M]^+_{obs}$ = 152.1074, $[M]^+_{calcd}$ = 152.1075.

2-Bromo-4-methoxy-1,3-dimethylbenzene (32) and 1,4-dibromo-2-methoxy-3,5-dimethylbenzene (35)

A round bottom flask at 0 °C was charged with HBr (4.67 g, 27.7 mmol), THF (60 mL), LiBr (1.14 g, 13.1 mmol), $NaNO_2$ (1.0 g, 14.5 mmol), and CuBr (2.26 g, 15.8 mmol). The ice bath was removed, and aniline **31** (3.0 g, 2.00 mmol) in THF (15 mL) was added dropwise. The reaction mixture was stirred at RT for an additional 1 h, followed by standard ethereal work-up, to give 3.43 g of a black oil which was predominantly bromide **32** along with dibromide **35**, which could not be separated. Albeit a mixture, the following data is for bromide **32**, the major component. ^{1}H (400 MHz) δ: 7.08 (d, J = 8.3 Hz, 1H), 6.75 (d, J = 8.3 Hz, 1H), 3.80 (s, 3H), 2.20 (s, 3H), 2.18 (s, 3H).

3-Methoxy-2,6-dimethylbenzaldehyde (33) and 2-methoxy-3,5-dimethylterephthalaldehyde (36)

To a solution of **32** and **35** (34 g) in THF (250 mL) at –78 °C was slowly added *t*-BuLi (180 mL, 306 mmol). This mixture was stirred at –78 °C for 2 h, followed by the addition of DMF (40 mL). The reaction mixture was warmed to RT and stirred overnight. Water (10 mL) was added slowly to quench the reaction, followed by standard ethereal work-up. Column chromatography (elution with pet. ether/EtOAc, 10:1) gave 1.22 g (37% over two steps) of aldehyde **33** (hexane/EtOAc, 4:1, R_f **33** = 0.66) as a

Can. J. Chem. Downloaded from www.nrcresearchpress.com by Renmin University of China on 09/02/12
For personal use only.

Can. J. Chem. Downloaded from www.nrcresearchpress.com by Renmin University of China on 09/02/12
For personal use only.

white solid. IR (film) λ_{max}: 2939, 1691, 1262 cm^{-1}. ^{1}H (400 MHz) δ: 10.6 (s, 1H), 7.03 (d, J = 8.4 Hz, 1H), 6.93 (d, J = 8.4 Hz, 1H), 3.83 (s, 3H), 2.51 (s, 3H), 2.46 (s, 3H). ^{13}C NMR (125 MHz) δ: 194.5 (d), 156.4 (s), 133.8 (s), 132.1 (s), 129.8 (s), 129.6 (d), 115.0 (d), 56.1 (q), 20.1 (q), 11.5 (q) ppm. HR-MS: $[M]^+_{obs}$ = 164.0840, $[M]^+_{calcd}$ = 164.0837. Further elution gave 0.31 g (8.1% over two steps) of *bis*-aldehyde **36** as a white solid (hexane/EtOAc, 4:1, R_f **36** = 0.45). Mp = 82.0–82.3 °C. IR (film) λ_{max}: 2930, 1691, 1409, 1232 cm^{-1}. ^{1}H (400 MHz) δ: 10.6 (s, 1H), 10.4 (s, 1H), 7.54 (s, 1H), 3.85 (s, 3H), 2.55 (s, 3H), 2.52 (s, 3H). ^{13}C NMR (100 MHz) δ: 193.7 (d), 190.1 (d), 160.4 (s), 138.8 (s), 136.2 (s), 134.9 (s), 131.4 (s), 128.9 (d), 63.8 (q), 19.9 (q), 11.8 (q) ppm. HR-MS: $[M]^+_{obs}$ = 192.0790, $[M]^+_{calcd}$ = 192.0786.

2-(Bromomethyl)-4-methoxy-1,3-dimethylbenzene (34)

A solution of aldehyde **33** (10.0 g, 61.0 mol) in Et_2O (150 mL) was cooled to 0 °C and LAH (2.55 g, 67.1 mmol) was added portion-wise. The ice bath was removed and the solution was stirred at RT for 1 h. The solution was poured into a 2 L Erlenmeyer flask containing Na_2SO_4 (20 g) and EtOAc (300 mL). Water was added slowly until the heterogeneous mixture turned to white. Standard ethereal work-up, followed by column chromatography (elution with pet ether/EtOAc = 4:1), afforded 9.60 g (95%) (3-methoxy-2,6-dimethylphenyl)methanol as a white solid (hexane/EtOAc, 4:1, R_f alcohol = 0.25). IR (film) λ_{max}: 3396, 2957, 1464, 1258 cm^{-1}. ^{1}H (400 MHz) δ: 7.02 (d, J = 8.8 Hz, 1H), 6.75 (d, J = 8.0 Hz, 1H), 4.75 (s, 2H), 3.82 (s, 3H), 2.38 (s, 3H), 2.31 (s, 3H). ^{13}C NMR (125 MHz) δ: 156.4 (s), 137.8 (s), 129.2 (s), 128.4 (d), 126.4 (s), 110.4 (d), 59.8 (t), 55.9 (q), 19.2 (q), 11.6 (q) ppm. HR-MS: $[M]^+_{obs}$ = 166.0999, $[M]^+_{calcd}$ = 166.0994.

A solution of the above alcohol (5.00 g, 30.1 mmol) in Et_2O (150 mL) was cooled to 0 °C and PBr_3 (3.1 mL, 33.1 mmol) was added dropwise. The resulting solution was removed from the ice bath and stirred at RT for 1 h. The resulting solution was cooled to 0 °C, and brine (30 mL) was added slowly. The aqueous phase was removed and the organic layer was dried over anhydrous magnesium sulfate. Filtration, followed by concentration at reduced pressure, and column chromatography (elution with pet ether/EtOAc, 15:1) afforded 6.69 g (97%) of bromide **34** as a white solid (hexane/EtOAc, 4:1, R_f **34** = 0.80). Mp = 62.3–62.5 °C. IR (film) λ_{max}: 3000, 2833, 1486, 1261 cm^{-1}. ^{1}H (400 MHz) δ: 7.03 (d, J = 8.4 Hz, 1H), 6.77 (d, J = 8.8 Hz, 1H), 4.60 (s, 2H), 3.83 (s, 3H), 2.40 (s, 3H), 2.33 (s, 3H). ^{13}C NMR (125 MHz) δ: 156.4 (s), 135.3 (s), 129.3 (s), 128.4 (d), 126.5 (s), 111.0 (d), 55.9 (q), 29.9 (t), 19.0 (q), 11.4 (q) ppm. HR-MS: $[M+H]^+_{obs}$ = 228.0140, $[M+H]^+_{calcd}$ = 228.0150.

3-Ethoxy-2-isopropyl-5-(3-methoxy-2,6-dimethylbenzyl)-5-methylcyclopent-2-en-1-one (37)

To a solution of diisopropylamine (2.40 mL, 17 mmol) in THF (20 mL) at –78 °C was added *n*-butyllithium (6.30 mL, 16 mmol) over a 5 min period. The resulting mixture was stirred at RT for 10 min then cooled to –78 °C. A solution of enone **19** (2.60 g, 14.3 mmol) and HMPA (2.60 g, 14.3 mmol) in THF (10 mL) was cannulated over a 5 min period. The resulting solution was stirred for 1 h at –78 °C then raised to –63 °C. A solution of bromide **34** (2.94 g, 17.2 mmol) in THF (10 mL) was cannulated into the reaction mixture over a 2 min period, and the resulting mixture was stirred overnight. Standard ethereal work-up, followed by column chromatography (elution with pet ether/EtOAc, 10:1), afforded 4.2 g (97%) of adduct **37** as a light yellow oil (hexane/EtOAc, 4:1, R_f **37** = 0.47). IR (film) λ_{max}: 2981, 1622, 1342, 1253 cm^{-1}. ^{1}H (400 MHz) δ: 6.94 (d, J = 8.4 Hz, 1H), 6.64 (d, J = 8.4 Hz, 1H), 3.99 (m, 1H), 3.87 (m, 1H), 3.79 (s, 3H), 3.28 (d, J = 14.8 Hz, 1H), 3.74 (d, J = 14.8 Hz, 1H), 2.71 (septet, J = 7.2 Hz, 1H), 2.38 (d, J = 17.2 Hz, 1H), 2.18 (s, 3H), 2.16 (d, J = 17.2 Hz, 1H), 2.10 (s, 3H), 1.28 (s, 3H), 1.19 (t, J = 7.2 Hz, 3H), 1.10 (d, J = 6.8 Hz, 3H), 1.08 (d, J = 7.2 Hz, 3H). ^{13}C NMR (100 MHz) δ: 209.3 (s), 181.9 (s), 156.3 (s), 137.9 (s), 129.7 (s), 128.0 (d), 126.4 (s), 122.9 (s), 108.5 (d), 64.9 (t), 55.8 (q), 46.9 (s), 36.8 (t), 36.4 (t), 27.9 (q), 23.0 (d), 21.0 (q), 20.3 (q), 20.3 (q), 15.1 (q), 13.5 (q) ppm. HR-MS: $[M+H]^+_{obs}$ = 331.2266, $[M+H]^+_{calcd}$ = 331.2273.

2-Isopropyl-4-(3-methoxy-2,6-dimethylbenzyl)-4-methyl-3-vinylcyclopent-2-en-1-one (24)

To a solution of vinyl bromide (3.2 mL, 45 mmol) in freshly distilled Et_2O (60 mL) at –78 °C, *t*-butyllithium (54 mL, 1.7 mol/L, 91 mmol) was added over a 15 min period. After stirring 2.5 h at RT, the vinyllithium mixture was cannulated into **37** (2.00 g, 6.1 mmol) in THF (60 mL) solution at –78 °C. The resulting mixture was warmed to RT and stirred for an additional 8 h. Hydrochloric acid (20.0 mL, 1.0 mol/L) was added dropwise at 0 °C, and the resulting mixture was stirred for 30 min. Standard ethereal work-up, followed by column chromatography (elution with pet ether/EtOAc, 8:1), gave 1.76 g (91%) of conjugated dienone **24** as a light yellow oil (hexane/EtOAc, 2:1, R_f **24** = 0.75). IR (film) λ_{max}: 2960, 1693, 1258, 1102 cm^{-1}. ^{1}H (400 MHz) δ: 6.96 (d, J = 8.0 Hz, 1H), 6.90 (dd, *J1* = 11.2 Hz, *J2* = 17.6 Hz, 1H), 6.66 (d, J = 8.4 Hz, 1H), 5.63 (d, J = 17.6 Hz, 1H), 5.47 (d, J = 11.2 Hz, 1H), 3.79 (s, 3H), 3.43 (m, 1H), 3.08 (dd, *J1* = 6.4 Hz, *J2* = 14.0 Hz, 1H), 2.93 (septet, J = 7.2 Hz, 1H), 2.57 (dd, *J1* = 10.0 Hz, *J2* = 14.0 Hz, 1H), 2.28 (m, 1H), 2.25 (s, 3H), 2.20 (s, 3H), 1.28 (s, 3H), 1.26 (d, J = 6.8 Hz, 1H), 1.22 (d, J = 6.8 Hz, 1H). ^{13}C NMR (125 MHz) δ: 208.3 (s), 166.9 (s), 156.4 (s), 145.0 (s), 138.1 (s), 130.4 (d), 128.4 (s), 128.3 (d), 125.2 (), 121.5 (t), 108.4 (d), 55.5 (q), 41.1 (t), 36.8 (d), 35.8 (t), 20.9 (q), 20.6 (q), 20.5 (q), 15.1 (q), 12.8 (q) ppm.

(3a*S*,8a*R*)-1-Isopropyl-3a,5,8a-trimethyl-3a,4,9,10-tetrahydrobenzo[*f*]azulene-2,6(3*H*,8a*H*)-dione (25)

To a solution of conjugated dienone **24** (200 mg, 0.641 mmol) in fresh distilled DCM (2 mL) at –78 °C was added $TiCl_4$ (10 μL, 0.91 mmol). The resulting mixture was stirred at –78 °C for 1 h, and the temperature was raised to –60 °C, then stirred for an additional 0.5 h. Water (5 mL) was added dropwise to quench the reaction, followed by standard ethereal work-up. Column chromatography (elution with pet ether/EtOAc, 4:1) afforded 115 mg (61%) of tricyclic enone **25** as a white solid (hexane/EtOAc, 2:1, R_f **25** = 0.41). IR (film) λ_{max}: 2963, 1738, 1693, 1658, 1627, 1379 cm^{-1}. ^{1}H (500 MHz) δ: 6.81 (d, J = 9.5 Hz, 1H), 6.31 (d, J = 9.5 Hz, 1H), 3.03 (d, J = 13.5 Hz, 1H),

Can. J. Chem. Downloaded from www.nrcresearchpress.com by Renmin University of China on 09/02/12
For personal use only.

2.74 (m, 1H), 2.67 (septet, J = 7.0 Hz, 1H), 2.35 (m, 3H), 2.17 (m, 1H), 1.96 (s, 3H), 1.71 (m, 1H), 1.59 (m, 1H), 1.22 (s, 3H), 1.13 (m, 6H), 1.09 (s, 3H). ^{13}C NMR (125 MHz) δ: 207.4 (s), 186.2 (s), 179.3 (s), 158.0 (s), 157.7 (d), 140.9 (s), 136.0 (s), 128.2 (d), 52.0 (t), 45.6 (t), 45.1 (s), 40.0 (t), 38.4 (t), 29.9 (q), 25.7 (q), 24.7 (d), 23.9 (t), 20.8 (q), 20.7 (q), 13.8 (q) ppm. HR-MS: $[M+H]^+_{obs}$ = 299.2010, $[M+H]^+_{calcd}$ = 299.2011.

(3a*R*,8a*R*)-1-Isopropyl-3a,5,8a-trimethyl-2,3,3a,4,9,10-hexahydrobenzo[*f*]azulen-6(8a*H*)-one (41)

To a solution of tricycle **25** (100 mg, 0.336 mmol) in freshly distilled DCM (10 mL) was added 10% TFA in DCM solution (5 mL), followed by $NaBH_4$ (64 mg, 1.7 mmol). The resulting mixture was stirred for 0.5 h. Water (5 mL) was added to quench the reaction, followed by standard ethereal work-up. Column chromatography (elution with pet ether/EtOAc, 10:1) gave 64 mg (67%) of dienone **41** as a light yellow oil (hexane/EtOAc, 4:1, R_f **41** = 0.55). IR (film) λ_{max}: 2963, 1658, 1462, 1151 cm^{-1}. ^{1}H (500 MHz) δ: 6.81 (d, J = 9.5 Hz, 1H), 6.31 (d, J = 9.5 Hz, 1H), 2.67 (septet, J = 7.0 Hz, 1H), 2.15–1.5 (m, 11H), 1.96 (s, 3H), 1.22 (s, 3H), 1.13 (m, 6H), 1.09 (s, 3H). HR-MS: $[M+H]^+_{obs}$ = 285.2222, $[M+H]^+_{calcd}$ = 285.2218.

(3a*R*,8a*R*)-1-Isopropyl-3a,5,8a-trimethyl-2,3,3a,4,8,8a,9,10-octahydrobenzo[*f*]azulen-6(7*H*)-one (42)

To a dry 20-mL round-bottomed flask was added tricycle **25** (100 mg, 0.336 mmol) under nitrogen atmosphere, followed by addition of anhydrous EtOAc (5 mL) and 5% of Pd/C (10 mg, 10% in weight). The nitrogen in the reaction flask was removed by bubbling H_2 into the reaction medium for a 5 min period. A balloon filled with H_2 was connected to the round-bottomed flask and the resulting mixture was stirred under H_2 for 2 h. The H_2 balloon was disconnected and the residue H_2 gas was removed by bubbling N_2 into the reaction mixture, followed by filtration through a short pad of silica gel to remove the catalyst. Standard ethereal work-up, followed by column chromatography (elution with pet ether/EtOAc, 4:1), gave 100 mg (99%) of *bis*-enone **42** as a white solid (hexane/EtOAc, 2:1, R_f **42** = 0.40). Mp = 147.0–147.2 °C. IR (film) λ_{max}: 3376, 2959, 1697, 1460, 1379, 1118 cm^{-1}. ^{1}H (400 MHz) δ: 2.87 (d, J = 13.2 Hz, 1H), 2.52–2.79 (m, 4H), 2.39 (d, J = 18.0 Hz, 1H), 2.30 (d, J = 18.8 Hz, 1H), 2.21 (m, 2H), 2.04 (m, 1H), 1.85 (s, 3H), 1.79 (m, 1H), 1.58 (m, 2H), 1.17 (m, 9H), 1.13 (s, 3H). ^{13}C NMR (100 MHz) δ: 207.3 (s), 198.5 (s), 179.5 (s), 160.6 (s), 140.6 (s), 135.3 (s), 52.0 (t), 44.5 (s), 41.0 (t), 40.1 (t), 34.9 (t), 34.4 (t), 26.6 (q), 25.5 (q), 24.7 (d), 22.5 (t), 20.9 (q), 20.8 (q), 13.7 (q) ppm. HR-MS: $[M+H]^+_{obs}$ = 301.2167, $[M+H]^+_{calcd}$ = 301.2168.

(3a*S*,8a*S*)-1-Isopropyl-3a,5,8a-trimethyl-3a,4,6,7,8,8a,9,10-octahydrobenzo[*f*]azulen-2(3*H*)-one (43) and (3a*R*,8a*S*)-1-isopropyl-3a,5,8a-trimethyl-2,3,3a,4,6,7,8,8a,9,10-decahydrobenzo[*f*]azulene (44)

To a solution of *bis*-enone **42** (153 mg, 0.510 mmol) in fresh distilled DCM (15 mL) was added 10% TFA in DCM solution (10 mL), followed by $NaBH_4$ (97 mg, 2.6 mmol). The resulting mixture was stirred for 0.5 h at RT. Water (5 mL) was added to quench the reaction, followed by standard ethereal work-up. Column chromatography (elution with pet ether/EtOAc, 10:1) gave 44 mg (30%) of diene **44** as a light yellow oil (hexane/EtOAc, 4:1, R_f **44** = 0.90). IR (film) λ_{max}: 2933, 1464, 1372 cm^{-1}. ^{1}H (400 MHz) δ: 1.70–2.35 (m, 17H), 1.67 (s, 3H), 1.13–1.19 (m, 6H), 1.10 (s, 3H), 0.98 (s, 3H). ^{13}C NMR (100 MHz) δ: 208.6 (s), 182.5 (s), 139.7 (s), 132.9 (s), 131.9 (s), 52.0 (t), 44.9 (s), 41.7 (t), 38.3 (s), 37.9 (t), 37.2 (t), 32.3 (t), 28.4 (q), 25.7 (q), 24.6 (d), 22.9 (t), 21.8 (q), 20.9 (q), 19.3 (t) ppm. HR-MS: $[M]^+_{obs}$ = 286.2295, $[M]^+_{calcd}$ = 286.2297. Further elution gave 76 mg (55%) of enone **43** as a light yellow oil (hexane/EtOAc, 4:1, R_f **43** = 0.55). ^{1}H (400 MHz) δ: 2.58–2.74 (m, 3H), 2.30 (d, J = 18.4 Hz, 1H), 2.20 (d, J = 18.0 Hz, 1H), 2.12 (m, 1H), 1.95 (m, 3H), 1.68–1.84 (m, 3H), 1.67 (s, 3H), 1.25–1.44 (m, 3H), 1.15 (m, 6H), 1.10 (s, 3H), 0.98 (s, 3H). ^{13}C NMR (100 MHz) δ: 208.6 (s), 182.5 (s), 139.7 (s), 132.9 (s), 131.9 (s), 52.0 (t), 44.9 (s), 41.7 (t), 38.3 (s), 37.9 (t), 37.2 (t), 32.3 (t), 28.4 (q), 25.7 (q), 24.6 (d), 22.9 (t), 21.8 (q), 20.9 (q), 19.3 (t) ppm. HR-MS: $[M+H]^+_{obs}$ = 287.2376, $[M+H]^+_{calcd}$ = 287.2375. Note: Allowing the reduction to proceed overnight (12 h) gave diene **44** in 73% yield.

(1*S*,3a*S*,8a*S*)-1-Isopropyl-3a,8a-dimethyl-5-methylenedecahydro-4a,10a-epoxybenzo[*f*]azulen-2(1H)-one (45)

A solution of **43** (10 mg, 0.034 mmol) and rose bengal (2.0 mg) in 5 mL of a solution of methanol/dichloromethane (1:9) was irradiated at –5 °C with a 500 W tungsten lamp, while oxygen was bubbled through the reaction mixture. After 40 min, the reaction mixture was treated with triethyl phosphite (0.3 mL) at RT for 1 h with vigorous stirring. After concentration, standard ethereal work-up provided a crude residue, which was purified by column chromatography (elution with pet ether: EtOAc, 10:1) and gave 9.9 mg (92%) of furan **45** (hexane: EtOAc, 4:1, R_f **45** = 0.45) as a colorless oil. IR (film) λ_{max}: 2933, 1740, 1075, 895 cm^{-1}. ^{1}H (400 MHz) δ: 4.76 (s, 1H), 4.66 (s, 1H), 2.93 (d, J = 17.6 Hz, 1H), 2.61–2.74 (m, 2H), 2.08–2.41 (m, 6H), 1.72–1.80 (m, 1H), 1.58–1.69 (m, 4H), 1.25–1.40 (m, 2H), 1.20 (m, 6H), 1.12 (s, 3H), 0.83 (s, 3H). ^{13}C NMR (100 MHz) δ: 217.0 (s), 148.7 (s), 103.1 (t), 90.9 (s), 86.6 (s), 59.2 (d), 54.6 (t), 46.6 (t), 44.9 (q), 36.2 (s), 35.8 (t), 32.8 (t), 31.4 (t), 25.7 (d), 24.4 (t), 21.9 (q), 21.2 (t), 19.9 (q), 18.8 (q), 18.1 (q) ppm. HR-MS: $[M+H]^+_{obs}$ = 303.2316, $[M+H]^+_{calcd}$ = 303.2324.

(1a*R*,4a*S*,9a*S*,10a*S*)-7-Isopropyl-1a,4a,9a-trimethyl-2,3,4,4a,5,6,9a,10-octahydro-1aH-azuleno[5′,6′:1,6]benzo[1,2-*b*]oxiren-8(9*H*)-one (46)

To a solution of diene **43** (35 mg, 0.12 mmol) in freshly distilled DCM (4 mL) under nitrogen atmosphere was added *m*-CPBA (77%, 33 mg, 0.15 mmol, 1.2 equiv.). The resulting mixture was stirred at RT for 1 h. Standard ethereal work-up, followed by column chromatography (elution with pet ether/EtOAc, 5:1), afforded 35.0 mg (95%) of epoxide **46** as a white foam (hexane/EtOAc, 2:1, R_f **46** = 0.49). IR (film) λ_{max}: 3006, 2918, 1717, 1364, 1224 cm^{-1}. ^{1}H (400 MHz) δ: 2.87 (m, 1H), 2.73 (septet, J = 7.2 Hz, 1H), 2.42 (m, 1H), 2.22 (d, J = 8.8 Hz, 2H), 1.90–2.12 (m, 3H), 1.64–1.83 (m, 3H), 1.39–1.52 (m, 3H), 1.37 (s, 3H), 1.29 (s, 3H), 1.20–

Can. J. Chem. Downloaded from www.nrcresearchpress.com by Renmin University of China on 09/02/12
For personal use only.

1.25 (m, 1H), 1.18 (s, 3H), 1.16 (s, 3H) 0.97 (s, 3H). ^{13}C NMR (100 MHz) δ: 207.3 (s), 179.4 (s), 141.2 (s), 68.6 (s), 65.3 (s), 53.3 (t), 42.8 (s), 42.2 (t), 37.7 (s), 36.8 (t), 36.7 (t), 31.4 (t), 25.9 (q), 24.8 (d), 24.2 t), 23.4 (q), 23.0 (q), 20.4 (q), 20.3 (q), 16.6 (q) ppm. HR-MS: $[M]^+_{obs}$ = 302.2243, $[M]^+_{calcd}$ = 302.2246.

(1a*R*,4a*S*,9a*R*,10a*S*)-7-Isopropyl-1a,4a,9a-trimethyl-2,3,4,4a,5,9,9a,10-octahydro-1a*H*-azuleno[5′,6′:1,6]benzo[1,2-*b*]oxirene (47)

To a solution of enone **46** (60 mg, 0.20 mmol) in freshly distilled Et_2O (10 mL) at 0 °C under nitrogen atmosphere was added LAH (7.6 mg, 0.20 mmol). The resulting reaction mixture was stirred for 1 h at RT. Water (4 mL) was slowly added to quench the reaction, followed by standard ethereal work-up. Concentration of the filtered organic phase afforded yellow oil. Silica gel was added to the bottle, and the resulting mixture was allowed to sit on the bench overnight. Column chromatography (elution with pet ether/EtOAc, 15:1) afforded 45.5 mg (80%) of diene **47** (hexane/EtOAc, 8:1, R_f **47** = 0.50) as a colorless oil. IR (film) λ_{max}: 3247, 2952, 1660, 1359, 1010 cm^{-1}. ^{1}H (500 MHz) δ: 5.60 (s, 1H), 5.45 (m, 1H), 2.90 (d, *J* = 15.0 Hz, 1H), 2.41 (m, 1H), 2.14–2.33 (m, 3H), 1.70–1.98 (m, 4H), 0.80–1.62 (m, 4H), 1.39 (s, 3H), 1.18 (s, 3H), 1.07–1.13 (m, 6H), 1.03 (s, 3H). ^{13}C NMR 154.5 (s), 149.5 (s), 125.6 (d), 113.6 (d), 70.4 (s), 65.8 (s), 49.6 (t), 43.5 (s), 39.2 (t), 37.9 (s), 37.2 (t), 34.8 (t), 30.1 (t), 25.7 (d), 24.0 (q), 23.7 (q), 23.3 (q), 22.3 (q), 22.3 (q), 16.7 (t) ppm. HR-MS: $[M]^+_{obs}$ = 286.2297, $[M]^+_{calcd}$ = 286.2297.

(3a*R*,4a*R*,8a*S*)-1-Isopropyl-3a,8a-dimethyl-5-methylene-3,3a,4,4a,5,6,7,8,8a,9-decahydrobenzo[*f*]azulen-4a-ol (48)

To a solution of diisopropylamine (0.70 mL, 5.0 mmol) in freshly distilled Et_2O (10 mL) at 0 °C was added *n*-butyllithium (2 mL, 5 mmol). The resulting mixture was stirred at RT for 10 min. Epoxide **47** (8.0 mg, 0.028 mmol) was transferred into a sealed tube, and 2 mL of the above LDA solution was added. The reaction vessel was closed, and it was heated to 50 °C and kept at this temperature for 36 h. Water (2 mL) was added to quench the reaction followed by standard ethereal work-up. Column chromatography (elution with pet ether/EtOAc, 15:1) afforded 7.4 mg (93%) of allylic alcohol **48** (hexane/EtOAc, 8:1, R_f **48** = 0.81) as a colorless oil. IR (film) λ_{max}: 3556, 2923, 1466, 1115 cm^{-1}. ^{1}H (500 MHz) δ: 5.74 (t, *J* = 7.0 Hz, 1H), 5.70 (s, 1H), 5.02 (s, 1H), 4.69 (s, 1H), 3.01 (s, 1H), 2.61 (d, *J* = 17.0 Hz, 1H), 2.44 (septet, *J* = 7.0 Hz, 1H), 2.36 (m, 2H), 2.27 (m, 1H), 2.12 (dd, *J*1 = 3.0 Hz, *J*2 = 16.5 Hz, 1H), 2.03 (dt, *J*1 = 12.5 Hz, *J*2 = 5 Hz, 1H), 1.83 (m, 2H), 1.40–1.62 (m, 3H), 1.44 (s, 3H), 1.13 (d, *J* = 7.0 Hz, 3H), 1.11 (s, 3H), 1.04 (d, *J* = 7.0 Hz, 3H), 0.96 (s, 3H). ^{13}C NMR (125 MHz) δ: 157.5 (s), 153.6 (s), 148.6 (s), 128.3 (d), 125.8 (d), 107.1 (t), 79.2 (s), 50.5 (t), 45.4 (t), 44.4 (s), 41.7 (t), 39.0 (t), 34.7 (t), 30.6 (q), 28.4 (q), 25.9 (d), 23.6 (t), 79.2 (s), 50.5 (t), 45.4 (t), 44.4 (s), 41.7 (t), 39.0 (t), 34.7 (t), 30.6 (q), 28.4 (q), 25.9 (d), 23.6 (t), 22.2 (q), 21.7 (q), 21.3 (q) ppm. HR-MS: $[M]^+_{obs}$ = 286.2300, $[M]^+_{calcd}$ = 286.2297.

(3a*S*,8a*R*)-1-Isopropyl-3a,5,8a-trimethyl-3a,4,8,8a,9,10-hexahydrobenzo[*f*]azulene-2,6(3*H*,7*H*)-dione (42) from enone (43)

To a solution of enone **43** (10 mg, 0.035 mmol) in acetone (2 mL) and H_2O (1 mL) was added *N*-bromosuccinimide (8.1 mg, 0.046 mmol, 1.3 equiv.) in one portion. The resulting mixture was stirred at RT for 5 min and was quenched with water (2 mL). Acetone was removed under vacuum using a rotary evaporator, followed by standard ethereal work-up. Column chromatographic purification (elution with pet ether/EtOAc, 4:1) gave 7.4 mg (71%) of *bis*-enone **42** (hexane/EtOAc, 2:1, R_f **42** = 0.40) as a white solid, which was identical to that previously characterized (i.e., the reduction of **25** to give **42**).

(3a*R*,8a*S*,10*S*)-1-Isopropyl-3a,5,8a-trimethyl-2,3,3a,4,6,7,8,8a,9,10-decahydrobenzo[*f*]azulen-10-ol (49)

To a solution of SeO_2 (9.1 mg, 0.089 mmol) in freshly distilled DCM (0.50 mL) was added *t*-BuOOH (37 μL, 0.36 mmol). The resulting mixture was stirred for 25 min at RT. Diene **44** (48 mg, 0.18 mmol) in DCM (0.50 mL) was added dropwise. The resulting mixture was stirred at RT for 8 h, followed by standard ethereal work-up. Column chromatography (elution with pet ether/EtOAc, 10:1) afforded 19 mg (40%) of triene **50** as a light yellow oil (hexane/EtOAc, 4:1, R_f **50** = 0.95). Further elution gave 23 mg (45%) of allylic alcohol **49** as a light yellow oil (hexane/EtOAc, 4:1, R_f **49** = 0.39).

(3a*R*,8a*S*)-1-Isopropyl-3a,5,8a-trimethyl-2,3,3a,4,7,8,8a,9-octahydrobenzo[*f*]azulen-10(6*H*)-one (51)

To a solution of allylic alcohol **49** (5.2 mg, 0.018 mmol) in CCl_4 (0.5 mL) was added MnO_2 (16 mg, 0.18 mmol). The resulting mixture was heated at 60 °C for 6 h. Standard ethereal work-up, followed by column chromatography (elution with pet ether/EtOAc, 12:1), gave 3.4 mg (65%) of enone **51** as a light yellow oil (hexane/EtOAc, 4:1, R_f **51** = 0.75). ^{1}H (400 MHz) δ: 3.34 (heptet, *J* = 7.2 Hz, 1H), 2.85 (d, *J* = 14.8 Hz, 1H), 2.57 (d, *J* = 14.0 Hz, 1H), 2.40 (t, *J* = 7.2 Hz, 2H), 2.22 (d, *J* = 14.8 Hz, 1H), 2.16 (d, *J* = 14.0 Hz, 1H), 2.01 (bs, 2H), 1.67 (s, 3H), 1.46–1.75 (m, 6H), 1.08 (s, 3H), 0.98–1.04 (m, 9H). ^{13}C NMR (125 MHz) δ: 202.7, 161.7, 142.9, 133.7, 129.0, 58.0, 48.7, 42.0, 40.8, 39.6, 36.1, 33.4, 29.1, 27.9, 25.6, 23.0, 20.9, 20.7, 20.7, 19.1 ppm.

Supplementary data

Supplementary data for this article are available on the journal Web site (www.nrcresearchpress.com/doi/suppl/10.1139/v11-116). The X-ray data for key intermediate **25**, CCDC 835868, has also been deposited with the Cambridge Crystallographic Data Centre. These data can be obtained, free of charge, via www.ccdc.cam.ac.uk/cgi-bin/catreq.cgi (or from the Cambridge Crystallographic Data Centre, 12 Union Road, Cambridge CB2 1Ez, UK; fax +44 1223 336033; or e-mail deposit@ccdc.cam.ac.uk).

Acknowledgments

Appreciation is extended to the NSF for partial support of this research (CHE-05064846) and to Dr. Pinrong Wang

(UGA) for carrying out the single crystal X-ray diffraction analysis.

References

(1) Faulkner, D. *Nat. Prod. Rep.* **1997** *14* (3), 259. doi:10.1039/np9971400259.

(2) Pettit, G. R.; Ode, R. H.; Herald, C. L.; Von Dreele, R. B.; Michel, C. *J. Am. Chem. Soc.* **1976** *98* (15), 4677. doi:10.1021/ja00431a072.

(3) Ochi, M.; Watanabe, M.; Miura, I.; Taniguchi, M.; Tokoroyama, T. *Chem. Lett.* **1980** *10* (10), 1229. doi:10.1246/cl.1980.1229.

(4) For the isolation of **3**, see:Crews, P.; Klein, T. E.; Hogue, E. R.; Myers, B. L. *J. Org. Chem.* **1982** *47* (5), 811. doi:10.1021/jo00344a012.

(5) For the isolation of **4**, see:Sun, H. H.; McConnell, O. J.; Fenical, W.; Hirotsu, K.; Clardy, J. *Tetrahedron*, **1981** *37* (6), 1237. doi:10.1016/S0040-4020(01)92057-5.

(6) Bowden, B. F.; Braekman, J.; Mitchell, S. J. *Aust. J. Chem.* **1980** *33* (4), 927. doi:10.1071/CH9800927.

(7) (a) Pattenden, G.; Robertson, G. M. *Tetrahedron Lett.* **1986** *27* (38), 399. doi:10.1016/S0040-4039(00)84029-0; (b) Begley, M. J.; Pattenden, G.; Robertson, G. M. *J. Chem. Soc., Perkin Trans. 1*, **1988** *5* (5), 1085. doi:10.1039/p19880001085.

(8) (a) Piers, E.; Friesen, R. W. *J. Org. Chem.* **1986** *51* (17), 3405. doi:10.1021/jo00367a042; (b) Piers, E.; Friesen, R. W. *J. Chem. Soc. Chem. Commun.* **1988** *2* (2), 125. doi:10.1039/c39880000125; (c) Piers, E.; Friesen, R. W. *Can. J. Chem.* **1992** *70* (4), 1204. doi:10.1139/v92-157.

(9) (a) Mehta, G.; Krishnamurthy, N. *Tetrahedron Lett.* **1987** *28* (47), 5945. doi:10.1016/S0040-4039(01)81097-2; (b) Mehta, G.; Krishnamurthy, N.; Karra, S. R. *J. Am. Chem. Soc.* **1991** *113* (15), 5765. doi:10.1021/ja00015a034.

(10) (a) Belmont, D. T.; Paquette, L. A. *J. Org. Chem.* **1985** *50* (21), 4102. doi:10.1021/jo00221a027; (b) Paquette, L. A.; Belmont, D. T.; Asu, Y. L. *J. Org. Chem.* **1985** *50* (24), 4667. doi:10.1021/jo00224a001; (c) Paquette, L. A.; Lin, H. S.; Belmont, D. T.; Springer, J. P. *J. Org. Chem.* **1986** *51* (25), 4807. doi:10.1021/jo00375a011.

(11) Williams, D. R.; Coleman, P. J. *Tetrahedron Lett.* **1995** *36* (1), 39. doi:10.1016/0040-4039(94)02164-7.

(12) (a) Majetich, G.; Song, J. S.; Ringold, C.; Nemeth, G. A. *Tetrahedron Lett.* **1990** *31* (16), 2239. doi:10.1016/0040-4039(90)80195-R; (b) Majetich, G.; Song, J. S.; Ringold, C.; Nemeth, G. A.; Newton, M. G. *J. Org. Chem.* **1991** *56* (12), 3973. doi:10.1021/jo00012a035.

(13) Bruson, H. A.; Kroeger, J. W. *J. Am. Chem. Soc.* **1940** *62* (1), 36. doi:10.1021/ja01858a008.

(14) (a) For our preliminary reports of this annulation strategy, see: Majetich, G.; Zhang, Y.; Feltman, T. L.; Belfoure, V. *Tetrahedron Lett.* **1993** *34* (34), 441. doi:10.1016/0040-4039(93)85097-G; (b) Majetich, G.; Siesel, D.; Liu, S.; Zhang, Y. *Tetrahedron Lett.* **1995** *36*, 4749; (c) For applications of this method in total synthesis, see:Majetich, G.; Zhang, Y.; Feltman, T. L.; Duncan, S. G., Jr. *Tetrahedron Lett.* **1993** *34* (34), 445. doi:10.1016/0040-4039(93)85098-H; (d) Majetich, G.; Wang, Y.; Li, Y.; Vohs, J. K.; Robinson, G. H. *Org. Lett.* **2003** *5* (21), 3847. doi:10.1021/ol035380i; (e) Majetich, G.; Li, Y.; Zou, G. *Heterocycles*, **2007** *73* (1), 217. doi:10.3987/COM-07-S(U)36; (f) Majetich, G.; Yu, J.; Li, Y. *Heterocycles*, **2007** *73* (1), 227. doi:10.3987/COM-07-S(U)37; (g) Majetich, G.; Zou, G.; Grove, J. *Org. Lett.* **2008** *10* (1), 85. doi:10.1021/ol701743c; (h) Majetich, G.; Zou, G. *Org. Lett.* **2008** *10* (1), 81. doi:10.1021/ol701800d; (i) Majetich, G.; Grove, J. L. *Org. Lett.* **2009** *11* (13), 2904. doi:10.1021/ol9009128.

(15) (a) Manchand, P. S.; Townsend, J. M.; Belica, P. S.; Wong, H. S. *Synthesis*, **1980** *1980* (05), 409. doi:10.1055/s-1980-29041; (b) Söderberg, B. C.; Fields, S. L. *Org. Prep. Proced. Int.* **1996** *28* (2), 221. doi:10.1080/00304949609356526.

(16) Tsukinoki, T.; Tsuzuki, H. *Green Chem.* **2001** *3* (1), 37. doi:10.1039/b008219h.

(17) Suzuki, N.; Kaneko, Y.; Nomoto, T.; Izawa, Y. *J. Chem. Soc. Chem. Commun.* **1984** (22), 1523. doi:10.1039/c39840001523.

(18) Majetich, G.; Fang, J. *Tetrahedron Lett.* **1998** *39* (46), 8381. doi:10.1016/S0040-4039(98)01931-5.

(19) Gribble, G. W.; Kelly, W. J.; Emery, S. E. *Synthesis*, **1978** *1978* (10), 763. doi:10.1055/s-1978-24884.

Can. J. Chem. Downloaded from www.nrcresearchpress.com by Renmin University of China on 09/02/12
For personal use only.

Tandem reaction of Morita–Baylis–Hillman alcohols derived from acrylic nitrile with 2-aminobenzimidazole in ionic liquid [BMIM]Cl/H_2O

Yan Wang, Li Liu, Dong Wang, and Yong-Jun Chen

Can. J. Chem. Downloaded from www.nrcresearchpress.com by Renmin University of China on 09/02/12
For personal use only.

Abstract: The tandem reaction of Morita–Baylis–Hillman (MBH) alcohols **1a**–**1l** derived from acrylic nitrile with 2-aminobenzimidazole (**2**) in ionic iquid (IL) [BMIM]Cl/H_2O without additional catalyst was developed for the efficient synthesis of benzimidazol[1,2-*a*]pyrimidin-7(8*H*)-imine compounds. The tandem reaction included aza-Michael addition and intramolecular addition of an amino group to the cyano group in one pot. The combination of ionic liquid and water was found to be the best reaction medium, which played a role for accelerating the tandem reaction.

Key words: Morita–Baylis–Hillman, ionic liquids, catalyst-free, aza-Michael addition.

Résumé : Comme méthode de synthèse efficace des dérivés de la benzimidazo[1,2-*a*]pyrimidine-7(8*H*)-imine, on a mis au point une réaction en tandem de Morita–Baylis–Hillman (MBH) d'alcools **1a**–**1l** dérivés de l'acrylonitrile avec du 2-aminobenzimidazole (**2**) dans un liquide ionique (LI) formé de chlorure de 1-butyl-3-méthylimidazolium (BMIM) et d'eau, sans addition de catalyseur. La réaction en tandem comporte une addition d'aza-Michael et une addition intramoléculaire du groupe amino sur le groupe cyano dans une réaction monotope. On a trouvé que la combinaison du liquide ionique et de l'eau est le meilleur milieu réactionnel qui joue un rôle d'accélérateur dans la réaction en tandem.

Mots-clés : Morita–Baylis–Hillman, liquides ioniques, sans catalyseur, addition d'aza-Michael.

[Traduit par la Rédaction]

Introduction

The Morita–Baylis–Hillman (MBH) reactions have proved to be one of the most successful methods for C–C bond-forming reactions. Since three functionalized groups, the hydroxyl group, the double bond, and the carbonyl (cyano) group, lie closely in one molecule, the MBH adducts are suitable precursors for the synthesis of many heterocycles and biologically active molecules.[1] Particularly, the Michael addition of the amine to the double bond of an MBH adduct's molecule and the subsequent functionalization have been employed in the synthesis of many aza-heterocycles.[2]

Imidazo[1,2-*a*]pyrimidines are very important intermediates and are widely used in the pharmaceutical chemistry, such as for the synthesis of the antianxiety drug divaplon (**A**) (Fig. 1).[3] Among them, several 7-amino-imidazo[1,2-*a*]pyrimidine derivatives also exhibited interesting biological activities including as $GABA_A$ receptors (**B**) (Fig. 1).[4] Recently, we reported the efficient synthesis of benzimidazo[1,2-*a*]pyrimidinone via a catalyst-free tandem reaction of MBH adducts bearing an ester unit with 2-aminobenzimidazole.[5] In general, the reaction containing the nitrile compound as a substrate is one of the most efficient approaches for introducing an amino group into a molecule. We envisioned that the tandem reaction of MBH alcohols derived from acrylic nitrile with 2-aminobenzoimidazole should be very interesting for the development of an efficient protocol accessible to the novel fused aza-heterocyclic compounds.

On the other hand, in recent years, ionic liquids (ILs) have attracted considerable attention as an alternative solvent in organic reactions because of their tunable physical properties, such as their almost nonvolatile nature, high thermal stability, strong solvating ability to a great number of organics, inorganics and polymers, reusability, and recyclability. Several ILs have been successfully used as solvents and promoters in a lot of chemical transformations.[6]

Herein, we will report a tandem reaction of MBH alcohols derived from acrylic nitrile and aldehydes with 2-aminobenzimidazole[7] in ILs with a small amount of water without any additional catalyst to produce novel fused aza-heterocyclic compounds.

Results and discussion

Initially, under the condition that is similar to the reaction of MBH alcohol derived from acrylic ester with 2-aminobenzimidazole (**2**),[5] the reaction of MBH alcohol **1h** derived from benzaldehyde and acrylic nitrile with **2** was carried

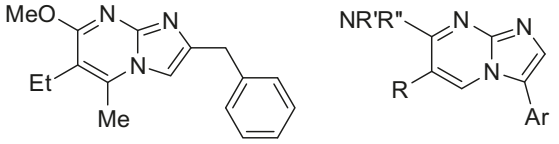
Received 16 March 2011. Accepted 30 May 2011. Published at www.nrcresearchpress.com/cjc on 1 November 2011.

Y. Wang, L. Liu, D. Wang, and Y.-J. Chen. Beijing National Laboratory for Molecular Sciences (BNLMS), CAS Key Laboratory of Molecular Recognition and Function, Institute of Chemistry, Chinese Academy of Sciences, Beijing 100190, P. R. China. Yan Wang Graduate School of Chinese Academy of Sciences, Beijing 100049, P. R. China.

Corresponding author: Li Liu (e-mail: lliu@iccas.ac.cn).

This article is part of a Special Issue dedicated to Professor Tak-Hang Chan.

Fig. 1. Divaplon (**A**) and $GABA_A$ receptors (**B**).



A, Divaplon **B**

out in dioxane at 80 °C (Table 1, entry 1). However, the yield of the product **3h** was very low. Although various organic solvents were used, the yields of **3h** were unsatisfactory either (Table 1, entries 2–6), even in the presence of K_2CO_3 as a catalyst (Table 1, entry 7). But the reaction of **1h** with **2** could proceed smoothly in water (Table 1, entry 8). Unfortunately, when the aqueous condition was employed to other substrates, such as **1a**, the reaction with **2** became sluggish and the products were complicated (Table 2, entries 1 and 2). This is probably attributed to the poor solubility and stability of the MBH alcohol **1a** in water at high temperature. To improve the solubility of the MBH alcohols and **2**, the ionic liquids were selected to be reaction media. If ionic liquid [BMIM]Cl was used as a medium for the reaction of **1a** with **2** at 100 °C, a homogeneous solution was formed and the product, 6-(4-chlorophenylhydroxylmethyl)-5,6-dihydro-benzimidazo-[1,2-*a*]pyrimidin-7(8*H*)-imine (**3a**), was obtained in 53% yield (Table 2, entry 3). To our delight, the addition of a small amount of water to the medium ([BMIM]Cl/H_2O = 11:1) led the yield of **3a** to increase (Table 2, entries 4 and 5). It was probably that the small amount of water could promote this reaction.[8] The tandem reaction did not need any additional catalyst for the high yield of the final product **3a**. However, when the water percentage in the reaction medium was increased to 4:1 ([BMIM]Cl/H_2O), the yield of **3a** was decreased sharply to 6%. It is proposed that the substrate **1a** decomposed under the conditions with such a large amount of water (Table 2, entry 6).

Based on these results, various ILs (Fig. 2) were employed in the reaction of **1a** with **2** as reaction media containing a small amount of water (IL/water = 11:1). As shown in Table 2 for the same cation ($[BMIM]^+$), the anions of the ILs used strongly influnced the yields of the product **3a** (Table 2, entry 5 vs entries 7–9). Moreover, with the same anion (BF_4^-) the molecular structure of the ammonium ion also has a strong effect on the reaction. It was found that $[EMIM]^+$ bearing an *N*-ethyl group and $[OMIM]^+$ bearing an *N*-octyl group provided poor yields of **3a** (Table 2, entries 10 and 11, respectively), but for $[BMIM]^+$ bearing an *N*-butyl group a 74% yield of **3a** was obtained (Table 2, entry 9). In comparison with $[BMIM]^+$, the change of the N′-substituent from a methyl to a vinyl group ($[BEIM]^+$) and introduction of a second methyl group ($[BDMIM]^+$) provided a complicated product mixture and very poor yield of **3a** (Table 2, entries 12 and 13) despite having the same core structure of imidazole. The employment of the pyridine unit ($[NBPD]^+$) as a cation part did not improve the yield of **3a** at all (Table 2, entry 14). Interestingly, the use of organic solvents with a small amount of water (Sol/H_2O = 11:1) also afforded a complicated mixture of the products (Table 2, entries 15 and 16). In summary, the IL [BMIM]Cl/water was determined to be the most efficient reaction medium for this tandem reaction.

With optimized conditions in hand, we examined the scope of the MBH alcohols derived from acrylic nitrile[9] with **2** in IL [BMIM]Cl/H_2O (11:1) at 100 °C in the absence of any additional catalyst (Scheme 1). The results are summarized in Table 3. As shown in Table 3, the reactions of various MBH alcohols (**1a**–**1l**) derived from acrylic nitrile proceeded smoothly in a period of 6 h to form the corresponding products **3a**–**3l** in good yields. The electronic properties of the substituents of MBH alcohols had no effect on the reaction. The MBH alcohol **1k** bearing the steric group also generated the product **3k** in 89% yield (Table 3, entries 11). Although much a longer reaction time (48 h) was needed, alkyl-substituted MBH alcohol **1l** could also give the expected product **3l** in good yield (75%) (Table 3, entry 12).

In terms of a plausible mechanism for the nucleophilic reaction with imidazole,[7b] the route of the reaction of MBH alcohols **1** derived from acrylic nitrile with 2-aminobenzimidazole (**2**) was proposed as shown in Scheme 2. In the first step, the nitrogen atom at the 3 position of 2-aminobenzimidazole attacked at the α,β-unsaturated carbon atom of the MBH alcohol in a Michael-addition manner to generate an intermediate **I** (path A). In this step, ILs, especially [BMIM]Cl containing a small amount of water, played the roles of both reaction medium and accelerator.[8] It was noteworthy that since the MBH alcohols **1** derived from acrylic nitrile were unstable to water and could be decomposed through retro-MBH reaction at high temperature, the water percentage in the IL was confined to a small range: H_2O:IL = 1:11 ~ <1:4. In the second step (path B), the intermediate **I** underwent an intramolecular addition reaction of an amino group to the cyano group, giving cyclization product **3**. In general, for the addition reaction of an amino group to the cyano group a suitable catalyst or a relatively higher reaction temperature were required. Thus, in a catalyst-free system a high reaction temperature (100 °C) had to be employed unavoidably.

Conclusion

In conclusion, we have developed an efficient method for the synthesis of fused aza-heterocyclic compounds, benzimidazo[1,2-*a*]pyrimi-din-7(8*H*)-imine derivatives in good to excellent yields via a tandem reaction of BMH alcohols (**1a**–**1l**) with 2-aminobenzoimidazole in IL/H_2O. The developed protocol was simple and catalyst free. The reaction underwent the Michael addition reaction, followed by intramolecular cyclization in a one-pot process. The produced fused heterocyclic compounds provided an opportunity to enhance the diversity of benzimidazo[1,2-*a*]pyrimidine compounds by further derivation.

Experimental

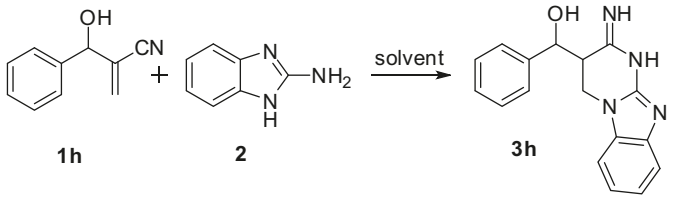
Typical procedure for the reaction of MBH alcohol (1) with 2-aminobenzimidazole (2)

To a solution of MBH alcohol **1a** (97 mg, 0.5 mmol) and **2** (100 mg, 0.75 mmol) in 0.5 mL of IL [BMIM]Cl was added water (40 μL, 2.5 mmol). The resulting mixture was heated at 100 °C until completion as indicated by TLC. Then the reaction mixture was extracted by ethyl acetate and

Can. J. Chem. Downloaded from www.nrcresearchpress.com by Renmin University of China on 09/02/12
For personal use only.

Can. J. Chem. Downloaded from www.nrcresearchpress.com by Renmin University of China on 09/02/12
For personal use only.

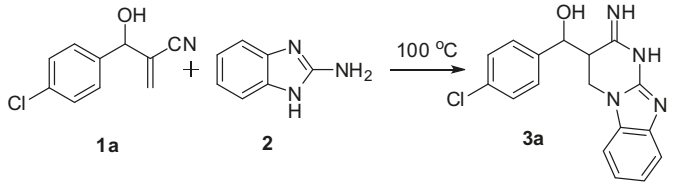
Table 1. The reaction of Morita–Baylis–Hillman (MBH) alcohol **1h** with **2**.



Entry	Solvent	*T* (°C)	Time (h)	Yield (%)[a]
1	Dioxane	80	14	45
2	MeOH	Reflux	14	10
3	THF	Reflux	14	18
4	DCM	Reflux	14	44
5	CH_3CN	80	14	18
6	Toluene	80	14	20
7[b]	Toluene	50	24	30[c]
8	H_2O	80	14	100

Note: Reaction conditions: **1h** (0.5 mmol), **2** (0.75 mmol), and solvent (0.5 mL).
[a]Determined by ^{1}H NMR.
[b]With K_2CO_3 (10 mol%).
[c]Isolated yield.

Table 2. The reaction of Morita–Baylis–Hillman (MBH) alcohol **1a** with **2**.



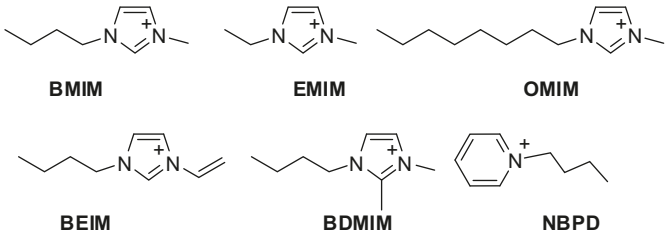
Entry	Reaction medium	Time (h)	Yield (%)[a]
1	H_2O	6	—[b]
2[c]	H_2O	6	—[b]
3	[BMIM]Cl	1	53
4[d]	[BMIM]Cl	1	66
5[d]	[BMIM]Cl	4	85
6[e]	[BMIM]Cl	4	6
7[d]	[BMIM]SbF_6	3	—[b]
8[d]	[BMIM]PF_6	3	46
9[d]	[BMIM]BF_4	3	74
10[d]	[EMIM]BF_4	4	50
11[d]	[OMIM]BF_4	4	—[b]
12 [d]	[BEIM]BF_4	4	—[b]
13[d]	[BDMIM]BF_4	4	—[b]
14 [d]	[NBPD]BF_4	4	—[b]
15 [d]	MeOH	6	—[b]
16 [d]	THF	5	—[b]

Note: Reaction conditions: **1a** (0.5 mmol), **2** (0.75 mmol), and solvent (0.5 mL), at 100 °C or reflux.
[a]Isolated yield.
[b]complicated products with poor yield of **3a**.
[c]At 80 °C.
[d]H_2O (2.5 mmol) was added.
[e][BMIM]Cl (0.4 mL) : H_2O (0.1 mL) = 4:1.

water. The organic phase was dried by Na_2SO_4 and purified by column chromatography over silica gel (eluent: DCM–MeOH = 100:2) to afford a light yellow solid **3a** (139 mg, 85%).

3a, light yellow solid, mp 161–163 °C. ν_{max} (KBr, cm^{-1}): 3471, 3371, 3055, 1547. δ_H (300 MHz, DMSO-d_6, TMS): 3.53–3.67 (1H, m, –CH), 4.21–4.54 (2H, m, –CH_2), 4.89–4.98 (1H, m, –CH), 6.47–6.56 (3H, m, –NH, –NH, –OH), 6.88–6.98 (2H_{arom}, m), 7.03–7.27 (2H_{arom}, m), 7.46–7.49 (4H_{arom}, m). δ_C (300 MHz. DMSO-d_6, TMS): 40.4, 41.2, 68.4, 70.3, 107.7, 107.8, 114.9, 118.0, 118.2, 118.3, 118.7, 120.7, 127.6, 128.2, 128.3, 128.6, 132.2, 132.7, 133.9,

Fig. 2. Ionic liquids employed in the reaction of Morita–Baylis–Hillman (MBH) alcohols with **2**.



134.2, 140.0, 141.0, 142.6, 142.7, 154.7, 154.8. HRMS (EI) *m/z* calcd for $C_{17}H_{16}ClN_4O$ $(M + 1)^+$: 327.1007; found: 327.1004.

3b, light yellow solid, mp 138–140 °C. ν_{max} (KBr, cm^{-1}): 3444, 3353, 3058, 1547. δ_H (300 MHz, DMSO-d_6, TMS): 3.57–3.59 (1H, m, –CH), 4.26–4.51 (2H, m, $–CH_2$), 4.91–5.00 (1H, m, –CH), 6.46–6.56 (3H, m, –NH, –NH, –OH), 6.88–6.98 ($2H_{arom}$, m), 7.04–7.59 ($6H_{arom}$, m). δ_C (300 MHz, DMSO-d_6, TMS): 40.5, 41.3, 68.4, 70.4, 107.8, 107.9, 114.8, 118.0, 118.4, 118.4, 118.7, 120.8, 124.4, 125.5, 125.7, 126.6, 127.6, 128.1, 130.1, 133.0, 133.1, 133.9, 134.2, 142.4, 142.6, 143.6, 144.5, 154.8. HRMS (EI) *m/z* calcd for $C_{17}H_{16}ClN_4O$ $(M + 1)^+$: 327.1007; found: 327.1007.

3c, light yellow solid, mp 108–110 °C. ν_{max} (KBr, cm^{-1}): 3444, 3353, 3060, 1546. δ_H (300 MHz, DMSO-d_6, TMS): 3.53–3.65 (1H, m, –CH), 4.47–4.55 (2H, m, $–CH_2$), 4.89–5.39 (1H, m, –CH), 6.44–6.57 (3H, m, –NH, –NH, –OH), 6.87–7.02 ($2.5H_{arom}$, m), 7.13–7.17 ($1H_{arom}$, m), 7.28–7.48 ($3.5H_{arom}$, m), 7.73–7.70 ($1H_{arom}$, m). δ_C (300 MHz, DMSO-d_6, TMS): 38.0, 38.3, 40.6, 65.2, 67.4, 107.6, 107.8, 114.9, 117.5, 118.3, 118.6, 118.7, 121.0, 127.3, 127.6, 128.0, 128.6, 129.1, 129.3, 129.6, 129.9, 130.1, 131.7, 133.7, 134.2, 138.2, 138.8, 142.2, 142.3, 154.7, 154.8. HRMS (EI) *m/z* calcd for $C_{17}H_{16}ClN_4O$ $(M + 1)^+$: 327.1007; found: 327.1003.

3d, light yellow solid, mp 149–151 °C. ν_{max} (KBr, cm^{-1}): 3477, 3371, 3054, 1546. δ_H (300 MHz, DMSO-d_6, TMS): 3.50–3.70 (1H, m, –CH), 4.20–4.53 (2H, m, $–CH_2$), 4.86–4.96 (1H, m, –CH), 6.45–6.54 (3H, m, –NH, –NH, –OH), 6.85–6.99 ($2H_{arom}$, m), 7.03–7.27 ($2H_{arom}$, m), 7.39–7.63 ($4H_{arom}$, m). δ_C (300 MHz, DMSO-d_6, TMS) 40.4, 41.2, 68.5, 70.3, 107.7, 107.9, 114.8, 114.8, 118.0, 118.2, 118.3, 118.7, 120.8, 121.3, 128.0, 129.0, 131.1, 131.2, 133.9, 134.2, 140.5, 141.4, 142.5, 142.7, 154.7, 154.8. HRMS (EI) *m/z* calcd for $C_{17}H_{16}BrN_4O$ $(M + 1)^+$: 371.0497; found: 371.0502.

3e, light yellow solid, mp 152–154 °C. ν_{max} (KBr, cm^{-1}): 3452, 3368, 3065, 1552. δ_H (300 MHz, DMSO-d_6, TMS): 3.57–3.69 (1H, m, –CH), 4.25–4.51 (2H, m, $–CH_2$), 4.89–4.96 (1H, m, –CH), 6.45–6.54 (3H, m, –NH, –NH, –OH), 6.88–6.99 ($2H_{arom}$, m), 7.02–7.73 ($6H_{arom}$, m). δ_C (300 MHz, DMSO-d_6, TMS): 41.0, 41.9, 68.9, 70.9, 108.3, 108.4, 115.4, 118.5, 118.9, 119.3, 121.3, 122.1, 122.3, 125.3, 126.4, 129.1, 130.0, 130.9, 131.0, 131.5, 134.4, 134.8, 143.0, 143.1, 144.3, 145.3, 155.3, 155.4. HRMS (EI) *m/z* calcd for $C_{17}H_{16}ClN_4O$ $(M + 1)^+$: 371.0497; found: 371.0502

3f, light yellow solid, mp 171–173 °C. ν_{max} (KBr, cm^{-1}): 3444, 3352, 3057, 1546. δ_H (300 MHz, DMSO-d_6, TMS) 3.48–3.71 (1H, m, –CH), 4.27–4.60 (2H, m, $–CH_2$), 4.81–5.32 (1H, m, –CH), 6.49–6.60 (3H, m, –NH, –NH, –OH), 6.86–6.99 ($2.3H_{arom}$, m), 7.12–7.16 ($1H_{arom}$, m), 7.22–7.34 ($1.7H_{arom}$, m), 7.45–7.54 ($1.7H_{arom}$, m), 7.65–7.74 (1.3Harom, m). δ_C (300 MHz, DMSO-d_6, TMS): 16.9, 37.2, 37.9, 38.3, 40.5, 67.3, 69.8, 107.6, 107.8, 114.8, 114.9, 117.3, 118.3, 118.5, 118.6, 118.7, 120.3, 120.9, 121.0, 122.2, 127.8, 128.1, 128.3, 128.8, 130.0, 130.3, 132.3, 132.6, 133.5, 133.7, 134.3, 139.7, 140.1, 142.1, 142.3, 154.4, 154.8. HRMS (EI) *m/z* calcd for $C_{17}H_{16}BrN_4O$ $(M + 1)^+$: 371.0497; found: 371.0502

3g, light yellow solid, mp 129–131 °C. ν_{max} (KBr, cm^{-1}): 3444, 3352, 3150, 1547. δ_H (300 MHz, DMSO-d_6, TMS): 3.52–3.66 (1H, m, –CH), 4.27–4.54 (2H, m, –CH2), 4.88–4.98 (1H, m, –CH), 6.42–6.56 (3H, m, –NH, –NH, –OH), 6.91–7.27 ($6H_{arom}$, m), 7.48–7.55 ($2H_{arom}$, m). δ_C (300 MHz, DMSO-d_6, TMS): 40.6, 41.2, 68.5, 70.3, 107.7, 107.8, 114.8, 118.0, 115.1, 115.2, 118.1, 118.2, 118.3, 118.8, 120.7, 127.7, 128.2, 127.8, 128.7, 128.8, 133.9, 134.3, 137.3, 138.1, 138.2, 142.6, 142.7, 154.7, 154.9, 160.0, 160.3. HRMS (EI) *m/z* calcd for $C_{17}H_{16}FN_4O$ $(M + 1)^+$: 311.1299; found: 311.1302.

3h, light yellow solid, mp 171–173 °C. ν_{max} (KBr, cm^{-1}): 3462, 3374, 3062, 1548. δ_H (300 MHz, DMSO-d_6, TMS): 3.51–3.69 (1H, m, –CH), 4.22–4.55 (2H, m, $–CH_2$), 4.85–4.95 (1H, m, –CH), 6.38–6.61 (3H, m, –NH, –NH, –OH), 6.86–7.01 ($2.5H_{arom}$, m), 7.13–7.16 ($1H_{arom}$, m), 7.24–7.45 ($5.5H_{arom}$, m). δ_C (300 MHz, DMSO-d_6, TMS): 41.1, 41.8, 69.4, 71.5, 108.3, 115.2, 118.7, 119.4, 121.3, 126.2, 127.2, 128.2, 128.7, 134.4, 134.7, 141.6, 142.5, 142.9, 155.2. HRMS (EI) *m/z* calcd for $C_{17}H_{17}N_4O$ $(M + 1)^+$: 293.1393; found: 293.1397.

3i, light yellow solid, mp 150–152 °C. ν_{max} (KBr, cm^{-1}): 3430, 3354, 3221, 1546. δ_H (300 MHz, DMSO-d_6, TMS): 3.53–3.67 (1H, m, –CH), 3.76–3.78 (3H, m, $–OCH_3$), 4.22–4.54 (2H, m, $–CH_2$), 4.83–4.94 (1H, m, –CH), 6.37–6.57 (3H, m, –NH, –NH, –OH), 6.89–7.34 ($8H_{arom}$, m). δ_C (300 MHz, DMSO-d_6, TMS): 39.3, 40.5, 41.3, 55.0, 55.0, 68.9, 70.9, 107.7, 107.8, 111.6, 112.2, 112.9, 113.7, 114.9, 117.9, 118.2, 118.9, 120.7, 129.3, 129.4, 134.0, 134.3, 131.5, 142.6, 142.7, 143.7, 154.7, 154.9, 159.2, 159.2 HRMS (EI) *m/z* calcd for $C_{18}H_{19}N_4O_2$ $(M + 1)^+$: 323.1498; found: 323.1503.

3j, light yellow solid, mp 173–175 °C. ν_{max} (KBr, cm^{-1}): 3444, 3354, 3053, 1546. δ_H (300 MHz, DMSO-d_6, TMS): 3.55–3.70 (3H, m, $–CH_3$), 3,81 (1H, s, –CH), 4.10–4.57 (2H, m, $–CH_2$), 4.82–5.30 (1H, m, –CH), 6.09–6.55 (3H, m, –NH, –NH, –OH), 6.81–7.27 ($7H_{arom}$, m), 7.53–7.55 ($1H_{arom}$, m). δ_C (300 MHz, DMSO-d_6, TMS): 14.0, 20.7, 37.8, 37.9, 40.8, 54.9, 55.4, 59.7, 63.4, 65.2, 107.4, 107.8, 110.2, 110.9, 114.8, 114.9, 118.2, 118.2, 118.3, 119.1, 120.2, 120.4, 120.7, 120.8, 126.2, 127.4, 128.7, 129.3, 129.7, 133.8, 134.3, 142.6, 142.7, 154.8, 154.9, 155.9. HRMS (EI) *m/z* calcd for $C_{18}H_{19}N_4O$ $(M + 1)^+$: 307.1549; found: 307.1553.

3k, light yellow solid, mp 168–170 °C. ν_{max} (KBr, cm^{-1}): 3444, 3353, 3221, 1546. δ_H (300 MHz, DMSO-d_6, TMS): 1.89 (1.5H, m, $–CH_3$), 2.30–2.33 (4.5H, m, $–CH_3$), 3.37–3.64 (1H, m, –CH), 4.34–4.60 (2H, m, $–CH_2$), 4.79–5.16 (1H, m, –CH), 6.17–6.59 (3H, m, –NH, –NH, –OH), 6.88–7.30 ($6H_{arom}$, m), 7.41–7.47 ($1H_{arom}$, m). δ_C (300 MHz, DMSO-d_6, TMS): 17.4, 18.5, 20.7, 20.9, 38.5, 40.5, 40.9, 65.0, 67.5, 107.7, 107.8, 114.9, 115.0, 118.0, 118.3, 118.5, 118.7, 120.8, 120.8, 126.4, 127.0, 128.1, 128.5, 130.1,

Can. J. Chem. Downloaded from www.nrcresearchpress.com by Renmin University of China on 09/02/12
For personal use only.

Scheme 1 The reactions of Morita–Baylis–Hillman (MBH) alcohols with **2**.

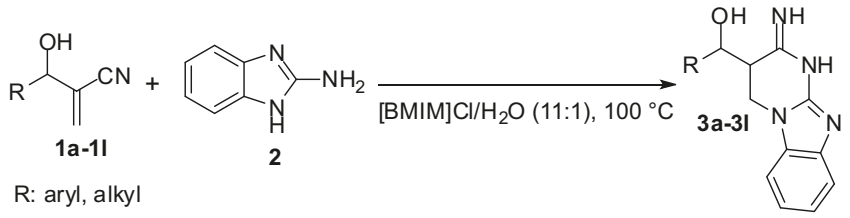
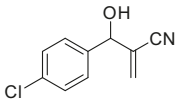
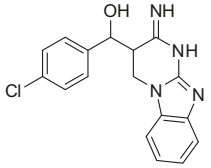
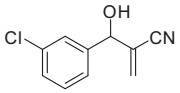
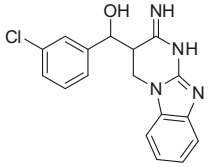
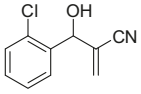
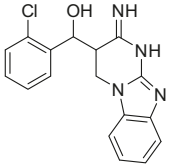
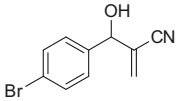
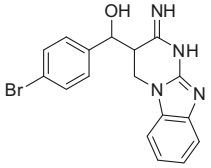
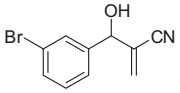
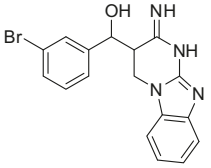
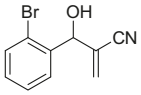
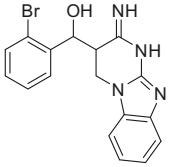
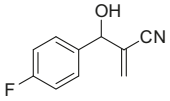
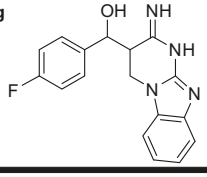


Table 3. The reaction of Morita–Baylis–Hillman (MBH) alcohols **1a**–**1l** with **2** in IL/H_2O without catalyst (IL, ionic liquid).

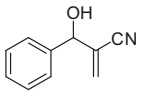
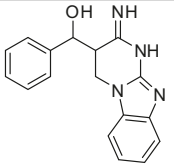
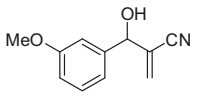
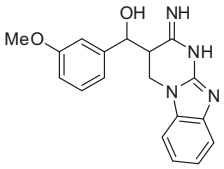
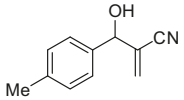
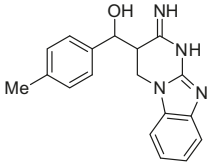
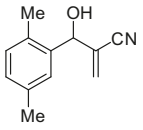
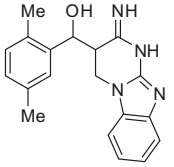
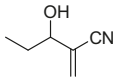
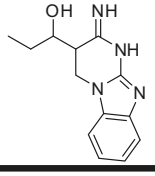
Entry	MBH alcohol	Time (h)	Product	Yield (%)
1	**1a** 	4	**3a** 	85
2	**1b** 	1.5	**3b** 	88
3	**1c** 	3	**3c** 	83
4	**1d** 	4	**3d** 	75
5	**1e** 	1.5	**3e** 	91
6	**1f** 	2	**3f** 	80
7	**1g** 	4	**3g** 	85

130.2, 131.9, 134.0, 134.4, 134.6, 135.0, 139.3, 139.6, 142.6, 142.8, 154.8, 155.0. HRMS (EI) *m/z* calcd for $C_{19}H_{21}N_4O$ $(M + 1)^+$: 321.1706; found: 321.1710.

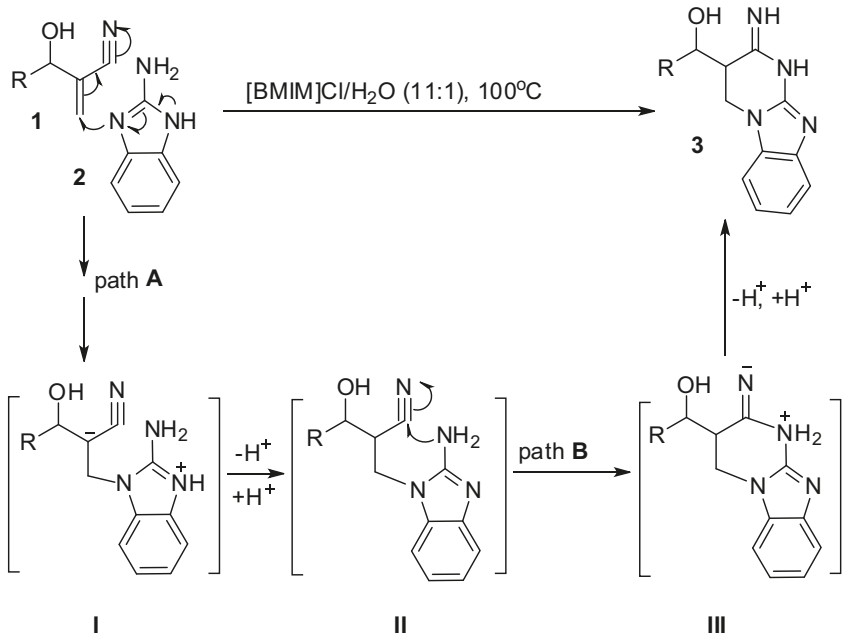
3l, light yellow solid, mp 110–112 °C. ν_{max} (KBr, cm^{-1}): 3430, 3352, 2966, 1547. δ_H (300 MHz, DMSO-d_6, TMS): 0.86–0.98 (3H, m, $–CH_3$), 1.46–1.76 (2H, m, $–CH_2$), 3.21 (1H, m, –CH), 3.51–3.59 (1H, m, –CH), 4.17–4.44 (2H, m, $–CH_2$), 5.48–5.60 (1H, m, –CH), 6.51 (3H, s, –NH, –NH, –OH), 6.88–6.99 ($2H_{arom}$, m), 7.41–7.24 ($2H_{arom}$, m). δ_C (300 MHz, DMSO-d_6, TMS): 10.0, 10.0, 16.8, 28.2, 37.7,

Can. J. Chem. Downloaded from www.nrcresearchpress.com by Renmin University of China on 09/02/12
For personal use only.

Table 3. (*concluded*).

Entry	MBH alcohol	Time (h)	Product	Yield (%)
8	**1h** 	5	**3h** 	83
9	**1i** 	4	**3i** 	88
10	**1j** 	3	**3j** 	76
11	**1k** 	6	**3k** 	89
12	**1l** 	48	**3l** 	75

Scheme 2. Plausible mechanism.



38.2, 39.8, 40.8, 68.7, 69.5, 107.9, 114.8, 114.9, 118.3, 118.3, 118.8, 119.3, 120.7, 120.8, 134.0, 134.2, 142.5, 142.7, 154.8, 154.8. HRMS (EI) *m/z* calcd for $C_{13}H_{16}N_4O$ $(M + 1)^+$: 245.1395; found: 245.1397.

Acknowledgement

We are grateful to the National Natural Foundation of China, Ministry of Science and Technology (No. 2009ZX09501-006), and the Chinese Academy of Sciences for financial support.

Can. J. Chem. Downloaded from www.nrcresearchpress.com by Renmin University of China on 09/02/12
For personal use only.

References

(1) (a) For selected reviews see Basavaiah, D.; Rao, K. V.; Reddy, R. J. *Chem. Soc. Rev.* **2007**, *36* (10), 1581. doi:10.1039/b613741p; (b) Singh, V.; Batra, S. N. *Tetrahedron* **2008**, *64* (20), 4511. doi:10.1016/j.tet.2008.02.087; (c) Lee, K.-Y.; Gowrisankar, S.; Kim, J.-N. *Bull. Korean Chem. Soc.* **2005**, *26* (10), 1481. doi:10.5012/bkcs.2005.26.10.1481; (d) Shi, Y. L.; Shi, M. *Org. Biomol. Chem.* **2007**, *5* (10), 1499. doi:10.1039/b618984a; (e) Basavaiah, D.; Rao, A. J.; Satyanarayana, T. *Chem. Rev.* **2003**, *103* (3), 811. doi:10.1021/cr010043d; (f) Ciganek, E. In *Organic Reactions;* Paquette, L. A. Ed.; John Wiley & Sons: New York, 1997; Vol. 51; p 201; (g) Declerck, V.; Martinez, J.; Lamaty, F. *Chem. Rev.* **2009**, *109* (1), 1. doi:10.1021/cr068057c.

(2) (a) Pathak, R.; Roy, A. K.; Batra, S. *Synlett* **2005**, *5*, 848; (b) Nag, S.; Pathak, R.; Kumar, M.; Shukla, P. K.; Batra, S. *Bioorg. Med. Chem. Lett.* **2006**, *16* (14), 3824. doi:10.1016/j.bmcl.2006.04.020; (c) Pathak, R.; Batra, S. *Tetrahedron* **2007**, *63* (38), 9448. doi:10.1016/j.tet.2007.06.115; (d) Yadav, L. D. S.; Srivastava, V. P.; Patel, R. *Tetrahedron Lett.* **2008**, *49* (39), 5652. doi:10.1016/j.tetlet.2008.07.069.

(3) (a) Clements-Jewery, S.; Danswan, G.; Gardner, C. R.; Matharu, S. S.; Murdoch, M. R.; Tully, W. R.; Westwood, R. *J. Med. Chem.* **1988**, *31* (6), 1220. doi:10.1021/jm00401a025; (b) Nag, S.; Mishra, A.; Batra, S. *Eur. J. Org. Chem.* **2008** (25), 4334. doi:10.1002/ejoc.200800448.

(4) Chambers, M. S.; Goodacre, S. C.; Hallett, D. J.; Jennings, A.; Jones, P.; Lewis, R. T.; Moore, K. W.; Russell, M. G. N.; Street, L. J.; Szekeres, H. J. WO Patent 2002074773, 2002.

(5) Wang, Y.; Shafiq, Z.; Liu, L.; Wang, D.; Chen, Y. J. *J. Heterocycl. Chem.* **2010**, *47* (2), 373.

(6) (a) For selected reviews see Welton, T. *Chem. Rev.* **1999**, *99* (8), 2071. doi:10.1021/cr980032t; (b) Dupont, J.; de Souza, R. F.; Suarez, P. A. Z. *Chem. Rev.* **2002**, *102* (10), 3667. doi:10.1021/cr010338r; (c) Sheldon, R. *Chem. Commun. (Camb.)* **2001** (23), 2399. doi:10.1039/b107270f; (d) Martins, M. A. P.; Frizzo, C. P.; Moreira, D. N.; Zanatta, N.; Bonacorso, H. G. *Chem. Rev.* **2008**, *108* (6), 2015. doi:10.1021/cr078399y.

(7) (a) The reaction of 2-aminobenzoimidazole with several electrophiles have been reported. Asobo, P. F.; Wahe, H.; Mbafor, J. T.; Nkengfack, A. E.; Fomum, Z. T.; Sopbue, E. F.; Döpp, D. *J. Chem. Soc., Perkin Trans. 1* **2001**, 457. doi:10.1039/b005511p; (b) Da Settimo, A.; Primofiore, G.; Da Settimo, F.; Marini, A. M.; Taliani, S.; Salermo, S.; Dalla Via, L. *J. Heterocycl. Chem.* **2003**, *40* (6), 1091. doi:10.1002/jhet.5570400620; (c) Shaabani, A.; Rahmati, A.; Naderi, S. *Bioorg. Med. Chem. Lett.* **2005**, *15* (24), 5553. doi:10.1016/j.bmcl.2005.08.101; (d) Karci, F.; Demircali, A.; Sener, I.; Tilki, T. *Dyes Pigm.* **2006**, *71* (2), 90. doi:10.1016/j.dyepig.2005.06.006; (e) Abdelhamid, A. O.; Riad, B. Y.; Aziz, S. I. *Arch. Pharm. (Weinheim)* **1987**, *320* (7), 642. doi:10.1002/ardp.19873200714.

(8) (a) For examples of ionic liquid (IL) and water-promoted aza-Michael reactions see Yang, L.; Xu, L. W.; Zhou, W.; Li, L.; Xia, C. G. *Tetrahedron Lett.* **2006**, *47* (44), 7723. doi:10.1016/j.tetlet.2006.08.103; (b) Xu, J. M.; Wu, Q.; Zhang, Q. Y.; Zhang, F.; Lin, A. F. *Eur. J. Org. Chem.* **2007** (11), 1798. doi:10.1002/ejoc.200600999; (c) Roy, S. R.; Chakraborti, A. K. *Org. Lett.* **2010**, *12* (17), 3866. doi:10.1021/ol101557t; (d) Xu, L.-W.; Li, J.-W.; Zhou, S.-L.; Xia, C.-G. *New J. Chem.* **2004**, *28* (2), 183. doi:10.1039/b312047c.

(9) According to the reference procedure, MBH alcohols **1a**–**1m** were prepared. Cai, J. X.; Zhou, Z. H.; Zhao, G. F.; Tang, C. C. *Org. Lett.* **2002**, *4* (26), 4723. doi:10.1021/ol027197f.

Can. J. Chem. Downloaded from www.nrcresearchpress.com by Renmin University of China on 09/02/12
For personal use only.

Development of a copper(II)-catalyzed three-component tandem synthesis of isoindolinone derivatives

Leon Xuetong Sun, Tieqiang Zeng, Dong Jiang, Li-Yi Dai, and Chao-Jun Li

Can. J. Chem. Downloaded from www.nrcresearchpress.com by Renmin University of China on 09/02/12
For personal use only.

Abstract: Isoindolinone derivatives are important pharmaceutical building blocks in medicinal chemistry. Isoindolo[2,1-*a*]quinolines are a class of interesting compounds that possess protective effects against N_2-induced hypoxia and inhibitory activities against human topoisomerase II and bacterial DNA-gyrase. The conventional methods for synthesizing these compounds are unsatisfactory because of their harsh reaction conditions, complex starting materials, and multistaged purification procedures. This synthesis of the propargyl-isoindolinone core features an aldehyde–alkyne–amine (A^3) coupling-based tandem strategy using methyl 2-formylbenzoate, primary aryl amine, and terminal alkyne under $Cu(OTf)_2$ catalysis.

Key words: aldehyde–alkyne–amine (A^3) coupling, propargyl-isoindolinone, isoindolo[2,1-*a*]quinoline, copper(II) catalysis, tandem reaction.

Résumé : Les dérivés de l'isoindolinone sont d'importants synthons en chimie médicinale. Les isoindolo[2,1-*a*]quinoléines font partie d'une classe intéressante de composés qui possèdent effets protecteurs contre l'hypoxie induite par N_2 et des activités inhibitrices contre la topoisomérase II humaine et la gyrase d'ADN bactérienne. Les méthodes de synthèse conventionnelles de ces composés ne sont pas satisfaisantes en raison de la sévérité de leurs conditions réactionnelles, de la nature complexes de leurs produits de départ et des méthodes de purification en plusieurs étapes. Cette synthèse du synthon propargyl-isoindolinone comporte un couplage d'aldéhyde, d'alcyne et d'amine (A^3) à base d'une stratégie en tandem impliquant du 2-formylbenzoate de méthyle, une amine aromatique primaire et un alcyne terminal sous l'influence d'un catalyseur de $Cu(OTf)_2$.

Mots-clés : couplage d'aldéhyde, d'alcyne et d'amine (A^3), propargyl-isoindolinone, isoindolo[2,1-*a*]quinoléine, catalyse par le cuivre(II), réaction en tandem.

[Traduit par la Rédaction]

Introduction

A tandem reaction, also called a cascade or domino reaction, is defined as a consecutive series of reactions that usually proceed via highly reactive intermediates; the product of each reaction acts as the substrate of subsequent reactions.[1] These reactions possess high synthetic value in the sense that they not only allow efficient construction of complex structures from simple precursors but also display overall reduced operations and better step economy, which translates into reduced labor time, energy input, and waste; therefore, they have been the subject of extensive investigations in recent years.[2]

Isoindoline derivatives are important pharmaceutical building blocks that possess unique medicinal properties. For instance, the diuretic activity of sulfonamide-functionalized isoindoline in Fig. 1 is 100 times more than for chlorothiazide.[3] Furthermore, isoindolylalkylphosphonium salts possess antitumour activities and have displayed substantial activity in the P-388 lymphocytic leukemia screen.[4] In some recent reports, these salts have been demonstrated to possess herbicidal activity[5] and to act as antagonists of the 5-hydroxytryptamine 2C ($5\text{-}HT_{2C}$) receptor,[6] as well as being candidates to treat various cancers.[7] There have also been some recent studies in applying isoindoline derivatives in pigments.[8]

One of the most common isoindoline derivatives is isoindolinone, which has also attracted much research interest owing to its substantial biological activities. N-Substituted isoindolinones of general structure **1** possess anxiolytic activity and are commonly applied as sedatives, hypnotics, and muscle relaxants.[9] Some examples, such as anxiolytics pazinaclone, pagoclone (Sanofi-Aventis and Pfizer, phase III

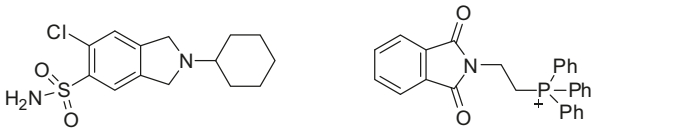
Received 27 April 2011. Accepted 14 June 2011. Published at www.nrcresearchpress.com/cjc on 10 November 2011.

L.X. Sun, T. Zeng, and C.-J. Li. Department of Chemistry, McGill University, 801 Sherbrooke Street West, Montreal, QC H3A 2K6. Canada.
D. Jiang. Department of Chemistry, McGill University, 801 Sherbrooke Street West, Montreal, QC H3A 2K6. Canada; Center for the Chemistry of Ionic Liquids, East China Normal University, Shanghai 20006, P. R. China.
L.-Y. Dai. Center for the Chemistry of Ionic Liquids, East China Normal University, Shanghai 20006, P. R. China.

Corresponding author: Chao-Jun Li (e-mail: CJ.Li@McGill.ca).

This article is part of a Special Issue dedicated to Professor Tak-Hang Chan.

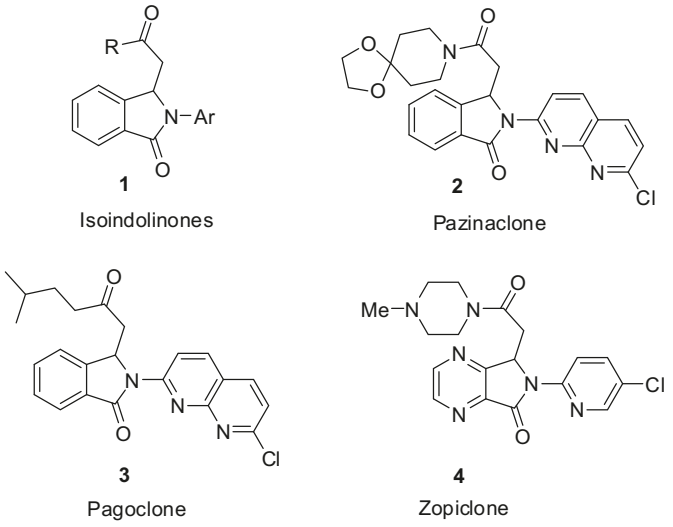
Fig. 1. Early discoveries of isoindoline and isoindolinone derivatives.[3,4]



Isoindoline synthesized in 1963 with high diuretic activity

Isoindolinone synthesized in 1977 with substantial activity in the P-388 lymphocytic leukemia screen

Fig. 2. Important N-substituted isoindolinone derivatives as pharmaceuticals.[9]



clinical trials), and the anticonvulsant zopiclone, are shown in Fig. 2.[10]

Conventional synthetic methods adopted in approaching polysubstituted isoindolinone derivatives are usually unsatisfactory because of their harsh reaction conditions, complex starting materials, and lengthy synthetic sequence.[11] In recent years, more and more cascade reactions have been devoted to the construction of the isoindolinone skeletons. For example, an elegant palladium(0)-catalyzed three-component carbonylation – amination – Michael addition was used by Grigg and et al.[9a] in 2005 in their synthesis of various isoindolinones. Nevertheless, the applications of cascade reactions are still quite limited.

While working on the aldehyde–alkyne–amine (A^3) methodology (A^3 coupling; Scheme 1) for the synthesis of monopropargyl amines,[12] we envisioned that the secondary amine formed in the product could also be utilized as a nucleophile to perform consecutive reactions. Under proper conditions, this nucleophilic nitrogen can be treated as the building block for a lactam ready to access various isoindolinone derivatives.

Results and discussion

Li and co-workers[13] developed the first copper-catalyzed addition as well as asymmetric addition of acetylenes to various imine and acylimines. This discovery has attracted much attention and also triggered intensive research in this area[14] because the final products are synthetically versatile building blocks for the preparation of many nitrogen-containing compounds that possess valuable biological activities. It has been proven that the A^3 coupling can be catalyzed by various types of transition-metal catalysts, including Cu(I), Cu(II), Ag(I), Au(I), and Au(III) salts and Cu/Ru bimetallic systems, etc.[12] Depending on the nature of the substrates, the reaction can proceed in organic solvent, water, or neat. We rationalized that from simple commercially available starting materials **5**, **6**, and **7**, under transition-metal catalysis, the A^3-coupling product **8** would quickly form in situ, and upon intramolecular cyclization, the isoindolinone core **9** would be constructed in one step (Scheme 2).

Our initial examination started by using 2-carboxybenzaldehyde, aniline, and phenyl acetylene as the starting materials, all of which are inexpensive readily available commercial substrates. Unfortunately, no desired product was obtained. ^{1}H NMR studies showed that 2-carboxybenzaldehyde mainly exists in its fused bicyclic form (Scheme 3). We believe that this form obstructs the formation of imine and thus prevents A^3 coupling from occurring. Another factor possibly responsible for the failure of the reaction is that the substrate does not contain a good leaving group to facilitate the cyclization of the amido ring.

To render a good leaving group into the substrate as well as converting it into its "open" form, we decided to use its methyl ester, "methyl 2-formylbenzoate", and re-subject it to the same sets of conditions examined previously; in this case, all metal catalysts offered the desired product in different yields, among which $Cu(OTf)_2$ had the highest product:impurities ratio. Upon systematic screening, the optimized conditions were determined to be 15 mol % of $Cu(OTf)_2$ at 100 °C for 12 h in toluene. One noteworthy fact is that the solvent is an essential component of the reaction, without which the conditions provided would be too harsh for the substrates used, and in most cases the phenylacetylene would be converted into acetophenone.

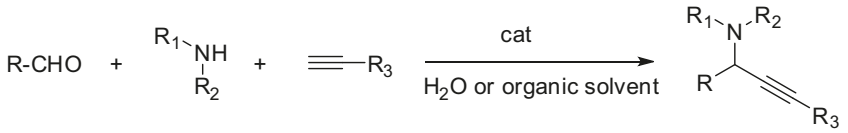
Various types of aniline derivatives were examined. Experimental results (Table 1) indicated that any ortho substituent on the aniline ring (**9g–9m**) impedes the formation of the desired product with no reaction observed, most likely because of steric hindrance. The presence of electron-withdrawing groups on the meta or para position (**9b–9f**) can reduce the yield compared with electron-donating groups.

Screening of the acetylene substrates proved to be challenging using this methodology. The results for the reactions tend to vary upon repetitions; thus, each yield reported in Table 2 is the averaged isolated yield among a few trials. Similar to the results of anilines, ortho-substitution patterns in aryl acetylenes (**9u** and **9z**) do not favour formation of desired products; most importantly, electronic characters of the aryl cycles do not seem to play a crucial role in the yield, despite the fact that in the para-substituted cases, electron-donating groups seem to offer a better yield than electron-withdrawing groups. Alkyl acetylenes (**9v** and **9w**) always provide higher yields than aryl acetylenes (**9n–9t**).

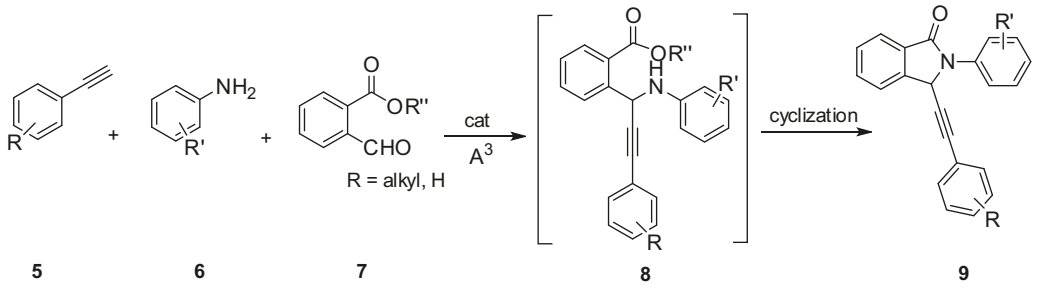
Two special situations have been observed. Firstly, when the aryl acetylene contains a nitrogen heterocycle, the yield diminishes to nearly zero. Based on the colour of the catalyst and the amount of starting materials recovered, we can clearly conclude that the catalyst is not turning over. We suspect that this is caused by the strong coordination and

Can. J. Chem. Downloaded from www.nrcresearchpress.com by Renmin University of China on 09/02/12
For personal use only.

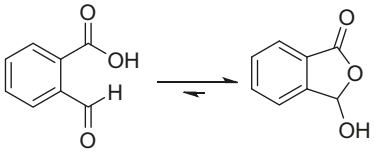
Scheme 1. Three-component coupling of aldehyde, alkyne, and amine (A^3 coupling).



Scheme 2. Proposed isoindoline synthesis via the A^3-coupling strategy.



Scheme 3. Equilibrium of 2-carboxybenzaldehyde.



complexation between the heterocyclic nitrogen and copper(II), which prevents the formation of copper acetylide. An elevated temperature or the addition of a catalytic amount of acid does not solve this problem. Secondly, when using propiolate as the alkyne, the desired isoindolinone core does not form; in this case, the mechanistic pathway is altered and the reaction exclusively yields the 1,4-dihydropyridine system (>90% isolated yield), as shown in Scheme 4. Initially, we were quite impressed by this outcome because previously known synthesis of 1,4-dihydropyridines either requires a microwave apparatus[15] or preformation of the imine with a rare earth metal catalyst (RE triflates, RE = Sc, Y, La, Ce, Pr, Nd, Sm, or Yb).[16] Unfortunately, upon careful review of the synthetic literature, we concluded that this methodology is not the greenest approach to date; as with our studies, Mai et al.[17] in 2009 used Brønsted acid as the catalyst and completed the same transformation in a one-pot tandem manner in the absence of any transition metal.

Conclusion

In summary, we have demonstrated a one-pot synthesis of the pharmaceutically interesting propargyl-isoindolinone core (**9**) based on the tandem A^3-coupling methodology, starting from methyl 2-formylbenzoate, aniline derivative, and alkynes as the precursors. Such methodology provides a simple and efficient access to a variety of isoindolinone building blocks from inexpensive starting materials readily. Within the scope of this reaction, two exceptions were observed: (*i*) using propiolates as the acetylene source provides 1,4-dihydropyridine as the only product and (*ii*) heterocyclic amines do not favour the formation of the desired product. For future work, chiral ligands shall be introduced into the reaction to generate enantio- or diastereo-selectivity. the isoindolinone core (**9**) can also be transformed into a series of biologically active compounds.

Experimental

All glassware used for moisture-sensitive reactions was flame-dried under vacuum and subsequently purged with nitrogen. All reagents were commercially available materials and were used without further purification unless specified. Standard column chromatography was performed on 20–60 μm silica gel (obtained from Silicycle Inc.) or on Sorbent silica gel (30–60 μm) using standard flash column chromatography techniques. Infrared analyses were recorded as a thin film on NaCl plates and solid compounds as KBr pellets. ^{1}H and ^{13}C NMR spectra were recorded on a Varian 400 MHz or 300 MHz spectrometer. Chemical shifts for ^{1}H NMR spectra were reported in parts per million (ppm) from tetramethylsilane with the solvent resonance as the internal standard (deuterated chloroform: δ 7.26 ppm, DMSO: δ 2.50 ppm). Chemical shifts for ^{13}C NMR spectra were reported in ppm from tetramethylsilane with the solvent resonance as the internal standard (deuterated chloroform: δ 77.0 ppm). Mass spectrometry (MS) data were obtained by using a Kratos MS25RFA mass spectrometer. High-resolution mass spectrometry electrospray ionization (HR-MS-ESI) measurements were performed at the McGill University MS Laboratory.

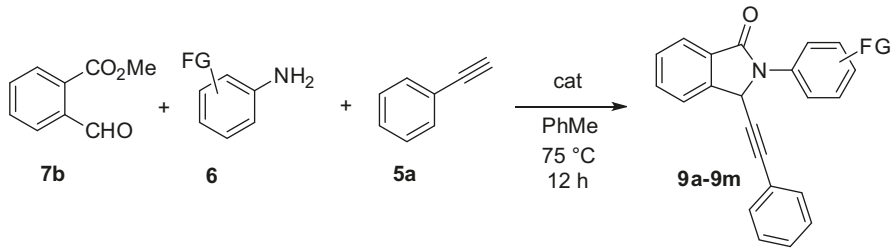
General procedure for the synthesis of isoindolinones

Under an argon atmosphere, acetylene (0.36 mmol), aniline (0.36 mmol), methyl 2-formylbenzoate (0.30 mmol), Cu $(OTf)_2$ (15 mol %), and anhydrous toluene (1 mL) were added into a tube and stirred at 75 °C for 12 h. After the reaction, 15 mL of ethyl acetate was added into the tube and the entire reaction mixture was filtered through a short plug of silica. The filtrate was concentrated in vacuo and then subjected to liquid column chromatography (hexane/EtOAc = 7:1 to 5:1 gradient elution). The solvent of the combined fractions was removed under reduced pressure to afford the desired isoindolinone compound as a viscous light yellow oil or semisolid.

Can. J. Chem. Downloaded from www.nrcresearchpress.com by Renmin University of China on 09/02/12
For personal use only.

Can. J. Chem. Downloaded from www.nrcresearchpress.com by Renmin University of China on 09/02/12
For personal use only.

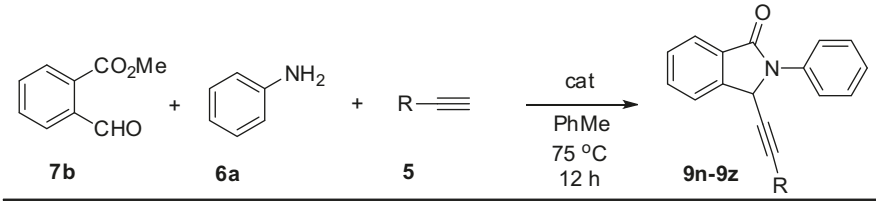
Table 1. The effect of various anilines on the reaction.



Entry	Aniline	Product	Isolated yield (%)
1	$C_6H_5NH_2$	**9a**	75
2	3-F-$C_6H_4NH_2$	**9b**	70
3	3-Cl-$C_6H_4NH_2$	**9c**	55
4	4-Cl-$C_6H_4NH_2$	**9d**	52
5	4-Br-$C_6H_4NH_2$	**9e**	66
6	4-NO_2-$C_6H_4NH_2$	**9f**	60
7	2-I-$C_6H_4NH_2$	**9g**	N.R.
8	2-NO_2-6-Me-$C_6H_3NH_2$	**9h**	N.R.
9	2-Cl-4-Cl-6-Cl-$C_6H_2NH_2$	**9i**	N.R.
10	2-OMe-5-OMe-$C_6H_3NH_2$	**9j**	N.R.
11	2-*i*-Pr-6-*i*-Pr-$C_6H_3NH_2$	**9k**	N.R.
12	2-Cl-4-Cl-$C_6H_3NH_2$	**9l**	<5
13	2-OMe-4-OMe-$C_6H_3NH_2$	**9m**	<5

Note: N.R. = no reaction. Conditions: phenylacetylene (0.36 mmol), aniline (0.36 mmol), methyl 2-formylbenzoate (0.30 mmol), and $Cu(OTf)_2$ (15 mol %) in 1 mL toluene, reacted for 12 h at 75 °C under argon.

Table 2. The effect of alkynes on the reaction.

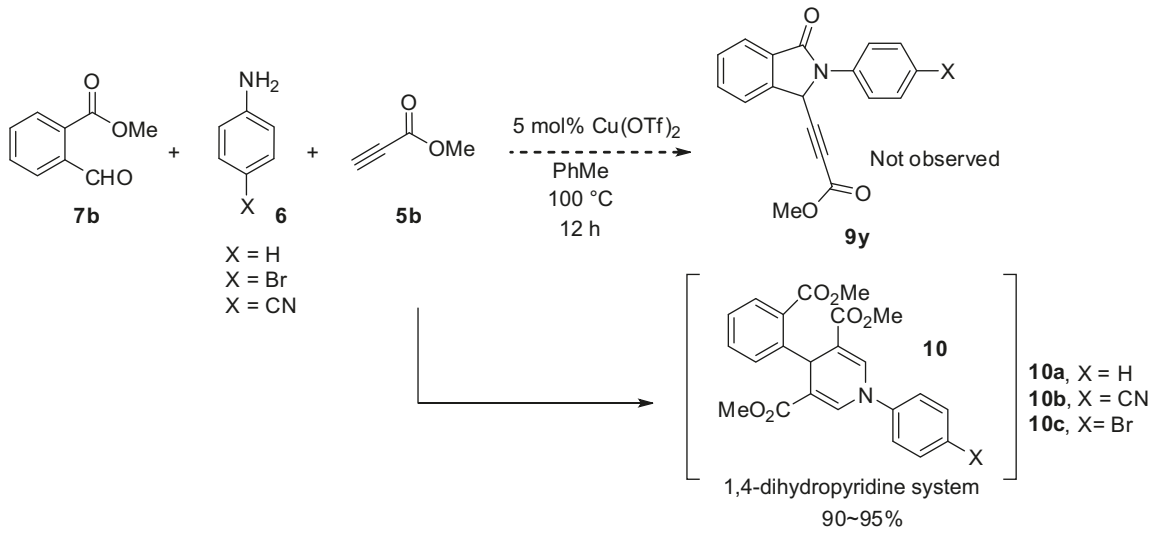


Entry	Acetylene	Product	Isolated yield (%)
1	4-Me-phenylacetylene	**9n**	31
2	4-OMe-phenylacetylene	**9o**	25
3	4-*t*-Bu-phenylacetylene	**9p**	35
4	4-*n*-Bu-phenylacetylene	**9q**	45
5	4-CF_3-phenylacetylene	**9r**	20
6	4-Ph-phenylacetylene	**9s**	20
7	3-F-phenylacetylene	**9t**	44
8	2-NO_2-phenylacetylene	**9u**	N.R.
9	Tetradec-1-yne	**9v**	55
10	5-Methylhex-1-yne	**9w**	60
11	Ethynyl-triisopropylsilane	**9x**	32
12	Methyl propiolate	**9y**[a]	0
13	2-Ethynylpyridine	**9z**	N.R

Note: N.R. = no reaction. Conditions: acetylene (0.36 mmol), aniline (0.36 mmol), methyl 2-formylbenzoate (0.30 mmol), and $Cu(OTf)_2$ (15 mol %) in 1 mL toluene, reacted for 12 h at 75 °C under argon.

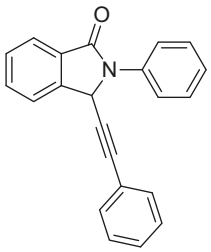
[a]Product **9y** does not bear an isoindolinone structure, instead it is a 1,4-dihydropyridine structure, noted as compound **10**.

Scheme 4. Formation of 1,4-dihydropyridine structural scaffolds.



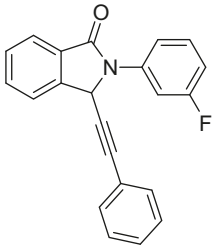
Can. J. Chem. Downloaded from www.nrcresearchpress.com by Renmin University of China on 09/02/12
For personal use only.

Characterization of products



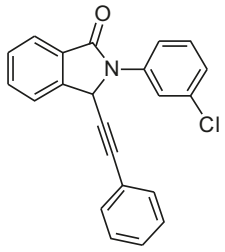
9a

^{1}H NMR (400 MHz, $CDCl_3$, ppm) δ: 7.96 (d, 1H, J = 7.6 Hz), 7.86 (dd, 2H, J = 7.8, 1.0 Hz), 7.72–7.68 (m, 2H), 7.58–7.45 (m, 3H), 7.32–7.26 (m, 6H), 6.04 (s, 1H). ^{13}C NMR (100 MHz, $CDCl_3$, ppm) δ: 166.7, 141.8, 137.7, 132.8, 131.8, 131.7, 129.3, 129.0, 128.9, 128.3, 125.3, 124.2, 123.0, 122.2, 121.7, 86.2, 83.5, 53.2. HR-MS (ESI) exact mass calcd. for $C_{22}H_{16}NO$ ([M + H]) m/z: 310.1237; found m/z: 310.1230.



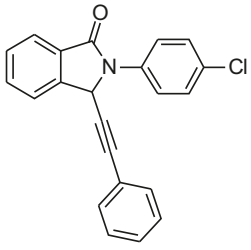
9b

^{1}H NMR (400 MHz, $CDCl_3$, ppm) δ: 7.96 (d, 1H, J = 7.6 Hz), 7.82–7.56 (m, 5H), 7.44–7.24 (m, 6H), 6.94 (td, 1H, J = 10.8, 2.6 Hz), 6.00 (s, 1H). ^{13}C NMR (100 MHz, $CDCl_3$, ppm) δ: 165.6 (d, J = 211.8 Hz), 161.3, 141.6, 139.3 (d, J = 13.9 Hz), 133.1, 131.8, 131.3, 130.1, 129.9, 129.4, 129.0, 128.3, 124.4, 123.1, 121.7, 116.6 (d, J = 4.3 Hz), 111.8 (d, J = 27.9 Hz), 108.9 (d, J = 35.2 Hz), 86.5, 83.0, 53.1. HR-MS (ESI) exact mass calcd. for $C_{22}H_{13}FNO$ ([M – H]) m/z: 326.0987; found m/z: 326.0988.



9c

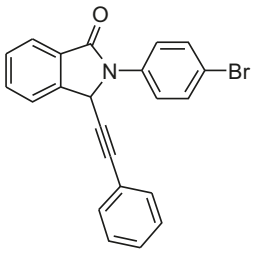
^{1}H NMR (400 MHz, $CDCl_3$, ppm) δ: 7.94 (d, 1H, J = 7.6 Hz), 7.84 (d, 2H, J = 8.8 Hz), 7.71–7.69 (m, 2H), 7.59–7.57 (m, 1H), 7.43 (d, 2H, J = 8.8 Hz), 7.33–7.26 (m, 5H), 5.99 (s, 1H). ^{13}C NMR (100 MHz, $CDCl_3$, ppm) δ: 166.6, 141.6, 138.9, 134.6, 133.1, 131.8, 131.3, 129.9, 129.4, 129.0, 128.3, 125.1, 124.4, 123.1, 121.7, 121.5, 119.5, 86.6, 82.9, 53.0. HR-MS (ESI) exact mass calcd. for $C_{22}H_{15}ClNO$ ([M + H]) m/z: 344.0837; found m/z: 344.0842.



9d

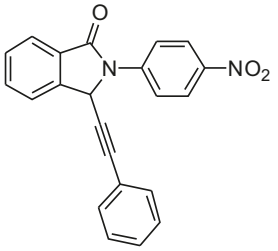
^{1}H NMR (400 MHz, $CDCl_3$, ppm) δ: 7.94 (d, 1H, J = 7.6 Hz), 7.84 (d, 2H, J = 8.8 Hz), 7.72–7.69 (m, 2H), 7.57–7.56 (m, 1H), 7.43 (dd, 2H, J = 7.0, 2.0 Hz), 7.30–7.26 (m, 5H), 6.00 (s, 1H). ^{13}C NMR (100 MHz, $CDCl_3$, ppm) δ: 166.6, 141.6, 136.3, 132.9, 131.8, 131.3, 130.4, 129.4, 129.1, 128.8, 128.3, 124.3, 123.1, 122.9. HR-MS exact mass calcd. for $C_{22}H_{14}ClNONa$ ([M + Na]) m/z: 366.0656; found m/z: 366.0664.

Can. J. Chem. Downloaded from www.nrcresearchpress.com by Renmin University of China on 09/02/12
For personal use only.



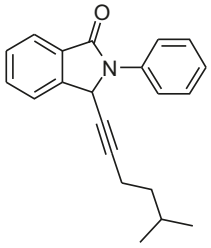
9e

^{1}H NMR (400 MHz, $CDCl_3$, ppm) δ: 7.94 (d, 1H, J = 7.2 Hz), 7.80 (d, 2H, J = 8.8 Hz), 7.79–7.67 (m, 2H), 7.59–7.56 (m, 3H), 7.33–7.25 (m, 5H), 5.99 (s, 1H). ^{13}C NMR (100 MHz, $CDCl_3$, ppm) δ: 166.6, 141.6, 136.8, 133.0, 131.9, 131.8, 131.3, 129.4, 129.0, 128.3, 124.3, 123.2, 123.1, 121.5, 118.2, 86.5, 82.9, 52.9. HR-MS (ESI) exact mass calcd. for $C_{22}H_{15}BrNO$ ([M + H]) m/z: 388.0332; found m/z: 388.0338.



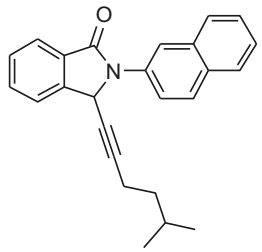
9f

^{1}H NMR (400 MHz, $CDCl_3$, ppm) δ: 8.34 (dd, 2H, J = 7.2, 2.0 Hz), 8.19 (dd, 2H, J = 9.6, 2.0 Hz), 7.90–7.50 (m, 4H), 7.34–7.29 (m, 5H), 6.09 (s, 1H). ^{13}C NMR (100 MHz, $CDCl_3$, ppm) δ: 166.9, 143.6, 143.5, 141.5, 133.8, 131.8, 130.7, 129.7, 129.3, 128.4, 124.8, 124.6, 123.2, 121.1, 119.9, 87.1, 82.4, 52.7. HR-MS (ESI) exact mass calcd. for $C_{22}H_{13}N_2O_3$ ([M – H]) m/z: 353.0932; found m/z: 353.0953.



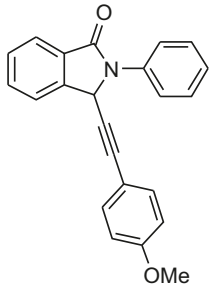
9w

^{1}H NMR (400 MHz, $CDCl_3$, ppm) δ: 7.91 (d, 1H, J = 7.6 Hz), 7.79 (d, 2H, J = 7.6 Hz), 7.67–7.62 (m, 2H), 7.58–7.51 (m, 1H), 7.46–7.42 (m, 2H), 7.26–7.21 (m, 1H), 5.79 (s, 1H), 2.13–2.09 (m, 2H), 1.51–1.43 (m, 1H), 1.28–1.23 (m, 2H), 0.86–0.76 (m, 6H). ^{13}C NMR (75 MHz, $CDCl_3$, ppm) δ: 166.6, 142.4, 137.7, 132.6, 131.6, 128.9, 128.8, 125.1, 124.1, 122.9, 122.2, 87.3, 74.4, 52.9, 36.9, 26.9, 22.0, 21.9, 16.6. HR-MS (ESI) exact mass calcd. for $C_{21}H_{22}NO$ ([M + H]) m/z: 304.1707; found m/z: 304.1698.



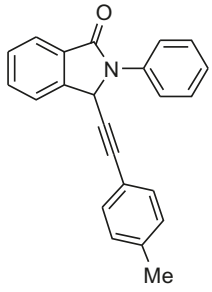
9w2

^{1}H NMR (400 MHz, $CDCl_3$, ppm) δ: 8.18 (d, 1H, J = 2 Hz), 8.02 (dd, 1H, J = 8.8, 2.4 Hz), 7.96–7.84 (m, 4H), 7.67 (dd, 1H, J = 2.8, 1.2 Hz), 7.58–7.44 (m, 3H), 5.94 (s, 1H), 2.10–2.06 (m, 2H), 1.38–1.33 (m, 1H), 1.25–1.18 (m, 2H), 0.68–0.64 (m, 6H). ^{13}C NMR (75 MHz, $CDCl_3$, ppm) δ: 166.6, 142.5, 135.3, 133.6, 132.6, 131.6, 131.1, 129.1, 128.6, 127.9, 127.5, 126.3, 125.5, 124.1, 122.9, 121.4, 119.8, 87.5, 74.5, 53.2, 36.9, 26.8, 21.8, 16.6. HR-MS (ESI) exact mass calcd. for $C_{25}H_{24}NO$ ([M + H]) m/z: 354.1852; found m/z: 354.1851.



9o

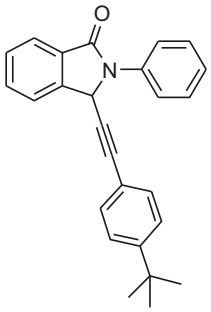
^{1}H NMR (400 MHz, $CDCl_3$, ppm) δ: 7.95 (d, 1H, J = 7.2 Hz), 7.86 (d, 2H, J = 8 Hz), 7.73–7.65 (m, 2H), 7.59–7.45 (m, 3H), 7.26–7.22 (m, 3H), 6.77 (d, 2H, J = 7.6 Hz), 6.02 (s, 1H), 3.77 (s, 3H). ^{13}C NMR (75 MHz, $CDCl_3$, ppm) δ: 166.7, 159.9, 142.0, 137.7, 133.3, 132.7, 131.6, 129.2, 128.9, 125.3, 124.2, 123.0, 122.2, 113.9, 86.2, 82.0, 80.2, 55.3, 53.4. HR-MS (ESI) exact mass calcd. for $C_{23}H_{18}NO_2$ ([M + H]) m/z: 340.1332; found m/z: 340.1333.



9n

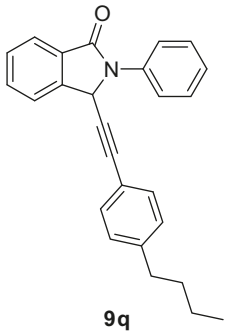
^{1}H NMR (400 MHz, $CDCl_3$, ppm) δ: 7.95 (d, 1H, J = 7.6 Hz), 7.87 (d, 2H, J = 8 Hz), 7.73–7.65 (m, 2H), 7.59–7.44 (m, 4H), 7.26–7.19 (m, 2H), 7.06 (d, 2H, J = 7.6 Hz), 6.02 (s, 1H), 3.31 (s, 3H). ^{13}C NMR (75 MHz, $CDCl_3$, ppm) δ: 166.7, 141.9, 139.1, 137.7, 132.7, 131.7, 129.2, 129.1, 129.0, 128.9, 125.3, 124.2, 123.1, 122.2, 119.4, 118.7, 86.4, 82.8, 53.3. HR-MS (ESI) exact mass calcd. for $C_{23}H_{16}NO$ ([M – H]) m/z: 322.1237; found m/z: 322.1231.

Can. J. Chem. Downloaded from www.nrcresearchpress.com by Renmin University of China on 09/02/12
For personal use only.



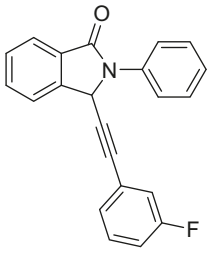
9p

^{1}H NMR (400 MHz, $CDCl_3$, ppm) δ: 7.95 (d, 1H, J = 7.6 Hz), 7.86 (d, 2H, J = 7.6 Hz), 7.73–7.65 (m, 2H), 7.57 (t, 1H, J = 7.6 Hz), 7.46 (t, 2H, J = 8.4 Hz), 7.30–7.22 (m, 5H), 6.03 (s, 1H), 1.27 (s, 9H). ^{13}C NMR (75 MHz, $CDCl_3$, ppm) δ: 166.7, 152.2, 141.9, 137.7, 132.7, 131.7, 131.6, 129.2, 128.9, 125.3, 125.2, 124.2, 123.0, 122.2, 118.7, 86.3, 82.8, 53.4, 34.8, 31.1. HR-MS (ESI) exact mass calcd. for $C_{26}H_{23}NONa$ ([M + Na]) *m*/*z*: 388.1672; found *m*/*z*: 388.1679.



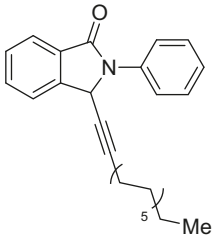
9q

^{1}H NMR (400 MHz, $CDCl_3$, ppm) δ: 7.95 (d, 1H, J = 7.6 Hz), 7.87 (d, 2H, J = 8 Hz), 7.73–7.65 (m, 2H), 7.59–7.55 (m, 1H), 7.49–7.45 (m, 2H), 7.26–7.22 (m, 3H), 7.07 (d, 2H, J = 8 Hz), 6.03 (s, 1H), 2.58–2.54 (m, 2H), 1.67–1.50 (m, 2H), 1.35–1.26 (m, 2H), 0.91–0.86 (m, 3H). ^{13}C NMR (75 MHz, $CDCl_3$, ppm) δ: 166.7, 144.1, 141.9, 137.7, 132.7, 131.7, 131.6, 129.2, 128.9, 128.4, 125.3, 124.2, 123.1, 122.2, 118.9, 86.4, 82.8, 53.3, 35.5, 33.3, 22.2, 13.9. HR-MS (ESI) exact mass calcd. for $C_{26}H_{23}NONa$ ([M + H]) *m*/*z*: 388.1672; found *m*/*z*: 388.1678.



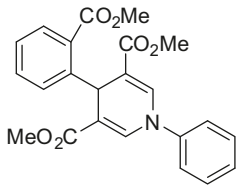
9t

^{1}H NMR (400 MHz, $CDCl_3$, ppm) δ: 7.97–7.83 (m, 3H), 7.71–7.66 (m, 1H), 7.60–7.41 (m, 4H), 7.27–7.20 (m, 2H), 7.07 (d, 1H, J = 8 Hz), 7.02–6.03 (m, 2H), 6.03 (s, 1H), 4.86 (s, 1H). ^{13}C NMR (75 MHz, $CDCl_3$, ppm) δ: 166.6, 141.5, 137.5, 132.8, 131.6, 129.9, 129.3, 129.2, 129.1, 129.0, 127.7, 127.6, 125.4, 124.3, 122.9, 122.1, 119.4, 118.6 (d, J = 22.5 Hz), 116.4, 116.3 (d, J = 21.9 Hz), 84.5 (d, J = 29 Hz), 53.1. HR-MS (ESI) exact mass calcd. for $C_{22}H_{13}FNO$ ([M – H]) *m*/*z*: 326.0987; found *m*/*z*: 326.0995.



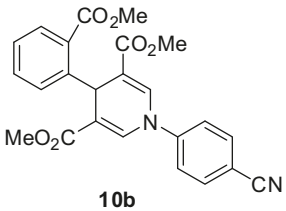
9v

^{1}H NMR (400 MHz, $CDCl_3$, ppm) δ: 7.91 (d, 1H, J = 7.6 Hz), 7.80 (d, 2H, J = 7.6 Hz), 7.64 (d, 2H, J = 2.4 Hz), 7.55–7.52 (m, 1H), 7.46–7.42 (m, 2H), 7.26–7.20 (m, 1H), 5.80 (s, 1H), 2.13–2.08 (m, 2H), 1.38–1.78 (m, 20H), 0.93–0.87 (m, 3H). ^{13}C NMR (75 MHz, $CDCl_3$, ppm) δ: 166.7, 142.4, 137.7, 134.4, 132.6, 131.5, 128.9, 128.8, 126.6, 125.1, 124.1, 123.7, 122.9, 122.1, 87.4, 74.5, 52.9, 31.9, 29.6, 29.4, 29.0, 28.6, 28.2, 22.7, 18.6, 14.1. HR-MS (ESI) exact mass calcd. for $C_{28}H_{36}NO$ ([M + H]) *m*/*z*: 402.2791; found *m*/*z*: 402.2801.



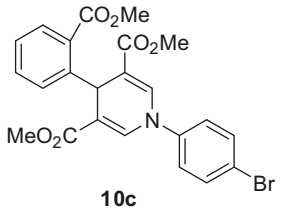
10a

^{1}H NMR (500 MHz, $CDCl_3$, ppm) δ: 7.75 (dd, 1H, J = 8 Hz, 1.5 Hz), 7.68 (s, 2H), 7.48–7.40 (m, 5H), 7.32–7.28 (m, 2H), 7.21 (m, 1H), 6.10 (s, 1H), 3.99 (s, 3H), 3.60 (s, 6H). ^{13}C NMR (75 MHz, $CDCl_3$, ppm) δ: 168.5, 167.0, 146.8, 143.0, 136.1, 131.9, 130.2, 130.1, 129.9, 129.7, 126.4, 126.3, 120.6, 111.4, 51.9, 51.4, 32.9. HR-MS (ESI) exact mass calcd. for $C_{23}H_{22}NO_6$ ([M + H]) *m*/*z*: 408.1442; found *m*/*z*: 408.1439.



10b

^{1}H NMR (400 MHz, $CDCl_3$, ppm) δ: 7.78–7.73 (m, 5H), 7.43–7.36 (m, 3H), 7.25–7.21 (m, 2H), 6.14 (s, 1H), 3.98 (s, 3H), 3.62 (s, 6H). ^{13}C NMR (75 MHz, $CDCl_3$, ppm) δ: 168.3, 166.5, 145.8, 145.7, 134.1, 134.0, 131.9, 130.3, 130.2, 129.9, 126.6, 119.8, 118.1, 113.5, 109.1, 52.02, 51.66, 32.97, 31.58, 22.65, 14.12. HR-MS (ESI) exact mass calcd. for $C_{24}H_{20}N_2O_6Na$ ([M + Na]) *m*/*z*: 455.1214; found *m*/*z*: 455.1206.



10c

^{1}H NMR (500 MHz, $CDCl_3$, ppm) δ: 7.75 (d, 1H, J = 8 Hz), 7.62 (s, 2H), 7.57 (dd, 2H, J = 6.8, 2 Hz), 7.42 (d, 2H, J = 4.4 Hz), 7.21–7.18 (m, 3H), 6.10 (s, 1H), 3.98 (s, 3H), 3.60 (s, 6H). ^{13}C NMR (75 MHz, $CDCl_3$, ppm) δ: 168.4, 166.9, 146.5, 142.0, 135.5, 133.0, 131.9, 130.2, 130.1, 129.7, 129.4, 126.4, 122.0, 111.9, 51.9, 51.5, 32.8. HR-MS (ESI) exact mass calcd. for $C_{23}H_{20}BrNO_6Na$ ([M + Na]) *m*/*z*: 508.0366; found *m*/*z*: 508.0371.

References

(1) For reviews, see (a) Tietze, L. F.; Brasche, G.; Gericke, K. M. *Domino Reactions in Organic Synthesis;* Wiley-VCH: Weinheim, Germany, 2006; p 3; (b) Tietze, L. F.; Beifuss, U. *Angew. Chem. Int. Ed. Engl.* **1993**, *32* (2), 131. doi:10.1002/anie.199301313; (c) Tietze, L. F. *Chem. Rev.* **1996**, *96* (1), 115. doi:10.1021/cr950027e; (d) Pellissier, H. *Tetrahedron* **2006**, *62* (10), 2143. doi:10.1016/j.tet.2005.10.041; (e) Ho, T. L. *Tandem Organic Reactions;* Wiley: New York, 1992; p 502; (f) Bunce, R. A. *Tetrahedron* **1995**, *51* (48), 13103. doi:10.1016/0040-4020(95)00649-S.

(2) (a) Ikeda, S. *Acc. Chem. Res.* **2000**, *33* (8), 511. doi:10.1021/ar9901016; (b) Enders, D. C.; Wang, J. W.; Bats, J. W. *Angew. Chem.* **2008**, *120* (39), 7649. doi:10.1002/ange.200802532.

(3) Cornish, E. J.; Lee, G. E.; Wragg, W. R. *Nature* **1963**, *197* (4874), 1296. doi:10.1038/1971296b0.

(4) (a) Dubois, R. J.; Lin, C.-C.; Beisler, J. A. *J. Med. Chem.* **1978**, *21* (3), 303. doi:10.1021/jm00201a016; (b) Bonfield, E. R.; Li, C.-J. *Adv. Synth. Catal.* **2008**, *350* (3), 370. doi:10.1002/adsc.200700500.

(5) Huang, M. Z.; Huang, K. L.; Ren, Y. G.; Lei, M. X.; Huang, L.; Hou, Z. K.; Liu, A. P.; Ou, X. M. *J. Agric. Food Chem.* **2005**, *53* (20), 7908. doi:10.1021/jf051494s.

(6) Hamprecht, D.; Micheli, F.; Tedesco, G.; Checchia, A.; Donati, D.; Petrone, M.; Terreni, S.; Wood, M. *Bioorg. Med. Chem. Lett.* **2007**, *17* (2), 428. doi:10.1016/j.bmcl.2006.10.029.

(7) (a) Muller, G. W.; Man, H. W. PCT Int. Appl. WO 2006025991, 2006; *Chem. Abstr.* **2006**, *144*, 269911; (b) Murakata, C.; Amishiro, N.; Atsumi, T.; Tamashita, Y.; Tanahashi, T.; Nakai, R.; Tagaya, H.; Takahashi, H.; Funahashi, J.; Yamamoto, J.; Fukuda, Y. PCT Int. Appl. WO 2006112479, 2006; *Chem. Abstr.* **2006**, *145*, 454932; (c) Funk, L. A.; Johnson, M. C.; Kung, P. P.; Meng, J. J.; Zhou, J. Z. PCT Int. Appl. WO 2006117669, 2006; *Chem. Abstr.* **2006**, *145*, 489014.

(8) Sasaki, D.; Fujiwara, T. Jpn. Kokai Tokkyo Koho JP 2005304565, 2006; *Chem. Abstr.* **2007**, *146*, 472371.

(9) (a) Grigg, R.; Gai, X.; Khamnaen, T.; Rajviroongit, S.; Sridharan, V.; Zhang, L.; Collard, S.; Keep, A. *Can. J. Chem.* **2005**, *83* (6–7), 990. doi:10.1139/v05-111; (b) Takahashi, I.; Kawakami, T.; Hirano, E.; Yokota, H.; Kitajima, H. *Synlett* **1996**, *1996* (04), 353. doi:10.1055/s-1996-5438.

(10) (a) Sorbera, L. A.; Leeson, P. A.; Silvestre, J.; Castaner, J. *Drugs Future* **2001**, *26* (7), 651. doi:10.1358/dof.2001.026.07.630003; (b) Anzini, M.; Cappelli, A.; Vomero, S.; Giorgi, G.; Langer, T.; Bruni, G.; Romeo, M. R.; Basile, A. S. *J. Med. Chem.* **1996**, *39* (21), 4275. doi:10.1021/jm960325j; (c) Gotor, V.; Limeres, F.; García, R.; Bayod, M.; Brieva, R. *Tetrahedron Asymmetry* **1997**, *8* (7), 995. doi:10.1016/S0957-4166(97)00090-6.

(11) (a) Zhu, C.; Falck, J. R. *Org. Lett.* **2011**, *13* (5), 1214. doi:10.1021/ol200093f; (b) Moreau, A.; Couture, A.; Deniau, E.; Grandclaudon, P.; Lebrun, S. *Tetrahedron* **2004**, *60* (29), 6169. doi:10.1016/j.tet.2004.05.033.

(12) Chen, L.; Li, C.-J. *Adv. Synth. Catal.* **2006**, *348* (12–13), 1459. doi:10.1002/adsc.200606090.

(13) (a) Li, C.-J.; Wei, C. *Chem. Commun. (Camb.)* **2002**, *2002* (3), 268. doi:10.1039/B108851N; (b) Wei, C.; Li, C.-J. *J. Am. Chem. Soc.* **2002**, *124* (20), 5638. doi:10.1021/ja026007t; (c) Wei, C.; Mague, J. T.; Li, C.-J. *Proc. Natl. Acad. Sci. U.S.A.* **2004**, *101* (16), 5749. doi:10.1073/pnas.0307150101; (d) Zhang, J.; Wei, C.; Li, C.-J. *Tetrahedron Lett.* **2002**, *43* (33), 5731. doi:10.1016/S0040-4039(02)01197-8.

(14) For reviews and recent examples, see (a) Li, C.-J. *Acc. Chem. Res.* **2010**, *43* (4), 581. doi:10.1021/ar9002587; (b) Wei, C.; Li, Z.; Li, C.-J. *Synlett* **2004**, *2004* (9), 1472. doi:10.1055/s-2004-829531; (c) Zeng, T.; Yang, L.; Hudson, R.; Song, G.; Moores, A. R.; Li, C.-J. *Org. Lett.* **2011**, *13* (3), 442. doi:10.1021/ol102759w; (d) Shore, G.; Yoo, W.-J.; Li, C.-J.; Organ, M. G. *Chem. Eur. J.* **2010**, *16* (1), 126. doi:10.1002/chem.200902396; (e) Zhang, Y.; Donahue, J. P.; Li, C.-J. *Org. Lett.* **2007**, *9* (4), 627. doi:10.1021/ol062918m; (f) Bonfield, E. R.; Li, C.-J. *Org. Biomol. Chem.* **2007**, *5* (3), 435. doi:10.1039/b613596j; (g) Zani, L.; Bolm, C. *Chem. Commun. (Camb.)* **2006**, *2006* (41), 4263. doi:10.1039/b607986p; (h) Yoo, W.-J.; Zhao, L.; Li, C.-J. *Aldrichim. Acta* **2011**, *44* (2), 43; (i) Zeng, T.; Chen, W.-W.; Cirtiu, C. M.; Moores, A.; Song, G.; Li, C.-J. *Green Chem.* **2010**, *12* (4), 570. doi:10.1039/b920000b; (j) Huang, B.; Yao, X.; Li, C.-J. *Adv. Synth. Catal.* **2006**, *348* (12–13), 1528. doi:10.1002/adsc.200606118.

(15) Balalaie, S.; Kowsari, E. *Monatsh. Chem.* **2001**, *132* (12), 1551. doi:10.1007/s007060170012.

(16) Kikuchi, S.; Iwai, M.; Murayama, H.; Fukuzawa, S. *Tetrahedron Lett.* **2008**, *49* (1), 114. doi:10.1016/j.tetlet.2007.11.003.

(17) Mai, A.; Valente, S.; Meade, S.; Carafa, V.; Tardugno, M.; Nebbioso, A.; Galmozzi, A.; Mitro, N.; De Fabiani, E.; Altucci, L.; Kazantsev, A. *J. Med. Chem.* **2009**, *52* (17), 5496. doi:10.1021/jm9008289.

Can. J. Chem. Downloaded from www.nrcresearchpress.com by Renmin University of China on 09/02/12
For personal use only.

Novel Zn(II) coordination polymer based on 1,2-bis (4-pyridyl)hydrazine — From two-dimensional to three-dimensional network

Huaishan Wang, Lap Szeto, Wesley Ting Kwok Chan, Ho-Lun Yeung, Ka-Leung Wong, and Wing-Tak Wong

Can. J. Chem. Downloaded from www.nrcresearchpress.com by Renmin University of China on 09/02/12
For personal use only.

Abstract: Two MOFs were reported based on Zn(II) with 1,2-bis(4-pyridyl)hydrazine (**L1**); a two-dimensional interpenetrating MOF **I** of formula $[Zn_2(\mathbf{L1})_2(\mathbf{L2})_2]_\infty$ was formed with terephthalic acid (**L2**) as an additional linker. A three-dimensional MOF **II** of formula $[Zn_2(\mathbf{L1})_2(\mathbf{L3})_2]_\infty$, was formed with the use of a larger spacer 2,6-naphthalenedicarboxylic acid (**L3**). MOF **II** consists of large porosity with a total volume of 3746 Å^3 that occupies 34.1% of the unit cell.

Key words: metal organic framework, coordination polymer, 1,2-bis(4-pyridyl)hydrazine, interpenetrating polymer, microporous, hydrogen bond.

Résumé : On rapporte les propriétés de deux charpentes organométalliques (COM) à base de Zn(II) et de 1,2-bis(4-pyridyl)hydrazine (**L1**); un COM bidimensionnelle imbriquée (**I**) de formule $[Zn_2(\mathbf{L1})_2(\mathbf{L2})_2]_\infty$ formé à l'aide d'acide téréphtalique (**L2**) utilisé comme coupleur additionnel. Il se forme aussi une COM tridimensionnelle (**II**) de formule $[Zn_2(\mathbf{L1})_2(\mathbf{L3})_2]_\infty$ lorsqu'on utilise l'acide naphtalène-2,6-dicarboxylique (**L3**) comme coupleur plus long. La charpente organométallique **II** possède une grande porosité, avec un volume total de 3746 A^3 qui occupe 34,1 % de la maille élémentaire.

Mots-clés : charpente organométallique, polymère de coordination, 1,2-bis(4-pyridyl)hydrazine, polymère imbriqué, microporeux, liaison hydrogène.

[Traduit par la Rédaction]

Introduction

Metal-organic frameworks (MOFs) have attracted much attention in the past decade because of their well-organized three-dimensional forms with permanent porosity, as well as their potential applications in adsorption, separation, and ion exchange processes,[1,2] catalysis,[3] and drug delivery.[4] Their specific chemical and physical properties are mainly dependent on the frameworks, which can be achieved by introducing different bridging ligands with geometrically predetermined metal centres. However, obtaining MOFs with desired topologies and functionalities is still a challenging task.

Organic linkers with C, N, O and S atoms or groups provide great opportunities to create functionalized porous frameworks with these heteroatoms exposed inside the pore space; this in turn can lead to materials tailor-made for specific applications. Among different linkers, nitrogen-containing linkers are of particular interest, with azo-ligand being one example.[5] Azo-ligand has shown good thermal stability and unique optical properties, which make it suitable for optical data storage and electro-optical devices.[5a,5b] Moreover, because of cis–trans isomerization of the N=N bond, azo-ligand is able to perform various kinds of molecular motions upon external stimuli.[5c–5e] By incorporating the azo functional groups into MOF, it may be possible to introduce interesting photochemical and physical properties in the product. Meanwhile, Zn has been demonstrated to be a versatile metal for the construction of MOFs. A recent example of a Zn MOF showed second-order nonlinear optical effects and a ferro-electric feature.[5g] Therefore, our initial attempt was to develop a Zn MOF with azo-linkers by performing reactions of $ZnCl_2$, 4,4′-azopyridine and terephthalic acid (**L2**) under (solvo)thermal conditions. Crystals suitable for X-ray single crystal characterization were obtained, and they showed a two-dimensional polymeric network. In the polymer $[Zn_2(\mathbf{L1})_2(\mathbf{L2})_2]_\infty$ (**I**), 1,2-bis(4-pyridyl)hydrazine (**L1**), which resulted from hydrogenation of 4,4′-azopyridines, was surprisingly observed. A similar reduction reaction in the presence of Ru ions was also reported.[6] Contrary to 4,4′-azopyridine, **L1** may provide excellent flexibility and functionality in the MOF structure. The single N–N bond of **L1** allows the flexibility to adopt various kinds of

Received 21 April 2011. Accepted 31 May 2011. Published at www.nrcresearchpress.com/cjc on 8 November 2011.

H. Wang, W.T.K. Chan, H.-L. Yeung, and W.-T. Wong. Department of Applied Biology and Chemical Technology, The Hong Kong Polytechnic University, Hung Hom, Hong Kong SAR.
L. Szeto. Department of Chemistry, The University of Hong Kong, Pokfulam, Hong Kong SAR.
K.-L. Wong. Department of Chemistry, Hong Kong Baptist University, Kowloon Tong, Hong Kong SAR.

Corresponding author: Wing-Tak Wong (e-mail: bcwtwong@polyu.edu.hk).

This article is part of a Special Issue dedicated to Professor Tak-Hang Chan.

Can. J. Chem. Downloaded from www.nrcresearchpress.com by Renmin University of China on 09/02/12
For personal use only.

Table 1. Crystal data and structure refinement parameters for **I** and **II.**

Crystal	**I**	**II**
Empirical formula	$C_{36}H_{28}N_8O_8Zn_2$	$C_{44}H_{32}N_8O_8Zn_2$
Formula mass	831.40	931.52
Crystal dimensions (mm)	0.16 × 0.02 × 0.02	0.45 × 0.24 × 0.22
Crystal system	Monoclinic	Monoclinic
Space group	*Pc*	*C*2/*c*
a (Å)	8.3585(8)	31.7790(5)
b (Å)	20.3147(9)	16.7618(3)
c (Å)	11.0912(10)	23.1651(4)
α (°)	90°	90°
β (°)	112.0460(10)°	116.4810(10)°
γ (°)	90°	90°
Volume (Å^3)	1745.6(2)	11044.8(3)
Z	2	8
Temperature (K)	300 (2)	296(2)
D_{calcd} (Mg m^{-3})	1.582	1.120
Collection ranges	$-11 \le h \le 9$, $-17 \le k \le 26$, $-14 \le l \le 14$	$-32 \le h \le 32$, $-16 \le k \le 16$, $-23 \le l \le 23$
θ range for data collection (°)	2.00–28.28	1.53–21.15
Radiation	Mo Kα (λ = 0.710 73 Å)	Mo Kα (λ = 0.710 73 Å)
F (000)	848	3808
Independent reflections	7698 (R_{int} = 0.0209)	6019 (R_{int} = 0.0537)
Total data	7698	6019
Unique data	488	559
Reflections collected, unique	12154, 7698	39582, 6019
Goodness of fit	0.988	1.051
Final *R* indices [$I>2\sigma(I)$]	R_1 = 0.0328, wR_2 = 0.0710	R_1 = 0.0355, wR_2 = 0.0878
R indices (all data)	R_1 = 0.0506, wR_2 = 0.0775	R_1 = 0.0471, wR_2 = 0.0922
Largest diff. peak and hole (e Å^{-3})	0.353 and –0.256	0.361 and –0.259

conformation when **L1** coordinates to metal ions. In contrast to the non-polar C–C bond, hydrazine units provide free basic centers to further interact with (*i*) metals in various coordination modes[7] or (*ii*) polar molecules through strong noncovalent interactions (e.g., hydrogen bonds).[8] The latter, having been found ubiquitously in biological systems, is considered one of the strong directional interactions for constructing coordination polymer with predictable features (molecular tectonics).[9] However, studies on hydrazine-containing MOFs are rare.[10] Moreover, to the best of our knowledge, there is no report on the development of **L1** for two- or three-dimensional network construction. We are interested in developing MOFs based on **L1**. Using the same synthetic strategy, a reaction of $ZnCl_2$, 4,4′-azopyridine, and a longer spacer, and 2,6-naphthalenedicarboxylic acids (**L3**) was attempted. Crystals were obtained, and the crystal structure showed a three-dimensional network, with formula $[Zn_2(\mathbf{L1})_2(\mathbf{L3})_2]_\infty$ (**II**).

Experimental

General

NMR spectra in solution were recorded on a Bruker Ultrashield 400 Plus MHz instrument, and the chemical shifts were referenced internally to residual solvent peaks in parts per million (ppm). Thermal gravimetric analysis data were recorded on a PerkinElmer Thermogravimetric Analyzer (TGA7) with a heating rate of 5 °C/min in an N_2 atmosphere. Infrared spectra were recorded on a Nicolet Nexus 470 FTIR spectrometer in the range 4000–400 cm^{-1}, by using dry KBr pellets containing about 1%–2% of the sample. Elemental analyses were recorded on a Vario EL elemental analyzer. Positive ion mass spectra were taken by Waters Quattro Ultima equipped with triple quadruple in electrospray mode.

X-ray crystallography

Measurements for crystal data were carried out on a Bruker Smart 1000 system equipped with an APEX II CCD device for **I** and **II**, with graphite monochromated Mo Kα radiation at room temperature. Multi-scan absorption correction was applied by SADABS program,[11] and the SAINT program was utilized for integration of the diffraction profiles.[12] The structures were solved by direct method and was refined by a full matrix least-squares treatment on F^2, using the SHELXTL programme system.[13,14] Finally, SQUEEZE–PLATON was used to remove the heavily disordered lattice solvents from refinement in **II**.[15] Crystal data, as well as details of data collection and refinement, for **I** and **II** are summarized in Table 1.

Synthesis and characterizations of MOF I, $[Zn_2(L1)_2(L2)_2]_\infty$

MOF **I** was synthesized by mixing 4,4′-azopyridine (13.8 mg, 0.075 mmol), terephthalic acid (**L2**) (8.3 mg, 0.05 mmol), and $Zn(NO_3)_2{\cdot}6H_2O$ (14.9 mg, 0.05 mmol) in DMF (4 mL) in an oven at 120 °C for 72 h, followed by slow cooling to room temperature at a rate of 10 °C h^{-1}. A mixture of solids and crystals resulted. Light-red crystals suitable for X-ray characterization and found to be MOF **I** were obtained. Yield: 15 mg (36%) on the basis of $Zn(NO_3)_2{\cdot}6H_2O$. The compound was characterized by single crystal X-ray

Can. J. Chem. Downloaded from www.nrcresearchpress.com by Renmin University of China on 09/02/12
For personal use only.

Fig. 1. (*a*) Asymmetric unit of **I**. (*b*) The basic repeating motif containing four zinc centres and four bridging ligands found in **I**. The highly twisted nature of **L1** can be clearly seen. Symmetry equivalent atoms were generated by the symmetry operation *x*, *y*, *z*.

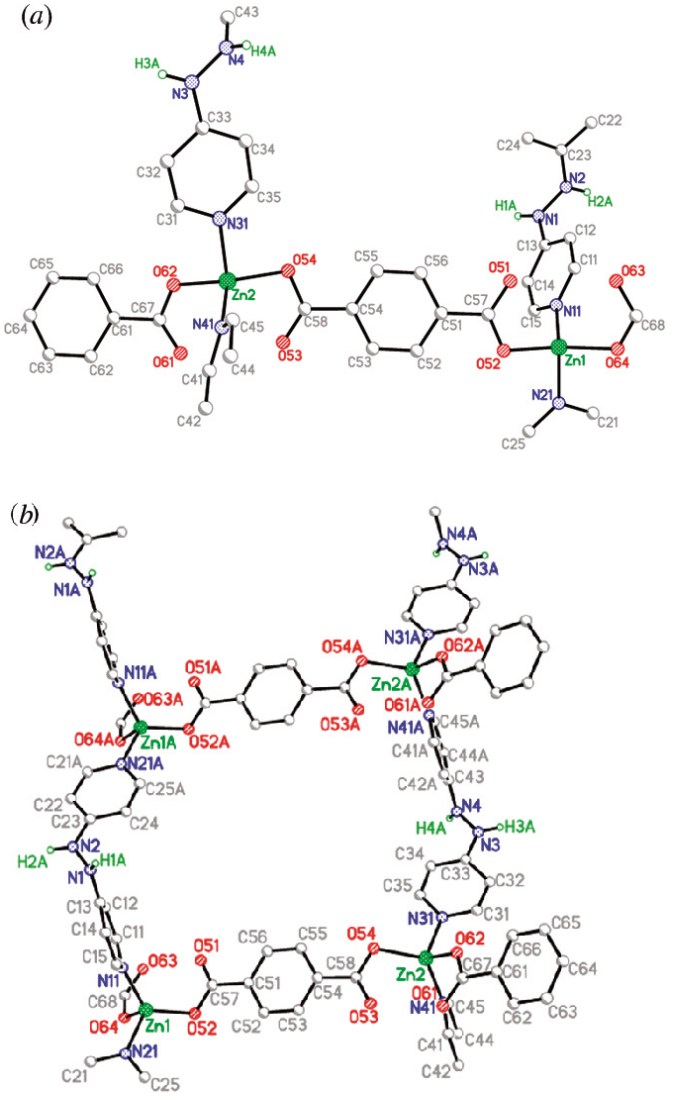


Fig. 2. An example of hydrogen bond (N-H1AA···O51) between neighboring asymmetric units of MOF **I**. Red (dark-grey oblique stripes in print version): oxygen; white: carbon; blue (light-grey dots in print): nitrogen (light-grey cross-hatch in print); green: Zn^{2+}.

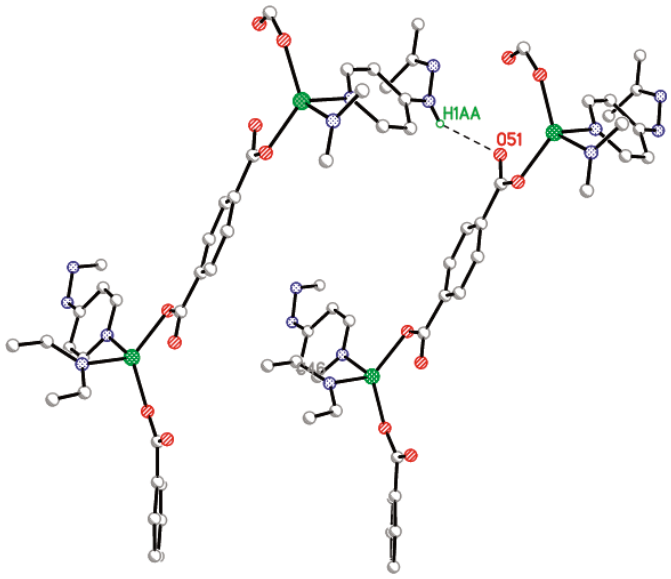
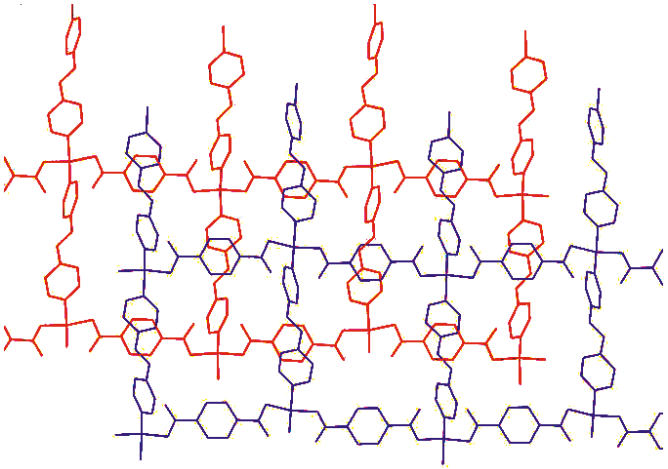


Fig. 3. The interpenetration between two layers of the 2D nets of **I**.



diffraction, powder X-ray diffraction (PXRD), thermogravimetric analysis (TGA), elemental analysis, and IR spectroscopy. IR (KBr pellet, ν, cm^{-1}): 3454.7 w, 3232.6 m, 1612.3 s, 1355.8 s, 1213.5 m, 1022.1 m, 821.5 m, 759.8 m. Elemental analysis (in wt%): calcd. for $Zn_2(\mathbf{L1})_2(\mathbf{L2})_2$: C 52.00, H 3.39, N 13.48; found: C 49.61, H 3.14, N 13.30.

Synthesis and characterizations of MOF II, $[Zn_2(L1)_2(L3)_2]_\infty$

MOF **II** was synthesized by mixing 4,4′-azopyridine (13.8 mg, 0.075 mmol), 2,6-naphthalenedicarboxylic acid (**L3**) (10.8 mg, 0.05 mmol), and $Zn(NO_3)_2{\cdot}6H_2O$ (14.9 mg, 0.05 mmol) in DMF (4 mL) in an oven at 120 °C for 72 h, followed by slow cooling to room temperature at a rate of 10 °C h^{-1}. A mixture of solids and crystals resulted. Light-red crystals suitable for X-ray characterization and found to be MOF **II** were obtained. Yield: 13 mg (31%) on the basis of $Zn(NO_3)_2{\cdot}6H_2O$. The compound was characterized by single crystal X-ray diffraction, powder X-ray diffraction (PXRD), thermogravimetric analysis (TGA), elemental analysis, and IR spectroscopy. IR (KBr pellet, ν, cm^{-1}): 3457.9 w, 3247.7 m, 1618.3 s, 1577.6 s, 1407.9 s, 1357.7 s, 1214.9 m, 1020.2 m, 790.7 m. Elemental analysis (in wt%): calcd. for $Zn_2(\mathbf{L1})_2(\mathbf{L3})_2{\cdot}2H_2O{\cdot}4DMF$: C 53.55, H 4.78, N 13.39; found: C 53.70, H 4.85, N 13.00.

Isolation and characterizations of L1 after MOF synthesis

A crude mixture of **I** was treated with 6N HCl (5 mL) for 2 h. The aqueous layer was extracted with Et_2O (20 mL) three times. The aqueous layer was then neutralized by 2M NaOH (15 mL) and further extracted with CH_2Cl_2 (20 mL) three times. The organic layer was obtained and dried with $MgSO_4$. The solvent was removed under reduced pressure. **L1** was isolated (yield: 30%) and characterized by ^1H NMR and ESI-MS. A similar procedure was applied to crude mixture

Fig. 4. Asymmetric unit of **II** showing the severely twisted nature of **L1**.

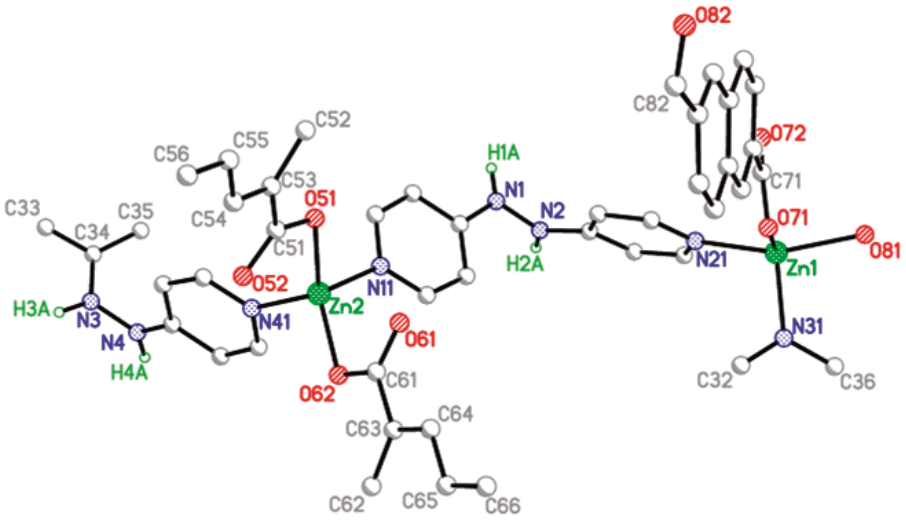


Fig. 5. Figure showing an example of hydrogen bond (N4A–H4AA···O61) between neighboring asymmetric units of MOF **II**. Red (dark-grey oblique stripes in print version): oxygen; dark line: carbon; blue (light-grey dots in print): nitrogen; green (light-grey cross-hatch in print): Zn^{2+}). Symmetry equivalent atoms were generated by: 0.5–*x*, 0.5+*y*, 0.5–*z*.

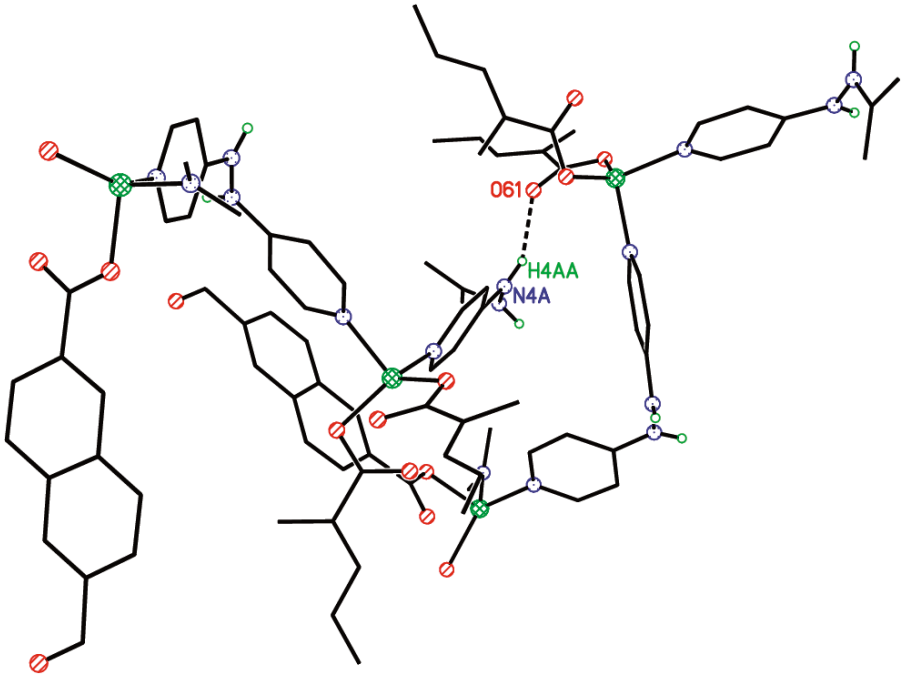


Table 2. Hydrogen bond distances and angles observed in **I** and **II**.

MOF	N–H···O	Distance (Å)	Angle (°)
I	N1–H1AA···O51	2.218	140.50
	N2–H2AA···O63	2.186	125.79
	N3–H3AA···O61	2.231	120.08
	N4–H4AA···O53	2.155	142.63
II	N1–H1AA···O72	2.272	121.35
	N2–H2AA···O52	2.030	156.91
	N4–H4AA···O61	2.011	148.78

of **II** (yield: 34%). ^{1}H NMR (400 MHz, d_6-DMSO) δ: 8.56 (s, 2H), 8.13 (d, 4H, J = 6.0 Hz), 6.60 (d, 4H, J = 6.0 Hz). ESI-MS *m/z* 187 $[M+H]^+$.

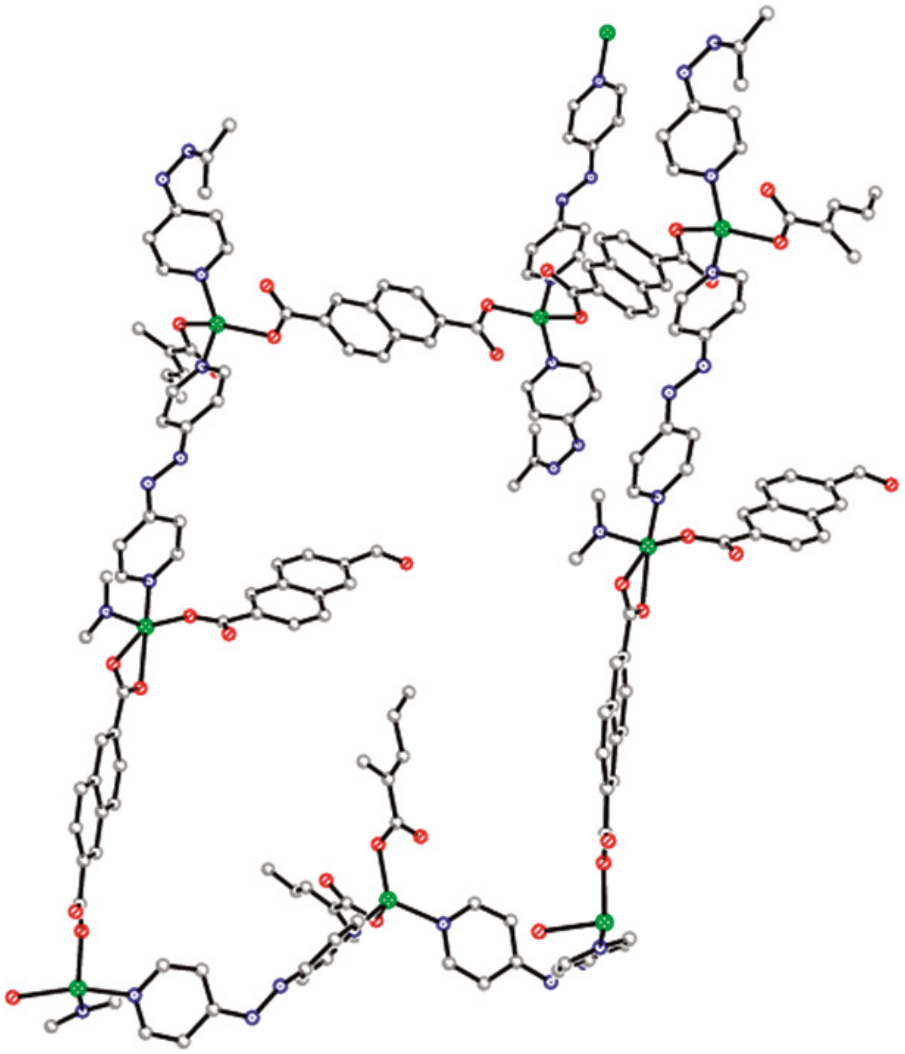
Results and discussion

Hydrogenation of 4,4′-azopyridine to form 1,2-bis(4-pyridyl)hydrazine

In the literature there are a variety of methods for the reduction of azo compounds to hydrazo compounds, commonly by metal-mediated reduction.[16] Conventional reduction of 4,4′-azopyridine to 1,2-bis(4-pyridyl)hydrazine required metal catalysts (e.g., Pd,[16a] Ni,[16b] Zn,[17] etc.) and in the presence of hydrogen donors such as formic acid,[18] ammonium formate,[19] and hydrazine.[20] Recently, an example of in situ formation of hydrazine ligands during MOF preparation by Zn-catalyzed hydration process was proposed.[10a] In our studies, 4,4′-azopyridines can be reduced to 1,2-bis(4-

Can. J. Chem. Downloaded from www.nrcresearchpress.com by Renmin University of China on 09/02/12
For personal use only.

Fig. 6. The basic repeating motif found within **II**.



Can. J. Chem. Downloaded from www.nrcresearchpress.com by Renmin University of China on 09/02/12
For personal use only.

pyridyl)hydrazines in the presence of Zn salts and organic acids under solvothermal conditions. In an attempt to understand the hydrogenation process from the azo group to hydrazine, control experiments were carried out. Firstly the reaction was carried out in the absence of Zn salt or organic acid, and secondly the reaction was carried out using all reactants at 120 °C under atmospheric pressure. The hydrazine product (**L1**) cannot be obtained in all these control reactions. Although the mechanism for the reduction and the role of Zn salts are not clear at this stage, these experiments indicated the importance of high pressure during hydrogenation process and suggested the source of hydrogen donors from carboxylic acids (**L2** or **L3**).

Structure of I

The single crystal X-ray diffraction study reveals that **I** crystallizes in the monoclinic space group *Pc*. The asymmetric unit (Fig. 1) consists of two zinc centers, both of them have a distorted tetrahedral geometry (average bond angles of 108.8° and 108.7°, respectively), and each coordinates with two pyridyl nitrogen atoms and two oxygen atoms from the monodentate carboxylate groups. Zn–E (E = N, O) bond lengths within the structure are found to be in agreement with literature values (1.940–2.043Å).[21]

As mentioned previously, 4,4′-azopyridine was found to have been hydrogenated to form **L1**. Initially, the presence of the amino protons could only be speculated through indirect evidence, as designation of proton purely based on residue peaks is often difficult. One such evidence is the largely twisted geometry of the whole ligand itself, with dihedral angles of 91.7° (between N(11) and N(21) pyridine rings) and 101.0° (between N(31) and N(41) pyridine rings), respectively. Furthermore, the extended N–N bonds (1.380 and 1.388 Å, compared with a typical N=N bond length of 1.25 Å)[22] also point to the hydrogenation of the azo group (Fig. 1*b*). Another subtle clue to the presence of the amino protons comes in the form of the C–O bond lengths found within the carboxylate groups. In a monodentate system, a difference in bond length between the two C–O bonds would normally be expected. However, while there is a minor difference between the bond length in general (1.212–1.306 Å), the bonds are still far shorter than the typical C–O bond length of 1.43 Å.[22] Thus the negative charge is still considered to be largely delocalized across the whole carboxylate group. Under this situation, the uncoordinated oxygen cannot

Can. J. Chem. Downloaded from www.nrcresearchpress.com by Renmin University of China on 09/02/12
For personal use only.

Fig. 7. A packing diagram of **II** showing the large volume of voids. The majority of hydrogen atoms are omitted for clarity.

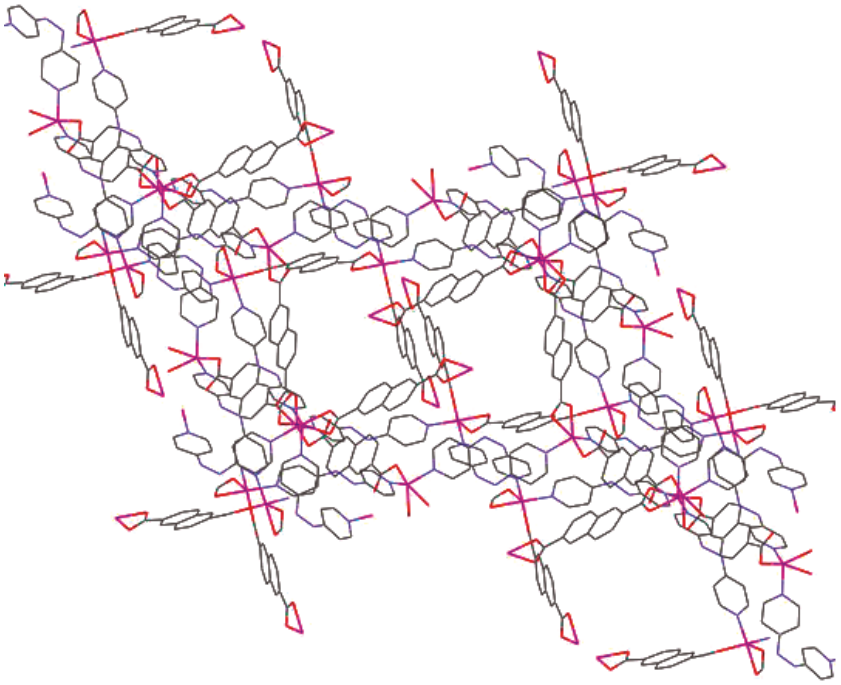


Fig. 8. Thermogravimetric curve of MOF (*a*) **I** and (*b*) **II**.

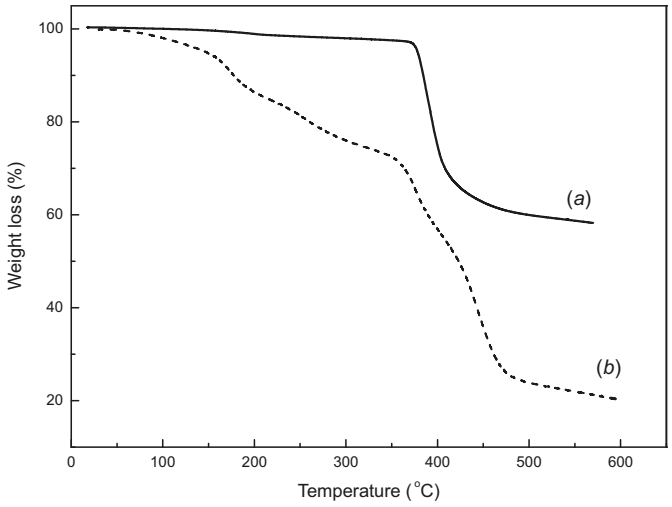
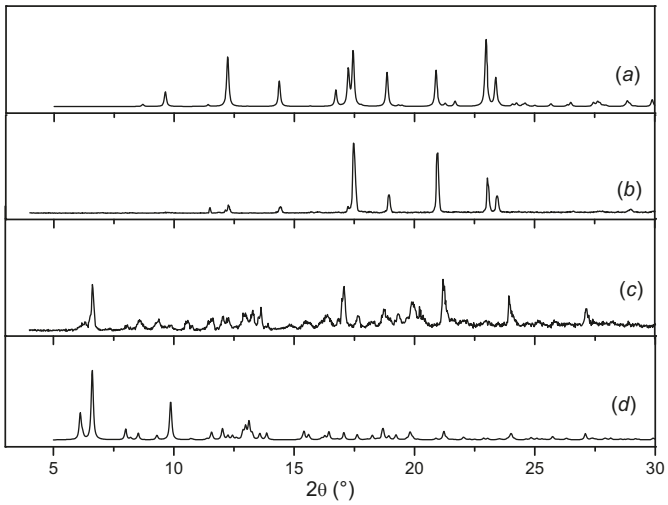


Fig. 9. Powder X-ray diffraction patterns of (*a*) simulation from a single crystal of MOF **I**, (*b*) crystals of MOF **I**, (*c*) crystals of MOF **II**, and (*d*) simulation from a single crystal of MOF **II**.



be truly unattached, and the amino proton is found to be within suitable distant and geometry to provide the necessary interaction through hydrogen bonding (Fig. 2). As **L1** is known to form a strong hydrogen bond,[8] the presence of the amino proton-oxygen hydrogen bonding is also potentially important to the way the carboxylate group is coordinated to the zinc center and in turn to the entire formation of the coordination polymer itself.

In the extended lattice, **L2** bridges over two crystallographically different zinc centers (i.e., between Zn(1) and Zn (2), and vice versa), whereas **L1** bridges across symmetrically equivalent zinc atoms (i.e., between neighboring Zn(1) atoms or neighboring Zn(2) atoms). The result is a ring with four bridges (two each of **L1** and **L2**), linking up four zinc metal centers as vertexes. This can then be seen to extend indefinitely, forming a 2D net. Because of the largely tetrahedral nature of the metal centers, a layer of the net has a distinctive zig-zag shape, this shape in turn allows for two sets of net to interpenetrate each other (Fig. 3). The aforementioned hydrogen bonding interactions are formed between these interpenetrating layers to provide stabilization. The interpenetrating arrangement means that no solvent accessible void can be found within any given layers; in fact, no lattice solvent could be located from the crystallographic data. The lack of lattice solvent would become one of the major differences between structure of **I** and **II**.

The structural analysis of **II** was severely hampered by the decomposition of the crystal during data collection. The solution could only be obtained after a number of attempts. **II** was found to crystallize in the centrosymmetric space group

Can. J. Chem. Downloaded from www.nrcresearchpress.com by Renmin University of China on 09/02/12
For personal use only.

of *C*2/*c*. Many features found in **I** can also be found in the analogous **II**. For example, the severely twisted nature of **L1** after the azo group was hydrogenated during the synthesis (dihedral angle of 72.6° and 99.0° between corresponding pyridine rings, respectively) (Fig. 4*a*), and hydrogen bonds between the amino proton and the uncoordinated oxygen on the carboxylate group can be observed too (Fig. 5). A comparison of hydrogen bonds in **I** and **II** is summarized in Table 2.

Unlike **I**, **L3** is seen to be bridging across symmetrically identical zinc atoms (i.e., Zn(1) to Zn(1) or Zn(2) to Zn(2)), whereas **L1** links together zinc centers of different environments (i.e., Zn(1) to Zn(2) and vice versa). More pertinently, the two types of zinc centers do have different coordination environments, as opposed to **I** whose two zinc centers have the same coordination mode. Zn(2) is four-coordinated, while Zn(1) is five-coordinated (Fig. 6).[23] Zn(2) is coordinated with two pyridyl N atoms and two O atoms from two carboxylate groups and takes up a distorted tetrahedral geometry (average bond angle of 108.9°), similar to the zinc centers found in **I**. The penta-coordinated Zn(1), on the other hand, arises from coordination with two pyridyl nitrogen atoms and three carboxylate oxygen atoms. One of the carboxylate groups is found to chelate to the zinc atom; as a result, the geometry at the zinc centre resembles an approximate trigonal bipyrimid. Steric hindrance is an issue surrounding chelation to the zinc center, as evident from the longer than typical O(81)–Zn(1) and O(82)–Zn(1) bond (2.142 and 2.268 Å, respectively), and perhaps unsurprisingly, no hydrogen bonding is observed for either oxygen atoms.

The larger **L3** ligand compared with **L2** and the difference in coordination environments allow for the formation of a 3D network as opposed to the 2D net seen in structure **I**. The basic motif is formed with eight zinc centers and eight bridges (four each of the **L1** and **L3** ligands). This motif extends throughout the lattice, where rings can be seen interpenetrating each other, making the overall structure rather complex (Fig. 7). Solvent accessible cavities can be found within the lattice, and these cavities occupy 33.9% of one unit cell volume (3746.1 $Å^3$ out of 11044.8 $Å^3$).[24] The crystal data show that solvent molecules such as DMF and water can be found inside the cavities, however, the heavily disordered nature made it difficult to determine the precise amount of each solvent present. The only satisfactory solution was obtained through the use of SQUEEZE (PLATON),[24] where the solvents were discounted from the lattice.

Thermal stabilities and powder XRD studies of I and II

To study the thermal stabilities of **I**, thermogravimetric analyses (TGAs) were performed on their polycrystalline samples (Fig. 8*a*). For MOF **I**, no weight loss was observed up to 385 °C. A significant weight loss was then observed at ca. 385–550 °C, indicating the framework decomposition of **I**. MOF **I** shows high thermal stability (>250 °C), and the lack of solvent capacity is consistent with its interpenetrating arrangement found in the crystal structure. The structural homogeneity of bulk powder samples of **I** was examined through comparison of experimental and simulated powder XRD patterns (Figs. 9*a* and 9*b*). The experimental pattern is in agreement with that of the simulated one generated from single-crystal X-ray diffraction data, which indicates the homogenous phase of final products.

However, during the sample preparation of **II** for TGA and powder XRD analysis, the compound lost its crystallinity gradually upon solvent removal and appeared to be decomposed slowly over a few hours. The TGA spectrum of **II** showed two major steps in the weight loss (Fig. 8*b*). The first obvious weight loss includes the release of water (2.75%) and DMF (23.10%) molecules at ca. 50–130 and 165–340 °C. The total weight loss of guest molecules is about 25.85% and closely matches the solvent amount calculated from the formula $[Zn_2(\mathbf{L1})_2(\mathbf{L3})_2]\cdot 2H_2O\cdot 4DMF$ (26.06%), which is based on the elemental analysis. A second obvious weight loss happened at ca. 360–470 °C, which shows decomposition of the solid-state framework. The powder XRD spectrum of **II** also showed the lost in crystalline nature and decomposition of the compound during the experiment (Figs. 9*c* and 9*d*), as it showed a difference in peak positions and intensities compared with the spectrum simulated from its single crystal.

Conclusion

We have demonstrated the use of flexible **L1** in the formation of two novel Zn metal-organic polymers. The use of larger **L3** over **L2**, as well as the coordination environment around the Zn ions, induces a significant change in the dimensions of the polymers, from 2D interpenetrating in **I** to 3D highly porous network in **II**. Moreover, extensive hydrogen bonds are observed between amino protons of **L1** and oxygens of carboxylate linkers in both polymers. This may play a prominent role in the formation of the two final solid-state organizations, and it opens up new strategy for well-defined supramolecular motif with porous architectures. Although the solid-state structures of MOF **II** are not stable enough for further application, the free basic centers in the structure have great potential to serve as the adsorption sites for guest molecules (e.g., metal ions and gases). We are extending the synthetic strategy to prepare other porous MOFs with the combination of **L1** and other carboxylate derivatives.

Supplementary data

Supplementary data for this article are available on the journal Web site (www.nrcresearchpress.com/doi/suppl/10.1139/v11-132). Crystallographic data CCDC 809663 and 809662 have also been deposited with the Cambridge Crystallographic Data Centre. These data can be obtained, free of charge, via www.ccdc.cam.ac.uk/cgi-bin/catreq.cgi (or from the Cambridge Crystallographic Data Centre, 12 Union Road, Cambridge CB2 1Ez, UK; fax +44 1223 336033; or e-mail deposit@ccdc.cam.ac.uk).

Acknowledgements

This work was financially supported by The Hong Kong Polytechnic University (Postdoctoral Fellowship Scheme No. G-YX1P) and The Hong Kong Research Grants Council.

References

(1) (a) Matsuda, R.; Kitaura, R.; Kitagawa, S.; Kubota, Y.; Belosludov, R. V.; Kobayashi, T. C.; Sakamoto, H.; Chiba, T.;

Can. J. Chem. Downloaded from www.nrcresearchpress.com by Renmin University of China on 09/02/12
For personal use only.

Takata, M.; Kawazoe, Y.; Mita, Y. *Nature*, **2005**, *436* (7048), 238. doi:10.1038/nature03852; (b) Phan, A.; Doonan, C. J.; Uribe-Romo, F. J.; Knobler, C. B.; O'Keeffe, M.; Yaghi, O. M. *Acc. Chem. Res.* **2010**, *43* (1), 58. doi:10.1021/ar900116g; (c) Rowsell, J. L. C.; Yaghi, O. M. *Angew. Chem. Int. Ed.* **2005**, *44* (30), 4670. doi:10.1002/anie.200462786.

(2) (a) Halper, S. R.; Do, L.; Stork, J. R.; Cohen, S. M. *J. Am. Chem. Soc.* **2006**, *128* (47), 15255. doi:10.1021/ja0645483; (b) Kawano, M.; Fujita, M. *Coord. Chem. Rev.* **2007**, *251* (21-24), 2592. doi:10.1016/j.ccr.2007.07.022.

(3) (a) Lee, J.; Farha, O. K.; Roberts, J.; Scheidt, K. A.; Nguyen, S. T.; Hupp, J. T. *Chem. Soc. Rev.* **2009**, *38* (5), 1450. doi:10.1039/b807080f; (b) Ma, L.; Abney, C.; Lin, W. *Chem. Soc. Rev.* **2009**, *38* (5), 1248. doi:10.1039/b807083k.

(4) (a) Norikane, Y.; Katoh, R.; Tamaoki, N. *Chem. Commun. (Cambridge)*, **2008**, *10* (16), 1898. doi:10.1039/b718813g; (b) Furusho, Y.; Tanaka, Y.; Maeda, T.; Ikeda, M.; Yashima, E. *Chem. Commun. (Cambridge)*, **2007**, (30): 3174. doi:10.1039/b705347a.

(5) (a) Egli, R. *Color Chemistry: The Design and Synthesis of Organic Dyes and Pigments*; A. T. Peters, H. S. Freeman, Eds.; Elservier, London, 1991; (b) Rau, R. In *Photochromism, Molecules and Systems*; H. Dürr, H. Bouas-Laurent, Eds.; Elsevier, Amsterdam, ch. 4, 1990; (c) Feringa, B. L. *Molecular Switches*; Wiley-VCH, Weinheim, 2001; (d) Yager, K. G.; Barrett, C. J. *J. Photochem. Photobiol. Chem.* **2006**, *182* (3), 250. doi:10.1016/j.jphotochem.2006.04.021; (e) Brown, E. V.; Granneman, G. R. *J. Am. Chem. Soc.* **1975**, *97* (3), 621. doi:10.1021/ja00836a025; (f) Venkataramani, S.; Jana, U.; Dommaschk, M.; Sönnichsen, F. D.; Tuczek, F.; Herges, R. *Science*, **2011**, *331* (6016), 445. doi:10.1126/science.1201180; (g) Wong, W.-Y.; Cheung, S.-H.; Lee, S.-M.; Leung, S.-Y. *J. Organomet. Chem.* **2000**, *596* (1-2), 36. doi:10.1016/S0022-328X(99)00536-7; (h) Liang, X.-Q.; Jia, J.-T.; Wu, T.; Li, D.-P.; Liu, L.; Tsolmon, ; Zhu, G.-S. *CrystEngComm*, **2010**, *12* (11), 3499. doi:10.1039/c0ce00329h.

(6) Launay, J.-P.; Tourrel-Pagis, M.; Lipskier, J.-F.; Marvaud, V.; Joachim, C. *Inorg. Chem.* **1991**, *30* (5), 1033. doi:10.1021/ic00005a029.

(7) (a) Yu, X.-Y.; Ye, L.; Zhang, X.; Cui, X.-B.; Zhang, J.-P.; Xu, J.-Q.; Hou, Q.; Wang, T.-G. *Dalton Trans.* **2010**, *39* (44), 10617. doi:10.1039/c002946g; (b) Crossland, J. L.; Zakharov, L. N.; Tyler, D. R. *Inorg. Chem.* **2007**, *46* (25), 10476. doi:10.1021/ic702007r; (c) Field, L. D.; Li, H. L.; Dalgarno, S. J. *Inorg. Chem.* **2010**, *49* (13), 6214. doi:10.1021/ic100821u.

(8) Du, M.; Zhang, Z.-H.; Wang, X.-G.; Wu, H.-F.; Wang, Q. *Cryst. Growth Des.* **2006**, *6* (8), 1867. doi:10.1021/cg0601812.

(9) (a) Hosseini, M. R. *Acc. Chem. Res.* **2005**, *38* (4), 313. doi:10.1021/ar0401799; (b) Zhang, X.-M.; Bai, C.-J.; Zhang, Y.-L.; Wu, H.-S. *Can. J. Chem.* **2004**, *82* (5), 616. doi:10.1139/v04-026; (c) Salazar–Mendoza, D.; Baudron, S. A.; Hosseini, M. W. *Inorg. Chem.* **2008**, *47* (3), 766. doi:10.1021/ic701949k; (d) Baudron, S. A.; Salazar–Mendoza, D.; Hosseini, M. W. *CrystEngComm*, **2009**, *11* (7), 1245. doi:10.1039/b901167f; (e) Pogozhev, D.; Baudron, S. A.; Hosseini, M. W. *CrystEngComm*, **2010**, *12* (7), 2238. doi:10.1039/b927348d; (f) Mouchaham, G.; Roques, N.; Imaz, I.; Duhayon, C.; Sutter, J.-P. *Cryst. Growth Des.* **2010**, *10* (11), 4906. doi:10.1021/cg1009785; (g) Yeung, H.-L.; Wong, W.-Y.; Wong, C.-Y.; Kwong, H.-L. *Inorg. Chem.* **2009**, *48* (9), 4108. doi:10.1021/ic802249f.

(10) (a) Fang, Z.-L.; Yu, R.-M.; He, J.-G.; Zhang, Q.-S.; Zhao, Z.-G.; Lu, C.-Z. *Inorg. Chem.* **2009**, *48* (16), 7691. doi:10.1021/ic9004533; (b) Huh, H. S.; Kim, S. H.; Yun, S. Y.; Lee, S. W. *Polyhedron*, **2008**, *27* (4), 1229. doi:10.1016/j.poly.2007.12.018.

(11) Sheldrick, G. M. *SADABS, Program for Empirical Absorption Correction of Area detector*; University of Göttingen, Germany, 1997.

(12) SAINT. *Version 7.34, Bruker*; Bruker AXS Inc., Madison, Wisconsin, USA, 2007.

(13) Sheldrick, G. M. *Acta Crystallogr. A*, **1990**, *46* (6), 467. doi:10.1107/S0108767390000277.

(14) Sheldrick, G. M. *SHELX-97, Programme for Crystal Structure Refinement*; University of Gottingen, 1990.

(15) Spek, A. L. *PLATON, A Multipurpose Crystallographic Tool*; Utrecht University, Utrecht, The Netherlands, 2005.

(16) (a) Bavin, P. M. G. *Can. J. Chem.* **1958**, *36* (1), 238. doi:10.1139/v58-032; (b) Furst, A.; Moore, R. E. *J. Am. Chem. Soc.* **1957**, *79* (20), 5492. doi:10.1021/ja01577a044; (c) Hornsby, S.; Peacock, W. L. *Chem. Ind. (London)*, **1958**, *27*, 858; (d) Vogel, A. I.; Watling, A.; Watling, J. *J. Chem. Educ.* **1958**, *35* (1), 40. doi:10.1021/ed035p40; (e) Gilchrist, T. L. *Comprehensive Organic Synthesis*; Fleming, I., Ed.; Pergamon Press: Oxford, UK, 1991; Vol. 8, Ch. 2.2, 381–402.

(17) Prasad, H. S.; Gowda, S.; Abiraj, K.; Gowda, D. C. *Synth. React. Inorg. Met. Org. Chem.* **2003**, *33* (4), 717. doi:10.1081/SIM-120020334.

(18) Gowda, D. C.; Gowda, A. S. P.; Baba, A. R.; Gowda, S. *Synth. Commun.* **2000**, *30*, 2885.

(19) Ram, S.; Ehrenkaufer, R. E. *Tetrahedron Lett.* **1984**, *25* (32), 3415. doi:10.1016/S0040-4039(01)91034-2.

(20) (a) Prasad, H. S.; Gowda, S.; Gowda, D. C. *Synth. Commun.* **2004**, *34* (1), 1. doi:10.1081/SCC-120027231; (b) Koppes, W. M.; Moran, J. S.; Oxley, J. C.; Smith, J. L. *Tetrahedron Lett.* **2008**, *49* (20), 3234. doi:10.1016/j.tetlet.2008.03.083.

(21) Search of the Cambridge Crystallography Data Base, using VISTA:Bruno, I. J.; Cole, J. C.; Edgington, P. R.; Kessler, M.; Macrae, C. F.; McCabe, P.; Pearson, J.; Taylor, R. *Acta Crystallogr. B*, **2002**, *58* (3-1), 389. doi:10.1107/S0108768102003324.

(22) Huheey, J. E.; Keiter, E. A.; Keiter, R. L. *Inorganic Chemistry*; Harper Collins; 4th ed., 1993.

(23) (a) For examples, see:Sreehari, N.; Varghese, B.; Manoharan, P. T. *Inorg. Chem.* **1990**, *29* (20), 4011. doi:10.1021/ic00345a020; (b) Zhang, L.; Ling, Y.; Peng, F.; Du, M. *J. Mol. Struct.* **2007**, *829* (1-3), 161. doi:10.1016/j.molstruc.2006.06.028; (c) Sun, X.-X.; Qi, C.-M.; Ma, S.-L.; Huang, H.-B.; Zhu, W.-X.; Liu, Y.-C. *Inorg. Chem. Commun.* **2006**, *9* (9), 911. doi:10.1016/j.inoche.2006.05.018.

(24) Spek, A. L. *PLATON, A Multipurpose Crystallographic Tool*; Utrecht University, Utrecht, The Netherlands, 2005.

Synthesis, structural characterization, and reactivity of late transition-metal complexes bearing linked cyclopentadienyl–carboranyl ligands

Dongmei Liu, Zaozao Qiu, Hoi-Shan Chan, and Zuowei Xie

Can. J. Chem. Downloaded from www.nrcresearchpress.com by Renmin University of China on 09/02/12
For personal use only.

Abstract: Late transition-metal complexes bearing linked cyclopentadienyl/indenyl–carboranyl ligands were synthesized and their reactivities were examined. Reaction of $Li_2[Me_2C(L)(C_2B_{10}H_{10})]$ (L = C_5H_4, C_9H_6, $Me_2NCH_2CH_2C_5H_3$) with $MCl_2(PPh_3)_2$ in Et_2O afforded $[\eta^5{:}\sigma\text{-}Me_2C(C_5H_4)(C_2B_{10}H_{10})]M(PPh_3)$ (M = Co (**4**), Ni (**5**)), $[\eta^5{:}\sigma\text{-}Me_2C(C_9H_6)(C_2B_{10}H_{10})]M(PPh_3)$ (M = Co (**6**), Ni (**7**)), and $[\eta^5{:}\sigma\text{-}Me_2C(Me_2NCH_2CH_2C_5H_3)(C_2B_{10}H_{10})]Ni(PPh_3)$ (**8**). Treatment of **4** or **5** with 2,6-dimethylphenylisocyanide, N-heterocyclic carbene (NHC), PCy_3, or 1,2-bis(diphenylphosphino)ethane (dppe) gave the corresponding PPh_3 displacement complexes $[\eta^5{:}\sigma\text{-}Me_2C(C_5H_4)(C_2B_{10}H_{10})]M(2,6\text{-}Me_2C_6H_3NC)$ (M = Co (**9**), Ni (**10**)), $[\eta^5{:}\sigma\text{-}Me_2C(C_5H_4)(C_2B_{10}H_{10})]M[1,3\text{-}(2,6\text{-}i\text{-}Pr_2C_6H_3)_2C_3N_2H_2]$ (M = Co (**11**), Ni (**12**)), $[\eta^5{:}\sigma\text{-}Me_2C(C_5H_4)(C_2B_{10}H_{10})]Ni(PCy_3)$ (**13**), or $\{[\eta^5{:}\sigma\text{-}Me_2C(C_5H_4)(C_2B_{10}H_{10})]Co\}_2(dppe)$ (**14**), respectively. These complexes were characterized by various spectroscopic techniques and elemental analyses. The molecular structures of **4**–**14** were further confirmed by single-crystal X-ray analyses.

Key words: carborane, cyclopentadienyl, cobalt complexes, nickel complexes, substitution reaction.

Résumé : On a effectué la synthèse de complexes de métaux de transition portant des ligands liés cyclopentadiényl/indényl-carboranyles et on en a examiné les réactivités. La réaction du $Li_2[Me_2C(L)(C_2B_{10}H_{10})]$ (L = C_5H_4, C_9H_6, $Me_2NCH_2CH_2C_5H_3$) avec le $MCl_2(PPh_3)_2$, dans l'éther, conduit à la formation des $[\eta^5{:}\sigma\text{-}Me_2C(C_5H_4)(C_2B_{10}H_{10})]M(PPh_3)$ (M = Co (**4**); Ni (**5**)), $[\eta^5{:}\sigma\text{-}Me_2C(C_9H_6)(C_2B_{10}H_{10})]M(PPh_3)$ (M = Co (**6**); Ni (**7**)) et $[\eta^5{:}\sigma\text{-}Me_2C(Me_2NCH_2CH_2CH_2C_5H_3)(C_2B_{10}H_{10})]Ni(PPh_3)$ (**8**). Le traitement des composés 4 et 5 avec de l'isocyanure de 2,6-diméthylphényle, des carbènes N-hétérocycliques (NHC), du PCy_3 ou du 1,2-bis(diphénylphosphino)éthane (dppe), conduit aux complexes correspondants avec remplacement du PPh_3, soit respectivement les $[\eta^5{:}\sigma\text{-}Me_2C(C_5H_4)(C_2B_{10}H_{10})]M(2,6\text{-}Me_2\text{-}C_6H_3NC)$ (M = Co (**9**); Ni (**10**)), $[\eta^5{:}\sigma\text{-}Me_2C(C_9H_6)(C_2B_{10}H_{10})]M[1,3\text{-}(2,6\text{-}i\text{-}Pr_2C_6H_3NC)_2(C_3N_2H_2]$ (M = Co (**11**); Ni (**12**)) $[\eta^5{:}\sigma\text{-}Me_2C(C_5H_4)(C_2B_{10}H_{10})]Ni(PCy_3)$ (**13**) ou $\{[\eta^5{:}\sigma\text{-}Me_2C(Me_2C_5H_4)(C_2B_{10}H_{10})]Co\}_2(dppe)$ (**14**). Ces complexes ont été caractérisés par diverses techniques spectroscopiques et par des analyses élémentaires. Les structures moléculaires des composés **4**–**14** ont de plus été confirmées par des diffractions de rayons-X sur des cristaux uniques.

Mots-clés : carborane, cyclopentadiényle, complexes du cobalt, complexes du nickel, réaction de substitution.

[Traduit par la Rédaction]

Introduction

Linked cyclopentadienyl/indenyl/fluorenyl–carboranyl ligands have been widely used for the synthesis of constrained-geometry transition-metal complexes,[1–3] in which the non-traditional metal–carbon(cage) (M–C_{cage}) bonds are generally inert toward electrophiles because of steric reasons.[1e,1f] On the other hand, they can offer transition-metal complexes unique features.[4] For example, the constrained-geometry ruthenium complexes, $[\eta^5{:}\sigma\text{-}Me_2C(C_5H_4)(C_2B_{10}H_{10})]Ru(L_2)$ (L = NHR_2, CH_3CN) can react with alkynes to produce Ru–carbene, –diene, and –bisvinylidene complexes bearing the $[Me_2C(C_5H_4)(C_2B_{10}H_{10})]^{2-}$ ligand.[4] In addition, $[\eta^5{:}\sigma\text{-}Me_2C(C_5H_4)(C_2B_{10}H_{10})]Ru(CH_3CN)_2$ can also react with 3 equiv of terminal alkynes ArC≡CH to form the unexpected tricyclic compounds with the activation of the incorporated C_5H_4 ring.[4f]

It has been documented that the Co and Ni complexes show some common features with the Ru ones in [2+2+2] cyclotrimerization of alkynes and C–C coupling reactions.[5] Connected to this and to understand the similarities and differences among late transition-metal complexes with linked cyclopentadienyl–carboranyl ligands, we extended our research to include cobalt and nickel metals. We report herein the synthesis, structure, and reactivity of Co and Ni complexes

Received 29 April 2011. Accepted 4 July 2011. Published at www.nrcresearchpress.com/cjc on 10 November 2011.

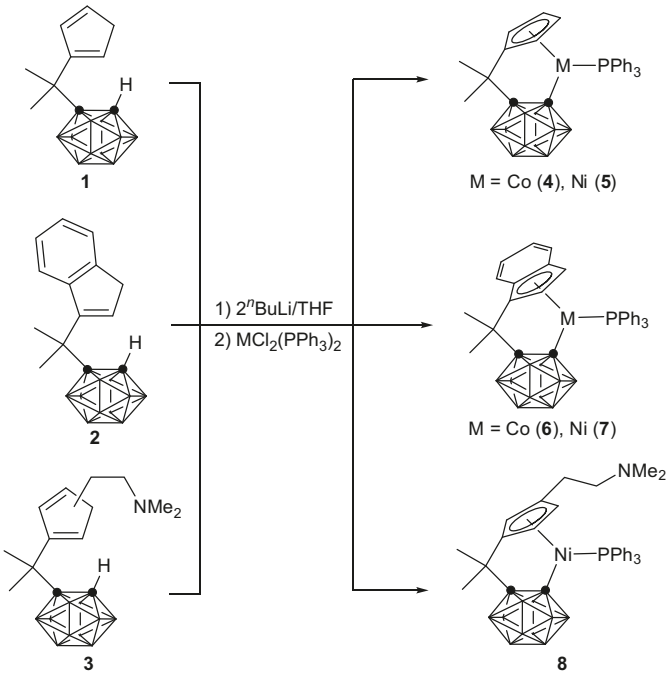
D. Liu, Z. Qiu, H.-S. Chan, and Z. Xie. Department of Chemistry and Center of Novel Functional Molecules, The Chinese University of Hong Kong, Shatin, New Territories, Hong Kong, China.

Corresponding author: Zuowei Xie (e-mail: zxie@cuhk.edu.hk).

This article is part of a Special Issue dedicated to Professor Tak-Hang Chan.

Can. J. Chem. Downloaded from www.nrcresearchpress.com by Renmin University of China on 09/02/12
For personal use only.

Scheme 1. Synthesis of cobalt and nickel complexes.



bearing carbon-linked cyclopentadienyl/indenyl–carboranyl ligands.

Results and discussion

Synthesis and structure

Treatment of $Li_2[Me_2C(C_5H_4)(C_2B_{10}H_{10})]$[2d] with 1 equiv of $MCl_2(PPh_3)_2$ (M = Co, Ni) in THF at room temperature afforded, after recrystallization from Et_2O, constrained-geometry transition-metal complexes $[\eta^5{:}\sigma\text{-}Me_2C(C_5H_4)(C_2B_{10}H_{10})]M(PPh_3)$ (M = Co (**4**) or Ni (**5**)) in ~90% isolated yields (Scheme 1). In a similar manner, complexes $[\eta^5{:}\sigma\text{-}Me_2C(C_9H_6)(C_2B_{10}H_{10})]M(PPh_3)$ (M = Co (**6**) or Ni (**7**)) and $[\eta^5{:}\sigma\text{-}Me_2C(Me_2NCH_2CH_2C_5H_3)(C_2B_{10}H_{10})]Ni(PPh_3)$ (**8**) were also synthesized from the interaction of $Li_2[Me_2C(C_9H_6)(C_2B_{10}H_{10})]$[2e] or $Li_2[Me_2C(Me_2NCH_2CH_2C_5H_3)(C_2B_{10}H_{10})]$ with 1 equiv of $MCl_2(PPh_3)_2$ in 63%–79% isolated yields, respectively (Scheme 1).

Complexes **4** and **6** were paramagnetic species, which did not provide useful NMR information. For complexes **5**, **7**, and **8**, the ^1H and ^{13}C NMR spectra showed the presence of the ligand and coordinated PPh_3 with an 1:1 molar ratio. Their ^{11}B NMR spectra exhibited the same 2:3:5 pattern. The ^{31}P NMR spectra displayed a singlet at 47.3 ppm for **5**, 33.8 ppm for **7**, and 36.5 ppm for **8**, respectively. The compositions of complexes **4**–**8** were confirmed by elemental analyses.

The solid-state structures of **4**–**8** as revealed by single-crystal X-ray analyses show that the metal atoms are η^5-bound to the cyclopentadienyl ligand (in **4**, **5**, and **8**) or indenyl ligand (in **6** and **7**), σ-bound to one cage carbon atom, and coordinated to a triphenylphosphine in a trigonal planar geometry, leading to the formation of 17 e^- cobalt and 18 e^- nickel complexes. The representative structures of **5**, **7**, and **8** are shown in Figs. 1–3, respectively. The selected bond

Fig. 1. Molecular structure of $[\eta^5{:}\sigma\text{-}Me_2C(C_5H_4)(C_2B_{10}H_{10})]NiPPh_3$ (**5**).

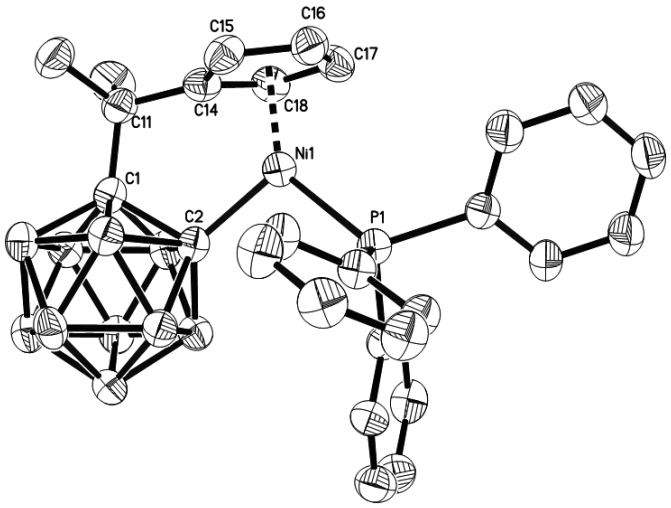
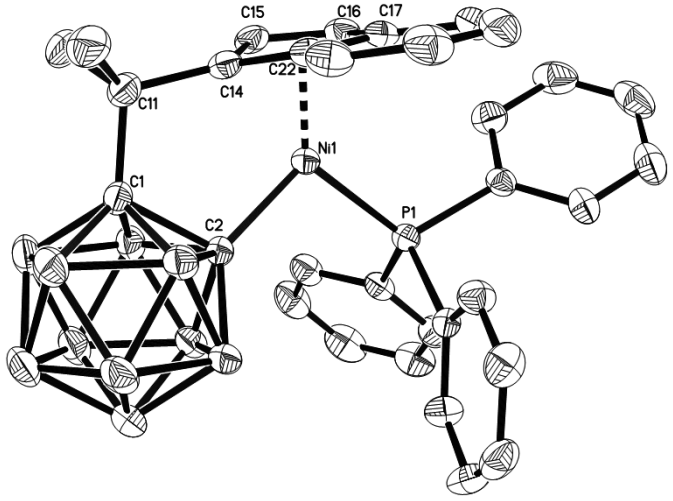


Fig. 2. Molecular structure of $[\eta^5{:}\sigma\text{-}Me_2C(C_9H_6)(C_2B_{10}H_{10})]NiPPh_3$ (**7**).



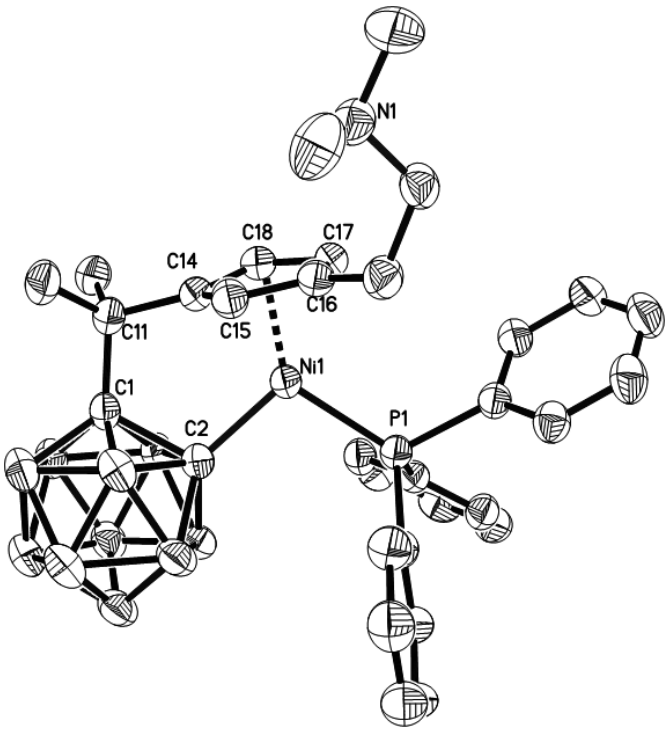
distances and angles around the metal atoms are listed in Table 1 for comparison. It is noted that the appended N atom in **8** does not substitute the P atom to form the intramolecular coordination to the Ni atom as the N atom is a harder base than the P atom.

The distances between the Co atom and the five-membered ring atoms ($Co–C_{ring}$) range from 2.028(3) to 2.126(3) Å in **4** and from 2.044(4) to 2.259(4) Å in **6**. These values are comparable to the 2.102(2) Å in $(\eta^5\text{-}C_5H_5)Co(PPh_3)[\eta^1(N)\text{-}N(O)Me]$,[6] to the 2.06(5) Å in $(\eta^5\text{-}C_5H_5)Co(S_2C_2B_{10}H_{10})$,[7] and to the 2.154(9) Å in $(\eta^5\text{-}C_9H_6)(C_3H_7)(PMe_3)_2CoI$.[8] The average $Ni–C_{ring}$ distances of 2.145(6) Å in **5**, 2.17 ± 0.01 Å in **7**, and 2.131(3) Å in **8** are very close to each other. They are also similar to the 2.102(6) Å in $[Ni(\eta^5\text{-}C_5H_5)(PPh_3)C{\equiv}CCHO]$,[9] to the 2.182(3) Å in $[(\eta^5\text{-}1\text{-}TMS\text{-}C_9H_5)NiCl(PPh_3)]$,[10] to the 2.114(7) Å in $(\eta^5{:}\eta^1\text{-}C_5H_4CH_2CH_2NMe_2)Ni(C_{12}H_8N)$,[11] and to the 2.098(9) Å in $[(\eta^5\text{-}C_5H_4CH_2CH_2NMe_2)Ni(dmpe)][PF_6]$.[12]

The metal – cage carbon distances ($M–C_{cage}$) between 1.95 and 2.01 Å for **4**–**8** are comparable to the 1.998(9)–2.013(9) Å in $[Ni\{(C_2B_{10}H_{10})_2\}_2]^{2-}$,[13] to the 2.051(12)–2.070(12) Å

Can. J. Chem. Downloaded from www.nrcresearchpress.com by Renmin University of China on 09/02/12
For personal use only.

Fig. 3. Molecular structure of [η^5:σ-$Me_2C(Me_2NCH_2CH_2C_5H_3)(C_2B_{10}H_{10})$]$NiPPh_3$ (**8**).



in $[Co\{(C_2B_{10}H_{10})_2\}_2]^{2-}$,[13] and to the 1.972(5) Å in $[\eta$:σ-$(2\text{-}C_5H_4NCH_2C_2B_{10}H_{10})]_2Ni$.[14]

The metal–phosphorus distances (M–P) in **4**–**8** fall in the range 2.19–2.25 Å. They are comparable to the 2.184(1) Å in (η^5-C_5H_5)$Co(PPh_3)[\eta^1(N)$-N(O)Me],[6] to the 2.146(1) Å in (η^5-C_9H_6)$Co(CO)(PPh_3)$,[15] to the 2.29(1)/2.20(1) Å in $(PPh_3)_2Ni(C_2B_{10}H_{10})$,[16] to the 2.211(2)/2.214(2) Å in $\{(PPh_3)_2Ni[\mu\text{-}(\eta^5\text{-}C_5H_4)CMe_2(\eta^5\text{-}C_5H_4)]Ni(PPh_3)_2\}\{PF_6\}_2$,[17] and to the 2.134(1) Å in $Cp^*Ni(PPh_3)(CH_2CO$*t*-Bu).[18]

Reactivity

The substitution reactions of **4** and **5** with various Lewis bases were examined to gain information on the lability of the PPh_3 ligand. The results showed that the PPh_3 in **4** and **5** were easily replaced by isocyanide, N-heterocyclic carbene (NHC), and other phosphines.

Treatment of **4** or **5** with 1 equiv of 2,6-dimethylphenylisocyanide at room temperature in toluene afforded, after recrystallization from Et_2O, the PPh_3 displacement products, [η^5:σ-$Me_2C(C_5H_4)(C_2B_{10}H_{10})$]$M(CNC_6H_3Me_2\text{-}2,6)$ (M = Co (**9**) or Ni (**10**)) in 77% and 59% isolated yield, respectively (Scheme 2). The reactions were monitored by ^{31}P NMR spectra. Complex **10** showed a distinct NMR spectrum from its parent complex **5**. Except for the resonances corresponding to the protons of the bridging ligand, signals in the range 6.66–6.51 ppm assignable to the aromatic protons and one singlet at 2.11 ppm attributable to the methyl protons on the phenyl ring were observed in the ^1H NMR spectrum. The characteristic resonance of the N=*C* at 162.8 ppm was observed in the ^{13}C NMR spectrum. The ^{11}B NMR spectrum showed a 1:2:3:4 pattern.

The structures of both **9** and **10** were confirmed by single-crystal X-ray analyses. They are isomorphous and isostructural with a trigonal planar geometry. The representative structure of **9** is shown in Fig. 4. The average $M–C_{ring}$ bond distances of 2.074(3)/2.099(4) Å in Co (**9**)/Ni (**10**) are comparable to those of 2.085(3)/2.145(6) Å observed in **4/5**, and the $M–C_{cage}$ bond distances of 1.922(3)/1.898(3) Å in **9/10** are slightly shorter than those of 1.989(3)/1.975(5) Å found in **4/5**. The M–C bond distances of 1.838(3)/1.790(3) Å in **9/10** compare to those of 1.87(1)/1.89(1) Å in $[Co(L_{C=O}:N_2(SO)_2)(CN$*t*-$Bu)_2]^-$,[19] to 1.772(18)/1.963(18) Å in $CoBr(PhCOCH)(CNC_6H_3Me_2\text{-}2,6)_6$,[20] to 1.787(3) Å in $Ni(triphos)(CNC_6H_3Me_2\text{-}2,6)$,[21] to 1.820(4) Å in $Ni\{S_2P(O)(OEt)\}(CNC_6H_3Me_2\text{-}2,6)(PCy_3)$,[22] and to 1.789(9)/1.789(8) Å in $[Ni(\mu\text{-}t\text{-}Bu_2As)(p\text{-tol-NC})_2]_2$.[23]

Reaction of **4** or **5** with 1 equiv of NHC (1,3-bis(2,6-diisopropylphenyl)-1,3-dihydro-2*H*-imidazol-2-ylidene) in toluene at room temperature afforded [η^5:σ-$Me_2C(C_5H_4)(C_2B_{10}H_{10})$]$M[C(2,6\text{-}i\text{-}Pr_2C_6H_3\text{–}NCH)_2]$ (M = Co (**11**) or Ni (**12**)) in 51% and 60% isolated yield, respectively (Scheme 2). The characteristic ^{13}C resonance at 163.1 ppm corresponding to the NHC carbene carbon was observed in the ^{13}C NMR spectrum of **12**. Its ^{11}B NMR spectrum showed a 2:3:5 pattern.

The structures of complexes **11** and **12** were confirmed by single-crystal X-ray analyses. They are isomorphous and isostructural. The metal atom is η^5-bound to the Cp ring, σ-bound to the cage carbon atom, and coordinated to the carbene atom in a trigonal planar geometry. The representative structure of **11** is shown in Fig. 5. The average $M–C_{ring}$/$M–C_{cage}$ bond distances of 2.143(3)/2.152(4) Å in **11** and 2.003(3)/1.945(3) Å in **12** are comparable to the corresponding values observed in **4** and **5**, respectively. The $Co–C_{NHC}$ bond distance of 2.011(2) Å in **11** is similar to that of 2.043(2)/2.019(2) Å in $[(TIMEN^{xyl})Co][BPh_4]_2$ (TIMEN = tris[2-(3-arylimidazol-2-ylidene)ethyl]amine; xyl = 2,6-dimethylphenyl))[24] and to 1.914(2) Å in (η^5-C_5H_4)$Co[C(2,6\text{-}i\text{-}Pr_2C_6H_3\text{–}NCH)_2]Me_2$.[25] The $Ni–C_{NHC}$ bond distance of 1.934(2) Å in **12** is somewhat longer than the 1.882(4) Å in $Cp[(\eta^2\text{:}\eta^2\text{-}CH_2{=}CHCH_2NCHCHNMe)]C]Ni$,[26] than the 1.886(3) Å in $(C_9H_7)[(i\text{-}PrNCH)_2C]NiCl$,[27] than the 1.888(4) Å in $(C_9H_7)[(i\text{-}PrNCH)_2C]NiBr$,[27] and than the 1.901(3) Å in $[(m\text{-}MeOC_6H_4CH_2NCHCHNCH_2CH_2PPh_2)C]_2NiCl_2$.[28]

Interaction of **5** with 1 equiv of PCy_3 (Cy = cyclohexyl) in refluxing toluene afforded [η^5:σ-$Me_2C(C_5H_4)(C_2B_{10}H_{10})$]$Ni(PCy_3)$ (**13**) in 57% isolated yield. The room-temperature reaction was very slow. An equimolar reaction of **4** with 0.5 equiv of dppe (1,2-bis(diphenylphosphino)ethane) gave $\{[\eta^5$:σ-$Me_2C(C_5H_4)(C_2B_{10}H_{10})]Co\}_2$(dppe) (**14**) in 62% isolated yield (Scheme 2). The substitution of PPh_3 in **5** by PCy_3 was confirmed by ^1H and ^{31}P NMR spectra. In addition to the resonances assignable to the protons of the bridging ligand, multiplets in the region 2.11–1.07 ppm corresponding to the cyclohexyl protons were observed in the ^1H NMR spectrum. Its ^{31}P NMR spectrum showed a singlet at 44.4 ppm compared with the 47.3 ppm in **5**.

The molecular structure of **13** is shown in Fig. 6. The Ni atom is η^5-bound to the cyclopentadienyl ring, σ-bound to one cage carbon atom, and coordinated to the P atom of the tricyclohexylphosphine in a trigonal planar geometry. The average $Ni–C_{ring}$/$Ni–C_{cage}$/Ni–P bond distances of 2.140(5)/1.949(5)/2.226(1) Å are very close to those of 2.145(6)/1.975(5)/2.210(1) Å in **5**. On the other hand, as revealed by

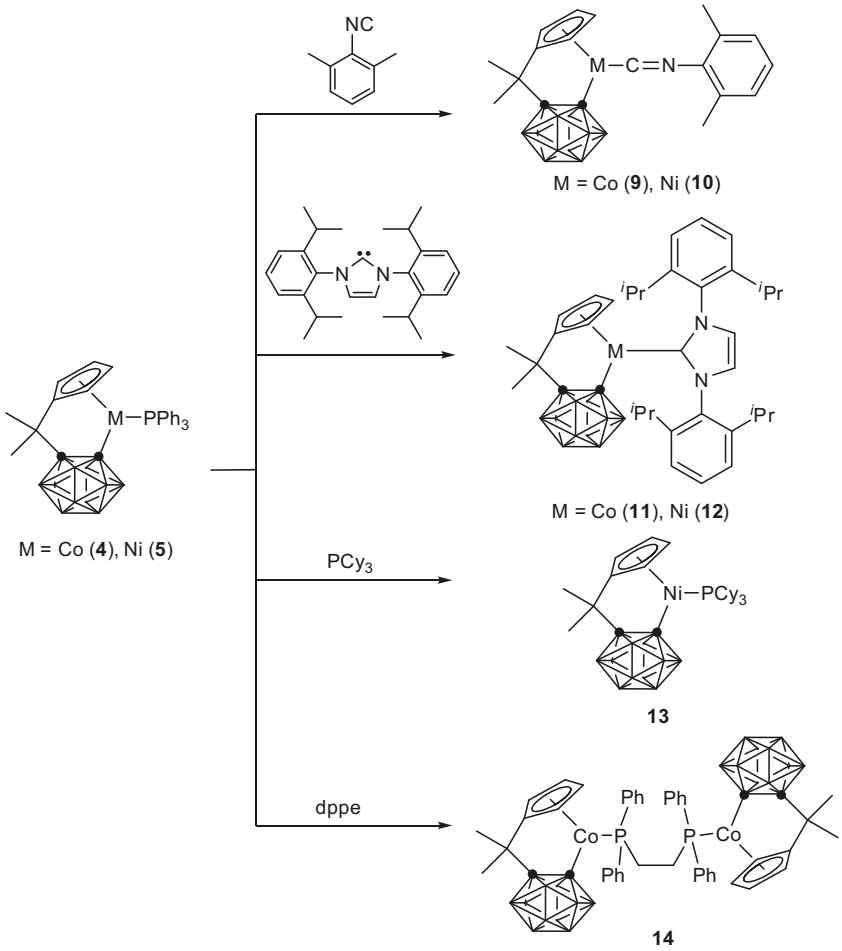
Can. J. Chem. Downloaded from www.nrcresearchpress.com by Renmin University of China on 09/02/12
For personal use only.

Table 1. Selected bond lengths (Å) and angles (°) in compounds **4**–**14**.

	Bond length (Å)				Bond angle (°)	
Compd.	M–C_{cage}	Av. M–C_{ring}	M–Cent[a]	M–X	Cent–M–C_{cage}[a]	C_{ring}–C_{bridge}–C_{cage}
4	1.989(3)	2.085(3)	1.706	2.209(1) (X = P)	122.6	113.9(2)
5	1.975(5)	2.145(6)	1.765	2.210(1) (X = P)	122.0	114.1(4)
6	2.008(5)	2.15±0.01	1.763	2.247(1) (X = P)	123.3	114.7(3)
7	1.950(3)	2.17±0.01	1.800	2.194(1) (X = P)	122.4	114.3(2)
8	1.960(2)	2.131(3)	1.752	2.188(1) (X = P)	122.0	114.4(2)
9	1.922(3)	2.074(3)	1.689	1.838(3) (X = C)	124.0	114.1(2)
10	1.898(3)	2.099(4)	1.722	1.790(3) (X = C)	123.4	114.0(2)
11	2.003(3)	2.143(3)	1.762	2.011(2) (X = C)	121.0	114.3(2)
12	1.945(3)	2.152(4)	1.786	1.934(2) (X = C)	120.5	114.2(2)
13	1.949(5)	2.140(5)	1.770	2.226(1) (X = P)	121.4	114.1(4)
14	1.951(3)	2.084(4)	1.697	2.216(1) (X = P)	123.4	114.3(2)

[a]Cent: the centroid of the five-membered ring.

Scheme 2. Reactivity of cobalt and nickel complexes.



single-crystal X-ray analyses, **14** is a dinuclear complex (shown in Fig. 7), in which two trigonal planar [η^5:σ-$Me_2C(C_5H_4)(C_2B_{10}H_{10})$]Co moieties are connected by a $Ph_2PCH_2CH_2PPh_2$ linkage resulting in the formation of a 17 e^- complex for each Co atom. The average Co–C_{ring}/Co–C_{cage}/Co–P bond distances of 2.084(4)/1.951(3)/2.216(1) Å are very similar to the 2.085(3)/1.989(3)/2.207(1) Å observed in **4**.

The aforementioned results show that the coordinated PPh_3 in complexes **4** and **5** is labile and can be replaced by Lewis bases. However, they are inert toward alkynes, nitriles, and H_2. Complexes **9** and **10** are also very thermally stable. The inertness of the M–C_{cage} σ bonds in these late transition-metal complexes can be ascribed to the steric hindrance of the icosahedral carborane cage.[1e,1f]

Conclusion

A series of cobalt and nickel complexes bearing carbon-bridged cyclopentadienyl/indenyl/$C_5H_3CH_2CH_2NMe_2$–carboranyl

Can. J. Chem. Downloaded from www.nrcresearchpress.com by Renmin University of China on 09/02/12
For personal use only.

Fig. 4. Molecular structure of $[\eta^5{:}\sigma\text{-}Me_2C(C_5H_4)(C_2B_{10}H_{10})]Co(CNC_6H_3Me_2\text{-}2,6)$ (**9**).

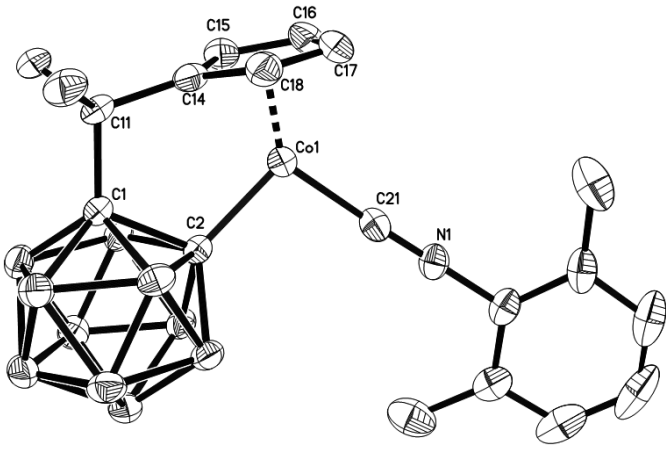
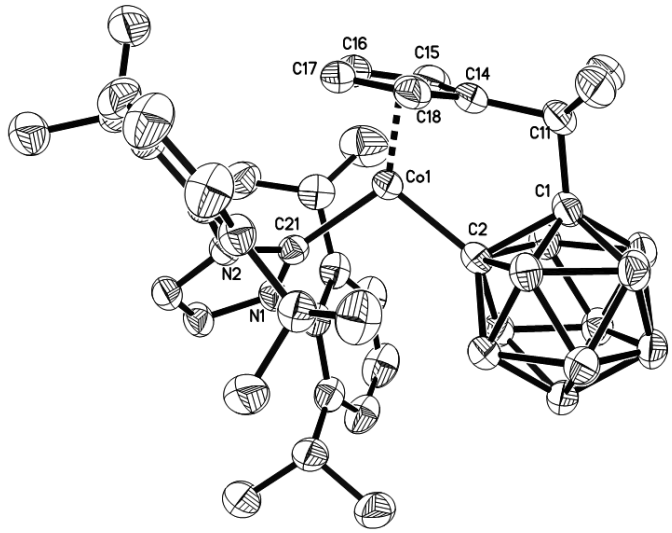


Fig. 5. Molecular structure of $[\eta^5{:}\sigma\text{-}Me_2C(C_5H_4)(C_2B_{10}H_{10})]Co[1,3\text{-}(2,6\text{-}i\text{-}Pr_2C_6H_3)_2C_3N_2H_2]$ (**11**).



ligands were synthesized via salt metathesis reactions between the dilithium salts of these ligands and metal halides. They adopt a trigonal planar geometry, leading to a 17 e– cobalt and a 18 e– nickel complex, respectively. The phosphines in $[\eta^5{:}\sigma\text{-}Me_2C(C_5H_4)(C_2B_{10}H_{10})]M(PPh_3)$ are labile and can be displaced by other Lewis bases. However, the $M–C_{cage}$ bonds in these complexes are inert toward electrophiles such as alkynes, nitriles, isonitriles, and H_2 because of the steric hindrance of the carboranyl ligand.

Experimental section

General procedures

All experiments were performed under an atmosphere of dry dinitrogen with the rigid exclusion of air and moisture using standard Schlenk or cannula techniques or in a glovebox. All organic solvents were refluxed over sodium benzophenone ketyl for several days and freshly distilled prior to use. All chemicals were purchased from either Sigma-Aldrich or Acros Chemical Co. and used as received unless otherwise noted. $Me_2NCH_2CH_2Cl$,[29] $Me_2NCH_2CH_2C_5H_3CMe_2$,[30] $Me_2C(C_5H_5)(C_2B_{10}H_{11})$,[2d] $Me_2C(C_9H_7)(C_2B_{10}H_{11})$,[2e]

Fig. 6. Molecular structure of $[\eta^5{:}\sigma\text{-}Me_2C(C_5H_4)(C_2B_{10}H_{10})]NiPCy_3$ (**13**).

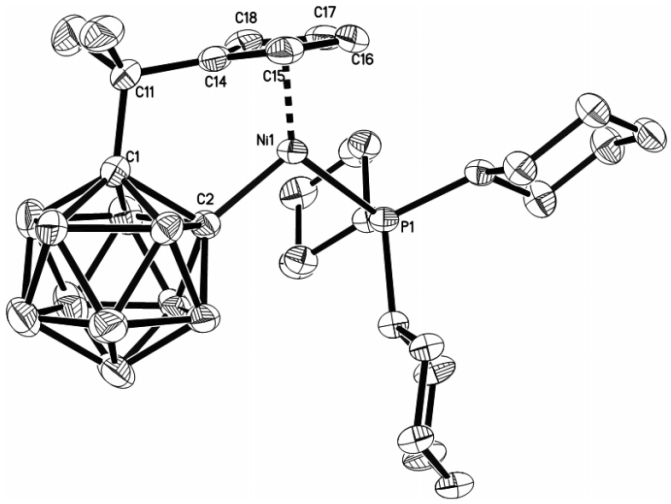
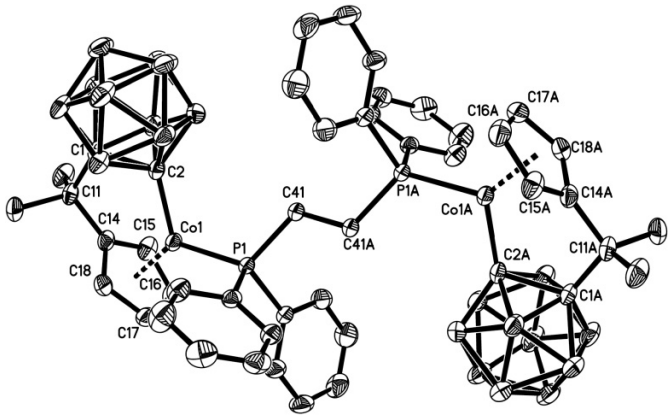


Fig. 7. Molecular structure of $\{[\eta^5{:}\sigma\text{-}Me_2C(C_5H_4)(C_2B_{10}H_{10})]Co\}_2(dppe)$ (**14**).



$NiCl_2(PPh_3)_2$,[31] and $CoCl_2(PPh_3)_2$[32] were prepared according to literature methods. Infrared spectra were obtained from KBr pellets prepared in the glovebox on a PerkinElmer 1600 Fourier transform spectrometer. ^1H and ^{13}C NMR spectra were recorded on a Bruker DPX 300 spectrometer at 300 and 75.5 MHz, respectively. ^{11}B and ^{31}P NMR spectra were recorded on a Varian Inova 400 spectrometer at 128 and 162 MHz, respectively. All chemical shifts were reported in δ units with references to the residual protons of the deuterated solvents for proton and carbon chemical shifts, to external $BF_3{\cdot}OEt_2$ (0.00 ppm) for boron chemical shifts, and to external 85% H_3PO_4 (0.00 ppm) for phosphorus chemical shifts. Elemental analyses were performed by the Shanghai Institute of Organic Chemistry, Chinese Academy of Sciences, China.

Preparation of $Me_2C(Me_2NCH_2CH_2C_5H_4)(C_2B_{10}H_{11})$ (3)

To a toluene/Et_2O (2:1) solution (15 mL) of $o\text{-}C_2B_{10}H_{12}$ (1.44 g, 10.0 mmol) was added a 1.60 mol/L solution of *n*-BuLi in hexane (12.6 mL, 20.2 mmol) at 0 °C, and the reaction mixture was warmed to room temperature and stirred for 2 h. The resulting $Li_2C_2B_{10}H_{10}$ solution was then cooled to 0 °C, to which was slowly added a solution

Can. J. Chem. Downloaded from www.nrcresearchpress.com by Renmin University of China on 09/02/12
For personal use only.

of dimethyl(dimethylaminoethyl)fulvene (2.12 g, 12.0 mmol) in a toluene/Et_2O (2:1) mixture (9 mL). The reaction mixture was maintained at 0 °C for 1 h, slowly warmed to room temperature, and then refluxed overnight. After removal of the solvent, Et_2O was added. The solution was quenched with a saturated NH_4Cl solution. The organic layer was separated and washed with water and then dried with anhydrous $MgSO_4$. After removal of the solvent by rotary evaporation, the residue was subjected to column chromatography on silica gel to give **3** as a yellow oil (2.66 g, 83%). IR (KBr, cm^{-1}) ν_{BH}: 2521 (vs). ^1H NMR ($CDCl_3$) δ: 6.25–5.70 (m, 3H) (vinylic *H*), 3.32 + 3.15 (s, 1H) (cage C*H*), 2.97 + 2.93 (s, 1H) (methylene *H* on Cp), 2.53 (m, 2H) ($CH_2CH_2N(CH_3)_2$), 2.43 (m, 2H) ($CH_2CH_2N(CH_3)_2$), 2.28 + 2.25 (s, 6H) ($CH_2CH_2N(CH_3)_2$), 1.58 + 1.50 (s, 6H) ($C(CH_3)_2$). $^{13}C\{^1H\}$ NMR ($CDCl_3$) δ: 150.1, 149.2, 133.2, 130.9, 127.1, 126.9, 126.3, 126.1 (vinylic *C*), 84.8 (cage *C*), 63.9, 63.4 ($N(CH_3)_2$), 59.5, 58.8 ($CH_2CH_2N(CH_3)_2$), 45.5, 42.9 ($CH_2CH_2N(CH_3)_2$), 44.3, 42.1 (methylene *C* on Cp), 42.1, 40.4 ($C(CH_3)_2$), 31.5, 30.8, 29.0, 28.3 ($C(CH_3)_2$). $^{11}B\{^1H\}$ NMR ($CDCl_3$): δ –3.9 (2B), –8.9 (2B), –11.3 (2B), –13.5 (4B). The ^1H and ^{13}C NMR data suggested that **3** was a mixture of isomers with the $Me_2NCH_2CH_2$ group bound to either the sp^2 or sp^3 carbon of the Cp ring.[2d]

Preparation of [η⁵:σ-Me₂C(C₅H₄)(C₂B₁₀H₁₀)]Co(PPh₃) (4)

An *n*-BuLi solution in *n*-hexane (1.60 mol/L, 1.25 mL, 2.0 mmol) was slowly added to a THF (10 mL) solution of $Me_2C(C_5H_5)(C_2B_{10}H_{11})$ (0.25 g, 1.0 mmol) at –78 °C and the mixture was warmed up to room temperature and then stirred for 3 h. The resulting solution was slowly added to a THF suspension (10 mL) of $CoCl_2(PPh_3)_2$ (0.65 g, 1.0 mmol) at room temperature, and the reaction mixture was stirred overnight. After removal of the solvent, the residue was extracted with Et_2O (2 × 25 mL). The Et_2O solution was concentrated to ~10 mL. Complex **4** was isolated as brown crystals after this solution stood at room temperature for 2 days (0.50 g, 87%). IR (KBr, cm^{-1}) ν_{BH}: 2579 (vs). Anal. calcd for $C_{28}H_{35}B_{10}CoP$ (**4**): C 59.04, H 6.19; found: C 59.08, H 6.61.

Preparation of [η⁵:σ-Me₂C(C₅H₄)(C₂B₁₀H₁₀)]Ni(PPh₃) (5)

This complex was prepared as green crystals from $Me_2C(C_5H_5)(C_2B_{10}H_{11})$ (0.25 g, 1.0 mmol), *n*-BuLi (1.60 mol/L, 1.25 mL, 2.0 mmol), and $NiCl_2(PPh_3)_2$ (0.65 g, 1.0 mmol) in THF (20 mL) using the same procedure as reported for **4**; yield: 0.53 g (93%). IR (KBr, cm^{-1}) ν_{BH}: 2581 (vs). ^1H NMR (C_6D_6) δ: 7.62 (m, 6H), 7.01 (m, 9H) (C_6H_5), 5.96 (br, 2H), 3.70 (br, 2H) (C_5H_4), 1.39 (s, 6H) ($(CH_3)_2C$). $^{13}C\{^1H\}$ NMR (C_6D_6) δ: 134.8, 134.7, 131.0, 128.9 (C_6H_5), 99.6, 88.2 (C_5H_4), 66.3 (cage *C*), 41.3 ($(CH_3)_2C$), 32.3 ($(CH_3)_2C$). $^{11}B\{^1H\}$ NMR (C_6D_6) δ: –3.5 (2B), –7.0 (3B), –9.8 (5B). $^{31}P\{^1H\}$ NMR (C_6D_6) δ: 47.3. Anal. calcd for $C_{28}H_{35}B_{10}NiP$ (**5**): C 59.07, H 6.20; found: C 58.51, H 6.25.

Preparation of [η⁵:σ-Me₂C(C₉H₆)(C₂B₁₀H₁₀)]Co(PPh₃) (6)

This complex was prepared as brown crystals from $Me_2C(C_9H_7)(C_2B_{10}H_{11})$ (0.30 g, 1.0 mmol), *n*-BuLi (1.60 mol/L, 1.25 mL, 2.0 mmol), and $CoCl_2(PPh_3)_2$ (0.65 g, 1.0 mmol) in THF (20 mL) using the same procedure as reported for **4**; yield: 0.49 g (79%). IR (KBr, cm^{-1}) ν_{BH}: 2593 (vs). Anal. calcd for $C_{32}H_{37}B_{10}CoP$ (**6**): C 62.03, H 6.02; found: C 62.30, H 6.17.

Preparation of [η⁵:σ-Me₂C(C₉H₆)(C₂B₁₀H₁₀)]Ni(PPh₃) (7)

This complex was prepared as green crystals from $Me_2C(C_9H_7)(C_2B_{10}H_{11})$ (0.30 g, 1.0 mmol), *n*-BuLi (1.60 mol/L, 1.25 mL, 2.0 mmol), and $NiCl_2(PPh_3)_2$ (0.65 g, 1.0 mmol) in THF (20 mL) using the same procedure as reported for **4**; yield: 0.43 g (69%). IR (KBr, cm^{-1}) ν_{BH}: 2581 (vs). ^1H NMR (C_6D_6) δ: 7.75 (d, J = 8.0 Hz, 1H), 6.78 (t, J = 8.0 Hz, 2H), 6.45 (d, J = 3.6 Hz, 1H), 5.13 (d, J = 8.0 Hz, 1H), 3.88 (t, J = 3.6 Hz, 1H) (C_9H_6), 7.32 (m, 6H), 6.99 (m, 9H) (C_6H_5), 1.60 (s, 3H), 1.54 (s, 3H) ($(CH_3)_2C$). $^{13}C\{^1H\}$ NMR (C_6D_6) δ: 135.0, 135.8, 134.4, 132.8, 132.7, 131.9, 130.9, 129.6, 126.6, 125.3, 123.8, 121.9, 117.3, 106.5 (C_9H_6 + C_6H_5), 64.5 (cage *C*), 44.1 ($(CH_3)_2C$), 32.3, 31.3 ($(CH_3)_2C$). $^{11}B\{^1H\}$ NMR (C_6D_6) δ: –3.2 (2B), –6.4 (3B), –9.3 (5B). $^{31}P\{^1H\}$ NMR (C_6D_6) δ: 33.8. Anal. calcd for $C_{32}H_{37}B_{10}NiP$ (**7**): C 62.05, H 6.02; found: C 62.07, H 5.80.

Preparation of [η⁵:σ-Me₂C(C₅H₃CH₂CH₂NMe₂)(C₂B₁₀H₁₀)]Ni(PPh₃) (8)

This complex was prepared as green crystals from $Me_2C(C_5H_4CH_2CH_2NMe_2)(C_2B_{10}H_{11})$ (0.32 g, 1.0 mmol), *n*-BuLi (1.60 mol/L, 1.25 mL, 2.0 mmol), and $NiCl_2(PPh_3)_2$ (0.65 g, 1.0 mmol) in THF (20 mL) using the same procedure as reported for **4**; yield: 0.40 g (63%). IR (KBr, cm^{-1}) ν_{BH}: 2587 (vs). ^1H NMR (C_6D_6) δ: 7.69 (m, 6H), 7.02 (m, 9H) (C_6H_5), 6.07 (d, J = 1.5 Hz, 1H), 5.87 (s, 1H), 3.76 (d, J = 2.4 Hz, 1H) (C_5H_3), 2.11 (m, 2H) ($CH_2CH_2NMe_2$), 1.90 (m, 2H) ($CH_2CH_2NMe_2$), 1.86 (s, 6H) ($N(CH_3)_2$), 1.45 (s, 3H), 1.40 (s, 3H) ($(CH_3)_2C$). $^{13}C\{^1H\}$ NMR (C_6D_6) δ: 135.5, 135.4, 134.8, 132.5, 132.1, 131.1, 109.8, 99.4, 97.7 (C_6H_5 + C_5H_3), 88.0 (cage *C*), 66.5 ($CH_2CH_2NMe_2$), 45.9 ($N(CH_3)_2$), 41.5 ($CH_2CH_2NMe_2$), 32.5 ($C(CH_3)_2$), 31.3, 30.7 ($C(CH_3)_2$). $^{11}B\{^1H\}$ NMR (C_6D_6) δ: –3.6 (2B), –6.8 (3B), –9.5 (5B). $^{31}P\{^1H\}$ NMR (C_6D_6) δ: 36.5. Anal. calcd for $C_{32}H_{44}B_{10}NNiP$ (**8**): C 60.01, H 6.92, N 2.19; found: C 60.35, H 6.83, N 2.06.

Preparation of [η⁵:σ-Me₂C(C₅H₄)(C₂B₁₀H₁₀)]Co(2,6-Me₂C₆H₃NC) (9)

To a toluene (5 mL) solution of [η⁵:σ-$Me_2C(C_5H_4)(C_2B_{10}H_{10})$]$Co(PPh_3)$ (**4**; 0.29 g, 0.50 mmol) was added 2,6-$Me_2C_6H_3NC$ (0.07 g, 0.50 mmol) at room temperature. The reaction mixture was stirred at room temperature overnight. After removal of the solvent, the residue was extracted with Et_2O (10 mL × 2). The combined Et_2O solutions were concentrated to ~5 mL. Complex **9** was isolated as brown crystals after this solution stood at room temperature for 1 day (0.17 g, 77%). IR (KBr, cm^{-1}) ν_{BH}: 2575 (vs). Anal. calcd for $C_{19}H_{29}B_{10}CoN$ (**9**): C 52.05, H 6.67, N 3.19; found: C 52.26, H 6.70, N 3.42.

Preparation of [η⁵:σ-Me₂C(C₅H₄)(C₂B₁₀H₁₀)]Ni(2,6-Me₂C₆H₃NC) (10)

This complex was prepared as green crystals from [η⁵:σ-$Me_2C(C_5H_4)(C_2B_{10}H_{10})$]$Ni(PPh_3)$ (**5**; 0.29 g, 0.50 mmol) and 2,6-$Me_2C_6H_3NC$ (0.07 g, 0.50 mmol) in toluene (5 mL)

Can. J. Chem. Downloaded from www.nrcresearchpress.com by Renmin University of China on 09/02/12
For personal use only.

Table 2. Crystal data and summary of data collection and refinement details for compounds **4**–**9**.

	Compound					
Parameter	**4**	**5**	**6**	**7**	**8**	**9**
Empirical formula	$C_{28}H_{35}B_{10}CoP$	$C_{28}H_{35}B_{10}NiP$	$C_{32}H_{37}B_{10}CoP$	$C_{32}H_{37}B_{10}NiP$	$C_{32}H_{44}B_{10}NNiP$	$C_{19}H_{29}B_{10}CoN$
Formula weight	569.6	569.3	619.6	619.4	640.5	438.5
Crystal size (mm)	0.50×0.40×0.10	0.50×0.30×0.20	0.50×0.40×0.10	0.50×0.40×0.40	0.40×0.30×0.20	0.40×0.30×0.30
Crystal system	Monoclinic	Monoclinic	Monoclinic	Monoclinic	Triclinic	Orthorhombic
Space group	$P2_1/c$	$P2_1/n$	$P2_1/c$	$P2_1/c$	$P(-1)$	$P2_12_12_1$
a (Å)	11.562(2)	11.720(2)	12.490(3)	12.322(2)	10.510(2)	12.585(5)
b (Å)	20.123(4)	20.529(4)	13.598(3)	13.403(2)	13.019(3)	12.826(5)
c (Å)	13.887(3)	13.938(3)	19.877(4)	19.755(3)	13.996(3)	14.284(6)
α (°)	90	90	90	90	101.90(3)	90
β (°)	114.60(3)	114.86(3)	90.00(3)	91.25(1)	106.00(3)	90
γ (°)	90	90	90	90	98.73(3)	90
V (Å^3)	2937.8(10)	3042.7(10)	3375.9(12)	3261.8(7)	1756.4(6)	2305.6(16)
Z	4	4	4	4	2	4
D_c (Mg m^{-3})	1.288	1.243	1.219	1.261	1.211	1.263
μ (mm^{-1})	0.658	0.709	0.578	0.667	0.622	0.752
Radiation (λ, Å)	Mo K (0.71073)	Mo K (0.71073)	Mo K (0.71073)	Mo K (0.71073)	Mo K (0.71073)	Mo K (0.71073)
F(000)	1180	1184	1284	1288	672	908
θ range (°)	1.9–25.6	1.9–25.4	1.6–25.0	1.6–25.0	1.5–25.5	2.0–28.0
Observed reflections	4864	4651	5388	5744	5630	5763
Parameters	361	361	397	397	406	280
R indices ($I > 2\sigma(I)$)[a]	$R_1 = 0.046$	$R_1 = 0.075$	$R_1 = 0.094$	$R_1 = 0.036$	$R_1 = 0.038$	$R_1 = 0.041$
	$wR_2 = 0.119$	$wR_2 = 0.189$	$wR_2 = 0.242$	$wR_2 = 0.085$	$wR_2 = 0.105$	$wR_2 = 0.086$
Goodness-of-fit (S)[b]	1.158	1.148	1.142	1.076	1.086	1.020

[a] $R_1 = \sum||F_0| - |F_c||/\sum|F_0|$; $wR_2 = \{\sum[w(F_0^2 - F_c^2)^2]/\sum[w(F_0^2)^2]\}^{1/2}$.

[b] $S = \{\sum[w(F_0^2 - F_c^2)^2]/(n - p)\}^{1/2}$ (n = No. of data; p = No. of parameters varied).

Published by NRC Research Press

Can. J. Chem. Downloaded from www.nrcresearchpress.com by Renmin University of China on 09/02/12
For personal use only.

Table 3. Crystal data and summary of data collection and refinement details for compounds **10**–**14**.

	Compound				
Parameter	**10**	**11**	**12**	**13**	**14**
Empirical formula	$C_{19}H_{29}B_{10}NNi$	$C_{37}H_{56}B_{10}CoN_2$	$C_{37}H_{56}B_{10}N_2Ni$	$C_{30}H_{58}B_{10}NiO_{0.5}P$	$C_{54}H_{84}B_{20}Co_2O_2P_2$
Formula weight	438.2	695.9	695.7	624.5	1161.2
Crystal size (mm)	0.50×0.40×0.30	0.50×0.40×0.40	0.50×0.40×0.30	0.30×0.20×0.10	0.40×0.30×0.20
Crystal system	Orthorhombic	Monoclinic	Monoclinic	Triclinic	Monoclinic
Space group	$P2_12_12_1$	$P2_1/n$	$P2_1/n$	$P(-1)$	$P2_1/c$
a (Å)	12.462(3)	10.585(2)	10.447(2)	10.233(2)	10.932(1)
b (Å)	12.866(3)	20.471(4)	20.103(4)	11.973(2)	16.750(2)
c (Å)	14.204(3)	19.337(4)	19.072(4)	15.377(2)	17.431(2)
α (°)	90	90	90	98.02(1)	90
β (°)	90	98.77(3)	90.86(3)	95.42(1)	103.11(1)
γ (°)	90	90	90	110.62(1)	90
V (Å^3)	2277.4(8)	4141.1(14)	3957.5(14)	1724.8(5)	3108.4(5)
Z	4	4	4	2	2
D_c (Mg m^{-3})	1.278	1.116	1.168	1.203	1.241
μ (mm^{-1})	0.859	0.442	0.519	0.631	0.625
Radiation (λ, Å)	Mo K (0.71073)	Mo K (0.71073)	Mo K (0.71073)	Mo K (0.71073)	Mo K (0.71073)
F(000)	912	1476	1480	670	1216
θ range (°)	4.0–51.2	3.0–50.6	3.0–50.0	2.7–50.0	3.4–56.0
Observed reflections	4056	6512	5968	6038	7716
Parameters	280	451	451	394	361
R indices ($I > 2\sigma(I)$)[a]	$R_1 = 0.040$	$R_1 = 0.052$	$R_1 = 0.048$	$R_1 = 0.055$	$R_1 = 0.054$
	$wR_2 = 0.110$	$wR_2 = 0.134$	$wR_2 = 0.124$	$wR_2 = 0.129$	$wR_2 = 0.129$
Goodness-of-fit (S)[b]	1.091	1.131	1.119	1.014	1.034

[a] $R_1 = \sum||F_0| - |F_c||/\sum|F_0|$; $wR_2 = \{\sum[w(F_0^2 - F_c^2)^2]/\sum[w(F_0^2)^2]\}^{1/2}$.
[b] $S = \{\sum[w(F_0^2 - F_c^2)^2]/(n-p)\}^{1/2}$ (n = No. of data; p = No. of parameters varied).

using the same procedure as reported for **9**; yield: 0.13 g (59%). IR (KBr, cm^{-1}) ν_{BH}: 2573 (vs). ^{1}H NMR (C_6D_6) δ: 6.66 (t, J = 7.8 Hz, 1H), 6.51 (d, J = 7.8 Hz, 2H) (C_6H_3), 5.65 (t, J = 2.4 Hz, 2H), 4.47 (d, J = 2.4 Hz, 2H) (C_5H_4), 2.11 (s, 6H) ((CH_3)$_2$C$_6$H$_3$), 1.29 (s, 6H) ((CH_3)$_2$C). ^{13}C{^{1}H} NMR (C_6D_6) δ: 162.7 (N=*C*), 132.8, 132.7, 132.0, 129.2 (*C*$_6$H$_3$), 98.5, 88.4 (*C*$_5$H$_4$), 32.3 ((CH$_3$)$_2$*C*), 30.6 ((*C*H$_3$)$_2$C$_6$H$_3$), 23.4 ((*C*H$_3$)$_2$C). ^{11}B{^{1}H} NMR (C_6D_6) δ: –2.03 (1B), –4.11 (2B), –6.79 (3B), –8.70 (4B). Anal. calcd for $C_{19}H_{29}B_{10}NNi$ (**10**): C 52.07, H 6.67, N 3.20; found: C 52.52, H 6.86, N 3.28.

Preparation of [η^5:σ-Me$_2$C(C$_5$H$_4$)(C$_2$B$_{10}$H$_{10}$)]Co[1,3-(2,6-*i*-Pr$_2$C$_6$H$_3$)$_2$C$_3$N$_2$H$_2$] (11)

To a toluene (5 mL) solution of [η^5:σ-Me$_2$C(C$_5$H$_4$)(C$_2$B$_{10}$H$_{10}$)]Co(PPh$_3$) (**4**; 0.29 g, 0.50 mmol) was added 1,3-(2,6-*i*-Pr$_2$C$_6$H$_3$)$_2$C$_3$N$_2$H$_2$ (0.20 g, 0.50 mmol) at room temperature, and the reaction mixture was stirred overnight. After removal of the solvent, the residue was extracted with Et$_2$O (10 mL × 2). The combined Et$_2$O solutions were concentrated to ~5 mL. Complex **11** was isolated as brown crystals after this solution stood at room temperature for 1 day (0.18 g, 51%). IR (KBr, cm^{-1}) ν_{BH}: 2570 (vs). Anal. calcd for $C_{37}H_{56}B_{10}CoN_2$ (**11**): C 63.86, H 8.11, N 4.03; found: C 63.35, H 7.67, N 4.01.

Preparation of [η^5:σ-Me$_2$C(C$_5$H$_4$)(C$_2$B$_{10}$H$_{10}$)]Ni[1,3-(2,6-*i*-Pr$_2$C$_6$H$_3$)$_2$C$_3$N$_2$H$_2$] (12)

This complex was prepared as green crystals from [η^5:σ-Me$_2$C(C$_5$H$_4$)(C$_2$B$_{10}$H$_{10}$)]Ni(PPh$_3$) (**5**; 0.29 g, 0.50 mmol) and 1,3-(2,6-*i*-Pr$_2$C$_6$H$_3$)$_2$C$_3$N$_2$H$_2$ (0.20 g, 0.50 mmol) in toluene (5 mL) using the same procedure as reported for **11**; yield: 0.21 g (60%). IR (KBr, cm^{-1}) ν_{BH}: 2573 (vs). ^{1}H NMR (C_6D_6) δ: 7.25 (m, 4H), 7.12 (m, 2H) (C_6H_3), 6.47 (s, 2H) ($C_3N_2H_2$), 5.77 (t, J = 2.4 Hz, 2H), 4.98 (d, J = 2.4 Hz, 2H) (C_5H_4), 3.66 (m, 2H), 3.09 (m, 2H) ((CH$_3$)$_2$C*H*), 1.62 (d, J = 6.6 Hz, 6H), 1.27 (d, J = 6.6 Hz, 6H), 1.01 (d, J = 6.6 Hz, 6H), 0.80 (d, J = 6.6 Hz, 6H) ((C*H*$_3$)$_2$CH), 1.24 (s, 6H) ((C*H*$_3$)$_2$C). ^{13}C{^{1}H} NMR (C_6D_6) δ: 163.1 (carbene *C* of NHC), 146.7, 144.8, 138.9, 130.8, 126.8, 125.5, 124.5, 120.6 (*C*$_6$H$_3$ + vinylic *C* of NHC), 98.6, 89.2 (*C*$_5$H$_4$), 40.5 ((CH$_3$)$_2$*C*), 30.7 ((*C*H$_3$)$_2$C), 29.4, 29.0 ((CH$_3$)$_2$*C*H), 26.1, 25.7, 23.5, 22.6 ((*C*H$_3$)$_2$CH). ^{11}B{^{1}H} NMR (C_6D_6) δ: –3.2 (2B), –6.3 (3B), –9.2 (5B). Anal. calcd for $C_{37}H_{56}B_{10}N_2Ni$ (**12**): C 63.88, H 8.11, N 4.03; found: C 63.86, H 8.19, N 4.25.

Preparation of [η^5:σ-Me$_2$C(C$_5$H$_4$)(C$_2$B$_{10}$H$_{10}$)]Ni(PCy$_3$) (13)

To a toluene (5 mL) solution of [η^5:σ-Me$_2$C(C$_5$H$_4$)(C$_2$B$_{10}$H$_{10}$)]Ni(PPh$_3$) (**5**; 0.29 g, 0.50 mmol) was added PCy$_3$ (0.14 g, 0.50 mmol) at room temperature. The reaction mixture was refluxed for 1 day. After removal of the solvent, the residue was extracted with Et$_2$O (10 mL × 2). The combined Et$_2$O solutions were concentrated to ~5 mL. Complex **13** was isolated as green crystals after this solution stood at room temperature for 1 day (0.18 g, 57%). IR (KBr, cm^{-1}) ν_{BH}: 2573 (vs). ^{1}H NMR (C_6D_6) δ: 5.94 (m, 2H), 4.23 (m, 2H) (C_5H_4), 2.11–1.07 (m, 33H) (Cy), 1.39 (s, 6H) ((C*H*$_3$)$_2$C). ^{13}C{^{1}H} NMR (C_6D_6) δ: 99.7, 90.2 (*C*$_5$H$_4$), 66.3 (cage *C*), 32.3, 31.2, 29.7, 28.1, 27.1, 23.4, 15.9 ((*C*H$_3$)$_2$*C* + P(*C*$_6$H$_{11}$)$_3$).

Can. J. Chem. Downloaded from www.nrcresearchpress.com by Renmin University of China on 09/02/12
For personal use only.

$^{11}B\{^1H\}$ NMR (C_6D_6) δ: –2.4 (5B), –6.0 (2B), –8.9 (3B). $^{31}P\{^1H\}$ NMR (C_6D_6) δ: 44.4. Anal. calcd for $C_{30}H_{58}B_{10}NiO_{0.5}P$ (**13** + $0.5Et_2O$): C 57.69, H 9.36; found: C 58.09, H 9.11.

Preparation of {[η⁵:σ-Me₂C(C₅H₄)(C₂B₁₀H₁₀)]Co}₂(dppe) (14)

This complex was prepared as brown crystals from [η⁵:σ-$Me_2C(C_5H_4)(C_2B_{10}H_{10})$]Co($PPh_3$) (**4**; 0.29 g, 0.50 mmol) and dppe (0.10 g, 0.25 mmol) in toluene (5 mL) using the same procedure as reported for **13**; yield: 0.19 g (62%). IR (KBr, cm^{-1}) ν_{BH}: 2573 (vs). Anal. calcd for $C_{46}H_{64}B_{20}Co_2P_2$ (**14** + $2Et_2O$): C 54.54, H 6.37; found: C 54.24, H 6.25.

X-ray structure determination

All single crystals were immersed in Paraton-N oil and sealed under N_2 in thin-walled glass capillaries. Data were collected at 293 K on a Bruker SMART 1000 CCD diffractometer using Mo Kα radiation. An empirical absorption correction was applied using the SADABS program.[33] All structures were solved by direct methods and subsequent Fourier difference techniques and refined anisotropically for all non-hydrogen atoms by full-matrix least-squares calculations on F^2 using the SHELXTL program package.[34] All hydrogen atoms were geometrically fixed using the riding model. Molecular structures of **13** and **14** showed the solvation of half and two Et_2O molecules, respectively. For the noncentrosymmetric structures **9** and **10**, the appropriate enantiomorph of **9** was chosen by refining Flack's parameter χ toward zero;[35] however, the appropriate enantiomorph of **10** was unable to be chosen as its $\chi \approx 0.5$ after refinement. Crystal data and details of data collection and structure refinements were given in Tables 2 and 3 (X-ray data can be found in the Supplementary data).

Supplementary data

Supplementary data are available for this article through the journal Web site at http://nrcresearchpress.com/doi/suppl/10.1139/v11-115. CCDC 823250–823260 contain the X-ray data in CIF format for this manuscript (compounds **4**–**14**). These data can be obtained, free of charge, via http://www.ccdc.cam.ac.uk/cgi-bin/catreq.cgi (Or from the Cambridge Crystallographic Data Centre, 12 Union Road, Cambridge CB2 1Ez, UK; fax +44 1223 336033; or e-mail deposit@ccdc.cam.ac.uk).

Acknowledgment

The work described in this article was supported by grants from the Research Grants Council of the Hong Kong Special Administration Region (Project No. 404609) and Direct Grant (Project No. 2060407).

References

(1) (a) For reviews, see Xie, Z. *Acc. Chem. Res.* **2003**, *36* (1), 1. doi:10.1021/ar010146i; (b) Xie, Z. *Coord. Chem. Rev.* **2002**, *231* (1–2), 23. doi:10.1016/S0010-8545(02)00112-1; (c) Xie, Z. *Coord. Chem. Rev.* **2006**, *250* (1–2), 259. doi:10.1016/j.ccr.2005.05.009; (d) Deng, L.; Xie, Z. *Coord. Chem. Rev.* **2007**, *251* (17–20), 2452. doi:10.1016/j.ccr.2007.02.009; (e) Shen, H.; Xie, Z. *Chem. Commun. (Camb.)* **2009** (18), 2431. doi:10.1039/b901549c; (f) Qiu, Z.; Xie, Z. *Sci. China Ser. B – Chem.* **2009**, *52*, 1544; (g) Hosmane, N. S.; Maguire, J. A. In *Comprehensive Organometallic Chemistry III;* Crabtree R. H.; Mingos, D. M. P., Eds.; Elsevier: Oxford, 2007; Vol. 3, Chapter 5.

(2) (a) Xie, Z.; Wang, S.; Zhou, Z.-Y.; Xue, F.; Mak, T. C. W. *Organometallics* **1998**, *17* (4), 489. doi:10.1021/om970860x; (b) Hong, E.; Kim, Y.; Do, Y. *Organometallics* **1998**, *17* (14), 2933. doi:10.1021/om9801150; (c) Xie, Z.; Wang, S.; Yang, Q.; Mak, T. C. W. *Organometallics* **1999**, *18* (13), 2420. doi:10.1021/om9809825; (d) Xie, Z.; Chui, K.; Yang, Q.; Mak, T. C. W. *Organometallics* **1999**, *18* (20), 3947. doi:10.1021/om990554e; (e) Wang, S.; Yang, Q.; Mak, T. C. W.; Xie, Z. *Organometallics* **2000**, *19* (3), 334. doi:10.1021/om990648o; (f) Zi, G.; Li, H.-W.; Xie, Z. *Organometallics* **2002**, *21* (6), 1136. doi:10.1021/om010973n; (g) Wang, H.; Li, H.-W.; Xie, Z. *Organometallics* **2003**, *22* (22), 4522. doi:10.1021/om0304255; (h) Wang, H.; Li, H.-W.; Huang, X.; Lin, Z.; Xie, Z. *Angew. Chem. Int. Ed.* **2003**, *42* (36), 4347. doi:10.1002/anie.200351892; (i) Wang, S.; Li, H.-W.; Xie, Z. *Organometallics* **2004**, *23* (10), 2469. doi:10.1021/om0498807.

(3) (a) Zi, G.; Li, H.-W.; Xie, Z. *Organometallics* **2002**, *21* (6), 1136. doi:10.1021/om010973n; (b) Zi, G.; Li, H.-W.; Xie, Z. *Organometallics* **2002**, *21* (19), 3850. doi:10.1021/om020325j; (c) Wang, H.; Wang, H.; Li, H.-W.; Xie, Z. *Organometallics* **2004**, *23* (4), 875. doi:10.1021/om034268l;; (d) Wang, H.; Chan, H.-S.; Xie, Z. *Organometallics* **2006**, *25* (10), 2569. doi:10.1021/om060082l.

(4) (a) Sun, Y.; Chan, H.-S.; Dixneuf, P. H.; Xie, Z. *Organometallics* **2004**, *23* (24), 5864. doi:10.1021/om0493816; (b) Sun, Y.; Chan, H.-S.; Dixneuf, P. H.; Xie, Z. *Chem. Commun. (Camb.)* **2004** (22), 2588. doi:10.1039/b409772f; (c) Sun, Y.; Chan, H.-S.; Xie, Z. *Organometallics* **2006**, *25* (17), 4188. doi:10.1021/om0604122; (d) Sun, Y.; Chan, H.-S.; Dixneuf, P. H.; Xie, Z. *J. Organomet. Chem.* **2006**, *691* (13), 3071. doi:10.1016/j.jorganchem.2006.03.022; (e) Sun, Y.; Chan, H.-S.; Xie, Z. *Organometallics* **2006**, *25* (14), 3447. doi:10.1021/om060249a; (f) Sun, Y.; Chan, H.-S.; Zhao, H.; Lin, Z.; Xie, Z. *Angew. Chem. Int. Ed.* **2006**, *45* (33), 5533. doi:10.1002/anie.200601650; (g) Liu, D.; Dang, L.; Sun, Y.; Chan, H.-S.; Lin, Z.; Xie, Z. *J. Am. Chem. Soc.* **2008**, *130* (47), 16103. doi:10.1021/ja8067098; (h) Qiu, Z.; Sun, Y.; Xie, Z. *Sci. China Chem.* **2010**, *53* (10), 2123. doi:10.1007/s11426-010-4111-z.

(5) Novák, P.; Pohl, R.; Kotora, M.; Hocek, M. *Org. Lett.* **2006**, *8* (10), 2051. doi:10.1021/ol060454m.

(6) O'Connor, J. M.; Bunker, K. D. *Organometallics* **2003**, *22* (25), 5268. doi:10.1021/om034083e.

(7) Kim, D.-H.; Ko, J.; Park, K.; Cho, S.; Kang, S. O. *Organometallics* **1999**, *18* (15), 2738. doi:10.1021/om990269v.

(8) Zhou, Z.; Jablonski, C.; Bridson, J. *J. Organomet. Chem.* **1993**, *461* (1–2), 215. doi:10.1016/0022-328X(93)83295-7.

(9) Gallagher, J. F.; Butler, P.; Hudson, R. D. A.; Manning, A. R. *J. Chem. Soc., Dalton Trans.* **2002** (1), 75. doi:10.1039/b104442g.

(10) Chen, Y.; Sui-Seng, C.; Boucher, S.; Zargarian, D. *Organometallics* **2005**, *24* (1), 149. doi:10.1021/om0494420.

(11) Segnitz, O.; Winter, M.; Fischer, R. A. *J. Organomet. Chem.* **2006**, *691* (22), 4733. doi:10.1016/j.jorganchem.2006.07.016.

(12) Segnitz, O.; Winter, M.; Merz, K.; Fischer, R. *Eur. J. Inorg. Chem.* **2000** *2000*, (9), 2077. doi:10.1002/1099-0682(200009)2000:9<2077::AID-EJIC2077>3.0.CO;2-P.

(13) Harwell, D. E.; McMillan, J.; Knobler, C. B.; Hawthorne, M. F. *Inorg. Chem.* **1997**, *36* (25), 5951. doi:10.1021/ic9706313.

(14) Wang, X.; Jin, G.-X. *Organometallics* **2004**, *23* (26), 6319. doi:10.1021/om0493356.
(15) Ng, S.; Goh, L.; Koh, L.; Leong, W.; Tan, G.; Ye, S.; Zhu, Y. *Eur. J. Inorg. Chem.* **2006**, *2006* (3), 663. doi:10.1002/ejic.200500785.
(16) Sayler, A. A.; Beall, H.; Sieckhaus, J. F. *J. Am. Chem. Soc.* **1973**, *95* (17), 5790. doi:10.1021/ja00798a074.
(17) Ascenso, J. R.; Dias, A. R.; Duarte, M. T.; Gomes, P. T.; Marote, J. N.; Ribeiro, A. F. G. *J. Organomet. Chem.* **2001**, *632* (1–2), 164. doi:10.1016/S0022-328X(01)00842-7.
(18) Burkhardt, E. R.; Bergman, R. G.; Heathcock, C. H. *Organometallics* **1990**, *9* (1), 30. doi:10.1021/om00115a007.
(19) Yano, T.; Wasada-Tsutsui, Y.; Arii, H.; Yamaguchi, S.; Funahashi, Y.; Ozawa, T.; Masuda, H. *Inorg. Chem.* **2007**, *46* (24), 10345. doi:10.1021/ic701107x.
(20) Yamamoto, Y.; Tanase, T.; Sugano, K. *J. Organomet. Chem.* **1995**, *486* (1–2), 21. doi:10.1016/0022-328X(94)05033-8.
(21) Hou, H.; Gantzel, P. K.; Kubiak, C. P. *Organometallics* **2003**, *22* (14), 2817. doi:10.1021/om030108y.
(22) Boíllos, E.; Miguel, D. *Organometallics* **2004**, *23* (11), 2568. doi:10.1021/om0343364.
(23) Jones, R. A.; Whittlesey, B. R. *Inorg. Chem.* **1986**, *25* (6), 852. doi:10.1021/ic00226a026.
(24) Hu, X.; Meyer, K. *J. Am. Chem. Soc.* **2004**, *126* (50), 16322. doi:10.1021/ja044271b.
(25) Simms, R. W.; Drewitt, M. J.; Baird, M. C. *Organometallics* **2002**, *21* (14), 2958. doi:10.1021/om020110+.
(26) Hahn, E. F.; Heidrich, B.; Hepp, A.; Pape, T. *J. Organomet. Chem.* **2007**, *692* (21), 4630. doi:10.1016/j.jorganchem.2007.04.025.
(27) Sun, H.; Shao, Q.; Hu, D.; Li, W.; Shen, Q.; Zhang, Y. *Organometallics* **2005**, *24* (2), 331. doi:10.1021/om049334d.
(28) Lee, C.-C.; Ke, W.-C.; Chan, K.-T.; Lai, C.-L.; Hu, C.-H.; Lee, H. M. *Chem. Eur. J.* **2007**, *13* (2), 582. doi:10.1002/chem.200600502.
(29) Dey, S.; Jain, V. K.; Chaudhury, S.; Knoedler, A.; Lissner, F.; Kaim, W. *Dalton Trans.* **2001**, 723.
(30) Müller, C.; Jutzi, P. *Synthesis* **2000**, *2000* (3), 389. doi:10.1055/s-2000-6341.
(31) Tayim, H. A.; Bouldoukian, A.; Awad, F. *J. Inorg. Nucl. Chem.* **1970**, *32* (12), 3799. doi:10.1016/0022-1902(70)80554-1.
(32) Grutters, M. M. P.; Müller, C.; Vogt, D. *J. Am. Chem. Soc.* **2006**, *128* (23), 7414. doi:10.1021/ja058095y.
(33) Sheldrick, G. M. *SADABS: Program for Empirical Absorption Correction of Area Detector Data;* University of Göttingen: Göttingen, Germany, 1996.
(34) Sheldrick, G. M. *SHELXTL 5.10 for Windows NT: Structure Determination Software Programs;* Bruker Analytical X-ray Systems, Inc.: Madison, WI, 1997.
(35) Flack, H. D. *Acta Crystallogr.* **1983**, *A39*, 876.

Can. J. Chem. Downloaded from www.nrcresearchpress.com by Renmin University of China on 09/02/12
For personal use only.

Low-temperature (293-60 K) Raman spectra of the crystalline *tert*-butylisocyanide complexes, $Cr(CO)_5$(CNBu-*t*) and *cis*-$Cr(CO)_4$(CNBu-*t*)$_2$ [1]

Honqi Li, Mirela M. Barsan, and Ian S. Butler

Can. J. Chem. Downloaded from www.nrcresearchpress.com by Renmin University of China on 09/02/12
For personal use only.

Abstract: Low-temperature (293–60 K) Raman spectra have been recorded in the 3500–50 cm^{-1} region for the crystalline *tert*-butylisocyanide (CNBu-t) complexes, $Cr(CO)_5$(CNBu-*t*) (**I**) and *cis*-$Cr(CO)_4$(CNBu-*t*)$_2$ (**II**). Several of the factor group splittings that are predicted for the ν_{CO}, ν_{CN}, ν_{CrC}, ν_{CrCN} and δ_{CrCO} modes on the basis of the $P2_1/a$ (C_{2h}^5) (**I**) and *Pccn* (D_{2h}^{10}) (**II**) crystallographic symmetries can be detected at very low temperatures. No phase transitions are observed for either complex throughout the temperature range investigated.

Key words: low-temperature Raman spectra, *tert*-butylisocyanide complexes, factor group analysis.

Résumé : Opérant à basse température (293–60 K), on a mesuré les spectres Raman dans la région de 3500–50 cm^{-1} de complexes cristallins de l'isocyanure *tert*-butyle (CNBu-*t*), soit le $Cr(CO)_5$(CNBu-*t*) (**I**) et le *cis*-$Cr(CO)_4$(CNBu-*t*)$_2$ (**II**). À des températures très basses, il est possible de détecter des dédoublements de facteur de groupe qui sont prédits sur la base des symétries cristallographiques $P2_1/a$ (C_{2h}^5) (**I**) et *Pccn* (D_{2h}^{10}) (**II**) pour les modes ν_{CO}, ν_{CN}, ν_{CrC}, ν_{CrCN} et δ_{CrCO}. Pour toute la plage de températures étudiée, il n'a pas été possible de détecter des transitions de phases pour l'un ou l'autre des complexes.

Mots-clés : spectres Raman à basse température. complexes de l'isocyanure de *tert*-butyle, analyse du facteur de groupe.

[Traduit par la Rédaction]

Introduction

Isocyanide ligands, CNR (R = alkyl or aryl), have attracted the attention of organometallic chemists for many years because of the close similarity of their bonding properties to those of the CO ligand. The pioneers in this organometallic field were Bigorgne and Bouquet,[2] whose initial isocyanide work with nickel and iron carbonyls was reported in the first volume of the *Journal of Organometallic Chemistry* in 1963. Isocyanides are considered to be better σ-donors but poorer π-acceptors than is CO, this conclusion being reached on the basis of molecular spectroscopic measurements on complexes such as the mixed carbonyl-isocyanide complexes, $Re_2(CO)_{10-n}(CNR)_n$ ($n = 1$–4)[3] and $M(CO)_{6-n}$(CNBu-*t*)$_n$ (M = Cr, Mo, W; Bu = *tert*-butyl; n = 1–3), at ambient temperature[4,5] and also under high external pressures.[6] There are now well-established procedures for the synthesis of these types of mixed carbonyl-isocyanide complexes.[7] In the cases of $Cr(CO)_5$(CNBu-*t*) (**I**) and *cis*-$Cr(CO)_4$(CNBu-*t*)$_2$ (**II**), evidence has been presented for pressure-induced, structural phase transitions occurring at about 11 and 6 kbar, respectively.[6] Since the unit cells of crystalline solids are known to contract dramatically upon compression and also with decreasing temperature, we decided it would be worthwhile investigating the low-temperature Raman spectra of these two complexes to see whether or not any related structural phase transitions would occur as the temperature was lowered. A further interest was to see if any factor group splittings could be detected in the spectra, and, if so, could these splittings be correlated to the known crystallographic space groups of the crystalline materials, i.e., complex **I** (monoclinic $P2_1/a$, C_{2h}^5)[8] and complex **II** (orthorhombic *Pccn*, D_{2h}^{10}).[9]

Experimental

Complexes **I** and **II** were prepared and purified by the literature methods.[5] All the solvents used in the syntheses were of reagent grade quality. Raman spectra were recorded at 1 cm^{-1} resolution on an Instruments S.A. U-1000 spectrometer. The 514.5 nm green line of a Spectra-Physics model 164 5-W argon-ion laser was used to excite the spectra; the power levels used were typically about 100 mW to avoid sample burning. The organometallic samples were sealed in glass capillary tubes and mounted onto the cold finger of a Displex closed-cycle helium cryostat fitted with a DE-202 expander and coupled to a HC-2D compressor for the low-temperature measurements. The temperature of the cryostat was measured and maintained with the aid of a 9650 Digital temperature

Received 29 April 2011. Accepted 25 July 2011. Published at www.nrcresearchpress.com/cjc on 22 November 2011.

H. Li, M.M. Barsan, and I.S. Butler. Department of Chemistry, McGill University, 801 Sherbrooke Street West, Montreal, QC H3A 2K6, Canada.

Corresponding author: Ian S. Butler (e-mail: ian.butler@mcgill.ca).

This article is part of a Special Issue dedicated to Professor Tak-Hang Chan.

Can. J. Chem. Downloaded from www.nrcresearchpress.com by Renmin University of China on 09/02/12
For personal use only.

Fig. 1. Variable-temperature Raman spectra of complex **I**, $Cr(CO)_5$ (CNBu-*t*), in the 2200–1900 and 500–50 cm^{-1} regions.

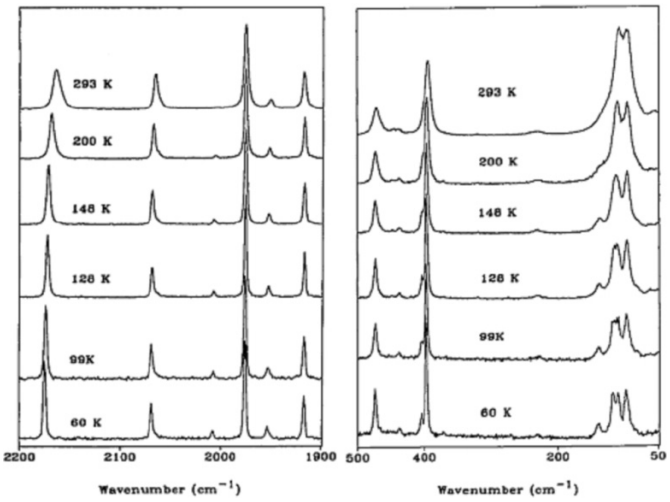
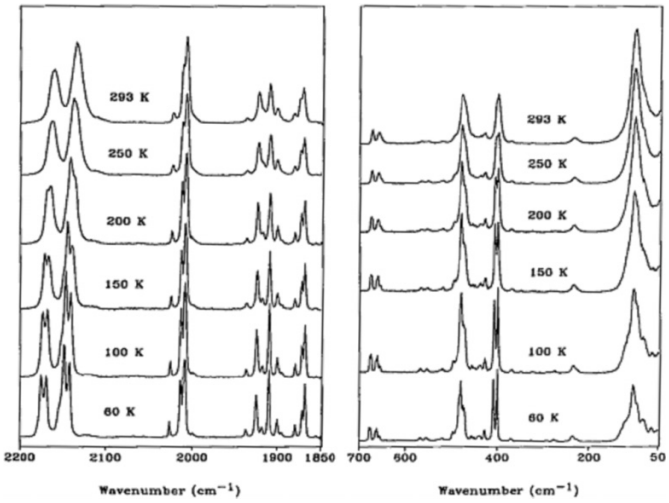


Fig. 2. Variable-temperature Raman spectra of complex **II**, $Cr(CO)_4$ (CNBu-*t*)$_2$, in the 2200–1850 and 700–50 cm^{-1} regions.



indicator–controller. Raman spectra were measured at about every 20 K in both the cooling and heating directions.

Results and discussion

The low-temperature Raman spectra of complexes **I** and **II** showed no evidence of any phase transitions down to 60 K. For the spectroscopic C_{2h}^5 space group of complex **I**,[8] the correlation between the local C_{4v} molecular, C_1 site and C_{2h} factor group symmetries indicates that the original Raman-active a_1 and b_1 modes would be expected to split into doublets, while the doubly degenerate *e* modes should give rise to quartets in the spectra. In the ν_{CN} and ν_{CO} region (2200–1800 cm^{-1}), none of the modes is split further, even at 60 K. There is one peak, however, which initially appears at 2008 cm^{-1} at ca. 220 K that gains intensity as the temperature is decreased. A similar peak appeared in the high-pressure Raman spectra at ca. 5 kbar.[6] This new peak is attributed to a combination of the a_1 ν_{CO} mode at 1917 cm^{-1} and the *e* δ_{CCrC} mode at 95 cm^{-1}. The temperature dependence of the intensity of the combination mode suggests that it is in Fermi resonance with the nearby *e* ν_{CO} fundamental at 1953 cm^{-1}.

On the basis of normal coordinate calculations for the closely related $M(CO)_6$ and $[M(CN)_6]^{3-}$ species,[10] the δ_{CrCO}, δ_{CrCN}, $\nu_{Cr\text{-}CO}$, and $\nu_{Cr\text{-}CN}$ modes of the mixed carbonyl–*tert*-butylisocyanide complexes should appear in the 700–300 cm^{-1} region. Specific vibrational assignments for this type of mixed ligand derivative are difficult because of the significant vibrational coupling that occurs. The Cr-CO and Cr-CN stretching modes are expected at lower wavenumbers than are the linear δ_{CrCO} and δ_{CrCN} bending modes. Moreover, since the Cr-CO force constants are larger than are those of Cr-CN, the δ_{CrCO} and $\nu_{Cr\text{-}CO}$ modes should appear at higher wavenumbers than do the δ_{CrCN} and $\nu_{Cr\text{-}CN}$ modes. Because of the vibrational coupling, however, substantial band overlap is almost certainly expected.

In the case of the low-energy Raman spectrum of complex **I**, the spectroscopic predictions are four $\nu_{Cr\text{-}CO}$, six δ_{CrCO}, one $\nu_{Cr\text{-}CN}$, and one δ_{CrCN} mode. A factor group analysis reveals that ten $\nu_{Cr\text{-}C(O\ and\ N)}$ and eighteen $\delta_{CrC(O\ and\ N)}$ modes would be expected in total. Twelve Raman-active bands are actually detected in the low-temperature Raman spectra of complex I. According to Farona et al.,[11] coupling between the $\nu_{Cr\text{-}CO}$, δ_{CrCO}, $\nu_{Cr\text{-}CN}$, and δ_{CrCN} vibrational modes leads to markedly reduced intensities for the $\nu_{Cr\text{-}CN}$ and δ_{CrCN} modes. The Raman pattern for complex **I** closely resembles those of the pentacarbonyl complexes, $Cr(CO)_5(CS)$ and $Mn(CO)_5X$ (X = Cl, Br, I). The four δ_{CrCO} modes are weak. In addition, two very weak peaks at ca. 372 and 438 cm^{-1}, which can only be seen clearly in the low-temperature spectra, are assigned to $\nu_{Cr\text{-}CN}$ and δ_{CrCN}, respectively. The strong b_1 $\nu_{Cr\text{-}CO}$ peak at 394 cm^{-1}, evidenced a shoulder initially at ca. 200 K, which gradually separated into a single peak at 403 cm^{-1}. This new band is attributed to a $\nu_{Cr\text{-}CO}$ mode. The two very strong bands at 96 and 107 cm^{-1} in the room temperature Raman spectrum are associated with the *e* and a_1 δ_{CCrC} modes, respectively. Another δ_{CCrC} mode (a_1) at 137 cm^{-1} is clearly resolved at 180 K, at which temperature the strong δ_{CCrC} band at 107 cm^{-1} has sharpened considerably. This latter mode is appreciably more temperature sensitive and shifts to much higher wavenumbers at lower temperatures than does the δ_{CCrC} mode at 95 cm^{-1}. At 150 K the 107 cm^{-1} mode has shifted to 113 cm^{-1}, while at 130 K it is split into two components at 111 and 115 cm^{-1}. Finally, three lattice modes become detectable at low temperatures at 82, 62 and 51 cm^{-1}, since the Rayleigh line has become much sharper (Fig. 1).

In the case of complex **II,** the observed vibrational bands obey the selection rules for C_{2v} local molecular symmetry very well in the ν_{CO} and ν_{CN} region (2200–1800 cm^{-1}). According to a factor group analysis for C_{2v} local symmetry, C_1 site symmetry, and C_{2h} crystal symmetry, each of the Raman-active ν_{CO}, $\nu_{Cr\text{-}CO}$, ν_{CN}, and $\nu_{Cr\text{-}CN}$ modes with a_1, b_1, and b_2 symmetry should split into doublets in the solid-state spectra. At ambient temperature, there is some splitting detected in the ν_{CO} bands, but none is observed for the ν_{CN} modes (Fig. 2). In the 2200–1800 cm^{-1} region, the a_1 and b_2 ν_{CN} modes begin to split into doublets at ca. 200 K, while all the ν_{CO} modes exhibit additional splitting upon lowering the temperature further. It is probable that the ν_{CN} modes do not exhibit any significant factor group splitting at ambient

Can. J. Chem. Downloaded from www.nrcresearchpress.com by Renmin University of China on 09/02/12
For personal use only.

conditions because of the large thermal motions of the *tert*-butyl groups. Methyl groups in molecular crystals are well-known to have large rotational motions even at ca. 100 K.[12] When the temperature of complex **II** is lowered or when external pressure is applied, however, the thermal motions of the *tert*-butyl group presumably become more restricted, thus obliterating the expected factor group splittings. The ν_{CN} modes are much more temperature sensitive than are the ν_{CO} modes — larger shifts to higher wavenumbers are observed upon decreasing the temperature. In the earlier high-pressure work, the ν_{CN} modes displayed much higher pressure dependences than did the ν_{CO} modes.[6] These observations reflect the changes in electron density distribution between the Cr atom and the ligands at low temperatures and high pressures.

Most vibrational modes in molecular crystals shift to higher wavenumbers when the crystal lattices and molecular bond distances shrink at lower temperatures. In our case, therefore, the CO, CN, Cr-CO, and Cr-CN force constants would be expected to increase as the temperature is lowered. However, as originally pointed out by the Adams group,[13,14] decreasing the M–CO bond distance in a metal carbonyl complex results in increased π-backbonding between the metal M and the π*-orbitals of the CO ligands. Any increase in the extent of π-backbonding will lead to a reduction in the force constants of the CO bonds. Consequently, the observed ν_{CO} band shifts are the net result of two opposing effects. In our case, the CNBu-*t* ligand is considered to be a weaker π-acceptor than is CO, so there should be less π-backbonding in the Cr–CN bonds than in the Cr–CO bonds when the Cr-ligand distances are reduced by either low temperatures or increasing pressure. The CN bond will not be weakened as much as the CO bonds. In addition, the electron-donating *tert*-butyl group, $-C(CH_3)_3$, should donate more electron density through its σ-framework to the CN ligand when the Cr–CN bond distance is being decreased as the result of the low-temperature or high-pressure effects.

In the low-energy region, two strong $\nu_{Cr\text{-}CO}$ bands at 400 and 478 cm^{-1} and a δ_{CrCO} band at 660 cm^{-1} are split into two components. Many other weak peaks, which could be assigned as ν_{CrCN} or δ_{CrCN} and modes, are clearly observed as the temperature is lowered. One strong δ_{CCrC} mode at 103 cm^{-1} also exhibits distinct components at low temperature.

In conclusion, (*i*) the low-temperature Raman spectra of complexes **I** and **II** do exhibit some of the splittings consistent with those predicted from the factor group analyses, and (*ii*) there are no phase transitions detected down to about 60 K.

Supplementary data

Supplementary tables for this article are available on the journal Web site (www.nrcresearchpress.com/doi/suppl/10.1139/v11-125).

Acknowledgement

This research was supported by operating and equipment grants from the NSERC (Canada).

References

(1) This research was presented, in part, at the XXI International Conference on Raman Spectroscopy, London, UK, August 17–22, 2008. N.B. Isocyanide ligands are also sometimes referred to in the literature as isonitriles.

(2) Bigorgne, M.; Bouquet, A. *J. Organomet. Chem.* **1963**, *1* (2), 101. doi:10.1016/S0022-328X(00)87442-2.

(3) Harvey, P. J.; Butler, I. S.; de C. Barreto, M.; Coville, N. J.; Harris, G. W. *Inorg. Chem.* **1988**, *27* (4), 639. doi:10.1021/ic00277a014.

(4) Li, H.; Butler, I. S.; Uhm, H. L. *J. Raman Spectrosc.* **1992**, *23* (8), 457. doi:10.1002/jrs.1250230806.

(5) Li, H.; Butler, I. S. *Appl. Spectrosc.* **1993**, *47* (2), 218. doi:10.1366/0003702934048244.

(6) Li, H.; Butler, I. S. *Inorg. Chem.* **1995**, *34* (5), 1193. doi:10.1021/ic00109a029.

(7) Albers, M. O.; Coville, N. J.; Uhm, H. L.; Butler, I. S. In *Syntheses: Reagents for Transition Metal Complex and Organometallic Syntheses*; R. J. Angelici, Ed.; Vol. 28; John Wiley & Sons, Inc., Hoboken, NJ. Chapter 37, 2007.

(8) The unit cell of complex **I** was determined by single-crystal X-ray diffraction: monoclinic P_{21}/a ($_{C2}^{h5}$); $Z = 4$; $a = 9.450(5)$, $b = 15.3346(4)$, $c = 9.519(23)$ Å; $\beta = 105.71(23)°$; $V = 1328.9(8)$ $Å^3$.

(9) Clegg, W.; Klingebiel, U.; Sheldrick, G. M. *Z. Naturforsch. C*, **1983**, *38b*, 260.

(10) (a) Jones, L. H. *Spectrochim. Acta [A]*, **1961**, *17*, 188; (b) Jones, L. H. *J. Chem. Phys.* **1957**, *27*, 665; (c) Waagejensen, P. *J. Mol. Struct.* **1973**, *17* (2), 377. and references cited therein. doi:10.1016/0022-2860(73)85179-8.

(11) Farona, M. F.; Grasselli, J. G.; Ross, B. L. *Spectrochim. Acta [A]*, **1983**, *23A*, 1875.

(12) Wood, K.; Tobias, D. J.; Kessler, B.; Gabel, F.; Oesterhelt, D.; Mulder, F. A.; Zaccai, G.; Weik, M. *J. Am. Chem. Soc.* **2010**, *132* (14), 4990, and refs. cited therein. doi:10.1021/ja910502g.

(13) Adams, D.; Davey, L. M.; Hatton, P. D.; Shaw, A. C. *J. Mol. Struct.* **1982**, *79*, 415. doi:10.1016/0022-2860(82)85093-X.

(14) Adams, D. M.; Ekejiuba, I. O. C. *J. Chem. Phys.* **1983**, *78* (9), 5408. doi:10.1063/1.445468.

Introduction of C(5/6) side chains onto 2-azabicyclo[2.1.1]hexanes via a 6-*anti*-bromo-5-*anti*-hydroxy derivative

Grant R. Krow, Fang Yu, Matthew Sender, Deepa Gandla, Guoliang Lin, Charles DeBrosse, and Charles W. Ross III

Can. J. Chem. Downloaded from www.nrcresearchpress.com by Renmin University of China on 09/02/12
For personal use only.

Abstract: Oxidation of the title bromoalcohol provided the strained ketone, 5-bromo-6-oxo-2-azabicyclo[2.1.1]hexane. Additions of nucleophiles to either this or the debrominated ketone have been used to introduce 5(6)-*syn*-alkyl and aryl groups, 5(6)-alkylidene linkages, and 5(6)-*anti*-alkyl and acyl substituents. Facial selectivity is for additions to the 6-bromo-5-ketone and 5-alkylidene azabicycles to occur from the face syn to the nitrogen atom. The bromine atom of the title alcohol has also been replaced by a 6-*anti*-(1-hydroxyethyl) substituent using a directed radical addition process. The stereoselective functionalization reactions expand the range of available methano-bridged pyrrolidines.

Key words: methanopyrrolidine, 6-oxo-2-azabicyclo[2.1.1]hexane, directed radical addition, facial selectivity and nucleophilic addition, strained ketone.

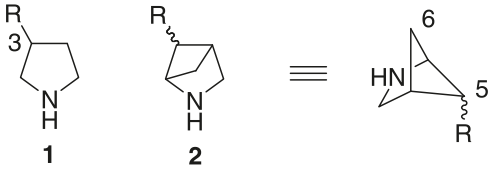
Résumé : L'oxydation du bromoalcool mentionné dans le titre conduit à une cétone tendue, le 5-bromo-6-oxo-2-azabicyclo [2.1.1]hexane. L'addition de nucléophiles aussi bien à ce produit qu'à la cétone débromée a été utilisée pour introduire des groupes 5(6)-*syn*-alkyles ou aryles, des liaisons 5(6)-alkylidènes et des substituants 5(6)-*anti*-alkyles ou acyles. La sélectivité faciale conduit à des additions sur les azabicycles avec des substituants 6-bromo et 5-cétone ou une chaîne 5-alkylidène qui se produisent par la face syn par rapport à l'atome d'azote. On a aussi remplacé l'atome de brome de l'alcool mentionné dans le titre par un substituant 6-*anti*-(1-hydroxyéthyle) en faisant appel à un processus d'addition radicalaire orienté. Les réactions de fonctionnalisations sélectives étendent la plage de pyrrolidines à pont méthano disponibles.

Mots-clés : méthanopyrrolidine, 6-oxo-2-azabicyclo[2.1.1]hexane, addition radicalaire orientée, sélectivité faciale, addition nucléophile, cétone tendue.

[Traduit par la Rédaction]

Introduction

Pyrrolidines **1** substituted with alkyl,[1,2] aryl,[3] or acyl[4] substituents at the 3-position, β to the nitrogen, are found in a number of molecules with interesting biological or structural properties. A 5-substituted 2-azabicyclo[2.1.1]hexane ring system (**2**) is a mimic of a pyrrolidine that has been constrained to exist in a single conformation in which a 2,4-methylene bridge forces the substituted C^{β} atom to be puckered out of the plane described by the other four atoms of its pyrrolidine ring. As part of a strategy to incorporate key pharmacophoric units into inflexible structures,[5] practical methods to introduce substituents in defined spatial orientations at one or both positions $C_{5(6)}$ of azabicycles such as **2** are of interest. Such molecules may prove to be valuable scaffolds for drug discovery and for incorporation into novel β-amino acids.[6]



2-Azabicyclo[2.1.1]hexanes **2** with alkyl, acyl, or aryl side chains attached at $C_{5(6)}$ are known, but effective syntheses for 5(6)-syn orientation of these groups predominate. Examples where only the C_5 bridge and the nitrogen atom have substituents are shown as follows.[7] The synthetic approaches to introduce alkyl groups include skeletal rearrangement (R = 6-*syn*-methyl, with heteroatoms in the other methylene bridge);[8] ring closure and subsequent manipulation (R = 5-*syn*-CH_2OH **3a** and R = 6-*syn*-CH_2NH_2, with a heteroatom in the 5-bridge).[9] There are photochemical cycloaddition

Received 11 March 2011. Accepted 10 July 2011. Published at www.nrcresearchpress.com/cjc on 16 November 2011.

G.R. Krow, F. Yu, M. Sender, D. Gandla, G. Lin, and C. DeBrosse. Department of Chemistry, Temple University, Philadelphia, PA 19122, USA.
C.W. Ross III. Department of Medicinal Chemistry, Merck Research Laboratories, Merck & Co., Inc., West Point, PA 19486-004, USA.

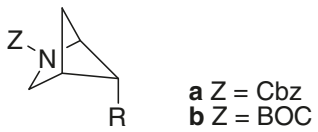
Corresponding author: Grant R. Krow (e-mail: Grkrow@temple.edu).

This article is part of a Special Issue dedicated to Professor Tak-Hang Chan.

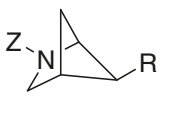
Can. J. Chem. Downloaded from www.nrcresearchpress.com by Renmin University of China on 09/02/12
For personal use only.

routes that introduce R/H = Me_2, along with a 1-aryl group;[10] R = $C(OR)_3$ or CH_2SiMe_3 along with acyl in the other methylene bridge;[11,12] and *R* = syn- or anti-oriented cyclohexane rings fused from C_5 to C_4 or cyclohexanone rings fused from C_5 to C_1.[13] Recently, alkylester **4b**, accompanied by some extended chain addition products, was prepared by methyl acrylate addition to radicals generated at C_5 from either a 5-*syn*-acid (**5b**) or 5-iodo-2-azabicyclo[2.1.1]hexane.[14] Phenyl substitution (R = 6-*syn*-Ph along with a 5-*anti*-heteroatom) was effected via a rearrangement route,[8] and also a 6:1 *syn*/*anti*-Ph mixture of **6b** and **7** were synthesized using a lead tetraacetate-initiated decarboxylative radical arylation of acid **5b**.[14] For 5-*syn*/*anti*-carbonyl substitution several photochemical syntheses introduced a 5-acetyl group[11,12,15] or 1,5-fused cyclohexanone ring systems.[16] Three routes to 5-carboxy azabicycles have been described. One somewhat lengthy route to the R = 5-*syn*-acid **5a** involves ring closure and subsequent modification of substituents.[9] A 6-acetyl-5-ester, of undefined stereochemistry, has been prepared from an azabicycle with an R = 5-*syn*-orthoester and a 6-*syn*-acetyl substituent using a photochemical ring closure sequence and subsequent synthetic modification of the orthoester.[11] We have described[17] a shorter approach to the preparation of R = 5-*syn*-**5b** and 5-*anti*-carboxy-2-azabicyclo[2.1.1]hexane (**8b**), useful for multigram quantities of the 5-*syn*-acid **5b**, from readily prepared and separable (9:1) 5-*syn*/*anti*-acetyl-2-azabicyclo[2.1.1]hexanes **9b/10** first described by Kwak and Winkler.[15] There remains a need for stereoselective synthetic routes that introduce 5-*anti*-alkyl and 5-*anti*-carboxy substituents onto 2-azabicyclo[2.1.1]hexanes.

A second synthetic challenge is the preparation of 2-azabicyclo[2.1.1]hexanes with functional groups and substituents on the same methylene bridge. There are two examples of such structures. These are the 6-*syn*-fluoro-6-*anti*-methyl-5-*anti*-alcohol **11** and the 6-*syn*-hydroxy-6-*anti*-methyl-5-*anti*-alcohol **12**.[8] There are no similar structures reported with the reversed stereochemistry at the tertiary carbon.

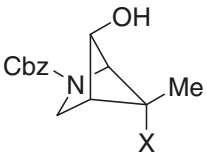


a Z = Cbz
b Z = BOC



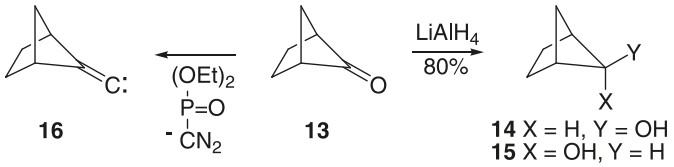
3 R = CH_2OH
4 R = $CH_2CH_2CO_2Me$
5 R = COOH
6 R = Ph
9 R = $COCH_3$

7 R = Ph
8 R = COOH
10 R = $COCH_3$



11 X = F
12 X = OH

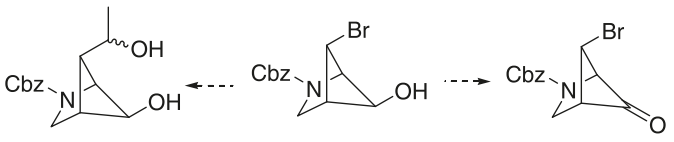
A disconnection of tertiary alcohol **12** suggested that an azabicyclic ketone might be a useful synthon for introduction of substituents at the C_5 position, although the stereochemistry of the addition to the ketone is an issue.[5a] The corresponding carbocycle (bicyclo[2.1.1]hexan-5-one **13**) has been synthesized[18] in an optimized 54% yield by alcohol oxidation,[18c] but only two nucleophilic addition reactions have been reported. Reduction of **13** gives and 82:18 exo/endo mixture of alcohols **14/15** in which the major product derives from hydride attack on the side of the ethylene bridge.[18a,18b] The only carbon nucleophile reported for reaction with ketone **13** was diethyl(diazomethyl)phosphonate; the transient alkylidene carbene **16** from this reaction does not retain evidence for the initial facial selectivity of nucleophilic attack.[19]



16 **13**

14 X = H, Y = OH
15 X = OH, Y = H

In this paper we show how a readily available pyridine-derived alcohol **17** can be oxidized to ketone **18**, and how subsequent carbonyl addition reactions provide solutions to the stereochemical problems outlined previously.[20] Stereocontrolled syntheses of tertiary alcohols with 5-*syn*-alkyl or 5-*syn*-aryl substituents, 5-*anti*-alkyl and 5-*anti*-carboxy compounds, as well as 5-*exo*-alkylidenes will be described. Additionally, we show how the bromoalcohol **17** can be used to incorporate a 6-*anti*-alkyl group onto the 2-azabicyclo [2.1.1]hexane skeleton to give diol **19** using a radical trapping process. Since 5(6)-substituents in these azabicycles are often compatible with subsequent introduction of substituents at the C_1 and C_3 positions, the functional group modifications described herein should prove useful in the preparation of more highly functionalized 5-substituted 2-azabicyclo[2.1.1]hexanes.[21]



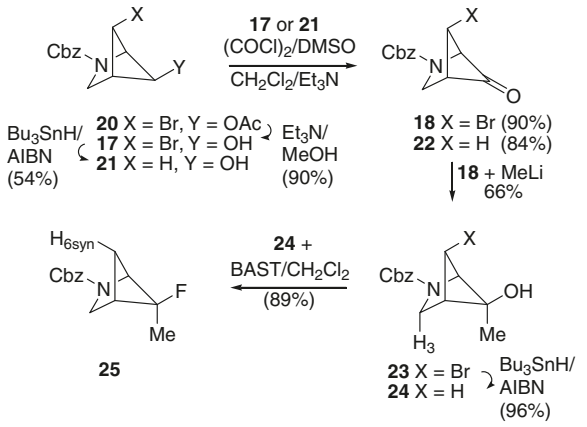
19 **17** **18**

Results and discussion

Hydrolysis of the bromoacetate **20**, prepared in three steps from pyridine,[20] afforded bromoalcohol **17** (90%), which was oxidized using Swern conditions (oxalyl chloride / DMSO / CH_2Cl_2 / Et_3N) to give the bromoketone **18** in 90% yield.[22] The ketone showed an IR carbonyl band at 1818 cm^{-1}. Debromination of bromoalcohol **17** using tributyltin hydride[23] gave alcohol **21** that was also oxidized to ketone **22** using the Swern procedure. The ketone **22** has an IR carbonyl stretch band at 1809 cm^{-1}. The parent carbocycle **13** has its carbonyl band at 1799 cm^{-1}.[18a]

Can. J. Chem. Downloaded from www.nrcresearchpress.com by Renmin University of China on 09/02/12
For personal use only.

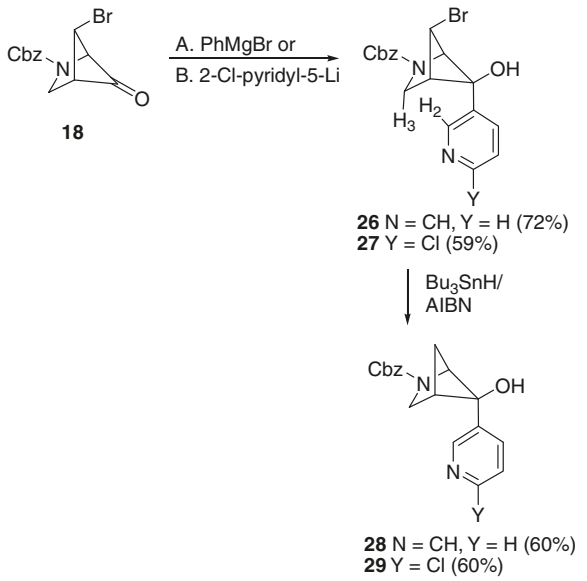
[1]



Addition of MeLi to ketone **18** afforded a single adduct **23** that was shown to have 6-*syn*-Me stereochemistry by NOE interaction of the methyl and an H_3 proton. Reductive removal of the bromine of **23** using tributyltin hydride[23] gave the alcohol **24**. Notably, the 5-*syn*-methyl and 5-*anti*-hydroxyl groups in **23** and **24** have complementary (inverted) stereochemistry relative to the tertiary alcohol **12** formed by a rearrangement pathway. The alcohol **24** was converted to the fluoride **25** by reaction with bis(2-methoxylethyl)aminosulfur trifluoride (BAST).[24] The absence of W-coupling between the 5-*anti*-fluorine atom and H_{6syn} enabled a stereochemical assignment for fluoride **25** that is consistent with precedent for retention of stereochemistry for an *anti*-alcohol displacement in this azabicyclic ring system.[25]

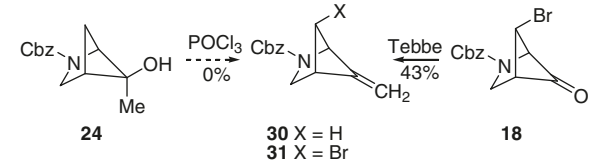
Addition of phenylmagnesium bromide or 2-chloro-pyridyl-5-lithium[26] to bromoketone **18** provided the arylalcohols **26** or **27**, respectively. The stereochemical assignment for both **26** and **27** were shown to be 6-*syn*-aryl by NOE interaction between H_2 of the respective aryl and pyridyl rings and H_3. The bromine atoms of **26** and **27** were reductively removed to give alcohols **28** and **29**; in the latter case with retention of the pyridyl chlorine atom. The syn relationship of the nitrogen atom in the attached chloropyridyl group at C_6 and the β-amino group embedded in the bicyclic ring is found also in epibatidine.[5a]

[2]



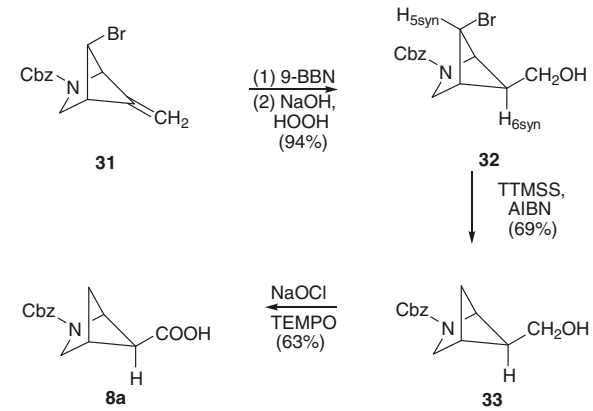
As part of an effort to prepare β-amino acids based on conformationally constrained pyrrolidines,[6] we desired a stereocontrolled synthetic route to the 5-*anti*-carboxylic acid **8b**. Toward this end, we attempted, unsuccessfully, to prepare 5-*exo*-methylene derivative **30** by dehydration of alcohol **24** using $POCl_3$/pyridine. Successful preparation of 5-*anti*-bromo-6-*exo*-methylene derivative **31** was achieved by reacting bromoketone **18** with the Tebbe reagent (48 h).[27] The Wittig reaction of bromoketone **18** with triphenylphosphonium methylide was unsuccessful as a route to 6-*exo*-methylene **31**.

[3]

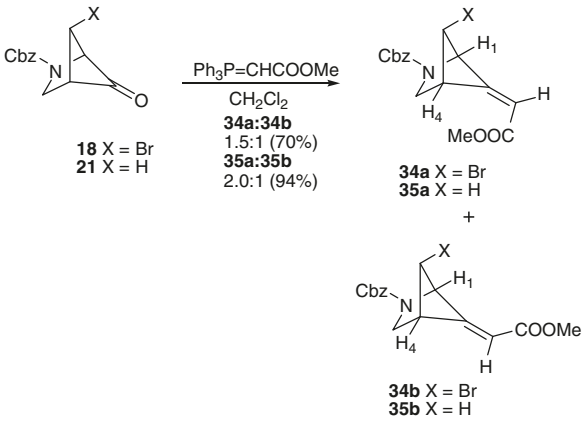


Alkene **31** was best converted to bromoalcohol **32** (94%) with 9-BBN at room temperature for 7 h, followed by basic hydrogen peroxide.[28] The 5-anti-6-anti- stereochemistry for **32** was shown by a W-plan coupling (J = 7.2 Hz) between H_{5syn} and H_{6syn}. Debromination of **32** with tris(trimethylsilyl) silane (TTMSS) gave alcohol **33** (69%)[29]; subsequent oxidation with NaOCl/TEMPO afforded the desired 5-*anti*-acid **8a**.[30]

[4]

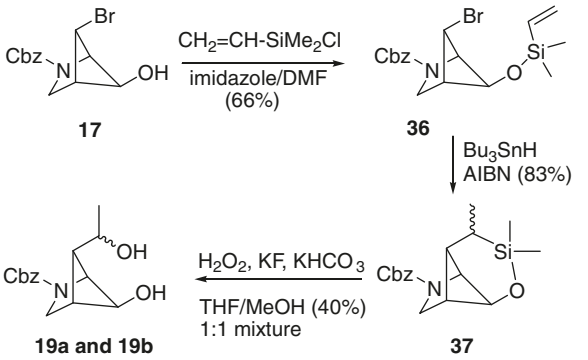


The difficulty in isolating useful product from the reaction of bromoketone **18** with $Ph_3P{=}CH_2$ was noted previously (see eq. [3]). Surprisingly, ketones **18** and **21** reacted with the conjugated ylide methyl(triphenylphosphoranylidene)acetate in CH_2Cl_2 to give mixtures of stereoisomeric esters **34a**–**34b** and **35a**–**35b**, respectively (eq. [5]).[31] This stable ylide generally reacts poorly, if at all, with ketones. The major isomers in both cases have the ester oriented toward C_4 (*E*-ester) as indicated by NOE experiments in which the vinylidene hydrogen interacts with H_1. In the minor isomer **34b**, NOE experiments indicate the vinylidene hydrogen is closer to H_4, whereas in the minor isomer **35b**, the *Z*-ester stereochemistry could not be confirmed by NOE experiments because of the overlap between H_1 and the vinylidene hydrogen.



[5]

The 5-anti-6-anti- substituents in bromoalcohol **17** are ideally situated to take advantage of an intramolecular cyclization approach to introduce a functionalized 5-*syn*-alkyl substituent by use of a silicon-containing tether.[32] Accordingly, alcohol **17** was reacted with dimethylvinylchlorosilane to afford the vinylsilyl ether **36**. The radical generated by abstraction of the bromine of **36** with tributyltin hydride (1.5 equiv) at reflux afforded tethered silyl ether **37** formed by 5-exo-cyclization (83%). Tamao oxidation of **37** gave a 1:1 mixture of alcohols **19a**–**19b** (40%), epimeric at the side-chain hydroxyl position.[33]



[6]

Conclusion

Addition reactions with bromoketone **18** and ketone **22** have been shown to extend the stereochemical diversity of alkyl-, acyl-, and aryl-substituted 2-azabicyclo[2.1.1]hexanes. It is now possible to access 2-azabicyclo[2.1.1]hexanes with 5(6)-*anti*-carboxy (or alkyl) groups and also 5(6)-*syn*-alkyl (or aryl) tertiary alcohols. Organolithium and organomagnesium carbonyl additions, as well as 9-BBN addition and catalytic hydrogenation of *exo*-alkylidines, have been shown to be stereoselective for attack from the face syn to the nitrogen-containing bridge.[34] In separate experiments the usefulness of the bromine substituent of bromoalcohol **17** for the introduction of 5-*anti*-alkyl groups by a tethering process has been demonstrated. The 5-bromine substituents in products derived from ketone **18** should prove useful in further synthetic manipulations of this azabicyclic ring system.[5a,35] The results have implications for development of bridged pyrrolidine-based pharmaceuticals and the preparation of β-amino acid oligomers with useful functionalities.

Experimental section

General procedures

Thin layer chromatography (TLC) was performed on precoated plates of silica gel GF 250–1000 μm. Column chromatography was performed on silica gel Merck grade 60 (230–400 mesh). Reagent chemicals were obtained from commercial suppliers, and reagent grade solvents were used without further purification. Both the ^{1}H and ^{13}C NMR spectra (see Supplementary data) are often complicated by the presence of carbamate conformers, and resonances are often presented as pairs. Chemical shifts are expressed in ppm relative to internal TMS (^{1}H) or solvent $CDCl_3$ (^{13}C). High-resolution mass spectra were performed at Merck Research Laboratories (West Point, Pennsylvania) using FAB ionization methods.

N-Benzyloxycarbonyl-6-*anti*-bromo-5-*anti*-hydroxy-2-azabicyclo[2.1.1]hexane (17)[20]

Triethylamine (20 mL) was added to the known[20] bromoacetate **20** (2.0 g, 5.6 mmol) in MeOH (10 mL) at room temperature (RT). The resulting mixture was stirred for 12 h. The solvent was removed, and purification of the resulting crude oil by column chromatography gave the known alcohol **17** (1.57 g, 90%) at R_f = 0.35 (2:1 hexanes/ether). ^{1}H NMR δ: 7.26 (s, 5H), 5.07 (s, 2H), 4.37 (d, J = 5.4 Hz, 1H), 4.19 (d, J = 7 Hz, 1H), 4.01 (d, J = 7.5 Hz, 1H), 3.53 (d, J = 8.8 Hz, 1H), 3.47 (d, J = 8.8 Hz, 1H), 3.5–3.4 (br, 1H), 2.92 (d, J = 7 Hz, 1H). ^{13}C NMR δ: 155.7, 136.5, 129.0, 128.7, 128.5, 85.4, 67.8, 66.4, 65.9, 52.4, 50.4, 49.7.

N-Benzyloxycarbonyl-5-*anti*-bromo-6-oxo-2-azabicyclo [2.1.1]hexane (18) — General procedure

Oxalyl chloride (360 mg, 2.76 mmol) dissolved in CH_2Cl_2 (10 mL) was placed in a 50 mL flask. The contents of the flask were cooled to –78 °C and DMSO (452 mg, 5.25 mmol) in CH_2Cl_2 (3 mL) was added dropwise over 5 min. Stirring was continued at –78 °C for 10 min followed by addition of the alcohol **17** (730 mg, 2.3 mmol) in CH_2Cl_2 (3 mL) over 10 min. The reaction mixture was stirred for 30 min, and triethylamine (1.16 g, 11.5 mmol) was added in over 10 min with stirring at –78 °C for 1 h. The cooling bath was removed and the reaction was stirred for an additional 3 h. Water (20 mL) was added at RT. After 10 min of stirring, the organic layer was separated. The aqueous layer was extracted with CH_2Cl_2 (3 × 20 mL), and the combined organic extracts were washed with brine, dried over $MgSO_4$, and filtered. The solvent was removed in vacuo. Column chromatography gave pure ketone **18** (642 mg, 90%) at R_f = 0.32 (1:1 hexanes / diethyl ether). ^{1}H NMR (500 MHz, $CDCl_3$) δ: 7.36 (m, 5H), 5.16 (s, 2H), 4.76 (d, J = 6.6 Hz, 1H, H_1), 3.90 (s, 1H, H_5), 3.77 (dd, J = 9.1, 1.4 Hz, 1H, H_3), 3.61 (dd, J = 9.0, 0.9 Hz, 1H, H_3), 3.49 (dbr, J = 6.6 Hz, 1H, H_4). ^{13}C NMR (100 MHz, $CDCl_3$) δ: 189.2 (C_6), 154.9 (C=O), 136.1, 129.1, 128.9, 128.7, 75.3 (C_1), 68.2 (CH_2Ph), 64.9 (C_4), 47.5 (C_5), 40.8 (C_3). HRMS m/z found: 310.0074; calcd for $C_{13}H_{13}{}^{79}BrNO_3$ (M + H)

Can. J. Chem. Downloaded from www.nrcresearchpress.com by Renmin University of China on 09/02/12
For personal use only.

Can. J. Chem. Downloaded from www.nrcresearchpress.com by Renmin University of China on 09/02/12
For personal use only.

310.0078; *m/z* found: 312.0053; calcd for $C_{13}H_{13}{}^{81}BrNO_3$ (M + H): 312.0058.

N-Benzyloxycarbonyl-6-*anti*-hydroxy-2-azabicyclo[2.1.1] hexane (21) — General procedure

Bromoalcohol **17** (300 mg, 0.96 mmol) dissolved in toluene (17 mL) was degassed for 30 min with argon. AIBN (16 mg, 0.96 mmol) and tristrimethylsilylsilane (0.59 mL, 1.92 mmol) were added and the reaction was heated to 100 °C for 2 h under argon.[23] The reaction was allowed to come to RT and the solvent was removed in vacuo. The resultant oil was purified by preparative silica gel TLC to yield alcohol **21** (150 mg, 67%) at $R_f = 0.38$ (1:1 ethyl acetate / hexanes). ^{1}H NMR (300 MHz, $CDCl_3$) δ: 7.39 (m, 5H), 5.19 (s, 2H), 4.26, 4.26 (2 d, J = 7.2, 7.5 Hz, 1H, H_1), 4.12 (d, J = 7.2 Hz, 1H, H_6), 3.45 (s, 2H, $2H_3$), 3.08 (br, 1H, OH), 2.97 (2 br, 1H, H_4), 2.72, 2.71 (2 d, J = 7.2, 7.2 Hz, 2H, H_{5x}), 1.68 (dd, J = 7.2, 7.2 Hz, H_{5n}). ^{13}C NMR (100 MHz, $CDCl_3$) δ: 156.2, 137.1, 128.9, 128.4, 128.2, 81.5 (C_6), 67.2 (CH_2Ph), 63.9 (C_1), 48.7 (C_3), 44.3 (C_4), 37.3 (C_6). HRMS *m/z* found: 256.0946: calcd for $C_{13}H_{15}NO_3Na$ (M + Na) *m/z*: 256.0950.

N-Benzyloxycarbonyl-5-oxo-2-azabicyclo[2.1.1]hexane (22)

According to the general procedure, oxalyl chloride (0.055 mL, 0.63 mmol) in dry CH_2Cl_2 (2 mL) was cooled to –78 °C. DMSO (0.09 mL, 1.26 mmol) was added by syringe, then stirred for 15 min. To this the alcohol **21** (74 mg, 0.32 mmol) dissolved in CH_2Cl_2 (1 mL) was added slowly over 15 min, followed by NEt_3 (0.18 mL, 1.26 mmol) over 10 min. After 15 min at –78 °C, the mixture was allowed to stir in a 0 °C bath for 2 h. The reaction was diluted with CH_2Cl_2 (6 mL) and washed with dilute HCl (3 × 3 mL, 0.1 N). Workup afforded ketone **22** as a pale yellow oil (64 mg, 84%) that remained at the origin when eluted with ether on a silica gel TLC plate. ^{1}H NMR (500 MHz, $CDCl_3$) δ: 7.37–7.30 (m, 5H), 5.16–5.14 (m, 2H, benzyl CH_2), 4.67 (d, J = 6.3 Hz, 1H, H_1), 3.62 (m, 2H, H_3), 3.30 (dd, J = 6.5, 3.2 Hz, 1H, H_4), 1.97 (dm, 1H, J = 8.9 Hz, H_{6anti}), 1.79 (bd, 1H, J = 8.9 Hz, H_{6syn}). ^{13}C NMR (126 MHz, $CDCl_3$) δ: 189.3, 155.2, 136.1, 128.5, 128.0, 69.6, 67.2, 55.8, 46.4, 29.6. HRMS *m/z* found: 232.0971; calcd for $C_{13}H_{14}NO_3$ (M + H) *m/z*: 232.0968.

N-Benzyloxycarbonyl-6-*anti*-bromo-5-*anti*-hydroxy-5-*syn*-methyl-2-azabicyclo[2.1.1]hexane (23)

MeLi (10.6 mg, 0.48 mmol) was added to cooled ether (5 mL, dry) at 0 °C with argon protection. After stirring for 5 min, bromoketone **18** (100 mg, 0.32 mmol) dissolved in ether (5 mL) was added dropwise over 10 min. Stirring was continued for 2 h. The cooling bath was removed and concd NH_4Cl (10 mL) was added at RT. The reaction mixture was stirred for an additional 5 min. The organic layer was separated, and the aqueous layer was extracted with ether (3 × 10 mL). The combined organic extracts were washed with brine, dried over $MgSO_4$, and filtered. The solvent was removed in vacuo and chromatography of the residue gave alcohol **23** (69 mg, 66%) at $R_f = 0.31$ (1:2 hexanes / diethyl ether). ^{1}H NMR (400 MHz, $CDCl_3$) δ: 7.26 (m, 5H), 5.16 (m, 2H), 4.36, 4.31 (2 d, J = 6.8 Hz, 1H, H_1), 4.01 (s, 1H, H_5), 3.62, 3.61 (2 s, 1H, OH), 3.53 (d, J = 9.2 Hz, 1H, H_3), 3.48 (d, J = 9.2 Hz, 1H, H_3), 2.83 (d, J = 6.8 Hz, 1H, H_4), 1.24, 1,21 (2 s, 3H, CH_3). ^{13}C NMR (100 MHz, $CDCl_3$) δ: 155.7, 136.4, 128.8, 128.5, 128.4, 128.2, 127.9, 86.9, 86.7 (C_6), 68.0, 67.8 (C_1), 67.4, 67.2 (CH_2Ph), 52.3 (C_3), 50.6, 50.3 (C_4), 49.2, 49.0 (C_5), 20.3 (CH_3). HRMS *m/z* found: 348.0203; calcd for $C_{14}H_{16}{}^{79}BrNNaO_3$ (M + Na): 348.0211; *m/z* found: 350.0185; calcd for $C_{14}H_{16}{}^{81}BrNNaO_3$ (M + Na): 350.0191. The stereochemistry at C_6 was confirmed by an NOE experiment that showed a Me/H_3 interaction.

N-Benzyloxycarbonyl-5-*anti*-hydroxy-5-*syn*-methyl-2-azabicyclo[2.1.1]hexane (24)

Following the general procedure, AIBN (12 mg, 0.07 mmol) was added to the bromoalcohol **23** (480 mg, 1.47 mmol) in benzene (20 mL) with argon protection. The resulting mixture was refluxed for 5 min, and Bu_3SnH (595 μL, 2.20 mmol) was added by syringe. The reaction was refluxed for an additional 10 h. The solvent was removed in vacuo and column chromatography of the residue gave alcohol **24** (350 mg, 96%) at $R_f = 0.18$ (1:2 hexanes / diethyl ether). ^{1}H NMR (400 MHz, $CDCl_3$) δ: 7.36 (m, 5H), 5.16 (s, 2H), 4.18, 4.15 (2 d, J = 6.8 Hz, 1H, H_1), 3.37 (d, J = 9.2 Hz, 1H, H_3), 3.34 (d, J = 9.2 Hz, 1H, H_3), 2.85 (d, J = 7.2 Hz, 1H, H_6), 2.55 (br, 1H, H_4), 2.42 (br, 1H, OH), 1.43 (d, J = 7.2 Hz, 1H, H_6), 1.17 (s, 3H, Me). ^{13}C NMR (100 MHz, $CDCl_3$) δ: 156.5, 155.9 (C=O), 137.0, 128.6, 128.1, 128.0, 83.8, 83.5 (C_5), 67.0, 66.9 (CH_2Ph), 65.9, 65.4 (C_1), 48.5 (C_3), 46.5 (C_4), 36.2, 36.0 (C_6), 19.1. HRMS *m/z* found: 248.1285; calcd for $C_{14}H_{18}NO_3$ (M + H): 248.1281; *m/z* found: 270.1090; calcd for $C_{14}H_{17}NNaO_3$ (M + Na): 270.1100.

N-Benzyloxycarbonyl-5-*anti*-fluoro-5-*syn*-methyl-2-azabicyclo[2.1.1]hexane (25)

A 50 wt % BAST solution in THF (299 μL, 0.8 mmol) was added dropwise to a solution of tertiary alcohol **24** (100 mg, 0.4 mmol) in CH_2Cl_2 (20 mL) at RT. The solution was stirred for 16 h. The solvent was removed in vacuo and column chromatography of the residue gave the fluoride **25** (90 mg, 89%) at $R_f = 0.44$ (1:1 hexanes / diethyl ether). ^{1}H NMR (300 MHz, $CDCl_3$) δ: 7.34 (m, 5H), 5.17 (s, 2H), 4.34. 4.30 (2 d, J = 7.2 Hz, 1H, H_1), 3.42 (d, J = 9.3 Hz, 1H, H_3), 3.34 (d, J = 9.3 Hz, 1H, H_3), 2.77 (br, 2H, H_4 and H_6), 1.56, 1.53 (2 d, J = 7.8 Hz, 1H, H_6), 1.30, 1.28 (2 d, J = 22.2 Hz, 3H, Me). ^{13}C NMR (100 MHz, $CDCl_3$) δ: 156.6, 156.0 (C=O), 137.1, 128.9, 128.8, 128.7, 128.6, 128.5, 128.3, 105.4, 103.4 (C_5), 67.4 (CH_2Ph), 64.8, 64.5, 64.2, 64.0 (C_1), 48.3 (C_3), 46.3, 46.2, 46.0 (C_4), 35.7, 35.6 (C_6), 15.9, 15.6 (CH_3). HRMS *m/z* found: 250.1233; calcd for $C_{14}H_{17}FNO_2$ (M + H): 250.1238.

N-Benzyloxycarbonyl-5-*anti*-bromo-6-*anti*-hydroxy-6-*syn*-phenyl-2-azabicyclo-[2.1.1]hexane (26)

Anhydrous diethyl ether (3 mL, dry) was added to bromoketone **18** (100 mg, 0.32 mmol) at 0 °C with argon protection. PhMgBr (87 mg, 0.48 mmol) was added to the mixture over 5 min. After stirring for 1 h, the cooling bath was removed and concd NH_4Cl (5 mL) was added at RT. The organic layer was separated, and the aqueous layer was extracted with diethyl ether (3 × 10 mL). The combined ether layers were dried over $MgSO_4$ and then filtered. Solvent

Can. J. Chem. Downloaded from www.nrcresearchpress.com by Renmin University of China on 09/02/12
For personal use only.

removal in vacuo and column chromatography of the residue gave pure bromide **26** (90 mg, 72%) at R_f = 0.45 (1:2 hexanes / diethyl ether). ^{1}H NMR (400 MHz, $CDCl_3$) δ: 7.33~6.96 (m, 10H, H on Ph), 5.09, 4.94, 4.93, 4.84 (4 d, J = 12.4, 12.4, 12.8, 12.8 Hz, 2H, CH_2Ph), 4.78, 4.74 (2 d, J = 7.2 Hz, 1H, H_1), 4.07, 4.05 (2 s, 1H, H_5), 3.40, 3.38 (2 br, 1H, OH), 3.33 (d, J = 9.2 Hz, 1H, H_3), 3.22, 3.21 (2 d, J = 7.2 Hz, 1H, H_4), 2.98 (d, J = 9.2 Hz, 1H, H_3). ^{1}H NMR (400 MHz, $CDCl_3$, 60 °C) δ: 7.21 (m, 5H), 5.11~4.86 (m, 2H), 4.78, 4.74 (2 d, J = 7.0, 7.1 Hz, 1H, H_1), 4.09 (s, 1H, H_5), 3.44, 3.42 (2 br, 1H, OH), 3.38 (d, J = 9.0 Hz, 1H, H_3), 3.24, 3.22 (2 d, J = 7.2 Hz, 1H, H_4), 3.03 (d, J = 9.0 Hz, 1H, H_3). ^{13}C NMR (100 MHz, $CDCl_3$) δ: 154.5, 154.4 (C=O), 140.1, 140.0, 136.6, 136.5, 129.2, 129.0, 128.7, 128.6, 128.5, 128.4, 128.2, 127.7, 125.9, 125.7 (C on Ph), 89.7, 89.5 (C_6), 67.6, 67.0 (CH_2Ph), 66.6, 65.9 (C_1), 51.7, 51.4 (C_4), 49.2, 49.0 (C_5), 48.9, 48.7 (C_3). HRMS *m/z* found: 388.0565; calcd for $C_{19}H_{19}{}^{79}BrNO_3$ (M + H): 388.0543.

N-Benzyloxycarbonyl-5-*anti*-bromo-6-*syn*-(6-chloro-3-pyridyl)-6-*anti*-hydroxy-2-azabicyclo[2.1.1]hexane (27)

At –78 °C, *n*-butyllithium in hexane (1.6 mol/L) (0.40 mL, 0.65 mmol) was added dropwise to a solution of 2-chloro-5-iodopyridine (0.155 g, 0.65 mmol) in dry THF (10 mL). The reaction was stirred for 30 min at –78 °C, whereupon the ketone **18** (0.200 g, 0.65 mmol) in dry THF (10 mL) was added slowly. The reaction was stirred at –78 °C for 0.5 h followed by 2 h at RT. The reaction was quenched with sat. aq ammonium chloride (10 mL), diluted with water (10 mL), and extracted with EtOAc (3 × 30 mL). The combined organic layers were washed with water, dried, and solvent was evaporated in vacuo to give the crude product. Column chromatography on silica gel, eluting with 1:1 hexanes / diethyl ether, gave the alcohol **27** (160 mg, 59%) at R_f = 0.27 (1:2 hexanes / diethyl ether). ^{1}H NMR (400 MHz, $CDCl_3$) δ: 8.11, 8.08 (2 br, 1H, H_2'), 7.30 (m, 5H), 7.04 (m, 2H, H_4' and H_5'), 4.95 (3 d, J = 12.0, 12.4, 12.8 Hz, 2H, CH_2Ph), 4.76 (br, 1H, H_1), 4.29 (br, 1H, OH), 4.08 (s, 1H, H_5), 3.40 (d, J = 9.2 Hz, 1H, H_{3n}), 3.25 (br, 1H, H_4), 2.88 (d, J = 9.2 Hz, 1H, H_{3x}). ^{13}C NMR (100 MHz, $CDCl_3$) δ: 154.6 (C=O), 151.4, 148.1, 137.2, 136.9, 136.3, 134.7, 129.2, 129.0, 128.7, 128.2, 125.9, 124.8, 87.6 (C_6), 68.1, 67.6 (CH_2Ph), 66.6, 65.9 (C_1), 52.0, 51.7 (C_4), 49.2 (C_3), 49.1, 48.7 (C_5). HRMS *m/z* found: 423.0105; calcd for $C_{18}H_{17}{}^{79}Br{}^{35}ClN_2O_3$ (MH): 423.0106.

N-Benzyloxycarbonyl-5-*anti*-hydroxy-5-*syn*-phenyl-2-azabicyclo[2.1.1]hexane (28)

Following the general procedure, AIBN (18 mg, 0.05 equiv) was added to the bromoalcohol **26** (0.84 g, 2.16 mmol) in benzene (25 mL) with argon protection. The resulting mixture was refluxed for 5 min and Bu_3SnH (0.87 mL, 1.5 equiv) was added. The reaction was refluxed for an additional 10 h. Workup and column chromatography gave the alcohol **28** (400 mg, 60%) at R_f = 0.32 (1:2 hexanes / diethyl ether). ^{1}H NMR (400 MHz, $CDCl_3$) δ: = 7.27~6.91 (m, 10H), 5.00, 4.87, 4.86, 4.74 (4 d, J = 12.8 Hz, 2H, CH_2Ph), 4.51 (multiple d, J = 7.2 Hz, 1H, H_1), 3.19 (br, 1H, OH), 3.13, 3.10 (2 d, J = 8.8 Hz, 1H, H_3), 2.89~2.80 (m, 3H, H_3, H_4, and H_6), 1.43 (d, J = 7.2 Hz, 1H, H_6). ^{13}C NMR (100 MHz, $CDCl_3$) δ: 155.4, 155.3 (C=O), 140.1, 137.3, 137.2, 129.1, 128.9, 128.7, 128.5, 128.4, 128.3, 128.0, 127.6, 126.5, 126.3, 87.3, 87.1 (C_6), 67.1, 66.5 (CH_2Ph), 64.4, 63.8 (C_1), 48.3, 48.1 (C_3), 46.1, 45.8 (C_4), 35.5, 35.3 (C_5). HRMS *m/z* found: 332.1251; calcd for $C_{19}H_{19}NNaO_3$ (M + Na): 332.1257.

N-Benzyloxycarbonyl-5-*syn*-(6-chloro-3-pyridyl)-5-*anti*-hydroxy-2-azabicyclo[2.1.1]hexane (29)

Following the general procedure, AIBN (2 mg, 0.05 equiv) was added to bromoalcohol **27** (0.130 g, 0.31 mmol) in 15 mL benzene with argon protection and Bu_3SnH (0.124 mL, 0.46 mmol) was added. After 10 h reflux, workup and column chromatography gave the alcohol **29** (60 mg, 60%) at R_f = 0.13 (1:2 hexanes / diethyl ether). ^{1}H NMR (400 MHz, $CDCl_3$) δ: 8.03, 7.99 (2 s, 1H, H_2'), 7.29 (m, 5H), 7.02 (m, 2H, H_4' and H_5'), 5.02, 4.95, 4.82 (3 d, J = 12.0, 12.0, 12.8 Hz, 2H, CH_2Ph), 4.58, 4.56 (2 d, J = 7.2 Hz, 1H, H_1), 3.60~3.00 (br, 1H, OH), 3.25, 3.24 (2 d, J = 9.2 Hz, 1H, H_{3n}), 2.98 (m, 2H, H_4 and H_6), 2.76 (d, J = 9.2 Hz, 1H, H_{3x}), 1.55 (d, J = 7.2 Hz, 1H, H_6). ^{13}C NMR (100 MHz, $CDCl_3$) δ: 155.3 (C=O), 151.2, 148.3, 148.1, 137.6, 137.4, 136.9, 134.8, 129.0, 128.6, 128.4, 127.9, 124.7, 84.8, 84.7 (C_5), 67.4, 66.9 (CH_2Ph), 64.4, 63.7 (C_1), 48.1, 47.9 (C_3), 46.4, 46.0 (C_4), 36.1, 35.8 (C_6). HRMS *m/z* found: 345.0989; calcd for $C_{18}H_{18}{}^{35}ClN_2O_3$ (MH): 345.1001. The stereochemistry on C_5 was confirmed by NOE. When $H_{2'}$ was irradiated, the signals of H_1, H_4, and H_{3x} were increased.

Attempted dehydration of alcohol 24 to give olefin 30

The tertiary alcohol **24** (200 mg, 0.6 mmol) in pyridine (5 mL) was placed in a 50 mL flask. To this stirred solution, phosphorus oxychloride (270 μL) was added at 0–5 °C, and the mixture was stirred for 14 h at RT. The reaction mixture was diluted with diethyl ether (10 mL) and slowly quenched with water (10 mL) to hydrolyze the excess phosphorus oxychloride. The layers were separated and the aqueous layer was extracted with diethyl ether (3 × 10 mL). The combined organic layers were washed with brine, dried over $MgSO_4$, and filtered. Solvent removal gave only 10 mg of crude oil that did not contain the desired alkene **30**.

N-Benzyloxycarbonyl-5-*anti*-bromo-6-methylene-2-azabicyclo[2.1.1]hexane (31)

To a solution of ketone **18** (1.26 mmol, 390 mg) in dry THF (15 mL) at 0 °C was added a toluene solution of the Tebbe reagent (2.52 mL of 0.5 mol/L solution, 1.26 mmol).[27] The mixture was allowed to warm to RT and stirred for 2 days, whereupon Et_2O (20 mL) was added followed slowly followed by 5 drops of aq NaOH (0.1 mol/L). After gas evolution ceased, the mixture was dried (Na_2SO_4) and filtered using a Celite pad. The solvent was removed in vacuo and purification of the residue by chromatography on silica gel (4:1 hexanes / diethyl ether) gave the bromoalkene **31** (165 mg, 43%) at R_f = 0.41 (1:1 hexanes / diethyl ether). ^{1}H NMR (400 MHz, $CDCl_3$) δ: 7.27 (m, 5H), 5.08 (s, 2H), 4.87 (br, 1H, $=CH_2$), 4.81 (s, 1H, $=CH_2$), 4.57 (br, 1H, H_1), 3.85 (s, 1H, H_5), 3.53 (d, J = 8.5 Hz, 1H, H_3), 3.42 (d, J = 8.5 Hz, 1H, H_3), 3.19 (d, J = 6.4 Hz, 1H, H_4). ^{13}C NMR (100 MHz, $CDCl_3$) δ: 155.7 (C=O), 148.5 (C_6), 136.7,

Can. J. Chem. Downloaded from www.nrcresearchpress.com by Renmin University of China on 09/02/12
For personal use only.

128.9, 128.8, 128.7, 128.5, 128.4 (Ph), 100.9 (=CH_2), 69.4 (C_1), 67.6, 67.4 (CH_2Ph), 54.5 (C_4), 50.2 (C_6), 49.6 (C_3). HRMS *m/z* found: 330.0094 (^{79}Br), 332.0070 (^{81}Br); calcd for $C_{14}H_{14}BrNO_2Na$ (MNa): 330.0100 (^{79}Br), 332.0080 (^{81}Br).

Wittig reaction of ketone 18 — Attempted synthesis of alkene 31

To a suspension of $CH_3{}^+PPh_3Br^-$ (77 mg, 0.22 mmol) in dry THF (1.1 mL) at –78 °C was added *n*-BuLi (135 μL, 0.215 mmol, 1.6 mol/L) by syringe, resulting in the appearance of a bright yellow color. After 30 min at –78 °C, ketone **18** (63 mg, 0.20 mmol) in dry THF (1.01 mL) was added slowly and allowed to rise to RT overnight. The reaction was quenched with water, and the solvent was removed in vacuo. The mixture was taken up in CH_2Cl_2 (6 mL) and washed with water (3 × 2 mL) and once with brine (1 × 2 mL). The solvent was removed in vacuo, and the resultant oil was purified by preparative TLC (4:1 hexanes/ether). Eight UV active bands were collected as fractions (63 mg total). No fraction corresponded to either starting material or the desired alkene **31**.

***N*-Benzyloxycarbonyl-5-*anti*-bromo-6-*anti*-(hydroxymethyl)-2-azabicyclo[2.1.1]-hexane (32)**

To a stirred solution of olefin **31** (150 mg, 0.49 mmol) in THF (10 mL) at 0 °C under an argon atmosphere was added 9-BBN (2.94 mL, 1.47 mmol, 0.5 mol/L solution in hexane). After the solution was stirred at RT for 7 h, 6 mol/L NaOH (1.3 mL) and 30% H_2O_2 (1.3 mL) were added at 0 °C. After stirring at RT overnight, the reaction mixture was diluted with water and extracted with diethyl ether (3 × 15 mL). The organic phase was washed with water, dried over Na_2SO_4, and concentrated under reduced pressure. Column chromatography of the residue (2:3 hexanes / diethyl ether) gave the alcohol **32** (150 mg, 94%) at R_f = 0.27 (1:1 hexanes / ethyl acetate). ^{1}H NMR (400 MHz, $CDCl_3$) δ: 7.36 (m, 5H), 5.16 (s, 2H), 4.54 (d, *J* = 7.2 Hz, 1H, H_1), 4,51 (d, *J* = 7.2 Hz, 2H, OCH_2), 3.96 (d, *J* = 7.2 Hz, 1H, H_{5syn}), 3.61 (d, *J* = 8.8 Hz, 1H, H_3), 3.54 (d, *J* = 8.8 Hz, 1H, H_3), 3.06 (d, *J* = 7.2 Hz, 1H, H_4), 2.44 (td, *J* = 7.2, 7.2 Hz, 1H, H_{6syn}), 2.00 (2 br, 1H, OH). ^{13}C NMR (100 MHz, $CDCl_3$) δ: 155.6 (C=O), 136.7, 128.9, 128.7, 128.5, 128.3, 67.5 (OCH_2), 65.3, 64.8 (C_1), 61.4 (CH_2Ph), 58.8 (C_3), 53.5 (C_5), 52.3 (C_4), 47.0 (C_6). HRMS *m/z* found: 326.0382; calcd for $C_{14}H_{17}{}^{79}BrNO_3$ (M + H): 326.0387.

***N*-Benzyloxycarbonyl-5-*anti*-(hydroxymethyl)-2-azabicyclo [2.1.1]hexane-2-carboxylate (33)**

To a toluene (15 mL) solution of bromide **32** (250 mg, 0.77 mmol) was added TTMSS (1.18 mL, 3.83 mmol) and a catalytic amount of AIBN. The resulting solution was refluxed under argon for 12 h until no starting material remained. The solvent was removed and purification of the residue by silica gel flash column chromatography gave alcohol **33** (130 mg, 69%) at R_f = 0.13 (1:1 hexanes / ethyl acetate). ^{1}H NMR (400 MHz, $CDCl_3$) δ: 7.34 (m, 5H), 5.16 (s, 2H, CH_2Ph), 4.35 (d, *J* = 7.2 Hz, 1H, H_1), 3.89 (d, *J* = 7.6 Hz, 2H, OCH_2), 3.46 (d, *J* = 8.4 Hz, 1H, H_3), 3.42 (d, *J* = 8.4 Hz, 1H, H_3), 2.74, 2.73 (2 d, *J* = 7.2 Hz, 1H, H_4), 2.41 (d, *J* = 8.0 Hz, 1H, H_6), 2.15 (td, *J* = 7.6, 7.6 Hz, H_5), 1.73 (br, 1H, OH), 1.51 (dd, *J* = 8.0, 7.6 Hz, 1H, H_6). ^{13}C NMR (100 MHz, $CDCl_3$) δ: 156.1, 137.1, 128.7, 128.5, 128.3, 128.1, 127.9, 66.9 (OCH_2), 61.7, 61.2 (C_1), 61.0 (CH_2Ph), 56.6 (C_3), 50.9 (C_5), 39.7 (C4), 38.0 (C_6). HRMS *m/z* found: 248.1274; calcd for $C_{14}H_{18}NO_3$ (M + H): 248.1281.

***N*-Benzyloxycarbonyl-5-*anti*-carboxy-2-azabicyclo[2.1.1] hexane (8a)**

To a stirred solution of alcohol **33** (60 mg, 0.24 mmol) in CH_2Cl_2 (3 mL) containing TEMPO (1 mg) was added $NaHCO_3$ (aq) (0.74 mL) containing KBr (3.0 mg) and Bu_4NCl (4.0 mg). The mixture was cooled to 0 °C and a solution of NaOCl (0.60 mL), $NaHCO_3$ (0.51 mL), and brine (0.55 mL) was added dropwise. After 1 h, the layers were separated. The organic layer was extracted with water (4 × 5 mL). The combined aqueous solution was acidified with 10% HCl. The resulting solution was extracted with EtOAc (4 × 10 mL). The combined organic solution was dried over Na_2SO_4. Removal of solvent and purification of the residue by column chromatography gave acid **8a** (40 mg, 63%) at R_f = 0.32 (90:10:1 CH_2Cl_2/MeOH/TFA). ^{1}H NMR (300 MHz, CD_3OD) δ: 7.41 (m, 5H), 5.20 (s, 2H), 4.58 (br, 1H, H_1), 3.48 (br, 2H, $2H_3$), 3.08, 3.06 (2 br, 1H, H_4), 2.61 (br, 2H, H_{6x} and H_5), 2.32 (t, *J* = 7.8 Hz, 1H, H_{6n}). ^{13}C NMR (100 MHz, $CDCl_3$) δ: 177.6 (COOH), 156.1 (C=O), 137.3, 137.0, 128.8, 128.6, 128.3, 128.1 (C on Ph), 67.1 (CH_2Ph), 63.3 (C_1), 58.7 (C_5), 50.8 (C_3), 42.3 (C_4), 39.4 (C_6). HRMS *m/z* found: 284.0898; calcd for $C_{14}H_{15}NO_4Na$ (M + Na): 284.0893. ^{1}H COSY showed couplings between H_1 and H_4 and H_{6x} and H_{6n}.

***N*-Benzyloxycarbonyl-5-[(methoxycarbonyl)methylene]-6-*anti*-bromo-2-azabicyclo[2.1.1]hexane (stereoisomers *E*-34a and *Z*-34b)**

Methyl(triphenylphosphoranylidene)acetate (582 mg, 1.74 mmol) was added to a solution of ketone **18** (360 mg, 1.16 mmol) in 20 mL CH_2Cl_2 at RT. The reaction mixture was stirred for 2 days. The solvent was removed in vacuo and purification of the residue by column chromatography on silica gel (4:1 hexanes / diethyl ether) provided stereoisomer **34a** (110 mg, 27%), stereioisomer **34b** (170 mg, 42%), and starting material (20 mg). Analytical data for product **34a** at R_f = 0.37 (1:1 hexanes / diethyl ether): ^{1}H NMR (400 MHz, $CDCl_3$) δ: 7.24 (m, 5H), 5.72 (s, 1H, =CH), 5.08 (s, 2H), 4.68 (br, 1H, H_1), 3.96 (d, *J* = 6.8 Hz, 1H, H_4), 3.94 (s, 1H, H_5), 3.67 (s, 3H, CH_3), 3.60 (d, *J* = 8.4 Hz, 1H, H_3), 3.50 (d, *J* = 8.4 Hz, 1H, H_3). ^{13}C NMR (100 MHz, $CDCl_3$) δ: 167.2, 159.7 (C_6), 155.5 (CO_2Bn), 136.5, 129.0, 128.8, 128.7, 128.6, 128.5, 108.4 (=CH), 68.9 (C_1), 67.8 (CH_2Ph), 55.2 (C_4), 52.0 (CH_3), 49.2 (C_3), 48.8 (C_5). HRMS *m/z* found: 388.0152; calcd for $C_{16}H_{16}{}^{79}BrNO_4Na$ (M + Na): 388.0155; *m/z* found: 390.0132; calcd for $C_{16}H_{16}{}^{81}BrNO_4Na$ (M + Na): 390.0134. Analytical data for product **34b** at R_f = 0.29 (1:1 hexanes / diethyl ether): ^{1}H NMR (400 MHz, $CDCl_3$) δ: 7.27 (m, 5H), 5.64 (s, 1H, =CH), 5.28 (d, 1H, *J* = 6.8 Hz, H_1), 5.09 (m, 2H, CH_2Ph), 3.93 (s, 1H, H_5), 3.61 (s, 3H, CH_3), 3.60 (d, *J* = 8.8 Hz, 1H, H_3), 3.59 (d, *J* = 8.8 Hz, 1H, H_3), 3.33 (d, *J* = 6.4 Hz, 1H, H_4). ^{13}C NMR (100 MHz, $CDCl_3$) δ: 165.8, 157.8 (C_6), 155.5 (CO_2Bn), 136.6, 128.9, 128.8, 128.7, 128.6, 128.3, 108.3 (=CH),

Can. J. Chem. Downloaded from www.nrcresearchpress.com by Renmin University of China on 09/02/12
For personal use only.

68.9 (C_1), 67.7, 67.6 (CH_2Ph), 54.7 (C_4), 52.0 (CH_3), 49.4 (C_3), 48.6 (C_5). HRMS *m/z* found: 388.0145; calcd for $C_{16}H_{16}{}^{79}BrNO_4Na$ (M + Na): 388.0155; *m/z* found: 390.0124; calcd for $C_{16}H_{16}{}^{81}BrNO_4Na$ (M + Na): 390.0134.

N-Benzyloxycarbonyl-5-[(methoxycarbonyl)methylene]-2-azabicyclo[2.1.1]hexane (stereoisomers *E*-35a and *Z*-35b)

According to the preceding procedure, methyl(triphenylphosphoranylidene)acetate (430 mg, 1.29 mmol) was added to a solution of ketone **21** (210 mg, 0.86 mmol) in CH_2Cl_2 (20 mL) at RT. After 36 h, workup and column chromatography on silica gel (3:1 hexanes / diethyl ether) provided alkene **35a** (155 mg, 62%) and alkene **35b** (80 mg, 32%). Analytical data for product **35a** at R_f = 0.34 (1:1 hexanes / diethyl ether): ^{1}H NMR (400 MHz, $CDCl_3$) δ: 7.25 (m, 5H), 5.38 (br, 1H, =CH), 5.07 (s, 2H), 4.66 (br, 1H, H_1), 3.89, 3.88 (2 d, J = 6.4, 6.8 Hz, 1H, H_4), 3.63 (s, 3H, CH_3), 3.45 (d, J = 8.0 Hz, 1H, H_3), 3.41 (d, J = 8.0 Hz, 1H, H_3). 1.89, 1.88 (2 d, J = 7.6 Hz, 1H, H_6), 1.68, 1.67 (2 d, J = 7.6 Hz, 1H, H_6). ^{13}C NMR (100 MHz, $CDCl_3$) δ: 167.2, 159.7 (C_5), 156.2, 137.0, 129.0, 128.9, 128.7, 128.6, 128.4, 128.3, 101.5 (=CH), 67.3 (CH_2Ph), 64.3 (C_1), 51.7 (CH_3), 49.2 (C_3), 47.3 (C_4), 36.9 (C_6). HRMS *m/z* found: 288.1229; calcd for $C_{16}H_{17}NO_4Na$ (M + Na): 288.1231. Analytical data for product **35b** at R_f = 0.27 (1:1 hexanes / diethyl ether): ^{1}H NMR (400 MHz, $CDCl_3$) δ: 7.26 (m, 5H), 5.29 (m, 2H, =CH and H_1), 5.09 (m, 2H, CH_2Ph), 3.60 (br, 3H, CH_3), 3.44 (d, J = 8.4 Hz, 1H, H_3), 3.36 (d, J = 8.4 Hz, 1H, H_3), 3.24 (2 d, J = 6.6 Hz, 1H, H_4), 1.89, 1.88 (2 d, J = 7.2 Hz, 1H, H_5), 1.68 (d, J = 7.2 Hz, 1H, H_5). ^{13}C NMR (100 MHz, $CDCl_3$) δ: 166.5, 158.9 (C_5), 156.2 (CO_2Bn), 137.1, 128.8, 128.6, 128.4, 128.3, 128.2 (C on Ph), 101.4 (=CH), 67.2 (CH_2Ph), 64.4 (C_1), 51.7 (CH_3), 49.2 (C_3), 46.8 (C_4), 36.9 (C_6). HRMS *m/z* found: 288.1230; calcd for $C_{16}H_{17}NO_4Na$ (M + Na): 288.1231.

N-Benzyloxycarbonyl-5-*anti*-bromo-6-*anti*-[dimethyl(vinyl) silyloxy]-2-azabicyclo[2.1.1]hexane (36)

Dimethylvinylchlorosilane (0.77 g, 6.4 mmol) was added to bromoalcohol **17** (2.0 g, 6.4 mmol) in DMF (1 mL) at RT followed by addition of imidazole (0.44 g, 6.4 mmol). The resulting mixture was stirred for 2 days. Diethyl ether (20 mL) and distilled water (20 mL) were added. The organic layer was separated and the aqueous layer was extracted with ether (3 × 20 mL). The combined organic extracts were washed with brine and then dried over $MgSO_4$. After filtration, the solvent was removed in vacuo and purification of the residue by column chromatography gave vinylsilane **36** (1.68 g, 66%) at R_f = 0.29 (4:1 hexanes / diethyl ether). ^{1}H NMR (400 MHz, $CDCl_3$) δ: 7.35 (m, 5H), 6.16 (dd, J = 20.0, 14.8 Hz, 1H, =CH), 6.05, 6.04 (2 d, J = 14.8, 14.4 Hz, 1H, $=CH_{2cis}$), 5.82, 5.81 (2 d, J = 20.0, 20.4 Hz, 1H, $=CH_{2trans}$), 5.14 (m, 2H, CH_2Ph), 4.36 (br, 1H, H_6), 4.27 (d, J = 6.4 Hz, 1H, H_1), 4.04 (d, J = 7.2 Hz, 1H, H_5), 3.53, 3.52 (2 d, J = 9.2, 8.8 Hz, 1H, H_3), 3.47 (d, J = 8.8 Hz, 1H, H_3), 2.90 (d, J = 6.4 Hz, 1H, H_4), 0.25 (s, 6H). ^{13}C NMR (100 MHz, $CDCl_3$) δ: 155.7, 155.2 (C=O), 137.0, 136.6 (=CH), 134.4 ($=CH_2$), 128.9, 128.5, 128.3, 83.7 (C_6), 67.5 (CH_2Ph), 66.4, 65.7 (C_1), 50.7 (C_4), 50.0 (C_5), 49.3 (C_3), –1.26, –1.55 ($2CH_3$). HRMS *m/z* found: 418.0436; calcd for $C_{17}H_{22}{}^{79}BrNaNO_3Si$ (M + Na): 418.0451; *m/z* found: 420.0423; calcd for $C_{17}H_{22}{}^{81}BrNO_3SiNa$ (M + Na): 420.0430.

N-Benzyloxycarbonyl-5-*anti*-oxy-6-*anti*-(1-ethyl)-2-azabicyclo[2.1.1]hexyl-dimethylsilane (37) (a 2,2,3-trimethyl-1,2-oxasilepane)

AIBN (3.0 mg, 0.02 mmol) was added to a solution of compound **36** (150 mg, 0.38 mmol) in benzene (20 mL) under argon. The resulting mixture was refluxed for 5 min and tributyltin hydride (165 mg, 0.57 mmol) was added immediately. The mixture was refluxed for an additional 5 h. The solvent was removed in vacuo to give a residue that after column chromatography gave tethered silane **37** (100 mg, 83%) at R_f = 0.32 (2:1 hexanes / diethyl ether). ^{1}H NMR (400 MHz, $CDCl_3$) δ: 7.30 (m, 5H), 5.11 (s, 2H), 4.15, 4.13 (2 d, J = 7.6, 7.2 Hz, 1H, H_6), 4.15, 4.08 (2 br, 1H, H_1), 3.40 (m, 2H, $2H_3$), 2.55 (br, 1H, H_5), 2.32, 2.30 (2 d, J = 7.6 Hz, 1H, H_4), 1.46 (m, 1H, CHSi), 1.05, 1.03 (2 d, J = 8.4, 7.6 Hz, 3H, CH_3), 0.20, 0.17, 0.16, 0.15 (4 s, 6H, $2CH_3$). ^{13}C NMR (100 MHz, $CDCl_3$) δ: 156.0 (C=O), 137.2, 128.9, 128.4, 128.2, 127.9, 84.5, 84.3 (C_6), 67.1 (CH_2Ph), 66.3, 65.7, 63.2, 62.6 (C_1), 57.9 (C_3), 49.5, 49.4 (C_4), 48.7, 48.2, 44.8, 44.5 (C_5), 19.6, 18.7 (SiCH), 15.8, 15.3 (CH_3), 1.87, 1.42 (CH_3), –1.12, –1.29 (CH_3). HRMS *m/z* found: 340.1344; calcd for $C_{17}H_{23}NO_3SiNa$ (M + Na): 340.1345.

N-Benzyloxycarbonyl-5-*anti*-hydroxy-6-*anti*-(1-hydroxyethyl)-2-azabicyclo[2.1.1]hexane stereoisomers (19)

Route A: To silylether **37** (30 mg, 0.095 mmol) in 1:1 THF/MeOH (0.2 mL) was added $KHCO_3$ (10 mg, 0.10 mmol) and KF (12 mg, 0.21 mmol). To this stirred suspension was added 30% H_2O_2 (50 mL, 0.45 mmol).[33] The suspension was stirred at RT open to the air for 28 h. Because of the small reaction volume, two additional portions of 1:1 THF/MeOH were added as the reaction solvent evaporated. The reaction was quenched by addition of 50% NaS_2O_3 (0.5 mL), and the solution (0.7 mL) was applied to a preparative silica gel TLC plate that was allowed to dry. Elution with 1:1 hexanes/Et_2O gave 6 mg (20%) of unreacted **37** (R_f = 0.5, 1:1 hexanes/Et_2O). A second elution with 2:1 EtOAc/hexanes yielded 17 mg (65%) of diols **19a** + **19b** at R_f = 0.3 (2:1 EtOAc/hexanes) taken as one fraction. The ratio of isomers was 45:55 by ^{1}H NMR based on integrations of unique peaks at δ 2.81 and 2.60. Route B: To a solution of compound **37** (520 mg, 1.64 mmol) in THF/MeOH (1:1, 15 mL), $KHCO_3$ (492 mg, 4.92 mmol), KF (190 mg, 3.28 mmol), and 90% H_2O_2 (0.78 mL, 39.36 mmol) were successively added. The resulting solution was stirred at RT for 20 h and then diluted with Et_2O. The solvent was filtered over Celite and concentrated in vacuo. Column chromatography gave diol **19a** (90 mg, 20% at R_f = 0.17, 2:1 ethyl acetate / hexanes) and diol **19b** (90 mg, 20% at R_f = 0.12, 2:1 ethyl acetate / hexanes). Spectral data for **19a**: ^{1}H NMR (400 MHz, $CDCl_3$) δ: 7.35 (br, 5H), 5.10 (br, 2H, CH_2Ph), 4.96, 4.84 (2 br, 1H, H_6), 4.34 (d, J = 7.2 Hz, 1H, H_1), 4.12 (d, J = 7.2 Hz, 1H, OCH), 3.85, 3.10 (2 br, 1H, OH), 3.49 (d, J = 8.8 Hz, 1H, H_3), 3.44 (d, J = 8.8 Hz, 1H, H_3), 2.60 (d, J = 7.2 Hz, 1H, H_4), 2.24 (br, 1H, OH), 2.14 (m, 1H,

H_5), 1.24 (d, J = 5.6 Hz, 3H, CH_3). ^{13}C NMR (100 MHz, $CDCl_3$) δ: 156.0, 137.0, 128.9, 128.4, 128.2, 83.3 (C_6), 67.3 (C_1), 66.5 (OCH), 63.7 (CH_2Ph), 63.0 (C_3), 50.8 (C_4), 46.0 (C_5), 23.2 (CH_3). HRMS *m/z* found: 300.1196; calcd for $C_{15}H_{19}NaNO_4$ (M + Na): 300.1206. Spectral data for **19b**: ^1H NMR (400 MHz, $CDCl_3$) δ: 7.34 (br, 5H), 5.14 (s, 2H), 4.79 (br, 1H, OCH), 4.14 (2 d, J = 7.2 Hz, H_1 and H_6), 3.53 (d, J = 8.8 Hz, 1H, H_3), 3.45 (d, J = 8.8 Hz, 1H, H_3), 3.00 (br, 1H, OH), 2.83 (d, J = 7.2 Hz, 1H, H_4), 2.16 (m, 1H, H_5), 1.82 (br, 1H, OH), 1.26 (d, J = 6.0 Hz, 3H, CH_3). ^{13}C NMR (100 MHz, $CDCl_3$) δ: 156.0, 137.0, 128.8, 128.6, 128.4, 128.2, 83.4 (C_6), 67.2 (OCH), 65.9 (C_1), 64.5 (CH_2Ph), 62.5 (C_3), 50.7 (C_4), 44.9 (C_5), 23.9 (CH_3). HRMS *m/z* found: 300.1217; calcd for $C_{15}H_{19}NaNO_4$ (M + Na): 300.1206.

Supplementary data

Supplementary data (copies of reported ^1H NMR and ^{13}C NMR spectra for all new compounds) are available with this article through the journal Web site at http://nrcresearchpress.com/doi/suppl/10.1139/v11-112.

Acknowledgment

Financial support was provided by the National Science Foundation (NSF, CHE 0515635 and CHE-0111208) and the donors of the Petroleum Research Fund, administered by the American Chemical Society. M.S. was supported by a Der Min Fan Fellowship and NSF (DGE-0841377) through a grant to Temple University. We thank A. Suffian for technical assistance.

References

(1) For a review of non-proteinogenic amino acids from *trans*-4-hydroxy-L-proline, see Remuzon, P. *Tetrahedron* **1996**, *52* (44), 13803. doi:10.1016/0040-4020(96)00822-8.

(2) (a) Del Valle, J. R.; Goodman, M. *J. Org. Chem.* **2003**, *68* (10), 3923. doi:10.1021/jo034214l; (b) For 4-phenyl or 4-cyclohexyl pralines, see Tamaki, M.; Han, G.; Hruby, V. J. *J. Org. Chem.* **2001**, *66* (10), 3593. doi:10.1021/jo005625u; (c) Krapcho, J.; Turk, C.; Cushman, D. W.; Powell, J. R.; DeForrest, J. M.; Spitzmiller, E. R.; Karanewsky, D. S.; Duggan, M.; Rovnyak, G.; Schwartz, J.; Natarajan, S.; Godfrey, J. D.; Ryono, D. E.; Neubeck, R.; Atwal, K. S.; Petrillo, E. W., Jr. *J. Med. Chem.* **1988**, *31* (6), 1148. doi:10.1021/jm00401a014.

(3) (a) Sonesson, C.; Wikstrom, H.; Smith, M. W.; Svennson, K.; Carlsson, A.; Waters, N. *Bioorg. Med. Chem. Lett.* **1997**, *7* (3), 241. doi:10.1016/S0960-894X(96)00618-X; (b) Ahn, K. H.; Lee, S. J.; Lee, C. H.; Hong, C. Y.; Park, T. K. *Bioorg. Med. Chem. Lett.* **1999**, *9* (10), 1379. doi:10.1016/S0960-894X(99)00201-2.

(4) (a) For leading references, see Schafmeister, C. E.; Brown, Z. Z.; Gupta, S. *Acc. Chem. Res.* **2008**, *41* (10), 1387. doi:10.1021/ar700283y; (b) Blanchet, J.; Pouliquen, M.; Lasne, M.-C.; Rouden, J. *Tetrahedron Lett.* **2007**, *48* (33), 5727, especially refs. 1–7 therein. doi:10.1016/j.tetlet.2007.06.106.

(5) (a) For leading references with bridged pyrrolidines, see Malpass, J. R.; Handa, S.; White, R. *Org. Lett.* **2005**, *7* (13), 2759. doi:10.1021/ol0510365; (b) Bunch, L.; Liljefors, T.; Greenwood, J. R.; Frydenvang, K.; Brauner-Osborne, H.; Krogsgaard-Larsen, P.; Madsen, U. *J. Org. Chem.* **2003**, *68* (4), 1489. doi:10.1021/jo026509p; (c) Hart, B. P.; Rapoport, H. *J. Org. Chem.* **1999**, *64* (6), 2050. doi:10.1021/jo982327c; (d) Han, W.; Pelletier, J. C.; Mersinger, L. J.; Kettner, C. A.; Hodge, C. N. *Org. Lett.* **1999**, *1* (12), 1875. doi:10.1021/ol990294x.

(6) Krow, G. R.; Liu, N.; Sender, M.; Lin, G.; Centafont, R.; Sonnet, P. E.; DeBrosse, C.; Ross, C. W., III; Carroll, P. J.; Shoulders, M. D.; Raines, R. T. *Org. Lett.* **2010**, *12* (23), 5438. doi:10.1021/ol1022917.

(7) For a review of synthetic approaches to 2-azabicyclo[2.1.1]hexanes, see Krow, G. R.; Cannon, K. C. *Heterocycles* **2004**, *62* (1), 877. doi:10.3987/REV-03-SR(P)1.

(8) Krow, G. R.; Lin, G.; Moore, K. P.; Thomas, A. M. C.; DeBrosse, C.; Ross, C. W., III; Ramjit, H. G. *Org. Lett.* **2004**, *6* (10), 1669. doi:10.1021/ol0494818.

(9) Lescop, C.; Mevellec, L.; Huet, F. *J. Org. Chem.* **2001**, *66* (12), 4187. doi:10.1021/jo001790y.

(10) Piotrowski, D. W. *Synlett* **1999**, *1999* (7), 1091. doi:10.1055/s-1999-2775.

(11) Winkler, J. D.; Fitzgerald, M. E. *Synlett* **2009**, *2009* (04), 562. doi:10.1055/s-0028-1087561.

(12) Ragains, J. R.; Winkler, J. D. *Org. Lett.* **2006**, *8* (20), 4437. doi:10.1021/ol061577+.

(13) (a) Ikeda, M.; Uchno, T.; Takahashi, M.; Ishibashi, H.; Tamura, Y.; Kido, M. *Chem. Pharm. Bull. (Tokyo)* **1985**, *33*, 3279; (b) Ikeda, M.; Takahashi, M.; Ohno, K.; Tamura, Y.; Kido, M. *Chem. Pharm. Bull. (Tokyo)* **1982**, *30*, 2269; (c) Toda, F.; Miyamoto, H.; Takeda, K.; Matsugawa, R.; Maruyama, N. *J. Org. Chem.* **1993**, *58* (23), 6208. doi:10.1021/jo00075a013.

(14) Krow, G. R.; Huang, Q.; Lin, G.; Centafont, R. A.; Thomas, A. M.; Gandla, D.; DeBrosse, C.; Carroll, P. J. *J. Org. Chem.* **2006**, *71* (5), 2090. doi:10.1021/jo052506b.

(15) Kwak, Y.-S.; Winkler, J. D. *J. Am. Chem. Soc.* **2001**, *123* (30), 7429. doi:10.1021/ja010542w.

(16) (a) Schell, F. M.; Cook, P. M.; Hawkinson, S. W.; Cassady, R. E.; Thiessen, W. E. *J. Org. Chem.* **1979**, *44* (9), 1380. doi:10.1021/jo01323a004; (b) Tamura, Y.; Ishibashi, H.; Hirai, M.; Kita, Y.; Ikeda, M. *J. Org. Chem.* **1975**, *40* (19), 2702. doi:10.1021/jo00907a002; (c) Swindell, C. S.; Patel, B. P.; DeSolms, S. J.; Springer, J. P. *J. Org. Chem.* **1987**, *52* (12), 2346. doi:10.1021/jo00388a002; (d) Tamura, Y.; Kita, Y.; Ishibashi, H.; Ikeda, M. *J. Chem. Soc. Chem. Commun.* **1971**, 1167; (e) Tamura, Y.; Kita, Y.; Ishibashi, H.; Ikeda, M. *Tetrahedron Lett.* **1972**, *13* (19), 1977. doi:10.1016/S0040-4039(01)84766-3.

(17) Krow, G. R.; Lin, G.; Herzon, S. B.; Thomas, A. M.; Moore, K. P.; Huang, Q.; Carroll, P. J. *J. Org. Chem.* **2003**, *68* (19), 7562. doi:10.1021/jo0348672.

(18) (a) Wiberg, K. B.; Lowry, B. R.; Colby, T. H. *J. Am. Chem. Soc.* **1961**, *83* (19), 3998. doi:10.1021/ja01480a013; (b) McDonald, R. N.; Reineke, C. E. *J. Org. Chem. Soc.* **1967**, *32* (6), 1888. doi:10.1021/jo01281a041; (c) Müller, P.; Blanc, J. *Helv. Chim. Acta* **1979**, *62* (6), 1980. doi:10.1002/hlca.19790620627; (d) Gassman, P. G.; Atkins, T. J. *J. Am. Chem. Soc.* **1970**, *92* (19), 5810. doi:10.1021/ja00722a084; (e) Wiberg, K. B.; Lowry, B. R.; Nist, B. J. *J. Am. Chem. Soc.* **1962**, *84* (9), 1594. doi:10.1021/ja00868a016.

(19) Gilbert, J. C.; Yin, J. *J. Org. Chem.* **2006**, *71* (15), 5658. doi:10.1021/jo060652r.

(20) Krow, G. R.; Lin, G.; Rapolu, D.; Fang, Y.; Lester, W. S.; Herzon, S. B.; Sonnet, P. E.. *J. Org. Chem.* **2003**, *68* (13), 5292. doi:10.1021/jo034394z.

(21) For C1 and (or) C3 α-functionalization reactions, see Krow, G.

Can. J. Chem. Downloaded from www.nrcresearchpress.com by Renmin University of China on 09/02/12
For personal use only.

R.; Herzon, S. B.; Lin, G.; Qiu, F.; Sonnet, P. E. *Org. Lett.* **2002**, *4*, 3151. doi:10.1021/ol026509b.
(22) Mancuso, A. J.; Huang, S.-L.; Swern, D. *J. Org. Chem.* **1978**, *43* (12), 2480. doi:10.1021/jo00406a041.
(23) Krow, G. R.; Lee, Y. B.; Lester, W. S.; Christian, H.; Shaw, D. A.; Yuan, J. *J. Org. Chem.* **1998**, *63* (23), 8558. doi:10.1021/jo9808472.
(24) (a) Lal, G. S.; Pez, G. P.; Pesaresi, R. J.; Prozonic, F. M. *J. Chem. Soc. Chem. Commun.* **1999**, 215; (b) Lal, G. S.; Pez, G. P.; Pesaresi, R. J.; Prozonic, F. M.; Cheng, H. *J. Org. Chem.* **1999**, *64* (19), 7048. doi:10.1021/jo990566+; (c) For a review see Krow, G.; Cannon, K. *e-EROS;* J. Wiley & Sons: New York; October, 2010.
(25) Jenkins, C. L.; Lin, G.; Duo, J.; Rapolu, D.; Guzei, I. A.; Raines, R. T.; Krow, G. R. *J. Org. Chem.* **2004**, *69* (25), 8565. doi:10.1021/jo049242y.
(26) (a) Fletcher, S. R.; Baker, R.; Chambers, M. S.; Herbert, R. H.; Hobbs, S. C.; Thomas, S. R.; Verrier, H. M.; Watt, A. P.; Ball, R. G. *J. Org. Chem.* **1994**, *59* (7), 1771. doi:10.1021/jo00086a030; (b) Hodgson, D. M.; Maxwell, C. R.; Wisedale, R.; Matthews, I. R.; Carpenter, K. J.; Dickenson, A. H.; Wonnacott, S. *J. Chem. Soc., Perkin Trans. 1* **2001**, *2001* (23), 3150. doi:10.1039/b107414h.
(27) (a) Pine, S. H.; Shen, G. S.; Hoang, H. *Synthesis* **1991**, *1991* (02), 165. doi:10.1055/s-1991-26406; (b) Barrett, A. G. M.; Damiani, F. *J. Org. Chem.* **1999**, *64* (4), 1410. doi:10.1021/jo9820972.
(28) Knights, E. F.; Brown, H. C. *J. Am. Chem. Soc.* **1968**, *90* (19), 5281. doi:10.1021/ja01021a047.
(29) Ballestri, M.; Chatgilialoglu, C.; Clark, K. B.; Griller, D.; Giese, B.; Kopping, B. *J. Org. Chem.* **1991**, *56* (2), 678. doi:10.1021/jo00002a035.
(30) Anelli, P. L.; Biffi, C.; Montanari, F.; Quici, S. *J. Org. Chem.* **1987**, *52* (12), 2559. doi:10.1021/jo00388a038.
(31) Isaacs, N. S.; El-Din, G. N. *Tetrahedron Lett.* **1987**, *28* (19), 2191. doi:10.1016/S0040-4039(00)96078-7.
(32) Shuto, S.; Kanazaki, M.; Ichikawa, S.; Matsuda, A. *J. Org. Chem.* **1997**, *62* (17), 5676. doi:10.1021/jo970867o.
(33) (a) Tamao, K.; Ishida, N.; Ito, Y.; Kumada, M. *Org. Synth.* **1990**, *69*, 96; (b) Blaszykowski, C.; Dhimane, A. L.; Fensterbank, L.; Malacria, M. *Org. Lett.* **2003**, *5* (8), 1341. doi:10.1021/ol034288j.
(34) Kaselj, M.; Chung, W.-S.; le Noble, W. J. *Chem. Rev.* **1999**, *99* (5), 1387. doi:10.1021/cr980364y.
(35) Krow, G. R.; Edupuganti, R.; Gandla, D.; Choudhary, A.; Lin, G.; Sonnet, P. E.; DeBrosse, C.; Ross, C. W., III; Cannon, K. C.; Raines, R. T. *J. Org. Chem.* **2009**, *74* (21), 8232. doi:10.1021/jo901725k.

Can. J. Chem. Downloaded from www.nrcresearchpress.com by Renmin University of China on 09/02/12
For personal use only.

Responsive properties of crystalline colloidal arrays formed by core-shell microspheres with pH and temperature sensitivities

Gwénaëlle Bazin and X.X. Zhu

Can. J. Chem. Downloaded from www.nrcresearchpress.com by Renmin University of China on 09/02/12
For personal use only.

Abstract: Polymeric microspheres responsive to pH and temperature changes have been prepared by a two-step surfactant-free emulsion polymerization with a polystyrene core and a hydrogel shell. The double sensitivity is achieved by the copolymerization in the shell layer of acrylic acid and *N*-isopropylacrylamide, which are pH- and thermo-responsive, respectively. Above a certain critical concentration, these microspheres are able to self-assemble into crystalline colloidal arrays, causing intense visible light diffraction. The behavior of these structures has been studied and correlated to the properties of the microspheres. The packing of these microspheres results in stimuli-sensitive colloidal crystals, with a behavior directly linked to the interactions between the particles and the surrounding media.

Key words: core-shell microspheres, surfactant-free emulsion polymerization, pH and thermo-sensitivity, crystalline colloidal arrays.

Résumé : Des microsphères doublement sensibles et composées d'un coeur de polystyrène entouré d'une couche d'hydrogel ont été synthétisées par polymérisation en émulsion sans tensioactif. La double sensibilité a été obtenue grâce à la copolymérisation de l'acide acrylique et du *N*-isopropylacrylamide, tous deux connus pour être sensibles respectivement au pH et à la température. Au dessus d'une concentration critique, ces microsphères sont capables de s'auto-assembler pour former des cristaux colloïdaux et affichent des couleurs intenses dues à la diffraction de la lumière visible. Le comportement de ces structures a été étudié en rapport avec les propriétés des particules. L'empilement de ces microsphères donne des cristaux colloïdaux sensibles à leur environnement, propriété qui semble être liée à la nature des interactions entre les particules.

Mots-clés : microsphères coeur-coquille, polymérisation en émulsion sans tensioactif, sensibilité au pH et à la température, cristaux colloïdaux.

Introduction

Polymer microspheres have been the subject of intense research interests for biosensor-related applications because of their high surface area, hence fast response and easy functionalization.[1] Stimuli-responsive microgels have proven to be particularly interesting because of their ability to swell or shrink, depending on their environment[2,3] or their interaction with an analyte, such as the complexation with a biological molecule.[4–6] Crystalline colloidal arrays (CCAs) may be formed through the self-assembly of these particles, and the stimuli-responsiveness combined to their visible light diffraction make these structures interesting and useful. CCAs may be used as photonic gap materials[7,8] and biosensors,[9,10] mainly in the form of polymerized crystalline colloidal arrays, where the self-assembled hard spheres are fixed inside a crosslinked hydrogel matrix, which is responsive toward the external stimulus. With this system, Asher and co-workers developed sensors for a large range of analytes from glucose to metal ions.[11,12]

For a direct response of the particles, stimuli sensitivity can be introduced into the particles. Lyon and co-workers have studied thermo-responsive poly(*N*-isopropylacrylamide) (PNIPAM) microgels, containing a very small fraction of acrylic acid monomers, and investigated the effect of temperature on their self-assembly,[13–15] noticing a loss of order above the lower critical solution temperature (LCST) of PNIPAM. The demand for more advanced properties also led to the development of particles with core-shell structures, often with a rigid core and a soft hydrophilic shell. Two kinds of stimuli-responsive core-shell particles have been synthesized, either with one responsive component[16–19] or even two or more components, forming multi-responsive systems.[20–22] The stimuli sensitivity can be introduced into the particles by adding a soft and responsive shell made of a hydrogel. Meng et al. showed the importance of the hydrophilic shell in the packing mechanism of core-shell particles with a polystyrene core.[17] They also showed the pH response of CCAs with a shell made of poly(acrylic acid). Li et al. investigated

Received 28 April 2011. Accepted 18 July 2011. Published at www.nrcresearchpress.com/cjc on 22 November 2011.

G. Bazin and X.X. Zhu. Département de Chimie, Université de Montréal, C.P. 6128, Succursale Centre-ville, Montréal, QC H3C 3J7, Canada.

Corresponding author: X.X. Zhu (e-mail: julian.zhu@umontreal.ca).

This article is part of a Special Issue dedicated to Professor Tak-Hang Chan.

Can. J. Chem. Downloaded from www.nrcresearchpress.com by Renmin University of China on 09/02/12
For personal use only.

the response to temperature using a poly(*N*-isopropylacrylamide) shell and noticed a shift of the diffraction peak.[18]

In this work, microspheres were synthesized by surfactant-free emulsion polymerization with a polystyrene core and a hydrogel shell. The shell was made of poly(acrylic acid) for pH-sensitivity and of a copolymer of acrylic acid and *N*-isopropylacrylamide for double sensitivity to both pH and temperature. These particles easily self-assemble into CCAs and display visible light diffraction. The packing mechanism and the properties of the CCAs in response to both pH and temperature changes have been studied and compared. The preliminary results indicate that the response is closely related to the kind of interactions that exist among the microspheres.

Experimental

Materials and synthesis of core-shell particles

Styrene, acrylic acid (AA), *N*-isopropylacrylamide (NIPAM), and potassium persulfate (KPS) were purchased from Sigma-Aldrich. Styrene and AA were distilled under reduced pressure. NIPAM was recrystallized from hexanes. The initiator KPS was used as received.

The core-shell microspheres were synthesized by a two-step surfactant-free emulsion polymerization in an aqueous medium following a procedure reported by Xiao et al.[23] and Meng et al.[17] In a 250 mL three-neck flask, equipped with a reflux condenser, 2.3 g of styrene and 0.2 g of hydrophilic monomers, either AA or a 1:1 mixture (weight ratio) of AA and NIPAM, were dissolved in 130 mL of milli-Q water. The system was degassed with nitrogen for 30 min while stirring with a mechanical stirrer at a speed of 300 rpm. The initiator KPS was then added with 20 mL of water, and the flask was heated to 70 °C in an oil bath. After 2 h of stirring, 1 g of the hydrophilic monomer or the mixture of hydrophilic monomers was added. The temperature and the stirring were maintained for an additional 22 h. The water–particle mixture was centrifuged, and the supernatant was removed and replaced by milli-Q water. The particles were redispersed by the use of a vortex and a sonicator. The centrifugation procedure was repeated three times, followed by dialysis against distilled water for one week at room temperature (RT) in a cellulose sack (MW cut off at 3200).

Characterization of the particles and the CCAs

The microsphere sizes were measured by dynamic light scattering on a Brookhaven BI-200SM instrument with a 532 nm green laser. The samples concentration was 0.02 wt %. For each sample, three measurements were taken. Our samples are composed of only one population of particles with a narrow distribution, the method of cumulants with a third-order fit was used to obtain the average size from the normalized autocorrelation function. The pH of the samples were adjusted by adding $HCl_{(aq)}$ or $NaOH_{(aq)}$ for the study of pH sensitivity. The temperature was controlled with a water bath, and the samples were allowed to equilibrate for 30 min before taking the measurements.

The particle packing was obtained with simple centrifugation before being studied by visible light diffraction, which was measured by the use of a home-assembled spectrophotometer (USB2000, Ocean Optics) equipped with a tungsten-halogen source (400–1000 nm), a backscattering probe (R200–7 VIS/NIR, Ocean Optics), and a cuvette holder with water circulation for temperature control. For pH studies, 5 samples of the same particle concentration but with different pH values were prepared with solutions of $HCl_{(aq)}$ or $NaOH_{(aq)}$.

Transmission electron microscopy (TEM) images of the particles were obtained with a Philips CM200 instrument at an acceleration voltage of 200 kV. TEM samples were prepared by depositing a 20 μL drop of particles solution of 0.1 wt% on a carbon-coated copper grid for 2 min before absorbing the excess with precision paper. The grids were then dried at RT overnight.

For scanning electron microscopy (SEM) of the CCAs, a concentrated solution of particles was drop-casted and dried at RT. The samples were coated with a layer of Pd–Au of 20 nm thickness and observed on a FE-SEM (Hitachi S-4700) with an accelerating voltage of 2 kV.

Results and discussion

Preparation and morphology of the polymer spheres

The two-step synthesis of the core-shell particles can be described as a surfactant-free emulsion polymerization followed by a seed polymerization. The first step is the synthesis of the microsphere core: the hydrophilic monomers start to polymerize in the aqueous medium, initiated by the water-soluble KPS. As more styrene units are incorporated, the oligomers become less water-soluble and start to form the core. The second step is the shell formation onto the cores, which serve as seed particles.

It has been shown that even one-step synthesis with a hydrophobic monomer and a hydrophilic one can yield core-shell structures to minimize unfavorable interactions between the hydrophobic units and water.[24] However, it has also been shown that the use of a second step gives better uniformity and a thicker shell.[19,23] The use of a more hydrophilic monomer in the first step helps stabilize the surface, leading to more particles smaller in size. However, larger amounts of hydrophilic monomers in the reaction medium can result in their polymerization in the solvent rather than their participation in the particles.

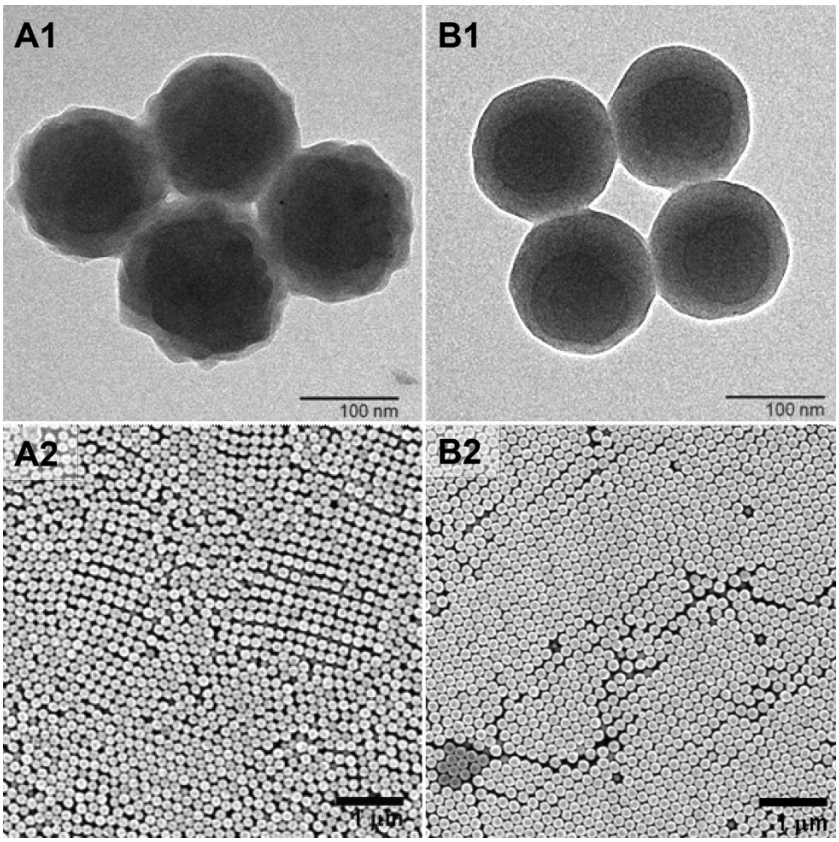
TEM images in Fig. 1 confirm that the core-shell structures of the particles and their uniformity in both size and shape. The surface of the P(S-AA-NIPAM) particles is smooth but the P(S-AA) particles are less regular, which is probably due to the solubility difference of the polymers in the shell at the temperature of preparation.

Double sensitivity toward pH and temperature

Figure 2A shows the pH effect on both kinds of microspheres. As expected, the P(S-AA) particles show a pH-induced transition characterized by a decrease in size at lower pH values, as the protonation facilitates hydrogen bonding between the carboxylic acid groups and thus the expulsion of water from the shell. The stimuli responsiveness of the hydrogel particles can be manifested by a volume phase transition (VPT), analogous to the cloud points of linear polymers. The VPT happens here between pH 6 and 7. The pK_a of the monomer is 4.3, but it is known that the polymerization, the chains entanglements, and the presence of hydrophobic units all may affect the value of

Can. J. Chem. Downloaded from www.nrcresearchpress.com by Renmin University of China on 09/02/12
For personal use only.

Fig. 1. TEM images (top) of (A) P(S-AA) and (B) P(S-AA-NIPAM) microspheres, showing the spherical and core-shell structures and SEM images (bottom) of the dried films showing the self-assembly of the particles into crystalline colloidal arrays.



the effective pK_a.[25,26] In this case, it may be shifted to a higher value. The P(S-AA-NIPAM) particles show a similar behavior versus pH with a decrease in size at acidic pH. The transition for the P(S-AA-NIPAM) microspheres versus pH at RT occurs over the same range of pH, but the change in size is less significant because of the smaller amount of AA in the shell in comparison to the P(S-AA) particles. At 46 °C, above the LCST of PNIPAM, the polymer becomes more hydrophobic and shrinks, causing a decrease in size. As a result, the particles are less pH-responsive with a broader transition and a smaller change in size than at lower temperatures.

In addition to the pH responsiveness, the P(S-AA-NIPAM) microspheres clearly demonstrate a temperature sensitivity, as shown in Fig. 2B. At pH 9, all the acrylic acid units are deprotonated, making the shell highly hydrophilic. There is a sharp VPT at ca. 30 °C, slightly under the known LCST of linear PNIPAM (32 °C), probably because the hydrophobic polystyrene core may lower the apparent hydrophilicity. The VPT at pH 3.5 (lower than the pK_a) is more gradual and spread over a temperature range of over 20 °C with a smaller change in size. Under this condition, PAA is protonated and less swollen, decreasing the hydrophilicity and making the particles less responsive to temperature. Matsuoka et al. showed that the addition of some ionic groups in PNIPAM particles sharpens the VPT compared with PNIPAM alone and attributed it to the presence of electrorepulsive force decreasing entanglements and interactions between the PNIPAM chains.[27]

Crystalline colloidal arrays

When the concentration is sufficiently high, both P(S-AA) and P(S-AA-NIPAM) microsphere samples can self-assemble into CCAs and exhibit intense color, which varies with the angle of the incident light, as a result of visible light diffraction. The diffraction of light by the CCAs formed by the microspheres follows Bragg's law:

$$[1] \qquad m\lambda = 2nd_{hkl}\sin\theta$$

where m is the order of diffraction, λ the wavelength of the diffracted light, n the refractive index of the CCAs, d_{hkl} the interplanar spacing for the lattice plane defined by the Miller indices (hkl), and θ the angle between the incident light and the diffracting lattice plane. The refractive index of a mixture, such as a solution of polymer in water, is regarded as additive and thus can be estimated from eq. [2]:

$$[2] \qquad n = n_{\mathrm{p}}\varphi_{\mathrm{p}} + n_{\mathrm{w}}(1 - \varphi_{\mathrm{p}})$$

where φ_{p} is the volume fraction of the particles and n_p and n_{w} are the refractive indices of the particles and water, respectively. The refractive index of the polymeric particles is estimated according to eq. [2] from the refractive indices of the corresponding homopolymers found in the literature[28–30] and the volume fractions of the core and shell as determined from TEM images. In the case of P(S-AA-NIPAM), the PAA/PNIPAM ratio in the shell is assumed to be identical to the feed ratio.

Light diffraction is observed over a wide range of particle concentrations, as shown in Figs. 3A and 3B, with the

Can. J. Chem. Downloaded from www.nrcresearchpress.com by Renmin University of China on 09/02/12
For personal use only.

Fig. 2. (A) Hydrodynamic diameters of P(S-AA) and P(S-AA-NIPAM) as a function of pH, and (B) hydrodynamic diameters of P(S-AA-NIPAM) as a function of temperature showing its double sensitivity.

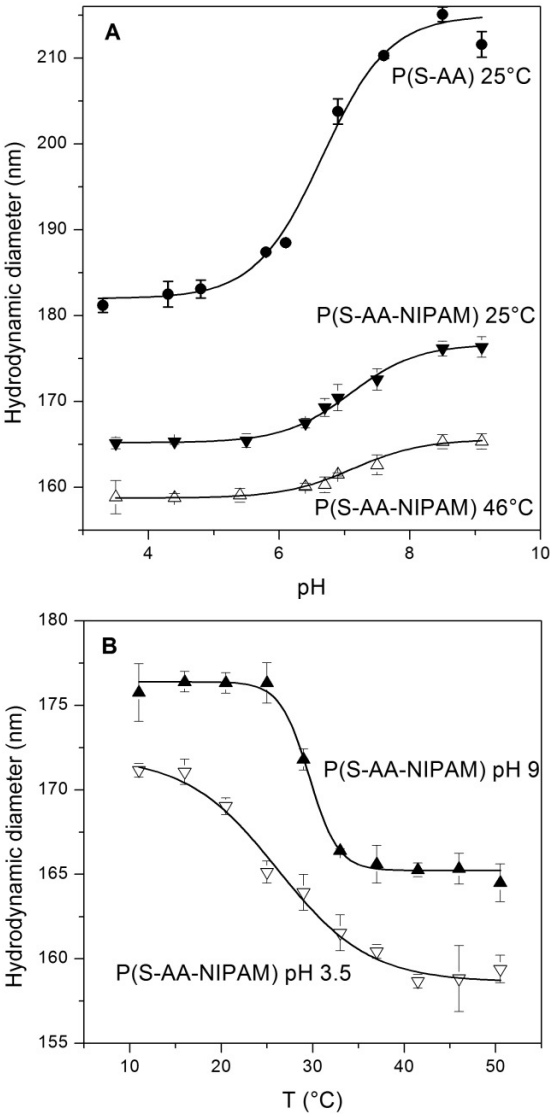
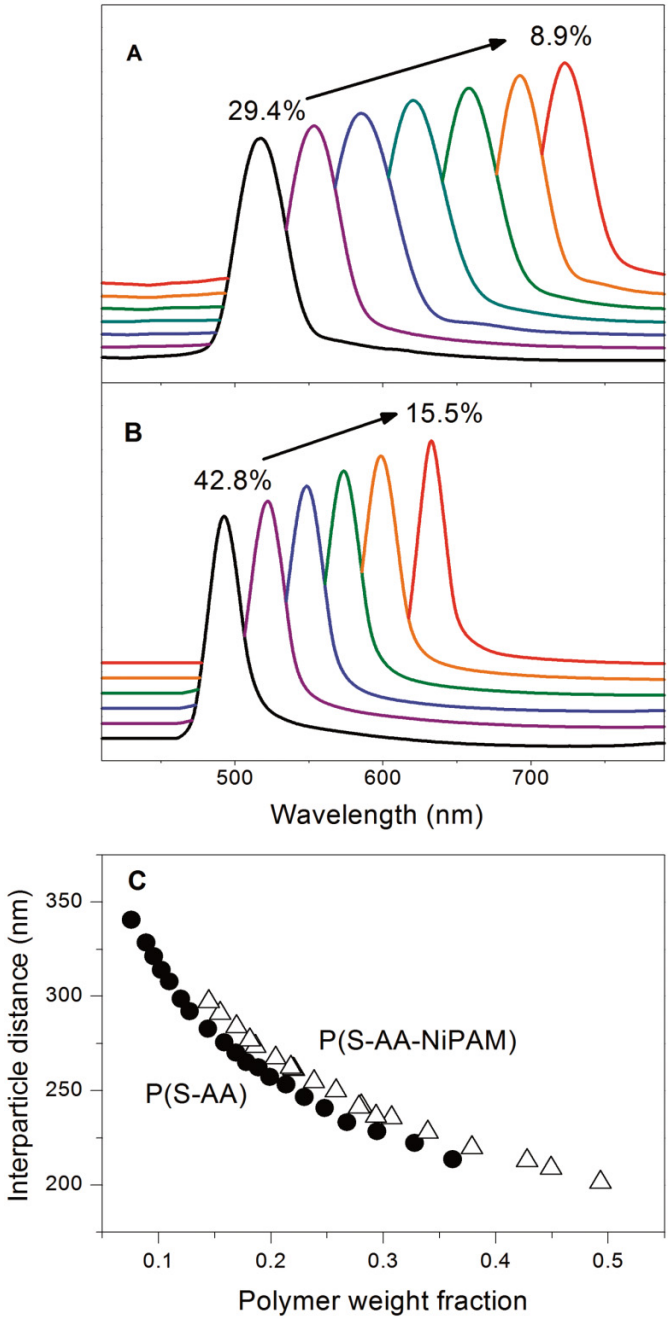


Fig. 3. Evolution of the diffraction spectra upon dilution of the CCAs of (A) P(S-AA) and (B) P(S-AA-NIPAM) particles. (C) The evolution of the estimated interparticle distance versus the polymer weight fraction. Spectra are normalized to the same intensity for the highest peak for better comparison. Weight percentages of particles in water are indicated in A and B.



diffraction peaks red-shifting upon dilution. Figure 3C shows the estimated interparticle distance versus the particle weight fraction. The interparticle distance was obtained through the lattice space given by Bragg's law (eq. [1]) by using the estimated values of refractive index (eq. [2]). It is interesting to compare the smallest interparticle distance, corresponding to the highest concentration obtained, to the microsphere size. The estimated interparticle distance for P(S-AA) CCAs at 36 wt% is 214 nm for a value of refractive index of 1.40. For P(S-AA-NIPAM) CCAs at 49 wt%, the estimated interparticle distance is 201 nm for a refractive index of 1.43. For both kinds of CCAs, these values are higher than the hydrodynamic diameters of the particles, 203 and 170 nm for P(S-AA) and P(S-AA-NIPAM), respectively. This may be an indicator that the CCAs are not close-packed, even at the highest concentrations obtained.

Figure 3C shows the same decreasing trend of the interparticle distances with the particle concentration for both kinds of particles. As the sample is diluted, the particles move further away from each other while maintaining the crystalline structure, leading to a larger interparticle distance and thus a higher wavelength of diffracted light. At some point of dilution (7 and 14 wt% for P(S-AA) and P(S-AA-NIPAM), respectively), the order is disrupted, highlighted by the disappearance of the diffraction peak. At this distance (estimated to be ca. 350 and 300 nm for P(S-AA) and P(S-AA-NIPAM), respectively) the electrostatic repulsion between

Can. J. Chem. Downloaded from www.nrcresearchpress.com by Renmin University of China on 09/02/12
For personal use only.

particles is not strong enough and is overcome by the Brownian motion, leading to a disordered suspension. As expected, with similar sizes, the P(S-AA) particles remain crystalline until 7 wt%, compared with only 14 wt% for the P(S-AA-NIPAM) particles: fewer charges mean weaker electrostatic interactions that are effective over shorter distances.

The P(S-AA-NIPAM) microspheres in dilute suspensions clearly demonstrate double sensitivity through their change in size. There is a greater complexity for more concentrated samples as the particles are packed into CCAs.

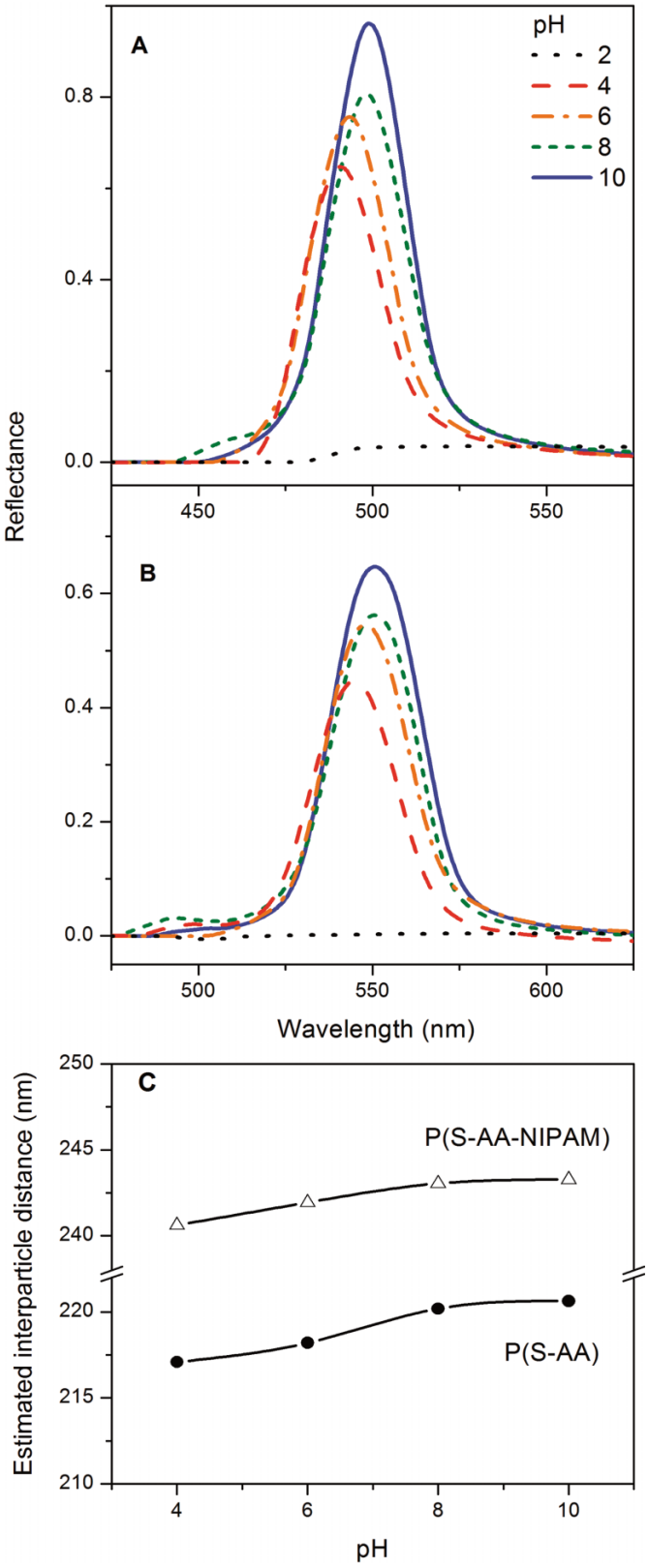
In Fig. 4, the effect of pH on CCA diffraction is shown. Both kinds of particles show the same trend. At pH 2, the acrylic acid residues chains are fully protonated decreasing the surface charge density. In addition, compared with pH 4, the aqueous medium at pH 2 has a higher ionic strength because of the $HCl_{(aq)}$ added to adjust the pH. The higher ionic strength results in weaker electrostatic interactions.[31,32] According to the DLS experiments, this happens for all pH values lower than 3, leading to the aggregation of particles in dilute suspensions. For the CCAs, the electrostatic repulsion is not strong enough to stabilize the system, causing a total loss of order. Between pH 4 and 10, the microspheres are organized into CCAs as shown by the presence of the diffraction peaks. At pH 10, the diffraction peaks are intense, while the PAA chains are fully deprotonated. As the pH decreases, the peaks become less intense and start to shift towards shorter wavelengths, indicating that the particles are closer to each other with a certain loss of order. Figure 4C summarizes the variation of the estimated interparticle distance as a function of pH. The same tendency is observed for both kinds of particles, but the changes seem to be larger for the P(S-AA) particles for which the variation of the surface charge density is more significant.

The thermo-responsiveness was also studied for the CCAs of P(S-AA-NIPAM), as shown in Fig. 5. First, a very concentrated sample at 49 wt% of the particles was studied at pH 7 (Fig. 5B). The increase in temperature causes a blue shift of the diffraction with a decrease of intensity, similar to the effect of pH. However, contrary to pH, the change in temperature does not affect the electrostatic repulsion but does affect the van der Waals interactions through the Hamaker constant, which increases from the swollen to the collapsed states of PNIPAM. At pH 4 (Fig. 5A), the shift is more significant, probably due to weaker electrostatic interactions, which make the system more sensitive to the van der Waals interactions. This proposed origin for the diffraction peak shift is further confirmed by the results obtained with a less concentrated sample (Fig. 5C). At this concentration (26 wt %), the particles are further away from each other and the van der Waals interactions are weaker between them, despite the increase of the Hamaker constant. As a result, the increase in temperature does not affect the interparticle distance to any significant extent, only a small decrease of the diffraction peak intensity due to the faster Brownian motion.

Conclusion

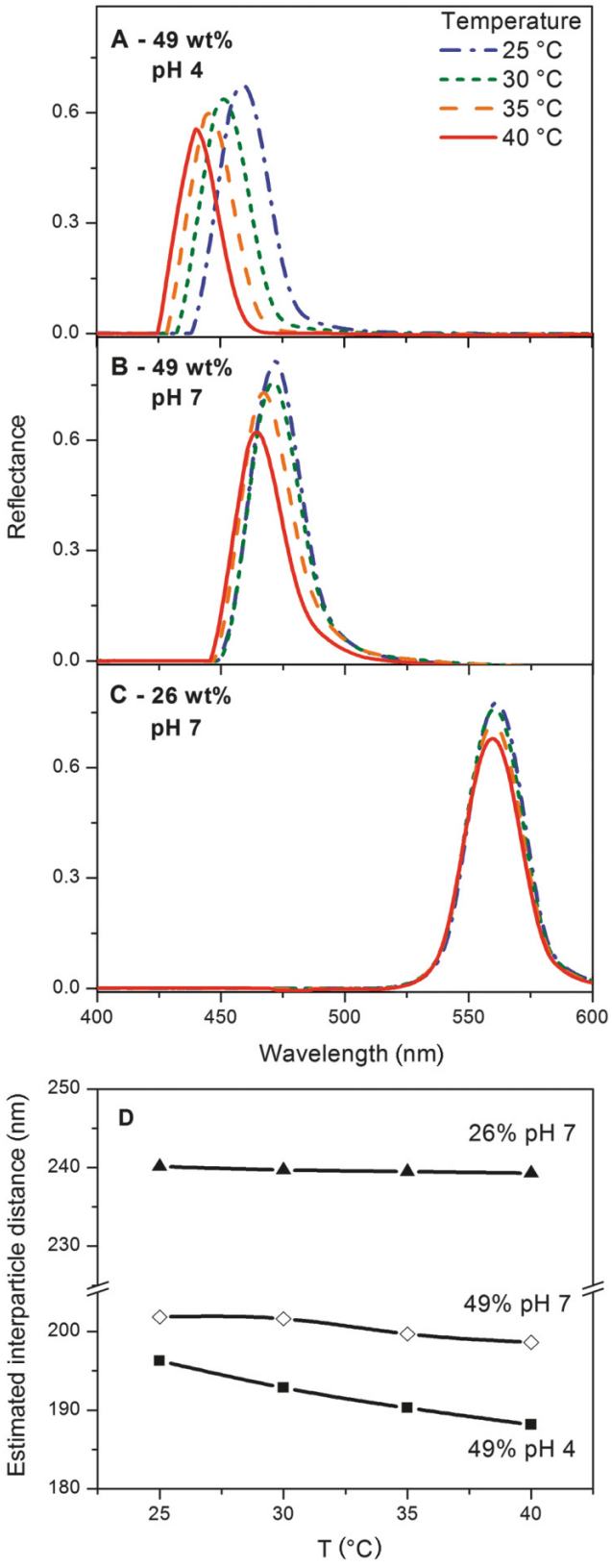
Core-shell microspheres with double sensitivity have been made via a simple two-step emulsion polymerization. The copolymerization of NIPAM and AA in the shell makes the particles responsive to changes in both pH and temperature.

Fig. 4. Diffraction spectra of the CCAs of (A) P(S-AA) and (B) P(S-AA-NIPAM) particles at different pH values with a particle concentration of 28 wt% at 25 °C. (C) The variation of the estimated interparticle distance as a function of pH.



Can. J. Chem. Downloaded from www.nrcresearchpress.com by Renmin University of China on 09/02/12
For personal use only.

Fig. 5. Diffraction spectra (A, B and C) of the CCAs of P(S-AA-NIPAM) particles at different temperatures under the specified conditions. (D) The variation of the estimated interparticle distance as a function of temperature. Notice the blue shift (towards shorter wavelengths) for the more concentrated samples.



It appears that the best sensitivity to temperature is obtained at high pH values, while the highest pH sensitivity is observed at low temperatures: the VPT is more intense and sharper when the shell is more hydrophilic. The CCAs obtained from these particles exhibit a good stability over a wide range of concentrations and also responsiveness to both temperature and pH stimuli. The increase of temperature and the decrease of pH both cause a decrease of the interparticle distance and a reduced order of the CCAs. These behaviors appear to be related to the nature and evolution of the interactions between particles rather than the change of particles size at the VPTs. The understanding of the self-assembly of the core-shell particles and the response of the CCAs toward the external stimuli is essential to their applications, especially in the design of biosensors by the use of such materials.

Acknowledgments

Financial support from Natural Sciences and Engineering Research Council of Canada, Le Fonds de recherche du Québec and the Canada Research Chair program is gratefully acknowledged. Merci à Messieurs Martin Lambert and Jean-François Myre pour leur aide dans la conception et fabrication du porte-cuvette permettant le contrôle de la température. XXZ is indebted to Professor T.H. Chan for encouragements during his graduate studies at McGill University.

References

(1) Kawaguchi, H. *Prog. Polym. Sci.* **2000**, *25* (8), 1171. doi:10.1016/S0079-6700(00)00024-1.
(2) Garcia, A.; Marquez, M.; Cai, T.; Rosario, R.; Hu, Z.; Gust, D.; Hayes, M.; Vail, S. A.; Park, C.-D. *Langmuir*, **2007**, *23* (1), 224. doi:10.1021/la061632n.
(3) Pelton, R. *Adv. Colloid Interface Sci.* **2000**, *85* (1), 1. doi:10.1016/S0001-8686(99)00023-8.
(4) Colonne, M.; Chen, Y.; Wu, K.; Freiberg, S.; Giasson, S.; Zhu, X. X. *Bioconjug. Chem.* **2007**, *18* (3), 999. doi:10.1021/bc060302b.
(5) Zhang, Y.; Guan, Y.; Zhou, S. *Biomacromolecules*, **2006**, *7* (11), 3196. doi:10.1021/bm060557s.
(6) Lapeyre, V.; Gosse, I.; Chevreux, S.; Ravaine, V. *Biomacromolecules*, **2006**, *7* (12), 3356. doi:10.1021/bm060588n.
(7) Foulger, S. H.; Kotha, S.; Sweryda-Krawiec, B.; Baughman, T. W.; Ballato, J. M.; Jiang, P.; Smith, D. W. J., Jr. *Opt. Lett.* **2000**, *25* (17), 1300. doi:10.1364/OL.25.001300.
(8) Gates, B.; Lu, Y.; Li, Z. Y.; Xia, Y. *Appl. Phys., A Mater. Sci. Process.* **2003**, *76* (4), 509. doi:10.1007/s00339-002-1893-7.
(9) Xu, X.; Goponenko, A. V.; Asher, S. A. *J. Am. Chem. Soc.* **2008**, *130* (10), 3113. doi:10.1021/ja077979+.
(10) Ding, Z.; Guan, Y.; Zhang, Y.; Zhu, X. X. *Polymer*, **2009**, *50* (17), 4205. doi:10.1016/j.polymer.2009.07.001.
(11) Ben-Moshe, M.; Alexeev, V. L.; Asher, S. A. *Anal. Chem.* **2006**, *78* (14), 5149. doi:10.1021/ac060643i.
(12) Goponenko, A. V.; Asher, S. A. *J. Am. Chem. Soc.* **2005**, *127* (30), 10753. doi:10.1021/ja051456p.
(13) Lyon, L. A.; Debord, J. D.; Debord, S. B.; Jones, C. D.; McGrath, J. G.; Serpe, M. J. *J. Phys. Chem. B*, **2004**, *108* (50), 19099. doi:10.1021/jp048486j.
(14) Debord, J. D.; Lyon, L. A. *Langmuir*, **2003**, *19* (18), 7662. doi:10.1021/la0342924.
(15) Debord, J. D.; Lyon, L. A. *J. Phys. Chem. B*, **2000**, *104* (27), 6327. doi:10.1021/jp001238c.

(16) Pelton, R. H. *J. Polym. Sci. A Polym. Chem.* **1988**, *26* (1), 9. doi:10.1002/pola.1988.080260102.
(17) Meng, Q.; Li, Z.; Li, G.; Zhu, X. X. *Macromol. Rapid Commun.* **2007**, *28* (16), 1613. doi:10.1002/marc.200700295.
(18) Li, G.; Pandya, P. D.; Seo, S. S. *Int. J. Polym. Anal. Charact.* **2009**, *14* (4), 351. doi:10.1080/10236660902875208.
(19) Santos, A. M.; Elaissari, A.; Martinho, J. M. G.; Pichot, C. *Polymer*, **2005**, *46* (4), 1181. doi:10.1016/j.polymer.2004.11.069.
(20) Berndt, I.; Richtering, W. *Macromolecules*, **2003**, *36* (23), 8780. doi:10.1021/ma034771+.
(21) Li, X.; Zuo, J.; Guo, Y.; Yuan, X. *Macromolecules*, **2004**, *37* (26), 10042. doi:10.1021/ma048658a.
(22) Chen, Y.; Gautrot, J. E.; Zhu, X. X. *Langmuir*, **2007**, *23* (3), 1047. doi:10.1021/la0624945.
(23) Xiao, X. C.; Chu, L. Y.; Chen, W. M.; Wang, S.; Xie, R. *Langmuir*, **2004**, *20* (13), 5247. doi:10.1021/la036230j.
(24) Polpanich, D.; Tangboriboonrat, P.; Elaïssari, A. *Colloid Polym. Sci.* **2005**, *284* (2), 183. doi:10.1007/s00396-005-1366-6.
(25) Mafé, S.; García-Morales, V.; Ramírez, P. *Chem. Phys.* **2004**, *296* (1), 29. doi:10.1016/j.chemphys.2003.09.033.
(26) Barba, A.; Dalmoro, A.; De Santis, F.; Lamberti, G. *Polym. Bull.* **2009**, *62* (5), 679. doi:10.1007/s00289-009-0040-4.
(27) Matsuoka, H.; Fujimoto, K.; Kawaguchi, H. *Polym. J.* **1999**, *31* (11–2), 1139. doi:10.1295/polymj.31.1139.
(28) Brandrup, J.; Immergut, E. H.; Grulke, E. A.; Abe, A.; Bloch, D. R. *Polymer Handbook*; 4th ed.; John Wiley and Sons, New York, 1999;2005; ISBN:0–471–47963–5.
(29) Nerapusri, V.; Keddie, J. L.; Vincent, B.; Bushnak, I. A. *Langmuir*, **2006**, *22* (11), 5036. doi:10.1021/la060252z.
(30) Reufer, M.; Dıaz-Leyva, P.; Lynch, I.; Scheffold, F. *Eur. Phys. J. E*, **2009**, *28* (2), 165. doi:10.1140/epje/i2008-10387-2.
(31) Li, Q.; Jonas, U.; Zhao, X. S.; Kappl, M. *Asia-Pac. J. Chem. Eng.* **2008**, *3* (3), 255. doi:10.1002/apj.144.
(32) Liang, Y.; Hilal, N.; Langston, P.; Starov, V. *Adv. Colloid Interface Sci.* **2007**, *134–135*, 151. doi:10.1016/j.cis.2007.04.003.

Can. J. Chem. Downloaded from www.nrcresearchpress.com by Renmin University of China on 09/02/12
For personal use only.

The role of magnetic nanoparticles (MNP) as reducing agents in an MNP-supported Pd–catalyst for the reductive homocoupling of aryl halides

Jie Zheng, Shengyue Lin, Bi-Wang Jiang, Todd B. Marder, and Zhen Yang

Can. J. Chem. Downloaded from www.nrcresearchpress.com by Renmin University of China on 09/02/12
For personal use only.

Abstract: A palladium pincer catalyst grafted onto the surface of magnetic nanoparticles (MNPs) has been developed. This material effectively catalyzes the reductive homocoupling of various aryl halide substrates, with the MNP support acting as the reducing agent. The catalyst can be recycled up to five times in the absence of additional reducing agent to give almost quantitative yields of biaryl homocoupling products. After the reducing power of the MNP has been depleted, the supported Pd complex remains an effective catalyst for Suzuki–Miyaura cross-coupling.

Key words: magnetic nanoparticles, reducing agent, supported Pd catalyst, reductive homocoupling, aryl halides.

Résumé : On a développé un catalyseur à tenaille à base de palladium greffé sur la surface de nanoparticules magnétiques (NPM). Ce matériau catalyse d'une façon efficace l'homocouplage réducteur de divers substrats d'halogénures d'aryle et les nanoparticules magnétiques agissent alors comme agent réducteur. Le catalyseur peut aussi être recyclé jusqu'à cinq fois, sans addition de nouvel agent réducteur, pour conduire à des rendements pratiquement quantitatifs de produits biaryles d'homocouplage. Une fois que le pouvoir réducteur des nanoparticules magnétiques a disparu, le complexe de palladium présent sur le support continue à être un catalyseur efficace pour la réaction de couplage croisé de Suzuki–Miyaura.

Mots-clés : nanoparticules, agent réducteur, catalyseur de palladium, réducteur, homocouplage.

[Traduit par la Rédaction]

Introduction

Palladium-catalyzed coupling reactions are among the most useful synthetic methods for the formation of carbon–carbon and carbon–heteroatom bonds and are widely utilized to assemble a vast range of important molecules in pharmaceutical, agricultural, natural product, and material sciences.[1] Using homogeneous palladium catalysis, a high reaction rate, turnover number (TON), selectivity, and yield are often possible after addition of the appropriate ligand.[2] However, the main drawback of homogeneous catalysis is associated with the separation and recycling of the catalyst. This aspect leads to a loss of expensive metal (and ligands), as well as to the presence of metal impurities in the products. The complete removal of residual metals is a major problem especially for pharmaceutical products, where carryover of metal impurities may cause serious problems in the production of many formulations.[3]

Recently, magnetic nanoparticles (MNPs)[4] have emerged as new catalyst supports because of their facile separation from the reaction mixture with the aid of an external magnet.[4] In this regard, we initiated a systematic program to develop novel types of grafted metal–catalysts on MNP,[5] and to apply them in metal-catalyzed reactions, as such types of catalysts not only can perform with superior catalytic activities compared with their corresponding bulk metals,[6] but also provide increased loading capacity. Herein, we report our new MNP-supported Pd pincer complex, which can catalyze the reductive homocoupling of aryl halides in high yields and can be recycled up to five times *in the absence of added reducing agents* without loss of activity. We show that Pd leaching is not responsible for the subsequent loss of activity for reductive homocoupling as the supported catalyst remains active for Suzuki–Miyaura cross-coupling catalysis.

Results and discussion

The MNPs utilized for immobilizing the Pd–catalyst were synthesized via a thermal decomposition approach according to the procedure reported by Cai and Wan.[7] Thus, the reaction of $Fe(acac)_3$ in triethylene glycol leads to the MNP. The formed MNPs were characterized by transmission electron microscopy (TEM), and the TEM image (Fig. 1) shows that they are relatively uniform with an average size of 6 ± 1 nm.

The synthesis of the NCN pincer ligand commenced as outlined in Scheme 1.

The commercially available 5-aminoisophthalic acid **1** was first converted to its diethyl ester **2**,[8] followed by $LiAlH_4$

Received 28 April 2011. Accepted 10 July 2011. Published at www.nrcresearchpress.com/cjc on 8 December 2011.

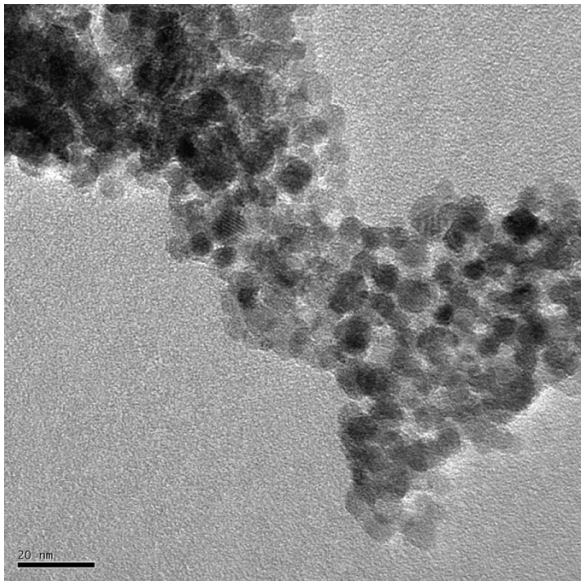
J. Zheng, S. Lin, B.-W. Jiang, and Z. Yang. Laboratory of Chemical Genomics and Nano-micro Material Research Center, School of Chemical Biology and Biotechnology, Shenzhen Graduate School of Peking University, Shenzhen, China, 518055.
T.B. Marder. Department of Chemistry, Durham University, South Road, Durham DH1 3LE, UK.

Corresponding authors: Todd B. Marder (e-mail: todd.marder@durham.ac.uk) and Zhen Yang (e-mail: zyang@pku.edu.cn)

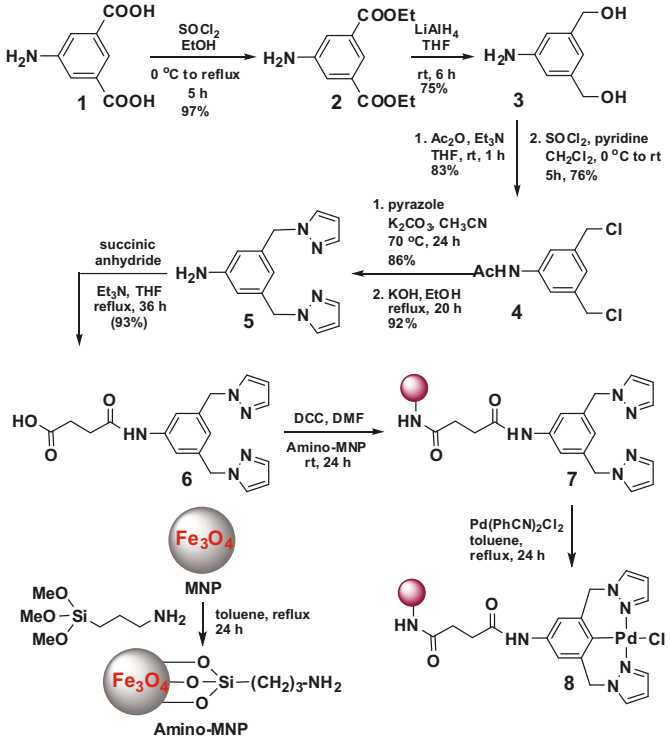
This article is part of a Special Issue dedicated to Professor Tak-Hang Chan.

Can. J. Chem. Downloaded from www.nrcresearchpress.com by Renmin University of China on 09/02/12
For personal use only.

Fig. 1. Transmission electron microscopy (TEM) image of magnetic nanoparticles (MNPs).

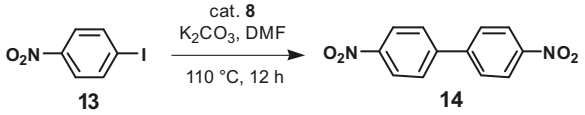


Scheme 1. Synthesis of magnetic nanoparticle (MNP) - grafted NCN pincer – Pd catalyst **8**.



reduction to afford diol **3** in 75% overall yield in two steps. An efficient acylation–chlorination sequence subsequently elaborated **3** into bis(chloromethyl)aniline **4** in 63% overall yield.[9] Compound **4** then underwent nucleophilic substitution of pyrazole, followed by hydrolysis to give bispyrazol-substituted aniline **5** in 79% yield (two steps). The substituted aniline **5** was then coupled with succinic anhydride in the presence of Et_3N to give amide **6** in 93% yield. Amide **6** was coupled to the MNP under standard conditions[7] to deliver **7**, which was then treated with $Pd(PhCN)_2Cl_2$ in refluxing toluene to afford the desired MNP-supported Pd–catalyst **8** as a black powder. The Pd loading level of the catalyst is 0.020 mmol/g, determined by elemental analysis.

Table 1. Homocoupling reaction of iodonitrobenzene.



Cycle	Conversion (%)[a]
1	>99
2	>99
3	>99
4	>99
5	>99

Note: All reactions were performed in DMF (3 mL) at 110 °C using MNP–Pd (300 mg, 2.0 mol % Pd loading), substrate (0.3 mmol), and K_2CO_3 (0.36 mmol). MNP, magnetic nanoparticle.

[a]Determined by ^{1}H NMR.

To test the efficiency and reactivity of the newly generated magnetic catalyst **8** in Pd-catalyzed coupling reactions, we first selected the Suzuki–Miyaura reaction because of its importance in the synthesis of unsymmetrical biaryls.[10]

Thus, when aryl iodide **9** was reacted with phenyl boronic acid **10** under typical Suzuki–Miyaura coupling conditions in the presence of catalyst **8**, the expected product **11** was obtained in 70% yield, together with the formation of 15% of the symmetrical biaryl product **12**, derived, surprisingly, from the reductive homocoupling of the aryliodide.

Symmetric biaryls Ar–Ar generated from oxidative homocoupling of the arylboronic acid $ArB(OH)_2$ are typically observed in Suzuki–Miyaura reactions, as they result from the process that reduces Pd(II) catalyst precursors to Pd(0) active catalysts.[10] However, the reductive homocoupling product derived from the aryl halide is seldom reported in Suzuki–Miyaura reactions.[11]

We attributed the formation of the homocoupling product **12** to the grafted magnetite nanocatalyst **8**. We also envisaged that the MNP derived from Fe_3O_4 might play the role of the reducing agent. We therefore decided to explore the feasibility of carring out the useful reductive homocoupling of aryl halides without the addition of any other reducing agents.

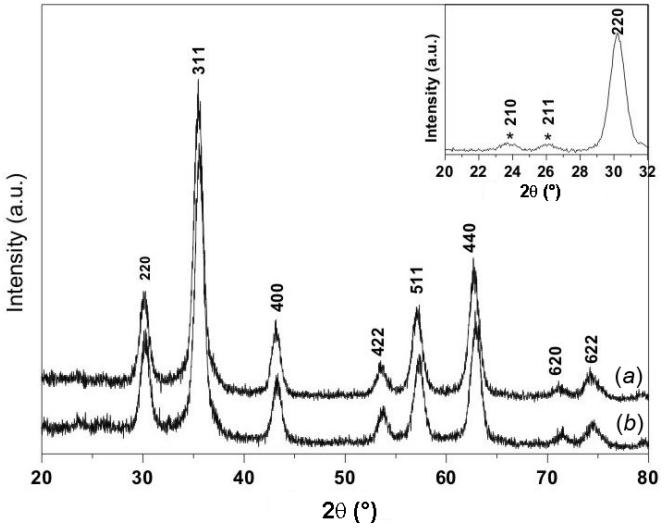
Thus, **13** was selected as the substrate, and the reaction was carried out in DMF for 12 h at 110 °C in the presence of K_2CO_3 and catalyst **8** (2.0 mol %). To our delight, the expected symmetric biaryl product **14** was obtained in quantitative yield (Table 1). It is noteworthy that the same catalyst could be recycled five times without loss of catalytic activity.

However, when the catalyst was continually applied to this reaction more than five times, the reductive homocoupling yield was decreased dramatically, indicating that the reducing capability of the MNPs had diminished. We also noticed that the color of the nanoparticles changed from black to red-brown after the homocoupling reaction, which suggested that Fe_3O_4 might be undergoing oxidation to Fe_2O_3. To prove our hypothesis, we characterized the nanoparticles by X-ray diffraction.

As shown in Fig. 2, the diffraction peaks indicate that the magnetite particles have been oxidized to maghemite after

Can. J. Chem. Downloaded from www.nrcresearchpress.com by Renmin University of China on 09/02/12
For personal use only.

Fig. 2. X-ray diffraction patterns. (*a*) The magnetic nanoparticles before catalytic reactions. (*b*) The magnetic nanoparticles after five catalytic cycles. The inset shows a magnification of the region 2θ = 20°–32° of curve (*b*).



five catalytic cycles, as evidenced by the observation of the enhancement of characteristic (210) and (211) diffraction peaks of maghemite in the XRD patterns of the nanoparticles after the coupling reaction.[12]

After the homocoupling reaction, catalyst **8** was simply attracted to the side of the vial by an external magnet (Fig. 3), the reaction mixture was transferred out of the flask, and the remaining catalyst was washed three times with CH_2Cl_2 before recharging with the substrate and the solvent.

To verify the role of MNP-grafted catalyst **8** in this coupling reaction, we then carried out comparison reactions. Thus, catalyst **8** was replaced with NCN pincer ligand and $Pd(PhCN)_2Cl_2$, respectively, to carry out the same reaction as depicted in Table 1. As a result, no coupling product **14** was observed, indicating that neither the NCN pincer ligand nor $Pd(PhCN)_2Cl_2$ can catalyze the observed homocoupling individually.

To clarify further if the leached Pd species is the active catalyst, we carried out the following reaction. Accordingly, the coupling reaction was carried out under the conditions listed in Table 1. After one catalytic cycle, the MNP-grafted catalyst **8** was removed with a magnet. The remaining solution was analyzed by GC–MS, and the result indicated that the conversion of the homocoupling reaction is 99%. To this solution were added the same amounts of **13** and K_2CO_3, and the formed mixture first underwent GC–MS analysis and then was heated at 110 °C for 12 h. The analytical results indicated that no homocoupling reaction proceeded by comparison of their GC–MS spectra before and after the reaction (Figs. 4–6). Thus, Pd species leached from the MNP-grafted catalyst **8** as an active catalyst could be precluded.

To profile the substrate scope, we selected nine additional substrates (**15**–**23**) for the homocoupling reactions under the conditions listed in Table 2. To our delight, all of the substrates gave essentially quantitative yields of the coupling products[13] (Table 2).

To evaluate whether the MNP plays a critical role in this reductive homocoupling process, we carried out the coupling

Fig. 3. Photograph of the system before and after reaction and separation of the magnetic nanoparticles.

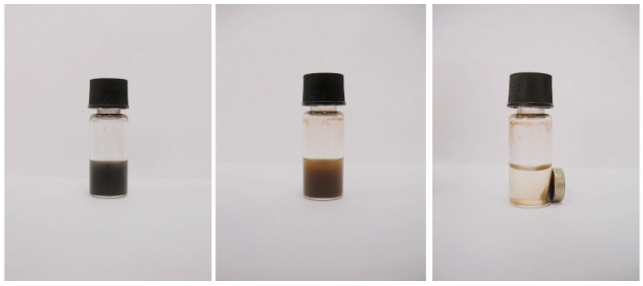
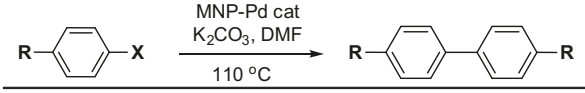


Table 2. Homocoupling reaction of aryl halides.

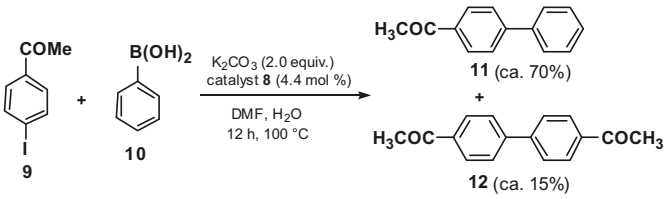


Entry	R	X	Time (h)	Yield (%)[a]
1	COOEt (**15**)	I	12	>99
2	COOMe (**16**)	I	12	>99
3	CF_3 (**17**)	I	12	>99
4	F (**18**)	I	12	>99
5	H (**19**)	I	12	>99
6	Me (**20**)	I	24	>99
7	OMe (**21**)	I	24	>99
8	NO_2 (**22**)	Br	24	>99
9	CHO (**23**)	Br	24	>99

Note: All reactions were performed in DMF (3 mL) at 110 °C using MNP–Pd (300 mg, 2.0 mol % Pd loading), substrate (0.3 mmol), and K_2CO_3 (0.36 mmol). MNP, magnetic nanoparticle.

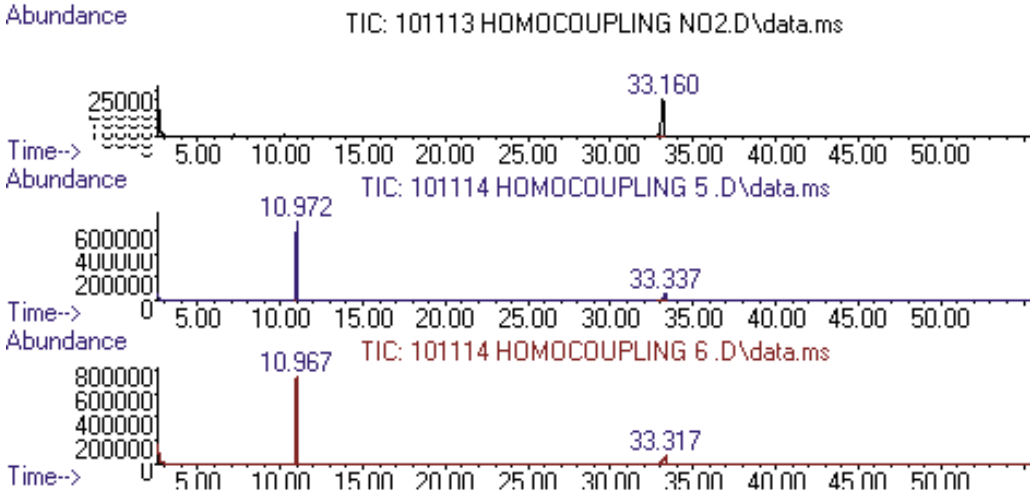
[a]Determined by NMR.

Scheme 2. Syntheses of compounds **11** and **12**.



reaction of **13** by replacing catalyst **8** with a combination of amino-MNP **6** and $PdCl_2(PhCN)_2$. The expected homocoupling indeed took place; however, considerable palladium aggregation was observed, and the catalyst system could not be recycled. Next, we also carried out the Suzuki–Miyaura reaction depicted in Scheme 2 with deactivated catalyst **8** (i.e., after five cycles in the homocoupling reaction). In this case, the coupling reaction between substrates **9** and **10** was catalyzed with deactivated catalyst **8** in the presence of DMF, K_2CO_3, and distilled water, the normal Suzuki–Miyaura product **12** was formed, and the previously observed homocoupling product **13** was not observed, indicating that (*i*) the MNPs in **8** serve as both the catalyst support and the reducing agent and (*ii*) Pd leaching is not responsible for the deactivation of the catalyst for the reductive homocoupling process.

Fig. 4. GC–MS spectra for the homocoupling reaction with or without magnetic nanoparticle (MNP) - grafted Pd–complex **8**. (Top) Spectra of the homocoupling product 4,4'-dinitrobiphenyl after one cycle with MNP-grafted Pd–complex **8** as catalyst. (Center) Spectra after removal of MNPs from the reaction mixture and addition of 1-iodo-4-nitrobenzene (0.3 mmol). The mixture was analyzed by GC–MS. (Bottom) After addition of K_2CO_3 (0.36 mmol) to the reaction mixture and the reaction was stirred at 110 °C for another 12 h. The mixture was analyzed by GC–MS.



Mechanistically, the formation of homocoupling products from aryl iodides might proceed through a process of sequential oxidative additions of aryl iodide to a MNP-grafted Pd–complex, accompanying by the in situ MNP-mediated reduction of the formed aryl palladium halide, and the generated MNP-grafted $PdAr_2$ species could undergo reductive elimination to give a reduced MNP-grafted Pd species and the biaryl, Ar–Ar. It is not useful at this time to speculate further on the nature of the Pd intermediates, as it is not clear whether a Pd(0)–Pd(II) or Pd(II)–Pd(IV) cycle is operating.

In summary, the Pd–pincer complex grafted onto MNP **8** exhibited good catalytic activity for the homocoupling of aryl halides to give symmetric biaryl compounds in the absence of additional reducing agents. This catalyst can be recycled up to five times without loss of catalytic activity. Our studies should stimulate further research in heterogeneous catalysis using MNP-grafted catalysts.

Experimental section

Materials and general procedure

All reactions were carried out under a nitrogen atmosphere with dry solvents under anhydrous conditions unless otherwise noted. All chemicals were commercially available and used without further purification. Solvents used in all the reactions were dried by standard procedures.

Reactions were monitored by thin-layer chromatography (TLC) carried out on 0.25 mm Tsingdao silica gel plates (60F-254) using UV light as the visualizing agent. Tsingdao silica gel (60, particle size 0.040–0.063 mm) was used for flash column chromatography.

Reagents were purchased at the highest commercial quality and used without further purification, unless otherwise stated. NMR spectra were recorded on a Brüker Avance 300 (^{1}H, 300 MHz; ^{13}C, 75.5 MHz) or a Brüker Avance 500 (^{1}H, 500 MHz; ^{13}C, 125 MHz). XRD was carried out on a D/max 2500PC X-ray diffractometer at room temperature.

Fig. 5. GC–MS spectrum report for Fig. 4.

```
 Signal      : TIC: 101113 HOMOCOUPLING NO2.D\data.ms

peak  R.T. first  max last  PK   peak      corr.    corr.    % of
  #   min   scan scan scan  TY  height     area     % max.   total
---  ----- ----- ---- ---- ---  -------   -------  ------  -------
 1  33.158  4491 4540 4573 BB 7   19809    2155337 100.00% 100.000%

                          Sum of corrected areas:     2155337
 Signal      : TIC: 101114 HOMOCOUPLING 5 .D\data.ms

peak  R.T. first  max last  PK   peak      corr.    corr.    % of
  #   min   scan scan scan  TY  height     area     % max.   total
---  ----- ----- ---- ---- ---  -------   -------  ------  -------
 1  10.972  1237 1246 1261 BB    768617  15835947 100.00%  68.218%
 2  33.340  4496 4567 4594 BB 7   60655   7377904  46.59%  31.782%

                          Sum of corrected areas:    23213851
 Signal      : TIC: 101114 HOMOCOUPLING 6 .D\data.ms

peak  R.T. first  max last  PK   peak      corr.    corr.    % of
  #   min   scan scan scan  TY  height     area     % max.   total
---  ----- ----- ---- ---- ---  -------   -------  ------  -------
 1  10.966  1231 1245 1254 BB    829221  16133377 100.00%  67.902%
 2  33.313  4493 4563 4597 BB 7   64243   7626288  47.27%  32.098%
```

Experimental procedures

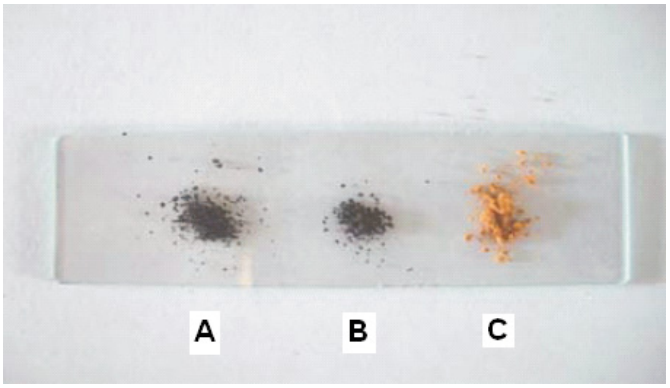
Synthesis of diethyl-5-(amino)isophthaloate (2)

To a stirred solution of 5-(amino)isophthalic acid **1** (5.0 g, 27.5 mmol) in absolute ethanol (100 mL) was added thionyl chloride (6.0 mL, 82.5 mmol) dropwise at 0 °C, and the formed mixture was stirred at reflux for 5 h. The solvent was removed in vacuum, the crude residue was dissolved in ethyl acetate, and the organic layer was washed with a saturated aqueous solution of sodium carbonate and then dried over sodium sulfate. The solvent was removed under vacuum to give diester **2** as a white solid in 97% yield. ^{1}H NMR (300 MHz, $CDCl_3$) δ: 8.07 (t, J = 1.2 Hz, 1H), 7.53 (d, J = 1.2 Hz, 2H), 4.39 (q, J = 7.2 Hz, 4H), 3.94 (bs, 2H), 1.41 (t, J = 7.2 Hz, 6H). ^{13}C NMR (75 MHz, $CDCl_3$) δ: 166.02, 146.58, 131.72, 120.50, 119.59, 61.14, 14.24. HRMS (*m/z*) calcd for $C_{12}H_{16}NO_4$ [M + H$^+$]: 238.1079; found: 238.1074.

Can. J. Chem. Downloaded from www.nrcresearchpress.com by Renmin University of China on 09/02/12
For personal use only.

Can. J. Chem. Downloaded from www.nrcresearchpress.com by Renmin University of China on 09/02/12
For personal use only.

Fig. 6. The color changes of MNP-grafted Pd–complex **8** before and after the homocoupling reaction. (*a*) Before reaction (black color). (*b*) MNP-grafted Pd–complex **8** heated to 110 °C in DMF for 60 h without color change (black color). (*c*) After the homocoupling reaction for five cycles, the color of MNP-grafted Pd–complex **8** was brownish.



Synthesis of 3,5-bis(hydroxymethyl)aniline (3)

To a slurry of $LiAlH_4$ (2.39 g, 63 mmol) in THF (200 mL), a solution of diethyl-5-(amino)isophthaloate (5.0 g, 21 mmol) in dry THF (100 mL) was added slowly at 0 °C with vigorous stirring. After this addition, the mixture was stirred initially at the same temperature for an additional 30 min and then at room temperature for 6 h. The reaction was quenched by the slow addition of ethyl acetate (20 mL) with vigorous stirring to consume the excess $LiAlH_4$. After stirring at the room temperature for 2 h, a saturated NH_4Cl solution (50 mL) was then added to hydrolyze the aluminum salt. After stirring for another 1 h, the resulting slurry was filtered through a pad of silica gel, and the pad was washed with ethyl acetate (3 × 100 mL). The filtrate was concentrated, and the residue was purified by flash chromatography on silica gel to give compound **3** (2.41 g) in 75% yield. ^{1}H NMR (300 MHz, DMSO-d_6) δ: 6.40 (s, 3H), 4.95 (t, J = 5.4 Hz, 4H,), 4.34 (br, 2H), 4.32 (br, 2H). ^{13}C NMR (75 MHz, DMSO-d_6) δ: 148.62, 143.21, 112.85, 111.01, 63.68. HRMS (*m*/*z*) calcd for $C_{12}H_{12}NO_2$ [M + H$^+$]: 154.0868; found: 154.0867.

Synthesis of* N*-acetyl-3,5-bis(chloromethyl)anilide (4)

To a solution of **3** (1.90 g, 12.4 mmol) in THF (100 mL) was sequentially added Et_3N (1.8 mol, 12.4 mmol) and acetic anhydride (1.2 mL, 12.4 mmol) at room temperature, and the mixture was stirred for 1 h. The reaction mixture was filtered, and the solid was washed with THF. The combined filtrates were concentrated and purified by flash chromatography on silica gel to give the amide (2.01 g) in 83% yield as a white solid. ^{1}H NMR (300 MHz, DMSO-d_6) δ: 9.85 (s, 1H), 7.41 (s, 2H), 6.92 (s, 1H), 5.15 (t, J = 5.7 Hz, 2H), 4.43 (d, J = 5.7 Hz, 4H), 2.02 (s, 3H). ^{13}C NMR (75 MHz, DMSO-d_6) δ: 168.51, 143.19, 139.43, 119.51, 115.84, 63.34, 24.40. HRMS (*m*/*z*) calcd for $C_{10}H_{14}NO_3$ [M + H$^+$]: 196.0974; found: 196.0964.

To a solution of the amide prepared above (1.84 g, 9.4 mmol) and pyridine (1.7 mL, 21 mmol) in CH_2Cl_2 (50 mL) was added thionyl chloride (1.5 mL, 21 mmol) in a dropwise manner at 0 °C, and the mixture was stirred at room temperature for 5 h. The reaction was quenched by the addition of water (30 mol), and the organic phase was then sequentially washed with water (2 × 30 mL), 1 N HCl (2 × 10 mL), and brine (2 × 10 mL), and the organic phase was finally dried over Na_2SO_4. The solvent was removed in vacuum, and the residue was purified by flash chromatography on silica gel to give **4** (1.66 g) in 76% yield. ^{1}H NMR (300 MHz, DMSO-d_6) δ: 7.53 (s, 2H), 7.16 (s, 1H), 4.54 (s, 4H), 2.19 (s, 3H). ^{13}C NMR (75 MHz, DMSO-d_6) δ: 168.51, 138.85, 138.54, 124.24, 119.65, 45.51, 24.53. HRMS (*m*/*z*) calcd for $C_{10}H_{12}Cl_2NO$ [M + H$^+$]: 232.0296; found: 232.0293.

Synthesis of 3,5-bis[(1*H*-pyrazol-1-yl)methyl]aniline (5)

To a solution of **4** (1.16 g, 5 mmol) in CH_3CN (30 mL) was added potassium carbonate (1.73 g, 12.5 mmol) and pyrazole (0.68 g, 10 mmol), and the mixture was refluxed for 24 h. The reaction mixture was filtered, and the solid was washed with CH_3CN (3 × 10 mL). The filtrate was concentrated in vacuum, and the residue was purified by flash chromatography on silica gel to give the intermediate dipyrazole (1.27 g) in 86% yield. ^{1}H NMR (300 MHz, $CDCl_3$) δ: 8.60 (s, 1H), 7.48–7.47 (m, 2H), 7.39–7.38 (m, 2H), 7.16 (s, 2H), 6.65 (s, 1H), 6.26–6.25 (m, 2H), 5.15 (s, 4H), 2.00 (s, 3H). ^{13}C NMR (75 MHz, $CDCl_3$) δ: 168.85, 139.67, 139.37, 137.97, 129.78, 121.47, 117.98, 106.05, 55.32, 24.18. HRMS (*m*/*z*) calcd for $C_{16}H_{18}N_5O$ [M + H$^+$]: 296.1511; found: 296.1511.

To a solution of the dipyrazole prepared above (1.18 g, 4 mmol) in 95% ethanol (50 mL) was added KOH (2.24 g, 40 mmol), and the mixture was refluxed for 20 h. The reaction mixture was neutralized by addition of a concentrated solution of HCl. The solvent was removed in vacuum, and the residue was extracted with CH_2Cl_2 (3 × 30 mL). The combined extracts were washed with a saturated solution of Na_2CO_3 (3 × 50 mL) and then dried over Na_2SO_4. The solvent was removed in vacuum, and the residue was purified by flash chromatography on silica gel to give **5** (0.93 g) in 92% yield. ^{1}H NMR (300 MHz, $CDCl_3$) δ: 7.54–7.53 (m, 2H), 7.38–7.37 (m, 2H), 6.46 (s, 1H), 6.38 (s, 2H), 6.28–6.27 (m, 2H), 5.19 (s, 4H), 3.69 (s, 2H). ^{13}C NMR (75 MHz, $CDCl_3$) δ: 147.34, 139.44, 138.43, 129.27, 116.61, 113.50, 105.88. 55.60. HRMS (*m*/*z*) calcd for $C_{14}H_{16}N_5$ [M + H$^+$]: 254.1406; found: 254.1403.

Synthesis of 4-{3,5-bis[(1*H*-pyrazol-1-yl)methyl] phenylamino}-4-oxobutanoic acid (6)

To a solution of **5** (0.76 g, 3 mmol) in dry THF (15 mL) was added triethylamine (0.5 mL, 3.5 mmol) and succinic anhydride (0.3 g, 3 mmol), and the mixture was refluxed for 36 h. A saturated solution of NH_4Cl (10 mL) was added, and the mixture was extracted with EtOAc (3 × 20 mL). The filtrate was concentrated in vacuum, and the residue was purified by flash chromatography on silica gel to give acid **6** (0.98 g) in 93% yield. ^{1}H NMR (500 MHz, DMSO-d_6) δ: 9.95 (s, 1H) 7.75–7.74 (m, 2H), 7.44–7.43 (m, 2H), 7.33 (s, 2H), 6.78 (s, 1H), 6.25–6.24 (m, 2H), 5.24 (s, 4H), 2.49–2.48 (m, 4H). ^{13}C NMR (125 MHz, DMSO-d_6) δ: 174.28, 170.74, 140.25, 139.56, 138.99, 130.69, 121.85, 117.84, 106.04, 55.20, 31.56, 29.35. HRMS (*m*/*z*) calcd for $C_{18}H_{20}N_5O_3$ [M + H$^+$]: 354.1566; found: 354.1561.

Can. J. Chem. Downloaded from www.nrcresearchpress.com by Renmin University of China on 09/02/12
For personal use only.

Synthesis of iron oxide nanocrystals

A typical procedure for the synthesis of MNPs was as follows: $Fe(acac)_3$ (7.1 g, 20 mmol) and triethylene glycol (250 mL) were directly added to a three-necked round-bottomed flask equipped with a condenser, mechanical stirrer, thermograph, and heating mantle, and the mixture was stirred under argon. The mixture was slowly heated to 180 °C first and kept at that temperature for 30 min and then quickly heated to reflux (~280 °C) and kept at reflux for another 30 min. After cooling to room temperature, a black homogeneous colloid (magnetite nanoparticles) was formed. To this solution was added ethyl acetate (500 mL), and the formed flocculation was separated from the solution with a magnet. The black precipitate was first redispersed in ethanol and then precipitated with ethyl acetate. This washing procedure was repeated twice to remove excess triethylene glycol and by-products completely, and the resulting MNPs were obtained by drying the precipitate in vacuum.

Synthesis of amino-functionalized iron oxide nanocrystals

Iron oxide nanocrystals (1.0 g) were refluxed with 3-aminopropyltrimethoxysilane (4.0 mL, 0.023 mmol) in dry toluene (6.0 mL) for 1 day, and the solids were separated by applying an external magnetic field and washed with dry acetone (6 × 30 mL). The resulting product was dried in vacuum for 1 h.

General procedure for the synthesis of MNP-supported palladium catalyst

To a solution of ligand **6** (0.043 g, 0.12 mmol) in DMF (4.0 mL) was added dicyclohexylcarbodimide (0.027 g, 0.13 mmol), and the resulting solution was stirred at room temperature for 1 h. To this solution was added the amine-terminated MNP (0.3 g), and the mixture was stirred at room temperature for 24 h. After the reaction, the solid was separated by applying an external magnetic field and washed with dry dichloromethane (6 × 10 mL). The residue was dispersed in dry toluene (10 mL), followed by addition of $Pd(PhCN)_2Cl_2$ (0.013 g, 0.017 mmol), and the resulting mixture was stirred at reflux for 24 h. The formed MNP-supported catalyst **8** was magnetically separated and washed with dry dichloromethane (6 × 10 mL).

Procedure for using the MNP-supported palladium catalyst in homocoupling reactions

To a solution of the aryl halide (0.3 mmol) and K_2CO_3 (50 mg, 0.36 mmol) in DMF (3 mL) was added catalyst **8** (0.300 g), and the mixture was heated at 110 °C for 12 or 24 h under a nitrogen atmosphere. After the reaction, a magnet was used to separate the catalyst, which was then washed with dry CH_2Cl_2 (10 mL). The combined organic phases were washed with water, dried with Na_2SO_4 and then evaporated. All of the coupling products have been previously reported.[13]

Synthesis of 4,4'-diacetylbiphenyl (12)

^{1}H NMR (300 MHz, $CDCl_3$) δ: 8.09 (d, 4H, J = 8.3 Hz), 7.75 (d, 4H, J = 8.3 Hz), 2.66 (s, 6H). ^{13}C NMR (75 MHz, $CDCl_3$) δ: 196.5, 143.3, 135.5, 127.9, 126.3, 25.6.[14]

Synthesis of 4,4'-dinitrobiphenyl (14)

^{1}H NMR (300 MHz, $CDCl_3$) δ: 8.37 (d, J = 8.1 Hz, 4H), 7.79 (d, J = 8.1 Hz, 4H). ^{13}C NMR (75 MHz, $CDCl_3$) δ: 148.00, 144.95, 128.31, 124.37.

Synthesis of 4,4'-diethylcarboxylatebiphenyl (15)

^{1}H NMR (300 MHz, $CDCl_3$) δ: 8.15–8.12 (m, 4H), 7.70–7.67 (m, 4H), 4.41 (q, J = 7.2 Hz, 4H), 1.42 (t, J = 7.2 Hz, 6H). ^{13}C NMR (75 MHz, $CDCl_3$) δ: 166.3, 144.2, 130.1, 129.9, 127.1, 61.0, 14.3. HRMS (*m*/*z*) calcd for $C_{18}H_{19}O_4$ [M^+]: 299.12834; found: 299.12738.

Synthesis 4,4'-dimethylcarboxylatebiphenyl (16)[14]

^{1}H NMR (300 MHz, $CDCl_3$) δ: 8.14–8.11 (m, 4H), 7.70–7.67 (m, 4H), 3.94 (s, 6H). ^{13}C NMR (75 MHz, $CDCl_3$) δ: 166.81, 144.29, 130.13, 129.64, 127.18, 52.15. HRMS (*m*/*z*) calcd for $C_{16}H_{15}O_4$ [M^+]: 271.09704; found: 271.09627.

Synthesis of 4,4'-ditrifluoromethylbiphenyl (17)[14]

^{1}H NMR (300 MHz, $CDCl_3$) δ: 7.74 (d, J = 8.3 Hz, 4H), 7.70 (d, J = 8.3 Hz, 4H). ^{13}C NMR (75 MHz, $CDCl_3$) δ: 143.2, 130.2 (q, J = 32.2 Hz), 127.5, 125.9 (q, J = 3.7 Hz), 122.2 (q, J = 272 Hz).

Synthesis of 4,4'-difluorobiphenyl (18)[14]

^{1}H NMR (300 MHz, $CDCl_3$) δ: 7.51 (m, 4H), 7.14 (t, 4H, J = 8.7 Hz). ^{13}C NMR (75 MHz, $CDCl_3$) δ: 164.00 (d, J = 246.4 Hz), 136.35 (d, J = 3.3 Hz), 128.5 (d, J = 8.1 Hz), 115.61 (d, J = 21.4 Hz).

Synthesis of biphenyl (19)[14]

^{1}H NMR (300 MHz, $CDCl_3$) δ: 7.85 (d, 4H, J = 7.5 Hz), 7.72 (t, 4H, J = 7.5 Hz), 7.52 (t, 2H, J = 7.3 Hz). ^{13}C NMR (75 MHz, $CDCl_3$) δ: 141.2, 128.7, 127.2, 127.1.

Synthesis of 4,4'-dimethylbiphenyl (20)[14]

^{1}H NMR (300 MHz, $CDCl_3$) δ: 7.47 (d, J = 8.1 Hz, 4H), 7.23 (d, 4H, J = 8.1 Hz), 2.38 (s, 6H). ^{13}C NMR (75 MHz, $CDCl_3$) δ: 138.22, 136.62, 129.36, 126.73, 20.99. HRMS (*m*/*z*) calcd for $C_{14}H_{13}$ (–): 181.10212; found: 181.10043.

Synthesis of 4,4'-dimethoxylbiphenyl (21)[14]

^{1}H NMR (300 MHz, $CDCl_3$) δ: 7.51 (d, 4H, J = 8.8 Hz), 6.97 (d, 4H, J = 8.8 Hz), 3.85 (s, 6H). ^{13}C NMR (75 MHz, $CDCl_3$) δ: 158.7, 133.5, 127.7, 114.1, 55.3.

Synthesis of 4,4'-diformylbiphenyl (23)

^{1}H NMR (300 MHz, $CDCl_3$) δ: 10.10 (s, 2H), 8.00 (d, J = 8.4 Hz, 4H), 7.81 (d, J = 8.4 Hz, 4H). ^{13}C NMR (75 MHz, $CDCl_3$) δ: 191.6, 145.5, 135.9, 130.3, 127.9. HRMS (*m*/*z*) calcd for $C_{14}H_{11}O_2$ ($M + H^+$): 211.07591; found: 211.07479.

Supplementary data

Supplementary data (experimental procedures and ^{1}H NMR and ^{13}C NMR spectra) are available with the article through the Journal Web site at http://nrcresearchpress.com/doi/suppl/10.1139/v11-133.

Acknowledgment

This work was funded by the National Science Foundation of China (Grants 20225318, 20325208, and 20902007). We

also thank the National Science and Technology Major Project "Development of Novel Vaccines, Antibodies and Therapeutic Agents against Influenza Infection" (2009ZX10004-016), the National Basic Research Program of China (973 Program, Grant No. 2010CB833201), and the Shenzhen Basic Research Program (Nos. JC200903160352A, JC201005260097A, and CXB201005260053A). T.B.M. thanks the Royal Society for a Wolfson Research Merit Award, the Engineering and Physical Sciences Research Council (EPSRC) for an Overseas Research Travel Grant, and the Royal Society of Chemistry for a Journals Grant for International Authors.

References

(1) Tsuji, J. *Palladium Reagents and Catalysts: New Perspectives for the 21st Century;* Wiley: Chichester, UK, 2004.

(2) Yin, L. X.; Liebscher, J. *Chem. Rev.* **2007**, *107* (1), 133. doi:10.1021/cr0505674.

(3) Welch, C. J.; Albaneze-Walker, J.; Leonard, W. R.; Biba, M.; DaSilva, J.; Henderson, D.; Laing, B.; Mathre, D. J.; Spencer, S.; Bu, X. D.; Wang, T. B. *Org. Process Res. Dev.* **2005**, *9* (2), 198. doi:10.1021/op049764f.

(4) (a) For a recent review on the applications of MNPs, see Lu, A. H.; Salabas, E. L.; Schuth, F. *Angew. Chem. Int. Ed.* **2007**, *46* (8), 1222. doi:10.1002/anie.200602866; (b) Jun, Y. W.; Choi, J. S.; Cheon, J. *Chem. Commun. (Camb.)* **2007** (12), 1203. doi:10.1039/b614735f; (c) Schätz, A.; Reiser, O.; Stark, W. J. *Chem. Eur. J.* **2010**, *16* (30), 8950. doi:10.1002/chem.200903462; (d) Yan, J.-M.; Zhang, X.-B.; Akita, T.; Haruta, M.; Xu, Q. *J. Am. Chem. Soc.* **2010**, *132* (15), 5326. doi:10.1021/ja910513h; (e) Yan, J.-M.; Zhang, X.-B.; Han, S.; Shioyama, H.; Xu, Q. *J. Power Sources* **2009**, *194* (1), 478. doi:10.1016/j.jpowsour.2009.04.023.

(5) Che, C.; Li, W. Z.; Lin, S. Y.; Chen, J. W.; Zheng, J.; Wu, J. C.; Zheng, Q. X.; Zhang, G. Q.; Yang, Z.; Jiang, B. W. *Chem. Commun. (Camb.)* **2009**, (40): 5990. doi:10.1039/b911999j.

(6) (a) Selected examples for the application of MNPs as catalyst supports, see Lu, A. H.; Schmidt, W.; Matoussevitch, N.; Bonnemann, H.; Spliethoff, B.; Tesche, B.; Bill, E.; Kiefer, W.; Schuth, F. *Angew. Chem. Int. Ed.* **2004**, *43* (33), 4303. doi:10.1002/anie.200454222; (b) Gardimalla, H. M. R.; Mandal, D.; Stevens, P. D.; Yen, M.; Gao, Y. *Chem. Commun. (Camb.)* **2005** (35), 4432. doi:10.1039/b504128g; (c) Hu, A.; Yee, G. T.; Lin, W. *J. Am. Chem. Soc.* **2005**, *127* (36), 12486. doi:10.1021/ja053881o; (d) Abu-Reziq, R.; Alper, H.; Wang, D. S.; Post, M. L. *J. Am. Chem. Soc.* **2006**, *128* (15), 5279. doi:10.1021/ja060140u; (e) Phan, N. T. S.; Gill, C. S.; Nguyen, J. V.; Zhang, Z. J.; Jones, C. W. *Angew. Chem. Int. Ed.* **2006**, *45* (14), 2209. doi:10.1002/anie.200503445; (f) Shokouhimehr, M.; Piao, Y. Z.; Kim, J.; Jang, Y. J.; Hyeon, T. *Angew. Chem. Int. Ed.* **2007**, *46* (37), 7039. doi:10.1002/anie.200702386; (g) Zhang, X. B.; Yan, J. M.; Han, S.; Shioyama, H.; Xu, Q. *J. Am. Chem. Soc.* **2009**, *131* (8), 2778. doi:10.1021/ja808830a; (h) Zhang, Y.; Zhao, Y. W.; Xia, C. G. *J. Mol. Catal. Chem.* **2009**, *306* (1–2), 107. doi:10.1016/j.molcata.2009.02.032.

(7) Cai, W.; Wan, J. Q. *J. Colloid Interface Sci.* **2007**, *305* (2), 366. doi:10.1016/j.jcis.2006.10.023.

(8) Aujard, I.; Baltaze, J. P.; Baudin, J. B.; Cogne, E.; Ferrage, F.; Jullien, L.; Perez, E.; Prevost, V.; Qian, L. M.; Ruel, O. *J. Am. Chem. Soc.* **2001**, *123* (34), 8177. doi:10.1021/ja010019h.

(9) Bergbreiter, D. E.; Osburn, P. L.; Liu, Y. S. *J. Am. Chem. Soc.* **1999**, *121* (41), 9531. doi:10.1021/ja991099g.

(10) (a) For reviews on the synthesis of biaryls, see Hassan, J.; Sevignon, M.; Gozzi, C.; Schulz, E.; Lemaire, M. *Chem. Rev.* **2002**, *102* (5), 1359. doi:10.1021/cr000664r; (b) Jutand, A.; Mosleh, A. *J. Org. Chem.* **1997**, *62* (2), 261. doi:10.1021/jo961464b.

(11) For an unusual reductive coupling of iodoacrylates, see Batsanov, A. S.; Knowles, J. P.; Samsam, B.; Whiting, A. *Adv. Synth. Catal.* **2008**, *350* (2), 227. doi:10.1002/adsc.200700464.

(12) Daou, T. J.; Pourroy, G.; Begin-Colin, S.; Greneche, J. M.; Ulhaq-Bouillet, C.; Legare, P.; Bernhardt, P.; Leuvrey, C.; Rogez, G. *Chem. Mater.* **2006**, *18* (18), 4399. doi:10.1021/cm060805r.

(13) (a) Wang, L. A.; Zhang, Y. H.; Liu, L. F.; Wang, Y. G. *J. Org. Chem.* **2006**, *71* (3), 1284. doi:10.1021/jo052300a; (b) Kuroboshi, M.; Waki, Y.; Tanaka, H. *J. Org. Chem.* **2003**, *68* (10), 3938. doi:10.1021/jo0207473; (c) Cepanec, I.; Litvic, M.; Udikovic, J.; Pogorelic, I.; Lovric, M. *Tetrahedron* **2007**, *63* (25), 5614. doi:10.1016/j.tet.2007.04.016.

(14) Moncomble, A.; Le Floch, P.; Gosmini, C. *Chem. Eur. J.* **2009**, *15* (19), 4770. doi:10.1002/chem.200900542.

Can. J. Chem. Downloaded from www.nrcresearchpress.com by Renmin University of China on 09/02/12
For personal use only.

Rational size control of gold nanoparticles employing an organometallic precursor [Au-C≡C- *t*-Bu]$_4$ and tunable thiolate-functionalized ionic liquids in organic medium

Kylie L. Luska and Audrey Moores

Can. J. Chem. Downloaded from www.nrcresearchpress.com by Renmin University of China on 09/02/12
For personal use only.

Abstract: Gold nanoparticles (Au NPs) stabilized with six different thiolate-functionalized ionic liquids (TFILs) were synthesized in an organic solvent. The size and optical properties of the TFIL-stabilized Au NPs can be rationally controlled by altering the *N*-alkyl chain length and (or) the counteranion of the TFIL-stabilizing ligand. Au NPs were prepared from the reduction of a gold precursor ($HAuCl_4$ or [Au-C≡C-*t*-Bu]$_4$) employing $NaBH_4$ in the presence of the different disulfide precursors. A model, based on Israelachvili theory, is proposed to account for the dependence of NP size on the *N*-alkyl chain length and the counteranion of the surfactantlike TFIL stabilizers.

Key words: gold nanoparticles, functionalized ionic liquids, gold(I) complexes, surface plasmon band, imidazolium salts.

Résumé : Des nanoparticules d'or (NPAu) stabilisées par six ioniques liquides fonctionnalisés par un thiolate (ILFT) ont été synthétisées dans un solvant organique. La taille et les propriétés optiques de ces NPAu stabilisées par des ILFT peuvent être contrôlées rationnellement en modifiant la longueur de la chaine *N*-alkyle et (ou) le contre-anion du ILFT. Les NPAu ont été préparées par réduction d'un précurseur d'or, $HAuCl_4$ ou [Au-C≡C-*t*-Bu]$_4$, à l'aide de $NaBH_4$, en présence de chacun des six précurseurs de disulfure. Un modèle, basé sur la théorie de Israelachvili, est avancé pour rendre compte de la relation entre la taille des NPAu et la longueur de la chaine *N*-alkyle et la taille du contre-anion du ILFT, qui agit comme stabilisant de la NP et surfactant.

Mots-clés : nanoparticules d'or, liquides ioniques fonctionnels, complexe d'or(I), bande plasmon de surface, sels d'imidazolium.

Introduction

Gold nanoparticles (Au NPs) are subject to intensive research because of their application in optical sensing,[1] surface-enhanced Raman spectroscopy,[2] and catalysis.[3,4] Optical[1] and catalytic[4] properties are governed by various factors including, among others, the size and shape of the NPs and the nature of the stabilizing ligand. Correlations between NP size and the properties of NPs are challenging to establish as different ligands are most often employed to achieve variance in the NP size,[5] which alter not only the size but also the electronics of the metal core. To establish such a relationship, it would be desirable to develop a family of stabilizing ligands, employed under identical reaction conditions,[6,7] that can control particle size. To reach this goal, we synthesized Au NPs of tunable size using the same class of ligand, thiolate-functionalized ionic liquids (TFILs), based on an imidazolium structure. This class of Au NP ligand was first proposed by Itoh et al.[8] and used for anion sensing. They were chosen here as (*i*) TFILs provide both electrostatic and covalent stabilization to metal NPs increasing their long-term stability[9–11] and (*ii*) alterations to the TFIL structure can be accomplished that do not involve changing the metal-binding moiety (i.e., *N*-alkyl chain length or counteranion), and thus preserve the electronic nature of the NP. Kim et al.[12] previously employed TFILs in the synthesis of Au and Pt NPs and demonstrated that the position and number of thiol moieties present in either the cation or anion of the TFIL ligands impacted the size of the Au and Pt NPs. Such ligand alterations dramatically influence both the electronic properties of the metal core and the organization of the ligand sphere, parameters that are proposed to remain constant in this study. Recent reports on Au NP synthesis have featured novel gold precursors (e.g., AuX (for X = Cl or Br),[13] $[AuN(SiMe_3)_2]_4$,[14] and $[NMe_4][Au(CF_3)_2]$[15]) in an effort to complement the well-established methodologies based on $HAuCl_4$[16] and to provide insight into the Au NP formation mechanism.[17] $[AuN(SiMe_3)_2]_4$ and $[NMe_4][Au(CF_3)_2]$ are interesting precursors as they eliminate the presence of halides in the reaction mixture, which have been shown to affect the properties of NPs.[18] For instance, a recent DFT study by Janiak and coworkers[19] demonstrated that the interaction between chloride anions and Au clusters possesses a large binding energy and thus Cl^- will play a role in stabilizing Au NPs if present in

Received 25 May 2011. Accepted 8 September 2011. Published at www.nrcresearchpress.com/cjc on 25 November 2011.

K.L. Luska and A. Moores. Department of Chemistry, McGill University, 801 Sherbrooke St. West, Montreal, QC H3A 2K6, Canada.

Corresponding author: Audrey Moores (audrey.moores@mcgill.ca).

This article is part of a Special Issue dedicated to Professor Tak-Hang Chan.

Can. J. Chem. Downloaded from www.nrcresearchpress.com by Renmin University of China on 09/02/12
For personal use only.

the synthetic mixture. Furthermore, in the context of IL chemistry, it was even more important to select a metal precursor that does not produce any ionic by-products that can undergo ion exchange with either of the IL ions.

Recently, the groups of Roucoux,[20] Hou,[21] and Dyson[22] studied the influence of various structural parameters of functionalized ionic liquid (FIL)-stabilized Rh and Pd NPs. Specifically, the concept of "supramolecular" arrangement of FILs at the surface of stabilized NPs was explored and evoked to rationalize such NP properties as catalytic activity.

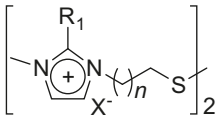
Herein, we propose the use of a family of disulfide TFIL precursors **1**–**6** (Scheme 1) in the formation of stable Au NPs with control of the NP size (Scheme 2) by reduction of gold precursors using $NaBH_4$. The TFILs act as surfactants, which stabilize the NPs through the anchoring of the thiol moiety to the metal surface. We also introduce a model to rationalize this control and study the impact of the ligands **1**–**6** onto the optical properties of the synthesized Au NPs. We also introduced a novel organometallic Au NP precursor, $[Au\text{-}C{\equiv}C\text{-}t\text{-}Bu]_4$,[23] to avoid the presence of halides during the NP synthesis and compared its performance with the more commonly used halide-based precursor, $HAuCl_4$. $[Au\text{-}C{\equiv}C\text{-}t\text{-}Bu]_4$ is expected to decompose under reducing conditions into Au(0) and volatile organic by-products, thus leaving the NP surface and the IL free of unwanted contaminants. Overall, our study suggests that FILs can act as surfactants to stabilize metal NPs and exert some level of size control over the final NP size.

Results and discussion

Synthesis of TFILs

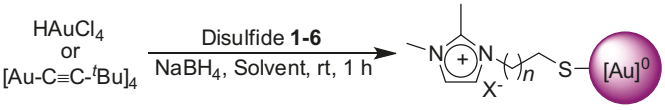
Compounds **1**–**6** are characterized by four parameters: (1) a thiolate function that binds to the Au particle, (2) an imidazolium unit, (3) an alkyl chain playing the role of spacer between the metal binding and imidazolium moiety, and (4) a counteranion (Scheme 2). In this study we altered both components (3) and (4) to impact the size of the particle while preserving (1) and (2) to have constant electronic and molecular structure, respectively. The procedure employed for the synthesis of **1**–**6** was adapted from that reported by Itoh et al.[8] (R_1 = H, n = 5, and X = Cl^-; Scheme 1) to prepare a series of TFIL precursors having differing *N*-alkyl chains (n = 5, 8, and 10) and counteranions (X^- = ^-OTf and $^-NTf_2$) (Scheme 3). Synthesis of the disulfide precursors **1**–**6** was achieved through the quaternization of ω-bromodisulfides with 1,2-dimethylimidazole, followed by an ion exchange of Br^- with either ^-OTf or $^-NTf_2$. 1,2-Dimethylimidazole was selected here instead of 1-methylimidazole, to ensure the stabilization of the NPs was provided solely by the TFILs **1**–**6**. NPs stabilized by 1-alkyl-3-methylimidazolium ILs may involve the formation of *N*-heterocyclic carbenes, which primarily occur at the C2 position on the imidazolium ring.[24–26] Thus, TFILs based on the 1-alkyl-2,3-dimethylimidazolium moiety were employed in this study to restrict the formation of carbene stabilizing species. Furthermore, ion exchange of Br^- to form disulfides **1**–**6** prior to NP synthesis allows for a better control of the properties of both the TFIL stabilizers and the resulting Au NPs. This contrasts with the work of Itoh et al.[8] as anion exchange was performed directly on the Au NPs. Their technique led to the development of a useful anion sensor; however, the extent of the full counteranion replacement within the NP ligand sphere, as well as the anion's impact during the synthesis of the NPs, was not determined. The present work used TFIL precursors composed of a known counterion and explored their influence on the properties of the resulting Au NPs.

Scheme 1. Ionic liquid disulfides **1**–**6** employed as precursors in the synthesis of thiolate-stabilized gold nanoparticles.[8]



R_1 = H; X = Cl^-; n = 5 (Itoh et al. precursor)
R_1 = CH_3; X = $^-OSO_2CF_3$ (^-OTf); n = 5 (**1**), n = 8 (**2**), n = 10 (**3**)
R_1 = CH_3; X = $^-N(SO_2CF_3)_2$ ($^-NTf_2$); n = 5 (**4**), n = 8 (**5**), n = 10 (**6**)

Scheme 2. Synthesis of thiolate-stabilized gold nanoparticles.



Nanoparticle synthesis and characterization

Synthesis of Au NPs was achieved by combining an organic solution of an Au precursor ($HAuCl_4$ or $[Au\text{-}C{\equiv}C\text{-}t\text{-}Bu]_4$, 0.100 and 0.025 mmol, respectively) with a methanol solution of one of disulfides **1**–**6** (0.20 mmol) and reducing the mixture with $NaBH_4$ (Scheme 2). The solution instantly changed colour from pale yellow to purple, indicating the formation of Au NPs. TEM analysis of the reaction mixtures showed the presence of well-dispersed Au NPs having mean diameters ranging from 3.0 to 4.3 nm depending on n and X^- (Fig. 1 and Table 1; see the Supplementary data for size and distribution data, Figs. S1 and S2). X-ray photoelectron spectrometry (XPS) analysis of the Au NPs (for $HAuCl_4$ and disulfide **1**) indicated the presence of gold, sulfur, carbon, nitrogen, oxygen, and fluorine, which signified the TFIL stabilization of the NPs (Supplementary data Figs. S3–S7). The $S2p_{(3/2)}$ binding energies (BEs) for disulfide **1** and the corresponding stabilized Au NPs are 163.7 and 162.3 eV respectively; a shift (–1.4 eV) that was in agreement with the binding of the thiolate functionality to the surface of the Au NPs.[27] Additional evidence for the presence of an Au–S bond was provided by the BEs of Au ($4f_{(7/2)}$ = 84.0 eV and $4f_{(5/2)}$ = 87.7 eV).[27,28] The Au:disulfide ratio was optimal at 1:2, affording small and well-dispersed NPs, whereas a smaller ratio (1:1) formed large Au aggregates and a larger ratio (1:4) produced clusters of small Au NPs that were not monodispersed. This ratio (1:2) was kept constant in all of the subsequent studies.

Size analysis and supporting model

The nature of the disulfide precursor, in terms of n and X^-, was found to influence the size of the Au NPs synthesized from $[Au\text{-}C{\equiv}C\text{-}t\text{-}Bu]_4$ (Table 1, entries 1–6). These results showed an increase in the NP size with an increase in the length of the *N*-alkyl chain (n) and a decrease in the NP size with an increase in the molecular volume of the counteranion

Scheme 3. Synthetic pathway for the preparation of disulfide ionic liquids **1–6** (for n = 5, 8, and 10 and X^- = $^-$OTf and $^-NTf_2$).

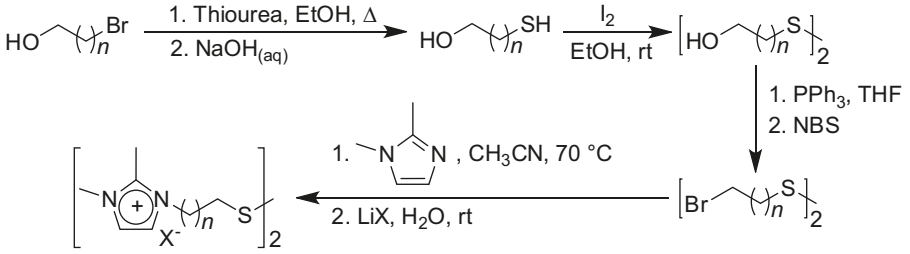
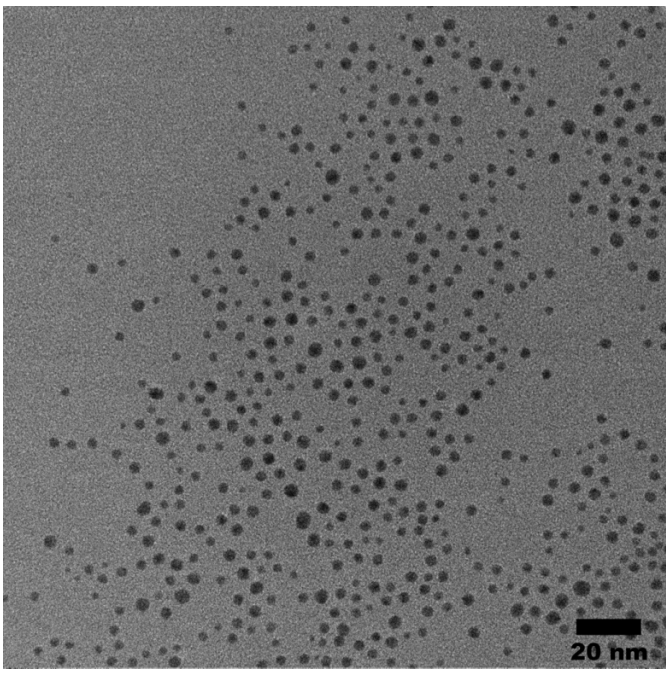


Fig. 1. Transmission electron micrograph of thiolate-stabilized gold nanoparticles, employing [Au-C≡C-*t*-Bu]$_4$ and disulfide **6**.



(X^-). The dependence of n and X^- on the size of the Au NPs can be justified by adapting the geometric theory proposed by Israelachvili[29] for the formation of spherical micelles (Scheme 4). This theory was adapted because of the intrinsic surfactant nature of the TFILs and their ability to bind strongly to the Au surface through their thiolate functionality. For a conventional micelle, (Scheme 4A) the radius (R) of a spherical micelle is dependent on the properties of the surfactant molecule such that $R = 3v/a_0$, where v is the volume of the hydrocarbon chain and a_0 is the area of the headgroup. This relationship can be extended to the formation of spherical NPs stabilized by TFILs **1–6** such that $R \propto v/a_0$, where R is now the radius of the structure containing the particle and the ligand shell, v is the volume of the hydrocarbon chain, including the thiolate moiety, and a_0 is the area of the imidazolium headgroup, including both the cation and the anion (Scheme 4B). According to this relationship, an increase in n would increase v, thus increase R, and ultimately the NP size. The TEM data obtained for Au NPs stabilized by thiolate ligands **1–6** (Table 1, entries 1–6) showed an increase in NP size when comparing n = 5, 8, and 10. In terms of the influence of X^-, this relationship predicts that an increase in a_0 would decrease the diameter of the NP. The molecular volume of the counteranions employed here are 0.131 and 0.232 nm^3 for $^-$OTf and $^-NTf_2$, respectively.[30] Therefore, the larger $^-NTf_2$ anion would increase a_0 and thus decrease the NP size. A comparison of the TEM data for thiolate-stabilized NPs with $^-$OTf (Table 1, entries 1–3) and $^-NTf_2$ (Table 1, entries 4–6) counteranions showed a consistently smaller size for the $^-NTf_2$ species.

The relationship between NP size and the TFIL counteranion was investigated already by Janiak and co-workers[30–32] in metal NPs synthesized directly in IL solvents. In their system, the relationship is opposite to what we observe, with an increase in NP diameter when the molecular volume of the anion was increased. Their results provided evidence that the NPs were stabilized by a classical electric double layer where anionic species stabilize the metal surface and thus govern the size of the NPs.[30] For our system, the size variation trends observed and the XPS measurements are both consistent with a covalent binding of the thiolate to the metal surface (as suggested by Itoh et al.[8] and shown in Scheme 2) and a global arrangement where the IL anion and cation pair are localized at the periphery of the ligand shell. These results, and especially the compliance to the Israelachvili model, suggest that there is a high level of organisation in the ligand shell resulting from the surfactant nature of the TFIL stabilizers. This is in accordance to what is expected from both imidazolium moieties[33] through electrostatic interactions and the *N*-alkyl chains through van der Waals interactions; the later being a similar phenomenon to that observed in the formation of self-assembled monolayers (SAMs) of long-chain alkanethiol on Au NPs.[34]

Influence of the gold precursor

Au NPs synthesized from [Au-C≡C-*t*-Bu]$_4$ were compared with NPs prepared employing $HAuCl_4$. [Au-C≡C-*t*-Bu]$_4$[23] is expected to decompose under reducing conditions to Au(0) and volatile organic by-products. TEM analysis of the thiolate-stabilized Au NPs showed well-dispersed NPs for the syntheses with either precursor, although slightly larger NPs were obtained from $HAuCl_4$ (Table 1, entries 7–12) compared with those from [Au-C≡C-*t*-Bu]$_4$ (Table 1, entries 1–6). This difference was attributed to the presence of Cl^- ions in the Au precursor, which may exchange with the counteranion of the TFIL stabilizer. According to our proposed model (Scheme 3), exchange of either $^-$OTf or $^-NTf_2$ with the smaller Cl^- species would decrease a_0 and increase the size of the resulting Au NPs. It was also observed that the trend between NP size and the properties of the disulfide ligand (n and X^-) were not as clear for particles synthesized from $HAuCl_4$. This discrepancy was most pronounced when

Can. J. Chem. Downloaded from www.nrcresearchpress.com by Renmin University of China on 09/02/12
For personal use only.

Can. J. Chem. Downloaded from www.nrcresearchpress.com by Renmin University of China on 09/02/12
For personal use only.

Table 1. Influence of the gold and disulfide precursors on the size and size distribution of thiolate-stabilized gold nanoparticles (Au NPs).

		Stabilizing ligand			
Entry	Au precursor	Disulfide	n	X^-	Au NP size (nm) (standard deviation σ)[a]
1	[Au-C≡C-*t*-Bu]$_4$	**1**	5	$^-$OTf	2.9(±0.6)
2		**2**	8	$^-$OTf	3.2(±0.6)
3		**3**	10	$^-$OTf	3.3(±0.6)
4		**4**	5	$^-$NTf$_2$	2.7(±0.5)
5		**5**	8	$^-$NTf$_2$	2.9(±0.4)
6		**6**	10	$^-$NTf$_2$	3.2(±0.6)
7	HAuCl$_4$	**1**	5	$^-$OTf	3.3(±0.6)
8		**2**	8	$^-$OTf	4.2(±0.7)
9		**3**	10	$^-$OTf	4.3(±0.7)
10		**4**	5	$^-$NTf$_2$	3.0(±0.4)
11		**5**	8	$^-$NTf$_2$	3.0(±0.3)
12		**6**	10	$^-$NTf$_2$	3.1(±0.5)

Note: Reaction conditions: [Au] = 0.1 mmol, disulfide = 0.2 mmol (2 equiv), $NaBH_4$ = 1.0 mmol (10 equiv), solvent = CH_3OH (for $HAuCl_4$), CH_3OH–CH_2Cl_2 (3:2, for [Au-C≡C-*t*-Bu]$_4$).

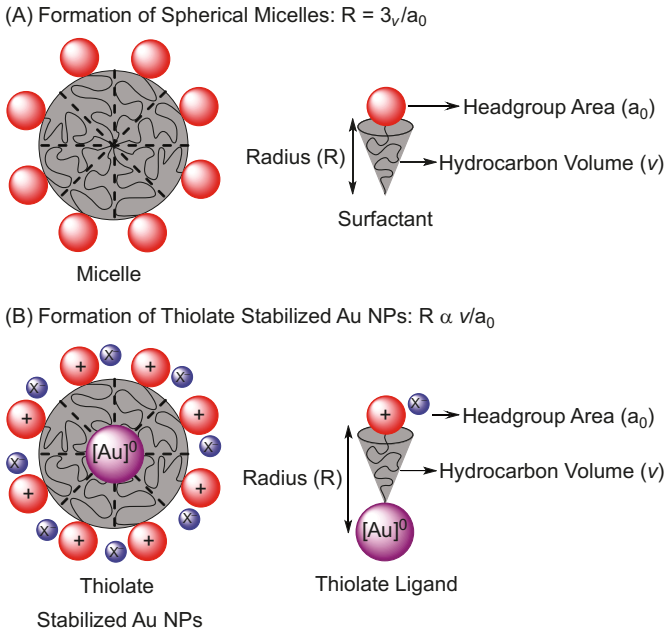
[a]Determined by TEM, measurement of >200 spherical particles.

comparing disulfides **2** (4.2 nm) to **3** (4.3 nm) (Table 1, entries 8 and 9) and **4** (3.0 nm) to **5** (3.0 nm) (Table 1, entries 10 and 11) as very little difference in size was observed for these NPs. The lack of correlation within the $HAuCl_4$ data was again accredited to anion exchange of the TFIL anion and thus emphasizes the importance of having well-defined systems in the synthesis of nanomaterials, including the use of halide-free metal precursors such as [Au-C≡C-*t*-Bu]$_4$.

Optical properties analysis

The optical properties of the synthesized Au NPs were analyzed using UV–vis spectroscopy. A surface plasmon band (SPB) was observed for Au NPs stabilized by TFILs **1**–**6** (λ_{max}(MeOH) = 535–650 nm) and was dependent on the nature of the thiolate employed (Fig. 2). The length of the alkyl chain was observed to influence the SPB as the longer chain thiolates, n = 8 and 10 (Fig. 2, curves b, c, e, and f), showed λ_{max} = 535 nm, whereas Au NPs synthesized from the shorter chain disulfides, n = 5 (Fig. 2, curves a and d), caused the λ_{max} to red shift to >535 nm. For TFIL **1** and **4** (n = 5) stabilized NPs, the distance between the particle surface and the IL environment is smaller than in the case of the longer chain TFIL-stabilized NPs. This shorter distance resulted in the NP perceiving a more polar environment and thus a globally higher dielectric medium at its surrounding. The theory predicts that the position of the SPB shifts toward the lower energy region as the surrounding medium refractive index increases,[1,35] which is consistent with the observed trend. A shorter chain disulfide (n = 2) was desired to further test this hypothesis; however, the synthesis of this disulfide could not be achieved. Aggregation of the NPs in solution could also be envisaged as the cause of this shift, in which case a red-shift is expected when the mean distance between particles decreases;[1,36] however, the TEM images obtained for all NPs are not consistent with significant aggregation in solution (Supplementary data Figs. S1 and S3). These results

Scheme 4. Schematic representation of (A) the size dependence of micelles on surfactant properties and (B) the size dependence of gold nanoparticles (Au NPs) on thiolate-functionalized ionic liquids (TFIL) properties.[29]



are supporting the idea that TFILs organize around the particle. Indeed, in the case of the longest alkyl spacers (n = 8 and 10), the respective blue-shift observed proves that the alkyl portion of the TFIL resides close to the surface of the particle, whereas the imidazolium cation and anion are maintained at the periphery of the ligand sphere. Moreover, the results obtained for n = 8 and 10 are virtually identical. This can be explained by the fact that changes happening far from the surface will not impact the perceived dielectric medium of the particle significantly. When the alkyl spacer is short (n = 5), the dielectric medium perceived by the Au NP is altered by the presence of the imidazolium cation and anion.

Can. J. Chem. Downloaded from www.nrcresearchpress.com by Renmin University of China on 09/02/12
For personal use only.

Conclusions

In conclusion, this report has outlined the synthesis of stable, well-dispersed Au NPs employing an organometallic Au precursor [Au-C≡C-*t*-Bu]$_4$ and TFIL stabilizers in a molecular solvent. This halogen-free Au complex allowed for the recognition of a relationship between the properties of the Au NPs, in terms of NP size and SPB, and two properties of the thiolate-stabilizing ligand, namely the length of the *N*-alkyl chain and the counteranion. A model, based on Israelachvili theory, was employed to explain the correlation between the size of Au NPs and the properties of the thiolate ligands. This model and XPS data evidenced a high level of organization inside these NPs where the TFILs interact with the particle surface through their thiolate functionalities. Functionalized ionic liquids act as surfactants for the synthesis of metal NPs with controlled properties leading to a novel bottom-up approach to the design of functional nanomaterials, as well as models to measure the influence of small size changes on the properties of NPs. Furthermore, [Au-C≡C-*t*-Bu]$_4$ has been shown to be an effective precursor in the synthesis of NPs featuring increased compositional purity and opens new opportunities for gaining an understanding in the role various stabilizing ligands play in the formation of Au NPs.

Experimental section

General remarks

All syntheses of ILs and NPs were carried out under an argon atmosphere employing Schlenk techniques. 6-Mercapto-1-hexanol,[37,38] 9-mercapto-1-nonanol,[37,39,40] 11-mercapto-1-undecanol,[37,41,42] bis(6-hydroxyhexyl)disulfide,[41] bis(11-hydroxyundecyl)disulfide,[37,41] bis(6-bromohexyl)disulfide,[42,43] and [Au-C≡C-*t*-Bu]$_4$[23,44] were prepared following known literature procedures. Tetrahydrofuran (distillation over Na and benzophenone) and acetonitrile (dried over 4 Å molecular sieves) were purified prior to use. All other chemicals and solvents were purchased from commercial sources and used without further purification. Melting points (mp) were determined on a Gallenkamp melting point apparatus and are uncorrected. Nuclear magnetic resonance (NMR) spectra were recorded on a 300 MHz Varian Mercury spectrometer. Mass spectra (MS) were recorded in positive electrospray mode with an IonSpec 7.0 tesla FTMS (IonSpec Corp., Lake Forest, California). TEM was performed on a Phillips CM 200 microscope. UV–vis spectra were recorded on a Jasco V-660 spectrophotometer. XPS was performed on a VG ESCALAB 3 MKII spectrometer (VG, Thermo Electron Corporation, UK) equipped with an Mg Kα source.

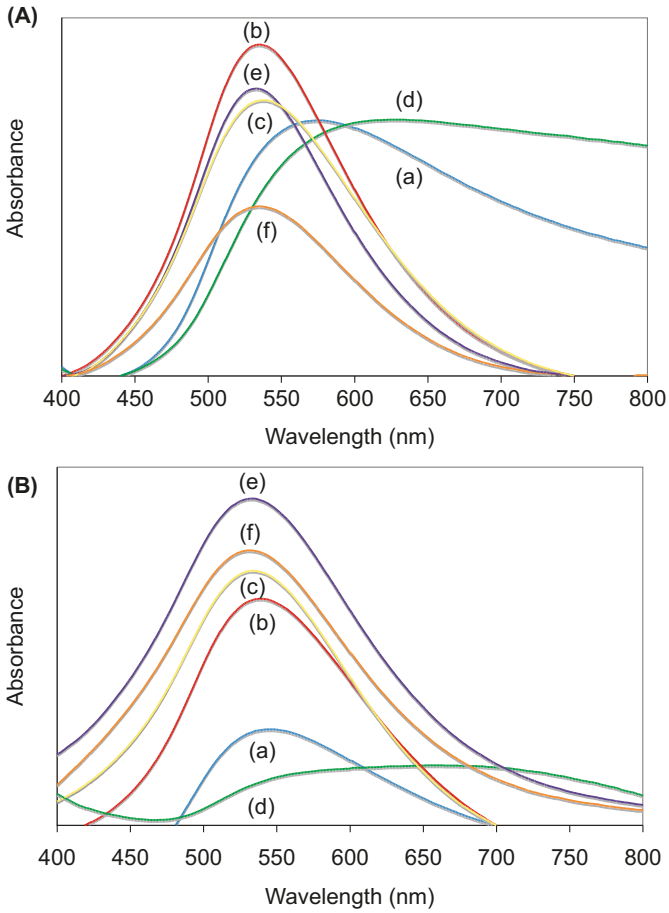
Synthesis of TFILs

The synthesis of disulfide ILs **1**–**6** followed a similar pathway to that reported by Itoh et al. (Scheme 1).[8] The synthesis and characterization data for all novel compounds are reported.

Bis(9-hydroxynonyl)disulfide

9-Mercapto-1-nonanol (7.81 g, 58.2 mmol) was dissolved in 12 mL MeOH and titrated with 0.5 mol/L methanolic iodine until the reaction turned from colourless to a persistent yellow colour. The mixture was allowed to stir at room temperature (rt) for 1 h. The reaction was quenched with 10% NaHSO$_3$(aq) and extracted with CH_2Cl_2 (3 × 50 mL). The organic phase was washed with 10% NaHSO$_3$(aq) and H_2O and dried over $MgSO_4$. The solvent was removed and the product was dried in vacuo to yield a white solid. Yield: 7.09 g (92%); mp 65–66 °C. ^{1}H NMR (300 MHz, $CDCl_3$, ppm) δ: 3.61(t, J = 6.2 Hz, 4H), 2.65 (t, J = 7.3 Hz, 4H), 1.64–1.28 (m, 30H). ^{13}C NMR (75.5 MHz, $CDCl_3$, ppm) δ: 63.2, 39.4, 33.0, 29.7, 29.6, 29.4, 29.4, 28.7, 25.9. MS (ESI$^+$) *m/z*: 351.2386 ($M^+ = [C_{18}H_{39}O_2S_2]^+$ requires 351.2385).

Fig. 2. UV–vis spectra of λ_{max}(MeOH) for gold nanoparticles (Au NPs) synthesized employing (A) $HAuCl_4$ and (B) [Au-C≡C-*t*-Bu]$_4$ as gold precursors stabilized by thiolates (a) n = 5, X^- = $^-$OTf; (b) n = 8, X^- = $^-$OTf; (c) n = 10, X^- = $^-$OTf; (d) n = 5, X^- = $^-$NTf$_2$; (e) n = 8, X^- = $^-$NTf$_2$; and (f) n = 10, X^- = $^-$NTf$_2$.



Bis(9-bromononyl)disulfide

Bis(9-hydroxynonyl)disulfide (3.55 g, 10.1 mmol) and PPh_3 (5.56 g, 21.2 mmol) were dissolved in 100 mL of distilled THF under an argon atmosphere. NBS (4.50 g, 25.3 mmol) was added in portions over 30 min. The mixture was stirred at rt for 1 h then heated to 50 °C for 18 h. The solvent volume was reduced, EtO_2 was added, and the mixture was cooled for 30 min to cause the precipitation of white solids. Upon filtration and solvent evaporation, the crude mixture was purified on silica employing EtOAc–hexanes. Bis(9-bromononyl)disulfide was obtained as a colourless liquid. Yield: 3.56 g (74%). ^{1}H NMR (300 MHz, $CDCl_3$, ppm) δ: 3.38 (t, J = 6.8 Hz, 4H), 2.65 (t, J = 7.4 Hz, 4H), 1.82 (pentet, J = 7.4 Hz, 4H), 1.64 (pentet, J = 7.1 Hz, 4H),

Can. J. Chem. Downloaded from www.nrcresearchpress.com by Renmin University of China on 09/02/12
For personal use only.

1.46–1.22 (m, 20H). ^{13}C NMR (75.5 MHz, $CDCl_3$, ppm) δ: 39.3, 34.2, 33.0, 29.7, 29.3, 29.3, 28.9, 28.6, 28.3.

Bis(11-bromoundecyl)disulfide

Bis(11-bromoundecyl)disulfide was obtained as a white solid. Yield: 2.93 g (52%). ^{1}H NMR (300 MHz, $CDCl_3$, ppm) δ: 3.39 (t, J = 6.9 Hz, 4H), 2.66 (t, J = 7.5 Hz, 4H), 1.83 (pentet, J = 7.2 Hz, 4H), 1.65 (pentet, J = 7.2 Hz, 4H), 1.45–1.21 (m, 28H). ^{13}C NMR (75.5 MHz, $CDCl_3$, ppm) δ: 39.4, 34.3, 33.0, 29.7, 29.7, 29.6, 29.4, 29.4, 29.0, 28.7, 28.4.

Disulfide 1

1,2-Dimethylimidazole (1.37 g, 14.3 mmol) was dissolved in 10 mL of MeCN. Bis(6-bromohexyl)disulfide (2.74 g, 6.99 mmol) was added and the mixture was stirred at 70 °C for 48 h. The solvent was removed in vacuo and the residual solid was washed with Et_2O (3 × 20 mL). Lithium trifluoromethanesulfonate (2.23 g, 14.3 mmol) was added in small portions to a solution of the crude product in 15 mL of H_2O. The mixture was stirred at rt for 1 h and 25 mL of CH_2Cl_2 was added. The organic phase was washed with H_2O and dried over $MgSO_4$. The solvent was removed and the product was dried in vacuo to yield a white solid. Yield: 3.63 g (72%); mp 104–106 °C. ^{1}H NMR (300 MHz, $(CD_3)_2CO$, ppm) δ: 7.65 (d, J = 2.0 Hz, 2H), 7.60 (d, J = 2.0 Hz, 2H), 4.28 (t, J = 7.5 Hz, 4H), 3.93 (s, 6H), 2.77 (s, 6H), 2.70 (t, J = 7.5 Hz, 4H), 1.88 (pentet, J = 7.5 Hz, 4H), 1.68 (pentet, J = 7.5 Hz, 4H), 1.52–1.28 (m, 8H). ^{13}C NMR (75.5 MHz, $(CD_3)_2CO$, ppm) δ: 145.6, 123.4, 122.3 (q, J_{CF} = 322.1 Hz), 122.0, 49.0, 38.9, 35.5, 30.4, 29.6, 28.5, 26.4, 9.8. MS (ESI$^+$) m/z: 212.1342 (M^{2+} = $[C_{22}H_{40}N_4S_2]^{2+}$ requires 212.1344).

Disulfide 2

The product was obtained as an amber oil. Yield: 3.19 g (80%). ^{1}H NMR (300 MHz, $(CD_3)_2CO$, ppm) δ: 7.65 (d, J = 2.0 Hz, 2H), 7.60 (d, J = 2.1 Hz, 2H), 4.27 (t, J = 7.5 Hz, 4H), 3.92 (s, 6H), 2.76 (s, 6H), 2.70 (t, J = 7.5 Hz, 4H), 1.86 (pentet, J = 7.5 Hz, 4H), 1.66 (pentet, J = 7.5 Hz, 4H), 1.48–1.25 (m, 20H). ^{13}C NMR (75.5 MHz, $(CD_3)_2CO$, ppm) δ: 145.6, 123.4, 122.3 (q, J_{CF} = 322.1 Hz), 121.9, 49.0, 39.3, 35.5, 30.5, 30.0, 29.8, 29.8, 29.7, 29.0, 26.8, 9.8. MS (ESI$^+$) m/z: 254.1811 (M^{2+} = $[C_{28}H_{52}N_4S_2]^{2+}$ requires 254.1809).

Disulfide 3

The product was obtained as an amber oil. Yield: 2.20 g (79%). ^{1}H NMR (300 MHz, $(CD_3)_2CO$, ppm) δ: 7.64 (d, J = 2.0 Hz, 2H), 7.61 (d, J = 2.0 Hz, 2H), 4.28 (t, J = 7.5 Hz, 4H), 3.93 (s, 6H), 2.77 (s, 6H), 2.71 (t, J = 7.5 Hz, 4H), 1.87 (pentet, J = 7.2 Hz, 4H), 1.67 (pentet, J = 7.2 Hz, 4H), 1.45–1.25 (m, 28H). ^{13}C NMR (75.5 MHz, $(CD_3)_2CO$, ppm) δ: 145.6, 123.4, 122.3 (q, J_{CF} = 322.1 Hz), 121.9, 49.1, 39.3, 35.5, 30.5, 30.2, 30.2, 30.2, 30.2, 29.8, 29.8, 29.1, 26.9, 9.8. MS (ESI$^+$) m/z: 282.2124 (M^{2+} = $[C_{32}H_{60}N_4S_2]^{2+}$ requires 282.2128).

Disulfide 4

The product was obtained as an amber oil. Yield: 2.91 g (90%). ^{1}H NMR (300 MHz, $(CD_3)_2CO$, ppm) δ: 7.60 (d, J = 2.1 Hz, 2H), 7.56 (d, J = 2.1 Hz, 2H), 4.27 (t, J = 7.5 Hz, 4H), 3.92 (s, 6H), 2.76 (s, 6H), 2.70 (t, J = 7.2 Hz, 4H), 1.89 (pentet, J = 7.4 Hz, 4H), 1.68 (pentet, J = 7.1 Hz, 4H), 1.54–1.30 (m, 8H). ^{13}C NMR (75.5 MHz, $(CD_3)_2CO$, ppm) δ: 145.5, 123.3, 121.8, 120.9 (q, J_{CF} = 321.6 Hz), 49.1, 38.8, 35.5, 30.3, 29.5, 28.5, 26.4, 9.7. MS (ESI$^+$) m/z: 212.1342 (M^{2+} = $[C_{22}H_{40}N_4S_2]^{2+}$ requires 212.1345).

Disulfide 5

The product was obtained as an amber oil. Yield: 3.90 g (79%). ^{1}H NMR (300 MHz, $(CD_3)_2CO$, ppm) δ: 7.62 (d, J = 2.1 Hz, 2H), 7.58 (d, J = 2.1 Hz, 2H), 4.27 (t, J = 7.5 Hz, 4H), 3.93 (s, 6H), 2.77 (s, 6H), 2.70 (t, J = 7.2 Hz, 4H), 1.83 (pentet, J = 7.4 Hz, 4H), 1.66 (pentet, J = 7.2 Hz, 4H), 1.50–1.24 (m, 20H). ^{13}C NMR (75.5 MHz, $(CD_3)_2CO$, ppm) δ: 145.6, 123.4, 121.9, 121.0 (q, J_{CF} = 321.4 Hz), 49.1, 39.2, 35.5, 30.5, 30.0, 29.8, 29.8, 29.7, 29.1, 26.9, 9.8. MS (ESI$^+$) m/z: 254.1811 (M^{2+} = $[C_{28}H_{52}N_4S_2]^{2+}$ requires 254.1813).

Disulfide 6

The product was obtained as a pale yellow oil. Yield: 3.39 g (58%). ^{1}H NMR (300 MHz, $(CD_3)_2CO$, ppm) δ: 7.62 (d, J = 2.1 Hz, 2H), 7.58 (d, J = 2.1 Hz, 2H), 4.27 (t, J = 7.5 Hz, 4H), 3.93 (s, 6H), 2.77 (s, 6H), 2.71 (t, J = 7.5 Hz, 4H), 1.88 (pentet, J = 7.2 Hz, 4H), 1.67 (pentet, J = 7.2 Hz, 4H), 1.45–1.25 (m, 28H). ^{13}C NMR (75.5 MHz, $(CD_3)_2CO$, ppm) δ: 145.6, 123.4, 121.9, 121.0 (q, J_{CF} = 321.6 Hz), 49.1, 39.3, 35.5, 30.5, 30.2, 30.2, 30.2, 30.2, 29.8, 29.8, 29.1, 26.9, 9.8. MS (ESI$^+$) m/z: 282.2124 (M^{2+} = $[C_{32}H_{60}N_4S_2]^{2+}$ requires 282.2128).

Synthesis of gold nanoparticles

From [Au-C≡C-t-Bu]$_4$

$[Au\text{-}C{\equiv}C\text{-}t\text{-}Bu]_4$ (27 mg, 0.025 mmol) was dissolved in 10 mL of degassed CH_2Cl_2 and the disulfide IL (0.20 mmol) was dissolved in 10 mL of degassed MeOH. Upon addition of the disulfide solution, the mixture was stirred for 30 min to form a light yellow solution. $NaBH_4$ (38 mg, 1.0 mmol) in 5 mL MeOH was added dropwise and stirred for 1 h. The precipitate was isolated via centrifugation (7500 rpm for 10 min), washed with acetone–pentane (2:1) (3 × 10 mL), and dried in vacuo. The crude mixture was employed for UV–vis and TEM analyses, while purified NPs were used for XPS.

From HAuCl$_4$

$HAuCl_4{\cdot}3H_2O$ (34 mg, 0.10 mmol) and the disulfide IL (0.20 mmol) were separately dissolved in 10 mL of degassed MeOH. Upon addition of the disulfide, the mixture was stirred for 30 min to form a light yellow solution. $NaBH_4$ (38 mg, 1.0 mmol) in 5 mL MeOH was added dropwise and stirred for 1 h. The precipitate was isolated via centrifugation (7500 rpm for 10 min), washed with acetone–pentane (2:1) (3 × 10 mL), and dried in vacuo. The crude mixture was employed for UV–vis and TEM analyses, while purified NPs were used for XPS.

Transmission electron microscopy

TEM of Au NPs was obtained on a Phillips CM 200 microscope operating at an accelerating voltage of 200 kV with a point resolution of 0.24 nm. Sample preparation included dilution of 10 drops of the Au NP solution in 20 drops of

i-PrOH, followed by deposition on a carbon-coated copper grid (400 mesh) at rt. The NP size distribution was determined from the measurement of >200 spherical particles chosen in arbitrary areas of enlarged micrographs.

UV–vis spectroscopy

Spectra were recorded on a Jasco V-660 spectrophotometer. Sample preparation included the dilution of 0.1 mL of the crude Au NP solution in 4.0 mL of MeOH. A correction of the raw data was employed to normalize the background.

Supplementary data

Supplementary data are available with the article through the journal Web site (http://nrcresearchpress.com/doi/suppl/10.1139/v11-146).

Acknowledgments

We acknowledge the Natural Sciences and Engineering Research Council of Canada (NSERC), the Canada Foundation for Innovation (CFI), the Fonds de recherche sur la nature et les technologies (FQRNT), the Canada Research Chairs, the Centre for Green Chemistry and Catalysis (CGCC), and McGill University for financial support. We also thank Dr. A. LeSimple (McGill University) for HRMS analysis and Dr. S. Poulin (École Polytechnique de Montréal) for XPS measurements. Drs. R.B. Lennox and I.S. Butler are acknowledged for fruitful comments.

References

(1) Moores, A.; Goettmann, F. *New J. Chem.* **2006**, *30* (8), 1121. doi:10.1039/b604038c.
(2) Barnes, W. L.; Dereux, A.; Ebbesen, T. W. *Nature* **2003**, *424* (6950), 824. doi:10.1038/nature01937.
(3) Della Pina, C.; Falletta, E.; Prati, L.; Rossi, M. *Chem. Soc. Rev.* **2008**, *37* (9), 2077. doi:10.1039/b707319b.
(4) Turner, M.; Golovko, V.; Vaughan, O.; Abdulkin, P.; Berenguer-Murcia, A.; Tikhov, M.; Johnson, B.; Lambert, R. *Nature* **2008**, *454* (7207), 981. doi:10.1038/nature07194.
(5) Kuhn, J. N.; Huang, W.; Tsung, C.-K.; Zhang, Y.; Somorjai, G. A. *J. Am. Chem. Soc.* **2008**, *130* (43), 14026. doi:10.1021/ja805050c.
(6) Zhang, Y.; Grass, M.; Habas, S.; Tao, F.; Zhang, T.; Yang, P.; Somorjai, G. *J. Phys. Chem. C* **2007**, *111* (33), 12243. doi:10.1021/jp073350h.
(7) Tsung, C.; Kuhn, J.; Huang, W.; Aliaga, C.; Hung, L.; Somorjai, G.; Yang, P. *J. Am. Chem. Soc.* **2009**, *131* (16), 5816. doi:10.1021/ja809936n.
(8) Itoh, H.; Naka, K.; Chujo, Y. *J. Am. Chem. Soc.* **2004**, *126* (10), 3026. doi:10.1021/ja039895g.
(9) Gao, S.; Zhang, H.; Wang, X.; Mai, W.; Peng, C.; Ge, L. *Nanotechnology* **2005**, *16* (8), 1234. doi:10.1088/0957-4484/16/8/042.
(10) Zhang, H.; Cui, H. *Langmuir* **2009**, *25* (5), 2604. doi:10.1021/la803347h.
(11) Wang, Z.; Zhang, Q.; Kuehner, D.; Ivaska, A.; Niu, L. *Green Chem.* **2008**, *10* (9), 907. doi:10.1039/b806453a.
(12) Kim, K.; Demberelnyamba, D.; Lee, H. *Langmuir* **2004**, *20* (3), 556. doi:10.1021/la0355848.
(13) Lu, X.; Tuan, H.-Y.; Korgel, B. A.; Xia, Y. *Chem. Eur. J.* **2008**, *14* (5), 1584. doi:10.1002/chem.200701570.
(14) Gajan, D.; Guillois, K.; Delichere, P.; Basset, J.-M.; Candy, J.-P.; Caps, V.; Coperet, C.; Lesage, A.; Emsley, L. *J. Am. Chem. Soc.* **2009**, *131* (41), 14667. doi:10.1021/ja903730q.
(15) Zopes, D.; Kremer, S.; Scherer, H.; Belkoura, L.; Pantenburg, I.; Tyrra, W.; Mathur, S. *Eur. J. Inorg. Chem.* **2011**, *2011* (2), 273. doi:10.1002/ejic.201000863.
(16) Brust, M.; Walker, M.; Bethell, D.; Schiffrin, D. J.; Whyman, R. *J. Chem. Soc. Chem. Commun.* **1994**, (7): 801. doi:10.1039/c39940000801.
(17) Goulet, P. J. G.; Lennox, R. B. *J. Am. Chem. Soc.* **2010**, *132* (28), 9582. doi:10.1021/ja104011b.
(18) Ott, L.; Finke, R. *Coord. Chem. Rev.* **2007**, *251* (9-10), 1075. doi:10.1016/j.ccr.2006.08.016.
(19) Redel, E.; Walter, M.; Thomann, R.; Vollmer, C.; Hussein, L.; Scherer, H.; Krüger, M.; Janiak, C. *Chem. Eur. J.* **2009**, *15* (39), 10047. doi:10.1002/chem.200900301.
(20) Léger, B.; Denicourt-Nowicki, A.; Olivier-Bourbigou, H.; Roucoux, A. *Tetrahedron Lett.* **2009**, *50* (47), 6531. doi:10.1016/j.tetlet.2009.09.039.
(21) Hu, Y.; Yu, Y.; Hou, Z.; Li, H.; Zhao, X.; Feng, B. *Adv. Synth. Catal.* **2008**, *350* (13), 2077. doi:10.1002/adsc.200800290.
(22) Dykeman, R. R.; Yan, N.; Scopelliti, R.; Dyson, P. J. *Inorg. Chem.* **2011**, *50* (3), 717. doi:10.1021/ic102041q.
(23) Manojlovic-Muir, L.; Henderson, A. N.; Treurnicht, I.; Puddephatt, R. J. *Organometallics* **1989**, *8* (8), 2055. doi:10.1021/om00110a037.
(24) Starkey Ott, L.; Campbell, S.; Seddon, K. R.; Finke, R. G. *Inorg. Chem.* **2007**, *46* (24), 10335. doi:10.1021/ic700976z.
(25) Starkey Ott, L.; Cline, M. L.; Deetlefs, M.; Seddon, K. R.; Finke, R. G. *J. Am. Chem. Soc.* **2005**, *127* (16), 5758. doi:10.1021/ja0423320.
(26) Scholten, J. D.; Ebeling, G.; Dupont, J. *Dalton Trans.* **2007**, (47): 5554. doi:10.1039/b707888a.
(27) Yee, C. K.; Ulman, A.; Ruiz, J. D.; Parikh, A.; White, H.; Rafailovich, M. *Langmuir* **2003**, *19* (22), 9450. doi:10.1021/la020628i.
(28) Tatumi, R.; Fujihara, H. *Chem. Commun. (Camb.)* **2005**, (1): 83. doi:10.1039/b413385d.
(29) Israelachvili, J. N. *Intermolecular and Surface Forces,* 2nd ed.; Academic Press: London, 1992.
(30) Redel, E.; Thomann, R.; Janiak, C. *Inorg. Chem.* **2008**, *47* (1), 14. doi:10.1021/ic702071w.
(31) Redel, E.; Thomann, R.; Janiak, C. *Chem. Commun. (Camb.)* **2008**, (15): 1789. doi:10.1039/b718055a.
(32) Krämer, J.; Redel, E.; Thomann, R.; Janiak, C. *Organometallics* **2008**, *27* (9), 1976. doi:10.1021/om800056z.
(33) Blesic, M.; Marques, M.; Plechkova, N.; Seddon, K.; Rebelo, L.; Lopes, A. *Green Chem.* **2007**, *9* (5), 481. doi:10.1039/b615406a.
(34) Badia, A.; Lennox, R.; Reven, L. *Acc. Chem. Res.* **2000**, *33* (7), 475. doi:10.1021/ar9702841.
(35) Underwood, S.; Mulvaney, P. *Langmuir* **1994**, *10* (10), 3427. doi:10.1021/la00022a011.
(36) Ung, T.; Liz-Marzan, L.; Mulvaney, P. *J. Phys. Chem. B* **2001**, *105* (17), 3441. doi:10.1021/jp003500n.
(37) Chang, Y. C.; Chiu, Y. H.; Wu, Y. W.; Tao, Y. T. *Biomaterials* **2005**, *26* (15), 2313. doi:10.1016/j.biomaterials.2004.06.043.
(38) Ramesha, A. R.; Chandresekaran, S. *J. Chem. Soc., Perkin Trans. 1* **1994**, (6): 767. doi:10.1039/p19940000767.
(39) Miller, C.; Cuendet, P.; Grætzel, M. *J. Phys. Chem.* **1991**, *95* (2), 877. doi:10.1021/j100155a072.

Can. J. Chem. Downloaded from www.nrcresearchpress.com by Renmin University of China on 09/02/12
For personal use only.

(40) Zong, K.; Brittain, S. T.; Bradwurm, D.; Kim, Y. *Synth. Commun.* **1997**, *27* (1), 157. doi:10.1080/00397919708004816.
(41) Khoshtariya, D. E.; Wei, J. J.; Liu, H. Y.; Yue, H. J.; Waldeck, D. H. *J. Am. Chem. Soc.* **2003**, *125* (25), 7704. doi:10.1021/ja034719t.
(42) Kubo, Y.; Uchida, S.; Kemmochi, Y.; Okubo, T. *Tetrahedron Lett.* **2005**, *46* (25), 4369. doi:10.1016/j.tetlet.2005.04.074.
(43) Harusawa, S.; Yoshida, K.; Kojima, C.; Araki, L.; Kurihara, T. *Tetrahedron* **2004**, *60* (51), 11911. doi:10.1016/j.tet.2004.09.109.
(44) Coates, G. E.; Parkin, C. *J. Chem. Soc.* **1962**, 3220. doi:10.1039/jr9620003220.

Can. J. Chem. Downloaded from www.nrcresearchpress.com by Renmin University of China on 09/02/12
For personal use only.

Surface etching of silicone elastomers by depolymerization

Michael A. Brook, Shigui Zhao, Lihua Liu, and Yang Chen

Can. J. Chem. Downloaded from www.nrcresearchpress.com by Renmin University of China on 09/02/12
For personal use only.

Abstract: Silicone elastomer surfaces that are rough at the nanometer to micron scales could be useful for biomaterials, but there are few efficient routes for their preparation. Silicones undergo depolymerization under equilibrating conditions. We demonstrate that surface roughness can be induced by depolymerizing silicone elastomers using triflic acid, tetrabutylammonium fluoride or KOH as catalysts. The efficiency of depolymerization, however, is decoupled from the roughness that develops. When the catalysts are dissolved in solvents that do not effectively swell silicones, the etching reaction can be mostly directed to the elastomer surface. Acid catalysis leads to slow, nearly homogenous surface erosion with surface roughnesses only increasing from 15 to about 125 nm root mean squared roughness. By contrast, once KOH partitions into the elastomer, the rate of erosion is more efficient than return of the catalyst to the solvent, leading to deep channels and roughnesses of up to ~850 nm. The use of fluoride requires good solvents for silicone, and leads to surfaces of intermediate roughness. Thus, judicious choice of catalyst and solvent permits independent control over depolymerization and the induction of surface roughness.

Key words: silicone, redistribution/equilibration, surface roughness.

Résumé : Des surfaces élastomères de silicone qui seraient dures aux échelles allant du nanomètre au micron pourraient être utiles comme biomatériaux, mais on ne connaît que peu de méthodes pour les préparer. Les silicones peuvent donner lieu à une dépolymérisation dans des conditions équilibrantes. Dans ce travail, on démontre que la rugosité de la surface peut être induite par une dépolarisation d'élastomères de silicone en utilisant de l'acide triflique, du fluorure de tétrabutylammonium ou du KOH comme catalyseurs. Toutefois, l'efficacité de la dépolymérisation est découplée de la rugosité qui se développe. Quand les catalyseurs sont dissous dans des solvants qui ne gonflent pas les silicones d'une façon efficace, la réaction d'attaque chimique peut être orientée principalement vers la surface de l'élastomère. La catalyse acide conduit à une érosion lente et pratiquement homogène de la surface qui ne fait passer la rugosité quadratique moyenne que d'environ 15 à 125 nm. À l'autre bout du spectre, une fois que le KOH a commencé la partition de l'élastomère, la vitesse d'érosion est beaucoup plus efficace que le retour du catalyseur dans le solvant et il en résulte qu'il y a formation de canaux et des rugosités allant jusqu'à environ 850 nm. L'utilisation du fluorure exige l'utilisation de bons solvants pour la silicone et conduit à des surfaces de rugosités intermédiaires. En peu en conclure qu'un choix judicieux de catalyseur et de solvant peut permettre d'avoir un contrôle indépendant sur la dépolarisation et l'induction d'une rugosité de surface.

Mots-clés : silicone, redistribution/équilibration, rugosité de surface.

[Traduit par la Rédaction]

Introduction

Silicone elastomers are widely used in a variety of biomaterials applications. The utility of such materials depends on the ability of the desired biological entities to populate the synthetic polymer surface. Various parameters affect the interactions between the silicone and local biology,[1] including the elastomer modulus, hydrophobicity, and surface roughness,[2] among others. Although the relationship between surface physical chemistry and cell adhesion and growth is not yet completely clear, polymer surface texture clearly affects cell adhesion, shape, proliferation, and function.[3,4] Some cell types prefer to adhere to rougher surfaces,[5–7] including on

Received 25 April 2011. Accepted 22 September 2011. Published at www.nrcresearchpress.com/cjc on 8 December 2011.

M.A. Brook, S. Zhao,* L. Liu,† and Y. Chen. Department of Chemistry and Chemical Biology, McMaster University, 1280 Main St. W., Hamilton, ON L8S 4M1, Canada.

Corresponding author: Michael A. Brook (email: mabrook@mcmaster.ca).

This article is part of a Special Issue dedicated to Professor Tak-Hang Chan. It is a tremendous pleasure to dedicate this paper to (Tak Hang) Bill Chan. I made lots of silicone polymers as undesired by-products while doing my Ph.D. in his lab. There is thus a certain irony in using this opportunity to report on degradation products when most of Bill's career has rather been associated with controlled synthesis. The subject was purposefully chosen, however. The element of surface control we attempt to describe in this paper was unexpected. Bill taught me to try and be a careful observer, to capture unexpected results, and to creatively (in his case) move them in new directions. I am extraordinarily grateful for his role as mentor.

*Present address: School of Materials Science & Engineering, Shandong University, 17923 Jingshilu, Jinan 250061, China.
†Present address: AB SCIEX Research and Development, 71 Four Valley Drive, Concord, ON L4K 4V8, Canada.

Can. J. Chem. Downloaded from www.nrcresearchpress.com by Renmin University of China on 09/02/12
For personal use only.

low-energy silicone surfaces,[8] although this trend is not universally followed.[9]

Surface roughness in silicone elastomers can be induced at various length scales. Silicones are very adept at accommodating details in complex molds and this serves as one strategy to make rough surfaces, for example, as stamps for microcontact printing.[10,11] However, we were interested in developing simple strategies that would randomly induce surface roughness at length scales ranging from ~10 nm to ~1 μm. These surfaces of pure dimethylsilicone could then be tested for their ability to facilitate cell adhesion and proliferation.

Silicones are known for their resistance to thermal and oxidative conditions. However, at pHs away from neutrality, silicones readily undergo chain scission in hydroxylic solvents.[12] Fluoride ion is similarly able to cleave Si–O bonds.[13] Once reactive chain ends form, reduction of the silicone polymer chain length occurs by backbiting, with concomitant ring formation. Both chain scission and backbiting lead to loss of molecular weight (Figs. 1A and 1B).

The equilibrium constant K_2 between chains and rings (Fig. 1B) is ~1 and is reduced by any factor that reduces the concentration of monomers in chains,[14] such as dilution by solvents or even by the presence of more voluminous side chains on the silicone backbone. One of the by-products of equilibration is D_4 $(Me_2SiO)_4$, which readily evaporates at room temperature and can further push the equilibrium towards depolymerization.[15]

The complete depolymerization of silicones by equilibration has previously been used to create porous media. For example, the silicone portion of block copolymers of silicone and polyisoprene leads to nanoporous foams[16] following erosion by tetrabutylammonium fluoride trihydrate (TBAF).[17]

The generation of rough surfaces on a silicone elastomer requires asymmetric depolymerization along the exposed surface. We report that random roughness between about 20 and 1000 nm can be readily induced in silicone elastomer surfaces by controlled depolymerization in an appropriate solvent using acid, base,[18] or fluoride catalysts, respectively: the three catalysts engender roughness quite differently.

Experimental section

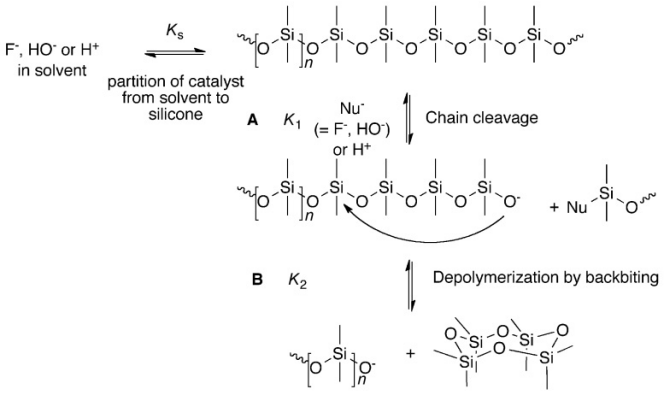
Materials

TBAF, KOH, and triflic acid (F_3CSO_3H, 98%) were purchased from Sigma-Aldrich and SylGard 184 (silicone elastomer kit) and poly(methylhydrosiloxane)($(MeHSiO)_n$, DC1107) were purchased from Dow Corning. The compounds and solvents (Caledon) 2-propanol (IPA), THF, hexanes, diethylene glycol dimethyl ether (diglyme), methanol, acetone, and dimethylformamide (DMF) were used as received.

Surface characterization

FTIR spectra (16 scans at 4 cm^{-1} resolution) of the surfaces prepared as described in the following were obtained using a Bio-Rad (Cambridge, MA) FTS-40 FTIR spectrometer with a fixed 45° angle attenuated total reflectance (ATR, ZnSe) cell attachment under N_2 purge. Thus, the samples were placed on an ATR cell and the FTIR scans were obtained; background runs were subtracted from the sample spectrum. The imaging data were analyzed with WinIR Pro software (Bio-Rad) and Excel software.

Fig. 1. Silicone equilibration.



The surface textures of both unmodified and modified elastomers were characterized by an optical profilometer and scanning electron microscopy (SEM). A Veeco WYKO NT1100 optical profiler (mode: VSI, objective 50×, FOV 2.0×), was used with Vision32 software. Three traces/images were recorded for each specimen in different locations to give an image of the profile and the root mean squared roughness (Rq) in nanometers. The images shown (Fig. 2) represent surfaces of approximately 225 μm × 300 μm.

PDMS discs were gold coated (25 nm) using a Gatan precision etching coating system (PECS), model 682, and then SEM images were taken with a Jeol 7000F microscope at different magnifications.

Silicone elastomers

Silicone elastomers were prepared following manufacturer's directions (two parts mixed in a 1:10 ratio of curing agent:base and allowed to cure at ambient temperature for 2 days in a Petri dish. Silicone elastomer slabs were punched into small circular discs of ~1.0 cm diameter × 0.3 cm thick using a coring tool.

Etching protocols

Surface-etching solutions were prepared by dissolving fixed weight fractions of the catalyst (TBAF, KOH, or triflic acid) into methanol, THF, or mixtures of these solvents with water (Table 1). The PDMS disks were placed into a vial normally containing 0.5–2 mL of the etching solution and shaken for various time periods at room temperature. Experiments were run in triplicate.

After etching, the elastomer discs were removed from the vials and washed extensively to remove any physically adhering materials. In a typical washing cycle, the rubber slabs were washed with acetone, THF, acetone, hexanes, acetone, water, acetone, and finally flushed with nitrogen and then placed in a vacuum chamber at room temperature overnight.

Preparation of Si–H surfaces

The reversibility of the etching process at the silicone interface was demonstrated by etching in the presence of a second silicone polymer. To a vial containing 5 mL absolute methanol and 3 mL poly(methylhydrosiloxane) (DC1107) was

Can. J. Chem. Downloaded from www.nrcresearchpress.com by Renmin University of China on 09/02/12
For personal use only.

Fig. 2. Surface profilometer images (Rq) of (A) unmodified PDMS (17 nm), (B) PDMS elastomer surface treated with DC1107 and 0.6 wt % trifluoromethanesulfonic acid (TfOH) in methanol for 420 min (120 nm), (C) PDMS elastomer surface treated with 2.0 mL of 0.10% TBAF/THF, for 2 h (435 nm), and (D) PDMS elastomer surface treated with 1.0% KOH/MeOH + 10% THF + 10% H_2O for 24 h (816 nm). SEM images of (E) PDMS treated with 2.0 mL of 0.10% TBAF/THF for 5 min (180) and (F) 5.0% KOH/MeOH + 10% THF + 10% H_2O for 5 h.

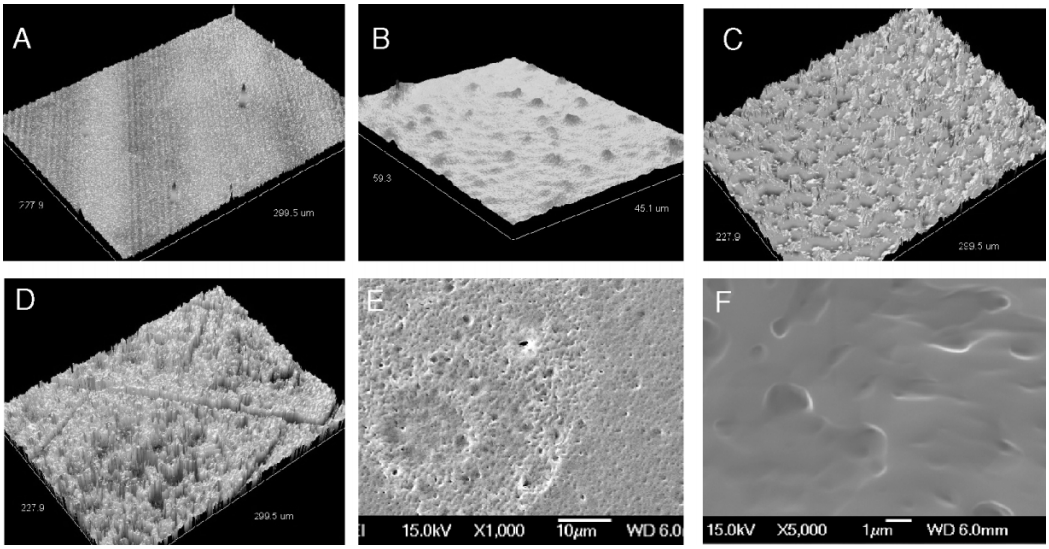


Table 1. Experimental protocols.

Catalyst	wt %	Solvent	Volume (mL)	Results
TBAF	0.001	THF	2	Fig. 3
	0.01	THF	2	
	0.1	THF	2	Fig. 4
	0.1	THF	0.5	Fig. 4
	0.1	THF/H_2O	2	Fig. 5
TfOH	0.6	MeOH	2	Fig. 6
	0.6	MeOH/DC1107	8	Fig. 7
KOH	1	MeOH/H_2O	2	Fig. 8
	5	MeOH/H_2O	2	Fig. 8
KOH	1	MeOH/H_2O/THF	2	Fig. 8
	5	MeOH/H_2O/THF	2	Fig. 8

Note: TfOH, trifluoromethanesulfonic acid; DC1107, poly(methylhydrosiloxane)$((MeHSiO)_n$.

added 1–30 PDMS discs and 50 μL trifluoromethanesulfonic acid (TfOH). After being vigorously shaken at room temperature, the discs were rinsed thoroughly with dry methanol and hexane to remove TfOH and unreacted DC1107 and then promptly blown dry with nitrogen followed by further drying under vacuum for 2 h. The presence of the SiH at the interface was shown by FTIR (cm^{-1}, neat: 2167 (Si–H)). IPA was an alternative solvent used for making the Si–H surface and led to a much more intense Si–H peak in the IR. However, the discs became brittle and a little bit cloudy after the process. Therefore, all the studies of Si–H materials described in the following were based on the recipe using methanol as the solvent.

The effect of reaction time on the roughness of the Si–H surface was investigated by varying the reaction duration from 1 to 35 min (1, 5, 10, 15, 20, 25, 30, and 35 min). Different concentrations of TfOH (5, 25, 50, and 125 μL in 8 mL of methanol and DC1107 mixture) were also used to study rates of surface modification.

Results

Silicone elastomers were prepared from a commercial kit: platinum-catalyzed addition cure was initiated simply by mixing the base and cross-linker. After mixing, the mobile mixture was placed in a Petri dish where it flowed before curing to give smooth elastomer films of ~3 mm thickness, which was completely cured over ~2 days at room temperature. These cured films exhibited a Rq[19] of ~15 nm as determined using a surface profilometer. We note that this technique is particularly convenient and rapid. However, it is often accompanied by large variations: it provides excellent resolution in the *Z* direction, but much less in the *X*–*Y* plane. In addition, error bars increase when nonregular features are present (e.g., the large cracks shown in Fig. 2D). Small cylindrical coupons of 1 cm diameter were cut from the cured films and used as substrates for surface modification. Etching and depolymerization were simultaneously performed by immersing one or more coupons in single or mixed solvents with one of three different catalyst types: the silicon-specific nucleophile (fluoride in TBAF), acid (triflic acid), or base (KOH) (Table 1).

Effect of solvent

Two classes of solvents were used to perform etching experiments. "Good" solvents that efficiently swell silicone elastomers include THF, diglyme, IPA, hexanes, and, to a lesser extent, DMF and acetone. Such solvents were required when fluoride was used as a depolymerization catalyst. However, these solvents were problematic when acid- or base-catalyzed depolymerization was examined because depolymerization was extremely efficient and difficult to control. After the exposure of elastomers to these conditions, degradation was easily observed as the formation of cracks along grain boundaries (Fig. 2D) and, ultimately, brittle structures. Controlled modification of the elastomer surface alone with these catalysts in good solvents was not generally possible in our hands. Therefore, poor or nonsolvents

Can. J. Chem. Downloaded from www.nrcresearchpress.com by Renmin University of China on 09/02/12
For personal use only.

for silicones, including water and methanol, were used for surface modification by acids or bases (for degrees of swelling of the elastomer in various solvents, see Fig. 9). The low solubility of the solvents and catalysts in silicones constrained reactions mostly to the external interface of the elastomer coupon.

Fluoride (TBAF) etch

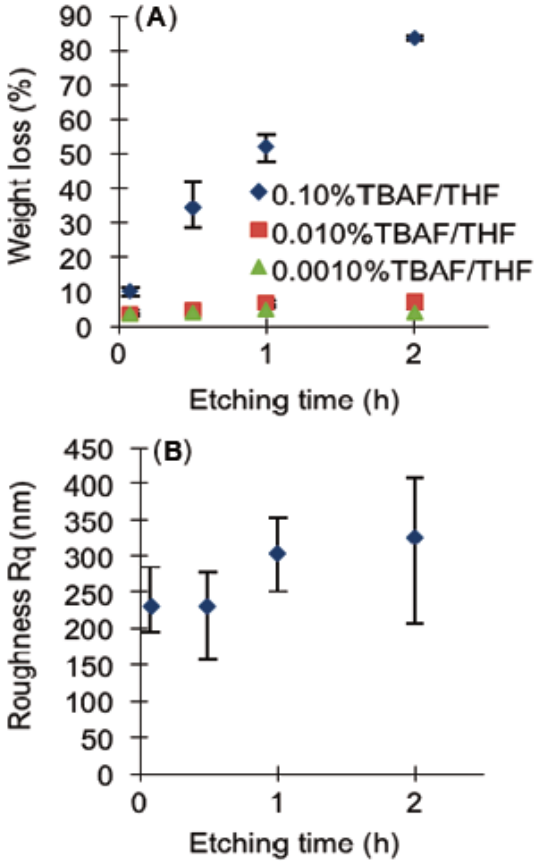
TBAF (Bu_4NF) is widely used as a source of organic-soluble fluoride ion to remove silyl ether protecting groups. While fluoride is a weak base, it is a powerful nucleophile for silicon both because of its small size (little steric barrier to attack at silicon) and the very high strength of the Si–F bond.[20] Fluoride can also facilitate the equilibration of silicone polymers under mild conditions.[21]

Attempts to modify the surface of silicone elastomers using TBAF in dry methanol, diglyme, or acetone were unsuccessful; even after reaction for 24 h at room temperature there was no change in surface roughness and significant weight loss was not observed. The fluoride was simply not an effective catalyst with these solvents. By contrast, etching in THF was efficient under these conditions, as shown by the efficient weight loss of the elastomer over time (Fig. 3A). Over longer etching times, the PDMS disc first became thinner then completely disappeared after etching for 3 h in 2.00 mL 0.10% TBAF/THF. Surprisingly, however, there was little concomitant change in surface roughness during this process. Following a rapid increase in Rq from ~15 to 230 nm, there was little further change over time as the elastomer decomposed (Fig. 3B). Profilometer and SEM images suggest that roughness is a result of asymmetric depolymerization along the surface in channels normal to the external surface (Figs. 2C and 2E).

The rate of degradation was also affected by the total volume of the TBAF/THF etching solution, not simply the concentration of the solution. For example, the use of 0.5 or 2 mL of the same 0.10% TBAF in THF solution, led to very different changes in the surface chemistry occurring on the elastomer surface. Higher volumes, thus more net fluoride and THF available to the elastomer, led to more profound changes in the surface roughness. This observation is consistent with a reaction mechanism in which, in addition to the rate of attack of the fluoride nucleophile at silicon, bond breaking is related to the rates of absorption of fluoride and (or) of swelling of the elastomer (see the following). The data in Fig. 4 further suggests that depolymerization of the silicone is decoupled from the induced surface roughness.

The efficiency of surface etching was also shown to depend strongly on the amount of water present in the reaction medium (Fig. 5). It is exceptionally difficult to completely dehydrate TBAF: most commercial samples are sold as a hydrate (we used the trihydrate). However, as the amount of water was increased from this low level, both the efficiency of depolymerization and resulting roughness were significantly reduced even in the presence of the good solvent, THF (Fig. 5). This suggests that water outcompetes silicone for the available fluoride, and no depolymerization of the silicone can result once the moisture content reaches a threshold value of ~4%.

Fig. 3. (A) Elastomer weight loss as a function of tetrabutylammonium fluoride trihydrate (TBAF) concentration. (B) Surface roughness as a function of etching time in 0.1% TBAF/THF (2.00 mL).



Acid-catalyzed etching

Triflic acid, which is commonly used to equilibrate silicones (particularly those containing Si–H groups that are degraded by basic conditions),[5] was added in various concentrations to methanol. Silicone elastomers exposed to acidic solutions for various periods of time changed very little from the starting roughness of ~15 nm Rq, as determined using profilometry (Fig. 6).

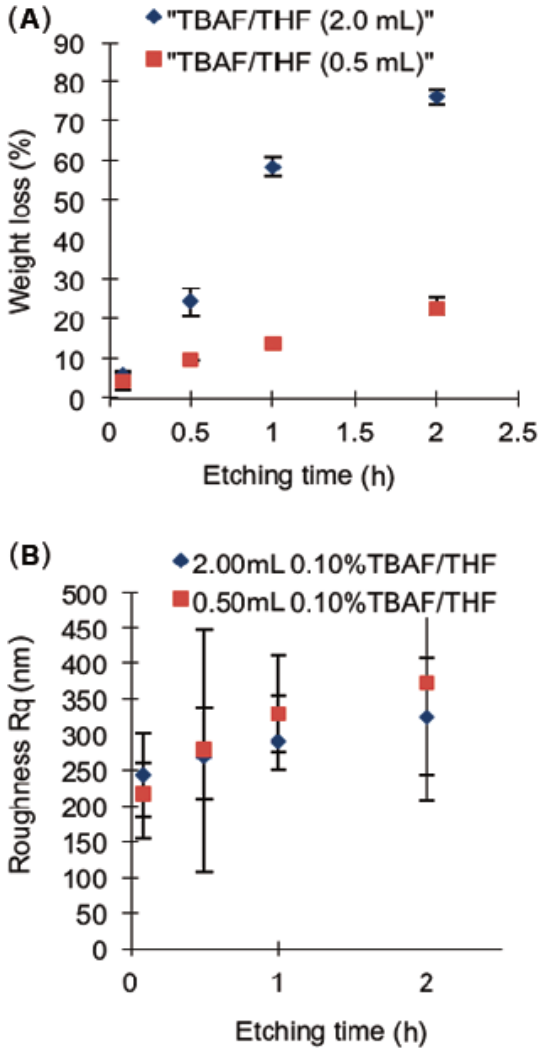
We were initially concerned that essentially no silicone reactions were taking place under these conditions. Therefore, a series of redistribution reactions between a silicone fluid and the silicone elastomer (rather the simple depolymerization, Fig. 7) was attempted using either the poor solvent methanol or the good solvent IPA.

Initially, the dimethylsilicone-based elastomer was exposed to a homogenous solution of DC1107 poly(methylhydrosiloxane) silicone oil and TfOH in IPA. This led rapidly to a silicone elastomer surface rich in Si–H groups as shown by a huge Si–H band at 2167 cm^{-1} (Fig. 7A). The visibly swollen elastomer rapidly developed cracks and then became brittle. This outcome at least demonstrated that reactions were occurring at the surface and internally in the presence of the acid in a good solvent for silicones (Fig. 10).

A dispersion of TfOH and DC1107 in the poorer solvent methanol was then used to modify the elastomer. Over a short period of time the surface became enriched with SiH groups, demonstrating that the silicone polymer was undergoing

Can. J. Chem. Downloaded from www.nrcresearchpress.com by Renmin University of China on 09/02/12
For personal use only.

Fig. 4. Effect of available tetrabutylammonium fluoride trihydrate (TBAF) on (A) weight loss and (B) roughness when etching silicone elastomers.

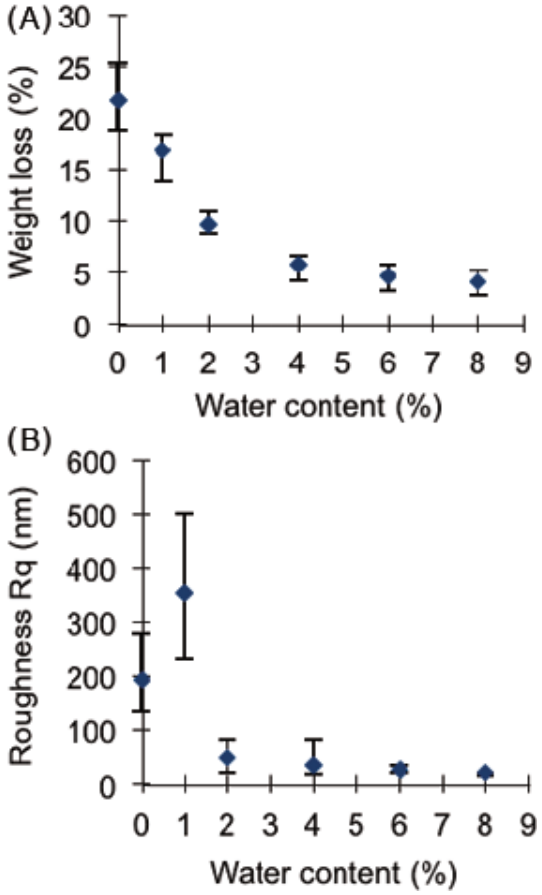


depolymerization/repolymerization at the interface leading to growth of new layers and (or) exchange of MeHSiO monomers with the Me_2SiO monomers of the silicone elastomer (Fig. 7B). The rate of surface enrichment in SiH groups also increased with the concentrations of TfOH (data not shown).[22] During these reactions, there was a gradual increase in surface roughness over time (Fig. 2B) that was accelerated with higher TfOH concentrations (Fig. 7C). The profilometer images suggest that more or less uniform etching of the surface is occurring, with the exception of some islands that resist degradation. That is, the surface roughness does not change a great deal during the etching process. An alternative explanation for smooth islands is the presence of adsorbed or absorbed silicone oil. This was discounted after extensive washing showed no change in the surface roughness.

Base-catalyzed etching

KOH is an effective catalyst for silicone equilibration.[22] In good solvents for silicone, degradation led to the rapid formation and propagation of cracks and very rough surfaces

Fig. 5. Effect of water concentration on (A) the rate of silicone degradation in THF and (B) resulting surface roughness.



(Fig. 2D). Surprisingly, even in solvent systems that were mostly water, a nonsolvent for silicones, very rough surfaces (Fig. 2C) rapidly evolved provided that even low concentrations of good solvents, such as acetone and particularly THF, were also present. The poor solvent methanol, to which water was added, was therefore used to preferentially direct reaction to the outer surface of the elastomer.

Unlike degradation catalyzed by fluoride or acid, almost no weight loss of PDMS was observed after etching for 5 h in 1.0% KOH/(MeOH + 10%H_2O), although a surface roughness of Rq 200 nm was obtained; further etching to 48 h did lead to further increases in surface roughness, although weight loss continued in a nearly linear fashion. Much higher roughness required higher catalyst loadings.

As with the case with fluoride, the eroded surface of the elastomer was comprised of pits (Fig. 2F). These pitted surfaces formed very early in the process, long before significant weight loss had occurred from the elastomer. At much later points during erosion, cracking processes and eventually complete degradation occurred.

Discussion

In solution, in the presence of any of the three catalysts examined, silicone polymers undergo random chain cleavage with concomitant reduction in the average molecular weight. This is the reverse process of the condensation process that leads to their formation (Fig. 1A). In the elastomeric structures

Can. J. Chem. Downloaded from www.nrcresearchpress.com by Renmin University of China on 09/02/12
For personal use only.

Fig. 6. Surface roughness of silicone elastomers exposed to (A) various concentrations of TfOH for 30 min and (B) 0.6 wt % trifluoromethanesulfonic acid (TfOH) in methanol over time.

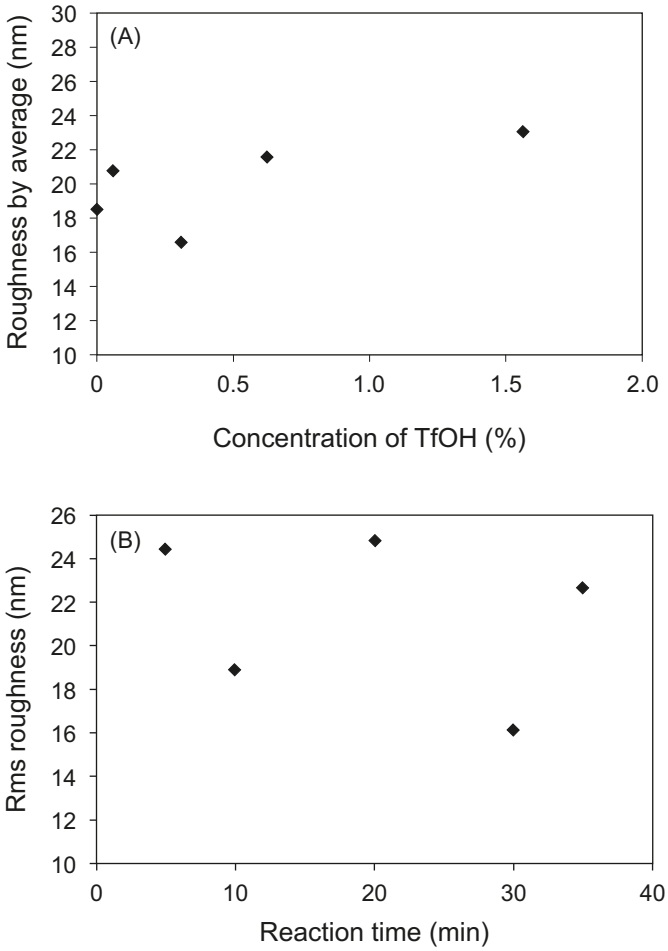
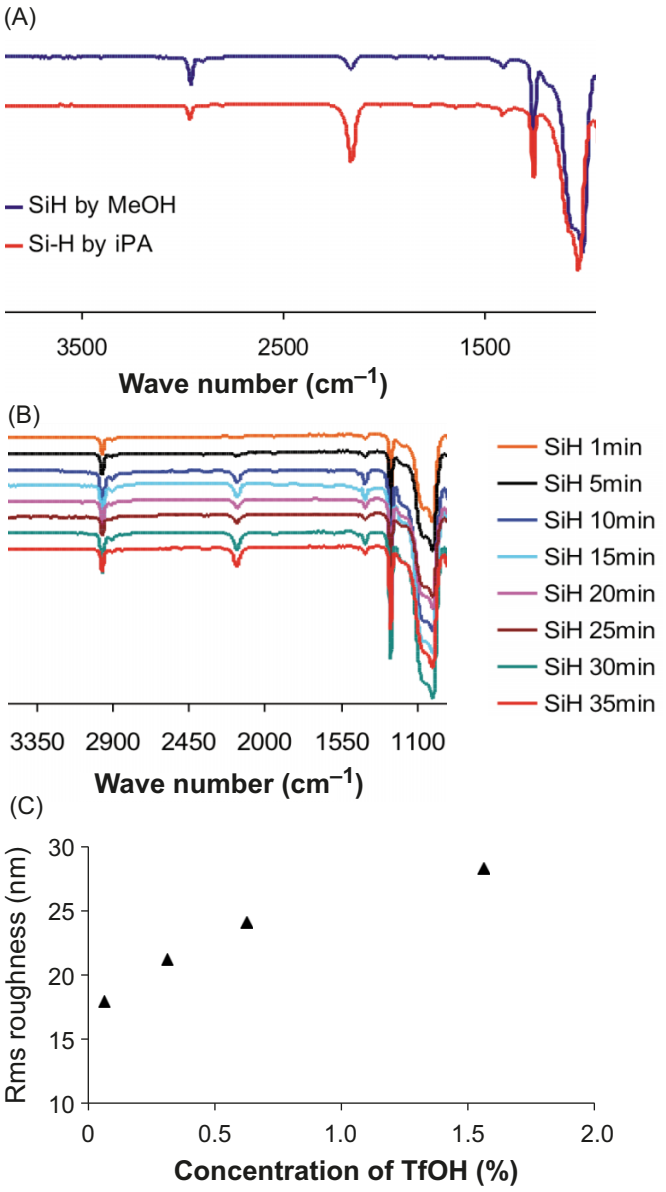


Fig. 7. Introduction of SiH groups (as shown by the IR band at 2167 cm^{-1}) on the PDMS elastomer surface with 0.6 wt % trifluoromethanesulfonic acid (TfOH) for 30 min (A) in alcohol and (B) in methanol over time. (C) Effect of TfOH concentration on induced roughness.



examined here, these processes cleave siloxane chains between cross-links. Chain cleavage is later accompanied by a depolymerization (unzipping) process through backbiting with concomitant loss of silicone cyclics (Fig. 1B).

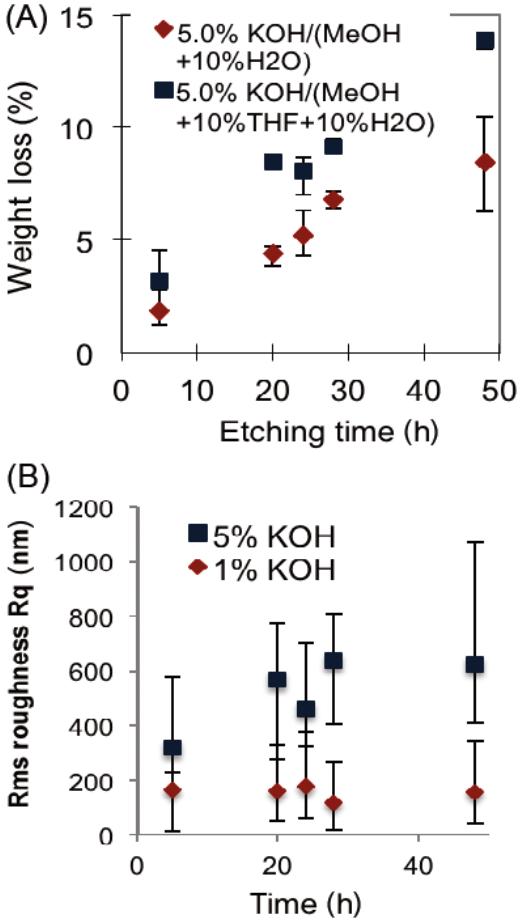
There is thus a temporal change in the cross-link density of the silicone elastomer. At the early stage of the degradative process, cleavage reduces the cross-link density, initially leading to softer elastomers. As depolymerization sets in, the loss of silicone monomers will increase the ratio of cross-links to chains leading to higher cross-link densities in the elastomer body. Cracking of the elastomer can result and, in the limit, low molecular weight linear and cyclic silicones and highly cross-linked resins are produced.

If the degradation processes were to occur uniformly across the elastomer surface (or uniformly within the silicone elastomer), loss of silicones from the elastomer would occur with little or no change in the surface roughness. That is, the elastomer would lose weight during degradation, but the surface roughness remains essentially unchanged. Such a situation was observed in the case of the acid catalyst in poor solvents for silicone. Aside from some "islands" that formed (Fig. 2B) — possibly because of pre-existing zones of higher cross-link density — slow and homogenous erosion from the outer surface was observed. Thus, the ability of the catalyst to facilitate degradation of the elastomer did not correlate with induced roughness.

The acid etch was performed in a poor solvent for silicones. In addition to the rates at which the decomposition equilibria are established in a given medium, the catalyst must partition between the solution and the silicone elastomer (K_s, Fig. 1), which exists as a distinct phase. The solvation equilibrium clearly favours the presence of the acid in solution rather than in the silicone. That is, the acid moves from solution to silicone, facilitates a small amount of silicone degradation, and then preferentially migrates back into solution. The process is then repeated at a different position on the surface such that more or less homogenous decomposition/depolymerization across the elastomer surface occurs with little change in surface roughness.

Can. J. Chem. Downloaded from www.nrcresearchpress.com by Renmin University of China on 09/02/12
For personal use only.

Fig. 8. Elastomers exposed to KOH in water/MeOH (optionally THF). (A) Weight loss. (B) Surface roughness.



The equilibration process under these conditions is inefficient. However, the ability to show that it is occurring was demonstrated by the redistribution of silicones in solution (hydrosilicones) with dimethylsilicones on the elastomer surface. Over time, the quantity of (grafted) SiH groups on the elastomer surface gradually increases as shown by IR spectroscopy (Fig. 7).

Etching with fluoride was not effective in poor solvents for silicones, suggesting that the fluoride does not efficiently leave solution to enter the silicone phase under these conditions. With a highly THF swollen silicone elastomer, by contrast, the fluoride enters the silicone phase and efficiently causes depolymerization of silicone. Very rapid decomposition was observed under these conditions, but not in a homogenous manner. Instead, the etching led to the formation of porous channels within the silicone (Fig. 2E). This observation is consistent with a process in which, once the fluoride has migrated into the silicone phase from THF, it remains there for a considerable period of time ($K_s > 1$, Fig. 1) causing "pockets" of degradation before returning to solution. If solvent conditions are such that the partition of catalyst into the silicone is disfavoured, it is possible to suppress degradation entirely: the efficiency of the catalyst drops dramatically with water content (Fig. 5), as has previously been observed.[23] Once the silicone degradation process is established, a rough surface is generated at a comparable rate to surface erosion such that the net surface roughness does not change (Fig. 3B), even if higher concentrations of catalyst are used (Fig. 4).

Fig. 9. Degree of swelling of the silicone elastomer in different solvents (DMF–MeOH and acetone–diglyme).

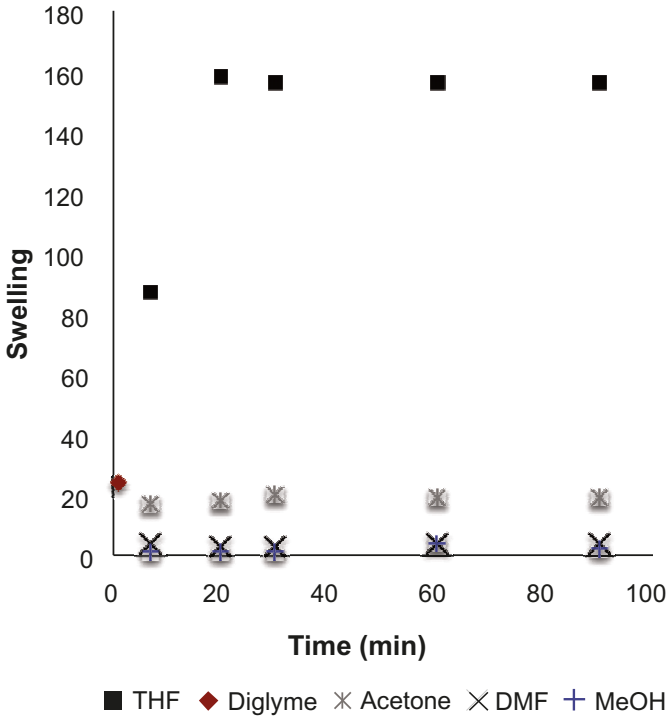
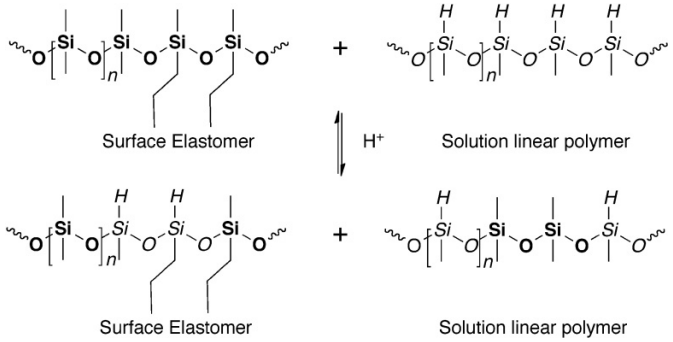


Fig. 10. Acid-catalyzed equilibration reaction between linear poly(methylhydrosiloxane) and elastomer polydimethylsiloxane.



KOH is promiscuous with regard to silicone degradation. Irrespective of solvent, efficient degradation of the elastomer body occurred. The erosion process was facilitated by the presence of even small quantities of good solvents for silicone, such as THF, even when diluted into water in small quantities (Figs. 2C and 2D).

As with fluoride, KOH leads to asymmetric degradation of the silicone elastomer such that as the silicone degrades, the surface becomes rougher. Once KOH partitions from solution into the elastomer body ($K_s >> 1$, Fig. 1), it remains there for extended periods of time "burrowing" (Fig. 2F) into the silicone leading to highly rough surfaces, prior to returning to the solution. With KOH, the relative amount of erosion to give rough surfaces, versus overall erosion, was highly concentration-dependent. Higher catalyst concentrations led to rougher surfaces.

Can. J. Chem. Downloaded from www.nrcresearchpress.com by Renmin University of China on 09/02/12
For personal use only.

The simple technology described previously allows silicone elastomer surfaces from ~15 to 1000 nm roughness to be generated with random features. Such a process would not be useful for creating fine patterns on a silicone elastomer surface. By contrast, it is an efficacious, simple, and reasonablly controllable method to manipulate large surfaces, as are found with stents, catheters, and other implantable silicone devices. With such materials in hand, it will be possible to establish optimum surface structures for proliferation of different cell types such that surfaces can be engineered for different biomaterials applications, which will be the subject of future reports.

Conclusion

Silicone elastomers are readily etched by catalysts that facilitate silicone redistribution. However, the catalysts examined (TfOH, TBAF, and KOH) exhibited different propensities to induce the formation of rough surfaces that were solvent-dependent. Fluoride required good solvents for silicone to induce significant changes in surface roughness at all. Under these conditions where silicones were swollen, degradation processes competed effectively with migration of the catalyst out of the silicone phase leading to significant losses of material in addition to induction of surface roughness. Otherwise, poor solvents for silicone were generally needed to limit reaction primarily to the elastomer surface. Acid slowly eroded the surface homogenously leading to only small changes in surface roughness over time because the catalyst preferentially resided in solution. By contrast, once KOH entered the silicone body, it continued to catalyze degradation burrowing into the silicone leading to large changes in roughness, but only relatively low losses of weight of the elastomer body. Thus, asymmetry in the elastomer surface can be controlled by the use of catalysts that preferentially partition from solution into silicone.

References

(1) Wong, J. Y.; Leach, J. B.; Brown, X. Q. *Surf. Sci.* **2004**, *570* (1–2), 119. doi:10.1016/j.susc.2004.06.186.

(2) Vianna-Soares, C. D.; Kim, C.-J.; Ciftci, K.; Borenstein, M. R. *Mater. Res.* **2004**, *7* (3), 473. doi:10.1590/S1516-14392004000300016.

(3) Koyano, T.; Minoura, N.; Nagura, M.; Kobayashi, K. *J. Biomed. Mater. Res.* **1998**, *39* (3), 486. doi:10.1002/(SICI)1097-4636(19980305)39:3<486::AID-JBM20>3.0.CO;2-7.

(4) Higuchi, A.; Tamiya, S.; Tsubomura, T.; Katoh, A.; Cho, C. S.; Akaike, T.; Hara, M. *J. Biomater. Sci. Polym. Ed.* **2000**, *11* (2), 149. doi:10.1163/156856200743625.

(5) Hallab, N. J.; Bundy, K. J.; O'Connor, K.; Moses, R. L.; Jacobs, J. J. *Tissue Eng.* **2001**, *7* (1), 55. doi:10.1089/107632700300003297.

(6) He, W.; Gonsalves, K. E.; Batina, N.; Poker, D. B.; Alexander, E.; Hudson, M. *Biomed. Microdevices* **2003**, *5* (2), 101. doi:10.1023/A:1024531010086.

(7) Chung, T. W.; Wang, Y. Z.; Huang, Y. Y.; Pan, C. I.; Wang, S. S. *Artif. Organs* **2006**, *30* (1), 35. doi:10.1111/j.1525-1594.2006.00178.x.

(8) (a) Fujisawa, N.; Poole-Warren, L. A.; Woodard, J. C.; Bertram, C. D.; Schindhelm, K. *Biomaterials* **1999**, *20* (10), 955. doi:10.1016/S0142-9612(98)00251-8; (b) Wilkerson, W. R.; Seegert, C. A.; Feinberg, A. W.; Zhao, L. C.; Callow, J. A.; Callow, M. E.; Brennan, A. B. *Polymer Prepr.* **2001**, *42* (1), 147.

(9) Prasad, B. R.; Brook, M. A.; Smith, T.; Zhao, S. G. I.; Chen, Y.; Sheardown, H.; D'Souza, R.; Rochev, Y. *Colloids Surf. B Biointerfaces* **2010**, *78* (2), 237. doi:10.1016/j.colsurfb.2010.03.006.

(10) Xia, N.; Thodeti, C. K.; Hunt, T. P.; Xu, Q. B.; Ho, M.; Whitesides, G. M.; Westervelt, R.; Ingber, D. E. *FASEB J.* **2008**, *22* (6), 1649. doi:10.1096/fj.07-090571.

(11) Xia, Y. N.; Whitesides, G. M. *Annu. Rev. Mater. Sci.* **1998**, *28* (1), 153. doi:10.1146/annurev.matsci.28.1.153.

(12) Huang, W.; Ikeda, Y.; Oku, A. *Polymer (Guildf.)* **2002**, *43* (26), 7295. doi:10.1016/S0032-3861(02)00713-9.

(13) (a) Greene, T. W. *Protective Groups in Organic Synthesis;* Wiley: New York, 1981; (b) Greene, T. W.; Wuts, P. G. M. *Protective Groups in Organic Synthesis,* 2nd ed., Wiley: New York, 1991; (c) McOmie, J. F. W., Ed. *Protecting Groups in Organic Synthesis;* Plenum: New York, 1973; (d) Kocienski, P. J. *Protecting Groups;* Thieme Verlag: Stuttgart, 1994.

(14) Chojnowski, J. Polymerization. In *Siloxane Polymers;* Clarson, S. J.; Semlyen, J. A.; Eds.; Prentice Hall: Englewood Cliffs, NJ, 1993; Chapter 1, p 5.

(15) Camino, G.; Lomakin, S. M.; Lageard, M. *Polymer (Guildf.)* **2002**, *43* (7), 2011. doi:10.1016/S0032-3861(01)00785-6.

(16) Hansen, M. S.; Vigild, M. E.; Berg, R. H.; Ndoni, S. *Polym. Bull.* **2004**, *51* (5–6), 403. doi:10.1007/s00289-004-0232-x.

(17) Cavicchi, K. A.; Zalusky, A. S.; Hillmyer, M. A.; Lodge, T. P. *Macromol. Rapid Commun.* **2004**, *25* (6), 704. doi:10.1002/marc.200300245.

(18) Brook, M. A.; Liu, L.; Zhao, S.; Mammo, Z. N. Etching of Silicone Elastomers: Controlled Manipulation of Surface Roughness. In *Synthesis and Properties of Silicones and Silicone-Modified Materials;* Clarson, S. J.; Fitzgerald, J. J.; Owen, M. J.; Smith, S. D.; Van Dyke, M. E., Eds.; American Chemical Society: Washington, DC, 2010; Vol. 1051, pp 147–155.

(19) Rq, the root mean square (rms) average between the height deviations and the mean line/surface, taken over the evaluation length/area. The mathematical formula used to calculate Rq is available from www.veeco.com.

(20) Brook, M. A. Extracoordination at Silicon. In *Silicon in Organic, Organometallic and Polymer Chemistry;* Wiley: New York, 2000; pp 97–114.

(21) Okamoto, M.; Suzuki, S.; Suzuki, E. *Appl. Catal. A Gen.* **2004**, *261* (2), 239. doi:10.1016/j.apcata.2003.11.005.

(22) (a) Chen, H.; Brook, M. A.; Sheardown, H. D.; Chen, Y.; Klenkler, B. *Bioconjug. Chem.* **2006**, *17* (1), 21. doi:10.1021/bc050174b; (b) Chen, H.; Brook, M. A.; Chen, Y.; Sheardown, H. *J. Biomater. Sci. Polym. Ed.* **2005**, *16* (4), 531. doi:10.1163/1568562053700183; (c) Chen, H.; Brook, M. A.; Sheardown, H. *Biomaterials* **2004**, *25* (12), 2273. doi:10.1016/j.biomaterials.2003.09.023.

(23) Hogrefe, R. I.; McCaffrey, A. P.; Borozdina, L. U.; McCampbell, E. S.; Vaghefi, M. M. *Nucleic Acids Res.* **1993**, *21* (20), 4739. doi:10.1093/nar/21.20.4739.

Quasi-classical trajectory calculation of the chemical reaction Ca + CF_3Br

Wenwen Xia, Li Yao, and Haiyang Zhong

Can. J. Chem. Downloaded from www.nrcresearchpress.com by Renmin University of China on 09/02/12
For personal use only.

Abstract: The dynamical properties of the product CaBr for the reaction Ca + CF_3Br were studied with the quasi-classical trajectory method based on the extended London–Eyring–Polanyi–Sato potential energy surface. In this paper, the results, such as vibrational distribution, reaction cross section, and rotational alignment of the product CaBr, were calculated and the reaction mechanism has been discussed. The peak value of the vibrational distribution is located at around $v = 3$ when the collision energy equals 0.55 eV. The result obtained in this paper agrees well with the experimental vibrational result. The reaction cross section and the product rotational alignment all decrease with the increasing collision energy, which changes from 0.1 to 1.0 eV.

Key words: QCT method, LEPS PES, Ca + CF_3Br reaction, dynamics property, reaction mechanism.

Résumé : Les propriétés dynamiques du produit CaBr résultant de la réaction Ca + CF_3Br ont été étudiées par la méthode de la trajectoire semi-classique à base de la surface d'énergie potentielle étendue de London–Eyring–Polanyi–Sato. Dans ce travail, on rapporte les résultats de calculs, telle la distribution vibrationnelle, la section droite de la réaction et l'alignement rotationnel du produit, et on discute du mécanisme réactionnel. La valeur maximale pour la distribution vibrationnelle se situe à environ $v = 3$, quand l'énergie de collision est égale à 0,55 eV. Les résultats obtenus dans ce travail sont en bon accord avec les valeurs vibrationnelles expérimentales. La section droite de la réaction et l'alignement rotationnel du produit diminuent tous avec une augmentation de l'énergie de collision qui passe de 0,1 à 1,0 eV.

Mots-clés : méthode de la trajectoire quasi-classique (TQC), surface d'énergie potentielle étendue de London–Eyring–Polanyi–Sato (SEP LEPS), réaction Ca + CF_3Br, propriété dynamique, mécanisme réactionnel.

[Traduit par la Rédaction]

Introduction

With the rapid development in experimental technology and theoretical studies, more and more people have studied the field of molecular reaction dynamics in recent decades, and the results obtained from the reaction are more exact than before. Especially, the reactions between alkaline earth metal atoms and halogenated methane have been widely studied in both experiment and theory.[1–15]

The main experimental technologies that have been used to measure the property of reaction is chemiluminescence (CL), laser-induced fluorescence (LIF), and cross molecular beam.[1,2] By means of these methods, distributions of the internal energy state, the velocity, and the space angle of the product can be detected.

In 1984, Munakata and Kasuya[3] measured the product-state distributions of reaction system Ba + CF_3Br by means of the LIF method in a crossed-beam configuration of the supersonic CF_3Br beam and the effusive Ba beam. They mainly studied the nascent vibrational distribution of the product BaBr and found that the vibrational distribution had a bimodal feature. They explained this phenomenon as that the reaction Ba + CF_3Br proceeded along two pathways. And later in 1993, Han et al.[4] measured the CL spectra, the collision cross sections, and the CL cross sections of reactions Ca(^{3}P) + CF_3I and Ca(^{3}P) + CH_3I in a beam-gas arrangement. They found that the vibrational excitation probability of product CaI ($A^2\prod$,$B^2\sum^+$) obtained from reaction Ca(^{3}P) + CF_3I was larger than that from reaction Ca(^{3}P) + CH_3I. Three years later, Stolte and co-workers[5] measured the continuous-wave LIF spectra of nascent products SrBr, SrI, and CaBr, which were formed in reactions of Sr with CH_3X and CF_3X (X = Br or I) and Ca with CH_3Br and CF_3Br. They obtained the vibrational distribution $P(v)$ and the rotational distribution $P_v(J)$ at a specific v value from the spectral simulations and found that the vibrational energy released into the monohalide product for reactions with CF_3X (X = Br or I) was larger than that for the corresponding reactions with CH_3X, and a detailed explanation was also given in their paper.[5] In the same year, Lendvay and co-workers[6] investigated the reactive properties of the O(^{1}D) + CF_3Br system via experimental and theoretical studies using the crossed molecular beam scattering measurement and the quasi-classical trajectory (QCT) method. They obtained the energy and angular distributions of the product OBr from the experiment. And from the theoretical study, they estimated the rate coefficients and scattering properties through classical trajectory calculations on a

Received 4 August 2011. Accepted 7 September 2011. Published at www.nrcresearchpress.com/cjc on 8 December 2011.

W. Xia, L. Yao, and H. Zhong. Institute of Computational Physics, Department of Physics, Dalian Maritime University, Dalian 116026, P. R. China.

Corresponding author: Li Yao (e-mail: yaoli@dlmu.edu.cn and haae@dlmu.edu.cn).

Can. J. Chem. Downloaded from www.nrcresearchpress.com by Renmin University of China on 09/02/12
For personal use only.

potential energy surface (PES) that was derived from spectroscopic and ab initio data. Later in 1999, Hou and co-workers[7] studied the same reaction as Lendvay.[6] The reaction in Hou's study was induced by photolysis of the CF_3Br–O_3 system under UV irradiation at 253.7 nm.

At the same time, from the theoretical study, the QCT, the semi-classical, and the quantum theory methods were the main methods that were used to study the molecular reaction dynamics. As we know, the molecular reaction dynamics had been studied by means of the QCT method during the 1930s[8] for the first time, which has undergone development since the 1960s.[9] Until now, the experimental result could be simulated, and the reaction mechanism could be further discussed and explained by means of the QCT method. Therefore, we can say that the QCT method is the most widely used now.

In 1996, van der Avoird and co-workers[10] investigated the energy dependence of the steric effect for reactions $Ca(^1D) + CH_3X$ (j,k,m = 1,1,1) with X = F, Cl, or Br by means of the semi-classical method and knew that products CaX were in the excited states $A^2\prod$, $B^2\sum^+$, and $A'^2\Delta$, respectively. Recently, Yao and co-workers,[11] using the QCT method, studied the dynamical properties of the product CaBr, which was formed in the reaction Ca + CH_3Br. They reported the results of vibrational distribution, rotational distribution, reaction cross section, and product rotational alignment for this reaction. And there were some other studies for reactions between alkaline earth metal atoms and halogenated methane that were related to the reaction Ca + CF_3Br; for example, Ba + CF_3Cl,[12] Sr + CF_3Cl,[13] and $O(^1D)$ + CF_3Cl.[14,15]

However, as we know up until now, no one has carried out a theoretical study on the reaction Ca + $CF_3Br \rightarrow$ CaBr + CF_3 by means of the QCT method. So, we will construct the extended London–Eyring–Polanyi–Sato (LEPS) PES for the reaction Ca + CF_3Br for the first time and apply the QCT method to calculate the vibrational distribution, reaction cross section, and product rotational alignment of the reaction in this paper, as well as analyze the reaction mechanism.

Theory

PES

The PES is the basis of the study and of the analysis of the reaction. Because of the absence of an accurate ab initio PES for the reaction Ca + CF_3Br, the LEPS PES is extended in this work to describe the reaction.

As for the reaction system A + BC → AB + C, the extended LEPS PES mentioned above can be interpreted for the ground state as follows.[16–18]

$$[1]\quad V(r_1, r_2, r_3) = Q_1 + Q_2 + Q_3 - (J_1^2 + J_2^2 + J_3^2 - J_1J_2 - J_2J_3 - J_1J_3)^{1/2}$$

where

$$[2]\quad Q_i = ({}^1E_i + {}^3E_i)/2$$

$$[3]\quad J_i = ({}^1E_i - {}^3E_i)/2$$

where ${}^1E_i$ is defined as the diatomic Morse potential function and ${}^3E_i$ stands for the anti-Morse function.

$$[4]\quad {}^1E_i = D_i\Big(\{1 - \exp[-\beta_i(r - r_0)]\}^2 - 1\Big)$$

$$[5]\quad {}^3E_i = {}^3D_i\Big(\{1 + \exp[-\beta_i(r - r_0)]\}^2 - 1\Big)$$

where

$$[6]\quad {}^3D_i = D_i(1 - S_i)/[2(1 + S_i)]$$

where S_i is an adjustable parameter (so-called Sato parameter) that has been used to achieve more reasonable LEPS PES. D_e, β_i, and R_i^0 are the Morse parameters of a diatomic molecule representing the classical dissociation energy, the spectrum constant, and the equilibrium bond length, respectively. Subscripts i = 1, 2, and 3 indicate Ca–Br, CF_3–Br, and Ca–CF_3, respectively, for the reaction Ca + CF_3Br. By means of these Morse parameters and through adjusting the Sato parameters S_i (i = 1, 2, or 3), whose values change from –1.0 to 1.0, the LEPS PES of the title reaction can be constructed to simulate the experimental results.[5]

The values of the Morse parameters can be obtained from eqs. [7]–[9] according to the data from the Gaussian 03 program on the MP2/6–311++G** level.[19] The configurations used in the calculations are all in the most stable states after being optimized. The optimizations of Ca–Br, CF_3–Br, and Ca–CF_3 were carried out and the energies were obtained. Then the frequency calculations of the three configurations were also given corresponding to stretching vibrational modes. After the data above was obtained, eqs. [7]–[9] were used to dispose these data to obtain the initial data used in the QCT calculation. In the calculation, group CF_3 is treated as a rigid group or an atom whose internal configuration almost does not change during the reaction, according to the Gaussian calculations, and the energy (E_{MP2}), equilibrium bond length (R_i^0), and force constant (Frc) were obtained.

$$[7]\quad D_e(\mathrm{AB}) = 27.2116[E_{MP2}(\mathrm{A}) + E_{MP2}(\mathrm{B}) - E_{MP2}(\mathrm{AB})]$$

$$[8]\quad K_e = 6.192\mathrm{Frc}$$

$$[9]\quad \beta_i = \sqrt{\frac{K_e}{2D_e}}$$

Here, D_e is in eV and E_{MP2} is in hartrees. In eq. [7], A stands for atom Ca and B stands for atom Br. Frc is in eV/Å^2. K_e is the vibrational force constant in mdyn/Å.

To study all of the collisions of an atom, the value of the maximum impact parameter (b_{max}) has to be found, although the calculation and only the calculation that has been carried out under the condition of $b \le b_{max}$ can ensure the accuracy of the result. All the results for the reaction Ca + CF_3Br can be given with the parameters presented in Tables 1 and 2.

Quasi-classical trajectory calculation

Hamilton's classical equations are numerically integrated for motion in three dimensions.[20] Since the arithmetical solutions of Hamilton's equations are difficult to obtain and the previous theoretical studies have already proved that the QCT method is good enough for the study of chemical reactions, the QCT method has been used to study the reaction in

Can. J. Chem. Downloaded from www.nrcresearchpress.com by Renmin University of China on 09/02/12
For personal use only.

Table 1. The parameters used to construct the London–Eyring–Polanyi–Sato potential energy surface (LEPS PES) for the reaction Ca + CF_3Br.

Species	D_e (eV)	β_i (Å^{-1})	R_i^0 (Å)	S_i
CaBr	3.3927	1.4238	2.6426	0.210
CF_3Br	3.0658	1.4708	1.9237	0.350
CF_3Ca	1.7830	1.3148	2.4832	0.420

Note: D_e, Morse parameter of a diatomic molecule representing the classical dissociation energy; β_i, Morse parameter of a diatomic molecule representing the spectrum constant; R_i^0, Morse parameter of a diatomic molecule representing the equilibrium bond length; S_i, Sato parameter. The values of D_e, β_i, and R_i^0 were obtained from the Gaussian 03 program at the MP2/6–311++G** level.

this paper, and the details are the same as the descriptions in refs. 21–24.

From simulation and comparison with the experimental results of the product state distributions for the reaction Ca + CF_3Br, the same initial conditions with the experiment (collision energy (E_{col}) = 0.55 eV) were chosen in this paper. A batch of 100 000 trajectories in the calculations was run for each of the collision energies for the reaction Ca + CF_3Br and the integration step size was chosen to be 0.1 fs, which would ensure the conservation of total energy and angular momentum. Trajectories were initiated at a Ca–CF_3Br internuclear separation of 15 Å and for the CF_3Br molecule at $v = 0$ and $j = 0$ levels.

Product rotational alignment

For a chemical reaction, the distribution of the product rotational angular momentum ($\mathbf{J}'$) relative to the reactant relative velocity vector ($\mathbf{K}$) can be described by the product rotational alignment ($\langle P_2(\mathbf{J}' \cdot \mathbf{K})\rangle$), and the computational method used in this paper was developed by Han et al.[16] and Costen et al.[25] Herein a brief description is shown.

During a reactive encounter, the total angular momentum is conserved ($\mathbf{J} + \mathbf{L} = \mathbf{J}' + \mathbf{L}'$), where $\mathbf{L}$ and $\mathbf{L}'$ are the reagent and product orbital momenta, respectively, and $\mathbf{J}$ is the reagent rotational angular momentum. When $\mathbf{J}$ is small (as is common), the product rotation can only result from $\mathbf{L}$. $\mathbf{J}'$ can be described by a function $f(\theta)$, where θ is the angle between $\mathbf{J}'$ and $\mathbf{K}$. $f(\theta)$ can be expanded in a set of Legendre polynomials.[16,26]

$$[10] \qquad f(\theta) = \sum a_l P_l(\cos\theta)$$

where

$$[11] \qquad a_l = \frac{2l+1}{l}\int_{-1}^{+1} P_l(\cos\theta) f(\cos\theta)\mathrm{d}\theta$$

The coefficients a_0, a_1, and a_2 are used to represent the isotropic distribution, product rotational orientation, and product rotational alignment, respectively.

$$[12] \qquad a_2 = 5\langle P_2(\cos\theta)\rangle = 5\langle P_2(\mathbf{J}' \cdot \mathbf{K})\rangle$$

and

$$[13] \qquad \langle P_2(\mathbf{J}' \cdot \mathbf{K})\rangle = \left\langle \frac{3\cos^2\theta - 1}{2} \right\rangle$$

Here P_2 denotes the second Legendre polynomial, $\langle \cos^2\theta \rangle$ can be obtained by averaging all the directions and parameters of collision, and the angular brackets indicate an average over the distribution of $\mathbf{J}'$ about $\mathbf{K}$.[26]

Apparently, the rotational alignment is determined by the average value of $P_2(\mathbf{J}'\cdot\mathbf{K})$ and the expected value is between 0.0 (randomly aligned) and –0.5 (completely aligned). The maximum product rotational alignment usually occurs when the conditions $|\mathbf{L}| >> |\mathbf{J}|$ and $|\mathbf{L}'| >> |\mathbf{J}'|$ are satisfied. The first condition is satisfied for reactions with large cross sections, whereas the typical Heavy + Heavy–Light (HHL) mass configuration leads to the second condition.[27] In other words, the phenomenon that product rotation is strongly aligned with the relative velocity of the reagent is mainly caused by the HHL mass combination, and the value of $\langle P_2(\mathbf{J}' \cdot \mathbf{K})\rangle$ should be equal to –0.5.

Results and discussions

PES

The construction of LEPS PES for the reaction Ca + CF_3Br is a precondition to obtain the dynamical properties of the reaction and study the reaction mechanism. The PES can be divided into two types according to the different types of energy released in the reaction A + BC → AB + C. One is attractive PES (energy is released in the process when atom A approaches molecule BC), and the other is repulsive PES (energy is released in the process when atom C is dissociated from molecule AB). The PES constructed in this paper belongs to the attractive PES. The specific method used to construct the LEPS PES is described in the second part of this paper and the parameters are given in Tables 1 and 2.

Figure 1 shows the contour plot of the LEPS PES for the reaction Ca + CF_3Br. Based on this extended LEPS PES, the dynamical properties, for example vibrational distribution, reaction cross section, and the product rotational alignment, were calculated by means of the QCT method and the results are shown in the following figures. The range of R is from 1.5 to 8.0 Å, as there are no significant barriers and wells in the entrance channel and exit channel at R from 0 to 1.5 Å and from 8.0 to 15.0 Å in Fig. 1. As can be seen from Fig. 1, the potential energy gradually decreases from the entrance ($R_{Ca,CF_3Br} = \infty$, corresponding to the reactants) to the exit ($R_{CaBr,CF_3} = \infty$, corresponding to the products). There is no reaction barrier involved in Fig. 1, whereas a shallow well exists in the entrance path of the LEPS PES. The position of the potential well on the LEPS PES is (2.7 Å, 2.3 Å) and the depth of the potential well is –10.45 erg × 10^{16}. The existence of this shallow well leads to the result that the reaction cross section decreases with the increasing collision energy.

Vibrational distribution

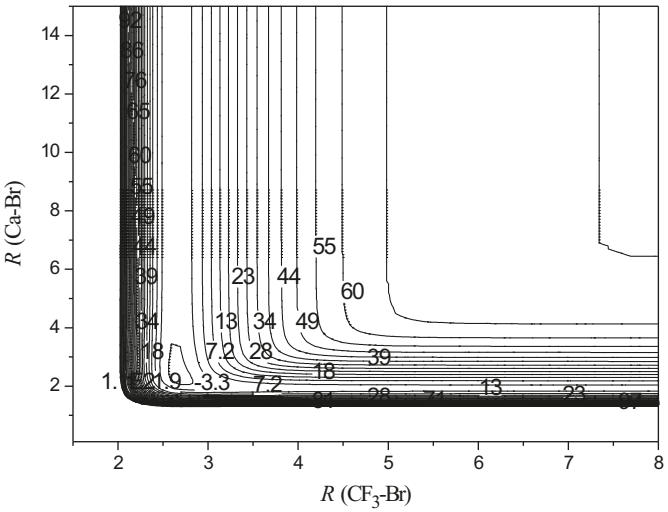
The vibrational distribution of product CaBr, which was obtained through the QCT calculations, is shown in Fig. 2 and it can be described as a function of vibrational quantum number. The vibrational distribution of the experiment is also shown in Fig. 2 for comparison and it is derived from Fig. 11 in ref. 5. To guarantee this comparison, an E_{col} of 0.55 eV was chosen according to the experiment, and the initial internal energy state of the reactant was set to be the ground state ($v = 0$, $j = 0$). As for the reaction Ca + CF_3Br, the QCT

Table 2. The values of the maximum impact parameter (b_{max}) for the reaction Ca + CF_3Br.

	E_{col} (eV)										
	0.1	0.2	0.3	0.4	0.5	0.55	0.6	0.7	0.8	0.9	1.0
b_{max}	5.70	5.40	5.25	5.15	5.00	5.00	5.00	4.90	4.80	4.70	4.70

The values of b_{max} for the reaction Ca + CF_3Br were calculated when the collision energy (E_{col}) changed.

Fig. 1. The plot of the London–Eyring–Polanyi–Sato potential energy surface (LEPS PES) for the reaction Ca + CF_3Br. The unit of R is Å and the unit of energy is erg × 10^{16} (1 erg = 1.4393 × 10^{13} kcal/mol; 1 cal = 4.184 J).



calculated product vibrational distribution of the CaBr shows a bell shape when the vibrational quantum number changes from 0 to 15. It can be seen from Fig. 2 that the vibrational distribution result rapidly increases to its maximum value and then decreases with the increasing v, with the condition that E_{col} = 0.55 eV. Both the experimental and theoretical product vibrational distributions reach peak values at around v = 3 for the product CaBr in Fig. 2. Obviously, the variational tendencies of the two vibrational distributions are similar with each other, and the QCT result obtained in this study is in good agreement with the experimental one.

The reactions between alkaline earth metal atoms (M) and halogenated alkanes have two pathways, which are the abstraction reaction and the insertion reaction. The collision energy cannot conquer the repellant when atom Ca attacks CF_3Br in the repulsive area, which closes to group CF_3, and then atom Ca shifts to the attractive area, which closes to atom Br. Under the conditions mentioned above, the insertion reaction occurs and the vibrational excitation of product CaBr is strong. When the collision energy is large enough, atom Ca and molecule CF_3Br can rapidly get close to each other and the C–Br bond fractures to form the product CaBr. This is the abstraction reaction that results in the weakness in vibrational excitation. The vibrational distribution is concentrated for the reactions between alkaline earth metal atoms (M) and halogenated alkanes. It mainly concentrates on the maximum value of the distribution. The vibrational distribution of the product has a strong dependence on the relative position of the halogen atom in the reactant and the direction from which the alkaline earth metal atom (M) approaches the halogenated alkane.

Unavoidably, there exist some differences between the experimental result and the theoretical one at high vibrational quantum numbers that are >4, since the theoretical simulation simplified the complex processing of the real world. The differences were caused by the single collision energy used in this work, by only considering the ground state in the QCT calculations, and by the single-particle approximation used for group CF_3. Although some of the differences can be seen in Fig. 2, we cannot neglect the merits of the QCT method, which are simple, illustrative, and accurate. It can deal with a big reaction system that cannot be treated by the quantum mechanics method and can obtain the dynamical results that were not given by Stolte and co-workers.[5]

Reaction cross section

The reaction cross section can be obtained with the QCT method and its equation can be written as follows.[28–30]

$$[14] \qquad \sigma_r = \pi b_{max}^2 (N_r/N)$$

where N is the number of total trajectories in the calculation and N_r is the number of reactive trajectories under the $b \leq b_{max}$ condition.

In this paper, the values of N, N_r, and b_{max} are obtained through the QCT calculations, and the results of reaction cross section versus collision energy are obtained by eq. [14] for the reaction Ca + CF_3Br and are shown in Fig. 3. As can be seen from Fig. 3, the reaction cross section regularly decreases from a maximum value of 27.466 Å^2 to a minimum value of 17.916 Å^2 when collision energy increases from 0.1 to 1.0 eV. This phenomenon indicates a kind of inverse relation that high reaction probabilities appear at low energies, whereas low reaction probabilities appear at high energies in the calculated results in Fig. 3.

The result that the reaction cross section decreases with the increasing collision energy agrees with the general behavior of chemical reactions that a potential well exists on the LEPS PES. This phenomenon is characteristic of the concurrent contraction of the capture radius with the increasing energy for systems with purely attractive PES.[31] In this study, the LEPS PES belongs to the attractive PES type and a shallow well can be seen on the LEPS PES in Fig. 1. The reaction cross section obtained in this paper can give a good description of the reaction Ca + CF_3Br.

Product rotational alignment

The product rotational alignment of the reaction Ca + CF_3Br versus collision energy has been calculated by means of the QCT method and the results are shown in Fig. 4. The values of the product rotational alignment $\langle P_2(\mathbf{J}' \cdot \mathbf{K})\rangle$ calculated in this paper have deviated overall from the kinematic limit (–0.5), and as the collision energy increases from 0.1 to 1.0 eV, the product rotational alignment steadily decreases

Can. J. Chem. Downloaded from www.nrcresearchpress.com by Renmin University of China on 09/02/12
For personal use only.

Can. J. Chem. Downloaded from www.nrcresearchpress.com by Renmin University of China on 09/02/12
For personal use only.

Fig. 2. Vibrational distribution of product CaBr obtained from the reaction Ca + CF_3Br when collision energy equals 0.55 eV. The experimental result was obtained from Fig. 11 in ref. 5.

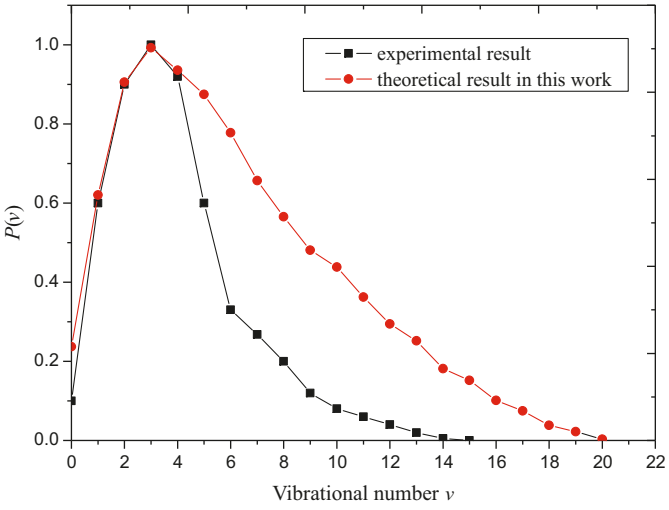
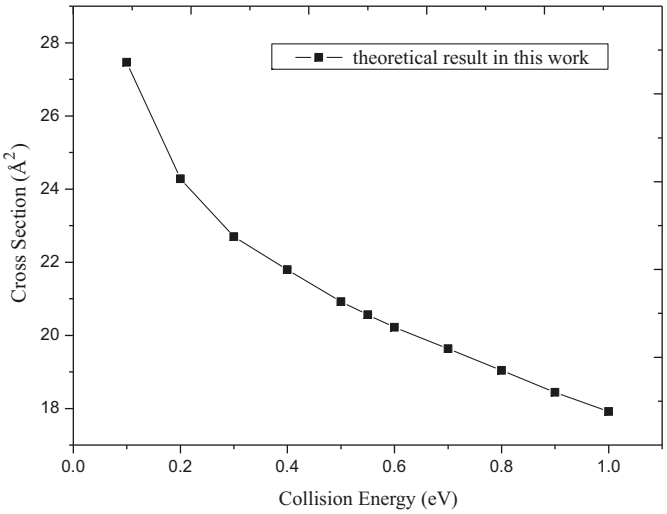


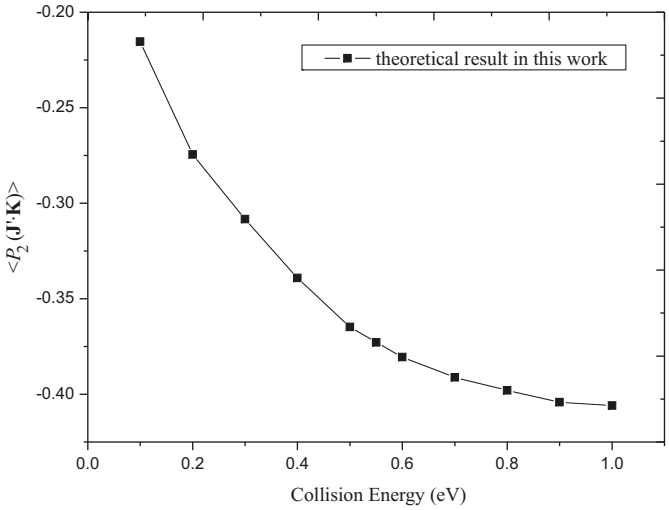
Fig. 3. The reaction cross section result versus collision energy for the reaction Ca + CF_3Br.



from –0.2154 to –0.4059. The result presents a falling trend and the alignment effect becomes strong.

The product rotational alignment is almost independent of the characters of PES, but can be influenced by the type of mass combination. The reaction Ca + CF_3Br studied in this paper belongs to the type of Light + Light–Light (LLL) mass combination and it can be found that the product rotational alignment shown in Fig. 4 is similar to the result of Fig. 4 in ref. 16. The LLL mass combination is similar to the HHH (Heavy + Heavy–Heavy) mass combination. The so-called LLL mass combination only refers to the mass ratio of three atoms and is approximately 1:1:1 and it does not mean that these three atoms are light atoms. The atomic mass of Ca is 40.08, the atomic mass of Br is 79.904, the atomic mass summation of the group CF_3 is 69.005 and the mass factor $\cos^2\beta$ ($\cos^2\beta = \frac{M_{Ca}M_{CF_3}}{M_{CaBr}M_{CaCF_3}}$, where M_{Ca} is the atomic mass of Ca, M_{CF_3} is the atomic mass summation of the group CF_3, M_{CaBr} is the mass of the product CaBr, and

Fig. 4. The product rotational alignment result versus collision energy for the reaction Ca + CF_3Br.



M_{CaCF_3} is the atomic mass summation of the group $CaCF_3$ of the reaction system and is 0.211. Here, the main consideration is the approximate mass proportion. Even so, for the $\langle P_2(\mathbf{J}' \cdot \mathbf{K})\rangle$ values of these two figures, there are some slight differences. The product rotational alignment of the reaction Ca + CF_3Br is smaller than the value of Fig. 4 at high collision energy, and the alignment effect is stronger than the low collision energy. The main reason for this phenomenon is that the mass proportion of this reaction slightly deviates from the LLL mass configuration.

Conclusions

In this paper, theoretical studies have been performed on the LEPS PES at different collision energies by means of the QCT method for the reaction Ca + CF_3Br. Some dynamical results such as the vibrational distribution, reaction cross section, and product rotational alignment were obtained.

The LEPS PES constructed for the reaction Ca + CF_3Br in this paper has a potential well in the entrance portion. The vibrational distribution first increases and then decreases with the increasing vibrational quantum number in both the experimental and theoretical results. The maximum value of the vibrational distribution appears at around $v = 3$ when the collision energy equals 0.55 eV. At the same time, the reaction cross section and the product rotational alignment were calculated for the title reaction when collision energy changes from 0.1 to 1.0 eV. The value of the reaction cross section decreases with the increasing collision energy and this phenomenon is due to the existence of a potential well on the LEPS PES. The result of product rotational alignment shows that the value decreases with the increasing collision energy and the relationship between the product rotational alignment and collision energy mainly depends on the mass combination. The reaction mechanism has been discussed in this paper through analyzing these calculated results.

As mentioned previously, from the related distributions of the reaction Ca + CF_3Br, it can be concluded that the theoretical results obtained by means of the QCT method are consistent with the experimental data and a reasonable interpretation is given for the experimental results.

Acknowledgements

This work was supported by the National Natural Science Foundation of China (Grant Nos. 10704012 and 11105022), the Natural Science Foundation of Liaoning Province (Grant Nos. L2010055 and L2010057), and the Fundamental Research Funds for the Central Universities (2011QN060, 2011QN151). The code used in this paper was provided by Professor K.L. Han.

References

(1) Prisant, M. G.; Rettner, C. T.; Zare, R. N. *J. Chem. Phys.* **1981**, *75* (5), 2222. doi:10.1063/1.442335.
(2) Lin, K.-C.; González-Ureña, A. G. *Int. Rev. Phys. Chem.* **2007**, *26* (2), 289. doi:10.1080/01442350701211180.
(3) Munakata, T.; Kasuya, T. *J. Chem. Phys.* **1984**, *81*, 5608. doi:10.1063/1.447664.
(4) Han, K. L.; He, G. Z.; Lou, N. Q. *Chin. J. Chem. Phys.* **1993**, *6*, 95.
(5) Keijzer, F.; Teule, J. M.; Bulthuis, J.; de Graaff, G. J.; Hilgeman, M. H.; Janssen, M. H. M.; Van Kleef, E. H.; Van Leuken, J. J.; Stolte, S. *Chem. Phys.* **1996**, *207* (2–3), 261. doi:10.1016/0301-0104(95)00369-X.
(6) Alagia, M.; Balucani, N.; Casavecchia, P.; Laganà, A.; Ochoa de Aspuru, G.; Van Kleef, E. H.; Volpi, G. G.; Lendvay, G. *Chem. Phys. Lett.* **1996**, *258* (3–4), 323. doi:10.1016/0009-2614(96)00810-X.
(7) Yu, Y.; Pan, X. X.; Li, C. M.; Hou, J.; Hou, H. Q. *Chem. J. Chin. Univ.* **1999**, *20*, 289.
(8) Eyring, H.; Polanyi, M. *Zh. Phys. Chem. (Leipzig) Abt. B* **1931**, *12*, 279.
(9) Aoiz, F. J.; Banares, L.; Herrero, V. J. *J. Chem. Soc., Faraday Trans.* **1998**, *94* (17), 2483. doi:10.1039/a803469i.
(10) Meijer, A. J. H. M.; Groenenboom, G. C.; van der Avoird, A. *J. Phys. Chem.* **1996**, *100* (40), 16072. doi:10.1021/jp961584n.
(11) Zhong, H. Y.; Xia, W. W.; Gu, L. Z.; Yao, L. *J. Theor. Comput. Chem.* **2009**, *8*, 861.
(12) Solarz, R. W.; Johnson, S. A. *J. Chem. Phys.* **1979**, *70* (8), 3592. doi:10.1063/1.437962.
(13) Sanchez Rayo, M. N.; Castaño, F.; Martinez, M. T.; Adams, J. W.; Carl, S. A.; Husain, D.; Schifino, J. *J. Chem. Soc., Faraday Trans.* **1993**, *89* (11), 1645. doi:10.1039/ft9938901645.
(14) Hu, W. H.; Shen, W. *J. Southwest China Normal University* **2005**, *30*, 893.
(15) Yu, Y.; Sun, W. M.; Pan, X. X.; Hou, H. Q. *Environ. Sci.* **2000**, *20*, 40.
(16) Han, K. L.; He, G. Z.; Lou, N. Q. *J. Chem. Phys.* **1996**, *105* (19), 8699. doi:10.1063/1.472651.
(17) Wang, M. L.; Han, K. L.; He, G. Z.; Lou, N. Q.; Bunsenges, X. *Ber. Phys. Chem.* **1997**, *101*, 1527.
(18) Zhang, X.; Xie, T. X.; Zhao, M. Y.; Han, K. L. *Chin. J. Chem. Phys.* **2002**, *15*, 169.
(19) Frisch, M. J.; Trucks, G. W.; Schlegel, H. B.; Scuseria, G. E.; Robb, M. A.; Cheeseman, J. R.; Montgomery, J. A., Jr.; Vreven, T.; Kudin, K. N.; Burant, J. C.; Millam, J. M.; Iyengar, S. S.; Tomasi, J.; Barone, V.; Mennucci, B.; Cossi, M.; Scalmani, G.; Rega, N.; Petersson, G. A.; Nakatsuji, H.; Hada, M.; Ehara, M.; Toyota, K.; Fukuda, R.; Hasegawa, J.; Ishida, M.; Nakajima, T.; Honda, Y.; Kitao, O.; Nakai, H.; Klene, M.; Li, X.; Knox, J. E.; Hratchian, H. P.; Cross, J. B.; Bakken, V.; Adamo, C.; Jaramillo, J.; Gomperts, R.; Stratmann, R. E.; Yazyev, O.; Austin, A. J.; Cammi, R.; Pomelli, C.; Ochterski, J. W.; Ayala, P. Y.; Morokuma, K.; Voth, G. A.; Salvador, P.; Dannenberg, J. J.; Zakrzewski, V. G.; Dapprich, S.; Daniels, A. D.; Strain, M. C.; Farkas, O.; Malick, D. K.; Rabuck, A. D.; Raghavachari, K.; Foresman, J. B.; Ortiz, J. V.; Cui, Q.; Baboul, A. G.; Clifford, S.; Cioslowski, J.; Stefanov, B. B.; Liu, G.; Liashenko, A.; Piskorz, P.; Komaromi, I.; Martin, R. L.; Fox, D. J.; Keith, T.; Al-Laham, M. A.; Peng, C. Y.; Nanayakkara, A.; Challacombe, M.; Gill, P. M. W.; Johnson, B.; Chen, W.; Wong, M. W.; Gonzalez, C.; Pople, J. A. *Gaussian 03, Revision A.1;* Gaussian Inc.: Wallingford, CT, 2003.
(20) Zhang, X.; Han, K. L. *Int. J. Quant. Chem.* **2006**, *106* (8), 1815. doi:10.1002/qua.20929.
(21) Porter, R. N.; Raff, M. L. *Dynamics of Molecule Collision, Part B;* Miller, W. H., Ed.; Plenum Press: New York, 1976.
(22) Wang, M.-L.; Han, K.-L.; He, G.-Z. *J. Phys. Chem. A* **1998**, *102* (50), 10204. doi:10.1021/jp981738u.
(23) Chen, M. D.; Wang, M. L.; Han, K. L.; Ding, S. L. *Chem. Phys. Lett.* **1999**, *301* (3–4), 303. doi:10.1016/S0009-2614(99)00052-4.
(24) Zhang, L.; Chen, M. D.; Wang, M. L.; Han, K. L. *J. Chem. Phys.* **2000**, *112* (8), 3710. doi:10.1063/1.480523.
(25) Costen, M. L.; Hancock, G.; Orr-Ewing, A. J.; Summerfield, D. *J. Chem. Phys.* **1994**, *100* (4), 2754. doi:10.1063/1.466470.
(26) Chen, M. D.; Han, K. L.; Lou, N. Q. *Chem. Phys. Lett.* **2002**, *357* (5–6), 483. doi:10.1016/S0009-2614(02)00585-7.
(27) Wang, W. L.; Han, K. L.; Zhan, J. P.; Wu, V. W. K.; He, G. Z.; Lou, N. Q. *Chem. Phys. Lett.* **1997**, *278* (4–6), 307. doi:10.1016/S0009-2614(97)01063-4.
(28) Xia, W. W.; Lu, N.; Zhong, H. Y.; Yao, L. *Can. J. Chem.* **2009**, *87* (8), 1103. doi:10.1139/V09-067.
(29) Yao, L.; Liu, Y. L.; Zhong, H. Y.; Cao, W. H. *J. Theor. Comput. Chem.* **2009**, *8*, 827.
(30) Xia, W. W.; Yao, L.; Chen, B. J. *J. Mol. Struct. (THEOCHEM)* **2010**, *962* (1–3), 56. doi:10.1016/j.theochem.2010.09.014.
(31) Yao, L.; Zhong, H. Y.; Liu, Y. L.; Xia, W. W. *Chem. Phys.* **2009**, *359* (1–3), 151. doi:10.1016/j.chemphys.2009.03.019.

Can. J. Chem. Downloaded from www.nrcresearchpress.com by Renmin University of China on 09/02/12
For personal use only.

Rapid synthesis of homoallylic alcohol from aldehyde with allyltributylstannane under solvent-free conditions

Pranjal P. Bora, H. Atoholi Sema, Barisha Wahlang, and Ghanashyam Bez

Can. J. Chem. Downloaded from www.nrcresearchpress.com by Renmin University of China on 09/02/12
For personal use only.

Abstract: A catalytic amount (2 mol %) of phosphotungstic acid (PTA) is sufficient to synthesize homoallylic alcohol in excellent yields from aldehyde with allyltributylstannane upon grinding under solvent-free reaction conditions. Easy handling, very short reaction time, solvent-free reaction conditions, and aqueous workup free isolation protocol may make our method very useful for synthetic chemists.

Key words: aldehyde, allyltributylstannane, homoallylic alcohol, phosphotungstic acid, grinding.

Résumé : Une quantité catalytique (2 mol %) d'acide phosphotungstique (APT) est suffisante pour effectuer la synthèse d'alcools homoallyliques, avec d'excellents rendements, par broyage d'un aldéhyde avec de l'allyltributylstannane dans des conditions réactionnelles sans solvant. La facilité de la manipulation, son temps de réaction très court, les conditions réactionnelles sans solvant et le protocole d'extraction en milieu aqueux pourrait en faire une méthode très précieuse pour les chimistes de synthèse.

Mots-clés : aldéhyde, allyltributylstannane, alcool homoallylique, acide phosphotungstique, broyage.

[Traduit par la Rédaction]

Introduction

In recent years, organic synthesis under solvent-free conditions has been considered to be one of the most important features for designing environmentally benign reaction protocols.[1,2] The solvent-free reactions can eliminate a commonly encountered solubility problem associated with reactivity and make the work-up process very easy by eliminating tedious aqueous workup and subsequent removal of solvents. Ironically, solvent accounts for the high *E* factor[3] of a reaction, which is a measure of the total waste generated during a reaction process. In recent years, phosphotungstic acid ($H_3PW_{12}O_{40}$) has found a lot of attention for being an environmentally benign and commercially available solid compound. Being a pseudoliquid,[4] phosphotungstic acid (PTA) is considered to be a better catalyst for organic transformations[5–9] than conventional inorganic and organic acids.

Homoallylic alcohols are considered as one of the most ubiquitous building blocks in organic synthesis and their applications in the field of organic total synthesis and pharmaceutical research[10–12] are well documented. With the advent of the ring-closing metathesis (RCM) approach,[13] homoallylic alcohols and amines are finding new impetus in the synthesis of bioactive natural products.[14–16] Acid-catalyzed reaction of aldehydes with allyltributylsatannanes is one of the most frequently exercised protocols for generation of homoallylic alcohols at room temperature. Among the Lewis acids,[17–28] $BF_3{\cdot}Et_2O$, $SnCl_4$, $TiCl_4$, etc., are highly moisture sensitive and hence require strictly anhydrous conditions, whereas transition-metal complexes such as AgOTf, $ReBr(CO)_5$, and $Sc(OTf)_3$ are very expensive, although water-tolerant. Although palladium and platinum complexes were also used as catalysts,[29–31] they are highly expensive and require high temperatures and long reaction times. The use of solid-supported reagents, such as polymer-bound sulfonamide,[32] silica–$Bi(OTf)_2$,[33] Ln–resins,[34] pincer bis(oxazolinyl)phenyl ligands on solid support,[35] and titanium-exchanged ZSM-5 catalyst[36] have also been reported, but those methods require catalyst preparation before use. Therefore, introduction of a new catalyst system that can address these drawbacks, as well as being efficient, selective, high yielding, and environmentally friendly, cannot be overlooked. As most of these reactions have considerably long reaction times and use hazardous organic solvents, we were looking for a catalyst to reduce the reaction time for this conversion and that could work in the absence of any solvent. Here, we wish to report PTA as an effective catalyst for the synthesis of homoallylic alcohol from aldehyde with allyltributylstannane.

Experimental

General remarks

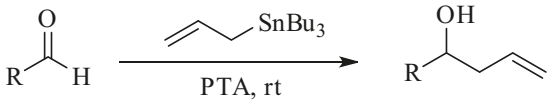
All reagents were commercially available and used without further purification. Most of the aldehydes were purchased from Sigma-Aldrich. The IR spectra were recorded on a PerkinElmer 983 spectrophotometer. For column chromatography, we employed Merck silica gel 60–120 mesh. ^1H NMR (400 MHz) and ^{13}C NMR (100 MHz) spectra were recorded

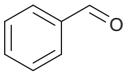
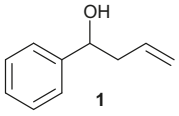
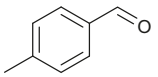
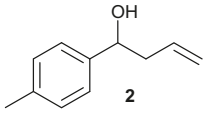
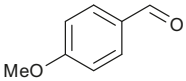
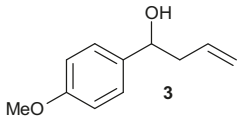
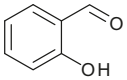
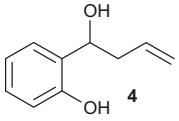
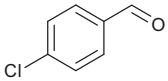
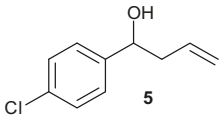
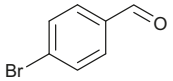
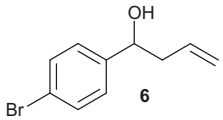
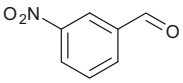
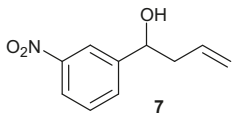
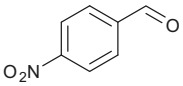
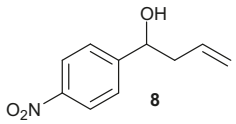
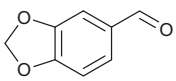
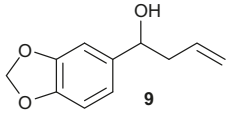
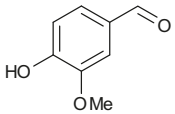
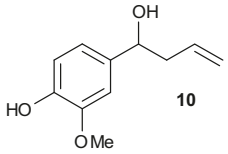
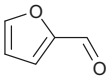
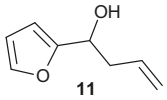
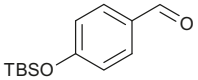
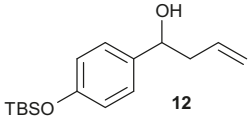
Received 23 July 2011. Accepted 2 October 2011. Published at www.nrcresearchpress.com/cjc on 12 December 2011.

P.P. Bora, H.A. Sema, B. Wahlang, and G. Bez. Department of Chemistry, North Eastern Hill University, Shillong-793022, India.

Corresponding author: Ghanashyam Bez (bez@nehu.ac.in).

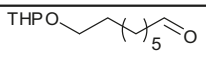
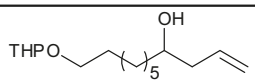
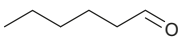
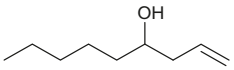
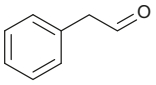
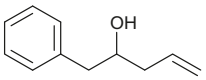
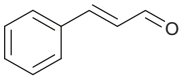
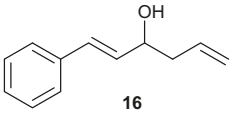
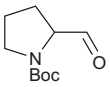
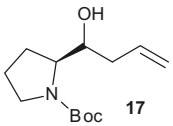
Table 1. Syntheis of homoallylic alcohols.



Entry	Substrate	Product	Time (min)	Yield (%)
1			10	90
2			10	91
3			12	81
4			10	83
5			7	95
6			7	96
7			5	97
8			5	99
9			8	82
10			20[a]	No reaction
11			10	89
12			10	88

Can. J. Chem. Downloaded from www.nrcresearchpress.com by Renmin University of China on 09/02/12
For personal use only.

Table 1. (*concluded*).

Entry	Substrate	Product	Time (min)	Yield (%)
13		 **13**	10	83
14		 **14**	10	93
15		 **15**	10	95
16		 **16**	10	92
17		 **17**	12	78

Note: Aldehyde–allyltributylstannane–PTA = 1:1.2:0.02, at room temperature. PTA, phosphotungstic acid.
[a]10 mol % of PTA.

Can. J. Chem. Downloaded from www.nrcresearchpress.com by Renmin University of China on 09/02/12
For personal use only.

on an AMX-400 MHz spectrometer using $CDCl_3$ as solvent and TMS as internal standard, unless otherwise stated. Mass spectra were obtained from a Waters ZQ 4000 mass spectrometer by the ESI method and the elemental analyses of the complexes were performed on a PerkinElmer-2400 CHN/S analyzer. Please see the Supplementary data for procedures and spectra.

Catalyst preparation

Phosphotungstic acid

Analytical grade $H_3PW_{12}O_{40}{\cdot}nH_2O$ was obtained commercially and used as a catalyst for the reaction.

Phosphotungstic acid/SiO_2

To a solution of $H_3PW_{12}O_{40}.nH_2O$ (0.5 g, 0.5 equiv by weight) in methanol (25 mL) was added silica gel (60–120 mesh, 4.5 g, 0.9 equiv by weight) and the mixture was stirred at room temperature for 6 h. Evaporation of methanol under reduced pressure gave a dry white powder. The catalyst was stored in a container for further use.

General procedure for phosphotungstic acid-catalyzed synthesis of homoallylic alcohol

A mixture of the aldehyde (1 mmol), allyltributylstannane (1.2 mmol), and phosphotungstic acid (0.02 mmol) was ground with a pestle in a mortar for the specified time (see Table 1). After complete conversion of the starting material, the crude mixture was dissolved in dichloromethane and directly loaded into a chromatography column charged with silica gel 60–120 mesh and eluted with a petroleum ether / ethyl acetate mixture as eluent in the appropriate ratio to obtain the pure product.

Spectral data for selected compounds

*1-(Benzo[*d*][1,3]dioxol-5-yl)but-3-en-1-ol (9)*

^{1}H NMR (400 MHz, $CDCl_3$, ppm) δ: 1.18 (s, 1H), 2.39 (t, J = 6.8 Hz, 2H), 4.57 (t, J = 6.4 Hz, 1H), 5.05–5.06 (d, J = 4.4 Hz, 1H), 5.07–5.10 (d, J = 11.2 Hz, 1H), 5.60 (m, 1H), 5.87 (s, 2H), 6.65–6.80 (m, 3H). ^{13}C NMR ($CDCl_3$, 100 MHz, ppm) δ: 43.8, 73.1, 100.9, 106.3, 108.0, 118.4, 119.2, 134.4, 137.9, 146.9, 147.7. ESI MS (*m*/*z*): 215 (M^+ + 23). Elemental anal. calcd for $C_{11}H_{12}O_3$: C 68.74, H 6.29; found: C 68.61, H 6.12.

*1-(4-*tert*-Butyldimethylsilyloxyphenyl)but-3-en-1-ol (12)*

^{1}H NMR (400 MHz, $CDCl_3$, ppm) δ: 0.00 (s, 6H), 0.78 (s, 9H), 1.42 (s, 1H), 2.30 (t, J = 6.8 Hz, 2H), 4.48 (t, J = 6.8 Hz, 1H), 4.93 (d, J = 5.2 Hz, 1H), 4.93 (d, J = 5.2 Hz, 1H), 4.97 (d, J = 14.0 Hz, 1H), 5.60 (m, 1H), 6.62 (d, J = 8.8 Hz, 2H), 7.02 (d, J = 8.4 Hz, 2H). ^{13}C NMR ($CDCl_3$, 100 MHz, ppm) δ: –4.4, 18.2, 25.6, 43.7, 73.0, 118.2, 119.9, 126.9, 134.6, 136.5, 115.0. ESI MS (*m*/*z*): 215 (M^+ + 23). Elemental anal. calcd for $C_{16}H_{26}O_2Si$: C 69.01, H 9.41; found: C 69.02, H 9.37.

*12-(Tetrahydro-2*H*-pyran-2-yloxy)dodec-1-en-4-ol (13)*

^{1}H NMR (400 MHz, $CDCl_3$, ppm) δ: 1.25–1.30 (m, 10H), 1.45–1.84 (m, 10H), 2.09–2.33 (m, 2H), 3.34–3.4 (m, 2H), 3.47–3.52 (m, 1H), 3.63 (s, 1H), 3.69–3.75 (m, 2H), 3.84–3.89 (m, 1H), 4.57 (d, J = 4 Hz, 1H), 5.11–5.15 (m, 1H), 5.77–5.88 (m, 1H). ^{13}C NMR (100 MHz, $CDCl_3$, ppm) δ: 19.7, 25.5, 25.6, 26.2, 29.4, 29.5, 29.6, 29.7, 30.7, 36.8, 41.3, 62.3, 67.6, 70.6, 98.8, 118, 134.9. ESI MS (*m*/*z*): 307.1 (M^+ + 23). Elemental anal. calcd for $C_{17}H_{32}O_3$: C 71.79, H 11.34; found: C 70.43, H 11.62.

Can. J. Chem. Downloaded from www.nrcresearchpress.com by Renmin University of China on 09/02/12
For personal use only.

Non-1-en-4-ol (14)

^{1}H NMR (400 MHz, $CDCl_3$, ppm) δ: 0.62 (t, J = 6.8 Hz, 3H), 1.02–1.10 (m, 4H), 1.13–1.20 (m, 4H), 1.74 (s, 1H), 1.79–1.91 (m, 1H), 2.01–2.06 (m, 1H), 3.36 (m, 1H), 4.86 (m, 2H) 5.57 (m, 1H). ^{13}C NMR (100 MHz, $CDCl_3$, ppm) δ: 13.9, 22.5, 25.3, 31.8, 36.7, 41.8, 70.6, 117.8, 134.9. ESI MS (*m*/*z*): 151.1 (M^+ + 23). Elemental anal. calcd for $C_9H_{18}O$: C 76.00, H 12.76; found: C 75.29, H 12.53.

1-Phenylhexa-1,5-dien-3-ol (16)

^{1}H NMR (400 MHz, $CDCl_3$, ppm) δ: 1.86 (s, 1H), 2.26–2.39 (m, 2H), 4.27 (q, J = 6.4 Hz, 1H), 5.07 (d, J = 4.4 Hz, 1H), 5.10 (d, J = 10.8 Hz, 1H), 5.77 (m, 1H), 6.16 (dd, J = 16.0, 6.4 Hz, 1H), 6.52 (d, J = 16 Hz, 1H), 7.11–7.30 (m, 5H). ^{13}C NMR (100 MHz, $CDCl_3$, ppm) δ: 42.0, 71.7, 118.5, 126.5, 127.6, 128.5, 130.3, 131.5, 134.0, 136.6. ESI MS (*m*/*z*): 173 (M^+ – 1), 172 (100). Elemental anal. calcd for $C_{12}H_{14}O$: C 82.72, H 8.10; found: C 82.49, H 7.85.

tert-*Butyl 2-(1-hydroxybut-3-enyl)pyrrolidine-1-carboxylate (17)*

^{1}H NMR (400 MHz, $CDCl_3$, ppm) δ: 1.40 (s, 9H), 1.68 (m, 2H), 1.81 (m, 2H), 2.09 (m, 2H), 3.18 (m, 3H), 3.45 (m, 1H), 3.82 (s, 1H), 5.01 (d, J = 9.2 Hz, 1H), 5.04 (d, J = 15.6 Hz, 1H), 5.83 (m, 1H). ^{13}C NMR ($CDCl_3$, 100 MHz, ppm) δ: 24.2, 27.4, 28.4, 37.1, 48.0, 62.6, 72.7, 79.9, 116.7, 135.6. ESI MS (*m*/*z*): 264 (M^+ + 23). Elemental anal. calcd for $C_{13}H_{23}NO_3$: C 64.70, H 9.61, N 5.80; found: C 64.41, H 9.85, N 6.19.

Results and discussion

Catalyst testing

In pursuance of our recent interests in PTA-catalyzed reactions,[37,38] we sought to use it for the allylation of aldehyde with allyltributylstannane. To achieve the stated objective, we stirred a mixture of *p*-nitrobenzaldehyde (1 mmol) with allyltributylstannane (1.2 equiv) in acetonitrile in the presence of 5 mol % of PTA. Upon constant monitoring by TLC, it was observed that the reaction was completed within 5 h to give 92% yield of the desired product.

As the surface area of PTA is smaller in comparison with its polyoxometalates, we wanted to know whether silica-supported PTA could reduce the reaction time. While using a PTA/SiO_2 reagent system, we initially opted to carry out the reaction in acetonitrile to mix the reacting species properly and found that the reaction was completed in 5 h to give 83% isolated yield of the desired product. Since the solvent is one of the most important contributors to the reaction rate, we wanted to use solvent-free conditions solely for carrying out the reaction.[39] When *p*-nitrobenzaldehyde (1 mmol) and allyltributylstannane (1.2 equiv) were stirred with the PTA/SiO_2 reagent system without using any solvent, complete conversion of the starting aldehyde took ~5 h. As these observations did not warrant any improvement over solution-phase stirring with PTA itself, we wanted to see the effect of grinding a mixture of aldehyde and allyltributylstannane with 5 mol % of the catalyst. To that effect, a mixture of *p*-nitrobenzaldehyde (1 mmol) and allyltributylstannane (1.2 equiv) was ground with a pestle in a mortar in the presence of 5 mol % of PTA. To our surprise, the reaction was completed within 5 min to give almost quantitative yield (Scheme 1).

Scheme 1. Synthesis of homoallylic alcohols.

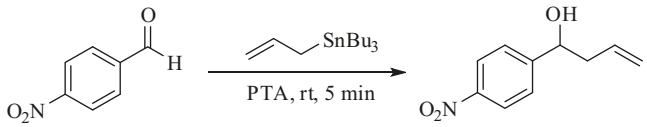


Table 2. Optimization of catalyst for the allylation of aldehyde.

Entry	Catalyst (mol %)	*p*-Nitrobenzaldehyde time (min)[a]	Hexanal time (min)[a]
1	1.0	120	300
2	1.5	15	25
3	2.0	5	10
4	4.0	5	9
5	5.0	5	9

Note: Aldehyde–allyltributylstannane, 1:1.2.
[a]The time for complete conversion.

Correlation of the catalyst ratio and reaction time

The fact that reaction proceeded slowly in the solution phase in the presence of PTA and silica-supported PTA suggests that the collision among the reactants upon grinding of the reaction mixture with PTA might have contributed to the shorter reaction time. It was observed that the reaction does not occur at room temperature, when a mixture of *p*-nitrobenzaldehyde and allyltributylstannane is ground in the absence of the catalyst. This established that there is no catalytic effect produced by the mortar and the pestle that might have contributed towards the shorter reaction time for completion. When complete conversion of the starting aldehyde was studied for the same reaction under catalytic conditions by varying the catalyst ratio, we found that 2 mol % of the catalyst is sufficient to complete the reaction within 5 min (Table 2). It was also observed that an amount of catalyst <2 mol % leads to increased reaction time for complete conversion, whereas an increased concentration of the catalyst up to 5 mol % could not reduce the reaction time significantly. We also tried to evaluate the reactivity pattern of aliphatic aldehyde by reacting a mixture of hexanal and allyltributylstannane in the presence of a catalytic amount of PTA (2 mol %) and found that the reaction takes a comparatively longer time.

Recovery of the catalyst

Since catalyst recovery is one of the most crucial components in catalytic reactions in general, we studied the reusability of the catalyst for successive batches for the reaction of *p*-nitrobenzaldehyde and allyltributylstannane using our reaction protocol. After completion of the reaction, diethyl ether was added to dissolve the product mixture and filtered to get the solid PTA residue. The PTA residue was washed thoroughly with diethyl ether and dried in an oven at 100 °C for 1 h and then cooled to room temperature. The recovered PTA catalyst obtained as mentioned was used for second, third, and fourth batches of the same reactants under similar reaction conditions without loss of appreciable activity in terms of reaction time and yield.

Can. J. Chem. Downloaded from www.nrcresearchpress.com by Renmin University of China on 09/02/12
For personal use only.

Generalization of the method

Having standardized the reaction parameters, such as the catalyst and the process, we set out to explore the general applicability of our method for both aromatic as well as aliphatic aldehydes[14] and its compatibility towards acid-sensitive functional groups (Table 1). It was observed that reaction worked exceedingly well for aromatic aldehydes having either +M or –M effect on the phenyl rings. The presence of phenolic an –OMe group in the para position of the aldehyde group did not have any noticable effect on the yield of the product, which is evident from the excellent yields of the products (Table 1, entry 3). Ironically, the vanillin (Table 1, entry 10) did not react despite the addition of 10 mol % of the catalyst under similar reaction conditions. It might be due to the poor electrophilicity of the aldehyde group resulting from the presence of the *p*-OH and *m*-OMe groups having +M effect on the phenyl ring. Several functional groups such as OTHP, methylenedioxy, etc., were hardly affected by the reaction conditions, as reflected by their excellent yields. From its excellent yield, we concluded that the OTBS (Table 1, entry 12) group is very stable under our reaction conditions. We did not observe any significant differences in reactivity for *m*- and *p*-nitrobenzaldehydes (Table 1, entries 7 and 8), as they took almost a similar reaction time for complete conversion. It is interesting to note that the aliphatic aldehydes (Table 1, entries 13–15) also gave excellent yields of their corresponding homoallylic alcohols upon grinding with allyltributylstannane in the presence of PTA. Excellent yield of homoallylic alcohol from cinnamaldehyde (Table 1, entry 16) shows that 1,2-addition is prefered in α,β-unsaturated aldehydes. *N*-Boc-pyrrolidine-2-carbaldehyde also generated its corresponding homoallylic alcohol (Table 1, entry 17) in good yield to verify the fact that the amide group, α to the aldehyde functionality, hardly has any negative impact on the efficiency of the reaction system.

Conclusion

This report introduces PTA as one of the most efficient catalysts for the allylation of aldehyde with allyltributylstannane. It has also established the fact that the catalytic activity increases manifold, resulting in a sharp reduction of reaction time, upon grinding the aldehyde and allyltributylstannane with PTA. Easy handling, very short reaction time, solvent-free reaction conditions, excellent yields, and a simple purification process devoid of aqueous workup may make our protocol very useful to synthetic chemists.

Supplementary data

Supplementary data are available with the article through the journal Web site (http://nrcresearchpress.com/doi/suppl/10.1139/v11-138).

Acknowledgment

The authors are grateful to the Department of Science and Technology (DST), New Delhi (Ref. No. SR/S1/OC-25/2007) and the University Grants Commission-Special Assistance Program (UGC-SAP), Department of Chemistry, North Eastern Hill University (NEHU), for financial help to carry out this work. Sophisticated Analytical Instrumentation Facility (SAIF)-NEHU is gratefully acknowledged for the analytical data.

References

(1) Walsh, P. J.; Li, H.; de Parrodi, C. A. *Chem. Rev.* **2007**, *107* (6), 2503. doi:10.1021/cr0509556.
(2) Horváth, I. T.; Anastas, P. T. *Chem. Rev.* **2007**, *107* (6), 2169. doi:10.1021/cr078380v.
(3) Sheldon, R. A. *Chem. Ind.* **1992**, 903.
(4) Mizuno, N.; Misono, M. *Chem. Rev.* **1998**, *98* (1), 199. doi:10.1021/cr960401q.
(5) Kozhevnikov, V. *Catalysts for Fine Chemical Synthesis. Catalysis by Polyoxometalates;* Derouane, E., Ed.; Vol. 2; Wiley: New York, 2002.
(6) Firouzabadi, H.; Iranpoor, N.; Nowrouzi, F. *Tetrahedron* **2004**, *60* (48), 10843. doi:10.1016/j.tet.2004.09.049.
(7) Firouzabadi, H.; Iranpoor, N.; Nowrouzi, F.; Amani, K. *Chem. Commun. (Camb.)* **2003**, (6): 764. doi:10.1039/b300775h.
(8) Bez, G.; Gogoi, D. *Tetrahedron Lett.* **2006**, *47* (29), 5155. doi:10.1016/j.tetlet.2006.05.057.
(9) Keri, R. S.; Hosamani, K. M.; Seetharama Reddy, H. R. *Catal. Lett.* **2009**, *131* (1–2), 321. doi:10.1007/s10562-009-9940-z.
(10) Davies, A. G. *Organotin Chemistry;* Wiley-VCH: Weinheim, Germany, 2004.
(11) (a) Marshall, J. A. *Chem. Rev.* **2000**, *100* (8), 3163. doi:10.1021/cr000003u; (b) Roush, W. R. In *Comprehensive Organic Synthesis;* Trost, B. M.; Fleming, I.; Heathcock, C. H., Eds.; Pergamon: Oxford, UK. 1991; Vol. 2.
(12) Hishashi, Y.; Koichiro, O. *Main Group Metals in Organic Synthesis;* Wiley-VCH: Weinheim, Germany, 2004; Vol. 2, pp. 621–720.
(13) Prunet, J. *Angew. Chem. Int. Ed.* **2003**, *42* (25), 2826. doi:10.1002/anie.200301628.
(14) Boruwa, J.; Barua, N. C. *Tetrahedron* **2006**, *62* (6), 1193. doi:10.1016/j.tet.2005.10.070.
(15) Pospíšil, J.; Markó, I. E. *Tetrahedron Lett.* **2008**, *49* (9), 1523. doi:10.1016/j.tetlet.2007.12.113.
(16) Chattopadhyay, S. K.; Biswas, T.; Biswas, T. *Tetrahedron Lett.* **2008**, *49* (8), 1365. doi:10.1016/j.tetlet.2007.12.097.
(17) Yanagisawa, A.; Nakashima, H.; Ishiba, A.; Yamamoto, H. *J. Am. Chem. Soc.* **1996**, *118* (19), 4723. doi:10.1021/ja9603315.
(18) Wang, C.-J.; Shi, M. *Eur. J. Org. Chem.* **2003**, *2003* (15), 2823. doi:10.1002/ejoc.200300099.
(19) Kobayashi, S.; Busujima, T.; Nagayama, S. *J. Chem. Soc. Chem. Commun.* **1998**, 19.
(20) Aspinall, H. C.; Bissett, J. S.; Greeves, N.; Levin, D. *Tetrahedron Lett.* **2002**, *43* (2), 323. doi:10.1016/S0040-4039(01)02116-5.
(21) Fernandes, R. A.; Stimac, A.; Yamamoto, Y. *J. Am. Chem. Soc.* **2003**, *125* (46), 14133. doi:10.1021/ja037272x.
(22) Kobayashi, S. *Eur. J. Org. Chem.* **1999**, *1999* (1), 15. doi:10.1002/(SICI)1099-0690(199901)1999:1<15::AID-EJOC15>3.0.CO;2-B.
(23) Choudary, B. M.; Chidara, S.; Sekhar, C. V. R. *Synlett* **2002**, (10): 1694. doi:10.1055/s-2002-34239.
(24) Nishiyama, Y.; Kakushou, S.; Sonoda, N. *Tetrahedron Lett.* **2005**, *46* (5), 787. doi:10.1016/j.tetlet.2004.12.022.
(25) Hachiya, I.; Kobayashi, S. *J. Org. Chem.* **1993**, *58* (25), 6958. doi:10.1021/jo00077a009.
(26) Kalita, H. R.; Borah, A. J.; Phukan, P. *Tetrahedron Lett.* **2007**, *48* (29), 5047. doi:10.1016/j.tetlet.2007.05.102.
(27) Yadav, J. S.; Reddy, B. V. S.; Kondaji, G.; Reddy, J. S. S. *Tetrahedron* **2005**, *61* (4), 879. doi:10.1016/j.tet.2004.11.029.

(28) Bartoli, G.; Bosco, M.; Giuliani, A.; Marcantoni, E.; Palmieri, A.; Petrini, M.; Sambri, L. *J. Org. Chem.* **2004**, *69* (4), 1290. doi:10.1021/jo035542o.
(29) Bedford, R. B. *Chem. Commun. (Camb.)* **2003**, (15): 1787. doi:10.1039/b211298c.
(30) Yao, Q.; Sheets, M. *J. Org. Chem.* **2006**, *71* (14), 5384. doi:10.1021/jo060456k.
(31) van der Boom, M. E.; Milstein, D. *Chem. Rev.* **2003**, *103* (5), 1759. doi:10.1021/cr960118r.
(32) Li, G.-l.; Zhao, G. *Org. Lett.* **2006**, *8* (4), 633. doi:10.1021/ol0528235.
(33) Sreekanth, P.; Park, J. K.; Kim, J. W.; Hyeon, T.; Kim, B. M. *Catal. Lett.* **2004**, *96* (3–4), 201. doi:10.1023/B:CATL.0000030121.59482.6d.
(34) Yu, L.; Chen, D.; Li, J.; Wang, P. G. *J. Org. Chem.* **1997**, *62* (11), 3575. doi:10.1021/jo961933+.
(35) Weissberg, A.; Portnoy, M. *Chem. Commun. (Camb.)* **2003**, (13): 1538. doi:10.1039/b301308a.
(36) Bhuyan, B. K.; Borah, A. J.; Senapati, K. K.; Phukan, P. *Tetrahedron Lett.* **2011**, *52* (21), 2649. doi:10.1016/j.tetlet.2011.03.056.
(37) Vanlaldinpuia, K.; Sema, H. A.; Rokhum, L.; Bez, G. *Chem. Lett.* **2010**, *39* (3), 228. doi:10.1246/cl.2010.228.
(38) Vanlaldinpuia, K.; Bez, G. *Tetrahedron Lett.* **2011**, *52* (29), 3759. doi:10.1016/j.tetlet.2011.05.050.
(39) The phrase "solvent-free conditions" is solely for the reaction only, not for purification of the products where solvents were used for purification by column chromatography.

Can. J. Chem. Downloaded from www.nrcresearchpress.com by Renmin University of China on 09/02/12
For personal use only.

Facile aqueous synthesis of functionalized CdTe nanoparticles and their application as fluorescence probes for determination of adenine and guanine

Li Li, Yaxiang Lu, Yaping Ding, Fenfen Zhang, and Yaping Wang

Can. J. Chem. Downloaded from www.nrcresearchpress.com by Renmin University of China on 09/02/12
For personal use only.

Abstract: Thioglycolic acid (TGA)-capped CdTe nanoparticles (NPs) were synthesized in aqueous medium, and their application as fluorescence probes in the detection of adenine and guanine was studied. The TGA-capped CdTe NPs were characterized by transmission electron microscopy, X–ray diffraction spectrometry, spectrofluorometry, Fourier transform infrared, and ultraviolet-visible spectrometry. Based on the significant enhancement of fluorescence emission of these CdTe fluorescence probes in the presence of adenine or guanine, a quantitative analysis method for these purines was proposed. Experimental conditions that govern the extent of fluorescence enhancement were optimized. Under the optimal conditions, the relative fluorescence intensity versus adenine or guanine concentrations gave a linear response, permitting the dynamic range of 7.0×10^{-7}–1.0×10^{-4} mol/L and 6.0×10^{-7}–9.0×10^{-5} mol/L for adenine and guanine, respectively. The method has also been applied successfully to the detection of adenine and guanine in synthetic samples with satisfactory results.

Key words: CdTe nanoparticles, fluorescence probe, adenine, guanine.

Résumé : Opérant dans un milieu aqueux, on a effectué la synthèse de nanoparticules (NP) de CdTe coiffées par d'acide thioglycolique (ATG) et on a étudié la possibilité de les utiliser comme sondes de fluorescence pour la détection de l'adénine et de la guanine. On a caractérisé ces nanoparticules de CdTd coiffées par d'acide thioglycolique (ATG) par microscopie électronique de transmission, par spectrométrie de diffraction des rayons-X, par spectrofluorométrie, par spectrométrie infrarouge à transformation de Fourier et par spectrométrie ultraviolette-visible. Sur la base de l'augmentation significative de l'émission de fluorescence de ces sondes de fluorescence à base de CdTe en présence d'adénine ou de guanine, on a proposé une méthode d'analyse quantitative pour ces purines. On a optimisé les conditions expérimentales qui favorisent une augmentation de la fluorescence. Dans les conditions optimales, on observe une corrélation linéaire entre l'intensité relative de la fluorescence en fonction des concentrations d'adénine ou de guanine et ceci établit que les plages dynamiques sont respectivement de $7{,}0 \times 10^{-7}$à $1{,}0 \times 10^{-4}$ mol/L et de $6{,}0 \times 10^{-7}$ à $9{,}0 \times 10^{-5}$ mol/L pour l'adénine et la guanine. La méthode a été appliquée avec succès à la détection de l'adénine et de la guanine dans des échantillons de synthèse.

Mots-clés : nanoparticules de CdTe, sonde de fluorescence, adénine, guanine.

[Traduit par la Rédaction]

1. Introduction

Semiconductor nanoparticles (NPs) are nanostructured materials,[1] also known as zero-dimensional materials or nanocrystallites.[2] These smart NPs are composed of atoms from groups II–VI, III–V or IV–VI elements in the periodic table.[3] Because of their quantum confinement of charge carriers in tiny spaces, NPs show some unique and fascinating optical properties, which are not available from either isolated molecules or bulk materials,[4,5] such as broad excitation wavelength range, narrow and symmetrical emission spectrum, size-tunable emission peak, longer fluorescence lifetime than organic fluorophores, high photobleaching threshold, and high resistance to optical and chemical degradation.[6–9] As the optical properties of NPs strongly depend on the nature of the surface, the interactions between specific analytes and the surface of the NPs can result in dramatic changes in their optical properties.[10] In addition, the high quantum yield makes them appealing for direct detection applications, removing the need for sample enrichment and amplification, making the prescribed technique more versatile and accessible.[11] Hence, functionalized NPs have been widely exploited for tracing biorecognition events or biocatalytic transformations,[12,13] and for biomolecule sensing strategies.[14]

Adenine and guanine are building blocks of both DNA and RNA that play a crucial role in protein biosynthesis and the storage of genetic information.[15] Adenine has important effects on physiological processes of human body. It controls blood flow, prevents cardiac arrhythmias, inhibits neurotransmitter release, affects cerebral circulation, and modulates activity of adenylate cyclase.[16] Guanine is believed to play a

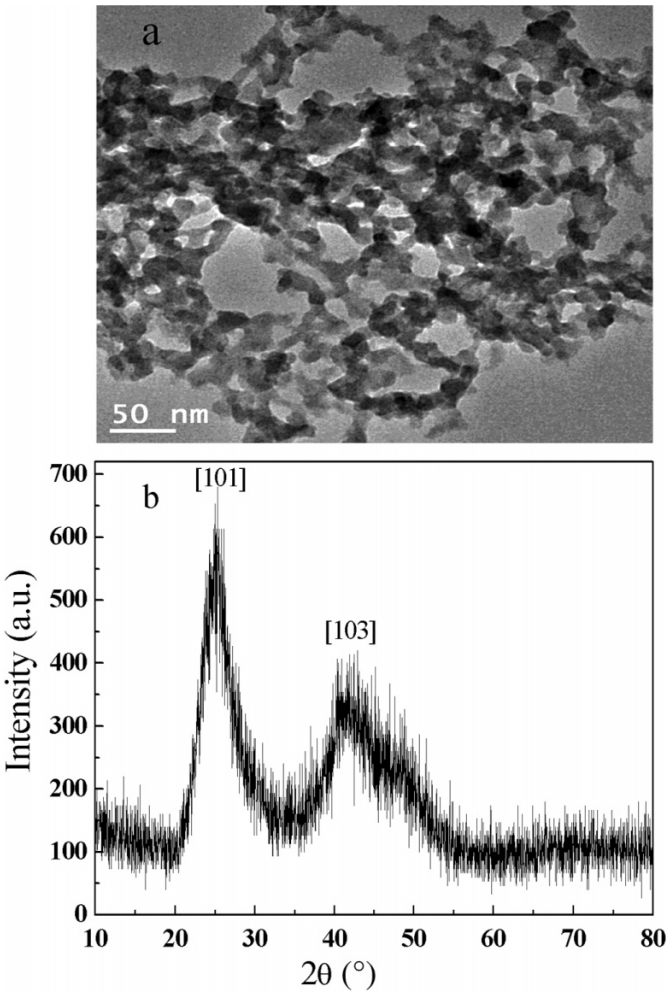
Received 16 April 2011. Accepted 30 September 2011. Published at www.nrcresearchpress.com/cjc on 13 December 2011.

L. Li, Y. Lu, Y. Ding, F. Zhang, and Y. Wang. Department of Chemistry, Shanghai University, Shanghai, 200444, P.R. China.

Corresponding author: Yaping Ding (e-mail: wdingyp@sina.com).

Can. J. Chem. Downloaded from www.nrcresearchpress.com by Renmin University of China on 09/02/12
For personal use only.

Fig. 1. (*a*) TEM image and (*b*) XRD pattern of the as-prepared TGA–CdTe nanoparticles.



key role in the oxidation of DNA by various types of oxidants and free radicals.[17] Thus, it can be used to predetermine physical and chemical mechanisms responsible for the degree, localization, and chemical impact of oxidative damage to DNA.[17,18] The importance of such a determination stems from the fact that abnormal concentrations of these purines in cells may reflect alterations in the activity of catabolic, anabolic, interconversion of enzymes, and the presence of various diseases.[19] Hence, quantitative analysis of adenine and guanine is very essential to bioscience and clinical diagnosis.

To date, various methods have been available for the determination of adenine and guanine. These include high performance liquid chromatography,[20] electrophoresis with spectroscopic and electrochemical detection,[21] electrochemical analysis,[22] liquid chromatography tandem mass spectroscopy,[23] flow injection chemiluminescence,[24] and surface-enhanced Raman spectroscopy.[25] However, each approach exhibits certain disadvantages. For example, chromatographic methods often require the isolation of matrix components, as well as derivatization steps,[26] while the electrochemical technique tends to suffer from irreversible adsorption on the electrode surface thus hampering the estimation.[19,27] In contrast, the fluorescence probe method appears to be a simple and fast experimental process, with

Fig. 2. (*a*) Absorption and (*b*) emission spectra of TGA–CdTe nanoparticles.

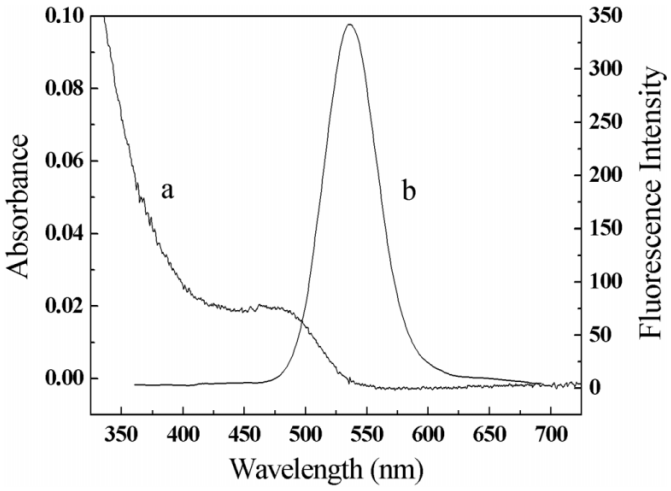
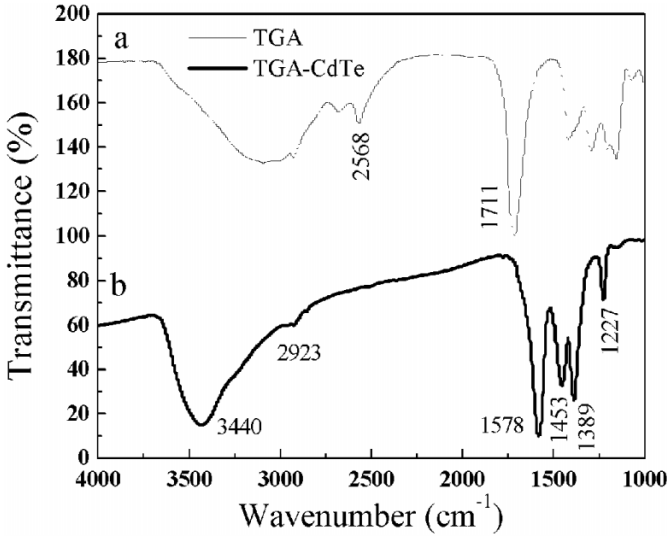


Fig. 3. (*a*) FTIR spectra of TGA and (*b*) TGA capped CdTe NPs.



high sensitivity for different fluorescent emission wavelengths corresponding to different molecular structures.[28]

In this paper, we present a simple, convenient and sensitive fluorescence emission method for the quantitative determination of adenine and guanine based on the interaction of CdTe NPs with adenine or guanine. The CdTe NPs were prepared in aqueous solution through a straightforward process by using safe inorganic salts as precursors and low-cost thioglycollic acid as the stabilizer. Under optimum conditions, the fluorescence of functionalized CdTe NPs was enhanced through binding with adenine or guanine, wherein the extent of the fluorescence intensity enhancement was proportional to the concentrations of the analytes. Interference tests using several metal ions and some small biomolecules demonstrated little impact on determination of the two purines.

2. Experimental

2.1 Reagents and materials

The chemicals used in the experiments included $CdCl_2 \cdot 2.5H_2O$ (analytical purity), sodium borohydride (96%),

Can. J. Chem. Downloaded from www.nrcresearchpress.com by Renmin University of China on 09/02/12
For personal use only.

Fig. 4. Effect of pH on the fluorescence intensity of TGA–CdTe system in the absence and presence of adenine or guanine.

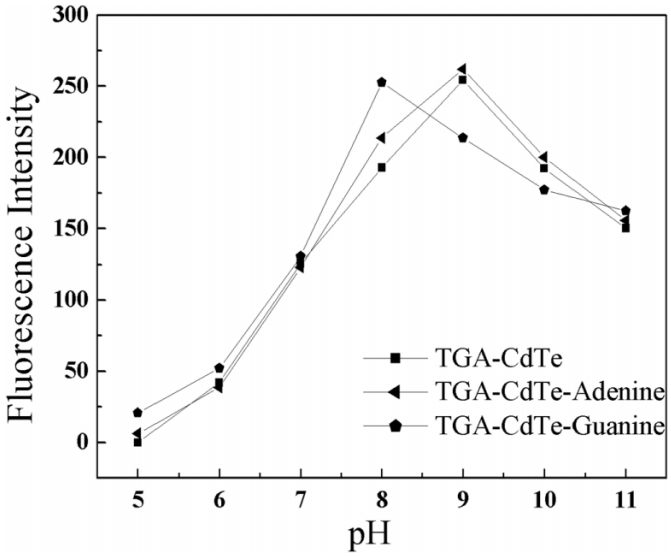
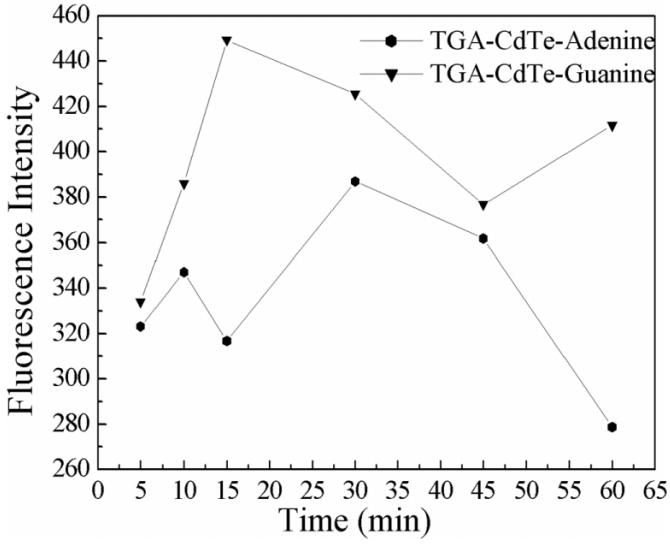


Fig. 5. Effect of reaction time on the fluorescence intensity of TGA–CdTe–adenine and TGA–CdTe–guanine systems.



tellurium powder (99.999%), adenine (biology reagent), guanine (biology reagent), and thioglycolic acid (TGA, purity). All chemicals were purchased from Shanghai Sinopharm Chemical Reagent Co. Ltd. (China) and used without further purification. Doubly distilled water (DDW) was used throughout. Stock solutions of adenine and guanine were prepared in 0.1 mol/L HCl at a concentration of 5 mmol/L and were further diluted with DDW whenever necessary. The phosphoric buffer solution (PBS) was prepared by adjusting 0.1 mol/L K_2HPO_4, KH_2PO_4, H_3PO_4, or NaOH accordingly.

2.2 Apparatus

Transmission electron microscopy (TEM) images were obtained using JEOL 200 CX transmission electron microscope. X–ray powder diffraction (XRD) spectra were taken on a Rigaku D/max 2550 X–ray diffractometer with Cu Kα radiation (λ = 0.15418 nm). The fluorescence emission spectra were measured by using a RF-5301PC spectrofluorometer with a 1 cm quartz cell. Absorption spectra were recorded on a UV-2501PC spectrometer. Infrared spectra were recorded by using an AVATAR 370 Fourier transform infrared (FTIR) spectrophotometer. The pH measurements were made with a pHS-3C pH meter. All optical measurements were carried out at room temperature under ambient conditions.

2.3 Synthesis of NaHTe

NaHTe solution was prepared using a modified literature procedure by treatment of Te powder with excess $NaBH_4$ at a molar ratio of 1:20.[29] To a small flask was loaded 151 mg (4 mmol) of $NaBH_4$ followed by the addition of 5 mL of DDW and 25.5 mg (0.2 mmol) of Te powder. The mixture was stirred under a N_2 atmosphere in ice-cooled water bath. During the course of the reaction, a small outlet connected to the flask was kept open to discharge the pressure from the N_2 and the resulting H_2. The NaHTe solution was obtained when the color of the solution changed from black to white.

2.4 Aqueous synthesis of TGA-capped CdTe nanoparticles

The synthesis of the colloidal CdTe NPs was carried out in a three-necked round-bottomed flask. Typically, 0.4 mmol of $CdCl_2{\cdot}2.5H_2O$ was dissolved in 100 mL DDW, and 0.96 mmol of TGA was added under stirring, followed by adjusting the pH to 11.2 by the addition of 1.0 mol/L NaOH solution dropwise. The resulted solution was degassed by N_2 bubbling for 30 min. Under vigorous stirring, 0.2 mmol of freshly prepared oxygen-free NaHTe was injected into the above solution. The molar ratio of Cd^{2+}/Te^{2-}/TGA was 2:1:4.8 in our experiments. The reaction between Cd^{2+} and NaHTe took place immediately upon the injection of NaHTe solution. The colorless solution changed to golden yellow. After being refluxed for 1 h at 95 °C, TGA-stabilized CdTe NPs exhibiting green fluorescence were obtained.

2.5 Determination of adenine and guanine with TGA–CdTe fluorescence probe

To determine the concentrations of adenine and guanine, a series of solutions prepared as follows were used to monitor the change of emission fluorescence intensity by means of spectrofluorometer. To a set of dry 25 mL calibrated flasks were added 400 μL of as-prepared TGA–CdTe solution and a series of known volumes of adenine or guanine standard solutions. The resulting solutions were diluted to the volume with PBS and mixed thoroughly. The mixtures were kept for a while in the dark prior to making the fluorescence measurements at room temperature. For emission measurements, the excitation wavelength was fixed at 351 nm, where neither adenine nor guanine possesses absorption. The fluorescence intensity was measured at 535 nm for adenine and 538 nm for guanine, respectively. Both slit widths of excitation and emission were 5 nm. The scanning bound was from 361 to 692 nm.

3. Results and discussion

3.1 Characterization of the prepared TGA–CdTe nanoparticles

The morphology of the prepared TGA–CdTe NPs was visualized by transmission electron microscopy. The typical TEM image (Fig. 1*a*) of TGA–CdTe NPs illustrates that

Can. J. Chem. Downloaded from www.nrcresearchpress.com by Renmin University of China on 09/02/12
For personal use only.

Fig. 6. (*a*) Fluorescence emission spectra of TGA–CdTe–adenine obtained in PBS (pH = 9.0) with excitation wavelength at 351 nm. $C_{adenine}$ (10^{-5} mol/L): (1) 0; (2) 0.1; (3) 3.0; (4) 5.0; (5) 7.0; (6) 9.0; (7) 10.0. (*b*) Fluorescence emission spectra of TGA–CdTe–guanine obtained in PBS (pH = 8.0) with excitation wavelength at 351 nm. $C_{guanine}$ (10^{-5} mol/L): (1) 0; (2) 0.08; (3) 0.9; (4) 3.0; (5) 5.0; (6) 7.0; (7) 9.0.

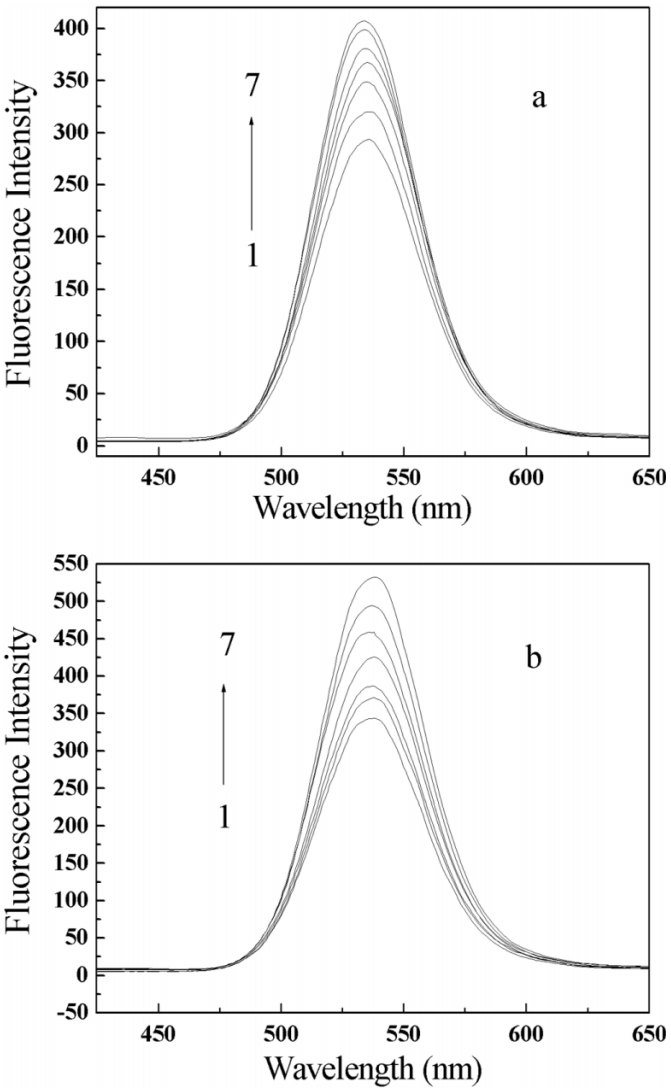
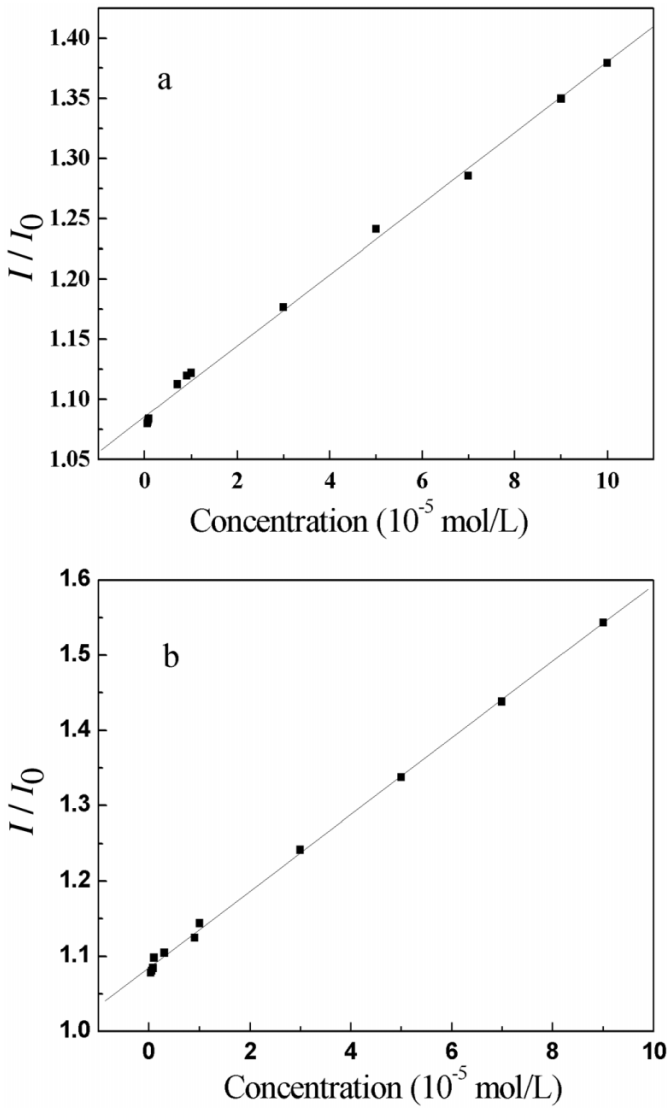


Fig. 7. Linear graph of the relative fluorescence intensity (I/I_0) versus the concentrations (C) of (*a*) adenine and (*b*) guanine.



these NPs are monodispersed, and the shape of them is close to regular spherical NPs with average diameters of approximately 30 nm. The XRD pattern (Fig. 1*b*) was obtained from TGA–CdTe powders precipitated from an aqueous solution of CdTe NPs with excess isopropanol. The XRD spectrum shows two main peaks at 25.3° and 41.7°, corresponding to the crystal planes 101 and 103, confirming that it has a hexagonal wurtzite crystalline structure. According to the Debye–Scherrer equation, $D = 0.89\lambda/\beta\cos\theta$, the average size of TGA–CdTe NPs is 30.8579 nm, which is in good agreement with the particle size estimated from the TEM image.

The optical properties of TGA–CdTe NPs were also characterized by using UV–vis absorption and fluorescence spectroscopy (Fig. 2). The absorption spectrum indicates that TGA–CdTe NPs have a wide range of absorption, and the excitonic absorption peak is at 475 nm. The emission spectrum displays an emission peak at 537 nm, and this spectrum is characterized by good symmetry and relatively narrow spectral width.

To demonstrate whether TGA has been capped onto CdTe NPs, FTIR studies were used to characterize the structure of TGA (Fig. 3*a*) and the TGA-modified CdTe NPs (Fig. 3*b*). Figure 3*b* clearly shows that the infrared absorption bands occur at 3440 cm^{-1} (OH stretching vibration), 2923 cm^{-1} (CH_2 symmetric stretching vibration), 1578 cm^{-1} (COO^- asymmetric stretching vibration), 1453 cm^{-1} (CH_2 scissoring vibration), 1389 cm^{-1} (COO^- symmetric stretching vibration), and 1227 cm^{-1} (CO stretching vibration).[30] It is noteworthy that the characteristic S–H vibrations in TGA at around 2568 cm^{-1} disappeared completely in the spectrum of TGA–CdTe NPs. Hence, it could be concluded that the S–Cd bonds were formed between TGA and CdTe core.[31] Besides, the asymmetric stretching vibration of the carboxyl group in TGA shifted from 1711 to 1578 cm^{-1}, indicating that TGA was absorbed onto Cd^{2+} as carboxylate after deprotonation.[32]

Table 1. Comparison of the proposed method with others.

Detection method	Purine	Linear range (10^{-6} mol/L)	LOD (10^{-6} mol/L)	r	Sensitivity	Reference
Voltammetry	adenine	0.37–37	0.03	0.9993	840 mA·L/mol·cm^{-2}	35
	guanine	0.07–20	0.006	0.9979	1 520 mA·L/mol·cm^{-2}	
Micellar electrokinetic chromatography	adenine	370–7400	8.58	0.9922	58.11 L/mol	15
	guanine	165–4960	1.92	0.9917	290.17 L/mol	
Ion-pair HPLC	adenine	37–370	12.95	0.9990	23 379.2 L/mol	20
	guanine	33.1–331	7.74	0.9990	44 130 L/mol	
LC/ESI–MS	adenine	14.8–1035	4.44	0.9970	8 378.7 L/mol	36
Flow-injection chemiluminescence	guanine	1.99–600	0.66	0.9956	3.175×10^6 L/mol	26
Fluorimetry	guanine	20–100	Not given	Not given	6 800 L/mol	37
Fluorimetry	adenine	0.7–100	0.14	0.9985	2 949 L/mol	This method
	guanine	0.6–90	0.08	0.9993	5 094 L/mol	

Table 2. Interference from some coexisted substances.

Coexisting substance	Coexisting concentration with adenine (10^{-5} mol/L)	Change of fluorescence intensity to adenine (%)	Coexisting concentration with guanine (10^{-5} mol/L)	Change of fluorescence intensity to guanine (%)
NH_4^+, Cl^-	100	+2.33	50	+1.64
K^+, NO_3^-	50	+2.55	50	+4.27
Na^+, I^-	50	+1.22	100	+1.68
Ca^{2+}, Cl^-	20	+1.94	50	–1.79
Zn^{2+}, SO_4^{2-}	5	–0.61	20	+3.52
Mg^{2+}, SO_4^{2-}	2.5	+2.72	5	+2.01
Co^{2+}, NO_3^-	2.5	–2.97	2	–4.90
Al^{3+}, NO_3^-	5	–4.94	5	+2.46
Glucose	20	+2.00	30	+2.75
Dopamine	10	–2.51	10	+1.98
Citric acid	20	–0.09	30	+0.41
Uric acid	5	–2.45	10	–0.11
Uracil	100	–2.99	100	+0.47
Thymine	100	–1.11	100	+3.87
L-cysteine	15	–4.99	30	+2.06
L-alanine	20	+0.88	5	+1.63
L-phenylalanine	5	+3.63	5	+4.21
L-tryptophan	20	+4.39	10	–3.75
L-leucine	10	–2.31	10	+2.34

3.2 Optimization of the general procedure

The fluorescence emission spectra of many matters are sensitive to their surrounding environment. To develop a sensitive and rapid spectrophotometric method for the determination of adenine and guanine, the test conditions were optimized by studying the effects of various factors such as pH value, incubation time, and temperature.

The effect of pH in a range between 4.0 and 11.0 was studied. PBS (0.1 mol/L) was used as the buffer to adjust the acidity of the aqueous medium. As shown in Fig. 4, pH influences the fluorescence intensity of NPs in the absence and presence of adenine or guanine. It can be seen clearly from Fig. 4 that the maximum fluorescence intensity of the TGA–CdTe–adenine system occurs at pH 9.0, whereas the optimal pH is 8.0 for the TGA–CdTe–guanine system. Therefore, pH of 9.0 and 8.0 was chosen to run the two systems, respectively.

The influence of reaction time on the fluorescence enhancement intensity was also studied. Fluorescence spectrum was recorded at different time intervals after the addition of adenine or guanine into the NPs solution. The results (in Fig. 5) show that the maximum fluorescence intensity is obtained when the reaction time is 30 min for adenine and 15 min for guanine. It was noted that temperature, as expected, had an effect on the fluorescence intensity of the TGA-capped CdTe NPs. Therefore, all analytical studies were conducted at room temperature (25 °C).

3.3 Spectral characteristics of fluorescence

A series of different concentrations of adenine or guanine were added to the TGA–CdTe NPs system. It was observed that the fluorescence intensity increased on the addition of adenine or guanine with no obvious spectra shift. Changes of the fluorescence emission spectra are given in Fig. 6. The

Can. J. Chem. Downloaded from www.nrcresearchpress.com by Renmin University of China on 09/02/12
For personal use only.

Table 3. Results of the analysis of synthetic samples ($n = 3$, $P = 95\%$).

Purine	Number	Amount (10^{-6} mol/L)	Addition of purine (10^{-6} mol/L)	Average recovery (%)	R.S.D. (%)
Adenine	1	20	10	98.03	1.96
	2	40	20	101.46	1.43
	3	80	20	97.67	1.16
Guanine	1	30	10	99.70	1.03
	2	50	15	100.31	2.01
	3	70	20	97.22	1.34

Can. J. Chem. Downloaded from www.nrcresearchpress.com by Renmin University of China on 09/02/12
For personal use only.

observed fluorescence band centers are at 535 nm (excitation 351 nm) for adenine and 538 nm (excitation 351 nm) for guanine. The possible mechanism of the interaction between TGA–CdTe NPs and the two purines is a hydrogen bond in nature.[33,34] The significant enhancement of fluorescence intensity offered the possibility of developing a sensitive method for quantitative assay of adenine and guanine based on spectrofluorometry.

3.4 Standard curve and detection limit

Under optimal experimental conditions, the enhancement effect of adenine or guanine on the fluorescence emission of TGA-capped CdTe NPs was concentration-dependent, which was best demonstrated in Fig. 7. There are good linear relationships between the relative fluorescence intensity ($\Delta I = I/I_0$) and the concentrations (C) of adenine and guanine, where I_0 and I are the fluorescence intensities at λ_{em} when excited at λ_{ex} in the absence and presence of purine solutions, respectively. The dynamic range of adenine is 7.0×10^{-7}–1.0×10^{-4} mol/L with a correlation coefficient (r) of 0.9985, and the dynamic range of guanine is 6.0×10^{-7}–9.0×10^{-5} mol/L with a correlation coefficient (r) of 0.9993. The calibration curve established the following equation, $\Delta I = 1.085 + 0.02949\ C$ (C, 10^{-5} mol/L) for adenine and $\Delta I = 1.084 + 0.05094\ C$ (C, 10^{-5} mol/L) for guanine. The detection limit was 1.4×10^{-7} mol/L for adenine and 8.0×10^{-8} mol/L for guanine. These analytical parameters are comparable or better than results reported for adenine or guanine detection (Table 1), which signifies that this method is sensitive.

3.5 Tolerance of foreign substances

Under the optimized conditions of assay, the effects of foreign substances on the fluorescence signals of CdTe NPs were investigated to evaluate the selectivity of this proposed method. Each foreign substance, of various concentrations, was mixed with 1.0×10^{-5} mol/L adenine or guanine prior to the detection. The tolerance limit was defined as the maximum concentration of the foreign substance that produced a determination error of less than 5% (Table 2). The results show that most of the substances examined have no obvious interference in determination, indicating that this method is selective and amenable to the detection of adenine and guanine in human or animal body fluid samples.

3.6 Analytical performance

The present method was applied to quantify adenine and guanine in three synthetic samples containing adenine or guanine and foreign substances whose concentrations were below the tolerance of coexisting species listed in Table 2. The average recovery (R) is defined by the equation $R = [(C_T - C_A)/C] \times 100\%$,[38] where C is the amount of purines (adenine or guanine) from synthetic samples, C_A is the added amount of standard solution of purines, and C_T is the amount of purines after the addition of standard solution of purines, which is obtained from the regression equation. The determination results and recovery tests are shown in Table 3. It can be seen that values acquired from the three samples are identical with the expected values. Moreover, the relative standard deviations (R.S.D.) are lower than 3%, showing good precision of this method. The average recovery ranges from 97.22% to 101.46%, which meets the requirement of micro-analysis. This indicates that our method is accurate, sensitive, and reproducible.

4. Conclusions

In this study, a novel fluorescence probe method based on TGA-capped CdTe NPs has been developed for the quantitative analysis of adenine and guanine. The TGA-capped CdTe NPs with excellent fluorescence properties were synthesized in aqueous solution through a straightforward process. The fluorescence intensity of the functionalized nanoparticles displayed a positive linear correlation with the concentrations of adenine or guanine. The use of TGA–CdTe NPs as fluorescence probes offered a particularly inexpensive, simple, and sensitive assay for adenine and guanine. These studies should provide valuable information in the design of fluorescence probes for the detection of other biomolecules. Finally, the CdTe nanoparticles may find more extensive applications in analytical biochemistry.

Acknowledgements

This research is supported by the National Natural Science Foundation of China (Nos. 20975066, 41140031), the Nano-Foundation of Science and Techniques Commission of Shanghai Municipality (No. 0952nm01500), the Leading Academic Discipline Project of Shanghai Municipal Education Commission (No. J50102), and the Graduate Innovation Foundation of Shanghai University (SHUCX112027).

References

(1) Niemeyer, C. M. *Angew. Chem. Int. Ed.* **2001**, *40* (22), 4128. doi:10.1002/1521-3773(20011119)40:22<4128::AID-ANIE4128>3.0.CO;2-S.

(2) Mao, H.; Yao, J. N.; Wang, L. N.; Liu, W. S. *J. Colloid Interface Sci.* **2008**, *319* (1), 353. doi:10.1016/j.jcis.2007.10.027.

(3) Chouhan, R. S.; Vinayaka, A. C.; Thakur, M. S. *Anal. Bioanal. Chem.* **2010**, *397* (4), 1467. doi:10.1007/s00216-009-3433-1.

Can. J. Chem. Downloaded from www.nrcresearchpress.com by Renmin University of China on 09/02/12
For personal use only.

(4) Weng, J. F.; Song, X. T.; Li, L. A.; Qian, H. F.; Chen, K. Y.; Xu, X. M.; Cao, C. X.; Ren, J. C. *Talanta*, **2006**, *70* (2), 397. doi:10.1016/j.talanta.2006.02.064.
(5) Kim, T.; Noh, M.; Lee, H.; Joo, S. W.; Lee, S. Y.; Lee, K. *J. Phys. Chem. B*, **2009**, *113* (43), 14487. doi:10.1021/jp906096a.
(6) Cai, Z. X.; Yang, H.; Zhang, Y.; Yan, X. P. *Anal. Chim. Acta*, **2006**, *559* (2), 234. doi:10.1016/j.aca.2005.11.061.
(7) Fu, A.; Gu, W.; Boussert, B.; Koski, K.; Gerion, D.; Manna, L.; Le Gros, M.; Larabell, C. A.; Alivisatos, A. P. *Nano Lett.* **2007**, *7* (1), 179. doi:10.1021/nl0626434.
(8) Ge, S. G.; Zhang, C. C.; Zhu, Y. N.; Yu, J. H.; Zhang, S. S. *Analyst (Lond.)*, **2010**, *135* (1), 111. doi:10.1039/b915622d.
(9) Michalet, X.; Pinaud, F. F.; Bentolila, L. A.; Tsay, J. M.; Doose, S.; Li, J. J.; Sundaresan, G.; Wu, A. M.; Gambhir, S. S.; Weiss, S. *Science*, **2005**, *307* (5709), 538. doi:10.1126/science.1104274.
(10) Chen, Y. J.; Yan, X. P. *Small*, **2009**, *5* (17), 2012. doi:10.1002/smll.200900291.
(11) Hunt, E. A.; Goulding, A. M.; Deo, S. K. *Anal. Biochem.* **2009**, *387* (1), 1. doi:10.1016/j.ab.2009.01.011.
(12) Gill, R.; Freeman, R.; Xu, J. P.; Willner, I.; Winograd, S.; Shweky, I.; Banin, U. *J. Am. Chem. Soc.* **2006**, *128* (48), 15376. doi:10.1021/ja066636t.
(13) Yuan, J.; Guo, W.; Wang, E. *Anal. Chem.* **2008**, *80* (4), 1141. doi:10.1021/ac0713048.
(14) Costa-Fernández, J. M.; Pereiro, R.; Sanz-Medel, A. *Trends Analyt. Chem.* **2006**, *25* (3), 207. doi:10.1016/j.trac.2005.07.008.
(15) Wang, W. P.; Zhou, L.; Wang, S. M.; Luo, Z.; Hu, Z. D. *Talanta*, **2008**, *74* (4), 1050. doi:10.1016/j.talanta.2007.06.047.
(16) Pietrzyk, A.; Suriyanarayanan, S.; Kutner, W.; Chitta, R.; Zandler, M. E.; D'Souza, F. *Biosens. Bioelectron.* **2010**, *25* (11), 2522. doi:10.1016/j.bios.2010.04.015.
(17) Ardakani, M. M.; Taleat, Z.; Beitollahi, H.; Salavati-Niasari, M.; Mirjalili, B. B. F.; Taghavinia, N. *J. Electroanal. Chem.* **2008**, *624* (1–2), 73. doi:10.1016/j.jelechem.2008.07.027.
(18) Hall, D. B.; Kelley, S. O.; Barton, J. K. *Biochemistry*, **1998**, *37* (45), 15933. doi:10.1021/bi981750c.
(19) Zen, J. M.; Chang, M. R.; Ilangovan, G. *Analyst (Lond.)*, **1999**, *124* (5), 679. doi:10.1039/a900532c.
(20) del Moral, P. G.; Arin, M. J.; Resines, J. A.; Diez, M. T. *J. Chromatogr. B Analyt. Technol. Biomed. Life Sci.* **2005**, *826* (1–2), 257. doi:10.1016/j.jchromb.2005.07.044.
(21) Tu, X. M.; Luo, X. B.; Luo, S. L.; Yan, L. S.; Zhang, F.; Xie, Q. J. *Mikrochim. Acta*, **2010**, *169* (1–2), 33. doi:10.1007/s00604-010-0307-3.
(22) Shen, Q.; Wang, X. M. *J. Electroanal. Chem.* **2009**, *632* (1–2), 149. doi:10.1016/j.jelechem.2009.04.009.
(23) Yang, F. Q.; Li, D. Q.; Feng, K.; Hu, D. J.; Li, S. P. *J. Chromatogr. A*, **2010**, *1217* (34), 5501. doi:10.1016/j.chroma.2010.06.062.
(24) Erbao, L.; Bingchun, X. *J. Pharm. Biomed. Anal.* **2006**, *41* (2), 649. doi:10.1016/j.jpba.2005.12.012.
(25) El Amri, C.; Baron, M. H.; Maurel, M. C. *J. Raman Spectrosc.* **2004**, *35* (2), 170. doi:10.1002/jrs.1126.
(26) Yang, M.; Liu, R.; Hou, D. Y.; Guo, Y. Y. *Luminescence*, **2005**, *20* (4–5), 307. doi:10.1002/bio.844.
(27) Wang, H. S.; Ju, H. X.; Chen, H. Y. *Anal. Chim. Acta*, **2002**, *461* (2), 243. doi:10.1016/S0003-2670(02)00297-0.
(28) Li, L.; Bian, R. X.; Ding, Y. P.; Yu, M. L.; Yu, D. W. *Mater. Chem. Phys.* **2009**, *113* (2–3), 905. doi:10.1016/j.matchemphys.2008.08.050.
(29) Zhao, W.; Fung, Y.; O, W.; Cheung, M. P. *Anal. Sci.* **2010**, *26* (8), 879. doi:10.2116/analsci.26.879.
(30) Abd El-Sadek, M. S.; Moorthy Babu, S. *Physica B*, **2010**, *405* (16), 3279. doi:10.1016/j.physb.2010.04.060.
(31) Hua, L.; Han, H.; Zhang, X. *Talanta*, **2009**, *77* (5), 1654. doi:10.1016/j.talanta.2008.09.061.
(32) Chen, H. I.; Li, R. B.; Lin, L.; Guo, G. S.; Lin, J. M. *Talanta*, **2010**, *81* (4–5), 1688. doi:10.1016/j.talanta.2010.03.024.
(33) Feng, X.; Shang, Q.; Liu, H.; Wang, H.; Wang, W.; Wang, Z. *J. Phys. Chem. C*, **2009**, *113* (17), 6929. doi:10.1021/jp806116m.
(34) Feng, X. J.; Shang, Q. K.; Liu, H. J.; Wang, W. L.; Wang, Z. D.; Liu, J. Y. *J. Lumin.* **2010**, *130* (4), 648. doi:10.1016/j.jlumin.2009.11.010.
(35) Liu, T.; Zhu, X. B.; Cui, L.; Ju, P.; Qu, X. J.; Ai, S. Y. *J. Electroanal. Chem.* **2011**, *651* (2), 216. doi:10.1016/j.jelechem.2010.11.026.
(36) Huang, L. F.; Wu, M. J.; Sun, X. J.; Guo, F. Q.; Liang, Y. Z.; Li, X. R. *J. Cent. South Univ. T.* **2004**, *11* (3), 295. doi:10.1007/s11771-004-0060-z.
(37) Chanu, T. I.; Negi, D. P. S. *Chem. Phys. Lett.* **2010**, *491* (1–3), 75. doi:10.1016/j.cplett.2010.03.068.
(38) Li, L.; Zhang, F. F.; Ding, Y. P.; Wang, Y. P.; Zhang, L. L. *J. Fluoresc.* **2009**, *19* (3), 437. doi:10.1007/s10895-008-0430-2.

Separation and determination of ephedra alkaloids in traditional Chinese medicine and human urines by capillary electrophoresis coupled with electrochemiluminescence detection

Yan-Ming Liu, Jie Li, Yang Yang, Junjun Du, and Lin Mei

Can. J. Chem. Downloaded from www.nrcresearchpress.com by Renmin University of China on 09/02/12
For personal use only.

Abstract: A new approach for the simultaneous determination of ephedrine, methylephedrine, and pseudoephedrine is developed, using capillary electrophoresis coupled with electrochemiluminescence detection with internal standard method. Separation efficiency and sensitivity were improved by use of an ionic liquid. Parameters affecting separation and detection were investigated in detail. Under optimum conditions, the three ephedra alkaloids were well separated and detected. The limits of detection (S/N = 3) of ephedrine, methylephedrine and pseudoephedrine are 4.0×10^{-8}, 6.5×10^{-8}, and 4.6×10^{-8} mol/L, respectively. The limits of quantitation (S/N = 10) in human urine are 5.3×10^{-7} mol/L for ephedrine, 9.1×10^{-7} mol/L for methylephedrine, and 6.9×10^{-7} mol/L for pseudoephedrine, respectively. The precision (RSD%) of the peak area and the migration time were from 2.2% to 2.5% and from 0.1% to 0.2% within a day and from 2.7% to 3.9% and from 0.4% to 0.8% in three days. The proposed method was successfully applied to the determination of three analytes in traditional Chinese medicine and human urine, and the monitoring of pharmacokinetics of pseudoephedrine in human body.

Key words: capillary electrophoresis, electrochemiluminescence, ephedra alkaloids, pharmacokinetics, traditional chinese medicine.

Résumé : On a développé une nouvelle méthode de détermination simultanée de l'éphédrine, de la méthyléphédrine et de la pseudoéphédrine par électrophorèse capillaire couplée à un détecteur à électrochimiluminescence, utilisant un standard interne. On a amélioré l'efficacité et la sensibilité de la séparation en utilisant un liquide ionique. On a étudié en détail les paramètres qui peuvent affecter la séparation et la détection. Dans des conditions optimales, les alcaloïdes de l'éphédra sont bien séparés et bien détectés. Les limites de détection (signal/bruit > 3) de l'éphédrine, de la méthyléphédrine et de la pseudoéphédrine sont respectivement de $4{,}0 \times 1^{-8}$, $6{,}5 \times 1^{-8}$ et $4{,}6 \times 1^{-8}$ mol/L. Les limites de quantification (signal/bruit > 10) dans l'urine humaine sont pour l'éphédrine, la méthyléphédrine et la pseudoéphédrine sont respectivement de $5{,}3 \times 10^{-7}$, $9{,}1 \times 10^{-7}$ et $6{,}9 \times 10^{-7}$ mol/L. Les précisions, écarts types relatifs (ETR%), de la surface sous les pics et des temps de migration varient de 2,2 % à 2,5 % et de 0,1 % à 0,2 % au cours d'une journée et de 2, 7 % à 3,9 % et de 0,4 % à 0,8 % en trois jours. La méthode proposée a été appliquée avec succès à la détermination des trois analytes dans des médicaments chinois traditionnels, dans l'urine humaine et au suivi pharmacocinétique de la pseudoéphédrine dans le corps humain.

Mots-clés : électrolyse capillaire, électrochimiluminescence, alcaloïdes de l'éphédra, pharmacocinétique, médicaments chinois traditionnels.

[Traduit par la Rédaction]

Introduction

Ephedrine (E), methylephedrine (ME), and pseudoephedrine (PE) are sympathomimetic amines with central nervous system stimulating properties.[1,2] These substances are ingredients of Ma Huang, which is a traditional Chinese medicine (TCM) derived from ephedrae herba that is used as a stimulant, diaphoretic, and anti-asthmatic.[3] They are also ingredients of many pharmaceuticals commonly used in the treatment of flu, rhinitis, colds, and allergy.[4] The International Olympic Committee[5] and most international sports federations have put the ephedrines on their list of prohibited doping substances and have adopted urinary threshold concentrations, above which an athlete is regarded as positive. Therefore, a fast, simple, and reliable method is needed for the simultaneous quantification of these substances. However, the simultaneous separation and detection of E, ME, and PE is difficult because of their similar chemical structure. Increasing concern on the part of both consumers and regulatory agencies of the safety of ephedra alkaloids has led to the development of a variety of analytical methods to measure these important drug ephedra alkaloids, such as gas chromatography (GC)[6,7] and liquid chromatography (LC).[8–10]

Received 14 August 2011. Accepted 26 September 2011. Published at www.nrcresearchpress.com/cjc on 13 December 2011.

Y.-M. Liu, J. Li, Y. Yang, J. Du, and L. Mei. College of Chemistry and Chemical Engineering, Xinyang Normal University, 237 Chang'an Road, Xinyang 464000, P. R. China.

Corresponding author: Yan-Ming Liu (e-mail: liuym9518@sina.com).

Can. J. Chem. Downloaded from www.nrcresearchpress.com by Renmin University of China on 09/02/12
For personal use only.

Capillary electrophoresis (CE) has been widely applied to the analysis of pharmaceutical compounds because of its high resolution, short analysis time, low reagent consumption, and easy automation.[11,12] Phinney et al.[13] reported a CE-UV method for the determination of E and PE enantiomers based on the cyclodextrin as additive. Li et al.[14] separated E and PE by CE, modified with a Cu (II)-L-lysine complex utilizing UV detection. Xie et al.[15] and Dong et al.[16] determined E and PE after derivatization by CE-LIF. Electrochemiluminescence (ECL) has become an attractive and powerful detection tool because of its advantages, such as high sensitivity, good selectivity, wide linear range, and low equipment cost.[17,18] Tris(2,2′-bipyridyl)ruthenium(II) ($Ru(bpy)_3^{2+}$) is the most efficient and widely used ECL reagent, because of its high luminescence efficiency and stability in aqueous media. Recently, CE coupled with ECL using $Ru(bpy)_3^{2+}$, has been proven to be a sensitive and efficient analytical technique and was successfully demonstrated in analyses of proteins,[19,20] amino acids,[21] and drugs.[22–24]

Ionic liquids (ILs) are new advanced materials consisting of entirely ionic species at ambient temperatures. They have some unique properties, compared with conventional organic solvents, such as nonvolatility, high chemical and thermal stability, a wide electrochemical window, good conductivity, and high viscosity.[25,26] ILs have played an important role as separation media in past decades in advancing research in GC,[27] LC,[28,29] and CE.[30,31] The wetting ability and the viscosity of ILs make them an ideal coating in stationary phases in GC. The addition of ILs as new mobile phase additives or chemical modifiers in LC could eliminate band broadening and tailing and improve resolution. ILs have been recognized as suitable background electrolytes in CE. Similar to LC, their use in CE has been shown to enhance resolution, peak efficiency, and peak symmetry.[32,33]

In this work, a sensitive CE-ECL method was developed for the simultaneous determination of E, ME, and PE with IL. To improve precision and obtain more accurate results, the internal standard method was adopted. The conditions for separation and detection were investigated in detail. The applicability of the proposed method was illustrated in the qualitative and quantitative analysis of three ephedra alkaloids in traditional Chinese medicine. The method was also applied to the determination of E, ME, and PE in human urine samples and the monitoring of pharmacokinetics for PE in the human body.

Experimental

Materials and reagents

E, ME, and PE were purchased from the National Institute for the Control of Pharmaceutical and Biological Products (Beijing, China). Tripropylamine (TPA) was obtained from Sigma-Aldrich Chemicals (Milwaukee, Wis., USA). PE sustained release capsules were acquired from Zhongmei Tianjin Shike Pharmaceutical Co. Ltd. (Tianjin, China). Xiao'er Qingre Zhike Koufuye (a kind of TCM for the treatment of colds, containing E, ME, and PE) was acquired from Hebei Sunstone Pharma (Tangshan, China). Tris(2,2′-bipyridyl) ruthenium(II) chloride hexahydrate was purchased from Alfa Aesar (A Johnson Matthey Company, Ward Hill, Mass., USA). 1-Butyl-3-methylimidazolium tetrafluoroborate ($BMIMBF_4$) was purchased from Wako Pure Chemical Industries (Japan). All chemicals and reagents were of analytical grade and used without further purification.

An amount of 5 mmol/L stock solutions of E, ME, PE, and TPA were prepared by dissolving each standard substance in pure water (18.2 MΩ cm) and processed with an Ultrapure Water System (Kangning Water Treatment Solution Provider, China). A series of working standard solutions were prepared by diluting the stock solution with pure water for calibration. All solutions were stored in a refrigerator at 4 °C and filtered through 0.22 μm cellulose acetate filters (Shanghai Xingya Purification Material Factory, China) prior to use.

CE-ECL apparatus

The CE-ECL experiments were performed on a model MPI-A CE ECL system (Xi'an Remax Electronic Science-Tech, Xi'an, China). The system provided a programmable high-voltage power supply (0–20 kV), an electrochemical potentiostat, a multifunction chemiluminescence detector, and a multichannel data collection analyzer. Output ECL intensity was amplified and recorded in a computer using the MPI-A software.

The end-column ECL detection cell was composed of a 500 μm Pt disk working electrode, an Ag/AgCl reference electrode (KCl saturated), and a Pt wire counter electrode. The surface of the working electrode was polished sequentially with 0.3 and 0.05 μm α-Al_2O_3 on a piece of polishing cloth until a mirror smooth surface appeared, and it was then sonicated for 10 min in water. The electrode was subjected to repeated cycling in the potential region of 0.2–1.25 V (versus Ag/AgCl) to obtain a reproducible cyclic voltammogram before the first use of every day. About 300 μL of 5 mmol/L $Ru(bpy)_3^{2+}$ with 50 mmol/L PBS solution at pH 8.5 was added into the cell before analysis and replaced every 6 h to eliminate depletion effects.

Procedure

All separations were performed in a 50 cm long fused-silica capillary, with 50 μm i.d. and 375 μm o.d. (Yongnian Reafine Chromatography, Hebei, China). The new capillary was rinsed sequentially with 2.0 mol/L CH_3OH-NaOH (2 g NaOH dissolved in 25 mL (4:1, *v*/*v*) CH_3OH/H_2O solution), 1.0 mol/L NaOH, 1.0 mol/L HCl, H_2O, and electrophoretic buffer for 30 min. At the beginning of each day, the capillary was flushed with 0.1 mol/L NaOH, HCl, H_2O, and equilibrated with the electrophoretic buffer for 5 min successively to maintain an active and reproducible inner surface. The capillary was rinsed sequentially with 0.1 mol/L NaOH, 0.1 mol/L HCl, H_2O, and electrophoretic buffer for 2 min after every five runs. The voltage of the photomultiplier tube (type CR105, Beijing Binsong Photonics, China) used to collect the ECL signal was set at –850 V during detection. The detection potential applied at the working electrode was fixed at 1.20 V. Electrokinetic injections were performed at 10 kV for 10 s. The inlet end of the capillary was held at a positive potential, and the outlet end was maintained at ground. Five mmol/L of $Ru(bpy)_3^{2+}$, prepared in 50 mmol/L phosphate buffer solution (PBS), was added to the detection cell. The peak area was used for the analysis.

Can. J. Chem. Downloaded from www.nrcresearchpress.com by Renmin University of China on 09/02/12
For personal use only.

Results and discussion

$Ru(bpy)_3^{2+}$ generated ECL with ME

ME was used as a model analyte to study the ECL performances of the ephedra alkaloids in this work. The results of CV of $Ru(bpy)_3^{2+}$ and ME showed that the CV wave of the ECL reaction of $Ru(bpy)_3^{2+}$ was observed with a peak voltage of 1.20 V. In presence of ME, the rise in the anodic current, a marker of the catalytic effect of $Ru(bpy)_3^{2+}$, were observed as the potential was scanned from 0.2 to 1.25 V. The possible mechanism for the enhanced ECL emission might occur as follows[18]:

[1] $$Ru(bpy)_3^{2+} - e^- \rightarrow Ru(bpy)_3^{3+}$$

[2] $$ME - e^- \rightarrow ME^{\bullet +}$$

[3] $$ME^{\bullet +} \rightarrow ME^{\bullet} + H^+$$

[4] $$Ru(bpy)_3^{3+} + ME^{\bullet} \rightarrow Ru(bpy)_3^{2+*} + \text{product}$$

[5] $$Ru(bpy)_3^{2+*} \rightarrow Ru(bpy)_3^{2+} + h\nu$$

Effect of electrophoretic buffer type

In CE, electrophoretic buffer has great influence on separation and detection. Four kinds of buffer, Tris-HCl, $Na_2B_4O_7$, PBS, and phosphate containing borax with the same concentration ($Na_2B_4O_7$-PBS), were examined separately and the results were shown in Fig. 1. It can be seen from Fig. 1 that the use of $Na_2B_4O_7$-PBS buffer can obtain good resolution (Rs) and high sensitivity.

Orthogonal experimental design for the electrophoretic buffer

Traditionally, separation conditions are optimized by a univariate study. This method can achieve certain satisfying performance. However, the best combination of every experimental parameter cannot be obtained when the interaction between some factors occurs. Combination investigation of all possible factors needs a large number of experiments.[34] To reduce the experiment number and gain the desired experimental results, orthogonal experimental design (OAD) can very efficiently and quickly generate useful information on key variables by arranging different factors for effective optimization of experimental conditions. In this work, the three main factors for electrophoretic buffer are pH, concentration of electrophoretic buffer, and percentage of IL ($BMIMBF_4$). The preliminary experiments showed that the addition of $BMIMBF_4$ as an additive to the electrophoretic buffer could improve the separation and detection sensitivity of the three drugs. The improvement in resolution and sensitivity is attributed to the interaction with analytes or by changing the conductivity, viscosity, and ionic strength of the background electrolytes.[35] Each factor in this OAD was evaluated at three levels, including pH at 9.0, 9.5, or 10, buffer concentration at 15, 20, or 25 mmol/L, and $BMIMBF_4$ at 0%, 0.2%, or 0.4% (*v*/*v*). The OAD results for the separation of E, ME, PE and TPA used as internal standard substance (IS) are shown in Fig. 2. Figure 2*e* shows that the Rs of E, ME, and PE mixtures were markedly improved, and ECL intensities of

Fig. 1. Effect of electrophoretic buffer type on resolution and sensitivity. Peaks are denoterd by, 1: E, 2: ME, 3: PE. Labels are denoted by, a: Tris-HCl, b: $Na_2B_4O_7$, c: PBS; d: $Na_2B_4O_7$-PBS. Conditions: detection potential, 1.2 V; electrophoretic buffer, 20 mmol/L $Na_2B_4O_7$-PBS at pH 9.5; electrokinetic injection, 10 kV × 10 s; separation voltage, 10 kV; ECL detection solution, 5 mmol/L $Ru(bpy)_3^{2+}$ with 50 mmol/L PBS at pH 8.5.

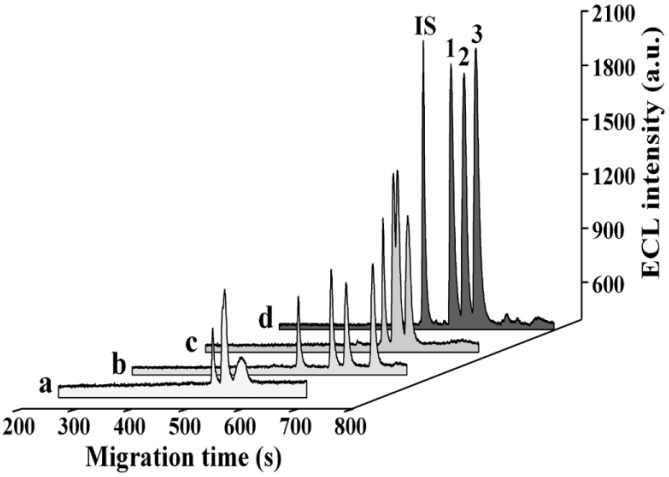


Fig. 2. The OAD CE-ECL electropherograms for the electrophoretic buffer. Other conditions are the same as in Fig. 1*d*.

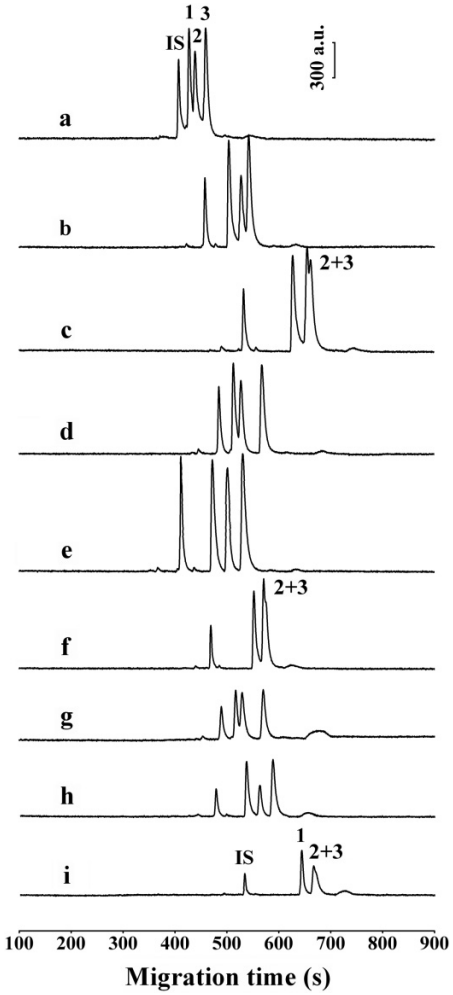


Table 1. The performance characteristics of the proposed method.

Analytes	Liner range (μmol/L)	Calibration curves				
		Slope	Intercept	*r*	LOD (mol/L)	LOQ (mol/L) in urine
E	0.2–100	11 338	16 981	0.9992	4.0×10^{-8}	5.3×10^{-7}
ME	0.5–150	10 502	–3 326	0.9994	6.5×10^{-8}	9.1×10^{-7}
PE	0.2–100	10 266	12 185	0.9994	4.6×10^{-8}	6.9×10^{-7}

Table 2. Study of the precision of the proposed method.

Analytes	RSD% for migration time of intraday ($n = 5$)		RSD % for area of intraday ($n = 5$)		RSD % for migration time of interday ($n = 15$)		RSD % for area of interday ($n = 15$)	
	External standard	Internal standard	External standard	Internal standard	External standard	Internal standard	External standard	Internal standard
E	0.6	0.1	3.5	2.2	1.3	0.4	4.9	2.7
ME	0.5	0.2	3.0	2.5	1.4	0.8	4.5	3.9
PE	0.8	0.2	3.1	2.4	1.3	0.6	5.4	3.7

three ephedra alkaloids were also increased (~3-fold) when 0.4% $BMIMBF_4$ was used in 20 mmol/L $Na_2B_4O_7$-PBS at pH 9.5. Under the optimum conditions, complete baseline separation within 10 min at a separation voltage of 10 kV could be obtained.

Effect of detection potential

ECL intensity is dependent on the rate of the light-emitting chemical reaction, which is in turn dependent on the potential applied to the electrode. The effect of the working potential on ECL responses in a potential range from 1.05 to 1.30 V was tested. The results showed that the ECL intensity for E, ME, and PE increased and reached maximum values at 1.20 V, and then decreased with the increasing detection potential from 1.05 to 1.30 V. Therefore, the optimum detection potential should be fixed at 1.20 V.

Effect of buffer pH in detection cell

The pH of buffer in detection cell also has a significant effect on the ECL response. The buffer pH range from 7.6 to 9.1 was examined. The results showed that the ECL intensity of the three analytes increased with the pH from 7.6 to 8.5, and then decreased. Thus, pH 8.5 was selected.

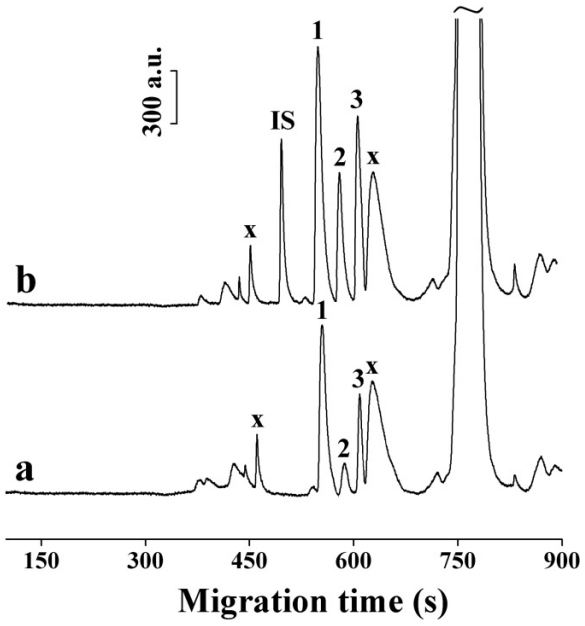
Effect of separation voltage

A study of the influence of the separation voltage on ECL intensity and Rs was carried out using the range 8 to 13 kV. ECL intensity increased as the separation voltage increased to 10 kV, and then decreased. Rs1 (E and ME) and Rs2 (ME and PE) decreased with increased the separation voltage, and Rs2 < 1.5 when the separation voltage was higher than 10 kV. Therefore, 10 kV was chosen.

Performance characteristics of the method

Under the optimized conditions, E, ME, PE and TPA used as IS were well separated. The typical electropherogram is shown in Fig. 2*e*. To evaluate the linearity of the established method, calibration curves were made by plotting peak area values against the analyte concentrations. The results obtained are listed in Table 1. It can be seen that the regression coefficients of the calibration curves are greater than 0.9992.

Fig. 3. Electropherograms of (*a*) TCM and (*b*) TCM spiked with 4.0×10^{-5} mol/L of E, 6.0×10^{-5} mol/L of ME, 5.0×10^{-5} mol/L of PE. Peaks are denoted by, 1: E, 2: ME, 3: PE, X: unknown compounds. Other conditions are the same as in Fig. 2*e*.



The limits of detection (LOD) in standard solution and the limits of quantitation (LOQ) in real samples were considered the minimum analyte concentrations yielding an S/N ratio equal to 3 and S/N ratio equal to 10, respectively. To reduce the irreproducibility associated with a complex sample matrix, sample injection volume, temperature, the properties of buffer and other factors, TPA was used as IS in this work. The ratios of the analyte peak (or migration time) to IS peak (or migration time) were used in the analysis.

The precision of the proposed method was evaluated in terms of repeatability and intermediate precision for the internal standard method and external standard method. The results are listed in Table 2. The repeatability was assessed on the same day by using five repetitive injections of a mixture standard solution of 5.0×10^{-7} mol/L of TPA, 4.0×10^{-6}

Can. J. Chem. Downloaded from www.nrcresearchpress.com by Renmin University of China on 09/02/12
For personal use only.

Can. J. Chem. Downloaded from www.nrcresearchpress.com by Renmin University of China on 09/02/12
For personal use only.

Table 3. Recoveries of three analytes in TCM at different spiking levels.

			RSD % of intraday		RSD % of interday	
Added (μmol/L)	Found (μmol/L)	Recovery (%)	External standard	Internal standard	External standard	Internal standard
E						
10	8.59	85.9	2.8	0.8	4.5	1.1
40	34.2	85.6	1.5	0.5	4.0	2.4
80	77.1	96.4	2.6	0.2	3.1	0.4
ME						
20	20.1	100.6	3.5	1.4	5.6	2.7
60	64.7	107.7	2.6	0.5	5.2	2.6
90	97.6	108.4	1.4	1.0	4.5	2.1
PE						
10	9.50	95.0	2.0	1.1	5.8	1.9
50	50.1	100.2	2.4	0.6	5.1	2.1
80	78.3	97.9	2.5	0.4	4.3	1.5

mol/L of E, 7.0×10^{-6} mol/L of ME, and 5.0×10^{-6} mol/L of PE. Intermediate precision was evaluated on three consecutive days with a similar procedure for repeatability evaluation. It can be seen in Table 2 that the precision of the internal standard method was better than that of external standard method.

Applications

The proposed CE-ECL method was applied to the determination of E, ME, and PE in a TCM, Xiao'er Qingre Zhike Koufuye. The preliminary experiments showed that satisfactory separation and detection can be achieved when samples were diluted 8-fold with pure water. The typical electropherograms of TCM, and TCM spiked with 1.0×10^{-5} mol/L of TPA, 4.0×10^{-5} mol/L of E, 6.0×10^{-5} mol/L of ME, and 5.0×10^{-5} mol/L of PE are illustrated in Figs. 3*a* and 3*b*, respectively. The content of the three ephedrines in TCM were determined to be 1.2×10^{-3} mol/L for E, 4.1×10^{-5} mol/L for ME, and 4.5×10^{-4} mol/L for PE. The recoveries of the three ephedrines in drugs were determined at three different spiked concentration levels, and the results are listed in Table 3. The RSDs for the measurement of peak areas were evaluated by the repeatability and intermediate precision for the internal standard method and the external standard method (also listed in Table 3).

The applicability was also examined by analyzing the three ephedrines in human urine. The urine was filtered through 0.22 μm cellulose acetate filters and then diluted 5-fold with pure water before CE-ECL analysis. The typical electropherograms of a blank urine sample from a healthy female person and also spiked with 2.0×10^{-6} mol/L of TPA, 1.0×10^{-5} mol/L of E, 1.2×10^{-5} mol/L of ME, and 1.0×10^{-5} mol/L of PE are illustrated in Figs. 4*a* and 4*b*, respectively. E, ME, PE, and TPA are not endogenous compounds, so they are not detected in the urine of healthy person and could be well separated and detected in spiked urine. Comparing with the published results in urine applications,[2,6] this CE-ECL method can realize good separation and sensitive detection for E, ME, and PE in human urine. The recoveries at three different spiked concentration levels (20, 200, and 400 μmol/L) were 101.5%–104.3% for E, 88.2%–101.3% for ME, and 97.6%–100.0% for PE, respectively. The RSDs of the peak area were less than 3.6%. The LOQs of E, ME, and PE in human

Fig. 4. Electropherograms of the (*a*) heathy human urine and (*b*) also spiked with 1.0×10^{-5} mol/L of E, 1.2×10^{-5} mol/L of ME, 1.0×10^{-5} mol/L of PE. Peaks are denoted by, 1: E, 2: ME, 3: PE, X: unknown compounds. Other conditions are the same as in Fig. 2*e*.

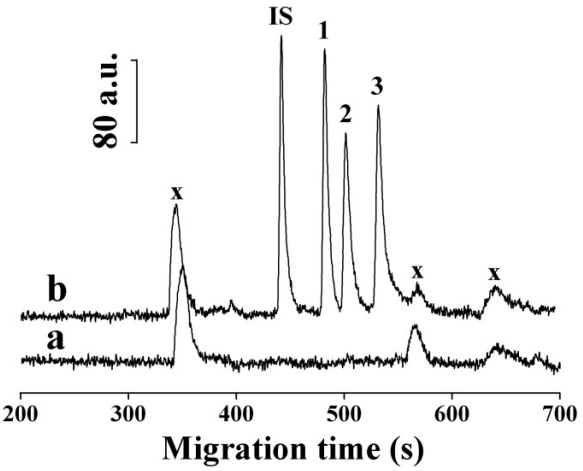
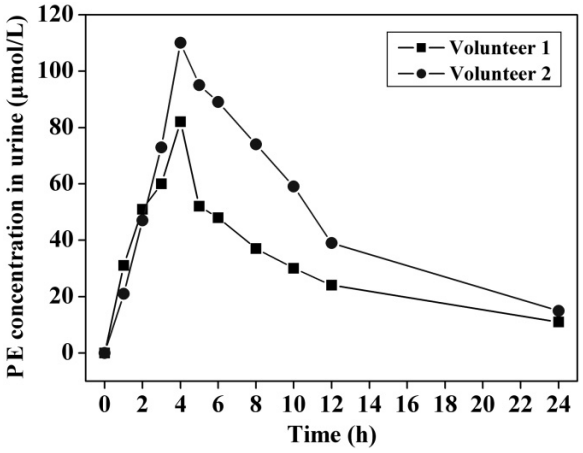


Fig. 5. PE concentration change in urine samples 0, 1, 2, 3, 4, 6, 8, 12, and 24 h after the ingestion of 90 mg of PE sustained release capsules to the volunteers. Other conditions are the same as in Fig. 2*e*.



urine were 5.3×10^{-7}, 9.1×10^{-7}, and 6.9×10^{-7} mol/L, respectively. These results indicated that the proposed method is accurate and reliable.

In the study of PE pharmacokinetics, two healthy female volunteers received an oral administration of 90 mg of PE sustained release capsules and were asked to drink sufficient and comparable amounts of water through the collection period. The urine samples were collected and analyzed immediately before the oral dose and again at 1, 2, 3, 4, 6, 8, 12 and 24 h after the oral dose. The results of the two volunteers are presented in the concentration time profile of Fig. 5. It can be seen that the maximal contents of PE in the urine samples from the two volunteers were achieved at about 4 h after receiving the oral dose and then subsequently decreased. The results also show that there is a difference in the content of PE in the urine of the two volunteers, which might be caused by metabolizability diversity between individuals.

Conclusions

This work proposes a simple, rapid, and sensitive method for the simultaneous determination of E, ME, and PE in TCM and human urine and the monitoring of pharmacokinetics for PE in the human body. Both separation efficiency and sensitivity can be improved by utilization of $BMIMBF_4$ as an additive in electrophoretic buffer. The use of TPA as IS improves the precision. The developed method has advantages of high separation efficiency, short analysis time, low sample consumption, simple operation, and high sensitivity. This method could be developed into a practical and valuable technique for the determination of ephedra alkaloids in clinical and biochemical analysis and pharmacokinetics study.

Acknowledgements

This work was supported by the National Natural Science Foundation of China (21075106), Henan Innovation Project for University Research Talents (2005126), and Natural Science Foundation of Henan Province of China (092300410122)

References

(1) van der Merwe, P. J.; Hendrikz, S. H. *J. Chromatogr. B Analyt. Technol. Biomed. Life Sci.* **1995**, *663* (1), 160. doi:10.1016/0378-4347(94)00429-9.

(2) Mateus-Avois, L.; Mangin, P.; Saugy, M. *J. Chromatogr. B Analyt. Technol. Biomed. Life Sci.* **2003**, *791* (1–2), 203.

(3) Sander, L. C.; Sharpless, K. E.; Satterfield, M. E.; Ihara, T.; Phinney, K. W.; Yen, J. H.; Wise, S. A.; Gay, M. L.; Lam, J. W.; McCooeye, M.; Gardner, G.; Fraser, C.; Sturgeon, R.; Roman, M. *Anal. Chem.* **2005**, *77* (10), 3101. doi:10.1021/ac0484530.

(4) Lam, J. H.; Gardner, G. J.; McCooeye, M.; Fraser, C. A.; Sturgeon, R. A. *Chromatographia*, **2005**, *383* (2), 268.

(5) International Olympic Committee. *List of prohibited classes of substances and prohibited methods*; Lausanne, Switzerland, 2001.

(6) Van Eenoo, P.; Delbeke, F. T.; Roels, K.; Backer, P. *J. Chromatogr. B Analyt. Technol. Biomed. Life Sci.* **2001**, *760* (2), 255. doi:10.1016/S0378-4347(01)00275-4.

(7) Lee, J. S.; Han, E. Y.; Lee, S. Y.; Kim, E. M.; Park, Y. H.; Lim, M. A.; Chung, H. S.; Park, H. S. *Forensic Sci. Int.* **2006**, *161* (2–3), 209. doi:10.1016/j.forsciint.2006.02.054.

(8) Okamura, N.; Miki, H.; Harada, T.; Yamashita, S.; Masaoka, Y.; Nakamoto, Y.; Tsuguma, M.; Yoshitomi, H.; Yagi, A. *J. Pharm. Biomed. Anal.* **1999**, *20* (1–2), 363. doi:10.1016/S0731-7085(99)00065-5.

(9) Ishida, M.; Abe, K.; Hashizume, M.; Kawamura, M. *Int. J. Pharm.* **2008**, *359* (1–2), 46. doi:10.1016/j.ijpharm.2008.03.034.

(10) Karakuş, S.; Küçükgüzel, İ.; Küçükgüzel, S. G. *J. Pharm. Biomed. Anal.* **2008**, *46* (2), 295. doi:10.1016/j.jpba.2007.10.018.

(11) Wang, X. W.; Zeng, S. *Curr. Pharm. Anal.* **2010**, *6* (1), 39. doi:10.2174/157341210790780221.

(12) Liu, Y. M.; Mei, L.; Yue, H. Y.; Shi, Y. M.; Liu, L. J. *Chromatographia*, **2010**, *72* (3–4), 337. doi:10.1365/s10337-010-1648-0.

(13) Phinney, K. W.; Ihara, T.; Sander, L. C. *J. Chromatogr. A*, **2005**, *1077* (1), 90. doi:10.1016/j.chroma.2005.04.068.

(14) Li, F.; Ding, Z. T.; Cao, Q. E. *Electrophoresis*, **2008**, *29* (3), 658. doi:10.1002/elps.200700334.

(15) Xie, J. P.; Zhang, J. Y.; Liu, J. Q.; Tian, J. N.; Chen, X. G.; Hu, Z. D. *J. Sep. Sci.* **2004**, *27* (14), 1211. doi:10.1002/jssc.200401756.

(16) Dong, Y. M.; Chen, Y. L.; Chen, X. G.; Hu, Z. D. *Biomed. Chromatogr.* **2006**, *20* (11), 1150. doi:10.1002/bmc.663.

(17) Yin, X. B.; Qiu, H. B.; Sun, X. H.; Yan, J. L.; Liu, J. F.; Wang, E. K. *Anal. Chem.* **2004**, *76* (13), 3846. doi:10.1021/ac049743j.

(18) Richter, M. M. *Chem. Rev.* **2004**, *104* (6), 3003. doi:10.1021/cr020373d.

(19) Li, T.; Li, B. L.; Dong, S. J.; Wang, E. K. *Chemistry*, **2007**, *13* (30), 8516. doi:10.1002/chem.200700275.

(20) Guo, L. H.; Qiu, B.; Xue, L. L.; Chen, G. N. *Electrophoresis*, **2009**, *30* (13), 2390. doi:10.1002/elps.200800715.

(21) Xu, Y. H.; Fang, L. Y.; Wang, E. K. *Electrophoresis*, **2009**, *30* (2), 365. doi:10.1002/elps.200800187.

(22) Hsieh, Y. C.; Whang, C. W. *J. Chromatogr. A*, **2006**, *1122* (1–2), 279. doi:10.1016/j.chroma.2006.05.078.

(23) Huang, Y.; Pan, W.; Guo, M. L.; Yao, S. Z. *J. Chromatogr. A*, **2007**, *1154* (1–2), 373. doi:10.1016/j.chroma.2007.02.029.

(24) Yuan, B. Q.; Huang, J. S.; Sun, J. Y.; You, T. Y. *Electrophoresis*, **2009**, *30* (3), 479. doi:10.1002/elps.200800253.

(25) Marsh, K. N.; Boxall, J. A.; Lichtenthaler, R. *Fluid Phase Equilib.* **2004**, *219* (1), 93. doi:10.1016/j.fluid.2004.02.003.

(26) Qi, S. D.; Cui, S. Y.; Chen, X. G.; Hu, Z. D. *J. Chromatogr. A*, **2004**, *1059* (1–2), 191. doi:10.1016/j.chroma.2004.09.090.

(27) Ding, J.; Welton, T.; Armstrong, D. W. *Anal. Chem.* **2004**, *76* (22), 6819. doi:10.1021/ac049144c.

(28) Berthod, A.; Ruiz-Angel, M. J.; Huguet, S. *Anal. Chem.* **2005**, *77* (13), 4071. doi:10.1021/ac050304+.

(29) Laremore, T. N.; Zhang, F. M.; Linhardt, R. J. *Anal. Chem.* **2007**, *79* (4), 1604. doi:10.1021/ac061688m.

(30) Qin, W. D.; Wei, H. P.; Li, S. F. Y. *J. Chromatogr. A*, **2003**, *985* (1–2), 447. doi:10.1016/S0021-9673(02)01844-7.

(31) Bao, Y.; Lantz, A. W.; Crank, J. A.; Huang, J. M.; Armstrong, D. W. *Electrophoresis*, **2008**, *29* (12), 2587. doi:10.1002/elps.200700719.

(32) Wu, X. P.; Wei, W. P.; Su, Q. M.; Xu, L. J.; Chen, G. N. *Electrophoresis*, **2008**, *29* (11), 2356. doi:10.1002/elps.200700746.

(33) Shamsi, S. A.; Danielson, N. D. *J. Sep. Sci.* **2007**, *30* (11), 1729. doi:10.1002/jssc.200700136.

(34) Guan, F. Y.; Wu, H. F.; Luo, Y. *J. Chromatogr. A*, **1996**, *719* (2), 427. doi:10.1016/0021-9673(95)00735-0.

(35) López-Pastor, M.; Simonet, B. M.; Lendl, B.; Valcárcel, M. *Electrophoresis*, **2008**, *29* (1), 94. doi:10.1002/elps.200700645.

Can. J. Chem. Downloaded from www.nrcresearchpress.com by Renmin University of China on 09/02/12
For personal use only.

Anharmonic effect of the decomposition reaction of the CF_3CCl_2O radical

Qian Li, Wenwen Xia, Li Yao, and Ying Shao

Can. J. Chem. Downloaded from www.nrcresearchpress.com by Renmin University of China on 09/02/12
For personal use only.

Abstract: The rate constant of the unimolecular decomposition reaction of the CF_3CCl_2O radical was calculated by using the method proposed by Yao and Lin (YL method). Two important channels of decomposition occurring via C–C and C–Cl bond scission were investigated. The results show that C–Cl bond scission is the dominant channel during the decomposition of the CF_3CCl_2O radical. Especially, the reasonable anharmonic effect on the decomposition reaction was investigated. The results show that the harmonic rate constants are higher than those of the anharmonic case in both microcanonical and canonical systems. The anharmonic effect is more evident with increasing energy.

Key words: anharmonic effect, unimolecular reaction, rate constant, YL method.

Résumé : Faisant appel à la méthode proposée par Yao et Lin (méthode YL), on a calculé la constante de vitesse de la réaction de décomposition unimoléculaire du radical CF_3CCl_2O. On a étudié deux voies importantes de décomposition se produisant par le biais de scissions des liaisons C–C et C–Cl. Les résultats montrent que la scission de la liaison C–Cl est la voie dominante durant la décomposition du radical CF_3CCl_2O. On a étudié particulièrement l'effet anharmonique raisonnable sur la réaction de décomposition. Les résultats montrent que les constantes de vitesse harmoniques sont plus élevées que celles du cas anharmonique tant dans le système microcanonique que dans le système canonique. L'effet anharmonique est plus évident avec une augmentation de l'énergie.

Mots-clés : effet anharmonique, réaction unimoléculaire, constante de réaction, méthode Yao et Lin (méthode YL).

[Traduit par la Rédaction]

Introduction

Many studies have indicated that the chemical and physical properties of chlorofluorocarbons (CFCs) along with their thermodynamic and transport properties made them suited for several industrial applications, but the stability of fully halogenated CFCs made them dangerous to the stratospheric ozone layer. As early as 1974, many scientists recognized that the release of CFCs into the stratosphere through a series of catalytic reactions leads to ozone-layer depletion, increasing global warming.[1–4] In 1987, with the threat of CFCs becoming more and more serious, the Montreal Protocol was developed to prohibit the production and use of CFCs. At the same time, there was an urgent need to develop acceptable substitutes that had similar properties to CFCs except for the environmental behaviors such as depletion of the ozone layer and global warming. After that, hydrofluorocarbons (HFCs) and hydrochlorofluorocarbons (HCFCs) were found to be substitutes for CFCs in refrigeration and air-conditioning systems.[5,6] Unlike CFCs, HFCs and HCFCs break down readily and react with the OH radical in the lower atmosphere, resulting in much shorter atmospheric lifetimes and a reduced potential to contribute to ozone depletion and to global warming in comparison with the CFCs.[7] One of the most widely used HCFCs is 2,2-dichloro-1,1,1-trifluoroethane (HCFC-123). It is not only used as a gaseous fire extinguisher but also as a metal and electronics cleaning agent. Although HCFC-123 contains chlorine, which is dangerous to the stratospheric ozone layer, its hydrogen-containing molecule decomposes primarily in the lower atmosphere before it can reach the ozone layer. Because the chlorine is dissipated at a lower altitude, HCFC-123 has relatively short atmospheric lifetimes and much lower ozone depletion potentials than CFCs. Thus, the haloalkoxy radicals formed by HCFC-123 in the atmosphere play an important role in the degradation mechanism of organic vapors in the troposphere.[8,9] Recently, considerable theoretical studies have been performed on similar haloalkoxy radicals.[10–14] Singh et al.[15] calculated the harmonic rate constant for C–C and C–Cl bond scission in CF_3CCl_2O decomposition for the canonical case at 298 K and 1 atm (1 atm = 101.325 kPa) pressure, obtaining the values $k_{C–C} = 6.7 \times 10^6$ s^{-1} and $k_{C–C} = 1.1 \times 10^8$ s^{-1}. The theoretical work suggested that C–Cl bond scission was favorable for the CF_3CCl_2O radical decomposition.[15] A literature survey indicated that there is no experimental data available on the CF_3CCl_2O radical.

On the other hand, many chemists had observed that the anharmonic effect played an important role in molecular systems, especially in those of molecules and clusters with highly flexible transition states.[16] In 1962, Schlag and Sandsmark[17]

Received 29 June 2011. Accepted 8 September 2011. Published at www.nrcresearchpress.com/cjc on 12 December 2011.

Q. Li, W. Xia, L. Yao, and Y. Shao. Institute of Computational Physics, Department of Physics, Dalian Maritime University, Dalian 116026, P. R. China.

Corresponding authors: Li Yao (e-mail: yaoli@dlmu.edu.cn) and Ying Shao (yshao@dlmu.edu.cn).

Can. J. Chem. Downloaded from www.nrcresearchpress.com by Renmin University of China on 09/02/12
For personal use only.

Fig. 1. The optimized geometries of the decomposition of CF_3CCl_2O at the B3LYP/6–311++G** level.

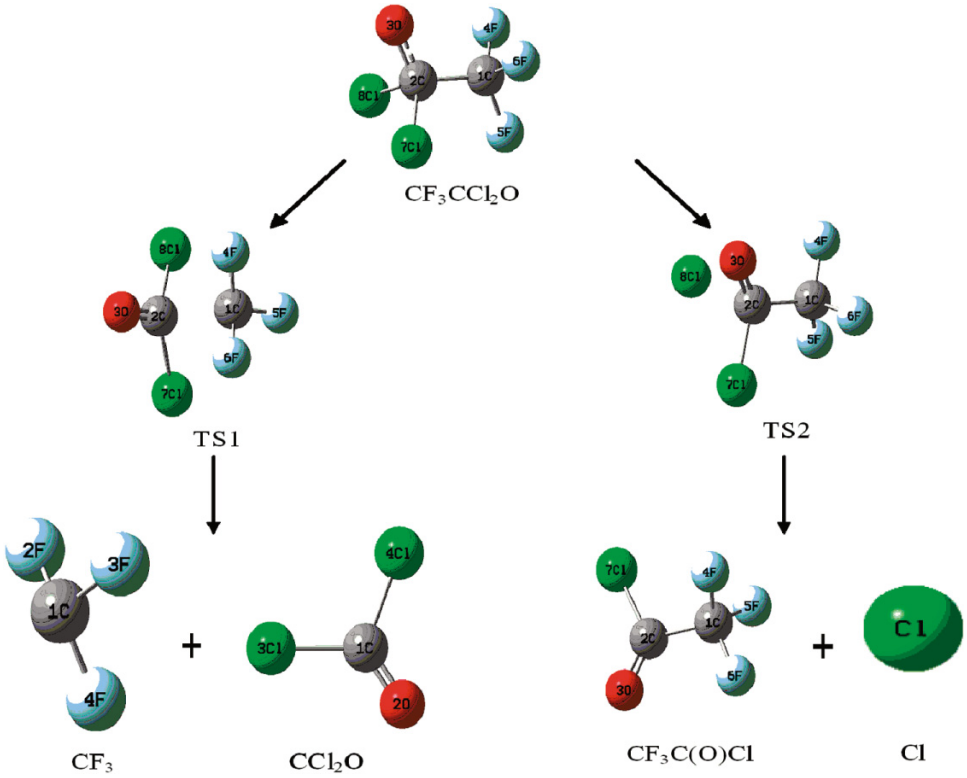


Table 1. Structural parameters of the reactant and transition states (TSs) involved in CF_3CCl_2O decomposition at the B3LYP/6–311++G** level.

Parameter	CF_3CCl_2O	TS1	TS2
Bond length (Å)			
R(1C–2C)	1.567	1.967	1.567
R(1C–4F)	1.336	1.310	1.332
R(1C–5F)	1.336	1.312	1.333
R(1C–6F)	1.340	1.310	1.343
R(2C–3O)	1.310	1.210	1.248
R(2C–7Cl)	1.805	1.820	1.782
R(2C–8Cl)	1.841	1.820	2.084
Bond angle (°)			
A(4F–1C–5F)	108.7	111.8	109.2
A(4F–1C–6F)	108.3	111.9	108.4
A(4F–2C–7Cl)	108.9	100.2	111.0
A(4F–2C–8Cl)	108.6	100.2	103.6
A(3O–2C–7Cl)	113.9	120.5	119.3
A(3O–2C–8Cl)	99.4	120.5	91.8

discovered that anharmonicity corrections may be significant in practice. Then, Haarhoff[18] considered the anharmonic corrections about the density of vibrational energy levels for a system of simple Morse oscillators. At present, many chemists have also observed that anharmonic effects are quite significant in the dissociation of clusters and molecular systems.[19–23] It is well-known that the characteristic features of the anharmonic effect contain an increase in the bond length and in the distance of bond dissociation and a decrease in vibrational bond-stretching frequencies. Several authors laid stress on the requirement for the anharmonic correction to previous reaction rate theories.[24–26] For this reason, using experimental thermodynamic data, Troe[27] presented a simple empirical method for generating anharmonic vibrational densities of states. Recently, a new method (Yao and Lin, YL method) that could carry out the first principle calculations about the rate constants of molecular reactions within the framework of transition-state theory has been proposed.[28] With this method, the anharmonic effect that is on the dissociation of molecular reaction was examined. The results mentioned above suggested that the YL method was appropriate for calculating rate constants of the unimolecular reaction and for investigating the anharmonic effect of the rate constant.

The purpose of this paper is to calculate the harmonic rate constants for the unimolecular decomposition of the CF_3CCl_2O radical and to investigate the anharmonic effect on this reaction. Therefore, we applied the YL method to examine the anharmonic effect on the unimolecular decomposition of the CF_3CCl_2O radical. The computational methods are described in detail in the Computational methods section. The Results and discussion section provides numerical results and detailed discussions. Finally, concluding remarks and a summary of this work are presented in the Conclusions.

Computational methods

Ab initio calculations

The two unimolecular decomposition channels of the CF_3CCl_2O radical are investigated (C–C and C–Cl bond scission) as given as follows:

$$CF_3CCl_2O \rightarrow CF_3 + C(O)Cl_2 \qquad (C-C \text{ bond scission})$$

Table 2. Parameters used in the rate constant calculations obtained from B3LYP/6–311++G** calculations.

Parameter	CF_3CCl_2O	TS1	TS2
Zero-point energy (B3LYP) (Hartree)	0.02418	0.02275	0.02347
Imaginary frequency	—	328.6*i*	350.3*i*
Energy (B3LYP) (Hartree)	–1371.47009	–1371.46055	–1371.46749
Single-point energy (CCSD(T)) (Hartree)	–1369.40440	–1369.38739	–1369.39834
Barrier (kcal/mol)		10.67	3.83

Note: TS1 and TS2 are the transition states corresponding to channels 1 and 2, respectively. The barriers are calculated at the CCSD(T)/6–311++G** level. 1 cal = 4.184 J).

Can. J. Chem. Downloaded from www.nrcresearchpress.com by Renmin University of China on 09/02/12
For personal use only.

$$CF_3CCl_2O \rightarrow CF_3C(O)Cl + Cl \qquad (C-Cl \text{ bond scission})$$

In the two reactions, the geometries of the reactant and transition states have been optimized using the B3LYP method with the 6–311++G** basis set. The vibrational harmonic and anharmonic frequencies, which were calculated at the same level, are used for characterization of stationary points, zero-point-energy (ZPE) corrections, and for the calculations of reaction rate constants using transition-state and Rice–Ramsperger–Kassel–Marcus (RRKM) theory. To obtain more accurate and reliable data, the single-point energies were recalculated by employing the CCSD(T) method with the 6–311++G** basis set. To confirm that the transition state connected smoothly to the reactant and the products, the transition state was subjected to an intrinsic reaction coordinate (IRC) with the same level of theory at which the optimization and frequency calculations were performed. The frequencies, energies of reactant, and transition-state (TS) structures in this paper were all calculated at 298 K and 1 atm pressure (room temperature). The Gaussian 03 program[29] was applied for all ab initio calculations.

RRKM theory

According to the RRKM theory, for the microcanonical system, the rate constant $k(E)$ for the unimolecular reaction can be expressed as[30]

$$[1] \qquad k(E) = \frac{\sigma}{h}\frac{W^{\neq}(E-E^{\neq})}{\rho(E)}$$

where σ is the symmetry factor (here we set $\sigma = 1$), h is Planck's constant, $\rho(E)$ represents the density of the state of the reactant, $W^{\neq}(E)$ stands for the total number of states for the transition state, and E and $E^{\neq}$ are the total energy and the activation energy in the microcanonical case, respectively.

In general, the definition of $W(E)$ and $\rho(E)$ can be expressed as[31–33]

$$[2] \qquad W(E) = \sum_i H(E-E_i)$$

$$[3] \qquad \rho(E) = \frac{\mathrm{d}W(E)}{\mathrm{d}E}$$

where $H(E - E_i)$ denotes Heaviside function and E_i are energy levels. $W(E)$ can be obtained by direct counting of those states that are less than or equal to E. The CF_3CCl_2O radical has 18 vibrational modes ($3N - 6$, N is the number of atoms in the reaction) for the reactants and 17 vibrational modes for TSs. The imaginary frequencies are excluded. The anharmonic effect was added in all the vibrational modes in the anharmonic calculations. The Laplace transformation was utilized for $W(E)$ and $\rho(E)$:[31–33]

$$[4] \qquad \int_0^{\infty} \mathrm{d}E e^{-\beta E} W(E) = \frac{Q(\beta)}{\beta} = L[W(E)]$$

$$[5] \qquad \int_0^{\infty} \mathrm{d}E e^{-\beta E} \rho(E) = Q(\beta) = L[\rho(E)]$$

where $\beta = 1/kT$, k is Boltzmann's constant, T is the temperature of the system, and $Q(\beta)$ is the partition function of the system. That is, when $Q(\beta)$ is obtained, $W(E)$ and $\rho(E)$ can be determined by eqs. [4] and [5] by applying the inverse Laplace transformation. The details can be found in ref. 28.

For a canonical system, the rate constant $k(T)$ for a unimolecular reaction is given by[31,33–35]

$$[6] \qquad k(T) = \frac{kT}{h}\frac{Q^{\neq}(T)}{Q(T)}e^{-\frac{E^{\neq}}{kT}}$$

where $Q(T)$ and $Q^{\neq}(T)$ are the partition functions of the reactant and the activated complex, respectively. In this case, we obtain

$$[7] \qquad Q^{\neq}(T) = \prod_i^{N-1} q_i^{\neq}(T)$$

$$[8] \qquad Q(T) = \prod_i^{N} q_i(T)$$

where N is the number of vibrational modes of the reactant and $q_i^{\neq}(T)$ and $q_i(T)$ represent the vibrational partition functions of the activated complex and the reactant, respectively.

According to the above discussion, we ascertain that the partition function plays a very important role in calculating the total number of states, the density of states, and the rate constant. To calculate the partition function of both microcanonical and canonical cases and to investigate the anharmonic effect on an unimolecular reaction, the Morse oscillator (MO) is taken as a simple form. For the MO we have

$$[9] \qquad E_{n_i} = (n_i + 1/2)\hbar\omega_i - x_i(n_i + 1/2)\hbar\omega_i$$

where n_i is the vibrational quantum number of the vibrational mode and ω_i is the frequency of the ith vibrational mode. Actually, the Morse and harmonic models give similar results at low energy, just like the equilibrium position of the stretching

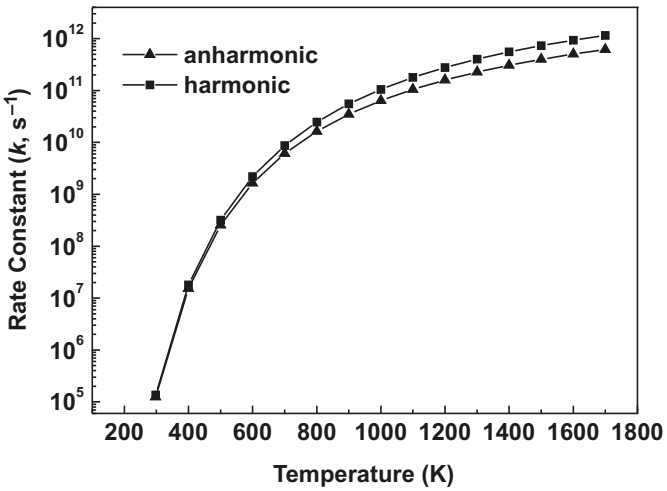
Can. J. Chem. Downloaded from www.nrcresearchpress.com by Renmin University of China on 09/02/12
For personal use only.

Table 3. The C–C scission rate constants of the CF_3CCl_2O radical at different temperatures for the canonical system.

	Temperature (K)									
Parameter	200	298	400	500	600	700	800	1000	1500	2000
Corresponding energy (kcal/mol)	1.38	3.13	5.45	8.05	10.89	13.90	17.02	23.51	40.44	57.83
Corresponding energy (cm^{-1})	483	1095	1906	2815	3809	4862	6016	8223	14144	20226
Anharmonic rate constant (l/s)	12.41	1.24×10^{5}	1.54×10^{7}	2.55×10^{8}	1.64×10^{9}	6.11×10^{9}	1.63×10^{10}	6.39×10^{10}	3.97×10^{11}	1.02×10^{12}
Harmonic rate constant (l/s)	12.87	1.36×10^{5}	1.80×10^{7}	3.19×10^{8}	2.19×10^{9}	8.72×10^{9}	2.46×10^{10}	1.05×10^{11}	7.33×10^{11}	1.93×10^{12}

Note: 1 cal = 4.184 J.

Fig. 2. The canonical rate constants for the C–C scission. The rate constant unit is s^{-1}.



bond. We can use the Morse model to simulate all the degrees of freedom, including nonstretching and stretching bonds of this reaction. x_i is the MO parameter, which is a measure of the deviation of the potential from the harmonic case. It is related to the dissociation energy and the energy of the fundamental transition. For $x_i = 0$, the anharmonic potential is reduced to the harmonic case. It can be expressed as $x_i = \hbar\omega_i/4D_{ie}$, where D_{ie} is the well depth of the MO, and the maximum of n_i is given by $n_i(m) = \frac{1}{2x_i} - \frac{1}{2}$. In this case, it is known that the anharmonic effect has two features: one is that the energy spacings are not equal and the other is that there is a maximum quantum number ($n_i(m)$) in the MO. In this paper, we shall discuss the anharmonic effect of the dissociation rate constant for the unimolecular decomposition reaction of the CF_3CCl_2O radical.

Results and discussion

For the unimolecular decomposition reaction of the CF_3CCl_2O radical, the optimized structure of the reactants, transition states, and products are illustrated in Fig. 1. Corresponding to Fig. 1, the geometric parameters are recorded in Table 1, from which it can be seen that the elongation of the C–C bond is found to be changed from 1.567 to 1.967 Å, together with a decrease in C–O bond distance from 1.309 to 1.210 Å. Similarly, the elongation of the C–Cl bond is found to be from 1.841 to 2.084 Å, together with a decrease in C–O bond distance from 1.309 to 1.247 Å. The information is obtained by way of employing the ab initio calculation of Gaussian 03 at the B3LYP/6–311++G** level. The energetic parameters of the reactant and the transition states calculated are shown in Table 2. From Table 2, the barrier height of the title reaction for channels 1 and 2 are 5.09 and 1.19 kcal/mol (1 cal = 4.184 J), respectively, with ZPE corrected. To obtain higher accuracy and reliability, we recomputed the single-point energies at the CCSD(T)/6–311++G** level, then got the values of the energy barriers as 10.67 and 3.83 kcal/mol. The results are different from the values given in ref. 15 because the optimized geometries of the reactants, transition states, and products used a different method and levels in ref. 15.

Can. J. Chem. Downloaded from www.nrcresearchpress.com by Renmin University of China on 09/02/12
For personal use only.

Table 4. The C–C scission rate constants of the CF_3CCl_2O radicals at different energies for the microcanonical system.

	Total energy (cm^{-1})									
Parameter	3809	4862	6016	7075	8223	9384	10811	11748	12944	14144
Corresponding total energy (kcal/mol)	10.89	13.90	17.02	20.23	23.51	26.83	30.19	33.59	37.01	40.44
Anharmonic $W(E)$ of TS	1.72	3.24×10^{3}	2.39×10^{5}	6.20×10^{6}	9.07×10^{7}	9.02×10^{8}	6.83×10^{9}	4.21×10^{10}	2.18×10^{11}	9.80×10^{11}
Anharmonic $\rho(E)$ of reactant ($1/cm^{-1}$)	4.60×10^{4}	4.45×10^{5}	3.46×10^{6}	2.24×10^{7}	1.24×10^{8}	5.95×10^{8}	2.53×10^{9}	9.74×10^{9}	3.40×10^{10}	1.09×10^{11}
Anharmonic rate constant (1/s)	1.12×10^{6}	2.18×10^{8}	2.07×10^{9}	8.28×10^{9}	2.19×10^{10}	4.54×10^{10}	8.08×10^{10}	1.30×10^{11}	1.92×10^{11}	2.09×10^{11}
Harmonic $W(E)$ of TS	1.86	2.35×10^{3}	1.50×10^{5}	3.59×10^{6}	4.96×10^{7}	4.70×10^{8}	3.39×10^{9}	1.20×10^{10}	9.92×10^{10}	4.27×10^{11}
Harmonic $\rho(E)$ of reactant ($1/cm^{-1}$)	1.92×10^{4}	1.66×10^{5}	1.16×10^{6}	6.85×10^{6}	3.48×10^{7}	1.55×10^{8}	6.14×10^{8}	2.22×10^{9}	7.37×10^{9}	2.26×10^{10}
Harmonic rate constant (1/s)	2.91×10^{6}	4.25×10^{8}	3.86×10^{9}	1.57×10^{10}	4.27×10^{10}	9.11×10^{10}	1.66×10^{11}	2.70×10^{11}	4.04×10^{11}	5.67×10^{11}

Note: TS, transition state; $\rho(E)$, the density of the state of the reactant; $W(E)$, total number of states for TS. 1 cal = 4.184 J.

Fig. 3. The microcanonical rate constants for the C–C scission. The rate constant unit is s^{-1}.

C–C bond scission

For the canonical system, the harmonic and anharmonic rate constants calculated by the YL method are presented in Table 3, with temperatures ranging from 200 to 2000 K. Corresponding to Table 3, the rate constants are also plotted in Fig. 2. From Table 3, the calculated harmonic rate constant is 1.36×10^5 s^{-1} at the 298 K. The result is different from the value given in ref. 15 because of the energy barrier we obtained differed from that given in ref. 15 In our work, the reactants, TSs, and products of the title reaction were optimized using the B3LYP method with the 6–311++G** basis set, and the single-point energies were recalculated by employing the CCSD(T) method with the 6–311++G** basis set with ZPE (calculated at the B3LYP/6–311++G** level) corrected. In Singh et al.'s[15] theoretical work, the reactants, TSs, and products of the CF_3CCl_2O radical decomposition were optimized at the B3LYP/6–311G(d,p) level, and the energy barrier was calculated using the G2M(CC,MP2) method. Therefore, we obtained the energy barrier of 10.67kcal/mol, whereas the value given in ref. 15 was 8.6 kcal/mol. On the other hand, it is clear that both the harmonic and anharmonic rate constants increase with increasing temperature. With the temperature increasing from 200 to 2000 K, the harmonic rate constant increased from 12.87×10^{12} to 1.93×10^{12} s^{-1}, whereas the anharmonic rate constant was in the range of 12.41×10^{12} to 1.02×10^{12} s^{-1}. The harmonic rate constants are higher than the anharmonic ones at all temperatures. When the temperature is 298 K, the anharmonic rate constant (1.24×10^5 s^{-1}) is 8.8% lower than the harmonic rate constant (1.36×10^5 s^{-1}), whereas the anharmonic rate constant (1.02×10^{12} s^{-1}) is 47.2% lower than the harmonic rate constant (1.93×10^{12} s^{-1}) at 2000 K. We can draw the conclusion that with increasing temperature the difference between the two cases is significant. In other words, the anharmonic effect becomes more significant with increasing temperature in the canonical system. It is worth noting in Table 3 that the first four energies are all lower than the calculated activation energy of 10.67 kcal/mol in this work. Hence, we had to calculate the rate constant in the microcanonical system at higher energy.

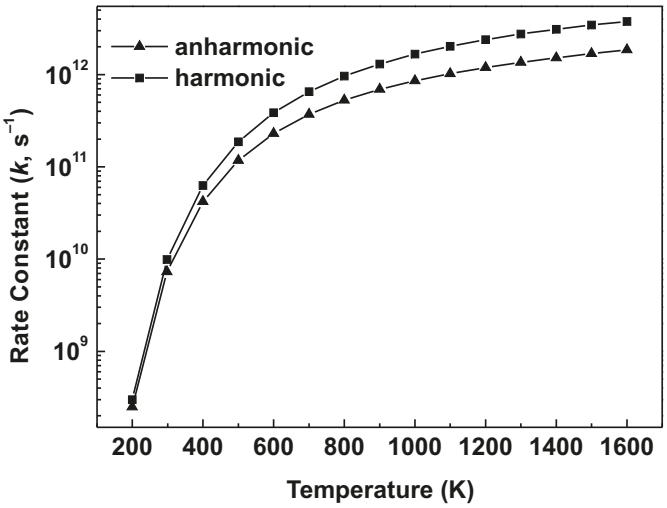
Can. J. Chem. Downloaded from www.nrcresearchpress.com by Renmin University of China on 09/02/12
For personal use only.

Table 5. The C–Cl scission rate constants of the CF_3CCl_2O radical at different temperatures for the canonical system.

	Temperature (K)									
Parameter	200	298	400	500	600	700	800	1000	1500	2000
Corresponding energy (kcal/mol)	1.38	3.13	5.45	8.05	10.89	13.90	17.02	23.51	40.44	57.83
Corresponding energy (cm^{-1})	483	1095	1906	2815	3809	4862	6016	8223	14144	20226
Anharmonic rate constant (1/s)	2.50×10^{8}	7.29×10^{9}	4.21×10^{10}	1.17×10^{11}	2.30×10^{11}	3.71×10^{11}	5.28×10^{11}	8.59×10^{11}	1.69×10^{12}	2.62×10^{12}
Harmonic rate constant (1/s)	2.99×10^{8}	9.89×10^{9}	6.29×10^{10}	1.87×10^{11}	3.88×10^{11}	6.53×10^{11}	9.64×10^{11}	1.66×10^{12}	3.44×10^{12}	4.95×10^{12}

Note: 1 cal = 4.184 J.

Fig. 4. The canonical rate constants for the C–Cl scission. The rate constant unit is s^{-1}.



To calculate the energy corresponding to the temperatures listed in Table 3, we employed the relation between the total energy of a microcanonical system and the temperature of a canonical system by

$$[10] \qquad E = -\left(\frac{\partial \ln Q}{\partial \beta}\right)$$

The energy in the microcanonical system can be obtained with eq. [10].

The total energies are 3 809, 4 862, 6 016, 7 075, 8 223, 9 384, 10 811, 11 748, 12 944, and 14 144 cm^{-1}, corresponding to the temperatures of 600, 700, 800, 900, 1000, 1100, 1200, 1300, 1400, and 1500 K. Table 4 shows the harmonic and anharmonic total number of states, density of states, and rate constants for channel 1. The rate constants with respect to the microcanonical total energies are also illustrated in Fig. 3.

From Table 4 and Fig. 3, we can see that for the microcanonical system the harmonic and anharmonic rate constants increase with increasing total energy. With the energy increasing from 3 809 to 14 144 cm^{-1}, the harmonic rate constant increases from 2.91×10^6 to 5.67×10^{11} s^{-1}, whereas the anharmonic rate constant is in the range of 1.12×10^6 to 2.09×10^{11} s^{-1}. The harmonic rate constants are higher than the anharmonic ones at all ranges of energy. When the total energy is 3809 cm^{-1}, the anharmonic rate constant (1.12×10^6 s^{-1}) is 61.5% lower than the harmonic rate constant (2.91×10^6 s^{-1}), whereas the anharmonic rate constant (2.09×10^{11} s^{-1}) is 65.0% lower than the harmonic rate constant (5.67×10^{11} s^{-1}) at a total energy of 14 144 cm^{-1}. It can be seen that, although the anharmonic effect is weak at low energy, it is obvious at higher energies. That is to say, with the increment of total energy, the anharmonic effect becomes more significant in the microcanonical system. Moreover, as seen from Tables 3 and 4, when the total energy is 14 144 cm^{-1}, the anharmonic rate constant (2.09×10^{11} s^{-1}) is 65.0% lower than the harmonic rate constant (5.67×10^{11} s^{-1}) for the microcanonical case, whereas the anharmonic rate constant (3.97×10^{11} s^{-1}) is 45.8% lower than the harmonic rate constant (7.33×10^{11} s^{-1}) for the canonical case. Thus,

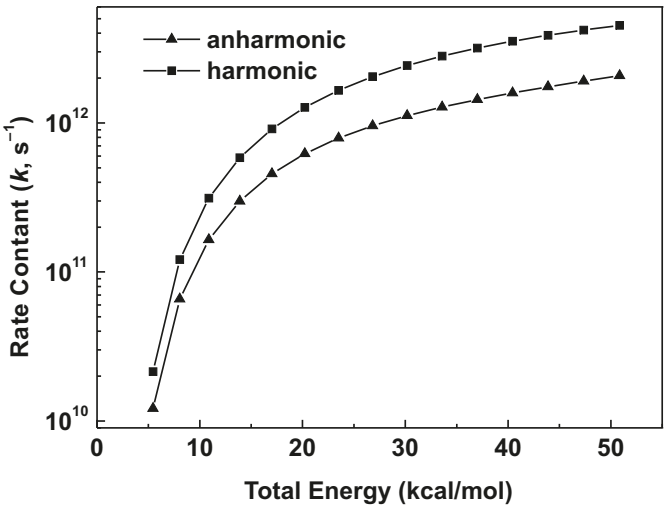
Can. J. Chem. Downloaded from www.nrcresearchpress.com by Renmin University of China on 09/02/12
For personal use only.

Table 6. The C–Cl scission rate constants of the CF_3CCl_2O radicals at different energies for the microcanonical system.

	Total energy (cm^{-1})								
Parameter	3 809	4 862	6 016	7 075	8 223	9 384	10 811	12 944	14 144
Corresponding total energy (kcal/mol)	10.89	13.90	17.02	20.23	23.51	26.83	30.19	37.01	40.44
Anharmonic $W(E)$ of TS	2.52×10^{5}	4.43×10^{6}	5.25×10^{7}	4.65×10^{8}	3.27×10^{9}	1.90×10^{10}	9.45×10^{10}	1.63×10^{12}	5.79×10^{12}
Anharmonic $\rho(E)$ of reactant ($1/cm^{-1}$)	4.60×10^{4}	4.45×10^{5}	3.46×10^{6}	2.24×10^{7}	1.24×10^{8}	5.95×10^{8}	2.53×10^{9}	3.40×10^{10}	1.09×10^{11}
Anharmonic rate constant (1/s)	1.64×10^{11}	2.99×10^{11}	4.55×10^{11}	6.22×10^{11}	7.91×10^{11}	9.56×10^{11}	1.12×10^{12}	1.43×10^{12}	1.59×10^{12}
Harmonic $W(E)$ of TS	2.00×10^{5}	3.23×10^{6}	3.53×10^{7}	2.91×10^{8}	1.92×10^{9}	1.05×10^{10}	4.98×10^{10}	2.08×10^{11}	7.81×10^{11}	2.66×10^{11}
Harmonic $\rho(E)$ of reactant ($1/cm^{-1}$)	1.92×10^{4}	1.66×10^{5}	1.16×10^{6}	6.85×10^{6}	3.48×10^{7}	1.55×10^{8}	6.14×10^{8}	2.22×10^{9}	7.37×10^{9}	2.26×10^{10}
Harmonic rate constant (1/s)	3.13×10^{11}	5.85×10^{11}	9.11×10^{11}	1.27×10^{12}	1.65×10^{12}	2.04×10^{12}	2.43×10^{12}	2.81×10^{12}	3.18×10^{12}	3.53×10^{12}

Note: TS, transition state; $\rho(E)$, the density of the state of the reactant; $W(E)$, total number of states for TS. 1 cal = 4.184 J.

Fig. 5. The microcanonical rate constants for the C–Cl scission. The rate constant unit is s^{-1}.



we can conclude that the rate constant is sensitive to the microcanonical system, but insensitive to the canonical system. That is, compared with the canonical case, the anharmonic effect in the microcanonical case is more obvious.

C–Cl bond scission

Similarly, for channel 2, the harmonic and anharmonic rate constants calculated for the canonical system using the YL method are all presented in Table 5, with the temperature ranging from 200 to 2000 K. Corresponding to Table 5, the rate constants are also plotted in Fig. 4. It is worth mentioning that from Table 5, when the temperature is lower than 298 K, the energies are all lower than the calculated activation energy of 3.83 kcal/mol. Hence, we have to calculate the rate constant in the microcanonical system at higher energy. Table 6 shows the the harmonic and anharmonic rate constants for the microcanonical case. Corresponding to Table 6, these data are illustrated in Fig. 5.

For the C–Cl bond scission reaction, from the results of Table 5 and at 298 K, the corresponding harmonic rate constant is 9.89×10^{9} s^{-1}. The result is different from the value given in ref. 15, the main reason being that the energy barrier we obtain differs from that given in ref. 15 In our work, the reactants, TSs, and products of the title reaction are optimized at the B3LYP/6–311++G** level, while in Singh et al.'s[15] theoretical work, the B3LYP method with the 6–311G(d,p) basis set was used. Therefore, we obtain an energy barrier of 3.83 kcal/mol, whereas the value given in ref. 15 is 6.5 kcal/mol. On the other hand, from Table 5 it is clear that the harmonic and anharmonic rate constants all increase with increasing temperature. With the temperature increasing from 200 to 2000 K, the harmonic rate constant is in the range of 2.99×10^{8} to 4.95×10^{12} s^{-1}, whereas the anharmonic rate constant increases from 2.50×10^{8} to 2.62×10^{12} s^{-1}. The anharmonic rate constants are lower than the harmonic ones at all ranges of temperature. When the temperature is 298 K, the anharmonic rate constant (7.29×10^{9} s^{-1}) is 26.3% lower than the harmonic rate constant (9.89×10^{9} s^{-1}), whereas the anharmonic rate constant (2.62×10^{12} s^{-1}) is 47.1% lower than the harmonic rate

Can. J. Chem. Downloaded from www.nrcresearchpress.com by Renmin University of China on 09/02/12
For personal use only.

constant (4.95×10^{12} s^{-1}) at 2000 K. Therefore, we can draw the conclusion that with increasing temperature the difference between the two cases becomes larger. That is to say, the anharmonic effect becomes more significant with increasing temperature in the canonical system. The results of Table 6 indicate that the rate constants basically increase with the increment of energy. With the energy increasing from 3 809 to 14 144 cm^{-1}, the harmonic rate constant increases from 3.13×10^{11} to 3.53×10^{12} s^{-1}, whereas the anharmonic rate constant is in the range of 1.64×10^{11} to 1.59×10^{12} s^{-1}. The harmonic rate constants are higher than the anharmonic ones at all ranges of temperature. When the total energy is 3809 cm^{-1}, the anharmonic rate constant (1.64×10^{11} s^{-1}) is 47.6% lower than the harmonic rate constant (3.13×10^{11} s^{-1}), whereas the anharmonic rate constant (1.59×10^{12} s^{-1}) is 55.0% lower than the harmonic rate constant (3.53×10^{12} s^{-1}) at a total energy of 14 144 cm^{-1}. Thus, we can see that, for microcanonical case, although the harmonic and anharmonic rate constants yield similar results at lower energy, the difference becomes increasingly obvious at higher energy. That is, with the increment of total energy the anharmonic effect becomes more and more obvious in the microcanonical system. Moreover, as can be seen from Tables 5 and 6, when the total energy is 14 144 cm^{-1}, the anharmonic rate constant (1.59×10^{12} s^{-1}) is 55.0% lower than the harmonic rate constant (3.53×10^{12} s^{-1}) for the microcanonical case, whereas the anharmonic rate constant (1.69×10^{12} s^{-1}) is 50.9% lower than the harmonic rate constant (3.44×10^{12} s^{-1}) for the canonical case. It can be seen that the rate constant is insensitive to the canonical case, but sensitive to the microcanonical case. In other words, compared with the canonical case, the anharmonic effect in the microcanonical system is more obvious.

From Figs. 2–5 and Tables 3–6, we can see that the rate constants for the C–Cl bond scission are all larger than those for the C–C bond scission. This means that the C–Cl bond scission is the predominant decomposition channel. The result is in reasonable agreement with that of Singh et al.'s[15] theoretical work. However, with increasing temperature and energy, the difference in the rate constants between the C–C and C–Cl bond scissions becomes smaller. In the canonical system, when the temperature is 2000 K, the differences in the harmonic and anharmonic rate constants between the C–C and C–Cl bond scissions decrease to 61.0% and 61.1%, respectively. In the microcanonical system, when the energy is 14 144 cm^{-1}, the difference in the harmonic and anharmonic rate constants between the C–C and C–Cl bond scissions decrease to 98.3% and 98.4%, respectively. Within both the C–C and C–Cl bond scissions, the difference between the harmonic and the anharmonic rate constants is rather small at lower energy and temperature, but it becomes large at a higher energy and temperature for both the canonical and microcanonical cases. For the C–C bond scission, the difference between the harmonic and the anharmonic rate constants for the canonical case increases from 3.6% to 47.2% and, for the microcanonical case, it increases from 61.5% to 65.0%. For the C–Cl bond scission, the difference between the harmonic and the anharmonic rate constants for the canonical case increases from 16.4% to 47.1% and from 47.6% to 55.0% for the microcanonical case. This indicates that the difference between the harmonic and the anharmonic rate constants increases with a total energy increase for either the C–C bond or C–Cl bond scission. Thus, we draw the conclusion that with an increment of temperature or total energy the anharmonic effect becomes more and more significant in both canonical and microcanonical systems. It is worth mentioning that the harmonic rate constants are all larger than the anharmonic ones for both the microcanonial and canonical systems.

Conclusions

In this paper, we calculated the harmonic and anharmonic rate constants of the unimolecular decomposition reaction of the CF_3CCl_2O radical using the YL method. We have only considered two unimolecular dissociation channels of the CF_3CCl_2O radical, i.e., C–C and the C–Cl bond scissions. Especially, we have investigated the anharmonic effect of the rate constant through comparing the anharmonic rate constants at different situations.

For the C–C bond scission, the calculated rate constant is 1.36×10^5 s^{-1} at 298 K for the harmonic case. Whereas for the C–Cl bond scission, the harmonic rate constants is 9.89×10^9 s^{-1} at 298 K. Our results differ from the values given in ref. 15 because of the values of the energy barriers for the two cases are different. There is no experimental data available in the literature for comparison. The rate constants of the C–Cl bond scission are all larger than those of the C–C bond scission. This indicates that the C–Cl bond scission is the dominating decomposition channel. The result is in reasonable agreement with that of Singh et al.'s[15] theoretical work.

Within both the C–C and C–Cl bond scissions, although the difference between the harmonic and the anharmonic rate constants is rather small at a lower energy and temperature, it becomes large at a higher energy and temperature for both the canonical case and microcanonical cases. This indicates that the difference between the harmonic and the anharmonic rate constants increases with increasing total energy. Thus, we can draw a conclusion that the anharmonic effect becomes more significant with increasing temperature or total energy for both the canonical and microcanonical cases.

In both canonical and microcanonical cases for two unimolecular decomposition channels, on one hand, the rate constants all basically increase with increasing total energy, but on the other hand, the harmonic and anharmonic rate constants give similar results when the temperature and energy are low. However, the difference between the two kinds of rate constants is quite large at a higher energy and temperature. Furthermore, the difference increases with increasing total energy. Therefore, we can conclude that the anharmonic effect becomes more significant with increasing total energy. Moreover, the results show that the difference between the harmonic rate constants and the anharmonic ones is rather small for the canonical case, whereas it is quite significant for the microcanonical case. That is to say, compared with the canonical case, the anharmonic effect in the microcanonical case is more obvious. The harmonic rate constants are all larger than the anharmonic ones in both canonical and microcanonical systems.

The present results indicate that within both microcanonical and canonical cases, the YL method works for investigating the rate constants of this type unimolecular decomposition.

Furthermore, the anharmonic effect of the title reaction, the unimolecular decomposition reaction of the CF_3CCl_2O radical, cannot be neglected.

Acknowledgements

This work was supported by the National Natural Science Foundation of China (Grant Nos. 11047110 and 11105022), The Natural Science Foundation of Liaoning Province (Grant Nos. L2010055 and L2010057) and The Fundamental Research Funds for the Central Universities (2011QN060, 2011QN151).

References

(1) Molina, M. J.; Rowland, F. S. *Nature* **1974**, *249* (5460), 810. doi:10.1038/249810a0.
(2) Wuebbles, D. J. *J. Geophys. Res.* **1983**, *88* (C2), 1433. doi:10.1029/JC088iC02p01433.
(3) Solomon, S. *Nature* **1990**, *347*, 347. doi:10.1038/347347a0.
(4) Rowland, F. S.; Molina, M. J. *Chem. Eng. News* **1994**, *8*, 72.
(5) Wayne, R. P. *Chemistry of Atmospheres;* Clarendon Press: Oxford, 2001.
(6) World Meteorological Organization, Scientific Assessment of Stratospheric Ozone. *Global Ozone Research and Monitoring Project Report;* No. 20; 1989; Vol. 11.
(7) Reizian-Fouley, A.; Dat, Y.; Rault, S. *Ecotoxicol. Environ. Saf.* **1997**, *36* (3), 197. doi:10.1006/eesa.1996.1467.
(8) Zellner, R. *Global Aspects of Atmospheric Chemistry;* Steinkopff: Darmstadt, Germany, 1999.
(9) Brasseur, G. P.; Orlando, J. J. *Atmospheric Chemistry and Global Change;* Oxford University Press: New York, 1999.
(10) Stevens, J. E.; Jabo Khayat, R. A.; Radkevich, O.; Brown, J. *J. Phys. Chem. A* **2004**, *108* (51), 11354. doi:10.1021/jp0468509.
(11) Wu, F.; Carr, R. W. *J. Phys. Chem. A* **2002**, *106* (24), 5832. doi:10.1021/jp013326i.
(12) Wu, F.; Carr, R. W. *J. Phys. Chem. A* **2003**, *107* (49), 10733. doi:10.1021/jp030566k.
(13) Hou, H.; Wang, B.; Gu, Y. *J. Phys. Chem. A* **2000**, *104* (7), 1570. doi:10.1021/jp9930999.
(14) Somnitz, H.; Zellner, R. *Phys. Chem. Chem. Phys.* **2001**, *3* (12), 2352. doi:10.1039/b009498f.
(15) Singh, H. J.; Mishra, B. K.; Gour, N. K. *Theor. Chem. Acc.* **2010**, *125* (1–2), 57. doi:10.1007/s00214-009-0659-0.
(16) (a) McDowell, S. A. C. *J. Mol. Struct. THEOCHEM* **2006**, *770* (1–3), 119. doi:10.1016/j.theochem.2006.05.037; (b) Bhuiyan, L. B.; Hase, W. L. *J. Chem. Phys.* **1983**, *78* (8), 5052. doi:10.1063/1.445373; (c) Peslherbe, G. H.; Hase, W. L. *J. Chem. Phys.* **1996**, *105* (17), 7432. doi:10.1063/1.472571.
(17) Schlag, E. W.; Sandsmark, R. A. *J. Chem. Phys.* **1962**, *37* (1), 168. doi:10.1063/1.1732944.
(18) Haarhoff, P. C. *Mol. Phys.* **1964**, *7* (2), 101. doi:10.1080/00268976300100871.
(19) (a) Krems, R.; Nordholm, S. *Z. Phys. Chem.* **2000**, *214* (11), 1467. doi:10.1524/zpch.2000.214.11.1467; (b) Shen, D.; Pritchard, H. O. *J. Chem. Soc., Faraday Trans.* **1996**, *92* (8), 1297. doi:10.1039/ft9969201297.
(20) Peslherbe, G. H.; Hase, W. L. *J. Chem. Phys.* **1996**, *105* (17), 7432. doi:10.1063/1.472571.
(21) Mitra, S. S.; Bhattacharyya, S. S. *J. Phys. At. Mol. Opt. Phys.* **1994**, *27* (9), 1773. doi:10.1088/0953-4075/27/9/015.
(22) Hobza, P.; Havlas, Z. *Chem. Rev.* **2000**, *100* (11), 4253. doi:10.1021/cr990050q.
(23) Song, K.; Hase, W. L. *J. Chem. Phys.* **1999**, *110* (13), 6198. doi:10.1063/1.478525.
(24) Hase, W. L. *Acc. Chem. Res.* **1998**, *31* (10), 659. doi:10.1021/ar970156c.
(25) Bagratashvili, V. N.; Letokhov, V. S.; Makarov, A. A.; Ryabov, E. A. *Laser Chem.* **1983**, *1* (5), 211. doi:10.1155/LC.1.211.
(26) Mitra, S. S.; Bhattacharyya, S. S. *J. Phys. At. Mol. Opt. Phys.* **1994**, *27* (9), 1773. doi:10.1088/0953-4075/27/9/015.
(27) (a) Troe, J. *J. Chem. Phys.* **1977**, *66* (11), 4758. doi:10.1063/1.433838; (b) Troe, J. *Chem. Phys.* **1995**, *190* (2–3), 381. doi:10.1016/0301-0104(94)00358-H; (c) Troe, J. *J. Phys. Chem.* **1979**, *83* (1), 114. doi:10.1021/j100464a019; (d) Troe, J. *J. Chem. Phys.* **1983**, *79* (12), 6017. doi:10.1063/1.445784; (e) Romanini, D.; Lehmann, K. K. *J. Chem. Phys.* **1993**, *98* (8), 6437. doi:10.1063/1.464808.
(28) (a) Yao, L.; Mebel, A. M.; Lu, H. F.; Neusser, H. J.; Lin, S. H. *J. Phys. Chem. A* **2007**, *111* (29), 6722. doi:10.1021/jp069012i; (b) Yao, L.; Liu, Y. L.; Lin, S. H. *Mod. Phys. Lett. B* **2008**, *22* (31), 3043. doi:10.1142/S0217984908017552; (c) Yao, L.; Lin, S. H. *Sci. China Ser. B* **2008**, *51* (12), 1146. doi:10.1007/s11426-008-0125-1; (d) Yao, L.; He, R. X.; Mebel, A. M.; Lin, S. H. *Chem. Phys. Lett.* **2009**, *470* (4–6), 210. doi:10.1016/j.cplett.2009.01.074; (e) Shao, Y.; Yao, L.; Lin, S. H. *Chem. Phys. Lett.* **2009**, *478* (4–6), 277. doi:10.1016/j.cplett.2009.07.051; (f) Yao, L.; Mebel, A. M.; Lin, S. H. *J. Phys. Chem. A* **2009**, *113* (52), 14664. doi:10.1021/jp9044379.
(29) Frisch, M. J.; Trucks, G. W.; Schlegel, H. B.; Scuseria, G. E.; Robb, M. A.; Cheeseman, J. R.; Montgomery, J. A., Jr.; Vreven, T.; Kudin, K. N.; Burant, J. C.; Millam, J. M.; Iyengar, S. S.; Tomasi, J.; Barone, V.; Mennucci, B.; Cossi, M.; Scalmani, G.; Rega, N.; Petersson, G. A.; Nakatsuji, H.; Hada, M.; Ehara, M.; Toyota, K.; Fukuda, R.; Hasegawa, J.; Ishida, M.; Nakajima, T.; Honda, Y.; Kitao, O.; Nakai, H.; Klene, M.; Li, X.; Knox, J. E.; Hratchian, H. P.; Cross, J. B.; Bakken, V.; Adamo, C.; Jaramillo, J.; Gomperts, R.; Stratmann, R. E.; Yazyev, O.; Austin, A. J.; Cammi, R.; Pomelli, C.; Ochterski, J. W.; Ayala, P. Y.; Morokuma, K.; Voth, G. A.; Salvador, P.; Dannenberg, J. J.; Zakrzewski, V. G.; Dapprich, S.; Daniels, A. D.; Strain, M. C.; Farkas, O.; Malick, D. K.; Rabuck, A. D.; Raghavachari, K.; Foresman, J. B.; Ortiz, J. V.; Cui, Q.; Baboul, A. G.; Clifford, S.; Cioslowski, J.; Stefanov, B. B.; Liu, G.; Liashenko, A.; Piskorz, P.; Komaromi, I.; Martin, R. L.; Fox, D. J.; Keith, T.; Al-Laham, M. A.; Peng, C. Y.; Nanayakkara, A.; Challacombe, M.; Gill, P. M. W.; Johnson, B.; Chen, W.; Wong, M. W.; Gonzalez, C.; Pople, J. A. *Gaussian 03, Revision C. 02;* Gaussian, Inc.: Wallingford, CT, 2004.
(30) Steinfeld, J. I.; Francisco, J. S.; Hase, W. L. *Chemical Kinetics and Dynamics;* Prentice-Hall: Englewood Cliffs, NJ, 1989.
(31) (a) Forst, W.; Prasil, Z. J. *Chem. Phys.* **1970**, *53*, 3065; (b) Forst, W. *Chem. Rev.* **1971**, *71* (4), 339. doi:10.1021/cr60272a001; (c) Forst, W. *Theory of Unimolecular Reactions;* Academic Press: New York, 1973.
(32) Hoare, M. R.; Ruijgrok, Th. W. *J. Chem. Phys.* **1970**, *52* (1), 113. doi:10.1063/1.1672655.
(33) Eyring, H.; Lin, S. H.; Lin, S. M. *Basic Chemical Kinetics;* Wiley-Interscience: Hoboken, NJ, 1980.
(34) Baer, T.; Hase, W. L. *Unimolecular Reaction Dynamics: Theory and Experiments;* Oxford University Press: New York, 1996.
(35) Gilbert, R. G.; Smith, S. C. *Theory of Unimolecular and Recombination Reactions;* Blackwell: Oxford, 1990.

Can. J. Chem. Downloaded from www.nrcresearchpress.com by Renmin University of China on 09/02/12
For personal use only.

Highly efficient one-pot synthesis of trisubstituted imidazoles under catalyst-free conditions

Najmadin Azizi, Nairreh Dado, and Alireza Khajeh Amiri

Abstract: Operationally simple, atom economical, and scalable synthesis of 2,4,5-trisubstituted imidazoles from benzil, aldehydes, and ammonium acetate is shown to proceed readily in methanol with high yield. The scope of the reaction is quite broad; a variety of aromatic and aliphatic activated and unactivated aldehydes have all been shown to be viable substrates for this reaction. Excellent yields and purity were obtained by washing the products with hot ethanol.

Key words: aldehyde, benzil, imidazole, atom economic, solvent effect, catalyst free.

Résumé : On a montré qu'un procédé simple, économique d'un point de vue atomique et d'échelle variable peut être appliqué à la synthèse, avec un rendement élevé, dans le méthanol, d'imidazoles 2,4,5-trisubstitués à partir du benzile, d'aldéhydes et d'acétate d'ammonium. Le domaine d'application de la réaction est étendu; on a en effet montré qu'une variété d'aldéhydes aromatiques et aliphatiques, activés et non activés, peuvent être utilisés comme substrats pour la réaction. On a obtenu rendements élevés et une pureté excellente en lavant les produits avec de l'éthanol bouillant.

Mots-clés : aldéhyde, benzile, imidazole, économique d'un point de vue atomique, effet de solvant, sans catalyseur.

[Traduit par la Rédaction]

Can. J. Chem. Downloaded from www.nrcresearchpress.com by Renmin University of China on 09/02/12
For personal use only.

Introduction

Imidazole derivatives play an important role in chemical and biological systems.[1] Many of the substituted imidazoles are known as inhibitors of fungicides and herbicides, plant growth regulators, and therapeutic agents.[2] Recent advances in green chemistry have extended the boundary of imidazoles as ionic liquids that can be used as electrolytes or green solvents because of their low vapor pressure and wide chemical stability.[3] Furthermore, imidazolylidene carbenes have been used in coordination chemistry, as ligands in transition-metal and metal-free catalysts for organic synthesis.[4,5]

Owing to the wide applicability of imidazoles, preparative methodologies for this class of compounds have been intensively developed in the literature.[6] Conventional methods for imidazole core synthesis usually involve the reaction of α-diketones and α-haloketones with formamide (Bredereck synthesis),[7] the base-promoted reaction of tosylmethyl isocyanides and aldimines or imidoyl chlorides,[8] and catalytic multicomponent coupling reactions in the presence of a Lewis acid[9] and an organocatalyst.[10]

However, the use of high temperatures, expensive instruments such as microwaves, and corrosive reagents limit these methods, and there are few reports on practical methods for preparing them, and no method is catalyst-free. Thus, highly efficient and flexible protocols for the synthesis of imidazoles are still in need as there is a scope for further improvement towards milder reaction conditions, development of simple workup, inexpensive reagents, convenient procedures, and higher product yields. In this article, a simple, rapid, and catalyst-free imidazole formation with excellent yield has been developed.

Results and discussion

Recently, we were interested in performing organic reactions in water, and we have shown that the aqueous medium can strongly favor the reactivity and selectivity, even when they are carried out under heterogeneous conditions.[11] Herein, we wish to report the simple synthesis of new imidazole derivatives with the reaction of 1,2-diketones and variety of aldehydes performed in methanol with excellent yields and without using any catalyst.

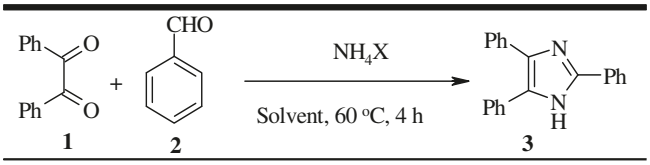
First, we embarked upon a series of experiments to establish the optimum conditions. The one-pot three-component reaction of benzaldehyde **2**, benzil **1**, and ammonium salts were studied (Table 1). First findings indicated that the presence of ammonium acetate in methanol was an excellent solvent without using any catalyst or promoter and 2,4,6-triphenyimidazole **3** crystals were obtained in 97% yield by reacting equimolar amounts of **1** and **2** at 60 °C for 4 h. Other ammonium salts such as fluoride, chloride, nitrate, and hydrogen sulfate and ammonia solution (32%) give low yields of desired products for these reaction conditions. We also investigated the effects of common organic solvents and the influence of different solvents on the rate and the course of these reactions. In dichloromethane, cyclohexane, and THF the reaction did not take place and the starting materials were recovered and low yield of the product was observed in acetonitrile, water, ethanol, and solvent-free conditions (Table 1).

Received 1 June 2011. Accepted 8 September 2011. Published at www.nrcresearchpress.com/cjc on 13 December 2011.

N. Azizi, N. Dado, and A.K. Amiri. Chemistry and Chemical Engineering Research Center of Iran, P.O. Box 14335-186, Tehran, Iran.

Corresponding author: Najmadin Azizi (e-mail: azizi@ccerci.ac.ir).

Table 1. Optimization of reaction conditions.



1 2 3

	Yield (%)
Solvent	
CH_2Cl_2	0
C_6H_{12}	0
CH_3CN	35
THF	5
SFC	60
H_2O	10
EtOH	70
MeOH	97
Amine/ammonium	
NH_3	20
NH_4F	40
NH_4Cl	0
NH_4NO_3	0
NH_4SO_4	15
NH_4OAc	97

Note: Reaction conditions: benzil (1 mmol), benzaldehyde (1 mmol), ammonium salts (3 mmol), and solvent (1 mL), 4 h.

With optimal conditions in hand, the reaction of benzil with different aldehydes was examined to explore the scope of the reaction. First, ammonium actate and benzil were used as model substrates (Table 2), and the results indicated that all commercially available aldehydes were good substrates for this system. Aromatic aldehydes bearing such functional groups as fluoro, chloro, bromo, methyl, or methoxy were able to effect the imidazole synthesis. We also observed that electronic effect on the aldehydes had little influence on the yield and the reaction conditions; that is, aryl aldehydes with electron-withdrawing groups reacted rapidly, whereas the substitution of electron-rich groups on the benzene ring did not decreased the reactivity. Moreover, a good yield for 3,5-dimethoxy benzaldehyde (Table 2, entry 24), the substrate with a strong electron-donating group, was observed. In addition, the 2-furaldehyde, (Table 2, entry 29), thiophenaldehyde (Table 2, entry 30), 2-naphthaldehyde (Table 2, entry 25), and 1-naphthaldehyde (Table 2, entry 26) also gave good yields of products. On the other hand, for the first time we have shown that fluorene-9-carbaldehyde (Table 2, entry 27), indole-3-carboxaldehyde (Table 2, entry 28), terephthaldehyde (Table 2, entry 31), isophthaldehyde (Table 2, entry 32), ferrocene carbaldehyde, (Table 2, entry 33), and aliphatic aldehydes still displayed high reactivity and clean reactions under these standard conditions.

It is noteworthy that the present method is very simple and that the process became even more attractive for large-scale applications when we found that it could be run at large scales without decreased yields and with the use of ethanol as the organic solvent in the workup without tedious column chromatography.

In summary, we have described a simple, highly efficient, and facile procedure for one-pot three-component synthesis of imidazole derivatives from readily available starting materials. To the best of our knowledge, this is the first report of the catalyst-free synthesis of imidazoles under very mild conditions. The procedure offers a simple experimental procedure and a short reaction time, is catalyst-free, is low cost, and provides efficient yields, which makes this method a useful and attractive strategy in view of economic and environmental advantages.

Experimental section

Instrumentation, analyses, and starting material

NMR spectra were recorded on a Bruker ACF 500 (^{1}H NMR at 500 MHz and ^{13}C NMR at 125 MHz) spectrometer in pure deuterated solvents with tetramethylsilane (Supplementary data). Melting points were determined in open capillary tubes in a Buchi-535 melting-point apparatus. All reagents, unless otherwise stated, were used as received from suppliers. Solvents were distilled before use.

General procedure for the synthesis of imidazole derivatives in methanol

To a well-stirred mixture of benzaldehyde (0.1 cm^3, 1 mmol) and benzil (0.21 g, 1 mmol) in methanol (1 cm^3) ammonium acetate was added (0.23 g, 3 mmol) and the reaction mixture was heated at 60 °C for 4–8 h. The reaction was allowed to cool and the resulting precipitates were recrystallized from ethanol to give pure imidazole derivatives.

Selected data for the new compounds

Table 1, entry 27

^{1}H NMR (500 MHz, DMSO-d_6) δ: 3.98 (s, 2H), 7.19–7.58 (m, 13H), 7.89 (d, J = 7.3 Hz, 1H), 7.94 (d, J = 7.9 Hz, 1H), 8.01 (d, J = 7.6 Hz, 1H), 8.29 (s, 1H), 12.66 (brs, NH, 1H). ^{13}C NMR (125 MHz, DMSO-d_6) δ: 121.0, 122.7, 124.9, 126.0, 127.3, 127.7, 127.8, 127.9, 128.6, 129.0, 129.2, 129.5, 129.7, 131.9, 136.1, 138.0, 141.6, 142.0, 144.2, 144.3, 146.7. Anal. calcd for $C_{28}H_{20}N_2$: C 87.47, H 5.24, N 7.29; found: C 86.55, H 5.10, N 6.30.

Table 1, entry 28

^{1}H NMR (500 MHz, DMSO-d_6) δ: 7.12–7.60 (m, 13H), 7.96 (s, 1H), 8.45 (s, 1H), 11.33 (brs, NH, 1H)), 12.23 (brs, NH, 1H). ^{13}C NMR (125 MHz, DMSO-d_6) δ: 107.7, 112.6, 120.5, 122.3, 122.7, 124.6, 125.9, 126.6, 127.0, 127.7, 128.2, 129.0, 129.5, 132.5, 136.2, 136.8, 137.12, 144.5. HRMS: 334 (M^+), 335 (100). Anal. calcd for $C_{23}H_{17}N_3$: C 82.36, H 5.11, N 12.53; found: C 81.90, H 4.88, N 12.01.

Table 1, entry 33

^{1}H NMR (500 MHz, DMSO-d_6) δ: 4.14 (s, 5H), 4.36 (t, J = 1.6 Hz, 3H), 4.96 (t, J = 1.9 Hz, 2H), 7.20–7.52 (m, 10H), 12.19 (brs, NH, 1H). ^{13}C NMR (125 MHz, DMSO-d_6) δ: 67.1, 69.5, 70.0, 76.6, 127.1, 127.8, 128.3, 128.9, 129.1, 129.4, 136.2, 146.8. HRMS: 404 (100).

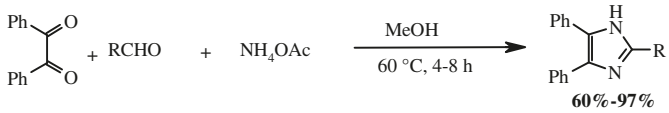
Supplementary data

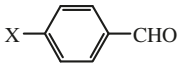
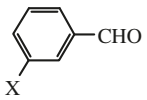
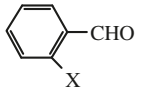
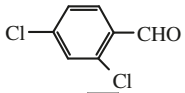
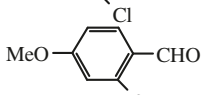
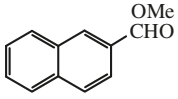
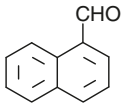
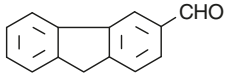
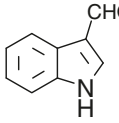
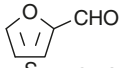
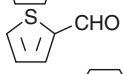
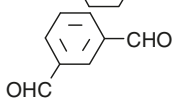
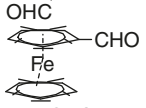
Supplementary data (experimental details and spectroscopic characterization (^{1}H and ^{13}C NMR and mass) of the compounds) are available with the article through the journal

Can. J. Chem. Downloaded from www.nrcresearchpress.com by Renmin University of China on 09/02/12
For personal use only.

Can. J. Chem. Downloaded from www.nrcresearchpress.com by Renmin University of China on 09/02/12
For personal use only.

Table 2. Practical synthesis of new imidazoles under catalyst-free conditions.



Entry	Aldehyde	X	Yield (%)	mp (°C) Found	mp (°C) Reported	Ref.
1		Cl	97	264	262–264	10c
2		F	95	242	188–190	10c
3		Br	90	260	265	9m
4		OH	80	235	232–233	10c
5		OCH_3	92	232	228–230	9n
6		CH_3	90	234	233–235	10c
7		C_2H_5	88	224	223–224	9o
8		C_3H_7	90	230	232–234	10c
9		CO_2CH_3	84	246	246–248	9o
10		NO_2	86	245	242	9m
11		H	97	275	276–278	9n
12		Cl	97	295–297	295	9m
13		Br	97	307–308	305–310	10c
14		OCH_3	97	263–265	267–268	9b
15		CH_3	95	298–299	300	9c
16		OH	92	258	259	9m
17		Cl	97	197–198	195–197	9n
18		F	97	256	254.5–255	9a
19		Br	97	206–207	206–208	9d
20		OCH_3	90	209–210	206–211	10c
21		CH_3	90	255	252.5–253.5	9a
22		NO_2	85	230–233	230–231	10c
23			80	176	178	9m
24			60	165–167	164–165	9e
25			72	279	277–278	9a
26			80	290	297	9m
27			75	281–283		
28			82	307		
29			80	245–247	242	9m
30			84	264–266	260–262	9m
31			70	>350	442	1d
32			74	288–290	294–296	1d
33			64	97–99		
34			62	248	246	9c
35			68	238	238–240	9p

Web site (http://nrcresearchpress.com/doi/suppl/10.1139/v11-141).

Acknowledgements

Financial support of this work by the Chemistry and Chemical Research Center of Iran is gratefully appreciated.

References

(1) (a) Lombardino, J. G.; Wiseman, E. H. *J. Med. Chem.* **1974**, *17* (11), 1182. doi:10.1021/jm00257a011; (b) Sundberg, R.; Martin, R. B. *Chem. Rev.* **1974**, *74* (4), 471. doi:10.1021/cr60290a003; (c) Katritzky, M. R. A. R.; Rees, C.; Scriven, E. F. V. In *Comprehensive Heterocycle Chemistry II;* Pergamon Press: Elmsford, NY, 1996; Vol. 3, pp 77–220; (d) Kimura, M.; Iwagaki, H.; Tsunenaga, M.; Inoue, S. US2007/112061 AI, 2007.

(2) (a) Doman, T. N.; McGovern, S. L.; Witherbee, B. J.; Kasten, T. P.; Kurumbail, R.; Stallings, W. C.; Connolly, D. T.; Shoichet, B. K. *J. Med. Chem.* **2002**, *45* (11), 2213. doi:10.1021/jm010548w; (b) Blum, C. A.; Zheng, X.; De Lombaert, S. *J. Med. Chem.* **2004**, *47* (9), 2318. doi:10.1021/jm030490g.

(3) (a) Welton, T. *Chem. Rev.* **1999**, *99* (8), 2071. doi:10.1021/cr980032t; (b) Herrmann, W. A.; Köcher, C. *Angew. Chem. Int. Ed. Engl.* **1997**, *36* (20), 2162. doi:10.1002/anie.199721621.

(4) Glorius, F. N-Heterocyclic Carbenes in Transition Metal Catalysis. In *Topics in Organometallic Chemistry;* Springer: Berlin, 2007; Vol. 2, pp 1–218.

(5) (a) Marion, N.; Diéz-González, S.; Nolan, S. P. *Angew. Chem. Int. Ed.* **2007**, *46* (17), 2988. doi:10.1002/anie.200603380; (b) Enders, D.; Balensiefer, T. *Acc. Chem. Res.* **2004**, *37* (8), 534. doi:10.1021/ar030050j.

(6) Kamijo, S.; Yamamoto, Y. *Chem. Asian J.* **2007**, *2* (5), 568. doi:10.1002/asia.200600418.

(7) (a) Little, T. L.; Webber, S. E. *J. Org. Chem.* **1994**, *59* (24), 7299. doi:10.1021/jo00103a021; (b) Li, B.; Chiu, C. K.-F.; Hank, R. F.; Murry, J.; Roth, J.; Tobiassen, H. *Org. Process Res. Dev.* **2002**, *6* (5), 682. doi:10.1021/op025552b; (c) Shilcrat, S. C.; Mokhallalati, M. K.; Fortunak, J. M. D.; Pridgen, L. N. *J. Org. Chem.* **1997**, *62* (24), 8449. doi:10.1021/jo971304f.

(8) (a) Nunami, K. I.; Yamada, M.; Fukui, T.; Matsumoto, K. *J. Org. Chem.* **1994**, *59* (25), 7635. doi:10.1021/jo00104a018; (b) Sisko, J. *J. Org. Chem.* **1998**, *63* (13), 4529. doi:10.1021/jo980248v; (c) Sisko, J.; Mellinger, M. *Pure Appl. Chem.* **2002**, *74* (8), 1349 and references therein. doi:10.1351/pac200274081349; (d) Illgen, K.; Nerdinger, S.; Behnke, D.; Friedrich, A. *Org. Lett.* **2005**, *7* (1), 39. doi:10.1021/ol0480269.

(9) (a) Wolkenberg, S. E.; Wisnoski, D. D.; Leister, W. H.; Wang, Y.; Zhao, Z.; Lindsley, C. W. *Org. Lett.* **2004**, *6* (9), 1453 and references therein. doi:10.1021/ol049682b; (b) Zuliani, V.; Cocconcelli, G.; Fantini, M.; Ghiron, C.; Rivara, M. *J. Org. Chem.* **2007**, *72* (12), 4551. doi:10.1021/jo070187d; (c) Kidwai, M.; Mothsra, P. *Tetrahedron Lett.* **2006**, *47* (29), 5029. doi:10.1016/j.tetlet.2006.05.097; (d) Khosropour, A. R. *Can. J. Chem.* **2008**, *86* (3), 264. doi:10.1139/v08-009; (e) Heravi, M. M.; Bakhtiari, K.; Oskooie, H. A.; Taheri, S. *J. Mol. Catal. Chem.* **2007**, *263* (1–2), 279. doi:10.1016/j.molcata.2006.08.070; (f) Heravi, M. M.; Zakeri, Z.; Karimi, N.; Saeedi, M.; Oskooie, H. A.; Tavakoli-Hosieni, N. *Synth. Commun.* **2010**, *40* (13), 1998. doi:10.1080/00397910903219377; (g) Sparks, R. B.; Combs, A. P. *Org. Lett.* **2004**, *6* (14), 2473. doi:10.1021/ol049124x; (h) Adib, M.; Sheibani, M.; Bijanzadeh, H. R.; Zhu, L.-G. *Tetrahedron* **2008**, *64* (47), 10681. doi:10.1016/j.tet.2008.09.002; (i) Adib, M.; Ansari, S.; Feizia, S.; Damavandi, J. A.; Mirzaei, P. *Synlett* **2009**, 3263; (j) Sadeghi, B.; Mirjalili, B. B. F.; Hashemi, M. M.; *Tetrahedron Lett.* **2008**, *49* (16), 2575. doi:10.1016/j.tetlet.2008.02.100; (k) Khalili, B.; Tondro, T.; Hashemi, M. M. *Tetrahedron* **2009**, *65* (34), 6882. doi:10.1016/j.tet.2009.06.082; (l) Mohammed, A. F.; Kokare, N. D.; Sangshetti, J. N.; Shinde, D. B. *J. Kor. Chem. Soc.* **2007**, *51* (5), 418. doi:10.5012/jkcs.2007.51.5.418; (m) Chary, M. V.; Keerthysri, N. C.; Vupallapati, S. V. N.; Lingaiah, N.; Kantevari, S. *Catal. Commun.* **2008**, *9* (10), 2013. doi:10.1016/j.catcom.2008.03.037; (n) Das Sharma, S.; Hazarika, P.; Konwar, D. *Tetrahedron Lett.* **2008**, *49* (14), 2216. doi:10.1016/j.tetlet.2008.02.053; (o) Wang, L.-M.; Wang, Y.-H.; Tian, H.; Yao, Y.-F.; Shao, J.-H.; Lio, B. *J. Fluor. Chem.* **2006**, *127* (12), 1570. doi:10.1016/j.jfluchem.2006.08.005; (p) Uçucu, Ü.; Karaburun, N. G.; Işikdağ, I. *Il Farmaco* **2001**, *56* (4), 285. doi:10.1016/S0014-827X(01)01076-X.

(10) (a) Murry, J. A.; Frantz, D. E.; Soheili, A.; Tillyer, D.; Grabowski, E. J. J.; Reider, P. J. *J. Am. Chem. Soc.* **2001**, *123* (39), 9696. doi:10.1021/ja0165943; (b) Zhong, Y. L.; Lee, J.; Reamer, R. A.; Askin, D. *Org. Lett.* **2004**, *6* (6), 929. doi:10.1021/ol036423y; (c) Samai, S.; Nandi, G. C.; Singh, P.; Singh, M. S. *Tetrahedron* **2009**, *65* (49), 10155. doi:10.1016/j.tet.2009.10.019.

(11) (a) Azizi, N.; Saidi, M. R. *Organometallics* **2004**, *23* (6), 1457. doi:10.1021/om0341505; (b) Azizi, N.; Saidi, M. R. *Org. Lett.* **2005**, *7* (17), 3649. doi:10.1021/ol051220q; (c) Azizi, N.; Aryanasab, F.; Torkiyan, L.; Ziyaei, A.; Saidi, M. R. *J. Org. Chem.* **2006**, *71* (9), 3634. doi:10.1021/jo060048g; (d) Azizi, N.; Torkiyan, L.; Saidi, M. R. *Org. Lett.* **2006**, *8* (10), 2079. doi:10.1021/ol060498v.

Can. J. Chem. Downloaded from www.nrcresearchpress.com by Renmin University of China on 09/02/12
For personal use only.

Four new triterpenoids from *Chisocheton paniculatus* and their anti-inflammatory activities

Ming-Hua Yang, Jun-Song Wang, Jian-Guang Luo, Xiao-Bing Wang, and Ling-Yi Kong

Can. J. Chem. Downloaded from www.nrcresearchpress.com by Renmin University of China on 09/02/12
For personal use only.

Abstract: As part of our continuing effort to discover new potential anti-inflammatory agents, four new triterpenoids, chisopanins L-O (**1**–**4**), were isolated from the twigs of *Chisocheton paniculatus*. Their structures were established on the basis of detailed analysis of spectroscopic data, including IR, NMR (1D and 2D NMR), and HR-ESI-MS. Their inhibitory effects against nitric oxide (NO) production were evaluated in an in vitro model of lipopolysaccharide (LPS)-stimulated RAW264.7 macrophages. Compounds **1**, **3**, and **4** were found to exhibit moderate activity with IC_{50} values less than 10 μmol/L.

Key words: Chisocheton paniculatus, triterpenoids, anti-inflammatory activity.

Résumé : Dans le cadre de nos travaux effectués dans le but de découvrir de nouveaux agents potentiellement anti-inflammatoires, on a isolé quatre nouveaux triterpénoïdes, les chisopanines L-O (**1**–**4**) des brindilles de *Chisocheton paniculatus*. On a déterminé leurs structures en se basant sur une analyse détaillée de données spectroscopiques, dont l'infrarouge, la résonance magnétique nucléaire uni- (RMN 1D) et bi-dimensionnelle (RMN 2D) et la spectrométrie de masse avec ionisation par électronébulisation et à haute résolution (SM-IEN-HR). On a évalué leurs effets d'inhibition contre la production d'oxyde nitrique (NO) dans un modèle in vitro de macrophages RAW264,7 stimulés par un lipopolysaccharide (LPS). Les composés **1**, **3** et **4** présentent une activité modérée avec des valeurs de IC_{50} inférieures à 10 μmol/L.

Mots-clés : Chisocheton paniculatus, triterpénoïdes, activité anti-inflammatoire.

[Traduit par la Rédaction]

Introduction

Chisocheton paniculatus Hiern (Meliaceae) is a rich source of protolimonoids and simple limonoids.[1,2] Several new C-*seco*-type tetranortriterpenoids and protolimonoids were isolated from this plant, showing significant anti-inflammatory activity in our previous reports.[3,4] Further investigation on fractions that exhibited anti-inflammatory activity led to the isolation of four new triterpenoids, chisopanins L-O (**1**–**4**). In this study, we describe the isolation and structural elucidation of these new compounds as well as their inhibitory activities against lipopolysaccharide (LPS)-induced NO production in RAW264.7 macrophages.

Results and discussion

The $CHCl_3$ extract of twigs of *C. paniculatus* was subjected to a silica gel column to yield several fractions, which was separated by repeated chromatography over MCI gel and silica gel columns, and finally by preparative HPLC to afford chisopanins L-O (**1**–**4**) (Fig. 1). The structures of these isolates were elucidated by analysis of their spectroscopic data, including IR, NMR (1D and 2D NMR), and HR-ESI-MS.

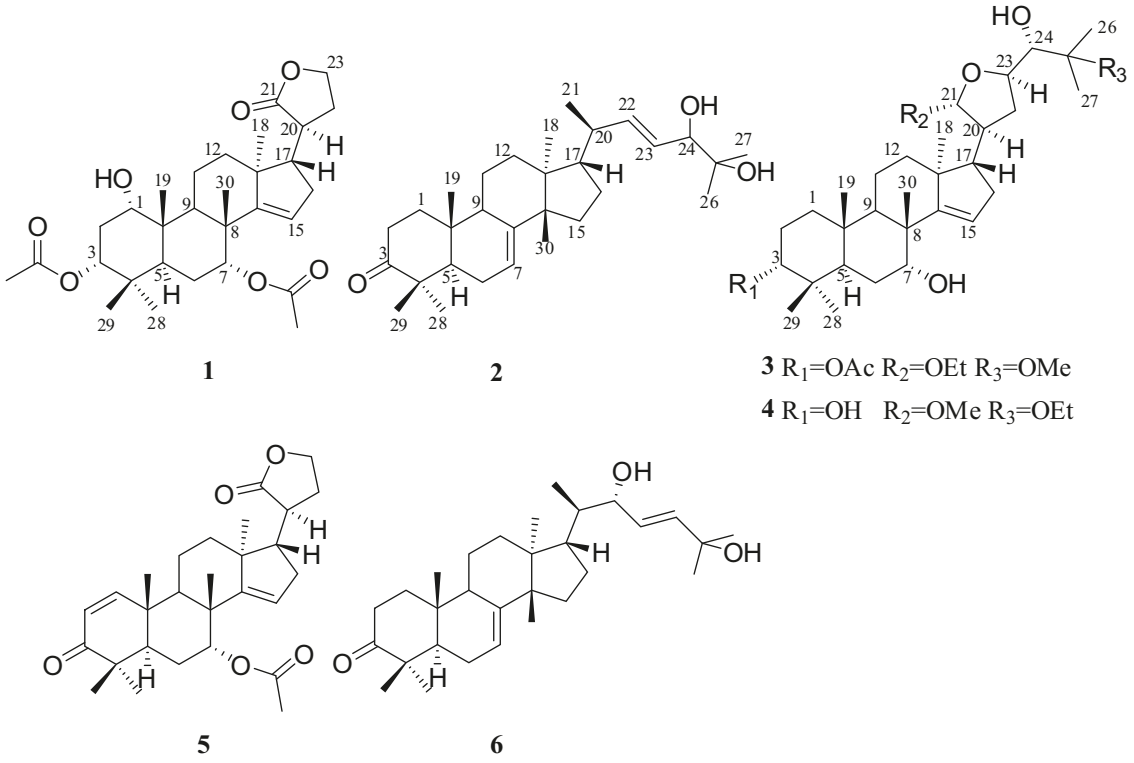
Chisopanin L (**1**) was isolated as a white amorphous powder. The $[M+Na]^+$ peak at *m/z* 534.3411 (calcd. for $C_{30}H_{44}O_7Na$, 534.3425) in the HR-ESI-MS indicated the molecular formula of $C_{30}H_{44}O_7$. Bands at 3579, 1784, and 1722 cm^{-1} in the IR spectrum revealed the existence of hydroxyl and carbonyl groups, respectively. The ^1H NMR spectrum (Table 1) showed the presence of 5 tertiary methyl groups (δ_H 0.80, 0.91, 0.92, 1.12, and 1.07, each 3H, s), two acetoxyl groups (δ_H 1.98, 2.11, each 3H, s), 5 oxygenated protons (δ_H 3.49, 3.90, 4.46, 4.94, and 5.18), and one olefinic proton (δ_H 5.26, t, 3.5 Hz). Except for the two acetoxyl groups, its ^{13}C NMR spectrum (Table 2) exhibited 26 carbons, including 5 methyls, 7 methylenes, 8 methines, and 6 quaternary carbons, featuring a tetranortriterpenoid skeleton. Similar to the known compound **5** (Fig. 1), the resonance of carbonyl signal at δ_C 176.7 in the ^{13}C NMR spectrum, along with the methylene proton signals at δ_H 4.46 and 3.90 (t, 8.5 Hz) in the ^1H NMR spectrum, indicated a γ-lactone nature of ring E, rather than a furan ring.[5] The observed HMBC correlations (Fig. 2) from H-23 (δ_H 3.90 and 4.46) to C-21 (δ_C 176.7), C-22 (δ_C 33.9), and C-17 (δ_C 58.1), from H-22a (δ_H 2.50) to C-21 (δ_C 176.7), and C-23 (δ_C 72.6), and from H-22b (δ_H 2.05) to C-17 (δ_C 58.1), C-20 (δ_C 37.6), and C-21 (δ_C 176.7), unambiguously confirmed the existence of a γ-lactone ring E. Further comparison with **5** revealed the absence of the characteristic α,β-unsaturated carbonyl moiety [δ_H 7.12 (d, 10 Hz), and 5.84 (d, 10 Hz); δ_C 204.3, 157.8, and 125.5] in **1**,[5] and instead, the appearance of two oxygen-

Received 3 June 2011. Accepted 19 September 2011. Published at www.nrcresearchpress.com/cjc on 21 December 2011.

M.-H. Yang, J.-S. Wang, J.-G. Luo, X.-B. Wang, and L.-Y. Kong. Department of Natural Medicinal Chemistry, China Pharmaceutical University, 24 Tong Jia Xiang, Nanjing 210009, P. R. China.

Corresponding author: Ling-Yi Kong (e-mail: cpu_lykong@126.com).

Fig. 1. Chemical structures of compounds **1**–**6**.



Can. J. Chem. Downloaded from www.nrcresearchpress.com by Renmin University of China on 09/02/12
For personal use only.

ated protons at C-1 and C-3 (δ_H 3.49 and 4.94),[6] which was confirmed by the HMBC correlations from H-19 (δ_H 0.92) and H-3 (δ_H 4.94) to C-1 (δ_C 71.3), and from H-28 (δ_H 0.80) and H-29 (δ_H 0.91) to C-3 (δ_C 78.7). Furthermore, the HMBC spectrum located the two acetoxyl groups at C-3 and C-7 by the cross peaks between the acetoxyl carbonyl signals (δ_C 169.4 and 170.2), and H-3 (δ_H 4.94), and H-7 (δ_H 5.18), respectively. The relative configuration of compound **1** was assigned by ROESY experiment (Fig. 3). In particular, the ROESY cross-peaks of Me-19/H-1, Me-30/H-7, and Me-29/H-3, as well as the small coupling constants, indicated the β-orientation for H-1, H-3, and H-7. Strong ROESY cross-peak between H-20 and Me-18 also revealed the α-orientation for H-20. Complete assignments of the proton and carbon resonances in **1** were made by the combined application of 1D and 2D NMR techniques, including HSQC, HMBC, and ROESY. Thus, the structure of **1** was determined to be as shown in Fig. 1.

Chisopanin M (**2**), a white amorphous powder, gave a $[M+Na]^+$ peak at *m*/*z* 479.3492 (calcd. for $C_{30}H_{48}O_3Na$, 479.3496) in the HR-ESI-MS, corresponding to the molecular formula of $C_{30}H_{48}O_3$. IR peaks at 3453 and 1699 cm^{-1} revealed the presence of hydroxyl and carbonyl groups. Seven tertiary and one secondary methyl groups in the ^1H NMR spectrum, in addition to 30 exhibited carbons in ^{13}C NMR, revealed a tirucallane skeleton of **2**. Further analysis suggested that compound **2** was an analogue of a known tirucallane triterpene **6**.[7] Both of them had one keto group at C-3 and one alkenyl at C-7, but differed in the side chain. The HMBC cross-peaks (Fig. 2) from H-22 (δ_H 5.61) to C-20 (δ_C 40.3), C-21 (δ_C 20.1), C-23 (δ_C 126.1), and C-24 (δ_C 79.7), together with the large coupling constant of H-22 (J = 15.3 Hz), revealed the existence of a trans-double bond between C-22 and C-23. The HMBC correlations from H-24 (δ_H 3.84) to C-23 (δ_C 126.1), C-25 (δ_C 72.9), C-26 (δ_C 26.4), and C-27 (δ_C 23.8) placed a hydroxyl group at C-24. The relative configuration of the tetracyclic core in **2** was assigned by a ROESY experiment and was identical to that of **6**. Despite the possible rotation at C-20, the observed NOE correlations of Me-18/H-20 and H-12β/Me-21 could still be used to suggest a preferred H-20α (C-20*S*) configuration and thus to confirm the tirucallane triterpene nature of **2**.[8,9] Thus, the structure of **2** was determined to be as shown in Fig. 1.

Chisopanin N (**3**) revealed a $[M+Na]^+$ peak at *m*/*z* 613.4057 (calcd. for $C_{35}H_{58}O_7Na$, 613.4075) in the HR-ESI-MS, corresponding to a molecular formula of $C_{35}H_{58}O_7$. All NMR data (Tables 1 and 2) were generally close to those of *apo*-tirucallol protolimonoids with a tetrahydrofuran ring E and an acetal group at C-21.[3] The ^1H NMR spectrum of **1** showed the presence of seven tertiary methyl groups (δ_H 0.86, 0.90, 0.91, 1.06, 1.11, 1.14, and 1.24, each 3H, s), one ethoxyl [δ_H 1.22 (3H, t, 7.1 Hz), 3.74 and 3.44 (each 1H, m)], one acetoxyl (δ_H 2.07, 3H, s), one methoxyl (δ_H 3.23, 3H, s), and one olefinic proton (δ_H 5.45, t, 2.0 Hz). The ^{13}C NMR spectrum indicated the presence of 10 methyls, 8 methylenes, 10 methines, and 7 quaternary carbons. Analysis of the HMBC spectrum positioned the ethoxyl at C-21 and the methoxyl at C-25. The location of the acetoxyl group was shown to be at C-3 by the HMBC cross peak between H-3 (δ_H 4.65) and the acetyl carbonyl at δ_C 171.0. The stereochemistry of **3** was determined on the basis of ROESY experiments. The observed ROESY correlations of H-21/H-17, Me-18/H-20, Me-18/H-21, Me-18/OEt-21, H-20/OEt-21, and

Table 1. ^{1}H NMR spectroscopic data (500 MHz in $CDCl_3$) for compounds **1**–**4** (*J* in Hz).

No.		**2**	**3**	**4**
1a	3.49, br s	1.99, m	1.36, m	1.38, m
1b		1.45, m	1.25, m	1.34, m
2a	2.30, dt (3.0, 16.5)	2.75, ddd (14.5, 7.2, 5.5)	1.90, m	1.70, m
2b	1.87, dt (3.0, 16.5)	2.26, m	1.58, m	1.70, m
3	4.94, t (3.0)		4.65, t (2.6)	3.40, t (2.8)
5	2.01, m	1.73, m	1.98, m	2.02, m
6a	1.78, m	2.09, m	1.72, m	1.92, m
6b	1.78, m	2.09, m	1.71, m	1.59, m
7	5.18, t (3.0)	5.31, d (3.1)	3.92, t (2.7)	3.90, br s
9	2.68, m	2.29, m	2.03, dd (7.5, 11.3)	2.01, m
11a	1.82, m	1.58, m	1.72, m	1.72, m
11b	1.52, m	1.58, m	1.50, m	1.49, m
12a	1.68, m	1.81, m	1.82, br d (11.7)	1.58, m
12b	1.44, m	1.64, m	1.43, m	1.47, m
15	5.26, t (3.5)	1.48, m	5.45, t (2.0)	5.45, t (2.6)
16a	2.16, m	1.80, m	2.17, ddd (3.5, 7.5, 11.0)	2.14, m
16b	2.05, m	1.27, m	2.12, dd (1.4, 10.7)	2.14, m
17	2.04, m	1.58, m	1.75, m	1.96, m
18	1.07, s	0.84, s	1.11, s	1.02, s
19	0.92, s	1.00, s	0.91, s	0.90, s
20	2.71, m	2.10, m	2.3, m	2.17, m
21		1.00, t (6.7)	4.90, d (3.8)	4.74, d (4.4)
22a	2.50, dd (8.0, 16.0)	5.61, dd (8.4, 15.3)	1.96, m	1.93, m
22b	2.05, m		1.60, m	1.80, m
23a	4.46, t (8.5)	5.44, dd (7.0, 15.3)	4.42, ddd (2.6, 4.7, 10.9)	4.47, ddd (2.6, 6.8, 9.6)
23b	3.90, t (8.5)			
24		3.84, d (7.0)	3.36, d (2.6)	3.26, d (2.6)
26		1.21, s	1.14, s	1.25, s
27		1.15, s	1.24, s	1.19, s
28	0.80, s	1.05, s	0.86, s	0.96, s
29	0.91, s	1.12, s	0.90, s	0.86, s
30	1.12, s	1.01, s	1.06, s	1.05, s
OAc	2.11, s; 1.98, s		2.07, s	
OMe			3.23, s	3.36, s
OEt			3.74, m; 3.44, m; 1.22, t (7.1)	3.45, 2H, m; 1.14, t (6.9)

Can. J. Chem. Downloaded from www.nrcresearchpress.com by Renmin University of China on 09/02/12
For personal use only.

H-23/OEt-21 were only possible in case of 20*S*, 21*R*, and 23*R* configuration.[3,10,11] The ROESY cross peaks of H-24/H-22 and H-24/H-23 and the small coupling constant ($J_{23,24}$ = 2.6 Hz) revealed a 24*R* configuration. From these observations, the structure of **3** was established as shown in Fig. 1.

Chisopanin O (**4**) exhibited a $[M+Na]^+$ peak at *m*/*z* 571.3988 (calcd. for $C_{33}H_{56}O_6Na$, 571.3969) in the HR-ESI-MS, corresponding to the molecular formula of $C_{33}H_{56}O_6$. Its NMR spectra were closely related to those of **3**, except for the absence of an acetoxyl group at C-3 in **4**, in accordance with having 42 mass units less than **3** in MS. The ethoxyl and methoxyl in **3** were confirmed to swap their positions in **4** by the observed HMBC cross-peaks from the ethoxylic methylene protons to C-25, and from the methoxyl protons to C-21. The configuration of **4** was also determined by a ROESY experiment to be identical to that of **3**. Thus, the structure of **4** was established as shown in Fig. 1.

Nitric oxide (NO) plays an important role in regulation of inflammatory processes, and compounds that inhibited NO release are thought to be potential anti-inflammatory agents.[12,13] Considering the exhibited anti-inflammatory activity of *C. paniculatus*,[3] these four triterpenoids were evaluated in vitro for their abilities to inhibit the NO release in LPS-stimulated mouse macrophages RAW 264.7. As shown in Table 3, compounds **1**, **3**, and **4** showed better inhibitory effects with IC_{50} values less than 10 μmol/L, as compared with other reported natural products,[14–16] most of which had effects that were several-fold higher. The NO release inhibitory effects of compounds **3** and **4**, together with previously reported other protolimonoids that excelled in this regards,[3] favored the investigation of this title plant for the discovery of lead compounds for new anti-inflammatory agent development.

Experimental

General

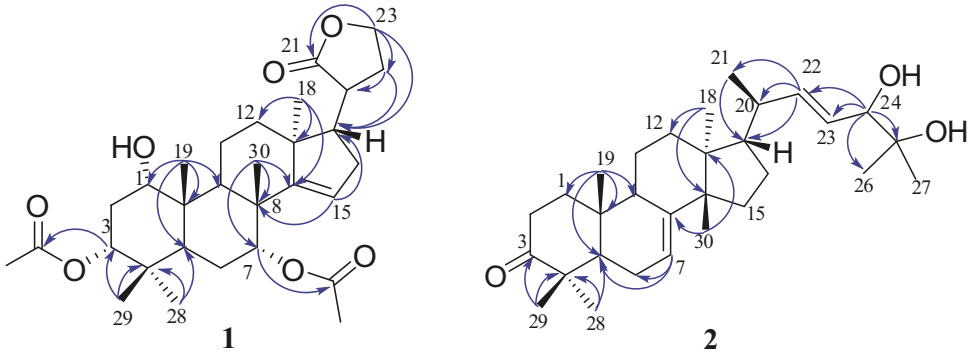
Optical rotations were carried out on a JASCO P-1020 polarimeter. IR (KBr disks) spectra were measured using a Bruker Tensor-27 spectrophotometer. NMR spectra were recorded on Bruker ACF-500 instrument (^{1}H: 500 MHz, ^{13}C: 125 MHz) using standard Bruker pulse programs. Chemical

Can. J. Chem. Downloaded from www.nrcresearchpress.com by Renmin University of China on 09/02/12
For personal use only.

Table 2. ^{13}C NMR spectroscopic data (125 MHz in $CDCl_3$) for compounds **1**–**4**.

No.	1	2	3	4
1	71.3	38.6	33.2	32.6
2	28.4	34.9	22.8	23.7
3	78.7	216.8	78.1	76.2
4	36.3	47.9	36.2	37.0
5	36.5	52.4	41.8	41.7
6	23.0	24.4	23.6	25.0
7	75.0	118.1	72.2	72.3
8	42.0	145.8	44.5	44.4
9	35.3	48.5	41.6	40.5
10	41.7	35.1	37.6	37.7
11	15.6	18.2	16.3	16.4
12	33.8	33.5	32.8	32.9
13	46.8	43.6	47.1	46.6
14	159.8	51.3	162.5	162.1
15	118.2	34.1	119.2	119.7
16	34.8	28.5	34.8	35.0
17	58.1	52.6	57.8	52.5
18	19.3	22.1	19.3	19.8
19	16.3	12.8	15.2	15.2
20	37.6	40.3	46.3	44.8
21	176.7	20.1	108.1	104.6
22	33.9	140.9	35.6	32.4
23	72.6	126.1	75.0	77.9
24		79.7	76.3	77.2
25		72.9	76.8	76.8
26		26.4	20.1	23.3
27		23.8	21.6	20.6
28	27.3	24.6	27.6	28.0
29	21.4	21.6	21.8	22.1
30	27.5	27.4	27.8	27.7
OAc	169.4, 21.3; 170.2, 21.2		171.0, 21.4	
OMe			49.1	54.9
OEt			63.8, 15.4	56.6, 16.2

Fig. 2. Key HMBC (H→C) correlations of compounds **1** and **2**.



shifts are given as δ-values with reference to tetramethylsilane (TMS) as an internal standard. Mass spectra were carried out on an Agilent Micro Q-TOF mass spectrometer. Silica gel (Qingdao Marine Chemical Co. Ltd.), C_{18} reverse-phased silica gel (150–200 μm, Merck), and MCI gel (CHP20P, 75–150 μm, Mitsubishi Chemical Industries Ltd.) were used for column chromatography. Silica gel GF_{254} plates (Qingdao Marine Chemical Co. Ltd.) were used for thin-layer chromatography, and spots were visualized by spraying with 10% H_2SO_4 followed by heating. Preparative HPLC was performed using Agilent 1100 series instrument with a Shim-Park RP-C_{18} column (200 mm × 20 mm i.d.).

Plant material

The twigs of *C. paniculatus* were collected in Xishuangbanna, Yunnan Province, China, in May 2007. The botanical identification was made by Professor Min-Jian Qin, Department of Medicinal Plants, China Pharmaceutical University,

Can. J. Chem. Downloaded from www.nrcresearchpress.com by Renmin University of China on 09/02/12
For personal use only.

Fig. 3. Selected ROESY (H↔H) correlations of compound **1**.

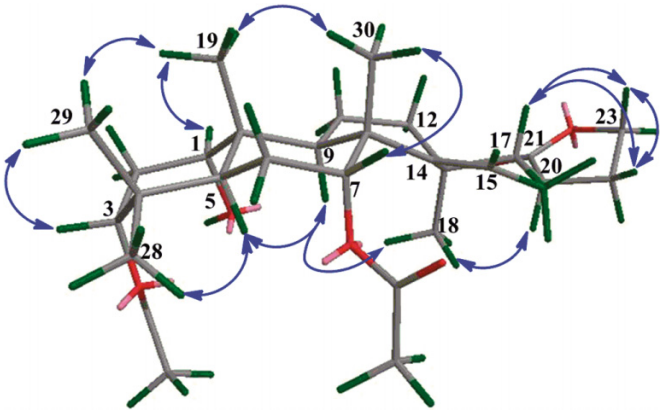


Table 3. Effects of compounds **1**–**4** on NO production in LPS-stimulated RAW 264.7 cells (n = 4).

	NO
Compounds	IC_{50} (μmol/L)
Chisopanin L (**1**)	6.6±0.1
Chisopanin M (**2**)	>50
Chisopanin N (**3**)	4.9±0.1
Chisopanin O (**4**)	4.4±0.2
Dexamethasone[a]	0.86±0.06

Note: A compound was regarded as inactive when IC_{50} > 50 μmol/L.
[a]Positive control.

Nanjing, China. A voucher specimen (No. 070705) is deposited in the Department of Natural Medicinal Chemistry, China Pharmaceutical University.

Extraction and isolation

The air-dried twigs of *C. paniculatus* (30 kg) were crushed into pieces (2 mm thick, QYD100II slicer, Shanghai TCM Machine) and extracted with 95% EtOH under reflux for 3 × 3 h. After concentration of the solution, the crude extract (1.5 kg) was suspended in water and then partitioned with $CHCl_3$ (6 × 2 L) and EtOAc (6 × 2 L) to afford a $CHCl_3$ layer (300 g) and an EtOAc layer (205 g). The $CHCl_3$ extract was chromatographed on a silica gel column eluted with gradient PE/EtOAc (100:0 to 1:1) to yield 10 fractions (CS1–CS10). Fraction CS2 (11 g) was chromatographed on a silica gel column eluted with PE/EtOAc (100:1 to 2:1) to mainly give three fractions, 2A–2C. Further purification of the fraction 2C by repeated preparative HPLC (MeCN/H_2O, 80:20) led to the isolation of **3** (3 mg). Fraction CS3 (9 g) was separated on a silica gel column with PE/EtOAc (50:1 to 2:1) to afford four fractions (3A–3D). Purification of the fraction 3B by MCI gel with MeOH/H_2O (70:30 to 100:0) and further preparation by HPLC (MeCN/H_2O, 85:15) afforded **2** (3 mg) and **4** (4 mg). Fraction CS8 (26 g) was subjected to chromatography over MCI gel (MeOH /H_2O, 30:70 to 100:0) and silica gel column ($CHCl_3$/MeOH, 100:0 to 50:1) to afford fractions 8A–8D. By repeated preparative HPLC (MeCN/H_2O, 45:55 and (or) MeOH/H_2O, 50:50), **1** (6 mg) were obtained from fraction 8A.

Chisopanin L (1)

White, amorphous powder; $[\alpha]_D^{25}$ –71.4 (c 0.550, $CHCl_3$). IR (KBr) ν_{max} (cm^{-1}): 3579, 3455, 2958, 1784, 1722, 1641, 1376, 1250, 1026. ^1H NMR see Table 1 and ^{13}C NMR see Table 2. HR-ESI-MS m/z: 534.3411 $[M+Na]^+$ (calcd. for $C_{30}H_{44}O_7Na$, 534.3425).

Chisopanin M (2)

White, amorphous powder; $[\alpha]_D^{25}$ –66.2 (c 0.090, $CHCl_3$). IR (KBr) ν_{max} (cm^{-1}): 3453, 2973, 1699, 1467, 1384. ^1H NMR see Table 1 and ^{13}C NMR see Table 2. HR-ESI-MS m/z: 479.3492 $[M+Na]^+$ (calcd. for $C_{30}H_{48}O_3Na$, 479.3496).

Chisopanin N (3)

White, amorphous powder; $[\alpha]_D^{25}$ –47.2 (c 0.290, $CHCl_3$). IR (KBr) ν_{max} (cm^{-1}): 3462, 2938, 2870, 1721, 1642, 1463, 1386, 1245, 1037. ^1H NMR see Table 1 and ^{13}C NMR see Table 2. HR-ESI-MS m/z: 613.4057 $[M+Na]^+$ (calcd. for $C_{35}H_{58}O_7Na$, 613.4075).

Chisopanin O (4)

White, amorphous powder; $[\alpha]_D^{25}$ –28.7 (c 0.340, $CHCl_3$). IR (KBr) ν_{max} (cm^{-1}): 3451, 2940, 1639, 1385. ^1H NMR see Table 1 and ^{13}C NMR see Table 2. HR-ESI-MS m/z: 571.3988 $[M+Na]^+$ (calcd. for $C_{33}H_{56}O_6Na$, 571.3969).

Measurement of NO production

This assay was performed as previously described.[3] Briefly, RAW 264.7 macrophages were cultured at 37 °C in 5% CO_2 in an RPMI 1640 medium, supplemented with 10% heated-deactivated fetal bovine serum (FBS), penicillin (100 U/mL), and streptomycin (15 μmol/L). The cells were incubated in 24-well cell culture plates at an initial density of 1×10^5 with 500 μL culture medium for 24 h and then pretreated with different compounds and lipopolysaccharide (LPS) (2 μg/mL) for 18 h. The amount of NO was assessed by determining the nitrite concentration in the cultured RAW 264.7 macrophage supernatants with Griess reagent (1% sulfanilamide and 0.1% naphthyl ethylene diamine dihydrochloride in 5% H_3PO_4). The absorbance at 540 nm was measured using a microplate reader.

Acknowledgments

This research work was supported by the Key Project of National Natural Science Foundation of China (No. 30830116), the Scaling Project for Innovation Scholars, Natural Science Foundation of Jiangsu Province, China (No. BK2008039), and the Project Funded by the Priority Academic Program Development of Jiangsu Higher Education Institutions.

References

(1) Connolly, J. D.; Labbé, C.; Rycroft, D. S.; Taylor, D. A. H. *J. Chem. Soc. Perkin Trans. 1*, **1979**, *12*, 2959. doi:10.1039/p19790002959.
(2) Bordoloi, M.; Saikia, B.; Mathur, R. K.; Goswami, B. N. *Phytochemistry*, **1993**, *34* (2), 583. doi:10.1016/0031-9422(93)80054-V.
(3) Yang, M. H.; Wang, J. S.; Luo, J. G.; Wang, X. B.; Kong, L. Y. *Bioorg. Med. Chem.* **2011**, *19* (4), 1409. doi:10.1016/j.bmc.2011.01.007.

(4) Yang, M. H.; Wang, J. S.; Luo, J. G.; Wang, X. B.; Kong, L. Y. *J. Nat. Prod.* **2009**, *72* (11), 2014. doi:10.1021/np900485t.
(5) Gunning, P. J.; Jeffs, L. B.; Isman, M. B.; Towers, G. H. N. *Phytochemistry*, **1994**, *36* (5), 1245. doi:10.1016/S0031-9422(00)89645-4.
(6) Rodríguez, B. *Magn. Reson. Chem.* **2003**, *41* (3), 206. doi:10.1002/mrc.1159.
(7) Mohamad, K.; Martin, M. T.; Litaudon, M.; Gaspard, C.; Sevenet, T.; Pais, M. *Phytochemistry*,**1999**, *52* (8), 1461. doi:10.1016/S0031-9422(99)00455-0.
(8) Wang, L. Y.; Wang, N. L.; Yao, X. S.; Miyata, S.; Kitanaka, S. *J. Nat. Prod.* **2003**, *66* (5), 630. doi:10.1021/np0205396.
(9) Liu, Y. H.; Abreu, P. *Phytochemistry*, **2006**, *67* (13), 1309. doi:10.1016/j.phytochem.2006.05.004.
(10) Mitsui, K.; Maejima, M.; Saito, H.; Fukaya, H.; Hitotsuyanagi, Y.; Takeya, K. *Tetrahedron*, **2005**, *61* (44), 10569. doi:10.1016/j.tet.2005.08.044.
(11) Mitsui, K.; Saito, H.; Yamamura, R.; Fukaya, H.; Hitotsuyanagi, Y.; Takeya, K. *Chem. Pharm. Bull. (Tokyo)*, **2007**, *55* (10), 1442. doi:10.1248/cpb.55.1442.
(12) Salvemini, D.; Wang, Z. Q.; Wyatt, P. S.; Bourdon, D. M.; Marino, M. H.; Manning, P. T.; Currie, M. G. *Br. J. Pharmacol.* **1996**, *118* (4), 829.
(13) Rahman, A. *Studies in Natural Products Chemistry*; Rios, J. L.; Recio, M. C.; Manez, S.; Giner, R. M., Eds; Elsevier: Amsterdam, 2000; Vol. 22, pp. 93–143.
(14) Yang, X. W.; Feng, L.; Li, S. M.; Liu, X. H.; Li, Y. L.; Wu, L.; Shen, Y. H.; Tian, J. M.; Zhang, X.; Liu, X. R.; Wang, N.; Liu, Y. H.; Zhang, W. D. *Bioorg. Med. Chem.* **2010**, *18* (2), 744. doi:10.1016/j.bmc.2009.11.055.
(15) Yodsaoue, O.; Karalai, C.; Ponglimanont, C.; Tewtrakul, S.; Chantrapromma, S. *Phytochemistry*, **2010**, *71* (14–15), 1756. doi:10.1016/j.phytochem.2010.06.016.
(16) Tewtrakul, S.; Subhadhirasakul, S.; Karalai, C.; Ponglimanont, C.; Cheenpracha, S. *Food Chem.* **2009**, *115* (2), 534. doi:10.1016/j.foodchem.2008.12.057.

Can. J. Chem. Downloaded from www.nrcresearchpress.com by Renmin University of China on 09/02/12
For personal use only.

Development of a solid polymer electrolyte membrane based on sulfonated poly(ether ether) ketone and polysulfone for fuel cell applications

Srinivasan Guhan, Rethinasabapathy Muruganantham, and Dharmalingam Sangeetha

Can. J. Chem. Downloaded from www.nrcresearchpress.com by Renmin University of China on 09/02/12
For personal use only.

Abstract: Polymer electrolyte membranes made of sulfonated poly(ether ether)ketone (SPEEK) and polysulfone (PSf) (2–10 wt %) were prepared by a solution casting method. The characteristic properties of the SPEEK/PSf polymer blend membranes were investigated using thermogravimetric analysis (TGA), scanning electron microscopy (SEM), and the AC impedance method. The SPEEK/PSf blend membranes showed good thermal and mechanical properties and appreciable ionic conductivity. It was revealed that the addition of PSf into the SPEEK matrix could markedly improve the electrochemical properties of the resulting membranes, which can be accomplished by a simple blend method. As a result, the SPEEK/PSf blends appear to be good candidates for the proton exchange membrane fuel cell (PEMFC) and direct methanol fuel cell (DMFC) applications. These blend membranes, having various amounts of PSf (2–10 wt %), were investigated in PEMFC and DMFC. The power densities were about 400 and 50 mW/cm^2 for PEMFC and DMFC, respectively. This makes PSf-based DMFC and PEMFC suitable for application in portable devices and transportation, respectively.

Key words: SPEEK, polysulfone, blend membranes, proton conductivity, polymer electrolyte.

Résumé : On a préparé des membranes de polymère électrolyte de poly(éther éther)cétone sulfonée (PEECS) et de polysulfone (PSf) (2 à 10 wt %) en procédant par la méthode de coulée à partir d'une solution. On a étudié les propriétés caractéristiques des membranes de polymères mixtes PEECS/PSf en faisant appel à l'analyse thermogravimétrique (ATG), la microscopie électronique à balayage (MEB) et la méthode d'impédance à courant alternatif. Les membranes de polymères mixtes PEECS/PSf présentent de bonnes propriétés thermiques et mécaniques ainsi qu'une conductivité appréciable. Leurs propriétés ont permis de montrer que l'addition de PSf dans la matrice de PEECS permet d'améliorer d'une façon marquée les propriétés électrochimiques des membranes qui en résultent et ceci peut être réalisé par une simple opération de mélange. On peut donc en conclure que les mélanges de PEECS de PSf pourraient être de bons candidats pour des applications dans une pile à combustible à membrane échangeuse de protons (PCAEP) et une pile à combustible à méthanol direct (PCMD). On a examiné les propriétés des membranes mixtes comportant diverses quantités de PSf (2 à 10 wt %) dans des systèmes de PCAEP et de PCMD. Les densités de puissance sont respectivement de 400 et de 50 mW/cm^2 pour la PCAEP et la PCMD. Ces caractéristiques suggèrent que les puissances des polymères mixtes, à base de PSf, dans des systèmes de PCAEP et de PCMD, pourraient respectivement être utilisables dans des dispositifs portables et pour le transport.

Mots-clés : polymère électrolyte de poly(éther éther)cétone sulfonée (PEECS), polysulfone, membranes mixtes, conductivité du proton, polymère électrolyte.

[Traduit par la Rédaction]

Introduction

In the past two decades, fuel cells have emerged as a feasible alternative to conventional hydrocarbon-based power sources because of their high power density and overall low emission levels.[1] The direct methanol fuel cell (DMFC) has been under development for applications over a broad range of power outputs in different operating environments. One of the key components that determines the efficiency of the fuel cell is the proton exchange membrane (PEM), which not only acts as a medium for the transportation of protons but also as a barrier that prevents mixing of the fuel gases (hydrogen and oxygen). The current fuel cell technology is based on perfluorosulfonic acid membranes as electrolytes such as Nafion,[2–4] which exhibits many attractive properties like excellent proton conductivity and high thermal and mechanical stabilities.

Among the diverse fuel cells, the proton exchange membrane fuel cells (PEMFCs) offer the advantages of high power density, low operating temperatures (60–100 °C) with consequent rapid start up, and dynamic response. However, the major barriers of PEM fuel cells using hydrogen as a fuel includes production, distribution, storage, humidification, etc. Also, the very low flash point of hydrogen (–423 F; 1 degree Fahrenheit = 5/9 K) causes increasing concerns about

Received 3 February 2011. Accepted 26 September 2011. Published at www.nrcresearchpress.com/cjc on 22 December 2011.

S. Guhan, R. Muruganantham, and D. Sangeetha. Department of Chemistry, Anna University Chennai, Chennai 600 025, India.

Corresponding author: Dharmalingam Sangeetha (e-mail: sangeetha@annauniv.edu).

Can. J. Chem. Downloaded from www.nrcresearchpress.com by Renmin University of China on 09/02/12
For personal use only.

the safety issues of hydrogen. All these limitations enabled researchers to think of other fuels that can be easily oxidized. Direct oxidation fuel cells using liquid methanol as a fuel has already attracted intensive research.[5–8]

The commercialization of the Nafion membrane was severely affected because of drawbacks such as (*i*) high cost; (*ii*) non eco-friendly nature; (*iii*) high crossover of methanol, especially in the case of the DMFC; (*iv*) dependence on relative humidity in maintaining proton conductivity; and (*v*) loss of proton conductivity at elevated temperatures, etc. To overcome these shortcomings associated with the Nafion and other similar perfluorinated membranes, several hydrocarbon-based aromatic polymers were considered for the synthesis of PEM. It includes sulfonated poly(ether ether)ketone (SPEEK),[9–11] sulfonated polyphenylene oxide (SPPO),[12,13] and sulfonated polybenzimidazole.[14–16] In all of these cases, the ionic conductivity at higher temperatures (>100 °C) must be improved, which implies that better water retention at higher temperatures is an absolute requirement. In this context, to enhance the water-retention property of the polymer electrolyte membranes and also to improve the stability of such membranes, various inorganic fillers such as silica, titania, zeolites, and montmorillonite (MMT) have been added into the polymer systems.[17–24] Among the various aromatic hydrocarbon-based polymers, SPEEK has been demonstrated to exhibit a stable performance that is comparable to Nafion in a fuel cell at 50 °C for more than 4300 h. To enhance the proton conductivity of SPEEK, the incorporation of several inorganic heteropolyacids was considered.[25–27]

In our current investigation, we tried to evaluate the performance of SPEEK membranes incorporated with various amounts of polysulfone (PSf). The ion-exchange capacity (IEC) was found to be appreciable. However, there is a decrease in the IEC values when the content of PSf was increased from 2% to 10%. Durability studies were performed and the membranes were stable for more than 6 h. All blend membranes were stable up to 200 °C for successful application as PEM in the PEMFC and the DMFC. The mechanical properties were found tincrease with increasing PSf content. The proton conductivity was found to be in the range of 10^{-3} S/cm, which is appreciable for the PEMFC and the DMFC.

Experimental

Materials and chemicals

PEEK was procured from Victrex, UK, and was dried overnight at 100 °C before use. PSf was kindly supplied by Sigma-Aldrich, USA. Sulfuric acid, *N*-methyl pyrollidone (NMP), and methanol were obtained from SRL Chemicals, India. Pt and Pt/Ru catalysts were procured from Arora Matthey, India.

Sulfonation of PEEK

The process of sulfonation is considered to be the most important stage during the synthesis of the polymer electrolyte. It not only provides the exchangeable protons to make the polymer capable of exchanging ions, especially protons, but also increases the hydrophilicity of the polymer electrolyte. An increase in the hydrophilic character is highly appreciable as it increases the water uptake capacity that in turn increases the proton conduction, the most characteristic property for the polymer electrolyte to be used in fuel cells.

The quantity of sulfuric acid for the desirable degree of sulfonation (40%) was calculated by carrying out the sulfonation reaction of PEEK with different amounts of sulfuric acid. The optimum amount was found to be 20 mL for 1 g of PEEK. In a typical process, ~10 g of dry PEEK was taken in a three-necked round-bottomed flask and 200 mL of sulfuric acid was added and the contents of the flask were vigorously stirred at room temperature. After the desired time, the contents of the flask were poured onto a large excess of crushed ice. The innumerable number of fibres that were formed was recovered by filtration. It was then washed several times with deionised water until the pH of the wash water fell between 6.5 and 7.0. It was then dried in an oven at 90 °C for 10 h. The resulting product was the sulfonated form of SPEEK.

Preparation of the blend membrane

To prepare the blend membranes, desired amounts of SPEEK and PSf were dissolved separately in NMP. After complete dissolution, the PSf solution was added slowly to the SPEEK solution. It was then kept under stirring for 6 h and degassed by ultrasonication. The solution was poured onto a clean Petri dish. The solution was kept in a hot air oven at 90 °C for 12 h. The blend membrane was obtained in the form of a clear, pale brown, transparent membrane. It was peeled off from the Petri dish and was stored for further investigation. The variations in the composition of the different blends are given in Table 1.

Characterization

The IEC indicates the number of mequiv of ions in 1 g of the dry polymer. It was determined by the titration method. The membrane in its acid form was weighed and then soaked in an aqueous solution containing a large excess of KCl to extract all the protons from the membrane. The electrolyte solution was then neutralized using a very dilute Na_2CO_3 solution of known concentration (0.01 N). The equivalent weight (EW) values were calculated from the dry weight of the membrane divided by the volume and the normality of the Na_2CO_3 solution. The IEC values were expressed as the number of milliequivalents of sulfonic groups per gram of dry polymer.

The amount of solvent intake by the membranes was studied. The dried membranes were weighed and soaked in water and methanol separately and allowed to get equilibrated at room temperature for 24 h, above which the weight was constant. The swollen membranes were then quickly weighed after blotting the surface water and the values noted. The swelling degree was determined using the formula

$$\mathrm{SW} = \frac{M_{\mathrm{wet}} - M_{\mathrm{dry}}}{M_{\mathrm{dry}}} 100$$

where M_{wet} = weight of the wet membrane and M_{dry} = weight of the dry membrane.

The measurements of proton conductivity (σ, S/cm) of the membranes were carried out using an Autolab potentiostat galvanostat impedance analyser. Membranes with the required dimensions were cut and pretreated with 0.01 N sulphuric

Can. J. Chem. Downloaded from www.nrcresearchpress.com by Renmin University of China on 09/02/12
For personal use only.

Table 1. Blend membrane code and composition.

Membrane code (SPX)	% Composition of SPEEK:PSf
SP 0	100:00
SP 2	98:02
SP 4	96:04
SP 6	94:06
SP 8	92:08
SP 10	90:10

Note: For SPX, S refers to sulfonated poly (ether ether)ketone (SPEEK), P refers to polysulfone (PSf), and X denotes the dosage of PSf in the blend membrane.

acid and kept in water for 100% hydration. Then they were placed between two silver electrodes with an area of 1.33 cm^2 with a uniform pressure applied to hold the system. The cell set-up was Ag/SPEEK + PSf/Ag. The resistance offered by the membrane was calculated and then converted to conductivity values using the formula

$$\sigma = L/(RA)$$

where R is the resistance offered by the membrane in Ω, L is the thickness of the membrane in cm, and A is the area of the membrane in cm^2.

The methanol permeability is a serious factor that reduces the efficiency of the fuel cell particularly in the case of DMFCs. The permeation not only allows the methanol fuel to the cathodic compartment, but also the mixing of the fuel with the incoming gas at the cathode. This drastically reduces the performance of the fuel cell. The methanol permeabilities of the blend membranes were analyzed using a diaphragm diffusion cell, consisting of two glass bottles that can be interconnected with a capacity of 50 cm^3. The membrane can be clamped between the two compartments. Initially, 25 mL of deionised water was taken in compartment A and 25 mL of 20% *v*/*v* methanol in water was taken in compartment B. As a result of the concentration difference between the two compartments, methanol flux arose across the membrane. The increase in the methanol concentration with respect to time in compartment A was followed using a PAL II digital refractometer.

NMR spectra were obtained with Bruker NMR spectrometer using deuterated dimethylsulfoxide as the solvent. The presence of the sulfonic acid group was confirmed from the NMR spectra.

The surface morphology of the blend membranes was investigated using a scanning electron microscope (SEM, JEOL 6360). A piece of membrane was vacuum sputtered with a thin layer of gold prior to SEM examination. The nature of the pores and the level of dispersion of PSf were examined.

For checking the durability of the blend membranes, the following procedure was adopted. Initially, a 4 ppm ferrous ammonium sulfate in 3% H_2O_2 solution was freshly prepared and the temperature of the solution was maintained at 80 °C. A 0.5 cm^2 membrane was cut and soaked in the solution. The time required for the physical disintegration of the blend membrane was carefully noted down and reported. The reaction was expected to occur by a free radical mechanism and the probable mechanism is shown in Scheme 1.

Thermogravimetric analysis (TGA) is mainly carried out to determine the thermal stability of the blend membranes. The change in weight of the membrane with an increase in temperature at a heating rate of 20 °C/min in a temperature range between 30 and 800 °C was followed using a SDT Q600 US analyser.

The mechanical properties were obtained from a Hounsfield universal testing machine. The sample size used was 5 mm × 50 mm as reported by Jung et al.[28] The cross-head speed was set at a constant speed of 10 mm/min. For each testing reported, at least three measurements were taken and the average value was reported.

The IR spectra (450–4000 cm^{-1}) for the dried membranes were recorded with a PerkinElmer FTIR spectrometer at 25 ± 2 °C. The samples were dried at 100 °C for 1 h before recording the spectrum.

X-ray diffraction (XRD) measurements were performed using an X'Pert Pro diffractometer. The dried samples were mounted on an aluminium sample holder. The scanning angle ranged from 1° to 80° with a scanning rate of 2°/min. All the spectra were taken at ambient temperature (25 ± 2 °C).

Membrane electrode assembly preparation

Membrane electrode assembly (MEA) was obtained by sandwiching the SPEEK/PSf blend membrane between the anode and cathode. For the PEMFC, the electrocatalyst used was 20 wt % Pt on Vulcan XC-72 for both the anode (loading 0.25 mg/cm^2) and cathode (loading 0.5 mg/cm^2) sides. For the DMFC, the electrocatalysts used were 40 wt % Pt:Ru (2:1) on Vulcan XC-72 and 20 wt % Pt on Vulcan XC-72 in the anode (loading 2.5 mg/cm^2) and in the cathode (loading 0.5 mg/cm^2), respectively. The catalyst layer was obtained by mixing the catalyst, isopropyl alcohol (IPA), deionised water, and Nafion solution as the binder and was coated on the carbon cloth. The electrode dimensions were 5 cm × 5 cm (total area, 25 cm^2). The MEA was fabricated uniaxially by hot pressing the anode and cathode onto the membrane at 95 °C and 150 kg/cm^2 for 3 min.

Single cell test

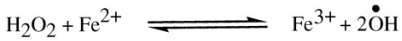
Performance of the fabricated membranes was measured via the PEMFC and DMFC test stations. A single cell with a 25 cm^2 active area was used in both the PEMFC and DMFC experiments. The external load was applied by means of an electronic load that was manually controlled. The fabricated MEA was placed in the test cell and the bolts were tightened with an equal torque on each bolt. In the PEMFC, the H_2 and O_2 flow rates were maintained at 40 mL/min in the anode and cathode, respectively, whereas ifor the DMFC, 2 mol/L methanol with a flow rate of 20 mL/min was fed into the anode side and O_2 with a flow rate of 40 mL/min was fed into the cathode side.

Results and discussion

The IEC values of the various blend membranes are given in Table 2. Although the IEC values were found to be decreasing with the content of PSf, all the membranes exhibit an IEC value better than Nafion 117, which was reported to

Scheme 1. Mechanism of durability testing.

Step 1



Step 2

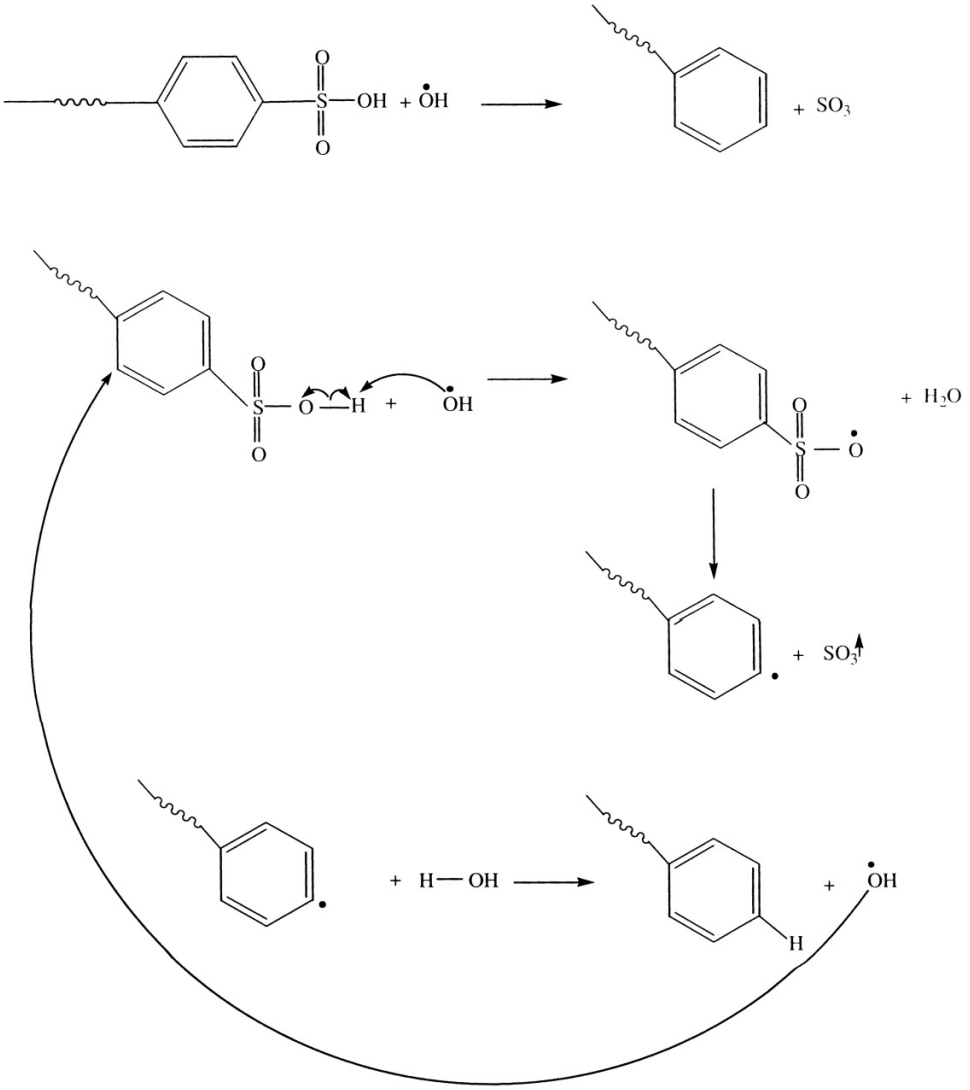


Table 2. Ion-exchange capapcity (IEC), absorption, and proton conductivity.

Sample No.	Membrane code (SPX)	IEC (mequiv/g)	Absorption (%)		Proton conductivity (mS/cm)
			Water	Methanol	
1	SPEEK	2.23	15.18	17.89	8.73
2	SP 2	2.01	14.54	13.67	7.40
3	SP 4	1.91	12.63	10.42	6.57
4	SP 6	1.79	10.83	7.91	6.09
5	SP 8	1.61	7.91	5.43	5.43
6	SP 10	1.45	5.98	3.11	4.81

Note: For SPX, S refers to sulfonated poly(ether ether)ketone (SPEEK), P refers to polysulfone (PSf), and X denotes the dosage of PSf in the blend membrane.

Can. J. Chem. Downloaded from www.nrcresearchpress.com by Renmin University of China on 09/02/12
For personal use only.

Scheme 2. Proton assignment in ^{1}H NMR.

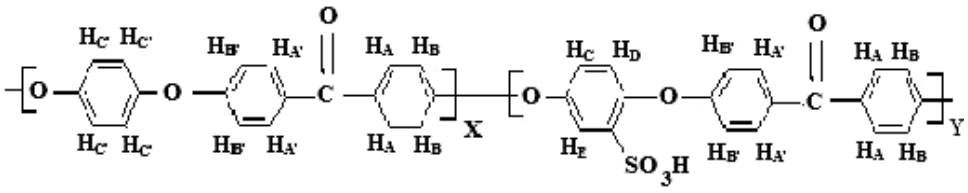


Table 3. Methanol permeability values of the blend membranes.

Membrane code (SPX)	Methanol permeability (%)
SP 0	21.0
SP 2	18.7
SP 4	16.8
SP 6	14.5
SP 8	13.1
SP 10	10.9

Note: For SPX, S refers to sulfonated poly(ether ether)ketone (SPEEK), P refers to polysulfone (PSf), and X denotes the dosage of PSf in the blend membrane.

be 0.91 mequiv/g.[29] Actually, the protons that are available in the sulfonic acid groupings of SPEEK were responsible for the exchange of ions. When the concentration of PSf is increased, the concentration of SPEEK decreases and, in other words, the effective concentrations of the sulfonic acid groupings decrease. This obviously accounts for the decreasing trend in IEC values.

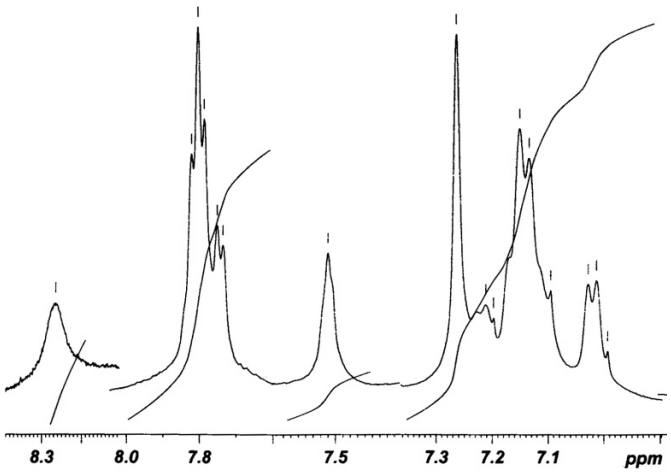
The water/alcohol absorption results are given in Table 2. The water uptake of Nafion 117 was reported to be 28.51%[30] and, in the case of the blend membranes, the water absorption was found to be decreasing with increasing content of PSf. The methanol absorption was also found to follow a similar trend like water absorption. This may be due to the reduction in the number of hydrophilic sulfonic acid groupings as the content of PSf is increased. The decreased methanol absorption content revealed that the blend membranes could be uitable candidates for use in DMFCs, when methanol is used as the fuel.

The results of the proton conductivity are given in Table 2. The proton conductivity of Nafion 117 was reported to be 2.95×10^{-2} S/cm. The proton conductivity of SPEEK tends to decrease with the addition of PSf. Water uptake plays an essential role in ionomer membrane properties. A possible reason that could be attributed to the reduction in the proton conductivity is that, as the content of PSf is increased in the blend, the effective concentration of SPEEK and hence the SO_3H groupings decreases. The protons of the sulfonic acid groupings are mainly responsible for the proton conductivity.

Methanol permeability plays a vital role in DMFCs. With an increase in the PSf loading, the methanol permeability decreases and the results are shown in Table 3. This may be due to the hydrophobic nature of PSf that prevents methanol from transferring through the membrane. The decrease in the methanol permeability makes these electrolyte blend membranes possible low cost alternatives to Nafion 117 for applications in DMFCs.

The ^{1}H NMR spectra of the SPEEK sample is shown in Fig. 1 and the numbering of various protons is shown in Scheme 2. In the spectra, the $H_{C'}$ of the unsubstituted hydroquinone ring of the PEEK repeat unit appears as a characteristic singlet at 7.26.[31] The presence of a sulfonic acid group causes a new peak at 7.51 that can be assigned to H_E and two doublets at 7.20 and 7.14 that may be assigned to the H_C and H_B protons in the sulfonated hydroquinone ring, respectively.

Fig. 1. ^{1}H NMR spectra of sulfonated poly(ether ether)ketone (SPEEK).



The SEM images of SPEEK and two representative blend membranes are given in Fig. 2. The SEM image looks dense, clear, and homogenous indicating a very good compatibility between the constituent polymers. Even at higher magnifications, the blend membranes showed no fissures, which may be due to the high boiling solvent used for the casting purpose. The evaporation of NMP solvent (boiling point 203 °C) was performed at 90 °C, indicating a very slow process of evaporation. On the other hand, if the evaporation was done at a faster rate or if a low boiling solvent was used, fissures could be observed.[32] The blend membranes appear to be pore-free even at higher magnification.

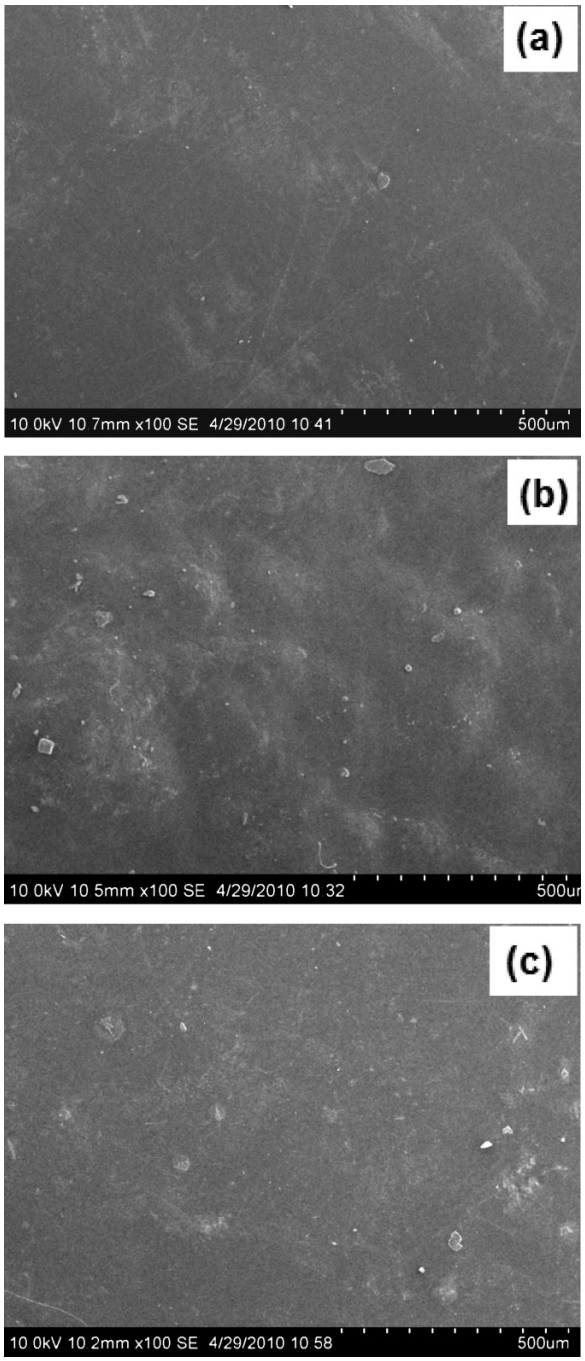
In the durability study, the time taken for the physical disintegration of the various blends was studied and the results are shown in Table 4. It is evident from the table that there is a gradual increase in the withstanding ability of the blends with increasing PSf content. An increase in the durability of the blend membranes indicates that the individual constituent polymeric materials in the blends are compatible with each other.

The TGA spectra of the blend membranes are given in Fig. 3. A three-stage degradation was observed. The initial loss up to 175 °C may be attributed to the loss of physically and chemically bound water along with a trace amount of residual solvent. The weight loss that occurs between 200 and

Can. J. Chem. Downloaded from www.nrcresearchpress.com by Renmin University of China on 09/02/12
For personal use only.

Can. J. Chem. Downloaded from www.nrcresearchpress.com by Renmin University of China on 09/02/12
For personal use only.

Fig. 2. Scanning electron microscopy (SEM) images of (*a*) sulfonated poly(ether ether)ketone (SPEEK), (*b*) SP 4, and (*c*) SP 10. For SPX, S refers to sulfonated poly(ether ether)ketone (SPEEK), P refers to polysulfone (PSf), and X denotes the dosage of PSf in the blend membrane.



375 °C may be due to the loss of sulfonic acid groupings. The third weight loss from 450 to 600 °C may be correlated to the main chain degradation.

The tensile strength and percentage elongation at the breaks of the various blend membranes are given in Table 4. There is an increase in the tensile strength with an increase in the content of PSf. One possible reason for this kind of behaviour in the mechanical properties may be due to the very good compatibility among the constituents, thus making the membrane stiffer. As a result, an increase in the tensile property was observed.

Table 4. Durability and mechanical properties.

Membrane code (SPX)	Durability (h)	Tensile strength (MPa)	Percentage elongation (%)
SP 0	2.5	24.6	28.7
SP 2	3.1	28.6	24.8
SP 4	3.5	31.3	22.1
SP 6	4.0	35.9	19.7
SP 8	4.4	38.5	15.4
SP 10	4.6	40.2	13.6

Note: For SPX, S refers to sulfonated poly(ether ether)ketone (SPEEK), P refers to polysulfone (PSf), and X denotes the dosage of PSf in the blend membrane.

Fig. 3. Thermal gravimetric analysis (TGA) spectra of (*a*) SP 2, (*b*) SP 4, (*c*) SP 6, (*d*) SP 8, and (*e*) SP 10. For SPX, S refers to sulfonated poly(ether ether)ketone (SPEEK), P refers to polysulfone (PSf), and X denotes the dosage of PSf in the blend membrane.

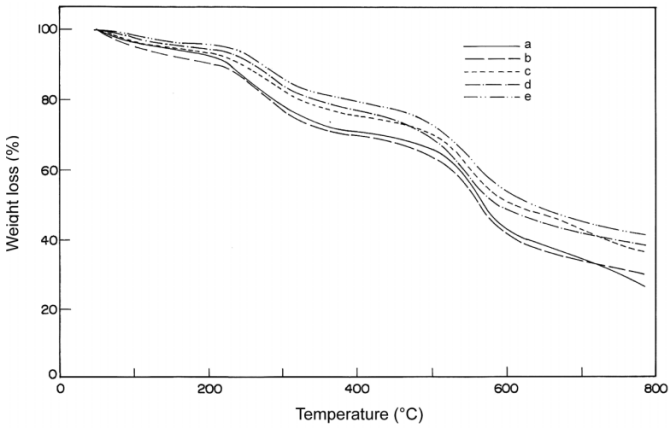
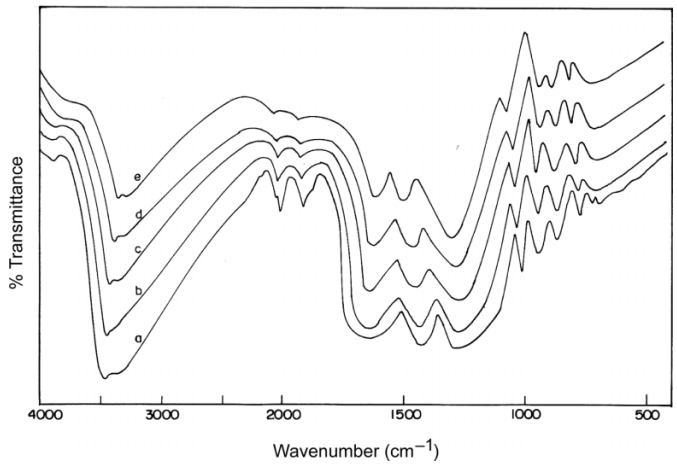


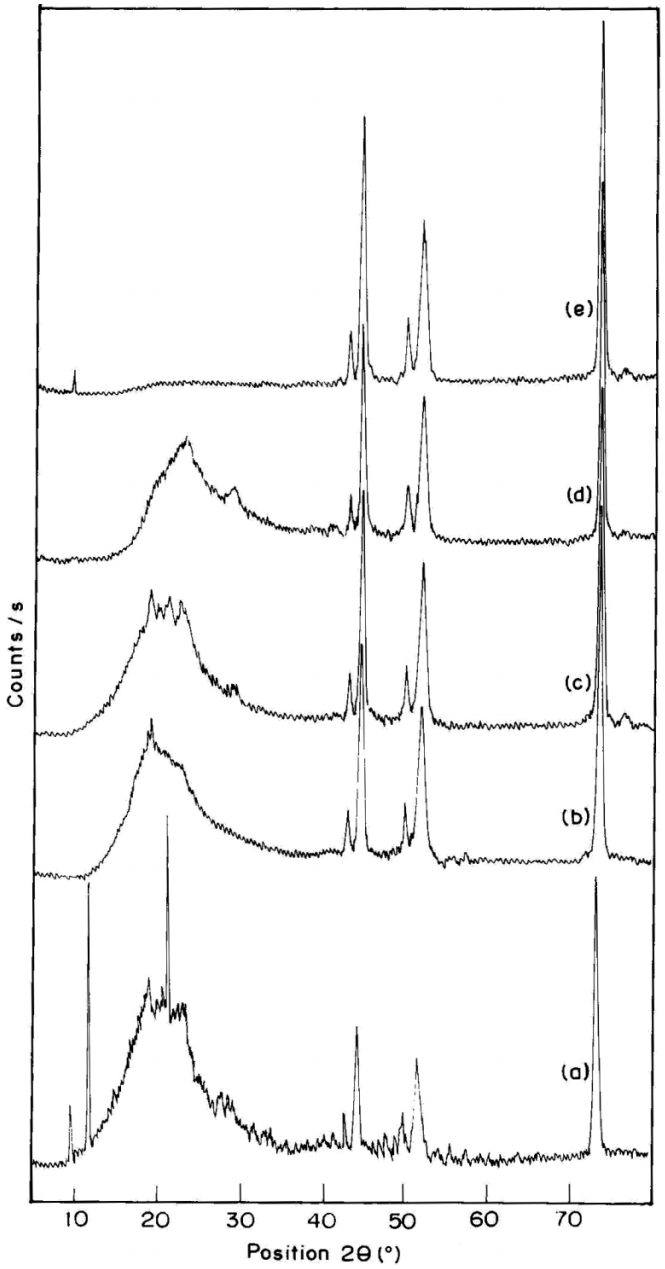
Fig. 4. FT-IR spectra of sulfonated poly(ether ether)ketone (SPEEK) blended with (*a*) 2% polysulfone (PSf), (*b*) 4% PSf, (*c*) 6% PSf, (*d*) 8% PSf, and (*e*) 10% PSf.



The FT-IR spectra of the various blends are shown in Fig. 4. There is a broad envelope in the high-energy region lying between 2100 and 3600 cm^{-1}. It includes the OH stretch of the SO_3H group of SPEEK and the C–H vibrations of the aromatic ring. The C=O vibration gives its peak at

Can. J. Chem. Downloaded from www.nrcresearchpress.com by Renmin University of China on 09/02/12
For personal use only.

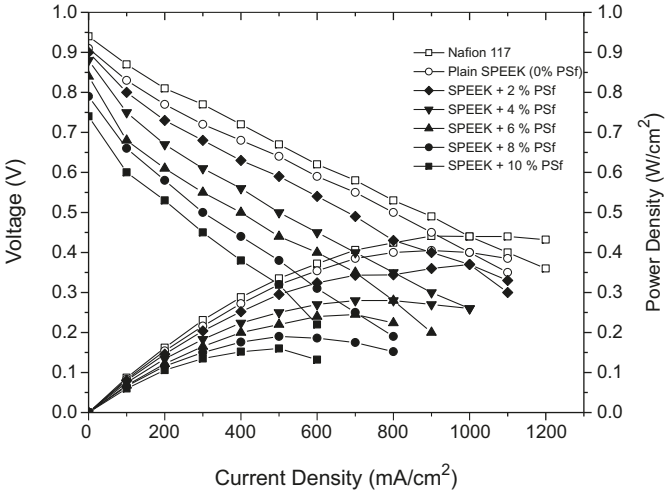
Fig. 5. X-ray diffraction (XRD) spectra of sulfonated poly(ether ether)ketone (SPEEK) with (*a*) 2% polysulfone (PSf), (*b*) 4% PSf, (*c*) 6% PSf, (*d*) 8% PSf, and (*e*) 10% PSf.



1640 cm^{-1}. Generally, this vibration occurs close to 1750 cm^{-1}, but because of the conjugation with the adjacent aromatic ring and phenolic oxygen, it is shifted to a very low value. The asymmetric O=S=O stretch of the sulfonic acid occurs close to 1260 cm^{-1}. There is a band at 1025 cm^{-1} that is due to the symmetric O=S=O stretch.

The XRD spectra of the blends are given in Fig. 5. In the case of the blend with 2% PSf, a broad envelope is observed between $2\theta = 10°–30°$. When the concentration of PSf was increased in the blend, the crystalline peak became broader and slowly disappeared when the concentration of PSf was elevated to 10%. Overall, the amorphous nature is enhanced with an increasing concentration of PSf, which could result in better mechanical properties, especially the tensile strength.

Fig. 6. Polarization curves of sulfonated poly(ether ether)ketone (SPEEK) with 2%–10% polysulfone (PSf) for proton exchange membrane fuel cells (PEMFCs).



Single cell performance in the PEMFC and the DMFC

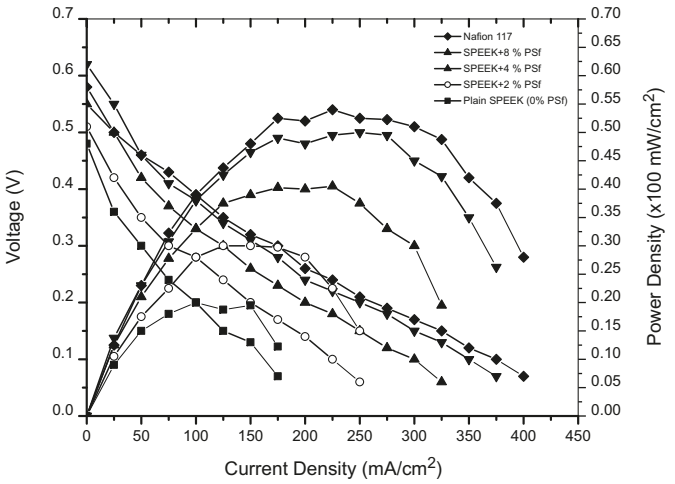
Figure 6 compares the polarization curves of the SPEEK/PSf blend membranes (2–10 wt %) with those of plain SPEEK and Nafion 117 membranes at room temperature in the PEMFC. For example, the SPEEK/PSf blend membranes show OCV values around 0.9 V, which is in comparison to that of plain SPEEK and Nafion 117 membranes. The maximum powers reached for the cell constructed with SPEEK/PSf membranes are 410, 340, 280, 224, 152, and 135 mW/cm^2 for the membranes with PSf loading of 0% (plain SPEEK), 2%, 4%, 6%, 8%, and 10%, respectively. The current density of the plain SPEEK membrane was 800 mA/cm^2 at 0.55 V, whereas that of SPEEK + 10% PSf blend was 220 mA/cm^2 under the same conditions. The reduction in the current density may be attributed to the resistance offered by the presence of PSf in the blend.

Figure 7 compares the polarization curves of SPEEK/PSf blend membranes (2–10 wt %) with those of plain SPEEK and Nafion 117 membranes at room temperature in the DMFC. The blend membranes show better performance in the DMFC than the plain SPEEK membrane because of low methanol crossover. The lower methanol crossover suppresses the catalyst poisoning and lowers the mixed potential at the cathode, resulting in an increase in the OCV under steady state conditions. The lower methanol crossover in the blend membrane could not only help lead to better long-term stability and performance but also to lower the Pt catalyst loading at the cathode. At 0.3 V, the maximum powesr reached for the cells constructed with SPEEK/PSf membranes are 51 and 37.5 mW/cm^2 for the membranes with a PSf loading of 8% and 4%, respectively, whereas under the same operating conditions, the maximum power densities offered by Nafion 117 and SPEEK (0% PSf) membranes are 46.5 and 16 mW/cm^2, respectively, at room temperature with a 2 mol/L methanol solution.

Conclusion

In the present study, blend membranes with SPEEK and PSf were synthesized. The blends were found to be mechanically

Fig. 7. Polarization curves of sulfonated poly(ether ether)ketone (SPEEK) with 2%–8% polysulfone (PSf) for the direct methanol fuel cell (DMFC).



stable. The SEM images revealed good compatibility between the constituents of the blend. The prepared membranes were found to be thermally stable upto 225 °C, which is highly suitable for the DMFC applications. The water retention capacity as well as the proton conductivity of the blend membranes was decreased due to the introduction of PSf. However, the proton conductivity was in the order of 10^{-3} S/cm. The presence of PSf has also influenced the durability of the membrane and it was found to be increasing. There was a very good reduction in the methanol permeability of the blends when compared to virgin SPEEK indicating a possible alternate for Nafion in the DMFC.

In the PEMFC, SPEEK/polysulphone blend membranes give the same results with that of Nafion 117 and exhibited OCV values around 0.9 V and the maximum power density obtained was around 400 mW/cm^2 and possesses excellent stability and performance. In the DMFC, the assistance of polysulphone enhances the resistivity to methanol crossover. The lower methanol crossover suppresses the catalyst poisoning and lowers the mixed potential at the cathode resulting in an increase in the OCV at steady state. The lower methanol crossover in the blend membrane could not only help lead to a better long-term stability and performance but also to lower the Pt catalyst loading at the cathode. The maximum power reached for the DMFC constructed with SPEEK/PSf membranes are around 50 mW/ cm^2, which is found to be most promising for the DMFC applications.

Can. J. Chem. Downloaded from www.nrcresearchpress.com by Renmin University of China on 09/02/12
For personal use only.

Acknowledgement

The authors would like to thank the Board of Research in Nuclear Sciences (BRNS), Mumbai, for their financial assistance via grant Nos. 2007/36/08-BRNS/597 and 2007/36/08-BRNS/0045.

References

(1) Kim, G. S.; Sui, P. C.; Shah, A. A.; Djilali, N. *J. Power Sources* **2010**, *195* (10), 3240. doi:10.1016/j.jpowsour.2009.11.110.

(2) Savinell, R.; Yeager, E.; Tryk, D.; Landau, U.; Wainright, J.; Weng, D.; Lux, K.; Litt, M.; Rogers, C. *J. Electrochem. Soc.* **1994**, *141* (4), L46. doi:10.1149/1.2054875.

(3) Miyake, N.; Wainright, J. S.; Savinell, R. F. *J. Electrochem. Soc.* **2001**, *148* (8), A898. doi:10.1149/1.1383071.

(4) Malhotra, S.; Datta, R. *J. Electrochem. Soc.* **1997**, *144* (2), L23. doi:10.1149/1.1837420.

(5) Wasmus, S.; Kuver, A. *J. Electroanal. Chem.* **1999**, *461* (1–2), 14. doi:10.1016/S0022-0728(98)00197-1.

(6) McNicol, B. D.; Rand, D. A. J.; Williams, K. R. *J. Power Sources* **1999**, *83* (1–2), 15. doi:10.1016/S0378-7753(99)00244-X.

(7) Baldauf, M.; Preidel, W. *J. Power Sources* **1999**, *84* (2), 161. doi:10.1016/S0378-7753(99)00332-8.

(8) Lamy, C.; Lima, A.; LeRhun, V.; Delime, F.; Countanceau, C.; Leger, J.-M. *J. Power Sources* **2002**, *105* (2), 283. doi:10.1016/S0378-7753(01)00954-5.

(9) Mikhailenko, S. D.; Zaidi, S. M. J.; Kaliaguine, S. *Catal. Today* **2001**, *67* (1–3), 225. doi:10.1016/S0920-5861(01)00290-5.

(10) Alberti, G.; Casciola, M.; Massinelli, L.; Bauer, B. *J. Membr. Sci.* **2001**, *185* (1), 73. doi:10.1016/S0376-7388(00)00635-9.

(11) Zaidi, S. M. J.; Mikhailenko, S. D.; Robertson, G. P.; Guiver, M. D.; Kaliaguine, S. *J. Membr. Sci.* **2000**, *173* (1), 17. doi:10.1016/S0376-7388(00)00345-8.

(12) Mohr, R.; Kudela, V.; Schauer, J.; Richau, K. *Desalination* **2002**, *147* (1–3), 191. doi:10.1016/S0011-9164(02)00533-7.

(13) Smitha, B.; Sridhar, S.; Khan, A. A. *J. Membr. Sci.* **2003**, *225* (1–2), 63. doi:10.1016/S0376-7388(03)00343-0.

(14) Weng, D.; Wainright, J. S.; Landau, U.; Savinell, R. F. *J. Electrochem. Soc.* **1996**, *143* (4), 1260. doi:10.1149/1.1836626.

(15) Jones, D. J.; Roziere, J. *J. Membr. Sci.* **2001**, *185* (1), 41. doi:10.1016/S0376-7388(00)00633-5.

(16) Staiti, P. *Mater. Lett.* **2001**, *47* (4–5), 241. doi:10.1016/S0167-577X(00)00241-X.

(17) Krishnan, P.; Park, J. S.; Kim, C. S. *J. Membr. Sci.* **2006**, *279* (1–2), 220. doi:10.1016/j.memsci.2005.12.010.

(18) Tricoli, V.; Nannetti, F. *Electrochim. Acta* **2003**, *48* (18), 2625. doi:10.1016/S0013-4686(03)00306-2.

(19) Tasaki, K.; Desousa, R.; Wang, H.; Gasa, J.; Venkatesan, A.; Pugazhendhi, P.; Loutfy, R. O. *J. Membr. Sci.* **2006**, *281* (1–2), 570. doi:10.1016/j.memsci.2006.04.052.

(20) Won, J.; Kang, Y. S. *Macromol. Symp.* **2003**, *204* (1), 79. doi:10.1002/masy.200351408.

(21) Gummaraju, R. V.; Moore, R. B.; Mauritz, K. A. *J. Polym. Sci., B, Polym. Phys.* **1996**, *34* (14), 2383. doi:10.1002/(SICI)1099-0488(199610)34:14<2383::AID-POLB8>3.0.CO;2-X.

(22) Shao, P. L.; Mauritz, K. A.; Moore, R. B. *Chem. Mater.* **1995**, *7* (1), 192. doi:10.1021/cm00049a029.

(23) Jung, D. H.; Cho, S. Y.; Peck, D. H.; Shin, D. R.; Kim, J. S. *J. Power Sources* **2003**, *118* (1–2), 205. doi:10.1016/S0378-7753(03)00095-8.

(24) Mauritz, K. A. *Mater. Sci. Eng.* **1998**, *C6*, 121.

(25) Guhan, S.; Kumar, N. A.; Sangeetha, D. *Chin. J. Polym. Sci.* **2009**, *27* (2), 157. doi:10.1142/S0256767909003789.

(26) Guhan, S.; Sangeetha, D. *Int. J. Polym. Mater.* **2009**, *58* (2), 87. doi:10.1080/00914030802565442.

(27) Guhan, S.; Sangeetha, D. *ICFAI Univ. J. Chem.* **2008**, *1*, 7.

(28) Jung, D. H.; Cho, S. Y.; Peck, D. H.; Shin, D. R.; Kim, J. S. *J. Power Sources* **2002**, *106* (1–2), 173. doi:10.1016/S0378-7753(01)01053-9.

(29) Rhee, C. H.; Kim, H. K.; Chang, H.; Lee, J. S. *Chem. Mater.* **2005**, *17* (7), 1691. doi:10.1021/cm048058q.

(30) Lee, H. C.; Hong, H. S.; Kim, Y. M.; Choi, S. H.; Hong, M. Z.; Lee, H. S.; Kim, K. *Electrochim. Acta* **2004**, *49* (14), 2315. doi:10.1016/j.electacta.2004.01.012.
(31) Gaowen, Z.; Zhentao, Z. *J. Membr. Sci.* **2005**, *261* (1–2), 107. doi:10.1016/j.memsci.2005.03.036.
(32) Ramya, K.; Velayutham, G.; Subramaniam, C. K.; Rajalakshmi, N.; Dhathathreyan, K. S. *J. Power Sources* **2006**, *160* (1), 10. doi:10.1016/j.jpowsour.2005.12.082.

Can. J. Chem. Downloaded from www.nrcresearchpress.com by Renmin University of China on 09/02/12
For personal use only.

Synthesis of 2,3,4-trisubstituted pyrroles via a facile reaction of vinyl azides and tosylmethyl isocyanide

Wenteng Chen, Jiaan Shao, Zhi Li, Marc A. Giulianotti, and Yongping Yu

Can. J. Chem. Downloaded from www.nrcresearchpress.com by Renmin University of China on 09/02/12
For personal use only.

Abstract: A facile synthesis of polysubstituted pyrroles from tosylmethyl isocyanide (TOSMIC) and readily synthesized vinyl azides was developed. The reaction proceeded under mild conditions in the presence of base. 2-Tosyl-substituted pyrroles were obtained in moderate to good isolated yields. Additionally, a base-initiated one-pot pyrrole synthesis also was developed using carboxaldehydes, ethyl 2-azidoacetate, and TOSMIC.

Key words: vinyl azides, 2,3,4-trisubstituted pyrroles, cyclization reaction, nucleophilic reaction, multicomponent reaction.

Résumé : On a développé une méthode facile de synthèse de pyrroles polysubstitués à partir de l'isocyanure de tosylméthyle (ICTOSM) et d'azotures de vinyles facilement accessibles. La réaction s'effectue dans des conditions douces, en présence d'une base. On a obtenu des 2-tosylpyrroles substitués avec des rendements en produits isolés allant de modérés à bons. De plus, on a mis au point une synthèse monotope de pyrroles initiée par une base et impliquant des carboxaldéhydes, du 2-azidoacétate d'éthyle et de l'isocyanure de tosylméthyle.

Mots-clés : azotures de vinyle, pyrroles 2,3,4-trisubstitués, réaction de cyclisation, réaction nucléophile, réaction à plusieurs composants.

[Traduit par la Rédaction]

Introduction

Substituted pyrroles are important heterocycles that are present as the core scaffolds in many natural products[1] and are reported to contribute to a wide spectrum of biological activities.[2] Thus, pyrroles are interesting synthetic targets for obtaining biologically active compounds. Over the past decades, a number of classical and new multicomponent reactions (MCRs) have been reported for the preparation of pyrroles, including the Hantzsch reaction,[3] the Paal–Knorr cyclization reaction of 1,4-dicarbonyl compounds and amines,[4] transition-metal-based strategies,[5] the Van Leusen cyclization,[6] and other cyclizations.[7–11] Despite the numerous approaches for the synthesis of pyrroles that have been developed so far, it is still challenging to prepare structurally diverse pyrroles from readily available building blocks.

Vinyl azide is a pivotal three-atom synthon for the formation of nitrogen-containing heterocycles (azaheterocycles). Especially, it has been reported that vinyl azide was employed with various transition metals in pyrrole synthesis.[9] Recently, we studied the base initial synthesis of polysubstituted pyrrolo[1,2-α]pyrazine using vinyl azides as the starting material.[12] As part of our ongoing studies on synthetic applications of vinyl azides, we present a facile and general synthesis from tosylmethyl isocyanide (TOSMIC) and vinyl azides, furnishing 2,3,4-trisubstituted pyrroles in the presence of base. In the previous studies, the azide group of vinyl azides lost nitrogen and incorporated the nitrogen atom into a newly formed molecule. In this report, however, the azide group of vinyl azides serves as a leaving group, which is crucial for the final aromatization of the intermediate to the final products. Meanwhile, in the Van Leusen synthesis, pyrroles are formed via elimination of sulfinic acid from the intermediate cycloadducts. Therefore, the present work would be a good addition to the synthetic application of Van Leusen's reagent. Moreover, previous reports on the use of vinyl azides as reaction partners for the preparation of 2-tosyl-substituted pyrroles are rare.

Results and discussion

The reaction of vinyl azide **1a**, derived from benzaldehyde, with TOSMIC was selected as a prototype reaction (Table 1) for the identification of the optimal reaction conditions for this synthesis. No reaction was observed when base was absent (Table 1, entry 1), but the transformation occurred in the presence of a variety of bases at room temperature to form **3a** as the major product (Table 1). Screening of the bases revealed

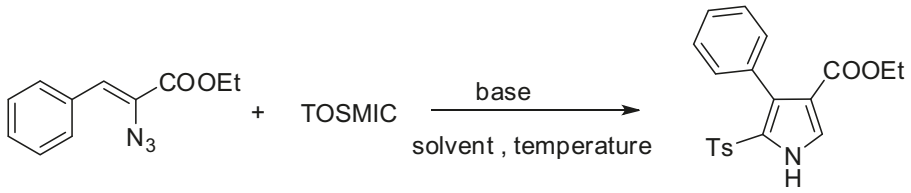
Received 28 May 2011. Accepted 8 September 2011. Published at www.nrcresearchpress.com/cjc on 22 December 2011.

W. Chen, J. Shao, and Z. Li. Institute of Materia Medica, College of Pharmaceutical Sciences, Zhejiang University, Hangzhou 310058, P. R. China.
M.A. Giulianotti. Torrey Pines Institute for Molecular Studies, 11350 Village Parkway, Port St. Lucie, FL 34987, USA.
Y. Yu. Institute of Materia Medica, College of Pharmaceutical Sciences, Zhejiang University, Hangzhou 310058, P.R. China; Torrey Pines Institute for Molecular Studies, 11350 Village Parkway, Port St. Lucie, FL 34987, USA.

Corresponding author: Yongping Yu (e-mail: yyu@zju.edu.cn).

Can. J. Chem. Downloaded from www.nrcresearchpress.com by Renmin University of China on 09/02/12
For personal use only.

Table 1. Optimization of reaction conditions.



graphic **1a** **2** **3a**

Entry	Base	Solvent	*t* (°C)	Yield (%)[a]
1	—	CH_3CN	25	n.r.
2	DBU	CH_3CN	25	24
3	*t*-BuOK	CH_3CN	25	30
4	Cs_2CO_3	CH_3CN	25	46
5	K_2CO_3	CH_3CN	25	26
6	NaH	CH_3CN	25	51
7	NaH	DMF	25	Trace
8	NaH	THF	25	n.r.
9	NaH	DCM	25	n.r.
10	NaH	Dioxane	25	n.r.
11	NaH	CH_3CN	40	35

Note: n.r, no result; DBU, 1,8-diazabicyclo[5.4.0]undec-7-ene. Reaction conditions: vinyl azide (0.2 mmol, 1.0 equiv), tosylmethyl isocyanide (TOSMIC, 0.4 mmol, 2.0 equiv), base (0.5 mmol, 2.5 equiv), 2 mL solvent, 24 h, room temperature.

[a]Isolated yield.

that NaH was the most efficient base (Table 1, entries 2–11). When 1,8-diazabicyclo[5.4.0]undec-7-ene (DBU), a strong base, was employed, the desired product **3a** was obtained with a yield of 24% (Table 1, entry 2). When the base was changed to Cs_2CO_3, the yield of **3a** was 46% (Table 1, entry 4). Other inorganic bases, such as *t*-BuOK and K_2CO_3 gave the product in low yields (Table 1, entries 3 and 5). Optimization of the solvent showed that acetonitrile (Table 1, entry 6) was superior to other solvents (Table 1, entries 6–10). This reaction was also tested at a higher temperature, but with a decrease in the yield (Table 1, entry 11). Based on this initial study, the optimal conditions were obtained in acetonitrile at room temperature when NaH was employed as a base (51%; Table 1, entry 6).

With the optimized reaction condition in hand, this methodology was evaluated using different substituted vinyl azides (**1**) with TOSMIC (**2**; Table 2). The vinyl azides (Table 2, entries 1–10) were readily prepared from the corresponding aromatic carboxaldehydes with ethyl 2-azidoacetate via a Knoevenagel condensation.[9] Additional vinyl azides (Table 2, entries 11–14) were prepared from the corresponding olefins by successive reaction with bromine then with sodium azide.[13]

As presented in Table 2, various substituted vinyl azides with TOSMIC worked well to provide the corresponding pyrroles in moderate to good isolated yields. The reaction could tolerate an array of R_1 substituents in the vinyl azides such as aryl, H, and the furyl moiety (Table 2). Vinyl azides bearing an electron-withdrawing group on the aryl ring gave good yields (62%–86%; Table 2, entries 4–9). The case is illustrated in Table 2, entry 8, where the vinyl azide with a NO_2 substituent at the aryl group gave a good isolated yield (86%). The influence of R_2 substituents in this reaction is also illustrated in Table 2 (entries 11–14). When an arylcarbonyl group occurred at the α-position of the vinyl azide, it lead to a sharp decrease in the yield (<45%; Table 2, entries 11–14), compared with entry 4 (75%; Table 2). The α-*N*-morpholinylcarbonyl-substituted vinyl azide greatly favored this process, providing the corresponding product in higher yield (94%; Table 2, entry 12).

α-Azidostyrene (Table 2, entry 11) was detrimental to the desired transformation, most probably because of its relatively low electron-withdrawing properties.

On the basis of the results presented above, we propose the following possible mechanism for this reaction, as shown in Scheme 1. First, it is expected to involve a Michael addition of TOSMIC **2** to the vinyl azides **1**, followed by an intramolecular cyclization reaction. The desired product **3** is generated via intramolecular proton transfer and the elimination of the N_3^- group.

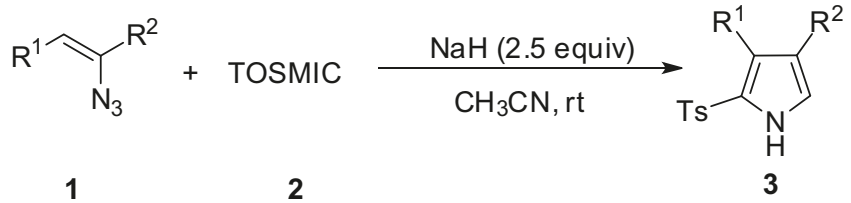
Multicomponent reactions have a couple of distinct advantages.[14] In this report, a one-pot three-component process was also investigated, where a mixture of 3-nitrobenzaldehyde and ethyl 2-azidoacetate was stirred under the Knoevenagel condensation conditions using NaH as the base for 2 h at –15 °C, followed by addition of TOSMIC. The reaction mixture was then stirred at room temperature (rt) for 24 h to give the desired product **3h** (Scheme 2) with a total yield of 54%.

Conclusions

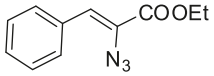
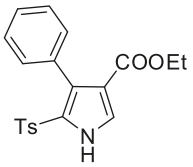
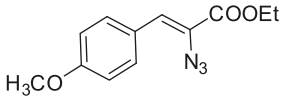
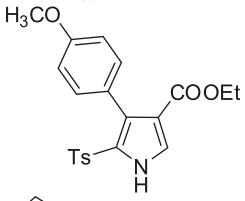
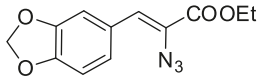
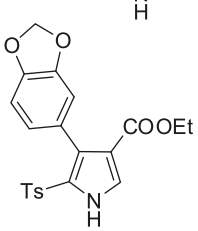
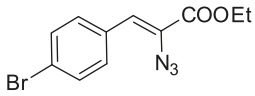
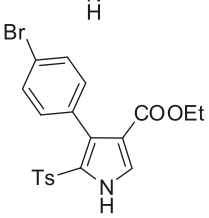
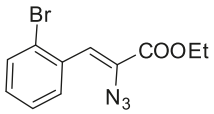
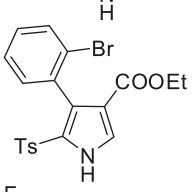
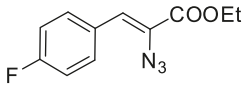
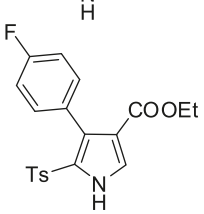
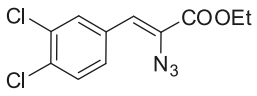
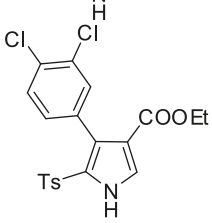
In conclusion, we have developed an efficient approach for the generation of 2,3,4-trisubstituted pyrroles in moderate to good yields. This reaction was realized through a domino process from TOSMIC and readily available vinyl azides. Expansion of the method to a one-pot, three-component protocol to generate pyrrole **3h** from commercially available aromatic carboxaldehyde, ethyl 2-azidoacetate, and TOSMIC

Can. J. Chem. Downloaded from www.nrcresearchpress.com by Renmin University of China on 09/02/12
For personal use only.

Table 2. Cyclization of tosylmethyl isocyanide (TOSMIC) with various vinyl azides.

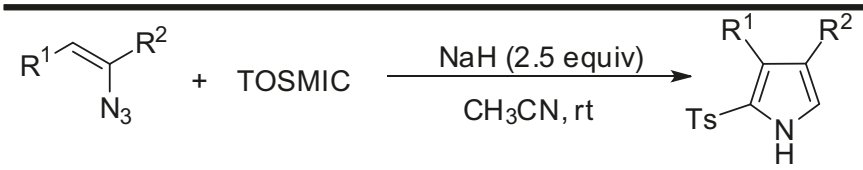


1 **2** **3**

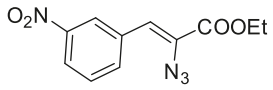
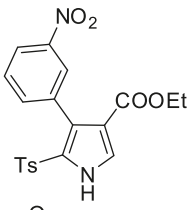
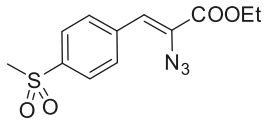
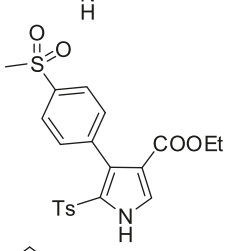
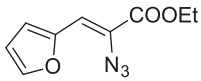
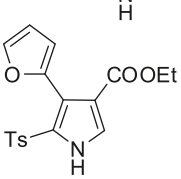
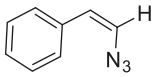
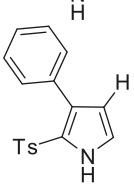
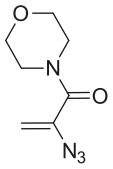
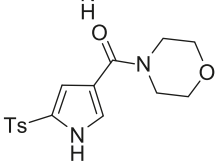
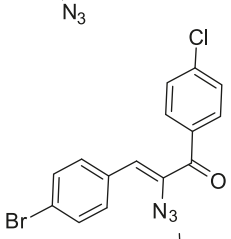
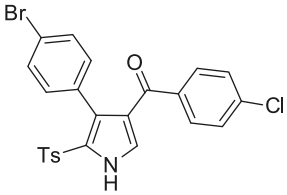
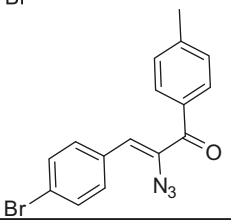
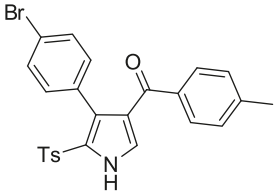
Entry	Substrate		Product		Yield (%)[a]
1		**1a**		**3a**	51
2		**1b**		**3b**	42
3		**1c**		**3c**	50
4		**1d**		**3d**	75
5		**1e**		**3e**	78
6		**1f**		**3f**	64
7		**1g**		**3g**	62

Can. J. Chem. Downloaded from www.nrcresearchpress.com by Renmin University of China on 09/02/12
For personal use only.

Table 2 (*concluded*).

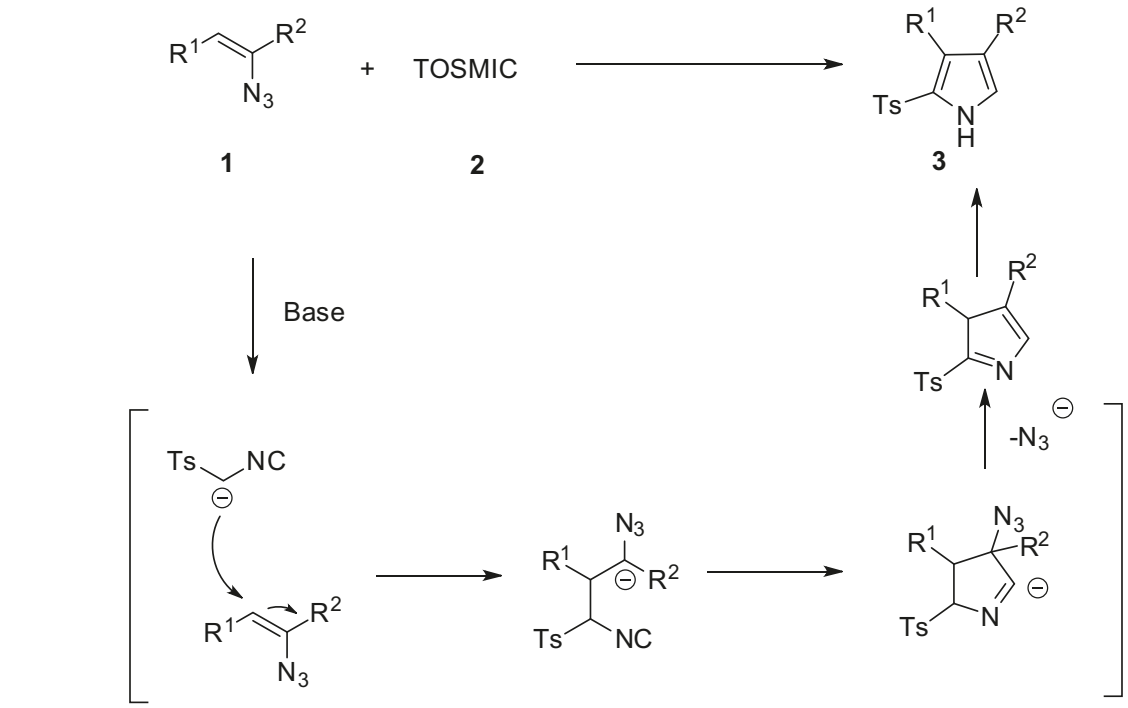


1 **2** **3**

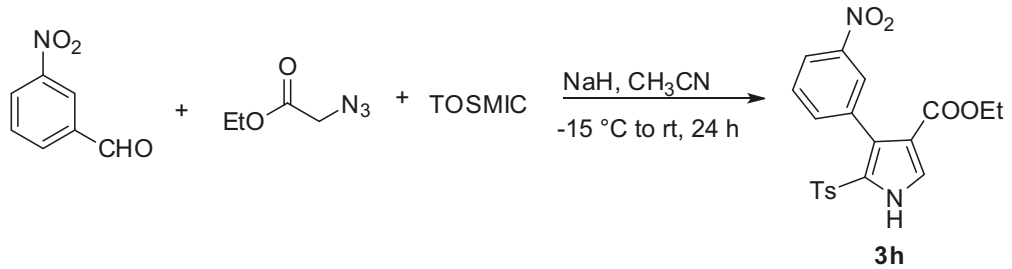
Entry	Substrate		Product		Yield (%)[a]
8		**1h**		**3h**	86
9		**1i**		**3i**	72
10		**1j**		**3j**	46
11		**1k**		**3k**	n.r.
12		**1l**		**3l**	94
13		**1m**		**3m**	45
14		**1n**		**3n**	36

Note: n.r., no result. Reactions were performed in anhydrous CH_3CN at room temperature with 2.0 equiv of TOSMIC **2** under an N_2 atmosphere.

Scheme 1. Proposed mechanism for the synthesis of pyrroles.



Scheme 2. One-pot three-component synthesis of polysubstituted pyrroles.



also was accomplished. The domino process includes a Knoevenagel condensation, a Michael addition, and intramolecular cycloaddition.

Experimental section

General methods

All solvents were purified according to standard methods prior to use. Reactions were run under an atmosphere of nitrogen unless mentioned otherwise. Purifications of the reaction products were carried out by chromatography using silica gel (200–300 mesh). Melting points were recorded on a BÜCHI B-540 melting point apparatus. Infrared spectra were recorded on an FTIR spectrophotometer. NMR spectra were recorded for ^{1}H NMR at 500 MHz and for ^{13}C NMR at 125 MHz. For ^{1}H NMR, tetramethylsilane (TMS) served as the internal standard ($\delta = 0$) and data are reported as follows: chemical shift, integration, multiplicity (s = singlet, d = doublet, t = triplet, q = quartet, and m = multiplet), and coupling constant(s) in Hz. For ^{13}C NMR, TMS ($\delta = 0$) or $CDCl_3$ ($\delta = 77.26$) was used as the internal standard and spectra were obtained with complete proton decoupling. LC–MS and HRMS data were obtained using ESI ionization.

General procedure A for the synthesis of 3

A mixture of vinyl azide **1** (1.0 mmol), TOSMIC **2** (2.0 mmol), and NaH (2.5 mmol) was stirred in anhydrous CH_3CN (2 mL) at rt under nitrogen for 24 h. The reaction mixture was quenched with water (10 mL) and then extracted three times with EtOAc (3 × 10 mL). The combined organic extracts were washed with brine (10 mL), dried over $MgSO_4$, and concentrated. The crude product was purified by chromatography (silica gel; petroleum ether:ethyl acetate = 3:1) to afford **3** and was crystallized from a mixture of EtOAc with hexanes.

General procedure B for the one-pot synthesis of 3h

A mixture of 3-nitrobenzaldehyde (1.0 mmol), ethyl 2-azidoacetate (5.0 mmol), and NaH (5.0 mmol) was stirred in anhydrous CH_3CN (5 mL) at –15 °C under nitrogen for 2 h. A solution of TOSMIC (3.0 mmol) and NaH (3.0 mmol) in anhydrous CH_3CN was then added into this mixture. The reaction was stirred at –15 °C to rt for 24 h. After the completion of the reaction, the resulting solution was quenched with saturated NH_4Cl solution (10 mL) and then extracted three times with EtOAc (3 × 10 mL). The combined organic extracts were washed with brine (10 mL), dried over $MgSO_4$,

Can. J. Chem. Downloaded from www.nrcresearchpress.com by Renmin University of China on 09/02/12
For personal use only.

Can. J. Chem. Downloaded from www.nrcresearchpress.com by Renmin University of China on 09/02/12
For personal use only.

and concentrated. The crude product was purified by chromatography (silica gel; petroleum ether:ethyl acetate = 3:1) to afford **3h** and was crystallized from a mixture of EtOAc with hexanes.

Ethyl 4-phenyl-5-tosyl-1*H*-pyrrole-3-carboxylate (3a)

Treatment of **1a** (217 mg, 1.0 mmol) with **2** (390 mg, 2.0 mmol) by General procedure A gave **3a** (188 mg, 51%) as a pale yellow solid (EtOAc/hexane); mp 168–170 °C. IR (KBr, cm^{-1}) ν: 3451, 3234, 2986, 1684, 770, 698, 661. ^{1}H NMR (500 MHz, $CDCl_3$) δ: 1.07 (3H, t, J = 7.0 Hz), 2.34 (3H, s), 4.08 (2H, q, J = 7.0 Hz), 7.07 (2H, d, J = 8.0 Hz), 7.14 (2H, d, J = 7.5 Hz), 7.25 (2H, d, J = 8.0 Hz), 7.30 (2H, t, J = 7.5 Hz), 7.34 (1H, d, J = 7.0 Hz), 7.58 (1H, d, J = 2.0 Hz), 10.07 (1H, brs). ^{13}C NMR (125 MHz, $CDCl_3$) δ: 14.1, 21.7, 60.2, 117.9, 126.4, 127.4, 127.7, 128.0, 130.0, 130.7, 130.8, 131.5, 138.2, 144.4, 163.5. LC–MS (ESI) m/z $[M + H]^+$: 370.3. HRMS (EI) m/z calcd for $C_{20}H_{19}NO_4S$ $(M)^+$: 369.1035; found: 369.1033.

Ethyl 4-(4-methoxyphenyl)-5-tosyl-1*H*-pyrrole-3-carboxylate (3b)

Treatment of **1b** (247 mg, 1.0 mmol) with **2** (390 mg, 2.0 mmol) by General procedure A gave **3b** (168 mg, 42%) as a pale yellow solid (EtOAc/hexane); mp 140–142 °C. IR (KBr, cm^{-1}) ν: 3451, 3236, 2987, 1674, 807, 768. ^{1}H NMR (500 MHz, $CDCl_3$) δ: 1.12 (3H, t, J = 7.0 Hz), 2.35 (3H, s), 3.86 (3H, s), 4.10 (2H, q, J = 7.0 Hz), 6.86 (2H, d, J = 8.5 Hz), 7.08–7.11 (4H, m), 7.28 (2H, d, J = 8.5 Hz), 7.56 (1H, d, J = 3 Hz), 10.13 (1H, brs). ^{13}C NMR (125 MHz, $CDCl_3$) δ: 14.1, 21.5, 55.3, 59.9, 112.8, 117.6, 123.4, 126.4, 127.2, 127.4, 129.4, 130.7, 131.8, 138.1, 144.2, 159.3, 163.4. LC–MS (ESI) m/z $[M + H]^+$: 400.4. HRMS (EI) m/z calcd for $C_{21}H_{21}NO_5S$ $(M)^+$: 399.1140; found: 399.1137.

Ethyl 4-(benzo[*d*][1,3]dioxol-5-yl)-5-tosyl-1*H*-pyrrole-3-carboxylate (3c)

Treatment of **1c** (261 mg, 1.0 mmol) with **2** (390 mg, 2.0 mmol) by General procedure A gave **3c** (207 mg, 50%) as a pale yellow solid (EtOAc/hexane); mp 173–175 °C. IR (KBr, cm^{-1}) ν: 3450, 3270, 2924, 1692, 810, 771. ^{1}H NMR (500 MHz, $CDCl_3$) δ: 1.14 (3H, t, J = 7.0 Hz), 2.37 (3H, s), 4.11 (2H, q, J = 7.0 Hz), 5.98 (2H, s), 6.57 (1H, d, J = 1.5 Hz), 6.62 (1H, dd, J_1 = 1.5 Hz, J_2 = 8.0 Hz), 6.76 (1H, d, J = 8.0 Hz), 7.13 (2H, d, J = 8.5 Hz), 7.36 (2H, d, J = 8.5 Hz), 7.56 (d, 1H, J = 3.5 Hz), 10.11 (1H, brs). ^{13}C NMR (125 MHz, $CDCl_3$) δ: 14.3, 21.8, 60.2, 101.2, 107.5, 111.3, 117.9, 124.4, 124.9, 126.5, 127.5, 127.8, 129.6, 130.4, 138.2, 144.6, 146.9, 147.4, 163.4. LC–MS (ESI) m/z $[M + H]^+$: 414.3. HRMS (EI) m/z calcd for $C_{21}H_{19}NO_6S$ $(M)^+$: 413.0933; found: 413.0935.

Ethyl 4-(4-bromophenyl)-5-tosyl-1*H*-pyrrole-3-carboxylate (3d)

Treatment of **1d** (296 mg, 1.0 mmol) with **2** (390 mg, 2.0 mmol) by General procedure A gave **3d** (336 mg, 75%) as a pale yellow solid (EtOAc/hexane); mp 185–187 °C. IR (KBr, cm^{-1}) ν: 3450, 3223, 2924, 1685, 818, 778. ^{1}H NMR (500 MHz, $CDCl_3$) δ: 1.11 (3H, t, J = 7.0 Hz), 2.37 (3H, s), 4.09 (2H, q, J = 7.0 Hz), 7.02 (2H, d, J = 8.5 Hz), 7.12 (2H, d, J = 8.5 Hz), 7.28 (2H, d, J = 8.5 Hz), 7.44 (2H, d, J = 8.5 Hz), 7.59 (1H, s), 9.87 (1H, brs). ^{13}C NMR (125 MHz, $CDCl_3$) δ: 14.2, 21.8, 60.3, 118.0, 122.4, 126.3, 127.5, 128.0, 129.3, 129.7, 130.5, 130.7, 132.5, 138.0, 144.8, 163.3. LC–MS (ESI) m/z $[M + H]^+$: 448.2. HRMS (EI) m/z calcd for $C_{20}H_{18}NO_4SBr$ $(M)^+$: 447.0140; found: 447.0147.

Ethyl 4-(2-bromophenyl)-5-tosyl-1*H*-pyrrole-3-carboxylate (3e)

Treatment of **1e** (296 mg, 1.0 mmol) with **2** (390 mg, 2.0 mmol) by General procedure A gave **3e** (350 mg, 78%) as an off-white solid (EtOAc/hexane); mp 179–181 °C. IR (KBr, cm^{-1}) ν: 3450, 3219, 2982, 1690, 763. ^{1}H NMR (500 MHz, $CDCl_3$) δ: 1.01 (3H, t, J = 7.0 Hz), 2.38 (3H, s), 4.00–4.11 (2H, m), 7.11 (2H, d, J = 8.5 Hz), 7.21–7.24 (1H, m), 7.28–7.32 (3H, m), 7.34–7.37 (1H, m), 7.45 (1H, d, J = 7.0 Hz), 7.61 (1H, d, J = 3.5 Hz), 9.92 (1H, brs). ^{13}C NMR (125 MHz, $CDCl_3$) δ: 14.0, 21.8, 60.2, 118.8, 125.3, 125.9, 126.7, 127.7, 128.7, 129.6, 129.7, 131.9, 132.8, 133.1, 137.4, 144.7, 163.3. LC–MS (ESI) m/z $[M + H]^+$: 448.2. HRMS (EI) m/z calcd for $C_{20}H_{18}NO_4SBr$ $(M)^+$: 447.0140; found: 447.0139.

Ethyl 4-(4-fluorophenyl)-5-tosyl-1*H*-pyrrole-3-carboxylate (3f)

Treatment of **1f** (235 mg, 1.0 mmol) with **2** (390 mg, 2.0 mmol) by General procedure A gave **3f** (248 mg, 64%) as a pale yellow solid (EtOAc/hexane); mp 183–185 °C. IR (KBr, cm^{-1}) ν: 3451, 3220, 2986, 1686, 808, 781. ^{1}H NMR (500 MHz, $CDCl_3$) δ: 1.10 (3H, t, J = 7.0 Hz), 2.36 (3H, s), 4.09 (2H, q, J = 7.0 Hz), 6.98–7.02 (2H, m), 7.10–7.14 (4H, m), 7.26–7.29 (2H, m), 7.59 (1H, s), 10.08 (1H, brs). ^{13}C NMR (125 MHz, $CDCl_3$) δ: 14.2, 21.8, 60.3, 114.5 (d, J = 21 Hz), 118.0, 126.5, 127.4, 127.9, 129.6, 129.7, 132.8 (d, J = 8 Hz), 138.1, 144.7, 162.8 (d, J = 245 Hz), 163.4. LC–MS (ESI) m/z $[M + H]^+$: 388.3. HRMS (EI) m/z calcd for $C_{20}H_{18}NO_4FS$ $(M)^+$: 387.0941; found: 387.0938.

Ethyl 4-(3, 4-dichlorophenyl)-5-tosyl-1*H*-pyrrole-3-carboxylate (3g)

Treatment of **1g** (286 mg, 1.0 mmol) with **2** (390 mg, 2.0 mmol) by General procedure A gave **3g** (272 mg, 62%) as a pale yellow solid (EtOAc/hexane); mp 191–193 °C. IR (KBr, cm^{-1}) ν: 3451, 3237, 2924, 1686, 770, 672. ^{1}H NMR (500 MHz, $CDCl_3$) δ: 1.11 (3H, t, J = 7.0 Hz), 2.39 (3H, s), 4.10 (2H, q, J = 7.0 Hz), 7.03 (1H, s), 7.07 (1H, d, J = 8.0 Hz), 7.16 (2H, d, J = 8.0 Hz), 7.33 (2H, d, J = 8.0 Hz), 7.40 (1H, d, J = 8.0 Hz), 7.60 (1H, s). ^{13}C NMR (125 MHz, $CDCl_3$) δ: 14.2, 21.8, 60.4, 118.0, 126.3, 127.6, 128.5, 129.5, 129.8, 130.3, 131.5, 131.6, 132.3, 132.4, 137.8, 145.1, 163.1. LC–MS (ESI) m/z $[M + H]^+$: 438.2. HRMS (EI) m/z calcd for $C_{20}H_{17}NO_4SCl_2$ $(M)^+$: 437.0255; found: 437.0258.

Ethyl 4-(3-nitrophenyl)-5-tosyl-1*H*-pyrrole-3-carboxylate (3h)

Treatment of **1h** (262 mg, 1.0 mmol) with **2** (390 mg, 2.0 mmol) by General procedure B gave **3h** (356 mg, 86%) as a pale yellow solid (EtOAc/hexane); mp 161–163 °C. IR (KBr, cm^{-1}) ν: 3451, 3250, 2984, 1689, 810, 737. ^{1}H NMR (500 MHz, $CDCl_3$) δ: 1.07 (3H, t, J = 7.0 Hz), 2.36 (3H, s), 4.08 (2H, q, J = 7.0 Hz), 7.13 (2H, d, J = 8.0 Hz), 7.32 (2H, d, J = 8 Hz), 7.54 (1H, t, J = 8.0 Hz), 7.62–7.64 (2H, m),

Can. J. Chem. Downloaded from www.nrcresearchpress.com by Renmin University of China on 09/02/12
For personal use only.

7.78 (1H, s), 8.22 (1H, d, J = 8.0 Hz). ^{13}C NMR (125 MHz, $CDCl_3$) δ: 14.2, 21.7, 60.5, 118.0, 122.9, 125.6, 126.7, 127.4, 127.7, 128.5, 129.9, 133.5, 137.2, 137.9, 145.3, 147.5, 163.1. LC–MS (ESI) m/z $[M + H]^+$: 415.3. HRMS (EI) m/z calcd for $C_{20}H_{18}N_2O_6S$ $(M)^+$: 414.0886; found: 414.0889.

Ethyl 4-(4-(methylsulfonyl)phenyl)-5-tosyl-1*H*-pyrrole-3-carboxylate (3i)

Treatment of **1i** (295 mg, 1.0 mmol) with **2** (390 mg, 2.0 mmol) by General procedure A gave **3i** (322 mg, 72%) as a pale yellow solid (EtOAc/hexane); mp 180–182 °C. IR (KBr, cm^{-1}) ν: 3452, 3266, 2986, 1684, 771. ^{1}H NMR (500 MHz, $CDCl_3$) δ: 1.11 (3H, t, J = 7.0 Hz), 2.36 (3H, s), 3.12 (3H, s), 4.10 (2H, q, J = 7.0 Hz), 7.11 (2H, d, J = 8.0 Hz), 7.27–7.28 (2H, m), 7.38 (2H, d, J = 8.0 Hz), 7.64 (1H, s), 7.88 (2H, d, J = 8.5 Hz). ^{13}C NMR (125 MHz, $CDCl_3$) δ: 14.2, 21.8, 44.8, 60.5, 117.8, 126.4, 126.5, 127.4, 128.3, 128.5, 129.8, 131.9, 137.8, 140.0, 145.1, 163.1. LC–MS (ESI) m/z $[M + H]^+$: 448.3. HRMS (EI) m/z calcd for $C_{21}H_{21}NO_6S_2$ $(M)^+$: 447.0810; found: m/z: 447.0815.

Ethyl 4-(furan-2-yl)-5-tosyl-1*H*-pyrrole-3-carboxylate (3j)

Treatment of **1j** (207 mg, 1.0 mmol) with **2** (390 mg, 2.0 mmol) by General procedure A gave **3j** (165 mg, 46%) as a yellow solid (EtOAc/hexane); mp 209–211 °C. IR (KBr, cm^{-1}) ν: 3451, 3225, 2988, 1685. ^{1}H NMR (500 MHz, $CDCl_3$) δ: 1.10 (3H, t, J = 7.0 Hz), 2.36 (3H, s), 4.09 (2H, q, J = 7.0 Hz), 6.99–7.02 (2H, m), 7.10 (2H, d, J = 8.0 Hz), 7.12–7.14 (1H, m), 7.26 (2H, d, J = 8.0 Hz), 7.59 (1H, s), 9.80 (1H, brs). ^{13}C NMR (125 MHz, $CDCl_3$) δ: 14.2, 21.8, 60.3, 114.4, 114.6, 118.1, 126.2, 127.5, 128.1, 129.6, 132.5, 132.6, 138.1, 144.7, 163.4. LC–MS (ESI) m/z $[M + H]^+$: 360.2. HRMS (EI) m/z calcd for $C_{18}H_{17}NO_5S$ $(M)^+$: 359.0827; found: 359.0826.

Morpholino(5-tosyl-1*H*-pyrrol-3-yl)methanone (3l)

Treatment of **1l** (182 mg, 1.0 mmol) with **2** (390 mg, 2.0 mmol) by General procedure A gave **3l** (314 mg, 94%) as an off-white solid (EtOAc/hexane); mp 202–204 °C. IR (KBr, cm^{-1}) ν: 3451, 3238, 2998, 1625. ^{1}H NMR (500 MHz, DMSO-d_6) δ: 2.37 (3H, s), 3.57 (8H, m), 6.96 (1H, d, J = 1.0 Hz), 7.41–7.43 (3H, m), 7.83 (2H, d, J = 8.5 Hz), 12.77 (1H, brs). ^{13}C NMR (125 MHz, DMSO-d_6) δ: 21.5, 66.7, 115.6, 119.7, 127.2, 127.3, 129.3, 130.5, 139.5, 144.5, 164.2. LC–MS (ESI) m/z $[M + H]^+$: 335.3. HRMS (EI) m/z calcd for $C_{16}H_{18}N_2O_4S$ $(M)^+$: 334.0987; found: 334.0978.

(4-(4-Bromophenyl)-5-tosyl-1*H*-pyrrol-3-yl)(4-chlorophenyl)methanone (3m)

Treatment of **1m** (363 mg, 1.0 mmol) with **2** (390 mg, 2.0 mmol) by General procedure A gave **3m** (232 mg, 45%) as an off-white solid (EtOAc/hexane); mp 225–227 °C. IR (KBr, cm^{-1}) ν: 3451, 1650. ^{1}H NMR (500 MHz, $CDCl_3$) δ: 2.36 (3H, s), 7.03–7.04 (2H, m), 7.11 (2H, d, J = 8.0 Hz), 7.29–7.30 (2H, m), 7.30–7.32 (4H, m), 7.36–7.37 (3H, m), 7.60–7.62 (2H, m). ^{13}C NMR (125 MHz, $CDCl_3$) δ: 21.8, 122.6, 125.2, 126.9, 127.4, 128.5, 128.8, 129.3, 129.8, 130.3, 130.9, 131.0, 132.4, 136.9, 137.8, 139.0, 145.0, 189.3. LC–MS (ESI) m/z $[M + H]^+$: 514.2. HRMS (EI) m/z calcd for $C_{24}H_{17}NO_3SClBr$ $(M)^+$: 512.9801; found: 512.9807.

(4-(4-Bromophenyl)-5-tosyl-1*H*-pyrrol-3-yl)(*p*-tolyl)methanone (3n)

Treatment of **1n** (342 mg, 1.0 mmol) with **2** (390 mg, 2.0 mmol) by General procedure A gave **3n** (178 mg, 36%) as a yellow solid (EtOAc/hexane); mp 180–182 °C. IR (KBr, cm^{-1}) ν: 3451, 1645. ^{1}H NMR (500 MHz, $CDCl_3$) δ: 2.35 (3H, s), 2.36 (3H, s), 7.05 (2H, d, J = 8.5 Hz), 7.10–7.14 (4H, m), 7.31 (2H, d, J = 8.5 Hz), 7.35–7.36 (3H, m), 7.58 (2H, d, J = 8.0 Hz), 10.05 (1H, brs). ^{13}C NMR (125 MHz, $CDCl_3$) δ: 21.8, 122.4, 125.7, 126.7, 127.4, 128.0, 129.1, 129.4, 129.7, 130.5, 130.9, 132.5, 135.9, 138.0, 143.5, 144.8, 190.3. LC–MS (ESI) m/z $[M + H]^+$: 494.3. HRMS (EI) m/z calcd for $C_{25}H_{20}NO_3SBr$ $(M)^+$: 493.0347; found: 493.0343.

Supplementary data

Supplementary data (including experimental procedures, characterization data, and copies of ^{1}H and ^{13}C NMR spectra for all products) are available with the article through the journal Web site at http://nrcresearchpress.com/doi/suppl/10.1139/v11-150.

Acknowledgements

We thank the National Natural Science Foundation of China (Grant Nos. 30772652 and 90813026) and the National Key Tech Project for Major Creation of New Drugs (Grant No. 2009ZX09501-010).

References

(1) (a) Larionov, O. V.; de Meijere, A. *Angew. Chem. Int. Ed.* **2005**, *44* (35), 5664. doi:10.1002/anie.200502140; (b) Smith, N. D.; Huang, D.; Cosford, N. D. P. *Org. Lett.* **2002**, *4* (20), 3537. doi:10.1021/ol0267073.

(2) (a) Silvestri, R.; La Regina, G.; De Martino, G.; Artico, M.; Befani, O.; Palumbo, M.; Agostinelli, E.; Turini, P. *J. Med. Chem.* **2003**, *46* (6), 917. doi:10.1021/jm0256124; (b) Kemnitzer, W.; Drewe, J.; Jiang, S.; Zhang, H.; Crogan-Grundy, C.; Labreque, D.; Bubenick, M.; Attardo, G.; Denis, R.; Lamothe, S.; Gourdeau, H.; Tseng, B.; Kasibhatla, S.; Cai, S. X. *J. Med. Chem.* **2008**, *51* (3), 417. doi:10.1021/jm7010657; (c) Pacorel, B.; Leung, S. C.; Stachulski, A. V.; Davies, J.; Vivas, L.; Lander, H.; Ward, S. A.; Kaiser, M.; Brun, R.; O'Neill, P. M. *J. Med. Chem.* **2010**, *53* (2), 633. doi:10.1021/jm901216v; (d) Plitt, P.; Gross, D. E.; Lynch, V. M.; Sessler, J. L. *Chemistry* **2007**, *13* (5), 1374. doi:10.1002/chem.200601514.

(3) Palacios, F.; Aparicio, D.; de los Santos, J. M.; Vicario, J. *Tetrahedron* **2001**, *57* (10), 1961. doi:10.1016/S0040-4020(01)00033-3.

(4) Bharadwaj, A. R.; Scheidt, K. A. *Org. Lett.* **2004**, *6* (14), 2465. doi:10.1021/ol049044t.

(5) Balme, G. *Angew. Chem. Int. Ed.* **2004**, *43* (46), 6238. doi:10.1002/anie.200461073.

(6) (a) Baxendale, I. R.; Buckle, C. D.; Ley, S. V.; Tamborini, L. *Synthesis* **2009**, *2009* (9), 1485. doi:10.1055/s-0028-1087991; (b) van Leusen, D.; van Echten, E.; van Leusen, A. M. *J. Org. Chem.* **1992**, *57* (8), 2245. doi:10.1021/jo00034a011; (c) van Leusen, A. M.; Siderius, H.; Hoogenboom, B. E.; van Leusen,

D. *Tetrahedron Lett.* **1972**, *13* (52), 5337. doi:10.1016/S0040-4039(01)85244-8.
(7) Robinson, G. M.; Robinson, R. *J. Chem. Soc. Trans.* **1918**, *113*, 639. doi:10.1039/ct9181300639.
(8) Nair, V.; Vinod, A. U.; Rajesh, C. *J. Org. Chem.* **2001**, *66* (12), 4427. doi:10.1021/jo001714v.
(9) (a) Chiba, S.; Wang, Y.-F.; Lapointe, G.; Narasaka, K. *Org. Lett.* **2008**, *10* (2), 313. doi:10.1021/ol702727j; (b) Wang, Y.-F.; Toh, K. K.; Chiba, S.; Narasaka, K. *Org. Lett.* **2008**, *10* (21), 5019. doi:10.1021/ol802120u.
(10) Minetto, G.; Raveglia, L. F.; Sega, A.; Taddei, M. *Eur. J. Org. Chem.* **2005**, *2005* (24), 5277. doi:10.1002/ejoc.200500387.
(11) (a) van Leusen, A. M.; Siderius, H.; Hoogenboom, B. E.; van Leusen, D. *Tetrahedron Lett.* **1972**, *13* (52), 5337. doi:10.1016/S0040-4039(01)85244-8; (b) ten Have, R.; Leusink, F. R.; van Leusen, A. M. *Synthesis* **1996**, *1996* (7), 871. doi:10.1055/s-1996-4306; (c) Dijkstra, H. P.; ten Have, R.; van Leusen, A. M. *J. Org. Chem.* **1998**, *63* (16), 5332. doi:10.1021/jo972216y.
(12) Chen, W.; Hu, M.; Wu, J.; Zou, H.; Yu, Y. *Org. Lett.* **2010**, *12* (17), 3863. doi:10.1021/ol101538x.
(13) Gilchrist, T. L.; Mendonca, R. *ARKIVOC* **2000**, *1*, 769.
(14) (a) Dömling, A.; Ugi, I. *Angew. Chem. Int. Ed.* **2000**, *39* (18), 3168. doi:10.1002/1521-3773(20000915)39:18<3168::AID-ANIE3168>3.0.CO;2-U; (b) Ruijter, E.; Scheffelaar, R.; Orru, R. V. A. *Angew. Chem. Int. Ed.* **2011**, *50* (28), 6234. doi:10.1002/anie.201006515.

Can. J. Chem. Downloaded from www.nrcresearchpress.com by Renmin University of China on 09/02/12
For personal use only.

Synthesis and intramolecular hydrogen bonding of *syn*-9-hydroxy-18-substituted [3.3]metacyclophanes

Kazuya Tazoe, Xing Feng, Bigyan Sharma, Shinpei Miyamoto, and Takehiko Yamato

Can. J. Chem. Downloaded from www.nrcresearchpress.com by Renmin University of China on 09/02/12
For personal use only.

Abstract: Various *anti*-9-methoxy[3.3]metacyclophane-2,11-diones are exclusively obtained by the coupling reaction of the corresponding 1,3-bis(bromomethyl)benzenes and 2,6-bis[2-isocyano-2-(tolylsulfonyl)ethyl]-4-*tert*-butylanisole in dimethylformamide (DMF) with an excess of sodium hydride, from which the corresponding *syn*-[3.3]metacyclophanes (MCPs) are synthesized via anti/syn-isomerization during the Wolff–Kishner reduction. Demethylation of *syn*-9-methoxy[3.3]MCPs with BBr_3 afforded the corresponding *syn*-9-hydroxy[3.3]MCPs in good yields. The existence of the strong intramolecular hydrogen bonding between the 9-hydroxy group and the 18-substituents, such as F, OH, and OMe groups at the opposing aromatic rings, are observed in solution and in the solid state. A distinct low-field shift of the phenolic OH proton was observed in the ^{1}H NMR spectrum compared with that of the 18-unsubstituted analog. Furthermore, O–H···F through-space coupling was observed.

Key words: metacyclophanes, conformation, anti/syn-isomerization, intramolecular hydrogen bonding, through-space coupling.

Résumé : Diverses *anti*-9-méthoxy[3,3]métacyclophane-2,11-diones peuvent être préparées à l'état pur par une réaction de couplage des 1,3-bis(bromométhyl)benzènes et du 2,6-bis[2-isocyano-2-(tolylsulfonyl)éthyl]-4-*tert*-butylanisole, dans le diméthylformamide (DMF), en présence d'un excès d'hydrure de sodium; ces dicétones, soumises à une réaction de Wolff–Kishner, conduisent aux *syn*[3,3]métacyclophanes (MCPs), par le biais d'une isomérisation anti/syn au cours de cette réduction. La déméthylation des *syn*-9-méthoxy[3,3]MCPs, à l'aide de BBr_3, conduit à la formation de *syn*-9-hydroxy[3,3]MCPs, avec de bons rendements. Il a été possible d'observer, tant en solution qu'à l'état solide, l'existence de fortes liaisons hydrogènes intramoléculaires entre le groupe hydroxyle en position 9 et les substituants en position 18, tels le F ou les groupes OH et OMe attachés aux noyaux aromatiques opposés. En RMN du ^{1}H, par comparaison avec l'analogue non substitué en position 18, on a observé un déplacement caractéristique à bas champ pour le proton du OH phénolique. De plus, on a observé un couplage O–H···F à travers l'espace.

Mots-clés : métacyclophanes, conformation, isomérisation anti/syn, liaison hydrogène intramoléculaire, couplage à travers l'espace.

[Traduit par la Rédaction]

Introduction

The synthesis and stereochemical aspects of conformationally mobile [3.3]MCPs (MCP = metacyclophane) have been of interest until now with particular attention[1–4] paid to dithia[3.3]MCPs, which possess an anti-stepped conformation. The pioneering work of the conformational investigation of 2,11-dithia[3.3]MCPs was reported by Vögtle and Schunder.[5] Shinmyozu et al.[6] reported the first preparation and conformational behavior in the carbocyclic [3.3]MCPs and their analogues (Fig. 1). [3.3]MCP exists in the syn geometry with a chair–chair arrangement of the trimethylene chains in the crystal state.[7–9] The preferred geometry of [3.3]MCP in solution is also a syn on the basis of the ^{1}H NMR spectrum, in which [3.3]MCP shows a strong temperature-dependent phenomenon at low temperature.[10–14]

Shinmyozu et al.[6] prepared [3.3]MCP using (*p*-tolylsulfonyl)methyl isocyanide (TosMIC) as the cyclization reagent, followed by Wolff–Kishner reduction. They made studies of syn/anti conversions in other [3.3]MCPs, especially in relation to the size of substituents such as halogens.[15] Like the parent compound, 9-halo[3.3]MCPs prefer the syn conformation, but the corresponding 2,11-diones favour the anti arrangement. Even one internal halogen substituent is sufficient to allow the isolation of a discrete syn- or anti-isomer. Although the effect on the ratio of syn- and anti-conformers of [3.3]MCPs was reported, it is still not clear what the effects are, not only properties of the internal substituents, but also having unsymmetrically substituted benzene rings arising from charge-transfer-type interactions between two benzene rings, as well as steric effects of substituents at the 6- and 15-positions.

Interestingly, all of the previously synthesized [3.3]MCPs are internally unsubstituted [3.3]MCP-2,11-diones and it is surprising that there are very few reports[16,17] on the preparation

Received 2 May 2011. Accepted 22 September 2011. Published at www.nrcresearchpress.com/cjc on 22 December 2011.

K. Tazoe, X. Feng, B. Sharma, S. Miyamoto, and T. Yamato. Department of Applied Chemistry, Faculty of Science and Engineering, Saga University, Honjo-machi 1, Saga 840-8502 Japan.

Corresponding author: Takehiko Yamato (e-mail: yamatot@cc.saga-u.ac.jp).

Can. J. Chem. Downloaded from www.nrcresearchpress.com by Renmin University of China on 09/02/12
For personal use only.

Fig. 1. syn- and anti-Conformers of [3.3]metacyclophane (MCP).

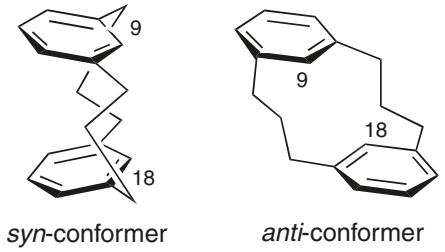
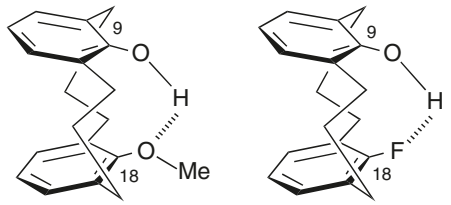


Fig. 2. Proposed intramolecular hydrogen bonding of *syn*-9-hydroxy-18-methoxy[3.3]MCP and *syn*-9-hydroxy-18-fluoro[3.3]MCP (MCP = metacyclophane).



of 9-methyl- or 9-methoxy analogues despite the fact that the chemical shift of the internal substituents, such as methyl and methoxy groups, provides a convenient probe for ^{1}H NMR studies of any possible conformational changes.

On the other hand, the cyclophane skeleton is suitable for realizing the ideal C–X (X = O, F)···H–O distance, angles, and evaluating the intramolecular hydrogen bond (Fig. 2). Especially, the C–F···H–O hydrogen bond is a new type of hydrogen bond, which was first proposed by Glusker and co-workers[18] in 1983. Following their work, research studies and discussions have been continued by many researchers who are still making efforts to confirm the hydrogen bonds using a variety of methods. Based on this speculation, we employed the cyclophane skeleton for investigating the C–F···H–O hydrogen bond. Phenol and fluorobenzene units in *syn*-9-hydroxy-18-fluoro[3.3]MCP could be fixed and close to each other. Here, we report the synthesis and stereochemical assignments of 9-methoxy-18-substituted [3.3]MCP-2,11-diones and their conversion to the corresponding 9-hydroxy-18-substituted [3.3]MCPs by Wolff–Kishner reduction followed by demethylation with BBr_3. The intramolecular hydrogen bonding between the 9-hydroxyl group and 18-substituents is also discussed.

Results and discussion

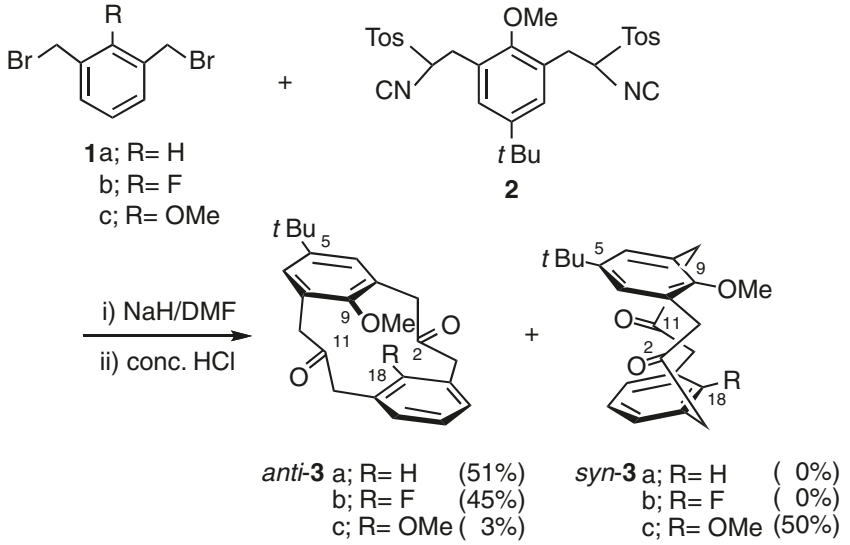
Vögtle and co-workers[19–21] reported the preparation of carbocyclic [3$_n$]MCPs using TosMIC[22,23] as the cyclization reagent, which was applied in a new cyclization procedure without phase-transfer conditions.[24–28] This strategy can be employed for the preparation of [3.3]MCP containing two benzene rings. However, the preparation of [3.3]MCPs using the TosMIC method is difficult because of its low yield as well as the difficulty of product separation from the other macrocyclic oligoketones, i.e., trimers and tetramers. Therefore, it has been very difficult to obtain sufficient amounts of the above compounds to investigate their chemical behavior.

Therefore, we selected the stepwise synthetic route, i.e., the preparation of the TosMIC adduct **2** first and then the cyclization of **2** with 1,3-bis(bromomethyl)-1-substituted benzenes **1** to prepare the desired cyclic dimer **3**. The preparation of 1,3-bis(bromomethyl)-1-substituted benzenes **1** are carried out by the treatment of 1,3-dimethyl-1-substituted benzenes with *N*-bromosuccinimide by the reported procedure.[29–31] The starting compound (2,6-bis(bromomethyl)-4-*tert*-butylanisole) was easily prepared by bromomethylation of 4-*tert*-butylanisole[32,33] using the *tert*-butyl group as a positional protecting group on the aromatic ring.[29–35] Although TosMIC adduct **2** was obtained in 78% yield by the reaction of 2,6-bis(bromomethyl)-4-*tert*-butylanisole with TosMIC as a mixture of two isomers, i.e., meso and dl, the attempted pure separation of these isomers of **2** failed. The cyclic diketones **3** were synthesized by coupling the 1,3-bis(bromomethyl)-1-substituted benzenes **1** with TosMIC adduct **2** under highly diluted conditions in DMF with an excess of sodium hydride as shown in Scheme 1. We have improved the addition procedure in Vögtle and co-workers' method.[19–21] Thus, to a suspension of NaH in DMF was dropped a solution of **1** and TosMIC adducts **2** in DMF at room temperature. This not only improves the yield of the desired ketones but also makes the handling of the base (solid NaH) easier. The ^{1}H NMR spectrum of **3** shows methoxy protons as a singlet except for diketone **3c**, which shows two kinds of methoxy protons, each as a singlet. By careful column chromatography (silica gel, Wako C-300), two conformers, *anti*-**3c** and *syn*-**3c**, were separated. They are thermally stable and do not interconvert at 150 °C in DMSO solution nor at 400 °C in the solid state.

The structures of **3** were elucidated by elemental analyses and spectral data. For instance, the mass spectral data for *anti*-**3a** (M^+ = 350) strongly supports a cyclic structure. The IR spectrum of *anti*-**3a** shows the absorption of the carbonyl stretching vibration around 1697 cm^{-1}. The ^{1}H NMR spectrum (in $CDCl_3$) of *anti*-**3a** exhibits two sets of doublets at δ 3.32 and 3.74 ppm (J = 14.2 Hz) and δ 3.33 and 3.48 ppm (J = 12.2 Hz) for the Ar*CH*$_2$CO*CH*$_2$Ar methylene protons and a singlet for the internal methoxy group at an upfield shift δ 3.33 ppm from anisole (δ 3.75 ppm) owing to the ring current of the opposing aromatic ring.[1,2,29,30,36–40] Similarly, the internal aromatic proton at the 18-position was observed at higher field, δ 5.39 ppm compared with that of the **1a** at δ 7.28 ppm. These observations strongly suggest that *anti*-**3a** adopts the anti-conformation. Similarly, the assignments of structures for other anti-conformers in *anti*-**3b** and *anti*-**3c** were readily apparent from their ^{1}H NMR spectra. Thus, upfield shifts of methoxy protons were observed at δ 3.13 ppm for *anti*-**3b** and δ 3.16 ppm for *anti*-**3c**. In contrast, the methoxy protons of *syn*-**3c** were observed at δ 3.55 and 3.56 ppm. Further, the aryl hydrogens at the 5,7-positions can clearly be seen to be shielded at δ 6.66 ppm by the adjacent ring, a common consequence of a face-to-face benzene ring.[36–45] Also the *tert*-butyl protons were observed at higher field, δ 1.12 ppm, compared with that of the *anti*-**3c** at δ 1.32 ppm owing to the strong shielding effect of the benzene ring. These observations strongly suggest that compound *syn*-**3c** adopts a syn-conformation.

Thus, the 9-methoxy analogue is exclusively formed as the anti-conformer independent of substituents R of 1,3-bis(bromomethyl)-1-substituted benzenes **1**, but the 9,18-dimethoxy

Scheme 1. Synthesis of *anti*-6-*tert*-butyl-9-methoxy-18-substituted [3.3]metacyclophane-2,11-diones **3**.



analogue **3c** is formed as a mixture of syn- and anti-conformers. Although the detailed reaction pathway of the formation of *syn*-**3c** is still not clear from the present results, one might propose the through-space interaction between the nonbonding electron pairs of the oxygen atom of both methoxy groups at the 9- and 18-positions and the opposite aromatic π-electrons, which may disfavour the formation of the anti-conformer.

The Wolff–Kishner reduction of *syn*- and *anti*-diketone **3c** afforded the desired *syn*- and *anti*-6-*tert*-butyl-9,18-dimethoxy[3.3]MCPs (**4c**) in 80% and 85% yields, respectively. No syn/anti-isomerization was observed under the reaction conditions used (Scheme 2).

In contrast, the attempted Wolff–Kishner reduction of *anti*-diketone *syn*-**3a**, carried out under the same reaction conditions as **3c**, led to *syn*-6-*tert*-butyl-9-methoxy[3.3]MCP (*syn*-**4a**) in 80% yield. No formation of the corresponding anti-conformer was observed under the reaction conditions used.

The structure of *syn*-**4a** has been elucidated by elemental analyses and spectral data. The ^{1}H NMR spectrum (in $CDCl_3$) of *syn*-**4a** exhibits a singlet at δ 3.67 ppm for the methoxy protons. Further, a singlet of the intra-annular proton H_{18} was observed at δ 7.18 ppm in addition to the resonances at δ 6.55 ppm for the 5,7-protons and at δ 6.54 and 6.73 ppm for the other three protons of the opposing aromatic rings, which clearly can be seen to be shielded by the adjacent ring, a common consequence of a face-to-face benzene ring.[36–45] Also, the *tert*-butyl protons were observed at higher field (δ 1.09 ppm) compared with that of the *anti*-**3a** at δ 1.35 ppm owing to the strong shielding effect of the benzene ring. These observations strongly suggest that compound *syn*-**4a** adopts a syn-conformation.

Interestingly, a similar result was obtained for the reduction of *anti*-**3b** to afford *syn*-6-*tert*-butyl-18-fluoro-9-methoxy[3.3]MCP (*syn*-**4b**) carried out under the same reaction conditions. anti/syn-Isomerization was observed under the reaction conditions used (Scheme 2). These findings strongly suggest that the ring inversion to the thermodynamically more stable syn-conformation is possible in the 9-methoxy[3.3]MCPs **4a** and **4b**.

On the other hand, as mentioned previously, we reported that *syn*-**3c** and *anti*-**3c** are thermally stable and do not interconvert at 150 °C in DMSO solution nor at 400 °C in the solid state. Although the detailed mechanistic conclusion to rationalize the present observation of anti-to-syn conversion is not clear, one might assume the similar behaviour that the [3.3]MCP exists in the syn geometry with a chair–chair arrangement of the trimethylene chains.[10]

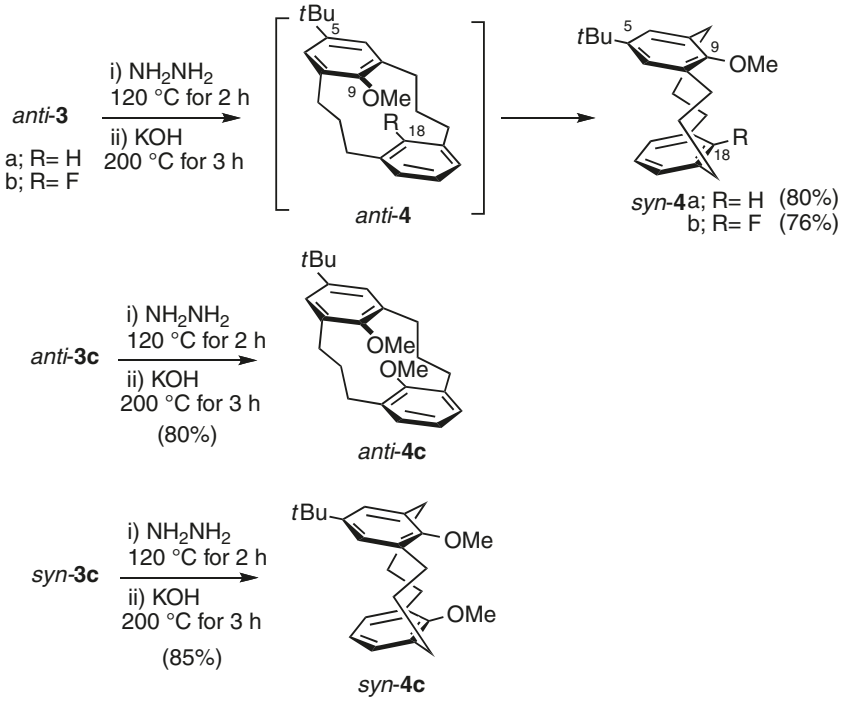
Demethylation of *syn*-9-methoxy[3.3]MCPs *syn*-**4a** and *syn*-**4b** with BBr_3 in dichloromethane affords the corresponding *syn*-9-hydroxy[3.3]MCPs *syn*-**5a** and *syn*-**5b** in 80% and 75% yields, respectively (Scheme 3). No formation of the corresponding anti-conformer was observed under the reaction conditions used. This finding suggests that the ring inversion to the thermodynamically stable anti-conformation is not possible in the 9-hydroxy[3.3]MCPs, which seem to have sufficient space for the conformational flipping as demonstrated by the molecular models. The same treatment of *syn*-9,18-dimethoxy[3.3]MCP *syn*-**4c** gives the corresponding *syn*-9,18-dihydroxy[3.3]MCP *syn*-**5c** in 85% yield.

The conformations of hydroxy[3.3]MCPs *syn*-**5** in solution, which have been prepared in the present work, are rigid and the signals of the methylene bridge do not coalesce below 130 °C in $CDBr_3$, the energy barriers to flipping being above 25 kcal mol^{-1} (1 cal = 4.184 J). The ^{1}H NMR spectrum (in $CDCl_3$) exhibits the signals for hydroxyl groups at around δ 4.61 ppm for *syn*-**5a** and at δ 4.81 ppm for *syn*-**5b**. The latter appeared as a doublet ($J_{H–F}$ = 6.6 Hz) that is coupled with the fluorine atom at the 18-position. These data show the existence of the intramolecular hydrogen bonding between two hydroxy groups among the opposing aromatic rings. The chemical shifts of the phenolic OH proton of *syn*-**5b** in $CDCl_3$ at concentrations of 1.0×10^{-1}, 1.0×10^{-2}, and 1.0×10^{-3} mol/L were the same within experimental error (δ_{OH} (*syn*-**5b**) = 4.81 ppm). Therefore, the C–F···H–O hydrogen bond is obvious in the ^{1}H NMR spectra. Moreover, specific phenomena were seen in the spectrum of *syn*-**5b**, viz., the OH signal appeared as a doublet ($J_{H–F}$ = 6.6 Hz), which shows the through-space coupling with the fluorine atom. By irradiation of the F atom, the coupling

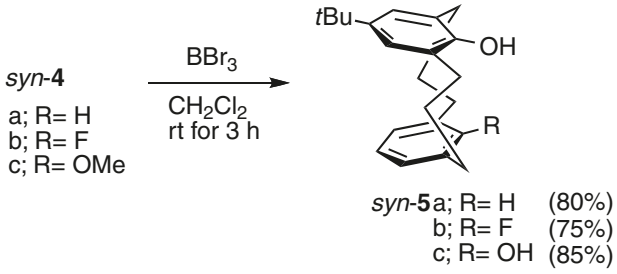
Can. J. Chem. Downloaded from www.nrcresearchpress.com by Renmin University of China on 09/02/12
For personal use only.

Can. J. Chem. Downloaded from www.nrcresearchpress.com by Renmin University of China on 09/02/12
For personal use only.

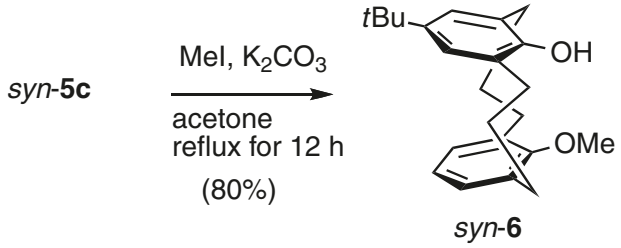
Scheme 2. Synthesis of *syn*- and *anti*-6-*tert*-butyl-9-methoxy-18-substituted [3.3]metacyclophanes **4**.



Scheme 3. Demethylation of *syn*-9-methoxy[3.3]metacyclophanes (*syn*-**4**) with BBr_3.



Scheme 4. O-Methylation of *syn*-6-*tert*-butyl-9,18-dihydroxy[3.3] metacyclophane (*syn*-**5c**).



disappeared and the doublet became a singlet. Furthermore, in a donating solvent such as [D_6]DMSO, the signal appeared as a singlet. This is further evidence of an O–H···F interaction.

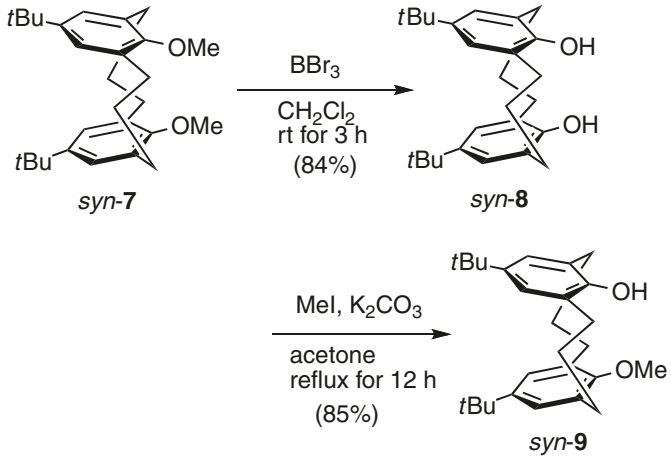
On the other hand for *syn*-9,18-dihydroxy[3.3]MCP (*syn*-**5c**), the signals of the OH protons were not observed clearly in $CDCl_3$ nor in benzene-d_6, different from those of *syn*-**5a** and *syn*-**5b**. This phenomena seems to be due to the faster exchange of intramolecular hydrogen bonding between unsymmetrical hydroxyl groups than NMR time scale. To studythe intramolecular hydrogen bonding of *syn*-**5c** in more detail, we attempted introduction of a methyl group to the one of the hydroxyl groups of *syn*-**5c**. Thus, reaction of *syn*-**5c** with methyl iodide was carried out in the presence of potassium carbonate in acetone reflux for 12 h. We succeeded in the preparation of the mono-O-methylation product *syn*-**6** in 80% yield (Scheme 4). The chemical shift of the phenolic OH proton of *syn*-**6** in $CDCl_3$ was observed at a lower magnetic field at δ 6.81 ppm owing to the intramolecular hydrogen bonding between 18-methoxy groups.

We have also carried out a similar partial O-methylation of the corresponding *syn*-6,15-di-*tert*-butyl-9,18-dihydroxy[3.3]MCP (*syn*-**8**; Scheme 5), which was prepared by demethylation of *syn*-6,15-di-*tert*-butyl-9,18-dimethoxy[3.3]MCP (*syn*-**7**)[46] with BBr_3, to afford the compound *syn*-**9** in 85% yield. Similarly, a distinct low-field shift of the phenolic OH proton was observed in the ^{1}H NMR spectrum of *syn*-**9** (δ 7.04 ppm) compared to that of the OMe-free analog *syn*-**5a** (δ 4.61 ppm).

Conclusions

Various anti-9-substituted [3.3]MCP-2,11-diones were exclusively obtained by the coupling reaction of the corresponding 1,3-bis(bromomethyl)-1-substituted benzenes **1** and 2,6-bis[2-isocyano-2-(tolylsulfonyl)ethyl]-4-*tert*-butylanisole **2** in DMF with an excess of sodium hydride. In the case of the coupling reaction of 1,3-bis(bromomethyl)anisole **1c** with **2**, a mixture of *anti*-**3c** and *syn*-**3c** was obtained owing to the repulsive interaction between the unshared electrons of the methoxy groups at the 9- and 18-positions and the opposite aromatic π-electrons, which may disfavour the formation of *anti*-**3c**. The corresponding *syn*-[3.3]MCPs *syn*-**4** were synthesized via anti/syn-isomerization by the Wolff–Kishner reduction. Demethylation of *syn*-9-methoxy[3.3]MCPs *syn*-**4** with BBr_3 afforded the corresponding *syn*-hydroxy[3.3]MCPs *syn*-**5** in good yields. The existence of

Scheme 5. O-Methylation of *syn*-6,15-di-*tert*-butyl-9,18-dihydroxy [3.3]metacyclophane (*syn*-**8**).



the strong intramolecular hydrogen bonding between the 9-hydroxy group and the 18-substituents at the opposing aromatic rings, such as the F atom and the OMe group, were observed in solution and in the solid state. Actually, evidence for the C–F···H–O hydrogen bond was obtained from the results of the crystallographic analysis. In the ^{1}H NMR spectrum, the O–H bond signal of *syn*-**5b** appears at a lower field than that of the fluorine-free analog *syn*-**5a**. Furthermore, through-space coupling between the F atom and the OH proton is observed. Similarly, a distinct lowfield shift of the phenolic OH proton was observed in the ^{1}H NMR spectrum of *syn*-**9** compared with that of the OMe-free analog *syn*-**5a**. Further studies on the chemical properties of *syn*-9-hydroxy-18-substituted [3.3]MCPs *syn*-**5**, *syn*-**6**, and *syn*-**9** are now in progress.

Experimental

All melting points are uncorrected. ^{1}H NMR spectra were recorded on a Nippon Denshi JEOL FT-300 spectrometer. Chemical shifts are reported as δ values (ppm) relative to internal Me_4Si. Mass spectra were obtained on a Nippon Denshi JIR-AQ2OM mass spectrometer at an ionization energy of 70 eV using a direct-inlet system through GLC; the *m*/*z* values reported include the parent ion peak. IR spectra were obtained on a Nippon Denshi JIR-AQ2OM spectrophotometer as KBr disks. Elemental analyses were performed by Yanaco MT-5. GLC analyses were performed on a Shimadzu GC (GC-14A); silicone OV-1, 2 m; programmed temperature rise, 12 °C min^{-1}; carrier gas nitrogen, 25 mL min^{-1}.

Materials

2,6-Bis(bromomethyl)-4-*tert*-butylanisole was prepared using the reported procedure.[32,33] The preparations of 1,3-bis(bromomethyl)-1-substituted benzenes (**1a**–**1c**) have been previously described.[47,48] *syn*-6,15-Di-*tert*-butyl-9,18-dimethoxy[3.3]metacyclophane (*syn*-**7**) was prepared using the reported procedure.[46]

Preparation of the TosMIC adduct 2 — Typical procedure

To a mixture of 20% aqueous NaOH (40 mL) and CH_2Cl_2 (50 mL) was added *n*-Bu_4NI (700 mg, 1.9 mmol) followed by a solution of TosMIC (8 g, 41 mmol) in CH_2Cl_2 (50 mL). After the reaction, the mixture was stirred at room temperature for 30 min and then a solution of 2,6-bis(bromomethyl)-4-*tert*-butylanisole (4.0 g, 11 mmol) in CH_2Cl_2 (50 mL) was added. The reaction mixture was stirred at room temperature for 2 h, quenched with water (100 mL), and was extracted with CH_2Cl_2 (3 × 100 mL). It was washed with water (100 mL), dried with Na_2SO_4, and concentrated in vacuo to leave a residue. To this residue methanol (100 mL) was added and the mixture was left overnight in the refrigerator to give 4.97 g (78%) of 2,6-bis[2-isocyano-2-(tolylsulfonyl)ethyl]-4-*tert*-butylanisole (**2**) as pale brown prisms (hexane), mp 150–151 °C. ν_{max} (KBr, cm^{-1}): 2134 (CN). δ_H ($CDCl_3$): 1.26, 1.27 (9H, each s, *t*-Bu), 2.49, 2.50 (6H, each s, *Me*), 2.87, 2.99 (2H, each dd, J = 11.7, 13.7 Hz, *CH*$_2$), 3.66, 3.77 (2H, each dd, J = 2.9, 13.7 Hz, *CH*$_2$), 3.76, 3.80 (3H, each s, *OMe*), 4.73, 4.83 (2H, each dd, J = 2.9, 11.7 Hz, *CH*), 7.19, 7.20 (2H, each s, Ar-*H*), 7.44, 7.46 (4H, d, J = 8.3 Hz, Ar-*H*), 7.87, 7.93 (4H, d, J = 8.3 Hz, Ar-*H*). *m*/*z*: 578 (M^+). Anal. calcd for $C_{31}H_{34}N_2O_5S_2$ (578.75): C 64.34, H, 5.92, N 4.84); found: C 64.56, H 5.87, N 4.73.

Stepwise cyclization of TosMIC adduct 2 and dibromide 1a

To a suspension of NaH (2.1 g, 51 mmol) in DMF (150 mL) a solution of **2** (4.7 g, 8.5 mmol) and **1a** (5.0 g, 8.5 mmol) in DMF (35 mL) was added dropwise over a period of 6 h. After the suspension was stirred for an additional 5 h at room temperature, it was quenched with ice water (300 mL). The reaction mixture was extracted with CH_2Cl_2 (3 × 100 mL), washed with water (200 mL), dried with Na_2SO_4, and concentrated in vacuo to 15 mL. Concentrated HCl (15 mL) was added and the solution was stirred for 15 min. The organic layer was again extracted with CH_2Cl_2 (3 × 100 mL), washed with water (2 × 100 mL), dried with Na_2SO_4, and concentrated and condensed under reduced pressure. The residue was chromatographed on silica gel using $CHCl_3$ as eluent to give crude *anti*-**3a** as a pale yellow solid. Recrystallization from methanol afforded *anti*-6-*tert*-butyl-9-methoxy[3.3]metacyclophane-2,11-dione (*anti*-**3a**, 1.52 g, 51%) as colourless prisms (MeOH), mp 110–111 °C. ν_{max} (KBr, cm^{-1}): 1698 (C=O). δ_H ($CDCl_3$): 1.35 (9H, s, *t*-Bu), 3.32 (2H, d, J = 14.2 Hz, *CH*$_2$), 3.33 (3H, s, O*Me*), 3.33 (2H, d, J = 12.2 Hz, *CH*$_2$), 3.48 (2H, d, J = 12.2 Hz, *CH*$_2$), 3.74 (2H, d, J = 14.2 Hz, *CH*$_2$), 5.55 (1H, s, Ar-*H*), 7.05–7.10 (3H, m, Ar-*H*), 7.25 (2H, s, Ar-*H*). *m*/*z*: 350 (M^+). Anal. calcd for $C_{23}H_{26}O_3$ (350.46): C 78.83, H 7.48; found: C 78.71, H 7.48.

Similarly, compound *anti*-**3b** was obtained in 45% yield.

anti-6-*tert*-Butyl-9-furuoro-18-methoxy[3.3]metacyclophane-2,11-dione (*anti*-**3b**) was obtained as colourless prisms (MeOH), mp 109–111 °C. ν_{max} (KBr, cm^{-1}): 1697 (C=O). δ_H ($CDCl_3$): 1.25 (9H, s, *t*-Bu), 3.13 (3H, s, OMe), 3.20 (4H, d, J = 14.9 Hz, *CH*$_2$), 3.67 (4H, d, J = 14.9 Hz, *CH*$_2$), 6.89 (1H, t, J = 6.0 Hz, Ar-*H*), 7.06 (2H, t, J = 7.2 Hz, Ar-*H*), 7.12 (2H, s, Ar-*H*). *m*/*z*: 368 (M^+). Anal. calcd. for $C_{23}H_{25}FO_3$ (368.44): C 74.98, H 6.84; found: C 74.64, H 7.00.

Stepwise cyclization of TosMIC adduct 2 and dibromide 1c

To a suspension of NaH (2.1 g, 51 mmol) in DMF (150 mL) a solution of **2** (4.7 g, 8.5 mmol) and **1c** (5.0 g, 8.5 mmol) in DMF (35 mL) was added dropwise over a

Can. J. Chem. Downloaded from www.nrcresearchpress.com by Renmin University of China on 09/02/12
For personal use only.

Can. J. Chem. Downloaded from www.nrcresearchpress.com by Renmin University of China on 09/02/12
For personal use only.

period of 6 h. After the suspension was stirred for an additional 5 h at room temperature, it was quenched with ice water (300 mL). The reaction mixture was extracted with CH_2Cl_2 (3 × 100 mL), washed with water (200 mL), dried with Na_2SO_4, and concentrated in vacuo to 15 mL. Concentrated HCl (15 mL) was added, and the solution was stirred for 15 min. The organic layer was extracted again with CH_2Cl_2 (3 × 100 mL), washed with water (2 × 100 mL), dried with Na_2SO_4, and concentrated and condensed under reduced pressure. The residue was chromatographed on silica gel using $CHCl_3$ as the eluent to give crude *anti*-**3c** as a pale yellow solid. The anti:syn ratio was determined as 5:95 by the ^{1}H NMR spectrum. The residue was chromatographed on silica gel using $CHCl_3$ as the eluent to give crude *anti*-**3c** and *syn*-**3c** as a pale yellow solid and a pale yellow oil, respectively. Recrystallization from hexane afforded *anti*-**3c** (96 mg, 3%). Crude *syn*-**3c** was again chromatographed on silica gel using $CHCl_3$ as the eluent to afford 1.62 g (50%) of *syn*-**3c** as a pale yellow oil.

anti-6-*tert*-Butyl-9,18-dimethoxy[3.3]metacyclophane-2,11-dione (*anti*-**3c**) was obtained as colourless prisms (hexane), mp 198–199 °C. ν_{max} (KBr, cm^{-1}): 1685 (C=O). δ_H ($CDCl_3$): 1.32 (9H, s, *t*-Bu), 3.16 (6H, s, O*Me*), 3.23 (4H, d, J = 14.6 Hz, CH_2), 3.60 (2H, d, J = 14.6 Hz, CH_2), 3.63 (2H, d, J = 14.6 Hz, CH_2), 6.93–6.99 (1H, m, Ar-*H*), 7.17 (2H, s, Ar-*H*) and 7.16–7.18 (2H, m, Ar-*H*). *m*/*z*: 380 (M$^+$). Anal. calcd for $C_{24}H_{28}O_4$ (380.49): C 75.75, H 7.42; found: C 75.56, H 7.54.

syn-6-*tert*-Butyl-9,18-dimethoxy[3.3]metacyclophane-2,11-dione (*syn*-**3c**) was obtained as a pale yellow oil. ν_{max} (NaCl, cm^{-1}): 1688 (C=O). δ_H ($CDCl_3$): 1.12 (9H, s, *t*-Bu), 3.32 (4H, d, J = 12.7 Hz, CH_2), 3.55 (3H, s, O*Me*), 3.56 (3H, s, O*Me*), 4.30 (4H, d, J = 12.7 Hz, CH_2), 6.48–6.54 (1H, m, Ar-*H*), 6.66 (2H, s, Ar-*H*), 6.65–6.68 (2H, m, Ar-*H*). *m*/*z*: 380 (M$^+$). Anal. calcd for $C_{24}H_{28}O_4$ (380.49): C 75.76, H 7.42; found: C 75.62, H 7.35.

Wolff–Kishner reduction of anti-*3a*

A mixture of *anti*-**3a** (1.20 g, 3.42 mmol), KOH (1.28 g, 23.0 mmol), 100% hydrazine hydrate (0.35 mL, 6.2 mmol), and triethylene glycol (3 × 50 mL) was heated at 120 °C for 2 h and then at 220 °C for 3 h. The cooled mixture was poured into water (50 mL), acidified with diluted HCl, extracted with CH_2Cl_2 (3 × 50 mL), washed with water (2 × 20 mL), dried with Na_2SO_4, and concentrated under reduced pressure. The residue was chromatographed on silica gel using hexane/benzene (1:1) as the eluent to give crude *syn*-**4a** as a colourless solid. Recrystallization from MeOH afforded *syn*-6-*tert*-butyl-9-methoxy[3.3]metacyclophane (*syn*-**4a**), which was obtained as colourless prisms (882 mg, 80%), mp 112–114 °C. δ_H ($CDCl_3$): 1.09 (9H, s, *t*-Bu), 1.70–1.82 (2H, m, CH_2), 2.30–2.37 (2H, m, CH_2), 2.47–2.76 (6H, m, CH_2), 3.00–3.09 (2H, m, CH_2), 3.67 (3H, s, O*Me*), 6.54 (2H, d, J = 7.0 Hz, Ar-*H*), 6.55 (2H, s, Ar-*H*), 6.73 (1H, t, J = 7.0 Hz, Ar-*H*), 7.18 (1H, s, Ar-*H*). *m*/*z*: 322 (M$^+$). Anal. calcd for $C_{23}H_{30}O$ (322.49): C 85.66, H 9.38; found: C 85.65, H 9.39.

Compounds *syn*-**4b** and *syn*-**4c** were similarly prepared in 76% and 85% yield, respectively.

syn-6-*tert*-Butyl-9-furuoro-18-methoxy[3.3]metacyclophane (*syn*-**4b**) was obtained as colourless prisms (MeOH), mp 146–148 °C. δ_H ($CDCl_3$): 1.06 (9H, s, *t*-Bu), 1.69–1.82 (2H, m, CH_2), 2.25–2.53 (6H, m, CH_2), 2.88–3.12 (4H, m, CH_2), 3.47 (6H, s, O*Me*), 6.41–6.50 (5H, m, Ar-*H*). *m*/*z*: 340 (M$^+$). Anal. calcd for $C_{23}H_{29}FO$ (340.49): C 81.14, H 8.59; found: C 81.21, H 8.70.

syn-6-*tert*-Butyl-9,18-dimethoxy[3.3]metacyclophane (*syn*-**4c**) was obtained as colourless prisms (hexane), mp 82–84 °C. δ_H ($CDCl_3$): 1.15 (9H, s, *t*-Bu), 1.81–1.89 (2H, m, CH_2), 2.45–2.52 (6H, m, CH_2), 3.03–3.13 (4H, m, CH_2), 3.48 (3H, s, O*Me*), 3.49 (3H, s, O*Me*), 6.48–6.56 (5H, m, Ar-*H*). *m*/*z*: 352 (M$^+$). Anal. calcd for $C_{24}H_{32}O_2$ (352.52): C 81.77, H 9.15; found: C 81.58, H 9.11.

Wolff–Kishner reduction of anti-*3c*

A mixture of *anti*-**3c** (1.20 g, 3.3 mmol), KOH (1.28 g, 23.0 mmol), 100% hydrazine hydrate (0.35 mL, 6.2 mmol), and triethylene glycol (3 × 50 mL) was heated at 120 °C for 2 h and then at 220 °C for 3 h. The cooled mixture was poured into water (50 mL), acidified with diluted HCl, extracted with CH_2Cl_2 (3 × 50 mL), washed with water (2 × 20 mL), dried with Na_2SO_4, and concentrated under reduced pressure. The residue was chromatographed on silica gel using hexane/benzene (1:1) as the eluent to give crude *anti*-**4c** as a colourless solid. Recrystallization from hexane afforded *anti*-6-*tert*-butyl-9,18-dimethoxy[3.3]metacyclophane (*anti*-**4c**) was obtained as colourless prisms (930 mg, 80%), mp 220–222 °C. δ_H ($CDCl_3$): 1.34 (9H, s, *t*-Bu), 2.05–2.15 (4H, m, CH_2), 2.31–2.42 (4H, m, CH_2), 2.57–2.69 (4H, m, CH_2), 3.10 (3H, s, O*Me*), 3.15 (3H, s, O*Me*), 6.85–6.88 (1H, m, Ar-*H*), 6.95–6.87 (4H, m, Ar-*H*). *m*/*z*: 352 (M$^+$). Anal. calcd for $C_{24}H_{32}O_2$ (352.52): C 81.77, H 9.15; found: C 81.69, H 9.04.

Reaction of syn-*4a with* BBr_3

To a solution of *syn*-**4a** (60 mg, 0.186 mmol) in CH_2Cl_2 (6 mL) at 0 °C was gradually added a solution of BBr_3 (0.087 mL, 0.922 mmol) in CH_2Cl_2 (0.1 mL). After the reaction mixture had been stirred at room temperature for 3 h, it was poured into ice water (10 mL) and then extracted with CH_2Cl_2 (10 mL × 3). The combined extracts were washed with water (2 × 10 mL), dried over Na_2SO_4, and concentrated in vacuo to leave a residue. The residue was chromatographed over silica gel (Wako C-300, 100 g) with hexane/$CHCl_3$ (4:1) as the eluent to give crude *syn*-**5a** as a colourless solid. Recrystallization from MeOH afforded *syn*-6-*tert*-butyl-9-hydroxy[3.3]metacyclophane (*syn*-**5a**) was obtained as a brown oil (46 mg, 80%). ν_{max} (NaCl, cm^{-1}): 3424 (OH). δ_H ($CDCl_3$): 1.03 (9H, s, *t*-Bu), 1.72–1.81 (2H, m, CH_2), 2.25–2.32 (2H, m, CH_2), 2.42–2.52 (2H, m, CH_2), 2.54–2.56 (2H, m, CH_2), 2.59–2.68 (2H, m, CH_2), 2.81–2.90 (2H, m, CH_2), 4.61 (1H, s, *OH*), 6.46 (2H, s, Ar-*H*), 6.48 (2H, d, J = 6.0 Hz, Ar-*H*), 6.72 (1H, t, J = 6.0 Hz, Ar-*H*). *m*/*z*: 308 (M$^+$). Anal. calcd for $C_{22}H_{28}O$ (308.46): C 85.66, H 9.15; found: C 85.56, H 9.31.

Compounds *syn*-**5b** and *syn*-**5c** were similarly prepared in 75% and 85% yield, respectively.

syn-6-*tert*-Butyl-18-furuoro-9-hydroxy[3.3]metacyclophane (*syn*-**5b**) was obtained as a pale yellow oil. ν_{max} (NaCl, cm^{-1}): 3354 (OH). δ_H ($CDCl_3$): 1.13 (9H, s, *t*-Bu), 1.80–1.92 (2H, m, CH_2), 2.33–2.43 (2H, m, CH_2), 2.52–2.65 (2H, m, CH_2), 2.52–2.65 (2H, m, CH_2), 2.95–3.01 (4H, m, CH_2), 4.81 (1H,

Can. J. Chem. Downloaded from www.nrcresearchpress.com by Renmin University of China on 09/02/12
For personal use only.

d, J = 6.6 Hz, *OH*), 6.49–6.98 (5H, m, Ar-*H*). *m/z*: 326 (M^+). Anal. calcd for $C_{22}H_{27}FO$ (326.46): C 80.94, H 8.34; found: C 80.76, H 8.35.

syn-6-*tert*-Butyl-9,18-dihydroxy[3.3]metacyclophane (*syn*-**5c**) was obtained as colourless prisms (hexane), mp 80–82 °C. ν_{max} (KBr, cm^{-1}): 3210 (OH). δ_H ($CDCl_3$): 1.15 (9H, s, *t*-Bu), 1.81–1.89 (2H, m, CH_2), 2.45–2.52 (6H, m, CH_2), 3.03–3.13 (4H, m, CH_2), 6.48–6.56 (5H, m, Ar-*H*). *m/z*: 324 (M^+). Anal. calcd $C_{22}H_{28}O_2$ (324.47): C 81.44, H 8.7; found: C 81.58, H 8.9.

O-Methylation of syn-*6-*tert-*butyl-9,18-dihydroxy[3.3] metacyclophane (*syn-*5c) in the presence of potassium carbonate*

A mixture of *syn*-**5c** (81 mg, 0.25 mmol) and potassium carbonate (86.4 mg, 1.25 mmol) in dry acetone (16 mL) was heated at reflux for 1.5 h under nitrogen. Then methyl iodide (0.16 mL, 2.5 mmol) was added and the mixture was heated at reflux for 6 h. After cooling of the reaction mixture to room temperature, it was filtered. The filtrate was concentrated to give a colourless oil, which was then chromatographed over silica gel (Wako, C-300; 100 g) with hexane/benzene (1:1) as the eluent to give a colourless solid, which was recrystallized from MeOH to afford *syn*-6-*tert*-butyl-9-hydroxy-18-methoxy[3.3]metacyclophane (*syn*-**6**) as colourless prisms (76 mg, 80%), mp 44–46 °C. ν_{max} (KBr, cm^{-1}): 3354 (OH). δ_H ($CDCl_3$): 1.11 (9H, s, *t*-Bu), 2.21–2.28 (4H, m, CH_2), 2.58–2.65 (4H, m, CH_2), 2.86–2.97 (4H, m, CH_2), 6.40–6.53 (3H, m, Ar-*H*), 6.60 (2H, s, Ar-*H*), 6.81 (1H, s, *OH*). *m/z*: 338 (M^+). Anal. calcd for $C_{23}H_{30}O_2$ (338.49): C 81.61 H 8.93; found: C 81.43, H 8.81.

Demethylation of syn-*6,15-di-*tert-*butyl-9,18-dimethoxy[3.3] metacyclophane (*syn-*7) with BBr_3*

To a solution of *anti*-**7**[46] (200 mg, 0.49 mmol) in CH_2Cl_2 (10 mL) at 0 °C was gradually added a solution of BBr_3 (1.0 mL, 10.6 mmol) in CH_2Cl_2 (1 mL). After the reaction mixture had been stirred at room temperature for 3 h, it was poured into ice water (20 mL), extracted with CH_2Cl_2 (2 × 10 mL), washed with water (2 × 10 mL), dried with Na_2SO_4, and concentrated in vacuo to give crude *syn*-**8** as a colourless solid. Recrystallization from methanol afforded 156 mg (84%) of *syn*-6,15-di-*tert*-butyl-9,18-dihydroxy[3.3] metacyclophane (*syn*-**8**). *syn*-**8** was obtained as colourless prisms (MeOH), mp 166–167 °C. ν_{max} (KBr, cm^{-1}): 3439 (OH). δ_H ($CDCl_3$): 1.11 (18H, s), 2.21–2.28 (4H, m), 2.58–2.65 (4H, m), 2.86–2.97 (4H, m), 5.30 (2H, s, OH), 6.62 (4H, s). *m/z*: 380 (M^+). Anal calcd for $C_{26}H_{36}O_2$ (380.58): C 82.06, H 9.53; found: C 82.33, H 9.51.

Compounds *syn*-**9** was similarly prepared in 85% yield by O-methylation of *syn*-**8** in the presence of potassium carbonate under the same conditions as *syn*-**5c**.

syn-6,15-Di-*tert*-butyl-9-hydroxy-18-methoxy[3.3]metacyclophane (*syn*-**9**) was obtained as colourless prisms (MeOH/$CHCl_3$, 1:1), mp 170–171 °C. ν_{max} (KBr, cm^{-1}): 3345 (OH). δ_H ($CDCl_3$): 1.11 (18H, s, *t*-Bu), 2.23–2.31 (4H, m, CH_2), 2.50–2.64 (4H, m, CH_2), 2.98–3.28 (4H, m, CH_2), 3.65 (3H, s, O*Me*), 6.54 (2H, s, Ar-*H*), 6.63 (2H, s, Ar-*H*), 7.04 (1H, s, *OH*). *m/z*: 394 (M^+). Anal calcd for $C_{27}H_{38}O_2$ (394.6): C 82.18, H 9.71; found: C 82.45, H 9.50.

Acknowledgement

This research was supported by a Grant-in-Aid for Scientific Research (C) (No. 22550040) from the Japan Society for the Promotion of Science.

References

(1) Vögtle, F. *Cyclophane Chemistry;* John Wiley & Sons Ltd.: Chicester, 1993.
(2) Gleiter, R.; Hopf, H. *Modern Cyclophane Chemistry;* Wiley-VCH: Weinheim, Germany, 2004.
(3) Semmelhack, M. F.; Harrison, J. J.; Young, D. C.; Gutiérrez, A.; Rafii, S.; Clardy, J. *J. Am. Chem. Soc.* **1985**, *107* (25), 7508. doi:10.1021/ja00311a047.
(4) Mitchell, R. H. *J. Am. Chem. Soc.* **2002**, *124* (10), 2352. doi:10.1021/ja0173977.
(5) Vögtle, F.; Schunder, L. *Chem. Ber.* **1969**, *102* (8), 2677. doi:10.1002/cber.19691020823.
(6) Shinmyozu, T.; Inazu, T.; Yoshino, T. *Chem. Lett.* **1976**, *5* (12), 1405. doi:10.1246/cl.1976.1405.
(7) Isaji, H.; Yasutake, M.; Takemura, H.; Sako, K.; Tatemitsu, H.; Inazu, T.; Shinmyozu, T. *Eur. J. Org. Chem.* **2001**, *2001* (13), 2487. doi:10.1002/1099-0690(200107)2001:13<2487::AID-EJOC2487>3.0.CO;2-F.
(8) Satou, T.; Shinmyozu, T. *J. Chem. Soc., Perkin Trans. 2* **2002**, *2002* (3), 393. doi:10.1039/b200402j.
(9) Shibahara, M.; Watanabe, M.; Iwanaga, T.; Ideta, K.; Shinmyozu, T. *J. Org. Chem.* **2007**, *72* (8), 2865. doi:10.1021/jo062220m.
(10) Sako, K.; Hirakawa, T.; Fujimoto, N.; Shinmyozu, T.; Inazu, T.; Horimoto, H. *Tetrahedron Lett.* **1988**, *29* (48), 6275. doi:10.1016/S0040-4039(00)82324-2.
(11) Sako, K.; Shinmyozu, T.; Takemura, H.; Suenaga, M.; Inazu, T. *J. Org. Chem.* **1992**, *57* (24), 6536. doi:10.1021/jo00050a031.
(12) Shinmyozu, T.; Wen, G.; Hirakawa, T.; Osada, S.; Takemura, H.; Sako, K.; Rudzinski, J. M. *Liebigs Ann.* **1996**, No. 2, 205. doi:10.1002/jlac199619960209.
(13) Sako, K.; Tatemitsu, H.; Onaka, S.; Takemura, H.; Osada, S.; Wen, G.; Shinmyozu, T.; Rudzinski, J. M. *Liebigs Ann.* **1996**, No. 10, 1645. doi:10.1002/jlac.199619961023.
(14) Ernst, L. *Prog. Nucl. Magn. Reson. Spectrosc.* **2000**, *37* (1–2), 47. doi:10.1016/S0079-6565(00)00022-4.
(15) Shinmyozu, T.; Inazu, T.; Yoshino, T. *Mem. Fac. Sci., Kyushu Univ. Ser. C* **1985**, *15*, 79.
(16) Osada, S.; Miyahara, Y.; Shinmyozu, T.; Inazu, T. *Mem. Fac. Sci., Kyushu Univ. Ser. C* **1993**, *19*, 39.
(17) Osada, S.; Miyahara, Y.; Shimizu, N.; Inazu, T. *Chem. Lett.* **1995**, *24* (12), 1103. doi:10.1246/cl.1995.1103.
(18) Murray-Rust, P.; Stallings, W. C.; Monti, C. T.; Preston, R. K.; Glusker, J. P. *J. Am. Chem. Soc.* **1983**, *105* (10), 3206. doi:10.1021/ja00348a041.
(19) Breitenbach, J.; Vögtle, F. *Synthesis* **1992**, *1992* (1/2), 41. doi:10.1055/s-1992-34171.
(20) (a) Breitenbach, J.; Ott, F.; Vögtle, F. *Angew. Chem.* **1992**, *104* (3), 360. doi:10.1002/ange.19921040339; (b) Breitenbach, J.; Ott, F.; Vögtle, F. *Angew. Chem. Int. Ed. Engl.* **1992**, *31* (3), 307. doi:10.1002/anie.199203071.
(21) Ott, F.; Breitenbach, J.; Nieger, M.; Vögtle, F. *Chem. Ber.* **1993**, *126* (1), 97. doi:10.1002/cber.19931260116.
(22) Possel, O.; van Leusen, A. M. *Tetrahedron Lett.* **1977**, *18* (48), 4229. doi:10.1016/S0040-4039(01)83472-9.
(23) van Leusen, D.; van Leusen, A. M. *Tetrahedron Lett.* **1977**, *18* (48), 4233. doi:10.1016/S0040-4039(01)83473-0.

(24) Kobiro, K.; Takahashi, M.; Nishikawa, N.; Kakiuchi, K.; Tobe, Y.; Odaira, Y. *Tetrahedron Lett.* **1987**, *28* (33), 3825. doi:10.1016/S0040-4039(00)96396-2.
(25) Kurosawa, K.; Suenaga, M.; Inazu, T.; Yoshino, T. *Tetrahedron Lett.* **1982**, *23* (50), 5335. doi:10.1016/S0040-4039(00)85832-3.
(26) Shinmyozu, T.; Hirai, Y.; Inazu, T. *J. Org. Chem.* **1986**, *51* (9), 1551. doi:10.1021/jo00359a033.
(27) Meno, T.; Sako, K.; Suenaga, M.; Mouri, M.; Shinmyozu, T.; Inazu, T.; Takemura, H. *Can. J. Chem.* **1990**, *68* (3), 440. doi:10.1139/v90-067.
(28) Sako, K.; Meno, T.; Shinmyozu, T.; Inazu, T.; Takemura, H. *Chem. Ber.* **1990**, *123* (3), 639. doi:10.1002/cber.19901230334.
(29) Tashiro, M.; Yamato, T. *J. Org. Chem.* **1981**, *46* (22), 4556. doi:10.1021/jo00335a047.
(30) Tashiro, M.; Yamato, T. *J. Org. Chem.* **1983**, *48* (9), 1461. doi:10.1021/jo00157a015.
(31) Yamato, T.; Miyazawa, A.; Tashiro, M. *J. Chem. Soc., Perkin Trans. 1* **1993**, No. 24, 3127. doi:10.1039/p19930003127.
(32) Tashiro, M.; Yamato, T. *Org. Prep. Proced. Int.* **1981**, *13* (1), 1. doi:10.1080/00304948109356494.
(33) Tashiro, M.; Yamato, T. *J. Org. Chem.* **1981**, *46* (8), 1543. doi:10.1021/jo00321a005.
(34) Yamato, T.; Matsumoto, J.; Tokuhisa, K.; Kajihara, M.; Suehiro, K.; Tashiro, M. *Chem. Ber.* **1992**, *125* (11), 2443. doi:10.1002/cber.19921251116.
(35) Yamato, T.; Miyazawa, A.; Tashiro, M. *Chem. Ber.* **1993**, *126* (11), 2505. doi:10.1002/cber.19931261126.
(36) Smith, B. H. In *Bridged Aromatic Compounds;* Academic Press: New York, 1964.
(37) (a) Vögtle, F.; Neumann, P. *Angew. Chem.* **1972**, *84* (3), 75. doi:10.1002/ange.19720840302; (b) Vögtle, F.; Neumann, P. *Angew. Chem. Int. Ed. Engl.* **1972**, *11* (2), 73. doi:10.1002/anie.197200731.
(38) Vögtle, F.; Neumann, P. *Synthesis* **1973**, *1973* (02), 85. doi:10.1055/s-1973-22137.
(39) Vögtle, F.; Höhner, G. *Top. Curr. Chem.* **1978**, *74*, 1. doi:10.1007/BFb0050144.
(40) Keehn, P. M.; Rosenfield, S. M., Eds. *Cyclophanes;* Academic Press: New York; Vol. 1, 1983.
(41) Mitchell, R. H.; Boekelheide, V. *Tetrahedron Lett.* **1970**, *11* (14), 1197. doi:10.1016/S0040-4039(01)97945-6.
(42) Mitchell, R. H.; Boekelheide, V. *J. Chem. Soc. Chem. Commun.* **1970**, 1555.
(43) Anker, W.; Bushnell, G. W.; Mitchell, R. H. *Can. J. Chem.* **1979**, *57* (23), 3080. doi:10.1139/v79-503.
(44) Mitchell, R. H.; Carruthers, R. J.; Mazuch, L.; Dingle, T. W. *J. Am. Chem. Soc.* **1982**, *104* (9), 2544. doi:10.1021/ja00373a036.
(45) Mitchell, R. H.; Boekelheide, V. *J. Am. Chem. Soc.* **1974**, *96* (5), 1547. doi:10.1021/ja00812a045.
(46) Yamato, T.; Doamekpor, L. K.; Koizumi, K.; Kishi, K.; Haraguchi, M.; Tashiro, M. *Liebigs Ann.* **1995**, *1995* (7), 1259. doi:10.1002/jlac.1995199507167.
(47) Tashiro, M.; Yamato, T. *J. Org. Chem.* **1985**, *50* (16), 2939. doi:10.1021/jo00216a026.
(48) Yamato, T.; Matsumoto, J.; Tokuhisa, K.; Tsuji, K.; Suehiro, K.; Tashiro, M. *J. Chem. Soc., Perkin Trans. 1* **1992**, (20): 2675. doi:10.1039/p19920002675.

Can. J. Chem. Downloaded from www.nrcresearchpress.com by Renmin University of China on 09/02/12
For personal use only.

A quasi-classical trajectory study of the reagent initial rotation quantum state effect on the reaction He + $T_2^+ \rightarrow HeT^+ + T$ using an improved ab initio potential energy surface

Ningjiu Zhao and Yufang Liu

Can. J. Chem. Downloaded from www.nrcresearchpress.com by Renmin University of China on 09/02/12
For personal use only.

Abstract: In this work, we employed the quasi-classical trajectory (QCT) method to study the vector correlations and the influence of the reagent initial rotational quantum number j for the reaction He + T_2^+ ($v = 0$, $j = 0$–3) → HeT^+ + T on a new potential energy surface (PES). The PES was improved by Aquilanti co-workers (Chem. Phys. Lett. 2009. **469:** 26–30). The polarization-dependent differential cross sections (PDDCSs) and the distributions of $P(\theta_r)$, $P(\phi_r)$, and $P(\theta_r, \phi_r)$ are presented in this work. The plots of the PDDCSs provide us with abundant information about the distribution of the product angular momentum polarization. The $P(\theta_r)$ is used to describe the correlation between **k** (the relative velocity of the reagent) and **j′** (the product rotational angular momentum). The distribution of dihedral angle $P(\phi_r)$ shows the **k**–**k′**–**j′** (**k′** refers to the relative velocity of the product) correlation. The PDDCS calculations illustrate that the product of this reaction is mainly backward scatter and it has the strongest polarization in the backward and sideways scattering directions. At the same time, the results of the $P(\phi_r)$ demonstrate that the product HeT^+ tends to be oriented along the positive direction of the y axis and it tends to rotate right-handedly in planes parallel to the scattering plane. Moreover, the distribution of the $P(\theta_r)$ manifests that the product angular momentum is aligned along different directions relative to **k**. The direction of the product alignment may be perpendicular, opposite, or parallel to **k**. Moreover, our calculations are independent of the initial rotational quantum number.

Key words: quasi-classical trajectory, vector correlations, steorodynamics, polarization-dependent differential cross sections (PDDCSs).

Résumé : Dans ce travail, on a utilisé la méthode de la trajectoire quasi-classiqe (TQC) pour étudier les corrélations des vecteurs ainsi que l'influence du nombre quantique initial du réactif, j, de la réaction He + T_2^+ ($v = 0$; $j = 0$–3) → HeT^+ + T sur une nouvelle surface d'énergie potentielle (SEP) . La surface d'énergie potentielle correspond à celle améliorée par Aquilanti et collègues (Chem. Phys. Lett. 2009. **469:** 26–30). Dans ce travail, on rapporte les valeurs de la différentielle des sections droites qui dépendent de la polarisation (DSDDP) ainsi que les distributions de $P(\theta_r)$, $P(\phi_r)$ et $P(\theta_r, \phi_r)$. Les courbes des valeurs de la DSDDP fournissent une information abondante concernant la distribution de la polarisation du moment angulaire du produit. On utilise le $P(\theta_r)$ pour décrire la corrélation entre **k** (la vitesse relative du réactif) et **j′** (le moment angulaire rotationnel du produit). La distribution du $P(\phi_r)$ dièdre permet de démontrer la corrélation **k**–**k′**–**j** (dans laquelle **k′** se réfère à la vitesse relative du réactif). Les calculs des valeurs de la DSDDP permettent d'illustrer que le produit de cette réaction donne principalement lieu à une rétrodiffusion et qu'elle est polarisée le plus fortement dans des directions de rétrodiffusion et de diffusion latérale. Parallèlement, les résultats obtenus pour les valeurs de $P(\phi_r)$ démontrent que le produit de HeT^+ tend à être orienté le long de la direction positive de l'axe y et que sa rotation tend vers la droite dans les plans parallèles au plan de diffusion. De plus, la distribution des valeurs de $P(\theta_r)$ démontre que l'alignement du produit peut être perpendiculaire, opposé ou parallèle à **k**. De plus, ces calculs sont indépendants de nombre quantique rotationnel initial.

Mots-clés : trajectoire quasi-classique, corrélations de vecteurs, stéréodynamique, différentielle des sections droites qui dépendent de la polarisation (DSDDP).

[Traduit par la Rédaction]

Introduction

During the development of ion–molecule reaction dynamics, the reaction He + H_2^+ and the isotopic reactions owing to its typical characteristics, have attracted more and more people to the study of the systems for dynamical progress. The experimental investigations have received considerable attention, as has theoretical study.[1–11] Being typical ion–molecule reactions, the reactions are regarded as the prototype systems for the testing of the quality of new theories and experiments. Therefore, it is necessary to obtain the dynamical

Received 13 May 2011. Accepted 8 July 2011. Published at www.nrcresearchpress.com/cjc on 12 January 2012.

N. Zhao and Y. Liu. Department of Physics, Henan Normal University, Xinxiang 453007, China.

Corresponding author: Yufang Liu(e-mail: yfliu126@126.com).

Can. J. Chem. Downloaded from www.nrcresearchpress.com by Renmin University of China on 09/02/12
For personal use only.

information of the reactions. In 1994, the ab initio calculations for the He + H_2^+ → HeH^+ + H was performed by Costen et al.[12] for the scattering energies near the threshold (21.91–26.52 kcal/mol; 1 cal = 4.184 J) at the MRCI level and the "exact" integral quantum reactive cross sections. Palmieri et al.[8] constructed the accurate potential energy surface, and the effect of the reagent vibration on the He + H_2^+ (v = 0–2, j = 0) → HeH^+ + H reaction was studied. The results implied that different vibrational quantum numbers made great differences on the reaction probability at the same collision energy and that the reaction cross sections generally increased as the vibrational number increased. Chu et al.[1] studied the He + H_2^+ reaction using the time-dependent quantum wave packet method, but this method was different from the former time-dependent quantum wave packet theory. Coriolis coupling was considered in this method. The conclusions regarding the reaction probability and reaction cross sections fundamentally agreed with the experimental results. Tiwari et al.[13] discussed the effect of reagent rotation on isotopic branching for the reaction He + HD^+ and the results showed that the branch ratios depended sensitively on the reagent rotation. Later, Tang et al.[9] investigated the reaction He + HD^+ (v = 0–3, j = 1) using time-dependent quantum wave packet method calculations, and the results were in excellent accordance with the experiments. Xu et al.[5,14] calculated the total integral reaction cross section as a function of the collision energy in the range of 0–46.12 kcal/mol and the isotope effect of He + H_2^+/D_2^+/T_2^+ on the stereodynamics at a collision energy of 50 kcal/mol by use of the quasi-classical trajectory (QCT) calculation. It should be mentioned that Aquilanti and co-workers[15] constructed a new potential energy surface (PES) of the He + H_2^+ → HeH^+ + H reaction. The stereodynamics and vector correlation information of the He + H_2^+ → HeH^+ + H reaction on the new PES have been less reported on. In addition, sufficient systematic reports have not been reported on the reaction He + T_2^+ → HeT^+ + T.

In recent years, the QCT method has played a key role in the study of molecule dynamics because of its precision and simplicity, especially the stereodynamics information.[11,16–31] As a consequence, we theoretically studied the He + T_2^+ → HeT^+ + T reaction using the QCT method.

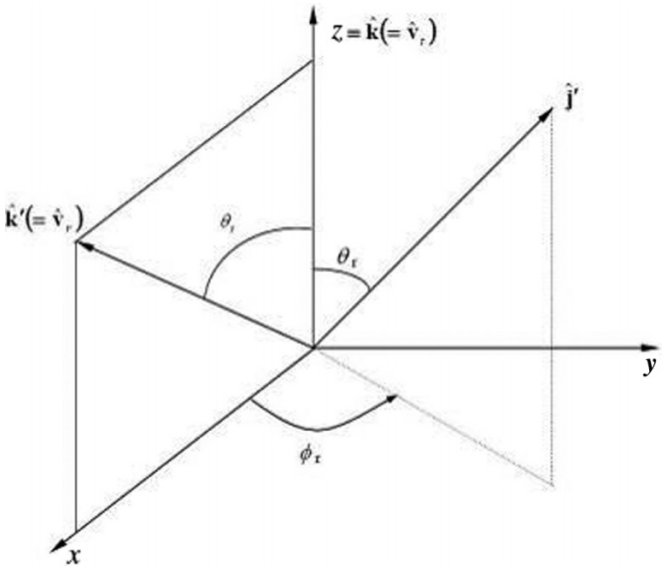
In this work, we will discuss the vector correlations of the reaction and the influence of reagent rotation states on the reaction by use of the QCT method on a new PES.[15] In our calculations, we set the reagent initial vibrational number (v) as 0, and the rotational quantum number (j) as 0–3. A collision energy of 3 eV was chosen. Apart from these, a batch of 10 000 trajectories was run and the integration step was chosen to be 0.1 fs.

Theoretical and computational method

The center-of-mass (CM) frame was chosen, in which the z axis was parallel to the reagent relative velocity **k** and the y axis was perpendicular to the x–z plane containing **k** and **k′**.

The fully correlated CM angular distribution is written as the sum[32–34]

Fig. 1. The center-of-mass coordinate system used to describe the **k**–**k′**–**j′** correlation.



$$[1]\qquad P(\cos\theta, \cos\theta_r, \phi_r) = \frac{1}{4\pi}\sum_{k=0}^{\infty}\sum_{q=-k}^{k}(2k+1) \times \frac{2\pi}{\sigma}\frac{d\sigma_{kq}}{d\omega}C_{kq}(\theta_r, \phi_r)$$

where $\omega = \theta$, ϕ and $\omega_r = \theta_r$, ϕ_r refer to the coordinates of the unit vectors **k′** and **j′** along the direction of the product relative velocity and rotational angular momentum vectors in the CM frame, respectively, and $C_{kq}(\theta_r, \phi_r)$ are modified spherical harmonics. $\frac{1}{\sigma}\frac{d\sigma_{kq}}{d\omega}$ represents the generalized polarization-dependent differential cross sections (PDDCSs).[32,35–40]

The PDDCSs are written as follows:

$$\frac{2\pi}{\sigma}\frac{d\sigma_{k0}}{d\omega} = 0$$

when k is odd,

$$\frac{2\pi}{\sigma}\frac{d\sigma_{kq+}}{d\omega} = \frac{2\pi}{\sigma}\frac{d\sigma_{kq}}{d\omega} = \frac{2\pi}{\sigma}\frac{d\sigma_{k-q}}{d\omega} = 0$$

when k is even, q is odd or k is odd q is even, and

$$\frac{2\pi}{\sigma}\frac{d\sigma_{kq-}}{d\omega} = \frac{2\pi}{\sigma}\frac{d\sigma_{kq}}{d\omega} - \frac{2\pi}{\sigma}\frac{d\sigma_{k-q}}{d\omega} = 0$$

when k and q are even or k and q are odd. We also can summarize it as[1,37,40,41–48]

$$[2]\qquad \frac{2\pi}{\sigma}\frac{d\sigma_{kq\pm}}{d\omega} = \sum_{k_1}\frac{[k_1]}{4\pi}S^{k_1}_{kq\pm}C_{k_1-q}(\theta, 0)$$

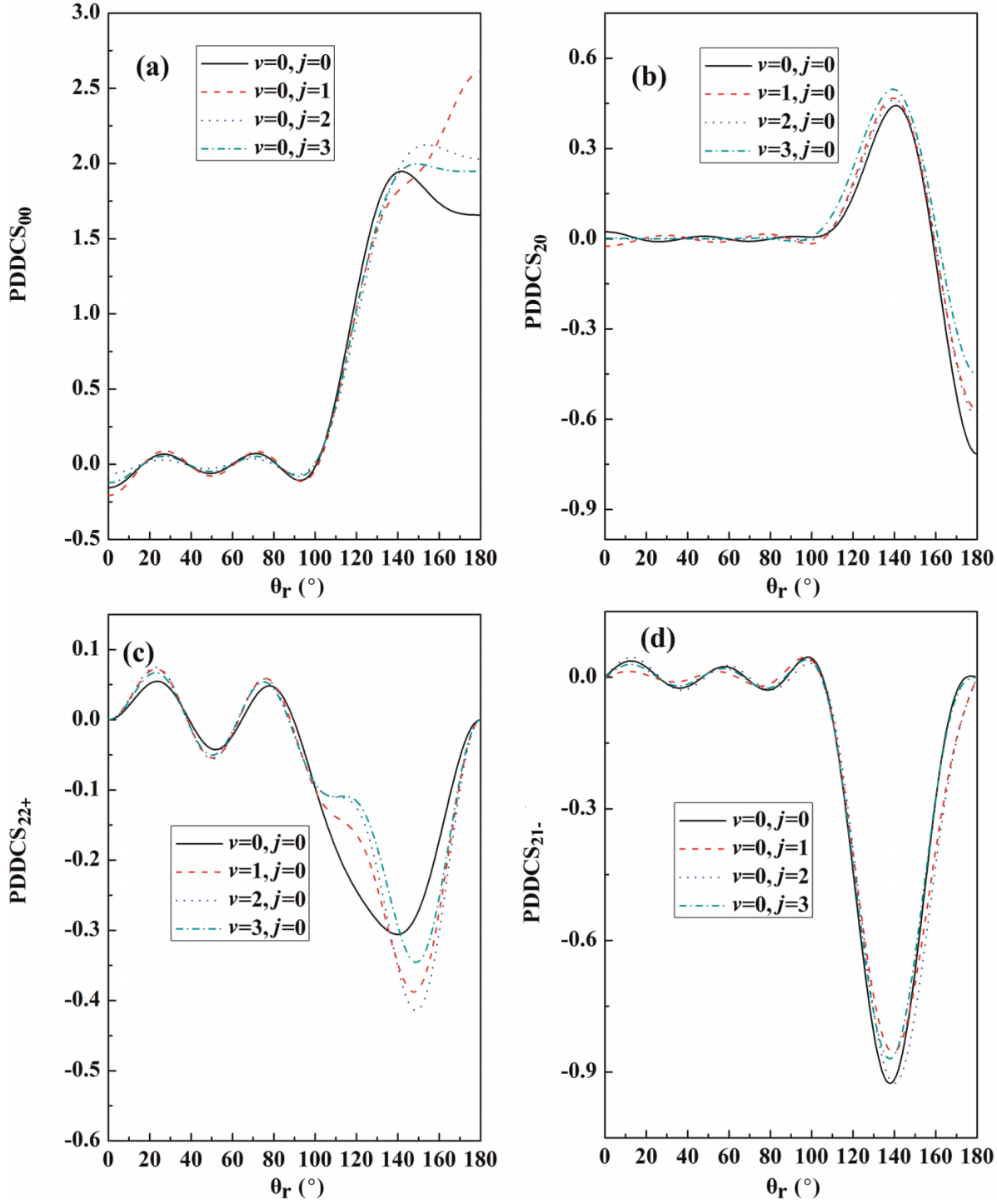
where $[k_1] = 2k_1 + 1$ and $S^{k_1}_{q\pm}$ can be expressed as

$$[3]\qquad S^{k_1}_{kq\pm} = \langle c_{k_1q}(\theta, 0)c_{kq}(\theta_r, 0)[(-1)^q e^{iq\phi_r} \pm e^{-iq\phi_r}]\rangle$$

Two vector correlations (**k**–**j′**, **k**–**k′**, or **k′**–**j′**) can be expanded into a series of Legendre polynomials (Fig. 1).[49–52] The $P(\theta_r)$ distribution corresponding to the **k**–**j′** correlation is written as

Can. J. Chem. Downloaded from www.nrcresearchpress.com by Renmin University of China on 09/02/12
For personal use only.

Fig. 2. Calculated polarization-dependent differential cross sections (PDDCSs) of the He + T_2^+ reaction at different initial states. (*a*) Indicating the $PDDCS_{00}$ of different rotational quantum numbers (from 0 to 3) at vibrational number 0. (*b*) Indicating the $PDDCS_{20}$ of different rotational quantum numbers (from 0 to 3) at vibrational number 0. (*c*) Indicating the $PDDCS_{22+}$ of different rotational quantum numbers (from 0 to 3) at vibrational number 0. (*d*) Indicating the $PDDCS_{21-}$ of different rotational quantum numbers (from 0 to 3) at vibrational number 0.



$$[4] \qquad P(\theta_r) = 1/2\sum_k [k] a_0^k P_k(\cos\theta_r)$$

The a_0^k coefficients (polarization parameters) are given by

$$a_0^k = P_k(\cos\theta_r)$$

The brackets represent an average over all the reactive trajectories. The dihedral angle distribution of the **k**–**k**′–**j**′ three-vector correlation is characterized by the angle $P(\theta_r)$. The distribution of the dihedral angle $P(\phi_r)$ could be expanded as a Fourier series

Can. J. Chem. Downloaded from www.nrcresearchpress.com by Renmin University of China on 09/02/12
For personal use only.

$$[5] \quad P(\phi_r) = \frac{1}{2\pi}\left(1 + \sum_{n\geq 2}^{\text{even}} a_n \cos n\phi_r + \sum_{n\geq 1}^{\text{odd}} b_n \sin\phi_r\right)$$

with a_n and b_n given by

$$a_n = 2\langle \cos n\phi_r \rangle$$

$$b_n = 2\langle \sin n\phi_r \rangle$$

In this work, convergence results were obtained when $P(\phi_r)$ was expended up to $n = 24$.

The joint of probability density function of angles θ_r and ϕ_r, which define the direction of $\mathbf{j}'$, can be written as

$$[6] \quad P(\theta_r, \phi_r) = \frac{1}{4\pi}\sum_{kq}[k]a_q^k C_{kq}(\theta_r, \phi_r)^* = \frac{1}{4\pi}\sum_k\sum_{q\geq 0}[a_{q\pm}^k \cos q\phi_r - a_{q\mp}^k i \sin q\phi_r]C_{kq}(\theta_r, 0)$$

The parameter a_q^k is evaluated as

$$[7] \quad a_{q\pm}^k = 2\langle C_{k|q|}(\theta_r, 0)\cos q\phi_r \rangle \quad k \text{ is even}$$

$$[8] \quad a_{q\pm}^k = 2i\langle C_{k|q|}(\theta_r, 0)\sin q\phi_r \rangle \quad k \text{ is odd}$$

During the calculation, $P(\theta_r, \phi_r)$ was expanded up to $k = 7$, which was sufficient for good convergence.

Results and discussion

Figure 2*a* presents the PDDCS ($(2\pi/\sigma)(d\sigma_{00}/d\omega_t)$), which is proportional to the general differential cross section (DCS). The PDDCS is not involved in the orientation and alignment effect of product angular momentum, however, it can give us the scattering direction of the product in this reaction or we can say that it describes the correlation of **k**–**k**′. From Fig. 2*a*, we can draw the conclusion that the product of this reaction is dominated by backward and sideways scattering. Comparing the different $PDDCSs_{00}$ of various j values, the forward and sideways scattering directions of the product are nearly unrelated to the rotational quantum numbers, whereas the backward scattering shows slight changes when the rotational quantum number increases. The PDDCS $(2\pi/\sigma)(d\sigma_{20}/d\omega_t)$ is shown in Fig. 2*b*, which represents the expectation value of the second Legendre moment $\langle P_2(\cos\theta)\rangle$. In addition, the $PDDCS_{20}$ is not opposite to the distribution of $PDDCS_{00}$, but it can tell us that the product angular momentum is strongly polarized in backward and sideways scattering directions. This phenomenon is different from the reaction He + H_2^+.[5] What has caused this difference remains to be further discussed, but we may also ascribe it to the mass factors according to ref. 22 or the properties of the new PES. It indicates that $\mathbf{j}'$ is preferentially polarized along the direction perpendicular to **k** at $\theta_t = 180°$ (θ_t is the angle between **k** and **k**′). It can be seen from Figs. 2*c* and 2*d* that all PDDCSs with $q \neq 0$ equal 0 at $\theta_t = 0°$ and 180°, and the PDDCSs

Fig. 3. Comparisons of the calculated angular distribution of $P(\theta_r)$ at different initial quantum states. The vibrational number is equal to 0 and the rotational quantum numbers range from 0 to 3.

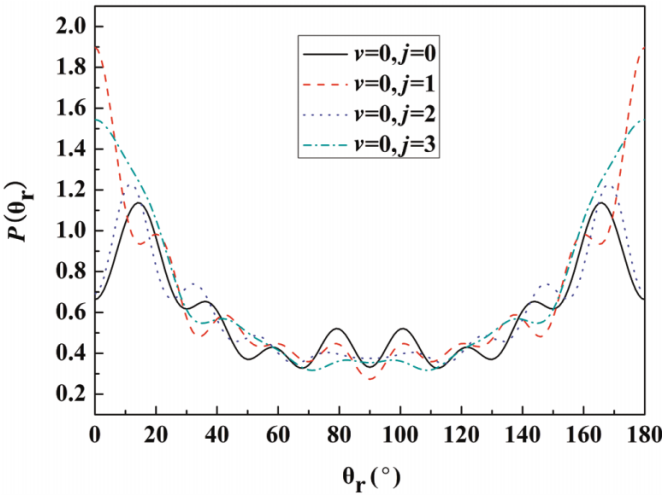
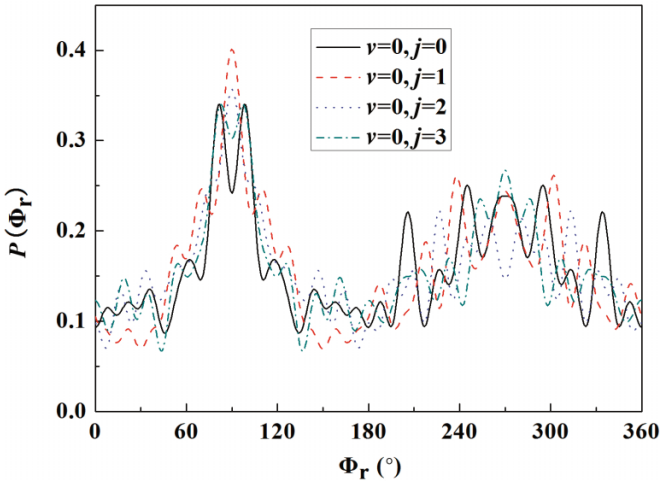


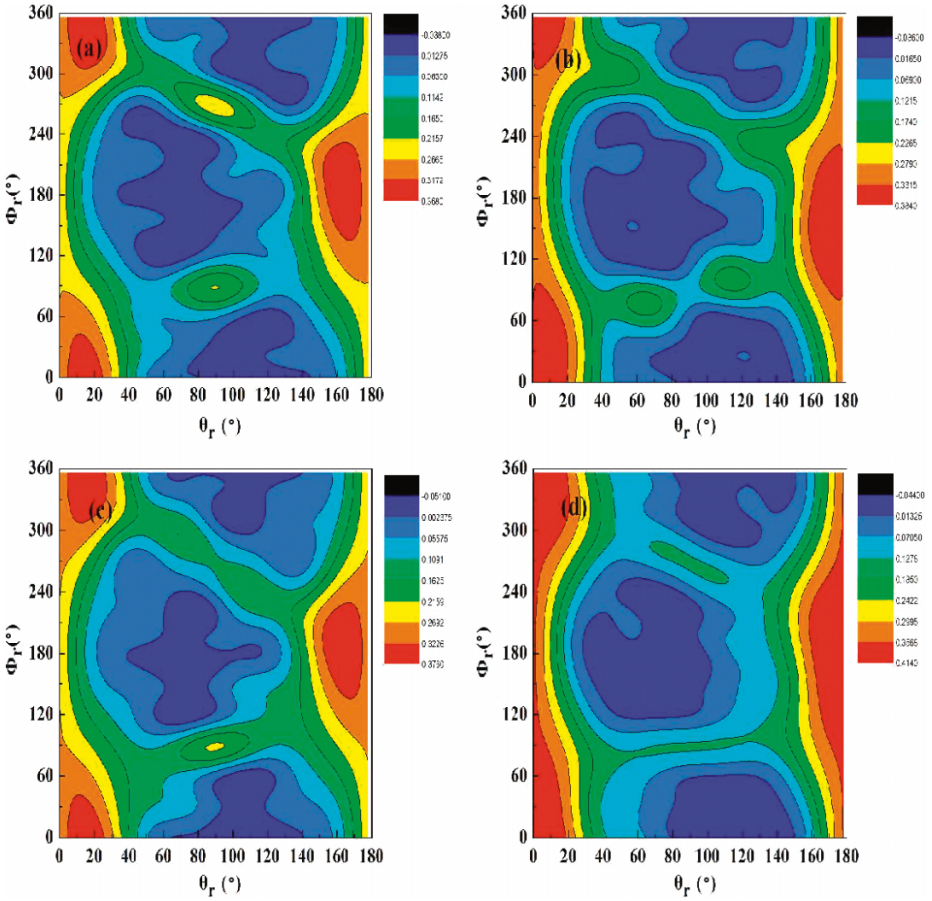
Fig. 4. The dihedral angle distribution of product rotational momentum $\mathbf{j}'$ regarding the **k**–**k**′ plane at different states of different rotational quantum numbers when the vibrational number equals 0, reflecting the correlations of **k**–**k**′–$\mathbf{j}'$.



$(2\pi/\sigma)(d\sigma_{22+}/d\omega_t)$ are nonzero at other majority portions of the scattering angles. However, the PDDCSs $(2\pi/\sigma)(d\sigma_{21-}/d\omega_t)$, which are related to $\langle \cos\theta_r \sin\theta_r \sin\phi_r \rangle$, are close to 0 when θ_t <100° and θ_t >170°. We can see that the $PDDCS_{22+}$ and $PDDCS_{21-}$ are both peaking at about θ_t = 140°. Moreover, as can be seen from (Fig. 2*d*), the polarization trends of the reaction in different initial states is displayed consistently. In addition, the distributions of the PDDCSs exhibit a trend of independence of the variation of j. What is interesting is that the PDDCSs ($q \neq 1$) are all different from the ones of the He + H_2^+/HD^+ reactions and presents different dynamical behaviors. The product of the former reaction is mainly backward and sideways scattered, however, the latter is mainly forward scattered[5] and the product angular momentum is strongly polarized in the backward and sideways scattering directions, whereas the product angular momentums of the latter reactions are forward scattered.

Can. J. Chem. Downloaded from www.nrcresearchpress.com by Renmin University of China on 09/02/12
For personal use only.

Fig. 5. Polar plots of the $P(\theta_r,\phi_r)$ distribution averaged over all scattering angles at each initial state. (*a*) Expression of the initial state $v = 0$, $j = 0$. (*b*) Expression of the initial state $v = 0$, $j = 1$. (*c*) Expression of the initial state $v = 0$, $j = 2$. (*d*) Expression of the initial state $v = 0$, $j = 3$.



For the reaction He + T_2^+, we also plot the $P(\theta_r)$ distribution in Fig. 3. Figure 3 clearly illustrates that the $P(\theta_r)$ distribution is symmetric with respect to 90° owing to the planar symmetry of this system. However, the peaks are not at the same angle. The peaks of the distribution $P(\theta_r)$ ($v = 0$, $j = 0$, 2) are at approximately 10° and 170°, whereas the peaks of the distribution $P(\theta_r)$ ($v = 0$, $j = 1$, 3) are both at 0° and 180°. The distributions $P(\theta_r)$, which represent the **k**–**j′** correlation, suggest that the product angular momentum vector is aligned along different directions relative to **k**. When the rotational quantum number is 0 or 2, the product rotational angular momentum is not aligned along a stationary direction, but could be aligned along the perpendicular, parallel, or opposite direction to **k**. Nonetheless, for the $v = 0$, $j = 1$, 3 states, the peaks at 0° and 180° demonstrate that the product rotational angular strongly aligns along the direction parallel and opposite to **k**.

Figure 4 shows the distributions of $P(\phi_r)$ in different quantum states. In this figure, a common feature exists for the $P(\phi_r)$ distributions in that they are prone to being asymmetric with respect to about $\phi_r = 180°$ (the scattering **k**–**k′** plane), with two distinct peaks emerging at $\phi_r = 90°$ and 270°. The peaks at 90° and 270° provide us with the information that the product tends to align along the direction of the *y* axis, which is perpendicular to the scattering plane. However, the differences between the peaks at 90° and 270° can be seen. Since the peaks at 90° are apparently stronger than the peaks at 270°, a conclusion can be mapped out that the products of the reaction of different *j* and $v = 0$ are not only aligned, but also oriented along the positive direction of the *y* axis. As well, the peak at 270° implies a preference for left-handed product rotation in planes parallel to the scattering plane; certainly, the peak at 90° indicates a preference for the right-handed product rotation. According to ref. 17, we will use the term "in-plane" to refer to this preference of the product rotating in the planes parallel to the scattering direction and the term "out-of-plane" to refer to the preference of the product rotating in planes parallel to the scattering plane simultaneously. With increasing *j*, no apparent variations were observed. That is to say, the product of the reaction He + T_2^+ ($v = 0$, $j = 0$–3) tends to right-hand rotate in planes parallel to the scattering plane.

The fact that the distribution $P(\phi_r)$ remains unchanged implies that the stereodynamic properties of this reaction at $v = 0$ are nearly independent of the rotational quantum number *j*. Figure 5 depicts the product angular momentum polarization in the form of polar plots θ_r and ϕ_r, which corresponds to the spatial distribution of the product rotational angular momentum. The spatial distribution is expressed by $P(\theta_r, \phi_r)$ distribution averaged over all scattering angles. What can we see from Fig. 5 is that, in regard to the reaction He + T_2^+ ($v = 0$, $j = 0$), the distribution of the $P(\theta_r,\phi_r)$ peaks is not only at

(90°, 90°), but also at (90°, 270°). They are in good agreement with the distributions of $P(\theta_r)$ and $P(\phi_r)$ of the products. However, Figs. 5*b* and 5*c* have a obvious distribution at around (90°, 90°) and a weak distribution at around (90°, 270°), and Fig. 4*d* has a relatively obvious distribution at around (90°, 270°) with a weak one at around (90°, 90°). They are also in good accordance with disributions of $P(\phi_r)$ and $P(\theta_r)$ of the products.

Conclusion

In this paper, the reaction He + T_2^+ (v = 0, j = 0–3) → HeT^+ + T has been theoretically calculated by use of the QCT method on a new PES at a collision energy of 3 eV. We have plotted the distribution curves of $P(\theta_r)$, $P(\phi_r)$, and $P(\theta_r, \phi_r)$. By investigating the angular distributions and comparing the changes with respect to j, we find that they are insensitive to the rotational quantum number j. The product rotational angular momentum is not aligned along a stationary direction. This is in agreement with the ref. 14, in which the effect of the HeT^+ product alignment along the direction perpendicular to k becomes weaker. The distribution of $P(\phi_r)$ reveals that the product rotational angular momentum vector is preferentially oriented along the positive direction of the y axis. Furthermore, the PDDCSs are calculated at the same time and compared among different j values. They demonstrate that the product of this reaction is dominated by backward and sideways scattering. In addition, they also perform an independent behavior on the initial rotational quantum number.

Acknowledgement

This Ppoject was supported by the National Natural Science Foundation of China (Grant Nos. 60977063 and 10574039), the Innovation Scientists and Technicians Troop Construction Projects of Henan Province of China (Grant No. 084100510011), and the Innovation Talents of Institution of Higher Education of Henan Province of China (Grant No. 2006KYCX002). The authors are grateful to Professors V. Aquilanti and C.N. Ramachandran for the new PES.

References

(1) Chu, T. S.; Lu, R. F.; Han, K. L.; Tang, X. N.; Xu, H.; Ng, C. Y. *J. Chem. Phys.* **2005**, *122* (24), 244322. doi:10.1063/1.1948380.
(2) Xu, W. W.; Liu, X. G.; Luan, S. X.; Sun, S. S.; Zhang, Q. G. *Chin. Phys. B* **2009**, *18* (1), 339. doi:10.1088/1674-1056/18/1/055.
(3) Xu, W. W.; Liu, X. G.; Zhang, Q. G. *Mol. Phys.* **2008**, *106* (14), 1787. doi:10.1080/00268970802290321.
(4) Chu, T. S.; Zhang, Y.; Han, K. L. *Int. Rev. Phys. Chem.* **2006**, *25* (1–2), 201. doi:10.1080/01442350600677929.
(5) Xu, W. W.; Liu, X. G.; Luan, S. X.; Zhang, Q. G. *Chem. Phys.* **2009**, *355* (1), 21. doi:10.1016/j.chemphys.2008.07.015.
(6) Aquilanti, V.; Capecchi, G.; Cavalli, S.; De Fazio, D.; Palmieri, P.; Puzzarini, C.; Aguilar, A.; Giménez, X.; Lucas, J. M. *Chem. Phys. Lett.* **2000**, *318* (6), 619. doi:10.1016/S0009-2614(00)00067-1.
(7) Tang, X. N.; Xu, H.; Zhang, T.; Hou, Y.; Chang, C.; Ng, C. Y.; Chiu, Y.; Dressler, R. A.; Levandier, D. J. *J. Chem. Phys.* **2005**, *122* (16), 164301. doi:10.1063/1.1883169.
(8) Palmieri, P.; Puzzarini, C.; Aquilanti, V.; Capecchi, G.; Cavalli, S.; De Fazio, D.; Aguilar, A.; Giménez, X.; Lucas, J. M. *Mol. Phys.* **2000**, *98* (21), 1835. doi:10.1080/00268970009483387.
(9) Tang, X. N.; Houchins, C.; Lau, K.-C.; Ng, C. Y.; Dressler, R. A.; Chiu, Y.-H.; Chu, T.-S.; Han, K. L. *J. Chem. Phys.* **2007**, *127*, 164318. doi:10-1063/1.2800009.
(10) Chupka, W. A.; Russel, M. E. *J. Chem. Phys.* **1968**, *49* (12), 5426. doi:10.1063/1.1670068.
(11) Aguado, A.; Paniagua, M. *J. Chem. Phys.* **1992**, *96* (2), 1265. doi:10.1063/1.462163.
(12) Costen, M. L.; Hancock, G.; Orr-Ewing, A. J.; Summerfield, D. *J. Chem. Phys.* **1994**, *100* (4), 2754. doi:10.1063/1.466470.
(13) Tiwari, A. K.; Panda, A. N.; Sathyamurthy, N. *J. Phys. Chem. A* **2006**, *110* (2), 389. doi:10.1021/jp051796x.
(14) Xu, W. W.; Liu, X. G.; Luan, S. X.; Zhang, Q. G. *Int. J. Quantum Chem.* **2007**, *110*, 860.
(15) Ramachandran, C. N.; De Fazio, D.; Cavalli, S.; Tarantelli, F.; Aquilanti, V. *Chem. Phys. Lett.* **2009**, *469* (1-3), 26. doi:10.1016/j.cplett.2008.12.035.
(16) Xie, T. X.; Zhang, Y.; Zhao, M. Y.; Han, K. L. *Phys. Chem. Chem. Phys.* **2003**, *5* (10), 2034. doi:10.1039/b300763d.
(17) Zhang, W. Q.; Cong, S.; Zhang, C.; Xu, X.; Chen, M. *J. Phys. Chem. A* **2009**, *113* (16), 4192. doi:10.1021/jp8105716.
(18) Kuntz, P. J. *Chem. Phys. Lett.* **1972**, *16* (3), 581. doi:10.1016/0009-2614(72)80429-9.
(19) Chu, T. S.; Zhang, X.; Han, K. L. *J. Chem. Phys.* **2005**, *122* (21), 214301. doi:10.1063/1.1924507.
(20) Yang, B. H.; Gao, H. T.; Han, K. L.; Zhang, J. Z. H. *J. Chem. Phys.* **2000**, *113* (4), 1434. doi:10.1063/1.481933.
(21) Wang, M. L.; Han, K. L.; He, G. Z. *J. Chem. Phys.* **1998**, *109* (13), 5446. doi:10.1063/1.476522.
(22) Wang, M. L.; Han, K. L.; He, G. Z. *J. Phys. Chem. A* **1998**, *102* (50), 10204. doi:10.1021/jp981738u.
(23) Xu, W. W.; Liu, X. G.; Zhang, Q. G. *Mol. Phys.* **2008**, *106* (14), 1787. doi:10.1080/00268970802290321.
(24) Li, Y. M. *Mol. Phys.* **2009**, *107* (13), 1331. doi:10.1080/00268970902873539.
(25) Chu, T. S.; Han, K. L. *J. Phys. Chem. A* **2005**, *109* (10), 2050. doi:10.1021/jp0451391.
(26) Zhang, H.; Zhu, R. S.; Wang, G. J.; Han, K. L.; He, G. Z.; Lou, N. Q. *J. Chem. Phys.* **1999**, *110* (6), 2922. doi:10.1063/1.477935.
(27) Ahmed, M.; Peterka, D. S.; Suits, A. *Chem. Phys. Lett.* **1999**, *301* (3–4), 372. doi:10.1016/S0009-2614(99)00048-2.
(28) Ransome, S. W.; Wright, J. S. *J. Chem. Phys.* **1982**, *77* (12), 6346. doi:10.1063/1.443810.
(29) Liu, Y. F.; Gao, Y. L.; Zhai, H. S.; Liu, R. Q. *J. At. Mol. Phys.* **2008**, *25*, 1063.
(30) Liu, X.; Lin, J. L.; Harich, S.; Yang, X. *J. Chem. Phys.* **2000**, *113* (4), 1325. doi:10.1063/1.481923.
(31) Hu, J.; Han, K. L.; He, G. Z. *Phys. Rev. Lett.* **2005**, *95* (12), 123001. doi:10.1103/PhysRevLett.95.123001.
(32) Han, K. L.; He, G. Z.; Lou, N. Q. *J. Chem. Phys.* **1996**, *105* (19), 8699. doi:10.1063/1.472651.
(33) Zhang, X.; Han, K. L. *Int. J. Quan. Chem.* **2006**, *106* (8), 1815. doi:10.1002/qua.20929.
(34) Han, K. L.; He, G. Z. *J. Photochem. Photobiol. Photochem. Rev.* **2007**, *8* (2), 55. doi:10.1016/j.jphotochemrev.2007.03.002.
(35) Xie, Z.; Bowman, J. M.; Zhang, X. B. *J. Chem. Phys.* **2006**, *125* (13), 133120. doi:10.1063/1.2238871.
(36) Christoffel, K. M.; Jin, Z.; Braams, B. J.; Bowman, J. M. *J. Phys. Chem. A* **2007**, *111* (29), 6658. doi:10.1021/jp068722l.
(37) Czakó, G.; Bowman, J. M. *J. Chem. Phys.* **2009**, *131* (24), 244302. doi:10.1063/1.3276633.

Can. J. Chem. Downloaded from www.nrcresearchpress.com by Renmin University of China on 09/02/12
For personal use only.

(38) Fu, B.; Kamarchik, E.; Bowman, J. M. *J. Chem. Phys.* **2010**, *133* (16), 164306. doi:10.1063/1.3488167.
(39) Chu, T. S.; Han, K. L.; Schatz, G. C. *J. Phys. Chem. A* **2007**, *111* (34), 8286. doi:10.1021/jp075173q.
(40) Han, K. L.; Zheng, X. L.; Sun, B. F.; He, G. Z.; Zhang, R. *Chem. Phys. Lett.* **1991**, *181* (5), 474. doi:10.1016/0009-2614(91)90383-K.
(41) Zhang, H.; Smith, S. C. *J. Chem. Phys.* **2001**, *115* (13), 5751. doi:10.1063/1.1400785.
(42) Joseph, T.; Sathyamurthy, N. *J. Chem. Phys.* **1987**, *86* (2), 704. doi:10.1063/1.452273.
(43) Zhang, H.; Smith, S. C. *J. Chem. Phys.* **2002**, *116* (6), 2354. doi:10.1063/1.1429951.
(44) Zhang, H.; Smith, S. C. *Phys. Chem. Chem. Phys.* **2001**, *3* (12), 2282. doi:10.1039/b008991p.
(45) Chen, M. D.; Tang, B. Y.; Han, K. L.; Lou, N. Q. *Chem. Phys. Lett.* **2001**, *337* (4-6), 349. doi:10.1016/S0009-2614(01)00219-6.
(46) Cramer, C. J.; Truhlar, D. G. *Chem. Rev.* **1999**, *99* (8), 2161. doi:10.1021/cr960149m.
(47) Honvault, P.; Launay, J. M. *J. Chem. Phys.* **2001**, *114* (3), 1057. doi:10.1063/1.1338973.
(48) Panda, A. N.; Sathyamurthy, N. *J. Chem. Phys.* **2005**, *122* (5), 054304. doi:10.1063/1.1839866.
(49) Maiti, B.; Kalyanaraman, C.; Panda, A. N.; Sathyamurthy, N. *J. Chem. Phys.* **2002**, *117* (21), 9719. doi:10.1063/1.1518002.
(50) Han, K. L.; He, G. Z.; Lou, N. Q. *Chin. Chem. Lett.* **1993**, *4*, 517.
(51) Chen, M. D.; Han, K. L.; Lou, N. Q. *J. Chem. Phys.* **2002**, *283*, 463.
(52) Chen, M.-D.; Wang, M.-L.; Han, K.-L.; Ding, S.-L. *Chem. Phys. Lett.* **1999**, *301* (3–4), 303. doi:10.1016/S0009-2614(99)00052-4.

Can. J. Chem. Downloaded from www.nrcresearchpress.com by Renmin University of China on 09/02/12
For personal use only.

Synthesis and 2D NMR characterization of Ni(II), Pd(II), and Cu(II) complexes with H2cdsalen (methyl-2{*N*-[2-(2′-hydroxyphenyl) methylidenenitrilo]ethyl}amino-1-cyclopentenedithiocarboxylate)

T.J. Morales-Juárez, M.C. Sánchez-López, R.M. Gómez-Espinosa, I. García-Orozco, and D. Corona-Becerril

Can. J. Chem. Downloaded from www.nrcresearchpress.com by Renmin University of China on 09/02/12
For personal use only.

Abstract: In this study we report on the preparation of Ni(II), Pd(II), Co(II), and Cu(II) complexes with H2cdsalen (methyl-2{*N*-[2-(2′-hydroxyphenyl)methylidenenitrilo]ethyl}amino-1-cyclopentenedithiocarboxylate)salicylaldehyde. The products were characterized using 1D NMR (^{1}H and ^{13}C) and 2D NMR (COSY, NOESY, and ROESY) techniques. The conformational studies of the complexes with Ni and Pd in solution have been performed with help of the nuclear Overhauser effect (NOE) and 2D ROESY experiments.

Key words: ROESY, conformational, H2cdsalen.

Résumé : On a effectué la préparation de complexes du Ni(II), Pd(II), Co(II) et Cu(II) avec le (méthyl-2-{*N*-[2-(2′-hydroxyphényl)méthylidènenitrilo]éthyl}amino-2-cyclopentènedithiocarboxylate)salicaldéhyde, H2cdsalen. Les produits ont été caractérisés par des techniques de RMN 1D du ^{1}H et du ^{13}C et de RMN 2D (« COSY », « NOESY », « ROESY »). On a réalisé des études conformationnelles des complexes du Ni et du Pd en solution en faisant appel à des mesures de l'effet Overhauser nucléaire (EON) et du « ROESY » 2D.

Mots-clés : ROESY, conformationnelle, H2cdsalen.

[Traduit par la Rédaction]

Introduction

The coordination compounds of transition metals have had great impact on numerous branches of science, from catalysis,[1–5] medicine,[6–10] or analytical chemistry[11–14] to the design and construction of materials with new properties (structural composites and metalloproteins).[15–18]

Recently, these synthetic and structural properties, in particular those of 2-amino 1-cyclopentene 1-carboxylic acid (ACDA) and its coordination derivatives, were studied.[19–21] In particular, the metal complexes of N- or S-alkylated ACDA derivatives have attracted considerable attention because of the specific bonding formed, which depends on the nature of the metallic core. The ACDA complexes with different transition metals have exhibited remarkable diversity in their coordination.[22] The steric orientation of the functional groups in the ACDA allows the formation of six-membered ring chelates with the metal, which is perhaps responsible for biological activity such as the antifungal action that is demonstrated by ACDA.[23] Because of its structure and chelating behavior, the ACDA molecule has been applied in vast domains for the determination of the ultra traces of the concentrations for metals such as copper, cadmium, nickel, and cobalt in water solutions of different origins, via flocculation or spectrophotometric analysis.[24–27] Thus, coordination compounds derived from ACDA play an important role, both biological and chemical, and it becomes interesting to study the influence of changing their binders and (or) coordination metals.

In this framework, our research group has studied the synthesis and conformational studies of metallic complexes from ACDA derivatives, mainly with the help of NMR.

Results and discussions

The ACDA (**2**) was prepared from cyclopentanone (**1**) through the methodology previously reported by Takeshima et al.[28] and purified by the Nag procedure.[29] The methylation of the obtained ACDA derivatives (**2**) using dimethyl sulfate under basic conditions yielded compound **3**, which immediately

Received 26 April 2011. Accepted 22 September 2011. Published at www.nrcresearchpress.com/cjc on 25 January 2012.

T.J. Morales-Juárez and M.C. Sánchez-López. Facultad de Química, Universidad Autónoma del Estado de México, Paseo Tollocan y Colón, 50120, Toluca Estado de México.
R.M. Gómez-Espinosa, I. García-Orozco, and D. Corona-Becerril. Centro Conjunto de Investigación en Química Sustentable UAEM-UNAM, Carretera Toluca-Ixtlahuaca Km 14.5, C.P. 50200, Toluca Estado de México.

Corresponding authors: T.J. Morales-Juárez (e-mail: jmoralesj@uaemex.mx) and D. Corona-Becerril (e-mail: dcoronab@uaemex.mx).

Scheme 1. Methodology for obtaining the H2cdsalen (methyl-2{*N*-[2-(2′-hydroxyphenyl)methylidenenitrilo]ethyl}amino-1-cyclopentene-dithiocarboxylate) (**5**).

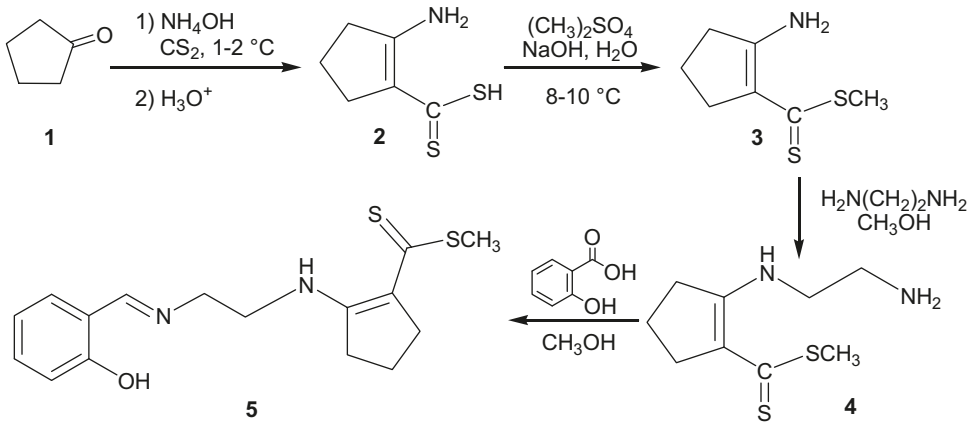
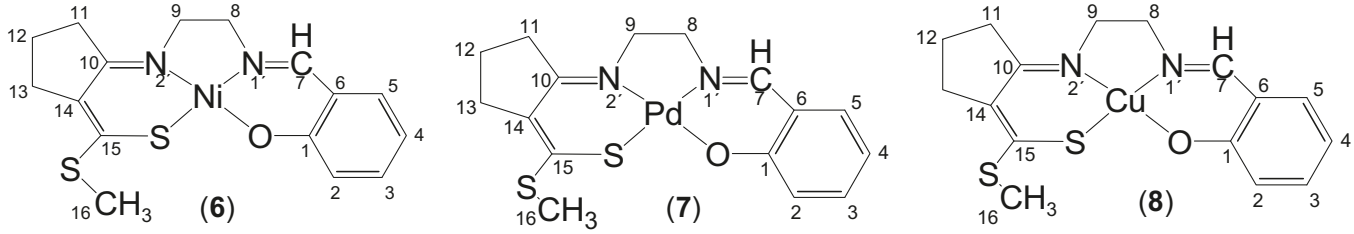


Fig. 1. Conformation proposed for complexes **6**–**8**.



reacted with diethylamine to produce the derivate **4**. Finally, the ligand **5** (H2cdsalen) was obtained through the reaction of amine **4** with salicylic acid (Scheme 1).

The synthesis of complexes **6**–**8** (Fig. 1) was realized using the Pereira methodology[30] with minor (Scheme 2) variations in the reaction conditions such as temperature and reaction time (see Experimental).

According to the literature,[31–33] it was possible to assume a square plane conformation for all four compounds synthesized, like the one shown in Fig. 1. The final conformations of the compounds as identified by the NMR ROESY experiments are consistent and fully agreed with a square-planar geometry.

Conformational studies

Since the derivatives **6**–**8** (Fig. 1) may be of some synthetic and structural interest, detailed studies of the structural properties, through the central metal and the peripheral moieties occurring in such compounds, was necessary.

To obtain more information on these structures, we performed conformational studies of the Ni(II), Pd(II), and Cu (II) complexes with H2cdsalen (methyl-2{*N*-[2-(2′-hydroxyphenyl)methylidenenitrilo]ethyl}amino-1-cyclopentenedithiocarboxylate derivatives, through the 2D NMR experiments (NOESY and ROESY).

First, Hcdsalen **5** and the molecules **6**–**8** were carefully identified using the usual high-resolution 1D and 2D NMR and techniques, which are shown in the Experimental section. Although these assignments are rather consistent and unambiguous, they will be briefly commented upon.

The high-resolution ^{1}H NMR spectrum ($CDCl_3$, 500 MHz) of H2cdsalen **5** (Supplementary data) showed the hydrogen on the methylene cyclopentane's C11, C12, and C13 at δ 1.84, 2.70, and 2.75 ppm, respectively, the singlet at δ 2.57 ppm was assigned to the hydrogen from the methyl dithioate moiety; the hydrogen from the methylene's C8 and C9 attached at the nitrogen atom appear at δ 3.71 and 3.84 ppm. In addition, we observed the aromatic protons from phenol at δ 6.85 (1H;C4), δ 6.95 (1H;C2), and 7.25 (1H;C5); a sharp singlet at δ 8.39 was assigned to the hydrogen's imine and two broad singlets at δ 12.38 and 12.85 ppm was assigned to the amine and alcohol moieties, respectively.

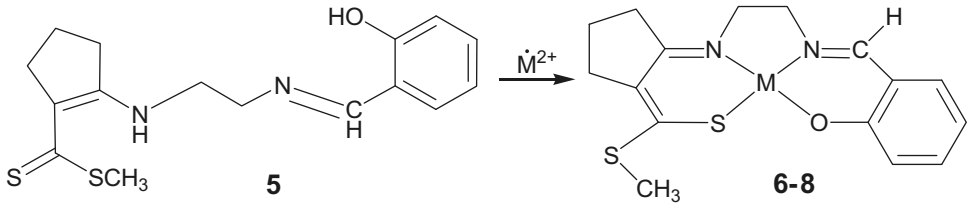
The high-resolution ^{1}H NMR spectrum ($CDCl_3$, 500 MHz) for complex **6** (see Fig. 1) shows a sextuple signal at δ 1.84 ppm for the methylene C12, a triple signal for the methylenes on C11 and C13 at δ 2.49 and 2.63 ppm, respectively. A singlet signal at δ 2.68 was assigned to the methyl dithioate. The signals for the methylenes on C8 and C9, both joined to a nitrogen atom, were assigned to δ 3.25 and 3.53 ppm, respectively. The aromatic protons of the phenol were designated in a multiple signal at δ 6.49 ppm (1H, C4), a double signal at δ 6.81ppm (1H, C2), a triple signal at δ 7.06 ppm (H1, C5), and a double from double signal at δ 7.13 ppm (1H, C3). Finally, the hydrogen from the imine was a single signal at δ 7.7 ppm.

Besides a few reports on the synthesis of these complexes (**6**–**8**),[24–30] there are not many studies related to their spatial behavior. For this very reason, we decided to perform a 2D NMR conformational study for these molecules, for example, the dipolar interactions between key protons through the space, using phase-sensitive NOESY and ROESY experiments.

Initially, a larger chemical shift difference between the protons of the imine in the H2cdsalen (**5**) and the imine in the compound **6** (δ 1.26) was observed, suggesting that the

Can. J. Chem. Downloaded from www.nrcresearchpress.com by Renmin University of China on 09/02/12
For personal use only.

Scheme 2. Complex formation. M: Ni, Pd, and Cu.



proton in **6** at δ 7.13 suffered diamagnetic shielding owing to the formation of a complex between the nickel and the ligand H2cdsalen (**5**). In addition, the signals for the hydrogens in the phenyl ring are shown at high frequency, this spectroscopic behavior is in accordance with the formation of complex **6**. The spectroscopic behavior for complex **7**, through the NMR spectroscopy, was similar.

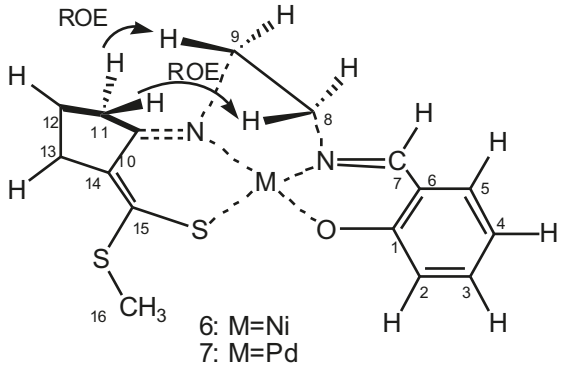
The conformational behavior of the derivatives **6–8** was then studied with help of the ROESY experiment. An interesting observation about the conformational study by the 2D NMR ROESY is the interaction between the methylene hydrogen from the cyclopentane and the methylene hydrogen in the lateral chain for the nickel and palladium compounds (Fig. 2). Unfortunately, it was not possible to obtain similar good quality 2D NMR ROESY spectra for the complex with copper. Nevertheless, it was possible to identify compound **8** through a crystal structure, showing a planar square conformation (see the Supplementary data).

For **6** in particular, the ROESY experiment (Fig. 3) shows two different interactions in space between the methylene hydrogen on C11 from the cyclopentane and the methylene hydrogen in the lateral chain on C8 and C9. This interaction is only possible if the methylene on C11 from the cyclopentane is placed out of the plane formed by the carbons C10–C14 in the same cyclopentane (see Fig. 3). In other words, the preferred conformation of this molecule is in an envelope, which is observed in some cyclopentane derivates. In addition, Bereman and co-workers[34,35] reported a distortion in the square-planar conformation for complexes containing Ni(II). This observation could be explained by the proximity of the hydrogen in the methylenes C8 and C9 and the hydrogen on C11 from the cyclopentane.

The shift for the methylene C11 with respect to methylene in the ligand is observed at 0.24 ppm high frequency, which supposes that the positive diamagnetic term increases because of its proximity to the methylenes C8 and C9. These methylenes (C11, C8, and C9) are the cornerstone of the conformational study of the metal–H2cdsalen (**5**) complexes, as its interaction in the ROESY experiment are the tools for understanding their behavior in solution.

For derivative **7**, its ROESY spectra experiment resembled the one observed for compound **6** (Fig. 4). The dipolar correlation between protons on C11/ C9, as well as the one observed for C11/C8, again suggested an envelope conformation for the cyclopentane moiety of these molecules. In other words, the carbons C10, C12, C13, and C14 are in a plane; whereas the hydrogen on carbon C11 is out-of-plane. According to the Bereman observations and interactions in the ROESY experiment, it is possible to propose a behavior for this family of metal complexes with H2cdsalen (**5**).

Fig. 2. Conformational behavior of Ni(II) and Pd(II) complexes with methyl-2{*N*-[2-(2′-hydroxyphenyl)methylidenenitrilo]ethyl}amino-1-cyclopentenedithiocarboxylate.



Conclusions

We were able to establish from a complete conformational behavior study of the Ni(II) and Pd(II) complexes with H2cdsalen (**5**) that their preferred conformation is an envelope for the cyclopentane moiety. The spatial proximity between the hydrogen on the methylene, carbons C8 and C9, with the hydrogen on the methylene C11 from the cyclopentane confirmed this observation.

Finally, the 2D NMR ROESY is a useful tool and important in the conformational study of small molecules. The information obtained from this experiment about the deviation from the fully planar conformation of these molecules enabled us to better understand the behavior of these complexes, which is important for determining their biological role and possible applications.

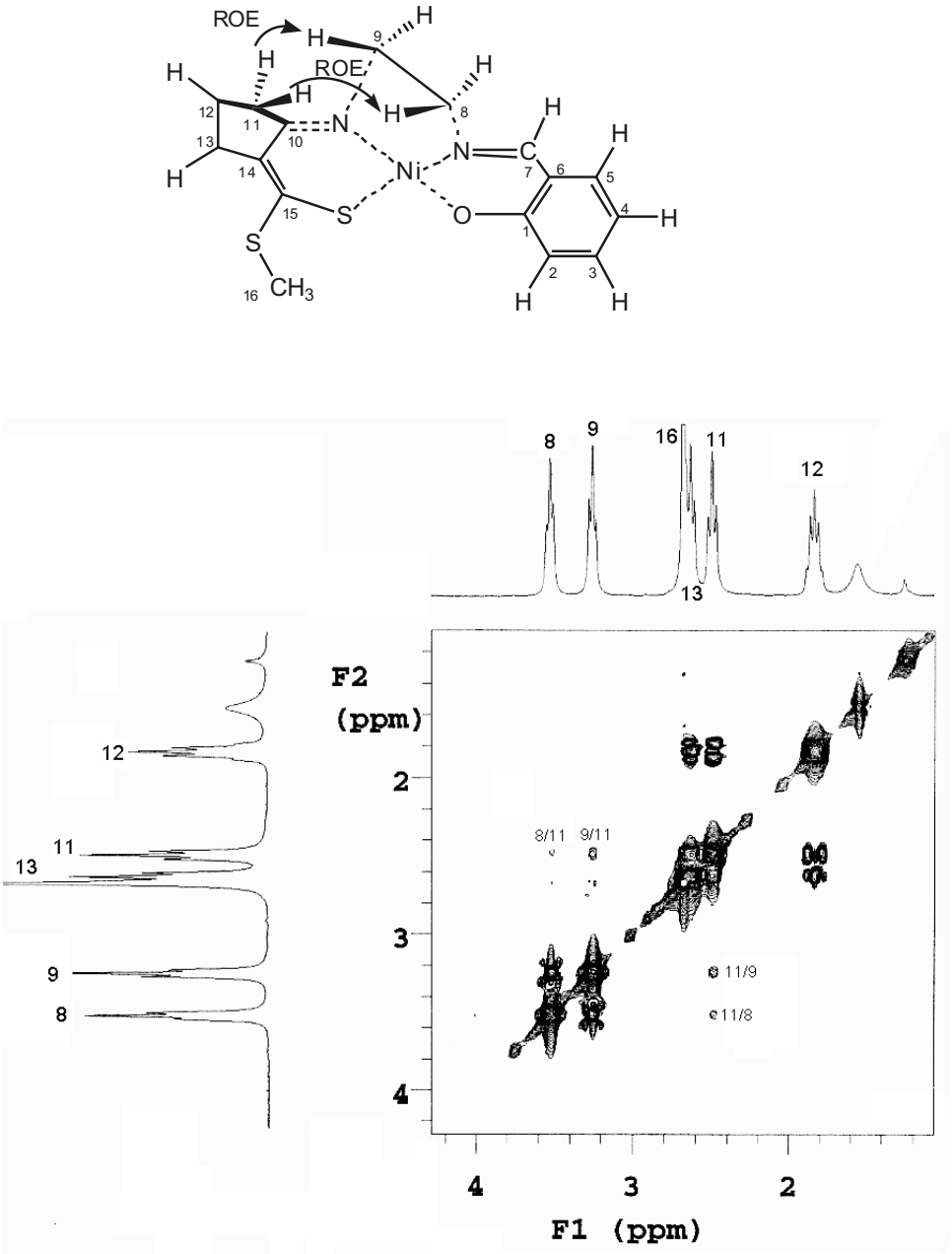
Experimental

Materials and physical measurements

All compounds used for the synthesis of the ligand and the complexes were purchased from Sigma-Aldrich and used without further purification. The ACDA,[13] Hcden,[5] and H_2cdsalen (**5**)[14] were synthesized by methods reported in the literature. Infrared spectra were recorded in the range 4000 to 400 cm^{-1} on a Nicolet FT-IR 510 spectrometer as KBr powder. The ^1H and ^{13}C spectra were recorded on a Varian Unity 10 for routine experiments and Varian Unity 500 spectrometers for 2D experiments (COSY, NOESY, and ROESY). The ^1H and ^{13}C chemical shifts (δ) are given in ppm relative to TMS as the internal standard (0.00 ppm). The mass spectra were recorded on a JEOL JMS-AX505HA via the EI/PI mode (70 eV; 200 °C direct probe for ligands) and fast atom bombardment ionization (FAB PI) was used for the complexes. Only molecular or protonated molecular ions (*m*/*z*) values are reported.

Can. J. Chem. Downloaded from www.nrcresearchpress.com by Renmin University of China on 09/02/12
For personal use only.

Fig. 3. ROESY spectrum of compound **6**.



Can. J. Chem. Downloaded from www.nrcresearchpress.com by Renmin University of China on 09/02/12
For personal use only.

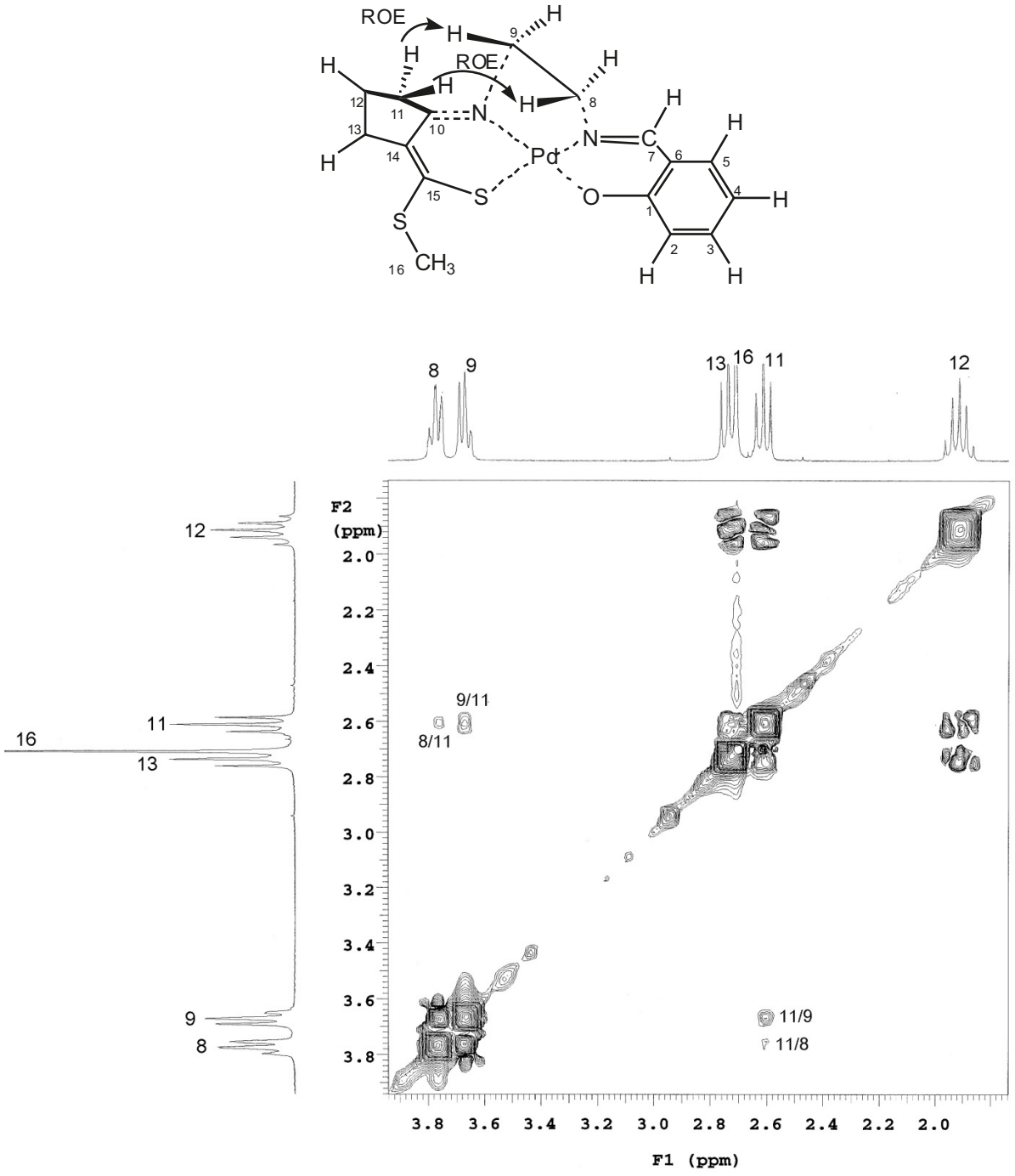
Nickel {methyl-2-{*N*-[2-(2′-phenolate)methylidynenitrilo] ethyl}aminato(-1)-1-cyclopentenedithiocarboxylate ([Ni(cdsalen)], 6)

To a solution of H_2cdsalen (methyl-2{*N*-[2-(2′-hydroxyphenyl)methylidenenitrilo]ethyl}amino-1-cyclopentenedithiocarboxylate; 0.2 g, 6.25×10^{-4} mol) in 12 mL of dichlorometane/methanol (2:1 *v*/*v*) was added a solution of $NiCl_2 \cdot 6H_2O$ (0.1485 g, 6.25×10^{-4} mol) in 10 mL of methanol. The mixture was stirred for 30 min and allowed to react at room temperature for 24 h. The resulting green powder was filtered off and washed with methanol several times. Yield: 0.179 g (76%); mp 237 °C. IR (KBr powder, cm^{-1}): 1622s ν(C=N), 1596m ν(C=C)/phenyl ring, 1316m $\nu(CH_3–S)$, 911m ν_{as}(CSS), 752s ν_{sym}(CSS), 618w ν(M–O), 462w ν(M–N). ^{1}H NMR in $CDCl_3$ (ppm) δ: 1.83 (m, 2H, CH_2(12)), 2.47 (t, 2H, CH_2(11)), 2.61 (t, 2H, CH_2(13)), 2.66 (s, 3H, CH_3(16)), 3.26 (t, 2H, CH_2(9)), 3.53 (t, 2H, CH_2(8)), 6.48 (t, 1H, CH4), 6.79 (d, 1H, CH2), 7.06 (d, 1H, CH5), 7.12 (t, 1H, CH3), 7.68 (s, 1H, CH7). ^{13}C NMR in $CDCl_3$ (ppm) δ: 16.37 (C16), 21.89 (C12), 32.11 (C11), 36.39 (C13), 56.24 (C9), 58.64 (C8), 114.87 (C2), 119.71 (C14), 122.22 (C4), 123.73 (C6), 132.20 (C3), 133.69 (C5), 160.08 (C10), 160.87 (C15), 164.14 (C1), 173.79 (C7), FAB$^+$–MS: *m*/*z*: 376 (M^+). HRMS (ESI) *m*/*z* calcd for $C_{16}H_{19}N_2OS_2Ni$ $[M + H]^+$: 377.0292; found: 377.0289.

Palladium {methyl-2-{*N*-[2-(2′-phenolate) methylidynenitrilo]ethyl}aminato(-1)-1-cyclopentenedithiocarboxylate ([Pd(cdsalen)], 7)

To a solution of H_2cdsalen (**5**) (0.1 g, 3.125×10^{-4} mol) in 120 mL of methanol was added a solution of $PdCl_2 \cdot 6H_2O$

Fig. 4. ROESY spectrum of compound **7**.



(0.0554 g, 3.125×10^{-4} mol) in 15 mL of ammonium hydroxide. The mixture was stirred for 3 days. The resulting yellow powder was filtered off and washed with methanol several times. Yield: 0.049 g (37%); mp 282–283 °C. IR (KBr powder, cm^{-1}): 1635s ν(C=N), 1311m $\nu(CH_3–S)$, 909m ν_{as}(CSS), 751s ν_{sym}(CSS), 612w ν(M–O), 464w ν(M–N). ^{1}H NMR in $CDCl_3$ (ppm) δ: 1.95 (m, 2H, CH_2(12)), 2.72 (s, 3H, CH_3(16)), 2.65 (t, 2H, CH_2(11)), 2.77 (t, 2H, CH_2(13)), 3.67 (t, 2H, CH_2(9)), 3.79 (t, 2H, CH_2(8)), 6.55 (t, 1H, CH4), 7.02 (d, 1H, CH2), 7.17 (d, 1H, CH5), 7.28 (t, 1H, CH3), 7.94 (s, 1H, CH7). ^{13}C NMR in $CDCl_3$ (ppm) δ: 17.45 (C16), 21.90 (C12), 33.12 (C11), 35.54 (C13), 58.57 (C9), 59.15 (C8), 114.64 (C2), 120.24 (C6), 122.47 (C4), 124.29 (C14), 134.31 (C3), 134.61 (C5), 158.61 (C10), 160.04 (C15), 165.38 (C1), 170.37 (C7). FAB$^+$–MS *m/z*: 424 (M^+). HRMS (ESI) *m/z* calcd for $C_{16}H_{19}N_2OS_2Pd$ $[M + H]^+$: 424.9974; found: 424.9966.

Copper {methyl-2-{*N*-[2-(2′-phenolate)methylidynenitrilo] ethyl}aminato(-1)-1-cyclopentenedithiocarboxylate ([Cu(cdsalen)], 8)

To a solution of H_2cdsalen (NrNr, 0.65 g, 2.0312×10^{-3} mol) in 40 mL of THF was added a solution of $Cu(OOC–CH_3)_2 \cdot H_2O$ (0.4054 g, 2.0312×10^{-3} mol) in 60 mL of THF. The mixture

Can. J. Chem. Downloaded from www.nrcresearchpress.com by Renmin University of China on 09/02/12
For personal use only.

was stirred for 24 h. The resulting brown needles were filtered off and washed with acetone several times. Yield: 0.5958 g (77%); mp 241–242 °C. IR (KBr powder, cm^{-1}): 1630s ν(C=N), 1573m ν(C=C)/phenyl ring, 1314m $\nu(CH_3–S)$, 902m ν_{as}(CSS), 751s ν_{sym}(CSS), 606w ν(M–O), 456w ν(M–N). EI-MS *m/z*: 381 (M^+). HRMS (ESI) *m/z* calcd for $C_{16}H_{19}N_2OS_2Cu$ $[M + H]^+$: 383.0074; found: 383.0066.

Supplementary data

Supplementary data are available with the article through the journal Web site (http://nrcresearchpress.com/doi/suppl/10.1139/v11-153). CCDC 842338 contains the X-ray data in CIF format for this manuscript. These data can be obtained, free of charge, via http://www.ccdc.cam.ac.uk/cgi-bin/catreq.cgi (or from the Cambridge Crystallographic Data Centre, 12 Union Road, Cambridge CB2 1Ez, UK; fax +44 1223 336033; or e-mail: deposit@ccdc.cam.ac.uk).

Acknowledgments

We would like to thank Universidad Autónoma del Estado de México (UAEMex) for sponsoring this work by a research grant to project 2608/2008U. We also thank Professor Rubén A. Toscano (Universidad Nacional Autónoma de México) for help with the X-ray crystallography.

References

(1) Solomon, E. I.; Sundaram, U. M.; Machonkin, T. E. *Chem. Rev.* **1996**, *96* (7), 2563. doi:10.1021/cr950046o.
(2) Latour, J. M. *Bull. Soc. Chim. Fr.* **1988**, 508.
(3) Sorrell, T. N. *Tetrahedron* **1989**, *45* (1), 3. doi:10.1016/0040-4020(89)80033-X.
(4) Vigato, P. A.; Tamburini, S.; Fenton, D. *Coord. Chem. Rev.* **1990**, *106*, 25. doi:10.1016/0010-8545(60)80002-1.
(5) Kitajima, N. *Adv. Inorg. Chem.* **1992**, *39*, 1. doi:10.1016/S0898-8838(08)60258-5.
(6) Schiffmann, R.; Heine, A.; Klebe, G.; Klein, C. D. *Angew. Chem. Int. Ed.* **2005**, *44* (23), 3620. doi:10.1002/anie.200500592.
(7) Navarro-Ranninger, C.; Ochoa, P.; Masaguer, J. R.; Pérez, J. M.; González, V. M.; Alonso, C. *J. Inorg. Biochem.* **1994**, *53* (3), 177. doi:10.1016/0162-0134(94)80003-0.
(8) Teixeira, L. J.; Seabra, M.; Reis, E.; Girão da Cruz, M. T.; Pedroso de Lima, M. C.; Pereira, E.; Miranda, M. A.; Marques, M. P. M. *J. Med. Chem.* **2004**, *47* (11), 2917. doi:10.1021/jm0311238.
(9) Abu-Surrah, A. S.; Kettunen, M.; Lappalainen, K.; Piironen, U.; Klinga, M.; Leskelä, M. *Polyhedron* **2002**, *21* (1), 27. doi:10.1016/S0277-5387(01)00952-4.
(10) Wheate, N. J.; Collins, J. G. *Curr. Med. Chem. Anticancer Agents* **2005**, *5* (3), 267. doi:10.2174/1568011053765994.
(11) Corduneanu, O.; Chiorcea-Paquim, A. M.; Diculescu, V.; Fiuza, S. M.; Marques, M. P. M.; Oliveira-Brett, A. M. *Anal. Chem.* **2010**, *82* (4), 1245. doi:10.1021/ac902127d.
(12) Mobin, S. M.; Sanghavi, B. J.; Srivastava, A. K.; Mathur, P.; Lahiri, G. K. *Anal. Chem.* **2010**, *82* (14), 5983. doi:10.1021/ac1004037.
(13) Del Pilar Taboada Sotomayo, M.; Tanaka, A. A.; Kubota, L. T. *Electrochim. Acta* **2003**, *48* (7), 855. doi:10.1016/S0013-4686(02)00777-6.
(14) Ebarvia, B. S.; Cabanilla, S.; Sevilla, S. F., III. *Talanta* **2005**, *66* (1), 145. doi:10.1016/j.talanta.2004.10.009.
(15) Neves, A.; Rossi, L. M.; Bortoluzzi, A. J.; Szpoganicz, B.; Wiezbicki, C.; Schwingel, E.; Haase, W.; Ostrovsky, S. *Inorg. Chem.* **2002**, *41* (7), 1788. doi:10.1021/ic010708u.
(16) Neves, A.; Rossi, L. M.; Bortoluzzi, A. J.; Mangrich, A. S.; Haase, W.; Werner, R. *J. Braz. Chem. Soc.* **2001**, *12* (6), 747. doi:10.1590/S0103-50532001000600010.
(17) Neves, A.; Erthal, S. M. D.; Drago, V.; Griesar, K.; Haase, W. *Inorg. Chim. Acta* **1992**, *197* (2), 121. doi:10.1016/S0020-1693(00)84953-1.
(18) dos Anjos, A.; Bortoluzzi, A. J.; Szpoganicz, B.; Caro, M. S. B.; Friedermann, G. R.; Mangrich, A. S.; Neves, A. *Inorg. Chim. Acta* **2005**, *358* (11), 3106. doi:10.1016/j.ica.2005.04.043.
(19) Shan, Z.; Wang, Y.; Liu, Q.; Zhang, N.; Yang, E.; Wei, J. *Inorg. Chim. Acta* **2010**, *363* (10), 2269. doi:10.1016/j.ica.2010.03.047.
(20) Bharadwaj, P. K.; Musker, W. K. *Inorg. Chem.* **1987**, *26* (9), 1453. doi:10.1021/ic00256a027.
(21) Bharadwaj, P. K.; Musker, W. K. *Inorg. Chem.* **1987**, *26* (9), 1453. doi:10.1021/ic00256a027.
(22) Tarassoli, A.; Sedaghat, T.; Neumüller, B.; Ghassemzadeh, M. *Inorg. Chim. Acta* **2001**, *318* (1–2), 15. doi:10.1016/S0020-1693(01)00368-1.
(23) Bordás, B.; Sohar, P.; Matolcsy, G.; Berencsi, P. *J. Org. Chem.* **1972**, *37* (11), 1727. doi:10.1021/jo00976a011.
(24) Bereman, R. D.; Churchill, M. R.; Shields, G. *Inorg. Chem.* **1979**, *18* (11), 3117. doi:10.1021/ic50201a032.
(25) Safavi, A.; Abdollahi, H.; Hormozi Nezhad, M. R.; Kamali, R. *Spectrochim. Acta A: Mol. Biomol. Spectrosc.* **2004**, *60* (12), 2897. doi:10.1016/j.saa.2004.02.001.
(26) Yokohama, M.; Takeshima, T. *Anal. Chem.* **1968**, *40*, 1345.
(27) Pereira, E.; Gomes, L.; de Castro, B. *J. Chem. Soc., Dalton Trans.* **1998**, (4): 629. doi:10.1039/a705685k.
(28) Takeshima, T.; Yokoyama, M.; Imamoto, T.; Akano, M.; Asaba, H. *J. Org. Chem.* **1969**, *34* (3), 730. doi:10.1021/jo01255a054.
(29) Nag, K.; Joardar, D. S. *Inorg. Chim. Acta* **1976**, *17*, 111. doi:10.1016/S0020-1693(00)81966-0.
(30) Pereira, E.; Gomes, L.; de Castro, B. *Inorg. Chim. Acta* **1998**, *271* (1–2), 83. doi:10.1016/S0020-1693(97)05904-5.
(31) Soloshonok, V. A.; Ono, H.; Ueki, T.; Vanthuyne, N.; Balaban, T. S.; Bürck, J.; Fliegl, H.; Klopper, W.; Naubron, J.; Bui, T. T. T.; Drake, A. F.; Roussel, C. *J. Am. Chem. Soc.* **2010**, *132* (30), 10477. doi:10.1021/ja103296g.
(32) Zhang, X.; Xi, Z.; Liu, A.; Chen, W. *Organometallics* **2008**, *27* (17), 4401. doi:10.1021/om8003674.
(33) Moon, D.; Kang, S.; Park, J.; Lee, K.; John, R. P.; Won, H.; Seong, S. H.; Kim, Y. S.; Kim, G. H.; Rhee, H.; Lah, M. S. *J. Am. Chem. Soc.* **2006**, *128* (11), 3530. doi:10.1021/ja060051h.
(34) Martin, E. M.; Bereman, R. D.; Singh, P. *Inorg. Chem.* **1991**, *30* (5), 957. doi:10.1021/ic00005a016.
(35) Bereman, R. D.; Shields, G. D.; Bordner, J.; Dorfman, J. R. *Inorg. Chem.* **1981**, *20* (7), 2165. doi:10.1021/ic50221a043.

Can. J. Chem. Downloaded from www.nrcresearchpress.com by Renmin University of China on 09/02/12
For personal use only.

The expected time to attain chemical equilibrium from a thermodynamic probabilistic analysis

Christopher Pastore and Moishe Garfinkle

Can. J. Chem. Downloaded from www.nrcresearchpress.com by Renmin University of China on 09/02/12
For personal use only.

Abstract: Employing a stochastic model, both Planck and Fokker proposed almost a century ago that stoichiometric chemical reactions proceed by a chain mechanism involving discrete reaction steps. To determine whether such a chain mechanism was in fact a valid mechanism for chemical reactions was the subject of a recent study (Garfinkle, M. 2002. *J. Phys. Chem.* **106A:** 490). Using a thermodynamic–probabilistic algorithm the stochastic reaction paths were found to be in excellent agreement with the observed reaction paths plotted from experimental data. This study was then extended to test the conclusions of Ehrenfest and Prigogine that a chain mechanism dictates that the number of discrete reaction steps required for a chemical reaction to attain equilibrium must be finite. The stochastic and empirical reaction paths were compared using experimental data for first-, second-, and third-order reactions as well as fractional order reactions. The empirical verification was excellent.

Key words: chemical thermodynamics, irreversible thermodynamics, reaction kinetics, mass action, natural path.

Résumé : En se basant sur un modèle stochastique, Plank et Fokker ont tous les deux proposé indépendamment, il y a pratiquement un siècle, que les réactions chimiques stoechiométriques se produisent par un mécanisme en chaîne impliquant des étapes réactionnelles distinctes. Un travail récent (Garfinkle, M. 2002. *J. Phys. Chem.* **106A:** 490) a été réalisé pour déterminer si un tel mécanisme en chaîne est un mécanisme valide pour les réactions chimiques. Sur la base d'un algorithme thermodynamique–probabilistique, on a trouvé que les voies réactionnelles stochastiques sont en excellent accord avec les voies réactionnelles observées sur la base de graphiques obtenus à partir de données expérimentales. Cette étude a alors été étendue pour vérifier la véracité des conclusions de Ehrenfest et Prigogine à l'effet qu'un mécanisme en chaîne impose un nombre déterminé d'étapes réactionnelles distinctes nécessaires pour qu'une réaction chimique atteigne un équilibre. On a comparé les voies réactionnelles stochastiques et empiriques à l'aide de données expérimentales pour des réactions d'ordre un, deux et trois ainsi que pour des réactions d'ordres fractionnaires. La vérification empirique est excellente.

Mots-clés : thermodynamique chimique, thermodynamique irréversible, cinétique réactionnelle, action de masse, voie naturelle.

[Traduit par la Rédaction]

Introduction

Classically, the progress of chemical reactions have been described by the empirical rate equations, first elucidated by Guldberg and Waage (see ref. 1) a century and a half ago. Their approach was strictly deterministic and depended on chemical concentrations. Its great success is testimony to its power to describe the reaction mechanisms involved in complex chemical reactions. The present study involves a parallel approach in which the chemical affinity, rather than the chemical concentrations, is used in describing the progress of chemical reactions. It is this thermodynamic–probabilistic approach that is described herein.

This study is a sequel to a work[2] describing the reaction path of homogeneous chemical reactions by a thermodynamic–probabilistic analysis. The agreement between the probabilistic and empirical reaction paths was excellent and is evident from the reaction plots of first-, second-, and third-order reactions as well as fractional order reactions including a 2/3 order free-radical chain mechanism.

The original analysis was then extended to elucidate the expected time to attain chemical equilibrium. Whether in fact this expected time required to attain equilibrium is quantifiable for chemical processes has been a subject of intense discussion for well over a century. Planck and Fokker (see refs. 3 and 4) concluded that the expected time was quantifiable. In contrast, chemical kineticists generally assert that the expected time to reach chemical equilibrium is infinite in accordance with the empirical rate equations first formulated by Guldberg and Waage,[1] a conclusion contrary to that arrived at by other investigators, including Prigogine et al.[5] and Ehrenfest and Ehrenfest.[6]

Equilibrium can be defined as a state whose microscopic properties are time-invariant, but this definition does not preclude microscopic fluctuations about the mean value of these properties. Boltzmann[7] argued that the energy probability

Received 4 August 2011. Accepted 19 September 2011. Published at www.nrcresearchpress.com/cjc on 25 January 2012.

C. Pastore. College of Design, Engineering, and Commerce, Philadelphia University, Philadelphia, PA 19144, USA.
M. Garfinkle. Department of Materials Engineering, Drexel University, Philadelphia, PA 19104, USA.

Corresponding author: Moishe Garfinkle (e-mail: garfinkm@drexel.edu).

Can. J. Chem. Downloaded from www.nrcresearchpress.com by Renmin University of China on 09/02/12
For personal use only.

distribution in an isolated system is itself an almost periodic function of time that never repeats itself. Hence, some displacement must always be present between a system approaching equilibrium and a state defined as equilibrium by virtue of its canonical distribution. In contrast, Prigogine et al.[5] argued that as long as the system has a finite volume encompassing a finite number of particles then the energy distribution must in time attain the canonical form. This would be in agreement with the statistical model of chain processes developed by Planck and Fokker (see refs. 3 and 4) and extended by Ehrenfest and Ehrenfest.[6]

From either of these arguments equilibrium is a special state that can be reached in either a finite time or not at all, depending on the investigator's proclivities. It is this view of equilibrium that is disputed in this study. Equilibrium can be viewed as just one discrete state in a succession of discrete states originating with reaction initiation and ending with reaction completion. This equilibrium state is distinguishable only probabilistically from other discrete states. This view is substantiated from a comprehensive empirical analysis.

Chemical reactions classically have been perceived as systems of discrete reacting particles. In this regard consider the homogeneous stoichiometric chemical reaction

$$[1] \qquad \sum [\nu_m M_m]_{T,V} = 0$$

proceeding in a closed system at fixed temperature T and volume V from reaction initiation towards reaction equilibrium along a specific reaction path, wherein ν_m is the stoichiometric coefficient and M_m is the molecular weight of reacting component m, with $\nu_m < 0$ for reactants. The process proceeds in discrete reaction steps wherein a set of reactant particles transforms to a set of product particles in strict accordance with reaction stoichiometry.

Deterministic approach

According to the classical approach, chemical kinetics as a formal study began with the empirical rate equations a century and a half ago using the kinetic mass action law.[1] The great utility of this approach has developed over the years, particularly with our understanding of molecular dynamics.[8] According to this mechanistic–deterministic approach reaction mechanisms can be elucidated, revealing the reaction rates of the specific steps that comprise the overall reaction. According to this deterministic approach, the reaction rate or velocity $v = [\delta c_m/\delta t]_{T,V}$ is equated to some function of the component concentration (c_m) depending on reaction mechanism.

The transformation rate for each chemical species is expressed as concentration change per unit time with the rate dependent on the concentration of each particular species c_m in the reaction volume. According to this formalism the forward reaction rate (v_f) decreases from its initial ($t = 0$) value of $v_f = v_0$ as the reaction proceeds according to

$$[2a] \qquad v_f = k_f \Pi [c_r]^{\nu_m}$$

In contrast the reverse reaction rate (v_r) increases from its initial ($t = 0$) value of $v_r = 0$ as the reaction proceeds according to

$$[2b] \qquad v_r = k_r \Pi [c_p]^{\nu_m}$$

where k_f and k_r are the forward and reverse reaction rate constants, respectively, and c_r and c_p designate the concentration of reactants and products, respectively. The overall reaction rate (v) is simply the difference $v = v_f - v_r$ and equilibrium is defined as the state at which $v_f = v_r$.

Upon summation of eqs. [2*a*] and [2*b*] and integration of the resultant concentration terms, c_r and c_p always appear as a logarithmic function directly proportional to the elapsed time. By inserting the equilibrium values of the concentrations of reactants and products (c_{eq}) into the integrated equation the expected time to attain equilibrium t_K is determined and is always found to be infinite according to this logarithmic formulation: $t_K = \infty$. The mechanistic–deterministic equilibrium is thus a static state for which overall $v = 0$: a direct outcome of its logarithmic formulation.

Probabilistic approach

The great utility of this thermodynamic–probabilistic analysis is its ability to elucidate the overall energetics of homogeneous stoichiometric chemical reactions independent of reaction mechanism. In this regard, the present comprehensive probabilistic analysis was conducted to (*i*) confirm the viability of this probabilistic description of stoichiometric chemical reactions, (*ii*) verify the probabilistic results by a comprehensive empirical analysis, and (*iii*) examine the approach to chemical equilibrium in relation to this empirical analysis.

Recapitulating the previous analysis[2] wherein the description and detail of the terms used are found, consider a chemical reaction in which the activity ratio Q_i at any state i between reaction initiation and equilibrium is classically defined as

$$[3a] \qquad Q_i = \Pi [r_m]^{\nu_m} [p_m]^{-\nu_m}$$

The same formalism is used to describe the equilibrium constant K by Guldberg and Waage (see ref. 1) as

$$[3b] \qquad K = \Pi [r_m]_{eq}^{\nu_m} [p_m]_{eq}^{-\nu_m}$$

Taking the ratio of eq. [3*a*] to eq. [3*b*] establishes an extent-of-reaction term as $\zeta_{Q_i} \equiv Q_i/K$, where $0 \leq \zeta_{Q_i} \leq 1$, indicating reaction initiation at one extreme ($\zeta_{Q_i} = 0$) and equilibrium at the other ($\zeta_{Q_i} = 1$).[9,10]

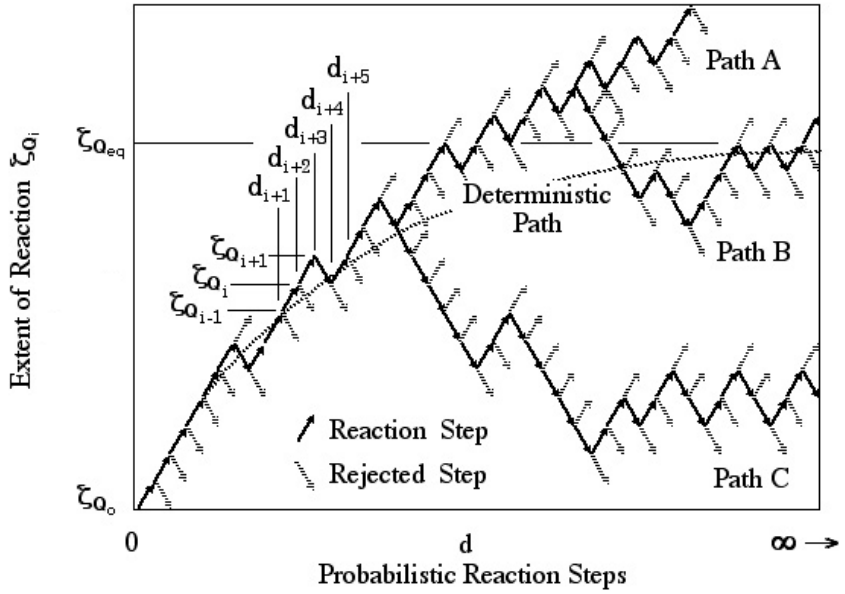
With the extent-of-reaction term (ζ_{Q_i}) defined we can now consider a probabilistic approach to the expected time to attain equilibrium for a finite chain mechanism for a chemical reaction between discrete particles. This probabilistic analysis requires that certain conditions be met:

1. The isothermal, isochoric reacting system is homogeneous in that all reacting species are uniformly distributed in a single fluid phase.
2. The reacting system is closed in that there is no mass transfer between the reacting system and its surroundings.
3. The reacting system involves a transformation between reactants and products in a strictly fixed stoichiometric ratio.

These are in fact a formal expression of the ordinary conditions under which stoichiometric chemical reactions are

Can. J. Chem. Downloaded from www.nrcresearchpress.com by Renmin University of China on 09/02/12
For personal use only.

Fig. 1. Chain mechanism depicting transformations along several possible reaction paths.



generally observed. Consider now the approach to equilibrium.[11] The thermodynamic–probabilistic approach is based on the linear assumption

$$[4] \qquad p_{i,i\pm1} \propto \zeta_{Q_i}$$

between the probability for reaction $p_{i,i\pm1}$ from the present state (ζ_{Q_i}) to either the following states (ζ_{Q_i+1}) or the previous state (ζ_{Q_i-1}).[2]

The specific linear equations describing a probabilistic reaction path can be derived from the following boundary conditions. At reaction initiation ($\zeta_{Q_i} = 0$) for the forward reaction step, $p_{0,0+1} = 1$, and for the reverse reaction step, $p_{0,0-1} = 0$. At equilibrium ($\zeta_{Q_{eq}} = 1$) for both the forward and reverse reaction steps, $p_{eq,eq\pm1} = 1/2$.

Using these boundary conditions for the reaction steps, the forward reaction expression takes the form

$$[5a] \qquad p_{i,i+1} = 1 - 1/2\zeta_{Q_i}$$

and the reverse reaction expression takes the form

$$[5b] \qquad p_{i,i-1} = 1/2\zeta_{Q_i}$$

and, consequently, $p_{i,i+1} + p_{i,i-1} = 1$, as would be expected.[2]

The determination of the validity of eqs. [5*a*] and [5*b*] required empirical verification. To place the probability data in a form amenable to empirical analysis, the chemical affinity A_i — a function of state introduced by De Donder[12] to quantify the driving force for a chemical reaction — can be readily calculated from both the calculated and experimental extent-of-reaction data.

$$[6] \qquad A_i = -RT \ln \zeta_{Q_i}$$

Almost 100 stoichiometric chemical reactions were examined, the kinetic data having been obtained from literature compilations or directly from kineticists, and from which each of the required (A_i:t_i) coordinate pairs were determined, where reaction initiation is defined as the state at which ∞:0 and equilibrium at which 0:t_K. These reactions included those with highly complex mechanisms in gaseous as well as aqueous and nonaqueous solutions. The agreement between the probabilistic and empirical reaction paths were excellent and it is evident from the published reaction plots of first-, second-, and third-order reactions as well as fractional order reactions (including a 2/3 order free-radical chain mechanism in addition to halogen exchange reactions), cyanohydrin formation reactions, and third-order tris(dipyridyl) ion reactions; pretty much covering the whole gamut of stoichiometric reaction mechanisms.[2]

With the validity of eqs. [5*a*] and [5*b*] established, the expected time to attain equilibrium can now be addressed using this thermodynamic–probabilistic approach. Immediately, we confront a basic departure from the classical mechanistic–deterministic approach wherein equilibrium is described as an invariant or static state at which $v = 0$. This classical approach, however, harbors a major inconsistency. Although it is generally agreed that chemical reactions are discrete particulate processes, the empirical rate equations themselves are continuous functions with their derivation involving integration. This discrepancy renders extreme extrapolation ($v_f - v_r \rightarrow 0$) uncertain.

The probabilistic approach, in contrast to the deterministic approach, describes a purely discontinuous or stepwise process. According to this stochastic model, equilibrium is simply the state at which $\zeta_{Q_i} = 1$ and therefore $p_{eq,eq-1} \rightarrow p_{eq,eq+1}$; a probabilistic or dynamic state is represented by $p_{eq,eq-1} - p_{eq,eq+1} = 0$. Using this approach, the expected time to attain equilibrium can now be considered.

Statistical analysis

Because the extent-of-reaction ζ_{Q_i} is directly proportional to the probabilities, the extent-of-reaction will be referred to for the remainder of this analysis. For stoichiometric chemical reactions to be amenable to this probabilistic analysis requires that the reaction path to be followed conforms to certain conditions:

Can. J. Chem. Downloaded from www.nrcresearchpress.com by Renmin University of China on 09/02/12
For personal use only.

1. The process must be discontinuous in that it proceeds in discrete steps between specific states ζ_{Q_i} and $\zeta_{Q_i\pm1}$.
2. The process must be periodic in that the number of reaction steps ($\Delta_{i,i+n}$) between point d_i and d_{i+n} required to return to any state ζ_{Q_i} from any other state $\zeta_{Q_i\pm n}$ is a multiple of some positive integer.
    1. The process must be irreducible in that the probabilities $p_{i,i\pm1}$ associated with the transformation of any present (t_i) state ζ_{Q_i} to any future (t_{i+1}) state ζ_{Q_i+1} must be independent of any past (t_{i-1}) state ζ_{Q_i-1}.

These conditions are really a natural consequence of a discrete kinetic formalism, specifically, a Markov[13] chain mechanism: a discrete form of a generalized Markov process.[14] Such a process is illustrated schematically in Fig. 1. For comparison, the deterministic path is shown, which gradually approaches, but never quite reaches, a static equilibrium state at $\zeta_{Q_{eq}}$.

The probability of a reaction step occurring is always greater than a rejected step except at equilibrium, where the probabilities are equal. The number of steps along any of the three probabilistic paths A, B, or C shown required to return to any specified prior state are the same and, consequently, the chain is periodic. For example, several reaction steps are designated d_{i+1}, d_{i+2}, d_{i+3}, d_{i+4}, d_{i+5}, and so forth, for any arbitrary state *i*. Various possible paths are shown by which the reaction can pass from state ζ_{Q_i-1} through state ζ_{Q_i} to state ζ_{Q_i+1}. This chain is irreducible if the probabilities associated with reaching either of the successive states ζ_{Q_i-1} or ζ_{Q_i+1} are independent of the path traversed to reach the present state ζ_{Q_i}.

Each reaction state shown in Fig. 1 can be specified by the coordinates (ζ_{Q_i},d_i). In the sequence of steps from d_{i+1} to d_{i+5} the extent-of-reaction term ζ_{Q_i} alternates from ζ_{Q_i-1} to ζ_{Q_i} then to ζ_{Q_i+1} then backwards to ζ_{Q_i} and then forwards to ζ_{Q_i+1}. This sequence of steps is periodic because any path chosen between steps (ζ_{Q_i-1},d_{i+1}) and (ζ_{Q_i+1},d_{i+5}) will always have the same number of transformations (in this example, four).

As the reaction progresses forward from state ζ_{Q_0} along path B the forward-reaction probability $p_{i,i+1}$ diminishes from 1 to 1/2 from step d_0 to the approach to equilibrium according to eq. [5*a*] for $\zeta_{Q_i} \rightarrow 1$. Accordingly, at each state ζ_{Q_i} the probability for transition to a state closer to equilibrium (ζ_{Q_i+1}) is always greater than the probability for a transition further from equilibrium (ζ_{Q_i-1}), regardless of which side of equilibrium the present state (ζ_{Q_i}) is on. Hence, path B is simply the expected path. However, inasmuch as the model is probabilistic, the reaction need never reach equilibrium as is evident from the possible path C. The reaction can cycle between several states indefinitely, although such an occurrence is highly unlikely. Alternatively, the reaction path can deviate progressively further from equilibrium toward completion as shown in path A, but again such an occurrence is highly unlikely. It is only the expected path with which we are concerned.

The classical kinetic model of equilibrium is essentially steady state with opposite reaction velocities equal. Instead, according to this probabilistic approach, the equilibrium state is not static, but a state in which the opposite reaction *probabilities* are equal and, consequently, in a continuing state of transformation, as is any other state. The reaction deviates from equilibrium according to local probability with the equilibrium state as the only expected state. Rarely, if ever, is the system precisely in its equilibrium state and even then it is a passing occurrence.

The use of stoichastic methods to examine the behavior of particulate processes is decidedly not recent. In 1907, Ehrenfest and Ehrenfest[6] developed a statistical model of atomic diffusion using chains that was shown to be in accordance with experimental evidence. The development of chain processes to account for physical behavior was due to Planck and Fokker (see refs. 3 and 4) In all of these cases the expected time to attain equilibrium was finite ($t_K < \infty$). This being the case, the next requirement is to determine the expected number of transformations needed to attain equilibrium.

Dynamic equilibrium

A principal requirement in describing a probabilistic reaction path for a chemical reaction is to determine the expected number of transformations ($\Delta_{i,j}$) required for the reaction to transition from any step d_i for a ζ_{Q_i} to any other step d_j for a ζ_{Q_j}, where $\Delta_{i,j} = d_j - d_i$. We are particularly interested in the expected number of transformations ($\Delta_{i,eq}$) required to attain the equilibrium step d_{eq} from any previous step d_i.

If one knows the expected number of transformations to reach equilibrium from a given step d_i, then, by induction, the number of steps required to reach equilibrium from the previous step d_{i-1} depends on the probability that the previous step will reach the given state ζ_{Q_i}.

If $\Delta_{i,j}$ represents the expected number of transformations required to reach state ζ_{Q_j} from any state ζ_{Q_i}, then $\Delta_{i,eq}$ represents the expected number of transformations required to reach equilibrium step d_{eq} from any step d_i. Similarly, $\Delta_{i-1,eq}$ is the expected number of transformations required to reach equilibrium from step d_{i-1}, which can be defined recursively in terms of the probability of state transformation as

$$[7] \qquad \Delta_{i-1,eq} = 1 + p_{i-1,i}\Delta_{i,eq} + p_{i-1,i-2}\Delta_{i-2,eq}$$

where obviously

$$[8] \qquad \Delta_{eq,eq} = 0$$

Similarly, it is clear that for the initial condition

$$[9] \qquad \Delta_{1,eq} = 1 + \Delta_{0,eq}$$

and that for the final condition

$$[10] \qquad \Delta_{i,eq} = 1 + \Delta_{i-1,eq}$$

It is now necessary to simultaneously solve eqs. [7]–[10] for $\Delta_{i,eq}$ to determine the number of transformations to the equilibrium step d_{eq} from step d_i. The usual and most convenient method for the solution of these multiple simultaneous linear equations is through matrix algebra.[15] By combining these linear recursive relationships, the system of simultaneous equations can be rewritten as the stochastic matrix expression

$$[11] \qquad \mathbf{Md} = \mathbf{c}$$

In this form **M** is a square matrix that represents the coefficients of the simultaneous linear system of relationships

given by eqs. [7]–[10], with **d** representing the column vector of $\Delta_{i,\mathrm{eq}}$ (the expected number of transformations required to achieve equilibrium d_{eq} from state d_i) and **c** is the column vector of constants. However, to solve for **d** requires that matrix **M** be represented in Jordan canonical form[4] and therefore invertible ($\mathbf{M} \neq 0$). The Jordan canonical form (also called the classical canonical form) is a special type of a square matrix comprised of discrete Jordan blocks.[16] For a reaction capable of achieving $n + 1$ states d_0 through d_n, these stochastic matrices can be fully expressed as

$$[12] \quad \mathbf{M} = \begin{bmatrix} 1 & -1 & 0 & \dots & 0 & 0 & 0 & \dots & 0 & 0 & 0 \\ -p_{2,1} & 1 & -p_{2,3} & \dots & 0 & 0 & 0 & \dots & 0 & 0 & 0 \\ 0 & -p_{3,2} & 1 & \dots & 0 & 0 & 0 & \dots & 0 & 0 & 0 \\ \dots & \dots & \dots & \dots & \dots & \dots & \dots & \dots & \dots & \dots & \dots \\ 0 & 0 & 0 & \dots & 1 & -p_{\mathrm{eq}-1,\mathrm{eq}} & 0 & \dots & 0 & 0 & 0 \\ 0 & 0 & 0 & \dots & 0 & 1 & 0 & \dots & 0 & 0 & 0 \\ 0 & 0 & 0 & \dots & 0 & -p_{\mathrm{eq}+1,\mathrm{eq}} & 1 & \dots & 0 & 0 & 0 \\ \dots & \dots & \dots & \dots & \dots & \dots & \dots & \dots & \dots & \dots & \dots \\ 0 & 0 & 0 & \dots & 0 & 0 & 0 & \dots & 1 & -p_{n-2,n-1} & 0 \\ 0 & 0 & 0 & \dots & 0 & 0 & 0 & \dots & -p_{n-1,n-2} & 1 & -p_{n-1,n} \\ 0 & 0 & 0 & \dots & 0 & 0 & 0 & \dots & 0 & -1 & 1 \end{bmatrix}$$

and

$$[13] \quad \mathbf{d} = \begin{bmatrix} d_{1,\mathrm{eq}} \\ d_{2,\mathrm{eq}} \\ d_{3,\mathrm{eq}} \\ \dots \\ d_{\mathrm{eq}-1,\mathrm{eq}} \\ d_{\mathrm{eq},\mathrm{eq}} \\ d_{\mathrm{eq}+1,\mathrm{eq}} \\ \dots \\ d_{n-2,\mathrm{eq}} \\ d_{n-1,\mathrm{eq}} \\ d_{n,\mathrm{eq}} \end{bmatrix} \quad \mathbf{c} = \begin{bmatrix} 1 \\ 1 \\ 1 \\ \dots \\ 1 \\ 0 \\ 1 \\ \dots \\ 1 \\ 1 \\ 1 \end{bmatrix}$$

Thus

$$[14] \quad \mathbf{d} = \mathbf{M}^{-1}\mathbf{c}$$

Equation [14] is solvable because only a matrix with coefficients in an algebraically closed field can be represented in Jordan canonical form. Obviously **M** is in this form. The matrix is thus nonsingular and, therefore, the stochastic matrix **M** is in fact invertible ($\mathbf{M} \neq 0$). Consequently, of the well-defined solutions for $\Delta_{i,\mathrm{eq}}$, all indicate without exception that the expected number of transformations required for rxn. [1] at any state ζ_{Q_i} to attain the equilibrium state $\zeta_{Q_{\mathrm{eq}}}$ cannot be infinite. Thus

$$[15] \quad 0 < \Delta_{i,\mathrm{eq}} < \infty$$

Accordingly, for a system of discrete reacting particles the expected number of transformations($\Delta_{0,\mathrm{eq}}$) required for rxn. [1] to reach its equilibrium step d_{eq} from its initial step d_0 must be finite.

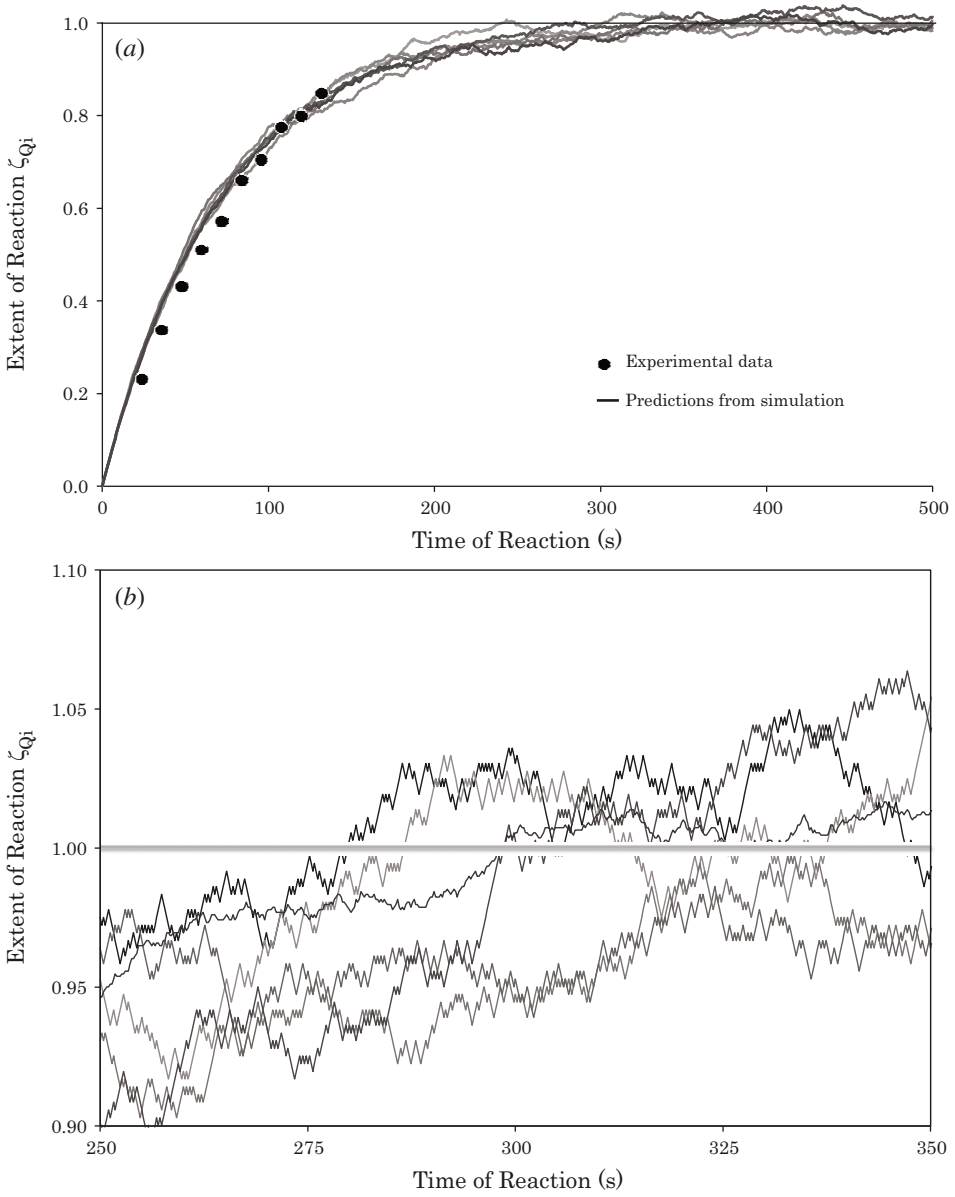
Elapsed time

Having established that the number of transformation steps required to attain equilibrium is finite, the expected time to attain equilibrium can now be considered. Because $\Delta_{0,\mathrm{eq}} < \infty$, the temporal progress of rxn. [1] can be expressed as a ratio $\Delta_{0,i}{:}\Delta_{0,\mathrm{eq}}$ between the number of steps required to reach any state i and the number required to reach the equilibrium state, where $\Delta_{0,i} < \Delta_{0,\mathrm{eq}}$. This ratio will now be related to the ratio of the elapsed time required to reach any state of the system (ζ_{Q_i}) to the expected time ($t_{0,\mathrm{eq}}$) required to attain equilibrium ($\zeta_{Q_{\mathrm{eq}}}$). Kineticists generally examine stoichiometric chemical reactions as interactions between chemical components as measured by concentration terms, but more precisely reaction rates are dependent on the chemical activities of the components rather than their concentrations. To circumvent this problem reactions are ordinarily observed under conditions of high dilution wherein partial pressures and concentrations closely approximate activities. Under these conditions of high dilution the relative number of collisions between reacting species in the reaction volume is insignificant compared with the total number of elastic collisions between all species present (diluent and reactant), and hence does not effect the overall collision rate. The accepted interpretation is that the Maxwell–Boltzmann energy distribution is not significantly disturbed by the meager number of reaction collisions.[17,18] Accordingly, because the overall collision rate is invariant at constant temperature, so must be the number of reaction collisions $\Delta_{i,i+n}$ per unit time from any step d_i to step d_{i+n}. Consequently, the elapsed time ($\mathrm{t}_{i,i+n}$) between each collision must be equally constant. Hence,

$$[16a] \quad t_{0,n} \propto \Delta_{0,n}$$

Can. J. Chem. Downloaded from www.nrcresearchpress.com by Renmin University of China on 09/02/12
For personal use only.

Fig. 2. (*a*) Time dependency of the extent-of-reaction for the reaction of styrene with iodine at 295 K. (*b*) Approach to equilibrium for the reaction of styrene with iodine at 295 K.



Can. J. Chem. Downloaded from www.nrcresearchpress.com by Renmin University of China on 09/02/12
For personal use only.

Inasmuch as the number of steps to attain equilibrium is finite, so must be the expected time to attain equilibrium, denoted $t_{0,eq}$. Because the overall collision rate is constant, then from eq. [16*a*]

$$[16b] \qquad t_{0,eq} \propto \Delta_{0,eq}$$

Taking the ratio of eq. [16*a*] to eq. [16*b*], where $t \equiv t_{0,n}$ and $t_K \equiv t_{0,eq}$, yields

$$[17] \qquad t/t_K = \Delta_{0,n}/\Delta_{0,eq}$$

Only if $t_K < \infty$ would the ratio of the transformations $\Delta_{0,n}/\Delta_{0,eq}$ be meaningful.

Empirical validation

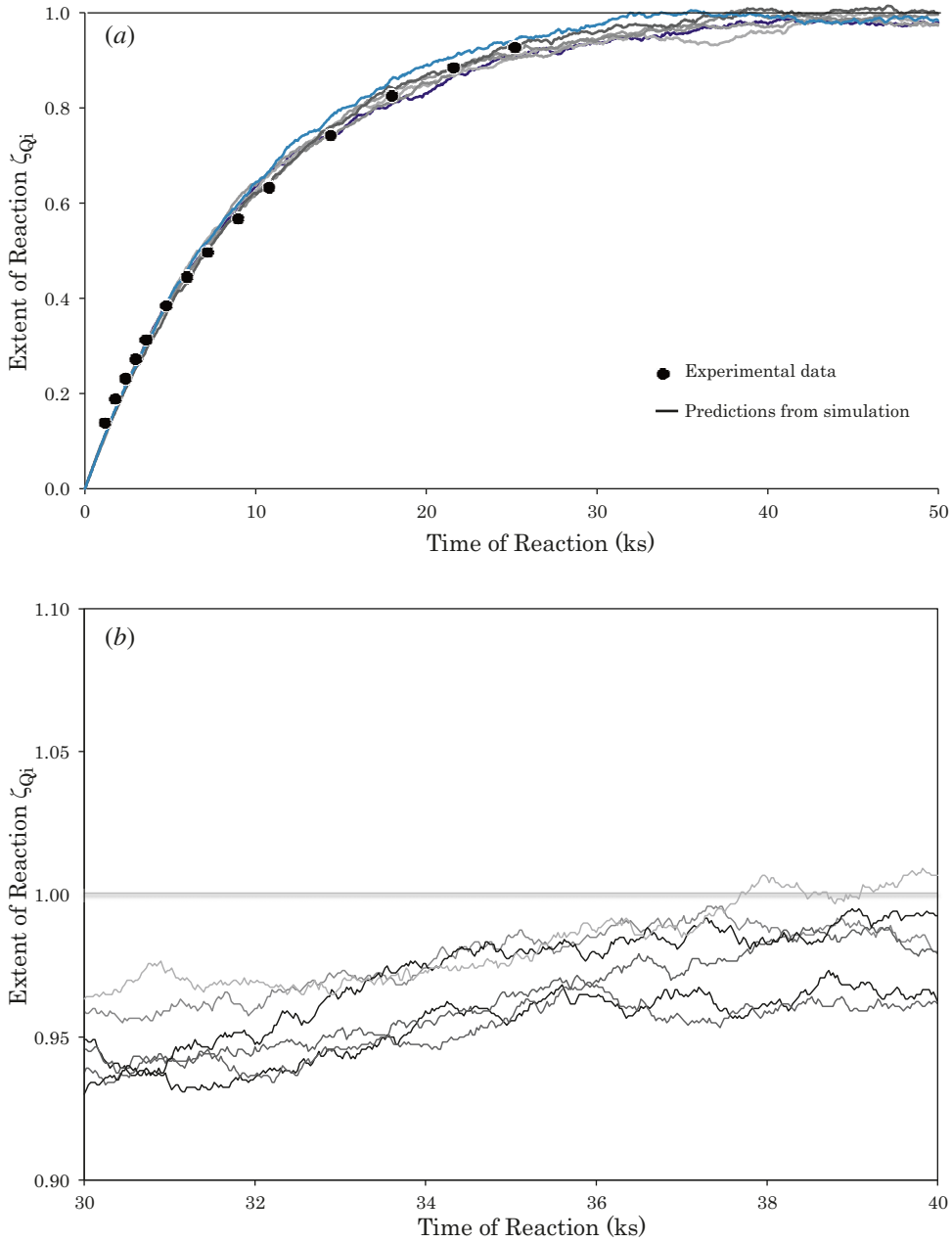
Although it is evident from this analysis that the expected time to attain equilibrium must be finite, the expected values of that elapse time must be probabilistic: it probably extends over an indeterminate, but finite range. To illustrate, consider the following empirical reaction data correlated by this probabilistic analysis according to eqs. [5*a*] and [5*b*] on approach to equilibrium. The probabilistic reaction paths were generated by an algorithm described in detail by Garfinkle[2] using a Microsoft Excel spreadsheet with an internal random-number generator. Thirty-six reaction plots were generated for each of the reactions cited and these were grouped into the six paths illustrated.

The reaction of styrene with iodine in carbon tetrachloride at 295 K is a highly complex process.[19]

$$[18] \qquad C_6H_5{-}CH{-}CH_2 + I_2 \rightarrow C_6H_5{-}CHI{-}CH_2I$$

The formation of styrene diiodide apparently involves both a free-radical chain mechanism that has a first-order dependency on iodine concentration and a 3/2 order dependency

Fig. 3. (*a*) Dehydrogenation of isobutane by iodine at 525 K. (*b*) Approach to equilibrium for the dehydrogenation of isobutane by iodine at 525 K.



on styrene concentration. The six reaction paths are illustrated in Fig. 2*a* with the empirical data points.

Figure 2*a* details the extrapolated reaction paths on approach to equilibrium, illustrating their probabilistic nature.

Apparently the time to attain equilibrium is >250 s. Probabilistically, however, equilibrium could be attained at any shorter time, but that time would not be the expected time.

The dehydrogenation of isobutane by iodine vapor at 525 K is exceedingly complex.

[19] $i\text{-}CH_6 + I_2 \rightarrow i\text{-}CH_4 + 2HI$

The reaction mechanism involves a free-radical chain reaction, with the postulated reaction rate depending on the equilibrium constant for iodine, where M is any molecule present.[20]

[20*a*] $I_2 + M \leftrightarrow 2I + M$

[20*b*] $i\text{-}BuH + I \rightarrow t\text{-}Bu + HI$

[20*c*] $t\text{-}Bu + I_2 \rightarrow t\text{-}BuI + I$

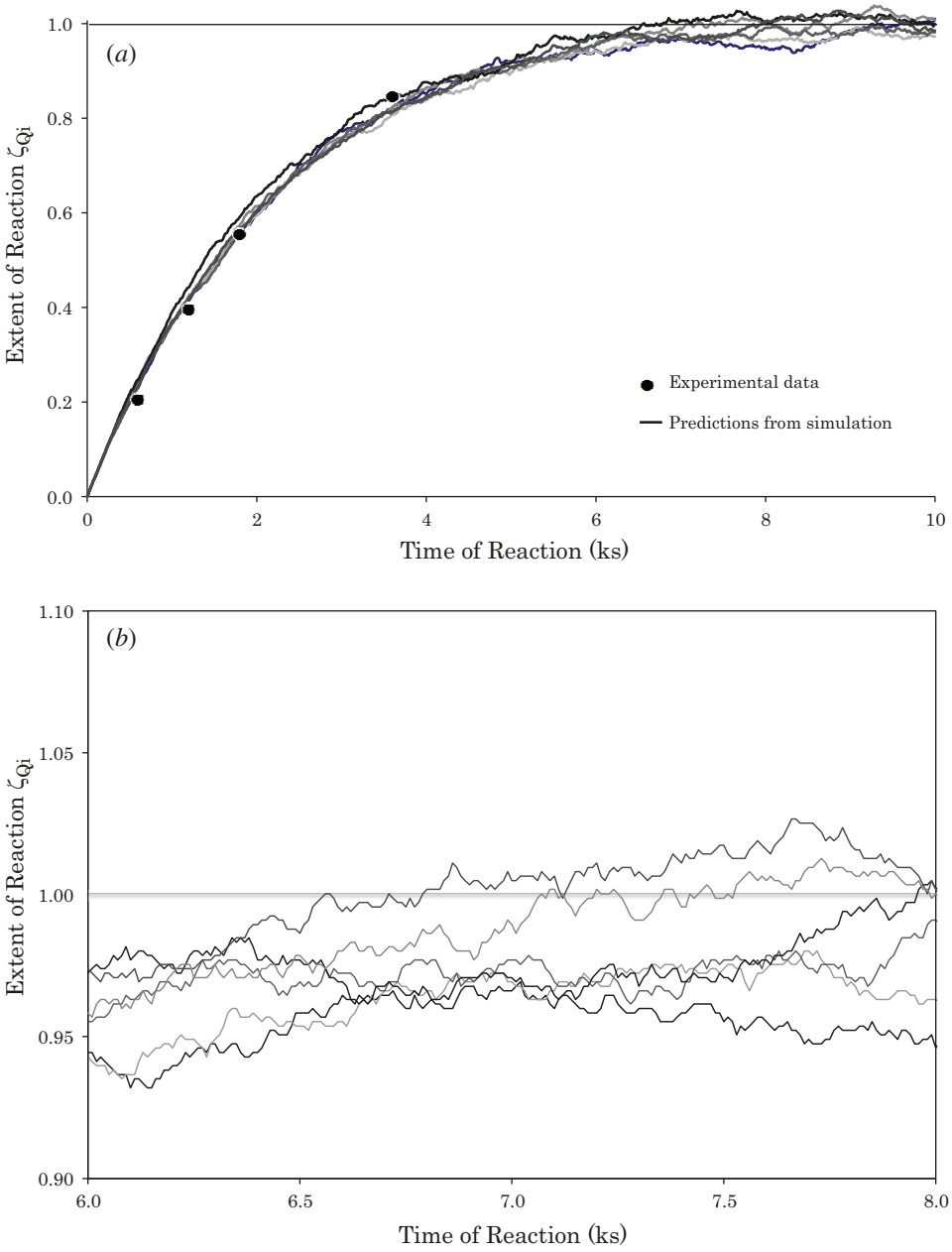
terminating in

[20*d*] $t\text{-}BuI \rightarrow i\text{-}Butene + HI$

It is immediately evident that the overall reaction rate depends on the concentrations of I_2 and HI molecules. The six

Can. J. Chem. Downloaded from www.nrcresearchpress.com by Renmin University of China on 09/02/12
For personal use only.

Fig. 4. (*a*) Time dependency of the extent-of-reaction for the biomination of platinic ammonia chloride at 308 K. (*b*) Approach to equilibrium for the biomination of platinic amomonia chloride at 308 K.



reaction paths are illustrated in Fig. 3*a* with the empirical data points.

Figure 3*b* details these six reaction paths on approach to equilibrium. Compare with Fig. 1.

The bromination of platinic ammonia chloride ion in KCl solution at 308 K is probably an elementary substitution reaction wherein

[21] $Pt(NH_3)Cl^+ + Br^- \rightarrow Pt(NH_3)Br^+ + Cl^-$

although an activated intermediate species is possibly involved.[21]

[22*a*] $Pt(NH_3)Cl^+ + Br^- \leftrightarrow Pt(NH_3)BrCl$

followed by

[22*b*] $Pt(NH_3)BrCl^{\ddagger} \rightarrow Pt(NH_3)Br^+ + Cl^-$

The six reaction paths are illustrated in Fig. 4*a* with the empirical data points. Figure 4*b* details these six reaction paths on approach to equilibrium.

Unexpectedly, the formation of acetone cyanohydrin in aqueous solution does not involve catalysis, as does many other such cyanohydrin formation processes.[22]

[23] $CH_3COCH_3 + HCN \rightarrow (CH_3)_2C(OH)CN$

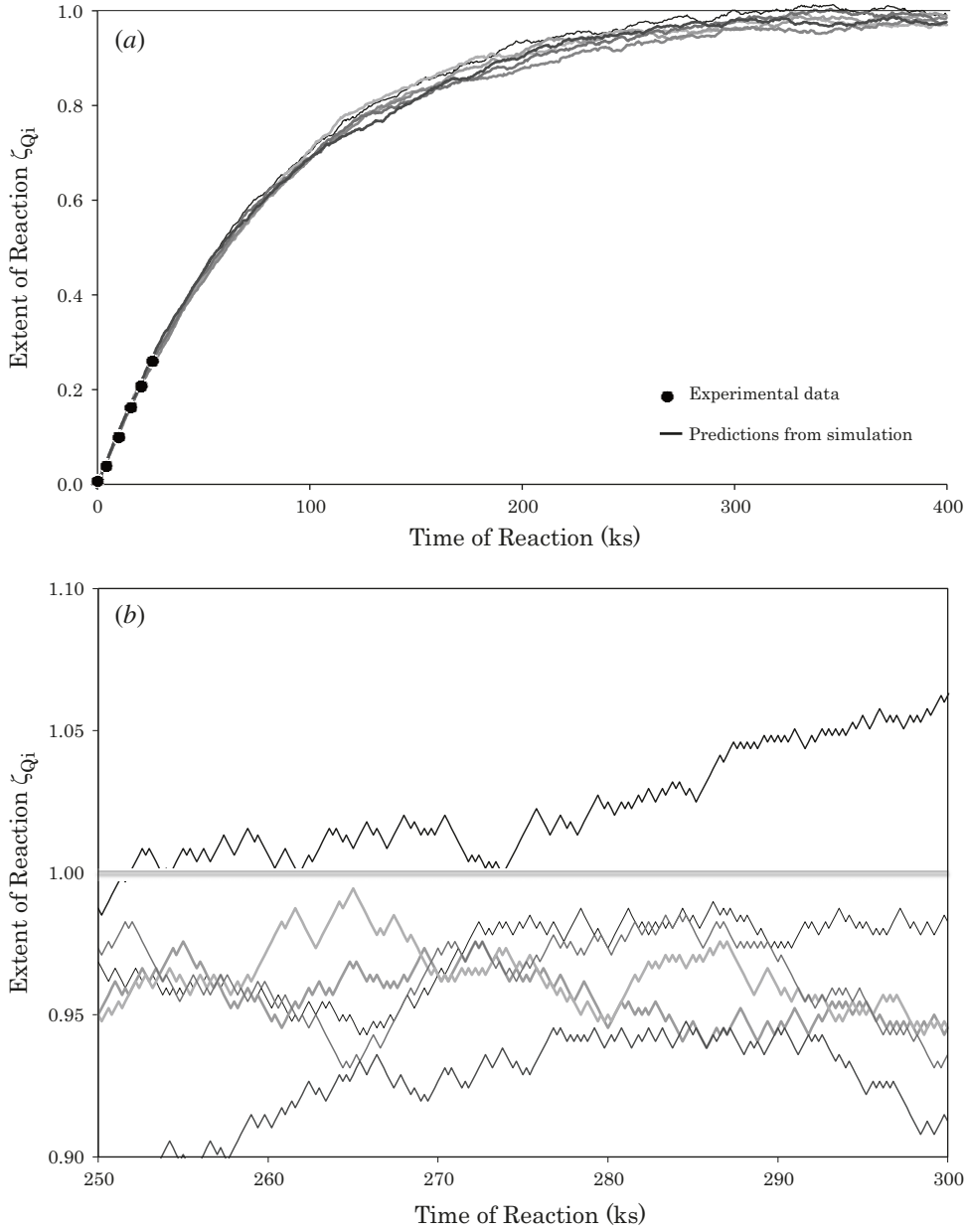
Instead, the formation reaction is a two-step process following ionization of HCN

[24*a*] $HCN \leftrightarrow H^+ + CN^-$

Can. J. Chem. Downloaded from www.nrcresearchpress.com by Renmin University of China on 09/02/12
For personal use only.

Can. J. Chem. Downloaded from www.nrcresearchpress.com by Renmin University of China on 09/02/12
For personal use only.

Fig. 5. (*a*) Formation of acetone cyanohydrin at 298 K. (*b*) Approach to equilibrium for the formation of acetone cyanohydrin at 298 K.



[24*b*] $CH_3COCH_3 + CN^- \rightarrow (CH_3)_3COCN^-$

[24*c*] $(CH_3)_3COCN^- + H^+ \rightarrow (CH_3)_3C(OH)CN$

with the slower reaction (eq. [24*b*]) controlling the overall reaction rate. The six reaction paths are illustrated in Fig. 5*a* with the empirical data points. Figure 5*b* details these six reaction paths on approach to equilibrium.

Discussion

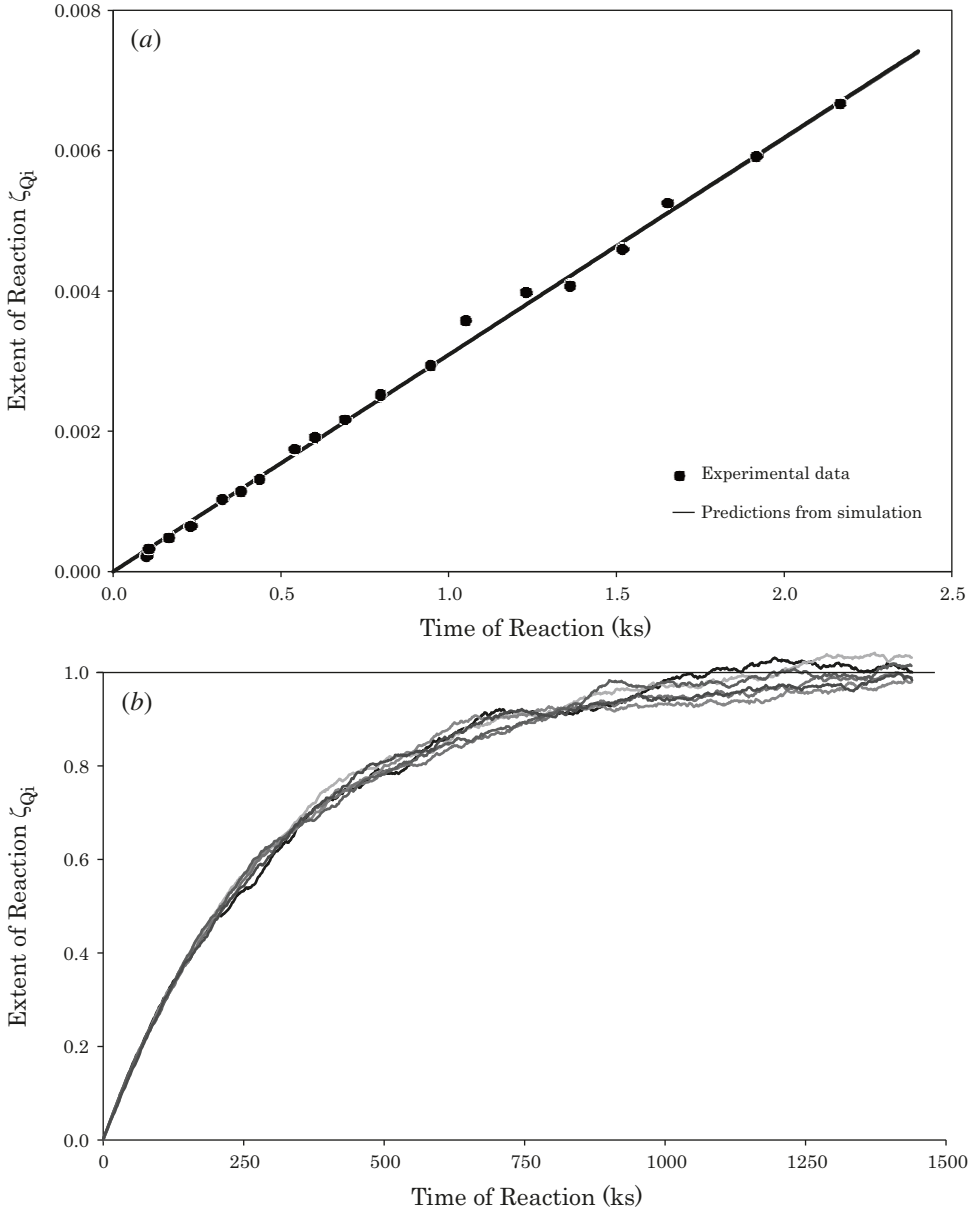
The multiple reactions paths plotted for the various reactions considered are in accordance with the schematic paths shown in Fig. 1 that illustrate a Markov[13] chain mechanism. A chain mechanism dictates that the expected time to attain equilibrium or any other state will be finite, which is in agreement with the matrix-algebra analysis. It is evident from these data correlations that given sufficient time the extent-of-reaction ζ_{Q_i} will attain some equilibrium value in a finite time as a passing occurrence. To quantify that expected time is considerably more difficult inasmuch as it involves a range of values. The expanded plots show the reaction paths as $\zeta_{Q_i} \rightarrow 1$. Accordingly, the only conclusion that has any validity is that $t_K < \infty$, in agreement with the stochastic argument.

For example, consider the formation of nitrosyl chloride at 333 K, which ostensibly depends on ternary collisions that are estimated to be about 100 times as rare as binary collisions.[23]

[25] $2NO + Cl_2 \rightarrow 2NOCl$

Can. J. Chem. Downloaded from www.nrcresearchpress.com by Renmin University of China on 09/02/12
For personal use only.

Fig. 6. (*a*) Time dependency of the extent-of-reaction for the formation of nitrosyl chloride at 333 K. (*b*) Time dependency of the extent-of-reaction for the formation of nitrosyl chloride at 333 K.



However, the reaction can be explained by a two-stage bimolecular process.[24]

[26*a*] $NO + Cl_2 \rightarrow NOCl + Cl\cdot$

[26*b*] $NO + Cl\cdot \rightarrow NOCl$

The six reaction paths for the formation of NOCl are illustrated in Fig. 6*a*.

On extrapolation using eq. [5*a*], the expected time to attain equilibrium was just under 10^5 s as shown in Fig. 6*b* (just over a quarter of a day: a relatively short period).

Now consider the quasi-unimolecular decomposition of nitrous oxide at 858 K.[25]

[27] $2N_2O \rightarrow 2N_2 + O_2$

This process probably involves an activated molecule

[28] $N_2O + M \rightarrow NO + N\cdot + M$

where M indicates collision activation. After activation, the probable sequence of steps is as follows:

[29*a*] $N\cdot + N_2O \rightarrow N_2 + NO$

The NO molecule then essentially drives the reaction

[29*b*] $NO + N_2O \rightarrow N_2 + O_2 + N\cdot$

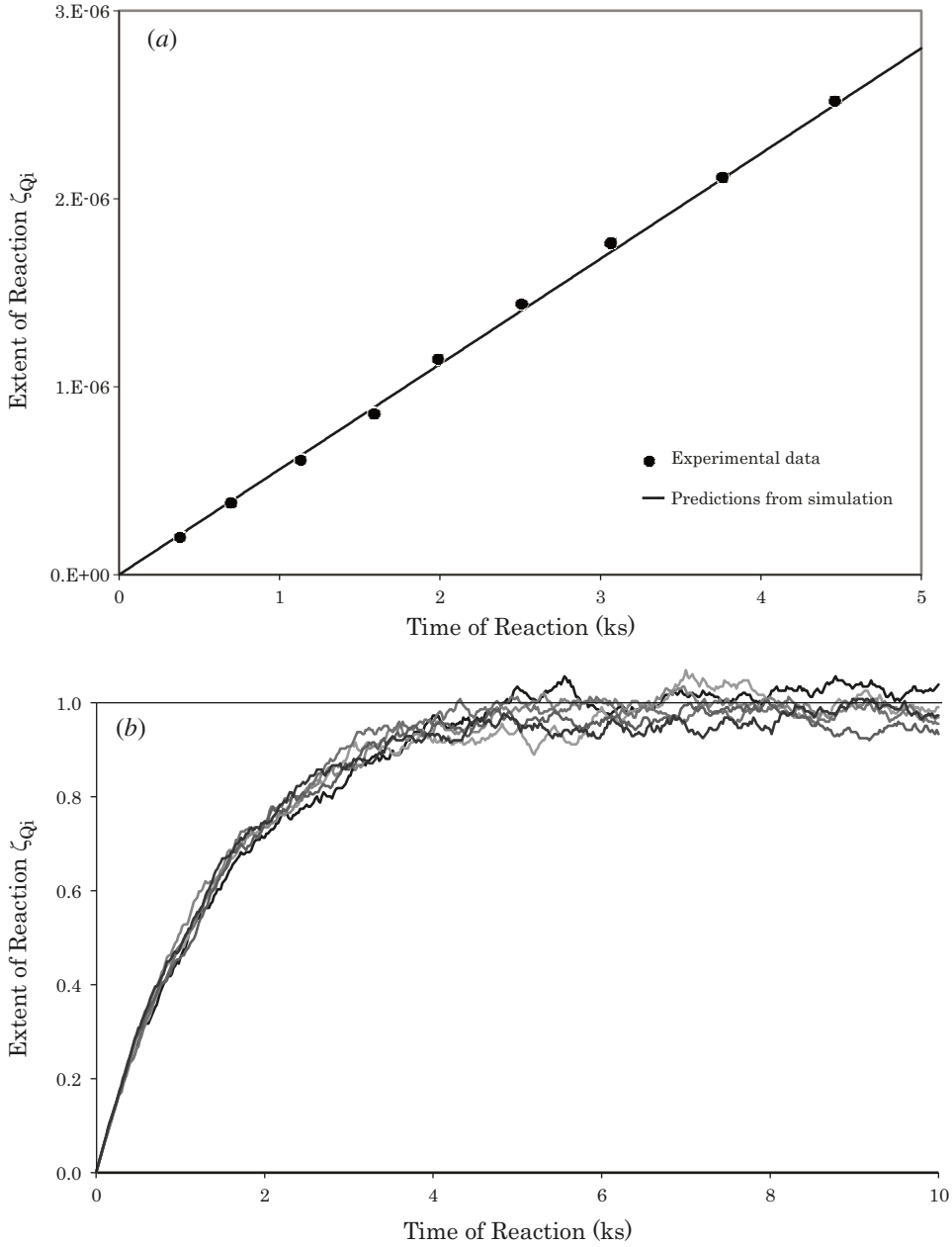
that terminates as

[29*c*] $N\cdot + NO \rightarrow N_2O$

The six reaction paths with data points are shown in Fig. 7*a*.

Can. J. Chem. Downloaded from www.nrcresearchpress.com by Renmin University of China on 09/02/12
For personal use only.

Fig. 7. (*a*) Decomposition of nitrous oxide at 858 K. (*b*) Approach to equilibrium for the decomposition of nitrous oxide at 858 K.



On extrapolation using eq. [5*a*], the expected time to attain equilibrium was roughly 10^9 s, just over a century as shown in Fig. 7*b*: well over an average lifetime, but still well short of infinity.

Of course, for most of the almost 100 reactions examined[10] the expected time to attain equilibrium was far beyond any practical observation time, and in fact beyond many lifetimes. For example, consider the oxidation of Fe(II) by Co(III) in perchloric acid solution at 298 K.[26]

[30] $\mathrm{Fe(II) + Co(III) \rightarrow Fe(III) + Co(II)}$

The ostensibly simple mechanism is really quite complex and probably involves the initial reaction

[31*a*] $\mathrm{Co^{3+} + OH^- \leftrightarrow CoOH^{2+}}$

followed by the hydroxyl transfer reaction

[31*b*] $\mathrm{Fe^{2+} + CoOH^{2+} \rightarrow FeOH^{2+} + Co^{2+}}$

and terminating in

[31*c*] $\mathrm{FeOH^{2+} \rightarrow Fe^{3+} + OH^-}$

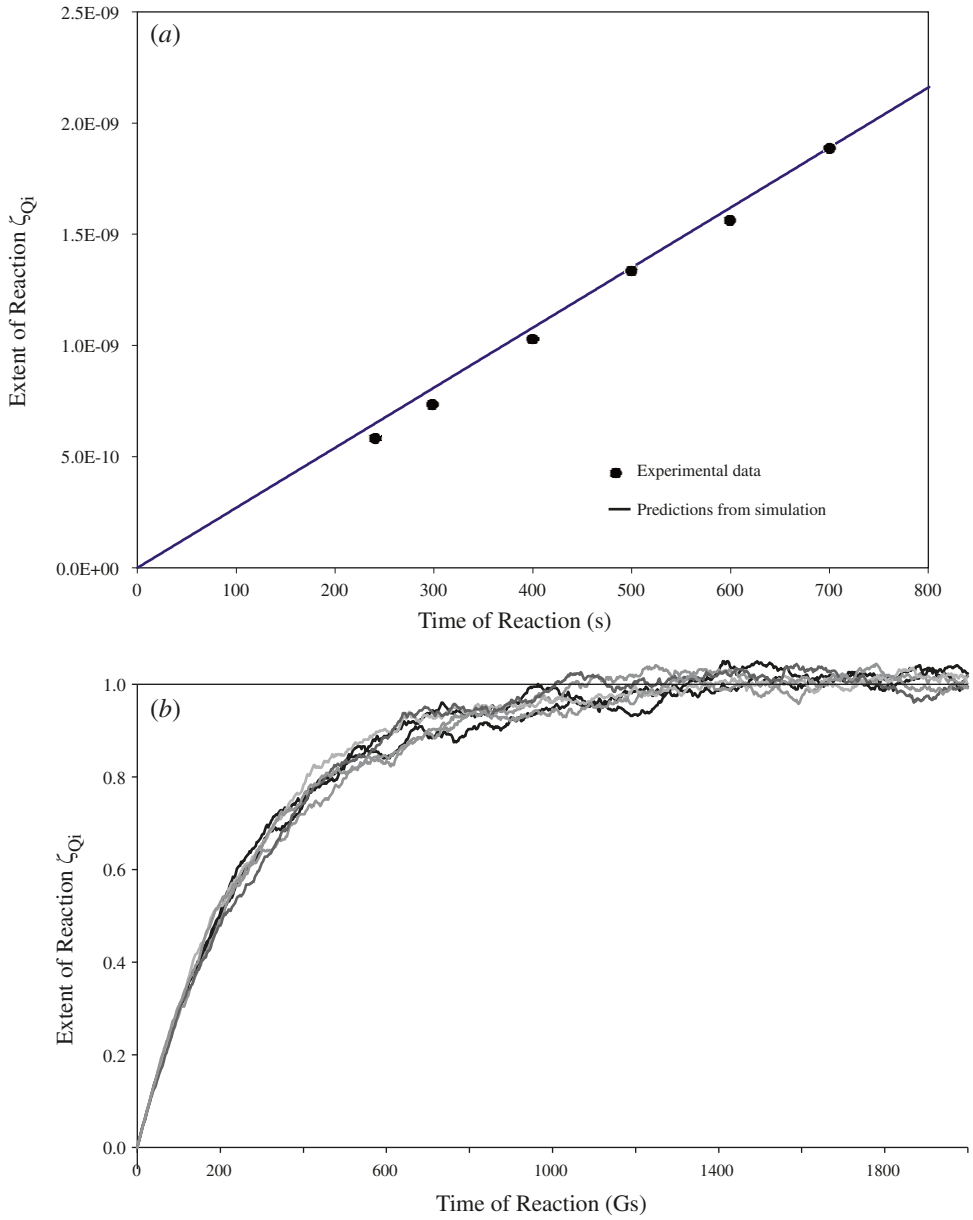
The reaction path is shown in Fig. 8*a*.

On extrapolation using eq. [5*a*], the expected time to attain equilibrium is well over 10^{11} s. This duration is roughly 5000 years; while a significant duration, nevertheless a value still considerably shy of infinity.

Conclusion

This thermodynamic–probabilistic parallels the approach of Guldberg and Waage, but this thermodynamic approach

Fig. 8. (*a*) Time dependency of the extent-of-reaction for the oxidation of Fe(II) by Co(III) at 298 K. (*b*) Time dependency of the extent-of-reaction for the oxidation of Fe(II) by Co(III) at 298 K.



depends on a discrete algorithm in contrast with the deterministic approach of the emprical rate equations. Whereas the probabilistic approach has been successfully applied to physical processes, it has now been shown by this study that it is equally valid for chemical reactions. This approach demonstrates that stoichiometric chemical reactions proceed by a Markov chain mechanism towards equilibrium as formulated by Planck and Fokker and that the expected number of discrete reaction steps is finite as predicted by Ehrenfest and Prigogine. Because the elapsed time to attain equilibrium is directly proportional to the number of reaction steps, the elapsed time must be also finite.

References

(1) Christianson, J. A. *The Law of Mass Action;* Norske Videnskaps-Academi: Oslo, 1964.
(2) Garfinkle, M. *J. Phys. Chem.* **2002**, *106* (3), 490. doi:10.1021/jp013048n.
(3) Loéve, M. *Probability Theory: Foundations, Random Sequences;* Van Nostrand: New York, 1955.
(4) Kolmogorov, A. *Math. Ann.* **1931**, *104*, 415. doi:10.1007/BF01457949.
(5) Prigogine, I.; Balescu, R.; Henin, F.; Resibois, P. *Physics* **1961**, *27*, 541.
(6) Ehrenfest, P.; Ehrenfest, T. *Phys. Z.* **1907**, *7*, 311.
(7) Percival, I. C. *J. Math. Phys.* **1961**, *2* (2), 235. doi:10.1063/1.1703705.
(8) Steinfeld, J. I.; Francisco, J. S.; Hase, W. L. *Chemical Kinetics and Dynamics;* Prentice Hall:, Upper Saddle River, NJ, 1998.
(9) Garfinkle, M. *J. Chem. Phys.* **1984**, *80* (8), 3640. doi:10.1063/1.447185.
(10) Garfinkle, M. *Discrete Dyn. Nat. Soc.* **2000**, *4* (2), 145. doi:10.1155/S1026022600000145.

Can. J. Chem. Downloaded from www.nrcresearchpress.com by Renmin University of China on 09/02/12
For personal use only.

(11) Baierlein, R. *Atoms and Information Theory;* Freeman: San Francisco, 1971; p 92.
(12) De Donder, T. *Acad. R. Belg. Bull. Cl. Sci.* **1922**, *5*, 197.
(13) Markov, A. *Izv. Akad. Nauk.* **1907**, *6*, 61.
(14) Kemeny, J. G.; Snell, J. L. *Finite Markov Chains;* Princeton Publishing Inc.: Princeton, IN, 1960.
(15) Wylie, C. *Advanced Engineering Mathematics;* McGraw-Hill Book Co.: New York, 1951.
(16) Strang, G. *Linear Algebra and its Applications,* 3rd ed.; Saunders: Philadelphia, 1988.
(17) Hinshelwood, C. N. *Kinetics of Chemical Change;* Oxford University Press: Oxford, 1940.
(18) Glasstone, S.; Laidler, K. J.; Eyering, H. *The Theory of Rate Processes;* McGraw-Hill: New York, 1941.
(19) Fraenkel, G.; Bartlett, P. D. *J. Am. Chem. Soc.* **1959**, *81* (21), 5582. doi:10.1021/ja01530a017.
(20) Svirbely, W. J.; Roth, J. F. *J. Am. Chem. Soc.* **1953**, *75* (13), 3106. doi:10.1021/ja01109a020.
(21) Espenson, J. H. *Chemical Kinetics and Reaction Mechanisms;* McGraw-Hill: New York, 1981; p 60.
(22) Teranishi, H.; Benson, S. W. *J. Am. Chem. Soc.* **1963**, *85* (19), 2887. doi:10.1021/ja00902a003.
(23) Benson, S. W. *Fundamental of Chemical Kinetics;* McGraw-Hill: New York, 1960; p 305.
(24) Sykes, A. G. *Kinetics of Inorganic Reactions;* Pergamon: Oxford, 1966; p 86.
(25) Pease, R. N. *J. Chem. Phys.* **1939**, *7* (9), 749. doi:10.1063/1.1750521.
(26) Bennett, L. E.; Sheppard, J. C. *J. Phys. Chem.* **1962**, *66* (7), 1275. doi:10.1021/j100813a015.

Can. J. Chem. Downloaded from www.nrcresearchpress.com by Renmin University of China on 09/02/12
For personal use only.

Stereodynamics study of the $O^+ + D_2$ ($v = 0, j = 0–2$) → $OD^+ + D$ reaction

Jiawu Chen, Xinguo Liu, and Qinggang Zhang

Can. J. Chem. Downloaded from www.nrcresearchpress.com by Renmin University of China on 09/02/12
For personal use only.

Abstract: The vector correlations between products and reagents for the ion–molecule reaction $O^+ + D_2 \rightarrow OD^+ + D$ with different rotational quantum numbers ($j = 0$, 1, or 2) were explored theoretically using the quasi-classical trajectory method (QCT) on a Martìnez–Millán–González (MMG) surface. The three angular distributions $P(\theta_r)$, $P(\phi_r)$, and $P(\theta_r,\phi_r)$, as well as four polarization-dependent differential cross sections (PDDCSs) were calculated. The results indicate that a reagent's rotational excitation greatly influences both the vector correlations of **k**–**k**′, **k**–**j**′, and **k**–**k**′–**j**′ and the PDDCSs of the title reaction, which means the reactivity is very sensitive to the rotational quantum number.

Key words: vector correlation, quasi-classical trajectory (QCT), stereodynamics, rotational excitation, polarization-dependent differential cross sections.

Résumé : On a fait appel à la méthode de la trajectoire quasi-classique (TQC) sur une surface MMG pour étudier d'une façon théorique la corrélation des vecteurs entre les produits et les réactifs pour la réaction ion–molécule $O^+ + D_2 \rightarrow OH^+ + D$ avec différents nombres quantiques rotationnels ($j = 0$, 1, ou 2). On a calculé respectivement les trois distributions angulaires $P(\theta_r)$, $P(\phi_r)$ et $P(\theta_r,\phi_r)$ ainsi que les quatre sections droites différentielles qui dépendent de la polarisation (SDDDP). Les résultats indiquent que l'excitation rotationnelle du réactif influence grandement la corrélation des vecteurs de **k**–**k**, **k**–**j**′ et **k**–**k**′–**j**′ ainsi que les sections droites différentielles qui dépendent de la polarisation (SDDDP) de la réaction mentionnée dans le titre, ce qui signifie que la réactivité est très sensible au nombre quantique rotationnel.

Mots-clés : corrélation des vecteurs, trajectoire quasi-classique (TQC), stéréodynamique, excitation rotationnelle, sections droites différentielles qui dépendent de la polarisation (SDDDP).

[Traduit par la Rédaction]

Introduction

Ion–molecule reactions are important processes that occur in many interesting situations, such as electric discharges, planetary ionospheres, interstellar space, and so on.[1–3] Being a very important ion–molecule reaction, the $O^+ + H_2 \rightarrow OH^+ + H$ system plays a key role in H_2-rich interstellar chemistry and in the Earth's ionosphere. As an isotopic variant reactivity of $O^+ + H_2 \rightarrow OH^+ + H$, the reaction

$$O^+ + D_2 \rightarrow OD^+ + D$$

can be regarded as a prototypical three-atom reaction system in the field of ion–molecule reaction dynamics and has received considerable attention both experimentally and theoretically. One of the most fascinating aspects of the reaction is that it is a moderately exothermic ion–molecule reaction. The reaction $O^+ + H_2 \rightarrow OH^+ + H$ is particularly important in dense interstellar clouds, where subsequent reactions of OH^+ with H_2 lead to the formation of H_2O^+ and H_3O^+ molecular ions, which are very important substances.[4]

In 2004, Rodrigo et al.[5] constructed a most accurate potential energy surface (PES) for $O^+ + H_2 \rightarrow OH^+ + H$. Subsequently, there have been many theoretical and experimental studies for $O^+ + H_2 \rightarrow OH^+ + H$ and its isotopic variants. Using the quasi-classical trajectory method (QCT), Rodrigo et al.[5] studied many scalar properties of the above reaction, such as the cross section, maximum impact parameter, and the reaction probability of $O^+ + H_2 \rightarrow OH^+ + H$. The results of QCT are in excellent agreement with the experimental results taken from Burley et al.[6] Recently, Sun et al.[7] studied the isotope effect of stereodynamics at collision energies of 1.0, 1.5, 2.0, and 2.5 eV. Besides the theoretical studies mentioned above, many experimental techniques, such as polarization-resolved chemiluminescence and polarized laser-induced fluorescence, have been used to measure the vector correlations between reagents and products.[8–10]

As mentioned, the reaction of $O^+ + H_2$ and its isotopic variants has been under considerable investigation, which, however, basically have dealt with scalar properties such as the rate constant, integral cross section, reaction probability, etc. Actually, it is at least equally important to study the vector properties if we want to fully understand the dynamics of the $O^+ + H_2$ system. Only by understanding both the scalar and vector properties can we have the fullest picture of the scattering dynamics.[11–17] As far as we know, although there have been several studies on the $O^+ + D_2 \rightarrow OD^+ + D$ reaction, the effects of different rotational quantum numbers on vector properties, which practically deserve further investigation,

Received 3 August 2011. Accepted 17 October 2011. Published at www.nrcresearchpress.com/cjc on 30 January 2012.

J. Chen, X. Liu, and Q. Zhang. College of Physics and Electronics, Shandong Normal University, 88 East Wenhua Road, Ji'nan, Shandong, Jinan 250014, China.

Corresponding author: Xinguo Liu (e-mail: liuxinguo@sdnu.edu.cn).

Can. J. Chem. Downloaded from www.nrcresearchpress.com by Renmin University of China on 09/02/12
For personal use only.

Fig. 1. The centre-of-mass coordinate system used to describe the **k**, **k**′, and **j**′ correlations.

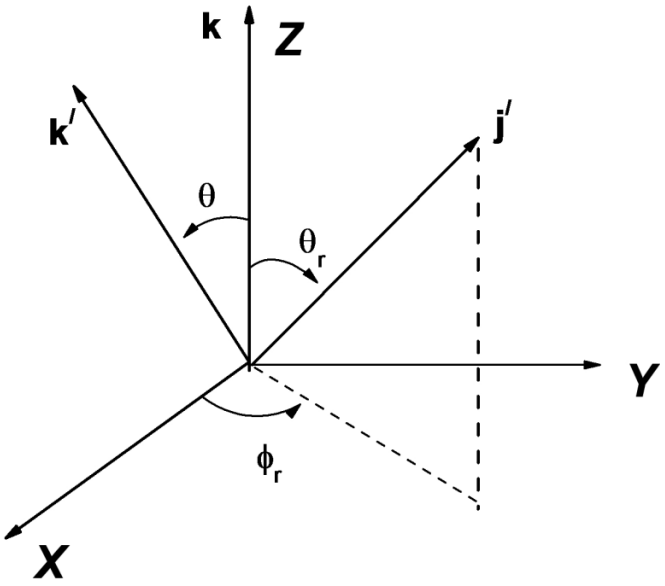
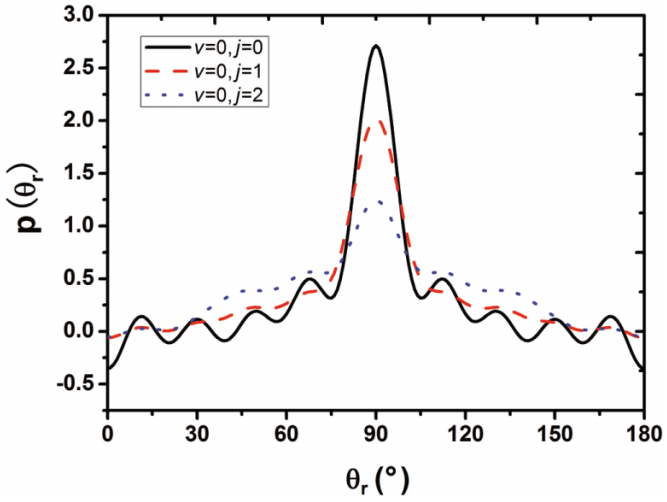


Fig. 2. The distribution of $P(\theta_r)$, reflecting the **k**–**j**′ correlation with $j = 0$–2.



have not been explored yet. That is why we carried out this theoretical calculation and feel that we have obtained some valuable results.

Theory

Product rotational polarization

For an atom–diatom reaction, a centre-of-mass (CM) frame is utilized in which the z axis lies in the direction of the reagent relative velocity (**k**). The reagent and product relative velocities are defined in terms of the reagent and product CM velocities as $\mathbf{k} = v_A - v_{BC}$, where v_A is the CM velocity of the reagent atom A and v_{BC} is the CM velocity of reagent diatom BC, and $\mathbf{k}' = v_{AB} - v_C$, where v_{AB} is the CM velocity of the product diatom AB and v_C is the CM velocity of the product atom C. We can see from Fig. 1 that **k** is parallel to the z axis and the x–z plane is the scattering plane that contains the initial and final relative velocity vectors. θ is the angle between the reagent and product relative velocity. θ_r and ϕ_r are the polar and azimuthal angles of the final rotational angular momentum **j**′.

Since the deduction process for the following formulae can be found in ref. 18, we will just summarize the formulae here.

The distribution function $P(\theta_r)$ describing the **k**–**j**′ correlation can be expanded into a series of Legendre polynomials[19–24]

$$[1] \qquad P(\theta_r) = \frac{1}{2}\sum_k (2k+1)a_0^{(k)}P_k(\cos\theta_r)$$

where

$$[2] \qquad a_0^{(k)} = \int_0^{\pi} P(\theta_r)P_k(\cos\theta_r)\sin\theta_r d\theta_r = \langle P_k(\cos\theta_r)\rangle$$

where k is the coefficient of the Legendre polynomials and P_k is part of the expression of the Legendre polynomials. The angular brackets represent an average over all trajectories. The expanding coefficients $a_0^{(k)}$ are called orientation (k is odd) and alignment (k is even) parameters.

Table 1. The product rotational alignment parameter $\langle P_2(\mathbf{j}'\cdot\mathbf{k})\rangle$ calculated with $j = 0$–2.

	Initial rotational No. (j)		
	0	1	2
$\langle P_2(\mathbf{j}'\cdot\mathbf{k})\rangle$	–0.410	–0.348	–0.245

Note: j, rotational quantum number; **j**′, product rotational angular momentum vector; **k**, relative velocity direction.

The angle distribution function $P(\theta_r)$ describing the **k**–**k**′–**j**′ correlation can be expanded into a Fourier series

$$[3] \qquad P(\phi_r) = \frac{1}{2\pi}\left(1 + \sum_{n\geq 2}^{\text{even}} a_n \cos n\phi_r + \sum_{n\geq 1}^{\text{odd}} b_n \sin\phi_r\right)$$

where n is the coefficient of the Fourier series.

$$[4] \qquad a_n = 2\langle\cos n\phi_r\rangle$$

$$[5] \qquad b_n = 2\langle\sin n\phi_r\rangle$$

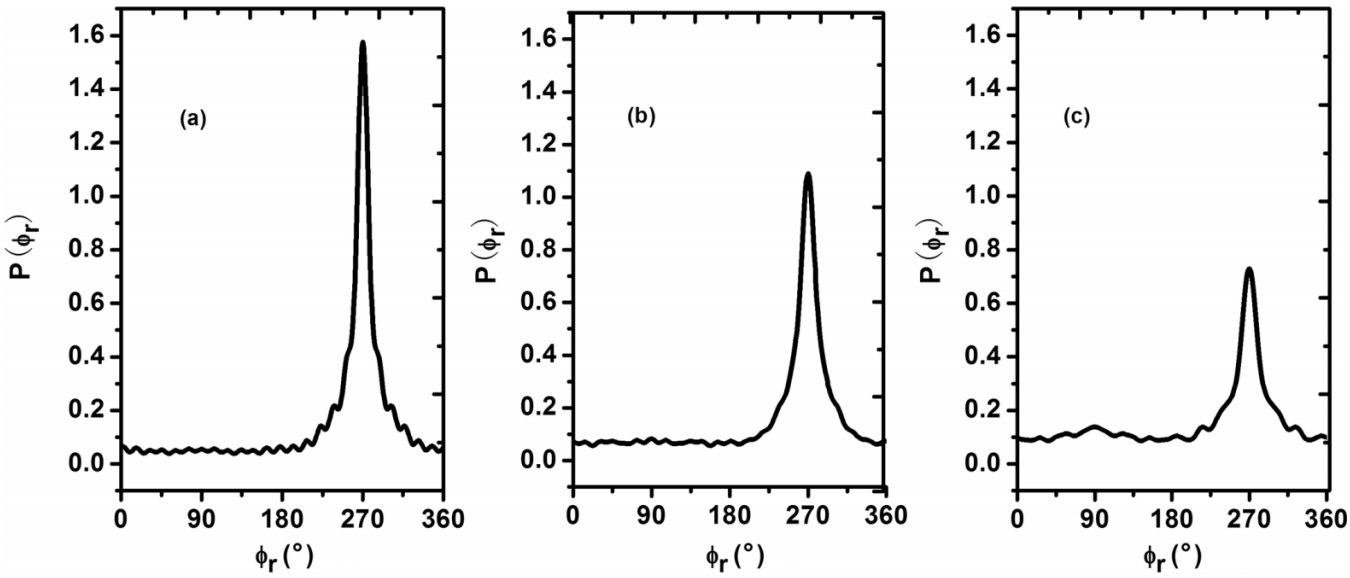
The angular brackets represent an average over all trajectories. In this calculation, $P(\phi_r)$ shows good convergence when it is expanded up to $n = 24$. The joint probability density function of angles θ_r and ϕ_r defining the direction of **j**′ can be written as

$$[6] \qquad P(\theta_r, \phi_r) = \frac{1}{4\pi}\sum_{kq}[k]a_q^k C_{kq}(\theta_r, \phi_r)^* = \frac{1}{4\pi}\sum_k\sum_{q\geq 0}[a_{q\pm}^k \cos q\phi_r - a_{q\mp}^k i\sin q\phi_r] \times C_{kq}(\theta_r, 0)$$

where q is the coefficient of the modified spherical harmonics and $C_{kq}(\theta_r, \phi_r) = \sqrt{4\pi/(2k+1)}Y_{kq}(\theta_r, \phi_r)$ (modified spherical harmonics), where Y_{kq} is the spherical harmonics. The polarization parameter is evaluated as

Can. J. Chem. Downloaded from www.nrcresearchpress.com by Renmin University of China on 09/02/12
For personal use only.

Fig. 3. The dihedral angle distribution of $\mathbf{j}'$ with respect to the $\mathbf{k}$–$\mathbf{k}'$ plane. Panels (*a*)–(*c*) describe the distributions with $j = 0$, 1, and 2, respectively.



$$[7] \qquad a^{k}_{q\pm} = 2\langle C_{k|q|}(\theta_r, 0)\cos q\phi_r\rangle \qquad (k \text{ is even})$$

$$[8] \qquad a_{q\mp} = 2i\langle C_{k|q|}(\theta_r, 0)\sin q\phi_r\rangle \qquad (k \text{ is odd})$$

In this calculation, $P(\theta_r,\phi_r)$ shows good convergence when it is expanded up to $k = 7$.

Polarization-dependent differential cross section (PDDCS)

The full three-dimensional angular distribution associated with $\mathbf{k}$–$\mathbf{k}'$–$\mathbf{j}'$ can be represented by a set of generalized PDDCSs in the CM frame. The fully correlated CM angular distribution is written as

$$[9] \qquad P(\omega_t, \omega_r) = \sum_{kq} \frac{[k]}{4\pi}\frac{1}{\sigma}\frac{d\sigma_{kq}}{d\omega_t}C_{kq}(\theta_r, \phi_r)^*$$

where ω_t is the coordinate of the unit vector $\mathbf{k}'$ along the direction of the product relative velocity, ω_r is the coordinate of the unit vector $\mathbf{j}'$ along the direction of the rotational angular momentum, and $\frac{1}{\sigma}\frac{d\sigma_{kq}}{d\omega_t}$ is a generalized PDDCS and $\frac{1}{\sigma}\frac{d\sigma_{kq}}{d\omega_t}$ yields

$$[10] \qquad \frac{1}{\sigma}\frac{d\sigma_{k0}}{d\omega_t} = 0 \qquad (k \text{ is odd})$$

$$[11] \qquad \frac{1}{\sigma}\frac{d\sigma_{kq+}}{d\omega_t} = \frac{1}{\sigma}\frac{d\sigma_{kq}}{d\omega_t} + \frac{1}{\sigma}\frac{d\sigma_{k-q}}{d\omega_t} = 0$$
$$(k \text{ is even and } q \text{ is odd or } k \text{ is odd and } q \text{ is even})$$

$$[12] \qquad \frac{1}{\sigma}\frac{d\sigma_{kq-}}{d\omega_t} = \frac{1}{\sigma}\frac{d\sigma_{kq}}{d\omega_t} - \frac{1}{\sigma}\frac{d\sigma_{k-q}}{d\omega_t} = 0$$
$$(k \text{ is even and } q \text{ is even or } k \text{ is odd and } q \text{ is odd})$$

The PDDCS may be written in a more compact form

$$[13] \qquad \frac{1}{\sigma}\frac{d\sigma_{kq\pm}}{d\omega_t} = \sum_{k_1}\frac{k_1}{4\pi}S^{k_1}_{kq\pm}C_{k_1q}(\theta_t, 0)$$

where the $S^{k_1}_{kq\pm}$ can be evaluated using the expected value expression

$$[14] \qquad S^{k_1}_{kq\pm} = \langle C_{k_1q}(\theta_t, 0)C_{kq}(\theta_r, 0)[(-1)^q e^{iq\phi_r} \pm e^{-iq\phi_r}]\rangle$$

where the angular brackets represent an average over all angles. With $q = 0$, the PDDCS can be represented as

$$[15] \qquad \frac{1}{\sigma}\frac{d\sigma_{k0}}{d\omega_t} = \frac{1}{4\pi}\sum_{k_1}[k_1]S^{k_1}_{k0}P_{k_1}(\cos\theta_t)$$

where $S^{k_1}_{k0}$ may be evaluated by the expected value expression

$$[16] \qquad S^{k_1}_{k0} = \langle P_{k_1}(\cos\theta_t)P_k(\cos\theta_r)\rangle$$

Many photon-initiated bimolecular reaction experiments are just sensitive to the polarization moments with $k = 0$ and $k = 2$. Therefore, we calculated the four PDDCSs: $(2\pi/\sigma)(d\sigma_{00}/d\omega_t)$, $(2\pi/\sigma)(d\sigma_{20}/d\omega_t)$, $(2\pi/\sigma)(d\sigma_{22}/d\omega_t)$, and $(2\pi/\sigma)(d\sigma_{21}/d\omega_t)$. In these calculations, the PDDCSs are expanded up to $k = 7$, which can show good convergence.

The distribution of the angular momentum $\mathbf{j}'$of the product molecule is described by a function $f(\theta_r)$, where θ_r is the angle between $\mathbf{j}'$ and $\mathbf{k}'$. $f(\theta_r)$ can be represented by the Legendre polynomial

$$[17] \qquad f(\theta_r) = \sum a_n P_n(\cos\theta_r)$$

with $n = 1$ indicating the product rotational alignment.

$$[18] \qquad \langle P_1(\mathbf{j}'\cdot\mathbf{k})\rangle = \langle\cos\theta_r\rangle$$

with $n = 2$ indicating the product rotational alignment.

$$[19] \qquad \langle P_2(\mathbf{j}'\cdot\mathbf{k})\rangle = \frac{1}{2}\langle 3\cos^2\theta_r - 1\rangle$$

Can. J. Chem. Downloaded from www.nrcresearchpress.com by Renmin University of China on 09/02/12
For personal use only.

PES

The PES used in this article was the Martìnez–Millán–González (MMG) surface.[5] The obtained analytical representation for the PES was employed by a many body expansion. The fitted values of the dissociation energy (D_e) for OH^+ and H_2 are 5.1268 and 4.7621 eV, respectively, which are in good agreement with the experimental results. It can be found that a barrier and two wells are observed with a decrease of the OHH angle. The height of the barrier becomes bigger and the energy of the wells decreases when the OHH angle decreases.

QCT calculations

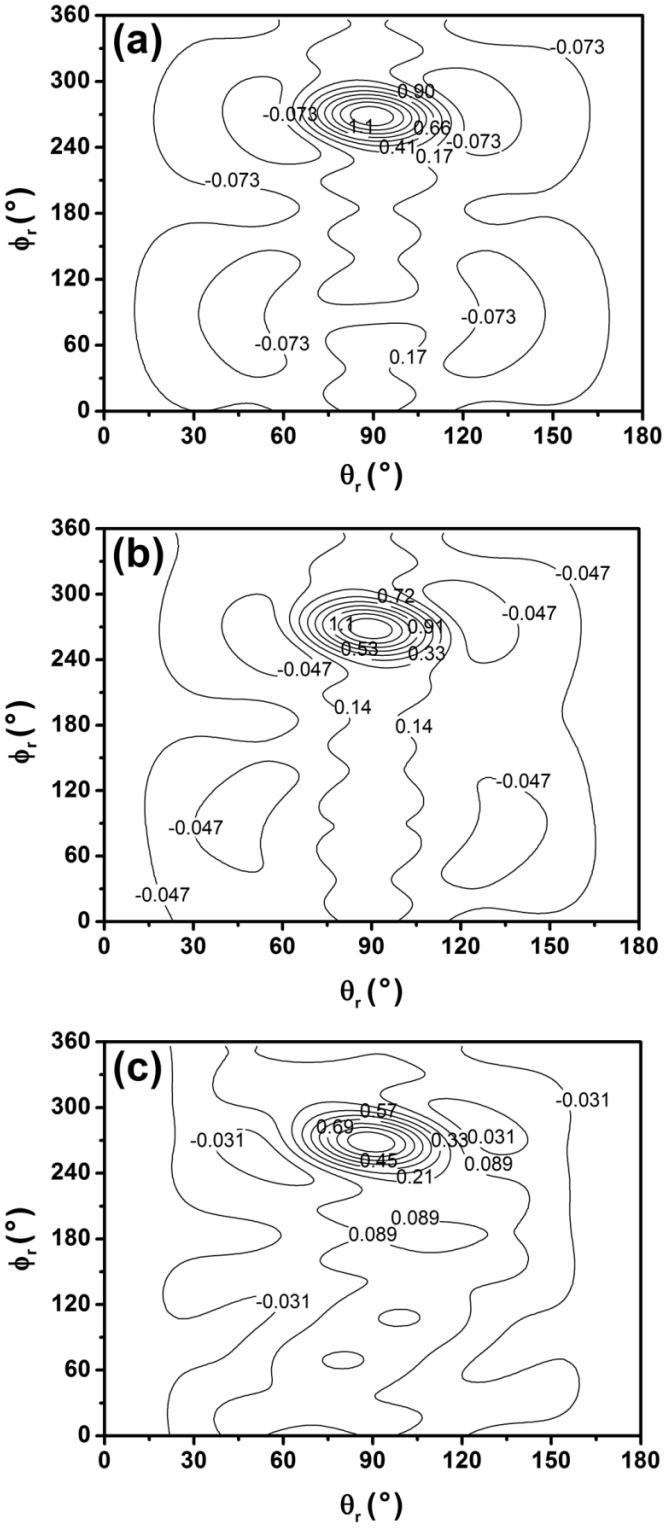
The QCT method was carried out to study the stereodynamics of the $O^+ + D_2 \rightarrow OD^+ + D$ reaction at a collision energy of 2.0 eV on the MMG surface.[5] The QCT calculation method we use here is the same as that found in refs. 17–20 and 25–27. The initial azimuthal orientation angle and polar angle of the reagent molecule internuclear axis are randomly sampled using the Monte Carlo method, and the ranges of the angles θ_r and ϕ_r are from 0° to 180° and from 0° to 360°, respectively. In the calculation, batches of 50 000 trajectories were run for each reaction and a 0.1 fs integration step size was chosen. All trajectories were started at an initial distance of 12.0 Å between the O^+ and the CM of the diatomic molecule. The impact parameter (b_{max}) for $j = 0$, 1, and 2 are 1.83, 1.85, and 1.88 Å, respectively.

Results and discussion

The $P(\theta_r)$ describing the $\mathbf{k}$–$\mathbf{j}'$ correlation is associated with the rotational quantum number and the calculated distributions of $P(\theta_r)$ for the $O^+ + D_2$ ($\upsilon = 0$, $j = 0$–2) reactivity are shown in Fig. 2, showing that the peak of $P(\theta_r)$ at $\theta_r = 90°$ is symmetric with respect to 90°, which means that $\mathbf{j}'$ is both strongly polarized and aligned along a direction perpendicular to $\mathbf{k}$. Clearly, Fig. 2 demonstrates that the peak of $P(\theta_r)$ becomes broader and lower as the rotational quantum number increases, which implies that the product rotational alignment effect becomes weaker with an increase of the rotational quantum number. From this discussion, it can be concluded that the rotational excitation of the reagent molecule D_2 has a great effect on the product rotational alignment. The CM frame alignment parameter $<P_2(\mathbf{j}'\cdot\mathbf{k})>$ is usually used to express the degree of product rotational polarization. The results presented in Table 1 agree well with the distribution of $P(\theta_r)$, namely, the smaller the expected value of $<P_2(\mathbf{j}'\cdot\mathbf{k})>$, the stronger the rotational alignment. It proves once again that the product rotational alignment is sensitive to the rotational quantum number.

A comparison of the $P(\theta_r)$ of the $O^+ + D_2 \rightarrow OD^+ + D$ reaction with $j = 0$, 1, and 2 is presented in Fig. 3, which clearly shows that the distributions of $P(\phi_r)$ tend to be asymmetric with respect to $\phi_r = 180°$, directly reflecting the strong polarization of the angular momentum for the three reactions. The $P(\phi_r)$ peaks appearing at both $\phi_r = 90°$ and 270° show that the rotational angular momentum vectors of the product of this reaction with $j = 0$, 1, and 2 are mainly aligned along the direction of y axis in the CM frame. Since the peak at $\phi_r = 90°$ is far lower than the one at $\phi_r = 270°$, we conclude that $\mathbf{j}'$ is not only aligned, but also oriented

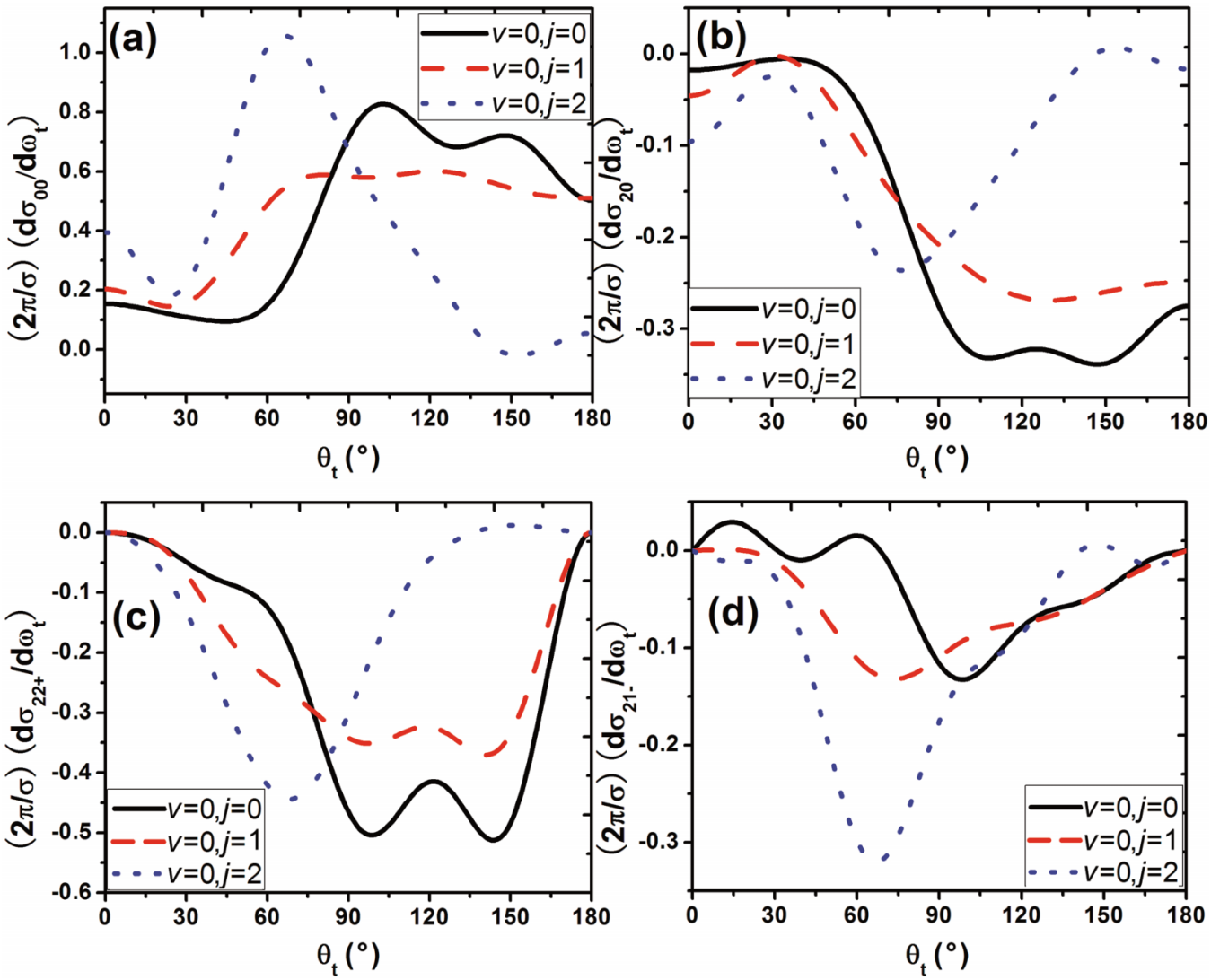
Fig. 4. Polar plots of the $P(\theta_r,\phi_r)$ distribution averaged over all scattering angles. Panels (*a*)–(*c*) describe the distributions with $j = 0$, 1, and 2, respectively.



along the opposite direction of the y axis. The results agree well with ref. 10, i.e., when the PES is repulsive for a heavy–light–light (HLL) system, $P(\phi_r)$ distributions usually show only one strong peak. It can also be found that the $P(\phi_r)$ peak for this reaction with $j = 0$ is the highest and the peak

Can. J. Chem. Downloaded from www.nrcresearchpress.com by Renmin University of China on 09/02/12
For personal use only.

Fig. 5. The polarization-dependent generalized differential cross sections for the reaction $O^+ + D_2$ ($v = 0$, $j = 0$–2). (*a*) $(2\pi/\sigma)(d\sigma_{00}/d\omega_t)$. (*b*) $(2\pi/\sigma)(d\sigma_{20}/d\omega_t)$. (*c*) $(2\pi/\sigma)(d\sigma_{22+}/d\omega_t)$. (*d*) $(2\pi/\sigma)(d\sigma_{21-}/d\omega_t)$.



with $j = 2$ is the lowest at $\phi_r = 270°$, and, to the contrary, the $P(\phi_r)$ peak for this reaction with $j = 0$ is the lowest and that with $j = 2$ is the highest at $\phi_r = 90°$, indicating that the distribution of $P(\phi_r)$ is very sensitive to j. The fact that the peaks $\phi_r = 270°$ of the three reactions are all strongly higher than those at $\phi_r = 90°$ implies that $\mathbf{j}'$ is preferentially oriented along the direction of the opposite direction of the y axis. Based on previous instantaneous collision theoretical studies[23,28] on the three-atom reaction, we have $\mathbf{j}' = \mathbf{L}\sin^2\beta + \mathbf{j}\cos^2\beta + \mathbf{J_1}m_B/m_{AB}$, where $\mathbf{L}$ is the reagent orbital angular momentum, m_B is the mass of atom B, m_{AB} is the total mass of atoms A and B, and $\mathbf{J_1} = \sqrt{\mu_{BC}R}(\mathbf{r}_{AB} \times \mathbf{r}_{CB})$, where $\mathbf{r}_{AB}$ and $\mathbf{r}_{CB}$ are unit vectors where B points to A and B points to C, respectively, μ_{BC} is the reduced mass of the BC molecule, and R is the repulsive energy. During the process of chemical bond formation and breakage for this reaction, the term $\mathbf{L}\sin^2\beta + \mathbf{j}\cos^2\beta$ in the equation is symmetric, whereas the left term of $\mathbf{j}'$ ($\mathbf{J_1}m_B/m_{AB}$) shows an appulsive direction as a result of the repulsive energy, which leads to the orientation of the product OD^+.

To get more valid stereodynamic information, the angular momentum polarizations in the form of polar plots are shown in Fig. 4. The three graphs show that the $P(\theta_r,\phi_r)$ distributions have a strong peak at (90°,270°) and a very weak peak at (90°,90°), which is in good agreement with the distributions of $P(\theta_r)$ and $P(\phi_r)$. The strong peak at (90°,270°) might result because the PES is a repulsive potential.

The PDDCS is used to describe the $\mathbf{k}$–$\mathbf{k}'$–$\mathbf{j}'$ correlation and the scattering direction of the product molecule. The calculated results for the $O^+ + D_2 \rightarrow OD^+ + D$ reaction with a chosen collision energy of 2.0 eV are presented in Fig. 5. The PDDCS $(2\pi/\sigma)(d\sigma_{00}/d\omega_t)$ is simply called the differential cross section (DCS), which is just used to describe the $\mathbf{k}$–$\mathbf{k}'$ correlation or the scattering direction of the product and is not related to the orientation and alignment of $\mathbf{j}'$. Clearly, Fig. 5*a* shows that the rotational quantum number has a great effect on the distribution of the PDDCS $(2\pi/\sigma)(d\sigma_{00}/d\omega_t)$, which indicates the intensity of the product molecule becomes stronger with an increase of the rotational quantum number when θ_t is <90°. To the contrary, it becomes weaker with an increase of the rotational quantum number when θ_t is

Can. J. Chem. Downloaded from www.nrcresearchpress.com by Renmin University of China on 09/02/12
For personal use only.

>90°. Furthermore, the product is sideways and backward scattering for $j = 0$ and 1 and totally forward scattering for $j = 2$. As ref. 10 indicates for a HLL combination reaction, the product mainly shows sideways and backward scattering when the PES is a repulsive surface; however, for $j = 2$, the product is totally forward scattering, from which we can deduce that a bigger rotational quantum number has a greater effect than the PES. The PDDCS $(2\pi/\sigma)(d\sigma_{20}/d\omega_t)$ is the expected value of the second Legendre moment, which is plotted in Fig. 5*b*. The tendency of $(2\pi/\sigma)(d\sigma_{20}/d\omega_t)$ is obviously opposite to that of $(2\pi/\sigma)(d\sigma_{00}/d\omega_t)$, indicating that $\mathbf{j}'$ is strongly aligned perpendicular to $\mathbf{k}$. In addition, the rotational quantum number has a strong influence on the angular distribution of PDDCSs with $q \neq 0$. In Fig. 5*c* the value of $(2\pi/\sigma)(d\sigma_{22+}/d\omega_t)$ is negative for all scattering angles, implying that the product is strongly aligned along the y axis. All PDDCSs with $q \neq 0$ equal to zero at the extremities of forward and backward scattering, which is determined by the fact that the average value of $\langle C_{k_1q}(\theta_t, 0)\rangle$ is 0 in eq. [14]. The strongest polarizations of the product of the three rotational quantum numbers ($j = 0$, 1, and 2) are at around 142°, 140°, and 70°, respectively. The distribution of $(2\pi/\sigma)(d\sigma_{21-}/d\omega_t)$ is shown in Fig. 5*d*. The polarization tendency is almost consistent with that of $(2\pi/\sigma)(d\sigma_{22+}/d\omega_t)$ with a small discrepancy. The strongest polarizations of the products of $j = 0$, 1, and 2 are at about 100°, 70°, and 65°, respectively.

Conclusions

In this paper we investigated the vector correlations for the chemical reaction $O^+ + D_2$ ($\upsilon = 0$, $j = 0$–2) using a QCT method on a MMG PES. The results demonstrate that the rotational polarization of the product shows diverse characteristics for different rotational quantum numbers. The $P(\theta_r)$ peak describing the $\mathbf{k}$–$\mathbf{j}'$ correlation becomes lower at 90° as the rotational quantum number increases, which indicates that the product rotational alignment effect becomes weaker with an increase of the rotational quantum number, and that the rotational excitation of the reagent molecule D_2 has a great effect on the product rotational alignment. The product rotational angular momentum vectors $\mathbf{j}'$ are not only aligned, but also preferentially oriented along the opposite direction of the y axis. The degree of orientation becomes lower with an increase of the rotational quantum number. In addition, at the same collision energy, the PDDCSs present distinct characteristics for different rotational quantum numbers, implying that the product rotational polarization is very sensitive to the rotational excitation of the reagent molecule.

Acknowledgement

This research was supported by the National Natural Science Foundation of China (grant Nos. 10504017 and 10874104) and the Key Project of the Chinese Ministry of Education (grant No. 206093). Special thanks to Professor K.L. Han for providing the QCT code for the stereodynamics.

References

(1) Martínez, R.; Lucas, J. M.; Giménez, X.; Aguilar, A.; González, M. *J. Chem. Phys.* **2006**, *124* (14), 144301. doi:10.1063/1.2179429.
(2) González, M.; Aguilar, A.; Gilibert, M. *Chem. Phys.* **1989**, *131* (2–3), 347. doi:10.1016/0301-0104(89)80181-8.
(3) Martínez, R.; Sierra, J. D.; Gray, S. K.; González, M. *J. Phys. Chem.* **2006**, *125* (16), 164305. doi:10.1063/1.2359727.
(4) Martínez, R.; Sierra, J. D.; González, M. *J. Chem. Phys.* **2005**, *123* (17), 174312. doi:10.1063/1.2098667.
(5) Martínez, R.; Millán, J.; González, M. *J. Chem. Phys.* **2004**, *120* (10), 4705. doi:10.1063/1.1638735.
(6) Burley, J. D.; Ervin, K. M.; Armentrout, P. B. *Int. J. Mass Spectrom. Ion Process.* **1987**, *80* (1–2), 153. doi:10.1016/0168-1176(87)87027-1.
(7) Sun, H. Z.; Liu, X. G.; Lv, J. J.; Liu, H. R. *J. Chem. Phys.* **2010**, *23* (5), 521. doi:10.1088/1674-0068/23/05/521-526.
(8) Aoiz, F. J.; Brouard, M.; Enriquez, P. A. *J. Chem. Phys.* **1996**, *105* (12), 4964. doi:10.1063/1.472346.
(9) Wang, M. L.; Han, K. L.; Zhan, J. P.; Wu, V. W. K.; He, G. Z.; Lou, N. Q. *Chem. Phys. Lett.* **1997**, *278* (4–6), 307. doi:10.1016/S0009-2614(97)01063-4.
(10) Wang, M. L.; Han, K. L.; He, G. Z. *J. Chem. Phys.* **1998**, *109* (13), 5446. doi:10.1063/1.476522.
(11) Prisant, M. G.; Rettner, C. T.; Zare, R. N. *J. Chem. Phys.* **1981**, *75* (5), 2222. doi:10.1063/1.442335.
(12) Lin, K.-C.; González-Ureña, A. *Int. Rev. Phys. Chem.* **2007**, *26* (2), 289. doi:10.1080/01442350701211180.
(13) Xu, W.-W.; Liu, X.-G.; Luan, S.-X.; Sun, S.-S.; Zhang, Q.-G. *Chem. Phys.* **2009**, *355* (1), 21. doi:10.1016/j.chemphys.2008.07.015.
(14) Xu, W. W.; Liu, X. G.; Luan, S. X.; Sun, S. S.; Zhang, Q. G. *Chin. Phys. B.* **2009**, *18* (1), 339. doi:10.1088/1674-1056/18/1/055.
(15) Xu, W. W.; Liu, X. G.; Zhang, Q. G. *Mol. Phys.* **2008**, *106* (14), 1787. doi:10.1080/00268970802290321.
(16) Wang, M. L.; Han, K. L.; Cong, S. L.; He, G. Z.; Lou, N. Q. *Chem. Phys.* **1998**, *238* (3), 481. doi:10.1016/S0301-0104(98)00326-7.
(17) Han, K. L.; He, G. Z.; Lou, N. Q. *J. Chem. Phys.* **1996**, *105* (19), 8699. doi:10.1063/1.472651.
(18) Aoiz, F. J.; Brouard, M.; Enriquez, P. A. *J. Chem. Phys.* **1996**, *105* (12), 4964. doi:10.1063/1.472346.
(19) Chen, M. D.; Han, K. L.; Lou, N. Q. *Chem. Phys. Lett.* **2002**, *357* (5–6), 483. doi:10.1016/S0009-2614(02)00585-7.
(20) Chen, M. D.; Han, K. L.; Lou, N. Q. *J. Chem. Phys.* **2003**, *118* (10), 4463. doi:10.1063/1.1545112.
(21) Ma, J. J.; Chen, M. D.; Cong, S. L.; Han, K. L. *Chem. Phys.* **2006**, *327* (2–3), 529. doi:10.1016/j.chemphys.2006.06.010.
(22) Li, W. L.; Wang, M. S.; Yang, C. L.; Liu, W. W.; Sun, C.; Ren, T. Q. *Chem. Phys.* **2007**, *337* (1–3), 93. doi:10.1016/j.chemphys.2007.06.041.
(23) Li, R. J.; Han, K. L.; Li, F. E.; Lu, R. C.; He, G. Z.; Lou, N. Q. *Chem. Phys. Lett.* **1994**, *220* (3–5), 281. doi:10.1016/0009-2614(94)00174-X.
(24) Aoiz, F. J.; Martinez, M. T.; Saez Rabanos, V. *J. Chem. Phys.* **2001**, *114* (20), 8880. doi:10.1063/1.1350916.
(25) Zhang, X.; Han, K. L. *Int. J. Quantum Chem.* **2006**, *106* (8), 1815. doi:10.1002/qua.20929.
(26) Zhang, W. Q.; Cong, S. L.; Zhang, C. H.; Xu, X. S.; Chen, M. D. *J. Phys. Chem. A* **2009**, *113* (16), 4192. doi:10.1021/jp8105716.
(27) Zhang, W. Q.; Li, Y. Z.; Xu, X. S.; Chen, M. D. *Chem. Phys.* **2010**, *367* (2–3), 115. doi:10.1016/j.chemphys.2009.11.006.
(28) Orr-Ewing, A. J.; Zare, R. N. *Annu. Rev. Phys. Chem.* **1994**, *45* (1), 315. doi:10.1146/annurev.pc.45.100194.001531.

Silicon and silicon oxide surface modification using thiamine-catalyzed benzoin condensations

Kelly A. Hoop, David C. Kennedy, Trevor Mishki, Gregory P. Lopinski, and John Paul Pezacki

Can. J. Chem. Downloaded from www.nrcresearchpress.com by Renmin University of China on 09/02/12
For personal use only.

Abstract: The benzoin condensation that involves the umpolung coupling of two aldehyde groups has been applied to the formation of functionalized silicon and silicon oxide surfaces using thiamine and other N-heterocyclic carbene (NHC) catalysis in water. This bioorthogonal conjugation of an aldehyde to a modified silicon or silicon oxide surface has been monitored and characterized using X-ray photoelectron spectroscopy and IR spectroscopy. NHC catalysis was found to be efficient in water mediating full conversion of the aldehyde functionalized silicon oxide surfaces at the interface.

Key words: "click" chemistry, benzoin condensation, silicon, surface functionalization.

Résumé : Dans le but de préparer des surfaces de silicium et d'oxydes de silicium fonctionnalisées, on a fait appel à une réaction de condensation de type benzoïne impliquant un couplage avec inversion de polarité de deux groupes aldéhydes, effectuée en solution aqueuse en présence de thiamine et d'autres carbènes N-hétérocycliques (CNH) utilisés comme catalyseurs. On a contrôlé la conjugaison bioorthogonale d'un aldéhyde à une surface de silicium ou d'oxyde de silicium modifiée et on l'a caractérisée en faisant appel à la spectroscopie photoélectronique des rayons-X et à la spectroscopie infrarouge. On a observé que la catalyse par des carbènes N-hétérocycliques est efficace dans l'eau pour conduire à une conversion complète des surfaces d'oxyde de silicium fonctionnalisées par un aldéhyde à l'interface.

Mots-clés : « chimie à clic », condensation de type benzoïne, silicium, fonctionnalisation d'une surface.

[Traduit par la Rédaction]

The development of organic reactions on silicon and silicon oxide surfaces is a highly active area of research because of the potential impact of the resulting new materials on applications in molecular electronics, biosensor development, and microarray technologies.[1] Considerable effort has been invested into building functional substrates onto silicon oxide surfaces at the nanoscale, leading to the development of several silicon oxide-bound systems for use on both particles and chips.[1,2] The most common techniques for the formation of monolayers on hydrogen-terminated silicon include: UV irradiation of alcohols and aldehydes, radical reactions of olefins using a radical initiator, or reactions with acylchlorides, which can then be further functionalized.[3] Silanes have been used for many years as a means to attach organic molecules to silicon oxide or glass and remain an important reagent in the fabrication of modified surfaces.[2] Currently, the techniques available to functionalize surfaces with biomolecules such as proteins are limited. Thus, there is a need to develop reactions that work well under aqueous conditions and that can be adapted to silicon surfaces.

Current strategies include physical, bioaffinity, and covalent immobilization.[4] Covalent immobilization, where a biomolecule such as a protein is directly attached to the surface via a newly formed covalent bond, offers advantages over other immobilization strategies. In particular, it allows for specific orientation of molecules at the surface and thus the generation of a homogenous surface. Also, unlike bioaffinity immobilization, the coupling partners employed in covalent immobilization can be relatively small, thus minimizing the chance that they will affect the structure and activity of the molecule being attached to the surface.

Covalent immobilization approaches for biomolecule attachment to silicon surfaces typically make use of highly specific bioorthogonal chemical reactions where functional groups not found in biology are used to specifically label and immobilize biomolecules.[4] While this approach offers many advantages, there exists only a handful of reactions that can be employed in a bioorthogonal manner.[4] The benzoin condensation, originally published in 1832 by Wöhler and Liebig,[5] represents a possible alternative for covalent coupling reactions onto silicon surfaces. The benzoin condensation involves the coupling of two aromatic aldehydes to form an α-hydroxy ketone via activation by cyanide.[5] The mechanism for this transformation was later elucidated by

Received 8 August 2011. Accepted 14 October 2011. Published at www.nrcresearchpress.com/cjc on 6 February 2012.

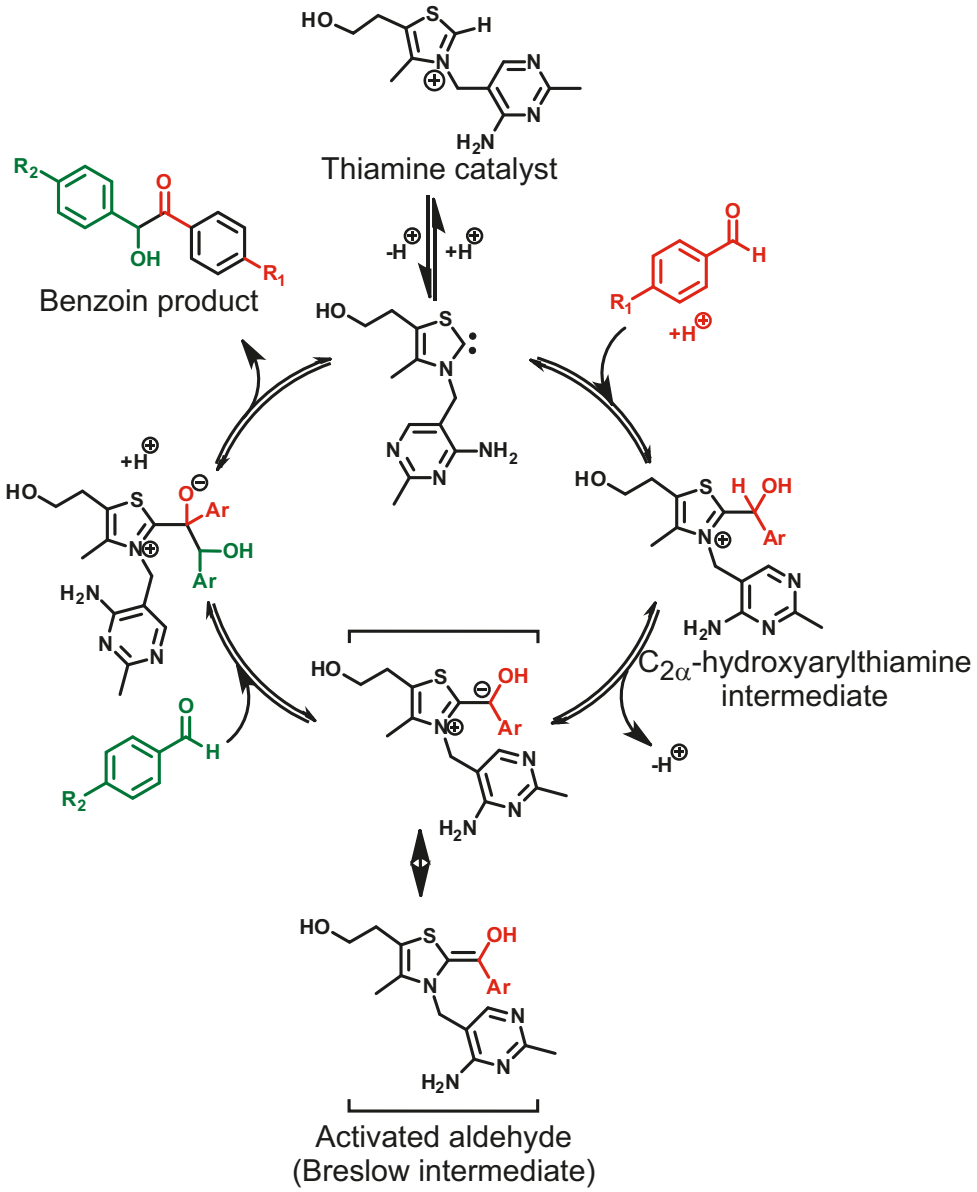
K.A. Hoop and J.P. Pezacki. Steacie Institute for Molecular Sciences, National Research Council of Canada, 100 Sussex Drive, Ottawa, ON K1A 0R6, Canada; Chemistry Department, University of Ottawa, 10 Marie-Curie, Ottawa, ON K1N 6N5, Canada.
D.C. Kennedy, T. Mishki, and G.P. Lopinski. Steacie Institute for Molecular Sciences, National Research Council of Canada, 100 Sussex Drive, Ottawa, ON K1A 0R6, Canada.

Corresponding author: John Paul Pezacki (e-mail: John.Pezacki@nrc-cnrc.gc.ca).

This paper is dedicated to Professor Ronald Kluger on the occasion of his 65th birthday.

Can. J. Chem. Downloaded from www.nrcresearchpress.com by Renmin University of China on 09/02/12
For personal use only.

Fig. 1. Catalytic cycle for thiamine-catalyzed benzoin condensation.



Lapworth in 1903.[6] Thiamine (vitamin B_1) is a naturally occurring water soluble compound that is also an effective catalyst for the benzoin reaction and was studied extensively by Breslow.[7] A reaction mechanism for the benzoin condensation catalyzed by thiamine is shown in Fig. 1. N-Heterocyclic carbenes (NHC) can also catalyze the benzoin reaction.[8–10]

Current research into benzoin-type reactions has shown that many NHCs similar to thiamine can also catalyze the reaction in polar protic solvents.[8,11,12] Moreover, recent advances have helped to make these transformations both asymmetric and also chemoselective for cross-coupled products.[9,10,13–17] Thiamine itself was also used to efficiently cross-couple different aldehydes as an enzyme complex with enzymes benzaldehyde lyase (BAL) and benzoylformate decarboxylase (BFD).[18] These findings suggest that the benzoin condensation may be a good candidate for further development as a reaction for covalent immobilization onto surfaces, since the catalysts are nontoxic, biocompatible, and aromatic aldehydes are functional groups not frequently found in commonly used model biological systems and offer an alternative to other click reactions.[19–37] A key nontrivial challenge is to determine the conditions under which the cross-coupling products are favoured in aqueous solution. We were interested in exploring conditions specifically for conjugating molecules to surfaces that have potential for future applications in biosensor and microarray functionalization. Herein, we describe the development of methodology using thiamine and NHC-catalyzed cross-coupling of aromatic aldehydes onto both hydrogen-terminated silicon and silicon oxide surfaces.

Results

Thiamine-catalyzed benzoin condensations were conducted on silicon oxide surfaces to determine the reactivity at the solid–liquid interface. Para-substituted benzaldehydes were used to test the electronic properties of the aldehydes for

Can. J. Chem. Downloaded from www.nrcresearchpress.com by Renmin University of China on 09/02/12
For personal use only.

rapid functionalization of the silicon surfaces. Benzaldehyde, 4-nitrobenzaldehyde, and 4-methoxybenzaldehyde were used in thiamine-catalyzed benzoin condensations on silicon oxide surfaces according to the sequence in Fig. 2 and are described in detail in the Experimental section. The optimal coupling involved reactions with 4-methoxybenzaldehyde by FTIR. No reactions were observed in the absense of catalyst or of 4-methoxybenzaldehyde.

FTIR analysis of samples

Thiamine was used to couple 4-methoxybenzaldehyde to the model surfaces of silicon oxide attenuated total reflection (ATR) chips to facilitate the measurement of changes in IR vibrational fequencies during the chemical reactions by FTIR. An ATR chip was prepared to afford the aldehyde surfaces shown in Fig. 2. Peaks in the FTIR spectrum (Fig. 3) of this surface agreed with the proposed bonding pattern with the peak at 1645 cm^{-1} corresponding to the imine C=N stretching mode,[38–40] the small peak observed at 1606 cm^{-1} associated with a vibrational mode of the phenyl ring, and the peak at 1703 cm^{-1} corresponding to the C=O stretching of the substituted benzaldheyde.[40] The ATR chip was then subjected to the benzoin condensation using the optimized reaction conditions with thiamine and 4-methoxybenzaldehyde and the reaction progress was monitored by FTIR (Fig. 3). After 4 h, the aldehyde peak at 1703 cm^{-1} was considerably reduced and, after 24 h, the aldehyde peak was no longer visible, whereas the peak at 1606 cm^{-1} had grown considerably, which is to be expected for the additional phenyl ring in the benzoin product. The carbonyl stretching vibration for the benzoin product[38,39] was masked by the imine peak of the linker. Control experiments were carried out where an imine-linker aldehyde surface ATR chip was immersed in benzoin reaction conditions including 4-methoxybenzaldehyde and TEA in water, but without the thiamine catalyst and separately without aldehyde. After 4 h under these conditions, the IR spectrum was unchanged, indicating that the changes in the IR spectra in Fig. 3 are the result of the benzoin condensation. The native oxide surface was exposed to the same reaction conditions to rule out nonspecific absorption. Again no new peaks were observed in the FTIR spectrum.

To test whether a bulkier group would be tolerated at the para position, a tether bearing electron-rich benzaldehyde 4-[2-(2-hydroxyethoxy)ethylamino]benzaldehyde was synthesized to mimic the electronics of the 4-methoxybenzaldehyde and to be a potential tether in future experiments. Thiamine was then used to catalyze the coupling of 4-[2-(2-hydroxyethoxy)ethylamino]benzaldehyde to the aldehyde-terminated ATR chip surface prepared according to Fig. 2. The reaction proceeded at a similar rate to that with 4-methoxybenzaldehyde. Again, the aldehyde carbonyl peak at 1703 cm^{-1} was greatly reduced after 4 h and no longer visible after 24 h (Fig. 4). A peak at 1605 cm^{-1} corresponding to the phenyl group was also present, as observed previously.

4-Fluorobenzaldehyde was also coupled to an aldehyde-terminated surface of an ATR chip using thiamine as a catalyst to test whether an electron-deficient aldehyde would affect the rate of the reaction. The reaction proceeded more slowly (Fig. 5), which was surprising given that it is more electrophilic. The reaction took approximately 6 times longer to reach completion. After 24 h the aldehyde carbonyl peak was no longer visible, and the remaining spectral features were consistent with those observed for the analogous reaction with 4-methoxybenzaldehyde.

A total of 11 NHCs,[3,7,41–46] all of which were already known catalysts of benzoin-type reactions in organic media, were tested in solution-based experiments towards the coupling of 4-methoxybenzaldehyde to the model surface. Of those tested, 1,3-bis(2,4,6-trimethylphenyl)imidazolium chloride (Fig. 6) was found to be the most efficient and was tested with the aldehyde surface in Fig. 2. Reaction conditions were adjusted to use only 1 equiv of base to fully deprotonate this NHC as opposed to the 2 equiv required with thiamine hydrochloride. After 4 h, the FTIR spectrum showed the reaction to be complete, since the aldehyde carbonyl peak at 1703 cm^{-1} was no longer visible and the phenyl peak at 1606 cm^{-1} had increased in intensity, corresponding to the increase of the second phenyl ring. The 1,3-bis(2,4,6-trimethylphenyl)imidazolium chloride catalyst appeared to be a better catalyst than thiamine for the cross-coupling of aldehydes at the solid–liquid interface.

X-ray photoelectron spectroscopy characterization of thiamine-catalyzed coupling reactions

The condensation of 4-fluorobenzaldehyde onto the surface was also monitored by using X-ray photoelectron spectroscopy (XPS). After 24 h under thiamine-catalyzed reaction conditions with 4-fluorobenzaldehyde, XPS scans of the imine-linker aldehyde surface (Fig. 5) showed the appearance of an F 1s signal at ~688 eV that is absent in scans of the surface prior to the reaction. A control experiment, where the surface was exposed to reaction conditions without thiamine, was carried out and detected fluorine at near background levels. To determine the amount of benzoin product formed on the surface, the N/F ratio of the final surface was determined. To calculate this ratio, sensitivity factors relative to carbon for both nitrogen (1.68) and fluorine (4) had to be considered.[47] The ratios were obtained by multiplying the observed intensity ratio from high-resolution scans by the inverse ratio of the sensitivity factors. The N/F ratio was found to be 4.7 for the benzoin-coated wafer (where the theoretical ratio should be 1) and 10.0 for the control wafer. The high N/F ratio indicates that not all of the terminal aldehydes reacted to form a benzoin product.

To enhance the fluorine reporter signal, 4-(trifluoromethyl) benzaldehyde was used in place of 4-fluorobenzaldehyde. In the survey scan of the reacted surface (Fig. 7), the F 1s signal at 688 eV was much larger than previously observed with 4-fluorobenzaldehyde. A high-resolution scan of the F 1s region showed that the reacted surface had a fourfold increase of fluorine emission over the control. The N/F ratio for the final functionalized surface was calculated to be 1.4 (the theoretical ratio should be 0.33) compared with 2.5 for the control wafer. Additionally, a high-resolution scan of the C 1s region showed an additional signal at 294 binding eV, which can be associated to a CF_3 carbon. An F/C_{CF_3} ratio of 3 was calculated (using sensitivity factors of 4 and 1 for F and C, respectively) which agrees with the theoretical value. Using the entire C 1s region between 282 and 295 binding eV, the calculated C/F ratio was 11.5 compared with a theoretical ratio of 6.3 for the benzoin product.

Can. J. Chem. Downloaded from www.nrcresearchpress.com by Renmin University of China on 09/02/12
For personal use only.

Fig. 2. Schematic of the reaction sequence for functionalizing silicon oxide surfaces using the thiamine-catalyzed benzoin condensation. The surfaces were first treated with 3-aminopropyltriethoxysilane (APTES) (step a), followed by reaction with 1 mmol/L aqueous terephthalaldehyde (step b), and benzoin condensation reactions were performed in an aqueous solution with substituted benzaldehydes, 1 equiv thiamine, and 2 equiv TEA with para-substituted aldehydes (substituents represented by X) as shown in step c.

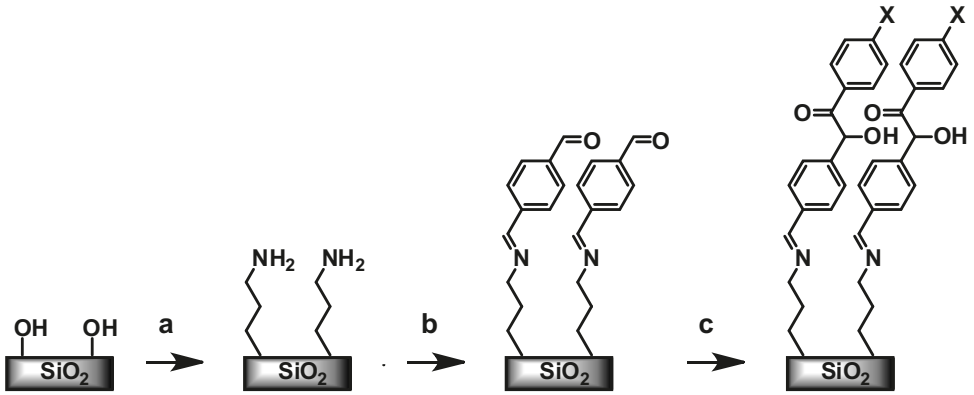


Fig. 3. FTIR characterization of thiamine-catalyzed coupling of 4-methoxybenzaldehyde to a model surface. Reaction progression at 0 h (bottom trace), 4 h (middle trace), and 24 h (top trace) of the conjugation reaction using thiamine as catalyst.

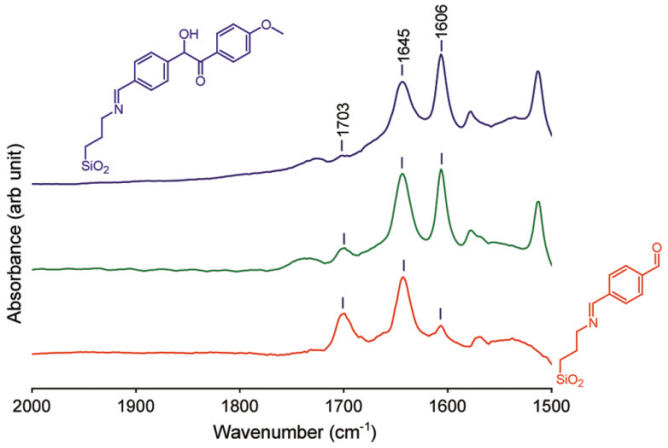
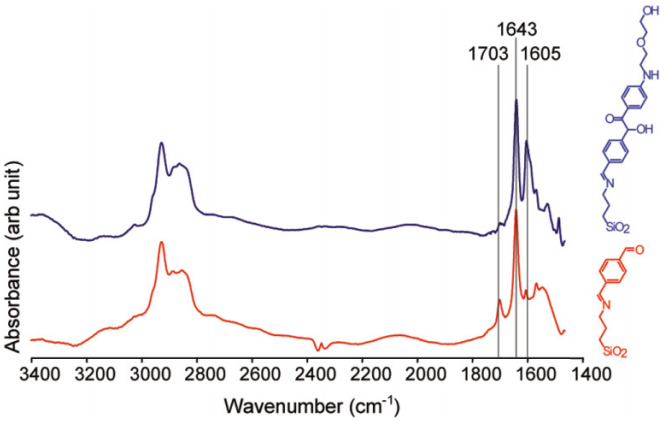


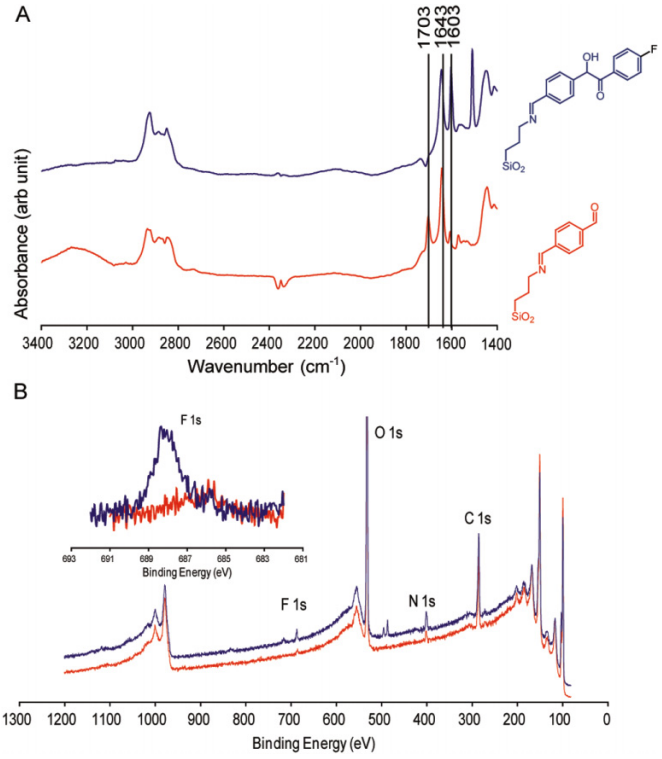
Fig. 4. FTIR characterization of thiamine-catalyzed coupling of 4-[2-(2-hydroxyethoxy)ethylamino]benzaldehyde to a model surface. Reaction progression at 4 h is shown.



Si(111) functionalization

Other surfaces were also tested to see whether the benzoin condensation reaction would be suitable for use in other applications where the use of glass or SiO_2 was not appropriate. A hydrogen-terminated (H-terminated) Si(111) ATR chip was prepared to provide the ether-linked aldehyde surface as in Fig. 8. Terephthaldialdehyde was directly attached to the H-terminated surface to yield the directly attached aldehyde to the Si(111) surface. The initial aldehyde-terminated surface provided a clean IR spectrum, with a peak at 1707 cm^{-1} corresponding to the C=O stretching of the benzaldehyde and a peak at 1612 cm^{-1} assigned to the phenyl. The directly attached

Fig. 5. Characterization of thiamine-catalyzed coupling of 4-fluorobenzaldehyde to a model oxide surface. (A) FTIR characterization at 0 h (bottom trace) and at 24 h (top trace). (B) X-ray photoelectron spectroscopy (XPS) survey scan(bottom trace: control, no catalyst; top trace: reaction after 24 h). The insert shows the XPS high resolution of the F 1s region (bottom trace: no catalyst; top trace: reaction after 24 h).



Can. J. Chem. Downloaded from www.nrcresearchpress.com by Renmin University of China on 09/02/12
For personal use only.

Fig. 6. Molecular structures 1,3-bis(2,4,6-trimethylphenyl)imidazolium chloride.

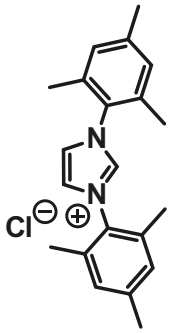
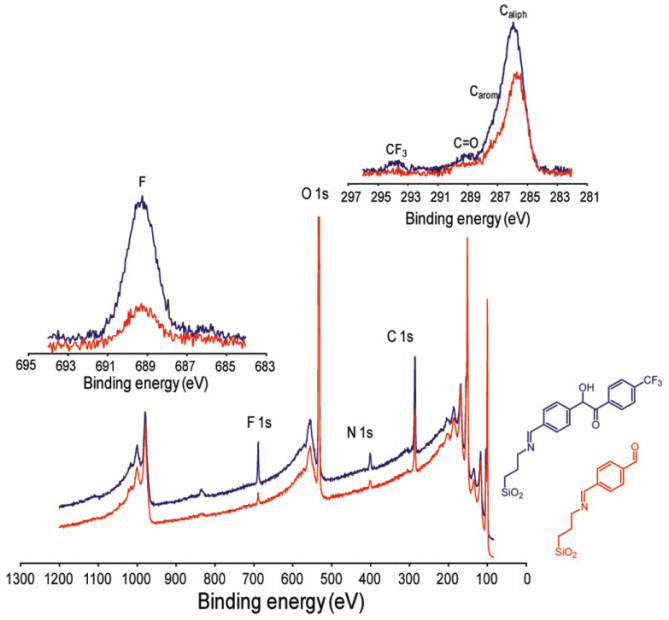


Fig. 7. X-ray photoelectron spectroscopy (XPS) characterization of thiamine-catalyzed coupling of 4-(trifluoromethyl)benzaldehyde to a model surface (bottom trace: control, no catalyst; top trace: reaction after 24 h). The spectrum from 1200 to 0 eV is shown. The upper left insert shows the F 1s region. The upper right insert shows the C 1s region.

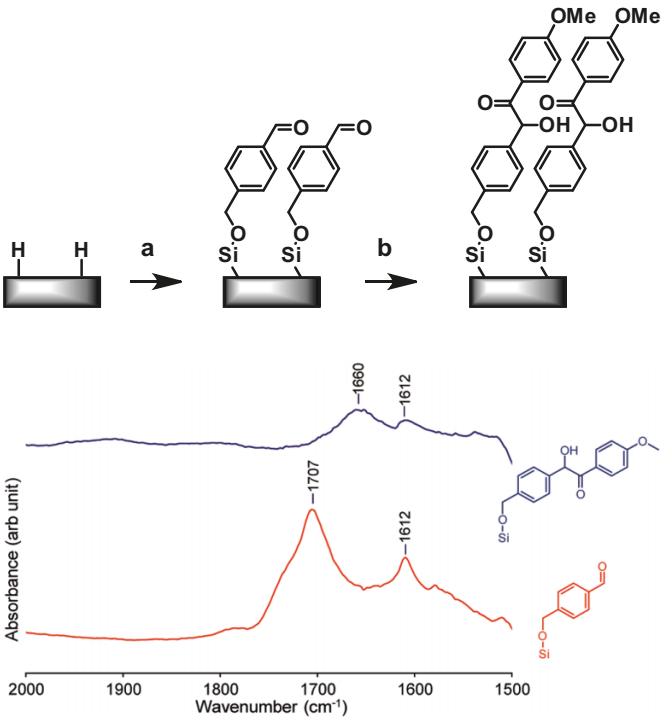


aldehyde surface was submitted to the same reaction conditions that were used to couple 4-methoxybenzaldehyde to silicon oxide surfaces using thiamine catalysis and monitored by FTIR (Fig. 8). After 4 h, the aldehyde carbonyl peak at 1707 cm^{-1} was significantly reduced and a new peak at 1655 cm^{-1} appeared, which was assigned to the C=O stretching of the benzoin carbonyl group. After 24 h, the aldehyde peak was no longer visible and only peaks assigned to the benzoin product remained.

Discussion

The thiamine-catalyzed benzoin condensation reaction was used to attach model aldehydes to surfaces. The reactions were generally observed to be faster and more chemoselective than those in solution. We hypothesize that the solid–liquid interface concentrates the organic reactants and acts similar to phase-transfer catalysis.[48–50] SiO_2 was chosen as the base substrate, since it is a common substrate in microarrays and has been extensively studied in such applications. Also, aldehyde coupling reactions provide new methods for bioconjugation given that a number of new methods exist for incorporating unnatural aldehyde groups into peptides and proteins.[51–54] Another advantage for performing methodology development on SiO_2 is that the surface also lends itself well to many spectroscopic techniques, including FTIR and XPS that were used extensively to characterize our modified surfaces.

Fig. 8. FTIR characterization of thiamine-catalyzed coupling of 4-methoxybenzaldehyde to hydrogen-terminated Si(111) surfaces. Directly attached aldehyde surface and reaction progression at 0 h (bottom trace) and 24 h (top trace).



Interestingly, we observed reactivity patterns that were different from those observed for NHC-catalyzed aldehyde cross-coupling reactions in solution. Usually electron-withdrawing substituents are favored for cross-coupling of benzaldehyde derivatives.[9,10,13–17] However, there are examples of analogous thiamine catalyzing cross-coupling reactions in water with methoxy-substituted benzaldehydes, where the thiamine catalyst is bound as a co-factor to an enzyme.[18] Interesting donor–acceptor relationships were established under these reaction conditions.[18] Others have postulated that differences between thiamine-dependent enzymatic catalysis and enzyme-free thiamine catalysis in solution may be due to desolvation and orientation of the thiamine co-factor on the enzyme.[55] A similar phenomenon may be happening for the catalysis on silicon surfaces where aromatic aldehydes are oriented with respect to the plane of the surface and where solvent behaviour is quite different from bulk solution.

(3-Aminopropyl)triethoxysilane (APTES) was chosen as the attachment molecule as it is a commonly used aminosilane for such purposes.[56,57] Although it is commonly used, it also has a complex reactivity profile because of its three reactive ethoxy groups. It can undergo the desired reaction of

Can. J. Chem. Downloaded from www.nrcresearchpress.com by Renmin University of China on 09/02/12
For personal use only.

covalent attachment with the surface through one, two, or three of the ethoxy groups; however, either vertical or horizontal polymerization are also possibilities with this substrate.[58] The latter, horizontal polymerization, can still be useful in surface functionalization, since it is possible that there is one ethoxy group still present and able to react with the SiO_2 even once it is polymerized and anchor the preassembled layer to the surface. APTES can also form hydrogen bonds to orient itself in several different arrangements on the surface.[58] This complex reactivity results in a nonhomogeneous surface and monolayers of APTES on SiO_2 that are difficult to consistently reproduce.

It has been previously shown that APTES quickly reacts with the surface at ambient temperature and pressure, without the need for any additional reagents or solvents.[59] An advantage to using ambient temperature and pressure vapour deposition is that we did not have to worry about excess water in the solvent causing uncontrollable polymerization of APTES. Reaction of the surface with APTES resulted in an amine-terminated surface. The terminal aromatic aldehyde was then installed by reacting the surface with an aqueous solution of terephthaldialdehyde as previously reported.[40] This provided an efficient means of reaching the terminal aldehyde without excess reagents, and the peak for the aldehyde (at ~1703 cm^{-1}) was clearly visible in the resulting IR spectrum of the surface.

The reaction progress between the aldehyde surface described in Fig. 3 and 4-methoxybenzaldehyde was followed by monitoring of the intensity of peaks of important functional groups in the FTIR spectrum. The shrinking of the aldehyde carbonyl peak at 1703 cm^{-1} was used to report on the consumption of the initial aldehyde-functionalized surface. The peak at 1606 cm^{-1} (a ring vibrational mode) was present in the initial aldehyde, but its intensity increased considerably upon formation of the benzoin product with the addition of a second phenyl ring on the surface. The peak at 1643 cm^{-1} (C=N stretching mode of the imine) remained unchanged after the benzoin reaction, evidence that the imine-linker was still intact. This suggests that the benzoin product was indeed being formed on the surface and giving rise to the observed changes in the IR spectrum.

It is interesting to note that, whereas the carbonyl peak for the benzoin products was not visible for the silicon oxide surfaces, the 4-methoxybenzoin surface derived from Si(111) did include a peak at ~1660 cm^{-1} that was assigned to the benzoin carbonyl peak. This suggests that the carbonyl peak of the benzoins on the model silicon oxide surfaces was in fact masked by the imine signal at 1643 cm^{-1}.

When 4-[2-(2-hydroxyethoxy)ethylamino]benzaldehyde was used, the reaction proceeded on the same time scale as the initial experiment; however, when 1,3-bis(2,4,6-trimethylphenyl)imidazolium chloride was used in place of thiamine, the 1703 cm^{-1} peak was no longer detectable after only 4 h (compared with 24 h with thiamine). This may be due to the increased stability and reactivity of the carbene formed after the deprotonation of the C_2 hydrogen. The presence of a phenyl ring on both heteroatoms as compared with only one with thiamine provide additional electron density to the C_2 site, stabilizing the resulting carbene.[12] The same system was also tested using an electron-poor aldehyde, 4-fluorobenzaldehyde. Fortuitously, we did see a reduction of the 1701 cm^{-1} peak and the emergence of a peak at 1603 cm^{-1}, which was assigned to the additional phenyl ring; however, this change in the spectrum was only apparent after 24 h. This observation does support our initial hypothesis that the electronics of the benzaldehydes play a role in determining the speed at which the reaction progresses. More evidence that the activated aldehyde species is forming with the electron-rich aldehyde is that when the imine-linked aldehyde-terminated surface is reacted with only catalyst and base, there is little change in the surface spectrum, where the 1703 cm^{-1} is only slightly decreased, but no additional peaks are observed.

The XPS data obtained from reactions involving aldehydes with fluorine substituents (4-fluorobenzaldehyde and 4-(trifluoromethyl)benzaldehyde) suggests that the main pathway for the incorporation of the fluoro signal at 688 eV is from the formation of the benzoin product on the surface. With reactions involving 4-fluorobenzaldehyde, the observed N/F ratio of 4.7 shows that under the reaction conditions, approximately one in five amines carried a benzoin product. The presence of a small F peak in the control can be attributed to either cross contamination or to 4-fluorobenzaldehyde reacting with free amines from unreacted APTES. With 4-(trifluoromethyl)benzaldehyde, the observed N/F ratio of 1.4 corresponds to approximately one in four amines carrying a benzoin product, which was very similar to the results in the previous system. The additional signal at 294 eV corresponding to the carbon of the CF_3 group and the observed F/C_{CF_3} ratio of 3 confirms that the entire F signal is associated with the incorporation of 4-(trifluoromethyl)benzaldehyde onto the surface. When considering the entire carbon region, the observed C/F ratio of 11.5 was much higher than the theoretical ratio of 6.3 for the benzoin product and much higher than the ratio of 3.7 for imine formation between unreacted APTES at the surface and 4-(trifluoromethyl)benzaldehyde. Since unreacted terminal aldehyde will increase the carbon content, this could indicate that only about 50% of the terminal aldehydes undergo benzoin condensation. The higher C/F ratio also indicated that the direct coupling of unreacted APTES at the surface and 4-(trifluoromethyl)benzaldehyde must be a negligible reaction pathway.

Conclusions

The benzoin condensation is an effective bioconjugation reaction to functionalize silicon and silicon oxide surfaces that proceeds using thiamine and NHC catalysts in water. Although we were able to demonstrate the condensation reactions using APTES-functionalized silicon oxide surfaces, more stable surfaces will be required to fully exploit this chemistry. Surfaces such as those generated by the reaction of terephthalaldehyde on H-terminated silicon surfaces, where the aromatic aldehyde is attached directly to the silicon surface through an Si–O–C bond, are stable and easily functionalized by the benzoin condensation. This method provides a new entry into the chemistry for functionalizing surfaces with biomolecules and has the potential to be exploited in the development of bioassays and in other applications.

Can. J. Chem. Downloaded from www.nrcresearchpress.com by Renmin University of China on 09/02/12
For personal use only.

Experimental

Materials and methods

Thiamine chloride hydrochloride, 1,3-bis(2,4,6-trimethylphenyl)imidazolium chloride, triethylamine, solvents, inorganic salts, and all benzaldehydes were used as received from Sigma-Aldrich unless otherwise stated in the text. Nuclear magnetic resonance spectra were recorded on a Bruker DRX-400 using a frequency of 400.13 MHz for ^{1}H and 100.61 MHz for ^{13}C and using a broadband direct detection probe. High-pressure liquid chromatography – mass spectrometry/mass spectrometry (HPLC–MS/MS) were carried out on a Waters system consisting of a Waters 996 photodiode array Ddetector, an Alliance HT – Waters 2795 separations module, and a Waters Micromass Z_{Q2000} unit equipped with a pneumatically assisted electrospray ionization source. Samples were run on a Waters Sunfire C18 (100 × 2.10 mm, 3.5 μm) column with a gradient of 10%–95% acetonitrile / 0.1% formic acid in H_2O / 0.1% formic acid over 15 min with a flow rate of 0.2 mL/min. MS data were collected in single-ion recording mode and processed using Masslynx. Attenuated total reflection Fourier transform IR (ATR-FTIR) spectra were recorded using a Nicolet MAGNA-IR 860 spectrometer at 4 cm^{-1} resolution. The ATR crystals were mounted in a purged sample chamber with the light focused normal to one of the 45° bevels. Background spectra were obtained using a blank surface (oxide surface or H-terminated surface depending on the experiment). XPS was performed on a PHI 5500 instrument using monochromated Al KR (1486 eV) radiation with detection on the surface normal. Spectra were fitted with Gaussian profiles using standard procedures. The positions of all peaks were normalized to C 1s at 285.0 eV. Experimental details for the benzoin compounds and the surface design are given in the Experimental section.

Silicon oxide elements

ATR elements were cleaned with piranha solution at 120 °C for 20 min and then rinsed with deionized water. To form the imine-linker aldehyde surface, the ATR element was exposed to APTES vapour for 10 min at room temperature. Once the free amine layer was formed, the ATR element was washed by sonicating in ethanol for 10 s, followed by rinsing with ethanol and then placement in a 1 mmol/L solution of terephthalaldehyde in water for 30 min at room temperature. The ATR element was then removed from the terephthalaldehyde solution and washed by sonicating in ethanol for 10 s, followed by rinsing with ethanol.

Silicon elements (H-terminated)

ATR elements were cleaned with piranha solution (96% H_2SO_4 and 30% H_2O_2, 3:1) at 120 °C for 20 min and then rinsed with deionized water. Samples were H-terminated by etching in degassed ammonium fluoride for 15 min, followed by a brief rinse in degassed water. To form the directly attached aldehyde surface, a 0.2 mol/L solution of terephthalaldehyde in toluene was degassed by bubbling with argon in a glass Schlenk tube for 10 min, followed by addition of the ATR element and heating of the solution at 90 °C for 1 h. The solution was cooled to room temperature and the ATR element removed and washed with 1,1,2-trichloroethane (TCE) in a Soxhlet extractor for 15–20 min and then further reacted as previously described.

Benzoin condensation on surfaces

Typically, 0.1 mmol of catalyst was dissolved in 1 mL of distilled water. To this, triethylamine (TEA) (27 μL, 0.2 mmol (with thiamine) or 18 μL, 0.1 mmol (with imidazolium catalyst)) was added. Para-substituted benzaldehyde (0.1 mmol) was added, and the solution was thoroughly mixed to form an emulsion. The reactions proceeded more slowly at lower catalyst concentrations and did not proceed at all in the absence of catalyst. The aromatic aldehyde-terminated ATR element was immersed in the solution and gently shaken. The reaction progression was monitored by ATR-FTIR. Gentle to vigorous washing was used as needed before scans to remove any noncovalently bound material.

Methoxybenzoins

Distributed among four 1.5 mL eppendorf vials, thiamine chloride hydrochloride (328 mg, 0.984 mmol) was dissolved in distilled water (2.4 mL) along with TEA (280 μL, 1.968 mmol). 4-Methoxybenzaldehye (160 μL, 0.984 mmol) and benzaldehyde (120 μL, 0.984 mmol) were added to the solution and the solution was shaken vigorously to form an emulsion. The vials were then placed in a centrifuge and spun for 3 days at 1400 rpm. The reactions were combined and 10 mL of water and 10 mL of ethyl acetate were added. The organic phase was isolated and the aqueous phase extracted 2 times with 10 mL of ethyl acetate. The organic fractions were combined, dried with magnesium sulfate, filtered, and concentrated. The resulting oil was purified by silica gel chromatography (4:1, hexanes – ethyl acetate, R_f = 0.32) to isolate the desired benzoin product as a mixture of regioisomers (3:1 based on NMR). The isomers were then separated by preparative HPLC (NovaPak C18 19 × 300 mm, iso 30% MeCN in H_2O, 20 min) in 41% total isolated yield.

2-Hydroxy-1-(4-methoxyphenyl)-2-phenylethanone[38]

Yield: 20 mg (33%). ^{1}H NMR (400 MHz, $CDCl_3$, ppm) δ: 7.93 (2H, d, J = 9.0 Hz), 7.39–7.25 (5H, m), 6.88 (2H, d, J = 9.0 Hz), 5.91 (1H, d, J = 5.8 Hz), 4.67 (1H, d, J = 6.0 Hz), 3.84 (3H, s). MS (positive ESI, M + 1) m/z 243.

2-Hydroxy-2-(4-methoxyphenyl)-1-phenylethanone

Prepared as previously described.[38] Yield: 8 mg (8%). ^{1}H NMR (400 MHz, $CDCl_3$, ppm) δ: 8.00–7.86 (2H, m), 7.54 (1H, dd, J = 4.3, 10.5 Hz), 7.42 (2H, t, J = 7.7 Hz), 7.30–7.24 (3H, m), 6.87 (2H, d, J = 8.7 Hz), 5.93 (1H, d, J = 6.0 Hz), 4.50 (1H, d, J = 6.0 Hz), 3.78 (3H, s). MS (positive ESI, M + 1) m/z 243.

4-[2-(2-Hydroxyethoxy)ethylamino]benzaldehyde

Prepared as previously described.[60] A mixture of 4-bromobenzaldehyde (925 mg, 5 mmol), 2-(2-aminoethoxy)ethanol (725 μL, 7.5 mmol), K_2CO_3 (1.38 g, 10 mmol), CuI (95 mg, 0.5 mmol), and L-proline (23 mg, 1 mmol) in 3 mL of DMF (dry) was heated to 80 °C for 48 h in a sealed flask under Ar. The cooled mixture was diluted with ethyl acetate and water. The organic layer was separated, and the aqueous layer was extracted with ethyl acetate. The combined organic layers were washed with brine, dried over Na_2SO_4, filtered, and con-

Can. J. Chem. Downloaded from www.nrcresearchpress.com by Renmin University of China on 09/02/12
For personal use only.

centrated. The residual oil was loaded on a silica gel column and eluted with ethyl acetate to afford 200 mg of the corresponding aniline (19% yield). ^{1}H NMR (400 MHz, $CDCl_3$, ppm) δ: 9.75 (1H, s), 7.72 (2H, d, J = 8.7 Hz), 6.66 (2H, d, J = 8.7 Hz), 4.80 (1H, s), 3.80 (2H, s), 3.78–3.72 (2H, m), 3.69–3.57 (2H, m), 3.44 (2H, q, J = 5.3 Hz), 2.01 (1H, s). ^{13}C NMR (100 MHz, $CDCl_3$, ppm) δ: 190.56 (CH), 153.45 (C), 132.54 (CH), 126.90 (C), 112.19 (CH), 72.49 (CH_2), 69.44 (CH_2), 62.01 (CH_2), 43.04 (CH_2). MS (positive ESI, M + 1) *m*/*z* 210.3; (negative ESI, M – 1) *m*/*z* 208.3.

4-Formyl-N-*[2-(2-hydroxyethoxy)ethyl]benzamide*

4-Carboxybenzaldehyde (1.015 g, 6.76 mmol) was dissolved in 16 mL of toluene. Once the aldehyde was dissolved, *p*-toluenesulfonic acid (38 mg, 0.20 mmol) and ethylene glycol (415 μL, 7.44 mmol) was added. The reaction was refluxed with a Dean–Stark apparatus overnight. Once the reaction was complete, the toluene was evaporated and the residual oil was dissolved in ethyl acetate (30 mL) and washed once with water (30 mL) and once with brine solution (30 mL). The organic phase was collected, dried over Na_2SO_4, and concentrated. The protected acid was recrystallized from hexanes – ethyl acetate to afford 1.22 g of 4-[1,3]dioxolan-2-yl-benzoic acid (92% yield). ^{1}H NMR (400 MHz, $CDCl_3$, ppm) δ: 8.02 (2H, d, J = 8.0 Hz), 7.49 (2H, d, J = 8.4 Hz), 5.78 (1H, s), 3.99 (4H, m). 4-[1,3]Dioxolan-2-yl-benzoic acid (123 mg, 0.633 mmol) was dissolved in 5 mL of DMF. Once the acid was dissolved, 2-(2-aminoethoxy)ethanol (7 μL, 0.697 mmol) was added along with DCC (196 mg, 0.950 mmol) and HOBt (128 mg, 0.950 mmol) and the reaction was allowed to stir at room temperature overnight. Once the reaction was complete, the mixture was dissolved in 10% sulfuric acid (5 mL) and left to stir at room temperature for 2 h to deprotect the aldehyde. Once the reaction was complete, the product was purified by flash chromatography (5%–10% methanol in dichloromethane) to afford 64 mg of the aldehyde (43% yield). ^{1}H NMR (400 MHz, $CDCl_3$, ppm) δ: 10.05 (1H, s), 7.92 (4H, s), 3.76 (2H, m), 3.69 (4H, m), 3.62 (2H, m). MS (positive ESI, M + 1) *m*/*z* 238.3; (negative ESI, M – 1) *m*/*z* 236.1.

Acknowledgements

This work has been generously supported by funding from Genome Canada and the Genomics and Health Initiative of the National Research Council of Canada. The authors thank Dr. J. Hulse, Dr. Z. He, and Ms. S. Moisa for XPS assistance.

References

(1) Minakata, S.; Komatsu, M. *Chem. Rev.* **2009**, *109* (2), 711. doi:10.1021/cr8003955.
(2) Ruckenstein, E.; Li, Z. F. *Adv. Colloid Interface Sci.* **2005**, *113* (1), 43. doi:10.1016/j.cis.2004.07.009.
(3) Boukherroub, R. *Curr. Opin. Solid State Mater. Sci.* **2005**, *9* (1–2), 66. doi:10.1016/j.cossms.2006.03.006.
(4) Rusmini, F.; Zhong, Z.; Feijen, J. *Biomacromolecules* **2007**, *8* (6), 1775. doi:10.1021/bm061197b.
(5) Wöhler, F.; Liebig, J. *Ann. Pharm.* **1832**, *3* (3), 249. doi:10.1002/jlac.18320030302.
(6) Lapworth, A. *J. Chem. Soc.* **1903**, *83*, 995.
(7) Breslow, R. *J. Am. Chem. Soc.* **1958**, *80* (14), 3719. doi:10.1021/ja01547a064.
(8) Enders, D.; Balensiefer, T. *Acc. Chem. Res.* **2004**, *37* (8), 534. doi:10.1021/ar030050j.
(9) Enders, D.; Niemeier, O.; Henseler, A. *Chem. Rev.* **2007**, *107* (12), 5606. doi:10.1021/cr068372z.
(10) Moore, J. L.; Rovis, T. Carbene Catalysts. In *Asymmetric Organocatalysis;* Springer-Verlag: Berlin, Heidelberg, 2010; pp 77–144.
(11) Enders, D.; Narine, A. A. *J. Org. Chem.* **2008**, *73* (20), 7857. doi:10.1021/jo801374j.
(12) Nair, V.; Bindu, S.; Sreekumar, V. *Angew. Chem. Int. Ed.* **2004**, *43* (39), 5130. doi:10.1002/anie.200301714.
(13) Baragwanath, L.; Rose, C. A.; Zeitler, K.; Connon, S. J. *J. Org. Chem.* **2009**, *74* (23), 9214. doi:10.1021/jo902018j.
(14) Jin, M. Y.; Kim, S. M.; Han, H.; Ryu, D. H.; Yang, J. W. *Org. Lett.* **2011**, *13* (5), 880. doi:10.1021/ol102937w.
(15) O'Toole, S. E.; Connon, S. J. *Org. Biomol. Chem.* **2009**, *7* (17), 3584. doi:10.1039/b908517c.
(16) O'Toole, S. E.; Rose, C. A.; Gundala, S.; Zeitler, K.; Connon, S. J. *J. Org. Chem.* **2011**, *76* (2), 347. doi:10.1021/jo101791w.
(17) Rose, C. A.; Gundala, S.; Connon, S. J.; Zeitler, K. *Synthesis* **2011**, (2), 190.
(18) Dünkelmann, P.; Kolter-Jung, D.; Nitsche, A.; Demir, A. S.; Siegert, P.; Lingen, B.; Baumann, M.; Pohl, M.; Müller, M. *J. Am. Chem. Soc.* **2002**, *124* (41), 12084. doi:10.1021/ja0271476.
(19) Jewett, J. C.; Sletten, E. M.; Bertozzi, C. R. *J. Am. Chem. Soc.* **2010**, *132* (11), 3688. doi:10.1021/ja100014q.
(20) Laughlin, S. T.; Baskin, J. M.; Amacher, S. L.; Bertozzi, C. R. *Science* **2008**, *320* (5876), 664. doi:10.1126/science.1155106.
(21) Sletten, E. M.; Bertozzi, C. R. *Angew. Chem. Int. Ed.* **2009**, *48* (38), 6974. doi:10.1002/anie.200900942.
(22) Best, M. D. *Biochemistry* **2009**, *48* (28), 6571. doi:10.1021/bi9007726.
(23) Hong, V.; Steinmetz, N. F.; Manchester, M.; Finn, M. G. *Bioconjug. Chem.* **2010**, *21* (10), 1912. doi:10.1021/bc100272z.
(24) Hsu, T. L.; Hanson, S. R.; Kishikawa, K.; Wang, S. K.; Sawa, M.; Wong, C. H. *Proc. Natl. Acad. Sci. U.S.A.* **2007**, *104* (8), 2614. doi:10.1073/pnas.0611307104.
(25) Lim, R. K. V.; Lin, Q. *Chem. Commun. (Camb.)* **2010**, *46* (10), 1589. doi:10.1039/b925931g.
(26) Soriano del Amo, D.; Wang, W.; Jiang, H.; Besanceney, C.; Yan, A. C.; Levy, M.; Liu, Y.; Marlow, F. L.; Wu, P. *J. Am. Chem. Soc.* **2010**, *132* (47), 16893. doi:10.1021/ja106553e.
(27) Faragher, R. J.; McKay, C. S.; Hoa, X. D.; Prikrylova, B.; Lopinski, G. P.; Figeys, D.; Veres, T.; Pezacki, J. P. *Can. J. Chem.* **2011**, *89* (5), 608. doi:10.1139/v11-015.
(28) Kennedy, D. C.; Lyn, R. K.; Pezacki, J. P. *J. Am. Chem. Soc.* **2009**, *131* (7), 2444. doi:10.1021/ja809451w.
(29) McKay, C. S.; Blake, J. A.; Cheng, J.; Danielson, D. C.; Pezacki, J. P. *Chem. Commun. (Camb.)* **2011**, *47* (36), 10040. doi:10.1039/c1cc13808a.
(30) Kolb, H. C.; Finn, M. G.; Sharpless, K. B. *Angew. Chem. Int. Ed.* **2001**, *40* (11), 2004. doi:10.1002/1521-3773(20010601)40:11<2004::AID-ANIE2004>3.0.CO;2-5.
(31) Presolski, S. I.; Hong, V.; Cho, S.-H.; Finn, M. G. *J. Am. Chem. Soc.* **2010**, *132* (41), 14570. doi:10.1021/ja105743g.
(32) Wu, P.; Malkoch, M.; Hunt, J. N.; Vestberg, R.; Kaltgrad, E.; Finn, M. G.; Fokin, V. V.; Sharpless, K. B.; Hawker, C. J. *Chem. Commun. (Camb.)* **2005**, *41* (46), 5775. doi:10.1039/b512021g.

(33) McKay, C. S.; Moran, J.; Pezacki, J. P. *Chem. Commun. (Camb.)* **2010**, *46* (6), 931. doi:10.1039/b921630h.
(34) Moran, J.; McKay, C. S.; Pezacki, J. P. *Can. J. Chem.* **2011**, *89* (2), 148. doi:10.1139/V10-112.
(35) Pezacki, J. P.; Blake, J. A.; Danielson, D. C.; Kennedy, D. C.; Lyn, R. K.; Singaravelu, R. *Nat. Chem. Biol.* **2011**, *7* (3), 137. doi:10.1038/nchembio.525.
(36) Lorello, G. R.; Legault, M. C. B.; Rakić, B.; Bisgaard, K.; Pezacki, J. P. *Bioorg. Chem.* **2008**, *36* (2), 105. doi:10.1016/j.bioorg.2007.12.006.
(37) Kennedy, D. C.; McKay, C. S.; Legault, M. C.; Danielson, D. C.; Blake, J. A.; Pegoraro, A. F.; Stolow, A.; Mester, Z.; Pezacki, J. P. *J. Am. Chem. Soc.* **2011**, *133* (44), 17993. doi:10.1021/ja2083027.
(38) Linghu, X.; Potnick, J. R.; Johnson, J. S. *J. Am. Chem. Soc.* **2004**, *126* (10), 3070. doi:10.1021/ja0496468.
(39) Linghu, X.; Johnson, J. S. *Angew. Chem. Int. Ed.* **2003**, *42* (22), 2534. doi:10.1002/anie.200250554.
(40) Rozkiewicz, D. I.; Ravoo, B. J.; Reinhoudt, D. N. *Langmuir* **2005**, *21* (14), 6337. doi:10.1021/la050438i.
(41) Reynolds, N. T.; Rovis, T. *J. Am. Chem. Soc.* **2005**, *127* (47), 16406. doi:10.1021/ja055918a.
(42) Iwamoto, K.-i.; Hamaya, M.; Hashimoto, N.; Kimura, H.; Suzuki, Y.; Sato, M. *Tetrahedron Lett.* **2006**, *47* (40), 7175. doi:10.1016/j.tetlet.2006.07.153.
(43) Murry, J. A.; Frantz, D. E.; Soheili, A.; Tillyer, R.; Grabowski, E. J. J.; Reider, P. J. *J. Am. Chem. Soc.* **2001**, *123* (39), 9696. doi:10.1021/ja0165943.
(44) Mattson, A. E.; Bharadwaj, A. R.; Zuhl, A. M.; Scheidt, K. A. *J. Org. Chem.* **2006**, *71* (15), 5715. doi:10.1021/jo060699c.
(45) Kano, T.; Sasaki, K.; Konishi, T.; Mii, H.; Maruoka, K. *Tetrahedron Lett.* **2006**, *47* (27), 4615. doi:10.1016/j.tetlet.2006.04.141.
(46) Arduengo, A. J.; Harlow, R. L.; Kline, M. *J. Am. Chem. Soc.* **1991**, *113* (1), 361. doi:10.1021/ja00001a054.
(47) Wagner, C. D.; Davis, L. E.; Zeller, M. V.; Taylor, J. A.; Raymond, R. H.; Gale, C. H. *Surf. Interface Anal.* **1981**, *3* (5), 211. doi:10.1002/sia.740030506.
(48) Almasi, D.; Alonso, D. A.; Najera, C. *Tetrahedron Lett.* **2007**, *18*, 299.
(49) Fedoryński, M. *Chem. Rev.* **2003**, *103* (4), 1099. doi:10.1021/cr0100087.
(50) Seayad, J.; List, B. *Org. Biomol. Chem.* **2005**, *3* (5), 719. doi:10.1039/b415217b.
(51) Banerjee, A.; Panosian, T. D.; Mukherjee, K.; Ravindra, R.; Gal, S.; Sackett, D. L.; Bane, S. *ACS Chem. Biol.* **2010**, *5* (8), 777. doi:10.1021/cb100060v.
(52) Carrico, I. S.; Carlson, B. L.; Bertozzi, C. R. *Nat. Chem. Biol.* **2007**, *3* (6), 321. doi:10.1038/nchembio878.
(53) Wu, P.; Shui, W. Q.; Carlson, B. L.; Hu, N.; Rabuka, D.; Lee, J.; Bertozzi, C. R. *Proc. Natl. Acad. Sci. U.S.A.* **2009**, *106* (9), 3000. doi:10.1073/pnas.0807820106.
(54) Xie, J. M.; Schultz, P. G. *Nat. Rev. Mol. Cell Biol.* **2006**, *7* (10), 775. doi:10.1038/nrm2005.
(55) Kluger, R.; Lam, J. F.; Pezacki, J. P.; Yang, C. M. *J. Am. Chem. Soc.* **1995**, *117* (46), 11383. doi:10.1021/ja00151a001.
(56) Pasternack, R. M.; Rivillon Amy, S.; Chabal, Y. J. *Langmuir* **2008**, *24* (22), 12963. doi:10.1021/la8024827.
(57) Simon, A.; Cohen-Bouhacina, T.; Porté, M. C.; Aimé, J. P.; Baquey, C. *J. Colloid Interface Sci.* **2002**, *251* (2), 278. doi:10.1006/jcis.2002.8385.
(58) Smith, E. A.; Chen, W. *Langmuir* **2008**, *24* (21), 12405. doi:10.1021/la802234x.
(59) Xu, D. X.; Densmore, A.; Delage, A.; Waldron, P.; McKinnon, R.; Janz, S.; Lapointe, J.; Lopinski, G.; Mischki, T.; Post, E.; Cheben, P.; Schmid, J. H. *Optics Exp.* **2008**, *16* (19), 15137. doi:10.1364/OE.16.015137.
(60) Zhang, H.; Cai, Q.; Ma, D. *J. Org. Chem.* **2005**, *70* (13), 5164. doi:10.1021/jo0504464.

Can. J. Chem. Downloaded from www.nrcresearchpress.com by Renmin University of China on 09/02/12
For personal use only.

Development of an avidin sensor based on the poly (methoxy amino-β-styryl terthiophene)-coated glassy carbon electrode

Hakim Mehenni

Can. J. Chem. Downloaded from www.nrcresearchpress.com by Renmin University of China on 09/02/12
For personal use only.

Abstract: In this study, a simple and direct biosensor was proposed, which was based on biotin immobilized onto a conducting polymer-coated electrode, for the determination of avidin, a highly stable glycoprotein found in egg whites. Biotin was immobilized onto the electrode by covalent coupling to the primary amine group on poly-3′-(2-methoxy-5-amino-β-styryl)-(2,2′:5′,2″-terthiophene) (PMAST), and the biotin–avidin interaction was monitored by square-wave voltammetry. Incubation of the PMAST/biotin-modified coated electrode with avidin in a phosphate-buffered saline solution caused a significant change to its square-wave voltammogram, which was explained by the binding of avidin by biotin, and resulted in restricted ion transfer to and from the conducting polymer. This change was then utilized to determine avidin. Importantly, we found a linear relationship for the avidin sensor in the range of 4×10^{-14} to 3×10^{-4} mol/L, and the detection limit was determined to be approximately 10^{-14} mol/L.

Key words: avidin, biosensor, electronic conducting polymer, cyclic voltammetry, electrode surface modification, square-wave voltammetry, biological functionalization.

Résumé : Dans cette étude, on propose l'utilisation d'un biosenseur simple et direct, qui est basé sur de la biotine immobilisée sur une électrode recouverte de polymère conducteur, pour la détermination de l'avidine, une glycoprotéine très stable qu'on retrouve dans les blancs d'oeufs. La biotine a été immobilisée sur l'électrode par un couplage covalent à un groupe amine primaire du poly-3′-(2-méthoxy-5-amino-β-styryl)-(2,2′:5′,2″-terthiophène (PMAST) et l'interaction biotine–avidine a été mesurée par voltampérométrie à onde carrée. Une incubation de l'électrode modifiée par une couche de PMAST / biotine avec de l'avidine, dans une solution saline tamponnée au phosphate, provoque un changement important dans le voltampérogramme qui est expliqué par une fixation de l'avidine par la biotine qui provoque une restriction dans le transfert d'ion vers et à partir du polymère conducteur. Ce changement a ensuite été utilisé pour déterminer l'avidine. De plus, on a trouvé qu'il existe une relation linéaire pour le senseur d'avidine dans la plage de concentrations allant de 4×10^{-14} à 3×10^{-4} mol/L et on a déterminé que la limite de détection est d'environ 10^{-14} mol/L.

Mots-clés : avidine, biosenseur, polymère conducteur d'électron, voltampérométrie cyclique, électrode à surface modifiée, voltampérométrie à onde carrée, fonctionnalisation biologique.

[Traduit par la Rédaction]

Introduction

Two types of biosensor formats (direct and indirect) were used and were based on the electrochemical techniques for the detection of proteins.[1] However, most indirect methods, where a sensitive and detectable label is combined with a protein of interest, are time-consuming and involve several steps. In contrast, direct electrochemical techniques are based on the measurement of potential, capacitance, and conductivity changes that are caused by specifically fixing the protein onto the surface of an electrode. Vital advantages of direct biosensors include the ability to perform single-stage reagentless analyses and the achievement of molecular recognition by sensing a specific bioreceptor–biomolecule interaction on the electrode surface. A successful electrochemical biosensor must be able to selectively recognize the desired biomolecule and produce a measurable electrochemical signal.[2] The conducting polymers, which are prepared from terthiophene, are known for their simple functionalization and relatively good stability in air in both neutral and oxidized states.[3,4] Consequently, oligo- and poly-thiophenes have been functionalized as advanced materials for electrode surface modifications, allowing for the development of biosensor devices. Indeed, DNA electrochemical sensors[5–7] and glucose sensors[8,9] have been recently developed. However, the development of protein biosensors has not been explored fully, but interesting works have been carried out to construct sensors for the avidin[10–12] and vitellogenin proteins.[13] In these two examples, a functionalized polyterthiophene was used as an electronic transducer by covalent immobilization of the bioreceptors

Received 14 June 2011. Accepted 2 October 2011. Published at www.nrcresearchpress.com/cjc on 6 February 2012.

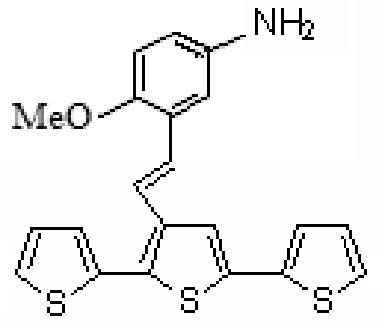
H. Mehenni. Laboratoires de Recherche sur les Matériaux organiques Avancés, INRS-Energie et Matériaux, 1650 Bd Lionel Boulet, Varennes, QC J3X 1S2, Canada; Functional Nanomaterials Laboratory, Department of Materials Science, King Abdullah University of Science and Technology, Thuwal 23955, Kingdom of Saudi Arabia.

Corresponding author: Hakim Mehenni (e-mail: hakim.mehenni@kaust.edu.sa).

Can. J. Chem. Downloaded from www.nrcresearchpress.com by Renmin University of China on 09/02/12
For personal use only.

(either biotin for the avidin electrode or an antibody to vitellogenin for the vitellogenin electrode) on a polyterthiophene-coated electrode. For the avidin sensor, functionalization of terthiophene by biotin was carried out by directly binding biotin to the central thiophene ring in the 3′ position by chemical synthesis. However, using chemical synthesis to biologically functionalize polythiophene was inconvenient because it limited the electrode to only a single target biomolecule. A second inconvenience was that the polythiophene redox signal was situated at a high potential, ~1 V vs Ag/AgCl, which usually led to biotin degradation. For the vitelloginin sensor, terthiophene was functionalized by adding a carboxylic acid group (–COOH) to the 3′ position of the central thiophene ring, resulting in terthiophene 3′-carboxylic acid (TCA). An advantage of biosensor systems that are based on poly(TCA) films is that they are not restricted to a single target biomolecule because various bioreceptors could be immobilized through an interaction with the free carboxylic acid groups present on the poly(TCA) film surface. However, the inconvenience of this biosensor system is that, again, the polythiophene backbone redox signal is situated at a high potential, which may cause the degradation of the immobilized bioreceptor on its surface.

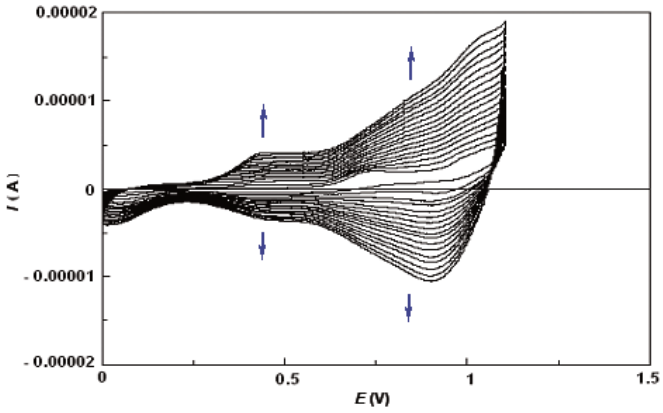
Herein, we report a simple and direct biosensor for the determination of avidin using square-wave voltammetry. This sensor was fabricated by covalent immobilization of biotin onto a conducting polymer-coated glassy carbon electrode, which was based on the 3′-(2-methoxy-5-amino-β-styryl)-(2,2′:5′,2″-terthiophene) (MAST) monomer.



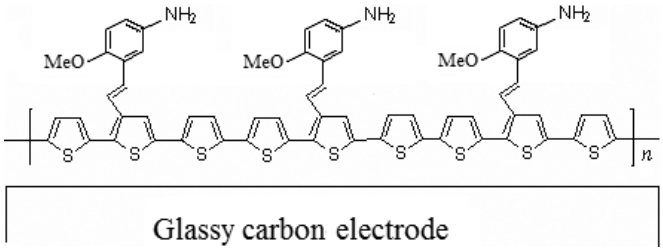
The MAST monomer

We investigated the possibility of using amino β-styryl-functionalized poly(terthiophene) in biosensor devices. For these types of sensors, the redox signal of the aminophenyl moiety was used as a transduction mechanism instead of the polyterthiophene redox signal. In this case, measurements at high oxidation potential were avoided, which could damage the biofunctionalization of the electrode at its surface, and polyterthiophene was used as a means of immobilization onto the electrode surface by electrodeposition. As the biotin–avidin interaction is known for this highly specific interaction, we began with the detection of avidin as a proof-of-concept experiment. Our group has recently described the preparation and characterization of the CAST monomer.[14] Among the principal advantages of this conducting polymer was the ability to change the nature of the immobilized bio-

Fig. 1. Growth of poly(3′-(2-methoxy-5-amino-β-styryl)-(2,2′:5′,2″-terthiophene)) (MAST) by repetitive scan cyclic voltammetry on a 7.068 mm^2 glassy carbon electrode between 0.0 and 1.1 V. Auxiliary electrode: Pt wire, reference electrode, Ag/AgCl; scan rate, 10 mV s^{-1}; 5 mmol/L MAST monomer; and 0.1 mol/L tetrabutylammonium perchlorate (TBAP) – dichloromethane (DCM). *E*, energy; *I*, current.



Scheme 1. Structure of the poly-3′-(3-methoxy-4-amino-β-styryl)-(2,2′:5′,2″-terthiophene) (PMAST) film that was electrodeposited onto a glassy carbon electrode.



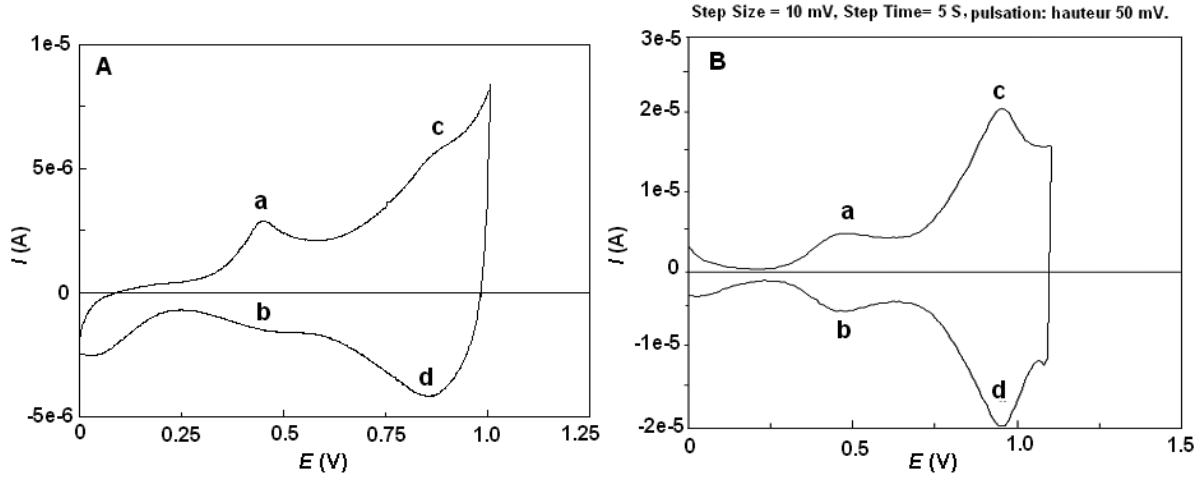
receptor through the formation of a covalent bond with the free primary amine groups on the polymer surface; hence, this polymer could be used as a biosensor for various biomolecule targets. Moreover, it was possible to observe the redox signal (oxidation peak) of the aminophenyl moiety in the square-wave voltammograms of the polymer MAST (PMAST) in organic medium.[14] We used the relative current measured at this oxidation peak, which is related to the concentration of avidin in a buffered medium, as the signal that is modified by the specific interaction of biotin–avidin on the surface electrode. Avidin is a highly stable glycoprotein (molecular mass ~68 000) found in egg whites. Avidin has been isolated as a tetramer, with each subunit containing a binding site for biotin that forms an exceedingly strong complex through noncovalent interactions ($K_a = 10^{15}$ $(mol/L)^{-1}$).[15,16]

Experimental

Reagents

The MAST monomer was synthesized according to our previous work.[14] The following chemicals were used: ethyl-3-(3-dimethylaminopropyl) carbodiimide (EDC), biotin, and tetrabutylammonium perchlorate (TBAP, electrochemical grade) from Sigma-Aldrich (Canada) and dichloromethane (DCM, HPLC grade), avidin from egg whites, and phosphate-

Fig. 2. (A) Cyclic voltammogram of the poly-3′-(3-methoxy-4-amino-β-styryl)-(2,2′:5′,2″-terthiophene) (PMAST) film between 0 and 1 V on a glassy carbon working electrode. Auxiliary electrode: Pt foil; reference electrode: Ag/AgCl; scan rate: 5 mV s^{-1}; in 0.1 mol/L tetrabutylammonium perchlorate (TBAP) – dichloromethane (DCM). (B) Square-wave voltammograms of the PMAST film between 0.0 and 1.0 V on a glassy carbon working electrode. Auxiliary electrode: Pt foil; reference electrode: Ag/AgCl; in 0.1 mol/L TBAP–DCM. *E*, energy; *I*, current.



Can. J. Chem. Downloaded from www.nrcresearchpress.com by Renmin University of China on 09/02/12
For personal use only.

buffered saline (PBS, 0.1 mol/L, pH 7.4 at 25 °C) from Fisher Scientific (Canada). All experimental solutions were prepared in double-distilled water obtained from a Milli-Q water system (18 MΩ cm^{-1}).

Modification of the electrode surface

The conducting polymer film on the polished glassy carbon electrode (area = 7.068 mm^2) was prepared by electropolymerization of 5 mmol/L of the MAST monomer in a 0.1 mol/L TBAP/CH_2Cl_2 solution by potential cycling between 0.0 and 1.1 V (vs Ag/AgCl) several times at 10 mV s^{-1}. After polymerization, the electrode surface was rinsed with CH_2Cl_2 to remove any excess monomers from the electrode surface. The poly-MAST (PMAST)-coated electrode was then immersed in a 0.1 mol/L PBS solution (pH 8) containing 0.05 mol/L EDC and 0.05 mol/L biotin for 24 h at 40 °C. Individual biotin molecules were then immobilized onto the PMAST film through the formation of a covalent bond with a free primary amine group on the polymer surface. The electrode was then rinsed thoroughly with the same buffer to remove any biotin that was not immobilized, and cyclic voltammograms (CVs) and square-wave voltammograms (SWVs) were recorded. Finally, the PMAST/biotin-modified electrode was incubated in a 0.1 mol/L PBS solution (pH 7.4) containing a known amount of avidin for 15 min at room temperature to block the active sites of avidin through a specific interaction with biotin. The electrode was then removed, rinsed with the same buffer to remove any avidin that had not reacted with biotin, and allowed to dry. CVs and SWVs were then recorded.

Instruments and electrochemical techniques

The measuring setup for all electrochemical experiments consisted of a three-electrode system, in which a glassy carbon electrode, an Ag/AgCl (saturated KCl) electrode, and a platinum foil (dimension, 1 cm × 1 cm; 0.025 mm^2 thickness) were used as the working, the reference, and the auxiliary electrodes, respectively. The CVs and the SWVs were recorded by employing a potentiostat/galvanostat (model EG & G, Princeton Applied Research, 273 A). All of the measurements were carried out in a 0.1 mol/L TBAP–DCM solution at room temperature.

Characterization techniques

The neutral PMAST and PMAST/biotin-modified sensors were characterized using a reflectance Fourier transform infrared (FT-IR) experiment and by X-ray photoelectron spectroscopy (XPS). FT-IR spectra of PMAST films on gold-coated glass electrodes were recorded on a NEXUS 670 FT-IR over the range 600–4000 cm^{-1}. XPS examination was carried out on the PMAST films grown on indium–tin–oxide (ITO)-coated glass electrodes using an Escalab 220i XL spectrometer (Vacuum Generator).

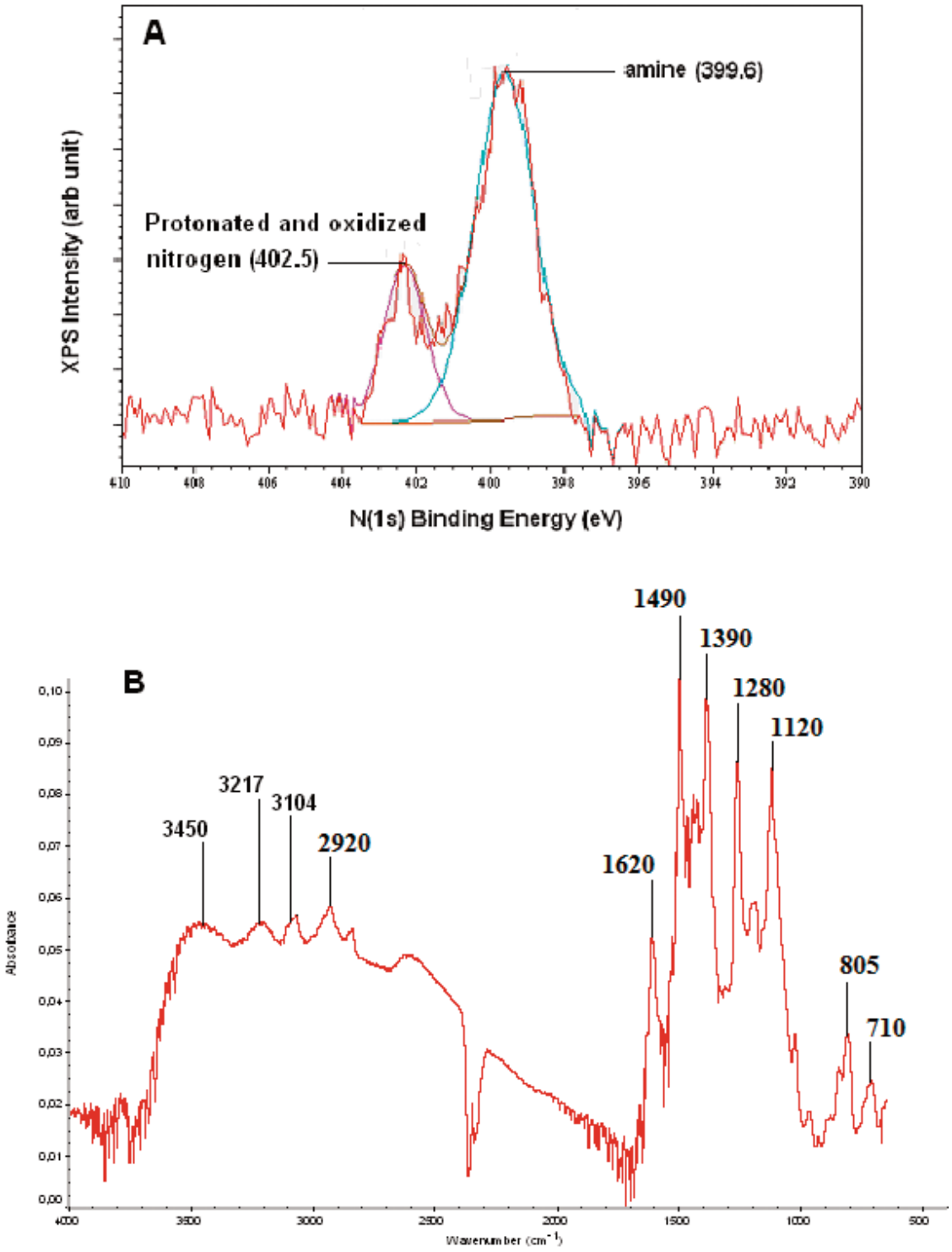
Results and discussion

Electrochemical polymerization of the MAST monomer and CVs and SWVs

Figure 1 shows the repetitive scan CVs for the formation of a PMAST film on a glassy carbon electrode. The CVs show the expected increase in current with increasing number of potential cycles, indicating the growth of an electronic conducting polymer (ECP). A robust and adherent black uniform polymer film was electrodeposited successfully onto the electrode surface. However, it was necessary to grow a thick polymer film to ensure that the polymer remained adherent during the transfers between aqueous and nonaqueous media; therefore, we made a film from 10 repetitive scans.

Scheme 1 shows the structure of the PMAST that was electrodeposited onto a glassy carbon electrode, and Fig. 2 shows the CVs and SWVs of PMAST on the glassy carbon working electrode. The CVs and SWVs clearly showed two redox couples, which can be assigned to the aminophenyl moiety redox potentials (labeled a and b, Fig. 2) at 0.5 V vs Ag/AgCl and the polythiophene backbone redox potentials (labeled c and d, Fig. 2) at 0.9 V vs Ag/AgCl. Indeed, we were able to determine the origin of the redox couples (a/b and c/d) by comparing the CVs and SWVs of a polyterthiophene

Fig. 3. X-ray photoelectron spectroscopy (XPS) (A) and Fourier transform infrared (FT-IR) (B) spectra of the poly-3′-(3-methoxy-4-amino-β-styryl)-(2,2′:5′,2″-terthiophene) (PMAST) film that had been grown on indium–tin–oxide (ITO)-coated glass and gold-coated glass, respectively, at room temperature.



film prepared under the same conditions and using the results from previously published studies that had analyzed polyterthiophene.[17] We found that the polaronic oxidation peak was situated toward 1.05 V vs SCE (corresponding to 1.09 V vs Ag/AgCl), and the anodic peak (a, Fig. 2) corresponded to the oxidation of the aminophenyl moiety. It has been reported that the aminophenyl moiety could be oxidized to give a radical cation.[18] This oxidation removes an electron from the free electron doublet of the nitrogen in its neutral state (NH_2), resulting in a radical nitrogen cation ($NH_2^{\cdot+}$).

Can. J. Chem. Downloaded from www.nrcresearchpress.com by Renmin University of China on 09/02/12
For personal use only.

Can. J. Chem. Downloaded from www.nrcresearchpress.com by Renmin University of China on 09/02/12
For personal use only.

Fig. 4. Schematic representation of the immobilization of the receptive biomolecule (biotin) via the activation of carboxylic functional groups (activated by ethyl-3-(3-dimethylaminopropyl) carbodiimide (EDC)) of the biotin.

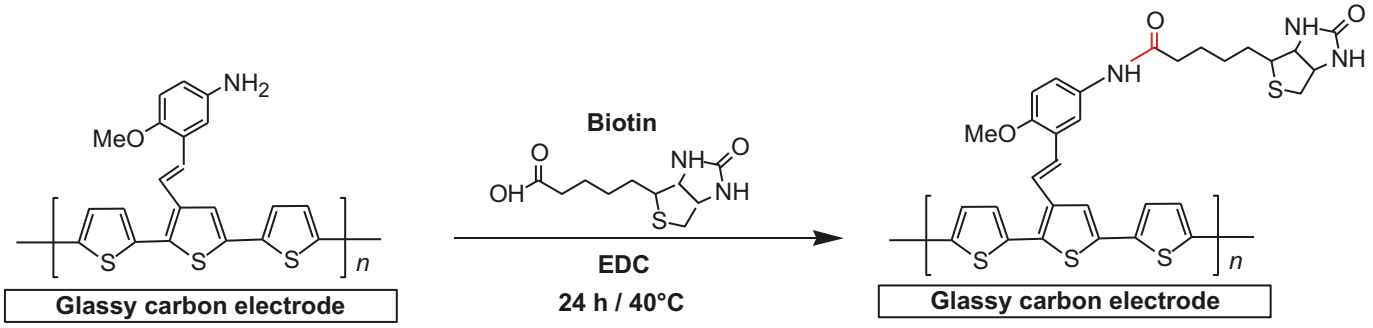
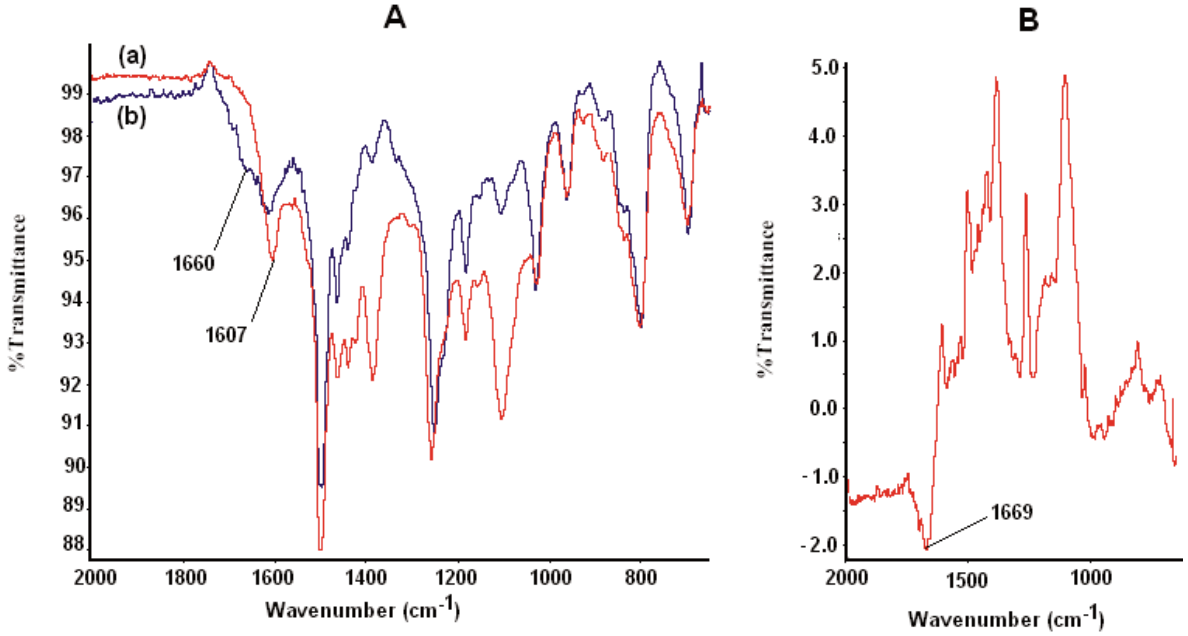


Fig. 5. (A) Fourier transform infrared (FT-IR) spectra of poly-3′-(3-methoxy-4-amino-β-styryl)-(2,2′:5′,2″-terthiophene) (PMAST) grown on gold-coated glass before (a) and after (b) modification with biotin in the range from 2000 to 600 cm^{-1}. (B) Subtraction spectrum of the PMAST/biotin-modified and the PMAST polymers.



Characterization by the XPS and FT-IR techniques

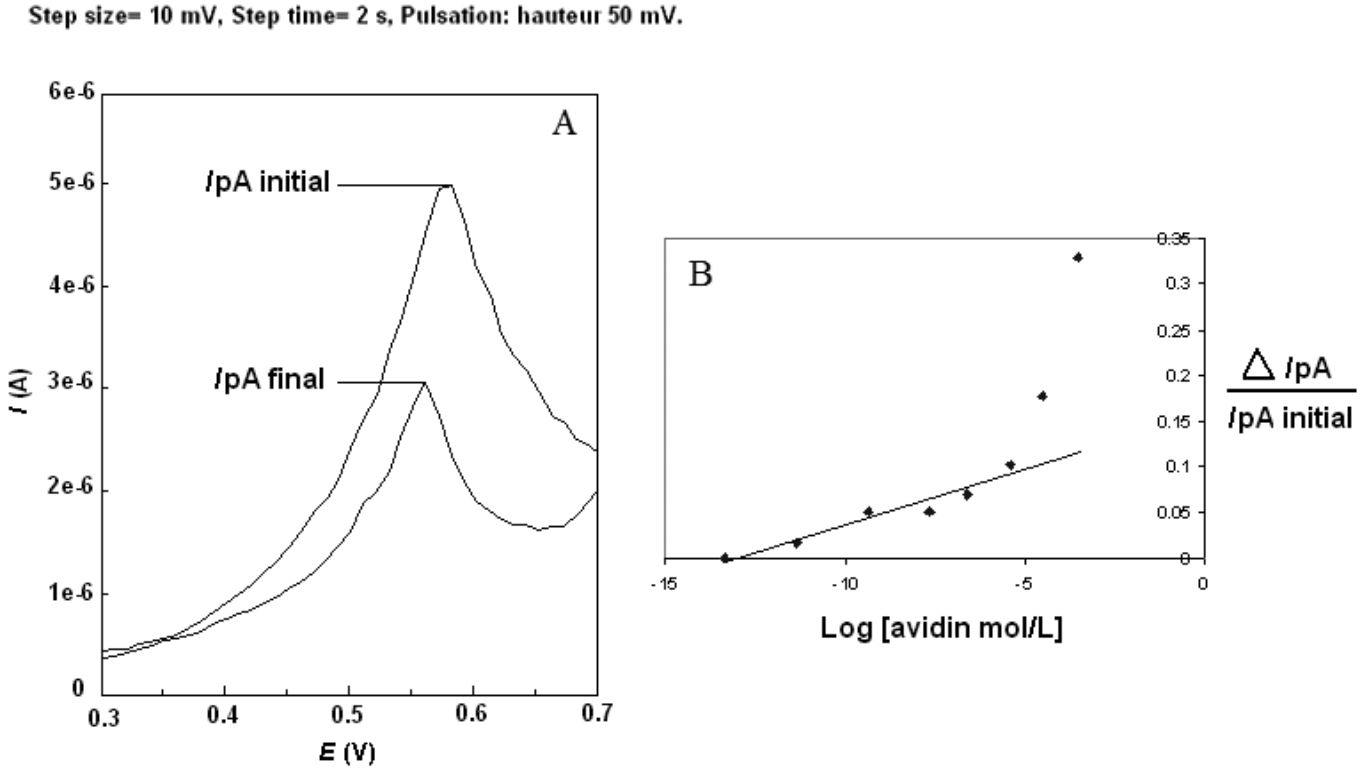
Studies of the PMAST film using the FT-IR and XPS techniques clearly showed the presence of free primary amine groups on the polymer film surface, and these groups were used in the next step of biofunctionalization of the PMAST surface. The XPS and the FT-IR spectra of the PMAST film are shown in Fig. 3. The XPS spectrum showed the deconvoluted N 1s spectrum for the surface of the PMAST film grown on an ITO-coated glass electrode. The two features seen at 402.5 and 399.6 eV were ascribed to a cationic nitrogen species (NH_3^+ and $NH_2^{\cdot+}$) and an amine I species (NH_2), respectively.[19,20] The FT-IR spectrum of the PMAST film grown on gold-coated glass showed two absorbance peaks at 3450 and 3217 cm^{-1} (amine I band, N–H stretching vibration),[21] which corresponded to the primary amine groups on the aminophenyl moiety. In addition, a C–H stretching vibration of the aromatic ring[22] was observed at 3104 cm^{-1}. Regarding the polythiophene backbone, the FT-IR spectrum showed a C–H stretching vibration band at 2920 cm^{-1}, a C=C stretching band at 1390–1620 cm^{-1}, a C–H plane-bending band at 1120 cm^{-1}, and a C–S bending band at 710 cm^{-1}.[23]

Surface modification with biotin

The step used to link biotin to the surface of the PMAST-coated electrode is summarized in Fig. 4. This procedure has the advantage of being performed under simple conditions and forms a covalent bond between the moieties.

A neutral PMAST film was grown on a gold-coated glass working electrode. Figure 5 shows the FT-IR spectra of the PMAST film before and after modification by biotin. Figure 5B clearly shows a new medium shoulder at 1660 cm^{-1} (amide II band, C=O stretching vibration) in the spectrum (b) after modification with biotin. The subtraction spectra of the PMAST/biotin-modified film (b) and PMAST film (a) clearly show an amide II band at 1669 cm^{-1} (C=O stretching vibration), which results from the amide II bond between biotin and the free primary amine groups on the PMAST film surface. It has been reported that the C=O stretching vibration

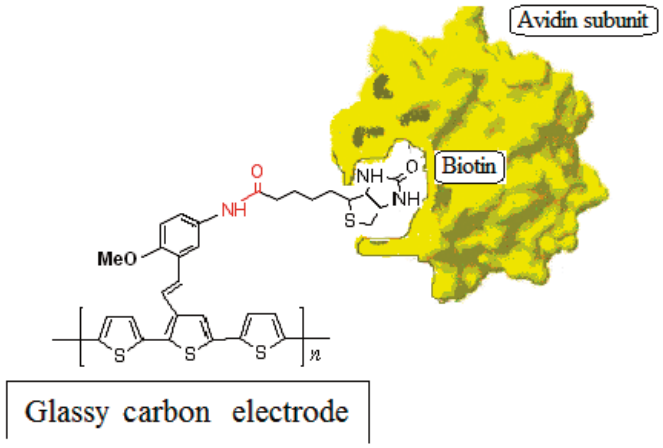
Fig. 6. (A) Square-wave voltammograms of the poly-3′-(3-methoxy-4-amino-β-styryl)-(2,2′:5′,2″-terthiophene) (PMAST) / biotin-modified coated glassy carbon working electrode, before (*I*pA initial) and after (*I*pA final) exposure to a solution of avidin (3×10^{-4} mol/L) in phosphate-buffered saline (PBS, 0.1 mol/L) for 15 min. Auxiliary electrode: Pt foil; reference electrode: Ag/AgCl; in 0.1 mol/L tetrabutylammonium perchlorate (TBAP) / dichloromethane (DCM). (B) Δ*I*pA / *I*pA initial as a function of log(avidin concentration in mol/L). *I*, current.



of an amide II in the solid phase is situated between 1680 and 1630 cm^{-1}.[24]

We also observed by cyclic and square-wave voltammetry that biotin immobilization on the PMAST/biotin-modified coated glassy carbon electrode caused a shift of the anodic peak toward a higher potential (from 0.5 to 0.575 V vs Ag/AgCl), which was initially attributed to the oxidation of the aminophenyl moiety. After biotin immobilization, the anodic peak corresponded to the oxidation of the amidophenyl on the polymer film surface. Indeed, it has been reported[25] that an amidophenyl moiety had a higher oxidation peak than its corresponding aminophenyl moiety. For example, a report[24] has stated that the acetoamidophenyl anodic peak was situated at +1.24 V vs Ag/AgCl, whereas the aminophenyl anodic peak was located at +0.98 V vs Ag/AgCl.

Scheme 2. Illustration of the direct electrochemical avidin sensor.



Effect of avidin exposure on the square-wave response of the PMAST/biotin-modified coated electrode and the linear relationship of the avidin sensor

The SWVs of the PMAST/biotin-modified coated working electrode, before and after exposure to a solution of 3×10^{-4} mol/L avidin in PBS (0.1 mol/L) for 15 min, are shown in Fig. 6A. We observed that exposure of the PMAST/biotin-modified coated working electrode to the avidin solution had a diminishing effect upon its electrochemical response, which caused a significant decrease in the oxidation current that was measured for the anodic peak (*I*pA). The current variation (Δ*I*pA) caused by avidin exposure corresponded to *I*pA initial – *I*pA final (Scheme 2).

In contrast, we observed no significant change when the PMAST/nonmodified coated working electrode was exposed to the avidin solution; thus, the electrochemistry of the PMAST/nonmodified film was unaffected by exposure to avidin. Therefore, avidin interacted specifically with the biotin moieties in the PMAST/biotin-modified film. This unusual voltammetry response after avidin exposure was consistent with the presence of avidin covering the polymer film surface, thus decreasing the number of amidophenyl moieties able to be oxidized during electrooxidation of the polymer film.

Can. J. Chem. Downloaded from www.nrcresearchpress.com by Renmin University of China on 09/02/12
For personal use only.

Can. J. Chem. Downloaded from www.nrcresearchpress.com by Renmin University of China on 09/02/12
For personal use only.

A plot of the relative variation of the current (ΔIpA / IpA initial) measured at the anodic peak potential (EpA) for the PMAST/biotin-modified film vs logavidin concentration) is shown in Fig. 6B to illustrate the possibility of constructing an avidin sensor using this system. We used various concentrations within the range of 4×10^{-14} to 3×10^{-4} mol/L, and the time of incubation was 15 min at room temperature. We observed a linear correlation of 0.97 between the concentrations of avidin from 4×10^{-6} to 4×10^{-4} mol/L. In contrast, there was a loss of this linear correlation at concentrations above 4×10^{-6} mol/L, which could be explained by the presence of an interaction between avidin and the modified surface electrode (other than the specific biotin–avidin interaction) caused by increasing avidin concentrations.

The plot is represented by the linear equation ΔIpA / IpA initial = 0.154 + 0.012 log(concentration). Finally, the minimum detectable concentration of avidin by this biosensor system was approximately 10^{-14} mol/L. Scheme 1 shows an illustration of the direct electrochemical avidin sensor that is based on the poly(methoxyamino-β-styryl terthiophene)-coated glassy carbon electrode.

Conclusion and prospects

In this study, we investigated the feasibility of a direct assay for avidin in a PBS solution. We have also illustrated the advantage of a simple procedure of biotin immobilization by covalent coupling to a primary amino group in a conducting polymer of a MAST-modified electrode, which did not hinder the specific biotin–avidin interaction. In principle, an avidin sensor could be constructed by electrogenerating a PMAST/biotin-modified coated glassy carbon working electrode. The biotin–avidin interaction was monitored by square-wave voltammetry, and a linear relationship for avidin for this sensor in the range of 4×10^{-14} to 3×10^{-4} mol/L was determined. Additionally, the detection limit was determined to be approximately 10^{-14} mol/L. Future work to investigate the possibility of using these PMAST films to target various biomolecules will focus on the biofunctionalization of its surface with various bioreceptors.

Acknowledgements

This work was supported by the National Institute of Scientific Research (INRS) and the Natural Sciences and Engineering Research Council of Canada (NSERC).

References

(1) Gizeli, E.; Lowe, C. R. *Immunosensors Anal. Biotechnol.* **1996**, *7*, 66.
(2) Teasdale, P. R.; Wallace, G. G. *Analyst (Lond.)* **1993**, *118* (4), 329. doi:10.1039/an9931800329.
(3) Daminelli, G.; Widany, J.; Di Carlo, A.; Lugli, P. *J. Chem. Phys.* **2001**, *115* (10), 4919. doi:10.1063/1.1391442.
(4) Roncali, J. *Chem. Rev.* **1992**, *92* (4), 711. doi:10.1021/cr00012a009.
(5) Ho, H. A.; Boissinot, M.; Bergeron, M. G.; Corbeil, G.; Dore, K.; Boudreau, D.; Leclerc, M. *ACS Symp. Ser.* **2004**, *888*, 359. doi:10.1021/bk-2005-0888.ch027.
(6) Uygun, A. *Talanta* **2009**, *79* (2), 194. doi:10.1016/j.talanta.2009.03.049.
(7) Higgins, J. S.; Mouffouk, F.; Brown, S. J.; Williams, D. R.; Cossins, A. R. *Sens. Actuators B Chem.* **2007**, *122* (1), 253. doi:10.1016/j.snb.2006.05.031.
(8) Uygun, A.; Yavuz, A.G.; Sen, S.; Omastová, M. *Synth. Met.* **2009**, *159* (19–20), 2022. doi:101.1016/j/synthmet.2009.07.009.
(9) Abasýyanýk, M. F.; Şenel, M. *J. Electroanal. Chem.* **2010**, *639* (1–2), 21.
(10) Kumpumbu-Kalemba, L.; Leclerc, M. *Chem. Commun. (Camb.)* **2000**, (19), 1847. doi:10.1039/a909744i.
(11) Mouffouk, F.; Brown, S. J.; Demetriou, A. M.; Higgins, S. J.; Nichols, R. J.; Gamini Rajapakse, R. M.; Reeman, S. *J. Mater. Chem.* **2005**, *15* (11), 1186. doi:10.1039/b413974g.
(12) Mouffouk, F.; Higgins, S. J. *Electrochem. Commun.* **2006**, *8* (1), 15. doi:10.1016/j.elecom.2005.10.009.
(13) Darain, F.; Park, D.-S.; Park, J.-S.; Shim, Y.-B. *Biosens. Bioelectron.* **2004**, *19* (10), 1245. doi:10.1016/j.bios.2003.11.014.
(14) Mehenni, H.; Dao, L. H. *Can. J. Chem.* **2008**, *86* (11), 1010. doi:10.1139/v08-136.
(15) Savage, M. D.; Mattson, G.; Desai, S.; Nielander, G. W.; Morgensen, S.; Conklin, E. J. *Avidin–Biotin Chemistry: A Handbook;* Pierce Chemical Co.: Rockford, Ill., 1992.
(16) Wilchek, M.; Bayer, E. A. In *Methods in Enzymology: Avidin–Biotin Technology;* Abelson, J. N., Simon, M. I., Eds.; Academic Press: San Diego, 1990; Vol. 184.
(17) Eales, R. M.; Hillman, A. R. *J. Mater. Sci.* **1990**, *25* (9), 3806. doi:10.1007/BF00582446.
(18) Gao, P.; Gosztola, D.; Weaver, M. J. *J. Phys. Chem.* **1989**, *93* (9), 3753. doi:10.1021/j100346a075.
(19) Moulder, J. F.; Stickle, W. F.; Sobol, P. E.; Bomben, K. D. In *Handbook of X-Ray Photoelectron Spectroscopy;* Physical Electronics: Eden Prairie, MN, 1992.
(20) Kang, E. T.; Neoh, K. G.; Huang, S. W.; Lim, S. L.; Tan, K. L. *J. Phys. Chem. B* **1997**, *101* (50), 10744. doi:10.1021/jp9727052.
(21) Vogel, A.I.; Tatchell, A.R.; Furnis, B.S.; Hannaford, A.J.; Smith, P.W.G. *Vogel's Textbook of Practical Organic Chemistry;* 5th ed.; Longman Scientific and Technical: UK, 1989; Table A2.7, p 1417.
(22) Vogel, A.I.; Tatchell, A.R.; Furnis, B.S.; Hannaford, A.J.; Smith, P.W.G. *Vogel's Textbook of Practical Organic Chemistry;* 5th ed.; Longman Scientific and Technical: UK, 1989; Table A2.3, p 1415.
(23) Gnanakan, S. R. P.; Rajasekhar, M.; Subramania, A. *Int. J. Electrochem. Sci.* **2009**, *4*, 1289.
(24) Vogel, A.I.; Tatchell, A.R.; Furnis, B.S.; Hannaford, A.J.; Smith, P.W.G. *Vogel's Textbook of Practical Organic Chemistry*; 5th ed.; Longman Scientific and Technical: UK, 1989; Table A2.8, p 1420.
(25) Garrido, E. M.; Lima, J. L. F. C.; Delerue-Matos, C.; Borges, F.; Silva, A. M. S.; Oliveira Brett, A. M. *Anal. Chim. Acta* **2001**, *434* (1), 35. doi:10.1016/S0003-2670(01)00817-0.

Synthesis and characterization of dendritic platinum bisferrocenylacetylide complexes

Qing Han, Li-Jun Chen, Hai-Bo Yang, Quan-Jie Li, Jiuming He, Hongwei Tan, Zeper Abliz, and Cui-Hong Wang

Can. J. Chem. Downloaded from www.nrcresearchpress.com by Renmin University of China on 09/02/12
For personal use only.

Abstract: A series of new dendritic platinum bisferrocenylacetylide complexes have been synthesized utilizing the coupling reaction of *trans*-Pt complexes with C–H bonds in alkynes as key steps. These new bimetallic dendrimers were fully characterized by multinuclear NMR (^{1}H, ^{13}C, and ^{31}P) and mass spectrometry (MALDI-TOF-MS and CSI-TOF-MS). Electrochemical studies of these complexes were carried out and revealed that all of the redox moieties are stable, independent, and electrochemically active. In addition, all metallodendrimers show one-electron reaction responses, and the increased sizes of these complexes did not exhibit a dramatic influence on the diffusion coefficient.

Key words: metallodendrimer, platinum biferrocenylacetylide complex, electrochemistry.

Résumé : On a réalisé la synthèse d'une série de nouveaux complexes dendritiques du bisferrocénylacétylure de platine en utilisant comme étapes clés une réaction de couplage de complexes *trans* du platine avec les liaisons C–H d'alcynes. Ces nouveaux dendrimères bimétalliques ont été complètement caractérisés par RMN multinucléaire (^{1}H, ^{13}C et ^{31}P) et par spectrométrie de masse en temps de vol (SM-TDV) avec ionisation par désorption au laser d'une matrice (« MALDI ») ou avec ionisation par nébulisation à froid (INF). On a effectué des études électrochimiques de ces complexes qui révèlent que toutes les portions redox sont stables, indépendantes et électrochimiquement actives. De plus, tous les métallodendrimères donnent des réponses avec des réactions un électron et l'augmentation de la taille de ces complexes n'influence pas d'une façon dramatique le coefficient de diffusion.

Mots-clés : métallodendrimère, complexe de bisferrocénylacétylure de platine, électrochimie.

[Traduit par la Rédaction]

Introduction

Dendrimers[1] are globular, highly branched macromolecules with a "well-defined" three-dimensional shape, size, and molecular weight. Usually, these branched macromolecules are comprised of several dendritic wedges extending outward from an internal core via interactive or stepwise procedures. In the past two decades, the design and synthesis of diverse dendrimers has received increasing attention,[2] not only because of their aesthetically pleasing structures but also as a result of their various applications in host–guest chemistry,[3] material science,[4] and membrane chemistry.[5] Since the pioneering work by Newkome et al.[6] and Balzani and co-workers[7] in the early 1990s, metallodendrimers[8,9] have evolved to be one of the most attractive fields within supramolecular chemistry. The incorporation of metal ions to the dendritic framework usually gives rise to new properties for the corresponding metallodendritic architectures, such as novel physical, optical, electrochemical, photochemical, biological, and catalytic properties.[10,11] Thus, numerous efforts have been taken to construct new metallodendrimers. For example, we reported the fabrication of a new family of metallodendrimers possessing well-defined and controllable cavities as cores via coordination-driven self-assembly.[12] Recently, our research interests have turned to the fabrication of heterometallic dendrimers connected by unsaturated carbon-rich bridges.

The carbon-rich organometallic complexes containing rigid π-conjugated chains have attracted considerable attention in the past few decades.[13] By taking advantage of the linear geometry of the alkynyl unit and its π-unsaturated character, the metal alkynyls have been extensively explored to prepare molecular wires and polymeric organometallic materials, which may possess interesting properties such as optical nonlinearity, luminescence, liquid crystallinity, and electrical conductivity.[14] In particular, the complexes with mixed-valence bimetallic skeletons have evolved to be important design targets for investigations into molecular electronic devices and chemical-sensing applications because of the possible charge delocalization along the entire conjugated backbone.[15,16]

Received 30 August 2011. Accepted 19 October 2011. Published at www.nrcresearchpress.com/cjc on 8 February 2012.

Q. Han, L.-J. Chen, H.-B. Yang, and C.-H. Wang. Shanghai Key Laboratory of Green Chemistry and Chemical Processes, Department of Chemistry, East China Normal University, Shanghai 200062, P.R. China.
Q.-J. Li and H. Tan. Department of Chemistry, Beijing Normal University, Beijing 100875, P.R. China.
J. He and Z. Abliz. Institute of Materia Medica, Chinese Academy of Medical Sciences and Peking Union Medical College, Beijing 100050, P.R. China.

Corresponding author: Cui-Hong Wang (e-mail: chwang@chem.ecnu.edu.cn)

Can. J. Chem. Downloaded from www.nrcresearchpress.com by Renmin University of China on 09/02/12
For personal use only.

Ferrocene, as a stable and readily oxidizable organometallic complex, has been widely utilized in multifunctional compounds because of its potential to be used in electroluminescence, information storage, and photochemical devices.[17,18] With their importance to material chemistry, there is increasing interest in the construction of novel ferrocenyl bimetallic oligomers or polymers.[19] For example, in the early 1990s, the synthesis and oxidation of Pt(II)–, Ru(II)–, Os (II)–, and Mn(I)–ferrocenylacetylide complexes were reported by the groups of Sato, Werner, Wong,[20] and Wolf.[21] After that the possibility of nonlinear optical response and the important role of the mixed-valence states in these complexes have been extensively investigated. For instance, Wolf and co-workers[21] synthesized a series of novel ruthenium(II) bisferrocenylacetylide complexes and investigated the effect of ancillaryl ligands on electronic delocalization.

In the past decade, the design and construction of platinum–acetylide dendrimers has attracted a great deal of attention because of their potential to provide new nano-sized organometallic materials.[18] For instance, Takahashi and coworkers[22a] reported the preparation of a new family of platinum–acetylide dendrimers possessing a porphyrin core. These novel dendrimers exhibited intramolecular energy transfer from platinum–acetylide moieties to the porphyrin core. Inspired in part by our successful results on the synthesis of platinum–acetylide building blocks,[12d,23b–23e] we envisioned that the synthesis of new platinum–bisferrocenylacetylide dendrimers with different spatial orientations would be realized by the proper choice of precursors with predefined angles and symmetry. It is noted that bimetallic metallodendrimers are of interest because of a variety of materials and synthetic applications.[22a,22b,23g] In addition, the possibility of fine-tuning the size and spatial orientation of the metallodendrimers would help provide enhanced understanding of the geometrical influence on the photo- and electro-chemical properties. Herein, we designed and synthesized two series of platinum–bisferrocenylacetylide dendrimers with different spatial orientations (60° and 120°) (Chart 1). The structures of all complexes were characterized by multinuclear NMR (^{1}H, ^{13}C, and ^{31}P) and mass spectrometry (MALDI-TOF-MS and CSI-TOF-MS), and their electrochemical behavior was investigated.

Results and discussion

Synthesis of dendritic platinum–bisferrocenylacetylide complexes

The acidity of C–H bonds in alkynes induced by transition metals has received considerable attention in organometallic chemistry.[23] Herein, we utilized the coupling reaction of *trans*-Pt complexes with C–H bonds in alkynes as key steps to the synthesis of all dendritic bimetallic complexes. Complexes **1a**–**1c** were easily prepared in five steps as indicated in Scheme 1. Fréchet-type dendrons were introduced by an etherification reaction of **3** with corresponding dendritic bromides. From dendritic 3,6-dibromophenanthrene derivatives **4a**–**4c**, dendritic 3,6-diethynylphenanthrenes **6a**–**6c** were obtained by the coupling reaction with (trimethylsilyl)acetylene, followed by deprotection with K_2CO_3 in a mixture of methanol and THF. Compounds **6a**–**6c** were then reacted with 4 equiv of *trans*-$PtI_2(PEt_3)_2$ to give diiodometal complexes **7a**–**7c**, by using similar procedures to those reported in previous studies.[22d,23d] Subsequent coupling reactions of **7a**–**7c** with ferrocenylacetylene resulted in the target Pt–Fe bimetallic dendrimers with a 60° orientation. Another series of 120° dendritic platinum–bisferrocenylacetylide complexes were obtained through similar procedures from known dendritic diiodometal complexes **8a**–**8c**[12d] as outlined in Scheme 2. In all cases, the desired complexes were purified by column chromatography on silica gel using dichloromethane as eluent and were obtained as yellow glassy solids with high purities. They exhibited good solubility in common organic solvents such as CH_2Cl_2 and $CHCl_3$. Moreover, these newly designed metallodendrimers are air- and humidity-stable at room temperature.

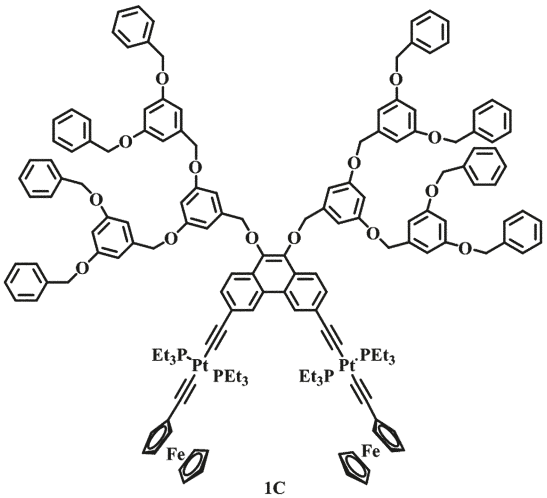
Structure characterization

Multinuclear NMR (^{1}H, ^{13}C, and ^{31}P) analysis of all bimetallic acetylide complexes revealed the formation of discrete highly symmetric species. The room-temperature ^{31}P NMR spectra of dendritic complexes **1a**–**1c** and **2a**–**2c** displayed a sharp singlet (ca. δ = 11.5 ppm) accompanied by platinum satellites (ca. $J_{Pt\text{-}P}$ = 2380 Hz), which is consistent with the trans configuration around the Pt(II) atom. It should be noted that the singlet in the ^{31}P NMR spectra of **1a**–**1c** and **2a**–**2c** exhibited a small downfield shift from the diiodometal precursors by ~2.3 ppm (Fig. 1). This change, as well as the increase in coupling of the flanking ^{195}Pt satellites (ca. ΔJ = +60 Hz), might be caused by the electron-withdrawing effect of the large π-conjugate bridges. Moreover, with the increase in the generation of dendrimers, ^{31}P NMR spectra of complexes do not display obvious changes. The ^{1}H NMR spectra of **1a**–**1c** exhibited characteristic phenanthrene proton resonances in the aromatic area, one singlet and two doublets. Compared with the diPt(II) precursors **7a**–**7c**, the ^{1}H NMR spectra of **1a**–**1c** show that some proton resonances in the phenanthrene ring displayed slight downfield shifts owing to the electron-withdrawing effect of the large π-conjugate bridges. For example, the singlet (δ 8.51 ppm) of **1c** showed an ~0.03 ppm downfield shift from 8.48 ppm in the spectrum of **7c**. Likewise, the analysis of the ^{1}H NMR spectra of **2a**–**2c** agrees well with the characterization of 120° bimetallic acetylide dendrimers.

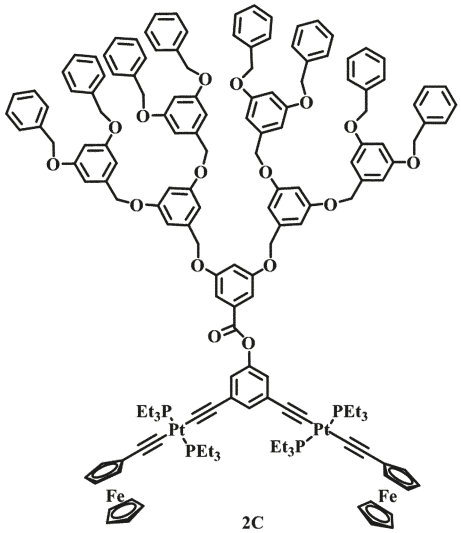
Usually MALDI-TOF-MS studies allow the complexes to remain intact during the analysis process and provide the high resolution required for the unambiguous determination of their absolute molecular weight and molecularity. MALDI-TOF-MS investigation of bimetallic acytelide dendrimers **1a**–**1c** and **2a**–**2c** were carried out first. Because of high molecular weights and complex isotope splitting of such multimetallic dendrimers, it is difficult to get strong mass signals even under the MALDI-TOF-MS conditions. With considerable effort, satisfactory high-resolution MALDI-TOF-MS results of **1a** and **2a** and **2b** were found, confirming the structure of such bimetallic complexes. To obtain the higher resolution of mass spectrometric studies for the other complexes, CSI-TOF-MS studies of **1b**, **1c**, and **2c** were performed. In the CSI-TOF-MS spectrum of **1b**, the peak at m/z = 2124.0, corresponding to the charge state $[M + H]^+$, was observed, and its isotopic resolution is in excellent agreement with the theoretical distribution (see Supplementary data). Moreover, the peaks at m/z = 1495.2 for

Can. J. Chem. Downloaded from www.nrcresearchpress.com by Renmin University of China on 09/02/12
For personal use only.

Chart 1.



1C



2C

1c and m/z = 1505.3 for **2c** were found in the CSI-TOF-MS spectra of [G-3] bimetallic acetylide dendrimers, which corresponds to the $[M + 2H]^{2+}$ charge state. These peaks were isotopically resolved and agree well with their theoretical distribution (Fig. 2).

Simulated molecular models

Flexible high-generation dendrimers often prove difficult to crystallize. All attempts to grow X-ray quality single crystals of dendritic bimetallic complexes **1a**–**1c** and **2a**–**2c** have proven to be unsuccessful to date. Thus, PM6 semiempirical molecular orbital method was employed to optimize the geometry of all dendritic platinum–bisferrocenylacetylide complexes. In the optimized structures of all bimetallic complexes, the ferrocene moieties and phenyl acetylides are σ-bonded to platinum in a trans configuration with 60° and 120° spatial orientations, respectively, whereas the dendrons position on the other side. Coordination around the platinum atoms is square-planar, with slight tetrahedral distortions. Moreover, the distance between two Fe atoms is about 1.7 nm for **1a**–**1c** and 2.4 nm for **2a**–**2c** (Fig. 3; also see Supplementary data).

Absorption and emission properties

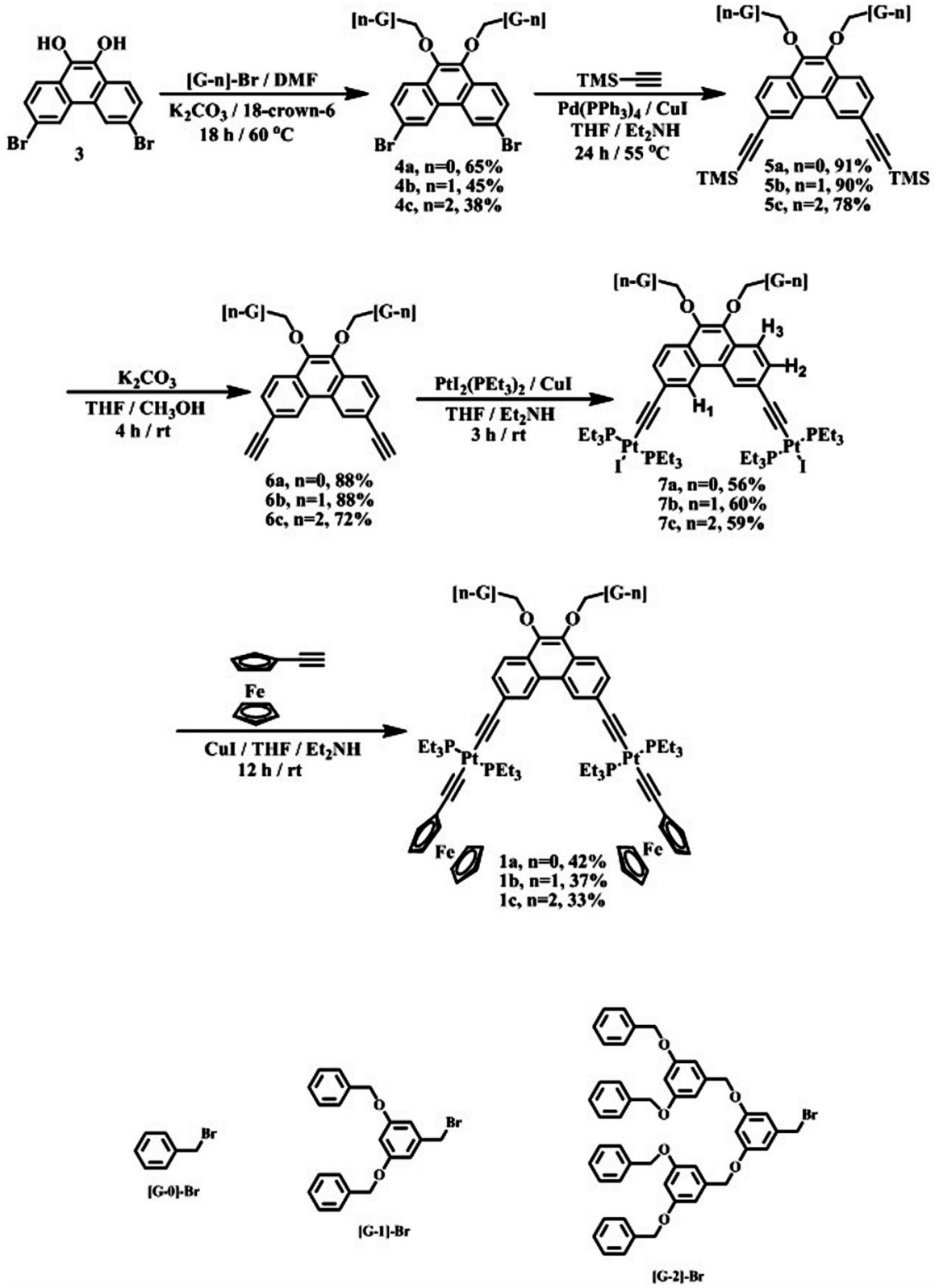
The absorption and emission properties of this series of platinum–acetylide biferrocenyl dendrimers were studied in dilute dichloromethane solution (ca. 10^{-5} mol/L) and the data are collected in Table 1. The electronic absorption spectra of metallodedrimers **1a**–**1c** displayed absorption bands in the range of 264–336 and 357–381 nm. Likewise, the absorption spectra of **2a**–**2c** were dominated by intense relatively broad bands in the near-UV region with strong transitions at higher energy. The dominant absorption band was described as metal-to-ligand charge transfer (MLCT) transitions according to a similar previous report.[24] Upon photo excitation, all metallodendrimers show weak luminescence in dichloromethane solution at room temperature. For example, upon being excited at 362 nm, **1a**–**1c** feature a band with a maximum at 406–409 nm in dilute dichloromethane solution (ca. 10^{-5} mol/L). Furthermore, in the emission spectrum of each compound, the approximate mirror symmetry with the respect to the lowest energy absorption bands was observed, which indicated that the same optical transition was involved in both absorption and emission processes. In addition, a small Stokes shift was found in each fluorescence spectrum, indicating that the emission emanates from the lowest singlet state. It should be noted that the emission bands are only slightly influenced by the increase of dendritic generations.

Electrochemistry properties

The electrochemical behavior of these platinum–acetylide biferrocenyl dendrimers has been investigated via cyclic voltammetry (CV) (Table 2). The study was performed in a dichloromethane solution of **1a**–**1c** and **2a**–**2c** containing 0.2 mol/L n-Bu_4NPF_6 as the supporting electrolyte at a ~7.0 mm^2 glassy carbon electrode. The cyclic voltammograms corresponding to the one-electron oxidation of the ferrocene groups yielded anodic to cathodic peak current ratios of $i_a/i_c \approx 1$ (Fig. 4; also see Supplementary data). Moreover, it was found that the oxidation of the ferrocene moieties in each complex was reversible, which was indicated by the nearly identical cathodic and anodic peak currents, as well as nearly scan-rate-independent peak potentials. The difference between the anodic and cathodic peak potentials (ΔE_p) measured at different scan rates was found to be larger than the theoretical value of 59 mV expected for a reversible one-electron redox reaction, a consequence of the solution ohmic resistance.

With the aim of obtaining the effects of dendron subunits in the electrochemical properties of ferrocenes, the further cyclic voltammetry of these complexes was carried out to gain the diffusion coefficients (D). Different from our previous reports,[12] the D values did not change dramatically with an increase in the molecular weight and molecular size in this study. These results indicate that the dendron moieties are located far from the electrochemical active centers and do not influence the electrochemical activity of ferrocenyl groups, which has been supported by the optimized structures.

Scheme 1. Synthetic route of complexes **1a**–**1c**.



Can. J. Chem. Downloaded from www.nrcresearchpress.com by Renmin University of China on 09/02/12
For personal use only.

Scheme 2. Synthetic route of complexes **2a**–**2c**.

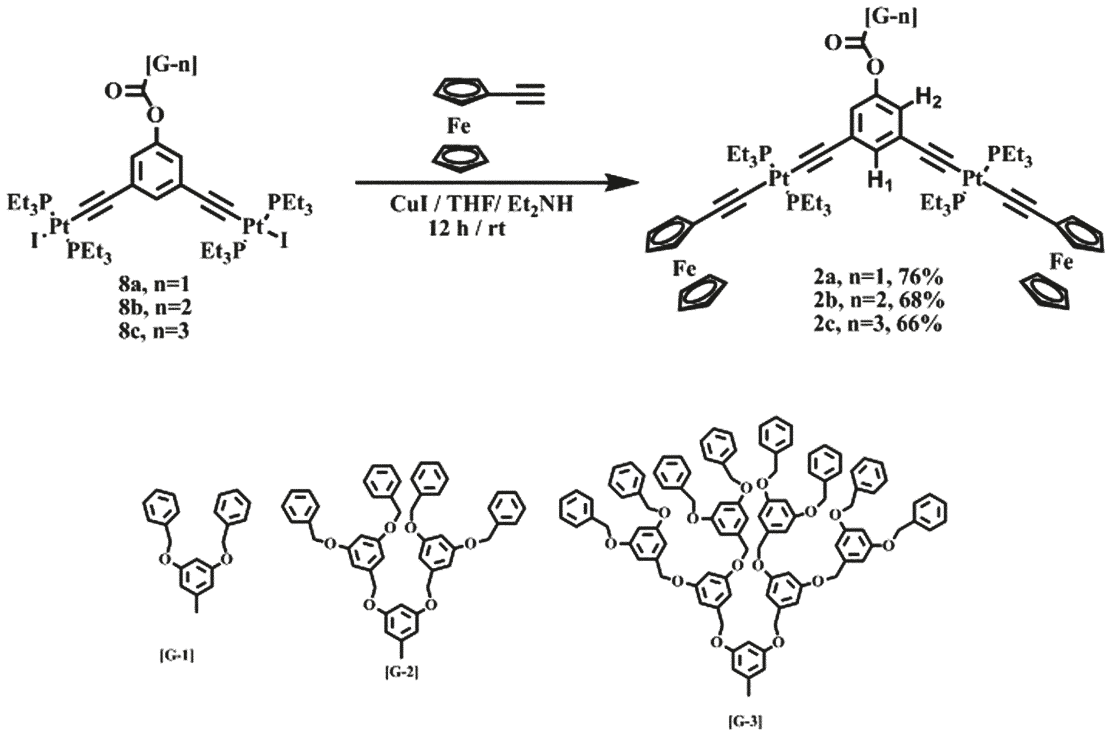
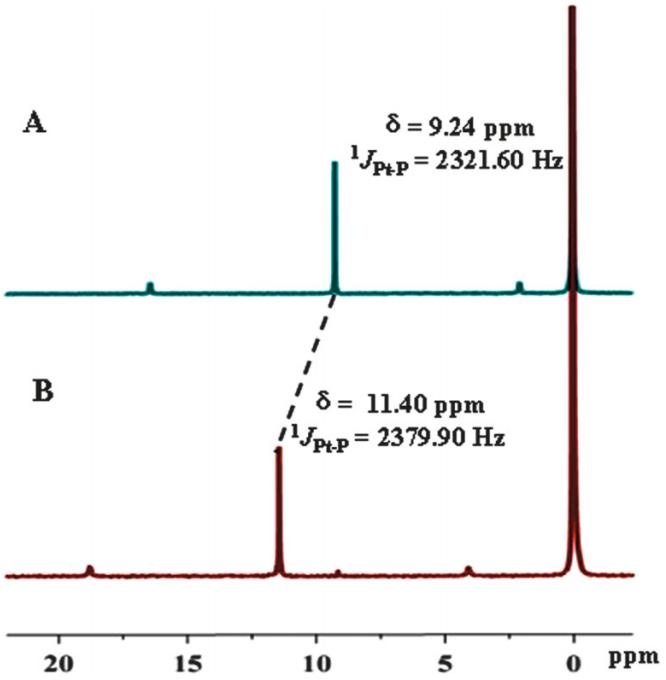


Fig. 1. Partial ^{31}P NMR (400 MHz, $CDCl_3$, 298 K) spectra of **7c** (A) and **1c** (B).



Experimental section

General comments

Materials and reagents

Toluene and THF was distilled from sodium and diethylamine was dried over potassium hydroxide. All solvents were degassed under N_2 for 30 min before use. NMR solvents ($CDCl_3$) and all other reagents were purchased and used without further purification.

Physical measurements and instrumentation

^1H, ^{13}C, and ^{31}P NMR spectra were recorded on a Bruker 300 MHz spectrometer (^1H: 300 MHz; ^{13}C: 75 MHz; and ^{31}P: 121.4 MHz) at 298 K or a 400 MHz spectrometer (^1H: 400 MHz; ^{13}C: 100 MHz; and ^{31}P: 162 MHz) at 298 K. The ^1H and ^{13}C NMR chemical shifts are reported relative to residual solvent signals, and ^{31}P NMR resonances are referenced to an internal standard sample of 85% H_3PO_4 (δ 0.0). Coupling constants (*J*) are in Hz and chemical shifts (δ) are in ppm. Multiplicities are denoted as follows: s = singlet, d = doublet, m = multiplet, and t = triplet. ESI-MS and EI -MS were recorded on an Agilent 5973N mass spectrometer using electrospray or electron ionization. MALDI-HRMS was recorded on a Waters GCT Premier mass spectrometer. CSI-TOF-MS was recorded on a JMS-T100LC mass spectrometer using electrospray ionization.

Spectroscopic measurements

UV–vis spectra were recorded on a Cary 50 Bio UV–vis spectrophotometer. Emission spectra were measured on a Cary Eclipse luminescence spectrometer. Samples for absorption and emission measurements were contained in 1 cm quartz cuvettes. CV was performed using a three-electrode cell and a RST electrochemical work station. The working electrode was a glassy carbon disk with a surface area of ~7.0 mm^2. A SCE electrode was used as reference electrode and a Pt wire as the counter electrode.

Synthesis of 4a–4c

Under an atmosphere of nitrogen, **3** (772 mg, 2.10 mmol), [G-*n*]-Br (for G0, 0.59 mL, 4.83 mmol; for G1, 1.85 g,

Can. J. Chem. Downloaded from www.nrcresearchpress.com by Renmin University of China on 09/02/12
For personal use only.

Can. J. Chem. Downloaded from www.nrcresearchpress.com by Renmin University of China on 09/02/12
For personal use only.

Fig. 2. Calculated (top trace) and experimental (bottom trace) CSI-TOF-MS spectra of [G-3] bimetallic dendrimers **1c** (A) and **2c** (B).

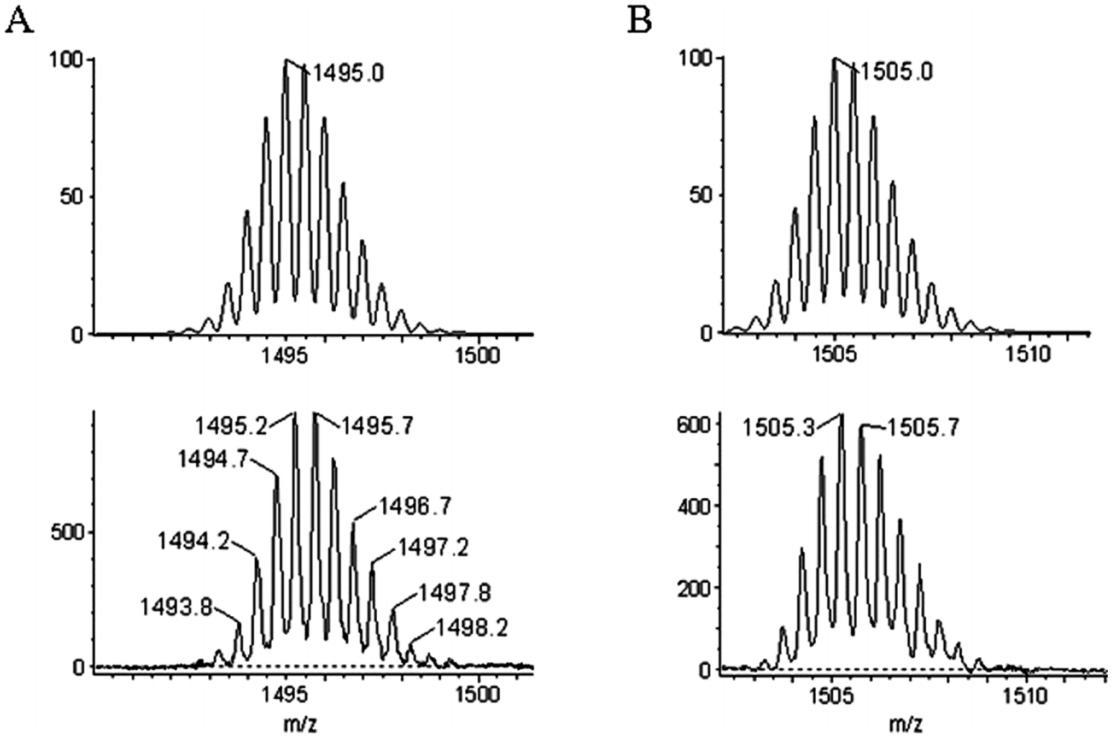


Fig. 3. Simulated molecular model of [G-3] complexes **1c** (A) and **2c** (B) optimized with the PM6 semiempirical molecular orbital method.

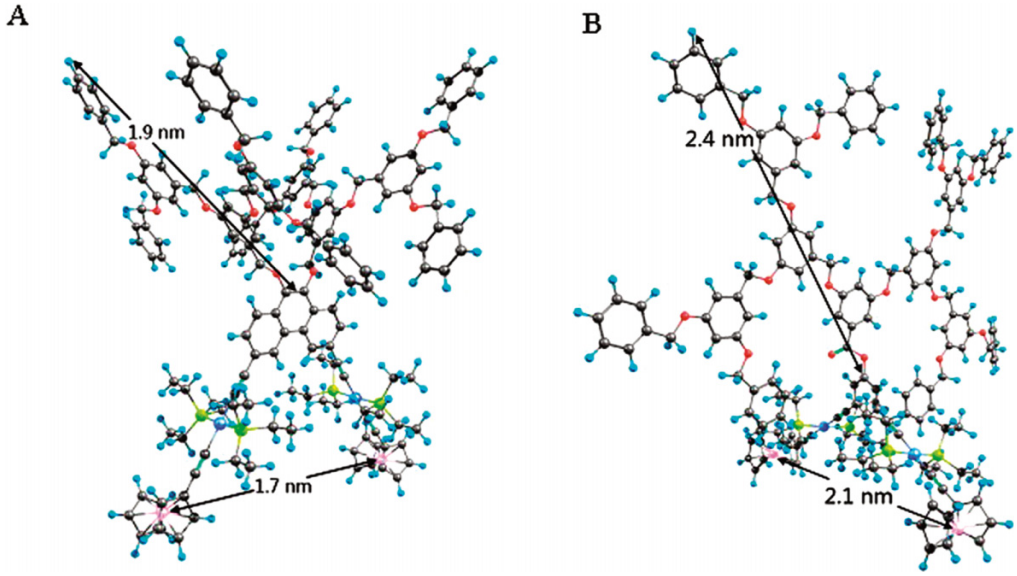


Table 1. UV–vis absorption and emission data for complexes **1a**–**1c** and **2a**–**2c**.

No.	Complex	Absorbance (λ_{max}, nm)	ε_0 ((mol/L)$^{-1}$ cm^{-1})	Emission (λ_{max}, nm)
1	**1a**	264, 335, 359, 378	56007, 42191, 40964, 37052	406, 420
2	**1b**	264, 336, 358, 381	54739, 40499, 39590, 35607	409
3	**1c**	265, 335, 357, 380	54247, 37567, 35417, 30815	408
4	**2a**	264, 288, 334	45204, 39842, 41519	405, 424
5	**2b**	265, 286, 335	47075, 42130, 41216	403, 422
6	**2c**	268, 285, 334	43241, 51956, 42752	409

Table 2. Cyclic voltammetry data for complexes **1a**–**1c** and **2a**–**2c** (CH_2Cl_2 with 0.2 mol/L *n*-Bu_4NPF_6, 298 K).

No.	Complex	$E_{1/2}$ (V vs SCE)	10^5 D (cm^2 s^{-1})
1	**1a**	0.339±0.002	1.19±0.02
2	**1b**	0.332±0.003	1.09±0.02
3	**1c**	0.323±0.002	1.07±0.02
4	**2a**	0.348±0.001	1.04±0.01
5	**2b**	0.340±0.001	1.04±0.01
6	**2c**	0.323±0.003	0.97±0.01

Note: $E_{1/2}$, half-wave potential; D, diffusion coefficient.

4.83 mmol; for G2, 3.9 g, 4.83 mmol), and K_2CO_3 (2.9 g, 21.0 mmol) were dissolved in DMF (25 mL). The mixture was heated at reflux for 18 h and then cooled to room temperature. Solvent was distilled and the resulting mixture was poured into water and extracted with methylene chloride (3 × 15 mL). The methylene chloride solution was washed with water, dried over anhydrous magnesium sulfate, and filtered. The crude products were purified by column chromatography on silica gel (dichloromethane / petroleum ether, ~1:1) to give compounds **4a**–**4c**.

4a

Yield (white solid): 0.58 g, 65%; mp 192 °C. R_f 0.74 (dichloromethane / petroleum ether, 1;1). ^{1}H NMR ($CDCl_3$, 300 MHz) δ: 8.66 (s, H_1, 2H), 8.10 (d, H_2, J = 8.7 Hz, 2H), 7.69 (d, H_3, J = 6.3 Hz, 2H), 7.52–7.49 (m, Ph*H*, 4H), 7.43–7.36 (m, Ph*H*, 6H), 5.27 (s, PhCH_2O, 4H). ^{13}C NMR ($CDCl_3$, 75 MHz) δ: 143.2, 136.9, 130.6, 129.0, 128.6, 128.4, 125.4, 124.3, 120.6, 75.5. MALDI-HRMS for **4a** *m*/*z* calcd for $C_{28}H_{20}Br_2O_2Na$ ([M + Na]$^+$): 568.97; found: 569.00.

4b

Yield (white glassy solid): 0.92 g, 45%; mp 152 °C. R_f 0.50 (dichloromethane / petroleum ether, 3:1). ^{1}H NMR ($CDCl_3$, 300 MHz) δ: 8.67 (d, H_1, J = 1.5 Hz, 2H), 8.08 (d, H_2, J = 8.7 Hz, 2H), 7.69 (d, H_3, J = 9.0 Hz, 2H), 7.37–7.29 (m, Ph*H*, 20H), 6.74 (d, Ph*H*, J = 2.1 Hz, 4H), 6.57 (t, Ph*H*, J = 2.1 Hz, 2H), 5.18 (s, PhCH_2O, 4H), 4.93 (s, PhCH_2O, 8H). ^{13}C NMR ($CDCl_3$, 75 MHz) δ: 160.1, 143.1, 139.3, 136.7, 130.7, 129.1, 128.6, 128.3, 128.0, 127.5, 125.5, 124.3, 120.7, 106.9, 101.9, 75.3, 70.1. MALDI-HRMS of **4b** *m*/*z* calcd for $C_{56}H_{44}Br_2O_6Na$ ([M + Na]$^+$): 993.14; found: 993.20.

4c

Yield (white glassy solid): 1.45 g, 38%; mp: 46 °C. R_f 0.36 (dichloromethane / petroleum ether, 4:1). ^{1}H NMR ($CDCl_3$, 400 MHz) δ: 8.65 (s, H_1, 2H), 8.09 (d, H_2, J = 8.8 Hz, 2H), 7.69 (d, H_3, J = 6.3 Hz, 2H), 7.34–7.28 (m, Ph*H*, 40H), 6.72 (s, Ph*H*, 4H), 6.62 (s, Ph*H*, 8H), 6.51 (s, Ph*H*, 6H), 5.15 (s, PhCH_2O, 4H), 4.93 (s, PhCH_2O, 16H), 4.82 (s, PhCH_2O, 8H). ^{13}C NMR ($CDCl_3$, 100 MHz) δ: 160.1, 160.0, 143.2, 139.4, 139.2, 136.7, 130.7, 129.1, 128.5, 128.3, 127.9, 127.5, 124.3, 120.8, 106.8, 106.4, 102.0, 101.6, 70.0, 69.9. MALDI-HRMS of **4c** *m*/*z* calcd for $C_{112}H_{92}Br_2O_{14}Na$ ([M + Na]$^+$): 1841.48; found: 1841.60.

Synthesis of 5a–5c

To a 50 mL round-bottomed Schlenk flask were added **4a**–**4c** (**4a**, 200 mg, 0.36 mmol; **4b**, 250 mg, 0.26 mmol; and **4c**, 300 mg, 0.16 mmol), trimethylsilylethyne (for G1, 0.41 mL, 2.88 mmol; for G2, 0.30 mL, 2.08 mmol; and for G3, 0.19 mL, 1.28 mmol), $Pd(PPh_3)_4$ (for G1, 42 mg; for G2, 30 mg; and for G3, 19 mg), and CuI (for G1, 7.0 mg; for G2, 5.0 mg; and for G3, 3.0 mg). Then a mixture of tetrahydrofuran (for G1, 4.0 mL; for G2, 3.0 mL; and for G3, 2.0 mL) and dry diethylamine (for G1, 4.0 mL; for G2, 3.0 mL; and for G3, 2.0 mL) was added under nitrogen. The solution was stirred at 66 °C for 24 h. The solvent was removed under vacuum and the resulting yellow residue was purified via column chromatography on silica gel (dichloromethane / petroleum ether, ~1:2) to provide compounds **5a**–**5c** (yields: G1, 91%; G2, 90%; and G3, 78%).

Synthesis of 6a–6c

Desilylation of **5a**–**5c** (**5a**, 105 mg, 0.18 mmol; **5b**, 182 mg, 0.18 mmol; and **5c**, 335 mg, 0.18 mmol) was achieved by stirring the compounds in a K_2CO_3 suspending solution of methanol–THF (100 mg in 20 mL methanol and 20 mL THF) for 4 h. The solution was carefully diluted with 30 mL of water and organic product was extracted with diethyl ether. Drying the ether phase over magnesium sulfate and subsequent filtration resulted in slightly yellow oil after removal of the solvent. Compounds **6a**–**6c** were obtained by column chromatography on silica gel (dichloromethane / petroleum ether, ~1:1).

6a

Yield (pale yellow solid): 92 mg, 88%; mp 138 °C. R_f 0.31 (dichloromethane / petroleum ether, 1:3). ^{1}H NMR ($CDCl_3$, 400 MHz) δ: 8.76 (s, H_1, 2H), 8.19 (d, H_2, J = 8.0 Hz, 2H), 7.68 (d, H_3, J = 8.8 Hz, 2H), 7.53–7.51 (m, H_3 and Ph*H*, 4H), 7.41–7.39 (m, Ph*H*, 6H), 5.28 (s, PhCH_2O, 4H), 3.22 (s, C≡C*H*, 2H). ^{13}C NMR ($CDCl_3$, 100 MHz) δ: 144.0, 137.1, 130.2, 129.5, 128.6, 128.4, 128.3, 127.8, 126.9, 122.7 119.8, 84.0, 77.9, 75.6. EI HRMS of **6a** *m*/*z* calcd for $C_{32}H_{22}O_2$: 438.1620 (M$^+$); found: 438.1623.

6b

Yield (pale yellow solid): 160 mg, 88%; mp 104 °C. R_f 0.31 (dichloromethane / petroleum ether, 1:1). ^{1}H NMR ($CDCl_3$, 400 MHz) δ: 8.77 (s, H_1, 2H), 8.17 (d, H_2, J = 8.4 Hz, 2H), 7.68 (d, H_3, J = 8.4 Hz, 2H), 7.36–7.33 (m, Ph*H*, 20H), 6.76 (s, Ph*H*, 4H), 6.56 (s, Ph*H*, 2H), 5.20 (s, PhCH_2O, 4H), 4.92 (s, PhCH_2O, 8H), 3.23 (s, C≡C*H*, 2H). ^{13}C NMR ($CDCl_3$, 100 MHz) δ: 160.1, 143.9, 139.4, 136.7, 130.3, 129.4, 128.6, 128.0, 127.5, 127.0, 122.6, 119.9, 106.9, 101.9, 84.0, 78.0, 75.3, 70.1. ESI HRMS of **6b** *m*/*z* calcd for $C_{60}H_{46}NaO_6$ ([M + Na]$^+$): 885.3187; found: 885.3175.

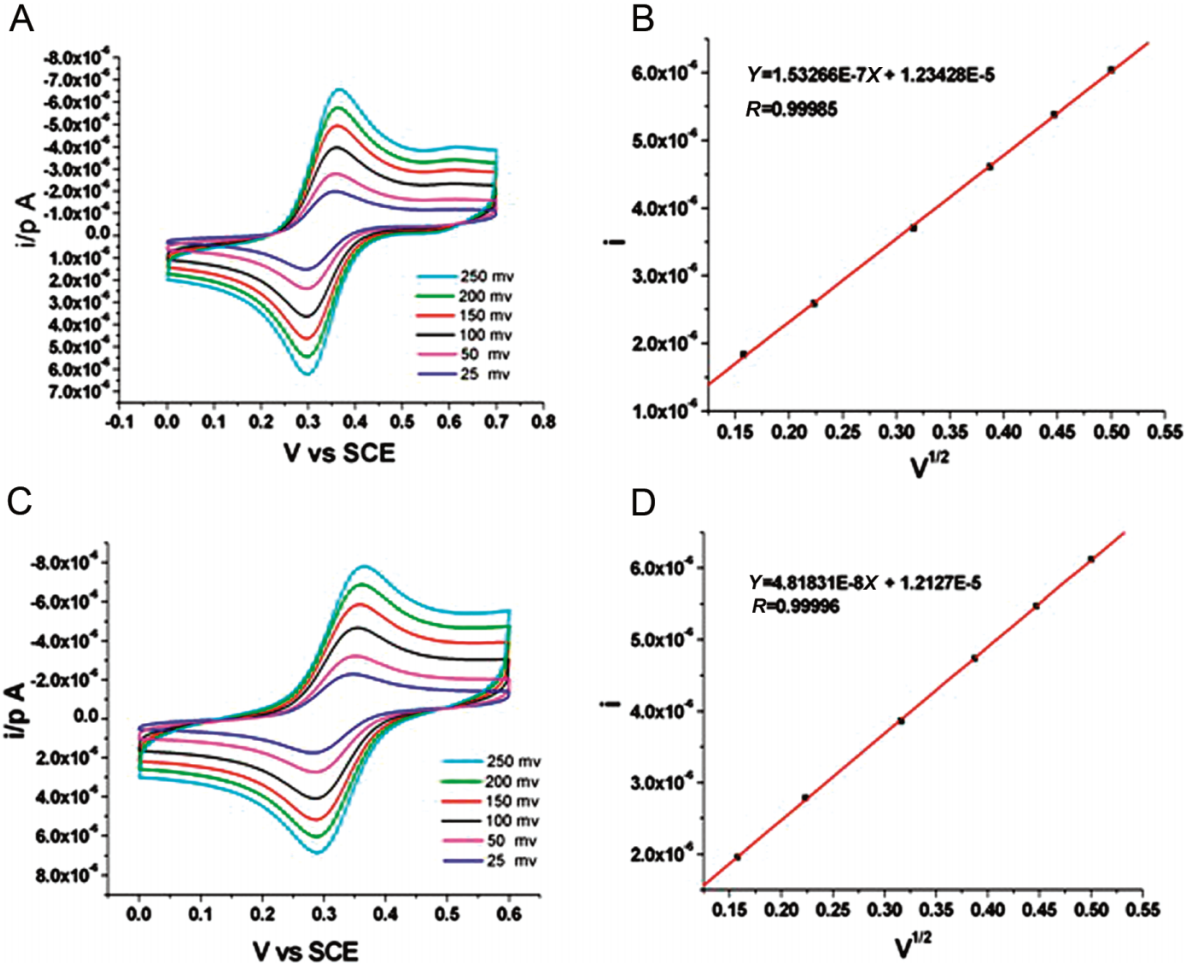
6c

Yield (pale yellow solid): 241 mg, 72%; mp 42 °C. R_f 0.38 (dichloromethane / petroleum ether, 3:1). ^{1}H NMR ($CDCl_3$, 400 MHz) δ: 8.76 (s, H_1, 2H), 8.19 (d, H_2, J = 6.8 Hz, 2H), 7.69 (d, H_3, J = 6.4 Hz, 2H), 7.34–7.30 (m, Ph*H*, 40H), 6.73 (s, Ph*H*, 4H), 6.63 (s, Ph*H*, 8H), 6.51 (s, Ph*H*, 6H), 5.17 (s, PhCH_2O, 4H), 4.93 (s, PhCH_2O, 16H), 4.82 (s, PhCH_2O, 8H), 3.20 (s, C≡C*H*, 2H). ^{13}C NMR ($CDCl_3$, 100 MHz) δ:

Can. J. Chem. Downloaded from www.nrcresearchpress.com by Renmin University of China on 09/02/12
For personal use only.

Can. J. Chem. Downloaded from www.nrcresearchpress.com by Renmin University of China on 09/02/12
For personal use only.

Fig. 4. Cyclic voltammograms of **1c** (A) and **2c** (C) at a scan rate of 25–250 mV/s and plot of the experimental ratio i vs $v^{1/2}$ at a scan rate of 25–250 mV/s (B for **1c** and D for **2c**). i, intensity of electric current; v, voltage.



160.1, 160.0, 143.9, 139.5, 139.2, 136.8, 130.3, 129.4, 128.5, 128.4, 127.9, 127.5, 127.0, 122.6, 120.0, 106.8, 106.4, 102.0, 101.6, 84.0, 78.1, 70.0, 69.9. MALDI-HRMS for ^{13}C NMR ($CDCl_3$, 100 MHz) δ: 160.1, 160.0, 143.9, 139.5, 139.2, 136.8, 130.3, 129.4, 128.5, 128.4, 127.9, 127.5, 127.0, 122.6, 120.0, 106.8, 106.4, 102.0, 101.6, 84.0, 78.1, 75.3, 70.0, 69.9. ESI HRMS of **6c** *m/z* calcd for $C_{116}H_{94}NaO_{14}$ ($[M + Na]^+$): 1733.6541; found: 1733.6473.

Synthesis of 7a–7c

To a solution of CuI (4 mg, 0.02 mmol) and $Pt(PEt_3)_2I_2$ (254 mg, 0.37 mmol) in 12 mL THF and 5 mL diethylamine was added dropwise to a solution of compound **6a**, **6b**, or **6c** (**6a**, 40 mg, 0.09 mmol; **6b**, 78 mg, 0.09 mmol; or **6c**, 154 mg, 0.09 mmol)) in THF (3 mL) under an atmosphere of nitrogen. The mixture was stirred at room temperature for 3 h. The solvent was removed in vacuo and the residue was purified via column column chromatography with dichloromethane as eluent afforded the products **7a**–**7c** as a yellow solid.

7a

Yield (pale yellow solid): 78 mg, 56%; mp 180 °C. R_f = 0.45 (dichloromethane / petroleum ether, 1:1). ^{1}H NMR ($CDCl_3$, 400 MHz) δ: 8.46 (s, H_1, 2H), 8.11 (d, H_2, J = 8.8 Hz, 2H), 7.55–7.49 (m, H_3 and Ph*H*, 6H), 7.43–7.36 (m, Ph*H*, 6H), 5.24 (s, PhCH_2O, 4H), 2.28–2.27 (m, PhCH_2CH$_3$, 24H), 1.25–1.18 (m, PhCH$_2$$CH_3$, 36H). ^{13}C NMR ($CDCl_3$, 100 MHz) δ: 143.2, 137.6, 129.7, 128.5, 128.3, 128.1, 127.1, 125.9, 124.2, 122.1, 75.4, 16.9, 16.7, 16.6, 8.5, 8.4, 8.2. ^{31}P NMR ($CDCl_3$, 161.9 Hz) δ: 9.18 (s, $^1J_{Pt–P}$ = 2323.3 Hz). MALDI-HRMS of **7a** *m/z* calcd for $C_{56}H_{81}I_2O_2P_4Pt_2$ ($[M + H]^+$): 1553.26; found: 1552.90.

7b

Yield (yellow solid): 107 mg, 60%; mp 55 °C. R_f 0.57 (dichloromethane / petroleum ether, 3:1). ^{1}H NMR ($CDCl_3$, 400 MHz) δ: 8.47 (s, H_1, 2H), 8.09 (d, H_2, J = 8.8 Hz, 2H), 7.51 (d, H_3, J = 8.0 Hz, 2H), 7.38–7.32 (m, Ph*H*, 20H), 6.80 (s, Ph*H*, 4H), 6.56 (s, Ph*H*, 2H), 5.19 (s, PhCH_2O, 4H), 4.93 (s, PhCH_2O, 8H), 2.28 (br, PhCH_2CH$_3$, 24H), 1.26–1.19 (m, PhCH$_2$$CH_3$, 36H). ^{13}C NMR ($CDCl_3$, 100 MHz) δ: 160.1, 143.0, 139.9, 136.8, 129.8, 128.5, 128.0, 127.6, 126.0, 124.2, 122.1, 106.9, 101.8, 90.9, 75.1, 70.1, 16.9, 16.7, 16.6, 8.4. ^{31}P NMR ($CDCl_3$, 161.9 Hz) δ: 9.17 (s, $^1J_{Pt–P}$ = 2323.3 Hz).

7c

Yield (yellow solid): 150 mg, 49%; mp 49 °C. R_f 0.54 (dichloromethane / petroleum ether, 6:1). ^{1}H NMR ($CDCl_3$,

Can. J. Chem. Downloaded from www.nrcresearchpress.com by Renmin University of China on 09/02/12
For personal use only.

400 MHz) δ: 8.48 (s, H_1, 2H), 8.12 (d, H_2, J = 8.4 Hz, 2H), 7.53 (d, H_3, J = 7.6 Hz, 2H), 7.34–7.29 (m, Ph*H*, 40H), 6.78 (s, Ph*H*, 4H), 6.63 (s, Ph*H*, 8H), 6.51 (s, Ph*H*, 6H), 5.16 (s, PhCH_2O, 4H), 4.93 (s, PhCH_2O, 16H), 4.82 (s, PhCH_2O, 8H), 2.27 (br, PhCH_2CH_3, 24H), 1.26–1.17 (m, PhCH$_2CH_3$, 36H). ^{13}C NMR ($CDCl_3$, 100 MHz) δ: 160.1, 143.1, 140.0, 139.2, 136.8, 129.9, 128.5, 128.3, 127.9, 127.5, 127.0, 122.0, 106.7, 106.5, 101.8, 101.6, 75.2, 70.0, 69.9, 16.9, 16.8, 16.6, 8.4. ^{31}P NMR ($CDCl_3$, 161.9 Hz) δ: 9.24 (s, $^1J_{Pt-P}$ = 2321.6 Hz).

Synthesis of 1a–1c

One of complexes **7a**–**7c** (**7a**, 93 mg, 0.06 mmol; **7b**, 119 mg, 0.06 mmol; or **7c**, 170 mg, 0.06 mmol) and ethynylferrocene (50 mg, 0.24 mmol) were dissolved in a mixture of THF (10 mL) and diethylamine (5 mL). CuI (2.0 mg) was added to this reaction mixture as a catalyst. The yellowish brown mixture was then stirred at room temperature for 12 h, and the solvent was removed under reduced pressure. The greenish yellow gummy residue was then purified by column chromatography on silica gel with dichloromethane as the eluent to afford a brownish yellow glassy solid of either **1a**, **1b**, or **1c**.

1a

Yield (brownish yellow glassy solid): 39 mg, 42%; mp 47 °C. R_f 0.58 (dichloromethane). ^{1}H NMR ($CDCl_3$, 400 MHz) δ: 8.48 (s, H_1, 2H), 8.08 (d, H_2, J = 8.0 Hz, 2H), 7.56–7.50 (m, Ph*H*, 6H), 7.41–7.36 (m, Ph*H*, 6H), 5.23 (s, PhCH_2O, 4H), 4.25 (s, Fc–*H,* 4H), 4.15 (s, Fc–*H*, 10H), 4.07 (s, Fc–*H*, 4H), 2.25–2.23 (m, PhCH_2CH_3, 24H), 1.33–1.27 (m, PhCH$_2CH_3$, 36H). ^{13}C NMR ($CDCl_3$, 100 MHz) δ: 167.7, 143.0, 137.6, 132.3, 130.9, 130.0, 128.8, 128.5, 128.3, 128.0, 126.8, 124.4, 121.8, 75.4, 70.3, 70.0, 69.4, 67.0, 65.5, 16.6, 16.5, 16.3, 8.5. ^{31}P NMR ($CDCl_3$, 161.9 Hz) δ: 11.5 (s, $^1J_{Pt-P}$ = 2381.5 Hz). MALDI-HRMS of **1a** m/z calcd for $C_{80}H_{99}Fe_2O_2P_4Pt_2$ ([M + H]$^+$): 1717.46; found: 1721.60.

1b

Yield (brownish yellow glassy solid): 48 mg, 37%; mp 49 °C. R_f 0.51 (dichloromethane). ^{1}H NMR ($CDCl_3$, 400 MHz) δ: 8.51 (s, H_1, 2H), 8.09 (d, H_2, J = 7.6 Hz, 2H), 7.54 (d, H_3, J = 8.0 Hz, 2H), 7.39–7.32 (m, Ph*H*, 20H), 6.82 (s, Ph*H*, 4H), 6.58 (s, Ph*H*, 2H), 5.20 (s, PhCH_2O, 4H), 4.94 (s, PhCH_2O, 8H), 4.27 (s, Fc–*H*, 4H), 4.17 (s, Fc–*H*, 10H), 4.09 (s, Fc–*H*, 4H), 2.27–2.26 (m, PhCH_2CH_3, 24H), 1.40–1.29 (m, PhCH$_2CH_3$, 36H). ^{13}C NMR ($CDCl_3$, 100 MHz) δ: 160.1, 140.1, 136.8, 130.2, 128.5, 128.4, 127.9, 127.6, 124.4, 121.8, 106.8, 101.8, 75.1, 70.3, 69.4, 67.0, 16.6, 16.5, 16.3, 8.5. ^{31}P NMR ($CDCl_3$, 161.9 Hz) δ: 11.5 (s, $^1J_{Pt-P}$ = 2379.9 Hz). CSI-TOF-MS of **1b** m/z calcd for $C_{108}H_{123}Fe_2O_6P_4Pt_2$ ([M + H]$^+$): 2141.63; found: 2142.00.

1c

Yield (brownish yellow glassy solid): 56 mg, 33%; mp: 50 °C. R_f 0.45(dichloromethane). ^{1}H NMR ($CDCl_3$, 400 MHz) δ: 8.51 (s, H_1, 2H), 8.11 (d, H_2, J = 8.4 Hz, 2H), 7.55 (d, H_3, J = 8.0 Hz, 2H), 7.35–7.30 (m, Ph*H*, 40H), 6.80 (s, Ph*H*, 4H), 6.65 (s, Ph*H*, 8H), 6.52 (s, Ph*H*, 6H), 5.17 (s, PhCH_2O, 4H), 4.94 (s, PhCH_2O, 16H), 4.82 (s, PhCH_2O, 8H), 4.26 (s, Fc–*H*, 4H), 4.16 (s, Fc–*H*, 10H), 4.08 (s, Fc–*H*, 4H), 2.35–2.33 (m, PhCH_2CH_3, 24H), 1.39–1.27 (m, PhCH$_2CH_3$, 36H). ^{13}C NMR ($CDCl_3$, 100 MHz) δ: 160.1, 160.0, 140.1, 139.2, 136.8, 128.5, 127.9, 127.5, 106.7, 106.5, 101.6, 70.3, 70.0, 69.9, 69.4, 67.0, 16.6, 16.4, 16.3, 8.5. ^{31}P NMR ($CDCl_3$, 161.9 Hz) δ: 11.4 (s, $^1J_{Pt-P}$ = 2379.9 Hz). CSI-TOF-MS of **1c** m/z calcd for $C_{164}H_{172}Fe_2O_{14}P_4Pt_2$ ([M + 2H]$^{2+}$): 1495.00; found: 1495.20.

Synthesis of 2a–2c

The synthetic procedure of **2a**–**2c** was similar to that for **1a**–**1c** except that 120° [G-1]–[G-3] dendritic precursors **8a**–**8c** were used and the brownish yellow glassy solids were obtained as desired products with moderate yields (G1, 76%; G2, 68%; and G3, 66%).

2a

Yield (brownish yellow glassy solid): 101 mg, 76%; mp: 49 °C. R_f 0.23 (dichloromethane / petroleum ether, 3:1). ^{1}H NMR ($CDCl_3$, 400 MHz) δ: 7.46–7.35 (m, Ph*H*, 12H), 7.12 (s, H_1, 1H), 6.87–6.85 (m, H_2 and Ph*H*, 3H), 5.11 (s, PhCH_2O, 4H), 4.23 (s, Fc–*H*, 4H), 4.14 (s, Fc–*H*, 10H), 4.06 (s, Fc–*H*, 4H), 2.17–2.18 (m, PhCH_2CH_3, 24H), 1.27–1.21 (m, PhCH$_2CH_3$, 36H). ^{13}C NMR ($CDCl_3$, 100 MHz) δ: 164.7, 159.9, 150.3, 136.4, 131.8, 131.2, 129.6, 128.6, 128.1, 127.5, 120.6, 109.0, 108.7, 108.5, 107.7, 105.1, 102.3, 72.8, 70.4, 70.2, 69.3, 66.9, 16.6, 16.4, 16.2, 14.1, 8.4. ^{31}P NMR ($CDCl_3$, 162 Hz) δ: 11.4 (s, $^1J_{Pt-P}$ = 2386.4 Hz). MALDI-HRMS of **2a** m/z calcd for $C_{79}H_{99}Fe_2O_4P_4Pt_2$ ([M + H]$^+$): 1737.45; found: 1736.50.

2b

Yield (brownish yellow glassy solid): 86 mg, 68%; mp 53 °C. R_f 0.67 (dichloromethane / ethyl acetate, 1:20). ^{1}H NMR ($CDCl_3$, 400 MHz) δ: 7.43–7.30 (m, Ph*H*, 22H), 7.11 (s, H_1, 1H), 6.84–6.82 (m, H_2 and Ph*H*, 3H), 6.69 (s, Ph*H*, 4H), 6.58 (s, Ph*H*, 2H), 5.04 (s, PhCH_2O, 12H), 4.22 (s, Fc–*H*, 4H), 4.18 (s, Fc–*H*, 10H), 4.05 (s, Fc–*H*, 4H), 2.16 (br, PhCH_2CH_3, 24H), 1.24–1.18 (m, PhCH$_2CH_3$, 36H). ^{13}C NMR ($CDCl_3$, 100 MHz) δ: 160.2, 159.8, 138.8, 136.8, 128.6, 128.0, 127.5, 109.0, 106.4, 101.8, 70.2, 69.4, 67.0, 16.6, 16.4, 16.2, 8.4. ^{31}P NMR ($CDCl_3$, 161.9 Hz) δ: 11.5 (s, $^1J_{Pt-P}$ = 2379.9 Hz). MALDI-HRMS of **2b** m/z calcd for $C_{107}H_{123}Fe_2O_8P_4Pt_2$ ([M + H]$^+$): 2161.62; found: 2161.60.

2c

Yield (brownish yellow glassy solid): 117 mg, 66%; mp 55 °C. R_f 0.67 (dichloromethane). ^{1}H NMR ($CDCl_3$, 400 MHz) δ: 7.44 (s, Ph*H*, 1H), 7.40–7.30 (m, Ph*H*, 42H), 7.10 (s, H_1, 1H), 6.84 (s, H_2 and Ph*H*, 3H), 6.67 (s, Ph*H*, 12H), 6.56 (s, Ph*H*, 6H), 5.01–4.95 (m, PhCH_2O, 28), 4.22 (s, Fc–*H*, 4H), 4.13 (s, Fc–*H*, 10H), 4.05 (s, Fc–*H*, 4H), 2.14 (br, Fc–*H*, 24H), 1.28–1.17 (m, Fc–*H*, 36H). ^{13}C NMR ($CDCl_3$, 100 MHz) δ: 160.2, 160.1, 159.8, 139.2, 136.8, 128.6, 128.0, 127.5, 106.5, 106.4, 106.7, 70.2, 70.1, 70.0, 69.4, 66.9, 16.6, 16.4, 16.2, 8.4. ^{31}P NMR ($CDCl_3$, 162 Hz) δ: 11.4 (s, $^1J_{Pt-P}$ = 2379.9 Hz). CSI-TOF-MS of **2c** m/z calcd for $C_{163}H_{172}Fe_2O_{16}P_4Pt_2$ ([M + 2H]$^{2+}$): 1505.00; found: 1505.30.

Can. J. Chem. Downloaded from www.nrcresearchpress.com by Renmin University of China on 09/02/12
For personal use only.

Conclusion

By employing the coupling reaction of *trans*-Pt complexes with C–H bonds in alkynes as key steps, we have successfully prepared a new family of dendritic platinum–bisferrocenylacetylide complexes from simple starting materials in satisfactory yields. Multinuclear NMR (^{1}H, ^{13}C, and ^{31}P) analysis of all metallodendrimers displayed very similar characteristics that are indicative of the generation of the desired species. The sharp NMR signals in both ^{31}P {^{1}H} and ^{1}H NMR spectra, along with the solubility of these species, ruled out the formation of oligomers. Moreover, mass spectrometric studies, including MALDI-TOF-MS and CSI-TOF-MS, provided further evidence for the unambiguous determination of their absolute molecular weight and molecularity. All bimetallic metallodendrimers exhibit remarkable solubility in common organic solvents, such as dichloromethane and chloroform. Furthermore, these newly designed metallodendrimers are air- and humidity-stable at room temperature. Electrochemical studies reveal that all of the redox moieties are stable, independent, and electrochemically active. In addition, all metallodendrimers show one-electron reaction responses and the increased size of the assemblies do not influence *D*. To the best of our knowledge, this is the first report on the synthesis of platinum–bisferrocenylacetylide dendrimers, which obviously enriches the library of heterometallic dendrimers connected by unsaturated carbon-rich bridges.

Supplementary data

Supplementary data are available with the article through the journal Web site http://nrcresearchpress.com/doi/suppl/10.1130/v11-159.

Acknowledgments

Professor C.-H. Wang thanks East China Normal University for financial support.

References

(1) (a) Fréchet, J. M. J.; Tomalia, D.A. *Dendrimers and Other Dendritic Polymers;* VCH-Wiley: New York, 2000; (b) Newkome, G. R.; Moorefield, C. N.; Vögtle, F. *Dendrimers and Dendrons: Concepts, Synthesis, Perspectives;* Wiley-VCH: Weinheim, 2001; (c) Zimmerman, S. C.; Lawless, L. J. *Supramolecular Chemistry of Dendrimers;* Topics in Current Chemistry 217; Springer: Berlin, 2001; p 95; (d) Matthews, O. A.; Shipway, A. N.; Stoddart, J. F. *Prog. Polym. Sci.* **1998**, *23* (1), 1. doi:10.1016/S0079-6700(97)00025-7.

(2) (a) Grayson, S. M.; Fréchet, J. M. J. *Chem. Rev.* **2001**, *101* (12), 3819. doi:10.1021/cr990116h; PMID:11740922; (b) Hecht, S.; Fréchet, J. M. J. *Angew. Chem. Int. Ed.* **2001**, *40* (1), 74. doi:10.1002/1521-3773(20010105)40:1<74::AID-ANIE74>3.0.CO;2-C; (c) Astruc, D.; Chardac, F. *Chem. Rev.* **2001**, *101* (9), 2991. doi:10.1021/cr010323t; PMID:11749398; (d) van Heerbeek, R.; Kamer, P. C. J.; van Leeuwen, P. W. N. M.; Reek, J. N. H. *Chem. Rev.* **2002**, *102* (10), 3717. doi:10.1021/cr0103874; PMID:12371900; (e) Crespo, L.; Sanclimens, G.; Pons, M.; Giralt, E.; Royo, M.; Albericio, F. *Chem. Rev.* **2005**, *105* (5), 1663. doi:10.1021/cr030449l; PMID:15884786; (f) Tomalia, D. A. *Prog. Polym. Sci.* **2005**, *30* (3–4), 294. doi:10.1016/j.progpolymsci.2005.01.007.

(3) (a) Baars, M. W. P. L.; Kleppinger, R.; Koch, M. H. J.; Yeu, S.-L.; Meijer, E. W. *Angew. Chem. Int. Ed.* **2000**, *39* (7), 1285. doi:10.1002/(SICI)1521-3773(20000403)39:7<1285::AID-ANIE1285>3.0.CO;2-F; (b) Hecht, S.; Vladimirov, N.; Fréchet, J. M. J. *J. Am. Chem. Soc.* **2001**, *123* (1), 18. doi:10.1021/ja003304u; (c) Marsitzky, D.; Vestberg, R.; Blainey, P.; Tang, B. T.; Hawker, C. J.; Carter, K. R. *J. Am. Chem. Soc.* **2001**, *123* (29), 6965. doi:10.1021/ja010020g; (d) Le Derf, F.; Levillain, E.; Trippé, G.; Gorgues, A.; Sallé, M.; Sebastian, R.-M.; Caminade, A.-M.; Majoral, J.-P. *Angew. Chem. Int. Ed.* **2001**, *40* (1), 224. doi:10.1002/1521-3773(20010105)40:1<224::AID-ANIE224>3.0.CO;2-O; (e) Gong, L.-Z.; Hu, Q.-S.; Pu, L. *J. Org. Chem.* **2001**, *66* (7), 2358. doi:10.1021/jo001565g.

(4) (a) Freeman, A. W.; Koene, C.; Malenfant, P. R. L.; Thompson, M. E.; Fréchet, J. M. J. *J. Am. Chem. Soc.* **2000**, *122* (49), 12385. doi:10.1021/ja001356d; (b) Weener, J.-W.; Meijer, E. W. *Adv. Mater. (Deerfield Beach Fla.)* **2000**, *12* (10), 741. doi:10.1002/(SICI)1521-4095(200005)12:10<741::AID-ADMA741>3.0.CO;2-6; (c) Newkome, G. R.; He, E.; Godínez, L. A.; Baker, G. R. *J. Am. Chem. Soc.* **2000**, *122* (41), 9993. doi:10.1021/ja001401h; (d) Lupton, J. M.; Samuel, I. D. W.; Beavington, R.; Burn, P. L.; Bässler, H. *Adv. Mater. (Deerfield Beach Fla.)* **2001**, *13* (4), 258. doi:10.1002/1521-4095(200102)13:4<258::AID-ADMA258>3.0.CO;2-9; (e) Maus, M.; De, R.; Lor, M.; Weil, T.; Mitra, S.; Wiesler, U.-M.; Herrmann, A.; Hofkens, J.; Vosch, T.; Müllen, K.; De Schryver, F. C. *J. Am. Chem. Soc.* **2001**, *123* (31), 7668. doi:10.1021/ja010570e.

(5) (a) Jansen, J. F. G. A.; de Brabander-van den Berg, E. M. M.; Meijer, E. W. *Science* **1994**, *266* (5188), 1226. doi:10.1126/science.266.5188.1226; PMID:17810265; (b) Jansen, J. F. G. A.; Meijer, E. W.; de Brabander-van den Berg, E. M. M. *J. Am. Chem. Soc.* **1995**, *117* (15), 4417. doi:10.1021/ja00120a032; (c) Kovvali, A. S.; Sirkar, K. K. *Ind. Eng. Chem. Res.* **2001**, *40* (11), 2502. doi:10.1021/ie0010520.

(6) Newkome, G. R.; Moorefield, C. N.; Baker, G. R.; Johnson, A. L.; Behara, R. K. *Angew. Chem. Int. Ed. Engl.* **1991**, *30* (9), 1176. doi:10.1002/anie.199111761.

(7) Denti, G.; Serroni, S.; Campagna, S.; Ricevuto, V.; Balzani, V. *Inorg. Chim. Acta* **1991**, *182* (2), 127. doi:10.1016/S0020-1693(00)90144-0.

(8) (a) Newkome, G. R.; Moorefield, F.; Vögtle, F. *Dendritic Molecules: Concepts, Synthesis, Properties;* VCH: Weinheim, Germany, 1996; (b) Constable, E. C. *Chem. Commun. (Camb.)* **1997**, *1073*. doi:10.1039/A605102B; (c) Zeng, F.; Zimmerman, S. C. *Chem. Rev.* **1997**, *97* (5), 1681. doi:10.1021/cr9603892; (d) Newkome, G. R.; He, E.; Moorefield, C. N. *Chem. Rev.* **1999**, *99* (7), 1689. doi:10.1021/cr9800659; (e) Bosman, A. W.; Janssen, H. M.; Meijer, E. W. *Chem. Rev.* **1999**, *99* (7), 1665. doi:10.1021/cr970069y; (f) Balzani, V.; Campagna, S.; Denti, G.; Juris, A.; Serroni, S.; Venturi, M. *Acc. Chem. Res.* **1998**, *31* (1), 26. doi:10.1021/ar950202d; (g) Gorman, C. B.; Smith, J. C. *Acc. Chem. Res.* **2001**, *34* (1), 60. doi:10.1021/ar000044c.

(9) (a) Astruc, D. *Acc. Chem. Res.* **2000**, *33* (5), 287. doi:10.1021/ar9901319; (b) Crooks, R. M.; Zhao, M.; Sun, L.; Chechik, V.; Yeung, L. K. *Acc. Chem. Res.* **2001**, *34* (3), 181. doi:10.1021/ar000110a; (c) Selby, H. D.; Roland, B. K.; Zheng, Z. *Acc. Chem. Res.* **2003**, *36* (12), 933. doi:10.1021/ar020134c; (d) Huck, W. T. S.; van Veggel, F. C. J. M.; Reinhoudt, D. N. *Angew. Chem. Int. Ed. Engl.* **1996**, *35* (11), 1213. doi:10.1002/

Can. J. Chem. Downloaded from www.nrcresearchpress.com by Renmin University of China on 09/02/12
For personal use only.

anie.199612131; (e) Enomoto, M.; Aida, T. *J. Am. Chem. Soc.* **1999**, *121* (4), 874. doi:10.1021/ja982282x; (f) Hwang, S.-H.; Shreiner, C. D.; Moorefield, C. N.; Newkome, G. R. *New J. Chem.* **2007**, *31* (7), 1192. doi:10.1039/B612656C; (g) Constable, E. C. *Chem. Soc. Rev.* **2007**, *36* (2), 246. doi:10.1039/B601166G; (h) Baytekin, H. T.; Sahre, M.; Rang, A.; Engeser, M.; Schulz, A.; Schalley, C. A. *Small* **2008**, *4* (10), 1823. doi:10.1002/smll.200800135.

(10) (a) Astruc, D.; Chardac, F. *Chem. Rev.* **2001**, *101* (9), 2991. doi:10.1021/cr010323t; (b) Becker, J. J.; Gagné, M. R. *Acc. Chem. Res.* **2004**, *37* (10), 798. doi:10.1021/ar000102u; (c) Astruc, D.; Ornelas, C.; Ruiz, J. *Acc. Chem. Res.* **2008**, *41* (7), 841. doi:10.1021/ar8000074; (d) Bonomi, R.; Selvestrel, F.; Lombardo, V.; Sissi, C.; Polizzi, S.; Mancin, F.; Tonellato, U.; Scrimin, P. *J. Am. Chem. Soc.* **2008**, *130* (47), 15744. doi:10.1021/ja801794t; (e) Enomoto, M.; Aida, T. *J. Am. Chem. Soc.* **1999**, *121* (4), 874. doi:10.1021/ja982282x; (f) Percec, V.; Dulcey, A. E.; Peterca, M.; Ilies, M.; Sienkowska, M. J.; Heiney, P. A. *J. Am. Chem. Soc.* **2005**, *127* (50), 17902. doi:10.1021/ja056313h.

(11) (a) Adronov, A.; Fréchet, J. M. J. *Chem. Commun.* **1701**, *2000*. doi:10.1039/B005993P; (b) Jiang, H.; Lee, S. J.; Lin, W. *Org. Lett.* **2002**, *4* (13), 2149. doi:10.1021/ol0259037; (c) Choi, M.-S.; Yamazaki, T.; Yamazaki, I.; Aida, T. *Angew. Chem. Int. Ed.* **2004**, *43* (2), 150. doi:10.1002/anie.200301665; (d) Mo, Y.-J.; Jiang, D.-L.; Uyemura, M.; Aida, T.; Kitagawa, T. *J. Am. Chem. Soc.* **2005**, *127* (28), 10020. doi:10.1021/ja042196z; (e) Maury, O.; Le Bozec, H. *Acc. Chem. Res.* **2005**, *38* (9), 691. doi:10.1021/ar020264l; (f) Hwang, S.-H.; Moorefield, C. N.; Newkome, G. R. *Chem. Commun. (Camb.)* **2008**, *2543*. doi:10.1039/B800825F.

(12) (a) Northrop, B. H.; Yang, H.-B.; Stang, P. J. *Chem. Commun. (Camb.)* **2008**, *5896*. doi:10.1039/B811712H; (b) Yang, H.-B.; Das, N.; Huang, F.; Hawkridge, A. M.; Muddiman, D. C.; Stang, P. J. *J. Am. Chem. Soc.* **2006**, *128* (31), 10014. doi:10.1021/ja063377z; PMID:16881621; (c) Yang, H.-B.; Hawkridge, A. M.; Huang, S. D.; Das, N.; Bunge, S. D.; Muddiman, D. C.; Stang, P. J. *J. Am. Chem. Soc.* **2007**, *129* (7), 2120. doi:10.1021/ja066804h; PMID:17256935; (d) Yang, H.-B.; Northrop, B. H.; Zheng, Y.-R.; Ghosh, K.; Lyndon, M. M.; Muddiman, D. C.; Stang, P. J. *J. Org. Chem.* **2009**, *74* (9), 3524. doi:10.1021/jo900067v. PMID:19344131.

(13) (a) Bunz, U. H. F. *Angew. Chem. Int. Ed. Engl.* **1994**, *33* (10), 1073. doi:10.1002/anie.199410731; (b) Diederich, F., Stang, P. J., Eds. *Modern Acetylene Chemistry;* VCH: Weinheim, Germany, 1995; p 443; (c) Bunz, U. H. F.; Rubin, Y.; Tobe, Y. *Chem. Soc. Rev.* **1999**, *28* (2), 107. doi:10.1039/a708900g; (d) Manners, I. *Angew. Chem.* **1996**, *108* (15), 1712. doi:10.1002/ange.19961081504.

(14) (a) Paul, F.; Lapinte, C. *Coord. Chem. Rev.* **1998**, *178–180*, 431. doi:10.1016/S0010-8545(98)00150-7; (b) Ziessel, R.; Hissler, M.; El-ghayoury, A.; Harriman, A. *Coord. Chem. Rev.* **1998**, *178–180*, 1251. doi:10.1016/S0010-8545(98)00060-5; (c) Nguyen, P.; Gómez-Elipe, X.; Manners, P. I. *Chem. Rev.* **1999**, *99* (6), 1515. doi:10.1021/cr960113u; PMID:11849001; (d) Dembinski, R.; Bartik, T.; Bartik, B.; Jaeger, M.; Gladysz, J. A. *J. Am. Chem. Soc.* **2000**, *122* (5), 810. doi:10.1021/ja992747z; (e) Long, N. J.; Williams, C. K. *Angew. Chem. Int. Ed.* **2003**, *42* (23), 2586. doi:10.1002/anie.200200537.

(15) (a) Le Narvor, N.; Toupet, L.; Lapinte, C. *J. Am. Chem. Soc.* **1995**, *117* (27), 7129. doi:10.1021/ja00132a013; (b) Le Narvor, N.; Lapinte, C. *Organometallics* **1995**, *14* (2), 634. doi:10.1021/om00002a010; (c) Stang, P. J.; Tykwinski, R. *J. Am. Chem. Soc.* **1992**, *114* (11), 4411. doi:10.1021/ja00037a063; (d) Weng, W.; Bartik, T.; Gladysz, J. A. *Angew. Chem.* **1994**, *106* (21), 2269. doi:10.1002/ange.19941062112; (e) Fyfe, H. B.; Mlekuz, M.; Zargarian, D.; Taylor, N. J.; Marder, T. B. *J. Chem. Soc. Chem. Commun.* **1991**, *188*. doi:10.1039/C39910000188.

(16) (a) Colbert, M. C. B.; Lewis, J.; Long, N. J.; Raithby, P. R.; Younus, M.; White, A. J. P.; Williams, D. J.; Payne, N. N.; Yellowlees, L.; Beljonne, D.; Chawdhury, N.; Friend, R. H. *Organometallics* **1998**, *17* (14), 3034. doi:10.1021/om970130p; (b) Sun, Y.; Taylor, N. J.; Carty, A. J. *Organometallics* **1992**, *11* (12), 4293. doi:10.1021/om00060a055; (c) Field, L. D.; George, A. V.; Hockless, D. C. R.; Purches, G. R.; White, A. H. *J. Chem. Soc. Dalton Trans.* **2011**, *1996*. doi:10.1039/DT9960002011; (d) Bunz, U. H. F.; Wiegelmann-Kreiter, J. E. C. *Chem. Ber.* **1996**, *129* (7), 785. doi:10.1002/cber.19961290709; (e) Jia, G.; Puddephatt, R. J.; Vittal, J. J.; Payne, N. C. *Organometallics* **1993**, *12* (2), 263. doi:10.1021/om00026a008.

(17) (a) van Staveren, D. R.; Metzler-Nolte, N. *Chem. Rev.* **2004**, *104* (12), 5931. doi:10.1021/cr0101510; (b) You, C.-C.; Wurthner, F. *J. Am. Chem. Soc.* **2003**, *125* (32), 9716. doi:10.1021/ja029648x; (c) Shoji, O.; Okada, S.; Satake, A.; Kobuke, Y. *J. Am. Chem. Soc.* **2005**, *127* (7), 2201. doi:10.1021/ja0445746; (d) Chebny, V. J.; Dhar, D.; Lindeman, S. V.; Rathore, R. *Org. Lett.* **2006**, *8* (22), 5041. doi:10.1021/ol061904d; (e) Collinson, M. M. *Acc. Chem. Res.* **2007**, *40* (9), 777. doi:10.1021/ar600029p; (f) Fréchet, J. M. J. *Science* **1994**, *263* (5154), 1710. doi:10.1126/science.8134834; (g) Rulkens, R.; Lough, A. J.; Manners, I.; Lovelace, S. R.; Grant, C.; Geiger, W. E. *J. Am. Chem. Soc.* **1996**, *118* (50), 12683. doi:10.1021/ja962470s.

(18) (a) Daniel, M.-C.; Ruiz, J.; Astruc, D. *J. Am. Chem. Soc.* **2003**, *125* (5), 1150. doi:10.1021/ja020833k; (b) Castro, R.; Cuadrado, I.; Alonso, B.; Casado, C. M.; Moran, M.; Kaifer, A. E. *J. Am. Chem. Soc.* **1997**, *119* (24), 5760. doi:10.1021/ja970922a; (c) Nguyen, P.; Gomez-Elipe, P.; Manners, I. *Chem. Rev.* **1999**, *99* (6), 1515. doi:10.1021/cr960113u; (d) Ikkala, O.; ten Brinke, G. *Science* **2002**, *295* (5564), 2407. doi:10.1126/science.1067794; (e) Stone, D. L.; Smith, D. K.; McGrail, P. T. *J. Am. Chem. Soc.* **2002**, *124* (5), 856. doi:10.1021/ja0117478; (f) Wang, F.; Xu, Y.; Ye, B.-X.; Song, M.-P.; Wu, Y.-J. *Inorg. Chem. Commun.* **2006**, *797*. doi:10.1016/j.inoche.2006.04.025.

(19) (a) Miller, J. S.; Epstein, A. J.; Reiff, W. M. *Chem. Rev.* **1988**, *88* (1), 201. doi:10.1021/cr00083a010; (b) Nalwa, H. S. *Appl. Organomet. Chem.* **1991**, *5* (5), 349. doi:10.1002/aoc.590050502.

(20) (a) Colbert, M. C. B.; Ingham, S. L.; Lewis, J.; Long, N. J.; Raithby, P. R. *J. Chem. Soc., Dalton Trans.* **1994**, *2215*. doi:10.1039/DT9940002215; (b) Sato, M.; Shintate, H.; Kawata, Y.; Sekino, M.; Katada, M.; Kawata, S. *Organometallics* **1994**, *13* (5), 1956. doi:10.1021/om00017a061; (c) Long, N. J.; Martin, A. J.; Vilar, R.; White, A. J. P.; Williams, D. J.; Younus, M. *Organometallics* **1999**, *18* (21), 4261. doi:10.1021/om980986+; (d) Lavastre, O.; Plass, J.; Bachmann, P.; Guesmi, S.; Moinet, C.; Dixneuf, P. H. *Organometallics* **1997**, *16* (2), 184. doi:10.1021/om960664a; (e) Wong, W. -Y.; Lu, G. -L.; Ng, K. -F.; Choi, K. -H.; Lin, Z. -Y. *J. Chem. Soc., Dalton Trans.* **2001**, *3250*. doi:10.1039/B105016H; (f) Wiedemann, R.; Fleischer, R.; Stalke, D.; Werner, H. *Organometallics* **1997**, *16* (5), 866. doi:10.1021/om960825a.

(21) Zhu, Y.-B.; Clot, O.; Wolf, M. O.; Yap, G. P. A. *J. Am. Chem. Soc.* **1998**, *120* (8), 1812. doi:10.1021/ja9732486.

(22) (a) Onitsuka, K.; Kitajima, H.; Fujimoto, M.; Iuchi, A.; Takei, F.; Takahashi, S. *Chem. Commun. (Camb.)* **2002**, *2576*. doi:10.1039/B206254B; (b) Onitsuka, K.; Iuchi, A.; Takahashi, S. *Chem. Commun. (Camb.)* **2003**, *280*. doi:10.1039/B210830E; (c) Onitsuka, K.; Fujimoto, M.; Ohshiro, N.; Takahashi, S. *Angew. Chem. Int. Ed.* **1999**, *38* (5), 689. doi:10.1002/(SICI)1521-3773(19990301)38:5<689::AID-ANIE689>3.0.CO;2-D; (d) Onitsuka, K.; Fujimoto, M.; Kitajima, H.; Ohshiro, N.; Takei, F.; Takahashi, S. *Chem. Eur. J.* **2004**, *10* (24), 6433. doi:10.1002/chem.200400544; (e) Leininger, S.; Stang, P. J.; Huang, S. *Organometallics.* **1998**, *17* (18), 3981. doi:10.1021/om980337y.

(23) (a) Tao, C.-H.; Zhu, N.-Y.; Yam, V. W. W. *Chem. Eur. J.* **2005**, *11* (5), 1647. doi:10.1002/chem.200400888; (b) Xu, X.-D.; Yang, H.-B.; Zheng, Y.-R.; Ghosh, K.; Lyndon, M. M.; Muddiman, D. C.; Stang, P. J. *J. Org. Chem.* **2010**, *75* (21), 7373. doi:10.1021/jo101648p; (c) Zhao, G.-Z.; Chen, L.-J.; Wang, C.-H.; Yang, H.-B.; Ghosh, K.; Zheng, Y.-R.; Lyndon, M. M.; Muddiman, D. C.; Stang, P. J. *Organometallics* **2010**, *29* (22), 6137. doi:10.1021/om1008605; (d) Yang, H.-B.; Northrop, B. H.; Zheng, Y.-R.; Ghosh, K.; Lyndon, M. M.; Muddiman, D. C.; Stang, P. J. *J. Org. Chem.* **2009**, *74* (9), 3524. doi:10.1021/jo900067v; (e) Ghosh, K.; Yang, H.-B.; Northrop, B. H.; Lyndon, M. M.; Zheng, Y.-R.; Muddiman, D. C.; Stang, P. J. *J. Am. Chem. Soc.* **2008**, *130* (15), 5320. doi:10.1021/ja711502t; (f) Berenguer, J. R.; Bernechea, M.; Fornies, J.; Lalinde, E.; Torroba, J. *Organometallics* **2005**, *24* (3), 431. doi:10.1021/om049208+; (g) Vicente, J.; Chicote, M.-T.; Alvarez-Falcon, M. M.; Jones, P. G. *Organometallics* **2005**, *24* (11), 2764. doi:10.1021/om0501273.

(24) (a) Sacksteder, L.; Baralt, E.; DeGraff, B. A.; Lukehart, C. M.; Demas, J. N. *Inorg. Chem.* **1991**, *30* (11), 2468. doi:10.1021/ic00011a004; (b) Choi, C. L.; Cheng, Y. F.; Yip, C.; Phillips, D.; Yam, L. *Organometallics* **2000**, *19* (16), 3192. doi:10.1021/om000135d; (c) Kwok, W. M.; Phillips, D. L.; Yeung, P. K. Y.; Yam, V. W. W. *J. Phys. Chem. A* **1997**, *101* (49), 9286. doi:10.1021/jp972374t.

Can. J. Chem. Downloaded from www.nrcresearchpress.com by Renmin University of China on 09/02/12
For personal use only.

Ionic-liquid-supported 1,5,7-triazabicyclo[4.4.0] dec-5-ene — An efficient and recyclable organocatalyst for Michael addition to α,β-unsaturated ketones

Manoj Kumar Muthyala, Bhupender S Chhikara, Keykavous Parang, and Anil Kumar

Can. J. Chem. Downloaded from www.nrcresearchpress.com by Renmin University of China on 09/02/12
For personal use only.

Abstract: A novel ionic-liquid-supported 1,5,7-triazabicyclo[4.4.0]dec-5-ene (IL–TBD) was synthesized and investigated for its ability to act as an active organocatalyst in the Michael addition of active methylene compounds and thiophenols to chalcones under solvent-free conditions. The IL–TBD afforded Michael addition products in excellent yields (82%–94%) at room temperature, and it was simply recycled and reused at least five times without significant loss of catalytic activity.

Key words: ionic liquid, supported catalysis, organocatalyst, Michael addition, α,β-unsaturated ketones.

Résumé : On a réalisé la synthèse d'un liquide ionique supporté par du 1,5,7-triazabicyclo[4.4.0]déc-5-ène (LI–TBD) et on a étudié ses capacités d'agir comme organocatalyseur dans l'addition de Michael de composés comportant des méthylènes actifs et des thiophénols à des chalcones, dans des conditions sans solvant. Le LI–TBD permet d'obtenir des produits d'addition de Michael avec d'excellents rendements (82 % à 94 %), à la température ambiante; il peut être recyclé facilement et réutilisé jusqu'à cinq fois sans perte significative de son activité catalytique.

Mots-clés : liquide ionique, catalyseur sur un support, organocatalyseur, addition de Michael, cétones α,β-insaturées.

[Traduit par la Rédaction]

Introduction

Organocatalyses have emerged as new and powerful tools in organic synthesis.[1–4] Lower cost, operational simplicity, easy availability, efficiency, and less toxicity make organocatalysts attractive alternatives to organometallic catalysts in organic synthesis. The major problems associated with most homogeneous organocatalyst systems are high organocatalyst loadings to afford efficient synthesis, long and tedious preparation steps, and separation and recycling of these catalysts. To overcome these difficulties catalysts have been immobilized on various solid supports. However, reaction rates are lower with solid-supported reagents and require longer validation times.

Ionic liquids (ILs) are fascinating materials for chemists as they offer new chemical and physical properties such as high thermal stability, very low to negligible vapor pressure, good solvating ability, a noncoordinating nature, and ease of recyclability.[5–10] In recent years, functionalized ionic liquids (FILs) synthesized with properties for specific desired chemical tasks have attracted the attention of chemists.[11,12] Several ILs functionalized with catalytically active groups have been developed and used effectively as recyclable organocatalysts for various organic transformations.[13–22] Imidazolium ILs functionalized with basic organic molecules such as proline[23–25] and pyrrolidine[26–32] have been extensively studied for Michael additions. FILs not only overcome the problems of lower reaction rate and longer validation reaction time but also provide reagents with tuneable properties and "green" credentials.

1,5,7-Triazabicyclo[4,4.0]dec-5-ene (TBD) is a versatile bicyclic guanidine with nucleophilic and basic properties that render this compound an extremely useful catalyst for many organic transformations.[33–37] Several methods have been reported for the preparation of heterogeneous basic catalysts in which TBD is covalently attached with polymer support or silica.[38–40] The solid-supported TBDs have efficiently promoted some fundamental base-catalyzed organic transformations such as the Nef reaction,[41] alkylation,[42] 1,2-epoxide ring opening,[43] aldol-type condensation,[43] Knoevenagel condensation,[43,44] Michael addition,[44] synthesis of thioureas,[45] aryl ether synthesis,[46] synthesis of benzofuran[47] and thiazoles,[48] and transesterification of soybean oil.[49] However, heterogeneous TBD usually suffers from the disadvantage of being only slightly recyclable, requires a compatible solvent for swelling, and has prolonged reaction times. In continuation of our effort to develop IL-based catalysts,[50] herein, we report the synthesis of a novel IL-functionalized TBD (IL–TBD)

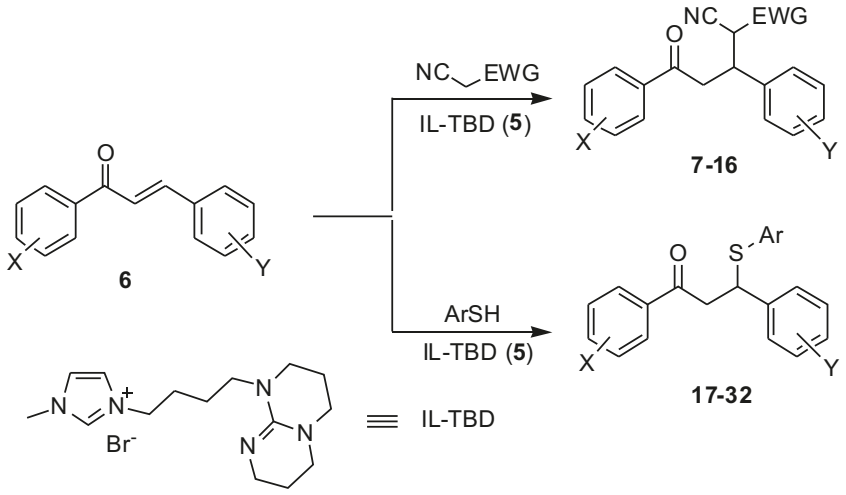
Received 10 July 2011. Accepted 30 November 2011. Published at www.nrcresearchpress.com/cjc on 14 February 2012.

M.K. Muthyala and A. Kumar. Department of Chemistry, Birla Institute of Technology and Science, Pilani 333 031 Rajasthan, India.
B.S. Chhikara and K. Parang. Department of Biomedical and Pharmaceutical Sciences, University of Rhode Island, Kingston, RI 02881, USA.

Corresponding author: Anil Kumar (email: anilkadian@gmail.com)

Can. J. Chem. Downloaded from www.nrcresearchpress.com by Renmin University of China on 09/02/12
For personal use only.

Scheme 1. Michael addition of active methylene compounds and thiophenols to chalcones. EWG, electron-withdrawing group.



and its use as an organocatalyst for the Michael addition of active methylene compounds and thiophenols to chalcones (Scheme 1).

Results and discussion

Synthesis of IL–TBD was achieved following the reaction sequences shown in Scheme 2. Initially, the reaction of 1-methylimidazole (**1**) with 1-bromo-4-chlorobutane (**2**) at room temperature afforded (4′-chlorobutyl)-3-methylimidazolium bromide (**3**). Subsequent reaction of **3** with 1.5 equiv of TBD (**4**) at 100 °C for 6 h gave IL–TBD **5** with bromide as the anion. The excess TBD was removed by washing with dichloromethane, and the IL–TBD was purified by column chromatography on silica gel. The structure of **5** was confirmed by ^{1}H NMR, ^{13}C NMR, and high-resolution mass spectrometry. The ^{1}H NMR spectrum showed multiplets in the range of 3.24 to 3.04, representing the methylene protons of TBD adjacent to nitrogens. In ^{13}C NMR, six carbons appeared in the aliphatic region in addition to methyl and methylene carbons of the IL, which corresponds to the methylene carbon of TBD. In HRMS peaks appeared at 356.1260 $[M]^+$, 358.1257 $[M + 2]^+$, and 276.1889 $[M - Br]^+$, which confirmed the structure of **5**.

The catalytic activity of IL–TBD as an organocatalyst was evaluated for the Michael addition of malononitrile to chalcones. The reaction conditions were optimized by taking the reaction of 3-(2-fluorophenyl)-1-(4-methoxyphenyl)prop-2-en-1-one with malononitrile to give **7** as model reaction (Table 1). Loading studies using different concentrations of catalyst showed the requirement of 50 mol % of IL–TBD to catalyze the reaction to maximum yields (Table 1, entries 1–4). The yield of Michael addition product was higher under solvent-free conditions (87%; Table 1, entry 3) as compared with the reaction in different organic solvents (58%–85%; Table 1, entries 5–9). The aqueous medium served as a poor system for this reaction giving no product over the period under similar reaction conditions (Table 1, entry 11). This may be due to the insolubility of both chalcone and the catalyst in water. The product yield was low (17%–20%) when the reaction was performed in ILs ([bmim]Br, [bmim]BF_4, and [bmim]PF_6) as solvents. The low yield in these ILs may

Scheme 2. Synthesis of ionic-liquid-supported 1,5,7-triazabicyclo [4.4.0]dec-5-ene (TBD) (IL–TBD).

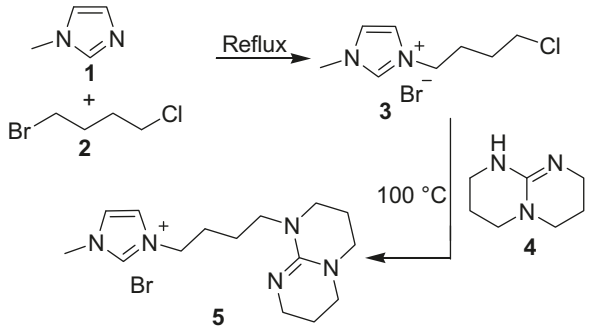


Table 1. Optimization of reaction conditions for Michael addition.

Entry	Catalyst (mol %)	Solvent	Time (h)	Yield (%)[a,b]
1	10	—	24	60
2	30	—	12	75
3	50	—	4	87
4	60	—	4	86
5	50	CH_3CN	4	85
6	50	CH_3OH	4	80
7	50	DMF	8	72
8	50	Ethanol	8	70
9	50	DCM	8	58
10	50	Toluene	36	70
11	50	H_2O	36	—[c]
12	50	[bmim]Br	12	18
13	50	[bmim]PF_6	12	17 (10)[d]
14	50	[bmim]BF_4	12	20

[a]Reaction conditions: chalcone (1 mmol), malononitrile (1 mmol), catalyst **5** (10–50 mol %), at room temperature.
[b]Isolated yield.
[c]No product formation was observed.
[d]Yield without catalyst.

Can. J. Chem. Downloaded from www.nrcresearchpress.com by Renmin University of China on 09/02/12
For personal use only.

probably be due to the slight acidic nature of the IL and the poor solubility of the reactant at room temperature in [bmim]Br. The role of IL–TBD as catalyst is confirmed by the fact that no product was formed in the absence of this catalyst. The reaction seems to proceed with a general base-catalyzed pathway. A plausible mechanism is shown in Scheme 3.

Furthermore, the catalyst was evaluated for its general application in Michael addition reactions by performing the reaction with different chalcones having electron-releasing and electron-withdrawing groups on either side as Michael acceptors and malononitrile and ethyl cyanoacetate as Michael donors (Table 2). It was observed that chalcones with both electron-withdrawing and electron-releasing groups resulted in high yields of Michael products. The presence of electron-withdrawing or electron-releasing groups had a negligible effect on the yield of the product. Malononitrile was found to be a better donor (Table 2, entries 1 and 8) when compared with ethyl cyanoacetate (Table 2, entries 9 and 10). The structure of the synthesized compound was confirmed by ^{1}H NMR and ^{13}C NMR.

The catalytic scope of the IL–TBD was also assessed for the thia-Michael addition to chalcones. As expected, thia-Michael addition of thiophenols to chalcones was extraordinarily fast with thiols in the presence of IL–TBD (10 mol %) and gave high yields with short reaction times (3–5 min) at room temperature (Table 3). Although the reaction also proceeded in [bmim][PF_6] alone to give **7** in 10% yield, the yield of product was greater (87%) and it required a shorter reaction time in the presence of a catalytic amount of IL–TBD under solvent-free conditions.

Finally, the recyclability of catalyst **5** was investigated in the model reaction. Addition of malononitrile to chalcone (3-(2-fluorophenyl)-1-(4-methoxyphenyl)prop-2-en-1-one) afforded **7**. After extracting **7**, the recovered **5** was again used for the model reaction and it was found that catalyst **5** can be efficiently reused for up to five cycles without much loss in the yield of **7** (Fig. 1).

Conclusion

We have described the synthesis of a novel IL–TBD and its ability to act as an active organocatalyst in the Michael addition of active methylene compounds and thiophenols to chalcones under solvent-free conditions. The IL–TBD afforded Michael addition products in excellent yields (82%–94%) at room temperature, and it was easily recycled and reused at least five times without significant loss of catalytic activity. This is the first example of an IL–TBD and its use in organic synthesis. The present study shows that high catalytic efficacy can be achieved by functionalizing ILs with organocatalysts under greener reaction conditions.

Experimental section

General

1-Methylimidazole, 1-bromo-4-chlorobutane, and TBD were purchased from Sigma-Aldrich, India. All other reagents and solvents were purchased from S. D. Fine, India, and used without further purification unless otherwise specified. Column chromatography was carried out over silica gel (60–120 mesh, S. D. Fine, India). NMR spectra were recorded on Brucker Heaven Avance 11 400 and Varian (500 MHz) spectrometers using $CDCl_3$ and DMSO-d_6 as solvents, and the chemical shifts are expressed in ppm. Mass spectra were recorded on a QSTAR ELITE LX/MS/MS mass spectrometer from Applied Biosystems. The purity of the products was determined on silica-coated aluminum plates (Merck).

Synthesis of 1-methyl-3-(4′-TBD-butyl)imidazolium bromide (IL–TBD) (5)

1-Bromo-4-chlorobutane (**2**, 2.09 g, 12 mmol) was added dropwise to 1-methylimidazole (**1**, 1.0 g, 12 mmol) at room temperature, and the reaction mixture was stirred for 4 h. The mixture turned viscous over this time. After completion of the reaction as indicated by thin-layer chromatography (TLC), the reaction mixture was extracted with ethyl acetate (3 × 10 mL) to remove unreacted starting materials. The trapped ethyl acetate was removed on a rotatory evaporator under reduced pressure to obtain the product **3** in 2.7 g (89% yield). IL **3** (2.7 g, 10.7 mmol) was added to TBD (**4**, 3.71 g 17.7 mmol) and the mixture was heated at 100 °C for 6 h. After completion of the reaction, the reaction mixture was cooled to room temperature and washed with DCM (5 × 15 mL) to remove unreacted TBD and TBD salt. The resulting IL was dried under reduced pressure to form a thick light yellow liquid, which was purified by column chromatography on silica gel to give **5**. Viscous liquid. Yield: 3.48 g (92%). ^{1}HNMR (500 MHz, DMSO-d_6) δ: 9.30 (s, 1H), 7.73 (s, 1H), 7.62 (s, 1H), 4.06 (t, J = 6.8 Hz, 2H), 3.69 (s, 3H), 3.24–3.19 (m, 2H), 3.13–3.04 (m, 6H), 3.00 (s, 2H), 1.74–1.56 (m, 6H), 1.32–1.23 (m, 2H). ^{13}C NMR (126 MHz, DMSO-d_6) δ: 150.2, 137.0, 123.9, 122.7, 48.9, 48.7, 47.7, 47.2, 46.1, 38.5, 36.2, 26.5, 23.6, 20.9, 20.7. HRMS calcd for $C_{15}H_{26}N_5Br$: 356.14; found: 356.1260 $[M]^+$, 358.1257 $[M + 2]^+$, 276.1889 $[M - Br]^+$.

General procedure for the Michael addition of active methylene compounds and thiophenols to chalcones

Malononitrile / ethyl 2-cyanoacetate / thiophenol (1.0 mmol) was added to a solution of chalcone (1.0 mmol) and **5** (0.5 mmol or 0.1 mmol for thiophenols). The reaction mixture was stirred vigorously until reaction completions (see Tables 2 and 3 for reaction times). The progress of the reaction was monitored by TLC. After completion of the reaction, the product was extracted from the catalyst by ethyl acetate (2 × 5 mL), leaving the IL–TBD catalyst in the flask. The ethyl acetate layer was evaporated and washed with diethyl ether to afford the pure product.

2-(1-(2-Fluorophenyl)-3-(4-methoxyphenyl)-3-oxopropyl) malononitrile (7)

^{1}H NMR (400 MHz, DMSO) δ: 7.87 (d, J = 7.4 Hz, 2H), 7.68–6.68 (m, 6H), 5.32 (d, J = 6.3 Hz, 1H), 4.58–4.19 (m, 1H), 3.80 (s, 3H), 3.71–3.57 (m, 1H). ^{13}C NMR (101 MHz, DMSO) δ: 194.81, 163.96, 161.93, 159.54, 130.92, 129.29, 125.24, 116.17, 116.00, 114.39, 113.63, 113.44, 56.00, 39.98, 33.72, 28.92. HRMS calcd for $C_{19}H_{15}FN_2O_2$: 322.1118; found: 323.1016 $[M]^+$.

Scheme 3. Plausible mechanism for the catalytic activity of ionic-liquid-supported 1,5,7-triazabicyclo[4.4.0]dec-5-ene (IL–TBD).

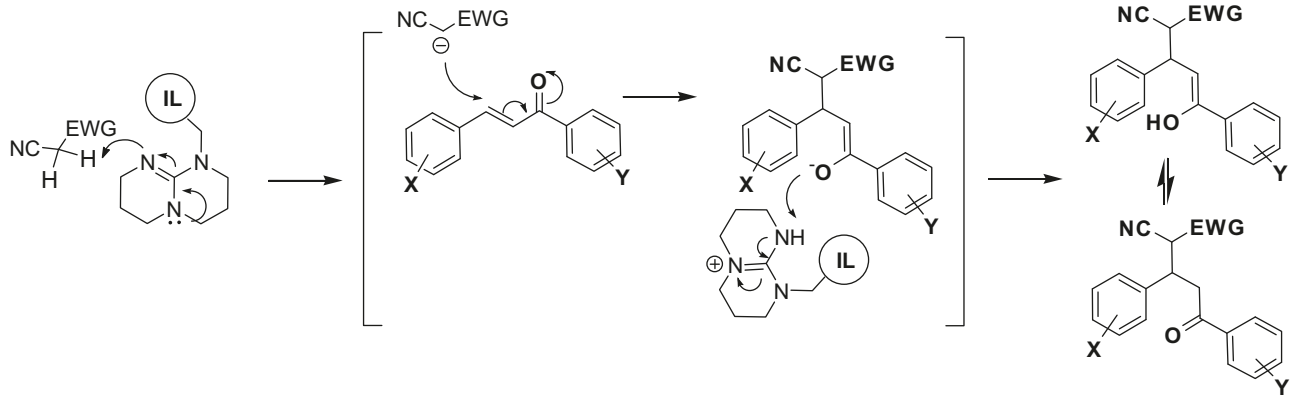


Table 2. Michael addition of active methylene compounds to chalcones catalyzed by **5**.

Product	X	Y	EWG	Time (h)	Yield (%)[a,b]
7	4-OCH_3	2-F	CN	4	87
8	4-Cl	2-F	CN	1.5	90
9	4-Cl	3-NO_2	CN	2	87
10	4-Cl	4-NO_2	CN	2	87
11	4-Cl	H	CN	2	92
12	4-OCH_3	4-NO_2	CN	4	86
13	4-OCH_3	4-OCH_3	CN	3	86
14	H	4-OCH_3	CN	3	85
15	4-Cl	H	CO_2Et	3	87
16	4-OCH_3	2-F	CO_2Et	6	82

Note: EWG, electron-withdrawing group.
[a]All the compounds showed satisfactory ^{1}H NMR and ^{13}C NMR.
[b]Isolated yield.

Table 3. Michael addition of thiophenols to chalcones catalyzed by **5**.

Product	X	Y	Ar	Time (min)	Yield (%)[a,b]
17	4-Cl	2-F	Ph	2	93
18	4-OCH_3	2-F	Ph	2	92
19	H	4-Cl	Ph	2	91
20	4-CH_3	H	Ph	2	92
21	4-OCH_3	3-NO_2	Ph	5	90
22	4-OCH_3	4-NO_2	Ph	5	92
23	4-CH_3	4-Cl	Ph	3	92
24	4-Cl	4-OCH_3	Ph	2	94
25	4-CH_3	4-OCH_3	Ph	2	93
26	4-OCH_3	4-OCH_3	Ph	2	92
27	4-Cl	H	Ph	4	92
28	4-NO_2	H	Ph	5	90
29	4-OCH_3	H	Ph	2	93
30	4-CH_3	3-NO_2	Ph	5	92
31	H	3-NO_2	Ph	5	91
32	4-Cl	H	4-CH_3OPh	4	90

[a]All the compounds showed satisfactory ^{1}H NMR and ^{13}C NMR.
[b]Isolated yield.

2-(3-(4-Chlorophenyl)-1-(2-fluorophenyl)-3-oxopropyl) malononitrile (8)

^{1}H NMR (500 MHz, DMSO) δ: 7.98 (d, J = 7.28 Hz, 2H), 7.60–7.58 (m, 3H), 7.40–7.35 (m, 1H), 7.26–7.20 (m, 2H), 5.25 (d, J = 6.5 Hz, 1H), 4.36–4.32 (m, 1H), 3.90 (dd, J = 18.3, 8.65 Hz, 1H), 3.69 (dd, J = 18.3, 5.4 Hz, 1H). ^{13}C NMR (126 MHz, DMSO) δ: 195.66, 139.03, 135.00, 130.76, 130.70, 130.45, 129.33, 125.25, 116.16, 115.98, 113.55, 113.35, 40.48, 33.60, 28.85. HRMS calcd for $C_{18}H_{12}ClFN_2O$: 326.0622; found: 327.0006 $[M]^+$.

2-(3-(4-Chlorophenyl)-1-(3-nitrophenyl)-3-oxopropyl) malononitrile (9)

^{1}H NMR (400 MHz, DMSO) δ: 8.00 (d, J = 6.8 Hz, 2H), 7.65–7.61 (m, 3H), 7.42–7.38 (m, 1H), 7.26 (d, J = 6.68 Hz, 2H), 5.26 (d, J = 6.5 Hz, 1H), 4.41–4.32 (m, 1H), 3.95–3.89 (m, 1H), 3.73–3.68 (m, 1H). ^{13}C NMR (101 MHz, DMSO) δ: 195.73, 139.09, 135.01, 130.84, 130.74, 130.54, 129.37, 125.29, 116.23, 115.98, 113.66, 113.43, 40.93, 33.52, 28.93. HRMS calcd for $C_{18}H_{12}ClN_3O_3$: 353.0567; found: 375.0487 $[M - H + Na]^+$.

2-(3-(4-Chlorophenyl)-1-(4-nitrophenyl)-3-oxopropyl) malononitrile (10)

^{1}H NMR (400 MHz, DMSO) δ: 8.26 (d, J = 7.27 Hz, 2H), 8.01 (d, J = 7.3 Hz, 2H), 7.82 (d, J = 7.3 Hz, 2H), 7.61 (d, J = 7.3 Hz, 2H), 5.32 (d, J = 6.3 Hz, 1H), 4.32–4.26 (m, 1H), 4.06–3.96 (m, 1H), 3.81–3.69 (m, 1H). ^{13}C NMR (101 MHz, DMSO) δ: 195.68, 147.86, 145.87, 139.15, 134.99, 130.57, 130.36, 129.39, 124.17, 113.60, 113.36, 40.47, 40.16, 29.30. HRMS calcd for $C_{18}H_{12}ClN_3O_3$: 353.0567; found: 375.0484 $[M - H + Na]^+$.

2-(3-(4-Chlorophenyl)-3-oxo-1-phenylpropyl)malononitrile (11)

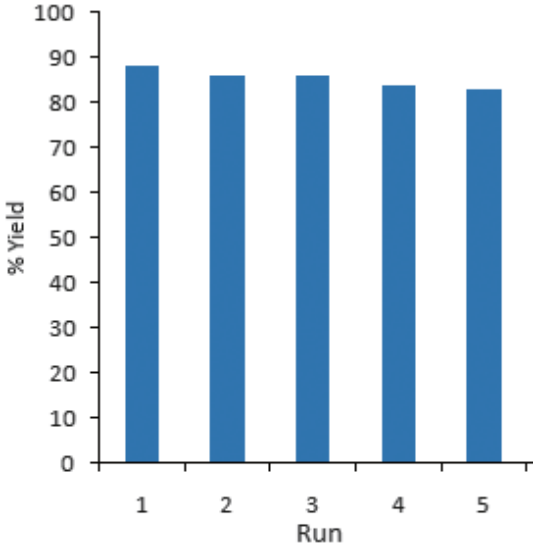
^{1}H NMR (400 MHz, DMSO) δ: 8.02–7.98 (m, 2H), 7.64–7.54 (m, 3H), 7.53–7.41 (m, 2H), 7.39–7.35 (m, 2H), 5.25–5.20 (m, 1H), 4.07–4.03 (m, 1H), 3.88–3.84 (m, 1H), 3.68–3.64 (m, 1H). ^{13}C NMR (101 MHz, DMSO) δ: 196.02, 139.07, 138.20, 135.18, 130.54, 129.37, 129.11, 128.74, 113.93, 113.65, 40.67, 40.50, 29.77. HRMS calcd for $C_{18}H_{13}ClN_2O$: 308.0716; found: 309.0701 $[M]^+$.

2-(3-(4-Methoxyphenyl)-1-(4-nitrophenyl)-3-oxopropyl) malononitrile (12)

^{1}H NMR (400 MHz, DMSO) δ: 8.22 (d, J = 7.12 Hz, 2H), 7.84 (d, J = 6.9 Hz, 2H), 7.43 (d, J = 6.9 Hz, 2H), 6.89 (d,

Can. J. Chem. Downloaded from www.nrcresearchpress.com by Renmin University of China on 09/02/12
For personal use only.

Fig. 1. Recycling of ionic-liquid-supported 1,5,7-triazabicyclo[4.4.0] dec-5-ene (IL–TBD) for the Michael addition reaction.



J = 7.1 Hz, 2H), 5.23 (d, J = 6.5 Hz, 1H), 4.43–4.36 (m, 1H), 4.01–3.96 (m, 1H), 3.83–3.72 (m, 1H), 3.78 (s, 3H). ^{13}C NMR (101 MHz, DMSO) δ: 195.78, 144.87, 143.97, 139.25, 135.69, 130.64, 130.23, 128.59, 128.23, 114.64, 113.86, 55.53, 40.87, 41.26, 29.45. HRMS calcd for $C_{19}H_{15}N_3O_4$: 349.1063; found: 371.0978 [M – H + Na]$^+$.

2-(1,3-Bis(4-methoxyphenyl)-3-oxopropyl)malononitrile (13)

^{1}H NMR (400 MHz, DMSO) δ: 8.01–7.96 (m, 2H), 7.45–7.37 (m, 2H), 7.04–7.02 (m, 2H), 7.01–6.98 (m, 2H), 5.21 (d, J = 6.5 Hz, 1H), 4.03–3.98 (m, 1H), 3.82 (s, 3H), 3.77–3.73 (m, 1H), 3.72 (s, 3H), 3.55–3.53 (m, 1H). ^{13}C NMR (101 MHz, DMSO) δ: 195.22, 163.92, 159.50, 130.95, 130.12, 129.88, 129.53, 114.41, 114.11, 113.80, 56.03, 55.50, 40.34, 40.31, 29.99. HRMS calcd for $C_{20}H_{18}N_2O_3$: 334.1317; found: 335.1187 [M]$^+$.

2-(1-(4-Methoxyphenyl)-3-oxo-3-phenylpropyl)malononitrile (14)

^{1}H NMR (400 MHz, DMSO) δ: 7.99 (d, J = 7.3 Hz, 2H), 7.71–7.62 (m, 1H), 7.60–7.49 (m, 2H), 7.45–7.36 (m, 2H), 7.03–6.89 (m, 2H), 5.24–5.05 (m, 1H), 4.06–3.98 (m, 1H), 3.82–3.78 (m, 1H), 3.73 (s, 3H), 3.63–3.57 (m, 1H). ^{13}C NMR (101 MHz, DMSO) δ: 196.95, 159.51, 136.54, 134.12, 130.06, 129.89, 129.28, 128.58, 114.43, 114.08, 113.76, 55.54, 40.78, 40.58, 29.98. HRMS calcd for $C_{19}H_{16}N_2O_2$: 304.1212; found: 333.1114 [M – H + K]$^+$.

Ethyl 5-(4-chlorophenyl)-2-cyano-5-oxo-3-phenylpentanoate (15)

^{1}H NMR (400 MHz, DMSO) δ: 8.01 (d, J = 7.5 Hz, 2H), 7.59 (d, J = 7.1 Hz, 2H), 7.35–7.26 (m, 5H), 4.69–4.46 (m, 1H), 4.08–3.97 (m, 3H), 3.72–3.65 (m, 2H), 1.08 (t, J = 7.1 Hz, 3H). ^{13}C NMR (101 MHz, DMSO) δ: 196.24, 165.75, 138.93, 135.39, 130.48, 129.39, 128.93, 128.57, 128.42, 128.20, 62.58, 44.11, 41.75, 40.86, 14.22. HRMS calcd for $C_{20}H_{18}ClNO_3$: 355.0975; found: 356.0798 [M]$^+$.

Ethyl 2-cyano-3-(2-fluorophenyl)-5-(4-methoxyphenyl)-5-oxopentanoate (16)

^{1}H NMR (400 MHz, DMSO) δ: 7.99 (d, J = 5.9, Hz, 2H), 7.62–7.58 (m, 2H), 7.53–7.45 (m, 1H), 7.35–7.30 (m, 1H), 7.18 (d, J = 6.6 Hz, 2H), 4.60 (d, J = 4.5 Hz, 1H), 4.37–4.28 (m, 1H), 4.11–4.04 (m, 2H), 3.88–3.57 (m, 2H), 1.01 (t, J = 6.7 Hz, 3H). ^{13}C NMR (101 MHz, DMSO) δ: 196.23, 165.85, 139.25, 135.49, 132.83, 130.46, 130.06, 129.50, 129.39, 125.22, 116.71, 115.94, 62.80, 43.49, 43.16, 41.60, 32.61, 14.09. HRMS calcd for $C_{21}H_{20}FNO_4$: 369.1376; found: 370.1288 [M]$^+$.

1-(4-Chlorophenyl)-3-(2-fluorophenyl)-3-(phenylthio) propan-1-one (17)

^{1}H NMR (400 MHz, DMSO) δ: 8.21–8. 13 (m, 1H), 7.97 (d, J = 6.9 Hz, 2H), 7.57–7.09 (m, 10H), 5.18–4.98 (m, 1H), 3.90–3.81 (m, 1H), 3.79–3.72 (m, 1H). ^{13}C NMR (101 MHz, DMSO) δ: 196.32, 138.93, 135.32, 133.89, 133.39, 132.49, 131.02, 130.48, 129.56, 129.35, 128.76, 125.43, 124.91, 116.09, 115.59, 43.36, 40.83. HRMS calcd for $C_{21}H_{16}ClFOS$: 370.0594; found: 392.0561 [M – H + Na]$^+$.

3-(2-Fluorophenyl)-1-(4-methoxyphenyl)-3-(phenylthio) propan-1-one (18)

^{1}H NMR (400 MHz, DMSO) δ: 7.95 (d, J = 6.87 Hz, 2H), 7.54–7.46 (m, 1H), 7.36–7.18 (m, 6H), 7.15–7.05 (m, 2H), 7.01 (d, J = 6.85 Hz, 2H), 5.21–5.08 (m, 1H), 3.83 (s, 3H), 3.83–3.78 (m, 1H), 3.72–3.58 (m, 1H). ^{13}C NMR (101 MHz, DMSO) δ: 195.48, 163.83, 161.33, 158.89, 134.17, 132.36, 130.92, 129.67, 129.55, 129.46, 129.04, 128.91, 128.07, 124.90, 115.82, 115.60, 114.40, 56.03, 42.87, 40.96. HRMS calcd for $C_{22}H_{19}FO_2S$: 366.1090; found: 367.1062 [M]$^+$.

3-(4-Chlorophenyl)-1-phenyl-3-(phenylthio)propan-1-one (19)

^{1}H NMR (400 MHz, $CDCl_3$) δ: 7.89 (d, J = 7.3 Hz, 2H), 7.59–7.55 (m, 1H), 7.46 (d, J = 7.5, 2H), 7.38–7.16 (m, 9H), 4.94–4.90 (m, 1H), 3.67–3.55 (m, 2H). ^{13}C NMR (101 MHz, $CDCl_3$) δ: 196.50, 139.62, 136.31, 133.47, 133.24, 132.78, 128.97, 128.77, 128.49, 128.38, 127.85, 127.63, 47.41, 44.27. HRMS calcd for $C_{21}H_{17}ClOS$: 352.0689; found: 353.0597 [M]$^+$.

3-Phenyl-3-(phenylthio)-1-*p*-tolylpropan-1-one (20)

^{1}H NMR (400 MHz, $CDCl_3$) δ: 7.79 (d, J = 7.4, 2H), 7.33–7.22 (m, 12H), 4.95 (t, J = 7.0 Hz, 1H), 3.63–3.50 (m, 2H), 2.39 (s, 3H). ^{13}C NMR (101 MHz, $CDCl_3$) δ: 195.63, 132.50, 129.09, 128.63, 128.23, 128.00, 127.60, 127.28, 127.13, 48.01, 44.27, 21.46. HRMS calcd for $C_{22}H_{20}OS$: 332.1235; found: 333.1187 [M]$^+$.

1-(4-Methoxyphenyl)-3-(3-nitrophenyl)-3-(phenylthio) propan-1-one (21)

^{1}H NMR (400 MHz, $CDCl_3$) δ: 8.18 (s, 1H), 8.04 (d, J = 6.5 Hz, 1H), 7.88 (d, J = 7.5 Hz, 2H), 7.62 (d, J = 6.7 Hz, 1H), 7.48–7.35 (m, 1H), 7.31–7.23 (m, 5H), 6.93 (d, J = 7.5 Hz, 2H), 5.01 (t, J = 6.0 Hz, 1H), 3.86 (s, 3H), 3.63 (d, J = 6.8 Hz, 2H). ^{13}C NMR (101 MHz, $CDCl_3$) δ: 194.46, 163.68, 143.64, 134.13, 133.19, 130.20, 129.14, 129.01,

Can. J. Chem. Downloaded from www.nrcresearchpress.com by Renmin University of China on 09/02/12
For personal use only.

Can. J. Chem. Downloaded from www.nrcresearchpress.com by Renmin University of China on 09/02/12
For personal use only.

128.88, 128.04, 122.42, 122.09, 113.69, 55.34, 47.64, 43.46. HRMS calcd for $C_{22}H_{19}NO_4S$: 393.1035; found: 394.0985 $[M]^+$.

1-(4-Methoxyphenyl)-3-(4-nitrophenyl)-3-(phenylthio) propan-1-one (22)

^{1}H NMR (400 MHz, DMSO) δ: 8.09 (d, J = 5.6 Hz, 2H), 7.95 (d, J = 5.2 Hz, 4H), 7.64 (d, J = 5.1 Hz, 2H), 7.31–7.19 (m 5H), 7.03 (d, J = 5.37 Hz, 2H), 5.07–4.98 (m, 1H), 3.83 (s, 3H), 3.73–3.68 (m, 2H). ^{13}C NMR (101 MHz, DMSO) δ: 195.27, 163.88, 150.24, 146.80, 133.74, 132.35, 130.99, 129.62, 128.12, 124.26, 123.79, 114.42, 47.42, 42.48. HRMS calcd for $C_{22}H_{19}NO_4S$: 393.1035; found: 394.0989 $[M]^+$.

3-(4-Chlorophenyl)-3-(phenylthio)-1-*p*-tolylpropan-1-one (23)

^{1}H NMR (400 MHz, $CDCl_3$) δ: 7.79 (d, J = 8.0 Hz, 2H), 7.42–7.14 (m, 11H), 4.91 (dd, J = 6.1, 7.8 Hz, 1H), 3.69–3.46 (m, 2H), 2.41 (s, 3H). ^{13}C NMR (101 MHz, $CDCl_3$) δ: 196.11, 144.13, 139.69, 133.87, 133.53, 132.74, 129.99, 129.16, 128.97, 128.74, 128.35, 127.98, 127.57, 47.47, 44.10, 21.48. HRMS calcd for $C_{22}H_{19}ClOS$: 366.0845; found: 367.0782 $[M]^+$.

1-(4-Chlorophenyl)-3-(4-methoxyphenyl)-3-(phenylthio) propan-1-one (24)

^{1}H NMR (400 MHz, $CDCl_3$) δ: 7.81 (d, J = 8.1 Hz, 2H), 7.48–7.17 (m, 9H), 6.79 (d, J = 8.1 Hz, 2H), 4.98–4.82 (m, 1H), 3.76 (s, 3H), 3.63–3.48 (m, 2H). ^{13}C NMR (101 MHz, $CDCl_3$) δ: 195.85, 158.57, 139.52, 132.65, 132.52, 129.28, 128.72, 128.69, 128.63, 127.35, 113.65, 55.01, 47.44, 44.58. HRMS calcd for $C_{22}H_{19}ClO_2S$: 382.0794; found: 383.0703 $[M]^+$.

3-(4-Methoxyphenyl)-3-(phenylthio)-1-*p*-tolylpropan-1-one (25)

^{1}H NMR (400 MHz, $CDCl_3$) δ: 7.79 (d, J = 8.1 Hz, 2H), 7.33–7.22 (m, 9H), 6.79 (d, J = 8.6 Hz, 2H), 4.94 (dd, J = 5.6, 8.4 Hz, 1H), 3.76 (s, 3H), 3.65–3.49 (m, 2H), 2.40 (s, 3H). ^{13}C NMR (101 MHz, $CDCl_3$) δ: 196.61, 158.48, 143.90, 134.06, 132.94, 132.41, 129.08, 128.67, 128.64, 128.00, 127.20, 113.59, 55.00, 47.45, 44.42, 21.46. HRMS calcd for $C_{23}H_{22}O_2S$: 362.1341; found: 363.1274 $[M]^+$.

1,3-Bis(4-methoxyphenyl)-3-(phenylthio)propan-1-one (26)

^{1}H NMR (400 MHz, $CDCl_3$) δ: 7.87 (d, J = 8.0 Hz, 2H), 7.32–7.13 (m, 7H), 6.90 (d, J = 7.9 Hz, 2H), 6.79 (d, J = 6.4 Hz, 2H), 4.94 (m, 1H), 3.85 (s, 3H), 3.75 (s, 3H), 3.63–3.50 (m, 2H). ^{13}C NMR (101 MHz, $CDCl_3$) δ: 195.49, 176.44, 163.37, 158.47, 132.98, 132.36, 130.19, 128.66, 127.17, 113.58, 113.52, 55.28, 55.00, 47.52, 44.16. HRMS calcd for $C_{23}H_{22}O_3S$: 378.129; found: 390.1205 $[M - H + Na]^+$.

1-(4-Chlorophenyl)-3-phenyl-3-(phenylthio)propan-1-one (27)

^{1}H NMR (400 MHz, $CDCl_3$) δ: 7.82 (d, J = 7.6 Hz, 2H), 7.42–2.24 (m, 12H), 4.94 (t, J = 7.8 Hz, 1H), 3.66–3.52 (m, 2H). ^{13}C NMR (101 MHz, $CDCl_3$) δ: 195.69, 140.77, 139.55, 134.78, 133.86, 132.60, 129.29, 128.74, 128.71, 128.32, 127.57, 127.44, 127.28, 48.02, 44.44. HRMS calcd for $C_{21}H_{17}ClOS$: 352.0689; found: 353.0582 $[M]^+$.

1-(4-Nitrophenyl)-3-phenyl-3-(phenylthio)propan-1-one (28)

^{1}H NMR (400 MHz, $CDCl_3$) δ: 8.26 (d, J = 8.80, 2H), 8.00 (d, J = 8.74 Hz, 2H), 7.37–7.17 (m, 10H), 4.90 (dd, J = 7.6, 6.0 Hz, 1H), 3.70–3.57 (m, 2H). ^{13}C NMR (101 MHz, $CDCl_3$) δ: 195.45 141.18, 139.45, 134.96, 133.98, 132.60, 129.64, 128.84, 128.61, 128.46, 127.12, 127.44, 127.28, 48.10, 44.42. HRMS calcd for $C_{21}H_{17}NO_3S$: 363.0929; found: 385.0879 $[M - H + Na]^+$.

1-(4-Methoxyphenyl)-3-phenyl-3-(phenylthio)propan-1-one (29)

^{1}H NMR (400 MHz, $CDCl_3$) δ: 8.00–7.79 (m, 2H), 7.34–7.24 (m, 10H), 6.98–6.84 (m, 2H), 4.97 (m, 1H), 3.85 (s, 3H), 3.61–3.51 (m, 2H). ^{13}C NMR (101 MHz, $CDCl_3$) δ: 195.32, 163.40, 141.08, 132.45, 130.20, 129.60, 128.64, 128.24, 127.61, 127.26, 127.12, 113.54, 55.29, 48.10, 44.02. HRMS calcd for $C_{22}H_{20}O_2S$: 348.1184; found: 349.1079 $[M]^+$.

3-(3-Nitrophenyl)-3-(phenylthio)-1-*p*-tolylpropan-1-one (30)

^{1}H NMR (400 MHz, $CDCl_3$) δ: 8.18 (s, 1H), 8.04 (d, J = 6.1 Hz, 1H), 7.90–7.74 (m, 2H), 7.62 (d, J = 6.3 Hz, 1H), 7.42–7.35 (m, 1H), 7.32–7.25 (m, 7H), 5.09–4.90 (m, 1H), 3.67–3.56 (m, 2H), 2.41 (s, 3H). ^{13}C NMR (101 MHz, $CDCl_3$) δ: 195.62, 147.98, 144.42, 143.59, 134.11, 133.59, 133.22, 132.65, 129.24, 129.02, 128.89, 128.07, 127.99, 122.44, 122.11, 47.58, 43.72, 21.49. HRMS calcd for $C_{22}H_{19}NO_3S$: 377.1086; found: 378.1023 $[M]^+$.

3-(3-Nitrophenyl)-1-phenyl-3-(phenylthio)propan-1-one (31)

^{1}H NMR (400 MHz, $CDCl_3$) δ: 8.18 (s, 1H), 8.05 (d, J = 7.1 Hz, H), 7.91 (d, J = 7.0 Hz, 2H), 7.71–7.54 (m, 2H), 7.54–7.36 (m, 3H), 7.36–7.17 (m, 5H), 5.01 (t, J = 6.7 Hz, 1H), 3.69 (d, J = 6.7 Hz, 2H). ^{13}C NMR (101 MHz, $CDCl_3$) δ: 196.00, 143.51, 136.03, 134.10, 133.46, 133.26, 129.05, 128.91, 128.58, 128.12, 127.86, 122.44, 122.15, 47.51, 43.90. HRMS calcd for $C_{21}H_{17}NO_3S$: 363.0929; found: 364.00875 $[M]^+$.

3-(4-Methoxyphenylthio)-1-(4-chlorophenyl)-3-phenylpropan-1-one (32)

^{1}H NMR (400 MHz, $CDCl_3$) δ: 7.79 (d, J = 8.6 Hz, 2H), 7.38 (d, J = 8.6 Hz, 2H), 7.29–7.17 (m, 7H), 6.74 (d, J = 8.7 Hz, 2H), 4.70 (m, 1H), 3.75 (s, 3H), 3.53–3.57 (m, 2H). ^{13}C NMR (101 MHz, $CDCl_3$) δ: 195.99, 159.92, 141.19, 139.69, 136.28, 135.11, 129.50, 128.93, 128.43, 127.80, 127.35, 124.06, 123.51, 121.93, 114.41, 55.29, 49.40, 44.26. HRMS calcd for $C_{22}H_{19}ClO_2S$: 382.0794; found: 404.0703 $[M - H + Na]^+$.

General procedure for recycling the catalyst

Malononitrile (1.0 mmol) was added to the solution of 3-(2-fluorophenyl)-1-(4-methoxyphenyl)prop-2-en-1-one and

IL–TBD (**5**) (0.5 mmol). The reaction mixture was stirred vigorously until reaction completion. The product was then extracted from the catalyst by ethyl acetate (2 × 5 mL) leaving the IL–TBD catalyst in the flask. The IL–TBD was washed with diethyl ether and dried under reduced pressure. The recovered IL was again used as a catalyst for a fresh batch of chalcone and malononitrile (1.0 mmol) under the same experimental conditions. The process was repeated five times without much loss in catalytic activity.

Can. J. Chem. Downloaded from www.nrcresearchpress.com by Renmin University of China on 09/02/12
For personal use only.

Acknowledgement

This work was financially supported by the Council of Scientific and Industrial Research (CSIR), New Delhi (Project No. 01(2214)/08/EMR-II) and the US National Science Foundation, Grant No. CHE 0748555. M.M.K. thanks CSIR, New Delhi, for a junior research fellowship.

References

(1) Dalko, P. I.; Moisan, L. *Angew. Chem. Int. Ed.* **2004**, *43* (39), 5138. doi:10.1002/anie.200400650.
(2) Dondoni, A.; Massi, A. *Angew. Chem. Int. Ed.* **2008**, *47* (25), 4638. doi:10.1002/anie.200704684.
(3) Yu, X.; Wang, W. *Chem. Asian J.* **2008**, *3* (3), 516. doi:10.1002/asia.200700415.
(4) List, B. *Chem. Rev.* **2007**, *107* (12), 5413. doi:10.1021/cr078412e.
(5) Wasserscheid, P.; Welton, T. *Ionic Liquids in Synthesis;* Wiley-VCH: Weinheim, Germany, 2008.
(6) Jain, N.; Kumar, A.; Chauhan, S.; Chauhan, S. M. S. *Tetrahedron* **2005**, *61* (5), 1015. doi:10.1016/j.tet.2004.10.070.
(7) Hallett, J. P.; Welton, T. *Chem. Rev.* **2011**, *111* (5), 3508. doi:10.1021/cr1003248.
(8) Sheldon, R. *Chem. Commun. (Camb.)* **2001** (23), 2399. doi:10.1039/b107270f.
(9) Kim, Y. J.; Varma, R. S. *Tetrahedron Lett.* **2005**, *46* (43), 7447. doi:10.1016/j.tetlet.2005.08.059.
(10) Ranu, B. C.; Jana, R. *J. Org. Chem.* **2005**, *70* (21), 8621. doi:10.1021/jo051373r.
(11) Miao, W.; Chan, T. H. *Acc. Chem. Res.* **2006**, *39* (12), 897. doi:10.1021/ar030252f.
(12) Lee, S. *Chem. Commun. (Camb.)* **2006** (10), 1049. doi:10.1039/b514140k.
(13) Visser, A. E.; Swatloski, R. P.; Reichert, W. M.; Mayton, R.; Sheff, S.; Wierzbicki, A.; Davis, J. H., Jr.; Rogers, R. D. *Chem. Commun. (Camb.)* **2001** (1), 135. doi:10.1039/b008041l.
(14) Bates, E. D.; Mayton, R. D.; Ntai, I.; Davis, J. H. *J. Am. Chem. Soc.* **2002**, *124* (6), 926. doi:10.1021/ja017593d.
(15) Ranu, B. C.; Banerjee, S. *Org. Lett.* **2005**, *7* (14), 3049. doi:10.1021/ol051004h.
(16) Audic, N.; Clavier, H.; Mauduit, M.; Guillemin, J.-C. *J. Am. Chem. Soc.* **2003**, *125* (31), 9248. doi:10.1021/ja021484x.
(17) Siyutkin, D. E.; Kucherenko, A. S.; Struchkova, M. I.; Zlotin, S. G. *Tetrahedron Lett.* **2008**, *49* (7), 1212. doi:10.1016/j.tetlet.2007.12.044.
(18) Zhao, D.; Fei, Z.; Geldbach, T. J.; Scopelliti, R.; Dyson, P. J. *J. Am. Chem. Soc.* **2004**, *126* (48), 15876. doi:10.1021/ja0463482.
(19) Mi, X.; Luo, S.; Cheng, J.-P. *J. Org. Chem.* **2005**, *70* (6), 2338. doi:10.1021/jo048391d.
(20) Xiao, J.-C.; Twamley, B.; Shreeve, J. M. *Org. Lett.* **2004**, *6* (21), 3845. doi:10.1021/ol048327i.
(21) Yao, Q.; Zhang, Y. *Angew. Chem. Int. Ed.* **2003**, *42* (29), 3395. doi:10.1002/anie.200351222.
(22) Siyutkin, D. E.; Kucherenko, A. S.; Zlotin, S. G. *Tetrahedron* **2009**, *65* (7), 1366. doi:10.1016/j.tet.2008.12.045.
(23) Miao, W.; Chan, T. H. *Adv. Synth. Catal.* **2006**, *348* (12–13), 1711. doi:10.1002/adsc.200606059.
(24) Luo, S.; Mi, X.; Zhang, L.; Liu, L.; Xu, H.; Cheng, J.-P. *Angew. Chem. Int. Ed.* **2006**, *45* (19), 3093–3097. doi:10.1002/anie.200600048.
(25) Luo, S.; Zhang, L.; Mi, X.; Qiao, Y.; Cheng, J.-P. *J. Org. Chem.* **2007**, *72* (24), 9350. doi:10.1021/jo7020357.
(26) Ni, B. K.; Zhang, Q. Y.; Headley, A. D. *Green Chem.* **2007**, *9* (7), 737. doi:10.1039/b702081c.
(27) Ni, B. K.; Zhang, Q. Y.; Headley, A. D. *Tetrahedron Lett.* **2008**, *49* (7), 1249–1252. doi:10.1016/j.tetlet.2007.12.024.
(28) Li, P.; Wang, L.; Zhang, Y.; Wang, G. *Tetrahedron* **2008**, *64* (32), 7633. doi:10.1016/j.tet.2008.05.039.
(29) Wu, L.-Y.; Yan, Z.-Y.; Xie, Y.-X.; Niu, Y.-N.; Liang, Y.-M. *Tetrahedron Asymmetry* **2007**, *18* (17), 2086. doi:10.1016/j.tetasy.2007.08.029.
(30) Zhang, Q.; Ni, B.; Headley, A. D. *Tetrahedron* **2008**, *64* (22), 5091. doi:10.1016/j.tet.2008.03.073.
(31) Ni, B. K.; Zhang, Q.; Dhungana, K.; Headley, A. D. *Org. Lett.* **2009**, *11* (4), 1037. doi:10.1021/ol900003e.
(32) Li, P.; Wang, P.; Wang, M.; Zhang, Y. *Eur. J. Org. Chem.* **2008**, *2008* (7), 1157. doi:10.1002/ejoc.200701037.
(33) Schroeder, G.; Brzezinski, B.; Podebski, D.; Grech, E. *J. Mol. Struct.* **1995**, *344* (1–2), 77. doi:10.1016/0022-2860(94)08427-J.
(34) Ye, W.; Xu, J.; Tan, C.-T.; Tan, C.-H. *Tetrahedron Lett.* **2005**, *46* (40), 6875. doi:10.1016/j.tetlet.2005.08.010.
(35) Bensa, D.; Rodriguez, J. *Synth. Commun.* **2004**, *34* (8), 1515. doi:10.1081/SCC-120030703.
(36) Cota, I.; Medina, F.; Sueiras, J. E.; Tichit, D. *Tetrahedron Lett.* **2011**, *52* (3), 385. doi:10.1016/j.tetlet.2010.11.032.
(37) Coles, M. P. *Chem. Commun. (Camb.)* **2009** (25), 3659. doi:10.1039/b901940e.
(38) Iijima, K.; Fukuda, W.; Tomoi, M. *J. Macromol. Sci. Pure Appl. Chem.* **1992**, *A29* (3), 249. doi:10.1080/00222339208052124.
(39) Tomoi, M.; Kato, Y.; Kakiuchi, H. *Makromol. Chem.* **1984**, *185* (10), 2117. doi:10.1002/macp.1984.021851007.
(40) Tomoi, M.; Watanabe, T.; Suzuki, T.; Kakiuchi, H. *Makromol. Chem.* **1985**, *186* (12), 2473. doi:10.1002/macp.1985.021861207.
(41) Ballini, R.; Fiorini, D.; Maggi, R.; Oro, C.; Palmieri, A.; Sartori, G. *Synlett* **2006**, *2006* (12), 1849. doi:10.1055/s-2006-947358.
(42) Xu, W.; Mohan, R.; Morrissey, M. M. *Tetrahedron Lett.* **1997**, *38* (42), 7337. doi:10.1016/S0040-4039(97)01782-6.
(43) Fringuelli, F.; Pizzo, F.; Vittoriani, C.; Vaccaro, L. *Chem. Commun. (Camb.)* **2004** (23), 2756. doi:10.1039/b409808k.
(44) Subba Rao, Y. V.; De Vos, D. E.; Jacobs, P. A. *Angew. Chem. Int. Ed. Engl.* **1997**, *36* (23), 2661. doi:10.1002/anie.199726611.
(45) Ballini, R.; Bosica, G.; Fiorini, D.; Maggi, R.; Righi, P.; Sartori, G.; Sartorio, R. *Tetrahedron Lett.* **2002**, *43* (47), 8445. doi:10.1016/S0040-4039(02)02100-7.
(46) Lizarzaburu, M. E.; Shuttleworth, S. J. *Tetrahedron Lett.* **2003**, *44* (26), 4873. doi:10.1016/S0040-4039(03)01117-1.

(47) Habermann, J.; Ley, S. V.; Smits, R. *J. Chem. Soc., Perkin Trans. 1* **1999**, (17): 2421. doi:10.1039/a904384e.
(48) Habermann, J.; Ley, S. V.; Scicinski, J. J.; Scott, J. S.; Smits, R.; Thomas, A. W. *J. Chem. Soc., Perkin Trans. 1* **1999**, (17): 2425. doi:10.1039/a905616e.
(49) Schuchardt, U.; Vargas, R. M.; Gelbard, G. *J. Mol. Catal.* **1996**, *109* (1), 37. doi:10.1016/1381-1169(96)00014-3.
(50) Chhikara, B. S.; Tehlan, S.; Kumar, A. *Synlett* **2005** (1), 63.

Can. J. Chem. Downloaded from www.nrcresearchpress.com by Renmin University of China on 09/02/12
For personal use only.

Cathodoluminescence, X-ray excited optical luminescence, and X-ray absorption near-edge structure studies of ZnO nanostructures

Olga Lobacheva, Patricia L. Corcoran, Michael W. Murphy, Jun Young Peter Ko, and Tsun-Kong Sham

Can. J. Chem. Downloaded from www.nrcresearchpress.com by Renmin University of China on 09/02/12
For personal use only.

Abstract: ZnO nanostructures of various morphologies and crystallinities were fabricated by thermal evaporation from Zn powder in a tube furnace in the presence of oxygen. It was found that the morphology of ZnO nanostructures was affected by synthesis parameters, such as growth temperature, carrier gas flow, and the presence of catalyst on the surface of the substrate. Representative ZnO nanostructures were studied by X-ray excited optical luminescence (XEOL) and cathodoluminescence (CL) methods. The luminescence from these samples exhibits a morphology dependence of the branching ratio of the near band gap (NBG) emission in the UV and defect emission in the green (GE). The appearance of the optical emission also depends on the excitation method. X-ray absorption near-edge structures (XANES) at the O K-edge and Zn L-edge are also presented and their implications discussed.

Key words: ZnO nanostructures, XEOL, XANES, cathodoluminescence.

Résumé : Faisant appel à une méthode d'évaporation thermique d'une poudre de Zn dans un four électrique à tube en présence d'oxygène, on a fabriqué des nanostructures de ZnO de morphologies et de cristallinités diverses. On a trouvé que la morphologie des nanostructures de ZnO est affectée par divers paramètres de la synthèse, telle la température de croissance, la vitesse d'écoulement du gaz et la présence de catalyseur sur la surface du substrat. On a étudié les structures de nanostructures de ZnO représentatives en faisant appel aux méthodes de luminescence optique excitée par rayons-X (LOEX) et de cathodoluminescence (CL). La luminescence dans ces échantillons présente, dans l'UV, une relation entre la morphologie sur le rapport de ramification et l'émission de la bande interdite rapprochée (BIR) et l'émission de défaut dans le vert (EV). L'apparition d'une émission optique dépend aussi de la méthode d'excitation. On a aussi déterminé les structures d'absorption des rayons-X près du seuil (« XANES ») au seuil K de l'oxygène et au seuil L du zinc et on discute de leurs implications.

Mots-clés : nanostructures du ZnO, luminescence optique excitée par rayons X (LOEX), structures d'absorption des rayons X près du seuil (« XANES »), cathodoluminescence.

[Traduit par la Rédaction]

Introduction

Zinc oxide, a versatile technological material for light emitting and photonic applications (e.g., solid-state lasers and LEDs), is a semiconductor with a wide band gap (~3.37 eV) and large free exciton energy (~60 meV). Its unique properties, availability in nature, and relatively low cost make it an attractive candidate for optoelectronic, lasing, and piezoelectronic as well as gas-sensing applications among other semiconducting materials with similar parameters.[1–3]

Previous studies have shown that the luminescence properties of ZnO nanostructures exhibit strong size and shape dependence.[4–10] Optical emission spectra of ZnO nanostructures usually show a sharp near-band-gap peak owing to excitonic transitions and a wide visible emission peak, which is usually ascribed to defect states within the band gap. Oxygen vacancies are commonly assigned as the origin of green emission in undoped ZnO crystals. The intensity of optical emission, branching ratio of the peaks, and position of the emission peaks (especially defect emission peaks) are affected by the morphology of ZnO nanostructures.[4–10]

On a nanoscale, as a rule, crystalline nanostructures tend to have superior crystal quality in terms of a lack of defects compared with bulk material. In nanostructures, defects tend to collect on the surface or in the near-surface region, which help reduce the strain in the crystal. As was shown in a cathodoluminescence (CL) study of ZnO nanostructures,[9] the

Received 27 July 2011. Accepted 8 September 2011. Published at www.nrcresearchpress.com/cjc on 9 February 2012.

O. Lobacheva, P.L. Corcoran, M.W. Murphy,* J.Y.P. Ko†, and T.-K. Sham. Departments of Chemistry, Earth Sciences, and Physics and Astronomy, The University of Western Ontario, London, ON N6A 5B7, Canada.

Corresponding author: Tsun-Kong Sham (e-mail: tsham@uwo.ca).

*Present address: HASYLAB / DESY, Notkestr. 85, 22603 Hamburg, Germany.
†Present address: Energy Materials Center, EMC^2, 173 ST Olin Lab, Cornell University, Ithaca, NY 14853, USA.

Can. J. Chem. Downloaded from www.nrcresearchpress.com by Renmin University of China on 09/02/12
For personal use only.

green emission is from defects. With the reduction of size and the increase of the surface-to-volume ratio, the surface and near-surface regions begin to play a prominent role in determining the optical properties of nanostructures.

Among other considerations, the optical spectra of nanostructures can be significantly affected by the nature of the excitation. For example, Liao et al.[11] observed a shift of the emission peaks and a difference in their branching ratio when probing emission properties of a ZnO nanostructure sample using CL and photoluminescence methods.

Here, we present a comparative study of the optical properties of ZnO nanostructures with different morphologies using two excitation methods: CL and X-ray excited optical luminescence (XEOL). The latter was conducted using synchrotron radiation with excitation energy tuned from below to above the O K- and Zn $L_{3,2}$-edges, providing site specificity by preferentially exciting the core levels of the O and Zn sites of the nanostructure, respectively. This provision was not available using CL and a laboratory laser or a UV lamp light source. We also present X-ray absorption near-edge structure (XANES) spectra obtained at the two absorption edges.

Experimental methods

ZnO nanostructure samples were synthesized from Zn powder by the chemical vapour deposition (CVD) method in a tube furnace in the presence of oxygen as described previously.[9] Morphology of the final product in this CVD process is strongly affected by synthesis parameters such as temperature, starting materials, carrier gas flow, nature of substrate, and the presence of catalyst. In this work, ZnO nanostructures were grown on a clean Si(100) slab substrate placed along the tube furnace, of which half of the substrate along the tube was covered with an Au catalyst.

XEOL and XANES spectra of ZnO samples were collected at the spherical grating monochromator (SGM) beam line of the Canadian Light Source (CLS), Saskatoon, Saskatchewan.[12] CL spectra were recorded using a Reliotron microscope stage-mounted CL instrument and spectrometer at the Department of Earth Sciences, The University of Western Ontario, London, Ontario.

CLS is a 2.9 GeV third-generation synchrotron light source. It produces a highly collimated and bright X-ray beam that can be finely tuned over a wide energy range (from IR to hard X-rays). The SGM beam line is equiped with an undulator providing soft X-ray photons in the energy range 250–2000 eV. Synchrotron-based spectroscopic methods such as XANES and XEOL were utilized in this experiment because they are especially suitable for probing the optical properties of nanostructured samples because of the tunability, brightness, and time structure of synchrotron radiation.

XEOL is an X-ray photon-in / optical photon-out method, converting the X-ray energy absorbed by the specimen into optical emission. Excitation of a specimen with X-ray photon energy tuned across the absorption edge of a particular element makes XEOL an element-, site-, and absorption-edge-specific technique under favourable conditions, since the absorption coefficient at an absorption edge of an element changes abruptly in favour of the element; this can provide more noticeable changes in the branching ratio. With the CL method, there is no such selectivity. The electron beam used for CL excites all of the possible emission channels via core excitation and secondary processes. CL results depend on the parameters of the electron beam such as the accelerating voltage and the beam current.[11,13] Thus, accelerating voltage determines the size of the excited volume inside the sample. Changes in the accelerating voltage lead to variation of the penetration depth of electrons. In general, the higher the energy (voltage) of the incident electron, the more penetrating the electron and the more energetic the secondary process, the longer the thermalization track for the secondary electrons and holes, which can recombined radiatively. As noted above, the near band-gap (exciton) and visible (defect) emission are relatively fast and slow processes, respectively, depending on the size and the crystallinity of the specimen.[9,10] They can also originate from various depth of the specimen, especially in nanostructures where the thermalization track may be truncated owing to the small size; therefore, the branching ratio of the peaks in the CL-induced optical spectrum of ZnO should depend somewhat on the accelerating voltage.[13]

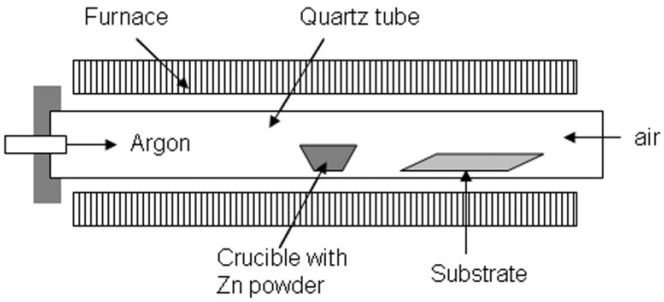


Fig. 1. Schematic for the fabrication process.

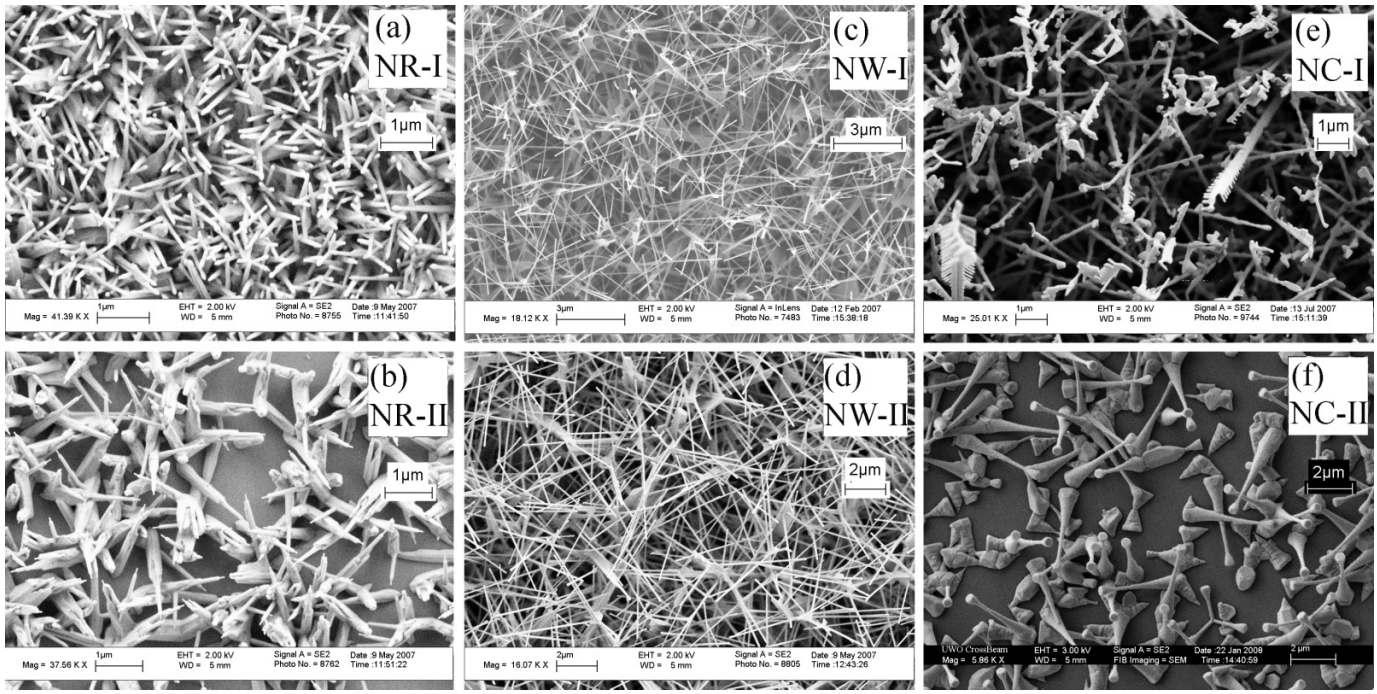
Synthesis of ZnO nanostructures

ZnO nanostructures were fabricated in a tube furnace from Zn powder (99.99%, Alfa Aesar) in the presence of oxygen. An alumina boat with starting material was placed in the centre of the quartz tube mounted into the furnace. The temperature in the furnace was increased at a rate of 10 °C/min to 550–570 °C and then kept constant for 45–60 min. At one end of the tube, a carrier gas (argon) was introduced into the system at a flow rate of 80 sccm. A silicon substrate (~0.5 in. wide (1 in. = 25.4 mm), 3 in. long slab of an Si(100) wafer) was placed downstream from the boat containing the starting material. The other end of the quartz tube was opened to ambient air (Fig. 1). At the synthesis temperature, Zn evaporated and reacted with ambient oxygen to form ZnO_x clusters ($x \leq 1$). The carrier gas transported Zn vapour and ZnO_x clusters toward the substrate where the nanostructures were formed.[13]

The Si wafer substrate was prewashed in acetone, alcohol, and distilled water. Half of the Si slab was covered along the length with colloidal gold (colloidal solution of thiol-capped gold nanoparticles), so that we could compare nanostructures grown with and without a catalyst. At an elevated temperature in the furnace the gold nanoparticles agglomerated into Au islands, which serve as catalysts for the subsequent growth of ZnO nanostructures by the vapour–liquid–solid (VLS) mechanism. On the clean part of the Si wafer, ZnO nanostructures were formed by the vapour–solid (VS) process.

Can. J. Chem. Downloaded from www.nrcresearchpress.com by Renmin University of China on 09/02/12
For personal use only.

Fig. 2. Scanning electron microscopy (SEM) of ZnO nanostructures: (*a*) and (*b*) nanorod samples NR-I and NR-II, respectively; (*c*) and (*d*) nanowire samples NW-I and NW-II, respectively; (*e*) and (*f*) nanocombs NC-I and nanocones NC-II, respectively. Upper row: nanostructures were grown on an Si wafer with Au catalyst; lower row: nanostructures were grown without catalyst on a clean Si wafer.



Although the presence of a catalyst is not a necessary condition for forming ZnO nanostructures, it affects the resulting morphology. The ZnO nanostructures thus formed appear as a grayish-white film on the surface of the Si wafer. When excited with an UV lamp the samples produced green light.

Several ZnO nanosamples with distinctly different morphologies along the substrate slab were chosen for characterization. Images of the selected samples were taken using a LEO 1530 scanning electron microscope (SEM) in the Nanofab Lab at The University of Western Ontario, London, Ontario.

Nanorod samples NR-I (Fig. 2*a*) and NR-II (Fig. 2*b*) were formed on Si wafer substrates with and without an Au catalyst, respectively, under the following synthesis conditions: temperature at the centre of the furnace, 550 °C; and Ar flow rate, 80 sccm. Sample NR-I contained ~350 nm nanorods with tips of ~70 nm in diameter, and sample NR-II was composed of ~300 nm nanorods with ~90 nm tips, terminating with even smaller spikes (~30 nm). Since the samples were collected at the same distance from the furnace centre, the experimental parameters, the growth temperature and the amount of Zn vapour, in the growth region can be considered identical. The influence of the Au catalyst led to the formation of nanorod structures with different dimensions, which is evident in the SEM images (Figs. 2*a* and 2*b*). When grown with the catalyst, ZnO formed a denser coverage on the substrate (sample NR-I, Fig. 2*a*), whereas the sample grown without a catalyst displayed bare Si wafer underneath the ZnO nanorods (sample NR-II, Fig. 2*b*).

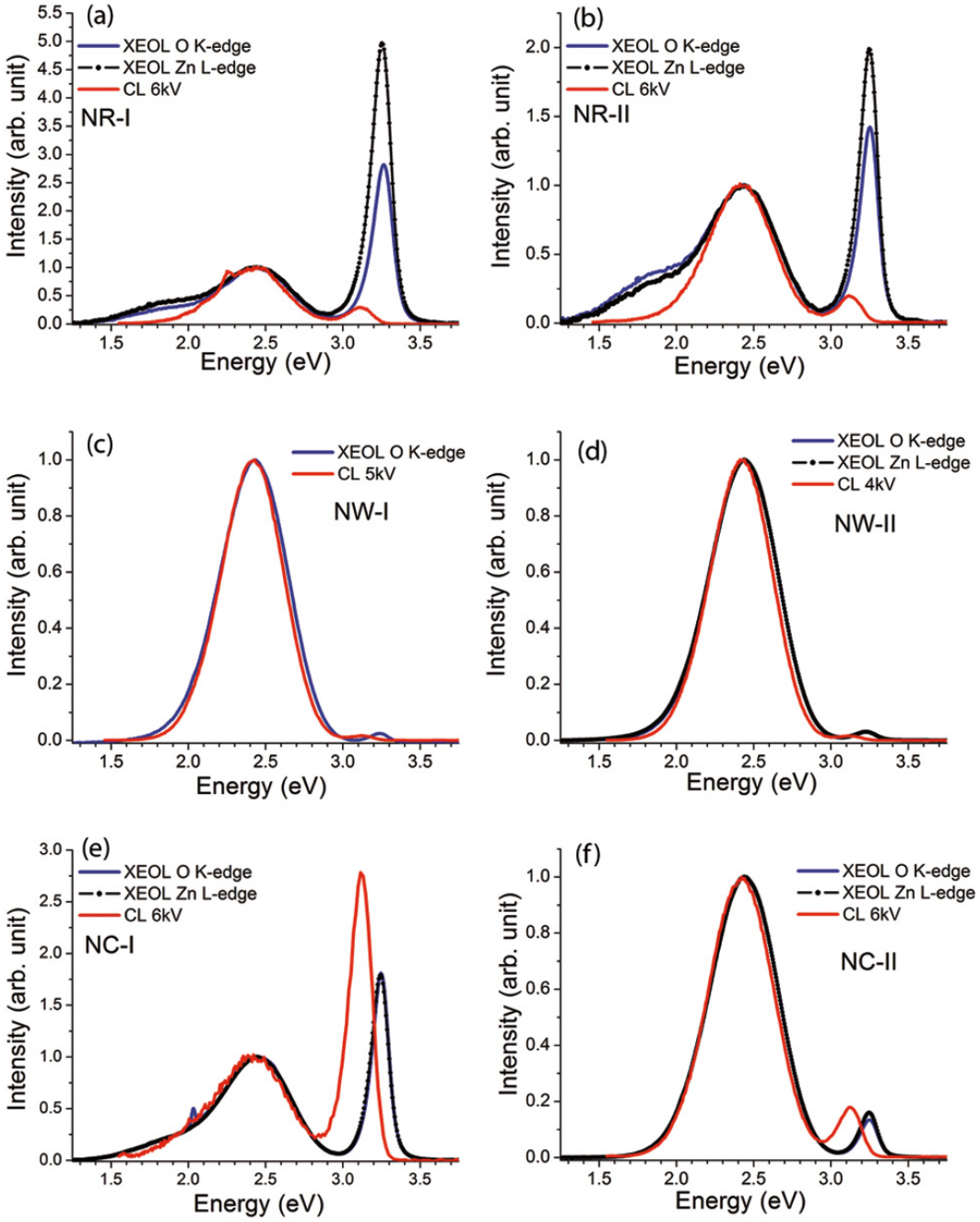
Nanowire samples NW-I (Fig. 2*c*) and NW-II (Fig. 2*d*) were fabricated using the same procedures at a temperature of 570 °C and at 75 sccm Ar flow with and without the Au catalyst, respectively. Sample NW-I was composed of nanowires ~50 nm in diameter, whereas sample NW-II was comprised of ~90 nm nanowires. Apparently, in this case, the concentration of Zn vapour was high enough to create a dense coverage of ZnO nanowires independent of the presence of catalyst.

The next two samples (nanocomb NC-I and nanocone NC-II) were fabricated using slightly a different growth scheme, i.e., the downstream end of the quartz tube was closed off to the atmosphere. The synthesis was performed at a temperature of 750 °C with a mixture of argon and oxygen (Ar (50 sccm) + O_2 (10 sccm)) as the carrier gas. This alteration of the synthetic procedure led to the formation of nanostructures with a very different morphology. Sample NC-I was grown on Si substrate with an Au catalyst. It consisted of a mixture of thinner nanowires, ~140 nm in diameter, and thicker rods, ~350 nm in diameter, with nanocombs formed on the ends (Fig. 2*e*). The nanocomb needlelike spikes are ~50–70 nm in diameter. Sample NC-II, which was grown on a clean Si surface, was composed of relatively large nanocones with a thick end of ~800–850 nm, a top of ~400–450 nm, and a neck measuring ~160 nm (Fig. 2*f*). Again the presence of the catalyst on the substrate led to denser growth of nanomaterials.

Results and discussion

Emission spectra of the aforementioned ZnO nanostructures were studied by XEOL and CL methods. XEOL spectra were excited with photon energy selected at just above the O K-edge (539 eV) and the Zn L-edge (1026 eV). The X-ray photon excitation energy was chosen in both cases so that a considerable fraction of photon flux was absorbed by the element of interest compared with situations just below the

Fig. 3. X-ray excited optical luminescence (XEOL) and cathodoluminescence (CL) of ZnO samples. (*a*) ZnO nanorod sample NR-I. (*b*) ZnO nanorod sample NR-II. (*c*) ZnO nanowire sample NW-I. (*d*) ZnO nanowire sample NW-II. (*e*) ZnO nanocomb sample NC-I. (*f*) ZnO nanocone sample NC-II.



edge. It should be noted that XEOL was done below and above the relevant absorption edges in many measurements we conducted previously on ZnO nanostructures.[9,10,12] There was no strong variation in the branching ratio for a given specimen, but the overall intensity varies because of an abrupt change of penetration depth that depends somewhat on the sample thickness, morphology, and degree of imperfection. In most cases, when the sample is thick compared with the one absorption length, the total luminescence yield with excitation across the O K-edge decreases, whereas at the Zn L-edge, the total luminescence yield increases; this is largely due to an interplay of penetration depth and the effective energy transfer of the Auger and secondary electrons to the optical channel. If Auger electrons are emitted in the surface region, they can escape the surface without contributing to the secondary process and, in turn, the luminescence. For most of the presented CL spectra we used an accelerating voltage of 6 kV. In the case of nanowire samples NW I and NW II, which produced very intense green emissions, the accelerating voltage was lowered (shown in the graph legend of Fig. 2). All the presented spectra are normalized to the intensity of the green emission peak for comparison.

XEOL and CL spectra of the nanorod sample NR-I are shown in Fig. 3*a*. XEOL collected at the O K-edge and at

Can. J. Chem. Downloaded from www.nrcresearchpress.com by Renmin University of China on 09/02/12
For personal use only.

Can. J. Chem. Downloaded from www.nrcresearchpress.com by Renmin University of China on 09/02/12
For personal use only.

Fig. 4. Cathodoluminescence (CL) of nanocomb (NC-I) and nanocone (NC-II) ZnO nanostructures excited with different electron energies (4–6 kV). The CL is normalized to the intensity of the green emission.

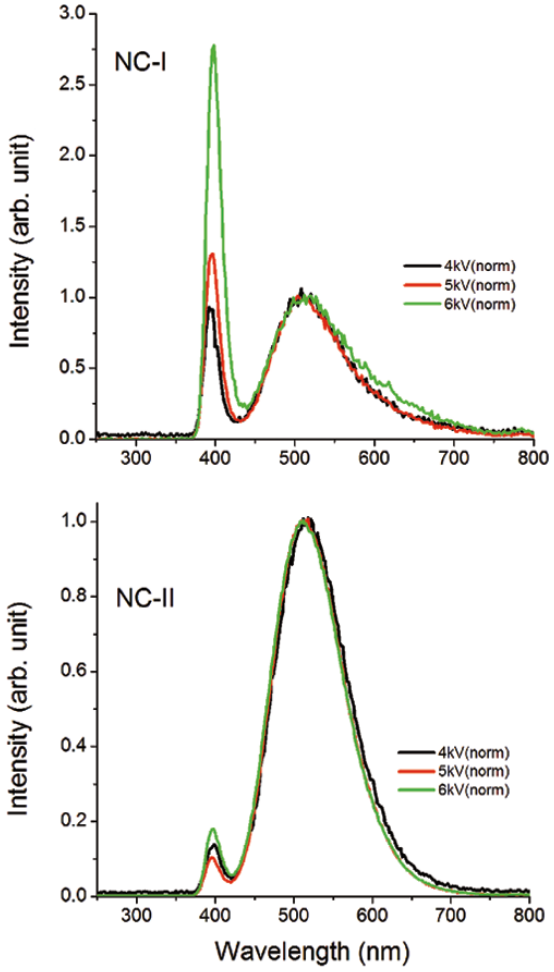
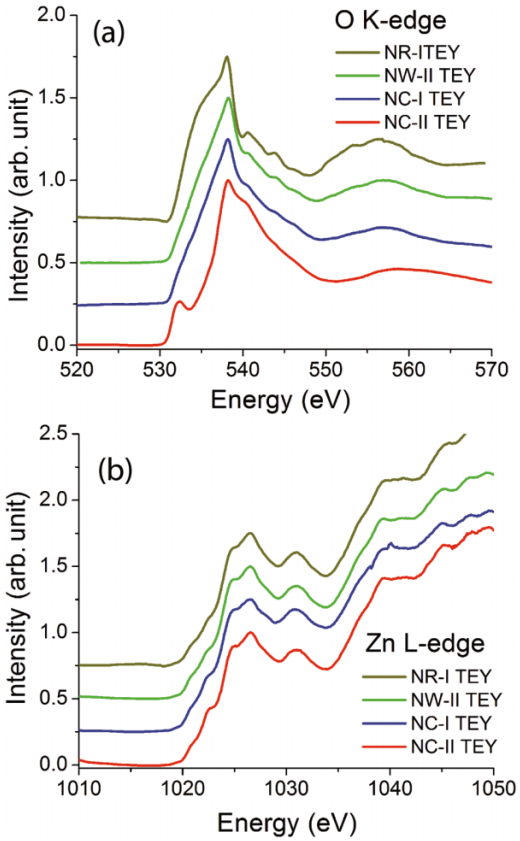


Fig. 5. X-ray absorption near-edge structure (XANES) total electron yield (TEY) of ZnO nanorod, nanowire, nanocomb, and nanocone samples. (*a*) O K-edge. (*b*) Zn L-edge.



the Zn L-edge show a sharp near-band-gap emission (NBG) peak at ~3.25 eV (381 nm), a broad green emission (GE) band at ~2.44 eV (508 nm) owing to defect states in the core, and a red shoulder at ~1.75 eV (710 nm) attributable to surface states. It has been shown that the branching ratio of the NBG and GE emission bands in XEOL is strongly dependent on the crystallinity and morphology of the nanostructure. Time-resolved experiments showed that, in general, the NBG is a very fast decay and can be dominant if the nanocrystal is near perfect (few defects).[9,10] The defect emission in the green is slow and is associated with defect concentration and the dynamics of the secondary processes in which energetic electrons thermalize in the solid. The observation of an intense NBG relative to GE indicates that NR-I is most crystalline among all samples investigated.[9,10] The branching ratio of the NBG peak is more intense for the XEOL spectrum recorded at the Zn L-edge (~1000 eV) than the spectrum at the O K-edge (~500 eV), although the overall behaviour of both curves is similar. This difference in NBG vs GE intensity is attributable to a relatively deeper probing depth in the Zn L-edge and a more effective truncation of the thermalization track of the secondary electrons and hole that are primarily responsible for the defect luminescence, so that the more energetic secondary electrons (e.g., associated with Zn $L_{3,2}$-edge decay) can escape the nanostructure effectively without contributing to the green emission. This argument applies to all situations with the same morphology.

The CL spectrum of sample NR-I has a weak NBG emission peak at ~3.11 eV (398 nm) and a more intensive broad green emission at ~2.44 eV (508 nm) (Fig. 3). This 3.11 eV peak is significantly lower in energy than the band gap and can be due to a self-trapped exciton with shallow electron traps that competes effectively with the NBG emission. It can also be due to band gap shrinkage from high excitation density resulting from irradiation of the high-energy electron beam, merging the shallow trapped states with the conduction band.[14] The spike at 2.25 eV is probably due to an electronic glitch or an impurity emission. As can be seen, the green emission peak is dominant and is more symmetric in the CL spectra than in the XEOL spectra. There is no red shoulder in the CL spectrum. As noted above, the NBG peak in the CL spectrum is red-shifted compared with the XEOL spectra. This appears to be a common feature for all our samples, and will be discussed further, whereas the green emission peaks are in good agreement with assignments in the literature and with the XEOL results. This confirms the general notion that the usually slow oxygen vacancy green emission is due to energy transfer via a secondary process independent of the excitation.

Can. J. Chem. Downloaded from www.nrcresearchpress.com by Renmin University of China on 09/02/12
For personal use only.

Optical emission spectra (XEOL and CL) of sample NR-II are shown in Fig. 3*b*. As in the previous case, the XEOL spectra have a NBG peak at ~3.25 eV, a GE peak at ~2.44 eV, and a red shoulder at ~1.75 eV. The CL spectrum displays a NBG peak at ~3.12 eV (397 nm), with an intensity lower than the corresponding XEOL peak, and a GE peak at ~2.43 eV (510 nm). Overall, the CL and XEOL spectra of NR-II have an appearance similar to that of sample NR-I, although the branching ratio of the two main peaks is slightly different: sample NR-II exhibits more intense defect (green) emissions for both XEOL and CL, indicating that it has a higher defect concentration than NR-I, although it is still highly crystalline. Again, the Zn L-edge excitation produces a higher branching ratio for the NBG emission, as expected for the same reason as discussed in the case of NR-I.

The emission spectra of the two nanowire samples (NW-I and NW-II) are in close agreement with each other (Figs. 3*c* and 3*d*, respectively). For both samples, the XEOL and CL emission curves exhibit very similar behaviour, but they are significantly different from those of NR-I and NR-II in that the green emission dominates with a relatively weak NBG emission. For sample NW-I (NWs of ~50 nm diameter), the XEOL collected at the O K-edge displays a weak NBG peak at ~3.23 eV (383 nm) and a very intensive GE peak at ~2.43 eV (510 nm) (Fig. 3*c*). In the CL spectrum, which was recorded at an accelerating voltage of 5 kV, the NBG peak is even weaker and red-shifted (~3.12 eV) as was the case for NR-I and NR-II. The green emission peak in the CL spectrum is at 2.43 eV, which is in agreement with the corresponding XEOL peak. These results suggest that these NW specimens have high defect concentrations enhancing an effective energy transfer to these sites at the expense of the NBG emission. These results are also in excellent agreement with previous findings that nanowires tend to have more defects than highly crystalline nanoneedles, nanorods, and nanoparticles and therefore emit in the green intensely.[9]

For sample NW-II (NWs of ~90 nm diameter), the normalized XEOL spectra excited at the O K-edge and the Zn L-edge practically coincide with each other: both have a very weak NBG peak at ~3.23 eV and an intensive GE peak at ~2.44 eV (Fig. 3*d*). CL collected at an accelerating voltage of 4 kV produces the same appearance as the XEOL spectra with a green peak at ~2.43 eV. The NBG peak is almost negligible (~3.12 eV), indicating that this is a defect abundant specimen and the excitonic energy transfers effectively to the defects.

The XEOL spectra of nanocomb sample NC-I exhibits a sharp NBG peak at ~3.25 eV and a weaker green emission peak at ~2.44 eV (Fig. 3*e*). It also displays a shoulder on the red side at ~1.75 eV, although it is not as prominent as the shoulder observed in the spectra of the nanorod samples. The CL spectrum of NC-I has an even higher branching ratio for the NBG peak compared with XEOL: the NBG peak is at 3.12 eV, again shifted to the red compared with the XEOL results, and the green emission peak is at 2.42 eV (512 nm). This result can be understood in terms of the more complex morphology of the sample. Close examination of the electron micrograph (Fig. 2*e*) reveals a mixed morphology situation with the presence of nanowires and nanorods (needles). The nanorods (needles) must be near perfect crystals, whereas the nanowires dominate the defect emission. The more intense and red-shifted NBG peak can result from band gap narrowing owing to high excitation (hence carrier) density when the sample is excited with a high-energy electron beam in contrast to quantum confinement where the band gap widens when the size decreases. This notion can be tested by varying the energy of the electrons in CL. One expects to see a more intense NBG emission if one lowers the excitation energy (decreasing the penetration depth). The results of such a test on the nanorod samples are shown in Fig. 4, where the NBG emission shifts to the red and the branching ratio of the NBG emission increases with increasing excitation energy.

For ZnO nanocones (sample NC-II), the green emission is more intense than the NBG emission in both the XEOL and CL spectra (Fig. 3*f*). In XEOL, the NBG peak is at ~3.25 eV and the GE peak is at ~2.44 eV. As observed for other samples, the NBG peak (~3.12 eV) on the CL spectrum of sample NC-II is red-shifted compared with that of XEOL at ~3.25 eV. The green peak is at ~2.42 eV in CL.

Based on these results, there are three types of emission bands: NBG emission, green emission, and red shoulder, corresponding to near band gap, bulk, and surface defects, respectively. Their relative intensities correlate with size, morphology, and crystallinity as described previously.[15–17] It appears that, for all ZnO samples except the thin nanowires, the XEOL spectra excited at the Zn L-edge have higher branching ratios for the NBG peak than the XEOL spectra at the O K-edge. For thin nanowires, the XEOL spectra excited at both absorption edges after being normalized are practically identical to each other, and the NBG emission is nearly quenched by the defects via energy transfer to the longer wavelength radiative channel. Several features are apparent for all samples examined: (*i*) in CL spectra, the NBG emission peak is red-shifted compared with the XEOL spectra; (*ii*) the defect emission in XEOL and CL spectra have almost the same energy position and profile; and (*iii*) the red shoulder, displayed in the XEOL spectra of nanorods (samples NR-I and NR-II) and nanocombs (sample NC-I), is not observed in the CL spectra, and the CL defect emission peak is more symmetric.

These results indicate that the variation in the excitation and energy-transfer mechanisms led to the different appearance of the XEOL and CL spectra, which depends on the crystallinity and morphology of the nanostructure. The probing depth was generally comparable for both methods because the size of the nanostructures is generally comparable to the probing depth of the excitation source. Most CL spectra were excited by an electron beam with an accelerating voltage of 4–6 kV. A rough estimate gives a value of 200–250 nm[19] for depth (inelastic scattering mean free path of electrons with a given energy) of the excited volume at these voltages. As for the XEOL spectra, the attenuation length of X-rays in ZnO is in the range of ~200–350 nm in the vicinity of the O K-edge and ~200–850 nm in the vicinity of the Zn L-edge.[20] For the samples examined, the X-ray attenuation length was greater than the diameter of the nanostructures (or at least comparable to it). The most important difference is that X-rays preferentially excite core electrons with site selectivity, whereas CL excites mostly valence and shallow core electrons with relatively little site selectivity. It should also be noted that the relatively poor vacuum conditiond in the CL measurements (mtorr) is most likely the reason for the

Can. J. Chem. Downloaded from www.nrcresearchpress.com by Renmin University of China on 09/02/12
For personal use only.

quenching of the red surface emission observed in XEOL, where the vacuum was about 10^{-8} torr (1 torr = 133.3224 Pa). What remains somewhat puzzling is the systematic red shift of the NBG peak in the CL spectra relative to the XEOL spectra, which was observed in all cases. We propose that in XEOL, the excitation of a core hole facilitates the formation of a more localized exciton that can decay rapidly, whereas in CL, the exciton becomes less localized in the absence of the core hole and the presence of shallow electron traps and high-density excitation. This notion needs to be confirmed with further investigations.

We have also tracked the structure and electronic behaviour of these materials by measuring their O K-edge and Zn $L_{3,2}$-edge XANES. Figure 5 shows some representative spectra at these edges.

Figure 5 displays the XANES collected in total electron yield (TEY) for four samples with distinctly different morphologies: nanorod (sample NR-I), nanowire (sample NW-II), nanocomb (sample NC-I), and nanocone (sample NC-II). At the O K-edge (Fig. 5*a*), all four samples have conformed TEY curves with the main absorption peak at 538 eV. The pre-edge peak in the TEY of sample NC-II can be assigned to silicon oxide on the surface of substrate. The SEM image (Fig. 2*f*) of the ZnO nanocones shows low packing density, and the surface of the Si wafer is clearly exposed. Comparison of the TEY curves of the four samples reveals that NR-I produces the most prominent and sharpest resonances on the TEY spectrum, whereas the TEY of the other samples are rather smooth. The sharpness of the resonance is associated with little disorder, while increasing broadening of these features can mean increasing disorder owing to increasing imperfection (disorder and defects, etc.) of the crystal as well as chemical inhomogeniety. The result suggests that the nanorod (sample NR-I) has a higher crystal quality than the other samples, and that crystal quality in the remaining samples decreases in thin nanowires (NW-II). Nanocombs (NC-I) and nanocones (NC-II) have mixed morphology, resulting in static disorder (inhomogeniety). The relative intensity of the NBG emission peak also supports this observation. The Zn $L_{3,2}$-edge XANES, however, do not exhibit significant changes, indicating that defects associated with oxygen play a more important role in the optical properties of these materials (Fig. 5*b*).

Summary

The emission properties of ZnO nanostructures with different morphologies were studied using XEOL and CL methods. XEOL spectra were obtained at the O K-edge and at the Zn L-edge.

Our results demonstrate that the optical emissions of ZnO nanostructures are dependent on their morphology and crystallinity. All samples had a sharp NBG (exciton) peak and a broad green (defect) emission peak, although the former is very sensitive to the presence of defects. The relative intensity (branching ratio) of the two emission peaks was very sensitive to nanostructures of different morphologies. Thus, ZnO nanowires have a very intense green emission peak compared with the NBG peak, suggesting that it has the most imperfect crystal structure, whereas the XEOL spectra of nanorods exhibits the most intense NBG emission owing to its near-perfect crystal structure, and finally the nanocombs and nanocombs with mixed morphology display both of the features shown for the nanowires and nanorods. In addition to the green emission, ZnO nanorods and nanocombs exhibit a red shoulder in the XEOL spectra and these are attributed to surface defects of a near-perfect crystal. If the nanostructure is defect abundant in the bulk, these surface features will be quenched because of the energy transfer to the bulk defects.

The appearance of the optical spectra also depends on the excitation method. For most samples, the green emission dominates in the CL spectra, presumably because of the high excitation density, which narrows the band gap and facilitates energy transfer to the defects, except for the nanocombs, which produce a more intense NBG peak and this can be attributed to the presence of highly crystalline nanorods (needles). Finally, no red emission shoulder was registered in the CL of the ZnO samples studied. Although the reason for this is not entirely clear, surface adsorption quenching could be one of the reasons for this difference.

XANES spectra at the O K-edge evidently reflect the difference in the morphology of the nanostructures and the local disorder (defect). The results suggest that ZnO nanorods have superior crystalline structures compared with the other samples. XANES spectra of the different nanosamples at the Zn L-edge are practically the same, indicating that oxygen plays a more significant role in the optical properties of these nanostructures.

Acknowledgements

Research at The University of Western Ontario was supported by the Natural Sciences and Engineering Research Council of Canada (NSERC), the Canada Foundation for Innovation (CFI), the Ontario Innovation Trust (OIT), and the Canada Research Chair (CRC) (T.K.S.). Synchrotron experiments were conducted at the Canadian Light Source, which is supported by NSERC, the National Research Council of Canada (NRC), the Canadian Institutes of Health Research (CIHR), and the University of Saskatchewan. The technical assistance of Tom Regier, Beamline Scientist for the SGM, is gratefully acknowledged.

References

(1) Pearton, S. J.; Lim, W. T.; Wright, J. S.; Tien, L. C.; Kim, H. S.; Norton, D. P.; Wang, H. T.; Kang, B. S.; Ren, F.; Jun, J.; Lin, J.; Osinsky, A. *J. Electron. Mater.* **2008**, *37* (9), 1426. doi:10.1007/s11664-008-0416-5.

(2) Basu, P. K.; Bhattacharyya, P.; Saha, N.; Saha, H.; Basu, S. *Sens. Actuators B Chem.* **2008**, *133* (2), 357. doi:10.1016/j.snb.2008.02.035.

(3) Barth, S.; Hernandez-Ramirez, F.; Holmes, J. D.; Romano-Rodriguez, A. *Prog. Mater. Sci.* **2010**, *55* (6), 563. doi:10.1016/j.pmatsci.2010.02.001.

(4) Djurišić, A. B.; Leung, Y. H. *Small* **2006**, *2* (8–9), 944. doi:10.1002/smll.200600134.

(5) Xu, C. X.; Sun, X. W.; Dong, Z. L.; Yu, M. B.; My, T. D.; Zhang, X. H.; Chua, S. J.; White, T. J. *Nanotechnology* **2004**, *15* (7), 839. doi:10.1088/0957-4484/15/7/022.

(6) Li, D.; Leung, Y. H.; Djurišic, A. B.; Liu, Z. T.; Xie, M. H.; Shi, S. L.; Xu, S. J.; Chan, W. K. *Appl. Phys. Lett.* **2004**, *85* (9), 1601. doi:10.1063/1.1786375.

(7) Red'kin, A. N.; Makovei, Z. I.; Gruzintsev, A. N.; Dubonos, S. V.; Yakimov, E. E. *Inorg. Mater.* **2007**, *43* (3), 253. doi:10.1134/S0020168507030089.
(8) Wang, Z. L. *J. Phys. Condens. Matter* **2004**, *16* (25), R829. doi:10.1088/0953-8984/16/25/R01.
(9) Sun, X. H.; Lam, S.; Sham, T. K.; Heigl, F.; Jürgensen, A.; Wong, N. B. *J. Phys. Chem. B* **2005**, *109* (8), 3120. doi:10.1021/jp044926v.
(10) Rosenberg, R. A.; Shenoy, G. K.; Tien, L. C.; Norton, D.; Pearson, S.; Sun, X. H.; Sham, T. K. *Appl. Phys. Lett.* **2006**, *89*, 093118(3). doi:10.1063/1.2245440.
(11) Liao, X.; Zhang, X. J. *PhysChemComm* **2007**, *111*, 9081.
(12) Regier, T.; Paulsen, J.; Wright, G.; Coulthard, I.; Tan, K. H.; Sham, T. K.; Blyth, R. I. R. In *Proceedings of the 9th International Conference on Synchrotron Radiation Instrumentation,* Daegu, Korea, 28 May – 3 June 2007; AIP, 2007; Vol. CP879, pp 473–476.
(13) Schmidt-Mende, L.; MacManus-Driscoll, J. L. *Mater. Today* **2007**, *10* (5), 40. doi:10.1016/S1369-7021(07)70078-0.
(14) Roth, A. P.; Webb, J. B.; Williams, D. F. *Phys. Rev. B* **1982**, *25* (12), 7836. doi:10.1103/PhysRevB.25.7836.
(15) Abrams, B. L.; Holloway, P. H. *Chem. Rev.* **2004**, *104* (12), 5783. doi:10.1021/cr020351r.
(16) Ichimiya, M.; Horii, T.; Hirai, T.; Sawada, Y.; Minamiguchi, M.; Ohno, N.; Ashida, M.; Itoh, T. *J. Phys. Condens. Matter* **2006**, *18* (6), 1967. doi:10.1088/0953-8984/18/6/012.
(17) Armelao, L.; Heigl, F.; Jürgensen, A.; Blyth, R. I. R.; Regier, T.; Zhou, X.-T.; Sham, T. K. *J. Phys. Chem. C* **2007**, *111* (28), 10194. doi:10.1021/jp071379f.
(18) Heigl, F.; Sun, X. H.; Lam, S.; Sham, T. K.; Gordon, R. A.; Brewe, D.; Rosenberg, R. A.; Shenoy, G. K.; Yablonskikh, M.; MacNaughton, J.; Moewes, A. *13th International Conference on X-ray Absorption Fine Structure, XAFS13,* Stanford, California, 9–14 July 2007; AIP Conference Proceedings, 2007; Vol. CP882, p 734.
(19) Potts, P. J. *A Handbook of Silicate Rock Analysis;* Blackie: Glasgow, and Chapman and Hall: New York, 1987; pp 336–337.
(20) Henke, B. L.; Gullikson, E. M.; Davis, J. C. *At. Data Nucl. Data Tables* **1993**, *54* (2), 181. doi:10.1006/adnd.1993.1013.

Can. J. Chem. Downloaded from www.nrcresearchpress.com by Renmin University of China on 09/02/12
For personal use only.

Oxidative transformation of N-substituted 2-aminophenols to 2-substituted benzoxazoles catalyzed by polymer-incarcerated and carbon-stabilized platinum nanoclusters

Woo-Jin Yoo, Hao Yuan, Hiroyuki Miyamura, and Shū Kobayashi

Can. J. Chem. Downloaded from www.nrcresearchpress.com by Renmin University of China on 09/02/12
For personal use only.

Abstract: The preparation of 2-substituted benzoxazoles was achieved through a sequential aerobic oxidation – enolization – oxidative cyclization reaction of N-substituted 2-aminophenols catalyzed by platinum nanoclusters supported on a polymer / carbon black composite material.

Key words: nanoparticles, platinum, oxidation, polymers, supported catalysis.

Résumé : La synthèse de benzoxazoles substitués en position 2 a été réalisée à partir de 2-aminophénols N-substitués à l'aide d'une séquence réactionnelle oxydation aérobie – énolisation – cyclisation oxydante catalysée par des nanoclusters de platine supportés sur un matériau composite polymère / noir de charbon.

Mots-clés : nanoparticules, platine, oxydation, polymères, catalyse supportée.

Introduction

The development of novel strategies for the efficient synthesis of compounds of high molecular complexity in an expedient manner is of great interest to the synthetic organic community. The utilization of catalysts for sequential reactions circumvents the necessary drain of resources caused by the act of isolation and purification of intermediates faced by traditional iterative synthetic methods.[1] Furthermore, the ability to perform one-pot tandem reactions would allow for the formation and use of highly reactive and (or) unstable intermediates in organic synthetic schemes. Whereas most sequential reactions are performed with homogenous catalysts, the use of heterogeneous catalysts would improve the synthetic utility of cascade reactions by facilitating its recovery and subsequent reuse. In addition to the ease of separation from the reaction mixture, heterogeneous systems for multicatalytic sequential reactions would allow for the use of mutually incompatible catalysts to coexist because of the site isolation of the catalytic species caused by the heterogeneous support.[2]

With our ongoing interest in the preparation of highly active immobilized metal catalysts, we have reported an efficient method for the immobilization of metal catalysts with styrene-based co-polymers through a process known as the polymer-incarcerated (PI) method.[3] We have demonstrated that various gold, platinum, and gold–bimetallic nanoclusters could be stabilized and immobilized by the polymer support and act as highly active heterogeneous catalysts for the aerobic oxidation of alcohols[4] and hydroquinones[5] under ambient pressure and temperature. Furthermore, these PI metal nanoclusters were utilized as catalysts for tandem reactions such as the oxidative esterification of alcohols[6] and sequential allylic oxidation – Michael addition reactions between 1,3-dicarbonyl compounds and allylic alcohols.[7]

As part of our continuing effort into developing aerobic oxidative reactions catalyzed by PI metal nanoclusters, we recently reported the use of platinum nanoclusters immobilized on a polymer / carbon black composite material (PI/CB–Pt) as an effective catalyst for the oxidative cyclization of phenolic and thiophenolic imines **1** to 2-substituted benzoxazoles and benzothiazoles **2** under ambient conditions (Scheme 1, eq. [1]).[8]

During the course of the aerobic oxidative cyclization reaction, we found trace amounts of *ortho*-quinones in the crude reaction mixture and believed these species to arise from the hydrolysis of *ortho*-quinone/thioquinone imines derived from the aerobic oxidation of 2-aminophenols/thiophenols. In a related work, Jiang et al.[9] described a *tert*-butyl hydroperoxide (TBHP) / I_2-mediated domino oxidative cyclization reaction with alkenes **3** and benzyl amines **4** to prepare polysubstituted oxazoles **5** (Scheme 1, eq. [2]). In their proposed mechanism, α-keto imine intermediate **6** was believed to enolize to **7** and was subsequently transformed to their desired oxazole **5** via cyclization and oxidation reactions. Inspired by the work of Jiang et al., we envisioned a similar mechanistic scenario in which N-substituted aminophenols **8** could be oxidatively converted to 2-substituted benzoxazoles **9** (Scheme 1, eq. [3]). Assuming that the PI/CB–Pt catalyst could oxidize **8** to *ortho*-quinone imine **10**, the enolization to phenolic

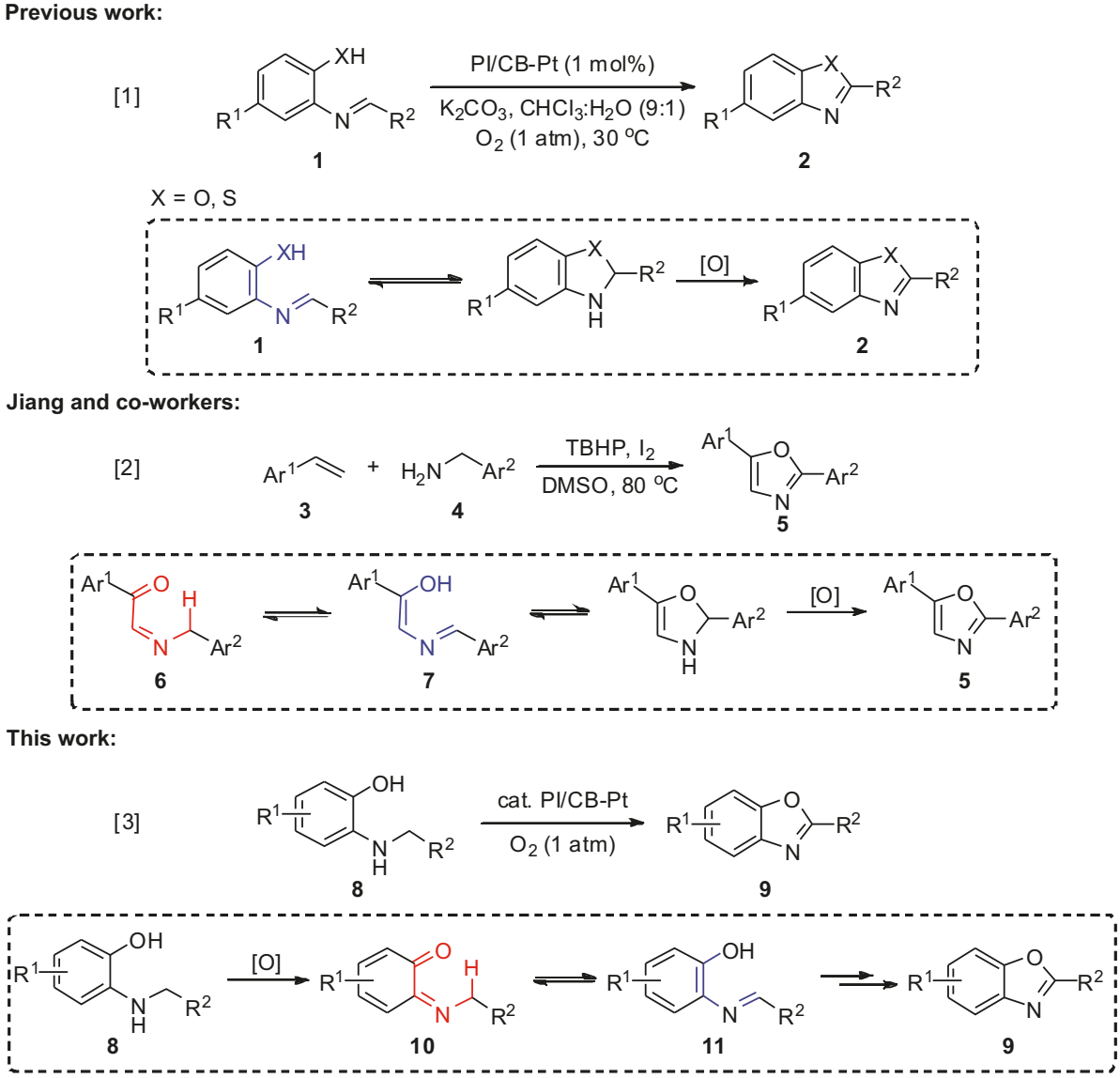
Received 20 June 2011. Accepted 2 October 2011. Published at www.nrcresearchpress.com/cjc on 1 March 2012.

W.-J. Yoo, H. Yuan, H. Miyamura, and S. Kobayashi. Department of Chemistry, School of Science, The University of Tokyo, Hongo, Bunkyo-ku, Tokyo 113-0033, Japan.

Corresponding author: S. Kobayashi (e-mail: shu_kobayashi@chem.s.u-tokyo.ac.jp).

Can. J. Chem. Downloaded from www.nrcresearchpress.com by Renmin University of China on 09/02/12
For personal use only.

Scheme 1. Oxidative preparation of oxazoles.



imine **11** should be highly favorable because of the rearomatization of the benzene ring.

In this paper, we report the preparation of benzoxazoles **9** from N-substituted 2-aminophenols **8** under mild aerobic oxidative conditions through a tandem reaction consisting of an aerobic oxidation – enolization – oxidative cyclization sequence catalyzed by polymer-supported platinum nanoclusters.

Results and discussion

We began our studies by preparing PI/CB–Pt catalyst (Pt particle size = 2.1 ± 0.7 nm; Fig. 1) following our previously reported procedure (Scheme 2) and attempted to perform the sequential oxidative transformation of aminophenol **8a** to 2-substituted benzoxazole **9a** (Table 1).

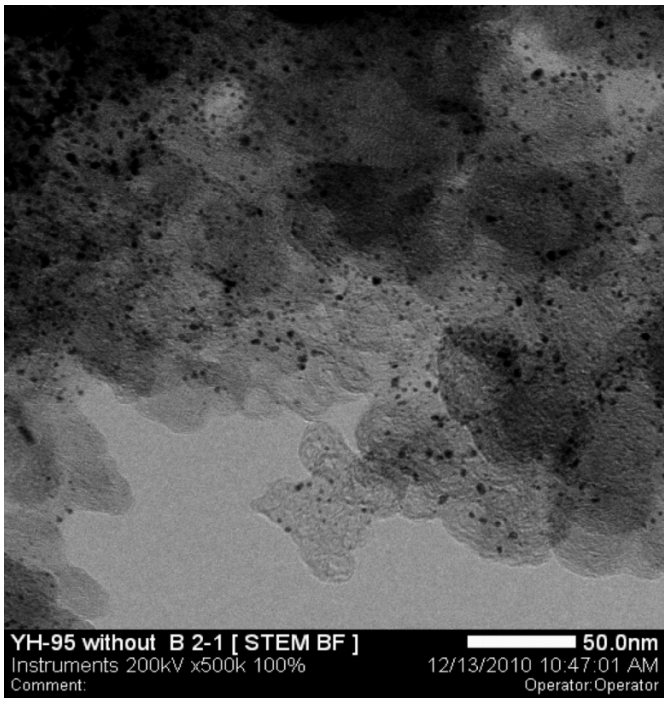
However, our initial attempts to synthesize benzoxazole **9a** by applying our previous conditions for the oxidative cyclization reaction failed, and only trace amounts of the desired product **9a** was observed (Table 1, entry 1). Since **8a** was fully converted and *ortho*-quinone was observed in the crude reaction mixture, we attributed this disappointing result to the relative instability of the reactive *ortho*-quinone imine intermediate. Thus, by introducing a substituent group to the aromatic ring of the aminophenol (**8b**) to stabilize the intermediate, 2-substituted benzoxazole **9b** was obtained with a poor yield (Table 1, entry 2). We found that, by diluting the reaction mixture (Table 1, entry 3) and reducing the amount of water (Table 1, entry 4), a modest improvement for the sequential oxidative transformation of **8b** was provided. However, it should be noted that water plays an important role and excluding water from the system reduces the ability of PI/CB–Pt to catalyze the aerobic oxidation reactions (Table 1, entry 5).

Next, we examined the scope of the tandem oxidative transformation reaction of N-substituted 2-aminophenols **8b**–**8l** (Table 2).

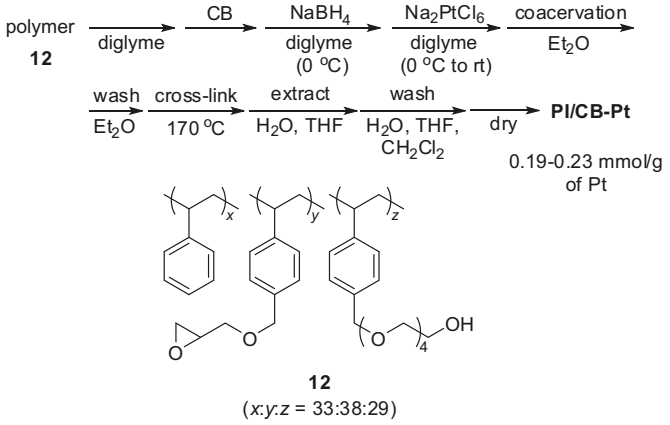
We initially examined the effect of the substituents on the aromatic ring of the 2-aminophenols and found that, by adjusting the position of the methyl group to be para to the

Can. J. Chem. Downloaded from www.nrcresearchpress.com by Renmin University of China on 09/02/12
For personal use only.

Fig. 1. Typical STEM image of platinum nanoclusters immobilized on a polymer / carbon black composite material (PI/CB–Pt).



Scheme 2. Synthetic procedure for the preparation of platinum nanoclusters immobilized on a polymer / carbon black composite material (PI/CB–Pt).



amine (**8c**), an improvement of the yield for benzoxazole **9c** (Table 2, entry 2) resulted, whereas the introduction of a more stabilizing group (*t*-Bu) lead to the quantitative conversion of **8d** to benzoxazole **9d** (Table 2, entry 3). Various 2-aryl benzoxazoles **9e**–**9h** bearing electron-rich and -poor substituents were prepared through the sequential oxidative transformation of N-substituted 2-aminophenols **8e**–**8h** with excellent yields (Table 2, entries 4–7). The synthesis of benzoxazoles with alkenyl (**9i**) and alkynyl (**9j**) substituents was achieved in moderate yields, but required a stoichiometric amount of base (Table 2, entries 8 and 9). Finally, benzoxazoles that possessed a primary aliphatic substituent at the 2-position (**9k** and **9l**) were prepared under our optimized reaction conditions with good results (Table 2, entries 10 and 11).

A tentative mechanism for the sequential oxidative transformation of N-substituted 2-aminophenols **8** to benzoxazoles **9** is shown in Scheme 3.

Based on our previous observations of the conversion of 2-aminophenols to *ortho*-quinones, we envisioned a reaction pathway in which N-substituted 2-aminophenol **8** would be oxidized to the corresponding *ortho*-quinone imine **10**, catalyzed by PI/CB–Pt. The facile enolization of **10** to phenolic imine **11** would restore aromaticity to the system and, after oxidative cyclization, would provide the desired benzoxazole **9**. Although the direct oxidation of **8** to **11** is a distinct possibility, this reaction pathway was discounted, since aerobic oxidation of amines to imines with metal nanoclusters is relatively difficult and requires high reaction temperatures.[10]

We also examined the possibility of an aerobic oxidation of **8** in the absence of the platinum catalyst. We performed control studies in which aminophenol **8d** was subjected to our optimized reaction conditions in the absence of PI/CB–Pt and also with our hybrid polymer / carbon black support material without platinum nanoclusters. In both cases, only trace amounts of **10** and **11** were detected by ^{1}H NMR of the crude reaction mixture.

Finally, we examined the possibility of recovery and reuse of our PI/CB–Pt catalyst for the sequential oxidative transformation of **8d**, and found that the catalyst could be reused for five cycles without noticeable loss of catalytic activity (Scheme 4).

Conclusion

In summary, we have developed a sequential aerobic oxidation – enolization – oxidative cyclization reaction of N-substituted 2-aminophenols to 2-substituted benzoxazoles catalyzed by platinum nanoclusters supported on a polymer / carbon black composite material. The reaction was shown to be remarkably mild and could be utilized to prepare 2-substiuted benzoxazoles with aryl, alkenyl, alkynyl, and aliphatic groups. Further investigations into improving the substrate scope and exploring additional oxidative methods towards the preparation of aromatic heterocycles are now in progress.

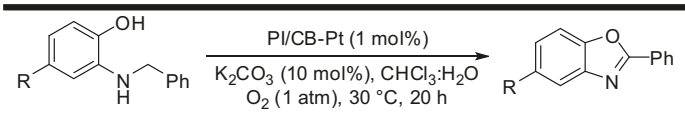
Experimental

Preparation method for PI/CB–Pt

Ketjen black (0.3751 g) was added to a solution of polymer **12** (0.3751 g) in diglyme (25 mL). After stirring the heterogeneous solution for 15 min, a solution of $NaBH_4$ (95.3 mg, 2.52 mmol) in diglyme (5.4 mL) was added dropwise, then a solution of $Na_2PtCl_6{\cdot}6H_2O$ (117.8 mg, 0.21 mmol) in diglyme (15 mL) was added dropwise at 0 °C. After stirring for 4 h at room temperature, Et_2O (200 mL) was added dropwise. The polymer-coated carbon black was washed several times with Et_2O and dried at room temperature. After light grinding with a motor and pestle, the recovered solid powder was heated at 170 °C for 4 h under a balloon of argon. After cooling to room temperature, the cross-linked polymer-coated carbon black was stirred in a THF–H_2O (1:1, 40 mL) mixture overnight. After being filtered and then washed with H_2O, tetrahydrofuran (THF), and dichloromethane (DCM), the recovered solid was dried

Can. J. Chem. Downloaded from www.nrcresearchpress.com by Renmin University of China on 09/02/12
For personal use only.

Table 1. Optimization of reaction conditions.



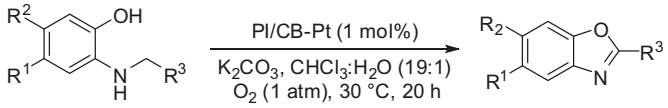
8a-8b **9a-9b**

Entry	Aminophenol	R	Ratio of $CHCl_3$–H_2O	Conc. (mol/L)	Product	Yield (%)[a]
1	**8a**	H	9:1	0.25	**9a**	<5
2	**8b**	Me	9:1	0.25	**9b**	28
3	**8b**	Me	9:1	0.05	**9b**	35
4	**8b**	Me	19:1	0.05	**9b**	48
5	**8b**	Me	1:0	0.05	**9b**	28

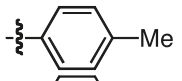
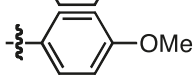
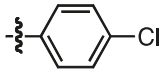
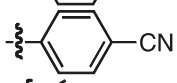
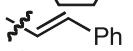
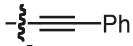
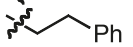
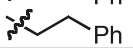
Note: Aminophenols **8a** and **8b** (0.25 mmol), K_2CO_3 (0.025 mmol), and platinum nanoclusters immobilized on a polymer / carbon black composite material (PI/CB–Pt) catalyst (1 mol%) in $CHCl_3$–H_2O at 30 °C under a balloon pressure of oxygen gas.

[a]Yield based on **8a** and **8b** and determined by ^{1}H NMR analysis of the crude reaction mixture using 1,1,2,2-tetrachloroethane as an internal standard.

Table 2. Substrate scope of the sequential oxidative transformation of N-substituted 2-aminophenols.



8b-8l **9b-9l**

Entry	Aminophenol	R^1	R^2	R^3	Product	Yield (%)[a]
1	**8b**	Me	H	Ph	**9b**	31
2	**8c**	H	Me	Ph	**9c**	65
3	**8d**	*t*-Bu	H	Ph	**9d**	Quant.
4	**8e**	*t*-Bu	H		**9e**	90
5	**8f**	*t*-Bu	H		**9f**	97
6	**8g**	*t*-Bu	H		**9g**	87
7	**8h**	*t*-Bu	H		**9h**	Quant.
8	**8i**	*t*-Bu	H		**9i**	70[b]
9	**8j**	*t*-Bu	H		**9j**	67[b]
10	**8k**	*t*-Bu	H		**9k**	79
11	**8l**	H	Me		**9l**	84

Note: Aminophenols **8b**–**8l** (0.25 mmol), K_2CO_3 (0.025 mmol), and platinum nanoclusters immobilized on a polymer / carbon black composite material (PI/CB–Pt) catalyst (1 mol%) in $CHCl_3$–H_2O (19:1, c = 0.05 mol/L) at 30 °C under a balloon pressure of oxygen gas.

[a]Yield based on **8b**–**8l** and determined by weight of the isolated products **9b**–**9l**.

[b]One equivalent of K_2CO_3 was used. Quant., quantitative.

under vacuum to provide the desired heterogeneous catalyst (PI/CB–Pt, 0.83 g; Pt loading, 0.2090 mmol/g).

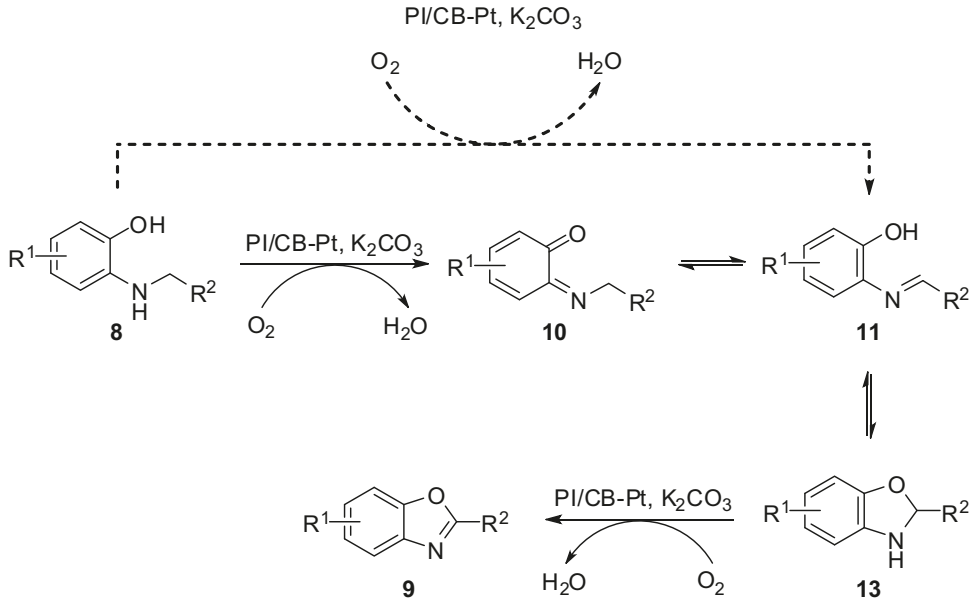
General experimental procedure for the preparation of N-substituted 2-aminophenols via reductive amination

Benzaldehyde (305 µL, 3.00 mmol) was added to a solution of 2-amino-4-*tert*-butylphenol (0.4857 g, 2.940 mmol) in EtOH (15 mL), and the reaction mixture was stirred for 4 h at room temperature. Then, $NaBH_4$ (0.1135 g, 3.00 mmol) was added portionwise and was allowed to stir for 1 h. After the reaction was completed, the reaction was quenched with H_2O (20 mL), extracted with CH_2Cl_2, and the combined organic layers were washed with a saturated brine solution. The extracted crude product was dried over $MgSO_4$, filtered, concentrated under reduced pressure, and then purified by column chromatography (EtOAc:hexane = 1:4) to provide the desired product **8d** (0.6130 g, 2.40 mmol, 82%) as a white solid.

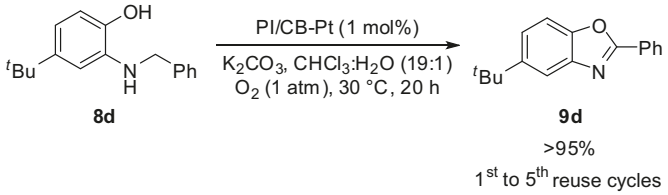
2-(Benzylamino)-4-methylphenol (8b)

mp 108 °C. IR (KBr, cm^{-1}): 3316 (m), 3090 (s), 3061 (s), 3035 (s), 2719 (s), 2342 (w), 1933 (w), 1851 (w), 1601 (s),

Scheme 3. Tentative mechanism for the platinum nanoclusters immobilized on a polymer / carbon black composite material (PI/CB–Pt)-catalyzed sequential oxidative transformation of N-substituted 2-aminophenols.



Scheme 4. Recovery and reuse of platinum nanoclusters immobilized on a polymer / carbon black composite material (PI/CB–Pt).



1362 (m), 1124 (s). ^{1}H NMR ($CDCl_3$, 600 MHz) δ: 7.35–7.28 (m, 4H), 7.22 (t, J = 7.6 Hz, 1H), 6.48–6.38 (d, J = 6.0 Hz, 3H), 4.75 (s, 1H), 4.27 (s, 2H), 2.19 (s, 3H). ^{13}C NMR ($CDCl_3$, 150 MHz) δ: 141.1, 139.3, 136.8, 131.0, 128.5, 127.3, 127.1, 118.0, 114.3, 113.2, 48.5, 21.1. DART-HRMS (*m*/*z*) calcd for $C_{14}H_{16}N_1O_1$ [(M + H)$^+$]: 214.12319; found: 214.12368.

2-(Benzylamino)-5-methylphenol (8c)

mp 102 °C. IR (KBr, cm^{-1}): 3312 (s), 3032 (s), 2918 (s), 2865 (s), 1934 (w), 1842 (w), 1722 (w), 1615 (m), 1524 (s), 1451 (s), 1123 (s). ^{1}H NMR ($CDCl_3$, 600 MHz) δ: 7.35–7.29 (m, 4H), 7.25–7.22 (t, J = 6.0 Hz, 1H), 6.59 (s, 2H), 6.46 (s, 1H), 4.67 (s, 1H), 4.26 (s, 2H), 2.16 (s, 3H). ^{13}C NMR ($CDCl_3$, 150 MHz) δ: 144.1, 139.4, 134.1, 128.5, 128.3, 127.6, 127.1, 121.6, 115.4, 113.5, 49.2, 20.5. DART-HRMS (*m*/*z*) calcd for $C_{14}H_{16}N_1O_1$ [(M + H)$^+$]: 214.12319; found: 214.12326.

2-(Benzylamino)-4-(*tert*-butyl)phenol (8d)

mp 99 °C. IR (KBr, cm^{-1}): 3460 (w), 3335 (m), 3207 (s), 2958 (s), 2870 (m), 1953 (w), 1852 (w), 1816 (w), 1604 (s), 1524 (s), 1410 (m), 1268 (s), 1132 (s). ^{1}H NMR ($CDCl_3$, 600 MHz) δ: 7.48–7.34 (m, 5H), 7.85–6.69 (d, J = 9.1 Hz, 3H), 5.27 (s, 1H), 4.41 (s, 2H), 1.35 (s, 9H). ^{13}C NMR ($CDCl_3$, 150 MHz) δ: 144.3, 141.4, 139.2, 136.1, 128.5, 127.7, 127.1, 114.7, 114.2, 110.5, 48.9, 33.9, 31.5. DART-HRMS (*m*/*z*) calcd for $C_{17}H_{22}N_1O_1$ [(M + H)$^+$]: 256.17014; found: 256.17079.

4-(tert-Butyl)-2-((4-methylbenzyl)amino)phenol (8e)

mp 73–74 °C. IR (KBr, cm^{-1}): 3326 (s), 2956 (s), 2900 (s), 1598 (s), 1466 (s), 1409 (s), 1348 (s), 1274 (s), 1183 (s), 1044 (s). ^{1}H NMR ($CDCl_3$, 600 MHz) δ: 7.24 (d, J = 7.6 Hz, 2H), 7.10 (d, J = 7.6 Hz, 2H), 6.73–6.58 (m, 3H), 4.25 (s, 2H), 2.31 (s, 3H), 1.23 (s, 9H). ^{13}C NMR ($CDCl_3$, 150 MHz) δ: 144.4, 141.6, 136.7, 136.4, 129.6, 129.2, 127.8, 127.2, 114.6, 110.4, 48.8, 33.8, 31.5, 21.0. DART-HRMS (*m*/*z*) calcd for $C_{18}H_{24}N_1O_1$ [(M + H)$^+$]: 270.18579; found: 270.18579.

4-(tert-Butyl)-2-((4-methoxybenzyl)amino)phenol (8f)

mp 87 °C. IR (KBr, cm^{-1}): 3513 (w), 3330 (s), 2953 (s), 2904 (s), 2867 (s), 1603 (s), 1520 (s), 1467 (m), 1362 (m), 1254 (s), 1184 (s), 1131 (s), 1041 (s). ^{1}H NMR ($CDCl_3$, 600 MHz) δ: 7.32 (d, J = 8.2 Hz, 2H), 6.90–6.63 (m, 5H), 4.64–4.20 (m, 3H), 3.80 (s, 3H), 1.27 (s, 9H). ^{13}C NMR ($CDCl_3$, 150 MHz) δ: 158.7, 144.4, 141.4, 136.2, 131.6, 129.0, 114.6, 113.9, 110.5, 55.3, 48.4, 33.7, 31.5. DART-HRMS (*m*/*z*) calcd for $C_{18}H_{24}N_1O_2$ [(M + H)$^+$]: 286.18070; found: 286.18094.

4-(tert-Butyl)-2-((4-chlorobenzyl)amino)phenol (8g)

mp 83 °C. IR (KBr, cm^{-1}): 3319 (s), 2961 (s), 2900 (s), 2864 (s), 1869 (w), 1739 (w), 1599 (s), 1518 (s), 1347 (m), 1185 (s), 1128 (s), 1048 (s). ^{1}H NMR ($CDCl_3$, 600 MHz) δ: 7.10 (d, J = 2.1 Hz, 4H), 6.56–6.39 (m, 3H), 4.91 (s, 1H), 4.12 (s, 2H), 1.10 (s, 9H). ^{13}C NMR ($CDCl_3$, 150 MHz) δ: 144.5, 141.3, 137.8, 135.8, 132.7, 128.9, 128.6, 114.9, 114.2, 110.5, 48.1, 34.2, 31.4. DART-HRMS (*m*/*z*) calcd for $C_{17}H_{21}N_1O_1Cl_1$ [(M + H)$^+$]: 290.12117; found: 290.13109.

4-(((5-(tert-Butyl)-2-hydroxyphenyl)amino)methyl) benzonitrile (8h)

mp 128 °C. IR (KBr, cm^{-1}): 3393 (s), 2961 (s), 2869 (s),

Can. J. Chem. Downloaded from www.nrcresearchpress.com by Renmin University of China on 09/02/12
For personal use only.

Can. J. Chem. Downloaded from www.nrcresearchpress.com by Renmin University of China on 09/02/12
For personal use only.

2232 (s), 1924 (w), 1705 (w), 1608 (s), 1523 (s), 1417 (s), 1275 (s), 1129 (s), 1012 (w). ^{1}H NMR ($CDCl_3$, 600 MHz) δ: 7.59 (d, J = 7.6 Hz, 2H), 7.49 (d, J = 7.6 Hz, 2H), 6.67–6.64 (m, 2H), 6.53 (s, 1H), 4.44 (s, 2H), 1.26 (s, 9H). ^{13}C NMR ($CDCl_3$, 150 MHz) δ: 145.7, 144.2, 141.1, 135.5, 132.3, 127.9, 118.8, 114.5, 113.8, 110.3, 109.6, 48.0, 34.1, 31.4. DART-HRMS (*m/z*) calcd for $C_{18}H_{21}N_2O_1$ [$(M + H)^+$]: 281.16539; found: 281.16648.

4-*(tert-*Butyl)-2-(cinnamylamino)phenol (8i)

mp 98–99 °C. IR (KBr, cm^{-1}): 3317 (s), 3061 (m), 2957 (s), 2861 (m), 1601 (s), 1521 (s), 1415 (s), 1364 (m), 1196 (s), 1133 (s), 1047 (w). ^{1}H NMR ($CDCl_3$, 600 MHz) δ: 7.45–7.31 (m, 5H), 6.97 (s, 1H), 6.77–6.70 (m, 3H), 6.44–6.40 (m, 1H), 5.62 (s, 1H), 4.31 (d, J = 5.5 Hz, 2H), 1.68 (s, 9H). ^{13}C NMR ($CDCl_3$, 150 MHz) δ: 144.1, 141.8, 136.8, 136.0, 131.8, 128.4, 127.3, 127.0, 126.3, 115.0, 114.3, 110.7, 46.9, 34.2, 31.6, 31.5. DART-HRMS (*m/z*) calcd for $C_{19}H_{24}N_1O_1$ [$(M + H)^+$]: 282.18579; found: 282.18705.

4-*(tert-*Butyl)-2-((3-phenylprop-2-yn-1-yl)amino)phenol (8j)

IR (NaCl, film, cm^{-1}): 3061 (m), 2959 (s), 2905 (s), 2868 (s), 2362 (w), 2337 (w), 1951 (w), 1885 (w), 1733 (s), 1604 (s), 1523 (s), 1489 (s), 1420 (s), 1250 (s), 1197 (s). ^{1}H NMR ($CDCl_3$, 600 MHz) δ: 7.30–7.21 (m, 2H), 7.16–7.09 (m, 3H), 6.83 (s, 1H), 6.57–6.54 (m, 2H), 4.13–3.97 (m, 2H), 1.19 (s, 9H). ^{13}C NMR ($CDCl_3$, 150 MHz) δ: 143.8, 142.4, 135.0, 128.1, 127.9, 122.9, 115.6, 114.0, 111.3, 86.6, 83.3, 34.9, 31.3, 20.9, 14.0. DART-HRMS (*m/z*) calcd for $C_{19}H_{22}N_1O_1$ [$(M + H)^+$]: 280.17014; found: 280.17017.

5-Methyl-2-((3-phenylpropyl)amino)phenol (8l)

mp 69–71 °C. IR (KBr, cm^{-1}): 3412 (w), 3285 (m), 2955 (s), 2852 (s), 2663 (s), 1901 (w), 1818 (w), 1746 (w), 1585 (s), 1478 (s), 1445 (s), 1371 (s), 1180 (s), 1084 (m). ^{1}H NMR ($CDCl_3$, 600 MHz) δ: 7.35–7.22 (m, 5H), 6.96 (t, J = 7.6 Hz, 1H), 6.80 (d, J = 8.2 Hz, 1H), 6.71 (d, J = 7.6 Hz), 2.92 (t, J = 6.8 Hz, 2H), 2.76 (t, J = 7.6 Hz, 2H), 2.29 (s, 3H), 2.00–1.94 (m, 2H). ^{13}C NMR ($CDCl_3$, 150 MHz) δ: 152.2, 141.5, 133.5, 132.8, 128.4, 128.3, 125.9, 125.4, 121.6, 111.8, 48.7, 33.4, 32.3, 17.3. DART-HRMS (*m/z*) calcd for $C_{16}H_{20}N_1O_1$ [$(M + H)^+$]: 242.15449; found: 242.15469.

Experimental procedure for the preparation of 4-(*tert*-butyl)-2-((3-phenylpropyl)amino)phenol (8k)

1-Bromo-3-phenylpropane (3.0 mL, 20 mmol) was added to a heterogeneous mixture of 2-amino-4-*tert*-butylphenol (6.573 g, 39.78 mmol) and $KHCO_3$ (8.763 g, 87.52 mmol) in DMF (10 mL), and the reaction mixture was stirred overnight at room temperature. The reaction mixture was diluted with EtOAc (30 mL) and H_2O (30 mL), extracted with EtOAc, and the combined organic layers were washed with a saturated brine solution. The extracted crude product was dried over $MgSO_4$, filtered, concentrated under reduced pressure, and then purified by column chromatography (EtOAc:hexane = 1:5) to provide the desired product **8k** (5.617 g, 19.82 mmol, 95%) as a white solid, mp 107–108 °C. IR (KBr, cm^{-1}): 3414 (s), 3330 (s), 3235 (s), 2959 (s), 2863 (s), 1940 (w), 1870 (w), 1806 (w), 1598 (s), 1522 (s), 1475 (s), 1417 (s), 1312 (m), 1208 (s), 1106 (m). ^{1}H NMR ($CDCl_3$, 600 MHz) δ: 7.34–7.21 (m, 6H), 6.74 (s, 2H), 2.77 (s, 2H), 2.00 (s, 2H), 1.31 (s, 9H). ^{13}C NMR ($CDCl_3$, 150 MHz) δ: 141.7, 128.4, 125.9, 33.3, 31.6. DART-HRMS (*m/z*) calcd for $C_{19}H_{26}N_1O_1$ [$(M + H)^+$]: 284.20144; found: 284.20186.

General experimental procedure for the sequential oxidative transformations of N-substituted 2-aminophenols

In a screw cap glass test tube, PI/CB–Pt (0.0210 g, 0.0025 mmol, 1 mol%), **8d** (0.0638 g, 0.250 mmol), and K_2CO_3 (0.0025 g, 0.025 mmol) were added and then partially dissolved in $CHCl_3$ (4.75 mL) and H_2O (0.25 mL). The reaction mixture was allowed to stir for 20 h at 30 °C under an O_2 balloon. After the completion of the reaction, the heterogeneous catalyst was removed by filtration and washed with CH_2Cl_2. $MgSO_4$ (0.02 g) was added to the resulting filtrate, and the dried crude reaction mixture was filtered again and then concentrated under reduced pressure. The crude product was purified by preparative thin-layer chromatography (EtOAc:hexane = 1:9) to provide **9d** (0.0626 g, 0.249 mmol, 100%) as a white solid.

5-Methyl-2-phenylbenzooxazole (9b)

^{1}H NMR ($CDCl_3$, 600 MHz) δ: 8.24–8.22 (m, 2H), 7.54–7.50 (m, 4H), 7.44 (d, J = 8.2 Hz, 1H), 7.14 (d, J = 8.2 Hz, 1H), 2.47 (s, 3H). ^{13}C NMR ($CDCl_3$, 150 MHz) δ 163.1, 149.0, 142.2, 134.4, 131.4, 128.9, 127.5, 127.3, 126.2, 119.9, 109.9, 21.5. This is a known compound and the spectral data are identical to those reported in the literature.[11]

6-Methyl-2-phenylbenzooxazole (9c)

^{1}H NMR ($CDCl_3$, 600 MHz) δ: 8.16 (s, 2H), 7.57 (d, J = 7.6 Hz, 1H), 7.45 (s, 1H), 7.09 (d, J = 8.2 Hz, 1H), 2.43 (s, 3H). ^{13}C NMR ($CDCl_3$, 150 MHz) δ: 162.5, 151.0, 139.8, 135.5, 131.3, 128.8, 127.4, 127.3, 125.8, 119.3, 110.7, 21.8. This is a known compound and the spectral data are identical to those reported in the literature.[12]

5-(*tert-*Butyl)-2-phenylbenzooxazole (9d)

^{1}H NMR ($CDCl_3$, 600 MHz) δ: 8.25–8.22 (m, 2H), 7.79 (d, J = 2 Hz, 1H), 7.52–7.47 (m, 4H), 7.41–7.39 (dd, J = 2 Hz, 1H), 1.38 (s, 3H). ^{13}C NMR ($CDCl_3$, 150 MHz) δ: 163.1, 148.7, 148.1, 142.0, 131.3, 128.9, 127.5, 127.3, 122.8, 116.5, 109.7, 34.9, 31.7. This is a known compound and the spectral data are identical to those reported in the literature.[13]

2-(4-Methylphenyl)-5-*tert-*butylbenzooxazole (9e)

^{1}H NMR ($CDCl_3$, 600 MHz) δ: 8.12 (d, J = 8.2 Hz, 2H), 7.78 (d, J = 1.4 Hz, 1H), 7.45 (d, J = 8.2 Hz, 1H), 7.39–7.36 (dd, J = 2 Hz, 1H), 7.29 (d, J = 8.3 Hz, 2H), 2.41 (s, 3H), 1.38 (s, 9H). ^{13}C NMR ($CDCl_3$, 150 MHz) δ: 163.4, 148.7, 148.0, 142.0, 141.8, 129.6, 127.4, 124.6, 122.5, 116.3, 109.5, 34.9, 31.7, 21.6. This is a known compound and the spectral data are identical to those reported in the literature.[14]

2-(4-Methoxylphenyl)-5-*tert-*butylbenzooxazole (9f)

mp 134.8 °C. IR (KBr, cm^{-1}): 3069 (m), 3003 (w), 2957 (s), 2372 (w), 2043 (w), 1898 (w), 1609 (s), 1499 (s), 1471

Can. J. Chem. Downloaded from www.nrcresearchpress.com by Renmin University of China on 09/02/12
For personal use only.

(m), 1337 (m), 1256 (s), 1170 (m), 1055 (m), 1026 (s). ^{1}H NMR ($CDCl_3$, 500 MHz) δ: 8.15 (d, J = 8.5 Hz, 2H), 7.75 (d, J = 1.7 Hz, 1H), 7.43 (d, J = 8.5 Hz, 1H), 7.34 (d, J = 8.5 Hz, 1H), 6.98 (d, J = 8.5 Hz, 2H), 3.84 (s, 3H), 1.37 (s, 9H). ^{13}C NMR ($CDCl_3$, 125 MHz) δ: 163.2, 162.1, 148.6, 147.8, 142.1, 129.2, 122.2, 119.8, 116.1, 114.2, 109.4, 55.3, 34.8, 31.7. DART-HRMS calcd for $C_{18}H_{20}N_1O_2$ [$(M + H)^+$]: 282.14940; found: 282.14963.

2-(4-Chlorophenyl)-5-*tert*-butylbenzooxazole (9g)

mp 167.1 °C. IR (KBr, cm^{-1}): 3061 (m), 2962 (s), 2905 (w), 2869 (w), 2369 (w), 1891 (s), 1600 (m), 1479 (s), 1399 (m), 1362 (m), 1275 (s), 1200 (m), 1088 (s), 1050 (s), 1009 (m). ^{1}H NMR ($CDCl_3$, 600 MHz) δ: 8.14 (d, J = 8.2 Hz, 2H), 7.77 (s, 1H), 7.47–7.44 (t, J = 8.2 Hz, 3H), 7.39 (d, J = 2 Hz, 1H), 1.38 (s, 9H). ^{13}C NMR ($CDCl_3$, 150 MHz) δ: 162.1, 148.7, 148.3, 141.9, 137.5, 129.2, 128.7, 125.8, 123.1, 116.5, 109.7, 35.0, 31.7. DART-HRMS calcd for $C_{17}H_{17}N_1O_1Cl_1$ [$(M + H)^+$]: 286.09987; found: 286.09902.

2-(4-Cyanophenyl)-5-*tert*-butylbenzooxazole (9h)

mp 207.2 °C. IR (KBr, cm^{-1}): 3061 (m), 2968 (s), 2905 (w), 2875 (m), 2225 (m), 1899 (w), 1746 (w), 1616 (m), 1573 (m), 1549 (m), 1479 (s), 1404 (s), 1367 (s), 1332 (s), 1278 (s), 1200 (m), 1133 (w), 1052 (s), 1013 (w). ^{1}H NMR ($CDCl_3$, 600 MHz) δ: 8.24 (d, J = 8.3 Hz, 2H), 7.74–7.70 (t, J = 8.3 Hz, 3H), 7.44–7.38 (m, 2H), 1.32 (s, 9H). ^{13}C NMR ($CDCl_3$, 150 MHz) δ: 160.9, 148.8, 148.7, 141.7, 132.6, 131.2, 127.7, 124.0, 118.2, 116.9, 114.4, 109.9, 34.9, 31.7. DART-HRMS calcd for $C_{18}H_{17}N_2O_1$ [$(M + H)^+$]: 277.13409; found: 277.13372.

5-(*tert*-Butyl)-2-styrylbenzooxazole (9i)

mp 93.6 °C. IR (KBr, cm^{-1}): 3030 (w), 2972 (w), 2950 (w), 2903 (w), 2868 (w), 2367 (w), 2341 (w), 1956 (w), 1886 (w), 1863 (w), 1741 (w), 1637 (m), 1608 (w), 1576 (m), 1531 (s), 1472 (w), 1450 (m), 1335 (m), 1265 (s), 1187 (s), 1121 (m), 1072 (m). ^{1}H NMR ($CDCl_3$, 600 MHz) δ: 7.77–7.72 (m, 2H), 7.58 (d, J = 7.6 Hz, 2H), 7.43–7.33 (m, 5H), 7.06 (d, J = 16.5 Hz, 1H), 1.38 (s, 9H). ^{13}C NMR ($CDCl_3$, 150 MHz) δ: 162.9, 148.4, 148.0, 142.1, 139.0, 135.2, 129.6, 128.9, 127.5, 123.0, 116.4, 114.1, 109.4, 34.9, 31.7. DART-HRMS calcd for $C_{19}H_{20}N_1O_1$ [$(M + H)^+$]: 278.15449; found: 278.15541.

5-(*tert*-Butyl)-2-phenylethynylbenzooxazole (9j)

mp 110.6 °C. IR (KBr, cm^{-1}): 3078 (w), 3037 (w), 2960 (s), 2867 (m), 2222 (s), 1891 (w), 1603 (w), 1543 (s), 1480 (s), 1362 (m), 1327 (m), 1299 (m), 1268 (m), 1149 (s), 1116 (m), 945 (s). ^{1}H NMR ($CDCl_3$, 600 MHz) δ: 7.74 (s, 1H), 7.64 (d, J = 8.2 Hz, 2H), 7.47–7.37 (m, 5H), 1.37 (s, 9H). ^{13}C NMR ($CDCl_3$, 150 MHz) δ: 148.6, 148.3, 147.8, 141.0, 132.2, 130.2, 128.6, 124.2, 120.3, 116.7, 109.7, 93.1, 77.7, 34.9, 31.7. DART-HRMS calcd for $C_{19}H_{18}N_1O_1$ [$(M + H)^+$]: 276.13884; found: 276.13927.

5-(*tert*-Butyl)-2-phenethylbenzooxazole (9k)

mp 42 °C. IR (KBr, cm^{-1}): 3068 (w), 3030 (w), 2953 (m), 2867 (w), 2492 (w), 2371 (w), 1618 (m), 1576 (s), 1477 (m), 1452 (m), 1365 (m), 1266 (m), 1226 (m), 1202 (w), 1161 (m), 1178 (m), 1077 (m), 1032 (w). ^{1}H NMR ($CDCl_3$, 600 MHz) δ: 7.62 (d, J = 1.4 Hz, 1H), 7.32–7.26 (m, 2H), 7.23–7.11 (m, 5H), 3.13 (s, 4H), 1.29 (s, 9H). ^{13}C NMR ($CDCl_3$, 150 MHz) δ: 166.3, 148.7, 147.6, 141.2, 140.1, 128.2, 126.4, 122.1, 116.1, 109.4, 34.8, 32.8, 31.7, 30.4. DART-HRMS calcd for $C_{19}H_{22}N_1O_1$ [$(M + H)^+$]: 280.17014; found: 280.17142.

6-Methyl-2-phenethylbenzooxazole (9l)

IR (KBr, cm^{-1}): 3061 (w), 3029 (m), 2925 (m), 2860 (w), 2362 (w), 1905 (w), 1608 (s), 1577 (s), 1495 (m), 1451 (m), 1242 (s), 1148 (m), 1037 (m). ^{1}H NMR ($CDCl_3$, 600 MHz) δ: 7.22 (t, J = 6.9 Hz, 3H), 7.17 (t, J = 7.6 Hz, 2H), 7.16–7.09 (m, 2H), 7.02 (d, J = 7.6 Hz, 1H), 3.19–3.10 (m, 4H), 2.53 (s, 3H). ^{13}C NMR ($CDCl_3$, 150 MHz) δ: 165.4, 150.5, 140.4, 140.2, 130.0, 128.6, 128.3, 126.4, 124.7, 124.2, 107.6, 33.1, 30.7, 16.5. DART-HRMS calcd for $C_{17}H_{16}N_1O_1$ [$(M + H)^+$]: 238.12319; found: 238.12273.

Acknowledgements

This work was partially supported by a Grant-in-Aid for Scientific Research from the Japan Society for the Promotion of Science (JSPS), the Global Centers of Excellence (COE) Program, The University of Tokyo, the Ministry of Education, Culture, Sports, Science and Technology - Japan (MEXT), and the New Energy and Industrial Technology Development Organization (NEDO). W.-J.Y. thanks JSPS for the JSPS Postdoctoral Fellowship for Foreign Researchers. We also thank Mr. N. Kuramitsu (The University of Tokyo) for STEM analysis and Dr. J.-F. Soulé for assistance during manuscript preparation.

References

(1) (a) Lee, J. M.; Na, Y.; Han, H.; Chang, S. *Chem. Soc. Rev.* **2004**, *33* (5), 302. doi:10.1039/b309033g; (b) Wasilke, J.-C.; Obrey, S. J.; Baker, R. T.; Bazan, G. C. *Chem. Rev.* **2005**, *105* (3), 1001. doi:10.1021/cr020018n; (c) Chapman, C. J.; Frost, C. G. *Synthesis* **2007**, (1): 1; (d) Shindoh, N.; Takemoto, Y.; Takasu, K. *Chem. Eur. J.* **2009**, *15* (45), 12168. doi:10.1002/chem.200901486; (e) Zhou, J. *Chem. Asian J.* **2010**, *5* (3), 422. doi:10.1002/asia.200900458.

(2) (a) Pittman, C. U., Jr; Smith, L. R. *J. Am. Chem. Soc.* **1975**, *97* (7), 1749. doi:10.1021/ja00840a022; (b) Bhanage, B. M.; Fujita, S.-i.; Yoshida, T.; Sano, Y.; Arai, M. *Tetrahedron Lett.* **2003**, *44* (17), 3505. doi:10.1016/S0040-4039(03)00688-9; (c) Pilling, A. W.; Boehmer, J.; Dixon, D. J. *Angew. Chem. Int. Ed.* **2007**, *46* (28), 5428. doi:10.1002/anie.200701079; (d) Gembus, V.; Bonnet, J.-J.; Janin, F.; Bohn, P.; Levacher, V.; Brière, J.-F. *Org. Biomol. Chem.* **2010**, *8* (14), 3287. doi:10.1039/c004704j.

(3) (a) For reviews on polymer-incarcerated metal catalysts see Akiyama, R.; Kobayashi, S. *Chem. Rev.* **2009**, *109* (2), 594. doi:10.1021/cr800529d; (b) Kobayashi, S.; Miyamura, H. *Chem. Rec.* **2010**, *10* (5), 271. doi:10.1002/tcr.201000026.

(4) (a) Miyamura, H.; Matsubara, R.; Miyazaki, Y.; Kobayashi, S. *Angew. Chem. Int. Ed.* **2007**, *46* (22), 4151. doi:10.1002/anie.200700080; (b) Miyamura, H.; Matsubara, R.; Kobayashi, S. *Chem. Commun.* **2008**, (17): 2031. doi:10.1039/b800657a; (c) Lucchesi, C.; Inasaki, T.; Miyamura, H.; Matsubara, R.; Kobayashi, S. *Adv. Synth. Catal.* **2008**, *350* (13), 1996. doi:10.1002/adsc.200800319; (d) Wang, N.; Matsumoto, T.; Ueno, M.; Miyamura, H.; Kobayashi, S. *Angew. Chem. Int. Ed.* **2009**, *121* (26), 4838. doi:10.1002/ange.200900565; (e) Kaizuka, K.;

Miyamura, H.; Kobayashi, S. *J. Am. Chem. Soc.* **2010**, *132* (43), 15096. doi:10.1021/ja108256h.
(5) (a) Miyamura, H.; Shiramizu, M.; Matsubara, R.; Kobayashi, S. *Chem. Lett.* **2008**, *37* (3), 360. doi:10.1246/cl.2008.360; (b) Miyamura, H.; Shiramizu, M.; Matsubara, R.; Kobayashi, S. *Angew. Chem. Int. Ed.* **2008**, *47* (42), 8093. doi:10.1002/anie.200802192; (c) Miyamura, H.; Maehata, K.; Kobayashi, S. *Chem. Commun.* **2010**, *46* (42), 8052. doi:10.1039/c0cc02865g.
(6) (a) Miyamura, H.; Yasukawa, T.; Kobayashi, S. *Green Chem.* **2010**, *12* (5), 776. doi:10.1039/b926877d; (b) Yasukawa, T.; Miyamura, H.; Kobayashi, S. *Chem. Asian J.* **2011**, *6* (2), 621. doi:10.1002/asia.201000624.
(7) Yoo, W.-J.; Miyamura, H.; Kobayashi, S. *J. Am. Chem. Soc.* **2011**, *133* (9), 3095. doi:10.1021/ja110142y.
(8) Yoo, W.-J.; Yuan, H.; Miyamura, H.; Kobayashi, S. *Adv. Synth. Catal.* **2011**, *353* (17), 3085. doi:10.1002/adsc.201100430.
(9) Jiang, H.; Huang, H.; Cao, H.; Qi, C. *Org. Lett.* **2010**, *12* (23), 5561. doi:10.1021/ol1023085.
(10) (a) For representative examples of aerobic amine oxidation catalyzed by metal nanoclusters see Zhu, B.; Lazar, M.; Trewyn, B. G.; Angelici, R. J. *J. Catal.* **2008**, *260* (1), 1. doi:10.1016/j.jcat.2008.08.012; (b) Grirrane, A.; Corma, A.; Garcia, H. *J. Catal.* **2009**, *264* (2), 138. doi:10.1016/j.jcat.2009.03.015; (c) Aschwanden, L.; Panella, B.; Rossbach, P.; Keller, B.; Baiker, A. *ChemCatChem* **2009**, *1* (1), 111. doi:10.1002/cctc.200900085; (d) So, M.-H.; Liu, Y.; Ho, C.-M.; Che, C.-M. *Chem. Asian J.* **2009**, *4* (10), 1551. doi:10.1002/asia.200900261; (e) Miyamura, H.; Morita, M.; Inasaki, T.; Kobayashi, S. *Bull. Chem. Soc. Jpn.* **2011**, *84* (6), 588. 10.1246/bcsj.20100300.
(11) Chen, Y.-X.; Qian, L.-F.; Zhang, W.; Han, B. *Angew. Chem. Int. Ed.* **2008**, *47* (48), 9330. doi:10.1002/anie.200803381.
(12) Ueda, S.; Nagasawa, H. *Angew. Chem. Int. Ed.* **2008**, *47* (34), 6411. doi:10.1002/anie.200801240.
(13) Xing, R.-G.; Li, Y.-N.; Liu, Q.; Meng, Q.-Y.; Li, J.; Shen, X.-X.; Liu, Z.; Zhou, B.; Yao, X.; Liu, Z.-L. *Eur. J. Org. Chem.* **2010**, *2010* (34), 6627. doi:10.1002/ejoc.201000985.
(14) Wang, B.; Zhang, Y.-C.; Li, P.-H.; Wang, L. *Chin. J. Chem.* **2010**, *28* (9), 1697. doi:10.1002/cjoc.201090287.

Can. J. Chem. Downloaded from www.nrcresearchpress.com by Renmin University of China on 09/02/12
For personal use only.

Microstructural study of cetyltrimethylammonium bromide / 1-butanol / salt / water system — SANS and 2D-NOESY analysis

K. Kuperkar, A. Patriati, E.G.R. Putra, K. Singh, D.G. Marangoni, and P. Bahadur

Can. J. Chem. Downloaded from www.nrcresearchpress.com by Renmin University of China on 09/02/12
For personal use only.

Abstract: Interaction of 1-butanol (BuOH) with a cationic surfactant, cetyltrimethylammonium bromide (CTAB) aggregate, in water and salt solution has been studied by viscometry, small-angle neutron scattering (SANS), and 2D-NMR techniques. The experimental results are interpreted in terms of a possible micellar growth occurring in the presence of added alcohol and salt. It was observed that the addition of BuOH strongly influences the viscosity of the CTAB/salt micellar system, reaching a peak viscosity at about 0.5% *w/v* of BuOH over a range of salt concentrations. Scattering measurements support the idea of a structural transformation by the observation of a spectral shift (broadening) as the total concentration of surfactant varies, indicating a decrease in the intermicellar distance and narrow size distribution. The chemical shift from ^{1}H NMR measurements gave complementary data on the solubilization of BuOH in CTAB micelles, whereas the expected locus (site) of the additive added to the surfactant including the dynamics of the molecules in micellar aggregates were successfully correlated by significant and positive cross peaks obtained from two-dimensional nuclear Overhauser effect spectroscopy (2D-NOESY).

Key words: micellar growth, solubilization, viscosity, SANS, 2D-NOESY.

Résumé : On a fait appel à des techniques de viscosimétrie, de diffraction de neutrons aux petits angles (DNPA) et de RMN bidimensionnelles pour étudier l'interaction entre le butan-1-ol (BuOH) et un agent de surface cationique, le bromure de cétyltriméthylammonium (BCTA) sous la forme d'agrégats dans l'eau et dans une solution de sel. On interprète les résultats expérimentaux en fonction d'une croissance micellaire potentielle qui se produirait en raison de la présence de l'alcool et du sel ajoutés. On a observé que l'addition de BuOH influence fortement la viscosité du système micellaire BCTA/sel alors que la viscosité atteint un maximum à environ 0.5 % p/V de BuOH sur une grande plage de concentrations de sel. En se basant sur le fait qu'on observe un élargissement du spectre avec une augmentation de la concentration totale de l'agent de surface, indiquant qu'il se produit une diminution dans la distance intermicellaire et une diminution de la distribution de la taille, les mesures de diffraction apportent un support à l'idée qu'il se produit une transformation de structure. Le déplacement chimique des mesures RMN du ^{1}H fournissent des données complémentaires sur la solubilization du BuOH dans des micelles de BCTA alors qu'on a établi une bonne corrélation avec les sites attendus de fixation de l'additif ajouté à l'agent de surface, y compris la dynamique des molécules dans les agrégats micellaires, grâce à des pics croisés significatifs et positifs obtenus par le biais de la spectroscopie de l'effet Overhauser nucléaire bidimensionnel (« 2D-NOESY »).

Mots-clés : croissance micellaire, solubilization, viscosité, diffraction de neutrons aux petits angles (DNPA), 2D-NOESY.

[Traduit par la Rédaction]

Introduction

Aqueous micellar solutions of cationic surfactants are well known to solubilize water insoluble or slightly soluble organic compounds. Such micellar systems have a wide range of applications, e.g., in the formation of microemulsions in tertiary oil recovery, as germicides in detergency, cosmetic preparations, dyeing operations, in the synthesis of mesoporous materials, in micellar catalysis, and as templates for the fabrication of nanostructures.[1–5]

Alcohols are either considered as cosurfactants (cosolutes) and (or) cosolvents. Depending on the chain length of the added alcohol, their amphipathic nature anchors them either in the surface region of aggregates or in the surrounding solution, altering the surfactant/solvent interfacial properties. The characteristics of surfactant/alcohol mixtures are dependent on the structure, length, and concentration of the alcohol chain. The addition of electrolytes to such surfactant/alcohol systems has been found to alter the existing micellar structures.[5] A number of reports can be found in the literature

Received 25 May 2011. Accepted 19 August 2011. Published at www.nrcresearchpress.com/cjc on 1 March 2012.

K. Kuperkar and P. Bahadur. Department of Chemistry, Veer Narmad South Gujarat University, Surat 395 007, India.
A. Patriati and E.G.R. Putra. Neutron Scattering Laboratory, National Nuclear Energy Agency of Indonesia, BATAN, Kawasan Puspiptek Serpong, Tangerang 15314, Indonesia.
K. Singh and D.G. Marangoni. Department of Chemistry, St. Francis Xavier University, Antigonish, NS B2G 2W5, Canada.

Corresponding author: Ketan C. Kuperkar (e-mail: ketankuperkar@gmail.com).

Can. J. Chem. Downloaded from www.nrcresearchpress.com by Renmin University of China on 09/02/12
For personal use only.

where the influence of added alcohol on the various fundamental micellar properties, including the critical micelle concentrations (the CMC value), aggregation number, the micellar charge, and the structure of aggregates composed of alkyltrimethylammonium bromide surfactants in aqueous solutions have been determined.[6–10]

The location and distribution of the alcohol between the aqueous and micellar pseudophases and its degree of solubilization are of both practical and academic interest. The addition of organic additives (electrolytes or polar compounds) influences the energy required for the transfer of the surfactant ion from the bulk solution to the micelle because of the screening effect on the micellar charge. It also alters the micellar morphology, depending upon the extent of their penetration and (or) intercalation into the micelles.[10,11] Alcohols that are partially miscible in water decrease the CMC for both ionic and nonionic surfactants, while completely miscible alcohols cause an increase of the CMC.[12–14] The literature also reports that, in concentrated micellar systems, morphological transformations of isotropically spherical micelles to more asymmetric shapes, such as ellipsoids (oblate or prolate) and even rods, results[13–19] in many cases, leading to viscoelastic effects in these systems. The occurrence of viscoelasticity over a certain range of either the surfactant or additive concentration is critically dependent on packing parameter considerations. Packing constraints are dependent on a number of factors in these systems, including the ionic strength, structure of the surfactant head group, the structure of counterions bound to the micelle, the degree of binding, and the location of these counterions in the aggregates, as well as the manner in which hydrophobic additives are solubilized.[10,13,14,19–21]

Although a number of studies dealing with the morphology of concentrated surfactant solutions have appeared in the literature,[8–17,22] a number of fundamental questions regarding the interactions that cause the transitions from spherical to wormlike or rodlike micelles remain. Systematic studies of the growth of micelles in the presence of additives could help understand the kinetics of micellar and mesophase growth. Recently, mesophasic structures have been identified as excellent templating agents for microspheres and nanoparticles of various types. Given the importance of mesophases in these applications, and the importance of the flow properties of surfactant solutions in a number of commercial products, we have embarked on a systematic and detailed investigation of the properties and the microstructure of a cationic micellar solution as a function of salt and alcohol concentration and temperature. In the present research paper, we obtained the viscosities of cetyltrimethylammonium bromide (CTAB) / salt solutions as a function of added 1-butanol (BuOH) and temperature. The micellar dimensions of CTAB aggregates as a function of alcohol and salt concentration were obtained from scattering techniques. 2D ^{1}H NMR (NOESY) spectra provided detailed information on the sites of alcohol encapsulation in the aggregates. These experiments give sensitive details about the molecular packing of the surfactants and the alcohol inside the aggregates. All these results provide important new insights in terms of the molecular interactions that lead to micellar growth and subsequent rheological behavior exhibited by these systems.

Experimental section

Materials and methods

Cationic surfactant CTAB was obtained from Sigma-Aldrich (USA). BuOH (Fluka) with a minimum 99.5% purity was used. Inorganic salts (NaBr or KBr) of AR grade were used in this study. Triple-distilled water was used for solution preparation. Deuterium oxide (D_2O) with 99.9% purity (Sigma-Aldrich) was used for small-angle neutron scattering (SANS) and ^{1}H NMR.

Viscosity experiments

Viscosity measurements were performed using an Ubbelohde suspended level capillary viscometer. This viscometer was cleaned and dried thoroughly before and after each measurement and was always suspended vertically in a thermostat with a temperature stability of ±0.1 °C in the investigated region. The flow time for a constant volume of solution through the capillary was measured with a calibrated stopwatch.[21]

SANS analysis

SANS measurements were conducted at the Neutron Scattering Laboratory (NSL) BATAN in Serpong, Indonesia, using a 36 m SANS spectrometer (SMARTer).[23] Each sample was measured at two detector distances (1.5 and 4 m) to cover a momentum transfer Q range of 0.025 to 0.3 Å^{-1}, with a neutron wavelength (λ) of 3.9 Å ($\Delta\lambda/\lambda$ = 13%). (We could not get the oscillation at high Q range because of the polydispersity of the micelles and the low resolution of the instrument; hence, all the SANS plots presented in this paper are plotted in a range of 0.02 to 0.14 Å^{-1}, as they appear more clear and distinct. SANS plots in the full Q range of 0.025 to 0.3 Å^{-1} are provided in the Supplementary data). All samples were dissolved in D_2O; the samples were then poured into 5 mm thick quartz cells and exposed to the neutron beam for a period of 30 min. For the concentration-dependent experiments, each sample was held at 30 °C to avoid any Krafft point issues. Scattering intensities of the samples were corrected for background noise, scattering by the solvent and quartz cell, and the sample's transmission using Graphical reduction and analysis SANS program (GRASP).[24] The corrected scattering intensity data at high Q range were normalized at the same level of the incoherent background. Then they were combined with the data at low Q range to cover the whole Q range of the experimental setup and then fitted using the SANS NIST data analysis program.[25]

The intensity $I(Q)$ of small-angle scattering as a function of momentum transfer Q for a homogeneous monodisperse interacting spherical micelle system can be expressed as

$$[1] \qquad I(Q) = n(\rho_m - \rho_s)^2 V^2 P(Q) S(Q)$$

where n denotes the number density of micelles and ρ_m and ρ_s are the scattering length densities of the micelle and the solvent, respectively. The term ($\rho_m - \rho_s$) is called contrast, V is the volume of a micelle, which is calculated by $V = 4\pi R(a)R(b)^2/3$, where $R(a)$ and $R(b)$ are the minor and major semi-axes, respectively. Equation [1] is used as an approximation for nonspherical and nonmonodisperse micelles. The form factor $P(Q)$ (also known as the intraparticle

Can. J. Chem. Downloaded from www.nrcresearchpress.com by Renmin University of China on 09/02/12
For personal use only.

structure factor) depends on the shape (cylinder, ellipsoid, or sphere) and the size of the micelles, and $S(Q)$ is the interparticle structure factor, which depends on the interaction potential and the number density. The expression derived by Hayter and Penfold was used.[26]

For an isotropic system, $S(Q)$ can be written as

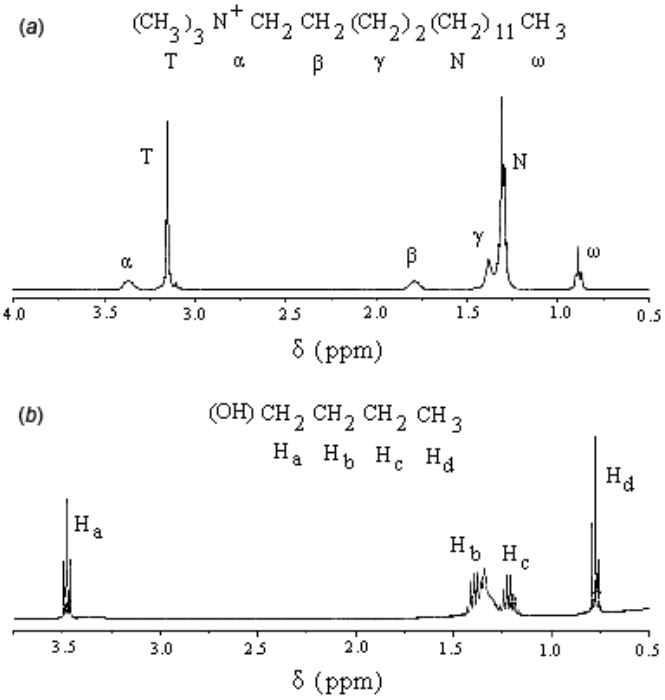
$$[2] \qquad S(Q) = 1 + 4\pi n \int [g(r) - 1] \frac{\sin Qr}{Qr} r^2 \mathrm{d}r$$

where $g(r)$ is the radial distribution function (the probability of finding another particle at a distance r from a reference particle centered at the origin).

^{1}H NMR and two-dimensional nuclear Overhauser effect spectroscopy (2D-NOESY)

1D and 2D NMR experiments (^{1}H, gradient COSY, and NOESY with and without solvent suppression) were performed with a Bruker AVANCE-II 400 MHz spectrometer at St. Francis Xavier University, Antigonish, Nova Scotia. The mixing and the delay times for the NOESY experiments were estimated from the spin-lattice relaxation time of a 5.0 wt % solution of BuOH in CTAB separately. To obtain 2D-NOESY spectra, acquisition delays of $\approx 3 \times T$ and mixing times of $\approx 1 \times T$ were used. Here, T is the acquisition time during which the signal is recorded. For the COSY experiments, the data were zero-filled once and multiplied by a sine-bell window in both dimensions prior to the 2DFT. In the gradient NOESY experiments, 256 transients of either 2 or 4 scans over 512 complex data points were acquired. All acquisitions were done in phase-sensitive mode, with and without the saturation of the water resonance at ~4.65 ppm. The data were zero-filled twice in dimension 1 and multiplied by a squared sine function in both dimensions before 2DFT.[20,27] Solutions were prepared directly in small sample vials, and these were dispensed into the NMR tubes with a volumetric pipette. Labeled ^{1}H spectra for CTAB and BuOH are given in Scheme 1.

Scheme 1. A plot of chemical shifts (δ) in ppm (x axis) versus signal intensity (y axis) showing structures, proton labellings, and the ^{1}H NMR spectrum of (*a*) cetyltrimethylammonium bromide (CTAB) and (*b*) 1-butanol (BuOH).



Results and discussion

Effect of additive concentration

According to the literature, the viscosities of certain cationic surfactant solutions are substantially altered when a medium chain length alcohol is added to the cationic micellar system in the presence of salt.[11,13,14] Figure 1 presents the viscosity measurements of a solution containing 0.10 mol/L CTAB mixed with varying amounts of NaBr as a function of the BuOH concentration.

It should be noted from Fig. 1 that there is very little change in the solution viscosity in the CTAB solution containing small amounts of NaBr over the range of alcohol concentrations investigated. This indicates that, in these systems, no significant aggregate growth was observed, indicating that these structures are essentially spherical micelles over the alcohol concentration range investigated. However, further additions of NaBr substantially influences the viscosity of the system, indicating significant growth in the aggregate size investigated at the higher salt concentrations. It is well-known in the literature that ionic surfactants tend to endure uniaxial growth upon the addition of salt,[8–17,22] leading to a wide array of aggregate morphologies ranging from oblate, prolate, or rodlike micelles, or even multiconnected wormlike micelles. An unusual highly viscoelastic solution was observed to form in the range of 0.2% to 2% *w/v* of added BuOH, indicating a significant structural transformation is occurring in this concentration range, which is attributed to the strong screening effect of the salt on the micellar charge and the partitioning of alcohol into the cationic micelles; the combination of these two factors leads to a substantial reduction in the aggregate charge density and, hence, reduced electrostatic repulsions. On further addition of salt, the viscosity decreases rapidly, which is likely due to the sliding over of cross-links or multiconnected networks.[10] Although the viscosity measurements provide a reasonable indication of structural changes occurring in the solution as a function of additive concentration, detailed information on the aggregate dimensions as a function of alcohol and salt concentration was obtained from a thorough quantitative analysis of the scattering data obtained from the SANS measurements.

SANS studies revealed the intensity dependence of the scattered neutrons on the additive concentration.[28,29] The scattering data were analyzed and fitted using a data analysis program for different micellar structures. The solid lines in the SANS plots represent the calculated scattering patterns as the best fits of the experimental data. Dimensional parameters such as semi-minor axis $R(a)$ and semi-major axis $R(b)$ were used as fitting variables. The correlation peak usually occurs at $Q_{max} = 2\pi/d$, where d is taken as the average distance between the micelles and Q_{max} is the value of Q at the peak position. Figures 2 and 3 explain the concentration-dependent study of 0.1 mol/L CTAB in D_2O solution as a function of BuOH and KBr concentration. The calculated distributions give peak positions that agree well with the

Can. J. Chem. Downloaded from www.nrcresearchpress.com by Renmin University of China on 09/02/12
For personal use only.

Fig. 1. Relative viscosity plot of 0.1 mol/L cetyltrimethylammonium bromide (CTAB) as a function of 1-butanol (BuOH) concentration (*%w/v*) in different NaBr concentrations at 30 °C.

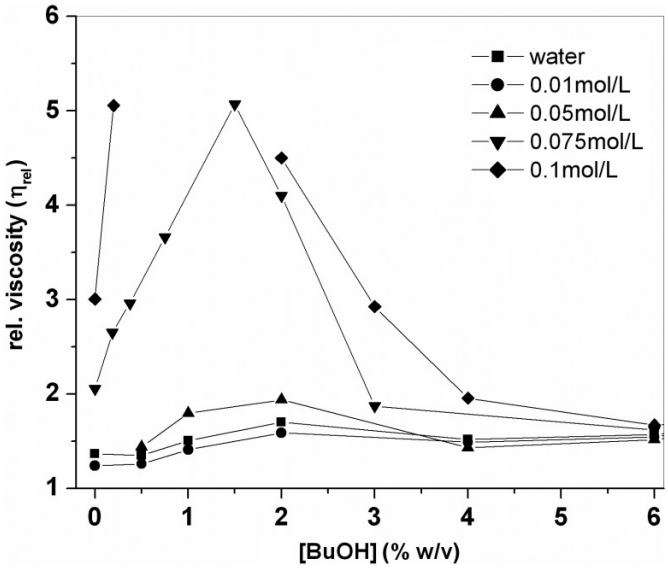
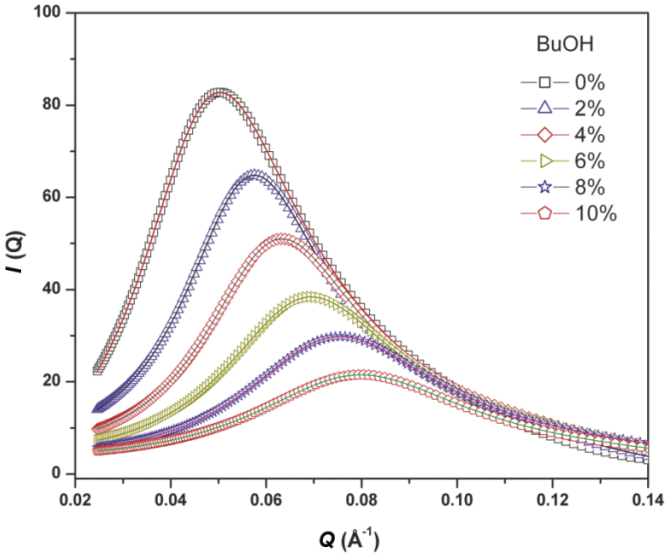


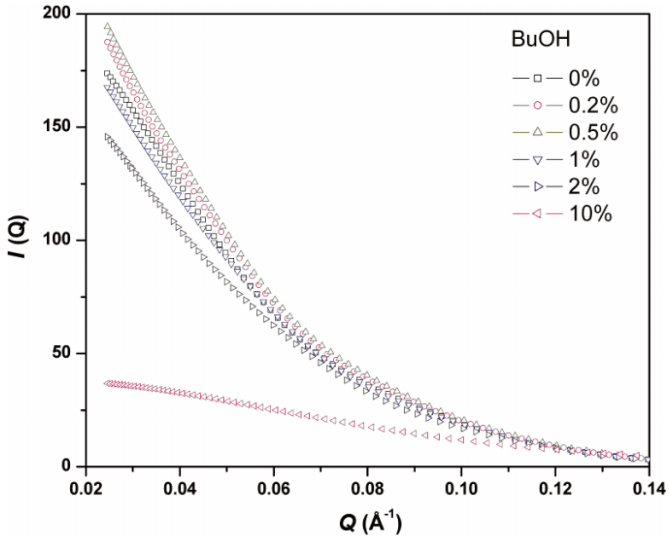
Fig. 2. Small-angle neutron scattering (SANS) plot of 0.1 mol/L cetyltrimethylammonium bromide (CTAB) solution as a function of 1-butanol (BuOH) concentration (*%w/v*) in the absence of salt at 30 °C. The symbols represent the experimental data and the solid line is the theoretical model calculation.



experimentally determined values for all the studied concentrations.

Figure 2 illustrates the scattering intensity of 0.10 mol/L CTAB solutions to which increasing amounts of BuOH are added. The shifts in the maximum of the scattering profile indicate changing concentrations of BuOH lead to the changes in the aggregate structure. It is well-known that, as alcohols solubilize inside micelles, the nonpolar hydroxyl group is interspersed amongst the charged surfactant headgroups and has a significant influence on the surface charge density of the aggregate. In micellar systems, this is manifested in changes in both the degrees of counterion binding as well as the surfactant aggregation number, i.e., both of

Fig. 3. Small-angle neutron scattering (SANS) plot of 0.1 mol/L cetyltrimethylammonium bromide (CTAB) solution in a fixed salt concentration (0.1 mol/L) as a function of 1-butanol (BuOH) concentration (*%w/v*) at 30 °C.



these parameters are known to substantially decrease as the amount of alcohol in the mixed solvent is increased in the dilute concentration range. At higher alcohol concentrations, micellar growth possible transitions owing to the modification of the electrostatic interactions between the micelles by the large amounts of alcohol incorporation into the aggregates. In the absence of additives, the scattering spectrum of the 0.10 mol/L CTAB solution shows a characteristic correlation peak owing to the repulsive intermicellar interactions between the positively charged CTAB micelles, signifying the presence of dense micelles in the system. We note that in the absence of salt (and with the increase in alcohol concentration of >2% *w/v*), the interparticle distances decrease and the peak shifts to higher *Q* values, indicating the change in micellar shape and size from a higher morphology structure to the lower ones.

Figure 3 shows the influence of changing both salt and BuOH concentrations on the mesophasic nature of CTAB solution. These results are consistent with the fact that for the self-assembly of the alcohol/surfactant system investigated here, the environment surrounding the cationic headgroups of CTAB is sensitive to the charge density of the aggregates and the "hardness" of the counterion. A number of studies recently have discussed the specific interactions that exist between charged headgroups of aggregating amphiphiles (i.e., forming micelles and vesicles) in terms of a lyotropic (Hofmeister) series: $OH^- < F^- < Cl^- < Br^-$. These ions are small in size and possess a high charge density and greatly influence the aggregation process depending on their location in the series.[19] In the present study, the formation of large stable aggregates in the cationic surfactant / alcohol / salt system was observed.

It was observed that with the addition of a fixed concentration of KBr (0.10 mol/L) to 0.10 mol/L CTAB in varying concentrations of BuOH, noticeable aggregate growth occurred (0.5% *w/v*) as the hydration shell of the Br^- ions was found to be more perturbed. We expect that the Debye

Can. J. Chem. Downloaded from www.nrcresearchpress.com by Renmin University of China on 09/02/12
For personal use only.

Table 1. Parameters obtained from the small-angle neutron scattering (SANS) fit for 0.1 mol/L cetyltrimethylammonium bromide (CTAB) in aqueous solution and in the presence of 0.1 mol/L KBr with varying 1-butanol (BuOH) concentrations (*%w/v*) at 30 °C.

	In water						In 0.1 mol/L KBr				
	BuOH concentration						BuOH concentration				
Parameters	0%	2%	4%	6%	8%	10%	0%	0.2%	0.5%	1%	2%
Volume fraction	0.036	0.036	0.031	0.031	0.031	0.031	0.038	0.038	0.038	0.038	0.038
R(*a*) rotation axis (Å)	18.73	18.73	20.62	18.64	17.08	16.92	20.89	20.89	20.89	20.89	20.89
R(*b*) (Å)	32.93	28.89	—	—	—	—	197.69	202.09	203.73	180.85	156.62
Polydispersity	—	—	0.17	0.19	0.20	0.16	—	—	—	—	—
Charge	20.88	20.26	19.53	18.72	18.37	18.88	49.10	42.73	41.73	41.26	40.37
Dielectric constant	164.85	29.72	57.29	54.35	50.11	27.88	179.11	108.38	186.30	82.15	24.09

Note: *R*(*a*) = semi-minor axis; *R*(*b*) = semi-major axis.

screening length decreases in this region because of an increase in the ionic strength of the medium by the addition of KBr. The correlation peak broadens and, as well, the Q_{max} shifts to lower Q values. Such a broadening of the correlation peak at a constant volume fraction of cationic aggregates indicates a significant decrease in the magnitude and the range of electrostatic interactions. The SANS scattering data are well described after fitting to the spherical model with a narrow particle size distribution for the investigated system. The parameters obtained from the fitting of the scattering profiles are shown in Table 1.

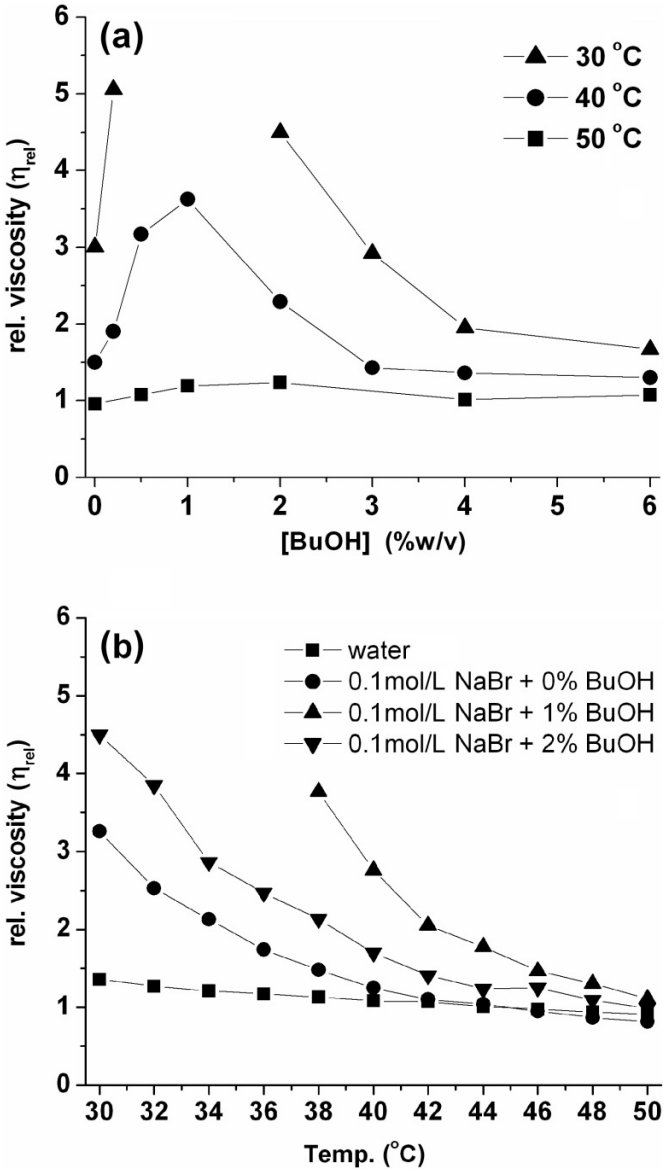
Effect of temperature

The effect of temperature on the relative viscosity of 0.10 mol/L CTAB solution in the presence of varying additive concentrations is shown in Fig. 4. It was found that, at lower temperature, the influence of salt and alcohol is more pronounced as the micellar growth is more inductive to higher dimensionality, leading to the formation of networks.[10,30]

When we examine Fig. 4, we can clearly infer the promotion of the volume fraction of CTAB micelles at 30 °C, which is attributed to the incorporation of alcohol in the interfacial region of aggregates, presumably with its –OH group in the Stern layer. It then reaches a maximum (~0.5% *w/v* BuOH) where shear thinning is observed at higher shear rates, indicating that these systems may be highly viscoelastic. Such behavior is characteristic of long rodlike or wormlike micelles.[10] As well, on increasing the alcohol content, we expect that the BuOH molecules will solubilize in the palisade region of the CTAB micelles and, with an increase in temperature, the viscosity of the system would decrease, which could be explained by the shear alignment of micelles as well as the thermal breakdown of the entangled micellar networks.

This interpretation of the relative viscosity results is found to be consistent with the SANS data as shown in Fig. 5. Here, the intensity of the scattered neutrons and aggregate length was found to decrease with increasing temperature, as they break down into smaller structures because of an increase in the degree of the dissociation of counterions, resulting in stronger repulsions between the charged head groups. Consequently, the effective head group area per surfactant molecule increases and causes the packing parameter to decrease, which affects the intermicellar separation and shifts the peak to larger Q values.[10] Table 2 provides a quantitative estimate of the micellar parameters obtained after model fitting.

Fig. 4. Viscosity plot of 0.1 mol/L cetyltrimethylammonium bromide (CTAB) solution in (*a*) the absence of salt and (*b*) in the presence of 0.1 mol/L NaBr (fixed) as a function of 1-butanol (BuOH) concentration (*%w/v*) at different temperatures.



Can. J. Chem. Downloaded from www.nrcresearchpress.com by Renmin University of China on 09/02/12
For personal use only.

Fig. 5. Small-angle neutron scattering (SANS) plot of 0.1 mol/L cetyltrimethylammonium bromide (CTAB) in 2% *w/v* 1-butanol (BuOH) at different temperatures.

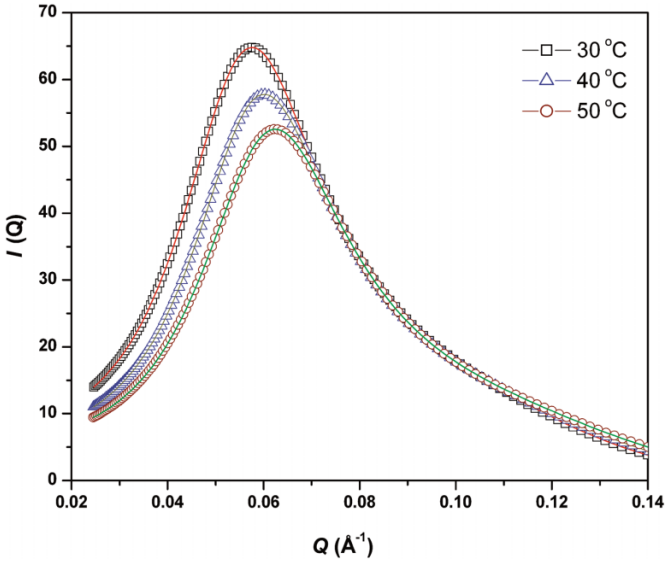


Table 2. Parameters obtained from the small-angle neutron scattering (SANS) fit for 0.1 mol/L cetyltrimethylammonium bromide (CTAB) in 2%*w/v* 1-butanol (BuOH) concentration at different temperatures.

	Temp. (°C)		
Parameter	30	40	50
R(*a*) rotation axis (Å)	18.73	18.73	18.73
R(*b*) (Å)	28.89	27.17	25.82
Charge	20.26	22.02	22.89
Dielectric constant	29.72	33.69	34.30

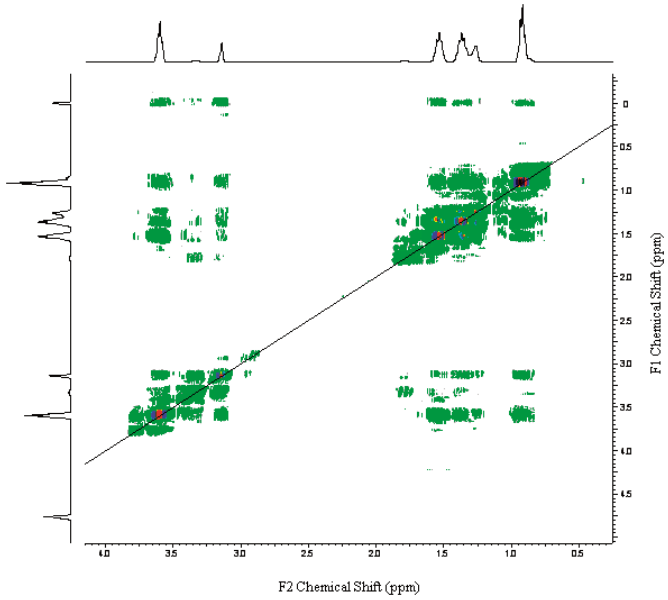
Note: *R*(*a*) = semi-minor axis; *R*(*b*) = semi-major axis.

Location of BuOH in the micelle

2D-NOESY experiments provide excellent insight into the fundamental nature of the self-assembly process in a wide array of self-assembled systems. Cross peaks observed in the 2D-NOESY spectra signify the spatial proximity (within 5 Å) of protons in the self-assembled aggregates. By measuring the cross-peak amplitudes, significant information on the encapsulation and location of the alcohol molecule in the surfactant micelle can be readily obtained.[20,27,31]

On examining the NOESY spectra of the CTAB/BuOH mixed system, a few similarities in the nature of the cross peaks were observed for these systems as well as for dodecyltrimethylammonium bromide (DTAB) / BuOH and sodium dodecylsulfate (SDS) / BuOH.[20] Figure 6 exhibits stronger cross peaks in the headgroup region of the CTAB/BuOH system, indicating a preferential solubilization of the alcohol near the palisade layer in the large cationic micelles. Additional cross peaks were also observed between the terminal $-CH_3$ group of CTAB and BuOH, consistent with the spatial proximity of these sets of protons. We also observed strong correlations between the β protons of CTAB with the H_a protons of BuOH (δ ~ 1.4 ppm) and the β and γ protons of CTAB with the H_b and H_c protons of BuOH. The $N-CH_3$ protons also had very strong interactions with the H_b and the H_c protons of BuOH. Some intramolecular

Fig. 6. Contour plot of the 2D-NOESY spectrum of 0.1 mol/L cetyltrimethylammonium bromide (CTAB) in 5%*w/v* 1-butanol (BuOH).



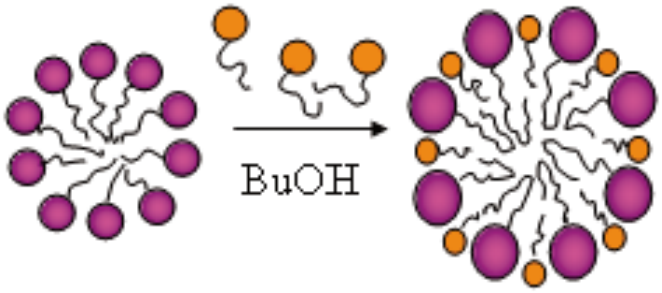
interactions between the H_b and H_c protons of the BuOH are consistent with some folding of the alcohol occurring in the palisade region of the micelle. These types of strong intramolecular interactions owing to the folding of surfactants in micelles have been discussed previously.[32]

We also observed a strong correlation between the $-CH_3$ protons of the alcohol-surfactant (δ ~ 0.9 ppm) and the first few chain protons of CTAB, as well as a number of other correlations in the region around 1–1.2 ppm that represent cross peaks between the ω-CH_3 peak of the cationic surfactant and the H_d alcohol peak. These cross peaks may be due to the folding of the carbon chains of CTA^+ cations in the interior of the micelles. This is consistent with the alcohol being located in the micelle palisade layer with its headgroup in intimate contact with CTAB headgroups located near the shell (hydration layer) or the palisade boundary, and its hydrocarbon chain pointed inwards towards the center of the aggregates. In the case of the higher alcohol concentrations investigated here, there is possibly some folding of the alcohol found in the headgroup region that may lead to the swelling of the aggregates in aqueous solution, consistent with the presence of the larger aggregates observed above. A probable encapsulation of BuOH occurring in the CTAB micelle from the analysis of the cross-peak locations and magnitudes is represented in Fig. 7.

Conclusions

Significant aggregate growth in a surfactant/alcohol/salt system has been verified through a combination of viscosity, SANS, and NMR NOESY experiments. Viscosity results appear to indicate a large change in the aggregate morphology in certain alcohol-rich regimes. SANS experiments also indicated that the interaggregate associations and significant surfactant incorporation into growing micelles, owing to favorable electrostatic and hydrophobic interactions, lead to significant viscosity enhancement in certain surfactant/salt/

Fig. 7. Encapsulation of 1-butanol (BuOH) in cetyltrimethylammonium bromide (CTAB) micelles.



alcohol concentrations. NMR NOESY experiments, being sensitive to molecular details, yielded important information on the location of the alcohol in the mixed aggregates and, hence, provided some indication of the folding and (or) encapsulation of the alcohol molecules in the micelles. All these results indicate that, in certain concentration ranges, organic additives like alcohols can serve as a partial substitute for salt with respect to the ability to thicken the surfactant solutions in aqueous medium.

Supplementary data

Supplementary data are available with the article through the journal Web site at http://nrcresearchpress.com/doi/suppl/10.1139/v11-155.

Acknowledgement

Financial assistance by the Board of Research in Nuclear Sciences (BRNS), BARC-INDIA under 2010/37C/31/BRNS is gratefully acknowledged. P.B. acknowledges St. Francis Xavier University, Antigonish, Nova Scotia, for the James Chair.

References

(1) Eicke, H.-F. Surfactants in Nonpolar Solvents, Aggregation and Micellization. In *Topics in Current Chemistry: Micelles;* Springer: Berlin, 1980; Vol. 87, pp 85–145.
(2) Rosen, M. J. *Surfactants and Interfacial Phenomena,* 3rd ed.; Wiley–Interscience: New York, 1982.
(3) Fainerman, V. B.; Miller, R.; Aksenenko, E. V. *Adv. Colloid Interface Sci.* **2002**, *96* (1–3), 339. doi:10.1016/S0001-8686(01)00088-4.
(4) Zana, R. *Adv. Colloid Interface Sci.* **1995**, *57*, 1. doi:10.1016/0001-8686(95)00235-I.
(5) Imae, T.; Abe, A.; Taguchi, Y.; Ikeda, S. *J. Colloid Interface Sci.* **1986**, *109* (2), 567. doi:10.1016/0021-9797(86)90338-3.
(6) Prasad, Ch. D.; Singh, H. N. *Colloids Surf.* **1990**, *50*, 37. doi:10.1016/0166-6622(90)80252-Y.
(7) (a) Candau, S.; Zana, R. *J. Colloid Interface Sci.* **1981**, *84* (1), 206. doi:10.1016/0021-9797(81)90277-0; (b) Zana, R.; Yiv, S.; Strazielle, C.; Lianos, P. *J. Colloid Interface Sci.* **1981**, *80* (1), 208. doi:10.1016/0021-9797(81)90177-6; (c) Candau, S.; Hirsch, E.; Zana, R.; , *J. Colloid Interface Sci.* **1982**, *88* (2), 428. doi:10.1016/0021-9797(82)90271-5.
(8) Attwood, D.; Mosquera, V.; Rodriguez, J.; Garcia, M.; Suarez, M. J. *Colloid Polym. Sci.* **1994**, *272* (5), 584. doi:10.1007/BF00653225.
(9) González-Pérez, A.; Czapkiewicz, J.; Del Castillo, J. L.; Rodríguez, J. R. *J. Colloid Interface Sci.* **2003**, *262* (2), 525. doi:10.1016/S0021-9797(03)00064-X.
(10) Kuperkar, K.; Abezgauz, L.; Danino, D.; Verma, G.; Hassan, P. A.; Aswal, V. K.; Varade, D.; Bahadur, P. *J. Colloid Interface Sci.* **2008**, *323* (2), 403. doi:10.1016/j.jcis.2008.04.040.
(11) Hoffmann, H.; Ebert, G. *Angew. Chem. Int. Ed. Engl.* **1988**, *27* (7), 902. doi:10.1002/anie.198809021.
(12) Kreke, P. J.; Magid, L. J.; Gee, J. C. *Langmuir* **1996**, *12* (3), 699. doi:10.1021/la9509662.
(13) Førland, G. M.; Samseth, J.; Høiland, H.; Mortensen, K. *J. Colloid Interface Sci.* **1994**, *164* (1), 163. doi:10.1006/jcis.1994.1154.
(14) (a) González-Pérez, A. J.; Galán, J.; Rodríguez, J. R. *Fluid Phase Equilib.* **2004**, *224* (1), 7. doi:10.1016/j.fluid.2004.06.039; (b) Galán, J. J.; Del Castillo, J. L.; González-Pérez, A.; Fuentes-Vázquez, V.; Rodríguez, J. R. *J. Therm. Anal. Calorim.* **2007**, *87* (1), 159. doi:10.1007/s10973-006-7818-5.
(15) Missel, P. J.; Mazer, N. A.; Benedek, G. B.; Young, C. Y.; Carey, M. C. *J. Phys. Chem.* **1980**, *84* (9), 1044. doi:10.1021/j100446a021.
(16) Lin, T. L.; Chen, S. H.; Gabriel, N. E.; Roberts, M. F. *J. Phys. Chem.* **1987**, *91* (2), 406. doi:10.1021/j100286a031.
(17) Manne, S.; Schaffer, T. E.; Huo, Q.; Hansma, P. K.; Morse, D. E.; Stucky, G. D.; Aksay, I. A. *Langmuir* **1997**, *13* (24), 6382. doi:10.1021/la970070s.
(18) Shiloach, A.; Blankschtein, D. *Langmuir* **1998**, *14* (25), 7166. doi:10.1021/la980646t.
(19) Abezgauz, L.; Kuperkar, K.; Hassan, P. A.; Ramon, O.; Bahadur, P.; Danino, D. *J. Colloid Interface Sci.* **2010**, *342* (1), 83. doi:10.1016/j.jcis.2009.08.045.
(20) Hawrylak, B. E.; Marangoni, D. G. *Can. J. Chem.* **1999**, *77* (7), 1241. doi:10.1139/v99-112.
(21) Kuperkar, K. C.; Mata, J. P.; Bahadur, P. *Colloids Surf. Physicochem. Eng. Aspects* **2011**, *380* (1–3), 60. doi:10.1016/j.colsurfa.2011.02.019.
(22) Rao, I. V.; Ruckenstein, E. J. *J. Colloid Interface Sci.* **1986**, *113* (2), 375. doi:10.1016/0021-9797(86)90173-6.
(23) (a) Putra, E. G. R.; Bharoto, E.; Santoso, A.; Ikram, J. *Nucl. Instrum. Methods Phys. Res. A* **2009**, *600* (1), 198. doi:10.1016/j.nima.2008.11.129; (b) Putra, E. G. R.; Ikram, A.; Santoso, E.; Bharoto, B. *J. Appl. Crystallogr.* **2007**, *40* (s1), s447. doi:10.1107/S002188980700605X; (c) Giri Rachman Putra, E.; Bharoto; Santoso, E.; Mulyana, Y. A. *Neutron News* **2007**, *18* (2), 23. doi:10.1080/10448630601148102.
(24) Dewhurst, C. *GRASP: Graphical Reduction and Analysis SANS Program for Matlab.* http://www.ill.eu/fileadmin/users files/Other Sites/lss-grasp/grasp_main.html; Institut Laue-Langevin: Grenoble, France, 2001–2007.
(25) Kline, S. R. *J. Appl. Crystallogr.* **2006**, *39* (6), 895. doi:10.1107/S0021889806035059.
(26) Hayter, J. B.; Penfold, J. *Colloid Polym. Sci.* **1983**, *261* (12), 1022. doi:10.1007/BF01421709.
(27) Yuan, H. Z.; Luo, L.; Zhang, L.; Zhao, S.; Mao, S. Z.; Yu, J. Y.; Shen, L. F.; Du, Y. R. *Colloid Polym. Sci.* **2002**, *280* (5), 479. doi:10.1007/s00396-001-0640-5.
(28) Shafiq Ullah, A. K. M.; Kamal, I. *BRAC Univ. J.* **2007**, *4* (1), 59.
(29) Chen, S. H.; Sheu, E. Y.; Kalus, J.; Hoffman, H. *J. Appl. Crystallogr.* **1988**, *21* (6), 751. doi:10.1107/S0021889888008052.
(30) Engelskirchen, S.; Acharya, D. P.; Garcia-Roman, M.; Kunieda, H. *Colloids Surf. A Physicochem. Eng. Asp.* **2006**, *279* (1–3), 113. doi:10.1016/j.colsurfa.2005.12.048.
(31) Mao, S. Z.; Du, Y. R. *Acta Phys. Chim. Sin.* **2003**, *19* (7), 675.
(32) McLachlan, A. A.; Singh, K.; Marangoni, D. *Colloid Polym. Sci.* **2010**, *288* (6), 653. doi:10.1007/s00396-009-2182-1.

Can. J. Chem. Downloaded from www.nrcresearchpress.com by Renmin University of China on 09/02/12
For personal use only.

$TiCl_4$-catalyzed synthesis of peroxyacetals from aldehydes

Chen-Yu Tsai, Lu-An Chen, and Kuangsen Sung

Can. J. Chem. Downloaded from www.nrcresearchpress.com by Renmin University of China on 09/02/12
For personal use only.

Abstract: Peroxyacetals **2a**–**2j** were prepared by $TiCl_4$-promoted nucleophilic addition of both *tert*-butyl hydroperoxide (TBHP) and an alcohol to the corresponding aldehyde. The reaction works well with a variety of aldehydes, but not with ketones. The magnitude of the equilibrium constant for hemiacetal formation plays an important role; a large constant enables high conversion to peroxyacetal.

Key words: peroxyaceta , aldehyde, titanium chloride, peroxide.

Résumé : On a préparé les peroxyacétals **2a**–**2j** par addition nucléophile catalysée par le $TiCl_4$ simultanée de l'hydroperoxyde de *tert*-butyle et d'un alcool sur l'aldéhyde correspondant. La réaction fonctionne bien avec un grand nombre d'aldéhydes, mais elle ne donne pas de bons résultats avec les cétones. La valeur de la constante d'équilibre de formation de l'hémiacétal joue un rôle important; avec une constante dont la valeur est élevée, on obtient un degré élevé de conversion en peroxyacétal.

Mots-clés : peroxyacétal, aldéhyde, chlorure de titane, peroxyde.

[Traduit par la Rédaction]

Introduction

The number of reported peroxide natural products continues to increase and some organic peroxides have been discovered to have antimalarial properties,[1] therefore, peroxide synthesis has been studied for a long time and is of continuing interest for chemists.[2–4,5,6] In last two decades, peroxyacetals have been used as substrates in the development of new methodology for peroxide synthesis. For example, neighboring iodo, alkoxy, acetoxy, and silyl groups impart useful levels of diastereoselection in the Lewis acid-mediated allylation of peroxyacetals, generating chiral peroxides.[2] Peroxyacetals undergo reaction with allyltrimethylsilane, silyl enol ethers, and silyl ketene acetals in the presence of Lewis acids, such as $TiCl_4$, $SnCl_4$, and trimethylsilyl triflate, to afford homoallyl peroxides, 3-peroxyketones, and 3-peroxyalkanoates, respectively.[3] Acid hydrolysis of peroxyacetals may generate alkyl hydroperoxides.[4] Hence, the synthesis of peroxyacetals has become interesting as well.

The major synthetic route to monoperoxyacetals or bisperoxyacetals is through the ozonolysis of alkenes or enol ethers, followed by alkylation or silylation of the resulting hydroperoxyacetals.[1c,4,7] The drawback of this general synthetic method is that the selectivity of ozonolysis is poor and cannot be used for substrates containing ozone-sensitive groups. Bisperoxyacetals and (or) ketals can be synthesized by another method, which involves the reaction of acetals or ketals with H_2O_2 in the presence of protic or Lewis acids, such as $BF_3{\cdot}OEt_2$, HCl, AcOH, and tungstic acid, followed by alkylation or silylation of the resulting dihydroperoxyacetals.[8] Bisperoxyacetals or ketals can also be directly synthesized by the reaction of acetals or ketals with alkyl hydroperoxides in the presence of protic or Lewis acids ($BF_3{\cdot}OEt_2$).[5] Recently, a newly developed methodology for monoperoxyacetals or bisperoxyacetals used iodine as a catalyst to peroxidize carbonyl compounds and, in this method, both ketones and aldehydes have the possibility of being converted into bisperoxyacetals or ketals or monoperoxyacetals or ketals.[6] In this paper, we will introduce a novel synthetic method that uses $TiCl_4$ as a catalyst and selectively converts an aldehyde into monoperoxyacetals. For this methodology, it is unnecessary to convert aldehydes into acetals or vinyl ethers before the preparation of peroxyacetals. In addition, this method for peroxyacetal synthesis works only for aldehydes, not for ketones, and that is quite different from ketal synthesis. To figure out what causes the difference, we propose a reaction mechanism for the $TiCl_4$-promoted peroxyacetal synthesis. A detailed analysis will lead us to the answer.

Results and discussion

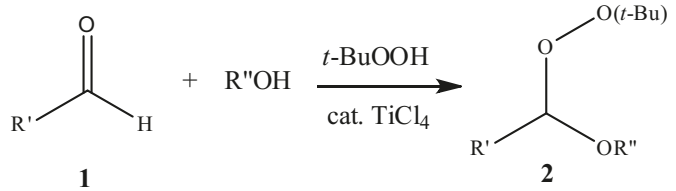
In this paper, we found that reaction of an aldehyde with 1 equiv of alcohol and 1.7 equiv of TBHP in the presence of a catalytic amount of $TiCl_4$ (0.1 equiv) in $CDCl_3$ solvent generated a peroxyacetal. To understand the scope of this reaction, we tested various aldehydes and alcohols for this type of reaction, and the results are shown in Table 1. First, we used an aromatic aldehyde (benzaldehyde) as an aldehyde substrate to react with a primary alcohol (*n*-BuOH), secondary alcohol (*i*-PrOH), benzyl alcohol, or tertiary alcohol (*t*-BuOH) for the peroxyacetal synthesis. What we found was that they

Received 23 August 2011. Accepted 19 October 2011. Published at www.nrcresearchpress.com/cjc on 9 March 2012.

C.-Y. Tsai, L.-A. Chen, and K. Sung. Department of Chemistry, National Cheng Kung University, Tainan, Taiwan.

Corresponding author: K. Sung (kssung@mail.ncku.edu.tw)

Table 1. $TiCl_4$-promoted synthesis of the peroxyacetals **2**.



1 **2**

Compound	R″	Product	Yield (%)
1a (R′ = Ph)	*n*-Bu	**2a**	88
1a (R′ = Ph)	*i*-Pr	**2b**	84
1a (R′ = Ph)	$PhCH_2$	**2c**	76
1a (R′ = Ph)	*t*-Bu	**2d**	58
1e (R′ = *i*-Pr)	$Ph(CH_2)_3$	**2e**	84
1f (R′ = *n*-Pr)	$Ph(CH_2)_3$	**2f**	82
1g (R′ = *p*-NO_2–Ph)	*n*-Bu	**2g**	89
1h (R′ = *m*-NO_2–Ph)	*n*-Bu	**2h**	94
1i (R′ = *p*-Cl–Ph)	*n*-Bu	**2i**	80
1j (R′ = *p*-MeO–Ph)	*n*-Bu	**2j**	79

Note: Reaction conditions: at room temperature over 1.5 days.

Can. J. Chem. Downloaded from www.nrcresearchpress.com by Renmin University of China on 09/02/12
For personal use only.

all generated the desired product in good yield, but a sterically hindered alcohol such as *t*-BuOH may result in a lower yield.

Afterwards, we used a primary alcohol ($Ph(CH_2)_3OH$) as a nucleophile to react with two types of aliphatic aldehydes (**1e** and **1f**). These two aliphatic aldehydes have different degrees of steric hindrance adjacent to their respective carbonyl groups, but they both worked well and similarly in the peroxyacetal synthesis.

We further explored electronic effects on this peroxyacetal synthesis. We used various substituted benzaldehydes as an aldehyde substrate to react with *n*-BuOH. The substituent includes *p*-NO_2, *m*-NO_2, *p*-Cl, and *p*-MeO, ranging from highly electron-withdrawing to highly electron-donating. What we found was that benzaldehyde with a highly electron-withdrawing substituent gave the peroxyacetal very easily and in high yield. Just like the synthesis of the other peroxyacetals mentioned above, they worked very well without using a dehydrating agent such as 4 Å molecular sieves. However, when we carried out the peroxyacetal synthesis for an aromatic aldehyde substrate with a strong electron-donating substituent such as *p*-MeO, conversion to the peroxyacetal was very low (<10%). This low conversion was significantly improved by using a very dry solvent and activated 4 Å molecular sieves.

In the $TiCl_4$-promoted nucleophilic addition of both TBHP and an alcohol to an aldehyde, we usually had acetal and bisperoxyacetal as by-products. When the ratio of the quantities for aldehyde, alcohol, and TBHP was 1:1:1 in the peroxyacetal synthesis, we obtained little of the acetal by-product. When the ratio was 1:1:2, we obtained little of the bisperoxyacetal. The best ratio for these substances was 1:1:1.7, where the major product was peroxyacetal with negligible acetal and bisperoxyacetal by-products.

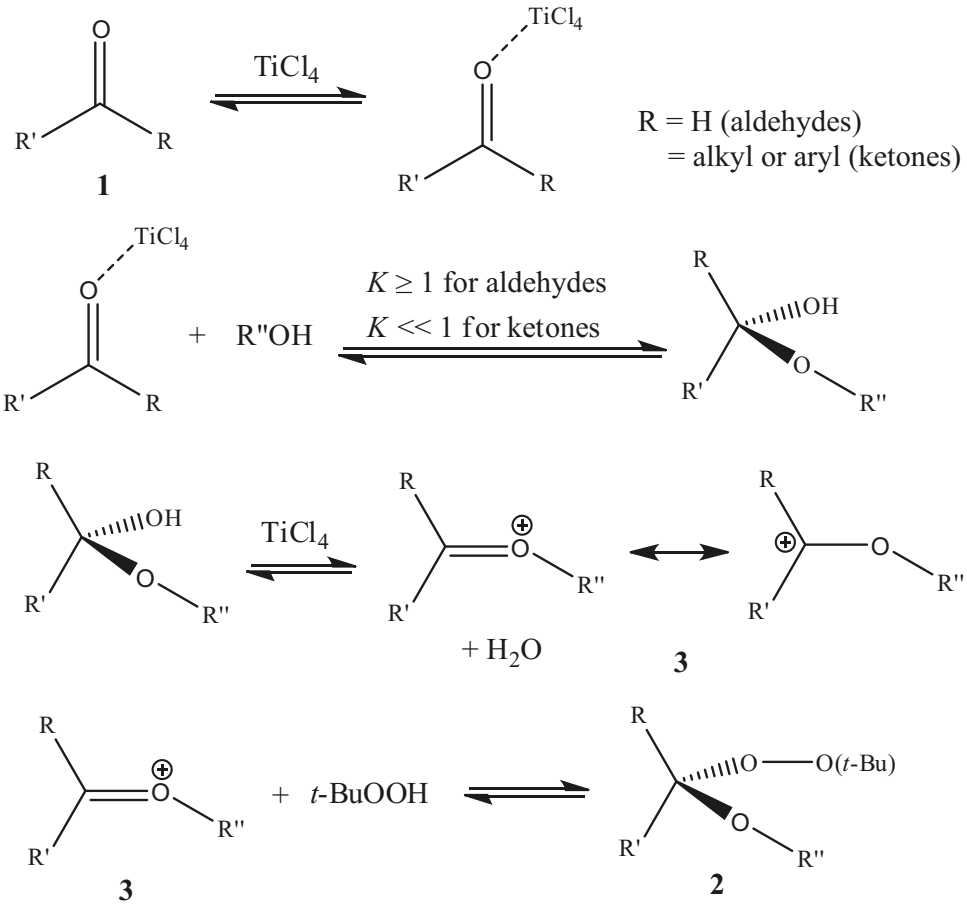
The limitation for the $TiCl_4$-promoted peroxyacetal synthesis is that the substrate cannot be a ketone. The ketone substrates we tried included acetone, acetaphenone, benzophenone, and benzil. This methodology did not work out for all the ketones even under very dry conditions and with a dehydration agent. This is quite different from ketal synthesis and that inspired us to analyze the reaction mechanism for the $TiCl_4$-promoted peroxyacetal synthesis.

Advantages of the $TiCl_4$-promoted peroxyacetal synthesis are as follows: (*i*) The method can be carried out at room temperature; (*ii*) Most peroxyacetal syntheses do not need a dehydrating agent and still achieve high yields, except for aldehyde substrates with highly electron-donating substituents. For aldehyde substrates with highly electron-donating substituents, one can still obtain peroxyacetals in high yield as long as a dried solvent and dehydrating agent are used; (*iii*) The peroxyacetal synthesis is selective for aldehyde substrates in the presence of ketone groups; (*iv*) It is unnecessary to convert aldehydes into acetals or vinyl ethers before preparation of peroxyacetals.

The mechanism for the $TiCl_4$-promoted peroxyacetal synthesis from an aldehyde substrate is assumed to be similar to that for acid-catalyzed acetal synthesis from an aldehyde substrate. Acid-catalyzed acetal synthesis from an aldehyde substrate usually involves two parts: (*i*) formation of hemiacetal from aldehyde and (*ii*) formation of acetal from hemiacetal. Then, the mechanism for the $TiCl_4$-promoted peroxyacetal synthesis from an aldehyde substrate is assumed to involve the same two parts (shown in Scheme 1). Chemists paid more attention to each of the two parts of the mechanism separately rather than the whole integrated mechanism.[9] In this paper, we will not only investigate each part of the mechanism, but also analyze the integrated mechanism as a whole.

For the second part of the mechanism, a hemiacetal intermediate may eliminate the OH group with the assistance of $TiCl_4$ activation,[10] forming a trigonal carbon and stabilized carbocation **3**. This ion will react very fast with an alcohol or TBHP to yield an acetal or ketal. The carbocation **3** is better stabilized by alkyl or aryl group than by H. If the formation of carbocation **3** is rate-limiting in the $TiCl_4$-promoted peroxyacetal synthesis, the activation energy for the formation of peroxyketal is supposed to be smaller than that for the formation of peroxyacetal. Therefore, we should have been

Scheme 1. Proposed mechanism for $TiCl_4$-promoted peroxyacetal synthesis.



able to prepare peroxyketal with this method, but we could not. This indicates that the second part of the mechanism (formation of acetal from hemiacetal) does not play the most important role in the $TiCl_4$-promoted peroxyacetal synthesis, but the first part of the mechanism (formation of hemiacetal from aldehyde) does.

The first part of the mechanism (formation of the hemiacetal or hemiketal) is similar to that for aldehyde or ketone hydration. Aldehyde hydration is usually thermodynamically favorable with an equilibrium constant close to or greater than 1, but ketone hydration is thermodynamically unfavorable with an equilibrium constant much smaller than 1. There are two pieces of evidence that support that the first part of the mechanism (formation of hemiacetal from aldehyde) plays the most important role in the $TiCl_4$-promoted peroxyacetal synthesis. The first piece of evidence is that peroxyketals cannot be prepared by this method. The possible explanation is that the thermodynamically unfavorable formation of hemiketal makes the formation of peroxyketal impossible in the $TiCl_4$-promoted peroxyacetal synthesis. The second piece of evidence is that the conversion to **2j** in the absence of a drying agent is much lower than the conversion to **2g** or **2h** under the same conditions. The possible explanation is that a strong electron-donating group (*p*-MeO) on **1j** and **2j** makes the formation of hemiacetal less thermodynamically favorable than a strong electron-withdrawing group (NO_2) and this causes the formation of peroxyacetal at low conversion levels. We solved the low-conversion problem by removing the water by-product with 4 Å molecular sieves, shifting the equilibrium position to the peroxyacetal product. This is usually found in the acetal synthesis, where azeotropic distillation is usually used as a way to remove the water by-product. However, azeotropic distillation is not a suitable way to remove water in the peroxyacetal synthesis because heat may further degrade the peroxyacetal product. Hence, the reason why the peroxyacetal synthesis does not work with ketones is that the formation constants from the ketones to the corresponding hemiketals in the first part of the reaction are too small to generate a large enough concentration of hemiketals for the second part of the reaction.

Conclusion

$TiCl_4$-promoted nucleophilic addition of both TBHP and an alcohol to an aldehyde generated a peroxyacetal. This methodology works selectively for aldehydes, but not for ketones. Various alcohols and aldehydes can be used in this peroxyacetal synthesis. To reduce the acetal and bisperoxyacetal by-products to a negligible amount, the best ratio of the quantities for aldehyde, alcohol, and TBHP in the peroxyacetal synthesis is 1:1:1.7. The equilibrium constant for the formation of hemiacetal plays the most important role in the $TiCl_4$-promoted peroxyacetal synthesis. The larger the formation constant of hemiacetal, the better conversion the peroxyacetal synthesis can reach.

Can. J. Chem. Downloaded from www.nrcresearchpress.com by Renmin University of China on 09/02/12
For personal use only.

Can. J. Chem. Downloaded from www.nrcresearchpress.com by Renmin University of China on 09/02/12
For personal use only.

Experimental section

General procedure for synthesis of peroxyacetals (2)

To aldehyde (1 mmol) and 4 Å molecular sieves (0.5 g) in $CHCl_3$ or $CDCl_3$ (2 mL) at room temperature was added $TiCl_4$ (0.1 mmol, 10% in $CHCl_3$ or $CDCl_3$). The mixture was stirred at room temperature for 1 h. Toluene solutions of TBHP (1.7 mmol) and alcohol (1 mmol) were added into the mixture, followed by stirring at room temperature for around 1–2 days. The reaction was monitored by ^{1}H NMR spectrometry until the reaction was complete. The product **2** was purified by column chromatography with silica gel as a stationary phase and hexane/EtOAc as a mobile phase.

(*tert*-Butylperoxybutoxymethyl)benzene (2a)

Colorless oil. ^{1}H NMR (300 MHz, $CDCl_3$) δ: 7.37–7.49 (m, 5H), 5.84 (s, 1H), 3.99 (dt, J = 9.6, 6.5 Hz, 1H), 3.67 (dt, J = 9.6, 6.7 Hz, 1H), 1.66 (m, 2H), 1.42 (m, 2H), 1.30 (s, 9H), 0.93 (t, J = 7.3 Hz, 3H). ^{13}C NMR (75 MHz, $CDCl_3$) δ: 136.9, 128.7, 128.1, 126.9, 106.0, 80.7, 69.3, 32.0, 26.5, 19.3, 13.8. The NMR data were in agreement with those previously reported for this compound (ref. 11). Anal. calcd for $C_{15}H_{24}O_3$: C 71.38, H 9.59; found: C 71.41, H 9.57.

(*tert*-Butylperoxyisopropoxymethyl)benzene (2b)

Colorless oil. ^{1}H NMR (300 MHz, $CDCl_3$) δ: 7.16–7.34 (m, 5H), 5.73 (s, 1H), 4.04 (m, 1 H), 1.17 (d, J = 6.1 Hz, 3H), 1.12 (s, 9H), 1.05 (d, J = 6.1 Hz, 3H). ^{13}C NMR (75 MHz, $CDCl_3$) δ: 137.5, 128.6, 128.1, 126.9, 104.4, 80.6, 71.5, 26.5, 23.0, 22.5. Anal. calcd for $C_{14}H_{22}O_3$: C 70.54, H 9.31; found: C 70.52, H 9.33.

(Benzyloxy-*tert*-butylperoxymethyl)benzene (2c)

Colorless oil. ^{1}H NMR (300 MHz, $CDCl_3$) δ: 7.27–7.52 (m, 5H), 5.97 (s, 1H), 5.02 (d, J = 12.3 Hz, 1H), 4.88 (d, J = 12.3 Hz, 1H), 1.31 (s, 9H). ^{13}C NMR (75 MHz, $CDCl_3$) δ: 138.2, 136.5, 128.8, 128.3, 128.2, 127.7, 127.5, 126.9, 105.1, 81.0, 70.9, 26.5. Anal. calcd for $C_{18}H_{22}O_3$: C 75.48, H 7.75; found: C 75.50, H 7.72.

(*tert*-Butoxy-*tert*-butylperoxymethyl)benzene (2d)

Colorless oil. ^{1}H NMR (300 MHz, $CDCl_3$) δ: 7.32–7.49 (m, 5H), 5.96 (s, 1H), 1.30 (s, 9H), 1.26 (s, 9H). ^{13}C NMR (75 MHz, $CDCl_3$) δ: 138.8, 128.5, 128.0, 127.1, 100.4, 80.4, 74.7, 28.8, 26.6. Anal. calcd for $C_{15}H_{24}O_3$: C 71.38, H 9.59; found: C 71.36, H 9.63.

(3-(1-*tert*-Butylperoxy-2-methylpropoxy)propyl)benzene (2e)

Colorless oil. ^{1}H NMR (300 MHz, $CDCl_3$) δ: 7.09–7.22 (m, 5H), 4.47 (d, J = 6.1 Hz, 1H), 3.90 (m, 1H), 3.49 (m, 1H), 2.64 (t, J = 6.9 Hz, 2H), 1.85 (m, 2H and 3H), 1.17 (s, 9H), 0.90 (d, J = 6.8 Hz, 6H). ^{13}C NMR (75 MHz, $CDCl_3$) δ: 142.2, 128.4, 128.2, 125.6, 110.4, 80.2, 69.5, 32.4, 31.7, 31.5, 26.5, 18.2, 17.9. Anal. calcd for $C_{17}H_{28}O_3$: C 72.80, H 10.07; found: C 72.83, H 10.04.

(3-(1-*tert*-Butylperoxybutoxy)propyl)benzene (2f)

Colorless oil. ^{1}H NMR (300 Hz, $CDCl_3$) δ: 7.21–7.33 (m, 5H), 4.90 (t, J = 5.6 Hz, 1H), 3.99 (m, 1H), 3.62 (m, 1H), 2.76 (t, J = 7.9, 2H), 1.98 (m, 2H), 1.69 (m, 2H), 1.49 (m, 2H), 1.29 (s, 9H), 0.99 (t, J = 7.3 Hz, 3H). ^{13}C NMR (75 MHz, $CDCl_3$) δ: 142.0, 128.4, 128.1, 125.6, 106.4, 80.0, 68.4, 34.4, 32.3, 31.5, 26.4, 18.2, 13.9. Anal. calcd for $C_{17}H_{28}O_3$: C 72.80, H 10.07; found: C 72.84, H 10.09.

1-(*tert*-Butylperoxybutoxymethyl)-4-nitrobenzene (2g)

Colorless oil. ^{1}H NMR (300 MHz, $CDCl_3$) δ: 8.21 (d, J = 8.1 Hz, 2H), 7.86 (d, J = 8.1 Hz, 2H), 5.85 (s, 1H), 4.05 (m, 1H), 3.71 (m, 1H), 1.65 (m, 2H), 1.46 (m, 2H), 1.25 (s, 9H), 0.93 (t, J = 7.2 Hz, 3H). ^{13}C NMR (75 MHz, $CDCl_3$) δ: 148.0, 143.8, 127.9, 123.3, 104.2, 81.0, 68.8, 31.8, 26.4, 19.2, 13.8. Anal. calcd for $C_{15}H_{23}NO_5$: C 60.57, H 7.80, N 4.71; found: C 60.54, H 7.81, N 4.70.

1-(*tert*-Butylperoxybutoxymethyl)-3-nitrobenzene (2h)

Colorless oil. ^{1}H NMR (300 MHz, $CDCl_3$) δ: 8.34 (s, 1H), 8.20 (d, J = 7.9 Hz, 1H), 7.83 (d, J = 7.9 Hz, 1H), 7.55 (t, J = 7.9 Hz, 1H), 5.86 (s, 1H), 4.06 (m, 1H), 3.72 (m, 1H), 1.69 (m, 2H), 1.47 (m, 2H), 1.39 (s, 9H), 0.93 (t, J = 7.2 Hz, 3H). ^{13}C NMR (75 MHz, $CDCl_3$) δ: 148.1, 139.2, 133.0, 129.0, 123.5, 122.2, 104.1, 81.0, 69.8, 31.8, 26.4, 19.2, 13.8. Anal. calcd for $C_{15}H_{23}NO_5$: C 60.57, H 7.80, N 4.71; found: C 60.56, H 7.84, N 4.72.

1-(*tert*-Butylperoxybutoxymethyl)-4-chlorobenzene (2i)

Colorless oil. ^{1}H NMR (300 MHz, $CDCl_3$) δ: 7.42 (d, J = 8.2 Hz, 2H), 7.33 (d, J = 8.2 Hz, 2H), 5.78 (s, 1H), 3.95 (m, 1H), 3.67 (m, 1H), 1.66 (m, 2H), 1.43 (m, 2H), 1.27 (s, 9H), 0.94 (t, J = 7.2 Hz, 3H). ^{13}C NMR (75 MHz, $CDCl_3$) δ: 135.4, 134.1, 128.3, 128.2, 105.1, 80.8. 69.4, 31.1, 26.5, 19.4, 13.8. Anal. calcd for $C_{15}H_{23}ClO_3$: C 62.91, H 8.10; found: C 62.89, H 8.12.

1-(*tert*-Butylperoxybutoxymethyl)-4-methoxybenzene (2j)

Colorless oil. ^{1}H NMR (300 MHz, $CDCl_3$) δ: 7.41 (d, J = 8.4 Hz, 2H), 6.89 (d, J = 8.4 Hz, 2H), 5.78 (s, 1H), 3.93 (m, 1H), 3.81 (s, 3H), 3.65 (m, 1H), 1.65 (m, 2H), 1.44 (m, 2H), 1.28 (s, 9H), 0.94 (t, J = 0.72 Hz, 3H). ^{13}C NMR (75 MHz, $CDCl_3$) δ: 159.8, 128.1, 114.2, 113.5, 105.9, 80.5, 69.2, 55.2, 32.0, 26.5, 19.3, 13.8. Anal. calcd for $C_{16}H_{26}O_4$: C 68.04, H 9.29; found: C 68.07, H 9.27.

Acknowledgment

Financial support from the National Science Council of Taiwan (NSC 98-2113-M-006-001-MY3 and NSC 100-3113-E-024-001-CC2) is gratefully acknowledged.

References

(1) (a) Casteel, D. A. *Nat. Prod. Rep.* **1999**, *16* (1), 55. doi:10.1039/a705725c; (b) Tang, Y. Q.; Dong, Y. X.; Vennerstrom, J. L. *Med. Res. Rev.* **2004**, *24* (4), 425. doi:10.1002/med.10066; (c) Kim, H. S.; Nagai, Y.; Ono, K.; Begum, K.; Wataya, Y.; Hamada, Y.; Tsuchiya, K.; Masuyama, A.; Nojima, M.; McCullough, K. J. *J. Med. Chem.* **2001**, *44* (14), 2357. doi:10.1021/jm010026g.

(2) Ahmed, A.; Dussault, P. H. *Tetrahedron* **2005**, *61* (19), 4657. doi:10.1016/j.tet.2005.02.071.

(3) Dussault, P. H.; Lee, I. Q.; Lee, H.-J.; Lee, R. J.; Niu, Q. J.; Schultz, J. A.; Zope, U. R. *J. Org. Chem.* **2000**, *65* (25), 8407. doi:10.1021/jo991714z.

(4) (a) Dussault, P. H.; Zope, U. R.; Westermeyer, T. A. *J. Org. Chem.* **1994**, *59* (26), 8267. doi:10.1021/jo00105a053; (b) Dussault, P.; Sahli, A. *J. Org. Chem.* **1992**, *57* (3), 1009. doi:10.1021/jo00029a043.
(5) Terent'ev, A. O.; Kutkin, A. V.; Troizky, N. A.; Ogibin, Y. N.; Nikishin, G. I. *Synthesis* **2005**, (13): 2215. doi:10.1055/s-2005-872093.
(6) Žmitek, K.; Zupan, M.; Stavber, S.; Iskra, J. *J. Org. Chem.* **2007**, *72* (17), 6534. doi:10.1021/jo0708745.
(7) (a) Kim, H. S.; Tsuchiya, K.; Shibata, Y.; Wataya, Y.; Ushigoe, Y.; Masuyama, A.; Nojima, M.; McCullough, K. J. *J. Chem. Soc., Perkin Trans. 1* **1999**, (13): 1867. doi:10.1039/a900826h; (b) Nakamura, N.; Nojima, M.; Kusabayashi, S. *J. Am. Chem. Soc.* **1987**, *109* (16), 4969. doi:10.1021/ja00250a034.
(8) (a) Ramirez, A.; Woerpel, K. A. *Org. Lett.* **2005**, *7* (21), 4617. doi:10.1021/ol051703u; (b) Terent'ev, A. O.; Kutkin, A. V.; Platonov, M. M.; Ogibin, Y. N.; Nikishin, G. I. *Tetrahedron Lett.* **2003**, *44* (39), 7359. doi:10.1016/S0040-4039(03)01844-6; (c) Opsenica, D.; Pocsfalvi, G.; Juranic, Z.; Tinant, B.; Declercq, J. P.; Kyle, D. E.; Milhous, W. K.; Solaja, B. A. *J. Med. Chem.* **2000**, *43* (17), 3274. doi:10.1021/jm000952f; (d) Jefford, C. W.; Li, Y.; Jaber, A.; Boukouvalas, J. *Synth. Commun.* **1990**, *20* (17), 2589. doi:10.1080/00397919008051466.
(9) (a) Anslyn, E. V.; Dougherty, D. A. *Modern Physical Organic Chemistry;* University Science: Sausalito, CA, 2006; pp 542–544; (b) Lowry, T. H.; Richardson, K. S. *Mechanism and Theory in Organic Chemistry;* Harper & Row: New York, 1987; pp 694–702.
(10) Tsai, C.-Y.; Sung, R.; Zhuang, B.-R.; Sung, K. *Tetrahedron* **2010**, *66* (34), 6869. doi:10.1016/j.tet.2010.06.046.
(11) (a) Ochiai, M.; Ito, T.; Takahashi, H.; Nakanishi, A.; Toyonari, M.; Sueda, T.; Goto, S.; Shiro, M. *J. Am. Chem. Soc.* **1996**, *118* (33), 7716. doi:10.1021/ja9610287; (b) Chen, L.-A.; Sung, K. *Org. Lett.* **2009**, *11* (15), 3370. doi:10.1021/ol901215y.

Can. J. Chem. Downloaded from www.nrcresearchpress.com by Renmin University of China on 09/02/12
For personal use only.

Aluminium heterogeneous speciation in natural waters

Igor Povar and Vasile Rusu

Can. J. Chem. Downloaded from www.nrcresearchpress.com by Renmin University of China on 09/02/12
For personal use only.

Abstract: The presence of aluminium in natural waters is of major concern at present because of the potential threat for the health of a number of species, including humans. In natural water, aluminium exists in different forms depending on the concentrations of various other species, organic matter, the types of minerals, the pH, etc. The aluminium species in the natural water – gibbsite system is considered in this work. The main approaches for estimating of the individual concentrations of the aluminium species involve the use of reliable thermodynamic data, together with experimental measurements of free or total concentrations of major components. The new type of diagrams based on graphical and computerized methods, which quantitatively describe the distribution of soluble and insoluble, inorganic, and organic, and monomeric and polymeric aluminium species in heterogeneous aquatic systems is presented. This approach utilizes thermodynamic relationships coupled with original mass balance constraints, where the mineral phases are explicitly expressed. The factors influencing the distribution of soluble and insoluble aluminium species in aquatic systems were analyzed. The new type of developed diagrams may be used to interpret data obtained within the framework of water-quality monitoring programs.

Key words: gibbsite, diagram of distribution, heterogeneous system, thermodynamic stability.

Résumé : La présence d'aluminium dans les eaux naturelles est maintenant une préoccupation majeure en raison des dangers potentiels que ce métal présente pour la santé d'un certain nombre d'espèces, dont les humains. Dans les eaux naturelles, l'aluminium existe sous diverses formes suivant, entre autres, les concentrations des diverses autres espèces, des matières organiques, des types de minéraux et du pH. Dans le présent travail, on considère la gibbsite comme l'espèce d'aluminium qui existe dans le système d'eau naturelle. Les principales approches utilisées pour évaluer les concentrations individuelles des espèces d'aluminium impliquent l'utilisation de données thermodynamiques fiables en relation avec des mesures expérimentales des concentrations libres ou totales des composants principaux. On a mis au point un nouveau type de diagrammes, basés sur des méthodes graphiques et des ordinateurs, qui permet de décrire d'une façon quantitative la distribution des espèces d'aluminium solubles et insolubles, inorganiques ou organiques, monomères ou polymères, dans des systèmes aquatiques hétérogènes. Cette approche utilise des relations thermodynamiques liées aux contraintes originales de balance des masses, dans lesquelles les phases minérales sont exprimées d'une façon explicite. On a analysé les facteurs qui influencent la distribution des espèces aluminium solubles et insolubles dans les systèmes aquatiques. Le nouveau type de diagramme qui a été mis au point peut être utilisé pour interpréter des données obtenues dans le cadre de programmes de surveillance de la qualité de l'eau.

Mots-clés : gibbsite, diagramme de distribution, système hétérogène, stabilité thermodynamique.

[Traduit par la Rédaction]

Introduction

Chemical forms of aluminium occurrence in natural waters are quite various, as Al^{3+} forms complexes with OH^-, SO_4^{2-}, F^-, and organic compounds. It is known that different chemical forms of aluminium possess different degrees of toxicity for live organisms in natural waters.[1–12] Furthermore, aluminium can play a toxic role in severe illnesses.[4–6] The identification and quantitative determination of the chemical forms of aluminium in situ, without any effect on chemical equilibrium of the system would be a crucial step. There are two general ways for fulfillment of the given problem: (*i*) experimental determination of individual chemical forms on the basis of their reactions with certain reagents with known physical and chemical properties or (*ii*) calculation of their distribution on the basis of the thermodynamic analysis and measurement of the total or equilibrium concentrations of metal and the most important ligands. Chemical modeling represents a unique method for the prediction of aluminium behavior in aqueous systems. Nevertheless, the majority of computer models include only inorganic mononuclear chemical forms (species) of aluminium, neglecting the formation of polynuclear and organic ones.[2] The equilibria and specification of individual chemical forms (species) of aluminium are represented in the form of various diagrams, basically diagrams of distribution or predominance.[5,8,13] Natural waters are in equilibrium with minerals, e.g., gibbsite, which affect the concentration of aluminium within certain limits.

Received 9 October 2011. Accepted 2 January 2012. Published at www.nrcresearchpress.com/cjc on 9 March 2012.

I. Povar and V. Rusu. Institute of Chemistry of the Academy of Sciences of Moldova, Academiei str. 3, MD-2028 Chisinau, Republic of Moldova.

Corresponding author: Igor Pover (e-mail: ipovar@yahoo.ca).

Can. J. Chem. Downloaded from www.nrcresearchpress.com by Renmin University of China on 09/02/12
For personal use only.

Consequently, it is necessary to consider natural waters in concert with solid phases.

The main objective of the present paper consists of the thermodynamic analysis and graphical representation of the distribution of various chemical forms of aluminium both in saturated aqueous solutions and solid phases. Initially, some assumptions similar to ref. 2, are made, including (*i*) the studied systems were considered in a stable state of chemical equilibrium, (*ii*) natural waters were analyzed as diluted solutions with a low ionic strength, (*iii*) the natural water was in balance with the mineral phase gibbsite, (*iv*) equilibrium reactions with the participation of Fe and Mn were not included in this model, (*v*) two chemical forms of aluminium – organic matter were considered (AlOrg and $AlHOrg^+$), (*vi*) the adsorption of anions (F^- and SO_4^{2-}) was not included in the model, (*vii*) Al phosphate complexes could be presented in the form of $AlH_2PO_4^{2+}$ and Al silicate complexes might be neglected. From the third assumption, the equilibrium concentration of aluminium ion [Al^{3+}] can be estimated as a function of pH using the following relations, where K_S is the equilibrium constant (solubility product).

$$[1] \qquad Al(OH)_3(s) + 3H^+ \Leftrightarrow Al^{3+} + 3H_2O, \qquad [Al^{3+}] = K_S[H^+]^3$$

The technical execution of the diagrams that explicitly specify the area of the loss of solid phases has been considered by the author.[5] However, such diagrams have a mainly qualitative character and are poorly suitable for some quantitative assessments. In this work, the new type of diagrams for the graphical representation of equilibrium in natural waters containing a mineral-phase gibbsite has been developed. Their construction is based on mass balance equations (MB) within the framework of the method of residual concentrations (RC)[14,15] and the thermodynamic delimitation of the stability of the solid phases.[16–19] Systems of liquid and solid phases, in which a series of chemical reactions proceeds concomitantly, shall be defined as heterogeneous and the constructed diagrams as diagrams of heterogeneous chemical equilibrium (DHCE). Outwardly, such diagrams are similar to the diagrams of distribution for homogeneous systems;[13] however, the principle of their construction differs radically from the last ones.

Theoretical

Besides the process of gibbsite dissolution (eq. [1]), a set of possible (probable) equilibria in the mineral phase – natural water system, presented in the Appendix (Table A1) is taken into account. The MB conditions in this system may be formulated on the basis of the method of residual concentrations (RC; see Appendix Table A2, eqs. [A1] and [A7]).[14,15] Quantities C_i^0 and C_i^r in eqs. [A1]–[A7] (Table A2) represent, respectively, the analytical and residual concentrations of the component *i* in the considered heterogeneous system.[14] In eq. [A7], C_H^0 denotes the excess of H^+ ions in relation to hydroxyl ions in a two-phase mixture $C_H^0 = -C_{OH}^0$.[14] From the stoichiometric composition of gibbsite $Al(OH)_3(s)$, the following ratio is obtained:

$$[2] \qquad 3 = \Delta C_{OH}/\Delta C_{Al}$$

Besides, within the RC method, the relations $\Delta C_{OH} = -\Delta C_H$ and $C_{OH}^r = -C_H^r$ are appropriate, and eq. [A7] (Table A2) becomes

$$[3] \qquad C_H^0 = -3\Delta C_{Al} + C_H^r$$

The equilibrium concentration of the Al^{3+} ion is determined from the equilibrium constant K_S (eq. [1]). From the equations of the conditions of mass balance (eqs. [A1]–[A7]) for a given pH and taking into account the relation in eq. [2]) and the equations of the law of mass action (LMA), a system of five equations with five unknown quantities [F], [Org], [SO_4], [PO_4], and ΔC_{Al} is derived, which may be easily solved numerically (eqs. [A1]–[A7], Table A2). Using the combined equations of LMA and MB, it is possible to calculate the diagrams of distribution of aluminium ion both in solid and liquid phases (species in aqueous solution), i.e., the diagrams of heterogeneous chemical equilibrium.

The following equations for calculation of the partial molar fractions of species γ_i in a heterogeneous system, where the reactions presented in Table A1 proceed concomitantly, can be written:

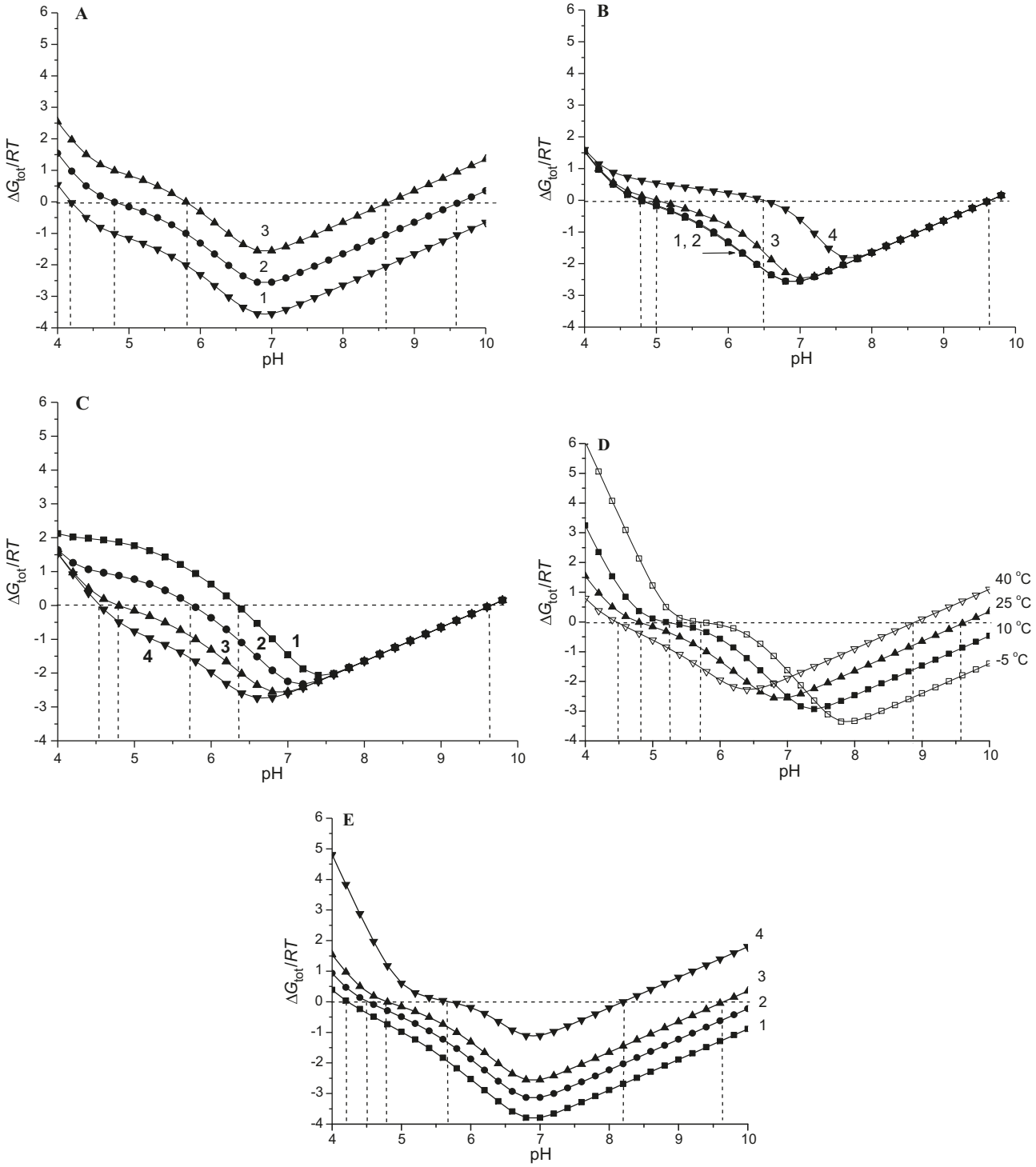
$$[4] \qquad \gamma_S = \frac{\Delta C_{Al}}{C_{Al}^0}, \gamma_{tot} = \frac{C_{Al}^r}{C_{Al}^0}, \gamma_{Al} = \frac{[Al]}{C_{Al}^0}, \quad \gamma_{i,j} = \frac{i[Al_i(OH)_j]}{C_{Al}^0}, \gamma_{f,j} = \frac{[AlF_j]}{C_{Al}^0}, \quad \gamma_{O1} = \frac{[AlOrg]}{C_{Al}^0}, \gamma_{O2} = \frac{[AlHOrg]}{C_{Al}^0}, \quad \gamma_{S1} = \frac{[AlSO_4]}{C_{Al}^0}, \gamma_{S2} = \frac{[Al(SO_4)_2]}{C_{Al}^0}, \quad \gamma_{PO_4} = \frac{[AlH_2PO_4]}{C_{Al}^0}$$

The index "tot" means the sum of the partial molar fractions of all the soluble particles. By comparing eq. [4] with eqs. [A1]–[7A] (Table A2), the following equation is valid.

$$[5] \qquad \gamma_S + \gamma_{tot} = \gamma_S + \gamma_{Al} + \sum_{i=1}\sum_{j=1}\gamma_{i,j} + \sum_{j=1}\gamma_{f,j} + \gamma_{O1} + \gamma_{O2} + \gamma_{S1} + \gamma_{S2} + \gamma_{PO_4}$$

The diagrams of the DHCE, outwardly, are similar to diagrams of species distribution in the homogeneous systems. The latter usually are fitted with the coordinates γ_i(pH), as in the absence of polynuclear complexes the partial molar fractions of species γ_i in aqueous solution (more frequently, notated as *f* or α) are functions only of the solution pH and do not depend on the initial concentrations of components. In the case of heterogeneous equilibria, the partial molar fractions of species also depend on the initial composition of the mixture and, for a given pH, are functions of five variables $\gamma_i = f(C_{Al}^0, C_F^0, C_{SO_4}^0, C_{Org}^0, C_{PO_4}^0)$. In this case, it is reasonable to fit diagrams with the coordinates (γ_i, pH) while the values of other quantities are constant.

Fig. 1. Variation of Gibbs energy depending on the pH in the system "saturated aqueous solution – gibbsite". (A) Concentrations (*M*): C^0_{Org}, $C^0_{PO_4}$, and $C^0_{SO_4}$, 1×10^{-4} mol/L; C^0_F, 5×10^{-6} mol/L; C^0_{Al}: (1) 1×10^{-3} mol/L, (2) 1×10^{-4} mol/L, (3) 1×10^{-5} mol/L. (B) Concentrations (*M*): C^0_{Al}, C^0_{Org}, $C^0_{PO_4}$, and $C^0_{SO_4}$, 1×10^{-4} mol/L; C^0_F: (1) 5×10^{-7} mol/L, (2) 5×10^{-6} mol/L, (3) 5×10^{-5} mol/L, (4) 5×10^{-4} mol/L. (C) Concentrations (*M*): C^0_{Al}, $C^0_{PO_4}$, $C^0_{SO_4}$, 1×10^{-4} mol/L; C^0_F, 5×10^{-6} mol/L; C^0_{Org}: (1) 1×10^{-2} mol/L, (2) 1×10^{-3} mol/L, (3) 1×10^{-4} mol/L, (4) 1×10^{-5} mol/L. (D) Variation of Gibbs energy depending on pH at various temperatures. Concentrations (*M*): C^0_{Al}, C^0_{Org}, $C^0_{PO_4}$, and $C^0_{SO_4}$, 1×10^{-4} mol/L; C^0_F, 5×10^{-6} mol/L; $C^0_{CO_3}$, 1×10^{-3} mol/L. (E) Variation of Gibbs energy depending on pH for various values of $\log K_S$: (1) 8.11, (2) 8.77, (3) 9.35, and (4) 10.80. Concentrations (*M*): C^0_{Al}, C^0_{Org}, $C^0_{PO_4}$, and $C^0_{SO_4}$, 1×10^{-4} mol/L; C^0_F, 5×10^{-6} mol/L; $C^0_{CO_3}$ 1×10^{-3} mol/L. Org, organic ligand.



Can. J. Chem. Downloaded from www.nrcresearchpress.com by Renmin University of China on 09/02/12
For personal use only.

Can. J. Chem. Downloaded from www.nrcresearchpress.com by Renmin University of China on 09/02/12
For personal use only.

The procedure for the construction of the DHCE includes following necessary stages:

i. Thermodynamic calculation of the gibbsite stability area. For this purpose, the Gibbs energy values for this complex process, where the reactions presented in Table A1 proceed concomitantly, are determined by the following equations:[16–19]

$$[6a] \qquad \Delta G_{\text{tot}} = -RT \ln \frac{C^r_{\text{Al}}}{C^0_{\text{Al}}} = -RT \ln \gamma_{\text{tot}} \qquad \text{or}$$

$$[6b] \qquad \Delta G_{\text{tot}} = -RT \ln (1 - \gamma_{\text{S}})$$

The solid-phase $Al(OH)_3(s)$ is stable if $\Delta G_{\text{tot}} > 0$. The condition $\Delta G_{\text{tot}} = 0$ corresponds to the beginning of its dissolution and (or) sedimentation.

i. Calculation of the partial molar fractions (γ_i) of all the chemical forms containing aluminium ion by eq. [4] for the gibbsite stability area established at previous stage.

ii. For completeness outside of this region, i.e., for a homogeneous aqueous solution, the partial molar fractions are computed by the usual equations used for the construction of distribution diagrams.[13] In this case, under conditions of only mononuclear complex species formation, the γ values do not depend on the initial concentration of the components.

It is worth mentioning that, by means of the partial molar fraction γ_S of the solid phase, it is possible to calculate the amount of the formed solid phase for a given initial concentration C^0_{Al} of the aluminium ion.

$$[7] \qquad \Delta C_{\text{Al}} = \gamma_{\text{S}} C^0_{\text{Al}}$$

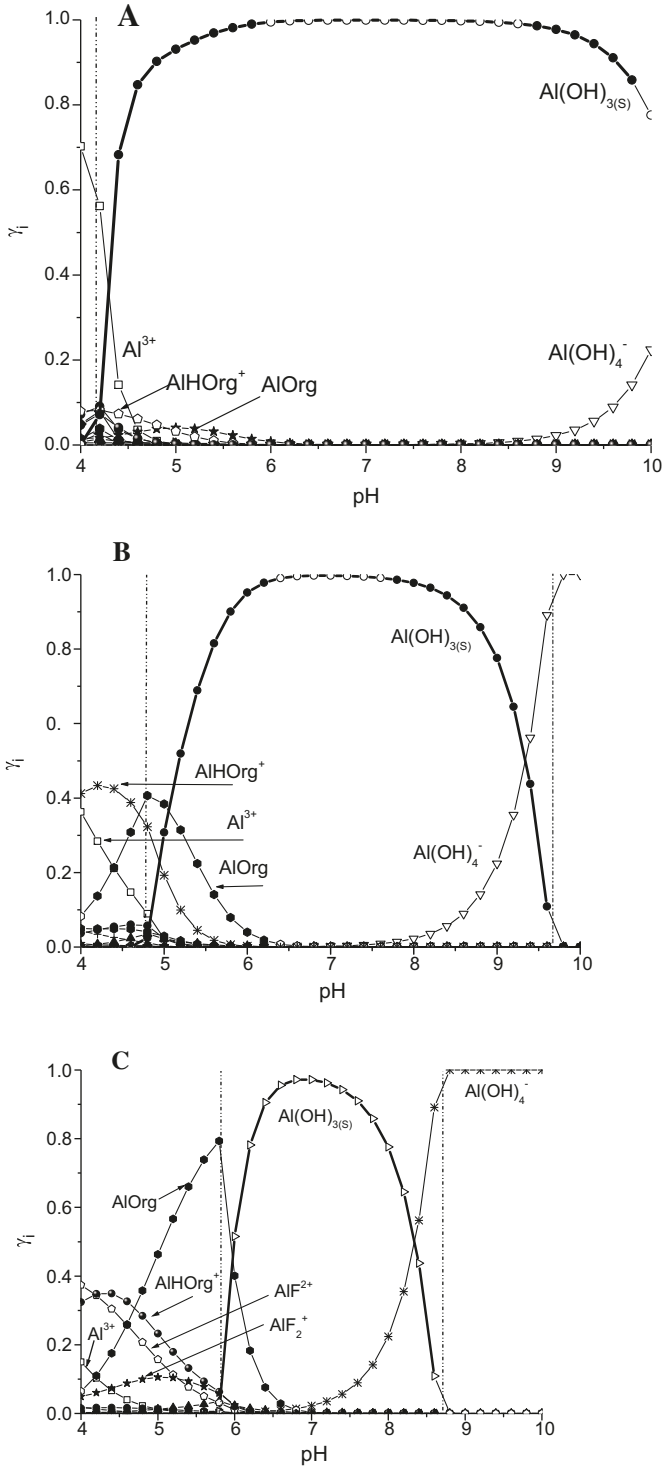
Results and discussion

It is well-known that pH value of saturated solutions is one of the major factors (master variable) influencing the distribution of insoluble aluminium hydroxide as well as its inorganic and organic forms. Figures 1A–1C show the variation in Gibbs energy depending on the pH in the system "saturated aqueous solution – gibbsite" for different concentrations of individual components of the investigated natural waters (NW). The diagrams for ΔG_{tot} (pH) allow for the easy definition of the gibbsite stability area.

The analysis of data presented in Fig. 1A shows that the thermodynamic stability area of gibbsite becomes considerably larger with an increase in the total (analytical) concentration of aluminium ion (C^0_{Al}). The presence of significant amounts of inorganic ligand, fluoride ion F^- (Fig. 1B), and organic ligand Org^{3-} (Fig. 1C) also significantly affects the solubility of gibbsite.

The DHCE for the investigated system at various concentrations of aluminium ion are represented in Fig. 1D. Such diagrams clearly reflect the distribution of various aluminium chemical forms both in the solid phase and saturated solutions. Partial molar fractions of soluble aluminium forms are changing strongly at the pH value of dissolution – formation of the solid phase. For a given total concentration of aluminium (C^0_{Al}) in acidic and neutral solutions the equilibrium concentrations of mononuclear hydroxo complexes are small (Figs. 2A–2C). Concomitantly, our calculations prove that the fraction of polynuclear hydroxocomplexes is negligible under the studied conditions. The partial molar fraction of free alu-

Fig. 2. Variation of heterogeneous chemical equilibria with pH in the saturated aqueous solution – gibbsite system. Concentrations (M): C^0_{Org}, $C^0_{\text{PO}_4}$, and $C^0_{\text{SO}_4}$ 1×10^{-4} mol/L; C^0_{F}, 5×10^{-6} mol/L; C^0_{Al}: (A) 1×10^{-3} mol/L; (B) 1×10^{-4} mol/L; (C) 1×10^{-5} mol/L. Org, organic ligand.



Can. J. Chem. Downloaded from www.nrcresearchpress.com by Renmin University of China on 09/02/12
For personal use only.

minium ions increases in a narrowed region of pH values as the total (analytical) concentration C^0_{Al} in saturated solution rises.

Moreover, the area of stability of the anionic hydroxo complex $Al(OH)_4^-$ gets narrower and, in alkalescent or alkaline media of heterogeneous systems, such species become the prevailing form. For concentrations $C^0_{Al} < 1 \times 10^{-3}$ mol/L in acescent or acidic media among soluble forms, the AlOrg and $AlHOrg^+$ species prevail.

At $[C^0_{Al}] = 1 \times 10^{-5}$ mol/L, an appreciable contribution is introduced by the complexes AlF^{2+} and AlF_2^+. The DHCE presented here differ significantly from the diagrams presented by Bi[2] as the latter considered the distribution of inorganic and organic forms only in aqueous solution.

Our calculations prove that aluminium complexes with sulfate and phosphate ions are formed in irrelevant quantities for the given composition of NWs, and this conclusion is in concordance with the work done by Bi.[2]

The effect of temperature on Gibbs energy variation is represented in Fig. 2. The equilibrium constants for different temperatures have been estimated on the basis of van't Hoff equation.

$$[8] \qquad \log K_2 = \log K_1 + (1/T_1 - 1/T_2)\Delta H/2.303R$$

The appropriate values of the enthalpies ΔH are listed in Table A1. Value T_1 has been chosen equal to 298 K ≡ 25 °C. It is supposed that the temperature insignificantly influences the ΔH values within the investigated temperature interval. The analysis of the curves proves that, in acidic media, the ΔG_{tot} value decreases with decreasing temperature and increases in alkaline media; however, in both media the area of maximal values of ΔG_{tot}, i.e., the area of maximal stability of the solid phase, is displaced by reducing the temperature towards higher values of pH.

One of the basic tasks concerning the calculations of chemical equilibria refers to the correct choice of equilibrium constants, i.e., their reliability and accuracy, from which the final results completely depend. As an example, the effect of accuracy of equilibrium constant values (K_S) on the functions ΔG_{tot}(pH) was considered. For various modifications of gibbsite, a series of values for K_S is known, e.g., 8.11, used for synthetic gibbsite; 8.77, used for natural gibbsite; 9.35, used for monocrystalline gibbsite; and 10.80, used for amorphous gibbsite.[2,3] As seen in Fig. 1E, the selection of an equilibrium constant for rxn. [1] has considerable effect on the gibbsite thermodynamic stability. By increasing the $\log K_S$ value, the range of pH values for the solid-phase thermodynamic stability becomes considerably narrower, with a concomitantly decrease in the ΔG_{tot} value.

Conclusions

A new type of diagram based on the thermodynamic analysis of the stability of natural mineral and original conditions of mass balance in the heterogeneous system saturated aqueous solution – gibbsite has been presented. Conditions of mass balance take into consideration all the chemical forms present in aqueous and solid phases, including inorganic and organic mononuclear and polynuclear forms. The effect of major factors influencing the distribution and concentration of soluble and insoluble species of aluminium in aquatic systems was analyzed. Our data regarding the factors influencing Al speciation, based on the constructed DHCE diagrams, are in good agreement with the previous results,[2,3] but they are more specific, taking explicitly into account the heterogeneous character of NWs.

References

(1) Achilli, M.; Ciceri, G.; Ferraroli, R.; Culivicchi, G.; Pieri, S. *Water Air Soil Pollut.* **1991**, *57–58* (1), 139. doi:10.1007/BF00282877.
(2) Bi, S. P. *Analyst (Lond.)* **1995**, *120* (7), 2033. doi:10.1039/an9952002033.
(3) Bi, S.; Chenyi Wang, C.; Cao, Q.; Zhang, C. *Coord. Chem. Rev.* **2004**, *248* (5–6), 441. doi:10.1016/j.ccr.2003.11.001.
(4) Driscoll, C. T. *Environ. Health Perspect.* **1985**, *63*, 93. doi:10.1289/ehp.856393.
(5) Kragten, Y. *Atlas of Metal–Ligand Equilibria in Aqueous Solutions;* Halsted Press: New York, 1978.
(6) Kvech, S.; Edwards, M. *Water Res.* **2002**, *36* (17), 4356. doi:10.1016/S0043-1354(02)00137-9.
(7) Schecher, W. D.; Driscoll, C. T. *Water Resour. Res.* **1987**, *23* (4), 525. doi:10.1029/WR023i004p00525.
(8) Stumm, W.; Morgan, J. J. *Aquatic Chemistry;* Wiley-Interscience: New York, 1981.
(9) Sullivan, T. J.; Cosby, B. J. *Water Air Soil Pollut.* **1998**, *105* (3/4), 643. doi:10.1023/A:1004957426629.
(10) (a) Fournier, A. C.; Shafran, K. L.; Perry, C. C. *Anal. Chim. Acta* **2008**, *607* (1), 61. doi:10.1016/j.aca.2007.11.026; (b) Müller, B.; Berg, M.; Yao, Z. P.; Zhang, X. F.; Wang, D.; Pfluger, A. *Sci. Total Environ.* **2008**, *402* (2–3), 232. doi:10.1016/j.scitotenv.2008.04.049.
(11) Moller, N.; Christov, C.; Weare, J. In *Proceedings of the 31st Workshop on Geothermal Reservoir Engineering,* Stanford University, Stanford, California, 30 January – 1 February; 2006, pp 1–8.
(12) Eriksson, G.; Konigsberger, E. *Pure Appl. Chem.* **2008**, *80* (6), 1293. doi:10.1351/pac200880061293.
(13) Butler, J. N.; Cogley, D. R. *Ionic Equilibrium: Solubility and pH Calculations;* John Wiley and Sons: New York, 1998.
(14) Povar, I. J. *Inorg. Chem.* **1996**, *41*, 1167 [In Russian].
(15) Povar, I. J. *Inorg. Chem.* **2000**, *45*, 1632 [In Russian].
(16) Fishtik, I.; Povar, I. *Zh. Obshch. Khim.* **1987**, *57*, 31.
(17) Fishtik, I.; Povar, I.; Vataman, I. *Zh. Obshch. Khim.* **1987**, *57*, 736.
(18) Povar, I. *Ukr. Khim. Zh.* **1994**, *60*, 371.
(19) Povar, I. *J. Anal. Chem.* **1998**, *53*, 1113.

Appendix

Table A1. Equilibrium constants and values of enthalpies (ΔH^2 (1 cal = 4.184 J).

Reaction	log$K$	ΔH (cal mol^{-1})	Symbol
$Al^{3+} + H_2O = AlOH^{2+} + H^+$	–4.99	11900	K_1
$Al^{3+} + 2H_2O = Al(OH)_2^+ + 2H^+$	–10.00	22000	K_2
$Al^{3+} + 4H_2O = Al(OH)_4^- + 4H^+$	–23.00	44060	K_4
$Al(OH)_3(s) + 3H^+ = Al^{3+} + 3H_2O$	9.35	–22800	K_S
$Al^{3+} + F^- = AlF^{2+}$	7.02	1100	K_{f1}
$Al^{3+} + 2F^- = AlF_2^+$	12.76	2000	K_{f2}
$Al^{3+} + 3F^- = AlF_3$	17.03	2500	K_{f3}
$Al^{3+} + 4F^- = AlF_4^-$	19.73	2200	K_{f4}
$Al^{3+} + 5F^- = AlF_5^{2-}$	20.92	1800	K_{f5}
$Al^{3+} + SO_4^{2-} = AlSO_4^+$	3.01	2150	K_{S1}
$Al^{3+} + 2SO_4^{2-} = Al(SO_4)_2^-$	4.90	2840	K_{S2}
$Al^{3+} + Org^{3-} = AlOrg$	8.39		K_{O1}
$Al^{3+} + H^+ + Org^{3-} = AlHOrg^+$	13.09		K_{O1}
$Org^{3-} + H^+ = HOrg^{2-}$	6.83		K_{g1}
$Org^{3-} + 2H^+ = H_2Org^-$	12.73		K_{g2}
$Org^{3-} + 3H^+ = H_3Org$	14.49		K_{g3}
$H^+ + F^- = HF$	3.17	3460	K_{HF}
$H_2O = H^+ + OH^-$	–14.00	13340	K_W
$2Al^{3+} + 2H_2O = Al_2(OH)_2^{4+} + 2H^+$	–6.3		K_{P1}
$3Al^{3+} + 4H_2O = Al_3(OH)_4^{5+} + 4H^+$	–12.1		K_{P2}
$Al^{3+} + H_2PO_4^- = AlH_2PO_4^{2+}$	3.1		K_{PO_4}
$PO_4^{3-} + H^+ = HPO_4^{2-}$	12.0		$K_{PO_4,1}$
$PO_4^{3-} + 2H^+ = H_2PO_4^-$	19.21		$K_{PO_4,2}$
$PO_4^{3-} + 3H^+ = H_3PO_4$	21.36		$K_{PO_4,3}$
$CO_3^{2-} + H^+ = HCO_3^-$	10.33	3617	K_{C1}
$CO_3^{2-} + 2H^+ = H_2CO_3$	16.68	5864	K_{C2}

Note: Org, organic ligand.

Can. J. Chem. Downloaded from www.nrcresearchpress.com by Renmin University of China on 09/02/12
For personal use only.

Can. J. Chem. Downloaded from www.nrcresearchpress.com by Renmin University of China on 09/02/12
For personal use only.

Table A2. Conditions of mass balance for the considered system.

Equation
[A1] $C^0_{Al} = C^r_{Al} + \Delta C_{Al} = \sum_{i=1}\sum_{j=0} i[Al_i(OH)_j^{3i-j}] + \sum_{j=1}[AlF_j^{3-j}] + [AlSO_4^+] + [Al(SO_4)_2^-] + [AlOrg^0] + [AlHOrg^+] + [AlH_2PO_4^{2+}] + \Delta C_{Al}$
$= K_S\sum_{i=1}\sum_{j=0} iK_{i,j}[H^+]^{3i-j} + K_S[H^+]^3\sum_{j=1}K_{f,i}[F^-]^j + K_SK_{S1}[H^+]^3[SO_4^{2-}]$
$+ K_S[H^+]^3K_{S2}[SO_4^{2-}]^2 + K_SK_{O1}[H^+]^3[Org^{3-}] + K_SK_{O2}[H^+]^4[Org^{3-}] + K_SK_{PO_4}[H^+]^5[PO_4^{3-}] + \Delta C_{Al}$
[A2] $C^0_F = [F^-] + [HF^0] + \sum_{j=1} j[AlF_j^{3-j}] = [F^-] + K_{HF}[H^+][F^-] + K_S[H^+]^3\sum_{j=1} jK_{f,j}[F^-]^j$
[A3] $C^0_{SO_4} = [SO_4^{2-}] + [AlSO_4^+] + 2[Al(SO_4)_2^-] = [SO_4^{2-}] + K_S[H^+]^3K_{S1}[SO_4^{2-}] + 2K_S[H^+]^3K_{S1}[SO_4^{2-}]^2$
[A4] $C^0_{Org} = \sum_{m=0}[H_mOrg^{m-3}] + [AlHOrg^+] + [AlOrg^0]$
$= [Org^{3-}] + [Org^{3-}]\sum_{m=1}K_{g,m}[H^+]^m + [Org^{3-}]K_S[H^+]^3K_{O1} + [Org^{3-}]K_SK_{O2}[H^+]^4$
[A5] $C^0_{CO_3} = [CO_3^{2-}] + [HCO_3^-] + [H_2CO_3^0] = [CO_3^{2-}] + K_{C1}[H^+][CO_3^{2-}] + K_C[H^+]^2[CO_3^{2-}]$
[A6] $C^0_{PO_4} = \sum_{l=0}[H_lPO_4^{l-3}] + [AlH_2PO_4^{2+}] = [PO_4^{3-}] + [PO_4^{3-}]\sum_{l=1}K_l[H^+]^l + [PO_4^{3-}]K_SK_{PO_4}[H^+]^5$
[A7] $C^0_H = C^r_H + \Delta C_H$
$= [H^+] - [OH^-] - \sum_{i=1}\sum_{j=1} j[Al_i(OH)_j^{3i-j}] + [AlHOrg^+] + 2[AlH_2PO_4^{2+}] + [HF^0] + \sum_{m=1} m[H_mOrg^{m-3}] + [HCO_3^-] + 2[H_2CO_3^0] + \sum_{l=1} l[H_lPO_4^{l-3}] + \Delta C_H$

Note: Org, organic ligand.

Complete basis set, hybrid-density functional theory study, and natural bond orbital interpretations of the conformational behavior of halocarbonyl, thiocarbonyl, and selenocarbonyl isocyanates

Seiedeh Negar Mousavi, Davood Nori-Shargh, Hooriye Yahyaei, and Kobra Mazrae Frahani

Can. J. Chem. Downloaded from www.nrcresearchpress.com by Renmin University of China on 09/02/12
For personal use only.

Abstract: Complete basis set CBS-QB3, hybrid-density functional theory (B3LYP/Def2-TZVPP) based methods and NBO interpretation were used to investigate the impacts of the stereoelectronic effects and electrostatic and steric interactions on the conformational properties of halocarbonyl isocyanates (halo = F (**1**), Cl (**2**), and Br (**3**)), halothiocarbonyl isocyanates (halo = F (**4**), Cl (**5**), and Br (**6**)), and haloselenocarbonyl isocyanates(halo = F (**7**), Cl (**8**), and Br (**9**)). Both methods showed that the Z-conformations of compounds **1**, **4**, and **7** are more stable than their corresponding E conformations, but the stability of the E conformations, when compared with the corresponding Z conformations, increases from compound **1** to compound **3**, compound **4** to compound **6**, and also from compound **7** to compound **9**. The NBO analysis showed that the generalized anomeric effect (GAE) is in favor of the Z conformations of compounds **1**, **4**, and **7**. The GAE values calculated (i.e., GAE_E–GAE_Z) increase from compound **1** to compound **3**, compound **4** to compound **6**, and also from compound **7** to compound **9**. On the other hand, there are none of the same trends between the calculated total dipole moment and the Gibbs free energy difference values between the E and Z conformations (i.e., $\Delta\mu_{E-Z}$ and ΔG_{E-Z}) of compounds **1**–**3**, **4**–**6**, and **7**–**9**. Accordingly, the GAE succeeds in accounting for the increase of the E conformation stability from compound **1** to compound **3**, compound **4** to compound **6**, and also from compound **7** to compound **9**. Therefore, the GAE associated with the electron delocalization, not the total dipole moment changes (i.e., $\Delta\mu_{E-Z}$), is a reasonable indicator of the total energy difference in compounds **1**–**3**, **4**–**6**, and **7**–**9**. There is a direct correlation between the calculated GAE and $\Delta[r_{2-6}(E) - r_{2-6}(Z)]$ parameters. Importantly, there are interesting through-space electron delocalizations ($LP_2X_6 \rightarrow \pi^*_{C4-O5}$) that justify the increase of the E conformation stability from compound **1** to compound **3**, compound **4** to compound **6**, and also from compound **7** to compound **9**, when compared with their corresponding Z conformations. The correlations between the GAE, bond orders, total steric exchange energies (TSEE), ΔG_{Z-E}, $\Delta\mu_{E-Z}$, structural parameters, and conformational behaviors of compounds **1**–**9** were investigated.

Key words: halocarbonyl isocyanates, stereoelectronic effect, molecular modeling, ab initio, NBO.

Résumé : On a fait appel à l'ensemble de base complet CBS-QB3, aux méthodes basées sur la théorie de la fonctionnelle de la densité hybride (B3LYP/Def2-TZVPP) et à une interprétation par les orbitales de liaison naturelle (OLN) pour étudier les impacts des effets stéréoélectroniques et des interactions électrostatiques et stériques sur les propriétés conformationnelles des isocyanates d'halogénocarbonyles (halogéno = F (**1**), Cl (**2**) et Br (**3**)), des isocyanates d'halogénothiocarbonyles (halogéno = F (**4**), Cl (**5**) et Br (**6**)) et des isocyanates d'halogénosélénocarbonyles (halogéno = F (**7**), Cl (**8**) et Br (**9**)). Les deux méthodes ont permis de montrer que les conformations Z des composés **1**, **4** et **7** sont plus stables que les conformations E, mais que la stabilité des conformations E, comparée celle des conformations Z, augmente du composé **1** au composé **3**, du composé **4** au composé **6** ainsi que du composé **7** au composé **9**. L'interprétation par les orbitales de liaison naturelle (OLN) montre que l'effet anomère généralisé (EAG) favorise les conformations Z des composés **1**, **4** et **7**. Les valeurs calculées pour l'effet anomère généralisé (EAG) (c'est-à-dire EAG_E–EAG_Z) augmente du composé **1** au composé **3**, du composé **4** au composé **6** ainsi que du composé **7** au composé **9**. Par ailleurs, il ne semble pas y avoir de tendances semblables pour les valeurs calculées pour les moments dipolaires totaux ou les différences d'énergie libre de Gibbs entre les conformations E et Z (c'est-à-dire $\Delta\mu_{E-Z}$ et ΔG_{E-Z}) pour les composés **1**–**3**, **4**–**6** et **7**–**9**. En conséquence, l'effet anomère généralisé (EAG) permet d'expliquer l'augmentation de stabilité de la conformation E du composé **1** au composé **3**, du composé **4** au composé **6** ainsi que du composé **7** au composé **9**. Il en ressort donc que l'effet anomère généralisé (EAG) associé à la délocalisation d'électron, et non pas les changements dans les moments dipolaires totaux (c'est-à-dire $\Delta\mu_{E-Z}$), est

Received 9 September 2011. Accepted 30 November 2011. Published at www.nrcresearchpress.com/cjc on 14 March 2012.

S.N. Mousavi, D. Nori-Shargh, and K.M. Frahani. Department of Chemistry, Arak Branch, Islamic Azad University, Arak, Iran.
H. Yahyaei. Department of Chemistry, Zanjan Branch, Islamic Azad University, Zanjan, Iran.

Corresponding author: Davood Nori-Shargh (e-mail: nori_ir@yahoo.com).

un indicateur raisonnable de la différence d'énergie totale dans les composés **1**–**3**, **4**–**6** et **7**–**9**. Il existe une corrélation directe entre l'effet anomère généralisé (EAG) et les paramètres $\Delta[r_{2\text{–}6}(E) - r_{2\text{–}6}(Z)]$. Il est aussi important de réaliser qu'il existe des délocalisations d'électrons intéressantes à travers l'espace ($LP_2X_6 \rightarrow \pi^*_{C4\text{–}O5}$) qui permet de justifier l'augmentation de la stabilité des conformations E du composé **1** au composé **3**, du composé **4** au composé **6** ainsi que du composé **7** au composé **9**, par comparaison avec les conformations Z correspondantes. On a aussi étudié les corrélations entre l'effet anomère généralisé (EAG), les ordres de liaison, les énergies d'échange stérique totales (EEST), $\Delta G_{E\text{–}Z}$, $\Delta\mu_{E\text{–}Z}$, paramètres structuraux et les comportements conformationnels des composés **1**–**9**.

Mots-clés : isocyanates d'halogénocarbonyles, effet stéréoélectronique, modelage moléculaire, ab initio, orbitales de liaison naturelle (OLN).

[Traduit par la Rédaction]

Can. J. Chem. Downloaded from www.nrcresearchpress.com by Renmin University of China on 09/02/12
For personal use only.

Introduction

The conformations of organic molecules can be determined by the electron delocalization from donor to acceptor and it is then referred to as stereoelectronic effects. The conformational behavior of molecules may be used to predict or explain the chemical reactivity of molecules on the basis of electronic activation or deactivation.[1,2] Esters of carboxylic acids, which have been the subject of extensive experimental and theoretical studies,[3,4] adopt a planar conformation, with a strong preference for the conformation in which the alkyl group attached to the ether oxygen is syn to the carbonyl oxygen. This planarity is predicted by overlapping between a nonbonding electron pair on the ether oxygen and the antibonding σ* orbital of the antiperiplanar C–O bond.[5] The internal rotation of the acetyl group around the C–C bond in chloroacetyl isocyanates in the condensed phase has been investigated using IR spectra.[6] The chemical reactivity and higher stability of the Z forms of acetyl isoicyanate and trichloroacetyl isocyanate have been examined using MO calculations.[7] Microwave[8] and electron diffraction[9] studies have showed that acetyl isocyanate only occurs in its Z form in the gas phase. UV, IR, and ^{13}C NMR techniques have been used to assign the Z and E forms of a large series of carbonyl and acyl isocyanates.[10]

In 1989, Mack et al.[11] used the gas electron diffraction (GED) approach to study the conformational properties of chlorocarbonyl isocyanate (**2**). The results from the GED study showed a mixture of E and Z isomers in a ratio of ~3:1 (ΔG = 0.7(3) kcal mol^{-1}, 1 cal = 4.184 J), which confirmed the interpretation of the vibrational spectra. Although the ab initio calculations (HF, MP2, and MP4(SDTQ) with different basis sets (4–31G*, 6–31G*, and D95*)) reproduced the experimental trans structure reasonably well, the relative stability of the two isomers is at variance with the experiment.

In 1991, Nguyen et al.[12] employed the MP2/6–31G(d,p) level of theory to investigate the conformations of chlorocarbonyl isocyanate (**2**). Their results showed that ab initio molecular orbital (MO) calculations at the MP2/6–31G** level of theory are reliable in determining the Z and E conformation differences of compound **2**. The results obtained at the MP2/6–31G** level of theory showed that the E conformer was prefered in compound **2** when compared with its Z conformation, which is in agreement with experiment. They stressed that the failure of the calculations by Mack et al.[11] to reproduce the Z and E conformation separation gap might be due to the geometrical parameters employed in their work. In addition, the MP2/6–31G(2d)//MP2/6–31G(d), MP2/6–311++G** results showed the E conformation of chlorocarbonyl isocyanate (**2**) is lower in energy than the Z isomer.[13,14] The results obtained at these levels of theory are in excellent agreement with experimental results obtained by gas-phase IR and electron-diffraction experiments. The importance of adding a sufficient number of polarization functions is emphasized.

In 1994, Durig et al.[15] used Raman and IR techniques for the study of the conformational preference of chlorocarbonyl isocyanate (**1**) in the gas and solid phases. They pointed out that the observed bands are assigned on the basis of the more stable Z conformation in the fluid states, but only the E conformation remains in the annealed solid.

In the same year, Klapstein and Nau[16] performed a variable-temperature approach for the study of the IR spectrum of chlorocarbonyl isocyanate (**2**) in the gas phase. They stressed that the higher stability of the E conformations for chloro- and bromo-carbonyl isocyanates are attributed to the high polarizabilities of the halogen atoms and explained as an electrostatic interaction between the heavy halides and the isocyanato carbon atom in the E conformation.

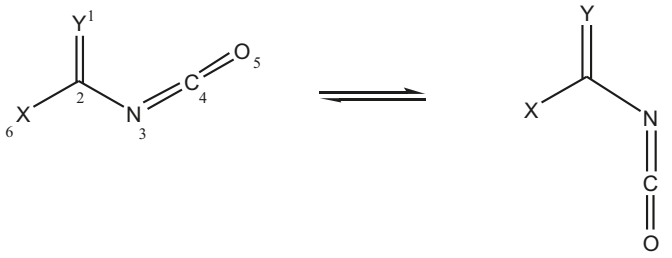
There is experimental and theoretical data for the conformational properties of some halocarbonyl isocyanate compounds,[6–19] but there is no published experimental and theoretical information about the donor–acceptor delocalization effects on the conformational properties of compounds **1**–**9** (see Scheme 1).

It should be noted that there is a stereoelectronic preference for conformations in which the best donor lone pair is antiperiplanar to the best acceptor bond.[20–34] Based on this argument, we could stress that the generalized anomeric effect (GAE), observable in acyclic compounds (such as dimethoxymethanes),[34] must be considered as the difference between the GAE of the E and Z conformations:

$$[1] \qquad GAE = GAE_E - GAE_Z$$

One of the goals of this work is the exploration of the argument stressed by Klapstein and Nau[16] about the higher stability of the E conformation for compounds **2** and **3** and also to give an answer to this question: Which factor has the most impact on the conformational behavior in compounds **1**–**9**? In this work, the stereoelectronic interactions associated with the GAE and also the conformational and structural properties of compounds **1**–**9** are investigated computationally

Scheme 1. Schematic representation of the conformations of compounds **1**–**9**.



Z-conformation *E*-conformation

[Numbering used for compounds **1**-**9** [Y=O, X=F (**1**), Cl (**2**), Br (**3**); Y=S, X=F (**4**), Cl (**5**), Br (**6**); Y=Se, X=F (**7**), Cl (**8**), Br (**9**)]

using the complete basis set - quadratic Becke3 composite method (CBS-QB3), hybrid - density functional theory (DFT) based methods, and natural bond orbital (NBO) analysis (see Scheme 1).[35–48]

The stabilization energies (E_2) associated with $LPN_3 \rightarrow \sigma^*_{C2-Y1}$, $LP_1Y_1 \rightarrow \sigma^*_{C2-N3}$, $LP_2Y_1 \rightarrow \sigma^*_{C2-N3}$, $LP_1X_6 \rightarrow \sigma^*_{C2-Y1}$, $LP_2X_6 \rightarrow \sigma^*_{C2-Y1}$, $LP_3X_6 \rightarrow \pi^*_{C2-Y1}$, $LP_2X_6 \rightarrow \pi^*_{C4-O5}$, $LP_1X_6 \rightarrow \sigma^*_{C2-N3}$, $LP_2X_6 \rightarrow \sigma^*_{C2-N3}$, and $LPN_3 \rightarrow \sigma^*_{C2-X6}$ electron delocalizations (see Fig. 1) and their influences on the conformational properties of compounds **1**–**9** were quantitatively investigated by NBO analysis. The stabilization energies associated with LP→σ* electron delocalizations are proportional to $S^2/\Delta E$ where S is the orbital overlap integral and ΔE is the energy differences between the LP and σ* orbitals.[49,50]

In addition, the E_2 associated with $i \rightarrow j$ delocalization is explicitly estimated by the following equation:

$$[2] \qquad E_2 = q_i \frac{F^2(i,j)}{\varepsilon_j - \varepsilon_i}$$

where q_i is the ith donor orbital occupancy, ε_i and ε_j are diagonal elements (orbital energies), and $F(i,j)$ represents off-diagonal elements associated with the NBO Fock matrix. Therefore, there is a direct relationship between $F(i,j)$ and S. It is known that the NBO analysis is a efficient approach for the investigation of the impacts of stereoelctronic interactions on the reactivity and dynamic behaviors of chemical compounds.[51,52]

Computational details

Composite complete basis set (CBS)[42–47] and hybrid-DFT calculations were carried out using the CBS-4 and B3LYP/Def2-TZVPP[35–41] levels of theory with the GAUSSIAN 03 package of programs.[35] The CBS models are compound methods that extrapolate to the CBS limit by using the $N - 1$ asymptotic convergence of MP2 pair energies calculated from pair natural orbital expansions.[42–47] The five-step CBS-QB3 series of calculations starts with a geometry optimization at the B3LYP[35–39] level, followed by a frequency calculation to obtain thermal corrections, zero-point vibrational energy, and entropic information. The next three computations are single-point calculations at the CCSD(T), MP4SDQ, and MP2 levels. It also corrects for spin contamination. The CBS extrapolation then computes the final energies.[46]

To quantitatively estimate the magnitude of the plausible donor–acceptor hyperconjugative interactions in Z and E conformations of compounds **1**–**9**, the NBO analysis was performed at the B3LYP/Def2-TZVPP level of theory by the NBO 5.G program contained in the PC-GAMESS interface.[48] The bonding and antibonding orbital occupancies in the Z and E conformations of compounds **1**–**9** and the stabilization energies associated with donor–acceptor electron delocalization were calculated using NBO analysis.

In the NBO analysis, the electronic wave functions are interpreted in terms of a set of occupied Lewis and a set of unoccupied non-Lewis localized orbitals. The delocalization effects (or donor–acceptor charge transfers) can be estimated from the presence of off-diagonal elements of the Fock matrix in the NBO basis. The NBO program searches for an optimal natural Lewis structure, which has the maximum occupancy of its occupied NBOs, and in general agrees with the pattern of bonds and lone pairs of the standard structural Lewis formula. Therefore, the new orbitals are more stable than pure Lewis orbitals, stabilizing the wave function and giving a set of molecular orbitals equivalent to canonical molecular orbitals.

Results and discussion

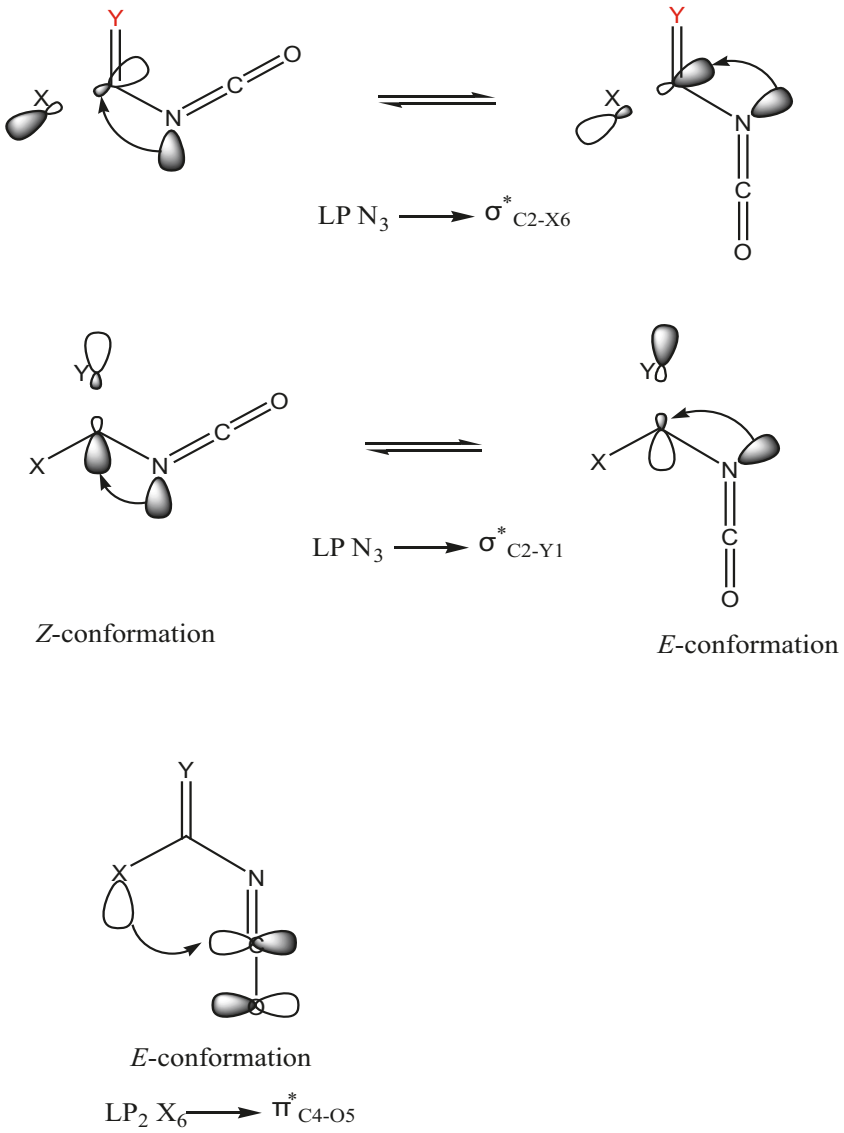
Conformation preference

The Gibbs free energy, enthalpy, and entropy differences (i.e., ΔG, ΔH, and ΔS) for the Z and E conformations of compounds **1**–**9**, as calculated at the B3LYP/Def2-TZVPP and CBS-QB3 levels of theory, are given in Table 1. It has to be noted that the absolute values of the thermodynamic properties certainly cannot be calculated at the accuracy level shown in Table 1. However, the quantities of interest here are the relative values of the thermodynamic functions for the Z and E conformations of the same molecule. Effectively, we expect that the errors in such differences will be very small and that even the corresponding errors between the different closely related compounds will be minimal. Accordingly, the smooth variation among the calculated values supports this expectation.

According to the B3LYP/Def2-TZVPP and CBS-QB3 results, the stability of the E conformation, when compared with the corresponding Z conformation, increases from compound **1** to compound **3**. The B3LYP/Def2-TZVPP method showed that the Z conformation of compound **1** is more

Can. J. Chem. Downloaded from www.nrcresearchpress.com by Renmin University of China on 09/02/12
For personal use only.

Fig. 1. Schematic representation of electron delocalizations between nonbonding and antibonding orbitals in the Z and E conformations of compounds **1**–**9**.



stable than its corresponding E conformation, while there is opposite trend for compound **3**. It has to be noted that there is no significant difference between the E and Z conformations of compound **2** (as calculated at the B3LYP/Def2-TZVPP level of theory). Except for compound **2**, the differences between the results of the CBS-QB3 method and B3LYP/Def2-TZVPP method are well within the uncertainty of CBS-QB3 as determined by tests of a group of standard molecules.[24] For compound **2**, CBS-QB3 shows an E conformation preference of 0.18 kcal mol^{-1} (1 cal = 4.184 J) in ΔG, whereas the B3LYP/Def2-TZVPP method has a 0.02 kcal mol^{-1} preference for the Z form. It has to be noted that the GED[11] results for compound **2** showed an E conformation preference of 0.7 kcal mol^{-1} in ΔG; therefore, the results of the CBS-QB3 method are is good agreement with the reported experimental data.

Similar to the trend observed for compounds **1**–**3**, the stability of the E conformation, when compared with the corresponding E conformation, increases from compound **4** to compound **6** and also from compound **7** to compound **9** (see Table 1). Klapstein and Nau[16] pointed out that the higher stability of the E conformations for chloro- and bromocarbonyl isocyanates are attributed to the electrostatic interaction between the heavy halides and the isocyanato carbon atom in the E conformation. It has to be noted that the negative charges of the halogen atoms decrease from the E conformations of compound **1** to compound **3** and also there are no significant differences between the positive charges of the isocyanato carbon atoms in these forms. Therefore, the electrostatic interaction associated with the attractive interactions between the negative charges of the halogen atoms and the isocyanato carbon atom in the E conformation is not responsible for the increase of the E conformation stability from compound **1** to compound **3**. The increasing polarizabilities of the halogen atoms may increase the attractive interaction between the halogen atoms and the isocyanato carbon atoms.

Can. J. Chem. Downloaded from www.nrcresearchpress.com by Renmin University of China on 09/02/12
For personal use only.

Can. J. Chem. Downloaded from www.nrcresearchpress.com by Renmin University of China on 09/02/12
For personal use only.

Table 1. Complete basis set - quadratic Becke3 (CBS-QB3)- and B3LYP/Def2-TZVPP-calculated thermodynamic parameters (ΔH, ΔG (in hartrees), and ΔS (in cal mol^{-1} K^{-1})), at 298 K and 1 atm (1 atm = 101.325 kPa), for the Z and E conformations of compounds **1**–**9**.

	CBS-QB3			B3LYP/ Def2-TZVPP		
Geometry	ΔH^a	ΔS^a	ΔG^a	ΔH^a	ΔS^a	ΔG^a
1-Z	0.000000	0.263	0.000000	0.000000	0.000	0.000000
	(0.00)[b]		(0.00)[b]	(0.00)[b]		(0.00)[b]
1-E	0.001162	0.000	0.001037	0.001301	0.427	0.001098
	(0.73)[b]		(0.65)[b]	(0.82)[b]		(0.69)[b]
	(0.74)[c]			(0.74)[c]		
2-Z	0.000173	0.232	0.000283	0.000000	0.000	0.000000
	(0.11)[b]		(0.18)[b]	(0.00)[b]		(0.00)[b]
			(0.7)[d]			(0.7)[d]
2-E	0.000000	0.000	0.000000	0.000114	0.173	0.000032
	(0.000)[b]		(0.00)[b]	(0.07)[b]		(0.02)[b]
3-Z	0.001346	0.034	0.001362	0.000759	0.000	0.000772
	(0.84)[b]		(0.85)[b]	(0.48)[b]		(0.48)[b]
3-E	0.00000	0.000	0.0000	0.0000000	0.028	0.0000000
	(0.00)[b]		(0.00)[b]	(0.00)[b]		(0.00)[b]
4-Z	0.000000	0.296	0.000000	0.000000	0.000	0.000000
	(0.00)[b]		(0.00)[b]	(0.00)[b]		(0.00)[b]
4-E	0.002324	0.000	0.002183	0.001905	0.454	0.001691
	(1.46)[b]		(1.37)[b]	(1.19)[b]		(1.06)[b]
5-Z	0.000000	0.000	0.000000	0.000000	0.000	0.000000
	(0.00)[b]		(0.00)[b]	(0.00)[b]		(0.00)[b]
5-E	0.001099	0.322	0.000946	0.000898	0.309	0.000752
	(0.69)[b]		(0.59)[b]	(0.56)[b]		(0.47)[b]
6-Z	0.000000	0.000	0.000000	0.00024	0.000	0.000133
	(0.00)[b]		(0.00)[b]	(0.15)[b]		(0.08)[b]
6-E	0.000264	0.248	0.000146	0.00000	0.226	0.0000000
	(0.17)[b]		(0.09)[b]	(0.00)[b]		(0.00)[b]
7-Z	0.000000	0.000	0.000000	0.000000	0.000	0.000000
	(0.00)[b]		(0.00)[b]	(0.00)[b]		(0.00)[b]
7-E	0.002920	0.313	0.002771	0.002214	0.55	0.001952
	(1.83)[b]		(1.74)[b]	(1.39)[b]		(1.22)[b]
8-Z	0.000000	0.000	0.000000	0.000000	0.000	0.000000
	(0.00)[b]		(0.00)[b]	(0.00)[b]		(0.00)[b]
8-E	0.001522	0.360	0.001351	0.00121	0.457	0.000993
	(0.96)[b]		(0.85)[b]	(0.76)[b]		(0.62)[b]
9-Z	0.000000	0.000	0.000000	0.000564	0.000	0.000000
	(0.00)[b]		(0.00)[b]	(0.35)[b]		(0.00)[b]
9-E	0.000643	0.310	0.000496	0.000000	0.397	0.000375
	(0.40)[b]		(0.31)[b]	(0.00)[b]		(0.23)[b]

[a]Relative to the most stable form.

[b]Numbers in parenthesis are in kcal mol^{-1} (1 cal = 4.184 J).

[c]From Raman and IR techniques, see ref. 15.

[d]From gas electron diffraction (GED), see ref. 11.

Stabilization energies and GAE

The NBO analysis shows that the E and Z conformations of compounds **1**–**9** benefit from the stabilization energies associated with the donor–acceptor electron delocalizations. Based on the optimized ground-state geometries using the B3LYP method, the NBO analysis of donor–acceptor (bond–antibond) interactions showed that the stabilization energies associated with $LPN_3 \rightarrow \sigma^*_{C2-Y1}$ electron delocalization for the Z conformations of compounds **1**–**3** are 8.81, 9.21, and 9.15 kcal mol^{-1}, respectively. Also, the stabilization energies associated with $LPN_3 \rightarrow \sigma^*_{C2-Y1}$ electron delocalization for the E conformations of compounds **1**–**3** are 1.97, 2.91, and 2.94 kcal mol^{-1}, respectively (see Table 2). Based on the results obtained, there are no significant differences between the stabilization energies associated with $LPN_3 \rightarrow \sigma^*_{C2-Y1}$ electron delocalization for the Z and E conformations of compounds **1**–**3**. Therefore, the stabilization energies associated with $LPN_3 \rightarrow \sigma^*_{C2-Y1}$ electron delocalizations cannot explain the increase of the E conformation stability from compound **1** to compound **3**. This fact can be seen in compounds **4**–**6** and **7**–**9** (see Tables 1 and 2).

Interestingly, the stabilization energy associated with $LPN_3 \rightarrow \sigma^*_{C2-X6}$ electron delocalization increases from the E conformation of compound **1** to compound **3**, compound **4**

Can. J. Chem. Downloaded from www.nrcresearchpress.com by Renmin University of China on 09/02/12
For personal use only.

Table 2. Natural bond orbital (NBO) calculated stabilization energies (E_2, in kcal mol^{-1}), generalized anomeric effects (GAEs, in kcal mol^{-1}), WBI), dipole moments (in debye), and total steric exchange energies (TSEEs, in kcal mol^{-1}) based on the calculated geometries using

	Compound							
Parameter	**1**		**2**		**3**		**4**	
	Z	E	Z	E	Z	E	Z	E
E_2								
$LPN_3 \rightarrow \sigma^*_{C2-Y1}$	9.10	1.97	9.36	2.91	9.27	2.94	9.64	0.84
$LP_1Y_1 \rightarrow \sigma^*_{C2-N3}$	2.35	2.85	2.27	2.47	2.27	2.41	4.55	4.69
$LP_2Y_1 \rightarrow \sigma^*_{C2-N3}$	25.57	24.39	26.13	24.61	25.07	23.62	12.98	12.16
$LP_1X_6 \rightarrow \sigma^*_{C2-Y1}$	1.01	0.98	1.42	0.96	1.34	0.77	1.53	1.51
$LP_2X_6 \rightarrow \sigma^*_{C2-Y1}$	8.36	7.54	5.98	5.55	4.67	4.41	6.60	6.15
$LP_3X_6 \rightarrow \pi^*_{C2-Y1}$	30.00	26.82	20.47	17.48	15.93	13.37	30.91	27.85
$LP_2X_6 \rightarrow \pi^*_{C4-O5}$	—	0.52	—	1.04	—	1.24	—	—
$LP_1X_6 \rightarrow \sigma^*_{C2-N3}$	—	—	0.57	0.58	0.54	0.58	—	—
$LP_2X_6 \rightarrow \sigma^*_{C2-N3}$	7.31	7.42	4.66	4.56	3.38	3.24	8.57	8.83
$LPN_3 \rightarrow \sigma^*_{C2-X6}$	6.16	12.51	2.97	15.49	2.70	17.55	9.25	14.50
GAE	89.86	85.00	73.83	75.65	65.17	70.13	84.03	76.53
GAE_{E-Z}	–4.86		1.82		4.96		–7.5	
Orbital occupancy								
LPN_3	1.68446	1.67733	1.68187	1.66771	1.67923	1.66427	1.66412	1.65168
σ^*_{C2-X6}	0.13500	0.15803	0.14847	0.18816	0.16573	0.21359	0.12269	0.14003
Orbital energy								
LPN_3	–0.40869	–0.40560	–0.40087	–0.39901	–0.39867	–0.39999	–0.39095	–0.38190
σ^*_{C2-X6}	0.21647	0.18538	0.06997	0.04144	0.01029	–0.01428	0.20311	0.17966
$\Delta(E\sigma^*_{C2-X6} - E_{LPN3})$	0.62516	0.59098	0.47084	0.44045	0.40896	0.38571	0.59406	0.56156
$F(i,j)$								
$LPN_3 \rightarrow \sigma^*_{C2-X6}$	0.058	0.080	0.035	0.077	0.031	0.076	0.070	0.085
Dipole moment								
μ	1.4914	1.7764	1.3091	1.6509	1.2573	1.5928	1.1551	1.1048
$\Delta\mu_{E-Z}$	0.2850		0.3418		0.3355		–0.0503	
Natural charge								
X_6	–0.33192	–0.35983	–0.00618	–0.06709	0.03895	–0.03484	–0.32140	–0.34354
C_4	0.91485	0.90661	0.91616	0.90836	0.91992	0.90797	0.92415	0.90054
Bond order (WBI)								
$C_2–X_6$	0.8797	0.8413	1.0151	0.9559	0.9836	0.9198	0.8892	0.8582
$\Delta(WBI(C_2–X_6)_{Z-E}$	0.0384		0.0592		0.0638		0.0310	
TSEE	155.01	153.45	165.28	151.50	168.88	149.86	183.61	192.11
$\Delta(TSEE_Z - TSEE_E)$	1.56		13.78		19.02		–8.5	

to compound **6**, and also from compound **7** to compound **9**. This follows the same trend with the increase of the stability of the E conformation, when compared with the corresponding Z conformation, from compound **1** to compound **3**, compound **4** to compound **6**, and also from compound **7** to compound **9**.

More interestingly, there is an intriguing through-space electron delocalization ($LP_2X_6 \rightarrow \pi^*_{C4-O5}$) in the E conformations of compounds **1**–**9** that justifies the increase of the stability of the E conformations, when compared with their corresponding Z conformations (see Fig. 1). The stabilization energies associated with $LP_2X_6 \rightarrow \pi^*_{C4-O5}$ electron delocalization for the E confrmations of compounds **1**–**3** are 0.52, 01.04, and 1.24 kcal mol^{-1}, respectively. Also, the NBO results show that the natural negative charges of the halogen atoms of the E conformations decrease on going from fluorine to bromine atoms (see Table 2). This fact can be attributed to the decrease of the electronegativity of the halogen atoms on going from fluorine to bromine atoms. Consequently, there are no increasing electrostatic stabilization interactions associated with the attractive interactions between the negative charges of the halogen atoms and the isocyanato carbon atom in the E conformations of compounds **1**–**3** (see Scheme 2).[11]

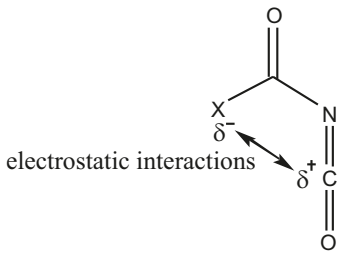
Based on eq. [2], the GAE values calculated (i.e., GAE_E–GAE_Z) associated with $LPN_3 \rightarrow \sigma^*_{C2-Y1}$, $LP_1Y_1 \rightarrow \sigma^*_{C2-N3}$, $LP_2Y_1 \rightarrow \sigma^*_{C2-N3}$, $LP_1X_6 \rightarrow \sigma^*_{C2-Y1}$, $LP_2X_6 \rightarrow \sigma^*_{C2-Y1}$, $LP_3X_6 \rightarrow \pi^*_{C2-Y1}$, $LP_2X_6 \rightarrow \pi^*_{C4-Y5}$, $LP_1X_6 \rightarrow \sigma^*_{C2-N3}$, $LP_2X_6 \rightarrow \sigma^*_{C2-N3}$, and $LPN_3 \rightarrow \sigma^*_{C2-X6}$ electronic delocalization for compounds **1**–**3** are –4.86, 1.82, and 4.96 kcal mol^{-1}, respectively (see Table 2). The GAE decreases from compound **1** to compound **3**. The stability of the E conformation, when compared with its corresponding Z conformation, increases from compound **1** to compound **3**, the rationalization of the conformational preference being accounted for solely in terms of the GAE. Similar to the trend observed for compounds **1**–**3**, the GAE succeeds in qualitatively accounting for the increase of the E conformation preferences from compound **4** to compound **6** and also from compound **7** to compound **9**.

Both methods revealed that the Z conformation preference in compounds **1**, **4**, and **7** increases from compound **1** to

off-diagonal elements ($F(i,j)$, in atomic units), orbital energies (in atomic units), orbital occupancies, bond orders (Wiberg bond index, B3LYP/Def2-TZVPP level of theory, for the conformations of compounds **1**–**9** (1 cal = 4.184 J).

5		**6**		**7**		**8**		**9**	
Z	E	Z	E	Z	E	Z	E	Z	E
10.33	1.39	10.34	1.44	10.05	0.89	10.90	1.60	10.90	1.71
5.34	5.09	5.91	5.34	4.81	4.88	5.70	5.19	6.33	5.59
13.90	12.71	13.03	12.11	9.53	8.88	10.20	9.42	9.55	8.94
2.96	2.49	3.05	2.40	1.54	1.55	3.17	2.81	3.38	2.82
4.96	4.78	3.81	3.91	6.56	6.11	5.06	4.79	3.88	3.87
23.29	20.40	18.50	16.16	31.89	28.75	25.04	22.10	20.20	17.72
—	0.70	—	0.83	—	—	—	0.54	—	0.63
0.60	0.88	0.56	0.89	—	—	0.64	0.96	0.63	1.01
6.31	6.44	4.79	4.70	8.81	9.09	6.82	7.03	5.31	5.28
5.42	17.48	5.45	20.10	9.50	15.02	5.70	17.80	5.73	20.44
73.11	72.36	65.44	67.88	82.69	75.17	73.23	72.24	65.91	68.01
–0.75		2.44		–7.52		–0.99		2.10	
1.65251	1.63403	1.64388	1.62750	1.65997	1.64333	1.64759	1.62164	1.63874	1.61470
0.12655	0.15896	0.14941	0.18969	0.10871	0.12470	0.10830	0.13752	0.12761	0.16491
–0.37866	–0.36959	–0.37328	–0.36782	–0.38917	–0.37625	–0.37493	–0.36138	–0.36971	–0.35917
0.07404	0.04864	0.01343	–0.00752	0.20828	0.18452	0.08227	0.05915	0.02094	0.00091
0.4527	0.41823	0.38671	0.3603	0.59745	0.56077	0.4572	0.42053	0.39065	0.36008
0.047	0.081	0.043	0.080	0.072	0.087	0.049	0.082	0.045	0.081
0.8234	0.8404	0.7327	0.7335	1.1072	0.9888	0.7469	0.7034	0.6598	0.5905
0.017		0.0008		–0.1184		–0.0435		–0.0693	
0.06562	0.01499	0.11885	0.05885	–0.32244	–0.34181	0.07935	0.03254	0.14094	0.08452
0.91413	0.89862	0.91231	0.90252	0.91881	0.89775	0.91588	0.89536	0.91237	0.89797
1.0442	0.9991	0.9995	0.9524	0.8985	0.8696	1.0697	1.0274	1.0289	0.9830
0.0451		0.0471		0.0289		0.0423		0.0459	
207.50	202.56	215.46	204.95	198.35	208.41	225.45	224.68	237.51	224.52
4.94		10.51		–10.06		0.77		12.99	

Scheme 2. Schematic representation of the electrostatic interactions between the halides and the isocyanato carbon atom in the E conformations



compound **7**. The CBS-QB3 calculated ΔG_{E-Z} values for compounds **1**, **4**, and **7** are 0.65, 1.37, and 1.74 kcal mol^{-1}, respectively. The B3LYP/Def2/TZVPP calculated ΔG_{E-Z} values for compounds **1**, **4**, and **7** are in agreement with the CBS-QB3 results (see Table 1). This fact can be attributed to an increase of the total GAE from compound **1** to compound **7**. The calculated GAE for compounds **1**, **4**, and **7** are –4.86, –7.50, and –7.52 kcal mol^{-1}, respectively.

Orbital occupancies

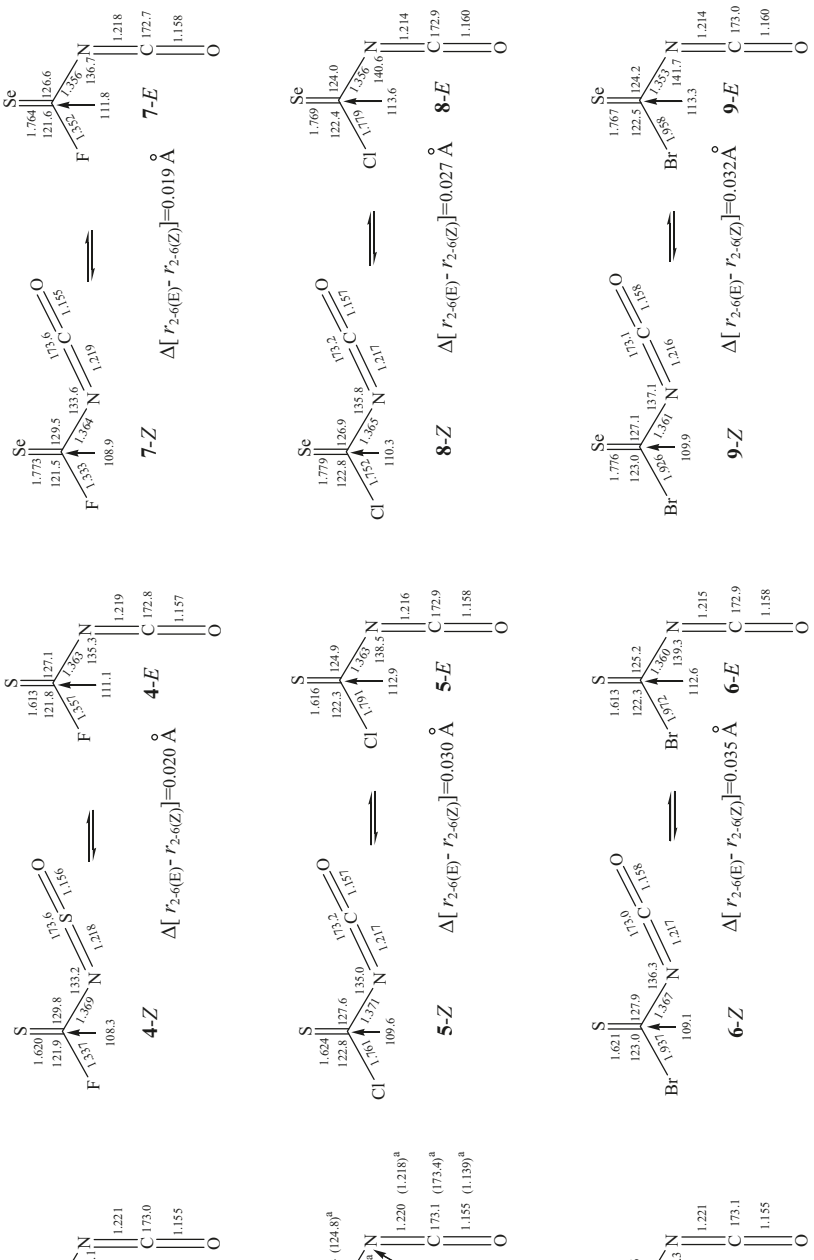
The orbital occupancies of the most effective electron delocalization that have the most impact on the GAE of the E conformations of compounds **1**–**9** (i.e., $LPN_3 \rightarrow \sigma^*_{C2-X6}$) have been investigated. The NBO results showed that the LPN_3 nonbonding orbital occupancies in the E conformations of compounds **1**–**3** are 1.677, 1.667, and 1.664, respectively. Also, the σ^*_{C2-X6} antibonding orbital occupancies in the E conformations of compounds **1**–**3** are 0.158, 0.188, and 0.214, respectively.

Similar to the trend observed for compounds **1**–**3**, the LPN_3 nonbonding orbital occupancies in the E conformations decreased from compound **4** to compound **6** and from compound **7** to compound **9**, and the σ^*_{C2-X6} antibonding orbital occupancies increased (see Table 2). This fact could be justified by the increase of the $LPN_3 \rightarrow \sigma^*_{C2-X6}$ electron delocalization from the E conformations of compound **1** to

Can. J. Chem. Downloaded from www.nrcresearchpress.com by Renmin University of China on 09/02/12
For personal use only.

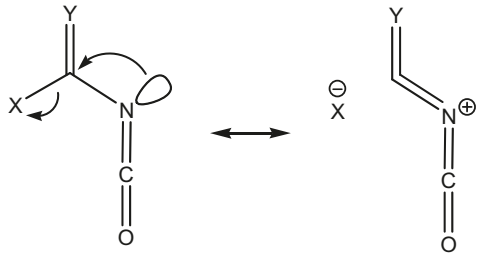
Can. J. Chem. Downloaded from www.nrcresearchpress.com by Renmin University of China on 09/02/12
For personal use only.

Fig. 2. B3LYP/6–311+G** calculated structural parameters for the Z and E conformations of compounds **1**–**9**. The calculated bond length and bond angle values are in Å and °, respectively. [a]From gas electron diffraction (GED). See ref. 11.



Can. J. Chem. Downloaded from www.nrcresearchpress.com by Renmin University of China on 09/02/12
For personal use only.

Scheme 3. Schematic representation of the $LPN_3 \rightarrow \sigma^*_{C2-X6}$ electron delocalization in the E conformations (as a no bond – double bond model).



compound **3**, compound **4** to compound **6**, and also from compound **7** to compound **9**.

Orbital energies and off-diagonal elements

It has to be noted that the stabilization energies associated with electron delocalization are proportional to $F_{i,j}^2/\Delta E_{ij}$ where $F_{i,j}$ is the orbital overlap integral (or off-diagonal elements of the secular determinant) and $\Delta E_{i,j}$ is the energy difference between the donor bonding (or nonbonding) and σ* (or π*) antibonding orbitals. The stereoelectronic orbital interactions are anticipated to be more effective for the anti rather than the syn or gauche arrangement between the donor and acceptor orbitals. Also, the stabilization (resonance) energy associated with the electron delocalization may increase as the acceptor orbital energy decreases and the donor orbital energy increases.

The energy differences between donor (E_{LPN_3}) and acceptor ($E\sigma^*_{C2-X6}$) orbitals (i.e., $\Delta(E\sigma^*_{C2-X6} - E_{LPN_3})$) for the E conformations of compounds **1–3** are 0.59098, 0.44045 and 0.38571, respectively, as calculated by the NBO analysis. The energy differences between LPN_3 (donor) nonbonding and σ^*_{C2-X6} (acceptor) antibonding orbitals (i.e., $\Delta(E\sigma^*_{C2-X6} - E_{LPaxM1})$) decrease from the E conformations of compound **1** to compound **3** (see Table 2). The strong acceptor antibonding orbital of the E conformation of compound **3** ($E\sigma^*_{C2-X6} = -0.01428$ atomic unit), when compared with those in compounds **2** and **1** (0.4144 and 0.18537 atomic unit, respectively), gives rise to strong $LPN_3 \rightarrow \sigma^*_{C2-X6}$ electron delocalization. On the other hand, the decrease of the *orbital overlap integral* (S) (i.e., off-diagonal elements ($F_{i,j}$)) values could reduce the $LPN_3 \rightarrow \sigma^*_{C2-X6}$ electron delocalization (see Table 2). NBO calculated $F_{i,j}$ values for the $LPN_3 \rightarrow \sigma^*_{C2-X6}$ electron delocalization for the E conformations of compounds **1–3** are 0.080, 0.077, and 0.076 atomic unit, respectively. The decrease of $F_{i,j}$ values could be justified by the increase of the X atom radius from compound **1** to compound **3**. Consequently, it seems that in the E conformations of compounds **1–3** the $\Delta(E\sigma^*_{C2-X6} - E_{LPaxM1})$ values could affect and control the order of the stabilization energies associated with $LPN_3 \rightarrow \sigma^*_{C2-X6}$ electron delocalizations. This conclusion can be generalized for compounds **4–6** and **7–9**.

Dipole moments

In the gas phase it is generally found that the conformation with the larger electrostatic energy (i.e., the larger dipole moment) has an increased overall energy.[53]

Liu and co-workers[54,55] pointed out that the total dipole moment change is a reasonable descriptor of the total energy difference; however, these correlations are not strong enough. It seems using any of the electron delocalization and electrostatic interactions alone is not adequately convincing to explain the general validity of the anomeric effect. Also, they stressed another explanation in terms of exchange–correlation and electrostatic interactions.

In this work, we have examined the contribution of the electrostatic interactions (by the calculation of the total dipole moment values)[53–56] on the total energy differences between the E and Z conformations of compounds **1–3**, **4–6**, and **7–9**. The calculated dipole moments for the E and Z conformations of compounds **1–3**, **4–6**, and **7–9** are given in Table 2. Using the dipole moments obtained, a "Δ" parameter could be found as $\Delta\mu_{E-Z}$. The corresponding $\Delta\mu_{E-Z}$ value increases from compound **1** to compound **2**, but decreases slightly from compound **2** to compound **3**. On the other hand, the calculated $\Delta\mu_{E-Z}$ value decreases from compound **4** to compound **6**. Interestingly, the calculated $\Delta\mu_{E-Z}$ value decreases from compound **7** to compound **8**, but increases from compound **8** to compound **9**. Therefore, the variations of the the calculated $\Delta\mu_{E-Z}$ value are not the same trend observed for the corresponding ΔG_{E-Z} values (i.e., the total energy differences). It seems the calculated $\Delta\mu_{E-Z}$ values fail to account for the increase of the calculated ΔG_{E-Z} values from compound **1** to compound **3**, compound **4** to compound **6**, and also from compound **7** to compound **9**. Therefore, the electrostatic interactions are not solely responsible for the total energy differences between the E and Z conformations of compounds **1–9** and it seems the GAE associated with the electron delocalization is a reasonable descriptor of the total energy differences between the E and Z conformations of compounds **1–9**.

Bond orders

The $LPN_3 \rightarrow \sigma^*_{C2-X6}$ electron delocalizations can affect the bond orders (e.g., Wiberg bond index, WBI: the sum of squares of off-diagonal density matrix elements between atoms, as formulated in terms of the natural atomic orbital (NAO) basis set) of C_2–X_6 bonds. In this regard, the differences between the WBI of C_2–X_6 bonds in the Z and E conformations (i.e., $\Delta(WBI(C_2-X_6)_{Z-E})$) increase from compound **1** to compound **3**, compound **4** to compound **6**, and also from compound **7** to compound **9** (see Table 2). The variation of the calculated $\Delta(WBI(C_2-X_6)_{Z-E})$ parameters are in accordance with the increase of the calculated GAE from compound **1** to compound **3**, compound **4** to compound **6**, and also from compound **7** to compound **9** (see Table 2).

Total steric exchange energies (TSEEs)

NBO analysis was used to calculate the steric exchange contributions in the Z and E conformations of compounds **1–9**. Contrary to the increase of the halogen atom radii from compounds **1→3**, **4→6**, and **7→9**, the differences between the calculated TSEE values for the Z and E conformations, $\Delta(TSEE_{Z-E})$, increase (see Table 2). The increase of the calculated $\Delta(TSEE_{Z-E})$ values can be justified by the increase of the C–X bond length from compounds **1→3**, **4→6**, and **7→9**. Therefore, the increase of the calculated $\Delta(TSEE_{Z-E})$ values

Can. J. Chem. Downloaded from www.nrcresearchpress.com by Renmin University of China on 09/02/12
For personal use only.

from compounds **1**→**3**, **4**→**6**, and **7**→**9** increases the relative stabilities of the E conformations compared with their corresponding Z conformations. Consequently, the variation of the calculated $\Delta(TSEE_{Z-E})$ values is in the same trend observed for the variation of the GAE values (see Table 2).

Structural parameters

Representative structural parameters for the E and Z conformations of compounds **1**–**9**, as calculated at the B3LYP/Def2-TZVPP level of theory, are shown in Fig. 2. Although it is not expected, in principle, to obtain exactly the experimental values because of the differences in the definition of bond length values, it is possible to carry out theoretical calculations, from which many properties and structures can be obtained with an accuracy that is competitive with experiment.

Importantly, the B3LYP/Def2-TZVPP results show that the C_2–X_6 bond lengths in the E conformations of compounds **1**–**9** are significantly longer than those of their corresponding Z conformations (see Fig. 2). In addition, the $\theta_{X6-C2-N3}$ bond angles of the Z conformations are smaller than those in the E conformations. This can be explained by the large $LPN_3 \rightarrow \sigma^*_{C2-X6}$ electron delocalization in the E conformations by increasing π-bond character of the N_3–C_2 bonds (see Scheme 3).

Using the structural parameters obtained, Δ parameters could be found as $\Delta[r_{2-6}(E) - r_{2-6}(Z)]$. The results obtained show that with the increase of the stabilization energies associated with $LPN_3 \rightarrow \sigma^*_{C2-X6}$ electron delocalizations in the E conformations of compounds **1**–**3**, **4**–**6**, and **7**–**9**, the calculated $\Delta[r_{2-6}(E) - r_{2-6}(Z)]$ parameter values increase from compound **1** to compound **3**, compound **4** to compound **6**, and also from compound **7** to compound **9** (see Table 2 and Fig. 2).

There is a direct correlation between the stabilization energies associated with $LPN_3 \rightarrow \sigma^*_{C2-X6}$ electron delocalizations and the calculated GAE values in compounds **1**–**9**. Consequently, the calculated $\Delta[r_{2-6}(E) - r_{2-6}(Z)]$ parameter could be proposed as a criterion for the evaluation of the GAE values in compounds **1**–**9**.

Conclusion

The CBS-QB3 and B3LYP/Def2-TZVPP calculations reported above and the NBO analysis provided a reasonable picture from structural, energetic, bonding, and stereoelectronic points of view for the conformational behavior in compounds **1**–**9**. Effectively, CBS-QB3 and B3LYP/Def2-TZVPP results revealed that the calculated ΔG_{E-Z} values increase from compound **1** to compound **3**, compound **4** to compound **6**, and also from compound **7** to compound **9**. A similar trend was observed for the calculated GAE (i.e., $GAE_E - GAE_Z$) and the differences between the calculated TSEE values for the Z and E conformations, $\Delta(TSEE_{Z-E})$. Accordingly, the correlations between the GAE, $\Delta(TSEE_{Z-E})$, and the calculated ΔG_{E-Z} values are strong enough. Consequently, the rationalization of the conformational preference in terms of the GAE and $\Delta(TSEE_{Z-E})$ succeeds in accounting for the increase of the E conformation stability from compound **1** to compound **3**, compound **4** to compound **6**, and also from compound **7** to compound **9**.

Importantly, the variations of the calculated $\Delta\mu_{E-Z}$ values from compound **1** to compound **3**, compound **4** to compound **6**, and also from compound **7** to compound **9** are not the same trend observed for the corresponding ΔG_{E-Z} values. Therefore, a reasonable correlation between the dipole moment differences and total energy differences was not found.

The longer C_2–X_6 bond lengths in the E conformations compared with those of their corresponding Z conformations can be explained by the large $LPN_3 \rightarrow \sigma^*_{C2-X6}$ electron delocalization in the E conformations by decreasing σ-bond character of the C_2–X_6 bonds. Importantly, the calculated $\Delta[r_{2-6}(E) - r_{2-6}(Z)]$ parameter could be proposed as a criterion for the evaluation of the GAE values in the E and Z conformations of compounds **1**–**9**.

References

(1) Deslongchamps, P. In *Stereoelectronic Effects in Organic Chemistry;* Baldwin, J. E., Ed.; Pergamon Press: Oxford, 1983.
(2) Kirby, A. J. *The Anomeric Effect and Related Stereoelectronic Effects;* Springer-Verlag: Berlin, 1983.
(3) Juarisi, E. *Introduction to Stereochemistry and Conformational Analysis;* Wiley: New York, 1991.
(4) Noe, E. A. Cf.; Sanders, T.; Garahi, M.; Hosseini, H.; Young, R. *J. Am. Chem. Soc.* **1985**, *107* (16), 4785. doi:10.1021/ja00302a034.
(5) Wiberg, K. B.; Laidig, K. E. *J. Am. Chem. Soc.* **1987**, *109* (20), 5935. doi:10.1021/ja00254a006.
(6) Yarkova, E. G.; Zobava, N. N.; Sagitova, R. N. *Zh. Strukt. Khim.* **1986**, *27*, 800 (English translation).
(7) Aminova, R. M.; Zobava, N. N.; Sagitova, R. N. *Dokl. Akad. Nauk SSSR* **1983**, *273*, 391 (English translation).
(8) Landsberg, B. M.; Iqbal, H. *J. Chem. Soc.* **1980**, *76* (2), 1208. doi:10.1039/F29807601208.
(9) Mack, H.-G.; Oberhammer, H.; Della Vedova, C. O. *J. Mol. Struct.* **1992**, *265* (3–4), 359. doi:10.1016/0022-2860(92)80113-V.
(10) Klapstein, D.; Nau, W. M. *Spectrochim. Acta A Mol. Biomol. Spectrosc.* **1994**, *50A*, 307. doi:10.1016/0022-2860(93)07865-T.
(11) Mack, H.-G.; Oberhammer, H.; Della Védova, C. O. *J. Mol. Struct. THEOCHEM* **1989**, *200*, 277. doi:10.1016/0166-1280(89)85060-2.
(12) Nguyen, M. T.; Hajnal, M. R.; Vanquickenborne, L. G. *J. Mol. Struct. THEOCHEM* **1991**, *231* (1–2), 185. doi:10.1016/0166-1280(91)85216-T.
(13) Jonas, V.; Frenking, G. *Chem. Phys. Lett.* **1991**, *177* (2), 175. doi:10.1016/0009-2614(91)90064-G.
(14) Al-Saadi, A. A.; Badawi, H. M. *J. Mol. Struct. THEOCHEM* **2002**, *582* (1–3), 11. doi:10.1016/S0166-1280(01)00776-X.
(15) Durig, J. R.; Guirgis, G. A.; Krutules, K. A.; Phan, H.; Stidham, H. D. *J. Raman Spectrosc.* **1994**, *25* (3), 221. doi:10.1002/jrs.1250250306.
(16) Klapstein, D.; Nau, W. M. *J. Mol. Struct.* **1994**, *317* (1–2), 59. doi:10.1016/0022-2860(93)07865-T.
(17) Mack, H.-G.; Della Védovab, C. O.; Willnerc, H. *J. Mol. Struct.* **1993**, *291* (2–3), 197. doi:10.1016/0022-2860(93)85045-V.
(18) Sullivan, J. F.; Nandy, S. K.; Lee, M. J.; Durig, J. R. *J. Mol. Struct.* **1992**, *266*, 271. doi:10.1016/0022-2860(92)80078-V.
(19) Campbell, N. L.; Gillis, C. J.; Klapstein, D.; Nau, W. M.; Balfour, W. J.; Fougère, S. G. *Spectrochim. Acta [A]* **1995**, *51* (5), 787. doi:10.1016/0584-8539(94)00199-L.

Can. J. Chem. Downloaded from www.nrcresearchpress.com by Renmin University of China on 09/02/12
For personal use only.

(20) Eliel, E. L.; Wilen, S. H. *Stereochemistry of Organic Compounds;* Wiley: New York, 1994.
(21) Juaristi, E.; Gonzalez, E. A.; Pinto, B. M.; Johnston, B. D.; Nagelkerke, R. *J. Am. Chem. Soc.* **1989**, *111* (17), 6745. doi:10.1021/ja00199a038.
(22) Pinto, B. M.; Johnston, B. D.; Nagelkerke, R.; Juaristi, E.; Gonza'lez, E. A. *Can. J. Chem.* **1989**, *67* (12), 2067. doi:10.1139/v89-321.
(23) Kirby, A. J. *The Anomeric Effects and Related Stereoelectronic Effects at Oxygen;* Springer-Verlag: Berlin, 1983.
(24) Praly, J.-P.; Lemieux, R. U. *Can. J. Chem.* **1987**, *65* (1), 213. doi:10.1139/v87-034.
(25) Salzner, U.; Schleyer, P. R. *J. Am. Chem. Soc.* **1993**, *115* (22), 10231. doi:10.1021/ja00075a044.
(26) Schleyer, P. R.; Jemmis, E. D.; Spitznagel, G. W. *J. Am. Chem. Soc.* **1985**, *107* (22), 6393. doi:10.1021/ja00308a041.
(27) Reed, A. E.; Weinstock, R. B.; Weinhold, F. *J. Chem. Phys.* **1985**, *83* (2), 735. doi:10.1063/1.449486.
(28) Reed, A. E.; Curtiss, L. A.; Weinhold, F. *Chem. Rev.* **1988**, *88* (6), 899. doi:10.1021/cr00088a005.
(29) Bailey, W. F.; Eliel, E. L. *J. Am. Chem. Soc.* **1974**, *96* (6), 1798. doi:10.1021/ja00813a025.
(30) Kleinpeter, E. In *Conformational Behavior of Six-Membered Rings;* Juaristi, E., Ed.; VCH Publishers, Inc.: New York, 1995.
(31) Alabugin, I. V. *J. Org. Chem.* **2000**, *65* (13), 3910. doi:10.1021/jo991622+.
(32) Juaristi, E.; Cuevas, G.; Vela, A. *J. Am. Chem. Soc.* **1994**, *116* (13), 5796. doi:10.1021/ja00092a034.
(33) Cuevas, G.; Juaristi, E. *J. Am. Chem. Soc.* **2002**, *124* (44), 13088. doi:10.1021/ja020317u.
(34) Roux, M. V.; Temprado, M.; Jiménez, P.; Dávalos, J. Z.; Notario, R.; Martín-Valcárcel, G.; Garrido, L.; Guzmán-Mejía, R.; Juaristi, E. *J. Org. Chem.* **2004**, *69* (16), 5454. doi:10.1021/jo049435l.
(35) Frisch, M. J.; Trucks, G. W.; Schlegel, H. B.; Scuseria, G. E.; Robb, M. A.; Cheeseman, J. R.; Montgomery, J. A.; Vreven, T.; Kudin, K. N.; Burant, J. C.; Millam, J. M.; Iyengar, S. S.; Tomasi, J.; Barone, V.; Mennucci, B.; Cossi, M.; Scalmani, G.; Rega, N.; Petersson, G. A.; Nakatsuji, H.; Hada, M.; Ehara, M.; Toyota, K.; Fukuda, R.; Hasegawa, J.; Ishida, M.; Nakajima, T.; Honda, Y.; Kitao, O.; Nakai, H.; Klene, M.; Li, X.; Knox, J. E.; Hratchian, H. P.; Cross, J. B.; Bakken, V.; Adamo, C.; Jaramillo, J.; Gomperts, R.; Stratmann, R. E.; Yazyev, O.; Austin, A. J.; Cammi, R.; Pomelli, C.; Ochterski, J. W.; Ayala, P. Y.; Morokuma, K.; Voth, G. A.; Salvador, P.; Dannenberg, J. J.; Zakrzewski, V. G.; Dapprich, S.; Daniels, A. D.; Strain, M. C.; Farkas, O.; Malick, D. K.; Rabuck, A. D.; Raghavachari, K.; Foresman, J. B.; Ortiz, J. V.; Cui, Q.; Baboul, A. G.; Clifford, S.; Cioslowski, J.; Stefanov, B. B.; Liu, G.; Liashenko, A.; Piskorz, P.; Komaromi, I.; Martin, R. L.; Fox, D. J.; Keith, T.; Al-Laham, M. A.; Peng, C. Y.; Nanayakkara, A.; Challacombe, M.; Gill, P. M. W.; Johnson, B.; Chen, W.; Wong, M. W.; Gonzalez, C.; Pople, J. A. *Gaussian 03,* Revision B.03; Gaussian Inc.: Wallingford, CT, 2004.
(36) Becke, A. D. *J. Chem. Phys.* **1993**, *98* (7), 5648. doi:10.1063/1.464913.
(37) Lee, C.; Yang, W.; Parr, R. G. *Phys. Rev. B* **1988**, *37* (2), 785. doi:10.1103/PhysRevB.37.785.
(38) Vosko, S. H.; Wilk, L.; Nusair, M. *Can. J. Phys.* **1980**, *58* (8), 1200. doi:10.1139/p80-159.
(39) Stephens, P. J.; Devlin, F. J.; Chabalowski, C. F.; Frisch, M. J. *J. Phys. Chem.* **1994**, *98* (45), 11623. doi:10.1021/j100096a001.
(40) Johnson, B. G. In *Modern Density Function Theory. A Tool for Chemistry;* Seminario, J. M., Politzer, P., Eds.; Elsevier: Amsterdam, 1995.
(41) Weigend, F.; Ahlrichs, R. *Phys. Chem. Chem. Phys.* **2005**, *7* (18), 3297. doi:10.1039/b508541a.
(42) Nyden, M. R.; Petersson, G. A. *J. Chem. Phys.* **1981**, *75* (4), 1843. doi:10.1063/1.442208.
(43) Petersson, G. A.; Al-Laham, M. A. *J. Chem. Phys.* **1991**, *94* (9), 6081. doi:10.1063/1.460447.
(44) Petersson, G. A.; Tensfeldt, T. G.; Montgomery, J. A., Jr. *J. Chem. Phys.* **1991**, *94* (9), 6091. doi:10.1063/1.460448.
(45) Ochterski, J. W.; Petersson, G. A.; Montgomery, J. A., Jr. *J. Chem. Phys.* **1996**, *104* (7), 2598. doi:10.1063/1.470985.
(46) Petersson, G. A.; Malick, D. K.; Wilson, W. G.; Ochterski, J. W.; Montgomery, J. A., Jr; Frisch, M. J. *J. Chem. Phys.* **1998**, *109* (24), 10570. doi:10.1063/1.477794.
(47) Montgomery, J. A., Jr; Frisch, M. J.; Ochterski, J. W.; Petersson, G. A. *J. Chem. Phys.* **1999**, *110* (6), 2822. doi:10.1063/1.477924.
(48) Glendening, E. D.; Badenhoop, J. K.; Reed, A. E.; Carpenter, J. E.; Bohmann, J. A.; Morales, C. M.; Weinhold, F. *NBO,* Version 5.G; Theoretical Chemistry Institute, University of Wisconsin: Madison, WI, 2004.
(49) Epiotis, N. D.; Yates, R. L.; Larson, R. J.; Kirmaier, C. R.; Bernardi, F. *J. Am. Chem. Soc.* **1977**, *99* (26), 8379. doi:10.1021/ja00468a001.
(50) Dionne, P.; St-Jacques, M. *J. Am. Chem. Soc.* **1987**, *109* (9), 2616. doi:10.1021/ja00243a012.
(51) Nori-Shargh, D.; Hassanzadeh, N.; Kosari, M.; Rabieikarahroudi, P.; Yahyaei, H.; Sharifi, S. *Can. J. Chem.* **2010**, *88* (7), 579. doi:10.1139/V10-022.
(52) Weinhold, F. *Angew. Chem. Int. Ed.* **2003**, *42* (35), 4188. doi:10.1002/anie.200351777.
(53) Wiberg, K. B.; Murcko, M. A. *J. Phys. Chem.* **1987**, *91* (13), 3616. doi:10.1021/j100297a030.
(54) Huang, Y.; Zhong, A. G.; Yang, Q.; Liu, S. *J. Chem. Phys.* **2011**, *134* (8), 084103. doi:10.1063/1.3555760.
(55) Liu, S. B. *J. Chem. Phys.* **2007**, *126* (24), 244103. doi:10.1063/1.2747247.
(56) Mo, Y. *Nat. Chem.* **2010**, *2* (8), 666. doi:10.1038/nchem.721.

Quasi-classical trajectory calculation of the chemical reaction Sr + CF_3I

Wenwen Xia, Xinting Huang, Li Yao, and Haiyang Zhong

Can. J. Chem. Downloaded from www.nrcresearchpress.com by Renmin University of China on 09/02/12
For personal use only.

Abstract: In this paper, the dynamical properties of the product SrI, which is formed in the reaction Sr + CF_3I, were studied by means of the quasi-classical trajectory method based on the extended London–Eyring–Polanyi–Sato potential energy surface. The vibrational distribution, rotational distribution, reaction cross section, and rotational alignment of the product SrI were calculated, and the mechanism of the title reaction has also been discussed. The calculated vibrational and rotational distributions show that their peak values are located at $v = 23$ and $J = 110$ at a collision energy of $E_{col} =$ 0.83 eV. These results are in good agreement with the results in Stolte's experiment. And the results obtained in this paper also indicate that the reaction cross section increases with increasing collision energy (from 0.5 to 1.5 eV), whereas the product rotational alignment decreases.

Key words: QCT method, LEPS PES, Sr + CF_3I reaction, dynamical property, reaction mechanism.

Résumé : Faisant appel à la méthode de la trajectoire quasi-classique basée sur la surface d'énergie potentielle étendue de London–Eyring–Polanyi–Sato, on a étudié les propriétés dynamiques du produit SrI qui se forme par la réaction Sr + CF_3I. On a calculé la distribution vibrationnelle, la distribution rotationnelle, la section droite de la réaction et l'alignement rotationnel du produit SrI et on discute aussi du mécanisme de la réaction mentionnée dans le titre. Les distributions vibrationnelle et rotationnelle montrent que leurs valeurs maximales se situent à $v = 23$ et $J = 110$, à une énergie de collision $E_{col} =$ 0,83 eV. Ces résultats sont en bon accord avec ceux obtenus dans l'expérience de Stolte. Et les résultats obtenus dans le présent travail indiquent aussi que la section droite de la réaction augmente avec une augmentation de l'énergie de collision de 0,5 à 1,5 eV, alors que l'alignement rotationnel du produit diminue.

Mots-clés : méthode de la trajectoire quasi-classique (TQC), surface d'énergie potentielle (SEP) étendue de London–Eyring–Polanyi–Sato (LEPS), réaction Sr + CF_3I, propriété dynamique, mécanisme de réaction.

[Traduit par la Rédaction]

Introduction

The CF_3I molecule is an important intermediate with fluoride that can introduce methyl fluoride into organic synthesis. Because of its strong reactivity, the CF_3I molecule can be dissociated easily in the lower atmosphere and usually does not reach the ozone layer. Therefore, its ozone depression potential (ODP) is zero and its global warming potential (GWP) is low.[1,2]

In recent years, the CF_3I molecule has been considered as a new type of environmentally friendly fire-extinguishing agent that can substitute for halon. As a result of the good oil soluble and material compatibility of the CF_3I molecule, it has been also considered as a latent substitute for refrigerants. At the same time, the CF_3I molecule has been widely applied to organic synthesis, biochemistry, surface active agents, dyes, and so on.[3] The electronic structure, the bonding properties, and the reactive property of the CF_3I molecule have become the focal point in experimental and theoretical studies.[4–11] Arai and co-workers[12] successfully developed a novel vapor-phase production process for CF_3I, which was obtained from the reaction of $CHF_3 + I_2$ with a unique catalyst in 2004. They found that the most effective catalyst for this reaction was alkali metal salt on an activated carbon carrier.[12]

The "dual-mode" mechanism was first postulated by Brooks et al.[13] in the study of the reaction K + $CF_3I \rightarrow$ KI + CF_3, which corresponded to the title reaction of this paper. A bimodal vibrational distribution of the product BaBr for the reaction Ba + CF_3Br was obtained by means of the laser-induced fluorescence (LIF) method by Munakata et al.[14] The reaction mechanism was also explained by the dual-mode mechanism, which has an analogy with the reaction K + CF_3I. The reaction between ground-state Sr and CF_3Cl was in tandem studied by Solarz and Johnson[15] in 1979 and Schifino and co-workers in 1993.[16] For the reaction Ba + CF_3I, Zare and co-workers[17,18] reported an analysis of the vibrational states of the product BaI using the LIF method. Lin et al.[19] deduced the recoil energy distributions and angular distributions for the reactions Ba + CH_3I, Ca + CH_3I, and Ba + CF_3I using a molecular beam apparatus.

Lou and co-workers[20,21] studied the reactions Ca + CH_3I and Ca + CF_3I and Ca(^{3}P) + CH_3I and Ca(^{3}P) + CF_3I in

Received 27 October 2011. Accepted 20 December 2011. Published at www.nrcresearchpress.com/cjc on 14 March 2012.

W. Xia, X. Huang, L. Yao, and H. Zhong. Institute of Computational Physics, Department of Physics, Dalian Maritime University, Dalian 116026, P.R. China.

Corresponding author: Li Yao (e-mail: yaoli@dlmu.edu.cn and haae@dlmu.edu.cn).

Can. J. Chem. Downloaded from www.nrcresearchpress.com by Renmin University of China on 09/02/12
For personal use only.

1988 and 1993. Energy partitioning, vibrational state distributions, and recoil momentum distributions of the product CaI were obtained from the studies of Ca + CH_3I and Ca + CF_3I.[20] The chemiluminescence (CL) spectra, collision cross sections, and CL cross sections of the reactions Ca(^{3}P) + CH_3I and Ca(^{3}P) + CF_3I were measured in a beam-gas arrangement.[21] Lou and co-workers[20,21] discovered that the sequence of the values of the cross sections for the reactions Ca(^{3}P) + CH_3I and Ca(^{3}P) + CF_3I was contrary to the results of the reactions Ca + CH_3I and Ca + CF_3I. Subsequently, the reaction of OH with CF_3I was investigated by Marshall and co-workers[22] via experimental and computational studies. The most correlative experiment with this work was the investigations of the reactions of Ca or Sr with CH_3X or CF_3X (X = Br or I) by Stolte and co-workers[23,24] With the LIF method, the experimental and simulated spectra and the vibrational and rotational distributions of nascent SrBr, SrI, and CaBr were measured.[23]

Recently, the exothermic reaction Sr + CH_3I was studied by means of the quasi-classical trajectory (QCT) method by Zhao and Li[25] They calculated the relationship of product energy disposal and product rotational alignment, respectively, with collision energy. The results for the reaction cross section and product vibrational distribution were also obtained in their work.[25]

As mentioned, there are a lot of experimental studies corresponding to the reaction Sr + CF_3I. In the previous papers,[26–28] some investigations for the reactions of alkaline earth metal atoms with halogenated methane were done by using the QCT method. However, there are no studies about the title reaction that have been carried out theoretically. Therefore, the QCT method based on an extended London–Eyring–Polanyi–Sato (LEPS) potential energy surface (PES) will be applied to study the dynamical properties of the reaction Sr + CF_3I in this paper.

Theory

Potential energy surface (PES)

Since constructing an accurate ab initio PES for the reaction Sr + CF_3I is difficult, an extended LEPS PES is employed in this work. In the QCT calculation, the LEPS PES is considered as a basis and can be described as follows:[29–31]

$$[1]\quad V(r_1, r_2, r_2) = Q_1 + Q_2 + Q_3 - (J_1^2 + J_2^2 + J_3^2 - J_1J_2 - J_2J_3 - J_1J_3)^{1/2}$$

where

$$[2]\quad Q_i = ({}^1E_i + {}^3E_i)/2$$

$$[3]\quad J_i = ({}^1E_i - {}^3E_i)/2$$

where ${}^1E_i$ is defined as the diatomic Morse potential function and ${}^3E_i$ stands for the anti-Morse function.

$$[4]\quad {}^1E_i = D_i\Big(\{1 - \exp[-\beta_i(r - r_0)]\}^2 - 1\Big)$$

$$[5]\quad {}^3E_i = {}^3D_i\Big(\{1 + \exp[-\beta_i(r - r_0)]\}^2 - 1\Big)$$

where

$$[6]\quad {}^3D_i = D_i(1 - S_i)/[2(1 + S_i)]$$

where S_i is an adjustable parameter (the so-called Sato parameter), whose value changes from –1.0 to 1.0. To achieve an exact LEPS PES, the Sato parameters have to be adjusted. First, they were adjusted to simulate the experimental result of the vibrational distribution in ref. 23. Once the theoretical result agreed with the experimental one, the obtained Sato parameters were used to calculate the other dynamical results of the reaction Sr + CF_3I. D_i, β_i, and R_i^0 are the Morse parameters of a semidiatomic molecule representing the classical dissociation energy, the spectrum constant, and the equilibrium nuclear separation, respectively. Subscripts i = 1, 2, and 3 indicate Sr–I, CF_3–I, and Sr–CF_3, respectively, for the title reaction.

In this paper, by means of these Morse parameters and Sato parameters, the LEPS PES of the title reaction can be constructed. Only the Morse parameters of Sr–I can be obtained from ref. 25, whereas the values of the other Morse parameters were not given in the corresponding literature.[1–25] Therefore, the Gaussian 03 program[32] was employed to calculate the Morse parameters of CF_3–I and Sr–CF_3 in this work.

The initial data in eqs. [7]–[9] were obtained by means of the Gaussian 03 program on the B3LYP/lanl2dz level.[32] The most stable configurations of CF_3–I and Sr–CF_3 can be found at the minimum energy level after the optimization. At the same time, the energy E_{HF} and equilibrium bond length R_i^0 can be obtained in the output files. Then from the frequency calculations of these configurations, the force constant (Frc) that corresponds to the stretching vibrational mode can be obtained in the output file. The Frc is a very important parameter that reflects the interactivity among atoms in a molecule (i.e., bond). The Frc is the second derivative of energy. It determines whether energy is becoming large or small. In other words, this can be described as uphill or downhill. Uphill indicates that the second derivative is negative, and downhill indicates that the second derivative is positive. Therefore, Frc has a relationship with molecular energy. In these calculations, the CF_3 group is treated as a rigid group because its internal configuration usually does not change during the reaction (checked by the Gaussian 03 program). After that, eqs. [7]–[9] were used to dispose of these initial data and obtain the Morse parameters.

$$[7]\quad D_i(\mathrm{AB}) = 27.2116[E_{\mathrm{HF}}(\mathrm{A}) + E_{\mathrm{HF}}(\mathrm{B}) - E_{\mathrm{HF}}(\mathrm{AB})]$$

$$[8]\quad K_e = 6.192\mathrm{Frc}$$

$$[9]\quad \beta_i = \sqrt{\frac{K_e}{2D_i}}$$

where K_e is the vibrational force constant.

For the reaction A + BC → AB + C, A stands for the Sr atom, B stands for the I atom, and C stands for the CF_3 group in this paper. In eq. [7], D_i is in eV and the single-point Hartree–Fock energy (E_{HF}) is in hartrees. In eq. [8], Frc is in mdyn/Å and K_e is in eV/Å^2. To use international units, the Gaussian system of units (mdyn/Å) has been

Table 1. The parameters used to construct the London–Eyring–Polanyi–Sato (LEPS) potential energy surface (PES) for the reaction Sr + CF_3I.

Species	D_i (eV)	β_i (Å^{-1})	R_i^0 (Å)	S_i (for $P(v)$)	S_i (for $P_v(J)$)
SrI	2.8210[25]	1.0100[25]	2.9800[25]	0.380	–0.100
CF_3I	2.1235	1.2657	2.1719	–0.350	–0.250
$SrCF_3$	1.8344	0.9446	2.6840	–0.055	–0.200

Note: S_i , Sato parameter; $P(v)$, vibrational distribution; and $P_v(J)$, rotational distribution. The values of D_i, β_i, and R_i^0 (Morse parameters for a semidiatomic molecule) were obtained from the Gaussian 03 program at the B3LYP/lanl2dz level and from ref. 25.

Table 2. The values of the maximum impact parameter (b_{max}) for the reaction Sr + CF_3I.

	E_{col} (eV)											
	0.5	0.6	0.7	0.8	0.83	0.9	1.0	1.1	1.2	1.3	1.4	1.5
b_{max}	2.55	2.60	2.70	2.75	2.75	2.80	2.85	2.80	2.80	2.80	2.80	2.80

Note: The values of b_{max} for the reaction Sr + CF_3I were calculated at different collision energies (E_{col}).

Can. J. Chem. Downloaded from www.nrcresearchpress.com by Renmin University of China on 09/02/12
For personal use only.

changed into kcal/mol/Å^2 (1 cal = 4.184 J). Because the unit of energy used in this paper is eV, the unit kcal/mol/Å^2 has been changed into eV/Å^2 (1 mdyn/Å = 144 × 4.3363 × 10^{-2} eV/Å^2 = 6.192 eV/Å^2).

To study all of the atomic collisions for the reaction Sr + CF_3I, the value of the maximum impact parameter (b_{max}) has to be determined during the calculation. The Morses and the Sato parameters of the reaction Sr + CF_3I are presented in Table 1. The values of b_{max} are listed in Table 2. All of the results of the reaction Sr + CF_3I can be obtained with these parameters.

Quasi-classical trajectory calculation

Hamilton's classical equations are numerically integrated by means of the conventional quasi-classical algorithm.[33,34] Previous theoretical studies[35–39] have already proven that the QCT method is good enough for the study of chemical reactions and has been chosen for this paper.

From a simulation and a comparison with the experimental results, the same collision energy with the experiment (0.83 eV) was chosen for use in this paper. In the calculations, a batch of 100 000 trajectories was sampled for each of the collision energies for the title reaction. The integration step size was chosen to be 0.1 fs for the conservation of total energy and angular momentum. Trajectories were initiated at an internuclear separation of 15 Å and for the CF_3I molecule at the ground-state level ($v = 0$, $j = 0$).

Product rotational alignment

In the study of a chemical reaction, the vector property also has to be considered. In this paper, the product rotational alignment of the reaction Sr + CF_3I was calculated with the method developed by Han and co-workers[29,40] A brief description is shown as follows.

During a reactive encounter, according to the conservation of the total angular momentum

$$[10] \qquad \mathbf{J} + \mathbf{L} = \mathbf{J}' + \mathbf{L}'$$

where $\mathbf{L}$ and $\mathbf{L}'$ are the reagent and product orbital momenta, respectively, and $\mathbf{J}$ and $\mathbf{J}'$ are the reagent and product rotational angular momenta, respectively. When $\mathbf{J}$ is small (as is common), the product rotation can only result from $\mathbf{L}$. $\mathbf{J}'$ can be described by a function $f(\theta)$, where θ is the angle between $\mathbf{J}'$ and the relative velocity vector $\mathbf{K}$. $f(\theta)$ can be expanded in a set of Legendre polynomials.[29,41]

$$[11] \qquad f(\theta) = \sum a_l P_l(\cos\theta)$$

where

$$[12] \qquad a_l = \frac{2l+1}{2}\int_{-1}^{+1} P_l(\cos\theta) f(\cos\theta) \mathrm{d}\theta$$

The coefficients a_0, a_1, and a_2 are used to represent the isotropic distribution, product rotational orientation, and product rotational alignment, respectively.

$$[13] \qquad a_2 = 5\langle P_2(\cos\theta)\rangle = 5\langle P_2(\mathbf{J}'\cdot\mathbf{K})\rangle$$

and

$$[14] \qquad \langle P_2(\mathbf{J}'\cdot\mathbf{K})\rangle = \left\langle \frac{3\cos^2\theta - 1}{2} \right\rangle$$

Here P_2 denotes the second item of the Legendre polynomial. The angular brackets in eq. [14] indicate an average over the distribution of $\mathbf{J}'$ about $\mathbf{K}$.[41]

The expected value of $\langle P_2(\mathbf{J}'\cdot\mathbf{K})\rangle$ is between 0.0 (randomly aligned) and –0.5 (completely aligned).[42] The maximum product rotational alignment usually occurs when the conditions $|\mathbf{L}| >> |\mathbf{J}|$ and $|\mathbf{L}'| >> |\mathbf{J}'|$ are satisfied. The first condition is satisfied for reactions with large cross sections, whereas the typical heavy + heavy–light (HHL) mass configuration leads to the second condition.[42] In other words, for the HHL mass combination, the product rotation is strongly aligned with the relative velocity of the reagent and the value of $\langle P_2(\mathbf{J}'\cdot\mathbf{K})\rangle$ should be equal to –0.5.[29]

Results and discussion

PES

The features of the LEPS PES constructed for the reaction Sr + CF_3I are the most basic conditions to obtain more precise results of the dynamical properties and study the reaction mechanism. Since the energy is released at different

Fig. 1. The plot of the London–Eyring–Polanyi–Sato (LEPS) potential energy surface (PES) for the reaction Sr + CF_3I. *R* is in Å and energy is in erg × 10^{16} (1 erg = 6.2415 × 10^{11} eV).

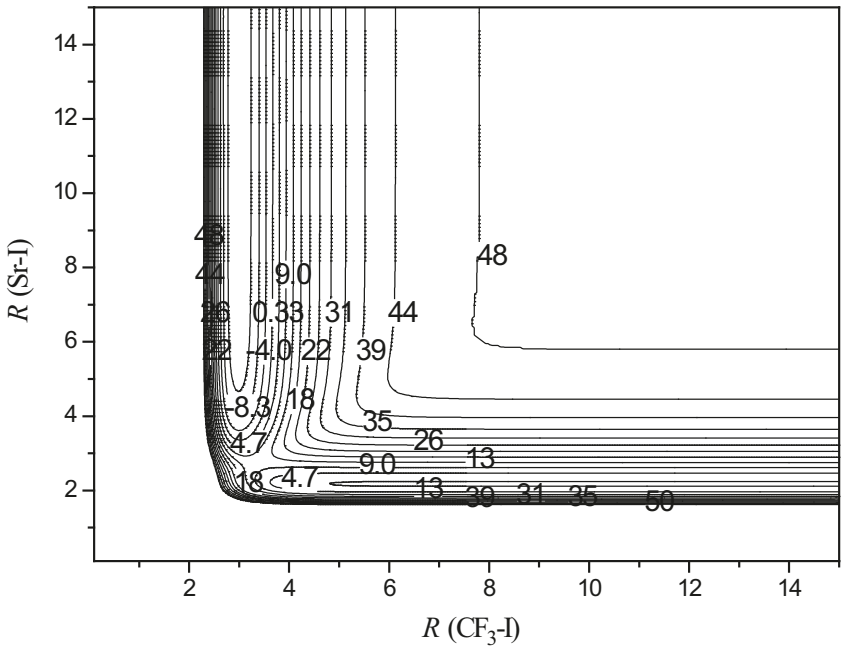
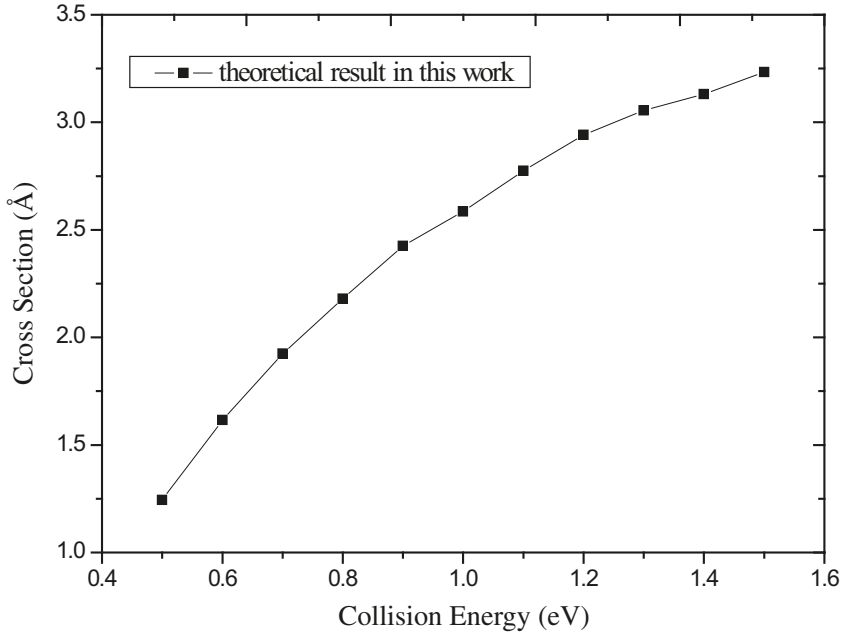


Fig. 2. The result of reaction cross section versus collision energy for the reaction Sr + CF_3I.



times in the reaction A + BC → AB + C, the PES can be divided into two types: attractive and repulsive PES. Energy is released when atom A approaches molecule BC for the attractive PES, and the potential energy is decreasing at the entrance valley of the reaction path. However, energy is released when atom C is dissociated from molecule AB for the repulsive PES, and the potential energy is decreasing at the exit valley. The LEPS PES of the title reaction was constructed using the method that is described in the theoretical part of this paper. The relevant parameters listed in Table 1 were obtained from ref. 25 and the Gaussian 03 program.

In this paper, the constructed PES is a repulsive PES and the contour plot of this extended LEPS PES is shown in Fig. 1. Based on it, the dynamical properties, just like the vibrational distribution, the rotational distribution, the reaction cross section, and the product rotational alignment, were calculated and the results are shown in the following section.

From Fig. 1, it can be seen that the potential energy gradually decreases along the minimum energy path, which is from the entrance ($R_{Sr,CF_3I} = \infty$, corresponding to the reactants) to the exit ($R_{SrI,CF_3} = \infty$, corresponding to the products). There is no potential well, but there is a reaction

Can. J. Chem. Downloaded from www.nrcresearchpress.com by Renmin University of China on 09/02/12
For personal use only.

Fig. 3. Vibrational distribution of product SrI obtained from the reaction Sr + CF_3I when the collision energy is 0.83 eV. The experimental result was obtained from Fig. 8 in ref. 23.

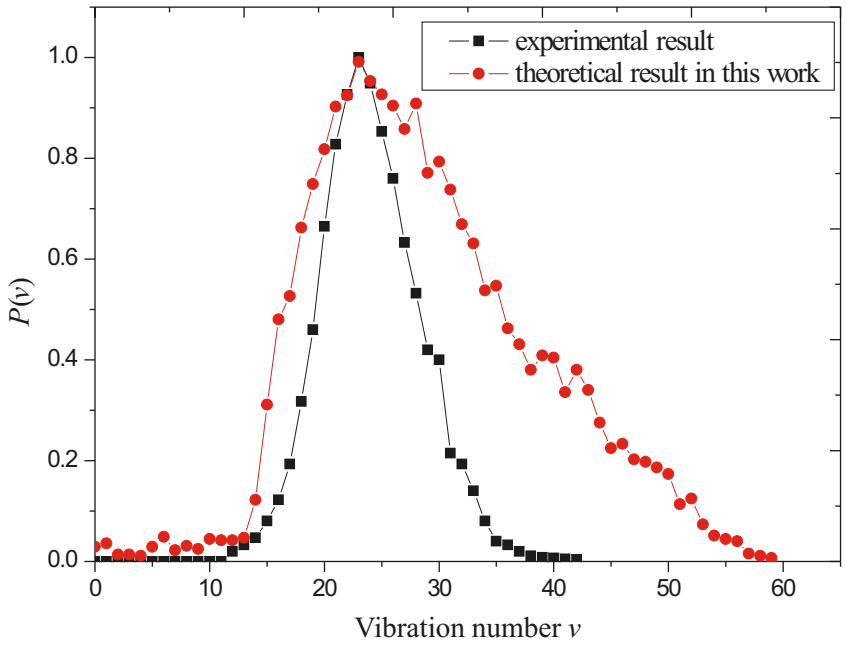
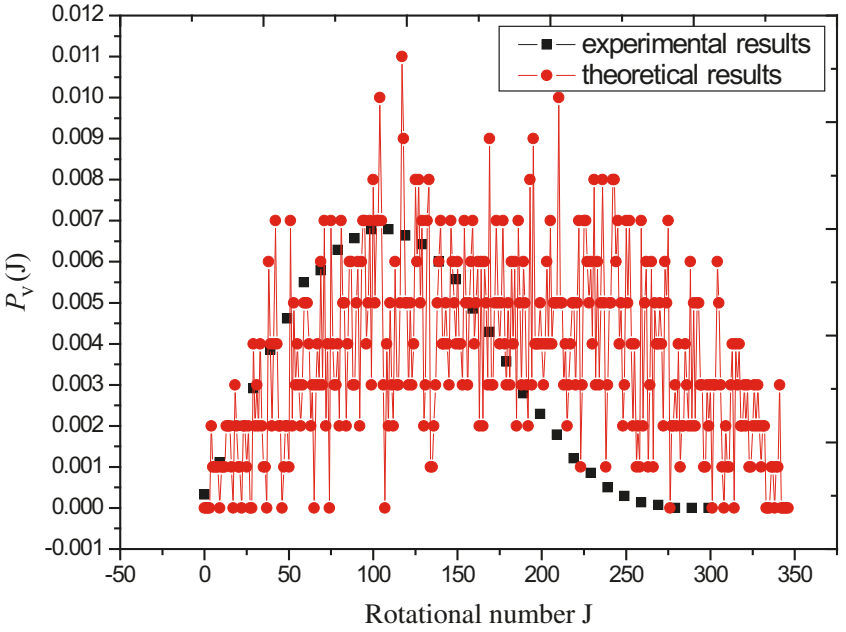


Fig. 4. Rotational distribution of product SrI obtained from the reaction Sr + CF_3I when the collision energy is 0.83 ev. The experimental result was obtained from Fig. 8 in ref. 23.



barrier with a value of 11.446 erg × 10^{16} (7.144 × 10^{-4} eV) existing in the entrance path of the LEPS PES in Fig. 1. This reaction barrier leads to the result that the reaction cross section increases with increasing collision energy, which is shown in Fig. 2.

Vibrational distribution

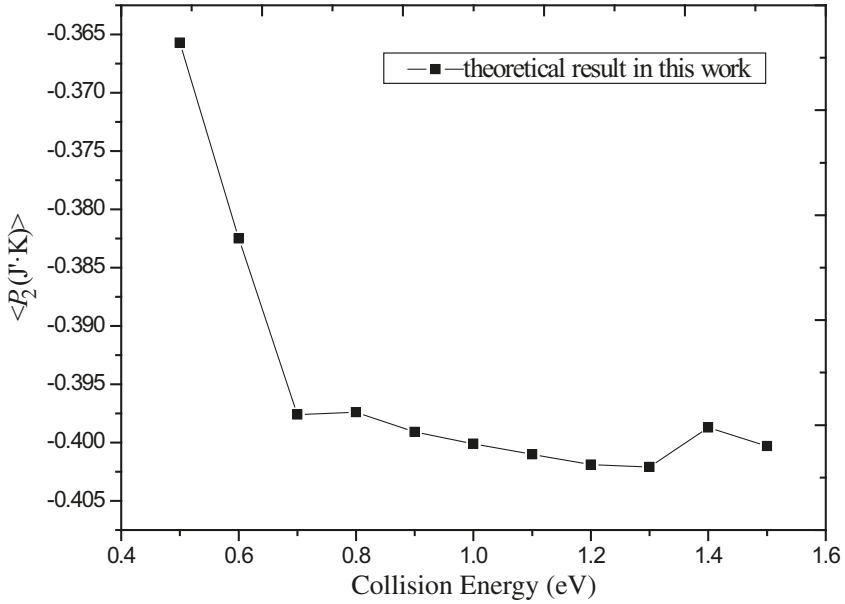
The theoretical result of the vibrational distribution for the reaction Sr + CF_3I is presented in Fig. 3 and it is compared with that of the experiment that is directly derived from Fig. 8 in ref. 23. The distribution can be described as a function of vibration quantum number. For the exactness of this comparison, the QCT calculation was carried out when the collision energy was equal to 0.83 eV and the trajectories were initiated at the ground state ($v = 0$, $j = 0$).

As for the title reaction, the QCT-calculated vibrational distribution of the product SrI is similar to a bell shape for the whole range of vibration quantum numbers $v = 0 \sim 60$. It can be seen from Fig. 3 that the value of the vibrational distribution changes from a regular increase to a decrease

Can. J. Chem. Downloaded from www.nrcresearchpress.com by Renmin University of China on 09/02/12
For personal use only.

Can. J. Chem. Downloaded from www.nrcresearchpress.com by Renmin University of China on 09/02/12
For personal use only.

Fig. 5. The result of product rotational alignment versus collision energy for the reaction Sr + CF_3I.



with increasing v. The peak values in the experimental and calculated results both appear when the value of v is equal to 23.

There are two pathways in the reactions of alkaline earth metal atoms (M) and halogenated alkanes, namely the abstraction reaction and the insertion reaction. If the repellant cannot be conquered by the collision energy in the process of the Sr atom attacking CF_3I in the repulsive area, which closes in on group CF_3, the insertion reaction will occur and thenthe Sr atom will shift to the attractive area, which closes in on atom I. But if the value of collision energy is large enough, the Sr atom and the CF_3I molecule can rapidly get close to each other and the C–I bond will fracture to form the product. This is the abstraction reaction. The vibrational distribution result strongly depends on the relative position of the halogen in the reactant and the direction of the M atom approaching the halogenated alkane.

It is necessary to draw a comparison between the theoretical result of the vibrational distribution and the experimental one. Unavoidably, some differences existing in the region around $v = 30 \sim 60$ are found in Fig. 3. Otherwise, the vibrational distribution of the product SrI calculated in this work agrees with the experimental result in ref. 23. These small differences in Fig. 3 are probably because the QCT calculation is taken at a single collision energy, only the ground state of reactants is considered, and the single-particle approximation for group CF_3 is used in this work. In other words, the complex process in the real reaction has been simplified in the theoretical simulation. Even so, the merits of the QCT method, which are simple, illustrative, and accurate, cannot be neglected by us. We often use the QCT method to treat some complex reaction systems instead of the quantum mechanics method. Generally speaking, the variational tendencies of these two results are similar to each other. The theoretical calculation in this work is still good for simulating the experimental result.

Rotational distribution

Figure 4 shows the experimental and the calculated rotational distributions of the product SrI formed in the reaction Sr + CF_3I by means of the QCT method when the collision energy is 0.83 eV. The corresponding experimental result is obtained from Fig. 8 in ref. 23. Stolte and co-workers[23] obtained the rotational distribution $P_v(J)$ at a specific v value from the spectrum simulation. In this paper, Fig. 4 is drawn for $v = 17$. From Fig. 4, it can be seen that when the rotational quantum number J increases, $P_v(J)$ first increases to its peak value and then decreases. In both the experimental and theoretical results, the peak values of $P_v(J)$ appear at around $J = 110$. However, the calculated rotational distribution of the product SrI has some differences in its "tail" when compared with the result in the experiment. The differences are caused by the same reasons for those of the vibrational distribution given in this paper. In summary, the shape of the theoretical result is nearly the same with that of the experimental result of Stolte and co-workers.[23]

Reaction cross section

The relative cross section can be obtained from the experiment,[23] whereas in the theoretical calculation, the absolute cross section can be obtained. In this paper, the reaction cross section is obtained from the following equation:[43]

$$[15] \qquad \sigma_r = \pi b_{max}^2 (N_r/N)$$

where N is the number of total trajectories in the calculation and N_r is the number of reactive trajectories under the $b \leq b_{max}$ condition. The values of these parameters can all be obtained in the output file of the QCT calculation.

The curve of the reaction cross section versus collision energy for the reaction Sr + CF_3I is depicted in Fig. 2 from which it can be seen that the reaction cross section shows a steady increase from a minimum value of 1.2439 Å^2 to a maximum value of 3.2329 Å^2 when the collision energy

Can. J. Chem. Downloaded from www.nrcresearchpress.com by Renmin University of China on 09/02/12
For personal use only.

changes between 0.5 and 1.5 eV. The relationship of the reaction cross section and the collision energy is considered directly proportional. The phenomenon that low reaction probabilities appear at low energies and high probabilities at high energies can be observed in the calculated results of this reaction cross section.

This indicates that a reaction barrier exists on the LEPS PES of the reaction Sr + CF_3I, which results in the reaction cross section increasing with increasing collision energy. The LEPS PES constructed for the title reaction belongs to the repulsive PES type, and the reaction barrier can be found in Fig. 1. It is clear that the results of the reaction cross section obtained here describe the reaction Sr + CF_3I well.

Product rotational alignment

The rotational alignment of the product SrI has been calculated versus a series of collision energies by means of the QCT method. Figure 5 shows the result of the reaction Sr + CF_3I. From the calculated product rotational alignment values, it can be seen that, overall, they have deviated slightly from –0.5, which is the kinematic limit value, and change from –0.3657 to –0.4003 versus the collision energy in the range of 0.5 to 1.5 eV. This result presents a falling trend: the product rotational alignment steadily decreases with increasing collision energy along which the alignment effect becomes strong.

Han et al. obtained the conclusion that the product rotational alignment is independent of the PES properties, but can be influenced by the type of mass combination.[29] According to the approximate mass ratio of the reactants, the Sr + CF_3I reaction can generally be regarded as an HHL mass combination. The result shown in Fig. 5 is similar to that of Fig. 2 in ref. 29. Since the product rotational angular momentum completely comes from the initial orbital angular momentum, the product rotation is strongly aligned about the relative velocity of the reactant and its value should be equal to –0.5.[29] However, the disposal of angular momentum into product orbital motion ($\mathbf{L} \rightarrow \mathbf{J}' + \mathbf{L}'$), particularly at lower collision energies, decreases the value of the product rotational alignment.[29] Therefore, it deviates from –0.5 and decreases with increasing collision energy for this mass combination. For $\langle P_2(\mathbf{J}' \cdot \mathbf{K}) \rangle$, it can be seen that the calculated result of the reaction Sr + CF_3I is bigger than the value of the product rotational alignment of the HHL mass combination shown in ref. 29. From the mass proportion of this reaction, it can be determined that the atomic mass of Sr is 87.62, the atomic mass of I is 126.905, and the atomic mass summation of the CF_3 group is 69.005. The mass ratio of this title reaction deviates slightly from the HHL mass configuration and between the HHL and the light + heavy–light (LHL) mass configurations. This is considered as the main reason for the phenomenon mentioned above.

Conclusions

In this paper, studies of the relationships of the vibrational distribution, rotational distribution, reaction cross section, and product rotational alignment with the collision energy for the reaction Sr + CF_3I have been carried out by means of the QCT method based on an extended LEPS PES.

There is a reaction barrier in the entrance part of the LEPS PES that is constructed for the title reaction. The result of the vibrational distribution shows that it first increases and then decreases in both the experimental and theoretical studies when the vibration quantum number continuously increases. Its maximum value appears at around $v = 23$ at a collision energy of 0.83 eV. In both the experimental and theoretical results of $P_v(J)$, their peak values all appear at around $J = 110$ and their changing tendencies basically agree. With increasing collision energy, the reaction cross section increases and this is caused by the reaction barrier on the LEPS PES. The product rotational alignment decreases with increasing collision energy and its value depends on the type of the mass combination of this reaction. The reaction mechanism has been discussed based on these conclusions and a reasonable interpretation is given. In summary, it can be concluded that the results in this paper are consistent with the experimental data for the exothermic reaction Sr + CF_3I.

Acknowledgements

This work was supported by the National Natural Science Foundation of China (Nos. 11047110 and 11105022), the Natural Science Foundation of Liaoning Province (Grant Nos. L2010055, L2010057, and 201102016), and the Fundamental Research Funds for the Central Universities (Nos. 2011QN060, 2011QN062, 2011JC021, and 2011QN151). The code used in this paper was provided by Professor K. Han.

References

(1) Li, Z. J.; Chen, X. J.; Shan, X.; Xue, X. X.; Liu, T.; Xu, K. Z. *Chem. Phys. Lett.* **2008**, *457* (1–3), 45. doi:10.1016/j.cplett.2008.04.007.
(2) Rattigan, O. V.; Shallcross, D. E.; Cox, R. A. *J. Chem. Soc., Faraday Trans.* **1997**, *93* (16), 2839. doi:10.1039/a701529a.
(3) Ma, Y. B.; Lv, J. *Chem. Prod. Tech.* **2007**, *14*, 8.
(4) Cvitas, T.; Gusten, H.; Klasinc, L.; Novadj, I.; Vancik, H. *Z. Naturforsch.* **1978**, *33a*, 1528.
(5) Yates, B. W.; Tan, K. H.; Bancroft, G. M.; Tse, J. S. *J. Chem. Phys.* **1986**, *85* (7), 3840. doi:10.1063/1.450904.
(6) Sheridan, J.; Gordy, W. *J. Chem. Phys.* **1952**, *20* (4), 591. doi:10.1063/1.1700499.
(7) Typke, V.; Dakkouri, M.; Onerhammer, H. *J. Mol. Struct.* **1978**, *44* (1), 85. doi:10.1016/0022-2860(78)85008-X.
(8) Cox, A. P.; Duxbury, G.; Hardy, J. A.; Kawashima, Y. *J. Chem. Soc. Faraday Trans. II* **1980**, *76*, 339. doi:10.1039/f29807600339.
(9) Simpson, M. J.; Tuckett, R. P.; Dunn, K. F.; Hunniford, C. A.; Latimer, C. J. *J. Chem. Phys.* **2009**, *130* (19), 194302. doi:10.1063/1.3137103.
(10) Xie, K. J.; Li, C. L.; Atom, J. *Mol. Phys.* **1986**, *3*, 113.
(11) Babushok, V.; Noto, T.; Burgess, D. R. F.; Hamins, A.; Tsang, W. *Combust. Flame* **1996**, *107* (4), 351. doi:10.1016/S0010-2180(96)00052-1.
(12) Nagasaki, N.; Morikuni, Y.; Kawada, K.; Arai, S. *Catal. Today* **2004**, *88* (3–4), 121. doi:10.1016/j.cattod.2003.11.007.
(13) Brooks, P. R. *Faraday Discuss. Chem. Soc.* **1973**, *55*, 299. doi:10.1039/dc9735500299.
(14) Munakata, T.; Kasuya, T. *J. Chem. Phys.* **1984**, *81* (12), 5608. doi:10.1063/1.447664.
(15) Solarz, R. W.; Johnson, S. A. *J. Chem. Phys.* **1979**, *70* (8), 3592. doi:10.1063/1.437962.
(16) Sanchez Rayo, M. N.; Castaño, F.; Martinez, M. T.; Adams, J. W.;

Can. J. Chem. Downloaded from www.nrcresearchpress.com by Renmin University of China on 09/02/12
For personal use only.

Carl, S. A.; Husain, D.; Schifino, J. *J. Chem. Soc., Faraday Trans.* **1993**, *89* (11), 1645. doi:10.1039/ft9938901645.
(17) Smith, G. P.; Whitehead, J. C.; Zare, R. N. *J. Chem. Phys.* **1977**, *67*, 1912.
(18) Allison, J.; Johnson, M. A.; Zare, R. N. *Faraday Discuss. Chem. Soc.* **1979**, *67*, 124.
(19) Lin, S. M.; Mims, C. A.; Herm, R. R. *J. Phys. Chem.* **1973**, *77* (5), 569. doi:10.1021/j100624a001.
(20) Han, K. L.; He, G. Z.; Lou, N. Q. *Chin. J. Chem. Phys.* **1993**, *6*, 95.
(21) He, G. Z.; Wang, J.; Tse, R. S.; Lou, N. Q. *Can. J. Chem.* **1988**, *66* (8), 1936. doi:10.1139/v88-312.
(22) Berry, R. J.; Yuan, J.; Misra, A.; Marshall, P. *J. Phys. Chem. A* **1998**, *102* (27), 5182. doi:10.1021/jp980645+.
(23) Keijzer, F.; Teule, J. M.; Bulthuis, J.; de Graaff, G. J.; Hilgeman, M. H.; Janssen, M. H. M.; van Kleef, E. H.; van Leuken, J. J.; Stolte, S. *Chem. Phys.* **1996**, *207* (2–3), 261. doi:10.1016/0301-0104(95)00369-X.
(24) Keijzer, F.; Bulthuis, J.; Winter, L. C. de; Van Kleef, E. H.; Stolte, S. *J. Mol. Spectrosc.* **1995**, *169*, 511.
(25) Zhao, X. X.; Li, Y. M. *J. At. Mol. Phys.* **2008**, *25*, 1345.
(26) Zhong, H. Y.; Xia, W. W.; Gu, L. Z.; Yao, L. *J. Theor. Comput. Chem.* **2009**, *8*, 861.
(27) Xia, W. W.; Yao, L.; Chen, B. J. *J. Mol. Struct. (THEOCHEM)* **2010**, *962* (1–3), 56. doi:10.1016/j.theochem.2010.09.014.
(28) Yao, L.; Zhong, H. Y.; Liu, Y. L.; Xia, W. W. *Chem. Phys.* **2009**, *359* (1–3), 151. doi:10.1016/j.chemphys.2009.03.019.
(29) Han, K. L.; He, G. Z.; Lou, N. Q. *J. Chem. Phys.* **1996**, *105* (19), 8699. doi:10.1063/1.472651.
(30) Wang, M. L.; Han, K. L.; He, G. Z.; Lou, N. Q. *Bunsenges. Ber. Phys. Chem.* **1997**, *101*, 1527.
(31) Zhang, X.; Xie, T. X.; Zhao, M. Y.; Han, K. L. *Chin. J. Chem. Phys.* **2002**, *15*, 169.
(32) Frisch, M. J.; Trucks, G. W.; Schlegel, H. B.; Scuseria, G. E.; Robb, M. A.; Cheeseman, J. R.; Montgomery, J. A., Jr.; Vreven, T.; Kudin, K. N.; Burant, J. C.; Millam, J. M.; Iyengar, S. S.; Tomasi, J.; Barone, V.; Mennucci, B.; Cossi, M.; Scalmani, G.; Rega, N.; Petersson, G. A.; Nakatsuji, H.; Hada, M.; Ehara, M.; Toyota, K.; Fukuda, R.; Hasegawa, J.; Ishida, M.; Nakajima, T.; Honda, Y.; Kitao, O.; Nakai, H.; Klene, M.; Li, X.; Knox, J. E.; Hratchian, H. P.; Cross, J. B.; Adamo, C.; Jaramillo, J.; Gomperts, R.; Stratmann, R. E.; Yazyev, O.; Austin, A. J.; Cammi, R.; Pomelli, C.; Ochterski, J. W.; Ayala, P. Y.; Morokuma, K.; Voth, G. A.; Salvador, P.; Dannenberg, J. J.; Zakrzewski, V. G.; Dapprich, S.; Daniels, A. D.; Strain, M. C.; Farkas, O.; Malick, D. K.; Rabuck, A. D.; Raghavachari, K.; Foresman, J. B.; Ortiz, J. V.; Cui, Q.; Baboul, A. G.; Clifford, S.; Cioslowski, J.; Stefanov, B. B.; Liu, G.; Liashenko, A.; Piskorz, P.; Komaromi, I.; Martin, R. L.; Fox, D. J.; Keith, T.; Al-Laham, M. A.; Peng, C. Y.; Nanayakkara, A.; Challacombe, M.; Gill, P. M. W.; Johnson, B.; Chen, W.; Wong, M. W.; Gonzalez, C.; Pople, J. A. *Gaussian 03,* Revision A.1; Gaussian Inc.: Pittsburgh, PA, 2003.
(33) Porter, R. N.; Raff, M. L. In *Dynamics of Molecule Collision, Part B;* Miller, W. H., Ed.; Plenum Press: New York, 1976; p 1.
(34) Truhlar, D. G.; Muckerman, J. T. In *Atom–Molecule Collision Theory;* Bernstein, R. B., Ed.; Plenum Press: New York, 1976; p 505.
(35) Zhao, D.; Zare, R. N. *J. Chem. Phys.* **1992**, *97* (9), 6208. doi:10.1063/1.463983.
(36) Wang, M.-L.; Han, K.-L.; He, G.-Z.; *J. Phys. Chem. A* **1998**, *102* (50), 10204. doi:10.1021/jp981738u.
(37) Chen, M. D.; Wang, M. L.; Han, K. L.; Ding, S. L. *Chem. Phys. Lett.* **1999**, *301* (3–4), 303. doi:10.1016/S0009-2614(99)00052-4.
(38) Zhang, L.; Chen, M. D.; Wang, M. L.; Han, K. L. *J. Chem. Phys.* **2000**, *112* (8), 3710. doi:10.1063/1.480523.
(39) Cai, M. Q.; Zhang, L.; Tang, B. Y.; Chen, M. D.; Yang, G. W.; Han, K. L. *Chem. Phys.* **2000**, *255* (2–3), 283. doi:10.1016/S0301-0104(00)00084-7.
(40) Li, R. J.; Han, K. L.; Li, F. L.; Lu, R. C.; He, G. Z.; Lou, N. Q. *Chem. Phys. Lett.* **1994**, *220* (3–5), 281. doi:10.1016/0009-2614(94)00174-X.
(41) Chen, M. D.; Han, K. L.; Lou, N. Q. *Chem. Phys. Lett.* **2002**, *357* (5–6), 483. doi:10.1016/S0009-2614(02)00585-7.
(42) Wang, W. L.; Han, K. L.; Zhan, J. P.; Wu, V. W. K.; He, G. Z.; Lou, N. Q. *Chem. Phys. Lett.* **1997**, *278* (4–6), 307. doi:10.1016/S0009-2614(97)01063-4.
(43) Xia, W. W.; Lu, N.; Zhong, H. Y.; Yao, L. *Can. J. Chem.* **2009**, *87* (8), 1103. doi:10.1139/V09-067.

Kinetic study on the linalool ozonolysis reaction in the atmosphere

Xiaomin Sun, Chenxi Zhang, Yuyang Zhao, Jing Bai, and Maoxia He

Can. J. Chem. Downloaded from www.nrcresearchpress.com by Renmin University of China on 09/02/12
For personal use only.

Abstract: In the atmosphere, linalool ozonolysis will generate a series of oxidation products and then form particles through nucleation. In this study, the linalool ozonolysis mechanisms were studied and some of the main products detected from experiment are verified. The Rice–Ramsperger–Kassel–Marcus (RRKM) theory and the canonical variational transition state theory (CVT) with small curvature tunneling effect (SCT) are used to calculate rate constants over the temperature range of 200~800 K. The total rate constant for the reaction of ozone with linalool is 4.50×10^{-16} cm^3 molecule^{-1} s^{-1}, and the addition of ozone to $(CH_3)_2C{=}CH{-}$ is the main ozone addition position. Furthermore, the Arrhenius formulas are fitted and the lifetimes of reaction species in the troposphere are discussed for the first time. The total atmospheric lifetime of linalool relative to O_3 is 2.30 h. The O_3-initiated atmospheric lifetimes of P1, P3, and P6 are 2.64 months, 16.67 days, and 15.5 h, respectively.

Key words: linalool, ozonolysis reaction, rate constants, atmospheric lifetime.

Résumé : Dans l'atmosphère, l'ozololyse du linalol conduit à la formation d'une série de produits d'oxydation qui, par nucléation, provoqueront la formation de particules. Dans cette étude, on a étudié les mécanismes d'ozonolyse du linalol et on a vérifié la nature de quelques-uns des produits principaux formés au cours de ces expériences. On a fait appel à la théorie de Rice–Rampsperger–Kassel–Marcus (RRKM) et la théorie de l'état de transition à variation canonique (TVC) modifiée par un léger effet tunnel de courbure (ETC) pour calculer les constantes de vitesse dans la plage de températures allant de 200 à 800 K. La constante de vitesse de réaction totale de l'ozone avec le linalol est de $4{,}50 \times 10^{-16}$ cm^3 molécule^{-1} s^{-1} et l'addition de l'ozone sur le linalol se fait principalement sur la portion $(CH_3)_2C{=}CH{-}$. De plus, pour la première fois, on a ajusté les formules d'Arrhenius et on discute des temps de vie des espèces réactives dans la troposphère. Le temps de vie total du linalol dans l'atmosphère, relatif à celui du O_3, est de 2,30 jours. Les temps de vie atmosphériques initiés par le O_3 des produits P1, P3 et P6 sont respectivement de 2,64 mois, 16,67 jours et 15,5 h.

Mots-clés : réaction d'ozonolyse du linalol, constantes de vitesse, temps de vie atmosphérique.

[Traduit par la Rédaction]

Introduction

Linalool ($(CH_3)_2C{=}CHCH_2CH_2C(CH_3)(OH)CH{=}CH_2$), a monoterpene compound with a floral scent, is released into the atmosphere from certain types of vegetation,[1–3] including tea, oranges, grapes, mangos, lemons, tomatos, basil, and lavender.[4] Linalool is used as a scent in 60%–80% of perfumed hygiene products and cleaning agents including soaps, detergents, shampoos, and lotions.

Linalool has a stereogenic center at C_3 that results in two stereoisomers: (*S*)- and (*R*)-linalool. There are different scents in these two stereoisomers, which contribute to the aroma of many common plants. (*S*)-Linalool has a scent associated with flowers and (or) orange, whereas (*R*)-linalool has a lavender scent and is typically found in lavender and basil. Since (*S*)- and (*R*)-linalool are equally stable,[5] the (*S*)-linalool (abbreviated to linalool) was choosen as an example.

In the troposphere it is easy for linalool to react with OH, NO_3, or O_3 to generate a series of oxidation products that lead to ambient secondary organic aerosol (SOA)[6]. SOA will have a great influence on atmospheric environment and human health. Thus, the studies on the mechanism for atmospheric oxidation of linalool are very important to reduce the formation of SOA. Among all of the atmospheric linalool oxidations, the ozonolysis reaction is particularly important. Many studies on linalool ozonolysis have been reported.[6–9] The products of linalool reacting with O_3 were investigated in ~6500–7900 L Teflon chambers using gas chromatography with mass spectrometry (GC–MS) and GC with Fourier transform infrared absorption spectroscopy (GC–FTIR) detection by Shu et al.[6] Acetone, formaldehyde, 4-hydroxy-4-methyl-5-hexenal, and 5-ethenyldihydro-5-ethyl-2(3*H*)-furanone are the main products, but the subsequent reactions of these products with ozone were not considered. Meera[8] studied linalool ozone reactions and analyzed the consequent reactive oxygen species using two chamber systems. At the same time, the rate constant for the linalool ozonolysis was found to be 3.49×10^{-16} cm^3 molecule^{-1} s^{-1}. Chen et al.[9]

Received 7 September 2011. Accepted 17 November 2011. Published at www.nrcresearchpress.com/cjc on 19 March 2012.

X. Sun. Environment Research Institute, Shandong University, Jinan 250100, P.R. China; State Key Laboratory of Solid Lubrication, Lanzhou Institute of Chemical Physics, Chinese Academy Of Science, Lanzhou 730000, P.R. China.
C. Zhang, Y. Zhao, J. Bai, and M. He. Environment Research Institute, Shandong University, Jinan 250100, P.R. China.

Corresponding author: Maoxia He (e-mail: hemaox@sdu.edu.cn).

Can. J. Chem. Downloaded from www.nrcresearchpress.com by Renmin University of China on 09/02/12
For personal use only.

used a dynamic system to study the SOA formation by linalool ozonolysis at room temperature. They only certified that linalool is less efficient in potential SOA formation yields compared with other terpene species like α-pinene, which has one endocyclic unsaturated carbon bond. However, the reaction mechanism of the linalool ozonolysis has still been neglected.

Our group has reported the reaction mechanism of linalool with ozone in the atmosphere using density functional theory (DFT).[10] The intermediates with H_2O were also discussed in detail. It was the first computational study to obtain a mechanistic understanding of how the detected products are generated, but the reaction rate of every elementary reaction was not calculated.

In this study, the geometrical parameters were optimized at the MPWB1K/6–31+G(d,p) level instead of at B3LYP/6–31G(d), with the calculation precision considered. It is well known that the B3LYP method underestimates barrier heights systematically. Furthermore, previous study has shown that the MPWB1K is an excellent method for the prediction of transition-state geometries.[11] On the basis of the quantum chemical information, the rate constants were calculated using the multichannel Rice–Ramsperger–Kassel–Marcus (RRKM) theory,[12] the transition-state theory (TST), and the canonical variational transition-state theory (CVT) with small-curvature tunneling (SCT) or zero-curvatue tunneling correction (ZCT)[13–15] over a wide temperature range of 200∼800 K.

Computational methods

Geometry optimization

The unrestricted MPWB1K method is used to treat systems with an even number of electrons but partial open-shell character, such as ozone or the criegee biradicals.[16,17] The geometrical parameters of stationary points are optimized at the MPWB1K/6–31+G(d,p) level. The vibrational frequencies were calculated at the same level to determine the nature of the stationary points. Each transition state was verified for their connection to the designated reactants and products by performing an intrinsic reaction coordinate (IRC) analysis.[18] A more flexible basis set, 6–311+G(3df,2p), was employed to calculate the single-point energies of various species. All quantum chemical calculations were performed with the Gaussian 03 programs.[19]

Kinetic calculations

The initial information obtained from ab initio calculations allowed us to calculate the rate constants including the tunneling effects. The kinetic calculations were carried out using RRKM theory and the CVT with SCT correction.

RRKM theory was used to calculate the rate constants of the bimolecular reaction. The kinetic program that had considered the pressure effect was supported by Hou et al.[12] The CVT with SCT correction is an effective method for the calculation of rate constants, but it fails to take the pressure change into consideration. In this paper, the CVT/SCT method was used to calculate the rate constants of the monomolecular isomerization over a suitable temperature range. Along the minimum energy path, approximately 40 points were selected. For each point, the frequency was calculated to obtain information on cartesian coordinates, gradients, and Hessian matrices. The kinetic calculations were carried out using the Polyrate 9.7 program.[20]

Results and discussion

The main reaction paths for linalool with O_3 are drawn in Fig. 1. The profiles of the potential energy surfaces are shownn in Figs. 2 and 3. The rate constants for the TST, CVT, CVT/ZCT, and CVT/SCT methods are presented in Fig. 4. Table 1 lists the rate constants of the elementary reaction at 200∼800 K (in s^{-1} and cm^3 $molecule^{-1}$ s^{-1} for unimolecular and bimolecular reactions, respectively). The Arrhenius formulas for elementary reactions over the temperature range are listed in Table 2. Table 3 presents the lifetimes of the reactant species in the atmosphere according to the rate constants.

Reaction mechanism

Linalool ozone reactions proceed through two possible routes because of the presence of the two double bonds in its chemical structure. The potential barriers of the initial addition of ozone to $(CH_3)_2C{=}CH$ and the addition of ozone to $CH_2{=}CH–$ are 0.27 and 2.36 kcal/mol (1 cal = 4.184 J), respectively. It agrees with the experiment study in which the ozone attacks $(CH_3)_2C{=}CH–$ more easily than it attacks $CH_2{=}CH–$.[6,9]

The primary ozonide is expected to undergo rapid decomposition into Criegee biradicals. The addition of ozone to $(CH_3)_2C{=}CH–$ (labeled as IM2) is used to explain the next part of the reaction mechanism. IM2 can decompose into 4-hydroxy-4-methyl-5-hexenal (P1) and $(CH_3)_2COO$ via TS2 with a barrier of 24.12 kcal/mol and also can produce biradical $CH_2{=}CHC(OH)(CH_3)CH_2CH_2C(H)OO$ (IM4) and acetone via TS5 with a barrier of 28.63 kcal/mol. P1 is more favored than IM4 by comparison. P1 will be cyclized and be named as 2-ethenyl-2-methyl-5-hydroxyterahydrofuran (P8). After IM4 reacts with H_2O, IM5 is produced and acid $CH_2{=}CHC(OH)(CH_3)CH_2CH_2COOH$ (P3) is obtained with the loss of a water molecule. Owing to the presence of the second double bond, P1 and P3 can further react with O_3 to give rise to secondary Criegee biradicals as suggested by Shu et al.,[6] Atkinson et al.,[21] and Calogirou et al.[22] It should be noted that P1 and P8 are the major products, which are in agreement with the previous study by Shu et al.[6] The primarily generated Criegee biradicals have seven carbon atoms and are expected to react with stable intermediates and then undergo nucleation and form particles.[9] These nucleate particles can be condensed and absorb volatile organics in the surroundings and grow in size, which will be the important constituents of SOA. The further attack of ozone on the second unsaturated carbon bond will lead to further fragmentation of carbon backbones, which yields products with even fewer carbon atoms, and therefore will be less likely to contribute to SOA formation and growth. Figure 1 shows the reaction sequence of the oxidation of linalool with ozone.

Rate constants

The RRKM, TST, and the CVT with SCT correction methods are used to calculate the rate constants. Given that the temperature ranges from –56 to 15 °C in the troposphere, a

Can. J. Chem. Downloaded from www.nrcresearchpress.com by Renmin University of China on 09/02/12
For personal use only.

Fig. 1. The reaction pathways of the oxidation of linalool with ozone at the MPWB1K/6–311+G(3df,2pd)// MPWB1K/6–31+G(d,p) level.

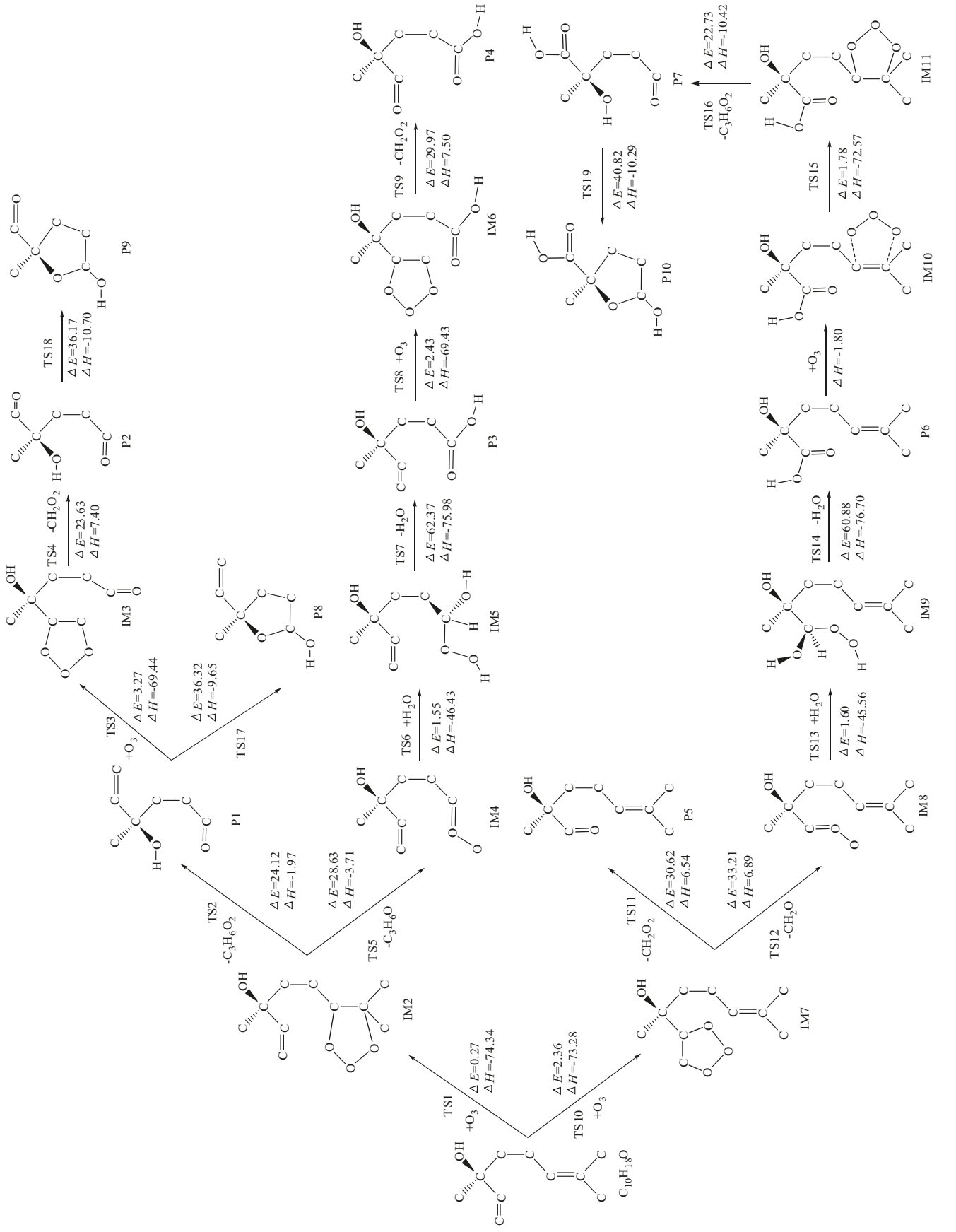


Fig. 2. The potential energy surface profile of the addition reaction for ozone to the $(CH_3)_2C=CH–$ group of linalool.

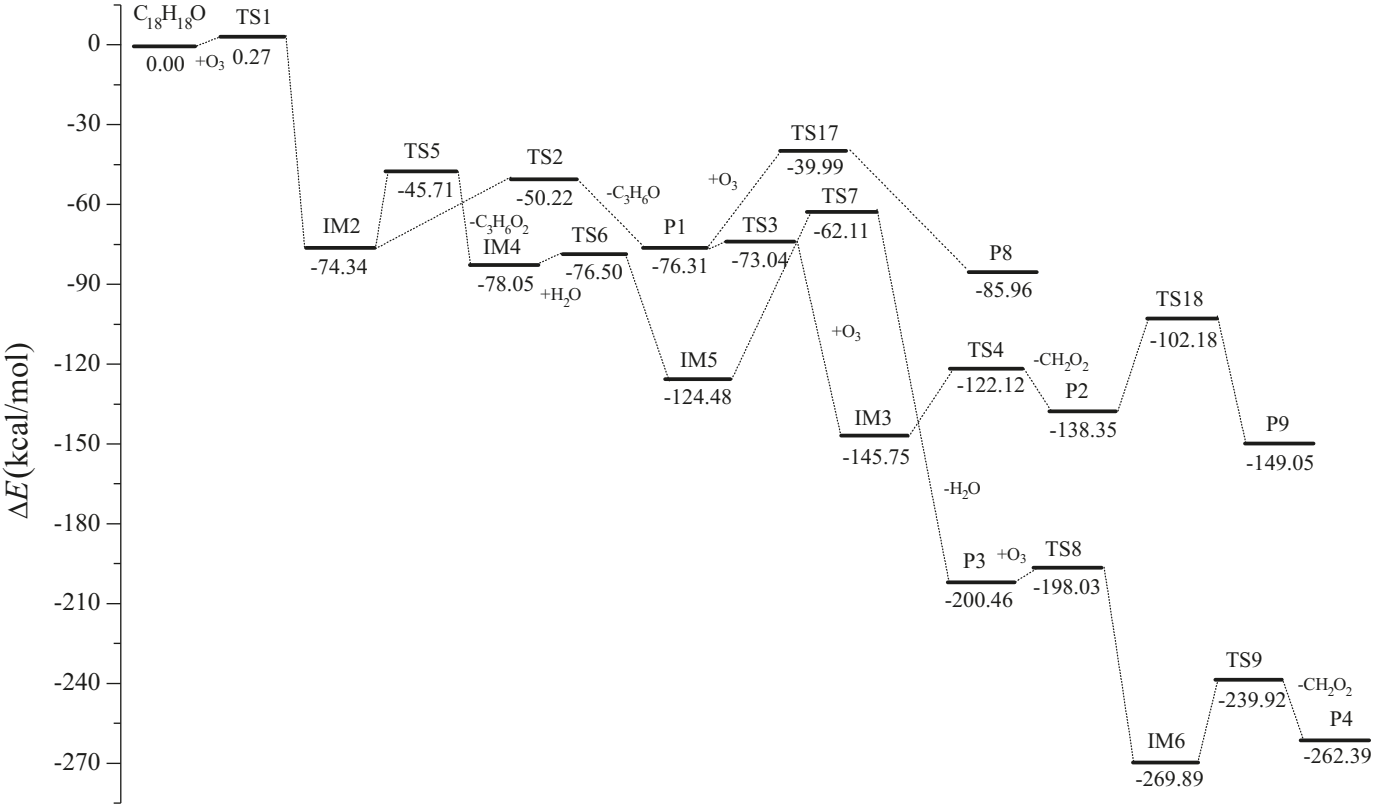
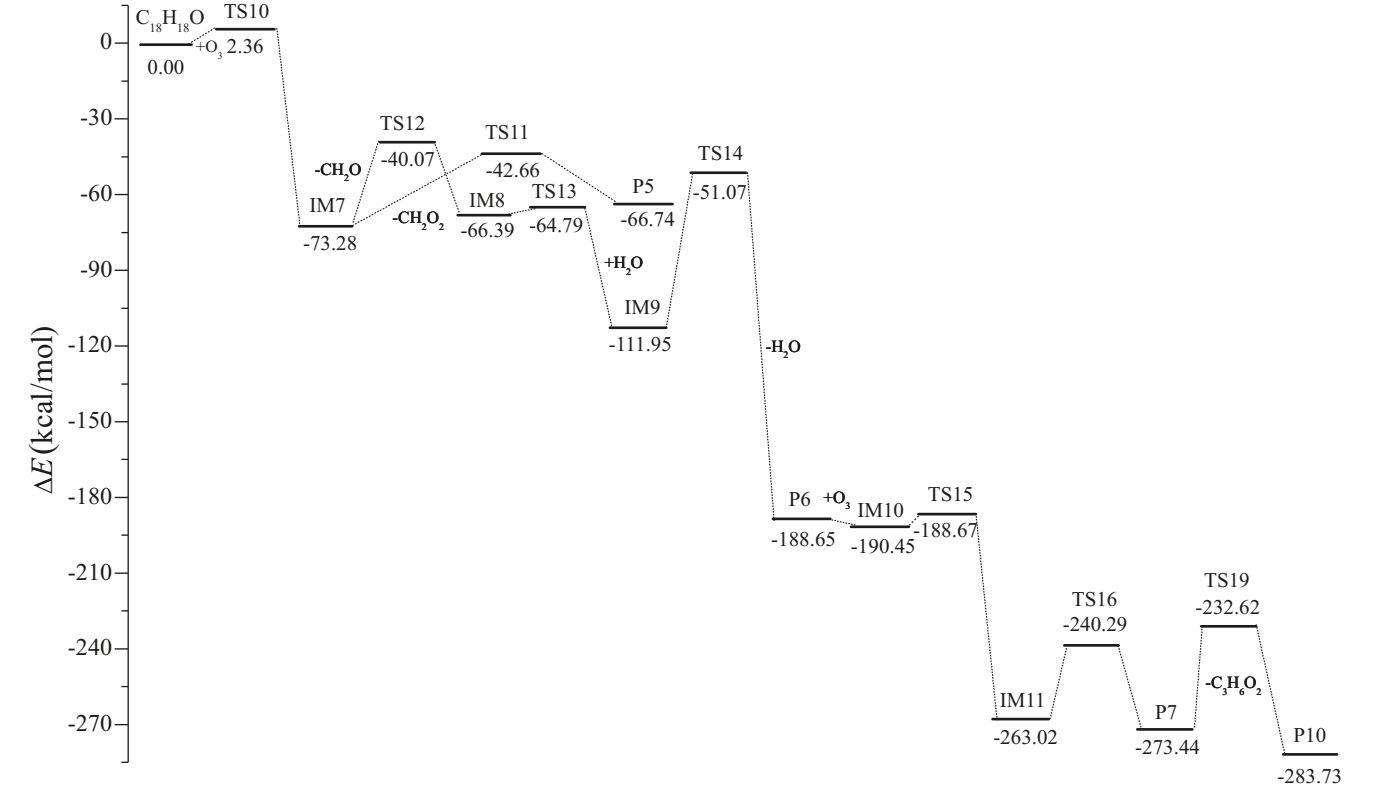


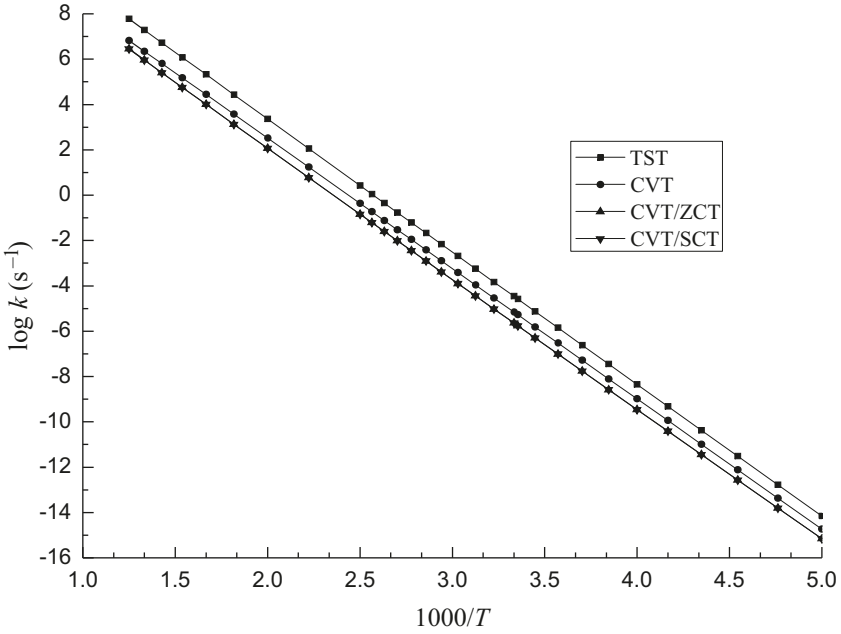
Fig. 3. The potential energy surface profile of the addition reaction for ozone to the $CH_2=CH–$ group of linalool.



Can. J. Chem. Downloaded from www.nrcresearchpress.com by Renmin University of China on 09/02/12
For personal use only.

Can. J. Chem. Downloaded from www.nrcresearchpress.com by Renmin University of China on 09/02/12
For personal use only.

Fig. 4. The rate constants of the elementary reaction 2 with TST and canonical variational transition-state theory (CVT) methods.



wider range of 200~800 K was chosen to study the relationship between temperature and rate constants. The reaction pressure was adopted at atmospheric pressure.

The RRKM method was used to calculate the rate constants in elementary reactions that have no barriers or very low barriers, such as elementary rxns. [1], [3], [6], [8], [10], [13], and [15]. The results are listed in Table 1.

For the primary ozonization, the rate constant for the ozonolysis reaction of $(CH_3)_2C{=}CH–$ (elementary rxn. [1]) is 3.83×10^{-16} cm^3 molecule^{-1} s^{-1} at 298.15 K, higher than that of the ozonization reaction of $CH_2{=}CH–$ (elementary rxn. [10]), 6.67×10^{-17} cm^3 molecule^{-1} s^{-1}. This result can be interpreted as that the preponderant ozone addition position is $(CH_3)_2C{=}CH–$. According to the rate constants of the addition reaction of ozone to $(CH_3)_2C{=}CH–$ and $CH_2{=}CH–$, the total rate constants for the ozonolysis reaction of linalool is 4.50×10^{-16} cm^3 molecule^{-1} s^{-1}, which is similar to 4.3×10^{-16} cm^3 molecule^{-1} s^{-1} found by Atkinson et al.[21] and 3.49×10^{-16} cm^3 molecule^{-1} s^{-1} found by Meera.[8]

For the secondary ozonization, such as elementary rxns. [3], [8], and [15], the rate constants at 298.15 K are 5.45×10^{-19}, 2.59×10^{-18}, and 6.39×10^{-16} cm^3 molecule^{-1} s^{-1}, respectively. It can be seen that the ozonization reactivity of P1 and P3 is lower than that of linalool, while the ozonization reactivity of P6 is higher than that of linalool. These rate constants range from 10^{-18} to 10^{-16} cm^3 molecule^{-1} s^{-1}. The calculated results are reasonable and acceptable.

As for the reactions involving water molecules, such as the elementary rxns. [6] and [13], the rate constants at 298.15 K are 1.83×10^{-20} and 3.15×10^{-22} cm^3 molecule^{-1} s^{-1}, respectively. Obviously, the rate constants are lower than those of the ozonolysis reaction.

The rate constants of TST share the same variation trend as that of CVT for the whole temperature range of 200~800 K studied, i.e., the higher the temperature, the larger the rate constant. The rate constants of elementary rxn. [2] are taken as an example.

In particular, the rate constant of the TST method is about 3.77 and 8.80 times of those of the CVT method at 200 K (TST, 7.02×10^{-15} s^{-1}; CVT, 1.86×10^{-15} s^{-1}) and at 800 K (TST, 5.87×10^{7}; CVT, 6.67×10^{6}), which suggests that the variational effect cannot be neglected in this reaction. Meanwhile, we can find that the higher the temprature, the greater the variational effect.

The tunneling effect is also taken into account in the computation of the rate constants. The CVT rate constants are larger than the CVT/ZCT and CVT/SCT ones over the temperature range of 200~800 K. For example, at 298.15 K, the CVT rate constant is 5.28×10^{-6} s^{-1}, whereas the CVT/ZCT and CVT/SCT rate constants are 1.72×10^{-6} and 1.73×10^{-6} s^{-1}, respectively. The former is 3.07 times the latter. The higher the temperature is, the less the ratio is, which suggests that the tunneling effect plays a more important role at low temperature than at high temperature for the calculation of the rate constants. As for TST and CVT/ZCT, the same trend is found. Another phenomenon that was observed was that the CVT/SCT rate constants come closer to the rate constants of TST and CVT in the higher temperature range. According to previous studies,[23,24] the CVT/SCT rate constants are in good agreement with experimental values in a large temperature range. Therefore, the results of the CVT/SCT method are reported for the other elementary reactions, which are also listed in Table 1.

Owing to the low barriers, elementary rxns. [4] and [16] occur easily. But the elementary rxns. [7] and [14] have barriers high above 60 kcal/mol and the rate constants are very low. The rate constants of elementary rxns. [2], [5], and [9] have similar orders of magnitudes with the expermental particle wall loss rate constants.[25–27] Elementary rxns. [12], [13], [17], [18], and [19] have the lower rate constants.

To be used more effectively, the calculated rate constants are fitted, and Arrhenius formulas $k(T) = a \times 10^b \exp(\Delta E/RT)$ for the crucial elementary reactions over the temperature

Can. J. Chem. Downloaded from www.nrcresearchpress.com by Renmin University of China on 09/02/12
For personal use only.

Table 1. The rate constants of elementary reactions [1]–[19] at 200~800 K.

	Reaction									
T (K)	1	2	3	4	5	6	7	8	9	10
200	1.72×10^{-17}	7.02×10^{-16}	8.84×10^{-21}	4.51×10^{-12}	1.97×10^{-16}	2.11×10^{-22}	7.89×10^{-47}	9.62×10^{-20}	2.00×10^{-17}	2.23×10^{-18}
220	3.90×10^{-17}	2.70×10^{-13}	2.68×10^{-20}	7.62×10^{-10}	9.08×10^{-14}	7.25×10^{-22}	1.78×10^{-41}	2.32×10^{-19}	1.05×10^{-14}	5.53×10^{-18}
240	7.87×10^{-17}	3.89×10^{-11}	6.85×10^{-20}	5.54×10^{-8}	1.53×10^{-11}	2.02×10^{-21}	5.16×10^{-37}	4.90×10^{-19}	1.96×10^{-12}	1.20×10^{-17}
260	1.45×10^{-16}	2.63×10^{-9}	1.54×10^{-19}	2.11×10^{-6}	1.19×10^{-9}	4.82×10^{-21}	3.09×10^{-33}	9.35×10^{-19}	1.66×10^{-10}	2.33×10^{-17}
280	2.48×10^{-16}	9.82×10^{-8}	3.10×10^{-19}	4.80×10^{-5}	4.99×10^{-8}	1.02×10^{-20}	5.38×10^{-30}	1.65×10^{-18}	7.52×10^{-9}	4.18×10^{-17}
298.15	3.83×10^{-16}	1.73×10^{-6}	5.45×10^{-19}	5.73×10^{-4}	9.70×10^{-7}	1.83×10^{-20}	1.98×10^{-27}	2.59×10^{-18}	1.55×10^{-7}	6.67×10^{-17}
300	4.00×10^{-16}	2.28×10^{-6}	5.78×10^{-19}	7.26×10^{-4}	1.29×10^{-6}	1.94×10^{-20}	3.48×10^{-27}	2.72×10^{-18}	2.07×10^{-7}	7.01×10^{-17}
320	6.16×10^{-16}	3.58×10^{-5}	1.00×10^{-18}	7.87×10^{-3}	2.23×10^{-5}	3.42×10^{-20}	1.01×10^{-24}	4.27×10^{-18}	3.78×10^{-6}	1.11×10^{-16}
340	9.09×10^{-16}	4.10×10^{-4}	1.65×10^{-18}	6.48×10^{-2}	2.77×10^{-4}	5.66×10^{-20}	1.50×10^{-22}	6.40×10^{-18}	4.94×10^{-5}	1.69×10^{-16}
360	1.30×10^{-15}	3.59×10^{-3}	2.59×10^{-18}	4.24×10^{-1}	2.62×10^{-3}	8.88×10^{-20}	1.28×10^{-20}	9.26×10^{-18}	4.88×10^{-4}	2.47×10^{-16}
380	1.80×10^{-15}	2.51×10^{-2}	3.91×10^{-18}	2.29	1.96×10^{-2}	1.33×10^{-19}	6.92×10^{-19}	1.30×10^{-17}	3.80×10^{-3}	3.49×10^{-16}
400	2.44×10^{-15}	1.45×10^{-1}	5.70×10^{-18}	1.05×10^{1}	1.21×10^{-1}	1.92×10^{-19}	2.51×10^{-17}	1.78×10^{-17}	2.42×10^{-2}	4.81×10^{-16}
450	4.74×10^{-15}	5.90	1.36×10^{-17}	2.61×10^{2}	5.64	4.23×10^{-19}	4.97×10^{-14}	3.52×10^{-17}	1.22	9.68×10^{-16}
500	8.36×10^{-15}	1.16×10^{2}	2.59×10^{-17}	3.48×10^{3}	1.24×10^{2}	8.09×10^{-19}	2.18×10^{-11}	6.29×10^{-17}	2.85×10^{1}	1.75×10^{-15}
550	1.37×10^{-14}	1.33×10^{3}	4.67×10^{-17}	2.91×10^{4}	1.57×10^{3}	1.40×10^{-18}	3.21×10^{-9}	1.04×10^{-16}	3.79×10^{2}	2.91×10^{-15}
600	2.11×10^{-14}	1.02×10^{4}	7.80×10^{-17}	1.72×10^{5}	1.31×10^{4}	2.24×10^{-18}	2.08×10^{-7}	1.62×10^{-16}	3.30×10^{3}	4.55×10^{-15}
650	3.10×10^{-14}	5.73×10^{4}	1.23×10^{-16}	7.78×10^{5}	7.90×10^{4}	3.38×10^{-18}	7.12×10^{-6}	2.39×10^{-16}	2.07×10^{4}	6.77×10^{-15}
700	4.39×10^{-14}	2.52×10^{5}	1.84×10^{-16}	2.85×10^{6}	3.71×10^{5}	4.87×10^{-18}	1.48×10^{-4}	3.41×10^{-16}	1.00×10^{5}	9.67×10^{-15}
750	6.03×10^{-14}	9.12×10^{5}	2.66×10^{-16}	8.77×10^{6}	1.42×10^{6}	6.77×10^{-18}	2.08×10^{-3}	4.69×10^{-16}	3.94×10^{5}	1.34×10^{-14}
800	8.06×10^{-14}	2.81×10^{6}	3.71×10^{-16}	2.35×10^{7}	4.61×10^{6}	9.13×10^{-18}	2.10×10^{-2}	6.29×10^{-16}	1.31×10^{6}	1.79×10^{-14}

Note: *T*, temperature. The units are s^{-1} and cm^3 $molecule^{-1}$ s^{-1} for unimolecular and bimolecular reactions, respectively.

Table 2. The lifetime(s) of reactant species in the atmosphere according to the rate constants at 200~800 K.

	Reaction									
T (K)	1[a]	2	3[a]	4	5	6[b]	7	8[a]	9	10[a]
200	2.16×10^{5}	1.42×10^{15}	4.21×10^{8}	2.22×10^{11}	5.08×10^{15}	8.82×10^{3}	1.27×10^{46}	3.87×10^{7}	5.00×10^{16}	1.67×10^{6}
220	9.54×10^{4}	3.70×10^{12}	1.39×10^{8}	1.31×10^{9}	1.10×10^{13}	2.57×10^{3}	5.62×10^{40}	1.60×10^{7}	9.52×10^{13}	6.73×10^{5}
240	4.73×10^{4}	2.57×10^{10}	5.43×10^{7}	1.81×10^{7}	6.54×10^{10}	9.21×10^{2}	1.94×10^{36}	7.59×10^{6}	5.10×10^{11}	3.10×10^{5}
260	2.57×10^{4}	3.80×10^{8}	2.42×10^{7}	4.74×10^{5}	8.40×10^{8}	3.86×10^{2}	3.24×10^{32}	3.98×10^{6}	6.02×10^{9}	1.60×10^{5}
280	1.50×10^{4}	1.02×10^{7}	1.20×10^{7}	2.08×10^{4}	2.00×10^{7}	1.82×10^{2}	1.86×10^{29}	2.25×10^{6}	1.33×10^{8}	8.90×10^{4}
298.15	9.71×10^{3}	5.78×10^{5}	6.83×10^{6}	1.75×10^{3}	1.03×10^{6}	1.02×10^{2}	5.05×10^{26}	1.44×10^{6}	6.45×10^{6}	5.58×10^{4}
300	9.30×10^{3}	4.39×10^{5}	6.44×10^{6}	1.38×10^{3}	7.75×10^{5}	9.59×10^{1}	2.87×10^{26}	1.37×10^{6}	4.83×10^{6}	5.31×10^{4}
320	6.04×10^{3}	2.79×10^{4}	3.72×10^{6}	1.27×10^{2}	4.48×10^{4}	5.44×10^{1}	9.90×10^{23}	8.71×10^{5}	2.65×10^{5}	3.35×10^{4}
340	4.09×10^{3}	2.44×10^{3}	2.25×10^{6}	1.54×10^{1}	3.61×10^{3}	3.29×10^{1}	6.67×10^{21}	5.81×10^{5}	2.02×10^{4}	2.20×10^{4}
360	2.86×10^{3}	2.79×10^{2}	1.44×10^{6}	2.36	3.82×10^{2}	2.10×10^{1}	7.81×10^{19}	4.02×10^{5}	2.05×10^{3}	1.51×10^{4}
380	2.07×10^{3}	3.98×10^{1}	9.51×10^{5}	4.37×10^{-1}	5.10×10^{1}	1.40×10^{1}	1.45×10^{18}	2.86×10^{5}	2.63×10^{2}	1.07×10^{4}
400	1.52×10^{3}	6.90	6.53×10^{5}	9.52×10^{-2}	8.26	9.69	3.98×10^{16}	2.09×10^{5}	4.13×10^{1}	7.73×10^{3}
450	7.85×10^{2}	1.69×10^{-1}	2.74×10^{5}	3.83×10^{-3}	1.77×10^{-1}	4.40	2.01×10^{13}	1.06×10^{5}	8.20×10^{-1}	3.84×10^{3}
500	4.45×10^{2}	8.62×10^{-3}	1.44×10^{5}	2.87×10^{-4}	8.06×10^{-3}	2.30	4.59×10^{10}	5.91×10^{4}	3.51×10^{-2}	2.13×10^{3}
550	2.72×10^{2}	7.52×10^{-4}	7.97×10^{4}	3.44×10^{-5}	6.37×10^{-4}	1.33	3.12×10^{8}	3.58×10^{4}	2.64×10^{-3}	1.28×10^{3}
600	1.76×10^{2}	9.80×10^{-5}	4.77×10^{4}	5.81×10^{-6}	7.63×10^{-5}	8.31×10^{-1}	4.81×10^{6}	2.30×10^{4}	3.03×10^{-4}	8.18×10^{2}
650	1.20×10^{2}	1.75×10^{-5}	3.02×10^{4}	1.29×10^{-6}	1.27×10^{-5}	5.50×10^{-1}	1.40×10^{5}	1.56×10^{4}	4.83×10^{-5}	5.50×10^{2}
700	8.47×10^{1}	3.97×10^{-6}	2.02×10^{4}	3.51×10^{-7}	2.70×10^{-6}	3.82×10^{-1}	6.76×10^{3}	1.09×10^{4}	1.00×10^{-5}	3.85×10^{2}
750	6.17×10^{1}	1.10×10^{-6}	1.40×10^{4}	1.14×10^{-7}	7.04×10^{-7}	2.75×10^{-1}	4.81×10^{2}	7.93×10^{3}	2.54×10^{-6}	2.78×10^{2}
800	4.62×10^{1}	3.56×10^{-7}	1.00×10^{4}	4.26×10^{-8}	2.17×10^{-7}	2.04×10^{-1}	4.76×10^{1}	5.91×10^{3}	7.63×10^{-7}	2.08×10^{2}

[a] O_3 concentration is ~2.688×10^{11} molecule/cm^3 (1.0×10^{-8} O_3 in the atmosphere).

[b] Water concentration is ~5.375×10^{17} molecule/cm^3 (2% H_2O in the atmosphere).

range of 200~800 K are listed in Table 2. The pre-exponential factor, the activation energy, and the rate constants can be obtained from these formulas. These formulas can provide helpful information for the atmospheric model study on the formation of SOA.

Atmospheric lifetimes

According to the rate constants of the elementary reactions, the atmospheric lifetimes of the reactants can be calculated. For the first-order reaction, the lifetime τ is the reciprocal of the rate constant k, that is, $\tau = \frac{1}{k}$. For the pseudo-first-order reaction, the lifetime is calculated according to $\tau = \frac{1}{k[x]_{const}}$, where the $[x]_{const}$ term is one of the reactant concentrations that can be taken as a constant in the troposphere. For the parallel reaction, the reciprocal of the total lifetime equals the sum of the reciprocal of the sublifetime, that is, $\frac{1}{\tau_{total}} = \sum_{i=1}^{m} \frac{1}{\tau_i}$. The m term is the number of parallel reactions. Then, the lifetime of the reactants in the 19 elementary rxns. can be obtained over the range of 200~800 K and

Can. J. Chem. Downloaded from www.nrcresearchpress.com by Renmin University of China on 09/02/12
For personal use only.

11	12	13	14	15	16	17	18	19
9.11×10^{-23}	5.58×10^{-25}	5.75×10^{-25}	2.58×10^{-46}	8.00×10^{-17}	3.95×10^{-13}	1.77×10^{-22}	1.41×10^{-25}	1.13×10^{-29}
1.42×10^{-19}	1.43×10^{-21}	3.30×10^{-24}	5.26×10^{-41}	1.35×10^{-16}	1.00×10^{-10}	2.11×10^{-19}	3.22×10^{-22}	6.12×10^{-26}
6.57×10^{-17}	9.99×10^{-19}	1.41×10^{-23}	1.41×10^{-36}	2.16×10^{-16}	1.02×10^{-8}	7.68×10^{-17}	2.02×10^{-19}	7.86×10^{-23}
1.20×10^{-14}	2.59×10^{-16}	4.80×10^{-23}	7.97×10^{-33}	3.26×10^{-16}	5.20×10^{-7}	1.12×10^{-14}	4.66×10^{-17}	3.34×10^{-20}
1.04×10^{-12}	3.06×10^{-14}	1.37×10^{-22}	1.32×10^{-29}	4.72×10^{-16}	1.52×10^{-5}	8.01×10^{-13}	4.93×10^{-15}	5.95×10^{-18}
3.62×10^{-11}	1.35×10^{-12}	3.15×10^{-22}	4.70×10^{-29}	6.39×10^{-16}	2.22×10^{-4}	2.34×10^{-11}	1.97×10^{-13}	3.59×10^{-16}
5.07×10^{-11}	1.93×10^{-12}	3.40×10^{-22}	8.21×10^{-27}	6.60×10^{-16}	2.86×10^{-4}	3.23×10^{-11}	2.79×10^{-13}	5.30×10^{-16}
1.52×10^{-9}	7.31×10^{-11}	7.56×10^{-22}	2.30×10^{-24}	8.95×10^{-16}	3.75×10^{-3}	8.17×10^{-10}	9.54×10^{-12}	2.68×10^{-14}
3.08×10^{-8}	1.82×10^{-9}	1.53×10^{-21}	3.34×10^{-22}	1.19×10^{-15}	3.66×10^{-2}	1.41×10^{-8}	2.14×10^{-10}	8.54×10^{-13}
4.49×10^{-7}	3.18×10^{-8}	2.87×10^{-21}	2.80×10^{-20}	1.54×10^{-15}	2.78×10^{-1}	1.77×10^{-7}	3.40×10^{-9}	1.85×10^{-11}
4.95×10^{-6}	4.13×10^{-7}	5.04×10^{-21}	1.48×10^{-18}	1.96×10^{-15}	1.71	1.70×10^{-6}	4.03×10^{-8}	2.89×10^{-10}
4.31×10^{-5}	4.16×10^{-6}	8.39×10^{-21}	5.29×10^{-17}	2.46×10^{-15}	8.81	1.30×10^{-5}	3.73×10^{-7}	3.42×10^{-9}
4.21×10^{-3}	5.55×10^{-4}	2.48×10^{-20}	1.02×10^{-13}	4.09×10^{-15}	2.83×10^{2}	9.49×10^{-4}	4.07×10^{-5}	6.31×10^{-7}
1.66×10^{-1}	2.82×10^{-2}	6.00×10^{-20}	4.40×10^{-11}	6.38×10^{-15}	4.59×10^{3}	2.93×10^{-2}	1.73×10^{-3}	4.09×10^{-5}
3.40	7.07×10^{-1}	1.25×10^{-19}	6.39×10^{-9}	9.45×10^{-15}	4.51×10^{4}	4.83×10^{-1}	3.72×10^{-2}	1.24×10^{-3}
4.23×10^{1}	1.04×10^{1}	2.34×10^{-19}	4.09×10^{-7}	1.34×10^{-14}	3.04×10^{5}	5.00	4.80×10^{-1}	2.13×10^{-2}
3.59×10^{2}	1.02×10^{2}	4.03×10^{-19}	1.39×10^{-5}	1.85×10^{-14}	1.53×10^{6}	3.61×10^{1}	4.17	2.37×10^{-1}
2.25×10^{3}	7.23×10^{2}	6.48×10^{-19}	2.89×10^{-4}	2.47×10^{-14}	6.15×10^{6}	1.97×10^{2}	2.67×10^{1}	1.86
1.11×10^{4}	3.96×10^{3}	9.89×10^{-19}	4.03×10^{-3}	3.24×10^{-14}	2.05×10^{7}	8.55×10^{2}	1.33×10^{2}	1.12×10^{1}
4.47×10^{4}	1.75×10^{4}	1.45×10^{-18}	4.07×10^{-2}	4.15×10^{-14}	5.88×10^{7}	3.10×10^{3}	5.44×10^{2}	5.36×10^{1}

11	12	13[b]	14	15[a]	16	17	18	19
1.10×10^{22}	1.79×10^{24}	3.24×10^{6}	3.88×10^{45}	4.65×10^{4}	2.53×10^{12}	5.65×10^{21}	7.09×10^{24}	8.85×10^{28}
7.04×10^{18}	6.99×10^{20}	5.64×10^{5}	1.90×10^{40}	2.76×10^{4}	1.00×10^{10}	4.74×10^{18}	3.11×10^{21}	1.63×10^{25}
1.52×10^{16}	1.00×10^{18}	1.32×10^{5}	7.09×10^{35}	1.72×10^{4}	9.80×10^{7}	1.30×10^{16}	4.95×10^{18}	1.27×10^{22}
8.33×10^{13}	3.86×10^{15}	3.88×10^{4}	1.25×10^{32}	1.14×10^{4}	1.92×10^{6}	8.93×10^{13}	2.15×10^{16}	2.99×10^{19}
9.62×10^{11}	3.27×10^{13}	1.36×10^{4}	7.58×10^{28}	7.88×10^{3}	6.58×10^{4}	1.25×10^{12}	2.03×10^{14}	1.68×10^{17}
2.76×10^{10}	7.41×10^{11}	5.91×10^{3}	2.13×10^{26}	5.82×10^{3}	4.50×10^{3}	4.27×10^{10}	5.08×10^{12}	2.79×10^{15}
1.97×10^{10}	5.18×10^{11}	5.47×10^{3}	1.22×10^{26}	5.64×10^{3}	3.50×10^{3}	3.10×10^{10}	3.58×10^{12}	1.89×10^{15}
6.58×10^{8}	1.37×10^{10}	2.46×10^{3}	4.35×10^{23}	4.16×10^{3}	2.67×10^{2}	1.22×10^{9}	1.05×10^{11}	3.73×10^{13}
3.25×10^{7}	5.49×10^{8}	1.22×10^{3}	2.99×10^{21}	3.13×10^{3}	2.73×10^{1}	7.09×10^{7}	4.67×10^{9}	1.17×10^{12}
2.23×10^{6}	3.14×10^{7}	6.48×10^{2}	3.57×10^{19}	2.42×10^{3}	3.60	5.65×10^{6}	2.94×10^{8}	5.41×10^{10}
2.02×10^{5}	2.42×10^{6}	3.69×10^{2}	6.76×10^{17}	1.90×10^{3}	5.85×10^{-1}	5.88×10^{5}	2.48×10^{7}	3.46×10^{9}
2.32×10^{4}	2.40×10^{5}	2.22×10^{2}	1.89×10^{16}	1.51×10^{3}	1.14×10^{-1}	7.69×10^{4}	2.68×10^{6}	2.92×10^{8}
2.38×10^{2}	1.80×10^{3}	7.50×10^{1}	9.80×10^{12}	9.10×10^{2}	3.53×10^{-3}	1.05×10^{3}	2.46×10^{4}	1.58×10^{6}
6.02	3.55×10^{1}	3.10×10^{1}	2.27×10^{10}	5.83×10^{2}	2.18×10^{-4}	3.41×10^{1}	5.78×10^{2}	2.44×10^{4}
2.94×10^{-1}	1.41	1.49×10^{1}	1.56×10^{8}	3.94×10^{2}	2.22×10^{-5}	2.07	2.69×10^{1}	8.06×10^{2}
2.36×10^{-2}	9.62×10^{-2}	7.95	2.44×10^{6}	2.78×10^{2}	3.29×10^{-6}	2.00×10^{-1}	2.08	4.69×10^{1}
2.79×10^{-3}	9.80×10^{-3}	4.62	7.19×10^{4}	2.01×10^{2}	6.54×10^{-7}	2.77×10^{-2}	2.40×10^{-1}	4.22
4.44×10^{-4}	1.38×10^{-3}	2.87	3.46×10^{3}	1.51×10^{2}	1.63×10^{-7}	5.08×10^{-3}	3.75×10^{-2}	5.38×10^{-1}
9.01×10^{-5}	2.53×10^{-4}	1.88	2.48×10^{2}	1.15×10^{2}	4.88×10^{-8}	1.17×10^{-3}	7.52×10^{-3}	8.93×10^{-2}
2.24×10^{-5}	5.71×10^{-5}	1.28	2.46×10^{1}	8.96×10^{1}	1.70×10^{-8}	3.23×10^{-4}	1.84×10^{-3}	1.87×10^{-2}

are listed in Table 3. The lifetimes at room temprature are taken as an example.

For the bimolecular reactions, such as elementary rxns. [1], [3], [6], [8], [10], [13], and [15], the atmospheric lifetimes can be calculated according to the pseudo-first-order reaction, since the concentrations of O_3 and H_2O can be taken as constant in atmosphere. Therefore, the total atmospheric lifetime of linalool relative to O_3 is 2.30 h. The O_3-initiated atmospheric lifetimes of P1, P3, and P6 are 2.64 months, 16.67 days, and 15.5 h, respectively. The atmospheric lifetimes of IM4 and IM8 relative to H_2O are 1.7 min and 1.64 h, respectively. For the pseudo-first-order reaction, the higher the constant concentration, the shorter the lifetime. In this case, high humidity can promote elementary rxns. [6] and [13].

For the monomolecular decomposition or isomerization reactions, the atmospheric lifetimes of the intermediate species vary greatly from seconds to years, such as IM2 (6.69 days), IM3 (2.92 min), IM6 (2.49 months), and IM11 (1.25 h). As for IM5 and IM9, the dehydration reactions from IM5 to P3 and IM9 to P6 have difficulty taking place as the barriers are very high. Therefore, the atmospheric lifetimes of IM5 and

Table 3. Arrhenius formulas for elementary reactions over the temperature range of 200–800 K.

Reaction	Arrhenius formula
R+O_3→TS1→IM2	$k(T) = 7.92\times10^{-13}$ exp(–2233.81/T)
IM2→TS2→P1+$C_3H_6O_2$	$k(T) = 3.93\times10^{13}$ exp(–13271.34/T)
P1+O_3→TS3→IM3	$k(T) = 7.86\times10^{-15}$ exp(–2816.74/T)
IM3→TS4→P2+CH_2O_2	$k(T) = 3.42\times10^{13}$ exp(–11497.23/T)
IM2→TS5→IM4+C_3H_6O	$k(T) = 1.09\times10^{14}$ exp(–13741.69/T)
IM4+H_2O→TS6→IM5	$k(T) = 2.41\times10^{-16}$ exp(–2816.05/T)
IM5→TS7→P3+H_2O	$k(T) = 1.09\times10^{13}$ exp(–27267.58/T)
P3+O_3→TS8→IM6	$k(T) = 7.08\times10^{-15}$ exp(–2319.91/T)
IM6→TS9→P4+CH_2O_2	$k(T) = 4.32\times10^{13}$ exp(–14013.91/T)
R+O_3→TS10→IM7	$k(T) = 2.19\times10^{-13}$ exp(–1376.40/T)
IM7→TS11→P5+CH_2O_2	$k(T) = 2.93\times10^{13}$ exp(–16393.21/T)
IM7→TS12→IM8+CH_2O	$k(T) = 4.58\times10^{13}$ exp(–17504.94/T)
IM8+H_2O→TS13→IM9	$k(T) = 1.55\times10^{-16}$ exp(–3900.93/T)
IM9→TS14→P6+H_2O	$k(T) = 1.68\times10^{13}$ exp(–27131.62/T)
P6+O_3→TS15→IM11	$k(T) = 1.88\times10^{-13}$ exp(–1647.99/T)
IM11→TS16→P7+$C_3H_6O_2$	$k(T) = 2.71\times10^{14}$ exp(–12397.10/T)
P1→TS17→P8	$k(T) = 8.41\times10^{11}$ exp(–1549272/T)
P2→TS18→P9	$k(T) = 8.83\times10^{11}$ exp(–16931.43/T)
P7→TS19→P10	$k(T) = 9.28\times10^{11}$ exp(–18827.26/T)

Note: Units are s^{-1} and cm^3 $molecule^{-1}$ s^{-1} for the unimolecular and bimolecular reactions, respectively.

IM9 are very long. As for the other species, IM7, P1, P2, and P7 also have long atmospheric lifetimes.

In the atmosphere, linalool ozonolysis will generate a series of oxidation products to form particles through nucleation. These nucleate particles can be condensed and absorb volatile organics to contribute to the formation of SOA. The longer the atmospheric lifetime, the more important the contribution to the SOA formation.

Acknowledgments

This work is supported by the National Natural Science Foundation of China (Nos. 20903062, 21177076, 20873074, and 20737001), the Natural Science Foundation of Shandong Province (No. Q2008B07), the Independent Innovation Foundation of Shandong University (No. 2010TS064), and the Open Project from State Key Laboratory of Environmental Chemistry and Ecotoxicology, Research Center for Eco-Environmental Sciences, Chinese Academy of Sciences (No. KF2009-10). The authors thank Professor Donald G. Truhlar for providing the POLYRATE 9.7 program and Professor Baoshan Wang for providing the RRKM program.

References

(1) Arey, J.; Corchnoy, S. B.; Atkinson, R. *Atmos. Environ.* **1991**, *25*, 1377.

(2) Konig, G.; Brunda, M.; Puxbaum, H.; Hewitt, C. N.; Duckham, S. G.; Rudolph, J. *Atmos. Environ.* **1995**, *29* (8), 861. doi:10.1016/1352-2310(95)00026-U.

(3) Grosjean, D.; Grosjean, E.; Williams, E. L. *Environ. Sci. Technol.* **1993**, *27* (12), 2478. doi:10.1021/es00048a026.

(4) Nakamura, A.; Fujiwara, S.; Matsumoto, I.; Abe, K. *J. Agric. Food Chem.* **2009**, *57* (12), 5480. doi:10.1021/jf900420g.

(5) Bäcktorp, C.; Johnson Wass, J. R. T.; Panas, I.; Sköld, M.; Börje, A.; Nyman, G. *J. Phys. Chem. A* **2006**, *110* (44), 12204. doi:10.1021/jp0603278.

(6) Shu, Y.; Kwok, E. S. C.; Tuazon, E. C.; Atkinson, R.; Arey, J. *Environ. Sci. Technol.* **1997**, *31* (3), 896. doi:10.1021/es960651o.

(7) Lee, A.; Goldstein, A. H.; Keywood, M. D.; Gao, S.; Varutbangkul, V.; Bahreini, R.; Ng, N. L.; Flagan, R. C.; Seinfeld, J. H. *J. Geophys. Res.* **2006**, *111*, D07302. doi:10.1029/2005JD006437.

(8) Meera, A. S. Ph.D. Dissertation, Syracuse University, New York, 2010.

(9) Chen, X.; Hopke, P. K. *Atmos. Environ.* **2009**, *43* (25), 3935. doi:10.1016/j.atmosenv.2009.04.033.

(10) Sun, T. L.; Wang, Y. D.; Zhang, C. X.; Sun, X. M.; Hu, J. T. *Acta Chim. Sin.* **2011**, *69*(17), 1965.

(11) Zhao, Y.; Truhlar, D. G. *J. Phys. Chem. A* **2004**, *108* (33), 6908. doi:10.1021/jp048147q.

(12) Hou, H.; Wang, B. S. *J. Chem. Phys.* **2007**, *127* (5), 054306. doi:10.1063/1.2756538.

(13) Baldridge, M. S.; Gordon, R.; Steckler, R.; Truhlar, D. G. *J. Phys. Chem.* **1989**, *93* (13), 5107. doi:10.1021/j100350a018.

(14) Gonzalez-Lafont, A.; Truong, T. N.; Truhlar, D. G. *J. Chem. Phys.* **1991**, *95* (12), 8875. doi:10.1063/1.461221.

(15) Liu, Y. P.; Lynch, G. C.; Truong, T. N.; Lu, D. H.; Truhlar, D. G.; Garrett, B. C. *J. Am. Chem. Soc.* **1993**, *115* (6), 2408. doi:10.1021/ja00059a041.

(16) Yang, J.; Li, Q. S.; Zhang, S. *Int. J. Quantum Chem.* **2007**, *107* (10), 1999. doi:10.1002/qua.21343.

(17) Yang, J.; Li, Q. S.; Zhang, S. W. *J. Comput. Chem.* **2008**, *29* (2), 247. doi:10.1002/jcc.20783.

(18) Fukui, K. *Acc. Chem. Res.* **1981**, *14* (12), 363. doi:10.1021/ar00072a001.

(19) Frisch, M. J.; Trucks, G. W.; Schlegel, H. B.; Scuseria, G. E.; Robb, M. A.; Cheeseman, J. R.; Montgomery, J. A., Jr.; Vreven, T.; Kudin, K. N.; Burant, J. C.; Millam, J. M.; Iyengar, S. S.; Tomasi, J.; Barone, V.; Mennucci, B.; Cossi, M.; Scalmani, G.; Rega, N.; Petersson, G. A.; Nakatsuji, H.; Hada, M.; Ehara, M.; Toyota, K.; Fukuda, R.; Hasegawa, J.; Ishida, M.; Nakajima, T.; Honda, Y.; Kitao, O.; Nakai, H.; Klene, M.;

Can. J. Chem. Downloaded from www.nrcresearchpress.com by Renmin University of China on 09/02/12
For personal use only.

Li, X.; Knox, J. E.; Hratchian, H. P.; Cross, J. B.; Bakken, V.; Adamo, C.; Jaramillo, J.; Gomperts, R.; Stratmann, R. E.; Yazyev, O.; Austin, A. J.; Cammi, R.; Pomelli, C.; Ochterski, J. W.; Ayala, P. Y.; Morokuma, K.; Voth, G. A.; Salvador, P.; Dannenberg, J. J.; Zakrzewski, V. G.; Dapprich, S.; Daniels, A. D.; Strain, M. C.; Farkas, O.; Malick, D. K.; Rabuck, A. D.; Raghavachari, K.; Foresman, J. B.; Ortiz, J. V.; Cui, Q.; Baboul, A. G.; Clifford, S.; Cioslowski, J.; Stefanov, B. B.; Liu, G.; Liashenko, A.; Piskorz, P.; Komaromi, I.; Martin, R. L.; Fox, D. J.; Keith, T.; Al-Laham, M. A.; Peng, C. Y.; Nanayakkara, A.; Challacombe, M.; Gill, P. M. W.; Johnson, B.; Chen, W.; Wong, M. W.; Gonzalez, C.; Pople, J. A. *Gaussian 03,* Revision B.03; Gaussian Inc.: Pittsburgh, PA, 2003.

(20) Zheng, J. J.; Zhang, S. X.; Lynch, B. J.; Corchado, J. C.; Chuang, Y. Y.; Fast, P. L.; Hu, W. P.; Liu, Y. P.; Lynch, G. C.; Nguyen, K. A.; Jackels, C. F.; Ramos, A. F.; Ellingson, B. A.; Melissas, V. S.; Villà, J.; Rossi, I.; Coitiño, E. L.; Pu, J. Z.; Albu, T. V.; Steckler, R.; Garrett, B.C; Truhlar, D. G. *POLYRATE version 2010-A;* 2010.

(21) Atkinson, R.; Tuazon, E. C.; Aschmann, S. M. *Environ. Sci. Technol.* **1995**, *29* (7), 1860. doi:10.1021/es00007a025.

(22) Calogirou, A.; Kotzias, D.; Kettrup, A. *Naturwissenschaften* **1995**, *82* (6), 288. doi:10.1007/BF01134526.

(23) Sun, T. L.; Zhang, Q. Z.; Qu, X. H.; Wang, W. X. *Chem. Phys. Lett.* **2005**, *407* (4–6), 527. doi:10.1016/j.cplett.2005.03.128.

(24) Zhang, Q. Z.; Zhang, R. Q.; Gu, Y. S. *J. Phys. Chem. A* **2004**, *108* (6), 1064. doi:10.1021/jp036446u.

(25) Sarwar, G.; Olson, D. A.; Corsi, R. L.; Weschler, C. J. *J. Air Waste Manage. Assoc.* **2004**, *54*, 367.

(26) Li, T. H.; Turpin, B. J.; Shields, H. C.; Weschler, C. J. *Environ. Sci. Technol.* **2002**, *36* (15), 3295. doi:10.1021/es015842s.

(27) Rohr, A. C.; Weschler, C. J.; Koutrakis, P.; Spengler, J. D. *Aerosol Sci. Technol.* **2003**, *37* (1), 65. doi:10.1080/02786820300892.

Can. J. Chem. Downloaded from www.nrcresearchpress.com by Renmin University of China on 09/02/12
For personal use only.

Two new one-dimensional coordination polymers containing $[N(CN)_2]^-$ — Syntheses, structures, and magnetic properties of $[M^{II}(3\text{-}Bzpy)_2(N(CN)_2)_2]$ (M = Mn (1) and Co (2) and 3-Bzpy = 3-benzoylpyridine)

Qianqian Bao, Yutao Ma, Qihua Zhao, Yanghui Luo, and Baiwang Sun

Can. J. Chem. Downloaded from www.nrcresearchpress.com by Renmin University of China on 09/02/12
For personal use only.

Abstract: The structures of two one-dimensional coordination complexes, $[M^{II}(3\text{-}Bzpy)_2(N(CN)_2)_2]$ (M = Mn (**1**) and Co (**2**) and 3-Bzpy = 3-benzoylpyridine), have been determined in this work. The two structures are isomorphous, crystallize in a monoclinic $P2_1/c$ space group, and show almost the same crystal structure. The magnetic measurements of the two compounds (2–300 K) indicate that antiferromagnetic exchanges exist between the metal ions of the two compounds.

Key words: dicyanamide, 1-D, structure, magnetic property.

Résumé : Dans ce travail, on a déterminé les structures de deux complexes de coordination unidimensionnels, $[M^{II}(3\text{-}Bzpy)_2(N(CN)_2)_2]$ (M = Mn (**1**) et Co (**2**) et 3-Bzpy = 3-benzoylpyridine). Les deux structures sont isomorphes, elles cristallisent dans le groupe d'espace monoclinique $P2_1/c$ et elles se présentent sous des formes cristallines pratiquement semblables. Des mesures magnétiques effectuées sur les deux composés (2–300 K) indiquent qu'il se produit des échanges antiferromagnétiques entre les ions métalliques des deux composés.

Mots-clés : dicyanamide, 1-D, structure, propriété magnétique.

[Traduit par la Rédaction]

Introduction

In the last 10 years, 1-D coordination polymers have been frequently investigated because of their magnetic characteristics.[1–3] The dicyanamide ligand $[N(CN)_2]^-$ is extremely popular as a building block in constructing coordination polymers, since it can act in a mono-, bi-, or tri-dentate coordination manner[4,5] and act as a molecular-based magnet precursor with several first-row transition ions such as Cu(II), Ni(II), Co(II), Mn(II), and Cr(II).[6–9] The introduction of N-based bridging and a terminal ligand into the metal $[N(CN)_2]^-$ system has led to many different structures with interesting magnetic properties. For example, when the metal/dca ratio is 1:2 and the metal is hexacoordinated, the dca ligand often acts as a tridentate ligand with the three nitrogen atoms and forms neutral three-dimensional compounds. If the metal is tetrachordinate, the dca ligand then acts as an end-to-end $\mu_{1,5}$ bidentate ligand.[10–13] It is interesting that the formation of the compounds in this family follow a strategy that their structural formulas can be expressed by $[ML_2(dca)_2]$, in which L may be two monodentate ligands or one bidentate ligand, and afford compounds with bidentate dca ligands.[11] Many such compounds have been reported, such as 1-D for $[M^{II}(pyr)_2(N(CN)_2)_2]$ (M = Mn (**1**) and Co (**2**) and pyr = 2-pyrrolidone)[14] and $Mn[N(CN)_2]_2(2,4'\text{-bpy})_2$ (2,4′-bpy = 2,4-bipyridine),[15] 2-D for $[M^{II}(N(CN)_2)_2(H_2O)]$phz (M = Co or Ni and phz = phenazine),[16] $Zn[N(CN)_2]_2$,[17] and 3-D for $M^{II}[N(CN)_2]_2$ (M = Cu, Co, Ni, or Mn)[6,18] and $M(dca)_2$(apym) (M = Co or Ni and apym = 2-aminopyrimidine).[19] In our previous work, we successfully introduced 3-benzoylpyridine as ancillary ligand of the dicyanamide system and obtained an interesting structure, $[Zn^{II}(3\text{-}Bzpy)_2(N(CN)_2)_2]$ (3-Bzpy = 3-benzoylpyridine).[20] Enlightened by this success, we report the structure and magnetic properties of two new 1-D coordination compounds of this family here, in which M is manganese(II) and cobalt(II) and the L_2 is two 3-benzoylpyridines with the formula $[M^{II}(3\text{-}Bzpy)_2(N(CN)_2)_2]$ (M = Mn (**1**) and Co (**2**)), where the dicyanamide anion bridged the metal ions in an end-to-end $\mu_{1,5}$ model as expected. The magnetic measurements indicate weak antiferromagnetic coupling with $J = -0.16$ for compound (**1**). It seems that weak antiferromagnetic coupling is the common gender of the manganese(II) complex in the double $\mu_{1,5}$-dicyanamide family,[21] but the magnetic properties of complex **2** are special from others in this family, and it shows significant orbital contribution at room temperature and obvious orbital angular momentum at lower temperatures.

Received 15 June 2011. Accepted 3 January 2012. Published at www.nrcresearchpress.com/cjc on 19 March 2012.

Q. Bao, Y. Luo, and B. Sun. Ordered Matter Science Research Center, Department of Chemistry and Chemical Engineering, Southeast University, Nanjing 210096, P.R. China.
Y. Ma and Q. Zhao. Department of Chemistry Key Laboratory of Medicinal Chemistry for Natural Resource Ministry of Education, Yunnan University, Kunming 650091, P.R. China.

Corresponding author: Baiwang Sun (e-mail: chmsunbw@seu.edu.cn).

Can. J. Chem. Downloaded from www.nrcresearchpress.com by Renmin University of China on 09/02/12
For personal use only.

Table 1. Crystallographic data for $[Mn(3\text{-}Bzpy)_2(N(CN)_2)_2]$ (**1**) and $[Co(3\text{-}Bzpy)_2(N(CN)_2)_2]$ (**2**) (3-Bzpy = 3-benzoylpyridine).

	Compound	
Parameter	**1**	**2**
Empirical formula	$C_{28}H_{18}MnN_8O_2$	$C_{28}H_{18}CoN_8O_2$
Formula weight	553.44	557.43
Crystal size (mm)	0.18×0.08×0.07	0.12×0.05×0.05
Crystal system	Monoclinic	Monoclinic
Space group	*P*2(1)/*c*	*P*2(1)/*c*
λ (Mo Kα) (Å)	0.71073	0.71073
a (Å)	6.3943(13)	6.4536(15)
b (Å)	7.5253(15)	7.4490(16)
c (Å)	26.517(6)	26.307(6)
α (°)	90	90.015(18)
β (°)	98.60(3)	98.027(18)
γ (°)	90	90.00(2)
V (Å^3)	1261.6(5)	1252.3(5)
Z	2	2
D_{calcd} (Mg m^{-3})	1.457	1.478
μ (mm^{-1})	0.567	0.729
F(000)	566	570
T (K)	293(2)	293(2)
θ range for data collection (°)	$3.11 \le \theta \le 25.00$	$3.1316 \le \theta \le 27.51$
Reflections collected	9597	12087
Unique reflections	2219	2870
Goodness-of-fit on F^2	1.066	1.097
Range (*h*,*k*,*l*)	$-7 \le h \le 7$, $-8 \le k \le 8$, $-31 \le l \le 31$	$-8 \le h \le 8$, $-9 \le k \le 9$, $-34 \le l \le 34$
R_1, wR_2 ($(I > 2\sigma(I))$)	0.0624, 0.1251	0.0529, 0.1396
R_1, wR_2 (all data)	0.1100, 0.1405	0.0783, 0.1564
$\Delta\rho_{min}$ and $\Delta\rho_{max}$ (e Å^{-3})	0.404, –0.276	0.297, –0.339

Note: $R_1 = \Sigma|F_o - F_c|/\Sigma F_o$ and $wR_2 = [\Sigma w(F_o - F_c)^2/\Sigma wF_o^2]^{1/2}$, where $w = 1/[\sigma^2(F_o^2) + (0.0808P)^2 + 0.17P]$ and $P = (\text{Max}(F_o^2, 0) + 2F_c^2)/3$ or $w = 1/[\sigma^2(F_o^2) + (0.0163P)^2 + 0.63P]$ and $P = (\text{Max}(F_o^2, 0) + 2F_c^2)/3$.

The crystal structure of compound **1** is very similar with the reported crystal structure: *trans*-$[Mn(4\text{-}Bzpy)_2(N(CN)_2)]$ (4-Bzpy = 4-benzoylpyridine),[21] which consists of chains with double $\mu_{1,5}$-dicyanamide bridges between neighboring manganese(II) atoms and shows weak antiferromagnetic coupling with $J = -0.3$. The differences of ancillary ligand L and magnetic behaviour between them indicate that any disparities of the ancillary ligand can lead to differences in the dicyanamide system both in topology structure and properties.

Experimental

Materials

All chemicals used (reagent grade) were commercially available. $Na[N(CN)_2]_2$ was purchased from the ACROS Company. Elemental analyses (C, H, and N) were carried out by using a Elementar Analysensysteme GmbH Vario EL instrument. The IR spectrum was recorded on a AThermo-Nicolet AVATAR FT-IR 360 spectrometer as KBr pellets in the 4000 ± 400 cm^{-1} region. The temperature-dependent magnetizations (M vs H) at 2.5 K of complexes **1** and **2** were measured by using a Quantum Design vibrating sample magnetometer (VSM) in the Physical property measurement system (PPMS).

Preparation of $[M^{II}(3\text{-}Bzpy)_2(N(CN)_2)_2]$ (M = Mn (1) and Co (2))

Complex (**1**) was prepared as follows: 3-Bzpy (21.96 mg, 0.12 mmol) was added slowly with stirring in an aqueous solution (5 mL) of $Mn(CH_3COO)_2{\cdot}4H_2O$ (30.00 mg, 0.12 mmol) and then sodium dicyanamide (21.36 mg, 0.24 mmol) in a methanol–water solution (5 mL) was added slowly. The resulting solution was continuously stirred for about 30 min at room temperature and then filtered. The filtrate was slowly evaporated at room temperature over several days, and yellowish needles crystals suitable for X-ray analysis were obtained. The yield was 80%. IR (KBr, cm^{-1}): 2308, 2229, 2171, 1650, 1596, 1450, 1425, 1371, 780, 703, 690, 650. Anal. calcd for $C_{28}H_{18}MnN_8O_2$ (%): C 60.77, N 20.25, H 3.28; found: C 61.23, N 20.12, H 3.34.

Compound **2** was synthesized exactly as for **1** but from $Co(Ac)_2{\cdot}4H_2O$. The crystal appeared as pink needles and the yield was 85%. IR (KBr, cm^{-1}): 2306, 2237, 2179, 1650, 1596, 1444, 1410, 1365, 780, 690, 703, 650. Anal. calcd for $C_{28}H_{18}CoN_8O_2$ (%): C 60.33, N 20.10, H 3.25; found: C 60.46, N 20.17, H 3.29.

Crystal data collection and refinement

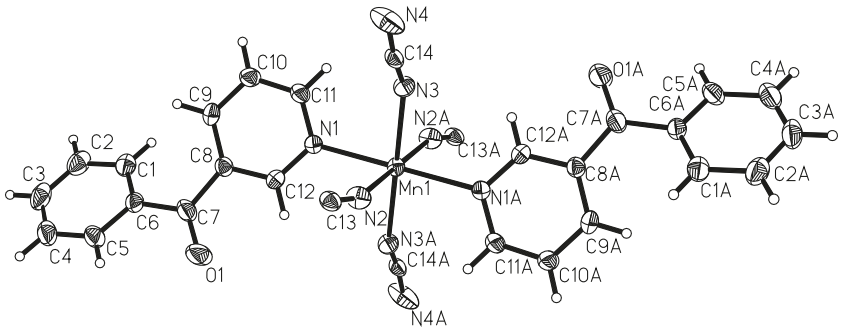
The structures of two compounds **1** and **2** were studied at the Sun B.W. Lab of Southeast University, Nanjing, P.R. China. Data were collected on a Rigaku Scxmini 1 K CCD area detector diffractometer with graphite-monochromated Mo Kα radiation (λ = 0.710 73 Å). The structural analyses show that they are isomorphous. Crystal data are summarized in Table 1. All the data were collected, processed, and corrected for Lorentz and polarization effects using the Bruker

Can. J. Chem. Downloaded from www.nrcresearchpress.com by Renmin University of China on 09/02/12
For personal use only.

Table 2. Selected bond distances (Å) and angles (°) for complexes **1** ($[Mn(3\text{-}Bzpy)_2(N(CN)_2)_2]$) and **2** ($[Co(3\text{-}Bzpy)_2(N(CN)_2)_2]$) (3-Bzpy = 3-benzoylpyridine).

Bond distance (Å)		Bond angle (°)	
Complex 1			
Mn1–N1	2.2078(37)	N1–Mn1–N1A	180.000(97)
Mn1–N2	2.2115(33)	N1–Mn1–N3	89.931(104)
Mn1–N3	2.2827(29)	N1–Mn1–N3B	90.069(104)
N2–C13	1.1241(58)	N1A–Mn1–N3	90.069(104)
N4A–C13	1.286(6)	N1A–Mn1vN3B	89.931(104)
N4A–C14A	1.2936(58)	N1–Mn1–N2	88.663(105)
N3–C14	1.1310(58)	N1–Mn1–N2B	91.337(105)
O1–C7	1.2118(62)	N1A–Mn1–N2	91.337(105)
C8–C7	1.4880(57)	N1A–Mn1–N2B	88.663(105)
C6–C7	1.4968(77)	N2–Mn1–N2B	180.000(136)
		N2–Mn1–N3	87.270(129)
Complex 2			
Co1–N1	2.175(2)	N1–Co1–N1A	180.000(1)
Co1–N2	2.135(2)	N1–Co1–N3	89.03(9)
Co1–N3	2.120(3)	N1–Co1–N3B	90.97(9)
N2–C13	1.148(3)	N1A–Co1–N3	90.97(9)
N4A–C13	1.2973(40)	N1A–Co1–N3B	89.03(9)
N4A–C14A	1.299(4)	N1–Co1–N2	89.76(9)
N3–C14	1.143(4)	N1–Co1–N2B	90.24(9)
O1–C7	1.218(5)	N1A–Co1–N2	90.24(9)
C8–C7	1.492(5)	N1A–Co1–N2B	89.76(9)
C6–C7	1.498(5)	N2–Co11–N2B	180.00(16)
		N2–Co1–N3	87.39(10)

Fig. 1. Structure of complex **1** ($[Mn(3\text{-}Bzpy)_2(N(CN)_2)_2]$; 3-Bzpy = 3-benzoylpyridine) with thermal ellipsoids drawn at the 50% probability level (hydrogen atoms are omitted for clarity).



SADABS program with the multiscan method. The structures were solved by direct methods and refined by a full-matrix least-squares technique based on F_2 using the SHELXL 97 program.[14] All non-hydrogen atoms were refined anisotropically, and hydrogen atoms were placed by calculation positions and refined isotropically.

Results and discussion

Crystallographic data for $[Mn(3\text{-}Bzpy)_2(N(CN)_2)_2]$ (**1**) and $[Co(3\text{-}Bzpy)_2(N(CN)_2)_2]$ (**2**), are listed in Table 1. Selected bond distances (Å) and angles (°) for complexes **1** and **2** are also listed in Table 2. Compounds **1** and **2** are one-dimensional coordination complexes. The structures of the two complexes are isomorphous and are exemplified by $[Mn(3\text{-}Bzpy)_2(N(CN)_2)_2]$ (see the Supplementary data).

A perspective view of the metal coordination environment in the crystals of complex **1** is presented in Fig. 1. It shows that the compound crystallizes in a monoclinic $P2_1/c$ space group. The Mn(II) ion, which lies on the inversion centre, is in an octahedral geometry with the four N atoms of different $[N(CN)_2]^-$ ligands in the equatorial plane. The another two N atoms of different 3-Bzpy ligands occupy the axial positions, since the bond angles of N1–Mn1–N1A, N2–Mn1–N2B, and N3–Mn1–N3B are all 180°, whereas, in the crystal structure of *trans*-$[Mn(4\text{-}Bzpy)_2(N(CN)_2)]$, the same bond angles are only 102.1(2)°.[13] This means that the disparity of the ancillary ligand can have a great affect on the topology structure of the dicyanamide system.

In the crystal structure, the Mn(II) atoms are bridged to form a 1-D chain by dicyanamide ligands (Fig. 2), which act

Can. J. Chem. Downloaded from www.nrcresearchpress.com by Renmin University of China on 09/02/12
For personal use only.

Fig. 2. A packing diagram of complex **1** ([Mn(3-Bzpy)$_2$(N(CN)$_2$)$_2$]) looking down the *b* axis showing how discrete 1-D Mn(3-Bzpy)$_2$(N(CN)$_2$)$_2$ coordination polymers are further extended into interesting 2-D supramolecular arrays through π-π stacking interactions (3-Bzpy = 3-benzoylpyridine). Displacement ellipsoids are drawn at the 50%, probability level and hydrogen atoms are omitted for clarity.

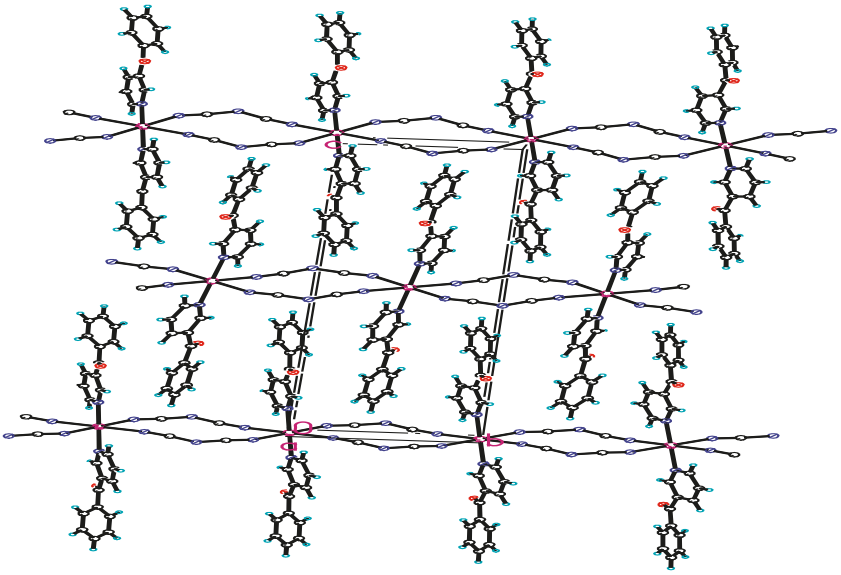
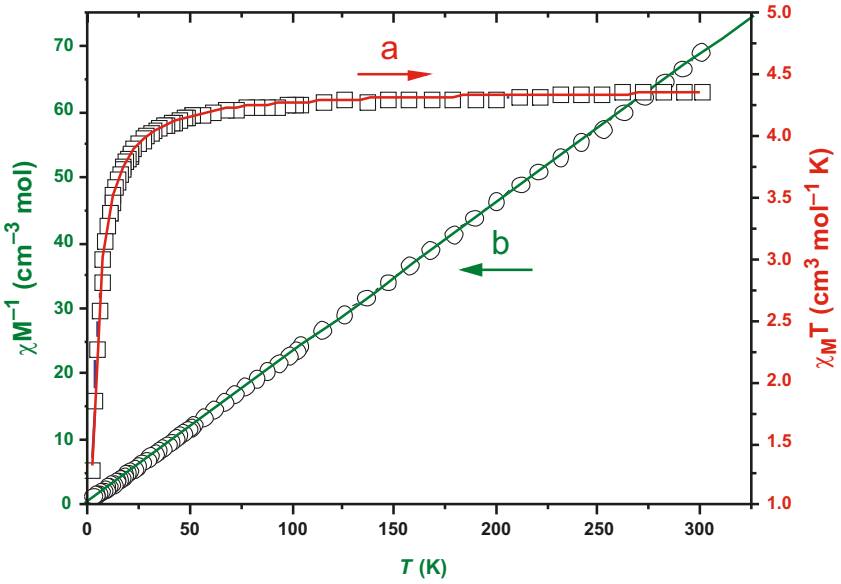


Fig. 3. Plots of the dependence of (*a*) $\chi_M T$ and (*b*) χ_M^{-1} on temperature for complex **1**([Mn(3-Bzpy)$_2$(N(CN)$_2$)$_2$]; 3-Bzpy = 3-benzoylpyridine). Circles and squares represent the experimental values and the solid lines represent the best calculated curves. χ_M is the molar magnetic susceptibility.



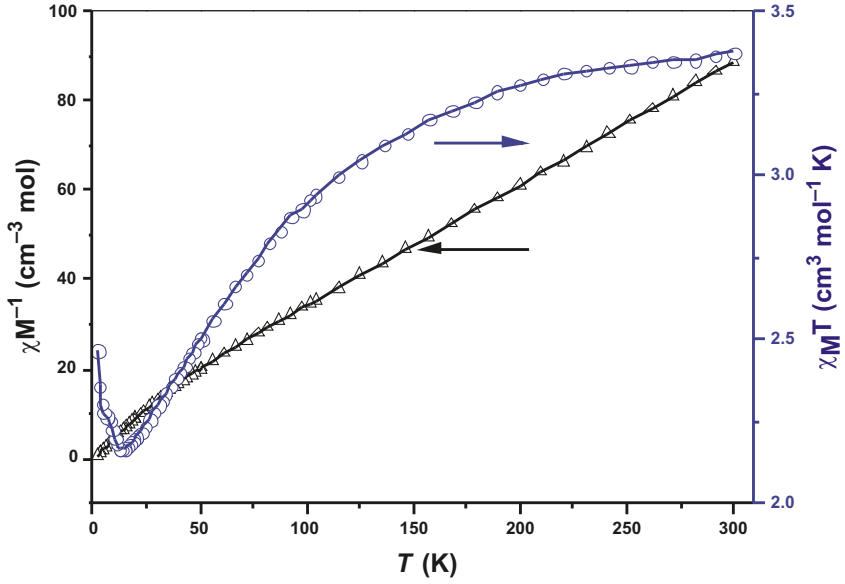
as bidentate bridging ligands by coordinating to adjacent Mn (II) centres through their two terminal nitrile N atoms. In addition, the shortest centroid-to-centriod distances between 3-Bzpy of adjacent chains are 4.000 and 4.118 Å, implying there are π–π stacking interactions among neighboring polymeric 1-D chains, which force the 1-D chains into interesting 2-D supramolecular arrays. Polymeric 1-D chains are generated parallel to the *b* axis, with adjacent chains staggered along the *b* axis and there are chains of metal ions bridged by the N atoms of the $[N(CN)_2]^-$ ligands, with Mn···Mn distances of 6.3943(13) Å. The Mn···Mn distance is shorter than that of [Mn(4-Bzpy)$_2$(N(CN)$_2$)] (7.584 Å)[13] and [Mn(pyr)$_2$(N(CN)$_2$)$_2$] (7.538 Å), since the bond angle of C13–N4–C14 is bigger than that in [Mn(pyr)$_2$(N(CN)$_2$)$_2$].[5]

The structure of **2** is very similar to that of [Mn(3-Bzpy)$_2$(N(CN)$_2$)$_2$], and it is necessary to note that the shortest intrachain distance between Co···Co was found as 7.4490(16) Å, and the shortest centroid-to-centroid distances between 3-Bzpy of adjacent chains are 3.969 and 4.105 Å.

Magnetochemistry

The temperature dependence of the molar magnetic susceptibility (χ_M) for complexes **1** and **2** was measured in the

Fig. 4. Plots of the dependence of (*a*) $\chi_M T$ and (*b* χ_M^{-1}) on temperature for complex **2** ([Co(3-Bzpy)$_2$(N(CN)$_2$)$_2$]). Circles and squares represent the experimental values and the solid lines represent the best calculated curves. χ_M is the molar magnetic susceptibility.



2–300 K temperature range, as shown in Figs. 3 and 4, in the forms of $\chi_M^{-1}$and $\chi_M T$ vs T. From the figures, we can see the two complexes both imply antiferromagnetic exchanges between the metal ions. According to the χ_M^{-1}–T line, the magnetic behaviors of **1** and **2** follow the Curie–Weiss law $\chi_M = C/(T - \theta)$ with Curie constant (C) values of 4.40 and 3.45 cm^3 mol^{-1} K and Weiss temperatures θ of –3.10 and –12.34 K. The value of $\chi_M T$ of **1** at 300 K is 4.371 cm^3 mol^{-1} K, and is perfectly agreement with the spin-only value expected for uncoupled high-spin $S = 5/2$ ions (4.37 cm^3 mol^{-1} K), so we can see the interactions between Mn^{2+} ions are very weak as expected. The magnetic susceptibility data were quantitatively analyzed by eq. [1], which is deduced from the Hamiltonian model with $H = -2JS_{Mn}S_{Mn}$ and derived from the Heisenberg infinite linear chain model.[22]

$$[1] \qquad \chi_M = \frac{Ng^2\mu_B{}^2S(S+1)}{3k_BT}\cdot\frac{1+u(K)}{1-u(K)}$$

where N is Avogadro's number, μ_B is the Bohr magneton, k_B is the Boltzman constant ($k_B = 0.695$), and J is the intrachain coupling constant of Mn^{2+} ions. From this, $N\beta^2/3k_B = 0.125$, $K = 2 \times J \times 2.5 \times 3.5/0.695/T$, where $u(K)$ and K are defined as

$$[2] \qquad u(K) = \coth K - \frac{1}{K}$$

$$[3] \qquad K = \frac{2JS(S+1)}{k_BT}$$

In eq. [2], coth K is expressed as

$$[4] \qquad \coth K = \frac{[\exp(K) + \exp(-K)]}{[\exp(K) - \exp(-K)]}$$

The values from eqs. [1]–[4] can be used to deduce the definite expression for χ_M.

$$[5] \qquad \chi_M = 1.1g^2 \times \frac{1 + [\exp(25.18J/T) + \exp(-25.18J/T) - T/25.18J]}{1 - [\exp(25.18J/T) - \exp(-25.18J/T)] + T/25.18J}$$

The best-fit parameters of the experimental data to the theoretical model were found to be $J = -0.16$ cm^{-1} and $g = 2.00$. The solid line in Fig. 3 represents the best-fit result. According to the single-crystal structure of complex **1**, the distance between Mn···Mn is 6.3943(13) Å and the pathway through a bridge of five atoms. This is one of the important reasons for the weak magnetic exchange interactions between the paramagnetic centres in the chains. Another reason for this phenomenon was proved by Mealli and Proserpio[23] based on MO calculation and confirms that the $\mu_{1,5}$-dicyanamide bridge should be assumed to be a very poor superexchange mediator. As for *trans*-[Mn(4-Bzpy)$_2$(N(CN)$_2$)], it shows the same magnetic profiles as **1** with a $\chi_M T$ of 4.20 cm^3 mol^{-1} K at 300 K.

Fig. 4 presents the $\chi_M T$–T curve of complex **2**. The $\chi_M T$ value gradually decreases from 3.38 to 2.20 cm^3 mol^{-1} K from 300 to 20 K because of antiferromagnetic exchange,but at lower temperature it increases more steeply to reach 2.47 cm^3 mol^{-1} K at 2 K, which is attributed to the orbital angular momentum of the Co atoms. The value of $\chi_M T$ per Co(II) ion at room temperature is greater than calculated for the spin-only case (1.87 cm^3 mol^{-1} K), revealing that a significant orbital contribution occurs.

Supplementary data

Supplementary data are available with the article through the journal Web site at http://nrcresearchpress.com/doi/suppl/10.1139/v2012-004. CCDC 841982 and CCDC 841981 contain the X-ray data in CIF format for compounds **1** and **2**. These data can be obtained, free of charge, via http://www.ccdc.cam.ac.uk/products/csd/request (or from the Cambridge Crystallographic Data Centre, 12 Union Road, Cambridge

Can. J. Chem. Downloaded from www.nrcresearchpress.com by Renmin University of China on 09/02/12
For personal use only.

CB2 1EZ, UK; fax: +44 1223 336 033; or e-mail: deposit@ccdc.cam.ac.uk).

Acknowledgment

This work was supported by the National Natural Science Foundation of China (Project 20671019).

References

(1) Miller, J. S. *Acta Crystallogr.* **1983**, *39*, 655.
(2) Gatteschi, D.; Kahn, O.; Miller, J. S.; Palacio, F. *Magn. Mol. Mater.* **1991**, *198*, 245.
(3) Escuer, A.; Mautner, F. A.; Sanz, N.; Vicente, R. *Inorg. Chem.* **2000**, *39* (8), 1668. doi:10.1021/ic990905h.
(4) Riggio, I.; van Albada, G. A.; Ellis, D. D.; Spek, A. L.; Reedijk, J. *Inorg. Chim. Acta* **2001**, *313* (1-2), 120. doi:10.1016/S0020-1693(00)00374-1.
(5) Li, B. L.; Li, B. Z.; Zhu, X.; Zhu, L. M.; Zhang, Y. *Acta Crystallogr. C* **2003**, *59* (9), m350. doi:10.1107/S0108270103012435.
(6) Batten, S. R.; Jensen, P.; Moubaraki, B.; Murray, K. S.; Robson, R. *Chem. Commun.* **1998**, (3), 439. doi:10.1039/A707264C.
(7) Kurmoo, M.; Kepert, C. J. *New J. Chem.* **1998**, *22* (12), 1515. doi:10.1039/a803165g.
(8) Manson, J. L.; Kmety, C. R.; Huang, Q. Z.; Lynn, J. W.; Bendele, G. M.; Pagola, S.; Stephens, P. W.; Liablesands, L. M.; Rheingold, A. L.; Epstein, A. J.; Miller, J. S. *Chem. Mater.* **1998**, *10* (9), 2552. doi:10.1021/cm980321y.
(9) Manson, J. L.; Kmety, C. R.; Epstein, A. J.; Miller, J. S. *Inorg. Chem.* **1999**, *38* (11), 2552. doi:10.1021/ic9901259.
(10) Manson, J. L.; Incarvito, C. D.; Rheingold, A. L.; Miller, J. S. *J. Chem. Soc., Dalton Trans.* **1998**, (22): 3705. doi:10.1039/a807788f.
(11) Manson, J. L.; Lee, D. W.; Rheingold, A. L.; Miller, J. S. *Inorg. Chem.* **1998**, *37* (23), 5966. doi:10.1021/ic980659u.
(12) Potocnák, I.; Dunaj-Jurco, M.; Miklos, D.; Kabesová, M.; Jäger, L. *Acta Crystallogr. C* **1995**, *51* (4), 600. doi:10.1107/S0108270194012084.
(13) Kozísek, J.; Paulus, H.; Danková, M.; Hvastijová, M. *Acta Crystallogr. C* **1996**, *52* (12), 3019. doi:10.1107/S0108270196010311.
(14) Sun, B. W.; Gao, S.; Ma, B. Q.; Wang, Z. M. *Inorg. Chem. Commun.* **2001**, *4* (2), 72. doi:10.1016/S1387-7003(00)00193-3.
(15) Liu, C. M.; Zhang, D. Q.; Zhu, D. B.; Jin, X. *Transition Met. Chem.* **2003**, *28* (3), 336. doi:10.1023/A:1022912419172.
(16) Kutasi, A. M.; Batten, S. R.; Moubaraki, B.; Murray, K. S. *J. Chem. Soc., Dalton Trans.* **2002**, (6): 819. doi:10.1039/b110920k.
(17) Batten, S. R.; Jensen, P.; Kepert, C. J.; Kurmoo, M.; Moubaraki, B.; Murray, K. S.; Price, D. J. *Chem. Commun.* **1999**, 177.
(18) Kurmoo, M.; Kepert, C. J. *New J. Chem.* **1998**, *22* (12), 1515. doi:10.1039/a803165g.
(19) Jensen, P.; Batten, S. R.; Moubaraki, B.; Murray, K. S. *Chem. Commun.* **2000**, (9), 793. doi:10.1039/a909067c.
(20) Yu, F.; Li., Z. S.; Sun,, B. W. *Acta Crystallogr. Sect. E Struct. Rep. Online* **2008**, *64* (8), m993. doi:10.1107/S1600536808019880.
(21) Sheldrick, G. M. *SHELX 97, Program for Crystal Structure Refinement;* University of Göttingen, Göttingen, Germany, 1997.
(22) Fisher, M. E. *Am. J. Phys.* **1964**, *32* (5), 343. doi:10.1119/1.1970340.
(23) Mealli, C.; Proserpio, D. M. *J. Chem. Educ.* **1990**, *67* (5), 399. doi:10.1021/ed067p399.

Can. J. Chem. Downloaded from www.nrcresearchpress.com by Renmin University of China on 09/02/12
For personal use only.

Bonding topology, hydrogen bond strength, and vibrational chemical shifts on hetero-ring hydrogen-bonded complexes — Theoretical insights revisited

Boaz G. Oliveira and Regiane C. M. U. Araújo

Can. J. Chem. Downloaded from www.nrcresearchpress.com by Renmin University of China on 09/02/12
For personal use only.

Abstract: This work presents a theoretical study about the interaction strength of the hydrogen-bonded complexes $C_2H_4O\cdots HF$, $C_3H_6O\cdots HF$, $C_2H_4O\cdots HCF_3$, and $C_3H_6O\cdots HCF_3$ at the B3LYP/6–311++G(d,p) level. The structures, hydrogen bond energies, charge transfers, and dipole moments of these complexes were analyzed in accordance with routine spectroscopy events, such as the red- and blue-shifts on the stretch frequencies of the proton donors (HF and HCF_3). The ChelpG atomic charges were used to quantify the charge-transfer fluxes from electron donor (O) towards to acceptors (HF or HCF_3). Moreover, the topological calculations on the basis of the quantum theory of atoms in molecules (QTAIM) approach were also used to unveil the hydrogen bond strength (O···H), mainly in the determination of their electronic densities and Laplacian shapes.

Key words: vibrational spectrum, oxirane, oxetane, ChelpG, QTAIM.

Résumé : Dans ce travail, on présente les résultats d'une étude théorique, effectuée au niveau B3LYP/6–311++G(d,p), sur la force des interactions dans les complexes comportant des liaisons hydrogènes, $C_2H_4O\cdots HF$, $C_3H_6O\cdots HF$, $C_2H_4O\cdots HCF_3$ et $C_3H_6O\cdots HCF_3$. On a analysé les structures, les énergies des liaisons hydrogènes, les transferts de charge et les moments dipolaires de ces complexes en relation avec des événements spectroscopiques de routine, tels les déplacements vers le bleu ou vers le rouge des fréquences d'élongation des donneurs de proton (HF et HCF_3). On a utilisé les valeurs des charges atomiques ChelpG pour quantifier les flux de transfert de charge du donneur d'électron (O) vers les accepteurs (HF et HCF_3). Des plus, on a aussi utilisé des calculs topologiques sur la base de l'approche de la théorie quantique des atomes dans les molécules (TQADM) pour déterminer la force des liaisons hydrogènes (O···H), particulièrement dans la détermination de leurs densités électroniques et des forces de leurs laplaciens.

Mots-clés : spectre vibrationnel, oxirane, oxétane, ChelpG, TQADM.

[Traduit par la Rédaction]

Introduction

It is well-known that many chemical, physical, and biological systems are formed by noncovalent interactions, of which the hydrogen bond is currently dominant.[1–3] Nowadays, the hydrogen bond has attained a high importance level owing to the immensity of phenomena originated from the contact between a proton donor and a center containing high charge density.[4] This statement can be verified in many studies, such as identification of intermediaries in reaction mechanisms,[5] determination of functionality of molecules into the bioorganic active sites,[6] and design of new compounds pharmacologically more potent.[7,8]

From the viewpoint of theoretical chemistry, the hydrogen bond can be analyzed in conformity with the contributions of the electrostatic potential, polarizability, exchange potential, dispersion forces, and charge transfer.[9] It should be kept in mind that the relative contributions of these parameters, which are quantified for each system albeit the redundant ratio of the electrostatic potential, is practically uncontestable.[10–12] Also, other studies have shown that the charge transfer is decisive for determination of the molecular stability,[13] and in some cases, the charge transfer is the greatest amount rather than electrostatic effects.[14]

In a historical background of the theoretical approaches implemented to study intermolecular systems, from the proposition of the energy and charge distribution decomposition (ECDD)[15] until symmetry-adapted perturbation theory (SAPT)[16], several works have been published with the persistent emphasis upon the formation of the hydrogen bonds for discovering the dominant term.[17] To shed light on this still unsolved question, it is quite recognized that the charge transfer drastically affects the proton donors, where the enhancement of their bond lengths is one of the most important

Received 14 October 2011. Accepted 2 December 2012. Published at www.nrcresearchpress.com/cjc on 26 March 2012.

B.G. Oliveira. Instituto de Ciências Ambientais e Desenvolvimento Sustentável, Universidade Federal da Bahia, 47801-100, Barreiras – BA, Brazil.
R.C.M.U. Araújo. Departamento de Química, Universidade Federal da Paraíba. 58059-900, João Pessoa, PB – Brazil.

Corresponding author: Boaz G. Oliveira (e-mail: boazgaldino@gmail.com).

Can. J. Chem. Downloaded from www.nrcresearchpress.com by Renmin University of China on 09/02/12
For personal use only.

characteristics.[18,19] In spectroscopy, these structural changes are titled bathochromic events or red-shift effects because the stretch frequencies of the proton donors are dislocated to downward values followed by increases on their absorption intensities.[20]

In the past, Pinchas[21] and Sandorfy and co-workers[22] were some of the pioneers in spectroscopy studies of intermolecular complexes. More recently, Hobza et al.[23] certified a novel interaction named as "opposite hydrogen bond" or "anti hydrogen bond", motivated by the detection of a blue-shift effect on the stretch frequency of the proton donor.[24–26] On the contrary to the hydrogen bonds with red-shift effects, systems with blue-shifts present a shortening of the bond lengths of the proton donors, and thereby their stretch frequencies are moved to upward values in the IR spectrum.[27,28] A classic example of a blue-shifting hydrogen bond is found in the heterocyclic system $C_2H_4O\cdots HCF_3$, whose spectroscopic properties have been well-defined by means of sophisticated ab initio calculations.[29] On the other hand, heterocyclic complexes formed by the association between oxirane (C_2H_4O) and oxetane (C_3H_6O) with monoprotic acids H–X (X = Cl, F, CN, NC, and CCH) have been exhaustively studied, and because of spectroscopic formalism, their red-shift effects were theoretically identified at the level of the density functional theory (DFT).[30,31]

To propose a theoretical interpretation to the IR chemical shifts in intermolecular complexes, Hermansson[32] showed the influence of the electric field (proton acceptors) on the dipole moment of proton donors, and, of course, this phenomenon affects the formation of the hydrogen bonds as well as their stretch frequencies. Therefore, it was noticed that blue-shifts are manifested when long hydrogen bonds are formed, in these cases where the derivative of the induced dipole moment is negative.[33] In total conformity with this scenario, it was also verified that unsaturated hydrocarbons are useful proton acceptors, yielding the formation of long and short hydrogen bond distances when blue- and red-shift effects were observed, respectively.[34,35] Although the electric field analysis has been widely used, it has not been established which parameter is the most adequate for the interpretation the hydrogen bond strength and its main vibrational characteristic, red- or blue-shifts, as commented above. In this context, the main goal of this work is focused on a theoretical study of hydrogen-bonded complexes formed by $C_nH_mO\cdots HX$ (for oxirane, $n = 2$ and $m = 4$; for oxetane, $n = 3$ and $m = 6$; for hydrofluoric acid, X = F; and for fluoroform, X = CF_3).[36–40]

Theoretical methods and level of analysis

The molecular properties and structures of hydrogen-bonded complexes have been the target of examination in a large number of theoretical works, and many of these examinations were performed through the application of hybrid functionals of exchange correlation.[41] However, the capability of B3LYP in investigations of the electronic structures of many system types has been shown over the years, mainly those formed via hydrogen bonds.[42] Because of this B3LYP functionality, we elected to use it in our investigation. Nevertheless, the formation of hydrogen complexes is conceived by means of the interaction between the HOMO and LUMO frontier orbitals, which represent the Lewis definitions of base (proton acceptors) and acid (proton donors), respectively. Although several atomic-charge approaches are available, such as Mulliken population analysis,[43] natural bond orbitals (NBO),[44] generalized polar atomic tensors (GAPT),[45] as well as the charges based on the Gasteiger[46] and Löwdin[47] methods, the evaluation of the charge transfer between the frontier orbitals is vital. By this context, it becomes necessary to keep in mind some criteria to choose a method with (*i*) satisfactory prediction of the charge transfer; (*ii*) low computational effort; and, if possible, (*iii*) a slight dependence from the ab initio basis sets. By taking into account these recommendations, ChelpG (charges derived from the electrostatic potential grid)[48] is the most appropriate method. In practice, the ChelpG charges have been widely used in studies of hydrogen complexes with quantification of the charge transfer[49] and prediction of the red- and blue-shift effects.[25–29,50]

Topological contribution

The works written by Koch and Popelier[51] Mosquera and co-workers,[52] Grabowski and Małecka,[53] Tang and Cui,[54] and others[55–59] show us that hydrogen bonds and their properties can be carefully predicted through the quantum theory of atoms in molecules (QTAIM).[60] Recently, Bader[61] revisited some QTAIM concepts, mainly the way in which the quantum basis can be adapted to describe the topological electronic density and the atomic behavior within the molecular environment.[62,63] By analyzing the QTAIM geneses, the construction of bond paths (BP)[64,65] and bond critical points (BCP)[66] model the chemical bonds and, in addition, these two topological descriptors try to explain an old unsolved question in chemistry: "Where is the atomic frontier localized into a chemical bond?" However, although Bader has warned that "bond paths are not chemical bonds",[67] the information obtained by means of topographic calculations developed at both the BCP and BP levels has aided in the interpretation of the chemical bonds and intermolecular interactions, such as hydrogen bonds and others.[40,68,69] The identification of the maxima and minima of the electronic density emerging from each BCP is performed when the zero flux is known.[70] In an overview, high and low charge density concentration can be interpreted through the Laplacian of the electronic density ($\nabla^2\rho$), whose profile can assume $\nabla^2\rho > 0$ to depression (intermolecular interactions) or $\nabla^2\rho < 0$ to accumulation (covalent bonds). By the fact that QTAIM is well-applied to heterocyclic structures,[68] we elected to use it on the $C_2H_4O\cdots HF$, $C_3H_6O\cdots HF$, $C_2H_4O\cdots HCF_3$, and $C_3H_6O\cdots HCF_3$ hydrogen-bonded complexes with the purpose of elucidating their hydrogen bond strengths (O···H), as well as the interpretation of the red- and blue-shifts on the proton donors HF and HCF_3.

Computational procedure

The optimized geometries of the hydrogen-bonded complexes $C_2H_4O\cdots HF$, $C_3H_6O\cdots HF$, $C_2H_4O\cdots HCF_3$, and $C_3H_6O\cdots HCF_3$ were obtained through the B3LYP/6–311++G(d,p) theoretical level. The calculations were carried out by GAUSSIAN software version 98W.[71] The ChelpG charges and QTAIM calculations were executed by GAUSSIAN 98W, although it should be highlighted that additional topological calculations were also executed by the AIM2000 1.0[72] program. The values of the hydrogen bond energies (ΔE) were determined

Can. J. Chem. Downloaded from www.nrcresearchpress.com by Renmin University of China on 09/02/12
For personal use only.

in conformity with the supermolecule approach.[9] The ΔE values were corrected through the results of the zero-point energy (ZPE)[73] and basis sets superposition error (BSSE).[74]

Results

Geometry

Figure 1 illustrates the optimized geometries of the $C_2H_4O\cdots HF$ (**I**), $C_3H_6O\cdots HF$ (**II**), $C_2H_4O\cdots HCF_3$ (**III**), and $C_3H_6O\cdots HCF_3$ (**IV**) hydrogen-bonded complexes. The small amount of data available for these systems from the little experimental research that has been done is still very useful for confirming the quality of our work. Actually, the experimental hydrogen bond distances of 1.70[75] and 1.66 Å[76] for **I** and **II**, respectively, are in good agreement with our theoretical results of 1.662 and 1.615 Å, respectively, obtained by means of the B3LYP/6–311++G(d,p) level. With regards to the $C_2H_4O\cdots HX$ complexes with X = F, Cl, CN, and CCH,[77] nonlinearities (θ) on their hydrogen bonds (O···H) are observed.[78] This structural distortion is manifested because of the secondary interactions between the electronegative centers (lone-electron pairs or π-electrons) of the proton donors and the axial hydrogen atoms of the hetero ring.[79] Not only theoretical, but experimental assays also prove the existence of this secondary interaction,[80–82] although at this time, we are not interested in this specific phenomenon. In fact, our objective is concentrated in the structural or vibrational deformations that occur upon the formation of the **I**, **II**, **III**, and **IV** complexes.[83]

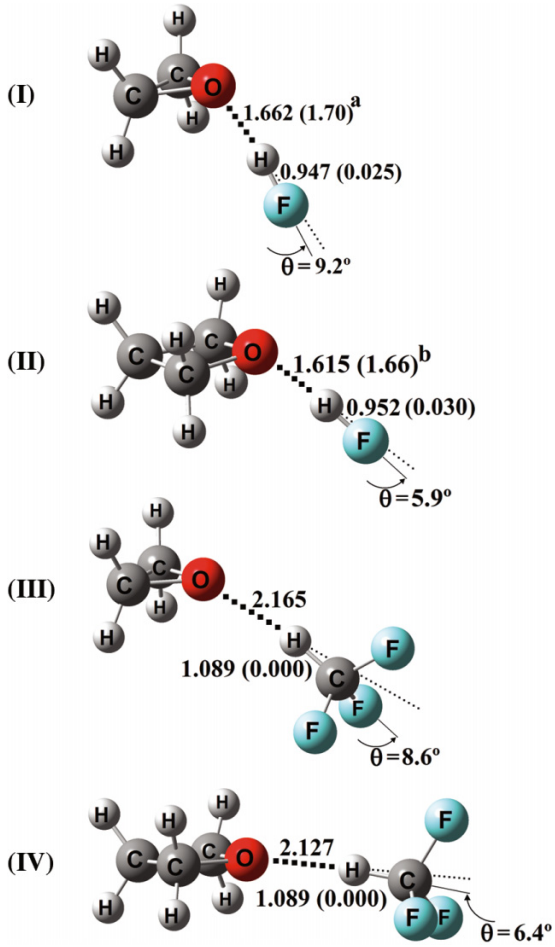
In a detailed analysis of the results pictured in Fig. 1, it can be easily perceived that **I** and **II** are the shortest bound systems, which is due to the high polarity of the hydrofluoric acid, as observed in other studies.[57] Regarding the H–F and H–C bond lengths of the proton donors, it can be emphasized that the enhanced results of 0.025 and 0.030 Å, respectively, corroborate the results of the hydrogen bond distances, i.e., the more stronger or shorter bound the complexes are, the more impressive the structural changes on the proton donors are observed. Note that the H–C changes slightly, which was already predicted by Hobza and Havlas,[29] by means of slight variations, in the range of 10^{-3}, when fluoroform binds with oxirane, and thereby the blue-shift on the stretch frequency is manifested.

IR spectrum analysis

Of course, incisive explanations about red- and blue-shift effects on the proton donors HF and HCF_3 can be formulated only after a circumstantial examination of their stretch frequencies,[84] whose values are listed in Table 1. This agrees with Alabugin et al.,[85] who stated that strong and weak bound complexes are vibrationaly identified by the emergence of red- and blue-shifts, respectively. As expected, the values of the red-shift effects are –535.2 and –654.7 cm^{-1} in **I** and **II**, respectively, whereas blue-shifts of +15.7 and +3.1 cm^{-1} are attributed to **III** and **IV**, respectively. We can see a systematic trend in the values of the absorption intensities listed in Table 1, in which increases and reductions of absorption ratios were found in the red- and blue-shift complexes,[86–88] respectively.

However, the hydrogen bond strength cannot be justly analyzed based only on the intermolecular distances and chemical shifts, but the values of the new vibrational modes listed in Table 1 are also considered great spectroscopy arguments in this regard.[89] By furnishing excellent agreement with all results discussed in this work, the spectroscopy criteria indicate that blue-shift complexes **III** and **IV** are weakly bound, either by the new vibrational modes of 94.1 and 82.3 cm^{-1}, respectively, or by the absorption intensities of 5.3 and 2.3 km mol^{-1}, respectively. In opposition to this, the $\upsilon^{Str}_{(O\cdots H-X)}$ values of 254.3 and 258 cm^{-1}, respectively, and $I^{Str}_{(O\cdots H-X)}$ values of 23.3 and 19.3 km mol^{-1}, respectively, are indications that red-shift complexes **I** and **II** are the strongest bonded.

Fig. 1. Optimized geometries of the $C_2H_4O\cdots HF$ (**I**), $C_3H_6O\cdots HF$ (**II**), $C_2H_4O\cdots HCF_3$ (**III**), and $C_3H_6O\cdots HCF_3$ (**IV**) complexes obtained from B3LYP/6–311++G(d,p) calculations.



Hydrogen bond energy and dipole moment

Through B3LYP/6–311++G(d,p) calculations, Table 2 lists the values of the total electronic energies (E), uncorrected results of the hydrogen bond energies (ΔE) and those with correction (ΔE^C), as well as the values of ΔZPE and BSSE for complexes **I**, **II**, **III**, and **IV**. The discovery of the most appropriate calculation level to reproduce or predict molecular properties is considered one of the most important objectives in theoretical chemistry,[90,91] although an old question still was not answered: "'Which is the most efficient method, between B3LYP and MP2, to be used in intermolecular studies?" This is not our focus at this time, but once

Can. J. Chem. Downloaded from www.nrcresearchpress.com by Renmin University of China on 09/02/12
For personal use only.

Table 1.. Values of the red- and blue-shifts, absorption intensity ratios, and new vibrational modes computed at the B3LYP/6–311++G(d,p) level of theory.

	Hetero-ring-bonded complex			
Parameter	**I**	**II**	**III**	**IV**
$\Delta\upsilon^{Str}_{(H–X)}$	–535.2	–654.7	+15.7	+3.1
$I^{Str}_{(H–X),C}$/ $I^{Str}_{(H–X),m}$	9.7	11.8	0.3	0.7
$\upsilon^{Str}_{(O\cdots H–X)}$	254.3[a]	258.0[b]	94.1[c]	82.3[c]
$I^{Str}_{(O\cdots H–X)}$	23.3[a]	19.3[b]	5.3[c]	2.3[c]

Note: Values of υ and I are given in cm^{-1} and km mol^{-1}, respectively.
[a]References 77 and 78.
[b]Reference 29.
[c]This work.

Table 2.. Values of the total energies (E), uncorrected (ΔE) and corrected (ΔE^C) hydrogen bond energies, zero-point energy (ΔZPE) and basis sets superposition error (BSSE) corrections, dipole moment enhancement ($\Delta\mu$), and ChelpG charge transfers (Δq^T and Δq^P).

	Hetero-ring-bonded complex			
Parameter	**I**	**II**	**III**	**IV**
E	–254.3348532	–293.6659414	–492.1914643	–531.5208797
ΔE	–42.90	–50.20	–16.17	–19.00
ΔZPE	9.87	9.92	2.09	1.96
BSSE	4.18	3.79	1.72	1.45
ΔE^C	–28.85	–36.49	–12.36	–15.59
Δq^T	–0.092	–0.119	–0.074	–0.090
Δq^P	–0.057	–0.085	–0.065	–0.071
$\Delta\mu$	0.45	0.97	0.49	0.89

Note: Values of E, ΔE, ΔE^C, ΔZPE, and BSSE are given in kJ mol^{-1}. Values of Δq^T and Δq^P are given in electrostatic units (esu). Values of $\Delta\mu$ are given in Debye (D).

Fig. 2. The relationship (ΔE^C = 37.5 R – 94.3 ; R^2 = 0.97) between the values of the corrected hydrogen bond energies and the hydrogen bond distances. All values were computed at the B3LYP/6–311++G(d,p) level of theory.

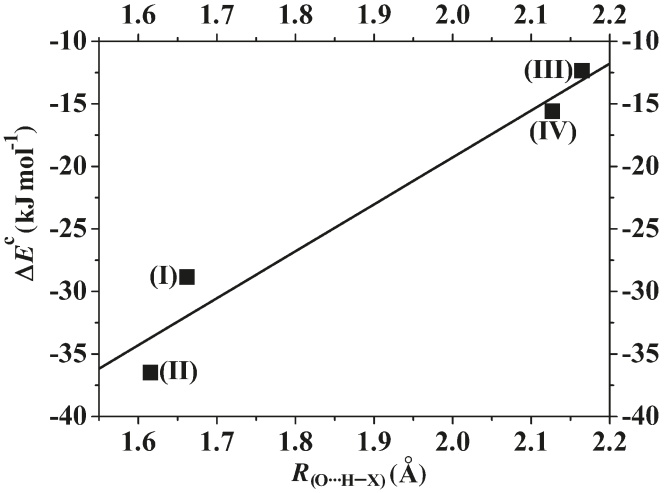
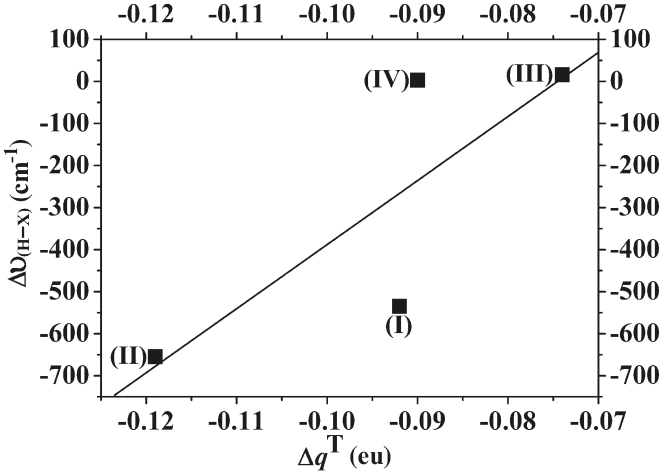


Fig. 3. The relationship ($\Delta\upsilon^{Str}_{(H–X)}$ = 15 234.5Δq^T + 1135.4; R^2 = 0.80) between the values of the red- and blue-shifts and the ChelpG charge transfer. All values were computed at the B3LYP/6–311++G(d,p) level of theory.



there are a large number of published works about this question, this could become a focus of our group.[30,92] However, by examining the values of the total electronic energies computed at the B3LYP/6–311++G(d,p) level, our result of –254.3348532 H for **I** is significantly more stable than the value of –253.77688 divulged by Chandra and Nguyen,[93] who used MP2/6–311++G(d,p) as their standard calculation method. Through the analysis of the hydrogen bond energies, Fig. 2 plots a close relationship between the ΔE^C values and the respective distances, $R_{(O\cdots H–X)}$. As noted in some works that energetic and structural parameters serve as the basis for predicting the interaction strength,[94,95] the amount of the hydrogen bond strength can be reliably observed by means of the relationship featured in Fig. 2, i.e., the computation of the higher ΔE^C energies and shorter

Can. J. Chem. Downloaded from www.nrcresearchpress.com by Renmin University of China on 09/02/12
For personal use only.

Table 3. Values of the electronic density (ρ) and the Laplacians ($\nabla^2\rho$) of the hydrogen bonds (O···H–X) and proton-donor bonds H–F and H–C.

	Hetero-ring hydrogen-bonded complex			
Parameter	**I**	**II**	**III**	**IV**
$\rho_{(O\cdots H-X)}$	0.047	0.053	0.015	0.017
$\nabla^2\rho_{(O\cdots H-X)}$	0.149	0.160	0.056	0.063
$\rho_{(H-X)}$	0.334	0.327	0.305	0.304
$\nabla^2\rho_{(H-X)}$	–2.43	–2.34	–1.116	–1.165

Note: Values of ρ and $\nabla^2\rho$ are given in e/a_0^3 and e/a_0^5, respectively. Values of ρ related to H–F (hydrofluoric acid monomer) and H–C (fluoroform monomer) bonds are 0.369 and 0.302 e/a_o^3, respectively. Values of $\Delta\rho_{(H-X)}$ computed for **I**, **II**, **III**, and **IV** are –0.035, –0.042, 0.003, and 0.002 e/a_0^3, respectively.

Fig. 4. The relationship ($\Delta E^C = -576.6\ \rho_{(O\cdots H-X)} - 4.17$; $R^2 = -0.98$) between the corrected hydrogen bond energies and the electronic density amounts.

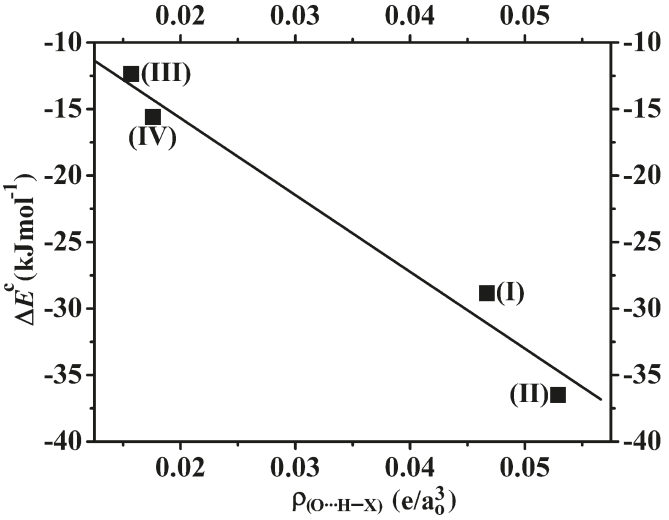
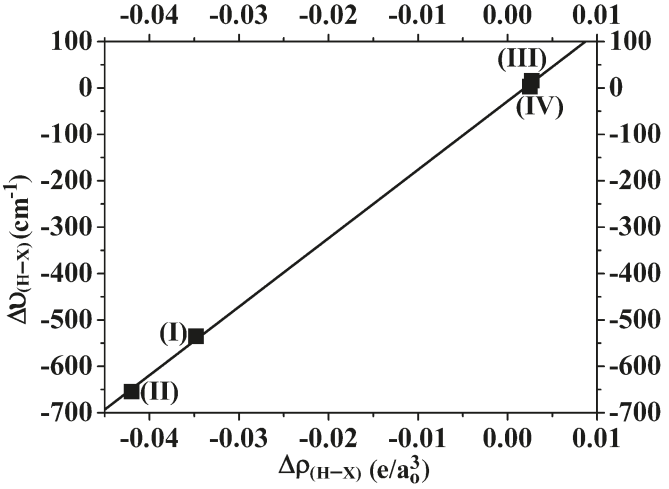


Fig. 5. The relationship ($\Delta\upsilon^{Str}_{(H-X)} = 14\,765\Delta\rho_{(H-X)} - 28.4$; $R^2 = 0.99$) between the values of the red- and blue-shifts versus the variations of the electronic densities of the H–X bonds.



$R_{(O\cdots H-X)}$ distances led us to affirm that blue-shift complexes are weakly bound in comparison with red-shift ones.

Analyzing Table 2, it can be seen that the values of the dipole moment enhancements (Δμ) are in good agreement with the hydrogen bond energies ΔE^C, i.e., ΔE^C (**II**) > ΔE^C (**I**) and Δμ (**II**) > Δμ (**I**), as well as ΔE^C (**IV**) > ΔE^C (**III**) and Δμ (**IV**) > Δμ (**III**). From the literature, Δμ is a measurement of the molecular distortion. Thus, it can be also used to interpret the interaction strength even indirectly, and indeed, the extension of the dipole moment enhancement is closely related with the charge transfer, as recently demonstrated by Stone and Misquita.[96] With this insight, it should be observed that charge transfer amounts from either Δq^T or Δq^P are in a good relationship with Δμ.

Charge transfer

It is well-known that the hydrogen bond energy is governed by the charge transfer between the molecular frontier orbitals, wherein the HOMO and LUMO are ascribed to the acceptor and donor of protons, respectively.[97] Here, it must be emphasized that the charge transference mechanism presents distinct profiles in both red- and blue-shift complexes. The charge fluxes in **I** and **II** are concentrated between hydrogen and fluorine on the hydrofluoric acid, whereas the charge transferred is dispersed among the carbon, hydrogen, and fluorine of the fluoroform in **III** and **IV**. To analyze these charge transference amounts, we decided that two measures should be done: (*i*) full charge transfer (Δq^T) along the proton donor molecule and (*ii*) partial charge transfer (Δq^P) on the hydrogen atom of the proton donors. Thus, we expect a clear justification about the formation of the red- and blue-shift effects, since the direct relationship between charge transfer and chemical shifts is well-known.[17,18,58,98] The Δq^T and Δq^P values are presented in Table 2. Throughout this work, it has been demonstrated that **I** and **II** are the stronger bound systems, which was also observed by means of the Δq^T values of –0.092 and –0.119 esu. Figure 3 demonstrates, however, that a satisfactory relationship between Δq^T and red- and blue-shifts could not be obtained.

However, if the charge transfer was partial (Δq^P), a good relationship could not be verified. For instance, the charge transfer values of –0.065 and –0.071 esu, respectively, are not in agreement with the respective blue-shift values of +15.7 and +3.1 cm^{-1}, respectively, in the **III** and **IV** systems. Furthermore, by comparing the Δq^P values of –0.057 and –0.065 esu, respectively, with the results for ΔE^C of –28.85 and –12.36 kJ mol^{-1}, respectively, once again, no direct relationship was obtained. It would be expected that the more stronger bonded the intermolecular system, the more intense the charge transfer should be, but this was not observed. In this context, it is necessary to use an alternative approach that can be efficiently used to validate the formation of the red- and blue-shifts of the hydrogen-bonded complexes **I**, **II**, **III**, and **IV**.

Bonding topology

When the QTAIM content and its applicability in studies of electronic structure was revisited,[99,100] the great capability of this theoretical method to evaluate the chemical bond and the electronic dynamism related to atomic interaction, either

Can. J. Chem. Downloaded from www.nrcresearchpress.com by Renmin University of China on 09/02/12
For personal use only.

in classical chemical bonds such as covalent or unsaturated ones,[101] and, of course, in the unusual intermolecular interactions, could be perceived.[102–105] The values in Table 3 demonstrate that low amounts of electronic density, in the range of 0.015–0.053 e/a_0^3, are associated with positive Laplacian values. These are two topological arguments of the QTAIM formalism used to characterize the hydrogen bonds O···H–F and O···H–C. As mentioned, the charge concentration on the H–F and H–C bonds is evidenced by the negative Laplacian values accompanied by high charge density, which also can be seen in Table 3. Nevertheless, a question still must be answered here: Owing to the failure of the ChelpG charge transfer in the interpretation of the red- and blue-shift effects, is it possible that another analysis yields more efficient results? From the values listed in Table 3, a reduction of the electronic density in the H–F bonds, with variations from 0.369 (hydrofluoric acid monomer) to 0.334 and 0.327 e/a_o^3 upon the formation of the red-shifted complexes **I** and **II**, can be observed. On the other hand, the electronic density of 0.302 e/a_0^3 of the H–C of the fluoroform monomer is constant, with values for **III** and **IV** of 0.305 and 0.304 e/a_0^3, respectively.

In this work, it has been demonstrated that stronger and weaker hydrogen bonds are characterized by the appearance of red- and blue-shift effects, although a new relationship was formulated between the hydrogen bond energies and electronic density amounts computed using the QTAIM. By this insight and the results plotted in Fig. 4, it is assumed that the alterations of the charge density of the H–F and H–C bonds are caused by the hydrogen bond strength.

Ideally, it can be perceived that weak hydrogen bonds cannot provoke significant changes in the electronic densities of the proton donors and vice-versa. In this context, the results illustrated in Fig. 5 show the relationship between the values of the red-shift and blue-shift and the variations in the electronic densities of the H–F and H–C bonds when **I**, **II**, **III**, and **IV** are formed.

As can be easily noted, an excellent relationship between ΔE^C and $\Delta\rho_{(H-X)}$ was obtained. In opposition to traditional studies of intermolecular systems, this result indicates that the charge transfer analysis does not always produce good results to validate the inherent phenomena of the hydrogen bonds, but the QTAIM electronic density behaves as a trusted parameter to this type of investigation, as already reported in recent work.[106]

Conclusions

In this work, a theoretical study of the molecular parameters of hydrogen-bonded complexes was presented. The structures $C_2H_4O\cdots HF$, $C_3H_6O\cdots HF$, $C_2H_4O\cdots HCF_3$, and $C_3H_6O\cdots HCF_3$ were conceived with prominence to the generation of the red- and blue-shifts on the stretch frequencies of the proton donors. Because of this, our discussion was dedicated to the inefficiency of the ChelpG in the evaluation of the charge transfer to be used in the interpretation of these chemical shifts. In conformity with traditional intermolecular systems studies, this is unusual as ChelpG is well-recognized as one of the most efficient approaches used in punctual charge calculations, but here we found that we had to apply an alternative procedure to this analysis type: the QTAIM topology. The structural and electronic analysis showed that the hydrogen bond strength can be interpreted through the direct relationship between distances and the corrected binding energies.

By taking into account the vibrational parameters, it was observed that red- and blue-shifts are closely related with stronger and weaker bound systems. Topologically, drastic and slight electronic density variations in the H–F and H–C bonds of the proton donors correlate with high and low binding energies, which is also correlated with red- and blue-shifted complexes. In this context, it a justification was proposed to the red- and blue-shifts based on the electronic density analysis. Henceforth, we expect that our results can be useful in further spectroscopy studies, mainly those composed of weak intermolecular systems with nontrivial vibrational characterization.

Supplementary data

Supplementary data are available with the article through the journal Web site http://nrcresearchpress.com/doi/suppl/10.1139/v2012-009.

Acknowledgement

The authors gratefully acknowledge partial financial support from the Brazilian funding agencies Coordenação de Aperfeiçoamento de Pessoal de Ensino Superior (CAPES) and Conselho Nacional de Desenvolvimento Científico e Tecnológico (CNPq).

References

(1) Grabowski, S. J. *Hydrogen Bonding — New Insights;* Springer: Amsterdam, 2006.
(2) Keefe, C. D.; Istvankova, Z. *Can. J. Chem.* **2011**, *89* (1), 34. doi:10.1139/V10-155.
(3) Bader, R. F. W. *Can. J. Chem.* **1964**, *42* (8), 1822. doi:10.1139/v64-274.
(4) Kojić-Prodić, B.; Molćanov, K. *Acta Chim. Slov.* **2008**, *55*, 692.
(5) Banks, H. D. *J. Org. Chem.* **2003**, *68* (7), 2639. doi:10.1021/jo0268411.
(6) Trylska, J.; Grochowski, P.; McCammon, J. A. *Protein Sci.* **2004**, *13* (2), 513. doi:10.1110/ps.03372304.
(7) Miño, G.; Contreras, R. *J. Phys. Chem. A* **2009**, *113* (19), 5769. doi:10.1021/jp902756x.
(8) Kuhn, B.; Mohr, P.; Stahl, M. *J. Med. Chem.* **2010**, *53* (6), 2601. doi:10.1021/jm100087s.
(9) Pople, J. A. *Faraday Discuss.* **1981**, *73*, 7.
(10) Grozema, F. C.; Zijlstra, R. W. J.; Swart, M.; van Duijhen, P. Th. *Int. J. Quantum Chem.* **1999**, *75* (4–5), 709. doi:10.1002/(SICI)1097-461X(1999)75:4/5<709::AID-QUA38>3.0.CO;2-N.
(11) Piquemal, J.-P.; Cisneros, G. A.; Reinhardt, P.; Gresh, N.; Darden, T. *J. Chem. Phys.* **2006**, *124* (10), 104101. doi:10.1063/1.2173256.
(12) Kenny, P. W. *J. Chem. Inf. Model.* **2009**, *49* (5), 1234. doi:10.1021/ci9000234.
(13) King, B. F.; Weinhold, F. *J. Chem. Phys.* **1995**, *103* (1), 333. doi:10.1063/1.469645.
(14) Alvarez-Rizzatti, M.; Mason, E. A. *J. Chem. Phys.* **1975**, *63* (12), 5290. doi:10.1063/1.431330.

Can. J. Chem. Downloaded from www.nrcresearchpress.com by Renmin University of China on 09/02/12
For personal use only.

(15) Umeyama, H.; Morokuma, K. *J. Am. Chem. Soc.* **1977**, *99* (5), 1316. doi:10.1021/ja00447a007.
(16) Pitoňák, M.; Riley, K. E.; Neogrády, P.; Hobza, P. *ChemPhysChem* **2008**, *9* (11), 1636. doi:10.1002/cphc.200800286.
(17) Jeziorski, B.; Moszynski, R.; Szalewicz, K. *Chem. Rev.* **1994**, *94* (7), 1887. doi:10.1021/cr00031a008.
(18) Araújo, R. C. M. U.; da Silva, J. B. P.; Ramos, M. N. *Spectrochim. Acta Part A* **1995**, *51* (5), 821. doi:10.1016/0584-8539(94)00194-G.
(19) Araújo, R. C. M. U.; Ramos, M. N. *J. Mol. Struct. THEOCHEM* **1996**, *366* (3), 233. doi:10.1016/0166-1280(96)04536-8.
(20) Nesbitt, D. J. *Chem. Rev.* **1988**, *88* (6), 843. doi:10.1021/cr00088a003.
(21) Pinchas, S. *Anal. Chem.* **1955**, *27* (1), 2. doi:10.1021/ac60097a002.
(22) Trudeau, G.; Dumas, J. M.; Dupuis, P.; Guérin, M.; Sandorfy, C. *Top. Curr. Chem.* **1980**, *93*, 91.
(23) Hobza, P.; Špirko, V.; Havlas, Z.; Buchhold, K.; Reimann, B.; Barth, H.-D.; Brutschy, B. *Chem. Phys. Lett.* **1999**, *299* (2), 180. doi:10.1016/S0009-2614(98)01264-0.
(24) Hobza, P.; Havlas, Z. *Chem. Rev.* **2000**, *100* (11), 4253. doi:10.1021/cr990050q.
(25) Hobza, P.; Špirko, V.; Selzle, H. L.; Schlag, E. W. *J. Phys. Chem. A* **1998**, *102* (15), 2501. doi:10.1021/jp973374w.
(26) Cubero, E.; Orozco, M.; Hobza, P.; Luque, F. J. *J. Phys. Chem. A* **1999**, *103* (32), 6394. doi:10.1021/jp990258f.
(27) Araújo, R. C. M. U.; Ramos, M. N. *J. Braz. Chem. Soc.* **1998**, *9* (5), 499. doi:10.1590/S0103-50531998000500016.
(28) Oliveira, B. G.; Vasconcellos, M. L. A. A. *J. Mol. Struct. THEOCHEM* **2006**, *774* (1–3), 83. doi:10.1016/j.theochem.2006.06.018.
(29) Hobza, P.; Havlas, Z. *Chem. Phys. Lett.* **1999**, *303* (3–4), 447. doi:10.1016/S0009-2614(99)00217-1.
(30) Kolboe, S.; Svelle, S. *J. Phys. Chem. A* **2008**, *112* (29), 6399. doi:10.1021/jp8027879.
(31) Ferreira, F. C.; Oliveira, B. G.; Ventura, E.; do Monte, S. A.; Braga, C. F.; Araújo, R. C. M. U.; Ramos, M. N. *Spectrochim. Acta Part A* **2006**, *64* (1), 156. doi:10.1016/j.saa.2005.07.010.
(32) Hermansson, K. *J. Phys. Chem. A* **2002**, *106* (18), 4695. doi:10.1021/jp0143948.
(33) Murray, J. S.; Concha, M. C.; Lane, P.; Hobza, P.; Politzer, P. *J. Mol. Model.* **2008**, *14* (8), 699. doi:10.1007/s00894-008-0307-y.
(34) Oliveira, B. G.; Araújo, R. C. M. U.; Ramos, M. N. *J. Mol. Struct. THEOCHEM* **2010**, *944* (1–3), 168. doi:10.1016/j.theochem.2009.12.032.
(35) Oliveira, B. G.; Araújo, R. C. M. U.; Ramos, M. N. *Orbital Elec. J. Chem.* **2009**, *1*, 156.
(36) Oliveira, B. G.; Santos, E. C. S.; Duarte, E. M.; Araújo, R. C. M. U.; Ramos, M. N.; Carvalho, A. B. *Spectrochim. Acta Part A* **2004**, *60* (8–9), 1883. doi:10.1016/j.saa.2003.10.006.
(37) Oliveira, B. G.; Duarte, E. M.; Araújo, R. C. M. U.; Ramos, M. N.; Carvalho, A. B. *Spectrochim. Acta Part A* **2005**, *61* (3), 491. doi:10.1016/j.saa.2004.04.023.
(38) Oliveira, B. G.; Pereira, F. S.; Araújo, R. C. M. U.; Ramos, M. N. *Chem. Phys. Lett.* **2006**, *427* (1–3), 181. doi:10.1016/j.cplett.2006.06.019.
(39) Oliveira, B. G.; Araújo, R. C. M. U.; Carvalho, A. B.; Lima, E. F.; Silva, W. L. V.; Ramos, M. N.; Tavares, A. M. *J. Mol. Struct. THEOCHEM* **2006**, *775* (1–3), 39. doi:10.1016/j.theochem.2006.06.028.
(40) Oliveira, B. G.; Ramos, M. N. *Int. J. Quantum Chem.* **2010**, *110* (2), 307. doi:10.1002/qua.21995.
(41) Geerlings, P.; De Proft, F.; Langenaeker, W. *Chem. Rev.* **2003**, *103* (5), 1793. doi:10.1021/cr990029p.
(42) Oliveira, B. G.; Araújo, R. C. M. U.; Carvalho, A. B.; Ramos, M. N. *Can. J. Chem.* **2010**, *88* (4), 338. doi:10.1139/V10-012.
(43) Mulliken, R. S. *J. Chem. Phys.* **1955**, *23* (10), 1833. doi:10.1063/1.1740588.
(44) Foster, J. P.; Weinhold, F. *J. Am. Chem. Soc.* **1980**, *102* (24), 7211. doi:10.1021/ja00544a007.
(45) Cioslowski, J. *J. Am. Chem. Soc.* **1989**, *111* (22), 8333. doi:10.1021/ja00204a001.
(46) Mortier, W. J.; van Genechten, K.; Gasteiger, J. *J. Am. Chem. Soc.* **1985**, *107* (4), 829. doi:10.1021/ja00290a017.
(47) Löwdin, P.-O. *Adv. Quantum Chem.* **1970**, *5*, 185. doi:10.1016/S0065-3276(08)60339-1.
(48) Breneman, C. M.; Wiberg, K. B. *J. Comput. Chem.* **1990**, *11* (3), 361. doi:10.1002/jcc.540110311.
(49) Oliveira, B. G.; Araújo, R. C. M. U.; Chagas, F. C.; Carvalho, A. B.; Ramos, M. N. *J. Mol. Model.* **2008**, *14* (10), 949. doi:10.1007/s00894-008-0337-5.
(50) Oliveira, B. G.; Araújo, R. C. M. U. *Quim. Nova* **2007**, *30* (4), 791. doi:10.1590/S0100-40422007000400007.
(51) Koch, U.; Popelier, P. L. A. *J. Phys. Chem.* **1995**, *99* (24), 9747. doi:10.1021/j100024a016.
(52) López, J. L.; Mandado, M.; González Moa, M. J.; Mosquera, R. A. *Chem. Phys. Lett.* **2006**, *422* (4–6), 558. doi:10.1016/j.cplett.2006.03.019.
(53) Grabowski, S. J.; Małecka, M. *J. Phys. Chem. A* **2006**, *110* (42), 11847. doi:10.1021/jp064997p.
(54) Tang, T.-H.; Cui, Y.-P. *Can. J. Chem.* **1996**, *74* (6), 1162. doi:10.1139/v96-130.
(55) Oliveira, B. G.; Araújo, R. C. M. U.; Ramos, M. N. *Struct. Chem.* **2008**, *19* (2), 185. doi:10.1007/s11224-007-9269-4.
(56) Oliveira, B. G.; Araújo, R. C. M. U.; Ramos, M. N. *Struct. Chem.* **2008**, *19* (4), 665. doi:10.1007/s11224-008-9344-5.
(57) Oliveira, B. G.; Araújo, R. C. M. U.; Carvalho, A. B.; Ramos, M. N. *J. Mol. Model.* **2009**, *15* (2), 123. doi:10.1007/s00894-008-0380-2.
(58) Oliveira, B. G.; Araújo, R. C. M. U.; Carvalho, A. B.; Ramos, M. N. *Chem. Phys. Lett.* **2007**, *433* (4–6), 390. doi:10.1016/j.cplett.2006.11.029.
(59) Oliveira, B. G.; Araújo, R. C. M. U. *Monatsh. Chem.* **2011**, *142* (9), 861. doi:10.1007/s00706-011-0540-4.
(60) Bader, R. F. W. *Atoms in Molecules — A Quantum Theory;* Oxford University Press: Oxford, 1980.
(61) Bader, R. F. W. *J. Phys. Chem. A* **2010**, *114* (28), 7431. doi:10.1021/jp102748b.
(62) Eberhart, M. *Can. J. Chem.* **1996**, *74* (6), 1229. doi:10.1139/v96-138.
(63) Tsirelson, V. G. *Can. J. Chem.* **1996**, *74* (6), 1171. doi:10.1139/v96-131.
(64) Bader, R. F. W. *J. Phys. Chem. A* **1998**, *102* (37), 7314. doi:10.1021/jp981794v.
(65) Runtz, G. R.; Bader, R. F. W.; Messer, R. R. *Can. J. Chem.* **1977**, *55* (16), 3040. doi:10.1139/v77-422.
(66) Bader, R. F. W. *Chem. Phys. Lett.* **2006**, *426* (1–3), 226. doi:10.1016/j.cplett.2006.05.072.
(67) Bader, R. F. W. *J. Phys. Chem. A* **2009**, *113* (38), 10391. doi:10.1021/jp906341r.
(68) Oliveira, B. G.; Araújo, R. C. M. U.; Carvalho, A. B.; Ramos, M. N. *J. Theor. Comput. Chem.* **2007**, *6* (4), 647. doi:10.1142/S0219633607003362.

Can. J. Chem. Downloaded from www.nrcresearchpress.com by Renmin University of China on 09/02/12
For personal use only.

(69) Oliveira, B. G.; Araújo, R. C. M. U.; Leite, E. S.; Ramos, M. N. *Int. J. Quantum Chem.* **2011**, *111* (1), 111. doi:10.1002/qua.22397.
(70) Keith, T. A.; Bader, R. F. W. *Can. J. Chem.* **1996**, *74* (2), 185. doi:10.1139/v96-022.
(71) Frisch, M. J.; Trucks, G. W.; Schlegel, H. B.; Scuseria, G. E.; Robb, M. A.; Cheeseman, J. R.; Zakrzewski, V. G.; Montgomery, J. A., Jr.; Stratmann, R. E.; Burant, J. C.; Dapprich, S.; Millam, J. M.; Daniels, A. D.; Kudin, K. N.; Strain, M. C.; Farkas, O.; Tomasi, J.; Barone, V.; Cossi, M.; Cammi, R.; Mennucci, B.; Pomelli, C.; Adamo, C.; Clifford, S.; Ochterski, J.; Petersson, G. A.; Ayala, P. Y.; Cui, Q.; Morokuma, K.; Rega, N.; Salvador, P.; Dannenberg, J. J.; Malick, D. K.; Rabuck, A. D.; Raghavachari, K.; Foresman, J. B.; Cioslowski, J.; Ortiz, J. V.; Baboul, A. G.; Stefanov, B. B.; Liu, G.; Liashenko, A.; Piskorz, P.; Komaromi, I.; Gomperts, R.; Martin, R. L.; Fox, D. J.; Keith, T.; Al-Laham, M. A.; Peng, C. Y.; Nanayakkara, A.; Challacombe, M.; Gill, P. M. W.; Johnson, B.; Chen, W.; Wong, M. W.; Andres, J. L.; Gonzalez, C.; Head-Gordon, M.; Replogle, E. S.; Pople, J. A. *Gaussian 98W,* Revision A.1; Gaussian, Inc.: Pittsburgh, PA, 1998.
(72) Biegler-König, F. *AIM 2000,* Version 1.0; Bielefeld, Germany, 2000.
(73) McQuarrie, D. A. *Statistical Thermodynamics;* Harper and Row: New York, 1973.
(74) Boys, S. B.; Bernardi, F. *Mol. Phys.* **1970**, *19* (4), 553. doi:10.1080/00268977000101561.
(75) Sanz, M. E.; Sanz, V. M.; López, J. C.; Alonso, J. L. *Chem. Phys. Lett.* **2001**, *342* (1–2), 31. doi:10.1016/S0009-2614(01)00568-1.
(76) Georgiou, A. S.; Millen, D. J.; Kisiel, Z.; Legon, A. C. *Chem. Phys. Lett.* **1989**, *155* (4–5), 447. doi:10.1016/0009-2614(89)87184-2.
(77) Oliveira, B. G.; Araujo, R. C. M. U.; Carvalho, A. B.; Ramos, M. N. *Spectrochim. Acta Part A* **2007**, *268* (3), 626. doi:10.1016/j.saa.2006.12.038.
(78) Oliveira, B. G.; Araujo, R. C. M. U.; Carvalho, A. B.; Ramos, M. N. *Spectrochim. Acta Part A* **2010**, *75* (2), 563. doi:10.1016/j.saa.2009.11.017.
(79) Oliveira, B. G.; Araújo, R. C. M. U.; Carvalho, A. B.; Ramos, M. N. *Quim. Nova* **2007**, *30* (5), 1167. doi:10.1590/S0100-40422007000500022.
(80) Atkins, M. J.; Legon, A. C.; Warner, H. E. *Chem. Phys. Lett.* **1994**, *229* (3), 267. doi:10.1016/0009-2614(94)01049-8.
(81) Legon, A. C.; Rego, C. A.; Wallwork, A. L. *J. Chem. Phys.* **1992**, *97* (5), 3050. doi:10.1063/1.463046.
(82) Kroon, J.; Kanters, J. A. *Nature* **1974**, *248* (5450), 667. doi:10.1038/248667a0.
(83) Oliveira, B. G.; Araújo, R. C. M. U.; Pereira, F. S.; Lima, E. F.; Silva, W. L. V.; Carvalho, A. B.; Ramos, M. N. *Quim. Nova* **2008**, *31* (7), 1673. doi:10.1590/S0100-40422008000700014.
(84) McDowell, S. A. C. *Phys. Chem. Chem. Phys.* **2003**, *5* (5), 808. doi:10.1039/b211014h.
(85) Alabugin, I. V.; Manoharan, M.; Weinhold, F. A. *J. Phys. Chem. A* **2004**, *108* (21), 4720. doi:10.1021/jp049723l.
(86) Oliveira, B. G.; Vasconcellos, M. L. A. A.; Olinda, R. R.; Filho, E. B. A. *Struct. Chem.* **2009**, *20* (1), 81. doi:10.1007/s11224-008-9401-0.
(87) Oliveira, B. G.; Leite, L. F. C. C. *J. Mol. Struct. THEOCHEM* **2009**, *915* (1–3), 38. doi:10.1016/j.theochem.2009.08.011.
(88) Barnes, A. J. *J. Mol. Struct. THEOCHEM* **2004**, *704*, 3.
(89) Araújo, R. C. M. U.; Soares, V. M.; Oliveira, B. G.; Lopes, K. C.; Ventura, E.; do Monte, S. A.; Santana, O. L.; Carvalho, A. B.; Ramos, M. N. *Int. J. Quantum Chem.* **2006**, *106* (13), 2714. doi:10.1002/qua.21132.
(90) Lozynski, M.; Rusinska-Roszak, D.; Mack, H.-G. *J. Phys. Chem. A* **1998**, *102* (17), 2899. doi:10.1021/jp973142x.
(91) Murashov, V. V.; Leszczynski, J. *J. Mol. Struct. THEOCHEM* **2000**, *529* (1–3), 1. doi:10.1016/S0166-1280(00)00524-8.
(92) Del Bene, J. E.; Person, W. B.; Szczepaniak, K. *J. Phys. Chem.* **1995**, *99* (27), 10705. doi:10.1021/j100027a005.
(93) Chandra, A. K.; Nguyen, M. T. *Chem. Phys. Lett.* **1998**, *283* (3–4), 152. doi:10.1016/S0009-2614(97)01345-6.
(94) Grabowski, S. J. *J. Mol. Struct.* **2000**, *553* (1–3), 151. doi:10.1016/S0022-2860(00)00576-7.
(95) Grabowski, S. J. *J. Mol. Struct.* **2001**, *562* (1–3), 137. doi:10.1016/S0022-2860(00)00863-2.
(96) Stone, A. J.; Misquitta, A. J. *Chem. Phys. Lett.* **2009**, *473* (1–3), 201. doi:10.1016/j.cplett.2009.03.073.
(97) Ratajczak, H.; Orville-Thomas, W. J.; Rao, C. N. R. *Chem. Phys.* **1976**, *17* (2), 197. doi:10.1016/0301-0104(76)80101-2.
(98) Ratajczak, H.; Orville-Thomas, W. J. *J. Mol. Struct.* **1973**, *19*, 237. doi:10.1016/0022-2860(73)85267-6.
(99) Bader, R. F. W. *Monatsh. Chem.* **2005**, *136* (6), 819. doi:10.1007/s00706-005-0307-x.
(100) Oliveira, B. G.; Araújo, R. C. M. U.; Ramos, M. N. *Quim. Nova* **2010**, *33* (5), 1155. doi:10.1590/S0100-40422010000500029.
(101) Bader, R. F. W. *Chem. Rev.* **1991**, *91* (5), 893. doi:10.1021/cr00005a013.
(102) Filho, E. B. A.; Ventura, E.; do Monte, S. A.; Oliveira, B. G.; Lima, C. G., Jr; Rocha, G. B.; Vasconcellos, M. L. A. A. *Chem. Phys. Lett.* **2007**, *449* (4–6), 336. doi:10.1016/j.cplett.2007.10.080.
(103) Oliveira, B. G.; Vasconcellos, M. L. A. A. *Inorg. Chem. Commun.* **2009**, *12* (11), 1142. doi:10.1016/j.inoche.2009.09.010.
(104) Oliveira, B. G.; Araújo, R. C. M. U.; Carvalho, A. B.; Ramos, M. N. *Struct. Chem.* **2009**, *20* (4), 663. doi:10.1007/s11224-009-9458-4.
(105) Oliveira, B. G.; Araújo, R. C. M. U.; Silva, J. J.; Ramos, M. N. *Struct. Chem.* **2010**, *21* (1), 221. doi:10.1007/s11224-009-9567-0.
(106) Oliveira, B. G.; Araújo, R. C. M. U.; Ramos, M. N. *J. Mol. Struct. THEOCHEM* **2009**, *908* (1–3), 79. doi:10.1016/j.theochem.2009.05.013.

Theoretical study on the aging and reactivation mechanism of tabun-inhibited acetylcholinesterase by using the quantum mechanical / molecular mechanical method

Yanwei Li, Likai Du, Yueming Hu, Xiaomin Sun, and Jingtian Hu

Can. J. Chem. Downloaded from www.nrcresearchpress.com by Renmin University of China on 09/02/12
For personal use only.

Abstract: The organophosphorous compound tabun is highly neurotoxic because of its irreversible inhibition on acetylcholinesterase (AChE). It is wildly used as a warfare agent in the military. In this work, the aging and reactivation mechanism of tabun-inhibited AChE were studied by using the quantum mechanical / molecular mechanical (QM/MM) method. Geometry optimization of the stationary points were performed at the B3LYP/6–31G(d) level. Single-point energies were computed at the B3LYP/6–311++G(d,p) level. On the basis of the QM/MM results, a conclusion that the C–O bond scission is caused by water attack on the ethoxy group in the aging mechanism can be drawn. The reactivation process initialed by the antidotes CH_2NO^- or HLÖ-7 consists of three elemental steps, the nucleophilic attack on the P atom by the antidote, the dephosphorylation process, and the decomposition of the antidote–tabun complex. The highest energy barriers of the aging reaction, CH_2NO^--induced reactivation, and HLÖ-7-induced reactivation are 19.9, 20.0, and 14.8 kcal/mol (1 cal = 4.184 J), respectively. The relative lower overall energy barrier of HLÖ-7-induced reactivation compared with that of the aging reaction indicates that HLÖ-7 is able to reactivate tabun-inhibited AChE. In addition, whether a newly designed antidote is able to reactivate tabun-inhibited AChE can be examined by the inequation $X < 19.9$ kcal/mol,where X means the highest energy barrier of the reactivation reaction of the newly designed antidote.

Key words: tabun, aging mechanism, reactivation mechanism, QM/MM method.

Résumé : Le tabun, un composé organophosphoré, est extrêmement neurotoxique en raison de son inhibition irréversible de l'acétylcholinestérase (AChE). Il a été utilisé comme arme chimique. Dans ce travail, faisant appel à la méthode de mécanique quantique / mécanique moléculaire (MQ/MM), on a étudié le vieillissement et le mécanisme de réactivation de de l'AChE inhibée par le tabun. On a effectué l'optimisation de la géométrie des points stationnaires au niveau B3LYP/6–31G(d) de la théorie. On a calculé les énergies des points uniques au niveau B3LYP/6–3111++G(d,p) de la théorie. Sur la base des résultats de méthode de MQ/MM, il est possible d'arriver à une conclusion à l'effet que, dans le mécanisme de vieillissement, la scission de la liaison C–O est causée par l'attaque d'une molécule d'eau sur le groupe éthoxy. Le processus de réactivation initié par les antidotes CH_2NO^- ou HLÖ-7 comporte trois étapes élémentaires, l'attaque nucléophile sur l'atome de phosphore par l'antidote, le processus de déphosphorylation et la décomposition du complexe antidote-tabun. La barrière d'énergie la plus élevée de la réaction de vieillissement, la réactivation induite par le CH_2NO^- et la réactivation induite par le HLÖ-7 sont respectivement de 19,9, 20,0 et 14,8 kcal/mol (1 cal = 4.184 J). Le niveau relativement plus bas de l'énergie d'activation globale pour la réactivation induite par le HLÖ-7 comparée à celle de la réaction de vieillissement indique que le HLÖ-7 peut réactiver l'AChE inhibée par le tabun. De plus, la possibilité qu'un nouvel antidote puisse réactiver l'AChE inhibée par le tabun a été examinée par l'inéquation $X < 19{,}9$ kcal/mol dans laquelle X correspond à la barrière d'énergie la plus élevée de la réaction de réactivation du nouvel antidote mis au point.

Mots-clés : tabun, mécanisme de vieillissement, mécanisme de réactivation, méthode MQ/MM.

[Traduit par la Rédaction]

Introduction

Organophosphorus (OP) compounds, such as paraoxon, methamidophos, VX, and tabun, have been used as insecticides in modern agriculture or as chemical warfare agents in the military. The broad distribution of OP compounds causes huge numbers of intoxications and thousands of deaths each year.[1,2] In addition, the OP chemical warfare agents are still widely used in the globalization and escalation of terrorist attacks as well as in other military conflicts since the 1990s. Tabun is the earliest synthesized chemical warfare agent and its output reached 10 000 – 12 000 tons during 1936–1944.[3,4] Because of its simple 3D structure, tabun can be a perfect model and representation for OP compounds in theoretical

Received 19 September 2011. Accepted 31 October 2011. Published at www.nrcresearchpress.com/cjc on 23 March 2012.

Y. Li, Y. Hu, X. Sun, and J. Hu. Environment Research Institute, Shandong University, Jinan 250100, P.R. China.
L. Du. Institute of Theoretical Chemistry, Shandong University, Jinan 250100, P.R. China.

Corresponding author: Jingtian Hu (e-mail: hjt@sdu.edu.cn).

Can. J. Chem. Downloaded from www.nrcresearchpress.com by Renmin University of China on 09/02/12
For personal use only.

study. Tabun can firmly combine with acetylcholinesterase (AChE; EC 3.1.1.7) and hinder its hydrolysis function towards the neurotransmitter acetylcholine (ACh). For example, Ser203, which is a critical amino acid in the active site of AChE, can be inhibited by tabun through nucleophillic attack. This inhibiting progress is also called "phosphonylation reaction". The inhibited AChE may spontaneously change into the "aged" state through an "aging reaction", making AChE irreversibly inactive. Successive accumulation of acetylcholine will paralyze neurotransmission and eventually lead to muscle fasciculation and respiratory failure. Without injecting the proper antidote immediately, people may die soon after the poisoning.[5] Actually, the inhibited AChE can be reactivated if a nucleophile attacks the P atom of tabun and removes it from the active site before the aging reaction.

There are two hypotheses about the aging mechanism of tabun-inhibited AChE: one suggests that the P–N bond breaks in the aging progress[6] and the other suggests that the aging reaction proceeds via O-dealkylation.[7] Both of the hypotheses are based on mass spectrometry studies. Kinetic analysis[8] and mechanisms[9] of reactivation and aging pathways by different phosphoramidates have also been reported. However, the aging and reactivate mechanisms of tabun-inhibited AChE have not been fully understood, and many details should be elucidated, such as the exact location of the antidotes, the structure information of the intermediates and transition states, and the movement and function of the critical amino acids in the active site. In the present work, the quantum mechanical / molecular mechanical (QM/MM) calculations were performed to clarify these issues. CH_2NO^- and HLÖ-7 were selected as the models. Some useful guidance in designing more efficient antidotes is also provided based on the computational results.

Computational methods

The QM/MM calculations were performed with the ChemShell package[10] integrating Turbomole[11] and DL-POLY programs.[12] The QM calculations were carried out by Turbomole with the aid of density functional theory (DFT).[13–15] The QM part was treated at the B3LYP/6–31G(d) level, and the single-point energies of the intermediates and transition states were calculated at the B3LYP/6–311++G(d,p) level, while the MM region was considered by the CHARMM22[16] force field. The QM and MM energies are considered complementary in our QM/MM calculations. The energy equation is as follows (E = entire, I = inner, O= outer, L = link, and Corr = corrections):[17]

$$E^{E}_{QM/MM} = E^{O}_{MM} + E^{I,L}_{QM} + E^{I,O}_{QM-MM} - E^{I,L}_{Corr}$$

An electronic embedding scheme[18] incorporating the MM charges into the one-electron Hamiltonian of the QM treatment and hydrogen link atoms with a charge shift model[19,20] were adopted for the QM/MM boundary. The default convergence criteria have been adopted in the QM/MM calculations with HDLC optimizers[21] for the reactant, intermediates, and product. The potential energy surface scan from reactant to product was employed in searching the transition state. Various potential energy surface (PES) scans (for example, P–O bond formation in the nucleophilic attack progress) were performed by constraining the relevant internal coordinates. The corresponding structure of the highest energy point during the PES was extracted and optimized before we confirmed its transition-state characteristics. All the structures were viewed through the VMD program.[22]

Refinement of the crystal structure

The simulation system was prepared on the basis of the crystal structure of mouse AChE (PDB code: 3DL7) obtained from the Protein Data Bank (http://www.pdb.org). According to the protein information in the file 3DL7.pdb, 11 residues are missing in the ChainA. The MODELLER[23] program was employed to replenish ChainA. The missing hydrogen atoms were added using the HBUILD facility in the CHARMM package.[24] CH_2NO^- was docked into the AChE enzyme using Accelrys Discovery Studio 2.1 (Accelrys Software Inc.). In fact, the crystal structure of the tabun–HLÖ-7–AChE complex (PDB code: 2JEZ) has been reported,[25] however, to make the results comparable, HLÖ-7 was extracted from 2JEZ and then docked with 3DL7 using Accelrys Discovery Studio 2.1. Together with the crystal water molecules, the antidote–AChE complex was initially placed in a cubic box with 42 875 water molecules. The cubic box was then modified to a sphere with a radius of 42 Å. The molecular dynamic simulation was done by the CHARMM program with the CHARMM22 force field for protein and the TIP3P model[26] for water. The force field for the antidote (CH_2NO^- and HLÖ-7) was built on the basis of the CHARMM General Force Field.[27] The system was then neutralized by nine sodium ions at random positions. The antidote was kept fixed while the others were allowed to move freely, then the constraints were removed. The system was first gradually heated from absolute zero to 298.15 K by 50 000 steps, then it was equilibrated thermally for 500 000 steps to reach the equilibration state, and then the canonical (NVT) ensemble was employed in the 2 ns simulation dynamics. The QM/MM calculation started with the last snapshot of the simulation dynamics. The analysis results (equilibration tendency of total energy and system stability) of the 2 ns simulation dynamics are shown in the Supplementary data (Figs. S1–S6).

Determination of the QM and movable MM regions

In the aging reaction, the QM subsystem is composed of key parts of residues Gly121, Gly122, Glu202, Sun203 (combination of Ser203 and tabun), Glu334, His447, and a water molecule with 77 atoms. It is labeled blue in Fig. 1A. In the reactivation reaction induced by CH_2NO^-, the QM subsystem, which is labeled blue in Fig. 1B, consists of 72 atoms. The MM region is selected within 6 Å of residues Gly121, Gly122, Sun203, Glu334, His44,7 and CH_2NO^-, with 1898 movable atoms. In the reactivation reaction induced by HLÖ-7, the QM subsystem consists of 106 atoms. All of the atoms within 20 Å of the P atom were selected to be the movable MM region, which contains 3993 atoms.

In the aging reaction, atoms within 6, 8, and 10 Å of residues Gly121, Gly122, Sun203, Glu334, and His447 were selected to be the movable MM region to test its contribution to the energy value of the optimizations. There are 1783, 2941, and 4684 movable atoms in the MM region, respectively. The results show that different scales for the MM region merely change the energy barrier of the reaction. Thus, although the movable atom number of the MM region is

Fig. 1. (A) Reaction center of the aging reaction. The quantum mechanical (QM) subsystem atoms are labeled in blue. The QM subsystem includes the whole amino acids Gly121, Gly122, and Ser203, and functional parts of the Glu202, Glu334, and His447 amino acids. (B) Reaction center of the reactivation reaction. Key distances are labeled in red. (C) The structures of CH_2NO^- and HLÖ-7. The colour version of this figure can be viewed with the article on the journal Web site.

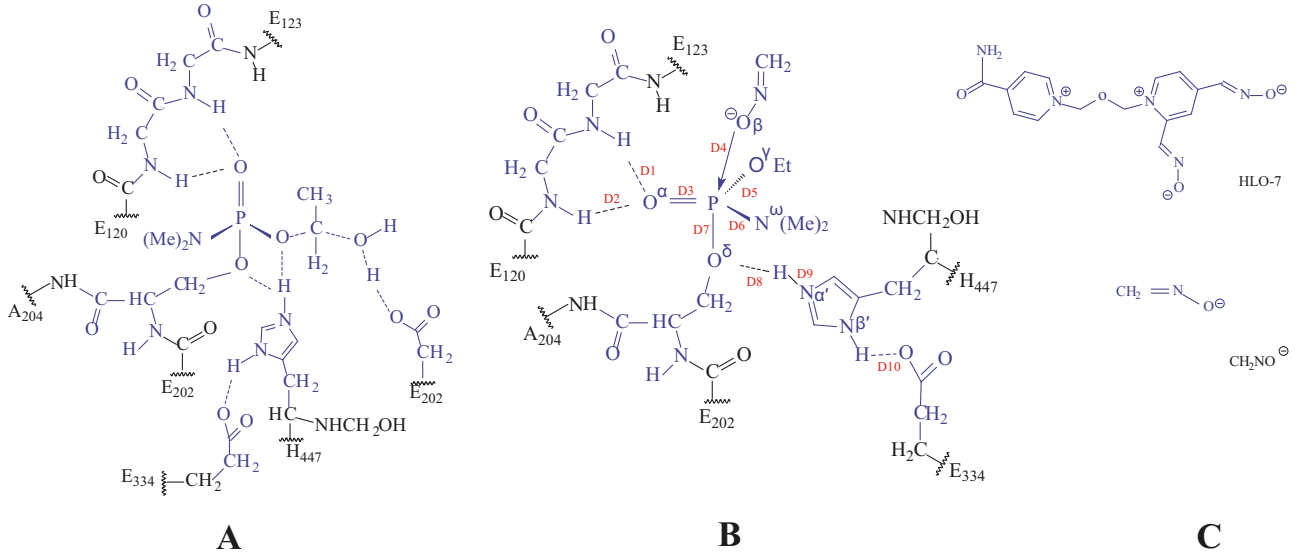
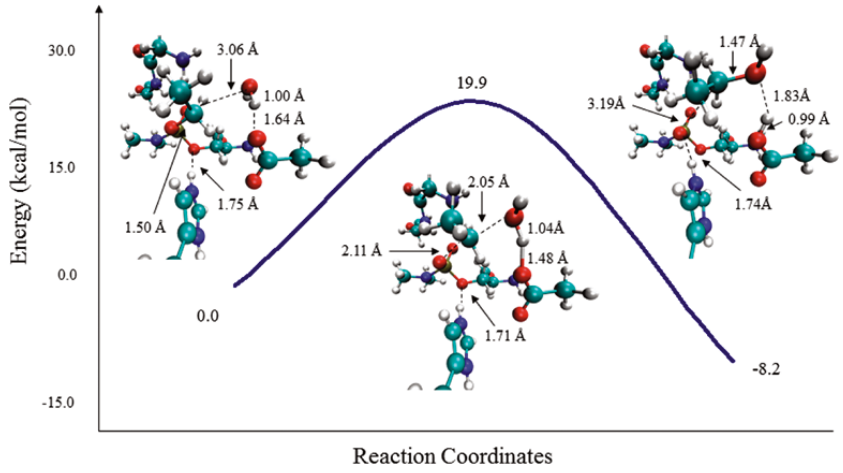


Fig. 2. Energy profile of the aging pathway determined by B3LYP/6–311++G(d,p) : CHARMM QM/MM method. In the 3D structure of the reaction center, carbon, nitrogen, oxygen, phosphorus, and hydrogen atoms are colored cyan, blue, red, tan, and white, respectively. Labeled figures are key distances of the reaction center. The colour version of this figure can be viewed with the article on the journal Web site.



different, the results obtained from the aging reaction and CH_2NO^-- or HLÖ-7-induced reactivation are comparable.

Results and discussion

Aging reaction initiated by a water molecule

A water molecule shown in Fig. 2 is involved in the aging reaction. This water molecule is supposed to be not far from the ethoxy moiety. Thus, it can easily attack the carbon atom of the ethoxy moiety. However, the crystal structure (PDB code: 3DL7) fails to provide the precise position of the water molecule because of low resolution or other unknown factors. We found the precise position of the water molecule by MD simulation using the CHARMM22 force field. An earlier study focused on the phosphonylation mechanism of tabun-inhibited AChE[28] and indicated that His447 should be at the protonated state and share a hydrogen bond with Sun203. Our optimized structure indicates that His447 is too far away from the water molecule to abstract an H atom from it. However, it can facilitate the aging reaction by gradually moving to the oxygen atom of the ethoxy moiety and attracting the electrons of the C–O bond, making it easier to break. On the other hand, Glu202 abstracts a hydrogen atom from the water molecule and promotes the nucleophilic attack on the carbon atom of the ethoxy moiety. The QM/MM results show that the aging reaction can occur easily (energy barrier 19.9 kcal/mol). This is consistent with the widely accepted idea that the aging reaction of tabun-inhibited AChE is spontaneous.

CH_2NO^--induced reactivation

Oximes are used as potential reactivators for OP-inhibited AChE. The simplest oxime, formaldehyde oximate anion (CH_2NO^-), was chosen as one model. In the present study, we mark the model that contains th eamino acid Glu334 in

Can. J. Chem. Downloaded from www.nrcresearchpress.com by Renmin University of China on 09/02/12
For personal use only.

Can. J. Chem. Downloaded from www.nrcresearchpress.com by Renmin University of China on 09/02/12
For personal use only.

Table 1. Key internuclear distances during the reactivation reaction of acetylcholinesterase (AChE) by CH_2NO^-.

	Internuclear distance (Å)																			
	D1		D2		D3		D4		D5		D6		D7		D8		D9		D10	
	Type																			
Structure	A	B	A	B	A	B	A	B	A	B	A	B	A	B	A	B	A	B	A	
Reactant	1.83	1.85	2.08	2.11	1.51	1.51	3.59	3.65	1.57	1.57	1.66	1.66	1.64	1.64	1.96	1.96	1.01	1.02	1.47	
TS-1	1.79	1.79	2.13	2.14	1.52	1.52	2.34	2.35	1.6	1.6	1.68	1.68	1.70	1.71	1.88	1.87	1.02	1.03	1.50	
INT-1	1.74	1.75	1.92	2	1.54	1.54	1.81	1.82	1.64	1.65	1.73	1.72	1.78	1.79	1.83	1.79	1.04	1.04	1.51	
TS-2	1.76	1.78	1.97	2.03	1.52	1.52	1.71	1.71	1.61	1.6	1.69	1.69	2.16	2.19	1.11	1.07	1.44	1.52	1.62	
INT-2	1.79	1.79	2.1	2.1	1.51	1.51	1.68	1.68	1.58	1.58	1.66	1.66	2.66	2.68	1.02	1.01	1.65	1.69	1.63	
Product	2.79	2.79	4.46	4.48	1.51	1.51	1.63	1.63	1.6	1.6	1.64	1.64	5.73	5.75	1.00	0.99	1.84	1.87	1.59	

Note: Types A and B refer to the model with Glu334 and without Glu334, respectively, in the QM subsystem.

Table 2. The relative energies of the transition states, intermediates, and products in reactivation reaction types A, B, C, and D at the B3LYP/6–311++G(d,p) level.

	Relative energy (kcal/mol)					
Type	Reactant	TS-1	INT-1	TS-2	INT-2	Product
A	0	15.3	11.3	20.0	14.9	–5.0
B	0	15.4	12.6	17.8	13.3	–5.8
C	0	10.0	8.3	14.8	7.5	1.4
D	0	11.3	10.2	13.9	8.7	3.0

Note: 1 cal = 4.184 J.

Table 3. The key angles of INT-1 of reactivation reaction types C and D.

	Angle (°)			
Type	O^{β}–P–O^{γ}	O^{α}–P–N^{ω}	N^{ω}–P–O^{γ}	O^{γ}–P–O^{α}
C	173.5	118.1	112.5	128.5
D	173.3	118.0	112.6	128.8

the QM subsystem as type A. The location of this oximate anion can be determined by MD simulation using the CHARMM force field together with the geometry optimization of the AChE–tabun–oximeate anion complex. The MD results show that the anion is stabilized by three surrounding water molecules.

The first step of the reactivate mechanism is the nucleophilic attack on the P atom by CH_2NO^-. This process should overcome an energy barrier of 15.3 kcal/mol. From Table 1, we find that the lengths of the O^{α}–P bond, O^{γ}–P bond, N^{ω}–P, and O^{δ}–P bond slightly increase during the nucleophilic attack. The angles of O^{β}–P–O^{γ}, O^{α}–P–N^{ω}, N^{ω}–P–O^{γ}, and O^{γ}–P–O^{α} are 170.1°, 114.5°, 118.6°, and 125.9°, respectively. The structure of intermediate 1 (INT-1) clearly shows the trigonal bipyramidal characteristic (Supplementary data Fig. S7). The second step is known as the dephosphorylation. His447 may steadily approach and donate a proton to the O^{δ} atom, which causes the H–O^{δ} bond formation and the P–O^{δ} bond scission. This process needs to overcome a barrier of 8.7 kcal/mol, which is lower than the first step. Comparing some key distances of the reactant with transition state 1 (TS-1), INT-1, TS-2, and INT-2, we find that distance 7 (D7), D8, and D9 change gradually while D1, D2, D3, D5, and D6 stay stable (Table 1; Supplementary data Figs. S7 and S8). The last step is the decomposition of the CH_2NO^-–tabun complex from the catalytic center of AChE. As a whole, the nucleophilic attack step is the rate-determining step (the energy barrier is 15.3 kcal/mol).

We mark the QM subsystem without Glu334 as type B. Type B is used to compare with type A to test the influence of the residue GLU334 on the reactivation reaction, especially on the energy barriers. This strategy has been adopted and explained in a former article.[29] In type B, the energy barrier of the nucleophilic attack step is 15.4 kcal/mol, which is almost the same as type A (15.3 kcal/mol). This indicates that including or not including Glu334 in the QM part has little impact on the nucleophilic attack step. However, the energy barrier of the dephosphorylation reaction is 5.2 kcal/mol in type B, which is 3.5 kcal/mol lower than that of type A.

Fig. 3. Energy profiles of reactivation reaction types A, B, C, and D. These reactions were determined by the B3LYP/6–311++G**: CHARMM quantum mechanical / molecular mechanical (QM/MM) method.

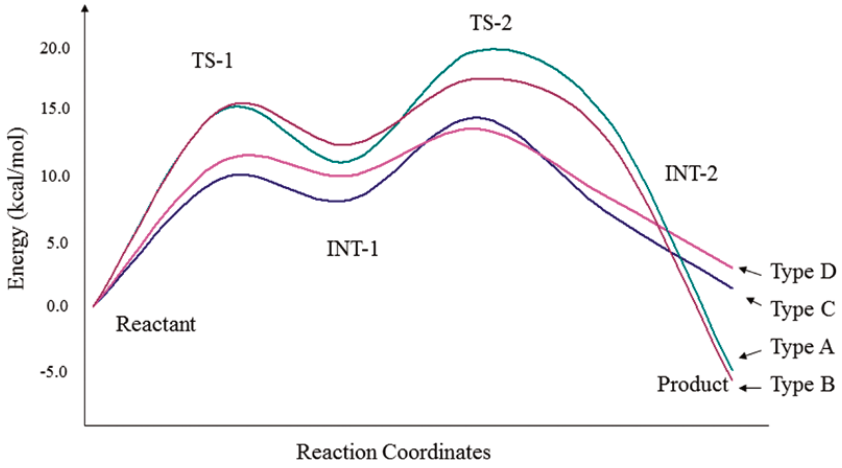
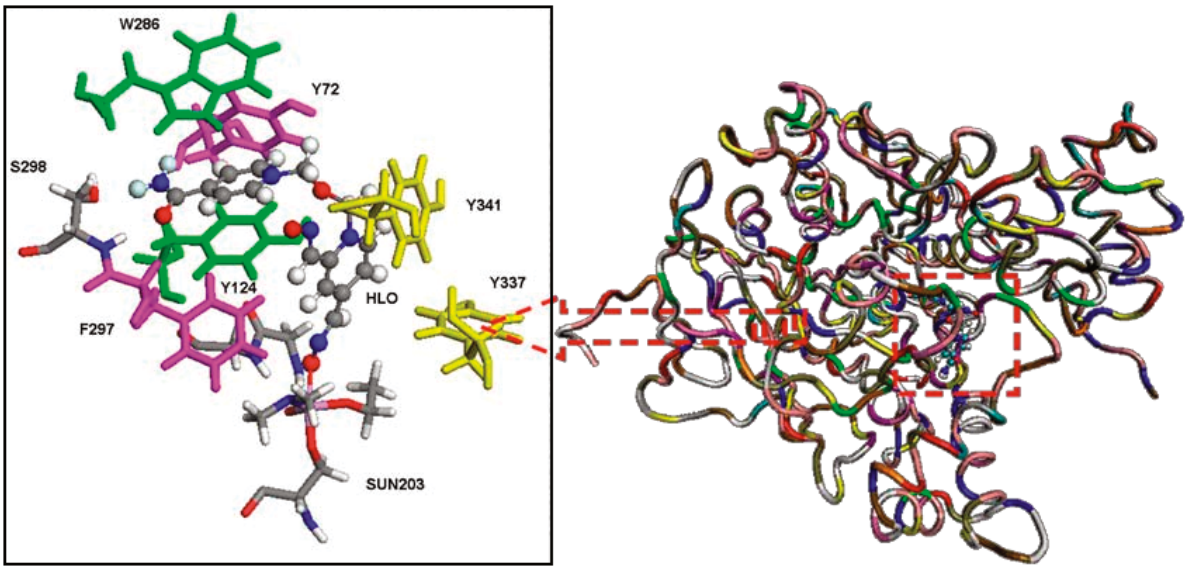


Fig. 4. The surrounding amino acids of HLÖ-7 and its location in acetylcholinesterase (AChE).



This means Glu334 does hinder the P–O$^{\delta}$ bond scission. Glu334 stabilizes INT-1 more than TS-2, consistent with the previous study; therefore, this glutamic acid facilitates the phosphonylation reaction.[30] The changes in D10 shown in Table 1 provide the information that Glu334 gradually leaves His447 without proton transfer. Energy profiles of reactivation reaction types A and B are shown in Fig. 3. The optimized structures are provided in the Supplementary data (Figs. S7 and S8). The computed single-point energies of each optimized structure along the reaction paths are shown in Table 2.

HLÖ-7-induced reactivation

One of the rings of HLÖ-7 is located near the ring of Trp286 and of Tyr124 by π-stacking interaction. Three hydrogen bonds are formed separately with Ser298, Phe297, and the amide group. The other ring is aligned by Tyr124, Tyr341, and Tyr337, shown in Fig. 4. In the study of HLÖ-7-induced reactivation, two models were built: one with Glu334 in the QM subsystem is defined as type C, the one without Glu334 in the QM subsystem is defined as type D. The INT-1 angles shown in Table 3 demonstrate its trigonal bipyramidal characteristics, which is in accordance with the results by da Silva Gonçalves et al.[20] Figure 5 shows the optimized structure information of the nucleophilic attack step of type C. In type C, the barrier of the reaction INT-1 → INT-2 is 6.5 kcal/mol, whereas it is 3.7 kcal/mol in type D. This reconfirms the conclusion above that Glu334 stabilizes INT-1 more than TS-2 in the dephosphorylation reaction. As shown in Fig. 3, the highest barriers of the HLÖ-7- and CH_2NO^--induced reactivation reactions are 14.8 and 20.0 kcal/mol, respectively. This distinctness may be caused by the structure difference of the two antidotes. The optimized structure information of the rest of the two steps are shown in Fig. 6.

The comparison of the aging reaction, CH_2NO^-- and HLÖ-7-induced reactivation

The CH_2NO^-- and HLÖ-7-induced reactivation mechanisms share two main common points: (*i*) They both consist of three steps: nucleophilic attack on the P atom, the dephosphorylation process, and the decomposition of the antidote–tabun

Can. J. Chem. Downloaded from www.nrcresearchpress.com by Renmin University of China on 09/02/12
For personal use only.

Can. J. Chem. Downloaded from www.nrcresearchpress.com by Renmin University of China on 09/02/12
For personal use only.

Fig. 5. The optimized structure of the active site for the nucleophilic attack step of reactivation reaction type C by the quantum mechanical / molecular mechanical (QM/MM) method. Carbon, nitrogen, oxygen, phosphorus, and hydrogen atoms are coloured cyan, blue, red, tan, and white, respectively. The unit of the distances given is Å. The colour version of this figure can be viewed with the article on the journal Web site.

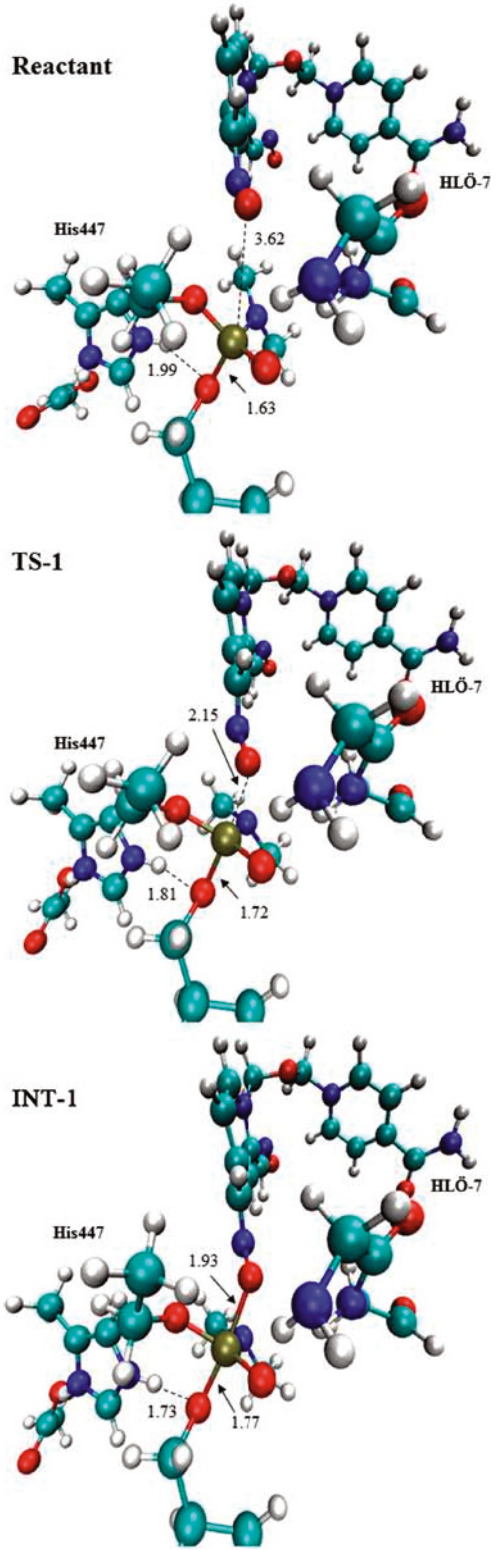
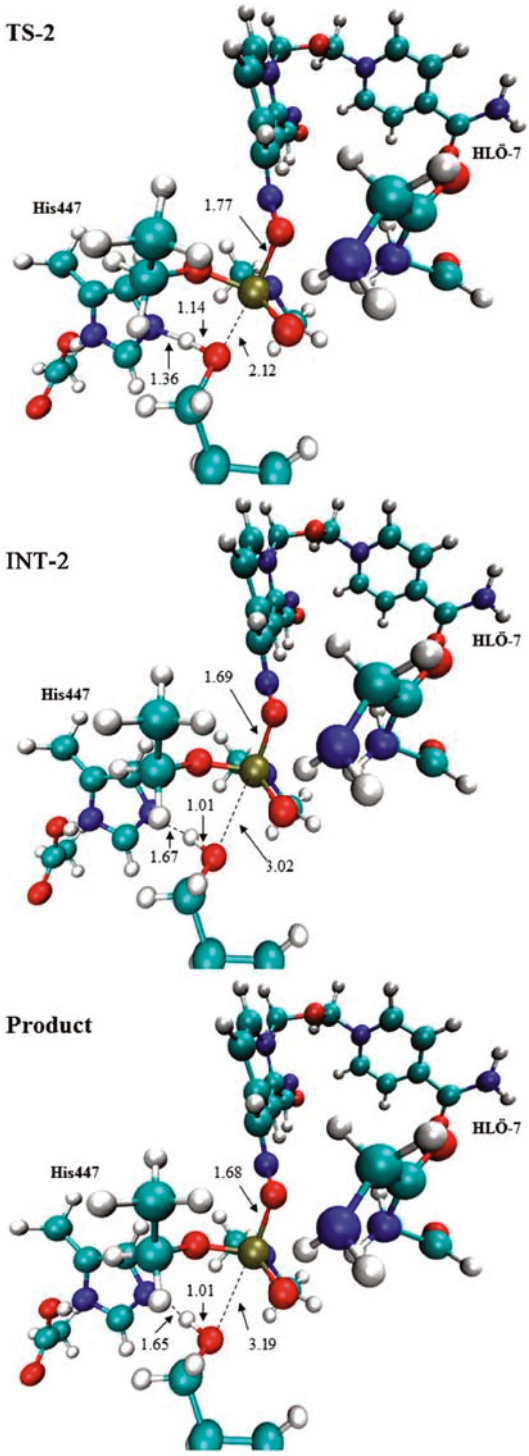


Fig. 6. The optimized structure of the active site for the dephosphorylation step of reactivation reaction type C by the quantum mechanical / molecular mechanical (QM/MM) method. Atoms are coloured in the same style as in Fig. 5. The unit of the distances given is Å. The colour version of this figure can be viewed with the article on the journal Web site.



complex from the active site; and (*ii*) They both have an intermediate with the trigonal bipyramidal characteristics.

One main difference is that the highest energy barrier of the CH_2NO^--induced reactivation reaction is 5.2 kcal/mol

Can. J. Chem. Downloaded from www.nrcresearchpress.com by Renmin University of China on 09/02/12
For personal use only.

higher than that of the HLÖ-7-induced reactivation reaction. An inequation can be drawn: $X < 19.9$ kcal/mol, where X means the overall energy barrier of the reactivation reaction by any antidotes, such as CH_2NO^-, HLÖ-7, pralidoxime, obidoxime, TMB-4, or HI-6.[31] The energy barrier of the aging reaction is 19.9 kcal/mol. If X is greater than 19.9 kcal/mol, the antidote will not be able to reactivate tabun-inhibited AChE. In addition, our results showed that the overall reactivation reaction by HLÖ-7 is endothermic, which indicates the reaction is reversible to some extent. Although the energy barrier is lower than 19.9 kcal/mol, it still seems that it is not a highly efficient oxime. The computational results are in accordance with the experiment data where maximum reactivation of tabun-inhibited AChE by HLÖ-7 is around 45%.[8] Thus, a second criterion of exothermicity is also useful for forecasting the reactivate efficacy of the newly designed antidote.

Conclusion

The aging mechanism and the reactivate mechanism were studied and elucidated in this work. HLÖ-7 was proved to be able to reactivate tabun-inhibited AChE by a QM/MM study. We provided an inequation ($X < 19.9$ kcal/mol) by two antidotes: CH_2NO^- and HLÖ-7. Besides this inequation, a second criterion of exothermicity is also introduced in forecasting the reactivate efficacy of the newly designed antidote. Of course, other already known useful antidotes should be tested using the same method to check the accuracy of the inequation.

Supplementary data

Supplementary data are available with the article through the journal Web site http://nrcresearchpress.com/doi/suppl/10.1139/v2012-007.

Acknowledgements

This work was supported financially by the National Nature Science Foundation of China (Project Nos. 21177077 and 20903062), the Independent Innovation Foundation of Shandong University (IIFSDU, project Nos. 2009JC016 and 2010TS064), the Open Project from the State Key Laboratory of Environmental Chemistry and Ecotoxicology, Research Center for Eco-Environmental Sciences, Chinese Academy of Sciences (No. KF2009-10).

References

(1) Alex, R.; Prasad, J.; Kuruvilla, A.; Jacob, K. S. *Br. J. Psychiatry* **2007**, *190* (3), 274. doi:10.1192/bjp.190.3.274a.

(2) da Silva Gonçalves, A.; França, T. C. C.; Wilter, A.; Figueroa-Villar, J. D. *J. Braz. Chem. Soc.* **2006**, *17* (5), 968. doi:10.1590/S0103-50532006000500022.

(3) Szinicz, L. *Toxicology* **2005**, *214* (3), 167. doi:10.1016/j.tox.2005.06.011.

(4) Delfino, R. T.; Ribeiro, T. S.; Figueroa-Villar, J. D. *J. Braz. Chem. Soc.* **2009**, *20* (3), 407. doi:10.1590/S0103-50532009000300003.

(5) Marrs, T. C. *Clinical and Experimental Toxicology of Organophosphates and Carbamates;* Butterworth & Heinemann: Oxford, 1992; pp 555–577.

(6) Barak, D.; Ordentlich, A.; Kaplan, D.; Barak, R.; Mizrahi, D.; Kronman, C.; Segall, Y.; Velan, B.; Shafferman, A. *Biochemistry* **2000**, *39* (5), 1156. doi:10.1021/bi992009n.

(7) Carletti, E.; Li, H.; Li, B.; Ekstrom, F.; Nicolet, Y.; Loiodice, M.; Gillon, E.; Froment, M. T.; Lockridge, O.; Schopfer, L. M.; Masson, P.; Nachon, F. *J. Am. Chem. Soc.* **2008**, *130* (47), 16011. doi:10.1021/ja804941z.

(8) Worek, F.; Aurbek, N.; Koller, M.; Becker, C.; Eyer, P.; Thiermann, H. *Biochem. Pharmacol.* **2007**, *73* (11), 1807. doi:10.1016/j.bcp.2007.02.008.

(9) Nachon, F.; Carletti, E.; Worek, F.; Masson, P. *Chem. Biol. Interact.* **2010**, *187* (1–3), 44. doi:10.1016/j.cbi.2010.03.053.

(10) Sherwood, P.; de Vries, A. H.; Guest, M. F.; Schreckenbach, G.; Catlow, C. R. A.; French, S. A.; Sokol, A. A.; Bromley, S. T.; Thiel, W.; Turner, A. J.; Billeter, S.; Terstegen, F.; Thiel, S.; Kendrick, J.; Rogers, S. C.; Casci, J.; Watson, M.; King, F.; Karlsen, E.; Sjøvoll, M.; Fahmi, A.; Schäfer, A.; Lennartz, C. *J. Mol. Struct. (THEOCHEM)* **2003**, *632* (1–3), 1. doi:10.1016/s0166-1280(03)00285-9.

(11) Ahlrichs, R.; Bär, M.; Häser, M.; Horn, H.; Kölmel, C. *Chem. Phys. Lett.* **1989**, *162* (3), 165. doi:10.1016/0009-2614(89)85118-8.

(12) Smith, W.; Forester, T. R. *J. Mol. Graph. Model.* **1996**, *14* (3), 136.

(13) Yu, W.; Hu, J.; Xu, F.; Sun, X.; Gao, R.; Zhang, Q.; Wang, W. *Environ. Sci. Technol.* **2011**, *45* (5), 1917. doi:10.1021/es103536t.

(14) Xu, F.; Yu, W.; Zhou, Q.; Gao, R.; Sun, X.; Zhang, Q.; Wang, W. *Environ. Sci. Technol.* **2011**, *45* (2), 643. doi:10.1021/es102660j.

(15) Xu, F.; Wang, H.; Zhang, Q.; Zhang, R.; Qu, X.; Wang, W. *Environ. Sci. Technol.* **2010**, *44* (4), 1399. doi:10.1021/es9031776.

(16) MacKerell, A.; Bashford, D.; Bellott, ; Dunbrack, R. L.; Evanseck, J. D.; Field, M. J.; Fischer, S.; Gao, J.; Guo, H.; Ha, S.; Joseph-McCarthy, D.; Kuchnir, L.; Kuczera, K.; Lau, F. T. K.; Mattos, C.; Michnick, S.; Ngo, T.; Nguyen, D. T.; Prodhom, B.; Reiher, W. E.; Roux, B.; Schlenkrich, M.; Smith, J. C.; Stote, R.; Straub, J.; Watanabe, M.; Wiórkiewicz-Kuczera, J.; Yin, D.; Karplus, M. *J. Phys. Chem. B* **1998**, *102* (18), 3586. doi:10.1021/jp973084f.

(17) Sherwood, P. In *Modern Methods and Algorithms of Quantum Chemistry;* Grotendorst, J., Ed.; NIC-Directors: Princeton, 2000; Vol. 3, pp 285.

(18) Bakowies, D.; Thiel, W. *J. Phys. Chem.* **1996**, *100* (25), 10580. doi:10.1021/jp9536514.

(19) de Vries, A. H.; Sherwood, P.; Collins, S. J.; Rigby, A. M.; Rigutto, M.; Kramer, G. J. *J. Phys. Chem. B* **1999**, *103* (29), 6133. doi:10.1021/jp9913012.

(20) da Silva Gonçalves, A.; França, T. C. C.; Figueroa-Villar, J. D.; Pascutti, P. G. *J. Braz. Chem. Soc.* **2011**, *22* (1), 155. doi:10.1590/S0103-50532011000100021.

(21) Billeter, S. R.; Turner, A. J.; Thiel, W. *Phys. Chem. Chem. Phys.* **2000**, *2* (10), 2177. doi:10.1039/a909486e.

(22) Humphrey, W.; Dalke, A.; Schulten, K. *J. Mol. Graph. Model.* **1996**, *14* (1), 33.

(23) Martí-Renom, M. A.; Stuart, A. C.; Fiser, A.; Sánchez, R.; Melo, F.; Sali, A. *Annu. Rev. Biophys. Biomol. Struct.* **2000**, *29* (1), 291. doi:10.1146/annurev.biophys.29.1.291.

(24) Brooks, B. R.; Bruccoleri, R. E.; Olafson, B. D.; States, D. J.; Swaminathan, S.; Karplus, M. *J. Comput. Chem.* **1983**, *4* (2), 187. doi:10.1002/jcc.540040211.

(25) Ekström, F. J.; Astot, C.; Pang, Y. *Clin. Pharmacol. Ther.* **2007**, *82* (3), 282. doi:10.1038/sj.clpt.6100151.

(26) Jorgensen, W. L.; Chandrasekhar, J.; Madura, J. D.; Impey, R.

W.; Klein, M. L. *J. Chem. Phys.* **1983**, *79* (2), 926. doi:10.1063/1.445869.
(27) Vanommeslaeghe, K.; Hatcher, E.; Acharya, C.; Kundu, S.; Zhong, S.; Shim, J.; Darian, E.; Guvench, O. P.; Vorobyov, I.; Mackerell, A. D. *J. Comput. Chem.* **2010**, *31* (4), 671.
(28) Kwasnieski, O.; Verdier, L.; Malacria, M.; Derat, E. *J. Phys. Chem. B* **2009**, *113* (29), 10001. doi:10.1021/jp903843s.
(29) Tian, B.; Strid, A.; Eriksson, L. A. *J. Phys. Chem. B* **2011**, *115* (8), 1918. doi:10.1021/jp111525p.
(30) Wang, J.; Gu, J.; Leszczynski, J. *J. Phys. Chem. B* **2008**, *112* (11), 3485. doi:10.1021/jp076974w.
(31) da Silva Gonçalves, A.; França, T. C. C.; Figueroa-Villar, J. D.; Pascutti, P. G. *J. Braz. Chem. Soc.* **2010**, *21* (1), 179. doi:10.1590/S0103-50532010000100025.

Can. J. Chem. Downloaded from www.nrcresearchpress.com by Renmin University of China on 09/02/12
For personal use only.

Reaction mechanism and kinetics of the atmospheric oxidation of 1,4-thioxane by NO_3 — A theoretical study

L. Sandhiya, P. Kolandaivel, and K. Senthilkumar

Can. J. Chem. Downloaded from www.nrcresearchpress.com by Renmin University of China on 09/02/12
For personal use only.

Abstract: Volatile organic compounds (VOCs) are emitted as pollutants into the atmosphere from many natural and artificial sources. The oxidation of VOCs by atmospheric species plays a key role in the degradation of VOCs. In the present investigation, the atmospheric degradation of a cyclic organosulfur compound, 1,4-thioxane, by an $NO_3^\bullet$ radical is studied. Pathways for the reaction of 1,4-thioxane with the $NO_3^\bullet$ radical were modeled through electronic structure calculations using density functional theory methods B3LYP, M06-2X, and MP2 with the 6–31G(d,p) basis set. The $NO_3^\bullet$-initiated reaction of 1,4-thioxane was found to proceed in three ways: by single-hydrogen atom abstraction, by direct transfer of the O atom of $NO_3^\bullet$ to the S atom moiety of 1,4-thioxane, or by two-hydrogen atom transfer reactions leading to the formation of a peroxy radical intermediate, which further undergoes secondary reactions with other atmospheric species. Structures, energies, and vibrational frequencies obtained from M06-2X/6–31G(d,p) electronic structure calculations were subsequently used to perform canonical variational transition-state theory calculations to determine the rate constants over the temperature range of 278–350 K and to study the lifetime of 1,4-thioxane in the atmosphere. The rate constant calculated for the reaction of 1,4-thioxane with the $NO_3^\bullet$ radical is in good agreement with the available experimental data.

Key words: 1,4-thioxane, atmospheric reactions, NO_3 radical, energy barrier, rate constant.

Résumé : Les composés organiques volatils (COVs) peuvent être émis dans l'atmosphère comme polluants émis par des sources naturelles et artificielles. L'oxydation de COVs par des espèces atmosphériques joue un rôle clé dans la dégradation des COVs. Dans le présent travail, on a étudié la dégradation atmosphérique d'un composé organosulfuré, le 1,4-thioxane, par le radical $NO_3^\bullet$. On a effectué une modélisation des voies possibles pour la réaction du 1,4-thioxane avec le radical $NO_3^\bullet$ et, à cette fin, on a fait appel à diverses méthodes de la théorie de la fonctionnelle de la densité, B3LYP, M06-2X et MP2 avec un ensemble de base 6–31G(d,p). On a trouvé que la réaction du 1,4-thioxane initiée par le $NO_3^\bullet$ pour s'effectuer suivant trois voies réactionnelles, par enlèvement d'un seul atome d'hydrogène, par transfert direct d'un atome d'oxygène du NO_3 à la portion sulfuré du 1,4-thoxane ou par des réactions de transfert de deux atomes d'hydrogène conduisant à la formation d'une intermédiaire radicalaire peroxy qui subit par la suite des réactions secondaires par réaction avec d'autres espèces atmosphériques. Les structures, les énergies et les fréquences vibrationnelles obtenues par calculs de structure électronique M06-2X/6–31G(d,p) ont subséquemment été utilisées pour effectuer des calculs selon la théorie de l'état de transition variationnel canonique dans le but de déterminer les constantes de vitesse pour la plage de température allant de 278 à 350 K et pour étudier le temps de vie du 1,4-thioxane dans l'atmosphère. La constante de vitesse calculée pour la réaction du 1,4-thioxane avec le radical $NO_3^\bullet$ est en bon accord avec les données expérimentales disponibles.

Mots-clés : 1,4-thioxane, réactions atmosphériques, radical NO_3, barrière d'énergie, constante de vitesse.

[Traduit par la Rédaction]

Introduction

Volatile organic compounds (VOCs) are emitted as pollutants into the atmosphere from anthropogenic and biogenic sources.[1–5] These compounds undergo a series of chemical reactions, leading to their removal from the troposphere or transformation into other compounds. The possible degradation process for these VOCs is their reactions with $OH^\bullet$ and $NO_3^\bullet$ radicals present in the atmosphere. The reactions of VOCs with these radicals can also lead to the formation of ozone, which is the major constituent of photochemical smog.[6] The $NO_3^\bullet$ radical is a common constituent of the atmosphere in the nighttime, and its maximum concentration is typically 10∼100 ppt.[7] The reaction of the $NO_3^\bullet$ radical with VOCs takes place during nighttime because $NO_3^\bullet$ rapidly photolyzes during the day time.[8] $NO_3^\bullet$ has been detected in both polluted and remote regions[9] of the atmosphere and thus the reaction of $NO_3^\bullet$ with VOCs acts as a driving force for the degradation of the VOCs. These reactions lead to the formation of products that are either harmless, do less harm, or are even hazardous to life on earth. Hence, it is very important to study the reaction between VOCs and the $NO_3^\bullet$

Received 18 October 2011. Accepted 13 January 2012. Published at www.nrcresearchpress.com/cjc on 23 March 2012.

L. Sandhiya, P. Kolandaivel, and K. Senthilkumar. Department of Physics, Bharathiar University, Coimbatore - 641 046, India.

Corresponding author: K. Senthilkumar (e-mail: ksenthil@buc.edu.in).

Can. J. Chem. Downloaded from www.nrcresearchpress.com by Renmin University of China on 09/02/12
For personal use only.

radical to know about the different degradation pathways. Also, the kinetics of the reactions are essential for finding the lifetimes of the VOCs emitted into the atmosphere and to understand the environmental implications.

The reaction kinetics of sulfur-containing VOCs have been studied and were reported on in various articles.[6,10–13] The cyclic organosulfur compound 1,4-thioxane is a breakdown product of a chemical weapon agent called mustard gas when it is disposed in the sea.[14,15] These organosulfur compounds are released into the atmosphere as a result of fossil fuel refining and combustion.[6] Recently, the kinetics of the reaction of 1,4-thioxane with NO_3• was evaluated experimentally by Aschmann et al.[16] The measured rate constant for the reaction of 1,4-thioxane with the NO_3• radical at room temperature is 5.9×10^{-14} cm^3 $molecule^{-1}$ s^{-1}. Except for this kinetic data, the reaction mechanism for the oxidation of 1,4-thioxane by the NO_3• radical and the reactions subsequent to the principal oxidation step have not been studied. As shown in previous studies, the formation of ozone is expected in the secondary reactions of the NO_3•-initiated reaction of VOCs.[1,8] Hence, the experimental study by Aschmann et al.[16] merits a theoretical study to analyze the reaction mechanism for 1,4-thioxane degradation by NO_3•.

In the present work, the interaction of the NO_3• radical with 1,4-thioxane was studied at two different C-atom sites, one at the C atom nearer to the O atom of 1,4-thioxane and the other at the C-atom site nearer to the S-atom of 1,4-thioxane. Previous studies[17–19] on the reactions of VOCs with the NO_3• radical have shown that the reactions involve two key intermediates, a peroxy radical and an alkoxy radical. In the present work, three possible reaction mechanisms are proposed for the NO_3•-initiated reactions of 1,4-thioxane. One of the mechanisms involves the abstraction of a single H atom from the CH_2 group of 1,4-thioxane by NO_3•, and the second mechanism involves the abstraction of two H atoms from the CH_2 group by NO_3•. The latter mechanism is characterized by an interesting proton-coupled electron transfer process. As shown in Figs. 1 and 2, the alkyl radical is formed through the abstraction of the hydrogen atoms of the CH_2 group in 1,4-thioxane. Furthermore, the alkyl radical reacts with O_2 to form alkyl peroxy radical as the first key intermediate. This alkyl peroxy radical interacts with NO and produces NO_2 and an alkoxy radical, which is the second key intermediate. The alkoxy radical further reacts with O_2 in the atmosphere and leads to the formation of ozone. Furthermore, a variety of potential secondary reaction paths are possible owing to the reaction between atmospheric species and the alkoxy radical. An important characteristic of the alkyl peroxy radical is its capability to undergo a self reaction.[20,21] The third reaction mechanism proceeds via the direct transfer of the O atom of NO_3 to the S-atom moiety of 1,4-thioxane.

To the best of our knowledge, the details of the reaction mechanisms of organosulfur compounds with the NO_3• radical are very limited. Except for the initial hydrogen atom abstraction step,[16] the reaction mechanisms and kinetics of secondary reactions for 1,4-thioxane with the NO_3• radical have not been studied. To determine the degradation pathways, a complete knowledge of the reaction mechanism is very essential. In view of the above-mentioned exposures, the aim of this work is to model the different reaction pathways for the degradation of 1,4-thioxane by the NO_3• radical using quantum chemical methods, and to determine the kinetics of the most favorable reactions using variational transition-state theory.[22]

Fig. 1. Reaction scheme for the interaction of NO_3• radical at the C-atom site adjacent to the O atom of 1,4-thioxane.

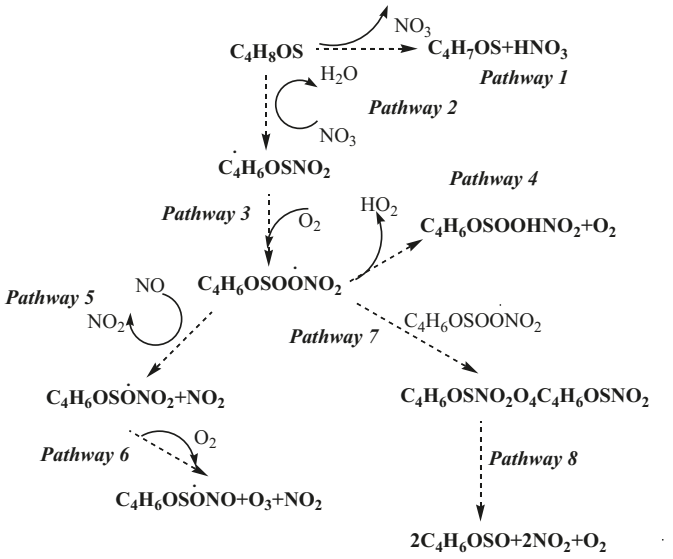
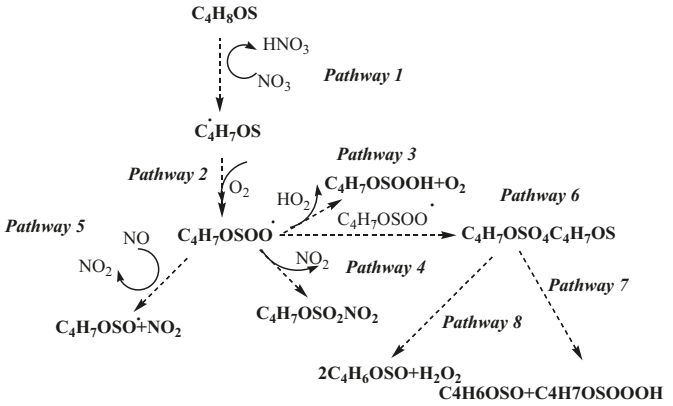


Fig. 2. Reaction scheme for the interaction of NO_3• radical at the C-atom site adjacent to the S atom of 1,4-thioxane.



Computational methods

The geometry of the minima and first-order saddle points on the potential energy surface of the reaction of 1,4-thioxane with the NO_3• radical were optimized using hybrid density functional theory methods, B3LYP[23,24] and M06-2X[25] with the 6–31G(d,p) basis set. Selected stationary points on the potential energy surface of the reaction system also were optimized at the MP2[26–28] level of theory with the 6–31G(d,p) basis set. At these levels of theory, the harmonic vibrational frequencies were calculated for all the optimized geometries to verify the nature of the stationary points. All minima were confirmed with positive frequencies and each transition state had one imaginary frequency confirming their location as maxima in one reaction coordinate. The connection of transition-state structure between designated reactant and product was confirmed in each case by intrinsic reaction coordinate

Can. J. Chem. Downloaded from www.nrcresearchpress.com by Renmin University of China on 09/02/12
For personal use only.

(IRC) calculations using the B3LYP and M06-2X methods using the second-order algorithm of Gonzalez and Schlegel.[29,30] The energy derivatives including gradients and hessians at stationary points along the minimum energy path (MEP) were also obtained. The enthalpy of a reaction and barrier height were calculated by including thermodynamic correction to the potential energy surface at a temperature of 298.15 K and 1 atm (1 atm = 101.325 kPa) pressure. All the electronic structure calculations were performed using the Gaussian09 program package.[31]

The theoretical rate constants for the most favorable reactions of 1,4-thioxane with the NO_3• radical were calculated using canonical variational transition-state theory (CVT).[32–34] The quantum effect correction for the CVT rate constant was made by small curvature tunneling (SCT) calculations.[35,36] The potential energy surface, gradients, and hessians obtained from M06-2X/6–31G(d,p) level electronic structure calculations were directly used to calculate the rate constants. Through CVT, the rate constant at temperature T is given by

$$[1] \qquad k^{\mathrm{CVT}}(T) = \min_s k^{\mathrm{GT}}(T, s)$$

where

$$[2] \qquad k^{\mathrm{GT}}(T, s) = \frac{\sigma k_{\mathrm{B}} T Q^{\mathrm{GT}}(T, s)}{h \quad \phi^{\mathrm{R}}(T)} e^{-V_{\mathrm{MEP}}(s)/k_{\mathrm{B}}T}$$

where $k^{\mathrm{GT}}(T,s)$ is the generalized transition-state theory rate constant at the dividing surface s, σ is the symmetry factor accounting for the possibility of more than one symmetry related reaction path, k_{B} is the Boltzmann constant, h is Planck's constant, $\phi^{\mathrm{R}}(T)$ is the reactant partition function per unit volume, $V_{\mathrm{MEP}}(s)$ is the classical potential energy at point s on the minimum energy path, and $Q^{\mathrm{GT}}(T,s)$ is the partition function of a generalized transition state at s. The partition functions for most of the vibrational modes were evaluated by treating them as quantum mechanically separable harmonic oscillators and the lowest vibrational mode was evaluated by hinder-rotor approximation.[37,38] The rate constant calculations were performed by using the GAUSSRATE 2009A[39] program, which is an interface between the Gaussian09 and POLYRATE 2010A[40] programs.

Results and discussion

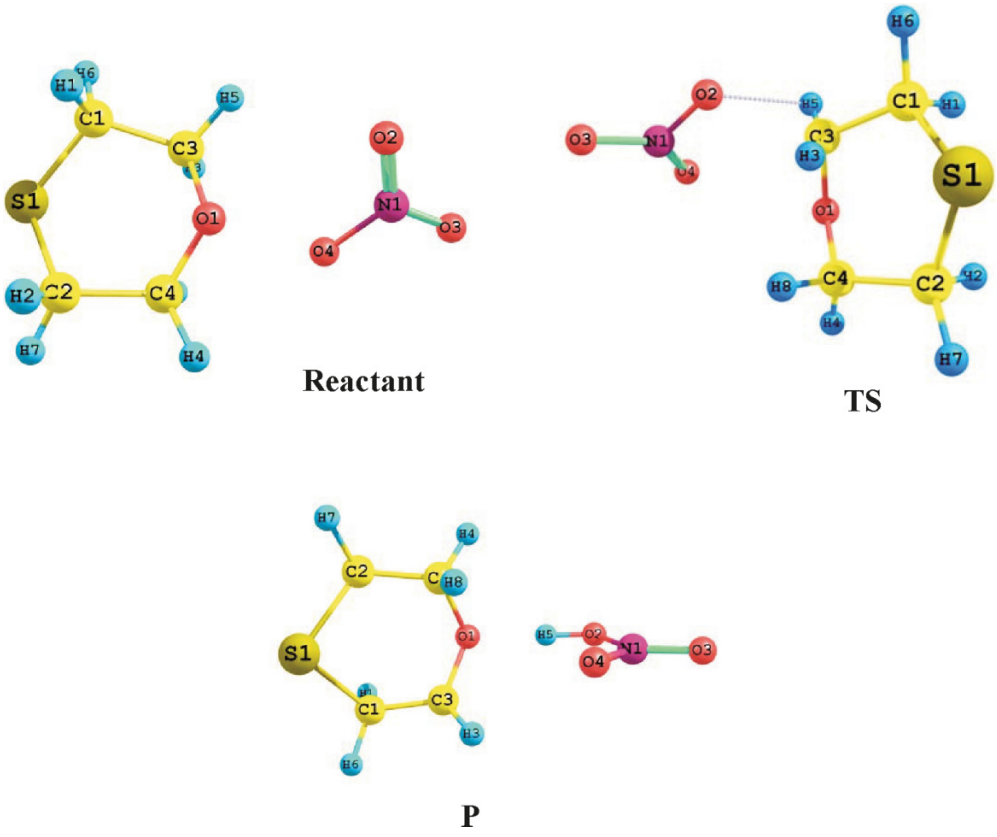
The NO_3•-initiated reaction of 1,4-thioxane proceeds in three different ways, a single H-atom abstraction from the CH_2 group of 1,4-thioxane by NO_3•, direct O-atom transfer to the S atom of 1,4-thioxane, or transfer of two hydrogen atoms from the CH_2 group of 1,4-thioxane to the O atom of NO_3•. It has been reported in various articles that the reaction of VOCs with NO_3• proceed mainly via single H-atom abstraction.[1,41,42] In this study, the pathway involving two-proton transfer and substitution of NO_2 as the initial step for NO_3• reactions with VOCs is reported for the first time. The interaction between the NO_3• radical and 1,4-thioxane was studied at two different C-atom sites, one at the C atom nearer to the O atom and the other at the C atom nearer to the S atom of 1,4-thioxane. The energy barrier for the reaction of single H-atom abstraction at the C atom adjacent to the O atom of 1,4-thioxane is 4.3 kcal/mol (1 cal = 4.184 J) and that at the C atom adjacent to the S atom of 1,4-thioxane is 13.1 kcal/mol, and the energy barrier for the two H-atom abstraction reaction is 22.51 kcal/mol. The calculated bond dissociation energy of the C–H bond adjacent to the O atom is 17.06 kcal/mol and that adjacent to the S atom is 39.64 kcal/mol. The dissociation energy of the C–H bond adjacent to the O atom is less when compared with that of the C–H bond adjacent to the S atom. This is due to the resonance of the C-radical site with the O atom. The direct transfer of the O atom from NO_3• to the S-atom moiety of 1,4-thioxane involves an energy barrier of 36 kcal/mol, which is quite large compared with the abstraction reactions. Hence, the subsequent reaction pathways corresponding to the initial H-atom abstraction reactions are studied in detail. The intermediates, transition states, and products are labeled as I, TS, and P, respectively, followed by a number.

Reaction mechanism and reaction pathways corresponding to the interaction of NO_3• radical at the C site nearer to the O atom of 1,4-thioxane

The reaction scheme corresponding to the reaction pathways involved in the reaction of the NO_3• radical with the C atom nearer to the O atom of 1,4-thioxane is illustrated in Fig. 1. The optimized structure of the reactive species corresponding to single H-atom abstraction reaction is given in Fig. 3. The structure of the stationary points optimized at M06-2X/6–31G(d,p) level of theory corresponding to the most favorable reaction pathway from the two H-atom abstraction reaction is illustrated in Fig. 4. The structure of the stationary points of the other reaction pathways is given in Fig. S1 of the Supplementary data. The energy profile corresponding to the favorable reaction pathway is illustrated in Fig. 5, and the energy profile for the other pathways is illustrated in Fig. S2 of the Supplementary data. The energy barrier (ΔE), enthalpy of the reaction (ΔH), and Gibb's free energy (ΔG) of the reactions calculated at the M06-2X/6–31G(d,p) level of theory are summarized in Table 1. The energetics obtained at the B3LYP/6–31G(d,p) level of theory are summarized in Table S1 of the Supplementary data. The structural parameters of the reactive species obtained from the two DFT methods and the MP2 method do not significantly differ from each other. For instance, the average root mean square deviation (rmsd) between the internal coordinates obtained at the above two exchange correlation functionals for the initial single H-atom abstraction reaction is 0.2 Å for the reactants, 0.07 Å for the transition state, and 0.1 Å for the product. The rmsd obtained with the MP2 and M06-2X methods are 0.1, 0.2, and 0.05 Å for the reactant, transition state, and product, respectively. Note that these rmsd values include both bonding and nonbonding interactions.

The single H-atom abstraction reaction results in the formation of nitric acid and thiooxonium radical (P) as products (pathway 1 in Fig. 1). This reaction proceeds through a TS with an energy barrier of 3.77, 4.3, and 7.2 kcal/mol, respectively, at the B3LYP, M06-2X, and MP2 level of theories. As expected, the B3LYP method underestimates the energy barrier for the single H-atom abstraction reaction. As shown in Fig. 3, in the TS, a weak hydrogen bonding exists between the H atom to be abstracted and the O atom of NO_3. The single H-atom abstraction reaction is exothermic by –16.61 kcal/mol

Fig. 3. The optimized structure of the reactive species corresponding to single H-atom abstraction at the C-atom site adjacent to the O atom of 1,4-thioxane.



and the reaction is exoergic by –16.98 kcal/mol at the M06-2X/6–31G(d,p) level of theory.

The reaction mechanism and reaction pathways corresponding to the two H-atom abstraction reaction was studied using the B3LYP and M06-2X functionals with the 6–31G(d,p) basis set. Several attempts were made to study these reactions using the MP2/6–31G(d,p) level of theory, but for many cases the optimization of the reactive species did not converge. Hence, the reactions corresponding to the two H-atom abstraction were studied and discussed using the results obtained from the M06-2X and B3LYP methods. The selected geometrical parameters of the reactive species corresponding to the most favorable reaction pathway from the two H-atom abstraction reaction obtained using DFT methods are summarized in Table S2 of the Supplementary data. The rmsd between the internal coordinates obtained at the B3LYP/6–31G(d,p) and M06-2X/6–31G(d,p) levels for the most favorable reaction pathway is 0.05 Å for the reactants, 0.1 Å for the TS, and 0.08 Å for the P. The structure and energetics obtained using the M06-2X functional with the 6–31G(d,p) basis set are discussed in detail and are used in further kinetic calculations.

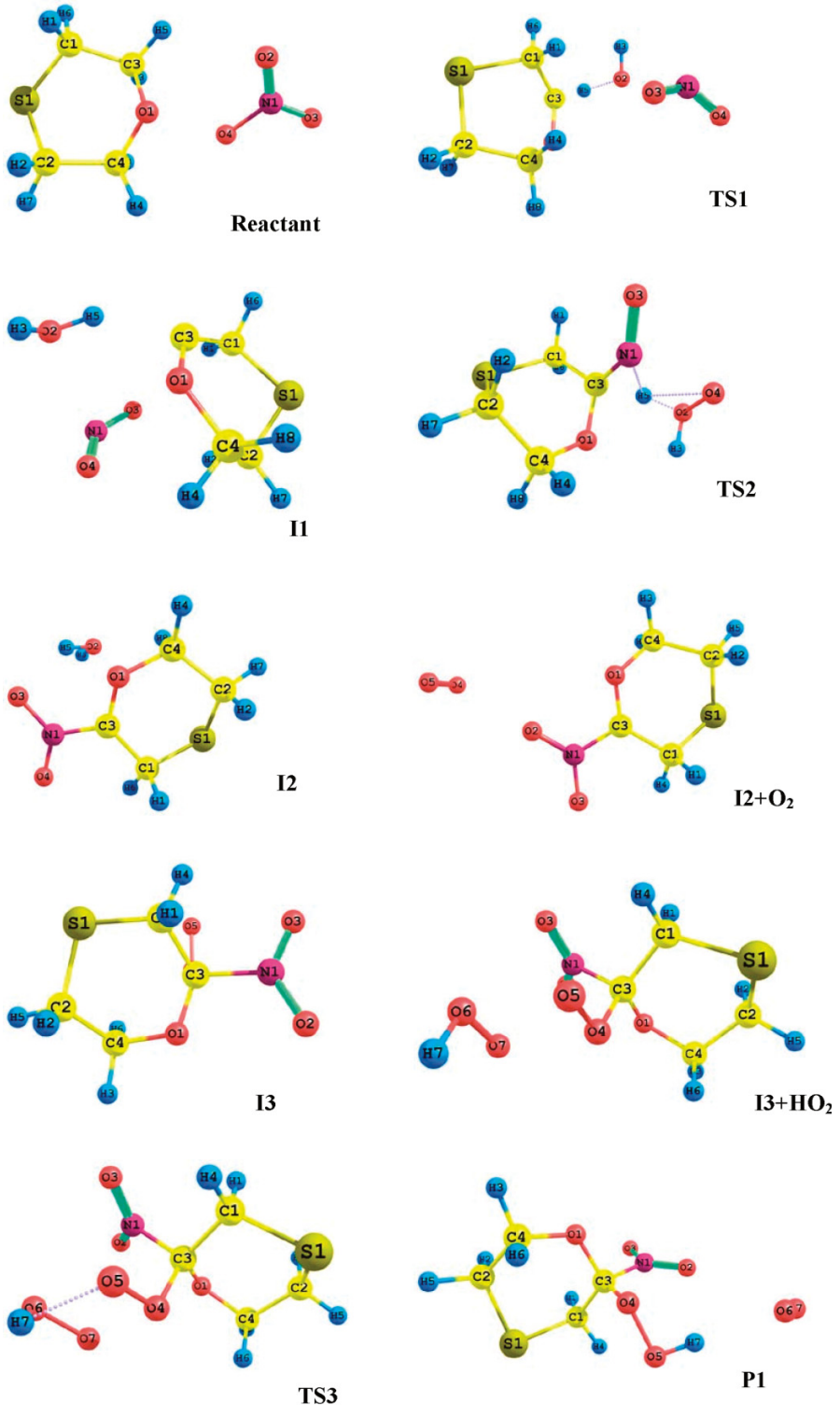
This second reaction mechanism involves the formation of an intermediate (I1) in which two H atoms of 1,4-thioxane are transferred to the O atom of NO_3 and thus a water molecule is eliminated (pathway 2 in Fig. 1). This initial reaction proceeds via TS1 with an energy barrier of 22.51 kcal/mol. TS1 shows a conserved character of the CH_2 and NO_3 groups with the distance between the O atom of NO_3 and the C atom of CH_2 reduced by 0.8 Å from that of the reactants (see Fig. 4). The reaction is exothermic by –1.3 kcal/mol and exoergic by –4.25 kcal/mol. In the next step, the NO_2 group binds with the carbon atom of the radical site of I1 and thus nitroso-thiooxonium radical I2 is formed through TS2. Thus, this reaction is a stepwise proton-coupled electron-transfer process. The barrier associated with TS2 is 50.83 kcal/mol. As reported in Table 1, the reaction is exothermic and exoergic by –46.36 and –43.24 kcal/mol, respectively.

As shown in Fig. 1 (pathway 3), the radical I2 reacts with O_2 to form nitroso-1,4-thioxane peroxy radical intermediate, I3. The oxygen molecule binds with the C atom of radical I2 in a barrierless reaction with a reaction enthalpy of –24.18 kcal/mol and a free energy of –18.8 kcal/mol. In the atmosphere, the I3 reacts with other atmospheric constituents and with itself and leads to multiple reaction pathways. The mechanisms of the reaction pathways to several dissociation products are discussed below.

The intermediate I3 further reacts with HO_2 in the atmosphere leading to the formation of 2-nitroso-1,4-thioxane-2-yl-hydroperoxide, P1, as a product (pathway 4 in Fig. 1). This product is formed because of the cleavage of the H–O bond of HO_2 and the cleaved H atom binds with the terminal O of the peroxy radical and O_2 is formed. This product formation is characterized by TS3 with a barrier of 1.92 kcal/mol. In TS3, the breaking O–H bond length is 1 Å and the newly formed H–O bond length in the product is 1.7 Å. As given in Table 1, this product formation is exothermic and exoergic with a ΔH of –35.02 kcal/mol and a ΔG of –38.4 kcal/mol.

Can. J. Chem. Downloaded from www.nrcresearchpress.com by Renmin University of China on 09/02/12
For personal use only.

Fig. 4. The optimized structures of the reactive species corresponding to the most favorable reaction pathway from the two H-atom abstraction reaction.



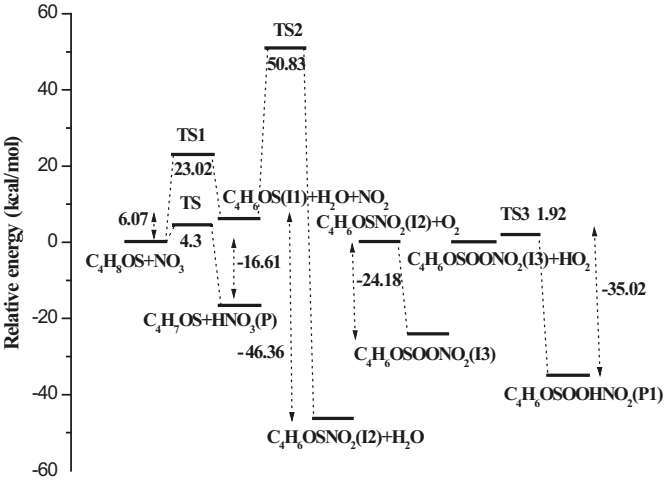
This pathway is energetically favorable because of the small barrier height.

As illustrated in Fig. 1, the intermediate I2 can oxidize NO and a nitro-alkoxy radical, I4, is formed as another intermediate (pathway 5). This intermediate is formed in a barrierless reaction with an exothermicity of –26.36 kcal/mol and the formation is exoergic with ΔG = –25.51 kcal/mol. As discussed before, the reaction of the $NO_3^{\bullet}$ radical with 1,4-thioxane is an important source for the formation of ozone (P2). The intermediate I3 along with NO_2 react with O_2 to form ozone (pathway 6 in Fig. 1). This reaction is characterized by TS4 with a barrier of 75.87 kcal/mol. In TS4, the N–O

Can. J. Chem. Downloaded from www.nrcresearchpress.com by Renmin University of China on 09/02/12
For personal use only.

Can. J. Chem. Downloaded from www.nrcresearchpress.com by Renmin University of China on 09/02/12
For personal use only.

Fig. 5. Relative energy profile for the most favorable reaction pathway from the two H-atom abstraction reaction.



bond of I3 is cleaved and the oxygen atom binds with O_2 to form a triangular structure, and the distance between the terminal O atoms of the triangular structure was found to be 0.2 Å greater than that of the product (see Fig. S1 of the Supplementary data). From TS4, O_3 is formed along with NO_2 and a coproduct. Here, the coproduct is a radical in which the N–O bond possesses a double bond character. This product channel is the most endothermic and endoergic with ΔH = 43.38 kcal/mol and ΔG = 44.02 kcal/mol. The repulsive interaction between the O atom of O_2 and that of I4 strengthens the endothermicity of the reaction.

The next most significant pathways are due to the self-reactions of hydroxyl-1,4-thioxane peroxy radicals. As illustrated in Fig. 1, the self reactions of peroxy radicals are characterized by the formation of a tetraoxide intermediate (pathway 7) and the geometry of this intermediate determines the pathway.[21] In the present case, the self reactions involved the formation of a linear tetraoxide intermediate, I5. I5 is formed in an endothermic reaction without any barrier and an enthalpy of 20.71 kcal/mol. This pathway is endoergic with a ΔG of 23.36 kcal/mol. I5 can further decompose into different products.

As shown in Fig. 1 (pathway 8), the self-reactions of nitroso peroxy radicals lead to the formation of neutral products 1,4-thioxane-2-one, O_2, and NO_2 (P3). This pathway involves TS5 with a barrier of 4.85 kcal/mol. In TS5, the oxygen molecule is cleaved and an increase in C–N bond length by 0.5 Å is observed over that of I5. The neutral products are formed when the C–N bond is cleaved and the C–O bond acquires double bond character. The reaction is exothermic and exergonic with a ΔH of –24.09 kcal/mol and a ΔG of –25.88 kcal/mol.

Thus, three different product channels were identified for the reactions of 1,4-thioxane with the NO_3• radical. Of all the pathways studied for the two H-atom transfer reaction, the reaction pathway leading to the formation of 2-nitroso-1,4-thioxane-2-yl-hydroperoxide (pathway 4, P1) was found to be the most favorable.

Kinetics

The reaction mechanisms and pathways corresponding to the interaction of NO_3• with the C-atom site nearer to the O atom of 1,4-thioxane discussed in the previous section show that the NO_3•-initiated reaction of 1,4-thioxane proceeds favorably in two ways as single H-atom abstraction from CH_2 group of 1,4-thioxane and also by a two H-atom transfer along with substitution reaction. The subsequent reactions studied for the two H-atom transfer reaction show that the formation of nitroso-1,4-thioxane peroxy radical intermediate (I33) is the key step in the reaction mechanism. Also, the formation of 2-nitroso-1,4-thioxane-2-yl-hydroperoxide along with O_2 (P1) is the most favorable reaction pathway. Hence, the rate constants are calculated for the formation of nitric acid and thiooxonium (P) product channels resulting from single H-atom abstraction reaction, and the intermediate channels (I1 and I2) of the two H-atom transfer reaction, the formation of nitroso-1,4-thioxane peroxy radical intermediate (I3) channel, and the formation of hydroperoxide along with the O_2 (P1) product channel of two H-atom abstraction reaction. The rate constants were calculated using CVT with SCT in a temperature range from 278 to 350 K with zero-point energy (ZPE)-corrected energies, gradients, and hessians calculated at the M06-2X/6–31G(d,p) level of theory. The rate constants for the single hydrogen abstraction channel (P), the formation of intermediate I1 and I2 channels, the formation of the peroxy radical intermediate channel (I3), and the product channel (P1) are designated as k_P, k_{I1}, k_{I2}, k_{I3} and k_{P1}, respectively, and are summarized in Table 2.

The calculated k_P for the single H-atom abstraction reaction at 298 K is 2.33×10^{-13} cm^3 molecule^{-1} s^{-1}. This value is comparable to the experimental value of 5.9×10^{-14} cm^3 molecule^{-1} s^{-1} by Aschmann et al.[16] The calculated rate constant agrees well with those obtained in previous studies.[41] The tunneling factor for this initial reaction is negligible because of the broad energy barrier as noted from the small imaginary vibrational frequency of the TS (–103 cm^{-1}). The rate constant k_{I1} for the two H-atom transfer reaction as the initial step is 4.71×10^{-18} cm^3 molecule^{-1} s^{-1} at 298 K. The calculated k_{I2} at 298 K for the intermediate I2 formation is 2.58×10^{-51} cm^3 molecule^{-1} s^{-1}. The small rate constant calculated for the formation of I2 shows that this reaction is not feasible in atmospheric chemistry. However, as observed in Table 2, k_{I2} shows positive temperature dependence and thus this reaction is important in the lower layer of the troposphere. The tunneling effect for this reaction is appreciable because of the high energy barrier (50.83 kcal/mol). That is, the formation of I2 is the rate-determining step for the whole reaction mechanism. Since I3 is formed without a potential barrier, the rate constant for this channel is obtained by variationally moving the reference position along the minimum energy path. The rate constant calculated for I3 at 298 K is 1.04×10^{-11} cm^3 molecule^{-1} s^{-1}. The rate constant k_{P1} calculated at 298 K for the formation of 2-nitroso-1,4-thioxane-2-yl-hydroperoxide along with the O_2 in product channel P1 is 2.16×10^{-16} cm^3 molecule^{-1} s^{-1}, and this is comparable to the estimated value based on the reported rate constants for $RO_2 + HO_2$ reactions.[43]

Reaction mechanism and reaction pathways corresponding to the interaction of NO_3• radical at the C site nearer to the S atom of 1,4-thioxane

The reaction scheme for the interaction of NO_3• at the C atom nearer to the S atom of 1,4-thioxane and the

Table 1. Energy barrier ΔE (in kcal/mol), enthalpy ΔH (in kcal/mol), and Gibb's free energy ΔG (in kcal/mol) for the proposed reactions of the interaction of $NO_3^\bullet$ radical at the C-atom site nearer to the O atom of 1,4-thioxane.

	Parameter		
Reaction	ΔE	ΔH	ΔG
$C_4H_8OS + NO_3 \rightarrow C_3H_6OSC^\bullet + H_2O + NO_2$ (I1)	22.51	–1.3	–4.25
$C_3H_6OSC^\bullet + H_2O + NO_2 \rightarrow C_3H_6OSC^\bullet NO_2$ (I2) + H_2O	50.83	–46.36	–43.34
$C_3H_6OSC^\bullet NO_2$ (I2) + $O_2 \rightarrow C_3H_6OSC(OO^\bullet)NO_2$ (I3)	No barrier	–24.18	–18.8
$C_3H_6OSC(OO^\bullet)NO_2 + HO_2 \rightarrow C_3H_6OSC(OOH)NO_2 + O_2$ (P1)	1.92	–35.02	–38.4
$C_3H_6OSC(OO^\bullet)NO_2 + NO \rightarrow C_3H_6OSCO^\bullet(NO_2)$ (I4) + NO_2	No barrier	–26.36	–25.51
$C_3H_6OSCO^\bullet(NO_2) + NO_2 + O_2 \rightarrow C_3H_6OSCO(NO) + O_3 + NO_2$ (P2)	75.87	43.38	44.02
$C_3H_6OSC(OO^\bullet)NO_2 + C_3H_6OSC(OO^\bullet)NO_2 \rightarrow C_3H_6OSNO_2CO_4CNO_2OSC_3H_6$ (I5)	No barrier	20.71	23.36
$C_3H_6OSNO_2CO_4CNO_2OSC_3H_6 \rightarrow 2C_3H_6OS(C{=}O) + 2NO_2 + O_2$ (P3)	4.85	–24.09	–25.88

Note: I, intermediate; P, product.

Table 2. Rate constants k_P, k_{I1}, k_{I2}, k_{I3}, and k_{P1} (in cm^3 $molecule^{-1}$ s^{-1}) for the initial single H-atom abstraction (P) step, two H-atom abstraction and substitution step (I1 and I2), peroxy radical (I3) formation step, and the formation of 2-nitroso-1,4-thioxane-2-yl-hydroperoxide along with the O_2 product channel (P1) resulting from the interaction of $NO_3^\bullet$ radical at the C-atom site nearer to the O atom of 1,4-thioxane.

	Rate constant (cm^3 $molecule^{-1}$ s^{-1})				
Temperature (K)	$k_P \times 10^{-13}$	$k_{I1} \times 10^{-18}$	k_{I2}	$k_{I3} \times 10^{-11}$	$k_{P1} \times 10^{-16}$
278	1.87	1.24	7.09×10^{-54}	1.02	1.77
288	2.09	2.56	1.49×10^{-52}	1.03	1.92
298	2.33	4.71	2.58×10^{-51}	1.04	2.16
308	2.58	6.42	3.70×10^{-50}	1.05	2.35
318	2.84	10.12	4.50×10^{-49}	1.06	2.41
328	3.12	14.78	4.70×10^{-48}	1.07	2.52
338	3.40	20.31	4.28×10^{-47}	1.08	2.63
348	3.70	27.92	3.43×10^{-46}	1.09	2.78
350	3.76	29.66	5.13×10^{-46}	1.09	2.82

Can. J. Chem. Downloaded from www.nrcresearchpress.com by Renmin University of China on 09/02/12
For personal use only.

corresponding pathways are given in Fig. 2. The reaction mechanism and reaction pathways corresponding to the interaction of the $NO_3^\bullet$ radical at the C-atom site adjacent to the S atom of 1,4-thioxane were studied using the B3LYP, M06-2X, and MP2 level of theories with the 6–31G(d,p) basis set. The structures of the stationary points optimized at the M06-2X/6–31G(d,p) level of theory corresponding to the most favorable pathway are shown in Fig. 6. The structure of the reactive species of the other pathways is given in Fig. S3 of the Supplementary data. The relative energy profile corresponding to the favorable reaction pathway calculated at the M06-2X level of theory is illustrated in Fig. 7. The energy profile of the other reaction pathways is shown in Fig. S4 of the Supplementary data. The energy barrier (ΔE), ΔH of the reaction, and ΔG of the reactive species calculated at the M06-2X level of theory are summarized in Table 3. The energetics obtained using the B3LYP and MP2 methods are summarized in Table S3 of the Supplementary data. The selected geometrical parameters of the reactive species corresponding to the most favorable reaction pathway calculated using the three methods are tabulated in Table S4 of the Supplementary data. The average rmsds between the internal coordinates obtained at the B3LYP and M06-2X functionals for the most favorable reaction pathway are 0.06, 0.4, and 0.1 Å for the reactants, transition state, and product, respectively. The rmsds obtained at the M06-2X and MP2 level of theories for the most favorable reaction pathway are 0.07 Å for the reactant, 0.1 Å for the transition state, and 0.09 Å for the products. The energy barriers calculated for the favorable reaction path are 4.09, 11.0, and 8.66 kcal/mol at the B3LYP, M06-2X, and MP2 level of theories, respectively. As expected, for a few cases, the energy barrier calculated from the DFT methods differed significantly from the results of the MP2 method. While comparing the results obtained for various reaction paths, it was observed that the relative importance of the studied reaction paths does not change with respect to the methods of calculation. For instance, both the DFT and MP2 methods predict that the reaction corresponding to the formation of 1,4-thioxane-2-yl nitroperoxoate is the favorable path. The structure and energetics obtained using the M06-2X functional with the 6–31G(d,p) basis set are discussed in detail and are used in further kinetic calculations.

The H-atom abstraction by the $NO_3^\bullet$ radical from the CH_2 group nearer to the S atom of 1,4-thioxane results in the formation of I1 and HNO_3 (pathway 1 in Fig. 2). This reaction occurs through transition state TS1 with an energy barrier of 13.1 kcal/mol. As given in Table 3, this reaction channel is formed with a small exothermicity of –0.93 kcal/mol in a mild exoergic reaction with ΔG = –3.0 kcal/mol. As explained for the previous reaction, the thiooxonium radical further reacts with O_2 in the atmosphere leading to the formation of I2 (pathway 2 in Fig. 2). This peroxy radical formation occurs in a barrierless reaction with a small reaction enthalpy of –1.58 kcal/mol and the reaction is exoergic

Can. J. Chem. Downloaded from www.nrcresearchpress.com by Renmin University of China on 09/02/12
For personal use only.

Fig. 6. The optimized structures of the reactive species corresponding to the most favorable reaction pathway from the single H-atom abstraction reaction.

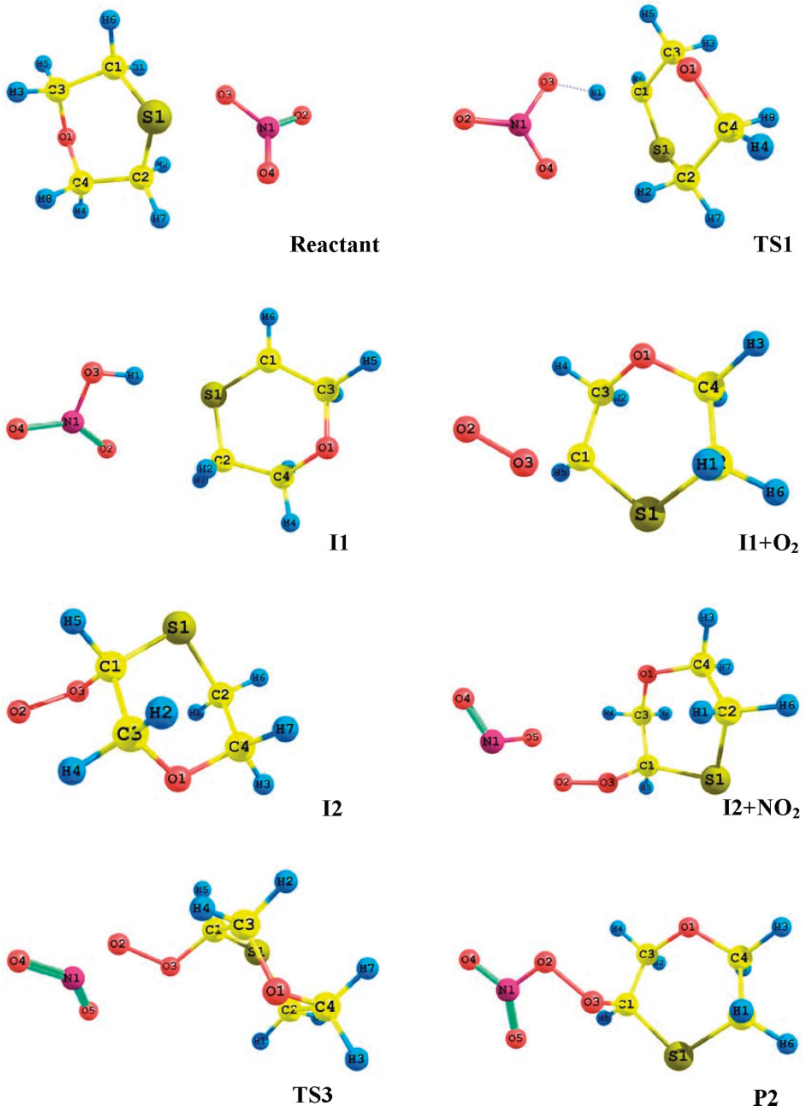
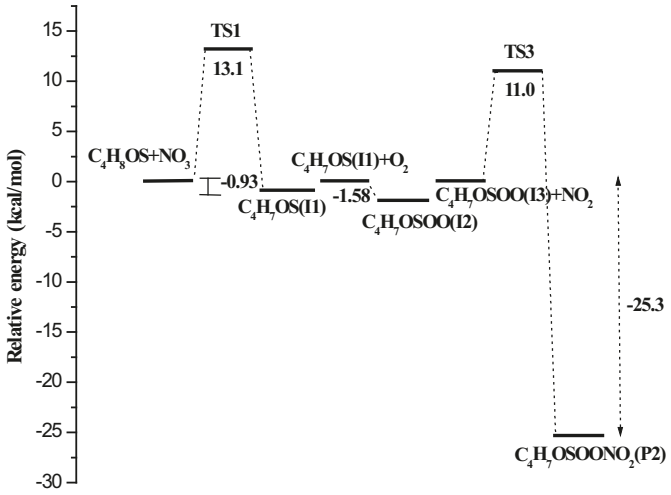


Fig. 7. Relative energy profile for the most favorable reaction pathway from the single H-atom abstraction reaction.



with $\Delta G = -1.0$ kcal/mol. As shown in Fig. 2, this peroxy radical can react in a variety of ways.

The peroxy radical reacts with HO_2 in the atmosphere leading to the formation of 2-hydroperoxy-1,4-thioxane (P1) and O_2 (pathway 3 in Fig. 2). These products are formed via TS2 with a large energy barrier of 47.78 kcal/mol, and the reaction is endothermic with a reaction enthalpy of 5.64 kcal/mol and a free energy of 4.12 kcal/mol. This reaction is not as feasible under atmospheric conditions because of the pronounced energy barrier of TS2.

The next pathway studied was the reaction of I2 with NO_2 in the atmosphere (pathway 4 in Fig. 2). This reaction is an important process during the oxidation of 1,4-thioxane because traces of nitrogen oxides are often present in the atmosphere, which may then be consumed in several atmospheric processes. This reaction may terminate the radical chain reactions and produce alkyl nitrates, where peroxy radicals act as NO_x reservoir compounds. In this reaction, the nitrogen atom of NO_2 is directly bonded with the oxygen atom of the peroxy radical (see Fig. 6) to form 1,4-thioxane-2-yl

Table 3. Energy barriers (ΔE in kcal/mol), enthalpy (ΔH in kcal/mol), and Gibb's free energy (ΔG in kcal/mol) for the proposed reactions of the interaction of the $NO_3^\bullet$ radical at the C-atom site nearer to the S atom of 1,4-thioxane.

	Parameter		
Reaction	ΔE	ΔH	ΔG
$C_4H_8OS + NO_3 \rightarrow C_4H_7OS$ (I1) + HNO_3	13.1	–0.93	–3.0
$C_4H_7OS + O_2 \rightarrow C_4H_7OSOO$ (I2)	No barrier	–1.58	–1.0
$C_4H_7OSOO + HO_2 \rightarrow C_4H_7OSOOH + O_2$ (P1)	47.78	5.64	4.12
$C_4H_7OSOO + NO_2 \rightarrow C_4H_7OSOONO_2$ (P2)	11.0	–25.3	–24.10
$C_4H_7OSOO + NO \rightarrow C_4H_7OSO$ (I3) + NO_2	No barrier	2.28	2.6
$C_4H_7OSOO + C_4H_7OSOO \rightarrow C_4H_7OSO_4C_4H_7OS$ (I4)	No barrier	–31.72	–31.17
$C_4H_7OSO_4C_4H_7OS \rightarrow C_4H_6OSO + C_4H_7OSOOOH$ (P3)	20.25	–57.05	–59.5
$C_4H_7OSO_4C_4H_7OS \rightarrow 2C_4H_6OSO + H_2O_2$ (P4)	11.42	–110.07	–114.86

Note: I, intermediate; P, product.

Table 4. Rate constants k_{I1}, k_{I2}, and k_{P2} (in cm^3 $molecule^{-1}$ s^{-1}) for the initial single H-atom abstraction (I1) step, the peroxy radical (I2) formation step, and the formation of the nitroperoxoate (P2) product channel resulting from the interaction of $NO_3^\bullet$ radical at the C-atom site nearer tothe S atom of 1,4-thioxane.

	Rate constant (cm^3 $molecule^{-1}$ s^{-1})		
Temperature (K)	$k_{I1} \times 10^{-19}$	$k_{I2} \times 10^{-11}$	$k_{P2} \times 10^{-12}$
278	2.52	1.28	7.10
288	4.77	1.28	7.23
298	8.65	1.28	7.35
308	15.13	1.28	7.48
318	25.59	1.28	7.59
328	41.96	1.28	7.70
338	66.90	1.27	7.81
348	77.03	1.27	7.91
350	89.13	1.27	7.93

Note: I, intermediate; P, product.

Can. J. Chem. Downloaded from www.nrcresearchpress.com by Renmin University of China on 09/02/12
For personal use only.

nitroperoxoate (P2). This reaction is characterized by TS3 with an energy barrier of 11 kcal/mol. In the transition-state structure, the distance between the terminal O atom of the peroxy radical and the N atom of NO_2 was reduced by 1.2 Å from that of the reactants. This reaction is exothermic and exoergic by $\Delta H = –25.3$ kcal/mol and $\Delta G = –24.1$ kcal/mol, respectively. This reaction is kinetically favorable because of the small energy barrier.

The peroxy radical I2 can be reduced by NO under atmospheric conditions (pathway 5 in Fig. 2). This reaction results in the formation of alkoxy radical I3 in a barrierless reaction with a reaction enthalpy of 2.28 kcal/mol and with an endoergicity of 2.6 kcal/mol. The self-reaction of the peroxy radical involves the formation of a linear tetraoxide intermediate (I4) as observed in the previous case (pathway 6 in Fig. 2). As given in Table 3, this intermediate is formed without any barrier and the reaction is exothermic by –31.72 kcal/mol and exoergic by –31.17 kcal/mol. As shown in Fig. 2 (pathway 7), this intermediate further dissociates into 1,4-thioxane-2-one and an hydroperoxy compound (P3) through TS4. In the transition-state structure, the tetraoxide bond is broken and the two O atoms in the tetraoxide intermediate weakly bind with the O atom of one of the self reactants, and the C–O bond length of the other self-reactant is 1.3 Å (see Fig. S3 of the Supplementary data). This pathway is exothermic by –57.05 kcal/mol and it passes through a barrier of 20.25 kcal/mol with an exoergicity of –59.05 kcal/mol.

Another important dissociation channel from I4 leads to the formation of hydroperoxide and two carbonyl compounds (P4) (pathway 8 in Fig. 2). This reaction occurs via TS5 with an energy barrier of 11.42 kcal/mol. As shown in Fig. S3 of the Supplementary data, in TS5 the tetraoxide bond is broken and two H atoms from the self-reactants are abstracted by the O atoms and weak hydrogen bonding exists between the H atoms and the O atoms. From this structure, the hydroperoxide is removed and two carbonyl products are formed. This reaction is very exothermic with a reaction enthalpy of –110.07 kcal/mol and is very exoergic with a free energy of –114.86 kcal/mol. This reaction is the lowest energy pathway and is kinetically favorable.

Thus, four different product channels were identified for the interaction of the $NO_3^\bullet$ radical at the C-atom site nearer to the S atom of 1,4-thioxane. Among the reaction pathways studied, the reaction of the peroxy radical with NO_2 leading to the formation of 1,4-thioxane-2-yl nitroperoxoate (P2) is the most favorable reaction.

Kinetics

The reaction mechanism for the interaction of the $NO_3^\bullet$ radical at the C-atom site nearer to the S atom of 1,4-thioxane

Can. J. Chem. Downloaded from www.nrcresearchpress.com by Renmin University of China on 09/02/12
For personal use only.

shows that the formation of P2 through I2 followed from the initial H-atom abstraction step (I1) is the most favorable reaction. Hence, the rate constants were calculated for the reaction channels involved in the formation of the product channel (P2). The rate constants k_{I1}, k_{I2}, and k_{P2} calculated in the temperature range of 278–350 K are summarized in Table 4. The rate constant k_{I1} calculated at 298 K is 8.65×10^{-19} cm^3 molecule^{-1} s^{-1}. The tunneling factor is negligible for this initial reaction channel. As observed in Table 4, the rate constant k_{I2} calculated for I2 formation remains the same for the whole temperature range studied with a value of 1.28×10^{-11} cm^3 molecule^{-1} s^{-1} at 298 K. The product channel (P2) is formed with a k_{P2} of 7.35×10^{-12} cm^3 molecule^{-1} s^{-1} at 298 K. The calculated rate constant k_{P2} does not show any significant variation with temperature. This value agrees well with the rate constant value calculated for the formation of nitroperoxoate in previous studies.[1]

Conclusions

The potential energy surface and the thermochemical and kinetic data for the atmospheric oxidation of 1,4-thioxane by the NO_3• radical were explored using quantum chemical methods and variational transition state theory. The results reveal several important aspects of organosulfur compounds in atmospheric chemistry. The following main conclusions were obtained.

1. The interaction of the NO_3• radical with 1,4-thioxane was studied at two different C-atom sites, one at the C atom nearer to the O atom and the other at the C atom nearer to the S atom of 1,4-thioxane. There are two possible ways favorable for the reaction between 1,4-thioxane and NO_3•, a single H-atom abstraction from the CH_2 group of 1,4-thioxane or a two H-atom transfer from CH_2 to NO_3• and subsequent binding of NO_2 with the thiooxonium radical.
2. The single H-atom abstraction reaction results in the formation of nitric acid and thiooxonium radical, whereas the two H-atom transfer reaction leads to the formation of a nitroso-thiooxonium radical and a water molecule.
3. The energy barrier for the single H-atom abstraction reaction from the C atom nearer to the O atom is 4.3 kcal/mol and the energy barrier for this abstraction from the C atom nearer to the S atom is 13.1 kcal/mol. This shows that the interaction of the NO_3• radical at the C-atom site nearer to the O atom is more favorable.
4. For two H-atom transfer reaction, the subsequent reaction pathways were studied and it was determined that the formation of the nitroso-1,4-thioxane peroxy radical is the major intermediate in the reaction pathways, and the most favorable secondary reaction pathway is the formation of 2-nitroso-1,4-thioxane-2-yl-hydroperoxide along with O_2.
5. The favorable reaction pathway from the single H-atom abstraction for the C atom adjacent to the S atom of 1,4-thioxane is the formation of 1,4-thioxane-2-yl nitroperoxoate (P2) with an energy barrier of 11 kcal/mol.
6. The rate constant for the single H-atom abstraction reaction from the C atom adjacent to the O atom is 2.33×10^{-13} cm^3 molecule^{-1} s^{-1} at 298 K and the rate constant for the two H-atom transfer reaction is 4.71×10^{-18} cm^3 molecule^{-1} s^{-1}. The rate constant calculated at 298 K for initial H-atom abstraction from the C-atom site adjacent to the S atom of 1,4-thioxane is 8.65×10^{-19} cm^3 molecule^{-1} s^{-1}. This result shows that the H-atom abstraction by the NO_3• radical from the C atom adjacent to the O atom of 1,4-thioxane is thermodynamically favored. The kinetic analysis carried out in this work agrees well with the available experimental results.

Supplementary data

Supplementary data are available with the article through the journal Web site http://nrcresearchpress.com/doi/suppl/10.1139/v2012-010. The energy barriers (ΔE), enthalpies (ΔH), and Gibbs free energies (ΔG) of the reactive species corresponding to the reaction pathways from the two H-atom abstraction reactions calculated at the B3LYP/6–31G(d,p) level of theory are summarized in Table S1. The selected structural parameters of the reactive species of the most favorable reaction pathway of this reaction system are summarized in Table S2. The optimized structures of the reactive species involved in this reaction mechanism are illustrated in Fig. S1 and the relative energy profile of the reaction pathways is shown in Fig. S2. The energy barriers (ΔE), enthalpies (ΔH), and Gibbs free energies (ΔG) of the reactive species corresponding to the reaction pathways from the single H-atom abstraction reactions calculated at the B3LYP/6–31G(d,p) and MP2/6–31G(d,p) levels of theory are summarized in Table S3. The selected structural parameters of the reactive species of the most favorable reaction pathway of this reaction system are summarized in Table S4. The optimized structures of the reactive species involved in this reaction mechanism are illustrated in Fig. S3 and the relative energy profile of the reaction pathways is shown in Fig. S4.

Acknowledgement

L.S. is thankful to Bharathiar University for providing a University Research Fellowship and the Department of Science and Technology (DST), India, for awarding an INSPIRE Fellowship. One of the authors (K.S.) is thankful to the DST for granting the research project under the DST-Fast track scheme for young scientists.

References

(1) Atkinson, R.; Arey, J. *Chem. Rev.* **2003**, *103* (12), 4605. doi:10.1021/cr0206420.
(2) Guenther, A.; Geron, C.; Pierce, T.; Lamb, B.; Harley, P.; Fall, R. J. *Atmos. Environ.* **2000**, *34* (12–14), 2205. doi:10.1016/S1352-2310(99)00465-3.
(3) Guenther, A.; Hewitt, C. N.; Erickson, D.; Fall, R.; Geron, C.; Graedel, T.; Harley, P.; Klinger, L.; Lerdau, M.; McKay, W. A.; Pierce, T.; Scholes, B.; Steinbrecher, R.; Tallamraju, R.; Taylor, J.; Zimmerman, P. *J. Geophys. Res.* **1995**, *100* (D5), 8873. doi:10.1029/94JD02950.
(4) Placet, M.; Mann, C. O.; Gilbert, R. O.; Niefer, M. J. *Atmos. Environ.* **2000**, *34* (12–14), 2183. doi:10.1016/S1352-2310(99)00464-1.
(5) Sawyer, R. F.; Harley, R. A.; Cadle, S. H.; Norbeck, J. M.; Slott, R.; Bravo, H. A. J. *Atmos. Environ.* **2000**, *34* (12–14), 2161. doi:10.1016/S1352-2310(99)00463-X.

Can. J. Chem. Downloaded from www.nrcresearchpress.com by Renmin University of China on 09/02/12
For personal use only.

(6) Wine, P. H.; Thompson, R. J. *Int. J. Chem. Kinet.* **1984**, *16* (7), 867. doi:10.1002/kin.550160707.
(7) Platt, U. F.; Winer, A. M.; Biermann, H. W.; Atkinson, R.; Pitts, J. N. *Environ. Sci. Technol.* **1984**, *18* (5), 365. doi:10.1021/es00123a015.
(8) Finlayson-Pitts, B. J.; Pitts, J. N., Jr. *Science* **1997**, *276* (5315), 1045. doi:10.1126/science.276.5315.1045.
(9) Atkinson, R.; Winer, A. M.; Pitts, J. N. *Atmos. Environ.* **1986**, *20* (2), 331. doi:10.1016/0004-6981(86)90035-1.
(10) Aschmann, S. M.; Atkinson, R. *J. Phys. Chem. A* **2006**, *110* (48), 13029. doi:10.1021/jp065382v.
(11) Daykin, E. P.; Wine, P. H. *Int. J. Chem. Kinet.* **1990**, *22* (10), 1083. doi:10.1002/kin.550221007.
(12) Martin, D.; Jourdain, J. L.; LeBras, G. *Int. J. Chem. Kinet.* **1985**, *17* (12), 1247. doi:10.1002/kin.550171202.
(13) Tuazon, E. C.; Aschmann, S. M.; Atkinson, R. *J. Phys. Chem. A* **2007**, *111* (5), 916. doi:10.1021/jp067274e.
(14) Brewer, P. G.; Nakayama, N. *Environ. Sci. Technol.* **2008**, *42* (5), 1394. doi:10.1021/es087088h.
(15) Zhang, X.; Hester, K. C.; Mancillas, O.; Peltzer, E. T.; Walz, P. M.; Brewer, P. G. *Environ. Sci. Technol.* **2009**, *43* (3), 610. doi:10.1021/es802283y.
(16) Aschmann, S. M.; Long, W. D.; Atkinson, R. *J. Phys. Chem. A* **2008**, *112* (51), 13556. doi:10.1021/jp8074018.
(17) Lightfoot, P. D.; Cox, R. A.; Crowley, J. N.; Destriau, M.; Hayman, G. D.; Jenkin, M. E.; Moortgat, G. K.; Zabel, F. *Atmos. Environ. Part A.* **1992**, *26* (10), 1805. doi:10.1016/0960-1686(92)90423-I.
(18) Wallington, T. J.; Dagaut, P.; Kurylo, M. J. *Chem. Rev.* **1992**, *92* (4), 667. doi:10.1021/cr00012a008.
(19) Tyndall, G. S.; Cox, R. A.; Granier, C.; Lesclaux, R.; Moortgat, G. K.; Pilling, M. J.; Ravishankara, A. R.; Wallington, T. J. *J. Geophys.Res.* **2001**, *106* (D11), 12157. doi:10.1029/2000JD900746.
(20) Feria, L.; Gonzalez, C.; Castro, M. *Int. J. Quantum Chem.* **2004**, *99* (5), 605. doi:10.1002/qua.10848.
(21) Feria, L.; Gonzalez, C.; Castro, M. *Int. J. Quantum Chem.* **2004**, *96* (4), 380. doi:10.1002/qua.10732.
(22) Isaacson, A. D.; Truhlar, D. G.; Rai, S. N.; Steckler, R.; Hancock, G. C.; Garrett, B. C.; Redmon, M. J. *Comput. Phys. Commun.* **1987**, *47* (1), 91. doi:10.1016/0010-4655(87)90069-5.
(23) Becke, A. D. *J. Chem. Phys.* **1993**, *98*, 5648. doi:10.1063/1.464913.
(24) Lee, C.; Yang, W.; Parr, R. G. *Phys. Rev. B* **1988**, *37* (2), 785. doi:10.1103/PhysRevB.37.785.
(25) Zhao, Y.; Truhlar, D. G. *Theor. Chem. Acc.* **2008**, *120* (1–3), 215. doi:10.1007/s00214-007-0310-x.
(26) Frisch, M. J.; Head-Gordon, M.; Pople, J. A. *Chem. Phys. Lett.* **1990**, *166* (3), 281. doi:10.1016/0009-2614(90)80030-H.
(27) Head-Gordon, M.; Head-Gordon, T. *Chem. Phys. Lett.* **1994**, *220* (1–2), 122. doi:10.1016/0009-2614(94)00116-2.
(28) Møeller, C.; Plesset, M. S. *Phys. Rev.* **1934**, *46* (7), 618. doi:10.1103/PhysRev.46.618.
(29) Fukui, K. *Acc. Chem. Res.* **1981**, *14* (12), 363. doi:10.1021/ar00072a001.
(30) Ishida, K.; Morokuma, K.; Kormornicki, A. *J. Chem. Phys.* **1977**, *66*, 2153.
(31) Frisch, M. J. G. W. T.; Schlegel, H. B.; Scuseria, G. E.; Robb, M. A.; Cheeseman, J. R.; Scalmani, G.; Barone, V.; Mennucci, B.; Petersson, G. A.; Nakatsuji, H.; Caricato, M.; Li, X.; Hratchian, H. P.; Izmaylov, A. F.; Bloino, J.; Zheng, G.; Sonnenberg, J. L.; Hada, M.; Ehara, M.; Toyota, K.; Fukuda, R.; Hasegawa, J.; Ishida, M.; Nakajima, T.; Honda, Y.; Kitao, O.; Nakai, H.; Vreven, T.; Montgomery, J. A., Jr.; Peralta, J. E.; Ogliaro, F.; Bearpark, M.; Heyd, J. J.; Brothers, E.; Kudin, K. N.; Staroverov, V. N.; Kobayashi, R.; Normand, J.; Raghavachari, K.; Rendell, A.; Burant, J. C.; Iyengar, S. S.; Tomasi, J.; Cossi, M.; Rega, N.; Millam, J. M.; Klene, M.; Knox, J. E.; Cross, J. B.; Bakken, V.; Adamo, C.; Jaramillo, J.; Gomperts, R.; Stratmann, R. E.; Yazyev, O.; Austin, A. J.; Cammi, R.; Pomelli, C.; Ochterski, J. W.; Martin, R. L.; Morokuma, K.; Zakrzewski, V. G.; Voth, G. A.; Salvador, P.; Dannenberg, J. J.; Dapprich, S.; Daniels, A. D.; Farkas, O.; Foresman, J. B.; Ortiz, J. V.; Cioslowski, J.; Fox, D. J. *Gaussian 09,* Revision A.02; Gaussian, Inc.: Wallingford CT, 2009.
(32) Garrett, B. C.; Truhlar, D. G. *J. Am. Chem. Soc.* **1979**, *101* (16), 4534. doi:10.1021/ja00510a019.
(33) Garrett, B. C.; Truhlar, D. G. *J. Chem. Phys.* **1979**, *70*, 1593.
(34) Garrett, B. C.; Truhlar, D. G.; Grev, R. S.; Magnuson, A. W. *J. Phys. Chem.* **1980**, *84* (13), 1730. doi:10.1021/j100450a013.
(35) Liu, Y. P.; Lynch, G. C.; Truong, T. N.; Lu, D. H.; Truhlar, D. G.; Garrett, B. C. *J. Am. Chem. Soc.* **1993**, *115* (6), 2408. doi:10.1021/ja00059a041.
(36) Lu, D.-h.; Truong, T. N.; Melissas, V. S.; Lynch, G. C.; Liu, Y.-P.; Garrett, B. C.; Steckler, R.; Issacson, A. D.; Rai, S. N.; Hancock, G. C.; Lauderdale, J. G.; Joseph, T.; Truhlar, D. G. *Comput. Phys. Commun.* **1992**, *71* (3), 235. doi:10.1016/0010-4655(92)90012-N.
(37) Chaung, Y. Y.; Truhlar, D. G. *J. Chem. Phys.* **2000**, *112*, 1221. doi:10.1063/1.480768.
(38) Truhlar, D. G. J. *J. Comput. Chem.* **1991**, *12* (2), 266. doi:10.1002/jcc.540120217.
(39) Zheng, J.; Zhang, S.; Corchado, J. C.; Chuang, Y. Y.; Coitino, E. L.; Ellingson, B. A.; Truhlar, D. G. *GAUSSRATE,* Version 2009; University of Minnesota: Minneapolis, MN, 2009.
(40) Zheng, J.; Zhang, S.; Lynch, B. J.; Corchado, J. C.; Chaung, Y. Y.; Fast, P. L.; Hu, W. P.; Liu, Y. P.; Lynch, G. C.; Nguyen, K. A.; Jackels, C. F.; Ramos, A. F.; Ellingson, B. A.; Melissas, V. S.; Villa, J.; Rossi, I.; Coitino, E. L.; Pu, J.; Albu, T. V. *POLYRATE,* Version 2010; University of Minnesota: Minneapolis, MN, 2010.
(41) Barnes, I.; Hjorth, J.; Mihalopoulos, N. *Chem. Rev.* **2006**, *106* (3), 940. doi:10.1021/cr020529+.
(42) Thüner, L. P.; Bardini, P.; Rea, G. J.; Wenger, J. C. *J. Phys. Chem.A* **2004**, *108* (50), 11019. doi:10.1021/jp046358p.
(43) Butkovskaya, N. I.; LeBras, G. *J. Phys.Chem.* **1994**, *98* (10), 2582. doi:10.1021/j100061a014.

Buffer capacity of heterogeneous chemical equilibria in natural waters

Igor Povar and Vasile Rusu

Can. J. Chem. Downloaded from www.nrcresearchpress.com by Renmin University of China on 09/02/12
For personal use only.

Abstract: A novel ion–molecular buffer approach for estimating buffer capacities for natural water – mineral equilibria has been developed. Using this approach, the buffer capacity for any component of the heterogeneous system can be assessed. A proportional relation between different capacities in relation to ions of the compound distributed between two phases has been found. The influence of major thermodynamic parameters, such as temperature, pH, and the main chemical component concentrations of natural waters upon system buffer capacities has been investigated. It is expected that this type of approach will help to predict long-term diminishing effects in natural waters as a remediation alternative. The obtained results are intended to provide users with a compulsory tool to set reliable limits of ion (including metal) levels in environmental systems.

Key words: buffer capacity, chemical equilibria, minerals, natural water, heterogeneous system.

Résumé : On a mis au point une nouvelle approche par tampon ion–moléculaire pour l'évaluation des capacités comme tampon de l'équilibre eau naturelle minérale. Utilisant cette approche, il est possible d'évaluer la capacité comme tampon par rapport à tout composant d'un système hétérogène. On a mis en évidence l'existence d'une relation proportionnelle entre les capacités différentes en relations avec les ions du composé distribué entre deux phases. On a étudié l'influence des paramètres thermodynamiques principaux, telle la température, le pH et les concentrations des principaux composants chimiques des eaux naturelles sur les capacités comme tampon du système. On peut s'attendre à ce qu'une telle approche pourra probablement être utile, comme alternative de réhabilitation, pour prédire les effets à long terme de diminution dans les eaux naturelles. Les résultats obtenus sont détaillés afin de fournir aux utilisateurs un outil obligatoire pour fixer des limites fiables pour les niveaux ioniques (y compris les métaux) dans les systèmes environnementaux.

Mots-clés : capacité comme tampon, équilibre chimique, minéraux, eau naturelle, système hétérogène.

[Traduit par la Rédaction]

Introduction

Under natural conditions the chemical composition of waters is regulated by natural processes, which preserve the chemical balance between the entry of chemical components into water and their elimination from it. The complexity of natural water (NW) composition, containing mineral phases and a huge set of chemical combinations, stimulates the capability of simultaneous occurring different chemical reactions and the capacity of mineral solid phases to be constant to a certain level in the aqueous solution composition. The property of a heterogeneous system to resist composition change, i.e., to maintain its chemical status at an invariable level at the flow outcome of chemical compounds of natural or anthropogenic character is called buffer action. Under real conditions, the buffer action of NW heterogeneous systems is expressed by the fact that, at the consumption of any element from solution, a partial dissolution of solid phases takes place and the solution composition is restored. If some excessive quantities of compounds come down from the outside in NW, the solid phase of the minerals bond such substances, again maintaining constant water composition. Therefore, the natural buffer action of natural systems is stipulated by a number of chemical reactions simultaneously taking place between aqueous solution and solid particles of minerals. Some of the basic physicochemical factors defining the stability of water systems under changing environmental conditions or at anthropogenic activity are (*i*) chemical composition and physicochemical properties of environmental objects, (*ii*) buffer action of waters and minerals, (*iii*) the water system acid-reduction function. Thus, NW in equilibrium with mineral phases not only geochemically accumulates geochemically the components of pollution, but also acts as a natural buffer that controls element and compound transfer and possesses the capacity to reduce negative effects of contaminants on vegetative and animal organisms. Such NW properties may be characterized by the concept of ion–molecular buffer action that is similar to acid–base buffering. Therefore, the concept of buffer capacity (or buffer intensity) can be expanded and used for the prediction of water system stability towards any other ions or neutral (molecular) compounds. In other words, the NWs are buffered not only towards the hydrogen ion (proton) concentration, but also in relation to the concentration of other NW-dissolved components. The processes of

Received 9 October 2011. Accepted 6 January 2012. Published at www.nrcresearchpress.com/cjc on 23 March 2012.

I. Povar and V. Rusu. Institute of Chemistry, Academy of Sciences of Moldova, 3 Academiei str., MD 2028 Chisinau, Republic of Moldova.

Corresponding author: Igor Pover (e-mail: ipovar@yahoo.ca).

Can. J. Chem. Downloaded from www.nrcresearchpress.com by Renmin University of China on 09/02/12
For personal use only.

Table 1. Equilibrium constants and values of enthalpies (ΔH).[2]

Reaction equation	log K	ΔH (cal mol^{-1})	Symbol
$Al^{3+} + H_2O = AlOH^{2+} + H^+$	–4.99	11900	K_1
$Al^{3+} + 2H_2O = Al(OH)_2^+ + 2H^+$	–10.00	22000	K_2
$Al^{3+} + 4H_2O = Al(OH)_4^- + 4H^+$	–23.00	44060	K_4
$Al(OH)_3(s) + 3H^+ = Al^{3+} + 3H_2O$	9.35	–22800	K_S
$Al^{3+} + F^- = AlF^{2+}$	7.02	1100	K_{F1}
$Al^{3+} + 2F^- = AlF_2^+$	12.76	2000	K_{F2}
$Al^{3+} + 3F^- = AlF_3$	17.03	2500	K_{F3}
$Al^{3+} + 4F^- = AlF_4^-$	19.73	2200	K_{F4}
$Al^{3+} + 5F^- = AlF_5^{2-}$	20.92	1800	K_{F5}
$Al^{3+} + SO_4^{2-} = AlSO_4^+$	3.01	2150	K_{S1}
$Al^{3+} + 2SO_4^{2-} = Al(SO_4)_2^-$	4.90	2840	K_{S2}
$Al^{3+} + Org^{3-} = AlOrg$	8.39	—[a]	K_{O1}
$Al^{3+} + H^+ + Org^{3-} = AlHOrg^+$	13.09	—	K_{O2}
$Org^{3-} + H^+ = HOrg^{2-}$	6.83	—	K_{g1}
$Org^{3-} + 2H^+ = H_2Org^-$	12.73	—	K_{g2}
$Org^{3-} + 3H^+ = H_3Org$	14.49	—	K_{g3}
$H^+ + F^- = HF$	3.17	3460	K_{HF}
$H_2O = H^+ + OH^-$	–14.00	13340	K_W
$2Al^{3+} + 2H_2O = Al_2(OH)_2^{4+} + 2H^+$	–6.3	—	K_{P1}
$3Al^{3+} + 4H_2O = Al_3(OH)_2^{5+} + 4H^+$	–12.1	—	K_{P2}
$Al^{3+} + H_2PO_4^- = AlH_2PO_4^{2+}$	3.1	—	K_{PO_4}
$PO_4^{3-} + H^+ = HPO_4^{2-}$	12.0	—	$K_{PO_4,1}$
$PO_4^{3-} + 2H^+ = H_2PO_4^-$	19.21	—	$K_{PO_4,2}$
$PO_4^{3-} + 3H^+ = H_3PO_4$	21.36	—	$K_{PO_4,3}$
$CO_3^{2-} + H^+ = HCO_3^-$	10.33	3617	K_{C1}
$CO_3^{2-} + 2H^+ = H_2CO_3$	16.68	5864	K_{C2}

Note: 1 cal = 4.184 J. Org, organic ligand.

[a]The — specifies the absence of experimental data.

dissolution and ionic exchange and complex formation, as well as biological activity, have their ion–molecular buffer action. Many slightly soluble components of NW systems, such as minerals, clay, and magmatic materials, contribute significantly to the buffer action of the given systems towards pH and other pX (where X is any ion, pX = –log[X]).

The buffer action of heterogeneous system mineral-saturated solutions depends on the chemical composition of the water solutions, as well as on the composition and properties of the mineral phases. We will examine a concrete real system (gibbsite-saturated solution), although the approach developed here can be applied for any other. As aluminium occurs in many minerals and materials, it is mostly present in all superficial waters. The average concentration of aluminium in river waters is 8.9×10^{-7} mol L^{-1} with a range from 3.7×10^{-7} up to 9.3×10^{-5} mol L^{-1}.[1] With an increase of the acidity of waters (up to a critical threshold of water biota survival; for example, for mollusks this threshold is pH 6.0 and for perches it is pH 4.5), the content of aluminium increases rapidly because of the interaction of aluminium hydroxide of natural materials with acid.

$$[1] \qquad Al(OH)_3(s) + 3H^+ \Leftrightarrow Al^{3+} + 3H_2O, \qquad K_S = [Al^{3+}][H^+]^{-3}$$

In eq. [1] K_S denotes the constant of equilibrium (solubility product). Even small concentrations of aluminium ions can be lethal to fishes. At the same time, phosphates provided by the evolution of phytoplankton and other water vegetation, combining with aluminium, become inaccessible to these organisms. In spite of the fact that the concept of buffer capacity towards all the components of solid phase has evident significance for the assessment of the NW composition stability in the presence of mineral phases, at present there is a limited number of works dedicated to this question.[2–8] In the literature, a few attempts of theoretical background development for the buffer action of heterogeneous systems towards the proton as the master variable can be found. For example, Bi and Yin[2] deduced the equation of buffer capacity towards the proton on the basis of classical systems of mass balance and electroneutrality equations. The latter equations in essence do not allow one to obtain the general expression of the buffer capacity (β_i^S; the superscript index S specifies the presence of the solid phase) for a wide range of considered heterogeneous systems. Besides, a number of limiting assumptions had been made by Bi and Yin[2] for their determination of the mathematical expressions.

Theory

As a criterion for the quantitative assessment of the intensity of buffer action of the studied multicomponent heterogeneous systems, the value of the buffer capacity deduced by us (β_i^S), which can be defined as a partial derivative,[4] was used

$$[2] \qquad \beta_i^S = \left(\frac{\partial C_i^0}{\partial \ln[i]}\right)_{C_j^0(j\neq i)}$$

where C_i^0 and $[i]$ are the initial concentration in heterogeneous mixture and the equilibrium concentration in solution

Can. J. Chem. Downloaded from www.nrcresearchpress.com by Renmin University of China on 09/02/12
For personal use only.

of the i component of solid phases, respectively; the subscript index C_j^0 shows that the initial concentrations of other components in the mixture remain constant.

Besides the process of gibbsite dissolution (eq. [1]), a set of possible equilibria in the system mineral phase – natural water, listed in Table 1,[2] has been taken into account.

The mass balance conditions in the heterogeneous system can be formulated on the basis of the method of residual concentrations:[6,7,9]

$$[3]\quad C^0_{Al} = C^r_{Al} + \Delta C_{Al} = \sum_{i=0}\sum_{j=1} i[Al_i(OH)_j] + \sum_{j=1}[AlF_j] + [AlSO_4] + [Al(SO_4)_2] + [AlOrg] + [AlHOrg] + [AlH_2PO_4] + \Delta C_{Al}$$

$$[4]\quad C^0_F = [F] + [HF] + \sum_{j=1} j[AlF_j]$$

$$[5]\quad C^0_{SO_4} = [SO_4] + [AlSO_4] + 2[Al(SO_4)_2]$$

$$[6]\quad C^0_{Org} = \sum_{m=0}[H_mOrg] + [AlHOrg] + [AlOrg]$$

where Org refers to organic ligand.

$$[7]\quad C^0_{CO_3} = [CO_3] + [HCO_3] + [H_2CO_3]$$

$$[8]\quad C^0_{PO_4} = \sum_{l=0}[H_lPO_4] + [AlH_2PO_4]$$

$$[9]\quad C^0_H = C^r_H + \Delta C_H = [H] - [OH] - \sum_{i=1}\sum_{j=1} j[Al_i(OH)_j] + [AlHOrg] + 2[AlH_2PO_4] + [HF] + \sum_{m=1} m[H_mOrg] - 3\Delta C_{Al} + [HCO_3] + 2[H_2CO_3] + \sum_{l=1} l[H_lPO_4]$$

For convenience, the charges of the species are omitted. The values C_i^0 and C_i^r in eqs. [3]–[8] are, respectively, the analytical and residual concentrations of a component i in the considered heterogeneous system.[6] In eq. [9], $C_H{}^0$ is the excess of H^+ ions in relation to hydroxyl ions in the two-phase mixture, $C_H{}^0 = -C_{OH}{}^0$.[6] Equation [9] also takes into account the stoichiometric composition of the solid phase.

$$3\Delta C_{Al} = \Delta C_{OH} = -\Delta C_H$$

The deduction of the expression for the buffer capacity towards the proton (or the proton buffer capacity) is presented in the Appendix. In the absence of polynuclear complexes, i.e., $i = 1$, the $\tilde{m}$ value coincides with the analytical concentration of aluminium in aqueous solution.

Taking into account the relation (eq. [A10], see the Appendix) one can obtain

$$[10]\quad \frac{\partial \Delta C_H}{\partial \ln[H]} = 9\tilde{m} + 3\tilde{i} + 3\sum_{j=1} j[AlF_j]\frac{\partial \ln[F]}{\partial \ln[H]} + 3([AlSO_4] + 2[Al(SO_4)_2])\frac{\partial \ln[SO_4]}{\partial \ln[H]} + 3([AlOrg] + [AlHOrg])\frac{\partial \ln[Org]}{\partial \ln[H]} + 3[AlH_2PO_4]\frac{\partial \ln[PO_4]}{\partial \ln[H]}$$

Substituting eq. [10] into the expression eq. [A1], taking into account the derivative (eqs. [A4]–[A8]), one can finally get

$$[11]\quad \beta^S_H = \tilde{h} + 6\tilde{i} + 9\tilde{m} - \frac{\left(\sum_{l=1} l[H_lPO_4] + 5[AlH_2PO_4]\right)^2}{C^0_{PO_4}} - \frac{([HCO_3] + 2[H_2CO_3])^2}{C^0_{CO_3}} - \frac{\left(\sum_{m=1} m[H_mOrg] + 3[AlOrg] + 4[AlHOrg]\right)^2}{C^0_{Org}} - \frac{9([AlSO_4] + 2[Al(SO_4)_2])^2}{[SO_4] + [AlSO_4] + 4[Al(SO_4)_2]} - \frac{\left([HF] + 3\sum_{j=1} j[AlF_j]\right)^2}{[F] + [HF] + \sum_{j=1} j^2[AlF_j]}$$

Similarly, it is possible to prove that, for the buffer capacity towards aluminium, the following expression is valid.

$$[12]\quad \beta^S_{Al} \equiv \left(\frac{\partial C^0_{Al}}{\partial \ln[Al]}\right)_{C_j^0} = \frac{1}{9}\tilde{h} + \frac{2}{3}\tilde{i} + \tilde{m} - \frac{\left(\frac{1}{3}\sum_{l=1} l[H_lPO_4] + \frac{5}{3}[AlH_2PO_4]\right)^2}{C^0_{PO_4}} - \frac{([HCO_3] + 2[H_2CO_3])^2}{9C^0_{CO_3}} - \frac{\left(\frac{1}{3}\sum_{m=1} m[H_mOrg] + [AlOrg] + \frac{4}{3}[AlHOrg]\right)^2}{C^0_{Org}} - \frac{\left([AlSO_4] + 2[Al(SO_4)_2]\right)^2}{[SO_4] + [AlSO_4] + 4[Al(SO_4)_2]} - \frac{\left(\frac{1}{3}[HF] + \sum_{j=1} j[AlF_j]\right)^2}{[F] + [HF] + \sum_{j=1} j^2[AlF_j]}$$

Can. J. Chem. Downloaded from www.nrcresearchpress.com by Renmin University of China on 09/02/12
For personal use only.

Comparing eqs. [11] and [12], an important interrelation between the buffer capacities of the heterogeneous saturated aqueous solution – gibbsite $Al(OH)_3(s)$ system can be identified.

$$[13] \qquad \beta_H^S = 9\beta_{Al}^S$$

In the case of the formation of the slightly soluble hydroxide $M(OH)_n(s)$, eq. [13] can be generalized.[6, 9]

$$[14] \qquad \beta_H^S = n^2\beta_M^S$$

Thus, the studied system containing the solid-phase gibbsite exhibits buffer properties towards both its components and, from eqs. [13] and [14], the buffer capacities are mutually proportional. Equations [11] and [12] allow the evaluation of the buffer action of the heterogeneous system in relation to components of the solid phase on the basis of equilibrium constants. It is worthy to mention that the obtained relations are only valid in the presence of the solid phase. The stability area of the latter is determined on the basis of the thermodynamic analysis of equilibriums in the studied systems.[6,7]

The proportionality of buffer capacities towards all the ions of the compound distributed between two phases is a general feature for heterogeneous systems. Similar relations were deduced for the liquid–liquid extraction systems.[10–13]

Results and discussion

The results of the calculations of the buffer capacities β_H^S as a function of pH for different compositions of the heterogeneous mixture are shown in Figs. 1–3. Obviously, an increase of the total concentration C_{Al}^0 (Fig. 1) augments the area of the buffer action because of the extension of the pH interval of the thermodynamic stability of the solid phase.

The curves of buffer capacities for separate components of the heterogeneous mixture, shown in Fig. 2, are calculated by the equations

$$[15] \qquad \beta_H^{Al} = \widetilde{h}_{Al} + 6\widetilde{i}_{Al} + 9\widetilde{m}_{Al}$$

where $\widetilde{h}_{Al} = \sum_{i=1}\sum_{j=1} j^2[Al_i(OH)_j]$, $\widetilde{i}_{Al} = -\sum_{i=1}\sum_{j=1} ij[Al_i(OH)_j]$, and $\widetilde{m}_{Al} = \sum_{i=0}\sum_{j=1} i^2[Al_i(OH)_j]$.

$$[16] \qquad \beta_H^F = \widetilde{h}_F + 9\widetilde{m}_F - \frac{\left([HF] + 3\sum_{j=1} j[AlF_j]\right)^2}{[F] + [HF] + \sum_{j=1} j^2[AlF_j]}$$

where $\widetilde{h}_F = [HF]$ and $\widetilde{m}_F = \sum_{j=1}[AlF_j]$.

$$[17] \qquad \beta_H^{Org} = \widetilde{h}_{Org} + 6\widetilde{i}_{Org} + 9\widetilde{m}_{Org} - \frac{\left(\sum_{m=1} m[H_mOrg] + 3[AlOrg] + 4[AlHOrg]\right)^2}{C_{Org}^0}$$

Here, $\widetilde{h}_{Org} = \sum_{m=1} m^2[H_mOrg] + [AlHOrg]$, $\widetilde{i}_{Org} = [AlHOrg]$, and $\widetilde{m}_{Org} = [AlOrg] + [AlHOrg]$.

Fig. 1. Buffer capacity β_H^S vs pH for the "saturated aqueous solution – gibbsite" system. Concentrations (mol/dm^3): C_{Org}^0, C_{PO4}^0, and $C_{SO4}^0 = 1 \times 10^{-4}$; $C_F^0 = 5 \times 10^{-6}$; $C_{CO3}^0 = 1 \times 10^{-3}$; C_{Al}^0: (*a*) 1×10^{-3}, (*b*) 1×10^{-4}, and (*c*) 1×10^{-5}. Org, organic ligand.

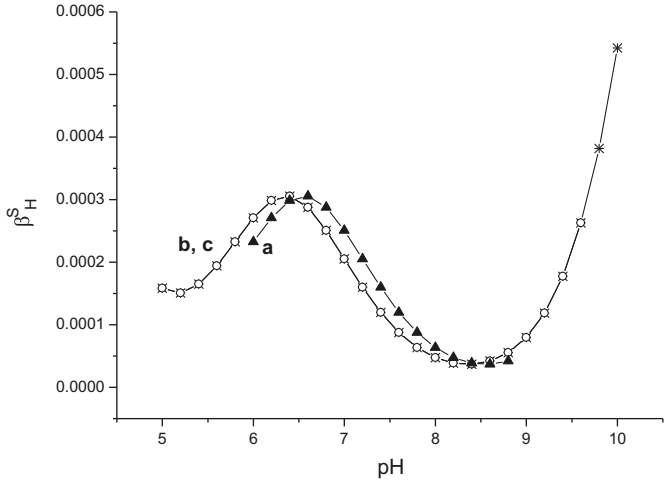
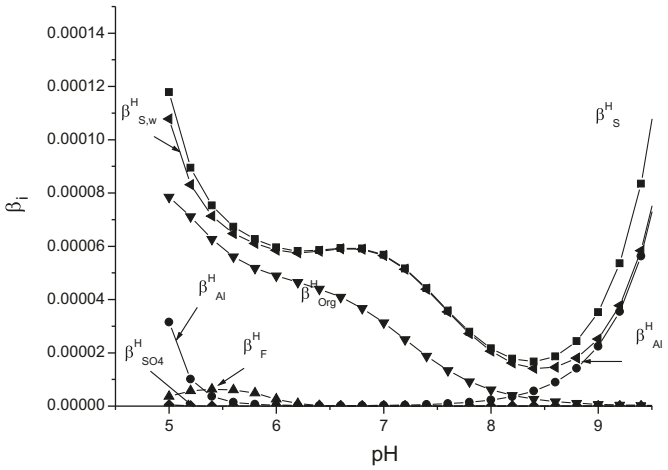


Fig. 2. The contribution of separate components of the heterogeneous mixture β_i (the composition is specified in the text) to the total buffer capacity β_H^S. $\beta_{H,W}^S$ value is the buffer capacity β_H^S disregarding the contribution of $[H^+]$ and $[OH^-]$.



$$[18] \qquad \beta_H^{SO_4} = 9\widetilde{m}_{SO_4} - \frac{9([AlSO_4] + 2[Al(SO_4)_2])^2}{[SO_4] + [AlSO_4] + 4[Al(SO_4)_2]}$$

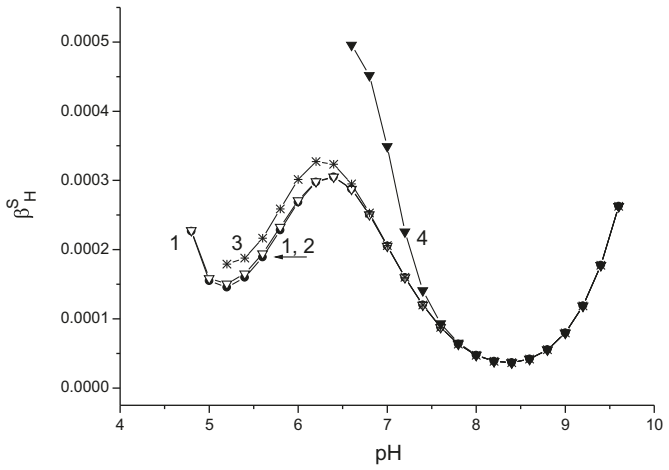
$$\widetilde{m}_{SO_4} = [AlSO_4] + [Al(SO_4)_2]$$

The following composition of the heterogeneous system has been used for the calculations: $C_{Al}^0 = 1 \times 10^{-4}$ mol/dm^3, $C_F^0 = 5 \times 10^{-6}$ mol/dm^3, $C_{Org}^0 = 1 \times 10^{-4}$ mol/dm^3, $C_{PO4}^0 = 1 \times 10^{-4}$ mol/dm^3, $C_{SO4}^0 = 1 \times 10^{-4}$ mol/dm^3, and $C_{CO3}^0 = 1 \times 10^{-5}$ mol/dm^3. One can state that the influence of H^+ in the studied pH interval may be neglected, and the OH^- ions exercise influence on β_H^S only at pH > 8.5. The aluminium ions and their hydroxocomplexes make a significant contribution in acid solutions up to pH 5.5 and at pH > 8 because of the predominance of the stable anionic hydroxocomplex $Al(OH)_4^-$.

The β_H^F value has a certain contribution within the pH range from 5 to 6, whereas the β_H^{SO4} value can be neglected in the whole interval of pH values. A quite significant contribution

Can. J. Chem. Downloaded from www.nrcresearchpress.com by Renmin University of China on 09/02/12
For personal use only.

Fig. 3. Buffer capacity $\beta_H{}^S$ vs pH for the "saturated aqueous solution – gibbsite" system. Concentrations (mol/dm^3): $C_{Al}{}^0$, $C_{Org}{}^0$, $C_{PO4}{}^0$, and $C_{SO4}{}^0 = 1 \times 10^{-4}$; $C_{CO3}{}^0 = 1 \times 10^{-3}$; $C_F{}^0$: (1) 5×10^{-7}, (2) 5×10^{-6}, (3) 5×10^{-5}, and (4) 5×10^{-4}. Org, organic ligand.



to the total buffer capacity $\beta_H{}^S$ has the value of $\beta_H{}^{Org}$ up to pH 8. At concentrations of fluoride ($C_F{}^0$) > 5×10^{-4} mol/dm^3, the $\beta_H{}^S$ value increases sharply in the range of pH values of the gibbsite dissolution–formation with a simultaneous narrowing of the total pH range of the buffer action (Fig. 3). As one can see from Fig. 4, the same effect is recorded with an increase of the $C_{Org}{}^0$ value, whereas the buffer capacity can increase many times.

The dependences of $\beta_H{}^S$ (pH) for different concentrations of carbonate ion are presented in Fig. 5. By taking into account the contribution of equilibria including carbonate ion in the total buffer capacity $\beta_H{}^S$, the $\beta_H{}^{CO3}$ value was calculated separately. In this case, the expression for $\tilde{h}$ (eq. [A2], see the Appendix) is simplified considerably.

$$[19] \qquad \tilde{h}_{CO_3} = [H] + [OH] + [HCO_3] + 4[H_2CO_3]$$

and

$$[20] \qquad \beta_H^{CO_3} = \tilde{h}_{CO_3} - \frac{([HCO_3] + 2[H_2CO_3])^2}{C^0_{CO_3}}$$

A comparison of the curves calculated by eqs. [A10] and [20] shows that equilibria with $CO_3{}^{2-}$ participation have a substantial contributionto $\beta_H{}^S$ at a $C_{CO3}{}^0 > 1 \times 10^{-4}$ mol/dm^3 (Figs. 6*a* and 6*b*). The contribution of the separate chemical species can be assessed from the diagrams of heterogeneous chemical equilibriums discussed in ref. 7.

The analysis of the obtained data presented in Figs. 1–5, taking into account eq. [13] allows us to conclude that the investigated heterogeneous system has a considerable buffer capacity towards to aluminium as well.

The influence of temperature on the value of the buffer capacity was also studied. The results of the calculations are presented in Fig. 7. The equilibrium constants for different temperatures have been estimated by the van't Hoff equation.

$$\log K_2 = \log K_1 + (1/T_1 - 1/T_2)\Delta H/2.303R$$

The necessary values of enthalpies (ΔH) are listed in Table 1. T_1 was set to 298 K = 25 °C. It was assumed that the

Fig. 4. Buffer capacity $\beta_H{}^S$ vs pH for the "saturated aqueous solution – gibbsite"system . Concentrations (mol/dm^3): $C_{Al}{}^0$, $C_{PO4}{}^0$, and $C_{SO4}{}^0 = 1 \times 10^{-4}$; $C_F{}^0 = 5 \times 10^{-6}$; $C_{CO3}{}^0 = 1 \times 10^{-3}$; $C_{Org}{}^0$: (1) 1×10^{-2}, (2) 1×10^{-3}, (3) 1×10^{-4}, and (4) 1×10^{-5}. Org, organic ligand.

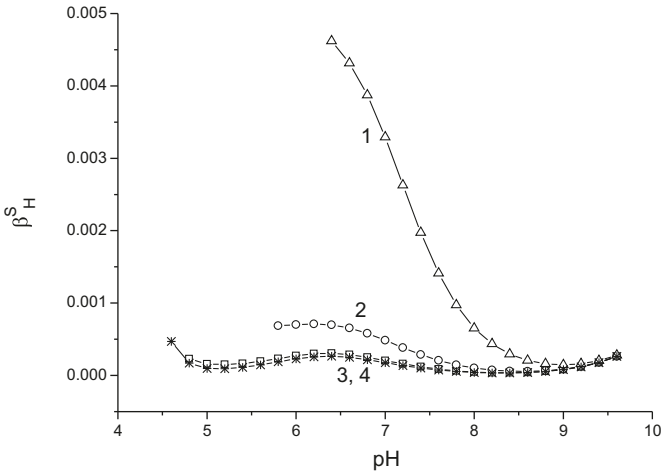
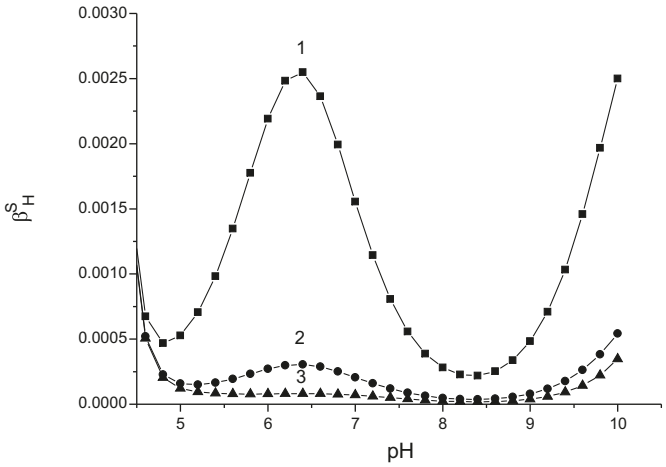


Fig. 5. Buffer capacity $\beta_H{}^S$ vs pH for the "saturated aqueous solution – gibbsite" system. Concentrations (mol/dm^3): $C_{Al}{}^0$, $C_{PO4}{}^0$, $C_{SO4}{}^0$, and $C_{Org}{}^0 = 1 \times 10^{-4}$; $C_F{}^0 = 5 \times 10^{-6}$; $C_{CO3}{}^0$: (1) 1×10^{-2}, (2) 1×10^{-3}, and (3) 1×10^{-4}. Org, organic ligand.



temperature insignificantly influences the ΔH values inside the investigated temperature range. AN analysis of the curves in Fig. 7 shows that the buffer capacity increases with a temperature decrease, whereas the pH interval of 5.5–7.0 of the maximum values of the buffer capacity displaces slightly.

Comparing the results of the calculation of ΔG_r with the $\beta_i{}^S$ calculation, one can see that the buffer capacity increases with an increase of the solubility of solid phase, i.e., the residual concentrations of ions in solution. Povar[6] remarked that at the pH of the total dissolution of the precipitate the buffer capacity changes sharply. Our obtained data correlate well with the experimental values of the buffer capacity $\beta_i{}^S$ presented in ref. 2, but their direct comparison is impossible because of the lack of experimental pH values in this reference. Thus, NW in equilibrium with mineral phases has a considerable potential reserve, by means of which the

Can. J. Chem. Downloaded from www.nrcresearchpress.com by Renmin University of China on 09/02/12
For personal use only.

Fig. 6. Total buffer capacity β_H^S vs pH, carbonate buffer capacity β_H^{CO3} vs pH, and their difference $\beta_H^S - \beta_H^{CO3}$. Concentrations (mol/dm^3): C_{Al}^0, C_{Org}^0, C_{PO4}^0, and $C_{SO4}^0 = 1 \times 10^{-4}$; $C_F^0 = 5 \times 10^{-6}$; C_{CO3}^0: (*a*) 1×10^{-3} and (*b*) 1×10^{-4}. Org, organic ligand.

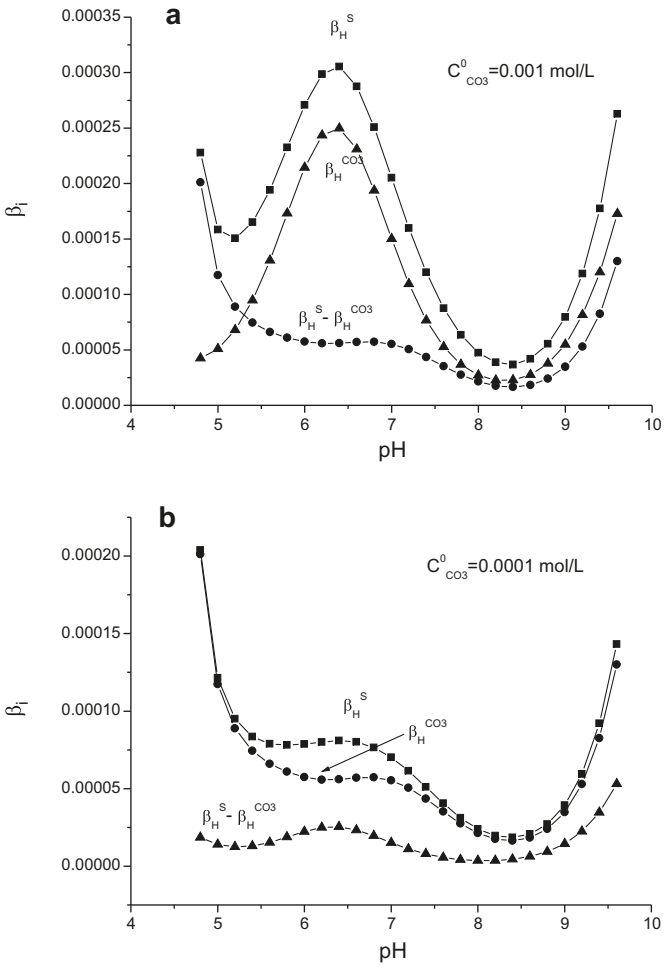
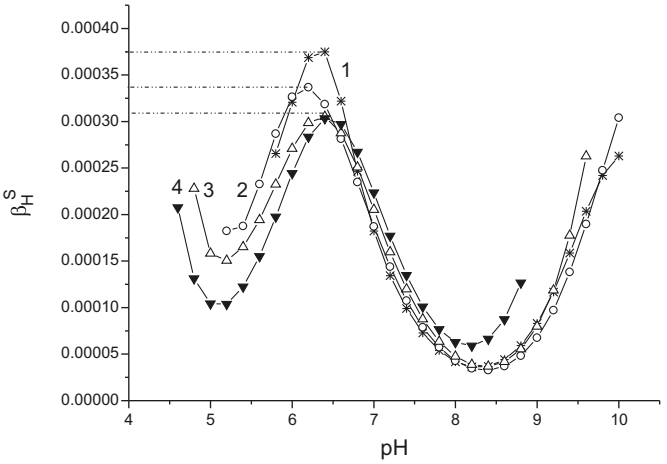


Fig. 7. Buffer capacity β_H^S vs pH for the "saturated aqueous solution – gibbsite" system at different temperatures (*t*, °C): (1) –5, (2) +10, (3) +25, and (4) +40. Concentrations (mol/dm^3): C_{Al}^0, C_{Org}^0, C_{PO4}^0, and $C_{SO4}^0 = 1 \times 10^{-4}$; $C_F^0 = 5 \times 10^{-6}$; $C_{CO3}^0 = 1 \times 10^{-3}$. Org, organic ligand.



equilibrium is regulated and one of its parameters is maintained constant.

Conclusions

On the basis of the method of residual concentrations, the original mathematical expressions for the quantitative calculation of buffer capacities towards both components of the mineral phase were deduced. The influence of different factors (temperature, pH, and concentrations of the main NW components) on the values of buffer capacities of the investigated heterogeneous systems was studied. It was established that NW in equilibrium with gibbsite has a certain potential reserve, by means of which the equilibrium is adjusted and one of its parameters is maintained constant. The presence of ligands that form stable complexes with ions of the solid phase promotes the amplification of the buffer actions of the heterogeneous systems. The presented approach can be used for research of the buffer action in the case of formation of one or several other solid phases in natural waters.

References

(1) Suess, M. J. *Examination of Water for Pollution Control. A Reference Handbook;* Pergamon Press: Oxford, 1982; Vol. 2, p 54.
(2) Bi, S.; Yin, W. *Analyst (Lond.)* **1995**, *120* (12), 2805. doi:10.1039/an9952002805.
(3) Charykov, A. K.; Osipov, N. N. *Karbonovye Kysloty i Karboksilatnye Kompleksy v Himicheskom Analize;* Khimiya: Leningrad, 1991; pp 204–207.
(4) Fishtik, I.; Povar, I. *Can. J. Chem.* **2006**, *84* (8), 1036. doi:10.1139/v06-127.
(5) Pfendt, L. B. *Analyst (Lond.)* **1995**, *120* (8), 2129. doi:10.1039/an9952002129.
(6) Povar, I. *Russ. J. Inorg. Chem.* **1996**, *41*, 1167.
(7) Povar, I.; Rusu, V. *Can. J. Chem.* This issue.
(8) Stumm, W.; Morgan, J. J. *Aquatic Chemistry;* Wiley-Interscience: New York, 1981; p 113.
(9) Povar, I. *Russ. J. Inorg. Chem.* **2000**, *45*, 1632.
(10) Povar, I.; Timbaliuc, N.; Cazac, T.; Chiriac, L. In Proceedings of the 2nd International Symposium on Sorption and Extraction, Vladivostok, Russia, 2009; pp 101–104.
(11) Povar, I.; Timbaliuc, N.; Cazac, T.; Chiriac, L. In Proceedings of the 2nd International Symposium on Sorption and Extraction, Vladivostok, Russia, 2009; pp 126–130.
(12) Povar, I.; Timbaliuc, N.; Blanaru, N.; Shepeli, D.; Cazac, T.; Spinu, O.; Chiriac, L. *pH and pA Buffer Properties of Monoprotic Carboxylic Acids in Bicomponent Two-Phase Extraction Systems,* In Proceedings of the 5th International Symposium "Chemistry and Chemical Education", Vladivostok, Russia, 2011; pp 100–103.
(13) Povar, I. *Dimerization of the Acid in the Organic Phase for Buffer Monocomponent Two-Phase Extraction Systems,* In Proceedings of the 5th International Symposium "Chemistry and Chemical Education"; Vladivostok, Russia, 2011; pp 107–109.

Appendix

A short deduction of the expression for the buffer capacity towards proton (or the proton buffer capacity) is examined below (a detail technique for the deduction of similar

Can. J. Chem. Downloaded from www.nrcresearchpress.com by Renmin University of China on 09/02/12
For personal use only.

expressions for slightly soluble salts of composition $M_mA_n(s)$ was elucidated in ref. A1).

[A1] $$\beta_H^S = \left(\frac{\partial C_H^0}{\partial \ln[H]}\right)_{C_j^0} = \widetilde{h} + 3\widetilde{i} + \frac{\partial \Delta C_H}{\partial \ln[H]} + ([AlHOrg] + \sum_{m=1} m[H_mOrg])\frac{\partial \ln[Org]}{\partial \ln[H]} + \left(2[AlH_2PO_4] + \sum_{l=1} l[H_lPO_4]\right)\frac{\partial \ln[PO_4]}{\partial \ln[H]} + [HF]\frac{\partial \ln[F]}{\partial \ln[H]} + ([HCO_3] + 2[H_2CO_3])\frac{\partial \ln[CO_3]}{\partial \ln[H]}$$

where

[A2] $$\widetilde{h} = [H] + [OH] + \sum_{i=1}\sum_{j=1} j^2[Al_i(OH)_j] + [AlHOrg] + 4[AlH_2PO_4] + [HF] + \sum_{m=1} m^2[H_mOrg] + [HCO_3] + 4[H_2CO_3] + \sum_{l=1} l^2[H_lPO_4]$$

[A3] $$\widetilde{i} = -\sum_{i=1}\sum_{j=1} ij[Al_i(OH)_j] + [AlHOrg] + 2[AlH_2PO_4]$$

For the deduction of the eq. [A1] the following relationships have been taken into account:

$$\frac{\partial [H]}{\partial \ln[H]} = [H]\frac{\partial \ln[H]}{\partial \ln[H]} = [H]$$

$$\frac{\partial [OH]}{\partial \ln[H]} = [OH]\frac{\partial \ln(K_W[H]^{-1})}{\partial \ln[H]} = -[OH]$$

$$\frac{\partial \ln[Al]}{\partial \ln[H]} = \frac{\partial \ln(K_S[H]^3)}{\partial \ln[H]} = 3$$

as

$$\frac{\partial \ln K_S}{\partial \ln[H]} = 0$$

For the determination of partial derivatives $\frac{\partial \ln[Org]}{\partial \ln[H]}$, $\frac{\partial \ln[PO_4]}{\partial \ln[H]}$, $\frac{\partial \ln[F]}{\partial \ln[H]}$, and $\frac{\partial \ln[CO_3]}{\partial \ln[H]}$, eqs. [4]–[8] (see text) are differentiated on ln[H], taking into account that the corresponding analytical concentrations of i components in the examined heterogeneous system do not depend on pH.

$$\left(\frac{\partial C_F^0}{\partial \ln[H]}\right)_{C_H^0, C_{Al}^0} = 0 = \left([F] + [HF] + \sum_{j=1} j^2[AlF_j]\right)\frac{\partial \ln[F]}{\partial \ln[H]} + [HF] + 3\sum_{j=1} j[AlF_j]$$

Hence,

[A4] $$\frac{\partial \ln[F]}{\partial \ln[H]} = -\frac{[HF] + 3\sum_{j=1} j[AlF_j]}{[F] + [HF] + \sum_{j=1} j^2[AlF_j]}$$

$$\left(\frac{\partial C_{SO_4}^0}{\partial \ln[H]}\right)_{C_{Al}^0} = 0 = \left([SO_4] + [AlSO_4] + 4[Al(SO_4)_2]\right) \times \frac{\partial \ln[SO_4]}{\partial \ln[H]} + 3\left([AlSO_4] + 2[Al(SO_4)_2]\right)$$

[A5] $$\frac{\partial \ln[SO_4]}{\partial \ln[H]} = -\frac{3([AlSO_4] + 2[Al(SO_4)_2])}{[SO_4] + [AlSO_4] + 4[Al(SO_4)_2]}$$

$$\left(\frac{\partial C_{Org}^0}{\partial \ln[H]}\right)_{C_{Al}^0, C_H^0} = 0 = C_{Org}^0\frac{\partial \ln[Org]}{\partial \ln[H]} + \sum_{m=1} m[H_mOrg] + [AlHOrg] + 3([AlOrg] + [AlHOrg])$$

[A6] $$\frac{\partial \ln[Org]}{\partial \ln[H]} = -\frac{\sum_{m=1} m[H_mOrg] + 3[AlOrg] + 4[AlHOrg]}{C_{Org}^0}$$

$$\left(\frac{\partial C_{CO_3}^0}{\partial \ln[H]}\right)_{C_H^0} = 0 = [HCO_3] + 2[H_2CO_3] + C_{CO_3}^0\frac{\partial \ln[CO_3]}{\partial \ln[H]}$$

[A7] $$\frac{\partial \ln[CO_3]}{\partial \ln[H]} = -\frac{[HCO_3] + 2[H_2CO_3]}{C_{CO_3}^0}$$

$$\left(\frac{\partial C_{PO_4}^0}{\partial \ln[H]}\right)_{C_{Al}^0, C_H^0} = 0 = C_{PO_4}^0\frac{\partial \ln[PO_4]}{\partial \ln[H]} + \sum_{l=1} l[H_lPO_4] + 2[AlH_2PO_4] + 3[AlH_2PO_4]$$

[A8] $$\frac{\partial \ln[PO_4]}{\partial \ln[H]} = -\frac{\sum_{l=1} l[H_lPO_4] + 5[AlH_2PO_4]}{C_{PO_4}^0}$$

The transformation of eq. [3] (see the text) and determination of the partial derivative $\frac{\partial \Delta C_H}{\partial \ln[H]}$ in eq. [A1] yields

[A9] $$C_{Al}^0 = \sum_{i=0}\sum_{j=1} i[Al_i(OH)_j] + \sum_{j=1}[AlF_j] + \sum_{k=1}[Al(SO_4)_k] + [AlHOrg] + [AlOrg] + [AlH_2PO_4] - \frac{1}{3}\Delta C_H$$

$$[A10]\quad \left(\frac{\partial C^0_{Al}}{\partial \ln[H]}\right)_{C^0_j} = 0 = 3\widetilde{m} + \widetilde{i} + \sum_{j=1} j[AlF_j]\frac{\partial \ln[F]}{\partial \ln[H]} + ([SO_4] + [AlSO_4] + 2[Al(SO_4)_2])\frac{\partial \ln[SO_4]}{\partial \ln[H]} + ([AlOrg] + [AlHOrg])\frac{\partial \ln[Org]}{\partial \ln[H]} + [AlH_2PO_4]\frac{\partial \ln[PO_4]}{\partial \ln[H]} - \frac{1\partial \Delta C_H}{3\partial \ln[H]}$$

where through $\widetilde{m}$ the following expression is noted.

$$[A11]\quad \widetilde{m} = \sum_{i=0}\sum_{j=1} i^2[Al_i(OH)_j] + \sum_{j=1}[AlF_j] + [AlSO_4] + [Al(SO_4)_2] + [AlOrg] + [AlHOrg] + [AlH_2PO_4]$$

Reference

(A1) Povar, I. *Russ. J. Inorg. Chem.* **1996**, *41*, 1167.

Can. J. Chem. Downloaded from www.nrcresearchpress.com by Renmin University of China on 09/02/12
For personal use only.

Computational study on the thermal decomposition and isomerization of the $CH_3OCF_2O^{\bullet}$ radical

Hari Ji Singh, Bhupesh Kumar Mishra, and Pradeep Kumar Rao

Can. J. Chem. Downloaded from www.nrcresearchpress.com by Renmin University of China on 09/02/12
For personal use only.

Abstract: The geometries of the reactant, products, and transition states involved in the decomposition pathways of the $CH_3OCF_2O^{\bullet}$ radical formed during the photooxidation of CH_3OCHF_2 (HFE-152a) have been optimized and characterized at the DFT-B3LYP level of theory using the 6–311G(d,p) basis set. Single-point energy calculations have been made at the G2M (CC,MP2) level of theory. Out of the four prominent decomposition channels considered, the β-C–O bond scission is found to be the dominant path involving a barrier height of 9.78 kcal mol^{-1} (1 cal = 4.184 J). The thermal rate constant for the above decomposition pathway is evaluated using canonical transition state theory (CTST) and was found to be 5.27×10^4 s^{-1} at 298 K and 1 atm (1 atm = 101.325 kPa).

Key words: HFE-152a, decomposition of HFE, potential energy surface, canonical transition state theory.

Résumé : Les géométries du réactif, du produit et des états de transition impliqués dans les voies de décomposition du radical $CH_3OCF_2O^{\bullet}$ qui se forme lors de la photooxydation du CH_3OCHF_2 (HFE-152a) ont été optimisées et caractérisées au niveau B3LYP de la théorie de la fonctionnelle de densité (TFD) en faisant appel à un ensemble de base 6–311G(d,p). On a aussi fait des calculs de points uniques au niveau G2M (CC,MP2) de la théorie. Des quatre voies principales de décomposition qui ont été considérées, on a trouvé que la scission de la liaison β-C–O est la voie dominante avec une barrière de 9,78 kcal mol^{-1} (1 cal = 4.184 J). Faisant appel à la théorie de l'état de transition canonique (TETC), on a évalué la constante thermique de vitesse pour cette voie de décomposition et on a trouvé qu'elle s'établit à $5,27 \times 10^4$ s^{-1}, à 298 K et 1 atm (1 atm = 101.325 kPa).

Mots-clés : HFE-152a, décomposition du HFE, surface d'énergie potentielle, théorie de l'état de transition canonique.

[Traduit par la Rédaction]

Introduction

Concern over the global environmental consequences of fully halogenated chlorofluorocarbons (CFCs) has created a need to determine the potential impact of other halogenated organic compounds on stratospheric ozone. The absence of an H-atom in the CFCs does not allow them to be oxidized or photolyzed in the troposphere. Thus, such compounds are transported into the stratosphere and their subsequent decomposition can lead to chlorine-catalyzed ozone depletion.[1–4] Because of the critical role played by CFCs in stratospheric ozone depletion, continuous efforts are being made to find replacement compounds. Hydrochlorofluorocarbons (HCFCs) and hydrofluorocarbons (HFCs) have been found to be an alternative and have gained wide industrial applications.[5,6] However, the release of HCFCs in the atmosphere has been attributed as leading to global warming because they possess significant absorbing potential for the IR radiation reflected from the Earth's surface and are thus called green house gases.[7,8] The physicochemical, environmental, and toxicological properties of HFCs are similar to CFCs and HCFCs and have been used as interim replacements for them. However, there are some environmental hazards and health risks involved in using HFCs[9,10] too. Studies performed with many of the HFCs and HCFCs have shown that these are not a viable solution for the protection of the ozone layer because they possess significant global warming potential (GWP).[11,12] Recently, attention has been paid to hydrofluoroethers (HFEs) for use as third-generation replacements to CFCs and which may find a place in the industry to be used as cleaning agents for electronic equipment, heat-transfer agents in refrigeration systems, and as carrier fluids for lubricant deposition.[13–15] One of the principal advantages of the HFEs is their shorter atmospheric lifetimes in comparison with HFCs.[16] The shorter lifetimes of these HFEs lead to lower GWPs.[17] The absence of chlorine atoms in HFEs would lead us to believe that such compounds would have little impact on stratospheric ozone and that they would possess a negligible ozone-depleting potential (ODP).[18,19] On the other hand, the presence of C–F and C–O bonds in HFEs may enhance the absorption features in the atmospheric IR region (800–1400 cm^{-1}) and could play a significant role as green house gases.[20] Therefore, it is pertinent to perform experimental and theoretical studies on the decomposition of HFEs to ascertain their suitability as replacement compounds

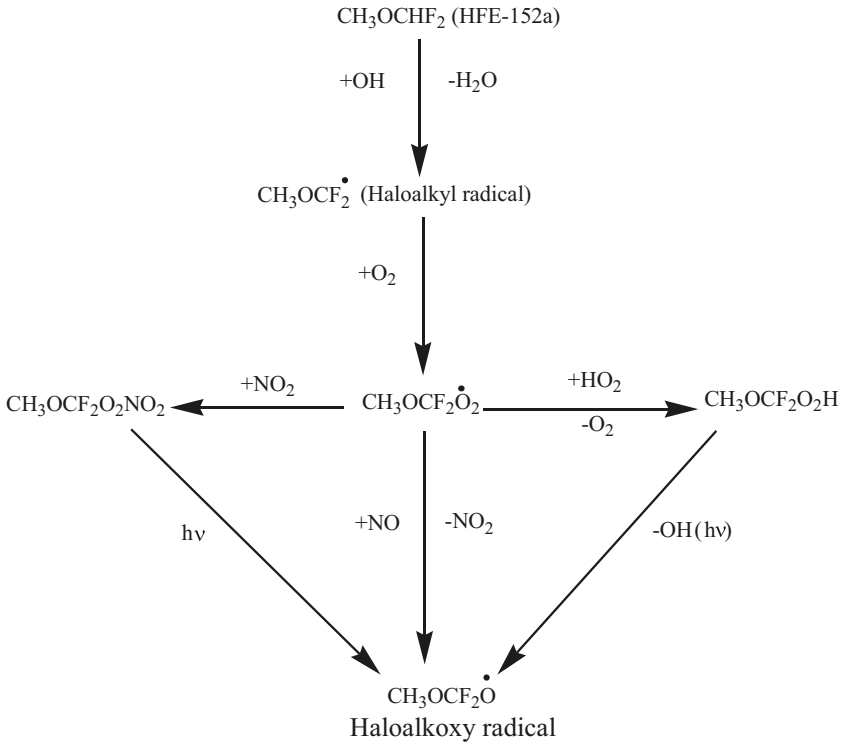
Received 26 July 2011. Accepted 11 October 2011. Published at www.nrcresearchpress.com/cjc on 28 March 2012.

H.J. Singh, B.K. Mishra, and P.K. Rao. Department of Chemistry, DDU Gorakhpur University, Gorakhpur - 273009, India.

Corresponding author: Hari Ji Singh (email: hjschem50@gmail.com).

Can. J. Chem. Downloaded from www.nrcresearchpress.com by Renmin University of China on 09/02/12
For personal use only.

Fig. 1. Tropospheric degradation mechanism of HFE-152a.



for HCFCs and HFCs.[21–24] A general mechanism of tropospheric degradation of HFE-152a is shown in Fig. 1, which is based on the fact that initial attack of the $OH^{\bullet}$ radical on HFE-152a leads to the formation of the haloalkyl radical ($CH_3OCF_2^{\bullet}$). The latter reacts with atmospheric O_2 to produce peroxy radicals ($CH_3OCF_2O_2^{\bullet}$). In a polluted atmosphere, the peroxy radicals thus formed may further react with other oxidizing species such as NO_2 and NO that ultimately lead to the formation of the haloalkoxy radical. On the other hand, the haloalkoxy radical may also be generated through another intermediate, the hydroperoxide ($CH_3OCF_2O_2H$) formed by the reaction of $CH_3OCF_2O_2$ and HO_2. The haloalkoxy radicals thus formed play a critical role in removing a variety of organic vapours present in the troposphere.[25] Several theoretical and experimental studies performed with a few HFEs such as CHF_2OCHF_2 (HFE-134), CF_3OCH_3 (HFE-143a), $CF_3CF_2OCH_3$ (HFE-245cb2), and $CF_3CF_2CF_2OCH_3$ (HFE-347mcc3) have shown that these HFEs possess favorable physical and chemical properties as that of CFCs, HCFCs, and HFCs.[26,27] The low ODP and shorter atmospheric life time (1.5 years) of difluoromethyl methyl ether CH_3OCHF_2 (HFE-152a) make it the most suitable replacement for CH_3CF_2Cl (HCFC-142b) as a refrigerant.[27] Christensen et al.[28] studied the degradation pathways of a similar hydrofluoroether, CF_3OCH_3 (HFE-143a), using a smog chamber / FTIR technique and concluded that the haloalkoxy radical, $CF_3OCH_2O^{\bullet}$ produced from HFE-143a, degraded primarily by reaction with O_2 in the atmosphere. In another study, Good et al.[29] also investigated the atmospheric oxidation mechanism of HFE-143a, HFE-134, and HFE-125 using experimental and ab initio methods and proposed that the H-atom abstraction reaction caused by photochemically produced hydroxyl radicals was the dominant path for removing these compounds from the troposphere. The studies performed by these groups[28,29] reflect the position that the F-atom on different carbon atoms in the HFEs changed the dominant pathways of decomposition.

Thus, studying the fate of haloalkoxy radicals formed from HFE-152a is important from the viewpoint of understanding its role in atmospheric chemistry. The literature survey reveals that no experimental or theoretical studies have been performed on HFE-152a with regards to its decomposition kinetics. There are four potential pathways of decomposition of $CH_3OCF_2O^{\bullet}$ produced from HFE-152a that involve bond scission and isomerization processes. These are represented as follows:

[1] $CH_3OCF_2O^{\bullet} \rightarrow CH_3O + CF_2O$

[2] $CH_3OCF_2O^{\bullet} \rightarrow CH_2O + CF_2O + H$

[3] $CH_3OCF_2O^{\bullet} \rightarrow CH_3OC(O)F + F$

[4] $CH_3OCF_2O^{\bullet} \rightarrow CH_2OCF_2OH$

In the present investigation, density functional theory (DFT) calculations on the decomposition pathways of the $CH_3OCF_2O^{\bullet}$ radical given by rxns. [1]–[4] were performed. Energetic calculations were performed using the modified G2 method, G2M(CC,MP2), and thermodynamic properties such as reaction enthalpies and free energies were calculated. Canonical transition state theory (CTST) was utilized to predict the rate constants for the above decomposition channels (rxns.[1]–[4]). Attempts were made to search and characterize transition states for the corresponding potential energy surfaces and energy barriers to decomposition were evaluated. The intrinsic reaction coordinate (IRC) calculation was also

Can. J. Chem. Downloaded from www.nrcresearchpress.com by Renmin University of China on 09/02/12
For personal use only.

performed to confirm the smooth transition from reactant to products through the respective transition states.

Computational method

Ab initio quantum mechanical calculations were performed with the Gaussian03 suite of programs.[30] Geometry optimizations of the reactant, products, and transition states were made using DFT employing Becke's three-parameter hybrid functional (B3LYP)[31,32] with the 6–311G (d,p) basis set. To determine the nature of different stationary points on the potential energy surface, vibrational frequencies were determined using the same level of theory at which the optimization was made. All the stationary points were identified to correspond to the minima with no imaginary frequency (NIMAG = 0), and the transition states were characterized by the presence of only one imaginary frequency (NIMAG = 1). To ascertain that the identified transition states connect reactant and products smoothly, IRC calculations[33] were performed at the UB3LYP/6–311G(d,p) level. To refine the energy values for various species involved in rxns. [1]–[4], a variant of the G-2 compound method,[34] G2M(CC,MP2), was utilized during the present study. Mebel et al.[35] suggested that the G2M(CC,MP2) method yielded accurate values of energy for the systems containing six to seven heavy atoms. According to the proposed scheme, geometry optimizations and frequency calculations were performed at the UB3LYP/6–311G (d,p) level and single-point energy calculations were completed at the MP2 and MP4 levels. CCSD(T)/6–311G(d,p) was substituted for the QCISD(T)/6–311G(d,p) calculation in the original G2 method. The G2M(CC,MP2) method yielded a composite energy value as described in the following:

$$E[\mathrm{G2M(CC,\,MP2)}] = E_{\mathrm{base}} + \Delta E(\mathrm{3df,2p}) + \Delta E(\mathrm{CC}) + \mathrm{HLC} + \mathrm{ZPE}$$

where

$$E_{\mathrm{base}} = E[\mathrm{MP4/6-311G(d,p)}]$$

$$\Delta E(\mathrm{3df,2p}) = E[\mathrm{MP2/6-311+G(3df,2p)}] - E[\mathrm{MP2/6-311G(d,p)}]$$

$$\Delta E(\mathrm{CC}) = E[\mathrm{CCSD(T)/6-311G(d,p)}] - E[\mathrm{MP4/6-311G(d,p)}]$$

HLC (high level correction) = $-0.00525n_\beta - 0.00019n_\alpha$ (n_α and n_β are the number of α and β valence electrons with $n_\alpha \geq n_\beta$), and ZPE = zero-point energy, obtained from the vibrational frequency calculation performed at UB3LYP/6–311G(d,p) level.

Results and discussion

The fate of haloalkoxy radical ($CH_3OCF_2O^\bullet$) during its thermal decomposition in the atmosphere is envisaged to occur via rxns. [1]–[4]. The detailed thermodynamic calculations for the decomposition channels (rxns. [1]–[4]) were performed at the UB3LYP/6–311G(d,p) level and the results obtained for the associated reaction enthalpies and free energies are listed in Table 1. Results show that the endothermicity of rxn. [3] is 10.03 kcal mol^{-1} (1 cal = 4.184 J) and it proceeds with a positive free energy change ($_r\Delta G^0(298)$ = 12.49 kcal mol^{-1}). This shows that rxn. [3] would be less probable in comparison with rxns. [1], [2], and [4]. Optimized geometries of the reactant, products, and transition states obtained at the UB3LYP/6–311G(d,p) level of theory are shown in Fig. 2, with the relevant bond lengths superimposed for the transition states. The detailed optimized structural parameters of the reactant, products, and transition states are given in Supplementary data Table S1. Transition states were searched on the potential energy surfaces of rxns. [1]–[4] and characterized as TS1, TS2, TS3, and TS4, respectively. The search was made along the minimum energy path on a relaxed potential energy surface, and the transition states were characterized by the presence of only one imaginary frequency. In the optimized structure of TS1, the elongation of the β-C–O bond is found to be from 1.381 to 1.758 Å (about a 27% increase) with a simultaneous shrinkage of the C–O• (C3–O4) bond by almost 9% (1.320–1.211 Å). The cleavage of the C–H bond (channel 2) leads to atomic hydrogen, CH_2O, and CF_2O. The corresponding transition state (TS2) shows larger structural changes than TS1, i.e., a substantial elongation (~45%) of the C–H (C1–H6) bond and a shortening (~16%) of the C–O bond (C1–O2). A similar analysis made on the optimized structure of TS3 reveals the elongation of the C–F (C3–F9) bond length from 1.365 to 1.862 Å, resulting in an increase of about 36% accompanied by a shrinkage of the β-C–O bond (C3–O2) from 1.381 to 1.304 Å (~6%). The only possible rearrangement pathway through a four-membered ring-type transition state (TS4) leads to the formation of CH_2OCF_2OH. The main structural characteristic in TS4 is the elongation of the C–H (C1–H7) bond by 14% and a decrease of the O(2)–C(1)–H(7) angle from 110.7 Å in CH_3OCF_2O to 97.9 Å in TS4, reflecting the migration of H(7) from C(1) to O(4).

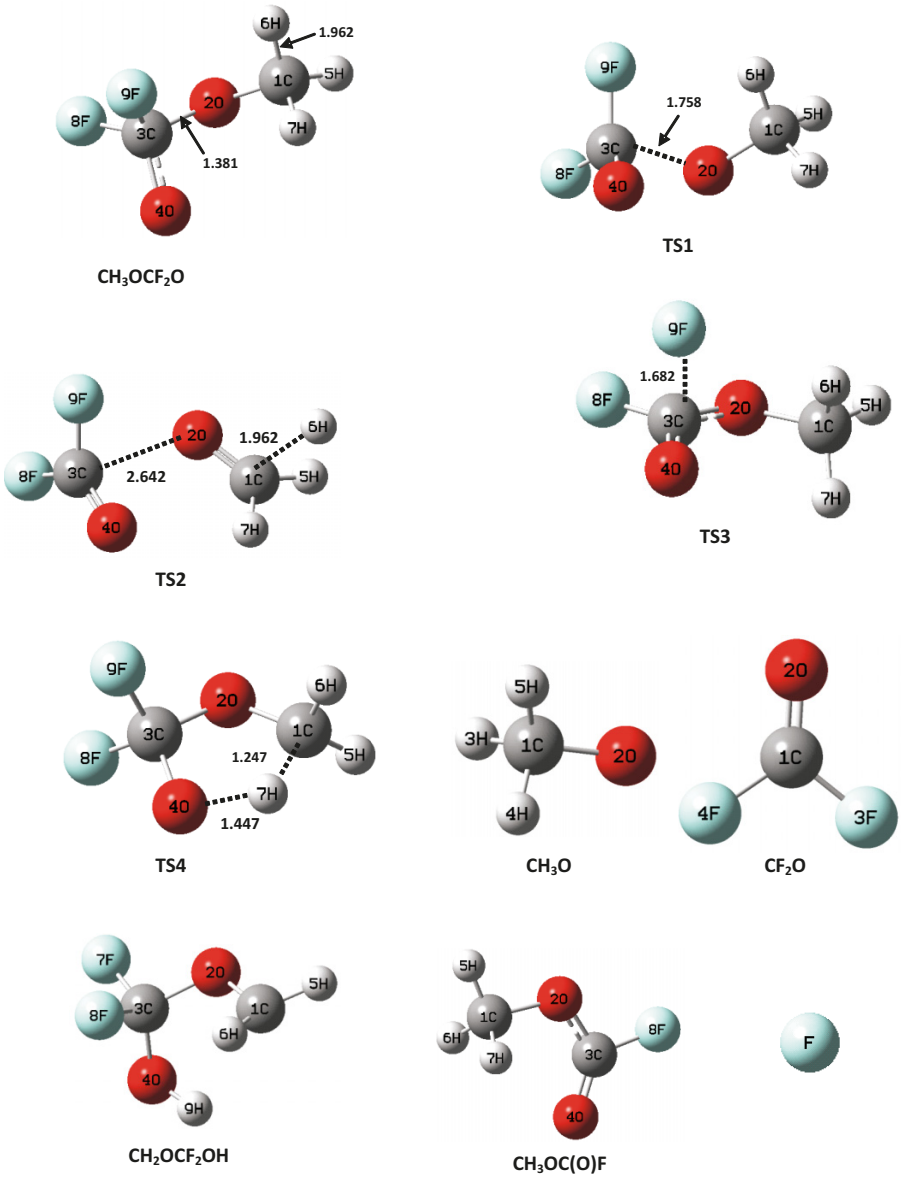
Results obtained during frequency calculations for the reactant, products, and transition states involved in rxns. [1]–[4] are recorded in Supplementary data Table S2. These results show that the reactant and products have stable minima on their potential energy surfaces characterized by the occurrence of only real and positive vibrational frequencies. The results recorded in Table S2 further show that the transition states are characterized by the occurrence of only one imaginary frequency obtained at 530, 610, 371, and 1543 cm^{-1} for TS1, TS2, TS3, and TS4, respectively. These frequencies were analyzed using the GaussView[36] visualization program, which revealed the smooth transition from reactant to products through the corresponding transition state. The existence of a transition state on the potential energy surface is ascertained by the IRC calculation performed at the same level of theory at which geometry optimization was made and performed using the Gonzalez–Schlegel steepest descent path[33] in the most weighted Cartesian coordinates, with a step size of 0.05 ($amu^{1/2}$-bohr). Force constants at 31 selected points (15 points in the reactant channel and 15 points in the product channel) were calculated, and the geometries were optimized at each point along the minimum energy path.

Single-point energy calculations of various species involved in the decomposition pathways were determined using

Table 1. Thermochemical data for the decomposition channels of $CH_3OCF_2O^{\bullet}$ calculated at the B3LYP/6–311G(d,p) level of theory.

Reaction channel	$_rΔH^0$ (298 K; kcal mol^{-1})	$_rΔG^0$ (298 K; kcal mol^{-1})
$CH_3OCF_2O^{\bullet} \rightarrow CH_3O + CF_2O$	–19.52	–25.45
$CH_3OCF_2O^{\bullet} \rightarrow CH_2O + CF_2O + H$	–5.42	–17.33
$CH_3OCF_2O^{\bullet} \rightarrow CH_3OC(O)F + F$	10.03	12.49
$CH_3OCF_2O^{\bullet} \rightarrow CH_2OCF_2OH$	–9.13	–9.24

Fig. 2. Optimized geometries of the species involved in the decomposition and isomerization of $CH_3OCF_2O^{\bullet}$ obtained at the UB3LYP/6–311G(d,p) level. Bond distances are given in Å.



the MP2, MP4, and CCSD(T) level of theories at the B3LYP/6–311G(d,p) optimized geometries and corrected for ZPE. The ZPE was calculated using B3LYP/6–311G(d,p) and corrected with a scale factor of 0.96 to partly eliminate the systematic errors.[37] To refine the energy values, these calculations were also performed using larger basis sets incorporating polarized and diffused basis functions. Zero-point-corrected total energies using standard and extended basis sets for various species and transition states involved are listed in Supplementary data Table S3. The data listed in Table S3 were used to calculate the energy barrier for β-C–O bond scission and the results are recorded in Table 2. The results show that the energy barrier for β-C–O bond scission falls in the range of 9–11 kcal mol^{-1}, whereas for F-elimination it is in the range of 22–27 kcal mol^{-1} depending on the level of theories involved during the calculations. No experimental

Can. J. Chem. Downloaded from www.nrcresearchpress.com by Renmin University of China on 09/02/12
For personal use only.

Can. J. Chem. Downloaded from www.nrcresearchpress.com by Renmin University of China on 09/02/12
For personal use only.

Table 2. Calculated energy barriers in kcal mol^{-1}.

	Transition state			
Method	TS1	TS2	TS3	TS4
MP2/6–311G(d,p)	10.80	14.77	25.43	15.67
MP2/6–311+G(3df,2p)	10.92	15.20	26.52	14.27
MP4/6–311G(d,p)	10.39	18.29	23.76	15.80
CCSD(T)/6–311G(d,p)	11.33	19.20	22.18	16.08
G2M(CC,MP2)	9.78	11.97	22.67	12.95

or theoretical data are available in the literature for comparison of the energy barriers associated with the decomposition channels of $CH_3OCF_2O^\bullet$ that were considered during the present investigation. However, to ascertain the reliability of the calculated values, a comparison was made with the energy values calculated at B3LYP/6–311+G(2d,2p)// B3LYP/6–31G(d) by Good et al.[29] for structurally similar compounds CF_3OCF_2O (HFE-125) and CHF_2OCF_2O (HFE-134), yielding the energy barriers for β-C–O bond scission of 9.4 and 10.30 kcal mol^{-1}, respectively, whereas the corresponding values for the F-elimination process were found to be 22.8 and 25.8 kcal mol^{-1}. The results obtained during the course of the present investigation for β-C–O bond scission and F-elimination (9.78 and 22.67 kcal mol^{-1} for $CH_3OCF_2O^\bullet$ radical decomposition using the G2M(CC, MP2) method) show a good agreement with the data obtained by Good et al.[29] for structurally similar hydrofluoroethers HFE-125 and HFE-134. This validates the use of the single-point energy calculation data obtained using the G2M(CC,MP2) method on the geometries optimized at the B3LYP/6–311G(d,p) level to construct a potential energy diagram for the decomposition channels of $CH_3OCF_2O^\bullet$ considered during the present study. The zero-point corrected total energies of various species obtained at G2M(CC,MP2) as listed in Table S3 were used relative to the ground-state energy of $CH_3OCF_2O^\bullet$ taken as zero. This energy diagram is shown in Fig. 3 and demonstrates that the barrier height of 9.78 kcal mol^{-1} for β-C–O bond scission is considerably lower than that for other decomposition pathways, and the dominance of the β-C–O bond scission in the decomposition of this haloalkoxy radical in the atmosphere is thus envisioned. Spin contamination was not important for the $CH_3OCF_2O^\bullet$ radical because $<S^2>$ was 0.76 before annihilation, which is only slightly larger than the expected value of $<S^2> = 0.75$ for doublets.

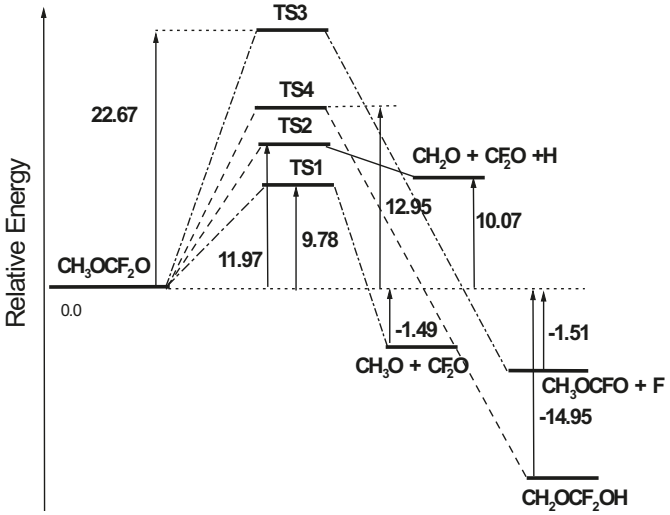
Rate constants

The rate constants for the decomposition channels shown by rxns. [1]–[4] of the $CH_3OCF_2O^\bullet$ radical were calculated using CTST[38] using the following expression:

$$[5] \qquad k = \Gamma(T)\frac{k_B T Q^{\ddagger}_{TS}}{h \quad Q_R}\exp\frac{-\Delta E}{RT}$$

where $\Gamma(T)$ is the tunneling correction factor at temperature T; $Q^{\ddagger}_{TS}$ and Q_R are the total partition functions for the transition state and reactant, respectively; ΔE is the barrier height including zero-point energy; k_B is the Boltzmann constant; and h is Planck's constant. Calculations for $\Gamma(T)$ were made using the expression of Wigner[39] as given by the following:

Fig. 3. Energy profile for $CH_3OCF_2O^\bullet$ unimolecular decomposition and isomerization at the G2M(CC,MP2) level. Energy values are given in kcal mol^{-1}.



$$[6] \qquad \Gamma(T) = 1 + \frac{1}{24}\left(\frac{h\nu^{\#}}{k_B T}\right)^2$$

where $\nu^{\#}$ is the imaginary frequency at the saddle point. However, $\Gamma(T)$ should be negligible for heavier atoms or groups as in the reactions studied. The partition functions for the respective transition state and reactant at 298 K are obtained from the vibrational frequency calculation made at the B3LYP/6–311G(d,p) level. The rate constant for β-C–O bond scission in $CH_3OCF_2O^\bullet$ decomposition occurring via rxn. [1] was calculated to be 5.27×10^4 s^{-1} at 298 K and 1 atm (1 atm = 101.325 kPa). A computational study performed by Henon et al.[40] on a structurally similar alkoxy radical ($CH_3OCH_2O^\bullet$) yielded a rate constant for β-C–O bond scission of 5.2×10^4 s^{-1}, which is in good agreement with the value of 5.27×10^4 s^{-1} calculated during the present investigation. Our modeling calculations for the A-factor for β-C–O bond scission in $CH_3OCF_2O^\bullet$ show it to be 0.78×10^{13} s^{-1}, which is also in good agreement with the value of 1×10^{13} to 2×10^{13} s^{-1} obtained by Good and Francisco[41] for β-C–O bond scission in the $CH_3OCH_2O^\bullet$ radical. The rate constants calculated during the present study for decomposition channels [2] and [4] were found to be 9.84×10^3 and 0.08×10^2 s^{-1}, respectively. Similar calculations performed to determine the rate constant for F-elimination occurring via rxn. [3] involving TS3 as the transition state yielded a value of 1.31×10^{-5} s^{-1} at 298 K and 1 atm with an associated A-factor of 5.59×10^{12} s^{-1}.

Can. J. Chem. Downloaded from www.nrcresearchpress.com by Renmin University of China on 09/02/12
For personal use only.

Conclusion

The most important stationary points on the potential energy surface for the thermal decomposition of the $CH_3OCF_2O^\bullet$ radical were investigated at the B3LYP/6–311G(d,p) level of theory. Energetic calculations performed at G2M (CC,MP2) revealed that the most dominant decomposition pathway for $CH_3OCF_2O^\bullet$ is the β-C–O bond scission that occurs with a barrier height of 9.78 kcal mol^{-1}. The other reaction pathways considered during the present investigation, such as H- and F-elimination and 1,5 H-transfer, occur with a barrier height in the range of 11.97–22.67 kcal mol^{-1}. Thus, the dominance of β-C–O bond scission in $CH_3OCF_2O^\bullet$ was established during the present investigation, and the thermal rate constants evaluated using conventional transition-state theory for this scission was estimated to be 5.27×10^4 s^{-1} with a corresponding A-factor of 0.78×10^{13} s^{-1} at 298 K and 1 atm pressure.

Supplementary data

Supplementary data for the geometrical parameters of the optimized geometries of the reactant, products, and transition states, and single-point energy data for various species involved in the decomposition channels (rxns. [1]–[4]) are listed in Tables S1–S3 and are available with this article through the journal Web site http://nrcresearchpress.com/doi/suppl/10.1139/v2012-005.

Acknowledgment

This work was performed under the project sponsored by the UP State Government under its Center of Excellence Program. Financial assistance from CSIR and UGC (DSA-II) to B.K.M. and P.K.R. is also acknowledged. Thanks are also due to the University Grants Commission for awarding the Rajiv Gandhi National Fellowship to one of the authors (P.K.R.).

References

(1) Solomon, S. *Nature* **1990**, *347* (6291), 347. doi:10.1038/347347a0.
(2) Molina, M. J.; Rowland, F. S. *Nature* **1974**, *249* (5460), 810. doi:10.1038/249810a0.
(3) Rowland, F. S.; Molina, M. J. *Chem. Eng. News* **1994**, *8*, 72.
(4) Wuebbles, D. J. *J. Geophys. Res.* **1983**, *88* (C2), 1433. doi:10.1029/JC088iC02p01433.
(5) World Meterological Organization (WMO). *Scientific Assessment of Stratospheric Ozone: 1989;* WMO, Global Ozone Research and Monitoring Project Report No. 20, 1991; WMO: Geneva, Switzerland; Vol. 11.
(6) Wayne, R. P. *Chemistry of Atmospheres;* Clarendon Press: Oxford, 2001.
(7) Dekant, W. *Environ. Health Perspect.* **1996**, *104*, 75.
(8) Hayman, G.; Derwent, R. D. *Environ. Sci. Technol.* **1997**, *31* (2), 327. doi:10.1021/es950775l.
(9) Tsai, W. T.; Chen, H. P.; Hsien, W. Y. *J. Loss Prev. Process Ind.* **2002**, *15* (2), 65. doi:10.1016/S0950-4230(01)00067-5.
(10) Tsai, W. T. *Chemosphere* **2005**, *61* (11), 1539. doi:10.1016/j.chemosphere.2005.03.084.
(11) Pinnock, S.; Hurley, M. D.; Shine, K. P.; Wallington, T. J.; Smyth, T. J. *J. Geophys. Res.* **1995**, *100* (D11), 23227. doi:10.1029/95JD02323.
(12) International Panel on Climate Change (IPCC). *Climate Change 1995: The Science of Climate Change;* Cambridge University Press: New York, 1996.
(13) Tsai, W. T. *J. Hazard. Mater.* **2005**, *119* (1–3), 69. doi:10.1016/j.jhazmat.2004.12.018.
(14) Fontana, G.; Causà, M.; Gianotti, V.; Marchionni, G. *J. Fluor. Chem.* **2001**, *109* (2), 113. doi:10.1016/S0022-1139(01)00366-9.
(15) Bivens, D. B.; Minor, B. H. *Int. J. Refrig.* **1998**, *21* (7), 567. doi:10.1016/S0140-7007(98)00027-9.
(16) Cooper, D. L.; Cunningham, T. P.; Allan, N. L.; McCulloch, A. *Atmos. Env. Part A* **1993**, *27* (1), 117. doi:10.1016/0960-1686(93)90077-C.
(17) Blowers, P.; Tetrault, K. F.; Trujillo-Morehead, Y. *Theor. Chem. Acc.* **2008**, *119* (4), 369. doi:10.1007/s00214-007-0394-3.
(18) Ravishankara, R. A.; Turnipseed, A. A.; Jensen, N. R.; Barone, S.; Mills, M.; Howard, C. J.; Solomon, S. *Science* **1994**, *263* (5143), 71. doi:10.1126/science.263.5143.71.
(19) Granier, C.; Shine, K. P.; Daniel, J. S.; Hansen, J. E.; Lal, S.; Stordal, F. Climate Effects of Ozone and Halocarbon Changes. In *Scientific Assessment of Ozone Depletion: 1998,* Global Ozone Research and Monitoring Project Report 44; World Meteorological Organization: Geneva, Switzerland, 1999.
(20) Good, D. A.; Francisco, J. S. *J. Phys. Chem.* **1998**, *102* (10), 1854. doi:10.1021/jp980048n.
(21) Chen, L.; Kutsuna, S.; Tokuhashi, K.; Sekiya, A. *J. Phys. Chem. A* **2006**, *110* (47), 12845. doi:10.1021/jp064917h.
(22) Urata, S.; Takada, A.; Uchimaru, T.; Chandra, A. K. *Chem. Phys. Lett.* **2003**, *368* (1–2), 215. doi:10.1016/S0009-2614(02)01718-9.
(23) Chen, L.; Kutsuna, S.; Tokuhashi, K.; Sekiya, A.; Takeuchi, K.; Ibusuki, T. *Int. J. Chem. Kinet.* **2003**, *35* (6), 239. doi:10.1002/kin.10124.
(24) Jogeshwari Devi, K.; Chandra, A. K. *Chem. Phys. Lett.* **2011**, *502* (1–3), 23. doi:10.1016/j.cplett.2010.12.011.
(25) Sekiya, A.; Misaki, S. *J. Fluor. Chem.* **2000**, *101* (2), 215. doi:10.1016/S0022-1139(99)00162-1.
(26) Smith, N. D. EPA-60/F-92-012, Springerfield, 1992.
(27) Satoh, K.; Nishiumi, H.; Kasatani, T. *Fluid Phase Equilib.* **1998**, *144* (1–2), 211. doi:10.1016/S0378-3812(97)00259-8.
(28) Christensen, L. K.; Wallington, T. J.; Guschin, A.; Hurly, M. D. *J. Phys. Chem. A* **1999**, *102*, 1854.
(29) Good, D. A.; Kamboures, M.; Santiano, R.; Francisco, J. S. *J. Phys. Chem.* **1999**, *103*, 9230.
(30) Frisch, M. J.; Trucks, G. W.; Schlegel, H. B.; Scuseria, G. E.; Robb, M. A.; Cheeseman, J. R.; Montgomery, J. A., Jr.; Vreven, T.; Kudin, K. N.; Burant, J. C.; Millam, J. M.; Iyengar, S. S.; Tomasi, J.; Barone, V.; Mennucci, B.; Cossi, M.; Scalmani, G.; Rega, N.; Petersson, G. A.; Nakatsuji, H.; Hada, M.; Ehara, M.; Toyota, K.; Fukuda, R.; Hasegawa, J.; Ishida, M.; Nakajima, T.; Honda, Y.; Kitao, O.; Nakai, H.; Klene, M.; Li, X.; Knox, J. E.; Hratchian, H. P.; Cross, J. B.; Bakken, V.; Adamo, C.; Jaramillo, J.; Gomperts, R.; Stratmann, R. E.; Yazyev, O.; Austin, A. J.; Cammi, R.; Pomelli, C.; Ochterski, J. W.; Ayala, P. Y.; Morokuma, K.; Voth, G. A.; Salvador, P.; Dannenberg, J. J.; Zakrzewski, V. G.; Dapprich, S.; Daniels, A. D.; Strain, M. C.; Farkas, O.; Malick, D. K.; Rabuck, A. D.; Raghavachari, K.; Foresman, J. B.; Ortiz, J. V.; Cui, Q.; Baboul, A. G.; Clifford, S.; Cioslowski, J.; Stefanov, B. B.; Liu, G.; Liashenko, A.; Piskorz, P.; Komaromi, I.; Martin, R. L.; Fox, D. J.; Keith, T.; Al-Laham, M. A.; Peng, C. Y.; Nanayakkara, A.; Challacombe, M.; Gill, P. M. W.; Johnson, B.; Chen, W.; Wong, M. W.; Gonzalez, C.; Pople, J. A.

Gaussian 03, Revision C.02; Gaussian Inc.: Pittsburgh, PA, 2003.
(31) Becke, A. D. J. *Chem. Phys.* **1993**, *98*, 5648.
(32) Lee, C.; Yang, W.; Parr, R. G. *Phys. Rev. B* **1988**, *37* (2), 785. doi:10.1103/PhysRevB.37.785.
(33) Gonzalez, C.; Schlegel, H. B. *J. Phys. Chem.* **1990**, *94* (14), 5523. doi:10.1021/j100377a021.
(34) Curtiss, L. A.; Raghavachari, K.; Trucks, G. W.; Pople, J. A. *J. Chem. Phys.* **1991**, *94* (11), 7221. doi:10.1063/1.460205.
(35) Mebel, A. M.; Morokuma, K.; Lin, M. C. *J. Chem. Phys.* **1995**, *103* (17), 7414. doi:10.1063/1.470313.
(36) Frisch, A.; Nielsen, A. B.; Holder, A. J. *GaussView Reference;* Gaussian, Inc.: Wallingford, CT, 2000.
(37) Scott, A. P.; Radom, L. *J. Phys. Chem.* **1996**, *100* (41), 16502. doi:10.1021/jp960976r.
(38) Truhlar, D. G.; Garrett, B. C.; Klippenstein, S. J. *J. Phys. Chem.* **1996**, *100* (31), 12771. doi:10.1021/jp953748q.
(39) Wigner, E. P. Z. *J. Phys. Chem* **1932**, *B19*, 203.
(40) Henon, E.; Bohr, F.; Sokolowski-Gomez, N.; Caralp, F. *Phys. Chem. Chem. Phys.* **2003**, *5* (24), 5431. doi:10.1039/b313251j.
(41) Good, D. A.; Francisco, J. S. *J. Phys. Chem. A* **2000**, *104* (6), 1171. doi:10.1021/jp9919718.

Can. J. Chem. Downloaded from www.nrcresearchpress.com by Renmin University of China on 09/02/12
For personal use only.

Characterizing the binding of nucleotide ATP on serum albumin by ^{31}P NMR diffusion

Zhiyan Song, Hua Zhao, Olarongbe Olubajo, Lewis B. Hall, Chauncey N. Orr, and Courtney B. Askew

Can. J. Chem. Downloaded from www.nrcresearchpress.com by Renmin University of China on 09/02/12
For personal use only.

Abstract: The pulsed-field-gradient (PFG) ^{31}P NMR diffusion spectra were measured under varied sample conditions to characterize the low-affinity binding of adenosine 5′-triphosphate (ATP) on human serum albumin (HSA) or bovine serum albumin (BSA). The NMR diffusion constants of ATP, ATP–HSA, or ATP–BSA were illustrated as function of ATP concentrations. The binding curves of ATP–HSA and ATP–BSA were identical but strikingly different from the ATP curve. Using a "Scatchard plot", the apparent binding constant (K) and number of ATP binding sites (n) on serum albumin were evaluated as $K = 75.25$ (mol/L)$^{-1}$ and $n = 10$, respectively. At a pH < 5.0 and a pH > 9.0 or a temperature > 45 °C, the diffusion data of ATP–HSA were found to increase remarkably, suggesting that the dissociation of ATP from HSA was largely enhanced, probably because of pH- or heat-induced protein structural change, degradation, or aggregation. In addition, our data indicated that ADP was strongly competitive with ATP for the low-affinity binding to HSA, but heptanone and Cl^- were essentially noncompetitive. These results are important for further elucidating the interaction of ATP with serum albumin and its possible effect on related bioprocesses. The method can be well applied to study the binding of other nucleotides/nucleosides on proteins.

Key words: NMR, ^{31}P, ATP, serum albumin, affinity, diffusion.

Résumé : Opérant des diverses conditions de l'échantillon, on a mesuré les spectres de diffusion de RMN du ^{31}P par la méthode du gradient de champ pulsé (GCP) dans le but de caractériser la faible affinité de fixation du 5′-triphosphate d'adénosine (TPA) sur de l'albumine sérique humaine (ASH) ou de l'albumine sérique bovine (ASB). Les constantes de diffusion de RMN du TPA et des agrégats TPA–ASH et TPA–ASB sont illustrées en fonction des concentrations du TPA. Les courbes de fixation des agrégats TPA–ASH et TPA–ASB sont identiques, mais ils diffèrent beaucoup de la courbe du TPA. Faisant appel à la « courbe de Scatchard », on a déterminé que la constante apparente de fixation (K) et le nombre des sites de fixation (n) du TPA sur l'albumine sérique sont respectivement de $K = 75{,}25$ (mol/L)$^{-1}$ et $n = 10$. À un pH < 5,0 et à un pH > 9,0 ou une température > 45 °C, on a observé que les données de diffusion pour de l'agrégat TPA–ASH augmentent d'une façon remarquable, ce qui suggère que la dissociation du TPA de l'ASH est fortement augmentée, probablement en raison de dégradations, d'agrégations ou changements structuraux dans la protéine induits par le pH ou la chaleur. De plus, nos données suggèrent que le diphosphate d'adénosine (DPA) offre une grande compétition au TPA pour la fixation de faible affinité avec l'ASH, mais que l'heptanone et l'ion Cl^- ne sont pas en compétition. Ces résultats sont importants pour une élucidation ultérieure de l'interaction du TPA avec l'albumine sérique et des ses effets potentiels sur les bioprocessus apparentés. La méthode peut facilement être appliquée à l'étude de la fixation d'autres nucléotides/nucléosides sur des protéines.

Mots-clés : RMN, ^{31}P, TPA, albumine sérique, affinité, diffusion.

[Traduit par la Rédaction]

Introduction

Human serum albumin (HSA) is a most abundant protein in blood plasma. It serves as a storage and transport protein for a variety of substances, such as drugs, hormones, fatty acids, metal ions, and flavor compounds.[1] The binding capacities of serum albumin are important for regulating the delivery, redistribution, and activities of its bound ligands.[1–5]

There are two major types of binding sites on serum albumin, i.e., the high- and low-affinity sites.[6] The high-affinity sites are also classified into three categories according to their ligand selectivity.[7–9] In general, the high-affinity sites may have relatively lower binding capacity for a specific ligand because the number of these sites is often small, whereas the low-affinity sites can have a higher binding capacity because of a larger number of the total sites. If the ligand concentration is sufficiently high, a ligand species may bind to both high- and low-affinity sites on serum albumin.[10]

Ligand binding to serum albumin has been widely studied using a variety of techniques, such as ultrafiltration,[9,11] HPLC,[12] electrophoresis,[13] optical spectroscopy,[14–23] ESR,[24–26]

Received 8 August 2011. Accepted 22 January 2012. Published at www.nrcresearchpress.com/cjc on 26 March 2012.

Z. Song, H. Zhao, O. Olubajo, L.B. Hall, C.N. Orr, and C.B. Askew. Department of Natural Sciences, Savannah State University, Savannah, GA 31404, USA.

Corresponding author: Zhiyan Song (e-mail: songz@savannahstate.edu).

Can. J. Chem. Downloaded from www.nrcresearchpress.com by Renmin University of China on 09/02/12
For personal use only.

and NMR.[10,27–35] Among these methods, NMR pulsed-field-gradient (PFG) diffusion is particularly useful for characterizing low-affinity binding, in which the weakly bound ligands undergo rapid exchange with the free ligands on the NMR chemical shift timescale, i.e., the exchange is fast relative to chemical shift differences between the free and bound species, thus, the observed ligand signals represent a weighted average for signals of free and bound ligands.[27,36] In contrast, if ligands are tightly bound to the high-affinity sites on protein, the NMR signals of bound ligands are often difficult to analyze because of much lowered spectral resolution and sensitivity.

Among other things, serum albumin can serve as a regulator in some adenosine 5′-triphosphate (ATP)-involved bioprocesses, such as G-protein signaling and muscle fiber functioning,[5] whereas the nucleotide ATP in blood plasma may have a role in regulation of coronary blood flow.[37,38] However, direct interactions of serum albumin with nucleotides have not yet been fully recognized, and a certain ambiguity or disagreement still exists in this regard. For instance, Jakob et al.[39] believed that nucleotides were incapable of binding to serum albumin; thus, in their fluorescence studies of ATP binding to Hsp90 and other proteins, bovine serum albumin (BSA) was used as a control, i.e., non-ATP-binding protein. In contrast, Bauer et al.[24] found from their ESR measurements that ATP was able to specifically bind to BSA. Furthermore, Takeda et al.[9] used ultrafiltration to verify that ATP binding to BSA was in a 1:1 molar ratio, and they also obtained different dissociation constants for ATP–BSA complexes under varied pH. These data may illustrate the binding capacity of ATP on a single high-affinity site of serum albumin. However, the low-affinity interactions between nucleotides and serum albumin have been unclear so far.

In this publication, we report a ^{31}P NMR-PFG diffusion investigation for the binding of ATP to HSA or BSA in aqueous solutions. ^{31}P NMR is able to produce sharp, well-separated spectral peaks. It has a greater resonance shift dispersion as compared with ^{1}H NMR, and a higher sensitivity than ^{13}C NMR because of the 100% natural abundance of the ^{31}P nucleus. The ^{31}P NMR-PFG diffusion technique can serve multiple purposes. For instance, it has been used for probing the strong interaction in some covalently bonded organophosphorus–protein complexes or for analyzing the formula weight of phosphorus-containing compounds.[40,41] Our ^{31}P diffusion study presented was focused on the low-affinity interaction between ATP and HSA or BSA. We measured ^{31}P diffusion spectra under varied sample conditions such as ATP concentrations, pH, or temperature, and from these spectra the observed diffusion constants (D_{obs}) were deduced. Some data were analyzed by the "Scatchard plot" to evaluate the apparent binding constant and number of ATP binding sites on serum albumin. In addition, the effect of pH or temperature on ATP affinity was verified, and competitive or noncompetitive binding was found in some ternary samples. These results are important for elucidating the weak-affinity interaction of ATP with serum albumin and its possible impact. The method can be applicable for investigating other nucleotide–protein interactions as well.

Experimental

The analytical grade chemicals (sodium salt of ATP, HSA, and BSA) were purchased from Sigma-Aldrich and used without further purification. NMR samples (ATP, ATP–HSA, or ATP–BSA) were prepared by fully dissolving solid ATP and HSA or BSA in D_2O solvent for the purpose of magnetic field lock. ATP concentrations were varied in the 5–75 mmol/L range, and HSA or BSA concentration was fixed at 1 or 5 mmol/L. Each sample had volume of 1 mL, suited for a 5 mm NMR tube. Sample pH was adjusted using 1 mol/L NaOH and HCl (accurate to pH 0.1), and no other pH buffers were added to avoid any interference by impurities. The prepared samples were "incubated" for a couple of hours prior to NMR acquisition to ensure that equilibrium was reached.

NMR experiments were carried out using a JEOL ECX-300 spectrometer equipped with a 5 mm broadband autotune probe, a PFG unit, and a temperature controller. To calibrate the PFG strength, the ^{1}H spectrum of a water sample was acquired using a single magnetic-field-gradient pulse, resulting in a nearly rectangular peak, and the peak width was measured in Hz then converted into PFG strength in T/m by the spectrometer. ^{31}P NMR-PFG diffusion spectra were measured using a standard stimulated spin-echo (SSE) pulse sequence with 256 scans and a 3 s repetition delay. Other acquisition parameters were typically set as follows: $\pi/2$ pulse length = 10.75 μs, diffusion time Δ = 200 ms, gradient-pulse duration δ = 4 ms, and gradient-pulse strength G incremented in 10 steps from 0.003 to 0.283 T/m, with the maximum strength of 0.3 T/m allowed for this instrument. Based on the relationship between the signal S and D, i.e., S is proportional to $(\gamma G\delta)^2 D(\Delta - \delta/3)$, in which γ is the magnetogyric ratio of the ^{31}P nucleus, the spectral peaks of α-, β-, and γ-phosphates were integrated, and the natural logarithms of the integrals (ln S) were graphed versus G^2. The observed ATP diffusion constants were deduced from the slopes of the linear graphs, i.e., D = slope/$[-\gamma^2\delta^2(\Delta - \delta/3)]$. We found that it was necessary to use peak integrals instead of peak heights for sufficiently accurate data fitting (with correlation coefficients of $R \approx 0.99$). The binding curve of ATP–HSA or ATP–BSA was also analyzed using a Scatchard plot,[42] from which the apparent K and n were obtained.

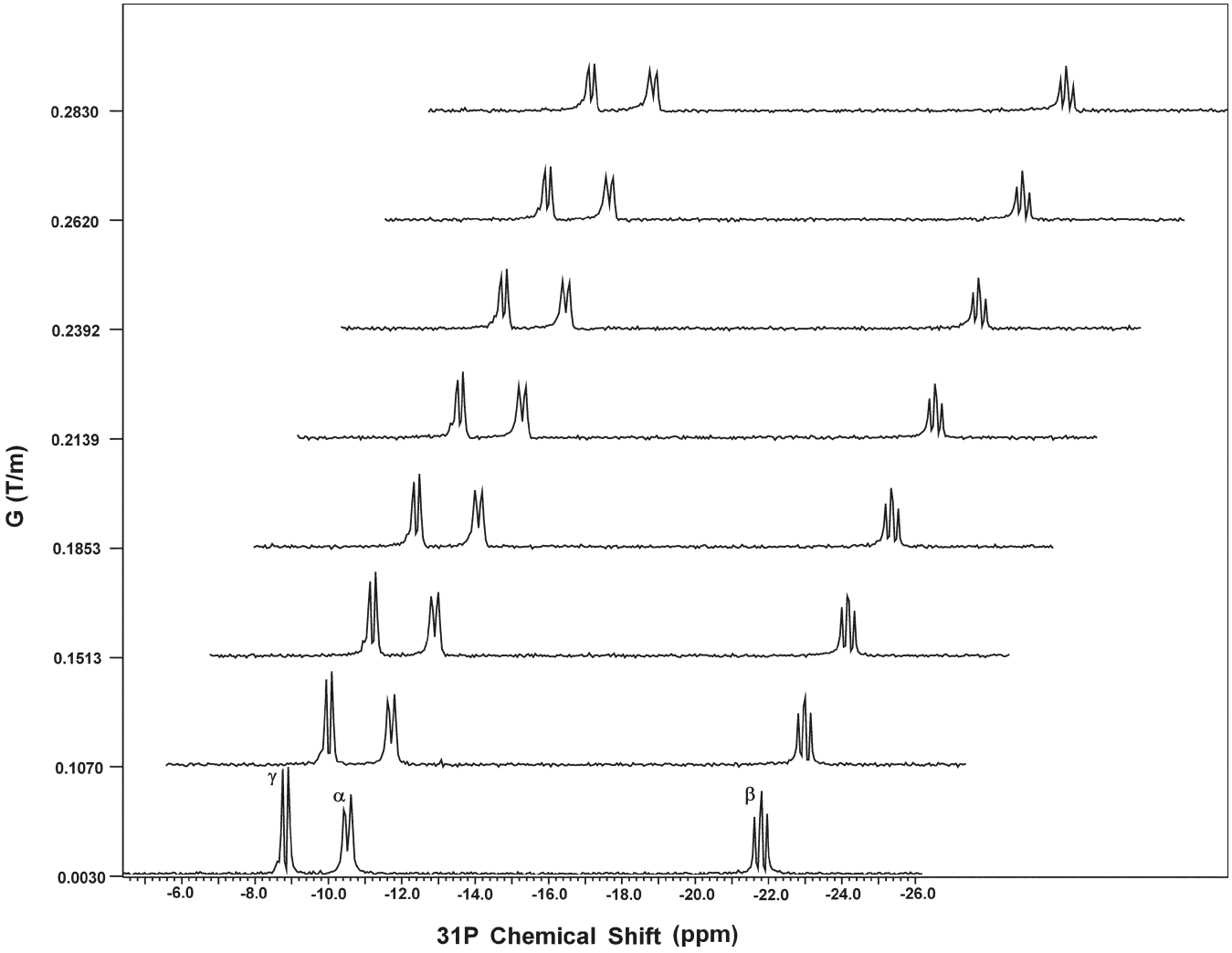
Results and discussion

^{31}P spectral features

Figure 1 shows a representative ^{31}P NMR-PFG diffusion spectrum of ATP–HSA, obtained at 25 °C and pH 5.5. The α-, β-, and γ-peaks of ATP are well-resolved. Across the slices, the peaks decay steadily under increased PFG strength (G) along the y axis. In Fig. 2, the natural logarithms of these peak integrals (ln S) are depicted as a function of G^2. It shows that the linear declines of the α-, β-, and γ-integrals are identical. In practice, D_{obs} can be derived from the line representing all three peaks.

Because of the lower sensitivity of the ^{31}P nucleus over that of the ^{1}H nucleus, ^{31}P-diffusion measurements often need more acquisition transients, and thus longer experimental time as compared with the conventional ^{1}H-diffusion measurements. However, there are several advantages in utilizing ^{31}P diffusions for our purpose. (*i*) In a ^{31}P-diffusion

Fig. 1. A representative ^{31}P NMR - pulsed-field-gradient (PFG) diffusion spectrum of adenosine 5′-triphosphate (ATP) – human serum albumin (HSA), acquired at 25 °C. The spectral slices show decays of α-, β-, and γ-peaks under increased PFG strength (*G*, T/m).



Can. J. Chem. Downloaded from www.nrcresearchpress.com by Renmin University of China on 09/02/12
For personal use only.

spectrum, the ATP peaks are exclusive and well-resolved, so the peak decays can be adequately described as a function of PFG strength. In contrast, in a ^{1}H-diffusion spectrum of ATP–HSA or ATP–BSA, the ^{1}H peaks of ATP would be severely overlapped by the overwhelming protein peaks, thus making the ATP data analysis rather difficult. (*ii*) The effect of phosphate spin-lattice relaxation (T_1) on the ^{31}P-diffusion experiment can be neglected. Unlike the spin-echo (SE) pulse sequence, which involves spin-spin relaxation (T_2), in the SSE experiment, the spin relaxation depends primarily on T_1 rather than T_2 relaxation.[43] However, as we verified during our investigation, the T_1 times of the α-, β-, and γ-phosphates of ATP–HSA and ATP–BSA samples were in the range of 1 to 2 s, and they were not affected greatly by varying ATP concentrations over 10–75 mmol/L. These T_1s are much longer with respect to the diffusion time (Δ = 200 ms) used in the SSE pulse sequence, so the signal attenuation caused by phosphate relaxations is not significant. With these spectral features, we are convinced that the observed diffusion constants can be accurately derived from our ^{31}P-diffusion experiments.

ATP concentration dependence

Various ^{31}P-diffusion spectra were acquired for ATP, ATP–HSA, and ATP–BSA samples under varied ATP concentrations and in the presence or absence of HSA and BSA. The D_{obs} for ATP were deduced from the spectra. These D_{obs} values were found to be strongly dependent on the ATP and protein concentrations. For instance, the obtained D_{obs} = 2.8×10^{-10} m^2/s for a sample containing 25 mmol/L ATP, $D_{obs} = 2.0 \times 10^{-10}$ m^2/s for 25 mmol/L ATP in 1 mmol/L BSA, and $D_{obs} = 0.7 \times 10^{-10}$ m^2/s for 25 mmol/L ATP in 5 mmol/L HSA or BSA. A comparison of these results indicates that the decrease in D_{obs} can be attributed to increased sample viscosity when protein content is increased, as well as the effect of ATP binding to HSA or BSA.

Figure 3 depicts the D_{obs} variations of ATP-only, ATP–HSA, and ATP–BSA samples under different ATP concentrations. As expected, the diffusion constants of ATP in ATP-only samples are larger than that in ATP–HSA and ATP–BSA over the entire concentration range because of the higher viscosity in HSA- and BSA-containing samples as well as ATP binding to the albumin. However, when ATP

Can. J. Chem. Downloaded from www.nrcresearchpress.com by Renmin University of China on 09/02/12
For personal use only.

Fig. 2. Linear relationships of the natural logaritm of the signal (ln S) and pulsed-field-gradient strength $(G)^2$, obtained from the integrals of α- (○), β- (□), and γ-peaks (Δ) in an adenosine 5′-triphosphate (ATP) – human serum albumin (HSA) diffusion spectrum (Fig. 1). The observed diffusion constant (D_{obs}) can be derived from the line (●) representing all peaks.

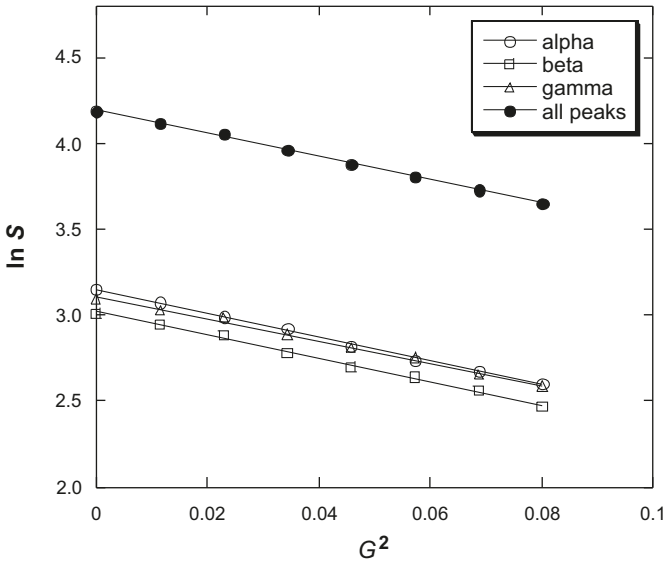
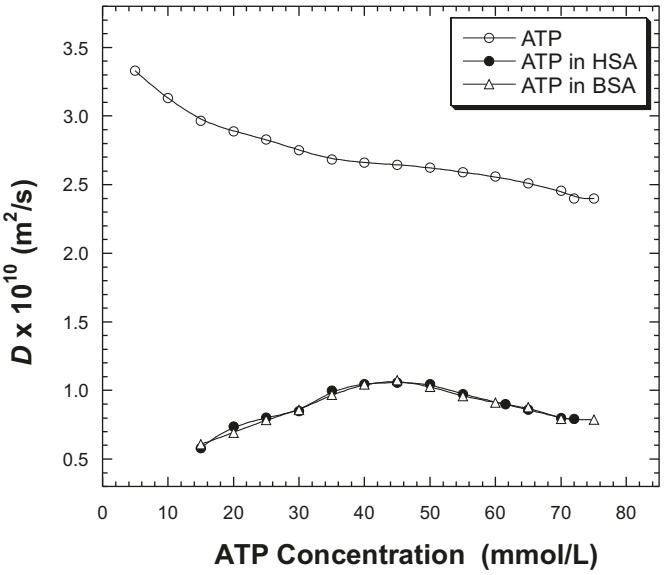


Fig. 3. The observed diffusion constants of adenosine 5′-triphosphate (ATP) (○), ATP – human serum albumin (HSA) (●), and ATP – bovine serum albumin (BSA) (△) obtained from ^{31}P NMR - pulsed-field-gradient (PFG) diffusions under varied ATP concentrations, with 5 mmol/L HSA or BSA, and at pH 5.5 and 25 °C.



concentrations were increased, a steady decrease of ATP self-diffusion was found for ATP-only samples. For instance, the NMR-derived ATP diffusion constants are reduced by ~20% when ATP was increased from 5 mmol/L (at which D_{obs} = 3.3×10^{-10} m²/s) to 75 mmol/L (at which $D_{obs} = 2.6 \times 10^{-10}$ m²/s). We believe that this is mainly due to the steadily increased ATP self-association at increased ATP concentration, resulting in a slower ATP diffusion rate. According to Sigel and Griesser,[44] the ATP self-association is pH-dependent with the self-association constant (K_{SA}) being approximately 2 $(mol/L)^{-1}$ at pH 5.5, and the percentage of ATP self-association also depends on ATP concentration, therefore, when increasing ATP concentration to ~75 mmol/L in a D_2O solution, the ATP monomer decreased from 100% to roughly 80% and the remaining 20% was mainly in the dimer state with a slight amount (~2%–3%) of the trimer. We believe that in this case, the D_{obs} can be assumed as a weighted average of the diffusion constants for the ATP monomer (D_1), dimer (D_2), and trimer (D_3), i.e., $D_{obs} = X_1D_1 + X_2D_2 + X_3D_3$, with $D_1 > D_2 > D_3$ and $X_1 + X_2 + X_3 = 1$. Therefore, as the fraction of monomer (X_1) decreases, but fractions of dimer (X_2) and trimer (X_3) increase under increased ATP concentrations, D_{obs} would decrease. Clearly, our diffusion results for ATP-only samples in Fig. 3 are consistent with the ATP self-association results of Sigel and Griesser.[44]

The D_{obs} curves of ATP–HSA and ATP–BSA in Fig. 3 were obtained from samples with varied ATP (15–75 mmol/L) but fixed 5 mmol/L HSA or BSA (i.e., [ATP]/[protein] = 3–15). We found that if ATP concentration was further lowered to 5–10 mmol/L, at which [ATP]/[protein] = 1–2, the resulting diffusion spectrum would have poor resolution and intensity, apparently because of ATP binding to the high-affinity sites of HSA or BSA under such a low [ATP]/[protein] ratio. In this case, an accurate diffusion constant was not obtainable.

In Fig. 3, the two curves of ATP–HSA and ATP–BSA are almost overlapped. This suggests that the ATP affinities on HSA and BSA are nearly the same. In particular, over the 15–45 mmol/L range (i.e., [ATP]/[protein] = 3–9), the D_{obs} of both ATP–HSA and ATP–BSA are increased under increased ATP concentrations. Such a trend variation is sharply contrary to that of ATP-only samples, characterizing the ATP binding to HSA or BSA. It indicates that, when the ATP concentration increases, the population of free ATP is increased more than that of the bound ATP. The curves of ATP–HSA and ATP–BSA reach a maximum at ~45 mmol/L ATP, suggesting that the binding of ATP to HSA or BSA is saturated around this point. Further increases of ATP result in steadily reduced D_{obs}, similar to that observed for ATP-only samples. This is understandable because increasing ATP concentration beyond the binding saturation of ATP–HSA or ATP–BSA simply means more addition of excess free ATP, which would further increase the ATP self-association and reduce its observed diffusion, as we determined previously.

Finally, it should be noted that the D_{obs} variations of blank ATP, ATP–HSA, and ATP–BSA samples (Fig. 3) are also consistent with what we have observed for blank guanosine 5′-triphosphate (GTP) and GTP–BSA or adesnosine 5′-monophosphate (AMP) and AMP–BSA (data not shown). These results support the conclusion that the nucleotides exhibit similar self-association, self-diffusion, and serum-albumin-binding properties.

The Scatchard plot

We analyzed the binding of ATP to HSA or BSA using a Scatchard equation[42]

$$[1] \qquad \frac{v}{L_f} = nK - Kv$$

where n is the number of binding sites on protein HSA or BSA, K is the apparent binding constant, v is the moles of

Can. J. Chem. Downloaded from www.nrcresearchpress.com by Renmin University of China on 09/02/12
For personal use only.

bound ligand (ATP) per mole of protein and it ranges from 0 to n, and L_f is the free ligand concentration. A set of L_f for eq. [1] was derived by

$$[2] \qquad L_f = L_0 X_f = L_0(1 - X_b)$$

where L_0 is the initial ligand concentration and X_f and X_b are the molar fractions of free and bound ligand, respectively. The X_b values in eq. [2] were evaluated from the diffusion data of ATP–HSA and ATP–BSA (shown in Fig. 3), i.e.,

$$[3] \qquad X_b = \frac{D_{max} - D_{obs}}{D_{max} - D_{min}}$$

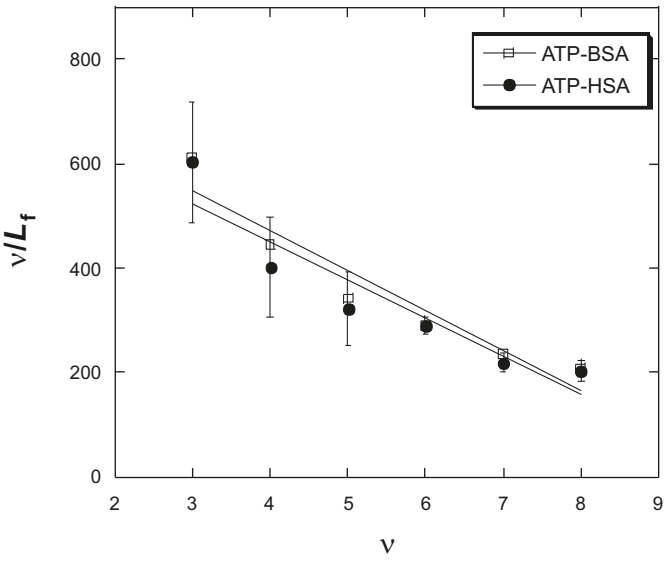
For this X_b calculation, D_{min} ($\approx 0.38 \times 10^{-10}$ m^2/s) was assessed by extrapolating the ATP–HSA or ATP–BSA curve to [ATP] = 0, D_{max} ($\approx 1.06 \times 10^{-10}$ m^2/s) was determined using the curve maximum in Fig. 3, and D_{obs} is the diffusion constant of either ATP–HSA or ATP–BSA observed prior to the binding saturation.

Figure 4 shows a Scatchard plot, i.e., ν/L_f vs ν for ATP–HSA and ATP–BSA, with the error bars assessed from the uncertainty in the D_{obs} measurements of ATP–HSA samples. In general, the data over the ν = 4–8 range show a reasonably good linear relationship, although the ν/L_f value at ν = 3 is overly high. The larger deviation of the latter may be attributed to several factors. First, ligand ATP has a stronger binding tendency at the lower ratio of [ATP]/[HSA] or [ATP]/[BSA], leading to reduced free ATP concentration (L_f) and thus a larger ν/L_f value. Second, the spectral sensitivity or signal-to-noise ratio in the ^{31}P NMR diffusion experiments was significantly reduced when the ATP concentration in the ATP–HSA or ATP–BSA system was relatively lower, inducing some uncertainty in the determination of D_{obs}, which in turn contributed to the larger error in the ν/L_f calculation.

In Fig. 4, we used all the data points for the linear fitting. From the slopes of two straight lines, the apparent binding constants (K = –slope) were derived as 73.60 (mol/L)$^{-1}$ (ATP–HSA) and 76.90 (mol/L)$^{-1}$ (ATP–BSA). The two values are close, consistent with the nearly overlapping curves in Fig. 3, and are averaged to 75.25 (mol/L)$^{-1}$. From the y intercepts, the number of binding sites (n = intercept/K) was derived as $n \approx 10$ for both samples. In fact, the number of ATP binding sites on serum albumin, derived from our ^{31}P NMR diffusion study, is comparable to the number of sites for the binding of alkanones (heptanone, octanone, or nonanone) to BSA ($n \approx$ 6–8) and for the binding of lipoic acid to BSA ($n \approx 10$), which were determined earlier by ^{1}H NMR.[28,45]

The low affinity binding of ATP to serum albumin may have its biological relevance. Albumin accounts for about 60% of the total protein in blood serum with an average of 42 g/L or 6.3×10^{-4} mol/L in concentration,[46] whereas the ATP concentration in human plasma is roughly 10^{-6} mol/L.[47] Assuming these quantities of albumin and ATP are available for their binding interaction, and considering that each albumin molecule is capable of binding 10 ATP molecules with an apparent binding constant of 75.25 (mol/L)$^{-1}$, we estimate that in theory about 3.2×10^{-7} mol/L of ATP, or nearly one-third of its total in blood plasma, could be weakly bound to serum albumin. Such binding might be significant for regulating the delivery, distribution, and activity of ATP in blood plasma, although the actual binding extent can be varied depending on the conditions and complexity in the biological systems.

Fig. 4. The Scatchard plots of adenosine 5′-triphosphate (ATP) – human serum albumin (HSA, ●) and ATP – bovine serum albumin (BSA, □) derived from the diffusion data in Fig. 3. The error bars are assessed from the uncertainty in the observed diffusion constant (D_{obs}) measurements of the ATP–HSA samples.



Effect of pH or temperature

Effect of pH or temperature on ATP affinity was verified by our ^{31}P NMR diffusion measurements of ATP–HSA, conducted under a fixed amount of ATP (30 mmol/L) and HSA (5 mmol/L), but varied pH or temperature.

Figure 5 shows the D_{obs} of ATP–HSA and ATP-only samples as a function of pH. Over the pH 5.0–9.0 range, variation of pH has no significant effect on the diffusion constants of ATP–HSA. The relatively low D_{obs} (~0.8×10^{-10} to 0.85×10^{-10} m^2/s) in this range are indicative of ATP binding on serum albumin. However, the observed diffusion constants are drastically increased in the pH < 5.0 and pH > 9.0 ranges ($D_{obs} \approx 1.4 \times 10^{-10}$ to 1.45×10^{-10} m^2/s at pH 4.0 or pH 11.0). This suggests that the ATP affinity on serum albumin is significantly reduced at low or high pH, apparently because of the pH-induced structural change of serum albumin or protein aggregation.[48] It is believed that serum albumin is capable of multiple pH-dependent transitions between different structural states (expanded ↔ fast ↔ normal ↔ basic ↔ aged), with a mid-point pH of the transition around 2.3, 4.3, 8.0, and 10.0, respectively.[49] Thus, in our experimental range of pH 5.0–9.0, serum albumin is in its normal and (or) basic forms. Our diffusion data demonstrates that only these two structural forms have the regular and identical capacity for low-affinity binding of ATP. It can also be noticed that the pH effect on the D_{obs} of ATP–HSA is quite distinctive as compared with ATP-only samples. The latter have a $D_{obs} \approx 2.7 \times 10^{-10}$ to 2.8×10^{-10} m^2/s over the entire pH range. That is, pH just slightly affects the self-diffusion of ATP-only samples. This outcome is expected and is consistent with the earlier ^{1}H-diffusion studies of ATP.[50,51]

Can. J. Chem. Downloaded from www.nrcresearchpress.com by Renmin University of China on 09/02/12
For personal use only.

Fig. 5. ^{31}P NMR - pulsed-field-gradient (PFG) diffusion constants of adenosine 5′-triphosphate (ATP, ○) and ATP – human serum albumin (HSA, ●) measured using 30 mmol/L ATP samples in the presence or absence of 5 mmol/L HSA at 25 °C and at varied pH.

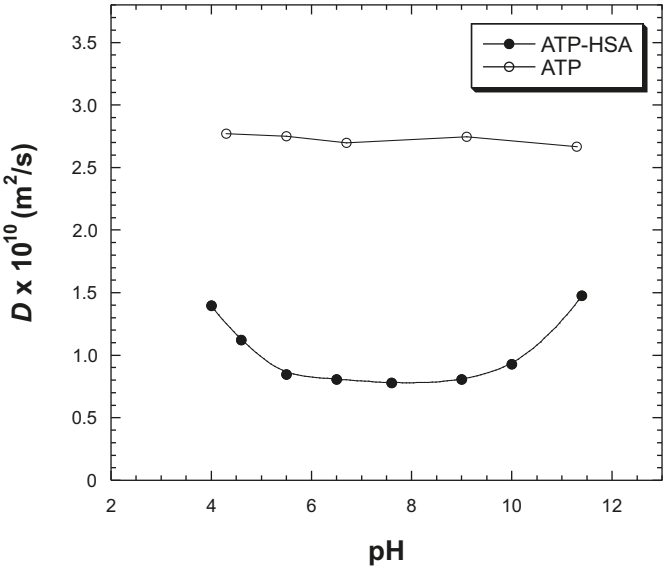


Fig. 6. ^{31}P NMR - pulsed-field-gradient (PFG) diffusion constants of adenosine 5′-triphosphate (ATP) – human serum albumin (HSA) measured using samples of 30 mmol/L ATP + 5 mmol/L HSA at pH 5.5 and at varied temperature.

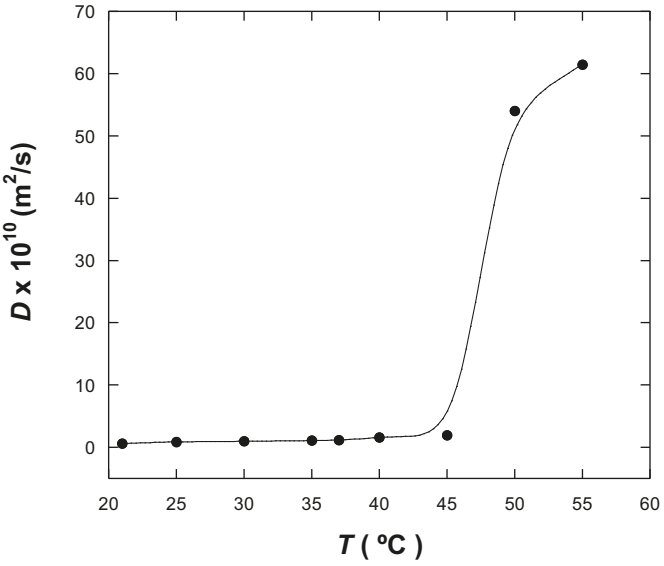


Figure 6 shows the diffusion constants of ATP–HSA as function of temperature. From 21 °C (at which D_{obs} = 0.60 × 10^{-10} m^2/s) to 45 °C (at which D_{obs} = 1.93 × 10^{-10} m^2/s), the diffusion constants steadily increased at elevated temperature. However, further heating above 45 °C lead to a drastic increase of D_{obs}. According to the Stokes–Einstein equation, $D = kT/(6\pi\eta a)$, which strictly applies to spherical particles, the diffusion constant (D) is directly proportional to temperature (T) and inversely related to viscosity (η) and dynamical size (a) of the species.[43] We believe that a steady increase of sample diffusion in the 21–45 °C range is mainly a direct consequence of temperature elevation and (or) viscosity lowering. Furthermore, the D_{obs} of ATP–HSA is a weighted average of bound ATP (D_b) and free ATP (D_f), i.e., $D_{obs} = D_bX_b + D_fX_f$. Therefore, a drastic increase in the diffusion constant over the T > 45 °C range can be attributed to the heat-induced conformation change, degradation, or aggregation of serum albumin,[52] all of which may significantly contribute to the ATP dissociation from HSA. It has been found that increasing temperature to ~50 °C results in an unfolding of the native serum albumin, i.e., a reversible separation of its structure domains I and II, while further increasing temperature to ~70 °C leads irreversibly to its complete denaturation, with an averaged melting temperature (T_m) around 63 °C.[53,54] Our result here indicates that even prior to the complete thermodenaturation, the unfolding of serum albumin in the ~45–60 °C range already causes a dramatic reduction of its ATP affinity.

ATP binding in ternary systems

Some other ligands may compete with ATP for binding to serum albumin. For instance, Bauer et al.[24] reported that the presence of amphiphilic fatty acids, such as palmitate and stearate, could reduce the ATP binding to BSA, and vice versa. Takeda et al.[9] also found that the Cl^- ion strongly inhibited the formation of a 1:1 complex of ATP–BSA; they suggested that ATP might compete with Cl^- for one high-affinity site on BSA. To verify whether the current ^{31}P NMR diffusion method is also effective for identifying binding competition, we did some preliminary measurements for ATP (5 mmol/L) + BSA (1 mmol/L) samples in the absence or presence of heptanone (30 mmol/L), NaCl (100 mmol/L), or adenosine 5′-diphosphate (ADP, 12 mmol/L). The following D_{obs} were obtained: 1.96 × 10^{-10} m^2/s (ATP–BSA), 1.95 × 10^{-10} m^2/s (ATP–BSA–heptanone), 2.02 × 10^{-10} m^2/s (ATP–BSA–NaCl), and 2.88 × 10^{-10} m^2/s (ATP–BSA–ADP). These results suggest that (*i*) the flavor compound heptanone, which has 7–8 low-affinity sites on serum albumin according to Jung et al.,[28] is a noncompetitive binding ligand with respect to ATP, (*ii*) Cl^- ion and ATP are essentially noncompetitive as well regarding their weak-affinity binding to serum albumin, although they can compete for one high-affinity site according to Takeda et al.,[9] and (*iii*) ADP is capable of strongly competing with ATP for binding on serum albumin, leading to a significant decrease of ATP binding and to a related D_{obs} increase in the ternary sample.

In conclusion, our ^{31}P NMR-PFG diffusion study is able to provide valuable information, including the characteristic binding parameters, i.e., apparent binding constant and number of binding sites of ATP on serum albumin, and dependences of ATP binding on various factors such as pH, temperature, and other ligands. These results are important for elucidating the low-affinity interaction of ATP with serum albumin and assessing its possible effect on related bioprocesses. It is also expected that the current NMR approach can be readily applied to the investigation of other nucleotide–protein binding interactions.

Acknowledgement

This research was supported by Grant No. S06GM060314 from the National Institutes of Health / National Institute of General Medical Sciences, Bethesda, Maryland, to Z.S.

Can. J. Chem. Downloaded from www.nrcresearchpress.com by Renmin University of China on 09/02/12
For personal use only.

References

(1) Curry, S. *Vox Sang.* **2002**, *83* (Suppl. 1), 315. doi:10.1111/j.1423-0410.2002.tb05326.x.
(2) Trigatti, B. L.; Gerber, G. E. *Biochem. J.* **1995**, *398* (1), 155.
(3) Du, Z.; Patel, T. B. *Arch. Biochem. Biophys.* **2003**, *415* (2), 221. doi:10.1016/S0003-9861(03)00263-7.
(4) Michel, A. D.; Xing, M.; Humphrey, P. P. *Br. J. Pharmacol.* **2001**, *132* (7), 1501. doi:10.1038/sj.bjp.0703968.
(5) Ponte, C. G.; Oliveira, C. F.; Suarez-Kurtz, G. *Braz. J. Med. Biol. Res.* **1997**, *30* (5), 675. doi:10.1590/S0100-879X1997000500017.
(6) Kragh-Hansen, U. *Pharmacol. Rev.* **1981**, *33* (1), 17.
(7) Sudlow, G.; Birkett, D. J.; Wade, D. N. *Mol. Pharmacol.* **1976**, *12* (6), 1052.
(8) Sudlow, G.; Birkett, D. J.; Wade, D. N. *Mol. Pharmacol.* **1975**, *11* (6), 824.
(9) Takeda, S.; Miyauchi, S.; Nakayama, H.; Kamo, N. *Biophys. Chem.* **1997**, *69* (2–3), 175. doi:10.1016/S0301-4622(97)00084-7.
(10) Oida, T. *J. Biochem.* **1986**, *100* (1), 99.
(11) Ishida, S.; Kinoshita, M.; Sakiya, Y.; Taira, Z.; Ichikawa, T. *Chem. Pharm. Bull. (Tokyo)* **1992**, *40* (1), 275. doi:10.1248/cpb.40.275.
(12) Hage, D. S.; Noctor, T. A.; Wainer, I. W. *J. Chromatogr. A* **1995**, *693* (1), 23. doi:10.1016/0021-9673(94)01009-4.
(13) Sun, P.; Hoops, A.; Hartwick, R. A. *J. Chromatogr. B Biomed. Appl.* **1994**, *661* (2), 335. doi:10.1016/0378-4347(94)00372-6.
(14) Meierhofer, T.; van den Elsen, J. M. H.; Cameron, P. J.; Muñoz-Berbel, X.; Jenkins, A. T. A. *J. Fluoresc.* **2010**, *20* (1), 371. doi:10.1007/s10895-009-0522-7.
(15) Wu, Q. H.; Wang, C.; Zhang, Z. H.; Zhang, M. Y.; Song, S. J.; Wang, Z. *Spectrosc. Spectr. Anal.* **2009**, *29* (4), 1060. PMID: 19626903.
(16) He, W. Y.; Chen, H. J.; Sheng, F. L.; Yao, X. J. *Spectrochim. Acta A Mol. Biomol. Spectrosc.* **2009**, *74* (2), 427. doi:10.1016/j.saa.2009.06.044.
(17) Jurasekova, Z.; Marconi, G.; Sanchez-Cortes, S.; Torreggiani, A. *Biopolymers* **2009**, *91* (11), 917. doi:10.1002/bip.21278.
(18) Guo, S.; Shi, X.; Yang, F.; Chen, L.; Meehan, E. J.; Bian, C.; Huang, M. *Biochem. J.* **2009**, *423* (1), 23. doi:10.1042/BJ20090913.
(19) Daneshgar, P.; Moosavi-Movahedi, A. A.; Norouzi, P.; Ganjali, M. R.; Madadkar-Sobhani, A.; Saboury, A. A. *Int. J. Biol. Macromol.* **2009**, *45* (2), 129. doi:10.1016/j.ijbiomac.2009.04.011.
(20) Chen, Z. Z.; Feng, F.; Yang, W. J.; Liang, W. J.; Li, R. J.; Wang, C. *Spectrosc. Spectr. Anal.* **2008**, *28* (7), 1612. PMID: 18844172.
(21) Sinha, S. S.; Mitra, R. K.; Pal, S. K. *J. Phys. Chem. B* **2008**, *112* (16), 4884. doi:10.1021/jp709809b.
(22) Guo, M.; Lu, W. J.; Li, M. H.; Wang, W. *Eur. J. Med. Chem.* **2008**, *43* (10), 2140. doi:10.1016/j.ejmech.2007.11.006.
(23) Maiti, T. K.; Ghosh, K. S.; Debnath, J.; Dasgupta, S. *Int. J. Biol. Macromol.* **2006**, *38* (3–5), 197. doi:10.1016/j.ijbiomac.2006.02.015.
(24) Bauer, M.; Baumann, J.; Trommer, W. E. *FEBS Lett.* **1992**, *313* (3), 288. doi:10.1016/0014-5793(92)81211-4.
(25) Gelos, M.; Hinderberger, D.; Welsing, E.; Belting, J.; Schnurr, K.; Mann, B. *Int. J. Colorectal Dis.* **2010**, *25* (1), 119. doi:10.1007/s00384-009-0777-0.
(26) da Silveira, V. C.; Caramori, G. F.; Abbott, M. P.; Gonçalves, M. B.; Petrilli, H. M.; da Costa Ferreira, A. M. *J. Inorg. Biochem.* **2009**, *103* (10), 1331. doi:10.1016/j.jinorgbio.2009.05.015.
(27) Luo, R.-S.; Liu, M.-L.; Mao, X.-A. *Spectrochim. Acta A Mol. Biomol. Spectrosc.* **1999**, *55* (9), 1897. doi:10.1016/S1386-1425(99)00052-9.
(28) Jung, D. M.; De Ropp, J. S.; Ebeler, S. E. *J. Agric. Food Chem.* **2002**, *50* (15), 4262. doi:10.1021/jf020229t.
(29) Fanali, G.; Pariani, G.; Ascenzi, P.; Fasano, M. *FEBS J.* **2009**, *276* (8), 2241. doi:10.1111/j.1742-4658.2009.06952.x.
(30) Henoumont, C.; Vander Elst, L.; Laurent, S.; Muller, R. N. *J. Biol. Inorg. Chem.* **2009**, *14* (5), 683. doi:10.1007/s00775-009-0481-0.
(31) Bergeron, S. J.; Henry, I. D.; Santini, R. E.; Aghdasi, A.; Raftery, D. *Magn. Reson. Chem.* **2008**, *46* (10), 925. doi:10.1002/mrc.2275.
(32) Shikii, K.; Sakurai, S.; Utsumi, H.; Seki, H.; Tashiro, M. *Anal. Sci.* **2004**, *20* (10), 1475. doi:10.2116/analsci.20.1475.
(33) Kitamura, K.; Kume, M.; Yamamoto, M.; Takegami, S.; Kitade, T. *J. Pharm. Biomed. Anal.* **2004**, *36* (2), 411. doi:10.1016/j.jpba.2004.06.027.
(34) Botta, M.; Quici, S.; Pozzi, G.; Marzanni, G.; Pagliarin, R.; Barra, S.; Geninatti Crich, S. *Org. Biomol. Chem.* **2004**, *2* (4), 570. doi:10.1039/b313677a.
(35) Cao, B.; Endsley, S.; Andersen, N. H. *Bioorg. Med. Chem.* **2003**, *11* (1), 69. doi:10.1016/S0968-0896(02)00324-3.
(36) Ji, Z. S.; Li, C. G.; Mao, X. A.; Liu, M. L.; Hu, J. M. *Chem. Pharm. Bull. (Tokyo)* **2002**, *50* (8), 1017. doi:10.1248/cpb.50.1017.
(37) Farias, M., III; Gorman, M. W.; Savage, M. V.; Feigl, E. O. *Am. J. Physiol. Heart Circ. Physiol.* **2005**, *288* (4), H1586. doi:10.1152/ajpheart.00983.2004.
(38) Gorman, M. W.; Rooke, G. A.; Savage, M. V.; Jayasekara, M. P.; Jacobson, K. A.; Feigl, E. O. *Am. J. Physiol. Heart Circ. Physiol.* **2010**, *299* (6), H1981. doi:10.1152/ajpheart.00611.2010.
(39) Jakob, U.; Scheibel, T.; Bose, S.; Reinstein, J.; Buchner, J. *J. Biol. Chem.* **1996**, *271* (17), 10035. doi:10.1074/jbc.271.17.10035.
(40) Segev, O.; Columbus, I.; Ashani, Y.; Cohen, Y. *J. Org. Chem.* **2005**, *70* (1), 309. doi:10.1021/jo0485942.
(41) Kagan, G.; Li, W.; Hopson, R.; Williard, P. G. *Org. Lett.* **2009**, *11* (21), 4818. doi:10.1021/ol9019106.
(42) Scatchard, G. *Ann. N. Y. Acad. Sci.* **1949**, *51* (4), 660. doi:10.1111/j.1749-6632.1949.tb27297.x.
(43) Johnson, C. S., Jr. *Progr. NMR Spectr.* **1999**, *34*, 203.
(44) Sigel, H.; Griesser, R. *Chem. Soc. Rev.* **2005**, *34* (10), 875. doi:10.1039/b505986k.
(45) Schepkin, V.; Kawabata, T.; Packer, L. *Biochem. Mol. Biol. Int.* **1994**, *33* (5), 879.
(46) Sadler, P. J.; Tucker, A. *Eur. J. Biochem.* **1992**, *205* (2), 631. doi:10.1111/j.1432-1033.1992.tb16821.x.
(47) Gorman, M. W.; Feigl, E. O.; Buffington, C. W. *Clin. Chem.* **2007**, *53* (2), 318. doi:10.1373/clinchem.2006.076364.
(48) Tominaga, T. T.; Yushmanov, V. E.; Borissevitch, I. E.; Imasato, H.; Tabak, M. *J. Inorg. Biochem.* **1997**, *65* (4), 235. doi:10.1016/S0162-0134(96)00137-7.
(49) Sadler, P. J.; Tucker, A. *Eur. J. Biochem.* **1993**, *212* (3), 811. doi:10.1111/j.1432-1033.1993.tb17722.x.
(50) Song, Z.; Parker, K. J.; Enoh, I.; Zhao, H.; Olubajo, O. *Magn. Reson. Chem.* **2010**, *48* (2), 123.
(51) Jiang, L.; Mao, X. A. *Spectrochim. Acta A Mol. Biomol. Spectrosc.* **2001**, *57* (8), 1711. doi:10.1016/S1386-1425(01)00442-5.
(52) Jordan, G. M.; Yoshioka, S.; Terao, T. *J. Pharm. Pharmacol.* **1994**, *46* (3), 182. doi:10.1111/j.2042-7158.1994.tb03774.x.
(53) Rezaei-Tavirani, M.; Moghaddamnia, S. H.; Ranjbar, B.;

Amani, M.; Marashi, S. A. *J. Biochem. Mol. Biol.* **2006**, *39* (5), 530. doi:10.5483/BMBRep.2006.39.5.530.

(54) Picó, G. *Biochem. Mol. Biol. Int.* **1995**, *36* (5), 1017.

Can. J. Chem. Downloaded from www.nrcresearchpress.com by Renmin University of China on 09/02/12
For personal use only.

Ring-opening polymerization of *rac*-lactide and ε-caprolactone using zinc and calcium salicylaldiminato complexes

Joshua B. L. Gallaway, Justin R. K. McRae, Andreas Decken, and Michael P. Shaver

Can. J. Chem. Downloaded from www.nrcresearchpress.com by Renmin University of China on 09/02/12
For personal use only.

Abstract: Tridentate Schiff base complexes of zinc and calcium were prepared and tested in the ring-opening polymerization of ε-caprolactone and *rac*-lactide to generate biodegradable polymeric materials from biocompatible metals. Alteration of the pendant donor arm attached to the imine backbone provides some control over catalyst composition and polymerization activity. Complexes of the formula [ONN]ZnN$(SiMe_3)_2$, where [ONN] = 2-(*N*-donor arm-imine)[4,6-di(*tert*-butyl)phenoxide], were isolated with ethyldimethylamine, ethylpiperidine, and ethylmorpholine substituents, while disproportionation led to the isolation of $[ONN]_2Zn$ complexes with methylpyridine, quinoline, and ethyldiisopropylamine derivatives, two of which were crystallographically characterized. Calcium complexes were more stable and novel [ONN]CaN$(SiMe_3)_2$ complexes with ethylpiperidine and ethyldiisopropylamine substituents were reported. Zinc and calcium catalysts coordinated to a single tridentate ligand were effective at initiating the polymerization of ε-caprolactone, but did not control the polymerizations, whereas the bis(ligand) complexes produced no polymer. These catalysts were effective at controlling the polymerization of *rac*-lactide. Coordinatively saturated complexes inhibit the polymerization, while initiation from either the amido or ligand alkoxide functionalities produces poly(lactic acid) with low polydispersities.

Key words: lactide, caprolactone, zinc, calcium, ring opening polymerization.

Résumé : On a préparé des complexes de zinc et de calcium avec des bases de Schiff tridentates et on a évalué la possibilité de les utiliser dans les polymérisations par ouverture de cycle de la ε-caprolactone et du *rac*-lactide conduisant à des matériaux polymères biodégradables à partir de produits métalliques biodégradables. L'altération du bras donneur pendant attaché au squelette de l'imine permet d'avoir un certain contrôle sur la composition du catalyseur et son activité dans la polymérisation. On a pu isoler des complexes de formule [ONN]ZnN$(SiMe_3)_2$ (dans lesquels [ONN] = 2-(imine avec bras *N*-donneur)[4,6-di(*tert*-butyl)phénolate] portant des substituants éthyldiméthylamine, éthylpipéridine et éthylmorpholine alors qu'une disproportionation permet d'isoler les complexes $[ONN]_2Zn$ avec les dérivés de la méthylpyridine, la quinoléine et l'éthyldiisopropylamine, dont deux ont été caractérisés par cristallographie. Les complexes du calcium sont plus stables et on a isolé pour la première fois les nouveaux complexes [ONN]CaN$(SiMe_3)_2$ avec des substituants éthylpipéridine et éthyldiisopropylamine. Les catalyseurs du zinc et du calcium ne comportant qu'une coordination à un ligand tridentate sont efficaces pour initier la polymérisation de la ε-caprolactone, mais ils ne permettent pas de contrôler les polymérisations alors que les complexes avec un bis(ligand) ne permettent pas de produire des polymères. Ces catalyseurs sont efficaces pour contrôler la polymérisation du *rac*-lactide. Les complexes à coordination saturée inhibent la polymérisation alors qu'une initiation par des groupes fonctionnels amido- ou un ligand alcoolate conduisent à la production d'acide polylactique avec de faibles polydispersités.

Mots-clés : lactide, caprolactone, zinc, calcium, polymérisation par ouverture de cycle.

[Traduit par la Rédaction]

Aliphatic poly(esters) such as poly(lactic acid) (PLA) and poly(ε-caprolactone) (PCL) have gained considerable interest in recent years because of their biodegradability and renewability.[1–4] These aliphatic polymers are also bioassimilable, as hydrolysis produces nontoxic components eliminated via the Krebs cycle as CO_2 and H_2O.[3] These poly(esters) have physical properties that can be tuned and varied during polymer processing by orientation, blending, branching, cross-linking, or plasticization, enabling the application of aliphatic poly(esters) to pharmaceuticals, microelectronics, and other fields.[5,6]

PLA is an important biodegradable polymer of high industrial potential because the lactide monomer can be acquired through the fermentation of renewable resources.[3] The most common application of PCL as a biodegradable polymer involves the development of pharmaceutical drugs such as Capronor, an implanted contraceptive delivery system.[7] PCL is synthesized from the monomer ε-caprolactone, which is

Received 23 November 2011. Accepted 21 January 2012. Published at www.nrcresearchpress.com/cjc on 4 April 2012.

J.B.L. Gallaway, J.R.K. McRae, and M.P. Shaver. Department of Chemistry, University of Prince Edward Island, 550 University Avenue, Charlottetown, PEI C1A 4P3, Canada.
A. Decken. Department of Chemistry, University of New Brunswick, P.O. Box 4400, Fredericton, NB E3B 5A3, Canada.

Corresponding author: Michael P. Shaver (email: mshaver@upei.ca).

Can. J. Chem. Downloaded from www.nrcresearchpress.com by Renmin University of China on 09/02/12
For personal use only.

traditionally produced by the Bayer–Villiger oxidation of cyclohexanone with peracids or hydrogen peroxide[8] but can also be produced from the fermentation of starch, suggesting renewability.[9]

Aliphatic poly(esters) are commonly synthesized through ring-opening polymerization (ROP) of the corresponding cyclic ester as it offers greater control over the resulting polymers.[1–4] While ROP of lactide has been accomplished with many metals, calcium and zinc are particularly promising for industrial applications, because of their low cost, high activity, and low toxicity.[10] Ligand sets supporting active zinc and calcium lactide catalysts include β-diketiminates, tris(pyrazol) hydroborates, anilido-oxazolinates, amino-bis(pyrazol)s, N-heterocyclic carbenes, heteroscorpionates, and others.[10] The best systems offer excellent conversions over a broad temperature range and polydispersity indexes (PDIs) as low as 1.1.[10]

ROP of ε-caprolactone with calcium and zinc catalysts is comparatively understudied, although simple organic amido calcium and zinc complexes, $H_2NCaOCHMe_2$ and $Zn(N(SiMe_3)_2)_2$, show high activity and poor control.[10,11] PCL synthesis is also efficiently mediated by heterobimetallic aluminum and zinc complexes with anilido-aldimine ligands[12] and some scorpionate-derived monometallic frameworks.[10]

Inspiration for this study, however, was derived from the work of Darensbourg et al.[13–16] who showed that a series of tridentate Schiff base complexes, shown in Fig. 1, of benign metals were effective in the ROP of cyclic esters. Complexes were variably effective, with pendant dimethylamine donors coordinated to calcium providing the best activity for lactide and trimethylene carbonate, whereas zinc complexes were less effective unless substituted with bulky amino acid derived ligands and used for lactide and ε-caprolactone polymerizations.

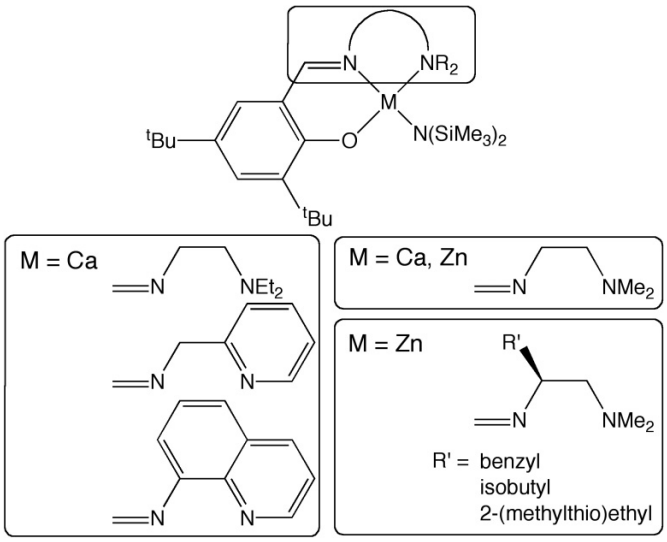
Herein we report an extension of this series of complexes, further examining the structure/activity relationships and the role the ligand plays in controlling the ROP of *rac*-lactide and ε-caprolactone. New substitutents include diisopropylamine ($N(i\text{-}Pr)_2$), piperidine (Pip), and morpholine (Mor) functionalities. Complexes substituted with a single tridentate ligand are effective catalysts for the ROP of *rac*-lactide.

Experimental

General experimental procedures

Chemicals and solvents used for the syntheses were purchased from Sigma-Aldrich, Fisher Chemicals, and Acros Chemicals. 3,5-Di-*tert*-butyl-2-hydroxybenzaldehyde (99% pure) and starting amine reagents were all used as received. Dry solvents including tetrahydrofuran (THF), toluene, pentane, and ether were obtained from an Innovative Technology glovebox system, which was fitted with a solvent purification system. The inline purification system was made up of alumina and a copper catalyst. These anhydrous solvents were degassed by three or four freeze–pump–thaw cycles, before taking them into an MBraun LABmaster sp. glovebox. Other solvents, including $CDCl_3$, C_6D_6, and hexamethyldisiloxane, were dried over CaH_2 for at least 24 h, before vacuum transferring or vacuum distilling. The MBraun glovebox was connected to a –35 °C freezer as well as [H_2O] and [O_2] analyzers. Air-sensitive reactions involving zinc and calcium

Fig. 1. Calcium and zinc Schiff base complexes previously developed for the polymerization of cyclic esters.[13–16]



were performed under an N_2 atmosphere in the glovebox or on a Schlenk line. The Schlenk reactions utilized a dual manifold Schlenk line with Kontes valves. All samples were characterized via ^1H and ^{13}C NMR spectroscopy. These spectra were obtained by running samples on a 300 MHz Bruker Avance spectrometer. Elemental analyses were performed at Guelph Analytical Laboratories. A Bruker AXS P4/SMART 1000 diffractometer was used to obtain crystallographic data. Polymerization data were obtained using a PolymerLabs GPC50 equipped with two Jordi Gel DVB mixed bed columns (300 mm × 7.8 mm). The mobile phase used in the system was HPLC grade THF and the polymer samples were dissolved in THF to create a solution for GPC analysis, at 50 °C, at a 1 mg/mL concentration, and at a 1 mL/min flow rate. Molecular weights were measured and corrected relative to styrene standards.[17]

Synthesis and characterization

Ligand frameworks

Ligands ^{NMe_2}[ONN]ME_2 (**1**), ^{Q}[ONN] (**2**), and ^{Py}[ONN] (**3**), where ^{R}[ONN] is 2-(*N*-donor arm-imine)(4,6-di(*tert*-butyl)phenoxide, were synthesized according to a literature procedure.[14]

Synthesis of $^{N(i\text{-}Pr)_2}$[ONN]$(i\text{-}Pr)_2{}^{N(i\text{-}Pr)_2}$[ONN] ***(4)***:

To a stirred solution of 3,5-di-*tert*-butyl-2-hydroxybenzaldehyde (2.51 g, 10.6 mmol) in methanol (25 mL) was added dropwise 2-(diisopropylamino) ethylamine (1.54 g, 10.6 mmol). The bright yellow solution was refluxed at 65 °C for approximately 10 h and then allowed to cool to room temperature. All volatiles were removed in vacuo to yield a bright yellow oil. The oil was dried under vacuum on the Schlenk line for 2 h and then purified by dissolving in cold pentane. The resulting solution was stored at –20 °C overnight, and the same purification process was repeated three times to give a dense yellow solid (1.37 g, 3.8 mmol, 36%). ^1H NMR ($CDCl_3$, ppm) δ:14.0 (1H, s, OH), 8.4 (1H, s, CH=N), 7.4–7.1 (2H, m, Ar–H), 3.6 (2H, t, J = 7 Hz, CH_2),

Can. J. Chem. Downloaded from www.nrcresearchpress.com by Renmin University of China on 09/02/12
For personal use only.

3.0 (2H, septet, J = 7 Hz, $CHMe_2$), 2.7 (2H, t, J = 7 Hz, CH_2), 1.5 (9H, s, $C(CH_3)_3$), 1.3 (9H, s, $C(CH_3)_3$), 1.0 (12H, d, J = 7 Hz, *i*-Pr CH_3). ^{13}C NMR ($CDCl_3$, ppm) δ: 166.3 (CH=N), 158.6, 140.0, 136.9, 126.9, 125.9, 118.1 (Ar), 61.6, 49.3, 35.2, 35.0, 34.7, 31.9, 31.8, 29.6. Elemental anal. calcd for $C_{23}H_{40}N_2O$ (%): C 76.61, H 11.18, N 7.77; found: C 76.81, H 11.11, N 7.77.

*Synthesis of ^{Pip}[ONN] (**5**):*

Ligand **5** was prepared analogously to **4**, using 3,5-di-*tert*-butyl-2-hydroxybenzaldehyde (2.56 g, 10.6 mmol), methanol (45 mL), and 4-(2-aminoethyl)piperidine (1.36 g, 10.6 mmol). This yielded a yellow powder (2.42 g, 10.6 mmol, 70%). ^{1}H NMR ($CDCl_3$, ppm) δ: 13.8 (1H, s, OH), 8.4 (1H, s, CH=N), 7.4 (1H, d, J = 2 Hz, Ar–H), 7.1 (1H, d, J = 2 Hz, Ar–H), 3.8 (2H, t, J = 7 Hz, CH_2), 2.7 (2H, t, J = 7 Hz, CH_2), 2.5 (4H, t, J = 5 Hz, CH_2), 1.6 (6H, m, CH_2), 1.5 (9H, s, $C(CH_3)_3$, 1.3 (9H, s, $C(CH_3)_3$). ^{13}C NMR ($CDCl_3$, ppm) δ: 166.75 (C=N), 158.3, 140.1, 136.9, 127.0, 126.0, 118.1 (Ar), 60.0, 57.3, 55.1, 35.4, 35.2, 34.3, 31.7, 26.2, 24.4 (CH_2). Elemental anal. calcd for $C_{22}H_{36}N_2O$ (%): C 76.69, H 10.53, N 8.13; found: C 76.90, H 10.45, N 8.10.

*Synthesis of ^{Mor}[ONN] (**6**):*

Ligand **6** was prepared analogously to **4**, using 3,5-di-*tert*-butyl-2-hydroxybenzaldehyde (2.56 g, 10.6 mmol), methanol (45 mL), and 4-(2-aminoethyl)morpholine (1.39 g, 10.6 mmol) to yield a pale yellow solid (3.82 g, 10.6 mmol, 85%). ^{1}H NMR ($CDCl_3$, ppm) δ: 13.7 (1H, s, OH), 8.4 (1H, s, CH=N), 7.4 (1H, d, J = 2 Hz, Ar–H), 7.1 (1H, d, J = 2 Hz), 3.73 (8H, t, J = 4 Hz, CH_2), 2.7 (2H, t, J = 7 Hz, CH_2), 2.5 (2H, t, J = 7 Hz, CH_2) 1.4 (9H, s, $C(CH_3)_3$), 1.3 (9H, s, $C(CH_3)_3$). ^{13}C NMR ($CDCl_3$, ppm) δ: 167.0 (C=N), 158.3, 140.2, 136.9, 127.1, 126.0, 118.1 (Ar), 67.2 (CH_2), 59.5, 57.0 (CH_2), 54.1 (CH_2), 35.2, 34.3 ($C(CH_3)_3$), 31.7, 29.6 ($C(CH_3)_3$). Elemental anal. calcd for $C_{21}H_{34}N_2O_2$ (%): C 72.79, H 9.89, N 8.08; found: C 72.84, H 9.91, N 8.15.

Zinc complexes

The complex ^{NMe_2}[ONN]ZnN$(SiMe_3)_2Me_2$ (**7**) was synthesized according to a literature procedure.[14]

*Synthesis of ^{Pip}[ONN]ZnN$(SiMe_3)_2$ (**8**):*

To a stirring solution of ^{Pip}[ONN] (2.00 g, 6.16 mmol) in THF (40 mL), a 1:1 stoichiometric ratio of $Zn(N(SiMe_3)_2)_2$ (2.38 g, 6.16 mmol) was added as a THF solution. After 2 h, the THF was removed in vacuo and the compound was isolated. To ensure complete dryness, the resulting solid was left under vacuum for several hours. To purify the solid, a pentane/toluene mixture was used to recrystallize the product. This yielded a yellow solid (1.97 g, 3.42 mmol, 58%). ^{1}H NMR ($CDCl_3$, ppm) δ: 8.2 (1H, s, CH=N), 7.4 (1H, d, J = 3 Hz, Ar–H), 6.9 (1H, d, J = 3 Hz, Ar–H), 3.7 (2H, t, J = 6 Hz, CH_2), 2.9 (2H, t, J = 6 Hz, CH_2), 2.7 (4H, t, J = 5 Hz, N–CH_2), 1.7 (6H, pentet, J = 5 Hz, CH_2), 1.5 (9H, s, $C(CH_3)_3$), 1.3 (9H, s, $C(CH_3)_3$), 0.1 (18H, s, $SiMe_3$). ^{13}C NMR ($CDCl_3$, ppm) δ: 170.1 (C=N), 167.6, 141.6, 134.7, 129.4, 128.0, 117.7 (Ar), 55.7, 55.5 (CH_2), 53.8, 52.6 (N–CH_2), 35.6, 33.8 ($C(CH_3)_3$), 31.3, 29.4 ($C(CH_3)_3$), 25.7, 23.7, 23.0 (CH_2), 5.6 ($Si(CH_3)_3$). Elemental anal. calcd for $C_{25}H_{44}N_3OSiZn$ (%): C 60.52, H 8.94, N 8.49; found: C 60.40, H 9.01, N 8.29.

*Synthesis of ^{Mor}[ONN]ZnN$(SiMe_3)_2$ (**9**):*

Complex **9** was prepared analogously to **8** using ^{Mor}[ONN] (1.01 g, 2.91 mmol), THF (40 mL), and $Zn(N(SiMe_3)_2)_2$ (1.12 g, 2.91 mmol). In contrast to **8**, **9** was mixed with 10 mL of THF and added to a stirring mixture of $Zn(N(SiMe_3)_2)_2$ in 30 mL THF. This synthesis yielded a light yellow solid (1.10 g, 1.92 mmol, 67%). ^{1}H NMR ($CDCl_3$, ppm) δ: 8.2 (1H, s, CH=N), 7.5 (1H, d, J = 3 Hz, Ar–H), 6.9 (1H, d, J = 3 Hz, Ar–H), 3.7 (4H, t, J = 6 Hz, O–CH_2), 2.9 (4H, t, J = 6 Hz, N–CH_2), 2.6 (2H, t, J = 7 Hz, CH_2), 1.9 (2H, t, J = 7 Hz, CH_2), 1.5 (9H, s, $C(CH_3)_3$), 1.3 (9H, s, $C(CH_3)_3$), 0.1 (18H, s, $SiMe_3$). ^{13}C NMR ($CDCl_3$, ppm) δ: 172.9 (C=N), 168.8, 141.7, 135.4, 130.0, 129.5, 117.2 (Ar), 68.2, 67.0 (O–CH_2), 59.0, 57.7 (CH_2), 35.8, 34.0 ($C(CH_3)_3$), 31.6, 29.7 ($C(CH_3)_3$), 5.1 ($SiMe_3$). Elemental anal. calcd for $C_{24}H_{42}N_3O_2SiZn$ (%): C 57.87, H 8.50, N 8.44; found: C 57.81, H 8.30, N 8.39.

*Synthesis of ^{Py}[ONN]$_2$Zn (**10**):*

Complex **10** was prepared analogously to **8**, leading to an impure reaction mixture. Recrystallization led to the isolation of the bis(ligand) complex in 20% yield. Altering reaction conditions to use 2 equiv of ^{Py}[ONN] (1.11 g, 3.42 mmol), THF (40 mL), and 1 equiv of $Zn(N(SiMe_3)_2)_2$ (0.66 g, 1.71 mmol) yielded a brown powder (**10**) in high yield (0.85 g, 1.54 mmol, 90%). ^{1}H NMR ($CDCl_3$, ppm) δ: 8.5 (2H, m, Ar–H), 8.2 (2H, s, CH=N), 7.3–6.8 (10H, m, Ar–H), 4.7 (4H, s, CH_2), 1.4 (18H, s, $C(CH_3)_3$), 1.3 (18H, s, $C(CH_3)_3$). ^{13}C NMR ($CDCl_3$, ppm) δ: 171.6 (C=N), 170.6, 157.1, 149.0, 141.8, 137.5, 133.5, 129.2, 129.1, 122.7, 122.3, 117.9 (Ar), 63.0 (CH_2), 35.8, 34.5 ($C(CH_3)_3$), 31.9, 29.9 ($C(CH_3)_3$). Elemental anal. calcd for $C_{42}H_{34}N_4O_2Zn$ (%): C 70.82, H 7.64, N 7.87; found: C 71.00, H 7.81, N 7.66.

*Synthesis of ^{Q}[ONN]$_2$Zn (**11**):*

Complex **11** was prepared analogously to **10** using ^{Q}[ONN] (3.00 g, 7.76 mmol), THF (40 mL), and $Zn(N(SiMe_3)_2)_2$ (1.40 g, 3.88 mmol). Complex **11** was recrystallized from a mixture of hexamethyldisiloxane and THF prior to use. The synthesis yielded a bright red solid (2.72 g, 34.6 mmol, 88%). ^{1}H NMR ($CDCl_3$, ppm) δ: 9.0 (2H, d, J = 5 Hz, Ar–H), 8.7 (2H, s, CH=N), 8.4 (2H, d, J = 5 Hz, Ar–H), 8.4–7.0 (12H, m, Ar–H), 1.6 (18H, s, $C(CH_3)_3$), 1.3 (18H, s, $C(CH_3)_3$). Elemental anal. calcd for $C_{48}H_{54}N_4O_2Zn$ (%): C 73.50, H 6.94, N 7.14; found: C 73.71, H 7.00, N 7.05.

*Synthesis of $^{N(i\text{-}Pr)_2}$[ONN]$_2$Zn(*i*-Pr)$_2$ (**12**):*

Complex **12** was prepared analogously to **10** using $^{N(i\text{-}Pr)_2}$[ONN](*i*-Pr)$_2$ (1.50 g, 4.15 mmol), THF (50 mL), and $Zn(N(SiMe_3)_2)_2$ (0.80 g, 2.07 mmol). The resulting product was a yellow solid (1.79 g, 3.02 mmol, 86%). ^{1}H NMR ($CDCl_3$, ppm) δ: 8.2 (2H, s, CH=N), 7.4 (2H, d, J = 3 Hz, Ar–H), 7.0 (2H, d, J = 3 Hz, Ar–H) 3.5 (4H, t, J = 9 Hz, CH_2), 2.9 (4H, septet, J = 4 Hz, $CH(CH_3)_2$), 2.7 (4H, t, J = 9 Hz, CH_2), 1.5 (18H, s, ($C(CH_3)_3$), 1.3 (18H, s, $C(CH_3)_3$), 0.9 (12H, d, J = 4 Hz, $CH(CH_3)_2$), 0.8 (12H, d, J = 4 Hz, $CH(CH_3)_2$). Elemental anal. calcd for $C_{46}H_{78}N_4O_2Zn$ (%): C 70.42, H 10.02, N 7.14; found: C 71.55, H 10.50, N 7.50. While repeated elemental analysis tests of isolated crystals were off, suggesting decomposition in shipping, crystals obtained from the same batch on which an X-ray diffraction

Can. J. Chem. Downloaded from www.nrcresearchpress.com by Renmin University of China on 09/02/12
For personal use only.

Fig. 2. Zinc complexes of Schiff base ligands.

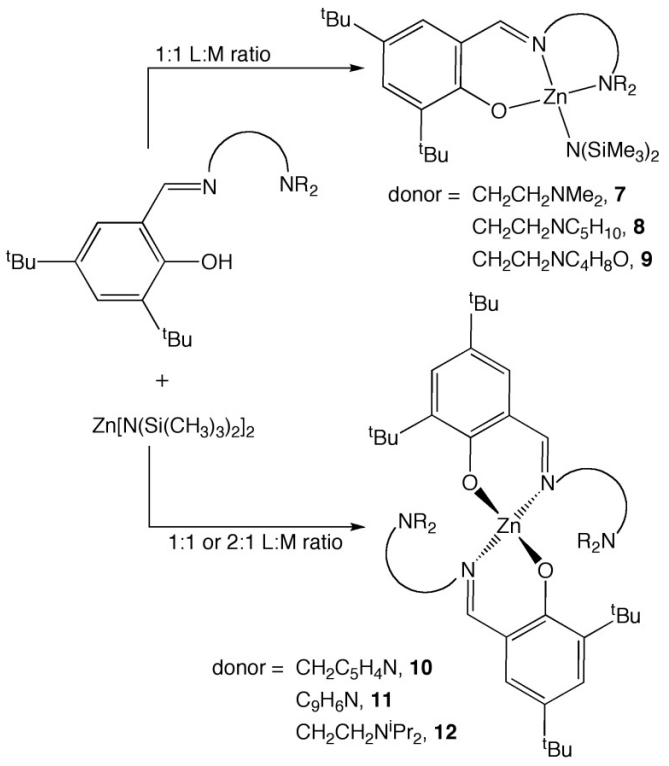
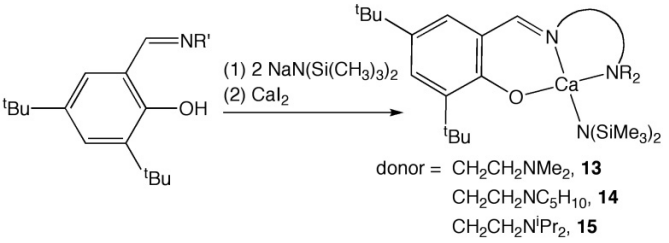


Fig. 3. Calcium complexes of Schiff base ligands.



study was performed were used in the reported polymerization reactions.

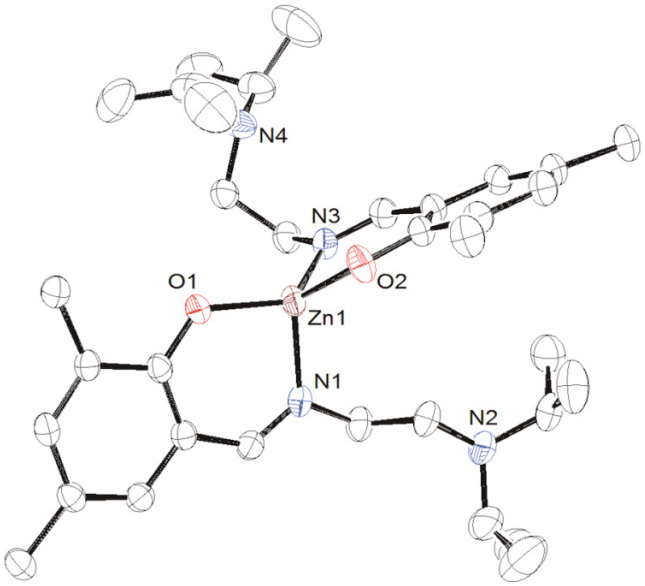
Calcium complexes

^{NMe_2}[ONN]CaNMe$_2$(SiMe$_3$)$_2$ (**13**) was synthesized according to a literature procedure.[14]

*Synthesis of ^{Pip}[ONN]CaN(SiMe$_3$)$_2$ (**14**):*

^{Pip}[ONN] (0.95 g, 2.76 mmol) and NaN(SiMe$_3$)$_2$ (1.01 g, 5.5 mmol) were dissolved in THF (10 mL) and stirred at room temperature for 5 h. A stirring suspension of CaI$_2$ (0.79 g, 2.68 mmol) in THF was added dropwise to this solution and allowed to stir for 12 h. The solvent was removed in vacuo and the product was dissolved in pentane and filtered through celite. Removal of the volatiles in vacuo afforded **13** as a yellow solid (0.50 g, 9.23 mmol, 33%). ^{1}H NMR (CDCl$_3$, ppm) δ: 8.1 (1H, s, CH=N), 7.7 (1H, d, J = 3 Hz, Ar–H), 7.2 (1H, d, J = 3 Hz, Ar–H), 3.3 (2H, t, J = 6 Hz, CH$_2$), 2.1 (2H, t, J = 6 Hz, CH$_2$), 1.9 (4H, t, J = 5 Hz, CH$_2$), 1.8 (9H, s, C(CH$_3$)$_3$), 1.5 (9H, s, C(CH$_3$)$_3$), 1.2 (6H, pentet, J = 5 Hz, CH$_2$), 0.5 (18H, s, SiMe$_3$). Elemental anal. calcd for C$_{25}$H$_{44}$N$_3$CaOSi (%): C 63.78, H 9.42, N 8.93; found: C 63.70, H 9.50, N 8.62.

Fig. 4. ORTEP drawing (spheroids at 50% probability) of ^{Q}[ONN]$_2$Zn (**11**). Protons and *tert*-butyl carbons are omitted for clarity.



*Synthesis of $^{N(i\text{-}Pr)_2}$[ONN]CaN(SiMe$_3$)$_2$(*i*-Pr)$_2$ (**15**):*

Complex **15** was prepared analogously to **14** using 1 equiv of $^{N(i\text{-}Pr)_2}$[ONN](*i*-Pr)$_2$ (1.01 g, 2.80 mmol), 2 equiv of NaN(SiMe$_3$)$_2$ (1.03 g, 5.60 mmol), THF (30 mL), and CaI$_2$ (0.82 g, 2.80 mmol), isolating **15** as a bright yellow solid (0.80 g, 1.43 mmol, 51%). ^{1}H NMR (CDCl$_3$) δ: 8.3 (1H, s, CH=N), 7.7 (1H, d, J = 3 Hz, Ar–H), 7.2 (1H, d, J = 3 Hz, Ar–H), 3.0 (2H, septet, J = 6 Hz, CH(CH$_3$)$_2$), 2.6 (4H, m, J = 9 Hz, C*H*$_2$), 1.5 (9H, s, C(CH$_3$)$_3$), 1.4 (9H, s, C(CH$_3$)$_3$), 1.0 (12H, d, J = 6 Hz, CH(CH$_3$)$_3$), 0.3 (18H, s, SiMe$_3$). Elemental anal. calcd for C$_{26}$H$_{48}$N$_3$CaOSi (%): C 64.14, H 9.94, N 8.63; found: C 64.07, H 10.01, N 8.47.

Crystal structure analyses

Crystals of **11** and **12** were grown by vapour diffusion using pentane and toluene at –35 °C. Single crystals were coated with Paratone-N oil, mounted using a polyimide MicroMount, and frozen in the cold nitrogen stream of the goniometer. A hemisphere of data was collected on a Bruker AXS P4/SMART 1000 diffractometer using ω and θ scans with a scan width of 0.3° and 10 s (**11**) or 30 s (**12**) exposure times. The detector distance was 5 cm. The data were reduced using SAINT[18] and corrected for absorption with SADABS.[19] The structure was solved by direct methods and refined by full-matrix least-squares on F2(SHELXTL).[20] For **11**, one of the *tert*-butyl groups, attached at C(4), was disordered and the site occupancies determined using an isotropic model at 0.7 (C(9)–C(11)) and 0.3 (C(9′)–C(11′) and fixed in subsequent refinement cycles. All non-hydrogen atoms were refined using anisotropic displacement parameters. Hydrogen atoms were included in calculated positions and refined using a riding model. Graphics were created using the ORTEP program.[21]

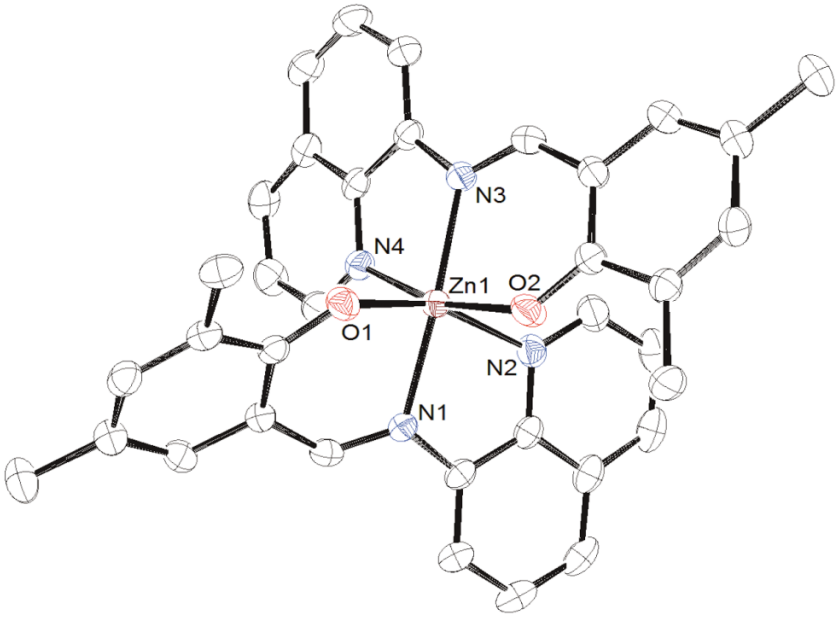
Results and discussion

Catalyst synthesis and characterization

Tridentate Schiff base ligands were readily synthesized via

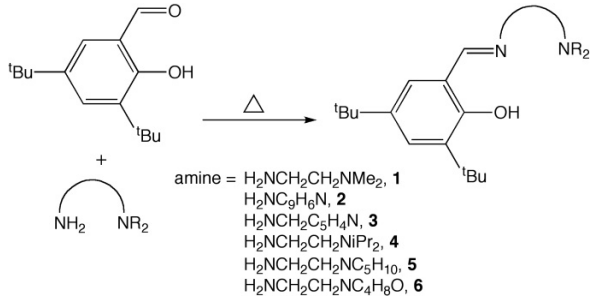
Can. J. Chem. Downloaded from www.nrcresearchpress.com by Renmin University of China on 09/02/12
For personal use only.

Fig. 5. ORTEP drawing (spheroids at 50% probability) of $^{N(i\text{-}Pr)_2}$[ONN]$_2$Zn(*i*-Pr)$_2$ (**12**). Protons and *tert*-butyl carbons are omitted for clarity.



imine condensation reactions and characterized by ^{1}H and ^{13}C NMR spectroscopy (eq. [1]). Six ligands were used in this study, substituted with dimethylamine, diisopropylamine, pyridine, quinoline, piperidine, and morpholine units.

[1]



Zinc catalysts were prepared by the dropwise addition of the proligand of choice to a stirring solution of bis(bis(trimethylsilyl)amide)zinc in THF. Filtration, drying, and recrystallization from a 1:3 toluene–pentane mixture accessed the desired products. Long recrystallizations promoted a transformation from the desired ^{R}[ONN]ZnN(SiMe$_3$)$_2$ complexes, observed in crude NMR spectra, to the bis(ligand) ^{R}[ONN]$_2$Zn species. This disproportionation reaction significantly lowered isolated yields of the desired products and in some cases prevented the isolation of a pure sample of the desired ^{R}[ONN]ZnN(SiMe$_3$)$_2$ catalyst. Improved yields of the ^{R}[ONN]$_2$Zn species could be obtained from purposefully using a 2:1 ligand–metal ratio. Ligands **1**–**6** and isolated complexes **7**–**12** are shown in Fig. 2. Complex formation was readily identified by a diagnostic shift in the imine resonance to δ 8.2 for alkyl-substituted nitrogen donor arms and δ 8.5 and 8.7 for pyridyl and quinolynyl donor arms, respectively, as well as the disappearance of the hydroxy signals. The integration and presence of N(SiMe$_3$)$_2$ protons at δ 0.1 was diagnostic for the formation of mono- or bis-ligated complexes.

Table 1. Selected bond distances (Å) and angles (°) for ^{Q}[ONN]$_2$Zn (**11**) and $^{N(i\text{-}Pr)_2}$[ONN]$_2$Zn (**12**).

	Complex	
	11	**12**
Bond distance (Å)		
Zn(1)–O(1)	2.0260(15)	1.9081(12)
Zn(1)–O(2)	2.0016(15)	1.9106(13)
Zn(1)–N(1)	2.1047(16)	2.0099(16)
Zn(1)–N(2)	2.2730(19)	—
Zn(1)–N(3)	2.1025(17)	2.0018(16)
Zn(1)–N(4)	2.2365(18)	—
Bond angle (°)		
O(1)–Zn(1)–N(1)	86.20(6)	95.08(6)
O(1)–Zn(1)–N(2)	158.42(6)	—
N(1)–Zn(1)–N(2)	75.36(7)	—
O(2)–Zn(1)–N(3)	88.52(6)	96.15(6)
O(2)–Zn(1)–N(4)	163.54(6)	—
N(3)–Zn(1)–N(4)	76.20(7)	—
(O1)–Zn(1)–O(2)	91.00(6)	113.69(6)

Calcium complexes were prepared via the ^{R}[ONN] sodium salt with 1 equiv of ligand and 2 equiv of NaN(SiMe$_3$)$_2$ reacted for 5 h in THF followed by dropwise addition of CaI$_2$ to the reaction mixture. Removal of solvent after 12 h followed by filtration and recrystallization from pentane afforded three desired complexes of the form ^{R}[ONN]CaN(SiMe$_3$)$_2$ characterized by ^{1}H and ^{13}C NMR spectroscopy (**13**–**15**, Fig. 3). Yields were moderate compared with the corresponding Zn complexes, potentially because of the relative stability of the CaI$_2$. Attempts to improve yields with longer reaction times and higher temperatures were unsuccessful and led to complex decomposition. Of note, pyridine and quinoline functionalities were not employed as the complexes had been previously tested, whereas morpholine substituents promoted the formation of an intractable mixture of solids. Again, the complex formation was noted in spectroscopic

Table 2. Selected crystallographic data and refinement details for $^{Q}[ONN]_2Zn$ (**11**) and $^{N(i\text{-}Pr)_2}[ONN]_2Zn$ (**12**).

	Complex	
Crystallographic parameters	**11**	**12**
Empirical formula	$C_{48}H_{54}N_4O_2Zn$	$C_{46}H_{78}N_4O_2Zn$
Formula mass	784.32	784.49
Colour, habit	Orange, rod	Colourless, rod
Dimensions (mm)	0.60×0.10×0.05	0.60×0.30×0.25
Crystal system	Triclinic	Monoclinic
Space group	*P*-1	*P*2(1)/*c*
Z	2	4
a, *b*, *c* (Å)	10.1627(17), 13.790(2), 16.511(3)	11.0836(13), 14.8067(18), 28.774(3)
α, β, γ (°)	104.350(2), 104.649(2), 99.769(2)	90, 93.411(2), 90
V (Å^3)	2101.1(6)	4713.7(10)
Temperature (K)	188(1)	188(1)
D_{calcd} (Mg m^{-3})	1.240	1.105
Radiation	Mo Kα	Mo Kα
μ (mm^{-1})	0.627	0.558
F(000)	832	1712
Reflections (obs.)	13846	32145
Reflections (ind.)	8955	10552
Data/restr./param.	8955 / 15 / 520	10552 / 0 / 498
Theta range (°)	1.57–27.49	1.42–27.50
Goodness-of-fit	1.052	1.027
R_1, wR_2	0.0413, 0.0822	0.0369, 0.0872
Largest peak/hole (e A^{-3})	0.330, –0.518	0.284, –0.275

Can. J. Chem. Downloaded from www.nrcresearchpress.com by Renmin University of China on 09/02/12
For personal use only.

studies by a shift in the imine resonance, the disappearance of hydroxyl resonances, and the presence and integration of $N(SiMe_3)_2$ signals.

Crystals suitable for X-ray diffraction studies were grown for **11** and **12** by vapour diffusion of pentane into toluene. The crystal structure of **11** (Fig. 4) indicates the complex has a distorted octahedral geometry with coordination of the quinoline nitrogens to afford a formally 22-electron complex. This six-coordinate complex, with both tridentate ligands arranged in a meridional geometry, contrasts with similar four-coordinate diphenolato complexes synthesized by Zhang et al.[23] In **11**, Zn–N bonds ranging from 2.10 to 2.27 Å contrast with the stronger Zn–O bonds of 2.00 and 2.03 Å. The structure of **12**, however, shows the Zn centre in a distorted T_d geometry (Fig. 5), similar to a previously published bidentate salicylaldimine structure.[23] A four-coordinate structure is favoured, correlating with the removal of the electron-withdrawing quinoline ring structure and the increased steric hindrance of the isopropyl substituents. As expected, the complex has shorter Zn–O (1.91 Å) and Zn–N (2.00, 2.01 Å) bond lengths compared with **11**. Selected bond distances, bond angles, and crystallographic parameters are provided in Tables 1 and 2.

Ring-opening polymerizations of *rac*-lactide and ε-caprolactone — Screening reactions

Polymerizations of ε-caprolactone mediated by complexes **7**–**15** are summarized in Table 3. Polymerizations with monomer–catalyst ratios of 100:1 were carried out in toluene (3 mL) at room temperature. No additional alcohol initiator was added to the reactions, so initiation from latent trimethylsilylamide or ligand alkoxide functionalities was expected. Temperatures were maintained at room temperature as higher temperatures and bulk polymerization led to significant transesterification and broadened molecular weight distributions, contrasting previous reports,[15,21] but supporting the poor activity of previously reported chiral variants.[22] None of the catalysts were effective at controlling the polymerization, however, certain trends can be highlighted. Complexes with a single ligand and bis(trimethylsilyl)amido initiating group initiate a productive PCL polymerization, however, polydispersities (PDIs) are high and observed molecular weights are higher than expected from monomer conversion. Complexes with two ligands, lacking the amido functionality, are unable to initiate the polymerization. The calcium complexes are significantly faster at polymerizing the ε-caprolactone monomer. Chromatographic analysis of these polymers still suggests a lack of control over this reaction, with multimodal molecular weight distributions. While disproportionation is possible for the monoligated complexes under polymerization conditions, which may explain the lack of control, no disproportionation was observed for **7**–**9** or **13**–**15** in coordinating solvents.

Polymerizations of *rac*-lactide mediated by complexes **7**–**15** are summarized in Table 4. Reactions were carried out at 70 °C in toluene for 30 or 240 min depending upon the observed reactivity of the complexes. Clear trends in catalyst performance are observed. Complexes **7**–**9**, ligated by a single tridentate ligand, produce PLAs of predictable molecular weights and low polydispersities. The fastest catalyst, capable of polymerizing nearly 100 equiv of *rac*-lactide in under 30 min, is the previously reported **7**, substituted with a sterically unencumbered dimethylamine donor arm. Increasing the steric bulk slows the polymerization, as expected. Both the rate of polymerization and the control of the polymerization are inhibited by the morpholine ligand, suggesting the pendant oxygen of the morpholine ring may block lactide coordination and ROP. Bis(ligand) complexes also initate and control the polymerization of lactide, likely inserting into one

Can. J. Chem. Downloaded from www.nrcresearchpress.com by Renmin University of China on 09/02/12
For personal use only.

Table 3. Polymerization of ε-caprolactone (ε-CL) mediated by complexes **7**–**15**.

[I]	Time (min)	Conv. (%)	M_n	$M_{n,th}$[a]	PDI
7	120	54	37898	6324	1.71
8	120	72	25150	8378	1.72
9	120	28	51714	3356	1.79
10	360	0	na	na	na
11	360	0	na	na	na
12	360	0	na	na	na
13	15	68	32841	7922	1.73
14	15	81	21544	9406	1.80
15	15	72	32583	8218	1.72

Note: Reactions carried out at 25 °C in 3 mL of toluene with monomer:catalyst ratios of 100:1. Molecular weights corrected for changes in relative retention times versus styrene standards. [I], initiator; M_n, number average molecular weight; $M_{n,th}$, theoretical molecular weight; PDI, polydispersity index; na, not available.

[a] $M_{n,th}$ = % conversion × MW ε-CL × 100 + MW $N(SiMe_3)_2$.

Table 4. Polymerization of *rac*-lactide mediated by complexes **7–15**.

[I]	Time (min)	Conv. (%)	M_n	$M_{n,th}$[a]	PDI
7	30	86	10079	12556	1.25
8	30	61	7374	8952	1.28
9	30	48	6338	7079	1.61
10	240	94	20508	13872	1.39
11	240	0	na	na	na
12	240	98	19878	14484	1.31
13	240	54	8321	7943	1.20
14	240	47	5987	6934	1.20
15	240	58	8986	8520	1.12
15[b]	400	58	18007	17040	1.25
15[c]	620	58	31998	34080	1.34

Note: Reactions carried out at 70 °C in 3 mL of toluene with monomer–catalyst ratios of 100:1. Molecular weights corrected for changes in relative retention times versus styrene standards. [I], initiator; M_n, number average molecular weight; $M_{n,th}$, theoretical molecular weight; PDI, polydispersity index; na, not available.

[a] $M_{n,th}$ = % conversion × MW *rac*-LA × 200 + MW initiating group.

[b] Ratio of 200:1 monomer–catalyst used.

[c] Ratio of 400:1 monomer–catalyst used.

of the zinc alkoxide bonds to the ligand.[23,24] Molecular weights were higher than theoretical, suggesting not all ligands may initiate the polymerization. Interestingly, the quinoline-substituted complex, which in the solid state had no open coordination sites, is completely unreactive towards lactide even at higher temperatures and longer reaction times, suggesting this octahedral coordination mode may be maintained in solution. No shift in lactide or catalyst resonances are noted in ^{1}H NMR spectra of 1:1 mixtures of **11** and *rac*-lactide, supporting this statement.

Finally, the calcium complexes prepared were all effective in the polymerization of *rac*-lactide, with similar levels of control regardless of the nature of the pendant donor arm. Reactions were slow, however, requiring longer reaction times to achieve higher conversions. Due to the inferior quality of the catalysts compared with industry standards, full reaction kinetics were not pursued. However, further evidence of polymerization control is offered by variation of [M]:[I] (monomer to initiator) ratios, as shown in Table 4 for catalyst **15**. When polymerizations are quenched at the same conversion, molecular weights increase linearly and correlate well with predicted values. A slight increase in PDI at longer reaction times suggest the catalysts may have limited thermal stability. All catalysts produced atactic PLA and showed no stereospecificity. Interestingly, the calcium complexes show lower activity, potentially because of their larger size and lower Lewis acidity, contributing to a lower overall reactivity.

Conclusions

Nine zinc and calcium complexes supported by phenoxy-imine ligands with various pendant donors were prepared, characterized, and screened as catalysts in the ROP of ε-caprolactone and *rac*-lactide. Seven of these catalysts are novel and include pendant piperidine, morpholine, diisopropylamine, pyridine, and quinoline donors to compare with first-generation catalysts substituted with dimethylamine donors. Zinc complexes have a tendency to disproportionate to form bis(ligand) species, which are ineffective for the polymerization of ε-caprolactone but initiate slowly to produce PLAs of controlled PDIs and molecular weights. Improved control was achieved through the use of zinc and calcium complexes coordinated to a single ligand framework with low PDI.

Acknowledgement

We thank the Natural Sciences and Engineering Research Council of Canada (NSERC) and the University of Prince Edward Island, Charlottetown, for financial support, and the Canada Foundation for Innovation and the Atlantic Canada Opportunities Agency for infrastructure. We would also like to thank NSERC for Undergraduate Student Research Awards to Justin McRae and Josh Gallaway.

References

(1) Stanford, M. J.; Dove, A. P. *Chem. Soc. Rev.* **2010**, *39* (2), 486. doi:10.1039/b815104k.
(2) Cameron, D. J. A.; Shaver, M. P. *Chem. Soc. Rev.* **2011**, *40* (3), 1761. doi:10.1039/c0cs00091d.
(3) Dove, A. P. *Chem. Commun. (Camb.)* **2008**, (48): 6446. doi:10.1039/b813059k.
(4) Dechy-Cabaret, O.; Martin-Vaca, B.; Bourissou, D. *Chem. Rev.* **2004**, *104* (12), 6147. doi:10.1021/cr040002s.
(5) Sinclair, R. G. *J. Macromol. Sci. Pure Appl. Chem.* **1996**, *A33* (5), 585. doi:10.1080/10601329608010880.
(6) Davis, K. A.; Burdick, J. A.; Anseth, K. S. *Biomaterials* **2003**, *24* (14), 2485. doi:10.1016/S0142-9612(02)00582-3.
(7) Dumitriu, S. *Polymeric Biomaterials;* Marcel Dekker: New York, 2002; Chapter 4.
(8) Arbaoui, A.; Redshaw, C. *Polym. Chem.* **2010**, *1* (6), 801. doi:10.1039/b9py00334g.
(9) Minami, M.; Kozaki, S. Method for Producing Aliphatic Polyester. U.S. Patent Appl. Publ. 20030023026 A1 20030130, 2003.
(10) Hayes, P. G.; Wheaton, C. A.; Ireland, B. J. *Dalton Trans.* **2009**, (25), 4832. doi:10.1039/b819107g.

(11) Tang, H.-Y.; Chen, H.-Y.; Huang, J.-H.; Lin, C.-C. *Macromolecules* **2007**, *40* (25), 8855. doi:10.1021/ma071540k.
(12) Gao, A.-H.; Yao, W.; Mu, Y.; Gao, W.; Sun, M.-T.; Su, Q. *Polyhedron* **2009**, *28* (13), 2605. doi:10.1016/j.poly.2009.05.037.
(13) Darensbourg, D. J.; Choi, W.; Richers, C. P. *Macromolecules* **2007**, *40* (10), 3521. doi:10.1021/ma062780n.
(14) Darensbourg, D. J.; Choi, W.; Karroonnirun, O.; Bhuvanesh, N. *Macromolecules* **2008**, *41* (10), 3493. doi:10.1021/ma800078t.
(15) Darensbourg, D. J.; Karroonnirun, O. *Inorg. Chem.* **2010**, *49* (5), 2360. doi:10.1021/ic902271x.
(16) Darensbourg, D. J.; Karroonnirun, O. *Macromolecules* **2010**, *43* (21), 8880. doi:10.1021/ma101784y.
(17) Kowalski, A.; Duda, A.; Penczek, S. *Macromolecules* **1998**, *31* (7), 2114. doi:10.1021/ma971737k.
(18) SAINT 7.23A. Bruker AXS, Inc., Madison, WI, 2006.
(19) Sheldrick, G. SADABS. Bruker AXS, Inc., Madison, WI, 2008.
(20) Sheldrick, G. M. *Acta Crystallogr.* **2008**, *A64* (1), 112. doi:10.1107/s0108767307043930.
(21) Farrugia, L. J. *J. Appl. Cryst.* **1997**, *30* (5), 565. doi:10.1107/S0021889897003117.
(22) Labourdette, G.; Lee, J.-C. D.; Patrick, B. O.; Ezhova, M. B.; Mehrkhodavandi, P. *Organometallics* **2009**, *28* (5), 1309. doi:10.1021/om800818v.
(23) Zhang, C.; Wang, Z.-X. *J. Organomet. Chem.* **2008**, *693* (19), 3151. doi:10.1016/j.jorganchem.2008.07.002.
(24) Bhunora, S.; Mugo, J.; Bhaw-Luximon, A.; Mapolie, S.; Van Wyk, J.; Darkwa, J.; Nordlander, E. *Appl. Organomet. Chem.* **2011**, *25* (2), 133. doi:10.1002/aoc.1728.

Can. J. Chem. Downloaded from www.nrcresearchpress.com by Renmin University of China on 09/02/12
For personal use only.

Citric acid as a trifunctional organocatalyst for thiocyanation of aromatic and heteroaromatic compounds in aqueous media

Ardeshir Khazaei, Mohammad Ali Zolfigol, Mohmmad Mokhlesi, and Mahtab Pirveysian

Can. J. Chem. Downloaded from www.nrcresearchpress.com by Renmin University of China on 09/02/12
For personal use only.

Abstract: A green and simple procedure for the thiocynation of aromatic and heteroaromatic rings in the presence of a catalytic amount of citric acid in water are described. The reactions proceed in high yields, with short reaction times and under mild conditions.

Key words: thiocyanation, citrc acid, organocatalyst, hydrogen peroxide, water.

Résumé : On a mis au point une méthode simple et écologique d'effectuer la thiocyanuration de noyaux aromatiques et hétéroaromatiques, en présence d'une quantité catalytique d'acide citrique, dans l'eau. Les réactions se font dans des conditions douces, de courts temps de réaction et avec des rendements élevés.

Mots-clés : thiocyanuration, acide citrique, catalyseur organique, peroxyde d'hydrogène, eau.

[Traduit par la Rédaction]

Introduction

Organocatalysis has emerged during the last decade as one of the major issues in the development of catalytic chemical technology.[1] As for conventional catalysis with transition-metal complexes, by using organic catalysts large quantities of products are expected to be prepared using a minimal amount of small organic molecules.[2] The recent organocatalytic protocols are particularly attractive because of the mildness of the reaction conditions, operational simplicity, the potential for the development of large scale production, and the ready availability and low toxicity of the organocatalysts.[3–12] A diverse set of organocatalytic reactions, including C–C, C–N, and C–O bond formation,[13] Diels–Alder,[14,15] Baylis–Hilman,[16,17] Mannich,[14,18–20] Michael,[14,21,22] Friedel–Crafts alkylation,[23] oxidation,[24,25] and carbohydrate synthesis,[26] has benefited from the developments in this area.[27–29] On the other hand, organocatalyzed reactions using water as a solvent have attracted a great deal of attention mainly because of the low cost, the safety, and the environmentally benign nature of water. The synthesis of organic molecules via reactions in water is an extensively investigated topic, which entails the additional challenge of water tolerance for a catalyst. Thus, the development of small organic molecules that catalyze reactions in water is currently an important goal amongst today's synthetic community.[30]

The thiocyanation reaction is one of the most useful carbon–sulfur bond-forming reactions. Thiocyanates have gained considerable importance in various areas of organosulfur chemistry.[31] For example, the thiocyanato group occurs as an important functionality in certain anticancer natural products formed by deglycosylation of glucosinolates derived from cruciferous vegetables.[32–36] On the other hand, thiocyano-substituted compounds are a useful precursor for the synthesis of organosulfur compounds, in which the thiocyanate group will be readily transferred to other functional groups such as sulfide,[35] aryl nitrile,[36] thiocarbamate,[37] and thionitrile.[38] Several methods have been developed for the thiocyanation of arenes by using various reagents[39–41] such as *N*-thiocyanatosuccinimide,[42] ceric ammonium nitrate (CAN),[43] acidic mont K10 clay,[44] iodine/methanol,[45] diethyl azodicarboxylate,[46] IL-$OPPh_2$,[47] pentavalent iodine,[48] IBX,[49] $FeCl_3$,[50] potassium peroxydizulfate – copper(II),[51] and Selectfluor.[52] However, most of the reported methods for the synthesis of aryl thiocyanates are associated with one or more of the following drawbacks such as low yields, long reaction times, the use of large amounts of catalyst, and the use of toxic or expensive catalysts. Thus, the search for finding an efficient, inexpensive, and nonpolluting method for the synthesis of this class of compounds is still of practical importance.

Because of these problems and the recent intense attention on environmentally benign protocols, the search for new and efficient catalysts that are able to promote organic reactions under green conditions is of interest for the production of aryl thiocyanates. In this regard, we report the synthesis of organo thiocyanate derivatives in the presence of a catalytic amount of citric acid in aqueous media.

Received 21 September 2011. Accepted 23 November 2011. Published at www.nrcresearchpress.com/cjc on 4 April 2012.

A. Khazaei, M.A. Zolfigol, M. Mokhlesi, and M. Pirveysian. Faculty of Chemistry, Bu-Ali Sina University, P.O. Box 6517838683, Hamedan, Iran.

Corresponding author: Ardeshir Khazaei (e-mail: akhazaei_1326@yahoo.com).

Can. J. Chem. Downloaded from www.nrcresearchpress.com by Renmin University of China on 09/02/12
For personal use only.

Results and discussion

For the synthesis of aryl thiocyanate, conversion of indole into its corresponding indole thiocyanate in water and room temperature has been considered as a model reaction (Scheme 1).

In an initial experiment, we examined the reaction of indole and KSCN in aqueous media by using different catalysts such as sodium citrate, benzenesulfonic acid, 1-(phenylthio) acetic acid, 4-chlorobenzoic acid, 4-methoxybenzoic acid, and citric acid. The results are summarized in Table 1. As Table 1 indicates, higher yield and shorter reaction times were obtained when citric acid was utilized as the catalyst. Brønsted acid organocatalysts such as benzenesulfonic acid, 1-(phenylthio)acetic acid, 4-chlorobenzoic acid, and 4-methoxybenzoic acid gave low yields of the corresponding 3-thiocyanato indole. The use of sodium citrate was also examined and a moderate yield of product was obtained. Citric acid very efficiently gave an excellent yield of the corresponding 3-thiocyanato indole in a shorter reaction time. This might be due to the solubility of citric acid in water, which could accelerate the reaction rate.

In the next step, the reaction of indole with H_2O_2 and KSCN was tested by using different amounts of citric acid at room temperature (Table 2). As shown in Table 2, the optimal amount of the catalyst was 10 mol %. In the absence of catalyst when indole was treated with hydrogen peroxide and KSCN, no product was obtained. When the amount of catalyst was less than 10 mol %, the yield of product was greatly reduced. Otherwise, increasing the catalyst loading from 10 to 15 mol % does not significantly change the yield. Also, the solvent effect was investigated using indole as a substrate. We carried out the reaction with the same concentration of the reactants in H_2O, MeOH, CH_3CN, CH_2Cl_2, THF, and AcOEt. Both the yields and the reaction times listed in Table 2 suggested that water was the most favorable solvent for the thiocyanation.

Consequently, 10 mol % citric acid was used in subsequent experiments. We then applied this reaction to a wide range of aromatic and heteroaromatic compounds; the results are summarized in Table 3.

A good range of aromatic and heteroaromatic compounds underwent thiocyanation with high regioselectivities and excellent yields being observed in all cases (Table 3). The reaction was mild and equally good for indoles, anilines, and N- substituted anilines.

As shown in Table 3, indole and electron-rich indoles gave the desired products in excellent yields (Table 3, entries 1–3). Also, electron-deficient indoles such as 5-bromoindole afforded the corresponding 5-bromo-3-thiocyanato indoles in good yields, but required longer reaction times (Table 3, entry 4). This observation can be attributed to the lower electron density of such substrates. The thiocyanation reaction was highly regioselective at the 3-position of the indole ring. Pyrrole was easily transformed into the monothiocyanated product within 15 min. After reviewing the reactions for the heterocycles, we examined the capability of aromatic amines in the thiocyanation reaction. Electron-rich amines such as *o*-toluidine and *m*-toluidine underwent reaction under the same conditions, leading to a high production efficiency (Table 3, entries 9 and 10). Our review showed that electron-deficient amines also carry out this reaction, but they need more time (Table 3, entries 11–14). In N-substituted amines some interesting results were achieved. In all cases, the substrate reacted and produced corresponding aryl thiocyanates (Table 3, entries 6–8 and 16–18). As shown in Table 3, the substitution was highly regioselective, occurring at the para position of the aromatics rings.

In comparison with the previously reported method using other reagents, which requires refluxing conditions for some substrates, the assistance of ultrasonic irradiation, and a toxic solvent or oxidant, this method is suitable and has mild and green reaction conditions.

In conclusion, we have developed an efficient, simple, and green-mediated thiocyanation of aromatic compounds with high regioselectivity. The described method has advantages such as a simple work-up, a short reaction time, is metal free, uses mild reaction conditions, and a clean production of the desired products in high yields.

Scheme 1. Thiocyanation of indole in the presence of citric acid.

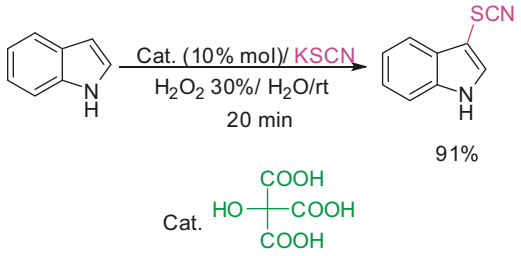


Table 1. Thiocyanation of indole using different catalysts (10 mol %).

Entry	Catalyst	Time (h)	Yield (%)
1	1-(Phenylthio)acetic acid	2.5	15
2	4-Methoxybenzoic acid	2.5	20
3	4-Chlorobenzoic acid	2.5	25
4	Citric acid	20 (min)	91
5	Sodium citrate	2.5	40
6	Benzenesulfonic acid	2	65

Table 2. Optimization of reaction conditions.

Entry	Catalyst (mol %)	Solvent	Time (h)	Yield (%)
1	1	H_2O	5	15
2	5	H_2O	3	35
3	10	H_2O	20 (min)	91
4	15	H_2O	20 (min)	90
5	10	MeOH	20 (min)	91
6	10	CH_3CN	20 (min)	90
7	10	CH_2Cl_2	2.5	40
8	10	AcOEt	2.5	55
9	10	THF	2.5	50

Experimental

All chemicals were purchased from Merck or Fluka Chemical Companies. All known compounds were identified by comparison of their melting points and spectral data with

Can. J. Chem. Downloaded from www.nrcresearchpress.com by Renmin University of China on 09/02/12
For personal use only.

Table 3. Substrate range in the thiocyanation reaction using KSCN / citric acid / H_2O_2 under mild conditions.

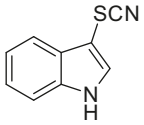
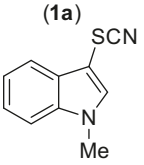
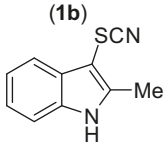
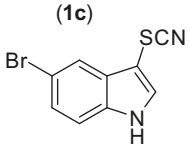
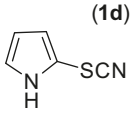
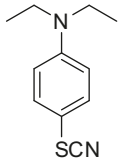
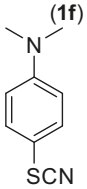
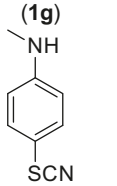
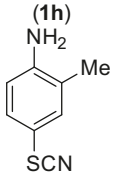
Entry	Product	Time (min)	Yield (%)[a]
1	 (**1a**)	20	91
2	 (**1b**)	20	82
3	 (**1c**)	7	88
4	 (**1d**)	25	85
5	 (**1e**)	15	93
6	 (**1f**)	60	75
7	 (**1g**)	60	79
8	 (**1h**)	60	81
9	 (**1i**)	15	85

Table 3 (*continued*).

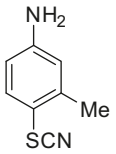
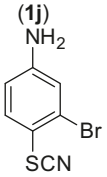
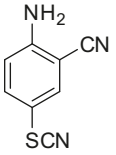
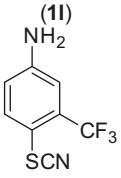
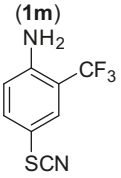
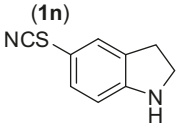
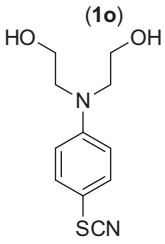
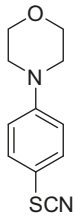
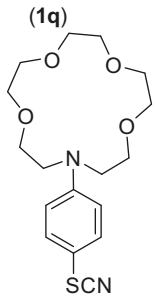
Entry	Product	Time (min)	Yield (%)[a]
10	 (**1j**)	35	88
11	 (**1k**)	45	60
12	 (**1l**)	5	78
13	 (**1m**)	50	72
14	 (**1n**)	35	77
15	 (**1o**)	45	89
16	 (**1p**)	45	83

Table 3 (*concluded*).

Entry	Product	Time (min)	Yield (%)[a]
17	 (**1q**)	60	65
18	 (**1r**)	40	79

Note: Reaction conditions: substrate, 1 mmol; H_2O_2 (30%), 3 mmol; KSCN, 3 mmol; citric acid, 10 mol %; H_2O, 3–5 mL; with stirring.
[a]Isolated yields.

those reported in the literature. Progress of the reactions was monitored by TLC using silica gel SIL G/UV 254 plates. The ^{1}H NMR (300 MHz) and ^{13}C NMR (75 MHz) were run on a Bruker Avance DPX-250 FT-NMR spectrometer (δ in ppm). Microanalysis was performed on a PerkinElmer 240-B microanalyzer. Melting points were recorded on a Büchi B-545 apparatus using open capillary tubes.

General procedure for the preparation of 3-thiocyanatoindole (1a)

A suspension of indole (0.117 g, 1 mmol), potassium thiocyanate (0.294 g, 3 mmol), and citric acid (0.0164 g, 10 mol %) in H_2O (3–5 mL) was stirred at room temperature for 5 min. Then H_2O_2 (30%, 3 mmol) was added dropwise (2–5 min). The progress of the reaction was monitored by TLC. After completion of the reaction, the reaction mixture was extracted with $CHCl_3$ (2 × 10 mL). Anhydrous Na_2SO_4 (3 g) was then added to the organic layer and filtered off after 20 min. $CHCl_3$ was removed and further purification was achieved by silica gel column chromatography with hexane/AcOEt (5:1).

Spectral data of the products

Note: Compounds **1f**, **1h**,**1k**, **1l**, **1m**, **1n**, **1o**, **1p**, **1q**, and **1r** are new. Selected product spectra can found in the Supplementary data.

3-Thiocyanatoindole (1a)

mp 71–73 °C (lit.[53] 70–71 °C). FT-IR (KBr): 2159 (SCN), 3289 (NH). ^{1}H NMR ($CDCl_3$) δ: 8.87 (br s, 1H), 7.83 (d, J = 8.8 Hz, 1H), 7.46–7.23 (m, 4H). ^{13}C NMR ($CDCl_3$) δ: 136.06, 131.2, 127.6, 123.8, 121.8, 118.6, 112.2, 91.7. MS (m/z) = 174 (M^+). Anal. calcd for $C_9H_6N_2S$: C 62.05, H 3.47, N 16.08; found: C 62.25, H 3.34, N 16.15.

1-Methyl-3-thiocyanatoindole (1b)

mp 79–81 °C (lit.[54] 80–81 °C). FT-IR (KBr): 2146 (SCN). ^{1}H NMR ($CDCl_3$) δ: 7.84–7.36 (m, 5H), 3.74 (s, 3H). ^{13}C NMR ($CDCl_3$) δ: 137.1, 135.2, 128.4, 123.4, 121.6, 118.8, 112.1, 110.3, 33.4. MS (m/z) = 188 (M^+). Anal. calcd for $C_{10}H_8N_2S$: C 63.80, H 4.28, N 14.88; found: C 64.01, H 4.15, N 14.92.

2-Methyl-3-thiocyanatoindole (1c)

mp 97–99 °C (lit.[55] 99–101 °C). FT-IR (KBr): 2151 (SCN), 3395 (NH), 3395. ^{1}H NMR ($CDCl_3$ δ): 8.55 (s, 1H), 7.71 (d, J = 6.9 Hz, 1H), 7.33–7.23 (m, 3H), 2.49 (s, 3H). ^{13}C NMR ($CDCl_3$) δ: 142.1, 135.1, 128.6, 122.9, 121.5, 118.0, 111.3, 88.7, 12.0. MS (m/z) = 188 (M^+). Anal. calcd for $C_{10}H_8N_2S$: C 63.80, H 4.28, N 14.88; found: C 63.65, H 4.41 N 14.80.

5-Bromo-3-thiocyanatoindole (1d)

mp 126–128 °C (lit.[53] 124–127 °C). FT-IR (KBr): 2146 (SCN), 3351 (NH). ^{1}H NMR ($CDCl_3$) δ: 8.87 (br s, 1H, NH), 7.90–7.15 (m, 5H). ^{13}C NMR ($CDCl_3$) δ: 134.6, 132.2, 129.3, 123.1, 121.2, 115.3, 113.7, 111.9, 102.2. MS (m/z) = 251 (M^+), 253 (M + 2). Anal. calcd for $C_9H_5BrN_2S$: C 42.71, H 1.99, N 11.07; found: C 42.55, H 2.12, N 11.07.

2-Thiocyanatopyrole (1e)

Liquid bp 175–176 °C (no literature value available). FT-IR (KBr): 2160 (SCN), 3247 (NH). ^{1}H NMR ($CDCl_3$) δ: 9.04 (s, 1H), 7.04–7.00 (m, 1H), 6.68–6.59 (m, 1H), 6.30–6.29 (m, 1H). ^{13}C NMR ($CDCl_3$ δ): 121.2, 120.2, 112.2, 110.9, 109.6. MS (m/z) = 124 (M^+).

4- Thiocyanato-*N*,*N*-diethylaniline (1f)

mp 82–84 °C (no literature value available). FT-IR (KBr): 2151 (SCN). ^{1}H NMR ($CDCl_3$) δ: 7.5–7.34 (m, 2H), 7.2–7.13 (m, 1H), 6.63–6.61 (m, 1H), 3.37(q, J = 7.12 Hz, 4H), 1.146 (t, J = 5.4 Hz, 6H). ^{13}C NMR ($CDCl_3$) δ: 149.1, 134.9, 125.2, 121.7, 112.6, 44.5, 12.3. MS (m/z) = 206 (M^+). Anal. calcd for $C_{11}H_{14}N_2S$: C 64.04, H 6.84, N 13.58; found: C 64.23, H 6.71, N 13.49.

4-Thiocyanato-*N*,*N*-dimethylaniline (1g)

mp 71–72 °C (lit.[55] 70–73 °C). FT-IR (KBr): 2146 (SCN). ^{1}H NMR ($CDCl_3$) δ: 7.44 (d, J = 8.7, 2H), 6.69 (d, J = 8.7, 2H), 3.00 (s, 6H). ^{13}C NMR ($CDCl_3$) δ: 151.6, 134.5, 113.1, 112.7, 106.3, 40.1. MS (m/z) = 178 (M^+). Anal. calcd for $C_9H_{10}N_2S$: C 60.64, H 5.65, N 15.72; found: C 60.45, H 5.84, N 15.65.

4-Thiocyanato-*N*-methylaniline (1h)

mp 45–48 °C (lit.[53] 46–47). FT-IR (KBr): 2153 (SCN), 3413 (NH). ^{1}H NMR ($CDCl_3$) δ: 7.15–7.12 (m, 2H), 7.06–6.82 (m, 2H), 4.70 (s, 1H), 3.32 (s, 3H). ^{13}C NMR ($CDCl_3$) δ: 150.9, 134.6, 132.8, 117.6, 116.4, 114.8, 113.6, 30.3. MS (m/z) = 164 (M^+). Anal. calcd for $C_8H_8N_2S$: C 58.51, H 4.91, N 17.06; found: C 58.71, H 4.79, N 17.12.

Can. J. Chem. Downloaded from www.nrcresearchpress.com by Renmin University of China on 09/02/12
For personal use only.

Can. J. Chem. Downloaded from www.nrcresearchpress.com by Renmin University of China on 09/02/12
For personal use only.

2-Methyl-4-thiocyanatoaniline (1i)

mp 62–64 °C (no literature value available). FT-IR (KBr): 2153 (SCN), 3369 and 3456 (NH_2). ^{1}H NMR ($CDCl_3$) δ: 6.64–7.37 (m, 3H), 3.987 (br s, 2H), 2.12 (s, 3H). ^{13}C NMR ($CDCl_3$) δ: 147.3, 135.1, 132.1, 123.9, 115.8, 112.8, 108.8, 17.2. MS (*m*/*z*) = 164 (M^+). Anal. calcd for $C_8H_8N_2S$: C 58.51, H 4.91, N 17.06; found: C 58.29, H 5.03, N 17.15.

3-Methyl-4-thiocyanatoaniline (1j)

mp 70–71 °C. FT-IR (KBr): 2146 (SCN), 3219 and 3337 (NH_2). ^{1}H NMR ($CDCl_3$) δ: 7.38 (d, *J* = 7.7 Hz, 1H), 7.65 (q, *J* = 6.52 Hz, 2H), 4.1 (br s, 2H), 2.34 (s, 3H). ^{13}C NMR ($CDCl_3$) δ: 149.7, 143.01, 136.3, 117.3, 112.4, 108.4, 21.2. MS (*m*/*z*) = 164 (M^+). Anal. calcd for $C_8H_8N_2S$: C 58.51, H 4.91, N 17.06; found: C 58.71, H 4.75, N 16.96.

3-Bromo-4-thiocyanatoaniline (1k)

mp 49–50 °C. FT-IR (KBr): 2156 (SCN), 3233 and 3376 (NH_2). ^{1}H NMR ($CDCl_3$) δ: 7.23–7.50 (m, 3H), 6.65 (s, 1H), 4.12 (s, 2H). ^{13}C NMR ($CDCl_3$) δ: 144.8, 134.5, 132.6, 117.5, 116.1, 112.7, 109.2. MS (*m*/*z*) = 228 (M^+), 230 (M + 2). Anal. calcd for $C_7H_5BrN_2S$: C 36.70, H 2.20, N 12.23; found: C 36.92, H 2.31, N 12.14.

2-Cyano-4-thiocyanatoaniline (1l)

mp 107–108 °C (no literature value available). FT-IR (KBr): 2156 (SCN), 2222 (CN), 3360 and 3444 (NH_2). ^{1}H NMR ($CDCl_3$) δ: 7.58–7.28 (m, 2H), 6.83 (s, 1H), 4.96 (br s, 2H). ^{13}C NMR ($CDCl_3$) δ: 151.7, 138.4, 137.2, 117.8, 116.3, 111.3, 109.3, 96.7. MS (*m*/*z*) = 175 (M^+). Anal. calcd for $C_8H_5N_3S$: C 54.84, H 2.88, N 23.98; found: C 55.05, H 2.75, N 23.88.

3-Trifluoromethyl-4-thiocyanatoaniline (1m)

mp 148–150 °C (no literature value available). FT-IR (KBr): 2160 (SCN), 3275 and 3369 (NH_2). ^{1}H NMR ($CDCl_3$) δ: 7.80–7.33 (m, 3H), 4.01 (br s, 2H). ^{13}C NMR ($CDCl_3$) δ: 144.6, 135.3, 125.5, 118.8, 117.4, 115.1, 111.7. MS (*m*/*z*) = 218 (M^+). Anal. calcd for $C_8H_5F_3N_2S$: C 44.04, H 2.31, N 12.84; found: C 44.26, H 2.43, N 12.75.

2-Trifluoromethyl-4-thiocyanatoaniline (1n)

mp 119–120 °C (no literature value available). FT-IR (KBr): 2158 (SCN), 3395 and 3435 (NH_2). ^{1}H NMR ($CDCl_3$) δ: 7.68–7.28 (m, 2H), 6.80 (s, 1H), 4.574 (br s, 2H). ^{13}C NMR ($CDCl_3$) δ: 146.7, 137.5, 131.9, 125.6, 114.3, 111.6, 109.2. MS (*m*/*z*) = 218 (M^+). Anal. calcd for $C_8H_5F_3N_2S$: C 44.04, H 2.31, N 12.84; found: C 43.85, H 2.40, N 12.79.

5-Thiocyanatoindoline (1o)

mp 59–60 °C (no literature value available). FT-IR (KBr): 2216 (SCN), 3420 (NH). ^{1}H NMR ($CDCl_3$) δ: 7.19–6.92 (m, 3H), 5.20 (br s, 1H), 4.02 (t, *J* = 9.7 Hz, 2H), 3.23 (t, *J* = 8.5 Hz, 2H). ^{13}C NMR ($CDCl_3$) δ: 142.1, 128.1, 127.8, 127.4, 122.3, 114.89, 110.3, 50.7, 28.51. MS (*m*/*z*) = 176 (M^+). Anal. calcd for $C_9H_8N_2S$: C 61.34, H 4.58, N 15.90; found: C 61.56, H 4.45, N 15.95.

4-Thiocyanato-*N*-phenyl-2,2-iminodiethanol (1p)

mp 66–69 °C (no literature value available). FT-IR (KBr): 2153, 3300. ^{1}H NMR ($CDCl_3$) δ: 7.43 (d, *J* = 6.5 Hz, 1H), 6.70 (d, *J* = 7.1 Hz, 2H), 3.75–3.60 (4H, m), 3.55–3.35 (m, 4H), 2.15 (s, 2H). ^{13}C NMR ($CDCl_3$) δ: 151.8, 132.1, 116.5, 114.3, 111.7, 58.7, 55.9. MS (*m*/*z*) = 238 (M^+). Anal. calcd for $C_{11}H_{14}N_2O_2S$: C 55.44, H 5.92, N 11.76; found: C 55.66, H 5.79, N 11.85.

4-Thiocyanato-*N*-phenylmorpholine (1q)

mp 74–76 °C (no literature value available). FT-IR (KBr): 2156 (SCN). ^{1}H NMR ($CDCl_3$) δ: 7.48 (d, *J* = 8.29 Hz, 2H), 6.92 (d, *J* = 8.42 Hz, 2H), 3.88 (t, *J* = 4.69 Hz, 4H), 3.24–3.21 (t, *J* = 4.83 Hz, 4H). ^{13}C NMR ($CDCl_3$) δ: 152.5, 133.7, 116.1, 111.9, 111.1, 67.1, 48.06. MS (*m*/*z*) = 220 (M^+). Anal. calcd for $C_{11}H_{12}N_2OS$: C 59.97, H 5.49, N 12.72; found: C 59.79, H 5.65, N 12.85.

4-Thiocyanato-*N*-phenyl-15-crown-5 (1r)

mp 77–80 °C (no literature value available). FT-IR (KBr): 2147 (SCN), 1094 (C–O), ^{1}H NMR ($CDCl_3$) δ: 7.35 (d, *J* = 5.5 Hz, 2H), 6.64 (d, *J* = 6 Hz, 2H), 3.57–3.72 (m, 20H). ^{13}C NMR ($CDCl_3$) δ: 149.3, 134.7, 112.8, 105.9, 112.6, 71.2, 70.2, 69.9, 68.01, 52.6. MS (*m*/*z*) = 352 (M^+). Anal. calcd for $C_{17}H_{24}N_2O_4S$: C 57.93, H 6.86, N 7.95; found: C 58.19, H 6.99, N 7.89.

Supplementary data

Supplementary data are available with the article through the journal Web site http://nrcresearchpress.com/doi/suppl/10.1139/v2012-013.

Acknowledgement

The authors acknowledge financial support for this work from the Research Affairs Office of Bu-Ali Sina University (Grant No. 32-1716 entitled: Development of chemical methods, reagent, and molecules), from the Iranian National Elites, and also from the Center of Excellence in Development of Chemical Method (CEDCM), Hamadan, I.R. Iran.

References

(1) Merino, P.; Marqués-López, E.; Tejero, T.; Herrera, R. P. *Tetrahedron* **2009**, *65* (7), 1219. doi:10.1016/j.tet.2008.11.020.
(2) (a) Dalko, P. I.; Moisan, L. *Angew. Chem. Int. Ed.* **2004**, *43* (39), 5138. doi:10.1002/anie.200400650; (b) Pellissier, H. *Tetrahedron* **2007**, *63* (38), 9267. doi:10.1016/j.tet.2007.06.024.
(3) Dekamin, M. G.; Sagheb-Asl, S.; Naimi-Jamal, M. R. *Tetrahedron Lett.* **2009**, *50* (28), 4063. doi:10.1016/j.tetlet.2009.04.090.
(4) Shen, Y.; Feng, X. M.; Li, Y.; Zhang, G.; Jiang, Y. *Tetrahedron* **2003**, *59* (30), 5667. doi:10.1016/S0040-4020(03)00908-6.
(5) Dekamin, M. G.; Mokhtari, J.; Naimi-Jamal, M. R. *Catal. Commun.* **2009**, *10* (5), 582. doi:10.1016/j.catcom.2008.10.036.
(6) Blanrue, A.; Wilhelm, R. *Synlett* **2004**, (14): 2621.
(7) Dekamin, M. G.; Karimi, Z. *J. Organomet. Chem.* **2009**, *694* (12), 1789. doi:10.1016/j.jorganchem.2009.01.058.
(8) (a) Raj, I. V. P.; Suryavanshi, G.; Sudalai, A. *Tetrahedron Lett.* **2007**, *48* (40), 7211. doi:10.1016/j.tetlet.2007.07.188; (b) Denmark, S. E.; Chung, W. *J. Org. Chem.* **2006**, *71* (10), 4002. doi:10.1021/jo060153q; (c) Tian, S. K.; Hong, R.; Deng, L.

Can. J. Chem. Downloaded from www.nrcresearchpress.com by Renmin University of China on 09/02/12
For personal use only.

J. Am. Chem. Soc. **2003**, *125* (33), 9900. doi:10.1021/ja036222p.
(9) Fetterly, B. M.; Verkade, J. G. *Tetrahedron Lett.* **2005**, *46* (46), 8061. doi:10.1016/j.tetlet.2005.09.032.
(10) (a) Suzuki, Y.; Abu Bakar, M. D.; Muramatsu, K.; Sato, M. *Tetrahedron* **2006**, *62* (17), 4227. doi:10.1016/j.tet.2006.01.101; (b) Song, J. J.; Gallou, F.; Reeves, J. T.; Tan, Z.; Yee, N. K.; Senanayake, C. H. *J. Org. Chem.* **2006**, *71* (3), 1273. doi:10.1021/jo052206u.
(11) Amurrio, I.; Córdoba, R.; Csákÿ, A.; Plumet, J. *Tetrahedron* **2004**, *60* (46), 10521. doi:10.1016/j.tet.2004.07.101.
(12) Wang, X.; Tian, S. K. *Synlett* **2007**, (9): 1416. doi:10.1055/s-2007-980366.
(13) Franzén, J.; Marigo, M.; Fielenbach, D.; Wabnitz, T. C.; Kjarsgaard, A.; Jørgensen, K. A. *J. Am. Chem. Soc.* **2005**, *127* (51), 18296. doi:10.1021/ja056120u.
(14) Notz, W.; Tanaka, F.; Barbas, C. F., III. *Acc. Chem. Res.* **2004**, *37* (8), 580. doi:10.1021/ar0300468.
(15) Liu, J.; Yang, Z.; Wang, Z.; Wang, F.; Chen, X.; Liu, X.; Feng, X.; Su, Z.; Hu, C. *J. Am. Chem. Soc.* **2008**, *130* (17), 5654. doi:10.1021/ja800839w.
(16) Masson, G.; Housseman, C.; Zhu, J. *Angew. Chem. Int. Ed.* **2007**, *46* (25), 4614. doi:10.1002/anie.200604366.
(17) Basavaiah, D.; Rao, K. V.; Reddy, J. R. *Chem. Soc. Rev.* **2007**, *36* (10), 1581. doi:10.1039/b613741p.
(18) Hayashi, Y.; Tsuboi, W.; Ashimine, I.; Urushima, T.; Shoji, M.; Sakai, K. *Angew. Chem. Int. Ed.* **2003**, *42* (31), 3677. doi:10.1002/anie.200351813.
(19) Liu, T.-Y.; Cui, H.-L.; Long, J.; Li, B.-J.; Wu, Y.; Ding, L.-S.; Chen, Y.-C. *J. Am. Chem. Soc.* **2007**, *129* (7), 1878. doi:10.1021/ja068703p.
(20) Rodríguez, B.; Bolm, C. *J. Org. Chem.* **2006**, *71* (7), 2888. doi:10.1021/jo060064d.
(21) Hayashi, Y.; Gotoh, H.; Tamura, T.; Yamaguchi, H.; Masui, R.; Shoji, M. *J. Am. Chem. Soc.* **2005**, *127* (46), 16028. doi:10.1021/ja055740s.
(22) Xie, H.; Zu, L.; Li, H.; Wang, J.; Wang, W. *J. Am. Chem. Soc.* **2007**, *129* (35), 10886. doi:10.1021/ja073262a.
(23) Herrera, R. P.; Sgarzani, V.; Bernardi, L.; Ricci, A. *Angew. Chem. Int. Ed.* **2005**, *44* (40), 6576. doi:10.1002/anie.200500227.
(24) Shibuya, M.; Tomizawa, M.; Suzuki, I.; Iwabuchi, Y. *J. Am. Chem. Soc.* **2006**, *128* (26), 8412. doi:10.1021/ja0620336.
(25) Imada, Y.; Iida, H.; Ono, S.; Murahashi, S.-I. *J. Am. Chem. Soc.* **2003**, *125* (10), 2868. doi:10.1021/ja028276p.
(26) Kazmaier, U. *Angew. Chem. Int. Ed.* **2005**, *44* (15), 2186. doi:10.1002/anie.200462873.
(27) Enders, D.; Grondal, C.; Hüttl, M. R. M. *Angew. Chem. Int. Ed.* **2007**, *46* (10), 1570. doi:10.1002/anie.200603129.
(28) McCooey, S. H.; Connon, S. J. *Angew. Chem. Int. Ed.* **2005**, *44* (39), 6367. doi:10.1002/anie.200501721.
(29) Clarke, M. L.; Fuentes, J. A. *Angew. Chem. Int. Ed.* **2007**, *46* (6), 930. doi:10.1002/anie.200602912.
(30) Pan, X.-Q.; Lei, M.-Y.; Zou, J.-P.; Zhang, W. *Tetrahedron Lett.* **2009**, *50* (3), 347. doi:10.1016/j.tetlet.2008.11.007.
(31) Guy, R. G. In *The Chemistry of the Cyanates and Their Thio Derivatives;* Patai, S., Ed.; Wiley Interscience: New York, 1977; p 819.
(32) Shahidi, F. *Sulphur Compounds in Foods;* Mussinan, C. J.; Keelan, M. E. Eds.; American Chemical Society: Washington, DC, 1994; Chapter 9, p 106.
(33) Mehta, R. G.; Liu, J.; Constantinou, A.; Thomas, C. F.; Hawthorne, M.; You, M.; Gerhäuser, C.; Pezzuto, J. M.; Moon, R. C.; Moriarty, R. M. *Carcinogenesis* **1995**, *16* (2), 399. doi:10.1093/carcin/16.2.399.
(34) Prakash, O.; Kaur, H.; Batra, H.; Rani, N.; Singh, Sh. P.; Moriarty, R. M. *J. Org. Chem.* **2001**, *66* (6), 2019. doi:10.1021/jo001504i.
(35) Billard, T.; Langlois, B. R.; Medebielle, M. *Tetrahedron Lett.* **2001**, *42* (20), 3463. doi:10.1016/S0040-4039(01)00514-7.
(36) Zhang, Z. H.; Liebeskind, L. S. *Org. Lett.* **2006**, *8* (19), 4331. doi:10.1021/ol061741t.
(37) (a) Riemschneider, R.; Wojahn, F.; Orlick, G. *J. Am. Chem. Soc.* **1951**, *73* (12), 5905. doi:10.1021/ja01156a552; (b) Riemschneider, R. *J. Am. Chem. Soc.* **1956**, *78* (4), 844. doi:10.1021/ja01585a038.
(38) Lee, Y. T.; Choi, S. Y.; Chung, Y. K. *Tetrahedron Lett.* **2007**, *48* (32), 5673 and references cited therein. doi:10.1016/j.tetlet.2007.06.041.
(39) Söderbäck, E. *Acta Chem. Scand.* **1954**, *8*, 1851. doi:10.3891/acta.chem.scand.08-1851.
(40) Grant, M. S.; Snyder, H. R. *J. Am. Chem. Soc.* **1960**, *82* (11), 2742. doi:10.1021/ja01496a023.
(41) Wu, G.; Liu, Q.; Shen, Y.; Wu, W.; Wu, L. *Tetrahedron Lett.* **2005**, *46* (35), 5831. doi:10.1016/j.tetlet.2005.06.132.
(42) Toste, F. D.; De Stefano, V.; Still, I. W. J. *Synth. Commun.* **1995**, *25* (8), 1277. doi:10.1080/00397919508012691.
(43) Nair, V.; George, T. G.; Nair, L. G.; Panicker, S. B. *Tetrahedron Lett.* **1999**, *40* (6), 1195. doi:10.1016/S0040-4039(98)02563-5.
(44) Chakrabarty, M.; Sarkar, S. *Tetrahedron Lett.* **2003**, *44* (44), 8131. doi:10.1016/j.tetlet.2003.09.032.
(45) Yadav, J. S.; Reddy, B. V. S.; Shubashree, S.; Sadashiv, K. *Tetrahedron Lett.* **2004**, *45* (14), 2951. doi:10.1016/j.tetlet.2004.02.073.
(46) Iranpoor, N.; Firouzabadi, H.; Khalili, D.; Shahin, R. *Tetrahedron Lett.* **2010**, *51* (27), 3508. doi:10.1016/j.tetlet.2010.04.096.
(47) Iranpoor, N.; Firouzabadi, H.; Azadi, R. *Tetrahedron Lett.* **2006**, *47* (31), 5531. doi:10.1016/j.tetlet.2006.05.145.
(48) Bhalerao, D. S.; Akamanchi, K. G. *Synlett* **2007**, (18): 2815. doi:10.1055/s-2007-991093.
(49) Yadav, J. S.; Reddy, B. V. S.; Krishna, B. B. M. *Synthesis* **2008**, *2008* (23), 3779. doi:10.1055/s-0028-1083636.
(50) Srihari, P.; Sirigh, A. P.; Jain, R.; Yadav, J. S. *Synthesis* **2005**, (6): 961. doi:10.1055/s-2005-861852.
(51) Kumar, A.; Ahamd, P.; Maurya, R. A. *Tetrahedron Lett.* **2007**, *48* (8), 1399. doi:10.1016/j.tetlet.2006.12.103.
(52) Yadav, J. S.; Reddy, B. V. S.; Reddy, Y. J. *Chem. Lett.* **2008**, *37* (6), 652. doi:10.1246/cl.2008.652.
(53) Memarian, H. R.; Mohammadpoor-Baltork, I.; Nikoofar, K. *Ultrason. Sonochem.* **2008**, *15* (4), 456. doi:10.1016/j.ultsonch.2007.09.010.
(54) Wu, J.; Wu, G. L.; Wu, L. M. *Synth. Commun.* **2008**, *38* (14), 2367. doi:10.1080/00397910802139254.
(55) Memarian, H. R.; Mohammadpoor-Baltork, I.; Nikoofar, K. *Can. J. Chem.* **2007**, *85* (11), 930. doi:10.1139/v07-092.

Polarized continuum model study of bond dissociation energies of the O–NO_2 bond — A density functional theory study and natural bond order analysis

Zhang Ruizhou, Fu Zhumu, Li Xiaohong, and Zhang Xianzhou

Can. J. Chem. Downloaded from www.nrcresearchpress.com by Renmin University of China on 09/02/12
For personal use only.

Abstract: Density functional methods (B3LYP, B3PW91, B3P86, and MPWB95) with 6–31G** basis sets and complete basis methods are employed to investigate the bond dissociation energies (BDEs) of the O–NO_2 bond for seven *O*-nitroalcohol compounds in acetonitrile solution. B3LYP/6–31+G**, (RO)B3LYP/6–311++G(2df,2p), and B3LYP/6–311G(d,p) methods are also used. By comparing the calculated results with the experimental values, B3LYP/6–31+G** is the most accurate method to compute the reliable BDEs for the studied compounds. The substituent effects on the O–NO_2 BDEs are analyzed. It is found that electron-withdrawing groups increase the BDE of the parent compound, whereas electron-donating groups decrease the BDE of the parent compound. Further, the natural bond orbital analysis shows that there exist good linear correlations between $E^{(2)}$ and Hammett constants, the BDE, and the difference of the second-order stabilization energies $E^{(2)}$ of $lpO_3 \rightarrow BD^*(O_1–N_1)$ and $lpO_3 \rightarrow BD^*(O_2–N_1)$.

Key words: density functional theory, polarized continuum model, *O*-nitroalcohol compounds, bond dissociation energy, natural bond orbital analysis.

Résumé : On a fait appel à des méthodes de la fonctionnelle de la densité (B3LYP, B3PW91, B3P86, MPWB95) et on a utilisé des méthodes avec des ensembles de base 6–31G** et des bases complètes pour étudier les énergies de dissociation de liaisons (EDL) O–NO_2 pour des composés sept *O*-nitroalcools en solution dans l'acétonitrile. On a aussi utilisé les méthodes B3LYP/6–31G**, (RO)B3LYP/6–311++G(2df,2p) et B3LY/6–311G(d,p). Par comparaison avec les données expérimentales, la méthode B3LYP/6–31+G** est la plus précise pour calculer des valeurs fiables pour les EDL des composés étudiés. On a analysé les effets de substituants sur les valeurs de EDL O–NO_2. On a observé que les groupes électro-attracteurs augmentent la valeur des EDL du produit de base alors que les groupes électro-répulsifs diminuent les valeurs de EDL du produit de base. De pus l'analyse des orbitales naturelles de liaison montre qu'il existe une bonne corrélation linéaire entre $E^{(2)}$ et les constantes de Hammett, l'EDL et la différence des énergies de stabilisation du deuxième ordre $E^{(2)}$ de $1pO_3 \rightarrow BD^*(O_1–N_1)$ et $1pO_3 \rightarrow BD^*(O_2–N_1)$.

Mots-clés : théorie de la fonctionnelle de la densité, modèle du continuum polarisé, composés *O*-nitroalcools, énergie de dissociation de liaison, analyse de l'orbitale naturelle de liaison.

[Traduit par la Rédaction]

Introduction

In the last two decades, the chemistry and biochemistry of nitrogen oxides (N*x*O*y*) have regained tremendous research attention,[1] because of the recent discoveries on the significant roles of N*x*O*y* in many important natural processes. Among various kinds of N*x*O*y*, nitric oxide (NO) is one of the smallest known biologically active messenger molecules and it plays key roles in regulating many important physiological functions in living bodies.[2–5] However, the importance of nitrogen dioxide (NO_2) has largely been overshadowed or even overlooked during the same period.

In chemistry, NO_2 is considered a strong oxidant and nitrating reagent for organic synthesis. Recent research shows that NO_2 is found to be associated with many destructive processes in living bodies, and the significant functions of NO_2 and nitrite ion (NO_2^-) in mammalian biology have slowly been accumulated.[6–9] Therefore, the research on the functions of NO_2 and NO_2^- has started to draw increasing attention recently. Espey et al.[10] and Pfeiffer[11] et al. thought that a wide spectrum of diseases is related to the exogenously and endogenously generated NO_2. In addition, NO_2^- plays a crucial role in many NO-mediated processes and gene expression.[12–14]

Received 30 November 2011. Accepted 2 February 2012. Published at www.nrcresearchpress.com/cjc on 4 April 2012.

Z. Ruizhou and L. Xiaohong. College of Physics and Engineering, Henan University of Science and Technology, Luoyang 471003, China.
F. Zhumu. Electronic and Information Engineering College, Henan University of Science and Technology, Luoyang 471003, China.
Z. Xianzhou. College of Physics and Information Engineering, Henan Normal University, Xinxiang, 453007, China.

Corresponding author: Li Xiaohong (e-mail: lorna639@126.com).

Can. J. Chem. Downloaded from www.nrcresearchpress.com by Renmin University of China on 09/02/12
For personal use only.

To understand the mechanistic details of NO_2 in chemical or biological processes, the basic information concerning quantitative energetic changes in NO_2-related bond cleavage in solution should be of great value because it provides the necessary information on the thermodynamic driving forces of NO_2 carrier molecules to release, capture, or transfer a NO_2 moiety.[15] The binding force of NO_2 with a particular active site can therefore be represented by the bond energy of the Y–NO_2 type, where Y represents the atom in a carrier to which NO_2 is directly attached. Recently, Li et al.[15] report a series of determined O–NO_2 homolytic bond energies of some *O*-nitroalcohols in acetonitrile solution by using titration calorimetry combined with relevant electrochemical data through proper thermodynamic cycles. The structures of the selected *O*-nitroalcohols are shown in Fig. 1.

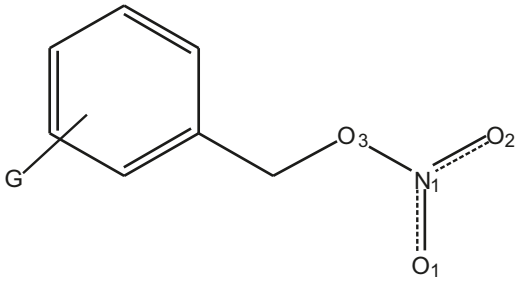
Because a rapid cleavage of the Y–NO_2 bond upon one-electron reduction of a nitro compound has been observed for years,[16–18] this kind of bond energy scale should also be useful for the study of the stability and shock sensitivity of the Y–NO_2-type energetic materials[19,20] and for estimating the nitrating ability of nitro-releasing compounds in synthetic chemistry.[21,22] However, our library survey shows that there are very few reports on the bond dissociation energies (BDEs) for the Y–NO_2 bond energies in any solvent system where the NO_2-related chemical and biological activities are likely to take place. If we can find an accurate calculational method to compute the BDEs of the Y–NO_2 bond, it would be possible to use this method to predict those molecules whose experimental BDEs are not available. In addition, the Y–NO_2 bond energy data bank can deepen our understanding of the board range of NO_2-related activities. This has also spurred us to initiate research on the O–NO_2 bond energies of molecules in solution.

Computational methods derived from density functional theory (DFT) are currently more practical for BDE calculation because of their favorable scaling and reasonable CPU cost. Among these DFT methods, B3LYP, B3PW91, and B3P86 are highly popular because of their advantages in BDE calculation. Previous research shows that the C–N BDEs for imidazole derivatives computed by the B3LYP/6–31G** method are in excellent agreement with their experimental values.[23] The B3P86 method revealed the best agreement with available experimental data in predicting the C–NO BDE.[24] Furthermore, Fu et al.[25] computed the BDEs of Y–NO bonds (Y = C, N, O, and S) for X–Y–NO (X = H, CH_3, C_2H_5, OCH_3, $COCH_3$, and Ph) molecules by the B3LYP method.

However, recent studies from a more general perspective demonstrated that these popular DFT methods could tend to underestimate BDEs by 2–6 kcal/mol (1 cal = 4.184 J).[26] Obviously, these failures are due to deficiencies of the approximate exchange-correlation functionality used for different calculating systems. So it is important to shed light on their systematic performance for a particular computational target.

In the present work, our objective was to perform a systematic comparison of the O–NO_2 BDEs of seven *O*-nitroalcohols compounds in acetonitrile solution. All the BDEs were calculated by employing hybrid DFT (B3LYP, B3PW91, B3P86, and MPWB95) methods and the complete basis set (CBS-4M) method. By comparing the calculated results with the available experimental values, a suitable method to compute O–NO_2 BDEs was obtained. The natural bond orbital (NBO) analysis was also performed for the title compounds.

Fig. 1. The structures of selected *O*-nitroalcohols.



G= 4-MeO, 4-Me, 4-H, 4-Cl, 4-Br, 4-CF_3, 4-NO_2

Theory and computational details

All calculations were performed with the Gaussian03 computational package.[27] Geometry optimizations and subsequent normal mode analyses were performed for the products of the different bond scission reactions in which a single NO_2 group was removed from the parent structure. The equilibrium geometries and BDEs were obtained at the Becke-style three-parameter DFT[28] with the Lee–Yang–Parr correlation function(LYP),[29,30] Perdew–Wang's 91 expression (PW91),[31] and Perdew's 86(P86).[32] One recently developed DFT method – one-parameter hybrid meta-GGA functional MPWB95[33] was also used in this paper. All calculations were performed at the 6–31G** basis set. The normal mode analysis for each structure resulted in no imaginary frequencies for the $3N - 6$ vibrational degrees of freedom, where N is the number of atoms in the system. This indicates that the structure of each molecule corresponds to a local minimum on the potential energy surface.

Generally, computed BDEs are reported for gas-phase conditions and it is expected that these values suffer variation in different environments such as those in living organisms. Therefore, it would be interesting to know what happens to these dissociation energies in the presence of a solvent such as acetonitrile.

The polarized continuum model (PCM) developed by Tomasi and co-workers[34–36] was employed. In this PCM model, the atomic radii of the spheres used to build the molecular cavity were adjusted by introducing chemical considerations such as hybridization, formal charge, and first-neighbor inductive effect. The effect of the escaped electronic charge outside the cavity was corrected with an additional set of charges on the cavity surface distributed according to the solute electronic density in each point of the surface.

For the CBS-4M model,[37–39] geometry optimization and zero-point energy computations were carried out first in Hartree–Fock theory. Then, the energy was evaluated with the second-order of Møller–Plesset (MP2) theory with a larger basis set and a CBS extrapolation to correct the energy through the second order. The MP4SDQ/6–31G calculation was used to approximate higher orders of contributions. There are also empirical corrections for spin contamination and a size-consistent higher order correction.

Can. J. Chem. Downloaded from www.nrcresearchpress.com by Renmin University of China on 09/02/12
For personal use only.

Table 1. The N_1–O_3 bond lengths (Å) of some *O*-nitroalcohol compounds (4-Y–C_6H_4–CH_2ONO_2) calculated by different DFT methods and the CBS-4M method (Y represents the atom in a carrier to which NO_2 is directly attached).

Method	Y = H	Y = CH_3	Y = Cl	Y = NO_2	Y = Br	Y = CF_3	Y = OCH_3	$C_2H_5ONO_2$[a]
B3LYP/6–31G**	1.393	1.393	1.395	1.398	1.396	1.397	1.392	1.391 (0.014)
B3PW91/6–31G**	1.381	1.381	1.384	1.387	1.384	1.385	1.379	1.379 (0.026)
B3P86/6–31G**	1.379	1.378	1.381	1.385	1.381	1.382	1.378	1.377 (0.028)
MPWB95/6–31G**	1.365	1.365	1.366	1.370	1.366	1.368	1.363	1.363 (0.042)
B3LYP/6–31+G**	1.389	1.388	1.391	1.395	1.392	1.393	1.387	1.386 (0.019)
CBS-4M	1.393	1.393	1.394	1.395	1.394	1.395	1.393	1.390 (0.015)
Expt.								1.405[b]
MP2/6–311G*[c]								1.411

[a]Values in parenthesis are deviations between computational results and experimental ones.
[b]See ref. 40.
[c]See ref. 41.

Table 2. Computed bond dissociation energies (BDEs, kcal/mol) in MeCN for the removal of an NO_2 group in *O*-nitroalcohol molecules by using various density functional theory (DFT) methods with the 6–31G** basis set (1 cal = 4.184 J).

		DFT method[a]			
Entry	Compound	B3LYP	B3PW91	B3P86	Expt.[b]
1	4-H–C_6H_4–CH_2ONO_2	37.7 (7.3)	40.5 (10.1)	42.2 (11.8)	30.4
2	4-CH_3–C_6H_4–CH_2ONO_2	37.5 (7.2)	40.3 (10.0)	42.0 (11.7)	30.3
3	4-Cl–C_6H_4–CH_2ONO_2	38.7 (7.9)	42.2 (11.4)	45.4 (14.6)	30.8
4	4-NO_2–C_6H_4–CH_2ONO_2	41.8 (2.2)	43.2 (3.6)	45.8 (6.2)	39.6
5	4-Br–C_6H_4–CH_2ONO_2	40.4 (9.3)	42.2 (11.1)	45.4 (14.3)	31.1
6	4-CF_3–C_6H_4–CH_2ONO_2	41.1 (9.7)	43.0 (11.6)	46.2 (14.6)	31.4
7	4-OCH_3–C_6H_4–CH_2ONO_2	37.2 (7.1)	39.4 (9.3)	41.7 (11.6)	30.1
Mean absolute deviation		7.2	9.6	12.1	

[a]The values in the parentheses are the deviations from the computed BDE for the experimental value.
[b]The data are from ref. 15.

The O–NO_2 bond strength was obtained by calculating the homolytic BDE, which is defined as the enthalpy change of the dissociation reaction

$$[1] \qquad R{-}X \rightarrow R^{\bullet} + X^{\bullet}$$

For the *O*-nitroalcohols studied here, the BDE is defined as the difference between the zero-point-corrected energy of the parent molecule and that of the products of the unimolecular dissociation in which a NO_2 group is removed. For example, for 4-CH_3–$C_6H_4CH_2O$–NO_2 the BDE is

$$[2] \qquad BDE_{O-NO_2} = E(C_8H_9O) + E(NO_2) - E(C_8H_9NO_3)$$

The average errors of the BDEs for the B3LYP, B3PW91, and B3P86 methods were determined by calculating the average absolute error (ε_{aae}), defined as

$$[3] \qquad \varepsilon_{aae} = \frac{1}{N}\sum_{i=1}^{N} |x_i - c_i|$$

where x_i represents the experimental data, c_i denotes the calculated values, and N is the number of experimental or calculated data.

Results and discussion

The N–O bond length

First, we examined the N_1–O_3 bond length of seven *O*-nitroalcohol compounds by various computational methods. The experimental equilibrium bond distances for the N_1–O_3 bond distances of the seven title compounds were not available. To have a comparison, we listed the N_1–O_3 experimental value[40] for $C_2H_5ONO_2$. It is noted from Table 1 that the N_1–O_3 bond lengths computed by the B3LYP functional are the biggest among those calculated by the B3LYP, B3PW91, B3P86, and MPWB95 methods with the 6–31G** basis set, and the N_1–O_3 bond lengths calculated by the MPWB95/6–31G** method are the smallest. The N_1–O_3 bond lengths computed by the CBS-4M method are slightly smaller than those computed by the B3LYP/6–31G** method except for 4-OCH_3–C_6H_4–CH_2ONO_2.

Compared with the corresponding experimental value, the B3LYP/6–31G** method produces the best result for $C_2H_5ONO_2$ with an N_1–O_3 bond length of 1.391 Å, only a 0.014 Å deviation from the experimental value, whereas the MPWB95/6–31G** method gives the worst result for $C_2H_5ONO_2$ with an N_1–O_3 bond length of 1.363 Å. In Table 1, we listed the results computed by Gong et al.[41] with the MP2/6–311G* method.

In addition, we computed the N_1–O_3 bond lengths of the selected compounds by using the BLYP/6–31+G**method. Through a comparison of the computational results, it is noted that the use of the diffuse function will improve the result. The deviation from the experimental value increases in the presence of the function.

Can. J. Chem. Downloaded from www.nrcresearchpress.com by Renmin University of China on 09/02/12
For personal use only.

Table 3. Computed bond dissociation energies (BDEs, kcal/mol; 1 cal = 4.1.84 J) in MeCN for the removal of an NO_2 group in *O*-nitroalcohol molecules by using the B3LYP/6–31+G**, CBS-4M, and MPWB95/6–31G** methods and the computed BDEs in MeCN for the removal of an NO_2 group in several *N*-nitroacylamides by using the B3LYP/6–31+G** method.

		Method[a]					Method[a]	
Entry	Compound	B3LYP/6–31+G**	MPWB95/6–31G**	CBS-4M	Expt.[b]	Compound	B3LYP/6–31+G**	Expt.[b]
1	4-H–C_6H_4–CH_2ONO_2	32.6 (2.2)	44.3 (13.9)	47.0 (16.6)	30.4	4-MeO–$C_6H_4CON(CH_3)NO_2$	34.0 (0.4)	33.6
2	4-CH_3–C_6H_4–CH_2ONO_2	32.4 (2.1)	44.0 (13.7)	46.8 (16.5)	30.3	4-CH_3–$C_6H_4CON(CH_3)NO_2$	33.8 (0.4)	33.4
3	4-Cl–C_6H_4–CH_2ONO_2	33.0 (2.2)	46.3 (15.5)	47.2 (16.4)	30.8	$C_6H_5CON(CH_3)NO_2$	33.3 (0.0)	33.3
4	4-NO_2–C_6H_4–CH_2ONO_2	34.9 (–4.7)	42.4 (2.8)	45.2 (5.6)	39.6	4-Cl–$C_6H_4CON(CH_3)NO_2$	33.3 (0.4)	32.9
5	4-Br–C_6H_4–CH_2ONO_2	34.6 (3.5)	46.3 (15.2)	49.5 (18.4)	31.1	4-Br–$C_6H_4CON(CH_3)NO_2$	33.6 (0.9)	32.7
6	4-CF_3–C_6H_4–CH_2ONO_2	34.8 (3.4)	43.2 (11.8)	44.8 (13.4)	31.4	4-NO_2–$C_6H_4CON(CH_3)NO_2$	32.4 (–0.2)	32.6
7	4-OCH_3–C_6H_4–CH_2ONO_2	32.1 (2.0)	43.8 (13.7)	46.4 (16.3)	30.1	$C_6H_5CON(C_2H_5)NO_2$	32.4 (–0.5)	32.9
Mean absolute deviation		2.9	12.4	14.7			0.4	

[a]The values in parentheses are the deviations from computed BDEs for the experimental values.
[b]The data are from ref. 15.

The BDEs of *O*-nitroalcohols in acetonitrile

The BDE results computed by using the B3LYP, B3P86, and B3PW91 three-parameter hybrid DFT methods with the 6–31G** basis set are presented in Table 2. The available experimental values[15] are also included. The BDEs of seven *O*-nitroalcohols are compared with the corresponding experimental results for the system. Detailed analysis reveals that the BDEs calculated by the B3LYP, B3P86, and B3PW91 methods all overestimated BDE, which disagrees with previous research asserting that DFT methods usually underestimate BDE systematically.

It is noted that the BDEs calculated by the B3P86 method for the seven molecules are all very poor, and all of the B3P86 calculated results overestimate the BDEs for the studied compounds. The O–NO_2 BDEs for the studied molecules have a considerable difference when compared with the experimental values. The average absolute difference for the B3P86 method is 12.1 kcal/mol, which is outside our desired target accuracy for chemical predictions. In Table 2, the largest error is found for 4-CF_3–C_6H_4–CH_2ONO_2 and 4-Cl–C_6H_4–CH_2ONO_2 (14.6 kcal/mol).

The mean absolute deviation between B3PW91 results and the experimental is 9.6 kcal/mol, which is smaller than that for the B3P86 method. From Table 2, we can see that the B3PW91 calculated results also overestimate the BDEs for the studied compounds. The maximum difference for the B3PW91 method is 11.6 kcal/mol for the BDE of compound 4-CF_3–C_6H_4–CH_2ONO_2. Thus, while the B3PW91 method with the 6–31G** basis set yields good results for some systems, it is clear that this method is not suitable for predicting accurate BDEs for the N_1–O_3 bond.

In Table 2, we can also see that the values obtained with the B3LYP method are closer to the experimental values than those obtained with the B3PW91 and B3P86 methods, with a mean absolute deviation between the B3LYP results and the experimental values of 7.3 kcal/mol. It is also noted that the mean absolute error reduces from 12.1 to 7.3 kcal/mol when the B3P86 method is replaced by the B3LYP method, which proves that the N_1–O_3 BDE for the studied compounds is sensitive to the calculational methods. Comparing the three DFT methods, it is noted that B3LYP method is the best procedure to compute the N_1–O_3 BDE among the selected methods, although the N_1–O_3 BDEs calculated by the B3LYP/6–31G** method for the studied molecules are considerably different when compared with the experimental values.

To determine whether the B3LYP method is sensitive to the basis sets, we computed the BDEs of the *O*-nitroalcohol compounds with the B3LYP method at the 6–31+G** basis set. In addition, to give an extensive comparison, the CBS-4M and MPWB95/6–31G** methods were also employed to predict the BDEs for the seven compounds. All calculated results are presented in Table 3.

As can be seen in Table 3, the N_1–O_3 BDEs performed by CBS-4M method are drastically deviated from the experimental values, with an average absolute deviation of 14.7 kcal/mol and a maximum deviation of 18.4 kcal/mol. For the seven compounds, the deviations between computational and experimental values are all greater than 3.0 kcal/mol. Therefore, the CBS-4M method is not suitable for predicting the BDEs for the studied compounds. For the

Can. J. Chem. Downloaded from www.nrcresearchpress.com by Renmin University of China on 09/02/12
For personal use only.

Table 4. Computed bond dissociation energies (BDEs, kcal/mol; 1 cal = 4.1.84 J) in MeCN for the removal of an NO_2 group in *O*-nitroalcohol molecules by using the (RO)B3LYP/6–311++G(2df,2p) and B3LYP/6–311G(d,p) methods.

		Method[a]		
Entry	Compound	(RO)B3LYP/6–311++G(2df,2p)	B3LYP/6–311G(d,p)	Expt.[b]
1	4-H–C_6H_4–CH_2ONO_2	32.9 (2.5)	34.2 (3.8)	30.4
2	4-CH_3–C_6H_4–CH_2ONO_2	34.7 (3.4)	35.6 (5.3)	30.3
3	4-Cl–C_6H_4–CH_2ONO_2	30.3 (–0.5)	35.7 (4.9)	30.8
4	4-NO_2–C_6H_4–CH_2ONO_2	31.4 (–8.2)	36.2 (–3.4)	39.6
5	4-Br–C_6H_4–CH_2ONO_2	35.0 (3.9)	35.5 (4.4)	31.1
6	4-CF_3–C_6H_4–CH_2ONO_2	35.0 (3.6)	35.8 (4.4)	31.4
7	4-OCH_3–C_6H_4–CH_2ONO_2	33.2 3.1)	33.3 (3.2)	30.1
Mean absolute deviation		3.6	4.2	

[a] The values in parentheses are the deviations from computed BDEs for the experimental values.
[b]The data are from ref. 15.

MPWB95/6–31G** method, the average absolute deviation is 12.4 kcal/mol, which is slightly smaller than that obtained by the CBS-4M method. For the B3LYP method, the use of the diffuse function can greatly improve the results. The deviations from experimental values drastically decrease in the presence of the diffuse function.

In view of the importance of the study on the BDEs of the Y–NO_2 type of compounds and whether the B3LYP/6–31+G** method can give satisfactory BDEs for other types of Y–NO_2 bonds, such as *N*-nitroacylamides, we computed the N–NO_2 BDEs of several *N*-nitroacylamides by the B3LYP/6–31+G** method. The computed results are listed in Table 3. From Table 3, it is noted that the B3LYP/6–31+G** method gave the better BDEs for the *N*-nitroacylamides. All the deviations are within 1.0 kcal/mol, the maximum deviation is 0.9 kcal/mol, and the mean absolute deviation is 0.4 kcal/mol.

Chandra et al.[42] estimated accurate S–H BDEs by using the (RO)B3LYP/6–311++G(2df,2p) method. Nam et al.[43,44] estimated accurate P–H BDEs by the (RO)B3LYP/6–311++G(2df,2p) method and C–H BDEs of toluene derivatives by using the (RO)B3LYP/6–311++G(2df,2p) and B3LYP/6–311G(d,p) methods. To determine whether the (RO)B3LYP/6–311++G(2df,2p) and B3LYP/6–311G(d,p) methods can obtain accurate O–N BDEs of the studied *O*-nitroalcohol compounds, we computed the O–N BDEs of the *O*-nitroalcohol compounds by using the (RO)B3LYP/6–311++G(2df,2p) and B3LYP/6–311G(d,p) methods. The computed results are all listed in Table 4. According to Table 4, it is interesting to point out that, although the (RO)B3LYP/6–311++G(2df,2p) and B3LYP/6–311G(d,p) methods gave accurate P–H BDEs and C–H BDEs, the two methods seem to give poor results for the studied molecules. For 4-NO_2–C_6H_4–CH_2ONO_2, the (RO)B3LYP/6–311++G(2df,2p) method produced a BDE of 31.4 kcal/mol, a 8.2 kcal/mol deviation from the experimental value. For the other six compounds, there are four compounds for which the deviations between computational and experimental values are greater than 3.0 kcal/mol. A similar analysis was made for the computed results by the B3LYP/6–311G(d,p) method.

Here, we should note that the B3LYP/6–31+G** method is able to accurately predict the BDE of the N–O bond for the selected alcohol compounds, but it is not a suitable method for estimating the transition metal – OH bond energies. Numerous studies show that the best method for calculating bond energies of transition-metal complexes is CCSD(T).[45] Dapprich et al.[46] calculated the BDEs of transition-metal complexes and found that CCSD(T) results were in good agreement with experimental data, whereas the bond energies at the HF level were too low and the MP2 results were too high.

Fig. 2. Dependence of the O_3–N_1 bond dissociation energy (BDE) on bond length for the title compounds in acetonitrile solution.

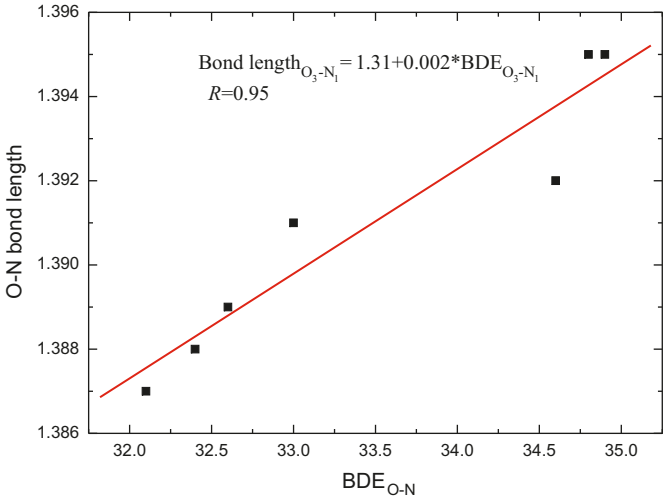


Table 5. Substituent effects on the bond dissociation energies (BDEs) of N_1–O_3 homolysis (kcal/mol; 1 cal = 4.1.84 J) by using the B3LYP/6–31+G** method for Y–C_6H_4–CH_2ONO_2 in acetonitrile (Y represents the atom in a carrier to which NO_2 is directly attached).

	Y–C_6H_4–CH_2ONO_2	
Y	BDE	ΔBDE
4-H	32.6	0
4-OCH_3	32.1	–0.5
4-CH_3	32.4	–0.2
4-Cl	33.0	0.4
4-Br	34.6	2.0
4-CF_3	34.8	2.2
4-NO_2	34.9	2.3

Can. J. Chem. Downloaded from www.nrcresearchpress.com by Renmin University of China on 09/02/12
For personal use only.

Table 6. The second-order perturbation theory analysis of the Fock matrix on the natural bond order (NBO) basis at the B3LYP/6–31+G** level.

Entry	Compound	$lpO_3 \rightarrow BD^*(O_1–N_1)$	$E(J) - E(I)^a$(au)	$F(i,j)^b$ (au)	$lpO_3 \rightarrow BD^*(O_2–N_1)$	$E(J) - E(I)^a$(au)	$F(i,j)^b$ (au)
1	4-H–C_6H_4–CH_2ONO_2	38.42	0.19	0.087	6.28	1.09	0.074
2	4-CH_3–C_6H_4–CH_2ONO_2	38.76	0.19	0.088	6.31	1.09	0.075
3	4-Cl–C_6H_4–CH_2ONO_2	37.83	0.19	0.087	5.64	1.23	0.075
4	4-NO_2–C_6H_4–CH_2ONO_2	36.24	0.19	0.086	7.01	1.09	0.073
5	4-Br–C_6H_4–CH_2ONO_2	37.79	0.19	0.087	6.19	1.09	0.074
6	4-CF_3–C_6H_4–CH_2ONO_2	37.18	0.19	0.086	6.11	1.09	0.074
7	4-OCH_3–C_6H_4–CH_2ONO_2	39.09	0.19	0.088	6.34	1.09	0.075

[a]Energy difference between donor (*i*) and acceptor (*j*) NBO orbitals.
[b]$F(i,j)$ is the Fock matrix element between *I* and *J* NBO orbitals.

From Tables 1 and 3, through analysis of the O_3–N_1 bond lengths and the BDEs calculated by the B3LYP/6–31+G** method, we found that the N_1–O_3 BDE is in a good linear relationship with the N_1–O_3 bond length and the correlated coefficient is 0.95. Figure 2 plots the correlation between the O_3–N_1 BDE and bond lengths.

Substituent effects on the BDEs of the O–NO_2 bond

From the analysis in the previous section, we know that B3LYP/6–31+G** is the best procedure for computing the dissociation energies for the N_1–O_3 bond in acetonitrile. Using this method, we studied the substituent effect on the N_1–O_3 BDEs for the studied molecules, where substituted groups include both the electron-donating and -withdrawing groups such as 4-Cl, 4-Br, 4-NO_2, 4-CH_3, and 4-CH_3O. The calculated BDEs for the selected compounds are shown in Table 5. The results show that the substituent effects on the BDEs of the selected compounds are insignificant.

An interesting point observed in the selected molecules is the change of BDEs and ΔBDE with the Hammett constant σ_p values of the substituent on the benzene. The Hammett constants[47] of the OCH_3, CH_3, H, Cl, Br, CF_3, and NO_2 groups are –0.27, –0.07, 0.00, 0.23, 0.23, 0.54, and 0.78, respectively. It is noted that electron-withdrawing groups increase the BDE of the parent compound 4-H–C_6H_4–CH_2ONO_2, while electron-donating groups decrease the BDE of the parent compound. On the one hand, we think this is because the benzene ring shows a strong negative inductive effect and a negative conjugative effect when the substituted group is connected with the benzene ring, which makes the density of the electric cloud change greatly and has an effect on the properties of the parent compound. On the other hand, it may occur because both groups may cause spin delocalization from the radical center formed by a single NO_2 group leaving the parent structure.

NBO analysis

NBO analysis provides an efficient method for studying intra- and inter-molecular bonding and interaction among bonds, and it also provides a convenient basis for investigating charge transfer or conjugative interaction in molecular systems. Some electron orbitals, acceptor orbitals, and the interacting stabilization energy that resulted from the second-order microdisturbance theory are reported.[48,49] The larger the $E^{(2)}$ value, the more intensive is the interaction between electron donors and electron acceptors, i.e., a tendency toward donating from electron donors to electron acceptors and a greater extent of conjugation of the whole system. Delocalization of the electron density between occupied Lewis-type (bond or lone pair) NBO orbitals and formally unoccupied (antibond or Rydberg) non-Lewis NBO orbitals correspond to a stabilizing donor–acceptor interaction. NBO analysis was carried out at the B3LYP/6–31+G** level to elucidate the intramolecular rehybridization and delocalization of electron density within the molecule. The important second-order stabilization energies ($E^{(2)}$) are reported in Table 6.

From Table 6, we can see that the $E^{(2)}$ of 4-OCH_3–C_6H_4–CH_2ONO_2 is the largest among the studied compounds. This shows that the interactions between electron donors and electron acceptors, $lpO_3 \rightarrow BD^*(O_1–N_1)$ and $lpO_3 \rightarrow BD^*(O_2–N_1)$, are

Can. J. Chem. Downloaded from www.nrcresearchpress.com by Renmin University of China on 09/02/12
For personal use only.

Fig. 3. Dependence of the second-order stabilization energy ($E^{(2)}$) on Hammett constants for the title compounds in acetonitrile solution.

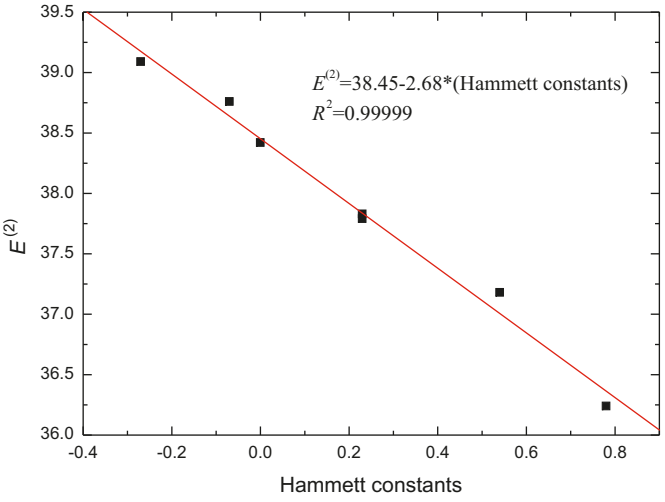
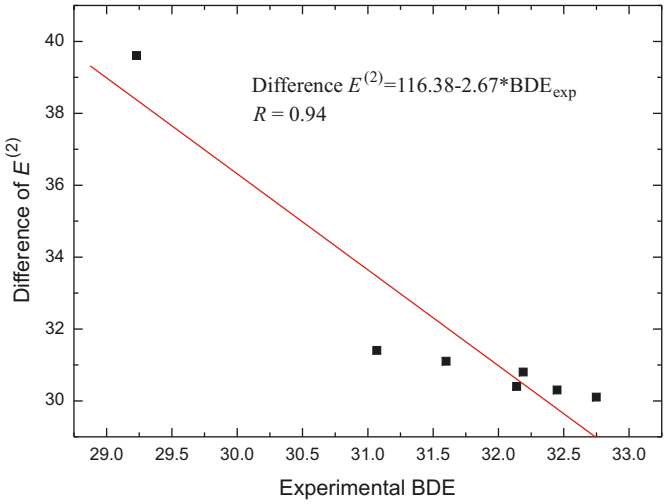


Fig. 4. Dependence of the difference of the second-order stabilization energy ($E^{(2)}$) on the experimental bond dissociation energies (BDEs) for the title compounds in acetonitrile solution.



very strong, which result in a shorter O_3–N_1 bond length. The Hammett constants[41] of the OCH_3, CH_3, H, Cl, Br, CF_3, and NO_2 groups are –0.27, –0.07, 0.00, 0.23, 0.23, 0.54, and 0.78, respectively. From the data in Table 6, it is noted that the $E^{(2)}$ of $lpO_3 \rightarrow BD^*(O_1–N_1)$ is successfully correlated with the Hammett constants. Figure 3 gives the correlation between $E^{(2)}$ and the Hammett constants.

In addition, it is noted that the BDEs of the title compounds have a better linear correlation with the difference between the $E^{(2)}$ of $lpO_3 \rightarrow BD^*(O_1–N_1)$ and $lpO_3 \rightarrow BD^*(O_2–N_1)$. The experimental BDE values of the title compounds are plotted against $E^{(2)}$ in Fig. 4. The correlation coefficient reached was 0.94.

Conclusions

In this paper, the BDEs of the O–NO_2 bonds for seven *O*-nitroalcohol compounds in acetonitrile solution were calculated by the B3LYP, B3PW91, B3P86, and MPWB95 methods with the 6–31G** basis set. The B3LYP/6–31+G**, (RO)B3LYP/6–311++G(2df,2p), B3LYP/6–311G(d,p), and CBS-4M methods were also used. By comparing all of the computed results with the experimental ones, we obtained the following conclusions:

1. The N_1–O_3 BDEs calculated by meta GGA functional MPWB95/6–31G** drastically deviate from the experimental values; the average absolute deviation is 12.4 kcal/mol.
2. Comparing the N_1–O_3 BDEs calculated by various methods, the B3LYP/6–31+G** method is the best procedure for computing dissociation energies for the N_1–O_3 BDE bonds among the selected methods; it has an average absolute deviation of 2.9 kcal/mol and a maximum deviation of 4.7 kcal/mol.
3. The analysis of substituent effects on the BDEs shows that electron-withdrawing groups increase the BDE of the parent compound 4-H–C_6H_4–CH_2ONO_2 and electron-donating groups decrease the BDE of the parent compound. The related reasons are further analyzed.
4. A good linear correlation exists between $E^{(2)}$ and the Hammett constants and a better correlation exists between the BDEs and the difference between the $E^{(2)}$ of $lpO_3 \rightarrow BD^*(O_1–N_1)$ and $lpO_3 \rightarrow BD^*(O_2–N_1)$.

We believe that such bond information should be useful in understanding the biological functions of nitrogen dioxide, especially its reactions with amino acids in vivo.

Acknowledgement

We gratefully thank the National Natural Science Foundation of China (Grant No. 10774039) and the Development Program in Science and Technology of Henan Province (Grant No. 112300410206), and Henan University of Science and Technology for Young Scholars (Grant No. 2009QN0032) for their support of this work.

References

(1) Augusto, O.; Bonini, M. G.; Amanso, A. M.; Linares, E.; Santos, C. C. X.; De Menezes, S. L. *Free Radic. Biol. Med.* **2002**, *32* (9), 841. doi:10.1016/S0891-5849(02)00786-4.

(2) Fukuto, J. M.; Ignarro, L. *J. Acc. Chem. Res.* **1997**, *30* (4), 149. doi:10.1021/ar960010y.

(3) Butler, A. R.; Williams, D. L. H. *Chem. Soc. Rev.* **1993**, *22* (4), 233. doi:10.1039/cs9932200233.

(4) Gnewuch, C. T.; Sosnovsky, G. *Chem. Rev.* **1997**, *97* (3), 829. doi:10.1021/cr941192h.

(5) Ignarro, L. J. *Annu. Rev. Pharmacol. Toxicol.* **1990**, *30* (1), 535. doi:10.1146/annurev.pa.30.040190.002535.

(6) Kurtikyan, T. S.; Ford, P. C. *Angew. Chem. Int. Ed.* **2006**, *45* (3), 492. doi:10.1002/anie.200502409.

(7) Kurtikyan, T. S.; Hovhannisyan, A. A.; Hakobyan, M. E.; Patterson, J. C.; Iretskii, A.; Ford, P. C. *J. Am. Chem. Soc.* **2007**, *129* (12), 3576. doi:10.1021/ja067245h.

(8) Kirsch, M.; Korth, H.-G.; Sustmann, R.; de Groot, S. H. *Biol. Chem.* **2002**, *383* (3–4), 389. doi:10.1515/BC.2002.043.

(9) Pfeiffer, S.; Mayer, B.; Hemmens, B. *Angew. Chem.* **1999**, *111* (12), 1824. doi:10.1002/(SICI)1521-3757(19990614)111:12<1824::AID-ANGE1824>3.0.CO;2-E.

(10) Espey, M. G.; Xavier, S.; Thomas, D. D.; Miranda, K. M.; Wink, D. A. *Proc. Natl. Acad. Sci. U.S.A.* **2002**, *99* (6), 3481. doi:10.1073/pnas.062604199.

Can. J. Chem. Downloaded from www.nrcresearchpress.com by Renmin University of China on 09/02/12
For personal use only.

(11) Pfeiffer, S.; Lass, A.; Schmidt, K.; Mayer, B. *FASEB J.* **2001**, *15* (13), 2355. doi:10.1096/fj.01-0295com.
(12) Gladwin, M. T.; Schechter, A. N.; Kim-Shapiro, D. B.; Patel, R. P.; Hogg, N.; Shiva, S.; Cannon, R. O.; Kelm, M.; Wink, D. A.; Espey, M. G.; Oldfield, E. H.; Pluta, R. M.; Freeman, B. A.; Lancaster, J. R.; Feelisch, M.; Lundberg, J. O. *Nat. Chem. Biol.* **2005**, *1* (6), 308. doi:10.1038/nchembio1105-308.
(13) Dejam, A.; Hunter, C. J.; Schechter, A. N.; Gladwin, M. T. *Blood Cells Mol. Dis.* **2004**, *32* (3), 423. doi:10.1016/j.bcmd.2004.02.002.
(14) Webb, A.; Bond, R.; Mclean, P.; Uppal, R.; Benjamin, N.; Ahluwalia, A. *Proc. Natl. Acad. Sci. U.S.A.* **2004**, *101* (37), 13683. doi:10.1073/pnas.0402927101.
(15) Li, X.; Zhu, X.-Q.; Zhang, F.; Wang, X.-X.; Cheng, J.-P. *J. Org. Chem.* **2008**, *73* (6), 2428. doi:10.1021/jo702364a.
(16) Hoffmann, A. K.; Hodgson, W. G.; Maricle, D. L.; Jura, W. H. *J. Am. Chem. Soc.* **1964**, *86* (4), 631. doi:10.1021/ja01058a019.
(17) Bowyer, W. J.; Evans, D. H. *J. Org. Chem.* **1988**, *53* (22), 5234. doi:10.1021/jo00257a008.
(18) Ruhl, J. C.; Evans, D. H.; Hapiot, P.; Neta, P. *J. Am. Chem. Soc.* **1991**, *113* (14), 5188. doi:10.1021/ja00014a007.
(19) Melius, C. F.; Bulusu, S. N. *Chemistry and Physics of Energetic Materials;* Kluwer: Dordrecht, 1990.
(20) Owens, F. *J. Mol. Struct. THEOCHEM* **1996**, *370* (1), 11. doi:10.1016/S0166-1280(96)04673-8.
(21) Park, Y. D.; Kim, H. K.; Kim, J. J.; Cho, S. D.; Kim, S. K.; Shiro, M.; Yoon, Y. J. *J. Org. Chem.* **2003**, *68* (23), 9113. doi:10.1021/jo0301503.
(22) Romea, P.; Aragones, M.; Garcia, J.; Vilarrasa, J. *J. Org. Chem.* **1991**, *56* (25), 7038. doi:10.1021/jo00025a017.
(23) Li, X.; Zhang, R.; Zhang, X. *J. Hazard. Mater.* **2010**, *183* (1–3), 622. doi:10.1016/j.jhazmat.2010.07.070.
(24) Li, X.-H.; Tang, Z.-X.; Yang, X.-D. *Int. J. Quantum Chem.* **2009**, *109* (6), 1403. doi:10.1002/qua.21952.
(25) Fu, Y.; Mou, Y.; Lin, B.-L.; Liu, L.; Guo, Q.-X. *J. Phys. Chem. A* **2002**, *106* (51), 12386. doi:10.1021/jp0217029.
(26) Van Speybroeck, V.; Marin, G. B.; Waroquier, M. *ChemPhysChem* **2006**, *7* (10), 2205. doi:10.1002/cphc.200600161.
(27) Frisch, M. J.; Trucks, G. W.; Schlegel, H. B.; Scuseria, G. E.; Robb, M. A.; Cheeseman, J. R.; Zakrzewski, V. G.; Montgomery, J. A.; Stratmann, R. E.; Burant, J. C.; Dapprich, S.; Millam, J. M.; Daniels, A. D.; Kudin, K. N.; Strain, M. C.; Farkas, O.; Tomasi, J.; Barone, V.; Cossi, M.; Cammi, R.; Mennucci, B.; Pomelli, C.; Adamo, C.; Clifford, S.; Ochterski, J.; Petersson, G. A.; Ayala, P. Y.; Cui, Q.; Morokuma, K.; Malick, D. K.; Rabuck, A. D.; Raghavachari, K.; Foresman, J. B.; Cioslowski, J.; Ortiz, J. V.; Baboul, A. G.; Stefanov, B. B.; Liu, G.; Liashenko, A.; Piskorz, P.; Komaromi, I.; Gomperts, R.; Martin, R. L.; Fox, D. J.; Keith, T.; Al-Laham, M. A.; Peng, C. Y.; Nanayakkara, A.; Gonzalez, C.; Challacombe, M.; Gill, P. M. W.; Johnson, B.; Chen, W.; Wong, M. W.; Andres, J. L.; Gonzalez, C.; Head Gordon, M.; Replogle, E. S.; Pople, J. A. *GAUSSIAN 03,* Revision B.02; Gaussian Inc.: Pittsburgh, PA, 2003.
(28) Becke, A. D. *J. Chem. Phys.* **1993**, *98* (7), 5648. doi:10.1063/1.464913.
(29) Lee, C.; Yang, W.; Parr, R. G. *Phys. Rev. B* **1988**, *37* (2), 785. doi:10.1103/PhysRevB.37.785.
(30) Miehlich, B.; Savin, A.; Stoll, H.; Preuss, H. *Chem. Phys. Lett.* **1989**, *157* (3), 200. doi:10.1016/0009-2614(89)87234-3.
(31) Perdew, J. P.; Wang, Y. *Phys. Rev. B* **1992**, *45* (23), 13244. doi:10.1103/PhysRevB.45.13244.
(32) Perdew, J. P. *Phys. Rev. B* **1986**, *33* (12), 8822. doi:10.1103/PhysRevB.33.8822.
(33) Zhao, Y.; Truhlar, D. G. *J. Phys. Chem. A* **2004**, *108* (33), 6908. doi:10.1021/jp048147q.
(34) Cossi, M.; Barone, V.; Cammi, R.; Tomasi, J. *Chem. Phys. Lett.* **1996**, *255* (4–6), 327. doi:10.1016/0009-2614(96)00349-1.
(35) Barone, V.; Cossi, M.; Tomasi, J. *J. Chem. Phys.* **1997**, *107* (8), 3210. doi:10.1063/1.474671.
(36) Mennucci, B.; Tomasi, J. *J. Chem. Phys.* **1997**, *106* (12), 5151. doi:10.1063/1.473558.
(37) Ochterski, J. W.; Petersson, G. A.; Montgomery, J. A., Jr. *J. Chem. Phys.* **1996**, *104* (7), 2598. doi:10.1063/1.470985.
(38) Montgomery, J. A., Jr; Frisch, M. J.; Ochterski, J. W.; Petersson, G. A. *J. Chem. Phys.* **1999**, *110* (6), 2822. doi:10.1063/1.477924.
(39) Montgomery, J. A., Jr; Frisch, M. J.; Ochterski, J. W.; Petersson, G. A. *J. Chem. Phys.* **2000**, *112* (15), 6532. doi:10.1063/1.481224.
(40) Shishkov, I. F.; Vilkov, L. V.; Bock, Ch. W.; Hargittai, I. *Chem. Phys. Lett.* **1992**, *197* (4–5), 489. doi:10.1016/0009-2614(92)85805-K.
(41) Gong, X. D.; Xiao, H. M.; Van de Graaf, B. *J. Mol. Struct. THEOCHEM* **1997**, *393* (1–3), 207. doi:10.1016/S0166-1280(96)04860-9.
(42) Chandra, A. K.; Nam, P.-C.; Nguyen, M. T. *J. Phys. Chem. A* **2003**, *107* (43), 9182. doi:10.1021/jp035622w.
(43) Nam, P.-C.; Nguyen, M. T.; Chandra, A. K. *J. Phys. Chem. A* **2004**, *108* (51), 11362. doi:10.1021/jp0467752.
(44) Nam, P.-C.; Nguyen, M. T.; Chandra, A. K. *J. Phys. Chem. A* **2005**, *109* (45), 10342. doi:10.1021/jp0534030.
(45) Frenking, G.; Antes, I.; Böhme, S.; Dapprich, S.; Ehlers, A. W.; Jonas, V.; Neuhaus, A.; Otto, M.; Stegman, R.; Veldkamp, A.; Vyboishchikov, S. F. *Reviews in Computational Chemistry;* Lipkowitz, K. B., Boyd, D. B., Eds. New York: VCH, 1996.
(46) Dapprich, S.; Pidun, U.; Ehlers, A. W.; Frenking, G. *Chem. Phys. Lett.* **1995**, *242* (4–5), 521. doi:10.1016/0009-2614(95)00759-W.
(47) Cao, C. Z. *Substituent Effects in Organic Chemistry;* Science Press: Beijing, 2003.
(48) James, C.; Amal Raj, A.; Reghunathan, R.; Jayakumar, V. S.; Joe, I. H. *J. Raman Spectrosc.* **2006**, *37* (12), 1381. doi:10.1002/jrs.1554.
(49) Liu, J.-N.; Chen, Z.-R.; Yuan, S.-F. *J. Zhejiang Univ. Sci.* **2005**, *6B* (6), 584. doi:10.1631/jzus.2005.B0584.

Synthesis and demethylation of 4,22-dimethoxy [2.10]metacyclophan-1-yne with BBr_3 to afford a novel [10](2,9)-5a,11a-benzofuro-5a-bora-11-bromochromenophane

Yuki Uchikawa, Kazuya Tazoe, Syogo Tanaka, Xing Feng, Taisuke Matsumoto, Junji Tanaka, and Takehiko Yamato

Can. J. Chem. Downloaded from www.nrcresearchpress.com by Renmin University of China on 09/02/12
For personal use only.

Abstract: 4,22-Dimethoxy[2.10]metacyclophan-1-yne was prepared by bromination of [2.10]metacyclophan-1-ene followed by the dehydrobromination of the bromine adduct with KOBu-*t*. Treatment of 4,22-dimethoxy[2.10]metacyclophan-1-yne with BBr_3 in CH_2Cl_2 at room temperature led to the demethylation and a successive intramolecular cyclization reaction to afford a novel [10](2,9)-5a,11a-benzofuro-5a-bora-11-bromochromenophane in good yield. Similar treatment of a mixture of the corresponding *meso*- and *dl*-1,2-dibromo-4,22-dimethoxy[2.10]metacyclophane with BBr_3 in CH_2Cl_2 under the same conditions described above afforded *cis*-4b,9b-dihydro[10]benzofuro[3,2-*b*]benzofuranophane in 83% yield.

Key words: metacyclophan-1-ene, dehydrobromination, metacyclophan-1-yne, double intramolecular cyclization, benzofuranophane.

Résumé : On a préparé le 4,22-diméthoxy[2,10]métacyclophan-1-yne par une bromuration du 4,22-diméthoxy[2,10]métacyclophan-1-ène suivie d'une déshydrobromuration de l'adduit bromé à l'aide de *tert*-butylate de potassium. La réaction du 4,22-diméthoxy[2,10]métacyclophan-1-yne avec du BBr_3, en solution dans le CH_2Cl_2, à la température ambiante, conduit successivement à une déméthylation et une réaction de cyclisation intramoléculaire qui fournit un nouveau [10](2,9)-5a,11a-benzofuro-5a-bora-11-bromochrométhénophane, avec un bon rendement. Un traitement semblable d'un mélange de *méso*- et de *dl*- 1,2-dibromo-4,22-diméthoxy[2,10]métacyclophane avec du BBr_3, en solution dans le CH_2Cl_2, dans les conditions décrites plus haut, conduit au 4b,9b-dihydro[10]benzofuro[3,2-*b*]benzofuranophane, avec un rendement de 83 %.

Mots-clés : métacyclophan-1-ène, déshydrobromuration, métacyclophan-1-yne, double cyclisation intramoléculaire, benzofuranophane.

[Traduit par la Rédaction]

Introduction

Cyclophanes belong to one of the remarkable compound classes that has attracted extensive studies.[1–3] In 1982, Psiorz and Hopf reported the identification of some elusive strained paracyclophyne intermediates, which were indirectly confirmed by the fact that giving Diels–Alder adducts were produced with dienophiles or that trimerization to the hexaphenyl benzene derivatives occurred.[4–8] Later, Meijere and Wong[5] reported the existence of the strained cyclophynes as an intermediate, which was established by a trapping method. Ramming and Gleiter[9] reported the syntheses of [*n*]MCP-diynes (MCP = metacyclophane) and their transformation of propargylic moieties into allenic moieties, as well as reactions with strong bases. Recently, Kawase and co-workers[10–12] reported the synthesis of [2_n]MCP-*n*-ynes by bromination–dehydrobromination of the corresponding MCP-*n*-enes, which were considerably strained with bent triple bonds. Although we attempted to prepare [2.3]- and [2.4]-MCP-1-ynes by the dehydrobromination of the corresponding 1,2-dibromo[2.3]- and [2.4]-MCPs,[13] no formations of the desired [2.3]- and [2.4]-MCP-ynes were observed because of the considerably strained bent triple bonds. Instead, only 1-bromo[2.3]- and [2.4]-MCP-1-enes, along with [2.3]- and [2.4]-MCP-1-ones, were obtained. On the other hand, we succeeded in preparing the larger ring sized 8,22-dimethoxy[2.8]- and 8,24-dimethoxy[2.10]-MCP-1-ynes with bent triple bonds by the bromination–dehydrobromination of the corresponding [2.*n*]MCP-1-enes.[13]

On the other hand, recently, Yamaguchi and co-workers[14–18] reported the double intramolecular cyclizations of diarylacetylenes to construct a series of fully ring-fused ladder π-conjugated skeletones with various main group elements, such

Received 4 November 2011. Accepted 16 January 2012. Published at www.nrcresearchpress.com/cjc on 4 April 2012.

Y. Uchikawa, K. Tazoe, S. Tanaka, X. Feng, and T. Yamato. Department of Applied Chemistry, Faculty of Science and Engineering, Saga University, Honjo-machi 1, Saga 840-8502, Japan.
T. Matsumoto and J. Tanaka. Institute for Material Chemistry and Engineering, Kyushu University, 6-1, Kasugakoen, Kasuga 816-8580, Japan.

Corresponding author: Takehiko Yamato (e-mail: yamatot@cc.saga-u.ac.jp).

Can. J. Chem. Downloaded from www.nrcresearchpress.com by Renmin University of China on 09/02/12
For personal use only.

as Si, B, P, and S, as the bridging moieties. Thus, there is substantial interest in the synthesis of the larger sized [2.*n*]MCP-1-ynes having nucleophilic substituents such as OH and OMe groups at the ortho position to the acetylenic linkage, which can afford convenient starting materials for the attempted preparation of a series of fully ring-fused [2.*n*]cyclophanes by the double intramolecular cyclizations of the diarylacetylene moiety (Scheme 1). In this paper, we describe the first preparation of 4,22-dimethoxy[2.10]MCP-1-ene using the low-valent titanium-induced McMurry reaction and their conversion to 4,22-dimethoxy[2.10]MCP-1-yne, which was treated with BBr_3 to afford a novel [10](2,9)-5a,11a-benzofuro-5a-bora-11-bromochromenophane by the intramolecular cyclizations of the diarylacetylene moiety.

Results and discussion

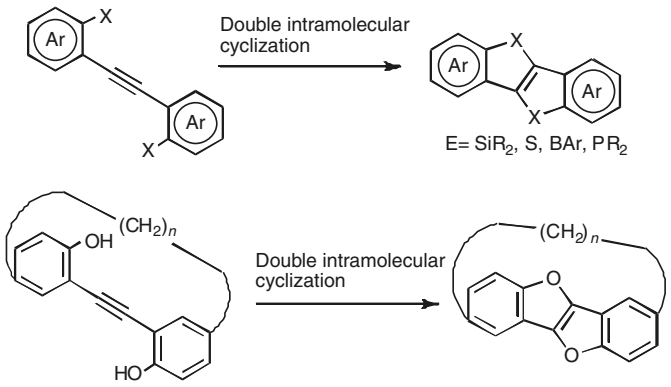
1,10-Bis(4-methoxyphenyl)decane (**2**) was prepared according to our previous reports.[19–24] The cross-coupling reaction of 4-methoxyphenylmagnesium bromide with 1,10-dibromodecane was carried out in the presence of cuprous bromide as a catalyst in a mixture of hexamethylphosphoric triamide (HMPA) and tetrahydrofuran (THF) at reflux temperature to give the desired 1,10-bis(4-methoxyphenyl)decane (**2**) in 82% yield. The $TiCl_4$-catalysed formylation of compound **2** with Cl_2CHOMe at 20 °C led to regioselective formylation at the meta positions of the 1,10-diphenylalkane, affording the desired 1,10-bis(3-formyl-4-methoxyphenyl) decane (**3**) in 83% yield. Compound **3** was subjected to reductive coupling by the McMurry reaction.[25–43] The novel desired [2.10]MCP-1-ene (**4**) was obtained in 94% yield along with the corresponding 1,2-diol (**5**). The ^{1}H NMR spectrum of **4** shows two kinds of methoxy protons, each as a singlet. By careful column chromatography (silica gel, Wako C-300), two isomers, (*E*)-**4** and (*Z*)-**4** (Scheme 2), were separated in 52% and 42% yield, respectively.

The structures of products (*E*)-**4** and (*Z*)-**4** were determined on the basis of their elemental analyses and spectral data. ^{1}H NMR signals of the olefinic protons for *E*- and *Z*-olefins should be observed at $\delta > 7.4$ ppm (*E*) and $\delta < 6.9$ ppm (*Z*).[44] The ^{1}H NMR spectrum of (*E*)-**4** in $CDCl_3$ shows a singlet at δ 7.36 ppm for olefinic protons and a doublet ($J = 2.4$ Hz) at δ 7.30 ppm for one aromatic proton ($H_{8,24}$), which is in a strongly deshielding region of the bridged double bond. In contrast, the ^{1}H NMR spectrum of (*Z*)-**4** in $CDCl_3$ shows a singlet at δ 6.70 ppm for olefinic protons and a set of doublets ($J = 2.4$ Hz) at δ 6.76, 6.98, and 7.03 ppm for the aromatic protons, which were observed at higher field owing to the strong shielding effect of the opposing benzene ring. These data strongly support that the structure of (*E*)-**4** is the E configuration and the structure of (*Z*)-**4** is the Z configuration, both having syn conformation. The structure of the syn-confomer is also readily assigned from the chemical shift of the internal proton Hi at δ 7.30 ppm for (*E*)-**4** and δ 7.03 ppm for (*Z*)-**4**.

Single-crystal X-ray diffraction structures of (*E*)-**4** recrystallized from hexane are illustrated in Fig. 1 with the atom-numbering system.

Compound (*E*)-**4** crystallized in the monoclinic space group *P*121/*a*. Compound (*E*)-**4** was located at general positions in the asymmetric unit of the crystal structure. The X-ray crystallographic analyses of (*E*)-**4** clearly show that the compound also adopts the anti conformation in the solid state. In addition, the double bond adopts the E configuration. These results seem to indicate that the double bond in (*E*)-**4** plays an important role in the fixation of the conformation in the solid state.

Scheme 1. Double intramolecular cyclization of diarylacetylenes and hydroxy[2.*n*]metacyclophan-1-ynes



In (*E*)-**4** the bond distance of C_1–C_2 is 1.341 Å, which is almost the same value as the distance between carbon atoms in ethylene. The bond distances of C_2–C_3 and C_1–C_{23} are 1.472 and 1.474Å, respectively, which are slightly shorter than those of C_7–C_9 (1.545 Å) and C_{18}–C_{19} (1.524 Å). The dihedral angles of C_9–C_{10}–C_{11}–C_{12}–C_{13}–C_{14}–C_{15}–C_{16}–C_{17}–C_{18}–C_1–C_2 between C_3–C_4–C_5–C_6–C_7–C_8 and C_{19}–C_{20}–C_{21}–C_{22}–C_{23}–C_{24} are different values, 3.15° and 0.15°, respectively, showing that the aromatic rings adopt the asymmetrical conformation in the molecule. This reflects the bond angles in the ethylenic bridge chain; the bond angles of C_1–C_2–C_3 and C_{23}–C_1–C_2 are different values (131.74° and 122.49°) that are larger than those of ethylene.

The structure of diol **5** was also determined on the basis of its elemental analyses and spectral data. Thus, we reported[44] the structure of *anti*-1,2-dihydroxy-6,13-dimethoxy[2.3]MCP and assigned it as a *trans*-diol with a exo–exo arrangement. We assigned the structure of **5** in a similar fashion. However, in the case of **5**, the similar upfield shift of the internal aromatic proton (δ 4.95 ppm for *anti*-1,2-dihydroxy-6,13-dimethoxy[2.3]MCP)[1–3,45,46] was not observed, but appeared in the normal aromatic region at δ 6.72 ppm ($J = 2.4$ Hz). This observation strongly suggests **5** adopts a syn conformation, different from that in *anti*-1,2-dihydroxy-6,13-dimethoxy[2.3]MCP. The other two aromatic protons was observed at δ 6.72 ($H_{5,21}$, $J = 8.4$ Hz) and 6.95 ($H_{6,20}$, $J = 2.4$, 8.4 Hz) ppm, respectively. Furthermore, the bridged methine protons show a downfield shift at δ 4.81 ppm as a doublet ($J = 2.1$ Hz), whereas those of 1,2-dihydroxy-6,13-dimethoxy[2.3]MCP are at δ 4.34 ppm. Thus, the bridged methine protons of **5** are in a strongly deshielding region of the oxygen atom of the methoxy groups on the benzene ring. These observations are strongly supported because the two OH groups are in an exo, exo arrangement and, therefore, **5** was found to be a *cis*-diol.

Attempted bromination of (*Z*)-4,22-dimethoxy[2.10]MCP-1-ene (*Z*)-**4** with an equimolar amount of benzyltrimethylammonium tribromide (BTMA Br_3), which was found to be a convenient solid brominating agent,[47] carried out in a

Can. J. Chem. Downloaded from www.nrcresearchpress.com by Renmin University of China on 09/02/12
For personal use only.

Scheme 2. Synthesis of (*Z*)- and (*E*)-4,22-dimethoxy[2.10]MCP-1-ene, (*Z*)-**4** and (*E*)-**4.**

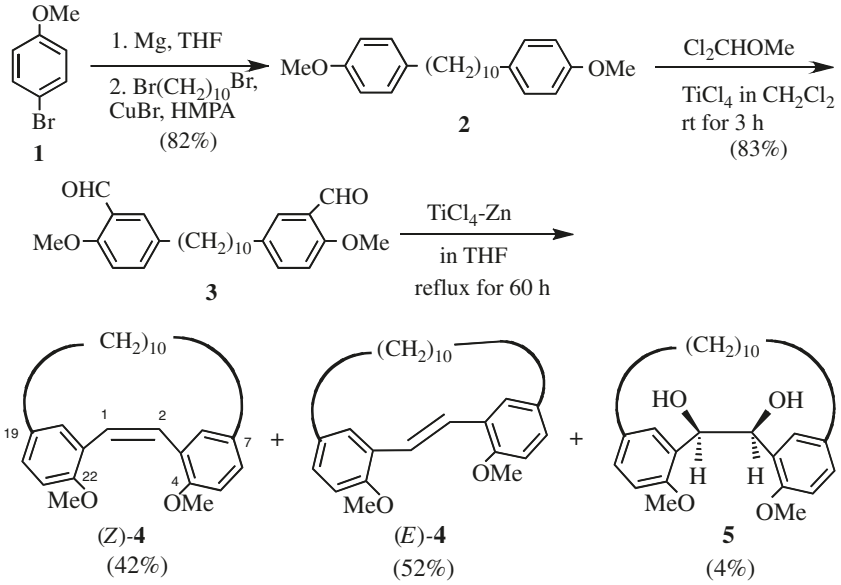
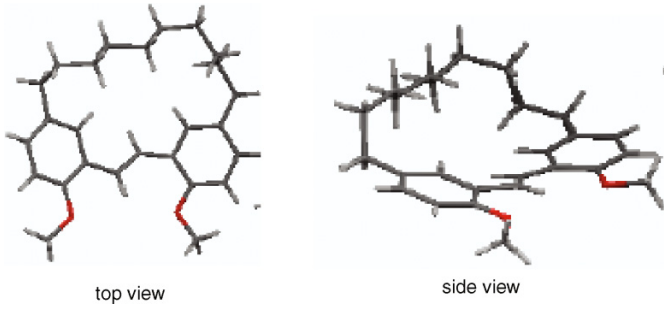
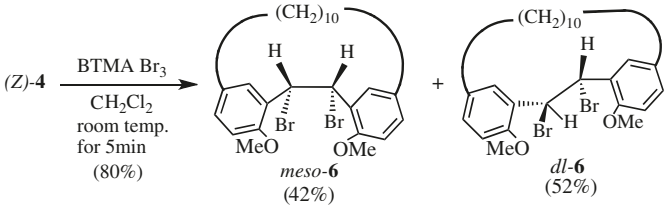


Fig. 1. Single-crystal X-ray diffraction structures of (*E*)-**4**. Hydrogen atoms are omitted for clarity.



Scheme 3. Bromination of (*Z*)-**4** with BTMA Br_3.



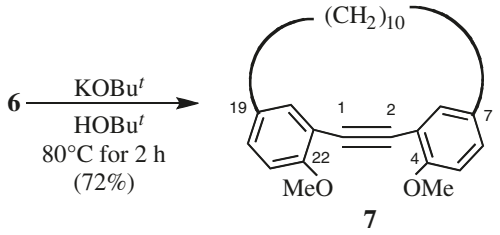
dichloromethane solution at room temperature for 5 min led to the expected cis- and trans-adducts **6** (*endo–endo*–Br and *endo–exo*–Br) to the bridged double bond in a ratio of 45:55 in 80% yield. Similar treatment of (*E*)-**4** with BTMA Br_3 under the same reaction conditions afforded a mixture of *meso*-**6** and *rac*-**6** (Scheme 3) in 91% yield in a ratio of 45:55.

When treated with potassium *tert*-butoxide in refluxing HOBu-*t* at 80 °C for 2 h, bromine adduct **6** gave the didehydrobromination product [2.10]MCP-1-yne (**7**) in 72% yield.

The structure of **7** was determined on the basis of its elemental analysis and spectral data. The ^{1}H NMR spectrum of **7** shows two internal protons as a doublet at δ 7.39 ($H_{8,24}$, J = 2.1 Hz) ppm and two aromatic protons at δ 6.78 ($H_{5,21}$, J = 8.4 Hz) and 7.03 ($H_{6,20}$, J = 2.1, 8.4 Hz) ppm. The chemical shift for the internal protons at normal aromatic protons strongly supports that the structure of **7** is the syn-conformer. A deshielded internal proton was observed in the NMR spectrum of **7** at δ 7.39 ppm in comparison with other aromatic protons, which is in a strongly deshielding region owing to the π-electrons of the triple bond. The chemical shifts of the ^{1}H and ^{13}C NMR signals arising from the benzene rings of **7** are comparable to those of the acyclic reference compound **11**,[13] which was prepared from 2-formyl-5-methylanisole (**8**) in three. steps, the same procedure as that for **7** (Scheme 4). Interestingly, the signals of the acetylenic carbons were observed at slightly lower field (δ 91.48 ppm for **7**) than that of **11** (δ 89.69 ppm, Scheme 5); this reflects the relatively small strain in the triple bond owing to bending and is almost the same value of that of [2_4]MCP-1,9,17,25-tetrayne (δ 92.20 ppm), but much lower than that of 1,5-cyclooctadiyne (δ 95.8 ppm)[48] or [2_3]MCP-1,9,17-triyne (δ 99.86 ppm).[11]

Single-crystal X-ray diffraction structures of **7** recrystallized from hexane are illustrated in Fig. 2 with the atom-numbering system. Compound **7** crystallized in the monoclinic space group $P21/a$ (Z = 8). All remaining hydrogen atoms are not shown for clarity. The structure was solved by direct-methods (Sir2002) and refined using the full-matrix least-squares method and Fourier synthesis. The X-ray structure determination of **7** clearly indicates that the structure of **7** is also the syn-conformer in the solid state, and the two methoxy groups are lying on the same side of the inner ring toward the outer direction to avoid steric repulsion with the bridge chain, the same as in (*E*)-**4**. The bond distance of C_1–C_2 is 1.20 Å, which is almost equal to the distance between carbon atoms in acetylene. The bond distances of C_2–C_3 and C_1–C_{23} are 1.43 and 1.43 Å, respectively, which are much shorter than those of C_7–C_9 (1.52 Å) and C_{18}–C_{19} (1.51 Å). Interestingly, the acetylenic moiety in the bridge chain does not adopt a different linear structurethan reference compound **11**; the bond angles of C_1–C_2–C_3 and C_2–C_1–C_{23} are unusual values, 169.6°and 170.2°. Thus, this clearly shows that **7** is a slightly bent molecule and supports the lower field shifts of

Scheme 4. Didehydrobromination of **6** with potassium *tert*-butoxide.



Scheme 5. Synthesis of acyclic reference compound **11**.

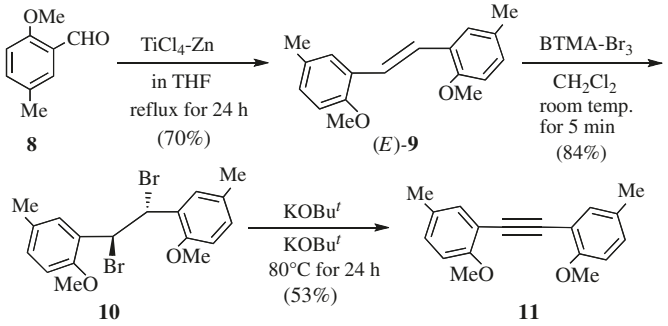
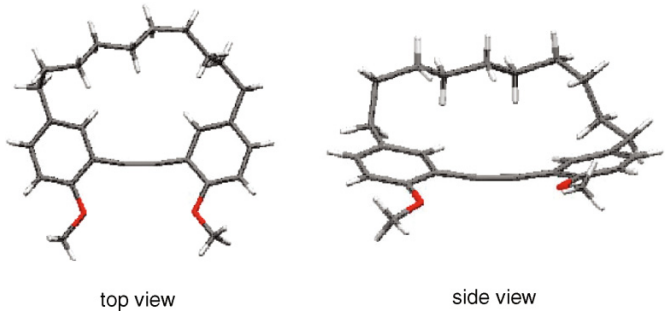


Fig. 2. Single-crystal X-ray diffraction structures of **7**. Hydrogen atoms are omitted for clarity.

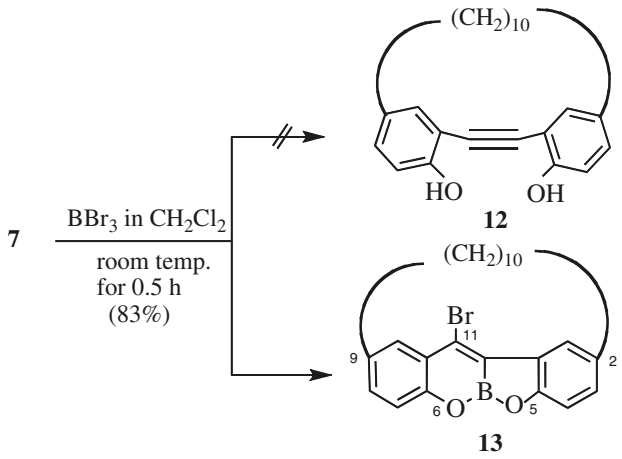


the signals of the acetylenic carbons in its ^{13}C NMR spectrum.

Attempted demethylation of **7** to afford **12** with trimethylsilyl iodide in acetonitrile solution[42–52] under various conditions failed. Only an intractable mixture of products was obtained. Interestingly, treatment of **7** with BBr_3 in CH_2Cl_2 at room temperature for 0.5 h afforded a novel [10](2,9)-5a,11a-benzofuro-5a-bora-11-bromochromenophane (**13**) in 83% yield (Scheme 6). No formations of the expected 4,22-dihydroxy[2.10]MCP-1-ene (**12**) or [10]benzofuro[3,2-*b*]benzofuranophane (Scheme 1) derived from the double intramolecular cyclizations of diarylacetylene and the OH groups of **12** were observed under the conditions used.

The structure of **13** was elucidated based on its elemental analysis and spectral data. Especially, the mass spectral data for **13** (M^+ = 435, 437) strongly supports one bromine atom containing product. The ^{1}H NMR spectrum in $CDCl_3$ exhibited six aromatic protons at δ 6.84 (d, J = 8.4), 6.86 (d, J = 2.4 Hz), 7.01 (dd, J = 2.4, 8.4 Hz), 7.18 (d, J = 8.4 Hz), 7.23 (dd, J = 1.2, 8.4 Hz), and 7.95 (d, J = 1.2 Hz) ppm, which were clearly associated with the unsymmetrical structure of **13**. On the basis of the spectral data, compound **13**

Scheme 6. Treatment of **7** with BBr_3 in CH_2Cl_2.



was assigned the structure, [10](2,9)-5a,11a-benzofuro-5a-bora-11-bromochromenophane.

Although the detailed mechanism of formation of [10]benzofurochromenophane (**13**) is not clear at the present stage, one might assume the reaction pathway as shown in Scheme 7. The present BBr_3-induced transformation from **7** to **13** probably occurred by demethylation of one methoxy group to afford the corresponding intermediate **A** followed by the second demethylation reaction along with the intramolecular cyclization reaction to afford the intermediate **B**, from which the electrophilic attack to the triple bond to generate the vinyl cation intermediate **C** occurred. Succesively, the nucleophilic attack to the vinyl cation intermediate **C** afforded compound **13** (Scheme 7). The present cyclization of the intermediate **B** to **C** might be attributable to conformational flexibility of the intermediate **B** and a short distance among the ethynyl group and boron atom as an electrophile owing to the *syn*-MCP skeletone. In fact, similar treatment of reference compound **11** with BBr_3 under the same conditions afforded only the intractable mixture of products. No formation of the corresponding benzofurochromene was observed under the conditions used.

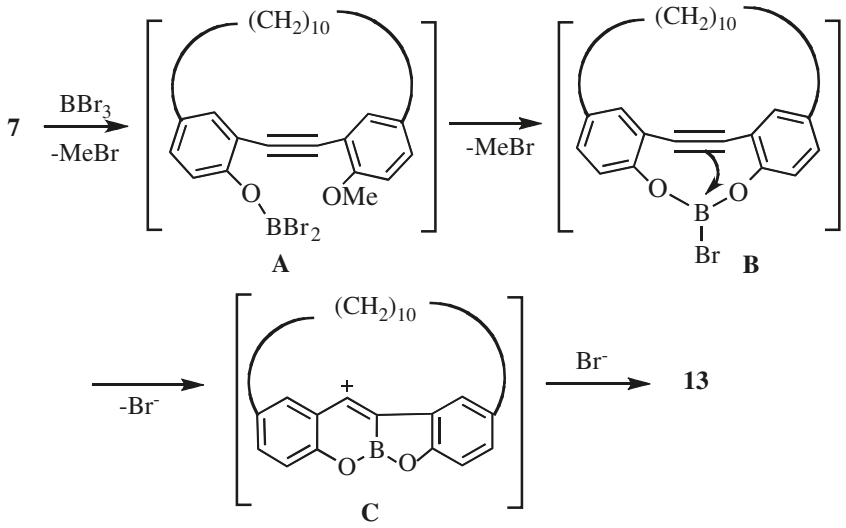
To study the present [10]benzofurochromenophane formation reaction in more detail, we attempted to carry out the treatment of dibromide **6** with BBr_3. In fact, the treatment of a mixture of *meso*- and *dl*-**6** with BBr_3 in CH_2Cl_2 under the same conditions described above afforded *cis*-4b,9b-dihydro [10]benzofuro[3,2-*b*]benzofuranophane (**15**) in 83% yield, but not [10]benzofurochromenophane (Scheme 8).

The present BBr_3-induced transformation from **6** to **15** probably occurred by the demethylation of methoxy groups to afford the corresponding phenol derivative **D**, followed by a nucleophilic attack by phenolic oxygen to the bromide carbon at the C_2 carbon to afford the benzofuran intermediate **E**, from which the second nucleophilic attack to the bromide carbon at the C_3 position of benzofuran occurred to afford benzofuro[3,2-*b*]benzofuranophane skeletone intermediate **G**. The second cyclization of the intermediate **E** to **F** might be attributable to conformational flexibility of the intermediate **E** around the diaryl linkage of 2-arylbenzofuran. Deprotonation from the intermediate **G** afforded compound **15** (Scheme 9). From this proposed reaction mechanism for the BBr_3-induced transformation of **6** to **15**, one might assume the importance

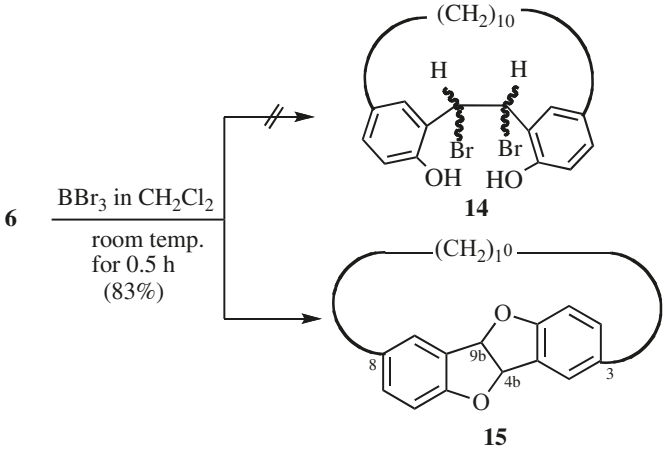
Can. J. Chem. Downloaded from www.nrcresearchpress.com by Renmin University of China on 09/02/12
For personal use only.

Can. J. Chem. Downloaded from www.nrcresearchpress.com by Renmin University of China on 09/02/12
For personal use only.

Scheme 7. Proposed reaction mechanism for the formation of **13**.



Scheme 8. Reaction of a mixture of *meso*- and *dl*-**6** with BBr_3 in CH_2Cl_2.



of the intramolecularly cyclized nine-membered intermediate **B** to afford **13** during the demethylation of **7** with BBr_3.

Conclusions

We have demonstrated a convenient preparation of 4,22-dimethoxy[2.10]MCP-1-yne (**7**) and conversion to a novel [10]benzofurochromenophane (**13**) by treatment with BBr_3 in CH_2Cl_2 at room temperature via demethylation and a successive intramolecular cyclization reaction. Interestingly, similar treatment of a mixture of the corresponding *meso*- and *dl*-1,2-dibromo-4,22-dimethoxy[2.10]MCP (**6**) with BBr_3 in CH_2Cl_2 under these same conditions afforded *cis*-4b,9b-dihydro[10]benzofuro[3,2-*b*]benzofuranophane (**15**) in 83% yield by double intramolecular cyclization. Further studies on the chemical properties of [10](2,9)-5a,11a-benzofuro-5a-bora-11-bromochromenophane **13** and *cis*-4b,9b-dihydro[10]benzofuro[3,2-*b*]benzofuranophane **15** are now in progress.

Experimental

All melting points were uncorrected. Proton nuclear magnetic resonance (^{1}H NMR) spectra were recorded on a Nippon Denshi JEOL FT-300 spectrometer. Chemical shifts are reported as δ values (ppm) relative to internal Me_4Si. Mass spectra were obtained on a Nippon Denshi JIR-AQ2OM mass spectrometer at an ionization energy of 70 eV using a direct-inlet system through GLC; *m*/*z* values reported include the parent ion peak. Infrared (IR) spectra were obtained on a Nippon Denshi JIR-AQ2OM spectrophotometer as KBr disks. Elemental analyses were performed with a Yanaco MT-5. Gas–liquid chromatograph (GLC) analyses were performed with a Shimadzu GC, GC-14A (silicone OV-1, 2 m; programmed temperature rise, 12 °C min^{-1}; carrier gas, nitrogen, 25 mL min^{-1}).

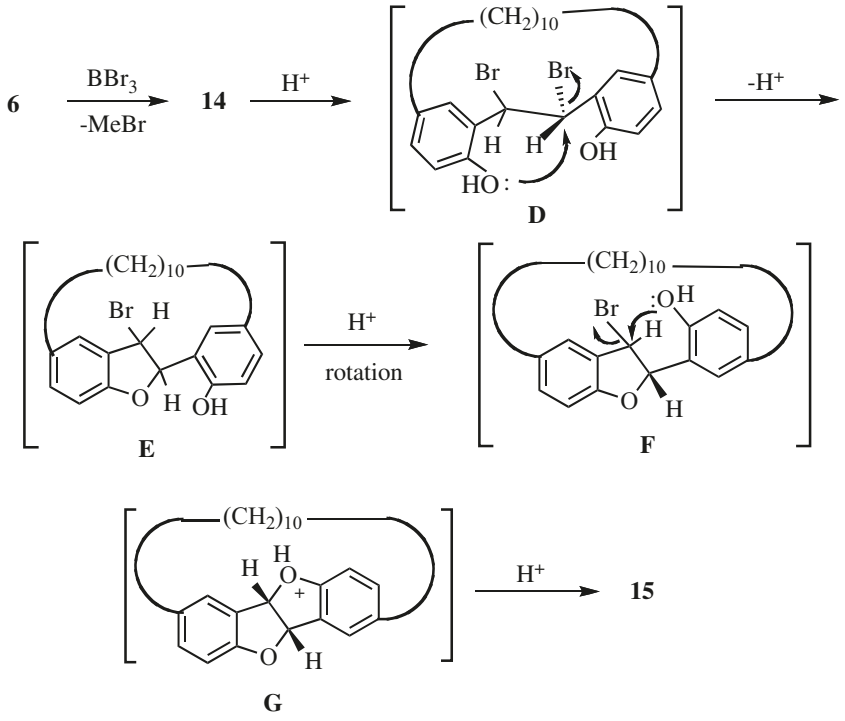
Preparation of 1,10-bis(4-methoxyphenyl)decane (2)

To a solution of 9.52 g (0.39 mol) of magnesium and a small amount of iodine in THF (10 mL) was added a solution of 4-bromoanisole (**1**) (33.7 g, 0.18 mol) in THF (40 mL) and the mixture was refluxed for 12 h. To a solution of 1,10-dibromodecane (18 g, 60 mmol) and CuBr (2.0 g, 14 mmol) in HMPA (10 mL) was added dropwise a solution of 4-methoxyphenylmagnesium bromide with gentle refluxing. After the reaction mixture was refluxed for an additional 24 h, it was quenched with a 10% aqueous ammonium chloride solution and extracted with CH_2Cl_2 (100 mL × 3). After the combined CH_2Cl_2 extracts were dried over Na_2SO_4, the solvent was evaporated in vacuo, and the residue was washed with methanol (100 mL) to afford 19 g of crude **2** as a colorless solid. Recrystallization from hexane gave **2** (17.5 g, 82%) as colorless prisms, mp 64–65 °C. ^{1}H NMR ($CDCl_3$) δ: 1.27 (broad s, 12H, *CH*$_2$), 1.54 (s, 4H, *CH*$_2$), 2.54–2.59 (m, 4H, *CH*$_2$), 3.78 (s, 6H, O*Me*), 6.82 (d, J = 8.8 Hz, 4H, Ar–*H*), 7.08 (d, J = 8.8 Hz, 4H, Ar–*H*). MS *m*/*z* (%): 354 (M^+). Anal. calcd for $C_{24}H_{34}O_2$ (354.53): C 81.31, H 9.67; found: C 81.42, H 9.54.

Preparation of 1,10-bis(3-formyl-4-methoxyphenyl)decane (3)

To a solution of 1,10-bis(4-methoxyphenyl)decane (**2**, 7.08 g, 20 mmol) and Cl_2CHOCH_3 (4.86 mL, 56 mmol) in CH_2Cl_2 (40 mL) was added a solution of $TiCl_4$ (6.7 mL,

Scheme 9. Proposed reaction mechanism for BBr_3-induced transformation from **6** to **15**.



61 mmol) in CH_2Cl_2 (40 mL) at 0 °C. After the reaction mixture was stirred at room temperature (rt) for 3 h, it was poured into a large amount of ice water (200 mL) and extracted with CH_2Cl_2 (100 mL × 2). The combined extracts were washed with water, dried with Na_2SO_4, and concentrated. The residue was chromatographed over silica gel (Wako C-300, 500 g) with hexane – ethylacetate (4:1) as eluent to give crude **3**. Recrystallization from hexane gave 6.82 g (83%) of 1,10-bis(3-formyl-4-methoxyphenyl)decane (**3**) as colorless prisms, mp 63–64 °C. IR (KBr, cm^{-1}) ν_{max}: 1683 (C=O). ^1H NMR ($CDCl_3$) δ: 1.26 (broad s, 12H, *CH*$_2$), 1.55 (s, 4H, *CH*$_2$), 2.54–2.59 (m, 4H, *CH*$_2$), 3.91 (s, 6H, *OMe*), 6.10 (d, *J* = 8.4 Hz, 2H, Ar*H*), 7.36 (dd, *J* = 2.1, 8.4 Hz, 2H, Ar*H*), 7.63 (d, *J* = 2.1 Hz, 2H, Ar–*H*), 10.4 (s, 2H, C*H*O). MS *m*/*z* (%): 410 (M^+). Anal. calcd for $C_{26}H_{34}O_4$ (410.56): C 76.06, H 8.35; found: C 76.14, H 8.27.

McMurry coupling reaction of 3

The McMurry reagent was prepared from $TiCl_4$ (13.75 mL, 125 mmol) and Zn powder (18 g, 275 mmol) in dry THF (500 mL), under nitrogen. A solution of 1,10-bis(3-formyl-4-methoxyphenyl)decane (**3**, 4.72 g, 11.5 mmol) in dry THF (250 mL) was added within 60 h to the black mixture of the McMurry reagent by using a high-dilution technique with continuous refluxing and stirring. The reaction mixture was refluxed for an additional 8 h, cooled to rt, and hydrolysed with aqueous 10% K_2CO_3 (500 mL) at 0 °C. The reaction mixture was extracted with CH_2Cl_2 (300 mL × 3). The combined extracts were washed with water, dried with Na_2SO_4, and concentrated. The residue was chromatographed over silica gel (Wako C-300, 500 g) with hexane – ethyl acetate (4:1) and ethyl acetate as eluents to give a mixture of (*E*)-**4** and (*Z*)-**4** as a colorless oil and **5** as a colorless solid. Recrystallization of hexane – ethyl acetate (4:1) eluents from hexane afforded (*E*)-**4** (2.28 g, 52%). The filtrate was condensed in vacuo to afford (*Z*)-**4** (1.83 g, 42%) as a colorless oil. The material obtained from the ethyl acetate eluent was recrystallized from hexane and afforded **5** (190 mg, 4%) as colorless prisms.

(*E*)-4,22-Dimethoxy[2.10]metacyclophan-1-ene ((*E*)-4)

(*E*)-**4** was obtained as colorless prisms (hexane), mp 102–103 °C. ^1H NMR ($CDCl_3$) δ: 1.46 (broad s, 12H, *CH*$_2$), 1.69 (broad s, 4H, *CH*$_2$), 2.55–2.67 (m, 4H, *CH*$_2$), 3.89 (s, 6H, O*Me*), 6.79 (d, *J* = 8.4 Hz, 2H, Ar*H*), 6.98 (dd, *J* = 2.4, 8.4 Hz, 2H, Ar–*H*), 7.30 (d, *J* = 2.4 Hz, 2H, Ar–*H*), 7.36 (s, 2H, =C*H*). ^{13}C NMR ($CDCl_3$) δ: 26.87, 28.35, 29.27, 29.99, 31.75, 55.47, 110.74, 126.62, 128.33, 128.53, 129.62, 133.41, 155.30. MS *m*/*z* (%): 378 (M^+). Anal. calcd for $C_{26}H_{34}O_2$ (378.55): C 82.49, H 9.05; found: C 82.41, H 8.99.

(*Z*)-4,22-Dimethoxy[2.10]metacyclophan-1-ene ((*Z*)-4)

(*Z*)-**4** was obtained as a colorless oil. ^1H NMR ($CDCl_3$) δ: 1.26 (m, 12H, *CH*$_2$), 1.43 (m, 4H, *CH*$_2$), 2.33–2.42 (m, 4H, *CH*$_2$), 3.69 (s, 6H, O*Me*), 6.70 (s, 2H, =C*H*), 6.76 (d, *J* = 8.4 Hz, 2H, Ar–*H*), 6.98 (dd, *J* = 2.4, 8.4 Hz, 2H, Ar–*H*), 7.03 (d, *J* = 2.4 Hz, 2H, Ar–*H*). MS *m*/*z* (%): 378 (M^+). Anal. calcd for $C_{26}H_{34}O_2$ (378.55): C 82.49, H 9.05; found: C 82.64, H 9.07.

1,2-Dihydroxy-4,22-dimethoxy[2.10]metacyclophane (5)

Compound **5** was obtained as colorless prisms (hexane), mp 116–117 °C. ^1H NMR ($CDCl_3$) δ: 1.24 (broad s, 12H, *CH*$_2$), 1.42–1.46 (m, 4H, *CH*$_2$), 2.37–2.44 (m, 4H, *CH*$_2$), 3.53 (s, 6H, O*Me*), 3.86 (d, *J* = 2.1 Hz, 2H, O*H*), 4.81 (d, *J* = 2.1 Hz, 2H, C*H*), 6.61 (d, *J* = 8.1 Hz, 2H, Ar–*H*), 6.72 (d, *J* = 2.4 Hz, 2H, Ar–*H*), 6.95 (dd, *J* = 2.4, 8.1 Hz, 2H, Ar–*H*). ^{13}C NMR ($CDCl_3$) δ: 26.3, 26.5, 29.7, 34.5, 55.2,

Can. J. Chem. Downloaded from www.nrcresearchpress.com by Renmin University of China on 09/02/12
For personal use only.

Can. J. Chem. Downloaded from www.nrcresearchpress.com by Renmin University of China on 09/02/12
For personal use only.

109.8 100.1, 127.3, 127.8, 128.1, 130.3, 155.2. MS *m/z* (%): 394 ($M^+ - H_2O$). Anal. calcd for $C_{26}H_{36}O_4$ (412.57): C 75.69, H 8.8; found: C 75.73, H 8.78.

Bromination of (*Z*)-4 with BTMA Br_3

To a solution of (*Z*)-**4** (200 mg, 0.53 mmol) in CH_2Cl_2 (20 mL) was added BTMA Br_3 (220 mg, 0.58 mmol) at rt. After the reaction mixture was stirred at rt for 5 min, it was poured into a large amount of ice water (50 mL) and extracted with CH_2Cl_2 (50 mL × 2). The combined extracts were washed with water, dried with Na_2SO_4, and concentrated. The residue was recrystallized from hexane and gave 228 mg (80%) of a mixture of 1-*endo*-bromo-2-*exo*-bromo-4,22-dimethoxy[2.10]metacyclophane (*rac*-**6**) and 1,2-di-*endo*-bromo-4,22-dimethoxy[2.10]-metacyclophane (*meso*-**6**) in a ratio of 55:45 as colorless prisms, mp 148–149 °C. ^{1}H NMR ($CDCl_3$) (*rac*-**6**) δ: 1.36 (broad s, 12H, *CH*$_2$), 1.45 (m, 4H, *CH*$_2$), 2.41–2.46 (m, 4H, *CH*$_2$), 3.73 (s, 3H, O*Me*), 3.78 (s, 3H, O*Me*), 5.64 (d, *J* = 10.2 Hz, 1H, *CH*), 6.60 (d, *J* = 7.8 Hz, 1H, *Ar–H*), 6.70 (d, *J* = 10.2 Hz, 1H, *CH*), 6.87–6.92 (m, 5H, Ar–*H*); *meso*-**6** δ: 1.36 (broad s, 12H, *CH*$_2$), 1.45 (m, 4H, *CH*$_2$), 2.41–2.46 (m, 4H, *CH*$_2$), 3.91 (s, 6H, O*Me*), 6.36 (s, 2H, *CH*), 6.65 (d, *J* = 7.8 Hz, 2H, *ArH*), 6.89 (dd, *J* = 1.2, 7.8 Hz, 2H, *Ar–H*), 7.08 (d, *J* = 1.2 Hz, 2H, Ar–*H*). MS *m/z* (%): 536, 538, 540 (M^+). Anal. calcd for $C_{26}H_{34}Br_2O_2$ (538.35): C 58.01, H 6.37; found: C 58.27, H 6.42.

Similar treatment of (*E*)-**4** with BTMA Br_3 under the same conditions as noted in the previous paragraph afforded a mixture of *rac*-**6** and *meso*-**6** in 91% yield in a ratio of 55:45 as colorless prisms.

Dehydrobromination of 6 with KOBu-*t*

To a solution of a mixture of *meso*- and *dl*-**6** (180 mg, 0.33 mmol) in HOBu-*t* (24 mL) was added KOBu-*t* (1.18 g, 10.5 mmol) at rt. After the reaction mixture was stirred at 80 °C for 2 h, it was poured into a large amount of ice water (50 mL) and extracted with CH_2Cl_2 (100 mL × 2). The combined extracts were washed with water, dried with Na_2SO_4, and concentrated. The residue was recrystallized from methanol and gave 89 mg (72%) of 4,22-dimethoxy[2.10]metacyclophan-1-yne (**7**) as colorless prisms, mp 113–114 °C. IR (KBr, cm^{-1}) ν_{max}: 2899, 2866, 2830, 2050 (C≡C), 1495, 1463, 1258, 1100, 1025, 802. ^{1}H NMR ($CDCl_3$) δ: 1.41 (m, 12H, *CH*$_2$), 1.60–1.72 (m, 4H, *CH*$_2$), 2.61–2.69 (m, 4H, *CH*$_2$), 3.89 (s, 6H, O*Me*), 6.78 (d, *J* = 8.4, 2H, Ar-*H*), 7.03 (dd, *J* = 8.4, 2.1 Hz, 2H, Ar*H*), 7.39 (d, *J* = 2.1 Hz, 2H, Ar–*H*). ^{13}C NMR ($CDCl_3$) δ: 26.65, 28.31, 29.17, 29.63, 31.76, 55.76, 91.48 (*sp*-C), 110.68, 112.11, 130.15, 133.52, 134.80, 156.56. MS *m/z* (%): 376 (M^+). Anal. calcd for $C_{26}H_{32}O_2$ (376.53): C 76.06, H 8.57; found: C 82.87, H 8.50.

McMurry coupling reaction of 8

The McMurry reagent was prepared from $TiCl_4$ (11.0 mL, 100 mmol) and Zn powder (14.4 g, 220 mmol) in dry THF (300 mL), under nitrogen. A solution of 2-formyl-5-methylanisole (**8**, 5.0 g, 33.3 mmol) in dry THF (70 mL) was added within 24 h to the black mixture of the McMurry reagent by using a high-dilution technique with continuous refluxing and stirring. The reaction mixture was refluxed for additional 8 h, cooled to rt, and hydrolysed with aqueous 10% K_2CO_3 (500 mL) at 0 °C. The reaction mixture was extracted with CH_2Cl_2 (300 mL × 3). The combined extracts were washed with water, dried with Na_2SO_4, and concentrated. The residue was treated with hexane (100 mL) to afford a colorless solid. Recrystallization from hexane afforded (*E*)-1,2-bis(2-methoxy-5-methylphenyl)ethene ((*E*)-**9**, 3.15 g, 70%) as colorless prisms, mp 123–125 °C. ^{1}H NMR ($CDCl_3$) δ: 2.34 (s, 6H, *CH*$_3$), 3.85 (s, 6H, O*Me*), 6.78 (d, *J* = 8.3 Hz, 2H, Ar–*H*), 7.02 (dd, *J* = 2.2, 8.3 Hz, 2H, Ar–*H*), 7.42 (s, 2H, =C*H*), 7.45 (d, *J* = 2.2 Hz, 2H, Ar*H*). ^{13}C NMR ($CDCl_3$) δ: 20.6, 55.6, 110.8, 123.1, 123.3, 126.9, 128.8, 129.8, 154.7. MS *m/z* (%): 268 (M^+). Anal. calcd for $C_{18}H_{20}O_2$ (268.36): C 80.56, H 7.51; found: C 80.41, H 7.69.

Bromination of (*E*)-9 with BTMA Br_3

To a solution of (*E*)-**9** (1.0 g, 3.73 mmol) in CH_2Cl_2 (100 mL) was added BTMA Br_3 (1.74 g, 4.46 mmol) at rt. After the reaction mixture was stirred at rt for 5 min, it was poured into a large amount of ice water (300 mL) and extracted with CH_2Cl_2 (100 mL × 2). The combined extracts were washed with water, dried with Na_2SO_4, and concentrated. The residue was treated with hexane (100 mL) to afford a colorless solid. Recrystallization from hexane afforded 1,2-bromo-1,2-bis(2-methoxy-5-methylphenyl)-ethane (**10**, 1.35 g, 84%) as colorless prisms, mp 146–148 °C. ^{1}H NMR ($CDCl_3$) δ: 2.18 (s, 6H, *CH*$_3$), 3.74 (s, 6H, O*Me*), 6.11 (s, 2H, *CH*), 6.52 (d, *J* = 8.1 Hz, 2H, Ar–*H*), 7.12 (dd, *J* = 2.0, 8.1 Hz, 2H, Ar–*H*), 7.38 (d, *J* = 2.0 Hz, 2H, Ar–*H*). MS *m/z* (%): 426, 428, 430 (M^+). Anal. calcd for $C_{18}H_{20}Br_2O_2$ (428.17): C 50.61, H 4.76; found: C 50.49, H 4.71.

Dehydrobromination of 10 with KOBu-*t*

To a solution of a mixture of **10** (680 mg, 1.59 mmol) in HOBu-*t* (68 mL) was added KOBu-*t* (1.78 g, 15.9 mmol) at rt. After the reaction mixture was stirred at 80 °C for 24 h, it was poured into a large amount of ice water (50 mL) and extracted with CH_2Cl_2 (100 mL × 2). The combined extracts were washed with water, dried with Na_2SO_4, and concentrated. The residue was chromatographed over silica gel (Wako C-300, 500 g) with hexane as eluents to give a colorless solid. Recrystallization from hexane afforded 1,2-bis(2-methoxy-5-methylphenyl)ethyne (**11**, 223 mg, 53%) as colorless prisms, mp 114–115 °C. ^{1}H NMR ($CDCl_3$) δ: 2.28 (6H, s, *CH*$_3$), 3.89 (s, 6H, O*Me*), 6.78 (d, *J* = 8.4 Hz, 2H, Ar*H*), 7.07 (dd, *J* = 2.4, 8.4 Hz, 2H, Ar–*H*), 7.33 (d, *J* = 2.2 Hz, 2H, Ar–*H*). ^{13}C NMR ($CDCl_3$) δ: 20.27, 56.04, 89.69 (*sp*-C), 110.6, 112.46, 129.60, 130.04, 133.96, 157.86. MS *m/z* (%): 266 (M^+). Anal. calcd for $C_{18}H_{18}O_2$ (266.34): C 81.17, H 6.81; found: C 81.03, H 6.92.

Reaction of 7 with BBr_3

To a solution of **7** (60 mg, 0.16 mmol) in CH_2Cl_2 (6 mL) at 0 °C was gradually added a solution of BBr_3 (0.087 mL, 0.922 mmol) in (0.1 mL). After the reaction mixture was stirred at rt for 0.5 h, it was poured into ice water (10 mL) and then extracted with CH_2Cl_2 (10 mL × 3). The combined extracts were washed with water (10 mL × 2), dried over Na_2SO_4, and concentrated in vacuo to leave a residue. The residue was chromatographed over silica gel (Wako C-300, 100 g) with hexane–$CHCl_3$ (4:1) as eluent to give crude **13** as a colorless solid. Recrystallization from EtOH gave

Can. J. Chem. Downloaded from www.nrcresearchpress.com by Renmin University of China on 09/02/12
For personal use only.

[10](2,9)-5a,11a-benzofuro-5a-bora-11-bromochromenophane (**13**, 58 mg, 83%) as colorless prisms, mp 207–208 °C. IR (KBr, cm^{-1}) ν_{max}: 2900, 2354, 1539, 1502, 1454. ^1H NMR ($CDCl_3$) δ: 1.27–1.35 (m, 12H, CH_2), 1.60 (s, 4H, CH_2), 2.64–2.67 (m, 2H, CH_2), 2.76–2.79 (m, 2H, CH_2), 6.84 (d, J = 8.4, 1H, Ar–*H*), 6.86 (d, J = 2.4 Hz, 1H, Ar–*H*), 7.01 (dd, J = 2.4, 8.4 Hz, 1H, Ar–*H*), 7.18 (d, J = 8.4 Hz, 1H, Ar–*H*), 7.23 (dd, J = 1.2, 8.4 Hz, 1H, Ar–*H*), 7.95 (d, J = 1.2 Hz, 1H, Ar*H*). MS *m*/*z* (%): 435, 437 (M^+). Anal. calcd for $C_{24}H_{26}BBrO_2$ (437.19): C 65.94, H 5.99; found: C 65.63, H 6.06.

Reaction of 6 with BBr_3

To a solution of **6** (60 mg, 0.11 mmol) in CH_2Cl_2 (6 mL) at 0 °C was gradually added a solution of BBr_3 (0.087 mL, 0.922 mmol) in CH_2Cl_2 (0.1 mL). After the reaction mixture was stirred at rt for 0.5 h, it was poured into ice water (10 mL) and then extracted with CH_2Cl_2 (10 mL × 3). The combined extracts were washed with water (10 mL × 2), dried over Na_2SO_4, and concentrated in vacuo to leave a residue. The residue was chromatographed over silica gel (Wako C-300, 100 g) with hexane–$CHCl_3$ (4:1) as eluent to give crude **15** as a colorless solid. Recrystallization from EtOH gave *cis*-4b,9b-dihydro[10]benzofuro[3,2-*b*]benzofuranophane (**15**, 32 mg, 83%) as colorless prisms, mp 163–164 °C. ^1H NMR ($CDCl_3$) δ: 0.25–1.26 (m, 16H, CH_2), 2.58–2.64 (m, 4H, CH_2), 6.08 (s, 2H, C*H*), 6.99 (dd, J = 8.1, 2.4 Hz, 2H, Ar–*H*), 7.00 (d, J = 8.1 Hz, 2H, Ar–*H*), 7.42 (d, J = 2.4 Hz, 2H, Ar–*H*). MS *m*/*z* (%): 348 (M^+). Anal. calcd for $C_{24}H_{28}O_2$ (348.49): C 82.72, H 8.10; found: C 82.63, H 8.03.

Crystallographic data for (*E*)-4 and 7

Crystal data for (E)-4

$C_{26}H_{34}O_2$, M = 378.55, monoclinic, $P121/a$, a = 17.192(7), b = 6.489(3), c = 39.947(17) Å, V = 4357(3) $Å^3$, β = 102.1256(11), Z = 8, D_c = 1.154 g cm^{-3}, μ (Mo Kα) = 0.071 mm^{-1}, T = 123.1 K, colourless prisms; 9519 reflections measured on a Rigaku Saturn CCD diffractometer, of which 6779 were independent, data corrected for absorption on the basis of symmetry equivalent and repeated data (min and max transmission factors: 0.849 and 0.998) and Lp effects, R_{int} = 0.087, structure solved by direct methods (Sir2002), F^2 refinement, R_1 = 0.156 for 6779 data with $F^2 > 2s(F^2)$, wR_2 = 0.4034 for all data, 8360 parameters.

Crystal data for 7

$C_{26}H_{32}O_2$, M = 376.52, monoclinic, $P21/a$, a = 16.7234(14), b = 6.422(4), c = 41.504(9) Å, V = 4370(3) $Å^3$, β = 101.363(14), Z = 8, D_c = 1.145 g cm^{-3}, μ (Cu Kα) = 0.543 mm^{-1}, T = 113 K, colourless prisms; 53 123 reflections measured on a Rigaku Saturn CCD diffractometer, of which 7933 were independent, data corrected for absorption on the basis of symmetry equivalent and repeated data (min and max transmission factors: 0.750 and 0.947) and Lp effects, R_{int} = 0.044, structure solved by direct methods (Sir2002), F^2 refinement, R_1 = 0.0577 for 7933 data with $F^2 > 2s(F^2)$, wR_2 = 0.1814 for all data, 569 parameters (crystallographic data (excluding structure factors) for the structures in this paper can be found in the Supplementary data).

Supplementary data

Supplementary data are available with the article through the journal Web site http://nrcresearchpress.com/doi/suppl/10.1139/v2012-014. CCDC 779075 and 819676 contain the X-ray data in CIF format for this manuscript. These data can be obtained, free of charge, via http://www.ccdc.cam.ac.uk/products/csd/request (Or from the Cambridge Crystallographic Data Centre, 12 Union Road, Cambridge CB2 1EZ, UK; fax: 144 1223 33603; or e-mail: deposit@ccdc.cam.ac.uk.

Acknowledgement

This work was performed under the Cooperative Research Program of the Network Joint Research Center for Materials and Devices, Institute for Materials Chemistry and Engineering, Kyushu University, Kasuga, Japan.

References

(1) Keehn, P. M., Rosenfield, S. M. Eds. *Cyclophanes;* Academic Press: New York, 1983; Vol. 1, Chapter 6, pp 428.
(2) Vögtle, F. *Cyclophane Chemistry;* Wiley: Chichester, UK, 1993.
(3) Gleiter, R.; Hopf, H. *Modern Cyclophane Chemistry;* Wiley-VCH, Weinheim, Germany, 2004.
(4) (a) Psiorz, M.; Hopf, H. *Angew. Chem.* **1982**, *21* (8), 623. doi:10.1002/anie.198206231; (b) Psiorz, M.; Hopf, H. *Angew. Chem. Int. Ed. Engl.* **1982**, *21* (8), 623. doi:10.1002/anie.198206231.
(5) (a) Reiser, O.; Reichow, S.; de Meijere, A. *Angew. Chem.* **1987**, *99* (12), 1285. doi:10.1002/ange.19870991213; (b) Reiser, O.; Reichow, S.; de Meijere, A. *Angew. Chem. Int. Ed. Engl.* **1987**, *26* (12), 1277. doi:10.1002/anie.198712771.
(6) (a) Wong, T.; Cheung, S. S.; Wong, H. N. C. *Angew. Chem.* **1988**, *100* (5), 716. doi:10.1002/ange.19881000516; (b) Wong, T.; Cheung, S. S.; Wong, H. N. C. *Angew. Chem. Int. Ed. Engl.* **1988**, *27* (5), 705. doi:10.1002/anie.198807051.
(7) (a) König, B.; Heinze, J.; Meerholz, K.; de Meijere, A. *Angew. Chem.* **1991**, *103* (10), 1350. doi:10.1002/ange.19911031017; (b) König, B.; Heinze, J.; Meerholz, K.; de Meijere, A. *Angew. Chem. Int. Ed. Engl.* **1991**, *30* (10), 1361. doi:10.1002/anie.199113611.
(8) Chan, C. W.; Wong, H. C. *J. Am. Chem. Soc.* **1988**, *110* (2), 462. doi:10.1021/ja00210a025.
(9) Ramming, M.; Gleiter, R. *J. Org. Chem.* **1997**, *62* (17), 5821. doi:10.1021/jo970327r.
(10) Kawase, T.; Ueda, N.; Oda, M. *Tetrahedron Lett.* **1997**, *38* (38), 6681. doi:10.1016/S0040-4039(97)01564-5.
(11) Utsumi, K.; Kawase, T.; Oda, M. *Chem. Lett.* **2003**, *32* (4), 412. doi:10.1246/cl.2003.412.
(12) Kawase, T. *Synlett* **2007**, *2007* (17), 2609. doi:10.1055/s-2007-991078.
(13) Yamato, T.; Fujita, K.; Abe, T.; Tsuzuki, H. *New J. Chem.* **2001**, *25* (5), 728. doi:10.1039/b010205i.
(14) Fukazawa, A.; Yamaguchi, S. *Chem. Asian J.* **2009**, *4* (9), 1386. doi:10.1002/asia.200900179.
(15) Fukazawa, A.; Yamada, H.; Yamaguchi, S. *Angew. Chem. Int. Ed.* **2008**, *47* (30), 5582. doi:10.1002/anie.200801834.
(16) Wakamiya, A.; Mori, K.; Araki, T.; Yamaguchi, S. *J. Am. Chem. Soc.* **2009**, *131* (31), 10850. doi:10.1021/ja905007s.
(17) Fukazawa, A.; Yamada, H.; Sasaki, Y.; Akiyama, S.;

Yamaguchi, S. *Chem. Asian J.* **2010**, *5* (3), 466. doi:10.1002/asia.200900517.
(18) Iida, A.; Yamaguchi, S. *J. Am. Chem. Soc.* **2011**, *133* (18), 6952. doi:10.1021/ja2019977.
(19) Yamato, T.; Matsumoto, J.-I.; Ide, S.; Suehiro, K.; Kobayashi, K.; Tashiro, M. *Chem. Ber.* **1993**, *126* (2), 447. doi:10.1002/cber.19931260223.
(20) (a) Yamato, T.; Sato, M.; Noda, K.; Matsumoto, J.; Tashiro, M. *J. Chem. Res. (S)* **1993**, *10*, 394; (b) Yamato, T.; Sato, M.; Noda, K.; Matsumoto, J.; Tashiro, M. *J. Chem. Res. (M)* **1993**, *10*, 2601.
(21) Yamato, T.; Matsumoto, J.; Ide, S.; Tokuhisa, K.; Suehiro, K.; Tashiro, M. *J. Org. Chem.* **1992**, *57* (19), 5243. doi:10.1021/jo00045a044.
(22) Yamato, T.; Matsumoto, J.-I.; Tokuhisa, K.; Kajihara, M.; Suehiro, K.; Tashiro, M. *Chem. Ber.* **1992**, *125* (11), 2443. doi:10.1002/cber.19921251116.
(23) Yamato, T.; Matsumoto, J.; Sato, M.; Noda, K.; Tashiro, M. *J. Chem. Soc., Perkin Trans. 1* **1995**, (10): 1299. doi:10.1039/p19950001299.
(24) Yamato, T.; Matsumoto, J.; Fujita, K. *J. Chem. Soc., Perkin Trans. 1* **1998**, (1): 123. doi:10.1039/a704105e.
(25) McMurry, J. E.; Fleming, M. P.; Kees, K. L.; Krepski, L. R. *J. Org. Chem.* **1978**, *43* (17), 3255. doi:10.1021/jo00411a002.
(26) McMurry, J. E. *Acc. Chem. Res.* **1983**, *16* (11), 405. doi:10.1021/ar00095a003.
(27) McMurry, J. E.; Haley, G. J.; Matz, J. R.; Clardy, J. C.; Van Duyne, G.; Gleiter, R.; Schaefer, W.; White, D. H. *J. Am. Chem. Soc.* **1984**, *106* (17), 5018. doi:10.1021/ja00329a071.
(28) McMurry, J. E. *Chem. Rev.* **1989**, *89* (7), 1513. doi:10.1021/cr00097a007.
(29) Mitchell, R. H.; Weerawarna, S. A. *Tetrahedron Lett.* **1986**, *27* (4), 453. doi:10.1016/S0040-4039(00)85503-3.
(30) Tanner, D.; Wennerström, O.; Chattopadhyaya, J.; Carlberg, G. E.; Sterner, O.; Wickberg, B. *Acta Chem. Scand. Ser. B.* **1983**, *37b*, 693. doi:10.3891/acta.chem.scand.37b-0693.
(31) Hopf, H.; Mlynek, C. *J. Org. Chem.* **1990**, *55* (4), 1361. doi:10.1021/jo00291a052.
(32) Grützmacher, H.-F.; Neumann, E. *Chem. Ber.* **1993**, *126* (6), 1495. doi:10.1002/cber.19931260635.
(33) Shukla, R.; Brody, D. M.; Lindeman, S. V.; Rathore, R. *J. Org. Chem.* **2006**, *71* (16), 6124. doi:10.1021/jo060817w.
(34) Debroy, P.; Lindeman, S. V.; Rathore, R. *J. Org. Chem.* **2009**, *74* (5), 2080. doi:10.1021/jo802579f.
(35) Yamato, T.; Matsumoto, J.; Ide, S.; Suehiro, K.; Tashiro, M. *J. Chem. Res. (S)* **1993**, 394.
(36) Yamato, T.; Fujita, K.; Okuyama, K.; Tsuzuki, H. *New J. Chem.* **2000**, *24* (4), 221. doi:10.1039/b001145m.
(37) Yamato, T.; Fujita, K.; Futatsuki, K.; Tsuzuki, H. *Can. J. Chem.* **2000**, *78* (8), 1089. doi:10.1139/v00-110.
(38) Yamato, T.; Fujita, K.; Tsuzuki, H. *J. Chem. Soc., Perkin Trans. 1* **2001**, (17): 2089. doi:10.1039/b010075g.
(39) Yamato, T.; Miyamoto, S.; Hironaka, T.; Miura, Y. *Org. Lett.* **2005**, *7* (1), 3. doi:10.1021/ol0483403.
(40) Yamato, T.; Hironaka, T.; Shiino, M.; Saisyo, T.; Miyamoto, S. *J. Chem. Res.* **2006**, *2006* (2), 110. doi:10.3184/030823406776330990.
(41) Yamato, T.; Okabe, R.; Miyamoto, S.; Miyazaki, M. *J. Chem. Res.* **2006**, *2006* (9), 593. doi:10.3184/030823406778521509.
(42) Saisyo, T.; Hironaka, T.; Shiino, M.; Yamato, T. *J. Chem. Res.* **2006**, *2006* (10), 661. doi:10.3184/030823406779173659.
(43) Saisyo, T.; Shiino, M.; Shimizu, T.; Paudel, A.; Yamato, T. *J. Chem. Res.* **2008**, *2008* (8), 479. doi:10.3184/030823408X338701.
(44) Merz, A.; Karl, A.; Futterer, T.; Stacherdinger, N.; Schneider, O.; Lex, J.; Luboch, E.; Biernat, J. F. *Liebigs Ann. Chem.* **1994**, *1994* (12), 1199. doi:10.1002/jlac.199419941211.
(45) Tashiro, M.; Yamato, T. *J. Org. Chem.* **1981**, *46* (22), 4556. doi:10.1021/jo00335a047.
(46) Tashiro, M.; Yamato, T. *J. Org. Chem.* **1983**, *48* (9), 1461. doi:10.1021/jo00157a015.
(47) Kajigaeshi, S.; Kakinami, T.; Tokiyama, H.; Hirakawa, T.; Okamoto, T. *Chem. Lett.* **1987**, *16* (4), 627. doi:10.1246/cl.1987.627.
(48) (a) Kloster-Jensen, E.; Wirz, J. *Angew. Chem.* **1973**, *85* (16), 723. doi:10.1002/ange.19730851608;; (b) Kloster-Jensen, E.; Wirz, J. *Angew. Chem. Int. Ed. Engl.* **1973**, *12* (8), 671. doi:10.1002/anie.197306711.
(49) Olah, G. A.; Narang, S. C.; Gupta, B. G. B.; Malhotra, R. *J. Org. Chem.* **1979**, *44* (8), 1247. doi:10.1021/jo01322a012.
(50) Olah, G. A.; Narang, S. C.; Gupta, B. G. B.; Malhotra, R. *Synthesis* **1979**, *1979* (01), 61. doi:10.1055/s-1979-28558.
(51) Yamato, T.; Matsumoto, J.; Tashiro, M. *J. Chem. Res.* **1994**, 178.
(52) Yamato, T.; Saruwatari, Y.; Yasumatsu, M.; Ide, S. *Eur. J. Org. Chem.* **1998**, *1998* (2), 309. doi:10.1002/(SICI)1099-0690(199802)1998:2<309::AID-EJOC309>3.0.CO;2-6.

Can. J. Chem. Downloaded from www.nrcresearchpress.com by Renmin University of China on 09/02/12
For personal use only.

Synthesis of β- and β,β-substituted Morita–Baylis–Hillman adducts using a two-step protocol

David I. Magee, Same Ratshonka, Jessica McConaghy, and Maggie Hood

Can. J. Chem. Downloaded from www.nrcresearchpress.com by Renmin University of China on 09/02/12
For personal use only.

Abstract: The synthesis of a large number of β- and β,β-substituted keto esters was successful by the use of the Knoevenagel condensation reaction. The stereoselectivity of these reactions was improved by alteration of various substituent groups. Although there were few examples of complete Z selectivity, the use of *tert*-butyl acetoacetate with either aromatic or aliphatic aldehydes afforded Z selectivity. The selective reductions of these substituted keto esters was successfully achieved by using a combination of $NaBH_4$ and $CeCl_3 \cdot 7H_2O$ or $Yb(OTf)_3$, which allowed a facile synthesis of a large number of stereochemically pure substituted Morita–Baylis–Hillman adducts, including β,β-substituted adducts.

Key words: Morita–Baylis–Hillman, Knoevenagel, reduction, β,β-substituted.

Résumé : On a effectué avec succès la synthèse d'un grand nombre d'esters β- et β,β-substitués en faisant appel à la condensation de Knoevenagel. On a amélioré la stéréosélectivité de ces réactions en procédant à l'altération de divers substituants. Même s'il n'y a que peu d'exemples de sélectivité Z complète, l'utilisation de l'acétoacétate de *tert*-butyle avec des aldéhydes aromatiques ou aliphatiques conduit à la formation de produits avec une sélectivité Z. On a effectué avec succès les réductions sélectives de ces cétoesters substitués en utilisant une combinaison de $NaBH_4$ et de $CeCl_3 \cdot 7H_2O$ ou de $Yb(OTf)_3$; ceci a permis de réaliser une synthèse facile d'un grand nombre d'adduits de Morita-Baylis-Hillman substitués et stéréochimiquement purs, y compris des adduits β,β-substitués.

Mots-clés : Morita–Baylis–Hillman, Knoevenagel, réduction, β,β-substitué.

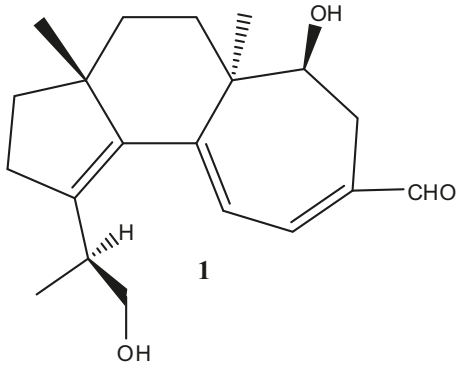
[Traduit par la Rédaction]

Introduction

There is significant interest in the field of natural product synthesis for the purpose of developing methodology for the synthesis of compounds with medicinal properties. Sarcodonin A (**1**) is a natural product found in the fungus *Sarcodon scabrosus*, which has been found to possess antibacterial and anti-inflammatory properties.[1] The cyanthane diterpenes are characterized by a fused 5,6,7-tricyclic array (Fig. 1), with most containing a C-3 isopropyl group that is not functionalized. Sarcodonin A is an exception, as it has an alcohol functionality at C-19, which generates a chiral centre at C-18. This increased level of oxidation makes the synthesis of sarcodonin A significantly more difficult than other members of the cyanthane family, since it requires controlling the configuration of a stereogenic centre on a pendant side chain relative to which it is attached. Since this particular type of stereochemical arrangement has been proven to be particularly troublesome to handle synthetically, this compound provides an interesting target to address this challenge.

Recently, the MaGee group[2] demonstrated that enantioselective deprotonation can be used to help address this problem. To implement this strategy for the synthesis of sarcodonin A, a potential symmetry in the molecule had to be delineated. Upon close examination it was envisioned that the left-hand portion of sarcodonin A could be constructed from the [3.2.1]-bicyclic diketone **4** (Scheme 1), thus, compounds like **2** became the lynchpin for our proposed synthesis.

Fig. 1. Sarcodonin A.



1

There appeared to be several approaches for the construction of this type of structure; these included: (1) addition of an allyl cation, or equivalent, to a conjugated diene;[3] (2) [3 + 3] carbocyclization of a nitroallylic ester and an enamine;[4] and (3) an α,α′-annulation strategy[5] involving reaction between a cyclic enamine and a biselectrophile (i.e., a compound that could serve as both an alkylation and Michael addition agent) (Fig. 2). For our purposes, however, each

Received 27 October 2011. Accepted 25 January 2012. Published at www.nrcresearchpress.com/cjc on 10 April 2012.

D.I. Magee, S. Ratshonka, J. McConaghy, and M. Hood. Department of Chemistry, P.O. Box 4400, University of New Brunswick, Fredericton, NB E3B 5A3, Canada.

Corresponding author: David I. MaGee (e-mail: dmagee@unb.ca).

Can. J. Chem. Downloaded from www.nrcresearchpress.com by Renmin University of China on 09/02/12
For personal use only.

Scheme 1. Retrosynthetic analysis of sarcodonin A.

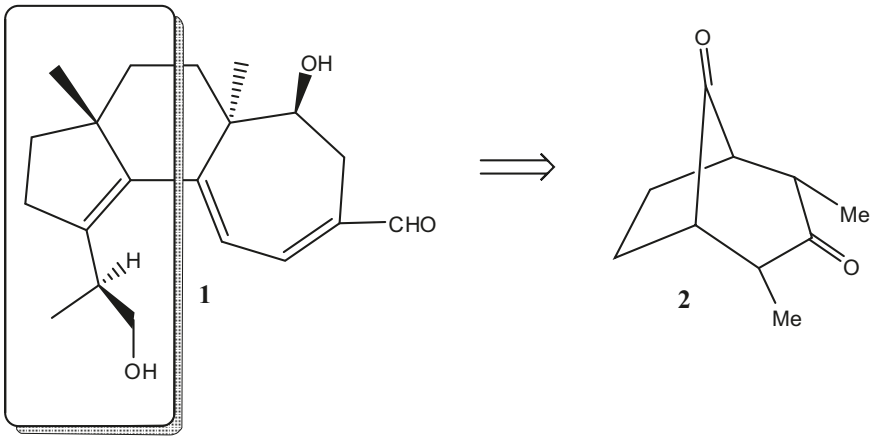
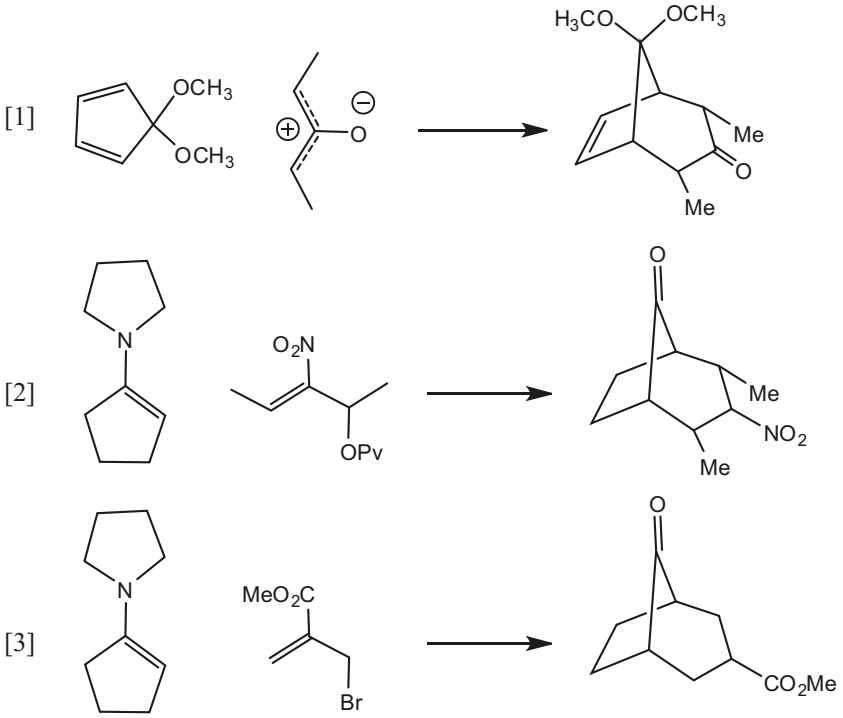


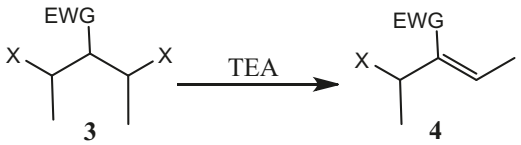
Fig. 2. Various approaches to construct [3.2.1]-bicyclic ketones.



approach had limitations. For instance, oxyallyl cation addition to 1,1-diethoxycyclopentadiene proceeds in very poor yield, which is unacceptable as the first step in a total synthesis. The [3 + 3]-carbocyclization route using nitroallylic esters proceeds in acceptable yields and is easily scaled up, however, all attempts to perform a Nef reaction failed.[6] Finally, the α,α′-annulation strategy efficiently generates compounds such as [3.2.1]-bicyclic ketones, however, it is underfunctionalized, and the ability to synthesize and use more highly substituted derivatives to participate in the annulation reaction has not been demonstrated.

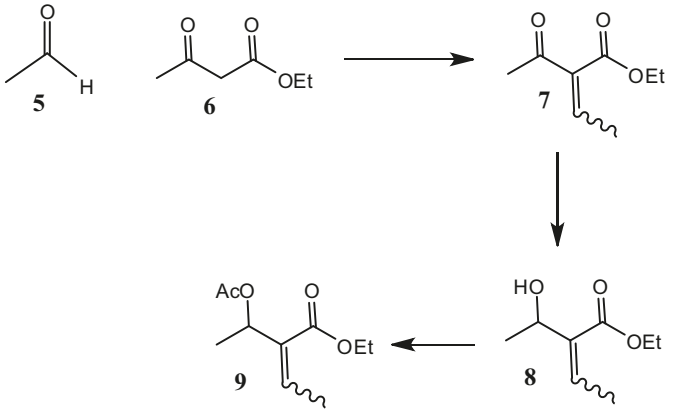
To solve the issue of underfunctionalization, compounds like **4** (Scheme 2) were required, and it was felt that these can potentially be accessed from Morita–Baylis–Hillman (MBH) adducts.[7] Unfortunately, β-branched MBH adducts are difficult to obtain using classical conditions, therefore, several chemical solutions have been reported.[8–15] Although each has their own advantages, they all have the limitation in requiring reactive organometallic and (or) toxic reagents and not being very amenable to scale up.

Scheme 2. An α,β-unsaturated compound suitably substituted for use in an α,α′-annulation sequence for sarcodonin A synthesis.



Given these limitations, an alternative route for the synthesis of the targeted annulation agent was sought. It was felt that the Knoevenagel reaction[16] between an aldehyde and ethyl acetoacetate would give rise to an α,β-unsaturated keto ester like **7**, and that upon reduction with an appropriate reducing agent would provide the MBH adduct **8** (Scheme 3). Although there was precedent for this approach,[17] in our

Scheme 3. Synthesis of Morita–Baylis–Hillman (MBH) adducts using the Knoevenagel condensation/reduction two-step protocol.



hands we routinely obtained low yields (>30%). If more substituted examples were used (e.g., Ph substituted on the alkene rather than methyl) then a much slower reduction occurred and did not have complete conservation of stereochemistry. Given these difficulties, we decided to investigate the breadth and scope of this reaction focusing on different substitution patterns, electron-withdrawing groups, and reduction conditions. Herein we report our study on the preparation of MBH adducts by this two-step protocol and show that it is rapid and generally applicable to the formation of β- and β,β-disubstituted MBH compounds.

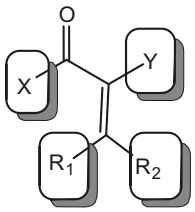
Results and discussion

The first step was the synthesis of the intermediate keto esters via a Knoevenagel condensation reaction. Literature reports have demonstrated this method to be appropriate for reactions between aromatic and aliphatic aldehydes, as well as different 1,3-dicarbonyl compounds[16] such as acetoacetates. The breadth of this reaction was attractive, since it would allow for the construction of a wide variety of adducts and thus permit the exploration of the scope of this two-step process.

In deciding what compounds should be generated, consideration was given to each quadrant of the alkene (Fig. 3). For instance, if Y were an ester then it could be easily varied from *tert*-butyl to methyl or benzyl to probe the sterics. It was also envisaged that electron-withdrawing groups (EWGs, Y) other than esters could be explored, such as a SO_2Ph, a ketone, or a cyano group. The ketone (X) could also be varied from a methyl to a branched or long-chain aliphatic ketone or to an aromatic ketone. Altering this quadrant allowed one to explore the effect of sterics on both the E:Z ratios obtained in the Knoevenagel condensations, as well as the ease of hydride reduction. Moving to the other quadrants of the double bond, R_1 and (or) R_2 could be replaced with branched or long-chain aliphatic or aromatic units. Finally, if both R_1 and R_2 were replaced with carbons then this would provide access to β,β-substituted adducts that could then be transformed into β,β-substituted MBH adducts; these are little known or studied compounds.

It is important to note that all of these alterations were important for obtaining a variety of substituted symmetrical and unsymmetrical compounds that have the potential to be very useful α,α′-annulation agents (biselectrophiles) for not only

Fig. 3. Different quadrants of the Knoevenagel condensation product.



the formation of substituted [3.2.1]-bicyclic diketones, but also a variety of other natural products. With this in mind, 18 different Knoevenagel products were synthesized following general procedures (Tables 1 and 2).

It was decided to first investigate what effect, if any, aromatic and aliphatic aldehydes had on the E and Z stereoselectivity when condensed with 1,3-dicarbonyl compounds. Thus, condensation of different acetoacetates with various aliphatic aldehydes (Table 1, entries 1–6) showed that regardless of whether a methyl, isopropyl, pentyl, or cyclohexyl group was on the terminus of the double bond, all condensations afforded roughly the same mixture of isomers (1.5–2.3:1) with Z being favoured over the E isomer in most cases. The exception to this was entry 6 where a *tert*-butyl group was able to confer complete stereochemical control, albeit in low chemical yield.

Other notable results obtained are entries 7–9 (Table 1), where the ester functionality was varied from methyl to *tert*-butyl to benzyl. It was found that increasing the bulk of the EWG group also increased the selectivity of the reaction in favour of the Z isomer. This was surprising, since it was expected that E stereoselectivity would be preferred as one increased the size of the ester group.[18] However, Tanikaga et al.[19] demonstrated that the stereoselectivity of the Knoevenagel product is affected by slight differences in steric requirements between the two EWGs and when the differences between X, Y, and R_2 (Fig. 3) are rather small then selectivity in favour of the Z isomer is preferred.

The effect of EWGs other than esters was also investigated. In entry 11 (Table 1), a sulfone was used for comparison and, as reported by Tanikaga et al.,[20] an overwhelming preference for the E-isomer was observed. However, as expected,[21] use of a cyano group (Table 1, entry 14) in place of an ester preferentially gave the Z-isomer.

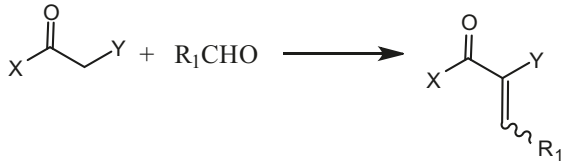
Continuing with this survey of different combinations, various alkyl groups were substituted on the ketone (Table 1, entries 10, 12, and 13) to assess if improved selectivity could be obtained and if the reduction would tolerate increased steric hindrance near the ketone. Not surprisingly, as the steric hindrance around the ketone increased there was an improvement in the stereochemical purity. This increase in stereoselectivity came at a price as the yield of Knoevenagel product decreased substantially as the acetoacetate became bulkier.

With a large number of aldehydes screened, a decision was made to look at the possibility of doing the condensation with a number of ketones ranging from straight-chain aliphatic (symmetric and unsymmetric), to cyclic aliphatic, to heterocyclic. These were condensed with ethyl acetoacetate to form β,β-substituted Knoevenagel products (Table 2).

Can. J. Chem. Downloaded from www.nrcresearchpress.com by Renmin University of China on 09/02/12
For personal use only.

Can. J. Chem. Downloaded from www.nrcresearchpress.com by Renmin University of China on 09/02/12
For personal use only.

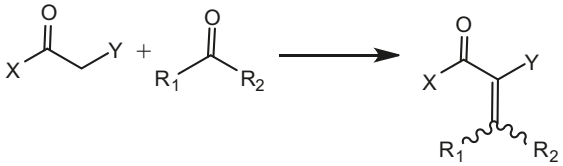
Table 1. Synthesis of β-substituted unsaturated keto esters by the Knoevenagel condensation reaction.



Entry	X	Y	R′	Time (h)	Product	Yield (%)	Isomer ratio (E:Z)	Method
1	Me	CO_2t-Bu	Me	12	10	83	1:2.3	A
2	Me	CO_2t-Bu	*i*-Pr	12	11	70	1:2.3	A
3	Me	CO_2t-Bu	$(CH_2)_4CH_3$	10	12	80	2:3	A
4	Me	CO_2Me	C_6H_{11}	4	13	84	2:3	A
5	Me	CO_2Me	$(CH_2)_4CH_3$	4	14	20	1:2	B
6	Me	CO_2Et	*t*-Bu	12	15	14	Z	B
7	Me	CO_2Me	Ph	3	16	80	1:1	B
8	Me	CO_2Bn	Ph	3	17	77	2:3	B
9	Me	CO_2t-Bu	Ph	10	18	50	Z	B
10	Ph	CO_2Et	Ph	3	19	70	Z	B
11	Ph	SO_2Ph	Ph	12	20	78	E	B
12	*i*-Pr	CO_2Me	Ph	3	21	60	1.8:1	B
13	*t*-Bu	CO_2Me	Ph	10	22	18	Z	B
14	Ph	CN	C_6H_{11}	48	23	50	Z	C

Note: Reagents: (A) CH_3COCH_2–Y; RCHO; piperidine; EtOH; 0 °C; (B) X–$COCH_2$–Y; RCHO; piperidine; AcOH; benzene; reflux; (C) $PhCOCH_2CN$; RCHO; proline; EtOH; room temperature (RT).

Table 2. Synthesis of β,β-substituted unsaturated keto esters by the Knoevenagel condensation reaction using the Lewis acids $ZnCl_2$ or $TiCl_4$.



Entry	X	Y	R′, R″	Time (h)	Product	Yield (%)
1	Me	OEt	Me, Me	72	24	42
2	Me	OEt	$(CH_2)_5$	16	25	28
3	Me	OEt	$(CH_2)_4$	16	26	38
4	Me	OEt	$C(C_2H_4)_2NCO_2CH_3$	16	27	32
5	Me	OEt	Me, C_7H_{15}	16	28	27

With a number of Knoevenagel condensation products in hand, the stage was set to look at the critical 1,2-hydride reduction. Upon examination of the literature there appeared to be several approaches. The first method to be studied was reduction using Luche conditions.[22] The advantage of this method was that selective 1,2-reduction could be obtained under conditions that did not affect other functional groups such as carboxylic acids, esters, amides, or nitro groups.[19] Furthermore, the reaction could be conducted at room temperature without the special exclusion of air or moisture. Even though there was a lot of precedent literature that consistently showed that Luche conditions were the appropriate choice for the selective 1,2-reduction of α-enones, it was not clear how it was going to perform on keto esters like **7**, as there were few reports of its use for the reduction of β′-oxocarbonyl compounds.[23] Regardless, following the procedure outlined by Luche, compounds **16** and **17** were treated with 1 mol equiv of sodium borohydride and cerium trichloride in methanol at 0 °C and room temperature (to assess the influence of temperature on the yield) to provide allylic alcohols **29** and **30** in 34%–80% overall yield (Table 3). From these results it was clear that effecting the reduction at room temperature gave the best results.

Of note in this preliminary investigation was the fact that, even though the reaction was started with a 1:1 mixture of isomers, the final stereoisomeric ratio of the products was found to be 2:3. There were several possibilities to account for this. Firstly, if the reduction of one isomer was faster than the other and the rate of isomerization of the starting materials was approximately the same as the reduction, then this would lead to a preponderance of one isomer. A second possibility was that there was some isomerization that took place after the reduction had occurred, presumably this would lead to a predominance of the thermodynamic product. Finally, it is possible that the reduction of one isomer was much more efficient than the other.

Can. J. Chem. Downloaded from www.nrcresearchpress.com by Renmin University of China on 09/02/12
For personal use only.

Table 3. Reduction of Knoevenagel condensation products **16** and **17** to allylic alcohols **29** and **30** using Luche conditions.

Starting material (E:Z isomer ratio)	Temp. (°C)	Time (h)	Product	Yield (%)	Isomer ratio (E:Z)
16 (1:1)	0	2	**29**	50	2:3
16 (1:1)	25	2	**29**	80	2:3
17 (2:3)	0	2	**30**	34	2:3
17 (2:3)	25	2	**30**	77	2:3

With the optimal conditions for the Luche reduction obtained, other reducing agents were investigated to see if greater success could be realized; these included lithium tri-*tert*-butoxyaluminium hydride (LATB-H),[24] borane methyl sulfide complex (BMS),[25] and $Yb(OTf)_3$[26] (Table 4). Of these, only $Yb(OTf)_3$ consistently reduced the ketone; however, the yields were substantially inferior to the yields under Luche conditions.

Based on the optimized conditions, all of the compounds in Tables 1 and 2 were reduced using the Luche method, and the results are summarized in Table 5. It was observed that as the substituent on the terminus of the alkene increased in size, the yield of the reduction product improved (Table 5, entries 1–7). This was presumably due to a diminution of competing side reactions such as Michael addition, self-condensation, or 1,4-reduction. This was especially true for the methyl-substituted compound (Table 5, entries 1 and 2) where it was observed that good yields could only be realized if the reduction was allowed to run for only a few seconds. It was also observed that in most cases it was possible to obtain pure isomers when starting with either pure E or Z starting material. The exception to this was the phenyl ketone **16**, for which the same isomer ratio of products was obtained after reduction regardless of the isomer ratio of the starting ketones.

Another notable result was the reduction of the cyano compound (Table 5, entry 18). It was found that the desired reduction product (Z-isomer) along with the fully reduced product, in which the double bond was also reduced, was obtained in approximately a 1:1 ratio. Although the desired product was present, the two compounds were found to be inseparable by column chromatography; thus, pure MBH adduct could not be achieved by this method.

Having succeeded with the reduction of the β-substituted Knoevenagel condensation products, the reduction of the β,β-substituted 1,3-dicarbonyl compounds was examined (Table 5). All the ketones (**24**–**28**) reduced very efficiently and in a short period of time (15 min) to produce the β,β-substituted MBH adducts in good to excellent yields. Of particular note is entry 23 (Table 5) where compound **52** was obtained in 71%; this result shows that additional functional groups may be present without adversely affecting the reduction.

α,α′-Annulation strategy for construction of the [3.2.1]-bicyclic ketone

With a suitable method available to generate amounts of alcohol **31** in hand, investigation into transforming it to the targeted annulation agent **57** was undertaken (Scheme 4). Fortunately, when alcohol **31** was treated with triphenylphosphine and *N*-bromosuccinimide (NBS)[27] at –30 °C, allylic bromide **55** was obtained in 48% yield as a 1:1 mixture of E- and Z-isomers. Alternatively, **31** could be efficiently acylated with acetyl chloride, pivaloyl chloride, and methyl chloroformate in 71%, 65%, and 73% yields, respectively.[4,17] Treatment of each of these biselectrophiles with 1-pyrrolidino-1-cyclopentene (**56**) with and without triethylamine in refluxing ethanol or acetonitrile provided variable success, with the desired cycloadducts, **57a** and **57b**, being most efficiently produced in 43% yield as a 1:1 mixture of isomers using bromide **55**.

Table 4. Reduction of selected Knoevenagel products with tri-*tert*-butoxyaluminium hydride (LATB-H), borane methyl sulfide complex (BMS), and $Yb(OTf)_3$.

Reducing agents	Starting material (E:Z isomer ratio)	Time (h)	Product	Yield (%)	Isomer ratio (E:Z)
LATB-H	**16** (1:1)	2	**29**	nr	—
	19 (0:1)	2	**43**	nr	—
BMS	**16** (1:1)	3	**29**	40	2:3
	17 (2:3)	3	**30**	27	2:3
	18 (0:1)	3	**42**	10	Z
	19 (0:1)	3	**43**	nr	—
	21 (2:1)	3	**45/46**	10	2:3
$Yb(OTf)_3$	**16** (1:1)	2	**29**	20	2:3
	17 (2:3)	2	**30**	10	2:3
	18 (0:1)	2	**42**	40	Z
	19 (0:1)	2	**43**	nr	—-

Note: nr, no reaction.

The isolated products were determined to be an approximately 50:50 mixture of symmetric and asymmetric esters based on an analysis of the ^1H and ^{13}C NMR spectra. The stereochemistries of the esters were assigned on the basis of correlations observed in the NOESY spectrum of the mixture. For the symmetric ester, the methine hydrogens on the carbons bearing the methyl groups were assigned as equatorial based on NOESY correlations observed between these hydrogens and the axial methylene hydrogens. The ester was assigned as axial based on NOESY correlations observed between the axial methyl hydrogens and the methine hydrogen on the carbon bearing the ester group (Fig. 4, **57a**).

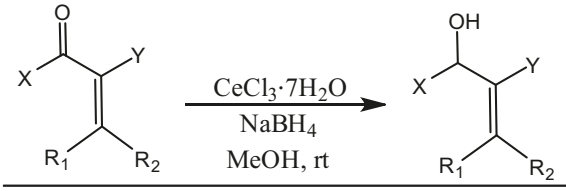
A similar analysis for the asymmetric ester determined the ester group to be axial. For the side of the molecule with the methyl group axial, NOESY correlations similar to those for the symmetric ester were observed, with an additional NOESY correlation observed between the methyl hydrogens and the axial methine hydrogen on the carbon bearing the equatorial methyl group. In addition, NOESY correlations were observed between the equatorial methyl hydrogens and one of the axial methylene hydrogens (Fig. 4, **57b**).

Conclusion

In conclusion, a large number of β- and β,β-substituted α,β-unsaturated keto esters were synthesized using the Knoevenagel condensation. For the synthesis of the β-keto esters, it was demonstrated that the stereoselectivity of the reaction was improved by alteration of various substituents on the ketone, ester group, and various aldehydes. From our results, a Z-selective Knoevenagel condensation can be achieved by the use of *tert*-butyl acetoacetate with either aromatic or aliphatic

Can. J. Chem. Downloaded from www.nrcresearchpress.com by Renmin University of China on 09/02/12
For personal use only.

Table 5. Reduction of the Knoevenagel condensation products using Luche conditions.



Entry	X	Y	R_1, R_2	Time	Product	Yield (%)	Isomer ratio (E:Z)
1	Me	CO_2t-Bu	Me, H	0.5 min	**31**	66	E
2	Me	CO_2t-Bu	H, Me	1 min	**32**	68	Z
3	Me	CO_2t-Bu	*i*-Pr, H	3 min	**33**	79	E
4	Me	CO_2t-Bu	H, *i*-Pr	3 min	**34**	66	Z
5	Me	CO_2t-Bu	$(CH_2)_4CH_3$, H	5 min	**35**	75	E
6	Me	CO_2t-Bu	H, $(CH_2)_4CH_3$	5 min	**36**	72	Z
7	Me	CO_2Et	*t*-Bu, H	3 min	**37**	92	Z
8	Me	CO_2Me	$(CH_2)_4CH_3$, H	2 h	**38**	40	E
9	Me	CO_2Me	H, $(CH_2)_4CH_3$	2 h	***ſ*39**	49	Z
10	Me	CO_2Me	C_6H_{11}, H	5 min	**40**	52	E
11	Me	CO_2Me	H, C_6H_{11}	5 min	**41**	56	Z
12	Me	CO_2t-Bu	Ph, H	2 h	**42**	60	Z
13	Ph	CO_2Et	Ph, H	2 h	**43**	77	Z
14	Ph	SO_2Ph	Ph, H	15 min	**44**	40	E
15	*i*-Pr	CO_2Me	Ph, H	2 h	**45**	65	E
16	*i*-Pr	CO_2Me	H, Ph	2 h	**46**	71	Z
17	*t*-Bu	CO_2Me	Ph, H	2 h	**47**	nr	—
18	Ph	CN	C_6H_{11}, H	5 min	**48**	52	Z
19	Me	CO_2Et	Me, Me	15 min	**49**	91	—
21	Me	CO_2Et	$(CH_2)_5$	15 min	**50**	91	—
22	Me	CO_2Et	$(CH_2)_4$	15 min	**51**	90	—
23	Me	CO_2Et	$(C_2H_4)_2NCO_2CH_3$	15 min	**52**	71	—
24	Me	CO_2Et	CH_3, nC_7H_{15}	15 min	**53**	82	Z
25	Me	CO_2Et	nC_7H_{15}, CH_3	15 min	**54**	82	E

Note: nr, no reaction.

Scheme 4. Synthesis of a [3.2.1]-bicyclic ketone using a Morita–Baylis–Hillman (MBH) adduct as a biselectrophile.

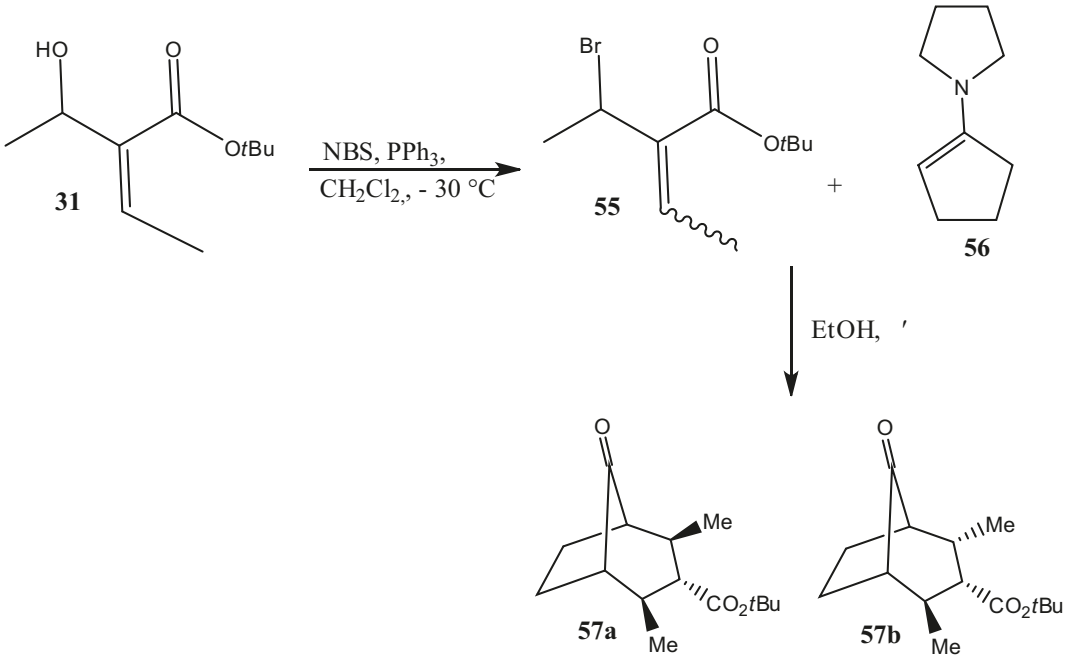
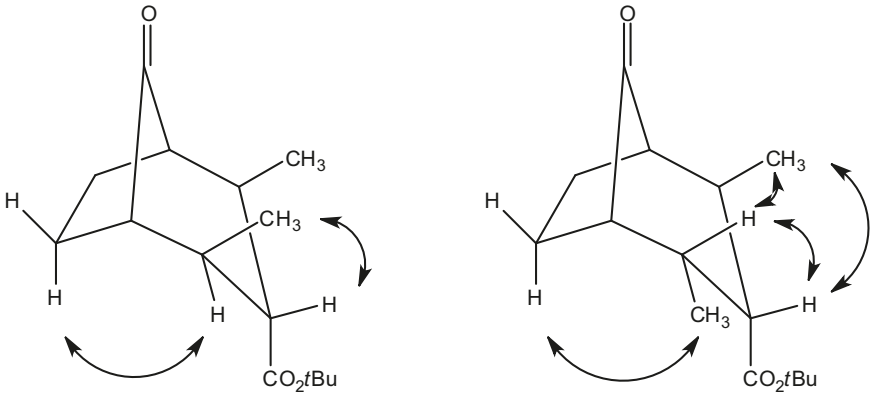


Fig. 4. Partial NOESY correlations observed for the (A) symmetric ester and (B) asymmetric ester.



57a **57b**

Can. J. Chem. Downloaded from www.nrcresearchpress.com by Renmin University of China on 09/02/12
For personal use only.

aldehydes. An added advantage of the *tert*-butyl ester derivatives was that it allowed for easy chromatographic separation of the stereoisomers. Although there were a few examples of complete Z selectivity, for the most part ratios of approximately 70:30 were routinely obtained. A number of β,β-substituted Knoevenagel condensation products were also obtained by the use of various symmetrical and unsymmetrical ketones with $TiCl_4$ or zinc chloride. In the case of an unsymmetrical ketone a 1:1 mixture of isomers was obtained.

These β- and β,β-substituted keto ester compounds were subjected to a variety of different reducing conditions to generate substituted MBH products, many of them previously unknown and inaccessible via traditional MBH methods. It was found that the reduction of these β-oxoesters was most successful using Luche conditions with good to excellent yields (40%–92%) being obtained within a few minutes at room temperature. In most cases, it was determined that there was no scrambling of the stereochemistry when either pure E- or Z-isomers were reduced. Since it is well-documented that Knoevenagel products are readily isomerized by simple heating,[28] this is important because, coupled with the ability to separate them by chromatography, it offers the potential of cycling both β-oxoester compounds to either MBH product in a stereochemically pure fashion.

Studies aimed at using these substituted MBH adducts for a variety of different synthetic endeavors are currently underway and results will be communicated in due course.

General experimental procedures

All reactions were carried out in flame-dried round bottom flasks (RBF) or in oven-dried glassware (pyrex) (140 °C, 1 h) unless stated otherwise. Temperatures indicated refer to an external bath. All reactions were magnetically stirred, unless stated otherwise. Standard techniques were used for solvent purifications. Anhydrous reaction solvents were available via the use of Grubbs-type columns. Air- and moisture-sensitive reagents were handled via standard techniques. Reagents were purchased from common suppliers and used as received unless stated otherwise. SiO_2 flash chromatography was performed using Silicycle silica gel (30–60 μm particle size). Nuclear magnetic resonance (NMR) spectroscopy was performed on a Varian INOVA 300 MHz or on a Varian UNITY 400 MHz (referred to proton resonance frequency). ^{1}H NMR spectroscopic data are presented in parts per million (δ) relative to tetramethylsilane as an internal standard. All proton–proton NMR coupling constants (*J*) are expressed in Hertz (Hz). ^{13}C NMR data are presented in parts per million (δ) relative to $CDCl_3$ (77.16 ppm) as an internal standard unless otherwise stated. Infrared spectra (IR) were recorded on a NEXUS 470 FTIR. Main peaks are reported as wavenumbers in cm^{-1}. High-resolution mass spectra (HRMS) were recorded using a Waters Xevo Q-Tof mass spectrometer. Samples were dissolved into a mixture of acetonitrile / deionized water / formic acid (50%:50%:0.1% composition), filtered on a 0.2 μm membrane filter, and then immediately introduced into the instrument by infusion at a rate of 10 μL/min. The ionization mode was electrospray positive (ESI+), which predominantly produced protonated cations ($[M + H]^+$ species). High-resolution spectra were acquired using a sodium formate solution as a lock mass reference solution and used as a mass correction when acquiring the sample spectra. ESI$^+$ conditions were optimized with a capillary voltage between 2 kV, a sample cone of 30, an extraction cone of 3.0, a source temperature of 120 °C, a desolvation temperature of 200 °C, a desolvation gas flow of 500 L/h, and a cone gas flow of 10 L/h. The MS data were acquired over a range of 20–1000 *m/z* with a scan duration of 1 s. Melting points were measured on a Gallenkamp melting point apparatus and all melting points are uncorrected.

General procedure for the synthesis of α,β-unsaturated dicarbonyl compounds 10–13

To a cooled (0 °C) mixture of aldehyde (50 mmol) and acetoacetate (15 mmol) was added a mixture of piperidine (0.03 mL) and EtOH (0.025 mL). The mixture was stirred at 0 °C for 12 h, and the reaction was quenched with cold aqueous 20% tartaric acid. The products were extracted with ethyl acetate, and the extracts were washed with brine, dried ($MgSO_4$), and concentrated under reduced pressure. The crude product was purified by column chromatography (SiO_2, hexane–AcOEt 10:1).

Preparation of tert*-butyl (*E*)- and (Z)-2-acetyl-but-2-enoate (10)*

Following the general procedure, esters **10a** and **10b** were formed in 83% yield (2.2 g) as a 1.2:3 mixture of E- and Z-isomers.[16]

Can. J. Chem. Downloaded from www.nrcresearchpress.com by Renmin University of China on 09/02/12
For personal use only.

Preparation of **tert-*butyl* (E)-** *and* **(Z)-2-acetyl-4-methylpent-2-enoate (11)**

Following the general procedure, esters **11a** and **11b** were formed in 70% yield (2.23 g) as a 1.2:3 mixture of E- and Z-isomers.[16]

Preparation of **tert-*butyl* (E)-** *and* **(Z)-2-acetyloct-2-enoate (12)**

Following the general procedure, esters **12a** and **12b** were formed in 80% yield as a 2:3 mixture of E- and Z-isomers. (Z)-Isomer **12a**: IR (neat, cm^{-1}): 2985, 1724, 1657, 1625, 1577, 1497, 1448, 1394, 1234, 1213, 1043, 949, 890, 757, 695. ^1H NMR ($CDCl_3$, 300 MHz) δ: 0.93 (t, 3H, J = 7.0 Hz), 1.21–1.51 (m, 8H), 1.52 (s, 9H), 2.31 (s, 3H), 6.82 (t, 1H, J = 9.5 Hz). ^{13}C NMR ($CDCl_3$, 300 MHz) δ: 22.0, 29.8, 52.0, 70.0, 126.0, 128.7, 129.6, 130.5, 133.3, 135.8, 139.9, 168.6. HRMS (M^+ + H) calcd for $C_{14}H_{25}O_3$: 241.1801; found: 241.1803. (*E*)-Isomer **12b**: IR (neat, cm^{-1}): 2985, 1724, 1657, 1625, 1577, 1497, 1448, 1394, 1234, 1213, 1043, 949, 890, 757, 695. ^1H NMR ($CDCl_3$, 300 MHz) δ: 0.89 (t, 3H, J = 6.8 Hz), 1.21–1.40 (m, 8H), 1.50 (s, 9H), 2.33 (s, 3H), 6.80 (t, 1H, J = 7.8 Hz). ^{13}C NMR ($CDCl_3$, 400 MHz) δ: 13.9, 22.3, 28.0, 29.1, 31.0, 31.4, 81.8, 137.2, 147.6, 163.7, 201.6. HRMS (M^+ + H) calcd for $C_{14}H_{25}O_3$: 241.1804; found: 241.1804.

Preparation of methyl **(E)-** *and* **(Z)-2-(cyclohexylmethylene)-3-oxobutanoate (13)**

Following the general procedure, esters **13a** and **13b** were formed in 84% yield as a 2:3 mixture of E- and Z-isomers.[23]

General procedure for the synthesis of α,β-unsaturated dicarbonyl compounds 14–22 using the Knoevenagel condensation reaction

1,3-Dicarbonyl compound (10 mmol), benzene (50 mL), aldehyde (10 mmol), glacial acetic acid (1 mmol), and piperidine (1 mmol) were placed in an oven-dried RBF equipped with a Dean–Stark apparatus. The mixture was heated to reflux and maintained there until TLC showed the complete consumption of starting material. Upon cooling to room temperature, the solution was diluted with diethyl ether (50 mL) and water (25 mL). The organic layer was separated and washed with water (25 mL), 1 mol/L HCl solution (2 × 25 mL), and then sodium hydrogen carbonate solution until neutrality was reached. The organic layer was dried (Na_2SO_4), filtered, and the solvent evaporated in vacuo. The crude product was purified by flash chromatography (hexane – diethyl ether).

Preparation of methyl **(E)-** *and* **(Z)-2-acetyloct-2-enoate (14)**

Following the general procedure, esters **14a** and **14b** were formed in 70% yield as a 1:2 mixture of E- and Z-isomers.[16]

Preparation of ethyl **(Z)-2-acetyl-4,4-dimethylpent-2-enoate (15)**

Following the general procedure, ester **15** was formed in 24% yield as a single Z-isomer.[29]

Preparation of methyl **(E)-** *and* **(Z)-2-benzylidene-3-oxobutanoate (16)**

Following the general procedure, esters **16a** and **16b** were formed in 80% yield as a 1:1 mixture of E- and Z-isomers.[16]

Preparation of benzyl **(E)-** *and* **(Z)-2-benzylidene-3-oxobutanoate (17)**

Following the general procedure, esters **17a** and **17b** were formed in 77% yield as a 2:3 mixture of E- and Z-isomers.[30]

Preparation of **tert-*butyl* 2-benzylidene-3-oxobutanoate (18)**

Following the general procedure, ester **18** was formed in 50% yield as a single Z-isomer.[31]

Preparation of ethyl **(Z)-2-benzoyl-3-phenylacrylate (19)**

Following the general procedure, ester **19** was formed in 70% yield as a single Z-isomer.[16,32]

Preparation of **(E)-1,3-diphenyl-2-(phenylsulfonyl)prop-2-en-1-one (20)**

Following the general procedure, ester **20** was formed as a brown solid that was recrystalized from ethanol to give 2.7 g (78% yield) of the E-isomer.[7] mp 135–136.5 °C (lit.[7] 136 °C).

Preparation of methyl **(E)-** *and* **(Z)-2-isobutyryl-3-phenylacrylate (21)**

Following the general procedure, ester **21** was formed in 60% yield as an 1.8:1 mixture of E- and Z-isomers.[16,33]

Preparation of methyl **2-benzylidene-4,4-dimethyl-3-oxopentanoate (22)**

Following the general procedure, ester **22** was formed in 18% yield as a Z-isomer.[34]

Preparation of (Z)-3-cyclohexyl-2 (benzo)acrylonitrile (23)

In a RBF under argon was added benzoylacetonitrile (1.45 g 10.0 mmol) and ethanol (30 mL). To this, L-proline (0.23 g, 2.0 mmol) and cyclohexane carboxaldehyde (1.21 mL, 10.0 mmol) were added. The mixture was allowed to stir at room temperature for 48 h. It was then concentrated in vacuo and purified via SiO_2 chromatography (15:1 hexane – ethyl acetate) to give 1.19 g (50% yield) of **23** as a clear yellow oil.[35]

Preparation of ethyl α-isopropylidine acetoacetate (24)

Ethyl acetoacetate (13.0 g, 0.100 mol), acetone (8.7 g, 0.15 mol), acetic anhydride (12.8 mL), and fused zinc chloride (1.9 g) were heated under reflux for 72 h. After cooling, diethyl ether (25 mL) was added and the resulting solution was washed with water (4 × 25 mL). The combined water washings were extracted with Et_2O (50 mL), and the combined organic extracts were dried with $MgSO_4$, filtered, and the solvent evaporated under reduced pressure. The oily residue was purified via SiO_2 chromatography (10:1 hexane – AcOEt) to give 7.42 g (42%) of **17** as a yellow oil.[36]

General procedure for the synthesis of α,β-unsaturated dicarbonyl compounds 25–28 using $TiCl_4$

CH_2Cl_2 (20 mL) and THF (20 mL) were placed in a RBF cooled to 0 °C. To this $TiCl_4$ (2.2 mL, 20 mmol) was carefully added dropwise, followed by ketone (10 mmol) and ethyl acetoacetate (1.08 mL, 10 mmol) in THF (5 mL). After complete addition, pyridine (3.2 mL, 40 mmol) was added and the solution was allowed to slowly warm to room temperature and stir for 16 h. The reaction mixture was diluted with H_2O and ethyl acetate (1:1, 100 mL) and the aqueous

Can. J. Chem. Downloaded from www.nrcresearchpress.com by Renmin University of China on 09/02/12
For personal use only.

phase was separated. The organic phase was washed with H_2O (3 × 50 mL), $NaHCO_3$, and brine and then dried over $MgSO_4$, filtered, and the solvent removed under reduced pressure. The oily residue was purified via SiO_2 chromatography (7:1 hexane – ethyl acetate).

Preparation of ethyl α-cyclohexylidine acetoacetate (25)

Following the general procedure, ester **18** was formed in 38% yield (0.75 g) as a pale yellow oil.[37]

Preparation of ethyl α-cyclopentylidine acetoacetate (26)

Following the general procedure, ester **19** was formed in 28% yield (0.55 g) as a pale yellow oil.[38]

Preparation of methyl 4-(1-(ethoxycarbonyl)-2-oxopropylidine)piperdine-1-carboxylate (27)

Following the general procedure, ester **20** was formed in 32% yield (0.8 g) as a pale yellow oil.[39]

Preparation of ethyl (*E*)- and (*Z*)-2-acetyl-3-methyldec-2-enoate (28)

Following the general procedure, esters **28a** and **28b** were formed in 27% yield (0.64 g) as colourless oils in a 1.25:1 mixture of E- and Z-isomers. *Z*-Isomer **28a**: IR (neat, cm^{-1}): 2954, 2929, 2857, 1725, 1700, 1624, 1466, 1354, 1225, 1119, 1053. ^1H NMR ($CDCl_3$, 300 MHz) δ: 0.88 (t, 3H, J = 7.1 Hz), 1.22–1.38 (m, 8H), 1.30 (t, 3H, J = 7.0 Hz), 1.42–1.55 (m, 2H), 1.95 (s, 3H), 2.28 (s, 3H), 2.34–2.42 (m, 2H), 4.24 (q, 2H, J = 7.2 Hz). ^{13}C NMR ($CDCl_3$, 300 MHz) δ: 14.3, 21.3, 22.8, 28.2, 29.2, 29.9, 30.8, 31.8, 31.9, 36.8, 60.9, 132.1, 157.4, 166.3, 200.3. HRMS (M^+ + H) calcd for $C_{15}H_{27}O_3$: 255.1961; found: 255.1960. *E*-Isomer **28b**: IR (neat, cm^{-1}): 2928, 2857, 1725, 1722, 1625, 1466, 1355, 1273, 1225, 1118, 1056. ^1H NMR ($CDCl_3$, 300 MHz) δ: 0.87 (t, 3H, J = 7.0 Hz), 1.18–1.35 (m, 8H), 1.29 (t, 3H, J = 7.2 Hz), 1.42–1.60 (m, 2H), 2.08 (s, 3H), 2.14–2.21 (m, 2H), 2.28 (s, 3H), 4.22 (q, 2H, J = 7.0 Hz). ^{13}C NMR ($CDCl_3$, 300 MHz) δ: 14.26, 14.3, 20.8, 22.8, 28.3, 29.2, 29.9, 31.2, 31.9, 37.1, 60.9, 132.2, 157.4, 165.9, 201.0. HRMS (M^+ + H) calcd for $C_{15}H_{27}O_3$: 255.1961; found: 255.1960.

General procedure for the reduction of Knoevenagel adducts using Luche conditions

Adducts **10**–**28** (1 mmol) and $CeC1_3{\cdot}7H_2O$ (1 mmol) were dissolved in methanol (2.5 mL) and $NaBH_4$ (38 mg, 1 mmol) was added in one portion with stirring. A vigorous gas evolution occurred and then stirring was continued for the specified time before the pH was adjusted to neutrality with dilute aqueous HCl. The mixture was extracted with diethyl ether (3 × 15 mL), the combined organic extracts were dried over $MgSO_4$, and the solvent evaporated under reduced pressure. The crude product was analyzed for quantitative isomer determination by ^1H NMR. It was then purified by column chromatography and identified by the usual spectroscopic methods.

Preparation of methyl (E)- and (Z)-2-benzylidene-3-hydroxybutanoate (29)

Following the general procedure (15 min), alcohols **29a** and **29b** were formed in 80% yield as a 2:3 mixture of E- and Z-isomers.[40]

Preparation of benzyl (E)- and (Z)-2-benzylidene-3-hydroxybutanoate (30)

Following the general procedure (15 min), alcohols **30a** and **30b** were formed in 77% yield as a 2:3 mixture of E- and Z-isomers. Z-Isomer **30a**: IR (neat, cm^{-1}): 3421, 3031, 2974, 1718, 1497, 1455, 1385, 1212, 1142, 1014, 921, 751, 697. ^1H NMR ($CDCl_3$, 300 MHz) δ: 1.44 (d, 3H, J = 6.5 Hz), 2.35 (d, 1H, J = 6.2 Hz), 4.64 (q, 1H, J = 6.3 Hz), 5.16 (s, 2H) 6.85 (s, 1H), 7.23–7.60 (m, 10H). ^{13}C NMR ($CDCl_3$, 400 MHz) δ: 22.4, 66.8, 69.9, 128.1, 128.2, 128.4, 128.5, 132.7, 135.0, 135.4, 137.5, 168.8. HRMS (M^+ + H) calcd for $C_{18}H_{19}O_3$: 283.1334; found: 283.1334. E-Isomer **30b**: IR (neat, cm^{-1}): 3421, 3031, 2974, 1718, 1497, 1455, 1385, 1212, 1142, 1082, 1014, 921, 751, 697. ^1H NMR ($CDCl_3$, 300 MHz) δ: 1.48 (d, 3H, J = 6.5 Hz), 2.20 (s, 1H, J = 6.3 Hz), 4.84 (q, 1H, J = 5.9 Hz), 5.16 (s, 2H), 7.21–7.43 (m, 10H), 7.85 (s, 1H). ^{13}C NMR ($CDCl_3$, 400 MHz) δ: 23.3, 65.0, 66.8, 128.3, 128.5, 128.6, 128.7, 128.9, 129.2, 134.5, 135.6, 140.0, 167.5. HRMS (M^+ + H) calcd for $C_{18}H_{19}O_3$: 283.1334; found: 283.1334.

Preparation of* tert-*butyl (E)-2-(1-hydroxyethyl)-but-2-enoate (31)

Following the general procedure (15 s), E-alcohol **31** was formed in 66% yield as a colourless oil. IR (neat, cm^{-1}): 3508, 2977, 2932, 1683, 1645, 1456, 1368, 1322, 1291, 1149, 1060, 988, 897, 761. ^1H NMR ($CDCl_3$, 300 MHz) δ: 1.39 (d, 3H, J = 6.7 Hz), 1.51 (s, 9H), 1.80 (d, 3H, J = 7.4 Hz), 3.80 (b, 1H), 4.70 (q, 1H, J = 6.7 Hz), 6.69 (q, 1H, J = 7.4 Hz). ^{13}C NMR ($CDCl_3$, 300 MHz) δ: 13.7, 23.4, 28.4, 64.9, 81.5, 136.2, 136.8, 166.9. HRMS (M^+ + H) calcd for $C_{10}H_{19}O_3$: 187.1334: found: 187.1332.

Preparation of* tert-*butyl (Z)-2-(1-hydroxyethyl)-but-2-enoate (32)

Following the general procedure (15 s), Z-alcohol **32** was formed in 68% yield as a colourless oil. IR (neat, cm^{-1}): 3462, 2977, 1684, 1645, 1456, 1368, 1291, 1148, 1104. ^1H NMR ($CDCl_3$, 300 MHz) δ: 1.34 (d, 3H, J = 6.5 Hz), 1.53 (s, 9H), 1.95 (d, 3H, J = 7.2 Hz), 4.40 (q, 1H, J = 6.5 Hz), 6.15 (q, 1H, J = 7.2 Hz). ^{13}C NMR ($CDCl_3$, 300 MHz) δ: 15.5, 22.5, 28.5, 70.3, 81.8, 134.7, 137.4, 167.4. HRMS (M^+ + H) calcd for $C_{10}H_{19}O_3$: 187.1334; found: 187.1332.

Preparation of* tert-*butyl (E)-2-(1-hydroxyethyl)-4-methylpent-2-enoate (33)

Following the general procedure (1 min), E-alcohol **33** was formed in 79% yield as a colourless oil. IR (neat, cm^{-1}): 3514, 2969, 2932, 2871, 1684, 1641, 1457, 1368, 1324, 1276, 1153, 1120, 1065, 900, 773. ^1H NMR ($CDCl_3$, 300 MHz) δ: 0.98 (d, 3H, J = 6.7 Hz), 1.03 (d, 3H, J = 6.7 Hz), 1.38 (d, 3H, J = 6.7 Hz), 1.50 (s, 9H), 2.60–2.75 (m, 1H), 3.71 (d, 1H, J = 10.9 Hz), 4.61–4.72 (m, 1H), 6.35 (d, 1H, J = 10.3 Hz). ^{13}C NMR ($CDCl_3$, 300 MHz) δ: 22.4, 22.5, 24.0, 27.3, 28.4, 65.3, 81.5, 133.1, 148.5, 167.3. HRMS (M^+ + H) calcd for $C_{12}H_{23}O_3$: 215.1647; found: 215.1647.

Can. J. Chem. Downloaded from www.nrcresearchpress.com by Renmin University of China on 09/02/12
For personal use only.

Preparation of* tert-*butyl (Z)-2-(1-hydroxyethyl)-4-methylpent-2-enoate (34)

Following the general procedure (1 min), Z-alcohol **34** was formed in 66% yield as a colourless oil. IR (neat, cm^{-1}): 3514, 2969, 2932, 2871, 1684, 1641, 1457, 1368, 1324, 1276, 1153, 1120, 1065, 900, 773. ^1H NMR ($CDCl_3$, 300 MHz) δ: 1.03 (d, 3H, J = 6.7 Hz), 1.38 (d, 3H, J = 6.7 Hz), 1.50 (s, 9H), 2.70 (d, 1H, J = 6.2 Hz), 3.00–3.06 (m, 1H), 4.61–4.72 (m, 1H), 6.35 (d, 1H, J = 10.3 Hz). ^{13}C NMR ($CDCl_3$, 300 MHz) δ: 22.65, 22.78, 22.79, 28.39, 28.44, 65.3, 81.8, 134.4, 146.0, 167.6. HRMS (M^+ + H) calcd for $C_{12}H_{23}O_3$: 215.1647; found: 215.1647.

Preparation of* tert-*butyl (E)-2-(1-hydroxyethyl)oct-2-enoate (35)

Following the general procedure (5 min), E-alcohol **35** was formed in 75% yield as a colourless oil. IR (neat, cm^{-1}): 3471, 2960, 2930, 2857, 1686, 1454, 1368, 1277, 1148, 1066, 850. ^1H NMR ($CDCl_3$, 300 MHz) δ: 0.91 (t, 3H, J = 7.0 Hz), 1.30–1.51 (m, 8H) 1.62 (s, 9H), 2.80 (bs, 1H) 2.28 (s, 3H), 4.41 (q, 1H, J = 6.5 Hz), 6.61 (t, 3H, J = 6.7 Hz). ^{13}C NMR ($CDCl_3$, 300 MHz) δ: 13.9, 22.5, 28.1, 28.3, 32.0, 82.2, 137.7, 146.9, 148.0, 163.1, 166.1, 195.0. HRMS (M^+ + H) calcd for $C_{14}H_{27}O_3$: 243.1961; found: 243.1961.

Preparation of* tert-*butyl (Z)-2-(1-hydroxyethyl)oct-2-enoate (36)

Following the general procedure (5 min), Z-alcohol **36** was formed in 72% yield as a colourless oil. IR (neat, cm^{-1}): 3430, 2960, 2930, 2859, 1713, 1458, 1368, 1250, 1153, 846. ^1H NMR ($CDCl_3$, 300 MHz) δ: 0.91 (t, 3H, J = 6.5 Hz), 1.20–1.51 (m, 8H) 1.52 (s, 9H), 2.28 (s, 3H), 2.80 (d, 1H, J = 6.3 Hz), 4.41 (q, 1H, J = 7.0 Hz) 6.10 (t, 1H, J = 6.7 Hz). ^{13}C NMR ($CDCl_3$, 300 MHz) δ: 13.9, 22.4, 26.9, 28.3, 32.0, 82.2, 138.2, 146.9, 148.0, 163.1, 165.1, 195.0. HRMS (M^+ + H) calcd for $C_{14}H_{27}O_3$: 243.1961; found: 243.1961.

Preparation of ethyl (Z)-2-(1-hydroxyethyl)-4,4-dimethylpent-2-enoate (37)

Following the general procedure (1 min), Z-alcohol **37** was formed in 66% yield as a colourless oil. IR (neat, cm^{-1}): 3441, 2959, 2872, 1725, 1661, 1464, 1380, 1271, 1235, 1194, 1140, 1071, 1028. ^1H NMR ($CDCl_3$, 300 MHz) δ: 1.15 (s, 9H), 1.35 (t, 2H, J = 7.2 Hz), 2.28 (s, 3H), 4.23 (q, 3H, J = 6.7 Hz), 5.65 (s, 1H). ^{13}C NMR ($CDCl_3$, 300 MHz) δ: 14.3, 22.5, 29.6, 33.3, 60.0, 61.0, 134.7, 141.3, 169.1. HRMS (M^+ + H) calcd for $C_{11}H_{21}O_3$: 201.1491; found: 201.1491.

Preparation of methyl (E)-2-(1-hydroxyethyl)oct-2-enoate (38)

Following the general procedure (15 min), E-alcohol **38** was formed in 40% yield as a colourless oil. IR (neat, cm^{-1}): 3447, 2959, 1718, 1496, 1436, 1367, 1226, 1139, 1012, 753, 697. ^1H NMR ($CDCl_3$, 300 MHz) δ: 0.85 (t, 3H, J = 6.9 Hz), 1.52–1.60 (m, 6H, J = 6.7 Hz), 1.39 (d, 3H, J = 6.5 Hz), 2.40 (q, 1H, J = 7.3 Hz), 2.59 (bs, 1H) 3.80 (s, 3H), 4.52 (t, 2H, J = 6.4 Hz), 6.79 (t, 1H, J = 7.4 Hz). ^{13}C NMR ($CDCl_3$, 300 MHz) δ: 13.0, 22.0, 33.0, 51.8, 80.5, 128.2, 129.0, 134.4, 135.4, 141.5, 167.0. HRMS (M^+ + H) calcd for $C_{11}H_{21}O_3$: 201.1491; found: 201.1491.

Preparation of methyl (Z)-2-(1-hydroxyethyl)oct-2-enoate (39)

Following the general procedure (15 min), Z-alcohol **39** was formed in 49% yield as a colourless oil. IR (neat, cm^{-1}): 3447, 2959, 1718, 1496, 1436, 1367, 1226, 1139, 1012, 753, 697. ^1H NMR ($CDCl_3$, 300 MHz) δ: 0.85 (t, 3H, J = 7.0 Hz), 1.51–1.60 (m, 6H), 1.39 (d, 3H, J = 6.5 Hz), 2.40 (q, 1H, J = 7.4 Hz), 2.59 (bs, 1H), 3.80 (s, 3H), 4.52 (t, 2H, J = 6.4 Hz), 6.19 (t, 1H, J = 7.7 Hz). ^{13}C NMR ($CDCl_3$, 300 MHz) δ: 13.0, 20.2, 33.5, 52.0, 74.8, 128.6, 129.0, 134.0, 135.2, 141.5, 167.4. HRMS (M^+ + H) calcd for $C_{11}H_{21}O_3$: 201.1491; found: 201.1491.

Preparation of methyl (E)-2-cyclohexzylidene-3-hydroxybutanoate (40)

Following the general procedure (5 min), E-alcohol **40** was formed in 52% yield as a colourless oil. IR (neat, cm^{-1}): 3447, 2959, 1718, 1496, 1436, 1367, 1226, 1139, 1012, 753, 697. ^1H NMR ($CDCl_3$, 300 MHz) δ: 0.80–1.38 (m, 10H), 1.40 (d, 3H, J = 6.7 Hz), 1.41–1.80 (m, 1H), 2.50 (bs, 1H) 3.80 (s, 3H), 4.71 (t, 1H, J = 9.9 Hz), 6.53 (d, 1H, J = 9.2 Hz). ^{13}C NMR ($CDCl_3$, 400 MHz) δ: 24.3, 25.6, 25.8, 26.0, 32.5, 37.4, 52.0, 65.5, 132.3, 148.6, 168.4. HRMS (M^+ + H) calcd for $C_{12}H_{21}O_3$: 213.1491; found: 213.1491.

Preparation of methyl (Z)-2-cyclohexzylidene-3-hydroxybutanoate (41)

Following the general procedure (5 min), Z-alcohol **41** was formed in 56% yield as a colourless oil. IR (neat, cm^{-1}): 3447, 2959, 1718, 1496, 1436, 1367, 1226, 1139, 1012, 753, 697. ^1H NMR ($CDCl_3$, 300 MHz) δ: 0.80–1.38 (m, 10H, J = 6.5 Hz), 1.39 (d, 3H, J = 6.5 Hz), 1.40–1.80 (m, 1H), 2.50 (bs, 1H) 3.80 (s, 3H), 4.71 (t, 1H, J = 9.7 Hz), 5.93 (d, 1H, J = 9.7 Hz). ^{13}C NMR ($CDCl_3$, 400 MHz) δ: 22.6, 25.5, 26.0, 26.1, 32.5, 37.9, 51.3, 69.5, 133.0, 146.4, 168.1. HRMS (M^+ + H) calcd for $C_{12}H_{21}O_3$: 213.1491; found: 213.1491.

Preparation of* tert-*butyl (Z)-2-benzylidene-3-hydroxybutanoate (42)

Following the general procedure (15 min), Z-alcohol **42** was formed in 50% yield.[41]

Preparation of ethyl (Z)-2-(hydroxyl(phenyl)methyl)-3-phenylacrylate (43)

Following the general procedure (15 min), (*Z*)-alcohol **43** was formed in 64% yield.[28]

Preparation of (E)-1,3-diphenyl-2-(phenylsulfonyl)prop-2-en-1-ol (44)

Following the general procedure (15 min), with the exception that a 4 mol equiv excess of sodium borohydride and cerium trichloride were used, alcohol **44** was formed in 40% yield as a colourless solid based on reacted starting material. mp 145–147 °C. IR (neat, cm^{-1}): 3478, 1619, 1493, 1446, 1298, 12589, 1142, 1089, 1049, 1029, 773, 698, 611. ^1H NMR ($CDCl_3$, 300 MHz) δ: 4.03 (bs, 1H), 6.09 (s, 1H), 7.02–7.14 (m, 4H), 7.25–7.32 (m, 3H), 7.38–7.54 (m, 8H),

Can. J. Chem. Downloaded from www.nrcresearchpress.com by Renmin University of China on 09/02/12
For personal use only.

8.14 (s, 1H). ^{13}C NMR ($CDCl_3$, 300 MHz) δ: 69.6, 126.0, 127.5, 127.6, 128.3, 129.0, 129.1, 129.6, 130.3, 132.7, 132.9, 139.2, 141.3, 143.0, 143.5. HRMS (M^+ + H) calcd for $C_{21}H_{19}O_3S$: 351.1055; found: 351.1055.

Preparation of methyl (E)-2-benzylidene-3-hydroxy-4-methylpentanoate (45)

Following the general procedure (15 min), E-alcohol **45** was formed in 65% yield as a colourless oil. IR (neat, cm^{-1}): 3447, 2959, 1718, 1496, 1436, 1367, 1226, 1139, 1012, 753, 697. ^{1}H NMR ($CDCl_3$, 300 MHz) δ: 0.69 (d, 3H, J = 6.7 Hz), 1.04 (d, 3H, J = 6.7 Hz), 2.03 (m, 1H), 3.22 (d, 1H, J = 2.7 Hz), 3.85 (s, 3H), 4.22 (t, 1H, J = 9.9 Hz), 7.26–7.43 (m, 5H), 7.80 (s, 1H). ^{13}C NMR ($CDCl_3$, 300 MHz) δ: 18.0, 19.5, 33.0, 51.8, 80.5, 128.2, 129.0, 134.4, 135.4, 141.5, 167.4. HRMS (M^+ + H) calcd for $C_{14}H_{19}O_3$: 235.1334; found: 235.1334.

Preparation of methyl (Z)-2-benzylidene-3-hydroxy-4-methylpentanoate (46)

Following the general procedure (15 min), Z-alcohol **46** was formed in 71% yield as a colourless oil. IR (neat, cm^{-1}): 3447, 2959, 1718, 1496, 1436, 1367, 1226, 1139, 1012, 753, 697. ^{1}H NMR ($CDCl_3$, 300 MHz) δ: 0.86 (d, 3H, J = 6.7 Hz), 1.02 (d, 3H, J = 6.7 Hz), 1.92 (m, 1H, J = 2.7 Hz), 2.10 (s, 1H), 3.63 (s, 3H), 4.06 (d, 1H, J = 9.9 Hz), 6.83 (s, 1H), 7.23–7.40 (m, 5H). ^{13}C NMR ($CDCl_3$, 300 MHz) δ: 19.6, 33.5, 52.0, 74.8, 128.6, 128.67, 129.0, 133.2, 134.0, 141.5, 167.4. HRMS (M^+ + H) calcd for $C_{14}H_{19}O_3$: 235.1334; found: 235.1334.

Preparation of (Z)-3-cyclohexyl-2-(hydroxy(phenyl)methyl) acrylonitrile (48)

Following the general procedure (5 min), alcohol **48** and its saturated analogue were formed in 52% yield as a yellow oil that was inseparable by SiO_2 chromatography. IR (neat, cm^{-1}): 3444, 3063, 3031, 2926, 2853, 2221, 1450, 1047, 701. ^{1}H NMR ($CDCl_3$, 400 MHz) δ: 1.67–1.76 (m, 10H), 2.17 (d, 1H, J = 4.0 Hz), 2.51–2.62 (m, 1H), 5.27 (d, 1H, J = 4.0 Hz), 6.37 (d, 1H, J = 10.0 Hz), 7.25–7.41 (m, 5H). ^{13}C NMR ($CDCl_3$, 400 MHz) δ: 25.4, 25.8, 32.1, 40.7, 74.6, 126.4, 126.5, 126.7, 128.9, 128.95, 129.0, 153.2. HRMS (M^+ + H) calcd for $C_{16}H_{20}NO$: 242.1546; found: 242.1545.

Preparation of methyl 2-(1-hydroxyethyl)-3-methylbut-2-enoate (49)

Following the general procedure (15 min), alcohol **49** was formed in 91% yield as pale yellow oil. IR (neat, cm^{-1}): 3450, 2970, 2931, 2856, 1715, 1448, 1372, 1300, 1253, 1210, 1146, 1108, 916, 733. ^{1}H NMR ($CDCl_3$, 300 MHz) δ: 1.34 (t, 3H, J = 7.1 Hz), 1.35 (d, 3H, J = 6.6 Hz), 1.83 (s, 3H), 1.9 (s, 3H), 2.80 (d, 1H, J = 1.4), 4.28 (q, 2H, J = 7.0 Hz), 4.74 (p, 1H, J = 6.9 Hz). ^{13}C NMR ($CDCl_3$, 300 MHz) δ: 14.4, 20.8, 22.5, 23.2, 60.5, 66.1, 131.9, 140.0, 169.3. HRMS (M^+ + H) calcd for $C_8H_{15}O_3$: 159.1021; found: 159.1021.

Preparation of ethyl 2-cyclohexylidene-3-hydroxybutanoate (50)

Following the general procedure (15 min), alcohol **50** was formed in 69% yield as a pale yellow oil. IR (neat, cm^{-1}): 3456, 2980, 2931, 2856, 1718, 1656, 1448, 1367, 1300, 1263, 1210, 1146, 1108, 1025, 916, 733. ^{1}H NMR ($CDCl_3$, 300 MHz) δ: 1.32 (d, 3H, J = 7.2 Hz), 1.36 (t, 3H, J = 6.8 Hz), 1.53–1.71 (m, 6H), 2.20–2.35 (m, 4H), 2.49 (d, 1H, J = 7.3 Hz), 4.26 (q, 2H, J = 7.2 Hz), 4.80 (p, 1H, J = 6.7 Hz). ^{13}C NMR ($CDCl_3$, 300 MHz) δ: 14.4, 23.0, 26.5, 28.0, 28.1, 30.4, 33.4, 60.6, 65.9, 129.6, 145.1, 169.8. HRMS (M^+ + H) calcd for $C_{12}H_{21}O_3$: 213.1491; found: 213.1491.

Preparation of ethyl 2-cyclopentylidene-3-hydroxybutanoate (51)

Following the general procedure (15 min), alcohol **51** was formed in 94% yield as a pale yellow oil. IR (neat, cm^{-1}): 3447, 2976, 2931, 2856, 1717, 1448, 1367, 1300, 1263, 1210, 1146, 1108, 916, 733. ^{1}H NMR ($CDCl_3$, 300 MHz) δ: 1.32 (t, 3H, J = 7.2 Hz), 1.39 (d, 3H, J = 6.7 Hz), 1.60–1.78 (m, 4H), 2.28–2.40 (m, 2H), 2.66–2.72 (m, 2H), 3.64 (d, 1H, J = 10.4 Hz), 4.24 (q, 2H, J = 7.0 Hz), 4.6 (p, 1H, J = 6.6 Hz). ^{13}C NMR ($CDCl_3$, 300 MHz δ): 14.2, 25.9, 26.1, 30.3, 34.8, 34.82, 60.8, 128.1, 166.4, 169.2, 199.2. HRMS (M^+ + H) calcd for $C_{11}H_{19}O_3$: 199.1334; found: 199.1334.

Preparation of methyl 4-(1-(ethoxycarbonyl)-2-hydroxypropylidene)piperidine-1-carboxylate (52)

Following the general procedure, alcohol **52** was formed in 71% yield as a pale yellow oil. IR (neat, cm^{-1}): 3455, 2980, 2873, 1684, 1456, 1412, 1371, 1213, 1132, 1095, 1071, 1024, 862, 769. ^{1}H NMR ($CDCl_3$, 300 MHz) δ: 1.32 (t, 3H, J = 7.0 Hz), 1.37 (d, 3H, J = 6.7 Hz), 2.54–2.46 (m, 5H), 3.46–3.58 (m, 4H), 3.70 (s, 3H), 4.26 (q, 2H, J = 7.2 Hz), 4.75 (p, 1H, J = 6.5 Hz). ^{13}C NMR ($CDCl_3$, 300 MHz) δ: 14.5, 23.1, 29.6, 32.0, 44.1, 44.4, 52.9, 61.0, 65.4, 132.2, 140.8, 156.0, 168.9. HRMS (M^+ + H) calcd for $C_{13}H_{22}NO_5$: 272.1498; found: 272.1498.

Preparation of ethyl (Z)-2-(1-hydroxyethyl)-3-methyldec-2-enoate (53)

Following the general procedure (15 min), Z-alcohol **53** was formed in 82% yield as a pale yellow oil. IR (neat, cm^{-1}): 3509, 3419, 2929, 2857, 1720, 1624, 1465, 1366, 1272, 1164, 1117, 1056, 967, 779, 722. ^{1}H NMR ($CDCl_3$, 300 MHz) δ: 0.88 (t, 3H, J = 7.2 Hz), 1.24–1.48 (m, 10H), 1.33 (t, 3H, J = 7.2 Hz), 1.35 (d, 3H, J = 6.7 Hz), 1.80 (s, 3H), 2.14–2.22 (m, 2H), 2.67 (d, 1H, J = 8.4 Hz), 4.25 (q, 2H, J = 7.2 Hz), 4.71 (p, 1H, J = 7.4 Hz). ^{13}C NMR ($CDCl_3$, 300 MHz) δ: 14.3, 14.5, 18.6, 22.6, 22.8, 28.4, 29.4, 29.8, 32.0, 37.1, 60.6, 66.3, 76.5, 132.0, 143.7, 169.4. HRMS (M^+ + H) calcd for $C_{15}H_{29}O_3$: 257.2117; found: 257.2118.

Preparation of ethyl (E)-2-(1-hydroxyethyl)-3-methyldec-2-enoate (54)

Following the general procedure (15 min), E-alcohol **54** were formed in 82% yield as a pale yellow oil. IR (neat, cm^{-1}): 3515, 3419, 2929, 2857, 1720, 1700, 1624, 1465, 1354, 1224, 1172, 1118, 1052, 970, 859, 781, 668, 646, 563. ^{1}H NMR ($CDCl_3$, 300 MHz) δ: 0.88 (t, 3H, J = 6.8 Hz), 1.32 (t, 3H, J = 7.0 Hz), 1.35 (d, 3H, J = 6.5 Hz), 1.88 (s, 3H), 2.04–2.22 (m, 2H), 2.81 (d, 1H, J = 8.0 Hz), 4.27 (q, 2H, J = 7.2 Hz), 4.72 (p, 1H, J = 6.3 Hz). ^{13}C NMR ($CDCl_3$, 300 MHz) δ: 14.3, 14.5, 21.4, 22.8, 28.4, 29.3, 29.9, 31.9,

Can. J. Chem. Downloaded from www.nrcresearchpress.com by Renmin University of China on 09/02/12
For personal use only.

35.0, 60.7, 65.9, 131.6, 144.8, 169.6. HRMS ($M^+ + H$) calcd for $C_{15}H_{29}O_3$: 257.2117; found: 257.2117.

General procedure for the reduction of Knoevenagel adducts using BMS

In a 50 mL three-neck flask equipped with a magnetic stirring bar and a reflux condenser, THF (3 mL) and β-keto ester (0.5 mmol) were added. To this well-stirred solution under an argon atmosphere was added BMS (0.50 mmol). After stirring for 75 min, excess hydride was quenched by the addition of methanol (0.5 mL), and the solution was diluted with water (25 mL) and extracted with diethyl ether (6 × 10 mL). The combined organic extracts was dried over $MgSO_4$ and, after filtration and evaporation of solvent, the crude product was purified by silica gel chromatography.

Preparation of methyl 2-benzylidene-3-hydroxybutanoate (29)

Two isomers were obtained: E and Z (2:3); 40% yield.

Preparation of* tert*-butyl 2-benzylidene-3-hydroxybutanoate (42)

1,2- and 1,4-addition products and two isomers (E and Z) were obtained in 10% yield.

Preparation of ethyl (Z)-2-(hydroxyl(phenyl)methyl)-3-phenylacrylate (43)

No reduction.

Preparation of methyl (E)- and (Z)-2-isobutyryl-3-phenylacrylate (45)

Two isomers were obtained (E and Z in a ratio of 2:3) in 10% yield, but they were not separable.

General procedure for the reduction of Knoevenagel adducts with sodium borohydride and $Yb(OTf)_3$

The keto ester (0.05 g, 1 mmol), MeOH (3 mL), and $Yb(OTf)_3$ (1.1 equiv) were added to a RBF and stirred at room temperature for 30 min. The solution was cooled to –78 °C and then $NaBH_4$ (1.1 equiv) was added slowly. The resulting mixture was stirred for 30 min at this temperature and then quenched by the addition of saturated aqueous ammonium chloride (10 mL). The reaction mixture was extracted with CH_2Cl_2 (3 × 5 mL), and the combined organic extract was dried over anhydrous $MgSO_4$. After filtering, the solvent was evaporated under reduced pressure and the product purified by flash column chromatography.

Preparation of methyl 2-benzylidene-3-hydroxybutanoate (29)

Two isomers were obtained: E and Z (2:3); 20% yield.

Preparation of* tert*-butyl 2-benzylidene-3-hydroxybutanoate (42)

The Z-isomer was obtained in 40% yield.

Preparation of ethyl (Z)-2-(hydroxyl(phenyl)methyl)-3-phenylacrylate (43)

No reduction.

Preparation of *tert*-butyl 2-(1-bromo-ethyl)-but-2-enoate (55)

To a RBF, under argon, was added alcohol **31** (3.29 g, 20.8 mmol) and CH_2Cl_2 (30 mL). The solution was cooled to –30 °C and triphenylphosphine (5.8 g, 22.1 mmol) was added, followed by NBS (3.9 g, 21.9 mmol). When the reaction was deemed complete using TLC, ~4 h at –30 °C, the solution was diluted with CH_2Cl_2, washed with $NaHCO_3$ (2×), brine, and then dried over $MgSO_4$. It was then filtered and solvent was removed in vacuo. The product was then purified via column chromatography using hexane – ethyl acetate (10:1) as eluent to yield bromide **55** as a yellow oil (2.2 g, 48%) that was immediately used in the next reaction. IR (neat, cm^{-1}): 2981, 2927, 1720, 1640, 1445, 1387, 1262, 1153, 1095, 1033, 913, 763, 734. ^1H NMR ($CDCl_3$, 300 MHz) δ: 6.92 (q, 0.33 H, J = 7.4 Hz) and 6.35 (qd, 0.66 H, J = 0.9, 7.2 Hz), 5.23 (q, 0.33H, J = 7.1 Hz), 5.11 (qt, 0.66 H, J = 0.9, 7.1 Hz), 4.29 (m, 2H), 2.05–1.85 (m, 6H), 1.32 (m, 3H). ^{13}C NMR ($CDCl_3$, 300 MHz) δ: 166.2, 140.3, 136.4, 60.8, 37.9, 24.3, 15.7, 14.2.

Preparation of 2,4-dimethyl-8-oxo-bicyclo[3.2.1]octane-3-carboxylic acid *tert*-butyl ester (57)

To a RBF, under argon, was added enamine **56** (1.36 g, 9.95 mmol), CH_3CN (15 mL), and triethylamine (1.2 g, 11.9 mmol). To this solution was then added bromoalkene **55** (2.2 g, 9.95 mmol) in CH_3CN (10 mL). After complete addition, the solution was heated at reflux for 20 h, cooled, and then water (15 mL) was added and heating at reflux was continued for 1.5 h. After cooling to room temperature, the solution was extracted with CH_2Cl_2 (4×). The combined organic phases were washed with brine, dried over $MgSO_4$, and filtered. The solvent was removed in vacuo to yield a brown oil that was purified via column chromatography using hexane – ethyl acetate (4:1) as eluent to yield ketone **57** as a yellow oil (0.79 g, 36%). IR (neat, cm^{-1}): 2975. ^1H NMR ($CDCl_3$, 300 MHz) δ: 2.76 (m, 0.5H), 2.63 (dp, J = 2.9, 7.4 Hz, 0.5H), 2.45 (m, 1H), 2.26 (dd, J = 2.6, 7.7 Hz, 0.5H), 2.16–1.94 (m, 3H), 1.92–1.78 (m, 2.5H), 1.71 (t, J = 8.4 Hz, 1H), 1.48 (s, 4.5H), 1.47 (s, 4.5H), 1.17 (d, J = 7.3 Hz, 1.5H), 1.08 (d, J = 7.1 Hz, 4.5H). ^{13}C NMR ($CDCl_3$, 300 MHz) δ: 220.1, 219.6, 174.7, 173.4, 81.0, 80.8, 52.2, 49.9, 49.5, 48.8, 48.4, 45.8, 43.0, 39.0, 28.23, 28.2, 25.1, 22.6, 22.0, 21.5, 17.7, 17.4. HRMS ($M^+ + H$) calcd for $C_{15}H_{25}O_3$: 253.1804; found: 253.1805.

Acknowledgments

Financial support from the Natural Sciences and Engineering Research Council of Canada (NSERC) for a Discovery Grant and the University of New Brunswick (UNB), Fredericton, New Brusnwick, is gratefully acknowledged. S.R. would like to thank the Botswana International University of Science and Technology (BIUST) for supporting her studies in Canada. Helpful discussions with Dr. Larry Calhoun (UNB) are gratefully acknowledged. We would like to thank Gilles Vautour for his assistance in running the mass specs and Elena McIntyre for her assistance in making some starting materials.

References

(1) (a) Kamo, T.; Imura, Y.; Hagio, T.; Makabe, H.; Shibata, H.; Hirota, M. *Biosci. Biotechnol. Biochem.* **2004**, *68* (6), 1362. doi:10.1271/bbb.68.1362; (b) Shibata, H.; Irie, A.; Morita, Y.

Can. J. Chem. Downloaded from www.nrcresearchpress.com by Renmin University of China on 09/02/12
For personal use only.

Biosci. Biotechnol. Biochem. **1998**, *62* (12), 2450. doi:10.1271/bbb.62.2450.

(2) MaGee, D. I.; Shannon, D. E. *Can. J. Chem.* **2004**, *82* (2), 333. doi:10.1139/v03-210.

(3) Rawson, D. I.; Carpenter, B. K.; Hoffmann, H. M. R. *J. Am. Chem. Soc.* **1979**, *101* (7), 1786. doi:10.1021/ja00501a025.

(4) Seebach, D.; Missbach, M.; Calderari, G.; Eberle, M. *J. Am. Chem. Soc.* **1990**, *112* (21), 7625. doi:10.1021/ja00177a026.

(5) (a) Nelson, R. P.; McEuen, J. M.; Lawton, R. G. *J. Org. Chem.* **1969**, *34* (5), 1225. doi:10.1021/jo01257a009; (b) Zhang, Y.; Schuster, G. B. *J. Org. Chem.* **1995**, *60* (22), 7192. doi:10.1021/jo00127a026.

(6) Hood, M. Investigations into the Synthesis of a [3.2.1]-Bicyclic Diketone. B.Sc. Honours Thesis, University of New Brunswick, Fredericton, New Brunswick, 2008.

(7) (a) Basavaiah, D.; Rao, A. J.; Satyanarayana, T. *Chem. Rev.* **2003**, *103* (3), 811. doi:10.1021/cr010043d; (b) Ma, G. N.; Jiang, J. J.; Shi, M.; Wei, Y. *J. Chem. Soc. Chem. Commun.* **2009**, 5496.

(8) (a) Sato, Y.; Takeuchi, S. *Synthesis* **1983**, *1983* (09), 734. doi:10.1055/s-1983-30492; (b) Reynolds, T. E.; Stern, C. A.; Scheidt, K. A. *Org. Lett.* **2007**, *9* (13), 2581. doi:10.1021/ol0710515; (c) Reynolds, T. E.; Bharadwaj, A. R.; Scheidt, K. A. *J. Am. Chem. Soc.* **2006**, *128* (48), 15382. doi:10.1021/ja0653674.

(9) (a) Marino, J. P.; Linderman, R. J. *J. Org. Chem.* **1981**, *46* (18), 3696. doi:10.1021/jo00331a023; (b) Marino, J. P.; Linderman, R. J. *J. Org. Chem.* **1983**, *48* (24), 4621. doi:10.1021/jo00172a036; (c) Ben Ayed, T.; Villiéras, J.; Amri, H. *Tetrahedron* **2000**, *56* (5), 805. doi:10.1016/S0040-4020(99)01079-0; (d) Dambrin, V.; Villiearas, M.; Janvier, P.; Toupet, L.; Amri, H.; Lebretona, J.; Villiearas, J. *Tetrahedron* **2001**, *57* (11), 2155. doi:10.1016/S0040-4020(01)00044-8; (e) Wei, H. X.; Willis, S.; Li, G. *Synth. Commun.* **1999**, *29* (17), 2959. doi:10.1080/00397919908086469.

(10) (a) Tsuda, T.; Yoshida, T.; Kawamoto, T.; Saegusa, T. *J. Org. Chem.* **1987**, *52* (8), 1624. doi:10.1021/jo00384a052; (b) Tsuda, T.; Yoshida, T.; Saegusa, T. *J. Org. Chem.* **1988**, *53* (5), 1037. doi:10.1021/jo00240a020; (c) Li, G.; Wei, H. X.; Willis, S. *Tetrahedron Lett.* **1998**, *39* (26), 4607. doi:10.1016/S0040-4039(98)00850-8.

(11) (a) Feit, B. A.; Melamed, U.; Schmidt, R. R.; Speer, H. *J. Chem. Soc., Perkin Trans. 1* **1981**, 1329. doi:10.1039/p19810001329; (b) Rollinson, S. W.; Amos, R. A.; Katzenellenbogen, J. A. *J. Am. Chem. Soc.* **1981**, *103* (14), 4114. doi:10.1021/ja00404a023; (c) Cha, J. H.; Pae, A. N.; Choi, K. I. I.; Cho, Y. S.; Koh, H. Y.; Lee, E. *J. Chem. Soc., Perkin Trans. 1* **2001**, 2079; (d) Davies, S. G.; Elend, D. L.; Jones, S.; Roberts, P. M.; Savory, E. D.; Smith, A. D.; Thomson, J. E. *Tetrahedron* **2009**, *65* (37), 7837. doi:10.1016/j.tet.2009.07.004.

(12) (a) Takai, K.; Kataoka, Y.; Utimoto, K. *J. Org. Chem.* **1990**, *55* (6), 1707. doi:10.1021/jo00293a008; (b) Takai, K.; Tezuka, M.; Utimoto, K. *J. Org. Chem.* **1991**, *56* (21), 5980. doi:10.1021/jo00021a005; (c) Kataoka, Y.; Miyai, J.; Tezuka, M.; Takai, K.; Utimoto, K. *J. Org. Chem.* **1992**, *57* (25), 6796. doi:10.1021/jo00051a023.

(13) Aoki, M.; Izumi, S.; Kaneko, M.; Ukai, K.; Takaya, J.; Iwasawa, N. *Org. Lett.* **2007**, *9* (7), 1251. doi:10.1021/ol070038h.

(14) Imamoto, T.; Kusumoto, T.; Tawarayama, Y.; Sugiura, Y.; Mita, T.; Hatanaka, Y.; Yokoyama, M. *J. Org. Chem.* **1984**, *49* (21), 3904. doi:10.1021/jo00195a006.

(15) Fang, F. G.; Horstmann, T. E.; Therrien, J. *Tetrahedron Lett.* **2010**, *51* (16), 2151. doi:10.1016/j.tetlet.2010.02.078.

(16) Antonioletti, R.; Bovicelli, P.; Malancona, S. *Tetrahedron* **2002**, *58* (30), 589. doi:10.1016/S0040-4020(01)01173-5.

(17) (a) Benfatti, F.; Cardillo, G.; Gentilucci, L.; Mosconi, E.; Tolomelli, A. *Tetrahedron Asymmetry* **2007**, *18* (18), 2227. doi:10.1016/j.tetasy.2007.09.002; (b) Benfatti, F.; Cardillo, G.; Gentilucci, L.; Mosconi, E.; Tolomelli, A. *Org. Lett.* **2008**, *10* (12), 2425. doi:10.1021/ol8006919; (c) Cardillo, G.; Gennari, A.; Gentilucci, L.; Mosconi, E.; Tolomelli, A.; Troisi, S. *Eur. J. Org. Chem.* **2009**, *2009* (34), 5991. doi:10.1002/ejoc.200900870.

(18) Happer, D. A. R.; Steenson, B. E. *Synthesis* **1980**, *1980* (10), 806. doi:10.1055/s-1980-29213.

(19) Tanikaga, R.; Konya, N.; Hamamura, K.; Kaji, A. *Bull. Chem. Soc. Jpn.* **1988**, *61* (9), 3211. doi:10.1246/bcsj.61.3211.

(20) Tanikaga, R.; Konya, N.; Kaji, A. *Chem. Lett.* **1985**, *14* (10), 1583. doi:10.1246/cl.1985.1583.

(21) (a) Zabicky, J. *J. Chem. Soc.* **1961**, 683. doi:10.1039/jr9610000683; (b) Schwarz, M. *J. Chem. Soc. Chem. Commun.* **1969**, 212.

(22) Gemal, A. L.; Luche, J. L. *J. Am. Chem. Soc.* **1981**, *103* (18), 5454. doi:10.1021/ja00408a029.

(23) Ward, D. E.; Rhee, C. K. *Can. J. Chem.* **1989**, *67* (7), 1206. doi:10.1139/v89-182.

(24) Brown, H. C.; Weissman, P. M. *Isr. J. Chem.* **1963**, *1*, 430.

(25) Mincione, E. *J. Org. Chem.* **1978**, *43* (9), 1829. doi:10.1021/jo00403a052.

(26) García Ruano, J. L.; Fernández-Ibáñez, M. Á.; Fernández-Salas, J. A.; Maestro, M. C.; Márquez-López, P.; Rodríguez-Fernández, M. M. *J. Org. Chem.* **2009**, *74* (3), 1200. doi:10.1021/jo802378s.

(27) Koval', I. V. *Russ. J. Org. Chem.* **2002**, *38* (3), 301. doi:10.1023/A:1016390721218.

(28) Inokuchi, T.; Okano, M.; Miyamoto, T. *J. Org. Chem.* **2001**, *66* (24), 8059. doi:10.1021/jo010575u.

(29) Takeughi, S.; Ohgo, Y.; Yoshimura, J. *Bull. Chem. Soc. Jpn.* **1974**, *47* (2), 463. doi:10.1246/bcsj.47.463.

(30) Mildenberger, H.; Maier, T.; Sachse, B. Ger. Offen, CODEN: GWXXBX, DE2836945, 1980.

(31) Fleming, I.; Ramarao, C. *Org. Biomol. Chem.* **2004**, *2* (10), 1504. doi:10.1039/b401435a.

(32) Mélot, J. M.; Texier-Boullet, F.; Foucaud, A. *Tetrahedron* **1988**, *44* (8), 2215. doi:10.1016/S0040-4020(01)81729-4.

(33) Roth, B. D.; Blankley, C. J.; Chucholowski, A. W.; Ferguson, E.; Hoefle, M. L.; Ortwine, D. F.; Newton, R. S.; Sekerke, C. S.; Sliskovic, D. R.; Wilson, M. *J. Med. Chem.* **1991**, *34* (1), 357. doi:10.1021/jm00105a056.

(34) Verhé, R.; De Kimple, N.; Courtheyn, D.; de Buyck, L.; Schamp, N. *Tetrahedron* **1982**, *38* (24), 3649. doi:10.1016/0040-4020(82)80073-2.

(35) Amancha, K. P.; Lai, Y.-C.; Chen, I.-C.; Liu, H.-J.; Zhu, J.-L. *Tetrahedron* **2010**, *66* (4), 871. doi:10.1016/j.tet.2009.11.105.

(36) Kazi, M. A.; Khan, I. H.; Khan, M. Y.; Kale, M. N.; Maccoll, A.; Horne, R. A.; Courant, R. A.; Frysinger, G. R.; Hotz, M. C. B.; Shaw, R.; Hallas, G.; Taylor, D. C.; Charalambous, J.; Frazer, M. J.; Gerrard, W.; Tidd, B. K.; Katritzky, A. R.; Waring, A. J.; Ellis, G. P.; King, J.; Lee, T. B.; Crofts, P. C.; Gosling, K.; Alder, R. W.; Whiting, M. C.; Abel, E. W.; Willey, G. R.; Jansen, A. B. A.; Stokes, P. J.; Mann, R. S.; Cole, A. R. H.; Osborne, G. A. *J. Chem. Soc.* **1964**, 1511. doi:10.1039/jr9640001511.

(37) Russell, G. A.; Mudryk, B.; Jawdosiuk, M. *Synthesis* **1981**, *1981* (1), 62. doi:10.1055/s-1981-29339.

(38) Nenitzescu, C. D.; Glats, A. M.; Gavet, M.; Pogany, I. *Izv. Akad. Nauk SSSR* **1963**, *27*, 332.
(39) Villemin, D.; Ben Alloum, A. *Synth. Commun.* **1991**, *21* (1), 63. doi:10.1080/00397919108020790.
(40) Aoki, M.; Izumi, S.; Kaneko, M.; Ukai, K.; Takaya, J.; Iwasawa, N. *Org. Lett.* **2007**, *9* (7), 1251. doi:10.1021/ol070038h.
(41) Chernega, A.; Davies, S. G.; Elend, D. L.; Smethurst, C. A. P.; Roberts, P. M.; Smith, A. D.; Smyth, G. D. *Tetrahedron* **2007**, *63* (30), 7036. doi:10.1016/j.tet.2007.05.015.

Can. J. Chem. Downloaded from www.nrcresearchpress.com by Renmin University of China on 09/02/12
For personal use only.

Highly efficient solvent-free acetylation of alcohols with acetic anhydride catalyzed by recyclable sulfonic acid catalyst (SBA-15–Ph–Pr–SO_3H) — An environmentally benign method

Daryoush Zareyee, Abdollah Razaghi Ghadikolaee, and Mohammad A. Khalilzadeh

Can. J. Chem. Downloaded from www.nrcresearchpress.com by Renmin University of China on 09/02/12
For personal use only.

Abstract: The catalytic activity of highly thermal stable, hydrophobic, and complete heterogeneous propylsulfonic acid functionalized nanostructured SBA-15 for excellent acetylation of alcohols and phenols with acetic anhydride at ambient temperature in solvent-free conditions was examined under environmentally benign reaction conditions. The salient features of this protocol are the absence of solvent, a green experimental procedure, and simple reusability of the catalyst (at least five reaction cycles).

Key words: solid sulfonic acid, SBA-15, heterogeneous catalyst, acetylation, solvent-free.

Résumé : Le SBA-15 est un produit nanostructuré à base d'acide propylsulfonique fonctionnalisé qui est très stable vis-à-vis de la chaleur, hydrophobe et totalement hétérogène. On a étudié son activité catalytique comme excellent catalyseur pour la réaction d'acétylation d'alcools et de phénols à l'aide d'anhydride acétique, à la température ambiante, dans des conditions expérimentales sans solvant et écologiques. Ce protocole est principalement caractérisé par l'absence de solvant, par son caractère écologique et la facilité de réutilisation du catalyseur (dans au moins cinq cycles réactionnels).

Mots-clés : acide sulfonique solide, SBA-15, catalyseur hétérogène, acétylation, sans solvant.

[Traduit par la Rédaction]

Introduction

The use of protecting groups is highly significant in organic synthesis and is often the key to the success of many synthetic enterprises. Among the various protecting groups used for the hydroxyl function, acetyl is the most common group in view of its facile introduction, being stable to the acidic reaction conditions, and also being easily removable by mild alkaline hydrolysis.[1] The acetylation of alcohols and phenols provides an efficient route for protecting –OH groups during oxidation, peptide coupling, and glycosidation reactions.[2] The most common and cheap acetylating regent is activated carboxylic acid derivative acetic anhydride[3] in the presence of amine bases like pyridine,[4] 4-diaminopyridine (DMAP),[5] triethylamine,[3] and 4-pyrrolidinopyridine.[4] Protic acids are also known to catalyze the acetylation process.[6] Additionally, various Lewis acids including $Sc(OTf)_3$,[7] $In(OTf)_3$,[8] $Ce(OTf)_3$,[9] $Gd(OTf)_3$,[10] $Al(OTf)_3$,[11] $Fe(ClO_4)_3$,[12] $Mn(OAc)_2$,[13] I_2,[14] $La(NO_3)_36H_2O$,[15] $Sn^{IV}(TPP)(BF_4)_2$,[16] $TiCl_3(OTf)$,[17] $H_{14}[NaP_5W_{29}MoO_{110}]$,[18] and borated zirconia[19] have also been investigated to meet the demand for more efficient methods. However, some of the base catalysts are toxic and possess offensive odours,[3–5] and the other methods have some serious drawbacks such as harsh reaction conditions, long reaction times, poor yields of the desired products, and tedious workup procedures. Another disadvantage is that most of these catalysts need organic solvents as media for acylation, thereby generating large amounts of corrosive and toxic waste. On the other hand, there are some toxicity and difficulties in separating conventional homogeneous catalysts from products.

One of the most promising solutions to these problems seems to be immobilization of catalysts or using ecofriendly solvent-free reaction conditions. Heterogeneous catalysts give generally higher selectivity and typically require easier workup procedures. Along this line, alumina-supported MoO_3,[20] $NaHSO_4{\cdot}SiO_2$,[21] polymer-supported $Gd(OTf)_3$,[22] cobalt(II) salen complex,[23] and sulfuric acid ([3-(3-silicapropyl)sulfanyl]propyl)ester[24] were also reported as heterogeneous catalysts for acylation of alcohols. Despite a number of improvements, some of these procedures still suffer from long reaction times,[22,23] high temperatures,[23] the use of toxic organic solvents,[21] and nonrecoverable catalysts,[21] which result in the generation of a large amount of toxic waste. Thus, introduction of inexpensive and green catalysts for this purpose is still in much demand.

Received 12 October 2011. Accepted 26 January 2012. Published at www.nrcresearchpress.com/cjc on 26 April 2012.

D. Zareyee, A.R. Ghadikolaee, and M.A. Khalilzadeh. Department of Chemistry, Qaemshahr Branch, Islamic Azad University, Qaemshahr, Iran.

Corresponding author: Daryoush Zareyee (e-mail: zareyee@gmail.com; zareyee.d@qaemshahriau.ac.ir).

Can. J. Chem. Downloaded from www.nrcresearchpress.com by Renmin University of China on 09/02/12
For personal use only.

Experimental section

General acetylation procedure

In a round-bottom flask (10 mL) equipped with a magnetic stirrer, SBA-15–Ph–Pr–SO_3H (12 mg, 2 mol %) was added to the substrate (1 mmol) and acetic anhydride (1.2 mmol), and the mixture was stirred at room temperature for the period of time indicated in Table 1. After completion of the reaction (TLC), the reaction mixture was filtered and the catalyst was rinsed with ethyl acetate and then was recovered. After the organic layer was washed with saturated $NaHCO_3$ and water, the aqueous layer was extracted with ethyl acetate and dried over anhydrous Na_2SO_4, filtered, and evaporated. The combined organic layer was subjected to column chromatography on silica gel to afford pure acetate. Characterization of some products was achieved by ^1H and ^{13}C NMR.

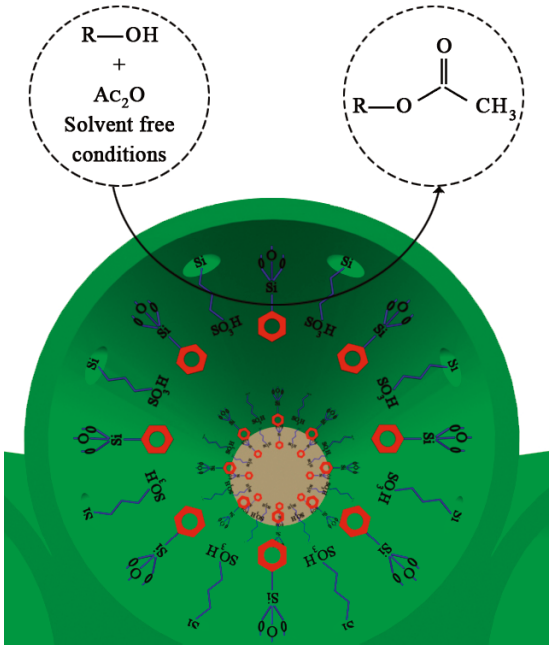
Results and discussion

Recently, we have prepared and used heterogeneous and hydrophobic sulfonic acid SBA-15–Ph–Pr–SO_3H as an efficient recoverable catalyst in some organic reactions.[25,26] Therefore, as a part of our continuing interest in the development and utility of this catalyst, having both acidic sites and phenyl groups inside the mesochannel of SBA-15, herein, we wish to report the applicability of SBA-15–Ph–Pr–SO_3H as an efficient, environmentally benign, and reusable catalyst in the promotion of the acetylation of alcohols and phenols with acetic anhydride. All reactions were performed in solvent-free reactions at room temperature and under complete heterogeneous reaction conditions in excellent yields (Scheme 1 and Table 1; also see the Supplementary data).

Initially, the effect of catalyst was investigated in the model reaction of benzyl alcohol with acetic anhydride, and several sets of reaction conditions were examined. Benzyl alcohol (1 mmol) was treated with acetic anhydride (1.2 mmol) in the absence of catalyst. As can be seen in Table 1, the corresponding product was obtained in 30% GC yield after 10 min (Table 1, entry 1). To evaluate the quantity of SBA-15–Ph–Pr–SO_3H, 1, 2, and 3 mol % of catalyst was used in the acetylation of benzyl alcohol for 10 min under solvent-free reaction conditions. It was observed that this reaction goes well in the presence of 2 mol % of catalyst (Table 1, entry 1). Use of a higher amount of catalyst (3 mol %) neither improves the yield nor the reaction time. Further studies have showed that all procedures work well with a 1:1.2 molar ratio of substrate to Ac_2O in the presence of 2 mol % of SBA-15–Ph–Pr–SO_3H without solvent at room temperature. On the basis of these results, we investigated the scope of the substrate alcohols and phenols with respect to the SBA-15–Ph–Pr–SO_3H catalyst-mediated acetylation, and the results obtained are summarized in Table 1.

The general efficiency of this reaction is evident from the fact that a variety of hydroxy compounds, including primary (aromatic and aliphatic), secondary (acyclic, cyclic, and benzylic), tertiary alcohols, and phenols, acetylated with acetic anhydride in the presence of 0.02 mmol of catalyst at room temperature were obtained in excellent yields during a short reaction time (Table 1). Primary benzylic alcohols with electron-releasing and electron-withdrawing groups were acylated, and the corresponding acetates were obtained in excellent yields (Table 1, entries 1–5). Secondary aromatic alcohols

Scheme 1. Schematic representation for solvent-free acylation of alcohols with Ac_2O using SBA-15–Ph–Pr–SO_3H.



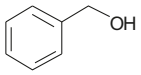
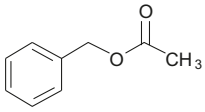
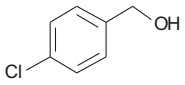
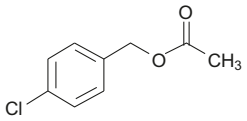
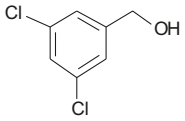
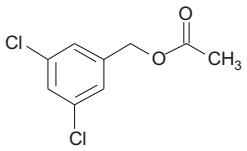
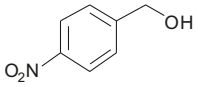
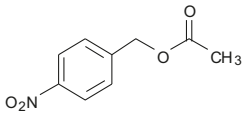
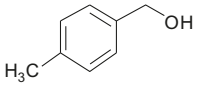
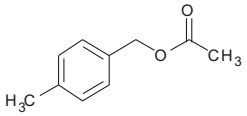
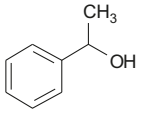
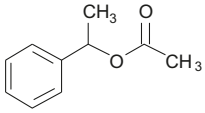
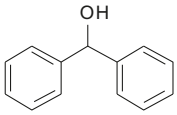
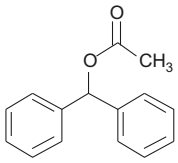
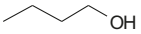
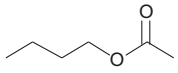
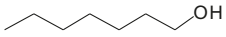
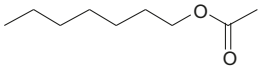
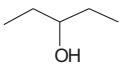
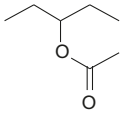
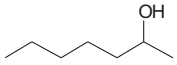
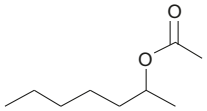
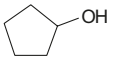
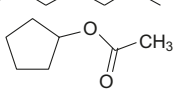
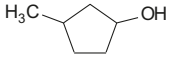
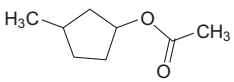
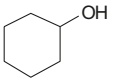
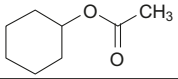
were also transformed to the respective acetates (Table 1, entries 6 and 7). Meanwhile, acetylation of primary and secondary aliphatic alcohols was performed in excellent yields in short reaction times (Table 1, entries 8–16). Phenol (Table 1, entry 17) and its derivatives (Table 1, entries 18–23) were also subjected to acetylation satisfactorily. It was also found that SBA-15–Ph–Pr–SO_3H effectively catalyzed the acetylation of diols and triols (Table 1, entries 24–26). Interestingly, adamantanol was also converted to the corresponding acetate as a model for acetylation of the hindered tertiary alcohols (Table 1, entry 27). The assigned structures were established from their spectral properties (^1H and ^{13}C NMR) and by comparison with available authentic data.

To clarify the merit of the catalyst, we compared the results of acetylation reaction of alcohols with some heterogeneous catalysts.[21–23] It can be concluded that the higher conversion of starting materials, shorter reaction times, and solvent-free reaction conditions for catalyst SBA-15–Ph–Pr–SO_3H might likely be attributed to the larger pore size of ordered SBA-15 and the beneficial influence of phenyl groups in close proximity to the sulfonic acid groups. Based on these observations, it is clear that the pore size and hydrophobic character of the catalyst are crucial parameters in the effectiveness of sulfonic acid based catalysts for the catalysis of the acetylation reaction, especially in solvent-free reaction conditions.

Reuse of the catalyst is an important aspect of any industrial process. Compared with traditional methods using volatile toxic solvents and nonrecoverable catalysts, which are energy consuming and environmentally malign, the ease of recycling is an attractive property of catalyst SBA-15–Ph–Pr–SO_3H for environmental protection and economic reasons. The catalyst could be stored and handled under open air conditions. To test the recyclability of the catalyst, the reaction was conducted with benzyl alcohol in the presence of catalyst

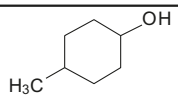
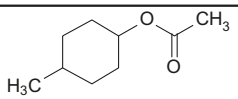
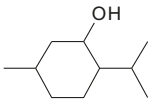
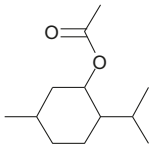
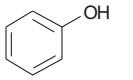
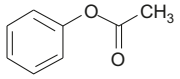
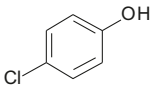
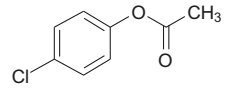
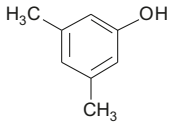
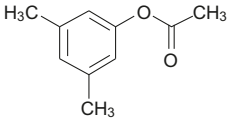
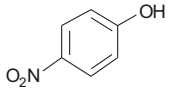
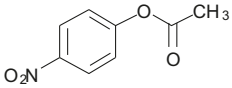
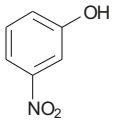
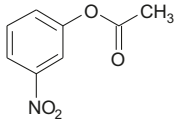
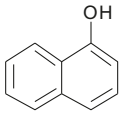
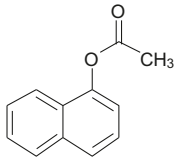
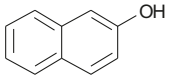
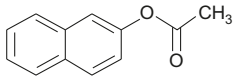
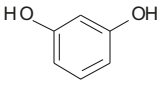
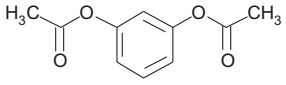
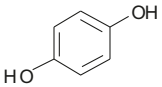
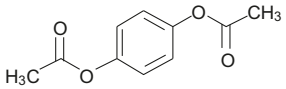
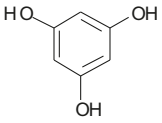
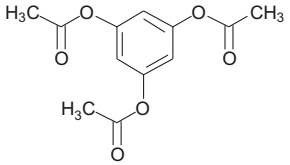
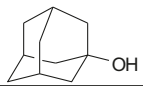
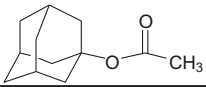
Can. J. Chem. Downloaded from www.nrcresearchpress.com by Renmin University of China on 09/02/12
For personal use only.

Table 1. Solvent-free acetylation of alcohols catalyzed by SBA-15–Ph–Pr–SO_3H at room temperature.

Entry	Substrate	Time (min)	Yield (%)[a,b]	Product
1		10	96 (30)[c]	
2		20	100	
3		25	95	
4		35	92	
5		10	98	
6		10	100	
7		30	91	
8		3	99	
9		3	99	
10		10	100	
11		5	100	
12		20	95	
13		20	97	
14		30	100	

for 10 min, which gave a conversion of 96%. The catalyst was quantitatively recovered by simple washing and filtration methods and proved to be reusable up to five times without any appreciable loss of catalytic activity. It is noteworthy that the catalyst-free solution was then left for 10 h, but no further reaction took place. This reusability demonstrates the high stability and turnover of catalyst under the conditions employed.

Table 1 (*concluded*).

Entry	Substrate	Time (min)	Yield (%)[a,b]	Product
15		30	100	
16		25	98	
17		15	100	
18		40	91	
19		10	100	
20		50	100	
21		45	100	
22		90	88	
23		70	100	
24		20	98	
25		17	97	
26		20	95	
27		25	98	

[a]Isolated yields.

[b]Reaction conditions: catalyst (0.02 mmol), alcohol (1 mmol), Ac_2O (1.2 mmol), room temperature, solvent-free conditions.

[c]Reaction performed in the absence of catalyst.

Conclusions

In summary, we have introduced highly efficient, hydrophobic, and reusable catalyst SBA-15–Ph–Pr–SO_3H as an active catalyst for solvent-free acetylation of alcohols at ambient temperature. In the presence of this catalyst, an almost stoichiometric amount of AC_2O is necessary. Moreover, this catalyst offers mild reaction conditions with short reaction

Can. J. Chem. Downloaded from www.nrcresearchpress.com by Renmin University of China on 09/02/12
For personal use only.

times, performing the acylation reactions under neat conditions. Besides, the catalyst kept its activity after five catalytic cycles. Accordingly, the methodology employed is a clean alternative for the acetylation reaction, tending toward ecoefficiency due to the use of solvent-free reaction conditions and recoverable catalyst, which can easily be prepared in the laboratory and stored for an extended period of time.

Supplementary data

Supplementary data are available with the article through the journal Web site at http://nrcresearchpress.com/doi/suppl/10.1139/v2012-018.

Acknowledgements

The authors acknowledge the Islamic Azad University of Qaemshahr Research Councils for support of this work.

References

(1) Green, T. W.; Wuts, P. G. M. *Protective Groups in Organic Synthesis;* 3rd ed.; John Wiley & Sons: New York, 1999; p 150.
(2) Hanson, J. R. *Protective Groups in Organic Synthesis;* Blackwell Science: Malden, MA, 1999.
(3) Zhdanov, R. I.; Zhenodarova, S. M. *Synthesis* **1975**, *1975* (4), 222. doi:10.1055/s-1975-23714.
(4) Tomohumi, S.; Kousaburo, O.; Takeshi, O. *Synthesis* **1999**, 1141.
(5) Höfle, G.; Steglich, V.; Vorbrüggen, H. *Angew. Chem. Int. Ed. Engl.* **1978**, *17* (8), 569. doi:10.1002/anie.197805691.
(6) Cope, A. C.; Herrick, E. C. In *Organic Syntheses Collective;* Wiley: New York, 1963; Vol. IV, p 304.
(7) Ishihara, K.; Kubota, M.; Kurihara, H.; Yamamoto, H. *J. Org. Chem.* **1996**, *61* (14), 4560. doi:10.1021/jo952237x.
(8) Chauhan, K. K.; Frost, C. G.; Love, I.; Waite, D. *Synlett* **1999**, *1999* (11), 1743. doi:10.1055/s-1999-2941.
(9) Dalpozzo, R.; De Nino, A.; Maiuolo, L.; Procopio, A.; Nardi, M.; Bartoli, G.; Romeo, R. *Tetrahedron Lett.* **2003**, *44* (30), 5621. doi:10.1016/S0040-4039(03)01358-3.
(10) Alleti, R.; Perambuduru, M.; Samantha, S.; Reddy, V. P. *J. Mol. Catal. A Chem.* **2005**, *226* (1), 57. doi:10.1016/j.molcata.2004.09.024.
(11) Kamal, A.; Khan, M. N. A.; Reddy, K. S.; Srikanth, Y. V. V.; Krishnaji, T. *Tetrahedron Lett.* **2007**, *48* (22), 3813. doi:10.1016/j.tetlet.2007.03.162.
(12) Heravi, M. M.; Behbahani, F. K.; Hekmat Shoar, R.; Oskooie, H. A. *Catal. Commun.* **2006**, *7* (3), 136. doi:10.1016/j.catcom.2005.09.011.
(13) Gowda, S.; Lokanatha Rai, K. M. *J. Mol. Catal. Chem.* **2004**, *217* (1–2), 27. doi:10.1016/j.molcata.2004.03.006.
(14) Phukan, P. *Tetrahedron Lett.* **2004**, *45* (24), 4785. doi:10.1016/j.tetlet.2004.04.076.
(15) Reddy, T. S.; Narasimhulu, M.; Suryakiran, N.; Mahesh, K. C.; Ashalatha, K.; Venkateswarlu, Y. *Tetrahedron Lett.* **2006**, *47* (38), 6825. doi:10.1016/j.tetlet.2006.07.059.
(16) Moghadam, M.; Tangestaninejad, S.; Mirkhani, V.; Mohammadpoor-Baltork, I.; Taghavi, S. A. *J. Mol. Catal. A Chem.* **2007**, *274* (1–2), 217. doi:10.1016/j.molcata.2007.05.012.
(17) Firouzabadi, M.; Iranpoor, N.; Farahi, S. *J. Mol. Catal. A Chem.* **2008**, *289*, 61.
(18) Romanelli, G.; Ruiz, D.; Vázquez, P.; Thomas, H.; Autino, J. C. *Chem. Eng. J.* **2010**, *161* (3), 355. doi:10.1016/j.cej.2009.12.029.
(19) Osiglio, L.; Romanelli, G.; Blanco, M. *J. Mol. Catal. A Chem.* **2010**, *316* (1–2), 52. doi:10.1016/j.molcata.2009.09.021.
(20) Joseph, J. K.; Jain, S. L.; Sain, B. *J. Mol. Catal. A Chem.* **2007**, *267* (1–2), 108. doi:10.1016/j.molcata.2006.11.026.
(21) Das, B.; Thirupathi, P. *J. Mol. Catal. A Chem.* **2007**, *269* (1–2), 12. doi:10.1016/j.molcata.2006.12.029.
(22) Yoon, H. J.; Lee, S. M.; Kim, J. H.; Cho, H. J.; Choi, J. W.; Lee, S. H.; Lee, Y. S. *Tetrahedron Lett.* **2008**, *49* (19), 3165. doi:10.1016/j.tetlet.2008.03.005.
(23) Rajabi, F. *Tetrahedron Lett.* **2009**, *50* (4), 395. doi:10.1016/j.tetlet.2008.11.024.
(24) Niknam, K.; Saberi, D. *Appl. Catal. A Gen.* **2009**, *366* (1), 220. doi:10.1016/j.apcata.2009.07.014.
(25) Karimi, B.; Zareyee, D. *Org. Lett.* **2008**, *10* (18), 3989. doi:10.1021/ol8013107. PMID:18702496.
(26) Karimi, B.; Zareyee, D. *J. Mater. Chem.* **2009**, *19* (45), 8665. doi:10.1039/b911388f.

Can. J. Chem. Downloaded from www.nrcresearchpress.com by Renmin University of China on 09/02/12
For personal use only.

Synthesis of new γ-lactones from preactivated monosubstituted pyrazines and TMS–ketene acetals

Azucena Garduño-Alva, M. Carmen Ortega-Alfaro, José G. López-Cortés, Isabel Chávez, Joaquin Barroso-Flores, Rubén A. Toscano, Henri Rudler, and Cecilio Álvarez-Toledano

Can. J. Chem. Downloaded from www.nrcresearchpress.com by Renmin University of China on 09/02/12
For personal use only.

Abstract: The double addition of bis(trimethylsilyl) ketene acetals (**1a**–**1b**, $R_1 = CH_3$, $-(CH_2)_5-$) to 2-substituted pyrazines promoted by triflic anhydride leads to γ-lactones in a single step. A systematic study involving electron-withdrawing and electron-donating groups (R_2 = CN, COOMe, PhCH=CH, Cl, Me, OMe) in the pyrazine ring reveals a strong dependence of electronic effects on the regiochemistry of nucleophilic addition.

Key words: pyrazines, γ-lactones, N-activation.

Résumé : La double addition des acétals de bis(trimethylsilyl) cétènes (**1a**–**1b**, $R_1 = CH_3$, $-(CH_2)_5-$) sur les pyrazines substituées en 2 et activées par l'anhydride triflique conduit à la formation de γ-lactones en une seule étape. Une étude systématique utilisant des substituants électro-attracteurs et des électro-donneurs (R_2 = CN, COOMe, PhCH=CH, Cl, Me, OMe) sur l'anneau de la pyrazine a révélé une forte dépendance des effets électroniques sur la régio-chimie de l'addition nucléophilique.

Mots-clés : pyrazines, γ-lactones, N-activation.

Introduction

Nitrogen heterocycles are abundant in nature and are of great significance to life because their structural subunits exist in many natural products such as vitamins, hormones, antibiotics, and alkaloids, as well as in pharmaceuticals, herbicides, and dyes.[1,2] The functionalization of azaheterocycles is therefore a powerful tool for synthesizing natural products and bioactive substances. Among the synthetic strategies that exist for carrying out such transformations, we have focused our efforts on the activation of the aromatic substrates by coordinating their double bonds to a transition metal and the activation of the aza-aromatics that occurs through nitrogen atoms via their pyridinium salts.[3] Following these approaches, we and other research groups have described the synthesis of functionalized γ- and δ-lactones via a double nucleophilic addition of bis(TMS)–ketene acetals to chromium(0) complexes,[4] allyl acetates,[5] tropylium ions,[6] and some azaheterocycles using methyl chloroformate[7] or triflic anhydride[8] as activating agents, and the appropriated halogen to induce the formation of the corresponding halolactones.

In the case of diazaheterocycles, there are important differences in their reactivity. When this reaction is extended to diazines such as pyrazine, quinoxaline, and pyrimidine, the ring-closure reaction takes place in one step (Scheme 1).[9–11]

In continuation of our studies on the activation of different diazaheterocyclic compounds and their reactivity towards nucleophiles, we herein report the full details on the regiochemistry of the nucleophilic addition of bis(TMS)–ketene acetals to different monosubstituted pyrazines previously activated with triflic anhydride. This systematic study involves both electron-withdrawing and electron-donating groups on the pyrazine ring.

Results and discussion

Reactivity of pyrazines containing electron-withdrawing groups

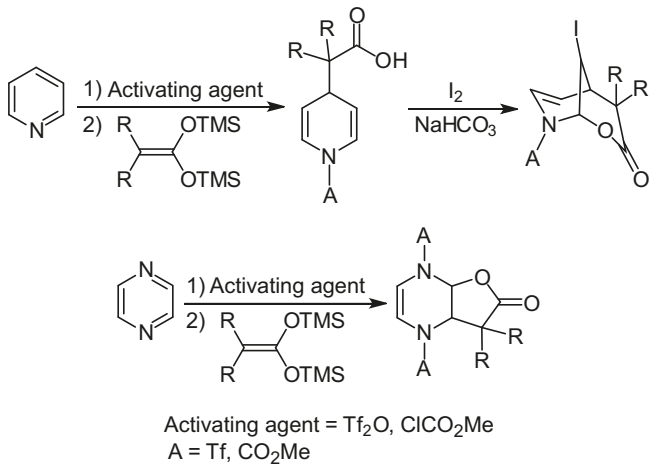
We started our study by using substituted pyrazines containing electron-withdrawing groups; thus, triflic anhydride (2 equiv) was added by syringe to a solution of corresponding pyrazine (**2**–**5**) in dry CH_2Cl_2 at –30 °C, followed by 2 equiv of bis(trimethylsilyl)ketene acetal **1**; the reaction

Received 4 August 2011. Accepted 26 January 2012. Published at www.nrcresearchpress.com/cjc on 26 April 2012.

A. Garduño-Alva, J.G. López-Cortés, I. Chávez, R.A. Toscano, and C. Álvarez-Toledano. Instituto de Química-UNAM, Circuito Exterior, Ciudad Universitaria, Coyoacán C. P. 04510, México, D. F.
M.C. Ortega-Alfaro. Instituto de Ciencias Nucleares-UNAM, Circuito Exterior, Ciudad Universitaria, Coyoacán C. P. 04510, México, D. F.
J. Barroso-Flores. Centro Conjunto de Investigación en Química Sustentable UAEM-UNAM. Car. Toluca-Atlacomulco, Km 14.5 Unidad San Cayetano. Personal de la UNAM. Toluca 50200, Estado de México, México.
H. Rudler. Institut Parisien de Chimie Moléculaire, UMR CNRS 7201, Université Pierre et Marie Curie, 4 place Jussieu, 75005 Paris CEDEX 5, France.

Corresponding author: C. Alvarez-Toledano (e-mail: cecilio@unam.mx).

Scheme 1.



mixture was stirred for 12 h (Scheme 2). The results are shown in Table 1. This reaction leads to the formation of two regioisomers (**A** and **A'**) depending on the nucleophilic attack of the TMS–ketene acetal. As can be seen, the reaction proceeds in a regioselective mode leading to products **A**. This behavior includes pyrazines containing strongly or moderated electron-withdrawing groups (Table 1, entries 1–8).

The assignment of the structure of all compounds was performed through spectroscopic methods. For example, the ^{1}H NMR spectrum of compound **2a** (mp 173 °C) confirms the double nitrogen activation and the ring closure in one step, leading to a *cis*-γ-lactone, which is consistent with two coupled signals shifted at 6.69 ppm (H6) and 5.12 ppm (H5) with $J = 8$ Hz. The ^{13}C NMR spectrum displays representative signals at 174.4 (lactone C=O), 85.9 (C6), 68.6 (C5), and 124.6 ppm (C3). Similar results were observed in the case of **2b** (mp 138 °C). Long-distance correlation (^3J) between H6 with C2, C7, and C8, as well as H5 with C3 using a heteronuclear multiple-bond correlation spectroscopy (HMBC) experiment, provides evidence of the correct position of the nitrile group, which is bonded to C2 (Fig. 1).

The structure of **4a** was fully established through an X-ray diffraction analysis (Fig. 2) and confirmed that a γ-lactone cis-fused to a tetrahydropyrazine had been formed.

In accordance with spectroscopic data, we can establish that the first nucleophilic attack toward pyrazine occurs on C5 once the nitrogen at position 4 has been activated, leading to intermediate **D**. This regiospecific activation is due to the fact that N4 is more basic as compared with N1, because of the neighboring electron-withdrawing group. A second activation promoted by another triflic anhydride molecule then takes place at N1, leading to **E**, which favors the ring-closure reaction, to give **2a** and **2b** (Scheme 3).

The introduction of chlorine as a substituent on the pyrazine ring leads to different behavior (Table 1, entries 7 and 8). As can be seen, products **5a** and **5b** were formed in moderate yield, and the new compounds **7a** and **7b**, containing an amide group in their structure (**B**), were also obtained. This is probably because the second nitrogen activation is not as fast, leading to a side reaction between the acetal **1** and triflic anhydride. The formation of **7a** and **7b** probably follows a similar reaction mechanism, as previously proposed by us in a related γ-lactone, using pyridazine as starting material and triflic anhydride as the activating agent (Scheme 4).[10]

The IR spectrum of product **7a** shows two absorption bands at 1791 and 1705 cm^{-1}, which indicates the presence of two different carbonyl groups. This result was confirmed in the ^{13}C NMR spectrum by the signals at 176.1 and 176.9 ppm, assigned to a lactone and an amide group, respectively. Two groups of signals shifted upfield in the ^{1}H NMR spectrum indicate the presence of four methyl groups, two of them as singlets, and the others as doublets coupled with a heptet signal shifted at 2.91 ppm, integration for one proton, which suggests an isopropyl group. This was in accordance with the introduction of 2 equiv of (TMS)–ketene acetal. The relative position of chlorine with respect to the lactone ring was assigned by the long-distance interaction observed in the HMBC experiment (Fig. 1).

The structure of **7a** was fully established through an X-ray diffraction analysis (Fig. 3) and confirmed that a γ-lactone cis-fused to a tetrahydropyrazine had been formed, one nitrogen bearing a trifluoromethanesulfonyl group, as expected from the NMR spectroscopic data, and the other surprisingly bearing an acyl group, which comes from an additional ketene acetal moiety.[10]

Reactivity of pyrazines containing electron-donating groups

To gain insight into the factor that controls the regiochemistry by electron-donating groups, we started screening this reaction using 2-methylpyrazine (**6**) and the (TMS)–ketene acetal **1a** (Table 1, entry 9) under similar reaction conditions. We obtained products **A** and **A'** in a 5:1 ratio, with a yield of 96%.[12] The major product was identified as **6a**, whose ^{1}H NMR spectrum showed two doublets at 6.53 and 4.79 ppm for H6 and H5 with $J = 8$ Hz, corresponding to a cis-fused lactone; this signal pattern concurs with previous results. Structure **6a'** was assigned to the minor product and, in this case, the vinyl protons H5 and H6 were displayed as a multiple signal with the integration of two protons. The ^{13}C NMR spectrum for this compound revealed a signal at 88.0 ppm assigned to quaternary carbon C2, consistent with a nucleophilic addition of (TMS)–ketene acetal over C3 and C2 of **6**. Two-dimensional NMR experiments are in agreement with the structure of **6a'**.

Similar to that observed for electron-withdrawing groups, the first activation occurs at the N4 despite increasing basic character in N1; we thought that the steric effect plays an important role in the first stage of the reaction. On the other hand, a loss in the selectivity of nucleophilic addition is observed and a mixture of products **6a** and **6a'** is obtained when acetal **1a** is used. When the same reaction was carried out with acetal **1b**, we only obtained the analogous compound **6b**. These results using the more sterically encumbered acetal substrate **1b** suggest that steric hindrance controls both the regioselectivity and yield of the nucleophilic addition product.

Finally, we carried out this reaction on 2-methoxypyrazine (**8**), which, once activated with triflic anhydride, led to three products after workup: two were identified as lactones **8'** and **9** and the other as carboxylic acid **10** (Scheme 5). The three products were formed by the regioselective nucleophilic addition of TMS–ketene acetal on C3, and in the case of **8'** and **9**

Can. J. Chem. Downloaded from www.nrcresearchpress.com by Renmin University of China on 09/02/12
For personal use only.

Scheme 2.

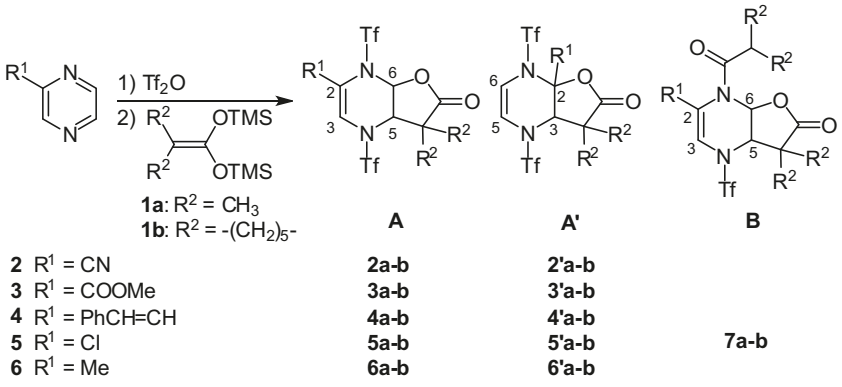
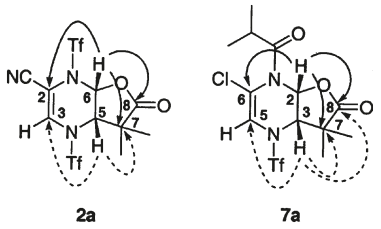


Table 1. Products obtained using 2-substituted pyrazines (**2**–**6**).

			Product (yield, %)		
Entry	R_1	R_2	**A**	**A'**	**B**
1	CN	Me	**2a** (60)	—	—
2	CN	$-(CH_2)_5-$	**2b** (36)	—	—
3	COOMe	Me	**3a** (89)	—	—
4	COOMe	$-(CH_2)_5-$	**3b** (84)	—	—
5	PhCH=CH	Me	**4a** (43)		
6	PhCH=CH	$-(CH_2)_5-$	**4b** (73)		
7	Cl	Me	**5a** (44)	—	**7a** (37)
8	Cl	$-(CH_2)_5-$	**5b** (37)	—	**7b** (25)
9	Me	Me	**6a** (80)	**6a'** (16)	—
10	Me	$-(CH_2)_5-$	**6b** (55)	—	—

Fig. 1. Heteronuclear multiple-bond correlation spectroscopy (HMBC) correlation for **2a** and **7a**.



with a ring-closure on C2, which is evidenced by the signals observed on the ^{13}C NMR spectra of these compounds around 100 ppm. These results reveal a high influence of the methoxy group in modifying the reactivity of the pyrazine. Additionally, a close relationship can be seen between the structure of **9a**–**9b** and the results obtained for compounds **7a**–**7b**, where an *N*-trifluoromethanesulfonyl moiety is bonded to an acyl group from 1 additional equiv of ketene acetal. The IR spectra of **9** showed two absorption bands around 1800 and 1700 cm^{-1}, consistent with a lactone and an amide group. The NMR spectroscopic data agree with this assessment. We fully confirmed the structure of **9a** through X-ray diffraction analyses (Fig. 4).

The IR spectra of the more polar compounds **10a** and **10b** showed the characteristic absorption band for the CO*OH* group, confirmed by the signals displayed in the ^1H NMR spectra at 10.70 and 10.08 ppm, respectively. We also observed the signals for the carboxyl groups in the ^{13}C NMR spectra at 179.8 and 178.9 ppm, respectively. A final assessment of the **10b** structure was obtained through an X-ray single crystal analysis (Fig. 5), which revealed that the first activation occurs on N4 of pyrazine followed by nucleophilic attack of the ketene acetal on C3; this compound is analogous to the first intermediate proposed in the reaction mechanism (**E**) (Scheme 3).

In accordance with the experimental results, a possible mechanism for the formation of **8'**, **9**, and **10** can be suggested (Scheme 6): the first nitrogen activation occurs on the nitrogen at the 4-position, then (TMS)–ketene acetal is nucleophilic added at the 3-position, leading to **F**, which is the key intermediate that gives rise to the three products. The hydrolysis of **F** thus leads to **10**. A subsequent nitrogen activation of **F** with a second equivalent of triflic anhydride favors the ring-closure reaction to **8'**. Alternatively, **F** might react with a second equivalent of ketene acetal, which is in excess, probably through a tandem reaction giving the amide **9**, as we have previously suggested.[10]

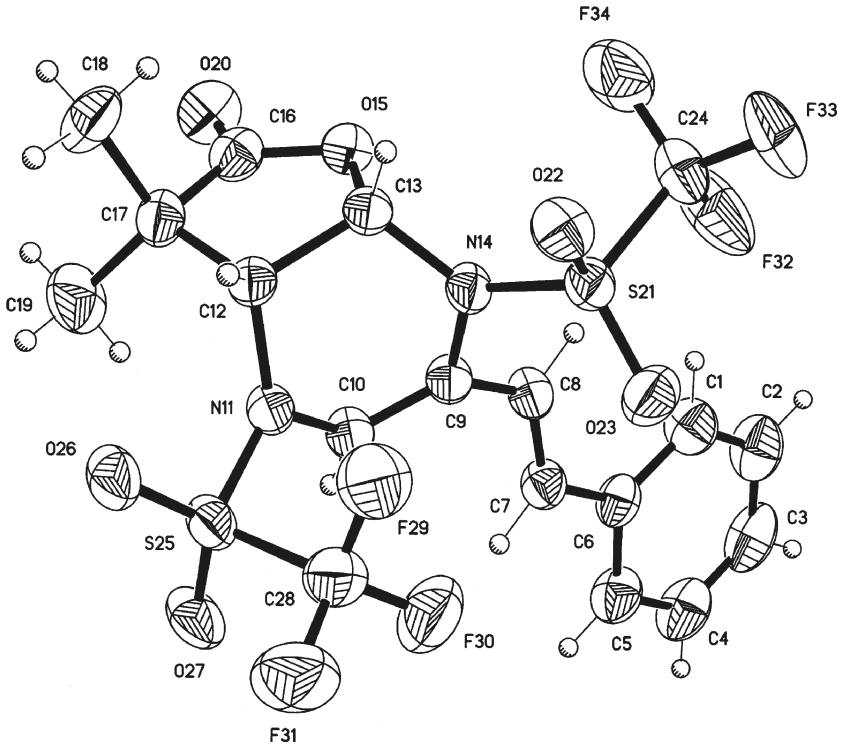
To understand the regiochemistry of the first nucleophilic addition on the pyrazines with triflic anhydride (C), we calculated the Fukui indices at the B3LYP/6–31G(d,p) level of theory. Figure 6 shows f^+ values for the substituted pyrazinium ions CN (**2C**), Me (**6C**), and MeO (**8C**). Geometry optimizations were carried out for each triflated compound.

On the basis of the calculated values for **2C** and **8C**, nucleophilic addition is carried out on C5 and C3, respectively. However, in the case of **6C**, we obtained close values of Fukui indices in both carbon atoms, showing a similar probability of nucleophilic attack by the TMS–ketene acetal. These theoretical findings agree with the experimental results and explain the loss of regioselectivity.

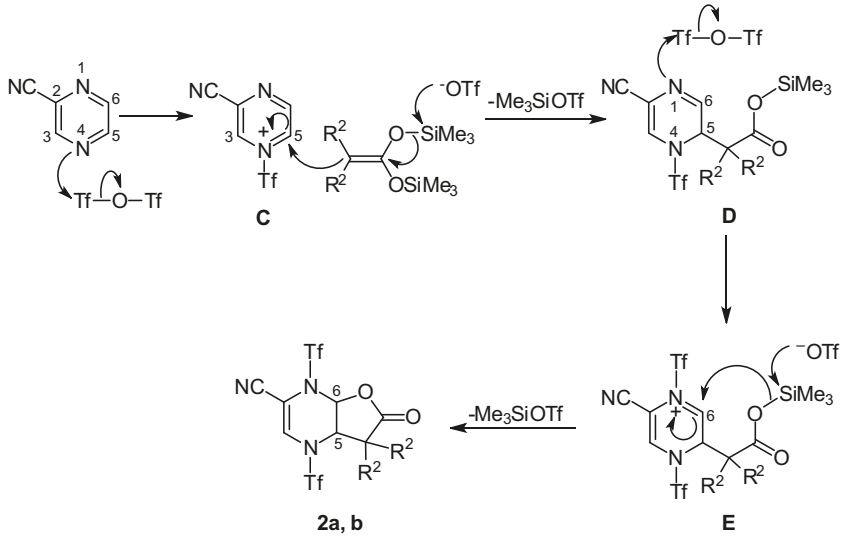
Can. J. Chem. Downloaded from www.nrcresearchpress.com by Renmin University of China on 09/02/12
For personal use only.

Can. J. Chem. Downloaded from www.nrcresearchpress.com by Renmin University of China on 09/02/12
For personal use only.

Fig. 2. ORTEP view of compund **4a**. Thermal ellipsoids at 30% probability level.



Scheme 3.



Mechanism insight

In an attempt to trap the intermediates proposed in the pathway to obtain **8**–**10**, we carried out three experiments in which we modified the stoichiometry of the ketene acetal as well as its structure. In the first assay, we performed the reaction using 1 equiv of triflic anhydride plus 2 equiv of ketene acetal **1b**. We obtained **10b** as the only product in 98% yield, thus confirming that **F** is the crucial intermediate in the reaction (Scheme 7).

Since the course of the reaction involves the formation of intermediate **F** as an initial step, we modified the structure of the ketene acetal by selecting the *O*-(TMS) ester **1c**. When we used an equimolar amount of Tf_2O and **1c**, the only product obtained was **11c**, which is formed through the nucleophilic addition at the 3-position on preactivated pyrazine (Scheme 8 and Table 2, entry 1). The spectroscopic data for **11c** confirms this result. In particular, the protons of the double bond gave the double signals at 6.37 and 6.09 ppm with $J = 5$ Hz and two singlets with the integration of three protons assigned to the methyl groups observed in the ^{1}H NMR spectrum. Furthermore, in the ^{13}C NMR spectrum we observed two signals at 172.7 and 157.8 ppm, assigned to an ester group and N=C, respectively. If the same reaction is carried out in a 2:1 ratio of Tf_2O–**1c** (Scheme 8 and Table 2, entry 2), **11c**, and **12c** were obtained in nearly equal amounts (38% and 48%, respectively). The IR spectrum

Scheme 4.

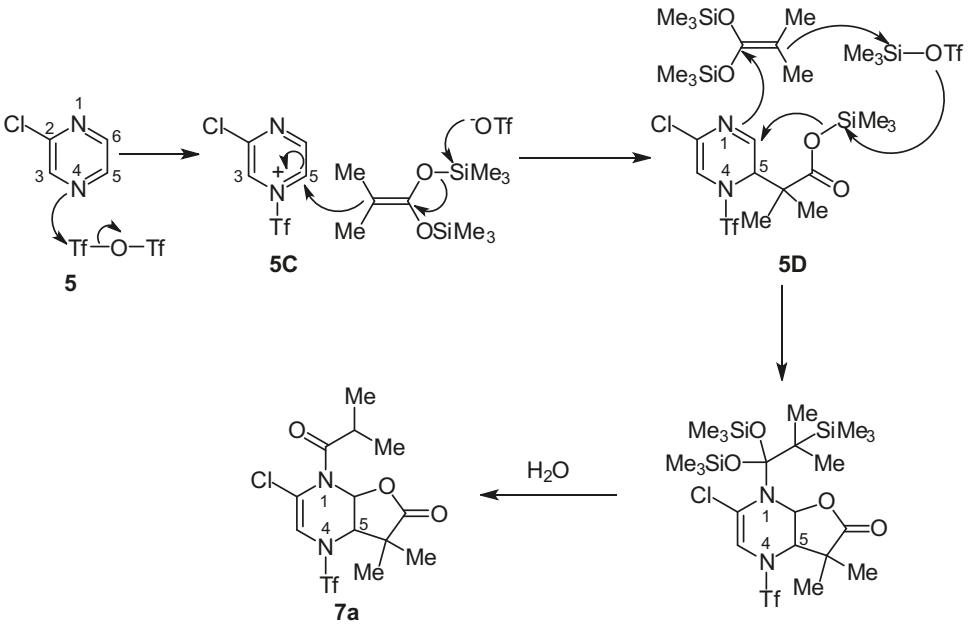
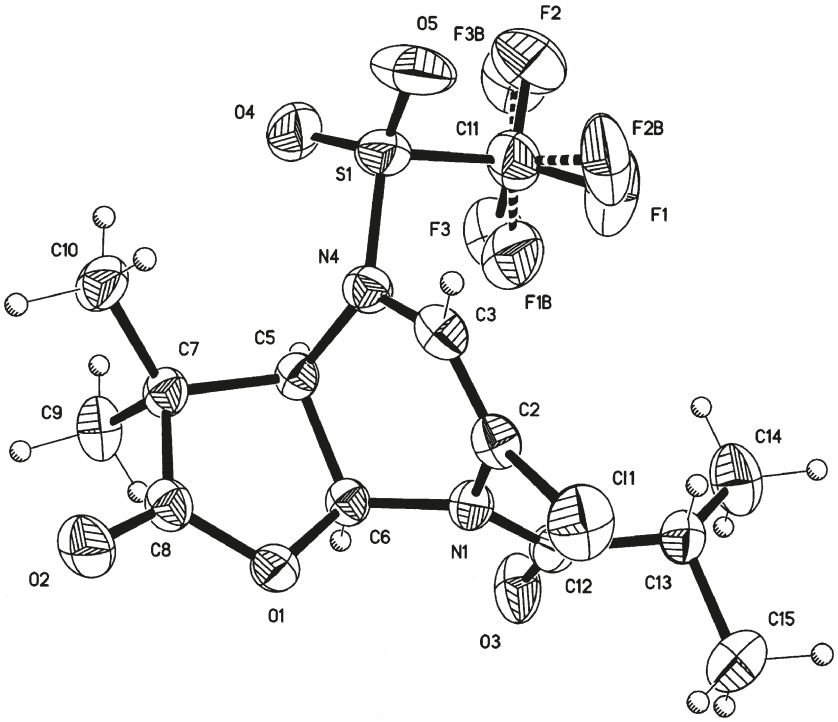


Fig. 3. ORTEP view of compound **7a**. Only one of two independent molecules is displayed. Thermal ellipsoids are at the 30% probability level.



of **12c** displays two absorption bands for carbonyl groups. As characteristic signals in the ^{1}H NMR spectrum, we observe those corresponding to the double bond C=C and the methyl group of the ester. The ^{13}C NMR spectrum shows two quartets with $J = 323$ Hz, indicating the presence of two different CF_3SO_2 bonded to both nitrogen atoms, which concurs with the mass spectrometry analysis. We can fully establish the structure of **12c** through X-ray diffraction analyses (Fig. 7).

These results confirm that the successive activation on the pyrazine ring takes place in steps, the crucial step being the formation of intermediate **F**, after which a consecutive activation promoted by a second molecule of triflic anhydride can promote the ring-closure reaction if a bis(TMS)–ketene acetal is used as a nucleophile.

For **12c**, we propose the following pathway (Scheme 9): as in preceding cases, the first nitrogen activation occurs on the nitrogen at the 4-position, then (TMS)–ketene acetal is nucleophilic-added at the 3-position, leading to **11c**, which reacts with a second equivalent of triflic anhydride, giving as a possible intermediate an iminiun salt that after work-up

Can. J. Chem. Downloaded from www.nrcresearchpress.com by Renmin University of China on 09/02/12
For personal use only.

Scheme 5.

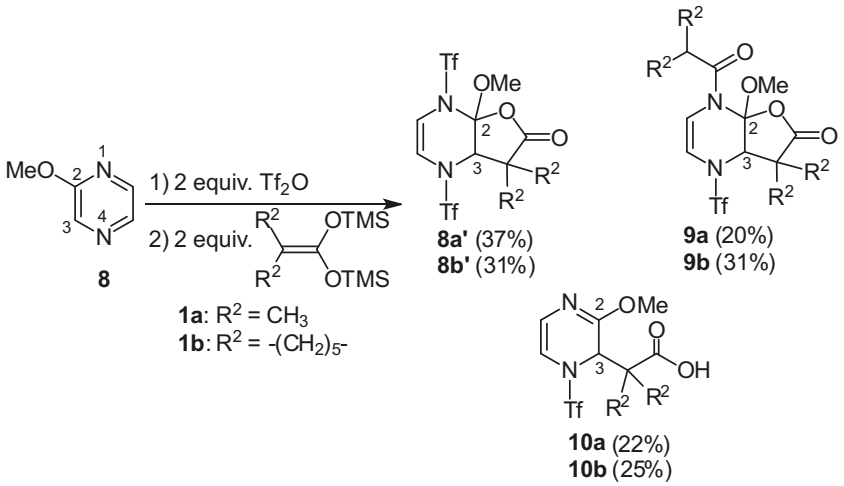
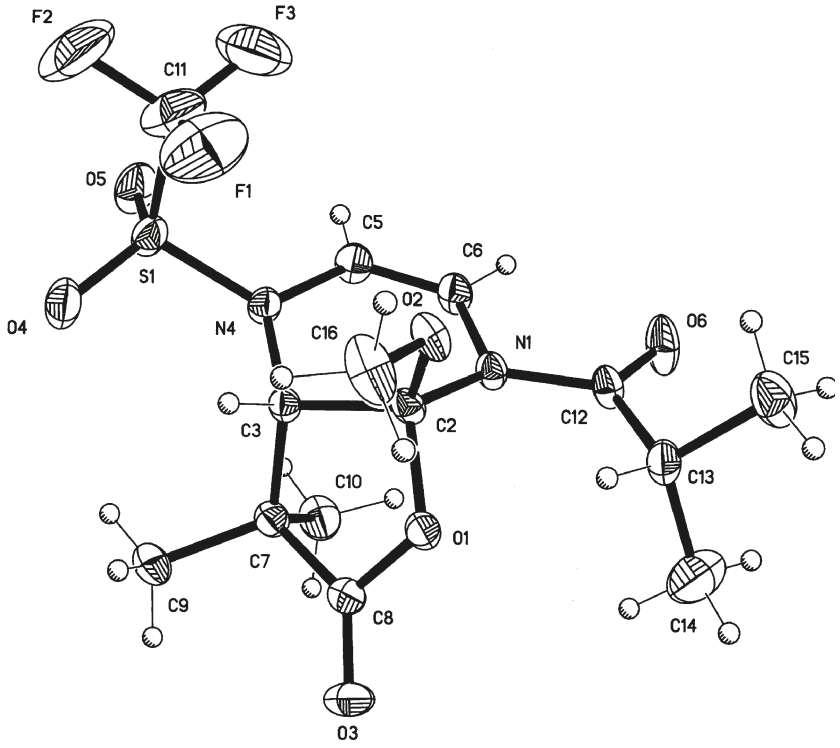


Fig. 4. ORTEP view of compound **9a**. Thermal ellipsoids are at the 30% probability level.



leads to the hemiacetal **G**, which after hidrolysis is transformed into the pyrazinone **12c**.

Conclusions

In all cases it was possible to obtain the γ-lactone through a one-pot reaction. The first N-activation of the diazine takes place on the nitrogen atom furthest from the substituent. This behavior can be attributed to the steric effect of the activating agent. The nucleophilic addition of the TMS–ketene acetal over the pyrazinium ring strongly depends on the substituents. Electron-withdrawing groups thus favor the addition on C5, even though strong donating groups such as methoxy modify the regiochemistry to the C3-position. In the case of the methyl group, we observe a loss of the regioselectivity of the nucleophilic addition. Calculated Fukui indices reflect the observed orientations upon the formation of the lactones through nucleophilic addition of the nucleophiles employed. Some suggested intermediates were trapped, which enabled us to propose a reasonable mechanism.

Experimental section

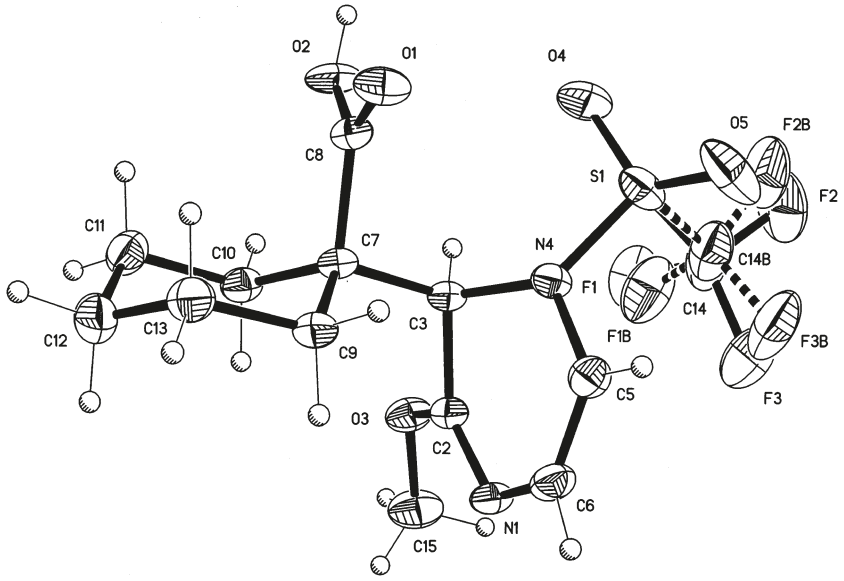
Materials

Anhydrous solvents were obtained by distillation under an inert atmosphere over sodium benzophenone for THF and anhydrous $CaCl_2$ for dichloromethane. Column chromatography was performed using 70–230 mesh silica gel. All reagents and solvents were obtained from commercial suppliers and used without further purification. All compounds were

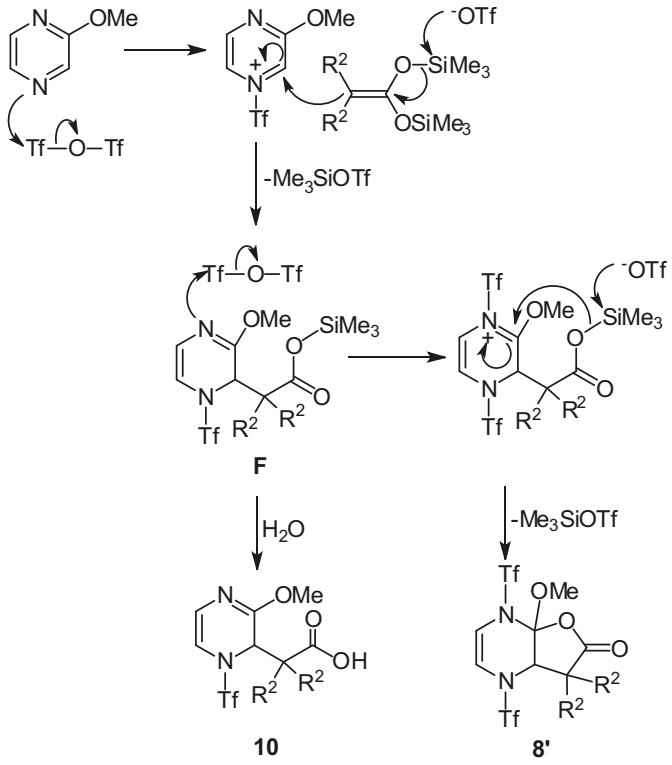
Can. J. Chem. Downloaded from www.nrcresearchpress.com by Renmin University of China on 09/02/12
For personal use only.

Can. J. Chem. Downloaded from www.nrcresearchpress.com by Renmin University of China on 09/02/12
For personal use only.

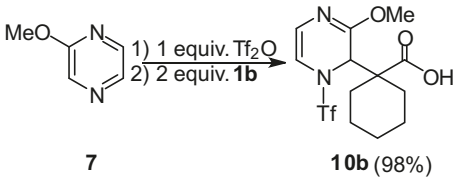
Fig. 5. ORTEP view of **10b**. Thermal ellipsoids are at the 30% probability level.



Scheme 6.



Scheme 7.



Scheme 8.

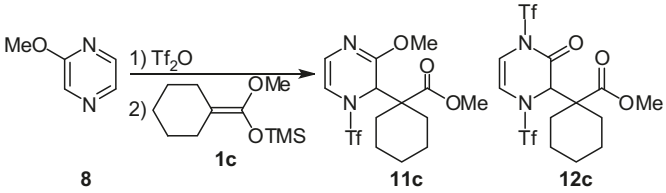
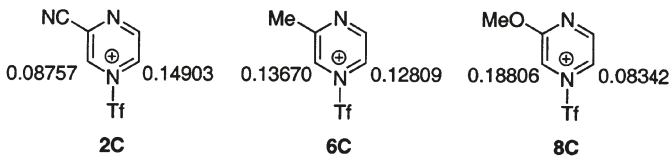


Table 2. Products obtained using 2-methoxypyrazine.

	Starting material		Yield (%)	
Entry	Tf_2O (equiv)	**1c** (equiv)	**11c**	**12c**
1	1	1.1	76	—
2	2	2	38	48

Fig. 6. Fukui f^+ indices for the parent compounds. Hydrogen atoms are omitted for clarity; only indexes for the ring-member atoms are displayed.



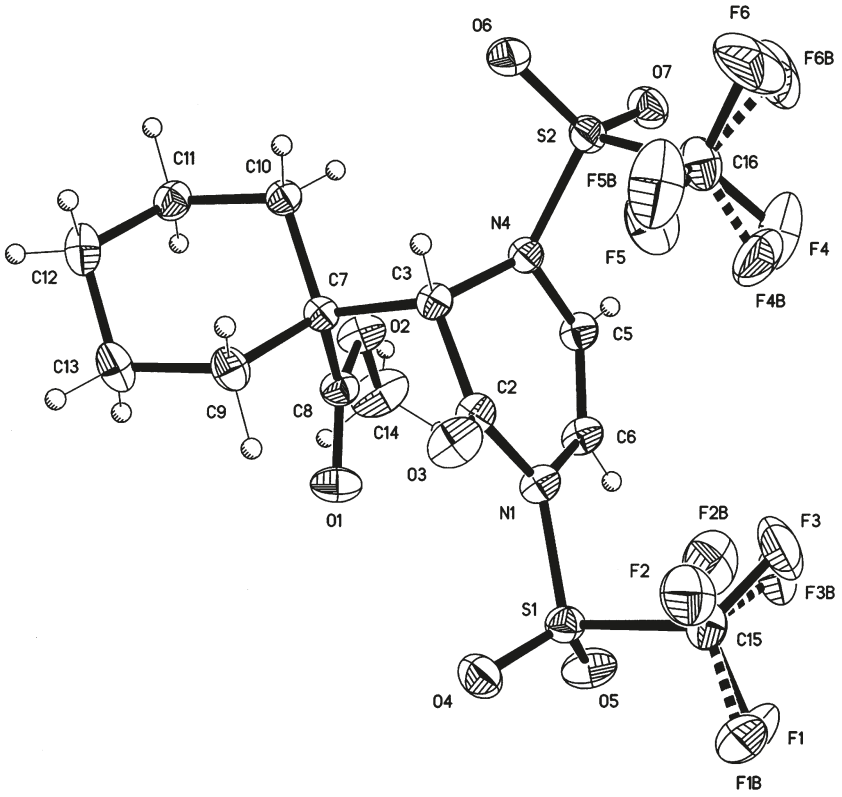
characterized by IR spectra, recorded on a PerkinElmer 283B or 1420 spectrophotometer using the KBr technique; all data are expressed in wavenumbers (cm^{-1}). Melting points were obtained on a Melt-Temp II apparatus and are uncorrected. NMR spectra were measured with a JEOL Eclipse +300 and a Varian Inova (500 MHz), using $CDCl_3$ and acetonitrile-D_3 as solvents. Chemical shifts are in ppm (δ) relative to TMS. The MS-FAB and MS-EI spectra were obtained on a JEOL SX 102A. The ketene acetals **1a–1c** were prepared according to published methods.[13]

Computational details

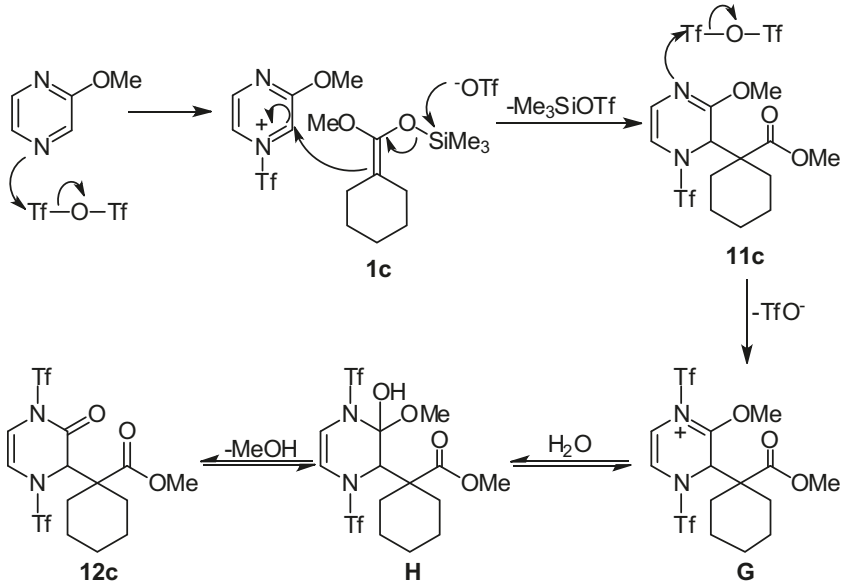
All computations were carried out using the Gaussian09 suite of programs.[14] Natural population analyses were performed with the NBO 3.1 program included in the aforementioned

Can. J. Chem. Downloaded from www.nrcresearchpress.com by Renmin University of China on 09/02/12
For personal use only.

Fig. 7. ORTEP view of **12c**. Thermal ellipsoids are at the 0% probability level.



Scheme 9.



Gaussian09 suite. The Berny optimization algorithm was employed in optimizing the geometry of all compounds. Fukui indices were later calculated for all the molecules following the regular procedure,[15] by using the results in the Natural Population Analysis (NPA).[16]

Structure determination by X-ray crystallography

Suitable X-ray quality **4a**, **7a**, **9a**, **10b**, and **12c** crystals were grown through slow evaporation of a dichloromethane–*n*-hexane solvent mixture at –5 °C. Single white crystals of compounds **4a**, **7a**, **9a**, **10b**, and **12c** were mounted on a glass fiber at room temperature. The crystals were then placed on a Bruker SMART APEX CCD diffractometer, equipped with Mo Kα radiation; decay was negligible in all cases. Data collections for all crystals were obtained at room temperature. Details of crystallographic data collected on compounds **4a**, **7a**, **9a**, **10b**, and **12c** are provided in Table 3. Systematic absences and intensity statistics were used in space group determination. The structures were solved using direct methods.[17] Anisotropic structure refinements were

Can. J. Chem. Downloaded from www.nrcresearchpress.com by Renmin University of China on 09/02/12
For personal use only.

Table 3. Crystal data and structure refinement parameters of **4a**, **7a**, **9a**, **10b**, and **12c**.

	Compound				
Parameter	**4a**	**7a**	**9a**	**10b**	**12c**
Formula	$C_{18}H_{16}F_6N_2O_6S_2$	$C_{13}H_{16}ClF_3N_2O_5S$	$C_{14}H_{19}F_3N_2O_6S$	$C_{13}H_{17}F_3N_2O_5S$	$C_{14}H_{16}F_6N_2O_7S_2$
MW (g mol^{-1})	534.45	404.798	400.37	370.35	502.41
Crystal size (mm)	0.42×0.40×0.26	0.39×0.28×0.24	0.39×0.19×0.14	0.50×0.25×0.13	0.37×0.36×0.13
Color	Colorless block	Colorless block	Colorless block	Colorless prism	Colorless prism
Crystalline system	Monoclinic	Triclinic	Monoclinic	Monoclinic	Triclinic
Space group	$P2_1/c$	P-1	$P2_1/n$	$P2_1/c$	P-1
Cell parameters					
a (Å)	15.180(1)	11.171(2)	8.294(1)	11.923(1)	7.678(1)
b (Å)	11.218(1)	11.550(2)	7.654(1)	7.894(1)	9.173(1)
c (Å)	14.197(1)	15.926(2)	28.814(4)	17.451(2)	16.308(2)
α (°)	90	97.247(2)	90	90	75.703(2)
β (°)	107.859(1)	103.735(2)	93.174(2)	95.063(2)	89.535(2)
γ (°)	90	110.879(2)	90	90	66.402(2)
V (Å^3)	2301.0(3)	1814(1)	1826.3(5)	1636.1(3)	1014.5(2)
Z	4	4	4	4	2
D_{calcd} (Mg m^{-3})	1.543	1.482	1.456	1.504	1.645
Reflections collected / R_σ	18466 / 0.0267	24689 / 0.0254	14037 / 0.0393	12725 / 0.0217	13897 / 0.0228
Ind. reflections, R_{int}	4215, 0.0321	6633, 0.0273	3321, 0.0419	2995, 0.0259	3687, 0.0247
Data/parameters	4215/309	6633/551	3321/240	2995/257	3687/337
Final R, $wR2$[I > 2σ(I)]	0.0487, 0.1211	0.0480, 0.1147	0.0668, 0.1581	0.0400, 0.1031	0.0423, 0.1084
$R1$, w$R2$ (all data)	0.0636, 0.1313	0.0637, 0.1237	0.0877, 0.1694	0.0470, 0.1087	0.0511, 0.1144
GoF on F^2	1.031	1.024	1.054	1.028	1.026

Published by NRC Research Press

Can. J. Chem. Downloaded from www.nrcresearchpress.com by Renmin University of China on 09/02/12
For personal use only.

achieved using full-matrix least-squares techniques on all non-hydrogen atoms. All hydrogen atoms — except H2 in compound **10b** — were placed in idealized positions, based on hybridization, with isotropic thermal parameters fixed at 1.2 or 1.5 times the value of the U_{eq} of the parent carbon atom. Structure solutions and refinements were performed using SHELXTL v 6.10 (see the Supplementary data).[18]

2-Benzylidene pyrazine (**4**) was prepared according to a modification of the reported method[19] as follows: In a 150 mL two-neck round-bottom flask fitted with a magnetic stirrer and reflux condenser, 1 equiv of potassium *tert*-butoxide (0.56 g, 5.5 mmol) was placed in 30 mL of anhydrous THF under nitrogen. After that, 1 equiv of 2-methylpyrazine (0.5 mL, 5.5 mmol) was added and the mixture was refluxed. Then, a solution of 1 equiv of benzaldehyde (0.6 mL, 5.5 mmol) in 20 mL of anhydrous THF was slowly added. The reaction mixture was refluxed for 24 h. Finally, 30 mL of brine was added and the product extracted with CH_2Cl_2 (2 × 50 mL). The combined organic layers were dried with anhydrous Na_2SO_4, and the solvent was removed in vacuo. The product was purified by neutral alumina chromatography. Elution with hexane – ethyl acetate (98:2). ($C_{12}H_{10}N_2$, M = 261 g/mol, white solid, mp 116–120 °C (0.68 g, 3.74 mmol, 68%). IR ν (cm^{-1}): 3031 (=CH–), 1630 (–C=N–). ^{1}H NMR (300 MHz, $CDCl_3$) δ: 8.64 (s, 1H, H5), 8.54 (s, 1H, H3), 8.40 (s, 1H, H6), 7.75 (d, 1H, H7 J = 16 Hz), 7.61–7.33 (m, 5H, H arom.), 7.16 (d, 1H, H8 J = 16 Hz). ^{13}C NMR (75 MHz, $CDCl_3$) δ: 151.3 (C2), 144.5 (C6) 143.8 (C3), 142.8 (C5), 136.0 (C9), 135.2 (C8), 129.0 (C11), 128.9 (C12), 127.4 (C10) 124.0 (C7). MS (EI$^+$, 70 eV) *m*/*z* (%): 182 (10) [M$^+$].

General procedure

Synthesis of lactones

In a 100 mL flask fitted with a magnetic stirrer, the corresponding monosubstituted pyrazine was dissolved in 30 mL of anhydrous dichloromethane and placed under nitrogen at –30 °C. After that 2 equiv of triflic anhydride were added, showing the formation of a precipitate, and subsequently 2 equiv of bis(trimethylsilyl)–ketene acetal **1** was added. The reaction mixture was allowed to reach room temperature and left stirring for 12 h. Finally, 40 mL of distilled water was added, the organic phase was recovered, and then dried with anhydrous sodium sulfate and filtered. The solvent was evaporated under vacuum. The products were purified using silica gel column chromatography, eluting with hexanes – ethyl acetate (98:2).

*6-Cyano-3,3-dimethyl-2-oxo-4,7-bis (trifluoromethanesulfonyl)-2,3,3a,4,7,7a-hexahydrofuro[2,3-*b*]pyrazine (2a)*

$C_{11}H_9F_6N_3O_6S_2$ (M = 457 g/mol) was prepared starting from pyrazine 2-carbonitrile (0.3 mL, 3.35 mmol), trifluoromethanesulfonic anhydride (1.2 mL, 6.7 mmol), and **1a** (1.6 mL, 6.7 mmol) and was obtained as a white solid, mp 173 °C (0.92 g, 2.01 mmol, 60%). IR ν (cm^{-1}): 2238 (CN), 1795 (C=O lactone). ^{1}H NMR (300 MHz, acetonitrile-D_3) δ: 7.58 (s, 1H, H3), 6.69 (d, 1H, H6, J = 8.2 Hz), 5.12 (d, 1H, H5, J = 8.2 Hz), 1.39 (s, 3H, H9), 1.36 (s, 3H, H10). ^{13}C NMR (75 MHz, acetonitrile-D_3) δ: 174.4 (C=O lactone), 133.8 (C3), 119 (q, *C*F_3, J = 322 Hz), 119 (q, CF_3, J = 320 Hz), 109.7 (*C*N), 103.0 (C2), 85.9 (C6), 68.6 (C5), 43.9 (C7), 24.3 (C9), 20.4 (C10). MS (EI$^+$, 70 eV) *m*/*z* (%): 457 (50) M$^+$, 324 (100) [M – 133]$^+$. HR-MS(FAB$^+$) calcd for $C_{11}H_9F_6N_3O_6S_2$: 456.9837; found: 456.9845.

*6'-Cyano-2'-oxo-4',7'-bis(trifluoromethanesulfonyl)spiro [cyclohexane-1,3'-2',3',3a',4',7',7a'-hexahydrofuro[2,3-*b*] pyrazine] (2b)*

$C_{14}H_{13}F_6N_3O_6S_2$ (M = 497 g/mol) was prepared starting from pyrazine 2-carbonitrile (0.3 mL, 3.35 mmol), trifluoromethanesulfonic anhydride (1.2 mL, 6.7 mmol), and **1b** (1.8 mL, 6.7 mmol) and was obtained as a white solid, mp 138 °C (0.60 g, 1.21 mmol, 36%). IR ν (cm^{-1}): 2240 (CN), 1798 (C=O lactone). ^{1}H NMR (300 MHz, acetonitrile-D_3) δ: 7.60 (s, 1H, H3), 6.61 (d, 1H, H6, J = 8 Hz), 5.14 (d, 1H, H5, J = 8 Hz), 2.00–1.20 (m, 10H, $H_{cyclohexyl}$). ^{13}C NMR (75 MHz, acetonitrile-D_3) δ: 173.8 (C=O lactone), 135.9 (C3), 119 (q, *C*F_3, J = 322 Hz), 119 (q, CF_3, J = 320 Hz), 110.4 (*C*N), 106.0 (C2), 87.7 (C6), 71.3 (C5), 46.4 (C7), 34.7, 30.1, 24.8 21.4, 21.0 ($C_{cyclohexyl}$). MS (EI$^+$, 70 eV) *m*/*z* (%): 497 (50) M$^+$, 364 (100) [M– 133]$^+$. HR-MS (FAB$^+$) calcd for $C_{14}H_{14}F_6N_3O_6S_2$: 498.0228; found: 498.0228.

*Methyl 3,3-dimethyl-2-oxo-4,7-bis (trifluoromethanesulfonyl)-2,3,3a,4,7,7a-hexahydrofuro[2,3-*b*]pyrazine-6-carboxylate (3a)*

$C_{12}H_{12}F_6N_2O_8S_2$ (M = 490 g/mol) was prepared starting from methyl 2-pyrazine carboxylate (0.3g, 2.17 mmol), trifluoromethanesulfonic anhydride (0.73 mL, 4.34 mmol), and **1a** (1.00 mL, 4.34 mmol) and was obtained as a white solid, mp 176 °C (0.94 g, 1.91 mmol, 89%). IR ν (cm^{-1}): 2991, 2946, 2870 (CH, CH_3), 1808 (C=O ester), 1747 (C=O lactone), 1410 years 1227 (SO_2), 1142 (CF_3). ^{1}H NMR (400 MHz, $CDCl_3$) δ: 7.51 (s, 1H, H3), 6.59 (d, 1H, H6, J = 8 Hz), 4.83 (d, 1H, H5, J = 8 Hz), 3.75 (s, 3H, H13), 1.35 (s, 3H, H9), 1.29 (s, 3H, H10).^{13}C NMR (100 MHz, $CDCl_3$) δ: 175.3 (C=O lactone), 159.6 (C=O ester), 131.3 (C3), 120.9 (C2), 119.2 (q, CF_3, J = 321 Hz), 87.7 (C6), 70.5 (C5), 53.1 (C13), 44.7 (C7), 25.5 (Me), 21.2 (Me). MS (IE$^+$, 70 eV) *m*/*z* (%): 590 (15) M$^+$, 357 (100) [M – 133]$^+$.

*Methyl 2'-oxo-4',7'-bis(trifluoromethanesulfonyl)spiro [cyclohexane-1,3'-2',3',3a',4',7',7a'-hexahydrofuro[2,3-*b*] pyrazine]-6'-carboxylate (3b)*

$C_{15}H_{16}F_6N_2O_8S_2$ (M = 530 g/mol) was prepared starting from methyl 2-pyrazine carboxylate (0.3 g, 2.17 mmol), trifluoromethanesulfonic anhydride (0.73 mL, 4.34 mmol), and **1b** (1.18 mL, 4.34 mmol) and was obtained as a white solid, mp 150 °C (0.97 g, 1.82 mmol, 84%). IR ν (cm^{-1}): 2959, 2941, 2870 (CH, CH_2, CH_3), 1798 (C=O ester), 1743 (C=O lactone), 1410 and 1225 (SO_2), 1150 (CF_3). ^{1}H NMR (300 MHz, $CDCl_3$) δ: 7.56 (s, 1H, H3), 6.56 (d, 1H, H6, J = 8 Hz), 4.84 (d, 1H, H5, J = 8 Hz), 3.87 (s, 3H, H17), 2.15–1.28 (m, 10H, $H_{cyclohexyl}$). ^{13}C NMR (75 MHz, $CDCl_3$) δ: 173.3 (C=O lactone), 159.7 (C=O ester), 131.7 (C3), 122.7 (C2), 119.4 (q, CF_3, J = 322 Hz), 119.3 (q, CF_3, J = 322 Hz), 88.1 (C6), 72.5 (C5), 53.3 (C17), 46.2 (C7), 35.3, 29.8, 24.4, 20.9, 20.5 ($C_{cyclohexyl}$). MS (IE$^+$, 70 eV) *m*/*z* (%): 530 (30) M$^+$, 109 (100) [M – 421]$^+$. HR-MS (FAB$^+$) calcd for $C_{15}H_{16}F_6N_2O_8S_2$: 530.0252; found: 530.0252.

Can. J. Chem. Downloaded from www.nrcresearchpress.com by Renmin University of China on 09/02/12
For personal use only.

6-(2-Phenyl-1E-ethenyl)-3,3-dimethyl-2-oxo-4,7-bis (trifluoromethanesulfonyl)-2,3,3a,4,7,7a-hexahydrofuro[2,3-b]pyrazine (4a)

$C_{18}H_{16}F_6N_2O_6S_2$ (M = 534 g/mol) was prepared starting from 2-benzylidene pyrazine (0.4 g, 2.2 mmol), trifluoromethanesulfonic anhydride (0.7 mL, 4.4 mmol), and **1a** (1 mL, 4.4 mmol) and was obtained as a white solid, mp 160 °C (0.51 g, 0.95 mmol, 43%). IR ν (cm^{-1}): 3105, 3085 (=C–H), 2985, 2920 (CH, CH_2), 1785 (C=O lactone), 1411 and 1230 (SO_2), 1017 (CF_3). ^{1}H NMR (400 MHz, $CDCl_3$) δ: 7.45–7.30 (m, 5H, $CH_{arom.}$) 6.75 (d, 1H, H13), 6.71 (s, 1H, H3) 6.60 (d,1H, H6, J = 8 Hz), 6.50 (d, 1H, H14), 4.85 (d, 1H, H5, J = 8 Hz), 1.42(d, 6H, H9 and H10). ^{13}C NMR (100 MHz, $CDCl_3$) δ: 175.6 (C=O lactone), 135.4 (C14), 134.8 (C15), 131.9 (C2), 129.5, 128.9, 127.2 ($C_{arom.}$), 120.9 (q, CF_3 J = 320 Hz), 118.1 (C13), 117.7 (q, CF_3 J = 320 Hz), 116.9 (C3), 87.8 (C6), 70.9 (C5), 44.4 (C7), 26.0, 21.0 (C9 and C10). MS (IE^+, 70 eV) m/z (%): 534 (5)[M], 401(15) $[M - 133]^+$, 268 (15) $[M - 133]^+$, 145 (100)[M – 123]. HR-MS (FAB^+) calcd for $C_{18}H_{16}F_6N_2O_6S_2$: 534.0354; found: 534.0357.

6'(2-Phenyl-1E-ethenyl)-3',3'-dimethyl-2'-oxo-4',7'-bis (trifluoromethanesulfonyl)spiro[cyclohexane-1,3'-2',3',3a',4',7',7a'-hexahydrofuro[2,3-b]pyrazine (4b)

$C_{21}H_{20}F_6N_2O_6S_2$ (M = 574 g/mol) was prepared starting from 2-benzylidene pyrazine (0.4 g, 2.2 mmol), trifluoromethanesulfonic anhydride (0.7 mL, 4.4 mmol), and **1b** (1.2 mL, 4.4 mmol) and was obtained as a white solid, mp 186 °C (0.90 g, 1.56 mmol, 71%). IR ν (cm^{-1}): 3095, 3061 (=C–H), 2936, 2868 (CH, CH_2), 1788 (C=O lactone), 1408 and 1212 (SO_2), 1011 (CF_3). ^{1}H NMR (400 MHz, $CDCl_3$) δ: 7.43–7.33 (m, 5H, $H_{arom.}$), 6.95 (d,1H, H16, J = 16 Hz), 6.65 (s,1H,H3), 6.56 (d, 1H, H6, J = 8 Hz), 6.49 (d,1H, H17, J = 16 Hz), 4.84 (d, 1H, H5, J = 8 Hz), 1.90–1.60 (m, 10H, $H_{cyclohexyl}$). ^{13}C NMR (100 MHz, $CDCl_3$) δ: 173.8 (C=O, lactone), 135.9 (C17), 134.7 (C18), 129.6 (C2), 128.9, 127.3, 127.2 ($C_{arom.}$), 119.6 (q, CF_3, J = 322 Hz), 119.1 (q, CF_3, J = 322 Hz), 117.9 (C16), 116.7 (C3), 87.9 (C6), 72.3 (C5), 45.9 (C7), 35.5, 29.5, 24.5, 21.0, 20.4 ($C_{cyclohexyl}$). MS (IE^+, 70 eV) m/z (%): 574 (40) [M^+], 441 (100) [M^+ – 133], 308 (40) [M^+ – 133], 181 (40)[M^+ – 127]. HR-MS (FAB^+) $C_{21}H_{20}F_6N_2O_6S_2$: 574.0667; found: 574.0659.

6-Chloro-3,3-dimethyl-2-oxo-4,7-bis (trifluoromethanesulfonyl)-2,3,3a,4,7,7a-hexahydrofuro[2,3-b]pyrazine (5a)

$C_{10}H_9ClF_6N_2O_6S_2$ (M = 466 g/mol) was prepared starting from 2-chloropyrazine (0.3 mL, 3.4 mmol), trifluoromethanesulfonic anhydride (1.15 mL, 6.8 mmol), and **1a** (1.58 mL, 6.8 mmol) and was obtained as a white solid, mp 144 °C (0.35 g, 0.749 mmol, 22%). IR ν (cm^{-1}): 1795 (C=O lactone). ^{1}H NMR (300 MHz, $CDCl_3$) δ: 6.71 (s, 1H, H3), 6.60 (d, 1H, H6, J = 7.5 Hz), 4.82 (d, 1H, H5, J = 7.5 Hz), 1.42 (s, 3H, H9), 1.40 (s, 3H, H10). ^{13}C NMR (75 MHz, $CDCl_3$) δ: 175.0 (C=O lactone), 124.6 (C2), 119.5 (q, CF_3, J = 322 Hz), 118.7 (q, CF_3, J = 319 Hz), 89.5 (C6), 71.3 (C5), 44.2 (C7), 25.9 (C9), 20.8 (C10). MS (EI^+, 70 eV) m/z (%): 466 (8) M^+, 69 (100) $[M - 397]^+$. HR-MS (FAB^+) calcd for $C_{10}H_9ClF_6N_2O_6S_2$: 465.9495; found: 465.9491.

6'-Chloro-2'-oxo-4'-7'-bis(trifluoromethanesulfonyl)spiro [cyclohexane-1,3'-2',3',3a',4',7',7a'-hexahydrofuro[2,3-b] pyrazine] (5b)

$C_{13}H_{13}ClF_6N_2O_6S_2$ (M = 506 g/mol) was prepared starting from 2-chloropyrazine (0.3 mL, 3.4 mmol), trifluoromethanesulfonic anhydride (1.15 mL, 6.8 mmol), and **1b** (1.85 mL, 6.8 mmol) and was obtained as a white solid, mp 142 °C (0.505 g, 0.99 mmol, 37%). IR ν (cm^{-1}): 2947, 2861 (CH, CH_2), 1801 (C=O lactone), 1426 and 1229 (SO_2), 1147 (CF_3). ^{1}H NMR (300 MHz, $CDCl_3$) δ: 6.66 (s, 1H, H3), 6.58 (d, 1H, H6, J = 7.4 Hz), 4.83 (d, 1H, H5, J = 7.4 Hz), 2.11–1.37 (m, 10H, $H_{cyclohexyl}$). ^{13}C NMR (75 MHz, $CDCl_3$) δ: 173.4 (C=O lactone), 126.56 (C2), 120.4 (C3), 119.7 (q, CF_3, J = 324 Hz), 118.8 (q, CF_3, J = 321 Hz), 89.8 (C6), 72.6 (C5), 45.9 (C7), 35.6, 29.6, 24.5, 21.0, 20.4 ($C_{cyclohexyl}$). MS (EI^+, 70 eV) m/z (%): 506 (30) M^+, 373 (100) $[M - 133]^+$. HR-MS (FAB^+) calcd for $C_{13}H_{13}ClF_6N_2O_6S_2$: 505.9808; found: 505.9812.

7-Isobutyroyl-6-chloro-3,3-dimethyl-2-oxo-4-trifluoromethanesulfonyl-2,3,3a,4,7,7a-hexahydrofuro[2,3-b]pyrazine (7a)

$C_{13}H_{16}F_3N_2O_5S$ (M = 404 g/mol) was prepared starting from 2-chloropyrazine (0.3 mL, 3.4 mmol), trifluoromethanesulfonic anhydride (1.58 mL, 6.8 mmol), and **1a** (1.85 mL, 6.8 mmol) and was obtained as a white solid, mp 140 °C (0.567 g, 1.09 mmol, 32%). IR ν (cm^{-1}): 1791 (C=O lactone), 1705 (C=O ester). ^{1}H NMR (300 MHz, $CDCl_3$) δ: 7.23 (d, 1H, H6, J = 7 Hz), 6.53 (s, 1H, H3), 4.65 (d, 1H, H5, J = 7 Hz), 2.91 (h, 1H, H13, J = 6.5 Hz), 1.40 (s, 3H, H9), 1.38 (s, 3H, H10), 1.28 (d, 3H, H14, J = 6.5 Hz), 1.17 (d, 3H, H15, J = 6.5 Hz). ^{13}C NMR (75 MHz, $CDCl_3$) δ: 176.1 (C=O lactone), 175.9 (C=O amide), 127.4 (C2), 119.7 (q, CF_3, J = 324 Hz), 118.8 (q, CF_3, J = 321 Hz), 117.3 (C3), 85.6 (C6), 71.7 (C5), 44.9 (C7), 34.5 (C13), 25.8 (C9), 20.9 (C10), 19.4 (C14), 19.3 (C15). MS (EI^+, 70 eV) m/z (%): 404 (2) M^+, 71 (100) $[M - 333]^+$. HR-MS (FAB^+) calcd for $C_{13}H_{17}ClF_3N_2O_5S$: 405.0499; found: 405.0495.

6'-Chloro-7'-cyclohexanecarbonyl-4'-trifluoromethanesulfonyl-spiro[cyclohexane-1,3'-2',3',3a',4',7',7a'-hexahydrofuro[2,3-b]pyrazine] (7b)

$C_{19}H_{24}ClF_3N_2O_5S$ (M = 484 g/mol) was prepared starting from 2-chloropyrazine (0.3 mL, 3.4 mmol), trifluoromethanesulfonic anhydride (1.15 mL, 6.8 mmol), and **1b** (1.85 mL, 6.8 mmol) and was obtained as a white solid, mp 146 °C (0.505 g, 0.844 mmol, 25%). IR ν (cm^{-1}): 1780 (C=O lactone), 1703 (C=O ester). ^{1}H NMR (300 MHz, $CDCl_3$) δ: 7.09 (s, 1H, H3), 6.40 (d, 1H, H6, J = 8 Hz), 4.57 (d, 1H, H5, J = 8 Hz), 2.44 (m, 1H, H16), 1.97–1.18 (m, 20H, $H_{cyclohexyl}$). ^{13}C NMR (75 MHz, $CDCl_3$) δ: 174.7 (C=O lactone), 174.5 (C=O ester), 129.4 (C2), 117.4 (C3), 85.7 (C6), 72.7 (C5), 46.2 (C16), 44.7 (C7), 35.3, 29.6, 29.4, 25.4, 25.3, 25.2, 24.6, 21.1, 20.4 ($C_{cyclohexyl}$). MS (EI^+, 70 eV) m/z (%): (IE, 70 eV) m/z (%): 484 (2) M^+, 83 (100) $[M - 401]^+$. HR-MS (FAB^+) calcd for $C_{19}H_{25}ClF_3N_2O_5S$: 485.1125; found: 485.1127.

3,3,6-Trimethyl-2-oxo-4,7-bis(trifluoromethanesulfonyl)-2,3,3a,4,7,7a-hexahydrofuro[2,3-b]pyrazine (6a)

$C_{11}H_{12}F_6N_2O_6S_2$ (M = 446 g/mol) was prepared starting

Can. J. Chem. Downloaded from www.nrcresearchpress.com by Renmin University of China on 09/02/12
For personal use only.

from 2-methylpyrazine (0.3 mL, 3.27 mmol), trifluoromethanesulfonic anhydride (1.1 mL, 6.6 mmol), and **1a** (1.53 mL, 6.6 mmol) and was obtained as a white solid, mp 104 °C (1.39 g, 3.13 mmol, 95%). IR ν (cm^{-1}): 1792 (C=O lactone). ^1H NMR (300 MHz, $CDCl_3$) δ: 6.53 (d, 1H, H6, J = 7.6 Hz), 6.35 (s, 1H, H3), 4.79 (d, 1H, H5, J = 7.6 Hz), 2.09 (s, 3H, H13), 1.39 (s, 3H, H9), 1.37 (s, 3H, H10). ^{13}C NMR (75 MHz, $CDCl_3$) δ: 175.7 (C=O lactone), 131.5 (C3), 119.7 (q, CF_3, J = 322 Hz), 118.9 (q, CF_3, J = 320 Hz), 117.7 (C2), 88.0 (C6), 70.5 (C5), 44.2 (C7), 25.9 (C9), 20.7 (C10), 17.7 (C13). MS (EI$^+$, 70 eV) *m/z* (%): 446 (30) M^+, 313 (100) $[M - 133]^+$. HR-MS (FAB$^+$) calcd for $C_{11}H_{12}F_6N_2O_6S_2$: 446.0041; found: 446.0042.

*6'-Methyl-2'-oxo-4',7'-bis(trifluoromethanesulfonyl)spiro[cyclohexane-1,3'-2',3',3a',4',7',7a'-hexahydrofuro[2,3-**b**]pyrazine] (6b)*

$C_{14}H_{16}F_6N_2O_6S_2$ (M = 486 g/mol) was prepared starting from 2-methylpyrazine (0.3 mL, 3.27 mmol), trifluoromethanesulfonic anhydride (1.1 mL, 6.6 mmol), and **1b** (1.8 mL, 6.6 mmol) and was obtained as a white solid, mp 138 °C (0.87 g, 1.79 mmol, 55%). IR ν (cm^{-1}): 1746 (C=O lactone). ^1H NMR (300 MHz, $CDCl_3$) δ: 6.49 (d, 1H, H6, J = 7.6 Hz), 6.29 (s, 1H, H3), 4.81 (d, 1H, H5, J = 7.6 Hz), 2.09 (s, 3H, C16), 2.00–1.61 (m, 10H, $H_{cyclohexyl}$). ^{13}C NMR (75 MHz, $CDCl_3$) δ: 174.0 (C=O lactone), 133.5 (C3), 119.8 (q, CF_3, J = 323 Hz), 118.9 (q, CF_3, J = 320 Hz), 117.9 (C2), 88.3 (C6), 71.6 (C5), 45.9 (C7), 35.4, 29.3, 24.5, 21.0, 20.3 ($C_{cyclohexyl}$), 17.7 (C16). MS (EI$^+$, 70 eV) *m/z* (%): 486 (20) M^+, 353 (100) $[M - 133]^+$. HR-MS (FAB$^+$) calcd for $C_{14}H_{16}F_6N_2O_6S_2$: 486.0354; found: 486.0350.

*7a-Methoxy-3,3-dimethyl-2-oxo-4,7-bis(trifluoromethanesulfonyl)-2,3,3a,4,7,7a-hexahydrofuro[2,3-**b**]pyrazine (8a')*

$C_{11}H_{12}F_6N_2O_7S_2$ (M = 462 g/mol) was prepared starting from 2-methoxypyrazine (0.3 mL, 3.1 mmol), trifluoromethanesulfonic anhydride (1.07 mL, 6.2 mmol), and **1a** (1.4 mL, 6.2 mmol) and was obtained as a white solid, mp 114 °C (0.535 g, 1.16 mmol, 37%). IR ν (cm^{-1}): 1817 (C=O lactone). ^1H NMR (300 MHz, $CDCl_3$) δ: 6.26 (dd, 2H, H5 and H6, J = 6.8 Hz), 4.53 (s, 1H, H3), 3.52 (s, 3H, H13), 1.48 (s, 3H, H9), 1.23 (s, 3H, H10). ^{13}C NMR (75 MHz, $CDCl_3$) δ: 172.4 (C=O lactone), 119.8 (q, CF_3, J = 323 Hz), 119.4 (q, CF_3, J = 322 Hz), 111.9 and 107.2 (C5 and C6), 105.1 (C2), 63.8 (C3), 52.8 (C13), 45.0 (C7), 24.5 (C9), 18.9 (C10). MS (EI$^+$, 70 eV) *m/z* (%): 462 (80) M^+, 301 (100) $[M - 161]^+$. HR-MS (FAB$^+$) calcd for $C_{11}H_{12}F_6N_2O_7S_2$: 461.9990; found: 461.9977.

*7a'-Methoxy-4',7'-bis(trifluoromethanesulfonyl)spiro[cyclohexane-1,3'-2',3',3a',4',7',7a'-hexahydrofuro[2,3-**b**]pyrazine] (8b')*

$C_{14}H_{16}F_6N_2O_7S_2$ (M = 502 g/mol) was prepared starting from 2-methoxypyrazine (0.3 mL, 3.1 mmol), trifluoromethanesulfonic anhydride (1.07 mL, 6.2 mmol), and **1b** (1.7 mL, 6.2 mmol) and was obtained as a white solid, mp 114 °C (0.485 g, 0.967 mmol, 31%). IR ν (cm^{-1}): 1812 (C=O lactone). ^1H NMR (300 MHz, $CDCl_3$) δ: 6.25 (dd, 2H, H5 and H6, J = 7 Hz), 4.40 (s, 1H, H3), 3.51 (s, 3H, H16), 2.19–1.25 (m, 10H, $H_{cyclohexyl}$). ^{13}C NMR (75 MHz, $CDCl_3$) δ: 170.2 (C=O lactone), 119.0 (q, CF_3, J = 320 Hz), 112.9 and 107.4 (C5 and C6), 104.9 (C2), 64.3 (C3), 52.6 (C16), 47.3 (C7), 32.7, 27.7, 24.5, 21.0, 20.5 ($C_{cyclohexyl}$). MS (EI$^+$, 70 eV) *m/z* (%): 502 (15) M^+, 153 (100) $[M - 349]^+$. HR-MS (FAB$^+$) calcd for $C_{14}H_{16}F_6N_2O_7S_2$: 502.0330; found: 502.0300.

*7-Isobutyroyl-7a-methoxy-3,3-dimethyl-2-oxo-4-trifluoromethanesulfonyl-2,3,3a,4,7,7a-hexahydrofuro[2,3-**b**]pyrazine (9a)*

$C_{14}H_{19}F_3N_2O_6S$ (M = 400 g/mol) was prepared starting from 2-methoxypyrazine (0.3 mL, 3.1 mmol), trifluoromethanesulfonic anhydride (1.07 mL, 6.2 mmol), and **1a** (1.4 mL, 6.2 mmol) and was obtained as a white solid, mp 170 °C (0.238 g, 0.595 mmol, 20%). IR ν (cm^{-1}): 1813 (C=O lactone), 1682 (C=O amide). ^1H NMR (300 MHz, $CDCl_3$) δ: 6.97 (d, 1H, H5, J = 7 Hz), 6.06 (d, 1H, H6, J = 7 Hz), 4.58 (s, 1H, H3), 3.48 (s, 3H, H16), 3.19 (h, 1H, H13, J = 7 Hz), 1.46 (s, 3H, H9), 1.21 (d, 3H, H14, J = 7 Hz), 1.20 (d, 3H, H15, J = 7 Hz), 1.19 (s, 3H, H10). ^{13}C NMR (75 MHz, $CDCl_3$) δ: 175.5 (C=O lactone), 173.3 (C=O amide), 119.0 (q, CF_3, J = 323 Hz), 112.4 (C6), 104.8 (C2), 104.1 (C5), 61.2 (C3), 51.8 (C16), 45.1 (C7), 34.4 (C13), 24.2 (C9), 20.4 (C10), 19.9 (C14), 19.3 (C15). MS (EI$^+$, 70 eV) *m/z* (%): 400 (5) M^+, 243 (100) $[M - 157]^+$. HR-MS (FAB$^+$) calcd for $C_{14}H_{19}F_3N_2O_6S$: 400.0916; found: 400.0924.

*7'-Cyclohexanecarbonyl-7a'-methoxy-4'-trifluoromethanesulfonyl-spiro[cyclohexane-1,3'-2',3',3a',4',7',7a'-hexahydrofuro[2,3-**b**]pyrazine] (9b)*

$C_{20}H_{27}F_3N_2O_6S$ (M = 480 g/mol) was prepared starting from 2-methoxypyrazine (0.3 mL, 3.1 mmol), trifluoromethanesulfonic anhydride (1.07 mL, 6.2 mmol), and **1b** (1.7 mL, 6.2 mmol) and was obtained as a white solid, mp 144 °C (0.465 g, 0.97 mmol, 31%). IR ν (cm^{-1}): 1799 (C=O lactone), 1698 (C=O amide). ^1H NMR (300 MHz, $CDCl_3$) δ: 6.98 (d, 1H, H6, J = 7 Hz), 6.06 (d, 1H, H5, J = 7 Hz), 4.46 (s, 1H, H3), 3.47 (s, 3H, H22), 2.88 (m, 1H, H16), 1.82–1.25 (m, 20H, $H_{cyclohexyl}$). ^{13}C NMR (75 MHz, $CDCl_3$) δ: 175.2 (C=O lactone), 171.4 (C=O amide), 119.0 (q, CF_3, J = 320 Hz), 113.0 and 104.3 (C5 and C6), 104.3 (C2), 61.9 (C3), 51.6 (C22), 47.3 (C7), 44.9 (C16), 32.5, 30.1, 29.9, 27.8, 25.9, 25.7, 25.6, 24.5, 21.2, 20.9 ($C_{cyclohexyl}$). MS (IE$^+$, 70 eV) *m/z* (%): 480 (3) M^+, 243 (100) $[M - 237]^+$. HR-MS (FAB$^+$) calcd for $C_{20}H_{27}F_3N_2O_6S$: 480.1542; found: 480.1545.

2-(3-Methoxy-1-trifluoromethanesulfonyl-1,2-dihydropyrazin-2-yl)-2-methylpropionic acid (10a)

$C_{10}H_{13}F_3N_2O_5S$ (M = 330 g/mol) was prepared starting from 2-methoxypyrazine (0.3 mL, 3.1 mmol), trifluoromethanesulfonic anhydride (1.4 mL, 6.2 mmol), and **1a** (1.7 mL, 6.2 mmol) and was obtained as a white solid, $mp_{(dec)}$ 128 °C (0.23 g, 0.696 mmol, 22%). IR ν (cm^{-1}): 3200–3000 (OH), 1726 (C=O carboxylic acid). ^1H NMR (300 MHz, $CDCl_3$) δ: 10.70 (s, 1H, O*H*), 6.36 (s, 1H, H5), 6.17 (s, 1H, H6), 4.79 (s, 1H, H3), 3.82 (s, 3H, H12), 1.34 (s, 3H, H9), 1.24 (s, 3H, H10). ^{13}C NMR (75 MHz, $CDCl_3$) δ: 179.8 (C=O carboxylic acid), 158.0 (C2), 126.4 (C5), 120.0 (q, CF_3, J = 323 Hz), 110.6 (C6), 60.1 (C3), 54.4 (C12), 47.2 (C7), 22.9 (C9),

Can. J. Chem. Downloaded from www.nrcresearchpress.com by Renmin University of China on 09/02/12
For personal use only.

20.7 (C10). MS (IE$^+$, 70 eV) *m/z* (%): 330 (5) M$^+$, 243 (100) [M – 87]$^+$. HR-MS (FAB$^+$) calcd for $C_{10}H_{14}F_3N_2O_5S$: 331.0576; found: 331.0574.

1-(3-Methoxy-1-trifluoromethanesulfonyl-1,2-dihydropyrazin-2-yl)-cyclohexane-1-carboxylic acid (10b)

$C_{13}H_{17}F_3N_2O_5S$ (*M* = 370 g/mol) was prepared starting from 2-methoxypyrazine (0.3 mL, 3.1 mmol), trifluoromethanesulfonic anhydride (0.52 mL, 3.1 mmol), and **1b** (1.7 mL, 6.2 mmol) and was obtained as a white solid, $mp_{(dec)}$ 120 °C (0.282 g, 0.762 mmol, 25%). IR ν (cm^{-1}): 3100–3000 (OH), 1726 (C=O carboxylic acid). ^{1}H NMR (300 MHz, $CDCl_3$) δ: 10.08 (s, 1H, O*H*), 6.39 (s, 1H, H5), 6.15 (s, 1H, H6), 4.54 (s, 1H, H3), 3.86 (s, 3H, H15), 2.19–1.62 (m, 10H, $H_{cyclohexyl}$). ^{13}C NMR (75 MHz, $CDCl_3$) δ: 178.9 (C=O carboxylic acid), 157.7 (C2), 126.9 (C5), 119.9 (q, CF_3, *J* = 324 Hz), 110.6 (C6), 60.9 (C3), 54.5 C15), 51.9 (C7), 31.6, 30.2, 30.2, 25.0, 22.9 ($C_{cyclohexyl}$). MS (EI$^+$, 70 eV) *m/z* (%): 370 (5) M$^+$, 243 (100) [M – 127]$^+$. HR-MS (FAB$^+$) calcd for $C_{13}H_{18}F_3N_2O_5S$: 371.0889; found: 371.0574.

Methyl 1-(3-methoxy-1-trifluoromethanesulfonyl-1,2-dihydropyrazin-2-yl)-cyclohexane-1-carboxylate (11c)

$C_{14}H_{19}F_3N_2O_5S$ (*M* = 384 g/mol) was prepared starting from 2-methoxypyrazine (0.3 mL, 3.1 mmol), trifluoromethanesulfonic anhydride (0.52 mL, 3.11 mmol), and **1c** (0.73 mL, 3.41 mmol) and was obtained as an oil (0.90 g, 2.35 mmol, 76%). IR ν (cm^{-1}): 1734 (C=O ester). ^{1}H NMR (300 MHz, $CDCl_3$) δ: 6.37 (d, 1H, H5, *J* = 5 Hz), 6.09 (d, 1H, H6, *J* = 5 Hz), 4.48 (s, 1H, H3), 3.84 (s, 3H, H14), 3.67 (s, 3H, H16), 2.20–1.12 (m, 10H, $H_{cyclohexyl}$). ^{13}C NMR (75 MHz, $CDCl_3$) δ: 172.7 (C=O ester), 157.8 (C2), 126.4, 110.0 (C5, C6), 119.9 (q, CF_3, *J* = 323 Hz), 61.0 (C3), 54.4 (C14), 52.4 C16), 51.8 (C7), 31.8, 30.4, 25.1, 23.1, 23.0 ($C_{cyclohexyl}$). MS (EI$^+$, 70 eV) *m/z* (%): 384 (4) M$^+$, 243 (100) [M – 141]. HR-MS (FAB$^+$) calcd for $C_{14}H_{20}F_3N_2O_5S$: 385.1045; found: 385.1050.

Methyl 1-(3-oxo-1,4-bis(trifluoromethanesulfonyl)-1,2,3,4-tetrahydropyrazin-2-yl)-cyclohexane-1-carboxylate (12c)

$C_{14}H_{16}F_6N_2O_7S_2$ (*M* = 502 g/mol) was prepared starting from 2-methoxypyrazine (0.3 mL, 3.1 mmol), trifluoromethanesulfonic anhydride (1.07 mL, 6.2 mmol), and **1c** (1.33 mL, 6.2 mmol) and was obtained as a white solid mp 108 °C (0.75 g, 1.49 mmol, 96%). IR ν (cm^{-1}): 1764 (C=O ester). ^{1}H NMR (300 MHz, $CDCl_3$) δ: 6.57 (d, 1H, H5, *J* = 5.7 Hz), 6.23 (d, 1H, H6, *J* = 5.7 Hz), 4.57 (s, 1H, H3), 3.71 (s, 3H, H14), 2.30–1.13 (m, 10H, $H_{cyclohexyl}$). ^{13}C NMR (75 MHz, $CDCl_3$) δ: 171.9 (C=O ester), 159.5 (C2), 115.3 and 110.7 (C5, C6), 119.9 (q, CF_3, *J* = 323 Hz), 67.4 (C3), 52.7 (C14), 50.3 (C7), 32.8, 30.9, 24.8, 22.8, 22.7 ($C_{cyclohexyl}$). MS (EI$^+$, 70 eV) *m/z* (%): 502 (10) M$^+$, 81 (100) [M – 421]$^+$. HR-MS (FAB$^+$) calcd for $C_{14}H_{16}F_6N_2O_7S_2$: 502.0303; found: 502.0299.

Supplementary data

Supplementary data (proton and carbon labels used in NMR characterization and complete tables with Fukui indices) are available with the article through the journal Web site (http://nrcresearchpress.com/doi/suppl/10.1139/v2012-016). CCDC 817202 (**4a**), CCDC 804199 (**7a**), CCDC 804200 (**9a**), CCDC 804201 (**10b**), and CCDC 804202 (**12c**) contain the X-ray data in CIF format for this manuscript. These data can be obtained, free of charge, via http://www.ccdc.cam.ac.uk/products/csd/request (Or from the Cambridge Crystallographic Data Centre, 12 Union Road, Cambridge CB2 1EZ, UK; fax: +44 1223 336033; or e-mail: deposit@ccdc.cam.ac.uk).

Acknowledgments

The authors would like to acknowledge the technical assistance provided by Rocio Patiño, Luis Velasco, and Javier Perez. They would also like to thank the Dirección General de Asuntos del Personal Académico - Programa de Apoyos a Proyectos de Investigación e Innovación Tecnológica (DGAPA-PAPIT) IN201211 and the Consejo Nacional de Cienca y Technología (CONACYT) 127796 projects and CONACYT for the Ph.D. grant extended to A.G.-A.

References

(1) Garuti, L.; Roberti, M.; Pizzirani, D. *Mini Rev. Med. Chem.* **2007**, *7* (5), 481. doi:10.2174/138955707780619626.

(2) Lee, S.; LaCour, T. G.; Fuchs, P. L. *Chem. Rev.* **2009**, *109* (6), 2275. doi:10.1021/cr800365m.

(3) Comins, D. L.; Joseph, S. P. In *Advances in Nitrogen Heterocycles;* Moody, C. J., Ed.; JAI Press: Greenwich CT, 1996; Volume 2, pp 251–294.

(4) (a) Bellassoued, M.; Chelain, E.; Collot, J.; Rudler, H.; Vaissermann, J. *Chem. Commun. (Camb.)* **1999**, (2): 187. doi:10.1039/a808072k; (b) Rudler, H.; Comte, V.; Garrier, E.; Bellassoued, M.; Chelain, E.; Vaissermann, J. *J. Organomet. Chem.* **2001**, *621* (1–2), 284. doi:10.1016/S0022-328X(00)00848-2; (c) Rudler, H.; Aldeco-Perez, E.; Parlier, A.; Alvarez, C.; Chaquim, P.; Herson, P.; Toscano, R. A.; Ramirez-Apan, M. T. *J. Mex. Chem. Soc.* **2008**, *52*, 145.

(5) (a) Rudler, H.; Parlier, A.; Cantagrel, F.; Harris, P.; Bellassoued, M. *Chem. Commun. (Camb.)* **2000**, (9): 771. doi:10.1039/b001175o; (b) Rudler, H.; Harris, P.; Parlier, A.; Cantagrel, F.; Denise, B.; Bellassoued, M.; Vaissermann, J. *J. Organomet. Chem.* **2001**, *624* (1-2), 186. doi:10.1016/S0022-328X(00)00905-0.

(6) Rudler, H.; Alvarez, C.; Parlier, A.; Perez, E.; Denise, B.; Xu, Y.; Vaissermann, J. *Tetrahedron Lett.* **2004**, *45* (11), 2409. doi:10.1016/j.tetlet.2004.01.068.

(7) (a) Rudler, H.; Denise, B.; Parlier, A.; Daran, J. C. *Chem. Commun. (Camb.)* **2002**, *2002* (9), 940. doi:10.1039/b201780f; (b) Rudler, H.; Denise, B.; Xu, Y.; Parlier, A.; Vaissermann, J. *Eur. J. Org. Chem.* **2005**, *2005* (17), 3724. doi:10.1002/ejoc.200500162; (c) Ullah, E.; Rotzoll, S.; Schmidt, A.; Michalik, D.; Langer, P. *Tetrahedron Lett.* **2005**, *46* (52), 8997. doi:10.1016/j.tetlet.2005.10.108; (d) Schmidt, A.; Michalik, D.; Rotzoll, S.; Ullah, E.; Fischer, C.; Reinke, H.; Görls, H.; Langer, P. *Org. Biomol. Chem.* **2008**, *6* (15), 2804. doi:10.1039/b804139c; (e) Xu, Y.; Aldeco-Pérez, E.; Rudler, H.; Parlier, A.; Alvarez, C. *Tetrahedron Lett.* **2006**, *47* (27), 4553. doi:10.1016/j.tetlet.2006.05.006; (f) Rudler, H.; Parlier, A.; Hamon, L.; Herson, P.; Chaquin, P.; Daran, J.-C. *Tetrahedron* **2009**, *65* (28), 5552. doi:10.1016/j.tet.2009.02.086.

(8) (a) Rudler, H.; Parlier, A.; Sandoval-Chavez, C.; Herson, P.; Daran, J.-C. *Angew. Chem. Int. Ed.* **2008**, *47* (36), 6843. doi:10.1002/anie.200801879; (b) Parlier, A.; Kadouri-Puchot, C.; Beaupierre, S.; Jarosz, N.; Rudler, H.; Hamon, L.; Herson,

P.; Daran, J.-C. *Tetrahedron Lett.* **2009**, *50* (52), 7274. doi:10.1016/j.tetlet.2009.10.038; (c) Gualo-Soberanes, N.; Ortega-Alfaro, M. C.; López-Cortés, J. G.; Toscano, R. A.; Rudler, H.; Alvarez-Toledano, C. *Tetrahedron Lett.* **2010**, *51* (24), 3186. doi:10.1016/j.tetlet.2010.04.030.

(9) (a) Rudler, H.; Denise, B.; Xu, Y.; Vaissermann, J. *Tetrahedron Lett.* **2005**, *46* (20), 3449. doi:10.1016/j.tetlet.2005.03.131; (b) Schmidt, A.; Gütlein, J.-P.; Langer, P. *Tetrahedron Lett.* **2007**, *48* (12), 2067. doi:10.1016/j.tetlet.2007.01.147; (c) Rotzoll, S.; Ullah, E.; Fischer, C.; Michalik, D.; Spannenberg, A.; Langer, P. *Tetrahedron* **2006**, *62* (51), 12084. doi:10.1016/j.tet.2006.09.072.

(10) Garduño-Alva, A.; Xu, Y.; Gualo-Soberanes, N.; López-Cortes, J.; Rudler, H.; Parlier, A.; Ortega-Alfaro, M. C.; Álvarez-Toledano, C.; Toscano, R. A. *Eur. J. Org. Chem.* **2008**, *2008* (21), 3714. doi:10.1002/ejoc.200800338.

(11) (a) Katritzky, A. R. *Comprehensive Heterocyclic Chemistry: The Structure, Reactions, Synthesis and Uses of Heterocyclic Compounds;* Pergamon Press: Bristol, 1984; Volume 3; (b) Palmer, M. H.; Arnold, E. *The Structure and Reactions of Heterocyclic Compounds;* Publishers Ltd.: London, 1967; Chapter 3.

(12) After conducting the purification by silica gel chromatography using different techniques, we were not able to separate them. The ratio of **6a** and **6a'** was determined through the integration of characteristic signals in the NMR spectrum.

(13) Ainsworth, C.; Kuo, Y. N. *J. Organomet. Chem.* **1972**, *73*, 34.

(14) Frisch, M. J.; Trucks, G. W.; Schlegel, H. B.; Scuseria, G. E.; Robb, M. A.; Cheeseman, J. R.; Scalmani, G.; Barone, V.; Mennucci, B.; Petersson, G. A.; Nakatsuji, H.; Caricato, M.; Li, X.; Hratchian, H. P.; Izmaylov, A. F.; Bloino, J.; Zheng, G.; Sonnenberg, J. L.; Hada, M.; Ehara, M.; Toyota, K.; Fukuda, R.; Hasegawa, J.; Ishida, M.; Nakajima, T.; Honda, Y.; Kitao, O.; Nakai, H.; Vreven, T.; Montgomery, J. A., Jr.; Peralta, J. E.; Ogliaro, F.; Bearpark, M.; Heyd, J. J.; Brothers, E.; Kudin, K. N.; Staroverov, V. N.; Kobayashi, R.; Normand, J.; Raghavachari, K.; Rendell, A.; Burant, J. C.; Iyengar, S. S.; Tomasi, J.; Cossi, M.; Rega, N.; Millam, J. M.; Klene, M.; Knox, J. E.; Cross, J. B.; Bakken, V.; Adamo, C.; Jaramillo, J.; Gomperts, R.; Stratmann, R. E.; Yazyev, O.; Austin, A. J.; Cammi, R.; Pomelli, C.; Ochterski, J. W.; Martin, R. L.; Morokuma, K.; Zakrzewski, V. G.; Voth, G. A.; Salvador, P.; Dannenberg, J. J.; Dapprich, S.; Daniels, A. D.; Farkas, O.; Foresman, J. B.; Ortiz, J. V.; Cioslowski, J.; Fox, D. J. *Gaussian 09,* Revision A.02; Gaussian, Inc.: Wallingford CT, 2009.

(15) Lewars, E. *Computational Chemistry. Introduction to the Theory and Applications of Molecular and Quantum Mechanics;* Kluwer Publishers: the Netherlands, 2003.

(16) Reed, A. E.; Curtiss, L. A.; Weinhold, F. *Chem. Rev.* **1988**, *88* (6), 899. doi:10.1021/cr00088a005.

(17) Altomare, G.; Cascarano, C.; Giacovazzo, A.; Burla, M. C.; Polidori, G.; Canalli, M. *J. Appl. Cryst.* **1994**, *27*, 435. doi:10.1107/S002188989400021X.

(18) Sheldrick, G. M. *Acta Crystallogr. Sect. A*, **2008**, *A64*, 112. doi:10.1107/S0108767307043930.

(19) Vanden Eynde, J. J.; Pascal, L.; Van Haverbeke, Y.; Dubois, P. *Synth. Commun.* **2001**, *31* (20), 3167. doi:10.1081/SCC-100105893.

Can. J. Chem. Downloaded from www.nrcresearchpress.com by Renmin University of China on 09/02/12
For personal use only.

Theoretical studies on clusters of carbonate with carbon dioxide, $CO_3^{1-/2-}(CO_2)_n$, for n = 1–5 — Comparison of carbonate clusters with sulfate clusters

Friedrich Grein and Daniel M. Chevrier

Can. J. Chem. Downloaded from www.nrcresearchpress.com by Renmin University of China on 09/02/12
For personal use only.

Abstract: Density functional theory (DFT) calculations were performed on the geometries and energies of $CO_3^{1-/2-}(CO_2)_n$ clusters with n = 1–5. For small clusters (n = 1 or 2), coupled cluster energies were obtained. Up to three CO_2 molecules are bound covalently to the dianion. Only weak electrostatic bonds were found in the monoanions. Calculated binding energies for the monoanions are in reasonable agreement with experimental values. The calculated adiabatic electron detachment energy for the dianion is –0.07 eV at n = 5, indicating that at least six CO_2 molecules will have to be added to CO_3^{2-} before the dianionic cluster becomes, in the gas phase, more stable than the monoanionic one. In comparison, for sulfate – carbon dioxide clusters, stabilization occurs at n = 2. Carbonate clusters are compared with sulfate clusters for three solvent molecules: CO_2, SO_2, and H_2O. Carbonate clusters have larger binding energies than sulfate clusters. For a given dianion, binding energies are largest for SO_2 and smallest for H_2O. However, in all cases, stabilization of the carbonate dianion by clustering is more difficult to achieve than stabilization of the sulfate dianion.

Key words: carbonate – carbon dioxide clusters, monoanions, dianions, density functional theory, dianion stabilization, solvation energies, binding energies, comparison with sulfate clusters.

Résumé : On a effectué des calculs suivant la théorie de la fonctionnelle de la densité sur les géométries et les énergies d'agrégats $CO_3^{1-/2-}(CO_2)_n$ dans lesquels n = 1–5. Pour les petits agrégats (n = 1 ou 2), il a été possible d'évaluer les énergies de couplage des agrégats. Le dianion peut se lier d'une façon covalente avec un maximum de trois molécules de CO_2. On n'a trouvé que de faibles liaisons électrostatiques dans les monoanions. Les énergies de liaisons calculées pour les monoanions sont en accord raisonnable avec les valeurs expérimentales. L'énergie calculée pour le détachement adiabatique d'un électron est de –0,07 eV pour n = 5; ceci indique que, en phase gazeuse, il faut ajouter au moins six molécules de CO_2 à l'anion CO_2^{2-} avant que l'agrégat dianionique devienne plus stable que l'agrégat monoanionique. Par comparaison, pour les agrégats sulfate – dioxyde de carbone, la stabilisation se produit avec n = 2. On a comparé les agrégats du carbonate avec ceux du sulfate pour trois molécules de solvant : CO_2, SO_2 et H_2O. Les énergies de liaison des agrégats du carbonate sont plus élevées que celles des agrégats du sulfate. Pour un dianion donné, les énergies de liaison sont les plus élevées pour le SO_2 et les plus faibles avec H_2O. Toutefois, dans tous les cas, la stabilisation du dianion carbonate par le biais de la formation d'agrégat se fait plus difficilement que la stabilisation du dianion sulfate.

Mots-clés : agrégats carbonate – dioxyde de carbone, monoanions, dianions, théorie de la fonctionnelle de la densité, stabilisation du dianion, énergies de solvatation, énergies de liaison, comparaison avec les agrégats du sulfate.

[Traduit par la Rédaction]

Introduction

Anionic clusters involving carbon dioxide have received considerable attention, with experiments going back to the 1970s. In 1977, Klots and Compton[1] obtained $(CO_2)_n^{1-}$ clusters for n = 2–6 by electron attachment to $(CO_2)_n$ in a time-of-flight mass spectrometer. More recent references report mass spectrometric, IR, and photoelectron work on clusters like $(CO_2)_n^{1-}$ and $O^-(CO_2)_n$;[2] $Cl^-(CO_2)_n$;[3] $F^-(CO_2)_n$;[4] $CO_3^{1-}(CO_2)_n$; $O_2^-(CO_2)_n$; $NO_2^{1-}(CO_2)_n$,[5] $O^-(CO_2)_n$, $(CO_2)_n^{1-}$;[6] $X^-(CO_2)$ with X = F, Cl, Br, and I;[7,8] $I_2^{1-}(CO_2)_n$;[9] $H_2O^{1-}(CO_2)_n$;[10] and $(CO_2)_n$.[11]

The present paper, dealing with anionic clusters of carbonate with carbon dioxide and of type $CO_3^{1-/2-}(CO_2)_n$, serves several purposes. For one, monoanionic clusters play an important role in the negative ion chemistry of the lower atmosphere.[12] Dianionic carbonate– carbon dioxide clusters, while not stable in the gas phase for small n, eventually become stabilized (more stable than corresponding monoanions) with

Received 5 December 2011. Accepted 2 February 2012. Published at www.nrcresearchpress.com/cjc on 2 May 2012.

F. Grein and D.M. Chevrier.* Department of Chemistry, University of New Brunswick, PO Box 4400, Fredericton, NB E3B 5A3, Canada.

Corresponding author: Friedrich Grein (e-mail: fritz@unb.ca).

*Present address: Chemistry Department, Dalhousie University, Halifax, NS B3H 4R2, Canada.

Can. J. Chem. Downloaded from www.nrcresearchpress.com by Renmin University of China on 09/02/12
For personal use only.

Table 1. Calculated B3PW91/6–311+G(3df) energies (a.u.) for the monoanions $CO_3(CO_2)_n^{1-}$(–1) and dianions $CO_3(CO_2)_n^{2-}$(–2).

	Energy (a.u.)			
Structure	E(–1)	ΔE(–1)	E(–2)	ΔE(–2)
0	–263.805799	—	–263.670269	—
Ia	–452.395651 (C_{2v})	–0.21	–452.340739 (C_s)	–2.40
Ib	—	—	–452.340711 (C_2)	–2.40
IIa	–640.984483 (C_{2v})	–0.39	–640.963280 (C_2)	–3.50
IIIa	–829.572276 (C_s)	–0.54	–829.561852 (C_2)	–3.95
IIIb	–829.572690 (D_{3h})	–0.56	–829.550998 (C_{3h})	–3.65
IVa	–1018.156342 (C_s)	–0.60	–1018.153238 (C_1)	–4.20
IVb	–1018.158302 (C_{2v})	–0.68	–1018.152582 (C_2)	–4.18
IVc	–1018.159355 (C_1)	–0.68	–1018.152192 (C_2)	–4.17
Va	–1206.745971 (C_1)	–0.80	–1206.743749 (C_2)	–4.43
Vb	–1206.746421 (C_2)	–0.81	–1206.742299 (C_1)	–4.39
Vc	–1206.746484 (C_s)	–0.81	–1206.742339 (C_1)	–4.39

Note: Binding energies (ΔE) are in eV. The energy of CO_2 is –188.582167 a.u.

Table 2. Adiabatic (ADE) and vertical electron (VDE) detachment energies (in eV) for the most stable $CO_3(CO_2)_n^{1-/2-}$ structures.

	B3PW91		CCSD		CCSD(T)	
Cluster	ADE	VDE	ADE	VDE	ADE	VDE
$CO_3^{1-/2-}$	–3.69	–3.56	–3.59	–3.38	–3.64	–3.55
$CO_3^{1-/2-}(CO_2)_1$	–1.49	–0.69	–1.46	–0.14	–1.62	–0.32
$CO_3^{1-/2-}(CO_2)_2$	–0.58	0.86	–0.73	1.82	–0.88	1.36
$CO_3^{1-/2-}(CO_2)_3$	–0.29	2.12				
$CO_3^{1-/2-}(CO_2)_4$	–0.17	2.32				
$CO_3^{1-/2-}(CO_2)_5$	–0.07	2.45				

Note: For B3PW91 calculations the basis set was 6–311+G(3df) and, for CCSD and CCSD(T) calculations, the 6–311+G(d) basis set was used.

the addition of a sufficient number of carbon dioxide molecules. A better knowledge of such clusters, in terms of binding energies, electron detachment energies, types of bonding, and covalent bonding versus electrostatic interactions, is of interest both for environmental reasons and for basic research. This knowledge also allows for comparison with related clusters, such as sulfate – carbon dioxide,[13] carbonate – sulfur dioxide,[14] and sulfate – sulfur dioxide[15] clusters, which were the subject of previous studies by this group.

A brief review of the literature pertinent to this investigation will be given. Keesee et al.[16] obtained gas-phase $\Delta H°$ and $\Delta S°$ values for the reaction $CO_3^{1-} + CO_2 \rightarrow CO_3^{1-}(CO_2)$, using high-pressure mass spectroscopy. Hiraoka and Yamabe[5] reported $\Delta H°$ values for the formation of $CO_3^{1-}(CO_2)_n$ clusters, with n = 1–7. The experimental $\Delta H°$ values will be given in the Results and discussion section and are compared with energies calculated in the present work. These authors also performed spin-restricted open-shell Hartree–Fock (ROHF) calculations to establish the structures of $CO_3^{1-}(CO_2)_n$ clusters with n = 1–3, all of which were found to have C_{2v} symmetry, with long chelate bonds (about 2.8 Å) coordinating the carbon of CO_2 with two oxygens of CO_3^{1-}. Shkrob[17] performed B3LYP/6–31G* geometry optimizations on CO_3^{1-} and $CO_3^{1-}(CO_2)$. Six starting geometries were tested for $CO_3^{1-}(CO_2)$. The lowest energies were obtained for C_s structures. In a recent paper by Bruna et al.,[18] structures of the dianionic clusters $CO_3^{2-}(CO_2)_n$ (n = 1–6) with C_2 symmetry were investigated by density functional theory (DFT) methods.

Table 3. Calculated incremental energy differences ($\Delta E_{n-1,n}$) vs. experimental incremental enthalpy differences ($\Delta H°_{n-1,n}$, kcal/mol; 1 cal = 4.184 J) for gas-phase clusters $CO_3(CO_2)_n^{1-}$.

Cluster	$\Delta E_{n-1,n}$	$\Delta H°_{n-1,n}$[a]
$CO_3^{1-}(CO_2)_1$	–4.83[b]	–5.94
$CO_3^{1-}(CO_2)_2$	–4.18	–5.73
$CO_3^{1-}(CO_2)_3$	–3.79	–5.50
$CO_3^{1-}(CO_2)_4$	–2.82	–5.22
$CO_3^{1-}(CO_2)_5$	–3.11	–4.80

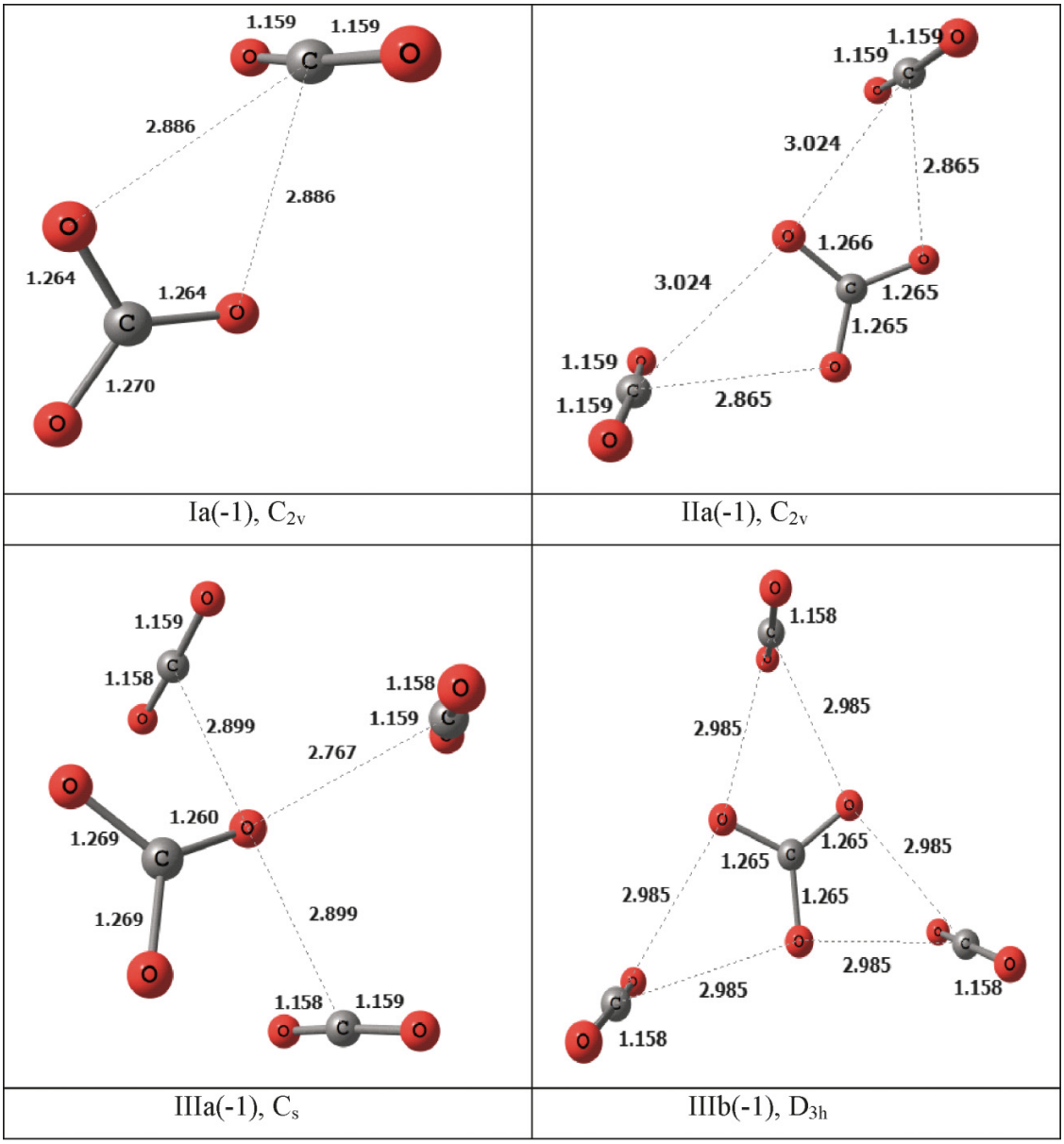
[a]See ref. 5 for experimental values.

[b]Calculated $\Delta H°_{1,2}$ = –3.97 kcal/mol. Enthalpies were not calculated for higher n values.

Experimental and theoretical studies were also reported on clusters of the anions CO_3^{1-} and CO_3^{2-} with molecules other than CO_2. Experimental $\Delta H°$ and $\Delta S°$ results are available for the reaction $CO_3^{1-} + nH_2O \rightarrow CO_3^{1-}(H_2O)_n$, n = 1–4.[19] Theoretical results for this reaction were obtained by Cappa and Elrod[20] and Pathak and Maity[21]; theoretical results for $CO_3^{2-} + nH_2O \rightarrow CO_3^{2-}(H_2O)_n$ were obtained by Pathak et al.;[22] and theoretical results for

Can. J. Chem. Downloaded from www.nrcresearchpress.com by Renmin University of China on 09/02/12
For personal use only.

Fig. 1. Structures of monoanions, $CO_3^{1-}(CO_2)_n$. Distances are in Å.



$CO_3^{1-/2-} + nSO_2 \rightarrow CO_3^{1-/2-}(SO_2)_n$, n = 1–4, were obtained by Grein et al.[14]

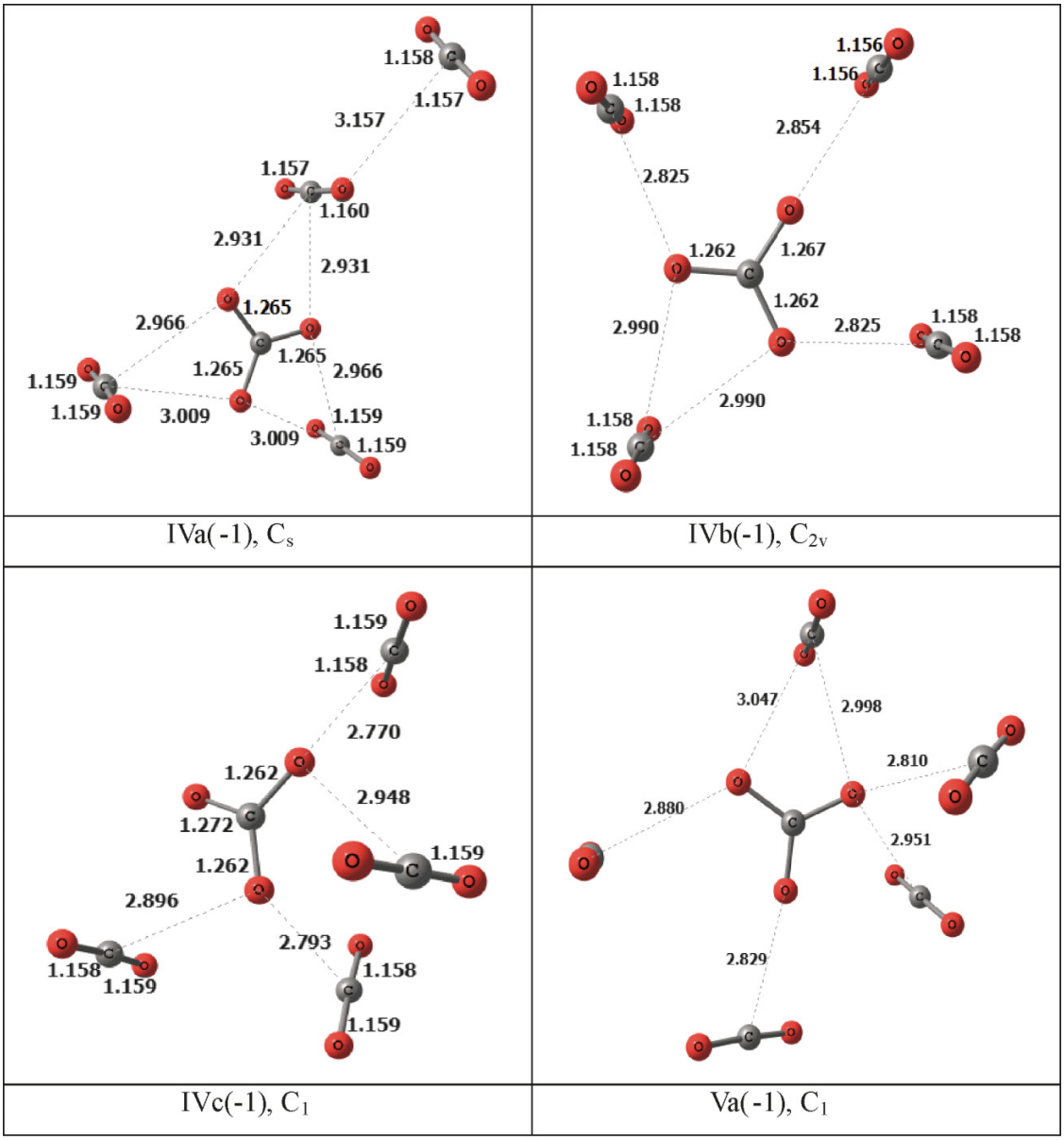
Methods

All DFT calculations were performed with the B3PW91[23,24] functional and the 6–31+G(3df) basis set, using the Gaussian03 computer programs.[25] For smaller clusters, coupled cluster methods with single, double (CCSD), and noniterative triple excitations (CCSD(T)) and second-order Møller–Plesset perturbation (MP2) methods, were applied. The choice of basis set, especially the use of diffuse functions, is critical for calculating geometries and energies of anions. Overly diffuse functions may lead to near separation of an electron from a dianion that is unstable in the gas phase, and therefore lead to energies and geometries close to that of the monoanion. On the other hand, diffuse functions are necessary for the description of stable anions. In the present case, as calculations on both mono- and di-anions are to be performed, a common basis set is required, and we chose a moderately diffuse basis set. We were encouraged in using such a basis set as theoretical values in the literature have been tested against experimental results. For example, Wang et al.[26] calculated ADE and VDE values for $SO_4^{2-}(H_2O)_n$, n = 1–6, using the aug-cc-pVTZ basis set, and obtained excellent agreement with experimental values for the stable clusters with n = 4–6.

Several starting geometries were used for the $CO_3^{1-}(CO_2)_n$ clusters, all initially having no symmetry constraints. Optimized structures were checked for symmetry, and the calculations were repeated with a symmetry constraint if found appropriate. Following the method described in previous papers,[13–15] the structures are labeled by a Roman numeral, indicating the number of CO_2 molecules added, and a small letter, where "a" is used for chainlike structures and "b" and "c" for branched structures. The energies listed in the tables

Can. J. Chem. Downloaded from www.nrcresearchpress.com by Renmin University of China on 09/02/12
For personal use only.

Fig. 1 (*continued*).



are electronic energies without zero-point vibrational corrections. In checking several cases, such corrections would decrease the binding energies by less than 0.1 eV (absolute). No imaginary frequencies were encountered when checking the most stable mono- and di-anionic clusters up to three additions.

Results and discussion

Structure of CO_3^{1-} and CO_3^{2-}

As described in the CO_3–SO_2 paper,[14] CO_3^{2-} is calculated by all methods to have D_{3h} symmetry, in agreement with experiment. However, the structure of CO_3^{1-} has been controversial. Hartree–Fock (HF) methods result in C_{2v} symmetry,[5] whereas DFT methods lead to D_{3h} symmetry.[14,17,20] It can be shown that HF and other methods are subject to symmetry breaking, from D_{3h} to C_{2v} symmetry. In a systematic investigation using methods from HF to MP2 to CCSD, CCSD(T), and DFT, Cappa and Elrod[20] concluded that the true ground state of CO_3^{1-} has D_{3h} symmetry, similar to that of the well-studied isoelectronic NO_3 radical.

Energies of carbonate – carbon dioxide clusters

In Table 1, B3PW91/6–311+G(3df) energies (E) and binding energies $\Delta E(-1)$ and $\Delta E(-2)$ are given for the optimized structures of $CO_3^{1-}(CO_2)_n$ and $CO_3^{2-}(CO_2)_n$, with n from 0 to 5. The binding energies are defined by

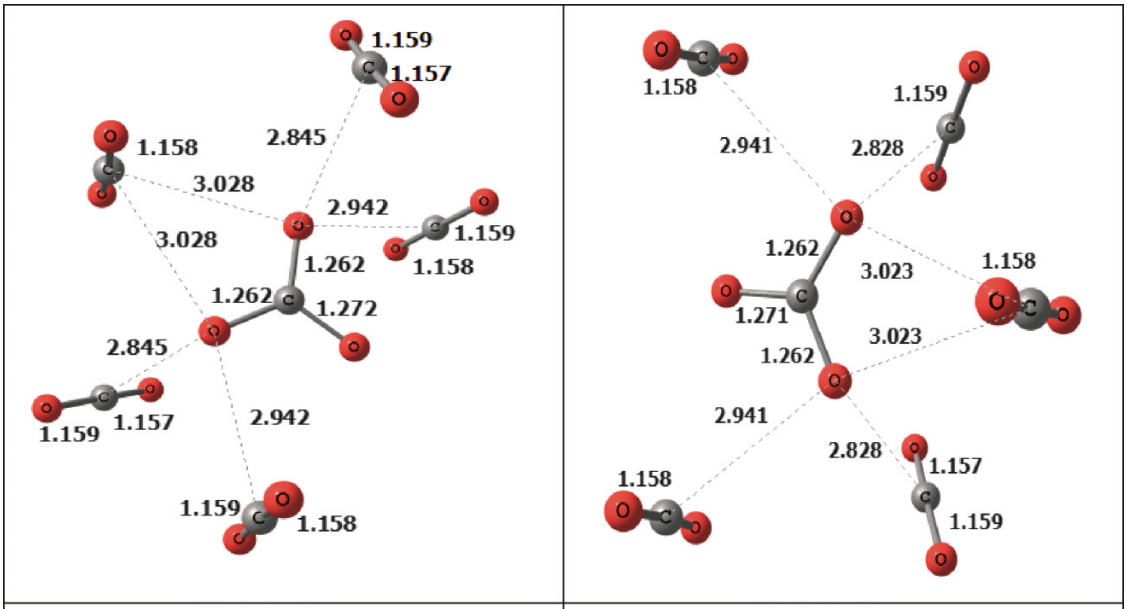
$$[1] \qquad \Delta E(-1) = E[CO_3{}^{1-}(CO_2)_n] - E[CO_3{}^{1-}] - nE[CO_2]$$

$$[2] \qquad \Delta E(-2) = E[CO_3{}^{2-}(CO_2)_n] - E[CO_3{}^{2-}] - nE[CO_2]$$

Symmetries are also indicated. Two structures are given for $n = 3$ and three each for $n = 4$ and 5.

Can. J. Chem. Downloaded from www.nrcresearchpress.com by Renmin University of China on 09/02/12
For personal use only.

Fig. 1 (*concluded*).



Vb(-1), C_2 | Vc(-1), C_s

Binding energies of the monoanions are small, ranging from –0.21 eV for $n = 1$ to –0.81 eV for $n = 5$. However, they are much larger for the dianions, with values from –2.40 to –4.43 eV. Differences in binding energies, for a given n, are small. Energies of the structures Va(–1) to Vc(–1) differ by only 0.01 eV, whereas energies of the corresponding dianionic clusters differ by 0.04 eV.

Adiabatic (ADE) and vertical (VDE) electron detachment energies are listed in Table 2. They are defined in eqs. [3] and [4], with

$$[3] \qquad \mathrm{ADE} = E_0[{CO_3}^{1-}(CO_2)_n] - E_0[{CO_3}^{2-}(CO_2)_n]$$

using the calculated energies (E_0) of the lowest energy structures of the mono- and di-anions, and

$$[4] \qquad \mathrm{VDE} = E_{\mathrm{vert}}[{CO_3}^{1-}(CO_2)_n] - E_0[{CO_3}^{2-}(CO_2)_n]$$

where the energy of the anionic cluster ${CO_3}^{1-}(CO_2)_n$ is calculated at the optimized geometry of the lowest energy dianion ${CO_3}^{2-}(CO_2)_n$ for the given n. As defined, ADE and VDE are negative if the dianion is less stable than the monoanion, and positive otherwise.

The ADE value (in DFT) is –3.69 eV for ${CO_3}^{2-}$, implying that ${CO_3}^{2-}$ is adiabatically 3.69 eV less stable than ${CO_3}^{1-}$. As expected, ADE values move toward zero as CO_2 molecules are added to ${CO_3}^{2-}$. However, contrary to ${SO_4}^{1-/2-}(CO_2)_n$[12] and other systems studied before, even at $n = 5$ ADE is still negative, although only by the small amount of 0.07 eV. (For the other systems studied in this series, the dianionic cluster stabilizes at $n = 2$ or 3.) VDE values are still negative at $n = 1$, but become positive starting with $n = 2$. This implies that ${CO_3}^{2-}(CO_2)_2$ is more stable than ${CO_3}^{1-}(CO_2)_2$ at the optimized geometry of ${CO_3}^{2-}(CO_2)_2$. Coupled cluster CCSD and CCSD(T) energies have been obtained at the DFT-optimized geometries for $n = 0$–2. They show the same trend as the DFT values. For $n = 2$, ADE is more negative by 0.2–0.3 eV. On the other hand, VDE values in CCSD and CCSD(T) are more positive. However, the switch from negative to positive VDEs still occurs at $n = 2$, as with DFT.

In Table 3, calculated incremental energies differences ($\Delta E_{n-1,n}$) for the monoanionic clusters are compared with experimental incremental enthalpy differences ($\Delta H°_{n-1,n}$) obtained by Hiraoka and Yamabe.[5] ΔH values were calculated for $n = 1$, but not for larger clusters. Calculated $\Delta E_{n-1,n}$ values are 1–2 kcal/mol (1 cal = 4.184 J) lower than experimental $\Delta H°_{n-1,n}$. As n increases, the drop-off in experimental enthalpies is much slower than that of the calculated energies. Theoretical values do not decrease in a regular fashion, and an irregular decrease is seen at $n = 4$. A search for $n = 4$ structures of ${CO_3}^{1-}(CO_2)_n$ with lower energy was not successful. Overall, however, considering such small energy differences, the agreement of theoretical with experimental values can be considered to be reasonable. Keesee et al.[16] obtained an enthalpy change of –7.1 ± 0.2 kcal/mol for ${CO_3}^{1-} + CO_2$, somewhat larger than that found by Hiraoka and Yamabe.[5]

Structure of monoanionic clusters

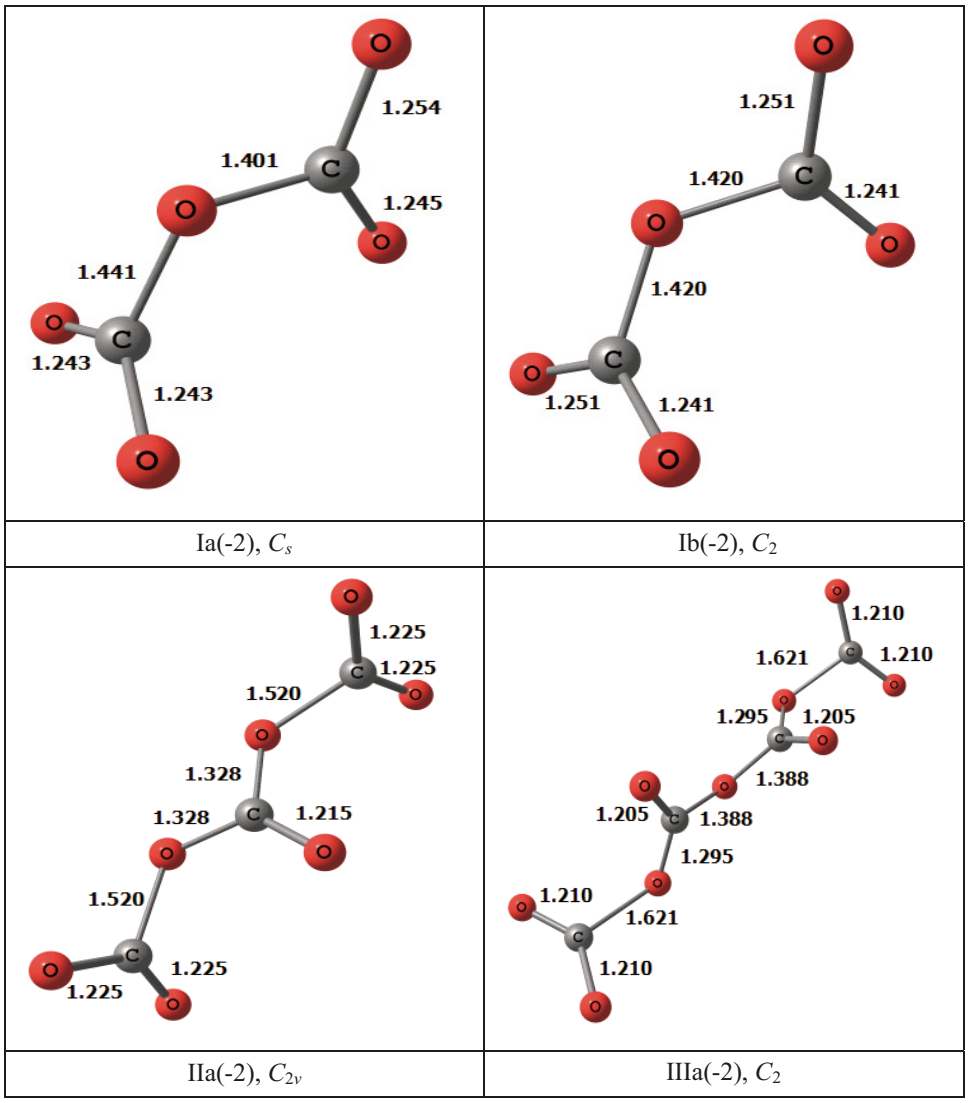
In all monoanionic clusters, shown in Fig. 1, the ${CO_3}^{1-}$ stays essentially intact, with weak electrostatic bonding (bond distances of 2.79–3.05 Å) to the carbon monoxides. As also seen for ${SO_4}^{1-}(CO_2)_n$,[12] the CO_2 molecules are slightly bent, with their oxygens pointing away from ${CO_3}^{1-}$, owing to electric repulsion of negative charges. Despite the long bonds, a remarkable number of clusters show symmetry, from C_s to D_{3h}. In agreement with the findings by Hiraoka and Yamabe,[5] the CO_2 carbons preferably bond to two oxygens of ${CO_3}^{1-}$. While these authors also found C_{2v} symmetry for the $n = 3$ clusters, in this work the D_{3h} structure for $n = 3$ optimized at lower energy.

Structure of dianionic clusters

The structures of dianionic clusters are displayed in Fig. 2.

Can. J. Chem. Downloaded from www.nrcresearchpress.com by Renmin University of China on 09/02/12
For personal use only.

Fig. 2. Structures of dianions, $CO_3^{2-}(CO_2)_n$. Distances are in Å.



Covalently bonded structures were found for dianions containing up to four carbon atoms. One to three oxygens of CO_3^{2-} are shared with neighboring CO_2 molecules, to form chainlike $O_2C–O–CO_2$, $O_2C–O–C(O)–O–CO_2$, and $O_2C–O–C(O)–O–C(O)–O–CO_2$ dianions, as well as a threefold paddlewheel structure (IIIb(–2)) with a carbon in the centre. The structures for $n = 4$ and 5 show one to three weakly bonded CO_2s. It is interesting that two structures for $[O_2C–O–CO_2]^{2-}$ ($n = 1$) have nearly identical energies, one being of C_s symmetry (Ia(–2)) and the other of C_2 symmetry (Ib(–2)). The central C–O bond distances are different in the C_s case (1.40 and 1.44 Å), but identical (1.42 Å) in the C_2 case. The most stable structures for each n have C_2 symmetry, in agreement with the structures found by Bruna et al.,[18] except for the C_1 structure IVa(–2), which is 0.02 eV lower than the C_2 structure IVb(–2).

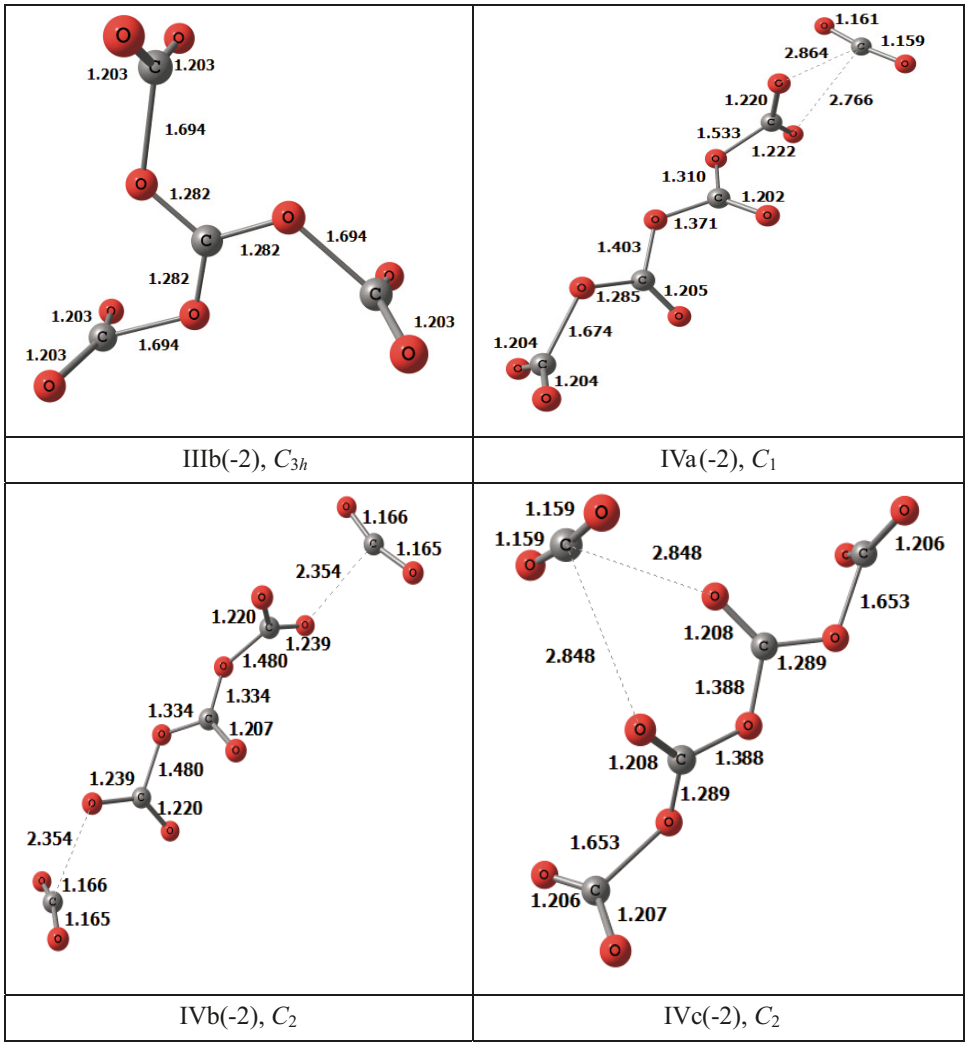
Comparison of carbonate – carbon dioxide with sulfate – carbon dioxide clusters

In Table 4, the results for the $CO_3^{1-/2-}(CO_2)_n$ (system **A**) clusters are contrasted to the $SO_4^{1-/2-}(CO_2)_n$ (system **B**) clusters from ref. 13. Both clusters have CO_2 as solvent, but differ in the anion. Table 4 shows that **A** has higher binding energies than **B**, both for the monoanions and the dianions. As n increases, the differences in binding energies between dianions and monoanions increase more strongly for system **A** than **B**. For system **A** such differences are about 2.2 eV for $n = 1$, rising up to 3.5 eV for $n = 4$. For system **B**, however, the differences are about 1.2 eV for $n = 1$ and 2.0 eV for $n = 4$. Despite the faster increase of the dianionic binding energies in system **A** compared with system **B**, it is more difficult to stabilize the dianion over the monoanion in system **A** because of the large ADE of CO_3^{2-} (–3.69 eV), compared with the much smaller (absolute) value for SO_4^{2-} (–1.75 eV).

Comparison of carbonate clusters with sulfate clusters

Earlier, carbonate clusters were compared with sulfate clusters, both having carbon dioxide as solvent. However, the problem of slower stabilization of carbonate clusters is not restricted to CO_2, but also applies to other solvents such as SO_2 and H_2O. Experimental and theoretical studies on $SO_4^{2-}(H_2O)_n$ clusters, for example, showed that here stabilization

Fig. 2 (*continued*).



IIIb(-2), C_{3h} | IVa(-2), C_1

IVb(-2), C_2 | IVc(-2), C_2

occurs at $n = 3$, with an experimental ADE at $n = 3$ of about 0.4 eV.[26] From the earlier discussion, one would predict that the carbonate–water clusters $CO_3^{2-}(H_2O)_n$ would stabilize at $n > 3$. No experimental studies of such clusters could be found in the literature. Pathak et al.[22] published theoretical results for IR spectra of $CO_3^{2-}(H_2O)_n$ clusters with n values from 1 to 6. However, for lower values of n such clusters are not expected to be stable in the gas phase, as they lose an electron by autodetachment. A calculation done here for $n = 1$ resulted in an ADE of –2.65 eV.

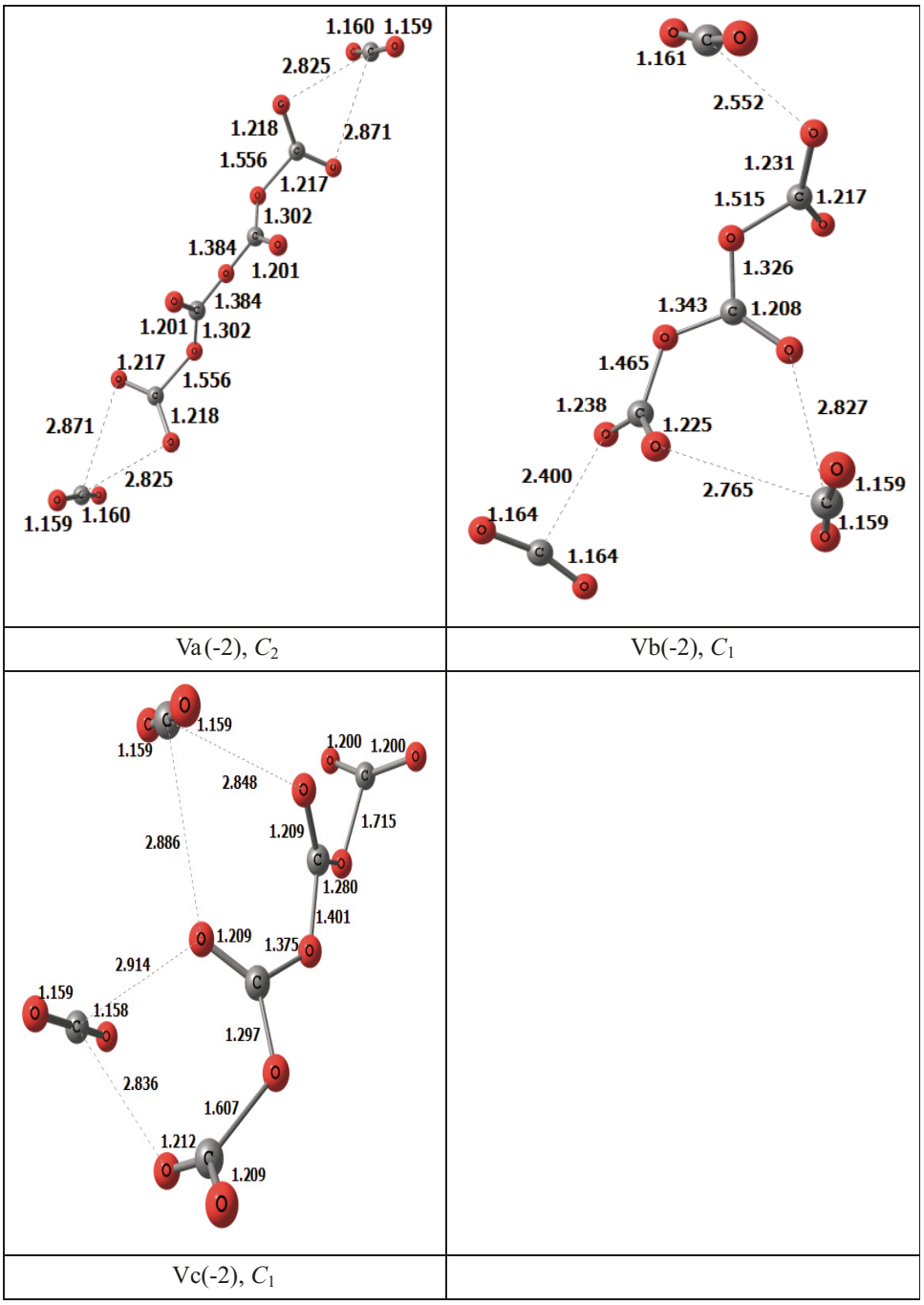
Based on the results obtained so far, we found it interesting to compare carbonate with sulfate clusters for the three solvent molecules CO_2, SO_2, and H_2O. These molecules span a wide range of dielectric constants, from a small 1.6 for CO_2 to a medium 15.4 for SO_2 and to a large 77.4 for H_2O. However, there are differences in bonding. Whereas dianionic clusters with CO_2 and SO_2 have mainly covalent bonding, those with water have hydrogen bonding.

The comparison is shown in Table 5. Data for $SO_4^{2-}(SO_2)_n$ are taken from Chan and Grein[15] and data for $CO_3^{2-}(SO_2)_n$ are taken from Grein et al.[14] Generally, the binding energies of the dianions are higher for the carbonate than for the sulfate clusters. For a given anion, the binding energies at $n = 1$ are highest for SO_2 and lowest for H_2O. Of the six clusters shown, $CO_3^{2-}(SO_2)$ has the highest binding energy and $SO_4^{2-}(H_2O)$ has the lowest binding energy. The ADEs for $n = 1$ are more negative for the carbonate than for the sulfate clusters, as was discussed earlier. For a given dianion, the water cluster has the most negative ADE. Overall, $CO_3^{2-}(H_2O)$ has the most negative ADE and $SO_4^{2-}(SO_2)$ has the least negative ADE at $n = 1$.

Solvation energies of dianions and monoanions in the three solvents were calculated with the PCM model.[27] They are shown in the last three columns of Table 5. Obviously, the solvation energies increase with the dielectric constant in the order CO_2, SO_2, and H_2O. For a given solvent, the solvation energies are higher for carbonates than for sulfates, both for the dianion and the monoanion. However, despite CO_3^{2-} in CO_2 solution having a higher solvation energy than SO_4^{2-} in CO_2 solution, such energy is not sufficient to overcome the large negative ADE of CO_3^{2-}. Contrary to the usual situation, where dianions in solution become stabilized over the monoanion, according to our calculations the dianion CO_3^{2-} solvated in CO_2 is less stable than the monoanion CO_3^{1-}

Can. J. Chem. Downloaded from www.nrcresearchpress.com by Renmin University of China on 09/02/12
For personal use only.

Fig. 2 (*concluded*).



solvated in CO_2. The last column of Table 5 shows the energy difference between the solvated dianion and monoanion (ΔE_{dian}), with positive numbers indicating that the solvated dianion is more stable. The value for CO_3^{2-}–CO_2 is –0.76 eV (3.92 – 0.99 – 3.69). The findings of solvation energy calculations for carbonate in CO_2 solution appear to disagree somewhat with the findings of our step-by-step calculations, whereby the carbonate dianion should eventually become stabilized (by the addition of about six CO_2 molecules).

On the other hand, calculations on $SO_4^{2-}(CO_2)_n$, which has a calculated reversal of stabilities at $n = 2$, show the solvation energy of SO_4^{2-} in CO_2 to be 3.64 eV, lower than the solvation energy of CO_3^{2-} in CO_2, but much in excess of –1.77 eV, the ADE of SO_4^{2-}. The total energy of the solvated dianion is lower than that of the solvated monoanion by 0.97 eV, in qualitative agreement with our step-by-step calculations.

The n value for which stabilization of the dianion first occurs (n_{Stabil}) is always higher for the carbonate than for the sulfate clusters and, within each group, it is highest for H_2O. For the carbonate clusters, n_{Stabil} was found to be 3 for SO_2,[14] and is predicted to be 6 for CO_2 (this work); it is estimated to be 4 or 5 for H_2O. This estimate of n_{Stabil} for $CO_3^{1-/2-}(H_2O)_n$ is based on the fact that it has to be greater than $n_{Stabil} = 3$,

Can. J. Chem. Downloaded from www.nrcresearchpress.com by Renmin University of China on 09/02/12
For personal use only.

Table 4. Comparison of results for $CO_3^{1-/2-}(CO_2)_n$ clusters (system **A**) with $SO_4^{1-/2-}(CO_2)_n$ clusters (system **B**, ref. 13).

	$CO_3^{1-/2-}(CO_2)_n$ (**A**)					$SO_4^{1-/2-}(CO_2)_n$ (**B**)			
Parameter	$n = 1$	$n = 2$	$n = 3$	$n = 4$	$n = 5$	$n = 1$	$n = 2$	$n = 3$	$n = 4$
$\Delta E(-1)$	–0.21	–0.39	–0.56	–0.68	–0.81	–0.11	–0.31	–0.44	–0.56
$\Delta E(-2)$	–2.40	–3.50	–3.95	–4.20	–4.43	–1.28	–2.04	–2.34	–2.59
ADE	–1.49	–0.58	–0.29	–0.17	–0.07	–0.59	–0.03	0.15	0.28
VDE	–0.69	0.86	2.12	2.32	2.45	0.37	1.68	1.86	1.97
cov(–1)	0	0	0	0	0	0	0	0	0
long(–1)	1	2	3	4	5	1	2	3	4
cov(–2)	1	2	3	3	3	1	2	2	2
long(–2)	0	0	0	1	2	0	0	1	2

Note: Adiabatic (ADE) and vertical (VDE) electron detachment energies and binding energies $\Delta E(-1)$ and $\Delta E(-2)$ are in eV. Number of covalent and long noncovalent bonds for monoanions, cov(–1) and long(–1), and for dianions, cov(–2) and long(–2). B3PW91/6–311+G(3df) values.

Table 5. Comparison of carbonate with sulfate clusters for solvent molecules CO_2, SO_2, and H_2O.

Cluster	ΔE_{bdg}	ADE	n_{Stabil}	$\Delta E_{solv}(-2)$	$\Delta E_{solv}(-1)$	ΔE_{dian}
$CO_3^{2-}CO_2$[a]	–2.40	–1.49	6[b]	–3.92	–0.99	–0.76
$CO_3^{2-}SO_2$[c]	–3.39	–1.96	3	–9.83	–2.48	3.66
$CO_3^{2-}H_2O$[a]	–1.58	–2.65	4 or 5[b]	–10.39	–2.62	4.08
$SO_4^{2-}CO_2$[d]	–1.28	–0.59	2	–3.64	–0.92	0.97
$SO_4^{2-}SO_2$[e]	–2.25	–0.52	2	–9.16	–2.30	5.10
$SO_4^{2-}H_2O$[f]	–1.21	–0.91	3	–9.68	–2.43	5.50

Note: Binding energy of dianions, ΔE_{bdg}; adiabatic electron detachment energy of dianions, ADE; value of n for which dianions become stabilized, n_{Stabil}; solvation energy, ΔE_{solv} of $CO_3^{2-}(-2)$ and $CO_3^{1-}(-1)$; and stability of the solvated dianion over the solvated monoanion, ΔE_{dian}. All energies are in eV. The ADE of CO_3^{2-} is –3.69 eV and the ADE of $SO_4^{2-}$is –1.77 eV.

[a]This work.

[b]Estimated, see text.

[c]Reference 14.

[d]Reference 13.

[e]Reference 15.

[f]Reference 26.

the value for hydrated sulfate, but not much greater owing to the large solvent stabilization energy of the dianion (ΔE_{dian} = 4.08 eV). The corresponding sulfate numbers are 2 for CO_2 and SO_2[13,15] and 3 for H_2O, as found experimentally and confirmed by calculations.[26]

According to Table 5, the (negative) binding energies for the dianionic clusters are ordered $SO_2 > CO_2 > H_2O$. However, combining the values given for the dianions with ADE(CO_3^{2-}) or ADE(SO_4^{2-}), shows that the binding energies of the monoanionc clusters are ordered $SO_2 > H_2O > CO_2$, with CO_2 and H_2O interchanged. The reason can be seen in the bonding character. Whereas clusters with SO_2 always have covalent bonding, the dianionic clusters with SO_2 and CO_2 have covalent bonding, and the monoanionic ones have only weak electrostatic bonds. Obviously, hydrogen bonds, while being weaker than covalent bonds, are still stronger than the electrostatic interactions.

Summary and conclusion

In this contribution, geometries were optimized for monoanionic and dianionic clusters of carbonate with carbon dioxide, using DFT methods. The monoanion CO_3^{1-} shows only weak electrostatic bonds with carbon dioxide molecules and corresponding small binding energies. The carbonate dianion, on the other hand, binds covalently to CO_2, up to a limit of three molecules. The binding energy is 2.4 eV for the first bond and rapidly declines for successive bonds. It will take at least six carbon dioxide molecules to stabilize the dianionic cluster over the monoanionic one.

This is the fourth paper in a series of studies exploring clusters of carbonate and sulfate with carbon dioxide and sulfur dioxide (for previous papers see refs. 13–15), allowing for a comparison of clusters and for extracting trends in properties. It was found that binding energies for dianionic clusters are higher for carbonates than for sulfates. Up to three CO_2s are covalently bonded in $CO_3^{2-}(CO_2)_n$ clusters, whereas only two are bonded in $SO_4^{2-}(CO_2)_n$. However, stabilization of dianionic clusters is more difficult for carbonates. Whereas sulfate – carbon dioxide clusters stabilize at $n = 2$ (addition of two CO_2s), carbonate – carbon dioxide clusters do not yet stabilize at $n = 5$. Calculated solvation energies on carbonate and sulfate dissolved in CO_2 confirm these trends.

In a more general comparison, clusters of carbonate and sulfate with water molecules have been added to clusters with CO_2 and SO_2. Clusters with water molecules have lower binding energies owing to hydrogen bonding compared with covalent bonding for the other systems. Stabilization requires

Can. J. Chem. Downloaded from www.nrcresearchpress.com by Renmin University of China on 09/02/12
For personal use only.

the addition of three H_2O molecules to sulfate and four or five to carbonate. Experimental results for dianionic clusters are available only for water as solvent. It is hoped that experiments will be conducted using other solvents such as SO_2 and CO_2.

Acknowledgments

The authors are indebted to the Natural Sciences and Engineering Research Council of Canada (NSERC) for continued financial support and to the Atlantic Computational Excellence Network (ACEnet) for the provision of excellent computing facilities. Thanks to Dr. Pablo Bruna and to the reviewers for valuable comments.

References

(1) Klots, C. E.; Compton, R. N. *J. Chem. Phys.* **1977**, *67* (4), 1779. doi:10.1063/1.435044.
(2) Stamatovic, A.; Stephan, K.; Märk, T. D. *Int. J. Mass Spectrom. Ion Process.* **1985**, *63* (1), 37. doi:10.1016/0168-1176(85)87039-7.
(3) Hiraoka, K.; Shoda, T.; Morise, K.; Yamabe, S.; Kawai, E.; Hirao, K. *J. Chem. Phys.* **1986**, *84* (4), 2091. doi:10.1063/1.450418.
(4) Hiraoka, K.; Mizuse, S.; Yamabe, S. *J. Chem. Phys.* **1987**, *87* (6), 3647. doi:10.1063/1.452962.
(5) Hiraoka, K.; Yamabe, S. J. *J. Chem. Phys.* **1992**, *97* (1), 643. doi:10.1063/1.463560.
(6) Lezius, M.; Rauth, T.; Grill, V.; Foltin, M.; Märk, T. D. *Z. Phys. D* **1992**, *24* (3), 289. doi:10.1007/BF01425751.
(7) Arnold, D. W.; Bradforth, S. E.; Kim, E. H.; Neumark, D. M. *J. Chem. Phys.* **1995**, *102* (9), 3493. doi:10.1063/1.468575.
(8) Arnold, D. W.; Bradforth, S. E.; Kim, E. H.; Neumark, D. M. *J. Chem. Phys.* **1995**, *102* (9), 3510. doi:10.1063/1.468576.
(9) Pathak, A. K.; Mukherjee, T.; Maity, D. K. *J. Phys. Chem. A* **2008**, *112* (47), 12037. doi:10.1021/jp805348q.
(10) Muraoka, A.; Inokuchi, Y.; Hammer, N. I.; Shin, J. W.; Johnson, M. A.; Nagata, T. *J. Phys. Chem. A* **2009**, *113* (31), 8942. doi:10.1021/jp903578e.
(11) Oliaee, J. N.; Dehghany, M.; Moazzen-Ahmadi, N.; McKellar, A. R. W. *Phys. Chem. Chem. Phys.* **2011**, *13* (4), 1297. doi:10.1039/c0cp02311f.
(12) Smith, D.; Spanel, P. *Mass Spectrom. Rev.* **1996**, *14* (4–5), 255. doi:10.1002/mas.1280140403.
(13) Grein, F.; Chevrier, D. M. *Theor. Chem. Acc.* **2012**, *131*, 1110. doi:10.1007/s00214-012-1110-5.
(14) Grein, F.; Chan, J. K.; Liko, I. *Can. J. Chem.* **2010**, *88* (11), 1125. doi:10.1139/V10-115.
(15) Chan, J.; Grein, F. *Comp. Theor. Chem.* **2011**, *966* (1–3), 225. doi:10.1016/j.comptc.2011.03.005.
(16) Keesee, R. G.; Lee, N.; Castleman, A. W., Jr. *J. Chem. Phys.* **1980**, *73* (5), 2195. doi:10.1063/1.440415.
(17) Shkrob, I. A. *J. Phys. Chem. A* **2002**, *106* (49), 11871. doi:10.1021/jp0214918.
(18) Bruna, P. J.; Grein, F.; Passmore, J. *Can. J. Chem.* **2011**, *89* (6), 671. doi:10.1139/v11-039.
(19) Keesee, R. G.; Lee, N.; Castleman, A. W., Jr. *J. Am. Chem. Soc.* **1979**, *101* (10), 2599. doi:10.1021/ja00504a015.
(20) Cappa, C. D.; Elrod, M. J. *Phys. Chem. Chem. Phys.* **2001**, *3* (15), 2986. doi:10.1039/b102981a.
(21) Pathak, A. K.; Maity, D. K. *J. Phys. Chem. A*, **2009**, *113* (48), 13443. doi:10.1021/jp907577j.
(22) Pathak, A. K.; Mukherjee, T.; Maity, D. K. *Syn. React. Inorg. Met. Org. Nano Met. Chem.* **2008**, *38*, 76.
(23) Becke, A. D. *J. Chem. Phys.* **1993**, *98* (7), 5648. doi:10.1063/1.464913.
(24) Perdew, J. P.; Burke, K.; Wang, Y. *Phys. Rev. B* **1996**, *54* (23), 16533. doi:10.1103/PhysRevB.54.16533.
(25) Frisch, M. J.; Trucks, G. W.; Schlegel, H. B.; Scuseria, G. E.; Robb, M. A.; Cheeseman, J. R.; Zakrzewski, V. G.; Montgomery, J. A., Jr.; Stratmann, R. E.; Burant, J. C.; Dapprich, S.; Millam, J. M.; Daniels, A. D.; Kudin, K. N.; Strain, M. C.; Farkas, O.; Tomasi, J.; Barone, V.; Cossi, M.; Cammi, R.; Mennucci, B.; Pomelli, C.; Adamo, C.; Clifford, S.; Ochterski, J.; Petersson, G. A.; Ayala, P. Y.; Cui, Q.; Morokuma, K.; Malick, D. K.; Rabuck, A. D.; Raghavachari, K.; Foresman, J. B.; Cioslowski, J.; Ortiz, J. V.; Stefanov, B. B.; Liu, G.; Liashenko, A.; Piskorz, P.; Komaromi, I.; Gomperts, R.; Martin, R. L.; Fox, D. J.; Keith, T.; Al-Laham, M. A.; Peng, C. Y.; Nanayakkara, A.; Gonzalez, C.; Challacombe, M.; Gill, P. M. W.; Johnson, B. G.; Chen, W.; Wong, M. W.; Andres, J. L.; Head-Gordon, M.; Replogle, E. S.; Pople, J. A. *Gaussian 03*; Gaussian, Inc.: Pittsburgh, PA.
(26) Wang, X.-B.; Nicholas, J. B.; Wang, L.-S. *J. Chem. Phys.* **2000**, *113* (24), 10837. doi:10.1063/1.1333703.
(27) Tomasi, J.; Mennucci, R.; Cammi, R. *Chem. Rev.* **2005**, *105* (8), 2999. doi:10.1021/cr9904009.

Can. J. Chem. Downloaded from www.nrcresearchpress.com by Renmin University of China on 09/02/12
For personal use only.

MINIREVIEW / MINISYNTHÈSE

Aromatic radical perfluoroalkylation reactions

Al Postigo

Can. J. Chem. Downloaded from www.nrcresearchpress.com by Renmin University of China on 09/02/12
For personal use only.

Abstract: This account intends to cover recent literature on radical perfluoroalkylation reactions of aromatic nuclei in organic and aqueous media. Emphasis will be placed on radical aromatic perfluoroalkylation reactions in water or aqueous media, with the aim of exploring aromatic radical reactivity in a benign environment.

Key words: radical perfluoroalkylation, radicals in aqueous media, aromatic radical perfluoroalkylation.

Résumé : Dans ce travail, on passe en revue la littérature récente sur les réactions de perfluoroalkylation radicalaires de noyaux aromatiques, dans des milieux organiques ou aqueux. On met l'emphase sur les réactions de perfluoroalkylation aromatiques dans l'eau ou les milieux aqueux afin d'évaluer la réactivité radicalaire des produits aromatiques dans un environnement bénin.

Mots-clés : perfluoroalkylation radicalaire, radicaux en milieu aqueux, perfluoroalkylation radicalaire aromatique.

[Traduit par la Rédaction]

Aromatic perfluoroalkylation reactions in organic conventional media

Introduction

Several important review articles involving radical perfluoroalkylation reactions of aromatic compounds have appeared in the literature in the past.[1,2] Radical metal-promoted aromatic perfluoroalkylation reactions are rare. Among them, the reactions where the metals employed (e.g., Cu, Zn, Fe)[2] are not directly involved in the Ar–R_f bond formation step, but are needed to generate the perfluoroalkyl radical from R_fX (X = I, Br), will not be the subject of this review article.

The $C_4F_9^\bullet$ and other perfluoroalkyl radicals show a clear-cut electrophilic character in aromatic substitution, as already reported for the addition to alkenes,[3,4] but the low regio- and chemo-selectivities suggest that the polar effect is not the main factor in determining the high reactivity of perfluoroalkyl radicals toward aromatics (10^5–10^6 $(mol/L)^{-1}$ s^{-1}, two to three orders of magnitude more reactive than alkyl radicals). The enthalpic factor, related to the involved bond energies, appears to be the major cause of the increased reactivity. The polar effect is considered as related more to the polarizability than to the polarity of a radical (the σ-perfluoroalkyl radicals are considered less polarizable and hence less sensitive to polar effects than σ-radicals).[5] Thus, it is not surprising that electron-rich aromatic nuclei showed the highest reactivity toward R_f radicals.

Aromatic radical perfluoroalkylation triggered by thermal initiators

Minischi and co-workers[5] used a series of initiation techniques to generate perfluoroalkyl radicals ($R_f^\bullet$) such as (*i*) benzoyl peroxide; (*ii*) *t*-BuOOH and Fe(III) salts; (*iii*) H_2O_2 and acetone; and (*iv*) H_2O_2, DMSO, and Fe(II) salt. Table 1 summarizes the perfluorobutylation of aromatics employing benzoyl peroxide as the radical initiation technique.

The reaction mechanism according to procedure (*i*) clearly involves homolytic decomposition of benzoyl peroxide with the formation of phenyl radical; the reaction of this according to eq. [1] appears to be much faster ($>10^8$ $(mol/L)^{-1}$ s^{-1}) than the hydrogen abstraction from the solvent (10^5 $(mol/L)^{-1}$ s^{-1}) or the addition to the aromatic ring (10^5 $(mol/L)^{-1}$ s^{-1}) because no significant aromatic phenylation was observed.

[1] $R_fI + Ph^\bullet \longrightarrow R_f^\bullet + PhI$

The radical $C_4F_9^\bullet$ adds to the aromatic ring, and the radical adduct is then oxidized in a chain process. The presence of a catalytic amount of Cu(II) salt increases the reaction rate because a redox chain is superimposed to the radical chain (Scheme 1).

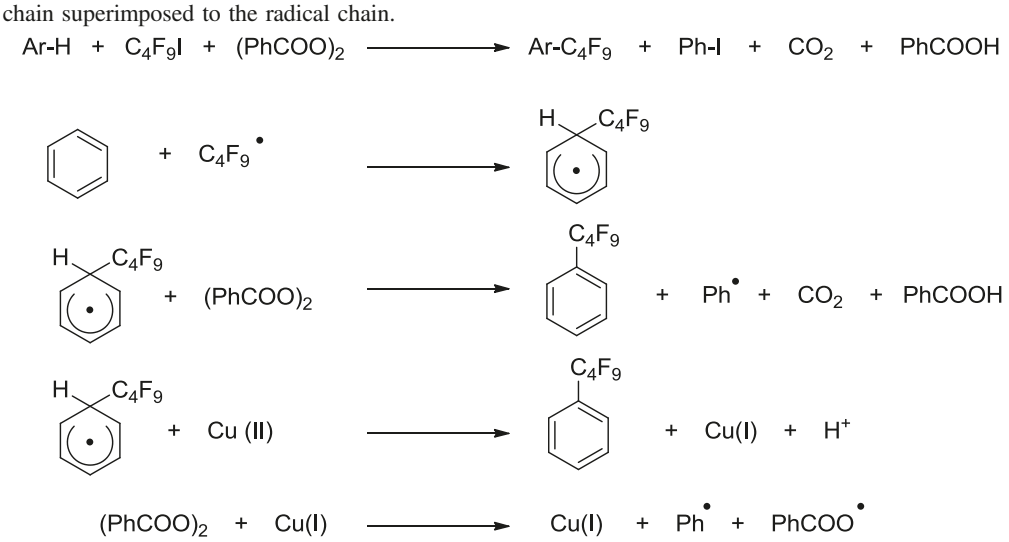
Minischi and co-workers[5] argue that the solvent is important for the efficiency of the aromatic perfluoroalkylation, because perfluoroalkyl radicals can effectively abstract hydrogen from C–H bonds of the solvent (the rates of abstraction by $Rf^\bullet$ are $>10^3$ larger than those of the analogue hydrocarbon radicals).[6]

Received 27 January 2012. Accepted 3 April 2012. Published at www.nrcresearchpress.com/cjc on 9 May 2012.

A. Postigo. Departamento de Química Orgánica, Facultad de Farmacia y Bioquímica, Universidad de Buenos Aires, Junín 954 CP 1113, Buenos Aires, Argentina.

E-mail for correspondence: apostigo@ffyb.uba.ar.

Scheme 1. Redox chain superimposed to the radical chain.



Thus, the rate of hydrogen abstraction by n-C_7F_{15}• from THF, whose α-C–H bond to the oxygen ring is particularly activated by both enthalpic and polar factors toward electrophilic radicals, has been evaluated at 6.1×10^5 $(mol/L)^{-1}$ s^{-1}. The authors[5] expected significantly lower rate constants for hydrogen abstraction from AcOH, DMSO, and MeCOMe by R_f•, always for enthalpic and polar reasons. The competition of hydrogen abstraction from the used solvents (AcOH, DMSO, and MeCOMe) appears to be negligible with activated aromatic substrates, and the efficiency of aromatic n-perfluoroalkylation is high, as shown by the comparable yields of PhI and n-C_4F_9–Ar.[1]

However, with deactivated aromatic substrates, such as $PhNO_2$ or PhCN,[5] the conversion of the aromatic compound is significantly lower than the yield, always high, of PhI; in these cases, it would appear that hydrogen abstraction from the solvent by n-C_4F_9• competes with the addition to the deactivated aromatic ring, even if an analysis of the volatile reaction products was not carried out.[5]

Aromatic substitution by procedures (*ii*)–(*iv*) is generally cleaner than the previously reported substitutions by thermolysis of R_fI or by homolysis of $(t\text{-BuO})_2$. The main reason is related to the lower efficiency of the rearomatization of the intermediate cyclohexadienyl radical, which, under these conditions, can also undergo disproportionation and dimerization leading to high-boiling derivatives.

The oxidation of cyclohexadienyl radicals by Cu(II) or Fe(III) are, on the contrary, very fast and selective in all cases, and they are always preferable when a catalytic redox chain can be achieved.

No substitution takes place with pyridine in AcOH solution,[5] whereas nitrobenzene and benzonitrile are attacked by the C_4F_9• radical. The fact that alkyl radicals, generated from alkyl iodides by the same procedures, do not react with homocyclic aromatic substrates suggested that perfluoroalkyl radicals must be much more reactive than alkyl radicals.[5]

On the other hand, protonated pyridine gives good results with alkyl radicals, but is quite unreactive toward C_4F_9• under the same conditions. This would indicate that alkyl and perfluoroalkyl radicals have opposite behavior because of their opposite polar character (electrophilic and nucleophilic, respectively, for perfluoroalkyl and alkyl radicals).

Table 1. Homolytic aromatic radical n-perfluoroalkylation.

Aromatic substrate	Orientation (%) relative substitution			Yield (%)
Benzene				94.7
Anisole	*o* (14.7)	*m* (45.5)	*p* (39.6)	93.3
Diphenyl ether	*o* (18.1)	*m* (24.4)	*p* (57.5)	90.9
Toluene	*o* (46.1)	*m* (30.3)	*p* (23.3)	90.1
Chlorobenzene	*o* (41.7)	*m* (39.6)	*p* (18.7)	47.1
Benzonitrile	*o* (20.5)	*m* (52.2)	*p* (27.3)	41.4
Nitrobenzne	*o* (31.1)	*m* (36.7)	*p* (32.2)	42.3
Biphenyl	*o* (25.1)	*m* + *p* (74.9)		97.2
Naphthalene	α (80.4)	β (19.6)		99.1
Thiophene	α (86.5)	β (13.1)		97.6

The electrophilic character of C_4F_9• radical is, however, scarcely reflected on the orientation of the substitution.

The ortho, meta, and para positions of toluene, chlorobenzene, anisole, diphenyl ether, benzonitrile, and nitrobenzene are substituted with low selectivity (Table 1), without a macroscopic influence of the polar character of the substituent, the ortho position being, obviously, affected by steric effects (e.g., the isomer distribution in chlorobenzene is characterized by 52% in the ortho position by CF_3•, but only 14% by the n-$C_{10}F_{21}$• radical). Substitution of naphthalene, biphenyl, thiophene, and pyrrole is, on the opposite, more selective. It would appear that the orientation is related more to the stabilization of the intermediate radical adducts than to the electron availability of the ring position.[5]

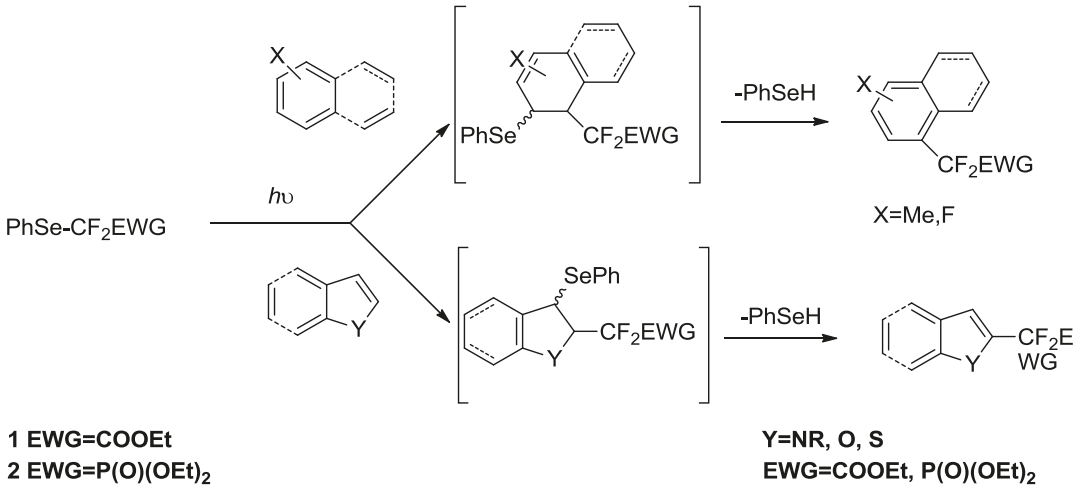
Aromatic radical perfluoroalkylation triggered by photochemical methods

A photochemical method was successfully employed to effect perfluoroalkylation reactions of aromatic and heteroaromatic compounds to provide substitutions with corresponding α-aryl-α,α-difluoroacetates and α-aryl-α,α-difluoromethylphosphonates in good to moderate yields.[7]

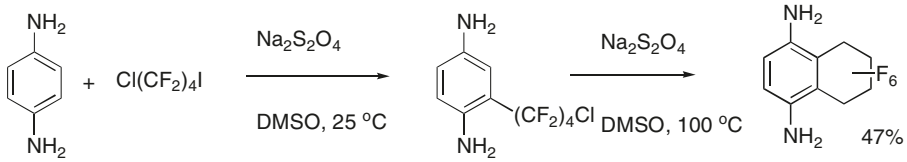
Aromatic and heteroaromatic substitutions with difluoromethyl radicals photogenerated from ethyl α-(phenylseleno)-α,α-difluoroacetate (**1**) and diethyl α,α-difluoromethyl-α-(phenylseleno)phosphonate (**2**) as shown in Scheme 2.

Can. J. Chem. Downloaded from www.nrcresearchpress.com by Renmin University of China on 09/02/12
For personal use only.

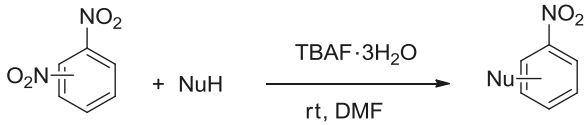
Scheme 2. Aromatic and heteroaromatic photo-substitutions with difluoromethyl radicals.



Scheme 3. Perfluoroalkylation of aromatic amines with $Cl(CF_2)_4I$ in DMSO.



Scheme 4. Introduction of polyfluoroalkoxy and polyfluoroalkylthio substituents in aromatic rings.



Aromatic radical perfluoroalkylation triggered by sulfinatodehalogenation reactions

Chen and co-workers[8] achieved the radical perfluoroalkylation reaction of aromatic amines by the substitution of aromatic H for R_f groups in DMSO as solvent, triggered through the decomposition of $Na_2S_2O_4$, according to Scheme 3 (see the Aromatic radical perfluoroalkylation reactions in aqueous media section for the mechanism of the sulfinatodehalogenation reactions).

A nonradical perfluoroalkylation reaction of activated ($ArNH_2$) aromatic nuclei has recently been accomplished through Pd catalysis in benzene as solvent.[9]

Aromatic radical perfluoroalkylation triggered by electron-transfer reactions

More recently, Yamakawa and co-workers[2h,10] accomplished the fluorination of aromatic compounds using Fenton reagent in DMSO as solvent. They attempted a series of simple substituted aromatic and heteroaromatic compounds with CF_3I and ethoxycarbonyl difluoromethyl bromide as fluorinating agents.

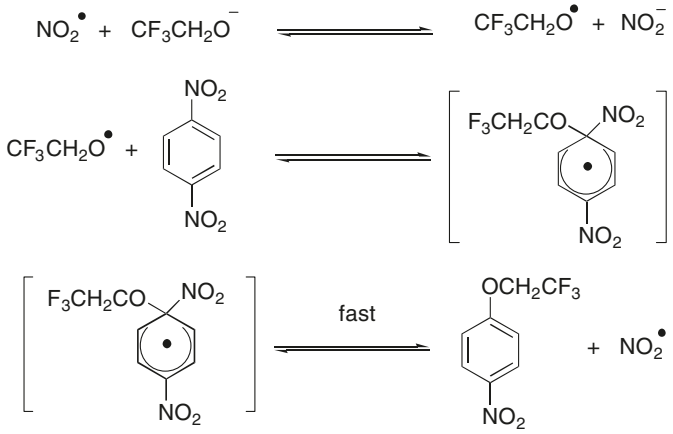
Introduction of polyfluoroalkoxy and polyfluoroalkylthio substituents in aromatic rings can be achieved with mild conditions and short times through the reaction of concentrated solutions of dinitrobenzenes in DMF with polyfluoroalcohols and polyfluorothiols in moderate excess in the presence of excess tetrabutylammonium fluoride as a base.[11] Terejo et al.[11]

Table 2. Introduction of polyfluoroalkoxy and polyfluoroalkylthio substituents in aromatic rings.

Entry	Substrate	Nucleophile	Product yield (%)	Rxn. time (h)
1	*p*-DNB	CF_3CH_2OH	98	1
2	*p*-DNB	$(CF_3)_2CHOH$	30	21
3	*p*-DNB	$CF_3(CF_2)_6CH_2OH$	89	2
4	*p*-DNB	CF_3CH_2SH	92	2
5	*o*-DNB	CF_3CH_2OH	76	1.5
6	*m*-DNB	CF_3CH_2OH	70	3
7	*m*-DNB	$CF_3(CF_2)_6CH_2OH$	—	24
8	*m*-DNB	CF_3CH_2SH	34	5

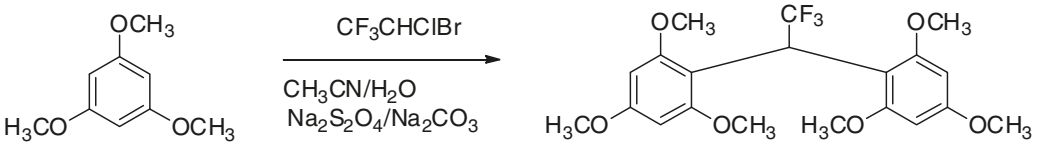
Note: DNB, dinitrobenzene.

Scheme 5. Radical propagation mechanism for the substitution of *p*-dinitrobenzene (DNB).

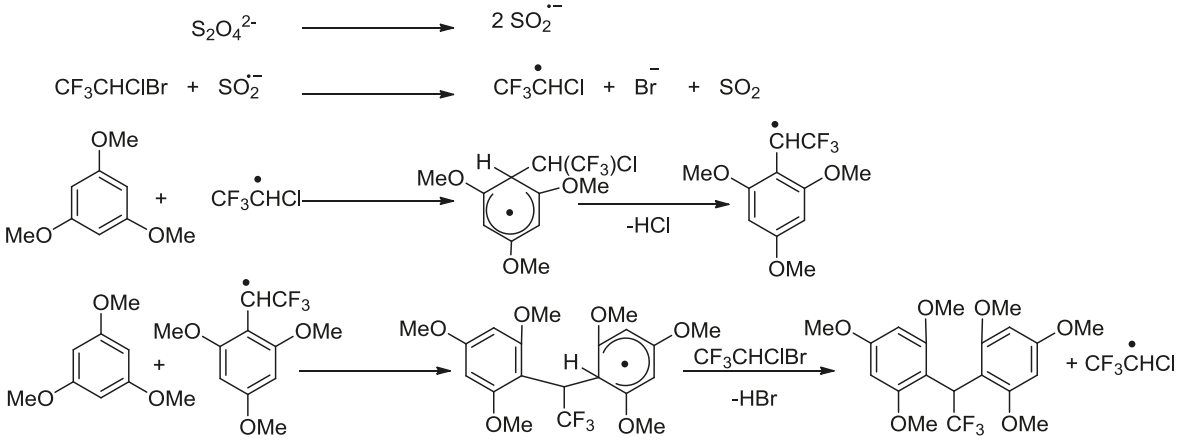


Can. J. Chem. Downloaded from www.nrcresearchpress.com by Renmin University of China on 09/02/12
For personal use only.

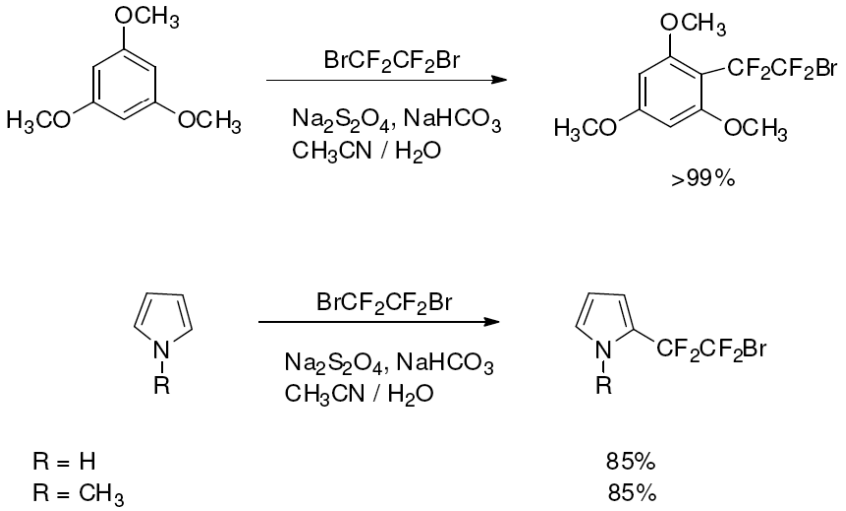
Scheme 6. Synthesis of trifluoromethyl-bis(2,4,6-trmethoxyphenyl)methane by sulfinatodehalogenation reaction.[19]



Scheme 7. Mechanism for the aromatic radical substitution reaction of H for R_f.[19]



Scheme 8. Radical aromatic substitution reactions of 1,3,5-trimethoxybenzene and pyrrols with $BrCF_2CF_2Br$ under sulfinatodehalogenation reaction conditions.[20]



postulated an operable fast radical chain mechanism. This mechanism is elicited from the oxidation of a Meisenheimer complex and proceeds through a radical aromatic substitution with the polyfluoroalkoxy or the polyfluoroalkylthio radicals as key intermediates. At low concentrations, entrainment can be achieved with the superoxide anion (Scheme 4).

The series of substituted products obtained under these conditions are illustrated in Table 2.

In Scheme 5, the proposed propagation mechanism is described, accounting for product formation.

Indeed, the mechanism corresponds to a typical radical aromatic substitution.[12] It is known that superoxide anion is a good oxidant for relatively acidic protic substrates to the corresponding radical through a process that includes dismutation.[13,14]

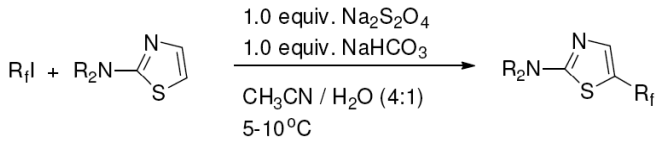
Terejo et al.[11] managed to generate the trifluoroethanol radical alternatively by the action of superoxide anion on trifluoroethanol ($pK_a = 23.6$ in DMSO).[15] The fast reaction between *p*-DNB and trifluoroethanol could be triggered by the addition of a catalytic amount of KO_2 (and an equimolecular amount of 18-crown-6 ether to achieve its solubilization in DMF). This represents a good example of entrainment, and considering the superoxide anion has no outer sphere electron-transfer oxidant properties,[13] this result strongly supports the operation of the trifluoroethoxy radical as an intermediate.

Aromatic radical perfluoroalkylation reactions in aqueous media

As opposed to radical perfluoroalkylation addition reactions of unsaturated compounds,[16,17] fluoroalkyl radical substitution

Can. J. Chem. Downloaded from www.nrcresearchpress.com by Renmin University of China on 09/02/12
For personal use only.

Scheme 9. Radical perfluoroalkylation of 2-aminothiazole derivatives.[21]



on the aromatic ring has received little attention. Furthermore, aromatic radical perfluoroalkylation in aqueous mixtures is restricted to a few examples of sulfinatodehalogenation reactions.

Recently, Barata-Vallejo and Postigo[18] summarized radical perfluoroalkylation reactions in aqueous media. In particular, activated aromatic nuclei, such as 1,3,5-trimethoxybenzene were employed in perfluoroalkyl substitution radical reactions in aqueous media. When a mixture of 1,3,5-trimethoxybenzene and 1-chloro-1-bromo-2,2,2-trifluoroethane was treated under sulfinatodehalogenation reaction conditions ($Na_2S_2O_4$/$NaHCO_3$ in CH_3CN/H_2O), a radical substitution reaction of H for R_f was achieved, as shown in Scheme 6.[19]

Dmowski et al.[19] postulated a radical mechanism such as that depicted in Scheme 7.

In another report by Dmowski et al.,[20] the aromatic substitution of trimethoxybenzenes and pyrrols with $BrCF_2CF_2Br$ was attempted as shown in Scheme 8.

More recently, Lu and co-workers[21] accomplished the polyfluoroalkylation of 2-aminothiazoles, as shown in Scheme 9. Reactions of 2-aminothiazole with *n*-C_4F_9I under sulfinatodehalogenation reaction conditions gave the substitution product in 80% yield with total selectivity at the 5-position of 2-aminothiazole (Scheme 9). A number of N-substituted 2-aminothiazoles also reacted with R_fI and R_fBr in yields ranging from 58% to 90%.[21]

While defluorination of polyfluoroalkyl-substituted arenes followed by nucleophilic attack from water has been well documented,[22] very few reductive defluorinations of polyfluoroalkyl-substituted arenes under mild conditions have been previously reported, and no other such reaction has been documented in aqueous media.

Conclusions

It becomes apparent that aromatic radical perfluoroalkylation reactions progress in good yields under different reaction and medium conditions. The types of reactions explored encompass simple aromatic radical substitutions triggered by the thermal decomposition of thermal initiators, photochemical initiation, metal-entrainment reactions, sulfinatodehalogenation reactions, and electron-transfer initiation. Remarkably, some of these initiations can be carried out in aqueous media, lowering the environmental impact of aromatic radical homolytic and ipso substitutions.

Acknowledgments

Thanks are given to Conicet, Consejo Nacional de Investigaciones Científicas y Técnicas, y Agencia Nacional de Promoción Científica y Técnica.

References

(1) Tomashenko, O. A.; Grushin, V. V. *Chem. Rev.* **2011**, *111* (8), 4475. doi:10.1021/cr1004293.

(2) (a) Furin, G. G. *Russ. Chem. Rev.* **2000**, *69* (6), 491. doi:10.1070/RC2000v069n06ABEH000353; (b) Fuchikami, T.; Ojima, I. *J. Fluor. Chem.* **1983**, *22* (6), 541. doi:10.1016/S0022-1139(00)81229-4; (c) Wakselman, C.; Tordeux, M. Eur. Pat. Appl. 206951, 1986; (d) Wakselman, C.; Tordeux, M. *J. Chem. Soc. Chem. Commun.* **1987**, 1701. doi:10.1039/c39870001701; (e) Tordeux, M.; Langlois, B.; Wakselman, C. *J. Chem. Soc., Perkin Trans. 1* **1990**, (8): 2293. doi:10.1039/p19900002293; (f) Moreno-Mañas, M.; Pleixats, R.; Villarroya, S. *Synlett* **1999**, *1999* (12), 1996. doi:10.1055/s-1999-2981; (g) Li, Y.; Li, C.; Yue, W.; Jiang, W.; Kopecek, R.; Qu, J.; Wang, Z. *Org. Lett.* **2010**, *12* (10), 2374. doi:10.1021/ol1007197; (h) Kino, T.; Nagase, Y.; Ohtsuka, Y.; Yamamoto, K.; Uraguchi, D.; Tokuhisa, K.; Yamakawa, T. *J. Fluor. Chem.* **2010**, *131* (1), 98. doi:10.1016/j.jfluchem.2009.09.007.

(3) Rong, X. X.; Pan., H.-Q.; Dolbier, W. R., Jr; Smart, B. E. *J. Am. Chem. Soc.* **1994**, *116* (10), 4521. doi:10.1021/ja00089a069.

(4) (a) Davis, C. R.; Burton, D. J.; Yang, Z.-Yu. *J. Fluor. Chem.* **1995**, *70* (1), 135. doi:10.1016/0022-1139(94)03102-6; (b) Le, T. D.; Arlauskas, R. A.; Weers, J. G. *J. Fluor. Chem.* **1996**, *78* (2), 155. doi:10.1016/0022-1139(96)03415-X; (c) Huang, X.-T.; Chen, Q.-Y. *J. Org. Chem.* **2001**, *66* (13), 4651. doi:10.1021/jo010178j.

(5) Bravo, A.; Bjørsvik, H.-R.; Fontana, F.; Liguori, L.; Mele, M.; Minisci, F. *J. Org. Chem.* **1997**, *62* (21), 7128. doi:10.1021/jo970302s.

(6) Dolbier, W. R., Jr. *Chem. Rev.* **1996**, *96* (5), 1557. doi:10.1021/cr941142c.

(7) Murakami, S.; Ishii, H.; Tajima, T.; Fuchigami, T. *Tetrahedron* **2006**, *62* (15), 3761. doi:10.1016/j.tet.2005.12.057.

(8) Cao, H. P.; Xiao, J.-C.; Chen, Q.-Y. *J. Fluor. Chem.* **2006**, *127* (8), 1079. doi:10.1016/j.jfluchem.2006.05.013.

(9) Loy, R. N.; Sanford, M. S. *Org. Lett.* **2011**, *13* (10), 2548. doi:10.1021/ol200628n.

(10) Ohtsuka, Y.; Yamakawa, T. *Tetrahedron* **2011**, *67* (12), 2323. doi:10.1016/j.tet.2011.01.049.

(11) Tejero, I.; Huertas, I.; Gonza'lez-Lafont, A.; Lluch, J. M.; Marquet, J. *J. Org. Chem.* **2005**, *70* (5), 1718. doi:10.1021/jo048354m.

(12) Tiecco, M. *Acc. Chem. Res.* **1980**, *13* (2), 51. doi:10.1021/ar50146a004.

(13) Sawyer, D. T.; Valentine, J. S. *Acc. Chem. Res.* **1981**, *14* (12), 393. doi:10.1021/ar00072a005.

(14) Nanni, E. J., Jr; Stallings, M. D.; Sawyer, D. T. *J. Am. Chem. Soc.* **1980**, *102* (13), 4481. doi:10.1021/ja00533a029.

(15) Bordwell, F. G. *Acc. Chem. Res.* **1988**, *21* (12), 456. doi:10.1021/ar00156a004.

(16) Barata-Vallejo, S.; Postigo, A. *J. Org. Chem.* **2010**, *75* (18), 6141. doi:10.1021/jo100901z.

(17) Slodowicz, M.; Barata Vallejo, S.; Vazquez, A.; Nudelman, N.; Postigo, A. *J. Fluor. Chem.* **2012**, *135*, 137. doi:10.1016/j.jfluchem.2011.10.002.

(18) Barata-Vallejo, S.; Postigo, A. *Eur. J. Org. Chem.* **2012**, *2012* (10), 1889. doi:10.1002/ejoc.201101808.

(19) Dmowski, W.; Urbanczyk-Lipkowska, Z.; Wójcik, D. *J. Fluor. Chem.* **2009**, *130* (5), 509. doi:10.1016/j.jfluchem.2009.02.011.

(20) Dmowski, W.; Piasecka-Maciejewska, K. *J. Fluor. Chem.* **2010**, *131* (7), 746. doi:10.1016/j.jfluchem.2010.01.009.

(21) Qi, Q.; Shen, Q.; Lu, L. *J. Fluor. Chem.* **2012**, *133*, 115. doi:10.1016/j.jfluchem.2011.07.005.

(22) Huang, W.; Ma, W. *Chin. J. Chem.* **1992**, *10* (32), 180.

Can. J. Chem. Downloaded from www.nrcresearchpress.com by Renmin University of China on 09/02/12
For personal use only.

Highly selective mono-N-benzylation and amidation of amines with alcohols or carboxylic acids using the Ph_2PCl/I_2/imidazole reagent system

Najmeh Nowrouzi and Mohammad Zareh Jonaghani

Can. J. Chem. Downloaded from www.nrcresearchpress.com by Renmin University of China on 09/02/12
For personal use only.

Abstract: Chlorodiphenylphosphine, imidazole, and molecular iodine in refluxing dichloromethane are used for the efficient preparation of amides under mild reaction conditions. This reagent system also shows excellent selectivity for mono-N-alkylation of amines with alcohols. In this system, the resulting phosphorus byproduct (diphenylphosphinic acid) is easily removed by extraction using an aqueous basic solution in the workup processes, which avoids the tedious and time-consuming chromatographic methods.

Key words: benzylation, amidation, imidazole, amine, alcohol, carboxylic acid, chlorodiphenylphosphine, iodine.

Résumé : On a utilisé un mélange de chlorodiphénylphosphine, d'imidazole et d'iode moléculaire dans le dichlorométhane au reflux pour préparer des amides d'une façon efficace, dans des conditions douces. Ce système de réactifs présente aussi une bonne sélectivité pour la mono-N-alkylation d'amines avec des alcools. Dans ce système, il est facile d'éliminer le sous-produit phosphoré, l'acide diphénylphosphinique, par extraction du mélange réactionnel à l'aide d'une solution basique aqueuse qui évite les méthodes chromatographiques lentes et ennuyeuses.

Mots-clés : benzylation, amidation, imidazole, amine, alcool, acide carboxylique, chlorodiphénylphosphine, iode.

[Traduit par la Rédaction]

Introduction

For many years, phosphines as reagents or catalysts have been employed for various organic transformations. Among these, soluble triphenylphosphine (TPP) has found significant attention, and several applications of this reagent have been demonstrated. This reagent has widespread use in organic chemistry in reactions such as the Staudinger reduction,[1] the Mitsunobu reaction,[2] the Wittig reaction,[3] halogenation of a hydroxyl group,[4] formylation reactions,[5] and nitrile and amide formation.[6] A common drawback of all these systems is the formation of stoichiometric amounts of phosphine oxides as byproducts, of which their separation from the reaction mixtures is usually a difficult task, and time-consuming chromatographic purification of the product is necessary to obtain pure compounds. Speed and efficiency in chemical separation are at the heart of parallel synthesis and combinatorial chemistry and are increasingly important in traditional synthesis as well.

As a solution to this problem, in recent years many efforts have been directed toward modifying TPP to facilitate the isolation and purification of the desired product. In this way, the use of expensive and not easily available reagents such as polymer-supported TPP,[7] PEG-supported (PEG = polyethyleneglycol) phosphine,[8] polystyryldiphenylphosphine,[9] diphenyl(2-pyridyl)phosphine,[10] (4-dimethylaminophenyl)diphenylphosphine,[11] Silphos,[12] tris[4-(1*H*,1*H*-perfluorooctyloxyphenyl)] phosphine[13] have been reported. Therefore, development of simple, efficient, and useful methods for the easy synthesis of organic compounds using readily available reagents is one of the major research demands in organic synthesis.

We have recently reported that chlorodiphenylphosphine (CDP), a commercially available reagent, is practically effective for the conversion of carboxylic acids, phenols, and thiols to their corresponding esters in the presence of molecular iodine.[14] In this system, the resulting phosphorus byproduct (diphenylphosphinic acid) is easily extracted with an aqueous basic solution in the workup processes without the need of using tedious and time-consuming chromatographic methods.

In continuation of our earlier work, we present a very easy and efficient method for N-alkylation and amidation of amines with alcohols or carboxylic acids.

The reaction of amines has been a topic of immense research owing to their synthetic utility and biological activity.[15] They are also widely used as intermediates to prepare solvents, fine chemicals, agrochemicals, and catalysts.[16]

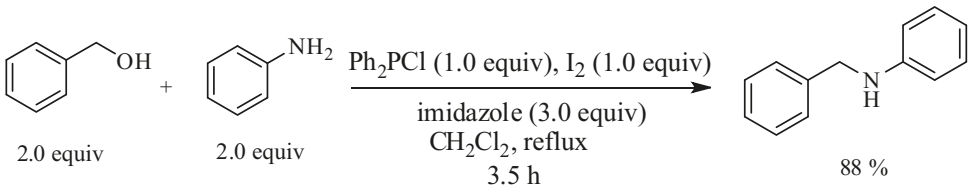
The nucleophilic attack of alkyl halides by primary amines is useful for the preparation of secondary amines, but the reaction is invariably slow and gives rise to a mixture of secondary and tertiary amines.[17] However, the toxicity of some

Received 19 June 2011. Accepted 2 February 2012. Published at www.nrcresearchpress.com/cjc on 9 May 2012.

N. Nowrouzi and M.Z. Jonaghani. Department of Chemistry, Faculty of Sciences, Persian Gulf University, Bushehr 75169, Iran.

Corresponding author: Najmeh Nowrouzi (email:nowrouzi@pgu.ac.ir).

Scheme 1. Formation of *N*-benzyl aniline using the Ph_2PCl/I_2/imidazole system.



alkylating agents and also the control of monoalkylation can be problematic. To obviate these problems, reductive amination of the carbonyl compounds,[18] amide reduction,[19] and the use of catalytic systems in the presence of alcohols, such as ruthenium, rhodium, iridium, zinc, palladium, and γ-alumina, have been reported. These conditions require strong reducing reagents or dangerous hydrogen gas and, in many cases, are not always selective and generate tertiary amines and (or) quaternary ammonium salts as byproducts. In addition, most of these catalytic systems require high reaction temperatures, and the applicable amines and alcohols are very restricted.[20] Recently, Iranpoor et al.[21] reported selective methods for N-monoalkylation of amines using the TPP system. In these methods, careful chromatography is necessary for isolation of the desired products from TPP oxide and the reaction mixture.

Due to the wide biological, synthetic, and industrial applications of amides, the amidation reaction is considered an important transformation in organic synthesis.[22,23] Different synthetic methodologies have been developed in the past two decades for the formation of an amide bond, with the focus on design and development of innovating coupling reagents. The most popular methods for the synthesis of amides involve the conversion of carboxylic acid to a more reactive functional group, such as acyl chloride, acyl azide, acylimidazoles, mixed anhydride, active esters, etc., followed by aminolysis with amine or via an in situ activation of the carboxylic group by using coupling reagents.[24] Although good results have been obtained with both approaches, they often need expensive coupling reagents, some of which are moisture-sensitive and sometimes lead to the formation of byproducts requiring further separation. These drawbacks usually limit their extensive application and give rise to the need for development of new types of condensing reagents.

Results and discussion

First, we investigated N-alkylation of aniline with benzyl alcohol using the Ph_2PCl/imidazole/I_2 system under various reaction conditions (Scheme 1). The optimization study revealed that 1.0 equiv of both Ph_2PCl and I_2 and 3.0 equiv of imidazole were sufficient to complete the reaction between 2.0 equiv of alcohol and 2.0 equiv of amine in refluxing dichloromethane. Similar to our previous work, it was observed that the presence of imidazole in the reaction mixture[14] not only neutralizes the liberated halogen acids, but also enhances the reactivity of the reagent system.

With the optimized conditions in hand, we screened a representative range of structurally different alcohols and amines for the reaction. Representative results are summarized in Table 1.

As shown by the data reported in Table 1, N-alkylation of anilines with benzyl alcohols bearing electron-donating and electron-withdrawing substituents at the aromatic ring proceeded to give benzyl aniline derivatives in good to excellent yields. As the results show, the reaction works best with the electron-rich benzyl alcohols. The electron-poor benzyl alcohols also provided the corresponding products, but with longer reaction times (Table 1, compare entries 5 and 9 with entries 6 and 10). In addition to the electronic factors, steric effects also affected the reaction in terms of time and yield. Comparison of entries 6 and 7 in Table 1 indicate that the existence of an ortho substituent on the phenyl ring slightly decreases the yield and increases the time of the reaction.

Treatment of 1-phenyl ethanol with this mixed reagent system (Table 1, entries 13–15) showed that this system is also suitable for the conversion of the secondary benzylic alcohols to their corresponding products. In the case of primary and secondary aliphatic alcohols such as 1-octanol and 2-octanol (Table 1, entries 20 and 21), no desired product was formed even after reflux in acetonitrile for a prolonged reaction time. These results exhibited that the reaction of non-benzylic alcohols with aniline in the presence of our reagent system does not occur.

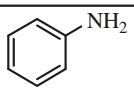
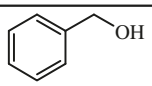
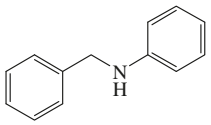
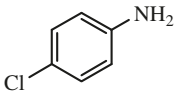
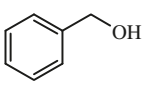
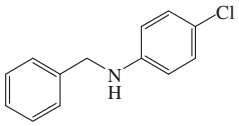
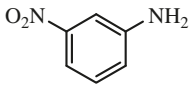
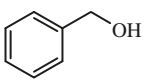
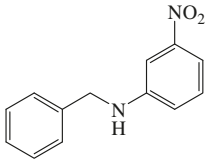
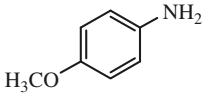
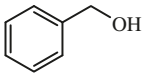
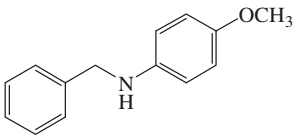
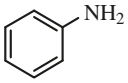
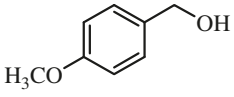
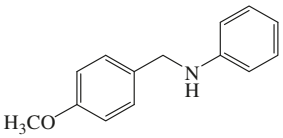
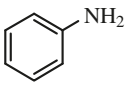
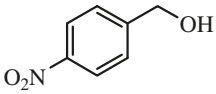
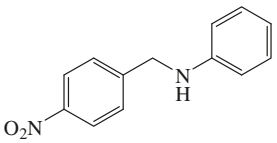
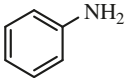
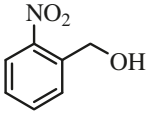
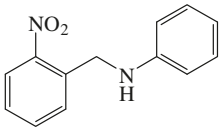
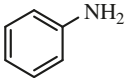
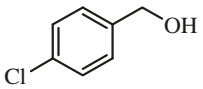
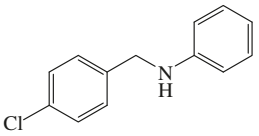
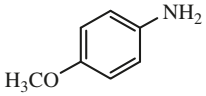
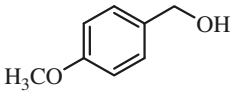
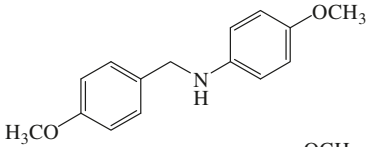
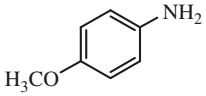
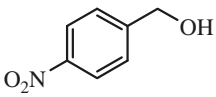
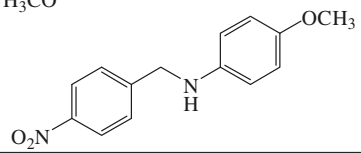
Similar to the alcohols, the nature of the substitution of the aromatic ring in aniline was also briefly studied. Both electron-donating and electron-withdrawing substituents react under our reaction conditions, and the overall yields in all cases are excellent. The reaction of benzyl alcohol with electron-rich anilines such as *p*-anisidine (Table 1, entry 4) gave the *N*-benzyl-4-methoxybenzenamine after 1.5 h, whereas a longer reaction time was observed for anilines bearing electron-withdrawing groups on the phenyl moiety (Table 1, entries 2 and 3).

In addition to this, in the reaction with benzyl alcohol, the more nucleophilic *N*-methylaniline produced better results as compared with the poor nucleophilic aromatic amines such as aniline (Table 1, compare entry 1 with entry 12).

Aliphatic amines were also tested to N-alkylation, but our attempts for alkylation of the primary aliphatic amines under the aforementioned conditions were unsuccessful, and the product was not obtained in this way even after refluxing in CH_3CN for 48 h. Secondary aliphatic amines (Table 1, entries 18 and 19) produced their corresponding tertiary amines in moderate yields. These reactions did not complete under the reaction conditions after 24 h and led to the desired product with lower yield possibly because of the steric effects. These results are not surprising based on the nucleophilicity of the amines. For the reaction to proceed, it is important to have amines as the reactive nucleophile and the secondary aliphatic amines are stronger nucleophiles than the primary amines. In the case of the aromatic amines, the stronger acidity of the amino group in aniline derivatives resulted in the easier formation of amine anions, which are strong nucleophiles.

Can. J. Chem. Downloaded from www.nrcresearchpress.com by Renmin University of China on 09/02/12
For personal use only.

Table 1. Benzylation of amines in the presence of the Ph_2PCl/imidazole/I_2 in CH_2Cl_2 at reflux conditions.

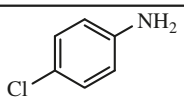
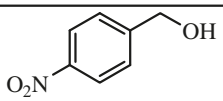
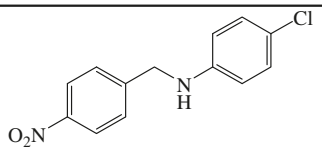
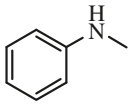
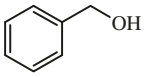
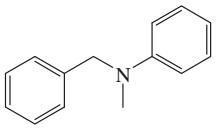
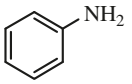
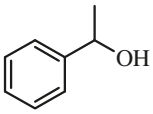
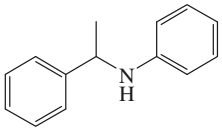
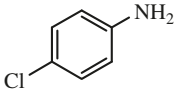
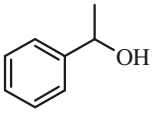
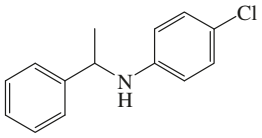
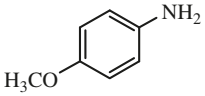
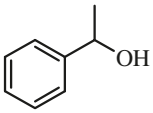
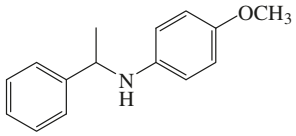
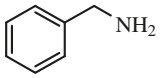
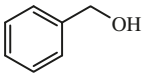
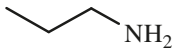
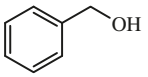
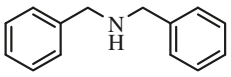
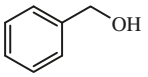
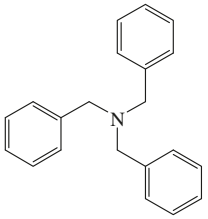
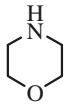
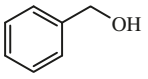
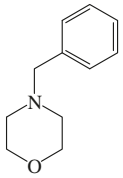
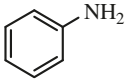
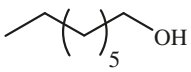
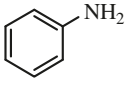
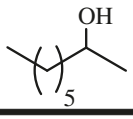
Entry	Amine	Alcohol	Product	Time (h)	Yield (%)[a]
1				3.5	88
2				7	90
3				8	88
4				1.5	93
5				3	92
6				5.5	90
7				8	80
8				4.5	89
9				15 min	94
10				5	87

To have more insight into the applicability, selectivity, and limitations of this new method, we performed an experiment using binary mixtures of equimolar amounts of aniline and different primary or secondary aliphatic amines and primary ones with benzyl alcohol. The results of this study are presented in Table 2.

As expected, reaction of a binary mixture of aniline and a primary aliphatic amine such as butyl amine proceeded smoothly to give the benzanilide as the single product in 90% yield (Table 2, entry 1). Benzyl amine was found to be unreacted under the reaction conditions (Table 2, entry 2). Furthermore, the alkylation of a secondary aliphatic amine in a dual mixture with benzyl amine as a primary aliphatic amine also proceeded to give tribenzylamine in moderate yield (Table 2, entry 3). The most important point regarding this method is that aromatic and secondary aliphatic amines

Can. J. Chem. Downloaded from www.nrcresearchpress.com by Renmin University of China on 09/02/12
For personal use only.

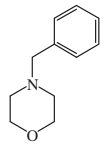
Table 1. (*concluded*).

Entry	Amine	Alcohol	Product	Time (h)	Yield (%)[a]
11				10	70
12				1	92
13				7	87
14				8.5	80
15				2	91
16			—	48	nr
17			—	48	nr
18				24	50
19				24	55
20			—	48	nr
21			—	48	nr

Note: nr, no reaction.

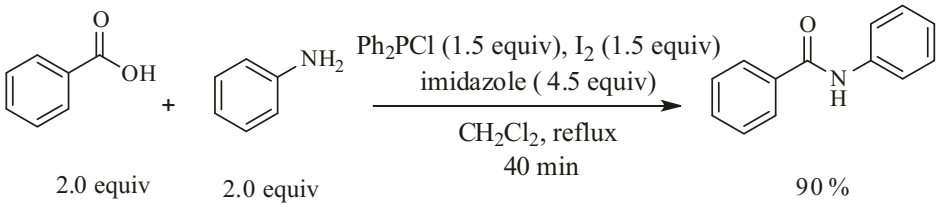
Can. J. Chem. Downloaded from www.nrcresearchpress.com by Renmin University of China on 09/02/12
For personal use only.

Table 2. Selective reaction of various amines with benzyl alcohol in binary mixtures usingthe Ph_2PCl/I_2/imidazole reagent system.

Entry	Alcohol	Binary mixture	Product	Time (h)	Yield (%)[a]
1	$PhCH_2OH$	$PhNH_2$–$CH_3CH_2CH_2NH_2$	$PhNHCH_2Ph$	3.5	90
2	$PhCH_2OH$	$PhNH_2$–$PhCH_2NH_2$	$PhNHCH_2Ph$	3.5	85
3	$PhCH_2OH$	$PhCH_2NHCH_2Ph$–$PhCH_2NH_2$	$(PhCH_2)_3N$	24	51
4	$PhCH_2OH$	Morpholine–$PhCH_2NH_2$		24	50

Note: The molar ratio of Ph_2PCl / imidazole / I_2 / $PhCH_2OH$ / binary mixture is 1.0:3.0:1.0:2.0:2.0:2.0.
[a]Isolated yield.

Scheme 2. Synthesis of benzanilide from the reaction of benzoic acid and aniline using the Ph_2PCl/I_2/imidazole system.



can be converted to their corresponding alkylated products in the presence of primary aliphatic amines in binary mixtures with excellent selectivity using the same stoichiometric amounts of the reagents and substrates as before.

To extend the applicability of our methodology and find out the limitations encountered in this new system, we sought conditions for performing direct amidation of carboxylic acids with amines, as an important transformation. In the amidation process, we examined the reaction of benzoic acid with aniline as a model reaction. Of the various stoichiometric amounts, the ratio of 1.5:4.5:1.5:2.0:2.0 for Ph_2PCl/imidazole/I_2/$PhCO_2H$/$PhNH_2$ in refluxing CH_2Cl_2 was found to be the best condition and resulted in benzanilide in 90% yield (Scheme 2). This transformation occurred conveniently with the easy removal of the produced phosphine oxide (diphenylphosphinic acid) by a simple extraction.

By using this system, the amidation of carboxylic acids with amines was also performed in a similar manner of amination and is shown in Table 3.

These results clearly demonstrate that the direct amidation was successful for both aliphatic and aromatic amines and acids.

With the variation of substituents in both acids and amines, it was observed that the reaction depended on the acidity of the benzoic acid derivatives and the nucleophilicity of the aromatic amines. As shown in Table 3, for most cases, better results were observed for the reaction of electron-withdrawing substituted aromatic acids (stronger aryl acids) with the activated aromatic amines carrying electron-donating substithents (stronger nucleophiles). For instance, reaction of *p*-nitrobenzoic acid with aniline proceeded to afford the desired product after 20 min (Table 3, entry 3), whereas longer reaction times were required when benzoic or *p*-methylbenzoic acid were employed in the reaction (Table 3, entries 1 and 2). Treatment of *p*-methoxyaniline and benzoic acid led to a clean reaction affording the desired amide after 30 min (Table 3, entry 4); however, the use of aniline bearing an electron-withdrawing group such as nitro, lead to the desired product in a relatively longer reaction time (2 h) and lower yield (75%) because of the low nucleophilicity of the amine (Table 3, entry 9).

As shown in Table 3, aliphatic amines (entries 10 and 11) and also aliphatic acids (Table 3, entry 15) are suitable substrates for synthesis of their corresponding amides. To show the generality of the present method, we examined the reaction of aliphatic and aromatic thiocarboxylic acids with aniline. In these cases, the successful transformation of thioacids to their corresponding thioamides was observed using the same reaction conditions as for carboxylic acids (Table 3, entries 16 and 17).

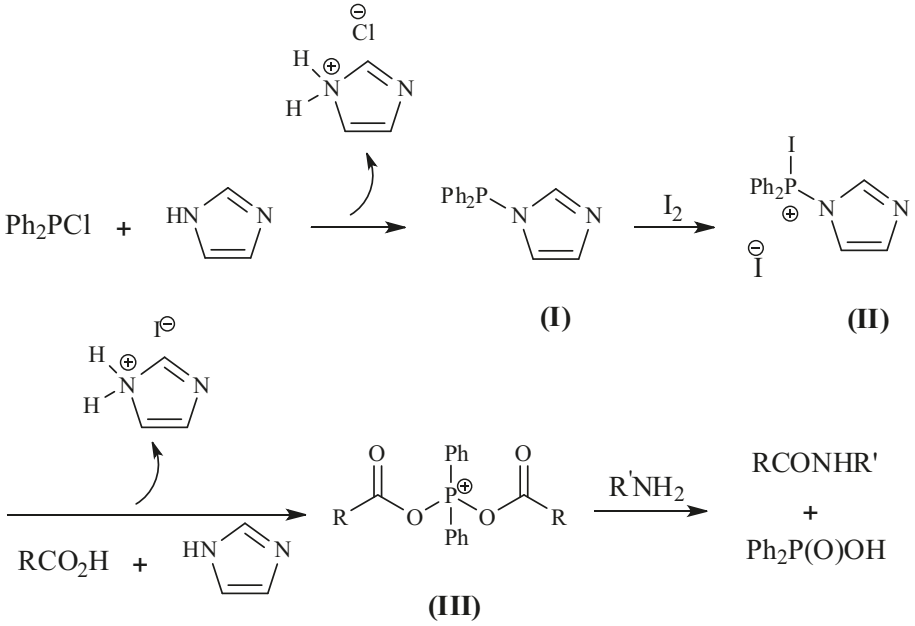
As previously reported,[14] we suggest that this reaction might be proceeding initially by formation of 1-(diphenylphosphino)imidazole (**I**), which in the second step reacts with iodine. The imidazole and iodine in the produced phosphonium salt are then exchanged by carboxylate anion to form the the acyloxyphosphonium ion (**III**). Finally the attack of the amine at the carbonyl carbon atom of this intermediate gives the corresponding amide along with diphenylphosphinic acid as a byproduct (Scheme 3).

Conclusion

In conclusion, we have developed a new, efficient, and mild method for mono-N-benzylation of amines with alcohols and also for amidation of carboxylic acids with aliphatic and aromatic amines. It should be noted that the present N-alkylation proceeds with high selectivity for mono-N-alkylation. In each reaction, monoalkylated aniline was formed as a single product and no formation of dialkylated aniline was observed. Therefore, one crucial feature embedded in this protocol is the excellent chemoselectivity. High yields, mild

Can. J. Chem. Downloaded from www.nrcresearchpress.com by Renmin University of China on 09/02/12
For personal use only.

Scheme 3. Proposed mechanism for the amidation reaction.



reaction conditions, a simple and convenient procedure, commercially availablity of the reagents, no need for a catalyst, and no prior activation in amidation are the advantages of this system. This system also has the further advantage that the reagent-derived byproduct (diphenylphosphinic acid) can be removed easily by a simple aqueous workup, which provides quick workup procedures instead of using the tedious and time-consuming chromatographic methods.

Experimental section

General methods

Solvents were dried and purified by standard procedures. Melting points were determined in open capillary tubes in a Buchi 530 circulating oil apparatus and are not corrected. NMR spectra were recorded on a Bruker Avance DPX-250 (^{1}H NMR, 250 MHz; ^{13}C NMR, 62.9 MHz) spectrometer in $CDCl_3$ or DMSO-d_6 using TMS as an internal standard. Determination of the purity of the products and the reaction monitoring were carried out on silica gel 254 analytical sheets or by GLC on a Shimadzu model GC-10A instrument. Column chromatography was carried out by silica gel 60 Merck (30–270). All compounds had been reported previously, and their identities were confirmed by comparison of their melting points and spectroscopic data with the reported data.

General procedure for the conversion of amines to *N*-benzyl amines

Benzyl alcohol (2.0 mmol) was added to a mixture of chlorodiphenylphosphine (1.0 mmol), imidazole (3.0 mmol), and iodine (1.0 mmol) in refluxing dichloromethane. Amine (2.0 mmol) was then added to the reaction mixture. After completion of the reaction, the residue was washed with saturated aqueous sodium carbonate (3 × 5 mL) until all diphenylphosphinic acid was removed from the organic phase. The aqueous phase was separated, and the organic phase was washed with aqueous sodium thiosulfate (2 × 5 mL) to remove the excess iodine and then washed with water, dried, and concentrated. Flash chromatography of the organic residue was performed on silica gel using *n*-hexane / ethyl acetate as eluent to give the pure products.

N-*Phenylbenzylamine*

mp 36 °C (lit.[25a] 37 °C). δ_H (250 MHz, $CDCl_3$): 7.22–7.43 (complex, 8H, Ph), 6.68–6.79 (complex, 2H, Ph), 4.38 (s, 2H, C*H*$_2$), 4.04 (s, 1H, N*H*). δ_C (62.9 MHz, $CDCl_3$): 148.2, 139.5, 129.3, 128.4, 127.6, 127.3, 117.6, 112.9, 48.4. HRMS (EI+) calcd for $C_{13}H_{13}N$: 183.1048; found: 183.045 (Table 1, entry 1).

N-*(4-Chlorophenyl)benzylamine*

mp 39 °C (lit.[25b] 39 °C). δ_H (250 MHz, $CDCl_3$): 7.14 (d, 2H, J = 7.2 Hz, Ph), 7.02–7.05 (m, 5H, Ph), 6.44 (d, 2H, J = 7.1 Hz, Ph), 4.37 (s, 2H, C*H*$_2$), 4.08 (s, 1H, N*H*). δ_C (62.9 MHz, $CDCl_3$): 150.2, 141.4, 128.7, 127.3, 127.0, 125.3, 119.5, 78.2, 49.2. HRMS (EI+) calcd for $C_{13}H_{12}ClN$: 217.0658; found: 217.0649 (Table 1, entry 2).

N-*(3-Nitrophenyl)benzylamine*

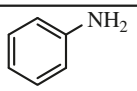
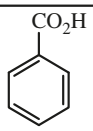
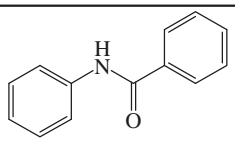
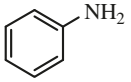
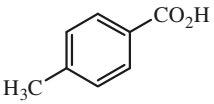
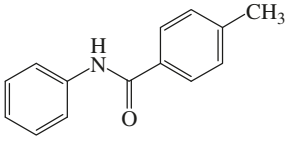
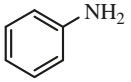
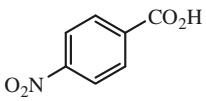
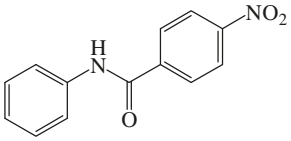
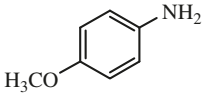
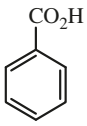
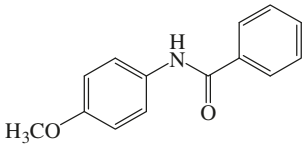
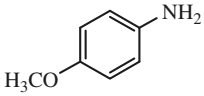
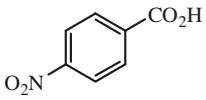
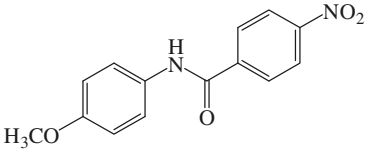
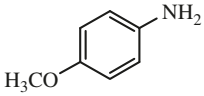
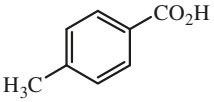
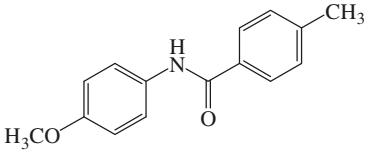
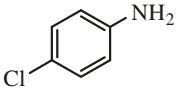
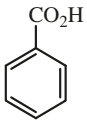
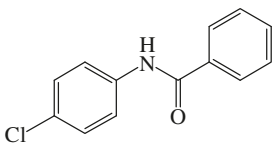
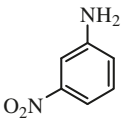
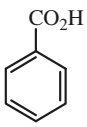
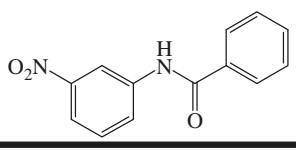
mp 104 °C (lit.[25c] 107 °C). δ_H (250 MHz, $CDCl_3$): 7.53–7.55 (m, 1H, Ph), 7.42 (s, 1H, Ph), 7.21–7.37 (m, 6H, Ph), 6.86–6.89 (m, 1H, Ph), 4.42 (s, 1H, N*H*), 4.36 (s, 2H, C*H*$_2$). δ_C (62.9 MHz, $CDCl_3$): 149.5, 148.9, 138.2, 139.8, 128.9, 127.7, 127.5, 118.8, 112.1, 106.6, 48.1. HRMS (EI+) calcd for $C_{13}H_{12}N_2O_2$: 228.0899; found: 228.0894 (Table 1, entry 3).

N-*(4-Methoxyphenyl)benzylamine*

mp 50 °C (lit.[25b] 51 °C). δ_H (250 MHz, $CDCl_3$): 7.17 (d, 2H, J = 7.3 Hz, Ph), 7.06–7.08 (m, 3H, Ph), 6.48 (d, 2H, J = 8.0 Hz, Ph), 6.34 (d, 2H, J = 7.9 Hz, Ph), 4.39 (s, 2H, C*H*$_2$), 4.11 (s, 1H, N*H*), 3.76 (s, 3H, O*Me*). δ_C (62.9 MHz, $CDCl_3$): 153.5, 141.2, 140.7, 127.8, 127.6, 127.0, 117.1, 115.3, 55.2, 50.1. HRMS (EI+) calcd for $C_{14}H_{15}NO$: 213.1154; found: 213.1147 (Table 1, entry 4).

Can. J. Chem. Downloaded from www.nrcresearchpress.com by Renmin University of China on 09/02/12
For personal use only.

Table 3. Synthesis of amides by the Ph_2PCl/imidazole/I_2 system in CH_2Cl_2 under reflux.

Entry	Amine	Acid	Product	Time (min)	Yield (%)[a]
1				40	90
2				50	93
3				20	90
4				30	89
5				10	94
6				40	91
7				55	87
8				80	77

Can. J. Chem. Downloaded from www.nrcresearchpress.com by Renmin University of China on 09/02/12
For personal use only.

4-Methoxy*-N-*phenylbenzylamine

mp 61 °C (lit.[25b] 63 °C). δ_H (250 MHz, $CDCl_3$): 7.31 (d, 2H, J = 7.5 Hz), 6.51–7.13 (m, 9H, Ph), 4.39 (s, 2H, C*H*$_2$), 3.91 (s, 1H, N*H*), 3.74 (s, 3H, O*Me*). δ_C (62.9 MHz, $CDCl_3$): 157.8, 149.1, 131.8, 129.9, 129.6, 128.3, 118.6, 115.5, 56.1, 49.7. HRMS (EI+) calcd for $C_{14}H_{15}NO$: 213.1154; found: 213.1150 (Table 1, entry 5).

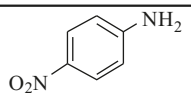
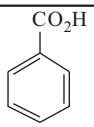
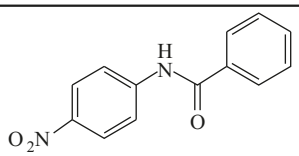
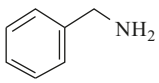
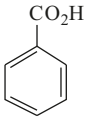
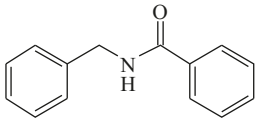
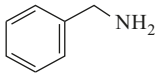
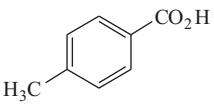
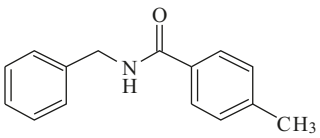
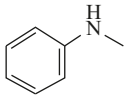
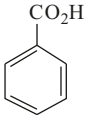
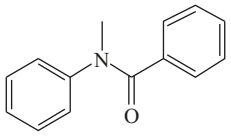
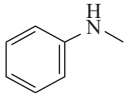
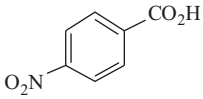
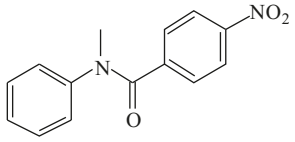
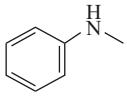
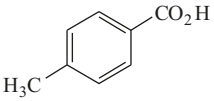
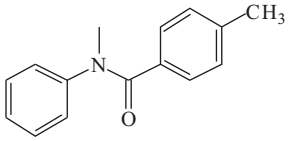
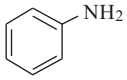
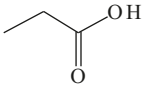
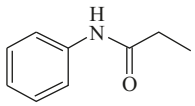
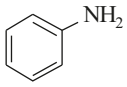
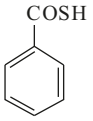
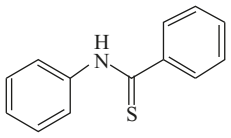
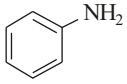
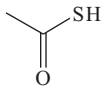
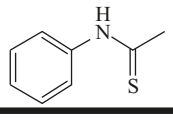
4-Nitro*-N-*phenylbenzylamine

mp 67 °C (lit.[25d] 67 °C). δ_H (250 MHz, $CDCl_3$): 8.13–8.18 (m, 2H, Ph), 7.56–7.71 (m, 2H, Ph), 7.23–7.37 (m, 2H, Ph), 6.68–6.84 (m, 3H, Ph), 4.38 (s, 2H, C*H*$_2$), 4.11 (s, 1H, N*H*). δ_C (62.9 MHz, $CDCl_3$): 146.4, 144.9, 143.7, 130.5, 128.4, 124.5, 117.7, 113.5, 48.9. HRMS (EI+) calcd for $C_{13}H_{12}N_2O_2$: 228.0899; found: 228.0885 (Table 1, entry 6).

2-Nitro*-N-*phenylbenzylamine

mp 45 °C (lit.[25e] 44 °C). δ_H (250 MHz, $CDCl_3$): 8.10 (d, 1H, J = 8.0 Hz, Ph), 7.74 (d, 1H, J = 8.0 Hz, Ph), 7.59 (t, 1H, J = 7.6 Hz, Ph), 7.44 (t, 1H, J = 7.8 Hz, Ph), 7.23 (t, 2H J = 8.0 Hz, Ph), 6.80 (t, 1H, J = 7.3 Hz, Ph), 6.63 (d, 2H, J = 8.4 Hz, Ph), 4.75 (s, 2H, C*H*$_2$), 4.42 (s, 1H, N*H*).

Table 3. (*concluded*).

Entry	Amine	Acid	Product	Time (min)	Yield (%)[a]
9				2 h	75
10				30	92
11				40	92
12				2.5 h	89
13				2 h	91
14				3 h	91
15				45	88
16				1 h	90
17				45	85

δ_C (62.9 MHz, $CDCl_3$): 148.25, 147.53, 135.78, 133.77, 129.81, 129.42, 128.03, 125.22, 118.03, 112.95, 45.76. HRMS (EI+) calcd for $C_{13}H_{12}N_2O_2$: 228.0899; found: 228.0891 (Table 1, entry 7).

4-Chloro-N-*phenylbenzylamine*

mp 47 °C (lit.[25f] 50 °C). δ_H (250 MHz, $CDCl_3$): 6.61–7.12 (m, 9H, Ph), 4.29 (s, 2H, C*H*$_2$), 3.92 (s, 1H, N*H*). δ_C (62.9 MHz, $CDCl_3$): 148.6, 139.1, 133.4, 129.8, 128.3, 128.0, 119.2, 114.5, 48.3. HRMS (EI+) calcd for $C_{13}H_{12}ClN$: 217.0658; found: 217.0641 (Table 1, entry 8).

N-*(4-Methoxybenzyl)-4-anisidine*

mp 90 °C (lit.[25g] 92 °C). δ_H (250 MHz, $CDCl_3$): 6.96 (d, 2H, J = 8.6 Hz, Ph), 6.65 (d, 2H, J = 8.8 Hz, Ph), 6.56 (d, 2H, J = 8.8 Hz, Ph), 6.35 (d, 2H, J = 8.7 Hz, Ph), 4.33 (s, 2H, C*H*$_2$), 3.71 (s, 6H, O*Me*). δ_C (62.9 MHz, $CDCl_3$): 158.8, 152.2, 142.5, 131.6, 128.8, 114.9, 114.1, 114.0, 55.8, 55.3, 48.7. HRMS (EI+) calcd for $C_{15}H_{17}NO_2$: 243.1259; found: 243.1248 (Table 1, entry 9).

N-*(4-Nitrobenzyl)-4-anisidine*

mp 97 °C (lit.[25h] 97 °C). δ_H (250 MHz, $CDCl_3$): 8.14 (dt,

Can. J. Chem. Downloaded from www.nrcresearchpress.com by Renmin University of China on 09/02/12
For personal use only.

Can. J. Chem. Downloaded from www.nrcresearchpress.com by Renmin University of China on 09/02/12
For personal use only.

2H, J = 8.8, 2.0 Hz, Ph), 7.52 (d, 2H, J = 8.8 Hz, Ph), 6.75 (dt, 2H, J = 9.0, 2.3 Hz, Ph), 6.53 (dt, 2H, J = 9.0, 2.3 Hz, Ph), 4.40 (s, 2H, CH_2), 3.71 (s, 3H, O*Me*). δ_C (62.9 MHz, $CDCl_3$): 152.2, 147.4, 146.8, 140.9, 127.6, 123.6, 114.5, 114.0, 55.9, 46.2. HRMS (EI+) calcd for $C_{14}H_{14}N_2O_3$: 258.1004; found: 258.1001 (Table 1, entry 10).

N-*(4-Nitrobenzyl)-4-chloroaniline*

mp 95 °C (lit.[25i] 97 °C). δ_H (250 MHz, $CDCl_3$): 8.07 (d, 2H, J = 8.5 Hz, Ph), 7.32 (d, 2H, J = 8.5 Hz, Ph), 7.05 (d, 2H, J = 8.8 Hz, Ph), 6.37 (d, 2H, J = 8.8 Hz, Ph), 4.32 (s, 2H, CH_2), 4.00 (s, 1H, N*H*). δ_C (62.9 MHz, $CDCl_3$): 147.8, 146.4, 145.7, 129.7, 127.9, 122.7, 120.9, 114.9, 46.2. HRMS (EI+) calcd for $C_{13}H_{11}ClN_2O_2$: 262.0509; found: 262.0493 (Table 1, entry 11).

N-*Methyl*-N-*phenylbenzylamine*

mp 37 °C (lit.[25j] 38 °C). δ_H (250 MHz, $CDCl_3$): 7.02–7.27 (m, 7H, Ph), 6.71–6.86 (m, 3H, Ph), 4.33(s, 2H, CH_2), 3.11 (s, 3H, *Me*). δ_C (62.9 MHz, $CDCl_3$): 149.4, 135.9, 129.7, 128.7, 126.0, 125.2, 117.4, 112.6, 59.3, 38.1. HRMS (EI+) calcd for $C_{14}H_{15}N$: 197.1204; found: 197.1193 (Table 1, entry 12).

N-*(1-Phenylethyl)aniline*

mp 52 °C (lit.[25k] 50 °C). δ_H (250 MHz, $CDCl_3$): 6.63–6.64 (m, 2H, Ph), 6.74–6.80 (m, 1H, Ph), 7.18–7.22 (m, 2H, Ph), 7.31–7.33 (m, 1H, Ph), 7.40–7.49 (m, 4H, Ph), 4.53 (q, 1H, J = 6.4 Hz, C*H*), 4.04 (s, 1H, N*H*), 1.50 (d, 3H, J = 6.4 Hz, *Me*). δ_C (62.9 MHz, $CDCl_3$): 147.2, 145.2, 129.1, 128.6, 126.8, 125.8, 117.2, 113.3, 53.2, 24.9. HRMS (EI+) calcd for $C_{14}H_{15}N$: 197.1204; found: 197.1196 (Table 1, entry 13).

4-Chloro*-N-*(1-phenylethyl)aniline

mp 59 °C (lit.[25k] 62 °C). δ_H (250 MHz, $CDCl_3$): 7.29–7.33 (m, 4H, Ph), 7.21–7.25 (m, 1H, Ph), 7.00–7.02 (m, 2H, Ph), 6.40–6.43 (m, 2H, Ph), 4.41 (q, 1H, J = 6.6 Hz, C*H*), 4.03 (s, 1H, N*H*), 1.53 (d, 3H, J = 6.6 Hz, *Me*). δ_C (62.9 MHz, $CDCl_3$): 145.7, 144.6, 128.9, 128.7, 127.0, 125.7, 121.8, 114.3, 53.5, 24.9. HRMS (EI+) calcd for $C_{14}H_{14}ClN$: 231.0815; found: 231.0809 (Table 1, entry 14).

***4-Methoxy*-N-*(1-phenylethyl)aniline*[25k]**

δ_H (250 MHz, $CDCl_3$): 7.20–7.38 (m, 5H, Ph), 6.66–6.69 (d, 2H, J = 8.4 Hz, Ph), 6.44–6.47 (d, 2H, J = 8.4 Hz, Ph), 4.42 (q, 1H, J = 6.6 Hz, C*H*), 3.60 (S, 3H, O*Me*), 1.47 (d, 3H, J = 6.6 Hz, *Me*). δ_C (62.9 MHz, $CDCl_3$): 151.9, 144.4, 141.5, 128.6, 126.8, 125.9, 114.7, 114.5, 55.7, 54.2, 25.0. HRMS (EI+) calcd for $C_{15}H_{17}NO$: 227.131; found: 227.130 (Table 1, entry 15).

Tribenzylamine

mp 91 °C (lit.[25l] 91 °C). δ_H (250 MHz, $CDCl_3$): 7.44–7.21 (m, 15H, Ph), 3.56 (s, 6H, CH_2). δ_C (62.9 MHz, $CDCl_3$): 140.1, 129.2, 128.6, 127.3, 58.3. HRMS (EI+) calcd for $C_{21}H_{21}N$: 287.1674; found: 287.1670 (Table 1, entry 18).

N-*Benzylmorpholine*

mp 168 °C (lit.[25l] 170 °C). δ_H (250 MHz, $CDCl_3$): 7.20–7.29 (m, 5H, Ph), 3.68 (t, 4H, J = 4.8 Hz, CH_2), 2.41 (t, 4H, J = 4.6 Hz, CH_2), 3.45 (s, 2H, PhCH_2). δ_C (62.9 MHz, $CDCl_3$): 137.7, 129.2, 128.2, 127.1, 67.0, 63.5, 53.6. HRMS (EI+) calcd for $C_{11}H_{15}NO$: 177.1154; found: 177.1148 (Table 1, entry 19).

General procedure for the conversion of acids to amides

To a stirred solution of Ph_2PCl (1.5 mmol) and imidazole (4.5 mmol) in 5 mL dichloromethane at reflux were added iodine (1.5 mmol) and acids (2.0 mmol), successively. Amines (2.0 mmol) were then added to the reaction mixture. After completion of the reaction, the organic layer was washed with saturated aqueous sodium carbonate (3 × 5 mL) and then aqueous sodium thiosulfate (2 × 5 mL), and then dried. The residue was subjected to flash chromatography over silica gel by using *n*-hexane / ethyl acetate as eluent to give the pure amides.

Benzanilide

mp 161 °C (lit.[25a] 163 °C). δ_H (250 MHz, $CDCl_3$): 7.15–8.08 (complex, 11H, Ph). δ_C (62.9 MHz, $CDCl_3$): 165.8, 137.9, 133.6, 131.8, 128.8, 128.4, 127.0, 124.6, 120.3. HRMS (EI+) calcd for $C_{13}H_{11}NO$: 197.0841; found: 197.0835 (Table 3, entry 1).

4-Methyl*-N-*phenylbenzamide

mp 147 °C (lit.[26a] 145 °C). δ_H (250 MHz, $CDCl_3$): 7.90 (s, 1H, N*H*), 7.68 (d, 2H, J = 8.0 Hz, Ph), 7.59 (d, 2H, J = 7.6 Hz, Ph), 7.42 (t, 2H, J = 7.8 Hz, Ph), 7.25 (d, 2H, J = 8.2 Hz, Ph), 7.23 (t, 1H, J = 7.4 Hz, Ph), 2.38 (s, 3H, *Me*). δ_C (62.9 MHz, $CDCl_3$): 167.2, 142.5, 137.8, 131.6, 129.5, 129.1, 128.4, 124.6, 119.8, 21.3. HRMS (EI+) calcd for $C_{14}H_{13}NO$: 211.0997; found: 211.0988 (Table 3, entry 2).

4-Nitro*-N-*phenylbenzamide

mp 211–213 °C (lit.[26b] 211–212 °C). δ_H (250 MHz, d_6-DMSO): 10.54 (s, 1H, N*H*), 8.36 (d, 2H, J = 8.8 Hz, Ph), 8.16 (d, 2H, J = 8.8 Hz, Ph), 7.76 (d, 2H, J = 8.3 Hz, Ph), 7.36 (m, 2H, Ph), 7.10–7.15 (m, 1H, Ph). δ_C (62.9 MHz, $CDCl_3$): 164.2, 157.5, 134.1, 133.8, 129.2, 128.7, 124.1, 123.5, 120.4. HRMS (EI+) calcd for $C_{13}H_{10}N_2O_3$: 242.0691; found: 242.0680 (Table 3, entry 3).

N-*(4-Methoxyphenyl)benzamide*

mp 154 °C (lit.[26c] 156–157 °C). δ_H (250 MHz, $CDCl_3$): 7.77 (d, 2H, J = 8.1 Hz, Ph), 7.64 (s, 1H, N*H*), 7.39–7.61 (m, 5H, Ph), 6.78 (d, 2H, J = 8.5 Hz, Ph), 3.85 (s, 3H, O*Me*). δ_C (62.9 MHz, $CDCl_3$): 165.7, 155.9, 137.1, 132.3, 131.2, 128.9, 127.5, 122.0, 114.9, 55.4. HRMS (EI+) calcd for $C_{14}H_{13}NO_2$: 227.0946; found: 227.0940 (Table 3, entry 4).

N-*(4-Methoxyphenyl)-4-nitrobenzamide*

mp 198–200 °C (lit.[26d] 199–201 °C). δ_H (250 MHz, d_6-DMSO): 10.45 (s, 1H, N*H*), 8.33 (d, 2H, J = 8.7 Hz, Ph), 8.16 (d, 2H, J = 8.7 Hz, Ph), 7.70 (d, 2H, J = 8.9 Hz, Ph), 6.93 (d, 2H, J = 8.9 Hz, Ph), 3.74 (s, 3H, O*Me*). δ_C (62.9 MHz, d_6-DMSO): 163.3, 155.8, 149.0, 140.6, 131.7, 129.0, 123.4, 122.0, 113.7, 55.1. HRMS (EI+) calcd for $C_{14}H_{12}N_2O_4$: 272.0797; found: 272.0785 (Table 3, entry 5).

N-*(4-Methoxyphenyl)-4-methylbenzamide*

mp 166 °C (lit.[26e] 166 °C). δ_H (250 MHz, $CDCl_3$): 9.35 (s, 1H, N*H*), 7.88 (d, 2H, J = 8.4 Hz, Ph), 7.73 (d, 2H, J = 9.3 Hz, Ph), 7.28 (d, 2H, J = 8.4 Hz, Ph), 6.90 (d, 2H, J =

Can. J. Chem. Downloaded from www.nrcresearchpress.com by Renmin University of China on 09/02/12
For personal use only.

9.3 Hz, Ph), 3.77 (s, 3H, O*Me*), 2.38 (s, 3H, *Me*). δ_C (62.9 MHz, $CDCl_3$): 164.8, 156.3, 141.8, 131.2, 129.2, 128.2, 127.4, 114.5, 55.9, 24.3. HRMS (EI+) calcd for $C_{15}H_{15}NO_2$: 241.1103; found: 241.1100 (Table 3, entry 6).

N-*(4-Chlorophenyl)benzamide*

mp 187 °C (lit.[26f] 188–190 °C). δ_H (250 MHz, $CDCl_3$): 7.75 (d, 2H, J = 7.0 Hz, Ph), 7.71 (s, 1H, N*H*), 7.64–7.52 (m, 5H, Ph), 7.43 (d, 2H, J = 8.7 Hz, Ph). δ_C (62.9 MHz, $CDCl_3$): 163.9, 137.3, 132.2, 128.9, 127.6, 126.7, 126.1, 121.6, 120.8. HRMS (EI+) calcd for $C_{13}H_{10}ClNO$:231.0451; found: 231.0442 (Table 3, entry 7).

N-*(3-Nitrophenyl)benzamide*

mp 155 °C (lit.[26g] 157 °C); δ_H (250 MHz, d_6-DMSO): 9.80 (s, 1H, N*H*), 7.52–7.55 (m, 1H, Ph), 7.42 (s, 1H, Ph), 7.23–7.37 (m, 6H, Ph), 6.86–6.89 (m, 1H, Ph). δ_C (62.9 MHz, $CDCl_3$): 164.8, 148.6, 136.8, 134.2, 132.2, 129.9, 128.9, 127.7, 127.5, 116.7, 115.5. HRMS (EI+) calcd for $C_{13}H_{10}N_2O_3$: 242.0691; found: 242.0684 (Table 3, entry 8).

N-*(4-Nitrophenyl)benzamide*

mp 197 °C (lit.[26h] 198–199 °C). δ_H (250 MHz, d_6-DMSO): 9.95 (s, 1H, N*H*),7.83–8.18 (d, 2H, J = 7.2 Hz, Ph), 7.69–7.76 (m, 3H, Ph), 7.39–7.55 (m, 4H, Ph). δ_C (62.9 MHz, d_6-DMSO): 164.0, 143.1, 141.4, 131.6, 129.2, 128.6, 128.1, 123.3, 120.0. HRMS (EI+) calcd for $C_{13}H_{10}N_2O_3$: 242.0691; found: 242.0681 (Table 3, entry 9).

N-*Benzylbenzamide*

mp 104–106 °C (lit.[26i] 103–104 °C). δ_H (250 MHz, $CDCl_3$): 7.70 (d, 2H, J = 8.4 Hz, Ph), 7.21–740 (m, 8H, Ph), 6.53 (s, 1H, N*H*), 4.54 (d, 2H, J = 5.7 Hz, CH_2). δ_C (62.9 MHz, $CDCl_3$): 167.4, 138.2, 134.4, 131.5, 128.8, 128.6, 127.9, 127.6, 127.0, 44.1. HRMS (EI+) calcd for $C_{14}H_{13}NO$: 211.0997; found: 211.0990 (Table 3, entry 10).

N-*Benzyl-4-methylbenzamide*

mp 137 °C (lit.[26j] 138 °C). δ_H (250 MHz, $CDCl_3$): 7.69 (d, 2H, J = 8.1 Hz, Ph), 7.36 (d, 4H, J = 4.3 Hz, Ph), 7.31–7.33 (m, 1H, Ph), 7.23–7.22 (m, 2H, Ph), 6.32 (s, 1H, N*H*), 4.65 (d, J = 5.6 Hz, 2H, CH_2), 2.39 (s, 3H, *Me*). δ_C (62.9 MHz, $CDCl_3$): 167.2, 141.9, 138.3, 131.5, 129.2, 128.7, 127.9, 127.6, 126.9, 44.1, 21.4. HRMS (EI+) calcd for $C_{15}H_{15}NO$: 225.1154; found: 225.1143 (Table 3, entry 11).

N-*Methyl*-N-*phenylbenzamide*

mp 104–106 °C (lit.[26k] 103–104 °C). δ_H (250 MHz, $CDCl_3$): 7.65 (d, 2H, J = 7.1 Hz, Ph), 7.14–7.47 (m, 3H, Ph), 6.71–6.93 (m, 5H, Ph), 3.52 (s, 3H, *Me*). δ_C (62.9 MHz, $CDCl_3$): 168.3, 142.7, 136.4, 129.1, 129.0, 128.7, 127.5, 126.7, 126.0, 39.6. HRMS (EI+) calcd for $C_{14}H_{13}NO$: 211.0997; found: 211.0987 (Table 3, entry 12).

N-*Methyl-4-nitro*-N-*phenylbenzamide*

mp 109–111 °C (lit.[26a] 106–107 °C). δ_H (250 MHz, $CDCl_3$): 8.01–8.33 (m, 4H, Ph), 6.63–6.82 (m, 5H, Ph), 3.46 (s, 3H, *Me*). δ_C (62.9 MHz, $CDCl_3$): 165.7, 150.6, 144.3, 141.3, 132.6, 130.8, 130.2, 128.7, 124.5, 37.8. HRMS (EI+) calcd for $C_{14}H_{12}N_2O_3$: 256.0848; found: 256.0832 (Table 3, entry 13).

4-Methyl*-N-*methyl*-N-*phenylbenzamide

mp 66 °C (lit.[26l] 68 °C). δ_H (250 MHz, $CDCl_3$): 7.21 (m, 4H, Ph), 7.13 (tt, 1H, J = 1.2, 6.6 Hz, Ph), 7.00 (d, 2H, J = 7.2 Hz, Ph), 6.94 (d, 2H, J = 7.8 Hz, *Me*), 3.46 (s, 3H), 2.24 (s, 3H, *Me*). δ_C (62.9 MHz, $CDCl_3$): 170.7, 145.2, 139.8, 132.9, 129.1, 128.9, 128.3, 126.8, 126.3, 38.5, 21.3. HRMS (EI+) calcd for $C_{15}H_{15}NO$: 225.1154; found: 225.1141 (Table 3, entry 14).

N-*Phenylpropionamide*

mp 97–99 °C (lit.[26m] 98–100 °C). δ_H (250 MHz, $CDCl_3$): 7.15 (s, 1H, N*H*), 7.07–7.52 (m, 5H, Ph), 2.39 (2H, q, J = 7.5 Hz, COCH_2), 1.25 (3H, t, J = 7.5 Hz, $COCH_2CH_3$). δ_C (62.9 MHz, $CDCl_3$): 172.0, 137.9, 128.9, 124.1, 119.7, 30.7, 9.6. HRMS (EI+) calcd for $C_9H_{11}NO$: 149.0841; found: 149.0834 (Table 3, entry 15).

N-*Phenylbenzothioamide*

mp 102–103 °C (lit.[26n] 100–101 °C). δ_H (250 MHz, $CDCl_3$): 9.00 (s, 1H, N*H*), 7.27–7.87 (m, 10H, Ph). δ_C (62.9 MHz, $CDCl_3$): 198.4, 142.8, 139.1, 131.3, 129.0, 128.5, 127.2, 127.0, 124.0. HRMS (EI+) calcd for $C_{13}H_{11}NS$: 213.0612; found: 213.0601 (Table 3, entry 16).

N-*Phenylethanethioamide*

mp 74–76 °C (lit.[26n] 75–76 °C). δ_H (250 MHz, $CDCl_3$): 9.51 (s, 1H, N*H*), 7.33–7.48 (m, 5H, Ph), 2.75 (s, 3H, *Me*). δ_C (62.9 MHz, $CDCl_3$): 200.7, 137.8, 128.8, 127.1, 124.4, 30.1. HRMS (EI+) calcd for C_8H_9NS: 151.0456; found: 151.0441 (Table 3, entry 17).

Acknowledgements

We thank the Persian Gulf University Research Council for generous partial financial support of this study.

References

(1) Gololobov, Y. G.; Zhmurova, I. N.; Kasukhin, L. F. *Tetrahedron* **1981**, *37* (3), 437. doi:10.1016/S0040-4020(01)92417-2.

(2) (a) Mitsunobu, O.; Yamada, M.; Mukaiyama, T. *Bull. Chem. Soc. Jpn.* **1967**, *40* (4), 935. doi:10.1246/bcsj.40.935; (b) Mitsunobu, O.; Eguchi, M. *Bull. Chem. Soc. Jpn.* **1971**, *44* (12), 3427. doi:10.1246/bcsj.44.3427.

(3) Wittig, G.; Schollkopf, U. *Chem. Ber.* **1954**, *87* (9), 1318. doi:10.1002/cber.19540870919.

(4) (a) Firouzabadi, H.; Iranpoor, N.; Sobhani, S. *Tetrahedron* **2004**, *60* (1), 203. doi:10.1016/j.tet.2003.10.058; (b) Hanessian, S.; Ponpipom, M. M.; Lavallee, P. *Carbohydr. Res.* **1972**, *24* (1), 45. doi:10.1016/S0008-6215(00)82258-2; (c) Iranpoor, N.; Firouzabadi, H.; Aghapour, G. *Synlett* **2001**, *2001* (7), 1176. doi:10.1055/s-2001-15157; (d) Iranpoor, N.; Firouzabadi, H.; Aghapour, G.; Vaes Zadeh, A. R. *Tetrahedron* **2002**, *58* (43), 8689. doi:10.1016/S0040-4020(02)01089-X.

(5) (a) Iranpoor, N.; Firouzabadi, H.; Chitsazi, M.; Jafari, A. A. *Tetrahedron* **2002**, *58* (35), 7037. doi:10.1016/S0040-4020(02)00699-3; (b) Barluenga, J.; Campos, P. J.; Gonzalez-Nunez, E.; Asensio, G. *Synthesis* **1985**, *1985* (04), 426. doi:10.1055/s-1985-31228; (c) Caputo, R.; Ferreri, C.; Palumbo, G. *Synth. Commun.* **1987**, *17* (13), 1629. doi:10.1080/00397918708057794.

(6) Iranpoor, N.; Firouzabadi, H.; Aghapour, G. *Synth. Commun.* **2002**, *32* (16), 2535. doi:10.1081/SCC-120005936.

Can. J. Chem. Downloaded from www.nrcresearchpress.com by Renmin University of China on 09/02/12
For personal use only.

(7) (a) Tunoori, A. R.; Dutta, D.; Georg, G. I. *Tetrahedron Lett.* **1998**, *39* (48), 8751. doi:10.1016/S0040-4039(98)01988-1; (b) Lizarzaburu, M. E.; Shuttleworth, S. J. *Tetrahedron Lett.* **2003**, *44* (26), 4873. doi:10.1016/S0040-4039(03)01117-1; (c) Gentles, R. G.; Wodka, D.; Park, D. C.; Vasudevan, A. *J. Comb. Chem.* **2002**, *4* (5), 442. doi:10.1021/cc010090j; (d) Choi, M. K. W.; He, H. S.; Toy, P. H. *J. Org. Chem.* **2003**, *68* (25), 9831. doi:10.1021/jo035226+.

(8) (a) Wentworth, P.; Vandersteen, A. M.; Janda, K. D. *Chem. Commun. (Camb.)* **1997**, 759; (b) Dickerson, T. J.; Reed, N. N.; Janda, K. D. *Chem. Rev.* **2002**, *102* (10), 3325. doi:10.1021/cr010335e.

(9) Amos, R. A.; Emblidge, R. W.; Havens, N. *J. Org. Chem.* **1983**, *48* (20), 3598. doi:10.1021/jo00168a058.

(10) Camp, D.; Jenkins, I. D. *Aust. J. Chem.* **1988**, *41* (12), 1835. doi:10.1071/CH9881835.

(11) von Itzstein, M.; Mocerino, M. *Synth. Commun.* **1990**, *20* (13), 2049. doi:10.1080/00397919008053136.

(12) (a) Iranpoor, N.; Firouzabadi, H.; Jamalian, A.; Kazemi, F. *Tetrahedron* **2005**, *61* (23), 5699. doi:10.1016/j.tet.2005.01.115; (b) Iranpoor, N.; Firouzabadi, H.; Jamalian, A. *Tetrahedron Lett.* **2005**, *46* (46), 7963. doi:10.1016/j.tetlet.2005.09.078; (c) Iranpoor, N.; Firouzabadi, H.; Jamalian, A. *Tetrahedron* **2006**, *62* (8), 1823. doi:10.1016/j.tet.2005.11.042.

(13) Desmaris, L.; Percina, N.; Cottier, L.; Sinou, D. *Tetrahedron Lett.* **2003**, *44* (41), 7589. doi:10.1016/j.tetlet.2003.08.064.

(14) Nowrouzi, N.; Mehranpour, A. M.; Ameri Rad, J. *Tetrahedron* **2010**, *66* (50), 9596. doi:10.1016/j.tet.2010.10.022.

(15) Rachinskii, F. Y.Potapenko, T. G.Shapilov, O. D.Osipyan, V. T.Krupenina, A. A. *Zh. Prikladnoi Khim.* **1968**, *41*, 1072.

(16) Seayad, A. M. A.; Klein, H.; Jackstell, R.; Gross, T.; Beller, M. *Science* **2002**, *297* (5587), 1676. doi:10.1126/science.1074801.

(17) Smith, M. B.; March, J. *March's Advanced Organic Chemistry: Reactions, Mechanisms, and Structure,* 6th ed.; Wiley: Hoboken, NJ, 2007; p 555.

(18) (a) Hamid, M. H. S. M.; Williams, J. M. J. *Chem. Commun. (Camb.)* **2007**, *2007* (7), 725. doi:10.1039/b616859k; (b) Chen, B. C.; Sundeen, J. A.; Guo, P.; Bednarz, M. S.; Zhao, R. *Tetrahedron Lett.* **2001**, *42* (7), 1245. doi:10.1016/S0040-4039(00)02257-7; (c) Szardenings, A. K.; Burkoth, T. S.; Look, G. C.; Campbell, D. A. *J. Org. Chem.* **1996**, *61* (19), 6720. doi:10.1021/jo960124n; (d) Fache, F.; Valot, F.; Milenkovic, A.; Lemaire, M. *Tetrahedron* **1996**, *52* (29), 9777. doi:10.1016/0040-4020(96)00503-0.

(19) Salomaa, S. In *The Chemistry of the Carbonyl Group;* Patai, S., Ed.; Wiley: New York, 1966; Vol. 1, p 177.

(20) (a) Fujita, K.; Li, Z.; Ozeki, N.; Yamaguchi, R. *Tetrahedron Lett.* **2003**, *44* (13), 2687. doi:10.1016/S0040-4039(03)00371-X; (b) Murty, M. S. R.; Jyothirmai, B.; Krishna, P. R.; Yadav, J. S. *Synth. Commun.* **2003**, *33* (14), 2483. doi:10.1081/SCC-120021838; (c) Kimura, M.; Futamata, M.; Shibata, K.; Tamaru, Y. *Chem. Commun. (Camb.)* **2003**, *2003* (2), 234. doi:10.1039/b210920d; (d) Valot, F.; Fache, F.; Jacquot, R.; Spagnol, M.; Lemaire, M. *Tetrahedron Lett.* **1999**, *40* (19), 3689. doi:10.1016/S0040-4039(99)00588-2; (e) Matloubi Moghaddam, F.; DokhtTaimoory, S. M.; Ismaili, H.; Rezanejade Bardajee, G. *Synth. Commun.* **2006**, *36*, 3599. doi:10.1080/00397910600943634; (f) Fujita, K.; Enoki, Y.; Yamaguchi, R. *Tetrahedron* **2008**, *64* (8), 1943. doi:10.1016/j.tet.2007.11.083.

(21) (a) Iranpoor, N.; Firouzabadi, H.; Nowrouzi, N.; Khalili, D. *Tetrahedron* **2009**, *65* (19), 3893. doi:10.1016/j.tet.2009.02.078; (b) Iranpoor, N.; Firouzabadi, H.; Khalili, D. *Bull. Chem. Soc. Jpn.* **2010**, *83* (8), 923. doi:10.1246/bcsj.20090269.

(22) (a) Lamberth, C.; Kempf, H. J.; Kriz, M. *Pest Manag. Sci.* **2007**, *63* (1), 57. doi:10.1002/ps.1308; (b) Navickiene, H. M. D.; Miranda, J. E.; Bortoli, S. A.; Kato, M. J.; Bolzani, V. S.; Furlan, M. *Pest Manag. Sci.* **2007**, *63* (4), 399. doi:10.1002/ps.1340.

(23) (a) Mabermann, C. E. In *Encyclopedia of Chemical Technology;* Wiley: New York, 1991; Vol. 1, p 251; (b) Lipp, D. In *Encyclopedia of Chemical Technology;* Wiley: New York, 1991; Vol. 1, p 266; (c) Opsahl, R. In *Encyclopedia of Chemical Technology;* Wiley: New York, 1991; Vol. 2, p 346.

(24) (a) For selected examples: Hassner, A.; Alexanian, V. *Tetrahedron Lett.* **1978**, *19* (46), 4475. doi:10.1016/S0040-4039(01)95256-6; (b) Ziegler, F. E.; Berger, G. D. *Synth. Commun.* **1979**, *9* (6), 539. doi:10.1080/00397917908060958; (c) Saigo, K.; Usui, M.; Kikuchi, K.; Shimada, E.; Mukaiyama, T. *Bull. Chem. Soc. Jpn.* **1977**, *50* (7), 1863. doi:10.1246/bcsj.50.1863; (d) Mukaiyama, T. *Angew. Chem. Int. Ed. Engl.* **1979**, *18* (10), 707. doi:10.1002/anie.197907073; (e) Inanaga, J.; Hirata, K.; Saeki, H.; Katsuki, T.; Yamaguchi, M. *Bull. Chem. Soc. Jpn.* **1979**, *52* (7), 1989. doi:10.1246/bcsj.52.1989; (f) Staab, H. A. *Angew. Chem. Int. Ed. Engl.* **1962**, *1* (7), 351. doi:10.1002/anie.196203511; (g) Diago-Meseguer, J.; Palomo-Coll, A. L.; Fernádez-Lizarbe, J. R.; Zugaza-Bilbao, A. *Synthesis* **1980**, *1980* (7), 547. doi:10.1055/s-1980-29116; (h) Shiina, I.; Ibuka, R.; Kubota, M. *Chem. Lett.* **2002**, *31* (3), 286. doi:10.1246/cl.2002.286; (i) Shiina, I.; Kubota, M.; Ibuka, R. *Tetrahedron Lett.* **2002**, *43* (42), 7535. doi:10.1016/S0040-4039(02)01819-1; (j) Montalbetti, C. A. G. N.; Falque, V. *Tetrahedron* **2005**, *61* (46), 10827. doi:10.1016/j.tet.2005.08.031; (k) Wakasugi, K.; Nakamura, A.; Iida, A.; Nishii, Y.; Nakatani, N.; Fukushima, S.; Tanabe, Y. *Tetrahedron* **2003**, *59* (28), 5337. doi:10.1016/S0040-4020(03)00734-8; (l) Yan, Z.; Tian, W.; Zeng, F.; Dai, Y. *Tetrahedron Lett.* **2009**, *50* (23), 2727. doi:10.1016/j.tetlet.2009.03.102; (m) Yamada, S.; Abe, M. *Tetrahedron* **2010**, *66* (45), 8667. doi:10.1016/j.tet.2010.09.016; (n) Ruan, Z.; Lawrence, R. M.; Cooper, C. B. *Tetrahedron Lett.* **2006**, *47* (43), 7649. doi:10.1016/j.tetlet.2006.08.024; (o) Saito, Y.; Ouchi, H.; Takahata, H. *Tetrahedron* **2008**, *64* (49), 11129. doi:10.1016/j.tet.2008.09.094; (p) Khalafi-Nezhad, A.; Parhami, A.; Soltani Rad, M. N.; Zarea, A. *Tetrahedron Lett.* **2005**, *46* (40), 6879. doi:10.1016/j.tetlet.2005.08.021.

(25) (a) Lide, D. R., Ed.*CRC Handbook of Chemistry and Physics;* 87th Ed.; CRC Press: London, 2006–2007; (b) Fujita, K.; Enoki, Y.; Yamaguchi, R. *Tetrahedron* **2008**, *64* (8), 1943. doi:10.1016/j.tet.2007.11.083; (c) Yang, M.; Liu, F. *J. Org. Chem.* **2007**, *72* (23), 8969. doi:10.1021/jo0712291; (d) Apodaca, R.; Xiao, W. *Org. Lett.* **2001**, *3* (11), 1745. doi:10.1021/ol015948s; (e) Tajbakhsh, M.; Hosseinzadeh, R.; Alinezhad, H.; Ghahari, S.; Heydari, A.; Khaksar, S. *Synthesis* **2011**, *2011* (03), 490. doi:10.1055/s-0030-1258384; (f) Heydari, A.; Khaksar, S.; Esfandyari, M.; Tajbakhsh, M. *Tetrahedron* **2007**, *63* (16), 3363. doi:10.1016/j.tet.2007.02.026; (g) Huang, Y.; Yi, W.; Cai, C. *J. Fluor. Chem.* **2010**, *131* (8), 879. doi:10.1016/j.jfluchem.2010.04.010; (h) Itoh, T.; Nagata, K.; Miyazaki, M.; Ishikawa, H.; Kurihara, A.; Ohsawa, A. *Tetrahedron* **2004**, *60* (31), 6649. doi:10.1016/j.tet.2004.05.096; (i) Zhu, C.; Akiyama, T. *Synlett* **2011**, 1251; (j) Zhang, M.; Moore, J. D.; Flynn, D. L.; Hanson, P. R. *Org. Lett.* **2004**, *6* (16), 2657. doi:10.1021/ol049209y; (k) Wang, Z.; Ye, X.; Wei, S.; Wu, P.; Zhang, A.; Sun, J. *Org. Lett.* **2006**, *8* (5), 999. doi:10.1021/ol060112g; (l) Hamid, M. H. S. A.; Allen, C. L.; Lamb, G. W.; Maxwell, A. C.; Maytum, H. C.; Watson, A. J.

A.; Williams, J. M. J. *J. Am. Chem. Soc.* **2009**, *131* (5), 1766. doi:10.1021/ja807323a.

(26) (a) Mohammadpoor-Baltork, I.; Memarian, H. R.; Bahrami, K. *Monatsh. Chem.* **2004**, *135*, 411; (b) Zacuto, M. J.; Xu, F. *J. Org. Chem.* **2007**, *72* (16), 6298. doi:10.1021/jo070553t; (c) Katritzky, A. R.; Cai, C.; Singh, S. K. *J. Org. Chem.* **2006**, *71* (9), 3375. doi:10.1021/jo052443x; (d) Yang, X.; Zeng, X.; Zhao, Y.; Wang, X.; Pan, Z.; Li, L.; Zhang, H. *J. Comb. Chem.* **2010**, *12* (3), 307. doi:10.1021/cc900135f; (e) Hwang, S.; Choi, S. Y.; Lee, J. H.; Kim, S.; In, J.; Ha, S. K.; Lee, E.; Kim, T. Y.; Kim, S. Y.; Choi, S.; Kim, S. *Bioorg. Med. Chem.* **2010**, *18* (15), 5602. doi:10.1016/j.bmc.2010.06.034; (f) Zhang, Z.; Yu, Y.; Liebeskind, L. S. *Org. Lett.* **2008**, *10* (14), 3005. doi:10.1021/ol8009682; (g) Ueda, S.; Nagasawa, H. *J. Org. Chem.* **2009**, *74* (11), 4272. doi:10.1021/jo900513z; (h) Prasad, A. K.; Kumar, V.; Malhotra, S.; Ravikumar, V. T.; Sanghvi, Y. S.; Parmar, V. S. *Bioorg. Med. Chem.* **2005**, *13* (14), 4467. doi:10.1016/j.bmc.2005.04.038; (i) Saito, Y.; Ouchi, H.; Takahata, H. *Tetrahedron* **2008**, *64* (49), 11129. doi:10.1016/j.tet.2008.09.094; (j) Huang, Z.; Reilly, J. E.; Buckle, R. N. *Synlett* **2007**, *2007* (7), 1026. doi:10.1055/s-2007-973890; (k) Itai, A.; Toriumi, Y.; Tomioka, N.; Kagechika, H.; Azumaya, I.; Shudo, K. *Tetrahedron Lett.* **1989**, *30* (45), 6177. doi:10.1016/S0040-4039(01)93335-0; (l) Baroudi, A.; Alicea, J.; Flack, P.; Kirincich, J.; Alabugin, I. V. *J. Org. Chem.* **2011**, *76* (6), 1521. doi:10.1021/jo102467j; (m) Singh, K.; Singh, K. *Tetrahedron* **2009**, *65* (50), 10395. doi:10.1016/j.tet.2009.10.037; (n) Liu, L.; An, N.; Pi, H.; Ying, J.; Du, W.; Deng, W. *Synlett* **2011**, 979.

Can. J. Chem. Downloaded from www.nrcresearchpress.com by Renmin University of China on 09/02/12
For personal use only.

Studies on the reaction of nitric oxide with α,β-unsaturated hydrazones

Desuo Yang, Xiaolin Luo, Haiyun Zhu, Yaning Guo, and Longmin Wu

Abstract: α,β-Unsaturated arylhydrazones (**1**) reacted with nitric oxide (NO) in the presence of a trace of oxygen to give α-(**2a**–**2c**, **2e**, and **2f**) or β-nitro (**2d** and **2g**) unsaturated hydrazones in good yield and with high stereoselectivity. The reaction occurs most likely by an electrophilic addition of NO_2 to the carbon–carbon double bond of **1** at its α- or β-position.

Key words: α,β-unsaturated hydrazone, nitric oxide, nitration reaction, electrophilic addition.

Résumé : Les arylhydrazones α,β-insaturées (**1**) réagissent avec l'oxyde nitrique (NO), en présence d'une trace d'oxygène pour conduire à la formation d'α- (**2a**–**2c**, **2e** et **2f**) ou de β-nitrohydrazones (**2d** et **2g**) insaturées, avec des bons rendements et une grande stéréosélectivité. La réaction se produit très probablement par une addition électrophile de NO_2 sur les positions α ou β de la double liaison carbone–carbone du composé **1**.

Mots-clés : hydrazone α,β-insaturée, oxyde nitrique, réaction de nitration, addition électrophile.

[Traduit par la Rédaction]

Can. J. Chem. Downloaded from www.nrcresearchpress.com by Renmin University of China on 09/02/12
For personal use only.

Introduction

Studies on nitric oxide (NO) associated with life processes have attracted more attention from scientists. The proper regulation of NO levels has been proposed as a desirable target for developing new medicines.[1] Therefore, intensive investigations have been directed toward reactions of NO with biological molecules[2] and various organic molecules, such as alkenes,[3] Schiff bases or oximes,[4] epoxides,[5] polycyclic aromatic hydrocarbons,[6] chalcone derivatives,[7] coumarins,[8] flavanones,[9] and hydrazones.[10]

Hydrazone compounds with an active imine double bond are widely used to construct chiral configurations and certain specific skeletons in organic synthesis.[11] In recent years, some hydrazones and their complexes have been found to have good bioactivity in the anticancer,[12] antimalarial,[13] and antiviral aspects.[14] As part of continuing efforts to explore biological applications of NO chemistry and ongoing studies on the reaction of NO with organic molecules, we studied the reaction of NO with saturated arylhydrazones in the presence of trace oxygen. It was found that the reaction of NO with aldehyde arylhydrazones provided exclusively C(1′)-nitrohydrazones with E-configurations,[15] and that ketone arylhydrazones afforded mononitrated azo-compounds.[16]

Gillis and LaMontagne[17] studied the oxidation of cinnamaldehyde monomethylhydrazone with lead tetraacetate and obtained the corresponding *N*-acetylcinnamic acid methylhydrazide. Kamitori et al.[18] reported that the trifluoroacetylation of dialkylhydrazones of α,β-unsaturated aldehydes occurred at the terminal carbon of the conjugate system. In conjunction with alkenes and simple hydrazones, the reaction of α,β-unsaturated hydrazones with NO is suggested to occur by a different mechanism from saturated hydrazones because of the existence of both C=C and C=N bonds in α,β-unsaturated hydrazones. In the present work we will report research on the reaction of NO with α,β-unsaturated aldehyde and ketone arylhydrazones.

α,β-Unsaturated arylhydrazones (**1**) were prepared by the reaction of an α,β-unsaturated ketone with 2,4-dinitrophenylhydrazine in ethanol. The crude products were obtained after removal of the solvent. Further purifications were done according to literature procedure.[19] The products were characterized by NMR, MS, and IR. The reaction of NO with **1** was examined in the presence of trace oxygen in CH_2Cl_2 at room temperature (Scheme 1). The unique products, α-nitrohydrazones (**2a**–**2c**, **2e**, and **2f**) or β-nitrohydrazones (**2d** and **2g**), were obtained in high yield. In the case of **1e** a small quantity of α-nitro alkenyl azo-compound (**2e′**) was also obtained. These results indicate that the reaction of NO with **1** occurs in a different way, compared with those of saturated hydrazones. It is proposed that the π bond of the C=C of **1** breaks during the reaction and a fresh C=C double bond is regenerated by an elimination reaction.

Results and discussion

Nitration reaction of NO with α,β-unsaturated arylhydrazones

Under similar conditions, compound **1** reacted with NO in the presence of minute amounts of oxygen affording a more complex pattern of products than the saturated hydrazones.[15,16] One hydrogen atom at the C=C bond of **1** was

Received 29 June 2011. Accepted 27 March 2012. Published at www.nrcresearchpress.com/cjc on 10 May 2012.

D. Yang, X. Luo, H. Zhu, and Y. Guo. Department of Chemistry & Engineering, Baoji University of Arts & Science, Baoji, 721013, P. R. China.
L. Wu. State Key Laboratory of Applied Organic Chemistry, Lanzhou University, Lanzhou, 730000, P.R. China.

Corresponding author: D. Yang (e-mail: yangds09@163.com).

Scheme 1.

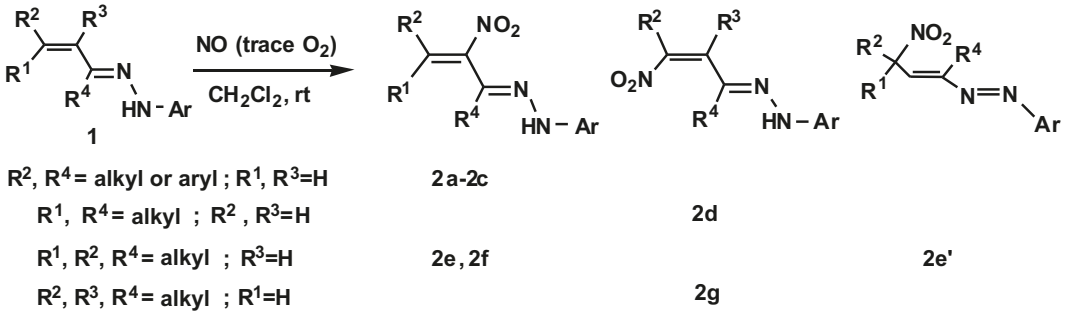
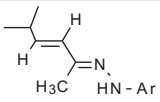
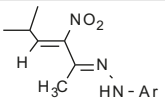
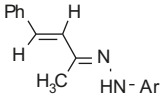
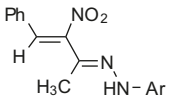
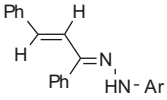
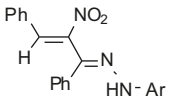
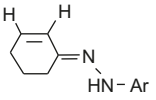
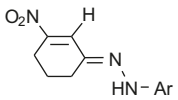
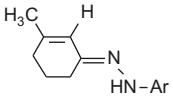
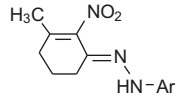
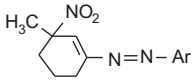
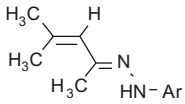
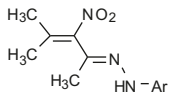
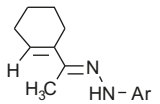
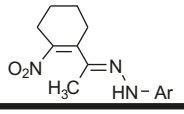


Table 1. Reaction of NO with α,β-unsatured hydrazones in CH_2Cl_2.

Entry	Substrate	Product	Time (h)*	Yield of **2** (%)†
a			11	84
b			8	82
c			9	71
d			13	76
			12	73
e		 **2e'**	12	14
f			8	89
g			14	86

*The reaction time.
†Yield of the isolated product.

exclusively substituted by a nitro group in all cases. It was also found that the nitro group replaces an α-hydrogen atom at the C=C bond with two hydrogen atoms in trans-positions (**2a**–**2c**), whereas the nitro group replaces a β-hydrogen atom (**2d**) when these two hydrogen atoms lay in cis-positions. It was found that **1e** reacted with NO to give **2e** and, in addition, a small amount of an α-nitro alkenyl azo-compound (**2e′**), where the substitution of a hydrogen atom at the C=C bond by a nitro group did not occur.

The nitration reaction of **1** with NO is assumed to occur by an electrophilic addition of NO_2 to the C=C double bond of **1**, most likely similar to that of alkenes.[3,20] At first, NO is oxidized with oxygen to give nitrogen dioxide (NO_2). NO_2 then undergoes an electrophilic addition to either the α-carbon (**1a**–**1c**, **1e**, and **1f**) or β-carbon (**1d** and **1g**) at the C=C bond of **1**, leading to the formation of a carbon radical. Afterwards, the resulting carbon radical couples with three molecules of NO to give a *N*-nitroso-*N*-nitrite compound,[15] followed by a rearrangement, an elimination of HNO_3, and an expulsion of N_2, giving compound **2** (Table 1).

As such, the amount of O_2 in the whole system would play a key role and is closely related to the composition of products and the reaction rate. No product was obtained when oxygen was rigorously excluded from the system.[15]

Can. J. Chem. Downloaded from www.nrcresearchpress.com by Renmin University of China on 09/02/12
For personal use only.

Fig. 1. gHSQC of **2b**.

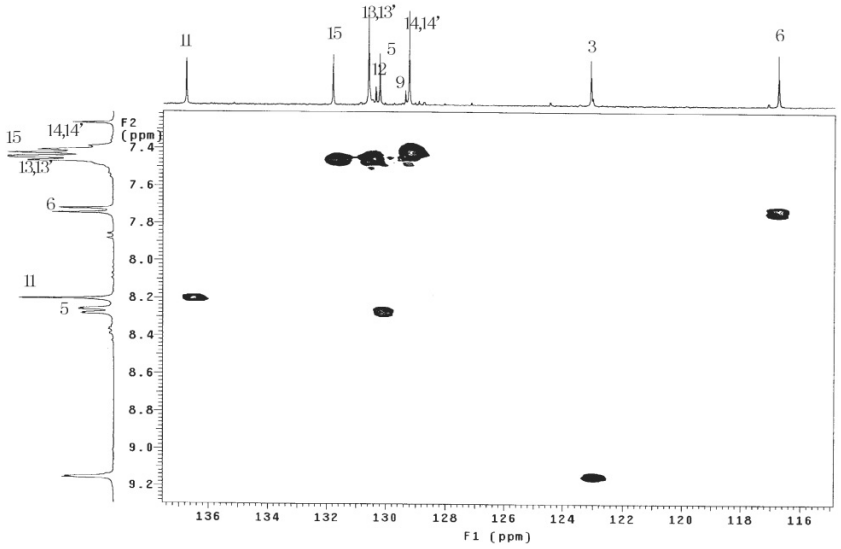
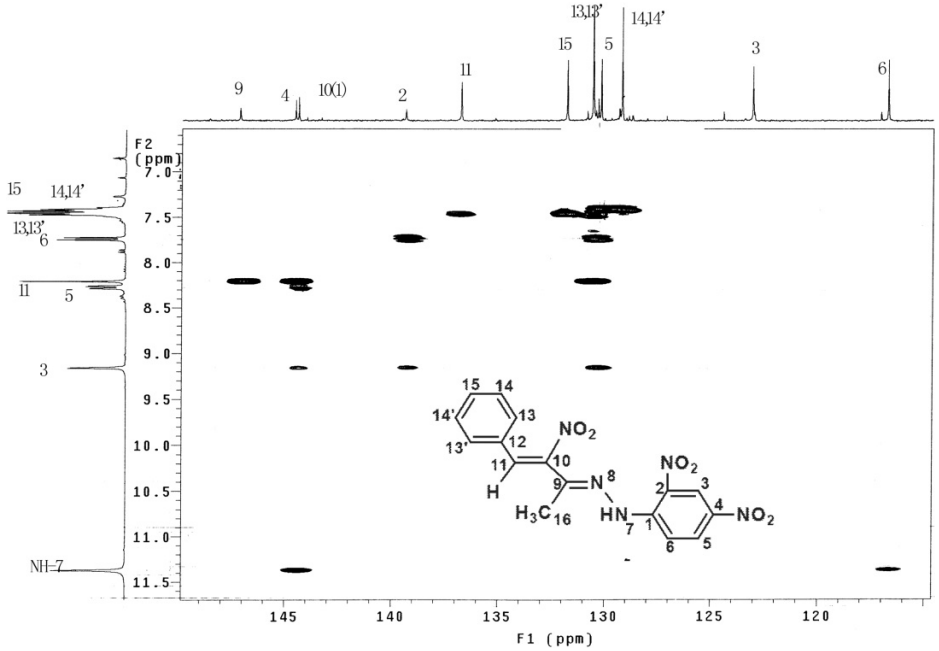


Fig. 2. HMBC of **2b**.



Can. J. Chem. Downloaded from www.nrcresearchpress.com by Renmin University of China on 09/02/12
For personal use only.

Identification of products

MS and HR-MS detections show that all the products were formed by loss of a hydrogen atom from **1** and by introduction of a nitro group. Except for **2e**′, the ν_{N-H} of –NH stretching bands is observed at ~3300 cm^{-1} in the IR spectra of **2**. The observations of a singlet peak at δ ~ 11.0 ppm for one hydrogen and another singlet peak and two doublet peaks at δ 7.2–9.2 ppm in the ^{1}H NMR spectra of **2** are assigned to –NH and 2,4-dinitrophenyl protons, respectively. ^{1}H NMR spectra of **2a**–**2d** also exhibit the loss of one hydrogen at the C=C bond in **1a**–**1d**. These detections indicate that the 2,4-dinitrophenylamino group remains unchanged, and the reaction occurs at the C=C bond rather than at the C=N bond.

A doublet peak at δ ~ 7.20 ppm and a multiplet peak at δ ~ 2.71 ppm are assigned to an isopropyl group (Scheme 1). An NOE enhancement was observed at the CH_3 (δ 2.30 ppm) protons in **2a** upon irradiation of the NH proton (δ 11.32 ppm). This indicates that NH is related to the $–CH_3$ at the C=N bond, i.e., $–CH_3$ and the NH–Ar groups are on the same side of the C=N bond with an E-configuration. When the =CH (δ 7.19 ppm) proton was irradiated, the signal of $–CH_3$ (δ 2.30 ppm) at the C=N bond was enhanced, indicating the nitro and the isopropyl groups are on the same sides of the C=C bond with a Z-configuration.

To determine the position of the nitro group at the C=C bond in **2b**, gHSQC and HMBC experiments were performed (Figs. 1 and 2). Three types of hydrogen, 2,4-dinitrophenyl (H3, H5, and H6), CH_3 (H16), and –NH (H7) in the ^{1}H NMR spectrum of **2b** are easily assigned. A singlet peak at δ ~ 8.20 ppm for one hydrogen is assigned to =CH (H11), and a group of multiple peaks at 7.39–7.49 ppm are assigned

Can. J. Chem. Downloaded from www.nrcresearchpress.com by Renmin University of China on 09/02/12
For personal use only.

to the hydrogens on the substituted phenyl (H13 and H13′, H14 and H14′, and H15). DEPT and gHSQC experiments indicate that H11 connects to C11 (~136.8 ppm). It can also be seen from the HMBC that H11 at the C=C bond is obviously related to a substituted phenyl (7.39–7.49 ppm) (Fig. 2). Similarly, C9 and C10 are relevant to H16 and H11, respectively. Thus, the nitro group can be deduced to lie at the α-position of **2b**. An NOE enhancement establishes the Z-configuration at the C=C bond.

The ^{1}H NMR spectrum of **2c** shows a singlet at δ 8.15 ppm assigned to the proton at the C=C double bond (=CH) and manifests, from its HMBC spectrum, that the =CH proton is related to the substituted phenyl protons (7.06–7.33 ppm). Therefore, the nitro group in **2c** is thought to be also connected to the α-position. NOE enhancements were observed at the phenyl protons of C=N bond upon irradiation of the NH proton (~11.38 ppm) and the proton at the C=C bond. These observations indicate that the phenyl and –NHAr groups are on the same side of the C=N bond and the $-NO_2$ and =CH groups are on opposite sides of the C=C bond. Therefore, a Z-configuration at the C=C bond of **2c** is assigned.

The ^{1}H NMR spectrum of **2d** shows a singlet at δ 7.66 ppm assigned to the =CH proton. Thus, the nitro group is thought to be connected to the β-position. An NOE enhancement was observed at the α-CH_2 protons (~2.64 ppm) of the C=N bond upon irradiation of the NH proton (~11.50 ppm). An E-configuration is assigned to the C=N bond of **2d**.

There is one hydrogen atom at the C=C bonds of **1e**–**1g**. ^{1}H NMR spectra of their products (**2e**–**2g**) display no proton linking at the C=C bond. The ^{13}C NMR spectra of **2e**–**2g** show that the proton of the double bond was replaced by a nitro group. An NOE experiment for **2e** shows its α-CH_2 proton (~2.68 ppm) at the C=N bond was related to the proton of NH (~11.20 ppm). Thus, the C=N group of **2e** with an E-configuration is established.

Compound **1e** reacted with NO to give a small amount of **2e**′ in addition to **2e**. MS and HR-MS detections show **2e**′ and **2e** have the same molecular formula. The ^{1}H NMR spectrum of **2e**′ displays a singlet at δ 7.28 ppm assigned to the =CH, and its ^{13}C NMR spectrum shows a singlet at δ_c 87.1 ppm assigned to a quaternary carbon associated with an NO_2. IR and ^{1}H NMR spectra indicate that there is no NH group in **2e**′. Therefore, product **2e**′ may be inferred to be an azo-compound.

Crystal structure of 2e

X-ray crystallography data for **2e** are shown in Table 2 (see the Supplementary data). Crystal structure and a packing diagram of **2e** are illustrated in Fig. 3, and the selected bond lengths and bond angles are summarized in Table 3. The analytical results indicate that the nitro group is linked at C-5, i.e., the α-carbon (Fig. 3*a*) and the N(3)–C(5) is a single bond (1.476(2) Å). Both the C(4)–C(5) bond length of 1.334(2) Å and the N(1)–C(6) bond length of 1.288(2) Å are assigned to an ethylenic bond and an imine double bond, respectively, in **2e**.

The C(1)–C(2)–C(3)–C(4)–C(5)–C(6) six-membered ring is an envelope-type structure. The vertical distance from C2 to the plane constructed by the remaining five carbon atoms is 0.5 Å. The dihedral angle between the nitro group at C5 (α-carbon) and the six-membered ring plane is 78°. A hydrogen bond exists between the hydrogen atom of NH and the oxygen atom of the *ortho*-nitro group on the benzene ring (Table 4; Fig. 3*b*).

Table 2. Crystal data and structure refinement of **2e**.

Parameter	
Empirical formula	$C_{13}H_{13}N_5O_6$
Formula weight	335.28
Temperature (K)	293 (2)
Wavelength (Å)	0.71073
Crystal system	Monoclinic
Space group	*P*2(1) /*c*
Unit cell dimensions	
a (Å)	14.501(2)
b (Å)	6.362(1)
c (Å)	17.166(2)
α (°)	90
β (°)	110.913(9)
γ (°)	90
Volume (Å^3)	1479.3(3)
Z	4
Density (calcd; g cm^{-3})	1.505
Absorption coefficient (mm^{-1})	0.122
F (000)	696
Crystal description	Needles
Crystal colour	Red
Crystal size (mm)	0.58×0.32×0.32
θ range for data collection (°)	1.50–25.25
Limiting indices	$0\le h\le 17$, $0\le k\le 7$, $-20\le l\le 19$
Reflections collected	3177
Independent reflections	2681 (R_{int} = 0.0145)
Absorption correction	None
Refinement method	Full-matrix least-squares on F^2
Data/restraints/parameters	2681/0/219
Goodness-of-fit on F^2	1.015
Final *R* indices (I > 2σ(*I*))	R_1 = 0.0530, wR_2 = 0.0928
R indices (all data)	R_1 = 0.0342, wR_2 = 0.0868
Extinction coefficient	0.0136(15)
Largest diff. peak and hole (e Å^{-3})	0.162 and –0.149

Conclusion

The present study reports that the reaction of NO with α,β-unsaturated arylhydrazones (**1**) in the presence of a trace of oxygen at room temperature gives α-nitro (**2a**–**2c**, **2e**, and **2f**) or β-nitro (**2d** and **2g**) unsaturated hydrazones in good yield and with high stereoselectivity. The nitration reaction is most likely initiated by an electrophilic addition reaction of NO_2 to the C=C double bond of substrate **1**. A small quantity of α-nitro alkenyl azo-compound (**2e**′) was also formed in the case of **1e**. The nitration reaction discussed herein offers an efficient method for preparing α,β-nitro unsaturated hydrazones and α,β-nitro unsaturated ketones.

Can. J. Chem. Downloaded from www.nrcresearchpress.com by Renmin University of China on 09/02/12
For personal use only.

Experimental

All solvents were distilled prior to use according to standard procedures. Methylene dichloride was dehydrated with CaH_2 by refluxing.

^1H and ^{13}C NMR spectra were recorded on a Bruker Avance 400 (^1H, 400 MHz; or ^{13}C, 100 MHz; δ downfield from TMS). IR analysis was performed on a Nicolet NEXUS 670 FT-IR. Mass data were obtained on a HP-5988A GC–MS, and HR-ESI-MS data were obtained on a Bruker Daltonics APEx II FT-ICR. Melting points were determined with an XT_4-100X micromelting point apparatus and not corrected.

X-ray analysis on single crystals was carried out at 293(2) K on a Nonius CAD4 automatic diffractometer using graphite-monochromated Mo Kα radiation (λ = 0.710 73 Å). Structural solutions and full-matrix least-squares refinements based on F^2 were performed with the SHELXS-97 and SHELXL-97 program packages,[21] respectively. All the non-hydrogen atoms were anisotropically positioned. Hydrogen atoms were placed in geometrical positions and constrained to ride on their parent atoms. Analytical expressions of neutral-atom scattering factors were employed, and anomalous dispersion corrections were incorporated (see the Supplementary data for crystallographic data (excluding structure factors)).[22]

General procedure for the synthesis of 2a–2g

A solution of **1** was prepared by dissolving **1** (0.5 mmol) in 100 mL of anhydrous dichloromethane. NO was produced by dropwise addition of 1 mol L^{-1} H_2SO_4 solution to a stirred saturated aqueous solution of $NaNO_2$ under an argon atmosphere. NO gas was purified by passing through a series of scrubbing bottles containing 4 mol L^{-1} NaOH, distilled water, and anhydrous $CaCl_2$ pellets in this order. The purified NO was bubbled through the stirred solution of **1**, which was previously degassed by argon for approx. 5–10 min and kept at a pressure of up to +10 mm H_2O column over local atmospheric pressure, at ambient temperature for 8–14 h. In the course of the reaction, the argon flow rate was controlled by regulating the flow meter at 0.8 L min^{-1}. A rough estimate of the total amount of NO passing through the solution was about 1000 mmol at the local atmosphere pressure using the ideal gas law. The progress of the reaction was monitored by TLC. After the reaction was complete, the mixture was dried over anhydrous $MgSO_4$, concentrated under vacuum, and purified by column chromatography on silica gel (200–300 mesh; ethyl acetate – petroleum ether, 1:6 v/v), giving pure product **2** (Table 1).

(E)-1-(2,4-Dinitrophenyl)-2-((Z)-5-methyl-3-nitrohex-3-en-2-ylidene)hydrazine (2a)

Yellow needles, mp 129–130 °C. ^1H NMR (400 MHz, $CDCl_3$, ppm) δ: 1.15(d, 6H, *J* = 4.6 Hz), 2.30 (s, 3H), 2.67–2.73 (m, 1H), 7.21 (d, *J* = 12.8 Hz, 1H), 7.89 (d, *J* = 9.6 Hz, 1H), 8.39 (dd, *J* = 9.6, 2.8 Hz, 1H), 9.18 (d, *J* = 2.8 Hz, 1H), 11.32 (s, 1H). ^{13}C NMR (100 MHz, $CDCl_3$, ppm) δ: 16.6, 22.1, 28.4, 63.4, 116.5, 123.2, 130.3, 130.4, 139.2, 144.4, 144.5, 146.9, 147.6. IR (KBr, cm^{-1}) ν_{max}: 3308, 3105, 2973, 2919, 2873, 2848, 1616, 1593, 1501, 1423, 1337, 1136, 1095, 953, 920, 831, 797, 740, 577, 505. HR-ESI-MS *m/z* calcd for $C_{13}H_{15}N_5O_6$ (M^+): 337.1022; found: 337.1011. EIMS *m/z*: 337(M^+), 320, 291, 278, 249, 181, 169, 122, 108, 93, 77, 67, 55.

(E)-1-(2,4-Dinitrophenyl)-2-((Z)-3-nitro-4-phenylbut-3-en-2-ylidene)hydrazine (2b)

Orange needles, mp 147–149 °C. ^1H NMR (400 MHz, $CDCl_3$, ppm) δ: 2.36 (s, 3H), 7.39–7.49 (m, 5H), 7.23 (d, *J* = 9.6 Hz, 1H), 8.20 (s, 1H), 8.26 (dd, *J* = 9.6, 2.4 Hz, 1H), 9.15 (d, *J* = 2.4 Hz, 1H), 11.36 (s, 1H). ^{13}C NMR (100 MHz, $CDCl_3$, ppm) δ: 16.7, 116.8, 123.0, 129.4, 130.2, 130.4, 130.6, 131.8, 136.8, 139.4, 144.4, 144.5, 147.1. IR (KBr, cm^{-1}) ν_{max}: 3308, 3107, 1652, 1615, 1514, 1333, 1139, 1095, 968, 935, 836, 743, 688, 581, 504. HR-ESI-MS *m/z* calcd for $C_{16}H_{17}N_6O_6$ (M + NH_4^+): 389.1209; found: 389.1218. EIMS *m/z*: 371 (M^+), 354, 336, 278, 232, 128, 102, 77, 63, 51, 43.

(E)-1-(2,4-Dinitrophenyl)-2-((E)-2-nitro-1,3-diphenylallylidene)hydrazine (2c)

Orange needles, mp 184–186 °C. ^1H NMR (400 MHz, $CDCl_3$, ppm) δ: 7.06–7.33 (m, 10H), 7.68 (d, *J* = 12.8 Hz, 1H), 8.15 (1H, s), 8.30 (d, *J* = 12.8 Hz, 1H), 9.03 (s, 1H), 11.38 (1H, s). ^{13}C NMR (100 MHz, $CDCl_3$, ppm) δ: 117.1, 119.7, 123.4, 126.1, 127.8, 128.1, 128.6, 129.6, 130.1, 130.6, 131.8, 136.5, 139.4, 144.2, 144.6, 147.7, 155.1. IR (KBr, cm^{-1}) ν_{max}: 3268, 3080, 2923, 2851, 1613, 1497, 1423, 1333, 1135, 1099, 919, 830, 767, 692, 632, 510. HR-ESI-MS *m/z* calcd for $C_{21}H_{15}N_5O_6$ (M^+): 433.1023; found: 433.1016. EIMS *m/z*: 433 (M^+), 403, 386, 294, 207, 189, 165, 135, 105, 77, 63, 51, 44, 39.

(E)-1-(2,4-Dinitrophenyl)-2-(3-nitrocyclohex-2-enylidene) hydrazine (2d)

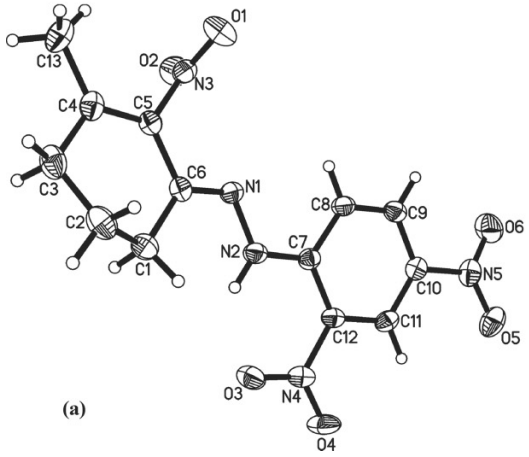
Orange needles, mp 216–217 °C. ^1H NMR (400 MHz, $CDCl_3$, ppm) δ: 2.15 (tt, *J* = 6.4, 6.8 Hz, 2H), 2.64 (t, *J* = 6.8 Hz, 2H), 2.90 (t, *J* = 6.4 Hz, 2H), 7.66 (s, 1H), 8.10 (d, *J* = 9.6 Hz, 1H), 8.42 (dd, *J* = 9.6, 2.8 Hz, 1H), 9.16 (d, *J* = 2.8 Hz, 1H), 11.50 (s, 1H). ^{13}C NMR (100 MHz, $CDCl_3$, ppm) δ: 20.3, 21.2, 22.9, 23.7, 29.7, 116.9, 123.1, 129.6, 130.4, 130.6, 139.6, 143.9, 149.7, 153.5. IR (KBr, cm^{-1}) ν_{max}: 3302, 3097, 2937, 1614, 1498, 1419, 1313, 1100, 925, 850, 792, 592, 518. HR-ESI-MS *m/z* calcd for $C_{12}H_{11}N_5O_6$ (M^+): 321.0709; found: 321.0721. EIMS *m/z*: 321 (M^+), 181, 152, 109, 77, 65, 55, 51, 44, 39.

(E)-1-(2,4-Dinitrophenyl)-2-(3-methyl-2-nitrocyclohex-2-enylidene)hydrazine (2e)

Red needles, mp 214–215 °C. ^1H NMR (400 MHz, $CDCl_3$, ppm) δ: 1.98 (s, 3H), 2.04–2.11 (m, 2H), 2.46 (t, *J* = 7.2 Hz, 2H), 2.68 (t, *J* = 8.8 Hz, 2H), 7.83 (d, *J* = 12.8 Hz, 1H), 8.32 (dd, *J* = 12.8, 2.4 Hz, 1H), 9.11 (d, *J* = 2.4 Hz, 1H), 11.20 (s, 1H). ^{13}C NMR (100 MHz, $CDCl_3$, ppm) δ: 19.7, 20.0, 23.7, 30.0, 117.0, 123.3, 130.3, 130.6, 139.1, 139.9, 144.4, 144.6, 146.7. IR (KBr, cm^{-1}) ν_{max}: 3305, 3105, 2963, 2938, 1611, 1501, 1427, 1333, 1306, 1137, 1113, 1062, 914, 848, 769, 739, 708, 680, 576, 556, 499. HR-ESI-MS *m/z* calcd for $C_{13}H_{13}N_5O_6Na$ (M + Na^+):

Can. J. Chem. Downloaded from www.nrcresearchpress.com by Renmin University of China on 09/02/12
For personal use only.

Fig. 3. (*a*) Crystal structure and (*b*) a packing diagram for **2e**.



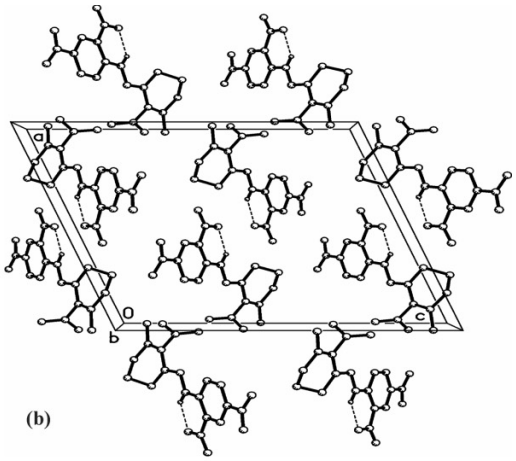


Table 3. Selected bond lengths (Å) and bond angles (°) of **2e**.

Bond lengths (Å)	
N(1)–C(6)	1.2884(19)
N(1)–N(2)	1.3686(17)
N(2)–C(7)	1.353(2)
N(3)–C(5)	1.4757(19)
N(3)–O(2)	1.2111(16)
N(3)–O(1)	1.2169(17)
C(4)–C(13)	1.490(2)
C(5)–C(6)	1.454(2)
C(4)–C(5)	1.334(2)
C(1)–C(6)	1.503(2)
C(3)–C(4)	1.504(2)
N(4)–C(12)	1.447(2)
N(5)–C(10)	1.460(2)
Bond angles (°)	
C(6)–N(1)–N(2)	116.30(13)
C(7)–N(2)–N(1)	120.02(12)
O(2)–N(3)–O(1)	124.08(14)
O(2)–N(3)–C(5)	118.58(14)
O(1)–N(3)–C(5)	117.33(13)
N(2)–C(7)–C(8)	120.75(14)
C(13)–C(4)–C(3)	118.00(15)
C(5)–C(4)–C(13)	123.87(16)
C(4)–C(5)–N(3)	118.23(14)
C(6)–C(5)–N(3)	114.97(13)
N(1)–C(6)–C(1)	127.51(15)
N(2)–C(7)–C(12)	122.59(14)
N(1)–C(6)–C(5)	116.51(14)
C(5)–C(6)–C(1)	115.95(14)
C(4)–C(5)–C(6)	126.71(15)
O(6)–N(5)–O(5)	123.74(16)
O(4)–N(4)–O(3)	121.83(14)

Table 4. Hydrogen bond geometry of **2e**.

D–H···A	D–H (Å)	H···A (Å)	D···A (Å)	D–H···A (°)
N2–H2N···O3	0.86	1.97	2.5993(17)	129.1

358.0758; found: 358.0769. EIMS *m/z*: 335 (M^+), 318, 288, 271, 241, 181, 167, 152, 121, 106, 91, 77, 65, 53, 41, 38.

1-(2,4-Dinitrophenyl)-2-(3-methyl-3-nitrocyclohex-1-enyl) diazene (2e′)

Orange needles, mp 173–175 °C. ^{1}H NMR (400 MHz, $CDCl_3$, ppm) δ: 1.77–2.02 (m, 6H), 2.35–2.39 (m, 1H), 2.49–2.53 (m, 1H), 2.63–2.66 (m, 1H), 7.28 (s, 1H), 7.68 (d, J = 11.8 Hz, 1H), 8.51 (dd, J = 11.8, 2.8 Hz, 1H), 8.79 (d, J = 2.8 Hz, 1H). ^{13}C NMR (100 MHz, $CDCl_3$, ppm) δ: 18.5, 21.9, 27.2, 34.1, 76.7, 87.1, 119.7, 120.1, 127.9, 141.6, 147.8, 148.6, 157.6. IR (KBr, cm^{-1}) ν_{max}: 3100, 2961, 2867, 1603, 1537, 1447, 1344, 1273, 1175, 1061, 906, 848, 741. HR-ESI-MS *m/z* calcd for $C_{13}H_{13}N_5O_6Na$ ($M + Na^+$): 358.0758; found: 358.0777. EIMS *m/z*: 335 (M^+), 289, 236, 208, 125, 115, 77, 65, 55, 51, 43, 39.

(E)-1-(2,4-Dinitrophenyl)-2-(4-methyl-3-nitropent-3-en-2-ylidene)hydrazine (2f)

Orange needles, mp 123–124 °C. ^{1}H NMR (400 MHz, $CDCl_3$, ppm) δ: 2.08 (s, 3H), 2.22 (s, 3H), 2.23 (s, 3H), 7.93 (d, J = 9.2 Hz, 1H), 8.36 (dd, J = 9.2, 3.2 Hz, 1H), 9.16 (d, J = 9.2 Hz, 1H), 11.25 (s, 1H); ^{13}C NMR (100 MHz, $CDCl_3$, ppm) δ: 15.9, 22.3, 23.2, 117.2, 123.2, 130.2, 139.0, 144.2, 144.6, 145.9, 146.6. IR (KBr, cm^{-1}) ν_{max}: 3298, 3116, 1645, 1617, 1589, 1515, 1492, 1417, 1366, 1331, 1296, 1266, 1132, 1103. HR-ESI-MS *m/z* calcd for $C_{12}H_{13}N_5O_6$ (M^+): 323.0866; found: 323.0877. EIMS *m/z*: 323 (M^+), 308, 277, 269, 230, 181, 79.

(E)-1-(2,4-Dinitrophenyl)-2-(1-(2-nitrocyclohex-1-enyl) ethylidene)hydrazine (2g)

Red needles, mp 202–204 °C. ^{1}H NMR (400 MHz, $CDCl_3$, ppm) δ: 1.79–1.81 (m, 2H), 1.86–1.89 (m, 2H), 2.22 (s, 3H), 2.52–2.54 (m, 2H), 2.71–2.74 (m, 2H), 7.86 (d, J = 9.2 Hz, 1H), 8.32 (dd, J = 9.2, 2.4 Hz, 1H), 9.14 (d, J = 2.4 Hz, 1H), 11.14 (s, 1H). ^{13}C NMR (100 MHz, $CDCl_3$, ppm) δ: 15.6, 21.1, 25.9, 29.6, 116.5, 123.3, 129.8, 130.0, 138.4, 140.1, 144.7, 147.5, 152.8. IR (KBr, cm^{-1}) ν_{max}: 3312, 3105, 2929, 2866, 2824, 1613, 1586, 1508, 1414, 1326, 1105, 1076, 978, 918, 835, 734, 674, 639, 590, 557, 527, 503. HR-ESI-MS *m/z* calcd for $C_{14}H_{15}N_5O_6Na$

(M + Na^+): 372.0914; found: 372.0927. EIMS *m/z*: 349 (M^+), 319, 303, 269, 238, 195, 154, 108, 100, 84, 55, 43.

Supplementary data

Supplementary data are available with the article through the journal Web site at http://nrcresearchpress.com/doi/suppl/10.1139/v2012-022. CCDC 220502 contains the X-ray data in CIF format for this manuscript. These data can be obtained, free of charge, via http://www.ccdc.cam.ac.uk/products/csd/request (Or from the Cambridge Crystallographic Data Centre, 12 Union Road, Cambridge CB2 1EZ, UK; fax: +44 1223 33603; or e-mail: deposit@ccdc.cam.ac.uk.

Acknowledgements

This work was financially supported by the Shaanxi Provincial Natural Science Foundation of China (Grant No. 2009K01-51) and the Phytochemistry Key Laboratory of Shaanxi Province (Grant No. 05JS43).

References

(1) (a) Hrabie, J. A.; Keefer, L. K. *Chem. Rev.* **2002**, *102* (4), 1135. doi:10.1021/cr000028t; (b) McCleverty, J. A. *Chem. Rev.* **2004**, *104* (2), 403. doi:10.1021/cr020623q; (c) Liu, Z.-Q.; Shang, X.-J.; Luo, H.-Q.; Zhou, B.; Wu, L. M. *Chin. J. Org. Chem.* **2006**, *26* (9), 1317; (d) DeRosa, F.; Keefer, L. K.; Hrabie, J. A. *J. Org. Chem.* **2008**, *73* (3), 1139. doi:10.1021/jo7020423; (e) Chakrapani, H.; Bartberger, M. D.; Toone, E. J. *J. Org. Chem.* **2009**, *74* (4), 1450. doi:10.1021/jo802517t.

(2) (a) Smith, R. C.; Tennyson, A. G.; Lim, M. H.; Lippard, S. J. *Org. Lett.* **2005**, *7* (16), 3573. doi:10.1021/ol0513903; (b) Masami, Y.; Takashi, I.; Masayuki, I.; Mie, S.; Katsumi, I.; Norikazu, T.; Tomoyuki, K. *J. Med. Chem.* **2005**, *48* (23), 7457. doi:10.1021/jm050623t.

(3) (a) Kelly, D. R.; Jones, S.; Adigun, J. O.; Koh, K. S. V.; Hibbs, D. E.; Hursthouse, M. B.; Jackson, S. K. *Tetrahedron* **1997**, *53* (50), 17221. doi:10.1016/S0040-4020(97)10202-2; (b) Brown, J. F., Jr. *J. Am. Chem. Soc.* **1957**, *79* (10), 2480. doi:10.1021/ja01567a035.

(4) (a) Hrabie, J. A.; Srinivasan, A.; George, C.; Keefer, L. K. *Tetrahedron Lett.* **1998**, *39* (33), 5933. doi:10.1016/S0040-4039(98)01218-0; (b) Mao, Y. Z.; Liu, Z. L.; Wu, L. M. *Chin. J. Chem.* **2000**, *18* (6), 789.

(5) (a) Wu, W. T.; Liu, Q.; Shen, Y. L.; Li, R.; Wu, L. M. *Tetrahedron Lett.* **2007**, *48* (9), 1653. doi:10.1016/j.tetlet.2006.12.095; (b) Fan, Y.; Shang, X. J.; Liu, Z. Q.; Wu, L. M. *Synth. Commun.* **2006**, *36* (21), 3149. doi:10.1080/00397910600908769; (c) Liu, Z. Q.; Li, R.; Yang, D. S.; Wu, L. M. *Tetrahedron Lett.* **2004**, *45* (7), 1565. doi:10.1016/j.tetlet.2003.11.084.

(6) Lei, L.-D.; Zhang, H.-R.; Yang, D.-S.; Wu, L.-M. *Chem. J. Chin. Univ.* **2004**, *25* (10), 1863.

(7) Li, R.; Liu, Z. Q.; Zhou, Y. L.; Wu, L. M. *Synlett* **2006**, (9): 1367.

(8) Lei, L. D.; Yang, D. S.; Liu, Z. Q.; Wu, L. M. *Synth. Commun.* **2004**, *34* (6), 985. doi:10.1081/SCC-120028628.

(9) Zhang, H.-R.; Wu, L.-M. *Chin. J. Org. Chem.* **2005**, *25* (10), 1248.

(10) Itoh, T.; Matsuya, Y.; Nagata, K.; Ohsawa, A. *Tetrahedron Lett.* **1997**, *38* (23), 4117. doi:10.1016/S0040-4039(97)00840-X.

(11) (a) Biechy, A.; Hachisu, S.; Quiclet-Sire, B.; Ricard, L.; Zard, S. Z. Z. *Tetrahedron* **2009**, *65* (33), 6730. doi:10.1016/j.tet.2009.04.027; (b) Dang, T. T.; Dang, T. T.; Fischer, C.; Görls, H.; Langer, P. *Tetrahedron* **2008**, *64* (9), 2207. doi:10.1016/j.tet.2007.12.024; (c) Wang, J. P.; Fu, Y. J.; Yin, W. P.; Wang, J. G.; Qin, J. H. *Chin. J. Org. Chem.* **2007**, *27* (4), 524; (d) Enders, D.; Voith, M.; Ince, S. J. *Synthesis* **2002**, *2002* (12), 1775. doi:10.1055/s-2002-33646; (e) Job, A.; Janeck, C. F.; Bettray, W.; Peters, R.; Enders, D. *Tetrahedron* **2002**, *58* (12), 2253. doi:10.1016/S0040-4020(02)00080-7.

(12) (a) Zhong, X.; Wei, H. L.; Liu, W. S.; Wang, D. Q.; Wang, X. *Bioorg. Med. Chem. Lett.* **2007**, *17* (13), 3774. doi:10.1016/j.bmcl.2007.04.006; (b) Morgan, L. R.; Jursic, B. S.; Hooper, C. L.; Neumann, D. M.; Kanappan, T.; LeBlanc, B. *Bioorg. Med. Chem. Lett.* **2002**, *12* (23), 3407. doi:10.1016/S0960-894X(02)00725-4.

(13) Melnyk, P.; Leroux, V.; Sergheraert, C.; Grellier, P. *Bioorg. Med. Chem. Lett.* **2006**, *16* (1), 31. doi:10.1016/j.bmcl.2005.09.058.

(14) Tian, B. H.; He, M. Z.; Tang, S. X.; Hewlett, I.; Tan, Z. W.; Li, J. B.; Jin, Y. X.; Yang, M. *Bioorg. Med. Chem. Lett.* **2009**, *19* (8), 2162. doi:10.1016/j.bmcl.2009.02.116.

(15) Yang, D. S.; Zhu, H. Y.; Guo, Y. N.; Wu, L. M. *Chin. J. Chem.* **2010**, *28* (7), 1193. doi:10.1002/cjoc.201090207.

(16) (a) Wu, W. T.; Su, G.; Lu, Z.; Wu, L. M. *Tetrahedron Lett.* **2007**, *48* (47), 8293. doi:10.1016/j.tetlet.2007.09.128; (b) Yang, D. S.; Lei, L. D.; Liu, Z. Q.; Wu, L. M. *Tetrahedron Lett.* **2003**, *44* (39), 7245. doi:10.1016/j.tetlet.2003.08.008.

(17) Gillis, B. T.; LaMontagne, M. P. *J. Org. Chem.* **1968**, *33* (2), 762. doi:10.1021/jo01266a056.

(18) Kamitori, Y.; Hojo, M.; Msuda, R.; Yoshida, T.; Ohara, S.; Yamada, K.; Yoshikawa, N. *J. Org. Chem.* **1988**, *53* (3), 519. doi:10.1021/jo00238a009.

(19) (a) Lin, E.-C.; Van De Mark, M. R. *J. Chem. Soc. Chem. Commun.* **1982**, (20): 1176. doi:10.1039/c39820001176; (b) Olah, G. A.; Ho, T.-L. *Synthesis* **1976**, *1976* (09), 610. doi:10.1055/s-1976-24138; (c) Lee, J. G.; Hwang, J. P. *Chem. Lett.* **1995**, *24* (7), 507. doi:10.1246/cl.1995.507.

(20) d'Ischia, M.; Rega, N.; Barone, V. *Tetrabedron* **1999**, *55* (30), 9297. doi:10.1016/S0040-4020(99)00491-3.

(21) (a) Sheldrick, G. M. *SHELXS-97: Program for Crystal Structures Determination;* University of Göttingen: Göttingen, Germany, 1997; (b) Sheldrick, G. M. *SHELXL-97: Program for Crystal Structure Refinement;* University of Göttingen: Göttingen, Germany, 1997.

(22) Wilson, A. J. C., Ed. In *International Tables for Crystallography,* Vol. C; Kluwer Academic Publishers: Dordrecht, 1992, Tables 4.2.6.8 and 6.1.1.4.

Can. J. Chem. Downloaded from www.nrcresearchpress.com by Renmin University of China on 09/02/12
For personal use only.

Preparation and application of copper hydroxide (oxide) / multiwalled carbon nanotubes nanocomposite-modified glassy carbon electrode as a nitrite sensor

Youqin Liu, Xiuying Tian, Yun Yan, and Yuehua Xu

Can. J. Chem. Downloaded from www.nrcresearchpress.com by Renmin University of China on 09/02/12
For personal use only.

Abstract: Copper hydroxide (oxide) / multiwalled carbon nanotubes nanocomposite-modified glassy carbon electrode ($Cu_{hydroxide/oxide}$/MWCNTs/GCE) was successfully prepared by a novel film plating / cyclic voltammetry (CV) method, which exhibited marked synergistic catalytic effects on the electro-oxidation of NO_2^-. The preparation process, impedance behavior, and surface morphology of $Cu_{hydroxide/oxide}$/MWCNTs/GCE were investigated by CV, electrochemical impedance spectroscopy, and scanning electron microscopy (SEM), respectively. The optimum preparation and test conditions for the electrode to have high catalytic activity were acquired. The linear range between the anodic current (Δi_a, μA) and NO_2^- concentration (c, mmol L^{-1}) was 1.0×10^{-4} to 14.0 mmol L^{-1}, and the corresponding calibration curve was $\Delta i_a = -0.1504 + 57.954c$ (R = 0.9990, n = 32) with a detection limit of 0.03 μmol L^{-1} (S/N = 3). The $Cu_{hydroxide/oxide}$/MWCNTs/GCE prepared in the optimal conditions showed good stability, high selectivity, low detection limit, and quick response (<0.2 s) to NO_2^- in phosphate buffer (pH 5.29) at 0.78 V, which has been successfully applied to the determination of NO_2^- in pickled vegetables with satisfactory results.

Key words: copper hydroxide / oxide, multi-walled carbon nanotube, nitrite, catalytic oxidation.

Résumé : On a réussi à préparer une électrode d'hydroxyde (oxyde) de cuivre / nanotubes de carbone vitreux multicloisonné nanocomposite modifié ($Cu_{hydroxyde/oxyde}$/MWCNTs/GCE) en faisant appel à une nouvelle méthode de plaquage de film / voltampérométrie cyclique (VC) qui présente des effets marqués de synergie catalytique sur l'oxydation électrolytique du NO_2^-. On a étudié le processus de préparation, le comportement d'impédance et la morphologie du $Cu_{hydroxyde/oxyde}$/MWCNTs/GCE en faisant appel respectivement à la VC, à spectroscopie d'impédance électrochimique et à la microscopie électronique à balayage. On a déterminé les conditions optimales de préparation et vérification pour que l'activité catalytique soit optimale. La plage linéaire entre le courant anodique (Δi_a, μA) et la concentration de NO_2^- (c, mmol L^{-1}) est de $1{,}0 \times 10^{-4}$ à 14,0 mmol L^{-1} et la courbe de calibration correspondante est décrite par l'équation $\Delta i_a = -0{,}1504 + 57{,}954\ c$ (R = 0,9990, n = 32), avec une limite de détection de 0,03 mmol L^{-1} (S/N = 3). Le $Cu_{hydroxyde/oxyde}$/MWCNTs/GCE préparé dans des conditions optimales présente une bonne stabilité, une sélectivité élevée, une limite de détection faible et un temps de réponse rapide (<0,2 s) vis-à-vis du NO_2^- dans un tampon de phosphate (pH de 5,29), à 0,78 V et il a été utilisé avec des résultats satisfaisants pour la détermination du NO_2^- dans des légumes marinés.

Mots-clés : hydroxyde / oxyde de cuivre, nanotube de carbone multicloisonné, nitrite, oxydation catalytique.

[Traduit par la Rédaction]

Introduction

Pollution to the soil and groundwater owing to the extensive use of nitrogenous fertilizer and nitrogen-containing pesticides results in a higher nitrate content in plants, especially leafy vegetables such as cabbage, kale, spinach, etc. During the storage of vegetables, nitrate can be reduced to nitrite by the nitrate reductase produced by the microorganisms propagated profusely in vegetables.[1] Vegetable pickling, one of the most common and most popular processing methods of fresh vegetables, will also produce a lot of nitrite in the pickled vegetables because of improper curing process control (inadequately pickled or deterioration).[2] Nitrite as a preservative and color fixative in meat processing (bacon, sausage, salted fish, etc.) is widely used to inhibit the propagation of *Clostridium botulinum* and produces a distinct color and flavor.[3] Nitrite may also indirectly enter the milk for a variety of reasons, such as the digestion of forage itself and feeding process.[4] Therefore, nitrite widely exists and is closely related to our daily lives.

However, numerous studies have shown that excessive nitrite is hazardous to human health. An intake of 0.2–0.5 g nitrite can lead to poisoning of an adult and ingestion of 3 g

Received 22 October 2011. Accepted 19 March 2012. Published at www.nrcresearchpress.com/cjc on 15 May 2012.

Y. Liu, X. Tian, Y. Yan, and Y. Xu. Institute of Biomaterial, College of Sciences, South China Agricultural University, Guangzhou 510642, P.R. China.

Corresponding author: Youqin Liu (e-mail: y.q.liu@eyou.com).

Can. J. Chem. Downloaded from www.nrcresearchpress.com by Renmin University of China on 09/02/12
For personal use only.

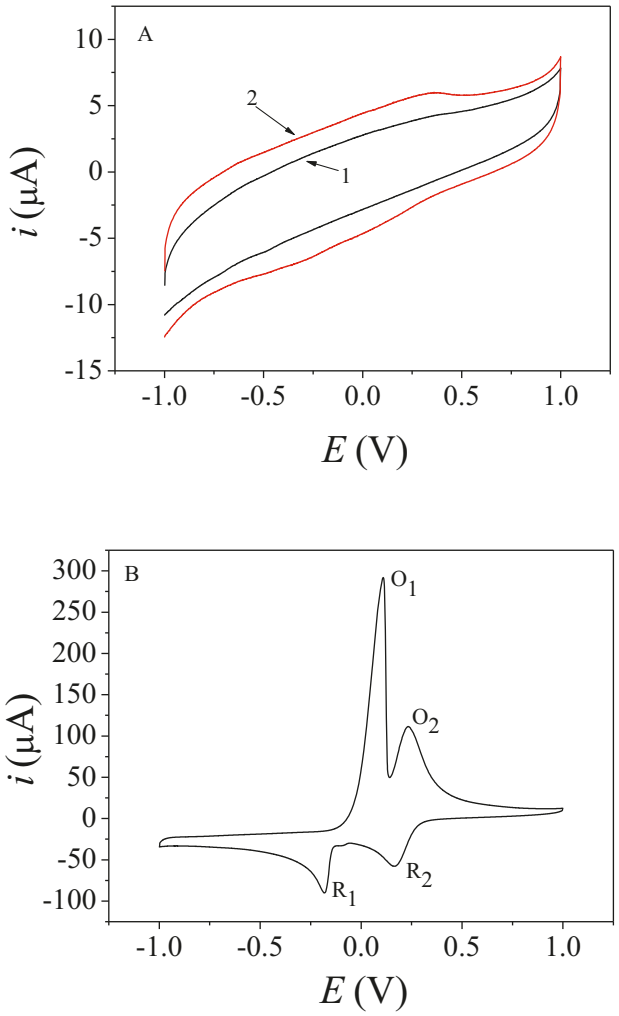
can lead to death. Nitrite in the blood can cause the irreversible oxidation of hemoglobin to methemoglobin, which lacks the capacity for oxygen transport and eventually will lead to death by respiratory failure.[5] Moreover, nitrite can react with amines and amides in the stomach to produce carcinogenic *N*-nitrosamine compounds, which mainly induce the digestive system canceration.[6] Nitrosamines also have teratogenic effects on the fetus, in particular on the central nervous system and the production of skeletal system abnormalities. To control the nitrite content in food and daily intake, it is of great importance to further develop a reliable alternative method for fast and sensitive determination of nitrite.

So far, many methods, such as UV–vis spectroscopy, fluorescence spectroscopy, chromatography, capillary electrophoresis, polarography, and potentiometry, have been used for nitrite determination in recent years.[7] However, most of these conventional approaches need complicated processes and expensive instruments. Furthermore, they are not suitable for the real-time monitoring of nitrite required for strict environmental control. In contrast, electrochemical methods for nitrite determination possess many unique advantages, such as simplicity, low cost, fast response, and the potential for real-time monitoring applications.[8] When the nitrite content was determined by measuring the current caused by the direct oxidation or reduction of nitrite on a substrate electrode, severe interferences could be produced because of the existence of higher overpotential.[9] At the same time, some species could poison the electrode surface and decrease the response sensitivity and reproducibility. To improve the selectivity of nitrite determination, the working electrode potential should be as close to zero as possible, which can be obtained by modifying a suitable electrocatalyst on the surface of the substrate electrode.

A variety of materials, such as metal nanoparticles,[10] metal oxides,[11] amino acids,[12] organic dyes,[13] conductive polymers,[14] carbon nanotubes (CNTs),[15] complexes,[16] and enzymes,[17] have been used to prepare chemically modified electrodes (CME) as sensors for nitrite determination. They all have demonstrated greater analytical performance than bare electrodes. In recent years, composite-modified electrodes have acquired increasing interest with quite different catalytic activity from those of single material. Some composites, such as CNTs/polyvanillin,[18] Pt nanoparticles / thionine / MWCNTs,[19] and Pt nanoparticles / poly(3-methylthiophene) nanorods,[20] have been reported for nitrite determination, which either improved the sensitivity, selectivity, and stability or extended the linear range of the calibration curve.

Transition-metal oxides as modified electrode materials show explicit characteristics of high activity, stability, and low cost, whereas CNTs exhibit high chemical stability, good electrical conductivity, and excellent biocompatibility, which makes them attractive for the construction of various electrochemical biosensors.[21,22] Based on the above considerations, we developed a copper hydroxide (oxide) / MWCNTs nanocomposite-modified glassy carbon electrode ($Cu_{hydroxide/oxide}$/MWCNTs/GCE) by a novel film plating / cyclic voltammetry (CV) method that was easier for the control of the number of active sites and made the film uniform and closely integrated with the electrode compared with the other methods reported. Marked synergistic catalytic effects on the electro-oxidation of NO_2^- were found. The effects of the preparation and testing conditions on the properties of the modified electrode were studied in detail. The results not only provided a sensitive electrochemical method for the determination of nitrite in real samples, but also embodied a novel idea for nanocomposite-modified electrode preparation and laid a good basis for the development of a high-performance miniature electrochemical sensor.

Fig. 1. (A) Cyclic voltammograms of glassy carbon electrode (GCE, curve 1) and multiwalled carbon nanotubes (MWCNTs) / GCE (curve 2) in 0.1 mol L^{-1} KCl solution. (B) Cyclic voltammogram of MWCNTs/GCE in 0.1 mol L^{-1} KCl solution containing 3.0 mmol L^{-1} $CuCl_2$ at 50 mV s^{-1}.



Results and discussion

Preparation of $Cu_{hydroxide/oxide}$/MWCNTs/GCE

Figure 1A shows the typical cyclic voltammograms of GCE (curve 1) and MWCNTs/GCE (curve 2) in 0.1 mol L^{-1} KCl. Non-Faradaic current at the MWCNTs/GCE increased significantly compared with that at GCE, indicating that MWCNTs had been successfully casted on the GCE surface. Figure 1B shows the cyclic voltammogram of $CuCl_2$ on MWCNTs/GCE in 0.1 mol L^{-1} KCl solution. Two pairs of well-defined redox peaks (O_1/R_1, O_2/R_2) were observed, which can be attributed to the quasi-reversible reaction of Cu^0/Cu^I and Cu^I/Cu^{II} redox couples, respectively. As can be

Can. J. Chem. Downloaded from www.nrcresearchpress.com by Renmin University of China on 09/02/12
For personal use only.

Fig. 2. Repetitive cyclic voltammograms of Cu / multiwalled carbon nanotubes (MWCNTs) / glassy carbon electrode (GCE) in 0.1 mol L^{-1} NaOH solution at 40 mV s^{-1}.

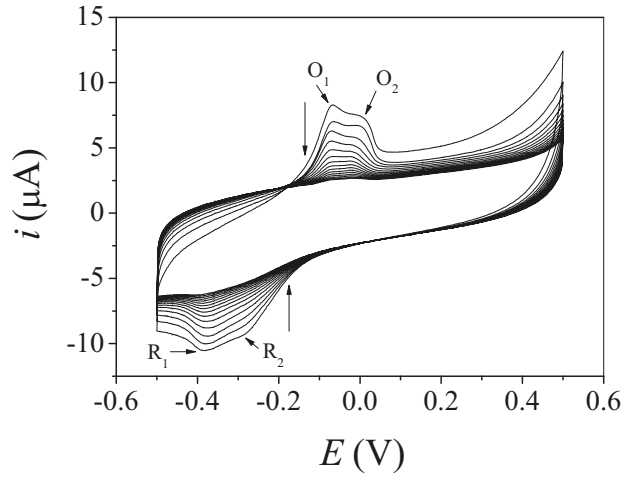
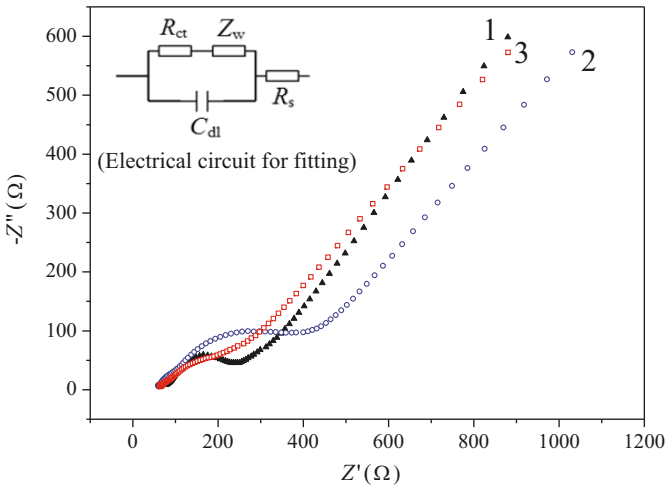


Fig. 3. Electrochemical impedance spectroscopy (EIS) of glassy carbon electrode (GCE, curve 1), $Cu_{hydroxide/oxide}$/GCE (curve 2), and $Cu_{hydroxide/oxide}$ / multiwalled carbon nanotubes (MWCNTs) / GCE (curve 3) in 0.1 mol L^{-1} KCl containing 10 mmol L^{-1} $[Fe(CN)_6]^{4-/3-}$ for 0.01–10^5 Hz at 0.28 V.



seen, Cu^{II} starts to be deoxidized at 0.30 V to Cu^{I}, which is further deoxidized to Cu^0 at –0.13 V, meaning that the deposition potential of Cu^0 particles on MWCNTs/GCE must be lower than –0.13 V.

Figure 2 shows the repetitive cyclic voltammograms of Cu/MWCNTs/GCE in 0.1 mol L^{-1} NaOH solution, by which $Cu_{hydroxide/oxide}$/MWCNTs/GCE was successfully prepared. As the potential scan proceeded, all redox peak current decreased, indicating that copper was converted to copper hydroxide / oxide on MWCNTs/GCE surface. The possible mechanism involving the electrochemical process can be expressed as follows: peak pair (O_1/R_1), $2Cu + 2OH^- - 2e = Cu_2O + H_2O$; peak pair ($O_2/R_2$), $2Cu_2O + 2OH^- + H_2O - 2e = 2Cu(OH)_2$.

Electrochemical impedance spectroscopy (EIS) is an efficient method for the investigation of electrochemical properties of modified electrode surface, with their graph comprising a semicircle and a straight line. The electron-

Fig. 4. Cyclic voltammograms of bare glassy carbon electrode (GCE, curve 1), $Cu_{hydroxide/oxide}$/GCE (curve 2), multiwalled carbon nanotubes (MWCNTs) / GCE (curve 3), and $Cu_{hydroxide/oxide}$/MWCNTs/GCE (curve 4) in 0.07 mol L^{-1} PBS + 0.2 mol L^{-1} KCl (pH 5.29) solution containing 2.5 mmol L^{-1} nitrite at 20 mV s^{-1}.

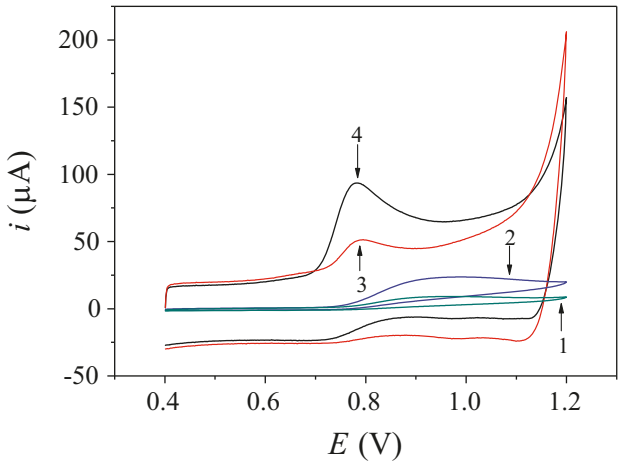
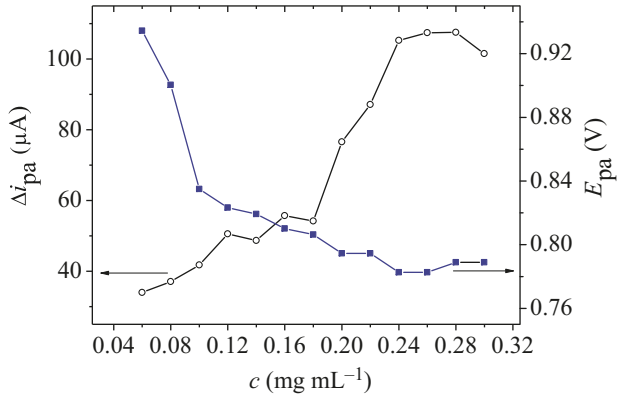


Fig. 5. The effect of multiwalled carbon nanotubes (MWCNTs) concentration on oxidation peak potential (E_{pa}) and current (Δi_{pa}) of 2 mmol L^{-1} nitrite on $Cu_{hydroxide/oxide}$ / MWCNTs / glassy carbon electrode (GCE) in 0.07 mol L^{-1} PBS (pH 5.29) + 0.2 mol L^{-1} KCl solution at 20 mV s^{-1}.

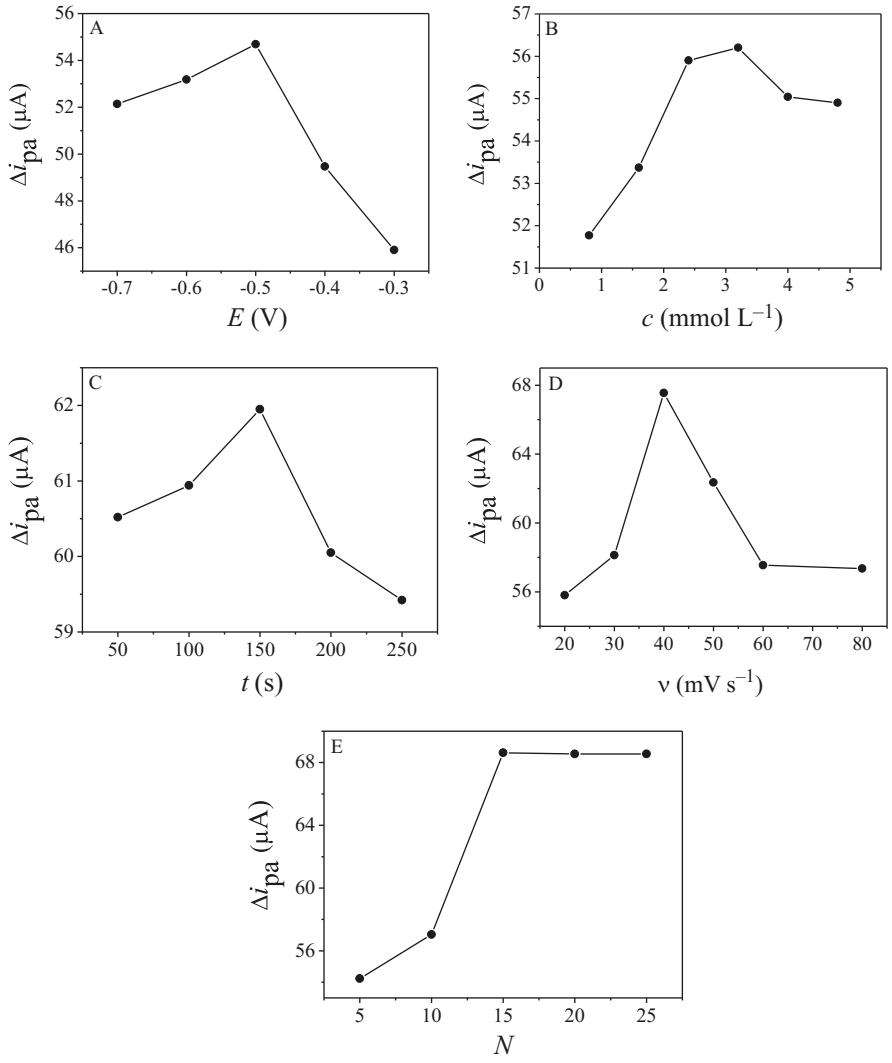


transfer resistance (R_{ct}) at the electrode surface is equivalent to the semicircle diameter. To obtain accurate R_{ct} values, an electrical circuit (inset, Fig. 3) was used to fit the EIS. Figure 3 shows the EIS measured on bare GCE (curve 1), $Cu_{hydroxide/oxide}$/GCE (curve 2), and $Cu_{hydroxide/oxide}$/MWCNTs/GCE (curve 3) in the presence of 10 mmol L^{-1} $[Fe(CN)_6]^{4-/3-}$ at 0.28 V. As shown, the EIS of $Cu_{hydroxide/oxide}$/GCE exhibited a larger semicircle portion (R_{ct} = 230.6 Ω) compared with that of bare GCE (R_{ct} = 145.9 Ω), suggesting that the resistance to the anion redox reaction increased at $Cu_{hydroxide/oxide}$/GCE. However, the semicircle portion (R_{ct} = 169.4 Ω) on $Cu_{hydroxide/oxide}$/MWCNTs/GCE significantly decreased because of the good conductivity of $Cu_{hydroxide/oxide}$/MWCNTs composite, which potentially improves the sensitivity of the sensor. The results from the EIS further proved that copper hydroxide / oxide was effectively deposited on MWCNTs surface.

Optimization of preparing conditions

Figure 4 shows the cyclic voltammograms obtained by four different GCEs in phosphate buffer solution (pH 5.29)

Fig. 6. Effects of copper deposition potential (A), Cu^{2+} concentration (B), deposition time (C), scan rate (D), and the number of scanning cycles (E) on the electrocatalytic activity of $Cu_{hydroxide/oxide}$ / multiwalled carbon nanotubes (MWCNTs) / glassy carbon electrode (GCE). Supporting electrolyte: 0.07 mol L^{-1} PBS (pH 5.29) + 0.2 mol L^{-1} KCl + 2 mmol L^{-1} $NaNO_2$.



containing 2.5 mmol L^{-1} nitrite at 20 mV s^{-1}. The nitrite underwent an irreversible oxidation. The peak potentials were about 0.97 V and the peak currents of nitrite oxidation on bare GCE and $Cu_{hydroxide/oxide}$/GCE were about 7.5 and 22.1 μA, respectively. The increase in peak current indicated that copper hydroxide / oxide had evident electrocatalytic activity toward the oxidation of nitrite. A remarkable shift in peak potential to the negative side (0.78 V) was noticed on MWCNTs/GCE, indicating that MWCNTs have strong electrocatalytic activity for nitrite oxidation. Interestingly, a larger increase in peak current (70.9 μA) was observed after electrodepositing copper hydroxide / oxide onto the MWCNTs/GCE, which can be attributed to the synergic catalytic effect of $Cu_{hydroxide/oxide}$/MWCNTs nanocomposite and the decrease of R_{ct}.

H^+ was proven to be involved in the catalytic reaction process, and the active species should be HNO_2 instead of NO_2^-. Nitrite is oxidized through a 2e process with the final product (NO_3^-) in aqueous solution. The mechanism for nitrite oxidation at solid electrodes is described as follows.[9,23,24]

$$H^+ + NO_2^- = HNO_2$$

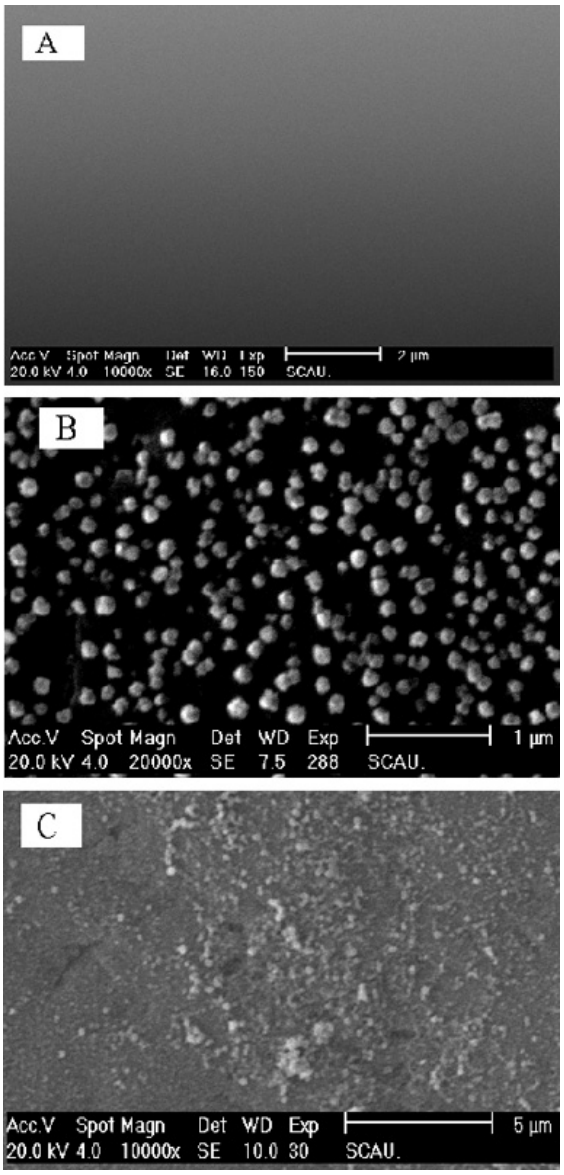
$$HNO_2 + H_2O - 2e = NO_3^- + 3H^+$$

The electrocatalytic activity of $Cu_{hydroxide/oxide}$/MWCNTs/GCE was affected by many factors such as the amount of MWCNTs, copper hydroxide / oxide, and electrochemical parameters. Figure 5 depicts the effect of MWCNTs concentration on the oxidation peak potential (E_{pa}) and current response to 2 mmol L^{-1} $NaNO_2$ at $Cu_{hydroxide/oxide}$/MWCNTs/GCE. With increasing MWCNTs concentration, the peak potential shifted to negative values and the peak current gradually increased. When the concentration of MWCNTs was in the range of 0.24–0.28 mg mL^{-1}, the peak potential and current had no significant changes, which might be due to the excellent synergistic effect of copper hydroxide / oxide and MWCNTs and lower R_{ct}. Insufficient or redundant MWCNTs may result in fewer active centers or the formation of clusters. Therefore, 0.24 mg mL^{-1} MWCNTs was chosen for subsequent experiments.

Can. J. Chem. Downloaded from www.nrcresearchpress.com by Renmin University of China on 09/02/12
For personal use only.

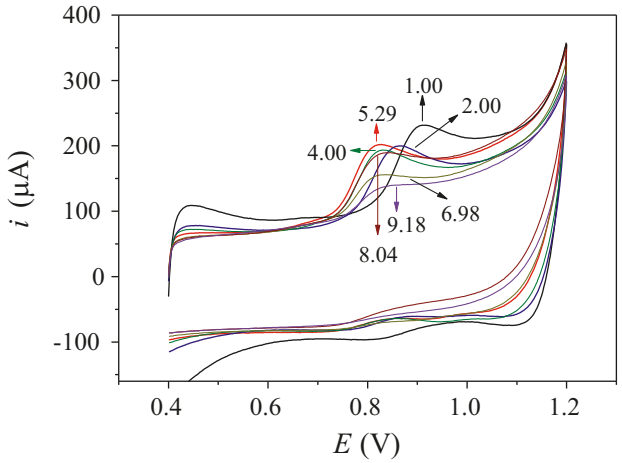
Can. J. Chem. Downloaded from www.nrcresearchpress.com by Renmin University of China on 09/02/12
For personal use only.

Fig. 7. Scanning electron microscopy (SEM) images of glassy carbon electrode (GCE; A), $Cu_{hydroxide/oxide}$/GCE (B), and $Cu_{hydroxide/oxide}$ / multiwalled carbon nanotubes (MWCNTs) / GCE (C).



The effect of copper particle deposition potential on the electrocatalytic activity is shown in Fig. 6A. The more negative the deposition potential, the higher the catalytic activity, indicating that the amount of copper hydroxide / oxide particles played a major role. However, the catalytic ability slowly decreased when the deposition potential was lower than –0.5 V, which may be attributed to the increase of resistance of ion transfer for charge balance in the process of film oxidation and reduction. The maximum response current was obtained at –0.5 V. Therefore, –0.5 V was selected as the optimum deposition potential. The Cu^{2+} concentration in the deposition bath had significant effect on the performance of the sensor. As can be seen from Fig. 6B, the peak current rises sharply with the increasing concentration of Cu^{2+} and the maximum response is approached at 3 mmol L^{-1}. Thus, 3 mmol L^{-1} Cu^{2+} was chosen as the optimal concentration for the sensor preparation. Figure 6C depicts the effect of

Fig. 8. Cyclic voltammograms of $Cu_{hydroxide/oxide}$ / multiwalled carbon nanotubes (MWCNTs) / glassy carbon electrode (GCE) in different pH solutions containing 1.5 mmol L^{-1} nitrite at 0.1 V s^{-1}.



electrodeposition time of copper particles on the electrocatalytic activity. The current response increases with the electrodeposition time increasing from 50 to 150 s and subsequently decreases, which further proves that the amount of copper hydroxide / oxide particles had a synergistic effect.

The influence of scan rate on the conversion of copper into copper hydroxide / oxide is shown in Fig. 6D. The magnitude of scan rate might influence the size, morphology, and uniform distribution of copper hydroxide / oxide particles on MWCNTs. The maximum response current was obtained at 40 mV s^{-1}. The function of the number of scanning cycles is to ensure the complete conversion of copper into copper hydroxide / oxide. The peak current increases sharply with an increase of the number of scanning cycles and the maximum response is approached after 15 cycles (Fig. 6E).

Characterization of $Cu_{hydroxide/oxide}$/MWCNTs/GCE

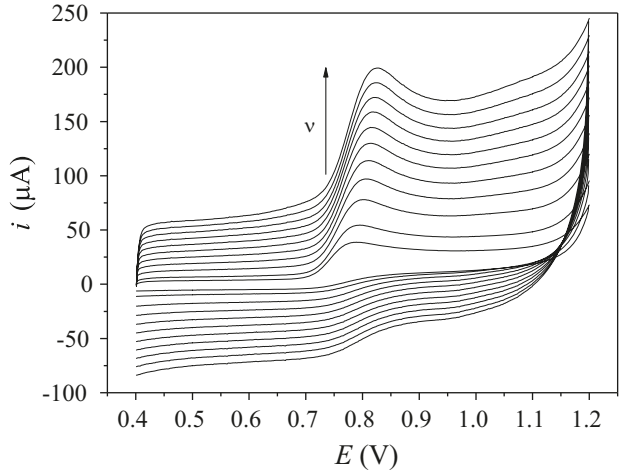
The surface morphology of $Cu_{hydroxide/oxide}$/MWCNTs/GCE (Fig. 7C) prepared in the optimized conditions was characterized by scanning electron microscopy (SEM). It can be seen that copper hydroxide/oxide particles were distributed homogeneously on MWCNTs with obvious differences to copper hydroxide/oxide particles directly deposited on GCE (Fig. 7B), which can be attributed to the completely different nucleation and growth process.

To find the optimal pH for nitrite oxidation on $Cu_{hydroxide/oxide}$/MWCNTs/GCE, cyclic voltammograms were recorded in different pH (1.00–9.19) solutions containing 1.5 mmol L^{-1} nitrite at 0.1 V s^{-1} (Fig. 8). The E_{pa} shifted negatively with increasing pH from 1.00 to 5.29 and remained stable at pH 5.29–9.18, indicating that H^+ takes part in the electrochemical reaction. Since a higher peak current was obtained at pH 5.29, pH 5.29 was selected for the subsequent experiments.

Figure 9 shows the cyclic voltammograms of $Cu_{hydroxide/oxide}$/MWCNTs/GCE in pH 5.29 PBS containing 2 mmol L^{-1} nitrite at various scanning rates (5–100 mV s^{-1}). The E_{pa} shifted positively with increasing scan rate, indicating a kinetic control for the oxidation of nitrite at the redox sites of $Cu_{hydroxide/oxide}$/MWCNTs/GCE electrode. The anodic peak current increased linearly with the square root of scan

Can. J. Chem. Downloaded from www.nrcresearchpress.com by Renmin University of China on 09/02/12
For personal use only.

Fig. 9. Cyclic voltammograms of $Cu_{hydroxide/oxide}$ / multiwalled carbon nanotubes (MWCNTs) / glassy carbon electrode (GCE) in 0.07 mol L^{-1} PBS (pH 5.29) + 0.2 mol L^{-1} KCl solution containing 2 mmol L^{-1} nitrite at scanning rates of 5, 10, 20, 30, 40, 50, 60, 70, 80, 90, and 100 mV s^{-1}.



rate (v) in the range of 5–100 mV s^{-1} (i_{pa} = –12.658 + 20.633$v^{1/2}$, R = 0.9954), suggesting that the kinetics of the overall process was controlled by diffusion.

Determination of NO_2^- on $Cu_{hydroxide/oxide}$/MWCNTs/GCE

Linear range and detection limit

Figure 10 shows the typical cyclic voltammograms obtained at $Cu_{hydroxide/oxide}$/MWCNTs/GCE in 0.07 mol L^{-1} PBS + 0.2 mol L^{-1} KCl solution containing different concentrations of $NaNO_2$. With the addition of $NaNO_2$, the peak current gradually increased and the potential was almost unchanged, suggesting that the sensor's response was very stable. A linear relationship between the peak current and the concentration of $NaNO_2$ was acquired in the range of 0.02–7.0 mmol L^{-1} (Δi_{pa} = 1.481 + 27.155c, R = 0.9993).

A current vs time curve at constant potential is a much more accurate and sensitive means for the determination of current than cyclic voltammetry (CV), which is usually employed to estimate the lower detection limit. Figure 11 shows a typical steady-state amperometric response of $Cu_{hydroxide/oxide}$/MWCNTs/GCE with the successive addition of $NaNO_2$ into the continuously stirred solution of PBS (pH 5.29) and KCl at 0.78 V. The linear regression equation is Δi_a = –0.1504 + 57.954c (R = 0.9990, n = 32) over the range of 1.0 × 10^{-4} to 14.0 mmol L^{-1} with a detection limit of 0.03 μmol L^{-1} (S/N = 3).

Effect of interferants

Selectivity is important in the practical use of sensors. The interference of foreign substances, such as Na_2SO_3, $CuSO_4$, $Mg(NO_3)_2$, and $(NH_4)_2CO_3$, on the determination of nitrite can be examined by adding them in turn into PBS solution (pH 5.29) (Fig. 12). When the tolerance limit was taken as the concentration of diverse species causing less than a 5% relative error, a 200-fold quantity of Na^+, K^+, Ca^{2+}, Mg^{2+}, Al^{3+}, Fe^{3+}, Zn^{2+}, Cu^{2+}, Ni^{2+}, F^-, Cl^-, Br^-, NO_3^-, SO_4^{2-}, CO_3^{2-}, PO_4^{3-}, glucose, fructose, L-glutamic acid, ethanol, and H_2O_2, and a 50-fold quantity of I^-, S^{2-}, SO_3^{2-}, SCN^-, L-tryptophan, and guanine, did not produce interference for 0.3 mmol L^{-1} nitrite. However, a 10 times greater presence of ascorbic acid, uric acid, dopamine, norepinephrine, and L-tyrosine in 0.3 mmol·L^{-1} nitrite interfered with the determination. In this case, differential pulse voltammetry could be used to determine the content of nitrite owing to their difference in peak potential. Therefore, the $Cu_{hydroxide/oxide}$/MWCNTs/GCE possessed high selectivity for nitrite.

Fig. 10. Cyclic voltammograms of $Cu_{hydroxide/oxide}$ / multiwalled carbon nanotubes (MWCNTs) / glassy carbon electrode (GCE) in 0.07 mol L^{-1} PBS (pH 5.29) + 0.2 mol L^{-1} KCl solution containing different concentrations (c) of NO_2^- at 20 mV s^{-1}. c (mmol L^{-1}): 0, 0.5, 1.0, 1.5, 2.0, 2.5, 3.0, 3.5, 4.0, 4.5, 5.0, 5.5, 6.0, 6.5, 7.0, 7.5, 8.0, 8.5, 9.0, 9.5, 10.0, 11.0, and 13.0.

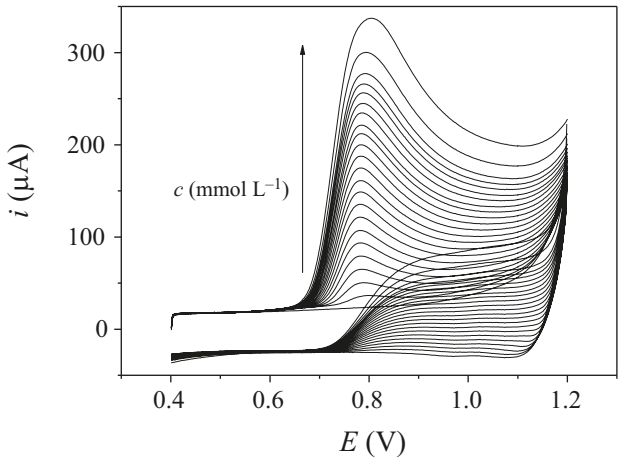
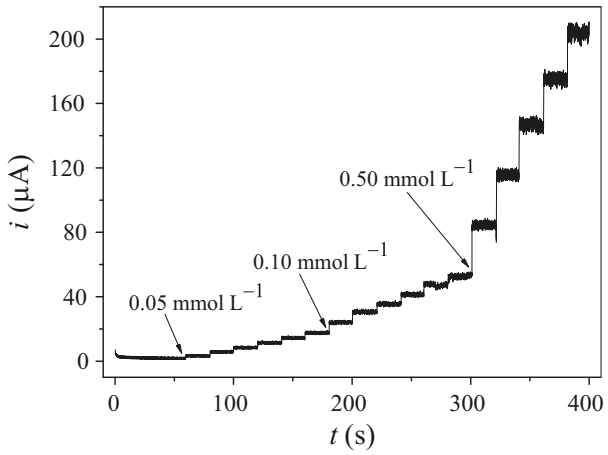


Fig. 11. A current vs time curve for nitrite oxidation on $Cu_{hydroxide/oxide}$ / multiwalled carbon nanotubes (MWCNTs) / glassy carbon electrode (GCE) in 0.07 mol L^{-1} PBS (pH 5.29) + 0.2 mol L^{-1} KCl at 0.78 V.

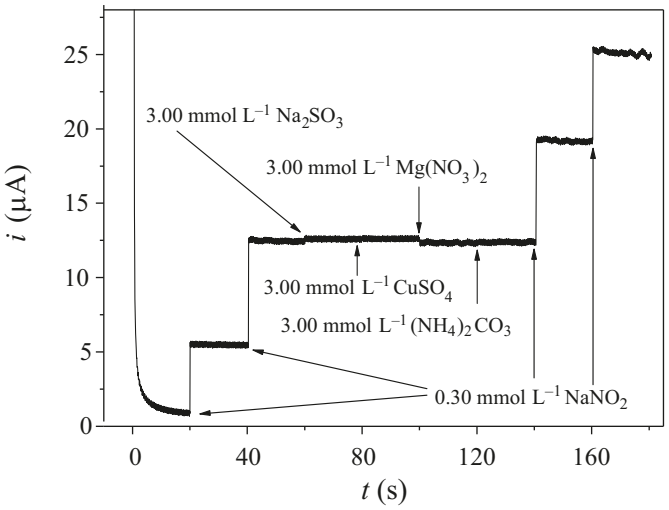


Response time and stability

The $Cu_{hydroxide/oxide}$/MWCNTs/GCE showed very fast response (<0.2 s) to the addition of nitrite at 0.78 V and produced a steady-state signal within 1 s (Fig. 13A). Figure 13B shows the amperometric response to 0.5 mmol L^{-1} $NaNO_2$ during a prolonged 3300 s experiment. The response remained stable throughout the experiment, indicating that the $Cu_{hydroxide/oxide}$/MWCNTs/GCE had high stability.

Can. J. Chem. Downloaded from www.nrcresearchpress.com by Renmin University of China on 09/02/12
For personal use only.

Fig. 12. A current vs time curve recorded on $Cu_{hydroxide/oxide}$ / multiwalled carbon nanotubes (MWCNTs) / glassy carbon electrode (GCE) in 0.07 mol L^{-1} PBS (pH 5.29) + 0.2 mol L^{-1} KCl by adding different species at 0.78 V. Arrows stand for the point of sample addition.



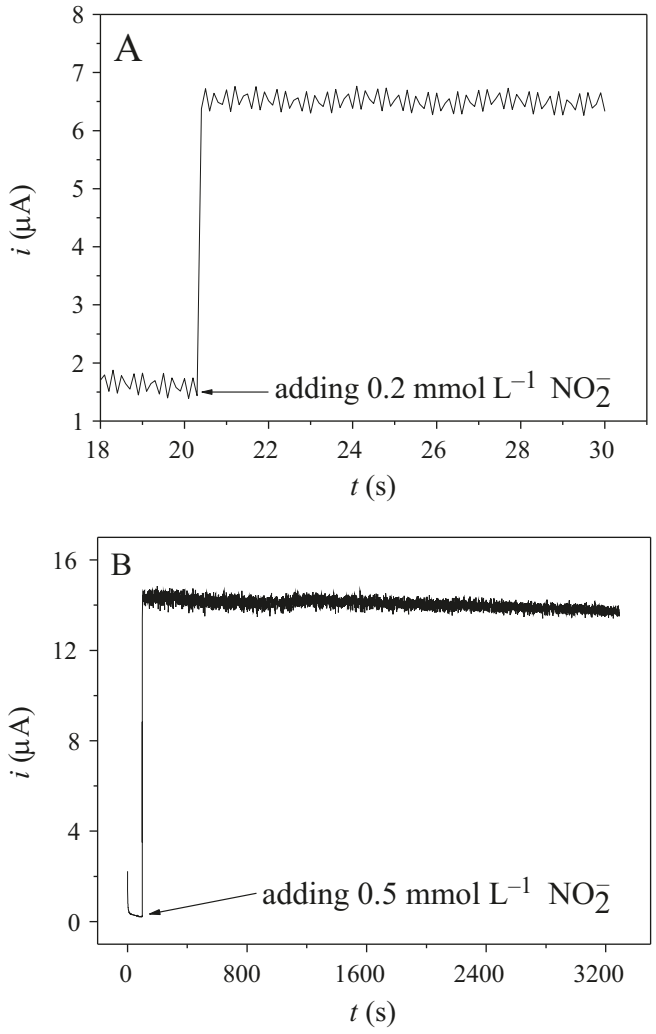
Five different $Cu_{hydroxide/oxide}$/MWCNTs/GCEs were prepared under the same conditions to estimate the fabrication reproducibility. The relative standard deviation (RSD) of amperometric responses to 0.20 mmol L^{-1} $NaNO_2$ was 2.2%, indicating that the reproducibility of electrode fabrication was excellent. The service life of $Cu_{hydroxide/oxide}$/MWCNTs/GCE electrode was evaluated by assaying 0.20 mmol L^{-1} $NaNO_2$ every day for 60 days and the relative change in current response was less than 5%. The storage stability of $Cu_{hydroxide/oxide}$/MWCNTs/GCE electrode was also investigated by placing it in a refrigerator (4 °C) after the first test. Six months later, the current response to 0.20 mmol L^{-1} $NaNO_2$ retained 92% of the initial value. In short, fast response and good stability provided a guarantee for the practical application.

Amperometric determination of $NaNO_2$ in real samples

To verify the performance and feasibility of the proposed method for the analysis of nitrite in pickled vegetables (purchased from local supermarkets), the $Cu_{hydroxide/oxide}$/MWCNTs/GCE was applied to the determination of nitrite in pickled radish, potherb mustard, and cucumber by a current vs time curve method at 0.78 V. The pickled vegetable was chopped and homogenized with a food mill. Two grams of the homogenized sample (weighed accurately to 0.1 mg) was placed in a 10 mL flask and extracted for 30 min by a supersonic method to keep the solid phase completely dispersed. The flask was kept in a water bath (75 °C) for 5 min to further promote the extraction of nitrite and then allowed to cool at ambient temperature. The sample was diluted with deionized water to the scale mark of the volumetric flask and filtered with filter paper. After the filtrate was centrifuged for 15 min at 10 000 rpm, the supernatant was used for electrochemical analysis.

Amperometric determinations were carried out by directly adding the standard sample and supernatant in turn into the electrochemical cell containing 10 mL of 0.07 mol L^{-1} PBS (pH 5.29) + 0.2 mol L^{-1} KCl. All the data presented are the means of five parallel determinations. Table 1 summarizes

Fig. 13. Response time (A) and stability (B) of $Cu_{hydroxide/oxide}$ / multiwalled carbon nanotubes (MWCNTs) / glassy carbon electrode (GCE) to 0.2 mmol L^{-1} (A) and 0.5 mmol L^{-1} $NaNO_2$ (B) in 0.07 mol L^{-1} PBS (pH 5.29) + 0.2 mol L^{-1} KCl at 0.78 V.



the results of the three samples. As can be seen, the RSD for each sample was less than 3%, and the recoveries ranged from 96.9% to 103.7%, indicating that the $Cu_{hydroxide/oxide}$/MWCNTs/GCE could be efficiently used for the determination of nitrite in food samples. To further estimate the efficiency of this sensor, a standard spectrophotometric method (*Chinese National Food Safety Standard*, GB 5009.33-2010) was adopted for the determination of nitrite in the same batch of samples and these results were consistent with those obtained by this work.

Conclusions

In this paper, we developed a copper hydroxide (oxide) / MWCNTs nanocomposite modified GCE by film plating / CV, which exhibited marked synergistic catalytic effects on the electrooxidation of NO_2^- in PBS (pH 5.29) solution. The concentration of MWCNTs, the thickness of the copper film, and the electrolyte pH had significant effects on electrocatalytic activity of GCE. The nitrite sensor possessed many advantages, such as easy preparation, fast response, long-term

Table 1. Nitrite content in pickled vegetables.

Sample	Initial nitrite content (mg kg^{-1})	Spiked nitrite content (mg kg^{-1})	Measured total nitrite content (mg kg^{-1})	RSD (%, $n = 5$)	Recovery (%)	Nitrite content obtained by the spectrophotometric method (mg kg^{-1})
Pickled radish	5.61	1.10	6.69	2.6	98.2	5.52
Pickled potherb mustard	7.36	5.80	12.98	3.0	96.9	7.41
Pickled cucumber	4.08	4.90	9.16	2.9	103.7	4.19

Note: RSD, relative standard deviation.

Can. J. Chem. Downloaded from www.nrcresearchpress.com by Renmin University of China on 09/02/12
For personal use only.

stability, high selectivity, wide linear range, and low detection limit. It has been applied to the determination of NO_2^- in pickled vegetables with satisfactory results.

Experimental section

Reagents

MWCNTs (purity, >97%; o.d., <10 nm; length, 5–15 μm) were purchased from Shenzhen Nanotech Port Co., Ltd., Shenzhen, P.R. China. Analytical grade $NaNO_2$, $CuCl_2{\cdot}2H_2O$, KCl, and *N*,*N*-dimethylformamide (DMF) were all purchased from Shanghai Chemical Reagent Company, Shanghai, P.R. China) and used without further purification. Stock solutions were all prepared with doubly distilled water.

Instrumentation

CV, EIS, and the current vs time curve method were carried out on a CHI 660C electrochemical analyzer (Shanghai Chenhua Co., P.R. China). A three-electrode configuration consisted of a modified GCE (3.0 mm diameter) as a working electrode, a reference electrode (Ag/AgCl satd. KCl), and a counterelectrode (Pt wire, 5 mm length, 1 mm diameter). Environmental SEM images (ESEM) were obtained on the GCE electrode with a detachable electrode tip using a XL-30 microscope (Philips Co., Netherlands). The solution pH values were determined on a pHS-3C meter (Precision Instruments Co., Ltd., Shanghai, P.R. China).

Preparation of $Cu_{hydroxide/oxide}$/MWCNTs/GCE and electrochemical measurement

The GCE surface was cleaned by ultrasonic cleaning in dilute nitric acid (1:1, *v*/*v*), ethanol, and deionized water, sucessively. First, a 10 μL suspension of MWCNTs in DMF obtained by ultrasound for 2 h was dripped on the GCE surface and dried at room temperature to obtain a MWCNTs/GCE. Then, copper nanoparticles were electrodeposited on MWCNTs/GCE surface by maintaining –0.5 V in 0.1 mol L^{-1} KCl solution containing $CuCl_2$. Last, the electrode was put in 0.1 mol L^{-1} NaOH solution to convert copper nanoparticles to copper hydroxide (oxide) by scanning repetitively.

The CV, current vs time curve, and EIS of $Cu_{hydroxide/oxide}$/MWCNTs/GCE were carried out in an electrochemical cell holding 10.0 mL different electrolyte solution. EIS measurements were carried out in the 0.01–10^5 Hz frequency range at 0.28 V. During all experiments, the electrolyte was prepurged with high-purity N_2 for 10 min to remove O_2, and a continuous flow of N_2 gas was maintained over the solution. All experiments were performed at room temperature (25 ± 1 °C).

Acknowledgments

This project was supported by the key Academic Program of the third phase "211 Project" of South China Agricultural University (Grant No. 2009B010100001) and the Scientific Research Starting Foundation for Drs., Natural Science Foundation of Guangdong Province, P.R. China (Grant No. 5300842).

References

(1) Anjana, S. U.; Iqbal, M. *Agron. Sustain. Dev* **2007**, *27* (1), 45. doi:10.1051/agro:2006021.
(2) Ji, F.-D.; Ji, B.-P.; Li, B.; Lu, F. *J. Food Process. Preserv.* **2009**, *33* (S1), 175. doi:10.1111/j.1745-4549.2008.00291.x.
(3) Honikel, K. O. *Meat Sci.* **2008**, *78* (1–2), 68. doi:10.1016/j.meatsci.2007.05.030.
(4) Reis Lima, M. J.; Fernandes, S. M. V.; Rangel, A. O. S. S. *Int. Dairy J.* **2006**, *16* (12), 1442. doi:10.1016/j.idairyj.2005.11.010.
(5) Kim-Shapiro, D. B.; Gladwin, M. T.; Patel, R. P.; Hogg, N. *J. Inorg. Biochem.* **2005**, *99* (1), 237. doi:10.1016/j.jinorgbio.2004.10.034.
(6) Huang, Y. G.; Ji, J. D.; Hou, Q. N. *Mutat. Res. Fundam. Mol. Mech. Mutagen* **1996**, *358* (1), 7. doi:10.1016/0027-5107(96)00087-5.
(7) Moorcroft, M. J.; Davis, J.; Compton, R. G. *Talanta* **2001**, *54* (5), 785. doi:10.1016/S0039-9140(01)00323-X.
(8) Di Matteo, V.; Esposito, E. *J. Chromatogr. A* **1997**, *789* (1–2), 213. doi:10.1016/S0021-9673(97)00851-0.
(9) Kozub, B. R.; Rees, N. V.; Compton, R. G. *Sens. Actuators B Chem.* **2010**, *143* (2), 539. doi:10.1016/j.snb.2009.09.065.
(10) Miao, P.; Liang, Z. Q.; Liu, L.; Chen, G. F. *Curr. Nanosci* **2011**, *7* (3), 354. [IDS: 784VV]. doi:10.2174/157341311795542345.
(11) Cao, X.; Cai, X.; Wang, N.; Guo, L. *Anal. Chim. Acta* **2011**, *691* (1–2), 43.
(12) Guan-Ping, J.; Xiang-Qin, L. *Chin. J. Chem.* **2005**, *23* (6), 673. doi:10.1002/cjoc.200590673.
(13) Chen, X.; Wang, F.; Chen, Z. *Anal. Chim. Acta* **2008**, *623* (2), 213. doi:10.1016/j.aca.2008.06.021.
(14) Liu, Z.; Xi, X.; Dong, S.; Wang, E. *Anal. Chim. Acta* **1997**, *345* (1–3), 147. doi:10.1016/S0003-2670(96)00631-9.
(15) Liu, P.; Hu, J. *Sens. Actuators B Chem.* **2002**, *84* (2–3), 194. doi:10.1016/S0925-4005(02)00024-2.
(16) Agboola, B.; Nyokong, T. *Anal. Chim. Acta* **2007**, *587* (1), 116. doi:10.1016/j.aca.2007.01.031.
(17) Salimi, A.; Noorbakhsh, A.; Ghadermarzi, M. *Sens. Actuators B Chem.* **2007**, *123* (1), 530. doi:10.1016/j.snb.2006.09.054.
(18) Zheng, D.; Hu, C.; Peng, Y.; Hu, S. *Electrochim. Acta* **2009**, *54* (21), 4910. doi:10.1016/j.electacta.2009.04.004.
(19) Yu, R.; Wang, L.; Xie, Q.; Yao, S. *Electroanalysis* **2010**, *22* (23), 2856. doi:10.1002/elan.201000296.

(20) Zhou, Y.; Xian, H.; Li, F.; Wu, S.; Lu, Q.; Li, Y.; Wang, L. *Electrochim. Acta* **2010**, *55* (20), 5905. doi:10.1016/j.electacta.2010.05.043.
(21) Rahman, M. M.; Ahammad, A. J. S.; Jin, J.-H.; Ahn, S. J.; Lee, J.-J. *Sensors (Basel Switzerland)* **2010**, *10* (5), 4855. doi:10.3390/s100504855.
(22) Vashist, S. K.; Zheng, D.; Al-Rubeaan, K.; Luong, J. H. T.; Sheu, F. S. *Biotechnol. Adv.* **2011**, *29* (2), 169. doi:10.1016/j.biotechadv.2010.10.002.
(23) Piela, B.; Wrona, P. K. *J. Electrochem. Soc.* **2002**, *149* (2), E55. doi:10.1149/1.1433751.
(24) Wang, P.; Mai, Z.; Dai, Z.; Li, Y.; Zou, X. *Biosens. Bioelectron.* **2009**, *24* (11), 3242. doi:10.1016/j.bios.2009.04.006.

Can. J. Chem. Downloaded from www.nrcresearchpress.com by Renmin University of China on 09/02/12
For personal use only.

Density functional theory for N–NO_2 bond dissociation energies of *N*-nitroacylamide compounds in acetonitrile — Theoretical method assessment and prediction

Xiaohong Li, Huixian Wang, Zhumu Fu, and Xianzhou Zhang

Can. J. Chem. Downloaded from www.nrcresearchpress.com by Renmin University of China on 09/02/12
For personal use only.

Abstract: The performance of various density functional theories (B3LYP, B3PW91, B3P86, B1LYP, BMK, MPWB1K, PBE0, and MPWB95) was examined for calculating N–NO_2 bond dissociation energies (BDEs) of 10 *N*-nitroacylamide compounds. The CBS-4M method was also used. By comparing the calculated results with the experimental values, it was observed that B1LYP/6–31G** and B3LYP/6–31+G** provided accurate BDEs. Especially, B3LYP/6–31+G** was recommended because of its smaller maximum absolute deviation. Further, substituent effects based on the B3LYP/6–31+G** method were analyzed. The result shows that an electron-donating group increases the BDE of the parent C_6H_5–$CON(CH_3)NO_2$, while an electron-withdrawing group decreases the BDE of the parent C_6H_5–$CON(CH_3)NO_2$. Subsequently, the BDEs of the other *N*-nitroacylamindes were estimated.

Key words: density functional theory, polarized continuum model, *N*-nitroacylamides compounds, bond dissociation energy, substituent effects.

Résumé : On a examiné les performances relatives de diverses variantes de la théorie de la fonctionnelle de la densité (B3LYP, B3PW91, B3P86, B1LYP, BMK, MPWB1K, PBE0 et MPWB95) pour calculer les énergies de dissociation de la liaison (EDL) N–NO_2 de composés de la famille de 10 *N*-nitroacylamides. On a aussi fait appel à la méthode CBS-4M. Une comparaison des résultats des calculs avec les résultats expérimentaux a permis d'observer que les méthodes B1LYP/6–31G** et B3LYP/6–31+G** conduisent aux énergies de dissociation de liaison les plus exactes. On recommande particulièrement la méthode B3LYP/6–31+G** en raison du fait que sa déviation absolue est la plus faible. On a de plus analysé l'effet de substituant par la méthode B3LYP/6–31+G**. Les résultats montrent qu'un groupe électrodonneur augmente l'énergie de dissociation de la liaison du composé fondamental, C_6H_5–$CON(CH_3)NO_2$, alors qu'un groupe électroattracteur la diminue. Finalement, on a aussi évalué les énergies de dissociation de liaison d'autres *N*-nitroacylamides.

Mots-clés : théorie de la fonctionnelle de la densité, modèle du continuum polarisé, composés de la famille des *N*-nitroacylamides, énergie de dissociation de la liaison, effets de substituant.

[Traduit par la Rédaction]

Introduction

Nitric oxide (NO) is a free-radical gas and one of the smallest known biologically active messenger molecules, which plays key roles in regulating a diverse range of physiological processes, including cellular differentiation and apotosis.[1–4] However, the importance of nitrogen dioxide (NO_2) has largely been overshadowed or even overlooked during the same period. Nitrogen dioxide has long been known in chemistry as a strong oxidant and nitrating reagent for organic synthesis, but not until very recently was it found to be associated with many destructive processes in living bodies. A wide spectrum of diseases has been suggested to be related to the exogenously and endogenously generated NO_2.[5,6] Conversely, it is also reported that NO_2^- plays a crucial role in many NO-mediated processes, such as hypoxic vasodilation and cytoprotection from cardiac and liver ischemia–reperfusion injury, and in gene expression.[7] Nitrite is also suggested to be a potential therapeutic in the treatment of various diseases.[8,9]

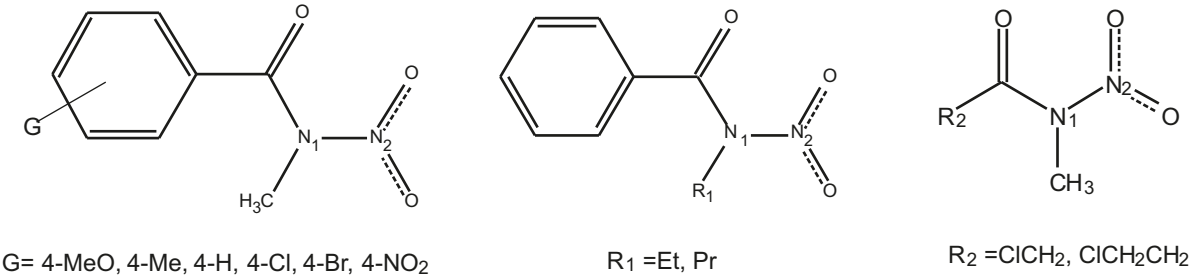
To understand the mechanistic details of NO_2 or NO_2^- in chemical or biological processes, the basic information concerning quantitative energetic changes in NO_2^- related bond cleavage in solution should be of great value because it provides the necessary information on the thermodynamic driving forces of NO_2^- carrier molecules to release, capture, or

Received 2 February 2012. Accepted 21 March 2012. Published at www.nrcresearchpress.com/cjc on 22 May 2012.

L. Li. College of Physics and Engineering, Henan University of Science and Technology, Luoyang 471003, China; Luoyang Key Laboratory of Photoelectric Functional Materials, Henan University of Science and Technology, Luoyang 471003, China.
W. Wang. College of Physics and Engineering, Henan University of Science and Technology, Luoyang 471003, China.
F. Fu. Electronic and Information Engineering College, Henan University of Science and Technology, Luoyang 471003, China.
Z. Zhang. College of Physics and Information Engineering, Henan Normal University, Xinxiang, 453007, China.

Corresponding author: Xiaohong Li (e-mail: lorna639@126.com).

Fig. 1. The structures of the selected *N*-nitroacylamide compounds.



Can. J. Chem. Downloaded from www.nrcresearchpress.com by Renmin University of China on 09/02/12
For personal use only.

transfer an NO_2 (or NO_2^-) moiety.[6] The binding force of NO_2 with a particular active site can therefore be represented by the bond energy of the Y–NO_2 type, where Y represents the atom in a carrier to which NO_2 is directly attached. Recently, Li et al.[10] reported the first series of experimentally determined N–NO_2 homolytic bond energy scales of some *N*-nitroacylamides compounds by using titration calorimetry in acetonitrile solution. The 10 *N*-nitroacylamide compounds are 4-MeO–$C_6H_4CON(CH_3)NO_2$ ($C_9H_{10}O_4N_2$), 4-CH_3–$C_6H_4CON(CH_3)NO_2$ ($C_9H_{10}O_3N_2$), $C_6H_5CON(CH_3)NO_2$ ($C_8H_8O_3N_2$), 4-Cl–$C_6H_4CON(CH_3)NO_2$ ($C_8H_7O_3N_2Cl$), 4-Br–$C_6H_4CON(CH_3)NO_2$ ($C_8H_7O_3N_2Br$), 4-NO_2–$C_6H_4CON(CH_3)NO_2$ ($C_8H_7O_5N_3$), $C_6H_5CON(C_2H_5)NO_2$ ($C_9H_{10}O_3N_2$), $C_6H_5CON(C_3H_7)NO_2$ ($C_{10}H_{12}O_3N_2$), $ClCH_2CON(CH_3)NO_2$ ($C_3H_5O_3N_2Cl$), and $ClCH_2CH_2CON(CH_3)NO_2$ ($C_4H_7O_3N_2Cl$). The structures of the selected *N*-nitroacylamide compounds are shown in Fig. 1.

Since a rapid cleavage of the Y–NO_2 bond (releasing a nitrite) upon one-electron reduction of a nitro compound has been observed for years,[11–13] this kind of bond energy scale should also be useful for the study of the stability and shock sensitivity of the Y–NO_2-type energetic materials[14,15] and for estimating the nitrating ability of nitro-releasing compounds in synthetic chemistry.[16,17] However, to our knowledge, no systematic work has been reported on the theoretical determinations of N–NO_2 bond energies in any solvent system where the NO_2-related chemical and biological activities are likely to take place.

Density functional theory (DFT) is currently more practical for bond dissociation energy (BDE) calculations because of their favorable scaling and reasonable CPU cost. Among these DFT methods, B3LYP, B3PW91, and B3P86 are highly popular because of their advantages in BDE calculation. Previous research has shown that the C–N BDEs for imidazole derivatives computed by the B3LYP/6–31G** method are in excellent agreement with their experimental values.[18] Furthermore, B3P86 values revealed the best agreement with available experimental data in predicting C–NO BDE.[19] Baciu and Gauld[20] obtained the best reliable BDEs for a range of *S*-nitrosothiols by the B3P86/6–311++G(2df,p) method, which is agreement with values obtained with higher accuracy methods, e.g., CBS-Q. However, recent cstudies from a more general perspective demonstrated that these popular DFT methods could tend to underestimate BDEs by 2–6 kcal/mol (1 cal = 4.184 J).[21] Obviously, the failures are due to deficiencies of the approximate exchange–correlation functionality used for different calculating systems. Therefore, it is important to shed light on their systematic performance for a particular computational target, particularly for the N–NO_2 BDEs of the title compounds.

In the present work, the performance of a variety of DFT functions, including B3LYP, B3PW91, B3P86, B1LYP, BMK, MPWB1K, PBE0 and MPWB95, was examined for the calculation of the N–N BDEs for several *N*-nitroacylamide compounds with the available experimental data. The complete basis set (CBS-4M) method is also used. The focus is on investigating their suitability and identifying low-cost alternative methods. If we can find an accurate calculational method to compute BDEs of the N–NO_2 bond, it would be possible to use this method to predict those molecules whose experimental BDEs are not available.

Computational methodology

All calculations were performed with the Gaussian03 computational package.[22] Geometry optimizations and subsequent normal-mode analyses at the corresponding equilibrium structures were performed for the products of the different bond scission reactions in which a single NO_2 group was removed from the parent structure. The equilibrium geometries and BDEs were obtained using the Becke-style three-parameter DFT[23] with the Lee–Yang–Parr correlation function (LYP),[24,25] the Perdew–Wang 91 expression (PW91),[26] and the Perdew 86 expression (P86).[27]

In addition, we applied two hybrid meta DFT methods called MPWB95 and MPWB1K, which were proposed by Zhao and Truhlar.[28] MPWB95 and MPWB1K have been developed in such a way that the functionals depend on the electron density, density gradient, Hartree–Fock exchange, and the Kohn–Sham orbitals in the form of a kinetic energy density, whereas the functionals of the hybrid DFT depend on the electron density, density gradient, and Hartree–Fock exchange only.[28] The MPWB1K method, which was developed for kinetics calculations, has been shown to be more accurate than the previously introduced MPW1K method.[28]

For the CBS-4M model,[29–31] a geometry optimization and a zero-point-energy computations were carried out in Hartree–Fock theory. Then, the energy was evaluated with the second-order of Møller–Plesset (MP2) theory with a larger basis set and a CBS extrapolation to correct the energy through the second order. The MP4SDQ/6–31G calculation was used to approximate higher orders of contributions. There are also empirical corrections for spin contamination and a size-consistent higher order correction. It must be noted that the new DFT method, the BMK functional, consists of modified original exchange and correlation functionalities. The BMK functionality is rather different from the others as it simulates a variable exact exchange by combining

Can. J. Chem. Downloaded from www.nrcresearchpress.com by Renmin University of China on 09/02/12
For personal use only.

exact exchange (42%) and terms depending on the kinetic energy density. This allows it to be developed for various applications, ranging from accurate heat of formation prediction to calculation of rate coefficients.[32]

In the PBE0 functional, there is only one coefficient, which is theoretically adjusted to 0.25, reflecting the mix of Hartree–Fock or exact exchange and the DFT exchange, which is represented by the PBE density functional.[33] The correlation part is also represented by the PBE correlation functional with the coefficient equal to one.

The polarized continuum model (PCM) developed by Tomasi and co-workers[34–36] was employed. In this PCM model, the atomic radii of the spheres used to build the molecular cavity were adjusted by introducing chemical consideration such as hybridization, formal charge, and first-neighbor inductive effect. The effect of the escaped electronic charge outside the cavity was corrected with an additional set of charges on the cavity surface distributed according to the solute electronic density in each point of the surface.

All calculations were performed at the 6–31G** basis set except the CBS-4M method. The normal mode analysis for each structure resulted in no imaginary frequencies for the $3N - 6$ vibrational degrees of freedom, where N is the number of atoms in the system. This indicates that the structure of each molecule corresponds to a local minimum on the potential energy surface.

Generally, computed BDEs are reported for gas-phase conditions and it is expected that these values suffer variation in different environments such as those in living organisms. So, it would be interesting to know what happens to these dissociation energies in the presence of a solvent such as acetonitrile.

The $N–NO_2$ bond strength is obtained by calculating the homolytic bond dissociation energy, which is defined as the enthalpy change of the dissociation reaction.

$$[1] \qquad R - X \rightarrow R^{\bullet} + X^{\bullet}$$

For the *N*-nitroacylamide compounds studied here, the BDE is defined as the difference between the zero-point-corrected energy (E) of the parent molecule and that of the products of the unimolecular dissociation in which an NO_2 group is removed. For example, for 4-CH_3–$C_6H_4CON(CH_3)NO_2$, the BDE is

$$[2] \qquad BDE_{N-NO_2} = E(C_9H_{10}ON) + E(NO_2) - E(C_9H_{10}O_3N_2)$$

The average error is determined by calculating the average absolute error (ε_{aae}), defined as

$$[3] \qquad \varepsilon_{aae} = \frac{1}{N}\sum_{i=1}^{N} |x_i - c_i|$$

where x_i represents the experimental data, c_i denotes the calculated values, and N is the number of experimental or calculated data.

Results and discussion

The N–N bond length

First, we examine the $N_1–N_2$ bond lengths of the 10 *N*-nitroacylamide compounds by various computational methods. For the $N_1–N_2$ bond distances of the 10 title compounds, the experimental equilibrium bond distances are not available. To have a comparison, we listed the N–N experimental bond distance[37] for NH_2NO_2.

It is noted from Table 1 that the $N_1–N_2$ bond lengths computed by the B3LYP functional are the largest among those calculated by various computational methods and the $N_1–N_2$ bond lengths calculated by the MPWB1K/6–31G** method are the smallest. The $N_1–N_2$ bond lengths computed by the CBS-4M method are slightly larger than those computed by the MPWB1K/6–31G** method. Compared with the corresponding experimental value, the B3LYP/6–31G** method produces the best result for NH_2NO_2 with an N–N bond length of 1.394 Å, only a 0.033 Å deviation from the experimental value. The CBS-4M method gives the worst result for NH_2NO_2 with an N–N bond length of 1.354 Å, because the method is based upon geometries optimized at the HF/3–21G* level of theory.

In addition, we computed the $N_1–N_2$ bond lengths of the selected compounds by using the B3LYP/6–31+G** method. Through a comparison of the computational results, it is noted that using diffuse function does not improve the result. The deviation from experimental value increases in the presence of diffuse function.

Performance of various computational methods for the $N–NO_2$ BDEs of *N*-nitroacylamides in acetonitrile

The BDE results computed by using the B3LYP, B1LYP, B3P86, and B3PW91 hybrid DFT methods with the 6–31G** basis set are presented in Table 2. The available experimental values[10] are also included. The BDEs of the 10 *N*-nitroacylamide compounds are compared with the corresponding experimental results for the system. Figure 2 gives the overall maximum and mean absolute deviations of the various methods.

It is noted from Table 2 and Fig. 2 that the B3PW91 and B3P86 methods failed to provide an accurate description of the N–O BDEs for the *N*-nitroacylamide compounds. The two methods deviated from the experimental data by as much as 13.9 kcal/mol, and the mean absolute deviations were 5.9 and 9.2 kcal/mol for the B3PW91 and B3P86 methods, respectively. Compared with the B3PW91 and B3P86 methods, the mean absolute deviation of the B3LYP method is 3.7 kcal/mol and the maximum deviation is 8.1 kcal/mol, which indicates that the B3LYP method is a better method for predicting the $N–NO_2$ BDEs among the three DFT methods. Table 2 also demonstrates that the B1LYP method gives the best BDEs for the $N–NO_2$ bonds of the title compounds. The maximum absolute and the mean absolute deviations are 5.68 and 1.2 kcal/mol, respectively.

In addition, detailed analysis reveals that the BDEs calculated by the B3LYP, B3P86 and B3PW91 methods were overestimated, which disagrees with previous research asserting that DFT methods usually underestimate BDE systematically. For example, the largest deviation (13.9 kcal/mol) between the BDEs and the experiment for the B3P86 method occurs for $ClCH_2CON(CH_3)NO_2$ ($C_3H_5O_3N_2Cl$). The maximum deviation between the B3PW91 computational results and the experimental values was 10.1 kcal/mol for $ClCH_2CON(CH_3)NO_2$ ($C_3H_5O_3N_2Cl$). The B1LYP method

Can. J. Chem. Downloaded from www.nrcresearchpress.com by Renmin University of China on 09/02/12
For personal use only.

Table 1. The N_1–N_2 bond lengths (Å) of some *N*-nitroacylamide compounds (4-Y-C_6H_4–$CON(CH_3)NO_2$) calculated by different DFT methods and the CBS-4M method.

	Bond length (Å)						
	Y						
Method	OCH_3	CH_3	H	Cl	Br	NO_2	NH_2NO_2[a]
B3LYP/6–31G**	1.388	1.392	1.393	1.397	1.396	1.405	1.394 (0.033)
B3PW91/6–31G**	1.381	1.384	1.387	1.390	1.390	1.397	1.384 (0.043)
B3P86/6–31G**	1.379	1.383	1.385	1.386	1.387	1.394	1.381 (0.046)
B1LYP/6–31G**	1.385	1.387	1.390	1.393	1.395	1.400	1.391 (0.036)
MPWB1K/6–31G**	1.361	1.362	1.364	1.367	1.366	1.370	1.361 (0.066)
BMK/6–31G**	1.379	1.386	1.388	1.391	1.392	1.397	1.389 (0.038)
PBE0/6–31G**	1.376	1.380	1.382	1.384	1.384	1.391	1.377 (0.05)
MPWB95K/6–31G**	1.372	1.375	1.376	1.381	1.379	1.384	1.373 (0.054)
B3LYP/6–31+G**	1.376	1.379	1.383	1.387	1.387	1.389	1.387 (0.04)
CBS-4M	1.366	1.366	1.367	1.370	1.369	1.377	1.354 (0.073)
Experimental							1.427[b]

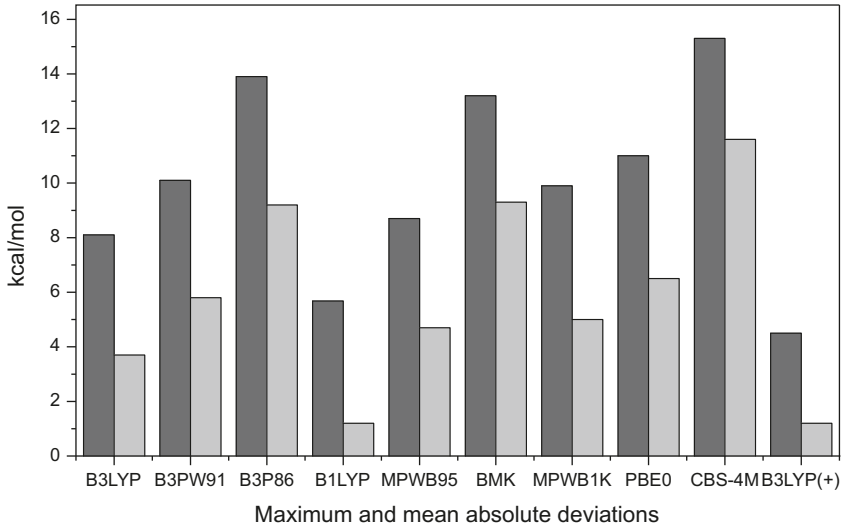
[a]Values in parentheses are the deviations between the computational results and the experimental ones.
[b]See ref. 32.

Table 2. Computed bond dissociation energies (BDEs, kcal/mol; 1 cal = 4.184 J) in MeCN for the removal of an NO_2 group in the studied molecules by using various density functional theory methods with the 6–31G** basis set.

Entry	Compound	B3LYP	B3PW91	B3P86	B1LYP	Expt.[a,b]
1	4-MeO–$C_6H_4CON(CH_3)NO_2$	36.8 (3.2)	38.8 (5.2)	42.2 (8.6)	33.6 (0.0)	33.6
2	4-CH_3–$C_6H_4CON(CH_3)NO_2$	36.7 (3.3)	38.7 (5.3)	42.1 (8.7)	33.5 (0.1)	33.4
3	$C_6H_5CON(CH_3)NO_2$	36.5 (3.2)	38.6 (5.3)	41.9 (8.6)	33.3 (0.0)	33.3
4	4-Cl–$C_6H_4CON(CH_3)NO_2$	35.9 (3.0)	38.1 (5.2)	40.9 (8.0)	32.9 (0.0)	32.9
5	4-Br–$C_6H_4CON(CH_3)NO_2$	35.7 (3.0)	37.9 (5.2)	41.5 (8.8)	32.5 (–0.2)	32.7
6	4-NO_2–$C_6H_4CON(CH_3)NO_2$	35.3 (2.7)	37.5 (4.9)	40.9 (8.3)	32.4 (–0.2)	32.6
7	$C_6H_5CON(C_2H_5)NO_2$	35.6 (2.7)	37.5 (4.6)	41.1 (8.2)	32.4 (–0.5)	32.9
8	$C_6H_5CON(C_3H_7)NO_2$	35.6 (2.0)	37.4 (3.8)	41.0 (7.4)	32.3 (–1.3)	33.6
9	$ClCH_2CON(CH_3)NO_2$	40.0 (8.1)	42.0 (10.1)	45.8 (13.9)	37.6 (5.7)	31.9
10	$ClCH_2CH_2CON(CH_3)NO_2$	39.3 (6.1)	41.2 (8.0)	44.6 (11.4)	37.2 (4.0)	33.2
Mean absolute deviation		3.7	5.8	9.2	1.2	

[a]Values in the parentheses are the deviations of the computed BDEs from the experimental ones.
[b]The data are from ref. 6.

Fig. 2. Overall maximum and mean absolute deviations of various methods. Dark gray bars represent the maximum deviations and the light gray bars represent the mean absolute deviations. B3LYP(+), B3LYP/6–31+G** method.



Can. J. Chem. Downloaded from www.nrcresearchpress.com by Renmin University of China on 09/02/12
For personal use only.

Table 3. Computed bond dissociation energies (BDEs, kcal/mol; 1 cal = 4.184 J) in MeCN for the removal of an NO_2 group in the studied molecules by using the B3LYP/6–31+G**, BMK, MPWB95, MPWB95, and PBE0 methods with the 6–31G** basis set and the CBS-4M method.

	Method[a]						
Compound	B3LYP /6–31+G**	BMK	MPWB95	MPWB1K	PBE0	CBS-4M	Expt.[b]
4-MeO–$C_6H_4CON(CH_3)NO_2$	34.0 (0.4)	42.5 (8.9)	37.4 (3.8)	37.5 (3.9)	39.1 (5.5)	44.7 (11.1)	33.6
4-CH_3–$C_6H_4CON(CH_3)NO_2$	33.8 (0.4)	42.0 (8.6)	37.3 (3.9)	37.4 (4.0)	39.1 (5.7)	44.6 (11.2)	33.4
$C_6H_5CON(CH_3)NO_2$	33.3 (0.0)	42.0 (8.7)	37.4 (4.1)	37.2 (3.9)	38.9 (5.6)	44.3 (11.0)	33.3
4-Cl–$C_6H_4CON(CH_3)NO_2$	33.3 (0.4)	41.5 (8.6)	36.8 (3.9)	36.9 (4.0)	38.5 (5.6)	44.0 (11.1)	32.9
4-Br–$C_6H_4CON(CH_3)NO_2$	33.0 (0.3)	41.2 (8.5)	36.9 (4.2)	36.8 (4.1)	38.4 (5.7)	43.8 (11.1)	32.7
4-NO_2–$C_6H_4CON(CH_3)NO_2$	32.4 (–0.2)	40.6 (8.0)	36.4 (3.8)	36.2 (3.6)	37.8 (5.2)	43.5 (10.9)	32.6
$C_6H_5CON(C_2H_5)NO_2$	32.4 (–0.5)	41.4 (8.5)	37.3 (4.4)	37.1 (4.2)	38.7 (5.8)	43.7 (10.8)	32.9
$C_6H_5CON(C_3H_7)NO_2$	32.0 (–1.6)	40.9 (7.3)	36.9 (3.3)	37.7 (4.1)	38.0 (4.4)	43.7 (10.1)	33.6
$ClCH_2CON(CH_3)NO_2$	36.4 (4.5)	45.1 (13.2)	40.6 (8.7)	41.8 (9.9)	42.9 (11.0)	47.2 (15.3)	31.9
$ClCH_2CH_2CON(CH_3)NO_2$	36.2 (3.0)	45.5 (12.3)	40.3 (7.1)	41.6 (8.4)	43.3 (10.1)	47.0 (13.8)	33.2
Mean absolute deviation	1.1	9.3	4.7	5.0	6.5	11.6	

[a]Values in parentheses are the deviations of the computed BDEs from the experimental ones.
[b]The data are from ref. 6.

gave both negative and positive deviations. Comparing the calculation results of the B1LYP and B3LYP methods, we can see that the B3LYP method did not give the better results, which means that not all of the complicated methods can obtain accurate results. For the different systems, it is important to found a suitable method to obtain the BDEs.

To determine whether the B3LYP method is sensitive to the basis set, we computed the BDEs of the *N*-nitroacylamides with the B3LYP method at the 6–31+G** basis set. In addition, to give an extensive comparison, the CBS-4M method and the BMK, MPWB95, MPWB1K, and PBE0 methods with the 6–31G** basis set were also employed to predict the BDEs for the 10 compounds. All calculated results are presented in Table 3.

As demonstrated in Table 3, the BMK, MPWB95, MPWB1K, PBE0 and CBS-4M methods all failed to provide accurate N–NO_2 BDEs. The mean absolute deviations of these methods versus the experiment are as follows: 9.3, 4.7, 5.0, 6.5, and 11.6 kcal/mol, respectively. Of the DFT methods, the B3LYP/6–31+G** method provides the best performance with the least mean absolute deviation. This shows that the use of diffuse functions can greatly improve the results. The deviations from experimental values drastically decrease in the presence of diffuse functions. As shown in Fig. 2, the maximum absolute deviations of B3P86 and BMK, B3PW91 and MPWB1K, and B3LYP and MPWB95 are almost at the same height, whereas the mean absolute deviation of MPWB95 is as large as that of MPWB1K. For PBE0, the maximum absolute deviation and mean absolute deviation are 11.0 and 6.5 kcal/mol, respectively. This shows that the PBE0 method is not the ideal method for the prediction of the N–NO_2 BDEs of *N*-nitroacylamide compounds.

From Fig. 2, it is clear that the B3LYP/6–31+G** and B1LYP/6–31G** methods are the ideal methods for estimating the N–NO_2 BDEs of the title compounds.

In summary, these DFT methods and the CBS-4M method exhibited different performances for calculating the N–NO_2 BDEs of the title compounds. The B3LYP/6–31+G** and B1LYP/6–31G** methods provided accurate values, and the B3LYP/6–31+G** method was found to be the best method because of the smaller maximum absolute deviation. Here, we must acknowledge that there are insufficient experimental data in the present work, specifically, the performance attributes for the particular computational targets.

From Tables 1 and 3, through analysis of the N_1–N_2 bond lengths and its BDEs calculated by the B3LYP/6–31+G** method, we found that the N_1–N_2 BDE is in a good linear relationship with the N_1–N_2 bond length and the correlated coefficient is 0.96. Figure 3 plots the correlation between the N_1–N_2 BDEs and bond lengths.

Substituent effects on the BDE of the N–NO_2 bond

In a comparison of the various computational methods from the analysis in the previous section, we know that the B3LYP method at the 6–31+G** basis set is the best procedure for the computation of the dissociation energies for the N–NO_2 bond in acetonitrile. Using this method, we studied the substituent effect on the N–NO_2 BDEs for the studied molecules, where substituted groups include both the electron-donating and -withdrawing groups such as 4-Cl, 4-Br, 4-NO_2, 4-CH_3, and 4-CH_3O. The calculated BDEs for the

Can. J. Chem. Downloaded from www.nrcresearchpress.com by Renmin University of China on 09/02/12
For personal use only.

Fig. 3. Dependence of N_1–N_2 bond dissociation energy (BDE) on bond length for some *N*-nitroacylamides in acetonitrile solution.

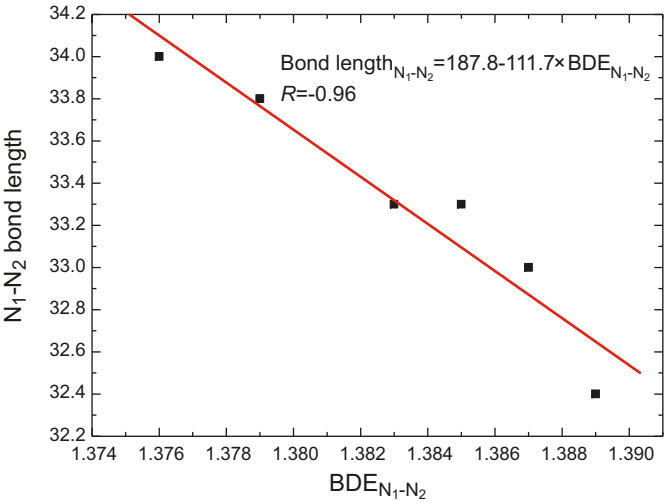


Table 4. Substituent effects on the bond dissociation energies (BDEs) of N–NO_2 homolysis (kcal/mol; 1 cal = 4.184 J) by using the B3LYP/6–31+G** method for Y–C_6H_4–CON(CH_3)NO_2, C_6H_5–CON(Y)NO_2, and Y–CON(CH_3)NO_2 in acetonitrile, where Y is 4-OCH_3, 4-CH_3, 4-H, 4-Cl, 4-Br, 4-NO_2, Et, Pr, $ClCH_2$, $ClCH_2CH_2$.

Y	BDE (kcal/mol)	ΔBDE (kcal/mol)
Y–C_6H_4–CON(CH_3)NO_2		
4-OCH_3	34.0	0.7
4-CH_3	33.8	0.5
4-H	33.3	0
4-Cl	33.3	0
4-Br	33.0	–0.3
4-NO_2	32.4	–0.9
C_6H_5–CON(Y)NO_2		
Et	32.4	0
Pr	32.0	–0.4
Y–CON(CH_3)NO_2		
$ClCH_2$	36.4	0
$ClCH_2CH_2$	36.2	–0.4

selected compounds are shown in Table 4. The results show that the substituent effects on the BDEs of the selected compounds are significant.

An interesting point observed in the selected molecules is the change of the BDEs and ΔBDE with the Hammett constant (σ_p) values of the substituent on the benzene. The Hammett constants[38] of the OCH_3, CH_3, H, Cl, Br, and NO_2 groups are –0.27, –0.17, 0.00, 0.23, 0.23, and 0.78, respectively. It is noted that BDE and ΔBDE decrease with the augment of the σ_p values for the 4-position substituted Y–C_6H_4–CON(CH_3)NO_2. Figure 4 plots the correlation between the N–NO_2 BDE of the 4-position substituted YC_6H_4–CON(CH_3)NO_2 and the Hammett constants. That is to say that an electron-donating group, such as 4-CH_3O, increases the BDE of the parent C_6H_5–CON(CH_3)NO_2, whereas an electron-withdrawing group, such as 4-NO_2, decreases the BDE of the parent C_6H_5–CON(CH_3)NO_2, because these groups always destabilize a radical.

Fig. 4. The correlation between the N–NO_2 bond dissociation energy (BDE) of the 4-position substituted Y–C_6H_4–CON(CH_3)NO_2 and the Hammett constant.

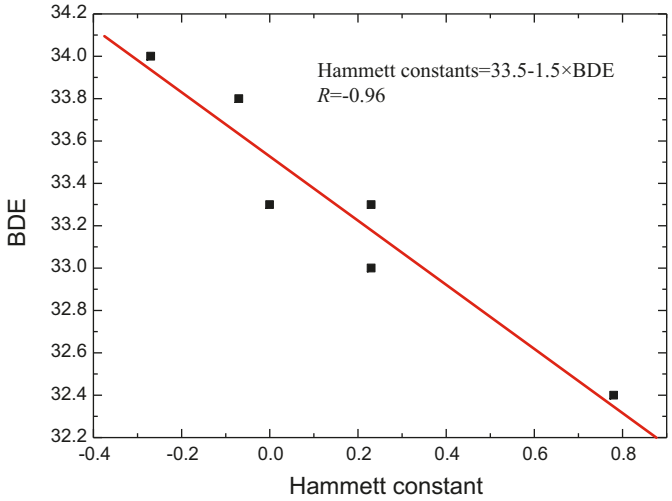


Table 5. Computed bond dissociation energies (BDEs, kcal/mol; 1 cal = 4.184 J) in MeCN for the removal of an NO_2 group in the other *N*-nitroacylamides by using B3LYP/6–31+G** methods.

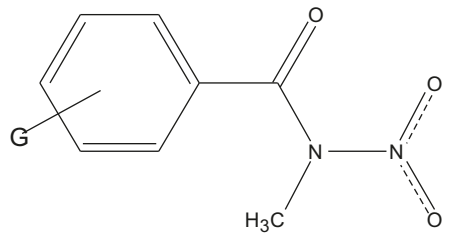
Compound	BDE (kcal/mol)
3-OMe–C_6H_4CON(CH_3)NO_2	34.7
3-CH_3–C_6H_4CON(CH_3)NO_2	32.8
3-Cl–C_6H_4CON(CH_3)NO_2	32.0
3-Br–C_6H_4CON(CH_3)NO_2	29.6
3-NO_2–C_6H_4CON(CH_3)NO_2	31.3
2-OMe–C_6H_4CON(CH_3)NO_2	33.0
2-Me–C_6H_4CON(CH_3)NO_2	33.0
2-Cl–C_6H_4CON(CH_3)NO_2	34.0
2-Br–C_6H_4CON(CH_3)NO_2	35.4
2-NO_2–C_6H_4CON(CH_3)NO_2	33.1

The polarization effects of the Et and Pr groups on the nitrogen atom are –0.49 and –0.54, respectively. Obviously, the BDE increases with the augment of the polarization effect. Similar analysis can be made on the Y–CON(CH_3)NO_2 compound, where Y is $ClCH_2CH_2$ or $ClCH_2$.

The prediction of the N–NO_2 BDEs of the other *N*-nitroacylamides in acetonitrile

In view of the importance of the study on the bond energies of the N–NO_2 type of compounds, this study aims not only to identify a suitable DFT method for *N*-nitroacylamides but also to estimate the BDEs of the other *N*-nitroacylamides through the chosen method, for which there are no experimental BDEs. The geometric molecular structures of the other *N*-nitroacylamides are optimized at the B3LYP/6–31+G** method. Their molecular structures are listed in Fig. 5. The N–NO_2 BDEs calculated by the B3LYP/6–31+G** method are listed in Table 5. It is noted that the BDE decreases with the augment of the σ_p value for the 3-position substituent groups, whereas the BDE changes slightly with the augment of the σ_p value for the 2-position substituent groups. In addition, comparing the calculated N–NO_2 BDEs of the 4-position substituted Y–C_6H_4–CON(CH_3)NO_2 compounds

Fig. 5. The structures of the other *N*-nitroacylamide compounds.



G= 3-Me, 3-OMe, 3-CH_2CH_3, 3-Cl, 3-Br, 3-NO_2
2-CH_2CH_3, 2-Me, 2-OMe, 2-Cl, 2-Br, 2-NO_2

listed in Table 3 with the calculated N–NO_2 BDEs in Table 5, we note that the position of the substituted groups has little effect on the BDEs.

Conclusion

In this paper, a systematic test was performed to study the performance of various DFT methods and the CBS-4M method for the N–NO_2 BDE calculation of *N*-nitroacylamide compounds. It was observed that the B1LYP/6–31G** and B3LYP/6–31+G** methods predicted accurate values and significantly outperformed CBS-4M and other popular DFT methods, including B3LYP, B3PW91, B3P86, BMK, MPWB1K, PBE0, and MPWB95 with the 6–31G** basis set. Because of the smaller maximum absolute deviation, we think that the B3LYP/6–31+G** method yields the most accurate BDEs compared with the experimental data; the mean absolute and maximum absolute deviations are 1.2 and 4.5 kcal/mol, respectively. The substituent effect shows that an electron-donating group increases the BDE of the parent C_6H_5–$CON(CH_3)NO_2$, whereas an electron-withdrawing group decreases the BDE of the parent C_6H_5–$CON(CH_3)NO_2$. Using the B3LYP/6–31+G** method, we estimated the BDEs of the other *N*-nitroacylamindes.

Acknowledgements

We gratefully thank the National Natural Science Foundation of China (Grant No. 60904023), the key project of the Henan Educational Committee (Grant No. 12A140004), and Henan University of Science and Technology for Young Scholars (Grant No. 2009QN0032) for their support of this work.

References

(1) Oliveira, F. S.; Ramos, T. M. B.; Oliveira, S. S. M.; Gaitani, C. M.; da Silva, R. S.; Marchetti, J. M. *Trends Inorg. Chem.* **2008**, *10*, 27.

(2) Koehler, J. J.; Zhao, J.; Jedlicka, S. S.; Porterfield, D. M.; Rickus, J. L. *J. Phys. Chem. B* **2008**, *112* (47), 15086. doi:10.1021/jp803276u.

(3) Wang, J.; Teng, Y.; Hao, Y.; Oh-Lee, J.; Mohanty, D. K. *Polym. J.* **2009**, *41* (9), 715. doi:10.1295/polymj.PJ2008335.

(4) de Santana, D. C. A. S.; Pupo, T. T.; Sauaia, M. G.; da Silva, R. S.; Lopez, R. F. V. *Int. J. Pharm.* **2010**, *391*, 21. doi:10.1016/j.ijpharm.2010.02.010.

(5) Espey, M. G.; Xavier, S.; Thomas, D. D.; Miranda, K. M.; Winkm, D. A. *Proc. Natl. Acad. Sci. U.S.A.* **2002**, *99* (6), 3481. doi:10.1073/pnas.062604199.

(6) Pfeiffer, S.; Lass, A.; Schmidt, K.; Mayer, B. *FASEB J.* **2001**, *15* (13), 2355. doi:10.1096/fj.01-0295com.

(7) Gladwin, M. T.; Schechter, A. N.; Kim-Shapiro, D. B.; Patel, R. P.; Hogg, N.; Shiva, S.; Cannon, R. O.; Kelm, M.; Wink, D. A.; Espey, M. G.; Oldfield, E. H.; Pluta, R. M.; Freeman, B. A.; Lancaster, J. R.; Feelisch, M.; Lundberg, J. O. *Nat. Chem. Biol.* **2005**, *1* (6), 308. doi:10.1038/nchembio1105-308.

(8) Pluta, R. M.; Dejam, A.; Grimes, G.; Gladwin, M. T.; Oldfield, E. H. *JAMA* **2005**, *293* (12), 1477. doi:10.1001/jama.293.12.1477.

(9) Hunter, C. J.; Dejam, A.; Blood, A. B.; Shields, H.; Kim-Shapiro, D. B.; Machado, R. F.; Tarekegn, S.; Mulla, N.; Hopper, A. O.; Schechter, A. N.; Power, G. G.; Gladwin, M. T. *Nat. Med.* **2004**, *10* (10), 1122. doi:10.1038/nm1109.

(10) Li, X.; Zhu, X.-Q.; Zhang, F.; Wang, X.-X.; Cheng, J.-P. *J. Org. Chem.* **2008**, *73* (6), 2428. doi:10.1021/jo702364a.

(11) Hoffmann, A. K.; Hodgson, W. G.; Maricle, D. L.; Jura, W. H. *J. Am. Chem. Soc.* **1964**, *86* (4), 631. doi:10.1021/ja01058a019.

(12) Bowyer, W. J.; Evans, D. H. *J. Org. Chem.* **1988**, *53* (22), 5234. doi:10.1021/jo00257a008.

(13) Ruhl, J. C.; Evans, D. H.; Hapiot, P.; Neta, P. *J. Am. Chem. Soc.* **1991**, *113* (14), 5188. doi:10.1021/ja00014a007.

(14) Melius, C. F.; Bulusu, S. N. *Chemistry and Physics of Energetic Materials;* Kluwer: Dordrecht, 1990.

(15) Owens, F. *J. Mol. Struct. THEOCHEM* **1996**, *370* (1), 11. doi:10.1016/S0166-1280(96)04673-8.

(16) Park, Y. D.; Kim, H. K.; Kim, J. J.; Cho, S. D.; Kim, S. K.; Shiro, M.; Yoon, Y. J. *J. Org. Chem.* **2003**, *68* (23), 9113. doi:10.1021/jo0301503.

(17) Romea, P.; Aragones, M.; Garcia, J.; Vilarassa, J. *J. Org. Chem.* **1991**, *56* (25), 7038. doi:10.1021/jo00025a017.

(18) Li, X.-H..; Zhang, R.-Z.; Zhang, X.-Z. *J. Hazard. Mater.* **2010**, *183*, 622. doi:10.1016/j.jhazmat.2010.07.070.

(19) Li, X.-H.; Tang, Z.-X.; Yang, X.-D. *J. Quant. Chem.* **2009**, *109*, 1403. doi:10.1002/qua.21952.

(20) Baciu, C.; Gauld, J. W. *J. Phys. Chem. A* **2003**, *107* (46), 9946. doi:10.1021/jp035205j.

(21) Van Speybroeck, V.; Marin, G. B.; Waroquier, M. *ChemPhysChem* **2006**, *7* (10), 2205. doi:10.1002/cphc.200600161.

(22) Frisch, M. J.; Trucks, G. W.; Schlegel, H. B.; Scuseria, G. E.; Robb, M. A.; Cheeseman, J. R.; Zakrzewski, V. G.; Montgomery, J. A.; Stratmann, R. E.; Burant, J. C.; Dapprich, S.; Millam, J. M.; Daniels, A. D.; Kudin, K. N.; Strain, M. C.; Farkas, O.; Tomasi, J.; Barone, V.; Cossi, M.; Cammi, R.; Mennucci, B.; Pomelli, C.; Adamo, C.; Clifford, S.; Ochterski, J.; Petersson, G. A.; Ayala, P. Y.; Cui, Q.; Morokuma, K.; Malick, D. K.; Rabuck, A. D.; Raghavachari, K.; Foresman, J. B.; Cioslowski, J.; Ortiz, J. V.; Baboul, A. G.; Stefanov, B. B.; Liu, G.; Liashenko, A.; Piskorz, P.; Komaromi, I.; Gomperts, R.; Martin, R. L.; Fox, D. J.; Keith, T.; Al-Laham, M. A.; Peng, C. Y.; Nanayakkara, A.; Gonzalez, C.; Challacombe, M.; Gill, P. M. W.; Johnson, B.; Chen, W.; Wong, M. W.; Andres, J. L.; Gonzalez, C.; Head Gordon, M.; Replogle, E. S.; Pople, J. A. *GAUSSIAN 03,* Revision B.02; Gaussian Inc.: Pittsburgh, PA, 2003.

(23) Becke, A. D. *J. Chem. Phys.* **1993**, *98* (7), 5648. doi:10.1063/1.464913.

(24) Lee, C.; Yang, W.; Parr, R. G. *Phys. Rev. B* **1988**, *37* (2), 785. doi:10.1103/PhysRevB.37.785.

(25) Miehlich, B.; Savin, A.; Stoll, H.; Preuss, H. *Chem. Phys. Lett.* **1989**, *157* (3), 200. doi:10.1016/0009-2614(89)87234-3.

(26) Perdew, J. P.; Wang, Y. *Phys. Rev. B* **1992**, *45* (23), 13244. doi:10.1103/PhysRevB.45.13244.

Can. J. Chem. Downloaded from www.nrcresearchpress.com by Renmin University of China on 09/02/12
For personal use only.

(27) Perdew, J. P. *Phys. Rev. B* **1986**, *33* (12), 8822. doi:10.1103/PhysRevB.33.8822.
(28) Zhao, Y.; Truhlar, D. G. *J. Phys. Chem. A* **2004**, *108* (33), 6908. doi:10.1021/jp048147q.
(29) Ochterski, J. W.; Petersson, G. A.; Montgomery, J. A., Jr. *J. Chem. Phys.* **1996**, *104* (7), 2598. doi:10.1063/1.470985.
(30) Montgomery, J. A., Jr; Frisch, M. J.; Ochterski, J. W.; Petersson, G. A. *J. Chem. Phys.* **1999**, *110* (6), 2822. doi:10.1063/1.477924.
(31) Montgomery, J. A., Jr; Frisch, M. J.; Ochterski, J. W.; Petersson, G. A. *J. Chem. Phys.* **2000**, *112* (15), 6532. doi:10.1063/1.481224.
(32) Vandeputte, A. G.; Sabbe, M. K.; Reyniers, M.-F.; Van Speybroeck, V.; Waroquier, M.; Marin, G. B. *J. Phys. Chem. A* **2007**, *111*, 11771. doi:10.1021/jp075132u.
(33) Perdew, J. P.; Burke, K.; Ernzerhof, M. *Phys. Rev. Lett.* **1996**, *77* (18), 3865. doi:10.1103/PhysRevLett.77.3865.
(34) Cossi, M.; Barone, V.; Cammi, R.; Tomasi, J. *Chem. Phys. Lett.* **1996**, *255* (4-6), 327. doi:10.1016/0009-2614(96)00349-1.
(35) Barone, V.; Cossi, M.; Tomasi, J. *J. Chem. Phys.* **1997**, *107* (8), 3210. doi:10.1063/1.474671.
(36) Mennucci, B.; Tomasi, J. *J. Chem. Phys.* **1997**, *106* (12), 5151. doi:10.1063/1.473558.
(37) Lin, M. H. *Calculation Model and Application of Quantum Chemistry [M];* Science and Technology Press: Beijing, 2004. [In Chinese.]
(38) Cao, C. Z. *Substituent Effects in Organic Chemistry;* Science Press: Beijing, 2003.

Can. J. Chem. Downloaded from www.nrcresearchpress.com by Renmin University of China on 09/02/12
For personal use only.

Effect of some surfactants on the chemiluminescent reactions of bis(2,4,6-trichlorophenyl)oxalate and bis(2-nitrophenyl) oxalate with hydrogen peroxide

Patrícia Dantoni, Ana Clara B. Rodrigues, Margareth Mie N. Matsuda, and Nina Coichev

Can. J. Chem. Downloaded from www.nrcresearchpress.com by Renmin University of China on 09/02/12
For personal use only.

Abstract: The chemiluminescent reactions of bis(2,4,6-trichlorophenyl)oxalate (TCPO) and bis(2-nitrophenyl)oxalate (2-NPO) with hydrogen peroxide in acetonitrile/water micellar systems (anionic, cationic, and non-ionic) and γ-cyclodextrin were studied in the presence of fluoranthene or 9,10-diphenylanthracene, imidazole, and two buffer solutions, $HTRIS^+$/TRIS and $H_2PO_4^-/HPO_4^{2-}$. The relative chemiluminenscence (CL) intensity is higher in the presence of the cationic (DDAB, CTAC, DODAC, and OTAC), anionic (SDS), and non-ionic (Tween 80) surfactants. In the presence of some non-ionic surfactants (Brij 35, Brij 76, and Tween 20), the CL intensity was partially quenched compared with the reaction with no surfactant. The sensitivity for hydrogen peroxide determination in the range 0.01×10^{-4} to 1.0×10^{-4} mol L^{-1}, considering the slope of the calibration curves (maximum peak height of CL vs. concentration), improved with the introduction of DDAH, CTAB, and SDS in $HTRIS^+$/TRIS buffer.

Key words: TCPO, 2-NPO, surfactant, chemiluminescence, hydrogen peroxide.

Résumé : On a étudié les réactions chimiluminescentes de l'oxalate de bis(2,4,6-trichlorophényle) (OTCP) et de l'oxalate de bis(2-nitrophényle) (O-2NP) avec le peroxyde d'hydrogène dans des systèmes micellaires d'acétonitrile/eau (anionique, cationique et non-ionique) et de γ-cyclodextrine, en présence de fluoranthène et de 9,10-diphényanthracène, d'imidazole et de deux solutions tampons, $HTRIS^+$/TRIS et $H_2PO_4^-/HPO_4^{2-}$. L'intensité relative de la chimiluminescence (CL) est plus élevée en présence des agents de surface cationiques (DDAB, CTAC, DODAC et OTAC), anionique (SDS) et non-ionique (Tween 80). En présence de quelques agents de surface non-ioniques (Brij 35, Brij 76 et Tween 20), l'intensité de CL est partiellement piégée par rapport à la réaction sans agent de surface. Si on se base sur la pente des courbes de calibration (hauteur maximale du pic de la CL vs. concentration), la sensibilité de la détermination du peroxyde d'hydrogène dans la plage de concentration allant de $0{,}1 \times 10^{-4}$ à $1{,}0 \times 10^{-4}$ mol L^{-1} augmente avec l'introduction de DDAH, de CTAB et de SDS dans le tampon $HTRIS^+$/TRIS.

Mots-clés : oxalate de bis(2,4,6-trichlorophényle) (OTCP), oxalate de bis(2-nitrophényle) (O-2NP), agent de surface, chimiluminescence, peroxyde d'hydrogène.

[Traduit par la Rédaction]

Introduction

The chemiluminescent reactions of bis(2,4,6-trichlorophenyl)oxalate (TCPO) and bis(2,4-dinitrophenyl)oxalate (DNPO) in the presence of hydrogen peroxide have been widely used for the detection of fluorescent compounds (fluorophores) at fmol levels. Most of the analytical applications of these systems refer to indirect methods for the determination of species, which generates hydrogen peroxide in a parallel reaction (for instance enzymes) or derivatization reaction using fluorophores as a label.[1–22]

Applications of the peroxyoxalate system, as a post-column reagent in chemiluminescence (CL) detection, in liquid chromatography,[23] and electrophoresis,[24] for clinical, pharmaceutical, environmental, and food analyses, combines the selectivity of the separation methods with the sensitivity of this detection technique.

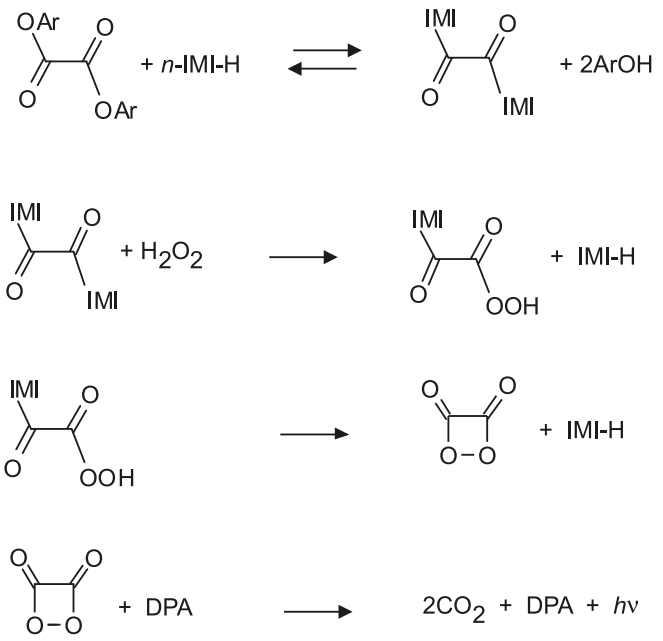
A critical review of the influence of Cr^{III}, Zn^{II}, and Pb^{II} on the chemiluminescent reactions of TCPO and bis(2-nitrophenyl)oxalate (2-NPO) with hydrogen peroxide in the presence of 3-aminofluoranthene, as fluorophore, and imidazole

Received 31 January 2012. Accepted 2 April 2012. Published at www.nrcresearchpress.com/cjc on 24 May 2012.

P. Dantoni and A.C.B. Rodrigues. Centro de Ciências Naturais e Humanas, Universidade Federal do ABC, R. Santa Adélia, 166, CEP 09210-270, Santo André, SP, Brazil.
M.M.N. Matsuda. Instituto de Pesquisas Energéticas e Nucleares (IPEN-CNEN/SP, Diretoria de Radio Farmácia), Av. Prof. Lineu Prestes, 2242, CEP 05508-900, São Paulo, SP, Brazil.
N. Coichev. Instituto de Química. Universidade de São Paulo, CP 26077, CEP 05513-970, São Paulo, SP, Brazil.

Corresponding author: Nina Coichev (e-mail: ncoichev@iq.usp.br).

Scheme 1. Simplified mechanism for the chemiluminescent reaction of bis(2,4,6-trichlorophenyl)oxalate (TCPO) with hydrogen peroxide, catalyzed by imidazole, in ethyl acetate anhydrous medium.[31] Ar = (2,4,6-trichlorophenyl) for TCPO and (2-nitrophenyl) for NPO.



(IMI), as catalyst, showed that the metal ions had no influence when the experiments were carried out in buffer solutions such as tris(hydroxymetyl)aminomethane ($HTRIS^+$/TRIS, pH 6.9–8.0) or $H_2PO_4^-/HPO_4^{2-}$ (pH 7.0–8.0).[25,26]

According to Motoyoshiya and Maruyama,[27] zinc and copper ions markedly enhanced the CL efficiencies in the presence of the chelator *N*-phenyl-*N*′,*N*′-bis(2-pyridinylmethyl)-1,2-ethanediamine, owing to the interaction of this ligand with the metal ion and the fluorophore.

A detailed study of several parameters such as acidity, water and acetonitrile (ACN) contents, and concentrations of TCPO, 2-NPO, IMI, hydrogen peroxide, and metal ions was reported by our group.[25,26] Among these factors, the catalytic effect of IMI depends very much on the unprotonated imidazole concentration and the acidity. The complex formation of these metal ions with IMI may change the acidity by disturbing the acid–base equilibrium of $HIMI^+$/IMI. As the CL efficiency sharply decreases at pH higher than 7.5, small variations of the acidity conditions can lead to several errors in the interpretation of the data. Some alternative methods described in the literature using flowing streams, such as continuous flow, flow injection[28–30] analysis, and liquid chromatography, require an appropriated optimization of the experimental parameters.

Some authors have intensively studied the possible mechanisms and intermediates for the chemiluminescent reaction of peroxyoxalate (PO-CL) catalyzed by IMI. The main reactions of the mechanism for the system TCPO, hydrogen peroxide, IMI, and 9,10-diphenylanthracene (DPA), in anhydrous ethyl acetate medium, involved the formation of an IMI-substituted peracid and an energy-rich intermediate (1,2-dioxetane-3,4-dione), which excited the fluorophore DPA, leading to light emission and CO_2 formation (Scheme 1).[31–34]

The main disadvantage of these systems is the insolubility of these compounds in water and their instability towards hydrolysis, which requires the use of organic solvents. The application of micelles has been studied to solve these problems, to use these systems for analytical purposes, decreasing the amount of organic solvents, or even avoiding IMI.

The results of the proposed CL systems in micellar media showed that enhancement on the CL intensity could arise by the solubilization of the reagents, the electrostatic effect of the ionic surfactant, and the alteration of the pH and the microenviroment of the CL reaction.[35,36]

There are some studies on analytical applications for the determination of fluorophores, proteins, and hydrogen peroxide in aqueous samples using the PO-CL reaction with the introduction of the micelles.[28–30,37–44]

Sodium dodecyl sulfate (SDS) micellar medium was used as a carrier to avoid the rapid degradation of TCPO in water in a flow-injection analysis,[28–30,41] allowing the use of TCPO in the absence of organic solvent.

Some groups have reported on the effect of micellar medium.[40,42,45] Steijger et al.[42] compared the stability of TCPO in ACN micellar systems and ACN/water phosphate buffer solution (80–20, *v*/*v*) with perylene as fluorophore. They investigated the effect of several types of surfactants, such as the anionic SDS and the cationic hexadecyltrimethylammonium bromide (CTAB). All analyzed micelles had a total or partial quencher effect compared with ACN buffer (no surfactant). The TCPO/H_2O_2 chemiluminescent reaction did not occur in CTAB, which may be the result of the quenching of CL intensity by the bromide ion of CTAB, and the intensity in SDS anionic micelles was appreciably less than that in neutral micellar solutions.

Based on the enhancement of PO-CL CL intensity by some surfactants in H_2O_2/TCPO/rhodamine, Wada et al.[43] proposed a method to detect commercially available detergent. The enhancement may occur by a notable change of pH by adding surfactants, such as a buffer solution was used. The effect of the buffer cations can be important because of the interaction of the polar surface of micelles and the cations, which can provide an electrostatic attraction for the hydrogen peroxide anions that penetrate into non-ionic micelles.[40] Several surfactants might play a catalytic effect, and the fluorescent impurities of some surfactants may contribute to this enhancement.[43]

Liang et al.[35] studied the synergetic effect of SDS, CTAB, and gold nanoparticles on the system H_2O_2 / TCPO / sodium citrate / Au nanoparticles. The CL intensity enhanced sharply with 5×10^{-3} mol L^{-1} CTAB and became reasonably constant when the concentration of 2.5×10^{-2} mol L^{-1} CTAB was used. However, a too high concentration of surfactant depressed the CL. According to the authors,[35] the CL of TCPO is enhanced by the cationic surfactant CTAB because the solubilities of TCPO and its excited intermediate in an aqueous micellar system are greater than that in pure ACN. The electrostatic effect of the ionic surfactant helps to concentrate the counterion, and the citrate anion was adsorbed onto the surface of the gold nanoparticles, which resulted in the stability of the Au colloid. In the presence of CTAB, Au nanoparticles are linked to CTAB by electrostatic attraction. The cage structure of the micelle is helpful for stabilizing the excited state and preventing it from quenching.

The present work reports the effect of different types of micelles (anionic, cationic, and non-ionic) and γ-cyclodextrin

Can. J. Chem. Downloaded from www.nrcresearchpress.com by Renmin University of China on 09/02/12
For personal use only.

Can. J. Chem. Downloaded from www.nrcresearchpress.com by Renmin University of China on 09/02/12
For personal use only.

(γ-CD; as further discussed) on the reaction of TCPO or 2-NPO with hydrogen peroxide in the presence of fluoranthene (FA) or DPA, as fluorophores, and two buffer solutions $HTRIS^+$/TRIS and $H_2PO_4^-/HPO_4^{2-}$. We carried out the experiments in three different media, with 25%, 37%, and 62% (*v*/*v*) ACN, since the stock solutions of TCPO, DPA, and IMI must be prepared in ACN. The CL intensity–time (*t*) profile was examined by varying the water content, acidity, IMI, hydrogen peroxide concentration, and fluorophore. Our results are reported in terms of the maximum peak height (I_{max}, relative light unit/second) and the area (*A*) under the curve of relative CL intensity (relative light unit) vs *t*. The total *t* refers to the time for the complete CL signal decay.

Experimental

Apparatus, reagents, and chemicals

All reagents were used as received without purification. Aqueous solutions were prepared with deionized water from the Milli-Q system (Millipore).

The buffers used were $HTRIS^+$/TRIS (0.12 mol L^{-1} tris(hydroxymethyl)aminomethane, pH 6.8, 8.3, and 8.7; (Kanto Chemical Co.) and $H_2PO_4^-/HPO_4^{2-}$ (0.10 mol L^{-1}, pH 6.6, 7.6, and 8.4; Kanto Chemical Co.). The pH of the buffers was adjusted with sodium hydroxide or nitric acid. The pH measurements were done with a pH meter (Metrohm, model 713) with a glass electrode (filled with saturated NaCl).

2-NPO was prepared according to the procedure in ref. 46.

Solutions of 4.5×10^{-4} mol L^{-1} TCPO (TCI Tokyo Kasei), 4.5×10^{-4} mol L^{-1} 2-NPO, 1.0×10^{-3} mol L^{-1} DPA (TCI Tokyo Kasei), 6.0×10^{-3} and 1.2×10^{-2} mol L^{-1} IMI (Sigma-Aldrich), and 1.0×10^{-3} mol L^{-1} FA (Nakalai Chemicals Ltd.) were prepared in ACN (Mallinckrodt) every day.

Diluted hydrogen peroxide solutions were prepared every day in water from hydrogen peroxide stock solution (30%, *m*/*m*, Merck). The stock solution of 0.100 mol L^{-1} hydrogen peroxide was standardized by titration with $KMnO_4$ standard solution in acid medium.

The surfactant (from Sigma-Aldrich, Kanto Chemical Co., and Merck) solutions were prepared in water or buffer solution (as indicated in the text): Brij 35 (polyoxyethylene(23) lauryl ether; critical micelle concentration (cmc) = 1×10^{-4} mol L^{-1}), Brij 76 (polyoxyethylene(10) stearyl ether; cmc = 3×10^{-3} mol L^{-1}), Tween 20 (polyoxyethylene (20) sorbitan monolaurate; cmc = 5×10^{-5} mol L^{-1}), Tween 80 (polyoxyethylene(20) sorbitan monooleate; cmc = 1.2×10^{-5} mol L^{-1}), TDTAB (tetradecyltrimethylammonium bromide; cmc = 3.5×10^{-3} mol L^{-1}), DDAB (dododecyldimethylammonium bromide; cmc = 1.8×10^{-4} mol L^{-1}), CTAC (cetyltrimethylammonium chloride; cmc = 1.3×10^{-3} mol L^{-1}), DODAC (dioctadecyldimethylammonium chloride) and OTAC (octadecyltrimethylammonium chloride; cmc = 3.4×10^{-4} mol L^{-1}), CTAB (cmc = 9×10^{-4} mol L^{-1}, SDS (cmc = 8.1×10^{-3} mol L^{-1}), DDAH, (3-(dimethyldodecylammonio)-propane-1-sulfonate; cmc = 1.2×10^{-3} mol L^{-1}).[47]

γ-CD (cyclooctaamylose, 0.01 mol L^{-1}; Sigma-Aldrich) solution was prepared in buffer medium.

Sample preparation

The experiments were done in the presence of two fluorophores, FA and DPA.

Table 1. Effect of some cationic surfactants on maximum emission intensity (I_{max}) in the reactions of bis(2-nitrophenyl)oxalate (2-NPO) or bis(2,4,6-trichlorophenyl)oxalate (TCPO) with H_2O_2.

	Oxalate			
	2-NPO		TCPO	
Surfactant	$I_{max}/10^4$	*t* (s)	$I_{max}/10^4$	*t* (s)
None	3.5	30	0.036	40
TDTAB	1.8	30	0.047	45
DDAB	10	45	0.19	45
CTAC	14	60	0.72	45
DODAC	18	60	1.8	60
OTAC	21	60	1.2	45

Note: [2-NPO] = 5.6×10^{-5} mol L^{-1}, [TCPO] = 5.6×10^{-5} mol L^{-1}, [H_2O_2] = 1.6×10^{-3} mol L^{-1}, [FA] = 1.2×10^{-4} mol L^{-1}, % ACN = 25, [surfactant] = 10cmc; *t* refers to the time for the complete chemiluminescence (CL) signal decay. TDTAB, tetradecyltrimethylammonium bromide; DDAB, dododecyldimethylammonium bromide; CTAC, cetyltrimethylammonium chloride; DODAC, dioctadecyldimethylammonium chloride; OTAC, octadecyltrimethylammonium chloride; FA, fluoranthene; ACN, acetonitrile.

Table 2. Effect of surfactant on maximum emission intensity (I_{max}) in the reaction of bis(2-nitrophenyl)oxalate (2-NPO) with H_2O_2.

Surfactant	Peak height ($I_{max}/10^4$)	*t* (s)
None	3.5	30
Non-ionic		
Brij 35	2.2	60
Brij 76	1.9	75
Tween 20	1.6	60
Tween 80	4.6	75
Anionic		
SDS	4.5	75

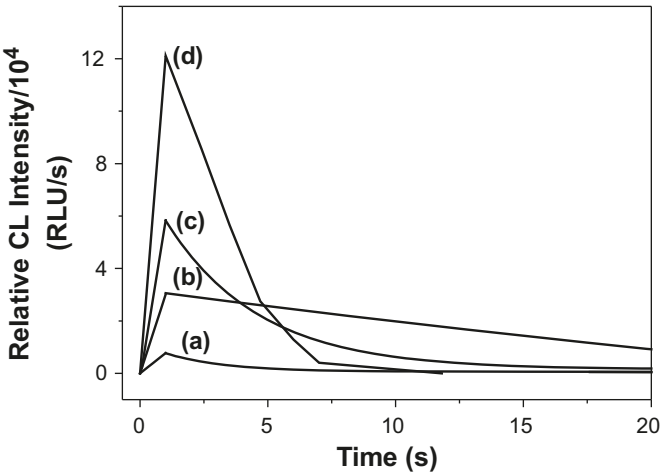
Note: [2-NPO] = 5.6×10^{-5} mol L^{-1}, [H_2O_2] = 1.6×10^{-3} mol L^{-1}, [FA] = 1.2×10^{-4} mol L^{-1}, % ACN = 25, [surfactant] = 10cmc; *t* refers to the time for the complete chemiluminescence (CL) signal decay. FA, fluoranthene; ACN, acetonitrile.

In the experiments with FA, the CL intensity profile was obtained with a Lumicounter 1000 (Microtec Nichi-on) and the signal recorded with a Shimadzu 135 recorder. The emission began just after the addition of the oxalate solution. The emission intensity is represented as the peak height (I_{max}) and the total emission time of reaction as (*t*). The sequence of the addition of the solutions was 0.1 mL of water, buffer, or surfactant solution (10 times the surfactant cmc), and 0.02 mL of 1.0×10^{-3} mol L^{-1} FA, 0.02 mL IMI (when used), 0.02 mL hydrogen peroxide, and 0.02 mL of 4.5×10^{-4} mol L^{-1} oxalate (2-NPO or TCPO). The sequence influences the emission intensity because the peroxyoxalates hydrolyze in aqueous solution. The concentrations of the final solutions (0.16 mL) are indicated in Tables 1 and 2.

In the experiments with DPA, the procedure for the CL intensity measurements involved mixing the reagents in a 3 mL glass flask placed in the luminometer (Lumat LB 9507, Berthold

Can. J. Chem. Downloaded from www.nrcresearchpress.com by Renmin University of China on 09/02/12
For personal use only.

Fig. 1. Relative chemiluminescence (CL) intensity in the presence of different surfactants in acetonitrile (ACN) / water (25% ACN). [TCPO] = 5.6×10^{-5} mol L^{-1}, [DPA] = 1.2×10^{-4} mol L^{-1}; $HTRIS^+$/TRIS pH 8.7; [H_2O_2] = 5.0×10^{-5} mol L^{-1}. (*a*) No surfactant or [γ-CD] = 6.2×10^{-3} mol L^{-1}. (*b*) Sodium dodecyl sulfate (SDS), 10cmc. (*c*) 3-(Dimethyldodecylammonio)-propane-1-sulfonate (DDAH), 10cmc. (*d*) Hexadecyltrimethylammonium bromide (CTAB), 10cmc. TCPO, bis(2,4,6-trichlorophenyl)oxalate; DPA, 9,10-diphenylanthracene; γ-CD, γ-cyclodextrin; cmc, critical micelle concentration; RLU, relative light unit.



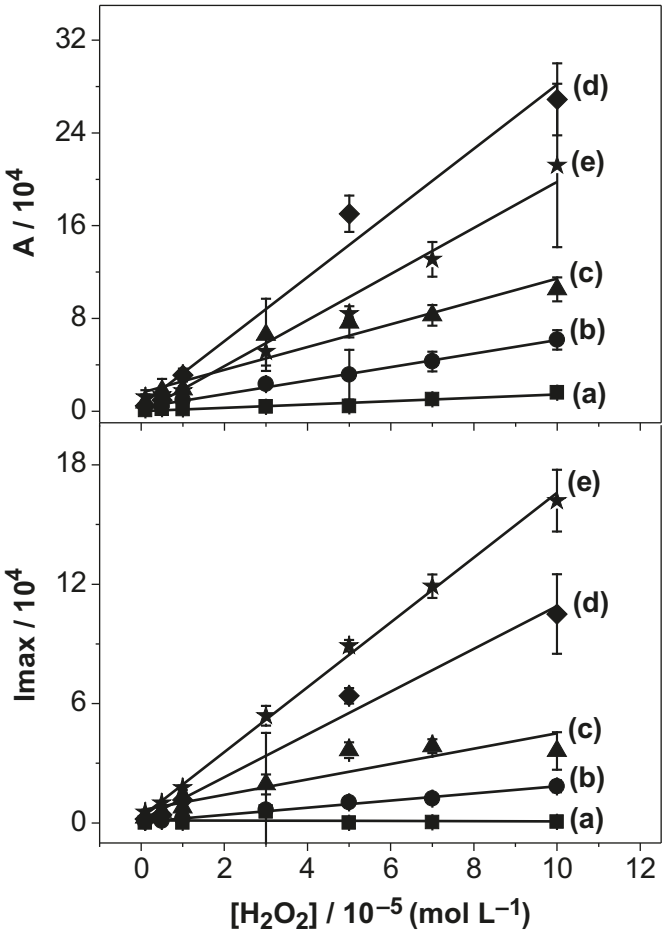
Technologies), positioned in front of the photomultiplier tube.

Because the peroxyoxalates hydrolyze in aqueous solution, the following mixing orders for the different reagents were used: 25% ACN (*v*/*v*): 50 μL of water or H_2O_2 (0.1×10^{-5} to 10×10^{-5} mol L^{-1}), 50 μL of 1.0×10^{-3} mol L^{-1} DPA, and 250 μL of surfactant (in water or buffer) were introduced into the glass flask, followed by automatic jet-injection, after 10 s, of 50 μL of 4.5×10^{-4} mol L^{-1}TCPO. As the DPA and TCPO solutions were prepared in ACN, the final solutions after mixing were 25% ACN (*v*/*v*); 37% ACN (*v*/*v*): 50 μL of water or H_2O_2 (0.1×10^{-5} to 10×10^{-5} mol L^{-1}), 50 μL of 1.0×10^{-3} mol L^{-1} DPA, 50 μL of 6.0×10^{-3} mol L^{-1} IMI, and 200 μL of water or surfactant (in water or buffer) were introduced into the glass flask, followed by automatic jet-injection, after 10 s, of 50 μL of 4.5×10^{-4} mol L^{-1} TCPO. As the DPA, TCPO, and IMI solutions were prepared in ACN, the final solutions after mixing were 37% ACN (*v*/*v*); 62% ACN (*v*/*v*): 50 μL of water or H_2O_2 (0.1×10^{-5} to 10×10^{-5} mol L^{-1}), 50 μL of 1.0×10^{-3} mol L^{-1} DPA, 100 μL of 1.2×10^{-2} mol L^{-1} IMI, 50 μL of ACN, and 100 μL of water or surfactant (in water or buffer) were introduced into the glass flask, followed by automatic jet-injection, after 10 s, of 50 μL of 4.5×10^{-4} mol L^{-1} TCPO. As the DPA, TCPO, and IMI solutions were prepared in ACN, the final solutions after mixing were 62% ACN (*v*/*v*). The concentrations of the final solutions (0.40 mL) are indicated in Figs. 1–4.

Results and discussion

The effects on the I_{max} and *A* values of different types of surfactants (anionic, cationic, and non-ionic), with different charged groups and hydrophobic chain lengths, were evaluated. We conducted experiments in the presence of fluorophores (FA or DPA) and oxalates (2-NPO or TCPO), as they were used in previous research[22] and showed different CL intensity–time profiles.

Fig. 2. Effect of pH and H_2O_2 concentration on maximum emission intensity (I_{max}) and emission area (*A*). Reaction of bis(2,4,6-trichlorophenyl)oxalate (TCPO) in acetonitrile (ACN) / water (25% ACN), at different pH values in $HTRIS^+$/TRIS and $H_2PO_4^-/HPO_4^{2-}$ buffers. No surfactant. [TCPO] = 5.6×10^{-5} mol L^{-1}, [DPA] = 1.2×10^{-4} mol L^{-1}. (*a*) Unbuffered medium (■). (*b*) $H_2PO_4^-/HPO_4^{2-}$, pH 6.6 (●). (*c*) $H_2PO_4^-/HPO_4^{2-}$, pH 7.6 (▲). (*d*) $HTRIS^+$/TRIS, pH 6.8 (◆). (*e*) $HTRIS^+$/TRIS, pH 8.7 (★). DPA, 9,10-diphenylanthracene.



Experiments in the presence of FA

The data for the 2-NPO reaction are reported in Tables 1 and 2. In the presence of the cationic surfactants (DDAB, CTAC, DODAC, and OTAC; Table 1) I_{max} and *t* increased. TDTAB and DDAB have bromide ions (reactive counterion), which can react with hydrogen peroxide in solution; even so, DDAB (with a larger hydrophobic chain length) had a positive effect on the CL intensity. The non-ionic Tween 80 and anionic SDS surfactants (Table 2) also showed higher I_{max}, whereas Brij 35, Brij 76, and Tween 20 had one partial quencher effect compared with the ACN/water systems with no surfactant.

The 2-NPO/H_2O_2 reaction was very much affected by the medium acidity and the buffer nature. Some experiments

Can. J. Chem. Downloaded from www.nrcresearchpress.com by Renmin University of China on 09/02/12
For personal use only.

Fig. 3. Effect of different surfactants and H_2O_2 concentration on maximum emission intensity (I_{max}) and emission area (A). Reaction of bis(2,4,6-trichlorophenyl)oxalate (TCPO) in acetonitrile (ACN) / water (25% ACN) in HTRIS$^+$/TRIS pH 8.7 buffer. [TCPO] = 5.6×10^{-5} mol L^{-1}, [DPA] = 1.2×10^{-4} mol L^{-1}. (*a*) DDAH 10cmc (▲). (*b*) CTAB, 10cmc (◆). (*c*) γ-CD, 6.2×10^{-3} mol L^{-1} (★). (*d*) SDS, 10cmc (►). DPA, 9,10-diphenylanthracene; DDAH, 3-(dimethyldodecylammonio)-propane-1-sulfonate; CTAB, hexadecyltrimethylammonium bromide; γ-CD, γ-cyclodextrin; SDS, sodium dodecyl sulfate; cmc, critical micelle concentration.

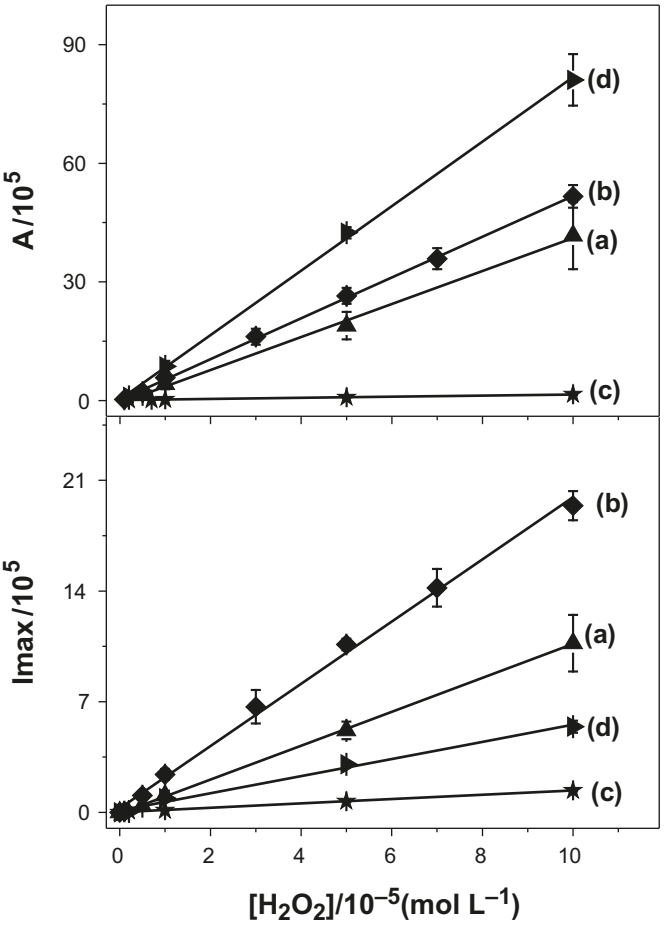
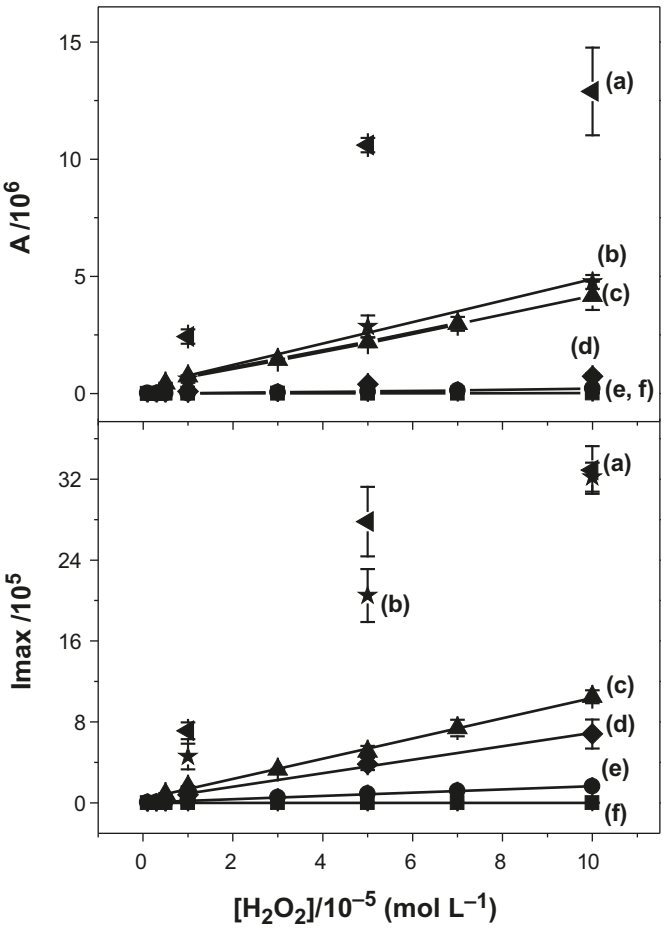


Fig. 4. Effect of imidazole (IMI) and H_2O_2 concentration on maximum emission intensity (I_{max}) and emission area (A). Reaction of bis (2,4,6-trichlorophenyl)oxalate (TCPO) in acetonitrile (ACN) / water and HTRIS$^+$/TRIS pH 8.7 buffer. No surfactant. [TCPO] = 5.6×10^{-5} mol L^{-1}. [DPA] = 1.2×10^{-4} mol L^{-1}. (*a*) 62% ACN, unbuffered medium, [IMI] = 3.0×10^{-3} mol L^{-1} (▲). (*b*) 62% ACN; HTRIS$^+$/TRIS, pH 8.7; [IMI] = 3.0×10^{-3} mol L^{-1} (★). (*c*) 37% ACN, unbuffered medium, [IMI] = 7.5×10^{-4} mol L^{-1} (▲). (*d*) 37% ACN; HTRIS$^+$/TRIS, pH 8.7; [IMI] = 7.5×10^{-4} mol L^{-1} (◆). (*e*) 25% ACN, unbuffered medium, no IMI (●). (*f*) 25% ACN; HTRIS$^+$/TRIS, pH 8.7; no IMI (■). DPA, 9,10-diphenylanthracene.



(data not shown) were carried out with 3.5×10^{-5} mol L^{-1} 2-NPO, 7.7×10^{-4} mol L^{-1} H_2O_2, and 7.7×10^{-5} mol L^{-1} FA in the presence of Brij 76 (10cmc) and HTRIS$^+$/TRIS (pH 8.3) or $H_2PO_4^-$/HPO_4^{2-} (pH 8.5) medium. In the presence of Brij 76 and HTRIS$^+$/TRIS buffer, the I_{max} value was twice the value of the one obtained in $H_2PO_4^-$/HPO_4^{2-} buffer.

The data reported in Table 1 show that, for the same experimental conditions, the reaction with 2-NPO has a higher I_{max} than the reaction with TCPO, in the presence or absence of cationic surfactants. In the cationic surfactants (especially CTAC, DODAC, and OTAC) intense peaks were observed for 2-NPO/ H_2O_2 and TCPO/H_2O_2 reactions, which had very low signals in the absence of surfactant.

Comparing the effect of the cationic micelles (CTAC and OTAC) (Table 1), CTAC, which has the smallest hydrophobic chain, showed a lower I_{max} value than OTAC. However, in DODAC medium, which forms vesicle micelles, the I_{max} value was in between CTAC and OTAC with a higher t. The increase of the hydrocarbon chain length of the surfactant results in an increase of both A and I_{max}). The length of the hydrocarbon chain of the surfactant influences the size of the micelles and the depth of penetration is different. This process may be favored by longer chain surfactants, which form looser micelles.

Experiments with TCPO in the presence of DPA

Additional experiments were carried out with DPA replacing FA. The acidity and micelle effects on the TCPO chemiluminescent reaction with hydrogen peroxide were investigated by analyzing the values of I_{max} and A.

Some CL intensity–time profiles, in the absence of IMI, are represented in Fig. 1. The emission began just after the addition of TCPO. The presence of 6.2×10^{-3} mol L^{-1} γ-CD had no effect. However SDS, DDAH, and CTAB increased the CL intensity. The results are shown in Figs. 2–5.

Can. J. Chem. Downloaded from www.nrcresearchpress.com by Renmin University of China on 09/02/12
For personal use only.

Fig. 5. Effect of H_2O_2 concentration on maximum emission intensity (I_{max}) and emission area (A). Reaction of bis(2,4,6-trichlorophenyl) oxalate (TCPO) in acetonitrile (ACN) / water (62% ACN) in unbuffered medium with different surfactants. [TCPO] = 5.6×10^{-5} mol L^{-1}, [DPA] = 1.2×10^{-4} mol L^{-1}, [IMI] = 3.0×10^{-3} mol L^{-1}. (*a*) [DDAH] = 10cmc (▲). (*b*) [CTAB] = 10cmc (◆). (*c*) [γ-CD] = 2.5×10^{-3} mol L^{-1} (★). (*d*) [SDS] = 10cmc (►). (*e*) No surfactant (●). DPA, 9,10-diphenylanthracene; IMI, imidazole; DDAH, 3-(dimethyldodecylammonio)-propane-1-sulfonate; CTAB, hexadecyltrimethylammonium bromide; γ-CD, γ-cyclodextrin; SDS, sodium dodecyl sulfate; cmc, critical micelle concentration.

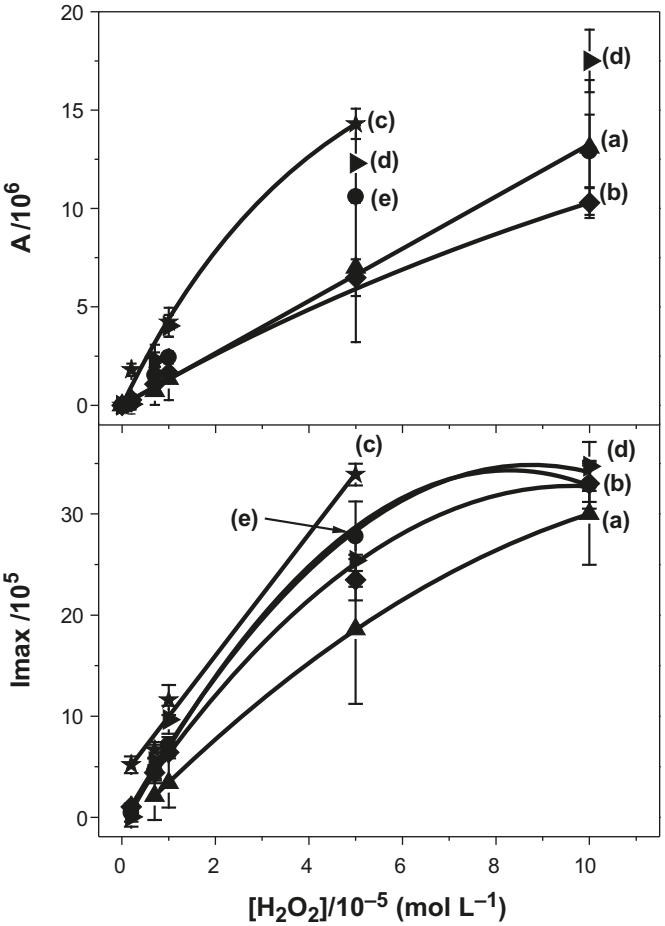


Figure 2 shows the effect of $H_2PO_4^-/HPO_4^{2-}$ and HTRIS+/TRIS buffers and the pH in the absence of surfactant. There was one smaller increase on the signals (I_{max} and A) in $H_2PO_4^-/HPO_4^{2-}$ medium compared with the unbuffered medium. The considerable enhancement in HTRIS+/TRIS buffer might be due to the catalytic effect of TRIS, as reported by Hayakawa et al.[37]

Figure 3 shows the effect of some of the surfactants. SDS (anionic) and γ-CD (0.01 mol L^{-1}) completely suppressed the signal in unbuffered and $H_2PO_4^-/HPO_4^{2-}$ media (data not shown). However, as TRIS has some catalytic effect, a relatively high increase occurs on the A and I_{max} values in HTRIS+/TRIS buffer solution (pH 8.7) in the presence of these surfactants (compare Figs. 1 and 2). The special combination of TRIS and CTAB (cationic) showed the highest increase of the I_{max} value (Fig. 2*b*). The following is the order for the I_{max} values: CTAB (cationic) > DDAH (amphiprotic) > SDS (anionic) > γ-CD; and the following is the order for the area (A): SDS (anionic) > CTAB (cationic) > DDAH (amphiprotic) > γ-CD.

Some relatively small signals were observed in the experiments in unbuffered medium in the presence of DDAH and CTAB (data not shown). When $H_2PO_4^-/HPO_4^{2-}$ (pH 7.6) was used, one relatively small signal was observed only in the presence of CTAB.

By comparing Figs. 2 (no surfactant) and 3, I_{max} and A were higher when the surfactants were present in HTRIS+/TRIS (pH 8.7), except when γ-CD was used (Fig. 2*c*). For the same hydrogen peroxide concentration, SDS had the most positive effect only on A, however, CTAB and DDAH also had good effects on I_{max} and A values, respectively.

1-Aroxalylimidazole and 1,1′-oxalyldiimidazole (Scheme 1) have been suggested as the relevant high-producing intermediates in aqueous ACN.[31,32] The catalytic effect of IMI on the TCPO/H_2O_2 reaction can be seen from the data in Fig. 3, as a large increase in the signals was observed.

As TCPO is easily hydrolyzed, I_{max} and A increase in the medium with the higher percentage of ACN. There is no linearity of I_{max} and A with the concentration of hydrogen peroxide in 62% ACN and HTRIS+/TRIS (Figs. 4*a* and 4*b*). However, in the presence of 37% and 25% ACN a linear dependence was observed (Figs. 4*c*–4*e*).

In the presence of IMI and 62% ACN, γ-CD had the highest effect on the I_{max} and A values (compare Figs. 3*c* and 5*c*); at 1×10^{-4} mol L^{-1} hydrogen peroxide, these values were so high that they could not be measured with the equipment that was used, showing one marked effect with the concentrations of hydrogen peroxide higher than 5×10^{-4} mol L^{-1}. In the presence of IMI the effect of surfactants is not marked (compare Fig. 5*e* without surfactant and Figs. 5*a* and 5*b* with DDAH and CTAB), since the catalytic effect of IMI (better than TRIS) is the dominant influence. There is no linearity of I_{max} and A with hydrogen peroxide concentration, which would not be suitable for analytical purposes.

The use of α-CD, γ-CD, and β-CD was suggested by Kojo et al.[38] to obtain better sensitivity in the analytical method for the determination of dansyl acid and glucose based on the glucose oxidase / H_2O_2 reaction in the presence of TCPO. γ-CD had better sensitivity in the phosphate buffer (pH 7.0), and the produced hydrogen peroxide was measured after 1 min with stirring at 37 °C. The detection limit corresponded to 1 pmol of hydrogen peroxide.

Inclusion in the CD cavity, which has a hydrophobic nature, is known to significantly affect the luminescent properties.[39] Woolf and Grayeski[39] reported the aqueous peroxyoxalate reactions of 4,4′-[oxalylbis[(trifluoromethylsulfonyl) imino]ethylene]bis[4-methylmorpholinium trifluoromethane sulfonate with hydrogen peroxide in the presence of several fluorophores and α-, γ- and β-CD. The enhancement due to the CDs was attributed to the increase in reaction rate and excitation and fluorescence efficiencies of the emitting species.

In Table 3, analytical parameters for H_2O_2 determination are represented for some selected experimental conditions. The detection limit is defined as three times the standard deviation of the linear coefficient divided by the angular coefficient value. The background signal and the standard deviation of the linear coefficient also increased, which restricts the improvement of the detection limits (10^{-6} mol L^{-1})

Table 3. Analytical parameters for H_2O_2 determination.

		Slope/10^{10}		Detection limit/10^6 (mol L^{-1})	
Medium/%ACN	Surfactant	I_{max}	A	I_{max}	A
HTRIS$^+$/TRIS (pH 8.7) / 25%	No	0.16	0.20	0.158	0.924
HTRIS$^+$/TRIS (pH 8.7) / 25%	DDAH	1.07	4.17	2.51	4.11
	CTAB	1.97	5.16	1.74	0.686
	γ-CD	0.14	0.14	2.09	7.80
	SDS	0.54	8.16	2.00	1.17
No buffer ([IMI] = 6.0×10^{-3} mol L^{-1}) / 37%	No	1.00	3.87	0.730	0.716
HTRIS$^+$/TRIS (pH 8.7) ([IMI] = 6.0×10^{-3} mol L^{-1}) / 37%	No	0.66	0.71	12.6	12.8

Note: Linear range 0.01×10^{-4} to 1.0×10^{-4} mol L^{-1}. IMI, imidazole; DDAH, 3-(dimethyldodecylammonio)-propane-1-sulfonate; CTAB, hexadecyltrimethylammonium bromide; γ-CD, γ-cyclodextrin; SDS, sodium dodecyl sulfate.

in the presence of the surfactants. In the presence of IMI, as a catalyst, the buffer HTRIS$^+$/TRIS had a negative effect; however, one better detection limit was obtained in the absence of surfactant and HTRIS$^+$/TRIS. The slopes of the calibration curves (A vs $[H_2O_2]$ and I_{max} vs $[H_2O_2]$), which represent the sensitivity, increase in the presence of DDAH, CTAB, and SDS in HTRIS$^+$ /TRIS buffer (pH 8.7, 25% ACN), whereas γ-CD had a small effect.

The analytical parameters reported by Dan et al.,[40] obtained for the chemiluminescent reaction of METQ with hydrogen peroxide in the presence of Brij 35 or CTAB, showed one detection limit of about 10^{-3} mol L^{-1}; so in the present work better results were obtained.

Conclusion

Under the experimental conditions of the present work, the presence of some surfactants causes an increase in the I_{max} and A signals. The effect on the increase is dependent on the nature of the fluorophore and hydrophobicity, charge differences, and concentration of the surfactant.

The effect of surfactants on the CL reaction is still unclear and depends on several parameters, and the comparison of different studies is not possible. The complexity of the system does not allow a definitive assignment of the species involved. However, based on the available literature and the data from Table 3, the sensitivity for hydrogen peroxide determination, considering the slope of the calibration curves (Table 3), improved with the introduction of some surfactants (DDAH, CTAB, and SDS) in HTRIS$^+$/TRIS buffer.

Acknowledgments

The authors acknowledge the financial support from the following Brazilian agencies: Fundação de Amparo à Pesquisa do Estado de São Paulo(FAPESP) and Conselho Nacional de Desenvolvimento Científico e Tecnológico (CNPq), and to Professor Masaaki Yamada (Tokyo Metropolitan University) for providing the equipment (Lumicounter 1000, Microtec Nichi-on) and facilities for the execution of some of the experiments.

References

(1) Hadd, A. G.; Birks, J. W. Selective Detectors. In *Chemical Analysis Series;* John Wiley: New York, 1995.
(2) Kwakman, P. J. M.; Brinkman, U. A. Th. *Anal. Chim. Acta* **1992**, *266* (2), 175. doi:10.1016/0003-2670(92)85041-4.
(3) Imai, K.; Matsunaga, Y.; Tsukamoto, Y.; Nishitani, A. *J. Chromatogr. A* **1987**, *400*, 169. doi:10.1016/S0021-9673(01)81610-1.
(4) Kobayashi, S. I.; Imai, K. *Anal. Chem.* **1980**, *52* (3), 424. doi:10.1021/ac50053a012.
(5) Sigvardson, K. W.; Birks, J. W. *Anal. Chem.* **1983**, *55* (3), 432. doi:10.1021/ac00254a006.
(6) Sigvardson, K. W.; Kennish, J. M.; Birks, J. W. *Anal. Chem.* **1984**, *56* (7), 1096. doi:10.1021/ac00271a011.
(7) Sigvardson, K. W.; Birks, J. W. *J. Chromatogr. A* **1984**, *316*, 507. doi:10.1016/S0021-9673(00)96179-X.
(8) Honda, K.; Miyaguchi, K.; Imai, K. *Anal. Chim. Acta* **1985**, *177*, 111. doi:10.1016/S0003-2670(00)82943-8.
(9) Nishitani, A.; Tsukamoto, Y.; Kanda, S.; Imai, K. *Anal. Chim. Acta* **1991**, *251* (1-2), 247. doi:10.1016/0003-2670(91)87143-U.
(10) Mann, B.; Grayeski, M. L. *Biomed. Chromatogr.* **1991**, *5* (1), 47. doi:10.1002/bmc.1130050111.
(11) Yan, B.; Lewis, S. W.; Worsfold, P. J.; Lancaster, J. S.; Gachanja, A. *Anal. Chim. Acta* **1991**, *250*, 145. doi:10.1016/0003-2670(91)85068-4.
(12) Andrew, K. N.; Sanders, M. G.; Forbes, S.; Worsfold, P. J. *Anal. Chim. Acta* **1997**, *346* (1), 113. doi:10.1016/S0003-2670(97)00052-4.
(13) Scott, G.; Seitz, W. R.; Ambrose, J. *Anal. Chim. Acta* **1980**, *115* (1), 221. doi:10.1016/S0003-2670(01)93160-5.
(14) van Zoonen, P.; Kamminga, D. A.; Gooijer, C.; Velthorst, N. H.; Frei, R. W.; Gübitz, G. *Anal. Chim. Acta* **1985**, *174*, 151. doi:10.1016/S0003-2670(00)84374-3.
(15) Van Zoonen, P.; Kamminga, D. A.; Gooijer, C.; Velthorst, N. H.; Frei, R. W. *Anal. Chim. Acta* **1985**, *167*, 249. doi:10.1016/S0003-2670(00)84427-X.
(16) Poulsen, J. R.; Birks, J. W.; Gübitz, G.; Van Zoonen, P.; Gooijer, C.; Velthorst, N. H.; Frei, R. W. *J. Chromatogr. A* **1986**, *360*, 371. doi:10.1016/S0021-9673(00)91686-8.
(17) Quaß, U.; Klockow, D. *Int. J. Environ. Anal. Chem.* **1995**, *60*, 361. doi:10.1080/03067319508042889.
(18) Honda, K.; Sekino, J.; Imai, K. *Anal. Chem.* **1983**, *55* (6), 940. doi:10.1021/ac00257a028.
(19) Van Zoonen, P.; Kamminga, D. A.; Gooijer, C.; Velthorst, N. H.; Frei, R. W. *Anal. Chem.* **1986**, *58* (6), 1245. doi:10.1021/ac00297a061.
(20) Van Zoonen, P.; Bock, H.; Gooijer, C.; Velthorst, N. H.; Frei, R. W. *Anal. Chim. Acta* **1987**, *200*, 131. doi:10.1016/S0003-2670(00)83764-2.
(21) Gooijer, C.; Velthorst, N. H. *Biomed. Chromatogr.* **1990**, *4* (3), 92. doi:10.1002/bmc.1130040303.
(22) Nakamura, M. M.; Coichev, N.; Lin, J. M.; Yamada, M. *Anal. Chim. Acta* **2003**, *484* (1), 101. doi:10.1016/S0003-2670(03)00327-1.
(23) Gámiz-Gracia, L.; García-Campaña, A. M.; Huertas-Pérez, J.

Can. J. Chem. Downloaded from www.nrcresearchpress.com by Renmin University of China on 09/02/12
For personal use only.

F.; Lara, F. J. *Anal. Chim. Acta* **2009**, *640* (1-2), 7. doi:10.1016/j.aca.2009.03.017.
(24) García-Campaña, A. M.; Lara, F. J.; Gámiz-Gracia, L.; Huertas-Pérez, J. F. *Trends Anal. Chem.* **2009**, *28*, 973.
(25) Nakamura, M. M.; Saraiva, S. A.; Coichev, N. *Anal. Lett.* **1999**, *32* (12), 2471. doi:10.1080/00032719908542982.
(26) Nakamura, M. M.; Saraiva, S. A.; Coichev, N. *Anal. Lett.* **2000**, *33* (3), 391. doi:10.1080/00032710008543060.
(27) Motoyoshiya, J.; Maruyama, T. *Luminescence* **2010**, *25* (2), 181. doi:10.1002/bio.1211.
(28) Lattanzio, G.; García-Campaña, A. M.; Soto-Chinchilla, J. J.; Gámiz-Gracia, L.; Girotti, S. *J. Pharm. Biomed. Anal.* **2008**, *46* (2), 381. doi:10.1016/j.jpba.2007.09.027.
(29) Fernández-Ramos, J. M.; García-Campaña, A. M.; Alés-Barrero, F.; Bosque-Sendra, J. M. *Talanta* **2006**, *69* (3), 763. doi:10.1016/j.talanta.2005.11.008.
(30) Gámiz-Gracia, L.; García-Campana, A. M.; Ales Barrero, F.; Cuadros Rodríguez, L. *Anal. Bioanal. Chem.* **2003**, *377*, 281. doi:10.1007/s00216-003-1958-2.
(31) Stevani, C. V.; Lima, D. F.; Toscano, V. G.; Baader, W. J. *J. Chem. Soc., Perkin Trans. 2* **1996**, (5): 989. doi:10.1039/p29960000989.
(32) Baader, W. J.; Stevani, C. V.; Bastos, E. L. In *Chemiluminescence of Organic Peroxides;* Rappoport, Z., Ed.; Wiley: Chichester, 2006; Vol. 2.
(33) Ciscato, L. F. M. L.; Bartoloni, F. H.; Bastos, E. L.; Baader, W. J. *J. Org. Chem.* **2009**, *74* (23), 8974. doi:10.1021/jo901402k.
(34) Tonkin, S. A.; Bos, R.; Dyson, G. A.; Lim, K. F.; Russell, R. A.; Watson, S. P.; Hindson, C. M.; Barnett, N. W. *Anal. Chim. Acta* **2008**, *614* (2), 173. doi:10.1016/j.aca.2008.03.009.
(35) Liang, S. X.; Li, H.; Lin, J. M. *Luminescence* **2008**, *23* (6), 381. doi:10.1002/bio.1049.
(36) Cao, Z.; Lau, C.; Lu, J. *Analyst (Lond.)* **2004**, *129* (12), 1262. doi:10.1039/b400574k.
(37) Hayakawa, K.; Minogawa, E.; Yokoyama, T.; Miyazaki, M.; Imai, K. *Biomed. Chromatogr.* **1992**, *6* (2), 84. doi:10.1002/bmc.1130060208.
(38) Kojo, S.; Tokumaru, S.; Kishida, E. *Clin. Chem.* **1992**, *38*, 788.
(39) Woolf, E. J.; Grayeski, M. L. *J. Lumin.* **1987**, *39* (1), 19. doi:10.1016/0022-2313(87)90005-6.
(40) Dan, N.; Lau, M. L.; Grayeski, M. L. *Anal. Chem.* **1991**, *63* (17), 1766. doi:10.1021/ac00017a021.
(41) Moreno-González, D.; García-Campaña, A. M.; González-Casado, A. *Anal. Lett.* **2010**, *43* (15), 2399. doi:10.1080/00032711003717406.
(42) Steijger, O. M.; van Mastbergen, H. M.; Holthuis, J. J. M. *Anal. Chim. Acta* **1989**, *217*, 229. doi:10.1016/S0003-2670(00)80405-5.
(43) Wada, M.; Abe, K.; Ikeda, R.; Harada, S.; Kuroda, N.; Nakashima, K. *Talanta* **2010**, *81* (3), 1133. doi:10.1016/j.talanta.2010.01.055.
(44) Orejuela, E.; Silva, M. *Analyst (Lond.)* **2002**, *127* (11), 1433. doi:10.1039/b207321h.
(45) Thompson, R. B.; McBee, S. E. S. *Langmuir* **1988**, *4* (1), 106. doi:10.1021/la00079a018.
(46) Rauhut, M. M.; Bollyky, L. J.; Roberts, B. G.; Loy, M.; Whitman, R. H.; Iannotta, A. V.; Semsel, A. M.; Clarke, R. A. *J. Am. Chem. Soc.* **1967**, *89* (25), 6515. doi:10.1021/ja01001a025.
(47) Hinze, W. L.; Srinivasan, N.; Smith, T. K.; Igarashi, S.; Hoshino, H. In *Advances in Multidimensional Luminescence;* JAI Press Inc.: Greenwich, CT, 1991.

Can. J. Chem. Downloaded from www.nrcresearchpress.com by Renmin University of China on 09/02/12
For personal use only.

Highly diastereoselective Mannich-type reaction of titanium enolate derived from 2′-hydroxypropiophenone

Guisheng Deng, Honghua Mo, Jing Luo, and Jingyuan Zou

Can. J. Chem. Downloaded from www.nrcresearchpress.com by Renmin University of China on 09/02/12
For personal use only.

Abstract: Mannich-type addition of the titanium enolate derived from 2′-hydroxypropiophenone to *N*-tosylimines provided the corresponding β-aminoketones in good to excellent yields (60%–90%) and with >99 : <1 anti diastereoselectivity. A model for synthesis of *anti* β-aminoketone as a predominant isomer based on the titanium enolate has been developed. High anti selectivity is not independent of the electron-donating and electron-withdrawing groups on the phenyl ring of the *N*-tosylimines. Noteworthy is the observation that the influence of a second Lewis acid on the Mannich-type reaction based on the titanium enolate is opposite to that obtained from other titanium enolates reported. A reasonable mechanism has been proposed to explain the high anti diastereoselectivity and the effect of a second Lewis acid on yield.

Key words: Mannich-type reaction, 2′-hydroxypropiophenone, titanium enolate, *N*-tosylimine.

Résumé : L'addition de type Mannich de l'énolate de titane obtenu à partir de la 2′-hydroxypropiophénone avec des *N*-tosylimines conduit à la formation des β-aminocétones correspondantes, avec des rendements allant de bons à excellents (60 % à 90 %) et un diastéréosélectivité anti >99 : <1. On a développé un modèle, basé sur l'utilisation d'un énolate de titane, qui permet de réalise la synthèse d'une β-aminocétone dans laquelle l'isomère anti est prépondérant. La sélectivitéanti élevée n'est pas indépendante du caractère électroaffinitaire ou électrodonneur des groupes présents sur le noyau phényle des *N*-tosylimines. Il est important de prendre note du fait que l'addition d'un second acide de Lewis au milieu réactionnel de la réaction de type Mannich déjà catalysée par un énolate de titane conduit à une influence opposée à celle obtenue avec d'autres énolates de titane. On propose un mécanisme raisonnable pour expliquer la diastéréosélectivité anti élevée et l'effet d'un deuxième acide de Lewis sur le rendement.

Mots-clés : réaction de type Mannich, 2′-hydroxypropiophénone, énolate de titane, *N*-tosylimine.

[Traduit par la Rédaction]

Introduction

The Mannich-type reaction is one of the most widely utilized chemical transformations for the construction of carbon–carbon bond.[1] High diasteroselectivity in the process is desirable. Numerous achievements have been accomplished in the area.[2,3a] Over the past 15 years, carbon–carbon bond-forming reactions involving additions of titanium enolates to the C=N bond of imines have emerged as powerful tools in organic synthesis.[3] In principle, these Mannich-type reactions of titanium enolates generate synthetically and biologically important β-aminocarbonyl compounds. Therefore, there is considerable attention on the development of methodologies for diastereocontrol. The ideal outcome is to form only syn- or anti-product with a series of imines. However, most of the reported addition reactions usually gave a mixture of syn- and anti-isomers, and high diastereoselectivity relied considerably on the substitution patterns of the imines.[4]

The aldol condensation of simple and commercially available propiophenone with aldehydes using $TiCl_4/Et_3N$ was reported by Harrison.[5] In the procedure, the enolization of the aromatic ketone gave the corresponding titanium enolates by treatment with $TiCl_4$ and triethylamine in CH_2Cl_2 at 0 °C, followed by the addition to aldehydes, affording aldol adducts with good to excellent diastereoselectivity. However, these conditions have not been applied to Mannich-type reactions with imines. We adopted the $TiCl_4$ / diisopropylethylamine (DIPEA) system and expanded it to Mannich-type reactions with *N*-tosylimines.

Results and discussion

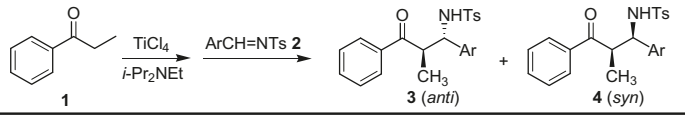
The initial investigation of the reaction of representative *N*-tosylimines (**2**) with the titanium enolate, derived from propiophenone by treating the aromatic ketone with $TiCl_4$/DIPEA at –20 °C in CH_2Cl_2, afforded the expected products (**3** and **4**) in acceptable yields as a mixture of anti- and syn-stereoisomers (Table 1, entries 1 and 2). The treatment of *N*-(furan-2-ylmethylene)-4-methylbenzenesulfonamide with titanium enolate gave the sole anti-isomer **3c** (Table 1, entry 3). It

Received 8 March 2011. Accepted 30 March 2012. Published at www.nrcresearchpress.com/cjc on 6 June 2012.

G. Deng, H. Mo, J. Luo, and J. Zou. College of Chemistry and Chemical Engineering, Hunan Normal University, Changsha, Hunan 410 081, P.R. China; Key Laboratory of Chemical Biology & Traditional Chinese Medicine Research (Ministry of Education of China), Hunan Normal University, Changsha, Hunan 410 081, P.R. China.

Corresponding author: Guisheng Deng (e-mail: gsdeng@hunnu.edu.cn).

Table 1. Mannich-type reaction of titanium enolate derived from propiophenone.



1 **3** (*anti*) **4** (*syn*)

Entry	Ar	Reaction time (h)	Yield (%)[a,b]	*anti*-**3**:*syn*-**4** (%)[c]	**3** and **4**
1	*p*-$CH_3C_6H_4$	10	38	75:25	**a**
2	*p*-ClC_6H_4	10	40	75:25	**b**
3	2-Furyl	10	34	>99:<1	**c**

Note: Propiophenone (1.0 mmol), $TiCl_4$ (1.0 mmol), diisopropylethylamine (DIPEA, 1.0 mmol), *N*-tosylimine (0.5 mmol), CH_2Cl_2 (15 mL), enolization at –20 °C, Mannich-type reaction at 0 °C.

[a]Overall isolated yield.

[b]Unreacted 2′-hydroxypropiophenone (**1**) and *N*-tosylimines (**2**) were almost recovered.

[c]Relative stereochemistry assigned by literature correlation and determined by ^{1}H NMR (500 MHz).

showed that diastereoselectivity of the Mannich-type reaction still depended on the substitution patterns of the imines. The levels of selectivity were similar to those possible with titanium enolates that were previously reported.

Recently, chemists have taken an interest in titanium-mediated Mannich-type reactions based on α- or β-functionalized carbonyl compounds, since high stereoselection of the addition reaction is easily achieved by the use of internal metal chelation. For example, titanium-mediated addition reactions of α-alkoxyacetate ester,[6] α-alkoxy amide,[7] β-silyloxy thioester,[8] β-hydroxy ester,[9] α-sulfenylacetates,[10] α-phenylseleno esters,[11] and α-chloro and cyanoethyl acetates[12] to imines, have been developed. The corresponding β-aminocarbonyl compounds have been prepared with predictably high stereoselectivity.

The recent success in the diastereoselective synthesis of *syn*- and *anti*-β-aminocarbonyl compounds by addition of titanium enolates to imines encouraged us to redesign a model of aromatic ketone for the acceleration of diastereoselection in the Mannich-type reaction. This idea was to introduce hydroxy at the 2-position on the phenyl ring of propiophenone. Although the titanium enolate, derived from 2′-hydroxypropiophenone, has been applied to diastereoselective synthesis of a 1-β-methylcarbapenem intermediate by condensation with 4-acetoxy-β-lactam,[13] diastereoselective Mannich-type reaction of the titanium enolate with *N*-tosylimines has not been exploited so far. Herein, we further describe Mannich-type reactions of 2′-hydroxypropiophenone (**5a**), compare its diastereoselection with that of the propiophenone. Although this resulted only in a moderate yield of the corresponding β-aminocarbonyl compound (Table 2, entry 1), the formation of the sole anti-product **6a** was attractive to us.

It is well-known that a Lewis acid activates an aldimine and that nucleophilic additions are accelerated.[14] Thus, we began to investigate the effect of a second Lewis acid on the addition reaction. In the condensation reaction of **5a** with imine **2a**, utilization of additive Lewis acids, such as $TiCl_4$, Ti(OPr-*i*)Cl_3, Ti(OPr-*i*)$_2Cl_2$, Ti(OPr-*i*)$_3$Cl, Ti(OPr-*i*)$_4$, $AlCl_3$, and BF_3·OEt_2, gave the sole anti product **6a** in all cases. In contrast with the results anticipated, yields were lower than those in the cases without any additive Lewis acids (Table 2, entries 2–8). In the absence of additive Lewis acid, Mannich-type reactions of the enolate derived from 2′-methoxypropiophenone (**5b**) with *N*-tosylimines **2a** and **2c** provided the corresponding products with high anti selectivity and in 47% and 49% yield, respectively (Table 2, entries 9 and 10). In contrary to those of the enolate derived from **5a**, yields were enhanced when using 1 equiv of additive Lewis acid such as titanium tetrachloride (Table 2, entries 11 and 12).

Under these optimal conditions, the Mannich-type reaction of the titanium enolate derived from **5a** occurred with a series of *N*-tosylimines as substrates, affording the expected products. The configuration to *anti*-**3** and *anti*-**6** and syn-isomers **4** was assigned on the basis of chemical shift and coupling constant trends and secured by comparison with similar ^{1}H NMR spectrum data already reported in the literature.[15–17] Furthermore, the relative stereochemistry was determined by decomposition of compound **6a** using ozone[13] into a known *anti*-β-amino acid (**8**) (Scheme 1).

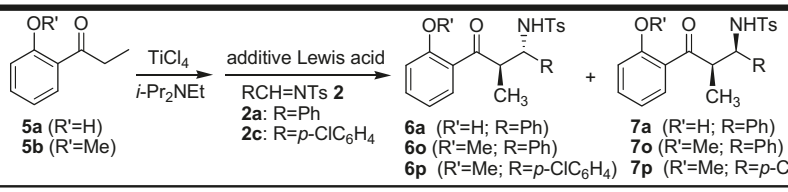
As shown in Table 3, the substituent group on the phenyl ring of the *N*-tosylimines did not have any influences on diastereoselectivity. Electron-donating and electron-withdrawing groups always gave the predominant anti-products **6** (Table 3, entries 1–12). Obviously, the hydroxy group at the ortho position on the phenyl ring of the aromatic ketone played an important role in the Mannich-type reaction, leading to higher anti selectivity.

The formation of the predominant *anti*-β-aminoketones **6** can be rationalized in terms of the addition of the *Z*-enolate[18] to the C=N double bond of the *N*-tosylimine via an accepted six-membered chelated chairlike transition state proposed by Zimmerman and Traxler.[19] In the transition state **TS-1** which is hexacoordinate at titanium,[20,21] the titanium center is coordinated to the enolate oxygen, phenol oxygen, and imine nitrogen, and has negative polarity as shown in Scheme 2. Thus, the enolate addition occurs from the anti-conformation[22] of the imine R with the titanium enolate methyl group to give the anti-product **6**.

As described in the previous paragraph, the Mannich-type reaction can be retarded by a second Lewis acid. Perhaps the most novel and interesting mechanistic issue arising from the current studies relates to the factors governing the sense of the reactive behavior in the carbon–carbon bond formation process. According to the literature,[20] we believe that the role of the second Lewis acid is to abstract chloride ion from the enolate-bound Ti(IV), thereby converting the trichlorotitanate transition state **TS-1** to the corresponding electroneutral dichlorotitanium enolate transition state **TS-2**, in which the enolate oxygen, phenol oxygen, imine nitrogen, and *N*-tosyl group oxygen are coordinated to titanium as

Can. J. Chem. Downloaded from www.nrcresearchpress.com by Renmin University of China on 09/02/12
For personal use only.

Table 2. Effect of a second Lewis acid on addition of titanium enolates derived from 2′-hydroxypropiophenone (**5a**) and 2′-methoxypropiophenone to *N*-tosylimines.



5a (R'=H)
5b (R'=Me)

6a (R'=H; R=Ph)
6o (R'=Me; R=Ph)
6p (R'=Me; R=*p*-ClC$_6$H$_4$)

7a (R'=H; R=Ph)
7o (R'=Me; R=Ph)
7p (R'=Me; R=*p*-ClC$_6$H$_4$)

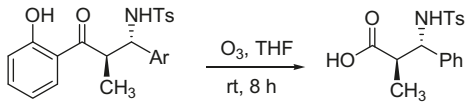
Entry	R′	R	Additive Lewis acid	Reaction time (h)	Yield (%)[a]	*anti*-**6**:*syn*-**7** (%)[b]
1	H, **5a**	Ph, **2a**	None	12	68	>99:<1
2	H, **5a**	Ph, **2a**	$TiCl_4$	12	40	>99:<1
3	H, **5a**	Ph, **2a**	Ti(OPr-*i*)Cl_3	12	22	>99:<1
4	H, **5a**	Ph, **2a**	Ti(OPr-*i*)$_2Cl_2$	12	20	>99:<1
5	H, **5a**	Ph, **2a**	Ti(OPr-*i*)$_3$Cl	12	22	>99:<1
6	H, **5a**	Ph, **2a**	Ti(OPr-*i*)$_4$	12	25	>99:<1
7	H, **5a**	Ph, **2a**	$AlCl_3$	12	20	>99:<1
8	H, **5a**	Ph, **2a**	$BF_3{\cdot}OEt_2$	12	32	>99:<1
9	Me, **5b**	Ph, **2a**	None	12	47	>99:<1
10	Me, **5b**	*p*-ClC$_6$H$_4$, **2c**	None	12	49	>99:<1
11	Me, **5b**	Ph, **2a**	$TiCl_4$	12	60	85:15
12	Me, **5b**	*p*-ClC$_6$H$_4$, **2c**	$TiCl_4$	12	64	>99:<1

Note: 2′-Hydroxypropiophenone (1.0 mmol), $TiCl_4$ (1.0 mmol), diisopropylethylamine (DIPEA; entries 1–8, 2.0 mmol; entries 9–12, 1.0 mmol), additive Lewis acid (1.0 mmol) (entries 2–8, 11, and 12), *N*-tosylimine (0.5 mmol), CH_2Cl_2 (15 mL), enolization at –20 °C, addition reaction at 0 °C.

[a]Isolated yield.

[b]Determined by ^{1}H NMR (500 MHz) of the crude mixture.

Scheme 1. Studies on the relative stereochemistry of compounds **6**.



Ar=Ph, **6a** (*anti*)
Ar=*p*-ClC$_6$H$_4$, **6c** (*anti*)

8 (*anti*)

outlined in Scheme 3. The new Ti(IV)-enolate species in **TS-2** are possibly different from that the Ti(IV)-enolate in **TS-1** initially formed. In **TS-2**, although the imine can be further activated because of the coordination of the *N*-tosyl group oxygen to titanium, the nucleophilicity of the electroneutral enolate moiety considerably decreases. Thus, the use of another second Lewis acid always results in poor Mannich-type reactions in our titanium enolate model.

With the titanium enolate derived from 2′-methoxypropiophenone, the effect of a second Lewis acid on yield is obviously different from those of **5a**. These results strongly suggest that the anti-isomers were obtained through a different pathway. It is known that $TiCl_4$ can form dimeric structures that involve bridging chlorine atoms[23,24]. Therefore, we speculate that the transition state **TS-3** formed in additive $TiCl_4$-mediated reactions in which the two chlorine atoms serve as bridges for the two transition metals (Scheme 4). In **TS-3**, the 2′-methoxy group oxygen on the phenyl ring of the enolate is not coordinated to titanium, and the elimination of Cl^- by MX_n should not occur. The aldimine would be activated by the coordination of the tosyl group oxygen with the additive Lewis acidic Ti(IV) center, resulting in higher yield.

Finally, while we have no direct information regarding the transition states of these reactions, Scheme 2, Scheme 3 and Scheme 4 depict simple models for rationalizing the observed anti stereochemistry and effect of a second Lewis acid on yield.

Conclusions

In summary, we have described a highly diastereoselective Mannich-type reaction of the titanium enolate derived from 2′-hydroxypropiophenone with a wide range of *N*-tosylimines. An efficient methodology for synthesis of *anti*-β-aminoketone as the sole isomer has been disclosed. The key to the success is the introduction of a hydroxy group at the ortho position on the phenyl ring of aromatic ketone. A working hypothesis based on the crucial role played by the stereochemistry of the enolate complexes has been proposed to account for the aforementioned results. The basic idea of controlling diasteroselectivity as shown here can be applied to many other nucleophilic addition reactions. Work along this line and the deprotection of the Ts group of products **6** are now in progress.

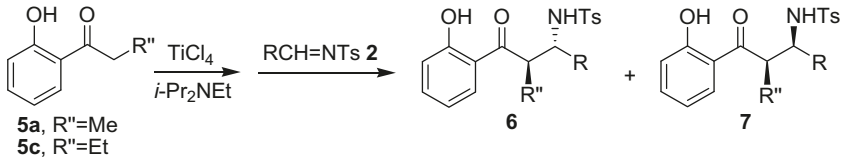
Experimental section

General procedures

The melting points reported are uncorrected and were determined using a super capillary point apparatus. IR spectra were recorded on a Nicolet Nexus TT-IR spectrophotometer. ^{1}H NMR and ^{13}C NMR spectra were recorded on a Bruker Avance-500 spectrometer with chloroform-*d* as a solvent and TMS as reference. EIMS and HRMS spectra were recorded on a GC–MS QP2010 and a Bruker APEX IV, respectively. Elemental analyses were obtained using a Thermofinnigan Flash-EA 1112 series apparatus. CH_2Cl_2 was dried on CaH_2, and other solvents were distilled prior to use.

Can. J. Chem. Downloaded from www.nrcresearchpress.com by Renmin University of China on 09/02/12
For personal use only.

Table 3. Mannich-type addition of titanium enolate derived from 2′-hydroxypropiophenone (**5a**) to a series of *N*-tosylimines.



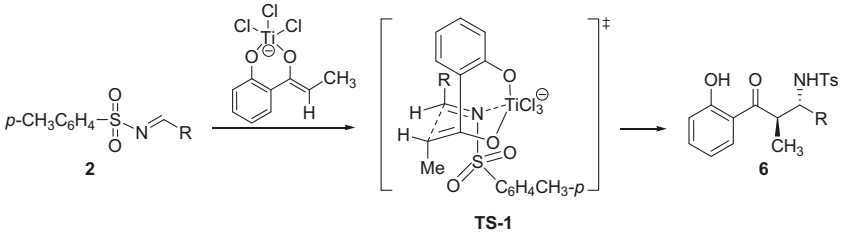
Entry	R″	*N*-Tosylimines **2**	R	Reaction time (h)	Yield (%)[a]	*anti*-**6**:*syn*-**7** (%)[b]
1	Me	**a**	Ph	12	68	>99:<1
2	Me	**b**	*p*-$CH_3C_6H_4$	10	65	>99:<1
3	Me	**c**	*p*-ClC_6H_4	10	70	>99:<1
4	Me	**d**	*p*-$O_2NC_6H_4$	10	70	>99:<1
5	Me	**e**	*p*-BrC_6H_4	10	76	>99:<1
6	Me	**f**	*p*-$CH_3OC_6H_4$	10	90	>99:<1
7	Me	**g**	*p*-^{i}BuOC_6H_4	12	70	>99:<1
8	Me	**h**	*o*-$CH_3OC_6H_4$	10	75	>99:<1
9	Me	**i**	3,4-$(CH_3O)_2C_6H_3$	10	72	>99:<1
10	Me	**j**	3,4-(Methylenedioxy)C_6H_3	12	85	>99:<1
11	Me	**k**	2-Furyl	10	60	>99:<1
12	Me	**l**	*E*-PhCH=CH	12	62	>99:<1
13	Et	**m**	*p*-ClC_6H_4	12	69	>99:<1
14	Et	**n**	*p*-BrC_6H_4	12	71	>99:<1

Note: 2′-Hydroxypropiophenone (1.0 mmol), $TiCl_4$ (1.0 mmol), diisopropylethylamine (DIPEA, 2.0 mmol), *N*-tosylimine (0.5 mmol), CH_2Cl_2 (15 mL), enolization at –20 °C, addition reaction at 0 °C.

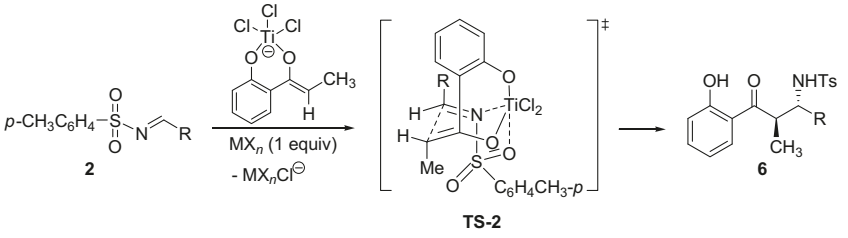
[a]Isolated yield.

[b]Determined by ^{1}H NMR (500 MHz) of the crude mixture.

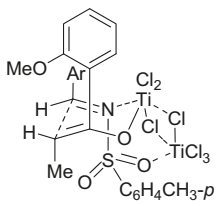
Scheme 2. Stereochemical model.



Scheme 3. Deactivation of the titanium enolate moiety with additive Lewis acid when using 2′-hydroxypropiophenone (**5a**).



Scheme 4. Activation of the titanium imine moiety with additive Lewis acid when using 2′-methoxypropiophenone.



Typical procedure for the synthesis of 3 and 4

To a stirred solution of the propiophenone **1** (1 mmol, 0.134 g, 134 μL) in dry CH_2Cl_2 (10 mL), cooled at –20 °C under N_2, was added $TiCl_4$ (1 mmol, 0.188 g, 110 μL). After 2 min, *i*-Pr_2NEt (1 mmol, 0.129 g, 165 μL) was added dropwise. After 1 h of stirring at –20 °C, a solution of (*E*)-*N*-benzylbenzenesulfonamide (0.5 mol, 0.137 g) in anhydrous CH_2Cl_2 (2 mL) was added and then stirring was continued for 10 h at 0 °C. The reaction was quenched by addition of

Can. J. Chem. Downloaded from www.nrcresearchpress.com by Renmin University of China on 09/02/12
For personal use only.

Can. J. Chem. Downloaded from www.nrcresearchpress.com by Renmin University of China on 09/02/12
For personal use only.

saturated NH_4Cl (5 mL), and the resulting slurry was washed with H_2O (50 mL). The combined organic extracts were dried over Na_2SO_4, filtered, and concentrated in vacuum to afford a brown solid. The residue was purified by flash chromatography on silica (petroleum ether / EtOAc, 7:1), to afford a mixture of **3a** and **4a** (0.078 g, 38%; **3a**:**4a** up to 75%:25%) as a colorless solid.

*2-Methyl-1-phenyl-3-(***p***-tolyl)-3-(tosylamino)propan-1-one (3a and 4a)*

Yield: 38% (anti:syn up to 75%:25%); colorless solid, mp 151–152 °C (hexane/EtOAc). Data for **3a**: ^{1}H NMR (500 MHz, $CDCl_3$, ppm) δ: 7.71 (d, J = 8.0 Hz, 2H), 7.45–7.49 (m, 3H), 7.33 (t, J = 7.5 Hz, 2H), 7.00 (d, J = 7.0 Hz, 2H), 6.91 (d, J = 8.0 Hz, 2H), 6.84 (d, J = 8.0 Hz, 2H), 6.47 (d, J = 5.5 Hz, 1H), 4.68 (dd, J = 6.5, 5.5 Hz, 1H), 3.90 (quintet, J = 6.5 Hz, 1H), 2.30 (s, 3H), 2.18 (s, 3H), 1.16 (d, J = 7.0 Hz, 3H). ^{13}C NMR (125.8 MHz, $CDCl_3$, ppm) δ: 203.65, 142.61, 137.95, 136.81, 136.35, 136.31, 133.38, 129.06, 128.87, 128.61, 128.27, 126.97, 126.66, 60.44, 46.05, 21.40, 20.93, 16.48. Data for **4a**: ^{1}H NMR (500 MHz, $CDCl_3$, ppm) δ: 7.71 (d, J = 8.0 Hz, 2H), 7.45–7.49 (m, 3H), 7.33 (t, J = 7.5 Hz, 2H), 7.00 (d, J = 7.0 Hz, 2H), 6.91 (d, J = 8.0 Hz, 2H), 6.84 (d, J = 8.0 Hz, 2H), 6.45 (d, J = 5.0 Hz, 1H), 4.66 (dd, J = 6.5, 5.0 Hz, 1H), 3.85 (quintet, J = 6.5 Hz, 1H), 2.25 (s, 3H), 2.08 (s, 3H), 1.18 (d, J = 7.0 Hz, 3H). ^{13}C NMR (125.8 MHz, $CDCl_3$, ppm) δ: 203.65, 142.61, 137.95, 136.81, 136.35, 136.31, 133.38, 129.06, 128.87, 128.61, 128.27, 126.97, 126.66, 60.44, 46.05, 21.40, 20.93, 16.48. Data for a mixture of **3a** and **4a**: IR (KBr, cm^{-1}): 3241, 1920, 1684, 1606, 1442, 1319, 1148, 971, 912, 847, 814, 742, 677, 578. MS (EI) 408 (M^+ + 1): 378, 332, 290, 274 (100), 236, 209, 167, 155, 118, 91, 77, 39: HRMS calcd for [$C_{24}H_{25}O_3S$ + H]: 408.1633; found: 408.1637. Anal. calcd for $C_{24}H_{25}O_3S$: C 70.73, H 6.18, N 3.44; found: C 70.68, H 6.20, N 3.48.

*2-Methyl-1-phenyl-3-(***p***-chlorophenyl)-3-(tosylamino) propan-1-one (3b and 4b)*

Yield: 40% (anti:syn up to 75%:25%); colorless solid, mp 126–127 °C (hexane/EtOAc). Data for **3b**: ^{1}H NMR (500 MHz, $CDCl_3$, ppm) δ: 7.80 (d, J = 8.0 Hz, 1H), 7.73 (d, J = 7.0 Hz, 2H), 7.45–7.51 (m, 3H), 7.36 (d, J = 8.0 Hz, 2H), 7.26 (d, J = 8.0 Hz, 1H), 6.96–7.05 (m, 4H), 6.60 (d, J = 9.5 Hz, 1H), 4.70 (dd, J = 9.5, 6.0 Hz, 1H), 3.89 (dq, J = 7.0, 6.0 Hz, 1H), 2.33 (s, 3H), 1.16 (d, J = 7.0 Hz, 3H). ^{13}C NMR (125.8 MHz, $CDCl_3$, ppm) δ: 203.26, 143.23, 139.25, 137.70, 136.05, 133.61, 133.07, 129.21, 128.71, 128.35, 128.29, 127.16, 126.94, 60.02, 45.84, 21.50, 16.50. Data for **4b**: ^{1}H NMR (500 MHz, $CDCl_3$, ppm) δ: 7.80 (d, J = 8.0 Hz, 1H), 7.68 (d, J = 7.0 Hz, 2H), 7.45–7.51 (m, 3H), 7.34 (d, J = 8.0 Hz, 2H), 7.26 (d, J = 8.0 Hz, 1H), 6.96–7.05 (m, 4H), 6.02 (d, J = 8.5 Hz, 1H), 4.60 (t, J = 8.5 Hz, 1H), 3.82 (qd, J = 8.5, 7.0 Hz, 1H), 2.31 (s, 3H), 1.25 (d, J = 7.0 Hz, 3H). ^{13}C NMR (125.8 MHz, $CDCl_3$, ppm) δ: 201.52, 143.45, 138.19, 137.93, 136.95, 133.35, 132.68, 129.68, 128.65, 128.30, 128.12, 127.13, 126.40, 59.21, 46.57, 21.39, 14.93. Data for a mixture of **3b** and **4b**: IR (KBr, cm^{-1}): 3241, 1688, 1592, 1495, 1437, 1328, 1154, 1089, 974, 916, 819, 664, 561. MS (EI): 428 (M^+), 384, 362, 322, 297, 294 (100), 272, 229, 178, 155, 134, 91, 77, 39. HRMS calcd for [$C_{23}H_{22}O_3S$ + H]: 408.1633; found: 408.1637. Anal. calcd for $C_{24}H_{25}O_3S$: C 70.73, H 6.18, N 3.44; found: C 70.68, H 6.20, N 3.48.

2-Methyl-1-phenyl-3-(2-furyl)-3-(tosylamino)propan-1-one (4c)

Yield: 38%; colorless solid, mp 88–90 °C (hexane/EtOAc). IR (KBr): 3340, 2964, 1668, 1593, 1521, 1455, 1209, 1167, 1023, 989, 820, 703, 559 cm^{-1}. ^{1}H NMR (500 MHz, $CDCl_3$, ppm) δ: 7.82 (d, J = 8.0 Hz, 2H), 7.63 (d, J = 8.0 Hz, 2H), 7.56 (t, J = 8.0 Hz, 1H), 7.43 (t, J = 8.0 Hz, 2H), 7.32 (d, J = 8.0 Hz, 1H), 7.18 (d, J = 8.0 Hz, 2H), 7.06 (d, J = 8.0 Hz, 1H), 6.13 (d, J = 9.0 Hz, 1H), 5.86 (d, J = 3.0 Hz, 1H), 4.79 (dd, J = 9.0, 5.0 Hz, 1H), 4.06 (dq, J = 7.0, 5.0 Hz, 1H), 2.37 (s, 3H), 1.24 (d, J = 7.0 Hz, 3H). ^{13}C NMR (125.8 MHz, $CDCl_3$, ppm) δ: 207.09, 154.83, 149.39, 143.08, 136.52, 129.89, 128.02, 128.73, 126.83, 126.35, 119.19, 118.62, 113.89, 53.92, 43.89, 21.50, 15.90. MS (EI): 383 (M^+), 314, 290, 274, 250, 237, 228, 198, 155, 133, 105 (100), 91, 77, 65, 51, 39. HRMS calcd for [$C_{21}H_{21}NO_4S$ + H]: 384.1270; found: 384.1273. Anal. calcd for $C_{21}H_{21}NO_4S$: C 65.78, H 5.52, N 3.65; found: C 65.79, H 5.49, N 3.67.

Typical procedure for the synthesis of 6 and 7

To a stirred solution of the 2′-hydroxyprophenone (1 mmol, 0.150 g, 138 μL) in dry CH_2Cl_2 (10 mL), cooled at –20 °C under N_2, was added $TiCl_4$ (1 mmol, 0.188 g, 110 μL). After 2 min, i-Pr_2NEt (2 mmol, 0.258 g, 330 μL) was added dropwise. After 1 h of stirring at –20 °C, a solution of *N*-tosylimines (0.5 mol, 0.130 g) in anhydrous CH_2Cl_2 (2 mL) was added, and the mixture was stirred for another 10 h at 0 °C. The reaction was quenched by addition of saturated NH_4Cl (5 mL), and the resulting slurry was washed with H_2O (50 mL). The combined organic extracts were dried over Na_2SO_4, filtered, and concentrated in vacuo to afford a brown solid. The residue was purified by flash chromatography on silica (petroleum ether / EtOAc, 7:1) to afford **6a** (0.140 g, 68%; **6a**:**7a** up to 100%:0%) as a colorless solid.

2-Methyl-1-(2-hydroxyphenyl)-3-phenyl-3-(tosylamino) propan-1-one (6a)

Yield: 68%; colorless solid, mp 116–117 °C (hexane/EtOAc). ^{1}H NMR (500 MHz, $CDCl_3$, ppm) δ: 12.00 (s, 1H), 7.52 (d, J = 8.5 Hz, 1H), 7.48 (d, J = 8.0 Hz, 2H), 7.38–7.42 (m, 1H), 7.08–7.10 (m, 3H), 7.04 (d, J = 8.0 Hz, 2H), 7.03 (d, J = 8.0 Hz, 2H), 6.91 (d, J = 8.5 Hz, 1H), 6.74–6.78 (m, 1H), 6.13 (d, J = 9.0 Hz, 1H), 4.72 (dd, J = 9.0, 6.0 Hz, 1H), 3.90 (dq, J = 7.0, 6.0 Hz, 1H), 2.31 (s, 3H), 1.21 (d, J = 7.0 Hz, 3H). ^{13}C-NMR (125.8 MHz, $CDCl_3$, ppm) δ: 208.84, 163.13, 142.90, 139.01, 137.69, 136.96, 129.79, 129.18, 128.39, 127.44, 126.93, 126.65, 119.02, 118.76, 60.44, 45.46, 21.39, 16.76. IR (KBr, cm^{-1}): 3300, 1719, 1619, 1432, 1325, 1160, 1082, 924, 760, 674, 575. MS (EI): 409 (M^+), 286, 260, 254, 238, 223, 207, 195, 181, 165, 155, 150, 134, 121, 104, 91 (100), 77, 65, 51, 39. HRMS calcd for [$C_{23}H_{23}NO_4S$ + H]: 410.1426; found: 410.1429. Anal. calcd for $C_{23}H_{23}NO_4S$: C 67.46, H 5.66, N 3.42; found: C 67.51, H 5.64, N 3.45.

Can. J. Chem. Downloaded from www.nrcresearchpress.com by Renmin University of China on 09/02/12
For personal use only.

2-Methyl-1-(2-hydroxyphenyl)-3-(p-tolyl)-3-(tosylamino) propan-1-one (6b)

Yield: 65%; colorless solid, mp 127–128 °C (hexane/EtOAc). ^{1}H NMR (500 MHz, $CDCl_3$, ppm) δ: 12.11 (s, 1H), 7.76 (d, J = 8.0 Hz, 1H), 7.63 (d, J = 7.0 Hz, 1H), 7.42 (d, J = 8.0 Hz, 2H), 7.37 (t, J = 8.0 Hz, 1H), 7.22 (d, J = 8.0 Hz, 1H), 6.96 (d, J = 8.0 Hz, 2H), 6.94 (d, J = 8.0 Hz, 2H), 6.90 (d, J = 8.0 Hz, 1H), 6.87 (d, J = 8.0 Hz, 2H), 6.72 (t, J = 7.5 Hz, 1H), 6.40 (d, J = 9.0 Hz, 1H), 4.67 (dd, J = 9.0, 8.0 Hz, 1H), 3.87 (qd, J = 8.0, 7.0 Hz, 1H), 2.30 (s, 3H), 2.20 (s, 3H), 1.03 (d, J = 7.0 Hz, 3H). ^{13}C NMR (125.8 MHz, $CDCl_3$, ppm) δ: 208.56, 162.99, 143.35, 142.80, 139.25, 137.40, 137.12, 136.79, 130.05, 129.09, 126.84, 126.35, 119.10, 118.79, 118.50, 60.05, 45.51, 21.41, 20.98, 16.48. IR (KBr, cm^{-1}): 3264, 1645, 1490, 1463, 1307, 1172, 970, 815, 754, 660. MS (EI): 423 (M^+), 378, 364, 341, 315, 291, 274 (100), 268, 237, 209, 195, 161, 155, 121, 118, 91, 65, 55, 39. HRMS calcd for [$C_{24}H_{25}NO_4S$ + H]: 424.1583; found: 424.1589. Anal. calcd for $C_{24}H_{25}NO_4S$: C 68.06, H 5.95, N 3.31; found: C 68.10, H 5.91, N 3.35.

2-Methyl-1-(2-hydroxyphenyl)-3-(p-chlorophenyl)-3-(tosylamino)propan-1-one (6c)

Yield: 70%; colorless solid, mp 161–162 °C (hexane/EtOAc). ^{1}H NMR (500 MHz, $CDCl_3$, ppm) δ: 12.03 (s, 1H), 7.56 (d, J = 8.0 Hz, 1H), 7.38 (dd, J = 8.0, 1.0 Hz, 2H), 7.34 (d, J = 8.0 Hz, 1H), 6.98–7.02 (m, 4H), 6.95 (d, J = 8.0 Hz, 2H), 6.89 (d, J = 8.0 Hz, 1H), 6.67 (t, J = 8.0 Hz, 1H), 6.53 (d, J = 9.0 Hz, 1H), 4.70 (dd, J = 9.0, 8.0 Hz, 1H), 3.84 (qd, J = 8.0, 7.0 Hz, 1H), 2.32 (s, 3H), 1.01 (d, J = 7.0 Hz, 3H). ^{13}C NMR (125.8 MHz, $CDCl_3$, ppm) δ: 208.06, 163.08, 143.18, 137.38, 137.24, 136.95, 133.32, 129.91, 129.19, 128.50, 128.43, 126.84, 126.34, 119.13, 118.58, 59.63, 45.26, 21.40, 16.58. IR (KBr, cm^{-1}): 3258, 1638, 1491, 1442, 1303, 1156, 1082, 812, 763, 673, 575. MS (EI): 444 (M^+ + 1), 384, 294, 275, 257, 229, 211, 178, 156, 155, 121, 91 (100), 75, 65, 39. HRMS calcd for [$C_{23}H_{22}ClNO_4S$ + H]: 444.1036; found: 444.1033. Anal. calcd. for $C_{23}H_{22}ClNO_4S$: C 62.23, H 4.99, N 3.16; found: C 62.28, H 4.90, N 3.20.

2-Methyl-1-(2-hydroxyphenyl)-3-(p-nitrophenyl)-3-(tosylamino)propan-1-one (6d)

Yield: 70%; colorless solid, mp 182–183 °C (hexane/EtOAc). ^{1}H NMR (500 MHz, $CDCl_3$, ppm) δ: 11.87 (s, 1H), 7.94 (d, J = 8.5 Hz, 2H), 7.52 (dd, J = 8.0, 1.0 Hz, 1H), 7.48 (d, J = 8.0 Hz, 2H), 7.40 (m, 1H), 7.29 (d, J = 9.0 Hz, 2H), 7.05 (d, J = 8.0 Hz, 2H), 6.90 (dd, J = 8.5, 1.0 Hz, 1H), 6.74 (m, 1H), 6.59 (d, J = 9.0 Hz, 1H), 4.82 (dd, J = 9.0, 7.0 Hz, 1H), 3.91 (quintet, J = 7.0 Hz, 1H), 2.32 (s, 3H), 1.01 (d, J = 7.0 Hz, 3H). ^{13}C NMR (125.8 MHz, $CDCl_3$, ppm) δ: 207.74, 163.21, 147.10, 146.50, 137.38, 137.18, 129.66, 129.39, 127.91, 126.86, 123.56, 119.25, 118.88, 118.29, 59.63, 45.05, 21.41, 16.84. IR (KBr, cm^{-1}): 3241, 1638, 1532, 1450, 1352, 1156, 812, 771, 698, 567. MS (EI): 454 (M^+), 436, 395, 335, 305, 283, 268, 239, 222, 193, 179, 150 (100), 121, 103, 91, 65, 39. HRMS calcd for [$C_{23}H_{22}ClNO_4S$ + H]: 455.1277; found: 455.1281. Anal. calcd for $C_{23}H_{22}NO_4S$: C 60.78, H 4.88, N 6.16; found: C 60.78, H 4.90, N 6.70.

2-Methyl-1-(2-hydroxyphenyl)-3-(p-bromophenyl)-3-(tosylamino)propan-1-one (6e)

Yield: 76%; colorless solid, mp 134–135 °C (hexane/EtOAc). ^{1}H NMR (500 MHz, $CDCl_3$, ppm) δ: 11.97 (s, 1H), 7.83 (d, J = 8.0 Hz, 1H), 7.58 (dd, J = 8.0, 1.0 Hz, 1H), 7.48 (d, J = 8.0 Hz, 2H), 7.42 (m, 1H), 7.31 (d, J = 8.0 Hz, 1H), 7.20 (d, J = 8.0 Hz, 2H), 7.06 (d, J = 8.0 Hz, 2H), 6.97 (d, J = 8.0 Hz, 2H), 6.86 (d, J = 9.0 Hz, 1H), 6.82 (m, 1H), 5.78 (d, J = 8.0 Hz, 1H), 5.06 (s, 1H), 4.60 (br t, J = 8.0 Hz, 1H), 3.84 (qd, J = 8.0, 7.0 Hz, 1H), 2.32 (s, 3H), 1.01 (d, J = 7.0 Hz, 3H). ^{13}C NMR (125.8 MHz, $CDCl_3$, ppm) δ: 206.88, 163.16, 143.52, 138.38, 136.90, 136.55, 131.46, 129.75, 129.42, 128.74, 127.03, 121.57, 119.08, 118.86, 117.95, 59.02, 45.80, 21.49, 14.59. IR (KBr, cm^{-1}): 3250, 1638, 1491, 1458, 1319, 1148, 1057, 902, 804, 680, 559. MS (EI): 490 (M^+ + 2), 488 (M^+), 430, 340, 332, 305, 286, 259, 237, 184, 155, 121 (100), 103, 91, 65, 39. HRMS calcd for [$C_{23}H_{22}BrNO_4S$ + H]: 488.0531; found: 488.0530. Anal. calcd for $C_{23}H_{22}BrNO_4S$: C 56.56, H 4.54, N 2.87; found: C 56.70, H 4.60, N 2.89.

2-Methyl-1-(2-hydroxyphenyl)-3-(p-methoxyphenyl)-3-(tosylamino)propan-1-one (6f)

Yield: 90%; colorless solid, mp 147–148 °C (hexane/EtOAc). ^{1}H NMR (500 MHz, $CDCl_3$, ppm) δ: 12.15 (s, 1H), 7.64 (dd, J = 8.0, 1.0 Hz, 1H), 7.40 (d, J = 8.0 Hz, 2H), 7.34 (m, 1H), 6.98 (d, J = 8.0 Hz, 2H), 6.92 (d, J = 8.0 Hz, 2H), 6.89 (dd, J = 8.0, 1.0 Hz, 1H), 6.69 (m, 1H), 6.57 (d, J = 8.0 Hz, 2H), 6.50 (d, J = 9.0 Hz, 1H), 4.69 (dd, J = 9.0, 8.0 Hz, 1H), 3.87 (qd, J = 8.0, 7.0 Hz, 1H), 3.67 (s, 3H), 2.28 (s, 3H), 0.97 (d, J = 7.0 Hz, 3H). ^{13}C NMR (125.8 MHz, $CDCl_3$, ppm) δ: 208.50, 162.94, 158.83, 142.69, 137.42, 136.74, 130.85, 130.10, 129.58, 129.07, 128.16, 126.88, 126.28, 119.11, 118.77, 118.40, 113.73, 59.74, 55.15, 45.58, 21.37, 16.41. IR (KBr, cm^{-1}): 3283, 1638, 1515, 1450, 1319, 1254, 1156, 1025, 976, 820, 755, 665, 575. MS (EI): 439 (M^+), 401, 375, 361, 333, 290 (100), 268, 253, 237, 210, 197, 165, 155, 134, 121, 91, 65, 39. HRMS calcd for [$C_{24}H_{25}NO_5S$ + H]: 440.1532; found: 440.1541. Anal. calcd for $C_{24}H_{25}NO_5S$: C 65.58, H 5.73, N 3.19; found: C 65.62, H 5.72, N 3.23.

2-Methyl-1-(2-hydroxyphenyl)-3-(p-isobutoxyphenyl)-3-(tosylamino)propan-1-one (6g)

Yield: 70%; colorless solid; mp 130–132 °C (hexane/EtOAc). ^{1}H NMR (500 MHz, $CDCl_3$, ppm) δ: 12.11 (s, 1H), 7.56 (dd, J = 8.0, 1.0 Hz, 1H), 7.44 (d, J = 8.0 Hz, 2H), 7.39 (m, 1H), 6.98 (d, J = 8.0 Hz, 2H), 6.91 (d, J = 8.0 Hz, 1H), 6.90 (d, J = 8.0 Hz, 2H), 6.74 (m, 1H), 6.56 (d, J = 8.0 Hz, 2H), 6.22 (dd, J = 8.0, 4.0 Hz, 1 H), 4.67 (br t, J = 7.0 Hz, 1H), 4.14 (m, 1H), 3.86 (quintet, J = 7.0 Hz, 1H), 2.29 (s, 3H), 1.51–1.72 (m, 2H), 1.20 (d, J = 7.0 Hz, 6H), 0.94 (d, J = 7.0 Hz, 3H). ^{13}C NMR (125.8 MHz, $CDCl_3$, ppm) δ: 208.87, 163.05, 157.44, 142.72, 136.86, 130.56, 129.92, 129.23, 129.08, 127.92, 126.94, 119.04, 118.77, 118.64, 74.87, 59.90, 45.64, 29.07, 21.42, 16.72, 9.81. IR (KBr, cm^{-1}): 3260, 2964, 1638, 1450, 1328, 1252, 1167, 822, 741, 666. MS (EI): 481 (M^+), 426, 332 (100), 310, 276, 239, 211, 176, 155, 150, 121, 92, 77, 65, 39. HRMS calcd for [$C_{27}H_{31}NO_5S$ + H]: 482.2001; found: 482.2002.

Can. J. Chem. Downloaded from www.nrcresearchpress.com by Renmin University of China on 09/02/12
For personal use only.

Anal. calcd for $C_{27}H_{31}NO_5S$: C 67.34, H 6.49, N 2.91; found: C 67.32, H 6.53, N 2.90.

2-Methyl-1-(2-hydroxyphenyl)-3-(o-methoxyphenyl)-3-(tosylamino)propan-1-one (6h)

Yield: 75%; colorless solid, mp 155–157 °C (hexane/EtOAc). ^{1}H NMR (500 MHz, $CDCl_3$, ppm) δ: 12.29 (s, 1H), 7.62 (dd, J = 8.0, 1.0 Hz, 1H), 7.35–7.39 (m, 3H), 7.06 (m, 1H), 6.94 (dd, J = 8.0, 1.0 Hz, 1H), 6.92 (d, J = 8.0 Hz, 1H), 6.88 (d, J = 8.0 Hz, 2H), 6.74 (m, 1H), 6.70 (t, J = 7.0 Hz, 1H), 6.58 (d, J = 8.0 Hz, 1H), 6.23 (d, J = 10.5 Hz, 1H), 4.82 (dd, J = 10.5, 9.0 Hz, 1H), 4.15 (qd, J = 9.0, 7.0 Hz, 1H), 3.72 (s, 3H), 2.25 (s, 3H), 0.94 (d, J = 7.0 Hz, 3H). ^{13}C NMR (125.8 MHz, $CDCl_3$, ppm) δ: 208.55, 162.96, 156.20, 142.58, 137.30, 136.52, 129.92, 128.86, 128.83, 126.72, 125.62, 120.45, 119.29, 118.92, 118.38, 110.40, 58.89, 55.19, 42.96, 21.37, 16.38. IR (KBr, cm^{-1}): 3261, 1632, 1501, 1436, 1324, 1246, 1154, 807, 749, 683, 559. MS (EI): 439 (M^+), 401, 375, 361, 333, 290 (100), 268, 253, 237, 210, 197, 165, 155, 134, 121, 91, 65, 39. HRMS calcd for [$C_{24}H_{25}NO_5S$ + H]: 440.1532; found: 440.1541. Anal. calcd for $C_{24}H_{25}NO_5S$: C 65.58, H 5.73, N 3.19; found: C 65.56, H 5.76, N 3.18.

2-Methyl-1-(2-hydroxyphenyl)-3-(3,4-dimethoxyphenyl)-3-(tosylamino)propan-1-one (6i)

Yield: 72%; colorless solid, mp 139–140 °C (hexane/EtOAc). ^{1}H NMR (500 MHz, $CDCl_3$, ppm) δ: 12.27 (s, 1H), 7.76 (d, J = 8.0 Hz, 1H), 7.64 (dd, J = 8.0, 1.0 Hz, 1H), 7.39 (d, J = 8.0 Hz, 3H), 7.22 (d, J = 8.0 Hz, 1H), 7.08 (ddd, J = 8.0, 1.0 Hz, 1H), 6.91–6.96 (m, 4H), 6.78 (d, J = 7.0 Hz, 1H), 6.70 (t, J = 8.0 Hz, 1H), 6.60 (d, J = 8.0 Hz, 1H), 6.22 (d, J = 10.5 Hz, 1H), 4.81 (dd, J = 10.5, 9.0 Hz, 1H), 4.15 (qd, J = 9.0, 7.0 Hz, 1H), 3.74 (s, 3H), 2.26 (s, 3H), 0.95 (d, J = 7.0 Hz, 3H). ^{13}C NMR (125.8 MHz, $CDCl_3$, ppm) δ: 208.57, 162.96, 156.21, 143.29, 142.70, 139.34, 137.23, 136.57, 129.93, 128.89, 127.73, 126.96, 126.36, 125.66, 120.49, 119.04, 118.43, 110.42, 59.90, 55.22, 42.96, 21.38, 16.38. IR (KBr, cm^{-1}): 3271, 1631, 1496, 1450, 1327, 1280, 1159, 761, 693. MS (EI): 469 (M^+), 410, 390, 375, 340, 319, 290 (100), 253, 237, 225, 210, 181, 164, 155, 121, 107, 91, 65, 51, 39. HRMS calcd for [$C_{25}H_{27}NO_6S$ + H]: 470.1637; found: 470.1639. Anal. calcd for $C_{25}H_{27}NO_6S$: C 63.95, H 5.80, N 2.98; found: C 63.93, H 5.82, N 3.00.

2-Methyl-1-(2-hydroxyphenyl)-3-(3,4-(methylenedioxy)phenyl)-3-(tosylamino)propan-1-one (6j)

Yield: 85%; colorless solid, mp 176–177 °C (hexane/EtOAc). ^{1}H NMR (500 MHz, $CDCl_3$, ppm) δ: 11.98 (s, 1H), 7.51 (dd, J = 8.0, 1.5 Hz, 1H), 7.43 (d, J = 8.0 Hz, 2H), 7.41 (ddd, J = 8.0, 1.5 Hz, 1H), 7.18 (dd, J = 7.0, 1.5 Hz, 2H), 7.02 (d, J = 8.0 Hz, 2H), 6.91–6.93 (m, 3H), 6.74–6.77 (m, 1H), 6.31 (d, J = 9.0 Hz, 1H), 4.67 (dd, J = 9.0, 6.0 Hz, 1H), 3.90 (dq, J = 7.0, 6.0 Hz, 1H), 2.35 (s, 3H), 1.17 (d, J = 7.0 Hz, 3H). ^{13}C NMR (125.8 MHz, $CDCl_3$, ppm) δ: 208.41, 163.17, 143.26, 137.97, 137.37, 137.16, 131.48, 129.73, 129.26, 128.54, 126.86, 121.44, 119.16, 118.82, 118.51, 59.82, 45.23, 21.45, 16.85. IR (KBr, cm^{-1}): 3258, 1630, 1491, 1458, 1303, 1139, 1082, 984, 820, 755, 665, 575. MS (EI): 453 (M^+), 430, 340, 301, 275, 237, 214, 184, 155, 150, 121 (100), 91, 77, 65, 39. HRMS calcd for [$C_{24}H_{23}NO_6S$ + H]: 454.1324; found: 454.1321. Anal. calcd for $C_{24}H_{23}NO_6S$: C 63.56, H 5.11, N 3.09; found: C 63.53, H 5.14, N 3.11.

2-Methyl-1-(2-hydroxyphenyl)-3-(2-furyl)-3-(tosylamino)propan-1-one (6k)

Yield: 60%; colorless solid, mp 80–81 °C (hexane/EtOAc). ^{1}H NMR (500 MHz, $CDCl_3$, ppm) δ: 12.06 (s, 1H), 7.85 (d, J = 8.0 Hz, 1H), 7.78 (d, J = 8.0 Hz, 1H), 7.56 (d, J = 8.0 Hz, 1H), 7.43 (m, 1H), 7.31 (d, J = 8.0 Hz, 1H), 7.23 (d, J = 8.0 Hz, 1H), 7.11 (d, J = 8.0 Hz, 2H), 7.02 (d, J = 8.0 Hz, 1H), 6.93 (d, J = 8.0 Hz, 1H), 6.83 (m, 1H), 6.17 (d, J = 9.0 Hz, 1H), 4.81 (dd, J = 9.0, 8.0 Hz, 1H), 4.15 (qd, J = 8.0, 7.0 Hz, 1H), 2.35 (s, 3H), 1.11 (d, J = 7.0 Hz, 3H). ^{13}C NMR (125.8 MHz, $CDCl_3$, ppm) δ: 207.97, 163.03, 155.83, 149.96, 143.08, 136.52, 129.84, 128.02, 128.83, 126.83, 126.33, 119.19, 118.62, 113.86, 108.09, 53.92, 43.39, 21.51, 15.97. IR (KBr, cm^{-1}): 3241, 1638, 1450, 1319, 1164, 984, 828, 763, 665, 567. MS (EI): 399 (M^+), 376, 340, 290, 250, 244, 213, 185, 155 (100), 121, 91, 77, 65, 39. HRMS calcd for [$C_{21}H_{21}NO_5S$ + H]: 400.1219; found: 400.1223. Anal. calcd for $C_{21}H_{21}NO_5S$: C 63.56, H 5.11, N 3.09; found: C 63.53, H 5.10, N 3.13.

2-Methyl-1-(2-hydroxyphenyl)-3-styryl-3-(tosylamino)propan-1-one (6l)

Yield: 62%; colorless solid, mp 131–133 °C (hexane/EtOAc). ^{1}H NMR (500 MHz, $CDCl_3$, ppm) δ: 12.08 (s, 1H), 7.70 (d, J = 8.0 Hz, 3H), 7.45 (m, 1H), 7.16–7.21 (m, 3H), 7.11 (d, J = 8.0 Hz, 2H), 7.00 (dd, J = 8.0, 1.0 Hz, 2H), 6.96 (dd, J = 8.0, 1.0 Hz, 1H), 6.86 (m, 1H), 6.18 (d, J = 16.0 Hz, 1H), 5.87 (d, J = 9.0 Hz, 1H), 5.77 (dd, J = 16.0, 8.0 Hz, 1H), 4.26 (dd, J = 9.0, 8.0 Hz, 1H), 3.78 (qd, J = 8.0, 7.0 Hz, 1H), 2.22 (s, 3H), 1.34 (d, J = 7.0 Hz, 3H). ^{13}C NMR (125.8 MHz, $CDCl_3$, ppm) δ: 208.98, 163.28, 143.27, 138.15, 137.07, 135.86, 132.91, 130.07, 129.50, 128.35, 127.88, 127.18, 126.42, 126.24, 119.20, 118.92, 118.49, 58.87, 44.80, 21.32, 15.89. IR (KBr, cm^{-1}): 3250, 1638, 1491, 1450, 1336, 1164, 976, 820, 755, 690, 575. MS (EI): 435 (M^+), 332, 286, 264, 249, 221, 207, 178, 155, 130, 121, 91 (100), 77, 65, 39. HRMS calcd for [$C_{25}H_{25}NO_4S$ + H]: 436.1583; found: 436.1580. Anal. calcd for $C_{25}H_{25}NO_4S$: C 68.94, H 5.79, N 3.22; found: C 68.90, H 5.82, N 3.23.

N-*(1-(4-Chlorophenyl)-2-(2-hydroxybenzoyl)butyl)-4-methylbenzenesulfonamide (6m)*

Yield: 69%; colorless solid, mp 165–166 °C. ^{1}H NMR (500 MHz, $CDCl_3$, ppm) δ: 12.10 (s, 1H), 7.48 (d, J = 7.5 Hz, 1H), 7.41 (d, J = 8.5 Hz, 2H), 7.38–7.34 (m, 1H), 7.00–6.90 (m, 5H), 6.90 (d, J = 8 Hz, 1H), 6.73 (t, J = 8 Hz, 1H), 6.51 (d, J = 10 Hz, 1H), 4.74 (dd, J = 10, 7 Hz, 1H), 3.70 (dt, J = 7, 7 Hz, 1H), 2.33 (s, 1H), 1.68–1.48 (m, 2H), 0.79 (t, J = 7.5 Hz, 3H). ^{13}C NMR (125.8 MHz, $CDCl_3$, ppm) δ: 208.67, 162.72, 143.04, 137.59, 137.36, 136.95, 133.11, 129.97, 129.10, 128.36, 128.08, 126.73, 119.82, 118.96, 118.45, 58.19, 51.74, 24.22, 21.27, 11.40. IR (KBr, cm^{-1}): 3251, 2967, 2879, 1735, 1488, 1441, 1333, 1156, 1090, 922, 811, 758, 673, 572. MS (EI): 460 (M^+ + 2), 458 (M^+), 294, 257, 241, 211, 164, 155, 121 (100), 91, 65, 39. HRMS calcd for [$C_{24}H_{24}ClNO_4S$ + H]: 458.1193;

Can. J. Chem. Downloaded from www.nrcresearchpress.com by Renmin University of China on 09/02/12
For personal use only.

found: 458.1190. Anal. calcd for $C_{24}H_{24}ClNO_4S$: C 62.94, H 5.28, N 3.06; found: C 62.90, H 5.20, N 3.20.

N-*(1-(4-Bromophenyl)-2-(2-hydroxybenzoyl)butyl)-4-methylbenzenesulfonamide (6n)*

Yield: 71%; colorless solid, mp 167–168 °C. ^{1}H NMR (500 MHz, $CDCl_3$, ppm) δ: 12.10 (s, 1H), 7.47 (d, J = 8 Hz, 1H), 7.40–7.33 (m, 3H), 7.13 (d, J = 8.5 Hz, 2H), 6.97 (d, J = 8 Hz 2H), 6.90–6.89 (m, 3H), 6.64 (t, J = 8 Hz, 1H), 6.50 (d, J = 10 Hz, 1H), 4.72 (dd, J = 10, 7 Hz, 1H), 3.69 (dt, J = 7, 7 Hz, 1H), 2.33 (s, 1H), 1.65–1.48 (m, 2H), 0.78 (t, J = 7.5 Hz, 3H). ^{13}C NMR (125.8 MHz, $CDCl_3$, ppm) δ: 208.60, 162.70, 143.10, 138.01, 137.26, 136.97, 131.31, 129.97, 129.11, 128.43, 126.71, 121.22, 119.79, 119.00, 118.45, 58.23, 51.65, 24.22, 21.33, 11.40. IR (KBr, cm^{-1}): 3249, 2961, 2880, 1638, 1485, 1333, 1159, 922, 835, 763, 663, 575. MS (EI): 504 (M^++2), 502 (M^+), 484, 430, 338, 301, 275 241, 211, 164, 155, 131, 121 (100), 91, 65, 39. HRMS calcd for [$C_{24}H_{24}BrNO_4S$ + H]: 502.0688; found: 502.0663. Anal. calcd for $C_{24}H_{24}BrNO_4S$: C 57.37, H 4.81, N 2.79; found: C 57.41, H 4.91, N 2.72.

N-*(3-(-Methoxyphenyl)-2-methyl-3-oxo-1-phenylpropyl)-4-methylbenzenesulfonamide (6o)*

Colorless solid, mp 112–113 °C (hexane/EtOAc). ^{1}H NMR (500 MHz, $CDCl_3$, ppm) δ: 7.48 (d, J = 8.5 Hz, 2H), 7.31–7.38 (m, 2H), 7.06–7.10 (m, 5H), 7.02 (d, J = 8.0 Hz, 2H), 6.82–6.89 (m, 2H), 6.40 (d, J = 8.5 Hz, 1H), 4.62 (t, J = 8.0 Hz, 1H), 3.91 (qd, J = 8.0, 7.0 Hz, 1H), 3.77 (s, 3H), 2.29 (s, 3H), 1.04 (d, J = 7.0 Hz, 3H). ^{13}C NMR (125.8 MHz, $CDCl_3$, ppm) δ: 206.51, 157.92, 142.66, 139.75, 137.87, 133.69, 130.27, 129.11, 128.09, 127.88, 127.06, 126.98, 126.38, 120.79, 111.56, 60.44, 55.59, 50.46, 21.41, 15.86. **7m**: ^{1}H NMR (500 MHz, $CDCl_3$, ppm) δ: 7.78 (d, J = 8.0 Hz, 2H), 7.22 (d, J = 8.0 Hz, 2H), 7.06–7.10 (m, 5H), 6.96 (d, J = 8.0 Hz, 2H), 6.82–6.89 (m, 2H), 5.85 (d, J = 7.0 Hz, 1H), 4.62 (t, J = 8.0 Hz, 1H), 3.86 (qd, J = 8.0, 7.0 Hz, 1H), 3.78 (s, 3H), 2.24 (s, 3H), 1.12 (d, J = 7.0 Hz, 3H). ^{13}C NMR (125.8 MHz, $CDCl_3$, ppm) δ: 204.75, 157.89, 143.16, 139.54, 136.96, 133.49, 130.37, 129.59, 128.40, 127.25, 127.23, 127.06, 126.38, 120.57, 111.32, 59.09, 55.48, 50.94, 21.50, 14.21. **6m** and **7m**: IR (KBr, cm^{-1}): 3280, 1670, 1590, 1460, 1340, 1160, 1100,1030, 760 671, 559. MS (EI): 426 (M^+ + 1), 427, 349, 324, 290, 268, 260, 237, 207, 195, 171, 155 135, 121, 91 (100), 77, 65, 39. Anal. calcd for $C_{24}H_{25}NO_4S$: C 68.06, H 5.95, N 3.31; found: C 68.05, H 5.60, N 3.29.

N-*(1-(4-Chlorophenyl)-3-(2-methoxyphenyl)-2-methyl-3-oxopropyl)-4-methylbenzenesulfonamide (6p)*

Colorless solid, mp 112–113 °C (hexane/EtOAc). ^{1}H NMR (500 MHz, $CDCl_3$, ppm) δ: 7.49 (d, J = 8.0 Hz, 2H), 7.38 (ddd, J = 8.0, 1.0 Hz, 1H), 6.99–7.08 (m, 6H), 6.90 (t, J = 8.0 Hz, 1H), 6.85 (d, J = 8.0 Hz, 1H), 6.40 (d, J = 8.5 Hz, 1H), 4.59 (t, J = 7.0 Hz, 1H), 3.91 (qd, J = 7.0, 7.0 Hz, 1H), 3.78 (s, 3H), 2.34 (s, 3H), 1.06 (d, J = 7.0 Hz, 3H). ^{13}C NMR (125.8 MHz, $CDCl_3$, ppm) δ: 206.23, 157.90, 142.97, 139.75, 138.48, 137.77, 133.89, 132.85, 130.31, 129.20, 128.45, 128.17, 128.05, 126.97, 111.55, 60.33, 55.58, 50.27, 21.44, 15.89. IR (KBr, cm^{-1}): 3276, 1671, 1583, 1457, 1340, 1160, 1097, 1020, 760, 671, 560. HRMS calcd for [$C_{24}H_{24}ClNO_4S$ + H]: 458.1193; found: 458.1184. Anal. calcd for $C_{24}H_{24}ClNO_4S$: C 62.94, H 5.28, N 3.06; found: C 62.90, H 5.22, N 3.13.

Procedure[13] for the transformation of 6a to methyl-3-(4-methylphenylsulfonamido)-3-phenylpropanoic acid (8)

A solution of **6a** (0.5 mmol, 0.205 g) in 50 mL of dichloromethane was added to 5.0 g of silica gel (80–120 mesh), followed by the removal of the solvent under reduced pressure. Ozone was passed through the silica gel preadsorbed with **6a** in a 500 mL Erlenmeyer flask at –78 °C for 15 min, followed by warming of the flask to room temperature. The silica gel was washed with ethyl acetate, filtered, and concentrated under reduced pressure. The residue was purified by flash chromatography on silica (petroleum ether / EtOAc, 2:1) to afford **8** (0.101 g, 61%) as a colorless solid, mp 132–133 °C (hexane/EtOAc) (lit[25] mp 131–133 °C). Spectral data (^{1}H and ^{13}C NMR and IR) of **8** are identical with those reported.[25] ^{1}H NMR (500 MHz, $CDCl_3$, ppm) δ: 7.48 (m, 2H), 7.11 (m, 3H), 7.03 (m, 4H), 6.19 (d, J = 9.2 Hz, 1H), 4.51 (dd, J = 7.2, 8.8 Hz, 1H), 2.89 (quint, J = 6.8 Hz, 1H), 2.28 (s, 3H), 1.17 (d, J = 6.8 Hz, 3H). ^{13}C NMR (125.8 MHz, $CDCl_3$, ppm) δ: 178.61, 143.32, 138.90, 138.02, 129.50, 128.72, 127.91, 127.33, 127.10, 60.49, 46.11, 21.70, 15.72. IR (KBr, cm^{-1}): 3265, 1715, 1162.

References

(1) (a) González, P. B.; Lopez, R.; Palomo, C. *J. Org. Chem.* **2010**, *75* (11), 3920. doi:10.1021/jo1005872; (b) Mizuta, S.; Shibata, N.; Goto, Y.; Furukawa, T.; Nakamura, S.; Toru, T. *J. Am. Chem. Soc.* **2007**, *129* (20), 6394. doi:10.1021/ja071509y; (c) Hatano, M.; Horibe, T.; Ishihara, K. *Org. Lett.* **2010**, *12* (15), 3502. doi:10.1021/ol101353r; (d) González, A. S.; Arrayás, R. G.; Carretero, J. C. *Org. Lett.* **2006**, *8* (14), 2977. doi:10.1021/ol060866v; (e) Wei, H.-L.; Yan, Z.-Y.; Niu, Y.-N.; Li, G.-Q.; Liang, Y.-M. *J. Org. Chem.* **2007**, *72* (22), 8600. doi:10.1021/jo7016235; (f) Hatano, M.; Horibe, T.; Ishihara, K. *J. Am. Chem. Soc.* **2010**, *132* (1), 56. doi:10.1021/ja909874b; (g) Hatano, M.; Maki, T.; Moriyama, K.; Arinobe, M.; Ishihara, K. *J. Am. Chem. Soc.* **2008**, *130* (50), 16858. doi:10.1021/ja806875c; (h) Zhang, Y.; Liu, Y.-K.; Kang, T.-R.; Hu, Z.-K.; Chen, Y.-C. *J. Am. Chem. Soc.* **2008**, *130* (8), 2456. doi:10.1021/ja7114844; (i) Li, Z.; Li, C.-J. *J. Am. Chem. Soc.* **2005**, *127* (11), 3672. doi:10.1021/ja050058j; (j) Yuan, Z.-L.; Jiang, J.-J.; Shi, M. *Tetrahedron* **2009**, *65* (31), 6001. doi:10.1016/j.tet.2009.05.080; (k) Hatano, M.; Ishihara, K. *Synthesis* **2010**, 3785 (l) Ma, Z.; Zhao, Y.; Jiang, N.; Jin, X.; Wang, J. *Tetrahedron Lett.* **2002**, *43* (17), 3209. doi:10.1016/S0040-4039(02)00498-7; (m) Zhao, Y.; Ma, Z.; Zhang, X.; Zou, Y.; Jin, X.; Wang, J. *Angew. Chem. Int. Ed.* **2004**, *43* (44), 5977. doi:10.1002/anie.200460730; (n) Zhao, Y.; Jiang, N.; Chen, S.; Peng, C.; Zhang, X.; Zou, Y.; Zhang, S.; Wang, J. *Tetrahedron* **2005**, *61* (27), 6546. doi:10.1016/j.tet.2005.04.054; (o) Dong, C.; Mo, F.; Wang, J. *J. Org. Chem.* **2008**, *73* (5), 1971. doi:10.1021/jo702275a.

(2) (a) Matsunaga, S.; Kumagai, N.; Harada, S.; Shibasaki, M. *J. Am. Chem. Soc.* **2003**, *125* (16), 4712. doi:10.1021/ja034787f; (b) Chen, Z.; Yakura, K.; Matsunaga, S.; Shibasaki, M. *Org. Lett.* **2008**, *10* (15), 3239. doi:10.1021/ol800965t; (c) Yin, L.; Kanai, M.; Shibasaki, M. *J. Am. Chem. Soc.* **2009**, *131* (28), 9610. doi:10.1021/ja9036675; (d) Matsunaga, S.; Yoshida, T.; Morimoto, H.; Kumagai, N.; Shibasaki, M. *J. Am. Chem. Soc.*

Can. J. Chem. Downloaded from www.nrcresearchpress.com by Renmin University of China on 09/02/12
For personal use only.

2004, *126* (28), 8777. doi:10.1021/ja0482435; (e) Harada, S.; Handa, S.; Matsunaga, S.; Shibasaki, M. *Angew. Chem. Int. Ed.* **2005**, *44* (28), 4365. doi:10.1002/anie.200501180; (f) Trost, B. M.; Terrell, L. R. *J. Am. Chem. Soc.* **2003**, *125* (2), 338. doi:10.1021/ja028782e; (g) Trost, B. M.; Jaratjaroonphong, J.; Reutrakul, V. *J. Am. Chem. Soc.* **2006**, *128* (9), 2778. doi:10.1021/ja057498v; (h) Córdova, A. *Asymmetric Bifunctional Catalysis Using Heterobimetallic and Multimetallic Systems in Catalytic Asymmetric Conjugate Reactions;* Córdova, A., Ed.; Wiley-VCH, Weinheim. 2010.

(3) (a) Córdova, A. *Acc. Chem. Res.* **2004**, *37* (2), 102. doi:10.1021/ar030231l; (b) Sakthivel, K.; Notz, W.; Bui, T.; Barbas, C. F., III. *J. Am. Chem. Soc.* **2001**, *123* (22), 5260. doi:10.1021/ja010037z; (c) Shimizu, M.; Kurokawa, H.; Nishiura, S.; Hachiya, I. *Heterocycles* **2006**, *70* (1), 57. doi:10.3987/COM-06-S(W)9; (d) Periasamy, M.; Suresh, S.; Ganesan, S. S. *Tetrahedron Asymmetry* **2006**, *17* (9), 1323. doi:10.1016/j.tetasy.2006.04.032; (e) Shimizu, M.; Tanaka, M.; Itoh, T.; Hachiya, I. *Synlett* **2006**, *2006* (11), 1687. doi:10.1055/s-2006-944220.

(4) (a) Annunziata, R.; Benaglia, M.; Cinquini, M.; Cozzi, F.; Ponzini, F.; Raimondi, L. *Tetrahedron* **1994**, *50* (9), 2939. doi:10.1016/S0040-4020(01)87005-8; (b) Periasamy, M.; Ganesan, S. S.; Suresh, S. *Tetrahedron Asymmetry* **2010**, *21* (4), 385. doi:10.1016/j.tetasy.2010.02.010.

(5) Harrison, C. R. *Tetrahedron Lett.* **1987**, *28* (36), 4135. doi:10.1016/S0040-4039(00)95559-X.

(6) Shimizu, M.; Ishida, T.; Fujisawa, T. *Chem. Lett.* **1994**, *23* (8), 1403. doi:10.1246/cl.1994.1403.

(7) Bravo, P.; Fustero, S.; Guidetti, M.; Volonterio, A.; Zanda, M. *J. Org. Chem.* **1999**, *64* (23), 8731. doi:10.1021/jo9909397.

(8) Annunziata, R.; Benaglia, M.; Cinquini, M.; Cozzi, F. *Tetrahedron Asymmetry* **1999**, *10* (24), 4841. doi:10.1016/S0957-4166(99)00566-2.

(9) Annunziata, R.; Benaglia, M.; Chiovato, A.; Cinquini, M.; Cozzi, F. *Tetrahedron* **1995**, *51* (36), 10025. doi:10.1016/0040-4020(95)00574-R.

(10) Fujisawa, T.; Sato, D.; Shimizu, M. *Bioorg. Med. Chem. Lett.* **1993**, *3* (11), 2343. doi:10.1016/S0960-894X(01)80952-5.

(11) Silveira, C. C.; Vieira, A. S.; Braga, A. L.; Russowsky, D. *Tetrahedron* **2005**, *61* (39), 9312. doi:10.1016/j.tet.2005.07.058.

(12) Kanwar, S.; Sharma, S. *Synth. Commun.* **2005**, *35* (16), 2149. doi:10.1080/00397910500181947.

(13) Lee, Y.-S.; Choung, W.-K.; Kim, K. H.; Kang, T. W.; Ha, D.-C. *Tetrahedron* **2004**, *60* (4), 867. doi:10.1016/j.tet.2003.11.048.

(14) (a) Kleinman, E. F. In *Comprehensive Organic Synthesis;* Trost, B. M., Ed.; Pergamon Press: New York, 1991; Vol. 2, Chapter 4.1; (b) Ojima, I.; Inaba, S.; Yoshida, K. *Tetrahedron Lett.* **1977**, *18* (41), 3643. doi:10.1016/S0040-4039(01)83315-3; (c) Guanti, G.; Narisano, E.; Banfi, L. *Tetrahedron Lett.* **1987**, *28* (37), 4331. doi:10.1016/S0040-4039(00)96501-8; (d) Mukaiyama, T.; Kashiwagi, K.; Matsui, S. *Chem. Lett.* **1989**, *8* (8), 1397. doi:10.1246/cl.1989.1397; (e) Mukaiyama, T.; Akamatsu, H.; Han, J. S. *Chem. Lett.* **1990**, *9* (6), 889. doi:10.1246/cl.1990.889; (f) Onaka, M.; Ohno, R.; Yanagiya, N.; Izumi, Y. *Synlett* **1993**, *1993* (02), 141. doi:10.1055/s-1993-22380; (g) Ishihara, K.; Funahashi, M.; Hanaki, N.; Miyata, M.; Yamamoto, H. *Synlett* **1994**, *1994* (11), 963. doi:10.1055/s-1994-23065; (h) Kobayashi, S.; Nagayama, S. *J. Org. Chem.* **1997**, *62* (2), 232. doi:10.1021/jo962010h; (i) Dong, C.; Deng, G.; Wang, J. *J. Org. Chem.* **2006**, *71* (15), 5560. doi:10.1021/jo0605039.

(15) Miura, K.; Tamaki, K.; Nakagawa, T.; Hosomi, A. *Angew. Chem. Int. Ed.* **2000**, *39* (11), 1958. doi:10.1002/1521-3773(20000602)39:11<1958::AID-ANIE1958>3.0.CO;2-4.

(16) Fujisawa, H.; Takahashi, E.; Mukaiyama, T. *Chemistry* **2006**, *12* (19), 5082. doi:10.1002/chem.200500821.

() (17) In general, the anti-isomers generally feature smaller C*H*(NHTs)–C*H*(CH_3) *J* values and larger C*H*(N*H*Ts) *J* values. Also, the C*H*(CH_3), C*H*(NHTs), and CH(N*H*Ts) generally resonate at lower field in the anti-isomer than in the syn-isomer.

(18) Bernardi, A.; Cavicchioli, M.; Marchionni, C.; Potenza, D.; Scolastico, C. *J. Org. Chem.* **1994**, *59* (13), 3690. doi:10.1021/jo00092a033.

(19) Zimmerman, H. E.; Traxler, M. D. *J. Am. Chem. Soc.* **1957**, *79* (8), 1920. doi:10.1021/ja01565a041.

(20) Crimmins, M. T.; King, B. W.; Tabet, E. A. *J. Am. Chem. Soc.* **1997**, *119* (33), 7883. doi:10.1021/ja9716721.

(21) Itoh, Y.; Yamanaka, M.; Mikami, K. *J. Am. Chem. Soc.* **2004**, *126* (41), 13174. doi:10.1021/ja046518a.

(22) Tang, T. P.; Ellman, J. A. *J. Org. Chem.* **2002**, *67* (22), 7819. doi:10.1021/jo025957u.

(23) (a) Brun, L. *Acta Crystallogr.* **1966**, *20* (6), 739. doi:10.1107/S0365110X66001786;; (b) Bassi, I. W.; Calcaterra, M.; Intrito, R. *J. Organomet. Chem.* **1977**, *127* (3), 305. doi:10.1016/S0022-328X(00)98067-7.

(24) Ng, S. W.; Barnes, C. L.; Hossain, M. B.; Van der Helm, D.; Zuckerman, J. J.; Kumar Das, V. G. *J. Am. Chem. Soc.* **1982**, *104* (20), 5359. doi:10.1021/ja00384a019.

(25) Davis, F. A.; Qiu, H.; Song, M.; Gaddiraju, N. V. *J. Org. Chem.* **2009**, *74* (7), 2798. doi:10.1021/jo9001504.

Gold cellular networks inside water-soluble sodium alginate sol

Jishi Wei, Jianmao Yang, and Shuyan Gao

Can. J. Chem. Downloaded from www.nrcresearchpress.com by Renmin University of China on 09/02/12
For personal use only.

Abstract: The present work demonstrates the fabrication of unique gold cellular networks inside water-soluble sodium alginate sol. In conjunction with control experiments, UV–vis spectra and TEM images structurally give a piece of robust evidence that Au(III) and sodium alginate combined with preparation parameters synergically favor the formation of gold cellular networks. From the viewpoint of green chemistry, the cheap and safe reactant sodium alginate and the friendly aqueous medium make the present method possible for applications in large-scale production of metallic cellular networks. Thus, coupled with facile and green creation, the gold cellular networks open new opportunities for noble metal nanostructures, with different morphologies, as biological labels, energy transfer pairs, and other nanoscale electronics.

Key words: biopolymer, cellular network, gold.

Résumé : Dans ce travail, on présente une méthode de préparation de réseaux cellulaires uniques d'or à l'intérieur d'un sol d'alginate de sodium soluble dans l'eau. En relation avec des expériences de contrôle, les spectres UV–vis et les images obtenues par microscopie électronique à transmission (MET) donnent un appui de taille au fait que le Au(III) et l'alginate de sodium se combinent avec des paramètres de préparation qui favorisent par synergie la formation des réseaux cellulaires d'or. Du point de vue de la chimie verte, l'alginate de sodium peu dispendieux et facilement accessible et le milieu réaction aqueux écologiquement correct font que la présente méthode pourrait s'appliquer sans problème à la production à grande échelle de réseaux cellulaires métalliques. Les réseaux cellulaires d'or, qui peuvent être obtenus facilement et d'une façon écologiquement correcte, ouvrent donc de nouvelles possibilités pour la production de nanostructures de métaux nobles comportant des morphologies différentes qui pourraient être utilisés comme marqueurs biologiques, paires de transfert d'énergie et d'autres combinaisons électroniques à l'échelle nano.

Mots-clés : biopolymère, réseau cellulaire, or.

[Traduit par la Rédaction]

Introduction

Nanoparticles are nanometer-size materials with unique physical and chemical properties and have been widely used for many years.[1] Meanwhile, it has been well-demonstrated that their physical and chemical properties are closely related to their size and shape.[2,3] Therefore, there has been an increasing interest in developing new methods for fabricating shape-controlled nanoparticles. For example, Ag and Au with different shapes such as nanorods,[3,4] nanoplates,[5–12] nanodisks,[13–16] sponges,[17] three-dimensional (3D) thorny nanostructures,[18] and hollow microspirals[19] have been synthesized. However, the procedure for porous metallic nanostructures is still a great challenge for materials scientists, although nanomaterials with very abundant pores have become increasingly attractive in the area of materials science,[20] which is fueled by their use in catalysis, gas storage, and separation.[21,22]

Biopolymers belong to a class of materials that can swell largely in water other than organic solvents and maintain their 3D network structure on a nanometer length scale in the swollen state. This makes them have many potential applications including high-surface-area supports for catalysts, separation media, and templates for the synthesis of other nanoscopic materials, which undoubtedly motivates the preparation of nanostructural materials inside biopolymers.[23,24] In fact, a sol-gel-derived 3D network of nanoscale particles (aerogel/ambigel),[25] and a 3D (hierarchically) ordered macroporous (3DOM) solid with an inverted opal structure have already been created by a combination of sol-gel chemistry and templating.[26,27] Among biopolymers that are widely used is Sodium alginate is a biopolymer that is widely in use. It is a popular additive and naturally derived linear anionic copolymer of 1,4-linked β-D-mannuronic acid (M block) and α-L-guluronic acid (G block) residues arranged in a nonregular blockwise pattern of varying proportionsof GG, MG, and MM blocks.[28–31] The chemical structure of sodium alginate is shown in Scheme 1. The extensive number of carboxyl groups present in sodium alginate can make cross-linked hydrogels form in the presence of cations via an ionic interaction between the acid groups on the G blocks and the chelating ions, generally, Ca^{2+}.[32,33] As a result, it is plausible

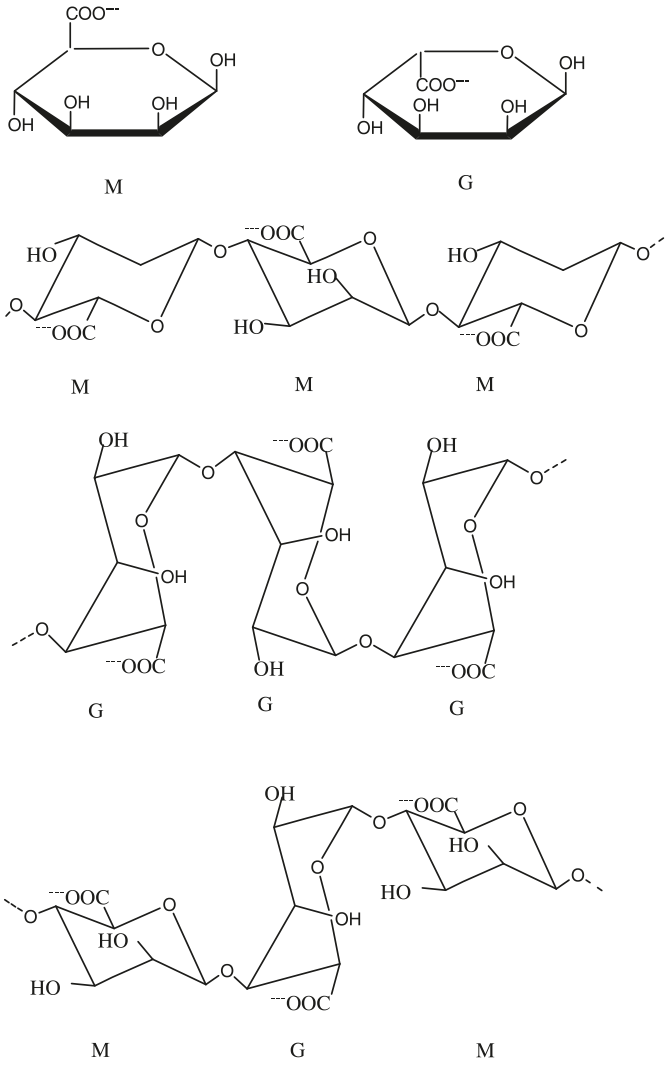
Received 13 February 2012. Accepted 13 April 2012. Published at www.nrcresearchpress.com/cjc on 6 June 2012.

J. Wei and S. Gao. College of Chemistry and Environmental Science, Henan Normal University, 46 Jianshe street, Xinxiang, 453007, Henan, P.R. China.
J. Yang. Research Center for Analysis and Measurement, Donghua University, Shanghai, 201620, P.R. China.

Corresponding author: Shuyan Gao (e-mail: shuyangao@htu.cn).

Can. J. Chem. Downloaded from www.nrcresearchpress.com by Renmin University of China on 09/02/12
For personal use only.

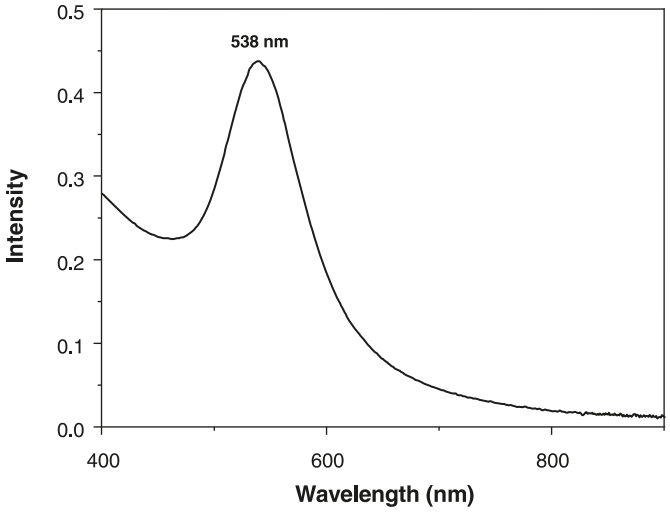
Scheme 1. Chemical structure units of sodium alginate (M = mannuronic acid and G = guluronic acid).



that Au(III) ions can play a significant role in guiding the supramolecular organization among sodium alginate sol, which results in the nanogold formation upon the reduction. That is to say, sodium alginate sol can act as nanoreactor to template and stabilize nanoparticles in the cross-linked system. However, little attention has been paid to the application of their cross-linked systems as nanoreactors.

In conjunction with the biocompatible nature and unique optical properties of gold nanoparticles, we report herein on the generation of gold cellular networks through the in situ reduction of the gold precursor existing inside the 3D network structure in sodium alginate sol. This bulky natural sodium alginate sol allows the stabilization of the porous nanostructues. UV–vis spectra and TEM images structurally witness the formation of gold cellular networks. Control experiments give a piece of robust evidence that Au(III) and the cheap and safe sodium alginate reactant combined with preparation parameters synerically favor the formation of gold cellular networks. Thus, coupled with facile and green creation, the gold cellular networks open new opportunities for noble metal nanostructures with different morphologies

Fig. 1. UV–vis absorption spectrum of the product.



as biological labels, energy transfer pairs, and other building blocks in nanoscale electronics.

Materials and methods

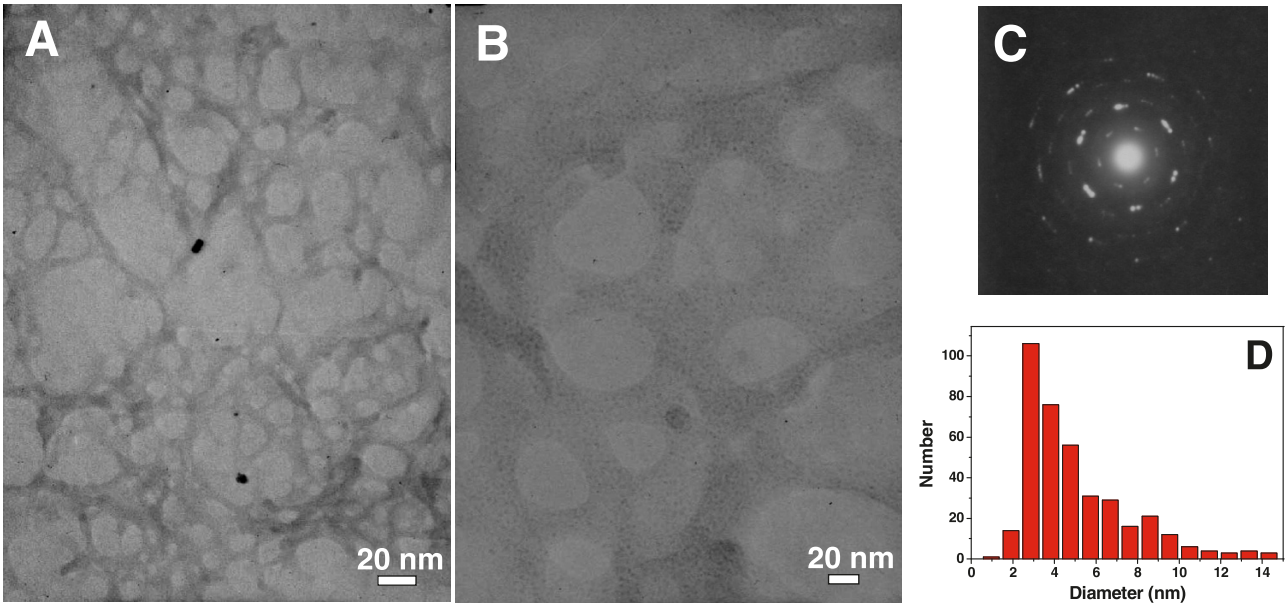
Sodium alginate was purchased from Sigma-Aldrich. All other reagents are of analytic grade and used as received without further purification. All water used in this investigation was deionized by a Nanopure filtration system to a resistivity of 18 MΩ cm. The preparation of gold cellular networks is quite straightforward. In a typical preparation, a 0.5 mL aliquot of a 0.0254 mol/L aqueous solution of $HAuCl_4$ was added to 10 mL of a 0.055% (wt) aqueous solution of soluble sodium alginate. The mixture was heated to 90 °C and was maintained at this temperature for 30 min. After the subsequent dropwise introduction of 0.2 mL of freshly prepared 0.1 mol/L aqueous sodium borohydride, the solution turned red, indicating the formation of gold nanoparticles. They were structurally investigated by UV–vis spectra, TEM images, selected area electron diffraction (SAED), and X-ray diffraction (XRD) to obtain detailed information on their nanometer-scale morphology. The UV–vis spectra were collected on a UV–vis spectrophotometer (Beijing Purkinje General Instrument Co., Ltd.). TEM and SAED measurements were made on a JEOL 2010 transmission electron microscope operated at an accelerating voltage of 200 kV. The XRD pattern was collected on a Rigaku-D/Max 2500 V/PC X-ray diffractometer using high-intensity Cu Kα1 radiation (λ = 1.54056 Å). Samples for TEM and XRD characterization were prepared by placing the gold colloidal sample on carbon-coated copper grid and glass substrates, respectively, and dried at room temperature.

Results and discussion

UV–vis absorption observations

The synthesis of gold cellular networks is carried out by the reduction of Au(III) to Au(0) in heated sodium alginate/$HAuCl_4$ aqueous solution. Gold nanoparticles exhibit strong plasmon resonance absorption that is dependent on particle size and shape. For roughly spherical gold nanoparticles, the fingerprint surface plasmon absorbance band generally falls

Fig. 2. Low magnification TEM Image (A), high magnification TEM image (B), SAED (C) of the gold cellular networks, and the size distribution (D).



between 520 and 530 nm.[27,34–36] The formation of gold colloid in our system was confirmed by the UV–vis spectrum, displaying a plasmon band maximum at 538 nm (2.31 eV) (shown in Fig. 1). The slight red shift to longer waves was observed for the sample, presumably stemming from the collective network behavior. It is worthwhile mentioning that the colloidal sample is stable for a month or longer without any observable aggregation, indicating that sodium alginate can serve as a very effective protective agent for the formation of gold colloid. There was quick color change from light yellow to purple, accompanied by the observable aggregation, for the control experiment with no sodium alignate in the solution performed. This simultaneously proved the protective agent role of sodium alginate in the formation of gold colloid.

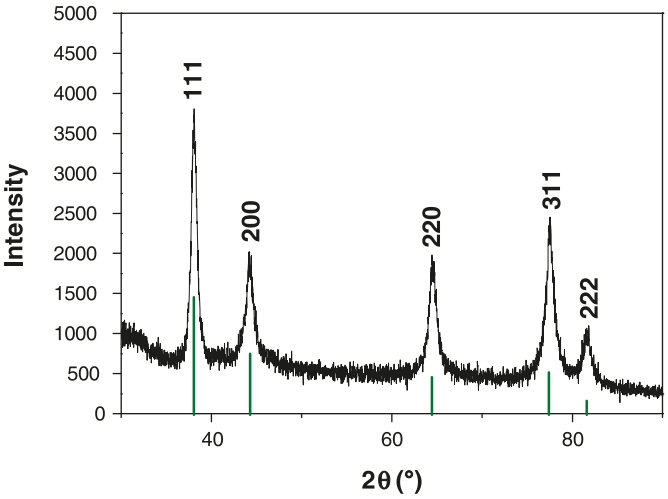
TEM measurements

Figure 2 shows the typical TEM images of the obtained gold cellular networks. The lower magnification image (Fig. 2A) indicates that the product consists of porous cellular networks. The higher magnification image (Fig. 2B) shows that the cellular networks are composed of discrete gold nanoparticles with average diameters of 3 nm. Figure 2D shows the size distributions. In general, the particles are isotropic (i.e., low aspect ratio) in shape. These results illustrate the synthesis of Au(0) nanoparticles through the reduction of Au(III) inside the cross-linked nanoscopic sodium alginate templates. The massive carboxyl groups act as stabilization and passivation contacts for the stabilization of the nanoparticles formed inside these templates. The related SAED pattern (Fig. 2C) obtained by focusing the electron beam on porous cellular networks on the TEM grid gives a piece of powerful evidence of the gold component. The SAED pattern reveals a ringlike pattern, suggesting that the gold nanoparticles are multicrystalline.

XRD measurement

Whereas SEM and TEM often sample only a small portion

Fig. 3. XRD pattern of the gold cellular networks. The vertical lines represent the data of JPCDS file, card No. 04-0784.



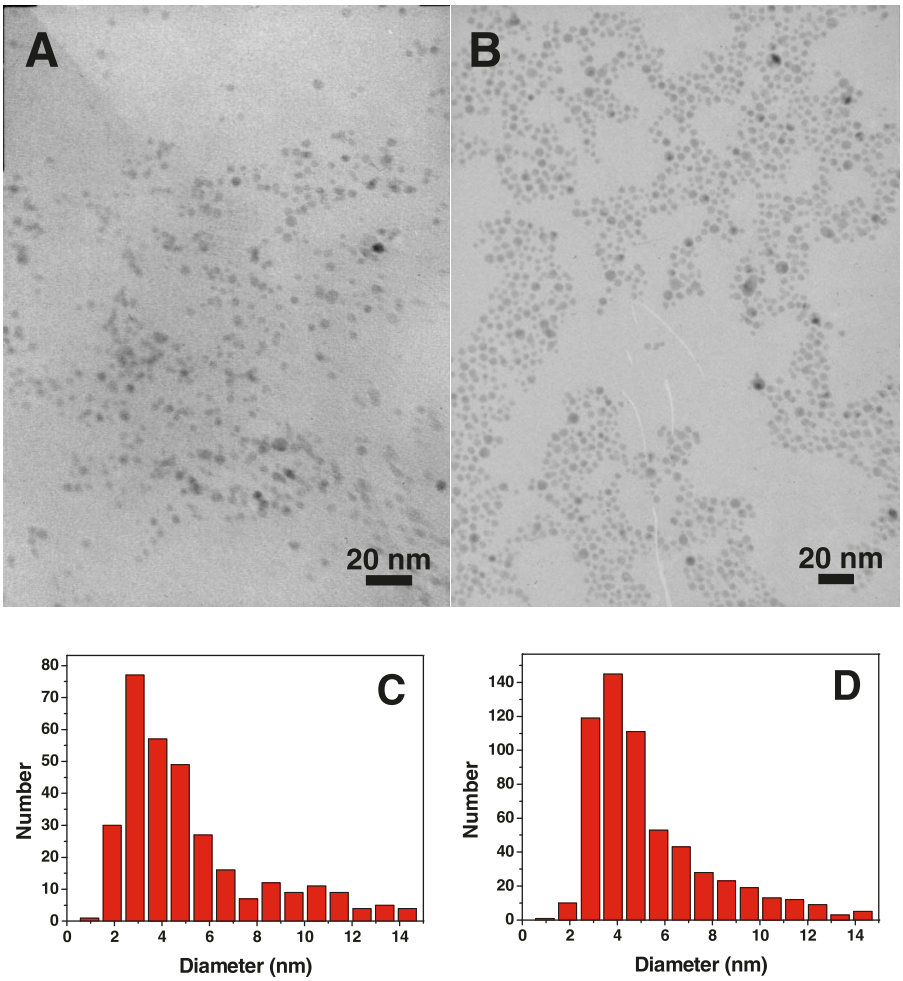
of the products, XRD can be used to assess the overall quality and purity of the product.[37] The XRD pattern recorded on the product is compiled in Fig. 3. The observed five Bragg reflections clearly correspond to the face-centered cubic structure of metallic gold with space group *Fm*3*m* (JPCDS file, card No. 04-0784). The observation of all the expected diffraction peaks substantiates the formation of crystalline gold.[38] The nanometer size of the gold crystallites is evidenced by the broad X-ray reflection peaks. From the well-known Scherrer formula, the average crystallite size (L) is

$$L = \frac{K\lambda}{B_m \cos\theta}$$

where λ is the X-ray wavelength, θ is the diffraction angle, B_m is the line width of the "pure" diffraction profile resulting from small crystallite size, and K is a constant approximately

Can. J. Chem. Downloaded from www.nrcresearchpress.com by Renmin University of China on 09/02/12
For personal use only.

Fig. 4. Representative TEM images when the reaction temperature is changed to room temperature (A) and to 50 °C (B) under the otherwise identical conditions and the corresponding size distributions: C from A and D from B.



Can. J. Chem. Downloaded from www.nrcresearchpress.com by Renmin University of China on 09/02/12
For personal use only.

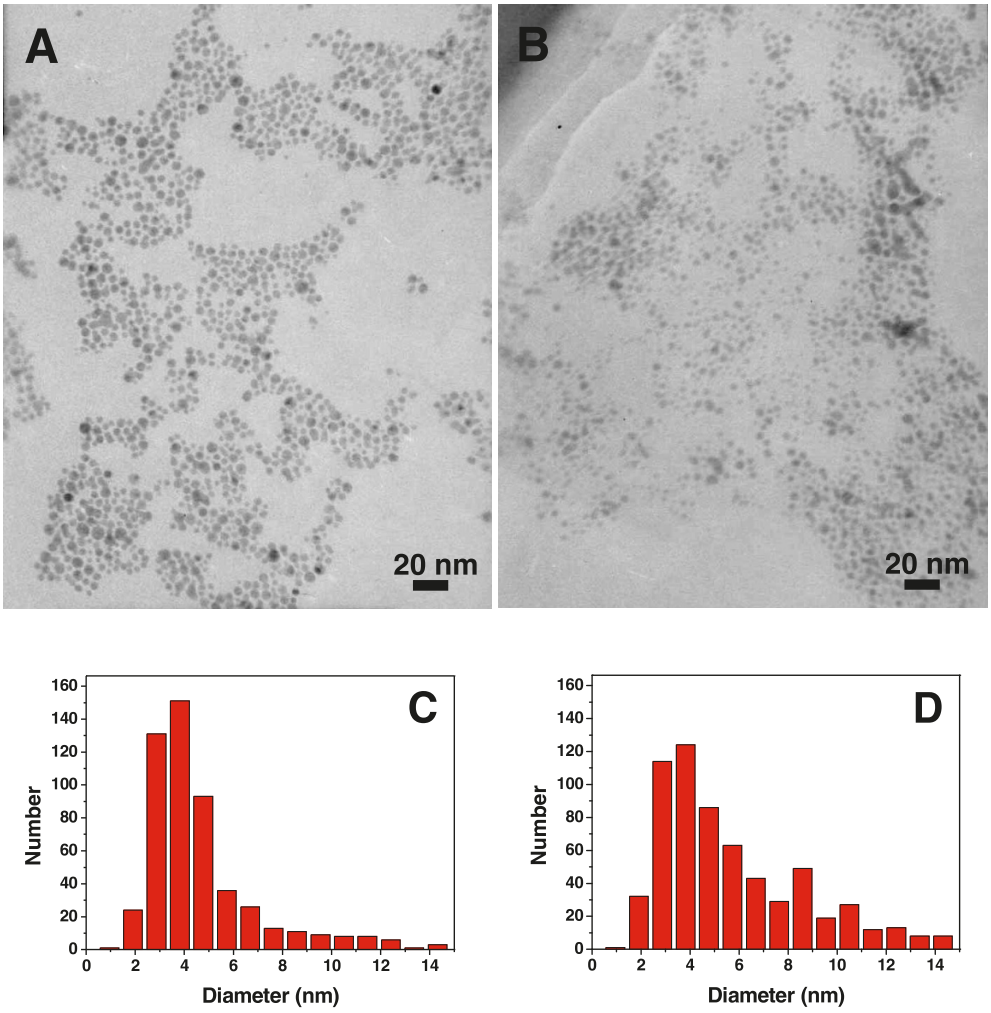
equal to unity and related to crystallite shape. According to the Scherrer formula, the average crystallite size of gold cellular networks is 5 nm, which is consistent with that calculated from the TEM images.

Control experiments

To clarify the effect of the reaction temperatures on the special morphology of the product, we conducted experiments by changing the reaction temperature to room temperature and 50 °C under otherwise identical conditions. The TEM image (Fig. 4) indicates that the particles invariably show 2D arrays consisting of close-packed and well-separated spherical particles, with an average particle size of 3.7 nm (Fig. 4A) and 4 nm (Fig. 4B), respectively. This indicates that the gold nanoparticles are capped by sodium alginate, which prevents physical contact between the particles and also provides sufficient hydrophobicity to the gold nanoparticles to enable their dispersion in water. More importantly, it suggests that the reaction temperature plays a vital role in the formation of cellular networks. This is presumably attributed to its well-stretched state resulting from heating treatment. The stretched state offers enough space for metal ions to approach carboxyl, thus facilitating the cross-linked system and the nanoparticles more stable. By this token, heat treatment in the present case is employed not only to increase the reaction velocity and narrow the particle-size distributions,[39] but also for the formation of the cross-linked system. This is a distinct feature superior to conventional stabilizers.

To make clear the role of the reactant concentrations in the formation of the porous networks, we also investigated the effect of the molar ratios of sodium alginate to Au on the morphology of the product, whereby we conducted the experiment by changing the molar ratio of sodium alginate / $HAuCl_4$ to 10:1 and 1:1 under otherwise identical conditions. The TEM image (Fig. 5) indicates that the particles also invariably show 2D arrays consisting of close-packed and well-separated spherical particles, with the average particle size of 4 nm (Fig. 5A) and 6.4 nm (Fig. 5B), respectively. This likewise indicates that the gold nanoparticles are capped by sodium alginate, which prevents physical contact between the particles and also provides sufficient hydrophobicity to the gold nanoparticles to enable their dispersion in water. The disappearance of cellular networks under the present conditions suggests that the molar ratios of sodium alginate to Au have evident effect on the formation of cellular networks. This is presumably attributed to the fact that the biopolymers swell enough to form the cross-linked system

Fig. 5. Representative TEM images when the molar ratios of sodium alginate/$HAuCl_4$ are changed to 1:1 (A) and 10:1 (B) under the otherwise identical conditions and the corresponding size distributions: C from A and D from B.



Can. J. Chem. Downloaded from www.nrcresearchpress.com by Renmin University of China on 09/02/12
For personal use only.

through metal ions bridging only at an appropriate concentration.

Conclusion

In conclusion, the results from UV-vis absorption spectra, TEM images,and XRD are in agreement, and provide robust evidence to support the successful fabrication of gold cellular networks. The cheap and safe of sodium alginate reactant combined with easy control of preparing parameters makes the present method possible for applications in large-scale production of metallic cellular networks. Control experiments show that both the reaction temperatures and reactant concentrations play a vital role in the formation of the cellular networks. Intense work aimed at supporting this sol-template-controlled synthesis strategy for other porous systems, particularly for nanomagnets is in progress.

A key issue in nanotechnology is the development of conceptually simple construction techniques for the mass fabrication of identical nanoscale structures. The present approach relies on the exploitation of specific cross-linking interactions between biopolymer and metal ions and is one of the key building principles of all living organisms. It is thus obvious to search for more biological structures that can be used as templates for directing and perfecting the self-assembly.[40]

Acknowledgement

This work was supported by the National Natural Science Foundation of China (Grant No. 21071047), the Program for New Century Excellent Talents in University (Grant No. NCET-11–0944), the Project Sponsored by the Scientific Research Foundation for the Returned Overseas Chinese Scholars, State Education Ministry of China, the Excellent Youth Foundation of He'nan Scientific Committee, and the Program for Science & Technology Innovation Talents in Universities of Henan Province (Grant No. 2011HASTIT010).

References

(1) Zhou, Y.; Yu, S. H.; Wang, C. Y.; Li, X. G.; Zhu, Y. R.; Chen, Z. Y. *Adv. Mater. (Deerfield Beach Fla.)* **1999**, *11* (10), 850. doi:10.1002/(SICI)1521-4095(199907)11:10<850::AID-ADMA850>3.0.CO;2-Z.

(2) Shao, L.; Fang, C. H.; Chen, H. J.; Man, Y. C.; Wang, J. F.; Lin, H.-Q. *Nano Lett.* **2012**, *12* (3), 1424. doi:10.1021/nl2041063.

(3) Chen, H. J.; Shao, L.; Ming, T.; Woo, K. C.; Man, Y. C.;

Wang, J. F.; Lin, H.-Q. *ACS Nano* **2011**, *5* (8), 6754. doi:10.1021/nn202317b.
(4) Edgar, J.; McDonagh, A. M.; Cortie, M. B. *ACS Nano* **2012**, *6* (2), 1116. doi:10.1021/nn203586j.
(5) Lee, B. H.; Hsu, M. S.; Hsu, Y. C.; Lo, C. W.; Huang, C. L. *J. Phys. Chem. C* **2010**, *114* (14), 6222. doi:10.1021/jp910100k.
(6) Yener, D. O.; Sindel, J.; Randall, C. A.; Adair, J. H. *Langmuir* **2002**, *18* (22), 8692. doi:10.1021/la011229a.
(7) Chen, S.; Carroll, D. L. *Nano Lett.* **2002**, *2* (9), 1003. doi:10.1021/nl025674h.
(8) Wang, F.; Ni, Y.; Ge, X.; Zhang, Z. *Chem. Lett.* **2002**, *31* (2), 196. doi:10.1246/cl.2002.196.
(9) Malikova, N.; Pastoriza-Santos, I.; Schierhorn, M.; Kotov, N. A.; Liz-Marzan, L. M. *Langmuir* **2002**, *18* (9), 3694. doi:10.1021/la025563y.
(10) Tsuji, M.; Hashimoto, M.; Nishizawa, Y.; Tsuji, T. *Chem. Lett.* **2003**, *32* (12), 1114. doi:10.1246/cl.2003.1114.
(11) Shao, Y.; Jin, Y.; Dong, S. *Chem. Commun. (Camb.)* **2004**, (9): 1104. doi:10.1039/b315732f.
(12) Sun, X.; Dong, S.; Wang, E. *Angew. Chem. Int. Ed.* **2004**, *43* (46), 6360. doi:10.1002/anie.200461013.
(13) Chen, S.; Fan, Z.; Carroll, D. L. *J. Phys. Chem. B* **2002**, *106* (42), 10777. doi:10.1021/jp026376b.
(14) Maillard, M.; Giorgio, S.; Pileni, M.-P. *Adv. Mater. (Deerfield Beach Fla.)* **2002**, *14* (15), 1084. doi:10.1002/1521-4095(20020805)14:15<1084::AID-ADMA1084>3.0.CO;2-L.
(15) Hao, E.; Kelly, K. L.; Hupp, J. T.; Schatz, G. C. *J. Am. Chem. Soc.* **2002**, *124* (51), 15182. doi:10.1021/ja028336r.
(16) Simakin, A. V.; Voronov, V. V.; Shafeev, G. A.; Brayner, R.; Bozon-Verduraz, F. *Chem. Phys. Lett.* **2001**, *348* (3–4), 182. doi:10.1016/S0009-2614(01)01136-8.
(17) Gao, S.; Zhang, H.; Wang, X.; Yang, J.; Zhou, L.; Peng, C.; Sun, D.; Li, M. *Nanotechnology* **2005**, *16* (11), 2530. doi:10.1088/0957-4484/16/11/012.
(18) Yuan, H.; Ma, W.; Chen, C.; Zhu, H.; Gao, X.; Zhao, J. *J. Phys. Chem. C* **2011**, *115* (47), 23256. doi:10.1021/jp205565y.
(19) Zhang, X.; Yu, M.; Liu, J.; Li, S. *Langmuir* **2012**, *28* (8), 3690. doi:10.1021/la204370x.
(20) Shin, H. C.; Liu, M. *Chem. Mater.* **2004**, *16* (25), 5460. doi:10.1021/cm048887b.
(21) Zhang, Y.; Cui, X.; Shi, F.; Deng, Y. *Chem. Rev.* **2012**, *112* (4), 2467. doi:10.1021/cr200260m.
(22) Férey, G. *Science* **2001**, *291* (5506), 994. doi:10.1126/science.1059200.
(23) Zhou, Y. *Curr. Nanosci.* **2006**, *2* (2), 123. doi:10.2174/157341306776875785.
(24) Zhou, Y. *Curr. Nanosci.* **2005**, *1* (81), 35. doi:10.2174/1573413052953174.
(25) Long, J. W.; Rhodes, C. P.; Young, A. L.; Rolison, D. R. *Nano Lett.* **2003**, *3* (8), 1155. doi:10.1021/nl0343598.
(26) Sakamoto, J. S.; Dunn, B. *J. Mater. Chem.* **2002**, *12* (10), 2859. doi:10.1039/b205634h.
(27) Poeppelmeier, K. R.; Barry, S. J.; Sorensen, E. M. Presented at the 204th Electrochemical Society Meeting, 2003; Electrochemical Society: Pennington, NJ, 2004; Abs. 1289.
(28) Haug, A.; Larsen, B.; Smidsrød, O.; Smidsrød, O.; Eriksson, G.; Blinc, R.; Paušak, S.; Ehrenberg, L.; Dumanović, J. *Acta Chem. Scand.* **1967**, *21*, 691. doi:10.3891/acta.chem.scand.21-0691.
(29) Martinsen, A.; Skjåk-Braek, G.; Smidsrød, O. *Biotechnol. Bioeng.* **1989**, *33* (1), 79. doi:10.1002/bit.260330111.
(30) Gombotz, W. R.; Wee, S. F. *Adv. Drug Deliv. Rev.* **1998**, *31* (3), 267. doi:10.1016/S0169-409X(97)00124-5.
(31) Moe, S. T.; Draget, K. I.; Skjak-Braek, G.; Smidsrod, O. In *Food Polysaccharides and Their Applications;* Stephen, A. M., Ed.; Marcel Dekker: New York, 1995; Vol. 67, p 245.
(32) Eiselt, P.; Yeh, J.; Latvala, R. K.; Shea, L. D.; Mooney, D. J. *Biomaterials* **2000**, *21* (19), 1921. doi:10.1016/S0142-9612(00)00033-8.
(33) Grant, G. T.; Morris, E. R.; Rees, D. A.; Smith, P. J. C.; Thom, D. *FEBS Lett.* **1973**, *32* (21), 195. doi:10.1016/0014-5793(73)80770-7.
(34) Jana, N. R.; Gearheart, L.; Murphy, C. J. *Langmuir* **2001**, *17* (22), 6782. doi:10.1021/la0104323.
(35) Jana, N. R.; Gearheart, L.; Murphy, C. J. *Chem. Mater.* **2001**, *13* (7), 2313. doi:10.1021/cm000662n.
(36) Shimizu, T.; Teranishi, T.; Hasegawa, S.; Miyake, M. *J. Phys. Chem. B* **2003**, *107* (12), 2719. doi:10.1021/jp026920g.
(37) Kim, F.; Connor, S.; Song, H.; Kuykendall, T.; Yang, P. *Angew. Chem. Int. Ed.* **2004**, *43* (28), 3673. doi:10.1002/anie.200454216.
(38) Gao, S.; Zhang, H.; Liu, X.; Wang, X.; Ge, L. *J. Colloid Interface Sci.* **2006**, *293* (2), 409. doi:10.1016/j.jcis.2005.06.077.
(39) Fan, H.; Yang, K.; Boye, D. M.; Sigmon, T.; Malloy, K. J.; Xu, H.; López, G. P.; Brinker, C. J. *Science* **2004**, *304* (5670), 567. doi:10.1126/science.1095140.
(40) Knez, M.; Bittner, A. M.; Boes, F.; Wege, C.; Jeske, H.; Maiβ, E.; Kern, K. *Nano Lett.* **2003**, *3* (8), 1079. doi:10.1021/nl0342545.

Can. J. Chem. Downloaded from www.nrcresearchpress.com by Renmin University of China on 09/02/12
For personal use only.

Decomposition of copper – amino acid complexes by oxalic acid dihydrate

Yi Liu, Genguang Jia, Xin Ling, Nuo Lan, Youguang Zheng, Sai Li, Ling Zhang, Ling Liu, Rongli Zhang, and Yunsheng Xue

Can. J. Chem. Downloaded from www.nrcresearchpress.com by Renmin University of China on 09/02/12
For personal use only.

Abstract: A facile approach to the synthesis of some side-chain-protected amino acids via oxalic acid dihydrate as the copper sequestering reagent is presented. The copper in the amino acid complex reacted with oxalic acid dihydrate to form insoluble cupric oxalate, with the free amino acid released. Compared with conventional methods, this method is convenient, inexpensive, and environmentally friendly.

Key words: side-chain-protected amino acid, oxalic acid dihydrate, cupric oxalate, synthesis.

Résumé : On a mis au point une approche simple à la synthèse des divers acides aminés à chaîne latérale protégée impliquant le dihydrate de l'acide oxalique comme réactif de séquestration de du cuivre. Le cuivre du complexe avec l'acide aminé réagit avec le dihydrate de l'acide oxalique pour former l'oxalate cuivrique insoluble et la libération de l'acide aminé libre. Par comparaison avec les autres méthodes conventionnelles, cette méthode est pratique, peu coûteuse et écologique.

Mots-clés : acide aminé à chaîne latérale protégée, dihydrate de l'acide oxalique, oxalate cuivrique, synthèse.

[Traduit par la Rédaction]

Introduction

Since the emergence of glycylglycine synthesis from a diketopiperazine by Fischer and Fourneau[1] in 1901, peptide synthesis has undergone tremendous progress and it is now possible to routinely synthesize a protein consisting of over 200 amino acids. However, when the amino acids involved are trifunctional, such as lysine, ornithine, etc., it is necessary to protect their side-chain functional groups. This is accomplished by first reacting the primary amino acids with cupric ions to form the stable chelate complex, followed by a reaction with acylation reagents to facilitate selective protection of the side-chain functional group.

To recover the side-chain-protected amino acids, it is necessary to decompose the copper – amino acid complexes, for which several methods are available involving several important reagents including EDTA,[2,3] potassium cyanide,[4] 8-quinolinol,[5] hydrogen sulfide,[6,7] thioacetamide,[8] sodium borohydride,[9] and sodium sulfide.[10] EDTA is one of the most widely employed copper-sequestering reagents. However, the resultant copper–EDTA complex during the course of the reaction is water-soluble, which can lead to effluent problems with the water-soluble side-chain-protected amino acids. When copper is removed from the complexes using KCN, H_2S, or thioacetamide, there is a marked drawback in that these reagents are highly toxic and, thioacetamide in particular, is a potential cancer-causing chemical. When copper is removed from the complexes employing 8-quinolinol, there is a low yield of protected amino acids, with the cost greatly increased. Similarly, in the case of copper removal using sodium borohydride, issues such as heat generation during bulk production of protected amino acids also result. Despite the fact that recent research has confirmed the efficiency of sodium sulfide in the detachment of copper from the complexes, its serious hazards to the environment are noteworthy.

Given the limitations of the methods concerning the copper(II) deprotection discussed previously, it is difficult to realize the industrialization. Several studies have shown that oxalic acid can be preferable for its inexpensiveness and friendliness to the environment and can form complexes with copper.[11–13] In this paper, we report a highly convenient and efficient method in which oxalic acid dihydrate is employed to detach the copper(II) complexes, to prepare the side-chain amino-protected acetyl, Boc, Fmoc, and Z (benzyloxy carbonyl) ornithines,and lysines, respectively.

Results and discussion

The behavior of copper in oxalic acid solutions has been well-studied. The results have shown that copper ions with oxalate can easily form complexes; however, the complexation ability in the solution depends on pH (1–1.5).[13] In continuation of our efforts towards the decoppering reaction, we employed oxalic acid dihydrate to sequester copper from the copper – amino acid complexes. In general, cupric oxalate is insoluble in water or diluted hydrochloric acid. To accelerate

Received 9 February 2012. Accepted 20 April 2012. Published at www.nrcresearchpress.com/cjc on 6 June 2012.

Y. Liu,* G. Jia,* X. Ling, N. Lan, Y. Zheng, S. Li, L. Zhang, L. Liu, R. Zhang, and Y. Xue. School of Pharmacy, Xuzhou Medical College, 84 West Huaihai Road, Xuzhou, 221002 Jiangsu, P.R. China.

Corresponding author: Yi Liu (e-mail: cbpe200902@163.com).

*Yi Liu and Genguang Jia are co-first authors.

Can. J. Chem. Downloaded from www.nrcresearchpress.com by Renmin University of China on 09/02/12
For personal use only.

Table 1. Preparation of the side-chain-protected amino acids.

Entry	Product[a]		Yield (%)	Purity (%)
1	H-Orn(Z)-OH	**a**	70	98.5
2	H-Orn(Fmoc)-OH	**b**	65	98.3
3	H-Orn(acetyl)-OH	**c**	78	97.9
4	H-Lys(Z)-OH	**d**	74	98.8
5	H-Lys(Fmoc)-OH	**e**	69	97.7
6	H-Lys(acetyl)-OH	**f**	65	98.0
7	H-Orn(Boc)-OH	**g**	59	97.1
8	H-Lys(Boc)-OH	**h**	63	96.9

[a]All compounds were characterized by ^{1}H NMR and elemental analysis.

the reaction, diluted hydrochloric acid was selected as the vehicle, with the concentrations of the acid investigated. It was observed that, with the acid maintained at a concentration of 0.01 mol/L, the method for the removal of copper ions by oxalic acid dihydrate was effective and could completely eradicate the sulfide problem during the course of the reaction (the pH of the solutions is ~1.1). The results in Table 1 show that the oxalic acid dihydrate-mediated detachment of copper ions from all the copper amino acid complexes resulted in protected amino acids of high purity with no racemization.

The copper complexes of the following amino acids were prepared in accordance with the methods in literature: N^{ε}-Boc–lysine,[14] N^{δ}-Boc–ornithine,[15] N^{ε}-*Z*–lysine, N^{δ}-*Z*–ornithine,[8] N^{ε}-Fmoc–lysine, N^{δ}-Fmoc–ornithine,[16] N^{δ}-acetyl–ornithine, and N^{ε}-acetyl–lysine.[17]

The copper – amino acid complexes were treated with oxalic acid dihydrate in diluted hydrochloric acid for 1–2 h at 80 °C to afford side-chain-protected amino acids **a**–**j** in yields of 55%–80% (Scheme1 and Table 1). The isolated products were characterized by ^{1}H NMR and elemental analyses.

Conclusion

In conclusion, we have confirmed that oxalic acid dihydrate is a useful reagent in removing copper from amino acid copper complexes during the preparation of several side-chain-protected amino acids. This method may also be applicable to bulk production of side-chain-protected amino acids.

Experimental

Melting points were measured in open capillaries and are uncorrected. Optical rotations were measured on a PerkinElmer model 341 automatic polarimeter. Elemental analysis was performed on a PerkinElmer CHNS analyzer. ^{1}H NMR spectra were recorded in CD_3SOCD_3 on a Bruker Avance 500 spectrometer; chemical shifts (δ) are reported in parts per million (ppm) relative to tetramethylsilane (TMS), serving as an internal standard. Solvents and reagents were purchased from respective suppliers and used without further purification.

General procedure for the preparation of side-chain-protected amino acids a–h

To dissolve the copper – amino acid complex (10.0 mmol) in a capped flask at ambient temperature, diluted hydrochloric acid (30 mL, 0.01 mol/L) was added, followed by the addition of oxalic acid dihydrate (10.3 mmol), and the resulting mixture was stirred at 80 °C (the pH of the solutions was ~1.1 at this time). At the end of stirring for 1–3 h, the consequent cupric oxalate precipitate was filtered. The filtrate was neutralized with dilute NaOH. The resulting precipitate was isolated by filtration and then rinsed with distilled water (50 mL × 4) to obtain the side-chain-protected amino acids **a**–**f**. The water-soluble products (**g**–**h**) were isolated by the removal of the solvent and extraction of the residue with acetone.

H-Orn (*Z*)-OH (compound a)

White crystals (70%), mp 248–250 °C, $[\alpha]_D^{20}$ +17.6° (lit.[18] mp 228–230 °C, $[\alpha]_D^{20}$ +17.5°, *c* 0.01, water/acetone = 1:1, and equal volumes of hydrochloric acid). ^{1}H NMR δ: 7.35–7.45 (m, 5H, Ar-H), 5.08 (s, 2H, Ar–CH_2), 3.37–3.44 (m, 1H, α-H), 3.19–3.23 (m, 2H, δ-H), 1.81–1.86 (m, 2H, γ-H), 1.65–1.70 (m, 2H, β-H). Anal. calcd for $C_{13}H_{18}N_2O_4$: C 58.63, H 6.81, N 10.52; found: C 58.57, H 6.84, N 10.48.

H-Orn (Fmoc)-OH (compound b)

White crystals (65%), mp 151–153 °C (lit.[19] mp 152–154 °C). ^{1}H NMR δ: 3.41–3.46 (m, 1H, α-H), 3.17–3.23 (m, 2H, δ-H), 1.78–1.84 (m, 2H, γ-H), 1.61–1.67 (m, 2H, β-H), 4.53–4.69 (m, 2H, $COOCH_2$), 4.31–4.37 (m, 1H, Fmoc-9H), 7.29–7.80 (m, 8H, Ar-H). Anal. calcd for $C_{20}H_{22}N_2O_4$: C 67.76, H 6.26, N 7.91; found: C 67.83, H 6.31, N 7.87.

H-Orn (Acetyl)-OH (compound c)

White crystals (78%), mp 246–249 °C (lit.[20] mp 248–250 °C). ^{1}H NMR δ: 3.38~3.45 (m, 1H, α-H), 3.18–3.24 (m, 2H, δ-H), 1.81–1.87 (m, 2H, γ-H), 1.58–1.65 (m, 2H, β-H), 2.01 (s, 3H, CH_3). Anal. calcd for $C_7H_{14}N_2O_3$: C 48.27, H 8.01, N 16.08; found: C 48.20, H 8.09, N 16.01.

H-Lys (Z)-OH (compound d)

White crystals (74%), mp 245–248 °C (lit.[8] mp 250 °C). ^{1}H NMR δ: 7.31–7.68 (m, 5H, Ar-H), 5.11 (s, 2H, Ar-CH_2), 3.13–3.22 (m, 2H, ε-H), 3.41–3.46 (m, 1H, α-H), 1.77–1.82 (m, 2H, β-H), 1.38–1.45 (m, 2H, γ-H), 1.57–1.64 (m, 2H, δ-H). Anal. calcd for $C_{14}H_{20}N_2O_4$: C 59.99, H 7.19, N 9.99; found: C 59.90, H 7.24, N 10.00.

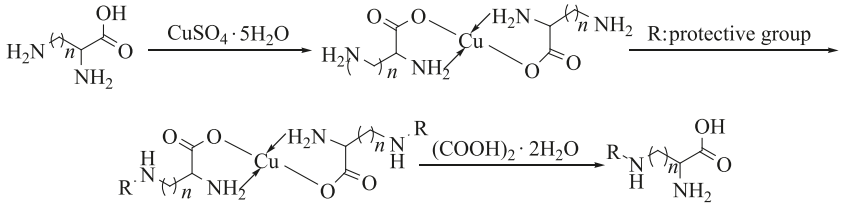
H-Lys (Fmoc)-OH (compound e)

White crystals (69%), mp 209–210 °C (lit.[19] mp 210–212 °C). ^{1}H NMR δ: 3.41–3.47 (m, 1H, α-H), 3.17–3.24 (m, 2H, ε-H), 1.32–1.39 (m, 2H, γ-H), 1.51–1.59 (m, 2H, δ-H), 1.79–1.85 (m, 2H, β-H), 4.74 (d, J = 3.21 Hz, 2H, OCH_2), 4.42 (t, J = 3.21 Hz, 1H, Fmoc-9H), 7.26~7.80 (m, 8H, Ar-H). Anal. calcd for $C_{21}H_{24}N_2O_4$: C 68.46, H 6.57, N 7.60; found: C 68.38, H 6.49, N 7.67.

H-Lys (Acetyl)-OH (compound f)

White crystals (65%), mp 245–249 °C (dec). ^{1}H NMR δ: 3.40–3.46 (m, 1H, α-H), 3.18–3.22 (m, 2H, ε-H), 1.30–1.38 (m, 2H, γ-H), 1.53–1.61 (m, 2H, δ-H); 1.73–1.85 (m, 2H, β-H), 2.00 (s, 3H, CH_3). Anal. calcd for $C_8H_{16}N_2O_3$: C 51.05, H 8.57, N 14.88; found: C 51.00, H 8.64, N 14.77.

Scheme 1.



a, H-Orn(Z)-OH: R=Z, *n*=3
b, H-Orn(Fmoc)-OH: R=Fmoc, *n*=3
c, H-Orn(Acetyl)-OH: R=Acetyl, *n*=3
g, H-Orn(Boc)-OH: R=Boc, *n*=3
d, H-Lys(Z)-OH: R=Z, *n*=4
e, H-Lys(Fmoc)-OH: R=Fmoc, *n*=4
f, H-Lys(Acetyl)-OH: R=Acetyl, *n*=4
h, H-Lys(Boc)-OH: R=Boc, *n*=4

H-Orn (Boc)-OH (compound g)

White crystals (59%), mp 210–213 °C, $[\alpha]_D^{20}$ +15.5° (lit.[21] mp 209.75 °C, $[\alpha]_D^{20}$ +15.2°,[17] *c* 1.0, acetic acid). ^{1}H NMR δ: 3.35–3.46 (m, 1H, α-H), 3.19–3.25 (m, 2H, δ-H), 1.81–1.92 (m, 2H, γ-H), 1.58–1.65 (m, 2H, β-H), 1.44 (s, 9H, 3 × CH_3). Anal. calcd for $C_{10}H_{20}N_2O_4$: C 51.71, H 8.68, N 12.06; found: C 51.66, H 8.60, N 12.11.

H-Lys (Boc)-OH (compound h)

White crystals (63%), mp 247–249 °C, $[\alpha]_D^{20}$ +17.1° (*c* 1, acetic acid). ^{1}H NMR δ: 3.37–3.44 (m, 1H, α-H), 3.14–3.21 (m, 2H, ε-H), 1.32–1.38 (m, 2H, γ-H), 1.50–1.58 (m, 2H, δ-H), 1.78–1.84 (m, 2H, β-H), 1.39 (s, 9H, 3 × CH_3). Anal. calcd for $C_{11}H_{22}N_2O_4$: C 53.64, H 9.00, N 11.37; found: C 53.70, H 8.95, N 11.33.

Acknowledgements

The authors are cordially indebted to these financial supports: "Qing-Lan" Project of Jiangsu Province, the Industrialization of Scientific Research Promotion Projects of Universities and Colleges in Jiangsu Province (Grant No. 2011-16), the Natural Science Fund for Universities and Colleges in Jiangsu Province (11KJB350005), the Project of Provincial Key Laboratory in Universities in Jiangsu Province (Grant Nos. JSBL0803, C0903, and C0904), the Science and Technology Plan Projects of Xuzhou (Grant Nos. XF11C037, XF11C062, and XF11C065), the Superiority Academic Discipline Construction Project of Jiangsu Higher Education Institutions, and the Six-Major-Talent-Summit Project of Jiangsu Province.

References

(1) Fischer, E.; Fourneau, E. *Ber. Dtsch. Chem. Ges.* **1901**, *34*, 2868. doi:10.1002/cber.190103402249.
(2) Zaoral, M. *Collect. Czech. Chem. Commun.* **1965**, *30*, 1853.
(3) Kuwta, S.; Watanabe, H. *Bull. Chem. Soc. Jpn.* **1965**, *38* (4), 676. doi:10.1246/bcsj.38.676.
(4) Zahn, H.; Zuber, H.; Ditscher, W.; Wegerle, D.; Meienhofer, J. *Chem. Ber.* **1956**, *89* (2), 407. doi:10.1002/cber.19560890234.
(5) Wiejak, S.; Masiukiewiez, E.; Rzeszotarska, B. *Chem. Pharm. Bull. (Tokyo)* **2001**, *49* (9), 1189. doi:10.1248/cpb.49.1189.
(6) Roeske, R.; Stewart, F. H. C.; Stedman, R. J.; Du Vigneaud, V. *J. Am. Chem. Soc.* **1956**, *78* (22), 5883. doi:10.1021/ja01603a047.
(7) Synge, R. L. M. *Biochem. J.* **1948**, *42*, 99.
(8) Taylor, U. F.; Dyckes, D. F.; Cox, J. R., Jr. *Int. J. Pept. Protein Res.* **1982**, *19* (2), 158. doi:10.1111/j.1399-3011.1982.tb02604.x.
(9) Sailaja, G.; Nowshuddin, S.; Rao, M. N. A. *Tetrahedron Lett.* **2004**, *45* (50), 9297. doi:10.1016/j.tetlet.2004.10.060.
(10) Nowshuddin, S.; Reddy, A. R. *Tetrahedron Lett.* **2006**, *47* (29), 5159. doi:10.1016/j.tetlet.2006.05.069.
(11) Gorantla, V. R. K.; Babel, A.; Pandija, S.; Babu, S. V. *Electrochem. Solid-State Lett.* **2005**, *8* (5), G131. doi:10.1149/1.1883873.
(12) Aksu, S. *J. Electrochem. Soc.* **2005**, *152* (12), G938. doi:10.1149/1.2121737.
(13) Liu, C. H.; Yang, T. Z.; Bin, W. D.; Pan, C. Q. *Hydrometallurgy of China* **1999**, *3*, 23.
(14) Scott, J. W.; Parker, D. R.; Parrish, D. R. *Synth. Commun.* **1981**, *11* (4), 303. doi:10.1080/00397918108063610.
(15) Wünsch, E.; Fries, G.; Zwick, A. *Chem. Ber.* **1958**, *91* (3), 542. doi:10.1002/cber.19580910312.
(16) Younghee, L.; Richerd, B. S. *Synthesis* **1999**, 1495.
(17) Neuberger, A.; Sanger, F. *Biochem. J.* **1943**, *37*, 515.
(18) Johansson, J.; Alto, P.; Skinner, W. A.; Valley, P. US Patent 3,754,027, 1973.
(19) Henczi, M.; Weaver, D. F. *Org. Prep. Proced. Int.* **1994**, *26* (5), 578. doi:10.1080/00304949409458061.
(20) Oka, Y.; Ogawa, T.; Sasaoka, K. *J. Nutr. Sci. Vitaminol. (Tokyo)* **1984**, *30* (1), 27. doi:10.3177/jnsv.30.27.
(21) Wiejak, S.; Masiukiewicz, E.; Rzeszotarska, B. *Chem. Pharm. Bull. (Tokyo)* **2001**, *49* (9), 1191. doi:10.1248/cpb.49.1189.

Can. J. Chem. Downloaded from www.nrcresearchpress.com by Renmin University of China on 09/02/12
For personal use only.

Extraction of s-block metals by nano-baskets of calix[4]crown-3

Bahram Mokhtari and Kobra Pourabdollah

Can. J. Chem. Downloaded from www.nrcresearchpress.com by Renmin University of China on 09/02/12
For personal use only.

Abstract: Three kinds of nano-baskets including 1,2-alternate and cone conformers of di-ionizable *p-tert*-butylcalix[4]arene-1,2-crown-3 and the cone conformer of *p-tert*-butylcalix[4]arene-1,2-thiacrown-3 were synthesized and the competitive solvent extractions of alkali and alkaline earth metal cations were studied. The novelty of this study is including three binding units of the calixarene's bowl, the crown ether's ring, and electron-donor ionizable moieties in a unique scaffold, in which their sizes were selected based upon their complexation ability to show equal binding tendency towards the cations. The objective of this work is to assess the extraction efficiency, selectivity, and $pH_{1/2}$ of such complexes. The results of solvent extraction experiments indicated that these compounds were effective extractants of alkali and alkaline earth metal cations. Their selectivities were greatly influenced by the acidity of the solution and the conformations of the calixcrown. One conformer was highly selective to Na^+ and the other to Ba^{2+} in acidic and basic solutions, respectively.

Key words: nano-baskets, competitive extraction, calix[4]crown-3, s-block metals.

Résumé : On a réalisé la synthèse de trois nouveaux types de nano-paniers, dont les conformères 1,2-alternés et à cône du *p-tert*-butylcalix[4]arène-1,2-couronne-3 et de son conformère en cône, le *p-tert*-butylcalix[4]arène-1,2-thiacouronne-3 et on en a étudié les capacités d'extraction compétitive par solvants de cations alcalins et alcalinoterreux. La nouveauté de cette étude réside dans le fait qu'elle inclut trois unités de fixation, soit le bol du calixarène, le noyau de l'éther couronne et les portions ionisables d'un électrodonneur dans un échafaudage unique dans lequel leurs grandeurs ont été choisies en raison de leur habilité à former à tous former des complexes avec les cations avec autant de facilité. L'objectif de ce travail était d'évaluer l'efficacité d'extraction, la sélectivité et le $pH_{1/2}$ de tels complexes. Les résultats des expériences d'extraction par les solvants indiquent que ces composés permettent d'extraire d'une façon efficace les cations métalliques alcalins et alcalino-terreux. Leurs sélectivités sont fortement influencées par l'acidité de la solution et de la conformation du calixarène couronne. Un conformère est très sélectif pour la Na^+ et l'autre pour la Ba^{2+} dans des solutions respectivement acides et basiques.

Mots-clés : nano-paniers, extraction compétitive, calix[4]couronne-3, métaux du bloc s.

[Traduit par la Rédaction]

Introduction

Nano-baskets of calixarenes and calixcrowns are a versatile class of macrocycles that have been subject to extensive research in the development of many extractants, transporters, and stationary phases (using a gas chromatograph, Teif Gostar Faraz Co.).[1–6] Functionalization of calix[4]arenes at both the upper rim and the lower rim has been extensively studied.[7,8] Attaching donor atoms to the lower rim of a calix[4]arene can improve the binding strength of the parent calixarene dramatically.[9–19] The two main groups of lower rim-functionalized calix[4]arenes are calix[4]arene podands and calixarene-crown ethers.[20,21] Distal hydroxyl groups can be connected to give 1,3-bridged calix[4]crowns, whereas connection between proximal hydroxyl groups leads to 1,2-bridged calix [4]crowns.

It was found that the 1,3-bridged calix[4]crowns exhibit high binding affinity and selectivity toward alkali and alkaline earth metal cations,[22] whereas the research on 1,2-bridged calix[4]crowns lags far behind. Combining crown ethers with calix[4]arenes increases the cation binding ability of the parent calixarenes, and control of the selectivity is obtained through the modulation of the crown ether size. Attachment of proton-ionizable groups to calixcrowns can further improve their extraction properties because the ionized group not only participates in metal ion coordination but also eliminates the need to transfer aqueous phase anions into the organic phase. Ungaro et al.[23] reported the first diproton-ionizable calix[4]crown-5 in 1984 and it showed a quite high efficiency in the extraction of divalent cations from water into dichloromethane. Combining crown ethers with calix[4]arenes increases the cation binding ability of the parent calixarenes.[24–26] The selectivity can be affected by the crown ether size, the identity of donor atoms on the crown ether moiety, and the conformation of the calixarene platform. To further explore the influence of these factors on the extraction characteristics of *p-tert*-butylcalix[4]arene-1,2-crown ethers toward metal ions, a series of di-ionizable *p-tert*-butylcalix[4]arene-1,2-crown-3 compounds in the cone

Received 17 June 2011. Accepted 26 September 2012. Published at www.nrcresearchpress.com/cjc on 6 June 2012.

B. Mokhtari and K. Pourabdollah. Razi Chemistry Research Center (RCRC), Shahreza Branch, Islamic Azad University, Shahreza, Iran.

Corresponding author: Kobra Pourabdollah (e-mail: pourabdollah@iaush.ac.ir).

Can. J. Chem. Downloaded from www.nrcresearchpress.com by Renmin University of China on 09/02/12
For personal use only.

and the 1,2-alternate conformations, as well as *p-tert*-butylcalix[4]arene-1,2-thiacrown-3 in the cone conformation, were synthesized.

There are two kinds of side chains in the calixcrown skeleton that were studied including two ionizable carboxylic acid moieties and the crown-ether moieties. The ionizable moieties not only participate in cooperative metal ion coordination but also eliminate the need to transfer the anions from the aqueous phase into the organic phase by operating in a cation-exchange mode with the metal cation. In this work, two proton-ionizable functional groups were incorporated into the calix[4]arene scaffold. A special feature of this modification is that the acidity of the ionizable moiety can be tunable by changing the functional group from hydroxyl to other groups because of the different electron-withdrawing abilities of the functional group. A wide range of pH environments can be examined when these ionizable groups are incorporated into the calixcrown skeleton. These extractants exhibit excellent extraction selectivity for alkali and alkaline earth metals.

In this work, three nano-baskets of calixcrowns with different proton-ionizable moieties were synthesized including cone *p-tert*-butylcalix[4]arene-1,2-crown-3 diacid, 1,2-alternate *p-tert*-butylcalix[4]arene-1,2-crown-3 diacid, and cone *p-tert*-butylcalix[4]arene-1,2-thiacrown-3 diacid. Competitive solvent extractions of alkali metal cations and alkaline earth metal cations were performed using these calixcrowns in which 1.0 mmol/L solutions of di-ionizable calix[4]arene ligands in chloroform as well as the plots of cation loading of the organic phase vs. the equilibrium pH of the aqueous phase were presented. In the following, the synthesis and the extraction procedures of the three conformers are presented.

Experimental methods

Materials and apparatus

Reagents were obtained from commercial suppliers and used directly, unless otherwise noted. Acetonitrile (MeCN) was dried over CaH_2 and distilled immediately before use. Tetrahydrofuran (THF) was dried over sodium with benzophenone as an indicator and distilled just before use. Cs_2CO_3 was activated by heating at 150 °C overnight under high vacuum and stored in a desiccator. Melting points were determined with a Mel-Temp melting point apparatus. Infrared (IR) spectra were recorded with a PerkinElmer model 1600 FT-IR spectrometer as deposits from CH_2Cl_2 solution on NaCl plates. The ^1H and ^{13}C NMR spectra were recorded with a Varian Unity INOVA 500 MHz FT-NMR (^1H, 500 MHz; and ^{13}C, 126 MHz) spectrometer in $CDCl_3$ with Me_4Si as internal standard unless mentioned otherwise. Chemical shifts (δ) are given in ppm downfield from TMS and coupling constants (*J*) are in Hz.

Preparation of *p-tert*-butylcalix[4]arene-1,2-crown-3 (**2**)

To a mixture of *p-tert*-butylcalix[4]arene (6.50 g, 10 mmol), diethylene glycol (1.59 g, 15 mmol), and triphenylphosphine (TPP, 8.00 g, 30 mmol) in 200 mL of toluene, a 40% solution of diethylazodicarboxylate (DEAD, 5.22 g, 30 mmol) in toluene was added dropwise. The mixture was stirred at room temperature for 0.5 h and then the solution was evaporated to dryness and the residue was extracted with hexane (3 × 30 mL) followed by evaporation and subsequent stirring in hexane and ethyl acetate. The precipitate was filtered and the filtrate was purified by chromatography on silica gel with hexane–EtOAc (9:1) as eluent to give a white solid (3.90 g, 54%) with mp 198–199 °C. IR (deposit from CH_2Cl_2 solution on a NaCl plate, cm^{-1}) ν_{max}: 3342 (O–H), 1249 and 1124 (C–O). ^1H NMR ($CDCl_3$) δ: 1.20 (s, 18H, CH_3), 1.21 (s, 18H, CH_3), 3.26–3.45 (m, 4H, $ArCH_2Ar$), 4.01 (t, J = 10.5 Hz, 2H, OCH_2CH_2O), 4.12 (t, J = 11.0 Hz, 2H, OCH_2CH_2O), 4.28–4.46 (m, 7H, OCH_2CH_2O, $ArCH_2Ar$), 4.82 (d, J = 12.0 Hz, 1H, $ArCH_2Ar$), 6.94–7.06 (m, 6H, ArH), 7.15 (d, J = 2.0 Hz, 2H, ArH), 8.87 (s, 2H, OH). ^{13}C NMR ($CDCl_3$) δ: 31.30, 31.50, 32.66, 33.01, 33.90, 34.18, 75.32, 125.31, 125.58, 125.60, 126.45, 128.32, 128.84, 129.15, 133.88, 134.62, 142.81, 147.42, 149.14, 150.34. Anal. calcd for $C_{48}H_{62}O_5$ (%): C 80.18, H 8.69; found: C 80.08, H 8.37.

Preparation of cone *p-tert*-butylcalix[4]arene-1,2-crown-3 diester (**3**)

p-tert-Butylcalix[4]arene-1,2-crown-3 (**2**) (5.00 g, 6.95 mmol) in 50 mL of THF was added dropwise into a mixture of NaH (0.85 g, 35.4 mmol) in 50 mL of THF. After stirring for 2 h, ethyl bromoacetate (6.95 g, 41.7 mmol) was added and the reaction mixture was stirred overnight. The reaction was monitored by TLC. After 48 h, the reaction was quenched by careful addition of dilute HCl and evaporated in vacuo. The residue was dissolved in CH_2Cl_2, the solution was washed with dilute HCl and water, dried over $MgSO_4$, and the solvent was evaporated in vacuo. Chromatographic purification on silica gel with hexane–EtOAc (2:8) as eluent gave an oil (3.81 g, 61%). IR (deposit from CH_2Cl_2 solution on a NaCl plate, cm^{-1}) ν_{max}: 1760 (C=O), 1253 and 1128 (CO). ^1H NMR ($CDCl_3$) δ: 1.04 (s, 18H, CH_3), 1.12 (s, 18H, CH_3), 1.34 (t, J = 7.0 Hz, 6H, OCH_2CH_3), 3.09 (d, J = 12.0 Hz, 1H, $ArCH_2Ar$), 3.18 (d, J = 12.0 Hz, 2H, $ArCH_2Ar$), 3.24 (d, J = 13.0 Hz, 1H, $ArCH_2Ar$), 3.83–3.92 (m, 2H, OCH_2CH_2O), 4.07 (d, J = 12.0, 2H, OCH_2CH_2O), 4.20 (m, 2H, OCH_2CH_2O), 4.27 (q, J = 7.0, 4H, OCH_2CH_3), 4.42 (d, J = 10.5 Hz, 2H, OCH_2CH_2O), 4.54–4.65 (m, 3H, $ArCH_2Ar$, OCH_2Ar), 4.88 (d, J = 15.5 Hz, 2H, OCH_2CO), 4.96 (d, J = 12.0 Hz, 1H, $ArCH_2Ar$), 6.76–6.84 (m, 4H, ArH), 6.86 (d, J = 2.5 Hz, 2H, ArH), 6.92 (d, J = 2.0 Hz, 2H, ArH). ^{13}C NMR ($CDCl_3$) δ: 14.33, 31.02, 31.32, 31.42, 33.82, 33.88, 53.42, 60.62, 72.03, 73.04, 75.24, 124.35, 125.39, 125.55, 132.72, 134.03, 134.35, 134.81, 144.84, 145.34, 152.88, 152.93, 170.28. Anal. calcd for $C_{56}H_{74}O_9$ (%): C 75.47, H 8.37; found: C 75.22, H 8.23.

Preparation of cone *p-tert*-butylcalix[4]arene-1,2-crown-3 diacid (**4**)

p-tert-Butylcalix[4]arene-1,2-crown-3 diester (**3**) (3.00 g, 3.05 mmol) in 60 mL of THF and 60 mL of 10% Me_4NOH was refluxed overnight. The solvent was evaporated in vacuo and the residue was dissolved in 100 mL of CH_2Cl_2. The organic layer was washed with 1 N HCl solution until pH 1 and then washed with 60 mL of brine and 60 mL of water, dried over $MgSO_4$, and evaporated in vacuo to give a white solid (2.49 g, 88%) with mp 255–256 °C. IR (deposit from CH_2Cl_2 solution on a NaCl plate, cm^{-1}) ν_{max}: 3217 (O–H),

Can. J. Chem. Downloaded from www.nrcresearchpress.com by Renmin University of China on 09/02/12
For personal use only.

1761 (C=O), 1203 and 1121 (C–O). ^{1}H NMR ($CDCl_3$) δ: 1.07 (s, 18H, CH_3), 1.11 (s, 18H, CH_3), 3.12 (d, J = 12.0 Hz, 1H, $ArCH_2Ar$), 3.22–3.36 (m, 3H, $ArCH_2Ar$), 3.81–3.92 (m, 2H, OCH_2CH_2O), 4.11 (d, J = 12.5 Hz, 2H, OCH_2CH_2O), 4.20 (t, J = 11.0 Hz, 2H, OCH_2CH_2O), 4.25–4.38 (m, 4H, OCH_2CH_2O, $ArCH_2Ar$), 4.49 (d, J = 13.0 Hz, 1H, $ArCH_2Ar$), 4.58 (d, J = 16.5 Hz, 2H, OCH_2CO), 4.79 (d, J = 16.5 Hz, 2H, OCH_2CO), 5.19 (d, J = 12.5 Hz, 1H, $ArCH_2Ar$), 6.83–6.91 (m, 4H, ArH), 6.93 (d, J = 2.0 Hz, 2H, ArH), 6.99 (d, J = 2.5 Hz, 2H, ArH). ^{13}C NMR ($CDCl_3$) δ: 30.30, 30.60, 30.80, 31.24, 31.34, 33.90, 33.98, 53.41, 71.62, 73.63, 124.49, 125.47, 126.11, 126.19, 133.12, 133.25, 133.54, 134.94, 145.45, 146.80, 151.23, 152.71, 171.56. Anal. calcd for $C_{52}H_{66}O_9$ (%): C 74.79, H 7.97; found: C 74.50, H 7.95.

Preparation of 1,2-alternate *p-tert*-butylcalix[4]arene-1,2-crown-3 diester (5)

Calix[4]arene-1,2-crown-3 (**2**) (6.00 g, 8.34 mmol) in 60 mL of THF was added dropwise to a mixture of KH (4.17 g, 40% in mineral oil, 41.7 mmol) in 60 mL of THF. After stirring for 2 h, ethyl bromoacetate (8.34 g, 50.04 mmol) was added and the reaction mixture was stirred for 3 days. The reaction was quenched by careful addition of dilute HCl. The mixture was washed with dilute HCl and water, dried over $MgSO_4$, and evaporated in vacuo. Chromatographic purification on silica gel with hexane–EtOAc (1:19) as eluent gave a white solid (3.60 g, 48%) with mp 205–206 °C. IR (deposit from CH_2Cl_2 solution on a NaCl plate, cm^{-1}) ν_{max}: 1760 (C=O), 1205 and 1132 (C–O). ^{1}H NMR ($CDCl_3$) δ: 1.09 (t, J = 7.0 Hz, 6H, SO_2CH_3), 1.31 (s, 18H, CH_3), 1.33 (s, 18H, CH_3), 2.48, (t, J = 10.0 Hz, 2H, OCH_2CH_2O), 3.15, (d, J = 12.5 Hz, 1H, $ArCH_2Ar$), 3.30–3.44 (m, 3H, $ArCH_2Ar$, OCH_2CH_2O), 3.53–3.65 (m, 6H, OCH_2CH_2O, OCH_2CO), 3.83 (d, J = 17.0 Hz, 2H, OCH_2CO), 3.89–4.04 (m, 6H, OCH_2CH_3, OCH_2CO), 4.07 (d, J = 16.5 Hz, 2H, $ArCH_2Ar$), 4.54 (d, J = 12.0 Hz, 1H, $ArCH_2Ar$), 4.77 (d, J = 13.5 Hz, 1H, $ArCH_2Ar$), 6.97 (d, J = 2.5 Hz, 2H, ArH), 7.07 (d, J = 2.0 Hz, 2H, ArH), 7.32 (d, J = 2.5 Hz, 2H, ArH), 7.42 (d, J = 2.0 Hz, 2H, ArH). ^{13}C NMR ($CDCl_3$) δ: 14.12, 29.20, 31.54, 31.58, 31.73, 34.07, 34.10, 39.14, 60.14, 69.37, 73.01, 74.43, 125.12, 125.43, 125.73, 125.89, 132.47, 133.06, 134.20, 135.24, 144.57, 145.57, 152.84, 152.96, 170.14. Anal. calcd for $C_{56}H_{74}O_9$ (%): C 75.47, H 8.37; found: C 75.50, H 8.06.

Preparation of 1,2-alternate *p-tert*-butylcalix[4]arene-1,2-crown-3 diacid (6)

The *p-tert*-butylcalix[4]arene-1,2-crown-3 diester (4.00 g, 4.07 mmol) in 150 mL of THF and 150 mL of 10% Me_4NOH was refluxed overnight. The solvent was evaporated in vacuo and the residue was dissolved in 200 mL of CH_2Cl_2. The organic layer was washed with 1 N HCl until pH 1 and then with brine (100 mL) and water (100 mL), dried over $MgSO_4$, and evaporated in vacuo to give a white solid (3.60 g, 96%) with mp > 300 °C. IR (deposit from CH_2Cl_2 solution on a NaCl plate, cm^{-1}) ν_{max}: 3391 (O–H), 1760 (C=O), 1207 and 1128 (C–O). ^{1}H NMR ($CDCl_3$) δ: 1.30 (s, 18H, CH_3), 1.33 (s, 18H, CH_3), 2.38, (t, J = 11.0 Hz, 2H, OCH_2CH_2O), 3.19, (d, J = 12.5 Hz, 1H, $ArCH_2Ar$), 3.24, (d, J = 13.0 Hz, 1H, $ArCH_2Ar$), 3.49, (t, J = 10.0 Hz, 2H, OCH_2CH_2O), 3.54–3.66 (m, 4H, OCH_2CH_2O), 3.85 (d, J = 17.5 Hz, 2H, $ArCH_2Ar$), 3.94 (t, J = 17.0 Hz, 2H, $ArCH_2Ar$), 4.09 (d, J = 15.5 Hz, 2H, OCH_2CO), 4.15 (d, J = 16.0 Hz, 2H, OCH_2CO), 4.55 (d, J = 12.0 Hz, 1H, $ArCH_2Ar$), 4.71 (d, J = 12.5 Hz, 1H, $ArCH_2Ar$), 6.98 (d, J = 2.0 Hz, 2H, ArH), 7.00 (d, J = 2.0 Hz, 2H, ArH), 7.34 (d, J = 2.5 Hz, 2H, ArH), 7.38 (d, J = 2.0 Hz, 2H, ArH). ^{13}C NMR ($CDCl_3$): 29.54, 31.40, 31.59, 34.13, 34.20, 38.98, 68.32, 72.80, 74.47, 124.40, 125.22, 125.57, 126.54, 131.40, 131.86, 134.18, 134.84, 146.49, 146.52, 151.45 152.13, 170.37. Anal. calcd for $C_{52}H_{66}O_9 \cdot 1.0C_6H_6$ (%): C 76.29, H 7.95; found: C 76.28, H 8.11.

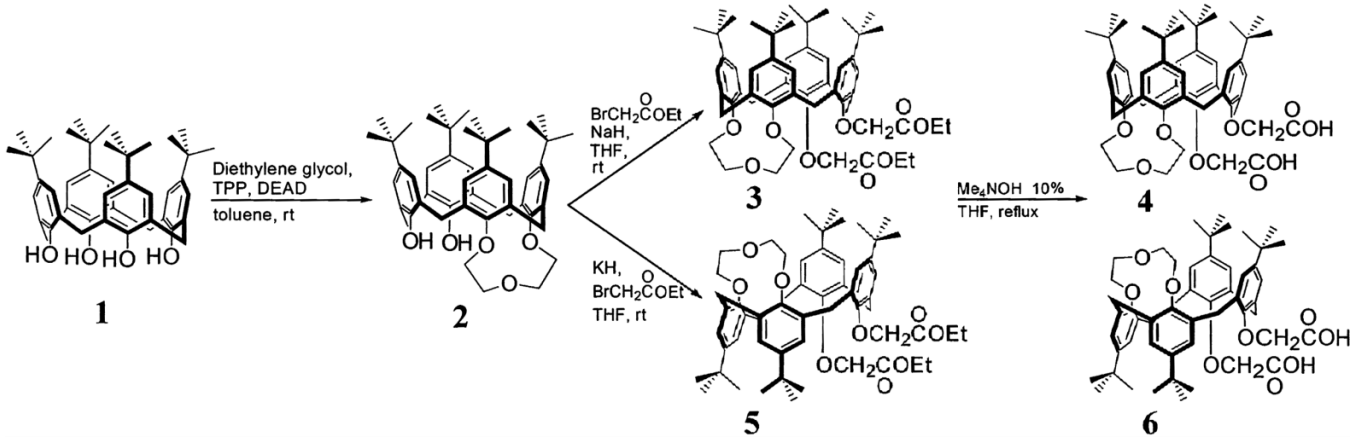
Preparation of cone *p-tert*-butylcalix[4]arene-1,2-thiacrown-3 (7)

To a mixture of *p-tert*-butylcalix[4]arene (**4**) (23.00 g, 35.49 mmol), 2,2′-thiodiethanol (6.49 g, 53.24 mmol), and TPP (27.92 g, 106.47 mmol) in 600 mL of toluene, a 40% solution of DEAD (46.35 g, 106.47 mmol) in toluene was added dropwise and the mixture was stirred at room temperature for 3 h. After the reaction was complete the solution was evaporated to dryness and the residue was extracted with hexane (3 × 300 mL). After filtration, the solvent was evaporated in vacuo. Purification by chromatography on silica gel with hexane–EtOAc (49:1) as eluent gave a white solid (7.55 g, 29%) with mp 110–115 °C. IR (deposit from CH_2Cl_2 solution on a NaCl plate, cm^{-1}) ν_{max}: 3338 (O–H), 1247 (CO). ^{1}H NMR ($CDCl_3$) δ: 1.19 (s, 18H, CH_3), 1.21 (s, 18H, CH_3), 3.17–3.26 (m, 2H, OCH_2CH_2S), 3.29–3.41 (m, 6H, $ArCH_2Ar$, OCH_2CH_2S), 3.93 (t, J = 10.0 Hz, 2H, OCH_2CH_2S), 4.33 (d, J = 13.0 Hz, 2H, $ArCH_2Ar$), 4.35 (d, J = 13.5 Hz, 1H, $ArCH_2Ar$), 3.62–4.68 (m, 2H, OCH_2CH_2S), 5.05 (d, J = 12.0 Hz, 1H, v), 6.99 (d, J = 2.5 Hz, 2H, ArH), 7.01 (d, J = 2.5 Hz, 2H, ArH), 7.02 (d, J = 2.5 Hz, 2H, ArH), 7.14 (d, J = 2.5 Hz, 2H, ArH), ^{13}C NMR ($CDCl_3$) δ: 31.21, 31.28, 31.49, 32.68, 33.00, 33.90, 34.17, 36.90, 53.36, 125.28, 125.54, 125.90, 126.36, 128.78, 128.90, 133.57, 134.75, 142.92, 147.48, 149.04, 150.19. Anal. calcd for $C_{48}H_{62}O_4S$ (%): C 78.43, H 8.50; found: C 78.75, H 8.41.

Preparation of cone *p-tert*-butylcalix[4]arene-1,2-thiacrown-3 diester (8)

p-tert-Butylcalix[4]arene-1,2-thiacrown-3 (**7**) (2.00 g, 2.72 mmol) in 40 mL of THF was added dropwise to a mixture of NaH (0.96 g, 8.16 mmol) in 40 mL of THF. After stirring for 2 h, ethyl bromoacetate (2.72 g, 16.32 mmol) was added and the reaction mixture was stirred overnight. The reaction mixture was monitored by TLC. The reaction was quenched with dilute HCl, washed with dilute HCl and water, dried over $MgSO_4$, and evaporated in vacuo. Chromatographic purification on silica gel with 3% EtOAc in hexanes gave a white solid (1.13 g, 46%) with mp 61–63 °C. IR (deposit from CH_2Cl_2 solution on a NaCl plate,cm^{-1}) ν_{max}: 1759 (C=O), 1248 and 1128 (C–O). ^{1}H NMR ($CDCl_3$) δ: 1.04 (s, 18H, CH_3), 1.12 (s, 18H, CH_3), 1.34 (t, J = 7.0 Hz, 6H, CH_2CH_3), 3.02–3.09 (m, 2H, OCH_2CH_2S), 3.12 (d, J = 12.5 Hz, 1H, $ArCH_2Ar$), 3.17 (d, J = 12.5 Hz, 2H, $ArCH_2Ar$), 3.25 (d, J = 12.5 Hz, 1H, $ArCH_2Ar$), 3.46–3.54

Scheme 1. Synthesis of *p-tert*-butylcalix[4]arene-1,2-crown-3 dicarboxylic acids (**4** and **6**).



(m, 2H, OCH_2CH_2S), 3.72–3.79 (m, 2H, OCH_2CH_2S), 4.24–4.32 (m, 4H, OCH_2CH_3), 4.50 (d, J = 13.0 Hz, 1H, $ArCH_2Ar$), 4.52 (d, J = 16.0 Hz, 2H, OCH_2CO), 4.71–4.77 (m, 2H, OCH_2CH_2S), 4.78 (d, J = 12.5 Hz, 2H, $ArCH_2Ar$), 4.90 (d, J = 16.0 Hz, 2H, OCH_2CO), 5.29 (d, J = 12.0 Hz, 1H, $ArCH_2Ar$), 6.78 (d, J = 2.5 Hz, 2H, ArH), 6.80 (d, J = 2.5 Hz, 2H, ArH), 6.86 (d, J = 2.5 Hz, 2H, ArH), 6.90 (d, J = 2.5 Hz, 2H, ArH). ^{13}C NMR ($CDCl_3$) δ: 14.33, 30.91, 31.33, 31.42, 31.50, 31.66, 31.76, 33.82, 33.89, 34.99, 60.70, 72.14, 75.87, 124.75, 125.17, 125.45, 125.60, 132.45, 133.96, 134.17, 134.97, 144.99, 145.44, 152.67, 152.95, 170.21. Anal. calcd for $C_{56}H_{74}O_8S \cdot 1.5H_2O$ (%): C 71.99, H 8.31; found: C 71.85, H 8.38.

Preparation of cone *p-tert*-butylcalix[4]arene-1,2-thiacrown-3 diacid (9)

p-tert-Butylcalix[4]arene diester (**8**) (1.13 g, 1.25 mmol) in 30 mL of THF and 30 mL of 10% Me_4NOH was refluxed overnight. The solvent was evaporated in vacuo and the residue was dissolved in 100 mL of CH_2Cl_2. The organic solution was washed with 1 N HCl solution until pH 1 and then with brine (100 mL) and water (100 mL), dried over $MgSO_4$, and the solvent was evaporated in vacuo to give a white solid (0.90 g, (85%) with mp 202–205 °C. IR (deposit from CH_2Cl_2 solution on a NaCl plate, cm^{-1}) ν_{max}: 3217 (O–H), 1760 (C=O), 1246 and 1127 (C–O). ^{1}H NMR ($CDCl_3$) δ: 1.07 (s, 18H, CH_3), 1.12 (s, 18H, CH_3), 3.07–3.14 (m, 2H, OCH_2CH_2S), 3.15 (d, J = 12.5 Hz, 1H, $ArCH_2Ar$), 3.27 (d, J = 13.0 Hz, 2H, $ArCH_2Ar$), 3.31 (d, J = 13.0 Hz, 1H, $ArCH_2Ar$), 3.67–3.75 (m, 2H, OCH_2CH_2S), 4.33 (d, J = 13.0 Hz, 2-H, $ArCH_2Ar$), 4.49 (d, J = 13.0 Hz, 1H, $ArCH_2Ar$), 4.58 (d, J = 16.5 Hz, 2H, OCH_2CO), 4.59–4.66 (m, 2H, OCH_2CH_2S), 4.78 (d, J = 16.0 Hz, 2H, OCH_2CO), 5.59 (d, J = 12.5 Hz, 1H, $ArCH_2Ar$), 5.29 (d, J = 12.0 Hz, 1H, $ArCH_2Ar$), 6.86 (d, J = 2.0 Hz, 2H, ArH), 6.88 (d, J = 2.5 Hz, 2H, ArH), 6.91 (d, J = 2.5 Hz, 2H, ArH), 6.97 (d, J = 2.5 Hz, 2H, ArH). ^{13}C NMR ($CDCl_3$) δ: 25.59, 30.63, 31.25, 31.35, 31.47, 31.60, 33.92, 33.97, 36.04, 67.96, 71.70, 77.59, 109.88, 124.80, 125.48, 125.93, 126.10, 133.09, 133.22, 133.33, 135.15, 145.64, 146.77, 151.40, 152.46, 171.58. Anal. calcd for $C_{52}H_{66}O_8S$ (%): C 73.38, H 7.82; found: C 73.12, H 7.54.

Results and discussion

Synthesis of calix[4]crown-3 conformers

The commonly employed method, which involves the reaction of *p-tert*-butylcalix[4]arene (**1**) and diethylene glycol ditosylate in the presence of strong base, failed to give *p-tert*-butylcalix[4]arene-1,2-crown-3 (**2**). Variations of the base, as well as elevating reaction temperature, were performed, but no detectable levels of compound **2** were found. Another entirely different method was utilized for the synthesis of compound **2** (Scheme 1). Under Mitsunobu reaction conditions, *p-tert*-butylcalix[4]arene (**4**) was treated with TPP and DEAD and reacted with diethylene glycol to form compound **2**. The reaction was quenched after 0.5 h and gave a 54% yield. Compared with the commonly used methods, the Mitsunobu reaction had a much shorter reaction time with a reasonable yield. Also, conversion of the diethylene glycol into diethylene glycol ditosylate was not necessary. Compound **2** was treated with sodium hydride in THF and reacted with ethyl bromoacetate at room temperature for 2 days to form *p-tert*-butylcalix[4]arene-1,2-crown-3 diester (**3**) in the cone conformation in 61% yield. The synthesis procedure is shown in Scheme 1. The resulting diester **3** was hydrolyzed with aqueous tetramethylammonium hydroxide in THF under reflux to give diacid **4** in 88% yield. Compound **2** was treated with KH in THF and reacted with ethyl bromoacetate at room temperature for 3 days to form *p-tert*-butylcalix[4]arene-1,2-crown-3 diester (**5**) in the 1,2-alternate conformation in 48% yield. The synthesis is depicted in Scheme 1. The resulting diester **5** was hydrolyzed with aqueous tetramethylammonium hydroxide in THF under reflux to give diacid **6** in 96% yield.

There were no peaks between 35–40 ppm in the ^{13}C NMR spectra for compound **4**, revealing that all four benzene rings have syn arrangements. In the ^{1}H NMR spectra for this compound, the bridging methylene protons are split into three pairs of doublets with an integration ratio of 1:2:1.

The ^{13}C NMR spectra for compound **6** showed peaks at both 31 and 38 ppm, revealing that the benzene rings have both syn and anti arrangements. In the ^{1}H NMR spectra for this compound, the bridging methylene protons are split into three pairs of doublets, with the integration ratio being 1:1:2.

Can. J. Chem. Downloaded from www.nrcresearchpress.com by Renmin University of China on 09/02/12
For personal use only.

Scheme 2. Synthesis of *p-tert*-butylcalix[4]arene-1,2-thiacrown-3 dicarboxylic acid (**9**).

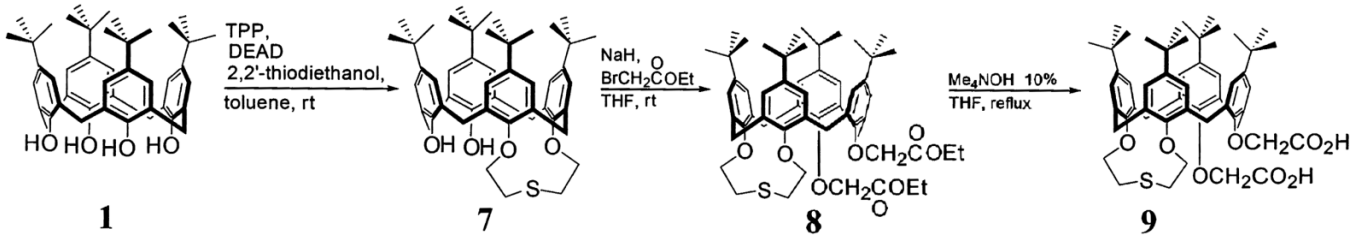


Fig. 1. Percentage of (*a*) metal loading vs. (*b*) equilibrium pH of the aqueous phase for competitive solvent extraction of alkali and alkaline earth metal ions into chloroform by conformer **4**.

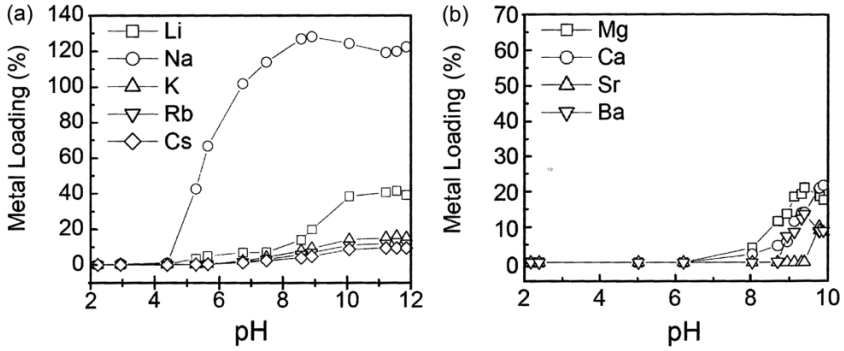
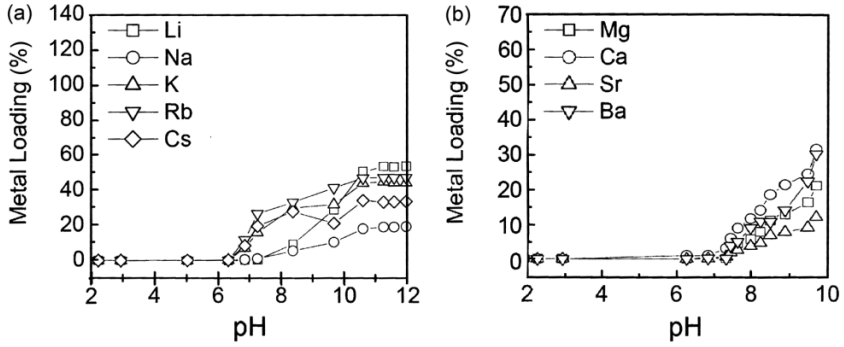


Fig. 2. Percentage of (*a*) metal loading vs. (*b*) equilibrium pH of the aqueous phase for competitive solvent extraction of alkali and alkaline earth metal ions into chloroform using conformer **6**.



Synthesis of cone calix[4]thiacrown-3

The *p-tert*-butylcalix[4]arene-1,2-thiacrown-3 (**7**) was synthesized following the method used for making compound **2** (Scheme 2). Under Mitsunobu reaction conditions, *p-tert*-butylcalix[4]arene (**1**) was treated with TPP and DEAD and reacted with 2,2′-thiodiethanol to form compound **7** in 29% yield.

Compound **7** was treated with sodium hydride in THF and reacted with ethyl bromoacetate at room temperature overnight to form *p-tert*-butylcalix[4]arene-1,2-thiacrown-3 diester (**8**) in the cone conformation in 61% yield. The synthesis is presented in Scheme 2. The resulting diester **8** was hydrolyzed with aqueous tetramethylammonium hydroxide in THF under reflux to give diacid **9** in 91% yield.

There are no peaks at 35–40 ppm in the ^{13}C NMR spectra for compound **9**, revealing that all four benzene rings have syn arrangements. In the ^{1}H NMR spectra for this compound, the bridging methylene group protons are split into three pairs of doublets, with an integration ratio of 1:2:1.

Competitive solvent extractions by ligand 4

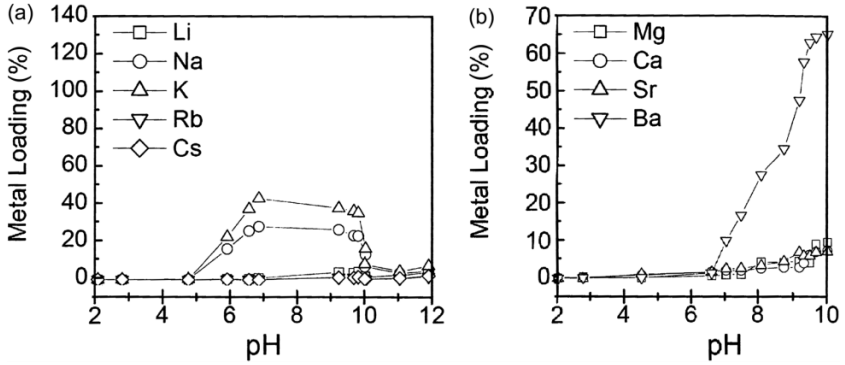
For competitive extraction of such metal cations, di-ionizable *p-tert*-butylcalix[4]arene-1,2-crown-3 ligand **4** exhibits very different selectivity from its *p-tert*-butylcalix[4]arene-1,2-crown-4 and -crown-5 analogues. All five alkali metal cations and four alkaline earth metal cations were detectably extracted into the chloroform phase and the selectivity order was $Na^+ > Li^+ > K^+ \approx Rb^+ \approx Cs^+$ and $Mg^{2+} > Ca^{2+} \approx Ba^{2+} > Sr^{2+}$ for ligand **4**, respectively. The pH for half loading ($pH_{1/2}$) is a measure of the acidity of the ligand. For compound **4**, the $pH_{1/2}$ value was 6 for binding to Na^+ and 9.6 for binding to Li^+, K^+, Rb^+, and Cs^+. The $pH_{1/2}$ values for binding to alkaline earth metal cations were determined to be in the range of 9–9.5. Figure 1 depicts the plots of metal ion loading of the organic phase vs. the equilibrium pH of the aqueous phase using ligands **4**.

Competitive solvent extractions by ligand 6

For competitive solvent extractions of aqueous alkali and

Can. J. Chem. Downloaded from www.nrcresearchpress.com by Renmin University of China on 09/02/12
For personal use only.

Fig. 3. Percentage of (*a*) metal loading vs. (*b*) equilibrium pH of the aqueous phase for competitive solvent extraction of alkali and alkaline earth metal ions into chloroform using conformer **9**.



alkaline earth metal cation (10.0 mmol/L in each) solutions by 1.0 mmol/L solutions of di-ionizable *p-tert*-butylcalix[4]arene-1,2-crown-3 ligand (**6**) in chloroform, plots of metal ion loading of the organic phase vs. the equilibrium pH of the aqueous phase are presented in Fig. 2.

For competitive extraction of alkali and alkaline earth metal cations, di-ionizable *p-tert*-butylcalix[4]arene-1,2-crown-3 ligand (**6**) exhibits versatile selectivities for alkali and alkaline earth metal ion species. All five alkali metal cations and four alkaline earth metal cations were detectably extracted into the chloroform phase. The selectivity order was $Li^+ > Rb^+ > K^+ > Cs^+ > Na^+$ and $Ca^{2+} > Ba^{2+} > Mg^{2+} > Sr^{2+}$ for ligand **6**, respectively. For compound **6**, the $pH_{1/2}$ value was 7 for binding to K^+, Rb^+, and Cs^+ and 9 for binding to Li^+ and Na^+. The $pH_{1/2}$ values for binding to alkaline earth metal cations were determined to be 8.5.

Competitive solvent extractions by ligand 9

Ligand **9** exhibited very different selectivity from its *p-tert*-butylcalix[4]arene-1,2-crown-3 analogues in cone and 1,2-alternate conformers. All five alkali metal cations and four alkaline earth metal cations were detectably extracted into the chloroform phase and the selectivity order was $K^+ > Na^+ >> Li^+ \approx Rb^+ \approx Cs^+$ and $Ba^{2+} >> Mg^{2+} \approx Ca^{2+} \approx Sr^{2+}$ for ligand **9**, respectively. The loading of K^+ and Na^+ passed through a maximum value and decreased to initial values, respectively. The peak points in the loading of K^+ and Na^+ by ligand **9** were determined to be 40% and 30%, respectively. These maximum loading conditions were observed in the pH range of 7–10. The $pH_{1/2}$ value was 6 for binding to Na^+ and K^+, whereas the other alkali metal cations (Li^+, Rb^+, and Cs^+) showed no loading. The $pH_{1/2}$ values for binding to alkaline earth metal cations were determined to be 9. Figure 3 shows the plots of metal ion loading of the organic phase vs. the equilibrium pH of the aqueous phase using ligands **9**.

Conclusions

1. Proton di-ionizable *p-tert*-butylcalix[4]arene-1,2-crown-3 conformers in the cone and the 1,2-alternate conformations, as well as a *p-tert*-butylcalix[4]arene-1,2-thiacrown-3 compound in the cone conformation, were synthesized as potential metal ion extractants.
2. The conformations and regio-selectivities of the new ligands were verified by ^1H and ^{13}C NMR spectroscopy, IR spectroscopy, and elemental analysis.
3. For each of the studied conformers, the average loading percentage for alkali metal cations were twice the loading percentage for alkaline earth metal cations.
4. Inserting the soft element of sulfur in the crown ether ring enhanced the loading percentage of soft cations (Ba^{2+}) dominantly.
5. Ligand **4** was selective to Na^+ at pH 8, ligand **6** was not selective to any cations at any pH points, and ligand **9** was selective for Ba^{2+} at pH 10.
6. The $pH_{1/2}$ values not only depended on the structures of the conformers but also were a function of the trapped cation.

Acknowledgements

This work was supported by Islamic Azad University (Shahreza branch) and the Iran Nanotechnology Initiative Council.

References

(1) Mokhtari, B.; Pourabdollah, K.; Dalali, N. *J. Incl. Phenom. Macrocycl. Chem.* **2011**, *69* (1–2), 1. doi:10.1007/s10847-010-9848-7.
(2) Mokhtari, B.; Pourabdollah, K.; Dalali, N. *J. Coord. Chem.* **2011**, *64* (5), 743. doi:10.1080/00958972.2011.555538.
(3) Mokhtari, B.; Pourabdollah, K.; Dallali, N. *J. Radioanal. Nucl. Chem.* **2011**, *287* (3), 921. doi:10.1007/s10967-010-0881-1.
(4) Mokhtari, B.; Pourabdollah, K.; Dalali, N. *Chromatographia* **2011**, *73* (9–10), 829. doi:10.1007/s10337-011-1954-1.
(5) Mokhtari, B.; Pourabdollah, K. *Asian J. Chem* **2011**, *23* (11), 4717.
(6) Mokhtari, B.; Pourabdollah, K. *Bull. Korean Chem. Soc.* **2011**, *32* (11), 3855. doi:10.5012/bkcs.2011.32.11.3855.
(7) Mokhtari, B.; Pourabdollah, K. *Bull. Korean Chem. Soc.* **2011**, *32* (11), 3979. doi:10.5012/bkcs.2011.32.11.3979.
(8) Mokhtari, B.; Pourabdollah, K. *J. Coord. Chem.* **2011**, *64* (17), 3081. doi:10.1080/00958972.2011.613462.
(9) Mokhtari, B.; Pourabdollah, K. *J. Coord. Chem.* **2011**, *64* (18), 3189. doi:10.1080/00958972.2011.616930.
(10) Mokhtari, B.; Pourabdollah, K. *J. Coord. Chem.* **2011**, *64* (23), 4029. doi:10.1080/00958972.2011.635790.
(11) Mokhtari, B.; Pourabdollah, K. *K. J. Coord. Chem.* **2011**, *64* (23), 4079. doi:10.1080/00958972.2011.636040.
(12) Mokhtari, B.; Pourabdollah, K. *J. Incl. Phenom. Macrocycl. Chem.* **2012**. Online First. doi:10.1007/s10847-011-0052-1.
(13) Mokhtari, B.; Pourabdollah, K. *J. Incl. Phenom. Macrocycl. Chem.* **2012**. Online First. doi:10.1007/s10847-011-0062-z.

Can. J. Chem. Downloaded from www.nrcresearchpress.com by Renmin University of China on 09/02/12
For personal use only.

(14) Mokhtari, B.; Pourabdollah, K. *J. Incl. Phenom. Macrocycl. Chem.* **2012**. Online First. doi:10.1007/s10847-011-0099-z.
(15) Mokhtari, B.; Pourabdollah, K. *Supramol. Chem.* **2011**, *23* (10), 696. doi:10.1080/10610278.2011.605452.
(16) Mokhtari, B.; Pourabdollah, K. *J. Electrochem. Soc.* **2012**, *159* (3), K61. doi:10.1149/2.048203jes.
(17) Mokhtari, B.; Pourabdollah, K. *Electroanalysis* **2012**, *24* (2), 219. doi:10.1002/elan.201100584.
(18) Mokhtari, B.; Pourabdollah, K. *J. Therm. Anal. Calorim.* **2012**. Online First. doi:10.1007/s10973-011-2014-7.
(19) Mokhtari, B.; Pourabdollah, K. *Drug Chem. Toxicol.* **2012**. Early Online. doi:10.3109/01480545.2011.653490.
(20) Salorinne, K.; Nissinen, M. *J. Incl. Phenom. Macrocycl. Chem.* **2008**, *61* (1–2), 11. doi:10.1007/s10847-008-9411-y.
(21) Kim, J. S.; Vicens, J. *J. Incl. Phenom. Macrocycl. Chem.* **2009**, *63* (1–2), 189. doi:10.1007/s10847-008-9503-8.
(22) Lamare, V.; Dozol, J. F.; Ugozzoli, F.; Casnati, A.; Ungaro, R. *Eur. J. Org. Chem.* **1998**, *1998* (8), 1559. doi:10.1002/(SICI)1099-0690(199808)1998:8<1559::AID-EJOC1559>3.0.CO;2-Y.
(23) Ungaro, R.; Pochini, A.; Andreetti, G. D. *J. Incl. Phenom. Molecul. Recogn. Chem.* **1984**, *2* (1–2), 199. doi:10.1007/BF00663257.
(24) Yang, Y.; Cao, X.; Surowiec, K.; Bartsch, R. A. *J. Incl. Phenom. Macrocycl. Chem.* **2010**, *66* (1–2), 163. doi:10.1007/s10847-009-9675-x.
(25) Arena, G.; Contino, A.; Longo, E.; Sciotto, D.; Spoto, G.; Torrisi, A. *J. Supramol. Chem* **2002**, *2* (6), 521. doi:10.1016/S1472-7862(02)00022-9.
(26) Lynch, J. A.; Mestayer, J. J.; Blanda, M. T. *J. Supramol. Chem* **2001**, *1* (3), 139. doi:10.1016/S1472-7862(02)00005-9.

Can. J. Chem. Downloaded from www.nrcresearchpress.com by Renmin University of China on 09/02/12
For personal use only.

A study of the Willgerodt–Kindler reaction to obtain thioamides and α-ketothioamides under solvent-less conditions

José Ernesto Valdez-Rojas, Hulme Ríos-Guerra, Alma Leticia Ramírez-Sánchez, Guadalupe García-González, Cecilio Álvarez-Toledano, José Guadalupe López-Cortés, Rubén A. Toscano, and José Guillermo Penieres-Carrillo

Can. J. Chem. Downloaded from www.nrcresearchpress.com by Renmin University of China on 09/02/12
For personal use only.

Abstract: In this paper, the results obtained in the synthesis of thioamides and α-ketothioamides by a modification of the Willgerodt–Kindler reaction, under solvent-free and noncatalyst conditions using IR energy as a source of activation, are presented. The use of IR energy in these reactions has been shown to lead to a mixture of thioamide and α-ketothioamide as the main products in most cases, with the latter predominating. The yields of α-ketothioamides from most of these reactions are better than those reported previously. To the best of our knowledge, this is the first time that IR energy has been applied to promote the Willgerodt–Kindler reaction.

Key words: Willgerodt–Kindler modification, α-ketothioamides, solvent-less conditions, IR energy, noncatalyst.

Résumé : Dans ce travail, on rapporte les résultats obtenus lors de la synthèse de thioamides et de α-cétothioamides, par le biais d'une modification de la réaction de Willgerodt–Kindler dans des conditions qui n'impliquent aucun solvant et aucun catalyseur et qui utilisent l'énergie infrarouge comme source d'activation. On a démontré que l'utilisation de l'infrarouge dans ces réactions conduit, dans la plupart des cas, à des mélanges contenant comme produits principaux un thioamide et un α-cétothioamide et que ce dernier est prédominant. Les rendements en α-cétothioamides, pour la plupart des réactions, sont meilleurs que ceux rapportés antérieurement. Au meilleur de nos connaissances, c'est la première fois que l'énergie de l'infrarouge a été utilisée pour la promotion de la réaction de Willgerodt–Kindler.

Mots-clés : modification de la réaction de Willgerodt-Kindler, α-cétothioamides, conditions expérimentales sans solvant, énergie infrarouge, sans catalyseur.

[Traduit par la Rédaction]

Introduction

Thioamides are among the most extensively studied chalcogen-containing compounds. They are known to demonstrate biological activity,[1] are used as synthetic intermediates in organic chemistry,[2] have been found in natural products, and have many applications in materials science and industrial processes.[3] They are also employed as insecticides[4] because they are well tolerated by plants and have low toxicity in higher animals, and they are used in medical applications, for example, in tuberculosis treatment,[5] as painkillers,[6] and as antioxidants.[7]

Currently, it is possible to find several methods for the synthesis of thioamides, most of which employ Lawesson's reagent.[8] However, there are also publications concerning the Willgerodt–Kindler method for the generation of these compounds,[9] but this method has some limitations, i.e., long reaction times are required and low yields are achieved. This reaction is characterized by the use of alkyl aryl ketones or aldehydes, elemental sulfur, and amines, with morpholine being the most commonly used amine. When ketones are used in this methodology, the carbonyl group is reduced to a methylene group and the terminal methyl group is oxidized to a thiocarbonyl group (**I**, Scheme 1).

Previous studies using thermal energy for the activation of reactions have yielded some unexpected results, with the most common problem being the failure to reduce the carbonyl group in the alkyl aryl ketone used, leading to the formation of the α-ketothioamide **II** as a reaction byproduct. Dauben and Rogan,[10] Harris et al.[11] Harrowven and Lucas,[12] and Liu et al.[13] encountered this problem and generated **II** in yields of 3%–20% when using reaction times of 8–24 h. In

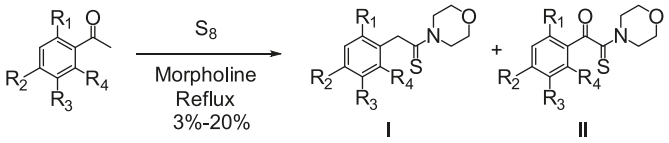
Received 31 October 2011. Accepted 27 March 2012. Published at www.nrcresearchpress.com/cjc on 12 June 2012.

J.E. Valdez-Rojas, H. Ríos-Guerra, A.L. Ramírez-Sánchez, G. García-González, and J.G. Penieres-Carrillo. Facultad de Estudios Superiores Cuautitlán-Universidad Nacional Autónoma de México, Sección de Química Orgánica, FESC, Campo 1, Avenida 1 de mayo s/n, Colonia Santa María Guadalupe Las Torres, Cuautitlán Izcalli, C. P. 54740, México.
C. Álvarez-Toledano, J.G. López-Cortés, and R.A. Toscano. Instituto de Química-Universidad Nacional Autónoma de México, Circuito Exterior, Ciudad Universitaria, Coyoacán, México D.F, C.P. 04510, México.

Corresponding author: José Guillermo Penieres-Carrillo (e-mail: penieres@unam.mx).

Can. J. Chem. Downloaded from www.nrcresearchpress.com by Renmin University of China on 09/02/12
For personal use only.

Scheme 1. General reaction conditions for the synthesis of thioamides. Dauben and Rogan:[10] Acetophenone (2.0 g, 12.3 mmol), elemental sulfur (0.40 g, 12.3 mmol), morpholine (1.08 g, 12.3 mmol); R_1 = Me, R_2 = Me, R_3 = H, R_4 = Me; yield (**II**) = 20%; 8 h. Harris et al.:[11] Acetophenone (5.0 g, 20.4 mmol), elemental sulfur (1.0 g, 31.25 mmol), morpholine (2.82 g, 32.4 mmol); R_1 = OC_6H_5, R_2 = H, R_3 = Cl, R_4 = H; yield (**I**) = 46%, **II** not isolated; 20 h. Harrowven and Lucas:[12] Acetophenone (23.3 g, 142 mmol), elemental sulfur (6.8 g, 213 mmol), morpholine (18.5 g, 213 mmol); R_1 = OMe, R_2 = Me, R_3 = H, R_4 = H; yield (**I**) = 57%, yield (**II**) = 10%; 24 h. Liu et al.:[13] Acetophenone (12.2 g, 100 mmol), elemental sulfur (4.8 g, 150 mmol), morpholine (11.3 g, 130 mmol); R_1 = R_2 = R_3 = R_4 = H; yield (**I**) = 66%, yield (**II**) = 3%; 20 h.



these reports, the reactions were performed at reflux, in the absence of solvent, employing acetophenones, elemental sulfur, and morpholine. However, the methodology developed in these studies cannot be considered to be a general synthetic route to α-ketothioamides **II**, because this unexpected product of the Willgerodt–Kindler reaction was only generated in isolated cases.

Other published routes to α-ketothioamides have employed α-chloroketones,[14] α-oxonitryl,[15] thioacetomorpholides,[16] pinacolone (3,3-dimethyl-2-butanone),[17] α-chlorosulfonyl and trisulfane intermediates,[18] or *N*,*N*-(dialkyl)aroylmethylamines.[19] However, like the Willgerodt–Kindler reaction, these methodologies are not general for the synthesis of α-ketothioamides. The reaction conditions employed are also dangerous or require expensive reagents and long reaction times. In general, thermal energy is used as the activation source for the Willgerodt–Kindler reaction. The use of alternative energy sources such as ultrasound[20] and microwaves[21] has recently been explored, and microwave activation has attracted particular attention. To the best of our knowledge, however, the use of IR energy as an activation source for the Willgerodt–Kindler reaction has not yet been reported. IR energy has been demonstrated to be useful in organic synthesis,[22] and has been used in the synthesis of 1,3,5-trioxanes from aldehydes,[23] in the Biginelli[24] and Knoevenagel[25] reactions, and for the synthesis of diindolylmethanes[26] and 3,4-dihydro-2(1*H*)-pyridones.[27] When investigating the synthesis of ε-caprolactam from cyclohexanone and hydroxylamine using bentonic clay under solvent-less conditions, we explored the use of several energy sources for activation of the reaction and found that IR energy performed better than thermal, microwave, or ultrasound energies.[28]

Results and discussion

We set out to explore the use of IR energy for the activation of the Willgerodt–Kindler reaction, employing acetophenone, elemental sulfur, and morpholine. After extensive experimentation, we found that a stoichiometric ratio for the starting materials of 1:1:1, solvent-less conditions, and irradiation with IR energy at a wavelength of 1100 nm (near-IR) for 1 h at 100 °C[29] were optimal conditions for the generation of the corresponding α-ketothioamide. In this way, the desired product was obtained exclusively in 56% yield.

This result encouraged us to study the reaction using other acetophenones and amines, to establish this method as a general route to synthesize α-ketothioamides **3** (Scheme 2).

We found that, under these conditions, this reaction ensured that the α-ketothioamides **3a**–**3h** (Table 1) were generated as the main products in most cases, and the yields were higher than those obtained (3%–20%) by other synthetic methods previously reported in the literature. The Willgerodt–Kindler products **4a**–**4h** were also detected in yields ranging from 0%–42% as a second product. Thus, with the methodology employed in this work, the outcome of the Willgerodt–Kindler reaction can be regarded as unclassical.

The products **3a**–**3h** were obtained in yields close to or higher than 50%, although when 2-methylpiperidine was used as the amine, a yield of only 20% was obtained, which may be attributed to steric factors. In entries 1–5 of Table 1, the products were synthesized from unsubstituted acetophenone, and the amine used was either morpholine, piperidine, or methylated regioisomers of the latter.

When the reaction was carried out with *p*-chloroacetophenone, a crystalline product was formed, and a single crystal could be used for X-ray diffraction study[30] (Fig. 1).

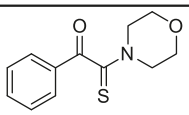
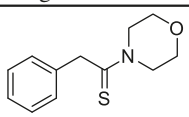
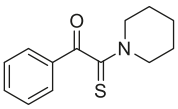
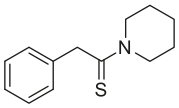
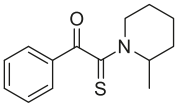
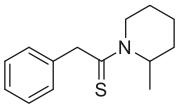
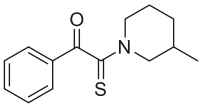
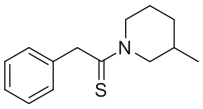
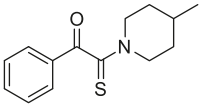
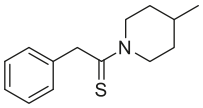
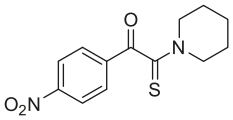
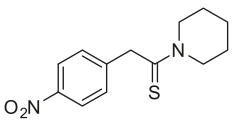
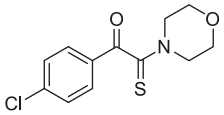
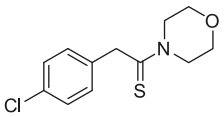
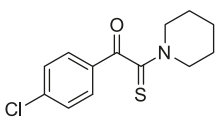
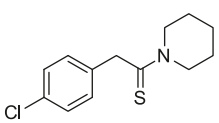
It is important to mention that the low yields of **3** shown in entries 7 and 8 in Table 1 were due to a competitive S_NAr reaction resulting in the formation of *p*-morpholino- or *p*-(1-piperidinyl)acetophenone[31] in yields of 20% and 19%, respectively, along with the corresponding thioamides from the Willgerodt–Kindler reaction, compounds **4g** and **4h** (Scheme 2; Table 1).

We also studied the reactions leading to the synthesis of **3a**–**3h** at room temperature, to determine the influence of temperature and energy source on their outcomes. The reactions were monitored for 48 h by TLC, and the conversion percentages were measured by gas chromatography coupled with mass spectrometry (Table 2). More than 50% of the acetophenone remained unreacted in some cases (Table 2, entries 7 and 8), and the behavior of these reactions was similar when IR energy was used. These results clearly demonstrated that the reactions proceeded better when activated with IR energy than when conducted at room temperature, and established the importance of IR energy in the synthesis of α-ketothioamides **3**. The formation of **4a**–**4h** was detected and the results are summarized in Table 2.

To compare the use of thermal conditions and IR energy for the synthesis of α-ketothioamides, we performed the reactions to obtain **3a** and **3b** under reflux conditions. After 5 h of reaction, with hourly monitoring by TLC, no formation of the corresponding α-ketothioamides could be detected. This behavior is consistent with the reported results by Liu et al.[13] for the reaction employing acetophenone, elemental sulfur, and morpholine at reflux temperature (83–85 °C), whereby **3** was obtained in just 3% yield after 20 h of reaction. In contrast, in the present study, the same compound (Table 1, entry 1) was obtained in 56% yield in a reaction time of 1 h. Moreover, Carmack et al.[32] reported similar reaction conditions to those used in the present paper (100 °C, elemental sulfur, morpholine, and solvent-less conditions) for

Can. J. Chem. Downloaded from www.nrcresearchpress.com by Renmin University of China on 09/02/12
For personal use only.

Table 1. Obtained results from the Willgerodt–Kindler reaction employing IR energy.

Entry	α-Ketothioamide	Yield(%)[a]	Willgerodt–Kindler product	Yield (%)[a]	Time (min)
1	 **3a**	56; 3;[13] 58;[b,14] 94[c,16]	 **4a**	Not formed; 50–81[21a]	60
2	 **3b**	50; 22;[b,14] 11[19]	 **4b**	39	60
3	 **3c**	20; 26[19]	 **4c**	Not formed	150
4	 **3d**	67	 **4d**	Not formed	60
5	 **3e**	48	 **4e**	Trace	60
6	 **3f**	54	 **4f**	Not formed	30
7	 **3g**	19; 83[c,16]	 **4g**	42; 40–55[21a]	60
8	 **3h**	12; 10[19]	 **4h**	11	60

[a]Purified product.

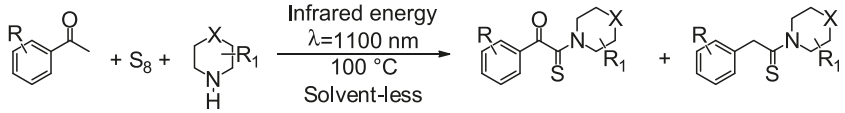
[b]From the linear synthesis (three steps); yield is for the last step.

[c]From the linear synthesis (two steps); yield is for the last step.

the reaction of linear and cyclic aliphatic ketones, using thermal energy, and obtained only the Willgerodt–Kindler product and carbonyl group isomerization products. Considering all of these results, it is proposed that IR energy is responsible for the synthesis of **3** as the principal product, and not the thermal heating that comes from the lamp employed in this work (see the Supplementary data).

The use of IR energy gives very efficient heat transfer similar

Scheme 2. Synthesis of thioamides from acetophenones, elemental sulfur, and heterocyclic amines.

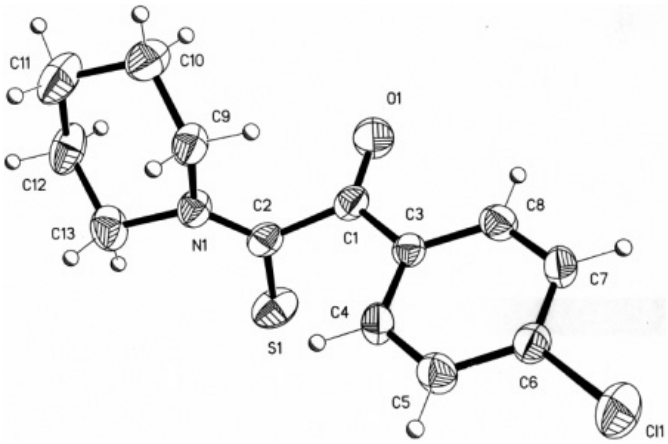


1a-1c **2a-2e** **3a-3h** 12%-67% **4a-4h** 0%-42%

1a H
1b *p*-NO_2
1c *p*-Cl

2a X=O, R_1=H
2b X=CH_2, R_1=H
2c X=CH_2, R_1=2-Me
2d X=CH_2, R_1=3-Me
2e X=CH_2, R_1=4-Me

Fig. 1. ORTEP for 1-(4-chlorophenyl)-2-piperidin-1-yl)-2-thioxo-ethanone (**3h**).



to that provided by microwave irradiation because both are electromagnetic waves and the behavior is comparable. The main effect produced by IR energy is thus an overheating in the reaction mixture that favors the formation of **3**. Mechanistically, we are in agreement with the reaction mechanism proposed by Darabi et al.[33]

Conclusion

In summary, we have described a new methodology for the synthesis of α-ketothioamides as the principal products, employing a multicomponent reaction activated by IR energy under solvent-less conditions. As far as we are aware, this is the first report of the use of IR energy for activation of the Willgerodt–Kindler reaction. We have established the utility of this method for the generation of α-ketothioamides, a reaction that could not previously be reliably accomplished by the Willgerodt–Kindler protocol when thermal energy was used. In all cases reported in this study, the α-ketothioamides were produced in yields ranging from moderate to good, depending on the substituents on the acetophenone aromatic ring.

This new methodology can be considered as a useful addition to the synthetic organic chemistry tool kit, as, to the best of our knowledge, no method has hitherto been reported to give α-ketothioamides in a one-pot reaction in yields better than those reported here.

Experimental section

General

All reagents were from Sigma-Aldrich and used from its commercial presentation, ^{1}H and ^{13}C NMR spectra were recorded by use of $CDCl_3$ or acetone-d_6 in Varian Mercury 200 and 300 MHz instruments, chemical shifts were reported in ppm from TMS with the solvent resonance as the internal standard, and coupling constants (*J*) are given in hertz, where s was assigned to single, d for doublet, t for triplet, m for multiple, and br for broad signals. The GC–MS analyses were conducted with gas chromatograph model 6850 and mass spectrometer 5975C by Agilent Technologies, employing a J&W HP-5MS capillary column. GC conditions: capillary column (30 m × 0.25 mm i.d., 0.25 μm film), helium as carrier gas at a constant flow velocity of 35 cm/s, and injector temperature 250 °C. MS data were reported as *m/z* (relative intensity). HRMS were recorded in an MStation JMS-700 JEOL at 70 eV. Melting points were obtained on a Fisher-Johns apparatus and are uncorrected. Analytical TLC was performed using Kieselgel 60 F_{254} silica gel plates (Merck, Darmstadt, Germany). A Buchi pump controller C-610 and a Buchi pump module C-601 were employed for flash chromatography. Elemental analyses were carried out with an Elementar Vario EL III element analyser.

IR equipment

The equipment used for irradiation with IR energy was created by employing an empty cylindrical metal vessel in which an Osram lamp (bulb model Thera-Therm, 250 W, 125 V) was inserted. This lamp is special short-wave IR lamp (IR-A) for use in body care and wellness applications, with a maximum radiation at a wavelength of about 1100 nm. The lamp instantly emits a full thermal output as soon as it is switched on. For controlling the temperature, a Digi-Sense variable-time power controller was used. This time controller turned the output load on and off and then repeated the cycle.

Typical procedure for the Willgerodt–Kindler reaction employing IR energy

For the synthesis of **3a**, the following were placed in a tube: acetophenone **1a** (100 mg, 0.83 mmol), elemental sulfur (27 mg, 0.83 mmol), and amine **2a** (73 mg, 0.83 mmol). This tube was then sealed and placed inside of the IR equipment at 3–5 cm above the IR lamp. The reaction mixture was irradiated at a wavelength of 1100 nm with IR energy at 100 °C for the appropriate time (30–150 min according to Table 1) and monitored using TLC. The products obtained as brown dark oils were purified using preparative plates or flash chromatography with silica gel as a stationary phase and a mixture of hexane – ethyl acetate as a mobile phase;

Can. J. Chem. Downloaded from www.nrcresearchpress.com by Renmin University of China on 09/02/12
For personal use only.

Can. J. Chem. Downloaded from www.nrcresearchpress.com by Renmin University of China on 09/02/12
For personal use only.

Table 2. Conversion percentages using acetophenones, elemental sulfur, and heterocyclic amines at room temperature.

Entry	Compound	Conversion (%)[a]	Compound	Conversion (%)[a]	Acetophenone (%)[b]
1	**3a**	19	**4a**	32	39
2	**3b**	12	**4b**	14	33
3	**3c**	10	**4c**	3	18
4	**3d**	43	**4d**	4	14
5	**3e**	36	**4e**	13	18
6	**3f**	30	**4f**	Not formed	37
7	**3g**	9	**4g**	12	56
8	**3h**	9	**4h**	10	55

[a]Percentage of conversion was measured by GC–MS.
[b]Unreacted raw material.

recrystallization processes were not necessary and pure products were characterized by ^{1}H and ^{13}C NMR and mass spectrometry. Syntheses of **3b**–**3h** were carried out with the same procedure. Products **4a**–**4h** were isolated and characterized from the mixture of the reactions for the synthesis of **3a**–**3h**.

Typical procedure for the Willgerodt–Kindler reaction at room temperature

For the formation of **3a**, elemental sulfur (184 mg, 5.7 mmol) was added to 500 mg (5.7 mmol) of amine **2a**, the reaction mixture was stirred for 2 h until the sulfur was completely dissolved in the amine, and then acetophenone **1a** (690 mg, 5.7 mmol) was added to the amine–sulfur mixture and stirred at room temperature for 48 h. The reaction was monitored by TLC and the conversion rates were determined by GC–MS. Compounds **3b**–**3h** were obtained, replacing the corresponding acetophenones **1a**–**1c** and amines **2a**–**2e** following the typical procedure for **3a**.

2-Morpholino-1-phenyl-2-thioxoethanone (3a)[13,14,16]

Yield: 109 mg (56%); pale yellow solid, mp 107–109 °C. R_f (70% Hex/AcOEt): 0.42. ^{1}H NMR (200 MHz, $CDCl_3$, Me_4Si) δ_H: 8.01–7.97 (2H, m), 7.34–7.31 (3H, m), 4.37–4.33 (1H, t, J = 9.8 Hz), 3.76–3.71 (1H, t, J = 9.8 Hz), 3.65–3.60 (1H, t, J = 9.6 Hz), 3.40–3.35 (1H, t, J = 9.6 Hz). ^{13}C NMR (50 MHz, $CDCl_3$) δ_C: 199.9 (C=S), 187.8 (C=O), 135.7, 128.9, 127.7, 127.1, 66.3, 50.7, 50.5, 50.1. MS (EI) m/z: 235 ($M^{+\bullet}$, 15%), 221 (100), 130 (35), 105 (5). HRMS-EI calcd for $C_{12}H_{13}O_2NS$: 235.0667; found: 235.0655.

1-Phenyl-2-(piperidin-1-yl)-2-thioxoethanone (3b)[14,19]

Yield: 97 mg (50%); pale yellow solid, mp 53–55 °C. R_f (90% Hex/AcOEt, eluted twice): 0.48. IR (KBr, cm^{-1}): 2944, 2862, 1666, 1590. ^{1}H NMR (300 MHz, $CDCl_3$, Me_4Si) δ_H: 7.99–7.96 (1H, m), 7.62–7.56 (2H, m), 7.50–7.44 (2H, m), 4.25–4.22 (2H, m), 3.54–3.50 (2H, m), 2.16 (2H, s), 1.82–1.73 (2H, br), 1.62–1.60 (2H, br). ^{13}C NMR (75 MHz, $CDCl_3$) δ_C: 194.2 (C=S), 187.9 (C=O), 134.1, 133.2, 129.6, 128.7, 52.9, 48.0, 26.3, 25.2, 23.9. MS (EI) m/z: 233 ($M^{+\bullet}$, 78.1%), 128 (100), 84 (53.1). HRMS-EI calcd for $C_{17}H_{22}O_2N_2S$: 233.0874; found: 233.0873.

2-(2-Methylpiperidin-1-yl)-1-phenyl-2-thioxoethanone (3c)[19]

Yield: 42 mg (20%); yellow solid,. mp 65–68 °C. R_f (90% Hex/AcOEt, eluted twice): 0.22. IR (KBr, cm^{-1}): 2928, 2860, 1737, 1667. ^{1}H NMR (300 MHz, $CDCl_3$, Me_4Si) δ_H: 8.01–7.94 (1H, m), 7.60–7.57 (2H, m), 7.51–7.46 (2H, m), 5.43–5.39 (1H, m), 4.09 (2H, m), 3.64–3.57 (2H, m), 1.99 (2H, m), 1.75 (2H, br), 1.25 (3H, s). ^{13}C NMR (75 MHz, $CDCl_3$) δ_C: 194.3 (C=S), 187.5 (C=O), 134.0, 133.4, 129.6, 128.7, 56.3, 49.7, 47.5, 41.9, 30.6, 29.6, 25.9, 25.3, 18.5, 18.3, 16.4, 14.7. MS (EI) m/z: 247 ($M^{+\bullet}$, 64.37%), 142 (75), 98 (62.5), 18 (100). HRMS-EI calcd for $C_{14}H_{17}ONS$: 247.1031; found: 247.1033.

2-(3-Methylpiperidin-1-yl)-1-phenyl-2-thioxoethanone (3d)

Yield: 138 mg (67%); yellow solid, mp 45 °C. R_f (90% Hex/AcOEt, eluted twice): 0.22. ^{1}H NMR (300 MHz, $CDCl_3$, Me_4Si) δ_H: 7.99–7.96 (1H, m), 7.62–7.57 (2H, m), 7.50–7.45 (2H, m), 5.33–5.21 (1H, m), 3.75–3.63 (2H, m), 3.28–3.07 (2H, m), 1.94–1.90 (2H, br), 1.82–1.68 (2H, br), 0.82–0.79 (3H, m). ^{13}C NMR (75 MHz, $CDCl_3$) δ_C: 194.4 (C=S), 187.8 (C=O), 134.0, 133.3, 129.7, 128.7, 58.9, 53.9, 52.4, 47.5, 32.5, 32.1, 31.2, 25.6, 24.4, 18.9, 18.5. HRMS-EI calcd for $C_{14}H_{17}ONS$: 247.1031; found: 247.1030.

2-(4-Methylpiperidin-1-yl)-1-phenyl-2-thioxoethanone (3e)

Yield: 99 mg (48%); yellow solid, mp 53–55 °C. R_f (90% Hex/AcOEt, eluted twice): 0.22. IR (KBr, cm^{-1}): 2928, 2860, 1737, 1667. ^{1}H NMR (300 MHz, $CDCl_3$, Me_4Si) δ_H: 7.98–7.94 (1H, m), 7.60–7.54 (2H, m), 7.49–7.43 (2H, m), 5.41–5.33 (1H, m), 3.78–3.70 (2H, m), 3.31–3.22 (2H, m), 1.96 (2H, m), 1.92–1.61 (2H, br), 1.22 (3H, s). ^{13}C NMR (75 MHz, $CDCl_3$) δ_C: 194.4 (C=S), 187.9 (C=O), 134.0, 133.3, 129.7, 128.7, 52.0, 47.3, 34.2, 33.2, 30.7, 21.1. MS (EI) m/z: 247 ($M^{+\bullet}$, 64.37%), 142 (75), 98 (62.5), 18 (100). HRMS-EI calcd for $C_{14}H_{17}ONS$: 247.1031; found: 247.1032.

1-(4-Nitrophenyl)-2-(piperidin-1-yl)-2-thioxoethanone (3f)

Yield: 91 mg (54%); yellow solid, mp 123–125 °C. R_f (66% Hex/acetone): 0.46. ^{1}H NMR (300 MHz, $CDCl_3$, Me_4Si) δ_H: 7.77–7.74 (2H, m), 6.62–6.59 (2H, m), 4.43 (2H, m), 4.23 (2H, m), 3.53 (2H, m), 1.77 (2H, br), 1.74 (2H, br). ^{13}C NMR (75 MHz, $CDCl_3$) δ_C: 195.5 (C=S), 187.7 (C=O), 152.6, 132.5, 122.8, 113.9, 53.0, 48.2, 26.5, 25.4, 24.1. MS (EI) m/z: 278 ($M^{+\bullet}$, 48%), 150 (6), 128 (100), 84 (96). Anal. calcd for $C_{13}H_{14}N_2O_3S$ (278.3): C 56.10, H 5.07, N 10.06; found: C 60.49, H 6.19, N 10.23.

Can. J. Chem. Downloaded from www.nrcresearchpress.com by Renmin University of China on 09/02/12
For personal use only.

1-(4-Chlorophenyl)-2-morpholino-2-thioxoethanone (3g)[16]

Yield: 33 mg (19%); yellow solid, mp 150–152 °C. R_f (73% Hex/AcOEt): 0.25. ^{1}H NMR (300 MHz, $CDCl_3$, Me_4Si) δ_H: 7.94–7.91 (2H, d, J = 8.7 Hz), 7.48–7.45 (2H, d, J = 9 Hz), 4.33–4.30 (1H, t, J = 9.9 Hz), 3.91–3.88 (1H, t, J = 9.9 Hz), 3.71–3.68 (1H, t, J = 9 Hz), 3.60–3.57 (1H, t, J = 9.3 Hz). ^{13}C NMR (50 MHz, $CDCl_3$) δ_C: 194.8 (C=S), 186.3 (C=O), 140.9, 131.1, 129.2, 125.7, 66.4, 66.3, 51.9, 47.1. MS (EI) *m/z*: 269 ($M^{+\bullet}$, 12%), 139 (33), 130 (100), 86 (76). Anal. calcd for $C_{12}H_{12}ClNO_2S$ (269.7): C 53.43, H 4.48, N 5.19; found: C 53.33, H 5.47, N 4.35.

1-(4-Chlorophenyl)-2-(piperidin-1-yl)-2-thioxoethanone (3h)[19]

Yield: 21 mg (12%); yellow solid, 120–122 °C. R_f (70% Hex/AcOEt): 0.18. IR (KBr, cm^{-1}): 2949, 2858, 1665, 1586. ^{1}H NMR (300 MHz, acetone-d_6, Me_4Si) δ_H: 8.00–7.97 (2H, d, J = 9 Hz), 7.61–7.58 (2H, d, J = 8.7 Hz), 4.26 (2H, m), 3.63–3.59 (2H, t, J = 11.4 Hz), 2 (2H, m) 1.81–1.77 (2H, m) 1.62 (2H, m). ^{13}C NMR (75 MHz, acetone-d_6) δ_C: 194.0 (C=S), 186.9 (C=O), 140.5, 133.3, 132.0, 129.9, 53.5, 48.4, 27.2, 25.9, 24.5. MS (EI) *m/z*: 267 ($M^{+\bullet}$, 30%), 138 (17), 128 (36), 84 (100). Anal. calcd for $C_{13}H_{14}ClNO_2S$ (267.7): C 58.31, H 5.27, N 5.23; found: C 58.20, H 7.26, N 2.91.

2-Phenyl-1-(piperidin-1-yl)ethanethione (4b)

Yield: 72 mg (39%); pale yellow solid, mp 55–57 °C. R_f (90% Hex/AcOEt, eluted twice): 0.51. ^{1}H NMR (300 MHz, $CDCl_3$, Me_4Si) δ_H: 7.33–7.18 (5H, m), 4.32 (2H, s), 4.26–4.23 (2H, m, J = 10.5 Hz), 3.57–3.53 (2H, m, J = 11.1 Hz), 2.02–1.97 (2H, bs), 1.64–1.61 (2H, m), 1.30–1.26 (2H, m). ^{13}C NMR (75 MHz, $CDCl_3$) δ_C: 198.1, 136.0, 128.7, 127.7, 126.7, 51.5, 50.9, 26.1, 25.1, 23.7. MS (EI) *m/z*: 219 ($M^{+\bullet}$, 100%), 128 (75), 91 (80). Anal. calcd for $C_{13}H_{17}NS$ (219.3): C 71.18, H 7.81, N 6.39; found: C 64.47, H 7.01, N 6.34.

2-(4-Chlorophenyl)-1-morpholinoethanethione (4g)

Yield: 69 mg (42%); yellow solid, mp 125–127 °C. R_f (73% Hex/AcOEt): 0.31. ^{1}H NMR (300 MHz, $CDCl_3$, Me_4Si) δ_H: 7.30–7.23 (5H, m), 4.34–4.31 (1H, t, J = 9.9 Hz), 4.28 (2H, s), 3.74–3.71 (1H, t, J = 9.9 Hz), 3.61–3.58 (1H, t, J = 9.6 Hz), 3.43–3.40 (1H, t, J = 9.9 Hz). ^{13}C NMR (50 MHz, $CDCl_3$) δ_C: 199.2, 134.1, 132.8, 129.1, 129.0, 66.2, 66.0, 50.6, 50.0, 49.6. MS (EI) *m/z*: 255 ($M^{+\bullet}$, 100%), 130 (55), 125 (35). Anal. calcd for $C_{12}H_{14}ClNOS$ (255.7): C 56.35, H 5.52, N 5.48; found: C 57.07, H 6.33, N 4.75.

Supplementary data

Supplementary data are available with the article through the journal Web site http://nrcresearchpress.com/doi/suppl/10.1139/v2012-030. CCDC 819515 contains the X-ray data in CIF format for this manuscript. These data can be obtained, free of charge, via http://www.ccdc.cam.ac.uk/products/csd/request (Or from the Cambridge Crystallographic Data Centre, 12 Union Road, Cambridge CB2 1EZ, UK; fax: 44 1223 336033; or e-mail: deposit@ccdc.cam.ac.uk.

Acknowledgments

The authors want to thank to Mr. L.B. Hernández Portilla and Dr. C.M. Flores Ortiz for GC–MS experiments done at Unidad de Biotecnología y Prototipos Facultad de Estudios Superiores (UBIPRO FES) - Iztacala Universidad Nacional Autónoma de México (UNAM) and Programa de Apoyo a Proyectos de Investigación e Innovación Tecnológica (PAPIT) for the project support (IN207208). J.E.V.-R. would like to thank CONACYT for support given through Ph.D. grant No. 226777.

References

(1) Freerksen, E. Synergistic Therapeutic Composition for the Treatment of Mycobacterioses. US Patent 4,005,207, January 25, 1977.

(2) Tsung-Ying, S; Dorn, K. P, Jr.; Witzel, B. E. Substituted Biphenyl Acetic Acid Derivatives. US Patent 3,624,142, November 30, 1971.

(3) (a) Banala, S.; Süssmuth, R. D. *ChemBioChem* **2010**, *11* (10), 1335. doi:10.1002/cbic.201000266; (b) Kramer, W.; Draber, W.; Timmler, H.; Forster, H. Process for the Preparation of α-Oxothiodimethylamide Compounds. US Patent 4,028,409, June 7, 1977; (c) Fusseneger, M.; Weber, W.; Schoenmakers, R. *US Patent Application.* **2011**, *US2011* (0053880), A1.

(4) (a) Searle, R. J. G.; Boyce, C. B. C.; Bay, H. Thioamide Pesticides. US Patent 4,096,275, June 20, 1978; (b) Fauss, R.; Findeisen, K.; Becker, B.; Hamman, I.; Homeyer, B. Pesticidal Novel Substituted Hydroxymalonic Acid Amide–Thiomides. US Patent 4,581,375, April 8, 1986.

(5) (a) Meltzer, R. I.; Lewis, A. D.; King, J. A. *J. Am. Chem. Soc.* **1955**, *77* (15), 4062. doi:10.1021/ja01620a029; (b) Wang, F.; Langley, R.; Gulten, G.; Dover, L. G.; Besra, G. S.; Jacobs, W. R.; Sacchettini, J. C. *J. Exp. Med.* **2007**, *204* (1), 73. doi:10.1084/jem.20062100.

(6) (a) Stiller, E. T.; Diassi, P. A.; Gerschutz, D.; Meikle, D.; Moetz, J.; Principe, P. A.; Levine, S. D. *J. Med. Chem.* **1972**, *15* (10), 1029. doi:10.1021/jm00280a009; (b) Gala, D.; Stamford, A.; Jenkins, J.; Kugelman, M. *Org. Process Res. Dev.* **1997**, *1* (2), 163. doi:10.1021/op960035c.

(7) Harrowven, D. C.; Lucas, M. C.; Howes, P. D. *Tetrahedron Lett.* **1999**, *40* (23), 4443. doi:10.1016/S0040-4039(99)00768-6.

(8) (a) Koketsu, M.; Ishihara, H. *Curr. Org. Synth.* **2007**, *4* (1), 15. doi:10.2174/157017907779981615; (b) Metzner, P. Thiocarbonyl Compounds as Specific Tools for Organic Synthesis. In *Topics in Current Chemistry;* Organosulfur Chemistry I, Vol. 204; Springer: New York, 1999; pp 127–181.

(9) Willgerodt, C. *Ber. Dtsch. Chem. Ges.* **1887**, *20* (2), 2467. doi:10.1002/cber.18870200278.

(10) Dauben, W.; Rogan, J. *J. Am. Chem. Soc.* **1956**, *78* (16), 4135. doi:10.1021/ja01597a075.

(11) Harris, T. W.; Smith, H. E.; Mobley, P. L.; Manier, D. H.; Sulser, F. *J. Med. Chem.* **1982**, *25* (7), 855. doi:10.1021/jm00349a018.

(12) Harrowven, D. C.; Lucas, M. C. *Tetrahedron* **1999**, *55* (4), 1187. doi:10.1016/S0040-4020(98)01096-5.

(13) Liu, W. W.; Zhao, Y. Q.; Xu, R. B.; Tang, L. J.; Hu, H. W. *Chin. J. Chem.* **2006**, *24* (10), 1472. doi:10.1002/cjoc.200690278.

(14) Asinger, F.; Schäfer, W.; Baumgarte, G.; Müting, P. F. *Liebigs Ann. Chem.* **1963**, *661* (1), 95. doi:10.1002/jlac.19636610108.

(15) Asinger, F.; Saus, A.; Offermanns, H.; Hahn, H. D. *Justus*

Liebigs Ann. Chem. **1966**, *691* (1), 92. doi:10.1002/jlac.19666910114.
(16) Moghaddam, F. H.; Mirjafary, Z.; Saeidian, H.; Javan, M. J. *Synlett* **2008**, *2008* (6), 892. doi:10.1055/s-2008-1042925.
(17) (a) Merz, W. Process for the Preparation of Alkali Metal Salts of 3,3-Dimethyl-2-oxo-butyric Acid. US Patent 4,113,767, September 12, 1978; (b) Merz, W. Process for the Preparation of 6-*tert*-Butyl-3-mercapto-4-amino-1,2,4-triazin-5(4*H*)-one. US Patent 4,151,355, April 24, 1979.
(18) Adiwidjaja, G.; Gunther, H.; Voss, J. *Angew. Chem. Int. Ed. Engl.* **1980**, *19* (7), 563. doi:10.1002/anie.198005631.
(19) Murata, S.; Suzuki, K.; Miura, M.; Nomura, M. *J. Chem. Soc., Perkin Trans. 1* **1990**, (2): 361. doi:10.1039/p19900000361.
(20) Raucher, S.; Klein, P. *J. Org. Chem.* **1981**, *46* (17), 3558. doi:10.1021/jo00330a041.
(21) (a) Nooshabadi, M.; Aghapoor, K.; Darabi, H. R.; Mojtahedi, M. M. *Tetrahedron Lett.* **1999**, *40* (42), 7549. doi:10.1016/S0040-4039(99)01600-7; (b) Olsson, R.; Hansen, H. C.; Andersson, C. M. *Tetrahedron Lett.* **2000**, *41* (41), 7947. doi:10.1016/S0040-4039(00)01360-5; (c) Aghapoor, K.; Darabi, H.; Tabar-Heydar, K.; Nakhshab, L. *Sulfur Lett.* **2002**, *25* (6), 259. doi:10.1080/02786110215846; (d) Zbruyev, O. I.; Stiasni, N.; Kappe, C. O. *J. Comb. Chem.* **2003**, *5* (2), 145. doi:10.1021/cc0200538; (e) Darabi, H. R.; Aghapoor, K.; Tajbakhsh, M. *Tetrahedron Lett.* **2004**, *45*, 4617; (f) Poupaert, J. H.; Duarte, S.; Colacino, E.; Depreux, P.; McCurdy, C. R.; Lambert, D. L. *Phosphorus Sulfur Silicon Relat. Elem.* **2004**, *179* (10), 1959. doi:10.1080/10426500490466995; (g) Holt, J. J.; Calitree, B. D.; Vincek, J.; Gannon, M. K.; Detty, M. R. *J. Org. Chem.* **2007**, *72* (7), 2690. doi:10.1021/jo070086f; (h) Darabi, H. R.; Aghapoor, K.; Balavar, Y.; Mobedi, E.; Farhangian, H.; Mohsenzadeh, F. *Z. Naturforsch.* **2008**, *63b*, 993.
(22) Miranda, R.; Noguez, O.; Velasco, B.; Arroyo, G.; Penieres, G.; Martínez, J. O.; Delgado, F. *Educ. Quim.* **2009**, *20* (4), 421.
(23) Camarena, R.; Cano, A. C.; Delgado, F.; Zúñiga, N.; Álvarez, C.; García, O. *Tetrahedron Lett.* **1993**, *34* (43), 6857. doi:10.1016/S0040-4039(00)91813-6.
(24) Salmón, M.; Osnaya, R.; Gómez, L.; Arroyo, G.; Delgado, F.; Miranda, R. *J. Mex. Chem. Soc.* **2001**, *45*, 206.
(25) (a) Delgado, F.; Tamariz, J.; Zepeda, G.; Landa, M.; Miranda, R.; García, J. *Synth. Commun.* **1995**, *25* (5), 753. doi:10.1080/00397919508011413; (b) Obrador, E.; Castro, M.; Tamaríz, J.; Zepeda, G.; Miranda, R.; Delgado, F. *Synth. Commun.* **1998**, *28* (24), 4649. doi:10.1080/00397919808004530; (c) Alcerreca, G.; Sanabria, R.; Miranda, R.; Arroyo, G.; Tamariz, J.; Delgado, F. *Synth. Commun.* **2000**, *30* (7), 1295. doi:10.1080/00397910008087151.
(26) Penieres-Carrillo, G.; García-Estrada, J. G.; Gutiérrez-Ramírez, J. L.; Álvarez-Toledano, C. *Green Chem.* **2003**, *5* (3), 337. doi:10.1039/b211011c.
(27) Noguez, M. O.; Marcelino, V.; Rodríguez, H.; Martín, O.; Martínez, J. O.; Arroyo, G. A.; Pérez, F. J.; Suárez, M.; Miranda, R. *Int. J. Mol. Sci.* **2011**, *12* (4), 2641. doi:10.3390/ijms12042641.
(28) Penieres, G.; Aceves, J. M.; Flores, A.; Mendoza, G.; Garcia, O.; Álvarez, C. *Heterocycl. Commun.* **1997**, *3* (6), 507. doi:10.1515/HC.1997.3.6.507.
(29) McNally, J. P.; Leong, V. S.; Cooper, N. J. Cannula Techniques for the Manipulation of Air-Sensitive Materials. In *Experimental Organometallic Chemistry;* Wayda, A.L., Darensbourg, M.Y., Eds.; ACS Symposium Series 357, Washington, DC, 1987; Chapter 2, pp 6–33.
(30) (a) Altomare, A.; Cascarano, G.; Giacovazzo, C.; Guagliardi, A.; Burla, M. C.; Polidori, G.; Canalli, M. *J. Appl. Cryst.* **1994**, *27*, 435; (b) Sheldrick, G. M. *SHELXL-97, Program for the Refinement of Crystal Structures;* University of Göttingen: Göttingen, Germany, 1997.
(31) (a) Lundstedt, T.; Thoren, P.; Carlson, R.; Norin, T.; Mörch, L. *Acta Chem. Scand. B* **1984**, *38b*, 717. doi:10.3891/acta.chem.scand.38b-0717; (b) Rais, A.; Ankati, H.; Biehl, E. J. *Heterocycl. Chem.* **2009**, *46* (4), 599. doi:10.1002/jhet.88.
(32) Carmack, M.; Behforouz, M.; Berchtold, G. A.; Berkowitz, S. M.; Wiesler, D.; Barone, R. *J. Heterocycl. Chem.* **1989**, *26* (5), 1305. doi:10.1002/jhet.5570260517.
(33) Darabi, H. R.; Aghapoor, K.; Nakhshab, L. *Z. Naturforsch.* **2004**, *59b*, 601.

Can. J. Chem. Downloaded from www.nrcresearchpress.com by Renmin University of China on 09/02/12
For personal use only.

M[P(1,2-$O_2C_6H_4)_3$] (M = K or Na) — Synthesis, characterization, and use in halide abstraction

Paul W. Siu and Derek P. Gates

Can. J. Chem. Downloaded from www.nrcresearchpress.com by Renmin University of China on 09/02/12
For personal use only.

Abstract: Alkali metal salts of the tris(*o*-phenylenedioxy)phosphate anion, K[P(1,2-$O_2C_6H_4)_3$] (K[**1**]) and Na[P(1,2-$O_2C_6H_4)_3$] (Na[**1**]), were prepared by treating Et_3NH[**1**] with KH or NaH, respectively. X-ray crystallographic analysis of K[**1**], crystallized in the presence of DMSO, revealed a dimeric structure of formulation $K_2(DMSO)_6$[**1**]$_2$·C_7H_8. In contrast, the crystal structure of K[**1**] grown from MeCN consists of fascinating hexagonal macrocycles with formulation {K$(MeCN)_2$[**1**]}$_6$ with an outside diameter of about 25 Å and a very small hole (≤2.5 Å). Remarkably, these hexagonal macrocycles stack one upon the other with a spacing of about 9.4 Å. The salt, K[**1**], is an effective halide abstraction agent reacting with (dppp)$PdCl_2$ (dppp = 1,3-bis(diphenylphosphino)propane) (1:1 ratio) or [(cod)RhCl]$_2$ (2:1 ratio) to afford [(dppp)Pd(μ-Cl)]$_2$[**1**]$_2$ and (cod)Rh[**1**], respectively. The molecular structures of each complex were determined.

Key words: anions, phosphorus, palladium, rhodium, macrocycles.

Résumé : On a préparé les sels de sodium et de potassium de l'anion tris(*o*-phénylènedioxy)phosphate, K[P(1,2-$O_2C_6H_4)_3$] (K[**1**]) et Na[P(1,2-$O_2C_6H_4)_3$] (Na[**1**]) par traitement du produit Et_3NH[**1**] respectivement avec du KH ou du NaH. Le composé K[**1**] recristallisé à partir du DMSO a fait l'objet d'une étude par diffraction des rayons-X et l'analyse des données révèle qu'il existe sous une structure dimère de formule $K_2(DMSO)_6$[**1**]$_2$·C_7H_8. Toutefois, la structure cristalline du composé K[**1**] obtenu par recristallisation à partir de l'acétonitrile est formée de macrocycles hexagonaux fascinants de formule {K$(MeCN)_2$[**1**]}$_6$ de diamètres extérieurs d'environ 25 Å et un très petit trou (≤2,5 Å). Il est remarquable que les macrocycles hexagonaux s'empilent les uns sur les autres avec un espacement de 9,4 Å. Le sel K[**1**] est un agent très efficace pour enlever des halogènes; il réagit avec le (dppp)$PdCl_2$ (dppp = 1,3-bis(disphénylphosphino)propane) (rapport de 1 :1) ou le [(cod)RhCl]$_2$ (rapport de 2 : 1) pour conduire à la formation respectivement de [(dppp)P(μ-Cl)]$_2$[**1**]$_2$ et de (cod)Rh[**1**]. On a déterminé les structures moléculaires de chaque complexe.

Mots-clés : anions, phosphore, palladium, rhodium, macrocycles.

[Traduit par la Rédaction]

Introduction

The development and investigation of hexacoordinate compounds of phosphorus is an area of widespread fundamental interest. Although such species can be cationic or neutral depending on the nature of the substituents,[1–3] by far the most prevalent are anionic species of the form $[PX_6]^-$, led by $[PF_6]^-$ and $[PCl_6]^-$. Within this subclass, the family of chiral hexacoordinate phosphorus(V)-based anions bearing chelating dianionic ligands such as tris(tetrachlorobenzenediolato) phosphate (TRISPHAT, **A**),[4a] bis(tetrachlorobenzenediolato) mono([1,1′]-binaphthalenyl-2,2′-diolato)phosphate (BINPHAT, **B**),[4b] and tris(oxalato)phosphate (TOP, **C**)[4c] (Chart 1) are of considerable interest.[5] Of these, perhaps the most widely studied is TRISPHAT (**A** in Chart 1),[6] which can be resolved into pure enantiomers and is employed in NMR enantiodifferentiation and resolution of chiral cations.[7,8] Interestingly, the non-halogenated tris(*o*-phenylenedioxy)phosphate anion, [**1**]$^-$, which was the first example of a hexacoordinate organophosphate anion,[9–11] cannot be resolved into pure enantiomers due to acid-catalyzed, one-ended dissociation leading to pseudorotation and racemization.[12] This parent system has received limited attention with the exception of some electrochemical studies of Li[**1**] pertaining to applications in lithium batteries,[13–15]

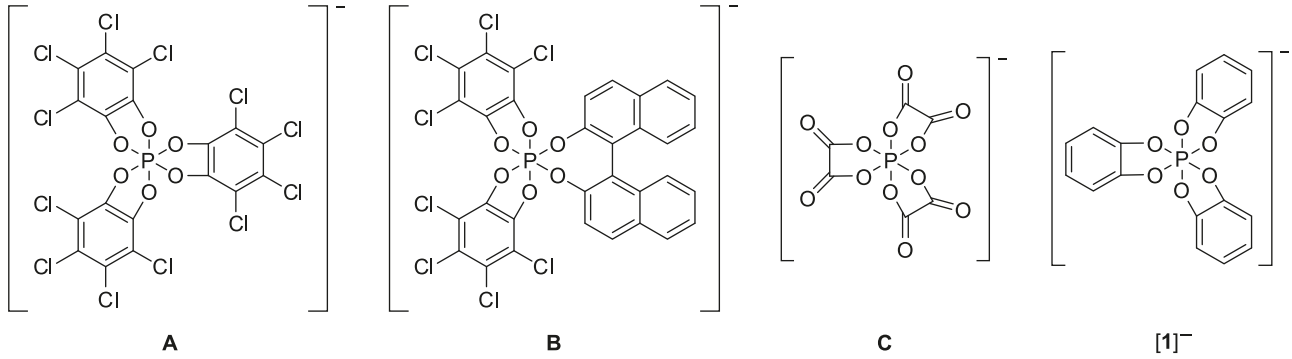
We have been interested in using [**1**]$^-$ as an anion for the stabilization of highly reactive cations and have synthesized and isolated Brønsted acids of [**1**]$^-$, namely $H(DMSO)_2$[**1**] and $H(DMF)_2$[**1**].[16] These compounds are attractive because of their simple and convenient synthesis from cheap and readily available starting materials and their potential utility in the generation of reactive cations in the presence of [**1**]$^-$, a relatively weakly coordinating anion. Indeed, we have shown that $H(DMF)_2$[**1**] may be utilized to protonate metal–alkyl bonds, a key step in the generation of numerous active catalyst species.[17–19] Based upon our investigation of the IR stretching frequencies of the ammonium salts, the coordination ability of [**1**]$^-$ should be comparable to that of $[BF_4]^-$.[16] Therefore, we hypothesized that alkali metal salts of [**1**]$^-$ may be of interest as halide abstracting reagents to generate reactive cations. Although the Li^+ salt of [**1**]$^-$ has been prepared,[15] the heavier alkali salts of [**1**]$^-$ have not been reported.

Received 26 February 2012. Accepted 6 April 2012. Published at www.nrcresearchpress.com/cjc on 28 June 2012.

P.W. Siu and D.P. Gates. Department of Chemistry, University of British Columbia, 2036 Main Mall, Vancouver, BC V6T 1Z1, Canada.

Corresponding author: Derek P. Gates (e-mail: dgates@chem.ubc.ca).

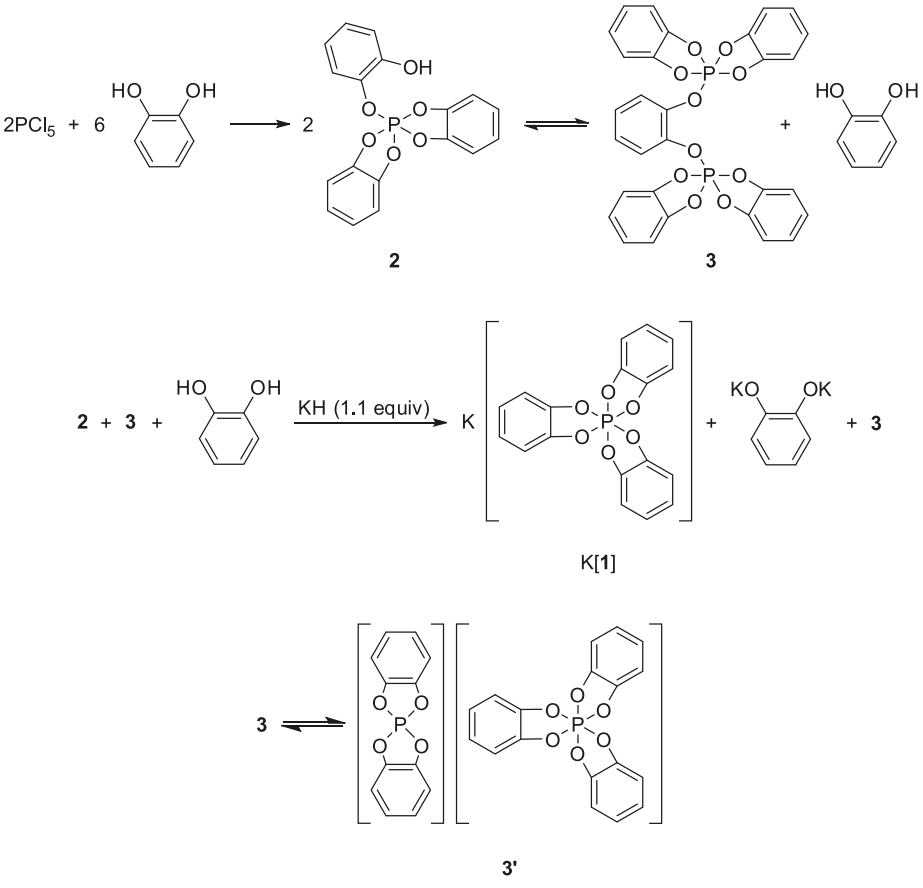
Chart 1. Selected samples of chiral hexacoordinate phosphorus(V)-based anions.



Herein, we report the synthesis and characterization of sodium and potassium salts of the anion [**1**]⁻ and our preliminary investigations of their use as halide abstracting reagents. The molecular structures of four new compounds containing [**1**]⁻ are reported: $K_2(DMSO)_6[\mathbf{1}]_2 \cdot C_7H_8$, $\{K(MeCN)_2[\mathbf{1}]\}_6$, $[(dppp)Pd(\mu\text{-}Cl)]_2[\mathbf{1}]_2$ (dppp = 1,3-bis(diphenylphosphino) propane), and (cod)Rh[**1**].

Discussion

It is well-established that the reaction of phosphorus(V) chloride with catechol (3 equiv) affords a mixture of **2** and **3**.[20] The salt Li[**1**] has previously been prepared by treating this mixture with *n*-BuLi.[14,15] Since *n*-BuK is not readily available, we attempted to prepare K[**1**] by treating a mixture of **2** and **3** in THF with potassium hydride (1.1 equiv). The ^{31}P NMR spectrum of the reaction mixture exhibits signals assigned to starting material **3** ($\delta = -27$)[20,21] and to a product with a chemical shift consistent with the [**1**]⁻ anion ($\delta = -83$),[15,16,22–25] tentatively assigned to K[**1**]. Interestingly, upon isolation and redissolution of the crude product in DMSO-d_6 the ^{31}P NMR spectrum showed signals at 13 and –83 ppm, suggesting the formation of the known **3′**.[20] Unfortunately, we have been unable to isolate pure K[**1**] from this mixture.

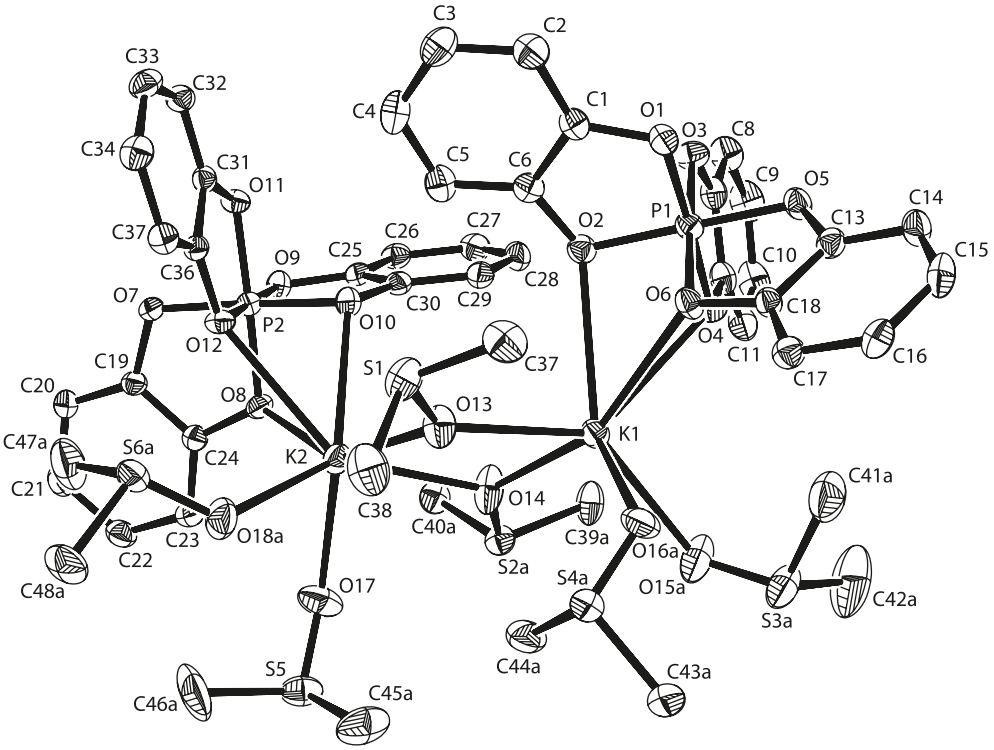


3'

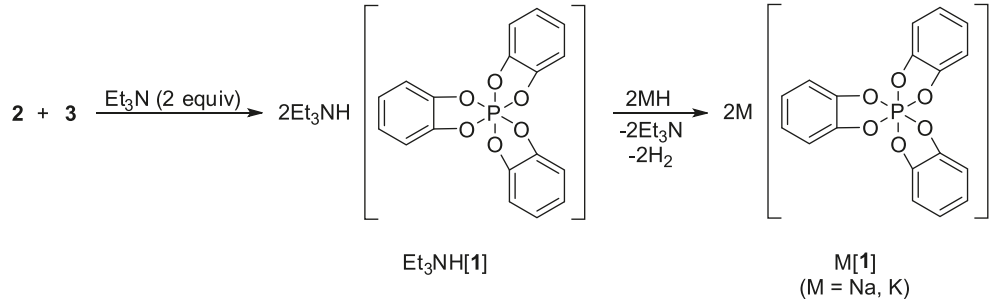
Can. J. Chem. Downloaded from www.nrcresearchpress.com by Renmin University of China on 09/02/12
For personal use only.

Can. J. Chem. Downloaded from www.nrcresearchpress.com by Renmin University of China on 09/02/12
For personal use only.

Fig. 1. Molecular structure of the Δ,Δ-$K_2(DMSO)_6[\mathbf{1}]_2$ (50% probability ellipsoids, the Λ,Λ-isomer is not shown). All hydrogen atoms and the solvent of crystallization (C_7H_8) are omitted for clarity. Selected bond lengths (Å): P(1)–O(1) = 1.714(1); P(1)–O(2) = 1.722(1); P(1)–O(3) = 1.707(1); P(1)–O(4) = 1.721(1); P(1)–O(5) = 1.708(1); P(1)–O(6) = 1.717(1); P(2)–O(7) = 1.710(1); P(2)–O(8) = 1.718(1); P(2)–O(9) = 1.708(1); P(2)–O(10) = 1.715(1); P(2)–O(11) = 1.708(1); P(2)–O(12) = 1.735(1); K(1)–O(2) = 2.876(1); K(1)–O(4) = 2.846(1); K(1)–O(6) = 2.801(1); K(1)–O(13) = 2.696(2); K(1)–O(14) = 2.666(2); K(1)–O(15A) = 2.766(5); K(1)–O(16A) = 2.779(7); K(2)–O(8) = 2.754(1); K(2)–O(10) = 2.965(1); K(2)–O(12) = 2.887(1); K(2)–O(13) = 2.678(2); K(2)–O(14) = 2.681(2); K(2)–O(17) = 2.670(2); K(2)–O(18A) = 2.729(8). Selected bond angles (°): O(1)–P(1)–O(2) = 90.88(6); O(3)–P(1)–O(4) = 91.04(6); O(5)–P(1)–O(6) = 90.67(6); O(7)–P(2)–O(8) = 90.51(6); O(9)–P(2)–O(10) = 91.44(6); O(11)–P(2)–O(12) = 90.76(6).



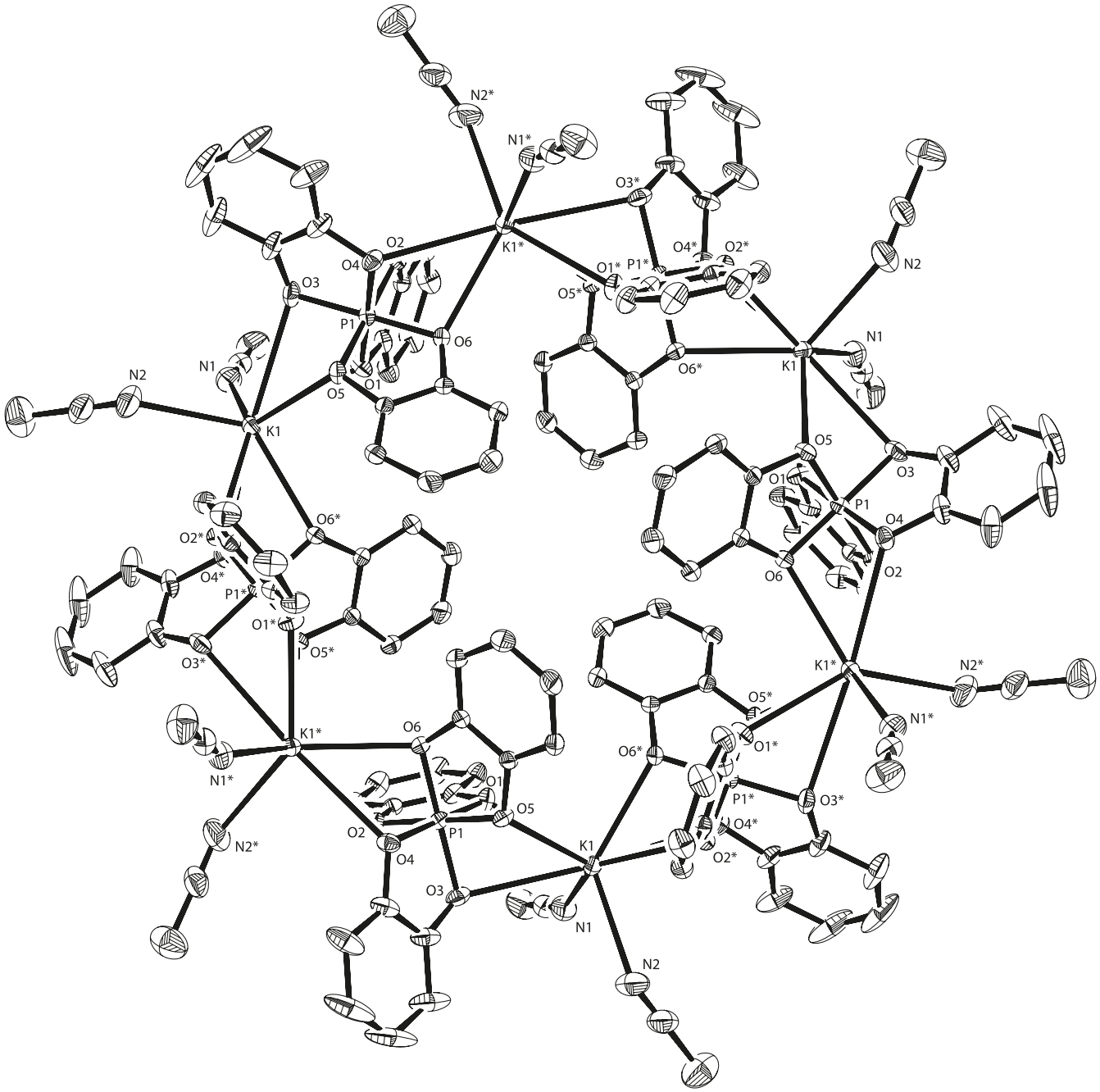
As an alternate strategy to synthesize K[**1**], the deprotonation of the known ammonium salt Et_3NH[**1**][9–11] with a slurry of KH (1.1 equiv) in acetonitrile was attempted. After workup, the desired product (K[**1**]) was obtained as a white solid. Characterization by ^{31}P NMR spectroscopy in CD_2Cl_2 revealed a singlet resonance at –86.1 ppm, consistent with the presence of the [**1**]$^-$ anion. The ^1H and $^{13}C\{^1H\}$ NMR spectra show only signals in the aromatic region as expected for K[**1**]. In particular, three signals are observed in the $^{13}C\{^1H\}$ NMR spectrum, which is consistent with the symmetrical [**1**]$^-$ anion. Satisfactory elemental microanalysis was obtained for K[**1**]. Following an analogous procedure, the sodium salt (Na[**1**]) was prepared and characterized by ^{31}P, ^1H, and $^{13}C\{^1H\}$ NMR spectroscopy and elemental analysis.



Efforts to obtain single crystals of K[**1**] from CH_2Cl_2 proved unsuccessful; however, crystals obtained from slow diffusion of toluene into a DMSO solution of the crude product were suitable for X-ray diffraction. The molecular structure is shown in Fig. 1 and reveals a dimeric structure of formulation $K_2(DMSO)_6[\mathbf{1}]_2{\cdot}C_7H_8$. Interestingly, each of the

Can. J. Chem. Downloaded from www.nrcresearchpress.com by Renmin University of China on 09/02/12
For personal use only.

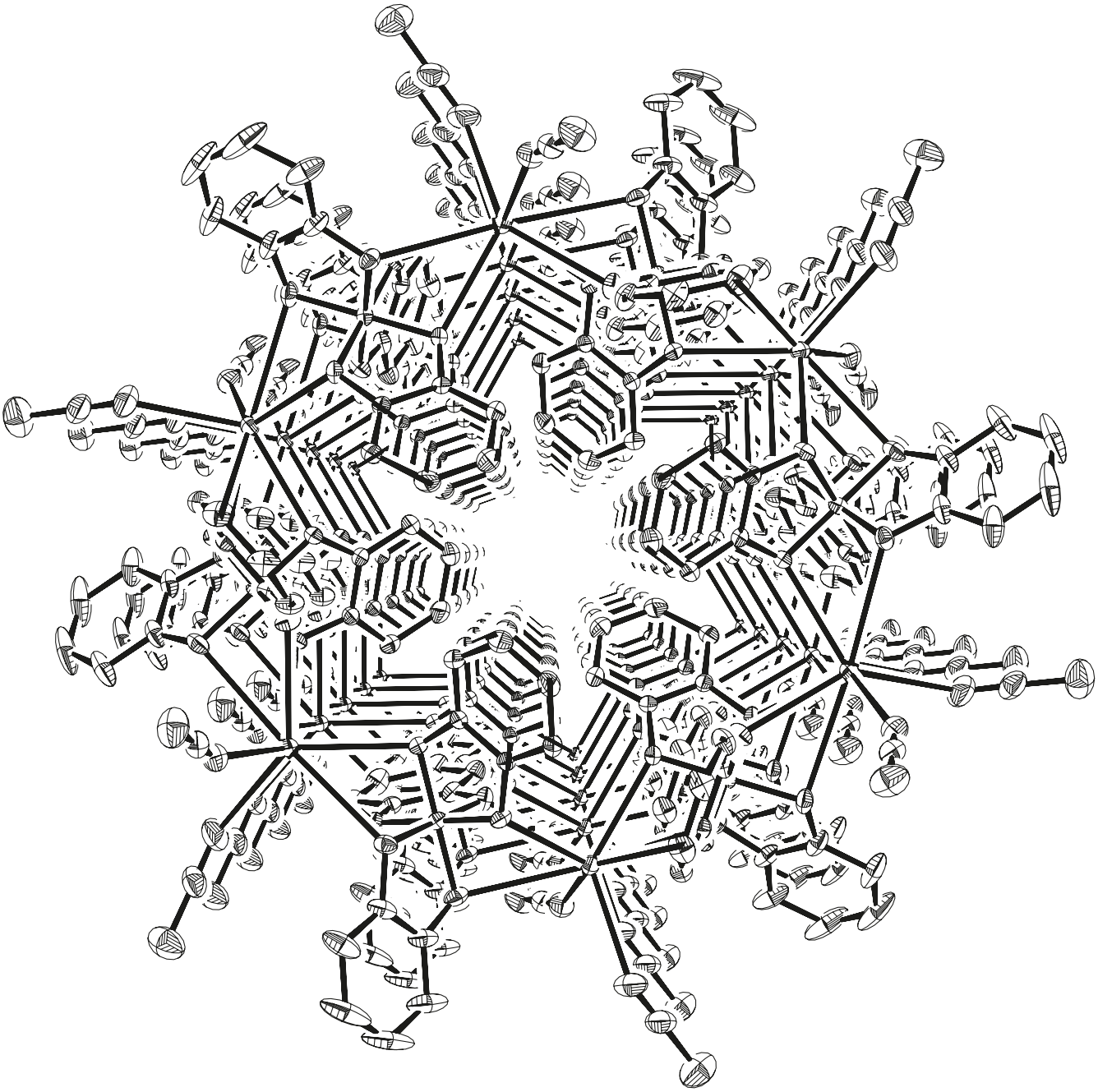
Fig. 2. Molecular structure of $\{K(MeCN)_2[\mathbf{1}]\}_6$ (50% probability ellipsoids). All hydrogen atoms are omitted for clarity. Selected bond lengths (Å): O(1)–P(1) = 1.7149(9); O(2)–P(1) = 1.7111(9); O(3)–P(1) = 1.7189(9); O(4)–P(1) = 1.7207(9); O(5)–P(1) = 1.7058(9); O(6)–P(1) = 1.7024(9); K(1)–O(1) = 2.7770(9); K(1)–O(3) = 3.019(1); K(1)–O(5) = 2.8244(9); K(1*)–O(2) = 2.8832(9); K(1*)–O(4) = 3.024(1); K(1*)–O(6) = 2.7705(9). Selected bond angles (°): O(1)–P(1)–O(2) = 91.06(4); O(3)–P(1)–O(4) = 91.11(5); O(5)–P(1)–O(6) = 91.53(4).



potassium ions are seven-coordinate, being bound by two terminal DMSO ligands, two bridging DMSO ligands, and three oxygen atoms of the $[\mathbf{1}]^-$ anion. The $[\mathbf{1}]^-$ anion is slightly perturbed by binding to K^+ with the three bound P–O bonds (avg. 1.721(3) Å, range 1.715(1) to 1.735(1) Å) being slightly longer than the three unbound P–O bonds (avg. 1.709(3) Å, range 1.707(1) to 1.714(1) Å). Overall, the average P–O bond (1.715(5) Å) and the average endocyclic O–P–O angle (90.9(2)°) within the anion $[\mathbf{1}]^-$ are similar to those found in previously reported compounds containing $[\mathbf{1}]^-$, namely: $Et_3NH[\mathbf{1}]$ (1.708(4) Å, 91.4(2)°),[11] $H(DMSO)_2[\mathbf{1}]$ (1.716(3) Å, 90.91(9)°),[16] $H(DMF)_2[\mathbf{1}]$ (1.711(3) Å, 90.8(1)°),[16] [(dppe)Pd(NCMe)Me][**1**] (dppe = 1,2-bis(diphenylphosphino)ethane; 1.709(7) Å, 91.0(2)°),[16] and $[(dppe)Pd(NCMe)_2][\mathbf{1}]_2$ (1.713(6) Å, 90.8(2)°).[16] The K–O distances involving the $[\mathbf{1}]^-$ ion (avg. 2.855(3) Å) are longer than those involving the DMSO moiety ($avg._{terminal}$ = 2.741(2) Å; $avg._{bridging}$ = 2.680(3) Å).

Recrystallization of K[**1**] from acetonitrile gave quite a different structure (Fig. 2). Remarkably, the molecular structure consists of fascinating macrocyclic hexamers of formulation $\{K(MeCN)_2[\mathbf{1}]\}_6$ with S_6 point group symmetry. The K^+ ions bridge two κ^3-bound $[\mathbf{1}]^-$ anions and have two acetonitrile

Fig. 3. Three-dimensional stacking of the $\{K(MeCN)_2[\mathbf{1}]\}_6$ (50% probability ellipsoids). All hydrogen atoms are omitted for clarity.

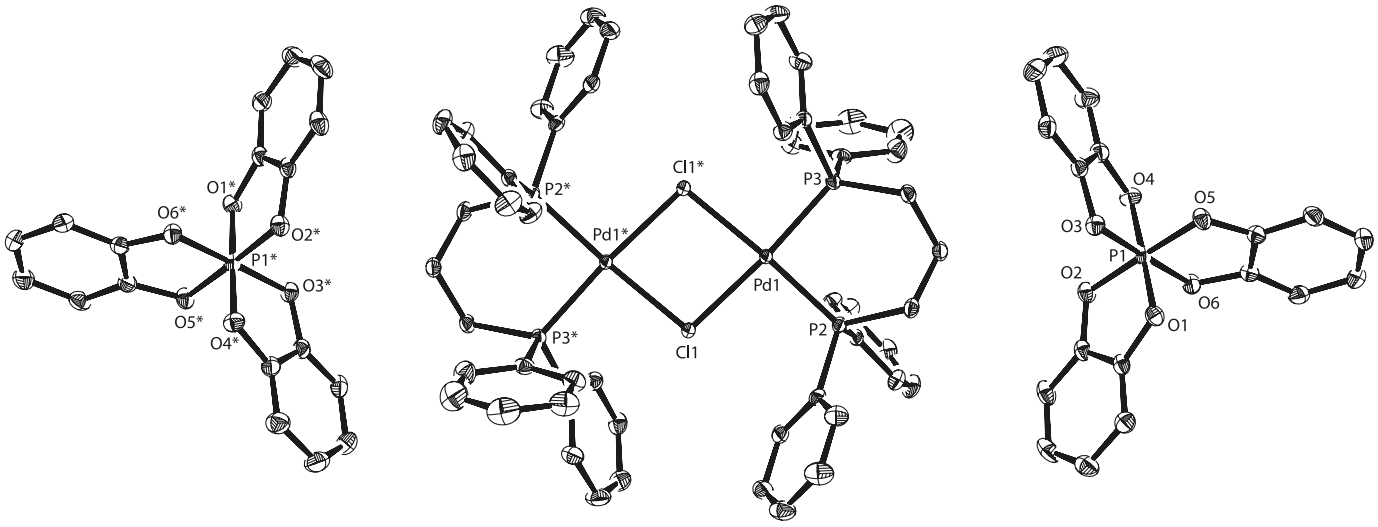


Can. J. Chem. Downloaded from www.nrcresearchpress.com by Renmin University of China on 09/02/12
For personal use only.

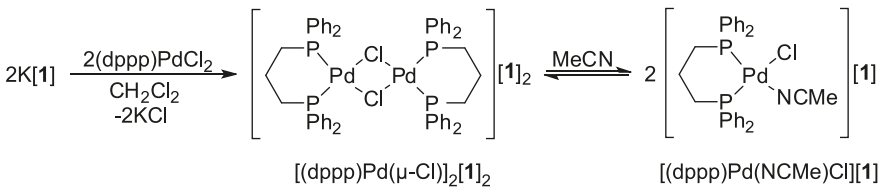
ligands making the K^+ ions eight coordinate. The K–O distances (avg. 2.883(2) Å) are slightly longer than the corresponding K–O distances in $K_2(DMSO)_6[\mathbf{1}]_2{\cdot}C_7H_8$ (avg. 2.855(3) Å). The $[\mathbf{1}]^-$ anions are situated at the vertices of a hexagon and their stereochemistry alternates between Λ and Δ around the ring. The metrical parameters within the anion $[\mathbf{1}]^-$ (avg. P–O = 1.712(2) Å and avg. O–P–O = 91.23(8)°) are comparable to those found in $K_2(DMSO)_6[\mathbf{1}]_2{\cdot}C_7H_8$ (avg. P–O = 1.715(5) Å and avg. O–P–O = 90.9(2)°). Particularly striking is the stacking of the hexagonal $\{K(MeCN)_2[\mathbf{1}]\}_6$ macrocycles one upon the other in the crystalline lattice (Fig. 3). The macrocycles each have an outside diameter of about 25 Å and a very small hole (≤2.5 Å) and are spaced by about 9.4 Å to form a one-dimensional array.

As a starting point to testing the efficacy of K[**1**] as a halide abstracting agent, a mixture of (dppp)$PdCl_2$ and solvent-free K[**1**] were mixed and dissolved in chloroform. The ^{31}P NMR spectrum of the yellow reaction solution, after filtration to remove KCl, showed singlet resonances at 12.4 and –84.2 ppm. Single crystals suitable for X-ray diffraction were obtained on slow evaporation of the reaction mixture. The molecular structure of the chloro-bridged dimer $[(dppp)Pd(\mu\text{-}Cl)]_2[\mathbf{1}]_2$ is shown in Fig. 4 and confirms the successful abstraction of a Cl^- ion with K[**1**]. There is a crystallographically imposed inversion centre between the Pd atoms. The metrical parameters of $[(dppp)Pd(\mu\text{-}Cl)]_2[\mathbf{1}]_2$ are unremarkable, being similar to those of related dimeric structures (e.g., $[(dppp)Pd(\mu\text{-}Cl)]_2[SO_4]_2$,[26] $[(dppe)Pd(\mu\text{-}Cl)]_2[X]_2$ (X = ClO_4^-,

Fig. 4. Molecular structure of $[(dppp)Pd(\mu_2\text{-}Cl)]_2[\mathbf{1}]_2$ (50% probability ellipsoids). All hydrogen atoms and the solvent of crystallization ($2 \times CHCl_3$) are omitted for clarity. Selected bond lengths (Å): P(1)–O(1) = 1.713(2); P(1)–O(2) = 1.710(2); P(1)–O(3) = 1.713(2); P(1)–O(4) = 1.708(2); P(1)–O(5) = 1.724(2); P(1)–O(6) = 1.720(2); Pd(1)–P(2) = 2.2489(5); Pd(1)–P(3) = 2.2598(5); Pd(1)–Cl(1) = 2.4024(5); Pd(1)–Cl(1*) = 2.4004(5). Selected bond angles (°): O(1)–P(1)–O(2) = 90.88(7); O(3)–P(1)–O(4) = 91.24(7); O(5)–P(1)–O(6) = 90.93(7); P(2)–Pd(1)–P(3) = 91.10(2); Cl(1)–Pd(1)–Cl(1*) = 83.22(2). dppp, 1,3-bis(diphenylphosphino)propane.



BF_4^-),[27,28] $[(dppen)Pd(\mu\text{-}Cl)]_2[CF_3SO_3]_2$ (dppen = 1,2-bis(diphenylphosphino)ethene),[29] $[(o\text{-}C_6H_4(CH_2PPh_2)_2)Pd(\mu\text{-}Cl)]_2[PF_6]_2$,[30] and $[(Ph_3P)_2Pd(\mu\text{-}Cl)]_2[BF_4]_2$).[31] Significantly, the molecular structure suggests weak interactions are present between the cation and the $[\mathbf{1}]^-$ anion. The closest contact is between an oxygen of the $[\mathbf{1}]^-$ anion and a hydrogen of the CH_2 moiety within the dppp ligand (O(1)···H(33b) = 2.208(1) Å) and is within the sum of the van der Waals radii for oxygen and hydrogen (r_{vdw} = 2.72 Å).[32] The metrical parameters within the anion $[\mathbf{1}]^-$ (avg. P–O = 1.715(4) Å and avg. O–P–O = 91.0(1)°) are consistent with those found in $K_2(DMSO)_6[\mathbf{1}]_2{\cdot}C_7H_8$ and $\{K(MeCN)_2[\mathbf{1}]\}_6$. Noteworthy is the fact that the molecular structure is consistent with the aforementioned ^{31}P NMR spectroscopic data for the reaction mixture with equivalent phosphine moieties of dppp (δ = 12.4) and the free $[\mathbf{1}]^-$ anion (δ = –84.2). It was not possible to dissolve the crystals in weakly coordinating solvents (e.g., $CDCl_3$ or CD_2Cl_2) so the crystals were dissolved in acetonitrile-d_3 for further spectroscopic analysis. Interestingly, the CD_3CN solution showed inequivalent phosphine moieties (δ = 15.1 (br s), 10.3 (br s)) and the $[\mathbf{1}]^-$ anion (δ = –81.7). These data are consistent with the solution structure being $[(dppp)PdCl(NCMe)][\mathbf{1}]$, which appears to be in equilibrium with $[(dppp)Pd(\mu\text{-}Cl)]_2[\mathbf{1}]_2$, since in some instances signals assigned to both species are observed.

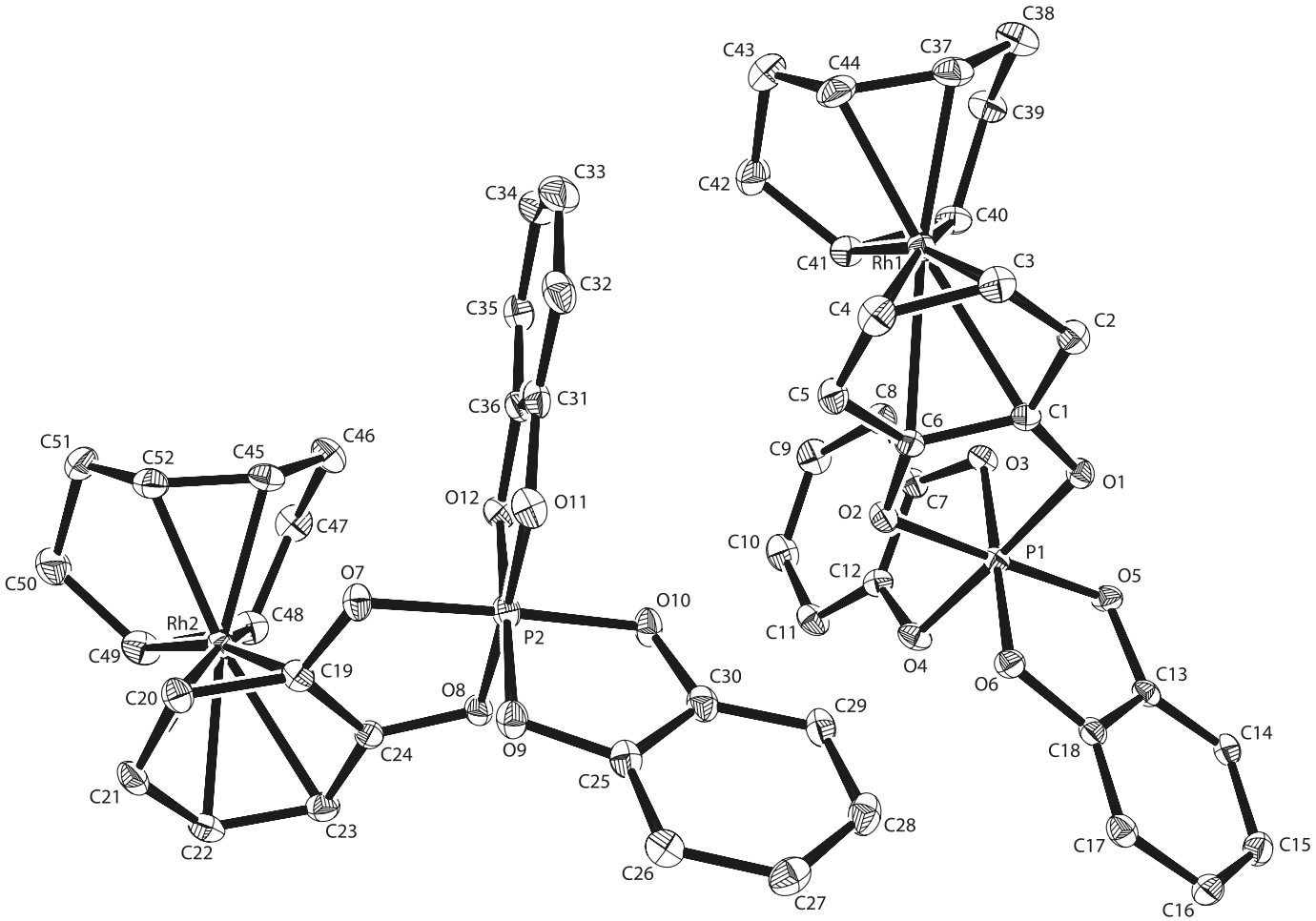


Given that K[**1**] is an effective halide abstraction agent for palladium(II) chloride bonds, we tested the efficacy of K[**1**] as a halide abstraction agent with the rhodium(I) dimer, $[(cod)RhCl]_2$. To a mixture of $[(cod)RhCl]_2$ with K[**1**] (2 equiv) was added acetonitrile and the yellow mixture was stirred overnight. Recrystallization of the crude product from dichloromethane afforded orange crystals. The molecular structure is shown in Fig. 5 and shows that the $[\mathbf{1}]^-$ anion is η^6-bound to the rhodium(I) centre to afford zwitterionic (cod)Rh[**1**]. Similar cation–anion interactions have been noted in the solid-state structures of similar rhodium(I) complexes containing the weakly coordinating anions $[BPh_4]^-$ and $[B(Ar_F)_4]^-$ (Ar_F = 3,5-bis(trifluoromethyl)phenyl).[33,34] The distance between the centroid of the η^6-bound aromatic ring and Rh(I) is approximately 1.9 Å and is similar to that found in Rh(dppe)$[BPh_4]$ and (cod)Rh$[B(Ar_F)_4]$. The anion–cation interaction results in a lowering of the symmetry about phosphorus with the four P–O bonds of the uncoordinated catechol (avg. 1.700(7) Å) being shorter than the P–O bonds of the coordinated catechol (avg. 1.745(4) Å). The crystals were further characterized by ^1H and ^{31}P NMR spectroscopy and elemental microanalysis. The ^{31}P NMR spectrum (CD_2Cl_2) displayed a singlet resonance at –79.9 ppm, which is shifted downfield compared with K[**1**] (δ = –86.1) and consistent with the retention of the coordination complex in solution. The ^1H NMR spectrum was consistent with a loss of symmetry for

Can. J. Chem. Downloaded from www.nrcresearchpress.com by Renmin University of China on 09/02/12
For personal use only.

Can. J. Chem. Downloaded from www.nrcresearchpress.com by Renmin University of China on 09/02/12
For personal use only.

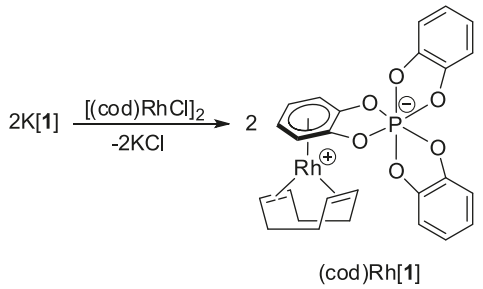
Fig. 5. Molecular structure of (cod)Rh[**1**]. Ellipsoids are drawn at the 50% probability level. All hydrogen atoms and solvents of crystallization (2.5 × CH_2Cl_2) are omitted for clarity. Selected bond lengths (Å): P(1)–O(1) = 1.747(3); P(1)–O(2) = 1.746(3); P(1)–O(3) = 1.695(2); P(1)–O(4) = 1.699(3); P(1)–O(5) = 1.706(3); P(1)–O(6) = 1.702(2); P(2)–O(7) = 1.746(3); P(2)–O(8) = 1.739(3); P(2)–O(9) = 1.703(2); P(2)–O(10) = 1.702(3); P(2)–O(11) = 1.697(3); P(2)–O(12) = 1.697(2); Rh(1)vC(1) = 2.405(4); Rh(1)–C(2) = 2.373(4); Rh(1)–C(3) = 2.262(3); Rh(1)–C(4) = 2.280(3); Rh(1)–C(5) = 2.355(4); Rh(1)–C(6) = 2.371(4); Rh(1)–C(37) = 2.127(5); Rh(1)–C(40) = 2.151(3); Rh(1)–C(41) = 2.136(3); Rh(1)–C(44) = 2.130(5); Rh(2)–C(19) = 2.364(3); Rh(2)–C(20) = 2.307(3); Rh(2)–C(21) = 2.286(3); Rh(2)–C(22) = 2.254(4); Rh(2)–C(23) = 2.357(5); Rh(2)–C(24) = 2.431(3); Rh(2)–C(45) = 2.125(4); Rh(2)–C(48) = 2.136(3); Rh(2)–C(49) = 2.124(3); Rh(2)–C(52) = 2.146(5). Selected bond angles (°): O(1)–P(1)–O(2) = 89.4(1); O(3)–P(1)–O(4) = 91.7(1); O(5)–P(1)–O(6) = 91.7(1); O(7)–P(2)–O(8) = 89.7(1); O(9)–P(2)–O(10) = 91.6(1); O(11)–P(2)–O(12) = 91.8(1).



the aryl H moieties and provides a further evidence that the complex structure of (cod)Rh[**1**] is retained in solution.

Summary

Synthetic procedures to access alkali metal salts containing the tris(*o*-phenylenedioxy)phosphate anion [**1**]$^-$, Na[**1**] and K[**1**], have been presented. Both compounds were characterized spectroscopically. In addition, X-ray crystallographic analysis of K[**1**], recrystallized in the presence of either DMSO or MeCN, revealed two distinct crystal structures: a dimeric structure of formulation $K_2(DMSO)_6[\mathbf{1}]_2 \cdot C_7H_8$ and a hexagonal macrocycle with formulation $\{K(MeCN)_2[\mathbf{1}]\}_6$. Solvent-free K[**1**] was shown to be an effective halide abstractor for (dppp)$PdCl_2$ (1:1) and $[(cod)RhCl]_2$ (2:1 ratio) to generate the dimeric $[(dppp)Pd(\mu\text{-}Cl)]_2[\mathbf{1}]_2$ and the zwitterionic (cod)Rh[**1**], both of which were structurally characterized.



(cod)Rh[**1**]

Experimental section

General procedures

All manipulations were performed using standard Schlenk or glove box techniques under nitrogen atmosphere. THF was

Can. J. Chem. Downloaded from www.nrcresearchpress.com by Renmin University of China on 09/02/12
For personal use only.

dried over sodium / benzophenone ketyl and distilled prior to use. Triethylamine, dichloromethane, acetonitrile, and CD_3CN (Cambridge Isotope Laboratories Inc.) were dried over calcium hydride and distilled prior to use. CD_2Cl_2 was purchased from Cambridge Isotope Laboratories Inc. in 1 g sealed ampules and used as received. DMSO was dried over 3 Å molecular sieves and distilled prior to use. Et_2O and toluene were deoxygenated with nitrogen and dried by passing through a column containing activated alumina. PCl_5 (Sigma-Aldrich) was sublimed prior to use. Potassium hydride (30 wt % dispersion in mineral oil) was purchased from Sigma-Aldrich, washed with hexanes, and dried in vacuo prior to use. Sodium hydride (dry, 95%) was purchased from Sigma-Aldrich and used as received. Mixture **2** / **3**[20] and [(dppp)$PdCl_2$][35] were prepared following literature procedures. ^{1}H, ^{13}C{^{1}H}, and ^{31}P NMR spectra were recorded at room temperature on Bruker Avance 300 or 400 MHz spectrometers. H_3PO_4 (85%) was used as an external standard (δ 0.0) for ^{31}P NMR spectra. ^{1}H NMR spectra were referenced to residual protonated solvent, and ^{13}C{^{1}H} NMR spectra were referenced to the deuterated solvent. Elemental analyses were performed in the University of British Columbia Chemistry Microanalysis Facility, Vancouver, British Columbia.

Synthesis of K[**1**]

To a stirred mixture of **2** and **3** (1.8 g, 5.1 mmol) in THF (15 mL) was added triethylamine (0.58 g, 5.7 mmol). An immediate precipitate was observed. The reaction mixture was stirred for 30 min, the precipitate was isolated by centrifugation and the solid was dried in vacuo. To a suspension of this colourless solid in acetonitrile (10 mL) was added potassium hydride (0.23 g, 5.7 mmol). The evolution of a gas was observed. After the mixture was stirred for 30 min, the solvent was removed in vacuo and the resultant white residue dissolved in THF (40 mL). The solution was filtered to remove insoluble salts and the filtrate was evaporated to dryness to afford a white solid. The solid was dissolved in minimal dichloromethane (3 mL) and Et_2O (100 mL) was added to precipitate the product, which was collected by filtration and dried in vacuo at 130 °C. Yield: 1.4 g (70%). ^{31}P NMR (121 MHz, CD_2Cl_2) δ: –86.1 (s). ^{1}H NMR (300 MHz, CD_2Cl_2) δ: 6.65–6.59 (m, 6H, Ar-*H*), 6.57–6.53 (m, 6H, Ar-*H*). ^{13}C{^{1}H} NMR (101 MHz, CD_2Cl_2) δ: 144.5 (d, J_{CP} = 4 Hz), 121.3 (s), 110.8 (d, J_{CP} = 16 Hz). Anal. calcd for $C_{18}H_{12}KO_6P$: C 54.82, H 3.07; found: C 54.58, H 3.20. X-ray quality crystals of $K_2(DMSO)_6$[**1**]$_2$ were obtained from slow diffusion of toluene into a DMSO solution of K[**1**] for about 1 week. X-ray quality crystals of {K(NCMe)$_2$[**1**]}$_6$ were obtained from slow evaporation of a concentrated solution of K[**1**] in toluene/MeCN for 8 days.

Synthesis of Na[**1**]

To a stirred mixture of **1** and **2** (0.55 g, 1.5 mmol) in THF (5 mL) was added triethylamine (0.18 g, 1.8 mmol). An immediate precipitate was observed. The reaction mixture was stirred for 15 min and the precipitate was isolated by centrifugation and the solid was dried in vacuo. To a suspension of this white solid in acetonitrile (10 mL) was added sodium hydride (0.039 g, 1.6 mmol). The evolution of a gas was observed. After the mixture was refluxed for 30 min, the solvent was removed in vacuo and the resultant white residue dissolved in THF (15 mL). The solution was filtered to remove insoluble salts and the filtrate was evaporated to dryness to afford a white solid. The solid was dried in vacuo at 120 °C. Yield: 0.47 g (80%). ^{31}P NMR (162 MHz, CD_3CN) δ: –82.9 (s). ^{1}H NMR (400 MHz, CD_3CN) δ: 6.67–6.65 (m, 12H, Ar-*H*). ^{13}C{^{1}H} NMR (101 MHz, CD_2Cl_2) δ: 146.4 (d, J_{CP} = 5 Hz), 120.5 (s), 110.5 (d, J_{CP} = 17 Hz). Anal. calcd for $C_{18}H_{12}NaO_6P$: C 57.16, H 3.20; found: C 57.50, H 3.44.

Synthesis of [(dppp)Pd(μ-Cl)]$_2$[**1**]$_2$

To a solid mixture of (dppp)$PdCl_2$ (50 mg, 0.085 mmol) and K[**1**] (34 mg, 0.086 mmol) was added chloroform (2 mL). The yellow reaction solution was stirred overnight and filtered through celite. The ^{31}P NMR spectrum of the reaction mixture showed singlet resonances at 12.4 and –84.2 ppm. Slow evaporation of the yellow solution afforded yellow crystals suitable for X-ray diffraction. The sample was dried in vacuo prior to analysis. Yield: 32 mg (41%). ^{31}P NMR (162 MHz, CD_3CN) δ: 15.1 (br s, dppp), 10.3 (br s, dppp), –81.7 (s, anion). ^{1}H NMR (400 MHz, CD_3CN) δ: 7.69–7.45 (m, 20H, Ar-*H* of dppp), 6.64–6.58 (m, 12H, Ar-*H* of anion), 2.67 (br s, 4H, PCH_2), 2.15–1.99 (m, 2H, $CH_2CH_2CH_2$). ^{13}C{^{1}H} NMR (101 MHz, CD_3CN) δ: 146.9 (d, J_{CP} = 5 Hz), 134.3 (d, J_{CP} = 11 Hz), 133.4 (s), 130.18 (s), 128.5 (s), 127.9 (s), 120.0 (s), 110.9 (d, J_{CP} = 17 Hz), 24.1 (br s), 19.2 (s). Anal. calcd for $C_{45}H_{38}ClO_6P_3Pd$: C 59.42, H 4.21; found: C 59.06, H 4.00.

Synthesis of (cod)Rh[**1**]

To solid mixture of K[**1**] (83 mg, 0.21 mmol) and [(cod)RhCl]$_2$ (51 mg, 0.10 mmol) was added acetonitrile (3 mL). The resulting cloudy yellow mixture was stirred overnight, followed by the removal of all volatiles in vacuo. The yellow residue was dissolved in dichloromethane (3 mL) and filtered to remove a small amount of insoluble material. Slow evaporation of the solution afforded orange crystals suitable for X-ray diffraction. Yield: 33 mg (52%). ^{31}P NMR (161 MHz, CD_2Cl_2) δ: –79.9 (s). ^{1}H NMR (400 MHz, CD_2Cl_2) δ: 6.94–6.91 (m, 2H, Ar-*H*), 6.76–6.64 (m, 8H, Ar-*H*), 5.56–5.50 (m, 2H, Ar-*H*), 5.33 (s, 1.25H, CH_2Cl_2), 4.69–4.39 (m, 4H, *H*C=C*H* in COD), 2.44–2.03 (m, 8H, CH_2 in COD). Anal. calcd for $C_{26}H_{24}O_6PRh \cdot 1.25CH_2Cl_2$: C 48.67, H 3.97; found: C 48.53, H 3.95.

X-ray crystallography

All single crystals were immersed in oil and were mounted on a glass fiber. Data were collected on a Bruker X8 APEX II diffractometer with graphite-monochromated Mo Kα radiation. All structures were solved by direct methods and subsequent Fourier difference techniques. Unless noted, all non-hydrogen atoms were refined anisotropically, whereas all hydrogen atoms were included in calculated positions but not refined. All data sets were corrected for Lorentz and polarization effects. Calculations were performed using PARST[36,37] and SHELXL-97.[38,39] All refinements were performed using the SHELXTL[39,40] crystallographic software package from Bruker-AXS.

The molecular structure of $K_2(DMSO)_6$[**1**]$_2$ contains five disordered molecules of DMSO bound to K(1) and K(2). Each of the disordered DMSO molecules was modeled in two orientations and refined with combinations of SADI,

Can. J. Chem. Downloaded from www.nrcresearchpress.com by Renmin University of China on 09/02/12
For personal use only.

Table 1. X-ray crystallographic data for $K_2(DMSO)_6[\mathbf{1}]_2$, $\{[K(MeCN)_2][\mathbf{1}]\}_6$, $[(dppp)Pd(\mu_2\text{-}Cl)]_2[\mathbf{1}]_2$, and (cod)Rh[**1**] (dppp = 1,3-bis(diphenylphosphino)propane).

	$K_2(DMSO)_6[\mathbf{1}]_2\cdot C_7H_8$	$\{K(MeCN)_2[\mathbf{1}]\}_6$	$[(dppp)Pd(\mu_2\text{-}Cl)]_2[\mathbf{1}]_2\cdot 2CHCl_3$	$2(cod)Rh[\mathbf{1}]\cdot 2.5CH_2Cl_2$
Formula	$C_{55}H_{68}K_2O_{18}P_2S_6$	$C_{132}H_{108}K_6N_{12}O_{36}P_6$	$C_{94}H_{80}\ Cl_{14}O_{12}P_6Pd_2$	$C_{54.50}H_{53}Cl_5O_{12}P_2Rh_2$
fw	1349.59	2858.72	2296.50	1344.98
Crystal system	Triclinic	Trigonal	Triclinic	Triclinic
Space group	$P\bar{1}$	$R\bar{3}$	$P\bar{1}$	$P\bar{1}$
Colour	Colourless	Colourless	Yellow	Yellow
a (Å)	11.145(1)	35.600(1)	13.6136(5)	13.479(1)
b (Å)	15.992(2)	35.600(1)	14.0099(5)	14.978(2)
c (Å)	19.375(2)	9.3796(2)	14.3587(5)	15.072(1)
α (°)	75.155(6)	90	67.568(2)	106.636(4)
β (°)	75.710(6)	90	87.784(2)	116.413(3)
γ (°)	86.784(6)	120	77.725(2)	90.610(4)
V (Å^3)	3234.6(6)	10294.9(4)	2470.7(2)	2577.2(4)
T (K)	173(2)	173(2)	173(2)	173(2)
Z	2	3	1	2
μ (Mo Kα) (mm^{-1})	0.456	0.342	0.898	1.027
Crystal size (mm^3)	0.50×0.45×0.40	0.75×0.70×0.65	0.60×0.15×0.05	0.45×0.45×0.10
D_{calcd} (Mg m^{-3})	1.386	1.383	1.543	1.733
2θ(max) (°)	55.8	60.0	60.0	55.8
No. of reflns.	50394	36207	78226	61859
No. of unique data	15240	6660	14338	12176
R(int)	0.0389	0.0231	0.0312	0.0296
Refln./param. ratio	16.62	22.89	24.85	17.78
R_1 ($I > 2\sigma(I)$)[a]	0.0410	0.0349	0.0337	0.0371
wR_2 (all data)[b]	0.0952	0.0914	0.0810	0.1040
GoF	1.028	1.030	1.048	1.168

[a] $R_1 = \Sigma||F_o| - |F_c||/\Sigma|F_o|$.

[b] $wR_2(F_2(\text{all data})) = \{\Sigma[w(F_o^2 - F_c^2)]^2/\Sigma[w(F_o^2)^2]\}^{1/2}$.

DANG, SIMU, and EADP where needed. Their respective populations were refined and the final occupancy of the major orientations are 0.802(2), 0.822(2), 0.855(2), 0.73(3), and 0.922(2).

(cod)Rh[**1**] crystallizes with two molecules of (cod)Rh[**1**] and 2.5 equiv of dichloromethane per the asymmetric unit. The other 0.5 equiv of dichloromethane is related through an inversion centre. Crystal data and refinement paramenters are listed in Table 1. Additional data are available in the Supplementary data.

Supplementary data

Supplementary data for this article are available with the article through the journal Web site at http://nrcresearchpress.com/doi/suppl/10.1139/v2012-028. CCDC 866633–866636 contain the X-ray data in CIF format for this manuscript. These data can be obtained, free of charge, via http://www.ccdc.cam.ac.uk/products/csd/request (Or from the Cambridge Crystallographic Data Centre, 12 Union Road, Cambridge CB2 1EZ, UK; fax: +44 1223 336033; or e-mail: deposit@ccdc.cam.ac.uk).

Acknowledgments

This work was supported by the Natural Science and Engineering Research Council (NSERC) of Canada, the Canada Foundation for Innovation (CFI), and the British Columbia Knowledge Development Fund (BCKDF). P.W.S. is grateful for an NSERC PGS D3 scholarship.

References

(1) Holmes, R. R. *Acc. Chem. Res.* **1998**, *31* (9), 535. doi:10.1021/ar9702583.
(2) Holmes, R. R. *Chem. Rev.* **1996**, *96* (3), 927. doi:10.1021/cr950243n.
(3) Wong, C. Y.; Kennepohl, D. K.; Cavell, R. G. *Chem. Rev.* **1996**, *96* (6), 1917. doi:10.1021/cr9410880.
(4) (a) Lacour, J.; Ginglinger, C.; Grivet, C.; Bernardinelli, G. *Angew. Chem. Int. Ed. Engl.* **1997**, *36* (6), 608. doi:10.1002/anie.199706081; (b) Lacour, J.; Londez, A.; Goujon-Ginglinger, C.; Buss, V.; Bernardinelli, G. *Org. Lett.* **2000**, *2* (26), 4185. doi:10.1021/ol006731l; (c) Wietelmann, U.; Bonrath, W.; Netscher, T.; Noth, H.; Panitz, J. C.; Wohlfahrt-Mehrens, M. *Chem. Eur. J.* **2004**, *10* (10), 2451. doi:10.1002/chem.200305208.
(5) Constant, S.; Lacour, J. *Top. Curr. Chem.* **2005**, *250*, 1.
(6) Lacour, J.; Ginglinger, C.; Favarger, F. *Tetrahedron Lett.* **1998**, *39* (27), 4825. doi:10.1016/S0040-4039(98)00943-5.
(7) Lacour, J.; Hebbe-Viton, V. *Chem. Soc. Rev.* **2003**, *32* (6), 373. doi:10.1039/b205251m.
(8) Lacour, J.; Moraleda, D. *Chem. Commun.* **2009**, (46), 7073. doi:10.1039/b912530b.
(9) Allcock, H. R. *J. Am. Chem. Soc.* **1963**, *85* (24), 4050. doi:10.1021/ja00907a045.
(10) Allcock, H. R.; Bissell, E. C. *Chem. Commun.* **1972**, (11), 676.
(11) Allcock, H. R.; Bissell, E. C. *J. Am. Chem. Soc.* **1973**, *95* (10), 3154. doi:10.1021/ja00791a013.
(12) Cavezzan, J.; Etemad-Moghadam, G.; Koenig, M.; Klaebe, A. *Tetrahedron Lett.* **1979**, *20* (9), 795. doi:10.1016/S0040-4039(01)86041-X.
(13) Nanbu, N.; Tsuchiya, K.; Sasaki, Y. *J. Power Sources* **2005**, *142* (1–2), 333. doi:10.1016/j.jpowsour.2004.09.003.
(14) Eberwein, M.; Schmid, A.; Schmidt, M.; Zabel, M.; Burgemeister, T.; Barthel, J.; Kunz, W.; Gores, H. J. *J. Electrochem. Soc.* **2003**, *150* (7), A994. doi:10.1149/1.1580821.
(15) Handa, M.; Suzuki, M.; Suzuki, J.; Kanematsu, H.; Sasaki, Y. *Electrochem. Solid-State Lett.* **1999**, *2* (2), 60. doi:10.1149/1.1390734.
(16) Siu, P. W.; Gates, D. P. *Organometallics* **2009**, *28* (15), 4491. doi:10.1021/om9003187.
(17) Krossing, I.; Raabe, I. *Angew. Chem. Int. Ed.* **2004**, *43* (16), 2066. doi:10.1002/anie.200300620.
(18) Ittel, S. D.; Johnson, L. K.; Brookhart, M. *Chem. Rev.* **2000**, *100* (4), 1169. doi:10.1021/cr9804644.
(19) Chen, E. Y. X.; Marks, T. J. *Chem. Rev.* **2000**, *100* (4), 1391. doi:10.1021/cr980462j.
(20) Koenig, M.; Klaebe, A.; Munoz, A.; Wolf, R. *J. Chem. Soc., Perkin Trans. 2* **1979**, 40.
(21) Schmidpeter, A.; von Criegern, T.; Sheldrick, W. S.; Schomburg, D. *Tetrahedron Lett.* **1978**, *19* (32), 2857. doi:10.1016/S0040-4039(01)94882-8.
(22) Gallagher, M.; Munoz, A.; Gence, G.; Koenig, M. *Chem. Commun.* **1976**, 321.
(23) Hellwinkel, D.; Wilfinger, H. J. *Chem. Ber.* **1970**, *103* (4), 1056. doi:10.1002/cber.19701030409.
(24) Munoz, A.; Gallagher, M.; Klaebe, A.; Wolf, R. *Tetrahedron Lett.* **1976**, *17* (9), 673. doi:10.1016/S0040-4039(00)74593-X.
(25) Ramirez, F.; Nowakowski, M.; Marecek, J. F. *J. Am. Chem. Soc.* **1977**, *99* (13), 4515. doi:10.1021/ja00455a058.
(26) Pelzer, G.; Herwig, J.; Keim, W.; Goddard, R. *Russ. Chem. Bull.* **1998**, *47* (5), 904. doi:10.1007/BF02498159.
(27) Kumar, J. S.; Singh, A. K.; Yang, J. C.; Drake, J. E. *J. Coord. Chem.* **1998**, *44* (3–4), 335. doi:10.1080/00958979808023085.
(28) Abu-Surrah, A. S.; Klinga, M.; Repo, T.; Leskela, M.; Debaerdemaeker, T.; Rieger, B. *Acta Crystallogr. C* **2000**, *56* (2), e44. doi:10.1107/S0108270100000639.
(29) Devic, T.; Batail, P.; Fourmigué, M.; Avarvari, N. *Inorg. Chem.* **2004**, *43* (10), 3136. doi:10.1021/ic035447y.
(30) Brown, M. D.; Levason, W.; Reid, G.; Watts, R. *Polyhedron* **2005**, *24* (1), 75. doi:10.1016/j.poly.2004.10.008.
(31) Ganguly, S.; Georgiev, E. M.; Mague, J. T.; Roundhill, D. M. *Acta Crystallogr. C* **1993**, *49* (6), 1169. doi:10.1107/S0108270192011855.
(32) Bondi, A. *J. Phys. Chem.* **1964**, *68* (3), 441. doi:10.1021/j100785a001.
(33) Albano, P.; Aresta, M.; Manassero, M. *Inorg. Chem.* **1980**, *19* (4), 1069. doi:10.1021/ic50206a059.
(34) Powell, J.; Lough, A.; Saeed, T. *Dalton Trans.* **1997**, (22), 4137.
(35) Lassahn, P. G.; Lozan, V.; Wu, B.; Weller, A. S.; Janiak, C. *Dalton Trans.* **2003**, (23), 4437. doi:10.1039/b302937a.
(36) Nardelli, M. *Comput. Chem.* **1983**, *7* (3), 95. doi:10.1016/0097-8485(83)85001-3.
(37) Nardelli, M. *J. Appl. Cryst.* **1995**, *28* (5), 659. doi:10.1107/S0021889895007138.
(38) Sheldrick, G. M. *SHELXL-97,* Release 97-2; University of Göttingen: Göttingen, Germany, 1997.
(39) Sheldrick, G. M. *Acta Crystallogr. Sect. A: Fundam. Crystallogr.* **2008**, *64* (1), 112. doi:10.1107/S0108767307043930.
(40) Sheldrick, G. M. *SHELXTL,* Version 5.1; Bruker AXS Inc.: Madison, WI, 1997.

Can. J. Chem. Downloaded from www.nrcresearchpress.com by Renmin University of China on 09/02/12
For personal use only.

Asymmetrically distorted structures of monosilacyclobutane and disilacyclobutane radical cations studied by ab initio and density functional theories

Z.J. Cai and Y.J. Shi

Can. J. Chem. Downloaded from www.nrcresearchpress.com by Renmin University of China on 09/02/12
For personal use only.

Abstract: The geometrical and electronic structures of a series of six monosilacyclobutane and 1,3-disilacyclobutane radical cations were systematically studied using ab initio and density functional theories. It was shown that all six radical cations possess an asymmetrically distorted structure in their ground electronic states. In the asymmetrically distorted C_1 structure of monosilacyclobutane cations, one Si–C bond was elongated and the other was shortened. For the disilacyclobutane cations, two ring bonds were elongated and the other two contracted. The asymmetrical distortion was enhanced by exocyclic methyl substitutions and weakened by endocyclic Si substitution. The unpaired electron was localized mainly in the elongated σ(Si–C) ring bond(s) in all six cations. Studies of the excited electronic states of the cations provided strong support that the asymmetrical distortion in the four-membered-ring cations originates from the second-order Jahn–Teller effect. It was found that the puckered ring structures in the monosilacyclobutane molecules were maintained upon ionization, whereas 1,3-disilacyclobutane cations changed to a planar ring structure. Examination of the potential energy surfaces of all six cations showed that the Si–C ring bond elongation is the main contributor to the significant difference in the geometry change between monosilacyclobutane and disilacyclobutane species upon ionization.

Key words: silacyclobutane, radical cation, second-order Jahn–Teller effect, potential energy surfaces, structures.

Résumé : Faisant appel à des calculs théoriques ab initio et d'autres dérivés de la théorie de la fonctionnelle de la densité, on a fait une étude systématique des structures géométriques et électroniques d'une série de six cations radicaux dérivés de monosilacyclobutanes et 1,3-disilacyclobutanes. Il a été permis de démontré que, dans leurs états électroniques fondamentaux, ces six cations radicaux possèdent une structure avec distorsion asymétrique. Dans la structure C_1 à distorsion asymétrique des cations radicaux du monosilacyclobutane, une des liaisons Si–C est allongée alors que l'autre est raccourcie. Dans le cas des cations radicaux du disilacyclobutane, les deux liaisons du cycle sont allongées alors que les deux autres sont contractées. La distorsion asymétrique est rehaussée par des substitutions de groupes méthyles exocycliques et affaiblie par une substitution endocyclique du silicium. Pour chacun des six cations radicaux, l'électron non apparié est principalement localisé dans les liaisons allongées σ(Si–C) du cycle. Les études des états électroniques excités des cations radicaux supportent fortement la distorsion dans les cations radicaux des cycles à quatre chaînons qui trouvent leur origine dans l'effet Jahn–Teller du deuxième ordre. On a trouvé que les structures repliées des cycles des molécules de monosilacyclobutane sont maintenues lors de l'ionisation alors que celles des cations radicaux dérivés du 1,3-disilacyclobutane se transforment en une structure dans laquelle le cycle est plan. L'examen des surfaces d'énergie potentielle des six cations radicaux montre que l'élongation de la liaison Si–C du cycle est la principale cause de la différence significative dans le changement de géométrie entre les espèces monosilacyclobutanes et disilacyclobutanes lors de leur ionisation.

Mots-clés : silacyclobutane, cation radical, effet Jahn–Teller du deuxième ordre, surfaces d'énergie potentielle, structures.

[Traduit par la Rédaction]

Introduction

The study of the geometrical and electronic structures of alkane radical cations has attracted much attention over the past few decades because of their fundamental chemical importance.[1–3] A variety of alkane radical cations, including both acylic[1,2,4,5] and cyclic[6–11] alkanes, have been studied by the low-temperature halocarbon matrix isolation electron spin resonance (ESR) spectroscopic techniques since the method was developed in the 1970s. Two types of electronic structures, i.e., a delocalized type and a localized type, were found based on the distributions of the unpaired electron. The *n*-alkane and unsubstituted cycloalkane (c-C_nH_{2n}, $3 \leq n \leq 8$) radical cations are characterized as delocalized σ-radical cations, in which the unpaired electron in the σ-molecular orbital delocalizes over the entire normal alkane chain and the equatorial plane of the cycloalkane ring, respectively. The

Received 20 March 2012. Accepted 25 April 2012. Published at www.nrcresearchpress.com/cjc on 27 June 2012.

Z.J. Cai and Y.J. Shi. Department of Chemistry, University of Calgary, Calgary, AB T2N 1N4, Canada.

Corresponding author: Y.J. Shi (e-mail: shiy@ucalgary.ca).

Can. J. Chem. Downloaded from www.nrcresearchpress.com by Renmin University of China on 09/02/12
For personal use only.

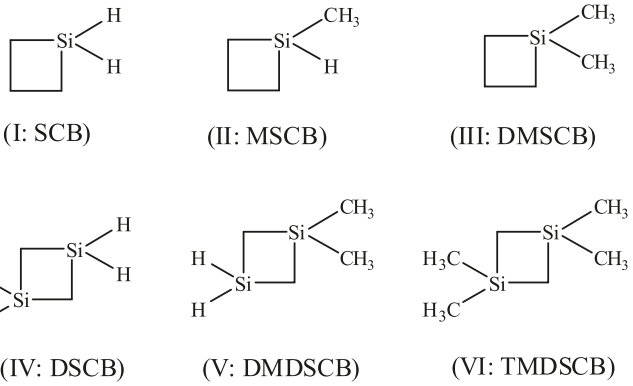
radical cations of branched alkanes and methyl-substituted cycloalkanes assume the localized electronic structure where the unpaired electron is more confined to a particular σ(C–C) bond.

The Jahn–Teller effect[12] plays an important role in determining the geometric structures of the alkane radical cations. Among the variety of acyclic and cyclic alkane cations studied, it has generally been found that the alkane molecules that are Jahn–Teller active, i.e., have a degenerate HOMO orbital, all undergo structure distortion by lowering the symmetry after one-electron oxidation to form the radical cations, whereas the geometric structures of the Jahn–Teller inactive alkane molecules can be maintained in their corresponding radical cations.[1–3,6] However, studies of methyl-substituted cycloalkane radical cations have revealed some interesting results. Shiotani and co-workers[7–11] found that, even if the precursor neutral molecules are Jahn–Teller inactive, their radical cations take an asymmetrically distorted geometrical structure in which one of the two ring C–C bonds connected to the methyl substituent is elongated and the symmetry of the cations is lowered.

Shiotani and co-workers then extended their low-temperature halocarbon matrix isolation ESR studies to silacycloalkane molecules, including silacyclohexane,[13] 1-methylsilacyclohexane,[14] and silacyclobutane and its methyl-substituted derivatives.[15] Theoretical studies of the ESR spectra and structures of silacyclobutane radical cations have also been reported recently.[16,17] It was found that removing one electron from these silacycloalkane molecules lowers the symmetry in the geometrical structures. The radical cations of the aforementioned silacycloalkanes possess an asymmetrically distorted C_1 structure with one of the Si–C bonds elongated where the unpaired electron mainly resides. The structural distortion observed in both methyl-substituted cycloalkane and silacycloalkane radical cations can be explained by the second-order Jahn–Teller theory, also known as the pseudo Jahn–Teller effect.[13,18–20] This theory predicts a specific way in which any molecule with electronic states that are close to each other (within about 4 eV) will react upon activation. In this case, the vibronic coupling, which is inversely proportional to the energy difference between the ground and excited electronic states, can induce the structural distortion of Jahn–Teller inactive molecules. The ESR studies of the radical cations of the open-chain ethylsilanes, including $SiEt_2H_2$, $SiEt_3H$, $SiEt_4$, and $SiEt_2MeH$ (Et, ethyl; Me, methyl), in low-temperature halocarbon matrices have confirmed that, owing to the pseudo Jahn–Teller effect, all cations adopt asymmetrically distorted structures with only one of the Si–C bonds elongated and the unpaired electron is largely localized in the elongated Si–C bond.[21] Toriyama et al.[22,23] revisited the radical cation structures of propane and *n*-pentane / branched pentane[24] and found that they also undergo similar structural distortion to those of ethylsilanes. Therefore, it is believed that the asymmetrically distorted structure originating from the pseudo Jahn–Teller effect is an intrinsic nature of the alkane and silaalkane radical cations whose precursor neutral molecules possess certain symmetry elements such as C_s, C_2, or C_{2v}.

The four-membered-ring silacycloalkane molecules have recently attracted a lot of research interest because of their wide range of applications in chemistry[25] and materials science.[26] The high ring strain energy and reactivity of these molecules have made them excellent choices as single-source precursors for producing silicon carbide thin films using chemical vapor deposition (CVD) techniques.[27–33] The structures of the neutral four-membered-ring silacycloalkane molecules have been extensively investigated by various experimental techniques and theoretical calculations.[34–38] Unlike their neutral equivalents, the structures of the radical cations of these four-membered-ring compounds are much less studied, although they are very important for their activities in the process of plasma-enhanced CVD[39] and other chemical reactions.[25] Only the ESR spectra accompanied by theoretical studies using ab initio and density functional theory (DFT) of silacyclobutane and its methyl-substituted derivatives have been reported in the literature.[15–17] The silacyclobutane radical cation possesses the asymmetrically distorted structure with one of the ring Si–C bonds elongated. However, the effect of the exocyclic methyl substitution on the electronic and geometric structures of silacyclobutane radical cation has not been systematically studied. Furthermore, it remains unclear how the asymmetrical distortion due to the pseudo Jahn–Teller effect changes in the radical cations upon introducing a second Si in the four-membered ring (endocyclic substitution).

In this work, to explore the effect of both exocyclic methyl substitution and endocyclic Si substitution on the structures of the radical cations of the four-membered-ring silacycloalkanes, we have systematically examined the electronic and geometric structures of a series of monosilacyclobutane (MonoSCB) and 1,3-disilacyclobutane (DiSCB) radical cations using ab initio and DFT methods. The three MonoSCB molecules investigated in this work include 1-silacyclobutane (SCB), 1-methyl-1-silacyclobutane (MSCB), and 1,1-dimethyl-1-silacyclobutane (DMSCB). 1,3-Disilacyclobutane (DSCB), 1,1-dimethyl-1,3-disilacyclobutane (DMDSCB), and 1,1,3,3-tetramethyl-1,3-disilacyclobutane (TMDSCB) belong to DiSCB molecules. The molecular structures of SCB (I), MSCB (II), DMSCB (III), DSCB (IV), DMDSCB (V), and TMDSCB (VI) are represented in the following.



The puckering potential energy surfaces (PESs) of all six cations were also studied to help understand the structural difference between MonoSCB and DiSCB radical cations. In addition, we studied some of the electronic transitions of the six radical cations. Comparison of the energy difference between the ground and excited electronic states of the radical cations provides strong support of the pseudo Jahn–Teller effect as the origin of the asymmetrical distortion in the four-membered-ring cations.

Can. J. Chem. Downloaded from www.nrcresearchpress.com by Renmin University of China on 09/02/12
For personal use only.

Computational details

All calculations in this work were performed using the Gaussian 03 program.[40] The previous studies from our group[38] and others[37] have shown that calculations using the second-order Møller-Plesset (MP2) perturbation theory work very well in predicting the geometric structures of neutral MonoSCB and DiSCB molecules, since the correlation energy is small in these single-bonded molecules. The structures of the six MonoSCB and DiSCB radical cations have not been reported in the literature except for that of SCB. The geometric structures of the SCB radical cation were investigated using MP2 and DFT with the B3LYP hybrid functional.[16,17] To confirm the lowest energy geometric structures of all six radical cations to be studied in this work, both MP2 and the B3LYP hybrid functional were used for the geometry optimization of radical cations using the 6–311++G(d,p) basis set. For all geometry optimizations, the frozen core approximation was employed. The frequency calculations at the harmonic level were performed on the optimized geometries to ensure that they belonged to the stable structures, not transition states.

Figure 1 shows the labels and numbering of atoms in both MonoSCB (compounds I–III) and DiSCB (compounds IV–VI) radical cations. The definitions of puckering angle (φ) and puckering coordinate (x) are shown in Fig. 2. φ is the dihedral angle between two planes, i.e., planes 1-2-4 and 3-2-4, in the ring, and x is half of the perpendicular distance between two ring diagonals. The PESs of the puckering motion and the barriers to planarity for each of the six radical cations were obtained by keeping the puckering dihedral angle, $\varphi(Si_1–C_2–C_4–C_3)$, at varied fixed values in the range of –60° to 60° at a step size of 5° while optimizing all the remaining parameters using MP2/6–311++G(d,p). The coordinate x was calculated at the optimized structures with different dihedral angles, so that the parameters of potential energy function could be obtained by polynominal fitting of the potential energy as a function of the x values.

To shed light on the origin of the asymmetrically distorted structures assumed by the radical cations, the first excited electronic states of all six radical cations were calculated on the MP2-optimized structures by time-dependent DFT, in which the hybrid functional B3LYP was employed with a basis set of 6–311++G(d,p).

Results and discussions

Geometry optimization — Asymmetrically distorted and localized ground electronic states

The search for the ground electronic states of the six radical cations was performed using the MP2 methods with the 6–311++G(d,p) basis set. From the geometry optimization of the SCB radical cation, two stable structures were found with C_1 and C_{2v} symmetry. The two structures are shown in Fig. 3. In the asymmetrically distorted C_1 structure, labeled as SCB$^{+\bullet}$-C_1 (Fig. 3*a*), one of the Si–C bonds was elongated and the other was contracted, whereas the C_{2v} structure shown in Fig. 3*b* has a planar ring structure with both Si–C bonds elongated to the same extent. The energy of SCB$^{+\bullet}$-C_1 is found to be 3.00 kcal/mol (1050 cm^{-1}) lower than that of SCB$^{+\bullet}$-C_{2v}. Therefore, the ground electronic state of the SCB radical cation has an asymmetrically distorted structure of C_1 symmetry with a puckered ring. This is in agreement with previous studies on the SCB radical cation[15–17] and other silaalkane cations.[13,14,21] The ground-state cationic structure for SCB was calculated using both MP2 and B3LYP methods. Comparison of the calculated structural parameters, including the bond lengths, bond angles, and puckering angles, for the ground electronic state of the SCB radical cation (SCB$^{+\bullet}$-C_1) using different methods can be found in Table 1. The results from previous calculations in the literature are also listed in Table 1. Our calculations show good agreements with those reported in the literature. All methods predict that the SCB radical cation has a puckered ring structure in its ground state. However, the DFT method seems to underestimate the dihedral angle by 7.6° when compared with the MP2 method. According to the previous results,[17] such underestimation was believed to be an artefact due to the B3LYP optimization. The calculated structural parameters were similar when using B3LYP and MP2 except for the underestimation of dihedral angle in the former. In addition, the energies for the ground-state SCB radical cation calculated at MP2/6–311++G(d,p) and B3LYP/6–311++G(d,p) were found to be –407.42276 and –408.33246 hartree, respectively. The energy calculated at the MP2 level of theory is much closer to the single-point energy of –407.52135 hartree calculated using CCSD(T)/6–311++G(3d,2p) on the optimized structure with MP2/6–311++G(d,p). Therefore, the following discussions will be based on the results from the MP2 calculations for consistency.

Similar asymmetrical distortions were found in the ground electronic structures of MSCB and DMSCB radical cations. MSCB has two conformers, i.e., the equatorial form (MSCB-*e*) and the axial form (MSCB-*a*). The geometry optimization found two stable structures with C_1 and C_s symmetry for the radical cation of each conformer. The C_1 structure shows an asymmetrical distortion with one of the ring Si–C bonds elongated and the other contracted, whereas both ring Si–C bonds are elongated in the planar C_s structure. The energy of the C_1 structure is 3.96 and 3.64 kcal/mol lower than that of the C_s structure for the MSCB-$e^{+\bullet}$ and MSCB-$a^{+\bullet}$, respectively. The MSCB-$a^{+\bullet}$-C_1 structure is calculated to be 0.33 kcal/mol (114 cm^{-1}) higher in energy than MSCB-$e^{+\bullet}$-C_1. Therefore, the ground electronic state of MSCB radical cation has an asymmetrically distorted C_1 structure in the equatorial form. The asymmetrically distorted C_1 structure of the ground-state DMSCB$^{+\bullet}$ is 4.54 kcal/mol lower in energy than the planar C_{2v} structure. The total energies for the different structures of the three MonoSCB radical cations calculated at MP2/6–311++G(d,p) and the energy difference between the two stable structures of each species are listed in Table 2.

Table 3 lists the calculated structural parameters of the ground electronic states (C_1) and the C_s/C_{2v} structures for the three MonoSCB radical cations. The structural parameters for the three neutral molecules are also listed for comparison. In the asymmetrically distorted C_1 structures, one Si–C ring bond ($r(Si_1–C_4)$ = 2.273–2.326 Å) was elongated by around 20% and the other Si–C ring bond ($r(Si_1–C_2)$ = 1.843–1.853 Å) was contracted a little when compared with the neutral MonoSCBs (r(Si–C) = 1.893–1.896 Å). The two unequal endocyclic bond angles ∠SiCC ($\angle Si_1–C_2–C_3$ = 79.1°–79.4°; $\angle Si_1–C_4–C_3$ = 92.5°–94.6°) in the C_1 structures also

Fig. 1. Numbering and labels of atoms of (*a*) monosilacyclobutane and (*b*) 1,3-disilacyclobutane radical cations. R represents either H or CH_3.

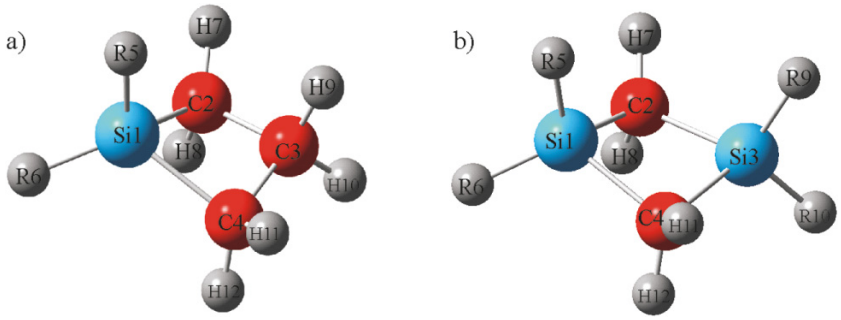
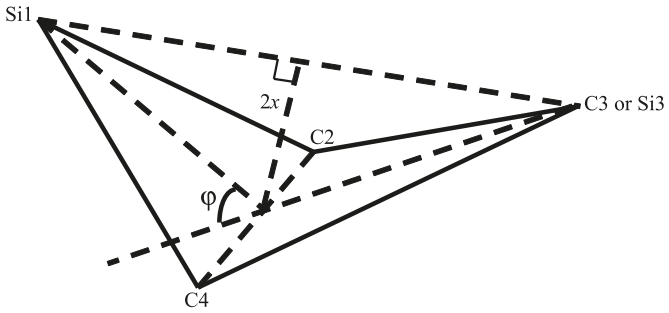


Fig. 2. Definitions of the ring puckering angle (φ) and the ring-puckering coordinate (x).



suggest the asymmetrical distortion of MonoSCB radical cations in comparison with the two equal bond angles in their neutral forms ($\angle Si_1–C_2–C_3 = \angle Si_1–C_4–C_3$ = 86.1°–86.4°). The similar puckering angles between the MonoSCB neutral and cationic C_1 structures indicate that the puckered structure was conserved upon ionization into the ground states. It is also interesting to note how the degree of asymmetrical distortion is affected by exocyclic methyl substitution in MonoSCB cations. The difference in the bond length between two Si–C ring bonds becomes larger with methyl substitution, as shown in Table 3, i.e., 0.430 Å for $SCB^{+\bullet}$; 0.452 Å for MSCB-$e^{+\bullet}$; and 0.473 Å for $DMSCB^{+\bullet}$. This type of trend implies that the distortion becomes slightly larger by replacing the exocyclic Si–H bonds with Si–CH_3 connections.

For the geometry optimization of the DSCB radical cation, the two stable structures shown in Figs. 4*a* and 4*b* were found with C_{2v} and D_{2h} symmetry, respectively. The former has an asymmetrically distorted structure with two elongated Si–C ring bonds and the other two shortened, whereas the latter has four elongated Si–C ring bonds to the same extent as compared with its neutral form. By comparing the energy between these two structures, the C_{2v} structure is 3.46 kcal/mol lower in energy than the one with D_{2h} symmetry. Thus, the ground electronic state of the DSCB radical cation has an asymmetrically distorted C_{2v} structure. Similar to $DSCB^{+\bullet}$, the ground electronic state of the $TMDSCB^{+\bullet}$ radical has an asymmetrically distorted C_{2v} structure that is 2.70 kcal/mol lower in energy than the D_{2h} structure. For the DMDSCB radical cation, the two optimized stable structures have C_s and C_{2v} symmetry, respectively, and are shown in Figs. 4*c* and 4*d*. The C_s structure is asymmetrically distorted with two elongated Si–C ring bonds, however, the two elongated Si–C bonds are of different lengths. The Si–C bond connected to the two methyl groups is more significantly elongated. The C_{2v} structure has all four Si–C ring bonds elongated, but not to the same extent. It was found that the $DMDSCB^{+\bullet}$-C_s structure is 3.78 kcal/mol lower in energy than its C_{2v} counterpart, and thus the asymmetrically distorted C_s structure is the ground state of the DMDSCB radical cation. The energy comparison for the different structures of the three DiSCB radical cations calculated at MP2/6–311++G(d,p) can be found in Table 2.

The calculated structural parameters of the ground electronic states (C_{2v} for $DSCB^{+\bullet}$ and $TMDSCB^{+\bullet}$ and C_s for $DMDSCB^{+\bullet}$) and the next higher energy stable structures for the three DiSCB radical cations are listed in Table 4. The structural parameters for the three neutral DiSCB molecules are also listed in the same table for comparison. In the asymmetrically distorted ground state of C_s symmetry for $DMDSCB^{+\bullet}$, one Si–C ring bond ($r(Si_1–C_4)$ = 2.243 Å) attached to the methyl groups was elongated by around 18%, but the other Si–C ring bond ($r(Si_1–C_2)$ = 1.841 Å) attached to the methyl groups was shortened. The $Si_3–C_4$ bond length was slightly elongated, whereas the remaining Si–C ring bond was almost unchanged with respect to the neutral DMDSCB (r(Si–C) = 1.899 Å). On the other hand, the ground electronic states for both $DSCB^{+\bullet}$ and $TMDSCB^{+\bullet}$ have two elongated Si–C ring bonds (2.058 Å for $DSCB^{+\bullet}$ and $TMDSCB^{+\bullet}$) to the same extent by ~8% in comparison with their neutral forms (1.901 Å for DSCB and 1.904 Å for TMDSCB), and the other two Si–C ring bonds contracted a little (1.862 Å for $DSCB^{+\bullet}$ and 1.866 Å for $TMDSCB^{+\bullet}$). Similar to the three MonoSCB radical cations, the asymmetric distortion in the ground cationic states of DiSCBs can be reflected in the two unequal endocyclic bond angles ∠Si–C–C. Furthermore, it is noted that the change in ring bond angles ∠C–Si–C upon ionization into the ground states is different among the three DiSCB radical cations. One ring bond angle (∠C–Si–C) changes significantly in $DMDSCB^{+\bullet}$ ($\angle C_2–Si_3–C_4$ = 99.2°) in comparison with its neutral ($\angle C_2–Si_3–C_4$ = 90.3°), and the other remains almost constant ($\angle C_2–Si_1–C_4$ = 90.9° and 89.9° for the cationic and neutral form, respectively). However, the two ring bond angles ∠C–Si–C are equal in $DSCB^{+\bullet}$ and $TMDSCB^{+\bullet}$ ($\angle C_2–Si_1–C_4 = \angle C_2–Si_3–C_4$ = 97.0° for $DSCB^{+\bullet}$; $\angle C_2–Si_1–C_4 = \angle C_2–Si_3–C_4$ = 96.4° for $TMDSCB^{+\bullet}$). This is due to the different asymmetric distortion assumed by DMDSCB and DSCB/TMDSCB radical cations. In $DMDSCB^{+\bullet}$-C_s, the two elongated Si–C ring bonds are of different lengths, whereas the symmetric plane crossing two ring C atoms was maintained in $DSCB^{+\bullet}$ and $TMDSCB^{+\bullet}$ with one pair of Si–C ring bonds elongated and another pair shortened, both to the same extent.

Can. J. Chem. Downloaded from www.nrcresearchpress.com by Renmin University of China on 09/02/12
For personal use only.

Fig. 3. Optimized C_1 (*a*) and C_{2v} (*b*) geometric structures of the 1-silacyclobutane (SCB I) radical cation calculated at the MP2/6–311++G(d,p) level. (A broken line indicates an elongated bond.)

a) $SCB^{+\bullet}$-C_1($\varphi = 34.6°$) b) $SCB^{+\bullet}$-C_{2v}($\varphi = 0°$)

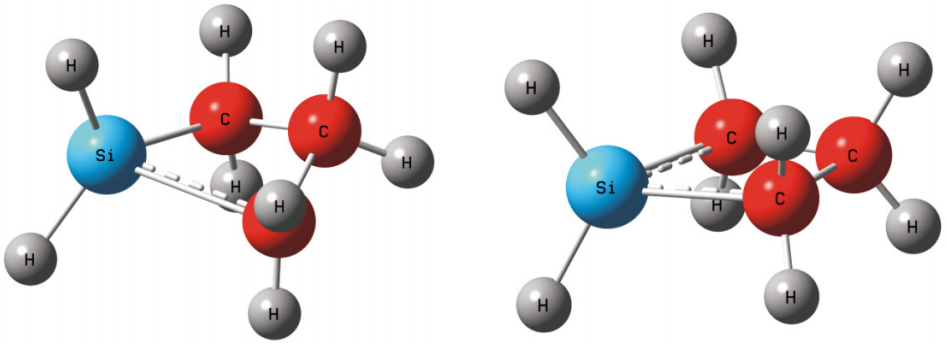


Table 1. Structural parameters in the ground electronic state of the 1-silacyclobutane (SCB) radical cation calculated by various methods.

	Method						
	B3LYP[a]	MP2[a]	B3LYP[b]	MP2[b]	B3LYP[c]	RI-MP2[c]	CCSD(T)[c]
	Basis set						
	6–311++G(d,p)	6–311++G(d,p)	6–31G(d,p)	6–31G(d,p)	cc-pVDZ	VTZPP	cc-PVDZ
Bond length (Å)							
$Si–C_2$	1.852	1.843	1.86	1.85	1.870	1.841	1.876
$Si–C_4$	2.281	2.273	2.27	2.27	2.300	2.255	2.311
$C_3–C_2$	1.594	1.580	1.60	1.57	1.590	1.577	1.587
$C_3–C_4$	1.498	1.503	1.50	1.50	1.499	1.497	1.514
$Si–R_5$	1.474	1.464			1.485	1.467	1.481
$Si–R_6$	1.475	1.465			1.485	1.467	1.481
$C_2–H_7$	1.090	1.091			1.100	1.087	1.105
$C_2–H_8$	1.087	1.092			1.099	1.086	1.104
$C_3–H_9$	1.089	1.091			1.098	1.086	1.103
$C_3–H_{10}$	1.098	1.099			1.106	1.094	1.110
$C_4–H_{11}$	1.090	1.088			1.100	1.087	1.105
$C_4–H_{12}$	1.090	1.091			1.097	1.083	1.102
Bond angle (°)							
$\angle C_2–Si–C_4$	73.0	72.6			71.6	73.2	71.3
$\angle C_2–C_3–C_4$	106.7	106.0			105.7	106.5	105.3
$\angle Si_1–C_2–C_3$	93.6	92.5			95.5	92.0	94.4
$\angle Si_1–C_4–C_3$	80.7	79.2			82.1	79.4	80.7
$\angle R_5–Si–R_6$	117.2	117.1					
Puckering angle (°)							
φ	27.0	34.6	27.0	34.0	24.7	33.1	31.5

Note: R_5, H_5; R_6, H_6.
[a]Results from this work.
[b]Calculations from ref. 16.
[c]Calculations from ref. 17.

One significant change in the geometry upon ionization for all three DiSCB species is that their dihedral angles were reduced to zero, i.e., all three $DiSCB^{+\bullet}$ have planar ring structures in their ground states. This is in sharp contrast to the behavior observed with the three MonoSCB cations where the puckered ring structures are maintained in the ground states. The reason for the difference in the geometry assumed by $MonoSCB^{+\bullet}$ and $DiSCB^{+\bullet}$ will be explained later. It is also interesting to note that the bond length difference of 0.196 Å between the two pairs of ring Si–C bonds in the ground-state $DSCB^{+\bullet}$ is much reduced as compared with 0.430 Å for the ground-state $SCB^{+\bullet}$. Moreover, the difference in the bond lengths of the two ring Si–C bonds connected to the methyl substituent is smaller in the ground-state $DMDSCB^{+\bullet}$ (0.402 Å) than in the ground-state $DMSCB^{+\bullet}$ (0.473 Å). Therefore, the endocyclic Si substitution seems to lessen the extent to which the four-membered ring undergoes the asymmetric distortion upon ionization.

Table 5 lists the calculated spin density distributions on the four ring atoms in the six asymmetrically distorted ground-state radical cations using DFT and MP2 with the 6–311++G(d,p) basis set. It is clear that most of the spin densities in the

Can. J. Chem. Downloaded from www.nrcresearchpress.com by Renmin University of China on 09/02/12
For personal use only.

Table 2. Energies of different structures of monosilacyclobutane (MonoSCB) and 1,3-disilacyclobutane (DiSCB) radical cations calculated at MP2/6–311++G(d,p).

	Ground state		Symmetrically distorted structure		Energy difference
Radical cations	Symmetry	Energy[a] (hartree)	Symmetry	Energy[a] (hartree)	(cm^{-1})
$SCB^{+\bullet}$	C_1	–407.42276	C_{2v}	–407.41797	1050
$MSCB^{+\bullet}$-*a*	C_1	–446.64560	C_s	–446.63980	1273
$MSCB^{+\bullet}$-*e*	C_1	–446.64612	C_s	–446.63980	1387
$DMSCB^{+\bullet}$	C_1	–485.86785	C_{2v}	–485.86060	1591
$DSCB^{+\bullet}$	C_{2v}	–658.45715	D_{2h}	–658.45164	1209
$DMDSCB^{+\bullet}$	C_s	–736.90009	C_{2v}	–736.89406	1322
$TMDSCB^{+\bullet}$	C_{2v}	–815.33736	D_{2h}	–815.33305	945

Note: SCB, 1-silacyclobutane; MSCB, 1-methyl-1-silacyclobutane; DMSCB, 1,1-dimethyl-1-silacyclobutane; DSCB, 1,3-disilacyclobutane; DMDSCB, 1,1-dimethyl-1,3-disilacyclobutane; TMDSCB, 1,1,3,3-tetramethyl-1,3-disilacyclobutane; *a*, axial; *e*, equatorial.

[a]Without zero-point energy corrections.

Can. J. Chem. Downloaded from www.nrcresearchpress.com by Renmin University of China on 09/02/12
For personal use only.

$MonoSCB^{+\bullet}$ with C_1 symmetry are localized mainly in the elongated σ(Si–C) ring bond as a result of the structural distortion. This agrees very well with the previous results that demonstrated that the unpaired electron resided predominately on the elongated σ(Si–C) ring bond(s) in silacyclobutane and silacyclohexane radical cations by low-temperature EPR studies.[13–17] The same was found for the $DMDSCB^{+\bullet}$-C_1 structure where the majority of the spin densities are confined to the one significantly elongated σ(Si–C) ring bond attached to the methyl groups. For the remaining two $DiSCB^{+\bullet}$, most of the total spin density is localized to the two σ(Si–C) ring bonds, i.e., Si_1–C_4 and Si_3–C_4. This is because both of the $DSCB^{+\bullet}$-C_{2v} and $TMDSCB^{+\bullet}$-C_{2v} structures have a pair of two Si–C ring bonds elongated. Therefore, all six radical cations form the localized asymmetrically distorted structures in their ground states.

Origin of the structure distortions — Pseudo Jahn–Teller effect

The structural distortion observed in the ground states of the six radical cations studied in this work can be explained by the pseudo Jahn–Teller effect. This theory suggests that the structural distortion in the radical cations of Jahn–Teller inactive molecules originates from the vibronic–electronic coupling, which is inversely proportional to the energy difference between the ground and excited electronic states. This is shown in the expression of the energy of a species, after a small distortion from the stable configuration, written as eq. [1] based on the second-order perturbation theory.[13,18–20]

$$[1] \qquad E = E_0 + \frac{Q^2}{2}\langle\psi_0|\frac{\partial^2 U}{\partial Q^2}|\psi_0\rangle + \sum_k \frac{\left(Q\langle\psi_0|\frac{\partial U}{\partial Q}|\psi_k\rangle\right)^2}{(E_0 - E_k)}$$

where E_0 is the energy of the structure without distortion, Q is the displacement of the normal coordinate from the original position, U is the nuclear–nuclear and nuclear–electronic potential energy, and ψ_0 and ψ_k are the wave functions for the ground electronic state and excited state, respectively. The first energy correction term in eq. [1] to the undistorted energy E_0 is always positive, and the second correction term is always negative. It is, therefore, the sum of the last two terms that determines whether a distorted structure is preferable or not; that is, when the sum is negative, the distorted structure is energetically favourable. As shown in eq. [1], the absolute value of the second correction term is inversely proportional to the energy difference between the ground state and the excited state. As Bader[18] suggested, the pseudo Jahn–Teller effect generally induces geometrical distortion when the energy difference between the electronic ground state and the low-lying electronic excited state is within 4 eV and that only the lowest lying excited state seems to be important in the summation of eq. [1].

Time-dependent DFT calculations were then used to calculate the electronic transition energy in the six radical cations. Table 6 lists the calculated electronic transition energy between the electronic ground state and the first excited electronic state for both MonoSCB and DiSCB radical cations at B3LYP/6–311++G(d,p). The lowest electronic transition energies calculated for the six neutral molecules are also listed in the same table for comparison. It was found that the lowest electronic transition mainly involves the HOMO and SOMO in the cations (97.3%–99.8%) and HOMO and LUMO in the neutral form (68.6%–70.1%). As shown in Table 6, the lowest electronic transition energy for the MonoSCB and DiSCB radical cations varies from 2.17 to 2.78 eV, which is less than 4 eV. Therefore, the predominant second energy-correction term in eq. [1] is expected to reduce the energy of the radical cations after structural distortion. In other words, the structures of MonoSCB and DiSCB cations get stabilized by the asymmetrical distortion in geometry. The lowest electronic transition energy for the six neutral molecules, on the other hand, ranges from 5.73 to 6.50 eV, which is significantly higher than those for the radical cations, and more importantly, higher than 4 eV. This explains why the structural distortion due to the pseudo Jahn–Teller effect does not occur in the neutral MonoSCBs and DiSCBs.

As mentioned in the previous section, the asymmetrical distortion is enhanced by exocyclic substitution of methyl groups on the ring Si atom and weakened by the endocyclic Si substitution for the six four-membered-ring radical cations. This type of trend was also observed in the radical cations of silacyclohexane and its methyl derivatives.[13] Creve and Nguyen[41] showed in their study of halogenated phosphine radical cations that an increasing number of substituents with high electronegativity can strengthen the pseudo Jahn–Teller effect. Since the C atom is more electronegative with respect to the Si atom, methyl substitution should result in a stronger

Can. J. Chem. Downloaded from www.nrcresearchpress.com by Renmin University of China on 09/02/12
For personal use only.

Table 3. Geometrical parameters for different structures of monosilacyclobutane (MonoSCB) radical cations calculated by MP2/6–311++G(d,p).

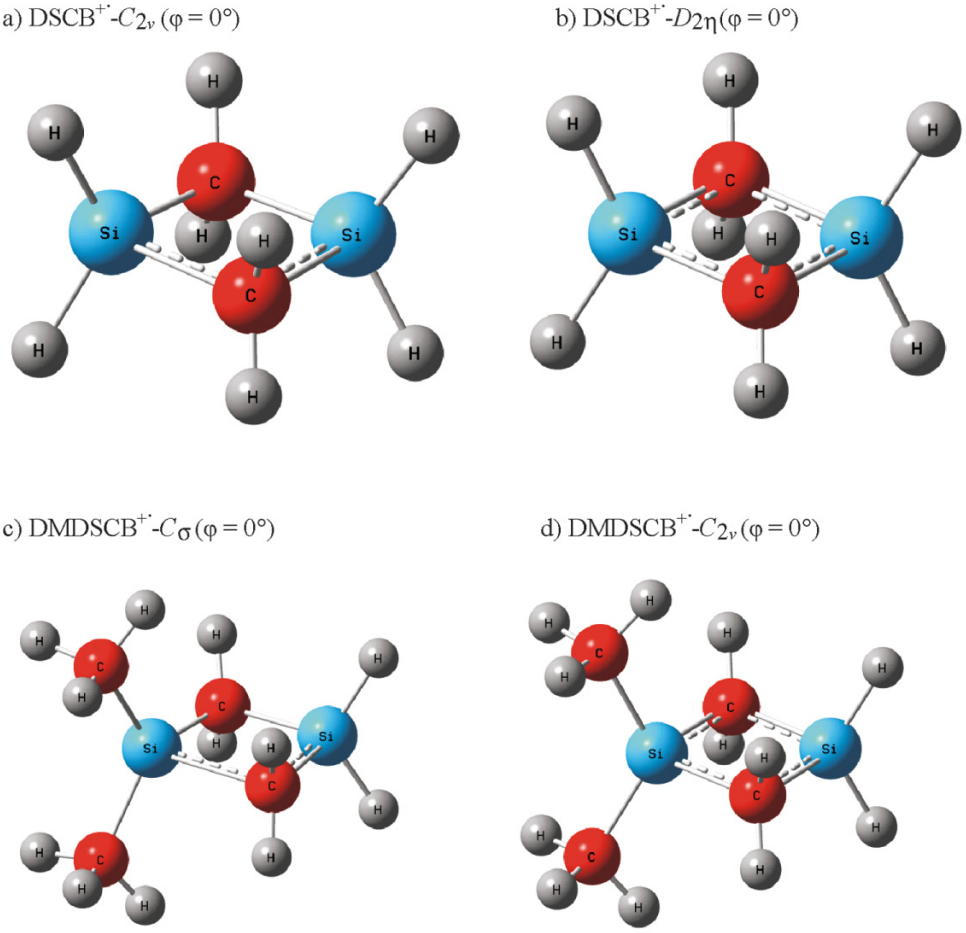
Molecule	SCB-C_s[a]	SCB$^{+\bullet}$-C_1	SCB$^{+\bullet}$-C_{2v}	MSCB-*e*-C_s[a]	MSCB$^{+\bullet}$-*e*-C_1	MSCB$^{+\bullet}$-*e*-C_s	DMSCB-C_s[a]	DMSCB$^{+\bullet}$-C_1	DMSCB$^{+\bullet}$-C_{2v}
Bond length (Å)									
Si–C_2	1.893	1.843	1.990	1.894	1.847	1.998	1.896	1.853	2.005
Si–C_4	1.893	2.273	1.990	1.894	2.299	1.998	1.896	2.326	2.005
C_3–C_2	1.562	1.580	1.532	1.562	1.576	1.531	1.563	1.574	1.530
C_3–C_4	1.562	1.503	1.532	1.562	1.504	1.531	1.563	1.504	1.530
Si–R_5	1.481	1.464	1.463	1.484	1.468	1.467	1.879	1.844	1.845
Si–R_6	1.481	1.465	1.463	1.875	1.838	1.840	1.877	1.843	1.845
C_2–H_7	1.091	1.091	1.095	1.092	1.092	1.094	1.093	1.092	1.094
C_2–H_8	1.096	1.092	1.095	1.096	1.093	1.094	1.096	1.093	1.094
C_3–H_9	1.096	1.091	1.088	1.096	1.091	1.088	1.096	1.091	1.089
C_3–H_{10}	1.095	1.099	1.088	1.095	1.098	1.088	1.095	1.097	1.089
C_4–H_{11}	1.091	1.088	1.095	1.092	1.088	1.094	1.093	1.088	1.094
C_4–H_{12}	1.096	1.091	1.095	1.096	1.091	1.094	1.096	1.090	1.094
Bond angle (°)									
∠C_2–Si–C_4	78.2	72.6	66.0	78.1	71.7	65.9	78.2	71.0	65.8
∠C_2–C_3–C_4	99.7	106.0	90.0	99.6	105.8	90.4	99.9	105.8	90.8
∠Si_1–C_2–C_3	86.1	92.5	102.0	86.2	93.3	101.9	86.4	94.6	101.7
∠Si_1–C_4–C_3	86.1	79.2	102.0	86.2	79.1	101.9	86.4	79.4	101.7
∠R_5–Si–R_6	108.7	117.1	116.0	109.9	117.8	116.6	110.0	118.2	117.0
Puckering angle (°)									
φ	34.2	34.6	0	34.2	35.0	0	32.6	33.3	0

Note: SCB, 1-silacyclobutane; MSCB, 1-methyl-1-silacyclobutane; DMSCB, 1,1-dimethyl-1-silacyclobutane; *e*, equatorial.

[a]Results from ref. 38.

Can. J. Chem. Downloaded from www.nrcresearchpress.com by Renmin University of China on 09/02/12
For personal use only.

Fig. 4. Optimized C_{2v} (*a*) and D_{2h} (*b*) geometric structures of the 1,3-disilacyclobutane (DSCB, IV) radical cation and C_s (*c*) and C_{2v} (*d*) structures of the 1,1-dimethyl-1,3-disilacyclobutane (DMDSCB, V) radical cation calculated at the MP2/6–311++G(d,p) level. (A broken line indicates an elongated bond.)



pseudo Jahn–Teller effect by further localizing the charge distribution on the elongated σ(Si–C) ring bond. Following the same argument, replacing a ring C atom with Si weakens the pseudo Jahn–Teller effect, consequently resulting in the structural distortion.

The asymmetrical distortion in the geometrical structures due to the pseudo Jahn–Teller effect generally lowers the molecular symmetry. For example, the radical cations of SCB, MSCB, and DMSCB all belong to the C_1 point group, which is lower than the C_s symmetry in their corresponding neutral forms. This is because the symmetric plane is distorted because of the pseudo Jahn–Teller effect upon ionization. However, the three DiSCB radical cations seem to escape from this general rule. The molecular symmetry is maintained upon ionization even though the ring structure has been asymmetrically distorted, which destroys the symmetry plane crossing the two ring Si atoms. This exception is due to the fact that the ring structure of the three DiSCB molecules changes from puckered to planar upon ionization.

Puckering potential energy surface (PES)

Although both MonoSCB and DiSCB cations possess the asymmetrically distorted structures in their ground states, there is one significant difference in the geometry change between these two types of species upon ionization. The puckered ring structures are maintained in MonoSCB cations, whereas DiSCB cations change to a planar ring structure. These two distinct structures are well-represented in the PESs as a function of dihedral angles, as shown in Fig. 5. In Fig. 5*a*, the puckered MonoSCB cations have double-well potential energy curves, in which the maximum energy structures correspond to the planar transition states. For SCB and DMSCB radical cations, the two minima are of equal energy. Two nonequivalent minima were found for the MSCB radical cation, and the equatorial conformer (MSCB-$e^{+\bullet}$) is more stable than the axial one (MSCB-$a^{+\bullet}$). The energy difference between the two conformers was determined to be 114 cm^{-1}. This is consistent with our previous calculation on the neutral molecule of MSCB, whose stable structure is also in equatorial form.[38] In Fig. 5*b*, the potential energy curves of the DiSCB cations have a single-well shape, which reflects the planar structure.

As has been well-established in the literature,[34] the puckering PES can be described by a one-dimensional potential energy function shown in eq. [2], if the planar ring has a plane of symmetry.

$$[2] \qquad V(x) = Ax^4 + Bx^2$$

where A is a positive constant, B can be either a positive or negative constant, and x is the puckering coordinate defined

Can. J. Chem. Downloaded from www.nrcresearchpress.com by Renmin University of China on 09/02/12
For personal use only.

Table 4. Geometrical parameters for different structures of 1,3-disilacyclobutane (DiSCB) radical cations calculated by MP2/6–311++G(d,p).

Molecule	DSCB-C_{2v}[a]	DSCB$^{+\bullet}$-C_{2v}	DSCB$^{+\bullet}$-D_{2h}	DMDSCB-C_s[a]	DMDSCB$^{+\bullet}$-C_s	DMDSCB$^{+\bullet}$-C_{2v}	TMDSCB-C_{2v}[a]	TMDSCB$^{+\bullet}$-C_{2v}	TMDSCB$^{+\bullet}$-D_{2h}
Bond length (Å)									
Si_1–C_2	1.901	1.862	1.933	1.905	1.841	1.939	1.904	1.866	1.931
Si_3–C_2	1.901	1.862	1.933	1.899	1.897	1.924	1.904	1.866	1.931
Si_1–C_4	1.901	2.058	1.933	1.905	2.243	1.939	1.904	2.058	1.931
Si_3–C_4	1.901	2.058	1.933	1.899	1.945	1.924	1.904	2.058	1.931
Si_1–R_5(Si_1–R_6)	1.480	1.466	1.470	1.877	1.847	1.868	1.879	1.856	1.869
Si_3–R_9(Si_3–R_{10})	1.480	1.466	1.470	1.481	1.468	1.471	1.879	1.856	1.869
C_2–H_7	1.091	1.091	1.091	1.092	1.092	1.092	1.094	1.093	1.093
C_2–H_8	1.096	1.091	1.091	1.097	1.092	1.092	1.097	1.093	1.093
C_4–H_{11}	1.091	1.090	1.091	1.092	1.090	1.092	1.094	1.092	1.093
C_4–H_{12}	1.096	1.090	1.091	1.097	1.090	1.092	1.097	1.092	1.093
Bond angle (°)									
∠C_2–Si_1–C_4	89.9	97.0	98.3	89.9	90.9	97.3	90.8	96.4	97.3
∠C_2–Si_3–C_4	89.9	97.0	98.3	90.3	99.2	98.2	90.8	96.4	97.3
∠Si_1–C_2–Si_3	87.4	88.1	81.7	87.5	91.1	82.2	87.8	88.6	82.7
∠Si_1–C_4–Si_3	87.4	78.0	81.7	87.5	78.8	82.2	87.8	78.6	82.7
∠R_5–Si_1–R_6	109.1	118.2	123.2	110.0	119.7	123.1	110.7	118.7	121.6
∠R_9–Si_3–R_{10}	109.1	118.2	123.2	108.8	116.6	121.4	110.7	118.7	121.6
Puckering angle (°)									
φ	25.5	0	0	23.7	0	0	17.5	0	0

Note: DSCB, 1,3-disilacyclobutane; DMDSCB, 1,1-dimethyl-1,3-disilacyclobutane; TMDSCB, 1,1,3,3-tetramethyl-1,3-disilacyclobutane.

[a]Results from ref. 38.

Can. J. Chem. Downloaded from www.nrcresearchpress.com by Renmin University of China on 09/02/12
For personal use only.

Table 5. Spin density distributions for the ring atoms of six radical cations (I–VI) calculated using B3LYP/6–311++G(d,p) and MP2/6–311++G(d,p).

	Spin density distribution					
Ring atom	$SCB^{+\bullet}$	MSCB-$e^{+\bullet}$	$DMSCB^{+\bullet}$	$DSCB^{+\bullet}$	$DMDSCB^{+\bullet}$	$TMDSCB^{+\bullet}$
At the B3LYP/6–311++G(d,p) level						
Si_1	0.21	0.2	0.17	0.05	0.15	0.06
C_2	0.02	0.01	0	0.06	0.06	0.03
C_3 (Si_3)[a]	0.01	0.01	0.01	0.05	–0.04	0.06
C_4	0.68	0.71	0.74	0.70	0.74	0.70
At the MP2/6–311++G(d,p) level						
Si_1	0.21	0.20	0.19	0.03	0.16	0.06
C_2	–0.01	–0.02	–0.04	0.01	0.03	0
C_3 (Si_3)[a]	–0.01	–0.02	–0.01	0.03	–0.06	0.06
C_4	0.78	0.80	0.82	0.88	0.87	0.86

Note: SCB, 1-silacyclobutane; MSCB, 1-methyl-1-silacyclobutane; DMSCB, 1,1-dimethyl-1-silacyclobutane; DSCB, 1,3-disilacyclobutane; DMDSCB, 1,1-dimethyl-1,3-disilacyclobutane; TMDSCB, 1,1,3,3-tetramethyl-1,3-disilacyclobutane; *e*, equatorial.

[a]C_3 in MonoSCB radical cations and Si_3 in DiSCB radical cations.

Table 6. The calculated energies and oscillator strengths for the lowest electronic transitions of monosilacyclobutane (MonoSCB) and 1,3-disilacyclobutane (DiSCB) radical cations using B3LYP/6–311++G(d,p) levels.

	Radical cations		Neutral molecules[a]	
Molecule	*E* (eV)	Osc. strength	*E* (eV)	Osc. strength
SCB	2.69	0.0013	6.50	0.0123
MSCB-*e*	2.72	0.0004	6.47	0.0079
DMSCB	2.78	0.0002	6.18	0.0207
DSCB	2.45	0.0133	6.06	0.0000
DMDSCB	2.48	0.0065	6.11	0.0319
TMDSCB	2.17	0.0059	5.73	0.0844

Note: SCB, 1-silacyclobutane; MSCB, 1-methyl-1-silacyclobutane; DMSCB, 1,1-dimethyl-1-silacyclobutane; DSCB, 1,3-disilacyclobutane; DMDSCB, 1,1-dimethyl-1,3-disilacyclobutane; TMDSCB, 1,1,3,3-tetramethyl-1,3-disilacyclobutane; *e*, equatorial.

[a]Results from ref. 38 calculated using the B3LYP/6–311++G(3df,p) level.

in Fig. 2. If B is negative, the function is a symmetric double-minimum type with an energy barrier height of $B^2/4A$ separating the equivalent minima. If B is positive, the function has only one minimum. The planar ring of $MSCB^{+\bullet}$ does not have a plane of symmetry. For this species, the asymmetry can be introduced into $V(x)$ by including the odd-powered terms of x. Since the maximum energy structure in the PES of $MSCB^{+\bullet}$ is planar coinciding with $x = 0$, the linear term can be omitted and the puckering potential energy for $MSCB^{+\bullet}$ can be represented by eq. [3].

$$[3] \qquad V(x) = Ax^4 + Bx^2 + Cx^3$$

where C is a constant. Among the six radical cations studied, C only has a nonzero value in $MSCB^{+\bullet}$. The potential function in eq. [3] has two nonequivalent minima. The sign of C determines which minimum is lower in energy than the other, and its magnitude reflects the energy difference between the two minima. The A, B, and C parameters in $V(x)$ for the six radical cations were determined in this work by fitting the calculated PES in the form of a polynomial function of x. The value of x at a specific dihedral angle was calculated using the corresponding geometric parameters, including the bond length and bond angles. The values of A, B, and C thus obtained for the six radical cations are listed in Table 7. The three parameters for the six neutral molecules are listed in the same table for comparison. The barrier height to planarity has also been reported with its corresponding dihedral angle and x value.

As shown in Table 7, the parameters of A remain positive upon ionization for all six species. The three MonoSCB radical cations have negative B values, which result in the puckered ring structures. However, the barrier heights are reduced in the cations as compared with their neutral counterparts. It is important to note that the B parameters for the DiSCBs change their sign from negative to positive upon ionization. The positive B values in the DiSCB cations suggest that they now have planar ring structures. The sign change in B originates from the fact that the balance between the torsional strain and the angle strain determines the ring planarity.[34] The torsional strain ordinarily favors a puckered ring to relieve the repulsion between hydrogen atoms in the eclipsed planar conformation, whereas the angle strain prefers to a planar ring in which the compressed and strained ring angles are at maximum.

The potential function in eq. [2] can be rewritten in terms of angle strain (V_d) and torsional strain (V_t).[34]

$$[4] \qquad V(x) = V_d + V_t = (A_d + A_t)x^4 + (B_d + B_t)x^2 = Ax^4 + Bx^2$$

where A_d and B_d are the angle strain contributions to the quartic and quadratic terms, respectively, and A_t and B_t are the torsional strain contributions to the quartic and quadratic terms, respectively. The expressions for the four constants are given in eqs. [5]–[8].

$$[5] \qquad A_d = \sum_i \frac{1}{2} k_i c_i$$

Can. J. Chem. Downloaded from www.nrcresearchpress.com by Renmin University of China on 09/02/12
For personal use only.

Fig. 5. Ring-puckering potential energy as a function of puckering angle (φ) for (*a*) monosilacyclobutane (MonoSCB) radical cations and (*b*) 1,3-disilacyclobutane (DiSCB) radical cations.

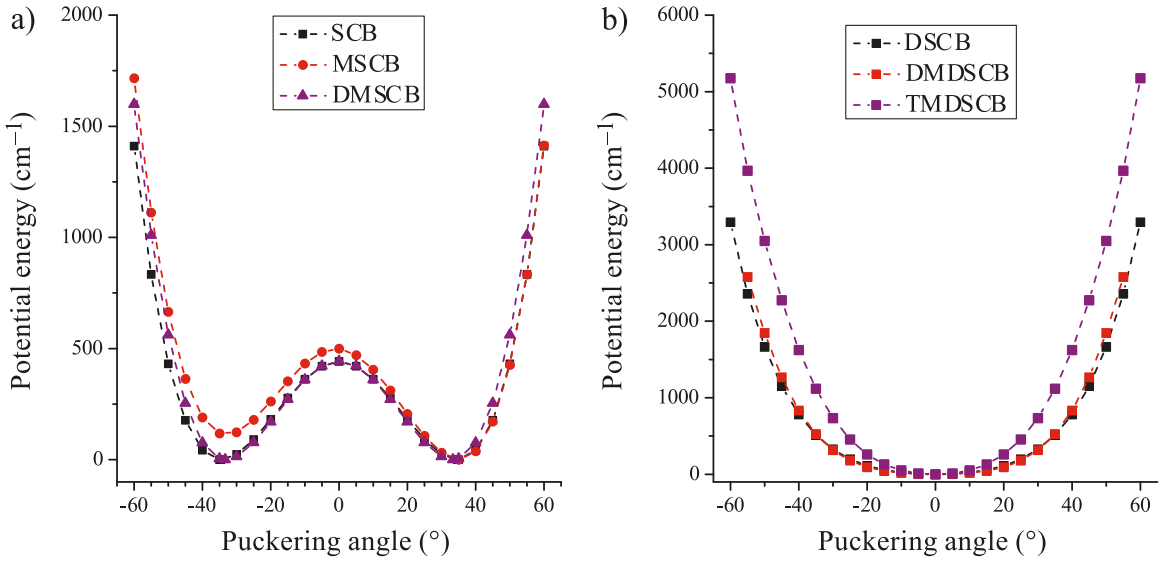


Table 7. Ring-puckering potential energy function parameters, barrier heights, puckering angles, and coordinate x for the monosilacyclobutane (MonoSCB) and 1,3-disilacyclobutane (DiSCB) radical cations calculated by MP2/6–311++G(d,p).

Molecule	A ($\times10^5$ cm^{-1} Å^{-4})[a]	B ($\times10^4$ cm^{-1} Å^{-2})[a]	C ($\times10^3$ cm^{-1} Å^{-3})[a]	Barrier (cm^{-1})	Puckering angle (°)	x (Å)
SCB[b]	6.990±0.066	–4.601±0.050	0	762.0	34.2	0.1753
SCB$^{+\bullet}$	4.504±0.018	–2.828±0.013	0	441.9	34.6	0.1747
MSCB[b]	8.155±0.137	–4.955±0.058	–7.549±0.831	773.4[c]	34.2	0.1758
MSCB$^{+\bullet}$	4.606±0.048	–2.850±0.034	–7.019±0.370	499.2[c]	35.0	0.1779
DMSCB[b]	7.715±0.080	–4.647±0.061	0	721.5	32.6	0.1673
DMSCB$^{+\bullet}$	4.738±0.042	–2.869±0.030	0	443.5	33.3	0.1696
DSCB[b]	3.868±0.059	–1.886±0.033	0	234.1	25.5	0.1483
DSCB$^{+\bullet}$	1.521±0.063	0.640±0.006	0	0	0	0
DMDSCB[b]	4.323±0.042	–1.752±0.024	0	186.1	23.7	0.1383
DMDSCB$^{+\bullet}$	1.570±0.022	0.569±0.020	0	0	0	0
TMDSCB[b]	5.819±0.108	–1.222±0.050	0	83.6	17.5	0.1018
TMDSCB$^{+\bullet}$	1.406±0.042	2.163±0.044	0	0	0	0

Note: SCB, 1-silacyclobutane; MSCB, 1-methyl-1-silacyclobutane; DMSCB, 1,1-dimethyl-1-silacyclobutane; DSCB, 1,3-disilacyclobutane; DMDSCB, 1,1-dimethyl-1,3-disilacyclobutane; TMDSCB, 1,1,3,3-tetramethyl-1,3-disilacyclobutane.

[a]The errors for the *A*, *B*, and *C* parameters (eq. [3]) were obtained from the polynomial fittings.

[b]Results from ref. 38.

[c]The barrier height was calculated from puckered MSCB-*e* (equatorial form) to its planar structure.

$$[6] \qquad A_t = \frac{27}{16}\sum_i h_i^4 V_3^i$$

$$[7] \qquad B_d = \sum_i k_i s_i c_i$$

$$[8] \qquad B_t = -\frac{9}{4}\sum_i h_i V_3^i$$

Here, i represents each single bond in a ring, k is the angle-bending force constant, s is the angle strain inherent in the planar ring, c and h are both positive constants, and V_3 is the torsional barrier to a torsional motion about a ring bond. According to eqs. [7] and [8], B_d is always positive, since s_i is positive for the four-membered rings, whereas B_t is always negative. Therefore, the sign of B is determined by the relative magnitudes of B_d and B_t.

As is seen from Table 7, the B constants are all negative in the six neutral molecules; this suggests that B_t predominates over B_d in the neutral forms. The magnitude of B_t is proportional to the torsional barrier height (V_3) about the ring bonds. The value of V_3 about a particular bond was reported to decrease with increasing bond length, as was illustrated in ethane (1013.069 cm^{-1}), methylsilane (591.370 cm^{-1}), and disilane (404.344 cm^{-1}).[42] Among these three molecules, the bond length increases with Si substitution, i.e., σ(C–C) < σ(Si–C) < σ(Si–Si).[43] As we discussed in our previous study,[38] the neutral DiSCB molecules are less puckered than

Can. J. Chem. Downloaded from www.nrcresearchpress.com by Renmin University of China on 09/02/12
For personal use only.

MonoSCBs, since there are four Si–C ring bonds in the former, but only two in the latter. This makes the *B* constants less negative in DiSCBs. Owing to the σ(Si–C) ring bond(s) elongation arising from the structural distortion, the V_3 values of all six molecules are expected to decrease in magnitude upon ionization. The resultant decrease in the magnitude of B_t leads to the overall positive *B* values in the DiSCB radical cations. The overall *B* values remain negative in MonoSCB radical cations, since the starting values of B_t are more negative in their neutral forms. Therefore, the Si–C ring bond elongation due to the pseudo Jahn–Teller effect upon ionization is believed to be the main reason why endocyclic Si substitution in silacyclobutane rings gives a planar ring in the DiSCB radical cations.

The exocyclic methyl substitution is found to affect the shape of the puckering PES. As shown in Fig. 5*b*, the TMDSCB radical cation has a larger curvature at the minimum when compared with the DSCB and DMDSCB radical cations. This is due to an increase in the magnitude of the positive *B* values upon exocyclic methyl substitution, as shown in Table 7. The change in *B* can again be understood by the change in V_3 upon methyl substitution. Previous studies of methyl-substituted silanes showed that the V_3 about the Si–C bond decreased upon methyl substitution, e.g., CH_3SiH_3 (V_3 = 591.370 cm^{-1}),[44] $(CH_3)_2SiH_2$ (V_3 = 577.437 cm^{-1}),[45] and $(CH_3)_4Si$ (V_3 = 476.476 cm^{-1}).[46] This leads to the decreasing magnitude of B_t, which in turn results in a more positive *B* value upon methyl substitution. Therefore, upon exocyclic methyl substitution the PESs of the DiSCB radical cations behave more like that of the harmonic oscillators.

Conclusions

A systematic study of the geometrical and electronic structures of three monosilacyclobutane (SCB, MSCB, and DMSCB) and three 1,3-disilacyclobutane (DSCB, DMDSCB, and TMDSCB) radical cations was performed using ab initio and DFT methods. The ground electronic states of all six radical cations have an asymmetrically distorted structure. Those of the MonoSCB radical cations are all of C_1 symmetry with one Si–C ring bond elongated and the other shortened. In the asymmetrically distorted structures of DiSCB radical cations, a pair of Si–C ring bonds are elongated and the other pair shortened. Of the three DiSCB radical cations, the pairs of bonds are elongated to the same extent in $DSCB^{+\bullet}$ and $TMDSCB^{+\bullet}$, whereas the two elongated Si–C bonds are of different lengths in $DMDSCB^{+\bullet}$. The next higher energy stable structures of the six radical cations all have a planar ring structure, where two ring Si–C bond lengths are increased to the same extent for MonoSCBs. The general feature in the geometry of the next higher energy stable structures of the three DiSCB radical cations is that all four ring Si–C bonds are elongated; however, all ring Si–C bonds are of the same length in $DSCB^{+\bullet}$ (D_{2h}) and $TMDSCB^{+\bullet}$ (D_{2h}), whereas the C_{2v} structure of $DMDSCB^{+\bullet}$ has two pairs of equal ring Si–C bonds.

In the asymmetrically distorted ground states, the unpaired electrons reside predominantly on the elongated σ(Si–C) ring bond(s) in the six radical cations, indicating a localized structure. This is in agreement with previous studies on silacycloalkane cations. In examining the effect of the exocyclic substitution of methyl groups on the ring Si atom and the replacement of a ring C atom by Si, it was found that the asymmetrical structural distortion is enhanced by exocyclic methyl substitution and weakened by endocyclic Si substituion. The asymmetrical structural distortions upon ionization of MonoSCBs and DiSCBs are believed to be due to the second-order Jahn–Teller effect. Our studies of the lowest lying excited electronic states of both MonoSCB and DiSCB radical cations using time-dependent DFT methods showed that they all lie above the ground states by an energy gap ranging from 2.17 to 2.78 eV. Therefore, the structural distortion due to the second-order Jahn–Teller effect stabilizes the cationic structures. It is also noted that there is one significant difference in the geometry change between MonoSCBs and DiSCBs upon ionization, i.e., the puckered ring structures are maintained in MonoSCB cations, whereas DiSCB cations change to a planar structure. The investigation on the PESs of the radical cations shows that MonoSCB cations possess double-well potential energy curves, whereas those of DiSCB cations are of a single-well shape. The difference is explained in terms of the competition between the torsional strain and the angle strain that determines the ring planarity. The elongation of Si–C ring bond(s) and the consequent decrease in the torsional barrier height lead to a planar ring structure in DiSCB radical cations.

Acknowledgments

The financial support for this work by the Natural Sciences and Engineering Research Council of Canada (NSERC), the Canadian Foundation for Innovations, and the University of Calgary is gratefully acknowledged. The authors would like to thank Professor Arvi Rauk for his helpful suggestions for this work.

References

(1) Iwasaki, M.; Toriyama, K.; Nunome, K. *J. Am. Chem. Soc.* **1981**, *103* (12), 3591. doi:10.1021/ja00402a066.
(2) Toriyama, K.; Nunome, K.; Iwasaki, M. *J. Chem. Phys.* **1982**, *77* (12), 5891. doi:10.1063/1.443863.
(3) Symons, M. C. R. *Chem. Soc. Rev.* **1984**, *13* (4), 393. doi:10.1039/cs9841300393.
(4) Toriyama, K.; Nunome, K.; Iwasaki, M. *J. Phys. Chem.* **1981**, *85* (15), 2149. doi:10.1021/j150615a001.
(5) Shiotani, M.; Yano, A.; Ohta, N.; Ichikawa, T. *Chem. Phys. Lett.* **1988**, *147* (1), 38. doi:10.1016/0009-2614(88)80220-3.
(6) Iwasaki, M.; Toriyama, K.; Nunome, K. *Faraday Discuss.* **1984**, *78*, 19. doi:10.1039/dc9847800019.
(7) Shiotani, M.; Ohta, N.; Ichikawa, T. *Chem. Phys. Lett.* **1988**, *149* (2), 185. doi:10.1016/0009-2614(88)87219-1.
(8) Lindgren, M.; Shiotani, M.; Ohta, N.; Ichikawa, T.; Sjoqvist, L. *Chem. Phys. Lett.* **1989**, *161* (2), 127. doi:10.1016/0009-2614(89)85043-2.
(9) Shiotani, M.; Lindgren, M.; Ichikawa, T. *J. Am. Chem. Soc.* **1990**, *112* (3), 967. doi:10.1021/ja00159a010.
(10) Shiotani, M.; Lindgren, M.; Ohta, N.; Ichikawa, T. *J. Chem. Soc., Perkin Trans. 2* **1991**, 711.
(11) Lindgren, M.; Komaguchi, K.; Shiotani, M.; Sasaki, K. *J. Phys. Chem.* **1994**, *98* (34), 8331. doi:10.1021/j100085a012.
(12) Jahn, H. A.; Teller, E. *Proc. R. Soc. Lond. A Math. Phys. Sci.* **1937**, *161* (905), 220. doi:10.1098/rspa.1937.0142.

Can. J. Chem. Downloaded from www.nrcresearchpress.com by Renmin University of China on 09/02/12
For personal use only.

(13) Komaguchi, K.; Shiotani, M. *J. Phys. Chem. A* **1997**, *101* (37), 6983. doi:10.1021/jp970958p.
(14) Shiotani, M.; Komaguchi, K.; Ohshita, J.; Ishikawa, M.; Sjoqvist, L. *Chem. Phys. Lett.* **1992**, *188* (1–2), 93. doi:10.1016/0009-2614(92)85094-Q.
(15) Komaguchi, K.; Shiotani, M.; Ishikawa, M.; Sasaki, K. *Chem. Phys. Lett.* **1992**, *200* (6), 580. doi:10.1016/0009-2614(92)80094-R.
(16) Fängström, T.; Lunell, S.; Engels, B.; Eriksson, L. A.; Shiotani, M.; Komaguchi, K. *J. Chem. Phys.* **1997**, *107* (2), 297. doi:10.1063/1.474441.
(17) Al Derzi, A. R.; Fau, S.; Bartlett, R. J. *J. Phys. Chem. A* **2006**, *110* (13), 4473. doi:10.1021/jp058164v.
(18) Bader, R. F. W. *Can. J. Chem.* **1962**, *40* (6), 1164. doi:10.1139/v62-178.
(19) Pearson, R. G. *J. Am. Chem. Soc.* **1969**, *91* (5), 1252. doi:10.1021/ja01033a058.
(20) Pearson, R. G. *J. Am. Chem. Soc.* **1969**, *91* (18), 4947. doi:10.1021/ja01046a001.
(21) Komaguchi, K.; Marutani, T.; Shiotani, M.; Hasegawa, A. *Phys. Chem. Chem. Phys.* **1999**, *1* (19), 4549. doi:10.1039/a905143k.
(22) Toriyama, K. *Chem. Phys. Lett.* **1991**, *177* (1), 39. doi:10.1016/0009-2614(91)90172-6.
(23) Toriyama, K.; Okazaki, M.; Nunome, K. *J. Chem. Phys.* **1991**, *95* (6), 3955. doi:10.1063/1.460802.
(24) Toriyama, K.; Okazaki, M. *J. Phys. Chem.* **1992**, *96* (17), 6986. doi:10.1021/j100196a026.
(25) Gusel'nikov, L. E. *Coord. Chem. Rev.* **2003**, *244* (1–2), 149. doi:10.1016/S0010-8545(03)00104-8.
(26) Johnson, A. D.; Perrin, J.; Mucha, J. A.; Ibbotson, D. E. *J. Phys. Chem.* **1993**, *97* (49), 12937. doi:10.1021/j100151a049.
(27) Larkin, D. J.; Interrante, L. V. *Chem. Mater.* **1992**, *4* (1), 22. doi:10.1021/cm00019a009.
(28) Wrobel, A. M.; Stanczyk, W. *Chem. Mater.* **1994**, *6* (10), 1766. doi:10.1021/cm00046a032.
(29) Loboda, M. J.; Seifferly, J. A.; Dall, F. C. *J. Vac. Sci. Technol. A* **1994**, *12* (1), 90. doi:10.1116/1.578864.
(30) Zaharias, G. A.; Duan, H. L.; Bent, S. F. *J. Vac. Sci. Technol. A* **2006**, *24* (3), 542. doi:10.1116/1.2194023.
(31) Shi, Y. J.; Lo, B.; Tong, L.; Li, X.; Eustergerling, B. D.; Sorensen, T. S. *J. Mass Spectrom.* **2007**, *42* (5), 575. doi:10.1002/jms.1186.
(32) Tong, L.; Shi, Y. J. *Thin Solid Films* **2009**, *517* (12), 3461. doi:10.1016/j.tsf.2009.01.058.
(33) Tong, L.; Shi, Y. J. *J. Mass Spectrom.* **2010**, *45* (2), 215. doi:10.1002/jms.1712.
(34) Legon, A. C. *Chem. Rev.* **1980**, *80* (3), 231. doi:10.1021/cr60325a002.
(35) Irwin, R. M.; Cooke, J. M.; Laane, J. *J. Am. Chem. Soc.* **1977**, *99* (10), 3273. doi:10.1021/ja00452a012.
(36) Novikov, V. P.; Tarasenko, S. A.; Samdal, S.; Vilkov, L. V. *J. Struct. Chem.* **2000**, *41* (2), 217. doi:10.1007/BF02741586.
(37) Rishard, M. Z. M.; Irwin, R. M.; Laane, J. *J. Phys. Chem. A* **2007**, *111* (5), 825. doi:10.1021/jp064480d.
(38) Cai, Z. J.; Shi, Y. J. *J. Mol. Spectrosc.* **2011**, *267* (1–2), 178. doi:10.1016/j.jms.2011.03.019.
(39) Stillahn, J. A.; Trevino, K.; Fisher, E. R. *Annu. Rev. Anal. Chem.* **2008**, *1* (1), 261. doi:10.1146/annurev.anchem.1.031207.112953.
(40) Frisch, M. J.; Trucks, G. W.; Schlegel, H. B.; Scuseria, G. E.; Robb, M. A.; Cheeseman, J. R.; Montgomery, J. A., Jr.; Vreven, T.; Kudin, K. N.; Burant, J. C.; Millam, J. M.; Iyengar, S. S.; Tomasi, J.; Barone, V.; Mennucci, B.; Cossi, M.; Scalmani, G.; Rega, N.; Petersson, G. A.; Nakatsuji, H.; Hada, M.; Ehara, M.; Toyota, K.; Fukuda, R.; Hasegawa, J.; Ishida, M.; Nakajima, T.; Honda, Y.; Kitao, O.; Nakai, H.; Klene, M.; Li, X.; Knox, J. E.; Hratchian, H. P.; Cross, J. B.; Bakken, V.; Adamo, C.; Jaramillo, J.; Gomperts, R.; Stratmann, R. E.; Yazyev, O.; Austin, A. J.; Cammi, R.; Pomelli, C.; Ochterski, J. W.; Ayala, P. Y.; Morokuma, K.; Voth, G. A.; Salvador, P.; Dannenberg, J. J.; Zakrzewski, V. G.; Dapprich, S.; Daniels, A. D.; Strain, M. C.; Farkas, O.; Malick, D. K.; Rabuck, A. D.; Raghavachari, K.; Foresman, J. B.; Ortiz, J. V.; Cui, Q.; Baboul, A. G.; Clifford, S.; Cioslowski, J.; Stefanov, B. B.; Liu, G.; Liashenko, A.; Piskorz, P.; Komaromi, I.; Martin, R. L.; Fox, D. J.; Keith, T.; Al-Laham, M. A.; Peng, C. Y.; Nanayakkara, A.; Challacombe, M.; Gill, P. M. W.; Johnson, B.; Chen, W.; Wong, M. W.; Gonzalez, C.; Pople, J. A. *Gaussian 03,* Revision B.01; Gaussian, Inc.: Wallingford, CT, 2004.
(41) Creve, S.; Nguyen, M. T. *J. Phys. Chem. A* **1998**, *102* (32), 6549. doi:10.1021/jp981083x.
(42) Moazzen-Ahmadi, N.; Horneman, V. M. *J. Chem. Phys.* **2006**, *124* (19), 194309. doi:10.1063/1.2198834.
(43) Haynes, W. M. (Ed.). *CRC Handbook of Chemistry and Physics,* 92nd ed.; CRC Press: Cleveland, OH, 2011.
(44) Moazzen-Ahmadi, N.; Ozier, I. *J. Mol. Spectrosc.* **1987**, *123* (1), 26. doi:10.1016/0022-2852(87)90260-8.
(45) Niide, Y.; Hayashi, M. *J. Mol. Spectrosc.* **2004**, *223* (2), 152. doi:10.1016/j.jms.2003.08.008.
(46) Campanelli, A. R.; Ramondo, F.; Domenicano, A.; Hargittai, I. *Struct. Chem.* **2000**, *11* (2–3), 155. doi:10.1023/A:1009213726034.

Stereoselective benzylic hydroxylation of ethylbenzene and propylbenzene using the mycelia of *Aspergillus flavus* MTCC-1783 and MTCC-1884

Saroj Yadav, R.S.S. Yadav, and K.D.S. Yadav

Can. J. Chem. Downloaded from www.nrcresearchpress.com by Renmin University of China on 09/02/12
For personal use only.

Abstract: The aim of this study was to provide syntheses of optically pure (*R*)-1-phenylethanol and (*R*)-1-phenylpropanol from ethylbenzene and propylbenzene, respectively, using the fungal mycelia of new fungal species, namely *Aspergillus flavus* MTCC-1783 and *Aspergillus flavus* MTCC-1884, as catalysts. The mycelia of *A. flavus* MTCC- 1783 and *A. flavus* MTCC-1884 were prepared by growing the fungal strains in liquid culture medium containing ethylmethylketone as the sole carbon source. The mycelia were suspended in potassium phosphate buffer pH 7.0. The suspensions of mycelia were used for the transformations of ethylbenzene and propylbenzene. Ethylbenzene and propylbenzene were converted to (*R*)-1-phenylethanol and (*R*)-1-phenylpropanol, in 100% and 99% ee, respectively. The mycelia of *A. flavus* MTCC-1783 and *A. flavus* MTCC-1884 can be used for the preparation of (*R*)-1-phenylethanol and (*R*)-1-phenylpropanol in 100% and 99% ee, respectively, from ethylbenzene and propylbenzene, respectively. The studies report convenient methods for the syntheses of optically pure isomers, (*R*)-1-phenylethanol and (*R*)-1-phenylpropanol, which are important chiral building blocks in the preparations of fine chemicals and pharmaceuticals. The reactions are ecofriendly, occur at 30 °C, and the time required was 24 h.

Key words: Aspergillus flavus, benzylic hydroxylation, biocatalyst, (*R*)-1-phenylethanol, (*R*)-1-phenylpropanol.

Résumé : On a réalisé la synthèse des (*R*)-1-phényléthanol et (*R*)-1-phénylpropanol, à partir respectivement de l'éthylbenzène et du propylbenzène, en présence de mycélium fongiques provenant de nouvelles espèces fongiques, soit l'*Aspergillus flavus* MTCC-1783 et l'*Aspergillus flavus* MTCC-1884, utilisées comme catalyseurs. Les mycélium d'*A. flavus* MTCC-1783 et d'*A. flavus* MTCC-1884 ont été préparés en procédant à la culture des souches fongiques dans des milieux de culture liquide ne contenant que de l'éthylméthylcétone comme source de carbone. Les mycélium ont été suspendus dans un tampon de sulfate de potassium, de pH 7,0. On a ensuite utilisé les suspensions de mycélium pour les transformations de l'éthylbenzène et du propylbenzène. L'éthylbenzène et le propylbenzène ont été convertis en (*R*)-1-phényléthanol et en (*R*)-(1)-phénylpropanol avec des excès énantiomères respectivement de 100 % et 99 %. En conclusion, les mycélium d'*A. flavus* MTCC-1783 et d'*A. flavus* MTCC-1884 peuvent être utilisés dans la préparation de (*R*)-1-phényléthanol et (*R*)-(1)-phénylpropanol avec des excès énantiomères respectivement de 100 % et 99 %, à partir respectivement l'éthylbenzène et du propylbenzène. Les études décrites dans ce travail rapportent la mise au point de méthodes commodes de synthèses d'isomères optiquement purs de (*R*)-1-phényléthanol et de (*R*)-(1)-phénylpropanol qui sont des synthons chiraux importants dans les préparations de produits chimiques fins et pharmaceutiques. Les réactions sont écologiques; elles se produisent à 30 °C et les temps requis sont de l'ordre de 24 heures.

Mots-clés : Aspergillus flavus, hydroxylation benzylique, biocatalyseur, (*R*)-1-phényléthanol, (*R*)-(1)-phénylpropanol.

[Traduit par la Rédaction]

Introduction

Chiral alcohols are important intermediates and are structural elements in the syntheses of biologically active compounds and natural products.[1–5] The optically active 1-phenylethanol is used as a chiral building block and synthetic intermediate in fine chemicals and in pharmaceutical industries.[6–8] (*R*)-1-Phenylethanol is widely used as a fragrance in the cosmetic industry because it has a mild floral odour. Other applications include use as a salvatochromic dye,[9] use as an opthalic preservative, and use as an inhibitor of cholesterol intestinal absorption.[10] β-Aminoalcohols have been used for the syntheses of 1-phenylethanol-2-[(2-phenyl-1-alkylethyl)amino]ethanol derivatives, a new important class of antidiabetic agents.[11] A large genus of mushroom flies has been reported to be attracted to 1-phenylethanol in field tests.[12] Thus, secondary alcohols act as pheromones also. However, the chemical methods for their syntheses are not

Received 2 December 2011. Accepted 20 April 2012. Published at www.nrcresearchpress.com/cjc on 3 July 2012.

S. Yadav, R.S.S. Yadav, and K.D.S. Yadav. Department of Chemistry, D.D.U. Gorakhpur University, Gorakhpur-273 009, India.

Corresponding author: Saroj Yadav (e-mail: s_saroj123@rediffmail.com).

Can. J. Chem. Downloaded from www.nrcresearchpress.com by Renmin University of China on 09/02/12
For personal use only.

convenient and ees are generally low.[13] On the other hand, biocatalytic methods are convenient and enantiomeric excesses are high.[14]

Several biocatalytic methods to synthesize enantiomeric pure secondary alcohols have been developed during the recent past owing to the increasing demand for these valuable compounds.[5] Stereoselective reduction of ketones[14] and enantioselective oxidation of racemic secondary alcohols have been studied for the preparations of pure enantiomeric secondary alcohols. Although the hydroxylation of nonactivated centres in hydrocarbons is one of the most useful biotransformations, so far it has been used mainly for the hydroxylation of steroids and terpeniods.[3,13] The biotransformation of ethylbenzene to 1-phenylethanol has rarely been studied.[15–20] The conversion of ethylbenzene and a number of its para-substituted derivatives to the corresponding optically active 1-phenylethanols with enantiomeric excesses varying between 5% and 40% using the fungus *Mortierella isabellina* have been reported.[15] The fungi *Cunninghamella echinulata* var. *elegans* and *Heminthosporium* were also capable of performing some of these transformations.[15] The hydroxylation of ethylbenzene almost exclusively at the secondary carbon atom giving 1-phenylethanols in the ratio 2:1 of the R and S isomers using cytochrome P450camp has been reported.[16] Seventeen fungi and two yeast species that could hydroxylate ethylbenzene and propylbenzene to 1-phenylethanol and 1-phenylpropanol, respectively, have been reported.[17] One potent strain, *Fusarium moniliforme*, oxidizes ethylbenzene and propylbenzene to the corresponding benzylic alcohols with enantiomeric excesses of 98% in the (R) (+) form.[17] The involvement of cytochrome P450 in this transformation has been demonstrated.[18] Szaleniec et al.[19] reported the oxidation of ethylbenzene to (*S*)-(–)-1-phenylethanol by the denitrifying bacterium *Azoarcus* species strain EbN1. A nobel Mo–Fe–S enzyme, anaerobic ethylbenzene dehydrogenase, has been isolated and characterized.[20] Keeping in mind the potential for the biotransformation of ethylbenzene to optically pure isomers of 1-phenylethanol, we initiated a search for the fungal strains that could carry out these useful transformations. In this communication, we report two fungal strains, namely *Aspergillus flavus* MTCC-1783 and *Aspergillus flavus* MTCC-1884, which transform ethylbenzene to (*R*)-1-phenylethanol and propylbenzene to (*R*)-1-phenylpropanol in 100% and 99% ee, respectively.

Materials and methods

Chemicals

Methylbenzene, ethylbenzene, propylbenzene, ethylmethylketone, racemic (±)-1-phenylethanol, (*R*)-1-phenylethanol, racemic (±)-1-phenylpropanol, and (*R*)-1-phenylpropanol were purchased from Sigma-Aldrich Chemicals Private Limited, New Delhi, India. All other chemicals were purchased either from S.D. Fine-chem Ltd., Mumbai, India, or from Qualigens Chemicals, Mumbai, India, and were used without further purification.

Fungal strains

Both fungal strains were procured from the Microbial Type Culture Collection Centre and Gene Bank, Institute of Microbial Technology, Chandigarh, India, and were maintained on Bennett's agar medium,[17] which consisted of 1.5% (*w*/*v*) glucose, 0.5% peptone, 0.2% yeast extract, 0.2% Ehlrich's beef extract, and 1.5% agar in tap water.

Preparation of mycelia

The microorganisms were cultivated in 100 mL of basal medium I (BM I) containing 1 mL of unsterilized ethylmethylketone (*v*/*v*) in 250 mL Erlenmeyer flasks at 30 °C on a rotary shaker at 150 rpm for 3 days. BM I contained 10 g of $NaNO_3$, 2 g of NH_4Cl, 2 g of KH_2PO_4, 3 g of K_2HPO_4, 2 g of NaCl, 0.2 g of $MgSO_4{\cdot}7H_2O$, 0.5 g of yeast extract, and 2 mL of metal solution having pH 7.0 in 1 L of deionized water. The metals solution consisted of 400 mg of $MnCl_2{\cdot}2H_2O$, 350 mg of $FeCl_2{\cdot}4H_2O$, 200 mg of $ZnCl_2$, 20 mg of $CoCl_2$, 20 mg of $CuCl_2{\cdot}H_2O$, 10 mg of $Na_2MoO_4{\cdot}2H_2O$, 10 mg of $Na_2B_4O_7{\cdot}10H_2O$, and 2 mL of concentrated HCl in 100 mL of deionized water. The mycelia were collected by filtration on ordinary filter papers, washed twice with 30 mL of 25 mmol/L potassium phosphate buffer (KPB, pH 7.0), and were used fresh.

Biotransformation reactions

The biotransformation reactions were performed using the reported method.[17] Wet mycelia (0.1 g) were suspended in 2 mL of 25 mmol/L KPB in test tubes (17 mm in diameter and 150 mm in height), and 200 μmol of ethylbenzene (21 μL) was added. The test tubes were closed with stoppers and incubated at 30 °C in a reciprocal shaker at 200 rpm. After 24 h, the reaction solutions were acidified by the addition of 0.2 mL of 6 N HCl. The products formed in the reaction solution were extracted thrice using 2.0 mL of *n*-hexane each time. Biotransformations of propylbenzene and methylbenzene were also studied using the above method. The extracts were analysed for 1-phenylethanol, 1-phenylpropanol, and benzylalcohol by using HPLC as mentioned in the following. In one typical scale-up experiment, 7.5 g of the mycelia of *A. flavus* MTCC-1884 suspended in 100 mL of 25 mmol/L KPB and 1.5 mL of ethylbenzene were reacted for 24 h at 25 °C and then extracted with 30 mL of *n*-hexane; 20 μL of the extract was subjected to HPLC analysis. In another experiment, 14 g of the mycelia of *A. flavus* MTCC-1783 suspended in 100 mL of KPB and 3.0 mL of ethylbenzene at 25 °C was reacted for 24 h, then extracted with 30 mL of *n*-hexane, and then 20 μL of the extract was subjected to HPLC analysis. Similar experiments were performed with propylbenzene.

HPLC analysis

HPLC analyses were done using a Waters HPLC (model 600E) and a Spherisorb C_{18} 5 UV (4.5 mm × 250 mm) column. The eluent phase was a methanol–water mixture in a 1:1 (*v*/*v*) ratio at 1 mL/min. The *n*-hexane extracts of the products (20 μL) were injected and the detections were made using a Waters UV detector (model 2487) at 254 nm.

Spectroscopic analysis

The identifications of the biotransformation products were done by IR and ^1H and ^{13}C NMR spectroscopic techniques.

^1H NMR

The ^1H NMR spectra of the biotransformation products

were recorded using a Jeol AL 300 MHz spectrometer in $CDCl_3$ using TMS as the internal standard reference at the Department of Chemistry, Banaras Hindu University, Varanasi, India.

^{13}C NMR

The ^{13}C NMR spectra of the biotransformation products were recorded on a Jeol-ECX 500 Hz spectrophotometer in $CDCl_3$ using TMS as the internal standard reference at the Department of Chemistry, Indian Institute of Technology, Kanpur, India. The chemical shift values were reported in ppm.

IR

The IR spectra of the biotransformation products were recorded on a Bruker IR-VERTEX Flash 70 spectrometer in the range of 400–4000 cm^{-1} at the Department of Chemistry, Indian Institute of Technology, Kanpur, India.

GC–MS

Products were analysed by GC–MS using an HP GC–MS model No. 5975C-inert MSDS with triple axis detector using helium gas (5 mL/min) as the mobile phase at the Department of Chemistry, Indian Institute of Technology, Kanpur, India.

Determination of ee

The ees were determined using a Chiralcel OD column (4.6 mm × 250 mm) manufactured by Daicel Chiral Technologies Pvt. Ltd. (Japan) using a 90:10 (*v*/*v*) mixture of *n*-hexane and isopropylalcohol as the eluent phase at a flow rate of 0.5 mL/min at the Department of Chemistry, Indian Institute of Technology, Kanpur, India.

Results and discusion

The results of the identification of the biotransformation products, (*R*)-1-phenylethanol and (*R*)-1-phenylpropanol, using the suspensions of fungal mycelia of the strains *A. flavus* MTCC-1783 and *A. flavus* MTCC-1884 are given in the Supplementary data. The fungal mycelia of *A. flavus* MTCC-1783 converted ethylbenzene to (*R*)-1-phenylethanol in 100% enantiomeric excess and propylbenzene to (*R*)-1-phenylpropanol in 99% enantiomeric excess. The reaction times were 24 h and no ethylbenzene and propylbenzene were detected at the end of transformation reactions showing that ethylbenzene and propylbenzene were fully transformed to their corresponding biotransformation products. Methylbenzene was also transformed to benzylalcohol by these two fungal strains showing that hydroxylations occur at benzylic carbon centre. In typical scale up experiments as mentioned in the materials and methods section (Biotransformation reactions) 1.5 mL of ethylbenzene and 3.0 mL of propylbenzene were fully converted to (*R*)-1-phenylethanol and (*R*)-1-phenylpropanol, respectively, showing the feasibility of the method on laboratory scale.

Supplementary data

Supplementary data are available with the article through the journal Web site at http://nrcresearchpress.com/doi/suppl/10.1139/v2012-034.

Acknowledgements

The financial support of CST, U.P., Lucknow, India, through project No. CST/SERPD/ D-2895/2008 is thankfully acknowledged. The academic support of Professor V.K. Yadav, Department of Chemistry, Indian Institute of Technology, Kanpur, India, in the determination of enantiomeric excess, and Professor R. Gurunath, of the same department, in GC–MS analysis is thankfully acknowledged.

References

(1) Theil, F. *Chem. Rev.* **1995**, *95* (6), 2203. doi:10.1021/cr00038a017.
(2) Nakamura, K.; Matsuda, T. *J. Org. Chem.* **1998**, *63* (24), 8957. doi:10.1021/jo9812779.
(3) Borgas, K. B.; de Souza Borges, W.; Durán-Patrón, R.; Pupo, M. T.; Bonato, P. S.; Collado, I. G. *Tetrahedron Asymmetry* **2009**, *20*, 385. doi:10.1016/j.tetasy.2009.02.009.
(4) Ou, L.; Xu, Y.; Ludwig, D.; Pan, J.; Xu, J. H. J. *Org. Process Res. Dev.* **2008**, *12* (2), 192. doi:10.1021/op700253t.
(5) Bisogno, F. R.; Lavandera, I.; Kroutil, W.; Gotor, V. *J. Org. Chem.* **2009**, *74* (4), 1730. doi:10.1021/jo802350f.
(6) Suginaka, K.; Hayashi, Y.; Yamamoto, Y. *Tetrahedron Asymmetry* **1996**, *7* (4), 1153. doi:10.1016/0957-4166(96)00121-8.
(7) Ivanov, A. E.; Schneider, M. P. *J. Mol. Catal. B: Enzym.* **1997**, *3* (6), 303. doi:10.1016/S1381-1177(97)00012-X.
(8) de los Ríos, A. P.; Hernández-Fernández, F. J.; Tomás-Alonso, F.; Gómez, D.; Víllora, G. *Can. J. Chem. Eng.* **2010**, *88*, 442. doi:10.1002/cjce.20285.
(9) Berglund, P. *Biomol. Eng.* **2001**, *18* (1), 13. doi:10.1016/S1389-0344(01)00081-8.
(10) Chua, L. S.; Sarmidi, M. R. *J. Mol. Catal. B: Enzym.* **2004**, *28* (2–3), 111. doi:10.1016/j.molcatb.2004.02.004.
(11) Lohse, O.; Spöndlin, C. *Org. Process Res. Dev.* **1997**, *1* (3), 247. doi:10.1021/op9600264.
(12) Kamm, J. A.; Buttery, R. G.; Robinson, W. H. *J. NewYork Entomol. Soc.* **1987**, *95*, 19.
(13) Faber, K. *Biotransformation Inorganic Chemistry;* 5th ed., Springer-Verlag: Berlin, 2004.
(14) Wu, X.; Xiao, J. J. *Chem. Commun. (Camb.)* **2007**, *24* (24), 2449. doi:10.1039/b618340a.
(15) Holland, H. L.; Bergen, E. J.; Chenchaiah, P. C.; Khan, S. H.; Munoz, B.; Ninniss, R. W.; Richards, D. *Can. J. Chem.* **1987**, *65* (3), 502. doi:10.1139/v87-087.
(16) Filipovic, D.; Paulsen, M. D.; Loida, P. J.; Sligar, S. G.; Ornstein, R. L. *Biochem. Biophys. Res. Commun.* **1992**, *189* (1), 488. doi:10.1016/0006-291X(92)91584-D.
(17) Uzura, A.; Katsuragi, T.; Tani, Y. *J. Biosci. Bioeng.* **2001**, *91*, 217.
(18) Uzura, A.; Katsuragi, T.; Tani, Y. *J. Biosci. Bioeng.* **2001**, *91*, 580.
(19) Szaleniec, M.; Hagel, C.; Menke, M.; Nowak, P.; Witko, M.; Heider, J. J. *Biochemistry* **2007**, *46* (25), 7637. doi:10.1021/bi700633c.
(20) Johnson, H. A.; Pelletier, D. A.; Spormann, A. M. *J. Bacteriol.* **2001**, *183* (15), 4536. doi:10.1128/JB.183.15.4536-4542.2001.

Can. J. Chem. Downloaded from www.nrcresearchpress.com by Renmin University of China on 09/02/12
For personal use only.

A thermoresponsive amphiphilic dendron — Synthesis, characterization, and self-assembled micelles for controlled drug release

Li Xu, Lidong Shao, Minqi Hu, Lin Chen, and Yunmei Bi

Can. J. Chem. Downloaded from www.nrcresearchpress.com by Renmin University of China on 09/02/12
For personal use only.

Abstract: A new third-generation thermoresponsive amphiphilic dendron consisting of a hydrophobic poly(benzyl ether) dendritic core and hydrophilic oligo(ethylene glycol) peripheries was synthesized by an efficient convergent approach. Its structure was confirmed by ^{1}H NMR, ^{13}C NMR, IR, GPC, MALDI-TOF MS, and elemental analysis. Turbidity and dynamic light scattering (DLS) measurements demonstrated that the dendron showed a reversible temperature-dependent phase-transition behavior in aqueous solution and its lower critical solution temperature (LCST) was lower than that of the corresponding second-generation dendron, indicating the dependence of LCSTs on the generation of dendrons. Fluorescent spectroscopy and TEM studies revealed that the dendron would self-assemble into nanospherical micelles with a very low critical micelle concentration (CMC) in water. The core-shell structure of the micelles was proved by ^{1}H NMR analyses of the micelles in D_2O. The drug-loading capacity of the dendron micelles is about 29 wt % for podophyllotoxin (POD) used as a model drug, and in vitro release tests showed a desired thermoresponsive drug-release behavior. These results indicate that the dendron is promising as stimuli-responsive material for biomedical applications.

Key words: amphiphilic dendron, poly(benzyl ether) dendritic core, oligo(ethylene glycol) peripheries, thermoresponsive micelles, controlled drug release.

Résumé : Utilisant une approche impliquant une synthèse efficace et convergente, on a réalisé la synthèse d'un nouveau dendron amphiphile thermosensible de troisième génération formé d'un coeur dendritique, un poly(éther benzylique) hydrophobe, et des périphéries hydrophiles à base d'oligo(éthylèneglycol). On en a confirmé la structure résonance magnétique nucléaire du ^{1}H et du ^{13}C, infrarouge, chromatographie en phase gazeuse, spectrométrie de masse en temps de vol avec ionisation par désorption au laser d'une matrice (« MALDI-TOF MS ») et par analyse élémentaire. Des mesures de turbidité et de diffusion de la lumière dynamique (DLD) ont permis de démontrer que, en solution aqueuse, le dendron donne lieu à un comportement impliquant une transition de phase réversible en fonction de la température et que sa température de solution critique la plus basse (TSCB) est plus basse que celle du dendron correspondant de deuxième génération, ce qui met en évidence que la température de solution critique la plus basse (TSCB) varie en fonction de la génération des dendrons. Des études de spectroscopie de fluorescence et de microscopie électronique de transmission (MET) mettent en évidence le fait que, dans l'eau, le dendron pourrait donner un auto-assemblage en micelles nanosphèriques avec une concentration micellaire critique (CMC) très basse. Faisant appel à des analyses de RMN du ^{1}H, on a pu déterminer que, dans le D_2O, la structure des micelles correspond à coeur en forme de coquille. La capacité de charge de médicament par les micelles de dendron est d'environ 29 % en poids pour la podophyllotoxine (POD) utilisée comme médicament modèle et des essais d'émission in vitro ont permis de démontrer un comportement recherché d'émission thermosensible des médicaments. Ces résultats indiquent que le dendron est un matériel stimuli-sensible prometteur pour des applications biomédicales.

Mots-clés : dendron amphiphile, poly(éther benzylique) à coeur dendritique, oligo(éthylèneglycol), périphéries, micelles thermosensibles, émission contrôlée de médicament.

[Traduit par la Rédaction]

Introduction

In recent years, a growing interest has been evident in the development of dendrimers that are responsive to external stimuli, such as pH,[1,2] temperature,[3,4] light,[5,6] and redox state.[7,8] One of the most appealing stimuli-responsive species is the thermoresponsive dendrimer, since such a system combines the advantages of temperature sensitivity and dendritic effect[9] for applications such as biomedicine and catalysis.[10–13] Thermoresponsive dendrimers can be constructed by attaching thermoresponsive groups or polymers to the periphery or the core of the dendrimer. Dendrimers with properly balanced hydrophilic and hydrophobic units can also act as temperature-sensitive dendrimers.[14] Poly(*N*-isopropylacrylamide) (PNIPAM) is a representative polymer exhibiting thermoresponsive behavior. It shows a dissolution–precipitation transition

Received 21 February 2012. Accepted 8 May 2012. Published at www.nrcresearchpress.com/cjc on 4 July 2012.

L. Xu, L. Shao, M. Hu, L. Chen, and Y. Bi. Yunnan Normal University, College of Chemistry and Chemical Engineering, Yunnan Normal University, Kunming 650092, P.R. China.

Corresponding author: Yunmei Bi (e-mail: yunmeibi@hotmail.com).

Can. J. Chem. Downloaded from www.nrcresearchpress.com by Renmin University of China on 09/02/12
For personal use only.

in aqueous solution at 32 °C. *N*-Isopropylacrylamide (NIPAM) has been incorporated into linear and dendritic macromolecules to obtain thermoresponsive copolymers and dendrimers.[15–20] For example, Kimura et al.[21] prepared the first thermoresponsive dendrimer by polymerization of NIPAM from the termini of a poly(propyleneimine) dendrimer with terminal thiol groups. The core of the dendrimer was a cobalt complex, which catalyzed oxidation of the thiol compounds.

Polyethylene glycol (PEG), an uncharged, nontoxic, and nonimmunogenic water-soluble polymer, has found diverse applications in biological sciences, personal care products, and industrial additives.[22] However, PEG possesses a lower critical solution temperature (LCST) above 100 °C, which is too high and may be a limitation to its widespread use in the biomedical field.[23] Recently, PEGylated polymers have been explored by incorporating PEG or oligo(ethylene glycol) (OEG) units into other macromolecules. They show lower LCSTs and are promising alternatives to PNIPAM for applications in drug delivery systems.[24–28] PEG is also useful for the preparation of temperature-sensitive dendrimers. For example, Li et al.[29] synthesized dendrimers containing temperature-sensitive oligoethylene glycol as a building block. These unique dendrimers showed fast and sharp transitions around their LCSTs. Their thermoresponsive behaviors are dependent on both the generation and the terminal structure.

Some amphiphilic PEGylated dendrons that are parts of dendrimers have temperature-dependent phase-transition behavior. Moreover, these dendrons, composed of hydrophobic and hydrophilic parts, can self-assemble into dendritic micelles. For instance, Asthmanikandan et al.[9] reported on thermosensitive biaryl-based dendrons with a pentaethylene glycol monomethyl ether and a decyl chain. These amphiphilic dendrons exhibited generation-dependent temperature sensitivity and were capable of forming micelles and reverse micelles in polar and apolar solvents, respectively. Chang and Dai[30] synthesized dendrons consisting of hydrophobic oligo (*p*-phenylene vinylene) core branches and hydrophilic oligo (ethylene oxide) terminal chains. These dendrons showed a LCST and the critical micellization behavior. The unusual properties of these amphiphilic PEGylated dendrons are attractive for potential application in controlled drug delivery systems.

Usually, the purification of synthesized dendrons or dendrimers requires column chromatography, which not only is tedious to perform but also unavoidably leads to losses of product. In this paper, we described the column-free synthesis, and thermoresponsive and micellar behaviors of a third-generation amphiphilic dendron containing a hydrophobic poly(benzyl ether) dendritic core and 27 hydrophilic diethylenoxy methyl ethers at its periphery. The controlled release of the model drug podophyllotoxin (POD) using the thermoresponsive micelles was also studied in detail.

Results and discussion

Synthesis and characterizations of dendrons

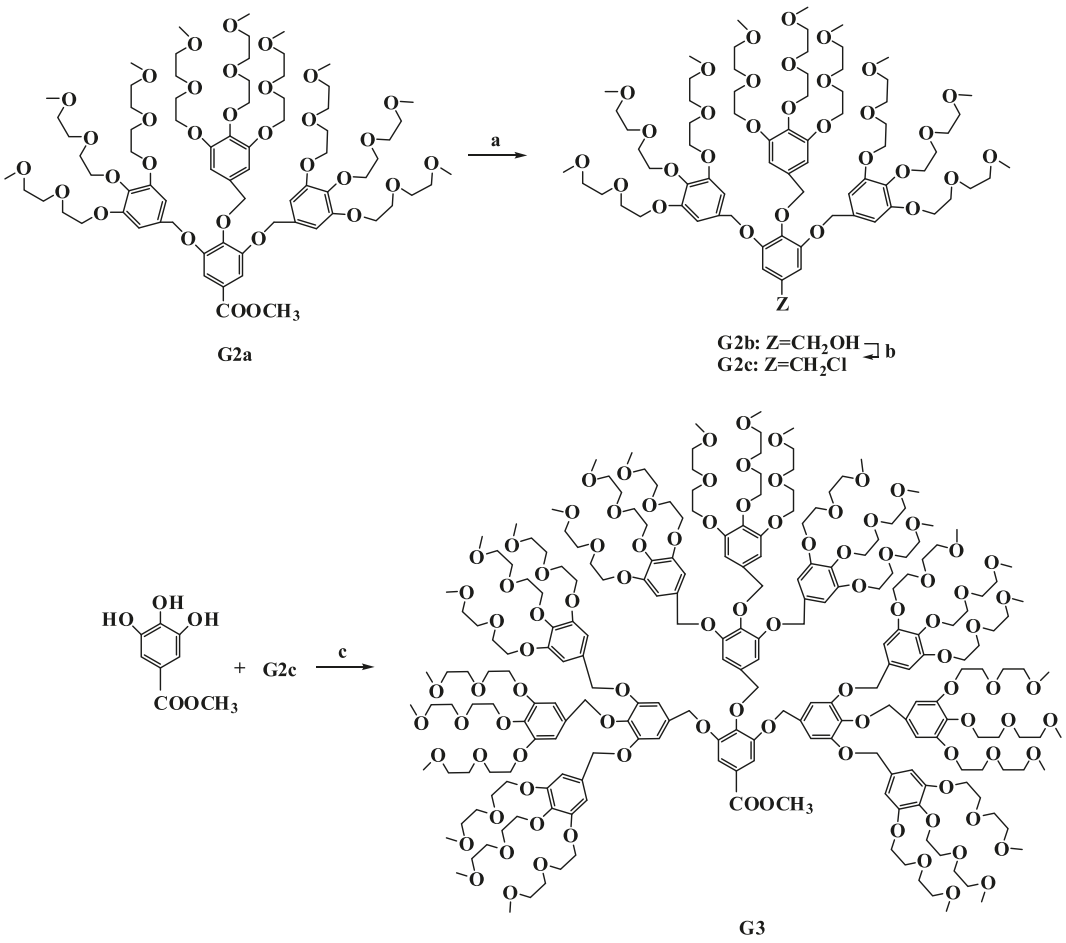
The synthetic procedures of the dendrons are summarized in Scheme 1. The second-generation dendron **G2a** was synthesized according to our previously reported method.[31] **G2a** was reduced with lithium aluminum hydride (LAH) to give the second-generation dendron alcohol **G2b**. Chlorination of **G2b** with $SOCl_2$ afforded the corresponding chloride **G2c**. In this study, each dendron was purified simply by solvent extraction or dialysis to remove the earlier generation dendron. Compared with the synthetic strategy of the corresponding first-generation dendron, the reaction conditions to synthesize **G2b** were modified by adjusting the molar ratio of LAH to **G2a** from 2:1 to 3:1 and prolonging the reaction time from 16 to 20 h. The reaction time of **G2b** with $SOCl_2$ was also prolonged from 3 to 4 h. As a result, the purification of **G2b** and **G2c** required only solvent extraction. The alkylation of methyl gallate with **G2c** by using K_2CO_3 as the base in *N*, *N*-dimethylformamide (DMF) provided analytically pure third-generation dendron **G3**, requiring only a dialysis workup. None of the dendrons required column chromatography for analytically pure material, thus facilitating scale-up. All new compounds were obtained as oily liquids and their structures were characterized by ^{1}H NMR and ^{13}C NMR spectra (Supplementary data Figs. S1–S3; Fig. 1), FT-IR, as well as ESI-MS or MALDI-TOF MS. **G3** was further characterized by GPC and elemental analysis. GPC analysis of **G3** showed a single peak (PDI = 1.05, Fig. 2). The M_n measured by GPC for **G3** was much lower than the calculated one using calibration with linear polystyrene. This is attributed to the difference between the hydrodynamic volumes of polystyrene and **G3** and is consistent with the studies of polyether dendrimers by Fréchet and coworkers.[32] However, MALDI-TOF MS of **G3** showed a single signal at m/z ($[M + Na]^+$) = 4624 (calcd mass, 4599), indicating the formation of **G3**.

Formation of micelles

The presence of a hydrophobic poly(benzyl ether) branch unit and hydrophilic oligo(ethyleneoxy) periphery means that these amphiphilic dendrons can potentially be precursors to nanoparticles with an oligo(ethyleneoxy) corona and a poly (benzyl ether) core upon dissolution in water, which is a selective solvent. The formation of the hydrophobic poly(benzyl ether) domain can be confirmed by ^{1}H NMR spectra with $CDCl_3$ and D_2O as locking solvents for **G3**. In $CDCl_3$, where micellar formation was not expected, all ^{1}H NMR resonances attributed to poly(benzyl ether) and oligo(ethyleneoxy) units were detected as shown in Fig. 1*a*. However, the ^{1}H NMR spectrum in D_2O showed an intensity reduction of poly(benzyl ether) resonances resulting from the suppressed molecular motion of the aggregated hydrophobic branch units (Fig. 1*b*). The small broad signals in the NMR spectrum indicate restricted motions of these protons within the core of nanoparticles. This result is evidence for a core-shell type formation with a hydrophobic inner core and a hydrophilic shell. Similar trends in ^{1}H NMR spectra are consistent with amphiphilic block copolymer systems.[33,34]

The formation of micelles from the third-generation dendron **G3** was also examined by the detection of critical micelle concentration (CMC) relying on a fluorescence technique with pyrene as the probe because pyrene preferentially partitions into the hydrophobic core of micelles from water.[35] The intensity ratio of I_{341}/I_{337} vs the logarithm of concentrations of **G3** in the pyrene excitation spectra was plotted in Fig. 3*a*. It is seen that the I_{341}/I_{337} ratios remain fairly constant below a certain concentration and then increase

Scheme 1. Synthesis of dendron **G3**. Reagents and conditions: (*a*) $LiAlH_4$ (LAH), tetrahydrofuran (THF), room temperature (rt), 20 h; (*b*) $SOCl_2$, *N*, *N*-dimethylformamide (DMF), dichloromethane (DCM), rt, 3 h; (*c*) K_2CO_3, DMF, 70 °C, 24 h.



Can. J. Chem. Downloaded from www.nrcresearchpress.com by Renmin University of China on 09/02/12
For personal use only.

remarkably above that concentration, indicating the formation of micelles. From this plot, a CMC of 7.7×10^{-6} mol/L was obtained from the intersection of two straight lines: the baseline and the rapidly rising I_{341}/I_{337} line (Fig. 3*b*), which is lower than the one of the second-generation dendron **G2a** (2.2×10^{-5} mol/L).[31] This could be attributed to the fact that **G3** is larger than **G2a**, which facilitates the aggregation of the dendron. These CMC values are comparable to those reported for some other amphiphilic dendrons and linear copolymers.[9,36] The low CMC values mean that the dendrons can self-assemble to form nanoscaled core-shell micelles at a lower compound concentration, which is suitable for drug delivery in very dilute aqueous milieux such as body fluids.[37]

Micelle morphology was investigated by transmission electron microscopy (TEM). It can be seen from Fig. 4 that dendron **G3** forms spherical micelles with a core-shell (corona) structure and an average diameter of about 60 nm. The micelles made from **G3** were bigger than those from **G2a**[31] because of its larger core and peripheries.

Thermoresponsive behavior

To investigate whether the third-generation dendron **G3** exhibits a thermal response, we examined the optical transmittance of a **G3** aqueous solution as a function of temperature. The concentration dependence of the LCST was also investigated in the range of 0.1–2.1 mg/mL and the results are plotted in Fig. 5. For comparison, the respective curve of dendron **G2a**[31] was also added (Fig. 5*b*). Dendron **G3** displayed an obvious phase transition in water and its LCST values decreased with increasing concentration from 0.3 to 1.5 mg/mL. Compared with dendron **G2a**, **G3** shows lower LCSTs at all concentrations tested, demonstrating the dependence of LCSTs on the generation of dendrons, which was in correspondence with the report by Aathimanikandan et al.[9] The reason may arise from the increased size of the dendrons with the increasing generation; thus, the interaction of the peripheral oligo(ethyleneoxy) groups would take place more efficiently with the increasing generation of the dendron, which leads to the dehydration of the terminal oligo (ethyleneoxy) groups at a lower temperature with increasing generation.[3]

The thermoresponsive behavior of dendrons **G2a** and **G3** was also analyzed by dynamic light scattering (DLS). The hydrodynamic diameter (D_h) of the dendrons are apparently influenced by the temperature, as shown in Fig. 6. At temperatures lower than the LCSTs, the two dendrons are easily solubilized in water so that the amphiphilic dendrons self-assemble into core-shell micelles with a low D_h of approximately 50–60 nm. However, a dramatic increase in D_h was

Can. J. Chem. Downloaded from www.nrcresearchpress.com by Renmin University of China on 09/02/12
For personal use only.

Fig. 1. ^{1}H NMR spectra of **G3** in $CDCl_3$ (*a*) and D_2O (*b*).

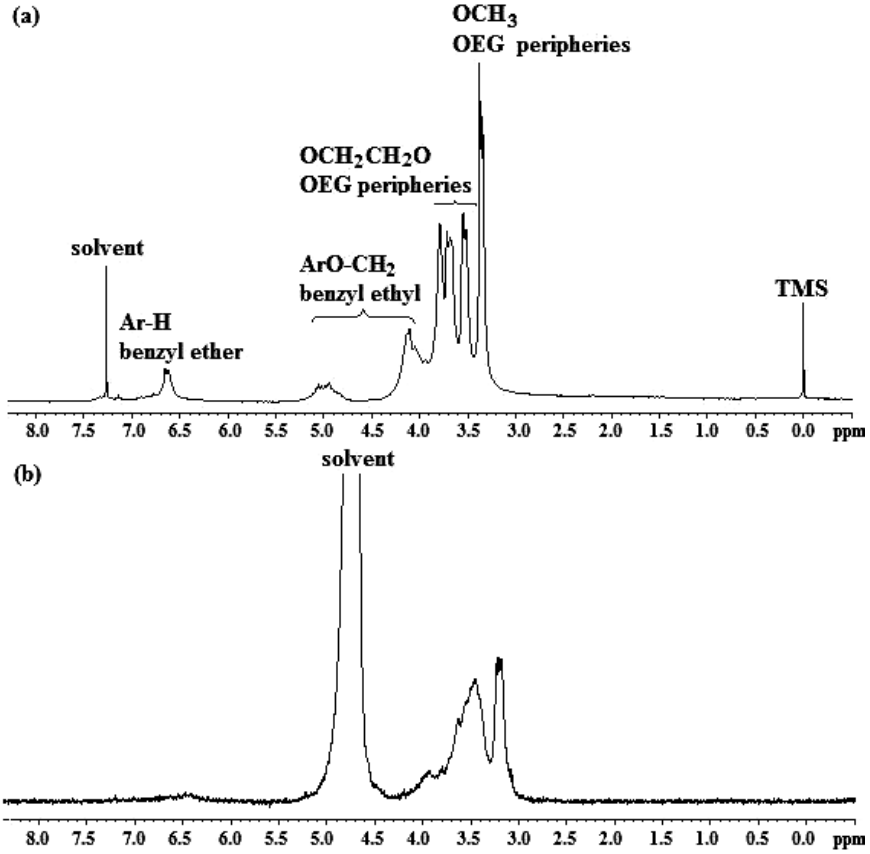
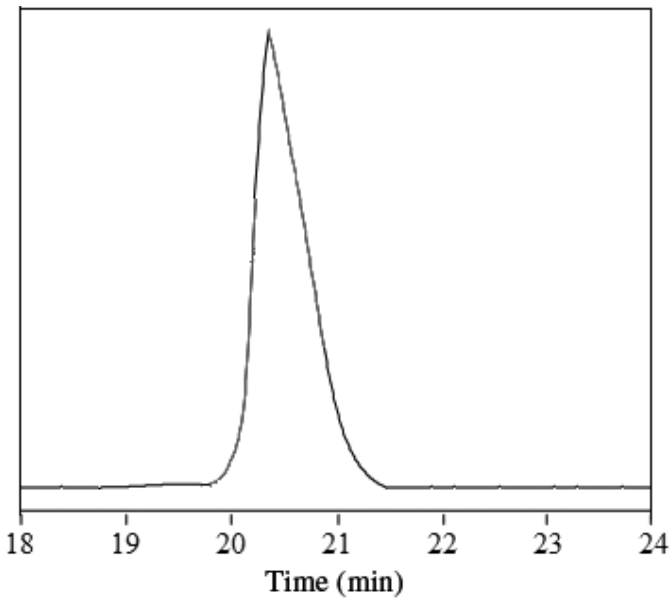


Fig. 2. GPC trace of **G3** with M_n (theory) = 4599 Da and M_n (GPC) = 1666.



observed once the temperature increased to near the LCST (58 and 54 °C, respectively), which indicated dendron aggregation. Dendron **G2a** requires a higher temperature to induce aggregation than dendron **G3** does. The aggregation process was completely reversible, and the aggregates became soluble again below the onset temperature. These are consistent with the results of turbidimetry measurement.

Controlled drug release

Hydrophobic drugs can be physically incorporated and stabilized in the micellar hydrophobic inner core by hydrophobic interaction. Podophyllotoxin (POD), an anticancer drug with poor solubility in water, was used as a model drug to investigate the potential application of dendron **G2a** and **G3** micelles in controlled drug release. The amount of drug incorporated into the micelles was measured by a UV spectrometer. The results showed that POD was successfully incorporated into micelles of **G2a** and **G3**, and the drug-loading content (DLC) and entrapment efficiency (EE) were about 21.24% and 77.81% for **G2a**, and 28.71% and 94.95% for **G3**, respectively, which are higher than those of the traditional micelles.[37] Furthermore, the amount of POD introduced into the micelle was dependent on the generation of the dendrons. The DLCs and EEs of **G3** with more hydrophobic phenyl groups are higher than those of **G2a** with fewer hydrophobic phenyl groups. To obtain information about the release of POD from **G2a** and **G3** micelles, the drug-loaded **G2a** and **G3** micelles were dissolved in PBS and dialyzed against PBS. Figure 7 shows the release profile of POD from **G2a** and **G3** micelles. In contrast with the rapid release of the free drug from a cellulose membrane (99% released in 4 h), the release from the dendritic micelles was slow and showed sustained characteristics. The generation of dendrons also affects drug release. The amount of drug released and the rate of release were greater for **G3** than for **G2a** micelles. This could be ascribed to steric hindrance of crowded end functional groups in higher generations and weaker interaction between these functional groups

Fig. 3. (*a*) Excitation spectra of pyrene in water at different concentrations of **G3**. (*b*) Plot of the intensity ratio I_{341}/I_{337} vs the logarithm of the concentration of **G3**.

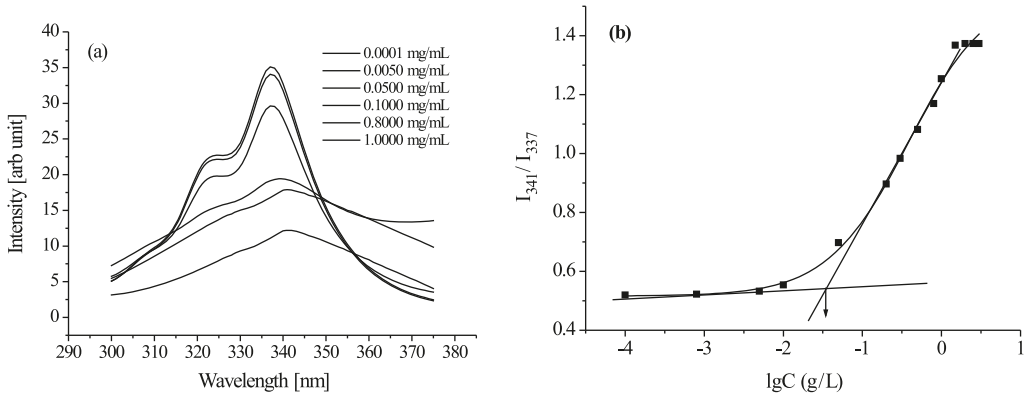
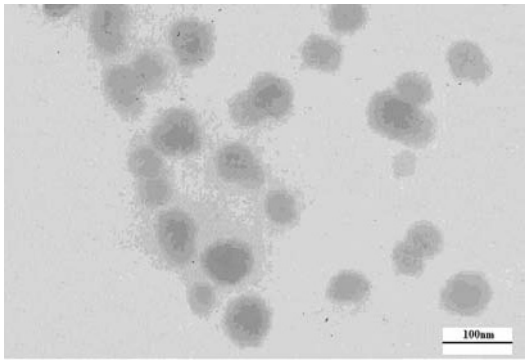


Fig. 4. Transmission electron microscopy (TEM) image of **G3** micelles.



and the drug molecules. A similar trend was observed in linear-dendrimer block copolymers containing PEG studied by Adeli et al.[38] To evaluate the effect of the temperature stimulus on release of POD from the thermoresponsive micelles, the POD release from **G3** micelles was examined in PBS solution at 25, 37, and 55 °C. As shown in Fig. 8, the POD release rate and amount increased with increasing temperature under constant pH (7.4) . A slow release was observed owing to the greater stability of micelles when the temperature was below the LCST (20 and 37 °C). However, when the temperature was above the LCST (55 °C), drug release was accelerated because of the temperature-induced structure change of the micelles. At a temperature above the LCST, the hydrophilicity of the micellar shell, comprised of oligo(ethyleneoxy) chains, was weakened, resulting in the deformation of the structure of the micelles. Thus, the drug release was faster above the LCST than below the LCST. Unfortunately, there was little change in the release rate of POD from **G3** micelles as a function of temperature, probably because the drug would be retained in the hydrophobic aggregates above the LCST. Therefore, this may not be an ideal system for thermally triggered drug release. However, it is expected that a less hydrophobic drug may be more readily released from **G3** micelles above the LCST.

Conclusions

We synthesized a novel third-generation thermoresponsive amphiphilic dendron with a hydrophobic poly(benzyl ether) dendritic core and hydrophilic oligo(ethylene glycol) peripheries using a simple convergent approach. The dendron exhibited a thermally induced phase transition in aqueous solution and its LCST increased with decreasing concentration over the range of 0.3–2.1 mg/mL of the dendron in aqueous solution. Studies of the association behavior of the synthesized dendron in aqueous solution revealed that the dendron is capable of forming spherical micelles of around 60 nm in diameter. Compared with its second-generation counterpart, the dendron exhibited lower LCST and CMC. The self-assembled dendron micelles exhibited high drug-loading capacity and thermoresponsive drug release behavior. These results indicate that the thermosensitive amphiphilic dendron possesses promising potential applications in the biomedical field.

Experimental

Instruments and materials

^{1}H NMR and ^{13}C NMR spectra were determined on a Bruker DRX-500 with TMS as internal standard. ESI-MS spectra were obtained on a Finnigan LCQ-Advantage mass spectrometer. Matrix-assisted laser desorption ionization (time of flight) mass spectrometry (MALDI-TOF MS) was carried out on a Bruker Biflex III MALDI-TOF spectrometer with α-cyano-4-hydroxylcinnamic acid (CCA) as the matrix. The GPC system consisted of a Waters 2690D separations module and a Waters 2414 refractive index detector (RI). Styragel HR1 THF and HR2 THF columns (Waters) were used at 40 °C with polystyrene as the standard and tetrahydrofuran (THF) as the mobile phase at a flow rate of 0.3 mL/min. FT-IR spectra were taken on a Nicolet AVATAR 360 FT-IR spectrometer.

Methyl 3,4,5-tris(3,4,5-tris(2-(2-methoxyethoxy)ethoxy) benzyloxy) benzoate (**G2a**) was synthesized according to the method previously reported.[31] Methyl gallate was purified by recrystallization from methanol. THF was refluxed on sodium and distilled from sodium benzophenone. DMF and dichloromethane (DCM) were distilled from anhydrous calcium chloride for drying. Other reagents were used as received.

Synthesis of 3,4,5-tris(3,4,5-tris(2-(2-methoxyethoxy) ethoxy)benzyloxy) benzyl alcohol (G2b)

Dendron **G2b** was prepared by the reduction of **G2a** with

Can. J. Chem. Downloaded from www.nrcresearchpress.com by Renmin University of China on 09/02/12
For personal use only.

Can. J. Chem. Downloaded from www.nrcresearchpress.com by Renmin University of China on 09/02/12
For personal use only.

Fig. 5. (*a*) Transmittance measurements as a function of temperature for different concentrations of **G3**. (*b*) Dependence of lower critical solution temperatures (LSCTs) on concentrations of **G3** and **G2a.**

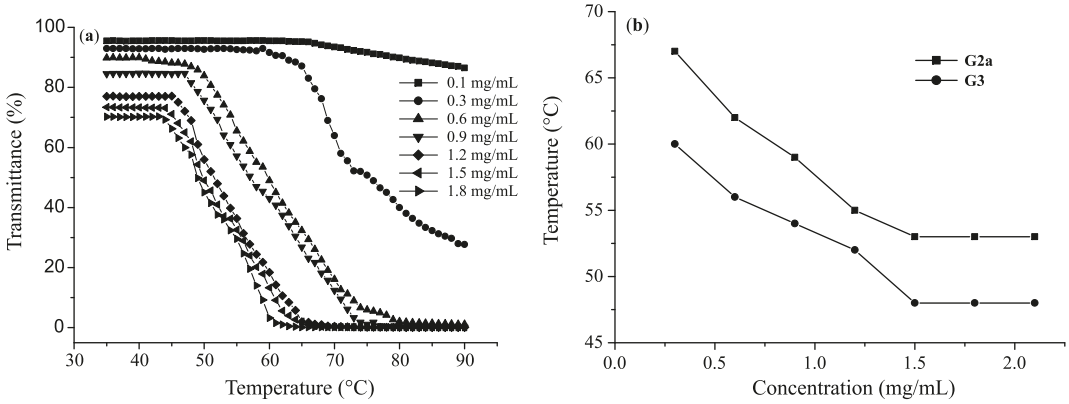


Fig. 6. Plots of hydrodynamic diameters (D_h) of the micelles from **G3** and **G2a** in aqueous solution as a function of temperature from dynamic light-scattering (DLS) measurements.

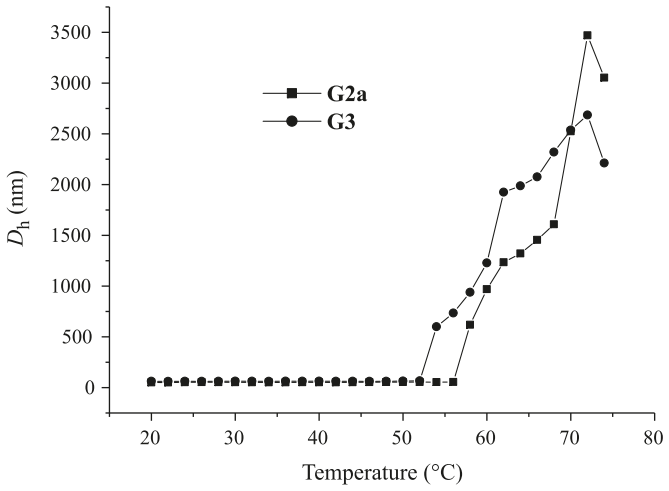
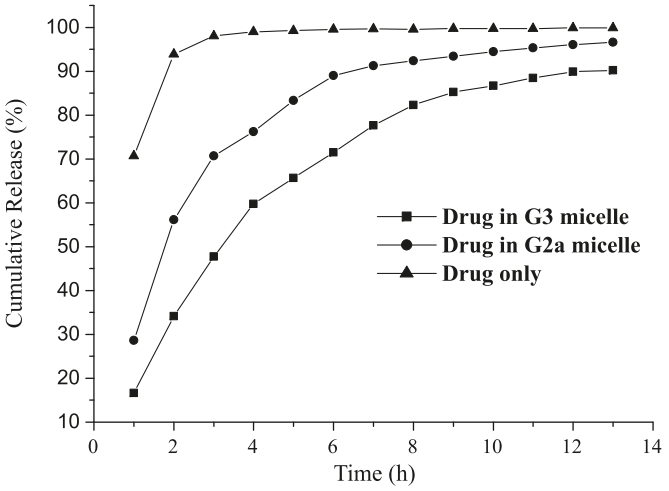
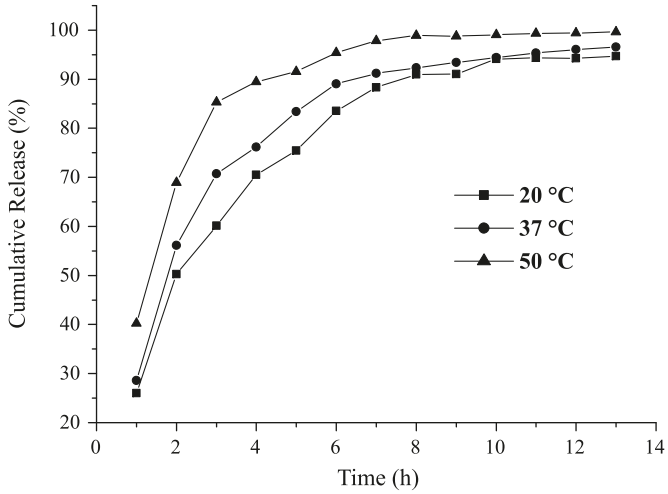


Fig. 7. In vitro release profile of podophyllotoxin from **G3** and **G2a** micelles at 37 °C.



LAH. To a solution of **G2a** (2.43 g, 1.6 mmol) in dry THF was added LAH (0.20 g, 5.2 mmol) at –5 °C. This mixture was stirred for 0.5 h, and then warmed to room temperature.

Fig. 8. Temperature-responsive drug release from **G3** micelles in phosphate-buffered saline solutions (PBS, pH 7.4) at 20, 37, and 55 °C, respectively.



After 20 h, the reaction was quenched by dropwise addition of 10% NaOH. The resulting precipitate was filtered and the THF was evaporated. The residue was dissolved in DCM and washed with saturated NaCl solution. The organic phase was dried over $MgSO_4$. After filtration, the DCM was rotoevaporated, affording **G2b** as a pale yellow oil, yield 80.5%. IR (KBr) *ν*: 3445 (m, ν(OH)), 2929 (s), 2879 (s), 1591 (s, ν(Ar)), 1501 (m, ν(Ar)), 1112 (s, ν_{as}(COC)). ^{1}H NMR (500 MHz, $CDCl_3$) δ: 6.64 (m, 8H, Ar H), 4.96–5.00 (m, 6H, CH_2), 4.53 (s, 2H, CH_2), 3.95–4.18 (m, 18H, CH_2), 3.77–3.85 (m, 18H, CH_2), 3.68–3.72 (m, 18H, CH_2), 3.53–3.55 (m, 18H, CH_2), 3.36–3.38 (m, 27H, CH_3). ^{13}C NMR (125 MHz, $CDCl_3$) δ: 152.95, 152.68, 138.19, 137.88, 133.74, 133.02, 108.23, 107.51, 107.02, 75.09, 72.65, 72.28, 72.22, 71.53, 70.84, 70.60, 69.95, 69.11, 64.73, 59.15. ESI-MS *m/z*: 1513 $[M + Na]^+$.

Synthesis of 3,4,5-tris(3,4,5-tris(2-(2-methoxyethoxy) ethoxy)benzyloxy) benzyl chloride (G2c)

G2c was obtained by chlorination of **G2b** with $SOCl_2$. **G2b** (3.88 g, 2.6 mmol) was dissolved in 50 mL of dry DCM. DMF (4.5 mL) and $SOCl_2$ (0.93 g, 7.8 mmol) was then added dropwise and the reaction mixture was stirred for

Can. J. Chem. Downloaded from www.nrcresearchpress.com by Renmin University of China on 09/02/12
For personal use only.

another 3 h. After being washed with aqueous $NaHCO_3$ solution and saturated NaCl, the organic phase was dried over $MgSO_4$ and filtered, and the solvent was rotoevaporated, affording **G2c** as a pale yellow oil, yield 92.4%. IR (KBr) *ν:* 2929 (s), 2879 (s), 1589 (s, ν(Ar)), 1499 (m, ν(Ar)), 1112 (s, ν_{as}(COC)). ^{1}H NMR (500 MHz, $CDCl_3$) δ: 6.63–6.65 (m, 8H, Ar H), 5.00 (s, 6H, CH_2), 4.46–4.49 (m, 2H, CH_2), 3.98–4.19 (m, 18H, CH_2), 3.77–3.87 (m, 18H, CH_2), 3.65–3.72 (m, 18H, CH_2), 3.51–3.64 (m, 18H, CH_2), 3.34–3.38 (m, 27H, CH_3). ESI-MS *m/z*: 1531 $[M + Na]^+$.

Synthesis of methyl 3,4,5-tris(3,4,5-tris(3,4,5-tris(2-(2-methoxyethoxy)ethoxy)benzyloxy)benzyloxy)benzoate (G3)

G3 was obtained by the alkylation of methyl gallate with **G2c**. A mixture of methyl gallate (0.09 g, 0.5 mmol), **G2c** (2.41 g, 1.6 mmol), and K_2CO_3 (0.69 g, 5.0 mmol) in dry DMF was stirred and heated to 70 °C for 24 h under a nitrogen atmosphere. After filtration and then evaporation of DMF in vacuo, the residue was dissolved in a small amount of distilled water, which was dialyzed against distilled water for 3 days. The water in the dialyzed solution was removed under reduced pressure, affording **G3** as a pale yellow oil, yield 62.3%. IR (KBr) *ν*: 2937 (m), 2878 (m), 1723 (m, ν(C=O)), 1589 (m), 1503 (m), 1110 (s, ν_{as}(COC)) ^{1}H NMR (500 MHz, $CDCl_3$) δ: 6.61–6.66 (m, 26H, Ar H), 4.94–5.07 (m, 24H, CH_2), 3.92–4.13 (m, 54H, CH_2), 3.78–3.79 (m, 57H, CH_2 + CH_3), 3.68–3.71 (m, 54H, CH_2), 3.52–3.55 (m, 54H, CH_2), 3.35–3.38 (m, 81H, CH_3). ^{13}C NMR (125 MHz, $CDCl_3$) δ: 166.72 (C=O), 154.66, 153.64, 153.02, 152.79, 151.85, 149.46, 142.49, 141.52, 138.31, 136.42, 133.74, 133.02, 132.71, 131.85, 131.65, 110.19, 109.60, 107.46, 107.05, 75.86, 75.33, 73.27, 72.89, 72.70, 72.34, 72.26, 70.87, 70.66, 69.99, 69.15, 60.46, 59.20, 58.29, 52.50. MALDI-TOF MS *m/z* calcd for $C_{227}H_{350}O_{95}$: 4599; found: 4624 $[M + Na]^+$. Anal. calcd for $C_{227}H_{350}O_{95}$: C 59.28, H 7.67; found: C 59.01, H 7.81.

Fluorescence measurements

Fluorescence spectra were obtained on a Hitachi F-4500 luminescence spectrophotometer using pyrene as a fluorescent probe. Aliquots of pyrene solution (5.9×10^{-6} mg/mL in acetone, 50 μL) were added to volumetric flasks and the acetone was evaporated overnight. Then, aqueous solutions of **G3** at different concentrations were added to the flasks. The final pyrene concentration in each sample was 5.9×10^{-7} mg/mL. The solutions were kept at room temperature for 24 h to equilibrate the pyrene and the micelles. The emission spectra were recorded from 250 to 500 nm with an excitation wavelength of 390 nm.

TEM measurements

A drop of aqueous dendron solution (1 mg/mL) was placed on a Formwar-coated copper grid and dried in air. TEM observation of the micelles was conducted on a Hitachi H-600 instrument operating at an acceleration voltage of 80 kV.

LCST measurement

The LCST was determined by cloud point measurement. Dendron **G3** was dissolved in deionized water at different concentrations. The temperature of the solutions was raised at a constant rate (0.4 °C/min) and the optical transmittance of the polymer solution was measured at 500 nm with a UV–vis spectrophotometer (Cary 50, Varian). The LCST was defined as the temperature corresponding to the initial break points in the resulting transmittance vs temperature curve.[39]

Dynamic light-scattering (DLS) experiments

The D_h of the micelles was determined by DLS as a function of temperature. The measurements were performed with a Zetasizer ZEN 3600 instrument (Malvern, UK) using a light-scattering apparatus equipped with a He–Ne laser. The scattering angle was kept at 173° (backscattering), and the wavelength in the vacuum was set as 633 nm during the whole experiment. Solutions of dendrons **G3** and **G2a** in deionized water (1.0 mg/mL) were filtered with a 0.45 μm filter prior to use. Three replicates were performed for each measurement and an average value was obtained.

Drug loading and in vitro release

Dendron **G2a** or **G3** (50 mg) and POD (15 mg) were dissolved in 10 mL of acetone. Deionized water (10 mL) was added dropwise to the solution under vigorous stirring. The solution was stirred in an open air system overnight to remove acetone by evaporation. The precipitate of unbound POD was removed by centrifugation at 4000 rpm for 30 min. The amount of POD entrapped in the dendron micelles was determined by measuring the absorbance at 292 nm, using a standard calibration curve experimentally obtained with POD–ethanol solutions. The DLCand EE were calculated from the following equations:[37] DLC (wt %) = 100(mass of POD in micelles / mass of POD-loaded micelles); EE (%) = 100(mass of POD in micelles / mass of POD initially loaded).

To study in vitro drug release, a dialysis bag (molecular weight cut off = 3500 Da) containing 15 mL of the drug-loaded micelles in suspension was immersed in a phosphate buffer solution (150 mL, 0.01 mol/L, pH 7.4) at 20, 37, or 55 °C. At predetermined time intervals, 2 mL aliquots of the aqueous solution were withdrawn from the release media for UV–vis analysis, and the same volume of a fresh buffer solution was added. The amount of drug released from micelles at different temperatures was measured by UV absorbance at 292 nm.

Supplementary data

Supplementary data are available with the article through the journal Web site http://nrcresearchpress.com/doi/suppl/10.1139/v2012-038.

Acknowledgements

The authors gratefully acknowledge support for this work of the National Natural Science Foundation of China (Grant No. 20864003), the Program for Changjiang Scholars and Innovative Research Team in University (PCSIRT), and the Natural Science Foundation of Yunnan Province (Grant No. 2009ZC064M). The authors also thank Professor Wenfu Fu for assistance with MALDI-TOF MS measurements.

Can. J. Chem. Downloaded from www.nrcresearchpress.com by Renmin University of China on 09/02/12
For personal use only.

References

(1) Medina, S. H.; El-Sayed, M. E. H. *Chem. Rev.* **2009**, *109* (7), 3141. doi:10.1021/cr900174j.

(2) Kannaiyan, D.; Imae, T. *Langmuir* **2009**, *25* (9), 5282. doi:10.1021/la8039847.

(3) Haba, Y.; Harada, A.; Takagishi, T.; Kono, K. *J. Am. Chem. Soc.* **2004**, *126* (40), 12760. doi:10.1021/ja047755g.

(4) Yang, Z.; Zhang, W.; Zou, J.; Shi, W. *Polymer (Guildf.)* **2007**, *48* (4), 931. doi:10.1016/j.polymer.2006.12.052.

(5) Nishiyama, N.; Morimoto, Y.; Jang, W. D.; Kataoka, K. *Adv. Drug Deliv. Rev.* **2009**, *61* (4), 327. doi:10.1016/j.addr.2009.01.004.

(6) Lai, P. S.; Lou, P. J.; Peng, C. L.; Pai, C. L.; Yen, W. N.; Huang, M. Y.; Young, T. H.; Shieh, M. J. *J. Control. Release* **2007**, *122* (1), 39. doi:10.1016/j.jconrel.2007.06.012.

(7) Kurtoglu, Y. E.; Navath, R. S.; Wang, B.; Kannan, S.; Romero, R.; Kannan, R. M. *Biomaterials* **2009**, *30* (11), 2112. doi:10.1016/j.biomaterials.2008.12.054.

(8) Navath, R. S.; Kurtoglu, Y. E.; Wang, B.; Kannan, S.; Romero, R.; Kannan, R. M. *Bioconjug. Chem.* **2008**, *19* (12), 2446. doi:10.1021/bc800342d.

(9) Aathimanikandan, S. V.; Savariar, E. N.; Thayumanavan, S. *J. Am. Chem. Soc.* **2005**, *127* (42), 14922. doi:10.1021/ja054542y.

(10) Haba, Y.; Kojima, C.; Harada, A.; Kono, K. *Macromolecules* **2006**, *39* (21), 7451. doi:10.1021/ma061019a.

(11) Yang, Z.; Xie, J.; Zhou, W.; Shi, W. *J. Biomed. Mater. A* **2009**, *89A* (4), 988. doi:10.1002/jbm.a.31881.

(12) Astruc, D.; Boisselier, E.; Ornelas, C. *Chem. Rev.* **2010**, *110* (4), 1857. doi:10.1021/cr900327d.

(13) Kailasan, A.; Yuan, Q.; Yang, H. *Acta Biomater.* **2010**, *6* (3), 1131. doi:10.1016/j.actbio.2009.08.036.

(14) Kojima, C. *Expert Opin. Drug Deliv.* **2010**, *7* (3), 307. doi:10.1517/17425240903530651.

(15) Heskins, J.; Guillet, J. E. *J. Macromol. Sci. Part A, Pure Appl. Chem.* **1968**, *2* (8), 1441. doi:10.1080/10601326808051910.

(16) Schild, H. G. *Prog. Polym. Sci.* **1992**, *17* (2), 163. doi:10.1016/0079-6700(92)90023-R.

(17) Dai, S.; Ravi, P.; Tam, K. C. *Soft Matter* **2009**, *5* (13), 2513. doi:10.1039/b821363.

(18) Li, Y. Y.; Zhang, X. Z.; Cheng, H.; Kim, G. C.; Cheng, S. X.; Zhuo, R. X. *Biomacromolecules* **2006**, *7* (11), 2956. doi:10.1021/bm060080k.

(19) Xu, J.; Luo, S. Z.; Shi, W. F.; Liu, S. Y. *Langmuir* **2006**, *22* (3), 989. doi:10.1021/la0522707.

(20) Luo, S. Z.; Xu, J.; Zhu, Z. Y.; Wu, C.; Liu, S. Y. *J. Phys. Chem. B* **2006**, *110* (18), 9132. doi:10.1021/jp061055b.

(21) Kimura, M.; Kato, M.; Muto, T.; Hanabusa, K.; Shirai, H. *Macromolecules* **2000**, *33* (4), 1117. doi:10.1021/ma9914671.

(22) Bailey, F. E.; Joseph, J.; Koleske, V. *Alkylene Oxide and Their Polymers;* Marcel Dekker: New York, 1990.

(23) Saeki, S.; Kuwahara, N.; Nakata, M.; Kaneko, M. *Polymer (Guildf.)* **1976**, *17* (8), 685. doi:10.1016/0032-3861(76)90208-1.

(24) Lutz, J.-F.; Akdemir, Ö.; Hoth, A. *J. Am. Chem. Soc.* **2006**, *128* (40), 13046. doi:10.1021/ja065324n.

(25) Lutz, J.-F.; Hoth, A. *Macromolecules* **2006**, *39* (2), 893. doi:10.1021/ma0517042.

(26) Hua, F. J.; Jiang, X. U.; Li, D. J.; Zhao, B. *J. Polym. Sci. A, Polym. Chem.* **2006**, *44* (8), 2454. doi:10.1002/pola.21357.

(27) Lutz, J.-F.; Andrieu, J.; Üzgün, S.; Rudolph, C.; Agarwal, S. *Macromolecules* **2007**, *40* (24), 8540. doi:10.1021/ma7021474.

(28) Becer, C. R.; Hahn, S.; Fijten, M. W. M.; Thijs, H. M. L.; Hoogenboom, R.; Schubert, U. S. *J. Polym. Sci. A, Polym. Chem.* **2008**, *46* (21), 7138. doi:10.1002/pola.23018.

(29) Li, W.; Zhang, A.; Chen, Y.; Feldman, K.; Wu, H.; Schlüter, A. D. *Chem. Commun.* **2008**, (45): 5948. doi:10.1039/b814192d.

(30) Chang, D. W.; Dai, L. *J. Mater. Chem.* **2007**, *17* (4), 364. doi:10.1039/b613278b.

(31) Xu, L.; Shao, L. D.; Chen, L.; Hu, M. Q.; Bi, Y. M. *Chem. Lett.* **2010**, *39* (11), 1177. doi:10.1246/cl.2010.1177.

(32) Mourey, T. H.; Turner, S. R.; Rubinstein, M.; Fréchet, J. M. J.; Hawker, C. J.; Wooley, K. L. *Macromolecules* **1992**, *25* (9), 2401. doi:10.1021/ma00035a017.

(33) Lee, J.; Cho, E. C.; Cho, K. *J. Control. Release* **2004**, *94* (2–3), 323. doi:10.1016/j.jconrel.2003.10.012.

(34) San Miguel, V.; Limer, A. J.; Haddleton, D. M.; Catalina, F.; Peinado, C. *Eur. Polym. J.* **2008**, *44* (11), 3853. doi:10.1016/j.eurpolymj.2008.07.056.

(35) Deng, C.; Chen, X. S.; Yu, H. J.; Sun, J.; Lu, T.; Jing, X. *Polymer (Guildf.)* **2007**, *48* (1), 139. doi:10.1016/j.polymer.2006.10.046.

(36) Chang, Y.; Park, C.; Kim, K. T.; Kim, C. *Langmuir* **2005**, *21* (10), 4334. doi:10.1021/la047036f.

(37) Qu, T. H.; Wang, A. R.; Yuan, J. F.; Shi, J. H.; Gao, Q. Y. *Colloids Surf. B* **2009**, *72* (1), 94. doi:10.1016/j.colsurfb.2009.03.020.

(38) Adeli, M.; Zarnegar, Z.; Dadkhah, A.; Hossieni, R.; Salimi, F.; Kanani, A. *J. Appl. Polym. Sci.* **2007**, *104* (1), 267. doi:10.1002/app.25583.

(39) Bi, Y.; Gong, X. ; He, F.; Xu, L.; Chen, L.; Zeng, X.; Yu, L. *Can. J. Chem.* **2011**, *89* (10), 1249. doi:10.1139/v11-102.

Electrochemical immunoassay of carcinoembryonic antigen based on TiO_2–graphene / thionine / gold nanoparticles composite

Ke-Jing Huang, Zhi-Wei Wu, Ying-Ying Wu, and Yan-Ming Liu

Can. J. Chem. Downloaded from www.nrcresearchpress.com by Renmin University of China on 09/02/12
For personal use only.

Abstract: A novel multilayer film based on gold nanoparticles (AuNPs), thionine (Thi), and TiO_2–graphene (TiO_2–Gr) was exploited to develop a highly sensitive amperometric immunosensor for detecting carcinoembryonic antigen (CEA). Firstly, Nafion–TiO_2–Gr homogeneous composite was dropped on the surface of a glassy carbon electrode (GCE). Then Thi was chemisorbed by the TiO_2–Gr–Nafion composite. Furthermore, the negative ly charged AuNPs were chemisorbed onto Thi film through the electrostatic force with the amino groups of Thi. Cyclic voltammetry (CV) was employed to characterize the assembly process and the performance of the immunosensor. Because of the synergistic effect of the AuNPs, Thi, and the unique properties of TiO_2–Gr, the obtained immunosensor exhibited a wide linear response to CEA in two ranges from 0.1 to 10.0 ng mL^{-1} and from 10.0 to 120.0 ng mL^{-1} with a relatively low detection limit of 0.01 ng mL^{-1} (S/N = 3), as well as good stability and repeatability.

Key words: TiO_2–graphene, gold nanoparticles, thionine, carcinoembryonic antigen, immunosensor.

Résumé : On a mis à profit un nouveau film à couches multiples, à base de nanoparticules d'or (NPAu), de thionine (Thi) et de TiO_2–graphène (TiO_2–Gr), pour développer une sonde immunologique ampérométrique ultrasensible pour la détection de l'antigène cancéroembryonique (ACE). Dans une première étape, le composite homogène Nafion–TiO_2–Gr est déposé sur la surface d'une électrode de carbone vitreux (ECV). La thionine est alors chimisorbée par le composite Nafion–TiO_2–Gr. Les nanoparticules d'or, chargées négativement, sont ensuite chimisorbées sur le film de thionine par la force électrostatique des groupes aminés de la thionine. On a fait appel à la cyclovoltampérométrie pour caractériser le processus d'assemblage et la performance de la sonde immunologique. En raison des effets de synergie des nanoparticules d'or, de la thionine et des propriétés uniques du TiO_2–Gr, la sonde immunologique obtenue présente des plages étendues de réponse linéaire à l'antigène cancéroembryonique (ACE) de 0,1 à 10,0 ng mL^{-1} et de 10,0 à 120,0 ng mL^{-1}, avec une limite de détection relativement faible de 0,01 ng mL^{-1} (S/N = 3), ainsi qu'une bonne stabilité et répétabilité.

Mots-clés : TiO_2–graphène, nanoparticules d'or, thionine, antigène cancéroembryonique, sonde immunologique.

[Traduit par la Rédaction]

Introduction

Increasing attention has been focused on the development of immunoassay because it has become a major analytical tool in clinical diagnosis. Many diseases are closely related to some proteins that are called as biomarkers, such as carcinoembryonic antigen (CEA) and α-fetoprotein (AFP). However, sensitive detection of protein biomarkers remains a great challenge as some biomarkers present at ultralow levels in the early stages of diseases.[1,2] It is very important to explore new methods for signal amplification to increase the sensitivity of the detection. Different methods for signal enhancement have been investigated such as enzyme labeling,[3] rolling circle amplification,[4] and nanomaterial labeling.[5] Among these methods, nanomaterial labeling is gaining growing interest because of the intrinsic advantages of nanomaterials, such as low cost, good thermal stability, and large surface area.[6,7]

3Graphene (Gr) has recently received attention from materials scientists because of its unique qualities including fast electron transportation and good biocompatibility, which result in promising applications in electrochemical sensors and biosensors.[8–10] However, many of the interesting and unique properties of Gr can only be realized after it is integrated into more complex assemblies. Some Gr-based hybrid materials have shown greater versatility as advanced electrode materials for the fabrication of electrochemical sensors and biosensors.[11,12]

TiO_2 is a metal oxide that has been widely used in the fabrication of electrochemical biosensors and biosensors[13,14] owing to its good biocompatibility and high conductivity. For example, TiO_2 was employed as a support matrix for immobilizing enzymes and the results showed that the TiO_2-based composite can facilitate the direct electron transfer and enhance the catalytic activity of enzymes.[15] Most recently, we

Received 7 December 2011. Accepted 1 May 2012. Published at www.nrcresearchpress.com/cjc on 4 July 2012.

K.-J. Huang, Z.-W. Wu, Y.-Y. Wu, and Y.-M. Liu. College of Chemistry and Chemical Engineering, Xinyang Normal University, Xinyang 464000, P.R. China.

Corresponding author: Ke-Jing Huang (e-mail: kejinghuang@163.com).

Can. J. Chem. Downloaded from www.nrcresearchpress.com by Renmin University of China on 09/02/12
For personal use only.

reported a TiO_2–graphene (TiO_2–Gr) nanocomposite used in electrochemical biosensor construction and its application in some biomolecule sensing, such as dopamine, glucose, adenine, and guanine.[16–18] TiO_2–Gr based analytical methods showed excellent performance, such as high selectivity, broad dynamic range, and low detection limit, owing to the characteristics and advantages of the TiO_2–Gr nanocomposite, and it opened a new platform for electrochemical sensor and biosensor design.

CEA, an acidic glycoprotein with a molecular weight of about 200 kDa, is one of the most extensively used tumor markers.[19] The normal range for CEA in an adult nonsmoker is <2.5 ng mL^{-1} and the normal range for a smoker is <5.0 ng mL^{-1}. An elevated CEA level in serum may be an early indication of lung cancer, ovarian carcinoma, colon cancer, breast cancer, and cystadenocarcinoma.[20,21] In this work, a sensitive electrochemical immunosensor for the detection of CEA based on a signal amplification of gold nanoparticles (AuNPs), thionine (Thi), and TiO_2–Gr is reported. Nafion–TiO_2–Gr composite was employed to form a stable and uniform film on the cleaned glassy carbon electrode (GCE) surface. Furthermore, Thi could be adsorbed on the Nafion–TiO_2–Gr film based on the electronic exchange between Nafion and cationic dye Thi. Moreover, AuNPs, which were utilized to immobilize the biomolecule for its biocompatibility and to provide satisfactory conductive capability, were adsorbed on Thi film through opposite-charged adsorption and the interaction between AuNPs and the amino groups of Thi. In this case, an efficiently conductive multilayer was formed on the electrode surface, which was responsible for the satisfactory current and amplified sensitivity. The whole route of this novel immunosensor immobilization was very simple and time-saving. This developed immunoassay showed good performance in areas such as high sensitivity, improved stability, good selectivity, and wider linear range owing to the synergic effects of TiO_2–Gr, Thi, and AuNPs. This strategy could be further developed for practical clinical detections of CEA and other important tumor markers.

Experimental

Materials

Chloroauric acid, sodium citrate, graphite powder, hydrazine solution (50 wt %), and ammonia solution (28 wt %) were obtained from the Shanghai Chemical Reagent Corporation (Shanghai, P.R. China). Bovine serum albumin (BSA), CEA, prostate-specific antigen (PSA), low-density lipoprotein (LDL), and human immunoglobulin (HIgG) were obtained from Sigma-Aldrich (Saint Louis, Missouri). AFP was purchased from Biocell (Zhengzhou, P.R. China). Gold nanoparticles were produced by reducing gold chloride tetrahydrate with citric acid.[22] The mean size of the prepared Au colloids was about 18 nm. The acetate buffer solutions with various pH values were prepared with 0.1 mol/L HAc–NaAc containing 0.1 mol/L KCl. Double-distilled water was used throughout this study

Instruments

A CHI660D electrochemical workstation (CH Instruments, Shanghai, P.R. China) and a standard three-electrode cell containing a platinum wire auxiliary electrode, a saturated calomel reference electrode (SCE), and a modified electrode as the working electrode were employed for the electrochemical studies. All of the potentials were with respect to the SCE. The pH measurements were made with a pH meter (MP 230, Mettler–Toledo, Greiffensee, Switzerland).

Preparation of TiO_2–Gr nanocomposite

Graphene oxide (GO) was prepared from graphite powder by the modified Hummers method.[22] Graphite was put into a mixture of 12 mL of concentrated H_2SO_4, 2.5 g of $K_2S_2O_8$, and 2.5 g of P_2O_5. The solution was heated to 80 °C and kept stirring for 5 h using an oil bath. Next, the mixture was diluted with deionized water (500 mL). The product was obtained by filtering using a 0.2 μm nylon film and then dried in air. The product was reoxidized by using the Hummers and Offeman method to produce the GO. Exfoliation was carried out by sonicating 0.1 mg/mL of the GO dispersion for 1 h. TiO_2–Gr nanocomposite was prepared according to the method provided in previous work.[16] In short, 20 mg of GO was dispersed in a mixed solution of H_2O (10 mL) and ethanol (5 mL) under ultrasonication for 1 h to get a homogenous colloidal suspension of exfoliated GO. Then, 0.2 mL of Ti(O*i*-Pr)$_4$ was added to the GO suspension and ultrasonicated for another 1 h. The resultant mixture was transferred to a 25 mL Teflon-sealed autoclave and kept at 130 °C for 12 h. The final product was isolated by filtration and rinsed thoroughly with water and then ethanol. After rinsing, the product was dried in vacuum. The TiO_2–Gr nanocomposite was obtained in the form of a black powder.

Fabrication of the immunosensor

One milligram of the as-prepared TiO_2–Gr nanocomposite was dispersed in 10.0 mL of 0.25 wt % Nafion solution under ultrasonication for 30 min to obtain a homogeneous, well-distributed suspension of Nafion–TiO_2–Gr composite. Prior to the modification, the bare GCE (3 mm diameter) was carefully polished to obtain a mirrorlike surface with 0.3 and 0.05 μm alumina slurries, followed by successive sonication in water and ethanol for 5 min and then the GCE was dried in air. Subsequently, 20 μL of the prepared Nafion–TiO_2–Gr was dropped on the clean GCE, which was then soaked in Thi solution (3 mmol/L) for 10 min. Following that it was incubated in gold colloids for 2 h. Twenty microlitres of anti-CEA antibody was then dropped on the surface of the AuNPs / Thi / Nafion–TiO_2–Gr / GCE and incubated for 6 h at 4 °C. The as-prepared immunosensor (assigned as anti-CEA / AuNPs / Thi / Nafion–TiO_2–Gr / GCE) was incubated in 0.25 wt % BSA for 60 min to eliminate nonspecific binding effects and block the remaining active groups. The process for the assembly of the immunosensor is presented in Scheme 1.

Electrochemical measurements

The immunosensor was then placed in an unstirred electrochemical cell containing 0.1 mol/L HAc–NaAc buffer (pH 5.0) at room temperature. The detection of the current response change before and after the antigen–antibody reaction was carried out by cyclic voltammetry (CV) measurements, with the potential range from –0.6 to 0.2 V (vs SCE). After

Scheme 1. The stepwise fabrication process of the immunosensor.

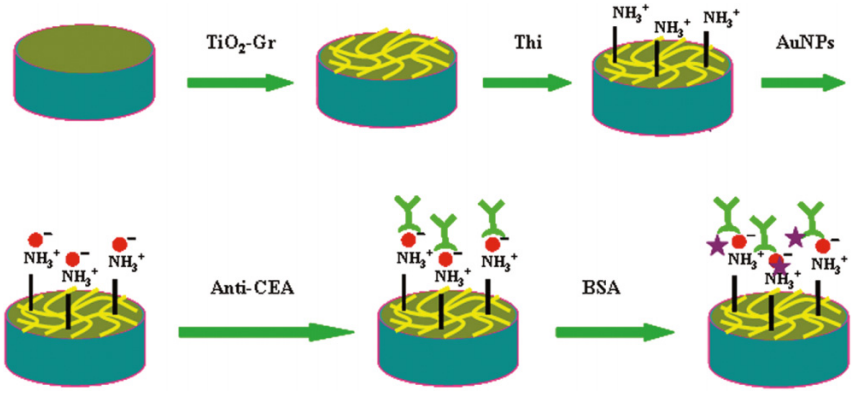
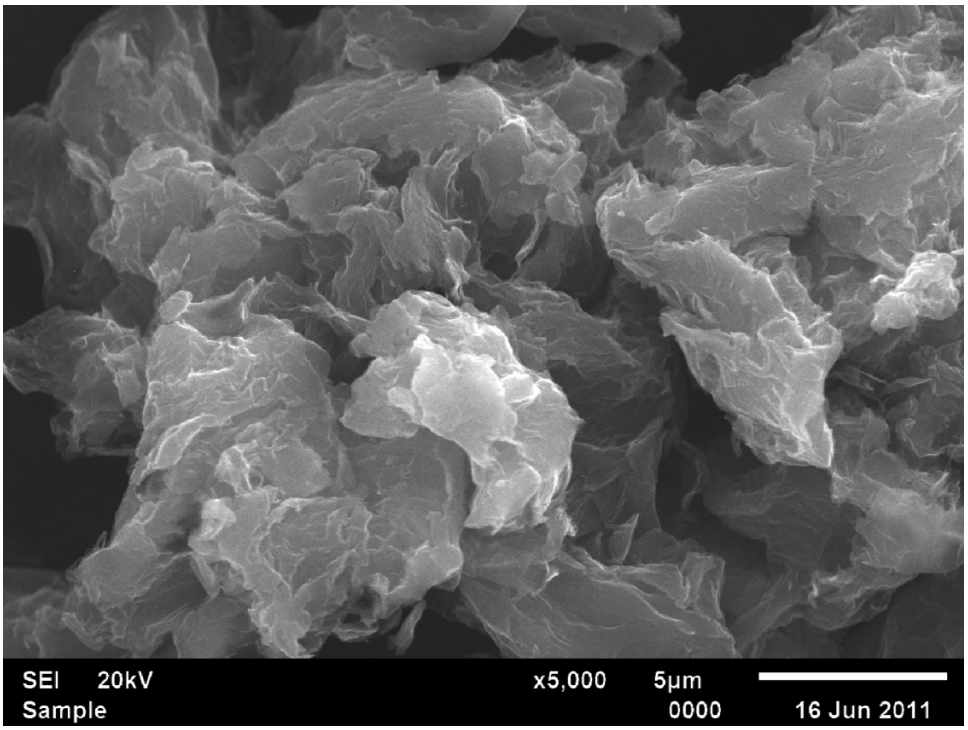


Fig. 1. SEM images of graphene (Gr).



incubation in antigen, the peak current response of the immunosensor was expected to decrease, because the antigen–antibody immunocomplex should hinder the access of the electron to the electrode. The amount of immunocomplex increased when the concentration of antigen increased, and this resulted in a decrease in the current response.

Results and discussion

Characteristics of Gr and TiO_2–Gr

The SEM image of the Gr (Fig. 1) reveals a typical crumpled and wrinkled Gr sheet structure. The integration between TiO_2 and Gr can be visualized from Fig. 2, in which TiO_2 nanoparticles of approximately 20–30 nm are uniformly and compactly embedded on the Gr substrate. The XRD patterns of the TiO_2–Gr are given in Fig. 3. The peaks in these diffraction patterns correspond to the anatase phase of TiO_2 (JCPDS file No. 21-1272), suggesting the complete formation of anatase TiO_2 during the hydrothermal process. However, the diffraction peaks of Gr are not distinguishable in the XRD patterns of TiO_2–Gr. This phenomena has also been observed in other relevant works, and it can be ascribed to the much lower crystalline extent of Gr than that of TiO_2, which results in the shielding of the Gr peaks by those of TiO_2.[23]

Electrochemical behaviors of modified electrodes

Cyclic voltammetrywas chosen to investigate the changes in the electrode behavior before and after each assembly step. Almost no CV peaks were detected at either the bare GCE or the Nafion–TiO_2–Gr modified GCE (Fig. 4, curves a and b). The background current of the TiO_2–Gr modified electrode is stronger than that of the bare GCE. This is most likely becaused the TiO_2–Gr nanocomposite could increase the effective surface area of the electrode. A pair of typical redox peaks can be observed after the adsorption of the electrochemically active Thi onto the Nafion–TiO_2–Gr film

Can. J. Chem. Downloaded from www.nrcresearchpress.com by Renmin University of China on 09/02/12
For personal use only.

Can. J. Chem. Downloaded from www.nrcresearchpress.com by Renmin University of China on 09/02/12
For personal use only.

Fig. 2. SEM images of TiO_2 – graphene (Gr).

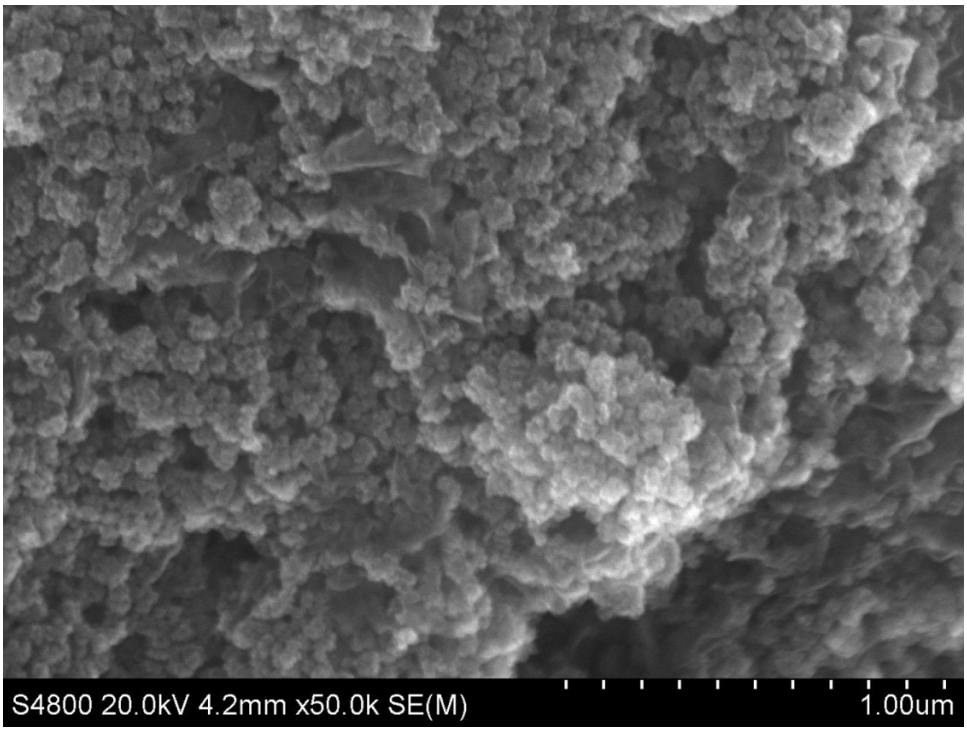
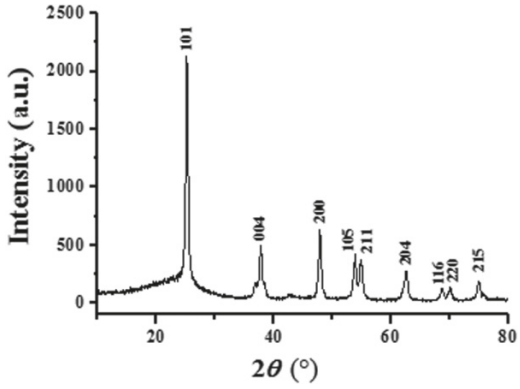


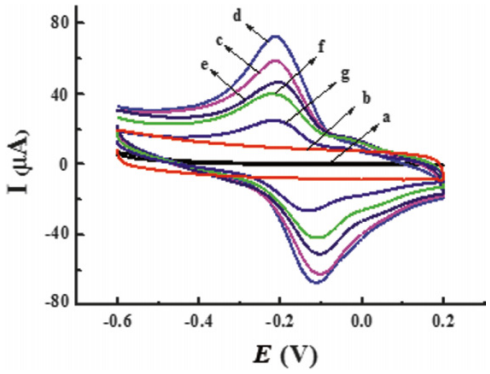
Fig. 3. XRD patterns of TiO_2 – graphene (Gr).



(Fig. 4, curve c). After the formation of the AuNPs monolayer on the modified electrode, the current response increases (Fig. 4, curve d). AuNPs can act as an electron shuttle, which makes it easier for the electron transfer to take place.[24] After the anti-CEA molecules are adsorbed onto the AuNPs, the peak currents obviously decrease, which suggests that the anti-CEA protein severely reduced the effective area and the active sites for electron transfer (Fig. 4, curve e). When BSA was immobilized to block the remaining active groups, a further decrease of the peak currents was found. This presumably was caused by the BSA hindrance of the access of Thi to the electrode surface, which resulted in a lower CV peak current. Lastly, a decrease of the peak current was found after CEA reactrf with BSA/anti-CEA/AuNPs/Thi/Nafion–TiO_2–Gr/GCE.

To further verify the conclusion previously mentioned and the electrochemical behaviors of the electrode during the modification, the electrochemical impedance spectroscopy (EIS) of variously modified electrodes wwas monitored in

Fig. 4. Cyclic voltammograms of different modified electrodes in BSA (pH 5.0). (*a*) Bare GCE. (*b*) Nafion–TiO_2–Gr/GCE. (*c*) Thi/Nafion–TiO_2–Gr/GCE. (*d*) AuNPs/Thi/Nafion–TiO_2–Gr/GCE. (*e*) Anti-CEA/AuNPs/Thi/Nafion–TiO_2–Gr/GCE. (*f*) BSA/anti-CEA/AuNPs/Thi/Nafion–TiO_2–Gr/GCE. (*g*) CEA/BSA/anti-CEA/AuNPs/Thi/Nafion–TiO_2–Gr/GCE. All potentials are given versus SCE and the scan rate was 50 mV s^{-1} from –0.6 to 0.2 V. BSA, bovine serum albumin; GCE, glassy carbon electrode; Gr, graphene; Thi, thionine; AuNPs, gold particles; CEA, carcinoembryonic antigen; SCE, saturated calomel reference electrode.



5 mmol/L $Fe(CN)_6^{3-/4-}$ solution containing 0.1 mol/L KCl (Fig. 5). The high-frequency region of the impedance plot shows a semicircle related to the redox probe $Fe(CN)_6^{3-/4-}$, followed by a Warburg line in the low-frequency region, which corresponds to the diffusion step of the overall process.[25] The bare GCE displays an almost straight line in the Nyquist plot of impedance spectroscopy, characteristic of a diffusion-limited electron-transfer process (Fig. 5, curve a). When Nafion–TiO_2–Gr was modified on the GCE surface, a high resistance was obtained (Fig. 5, curve b). The resistance

Can. J. Chem. Downloaded from www.nrcresearchpress.com by Renmin University of China on 09/02/12
For personal use only.

Fig. 5. Electrochemical impedance spectroscopy (EIS) of different modified electrodes in 5 mmol/L $Fe(CN)_6^{3-/4-}$ solution containing 0.1 mol/L KCl: (*a*) bare GCE, (*b*) Nafion–TiO_2–Gr/GCE, (*c*) Thi/Nafion–TiO_2–Gr/GCE, (*d*) AuNPs/Thi/Nafion–TiO_2–Gr/GCE, (*e*) anti-CEA/AuNPs/Thi/Nafion-–TiO_2–Gr/GCE, (*f*) BSA/anti-CEA/AuNPs/Thi/Nafion–TiO_2–Gr/GCE, and (*g*) CEA/BSA/anti-CEA/AuNPs/Thi/Nafion–TiO_2–Gr/GCE. The frequency range isfrom 1×10^{-2} to 1×10^6 Hz with a perturbation amplitude of 5 mV. The initial potential is –0.16 V. The inset is the equivalent circuit used to model impedance data in the presence of the redox couple. GCE, glassy carbon electrode; Gr, graphene; Thi, thionine; AuNPs, gold particles; CEA, carcinoembryonic antigen. Rs, Zw, Ret, and Cdl represent the solution resistance, the Warburg diffusion resistance, the electron-transfer resistance, and the double-layer capacitance, respectively.

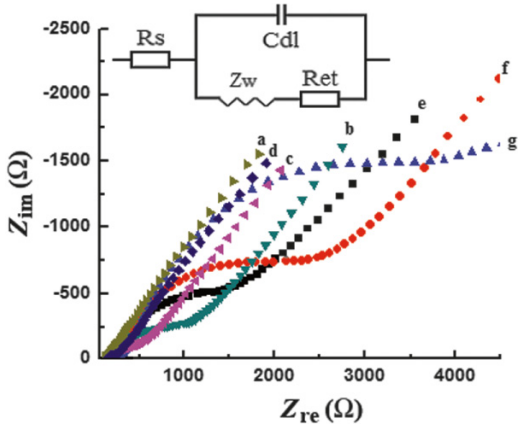
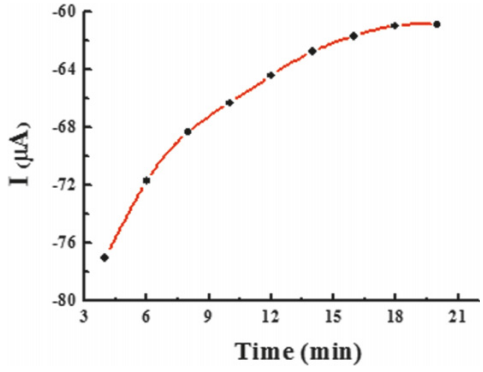


Fig. 6. Influence of incubation time.



decreased after Thi was assembled on the surface of Nafion–TiO_2–Gr (Fig. 5, curve c). This may occur because Thi as a mediator could facilitate the electron transfer and the positively charged Thi could attract the negatively charged Fe $(CN)_6^{3-/4-}$. In contrast, the resistance decreased again at the AuNPs/Thi/Nafion–TiO_2–Gr/GCE (Fig. 5, curve d), which is mainly attributed to the high conductivity of AuNPs. Anti-CEA antibody is a biomacromolecule with weak electroactivity and its assembly resulted in a resistance increase (Fig. 5, curve e). After the electrode was blocked with BSA, the resistance increased (Fig. 5, curve f), which can be attributed to the fact that the outer protein membrane insulates the conductive support and counteracts the interfacial electron transfer. After immobilization of CEA onto the electrode surface, a remarkable increase in the resistance was observed (Fig. 5, curve g). The reason is that the immunocomplex layer on the electrode acts as the electron communication and mass-transfer blocking layer, further insulating the conductive support and significantly hindering the access of the redox probe to the electrode surface.

Fig. 7. The immunosensor response in the detection solution (BSA) at various pH values (4.0, 4.5, 5.0, 5.5, 6.0, 6.5, and 7.0).

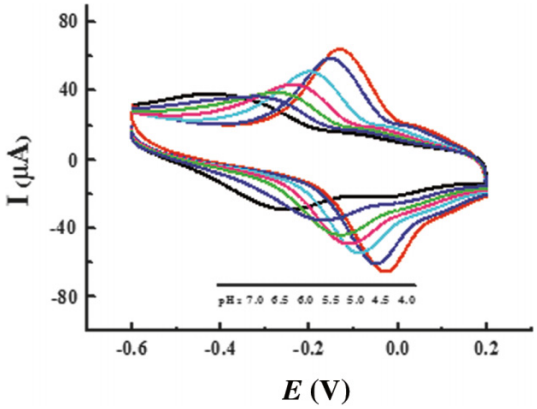
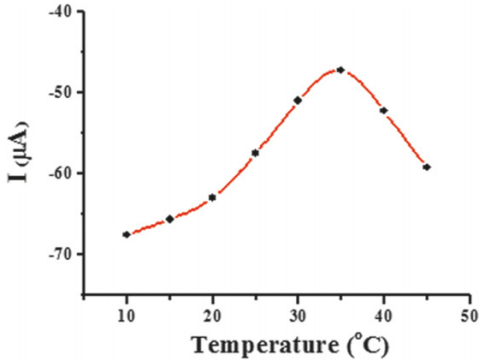


Fig. 8. Influence of incubation temperature on current response. All potentials are given versus a saturated calomel reference electrode (SCE) and the scan rate was 50 mV s^{-1}.



Optimizing conditions for immunoassay

The incubation time is a block to the improvement of immunoassay efficiency, which is usually controlled by the mass transport of immunoreagents and the kinetics of immunoreaction. Figure 6 displays the electrochemical responses of the immunosensor in pH 5.0 BSA after incubation with 30 ng mL^{-1} CEA for various times. The peak currents increase with the increasing incubation time and then tends to level off after 18 min, and a longer incubation time does not improve the response. Thus, 18 min was used for the antigen–antibody reaction. Figure 5*b* shows the CVs of the immunosensor in 0.1 mol/L BSA with various pH values at 50 mV s^{-1} after incubation with 30 ng mL^{-1} CEA. As indicated in Fig. 7, the peak currents decrease with an increase in pH from 4.0 to 7.0, while the potential separation of the anodic peak and cathodic peak increases. At BSA pH 5.0, the electrochemical immunosensor exhibits a quasireversible redox process. Meanwhile, we also considered that higher or lower pH might affect the bioactivity of the immobilized proteins. So, ABS pH 5.0 was selected for the detection of CEA. The effect of incubation temperature on the peak currents

Table 1. Comparison of different electrochemical immunosensors for the determination of carcinoembryonic antigen (CEA).

Modified electrode	Linear range (ng mL^{-1})	Detection limit (ng mL^{-1})	Reference
Anti-CEA/AuNPs/poly-*o*-aminophenol	0.5–20	0.1	26
Anti-CEA/AuNPs	0.50–25	0.25	27
Anti-CEA / AuNPs / polysulfanilic acid / HP	0.5–5.0	—	28
Anti-CEA/core-shell Fe_3O_4/SiO_2	1.6–60	0.5	29
Anti-CEA/Thi/HP	0.6–200	0.2	30
Anti-CEA/HP/sol-gel	0.5–120	0.4	31
Anti-CEA/AuNPs/(3-mercaptopropyl)trimethoxysilane/ Fe_3O_4	1.0–55	0.13	32
Anti-CEA / 3-aminophenylboronic,11-mercaptoundecanoic acid / HP	2.0–40.0	1.1	33
Anti-CEA/AuNPs/Chit/NG	0.2–120.0	0.06	34
Anti-CEA/AuNPs/Thi/Nafion–TiO_2–Gr	0.1–10 and 10–120	0.01	This work

Note: AuNPs, gold particles; Thi, thionine; Gr, graphene; HP, horseradish peroxidase; Chit, chitosan; NG, nanostructure gold.

Table 2. Interference studies with the immunosensor ($n = 6$).

Interference	Current ratio	Interference	Current ratio
PSA	0.94±0.02	Ascorbic acid	1.03±0.07
AFP	0.89±0.05	Dopamine	0.90±0.05
HIgG	0.92±0.06	Glucose	0.96±0.02
BSA	1.04±0.01	Tryptophan	0.95±0.02
LDL	0.96±0.02	Tyrosine	1.03±0.05
Arginine	1.01±0.06	Histidine	0.98±0.03

Note: PSA, prostate-specific antigen; LDL, low-density lipoprotein; HIgG, human immunoglobulin; AFP, α-fetoprotein; BSA, bovine serum albumin.

was studied over a temperature range from 10 to 45 °C. The maximum response appears at an incubation temperature of 35 °C (Fig. 8). However, considering the activity of the biomolecule and the lifetime of the immunosensor, a temperature of 25 °C was used for the experiment.

Analytical performance of the immunosensor

Under optimal conditions, the immunosensor was incubated in a CEA solution of different concentrations for 18 min and then the measurements were performed at a scan rate of 50 mV s^{-1} in BSA (pH 5.0) at 25 °C. The calibration graph for the determination of CEA was obtained using BSA/anti-CEA/AuNPs/Thi/Nafion–TiO_2–Gr/GCE as an immunosensor. The results show that the decrease in peak current is proportional to CEA concentration in two ranges, from 0.1 to 10.0 ng mL^{-1} and from 10.0 to 120.0 ng mL^{-1}, with correlation coefficients of 0.990 and 0.995, respectively. The detection limit was 0.01 ng mL^{-1} (S/N = 3). The results are compared with those of other immunoassay biosensing systems, which have been developed to monitor the levels of CEA, as shown in Table 1. The comparative data suggests the superiority of the present sensor over some earlier reported immunosensors, especially the characteristics of sensitivity and the detection limit. The possible reason is that Nafion–TiO_2–Gr and AuNPs/Thi film may increase the electrocatalytic active area and the immobilization amount of anti-CEA, as well as promote electron transfer between multilayer films and the electrode.

Stability, repeatability, reproducibility, and specificity

The reproducibility of the immunosensor was evaluated by intra-assay and interassay coefficients of variation (CVs). The intra-assay precision was evaluated by assaying the CEA level for 20 determinations of 1 sample with the same immunosensor. The intra-assay CVs of this method were 6.9% and 4.8% at CEA concentrations of 1 and 10 ng mL^{-1}, respectively. The interassay precision was estimated by determining the CEA level in one sample with six immunosensors. The interassay CV was 6.1% at a CEA concentration of 10 ng mL^{-1}. Thus, the precision and reproducibility of the proposed immunosensor were acceptable.

The storage stability of the sensors was evaluated over a period of 30 days by storing the sensor in 0.01 mol/L phosphate-buffered solutions (PBS, pH 7.0) at 4 °C. No obvious amperometric changes were observed after storage. The sensor retained about 98.1%, 96.2%, and 86.3% of the original value after storage periods of 10, 20, and 30 days, respectively. The good stability may be ascribed to the fact that the anti-CEA molecules were absorbed firmly on the surface of the AuNPs/Thi/Nafion–TiO_2–Gr composite film, which provided a good biocompatible microenvironment.

The reproducibility of the immunosensor plays a key factor in the development of a practical immunosensor. A regeneration study of the prepared immunosensor was implemented by using regeneration solutions to break the antibody–antigen linkage. In this study, the immunosensor that had been incubated in 10 ng mL^{-1} CEA for 18 min was immersed in a stirred 0.2 mol/L glycine–hydrochloric acid (Gly–HCl) solution (pH 2.8) and a stirred 4 mol/L urea solution for 5 min, in succession. A relative standard deviation (RSD) of 4.0% was acquired (five regenerations and measurement).

Selective determination of target analytes plays an important role in analyzing biological samples in situ without separation. The effect of substances that might interfere with the response of the immunosensor was investigated. The evaluation of the selectivity of the immunosensor was carried out by incubating the immunosensor in 10.0 ng mL^{-1} CEA containing some potential co-existing species with CEA, such as PSA, AFP, HIgG, LDL, BSA, ascorbic acid, dopamine, L-glucose, arginine, histidine, tryptophan, and tyrosine. The

Can. J. Chem. Downloaded from www.nrcresearchpress.com by Renmin University of China on 09/02/12
For personal use only.

Table 3. Comparison of the results of the analyses of serum samples using two different methods.

	Sample (ng mL^{-1})				
Method	1	2	3	4	5
ELISA	5.1±0.2	14.3±0.2	21.6±0.6	40.4±0.5	70.3±0.8
Method described in this work	4.8±0.3	14.9±0.6	20.2±0.3	42.9±0.5	74.1±0.7
Relative standard deviation (%)	–5.9	4.2	–6.5	6.2	5.4

degree of interference from these substances can be judged from the value of the current ratio. Herein, the current ratios can be obtained from the current reading of the immunosensor incubated in 10.0 ng mL^{-1} CEA and 10.0 ng mL^{-1} interfering substances versus the current reading with the immunosensor incubated in 10.0 ng mL^{-1} CEA. The results are listed in Table 2. The results suggested that the substance selected did not interfere remarkably. Moreover, these nonspecific species did not lead to a significant current shift or current change. Therefore, the immunosensor had a good selectivity to CEA.

Application

To investigate the reliability of the immunosensor for actual samples, six human serum samples were diluted to different concentrations with PBS (pH 7.0) and were assayed using the immunosensor with reference to the ELISA method. The results are shown in Table 3. The relative deviations of the two methods ranged from –6.5% to 6.2%, which indicated that the results obtained by the immunosensor were in agreement with that obtained by the ELISA. Therefore, the proposed immunosensor could be reasonably applied in assaying actual samples.

Conclusions

This work developed a novel strategy for an amperometric immunosensor for CEA based on the antibody adsorbed in AuNPs/Thi/Nafion–TiO_2–GR/GCE. The combination of the good conductivity and a large surface area with TiO_2–Gr, and the advantages of the AuNPs/Thi film, including biocompatibility and amplification, significantly enhanced the sensitivity of the immunosensor. The biosensor possesses good bioactivity, comparable detection limit and linear range, and acceptable storage stability. The results showed that the method was simple and sensitive enough for determination of CEA in human serum samples with good precision and accuracy. A new goal based on this work is to construct a new TiO_2–Gr-based bionanolabel for the amplification of the assay signal. This research could open new avenues in the application of TiO_2–Gr-based nanocables for clinical immunoassays, and could provide a convenient platform to modify for clinical testing and drug screening.

Acknowledgments

This work was supported by the National Natural Science Foundation of China (Grant No. 21075106), the Program for Science & Technology Innovation Talents in Universities of Henan Province (Grant No. 2010HASTIT025), and the Excellent Youth Foundation of He'nan Scientific Committee (Grant No. 104100510020).

References

(1) Zhang, B.; Zhang, X.; Yan, H. H.; Xu, S. J.; Tang, D. H.; Fu, W. I. *Biosens. Bioelectron.* **2007**, *23* (1), 19. doi:10.1016/j.bios.2007.03.007.
(2) Wu, J.; Fu, Z. F.; Yan, F.; Ju, H. X. *Trends Anal. Chem.* **2007**, *26* (7), 679. doi:10.1016/j.trac.2007.05.007.
(3) Yang, M. H.; Li, H.; Javadi, A.; Gong, S. Q. *Biomaterials* **2010**, *31* (12), 3281. doi:10.1016/j.biomaterials.2010.01.033.
(4) Zhou, L.; Ou, L. J.; Chu, X.; Shen, G. L.; Yu, R. Q. *Anal. Chem.* **2007**, *79* (19), 7492. doi:10.1021/ac071059s.
(5) Wan, Y.; Wang, Y.; Wu, J. J.; Zhang, D. *Anal. Chem.* **2011**, *83* (3), 648. doi:10.1021/ac103047c.
(6) Wang, J. X.; Zhu, X.; Tu, Q. Y.; Guo, Q.; Zarui, C. S.; Momand, J.; Sun, X. Z.; Zhou, F. M. *Anal. Chem.* **2008**, *80* (3), 769. doi:10.1021/ac0714112.
(7) Wang, J.; Meng, W. Y.; Zheng, X. F.; Liu, S. L.; Li, G. X. *Biosens. Bioelectron.* **2009**, *24* (6), 1598. doi:10.1016/j.bios.2008.08.030.
(8) Shan, C.; Yang, H.; Han, D.; Zhang, Q.; Ivaska, A.; Niu, L. *Biosens. Bioelectron.* **2010**, *25* (5), 1070. doi:10.1016/j.bios.2009.09.024.
(9) Savchenko, A. *Science* **2009**, *323* (5914), 589. doi:10.1126/science.1169246.
(10) Zhou, M.; Zhai, Y. M.; Dong, S. J. *Anal. Chem.* **2009**, *81* (14), 5603. doi:10.1021/ac900136z.
(11) Guo, S. J.; Wen, D.; Zhai, Y.; Dong, S. J.; Wang, E. K. *ACS Nano* **2010**, *4* (7), 3959. doi:10.1021/nn100852h.
(12) Shan, C.; Yang, H.; Han, D.; Zhang, Q.; Ivaska, A.; Niu, L. *Biosens. Bioelectron.* **2010**, *26* (7), 3181.
(13) Jiang, L. C.; Zhang, W. D. *Electroanalysis* **2009**, *21* (8), 988. doi:10.1002/elan.200804502.
(14) Lin, H. G.; Ji, X. B.; Chen, Q. Y.; Zhou, Y. K.; Banks, C. E.; Wu, K. B. *Electrochem. Commun.* **2009**, *11* (10), 1990. doi:10.1016/j.elecom.2009.08.034.
(15) Bao, S. J.; Li, C. M.; Zang, J. F.; Cui, X. Q.; Qiao, Y.; Guo, J. *Adv. Funct. Mater.* **2008**, *18* (4), 591. doi:10.1002/adfm.200700728.
(16) Fan, Y.; Lu, H. T.; Liu, J. H.; Yang, C. P.; Jing, Q. S.; Zhang, Y. X.; Yang, X. K.; Huang, K. J. *Colloids Surf. B Biointerfaces* **2011**, *83* (1), 78. doi:10.1016/j.colsurfb.2010.10.048.
(17) Fan, Y.; Huang, K.-J.; Niu, D.-J.; Yang, C.-P.; Jing, Q.-S. *Electrochim. Acta* **2011**, *56* (12), 4685. doi:10.1016/j.electacta.2011.02.114.
(18) Sun, J.-Y.; Huang, K.-J.; Zhao, S.-F.; Fan, Y.; Wu, Z.-W. *Bioelectrochemistry* **2011**, *82* (2), 125. doi:10.1016/j.bioelechem.2011.06.007.
(19) Gao, X.; Zhang, Y. M.; Chen, H.; Chen, Z. C.; Lin, X. F. *Anal. Biochem.* **2011**, *414* (1), 70. doi:10.1016/j.ab.2011.03.005.
(20) Sato, K.; Tokeshi, M.; Kimura, H.; Kitamori, T. *Anal. Chem.* **2001**, *73* (6), 1213. doi:10.1021/ac000991z.
(21) Li, J. P.; Gao, H. L.; Chen, Z. Q.; Wei, X. P.; Yang, C. F. *Anal. Chim. Acta* **2010**, *665* (1), 98. doi:10.1016/j.aca.2010.03.020.
(22) Kovtyukhova, N. I.; Ollivier, P. J.; Martin, B. R.; Mallouk, T. E.; Chizhik, S. A.; Buzaneva, E. V.; Gorchinskiy, A. D. *Chem. Mater.* **1999**, *11* (3), 771. doi:10.1021/cm981085u.

Can. J. Chem. Downloaded from www.nrcresearchpress.com by Renmin University of China on 09/02/12
For personal use only.

(23) Zhang, H.; Lv, X.; Li, Y.; Wang, Y.; Li, J. *ACS Nano* **2010**, *4* (1), 380. doi:10.1021/nn901221k.
(24) Chen, H.; Jiang, J. H.; Huang, Y.; Deng, T.; Li, J. S.; Shen, G. L.; Yu, R. Q. *Sens. Actuators B Chem.* **2006**, *117* (1), 211. doi:10.1016/j.snb.2005.11.026.
(25) Atta, N.; El-Kady, M. *Talanta* **2009**, *79* (3), 639. doi:10.1016/j.talanta.2009.04.040.
(26) Tang, H.; Chen, J.; Nie, L.; Kuang, Y.; Yao, S. *Biosens. Bioelectron.* **2007**, *22* (6), 1061. doi:10.1016/j.bios.2006.04.027.
(27) Wu, J.; Tang, J.; Dai, Z.; Yan, F.; Ju, H.; Murr, E. N. *Biosens. Bioelectron.* **2006**, *22* (1), 102. doi:10.1016/j.bios.2005.12.008.
(28) Li, X.; Yuan, R.; Chai, Y.; Zhang, L.; Zhuo, Y.; Zhang, Y. *J. Biotechnol.* **2006**, *123* (3), 356. doi:10.1016/j.jbiotec.2005.11.023.
(29) Pan, J.; Yang, Q. *Anal. Bioanal. Chem.* **2007**, *388* (1), 279. doi:10.1007/s00216-007-1224-0.
(30) Dai, Z.; Chen, J.; Yan, F.; Ju, H. *Cancer Detect. Prev.* **2005**, *29* (3), 233. doi:10.1016/j.cdp.2004.12.003.
(31) Tan, F.; Yan, F.; Ju, H. *Electrochem. Commun.* **2006**, *8* (12), 1835. doi:10.1016/j.elecom.2006.08.026.
(32) Tang, D.; Xia, B. *Microchim. Acta* **2008**, *163* (1–2), 41. doi:10.1007/s00604-007-0918-5.
(33) Zhang, X.; Wu, Y.; Tu, Y.; Liu, S. *Analyst (Lond.)* **2008**, *133* (4), 485. doi:10.1039/b714896h.
(34) He, X.; Yuan, R.; Chai, Y.; Shi, Y. *J. Biochem. Biophys. Methods* **2008**, *70* (6), 823. doi:10.1016/j.jbbm.2007.06.002.

Can. J. Chem. Downloaded from www.nrcresearchpress.com by Renmin University of China on 09/02/12
For personal use only.

Nonperturbative time-dependent density functional theory (TDDFT) and time-dependent electron localization function (TDELF) study of the ionization of OCS and CS_2 with ultrashort intense laser pulses — Orientational effects

Emmanuel Fowe Penka and André Dieter Bandrauk

Abstract: The nonlinear nonperturbative response of OCS and CS_2 to ultrashort (few cycles) intense laser pulses was studied numerically by time-dependent density functional theory (TDDFT) methods to understand molecular ionization as a function of laser–molecule orientation. A time-dependent electron localization function(TDELF) was used to visualize the nonlinear nonperturbative electron transfer occurring during the laser pulse. It was found that, for intensities $I > 3.5 \times 10^{14}$ W/cm^2, the inner shell Kohn–Sham (KS) molecular orbitals contribute significantly to the ionization, whereas for the intensity $I < 3.5 \times 10^{14}$ W/cm^2, the highest occupied molecular orbital (HOMO) shows the dominant response to the field. In general, the ionization rate maxima correspond to the alignment of maximum KS orbital densities with the laser pulse polarization instead of orbital ionization potentials (IP). These findings are corroborated through analysis of the TDELF images, where the ionization occurs from the lone pair or bond regions of the corresponding molecules.

Key words: molecular ionization, ionization potential, electron localization function, density functional theory.

Résumé : Faisant appel aux méthodes de la théorie de la densité fonctionnelle dépendante du temps (TDFDT), nous avons étudié d'une façon numérique la réponse non linéaire et non perturbatrice du OCS et du CS_2 aux pulsations laser ultracourtes (quelques cycles) et intenses dans le but d'étudier l'ionisation moléculaire en fonction de l'orientation laser–molécule. Nous avons utilisé la fonction de localisation de l'électron dépendante du temps (FLEDT) pour visualiser le transfert d'électron non linéaire et non perturbé qui se produit au cours de la durée du pulse laser. On a trouvé que, pour des intensités $I > 3{,}5 \times 10^{14}$ W/cm^2, les orbitales moléculaires Kohn–Sham (KS) de la couche interne contribuent d'une façon significative à l'ionisation alors que, lorsque l'intensité $I < 3{,}5 \times 10^{14}$ W/cm^2, c'est l'orbitale moléculaire haute occupée (OMHO) qui provoque la réponse dominante du champ. En général, les maxima du taux d'ionisation correspondent à un alignement des densités des orbitales KS avec la polarisation de la pulsation laser plutôt que les potentiels d'ionisation (PI) des orbitales. Ces observations sont corroborées par une analyse des images de la fonction de localisation de l'électron dépendante du temps (FLEDT) dans lesquelles l'ionisation se produit à partir d'une paire non partagée ou des régions de liaisons des molécules correspondantes.

Mots-clés : ionisation moléculaire, potentiel d'ionisation, fonction de localisation d'électron, théorie de la fonctionnelle de la densité.

[Traduit par la Rédaction]

Introduction

Recent developments in the generation and characterization of ultrashort laser pulses[1,2] provide the tools necessary for investigating electron dynamics in atoms and molecules at the electron's natural time scale, the attosecond (1 as = 10^{-18} s).[2] Such ultrashort pulses offer the possibility of creating coherent electron wavepackets (CEWPs) inside molecules on the as time scale and subnanometer size.[3] Currently, the main source of as pulses is high-order harmonic generation (HHG) from atoms and (or) molecules exposed to ultrashort (few cycles) laser pulses at intensities $I \geq 10^{14}$ W/cm^2 and IR frequencies ($\omega = 0.0567$ au, $\lambda = 800$ nm). The atomic unit, au of intensity $I = 3.54 \times 10^{16}$ W/cm^2, corresponds to the au of electric field strength, $E = 5 \times 10^9$ V/cm, the field at the au of radius $a_0 = 0.0525$ nm of the H atom. Current laser intensities approach the au of I, thus requiring nonlinear nonperturbative treatments of laser–molecule interactions. A most promising approach to treating such problems is a nonlinear

Received 5 November 2011. Accepted 13 January 2012. Published at www.nrcresearchpress.com/cjc on 11 July 2012.

E.F. Penka and A.D. Bandrauk.* Laboratoire de Chimie Théorique, Faculté des Sciences, Université de Sherbrooke, Sherbrooke, QC J1K 2R1, Canada.

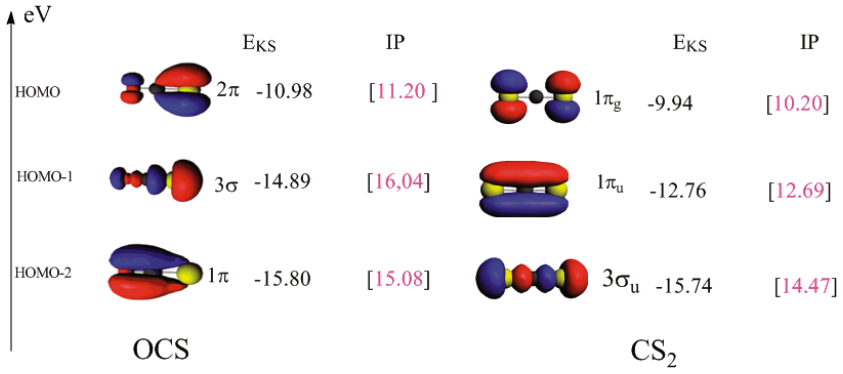
Corresponding author: Emmanuel Fowe Penka (e-mail: emmanuel.penka@usherbrooke.ca).

*Canada Research Chair – Computational Chemistry and Molecular Photonics.

Can. J. Chem. Downloaded from www.nrcresearchpress.com by Renmin University of China on 09/02/12
For personal use only.

Can. J. Chem. Downloaded from www.nrcresearchpress.com by Renmin University of China on 09/02/12
For personal use only.

Fig. 1. DFT/LB94 orbital energies (E_{KS}) and experimental ionization potentials (IPs) of the molecular orbitals of OCS and CS_2. Only the three highest relevant occupied molecular orbitals, HOMO, HOMO-1, and HOMO-2, are shown. Atom colours: carbon (black), sulfur (yellow), and oxygen (red) (please see the Web version of this paper for the colour figure).



nonperturbative time-dependent density functional theory method (TDDFT), using functionals that can accurately give ionization potentials (IPs) of molecular orbitals.[4] Such an approach has also been generalized to introduce coherent control algorithms for optimizing laser–molecule responses.[5] In the present work, we extend our previous study[6] of CO_2 in intense laser fields to CS_2 and the nonsymmetric OCS to compare the nonlinear nonperturbative laser–molecule response of symmetric and nonsymmetric systems. Effective single active electron (SAE) models are currently used for orbital imaging of CO_2 in intense laser fields.[7] TDDFT methods will allow us to address the accuracy of these models and include inner shell excitation–ionization shown previously to be non-negligible at high intensities.[8]

Methods — Nonperturbative TDDFT Kohn–Sham formalism

The TDDFT method provides the most detailed and feasible ab initio approach for tackling many-body problems in external time-dependent fields. DFT, as first introduced by Hohenberg and Kohn,[9] and extended by Kohn and Sham[10] (KS), is based on the existence of an exact mapping between one-particle density and external potentials. This leads to the density of the interacting system being obtained from the density of an auxiliary system of noninteracting particles moving in an effective local single-particle potential. A time-dependent generalization of DFT was provided by Runge and Gross,[11] showing that there is a one-to-one correspondence between the external (time-dependent) potential, $\upsilon_{ext}(r, t)$, and the time-dependent one-electron density, $n(r, t)$ for many-body systems evolving from a fixed initial state. The time-dependent electronic density is written as[12]

$$[1] \qquad n(r,t) = \sum_{\sigma=\uparrow,\downarrow} n_\sigma(r,t) = \sum_{\sigma=\uparrow,\downarrow} \sum_{i}^{N_\sigma} |\psi_{i\sigma}(r,t)|^2$$

where N_σ is the number of the occupied KS orbital in spin state σ and $\psi_{i\sigma}(r,t)$ is the orbital obtained through the time-dependent KS equations (in au)

$$[2] \qquad i\frac{\partial}{\partial t}\psi_{i\sigma}(r,t) = \left[-\frac{1}{2}\nabla^2 + \upsilon_{\text{eff}}(r,t)\right]\psi_{i\sigma}(r,t)$$

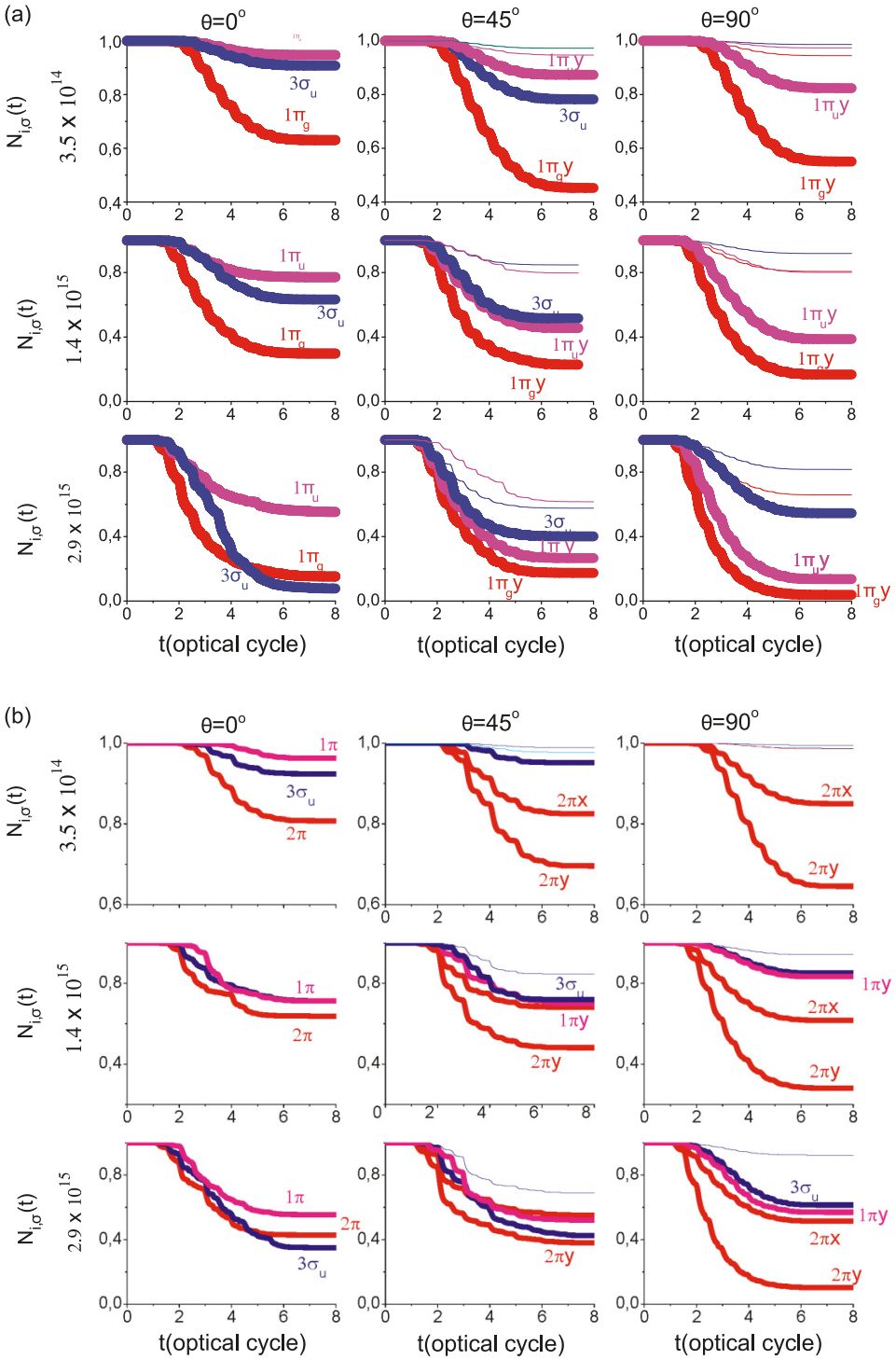
where

$$\upsilon_{\text{eff}}(r,t) = \upsilon_{\text{ext}}(r,t) + \upsilon_h(r,t) + \upsilon_{\text{xc},\sigma}(r,t)$$

The first term is the external potential due to the interaction of the electron with an external laser field and the nuclei, the second term accounts for the classical Hartree electrostatic interaction between electrons, and the third term is the exchange correlation potential (υ_{xc}), which includes all nontrivial many-body effects, and has an extremely complex (and essentially unknown) functional dependence on the density. When an intense low-frequency electric field is applied to a molecule, electrons tend to ionize from the higher ionization potential (IP) orbitals. Therefore, the choice of an approach that accurately reproduces the experimental IP is essential for analysis of ionization processes. In this work, we have used the Van Leeuwen and Baerends[13] potential (LB94), which introduces a gradient correction to the LDA exchange correlation so as to reproduce the Coulomb asymptotic behaviour of the potential. The LB94 potential yields excellent estimates of the IP for atoms and small molecules, as shown in Fig. 1, especially in the framework of the linear response TDDFT excitation energy.[14] This model potential significantly corrects the higher moments of the density, notably for diffuse outer orbitals involved in excitations and, in our case, in ionization. The LB94 also includes partial and considerable self-interaction correction (SIC) resulting from an interaction of an electron with itself, of importance to electronic transport.[15] Such corrections can produce spurious oscillations in photoionization calculations,[16] but little is known about the corrections for strong fields in the nonperturbative regime. We focus on the LB94 potential generally, which offers accurate IPs for most molecular orbitals, an essential starting point for accurate ionization. Previous other approaches have used optimized effective potentials[17] (OEP) with exact exchange and also effective local potentials for excited states.[18,19] Furthermore, at high intensities, excited states have very short lifetimes, thus reducing considerably the nonadiabatic effects. The neglect of nonadiabatic effects, which is a major difficulty of linear TDDFT, is implicit in the strong field approximation (SFA)[20] a current simple nonperturbative model that neglects excited states. The generally accurate KS orbital IPs with the LB94 potential suggest that these orbitals simulate Dyson orbitals[21] for which no exact

Can. J. Chem. Downloaded from www.nrcresearchpress.com by Renmin University of China on 09/02/12
For personal use only.

Fig. 2. (*a*) TDDFT/LB94 orbital population ($N_{i,\sigma}(t)$) of CS_2 at different laser intensities for a selective fixed angle (θ) between the molecular *z* axis and the laser polarization direction. Only the relevant Kohn–Sham (KS) orbitals that possess an important response to the laser field are shown with their labels. (*b*) TDDFT–LB94 orbital population ($N_{i,\sigma}(t)$) of OCS at different laser intensities for a selective fixed angle (θ) between the molecular *z* axis and the laser polarization direction. Only the relevant KS orbitals that possess an important response to the laser field are shown with their labels (please see the Web version of this paper for the colour figure).



time-dependent theory is available currently. We therefore use the LB94 potential in the present TDELF work, as we have shown that it provides a feasible approach to studying strong field effects in CO_2.[6]

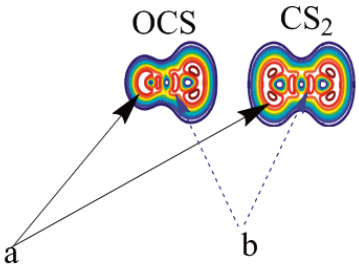
Computational methods

Ionization in KS orbitals

In the present work, the TDDFT KS equation was discretized

Can. J. Chem. Downloaded from www.nrcresearchpress.com by Renmin University of China on 09/02/12
For personal use only.

Fig. 3. DFT/LB94 representation of the ground-state electron localization function (ELF) of the OCS and CS_2 molecules. The lone-pair and the chemical-bond regions are shown.



a: Lone pair region, b: Chemical bond region

in space using finite-difference (FD) grid techniques as reported in our previous work.[6] The bond length was set to its experimental[22–25] value. For OCS, bond lengths are CS = 0.156 nm, CO = 0.1157 nm, and CS= 0.155 nm for CS_2 as compared with CO_2.[6] The molecule was placed in a large three-dimensional (3D) rectangular grid cell (au are used) of dimension $|z_{max}| = 90$ au (1 au = 0.0529 nm) and $|x_{max}| = |y_{max}| = 25$ au if the laser is oriented parallel to the molecular z axis. The uniform FD grid spacing ($\Delta z = \Delta x = \Delta y = 0.34$ au) was used and the convergence of the calculations was checked against results that used a larger grid spacing. The size of the grid was determined by the maximum radius $\alpha = E/m\omega^2$ of an electron in a time-dependent electric field of maximum amplitude E. Thus, at $E = 0.1$ au corresponding to an intensity $I = 3.50 \times 10^{14}$ W/cm^2, $\alpha = 30$ au at $\lambda = 800$ nm and $\omega = 0.057$ au. Thus, since α is the size of the recolliding electron trajectory, $z_{max} = 90$ au >> α ensures that all recolliding electrons are collected in the numerical procedure.[26] The laser intensity is related to the field strength by $I = \frac{1}{2}\varepsilon_o cE^2$, where ε_o is the permittivity of free space and c is the speed of light. The angle (θ) between the linear polarized laser and the main molecular z axis varies from 0° to 90°. The total pulse area condition $\int_{-\infty}^{+\infty} E(t)dt = 0$ was verified to ensure no spurious static effects for pulses satisfying Maxwell's equations.[26,27] The external potential created by an intense laser field is assumed to arise from an oscillating electric field with a cosine envelope. When the laser is linearly polarized parallel to the molecular axis z, $\upsilon_{ext}(r, t)$ is given by

$$[3] \qquad \upsilon_{ext}(r,t) = zE\cos^2\left(\frac{\pi t}{T}\right)\sin(\omega t) \qquad (0 \prec t \prec T)$$

T determines the laser pulse duration. The time-dependent equations (eq. [2]) are solved using the Crank–Nicolson scheme,[22,24] with $\Delta t = 0.02$ au (1 au = 24×10^{-18} s) as the time step. All calculations were done using eight optical cycle pulse duration on an Intel multiprocessor parallel machine at Compute Canada's Sherbrooke centre. To absorb the ionized charge density and avoid reflections at the boundary of the box owing to ionization during the propagation, we employ a mask function. By using this technique, the KS wave function is multiplied at each time step at grid boundaries by a function $M(z)$, which is 1 in the inner simulation region and gradually goes to 0 at the boundaries. The time-dependent ionization probability ($P_{i,\sigma}(t)$) of an individual KS spin orbital is calculated as[4]

$$[4] \qquad P_{i,\sigma}(t) = 1 - N_{i,\sigma}(t)$$

where $N_{i,\sigma}(t) = \langle\psi_{i,\sigma}(r,t)|\psi_{i,\sigma}(r,t)\rangle$ is the time-dependent population (survival probability) of the i,σ-th occupied spin population.

Time-dependent electron localization function (TDELF)

The ELF is a method for the mapping of the pair-electron probability in multielectron systems. It was first introduced by Becke and Edgecombe[28] as a descriptor of electronic localization, using arguments based on the conditional same-spin pair-probability function. Our recent work shows that the ELF is a useful tool for identifying and visualizing lone-pair and bonding-pair electrons.[6] Here, we briefly recall the definitions of the extension of the ELF for time-dependent processes. The time-dependent ELF, or TDELF ($\eta(r, t)$) is given as

$$[5] \qquad \eta(r,t) = \frac{1}{1 + \left(\frac{C(r,t)}{C_h(r,t)}\right)^2}$$

where

$$[6] \qquad C(r,t) = \sum_\sigma \left\{ \sum_{i=1}^{N_\sigma} |\nabla\psi_{i\sigma}(r,t)|^2 - \frac{1}{4}\frac{[\nabla n_\sigma(r,t)]}{n_\sigma(r,t)} - \frac{j_\sigma^2(r,t)}{n_\sigma(r,t)} \right\}$$

$$[7] \qquad C_h(r,t) = \frac{3}{5}(6\pi^2)^{2/3} n_\sigma(r,t)^{5/3}$$

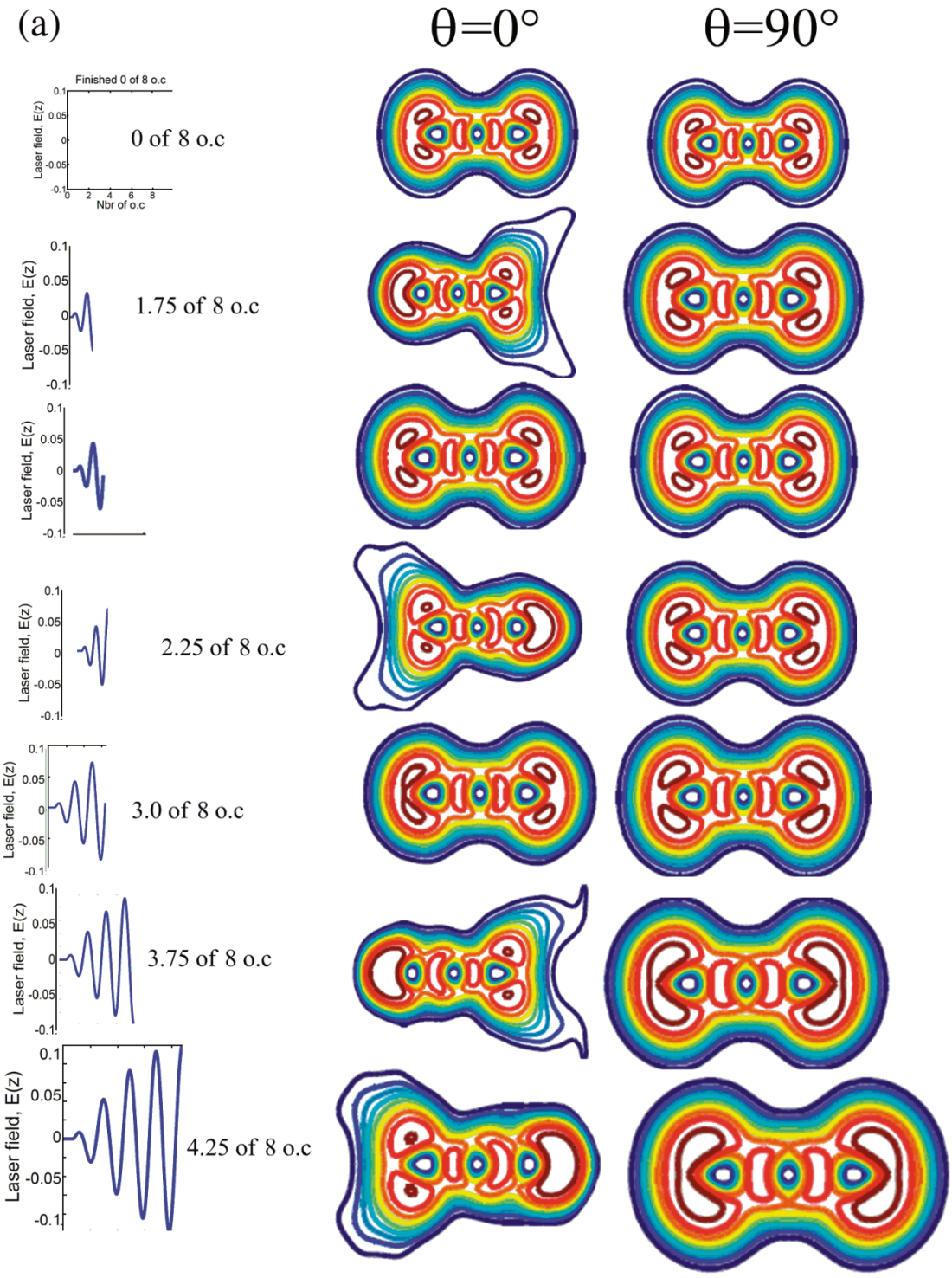
The term j_σ^2 is the squared modulus of the current density depending on the phase of the orbitals and is the time-dependent correction to the original ELF.[28] $C(r, t)$ measures the probability of finding one electron in the near vicinity of a reference like-spin electron at position r and time t. Thus, the Pauli repulsion between two like-spin electrons, described by the smallness of $C(r, t)$, is taken as a measure of the electron localization. $C_h(r, t)$ is the corresponding factor found for a uniform electron gas, i.e., a homogeneous electron gas whose density is the same as that of the real system. The TDELF would be used for the time-resolved observation of the molecular ionization and can thus provide a visual understanding of the electron-transfer dynamics (most notably lone-pair and bond electrons) under strong laser pulses.

Results and discussion

Electronic analysis and ionization

The electronic structure from the DFT–KS calculation is depicted in Fig. 1, where the three highest occupied KS MOs HOMO, HOMO-1, and HOMO-2 with their phases and energies, are presented. For the CS_2 molecule, one finds that the HOMO is an antibonding type ($1\pi_g$) formed of π lobes lying perpendicular to the internuclear axis and located on the sulfur atoms for CS_2, whereas the orbitals forming the HOMO (2π) of OCS are mostly located on the sulfur atom. One sees that the computed KS orbital energies are, except

Fig. 4. (*a*) Snapshot of the isosurface of the TDELF images for $I = 3.5 \times 10^{14}$ W/cm^2 as the CS_2 molecule evolves in a laser field of eight optical cycles (o.c.). Calculations are done for with $\theta = 0°$ and 90°. (*b*) Snapshot of the isosurface of the TDELF images for $I = 3.5 \times 10^{14}$ W/cm^2 as the OCS molecule evolves in a laser field of eight optical cycles (o.c.). Calculations are done for with $\theta = 0°$ and 90° (including the ionized distribution on right-hand side).

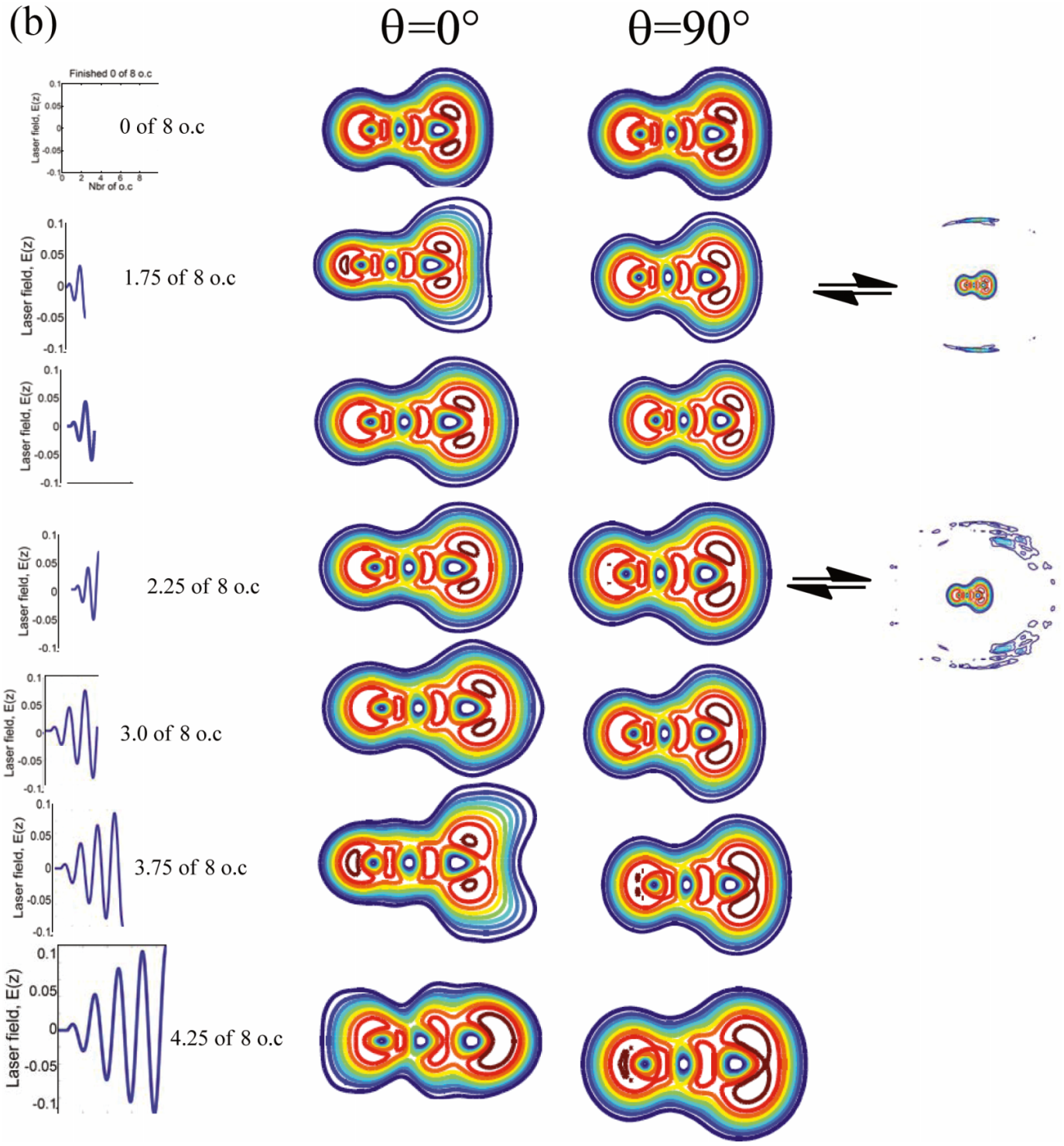


for OCS, in general in agreement with the available experimental IPs. Thus, the CS_2 KS orbital energies respect the experimentally observed IP order, whereas, for OCS, the order between the 3σ and 1π orbitals is inverted, but the energy separation of 1 eV is the same. We further investigated the time evolution in the presence of intense pulses of some relevant KS orbitals using eq. [4]. Three angular orientations were considered ($\theta = 0°$, 45 °, and 90°), where θ is the angle between the molecular *z* axis and the laser polarization.

Time-dependent KS populations, ($N_{i,\sigma}(r, t)$) using three laser intensities ranging from 3.50×10^{14} to 3.0×10^{15} W/cm^2, are displayed in Figs. 2*a* and 2*b* for, respectively, the CS_2

Can. J. Chem. Downloaded from www.nrcresearchpress.com by Renmin University of China on 09/02/12
For personal use only.

Fig. 4. (*concluded*).



and the OCS molecules. Evidence of a strong dependence of the KS remaining orbital population on the laser intensity was observed. It emerges that, in general, the KS MO ionization is the most important for CS_2 owing to its lower IP as compared with OCS. When $\theta = 0°$, for symmetry reasons the two components of each 2π or $1\pi_g$ orbital have the same behaviour because they are degenerate. For the lower laser intensity $I = 3.50 \times 10^{14}$ W/cm^2, one sees that the HOMO shows the dominant response to the laser field, as expected. It is followed, respectively, by the inner shell orbitals $3\sigma/3\sigma_u$ (HOMO-1 for OCS and HOMO-2 for CS_2). As the laser intensity increases, it emerges that the HOMO does not remain the most affected by the external laser field. Instead, our calculation shows that the ionization of the inner $3\sigma/3\sigma_u$ molecular orbital dominates. Such relatively small ionizations of the HOMOs under high laser intensity is related to their nodal plane containing the molecular axis. This gives rise to a low ionization yield when aligned parallel to the laser electric

Can. J. Chem. Downloaded from www.nrcresearchpress.com by Renmin University of China on 09/02/12
For personal use only.

Can. J. Chem. Downloaded from www.nrcresearchpress.com by Renmin University of China on 09/02/12
For personal use only.

field, whereas $3\sigma_u/3\sigma$ has the right symmetry (MO shape) to interact with the laser field as its density is maximum parallel to the field. At angles $\theta = 45°$ and 90°, the symmetry behaviour of the different components of the π orbitals is broken (i.e., degeneracy is removed) and we have renamed them as follows: components of the $1\pi_g$ of CS_2 are $1\pi_g x$ and $1\pi_g y$ and those of the 1π of the OCS are $1\pi x$ and $1\pi y$. When $\theta = 45°$, the main ionization occurs from the HOMO, followed by that of the inner $1\pi_u/1\pi$ and $3\sigma_u/3\sigma$ MO orbital. The enhanced ionization of the HOMO is the result of the combined effects of its lower IP and its alignment along the laser polarization axis at $\theta = 45°$ as reported[29] previously in H_2^+. Finally, when $\theta = 90°$, once again, one finds that the KS MOs of CS_2 ionize more than in OCS and the HOMO remains the most affected by the field at lower intensity. For higher laser-peak intensities, the ionization is dominated by the bonding $1\pi_u/1\pi$ orbital. We find that those orbitals that have maximum density in the direction of laser polarization will most strongly influence or dominate in ionization and in the MHOHG processes. However, for the OCS molecule, one sees that as the laser intensity is increasing, the two components of the HOMO ($2\pi y$, $2\pi x$) present the dominant response to the laser field. This is because in comparison with the CS_2 MOs, the HOMO and the HOMO-2 of the OCS have almost the same shape (density). As a consequence, its HOMO ionizes faster as the laser intensity is increasing owing to its lower IP.

In conclusion, we find that the KS HOMO ionization increases from $\theta = 0°$ and reaches a maximum when the molecule is aligned at an angle around 45° with respect to the direction of the laser polarization, and then decreases at larger angles towards 90°. The ionization rate maxima as a function of the angle follow the maxima in electron density, and the minima reflect the nodal structure of the orbitals. Such a nonlinear response in ionization at high intensities has been predicted by the tunnelling ionization model.[30]

Electron localization analysis

ELF versus density

In Fig. 3*a*, we display the field free ELF of OCS and CS_2 molecules in a plane containing the three atoms. The bond (b) and the lone pair location (a) are shown.

The ELF value for the lone pair is higher than for the chemical bond. This arises from the fact that the lone pair (HOMO) is more localized than the CO bond (HOMO-1 and HOMO-2) as shown in Fig. 1. The lone pair electron density HOMO ($1\pi_g/2\pi$ region (a)), is visible, whereas the HOMO-1 and the HOMO-2 are essentially located in bonding region (b). Such clear separation between the HOMO and the relevant inner orbitals enables us to get a deep insight into the real time MO behaviour when the molecule is under an external field. The angles $\theta = 0°$ and $\theta = 90°$ weren considered and the results are shown next. We note that, in the CS moiety, the lone pair appears as two distinct regions at angles of 45° with respect to the molecular z axis. This reflects the major density of the π orbitals of the sulfur atoms.

TDELF of CS_2

At $\theta = 0°$, the laser polarization is parallel to the molecular z axis and, at the initial time step, the ELF picture corresponds to the ground-state image. As the time propagation evolves, the first major laser perturbation occurs on the lone-pair region of the sulfur (Fig. 3*b*) after 1.75 optical cycles (o.c.).

The electric field being negative, the major perturbation consists of a lengthening of the lone-pair region followed by the appearance of a hole in the left atom, reflecting the depletion by ionization or the electron transfer (ET) of the electron density. At 2.25 o.c., where the electric field is positive, a perturbation as exactly described in the folllowing arises on the right atom. The same asymmetric perturbation behaviour is observed, respectively, at 3.75 and 4.25 o.c., where the size of the perturbation increases with the electric field. The observed nonsymmetrical perturbation of the electron density on the two sulfur (CS_2) atoms indicates that these atoms feel the presence of the external field differently. The images show that the major part of the perturbation is located in the region corresponding to the lone-pair region (HOMO) of the molecule. As the time propagation evolves, the intensity of the perturbation in the lone-pair region increases as well, reaching a maximum for the field extrema (minimum, i.e., 3.75 o.c. ($E < 0$); or maximum, i.e., 4.25 o.c. ($E > 0$)) of the external electric field and seems to disappear around the zero values of the external field (e.g., at 3.0 o.c.). Classical models of electron recollision predict such recollisions to occur near zero fields.[31,32] For the perpendicular configuration $\theta = 90°$, the first noticeable perturbation occurs after 1.75 o.c., where the field is negative. This is manifested by the lengthening or increased diffuseness of the lone-pair region on the sulfur atoms for CS_2. The perturbation is found symmetrically distributed; this effect reflects the fact that the sulfur atoms feel simultaneously or instantaneously the same effect of the laser field. As the time propagation evolves (3.75 and 4.25 o.c.), one sees that the dominant response comes from the lone-pair region. Most notably, one observes that, during the propagation, the electronic perturbation is characterized by an interaction between the outer lone pair and the inner bonding CS region and the perturbation disappears whenever the external electric field vanishes. Large depletion of electron density occurs at 2.25 and 4.25 o.c. in the opposite direction to that of the field and is illustrated as dark "holes" in Fig. 4*a*. Thus, in CS_2, the loss of an electron via ionization occurs in the lone-pair sp^2 hybrids of S. Simultaneously, the bonding C–S region expands opposite to the whole region.

TDELF of OCS

One of the most interesting points in the study of the OCS molecule with the TDELF function lies in the fact that its HOMO is nonsymmetric (as opposed to the CS_2 case) and is mainly located on two different atoms, oxygen (nearly 20%) and sulfur (nearly 70%), each bearing a different IP. In Fig. 4*b*, the oxygen is easily recognized by having one lobe, whereas the sulfur bears two owing to considerable sp^2 hybridization. For $\theta = 0°$, where the laser polarization and molecular axis are parallel, at 1.75 o.c. ($E < 0$) with a negative electric field and with electron displacement toward S, the perturbation appears on the lone-pair position of the oxygen atom. At 4.25 o.c. ($E > 0$) with a positive electric field, the results show that the perturbation now appears on the lone-pair region of the sulfur atom, whereas the corresponding lone-pair region on the oxygen atom has expanded owing to

Can. J. Chem. Downloaded from www.nrcresearchpress.com by Renmin University of China on 09/02/12
For personal use only.

electron transfer in that direction. As the propagation is evolving, the intensity of the perturbation on the lone-pair region is increasing as well, reaching a maximum at the electric field maxima or minima.

For $\theta = 90°$, the two atoms are feeling exactly the same laser intensity at the same time, and the ionization (see 1.75 and 2.25 o.c.) is much higher from the sulfur moiety than from the oxygen one, owing to the IP difference of the sulfur and the oxygen atoms. As expected, the perturbation on the different lone-pair regions is getting higher as the laser intensity is increasing. Figure 4*b* shows that the OCS behaves in the presence of the laser as a superposition of the moieties, one from CS_2 and the other from CO_2, giving rise to a nonsymmetric perturbation on the system when the laser is oriented parallel ($\theta = 0°$) or perpendicular ($\theta = 90°$) to the laser field. On the latter, a double-hole structure appears on the O moiety, as observed before in CO_2,[6] suggesting increasing sp^2 hybridization.

In conclusion, we find that at the lower intensity ($I = 3.50 \times 10^{14}$ W/cm^2) laser-peak intensity, the lone-pair region (HOMO) of linear molecules is the most affected by the field, in good agreement with our finding in the KS–MO ionization analysis in the previous section. For CS_2, the lower IP of the sulfur orbitals shows that these holes remain localized (Fig. 4*a*), reflecting rapid electron ionization (Fig. 2*b*) in the opposite direction to that of the laser-field phase. For the perpendicular orientation ($\theta = 90°$), the holes on each atom are split symmetrically as seen in Figs. 4*a* (CS_2) and 4*b* (OCS). On the latter, the O lone-pair distribution behaves distinctly differently from that of S owing to the smaller radius of the O orbitals.

Conclusion

The nonlinear nonperturbative TDDFT calculations presented in this paper for symmetric CS_2 and nonsymmetric OCS triatomics present a TDELF analysis of MO ionization at high laser intensities where linear TDDFT is not applicable. As major results, we find that at equilibrium distance R and at intensities $I > 3.5 \times 10^{14}$ W/cm^2, lower inner highest occupied molecular orbitals contribute significantly to ionization. This is due to the symmetry of these orbitals, even though such lower inner shell orbitals have higher IPs. At particular angles, ionization probabilities of different orbitals cross in magnitude. These findings are confirmed with the TDELF representation through the analysis in terms of density perturbations appearing on the TDELF images of each molecule. For $\theta = 0°$ and at a lower laser intensity ($I = 10^{14}$ W/cm^2), one sees that the HOMO is the most affected by the laser field and a large asymmetric density is found, i.e., one finds that during each half cycle, the laser perturbation occurs alternatively from one nucleus to another (favouring minimal interference), whereas for $\theta = 90°$, both nuclei simultaneously feel the same perturbation from the laser field (favouring maximal interference).[33] Our simulations also show that the local LB94 potential gives reliable orbital energies,[34] and IPs in near agreement with experimental data of individual orbitals, thus suggesting that the KS orbitals are close to Dyson orbitals,[21] which are the exact many-body orbitals for ionization. The relation between time-dependent Dyson and LB94 KS orbitals requires further exploration and also the effect of long range – short range correlation models on the nonlinear nonperturbative response[35] of molecules to intense laser pulses.

References

(1) Brabec, T.; Krausz, F. *Rev. Mod. Phys.* **2000**, *72* (2), 545. doi:10.1103/RevModPhys.72.545.
(2) Krausz, F.; Ivanov, M. Y. *Rev. Mod. Phys.* **2009**, *81* (1), 163. doi:10.1103/RevModPhys.81.163.
(3) Chelkowski, S.; Yudin, G. L.; Bandrauk, A. D. *J. Phys. At. Mol. Opt. Phys.* **2006**, *39* (13), S409. doi:10.1088/0953-4075/39/13/S14.
(4) Ullrich, C. A.; Bandrauk, A. D. In *Time-Dependent Density Functional Theory;* Marques, M. A. L.; Nogueira, F.; Rubio, A.; Burke, K.; Ullrich, C.A.; Gross, E. K. U., Eds.; Springer: Berlin, 2006; pp 357–374.
(5) Castro, A.; Werschnik, J.; Gross, E. K. U. Controlling the Dynamics of Many-Electron Systems from First Principles: A Marriage of Optimal Control and Time-Dependent Density-Functional Theory. Available from http://arxiv.org/abs/1009.2241, 2010.
(6) Fowe, E. P.; Bandrauk, A. D. *Phys. Rev. A* **2010**, *81* (2), 023411. doi:10.1103/PhysRevA.81.023411.
(7) Peters, M.; Nguyen-Dang, T.; Cornaggia, C.; Saugout, S.; Charron, E.; Keller, A.; Atabek, O. *Phys. Rev. A* **2011**, *83* (5), 051403. doi:10.1103/PhysRevA.83.051403.
(8) Talebpour, A.; Bandrauk, A. D.; Yang, J.; Chin, S. L. *Chem. Phys. Lett.* **1999**, *313* (5-6), 789. doi:10.1016/S0009-2614(99)01075-1.
(9) Hohenberg, P.; Kohn, W. *Phys. Rev.* **1964**, *136* (3B), B864. doi:10.1103/PhysRev.136.B864.
(10) Kohn, W.; Sham, L. J. *Phys. Rev.* **1965**, *140* (4A), A1133. doi:10.1103/PhysRev.140.A1133.
(11) Runge, E.; Gross, E. K. U. *Phys. Rev. Lett.* **1984**, *52* (12), 997. doi:10.1103/PhysRevLett.52.997.
(12) Nguyen, H. S.; Bandrauk, A. D.; Ullrich, C. A. *Phys. Rev. A* **2004**, *69* (6), 063415. doi:10.1103/PhysRevA.69.063415.
(13) van Leeuwen, R.; Baerends, E. J. *Phys. Rev. A* **1994**, *49* (4), 2421. doi:10.1103/PhysRevA.49.2421.
(14) Banerjee, A.; Harbola, M. K. *Phys. Rev. A* **1999**, *60* (5), 3599. doi:10.1103/PhysRevA.60.3599.
(15) Toher, C.; Filippetti, A.; Sanvito, S.; Burke, K. *Phys. Rev. Lett.* **2005**, *95* (14), 146402. doi:10.1103/PhysRevLett.95.146402.
(16) Madjet, M. E.; Chakraborty, H. S.; Rost, J. M. *J. Phys. B* **2001**, *34* (10), L345. doi:10.1088/0953-4075/34/10/106.
(17) Otobe, T.; Yabana, K.; Iwata, J.-I. *Phys. Rev. A* **2004**, *69* (5), 053404. doi:10.1103/PhysRevA.69.053404.
(18) Wijewardane, H. O.; Ullrich, C. A. *Phys. Rev. Lett.* **2008**, *100* (5), 056404. doi:10.1103/PhysRevLett.100.056404.
(19) Staroverov, V. N.; Glushkov, V. N. *J. Chem. Phys.* **2010**, *133* (24), 244104. doi:10.1063/1.3521492.
(20) Lewenstein, M.; Balcou, P.; Ivanov, M.; L'Huillier, A.; Corkum, P. *Phys. Rev. A* **1994**, *49* (3), 2117. doi:10.1103/PhysRevA.49.2117.
(21) Ortiz, J. V. *Int. J. Quantum Chem.* **2004**, *100* (6), 1131. doi:10.1002/qua.20204.
(22) Brundle, C. R.; Baker, C.; Brundle, C. R.; Turner, D. W. *Int. J. Mass Spectrom. Ion Phys.* **1968**, *1* (4–5), 285. doi:10.1016/0020-7381(68)85005-3.
(23) Turner, D. W.; May, D. P. *J. Chem. Phys.* **1967**, *46* (3), 1156. doi:10.1063/1.1840783.
(24) Brundle, C. R.; Turner, D. W. *Int. J. Mass Spectrom. Ion Phys.* **1969**, *2* (3), 195. doi:10.1016/0020-7381(69)80018-5.

(25) Al-Joboury, M. I.; May, D. P.; Turner, D. W. *J. Chem. Soc.* **1965**, 6350. doi:10.1039/jr9650006350.
(26) Bandrauk, A. D.; Barmaki, S.; Kamta, G. L. In *Progress in Ultrafast Intense Laser Science;* Yamanouchi, K.; Chin, S. L.; Agostini, P.; Ferrante, G., Eds.; Springer: Tokyo, 2008; Vol. III.
(27) Brabec, T.; Coté, M.; Boulanger, P.; Ramunno, L. *Phys. Rev. Lett.* **2005**, *95* (7), 073001. doi:10.1103/PhysRevLett.95.073001.
(28) Becke, A. D.; Edgecombe, K. E. *J. Chem. Phys.* **1990**, *92* (9), 5397. doi:10.1063/1.458517.
(29) Lagmago Kamta, G.; Bandrauk, A. D. *Phys. Rev. A* **2007**, *75* (4), 041401. doi:10.1103/PhysRevA.75.041401.
(30) Tong, X.; Zhao, Z.; Lin, C. *Phys. Rev. A* **2002**, *66* (3), 033402. doi:10.1103/PhysRevA.66.033402.
(31) Corkum, P. B. *Phys. Rev. Lett.* **1993**, *71* (13), 1994. doi:10.1103/PhysRevLett.71.1994.
(32) Bandrauk, A. D.; Chelkowski, S.; Goudreau, S. *J. Mod. Opt.* **2005**, *52* (2–3), 411. doi:10.1080/09500340410001729582.
(33) Zuo, T.; Bandrauk, A. D.; Corkum, P. B. *Chem. Phys. Lett.* **1996**, *259* (3–4), 313. doi:10.1016/0009-2614(96)00786-5.
(34) Son, S.-K.; Chu, S.-I. *Chem. Phys.* **2009**, *91*, 366.
(35) Toulouse, J.; Colonna, F.; Savin, A. *Phys. Rev. A* **2004**, *70* (6), 062505. doi:10.1103/PhysRevA.70.062505.

Can. J. Chem. Downloaded from www.nrcresearchpress.com by Renmin University of China on 09/02/12
For personal use only.

Preparation of (*Z*)-1,2-dichloroalkenes from terminal alkynes

Ningzhang Zhou, Qiang Wang, Alan J. Lough, and Hongbin Yan

Can. J. Chem. Downloaded from www.nrcresearchpress.com by Renmin University of China on 09/02/12
For personal use only.

Abstract: (*Z*)-1,2-Dihaloalkenes are thermodynamically disfavoured of the two stereoisomers. This paper reports the synthesis of some (*Z*)-1,2-dichloroalkene analogues from mucochloric acid. A more versatile approach involved the chloroboration of terminal alkynes to yield corresponding (*Z*)-chloroboronic acid as a first step. Treatment of the organoboronic acid with potassium hydrogen difluoride followed by tetrabutylammonium trichloride gave (*Z*)-1,2-dichloroalkenes in moderate to good yields in a stereospecific manner.

Key words: cis-dichloroalkene, chloroboration, chlorodeboronation, NOE, terminal alkyne.

Résumé : Dans les séries de 1,2-dihalogénoalcènes, les isomères (*Z*)- sont thermodynamiquement défavorisés. Dans ce travail, on a réalisé la synthèse de quelques analogues de (*Z*)-1,2-dichloroalcènes à partir de l'acide mucochlorique. Une approche encore plus versatile implique une première étape de chloroboration d'alcynes terminaux qui conduit à l'acide (*Z*)-chloroboronique correspondant. Le traitement de l'acide organoboronique avec du difluorure de potassium et d'hydrogène, suivi d'une réaction avec du trichlorure de tétrabutylammonium fournit les (*Z*)-1,2-dichloroalcènes d'une manière stéréospécifique, avec des rendements allant de modérés à bons.

Mots-clés : cis-dichloroalcène, chloroboration, chlorodéboronation, effet Overhauser nucléaire (EN), alcyne terminal.

[Traduit par la Rédaction]

Introduction

1,2-Dihaloalkenes are useful precursors in organic synthesis, particularly in the carbon–carbon bond-forming reactions.[1] Of the two stereoisomers, (Z)-isomers have found applications in reactions such as the Bergman cyclization.[2] In this respect, challenges remain in the preparation of 1,2-(*Z*)-dihaloalkenes as the (E)-isomers are thermodynamically favoured and are formed predominantly in direct electrophilic halogenation of alkynes.[3–5] A few methods have been reported for the stereoselective synthesis of 1,2-dihaloalkenes,[6–9] including a recent report on the synthesis of (*Z*)-dibromoalkenes by a bromodeboronation sequence of potassium bromoalkenyl – trifluoroborates;[10] however, as far as we are concerned, the only known reliable stereospecific approach to (*Z*)-1,2-dichloroalkene derivatives is the use of mucochloric acid (**1**) as the starting material.[11] We now report a chlorodeboronation methodology that is applicable to the synthesis of (*Z*)-1,2-dichloroalkenes.

Results and discussion

Synthesis of (*Z*)-1,2-dichloroalkenes from mucochloric acid

As mentioned previously, the only known stereospecific method for the preparation of (*Z*)-1,2-dichloroalkenes utilized mucochloric acid (**1**) as starting material. Upon treatment with sodium hydroxide, 2,3-(*Z*)-dichloropropenoic acid (**2**) was obtained. This latter compound can be transformed into corresponding alcohol **3**, allyl chloride **4**, anhydride **5**, or ester **6** (Scheme 1). However, this process is rather limited in scope, requiring complex transformations to access higher carbon derivatives.

Stereoselectivity of bromodeboronation reaction from potassium bromoalkenyl – trifluoroborates

It was recently shown[10] that (*Z*)-1,2-dibromoalkenes can be prepared in a stereospecific manner from a sequence of transformations using terminal alkynes as starting materials. This approach (Scheme 2) begins with the addition of boron tribromide across the triple bond to give (*Z*)-bromovinylboron dibromide (**8**).[12] Upon hydrolysis, bromovinylboronic acid (**9**) was obtained, which was subsequently transformed into corresponding potassium trifluoroborate (**10**) by treatment with potassium hydrogen difluoride.[10,12] Final bromodeboronation with tetrabutylammonium tribromide gave (*Z*)-1,2-dibromoalkenes (**11**) with retention of stereochemistry.[10]

With a model compound ((*Z*)-3,4-dibromobutenyl *p*-tosylate, **12**), we were able to confirm the stereochemistry with crystal

Received 20 January 2012. Accepted 15 May 2012. Published at www.nrcresearchpress.com/cjc on 11 July 2012.

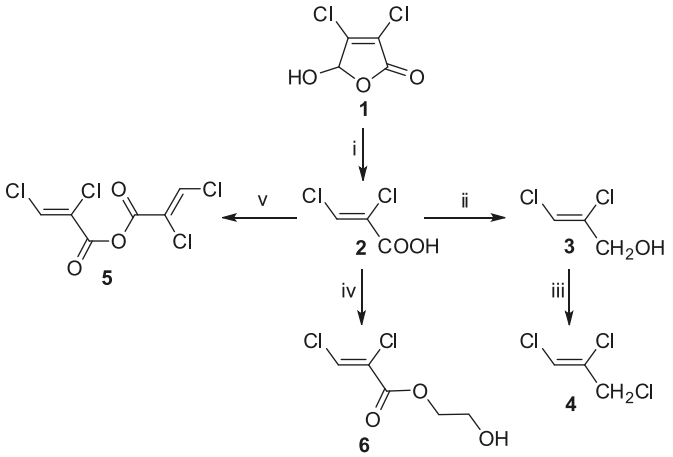
N. Zhou* and H. Yan. Department of Chemistry, Brock University, 500 Glenridge Ave, St. Catharines, ON L2S 3A1, Canada.
Q. Wang.* Department of Chemistry, Brock University, 500 Glenridge Ave, St. Catharines, ON L2S 3A1, Canada; Current address: School of Chemistry and Chemical Engineering, Wuhan Textile University, Wuhan 430073, China.
A.J. Lough. Department of Chemistry, University of Toronto, 80 St. George Street, Toronto, ON M5S 3H6, Canada.

Corresponding author: Hongbin Yan (e-mail: tyan@brocku.ca).

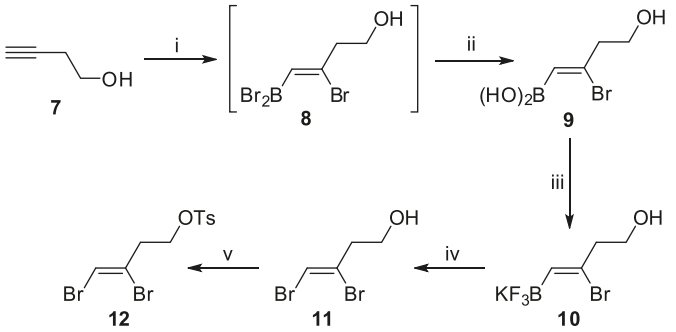
*These authors contributed equally to this work.

Can. J. Chem. Downloaded from www.nrcresearchpress.com by Rennmin University of China on 09/02/12
For personal use only.

Scheme 1. Reagents and conditions: (*i*) aq NaOH and then aq HCl; (*ii*) $LiAlH_4$, Et_2O; (*iii*) $SOCl_2$, C_5H_5N, CH_2Cl_2; (*iv*) $HOCH_2CH_2OH$, DCC; (*v*) DCC, Et_2O.



Scheme 2. Reagents and conditions: (*i*) BBr_3, CH_2Cl_2; (*ii*) aq $NaHCO_3$; (*iii*) KHF_2, CH_3OH, H_2O; (*iv*) $Bu_4N^+Br_3^-$, aq THF; (*v*) TsCl, C_5H_5N.



structure (Fig. 1), where the two bromines are clearly in a Z-configuration.

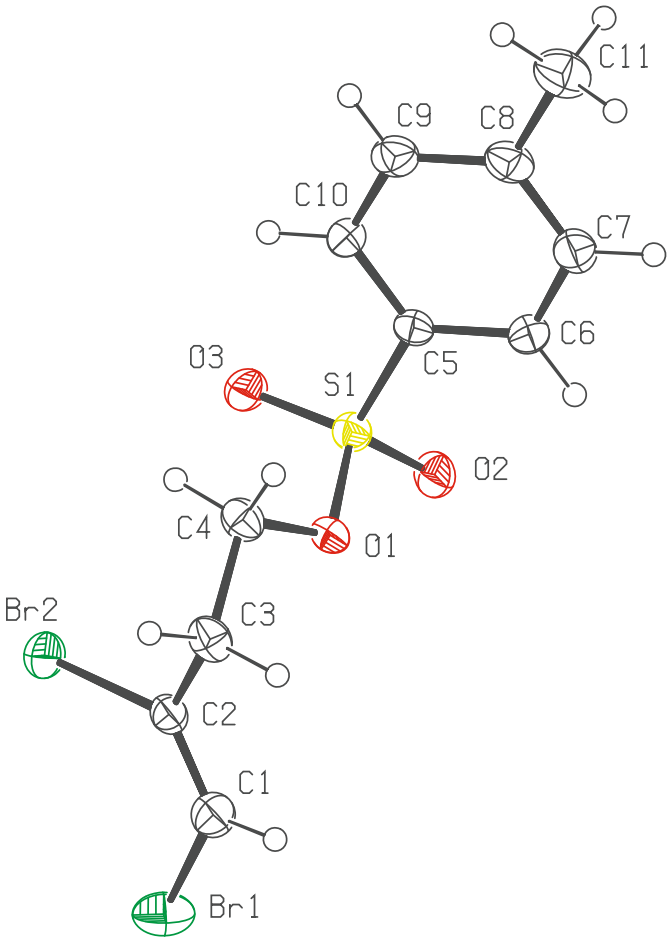
The chemistry described in this section extends its scope to both aliphatic and aromatic alkynes and therefore represents a versatile approach for the access of (*Z*)-1,2-dibromoalkenes.

Preparation of (*Z*)-1,2-dichloroalkenes from terminal alkynes

In our search for suitable 1,2-dihaloalkenes as Sonogashira reaction precursors, a versatile approach for the synthesis of (*Z*)-1,2-dichloroalkenes was required. It occurred to us that it is highly likely that a strategy similar to the bromodeboronation sequence described previously would provide access to the desired (*Z*)-1,2-dichloroalkenes. Indeed, it was reported previously that treatment of phenylacetylene with boron trichloride gave corresponding (2-chloro-2-phenylvinyl)dichloroborane.[14] To our satisfaction, this approach gave (*Z*)-1,2-dichloroalkenes from terminal alkynes in moderate to good yields and in a stereospecific manner (Scheme 3).

The transformations began with the treatment of terminal alkynes with boron trichloride, followed by hydrolysis to give corresponding chlorovinylboronic acid (**15**). Upon formation of the corresponding potassium trifluoroborate (**16**), chlorodeboronation was effected using tetrabutylammonium

Fig. 1. The molecular structure of (*Z*)-3,4-dibromobutenyl *p*-tosylate (**12**) with 30% probability displacement ellipsoids (prepared with PLATON).[13]



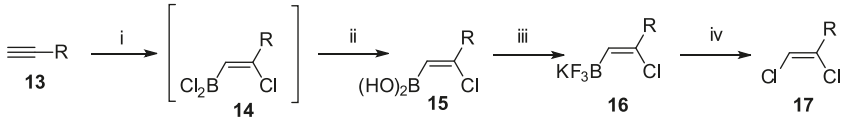
trichloride. This latter reagent is not commercially available, however, it can be readily prepared as a stable solid by bubbling chlorine gas into a solution of tetrabutylammonium chloride in dichloromethane.[15,16] The results for chlorodeboronation of some substrates are shown in Table 1. It is noted that some of the lower yields shown in Table 1 were most likely due to the relatively low boiling points of the products.

To illustrate the stereochemistry of the transformations, 3,4-(*E*)-dichlorobutenol (**18**) was prepared using a literature procedure.[3] Thus, treatment of 3-alkynol with copper(II) chloride and lithium chloride (Scheme 4) gave **18** almost as the sole product.

The two stereoisomers **17a** and **18** displayed different ^1H NMR chemical shifts (Fig. 2*a*), and in NOE experiments, the clear NOE signal present in **17a**, which is absent in **18**, clearly confirmed the (Z)-configuration.

The utility of this method can be extended to the preparation of 1,2-(*Z*)-bromochloro (or chlorobromo) alkenes from 1,2-terminal alkynes. As exemplified in Scheme 5, treatment of 4-bromo-1-butyne (**19**) with either BCl_3 or BBr_3 followed by hydrolysis gives the corresponding (*Z*)-2-chloro-4-bromo-1-butenylboronic acid (**15e**) or (*Z*)-2-bromo-4-bromo-1-butenylboronic acid (**20**). Transformation of these two organoboronic acids into the corresponding potassium trifluoroborates

Scheme 3. Reagents and conditions: (*i*) BCl_3, CH_2Cl_2; (*ii*) H_2O; (*iii*) KHF_2, CH_3OH, H_2O; (*iv*) $Bu_4N^+Cl_3^-$, aq THF.

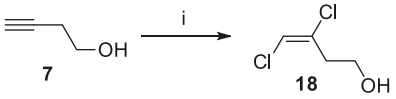


a) R = -CH_2CH_2OH; **b)** R = -Ph; **c)** R = -CH_2OH;
d) R = -$(CH_2)_5CH_3$; **e)** R = -CH_2CH_2Br

Table 1. Chlorodeboronation **16** → **17**.

Entry (product)	R	Yield (%)
1 (**17a**)	–CH_2CH_2OH	51
2 (**17b**)	–Ph	84
3 (**17c**)	–CH_2OH	45
4 (**17d**)	–$(CH_2)_5CH_3$	77
5 (**17e**)	–CH_2CH_2Br	62

Scheme 4. Reagents and conditions: (*i*) $CuCl_2$, LiCl, CH_3CN.



16e and **21**, respectively, was readily effected by treatment with potassium hydrogen difluoride. Subsequent bromo- (or chloro-) deboronation gave 1,2-(*Z*)-bromochloro (or chlorobromo) alkenes **23** and **22**, respectively. It is anticipated that these 1,2-(*Z*)-dihaloalkenes could find synthetic utilities in sequential coupling reactions because of the different reactivity between vinyl chlorides and bromides. This aspect of the application is being explored in our laboratory to access the enediyne moieties with different substituents on 1,2-alkenes.

Conclusion

In conclusion, tetrabutylammonium trichloride-based chlorodeboronation of potassium bromoalkenyl trifluoroborates represents an efficient approach to the synthesis of (*Z*)-1,2-dichloroalkenes from terminal alkynes. This method provides access to these thermodynamically less stable alkenes as important synthetic intermediates.

Experimental details

^1H NMR spectra were measured at 300 and 600 MHz with Bruker AV300 and AV600 spectrometers, respectively; tetramethylsilane was used as an internal standard; *J* values are given in Hz. ^{13}C NMR spectra were measured at 75.5 or 150.9 MHz with the same spectrometers. Chemical shifts are given in ppm. Low- and high-resolution mass spectra were obtained with a Kratos Concept 1S high-resolution mass spectrometer using electron impact or fast atom bombardment sources interfaced with a DART 32 bit acquisition system through a Sun Sparcstation 10 and Mach 3 software. Desican 230–400 mesh silica gel 60 was used for flash column chromatography. Chemicals were purchased from Sigma-Aldrich or TCI America and used without further purification unless stated otherwise. Dichloromethane, diethyl ether, and tetrahydrofuran were purified by a Pure-Solv solvent purification system (Innovative Technology), and stored over activated 4 Å molecular sieves.

Experimental procedures for the synthesis of **17a** and corresponding intermediates are described in the following. Synthetic procedures for **17b–17d** and corresponding intermediates can be found in the Supplementary data.

(*Z*)-2-Chloro-4-hydroxy-1-butenylboronic acid (15a)

To a solution of boron trichloride in dichloromethane (1 mol/L, 8.0 mL, 8.0 mmol) was added dropwise a solution of 3-butyn-1-ol (0.48 g, 6.85 mmol) in dry dichloromethane (10 mL) at 0 °C under nitrogen. After the reaction mixture was stirred for 20 h at room temperature, the products were transferred via cannulation to a stirred mixture of diethyl ether and water (20 mL, 1:1 *v*/*v*) at 0 °C. The resulting mixture was stirred for 4 h at room temperature and then concentrated to dryness under reduced pressure. The residue was purified by column chromatography on silica gel. The appropriate fractions, which were eluted with dichloromethane, were pooled and concentrated under reduced pressure to yield the title compound as a colourless oil (0.48 g, 47%). δ_H (D_2O): 2.47 (2 H, t, J = 5.8 Hz), 3.63 (2 H, t, J = 5.9 Hz), 5.49 (s, 1H). δ_C (D_2O): 43.9, 58.5, 120.6 (br), 145.6.

Potassium (*Z*)-2-chloro-4-hydroxy-1-butenyl trifluoroborate (16a)

To a solution of the organoboronic acid **15a** (0.31 g, 2.06 mmol) in methanol (8 mL) was added dropwise a solution of potassium hydrogen difluoride (0.80 g, 10.2 mmol) in water (8 mL) at 0 °C. After the reaction mixture was stirred at room temperature for 3 h, the products were concentrated to dryness under reduced pressure. The resulting solid was extracted with acetone (5 × 30 mL), aided by sonication. The acetone extracts were combined and evaporated at room temperature under reduced pressure to give the title compound as a light brown solid (0.31 g, 1.44 mmol, 71%). δ_H (D_2O): 2.48 (2 H, t, J = 6.1 Hz), 3.69 (2 H, t, J = 6.1 Hz), 5.44 (1 H, q, J = 4.5 Hz). δ_C (D_2O): 44.1, 59.0, 129.0 (br), 138.7 (q).

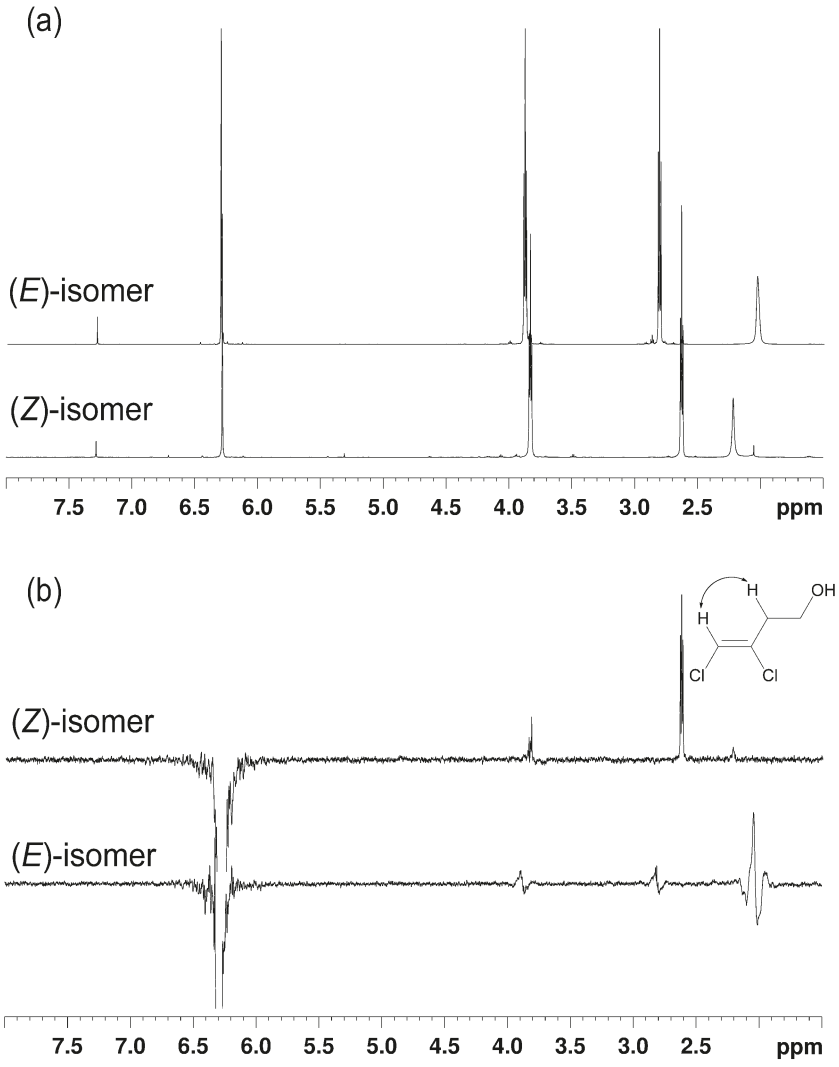
(*Z*)-3,4-Dichloro-3-buten-1-ol (17a)

To a solution of potassium trifluoroborate **16a** (0.20 g, 0.94 mmol) in aqueous tetrahydrofuran (12 mL, 1:1 *v*/*v*) was added tetrabutylammonium trichloride (0.68 g, 1.95 mmol) at room temperature. After the mixture was stirred for 3 h, the products were diluted with water (20 mL) and extracted with dichloromethane (3 × 30 mL). The combined organic layers were dried ($MgSO_4$) and concentrated under reduced pressure. The residue was purified by column chromatography on silica gel. Evaporation of the combined fractions, which

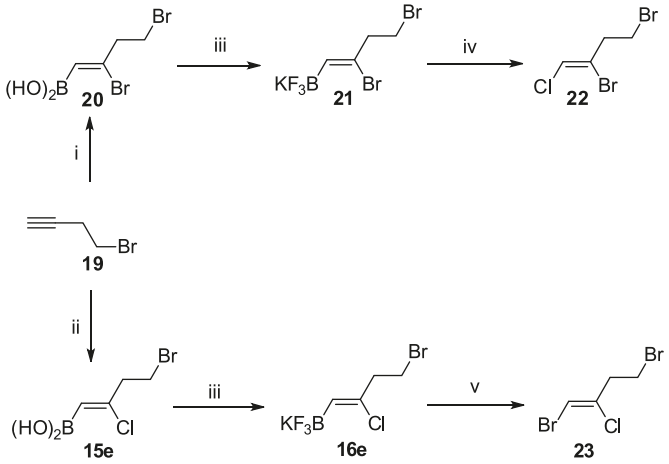
Can. J. Chem. Downloaded from www.nrcresearchpress.com by Renmin University of China on 09/02/12
For personal use only.

Can. J. Chem. Downloaded from www.nrcresearchpress.com by Renmin University of China on 09/02/12
For personal use only.

Fig. 2. NMR spectra of the (Z)- and (E)-stereoisomers **17a** and **18**. (*a*) ^{1}H NMR spectra of **17a** and **18**. (*b*) NOE of **17a** and **18**.



Scheme 5. Reagents and conditions: (*i*) (*a*) BBr_3, CH_2Cl_2; (*b*) H_2O; (*ii*) (*a*) BCl_3, CH_2Cl_2; (*b*) H_2O; (*iii*) KHF_2, CH_3OH, H_2O; (*iv*) $Bu_4N^+Cl_3^-$, aq THF; (*v*) $Bu_4N^+Br_3^-$, aq THF.



were eluted with hexanes – ethyl acetate (9:1 *v*/*v*), gave the title compound as a colourless oil (68 mg, 51%). δ_H ($CDCl_3$): 2.18 (1 H, s), 2.62 (2 H, t, J = 5.8 Hz), 3.83 (2 H, t, J = 5.9 Hz), 6.28 (s, 1H). δ_C ($CDCl_3$): 40.7, 59.2, 115.7, 133.8. HR-MS (EI) calcd for $C_4H_6Cl_2O$: 139.97957; found: 139.97914.

(*Z*)-2,3-Dichloropropenoic acid (**2**)

To a cooled (ice water bath) solution of sodium hydroxide in distilled water (24.00 g NaOH in 120 mL water, 0.600 mol) was added mucochloric acid (40.00 g, 0.237 mol) in small portions to maintain a light yellow mixture. The resulting clear yellow solution was heated at 50 °C for 2 h. Upon cooling (ice water bath), concentrated hydrochloric acid (37%, 40 mL) was added slowly under stirring. After the reaction mixture was stirred for 1 h at 0 °C, the solid that formed was collected by filtration, followed by washing with small portions of ice-cold water (2 × 30 mL). The pale yellow solid was dissolved in diethyl ether (50 mL) and dried ($MgSO_4$). Evaporation of solvents under reduced pressure gave the title compound as a yellow oil that solidified upon standing as a creamy solid (23.3 g, 70%). δ_H ($CDCl_3$): 7.83 (1 H, s), 10.57 (1 H, s). δ_C ($CDCl_3$): 126.8, 135.4, 166.3. HR-MS (EI) calcd for $C_3H_2O_2Cl_2$: 139.94318; found: 139.94348.

Can. J. Chem. Downloaded from www.nrcresearchpress.com by Renmin University of China on 09/02/12
For personal use only.

Reduction of (*Z*)-2,3-dichloropropenoic acid (2) to (*Z*)-1,2-dichloro-3-hydroxy-1-propene (17c or **3**)

To a cooled (ice water bath) suspension of lithium aluminum hydride (0.84 g, 95% purity, 21 mmol) in dry diethyl ether (20 mL) was added dropwise a solution of (*Z*)-2,3-dichloropropenoic acid (**2**, 3.00 g, 21.3 mmol) in dry diethyl ether (20 mL). After stirring, first at 0 °C for 20 min and then at room temperature for 2 h, the reaction mixture was cooled (ice water bath), followed by sequential addition of methanol (0.5 mL) and water (20 mL). When the evolution of hydrogen gas ceased, dilute hydrochloric acid (approximately 3 N) was added to acidify the mixture until all precipitate dissolved. The layers were separated and the aqueous layer was back-extracted with diethyl ether (50 mL). The combined organic layers were washed with brine (2 × 20 mL), dried ($MgSO_4$), and evaporated under reduced pressure. The residue was distilled to give (*Z*)-1,2-dichloro-3-hydroxy-1-propene as a colourless oil (1.62 g, 45–48 °C/2 mm Hg (1 mm Hg = 133.3224 Pa), 61%). The NMR spectra were identical to those of **17c**.

(*Z*)-1,2,3-Trichloro-propene (4)

To a cooled (ice water bath) solution of (*Z*)-1,2-dichloro-3-hydroxy-1-propene (**3**, 3.00 g, 23.6 mmol) in dry dichloromethane (12 mL) and dry pyridine (2.7 mL) was added dropwise thionyl chloride (2.4 mL, 33 mmol). After the reaction mixture was stirred, first at 0 °C for 20 min and then at room temperature for 2 h, nitrogen gas was bubbled into the reaction mixture. The products were then evaporated under reduced pressure, and the residue was extracted with diethyl ether (3 × 50 mL). The combined ether layers were concentrated under reduced pressure. The residue was purified by column chromatography on silica gel. The appropriate fractions, which were eluted with hexanes–dichloromethane (3:2 *v*/*v*), were evaporated under reduced pressure to give the title compound as a colourless oil (1.30 g, 38%). δ_H ($CDCl_3$): 4.67 (2 H, s), 6.64 (1 H, s). δ_C ($CDCl_3$): 63.5, 120.9, 130.7. HR-MS (EI) calcd for $C_3H_3Cl_3$: 143.93003; found: 143.92975.

(*Z*)-3,4-Dibromo-3-buten-1-tosylate (12)

To a cold (ice water bath) solution of (*Z*)-3,4-dibromo-3-buten-1-ol (**11**,[10] 0.20 g, 0.87 mmol) in dry pyridine (3.5 mL) was added *p*-tosyl chloride (0.33 g, 1.73 mmol). After 24 h, the products were concentrated under reduced pressure, and the residue was taken up in dichloromethane (20 mL) and washed successively with water (20 mL) and brine (20 mL), and dried ($MgSO_4$). Evaporation of solvents gave a yellow oil that was purified by column chromatography on silica gel. The appropriate fractions, which were eluted with petroleum ether – ethyl acetate (9:1 *v*/*v*), were combined and evaporated under reduced pressure to give the title compound as a colourless oil that solidified upon standing (0.15 g, 45%). δ_H ($CDCl_3$): 2.47 (3 H, s), 2.84 (2 H, dt, J = 1.1 and 6.0 Hz), 4.21 (2 H, t, J = 6.0 Hz), 6.69 (1 H, t, J = 1.1 Hz), 7.27 (2 H, d, J = 8.0 Hz), 7.78 (2 H, d, J = 8.0 Hz). δ_C ($CDCl_3$): 21.7, 40.5, 66.6, 109.6, 127.2, 128.0, 130.0, 132.7, 145.1. HR-MS (EI) calcd for $C_{11}H_{12}O_3Br_2S$: 383.88547; found: 383.88595.

Single crystal growth: Single crystals of the tosylate **12** were obtained by slow evaporation of a solution of **12** in hexanes.

X-ray diffraction experiment

Data were collected on a Nonius Kappa-CCD diffractometer using monochromated Mo Kα radiation and were measured using a combination of ϕ scans and ω scans with κ offsets, to fill the Ewald sphere. The data were processed using the Denzo-SMN package.[17] Absorption corrections were carried out using SORTAV.[18] The structure was solved and refined using SHELXTL V6.1[19] for full-matrix least-squares refinement that was based on F^2. All H atoms were included in the calculated positions and allowed to refine in riding-motion approximation with U_{iso} tied to the carrier atom.

Supplementary data

Supplementary data are available with the article through the journal Web site at http://nrcresearchpress.com/doi/suppl/10.1139/v2012-041. CCDC 859121 contains the X-ray data in CIF format for this manuscript. These data can be obtained, free of charge, via http://www.ccdc.cam.ac.uk/products/csd/request (Or from the Cambridge Crystallographic Data Centre, 12 Union Road, Cambridge CB2 1EZ, UK; fax: +44 1223 33603; or e-mail: depost@ccdc.cam.ac.uk.

Conclusion

In conclusion, an approach for the synthesis of the thermodynamically disfavoured (*Z*)-1,2-dichloroalkenes was developed. Chloroboration of terminal alkynes gives corresponding (*Z*)-chloroboronic acids, which are readily transformed into potassium trifluoro organoborate. Subsequent chlorodeboronation gives (*Z*)-1,2-dichloroalkenes in a stereospecific manner.

Acknowledgments

The authors thank the Natural Sciences and Engineering Research Council of Canada (NSERC) for funding this work.

References

(1) Nubbemeyer, U. *Sci. Synth.* **2008**, *32*, 57.
(2) Basak, A.; Mandal, S.; Bag, S. S. *Chem. Rev.* **2003**, *103* (10), 4077. doi:10.1021/cr020069k.
(3) Uemura, S.; Okazaki, H.; Onoe, A.; Okano, M. *J. Chem. Soc., Perkin Trans. 1* **1977**, (6), 676. doi:10.1039/p19770000676.
(4) Uemura, S.; Okazaki, H.; Okano, M. *J. Chem. Soc., Perkin Trans. 1* **1978**, (11), 1278. doi:10.1039/p19780001278.
(5) Kodomari, M.; Sakamoto, T.; Yoshitomi, S. *Bull. Chem. Soc. Jpn.* **1989**, *62* (12), 4053. doi:10.1246/bcsj.62.4053.
(6) Hénaff, N.; Whiting, A. *J. Chem. Soc., Perkin Trans. 1* **2000**, (3), 395. doi:10.1039/a906832e.
(7) Hara, S.; Kato, T.; Shimizu, H.; Suzuki, A. *Tetrahedron Lett.* **1985**, *26* (8), 1065. doi:10.1016/S0040-4039(00)98513-7.
(8) Chen, Z.; Jiang, H.; Li, Y.; Qi, C. *Chem. Commun. (Camb.)* **2010**, *46* (42), 8049. doi:10.1039/c0cc02156c.
(9) Chen, D.; Cao, Y.; Yuan, Z.; Cai, H.; Zheng, R.; Kong, L.; Zhu, G. *J. Org. Chem.* **2011**, *76* (10), 4071. doi:10.1021/jo102406j.
(10) Yao, M.-L.; Reddy, M. S.; Yong, L.; Walfish, I.; Blevins, D. W.; Kabalka, G. W. *Org. Lett.* **2010**, *12* (4), 700. doi:10.1021/ol9027144.

(11) Schaefer, B., Haunert, F., Goetz, N. 2007. US 2007/0037978: A1.
(12) Yao, M.-L.; Reddy, M. S.; Zeng, W.; Hall, K.; Walfish, I.; Kabalka, G. W. *J. Org. Chem.* **2009**, *74* (3), 1385. doi:10.1021/jo802207y.
(13) Spek, A. L. *Acta Crystallogr. D Biol. Crystallogr.* **2009**, *65* (2), 148. doi:10.1107/S090744490804362X.
(14) Lappert, M. F.; Prokai, B. *J. Organomet. Chem.* **1964**, *1* (5), 384. doi:10.1016/S0022-328X(00)80030-3.
(15) Schlama, T.; Gabriel, K.; Gouverneur, V.; Mioskowski, C. *Angew. Chem. Int. Ed. Engl.* **1997**, *36* (21), 2342. doi:10.1002/anie.199723421.
(16) Kajigashi, S.; Shimizu, M.; Moriwaki, M.; Fujisaki, S.; Kakinami, T. *Yamaguchi Univ. Tech. Rep.* **1989**, *4* (3), 237.
(17) Otwinowski, Z.; Minor, W. *Methods in Enzymology;* Macromolecular Crystallography, Part A, Vol. 276; Carter, C. W., Sweet, R. M., Eds.; London: Academic Press, 1997; pp 307–326.
(18) Blessing, R. H. *Acta Crystallogr. A* **1995**, *51* (1), 33. doi:10.1107/S0108767394005726.
(19) Sheldrick, G. M. *Acta Crystallogr. A* **2008**, *64* (1), 112. doi:10.1107/S0108767307043930.

Can. J. Chem. Downloaded from www.nrcresearchpress.com by Renmin University of China on 09/02/12
For personal use only.

Ab initio calculation of the low-lying electronic states of the ZrN molecule

A. Farhat, M. Korek, M.A.L. Marques, and S.N. Abdul-Al

Can. J. Chem. Downloaded from www.nrcresearchpress.com by Renmin University of China on 09/02/12
For personal use only.

Abstract: An ab initio calculation of the low-lying electronic states of zirconium nitride (ZrN) were performed by using a complete active space self-consistent field with multireference single and double excitation configuration interaction (MRSDCI). The potential energy curves of 21 low-lying electronic states of the ZrN molecule with different spin and spatial symmetries, in the representation $^{2s+1}\Lambda^{(+/-)}$ and below 30 000 cm^{-1}, were identified. The harmonic frequency (ω_e), the equilibrium internuclear distance (R_e), the rotational constants (B_e), the electronic energy with respect to the ground state (T_e), and the permanent dipole moment (μ) were calculated for the considered electronic states. The comparison of these values with those available in the literature shows a very good agreement with either theoretical or experimental data. Fifteen new electronic states were studied here for the first time.

Key words: ab initio calculation, electronic structure, spectroscopic constants, potential energy curves.

Résumé : On a fait des calculs ab initio des états électroniques de faible intensité du nitrure de zirconium (ZrN) en utilisant un champ auto-cohérent avec un espace complètement actif et des interactions de configuration à excitation simple et double à multiples références (« MRSDCI »). On a identifié les courbes d'énergie potentielle de vingt et un états électroniques de faible intensité de la molécule de ZrN avec divers spins et symétries spatiales, de représentation $^{2s+1}\Lambda^{(+/-)}$ et apparaissant en-dessous de 30 000 cm^{-1}. On a calculé la fréquence harmonique (ω_c), la distance internucléaire d'équilibre (R_c), les constantes rotationnelles (B_c), l'énergie électronique par rapport à l'état fondamental (T_c), ainsi que le moment dipolaire permanent (μ), de chacun des états électroniques considérés. La comparaison de ces valeurs avec celles rapportées dans la littérature montre qu'il existe un bon accord entre les valeurs expérimentales et théoriques. Quinze nouveaux états électroniques ont été étudiés pour la première fois.

Mots-clés : calculs ab initio, structure électronique, constantes spectroscopiques, énergie potentielle, courbes.

[Traduit par la Rédaction]

Introduction

The zirconium nitride molecule (ZrN) is one of the transition-metal nitrides (TMNs), which are metallic compounds with outstanding physical properties. They are chemically very stable with high corrosion resistance, high melting temperatures, and are extremely hard.[1] These TMNs are widely used in information storage technology, cutting tools, high power energy industry, and optoelectronics. ZrN has a cubical crystal structure where the metallic atoms form the face-centered cubic lattice and nonmetallic atoms occupy the interstitial positions.[2–13] The nitrides of group IV metals are finding increased importance in the semiconductor industry. Titanium, zirconium, and hafnium nitrides are excellent diffusion barrier layers in silicon semiconductors because of their slow diffusion rates and high conductivity. In recent years, the electronic structures, dynamics of formation, and bonding in bulk and gas-phase cluster materials have become of significant interest to materials scientists and chemists.[14–17] In industrial processes, ZrN is one of the materials that has the best mechanical properties and is deposited by physical vapor deposition to coat medical devices, industrial parts, automotive and aerospace components, and other parts subject to high wear and corrosive environments.[18–21]

Some of the transition-metal elements are known to occur in S- and M-type stars in the form of metal monoxides.[22] It is possible that the corresponding TMNs are also present in a stellar atmosphere. Transition-metal-containing diatomics represent simple metal systems where d electrons participate in the bonding.[22] These molecules provide models for understanding the bonding and reactivity in transition-metal systems.[23] The spectroscopic study of this transition-metal diatomic is difficult particularly because of the high density of the low-lying electronic states associated with partially occupied d orbitals[24,25] to the large nuclear spin associated with transition-metal atoms, which could give rise to complex magnetic hyperfine structure patterns in the spectra of these molecules.[26–28] Although the electronic structure of many gaseous transition-metal oxides, carbides, and hydrides are relatively well-characterized, only a few nitrides are known.

Received 12 March 2012. Accepted 26 April 2012. Published at www.nrcresearchpress.com/cjc on 11 July 2012.

A. Farhat and M.A.L. Marques. Université de Lyon, F-69000 Lyon, France and LPMCN, CNRS, UMR 5586, Université Lyon 1, F-69622 Villeurbanne, France.
M. Korek. Faculty of Science, Beirut Arab University, P.O. Box 11-5020 Riad El Solh, Beirut 1107 2809, Lebanon.
S.N. Abdul-Al. Faculty of Science, Lebanese International University, Museitbeh, Beirut, Lebanon.

Corresponding author: M. Korek (e-mail: fkorek@yahoo.com).

Can. J. Chem. Downloaded from www.nrcresearchpress.com by Renmin University of China on 09/02/12
For personal use only.

Table 1. Calculated spectroscopic constants for the lowest lying 20 doublet and quartet states of the ZrN molecule.

State	T_e (cm^{-1})	$\Delta T_e/T_e$ (%)	ω_e (cm^{-1})	$\Delta\omega_e/\omega_e$ (%)	$B_e \times 10$ (cm^{-1})	$\Delta B_e/B_e$ (%)	$D_e \times 10^7$ (cm^{-1})	$\Delta D_e/D_e$ (%)	R_e (Å)	$\Delta R_e/R_e$ (%)
$X^2\Sigma^+$	0[a]		982.79[a]		4.6258		4.0939		1.7314[a]	
	0[b–k]		1015[Theo.b]	3.1	4.7816[Exp.e]	3.2	4.55[Exp.e]	10	1.7023[Exp.b]	1.7
			1002.6[Exp.c]	1.9	4.8052[Exp.f]	3.7	4.54[Exp.f]	9.8	1.6943[Exp.e]	2.1
			1002.2[Exp.d]	1.9	4.7981[Exp.g]	3.5	4.515[Exp.g]	9.3	1.6954[Exp.h]	2.1
			1030[Exp.d]	4.5	4.8406[Exp.h]	4.4	4.53[Exp.h]	9.6	1.7[Exp.i]	1.8
			991[Exp.j]	0.8	4.83[Exp.i]	2.1				
$(1)^2\Delta$	7580.02		920.97		4.5095		4.3219		1.7545	
	8531[Theo.b]	11	944[Theo.b]	2.4					1.7228[Theo.b]	1.8
$(1)^2\Pi$	16317.00		929.20		4.6209		4.5793		1.7325	
	16747[Theo.b]	2.5	1004[Theo.b]	7.4	4.5870[Exp.b]	3.4	5.61[Exp.e]	18.3	1.7000[Theo.b]	1.9
	17401[Exp.k]	6.2	973[Exp.d]	4.5	4.7508[Exp.e]	2.7	5.54[Exp.f]	17	1.7062[Exp.d]	1.5
	17318.76[Exp.e]	5.7			4.7601[Exp.f]	2.9				
	16905.1[Exp.f]	3.4								
$(1)^4\Delta$	16477.72		844.59		4.1450		3.9891		1.8303	
	17026[Theo.b]	3.2	828[Theo.b]	2.0					1.8033[Theo.b]	1.4
$(1)^4\Pi$	16621.60		763.27		3.8515		3.9298		1.8989	
$(1)^4\Phi$	16708.48		768.29		3.8327		3.8202		1.9032	
$(1)^2\Phi$	16879.49		746.89		3.7785		3.8696		1.9163	
$(2)^2\Delta$	17494.25		727.12		4.1080		5.3288		1.8385	
$(2)^2\Sigma^+$	17595.15		959.83		4.1331		3.0601		1.8329	
	16228[Theo.b]	8.4	935[Theo.b]	2.6	4.587[Exp.i]	9.8			1.7789[Theo.b]	3.0
$(2)^2\Pi$	17904.42		1415.93		4.1840		1.4680		1.8216	
$(3)^2\Pi$	19155.01		1408.58		4.0097		1.3130		1.8607	
$(3)^2\Delta$	20905.95		867.13		4.1563		3.7985		1.8282	
$(2)^2\Phi$	20924.10		778.16		3.8571		3.7926		1.8972	
$(4)^2\Pi$	21992.86		948.11		3.9070		2.6448		1.8847	
$(3)^2\Sigma^+$	23604.08		783.84		4.4609		5.7807		1.7668	
	25844[Theo.b]	8.6	830[Theo.b]	5.5	4.587[Exp.b]	2.7			1.7247[Theo.b]	2.4
	24670.06[Exp.b]	4.3								
	24670[Exp.k]	4.3								
$(1)^4\Sigma^+$	23730.45		723.81		3.6972		3.7325		1.9388	
$(2)^4\Delta$	26833.38		764.83		3.7858		3.6894		1.9152	
$(2)^4\Pi$	26841.14		787.26		4.0562		4.4064		1.8494	
$(3)^4\Pi$	27476.45		974.42		3.8178		2.3471		1.9071	
$(3)^4\Delta$	29763.96		802.67		3.7124		4.1258		1.9306	
$(2)^4\Phi$	30054.29		780.77		4.0345		4.2890		1.8556	

Note: Theo. and Exp. represent theoretical and experimental results in references. T_e, transition energy relative to the ground state; ω_e, harmonic frequency around the equilibrium; B_e, rotational constant; D_e, centrifugal distortion constant; R_e, equilibrium internuclear distance.

[a]The first entry is for the values of the present work.
[b]Reference 29.
[c]Reference 36.
[d]Reference 33.
[e]Reference 34.
[f]Reference 31.
[g]Reference 32.
[h]Reference 30.
[i]Reference 38.
[j]Reference 37.
[k]Reference 35.

Can. J. Chem. Downloaded from www.nrcresearchpress.com by Renmin University of China on 09/02/12
For personal use only.

Fig. 1. Potential energy curves for the $^2\Sigma^+$ and $^2\Delta$ states of the ZrN molecule.

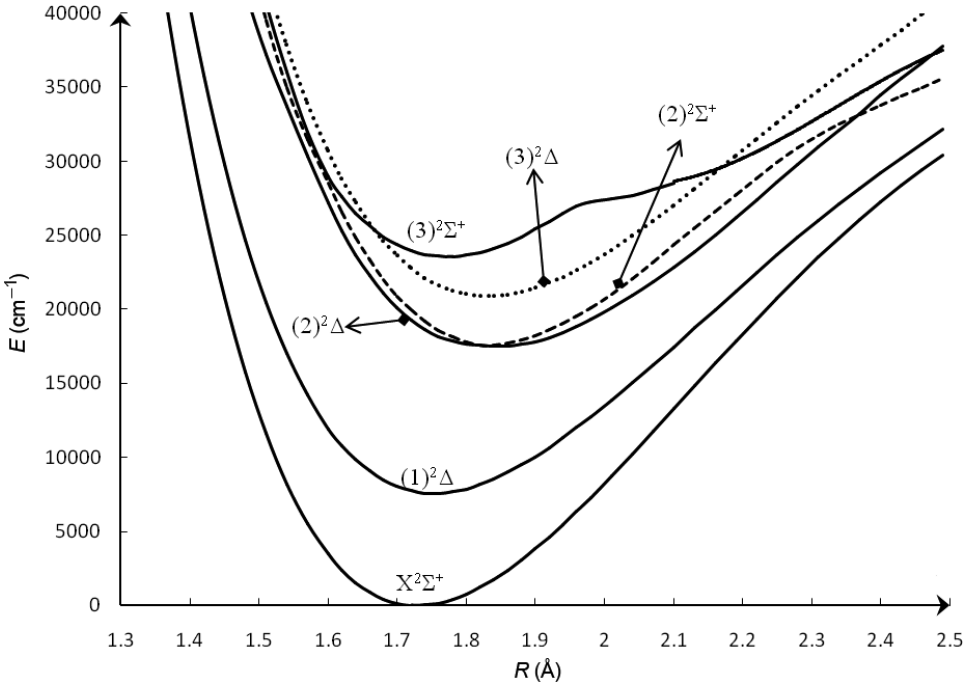
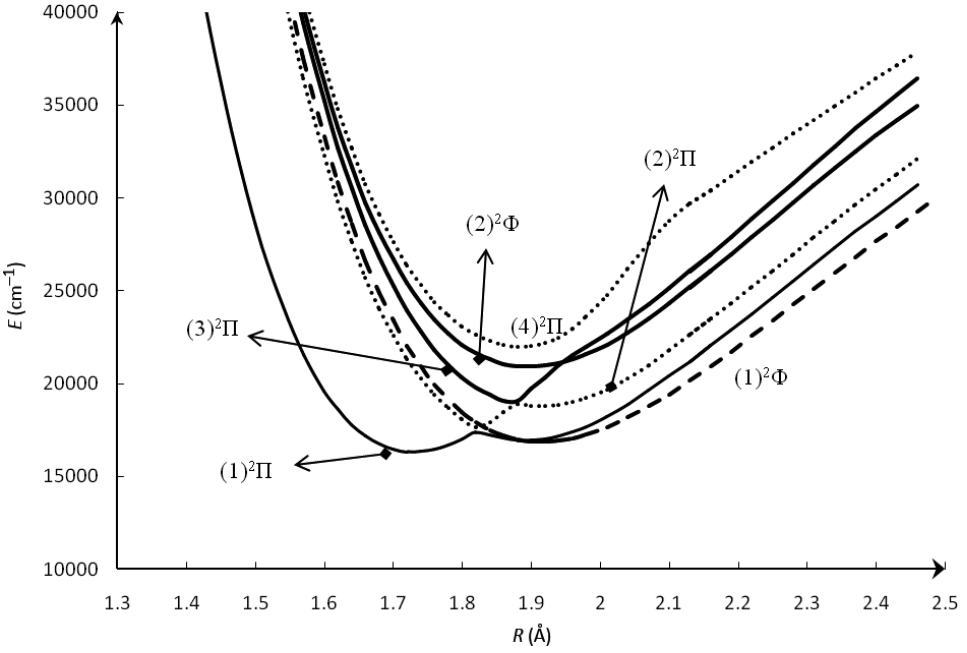


Fig. 2. Potential energy curves for the $^2\Pi$ and $^2\Phi$ states of the ZrN molecule.



The theoretical ab initio methods are helpful in this respect, since they provide the experimentalist with useful and accurate data on the electronic structure of this class of molecules.

In the literature, most of the bands (0,0),[28,29] (1,1),[30–32] (2,2)[32,33] of the vibrational transitions $A^2\prod \leftarrow X^2\sum$ and $B^2\sum^+ \leftarrow X^2\sum$ of the ZrN molecule were heavily perturbed, and thus only partial analysis of the spectrum was performed.[32–34] Li et al.[35] studied the magnetic hyperfine structure of the $X^2\sum^+$ state for the isotopomer ^{91}ZrN, recording the laser-induced fluorescence spectrum of the $A^2\prod - X^2\sum^+$ vibrational transition (0 – 0). DeVore and Gallaher[36] performed an IR spectroscopic and density functional investigation for the reaction between transition metals Ti, Zr, and Hf and nitrogen atoms. Kushto et al.[37] performed an IR vibrational spectroscopy of the group IV transition-metal diatomic gaseous nitrides TiN, ZrN, and HfN. The ZrN molecule is isoelectronic with YO[38] and has a valence electronic configuration similar to TiN[39–41] and ScO;[42–45] in view of the perturbations observed in the spectra of these isovalent molecules,

Can. J. Chem. Downloaded from www.nrcresearchpress.com by Renmin University of China on 09/02/12
For personal use only.

Fig. 3. Potential energy curves for the $^4\Sigma^+$ and $^4\Delta$ states of the ZrN molecule.

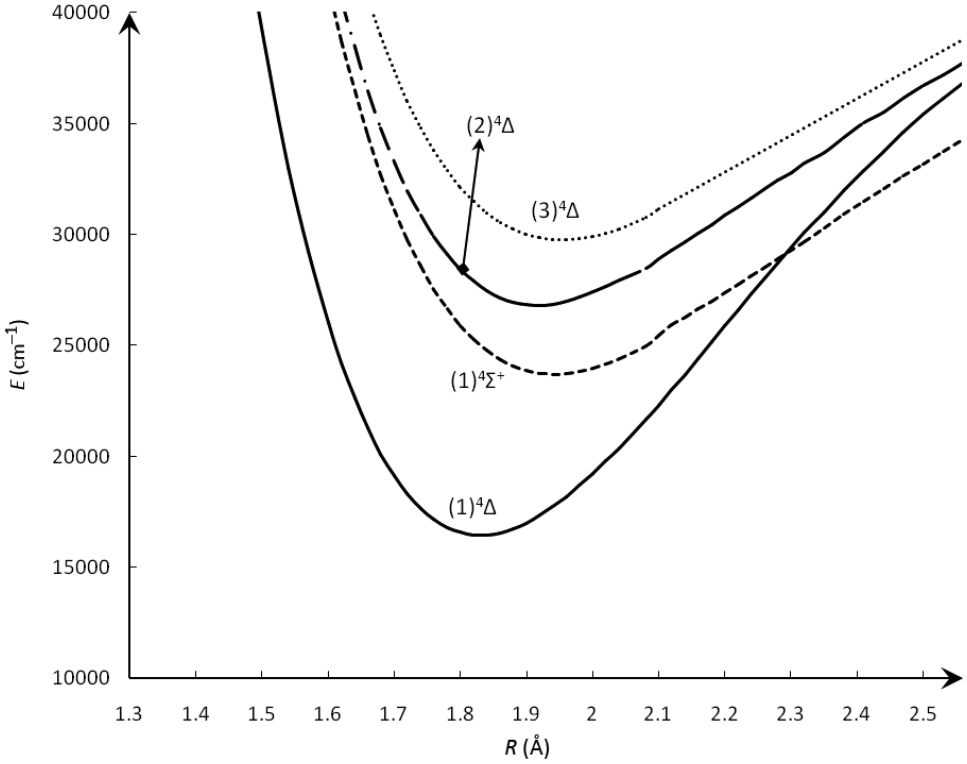
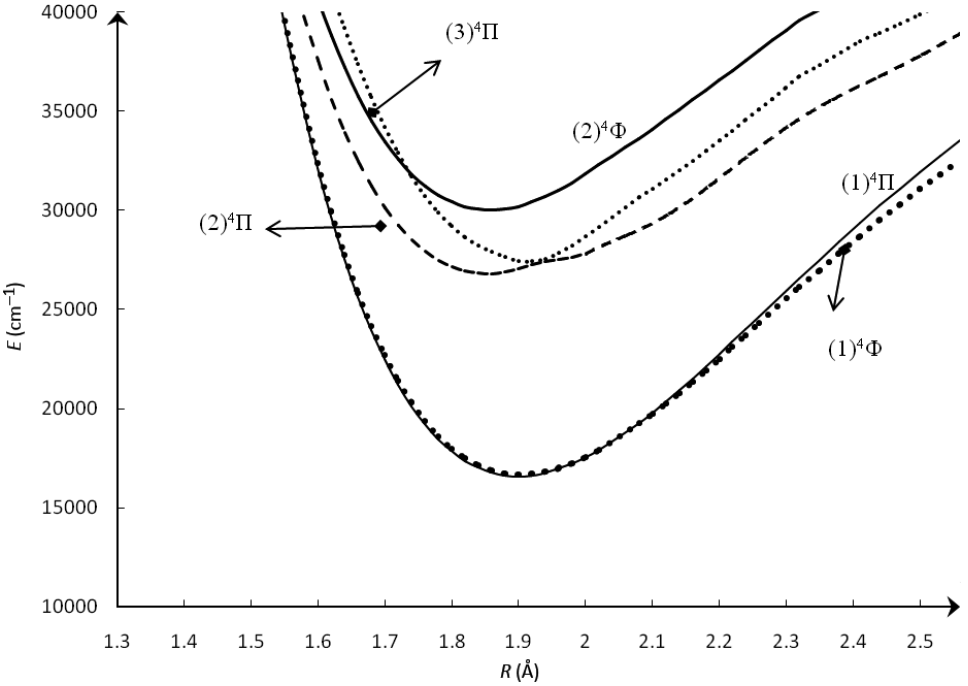


Fig. 4. Potential energy curves for the $^4\Pi$ and $^4\Phi$ states of the ZrN molecule.



it is not surprising that the spectrum of ZrN is also perturbed. Chen et al.[28] conducted a theoretical study on the ZrN molecule on the six lowest lying electronic states.

The important connection between energy relations of solids and molecules[46] and the absence of theoretical study of the higher excited states of the ZrN molecule stimulated us, in the present work, to investigate more extensive ab initio calculation of ZrN. Based on our previous theoretical calculations,[47–53] the potential energy curves and the spectroscopic constants of the 21 low-lying electronic states were calculated where 15 new electronic states have been studied here for the first time.

Calculation method

The energies of the ground and low-lying excited states of

Can. J. Chem. Downloaded from www.nrcresearchpress.com by Renmin University of China on 09/02/12
For personal use only.

Table 2. Leading configurations with percent composition of the parent electronic states $^{2s+1}\Lambda^{\pm}$ in the ZrN molecule.

Electronic state	Weight
$X^2\sum^+$	89% $1\sigma^2 1\pi^4 2\sigma^1$
$(2)^2\sum^+$	88% $1\sigma^2 1\pi^4 3\sigma^1$
$(3)^2\sum^+$	95% $1\sigma^1 1\pi^4 2\sigma^1 3\sigma^1$
$(1)^2\Delta$	86% $1\sigma^2 1\pi^3 3\sigma^1 3\pi^1$
$(2)^2\Delta$	72% $1\sigma^2 1\pi^3 2\sigma^1 2\pi^1$, 12% $1\sigma^2 1\pi^3 3\sigma^1 2\pi^1$
$(1)^2\prod$	85% $1\sigma^2 1\pi^4 2\pi^1$, 3% $1\sigma^2 1\pi^4 3\pi^1$
$(2)^2\prod$	66% $1\sigma^2 1\pi^3 2\sigma^2$, 13% $1\sigma^2 1\pi^3 2\sigma^1 4\sigma^1$
$(1)^2\Phi$	50% $1\sigma^2 1\pi^3 2\sigma^1 4\sigma^1$, 49% $1\sigma^2 1\pi^3 2\sigma^1 1\delta^1$
$(3)^2\prod$	41% $1\sigma^2 1\pi^3 2\sigma^1 3\sigma^1$, 40% $1\sigma^2 1\pi^3 2\sigma^1 1\delta^1$, 16% $1\sigma^2 1\pi^3 2\sigma^2$
$(2)^2\Phi$	47% $1\sigma^2 1\pi^3 2\sigma^1 3\sigma^1$, 45% $1\sigma^2 1\pi^3 2\sigma^1 1\delta^1$
$(4)^2\prod$	41% $1\sigma^2 1\pi^3 2\sigma^1 3\sigma^1$, 44% $1\sigma^2 1\pi^3 2\sigma^1 1\delta^1$
$(1)^4\Delta$	90% $1\sigma^2 1\pi^2 2\sigma^1 3\sigma^2$
$(1)^4\sum^+$	84% $1\sigma^2 1\pi^3 2\sigma^1 2\pi^1$, 5% $1\sigma^2 1\pi^3 3\sigma^1 2\pi^1$, 5% $1\sigma^2 1\pi^3 2\pi^1 1\delta^1$
$(2)^4\Delta$	70% $1\sigma^2 1\pi^3 2\sigma^1 2\pi^1$, 25% $1\sigma^2 1\pi^3 3\sigma^1 2\pi^1$
$(3)^4\Delta$	50% $1\sigma^2 1\pi^3 3\sigma^1 2\pi^1$, 22% $1\sigma^2 1\pi^3 2\sigma^1 2\pi^1$, 20% $1\sigma^2 1\pi^3 2\pi^1 1\delta^1$
$(1)^4\prod$	98% $1\sigma^2 1\pi^3 2\sigma^1 3\sigma^1$
$(1)^4\ \Phi$	99% $1\sigma^2 1\pi^3 2\sigma^1 3\sigma^1$
$(2)^4\prod$	88% $1\sigma^1 1\pi^4 2\sigma^1 2\pi^1$, 9% $1\sigma^1 1\pi^4 3\sigma^1 2\pi^1$
$(3)^4\prod$	48% $1\sigma^1 1\pi^4 3\sigma^1 2\pi^1$, 48% $1\sigma^1 1\pi^4 2\pi^1 1\delta^1$
$(2)^4\ \Phi$	43% $1\sigma^1 1\pi^4 3\sigma^1 2\pi^1$, 43% $1\sigma^1 1\pi^4 2\pi^1 1\delta^1$, 10% $1\sigma^1 1\pi^4 2\pi^1 1\delta^1$

Note: Weights (in percent) are obtained from the square of the corresponding configuration interaction coefficients (CMRCI); weights lower than 2% are not reported.

Table 3. Permanent dipole moments (μ) for the electronic states of the molecule ZrN at $R = 1.72$Å.

State $^{2s+1}\Lambda$	|μ| (D)	State $^{2s+1}\Lambda$	|μ| (D)
$X^2\Sigma^+$	3.190	$(4)^2\Pi$	0.983
$(1)^2\Delta$	6.489	$(1)^4\Delta$	1.954
$(2)^2\Delta$	2.063	$(1)^4\Sigma^+$	0.730
$(2)^2\Sigma^+$	0.603	$(2)^4\Delta$	1.270
$(3)^2\Sigma^+$	0.827	$(3)^4\Delta$	2.977
$(3)^2\Delta$	4.399	$(1)^4\Pi$	2.246
$(1)^2\Pi$	4.712	$(1)^4\Phi$	2.222
$(2)^2\Pi$	1.324	$(2)^4\Pi$	0.778
$(1)^2\Phi$	1.805	$(3)^4\Pi$	3.255
$(3)^2\Pi$	1.499	$(2)^4\Phi$	4.029
$(2)^2\Phi$	0.765		

ZrN were calculated by employing the complete active space self-consistent method (CASSCF) to generate the orbitals for the multireference single and double excitation configuration interaction (MRSDCI) computation. The CASSCF method included a full CI space of configurations within the active space chosen, obtained by distributing seven valence electrons of ZrN among the Zr (4d, 5s, 5p) and N (2s, 2p) orbitals. As the CASSCF method does not include dynamic correlation, we performed MRSDCI calculations to provide DCI optimizations. The Davidson correction, noted as MRSDCI + Q, was then invoked to account for quadruple excitations.

The spectroscopic constants R_e, ω_e, T_e, D_e, and B_e obtained from all of these curves are given in Table 1, where R_e is the equilibrium internuclear distance, ω_e is the harmonic frequency around the equilibrium, T_e is the transition energy relative to the ground state, B_e is the rotational constant, and D_e is the centrifugal distortion constant. These constants were calculated by fitting the potential energy curves around the internuclear distance at equilibrium R_e. All of the calculations were carried out in the C_{2v} symmetry with the ZrN molecular axis lying along the z axis of the coordinate system. The CASSCF active space contains 4σ(Zr, 5s, $4d_0$, $5p_z$; N, $2p_z$), 3π(Zr, $4d_{\pm2}$, $5p_{x,y}$; N, $2p_{x,y}$), and 1δ(Y, $4d_{\pm1}$) orbitals, this corresponds to five $a1$, three $b2$, three $b1$, and one $a2$ orbitals [5,3,3,1]. The potential energy curves of 21 low-lying electronic states of ZrN were generated using the MRSDCI + Q calculations. The zirconium species is treated in an all electron scheme; the 40 electrons of the Zr atom are considered using the contracted Huzinaga basis set from the literature[54,55] for s, p, and d functions; this basis set (27s, 20p, 17d) was contracted to (18s, 16p, 11d) and to which we have added one f function (18s, 16p, 11d, 1f). The exponent of this f function was taken to be 0.08. The nitrogen species was treated as a system of seven electrons by using the Rydberg2 (Dunning–Hay DZP + Rydberg)[56] basis set for s, p, and d functions (9s, 5p, 1d). Among the 47 electrons considered for the ZrN molecule, 40 electrons were frozen in subsequent calculations so that seven valence electrons were distributed over all the active molecular orbitals. Although the atomic structure of the nitrogen atom is relatively simple, with ^{4}S state for its ground electronic state and ^{2}D for the first excited state at about 19174.22 cm^{-1} higher,[57] the electronic states of the zirconium atom are more complicated. The lowest electronic state of Zr is ^{3}F, but the first excited state, namely, ^{3}P ($4d^25s^2$), lies at about 4269.89 cm^{-1} higher.[57] The doublet and quartet low-lying electronic states $\sum^+$, $\prod$, Φ, Δ, and Γ of ZrN have been obtained by the combination of the atoms Zr and N. It is obvious that even if we consider the nitrogen atom only in its ground state, there will be a plenty of electronic states generated from the low-lying atomic Zr electronic states, which could also split further by

Table 4. Positions of the crossing and avoided crossings between the different electronic states of the ZrN molecule.

		Crossing	Avoided crossing				Crossing	Avoided crossing	
State 1	State 2	r_c (Å)	r_{av} (Å)	ΔE_{av} (cm^{-1})	State 1	State 2	r_c (Å)	r_{av} (Å)	ΔE_{av} (cm^{-1})
$(1)^2\Sigma^+$	$(1)^2\Phi$	2.43			$(3)^2\Sigma^+$	$(2)^2\Pi$	1.66		
$(1)^2\Delta$	$(1)^2\Phi$	2.24				$(1)^2\Phi$	1.67		
	$(1)^4\Pi$	2.30				$(3)^2\Pi$	1.72		
	$(1)^4\Phi$	2.28				$(2)^2\Phi$	1.76		
$(2)^2\Delta$	$(2)^2\Sigma^+$	2.37				$(4)^2\Pi$	1.77		
	$(1)^2\Phi$	1.83				$(1)^4\Sigma^+$	1.84		
	$(2)^2\Pi$	1.97				$(2)^4\Delta$	1.94		
	$(1)^4\Delta$	1.51				$(1)^4\Pi$	1.67		
	$(1)^4\Pi$	1.80				$(1)^4\Phi$	1.68		
	$(1)^4\Phi$	1.81			$(2)^2\Phi$	$(1)^4\Sigma^+$	2.21		
	$(2)^4\Pi$	2.49			$(1)^2\Pi$	$(1)^2\Phi$	1.86		
$(2)^2\Sigma^+$	$(1)^2\Phi$	1.83				$(1)^4\Delta$	1.79/1.89		
	$(2)^2\Phi$	2.09				$(1)^4\Pi$	1.82		
	$(1)^4\Sigma^+$	2.16				$(1)^4\Phi$	1.82		
	$(1)^4\Phi$	1.81				$(2)^2\Pi$		1.82	285
	$(1)^4\Pi$	1.81			$(2)^2\Pi$	$(3)^2\Pi$		1.88	186
	$(3)^2\Sigma^+$		1.6	383		$(1)^2\Phi$	1.83		
$(3)^2\Delta$	$(3)^2\Sigma^+$	1.67/2.15				$(1)^4\Delta$	2.03		
	$(2)^2\Pi$	1.65			$(1)^2\Phi$	$(1)^{4\Delta}$	1.90		
	$(1)^2\Phi$	1.68				$(1)^4\Pi$	1.96		
	$(3)^2\Pi$	2.76				$(1)^4\Phi$	1.96		
	$(2)^2\Phi$	1.87			$(3)^2\Pi$	$(2)^2\Phi$	1.94		
	$(4)^2\Pi$	2.25				$(1)^4\Sigma^+$	2.12		
	$(1)^4\Sigma^+$	2.01				$(2)^4\Pi$	1.56		
	$(2)^4\Delta$	2.19			$(1)^4\Pi$	$(1)^4\Phi$	1.87		
	$(3)^4\Delta$	2.29			$(2)^4\Pi$	$(1)^4\Sigma^+$	1.73		
	$(1)^4\Phi$	1.64				$(2)^4\Delta$	1.89		
	$(1)^4\Pi$	1.64				$(3)^4\Pi$		1.94	101
	$(2)^4\Pi$	2.28			$(2)^4\Phi$	$(1)^4\Sigma^+$	1.61		
	$(3)^4\Pi$	2.42				$(2)^4\Delta$	1.69		
$(4)^2\Pi$	$(1)^4\Sigma^+$	1.99				$(3)^4\Delta$	1.88		
	$(2)^4\Delta$	2.10			$(3)^4\Pi$	$(2)^4\Delta$	1.54		
	$(3)^4\Delta$	2.333				$(3)^4\Delta$	2.18		
	$(2)^4\Pi$	1.59							
$^4\Delta$	$(1)^4\Pi$	1.86							

Can. J. Chem. Downloaded from www.nrcresearchpress.com by Renmin University of China on 09/02/12
For personal use only.

spin orbit coupling.[58,59] To facilitate a thorough exploration of the complicated manifold of electronic states of the ZrN molecule, multiple roots for every possible multiplicity were considered for each symmetry in the C_{2v} group at the CASSCF/MRSDCI level. Depending on the space and spin symmetries of the electronic states, the size of the wave functions used varied from 10 248 to 14 251 configuration state functions in CASSCF calculations and from 770 000 to 977 500 configuration state functions in MRSDCI calculations.

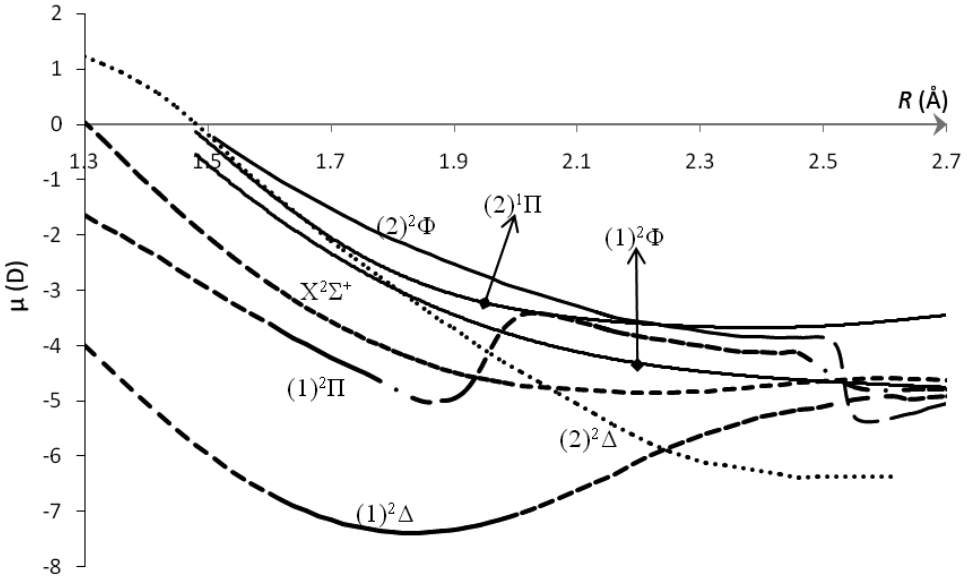
Results

The potential energy curves for 21 low-lying electronic states in the representation $^{2s+1}\Lambda^{(\pm)}$ of the ZrN molecule were obtained from MRSDCI + Q calculations performed at 40 internuclear distances equally distributed between 1.3 and 2.5 Å. Figures 1–4 show the potential curves of 12 low-lying doublet and 9 low-lying quartet states, respectively. The energy scale of all figures is relative to the energy minimum of the ground electronic states predicted here to be $^2\sum^+$. The ground state of ZrN is $X^2\sum^+$, resulting from the distribution of seven valence electrons over molecular orbitals $1\sigma^2 1\pi^4 2\sigma^1$, leading to a $\Lambda = 0$, with one unpaired electron ($S = 1/2$), giving a doublet multiplicity (2s+1) ground state.

The comparison between the values of the present work with the theoretical results available in the literature[30] shows a very good agreement with a percentage relative difference of $3.2\% \leq \delta T_e/T_e \leq 11\%$, $2.4\% \leq \delta\omega_e/\omega_e \leq 7.4\%$, and $1.4\% \leq \delta R_e/R_e \leq 3\%$ for the states $X^2\Sigma^+$, $(1)^2\Delta$, $(2)^2\Sigma^+$, $(3)^2\Sigma^+$, $(1)^2\Pi$, and $(1)^4\Delta$. The experimental results available in the literature for ZrN for the states $X^2\Sigma^+$, $(3)^2\Sigma^+$, and $(1)^2\Pi$ are reproduced in our calculations with a percentage relative difference of 3.4% (ref. 31) $\leq \delta T_e/T_e \leq$ 6.2% (ref. 35), 0.8% (ref. 37) $\leq \delta\omega_e/\omega_e \leq$ 4.5% (ref. 33), 2.1% (ref. 38) $\leq \delta B_e/B_e \leq$ 9.8% (ref. 38), and 1.5% (ref. 33) $\leq \delta R_e/R_e \leq$ 2.1% (ref. 30). The experimental values[30–32,34] of the rotational constant D_e are in good agreement with our results for the ground $X^2\Sigma^+$ state, with a relative difference of 9.3% (ref. 32) $\leq \delta D_e/D_e \leq$ 10% (ref. 34); this agreement becomes less for the $(1)^2\Pi$ state, where the relative difference is 17% (ref. 31) $\leq \delta D_e/D_e \leq$ 18.3% (ref. 34). In Table 1, the experimental value of the transition energy T_e for the state

Can. J. Chem. Downloaded from www.nrcresearchpress.com by Renmin University of China on 09/02/12
For personal use only.

Fig. 5. Permanent dipole moments (μ) of the ground and doublet excited considered electronic states of the ZrN molecule.



$(1)^2\prod$ reported in ref. 31 was estimated by using the relation $T_e = T_v - \omega_e (v+1/2)$, and the energy value 17318.76 was averaged over the two spin components $\prod_{1/2}$ and $\prod_{3/2}$ reported in ref. 34. Table 2 gives a list of 24 configurations labeled from (A) to (Z), which have weight ≥ 2% in the CMRCI wave functions as detailed in Table 3. The configuration weights are calculated as the squares of the corresponding CI coefficients. Table 2 characterizes each configuration in terms of electron promotions with respect to the ground configuration ($1\sigma^2 1\pi^4 2\sigma^1$) and also reports the arising electronic states. The $(1)^2\prod$ state arises from the promotion of the $2\sigma^1$ electron into a $2\pi^1$ orbital with an increase in energy of about 16 298.08 cm^{-1}. The $(2)^2\sum^+$ state ($1\sigma^2 1\pi^4 3\sigma^1$) arises from the promotion of a 2σ electron to a 3σ orbital, which corresponds to an energy increase of 17 562.94 cm^{-1}, whereas the $(3)^2\sum^+$ state ($1\sigma^1 1\pi^4 2\sigma^1 3\sigma^1$) arises from the promotion of the 1σ electron into the 3σ orbital with an energy increase of 23 524.67 cm^{-1}. The lowest quartet state $(1)^4\Delta$ ($1\sigma^2 1\pi^2 2\sigma^1 3\sigma^2$) arises from the promotion of two 1π electrons into a 3σ orbital with an energy change of 16 435.04 cm^{-1}. In this study, we calculated the spectroscopic properties of the low-lying $(1)^4\Pi$ and $(1)^4\Phi$ states for which a heavy mixing was reported in ref. 30 The $(1)^4\Pi$ state was found to be 86 cm^{-1} separated from the $(1)^4\Phi$ state; this is not surprising, since both states have the same electronic configuration ($1\sigma^2 1\pi^3 2\sigma^1 3\sigma^1$) that arises from the excitation of a 1π electron into a 3σ orbital with an average energy change of 16 652.57 cm^{-1}.

Chen et al.[25] studied the (0,0) band of the $(3)^2\sum^+ \leftarrow X^2\sum^+$ transition through the laser spectroscopy technique, reporting the presence of severe perturbations in the rotational energy spectra of the investigated transition. As the nature of the perturbing state could not be identified, this suggests that the $(3)^2\sum^+$ state and its perturbing state have close potential energy curves with a low vibrational $v = 0$ quantum number for this perturbing state. From the potential energy curves of the present work, we identified the nature of the perturbing state to be a $(3)^2\Delta$ state whose potential energy curve crosses that of the $(3)^2\sum^+$ state at $r = 1.66$ Å.

Recent experimental studies of photodissociation dynamics show that the potential energy curve crossing plays a deterministic role in the choice of the channel of dissociation.[48] Then, in the range of r considered, some crossings and avoided crossings between the different electronic states occur; these are reported in Table 4 with the position of the crossings r_c and avoided crossings r_{av} together with their energy gap separation, ΔE_{av}. Several perturbations have been detected experimentally in the vibronic band systems for $v = 0$, 1, and 2 for the $(1)^2\prod$ electronic state.[26,27,33] These perturbations were not clear, since the nature of the perturbing states could not be resolved. Our theoretical potential energy curves show the avoided crossing of the $(1)^2\prod$ state with the $(2)^2\prod$ state at $r = 1.83$ Å and the crossing with the $(1)^2\Phi$ state at $r = 1.84$ Å. This crossing and avoided crossing may be responsible for the experimental vibrational perturbations occurring in the spectra of the $(1)^2\prod$ electronic state. A similar avoided crossing has been detected between the $(1)^2\prod$ and the $(2)^2\prod$ states in the YO molecule,[22] which is isoelectronic to the ZrN molecule.

For the ground and the considered doublet electronic states, the permanent dipole moments were calculated in terms of the internuclear distance (R) and are plotted in Fig. 5. In this figure we notice that the $(1)^2\Delta$ state attains the largest dipole moment of 7.385 D at $R = 1.82$ Å. The permanent dipole moments at the equilibrium internuclear distances for the studied states are given in Table 3. The comparison of these values with other results in the literature is not possible, since, to the best of our knowledge, these values are given here for first time.

Conclusion

The potential energy curves of 21 low-lying electronic states of the ZrN molecule were computed using the CASSCF and MRSDCI + Q methods. To the best of our knowledge, only six states have been characterized in the literature. Several experimental perturbations in the vibronic structures of the $(3)^2\sum^+ \leftarrow X^2\sum^+$ and $(1)^2\prod \leftarrow X^2\sum^+$ systems

have been resolved as the identities of the perturbing states were revealed. Many low-lying quartet states ($^4\prod$ and $^4\Phi$) were detected for the first time. The potential energy curves and the spectroscopic constants were obtained for the investigated states where the comparison with the available experimental and theoretical data in the literature showed very good agreement. In this work, 15 new low-lying electronic states in the doublet and quartet manifolds were studied for the first time. Because of the importance of the ZrN molecule in several areas of science, we expect that the results of the present work will invoke further experimental investigations of the electronic structure of the ZrN molecule. The values of the permanent dipole moments of the investigated electronic states are reported here for the first time.

References

(1) Greenwood, N. N.; Earnhsaw, A. *Chemistry of the Elements;* Pergamon: Oxford, 1984.
(2) Barrett, C. S.; Massalski, T. B. *Structure of Metals;* Pergamon: New York, 1980.
(3) Toth, L. E. *Transition Metal Carbides and Nitrides;* Academic: New York, 1971.
(4) Storms, E. K. *The Refractory Carbides;* Academic: New York, 1967.
(5) Gubanov, V. A.; Ivanovsky, A. L.; Zhukov, V. P. *Electronic Structure of Refractory Carbides and Nitrides;* Cambridge University Press: Cambridge, 1994.
(6) Weber, W. In *The Electronic Structure of Complex Systems;* NATO ASI Series, Vol. 113; Phariseau, P., Temmerman, W. M., Eds.; Plenum: New York, 1995.
(7) Häglund, J.; Grimvall, G.; Jarlborg, T.; Fernández Guillermet, A. *Phys. Rev. B* **1991**, *43* (18), 14400. doi:10.1103/PhysRevB.43.14400.
(8) Fernández Guillermet, A.; Häglund, J.; Grimvall, G. *Phys. Rev. B* **1992**, *45* (20), 11557. doi:10.1103/PhysRevB.45.11557.
(9) Guillermet, A. F.; Häglund, J.; Grimvall, G. *Phys. Rev. B* **1993**, *48* (16), 11673. doi:10.1103/PhysRevB.48.11673.
(10) Stampfl, C.; Mannstadt, W.; Asahi, R.; Freeman, A. J. *Phys. Rev. B* **2001**, *63* (15), 155106. doi:10.1103/PhysRevB.63.155106.
(11) Takeuchi, N. *Phys. Rev. B* **2002**, *65* (4), 045204. doi:10.1103/PhysRevB.65.045204.
(12) Viñes, F.; Sousa, S.; Liu, P.; Rodriguez, J. A.; Illas, F. *J. Chem. Phys.* **2005**, *122* (17), 174709. doi:10.1063/1.1888370.
(13) Isaev, E. I.; Simak, S. I.; Abrikosov, I. A.; Ahuja, R.; Vekilov, Yu. Kh.; Katsnelson, M. I.; Lichtenstein, A. I.; Johansson, B. *J. Appl. Phys.* **2007**, *101* (12), 123519. doi:10.1063/1.2747230.
(14) Weiller, B. H. *J. Am. Chem. Soc.* **1996**, *118* (21), 4975. doi:10.1021/ja953468o.
(15) Cundari, T. R.; Li, Y. *Int. J. Quantum Chem.* **1995**, *55* (4), 315. doi:10.1002/qua.560550403.
(16) Häglund, J.; Fernández-Guillermet, A.; Grimvall, G.; Körling, M. *Phys. Rev. B* **1993**, *48* (16), 11685. doi:10.1103/PhysRevB.48.11685.
(17) Reddy, B. V.; Khanna, S. N. *Phys. Rev. B* **1996**, *54* (3), 2240. doi:10.1103/PhysRevB.54.2240.
(18) Mei, F. H.; Shao, N.; Wei, L.; Dong, Y. S.; Li, G. Y. *Appl. Phys. Lett.* **2005**, *87* (1), 011906. doi:10.1063/1.1951047.
(19) Hock, M.; Schäffer, E.; Döll, W.; Kleer, G. *Surf. Coat. Tech.* **2003**, *163–164*, 689. doi:10.1016/S0257-8972(02)00658-8.
(20) Li, D. J.; Wang, M. X.; Zhang, J. J. *Mater. Sci. Eng. A* **2006**, *423* (1–2), 116. doi:10.1016/j.msea.2005.11.068.
(21) Hsu, C. H.; Chen, M. L.; Lai, K. L. *Mater. Sci. Eng. A* **2006**, *421* (1–2), 182. doi:10.1016/j.msea.2005.12.014.
(22) Sauval, A. J. *Astron. Astrophys.* **1978**, *62*, 295.
(23) Langhoff, S. R.; Bauschlicher, C. W., Jr; Partridge, H. *J. Chem. Phys.* **1988**, *396*, 89.
(24) Langhoff, S. R.; Bauschlicher, C. W., Jr. *Annu. Rev. Phys. Chem.* **1988**, *39* (1), 181. doi:10.1146/annurev.pc.39.100188.001145.
(25) Morse, M. D. *Chem. Rev.* **1986**, *86* (6), 1049. doi:10.1021/cr00076a005.
(26) James, A. M.; Fournier, R.; Simard, B.; Campbell, M. D. *Can. J. Chem.* **1993**, *71* (10), 1598. doi:10.1139/v93-200.
(27) Ram, R.; Bernath, P. *J. Mol. Spectrosc.* **1994**, *165* (1), 97. doi:10.1006/jmsp.1994.1113.
(28) Chen, H.; Li, Y.; Mok, D. K.; Cheung, A. *J. Mol. Spectrosc.* **2003**, *218* (2), 213. doi:10.1016/S0022-2852(02)00086-3.
(29) Cheung, A. S. C.; Li, H.; Jiang, H.; Chen, H. *J. Mol. Spectrosc.* **2001**, *210* (1), 84. doi:10.1006/jmsp.2001.8456.
(30) Chan, C. M. T.; Li, H.; Sze, N. S.-K.; Cheung, A. S. C. *J. Mol. Spectrosc.* **1996**, *180* (1), 145. doi:10.1006/jmsp.1996.0233.
(31) Jiang, H.; Ma, C.; Tong, G. S. M.; Cheung, A. S. C. *J. Mol. Spectrosc.* **1999**, *480*, 277.
(32) He, J.; Ma, C.; Cheung, A. S. C. *Chem. Phys. Lett.* **1998**, *295*, 535. doi:10.1016/S0009-2614(98)00993-2.
(33) Chan, C. M.-T.; Li, H.; Cheung, A. S. C. *Chem. Phys. Lett.* **1997**, *269* (1–2), 49. doi:10.1016/S0009-2614(97)00239-X.
(34) Bates, J. K.; Dunn, T. M. *Can. J. Phys.* **1976**, *54* (12), 1216. doi:10.1139/p76-145.
(35) Li, H.; Chan, C. M.-T.; Cheung, A. S.-C. *J. Mol. Spectrosc.* **1996**, *176*, 219. doi:10.1006/jmsp.1996.0079.
(36) DeVore, T. C.; Gallaher, T. N. *J. Chem. Phys.* **1979**, *70* (7), 3497. doi:10.1063/1.437885.
(37) Kushto, G.; Souter, P.; Chertihin, G.; Andrews, L. *J. Chem. Phys.* **1999**, *110* (18), 9020. doi:10.1063/1.478822.
(38) Childs, W. J.; Poulsen, O.; Steimle, T. C. *J. Chem. Phys.* **1988**, *88* (2), 598. doi:10.1063/1.454186.
(39) Bauschlicher, C. W., Jr. *Chem. Phys. Lett.* **1983**, *100* (6), 515. doi:10.1016/0009-2614(83)87419-3.
(40) Dunn, T. M.; Hanson, L. K.; Rubinson, K. A. *Can. J. Phys.* **1970**, *48* (14), 1657. doi:10.1139/p70-209.
(41) Athénour, C.; Féménias, J.-L.; Dunn, T. M. *Can. J. Phys.* **1982**, *60* (2), 109. doi:10.1139/p82-015.
(42) Adams, A.; Klemperer, W.; Dunn, T. M. *Can. J. Phys.* **1968**, *46* (19), 2213. doi:10.1139/p68-569.
(43) Akerlind, , L. A. *Ark. Fys.* **1962**, *22*, 41.
(44) Stringat, R.; Athénour, C.; Féménias, J.-L. *Can. J. Phys.* **1972**, *50* (4), 395. doi:10.1139/p72-057.
(45) Huzinaga, S.; Klobukowski, M.; Sakai, Y. *J. Phys. Chem.* **1984**, *88* (21), 4880. doi:10.1021/j150665a015.
(46) Smith, J. R.; Schlosser, H.; Leaf, W.; Ferrante, J.; Rose, J. H. *Phys. Rev. A* **1989**, *39*, 414.
(47) Korek, M.; Moghrabi, Y. A.; Allouche, A. R. *J. Chem. Phys.* **2006**, *124* (9), 094309. doi:10.1063/1.2173239.
(48) Korek, M.; Bleik, S.; Allouche, A. R. *J. Chem. Phys.* **2007**, *126* (12), 124313. doi:10.1063/1.2710257.
(49) Taher-Mansour, F.; Allouche, A. R.; Korek, M. *J. Mol. Spectrosc.* **2008**, *248* (1), 61. doi:10.1016/j.jms.2007.11.012.
(50) Korek, M.; Kontar, S.; Taher-Mansour, F.; Allouche, A. R. *Int. J. Quantum Chem.* **2009**, *109* (2), 236. doi:10.1002/qua.21779.
(51) Korek, M.; Younes, G. A.; Al-Shawa, S. *J. Mol. Struct. THEOCHEM* **2009**, *899* (1–3), 25. doi:10.1016/j.theochem.2008.12.006.
(52) Hamdan, A.; Korek, M. *Chem. Phys.* **2010**, *369* (1), 13. doi:10.1016/j.chemphys.2010.01.023.

Can. J. Chem. Downloaded from www.nrcresearchpress.com by Renmin University of China on 09/02/12
For personal use only.

(53) Hamdan, A.; Korek, M. *Int. J. Quantum Chem.* **2011**, *111* (12), 2960. doi:10.1002/qua.22602.
(54) Huzinaga, S.; Klobukowski, M. *Chem. Phys. Lett.* **1993**, *212* (3–4), 260. doi:10.1016/0009-2614(93)89323-A.
(55) Huzinaga, S.; Miguel, B. *Chem. Phys. Lett.* **1990**, *175* (4), 289. doi:10.1016/0009-2614(90)80112-Q.
(56) Dunning, T. H., Jr.; Hay, P. J. In *Methods of Electronic Structure Theory;* Vol. 2; Schaefer, H. F., III, Ed.; Plenum Press: New York, 1977.
(57) Moore, C. E. *Atomic Energy Levels;* Natl. Bur. Stand. (US) Circ. 467, Vol. II, 1952.
(58) Balasubramanian, K. *Relativistic Effects in Chemistry Part A: Theory and Techniques;* Wiley Interscience: New York, 1997; p 301.
(59) Balasubramanian, K. *Relativistic Effects in Chemistry Part B: Applications to Molecules and Clusters;* Wiley Interscience: New York, 1997; p 527.

Can. J. Chem. Downloaded from www.nrcresearchpress.com by Renmin University of China on 09/02/12
For personal use only.

Prediction of gas-phase reduced ion mobility constants (K_0) from three-dimensional molecular structure representation

Jing Song, Ying Zhang, Hui Hu, Hui Zhang, Lin Lin, and Jie Xu

Can. J. Chem. Downloaded from www.nrcresearchpress.com by Renmin University of China on 09/02/12
For personal use only.

Abstract: Quantitative structure–property relationship (QSPR) studies were performed for the prediction of gas-phase reduced ion mobility constants (K_0) of diverse compounds based on three-dimensional (3D) molecular structure representation. The entire set of 159 compounds was divided into a training set of 120 compounds and a test set of 39 compounds according to Kennard and Stones algorithm. Multiple linear regression (MLR) analysis was employed to select the best subset of descriptors and to build linear models, whereas nonlinear models were developed by means of an artificial neural network (ANN). The obtained models with five descriptors involved show good predictive power for the test set: a squared correlation coefficient (R^2) of 0.9029 and a standard error of estimation (s) of 0.0549 were achieved by the MLR model, whereas by the ANN model, R^2 and s were 0.9292 and 0.496, respectively. The results of this study compare favorably to previously reported prediction methods for the ion mobility constants. In addition, the descriptors used in the models are discussed with respect to the structural features governing the mobility of the compounds.

Key words: QSPR, ion mobility constants, three-dimensional descriptors, multiple linear regression, artificial neural network.

Résumé : On a effectué des études de relation structure/propriétés quantitatives (RSPQ) dans le but de prédire les constantes de mobilité ionique réduites en phase gazeuse (K_0) de divers composés en fonction de la représentation tridimensionnelle (3D) de leur structure moléculaire. On a fait appel à l'algorithme de Kennard et Stones pour diviser un ensemble de 159 composés en bloc de 120 composés utilisés pour développer la méthode et un autre bloc de 39 composés utilisés pour la vérifier. On a utilisé une méthode d'analyse de régression linéaire multiple (RLM) pour choisir le meilleur sous-ensemble des descripteurs et pour développer les modèles linéaires; les modèles non-linéaires ont été développés à l'aide d'un réseau neural artificiel (RNA). Les modèles obtenus en impliquant cinq descripteurs permettent d'obtenir un bon pouvoir de description pour l'ensemble à vérifier : faisant appel à une analyse de régression multiple, le coefficient de corrélation quadratique (R^2) est égal à 0,9029 et l'erreur d'évaluation standard (s) est égale à 0,0549 alors que, par l'utilisation du réseau neural artificiel conduit à des valeurs de R^2 et s de 0,0202 et de 0 496 respectivement. Les résultats de cette étude se comparent favorablement avec les résultats rapportés antérieurement à l'aide d'autres méthodes de prédiction des constantes de mobilité ionique. De plus, on discute des descripteurs utilisés dans les modèles en fonction des caractéristiques structurales qui gouvernent la mobilité des composés.

Mots-clés : relation structure–propriétés quantitatives (RSPQ), constantes de mobilité ionique, descripteurs tridimensionnels, régression linéaire multiple, réseau neural artificiel.

[Traduit par la Rédaction]

Introduction

The use of ion mobility spectrometry (IMS) has attracted significant interest as a tool for the separation of mixtures of components because of its high speed, excellent detection limits, amenability to miniaturization, and ruggedness for field operation.[1–3] When coupled with time-of-flight mass spectrometry, IMS also can be used for high-throughput drug screening,[4] proteomics,[5–7] glycomics,[8,9] and metabolomics studies.[10]

The basic concept of IMS is that an ion will drift at a constant velocity when exposed to an electric field at ambient pressure. The ion accelerates in the electric field before colliding with a neutral molecule and stopping.[11] The continuous series of accelerations and collisions leads to the apparent constant velocity. Ion mobility (K) is the ratio of

Received 23 March 2012. Accepted 4 June 2012. Published at www.nrcresearchpress.com/cjc on 19 July 2012.

J. Song. College of Accounting, Wuhan Textile University, 430073, Wuhan, P.R. China.
Y. Zhang. College of Finance and Economics, Wuhan Textile University, 430073, Wuhan, P.R. China.
H. Hu, H. Zhang, and L. Lin. International Business Economic College, Wuhan Textile University, 430073, Wuhan, P.R. China.
J. Xu. College of Materials Science and Engineering, State Key Laboratory of New Textile Materials and Advanced Processing Technology, Wuhan Textile University, 430073, Wuhan, P.R. China.

Corresponding author: Jie Xu (e-mail: xujie0@ustc.edu).

Can. J. Chem. Downloaded from www.nrcresearchpress.com by Renmin University of China on 09/02/12
For personal use only.

the ion drift velocity (v) to the applied electric field (E), which is the most important parameter governing the separation of solutes in IMS. The value of K in most IMS instruments can be derived from the following equation:[12]

$$[1] \qquad K = \frac{L^2}{Vt}$$

where L is the length of the drift tube region of the spectrometer, V is the applied voltage, and t is the drift time of the ion. For the purpose of standardization, the reduced mobility constant (K_0) is typically reported for any particular analyte ion. K_0 values are calculated using the following equation:[12]

$$[2] \qquad K_0 = K\left(\frac{273}{T}\right)\left(\frac{P}{760}\right)$$

where T is the operating temperature of the instrument and P is the current ambient pressure. Direct comparison and estimation of K_0 values measured under different conditions are made possible by using this normalization.

The ability to predict K_0 values is of great importance for several reasons.[13] First, the determination of K_0 values by experiment is often expensive and time-consuming. Second, the reported experimental K_0 values are limited. Third, the predicted K_0 values can provide an initial value for algorithms used to calibrate instrument-specific measurements. Finally, a prediction equation could provide valuable insights into the principle dynamics that have the greatest effects on ion mobility.

The mass/inverse mobility correlation has been used to predict the K_0 of homogeneous series of compounds with some success. However, the obtained results were not satisfactory when applied to a diverse set of compounds.[14–17] The quantitative structure–property relationship (QSPR) provides an alternative method for predicting K_0 using descriptors derived solely from the molecular structure to fit experimental data. The QSPR method is based on the assumption that the variation of the behavior of the compounds, as expressed by any measured properties, can be correlated with numerical changes in structural features of all compounds, termed "molecular descriptors".[18–24] The advantage of this method lies in the fact that it requires only the knowledge of the chemical structure and is not dependent on any experimental properties. The QSPR method has been successfully applied to predict the chemical and physical properties of compounds. Wessel and Jurs[25] developed an artificial neural network (ANN) model, which predicted K_0 values with over 99% accuracy for a defined set of relatively simple compounds and a somewhat lower (i.e., 91.1%) accuracy for an expanded set containing more diverse compounds.[12] Although this model has good predictive ability, it is difficult to interpret the relationship between the inputs and response. Tolley and co-workers[1] built several models using the multiple linear regression (MLR) method for different series of compounds. A squared correlation coefficient (R^2) value of 80.1% between the calculated K_0 values and measured K_0 values was obtained for 162 compounds. These models are difficult to generalize because different equations are proposed for different groups of compounds. In addition, these models were not tested with the external set, thus, their true prediction ability for new compounds not used for model development was not clear. Actually, the external validation is a crucial aspect of any QSPR modeling.[26] Recently, Yao and co-workers[13] developed linear and nonlinear models for predicting K_0 of diverse compounds based on the descriptors calculated from the CODESSA software. Although much has been done, the accuracy and cost of predictions, as well as their clear physical interpretations, are still matters of concern.

Molecular descriptors can be defined as the final result of a logic and mathematical procedure that transforms chemical information encoded within a symbolic representation of a molecule into a useful number.[27] Molecular descriptors play an important role in the quantitative description of chemical structure to find appropriate predictive models. Based on the dimensionality of the molecular representation, molecular descriptors can be classified into zero-dimensional (0D), one-dimensional (1D), two-dimensional (2D), three-dimensional (3D), and even higher dimensional groups. The good predictive abilities of 3D descriptors in QSPR studies have been demonstrated in recent years,[28–35] since the higher dimensional structure of a molecule contains more information.

No reports on 3D descriptors for QSPR studies on ion mobility constants can be found in the literature. The scope of this work is to evaluate the explanatory ability of 3D descriptors to represent the effect of molecular structure on the ion mobility. A diverse set of 159 compounds previously collected were re-examined. Linear and nonlinear models are developed by means of MLR and ANN. Furthermore, the structural factors affecting the mobility behavior of these compounds in ion mobility spectrometry are discussed in detail on the basis of descriptor contribution analysis.

Materials and method

Data set

The K_0 values of 162 compounds with diverse structures were taken from the literature.[1] Chloroacetophenone, 3-xylyl bromide (3-methylbenzyl bromide), and dichloro(2-chlorovinyl) arsine were excluded from the data set,[13] and the rest of the 159 compounds with K_0 values ranging from 1.23 to 2.97 (Table 1) were studied.

Descriptor generation

The molecular structures of these compounds were optimized using the MM+ molecular mechanics method (Polak–Ribiere algorithm) and the semiempirical AM1 method at a restricted Hartree–Fock level with no configuration interaction in the HYPERCHEM program (version 6.01).[36] A gradient norm limit of 0.01 kcal $Å^{-1}$ mol^{-1} (1 cal = 4.184 J) was chosen as the stopping criterion for the optimization. The resulting lowest energy geometry for each compound was then submitted to the DRAGON software (version 5.4)[37] for calculation of the 735 3D descriptors.

To reduce redundant and nonuseful information, constant or near constant values and descriptors found to be highly correlated pairwise (one of any two descriptors with a correlation greater than 0.99[38]) were excluded in a prereduction step. Consequently, 404 descriptors remained to undergo subsequent descriptor selection.

Kennard and Stones algorithm

Kennard and Stones algorithm[39] has been considered as

Can. J. Chem. Downloaded from www.nrcresearchpress.com by Renmin University of China on 09/02/12
For personal use only.

Table 1. Experimental and calculated K_0 values of compounds used in this study.

		K_0		
			Calcd.	
No.	Compound	Expt.	MLR	ANN
1	1,2,4,5-Tetramethylbenzene	1.98	1.92	1.95
2	1,2,4-Trimethylbenzene	1.87	1.83	1.85
3	1,2-Dimethylcyclohexane	1.87	1.90	1.89
4	1,3-Dimethylcyclohexane*	1.87	1.86	1.84
5	2-(2-Hydroxyethyl)pyridine	1.86	1.75	1.82
6	2,2,3,3-Tetramethylbutane	2.02	1.90	1.97
7	2,2,4-Trimethylpentane	1.82	1.84	1.80
8	2,2-Dimethylhexane	1.82	1.80	1.80
9	2,4,6-Trimethylpyridine	1.84	1.80	1.84
10	2,4-Lutidine	1.95	1.87	1.86
11	2,5-Dimethyl-1,5-hexadiene	1.78	1.81	1.84
12	2-Butanol	1.85	1.89	1.87
13	2-Butanone*	2.00	2.02	1.95
14	2-Ethoxyethylacetate	1.86	1.75	1.76
15	2-Ethyl-1-butanol	1.66	1.78	1.73
16	2-Ethyl-1-hexene	1.84	1.80	1.83
17	2-Ethylbutanioc acid methyl ester	1.74	1.71	1.72
18	2-Heptanone*	1.69	1.69	1.69
19	2-Hexanol	1.69	1.70	1.69
20	2-Hexanone	1.79	1.79	1.80
21	2-Methyl-1-butanol	1.72	1.78	1.78
22	2-Methyl-1-propanol	1.84	1.84	1.85
23	2-Methyl-2-propanol	1.83	1.91	1.88
24	2-Methyl-3-hexanone	1.79	1.76	1.72
25	2-Methylbutanal*	1.81	1.84	1.83
26	2-Methylcyclohexanone	1.82	1.81	1.81
27	2-Methylheptane*	1.80	1.72	1.80
28	2-Methylhexane	1.90	1.79	1.85
29	2-Methylpentanal	1.73	1.72	1.75
30	2-Methylpentanoic acid methyl ester	1.72	1.68	1.70
31	2-Methylpropanal	1.93	1.90	1.85
32	2-Octanone	1.60	1.61	1.59
33	2-Pentanone	1.88	1.90	1.87
34	2-Propanol	1.98	1.95	1.97
35	3,3-Dimethyl-2-butanol	1.84	1.84	1.76
36	3,5,5-Trimethyl-1-hexene	1.77	1.80	1.76
37	3-Amyl acetate*	1.68	1.73	1.70
38	3-Heptanone*	1.75	1.75	1.73
39	3-Hexanol*	1.71	1.73	1.72
40	3-Methyl-5-hexanone	1.72	1.68	1.69
41	3-Methylbutanal	1.81	1.83	1.82
42	3-Methylcyclohexanone*	1.76	1.74	1.80
43	3-Methylhexane	1.91	1.78	1.85
44	3-Octanone*	1.70	1.67	1.58
45	3-Pentanol	1.78	1.82	1.82
46	3-Pentanone	1.88	1.91	1.87
47	4-Heptanone*	1.76	1.76	1.73
48	4-Methylcyclohexanone	1.76	1.76	1.79
49	4-Methylheptane	1.81	1.71	1.80
50	5-Methyl-2-hexanone	1.70	1.67	1.71
51	Acetic acid	2.03	2.12	2.06
52	Acetone	2.13	2.05	2.10
53	Ammonia	2.97	2.97	2.97
54	Aniline	1.86	1.88	1.86
55	Benzaldehyde	1.85	1.77	1.83

Table 1 (*continued*).

		K_0		
			Calcd.	
No.	Compound	Expt.	MLR	ANN
56	Benzene	1.94	1.98	1.90
57	Benzylamine	1.74	1.87	1.86
58	Biphenylene	1.72	1.74	1.81
59	Butanal	1.83	1.89	1.83
60	Butylbenzene	1.89	1.76	1.79
61	Butylcyclohexane	1.68	1.69	1.68
62	Butyl propanoate*	1.68	1.68	1.69
63	Carbonic dichloride*	2.77	2.59	2.67
64	Chlorobenzene	1.83	1.93	1.83
65	Cumene	1.86	1.79	1.83
66	Cyanogen chloride	2.50	2.58	2.51
67	Cycloheptane*	1.96	1.90	1.89
68	Cyclohexanone	1.84	1.81	1.84
69	Cyclohexene	1.83	1.94	1.89
70	Cyclohexylamine	1.82	1.88	1.85
71	Decanal	1.38	1.38	1.40
72	Decanol	1.34	1.40	1.29
73	Dicylopentadiene	1.79	1.86	1.87
74	Diethyl phthalate	1.49	1.53	1.52
75	Diisobutylamine	1.70	1.79	1.79
76	Diisopropylamine	1.90	1.91	1.94
77	Dimethyl methylphosphonate	1.91	1.94	1.90
78	Di-*n*-butylamine	1.67	1.67	1.68
79	Di-*n*-propylamine	1.86	1.82	1.87
80	Ethanol	2.06	2.05	2.05
81	Ethyl *N*,*N*-dimethylphosphoroamidocyanidate	1.57	1.67	1.59
82	Ethyl acetate*	1.93	1.95	1.91
83	Ethylbenzene	1.97	1.87	1.86
84	Ethyl butanoate*	1.79	1.79	1.82
85	Ethylcyclohexane	1.86	1.82	1.82
86	Ethylcyclopentane	1.94	1.93	1.91
87	Ethyl ether	1.98	2.02	2.00
88	Ethyl hexanoate*	1.63	1.53	1.56
89	Ethyl octanoate	1.47	1.37	1.41
90	Ethyl propanoate*	1.86	1.91	1.87
91	Glutaraldehyde	1.97	2.04	1.97
92	Heptanal*	1.60	1.61	1.62
93	Heptanol	1.54	1.61	1.57
94	Hexanal	1.69	1.69	1.68
95	Hexanol	1.62	1.69	1.68
96	Hydrogen cyanide	2.50	2.44	2.49
97	Isoamyl acetate	1.64	1.61	1.67
98	Isoamyl alcohol	1.72	1.78	1.82
99	Isoamylamine	1.84	1.83	1.82
100	Isobutyl acetate*	1.72	1.69	1.74
101	Isobutylbenzene*	1.75	1.80	1.80
102	Isobutyric acid	1.86	1.88	1.93
103	Isopropyl methylphosphonofluoridate	1.68	1.70	1.67
104	Isopropyl acetate	1.83	1.84	1.81
105	Isopropylcyclohexane	1.78	1.84	1.77
106	Mesitylene	1.60	1.49	1.55
107	Methyl anteisovalerate	1.80	1.75	1.78
108	Methyl butanoate	1.86	1.78	1.84
109	Methylcyclohexane*	1.95	1.91	1.90
110	Methyl heptanoate	1.60	1.44	1.61

Can. J. Chem. Downloaded from www.nrcresearchpress.com by Renmin University of China on 09/02/12
For personal use only.

Can. J. Chem. Downloaded from www.nrcresearchpress.com by Renmin University of China on 09/02/12
For personal use only.

Table 1 (*concluded*).

		K_0		
			Calcd.	
No.	Compound	Expt.	MLR	ANN
111	Methyl hexanoate	1.68	1.53	1.65
112	Methyl isobutyrate	1.87	1.82	1.81
113	Methyl isocaproate*	1.67	1.65	1.69
114	Methyl *tert*-valerate*	1.82	1.75	1.71
115	*m*-Xylene*	1.96	1.90	1.88
116	*N*,*N*-Diethylaniline	1.70	1.65	1.71
117	*N*,*N*-Dimethylaniline	1.81	1.86	1.85
118	*n*-Amylamine	1.79	1.81	1.81
119	Naphthalene	1.86	1.80	1.83
120	*n*-Butylamine	1.92	1.90	1.90
121	*n*-Decane	1.63	1.59	1.59
122	*n*-Heptane	1.90	1.80	1.87
123	*n*-Heptylamine	1.58	1.65	1.51
124	*n*-Hexane*	2.00	1.88	1.95
125	*n*-Hexylamine	1.68	1.73	1.67
126	Nitrochloroform	2.70	2.57	2.69
127	*n*-Nonane	1.72	1.74	1.74
128	*n*-Octane*	1.80	1.73	1.77
129	Nonanal	1.44	1.45	1.48
130	Nonanol	1.40	1.46	1.36
131	Octanal	1.51	1.53	1.56
132	Octanol*	1.47	1.54	1.46
133	*o*-Ethyl-*S*-(2-diisopropylaminoethyl)methylphosphonothiolate	1.23	1.38	1.22
134	*o*-Toluidine	1.80	1.93	1.88
135	*o*-Xylene	1.96	1.91	1.87
136	Parathion	1.27	1.38	1.32
137	*p*-Cymene	1.76	1.76	1.83
138	*p*-Diisopropylbenzene	1.59	1.67	1.66
139	Pentanal*	1.80	1.79	1.75
140	Pentane*	2.02	1.97	2.00
141	Pinacolyl methylphosphonofluoridate	1.52	1.48	1.51
142	Propanal	1.93	1.96	1.95
143	Propanol*	1.93	1.96	1.95
144	Propionic acid*	1.94	1.90	1.86
145	Propyl methanoate*	1.87	1.79	1.76
146	Propylbenzene*	1.85	1.81	1.83
147	Propyl butanoate	1.71	1.74	1.71
148	Propylcyclohexane*	1.77	1.76	1.76
149	Propyl propanoate*	1.77	1.78	1.77
150	*sec*-Amyl acetate*	1.66	1.66	1.68
151	*sec*-Butyl acetate	1.75	1.75	1.73
152	*sec*-Butylbenzene	1.75	1.83	1.79
153	*tert*-Amyl alcohol*	1.67	1.85	1.82
154	*tert*-Butyl acetate	1.75	1.83	1.79
155	*tert*-Butylamine	2.00	1.96	1.95
156	Toluene*	1.87	1.99	1.91
157	Triethylamine	1.95	1.87	1.88
158	Tri-*n*-butylamine	1.46	1.54	1.49
159	Tri-*n*-propylamine	1.69	1.73	1.75

Note: ANN, artificial neural network; MLR, multiple linear regression.

*Compounds in the test set.

one of the best ways to build training and test sets.[40,41] The advantages of this algorithm are that the training samples always map the measured region of the input variable space completely with respect to the induced metric and that the no test samples fall outside the measured region. Using Kennard and Stones algorithm, the entire data set was divided into two subsets: a training set of 120 compounds and a test set including the remaining 39 compounds.

Can. J. Chem. Downloaded from www.nrcresearchpress.com by Renmin University of China on 09/02/12
For personal use only.

Model development and validation

Linear models were developed by applying stepwise MLR analysis with leave-one-out (LOO) cross-validation to the training set. The quality of the models was measured by the R^2, the adjusted R^2, the cross-validated R^2, the F ratio values, the standard error of estimation (s), and the significance level value (p). A variance inflation factor (VIF) was calculated to test if multicollinearities existed among the descriptors, which is defined as

$$[3] \qquad \mathrm{VIF} = \frac{1}{1 - R^2_j}$$

where R^2_j is the squared correlation coefficient between the jth coefficient regressed against all the other descriptors in the model. Models would not be accepted if they contained descriptors with VIF above a value of five.[42] To exclude the possible existence of fortuitous correlations, the proposed MLR model was also checked by Y-randomization tests.

Nonlinear models were then developed by submitting the selected descriptors from MLR to a three-layer, fully connected, feed-forward ANN. The number of input neurons was equal to that of the descriptors in the linear model. The number of hidden neurons was optimized by a trial and error procedure on the training process. One output neuron was used to represent the experimental K_0. The network was trained using the quasi-Newton Broyden–Fletcher–Goldfarb–Shanno (BFGS) algorithm.[25] To avoid overtraining, one-tenth of the data from the training set were randomly selected as a separate validation set for monitoring the training process, i.e., during the training of the network the performance was monitored by predicting the values for the systems in the validation set. When the results for the validation set ceased to improve, the training was stopped.

Validation of the linear and nonlinear models was further performed by using the external test set composed of data not used to develop the prediction model. The external $R^2_{\mathrm{CV,ext}}$ for the test sets was determined as

$$[4] \qquad R^2_{\mathrm{CV,ext}} = 1 - \frac{\sum (y_i - \tilde{y}_i)^2}{\sum (y_i - \bar{y}_{\mathrm{tra}})^2}$$

where y_i and $\tilde{y}_i$ are the observed and the calculated values, respectively, and $\bar{y}_{\mathrm{tra}}$ is the averaged value for the response variable of the training set. According to Tropsha and coworkers,[26,40] a QSPR model is successful if it satisfies several criteria as follows:

$$[5a] \qquad R^2_{\mathrm{CV,ext}} > 0.5$$

$$[5b] \qquad r^2 > 0.6$$

$$[5c] \qquad (r^2 - r_0^2)/r^2 < 0.1 \quad \text{or} \quad (r^2 - r_0'^2)/r^2 < 0.1$$

$$[5d] \qquad 0.85 \leq k \leq 1.15 \quad \text{or} \quad 0.85 \leq k' \leq 1.15$$

where r is the correlation coefficient between the calculated and experimental values in the test set, r_0^2 (calculated versus observed values) and $r_0'2$ (observed versus calculated values) are the coefficients of determination, and k and k' are the slopes of the regression lines through the origin of the calculated versus observed values and the observed versus calculated values, respectively. Detailed mathematical definitions of these parameters can be found in Golbraikh and Tropsha.[26]

Applicability domain analysis

The applicability domain (AD) of a QSPR model[40,43] must be defined if the model is to be used for screening new compounds. In this work, the structural AD was verified by the leverage approach. The leverage (h_i)[43] is defined as follows:

$$[6] \qquad h_i = \mathbf{x}_i^{\mathrm{T}} (\mathbf{X}^{\mathrm{T}} \mathbf{X})^{-1} \mathbf{x}_i$$

where $\mathbf{x}_i$ is the descriptor row-vector of the ith compound, $\mathbf{x}_i^{\mathrm{T}}$ is the transpose of $\mathbf{x}_i$, $\mathbf{X}$ is the descriptor matrix, and $\mathbf{X}^{\mathrm{T}}$ is the transpose of $\mathbf{X}$. The warning leverage (h^*) is, generally, fixed at $3(m + 1)/n$, where n is the total number of samples in the training set and m is the number of descriptors involved in the correlation.

The Williams plot (the plot of leverage values versus standardized residuals) was used to give a graphical detection of both the response outliers (Y outliers) and the structurally influential compounds (X outliers). In this plot, the two horizontal lines indicate the limit of normal values for Y outliers (i.e., samples with standardized residuals greater than 3.0 SD units, $\pm 3.0s$); the vertical straight lines indicate the limits of normal values for X outliers (i.e., samples with leverage values greater than the threshold value, $h > h^*$). For a sample in the external test set whose leverage value is greater than h^*, its prediction is considered unreliable, because the prediction is the result of a substantial extrapolation of the model. Conversely, when the leverage value of a compound is lower than the critical value, the probability of accordance between predicted and experimental values is as high as that for the compounds in the training set. It is noteworthy that the response outliers can be highlighted only for compounds with known responses and the possibility of a compound to be out of the structural AD of a model can be verified for every new compound, the only knowledge needed being the molecular structure information represented by the molecular descriptors selected in the model.

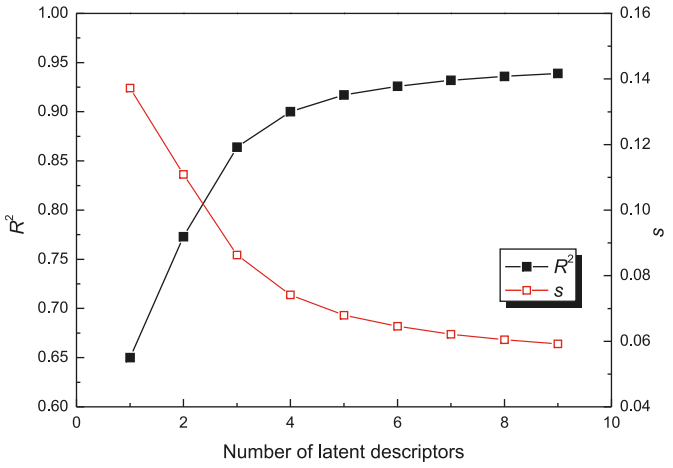
Results and discussion

MLR model

Stepwise MLR analysis with LOO cross-validation was used to develop linear models from the training set, and the number of descriptors in the final model was determined on the basis of the R^2, the adjusted R^2, the cross-validated R^2, the significance test F, and the standard error s. The plots of R^2 and s versus the number of the latent descriptors are shown in Fig. 1. The R^2 value increased gradually with an increasing number of descriptors. The optimum subset size was reached when the addition of another descriptor did not significantly improve the performance of the model. To avoid overparameterization of the models, such as those that contain an excess of descriptors and are difficult to interpret in terms of physical interactions, an increase of the R^2 value of less than 0.01 was chosen as the breakpoint criterion. Thus,

Can. J. Chem. Downloaded from www.nrcresearchpress.com by Renmin University of China on 09/02/12
For personal use only.

Fig. 1. R^2 and standard error (s) vs the number of latent descriptors in the best multiple linear regression (MLR) models.



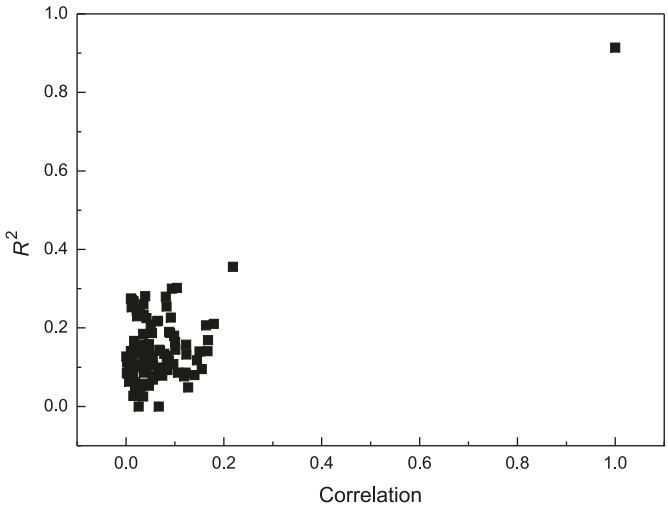
the five-parameter model was selected as the best model, which can be described as

$$[7] \quad K_0 = -0.637(\text{DISPe}) - 0.0326(\text{RDF050m}) + 0.421(\text{E3p}) + 0.485(\text{Dm}) - 0.243(\text{HIC}) + 2.748$$

for $n = 120$, $R^2 = 0.9171$, $R_{CV}{}^2 = 0.9056$, $R_{adj}{}^2 = 0.9107$, $s = 0.0680$, $F = 252.3$, and $p < 0.0001$. Here, DISPe is the d COMMA2 value / weighted by atomic Sanderson electronegativities, RDF050m is the radial distribution function – 5.0 / weighted by atomic masses, E3p is the third component accessibility directional weighted holistic invariant molecular (WHIM) index / weighted by atomic polarizabilities, Dm is the D total accessibility index / weighted by atomic masses, and HIC is the mean information content on the leverage magnitude. More information about these descriptors can be found in the DRAGON software user's guide[37] and the refs. therein.

In general, the larger the magnitude of the F ratio, the better the model prediction of the property values in the training set. The large F ratio of 252.3 indicates that eq. [7] does an excellent job of predicting the K_0 values of the training set. Equation [7] has an adjusted R^2 value of 0.9107, which indicates good agreement between the correlation and the variation in the data. The cross-validated correlation coefficient $R_{CV}{}^2 = 0.9056$ illustrates the reliability of the model by focusing on the sensitivity of the model to the elimination of any single data point. The model was further validated by applying the randomization tests, and the obtained R^2 vs the correlation coefficient between the original and permuted response data are plotted in Fig. 2. The lower R^2 values indicate that the good results of the original model are not due to chance correlation or structural dependency of the training set. Some important statistical parameters shown in Table 2 were used to valuate the involved descriptors. The t value of a descriptor measures the statistical significance of the regression coefficients. The high absolute t values shown in Table 2 express that the regression coefficients of the descriptors involved in the MLR model are significantly larger than the standard deviation. The t probability of a descriptor can describe the statistical significance when combined together within an overall collective QSPR model (i.e., descriptors' interactions). Descriptors with t probability values

Fig. 2. R^2 vs the correlation coefficient between the original and permuted response data (average value of R^2 is 0.138).



below 0.05 (95% confidence) are usually considered statistically significant in a particular model, which means that their influence on the response variable is not merely by chance.[44] The smaller t probability suggests the more significant descriptor. The t probability values of the 5 descriptors are very small, indicating that all of them are highly significant descriptors. Furthermore, all the VIF values are less than five, suggesting that these descriptors are weakly correlated with each other. Thus, the model can be regarded as an optimal regression equation.

The calculated K_0 values from the MLR model for the training and test sets are shown in Table 1 and Fig. 3. The errors are distributed on both sides of the zero point; thus, one may conclude that there is no systematic error in the model development. The following statistical parameters were obtained for the test set ($s = 0.0549$), which obviously satisfy the generally accepted condition and thus demonstrate the predictive power of the present model.

$$R^2{}_{CV,ext} = 0.8945 > 0.5$$
$$r^2 = 0.9029 > 0.6$$
$$(r^2 - r_0{}^2)/r^2 = (0.9029 - 0.9919)/0.9029 < 0.1$$
$$\text{or} \quad (r^2 - r_0'^2)/r^2 = (0.9029 - 0.9952)/0.9029 < 0.1$$
$$0.85 \le k = 1.007 \le 1.15$$
$$\text{or} \quad 0.85 \le k' = 0.992 \le 1.15$$

ANN model

The ANN has become an important and widely used nonlinear modeling technique for QSPR studies. The mathematical adaptability of ANN commends it as a powerful tool for pattern classification and building predictive models. A particular advantage of ANN is its inherent ability to incorporate nonlinear dependencies between the dependent and independent variables without using an explicit mathematical function. Among the neural network learning algorithms, the back-propagation (BP) method[45] is one of the most commonly used methods. The drawback of BP is that the training processes slowly, because the gradient-descent algorithm is usually

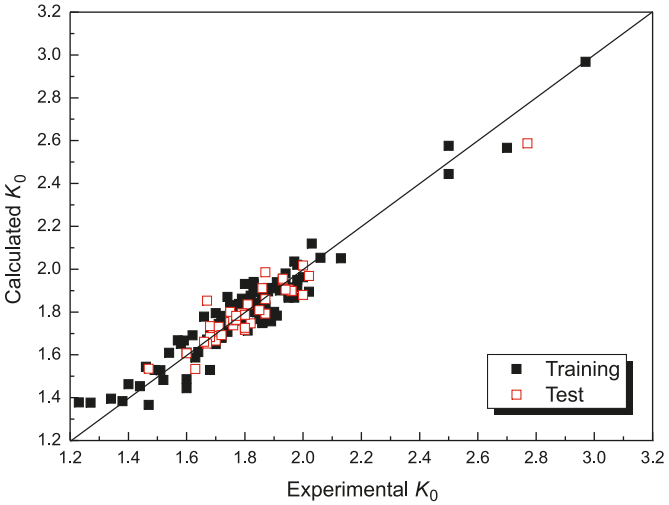
Can. J. Chem. Downloaded from www.nrcresearchpress.com by Renmin University of China on 09/02/12
For personal use only.

Table 2. Characteristics of the descriptors selected in the optimal multiple linear regression (MLR) model.

Descriptor	Descriptor type	Coefficient	Error	*t* value	*t* probability	VIF
Constant		2.748	0.065	42.396	0.0000	
DISPe	Geometrical descriptors	–0.637	0.050	–12.789	0.0000	1.139
RDF050m	RDF descriptors	–0.0326	0.004	–7.903	0.0000	1.632
E3p	WHIM descriptors	0.421	0.093	4.518	0.0002	2.175
Dm	WHIM descriptors	0.485	0.101	4.788	0.0000	2.569
HIC	GETAWAY descriptors	–0.243	0.016	–15.627	0.0000	2.451

Note: VIF, variance inflation factor; DISPe, d COMMA2 value / weighted by atomic Sanderson electronegativities; RDF050m, radial distribution function – 5.0 / weighted by atomic masses; E3p, third component accessibility directional WHIM index / weighted by atomic polarizabilities; Dm, D total accessibility index / weighted by atomic masses; and HIC is the mean information content on the leverage magnitude; GETAWAY, geometry, topology, and atom-weights assembly. The *t* value of a descriptor measures the statistical sifnificance of the regression coefficients. The *t* probability of a descriptor can describe the statistical significance when combined together within an overall collective quantitative structure–property relationship (QSPR) model.

Fig. 3. Calculated vs experimental reduced mobility constant (K_0) values by the multiple linear regression (MLR) model.



used for minimizing the sum-of-squares error. In this study, the quasi-Newton BFGS algorithm[25] was used to develop nonlinear models. The advantages of the BFGS algorithm are that specifying rate or momentum is not necessary and the training is much more rapid.[46] The five descriptors from the MLR model were used as inputs to the network. The number of hidden neurons is an important parameter influencing the performance of the ANN. The usual rule of thumb is that the weights and biases should be less than the samples so that the model achieved by the network is stationary.[47] Consequently, a 5–5–1 network configuration, which gives the best prediction, was obtained after the trial and error procedure.

The present three-layer feed forward neural network with the sigmoidal transfer function can be simplified in the form of eq. [8].

$$[8] \qquad y_{\text{calcd}}(i) = \{\mathbf{W}_2[1.2/\left(1 + e^{-(\mathbf{W}_1\mathbf{T}_i)-\mathbf{b}_1}\right) - 0.1]\} + \mathbf{b}_2$$

where $\mathbf{T}$ is the input matrix of dimension of $m \times n$, where m is the number of molecular descriptors involved and n is the number of compounds available in the training set; $\mathbf{T}_i$ is the ith-column of $\mathbf{T}$; $\mathbf{W}_1$ is the first weight matrix of the three-layer network and has the dimension nhidden $\times$ m, where nhidden is the number of neurons in the hidden layer; $\mathbf{b}_1$ is the first bias matrix of dimension nhidden $\times$ 1; $\mathbf{W}_2$ is the second weight matrix of the output layer and has the dimension 1 $\times$ nhidden; $\mathbf{b}_2$ is the second bias matrix of the output layer, which is a number; and $y_{\text{calcd}}(i)$ is the ith output of this network, which must be compared with the ith response. The values of $\mathbf{W}_1$, $\mathbf{W}_2$, $\mathbf{b}_1$, and $\mathbf{b}_2$ (shown in Table 3) were obtained by the minimization of an objective function, which is commonly the mean-squared error between the outputs of the neural network and the target values.

The predictive results from the ANN model for the entire data set are given in Table 1 and Fig. 4. The R^2, R_{CV}^2, and s for the training set are 0.9631, 0.9622, and 0.0446, respectively. The proposed ANN model is predictive as it satisfies the conditions for the test set ($s = 0.0496$).

$$R^2_{\text{CV,ext}} = 0.9215 > 0.5$$
$$r^2 = 0.9292 > 0.6$$
$$(r^2 - r_0^2)/r^2 = (0.9292 - 0.9896)/0.9029 < 0.1$$
$$\text{or} \quad (r^2 - r_0'^2)/r^2 = (0.9292 - 0.9922)/0.9029 < 0.1$$
$$0.85 \le k = 1.009 \le 1.15$$
$$\text{or} \quad 0.85 \le k' = 0.990 \le 1.15$$

By comparison of the models obtained by MLR and ANN, it can be seen that the performance of ANN is better than that of MLR, which confirms the nonlinear relationship between the structural information and the K_0. To further test the suitability of the proposed models, the obtained results were compared with those calculated by other reported models[13] (Table 4) for the same set of compounds. The present models developed on the basis of 3D molecular representation are comparable in quality to the models described by Yao and co-workers[13] This fact confirms the potency of 3D descriptors as a useful tool for the structural characterization and prediction of the mobility behavior in IMS.

Applicability domain

It needs to be pointed out that no matter how robust, significant, and validated a QSPR model may be, it cannot be expected to reliably predict the modeled property for the entire universe of compounds. Therefore, before a QSPR model is put into use for screening compounds, its AD must be defined and predictions for only those compounds that fall in this domain can be considered as reliable. The model AD was analyzed in the Williams plot (shown in Fig. 5). Three

Can. J. Chem. Downloaded from www.nrcresearchpress.com by Renmin University of China on 09/02/12
For personal use only.

Table 3. Weight and bias matrices of the obtained neural network.

Weight matrix					Bias matrix
$\mathbf{W_1}$					$\mathbf{b_1}$
1.7734	3.8274	0.6634	0.2844	1.7280	–0.9686
0.7611	0.9290	0.3222	–0.1644	–0.0345	–1.7603
–0.1924	–1.2679	0.3603	–2.3922	–1.7971	–1.2790
–0.0960	2.1991	–0.4850	0.1874	–0.0661	3.6437
0.2519	–0.3336	–0.8367	–2.5291	–0.4017	4.6772
$\mathbf{W_2}$					$\mathbf{b_2}$
–2.8285	1.1903	1.9530	1.4593	–2.7607	1.5991

Note: $\mathbf{W}_1$, first weight matrix of the three-layer network with the dimension nhidden × m, where nhidden is the number of neurons in the hidden layer; $\mathbf{b}_1$, first bias matrix of dimension nhidden × 1; $\mathbf{W}_2$, second weight matrix of the output layer with the dimension 1 × nhidden; $\mathbf{b}_2$, second bias matrix of the output layer, which is a number.

Fig. 4. Calculated vs experimental K_0 values by the artificial neural network (ANN) model.

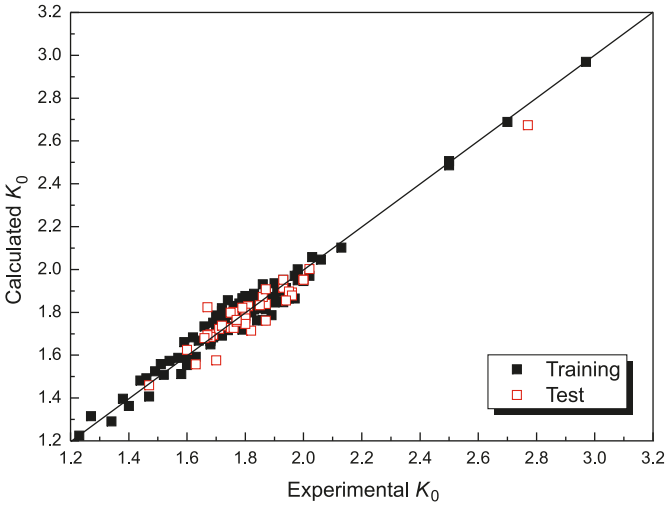


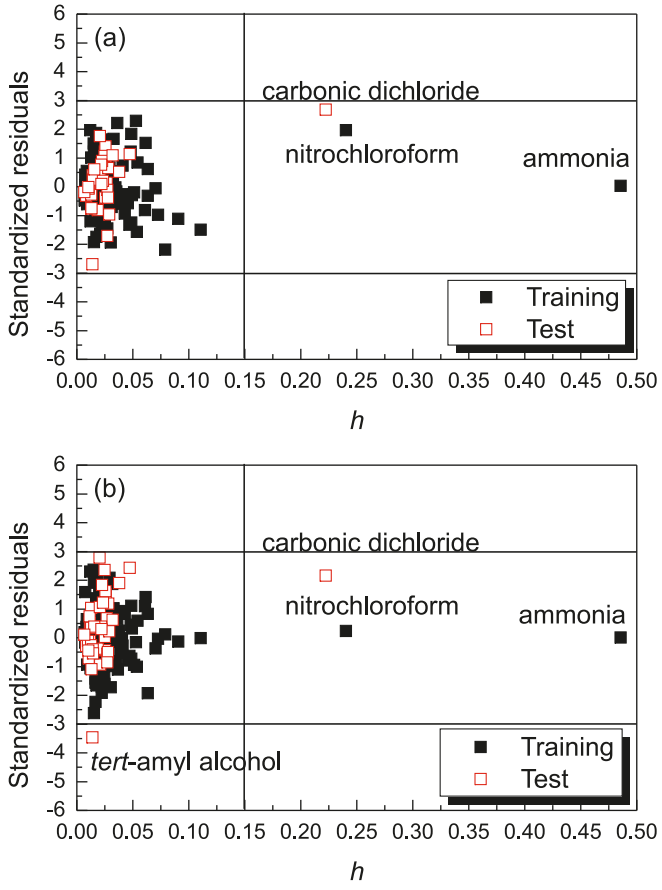
Table 4. Performance comparison between different quantitative structure–property relationship (QSPR) models for the prediction of the reduced mobility constant (K_0).

	Training set		Test set	
Model	R^2	s	R^2	s
Present MLR	0.9171	0.0680		0.0549
Present ANN	0.9631	0.0446		
Reference 13 (MLR)	0.9116	0.0693	0.9067	0.9029
Reference 13 (PPR)	0.9337	0.0566	0.9569	0.0469

Note: MLR, multiple linear regression; ANN, artificial neural network; PPR, projection pursuit regression.

compounds (carbonic dichloride, nitrochloroform, and ammonia) were found to be X outliers (with leverage values higher than the warning leverage limit of 0.150). In the Williams plot, X outliers can be explained as compounds with peculiar features poorly represented in the data set, which could affect the variable selection for a better modeling of those compounds. Ammonia is the only inorganic compound in the data set, nitrochloroform is the unique nitro compound with strong polarity, and arbonic dichloride is of the unstable structure feature. These three compounds were well predicted by the present models and thus reinforced the models.

Fig. 5. Williams plots of the developed models: (*a*) multiple linear regression (MLR) and (*b*) artificial neural network (ANN).



Generally, if the residual value is larger than ±3.0s, the sample can be considered a response outlier (Y outlier), which could be associated with errors in the experimental values. On analyzing the AD of the developed models in the Williams plot, there is no response outlier for the MLR model. For the ANN model, *tert*-amyl alcohol would be recognized as a response outlier and it also shows a relatively large standard residual (close to 3s) for the MLR model. However, the majority of the samples within the model AD were calculated accurately, which provided another indication of the reliability of the predictions.

Because of their high predictive abilities, the proposed models could be used to screen existing databases or virtual

Can. J. Chem. Downloaded from www.nrcresearchpress.com by Renmin University of China on 09/02/12
For personal use only.

chemical structures to identify compounds with the desired ion mobility constants. In this case, the AD will serve as a valuable tool to filter out "dissimilar" chemical structures.

Descriptor contribution analysis and interpretation

The descriptors appearing in the present models encode 3D aspects of the molecular structure and can be classified as follows: (1) a geometrical descriptor, DISPe; (2) an RDF descriptor, RDF050m; (3) two WHIM descriptors, E3p and Dm; and (4) a GETAWAY (geometry, topology, and atom-weights assembly) descriptor, HIC.

It is not a trivial task to interpret the nonlinear models because of their complex modeling procedure and vague output, although the nonlinear models could give better predictive results. Thus, the descriptor interpretation was carried out on the basis of the MLR model. Based on a previously described procedure,[48] the relative contributions of the five descriptors to the MLR model were determined and are plotted in Fig. 6. The significance of the descriptors involved in the MLR model decreases in the following order: DISPe (23.5%) > HIC (19.9%) > RDF050m (19.7%) > Dm (19.0%) > E3p (17.9%). The difference in descriptor contribution between any two descriptors used in the models is not significant, indicating that all of the descriptors are indispensable in generating the predictive models.

The most significant descriptor in the MLR model is DISPe, a COMMA2[49] descriptor. DISPe is a measure of displacement between the geometric and the electronegativity (e) centers in the molecule, calculated with respect to the molecular principal axes. This descriptor can reflect how charge is distributed in the molecule and loosely show molecular size as well. The negative regression coefficient of this descriptor suggests that an increasing separation between geometric and electronegativity centers is detrimental to the K_0. Thus, this descriptor could be an indicator for compounds that have a small K_0 value.

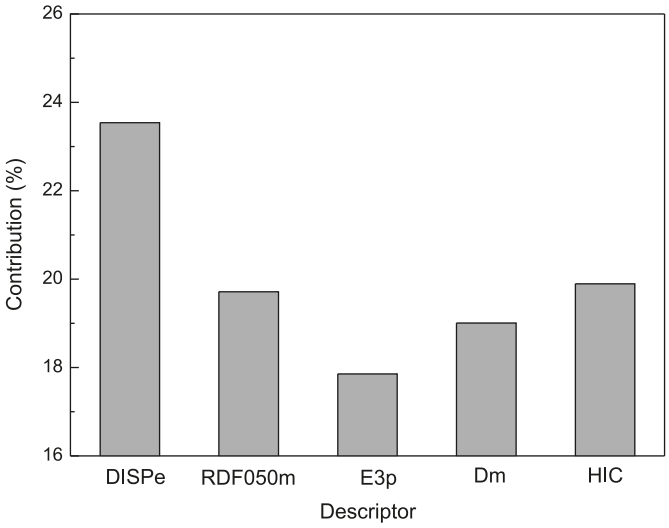
The second important descriptor is HIC, the mean information content on the leverage magnitude. HIC is calculated as follows:[50]

$$[9] \qquad \mathrm{HIC} = -\sum_{i=i}^{n\mathrm{AT}} \frac{h_{ii}}{D} \log_2 \frac{h_{ii}}{D}$$

where nAT is the number of molecule atoms, D is the rank of the molecular matrix equal to 1, 2, and 3 for linear, planar, and nonplanar molecules, respectively. This descriptor is able to catch more specific information with regard to molecular complexity than the total and standardized information content on the leverage equality. For example, HIC can recognize the different substituents in a series of monosubstituted benzenes. HIC is also sensitive to the presence of multiple bonds. The emergence of HIC in the model reflects the importance of molecular shape of a compound during the IMS separation process.

The third descriptor, RDF050m, is one of the RDF descriptors, which have been proposed based on a radial distribution function. The RDF descriptors can be interpreted as the probability distribution of finding an atom in a spherical volume of radius r. The general form of the radial distribution function is represented by

Fig. 6. Relative contributions of the descriptors to the multiple linear regression (MLR) model.



$$[10] \qquad \mathrm{RDF}rw = f \sum_{i=1}^{n\mathrm{AT}-1} \sum_{j=i+1}^{n\mathrm{AT}} w_i w_j e^{-\beta(r-r_{ij})^2}$$

where f is a scaling factor (assumed equal to one in the calculations) and w is the characteristic property of the atom.[51] RDFrw is generally calculated at a number of discrete points with defined intervals. Besides information about interatomic distances in the entire molecule, RDF050m provides further information about atomic masses. The negative correlation coefficient for RDF050m indicates that a compound with a larger value for this descriptor would have smaller K_0 value.

WHIM descriptors[52,53] are based on principal component analysis of the weighted covariance matrix obtained from the atomic Cartesian coordinates. WHIM descriptors can capture 3D information regarding molecular size, shape, symmetry, and atom distribution with respect to the molecule as a whole. E3p and Dm were calculated by eqs. [11] and [12], respectively, where λ refers to eigenvalues of the weighted covariance matrix and t refers to atomic coordinates with respect to the principal axes.

$$[11] \qquad Ekw = \frac{\lambda_k^2 n\mathrm{AT}}{\sum t_{jk}^4}$$

$$[12] \qquad D = E1w + E2w + E3w$$

Dm indicates a global measure of the degree of participation in intermolecular interactions, based on the projections of the atoms through principal axes or principal components. This descriptor points to the influence of the molecular conformation during the IMS separation process. The coefficient of Dm is positive, meaning that the K_0 increases when this descriptor increases. E3p conveys information about the distribution of electronic charge within the molecule, which has a positive effect on K_0.

Can. J. Chem. Downloaded from www.nrcresearchpress.com by Renmin University of China on 09/02/12
For personal use only.

Conclusions

In this paper, the QSPR method was employed to predict the ion mobility constants of 159 diverse compounds based on 3D descriptors. A five-parameter linear model was developed by MLR, with $R^2 = 0.9171$ and $s = 0.0680$ for the training set. The nonlinear model built by ANN appeared to be more reliable than the linear model, where R^2 was 0.9631 and s was 0.0446 for the training set. Satisfactory prediction results for the test set were obtained with both the linear and nonlinear models. The descriptors involved in the models indicate that the major factors determining the mobility of the compounds are molecular size, shape, and charge distribution. The proposed models are predictive and could be used to estimate the ion mobility constants of compounds in IMS because all the descriptors involved can be directly calculated from the molecular structure.

Acknowledgements

This work was supported by the Natural Science Foundation of China (Grant No. 51003082) and the Educational Commission of Hubei Province (Grant No. Q20101606). The authors gratefully wish to express their thanks to the reviewers for critically reviewing the manuscript and making important suggestions.

References

(1) Agbonkonkon, N.; Tolley, H. D.; Asplund, M. C.; Lee, E. D.; Lee, M. L. *Anal. Chem.* **2004** *76* (17), 5223. doi:10.1021/ac030403s.
(2) Steiner, W. E.; Clowers, B. H.; Matz, L. M.; Siems, W. F.; Hill, H. H. *Anal. Chem.* **2002** *74* (17), 4343. doi:10.1021/ac025687f.
(3) Bota, G. M.; Harrington, P. B. *Talanta* **2006** *68* (3), 629. doi:10.1016/j.talanta.2005.05.001.
(4) Myung, S.; Lee, Y. J.; Moon, M. H.; Taraszka, J.; Sowell, R.; Koeniger, S.; Hilderbrand, A. E.; Valentine, S. J.; Cherbas, L.; Cherbas, P.; Kaufmann, T. C.; Miller, D. F.; Mechref, Y.; Novotny, M. V.; Ewing, M. A.; Sporleder, C. R.; Clemmer, D. E. *Anal. Chem.* **2003** *75* (19), 5137. doi:10.1021/ac030107f.
(5) McLean, J. A.; Russell, D. H. *J. Proteome Res.* **2003** *2* (4), 427. doi:10.1021/pr034004p.
(6) Valentine, S. J.; Plasencia, M. D.; Liu, X.; Krishnan, M.; Naylor, S.; Udseth, H. R.; Smith, R. D.; Clemmer, D. E. *J. Proteome Res.* **2006** *5* (11), 2977. doi:10.1021/pr060232i.
(7) Liu, X.; Valentine, S. J.; Plasencia, M. D.; Trimpin, S.; Naylor, S.; Clemmer, D. E. *J. Am. Soc. Mass Spectrom.* **2007** *18* (7), 1249. doi:10.1016/j.jasms.2007.04.012.
(8) Hoaglund, C. S.; Valentine, S. J.; Clemmer, D. E. *Anal. Chem.* **1997** *69* (20), 4156. doi:10.1021/ac970526a.
(9) Jin, L.; Barran, P. E.; Deakin, J. A.; Lyon, M.; Uhrín, D. *Phys. Chem. Chem. Phys.* **2005** *7* (19), 3464. doi:10.1039/b508644b.
(10) Dwivedi, P.; Wu, P.; Klopsch, S. J.; Puzon, G. J.; Xun, L.; Hill, H., Jr. *Metabolomics* **2008** *4* (1), 63. doi:10.1007/s11306-007-0093-z.
(11) Hill, Jr., H. H. *Anal. Chem.* **1990** *62*, 1201A.
(12) Wessel, M. D.; Sutter, J. M.; Jurs, P. C. *Anal. Chem.* **1996** *68* (23), 4237. doi:10.1021/ac960466t.
(13) Liu, H.; Yao, X.; Liu, M.; Hu, Z.; Fan, B. *Talanta* **2007** *71* (1), 258. doi:10.1016/j.talanta.2006.03.058.
(14) Griffin, G. W.; Dzidic, I.; Carroll, D. I.; Stillwell, R. N.; Horning, E. C. *Anal. Chem.* **1973** *45* (7), 1204. doi:10.1021/ac60329a026.
(15) Lin, S. N.; Griffin, G. W.; Horning, E. C.; Wentworth, W. E. *J. Chem. Phys.* **1974** *60* (12), 4994. doi:10.1063/1.1681013.
(16) Benezra, S. A. *J. Chromatogr. Sci.* **1976** *14*, 122.
(17) Karasek, F. W.; Kim, S. H.; Rokushika, S. *Anal. Chem.* **1978** *50* (14), 2013. doi:10.1021/ac50036a019.
(18) Yao, X. J.; Wang, Y. W.; Zhang, X. Y.; Zhang, R. S.; Liu, M. C.; Hu, Z. D.; Fan, B. T. *Chemom. Intell. Lab. Syst.* **2002** *62* (2), 217. doi:10.1016/S0169-7439(02)00017-5.
(19) Xu, J.; Guo, B.; Chen, B.; Zhang, Q. *J. Mol. Model.* **2005** *12* (1), 65. doi:10.1007/s00894-005-0006-x.
(20) Devillers, J.; Balaban, A. T., Eds. *Topological Indices and Related Descriptors in QSAR and QSPR;* Gordon and Breach: The Netherlands, 1999.
(21) Karelson, M. *Molecular Descriptors in QSAR/QSPR;* Wiley-Interscience: New York, 2000.
(22) Todeschini, R.; Consonni, V. *Molecular Descriptors for Chemoinformatics,* 2nd ed.; Wiley-VCH: Weinheim, 2009.
(23) Xu, J.; Zhang, H.; Wang, L.; Ye, W.; Xu, W.; Li, Z. *Fluid Phase Equilib.* **2010** *291* (2), 111. doi:10.1016/j.fluid.2009.12.032.
(24) Xu, J.; Wang, L.; Wang, L.; Shen, X.; Xu, W. *J. Comput. Chem.* **2011** *32* (15), 3241. doi:10.1002/jcc.21907.
(25) Wessel, M. D.; Jurs, P. C. *Anal. Chem.* **1994** *66* (15), 2480. doi:10.1021/ac00087a012.
(26) Golbraikh, A.; Tropsha, A. *J. Mol. Graph. Model.* **2002** *20* (4), 269. doi:10.1016/S1093-3263(01)00123-1.
(27) Todeschini, R.; Consonni, V. *Handbook of Molecular Descriptors;* Wiley-VCH: Weinheim, 2000.
(28) Estrada, E.; Molina, E. *J. Chem. Inf. Comput. Sci.* **2001** *41* (3), 791. doi:10.1021/ci000156i.
(29) Consonni, V.; Todeschini, R.; Pavan, M.; Gramatica, P. *J. Chem. Inf. Comput. Sci.* **2002** *42* (3), 693. doi:10.1021/ci0155053.
(30) Cruz, V.; Ramos, J.; Munoz-Escalona, A.; Lafuente, P.; Pena, B.; Martinez-Salazar, J. *Polymer (Guildf.)* **2004** *45* (6), 2061. doi:10.1016/j.polymer.2003.12.059.
(31) Saíz-Urra, L.; Pérez González, M.; Teijeira, M. *Bioorg. Med. Chem.* **2006** *14* (21), 7347. doi:10.1016/j.bmc.2006.05.081.
(32) Saíz-Urra, L.; Pérez González, M.; Fall, Y.; Gómez, G. *Eur. J. Med. Chem.* **2007** *42* (1), 64. doi:10.1016/j.ejmech.2006.08.005.
(33) Cabrera-Pérez, M. A.; Castillo-González, D.; Pérez-González, M.; Durán-Martínez, A. *QSAR Comb. Sci.* **2009** *28* (5), 526. doi:10.1002/qsar.200860042.
(34) D'Archivio, A. A.; Maggi, M. A.; Mazzeo, P.; Ruggieri, F. *Anal. Chim. Acta* **2008** *628* (2), 162. doi:10.1016/j.aca.2008.09.018.
(35) Xu, J.; Wang, L.; Wang, L.; Liang, G.; Shen, X.; Xu, W. *Chemom. Intell. Lab. Syst.* **2011** *107* (1), 178. doi:10.1016/j.chemolab.2011.03.006.
(36) *Hyperchem,* version 6.01; Hypercube, Inc.: Gainesville, 2000.
(37) Todeschini, R.; Consonni, V.; Mauri, A.; Pavan, M. *DRAGON for Windows (Software for Molecular Descriptor Calculations),* version 5.4; TALETE srl: Milan, Italy, 2006.
(38) Liu, H.; Gramatica, P. *Bioorg. Med. Chem.* **2007** *15* (15), 5251. doi:10.1016/j.bmc.2007.05.016.
(39) Kennard, R. W.; Stone, L. A. *Technometrics* **1969** *11*, 137.
(40) Tropsha, A.; Gramatica, P.; Gombar, V. K. *QSAR Comb. Sci.* **2003** *22* (1), 69. doi:10.1002/qsar.200390007.
(41) Wu, W.; Walczak, B.; Massart, D. L.; Heuerding, S.; Erni, F.; Last, I. R.; Prebble, K. A. *Chemom. Intell. Lab. Syst.* **1996** *33* (1), 35. doi:10.1016/0169-7439(95)00077-1.

(42) Holder, A. J.; Yourtee, D. M.; White, D. A.; Glaros, A. G.; Smith, R. *J. Comput. Aided Mol. Des.* **2003** *17* (2/4), 223. doi:10.1023/A:1025382226037.
(43) Atkinson, A. *Plots, Transformations, and Regression;* Clarendon Press: Oxford, UK, 1985.
(44) Ramsey, L. F.; Schafer, W. D. *The Statistical Sleuth;* Wadsworth Publishing Company: Beverly, MA, 1997.
(45) Jansson, P. A. *Anal. Chem.* **1991** *63* (6), 357A. doi:10.1021/ac00006a739.
(46) Xu, L.; Ball, J. W.; Dixon, S. L.; Jurs, P. C. *Environ. Sci. Chem.* **1994** *13*, 841.
(47) Qi, Y.-H.; Zhang, Q.-Y.; Xu, L. *J. Chem. Inf. Comput. Sci.* **2002** *42* (6), 1471. doi:10.1021/ci020027x.
(48) Zheng, F.; Bayram, E.; Sumithran, S. P.; Ayers, J. T.; Zhan, C.-G.; Schmitt, J. D.; Dwoskin, L. P.; Crooks, P. A. *Bioorg. Med. Chem.* **2006** *14* (9), 3017. doi:10.1016/j.bmc.2005.12.036.
(49) Silverman, B. D. *J. Chem. Inf. Comput. Sci.* **2000** *40* (6), 1470. doi:10.1021/ci000457s.
(50) Consonni, V.; Todeschini, R.; Pavan, M. *J. Chem. Inf. Comput. Sci.* **2002** *42* (3), 682. doi:10.1021/ci015504a.
(51) Hemmer, M. C.; Steinhauer, V.; Gasteiger, J. *Vibrat. Spect.* **1999** *19* (1), 151. doi:10.1016/S0924-2031(99)00014-4.
(52) Todeschini, R.; Lasagni, M.; Marengo, E. *J. Chemometr.* **1994** *8* (4), 263. doi:10.1002/cem.1180080405.
(53) Todeschini, R.; Gramatica, P.; Provenzani, R.; Marengo, E. *Chemom. Intell. Lab. Syst.* **1995** *27*, 221.

Can. J. Chem. Downloaded from www.nrcresearchpress.com by Renmin University of China on 09/02/12
For personal use only.

Composition of *Dithyrea wislizenii* fruit extract and free-radical scavenging activity of its constituents

Sabine Montaut, Julie Grandbois, Laura S. Rossi, Sonia Kamal, James Khouri, Melissa G. Ménard, and Hélène A. Joly

Can. J. Chem. Downloaded from www.nrcresearchpress.com by Renmin University of China on 09/02/12
For personal use only.

Abstract: Glucolesquerellin (**2**), glucohesperin (**3**), quercetin 3-*O*-sophoroside (**4**), and quercetin 3-*O*-sophoroside-7-*O*-glucoside (**5**), isolated from the fruit of *Dithyrea wislizenii*, were quantified by HPLC. The fruit extract and flavonoids were not found to be toxic by using a brine shrimp lethality assay. The fruit extract and the flavonoids and glucosinolates were submitted to a free-radical scavenging activity assay with the diphenylpicrylhydrazyl radical (DPPH$^{\bullet}$). The concentration of quercetin (**6**) (a positive control for the flavonoids) able to scavenge 50% of DPPH$^{\bullet}$ (SC_{50}) was 32 ± 2 μmol/L (or 4 ± 1 μg/mL), which was about 27 times more potent than the crude extract. Compounds **4** and **5** had a SC_{50}, the concentration of the compound required to scavenge 50% of the DPPH$^{\bullet}$, of 78 ± 1 μmol/L and 113 ± 10 μmol/L, respectively. The positive control for the glucosinolates, glucoraphasatin, (**1**) had a SC_{50} of 1768 ± 60 μmol/L. The glucosinolates **2** and **3** had a SC_{50} of 7819 ± 1968 and 970 ± 63 μmol/L, respectively.

Key words: Dithyrea wislizenii, Brassicaceae, flavonoids, glucosinolates, free-radical scavengers.

Résumé : La glucolesquerelline (**2**), la glucohespérine (**3**), la quercétine 3-*O*-sophoroside (**4**), et la quercétine 3-*O*-sophoroside-7-*O*-glucoside (**5**), isolées à partir des fruits de *Dithyrea wislizenii*, ont été quantifiés par HPLC. L'extrait de fruit et les flavonoïdes n'ont pas montré de toxicité en utilisant le test de mortalité de la crevette de saumure. L'extrait de fruit, les flavonoïdes et les glucosinolates ont été soumis à un test d'activité anti-radicalaire à l'aide du radical diphénylpicrylhydrazyle (DPPH$^{\bullet}$). La concentration de quercétine (**6**) (un contrôle positif pour les flavonoïdes) capable de piéger 50 % de DPPH$^{\bullet}$ (SC_{50}) était 32 ± 2 μmol/L (ou 4 ± 1 μg/mL), ce qui était environ 27 fois plus puissant que l'extrait brut. Les composés **4** et **5** avaient des SC_{50} de 78 ± 1 μmol/L et 113 ± 10 μmol/L, respectivement. Le contrôle positif pour les glucosinolates, la glucoraphasatine, (**1**) avait une SC_{50} de 1768 ± 60 μmol/L. Les glucosinolates **2** et **3** avaient des SC_{50} de 7819 ± 1968 et 970 ± 63 μmol/L, respectivement.

Mots-clés : Dithyrea wislizenii, Brassicaceae, flavonoïdes, glucosinolates, piégeurs de radicaux libres.

Introduction

The antioxidant properties of plant extracts originating from members of the Brassicaceae family were first attributed to polyphenolic compounds.[1] However, there have been reports that nonphenolic compounds can also contribute to the antioxidant activity of some *Brassica* sp.[2] In fact, the glucosinolate (GL), 4-methylsulfanyl-3-butenylGL (**1**), was shown to have free-radical scavenging activity towards the radical cation 2,2′-azino-bis(3-ethylbenzthiazoline-6-sulfonic acid) (ABTS$^{\bullet+}$) and the diphenylpicrylhydrazyl (DPPH$^{\bullet}$) free radical.[3,4]

Dithyrea wislizenii Engelm. (Brassicaceae) (syn. *Dimorphocarpa wislizenii* (Engelm.) Rollins), an endemic annual plant found in Nevada, Colorado, Utah, Arizona, New Mexico, and Texas, grows in open sandy soil of dry grasslands and deserts. This branched or unbranched, greyish, hairy plant has pinnately lobed leaves, white flowers in dense, thick racemes, and is commonly referred to as "spectacle pod".[5] Many Native American tribes used this plant as food for animals,[6] as a drug to reduce swelling, to treat delirium, on wounds, and in miscellaneous ceremonies.[7]

In previous phytochemical studies, the fatty acid content of the seed oil of *D. wislizenii* was investigated.[8,9] In addition, a GC analysis of the hydrolysis products of the compounds extracted from the seeds showed the presence of 5-methylsulfanylpentyl-, 6-methylsulfanylhexyl-, 7-methylsulfanylheptyl-, 5-methylsulfinylpentyl-, and 6-methylsulfinylhexyl isothiocyanates (ITCs), which suggests that the seeds contain the parent GLs.[10] Recently, our group analyzed the fruit extract of *D. wislizenii* for desulfoGLs and intact GLs using HPLC–APCI-MS and HPLC–ESI-MS, respectively. 2-PropenylGL (sinigrin) was shown to be present in the extract. 6-MethylsulfanylhexylGL (glucolesquerellin, **2**), 6-methylsulfinylhexylGL (glucohesperin, **3**), 7-methylsulfanylheptylGL, and 5-methylsulfanylpentylGL (glucoberteroin) were isolated from the extract and characterized by UV, IR, and NMR spectroscopies, and mass spectrometry.[11] Finally, the indole alkaloid, dithyreanitrile (7-methoxy-α,α-bis(methylsulfanyl)-1*H*-indole-3-acetonitrile), was isolated from the seeds of

Received 2 April 2012. Accepted 2 June 2012. Published at www.nrcresearchpress.com/cjc on 19 July 2012.

S. Montaut, J. Grandbois, L.S. Rossi, S. Kamal, J. Khouri, M.G. Ménard, and H.A. Joly. Department of Chemistry and Biochemistry, Laurentian University, 935 Ramsey Lake Road, Sudbury, ON P3E 2C6, Canada.

Corresponding author: Sabine Montaut (e-mail: smontaut@laurentian.ca).

Can. J. Chem. Downloaded from www.nrcresearchpress.com by Renmin University of China on 09/02/12
For personal use only.

D. wizlizenii. This compound was shown to inhibit the feeding of the fall armyworm (*Spodoptera frugiperda* Smith) and the European corn borer (*Ostrinia nubilalis* Hbn.) larvae.[12]

Here we report the isolation, structure elucidation, and quantification of two flavonoids present in the fruit extract of *D. wislizenii*. In addition, we have quantified the two major GLs (**2** and **3**) in the extract. The toxicity on brine shrimp larvae of the fruit extract and of the flavonoids was probed. The free-radical scavenging activity of the fruit extract and of the isolated flavonoids was evaluated by electron spin resonance (ESR) spectroscopy. Seeing that some GLs have been implicated in the free-radical scavenging activity of plant extracts, but not many have been studied, we determined the free-radical scavenging activity of the GLs found in the fruit extract of *D. wislizenii*.

Results and discussion

To use the plant extract in health-benefit applications or in animal and human nutrition, its lack of lethality was probed against *Artemia salina* L. (brine shrimp) larvae. The brine shrimp lethality test showed that the fruit extract was not lethal against *A. salina* larvae at the tested concentrations.[13] This was expected, since this plant was given to animals as food.[6]

To test free-radical scavenging activity, the *D. wislizenii* fruit extract was added to solutions containing a known concentration of the stable free radical, DPPH•. The average amount of *D. wislizenii* fruit extract able to scavenge 50% of the DPPH• (SC_{50}) was 110 ± 11 μg/mL (Table 1). We decided to determine which natural products contributed to this activity; hence, we have isolated the major secondary metabolites in the extract and probed their free-radical scavenging activity.

Several peaks were detected in the HPLC chromatogram of the extract of *D. wislizenii* fruit (Fig. S1, Supplementary data), using the experimental conditions described in the literature.[14] In addition to the previously reported occurrence of sinigrin, glucohesperin, glucoberteroin, glucolesquerellin, and 7-methylsulfanylheptylGL,[11] the plant extract contained two compounds eluting at retention times (t_R) of 36.8 min (compound **4**) and 29.8 min (compound **5**). These two compounds were isolated from the extract using the chromatographic separations outlined in the Experimental section. The spectroscopic data of compound **4** were in agreement with those published in the literature for the 3-*O*-β-D-(2-*O*-β-D-glucopyranosyl)glucopyranoside of quercetin, also known as quercetin 3-*O*-sophoroside (**4**)[15–19] (Fig. 1; Table S1, Supplementary data) and the data of compound **5** were in agreement with those published in the literature for quercetin 3-*O*-sophoroside-7-*O*-glucoside (**5**) (Fig. 1; Table S1, Supplementary data).[15–17,20,21]

Although **4** and **5** have been found in several members of the Brassicaceae family, it is the first time that they have been observed in the *Dithyrea* sp. For example, quercetin 3-*O*-sophoroside has been previously identified in the genus *Brassica*[22] and in watercress,[23] and quercetin 3-*O*-sophoroside-7-*O*-glucoside has been found in canola and tronchuda cabbage.[19–21,24–28]

The major compounds found in the *D. wislizenii* extract, namely **2**–**5** were quantified by HPLC. The quantities of **2**, **3**, **4**, and **5** in the plant extract were estimated to be 12.4, 6.0, 2.1, and 18.0 μmol/g of dried fruit, respectively.

The free-radical scavenging activities of the natural products isolated from *D. wislizenii* were tested (Table 1). Quercetin (**6**) and glucoraphasatin (**1**), compounds known to have free-radical scavenging activity against DPPH•, were used as the positive control for the flavonoids and GLs isolated from *D. wislizenii*, respectively. The SC_{50} of **6** has been expressed in both μg/mL and μmol/L to allow for comparison with the activity of the crude extract and the isolated flavonoids and GLs. The SC_{50} of compound **6** is 27 times smaller than that of the crude extract of *D. wislizenii*. This means that compound **6** scavenges DPPH• better than the crude extract. This is not surprising as the extract is a complex mixture of compounds, many of which do not possess free-radical scavenging activity. Flavonoids **4** and **5** have weaker free-radical scavenging activities than **6** (Table 1). Compound **6** is 2.5 times better at scavenging free-radicals than **4**, and 3.6 times better than **5**. This finding is consistent with the trolox equivalent antioxidant capacity (TEAC) values obtained for **6** and **4**. The TEAC value of **6** was reported to be 3 times higher than that of **4**.[1] Furthermore, in our investigation, **4** was found to be 1.5 times better at scavenging free-radicals than **5**, which means that the latter had the weakest free-radical scavenging activity among the flavonoids tested.

The three main structural features in flavonoids that determine their overall free-radical scavenging activity are (*i*) the *o*-dihydroxyl groups in the B ring, (*ii*) the double bond between C(2) and C(3) in the C ring, which is conjugated to the 4-oxo group (C=O) in the C ring, and (*iii*) the presence of additional OH groups at positions 3 and 5.[29] The presence of these three main structural features in **6** explains why it possesses a high free-radical scavenging activity. The substituents at positions 3 and 7 are glucose residues that affect the ability of the B-ring hydroxyl groups to donate one hydrogen in **4** and **5**.

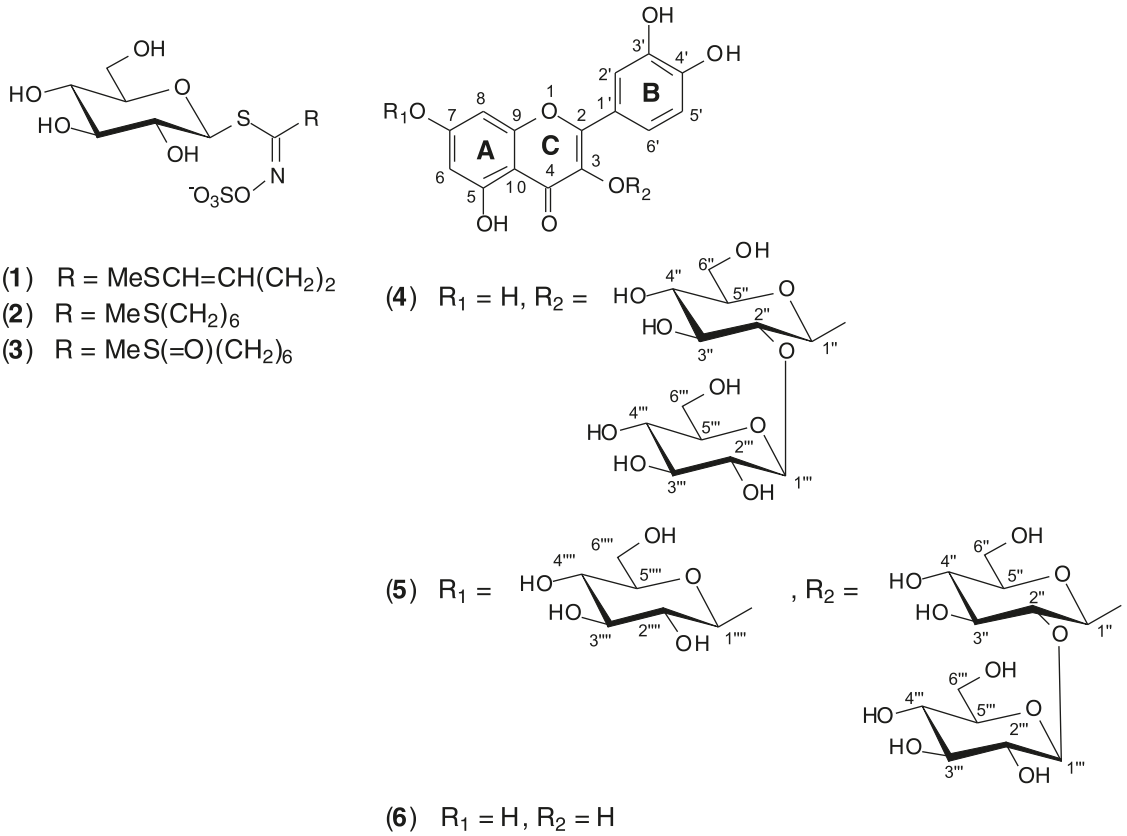
The SC_{50} of **1** was found to be 4 times smaller than that of **2**, whereas the SC_{50} of **3** was 2 times lower than the SC_{50} of **1** and 8 times smaller than that of **2**. This means that **3** is a better free-radical scavenger than **1** and that **1** is a better scavenger than **2** (Table 1). The SC_{50} of **2** has a relatively large standard deviation because it demonstrated relatively weak free-radical scavenging activity. Although the mechanism for the reaction of DPPH• with GLs is not known, Barillari and co-workers[4] proposed that the reaction of DPPH• with 4-methylsulfanyl-3-butenyl ITC, also called raphasatin, the degradation product of **1**, proceeds via two pathways (Fig. 2). These involve abstraction of the hydrogen atom α to the allylic functional group, –CH=CHSCH$_3$, (path 1) and abstraction of the hydrogen atom that is α to the –N=C=S (path 2). Presumably, –CH=CHSCH$_3$ and –N=C=S are responsible for the weakening of the respective C–H bonds. Abstraction of a second hydrogen in both of the proposed pathways leads to a conjugated ITC. In the case of the intact GLs used in the present study, one could propose a similar mechanism (Fig. 3). The hydrogen atoms most likely to react with the DPPH• are those α to the *O*-sulfated *Z*-thiohydroximate functional group as well as those α to –CH=CHSCH$_3$ (for **1**), SCH$_3$ (for **2**), and SOCH$_3$ (for **3**). For **2** and **3**, the sulfanyl and sulfinyl groups are separated from the *O*-sulfated

Table 1. Free-radical scavenging activities of the fruit extract of *Dithyrea wislizenii*, glucolesquerellin (**2**), glucohesperin (**3**), quercetin 3-*O*-sophoroside (**4**), and quercetin 3-*O*-sophoroside-7-*O*-glucoside (**5**), against diphenylpicrylhydrazyl (DPPH•).

Extract/product	DPPH[a]	Average SC_{50} ± SD (% error)[b]
Quercetin (**6**)	160	4±1 μg/mL (21.8)
Dithyrea wislizenii fruit extract	160	110±11 μg/mL (10.2)
Quercetin (**6**)	350	32±2 μmol/L (7.6)
Quercetin 3-*O*-sophoroside (**4**)	350	78±1 μmol/L (1.3)
Quercetin 3-*O*-sophoroside-7-*O*-glucoside (**5**)	350	113±10 μmol/L (9.1)
Glucoraphasatin (**1**)	350	1768±60 μmol/L (3.4)
Glucolesquerellin (**2**)	350	7819±1968 μmol/L (25.2)
Glucohesperin (**3**)	350	970±63 μmol/L (6.5)

Note: SC_{50}, the concentration of the compound required to scavenge 50% of the DPPH•.
[a]Concentration of DPPH• in the capillary in μmol/L.
[b]Tested in triplicate from three independent experiments.

Fig. 1. Structure of glucolesquerellin (**2**), glucohesperin (**3**), quercetin 3-*O*-sophoroside (**4**), and quercetin 3-*O*-sophoroside-7-*O*-glucoside (**5**) isolated from *Dithyrea wislizenii*.



Z-thiohydroximate functional group by six methylene groups. The effect of the *O*-sulfated *Z*-thiohydroximate functional group, if any, on the α-C–H bond strength would be comparable. Therefore, the difference in the SC_{50} must be primarily dependent on the SCH_3 and $SOCH_3$ groups. The sulfinyl group is more electron-withdrawing than the sulfanyl group, which makes the adjacent hydrogen atoms in **3** more acidic than in **2**.[30] Furthermore, the S=O bond will delocalize the unpaired electron over the π bond. This allows **3** to donate the hydrogen atoms easily, resulting in a higher free-radical scavenging activity than those of **2** and **1**. For **1**, the C=C bond is electron-withdrawing and will make the adjacent hydrogen atom more acidic and easier for the free radical to abstract. Moreover, the C=C bond allows the free electron to be delocalized over the π bond. This results in a higher free-radical scavenging activity than that of **2**. Our observations suggest that the presence of a sulfinyl group and C=C bond contributes to the overall scavenging activity of certain GLs. Papi et al.[4] studied the free-radical scavenging activity of raphasatin and its intact GL (**1**) towards DPPH• and found the ITC to be 3 times more active than the intact GL. This suggests that the ITC group is the major contributor to this

Can. J. Chem. Downloaded from www.nrcresearchpress.com by Renmin University of China on 09/02/12
For personal use only.

Fig. 2. Proposed mechanisms of the reaction of 4-methylsulfanyl-3-butenyl isothiocyanate with diphenylpicrylhydrazyl radical (DPPH•).[4]

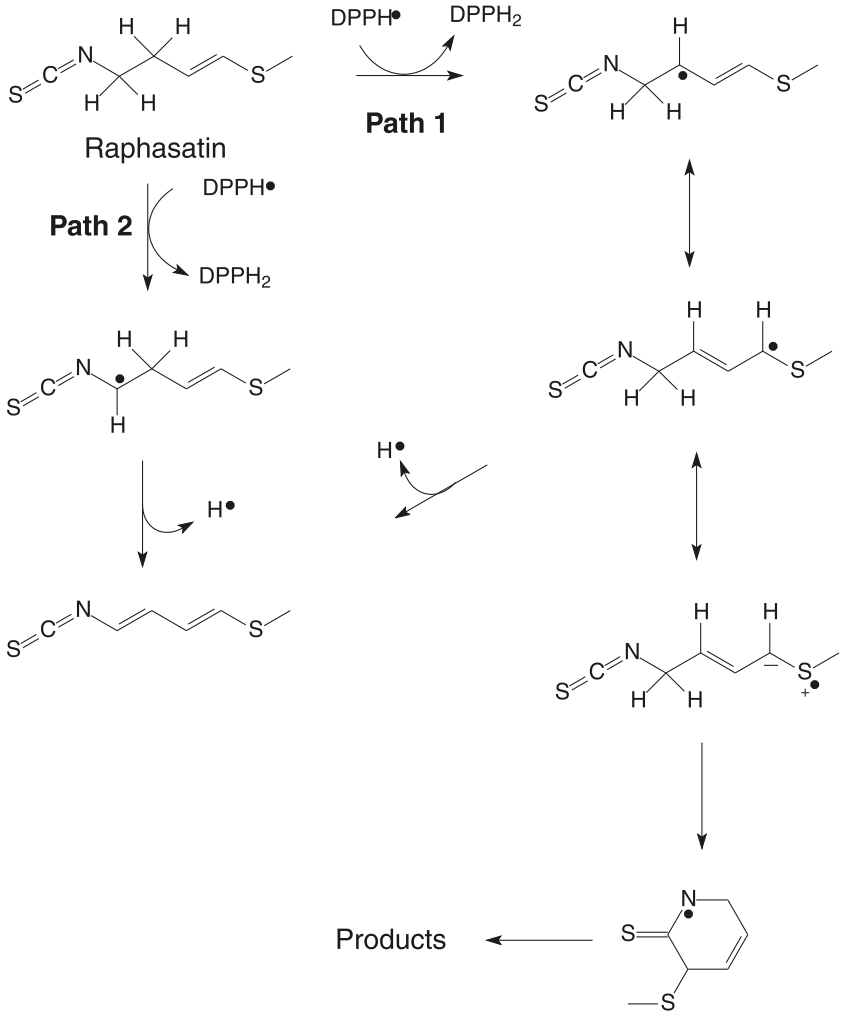
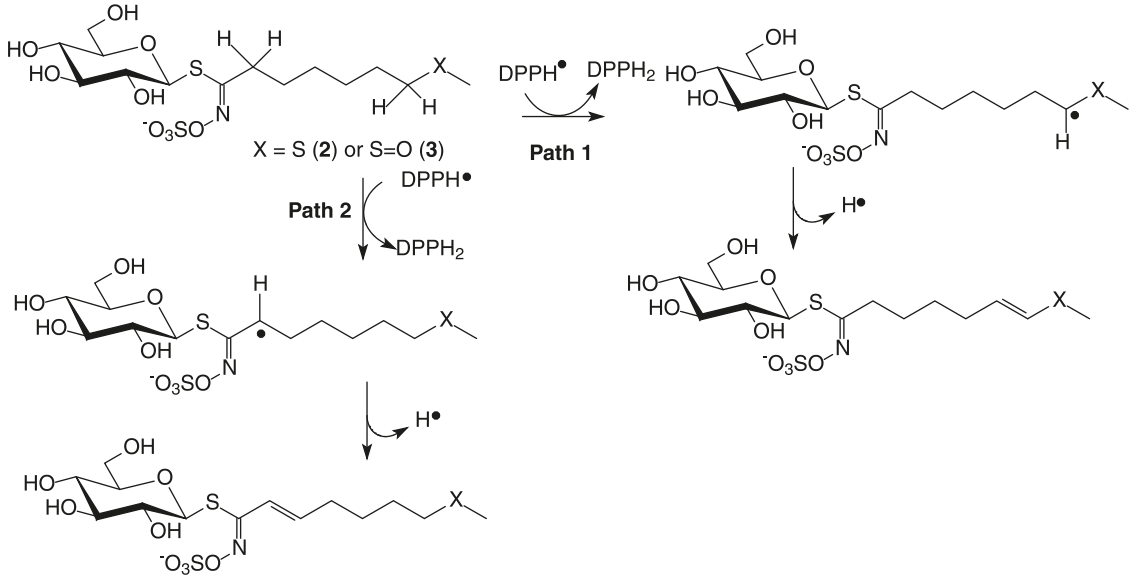


Fig. 3. Proposed mechanisms of the reactions of glucolesquerellin (**2**) and glucohesperin (**3**) with diphenylpicrylhydrazyl radical (DPPH•).



Can. J. Chem. Downloaded from www.nrcresearchpress.com by Renmin University of China on 09/02/12
For personal use only.

Can. J. Chem. Downloaded from www.nrcresearchpress.com by Renmin University of China on 09/02/12
For personal use only.

increased activity. Because **3** was found to be twice as active as **1**, we expect that its corresponding ITC hesperin would be twice as active as raphasatin.

It is worth noting that other natural products, such as the ones in garlic containing a sulfoxide functional group such as alliin and thiosulfinates such as allicin, have also been shown to possess some free-radical scavenging properties.[31] Finally, all the GLs we tested were weaker free-radical scavengers than the flavonoids we analyzed. Glucohesperin (**3**), the best GL among the ones we tested, was 8.6 times less active than **5**, the poorest free-radical scavenger among the flavonoids we tested. Overall, our results indicated that the flavonoids strongly contributed to the free-radical scavenging activity of *D. wislizenii* fruit extract, whereas the GLs contributed to the activity to a lesser extent.

Conclusions

In this study, we have isolated and identified quercetin 3-*O*-sophoroside (**4**) and quercetin 3-*O*-sophoroside-7-*O*-glucoside (**5**) representing the first report of the presence of flavonoids in a *Dithyrea* species. The crude extract, **4**, and **5** were not lethal against *A. salina* at the concentrations tested. Both isolated flavonoids and GLs contributed to the free-radical scavenging activity of *D. wislizenii*. It was revealed that the flavonoids were stronger free-radical scavengers than the GLs and, hence, the major contributors to the free-radical scavenging activity of *D. wislizenii*. From the structures of the flavonoids, we confirmed that the more glycosylated the flavonoid, the weaker its free-radical scavenging activity. From the structures of the GLs, we proposed that the presence of the sulfanyl and sulfinyl groups would contribute to the free-radical scavenging activity of the tested GLs. Further investigations of the free-radical scavenging activity of the plant extract and of the major natural products isolated should be carried out against the superoxide anion ($O_2^{\bullet -}$) and hydroxyl radical ($HO^{\bullet}$). Such a study could contribute to understanding the anti-inflammatory properties of the plant metabolites (most probably the flavonoids) initially observed by many Native North American tribes who used the plant to reduce swelling. Because the plant extract and its components display free-radical scavenging ability, other studies could be directed towards probing the potential cancer-preventive effects of *D. wislizenii*. Furthermore, the free-radical scavenging activity of lesquerellin and hesperin, the ITCs of **2** and **3**, could be investigated as they are expected to be better scavengers than their parent GLs. In fact, raphasatin, the glucoraphasatin ITC, has been shown to be 3 times more potent as a scavenger of $DPPH^{\bullet}$ than glucoraphasatin.[4] In conclusion, *D. wislizenii* is a good source of free-radical scavengers.

Experimental

Materials

All solvents were ACS grade and used as such except for $CHCl_3$, which was redistilled. All deuterated solvents were purchased from Cambridge Isotopes Laboratories, Inc. (Andover, Massachusetts). Formic acid, L-(+)-arabinose, D-(+)-galactose, D-glucose, D-(+)-xylose, NaOH, and EtOAc were purchased from BDH (Toronto, Ontario). HPLC-grade MeOH, absolute EtOH, and triethylamine (reagent grade) were purchased from Fisher Scientific (Whitby, Ontario). Sinigrin, D-(+)-mannose, DMSO, NaOAc, and quercetin dihydrate were purchased from Sigma-Aldrich (Oakville, Ontario). $DPPH^{\bullet}$ was purchased from Sigma-Aldrich and stored at 5 °C. Glacial AcOH was purchased from Anachemia Canada Inc. (Montreal, Quebec). HCl was purchased from Stanchem (Etobicoke, Ontario). H_3BO_3 was bought from Matheson, Coleman, and Bell Manufacturing Chemists (Norwood, Ohio). $AlCl_3$ was from the McArthur Chemical Co., Ltd. (Montreal, Quebec). Isopropanol and thymol were purchased from EM Science (Gibbstown, New Jersey). HPLC-grade H_2O was generated in the laboratory through a Nanopure Diamond Ultrapure water system by Barnstead (Dubuque, Iowa). Kieselgel 60 F_{254} analytical TLC aluminum sheets were purchased from EM Science; compounds were visualized under UV light and by dipping the plates in sulfuric thymol solution containing 1% (*w*/*v*) thymol, 10% (*v*/*v*) H_2SO_4, and 95% EtOH, followed by heating. Flash column chromatography (FCC) was carried out using 70–230 mesh 60 Å normal-phase silica gel (Sigma-Aldrich). Sephadex LH-20 was purchased from Pharmacia Fine Chemicals (Uppsala, Sweden). C-18 silica gel was purchased from Alltech (Guelph, Ontario). C-18 silica gel cartridges (Mega Bond Elut Flash, 10 g sorbent mass, 60 mL volume) were obtained from Varian, Inc (Mississauga, Ontario).

Instrumentation

UV spectra were recorded on a Biochrom Ultrospec 2100 pro UV–vis spectrophotometer (Cambridge, UK). Specific rotations ($[\alpha]_D$) were measured with a Rudolph Research Corporation Autopol II automatic polarimeter (Flanders, New Jersey) at ambient temperature using a 20 cm path length cell; the units are 10^{-1}deg cm^2 g^{-1} and the concentrations (*c*) are reported in grams per 100 millilitres. IR spectra were recorded with a PerkinElmer Paragon 1000PC IR spectrometer (Waltham, Massachusetts) or a Bruker Optics Tensor 27 FTIR instrument (Boston, Massachusetts) using KBr disks. NMR spectra were recorded on a Bruker Avance spectrometer at 600 MHz (^{1}H) and 150 MHz (^{13}C) at the Saskatchewan Structural Science Centre (Saskatoon, Saskatchewan), or on a Bruker DRX 500 spectrometer at 500 MHz (^{1}H) and 125 MHz (^{13}C) at Laurentian University (Sudbury, Ontario); δ values were referenced to D_2O at 4.80 ppm and to DMSO-d_6 at 2.50 ppm for ^{1}H NMR spectra and at 39.5 ppm for ^{13}C NMR spectra. High-resolution electrospray mass spectrometric (HR-ESI-MS) measurements were recorded using an API Qstar XL mass spectrometer at the Saskatchewan Structural Science Centre. A Varian E109 EPR spectrometer operating at X-band was used to measure the free-radical scavenging activity of the antioxidants. ESR spectra were recorded at room temperature (21–23 °C) at centre field, 3257; field sweep, 100 G; and microwave power, 2 mW. For a given experiment, the receiver gain was kept constant.

Plant material

Dry *Dithyrea wislizenii* fruit was obtained from the Plants of the South West company (Santa Fe, New Mexico). A voucher (No. 21023) was deposited at the Department of Biology Herbarium, Laurentian University. Cherry Belle radish

Can. J. Chem. Downloaded from www.nrcresearchpress.com by Renmin University of China on 09/02/12
For personal use only.

seeds (Gardener's choice) were purchased from a local store in Sudbury, Ontario.

HPLC-ESI-MS analysis

Dithyrea wislizenii extract (50 mg) was dissolved in 2 mL of MeOH and filtered through a plug of cotton prior to analysis by HPLC. Analysis was performed by injecting a 20 μL aliquot of the solution of crude extract into an Agilent Technologies HP 1100 (New Castle, Delaware) HPLC equipped with a quaternary pump, automatic injector, diode-array detector (wavelength range 190–600 nm), degasser, and a Hypersil ODS column (5 μm, 4.6 mm × 200 mm). The two mobile-phase solvents, MeOH and H_2O, were prepared with 0.15% triethylamine and 0.18% formic acid added as ion-pairing reagents. Both solutions were filtered using 0.45 μm nylon membranes. The initial mobile phase was 100% HPLC-grade H_2O. At 10 min, the mobile phase was switched to a linear gradient of 100% H_2O to 100% MeOH over 60 min.[14] After each run, the initial mobile-phase conditions were set and the system was allowed to equilibrate. The flow rate was kept constant at 1 mL/min. The column temperature was held at room temperature. The HPLC was interfaced to an Agilent model 6120 MS with a Chemstation data system (LC–MSD B.03.01). The ES interface was a standard ES source operating with a capillary voltage of 4 kV and temperature of 350 °C. The system was operated in the negative and positive ion ES modes. Nitrogen was used as nebulizing and drying gas at a flow of 10 L/min (35 psig, 1 psi = 6.894 kPa). The MS was programmed to perform full scans between *m/z* 100 and 1000 amu.

Extraction and isolation

Dithyrea wislizenii fruits (347 g) were frozen in liquid N_2, ground in a mortar, and immediately extracted 3 times with boiling MeOH (1.4 L for the first extraction and 1.05 L for the other extractions) for 30 min. The methanolic solution was filtered and concentrated to dryness (33 g). This extract was dissolved in H_2O (200 mL) and submitted to liquid–liquid extractions with solvents of increasing polarity, $CHCl_3$, EtOAc, and BuOH. Each organic layer was concentrated ($CHCl_3$ fraction, 15.2 g; EtOAc fraction, 1.2 g; and BuOH fraction, 6.1 g) and the aqueous layer was lyophilized (11.7 g). The BuOH fraction (3.6 g) was fractionated by FCC (normal phase; gradient $CHCl_3$/MeOH 8:2, 7:3, and 0:10 *v/v*; 25 mL fractions). Fractions 22–35, obtained from the FCC column, eluted with $CHCl_3$/MeOH 7:3 (*v/v*), were combined (210 mg) and fractionated on a Sephadex LH-20 column (H_2O/MeOH 10:0 and 0:10 *v/v*, 5 mL fractions). Fractions eluted with MeOH were combined and yielded quercetin 3-*O*-sophoroside (**4**, 64.6 mg). Fractions 126–177, obtained from the FCC (normal phase) mentioned previously, eluted with MeOH, were combined (611 mg) and subjected to Sephadex LH-20 column (H_2O/MeOH 10:0 and 0:10 *v/v*, 5 mL fractions) fractionations. Fractions 4–8, eluted with H_2O from the Sephadex LH-20 column, were combined (175 mg) and submitted to a solid-phase separation (C18 cartridge; H_2O/MeOH 100:0, 95:5, 90:10, 80:20, and 0:100 *v/v*; 5 mL fractions). Fractions 69–82, eluted with H_2O/MeOH 80:20 (*v/v*), yielded quercetin 3-*O*-sophoroside-7-*O*-glucoside (**5**, 56.6 mg).

Acid hydrolysis of flavonoids and identification of aglycones and carbohydrates

The flavonoid was mixed with 6% aq HCl (5 mL). The solution was heated for 45 min. After cooling, the solution was extracted 3 times with EtOAc (3 × 5 mL). Evaporation of the aqueous layer yielded the sugars that were analysed by TLC (isopropanol/AcOH/H_2O, 3:1:0.5 *v/v/v*). The carbohydrate composition was determined according to the TAPPI test method T249-cm-85 by FPInnovations-Paprican division (Pointe-Claire, Quebec).[17] Arabinose, xylose, mannose, galactose, and glucose were used as reference compounds. The organic layer, after drying over sodium sulfate, was evaporated. Quercetin was identified in this layer by LC–MS analysis by comparison of the t_R, UV, and mass spectra with those of a commercial standard.

Quercetin 3-O-sophoroside (4H-1-benzopyran-4-one, 2-(3,4-dihydroxyphenyl)-3-[(2-O-β-D-glucopyranosyl-β-D-glucopyranosyl)oxy]-5,7-dihydroxyflavone; 4)

Yellow amorphous powder. HPLC, t_R = 36.8 min. $[\alpha]^{26}_D$ – 147 (*c* 0.08, MeOH). UV (MeOH) λ_{max} (nm, log ε): 206 (4.5), 258 (4.2), 356 (4.1); + NaOH: 273, 408; + $AlCl_3$: 275, 429; + $AlCl_3$ + HCl: 270, 355, 390; + NaOAc: 270, 350; + NaOAc + H_3BO_3: 259, 358. FTIR (KBr, cm^{-1}): 3408 (OH), 2927 (CH), 2341, 1656 (α,β-unsaturated C=O), 1607, 1507, 1455, 1361, 1305, 1198, 1168, 1075 (C-O). For ^1H and ^{13}C NMR data see Table S1. HR-ESI$^-$-MS *m/z* calcd for $C_{27}H_{29}O_{17}^-$: 625.1410; found: 625.1406 [M – H]$^-$. HR-ESI$^+$-MS *m/z* calcd for $C_{27}H_{31}O_{17}^+$: 627.1556; found: 627.1573 [M + H]$^+$.

Quercetin 3-O-sophoroside-7-O-glucoside (4H-1-benzopyran-4-one, 2-(3,4-dihydroxyphenyl)-3-[(2-O-β-D-glucopyranosyl-β-D-glucopyranosyl)oxy]-7-(β-D-glucopyranosyloxy)-5-hydroxyflavone; 5)

Yellow amorphous powder. HPLC, t_R = 29.8 min. $[\alpha]^{22}_D$ – 98 (*c* 0.02, MeOH). UV (MeOH) λ_{max} (nm, log ε): 206 (4.5), 256 (4.2), 356 (4.0); + NaOH: 275, 418; + $AlCl_3$: 274, 295, 334, 436; + $AlCl_3$ + HCl: 268, 351, 400; + NaOAc: 263, 352; + NaOAc + H_3BO_3: 261, 354. FTIR (KBr, cm^{-1}): 3416 (OH), 2923 (CH), 2360, 2341, 1656 (α,β-unsaturated C=O), 1600, 1492, 1271, 1203, 1174, 1074 (C-O). For ^1H and ^{13}C NMR data see Table S1. HR-ESI$^-$-MS *m/z* calcd for $C_{33}H_{39}O_{22}^-$: 787.1938; found: 787.1909 [M – H]$^-$.

Purification of glucoraphasatin (1)

Cherry Belle radish seeds were soaked for 1 min in 1% sodium hypochlorite and rinsed with distilled H_2O. Seeds were laid on two sheets of filter paper in Petri dishes and were incubated at room temperature (23 ± 2 °C) under an 8 h day / 16 h night photoperiod. The sprouts were watered twice a day with H_2O. Fresh nine-day-old Cherry Belle radish seedlings (899 g) were frozen in liquid N_2, ground in a mortar, and immediately extracted 3 times with boiling MeOH (3 × 3 L) for 30 min. The methanolic solution was filtered and concentrated to dryness (35 g). This extract was dissolved in H_2O (100 mL) and subjected to liquid–liquid extractions with solvents of increasing polarity, EtOAc and BuOH. Each organic layer was concentrated (EtOAc fraction, 1.1 g; and BuOH fraction, 3.4 g) and the aqueous layer was dried (29.4 g). The aqueous fraction (3 g) was purified using column

Can. J. Chem. Downloaded from www.nrcresearchpress.com by Renmin University of China on 09/02/12
For personal use only.

chromatography (C18 reverse phase, gradient H_2O/MeOH 10:0 and 0:10 *v*/*v*, 23 mL fractions). Fractions 18–84, eluted with H_2O from the C18 reverse-phase column, were combined (232 mg) and subjected to solid-phase separation (C18 cartridge, H_2O/MeOH 10:0 and 0:10 *v*/*v*, 3 mL fractions). Fractions 7–34, eluted with H_2O yielded glucoraphasatin (**1**, 101 mg). The purity of the amorphous solid **1** was assessed by HPLC, and the compound was characterized by ^{1}H and ^{13}C NMR spectroscopies. The spectroscopic data were consistent with the ones previously published.[3]

Purification of glucolesquerellin (2) and glucohesperin (3)

These GLs were isolated and characterized as previously reported.[11]

Flavonoid and glucosinolate quantification

Several solutions of **2** and **3** (5×10^{-3}, 10^{-3}, 2×10^{-4}, and 4×10^{-5} mol/L), **4** (9.8×10^{-4}, 4.9×10^{-4}, and 2.45×10^{-4} mol/L), and **5** (10^{-2}, 5×10^{-3}, 10^{-3} mol/L) were prepared via serial dilution in MeOH. Each solution was injected (20 µL) into the HPLC. Calibration curves were then constructed using Microsoft Excel from data obtained from three independent experiments run in triplicate.

Brine shrimp lethality assay

Brine shrimp eggs were obtained from a local store and were hatched in artificial sea water. The hatching, harvesting, and dispensing of nauplii were performed in a manner similar to that of Solis et al.[13] *Artemia salina* eggs were hydrated in a 200 mL beaker containing artificial sea water (table salt, 38 g/L). Eggs were sprinkled into the darkened half of the beaker and separated from the aerated, illuminated other half by a plastic divider. The hatching time was ~48 h. *Artemia salina* nauplii that accumulated in the illuminated part of the beaker were transferred into a 96 well microplate (VWR International Inc., Mississauga, Ontario) (10 nauplii per 100 microlitres of artificial sea water per well). *Dithyrea wislizenii* fruit extract, **4**, and **5** were added to live nauplii and, after a 24 h exposure time at 22 °C, the brine shrimp lethality was measured by counting the number of dead (nonmotile) nauplii per well, using a binocular microscope. One hundred microlitres of MeOH were then added to each well and, after 15 min, the total number of shrimp in each well was counted. The crude extract was tested at 125, 250, and 500 ppm. Compounds **4** and **5** were tested at 125, 250, 500, and 1000 µmol/L. Sea water was used as the control. A positive assay was the death of all brine shrimp with 100 µmol/L of thymol. The results were obtained from three independent experiments in triplicate.

DPPH• assay

Solution preparation

The SC_{50} for **6** (positive control for flavonoids), **1** (positive control for GLs), and compounds **2**–**5** were extracted from the linear regression line of plots of % scavenging activity (SA) vs compound concentration (µmol/L). The SC_{50} was determined from the linear regression line. SC_{50} values represent the mean of three independent experiments, run in triplicate, and are expressed as the mean ± SD, calculated using Microsoft Excel. The solutions tested for SA using the ESR method outlined as follows were prepared by the serial dilution of stock solutions of **1**–**6**. EtOH was used as the solvent in the dilutions. A 981.5 µmol/L quercetin (**6**) stock solution was used to prepare five solutions with concentrations between 12.6 and 196.3 µmol/L. A 6900 µmol/L stock solution of **4** in DMSO was used to prepare four solutions with concentrations between 22.8 and 284.3 µmol/L. A 172 µmol/L stock solution of **5** in DMSO was used to prepare four solutions with concentrations between 22 and 275 µmol/L. A 7129 µmol/L stock solution of **1** in DMSO was used to prepare four solutions with concentrations between 1643 and 4277 µmol/L. A stock solution (about 26 227 µmol/L) of **2** was prepared in DMSO. From the stock solution, three serial dilutions in EtOH resulted in solution concentrations between 7 787 and 22 958 µmol/L. The stock solution and the three solutions were tested for free-radical scavenging activity. A 3147 µmol/L stock solution of **3** in DMSO was used to prepare three solutions with concentrations ranging from 201 to 1259 µmol/L. These as well as the stock solution were tested for free-radical scavenging activity.

General procedure

In general, 100 µL of a 700 µmol/L DPPH• solution was transferred to a 4 mL vial (Supelco 2-7138) containing a stirring bar. The antioxidant solution (100 µL) being tested was added to the vial. The timer was started and the vial was capped and placed on the stir plate. The reaction was carried out at room temperature (21–23 °C). At the 30 min mark, a portion of the contents of the vial were transferred with a glass syringe (Hamilton 80801) to a 3 cm long capillary tube (fabricated by cutting a Kimble No. 345059 (VWR) capillary tube to the desired length). The capillary tube was sealed with paraffin. The capillary was placed in an ESR tube (Wilmad), which was subsequently inserted in the cavity of the Varian X-band ESR spectrometer. The ESR spectrum was recorded at a frequency of ~9120 MHz and a microwave power of 2 mW. The center field and field sweep were set at 3257 and 100 G, respectively. The area under the ESR spectrum of DPPH• was determined by using the double integration (DI) feature in the ESR software known as EPRware (Scientific Software Services, Northville, Michigan). The DI is related to the concentration of DPPH• in the tube. The %SA is defined as shown in eq. [1].

$$[1] \qquad \%SA = 100(1 - DI_S/DI_{NC})$$

DI_S and DI_{NC} are the double integration of the DPPH• spectrum in the presence and absence, respectively, of the compound being tested for the free-radical scavenging activity.

Supplementary data

Supplementary data (Fig. S1 and Table S1) are available with the article through the journal Web site at http://nrcresearchpress.com/doi/suppl/10.1139/v2012-042.

Acknowledgements

Financial support from the Natural Sciences and Engineering Research Council of Canada (NSERC Discovery Grant), Laurentian University (Start-up funds and Career and Employment Centre), the Canadian Foundation for Innovation (Leaders Opportunity Fund)-Ontario Research Fund, Human

Resources and Skills Development Canada (Canada Summer Jobs program), and the Ontario Ministry of Northern Development and Mines (Summer Jobs Service Program) are gratefully acknowledged by S.M. The authors also thank Dr. J. Gray-Munro for the use of the FTIR instrument. The technical assistance provided by J. Feola, M. Myre, and F. Desmarais (ESR operation), and W. Beckerleg (isolation of glucoraphasatin) is greatly appreciated.

References

(1) Plumb, G. W.; Price, K. R.; Rhodes, M. J. C.; Williamson, G. *Free Radic. Res.* **1997**, *27* (4), 429. doi:10.3109/10715769709065782.

(2) Nilsson, J.; Olsson, K.; Engqvist, G.; Ekvall, J.; Olsson, M.; Nyman, M.; Åkesson, B. *J. Sci. Food Agric.* **2006**, *86* (4), 528. doi:10.1002/jsfa.2355.

(3) Barillari, J.; Cervellati, R.; Paolini, M.; Tatibouët, A.; Rollin, P.; Iori, R. *J. Agric. Food Chem.* **2005**, *53* (26), 9890. doi:10.1021/jf051465h.

(4) Papi, A.; Orlandi, M.; Bartolini, G.; Barillari, J.; Iori, R.; Paolini, M.; Ferroni, F.; Fumo, M. G.; Pedulli, G. F.; Valgimigli, L. *J. Agric. Food Chem.* **2008**, *56* (3), 875. doi:10.1021/jf073123c.

(5) MacMahon, J. A. *Deserts: The Audubon Society Nature Guides;* Knopf: New York, 1985; p 375.

(6) Rosiere, R. E.; Beck, R. F.; Wallace, J. D. *J. Range Manage.* **1975**, *28* (2), 89. doi:10.2307/3897435.

(7) Moerman, D. E. *Native America Ethnobotany;* Timber Press; Portland, OR, 1998; pp 200–201.

(8) Earle, F. R.; Jones, Q. *Econ. Bot.* **1962**, *16* (4), 221. doi:10.1007/BF02860181.

(9) Miller, R. W.; Earle, F. R.; Wolff, I. A.; Jones, Q. *J. Am. Oil Chem. Soc.* **1965**, *42* (10), 817. doi:10.1007/BF02541165.

(10) Daxenbichler, M. E.; Spencer, G. F.; Carlson, D. G.; Rose, G. B.; Brinker, A. M.; Powell, R. G. *Phytochemistry* **1991**, *30* (8), 2623. doi:10.1016/0031-9422(91)85112-D.

(11) Montaut, S.; Grandbois, J.; Righetti, L.; Barillari, J.; Iori, R.; Rollin, P. *J. Nat. Prod.* **2009**, *72* (5), 889. doi:10.1021/np800738w.

(12) Powell, R. G.; Mikolajczak, K. L.; Zilkowski, B. W.; Lu, H. S. M.; Mantus, E. K.; Clardy, J. *Experientia* **1991**, *47* (3), 304. doi:10.1007/BF01958168.

(13) Solis, P. N.; Wright, C. W.; Anderson, M. M.; Gupta, M. P.; Phillipson, J. D. *Planta Med.* **1993**, *59* (3), 250. doi:10.1055/s-2006-959661.

(14) Zrybko, C. L.; Fukuda, E. K.; Rosen, R. T. *J. Chromatogr. A* **1997**, *767* (1-2), 43. doi:10.1016/S0021-9673(96)01068-0.

(15) Mabry, T. J.; Markham, K. R.; Thomas, M. B. *The Systematic Identification of Flavonoids;* Springler-Verlag: New York, 1970; p 24.

(16) Weckerle, B.; Michel, K.; Balázs, B.; Schreier, P.; Tóth, G. *Phytochemistry* **2001**, *57* (4), 547. doi:10.1016/S0031-9422(01)00059-0.

(17) Cao, B.; Tschirner, U.; Ramaswamy, S.; Webb, A. *Tappi J.* **1997**, *80* (9), 193.

(18) Nørbæk, R.; Kondo, T. *Phytochemistry* **1999**, *51* (8), 1113. doi:10.1016/S0031-9422(99)00109-0.

(19) Price, K. R.; Casuscelli, F.; Colquhoun, I. J.; Rhodes, M. J. C. *J. Sci. Food Agric.* **1998**, *77* (4), 468. doi:10.1002/(SICI)1097-0010(199808)77:4<468::AID-JSFA66>3.0.CO;2-B.

(20) Pedras, M. S. C.; Zheng, Q.-A.; Gadagi, R. S.; Rimmer, S. R. *Phytochemistry* **2008**, *69* (4), 894. doi:10.1016/j.phytochem.2007.10.019.

(21) Nielsen, J. K.; Olsen, C. E.; Petersen, M. K. *Phytochemistry* **1993**, *34* (2), 539. doi:10.1016/0031-9422(93)80042-Q.

(22) Wilson, K. E.; Wilson, M. I.; Greenberg, B. M. *Photochem. Photobiol.* **1998**, *67* (5), 547. doi:10.1111/j.1751-1097.1998.tb09092.x.

(23) Boyd, L. A.; McCann, M. J.; Hashim, Y.; Bennett, R. N.; Gill, C. I. R.; Rowland, I. R. *Nutr. Cancer* **2006**, *55* (2), 232. doi:10.1207/s15327914nc5502_15.

(24) Ferreres, F.; Sousa, C.; Valentão, P.; Pereira, J. A.; Seabra, R. M.; Andrade, P. B. *Phytochemistry* **2007**, *68* (3), 361. doi:10.1016/j.phytochem.2006.10.020.

(25) Wilson, K. E.; Thompson, J. E.; Huner, N. P. A.; Greenberg, B. M. *Photochem. Photobiol.* **2001**, *73* (6), 678. doi:10.1562/0031-8655(2001)073<0678:EOUAEO>2.0.CO;2.

(26) Vallejo, F.; Tomás-Barberán, F. A.; Ferreres, F. *J. Chromatogr. A* **2004**, *1054* (1–2), 181. doi:10.1016/j.chroma.2004.05.045.

(27) Robbins, R. J.; Keck, A.-S.; Banuelos, G.; Finley, J. W. *J. Med. Food* **2005**, *8* (2), 204. doi:10.1089/jmf.2005.8.204.

(28) Francisco, M.; Moreno, D. A.; Cartea, M. E.; Ferreres, F.; García-Viguera, C.; Velasco, P. *J. Chromatogr. A* **2009**, *1216* (38), 6611. doi:10.1016/j.chroma.2009.07.055.

(29) Bors, W.; Heller, W.; Michel, C.; Saran, M. *Methods Enzymol.* **1990**, *186*, 343. doi:10.1016/0076-6879(90)86128-I.

(30) Bordwell, F. G.; Liu, W.-Z. *J. Phys. Org. Chem.* **1998**, *11* (6), 397. doi:10.1002/(SICI)1099-1395(199806)11:6<397::AID-POC10>3.0.CO;2-B.

(31) Lynett, P. T.; Butts, K.; Vaidya, V.; Garrett, G. E.; Pratt, D. A. *Org. Biomol. Chem.* **2011**, *9* (9), 3320. doi:10.1039/c1ob05192j.

Can. J. Chem. Downloaded from www.nrcresearchpress.com by Renmin University of China on 09/02/12
For personal use only.

A new, simple hydrothermal synthesis of magnetic nano-octahedrons — Application to hyperthermia cancer cell killing

Md. Abdulla-Al-Mamun, Yoshihumi Kusumoto, and Md. Shariful Islam

Can. J. Chem. Downloaded from www.nrcresearchpress.com by Renmin University of China on 09/02/12
For personal use only.

Abstract: Surfactant-free magnetic nano-octahedrons were successfully synthesized by the alkaline hydrothermal decomposition of ferric nitrate salt ($Fe(NO_3)_3{\cdot}9H_2O$) in a water–ethanol mixed solvent with a variety of alkaline concentrations. High-resolution scanning electron microscope (SEM) pictures demonstrated the formation of octahedron-structured magnetic nanoparticles at a 10 mol/L alkaline concentration. A possible synthesis mechanism of the magnetic nano-octahedron was discussed. An alternating current magnetic field to induce hyperthermia cancer cell killing was investigated. Maximum hyperthermia cancer cell killing (~100%) was found with 10 mol/L alkaline-synthesized nano-octahedrons, whereas that with 2 mol/L alkaline gave ~40%.

Key words: magnetic materials, chemical synthesis, electron microscopy, X-ray diffraction, magnetic properties, hyperthermia cancer cell killing.

Résumé : On a réalisé avec succès la synthèse de nanoparticules magnétiques à structure octaédrique ne comportant aucun agent de surface en procédant à la décomposition hydrothermique alcaline du sel de nitrate ferrique (($Fe(NO_3)_3{\cdot}9H_2O$) dans un mélange eau–éthanol agissant comme solvant pour des concentrations variées de produit alcalin. Des images obtenues par microscopie électronique à balayage (MEB) à haute résolution ont permis de démontrer la formation de nanoparticules magnétiques à structure octaédrique lors des traitements par des solutions alcalines à une concentration de 10 mol/L. On discute aussi du mécanisme de synthèse potentiel des nanoparticules magnétiques à structure octaédrique. On a examiné la possibilité de détruire des cellules cancéreuses par hyperthermie induite par un champ magnétique à courant alternatif. La destruction maximale des cellules cancéreuses par hyperthermie (environ 100 %) a été observée avec les nanoparticules magnétiques à structure octaédrique obtenues lors de la synthèse à l'aide d'une solution alcaline à concentration de 10 mol/L alors que la destruction observée avec celles obtenues à une concentration de 2 mol/L n'est que d'environ 40 %.

Mots-clés : matériaux magnétiques, synthèse chimique, microscopie électronique, diffraction des rayons X, propriétés magnétiques, destruction de cellules cancéreuses par hyperthermie.

[Traduit par la Rédaction]

Introduction

Magnetic nanostructural materials have been studied as novel imaging, diagnostic, and therapeutic agents due to their unique properties.[1] Magnetic nanoparticles (MNPs) have attracted tremendous attention because of their various biomedical applications.[2] In particular, magnetite (Fe_3O_4) has been considered recently as an ideal candidate for biological applications, both as a tag for sensing and imaging and as an activity agent for antitumor therapy.[3] Magnetic properties of magnetite nanoparticles are particularly attractive for application in cancer cell killing and magnetic recording.

A number of preparation techniques have been reported for high-quality magnetite nanoparticles, such as the reduction of Fe_2O_3,[4] microwave hydrothermal reaction,[5] coprecipitation method,[6] sonochemical reduction,[7] etc. The traditional approach to iron oxide colloids has relied on the aqueous precipitation or hydrolysis of Fe^{2+} and (or) Fe^{3+} salt(s); these materials can be poorly crystalline and polydispersive in many cases.[8] In general, among almost all the methods, stabilizing reagents are introduced during the preparation for acquiring colloidal dispersions. In our case, we used only the hydrothermal method without using any stabilizing agent or surfactant.

We have studied how to grow nano-sized single crystals of magnetic materials in a mixed solvent of ethanol and water. A thorough literature search revealed that no single crystals of magnetic materials were grown in a large scale production using KOH hydrothermal reduction of ferric nitrate. To grow bulk-scale single crystals, the growth conditions have to be optimized accordingly. Hence, in the present work, attempts have been made to investigate the nucleation parameters of magnetic nanomaterials, which are the prerequisite for investigating the growth mechanism of bulk-scale single crystals. The magnetic octahedron-shaped nanoparticles in a mixture

Received 31 January 2012. Accepted 25 April 2012. Published at www.nrcresearchpress.com/cjc on 23 July 2012.

M. Abdulla-Al-Mamun, Y. Kusumoto, and M.S. Islam. Department of Chemistry and Bioscience, Graduate School of Science and Engineering, Kagoshima University, 1-21-35 Korimoto, Kagoshima 890-0065, Japan.

Corresponding author: Yoshihumi Kusumoto (e-mail: kusumoto@sci.kagoshima-u.ac.jp).

Can. J. Chem. Downloaded from www.nrcresearchpress.com by Renmin University of China on 09/02/12
For personal use only.

of alcohol and water were prepared for the first time and thereby the possibility of growing bulk-scale magnetic single crystals was also examined. In addition, the effects of reaction conditions such as the molar concentration of alkali on morphology and magnetic properties of magnetic octahedron-structured nanoparticles were investigated. The ability to create octahedron-shaped morphologies with interesting magnetic properties enhances the prospects for application of magnetic nanostructures in a wide range of scientific and technological fields, including medicine, biochemistry, and electronics.

Here, we report a new generation of compact, uniform, surfactant-free magnetic nano-octahedrons and their successful utilization for hyperthermia cancer cell killing under an alternating current (AC) magnetic field. Moreover, the magnetic octahedron-shaped nanoparticles in a mixture of alcohol and water were prepared for the first time and their hyperthermia cytotoxicity is also reported for the first time.

Experimental

Material and methods

Ferric(III) nitrate nonahydrate ($Fe(NO_3)_3{\cdot}9H_2O$), ethanol, methanol, and potassium hydroxide (KOH) were purchased from Wako Pure Chemical Industries Ltd. All chemicals were used as received without further purification. The water used was purified through a Millipore system. The magnetic nanoparticles were synthesized using a hydroxide oxidation–reduction method under autoclave hydrothermal conditions.

Preparation

MNPs were synthesized using ferric(III) nitrate fixed at 0.03 mol/L and the concentration of KOH was varied at 2, 4, 6, 8, and 10 mol/L. $Fe(NO_3)_3{\cdot}9H_2O$ (0.03 mol/L) was dissolved in a 40 vol% ethanol–water solution. Under vigorous stirring, fresh KOH was mixed with the $Fe(NO_3)_3{\cdot}9H_2O$ containing water–ethanol solution. Finally, the mixture was transferred into a Teflon-lined stainless steel autoclave with a capacity of 200 mL for hydrothermal treatment at 200 °C for 12 h. After the reduction was complete, the autoclave was allowed to cool to room temperature. Next, the solution was centrifuged and the particles were separated by washing with distilled water and absolute methanol and dried in a vacuum at 80 °C.

Characterization

The UV–vis reflectance spectra of the MNPs were recorded with a UV–vis spectrophotometer (Shimadzu Corporation, UV-2450, Japan) and barium sulfate ($BaSO_4$) was used as a standard. The reflectance band was automatically changed to the absorption band by UV-2450 instrument software. The average diameters and size distributions of the magnetic nanoparticles were obtained from the enlarged photographs of a scanning electron microscope (SEM) (SU-70, Hitachi). The crystal structure identification was made by X-ray diffraction (XRD) using a PANalytical Advance X-ray diffractometer with Cu Kα radiation. The quantitative chemical composition of the nanoparticles' surface was also measured using an energy dispersive X-ray spectrometer (EDX) attached to the SEM. Magnetic measurements were performed using a superconducting quantum interference device (SQUID) magnetometer (Quantum Design model MPMS-5).

Cancer cell culture and killing method

Potential cancer cell killing effects of MNPs towards a human carcinoma (HeLa) cell line were studied by incubating the cells in different concentrations of MNPs. HeLa cells were cultured in a minimum essential medium (MEM) solution with 10% newborn calf serum (NBS) in a humidified incubator under an atmosphere of 5% CO_2 in air at 37 °C. The HeLa cells were plated at a concentration of about 3×10^5 in 40 mm Petri dishes and allowed to grow for 2 days. An AC magnetic field (handmade, picture shown in the Supplementary data as Fig. S4, frequency 560 kHz, AC voltage 7 V, AC current 0.8 A, monitor voltage 3.2 Vp (6.2 mT = 5 kA/m)) was induced for 10 min for the hyperthermia effect on HeLa cells. Hyperthermia-elevated temperature for every dish was measured by using a digital thermometer (^{SK}SATO, Model SK-250WP II-R). After the AC magnetic field was induced, the medium was removed and the cells were washed twice with phosphate-buffered saline (PBS) and the cells were counted using an automated cell counter (Bio-Rad, Model TC 10) with trypan blue staining. The images were taken using an Olympus inverted CKX41 microscope with an attached digital camera (DP21).

Results and discussion

UV–vis reflectance absorption spectra analysis of magnetic nanoparticles

The UV–vis reflectance spectra of MNPs are shown in Fig. S1 in the Supplementary data. The characteristic absorption shoulders are found at around 600–700 nm. The shoulder bands may depend on the individual particle property including size, shape, and solvents and reducing agents employed. Figure S1 (Supplementary data) shows that the absorption shoulders increase with increasing KOH alkaline agent (absorption band b–f in Fig. S1). The alkaline agent (KOH) can impact the absorption properties of MNPs as shown in Fig. S1 (Supplementary data). The broadness of the absorption shoulders (Fig. S1 in the Supplementary data) probably arises from the wide size distribution of MNPs at the high alkaline concentration (10 mol/L). The comparison of absorption spectra with reference commercial α-Fe_2O_3 and Fe_3O_4 are also shown in Figs. S1*a* and S1*g* (Supplementary data), respectively.

Morphological and structural characterization of MNPs

The SEM images for the MNPs are shown in Fig. S2 and reveal many irregular particles (Figs. S2*a*–S2*d*; Supplementary data) when the KOH concentration was varied in aqueous solution, keeping other conditions constant. This difference suggests that the KOH concentration plays an important role in the formation of octahedron MNPs. As seen in Figs. S2*e*–S2*f* (Supplementary data; [KOH] = 10 mol/L), the average sizes of most of the particles are less than or around 400 nm and the nanocrystals have an octahedron structure. Very small amounts of spherical nanocrystals and triangles were also observed in some images. The reproducibility of the formation of the nano-octahedron was observed through independent experiments under identical conditions at

Can. J. Chem. Downloaded from www.nrcresearchpress.com by Renmin University of China on 09/02/12
For personal use only.

Fig. 1. The X-ray powder diffraction (XRD) patterns of 2–10 mol/L alkali-synthesized nanoparticles. H, hematite; M, magnetite.

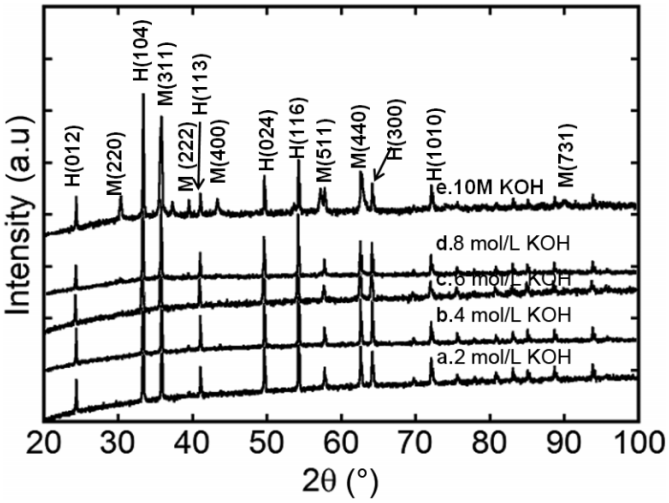
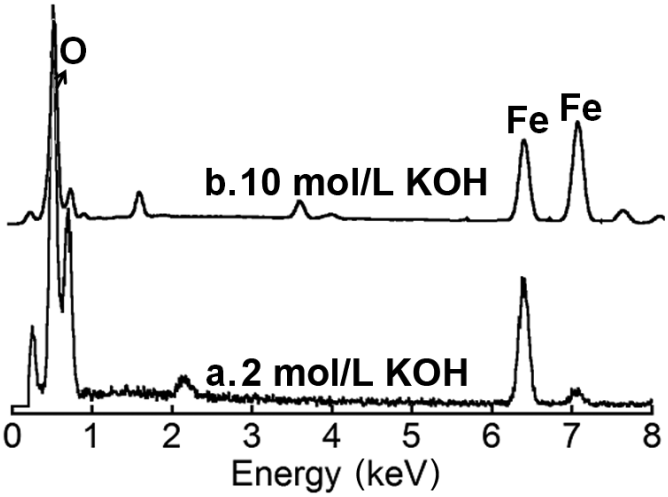


Fig. 2. Energy dispersive X-ray spectrometer (EDX) spectrum of (*a*) 2 mol/L and (*b*) 10 mol/L alkali-synthesized nano-octahedron.

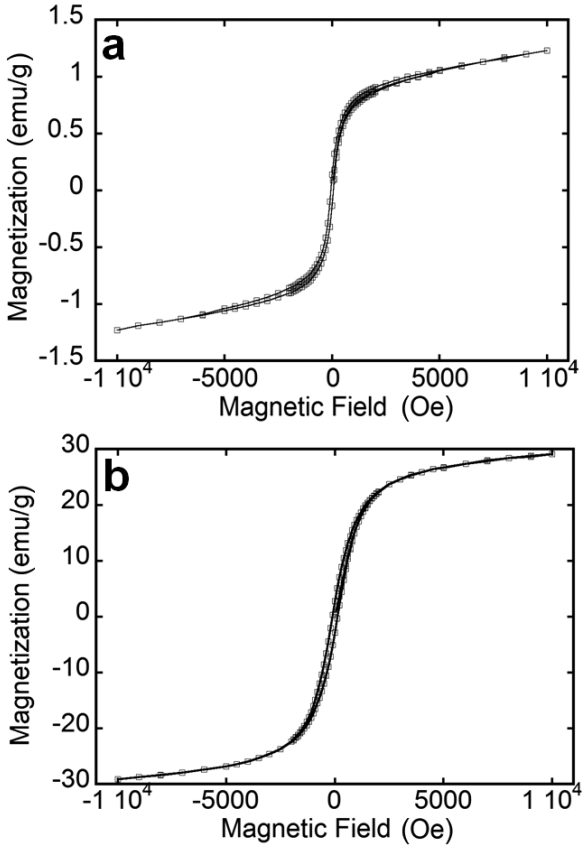


[KOH] = 10 mol/L. The shape of these structures is characteristic of the face-centered cubic (fcc) structure of MNPs. Magnetite has a cubic inverse spinel structure with oxygen forming fcc closed packing and Fe cations occupying interstitial tetrahedral sites and octahedral sites.[9]

The X-ray diffraction patterns of the MNPs synthesized at different alkaline concentrations are shown in Fig. 1. The peaks at the (220), (311), (222), (400), (511), (440), and (731) planes belong to the fcc metallic magnetite (Joint Committee on Powder Diffraction Standards (JCPDS) file No. 01-075-0033) as shown in Fig. 1*e*. The other peaks (Fig. 1*e*) and the spectra peaks of Figs. 1*a*–1*d* belong to hematite (JCPDS file No. 00-013-0534), indicating that hematite also partly coexists with magnetite particles. It can be seen that hematite (α-Fe_2O_3) products are obtained when the KOH concentration is less than 8 mol/L as shown in Figs. 1*a*–1*d* and, when the KOH concentration is 10 mol/L, the product is almost completely changed to magnetite (Fe_3O_4) withsome α-Fe_2O_3 coexisting as shown in Fig. 1*e*.

EDX was employed to obtain the quantitative elemental information of the amount and the distribution of Fe and O species in the sample. The elemental analysis by EDX (Fig. 2) confirms the presence of Fe and O elemental signatures of the product obtained at 2 (Fig. 2*a*) and 10 mol/L (Fig. 2*b*) KOH reduction. The elemental analysis showed that the products have iron oxides with the atomic ratios of 68.49:30.48 and 72.61:27.39 (%) for Fe/O at 2 and 10 mol/L KOH reduction materials, respectively, as expected for the nearly stoichiometric composition of magnetite with coexisting hematite.

Fig. 3. Magnetic hysteresis curves measured at room temperature for (*a*) 2 mol/L alkali-synthesized nanoparticles and (*b*) 10 mol/L alkali-synthesized nano-octahedrons.



Magnetic measurement of MNPs

The magnetic properties of 2 and 10 mol/L alkali-synthesized MNPs were investigated at room temperature. A change of magnetic saturation was observed when the alkaline concentration was varied from 2 to 10 mol/L. Figure 3 shows that the magnetic saturation value (M_s) is 0.9 emu/g for 2 mol/L alkali-synthesized (Fig. 3*a*) nanoparticles, whereas it is 24 emu/g for 10 mol/L alkali-synthesized (Fig. 3*b*) nano-octahedrons. Such phenomena can be closely related to the phase change of magnetic particles from hematite to magnetite. The magnetic state hysteresis residual magnetization at a zero external field was also varied by the alkaline concentration. The remanent magnetization (M_r) was found to be 0.13 emu/g for 2 mol/L and 3.33 emu/g for 10 mol/L, and coercivity (H_c) was 59.0 Oe for 2 mol/L and 111.00 Oe for 10 mol/L, respectively, as shown in the Supplementary data (Figs. S3*a* and S3*b*). Hysteresis loops of the nano-octahedron show

Can. J. Chem. Downloaded from www.nrcresearchpress.com by Renmin University of China on 09/02/12
For personal use only.

that the octahedron is ferromagnetic (Hc = 111.00 Oe) at room temperature.

An XRD study also proved that the magnetite particles are partially replaced in place of hematite at the 10 mol/L alkaline concentration, which results in an increase in the magnetization. The experimental results also indicate that the MNPs alkalization at the higher 10 mol/L possesses high magnetization. It is reasonable to conclude that the alkaline concentration also has tunable properties for the magnetization.

Synthesis mechanism of MNPs

We prepared the ferromagnetic nanoparticles by the oxidation–reduction of ferric nitrate salt in the ethanol–water solvent. Firstly, $Fe(NO_3)_3{\cdot}9H_2O$ dissociates slowly into Fe^{3+} and NO_3^- ions due to their weak dissociation tendency under the aqueous hydrothermal conditions.

$$[1] \quad Fe(NO_3)_3 \rightarrow Fe^{3+} + 3NO_3^-$$

Also, most of the metal nitrate salts (e.g., $Fe(NO_3)_3$) decompose via hydrolysis to the hydroxides.[10]

$$[2] \quad Fe(NO_3)_3 + 3H_2O \rightarrow Fe(OH)_3 + 3HNO_3$$

Or, the available Fe^{3+} ions (eq. [1]) are subsequently depleted to form $Fe(OH)_3$ or FeOOH in an alkaline condition.

$$[3] \quad Fe^{3+} + H_2O \rightarrow Fe(OH)_3 \rightarrow FeO(OH) \quad (H_2O \text{ oxidation})$$

The resulting $Fe(OH)_3$ or FeOOH quickly decomposes into α-Fe_2O_3 in an alkaline solution.

$$[4] \quad Fe(OH)_3/FeO(OH) \rightarrow \alpha\text{-}Fe_2O_3$$

Finally, α-Fe_2O_3 can be transformed into Fe_3O_4 in the reaction of an alkaline solution under high temperature and pressure.

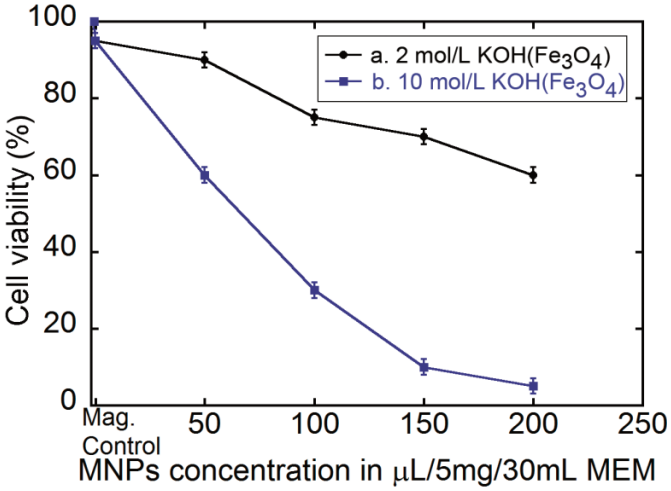
$$[5] \quad \alpha\text{-}Fe_2O_3 \rightarrow Fe_3O_4 \quad (\text{Reduction})$$

Through the experiments we find that the concentration of the alkali has a key influence on the octahedron-shape growth morphology. When the alkaline concentration (10 mol/L) is high in the reaction, mainly Fe_3O_4 nano-octahedrons and some coexisting Fe_2O_3 particles can be produced (Fig. 1*e*). This is in good agreement with the synthesis of the alkali-tunable ferromagnetic nanoparticles (Fig. 1).

Enhanced magnetic hyperthermia cancer cell killing

It is also well-known that hematite shows antiferromagnetic behavior. In our case, 10 mol/L alkali-synthesized magnetic nano-octahedrons also have some coexisting hematite as shown in the XRD data (Fig. 1*e*). The ferromagnetic (Fe_3O_4) and antiferromagnetic (α-Fe_2O_3) behavior of nanoparticles can increase the localized temperature (hyperthermia) inside a tumor,[11] which promotes cancer cell death. From the comparative studies (Fig. 4) on cancer treatments, the cancer cell killing efficiency was found to be ~40% (Fig. 4*a*) for 2 mol/L synthesized MNPs with a hyperthermia temperature (~45 °C), whereas for 10 mol/L synthesized MNPs it was found to be ~100% (Fig. 4*b*) with a hyperthermia temperature of ~50 °C. To investigate the colloidal stability of MEM-containing MNPs, the MNPs (5 mg) were dispersed in MEM (10 mL) by sonication. As shown in the Supplementary data in the absence (Fig. S5*a*) and presence (Fig. S5*b*) of a permanent magnetic field, as-prepared nano-octahedrons are well dispersed in the MEM media without any aggregation and (or) precipitation and firmly dragged by the permanent magnetic force.

Fig. 4. Surviving fractions of HeLa cells in the presence of 2 mol/L alkaline-synthesized nanoparticles and 10 mol/L alkaline-synthesized magnetic nanoparticles (MNPs). One hundred percent of cells were killed in the presence of 200 μL of the 10 mol/L alkaline-synthesized MNPs solution, whereas the 2 mol/L alkaline-synthesized nanoparticles gave only 40%. In the vertical scale, 100% means the control dish, bars represent the average region of three times the measured data, and the points represent the mean value from three measurements.



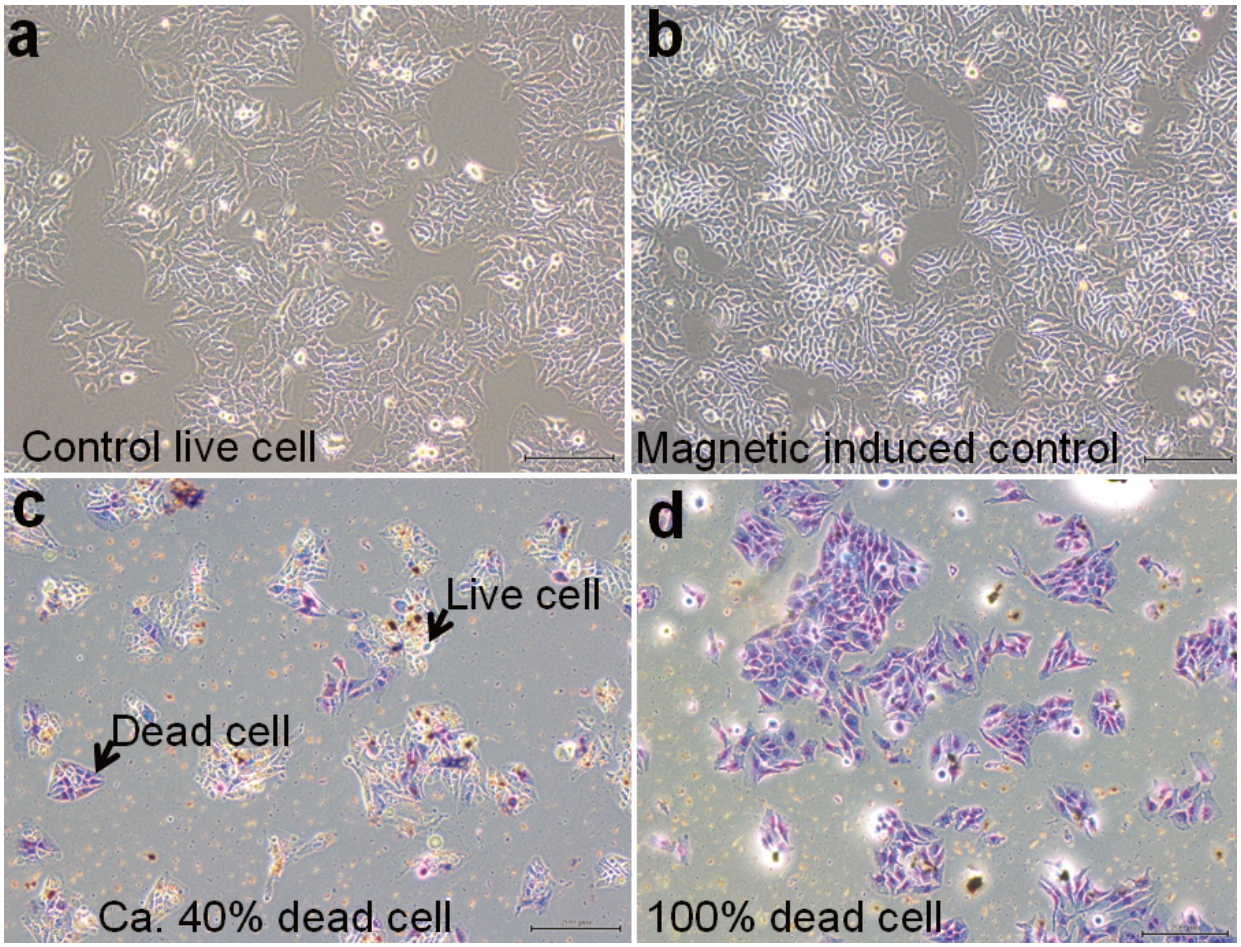
MNPs (5 mg) were dispersed in 30 mL of MEM supplemented with 10% NBS. Then the solution was sonicated for about 5 min and the nanoparticle-containing solution was filtered by a 40 μm cell strainer (BD Falcon). To compare the magnetic field induced cell killing, cell dishes were incubated for 24 h with different amounts of MEM-containing MNPs solutions (50, 100, 150, and 200 μL), and another dish without a nanoparticle solution (magnetic-induced control dish) was also incubated for 24 h. The cell viability under a 10 min AC magnetic field induction without MNPs (magnetic control) was more or less 95%. The cell killing ability under a 10 min AC magnetic field induced with 200 μL MEM containing 2 mol/L alkaline-synthesized nanoparticles and 10 mol/L alkaline-synthesized nanoparticles was ~40% and ~100%, respectively (Fig. 4).

The microscopic images of HeLa cells before and after magnetization induction are shown in Figs. 5*a* and 5*b*–5*d*, respectively. Figures 5*a* and 5*b* show that the cell morphology is largely unchanged after a 10 min magnetization. Figures 5*c* and 5*d* show that the HeLa cells suffer severe hyperthermia injury under a 10 min magnetization with the MNPs, indicated by the trypan blue stain, which confirms cell death.

Conclusions

In summary, we synthesized surfactant-free octahedron-shaped Fe_3O_4 with coexisting Fe_2O_3 under variable alkaline

Fig. 5. Microscopic images of HeLa cells. (*a*) No nanoparticles nor magnetization. (*b*) After a 10 min magnetic field induction without nanoparticles. (*c*) After a 10 min magnetic field induction with 2 mol/L alkaline-synthesized nanoparticles; trypan blue stained image. (*d*) After a 10 min magnetic field induction with 10 mol/L alkaline-synthesized nanoparticles; trypan blue stained image. Scale bars show 200 μm.



concentrations by hydrothermal decomposition of $Fe(NO_3)_3 \cdot 9H_2O$ in a water–ethanol mixed solvent. Through the experiments we found that the concentration of alkali has a key influence on the octahedron-shape growth morphology. The study also revealed that these alkaline concentrations influence the phase, shape, and magnetization of nanoparticles. We found a reproducible octahedron shape with high magnetization of nanoparticles synthesized at high alkaline concentration (10 mol/L). Also, we found that the cancer cell killing with high alkaline (10 mol/L) synthesized nanoparticles was more efficient than that with lower alkaline (2 mol/L) synthesized nanoparticles.

Supplementary data

Supplementary data are available with the article through the journal Web site http://nrcresearchpress.com/doi/suppl/10.1139/v2012-046.

Acknowledgement

This research was partly supported by a Grant-in-Aid for Challenging Exploratory Research (No. 23655204) and a Grant-in-Aid for Fellows (No. 22-10083) from the Japan Society for the Promotion of Science (JSPS). The authors wish to thank Assistant Professor Hirotaka Manaka for kindly permitting the use of the magnetometer in his laboratory at Kagoshima University.

References

(1) Rosi, N. L.; Mirkin, C. A. *Chem. Rev.* **2005**, *105* (4), 1547. doi:10.1021/cr030067f.
(2) Gao, J.; Gu, H.; Xu, B. *Acc. Chem. Res.* **2009**, *42* (8), 1097. doi:10.1021/ar9000026.
(3) Perez, J. M.; O'Loughlin, T.; Simeone, F. J.; Weissleder, R.; Josephson, L. *J. Am. Chem. Soc.* **2002**, *124* (12), 2856. doi:10.1021/ja017773n.
(4) Osterhout, V. *Magnetic Oxides;* John Wiley & Sons: New York, 1975.
(5) Dhage, S. R.; Khollam, Y. B.; Potadr, H. S.; Deshpande, S. B.; Bakare, P. P.; Sainkar, S. R.; Date, S. K. *Mater. Lett.* **2002**, *57* (2), 457. doi:10.1016/S0167-577X(02)00811-X.
(6) Fried, T.; Shemer, G.; Markovich, G. *Adv. Mater. (Deerfield Beach Fla.)* **2001**, *13* (15), 1158. doi:10.1002/1521-4095(200108)13:15<1158::AID-ADMA1158>3.0.CO;2-6.
(7) Kumar, R. V.; Koltypin, Yu.; Cohen, Y. S.; Cohen, Y.; Aurbach, D.; Palchik, O.; Felner, I.; Gedanken, A. *J. Mater. Chem.* **2000**, *10* (5), 1125. doi:10.1039/b000440p.
(8) Ziolo, R. F.; Giannelis, E. P.; Weinstein, B. A.; O'Horo, M. P.; Ganguly, B. N.; Mehrotra, V.; Russell, M. W.; Huffman, D. R.

Can. J. Chem. Downloaded from www.nrcresearchpress.com by Renmin University of China on 09/02/12
For personal use only.

Science **1992**, *257* (5067), 219. doi:10.1126/science.257.5067.219.
(9) Liu, X. M.; Fu, S. Y.; Xiao, H. M. *Mater. Lett.* **2006**, *60* (24), 2979. doi:10.1016/j.matlet.2006.02.027.
(10) Cabañas, A.; Poliakoff, M. *J. Mater. Chem.* **2001**, *11* (5), 1408. doi:10.1039/b009428p.
(11) Islam, M. S.; Kusumoto, Y.; Abdulla-Al-Mamun, M.; Horie, Y. *Chem. Lett.* **2011**, *40* (7), 773. doi:10.1246/cl.2011.773.

Can. J. Chem. Downloaded from www.nrcresearchpress.com by Renmin University of China on 09/02/12
For personal use only.

The use of Ebonex electrodes for the electrochemical removal of nitrate ion from water

David Kearney, Dorin Bejan, and Nigel J. Bunce

Can. J. Chem. Downloaded from www.nrcresearchpress.com by Renmin University of China on 09/02/12
For personal use only.

Abstract: This work addresses the remediation of nitrate-contaminated water using electrodes made of Ebonex (a titanium oxide ceramic with a wide range of potential stability). The objective was the complete denitrification of solutions containing nitrate ion. Denitrification was achieved in about 50% yield with unreactive supporting electrolytes when Ebonex was used as both cathode and anode, the remaining product being ammonia. Ammonia could be re-oxidized at the Ebonex anode, but this was much less efficient than the reduction step. A more efficient electrolytic denitrification was possible for solutions containing chloride; this is oxidized anodically to hypochlorite, which then oxidizes ammonia chemically to N_2. The overall rate of denitrification was highest at moderate concentrations of chloride ion, because hypochlorite also re-oxidizes reduction intermediates such as nitrite back to nitrate. Complete denitrification was achieved at all stages of the reaction using Ebonex cathode and a dimensionally stable anode based on Ti/IrO_2 or Ti/RuO_2, because the DSA oxidizes chloride ion more efficiently than Ebonex. Cathode fouling by water sources that are high in hardness cations can be prevented by using one DSA and a pair of Ebonex electrodes that undergo periodic polarity reversal.

Key words: nitrate reduction, Ebonex cathode, reverse polarity, electrolytic denitrification.

Résumé : Ce travail a pour but de présenter une méthode de réhabilitation de l'eau contaminée par des nitrates en faisant appel à des électrodes faites à partir d'Ebonex (de la céramique à base d'oxyde de titane qui présente une stabilité de potentiel sur une très grande plage). L'objectif était d'obtenir une dénitrification complète de solutions contenant l'ion nitrate. Lorsque l'Ebonex a été utilisé soit comme cathode ou comme anode avec des électrolytes de support non réactifs, la dénitrification a été réalisée avec un rendement d'environ 50 % et le produit résiduel était l'ammoniac. L'ammoniac ne peut pas être réoxydé sur une anode d'Ebonex, mais ce processus est beaucoup moins efficace que l'étape de réduction. Une dénitrification électrolytique plus efficace est possible avec les solutions contenant l'ion chlorure qui est oxydé à l'anode en hypochlorite et qui oxyde ensuite l'ammoniac d'une façon chimique en N_2. Le taux maximal de dénitrification est maximal avec des concentrations modérées d'ion chlorure, parce que l'hypochlorite reoxyde aussi des intermédiaires de la réduction, tel le nitrite en nitrate. On a réalisé une dénitrification totale à toutes les étapes de la réaction en utilisant une cathode d'Ebonex et une anode de dimension stable à base de Ti/IrO_2 ou Ti/RuO_2, parce que le DSA (Dirty Sandstone Acid)™ oxyde l'ion chlorure d'une façon plus efficace que l'Ebonex. Il est possible de prévenir l'encrassement de la cathode par des eaux de source riches en cations provoquant de la dureté en utilisant un DSA et une paire d'électrodes Ebonex qui est soumise périodiquement à une inversion de polarité.

Mots-clés : réduction de nitrates, cathode Ebonex, inversion de polarité dénitrification.

[Traduit par la Rédaction]

Introduction

Nitrate is an almost ubiquitous contaminant of ground water in areas of intensive agriculture due to run off from fertilizer and to biological transformation of nitrogenous runoff from feedlots. This poses a toxicity problem when ground water is to be used as a source of drinking water for both municipal consumers and those with residential wells.[1,2] The toxicity of nitrate is of special concern for young children, because the fetal and infant form of hemoglobin binds to nitrate to produce an inefficient oxygen transport molecule, leading to the condition methemoglobinemia. In most jurisdictions, the maximum allowable level for nitrate in drinking water is 45 mg L^{-1}, often expressed as 10 mg N L^{-1}. A further problem is the release of the potent greenhouse gas N_2O as a result of incomplete denitrification.[3,4] Other sources of nitrate contamination include industrial and nuclear processing waste waters.[5]

Electrochemical reduction of nitrate has been studied for many different cathodes as a possible remediation method for waters that contain sufficient electrolytes to carry the current.[5–7] The optimal outcome would be the complete elimination of nitrogen in the form of N_2, especially for potable water, but in most cases the major reduction product is ammonia, and elemental nitrogen is only a minor product (eqs. [1]–[2]). This has the effect of exchanging one pollutant for another. The options for an electrochemical technology to

Received 23 December 2011. Accepted 25 April 2012. Published at www.nrcresearchpress.com/cjc on 23 July 2012.

D. Kearney, D. Bejan, and N.J. Bunce. Electrochemical Technology Centre, Chemistry Department, University of Guelph, Guelph, ON N1G 2W1, Canada.

Corresponding author: Nigel J. Bunce (e-mail: nbunce@uoguelph.ca).

Can. J. Chem. Downloaded from www.nrcresearchpress.com by Renmin University of China on 09/02/12
For personal use only.

remove nitrate are to find conditions that favour the formation of N_2 over NH_3 or to couple the electrochemical reduction of nitrate with a process for removing ammonia as it is formed.

[1] $NO_3^- + 10H^+ + 8e^- \rightarrow NH_4^+ + 3H_2O$

[2] $NO_3^- + 6H^+ + 5e^- \rightarrow 1/2N_2 + 3H_2O$

Kyriacou and Katsounaros[6] have summarized the results of nitrate electroreduction for a wide variety of cathodes. The proportions of N_2 and NH_3 depend on the choice of cathode, the cathode potential, and the supporting electrolyte. The best yield of nitrogen reported, 92% N_2 and 6% N_2O, was found at a tin cathode, at very negative potentials.[8] The detailed chemistry is complex because of the large number of nitrogenous species of different oxidation states that must be considered as possible intermediates.

Although the ammonia product can be removed from aqueous solutions by gas stripping, this process is most effective when pH > pK_a of NH_4^+ (9.25), which is outside the pH range of drinking water. It would be impractical to implement domestically, while for municipal or industrial applications there would remain the problem of treating the volatilized ammonia to avoid air pollution.

The 3-electron electrochemical oxidation of ammonia to nitrogen (eq. [3]) can in principle be coupled to the 8-electron reduction of nitrate ion to ammonium ion (eq. [1]).

[3] $NH_3 \rightarrow 1/2N_2 + 3H^+ + 3e^-$

The oxidation of ammonia to elemental nitrogen is also much more facile in alkaline solution, because NH_3 is much more easily oxidized than NH_4^+[9]. High chemical and current efficiencies are possible using noble metal anodes, such as platinized platinum, and carefully controlled potential.[9] Attempts to use anodes not based on noble metals at pH values relevant to drinking water have had limited success.[9,10] Recently, denitrification has been studied with pairs of identical electrodes made of Cu-Ni alloy[11] or boron-doped diamond[12] using polarity reversal. In the latter case, low (but not zero) concentrations of ammonia were achieved in the remediation of high nitrate – low chloride waste water from hydroponic operations.

Break-point chlorination (eqs. [4]–[5]) is routinely used to remove ammonia from potable water simultaneously with disinfection.[13,14] Analogous chemistry can be initiated by electrochemical oxidation of chloride ion to HOCl.[15–18] The combination of cathodic reduction of nitrate and chloride-mediated electrochemical oxidation achieves the desired conversion of NO_3^- to N_2, although chloride salts cannot be added to potable water. In addition, the cycle eq. [6]–eq. [5] is not entirely catalytic in chloride: further oxidation of hypochlorite gives toxic chlorine oxyanions: ClO_2^- promotes erythrocyte lysis;[19] ClO_3^- is a nitrate antagonist in plants;[20] ClO_4^- is a thyroid hormone mimic.[21,22]

[4] $Cl_2 + H_2O \rightarrow HCl + HOCl$

[5] $3HOCl + 2NH_3 \rightarrow N_2 + 3HCl + 3H_2O$

[6] $Cl^- + H_2O \rightarrow HOCl + H^+ + 2e^-$

The present research was initially directed towards the use of Ebonex electrodes for the simultaneous reduction of nitrate and oxidation of ammonia, as a possible one-step chloride-free denitrification. Ebonex is a conductive and corrosion-resistant ceramic with optimal electrical conductivity at the composition Ti_4O_7, which is usually conceptualized as alternating layers of TiO: $3TiO_2$.[23,24] Ebonex has excellent stability with respect to water decomposition under both anodic (>2 V vs. SCE) and cathodic (~ –1.4 V vs. SCE) polarization and is extremely corrosion-resistant,[25–28] suggesting its possible use as both anode and cathode for such a process. In practice, the combination of Ebonex cathode – Ebonex anode was rather inefficient. Instead, a novel chloride-mediated protocol was developed — a Ti/RuO_2 anode promoted efficient oxidation of chloride, and a pair of Ebonex electrodes was used with periodic polarity reversal. This gave efficient reduction, even in the presence of hardness cations, which otherwise foul the cathode.

Materials and methods

Sodium hydroxide, sodium chloride, calcium chloride, sodium nitrate, and sodium nitroprusside were obtained from Fisher Scientific (Toronto, Ontario, Canada). Sigma-Aldrich (Oakville, Ontario, Canada) provided ammonium sulfate, sodium sulfate, sodium citrate, sodium perchlorate, and phenol. Commercial Alcohols Inc. (Brampton, Ontario, Canada) supplied ethanol, and Ultra Bleach (sodium hypochlorite) was obtained from Loblaws (Toronto, Ontario, Canada). The Ebonex electrode materials were obtained from Vector Corrosion (Stoney Creek, Ontario, Canada), and Ti/IrO_2-Ta_2O_5 and Ti/RuO_2 electrodes were supplied by ELTECH Systems Corporation (Painesville, Ohio, USA). All solutions were prepared using deionized water.

Electrolyses using Ebonex as both the cathode and anode were performed in a rectangular Plexiglas cell (internal dimensions: 2.9 cm × 2.9 cm × 7.5 cm) whose lid (also Plexiglas) held four cylindrical Ebonex electrodes (7.5 cm length and 1 cm diameter, external dimensions), with each immersed area of 20 cm^2. The electrodes were connected in diagonal pairs and operated (in most experiments) with periodically reversed polarity. In this cell, for example, an applied current of 40 mA represents a current density of 1 mA cm^{-2}. The inter-electrode gap was 5 mm between cathode and anode, and 10 mm between the 2 anodes or the 2 cathodes. A Princeton Applied Research Model 363 Potentiostat Galvanostat was used as the power supply, with a Siemens LOGO! 12/24 RC switcher used to reverse polarity between the electrodes. Cell voltage was monitored using a Wavetek DM5XL multimeter.

Batch electrolyzes using a Ti/RuO_2 anode (surface area of 6 cm^2 immersed in solution) were performed in a 100 mL Pyrex beaker, using 38 mL of solution in each experiment. An Ebonex cathode was used (7.5 cm length × 1 cm diameter), with an inter-electrode gap of 1 cm. In this cell, the cathode current density for 40 mA applied current was 2 mA cm^{-2}, and the anode current density was 6.7 mA cm^{-2}. Electrolyses were carried out amperostatically and under gentle

Can. J. Chem. Downloaded from www.nrcresearchpress.com by Renmin University of China on 09/02/12
For personal use only.

stirring, using a magnetic stir bar and a Fisher Scientific Thermix stirrer.

The progress of the electrolyzes was monitored by taking 0.5 mL samples every hour, diluting the sample to 10 mL with deionized water, and analyzing the sample for total nitrogen with a Shimadzu TOC analyzer, using the TOC + TN method. The analyzer gave a result in ppm of nitrogen, which was converted to mmol L^{-1} of N after dividing by the molar mass of nitrogen (14 g mol^{-1}) and multiplication by the 20× dilution factor.

Ammonia concentrations were determined spectrophotometrically,[29] using phenol, nitroprusside, and alkaline citrate to form indophenol blue, whose intensity at 640 nm is proportional to the ammonia concentration. A Pharmacia LKB-Novaspec II spectrophotometer was used to measure absorbance. A calibration curve was produced using standards, from which absorbance values of unknown samples could be converted to ammonia concentration.

Nitrate concentration was determined by subtracting the concentration of ammonia from the concentration of TN for a given sample. In some cases, nitrate concentration was also determined spectrophotometrically,[30] with agreement always observed between the two methods. A Shimadzu UV 160U Spectrophotometer was used to measure the absorbance of the samples at 275 and 220 nm.

Results and discussion

Ebonex cathode and Ebonex anode in the absence of chloride

Cyclic voltammetry at an Ebonex electrode revealed that there was no cathodic current until –1.8 V vs. Pt wire reference electrode, and that the current was independent of the nitrate concentration (Fig. 1A). This observation is compatible with the conclusions of Katsounaros and Kyriacou for tin,[31] where there is a high overvoltage for hydrogen evolution, and the cathodic current is ascribed to the formation of sorbed hydrogen rather than reduction of nitrate. Tentatively, a similar explanation may be applicable to Ebonex. For graphite, in contrast, the onset of the cathodic current began at less negative potentials, and the current increased with the nitrate concentration (Fig. 1B).

Preliminary electrolyzes showed that reduction of nitrate was efficient at Ebonex, but oxidation of ammonia was inefficient. These experiments employed Ebonex as both anode and cathode, and the polarity was reversed every 30 min, because we have previously shown that an Ebonex anode otherwise loses its activity through oxidation of the surface.[32,33] Anodic deactivation can be conceptualized as oxidation of the Ti_4O_7 surface layer to Ti_4O_8 (= TiO_2), in competition with oxidation of water or other substrate. Periodic reversal of the polarity allowed the activity of a pair of Ebonex electrodes to be sustained, with the additional advantage of avoiding the deposition of carbonate scale on the cathode when the supporting electrolyte contains hardness cations. Cathode fouling is the result of high pH near the cathode surface due to the reduction of water to H_2 and OH^-.[34] A control electrolysis without nitrate, in which the supporting electrolyte contained calcium (0.5 mol/L $CaCl_2$), indeed showed the development of a lime deposit unless the polarity was reversed.

Fig. 1. Cyclic voltammetry at 50 mV/s using 50 mmol/L $NaClO_4$ of supporting electrolyte: 1, background; 2, 25 mmol/L $NaNO_3$; 3, 0.5 mol/L $NaNO_3$. (A) Ebonex electrode (8 mm^2). (B) Graphite pencil lead electrode (63 mm^2).

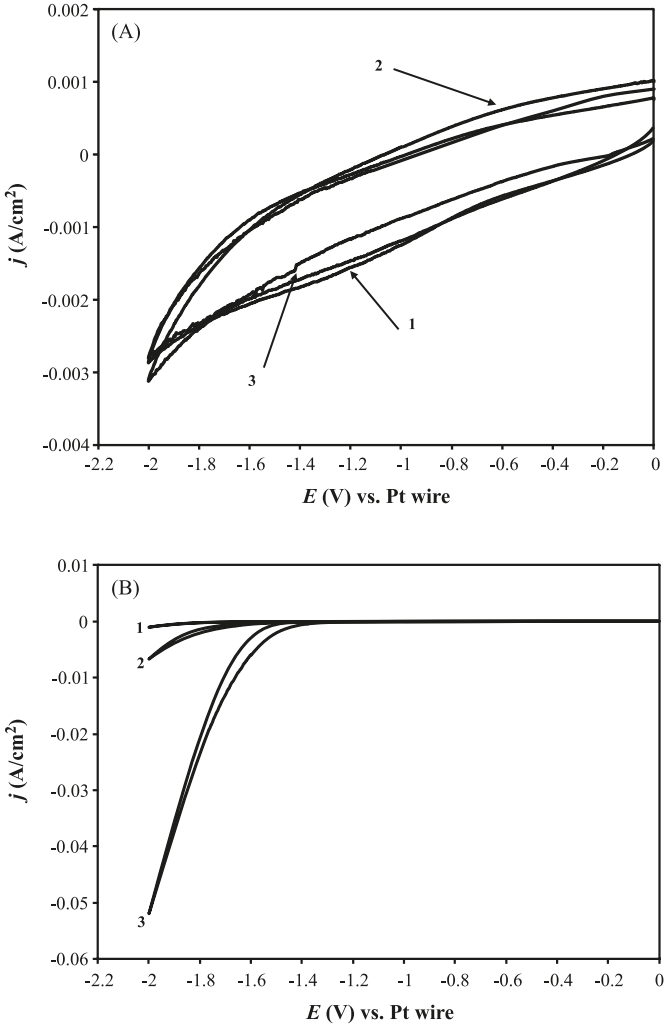
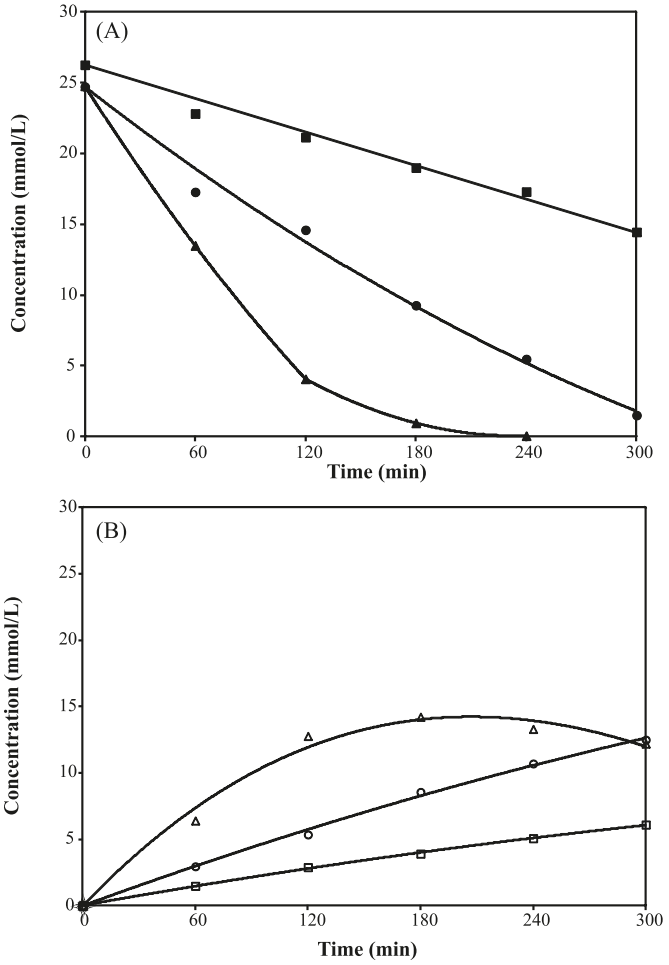


Figure 2 shows the results of electrolysis of 25 mmol/L $NaNO_3$ at different currents, with 0.1 mol/L $NaClO_4$ as an unreactive supporting electrolyte. Ammonia was in all cases a significant product, as observed at most other cathodes.[6] Loss of total nitrogen (TN) is a direct measure of denitrification. The loss of nitrate, represented by the difference between TN and $c(NH_3)$, followed the expected nearly zero order (current-controlled) kinetics until late in the reaction because of the low current densities (0.67 to 3.0 mA cm^{-2}). This was shown by the initial rates (linear portion of Fig. 2, panel A) of 0.038 ± 0.001, 0.081 ± 0.010, and 0.17 ± 0.01 mmol/L min^{-1} at 30, 60, and 120 mA, which were proportional to the applied current (Supplementary data Fig. S1). When $c(NO_3^-)$ was measured directly, there was no difference between this value and [TN - $c(NH_3)$], showing that significant concentrations of other nitrogen species were not present. An experiment in which 25 mmol/L $NaNO_3$ was electrolyzed in 0.1 mol/L $NaClO_4$ supporting electrolyte at 120 mA, with or without reversing the polarity, showed that the reduction of nitrate was not affected by polarity reversal. From this, we conclude that Ebonex cathodes are not inactivated by

Can. J. Chem. Downloaded from www.nrcresearchpress.com by Renmin University of China on 09/02/12
For personal use only.

Fig. 2. Electrolysis of 25 mmol/L $NaNO_3$ with 0.1 mol/L $NaClO_4$ supporting electrolyte at different currents. (A) Nitrate. (B) Ammonia. 120 mA (▲/△), 60 mA (●/○), 30 mA (■/□)



"over-reduction" in the way that Ebonex anodes are inactivated by overoxidation.[32] Periodic polarity reversal is not detrimental to the current efficiency, however, and is useful when solutions contain hardness cations.

In the foregoing experiment at 120 mA, the concentration of ammonia was 14 mmol/L after 3 h; this accounted for almost all the TN (the residual concentration of nitrate was ~1 mmol/L). Of the total 1296 C (0.0134 mol electrons), 4.3×10^{-3} mol e^- were used to form ammonia according to eq. [1] and 2.7×10^{-3} mol e^- for forming N_2 by eq. [2], for a total current efficiency of 52%. The product ratio NH_3:N_2 was independent of current, namely 1.1, 1.2, and 1.0 for 30, 60, and 120 mA, respectively. In experiments that were continued overnight, the residual ammonia concentrations were zero at 120 mA, 9 mmol/L at 60 mA, and 10 mmol/L at 30 mA. These experiments were carried out under conditions where any ammonia stripped from the solution was trapped — there was no significant loss of ammonia by this route. The rate of oxidation of ammonia was at least 10-fold slower than the reduction of nitrate; therefore, the initial phase of denitrification cannot be explained by a mechanism in which nitrate is reduced to ammonia at the cathode and then reoxidized at the anode. This conclusion was confirmed in experiments starting with ammonia, again using Ebonex as both anode and cathode, even when the reaction conditions were modified to the highly alkaline pH values that are customarily used at noble metals. For example, there was still 7 mmol/L ammonia remaining even after 21 h electrolysis of 25 mmol/L ammonia (in the form of ammonium perchlorate) at 120 mA in alkaline solution (Supplementary data Fig. S2).

Voltammetry does not offer straightforward answers concerning the mechanism of cathodic reduction of nitrate. A clear reduction peak for nitrate was seen at Pt in acidic solution.[35] A complication is that the progress and mechanism of nitrate reduction are pH dependent, as emphasized by Milhano and Pletcher.[5,44] In other work, no reduction current was seen unless the solution also contained a small concentration of nitrite ion, and the second cycle of a cyclic voltammogram gave larger currents than the first, suggesting that nitrite formation causes the reduction to be autocatalytic.[36] Katsounaros and Kyriacou found that the reduction current, in neutral solution at a tin cathode, commenced at ~ –1.5 V vs. Ag/AgCl and increased with the concentration of $NaNO_3$, but no peak current was seen even at –2.2 V.[31]

A high overpotential for hydrogen formation is not the only factor that determines the selectivity between N_2 and NH_3. Tin, Ebonex, and boron-doped diamond all have a high overpotential for hydrogen evolution, but only tin has a high selectivity for N_2.[6,8] The electrochemical reduction of nitrate (and the analogous biological process)[37] are mechanistically complex, not least because many intermediates exist as acid-base conjugates.[5,6]

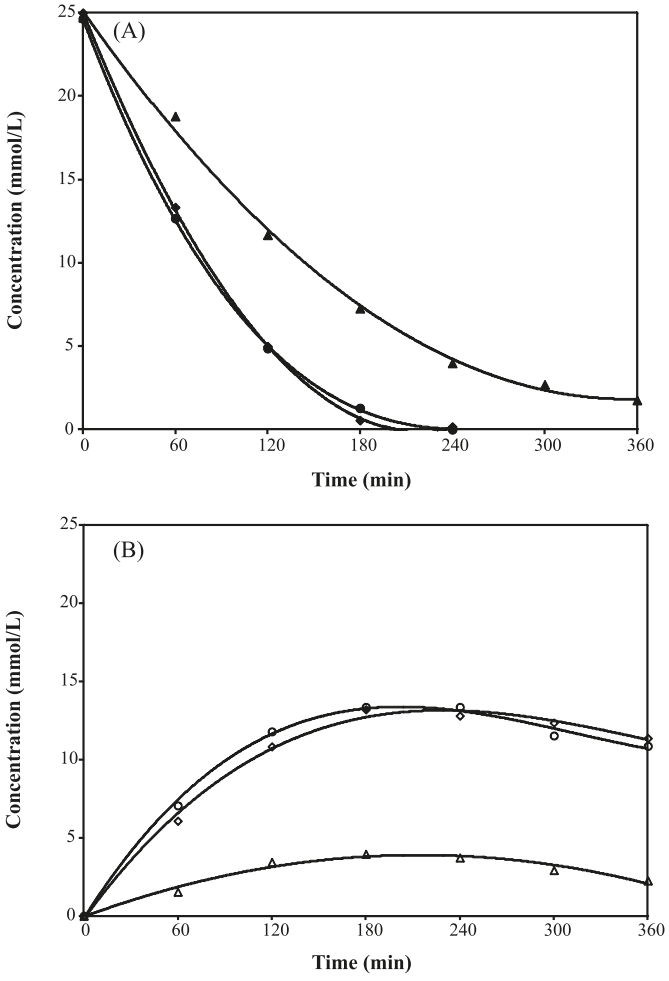
At most cathodes, the initial product of nitrate reduction is nitrite ion, initiated by addition of e^-/H^+. For tin, no hydrogen gas was evolved until well into the electrolyzes, especially at higher initial concentrations of nitrate, suggesting that nascent hydrogen, assumed to be equivalent to a sorbed hydrogen atom, is the active reductant under these conditions.[31] The intermediate product is NO_2, which is reduced to nitrite by either e^- or H(ads). Analogous reactions can convert nitrite to NO and thence HN=O (nitroxyl). Nitroxyl is the key intermediate in determining whether the final product is monomeric (NH_4^+) or dimeric (N_2O and (or) N_2) both electrochemically and biologically.[37] HNO dimerizes rapidly in aqueous solution to give hyponitrous acid $H_2N_2O_2$.[38] Katsounaros and Kyriacou showed experimentally that $H_2N_2O_2$ is formed during the reduction of nitrate at a tin cathode and proposed that it spontaneously produces N_2O, which can reduce further to N_2.[39] However, HNO also undergoes a pair of e^-/H^+ reactions that lead to hydroxylamine (which is reducible to ammonium ion); in addition, HNO is a reaction partner for hydroxylamine, forming N_2. The reaction between ammonium ion and nitrite (N_2O_3 is the active nitrosating agent at moderate pH values) (eq. [7]), is too slow to account for significant loss of TN from the solution on the time-scale and reactant concentrations of our experiments.[40]

$$[7] \qquad NO_2^- + NH_4^+ \rightarrow N_2 + 2H_2O$$

Katsounaros and Kyriacou observed that the relative yield of nitrogen and the total faradaic current efficiency were concentration-dependent, increasing from 70% to 83% as the concentration of nitrate was raised from 100 to 1500 mg L^{-1}.[31] Taking into account that the highly negative polarization of the tin cathode (–2.8 V vs. Ag/AgCl) would repel the

Can. J. Chem. Downloaded from www.nrcresearchpress.com by Renmin University of China on 09/02/12
For personal use only.

Fig. 3. Electrolysis of $NaNO_3$ 25 mmol/L at 120 mA with different supporting electrolytes. (A) Nitrate. (B) Ammonia. NaCl 0.05 mol/L (▲/△), $NaClO_4$ 0.05 mol/L (●/○), Na_2SO_4 0.05 mol/L (◆/◇).



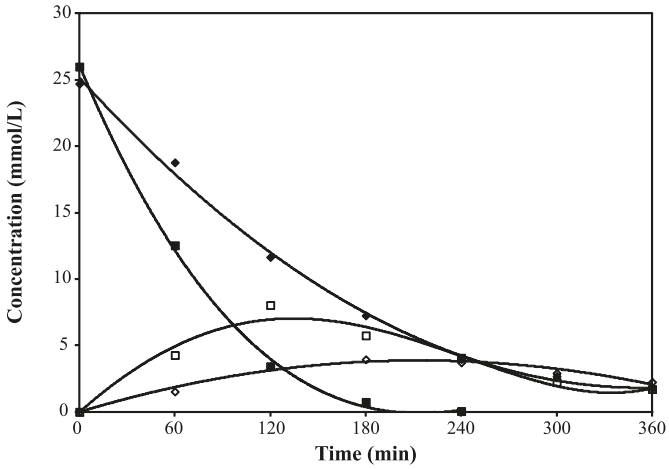
approach of nitrate anions, they proposed a mechanism involving the approach of $M^+\cdots NO_3^-$ ion pairs to the cathode and fitted the concentration dependence of the rate of reduction at constant potential to a Langmuir association model.[39]

To conclude this section, our experiments show that it is possible to achieve complete electrochemical denitrification of a nitrate solution using Ebonex as both anode and cathode, although the overall current efficiency is disappointingly low.

Ebonex cathode and Ebonex anode in the presence of chloride

Figure 3 compares electrolyzes of 25 mmol/L nitrate in 0.05 mol/L supporting electrolytes $NaClO_4$, Na_2SO_4, and NaCl. The NaCl solution gave the fastest loss of TN, the slowest rate of loss of nitrate, and the lowest chemical yield of ammonia. These observations are consistent with the well-known intervention of oxidation to hypochlorite and a mediated oxidation in the presence of chloride. The explanation for the slower reduction of nitrate in the presence of chloride is that hypochlorite re-oxidizes partly reduced intermediates back to nitrate. As in the chloride-free solutions, the measured $c(NO_3^-)$ was equal to [TN – $c(NH_3)$], showing the absence of significant concentrations of other nitrogen species. The apparent current efficiency in NaCl solution was 30%. The current efficiency for N_2 was calculated on the basis of a $5e^-$ change (not $8e^-$ followed by reoxidation), both to compare with the chloride-free system and because the ultimate practicality of such as remediation method is kWh per kg nitrate, irrespective of the reaction mechanism.

Fig. 4. 25 mmol/L $NaNO_3$ + 50 mmol/L NaCl electrolyzed at 120 mA. Nitrate (black shapes), ammonia (white shapes). Polarity reversal every 180 min (■/□), polarity reversal every 30 min (◆/◇).



In contrast with chloride-free solution, polarity reversal every 30 min decreased the rate of reduction of nitrate and increased the yield of ammonia ($[Cl^-]$ = 500 mmol/L; $[NO_3^-]$ = 25 mmol/L) (Fig. 4). This observation is consistent with observations on the oxidation of sulfide at Ebonex anodes.[33] Polarity reversal maintains the activity of the anode towards oxidation of chloride to hypochlorite, giving a higher steady-state concentration of hypochlorite, and thus increasing the rate of oxidation of ammonia to N_2. It also speeds up re-oxidation of partly reduced intermediates to nitrate, so the net rate of reduction of nitrate is slower.

In a series of experiments carried out in the cell with two pairs of Ebonex electrodes at $[Cl^-]$ = 500 mmol/L; $[NO_3^-]$ = 25 mmol/L, the initial (linear) rates of loss of TN for currents 20, 40, 60, 120 mA (= 1:2:3:6) were 0.012, 0.022, 0.033, and 0.080 mmol/L min^{-1} = 1:1.8:2.7:6.7; those for loss of nitrate were similar: 0.014, 0.032, 0.044, and 0.109 min^{-1} = 1:2.4:3.1:7.8 (Fig. 5). The increasing curvature of the data with increasing current suggests a current controlled reaction at low current, moving towards mixed and (or) mass transport control at 120 mA. As in the absence of chloride, the ammonia concentration only begins to decline once $c(NO_3^-)$ has become negligible, showing that nitrate reduction is more efficient than ammonia oxidation. Throughout the reaction, TN ~ $c(NH_3)$.

A study of the effect of the chloride concentration at constant $[NO_3^-]$ and constant current (120 mA) indicated an optimum range for $c(Cl^-)$. Our initial experiments were carried out without controlling the ionic strength (Supplementary data Fig. S3), at which the rate of ammonia formation followed the order: Control < 0.01 < 0.05, 0.2, and 0.5 mol/L NaCl. At a constant ionic strength of 500 mmol/L, varying from 100% $NaClO_4$ to 100% NaCl, there was little change in

Can. J. Chem. Downloaded from www.nrcresearchpress.com by Renmin University of China on 09/02/12
For personal use only.

Fig. 5. Electrolysis of $NaNO_3$ 25 mmol/L with NaCl 0.5 mol/L supporting electrolyte. Nitrate (filled symbols), ammonia (open symbols). 20 mA (■/□), 40 mA (◆/◇), 60 mA (▲/△), 120 mA (●/○).

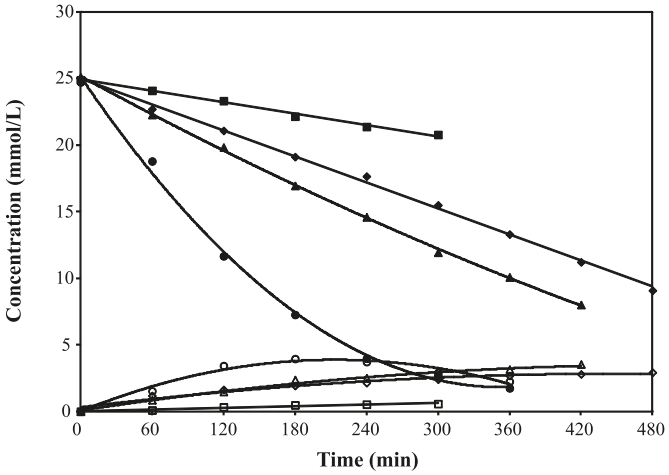


Fig. 6. Electrolysis of $NaNO_3$ 25 mmol/L at 120 mA and constant 500 mmol/L ionic strength. (A) Nitrate; (B) ammonia. 500 mmol/L $NaClO_4$ (▲/△), 10 mmol/L NaCl + 490 mmol/L $NaClO_4$ (◆/◇), 50 mmol/L NaCl + 450 mmol/L $NaClO_4$ (■/□), 500 mmol/L NaCl (●/○).

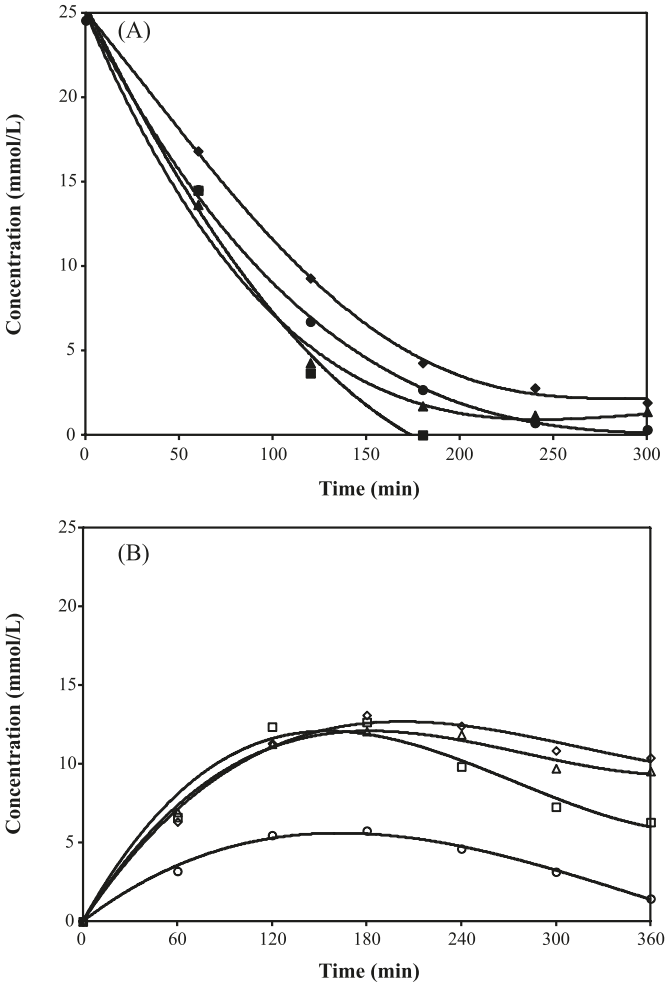
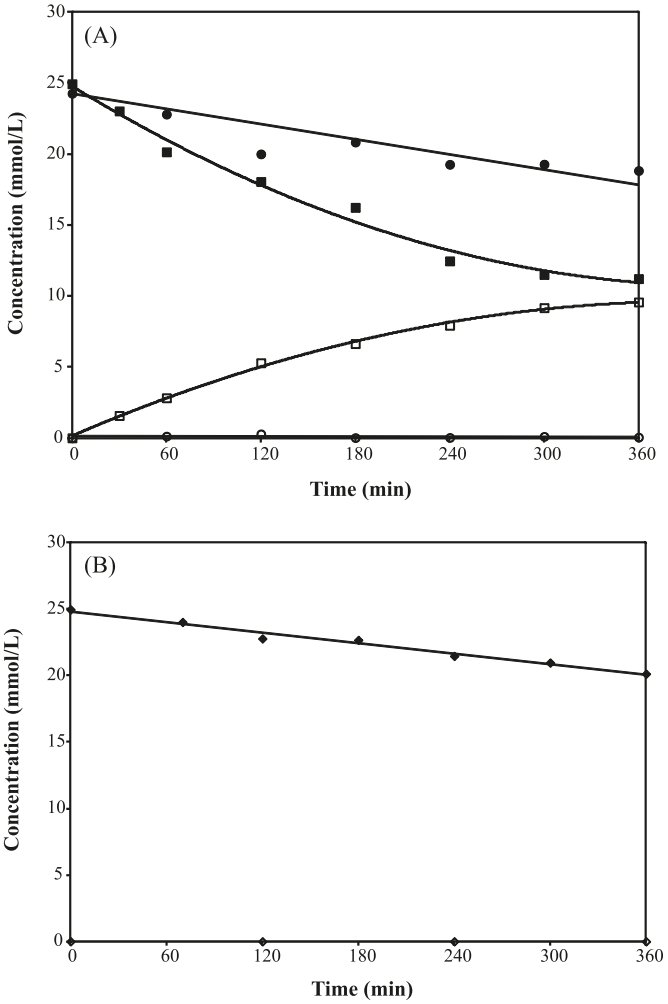


Fig. 7. Electrolysis of $NaNO_3$ 25 mmol/L at 40 mA with one Ebonex. Nitrate (filled symbols), ammonia (open symbols). (A) Ti/IrO_2-Ta_2O_5 anode/Ebonex cathode, (B) Ti/RuO_2 anode/ Ebonex cathode. NaCl 0.5 mol/L (●/○), Na_2SO_4 0.5 mol/L (■/□).



the rate of reduction of nitrate and a gradual (but incomplete) reduction in the build-up of ammonia at intermediate stages of denitrification (Fig. 6).

Ebonex cathode and dimensionally stable anode in the presence of chloride

Because the inefficiency of ammonia oxidation in the foregoing experiments can be attributed to the relative inefficiency of Ebonex as an anode material, we carried out experiments with an Ebonex cathode and either Ti/IrO_2-Ta_2O_5 or Ti/RuO_2 anode. On the anode side, DSAs have previously been used in this application by Li et al.[41] Reversal of polarity was not employed in these experiments, because it is unnecessary for the Ebonex cathode (see above) and inappropriate for the metal oxide-based anodes. In a series of experiments using 500 mmol/L [Cl^-], 25 mmol/L [NO_3^-], and an applied current of 40 mA, the loss of nitrate was 0.014 and 0.013 mmol/L min^{-1} at Ti/RuO_2 or Ti/IrO_2-Ta_2O_5 anodes, respectively, and total denitrification was achieved at all stages of the electrolyzes (Figs. 7A and 7B). For comparison, the loss of nitrate (initial rate 0.048 mmol/L min^{-1}) at Ti/IrO_2-Ta_2O_5 in 500 mmol/L Na_2SO_4 was faster than in

Table 1. Comparison of DSA and Ebonex anodes (Ebonex cathode) in the reduction of nitrate in unreactive supporting electrolytes and in NaCl.

Anode	Supporting electrolyte	Initial rate (mmol/L min^{-1})	Ammonia concentration	Notes
Ebonex	0.1 mol/L $NaClO_4$	0.050	5 mmol/L at 180 min	Interpolated from Figs. S1 and 2B
Ebonex	0.5 mol/L NaCl	0.032	2 mmol/L at 180 min	Figure 5
Ti/IrO_2-Ta_2O_5	0.5 mol/L Na_2SO_4	0.048	6 mmol/L at 180 min	Figure 7A
Ti/IrO_2-Ta_2O_5	0.5 mol/L NaCl	0.013	Zero throughout	Figure 7A
Ti/RuO_2	0.5 mol/L NaCl	0.014	Zero throughout	Figure 7B

Can. J. Chem. Downloaded from www.nrcresearchpress.com by Renmin University of China on 09/02/12
For personal use only.

Fig. 8. 50 mmol/L $NaNO_3$ + 50 mmol/L NaCl + 425 mmol/L $NaClO_4$ in a batch cell at varying currents. Ti/RuO_2 anode; pair of Ebonex cathodes with polarity reversal every 30 min. Nitrate (filled symbols), ammonia (open symbols). 120 mA (♦ /◇), 60 mA (■/□), 30 mA (▲/△).

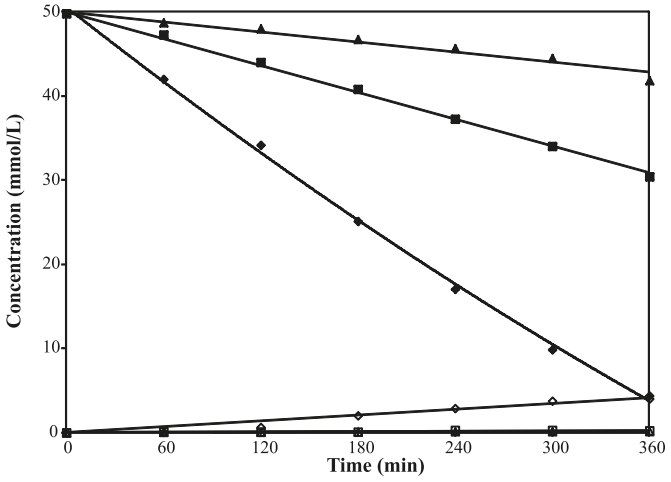
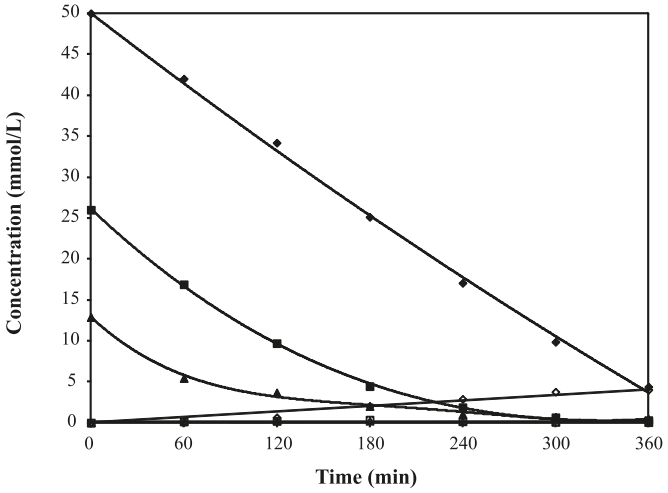


Fig. 9. Batch cell electrolysis at 120 mA. Ti/RuO_2 anode; pair of Ebonex cathodes with polarity reversal every 30 min. Nitrate (filled symbols), ammonia (open symbols). 50 mmol/L $NaNO_3$ + 50 mmol/L NaCl + 425 $NaClO_4$ (♦ /◇), 25 mmol/L $NaNO_3$ + 50 mmol/L NaCl + 450 mmol/L $NaClO_4$ (■/□), 12.5 mmol/L $NaNO_3$ + 50 mmol/L NaCl + 462.5 mmol/L $NaClO_4$ (▲/△).



NaCl, but ammonia was present at intermediate stages of electrolysis. As explained previously, anodic formation of hypochlorite promotes the oxidation of both ammonia to N_2 and reduction intermediates back to nitrate, lowering the net rate of reduction of nitrate.

Table 1 summarizes results at 40 mA, 500 mmol/L [Cl^-], 25 mmol/L [NO_3^-] for the systems Ebonex–Ebonex and DSA–Ebonex for loss of nitrate, along with the ammonia concentrations at an arbitrarily chosen reaction time of 180 min. The rate of loss of nitrate was consistently slower when an unreactive supporting electrolyte was replaced by NaCl, as explained by re-oxidation of intermediate reduction products. The DSAs catalyze the oxidation of ammonia and reduction intermediates of nitrate through the hypochlorite reaction more efficiently than Ebonex. At the DSAs, ammonia is absent at all stages of the reaction when NaCl is present, unlike at Ebonex anodes. However, the net rate of nitrate reduction is slower using the DSA than at Ebonex for the same chloride concentration.

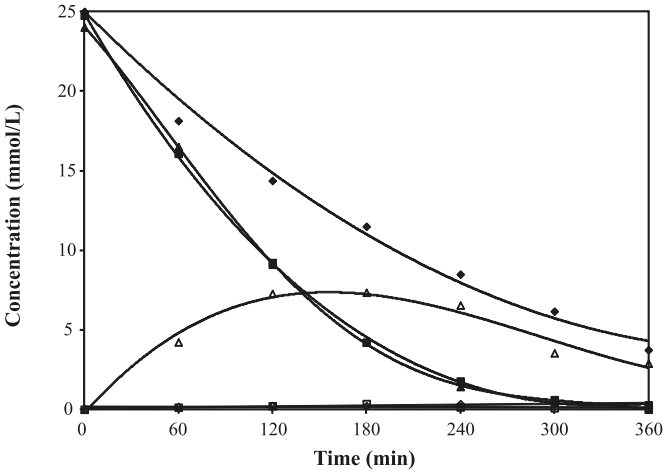
Two Ebonex electrodes with periodic polarity reversal and one DSA in the presence of chloride

In this section, we introduce the idea of using Ti/RuO_2 as the anode, without polarity reversal, and a pair of Ebonex electrodes that switched between cathodic and anodic polarization every 30 min. This method combines the superior efficiency of Ti/RuO_2 over Ebonex for oxidizing chloride to hypochlorite, with the ability to reverse the polarity to prevent the accumulation of lime deposits on the cathode when the water contains hardness ions.[11,12,42] Its high stability under both anodic and cathodic polarization makes Ebonex a good choice for this application.

Figure 8 shows the influence of changing the applied current in the system 50 mmol/L $NaNO_3$, 50 mmol/L NaCl, and 425 mmol/L $NaClO_4$. For currents 30, 60, and 120 mA, the rate of loss of nitrate was proportional to the current (Supplementary data Fig. S4). Ammonia was completely absent from the solution at all stages of the reaction at 30 and 60 mA but built up late in the reaction at 120 mA, presumably because the oxidation of chloride could not keep pace with the reduction of nitrate at this low chloride concentration. Overall current efficiencies (again based on $5e^-$ for nitrate to N_2 and $8e^-$ for nitrate to ammonia) were 26%, 29%, and 38% at 30, 60, and 120 mA. Consistent with this explanation, a series of electrolyses at constant current (120 mA), chloride (50 mmol/L), and $NaClO_4$ adjusted to keep the ionic strength constant showed that lowering the starting concentration of nitrate led to complete denitrification even at 120 mA (Fig. 9). The initial rates of loss of nitrate (first 60 min) were almost independent of the nitrate concentration.

Can. J. Chem. Downloaded from www.nrcresearchpress.com by Renmin University of China on 09/02/12
For personal use only.

Fig. 10. Batch cell electrolysis of 25 mmol/L $NaNO_3$ at 120 mA in different concentrations of NaCl. Ti/RuO_2 anode; pair of Ebonex cathodes with polarity reversal every 30 min. Nitrate (filled symbols), ammonia (open symbols). All solutions electrolyzed were at equal ionic strength ($NaClO_4$ was used). 0.5 mol/L NaCl (◆/◇), 0.05 mol/L NaCl (■/□), 0.01 mol/L NaCl (▲/△).



As observed in the Ebonex cathode – Ebonex anode experiments above, the rate of loss of nitrate was slower in NaCl solution than in $NaClO_4$ or Na_2SO_4 at the same ionic strength, and there was a significant build-up of ammonia (maximum 9–10 mmol/L from 25 mmol/L $NaNO_3$ in the latter two experiments) at intermediate conversion of nitrate (Supplementary data Figs. S5A and S5B).

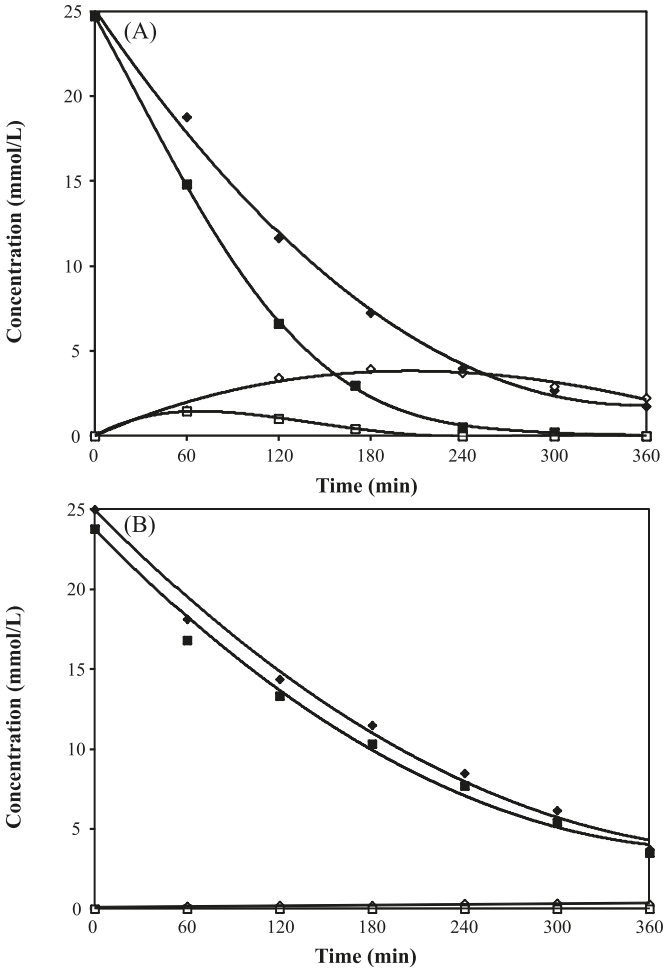
Figure 10 (which represents an series of experiments parallel to those in Fig. 6 for Ebonex–Ebonex) illustrates the effect of changing the chloride concentration at constant nitrate (25 mmol/L) and current (120 mA). At and above 50 mmol/L chloride, no ammonia is formed at any stage of the reaction. The net rate of loss of nitrate is independent of the chloride concentration at the two lower chloride concentrations but is inhibited at the high chloride concentration of 500 mmol/L. Finally, Fig. 11 gives a comparison of experiments carried out at 250 mmol/L $CaCl_2$ and 500 mmol/L NaCl for both Ebonex anode – Ebonex cathode and Ti/RuO_2 anode – two Ebonex electrodes with reversing polarity. The presence of the hardness cation Ca^{2+} slowed the reduction of nitrate and the overall rate of denitrification at Ebonex–Ebonex due to the accumulation of a lime deposit (Fig. 11A), but there was no inhibition of either process for Ti/RuO_2 anode/two Ebonex electrodes (Fig. 11B).

Conclusions

The use of Ebonex as both cathode and anode allowed a partial solution to the problem of remediating nitrate without the use of chloride. The reduction step gave ammonia in maximum yields of about 50% of the starting concentration of nitrate. Re-oxidation of ammonia at the Ebonex anode allowed complete denitrification, but the oxidation step was considerably more demanding in terms of the total charge required.

A simpler and more efficient electrolytic process was possible for solutions that contain chloride. Reduction at the Ebonex cathode once again gave a mixture of ammonia and

Fig. 11. Electrolysis of 25 mmol/L $NaNO_3$ at 120 mA with different supporting electrolytes: (A) Ebonex anode–Ebonex cathode; (B) Ti/RuO_2 anode and two Ebonex electrodes with periodically reversed polarity. Nitrate (filled symbols), ammonia (open symbols). NaCl 0.5 mol/L (◆/◇), $CaCl_2$ 0.25 mol/L (■/□).



N_2, but anodic oxidation of chloride to hypochlorite allowed efficient removal of ammonia. The hypochlorite-mediated process could be achieved using Ebonex cathode and anode as before, but even more efficiently if the anode was a dimensionally stable anode based on Ti/IrO_2 or Ti/RuO_2 — the types of anodes used for the industrial oxidation of chloride. The presence of chloride inhibited the apparent rate of loss of nitrate, because the hypochlorite thus formed re-oxidized reduction intermediates such as nitrite back to nitrate, and so the overall efficiency of denitrification was highest at moderate concentrations of chloride ion. The use of one DSA and two Ebonex electrodes, with the polarity of the Ebonex electrodes being periodically reversed, prevented cathode fouling for water sources that are high in hardness cations. The advantage of using Ebonex in this application is the ability to reverse the polarity, and hence to operate with an undivided cell, which avoids the need for a membrane that can be subject to fouling. A slightly different approach to indirect reduction has been described by Wang et al.,[43] who produced Ti(II) and Ti(III) species at a sacrificial titanium anode. The soluble titanium species can reduce nitrate anion in the bulk solution.

Can. J. Chem. Downloaded from www.nrcresearchpress.com by Renmin University of China on 09/02/12
For personal use only.

Supplementary data

Supplementary data are available with the article through the journal Web site at www.nrcresearchpress.com/doi/suppl/10.1139/v2012-048.

Acknowledgement

We thank the Natural Sciences and Engineering Research Council of Canada for supporting this work financially.

References

(1) Torok, J. *Protectio Vitae* **1971**, *16* (6), 253.
(2) Faivre, J.; Faivre, M.; Klepping, C.; Roche, L. *Ann. Nutr. Aliment.* **1976**, *30* (5–6), 831.
(3) Makris, K. C.; Sarkar, D.; Andra, S. S.; Bach, S. B. H.; Datta, R. *Environ. Pollut. (Oxford, UK)* **2009**, *157* (6), 1957. doi:10.1016/j.envpol.2009.01.01910.1016/j.envpol.2009.01.019.
(4) VanderZaag, A. C.; Jayasundara, S.; Wagner-Riddle, C. *Anim. Feed Sci. Technol.* **2011**, *166–167*, 464. doi:10.1016/j.anifeedsci.2011.04.034.
(5) Milhano, C.; Pletcher, D. *The Electrochemistry and Electrochemical Technology of Nitrate*; In *Modern Aspects of Electrochemistry, No. 45;* White, R.E. Ed.; Springer Science, 2009; pp. 1–61.
(6) Kyriacou, G.; Katsounaros, I. *Electrolysis: Theory, Types, and Applications;* Kuai S., Meng, J., Eds.; Nova Science Publishers, 2011; pp. 327–354.
(7) Haque, Inam Ul; Tariq, M. *J. Chem. Soc. Pak.* **2010**, *32* (3), 396.
(8) Katsounaros, I.; Ipsakis, D.; Polatides, C.; Kyriacou, G. *Electrochim. Acta* **2006**, *52* (3), 1329. doi:10.1016/j.electacta.2006.07.034.
(9) Bunce, N. J.; Bejan, D. *Electrochim. Acta* **2011**, *56* (24), 8085. doi:10.1016/j.electacta.2011.07.078.
(10) Kapalka, A.; Joss, L.; Anglada, A.; Comninellis, C.; Udert, K. M. *Electrochem. Commun.* **2010**, *12* (12), 1714. doi:10.1016/j.elecom.2010.10.004.
(11) Reyter, D.; Bélanger, D.; Roué, L. *J. Hazard. Mater.* **2011**, *192* (2), 507. doi:10.1016/j.jhazmat.2011.05.054.
(12) Georgeaud, V.; Diamond, A.; Borrut, D.; Grange, D.; Coste, M. *Water Sci. Technol.* **2011**, *63* (2), 206. doi:10.2166/wst.2011.03410.2166/wst.2011.034.
(13) Stumm, W.; Morgan, J. J. *Aquatic Chemistry: Chemical Equilibria and Rates in Natural Waters;* 3rd ed.; Wiley-Interscience, New York, 1995; p. 700.
(14) Singer, P. C.; Reckhow, D. A. *Chemical Oxidation*; In *Water Quality & Treatment: A Handbook on Drinking Water;* 6th ed.; Edzwald, J.K., Ed.; McGraw Hill, New York, 2011; pp. 7.15–7.20.
(15) Kim, K.-W.; Kim, Y.-J.; Kim, I.-T.; Park, G.-I.; Lee, E.-H. *Electrochim. Acta* **2005**, *50* (22), 4356. doi:10.1016/j.electacta.2005.01.046.
(16) Kim, K.-W.; Kim, Y.-J.; Kim, I.-T.; Park, G.-I.; Lee, E.-H. *Water Res.* **2006**, *40* (7), 1431. doi:10.1016/j.watres.2006.01.042.
(17) Kim, K.-W.; Kim, I.-T.; Park, G.-I.; Lee, E.-H. *J. Appl. Electrochem.* **2006**, *36* (12), 1415. doi:10.1007/s10800-006-9234-8.
(18) Li, L.; Liu, Y. *J. Hazard. Mater.* **2009**, *161* (2–3), 1010. doi:10.1016/j.jhazmat.2008.04.047.
(19) Harrington, R. M.; Romano, R. R.; Gates, D.; Ridgway, P. *J. Am. Coll. Toxicol.* **1995**, *14* (1), 21. doi:10.3109/10915819509008678.
(20) Agaev, R.A.; Danilov, V.B.; Khachaturov, V.A.; Kasymov, B. Kh.; Tishabaev, B.Sh. *Uzbekskii Biologicheskii Zhurnal.* 1986, (1), 40.
(21) Liu, F.-J.; Wang, J.-S.; Theodorakis, C. W. *Environ. Sci. Technol.* **2006**, *40* (10), 3429. doi:10.1021/es052538g.
(22) US Department of Health and Human Services. *Toxicological Profile for Perchlorates (Syrcause Research Corp. Contract 200–2004–09793),* 2008; 256 pp.
(23) Hayfield, P. C. S. *Development of a New Material, Monolithic Ti_4O_7 Ebonex Ceramic;* Royal Society of Chemistry, Cambridge, UK, 2002; Chapters 1 and 2.
(24) Walsh, F. C.; Wills, R. G. A. *Electrochim. Acta* **2010**, *55* (22), 6342. doi:10.1016/j.electacta.2010.05.011.
(25) Graves, J. E.; Pletcher, D.; Clarke, R. L.; Walsh, F. C. *J. Appl. Electrochem.* **1991**, *21* (10), 848. doi:10.1007/BF01042450.
(26) Miller-Folk, R. R.; Noftle, R. E.; Pletcher, D. *J. Electroanal. Chem. Interfacial Electrochem.* **1989**, *274* (1–2), 257. doi:10.1016/0022-0728(89)87047-010.1016/0022-0728(89)87047-0.
(27) Pollock, R. J.; Houlihan, J. F.; Bain, A. N.; Coryea, B. S. *Mater. Res. Bull.* **1984**, *19* (1), 17. doi:10.1016/0025-5408(84)90005-9.
(28) Scott, K.; Cheng, H. *J. Appl. Electrochem.* **2002**, *32* (6), 583. doi:10.1023/A:1020107631326.
(29) Clesceri, L. S.; Greenberg, A. E.; Eaton, A. D., Eds. *Standard methods for the examination of water and wastewater;* 20th ed.; American Public Health Association, Washington, DC, 1998; Method 4500- NH_3 F.
(30) Clesceri, L. S.; Greenberg, A. E.; Eaton, A. D., Eds. *Standard methods for the examination of water and wastewater;* 20th edn.; American Public Health Association, Washington, DC, 1998; Method 4500- NO_3^- B.
(31) Katsounaros, I.; Kyriacou, G. *Electrochim. Acta* **2008**, *53* (17), 5477. doi:10.1016/j.electacta.2008.03.018.
(32) Bejan, D.; Malcolm, J. D.; Morrison, L.; Bunce, N. J. *Electrochim. Acta* **2009**, *54* (23), 5548. doi:10.1016/j.electacta.2009.04.057.
(33) El-Sherif, S.; Bejan, D.; Bunce, N. J. *Can. J. Chem.* **2010**, *88* (9), 928. doi:10.1139/V10-081.
(34) Kraft, A. *Platin. Met. Rev.* **2008**, *52* (3), 177. doi:10.1595/147106708X329273.
(35) Dima, G. E.; de Vooys, A. C. A.; Koper, M. T. M. *J. Electroanal. Chem.* **2003**, *554–555*, 15.
(36) de Groot, M. T.; Koper, M. T. M. *J. Electroanal. Chem.* **2004**, *562* (1), 81. doi:10.1016/j.jelechem.2003.08.011.
(37) Rosca, V.; Duca, M.; de Groot, M. T.; Koper, M. T. M. *Chem. Rev.* **2009**, *109* (6), 2209. doi:10.1021/cr8003696.
(38) Bazylinski, D. A.; Hollocher, T. C. *Inorg. Chem.* **1985**, *24* (25), 4285. doi:10.1021/ic00219a017.
(39) Katsounaros, I.; Kyriacou, G. *Electrochim. Acta* **2007**, *52* (23), 6412. doi:10.1016/j.electacta.2007.04.050.
(40) Da Silva, G.; Dlugogorski, B. Z.; Kennedy, E. M. *Int. J. Chem. Kinet.* **2007**, *39* (12), 645. doi:10.1002/kin.20280.
(41) Li, M.; Feng, C.; Zhang, Z.; Yang, S.; Sugiura, N. *Bioresour. Technol.* **2010**, *101* (16), 6553. doi:10.1016/j.biortech.2010.03.076.
(42) Reyter, D.; Bélanger, D.; Roué, L. *Water Res.* **2010**, *44* (6), 1918. doi:10.1016/j.watres.2009.11.037.
(43) Wang, D. M.; Lin, H. Y.; Shah, S. I.; Ni, C. Y.; Huang, C. P. *Separ. Purif. Tech.* **2009**, *67* (2), 127. doi:10.1016/j.seppur.2009.03.008.
(44) Although there is an extensive literature on the mechanism of reduction of nitrate at copper cathodes, this is not germane to Ebonex, which, unlike copper, does not dissolve.

Identification of new checkpoint kinase-1 (Chk1) inhibitors by docking, 3D-QSAR, and pharmacophore-modeling methods

Premlata K. Ambre, Raghuvir R. S. Pissurlenkar, Evans C. Coutinho, and Radhakrishnan P. Iyer

Can. J. Chem. Downloaded from www.nrcresearchpress.com by Renmin University of China on 09/02/12
For personal use only.

Abstract: Inhibition of checkpoint kinase-1 (Chk1) by small molecules is of great therapeutic interest in the field of oncology and for understanding cell-cycle regulations. This paper presents a model with elements from docking, pharmacophore mapping, the 3D-QSAR approaches CoMFA, CoMSIA and CoRIA, and virtual screening to identify novel hits against Chk1. Docking, 3D-QSAR (CoRIA, CoMFA and CoMSIA), and pharmacophore studies delineate crucial site points on the Chk1 inhibitors, which can be modified to improve activity. The docking analysis showed residues in the proximity of the ligands that are involved in ligand–receptor interactions, whereas CoRIA models were able to derive the magnitude of these interactions that impact the activity. The ligand-based 3D-QSAR methods (CoMFA and CoMSIA) highlight key areas on the molecules that are beneficial and (or) detrimental for activity. The docking studies and 3D-QSAR models are in excellent agreement in terms of binding-site interactions. The pharmacophore hypotheses validated using sensitivity, selectivity, and specificity parameters is a four-point model, characterized by a hydrogen-bond acceptor (A), hydrogen-bond donor (D), and two hydrophobes (H). This map was used to screen a database of 2.7 million druglike compounds, which were pruned to a small set of potential inhibitors by CoRIA, CoMFA, and CoMSIA models with predicted activity in the range of 8.5–10.5 log units.

Key words: anticancer agents, checkpoint kinase-1 (Chk1), docking, CoRIA, CoMFA, CoMSIA, pharmacophore modeling, database screening.

Résumé : L'inhibition de la kinase-1 du point de vérification (Chk-1) par de petites molécules est d'un grand intérêt dans le domaine de l'oncologie et dans la compréhension de la régulation du cycle cellulaire. Dans ce travail on a mis au point un modèle avec des éléments de jonction, de cartographie pharmacophore, des approches de relation quantitative structure activité tridimensionnelle (RQSA-3D) telle l'analyse comparative de champ moléculaire (ACoCM), l'analyse comparative des indices de similarité moléculaire (ACoISM), l'analyse comparative des interactions entre résidus (ACoIR) et une visualisation virtuelle afin d'identifier de nouvelles touches pour l'inhibition de la kinase-1 du point de vérification (Chk-1). Les éléments de jonction, les approches de relation quantitative structure activité tridimensionnelle (RQSA-3D) (analyse comparative de champ moléculaire (ACoCM), analyse comparative des indices de similarité moléculaire (ACoISM), analyse comparative des interactions entre résidus (ACoIR)) et les études de pharmacophore ont permis de délimiter les sites ponctuels critiques des inhibiteurs Chk-1 qui peuvent être modifiés pour en améliorer l'activité. Les analyses des éléments de jonction ont permis de préciser la nature des résidus à proximité des ligands qui sont impliqués dans les interactions ligand–récepteur alors que les analyses comparatives des interactions entre résidus (ACoIR) ont permis de déterminer l'amplitude des interactions qui influencent l'activité. Les méthodes de relation quantitative structure activité tridimensionnelle (RQSA-3D) basées sur des ligands, telle l'analyse comparative de champ moléculaire (ACoCM) et l'analyse comparative des indices de similarité moléculaire (ACoISM), permettent de mettre en évidence superficies clés des molécules qui ont des effets avantageux et (ou) préjudiciables à leur activité. Les études des éléments de jonction et les méthodes RQSA-3D sont en excellent accord en termes d'interactions de sites de liaisons. Les hypothèses tirées de la cartographie pharmacophore et validées en faisant appel à des paramètres de sensibilité, de sélectivité et de spécificité correspondent à un modèle à quatre points qui est caractérisé par un accepteur de liaison hydrogène (A), un donneur de liaison hydrogène (D) et deux hydrophobes (H). On a utilisé cette carte pour évaluer une base de données de 2,7 millions de composés ressemblant à des médicaments qui ont été élagués par l'analyse comparative de champ moléculaire (ACoCM), l'analyse comparative des indices de similarité moléculaire (ACoISM) et l'analyse comparative des interactions entre résidus (ACoIR) de façon à obtenir un petit ensemble d'inhibiteurs potentiels avec une activité prédite de 8,5 à 10,5 unités logarithmiques.

Received 30 March 2012. Accepted 31 May 2012. Published at www.nrcresearchpress.com/cjc on 24 July 2012.

P.K. Ambre, R.R.S. Pissurlenkar, and E.C. Coutinho. Molecular Simulations Group, Department of Pharmaceutical Chemistry, Bombay College of Pharmacy, Kalina, Santacruz (East), Mumbai 400 098 India.
R.P. Iyer. Spring Bank Pharmaceuticals Inc., 113 Cedar Street, Milford, MA 01757, USA.

Corresponding author: Raghuvir R. S. Pissurlenkar (e-mail. raghuvir@bcpindia.org and raghuvir@bcp.edu.in).

Mots-clés : agents anticancéreux, kinase-1 du point de vérification (Chk-1), éléments de jonction, analyse comparative des interactions entre résidus (ACoIR) analyse comparative de champ moléculaire (ACoCM), analyse comparative des indices de similarité moléculaire (ACoISM), modélisation pharmacophore, évaluation d'une banque de données.

[Traduit par la Rédaction]

Can. J. Chem. Downloaded from www.nrcresearchpress.com by Renmin University of China on 09/02/12
For personal use only.

Introduction

The cellular response to DNA damage involves a delay in the cell cycle and an increase in repair and apoptosis.[1] Many of the current cancer therapies are based upon apoptosis as an outcome of induced DNA damage by the anticancer agents, but the development of resistance is a significant limitation in treatment. One important mechanism of drug resistance is the result of cell-cycle delays, which provide opportunities for cancer cells to repair DNA damage. A number of kinases respond to DNA damage in normal cells so as to arrest cycle progression. This allows the repair of DNA damage to occur either at the cell-cycle G1 phase mediated by the tumor suppressor protein p53 and (or) at the G2 and S phases mediated by the checkpoint kinase-1 (Chk1). However, tumor cells often are deficient in DNA repair at the G1 phase due to loss of the p53 function (an estimated 50%–70% of all cancers) and relies on Chk1 to induce arrest at the S and G2 phases for survival. Consequently, p53-deficient cancers are more vulnerable to Chk1 inhibition, which results in abrogation of DNA-damage-induced arrest and premature progression into mitosis, resulting in mitotic damage and apoptosis.

Several chemical classes of natural and synthetic origin have been reported as Chk1 inhibitors, for example, debromohymenialdisine,[1–3] 9-staurosporine,[4,5] 3-ethylidene-1,3-dihydro-indol-2-ones,[6] 1,4-dihydroindeno[1,2-*c*]pyrazoles,[7] 3-(indol-2-yl)indazoles,[8] thioquinazolinones,[9] pyrazoloquinolinones,[10] 6-substituted indolylquinolinones,[11] and substituted furo[2,3-*d*]pyrimidines.[12] In spite of the diverse classes of Chk1 inhibitors that have been identified, there is a need to identify inhibitors that can be developed as drugs.

Molecular modeling studies have provided insights into the ligand–Chk1 receptor recognition process and in the development of potential Chk1 inhibitors. Many such endeavors include computational studies such as classical and multidimensional quantitative structure–activity relationships (QSARs),[13] docking, de novo drug design,[14] molecular dynamics (MD) simulations,[15] and pharmacophore modeling.[16–19] Comprehensive reviews have been published recently that summarize the use of computational techniques in the development of Chk1 inhibitors.[12,18,20,21] Although a few studies[12,18,21] have hypothesized the involvement of selected amino acid residues in the receptor to be vital for ligand binding, the important residue types and the nature of interactions involved in ligand–receptor binding remain to be established.

Chen et al.[18] reported a ligand-based, four-point pharmacophore model for a set of active Chk1 inhibitors (22 molecules with an activity span of 4 log units). The model is comprised of a hydrogen-bond acceptor, a hydrogen-bond donor, and two hydrophobes along with an excluded volume. Chen et al.[19] also proposed a pharmacophore model based on a consensus study of an overlay of 35 X-ray crystal structures, with additional information extracted from the target enzyme of Chk1. Although both the reported models have the same four features, the second hypothesis includes shape and 12 excluded volume features. The hydrogen-bond features located on the ligand are designed to bond with the backbone CO of Glu85 and the backbone NH of Cys87 of Chk1, whereas the two hydrophobes were mapped to the aromatic cores of the molecule.

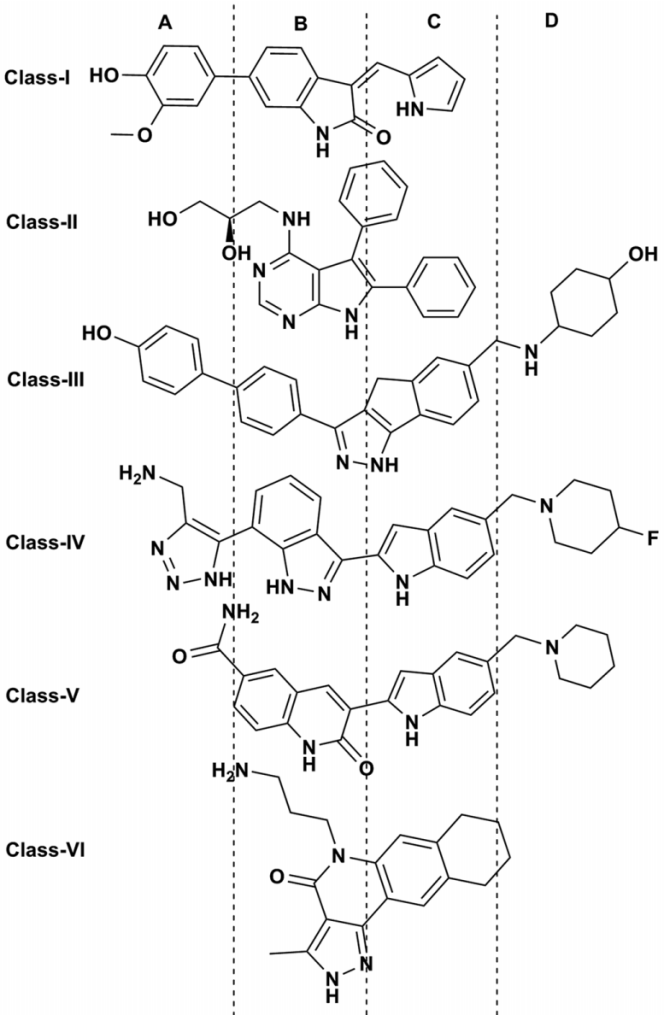
The present study is a step-by-step approach to identify novel Chk1 inhibitors. To state briefly, 70 molecules from different structural classes were docked into the active site of Chk1 to identify probable binding poses. Models equating the activity to interaction elements like van der Waals (vdW), coulombic forces, and hydrogen bonding were built using the 3D-QSAR tool, comparative residue–ligand interaction analysis (CoRIA).[22–24] Several other activity models using only ligand features were recognized with the 3D-QSAR tools, comparative molecular field analysis (CoMFA)[25] and comparative molecular similarity indices analysis (CoMSIA),[26] based on the alignment strategy derived by the previously conducted docking studies. Having built the necessary models to predict active molecules, we extended the studies to develop pharmacophore models that could be used to screen databases of druglike molecules not amenable to 3D-QSAR approaches. The pharmacophore models for Chk1 were developed using both the receptor- and ligand-based approaches to realize similarities and differences in the two approaches. The hypotheses were developed based upon five different crystal structures of Chk1 bound with potent ligands and were validated using a database of both active and inactive molecules. Subsequently, the same set of ligands was used to build further hypotheses using the ligand-based pharmacophore approach involving (*i*) the receptor-bound conformations of the ligand ignoring the receptor conformation and (*ii*) generation of multiple conformers. All hypotheses (receptor- and ligand-based) were screened against a decoy data set spiked with actives, and the resulting enrichment factor (EF) was calculated. Finally, a large database of druglike compounds was screened using the best hypothesis (receptor-based) leading to a set of virtual hits, whose activities were predicted using the earlier developed CoMFA, CoMSIA, and CoRIA models. The ligands predicted to be active are suitable for experimental investigations based on the predicted absorption, distribution, metabolism, and excretion (ADME) properties.

Materials and methods

The docking studies were carried out with the docking program Glide v5.6[27–29] in the Schrödinger Suite 2010 (Schrödinger LLC, USA) running on an Intel Xeon processor-based workstation with CentOS Enterprise Linux 5.5. The CoRIA models were built based on the docked poses of

Can. J. Chem. Downloaded from www.nrcresearchpress.com by Renmin University of China on 09/02/12
For personal use only.

Fig. 1. Dissection of molecules belonging to different classes into the basic fragments A, B, C, and D.



the ligands with Cerius2 (v4.11; Accelrys Inc., USA) running on an AMD Athlon processor-based workstation with CentOS Enterprise Linux 4.9. The 3D-QSAR (CoMFA and CoMSIA) studies were accomplished with Sybyl v7.1 (Tripos Inc., USA) running on an AMD Athlon processor-based workstation with CentOS 4.9 Enterprise Edition Linux 4.9. Pharmacophore mapping and database screening were done with the pharmacophore module in Discovery Studio (v3.0; Accelrys Inc.) running on an eight-node high-performance computing cluster (HCL Infosystems Ltd., India) with an Intel Xeon processor and CentOS Enterprise Linux 5.4.

Chk1 inhibitors

Chk1 inhibitors and their activities were compiled from literature reports.[6–8,10–12,21] Six different classes of Chk1 inhibitors were considered for this study (Fig. 1 and Table 1): class I, 3-ethylidene-1,3-dihydroindol-2-ones; class II, substituted furo[2,3-*d*]pyrimidines; class III, 1,4-dihydroindeno [1,2-*c*]pyrazoles; class IV, 3-(indol-2-yl)indazoles; class V, 6-substituted indolylquinolinones; and class VI, pyrazoloquinolinones, along with other miscellaneous compounds that exhibit pronounced Chk1 inhibition (Table 1). The molecules were then partitioned into training (50) and test (20) sets with the ratio of molecules at approximately 3:1. The segregation of molecules into training and test sets was based on structural diversity, physicochemical properties, and span of activity and was carrid out with the "ligand diversity selection" tool in Discovery Studio v3.0. The structures of the molecules in the training (50) and test (20) sets are provided in Table S1 of the Supplementary data.

Protein and ligand preparation

The X-ray crystal structures (PDB codes: 2AYP, 2BRB, 2C3L, 2C3K, 2C3J, 2E9O, 2HOG, 2HY0, and 2QHN) of Chk1 bound to different inhibitors were obtained from the Protein Data Bank (http://www.rcsb.org/pdb). The structures were prepared for the docking studies with the Protein Preparation Wizard in the Schrödinger Suite of programs. The crystal waters were removed, hydrogen atoms were added, and atom types and partial charges were assigned based on the OPLS2005 force field. The formal charges for the acidic and basic amino acids were set according to the physiological pH 7.4. The N- and the C-terminii were capped with the acetyl (ACE) and the *N*-methylamino (NMA) groups, respectively. Subsequently, the system was relaxed using energy minimization until an energy gradient of 0.01 kcal/mol/Å (1 cal = 4.184 J) was reached with the OPLS2005 force field.

The Chk1 inhibitors used in docking studies were prepared using the LigPrep v2.4 in Maestro (Schrödinger 2010 Suite). The atom types and partial charges were assigned based on the OPLS2005 force field, corresponding to the physiological pH 7.4. A set of diverse conformations and tautomeric states were generated for the ligands using the LigPrep in Schrödinger Suite.

Docking studies

In the initial phase of docking, the grid was generated with the bound ligand defining the grid center. The inner grid box was set to 10 Å and the outer grid was set to 20 Å in size, thus providing ample space for the generation of diverse ligand conformations in the binding pocket by the search and score algorithm. The vdW radius was scaled to 1.0 Å to soften the potential over the nonpolar areas of the enzyme that lie within the grid extents and the partial atomic charges were set to 0.25 of the exact value. The receptor atoms beyond the extent of the grid were unscaled. To maximize the probability of forming hydrogen bonds between the residues in the enzyme active site and the ligand, the side-chain hydroxyl groups of the amino acids serine, threonine, and tyrosine were allowed to rotate. The docking settings were validated based on the protocol's ability to reproduce the X-ray conformation of the bound ligand in the enzyme active site. On optimization of the protocol, the Chk1 inhibitors were docked to find the best poses, which were scored on-the-fly with scoring function GlideScore SP. Energies associated with electrostatic, van der Waals, and hydrogen-bonding interactions were computed between every amino acid in the active site and the ligand. These energies formed the input for the development of the CoRIA models.

CoRIA studies

The amino acids in the active site of Chk1, which form crucial electrostatic, vdW, and hydrogen-bond interactions

Can. J. Chem. Downloaded from www.nrcresearchpress.com by Renmin University of China on 09/02/12
For personal use only.

Table 1. The cores of the six classes of checkpoint kinase-1 (Chk1) inhibitors showing the sites of substitutions (R groups) (complete structures and pIC_{50} ($-\log(IC_{50})$ in molar concentration) activities of the six classes of Chk1 inhibitors are given in Supplementary data Table S1).

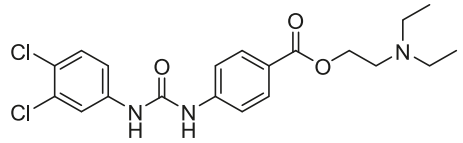
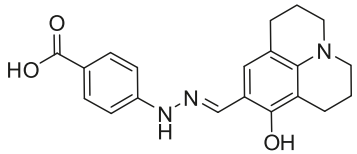
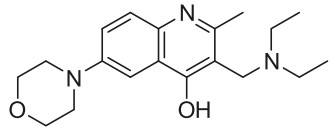
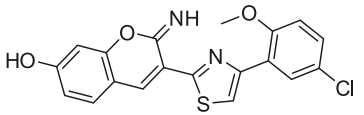
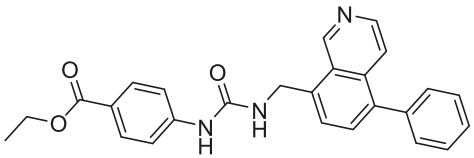
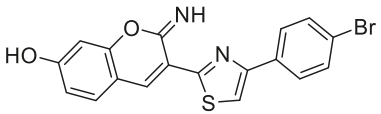
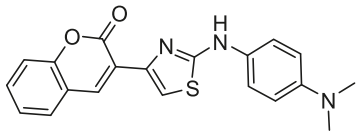
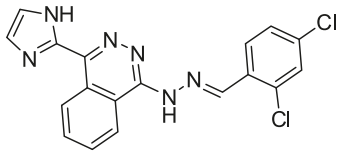
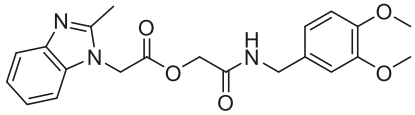
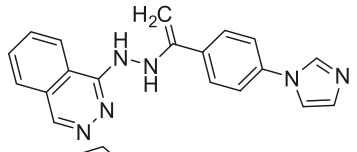
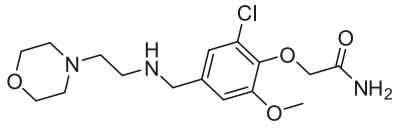
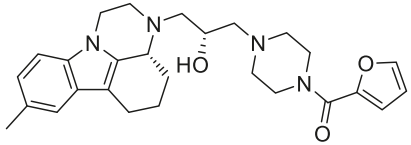
Class	Chk1 inhibitor	Structure
I	1-Ethylidene-1,3-dihydroindol-2-ones	
II	Substituted furo[2,3-*d*]pyrimidines	
III	1,4-Dihydroindeno[1,2-*c*]pyrazoles	
IV	3-(Indol-2-yl)indazoles	
V	6-Substituted indolylquinolinones	
VI	Pyrazoloquinolinones	

A B C D E

Published by NRC Research Press

Can. J. Chem. Downloaded from www.nrcresearchpress.com by Renmin University of China on 09/02/12
For personal use only.

Table 2. Hits from virtual screening predicted as active by the comparative residue–ligand interaction analysis (CoRIA), comparative molecular field analysis (CoMFA), and comparative molecular similarity indices analysis (CoMSIA) models.

Virtual hits	Structure	Predicted pIC_{50}	Virtual hits	Structure	Predicted pIC_{50}
D1		8.63	D7		8.73
D2		9.22	D8		9.14
D3		9.02	D9		9.02
D4		9.17	D10		10.51
D5		9.19	D11		9.14
D6		8.59	D12		9.55

Note: pIC_{50}, –log (IC_{50}) in molar concentration.

Can. J. Chem. Downloaded from www.nrcresearchpress.com by Renmin University of China on 09/02/12
For personal use only.

with the inhibitors, were probed with CoRIA.[22–24] The CoRIA descriptors, i.e., the nonbonded interaction energies (vdW, coulombic (Coul), and hydrogen bond) of Chk1 inhibitors with individual residues in the active site of the Chk1, were computed using Glide v5.6 on the individual enzyme–ligand complexes. These descriptors were then correlated with the biological activity using G/PLS as the chemometric method in Cerius2 v4.11.[30,31] Initially, 500 equations were randomly generated on a training set of 50 molecules. These solutions were evolved for 20 000 generations through a process of crossover and mutation to generate the final models. The models were optimized for the number of PLS components and the length of the equations, which were varied from 2 to 6 and 4 to 10, respectively. The final models were validated using leave-group-out (LGO) and randomization. The models were also tested for their predictive power on an external test set of 20 molecules.[30,31] Additional metrics like r^2_m (for training and test sets) and r^2_p (for randomization) were implemented to assess the robustness of the models.[32,33]

CoMFA and CoMSIA studies

The 3D-QSAR studies CoMFA[25] and CoMSIA[26,34–36] were carried out on the receptor-based alignment, an overlay of the molecules obtained from the docking studies. The steric and electrostatic fields were computed with the default settings of the 3D cubic lattice, grid spacing, the probe atom, and the cutoff. For the CoMFA studies, only steric and electrostatic fields were computed, whereas, for CoMSIA, hydrophobic, and hydrogen-bond donor and acceptor fields were computed in addition to the steric and electrostatic fields. The CoMFA and CoMSIA descriptors were used as independent variables and the pIC_{50} ($-\log(IC_{50})$ in molar concentration) values as the dependent variable in a partial least-squares (PLS) regression analysis[37] to derive the 3D-QSAR models. The optimal number of components was determined by SAMPLS,[38] which was subsequently used to derive the final QSAR models. In addition to q,[2] the conventional correlation coefficient r^2, the standard errors (SE), and the F value were also computed. The robustness of the models was gauged by cross-validation using the leave-one-out (LOO) and the LGO of 10 groups and bootstrap[30,39] carried out with 100 runs. Additional validation metrics as suggested by Roy and co-workers[32,33] were also carried out.

Pharmacophore modeling

Pharmacophore generation

The pharmacophore models were built in Discovery Studio v3.0 using two approaches. The first approach, referred to as the receptor–ligand pharmacophore generation protocol, is a receptor-dependent technique that dwells on the information on features extracted from enzyme–ligand complexes. In the present study, the pharmacophore hypotheses were developed using the X-ray structures with PDB codes 2AYP, 2E9O, 2HOG, 2HY0, and 2QHM. In the pharmacophore modeling, all standard features, i.e., hydrogen-bond acceptor, hydrogen-bond donor, hydrophobic feature, negative and positive ionizable features, and aromatic ring, were considered. The minimum number of features was set to 4 and the maximum to 10. The pharmacophore models were ranked using a rule-based scoring function. The scoring function is based on a GFA model, which is a function of all the features in the pharmacophore model and the corresponding distances between them. The effect of the shape constraint was also evaluated during the study. The pharmacophore models were validated using a defined set of active and inactive ligands. A flexible-fit approach was used to achieve correspondence between the ligands used for validation and the pharmacophoric features of the models. A ligand-dependent technique known as common feature pharmacophore was also used as a complementary approach. The hypotheses were generated either from the receptor-bound conformations or from multiple conformations of the ligands generated by a systematic search ensuring maximum coverage of conformational space. A set of 10 hypotheses was generated in each case.

Validation of pharmacophore hypotheses

The selectivity and sensitivity of the hypotheses were determined based on the efficiency of the models to select known actives and inactives for the target enzyme (Chk1). Also, all hypotheses were screened against a decoy data set of 2000 molecules with an average MW of 300, which was spiked with 25 actives ($pIC_{50} \geq 6.0$). Subsequently, the enrichment ratio (EF) was determined for all hypotheses as given by

$$[1] \qquad EF = (H_a D_t)/(H_t D_a)$$

where H_a is the number of actives, H_t is the total number of hits, D_t is the total number of molecules in the database, and D_a is the total number of active molecules in the database.

Database screening

The best pharmacophore model (receptor-based model) was used to screen the '"iResearch Database" (ChemNavigator, USA) having approximately 2.7 million druglike compounds. The fished out virtual hits were docked into the active site of Chk1 in their pharmacophore-constrained conformation. The activities of the hits were further predicted by the previously validated 3D-QSAR models of CoRIA, CoMFA, and CoMSIA. A few representative molecules with activities (consensus) predicted in the 8.5–10.5 range are depicted in Table 2. The hits obtained from the virtual screen have a Tanimoto similarity coefficient in the range 0.4–0.6 with reference to the training set molecules.

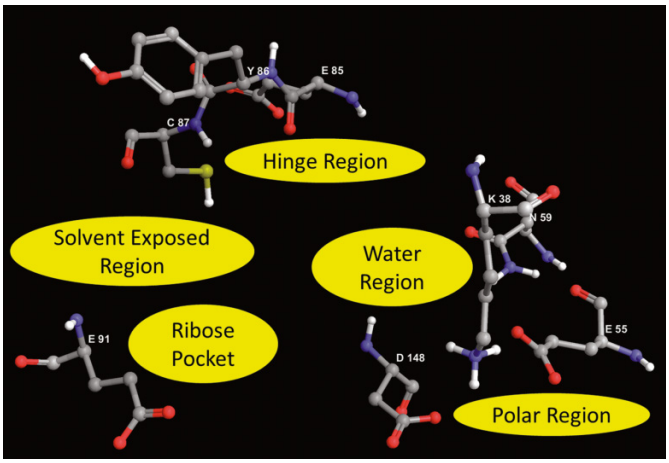
Results and discussion

The ATP-binding pocket of Chk1 can be roughly divided into five regions: the solvent-exposed region, the hinge region, the water pocket, the polar region, and the ribose-binding pocket (Fig. 2). The solvent-exposed region is adjacent to the hinge region, and the introduction of the polar group in this region is expected to enhance kinase activity and also improve biophysical characteristics.

The water pocket, which is unique to Chk1, is occupied by three water molecules and buried at the periphery of the ATP binding site. It has been demonstrated that filling this pocket with functional groups can confer ligands with an enhanced affinity for Chk1. In addition, to obtain high potency, it is required that the ligands form hydrogen bonds with amino acid residues in the polar region. Ligands that can participate in ionic interactions with the acidic residue Glu91 or form

Can. J. Chem. Downloaded from www.nrcresearchpress.com by Renmin University of China on 09/02/12
For personal use only.

Fig. 2. The ATP binding site of checkpoint kinase-1 (Chk1) depicting critical regions of amino acids that bind ligands and water molecules.



hydrogen bonds with the side-chain carbonyl oxygen of Glu91, situated in the ribose binding pocket, can potentially enhance the potency of the compound. It has been revealed that this region is of great significance, since functional groups designed to interact with residues in or in proximity to the ribose-binding pocket are desirable, although not a specific requirement for inhibition of Chk1.

The docking and 3D-QSAR studies reported by Du et al.[13] were based on 5,10-dihydrodibenzo[*b*,*e*]-1,4-diazepin-11-ones as Chk1 inhibitors. The study revealed strong hydrophobic interactions between the inhibitors and residues Leu15, Val23, Tyr86, Leu137, and Asp148 in the enzyme. The molecules also form hydrogen bonds with the backbone CO or NH groups of the amino acids Thr14 and Cys87. The CoMFA analysis also highlighted the fact that amine or amide groups placed at the terminal fragment of the molecules (polar region) strongly modulate the activity.

Chen et al.[18] reported a five-point pharmacophore model with a hydrogen-bond acceptor, hydrogen-bond donor, two hydrophobes, and an excluded volume, which was developed by a multiple conformation approach. These features were mapped onto the active site of Chk1 using (*i*) the hydrogen-bond interactions in the hinge region involving the carbonyl group at the second position on the quinolin-2(1*H*)-one moiety with the backbone NH of Cys87 and (*ii*) the N^1H of the quinolin-2(1*H*)-one with the backbone CO of amino acid Glu85, which make up the hydrogen-bond acceptor and donor features, respectively. The two hydrophobic regions are mapped to the aromatic ring (fragment C in Fig. 1) that binds in the pocket formed by Leu15, Gly89, and Gly90. The second hydrophobic region is located on the 6-chlorine substitution on the quinol-2-one nucleus (fragment B in Fig. 1), which binds in the region lined by the amino acids Val40, Val68, Phe70, Leu82, and Leu84. Another pharmacophore hypothesis by Chen et al.[18] was developed by clustering multiple structure-based pharmacophore models that have been derived from different Chk1 ligand complexes in comparable binding modes. Similar to the earlier model, the hydrogen-bond acceptor and donor features were positioned in the hinge region of the active site, whereas one hydrophobe was located near the amino acids Tyr20 and Val23 and the other near Leu15 and Leu137. In addition, Chen et al.[18] also proposed that the positive ionizable feature on the ligand that interacts with the ribose-binding site had no significant contribution to activity. In our study, the quality of the hypothesis has been further improved by the inclusion of excluded volumes.

Docking studies

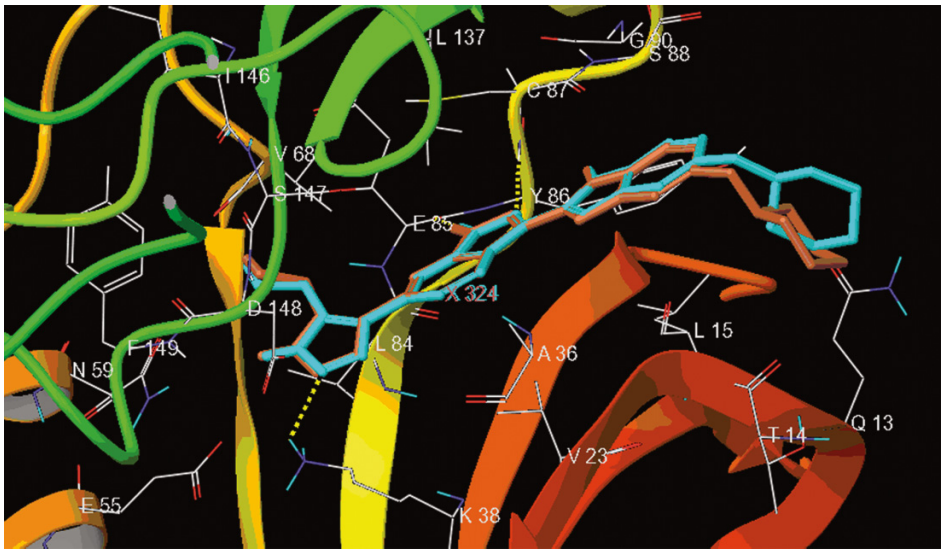
In our study, the binding modes were analyzed and compared based on the six structural classes by docking the inhibitors into the active site of Chk1. The active site of Chk1 is a groove that is formed by a bundle of β-strands and an α-helix composed of hydrophobic amino acids, namely, Leu15, Val23, Ala36, Val68, Leu84, Cys87, Gly90, Leu137, and Phe149, a positively charged amino acid Lys38, negatively charged amino acids Glu55, Glu85, and Asp148, and polar amino acids Gln13, Thr14, Tyr86, Ser88, Asn135, and Ser147. Before docking the inhibitors, the protocol was tested on the X-ray crystal structures with PDB codes 2AYP, 2BRB, 2E9O, 2HOG, 2HY0, and 2QHN.[6–8,10–12,21] Upon analysis, it was observed that the docking poses had a root-mean-squared displacement (RMSD) less than 1.0 from the crystal pose (Fig. 3). Following this, all Chk1 ligands (structures provided in Supplementary data Table S1) were docked and the classwise binding interactions analyzed (Table 3).

Based on the overlay of the crystal structures, the binding-site analysis revealed that fragment A of ligands with groups such as hydroxy, hydroxymethyl, amine, or methylamine are able to interact with various amino acids in the polar region through prominent and regular hydrogen bonds, namely, with the ω-nitrogen of Lys38 and the δ-carboxylate of Glu55 and hydrogen bonds with the γ-carboxamide of Asn59, β-hydroxy of Ser147, and the backbone NH of Asp148 and Phe149. For most ligands, fragment A is surrounded by hydrophobic amino acids (Leu62, Val68, Leu82, Leu84, Ile146, and Phe149), of which the prominent interactions were with Val68, Leu84, and Phe149. However, these interactions are missing in class VI molecules as they do not have fragment A. Hydrogen-bond interactions involving fragment B are seen in the hinge region of the Chk1 active site formed by the backbone of amino acids Glu85 and Cys87. This is a crucial interaction for Chk1 inhibition irrespective of the class, which has also been highlighted by Chen et al.[18] Hydrophobic interactions of fragment B are seen with Val23, Ala36, and Leu137. The hydrogen-bonding interactions for fragment C are sparse and almost absent for fragment D. The hydrophobic amino acids Leu15, Val23, and Tyr86 are in close proximity to fragment C. Fragment D is seen to surface out from the binding pocket of Chk1 as a result of which the binding-site analysis does not reveal any specific interaction for fragment D. However, it can be noted that the molecules bearing fragment D have pIC_{50} values greater than 8 log units. The presence of fragment D in a molecule simply alters the partition coefficient through an increase in the hydrophobicity and this causes an increase in the activity. This aspect cannot be deciphered from the docking studies.

CoRIA studies

CoRIA models were developed using the interaction energies Coul, vdW, hydrogen bond, and total energy (E_{Int}) between the

Fig. 3. A view of the docking pose in relation to the crystal structure for the ligand 5-{3-[5-(piperidin-1-yl-methyl)-1*H*-indol-2-yl]-1*H*-indazol-6-yl}-2*H*-1,2,3-triazol-4-yl)methanol.



ligands and residues in the enzyme active site as descriptors. These were correlated to the biological activity through G/PLS.[30,31] Statistically significant models were obtained by optimization of the training-set molecules, the number of PLS components, and the length of the equations. The best models were obtained on a training set of 50 diverse sites (structural fingerprints and physicochemical properties), with four and five PLS components and with five to eight terms, respectively. The CoRIA models have acceptable regression coefficients (r^2), which lie in the range 0.81–0.87, and cross-validation coefficients (q^2) between 0.69–0.71. Some representative CoRIA models along with their statistics are presented in Table 4. Additional computed metrics, such as r^2_m and r^2_p, also have values greater than 0.5, indicating robustness of the model[32,33] (Table 4). The plots for experimental versus predicted activity are given in Fig. 4.

The use of a genetic algorithm in model building permitted the visualization of the rise and decay of descriptors (the evolution) during the model-building process. The descriptors that were retained after genetic evolution and formed part of the final CoRIA models helped in analysing and interpreting the type and point of interaction between the ligands and amino acids in the active site. The significant descriptors evolved over the 500 models were classified into two groups (major and minor) based on their frequency of appearance in the models so as to understand their influence on the activity.

The amino acids that predominantly appeared with coulombic interactions with the inhibitors are Tyr20, Gly21, Val35, Ile39, Val68, Lys132, and Leu137, whereas Asn143, Leu144, Lys145, and Ser147 exhibited vdW interactions that enveloped fragments A and B. The amino acids Leu15, Gly21, Leu64, Glu85, Thr170, and Ser193 exhibited both Coul and vdW interactions. Analysis of models 1 and 2 given in Table 4, showed that the total E_{Int} with amino acids Leu15 and Gly21 had a negative coefficient, which indicates that enhancing this interaction would improve the activity. Amino acids Leu15 and Gly21, which appeared in the vicinity of fragments C and D and resulting in classes II and VI molecules being devoid of fragment D, showed lower activity. The coefficients of terms associated with vdW interaction, e.g., for Tyr20 and Lys145, were positive and negative, respectively. This meant that vdW interaction with Tyr20 can have a negative impact on the activity owing to a steric clash with fragment A. On the other hand, the Coul interaction of molecules with Val35 had a positive impact on the activity.

Statistical analysis revealed that there are two molecules predicted as outliers by model 2 (Table 4) and one molecule by model 1 (Table 4), by 2 log order deviation from the reported experimental activity. This residual in the prediction arises from the large vacuous nature of the binding pocket. This means that the outlier molecules have adopted conformations different from similar molecules in their series. This deviation in the binding pose has a direct impact on the computed binding site interactions, which further impacts the activity predicted by the QSAR models.

In summary, our studies suggest that structural modifications that enhance the E_{Int} for fragment C with residues Leu15 and Gly21 (characteristic for most active molecules) and decrease the vdW interaction of fragment A with Tyr20 (prominent in the low active molecules) will help in improving the activity (Table 5).

3D-QSAR (CoMFA and CoMSIA) studies

The CoMFA and CoMSIA models were generated over a training set of 50 Chk1 inhibitors belonging to six classes. The molecules in the training and test sets were aligned based on the receptor-based overlay,[40] a technique that has been proven better over the standard atom-fit alignment. The standard atom-fit alignment cannot be implemented for the Chk1 inhibitors as their cores are structurally diverse, and hence the 3D-QSAR studies were carried out on the receptor-based alignment (Fig. 5). Different models were generated using Gasteiger, Gasteiger–Hückel, and MMFF94 charges. All models were internally validated by LOO, LGO, and bootstrap analysis. The results indicate that CoMFA models have poor statistics compared with CoMSIA models, which is probably because of the inability of CoMFA to explicitly

Can. J. Chem. Downloaded from www.nrcresearchpress.com by Renmin University of China on 09/02/12
For personal use only.

Can. J. Chem. Downloaded from www.nrcresearchpress.com by Renmin University of China on 09/02/12
For personal use only.

Table 3. Types of interactions between ligands belonging to different classes and active-site residues in checkpoint kinase-1 (Chk1).

Structure No.	Class	H-bond interaction (D–H···A)	Hydrophobic interaction
1	1-Ethylidene-1,3-dihydroindol-2-one	(FragA):OH···CO($^{\delta}$COO^{-}:Glu55)	FragA: Val67, Val68, Leu82, Leu84, Phe149
		(Asn59):$^{\gamma}$CONH$_2$···OH^4(FragA)	
		(Phe149):^{bkbn}NH···OH^4(FragA)	FragB: Val23, Ala36, Leu137, Ile146
		(FragB):NH^1...^{bkbn}CO(Glu85)	
		(Cys87):^{bkbn}NH^{2}CO(FragB)	FragC: Leu15, Tyr86
2	Furo[2,3-*d*]pyrimidine	(FragA):CHOH···OH(Ser147)	FragB/C: Leu15, Val23, Ala36, Val68, Leu84, Tyr86, Leu137
		(Cys87):^{bkbn}NH···N^3(FragB)	
		(FragB):NH^4...^{bkbn}CO(Cys87)	
3	1,4-Dihydroindeno[1,2-*c*]pyrazoles	(Lys38):$^{\omega}$NH$_3^+$···O$^{-(4)}$(COO$^-$:FragA)	FragA: Val68, Leu84, Phe149
		(Asp148):^{bkbn}NH···CO^4(COO$^-$:FragA)	FragB: Val23, Ala36, Leu137
		(FragD):NH···^{bkbn}CO(Leu15)	FragC/D: Leu15, Val23, Tyr86
4	3-(Indol-2-yl)indazole	(Lys38):$^{\omega}$NH$_3^+$···N^2(FragA)	FragA: Leu62, Val68, Leu82, Leu84, Ile146, Phe149
		(Asp148):^{bkbn}NH···OH^5(FragA)	
		(FragB):NH^1...^{bkbn}CO(Glu85)	FragB: Val23, Ala36, Tyr86, Leu137
		(Cys87):^{bkbn}NH···N^2(FragB)	FragC: Leu15, Val23, Tyr86
5	6-Substituted indolylquinolinone	(Lys38):$^{\omega}$NH$_3^+$···N^2(FragA)	FragA: Val68, Leu84, Phe149
		(FragA):NH^1···O$^-$($^{\delta}$COO$^-$:Glu55)	FragB: Val23, Ala36, Leu137
		(FragB):NH^1...^{bkbn}CO(Glu85)	FragC: Leu15, Val23, Tyr86
		(Cys87):^{bkbn}NH···CO^2(FragB)	
		(FragC):NH^1...^{bkbn}CO(Cys87)	
6	Pyrazoloquinolinone	(Cys87):^{bkbn}NH···CO^2(FragB)	FragB/C: Leu15, Val23, Ala36, Val68, Leu84, Tyr86, Leu137
		(FragB):NH^1...^{bkbn}CO(Cys87)	

Note: Frag, fragment.

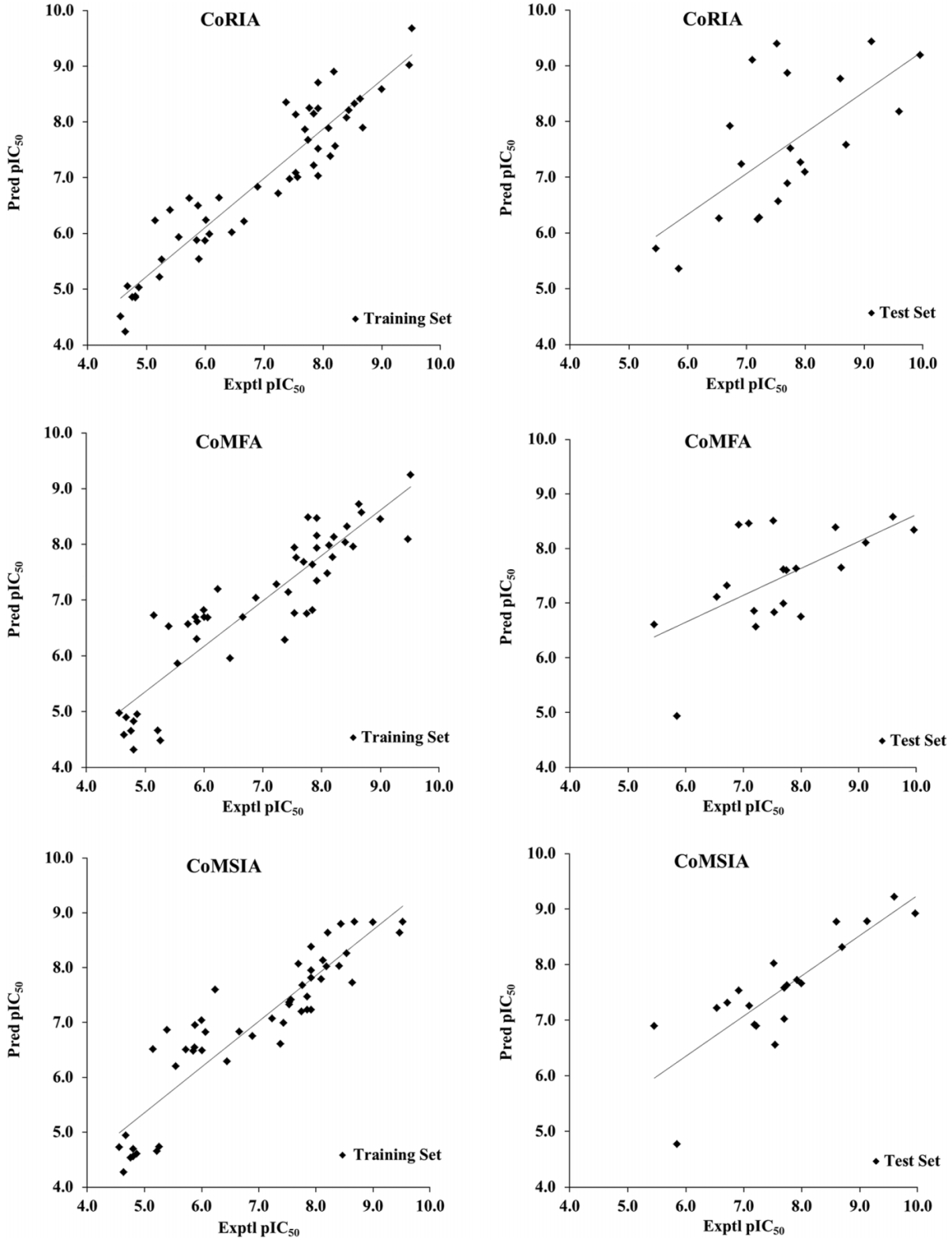
Table 4. Comparative residue–ligand interaction analysis (CoRIA) models and their statistics.

Structure No.	CoRIA model	n	PLS	No. of Terms	r^2	r^2_{CV} (LOO)	r^2_{CV} (LGO)	r^2_{BS}	r^2_{rand}	r^2_{pred}	r^2_m Overall	r^2_m Training	r^2_m Test	r^2_p
1	$pIC_{50} = 2.08 - 0.47Leu15_{EInt} + 1.68Tyr20_{vdW} - 4.11Gly21_{EInt} - 1.10Ser147_{vdW}$	50	4	5	0.81	0.69	0.56	0.79 (±0.002)	0.10	0.56 (1 out)	0.59	0.64	0.43	0.68
2	$pIC_{50} = -0.27 - 0.53Leu15_{EInt} - 12.86Lys145_{vdW} + 19.17Thr170_{EInt} - 0.84Ser147_{vdW} + 2.44Val35_{Coul} - 5.69Gly21_{EInt} + 9.31Val40_{EInt}$	50	5	8	0.87	0.71	0.51	0.74 (±0.042)	0.23	0.66 (2 out)	0.66	0.77	0.33	0.70

Note: LOO, leave one out; LGO, leave group out; r^2_{CV}, cross-validation coefficient; r^2_{BS}, boot-strapping coefficient; EInt, total energy; vdW, van der Waals; Coul, coulombic.

Can. J. Chem. Downloaded from www.nrcresearchpress.com by Renmin University of China on 09/02/12
For personal use only.

Fig. 4. Predicted versus experimental activity for training and test molecules based on the 3D-QSAR models comparative residue–ligand interaction analysis (CoRIA), comparative molecular field analysis (CoMFA), and comparative molecular similarity indices analysis (CoMSIA).



account for hydrophobic and hydrogen-bond features. Additional validation with metrics suggested by Roy et al.[33] indicate that all CoMSIA models are sufficiently robust (Table 6). The statistics and the respective field contributions for the best models are provided in Table 6.

The plots for experimental versus predicted activity are given in Fig. 4. Among the different charge-assignment models, decent QSAR models were developed when the molecules were assigned with Gasteiger charges, and thus only these models are discussed here. The contours were analyzed

Can. J. Chem. Downloaded from www.nrcresearchpress.com by Renmin University of China on 09/02/12
For personal use only.

Table 5. Comparison of the trend in activity with the interaction energetics.

Structure No.	Molecule	pIC_{50}	(–)Leu15$_{EInt}$	(+)Tyr20$_{vdW}$	(–)Gly21$_{EInt}$	(+)Val35$_{Coul}$	(+)Val40$_{EInt}$	(–)Lys145$_{vdW}$	(–)Ser147$_{vdW}$	(+)Thr170$_{EInt}$
1	Class I	8.16	–4.739	–0.205	–0.014	0.162	0.010	–0.200	–2.921	–0.017
2	Class II	5.85	–6.055	–0.573	–0.175	–0.218	–0.019	–0.158	–0.799	–0.029
3	Class III	7.70	–8.701	–0.376	–0.012	–0.729	–0.051	–0.162	–2.391	0.138
4	Class IV	9.52	–7.928	–0.233	–0.040	0.333	–0.076	–0.213	–2.934	–0.006
5	Class V	9.19	–8.799	–0.196	–0.188	0.182	–0.059	–0.151	–1.631	0.005
6	Class VI	6.01	–5.829	–0.010	–0.075	0.164	–0.022	–0.147	–0.972	0.005

Note: pIC_{50}, –log (IC_{50}) in molar concentration; EInt, total energy; Coul, coulombic; vdW, van der Waals.

with respect to the most active and least active molecules in the training set to understand differences in the field distribution associated with the different fragments and their correlation with the activity of the molecules. The contours are depicted in Figs. 6 and 7 for the CoMFA and CoMSIA models, respectively. The steric and electrostatic contours positioned in the Chk1 active site show that the nature of the contours complements the nature of the amino acids over which they superimpose, and it now becomes possible to comprehend the 3D-QSAR results in light of the protein–ligand interactions (Fig. 8).

Steric field

The CoMFA steric fields around the molecule are represented by green and yellow contours that differentiate bulk in a favourable or unfavourable way, respectively (Fig. 6). Inspection of the contours around the most active molecule reveals that bulk is favoured around fragment D; this fragment, which is absent in classes I, V, and VI, is responsible for their low activity, which is <5 log units. In Fig. 6, patches of green in the vicinity of the terminal portion of fragment A indicate that fragments with one or two carbon units, namely, methyl or ethyl, can be accommodated in this region. This observation is supported by the more active molecules. The yellow contours, which represent the disfavoured bulk brackets of the molecule at fragments B and C, indicating that the substitution at this area would cause steric hindrance as the fragment B–C itself snugly fits among hydrophobic residues in this region of the active site of Chk1. Similar steric contours are seen in case of the CoMSIA model (Fig. 7).

Electrostatic field

The Chk1 inhibitors studied here have fragments B and C composed of heteroaromatic rings that are linearly linked to each other. The blue electrostatic contours (Fig. 6) seen in these fragments arise from the acidic nitrogen atoms in the heteroaromatic cores. This part of the molecule is involved in hydrogen-bond interaction with the amino acids Glu85 and Cys87, which form the part of the hinge region in the active site. In the least active molecules, fragments B–C have electronegative groups (e.g., NO_2), which are incompatible with the blue contours in CoMFA. The electrostatic contours in CoMSIA (Fig. 7) depict small red patches that represent electronegative atoms near fragment A, which has electronegative groups, e.g., the electronegative pyrazole ring atoms in the more active molecules. This represents the electronegative microenvironment that is desirable for interaction (hydrogen bonds) with the positively charged amino acid Lys38.

Hydrophobic field

CoMSIA contours provide information about the hydrophobic characteristics of Chk1 molecules. The yellow contours (Fig. 7) that characterize hydrophobic fields enclose the aromatic cores of fragments A, B, and C, which snugly fit the active site. The contours that represent hydrophilic fields (white) are concentrated near the heteroatoms of fragments A and B. The hydrophilic contours are in line with the characteristics of the Chk1 active site, which has an anchoring polar site, a water region (with Lys38), and a hinge

Can. J. Chem. Downloaded from www.nrcresearchpress.com by Renmin University of China on 09/02/12
For personal use only.

Fig. 5. Receptor-based alignment of (*a*) 1-ethylidene-1,3-dihydroindol-2-ones, (*b*) furo[2,3-*d*]pyrimidines, (*c*) 1,4-dihydroindeno[1,2-*c*]pyrazoles, (*d*) 3-(indol-2-yl)indazoles, (*e*) 6-substituted indolylquinolinones, and (*f*) pyrazoloquinolinones (these classes have been shown separately for clarity).

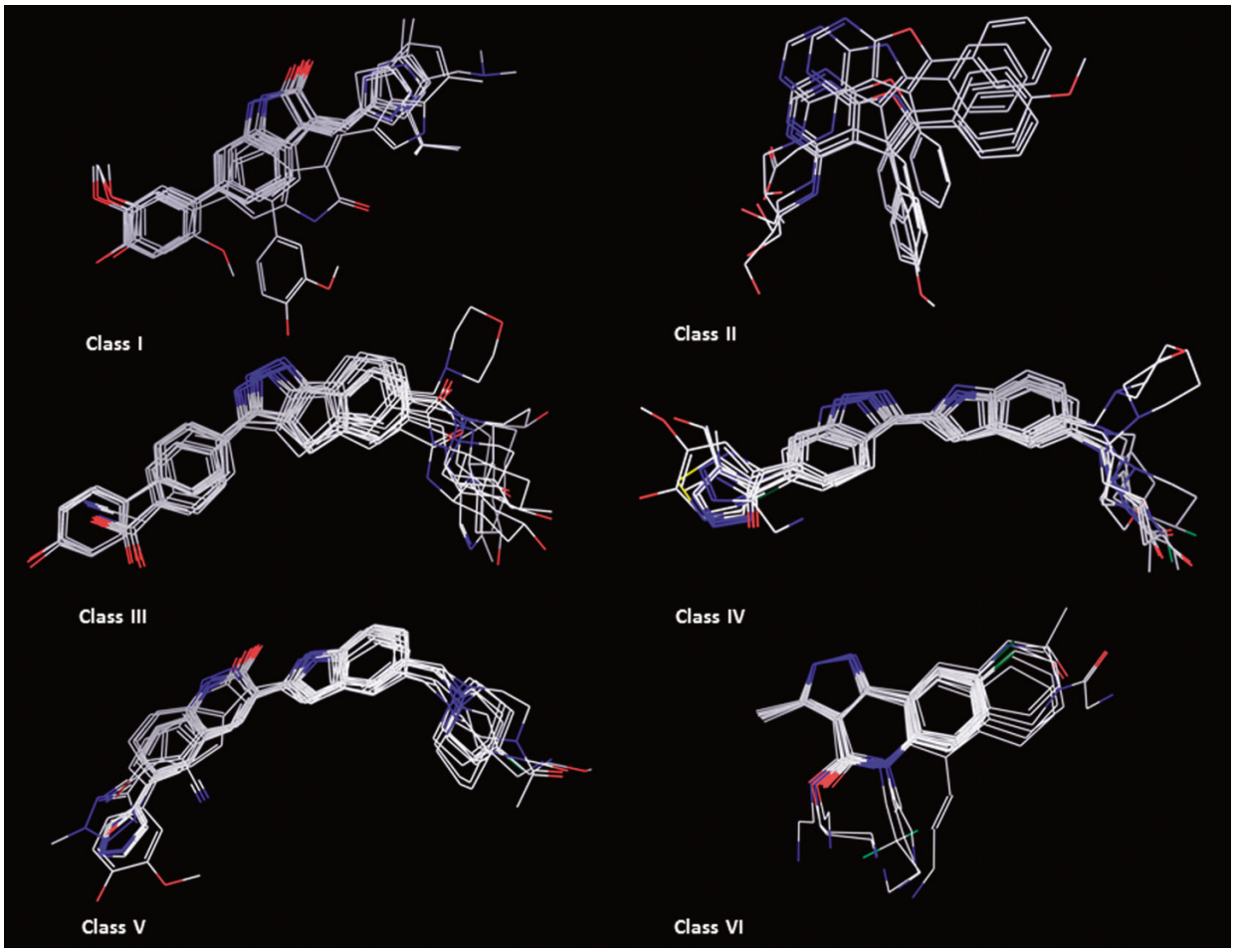


Table 6. The statistics of comparative molecular field analysis (CoMFA) and comparative molecular similarity indices analysis (CoMSIA) models generated using different charge methods.

	CoMFA			CoMSIA		
Statistic	Gasteiger	Gasteiger–Hückel	MMFF94	Gasteiger	Gasteiger–Hückel	MMFF94
r^2	0.67	0.83	0.70	0.81	0.79	0.81
r^2_{CV} (LOO)	0.51	0.40	0.49	0.49	0.47	0.49
r^2_{CV}(LGO)	0.51	0.40	0.49	0.49	0.47	0.49
r^2_{BS}	0.72	0.87	0.79	0.88	0.85	0.86
r^2_{pred}	0.33	0.29	0.31	0.78	0.49	0.52
r^2_m (training)	0.41	0.69	0.46	0.68	0.61	0.65
r^2_m (test)	0.13	0.11	0.13	0.49	0.12	0.15
r^2_m (overall)	0.33	0.51	0.37	0.65	0.49	0.53
F test	48.35	76.92	55.28	94.91	89.68	102.54
SEE	0.84	0.60	0.80	0.66	0.67	0.63
PLS	2	3	3	3	2	2
Field contribution						
Steric	0.537	0.482	0.475	0.126	0.135	0.135
Electrostatic	0.463	0.518	0.525	0.204	0.201	0.200
Hydrophobic	—	—	—	0.207	0.201	0.197
H-bond donor	—	—	—	0.227	0.212	0.213
H-bond acceptor	—	—	—	0.236	0.252	0.255

Fig. 6. The comparative molecular field analysis (CoMFA) contours around the most active molecule (A) electrostatic contours (electropositive, blue; and electronegative, red) and (B) steric contours (favoured, green; and disfavoured, yellow). (Please see the online article for the colour figure).

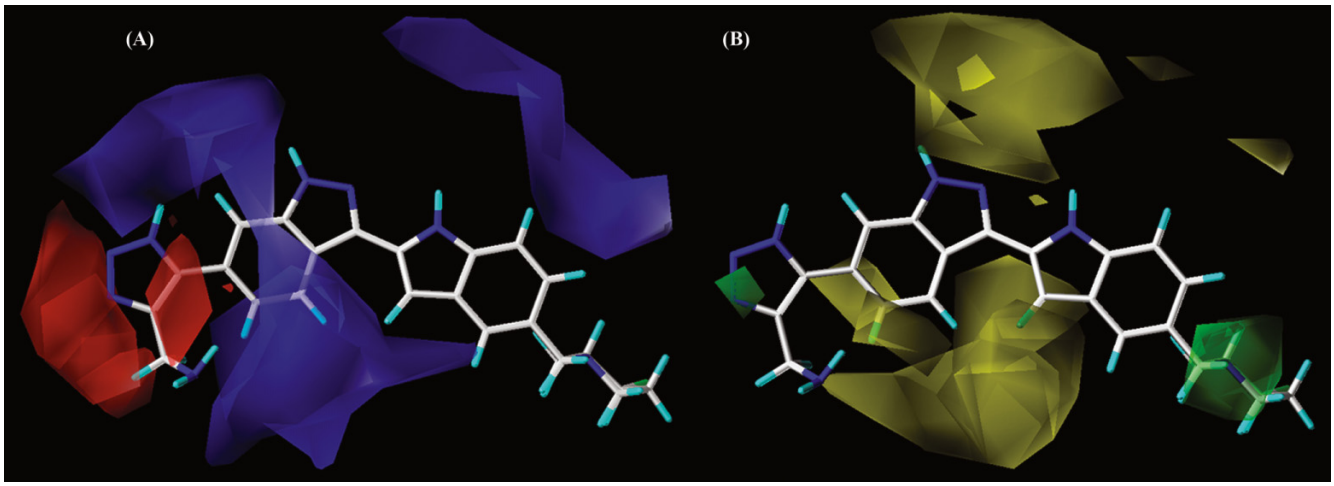
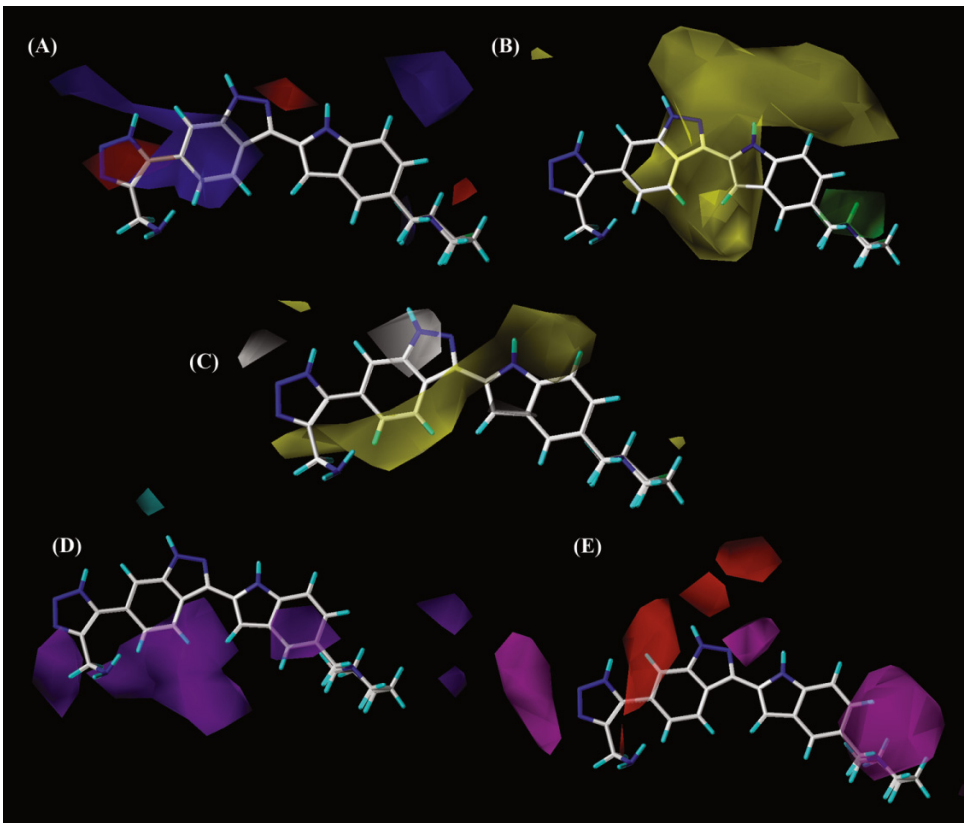


Fig. 7. The comparative molecular similarity indices analysis (CoMSIA) contours around the most active molecule (A) electrostatic contours (electropositive, blue; and electronegative, red); (B) steric contours (favoured, green; and disfavoured, yellow); (C) hydrophobic contours (favoured, yellow; and disfavoured, white); (D) H-donor contours (favoured, cyan); and (E) H-acceptor contours (favoured, magenta; disfavoured, purple; and disfavoured, red). (Please see the online article for the colour figure).



region (with Glu85 and Cys87). A relationship also exists between the hydrophobic contours and the remaining portion of the active site.

Hydrogen-bond donor and acceptor fields

The Chk1 inhibitors interact with the active-site residues using significant numbers of hydrogen-bonding interactions. Thus, QSAR contours that depict hydrogen bonds and their characteristics (acceptor or donor) can help correlate the relationship between H-bonding interactions and biological activity.

The hydrogen-bond donor fields are represented by cyan and purple contours (Fig. 7). Cyan-coloured contours are seen near the heteroatom (acidic nitrogen atom) on fragment

Can. J. Chem. Downloaded from www.nrcresearchpress.com by Renmin University of China on 09/02/12
For personal use only.

Fig. 8. Comparative molecular field analysis (CoMFA) contours for (A) steric and (B) electrostatic contours positioned in the binding site of checkpoint kinase-1 (Chk1).

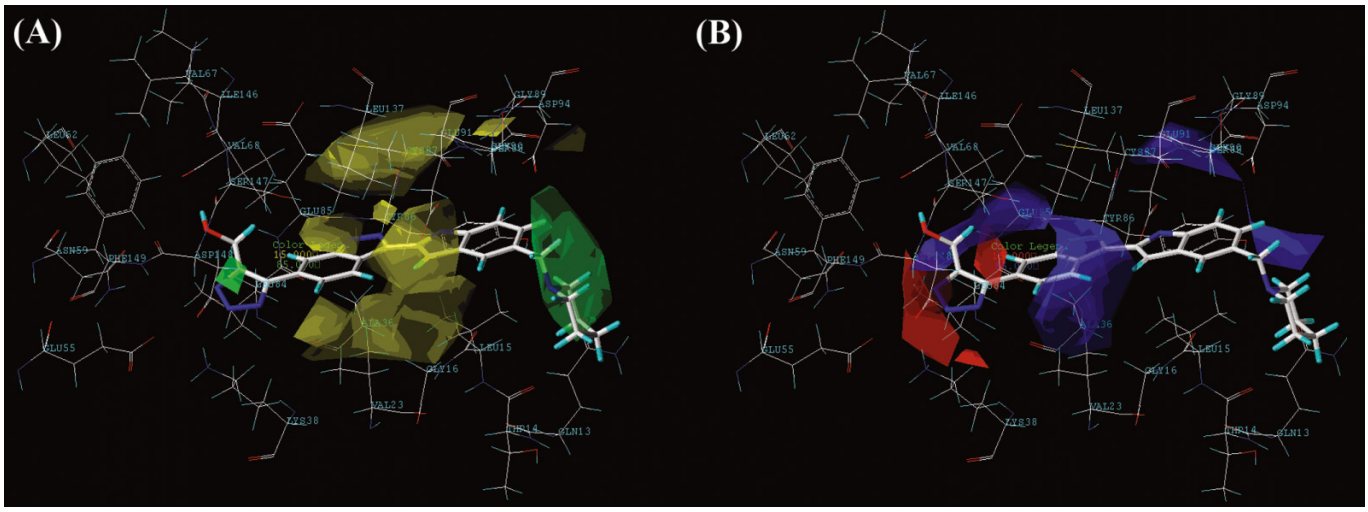
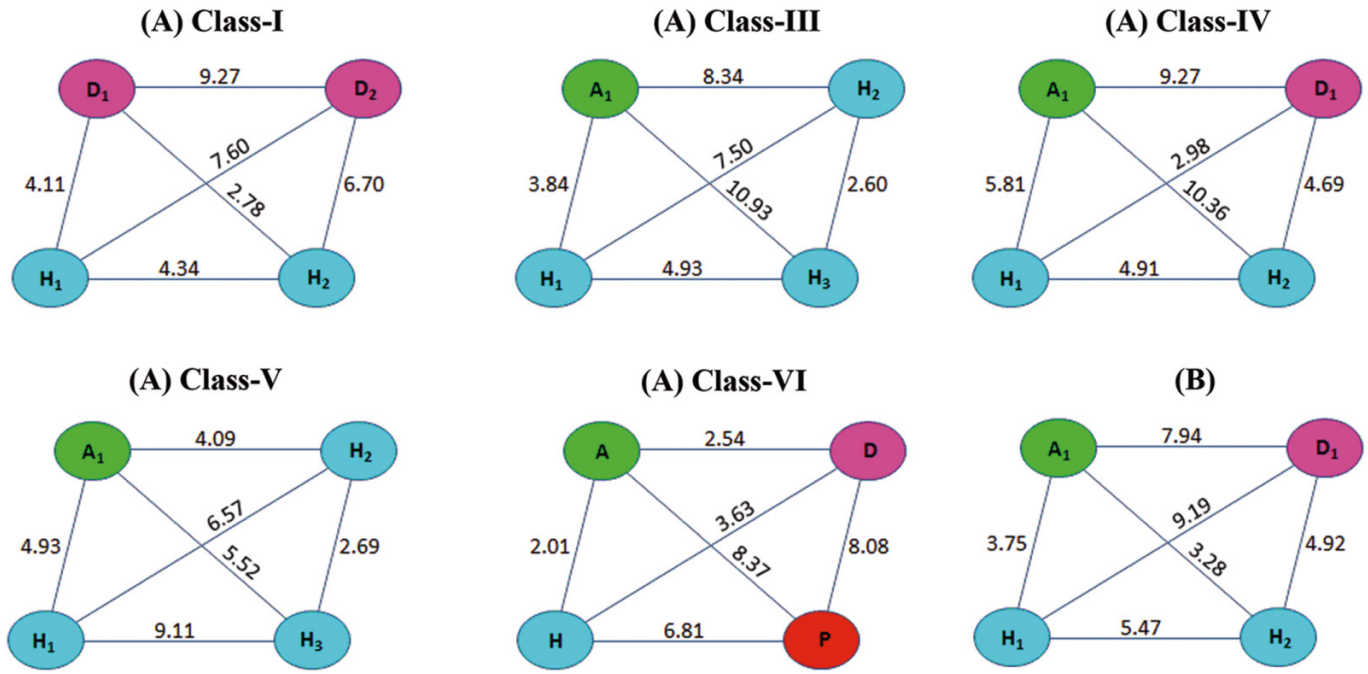


Table 7. Statistics of the different pharmacophore hypotheses.

Class	No. of true positives	No. of false positives	Enrichment ratio	Feature	Selectivity	Sensitivity	Specificity	ROC
I	18	7	57.92	DDHH	1.75	0.72	1.00	0.76
III	19	6	61.13	AHHH	0.477	0.76	1.00	0.6
IV	23	2	74.00	ADHH	1.114	0.92	1.00	0.72
V	24	1	77.22	AHHH	0.477	0.96	1.00	0.8
VI	2	23	6.44	ADHP	0.829	1.00	0.800	0.8
Ligands I	25	0	80.44	AHH	—	1.00	1.00	—
Ligands II	23	2	74.00	ADHH	—	0.92	1.00	—

Note: Total actives, 25; total molecules, 2011; total inactives, 1986. ROC, receiver operating characteristic; D, donor; H, hydrophobe; A, acceptor; P, pharmacophore.

Fig. 9. Features and distances for the pharmacophore hypotheses developed by (A) the receptor-based approach and (B) the ligand-based approach.



Can. J. Chem. Downloaded from www.nrcresearchpress.com by Renmin University of China on 09/02/12
For personal use only.

Fig. 10. Dendrogram showing the clustering of the seven pharmacophore hypotheses.

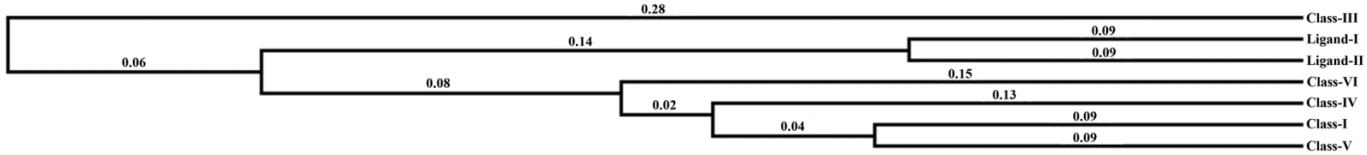
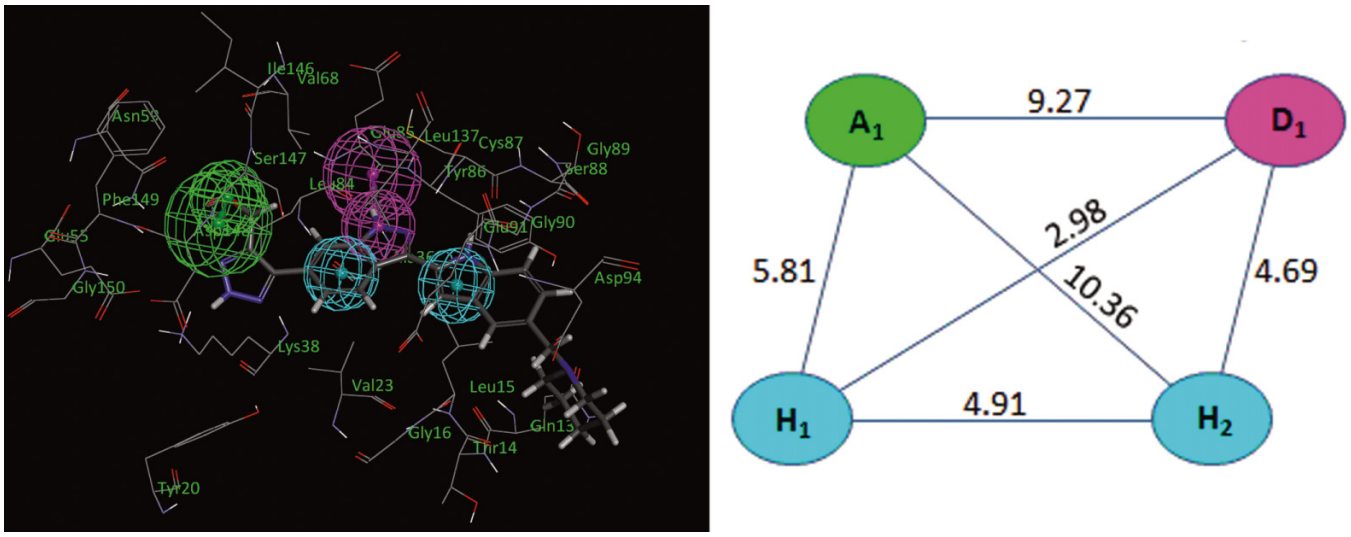


Fig. 11. Features and distances for the best pharmacophore hypotheses (ADHH). A, hydrogen-bond acceptor; D, hydrogen-bond donor; and H, hydrophobe.



B, which can be correlated with the hydrogen bond with the backbone CO of Glu85 (Fig. 7 and Table 3). There seems to be no additional requirement for hydrogen-bond donor groups in the remaining region of the molecule as seen by the absence of purple contours.

Extending the analysis further to hydrogen-bond acceptor fields, magenta contours are concentrated at the basic nitrogen or oxygen atoms on fragments A and B and the amine (–NH–) bridge that links fragment C with D. This primarily represents the interaction of Chk1 inhibitors with amino acids like Lys38, the backbone NH of Asp148 or Phe149 for fragment A, and the backbone NH of Cys87 for fragment B (Fig. 7 and Table 3).

Pharmacophore-modeling studies

The current study used both receptor-dependent and -independent techniques to develop pharmacophore models. In the receptor-based technique, the features in the Chk1 ligand complexes that correspond to significant interactions were transformed into hypotheses. In the ligand-based approach, models were developed using both rigid and flexible conformations for a selected set of active ligands. Overall, it was found that, irrespective of the approach used for hypothesis development, the models possessed the same set of pharmacophoric features, namely, hydrogen-bond donor, hydrogen-bond acceptor, and two hydrophobes, which also correspond to the models reported by Chen et al.[18] However, the major differences between the hypothesis generated in the current study and that reported by Chen et al.[18] are related to the spatial location and interfeature distances. The specificity and selectivity of these models were computed for a set of Chk1 analogs categorized as actives and inactives. A comparative analysis of the pharmacophores developed by the two approaches shows that the receptor-based pharmacophore evolves as a superior hypothesis, which is attributed to the fact that the method captures crucial ligand–receptor interactions besides ligand configuration.

Receptor–ligand pharmacophore

Based on the ligand features that correspond to receptor–ligand interactions, a set of pharmacophoric hypotheses were generated for each of the five X-ray crystal structures (PDB codes 2AYP, 2E9O, 2HOG, 2HY0, and 2QHM). The hypotheses were subsequently validated using a set of both active and inactive ligands. The pharmacophore hypothesis generated for each class is discussed as follows.

Class I (3-ethylidene-1,3-dihydroindol-2-ones)

Among 18 pharmacophoric features that were detected for the ligand 2AYP, only seven involved interactions with amino acids in the Chk1 active site. Among the set of 10 pharmacophore hypotheses generated, the DDHH hypothesis was mapped most frequently to the ligand and its interactions with the active site (Table 7). The best four-point model (DDHH, Fig. 9) mapped to the ligand (3*Z*)-6-(4-hydroxy-3-methoxyphenyl)-3-[(1*H*-pyrrol-2-yl)methylene]-1,3-dihydro-2*H*-indol-2-one (class I, Fig. 1) has two hydrogen-bond donor features (D) that involve the 4-hydroxyl group of the phenyl ring (fragment A) and the 1-NH group of the indol-2-one ring (fragment B) with one vector oriented towards the δ-carboxylate of the amino acid Glu55 (polar region) and the second vector pointing to the carbonyl group in of the backbone of Glu85 (hinge region). The two hydrophobes (H) are closely spaced and appear on the phenyl ring (fragment A) and the 3-methoxy substituent that interacts with

Can. J. Chem. Downloaded from www.nrcresearchpress.com by Renmin University of China on 09/02/12
For personal use only.

Can. J. Chem. Downloaded from www.nrcresearchpress.com by Renmin University of China on 09/02/12
For personal use only.

Asn59, Val68, Phe70, and Phe149. Validation of this hypothesis using a decoy data set showed an above average (>0.60) sensitivity and excellent selectivity (>0.90), (Table 7). The EF for this model is, however, in the range of average acceptable value (<0.60). A set of 30 excluded volume features were found to align the binding pocket of the Chk1 active site, except for the areas where the significant amino acids that interact with the ligand are located.

No validated pharmacophore hypothesis could be generated for class II ligands using the receptor-based approach and will not bediscussed further.

*Class III (1,4-dihydroindeno[1,2-*c*]pyrazoles)*

Of the 19 pharmacophoric features identified for the Chk1 ligand complexes, five could be mapped to significant enzyme–ligand interactions, namely, AHHH, where A is the hydrogen-bond acceptor. This gives two models, each with four features that map the ligand interactions with the active site. The statistically acceptable four-point model (AHHH) is mapped to the ligand 4-(6-{[(4-methylcyclohexyl)amino]methyl}-1,4-dihydroindeno[1,2-*c*]pyrazol-3-yl)benzoic acid as follows: the hydrogen-bond acceptor feature is mapped to the 4-carboxylate group on fragment A that associates as an hydrogen bond with the side-chain NH_3^+ group in Lys38. The hydrophobes are located over the centroid of the phenyl ring (fragment A) and the centroid of the dihydroindeno[1,2-*c*]pyrazole nucleus (fragment B/C). The interacting hydrophobic amino acids are Leu15, Val23, Ala36, Val68, Leu84, Tyr86, and Leu137. In all, 25 excluded volumes were mapped to the binding pocket for residues that do not have any significant interactions. The class III hypothesis (AHHH) is different from the class I hypothesis (DDHH). In this case, statistics reveal an EF value with sensitivity and specificity above average (>0.70).

Class IV (3-(indol-2-yl)indazoles)

The most active Chk1 inhibitors belong to class IV. Seven significant features, namely, AADDHHH, which represent the essential receptor–ligand interactions, were mapped to the ligand 5-{3-[5-(piperidin-1-yl-methyl)-1*H*-indol-2-yl]-1*H*-indazol-6-yl}-2*H*-1,2,3-triazol-4-yl)methanol from among the 33 pharmacophoric features. All the 10 hypotheses are different, but as per the statistics, ADHH is the best-fit hypothesis developed for this class, which was also reported by Chen et al.[18,19] However, these features appear to be located at different sites in the ligand with different interfeature distances in comparison with the model reported and discussed by Chen et al.[18,19] A has been mapped to the hydroxymethyl group on the triazole nucleus (fragment A), which forms a hydrogen bond with the backbone NH of Asp148, whereas D is the NH^1 group of indazole (fragment B), which interacts with the backbone CO of Glu85. The two Hs are present on the phenyl ring of indazole (fragment B) and the pyrrole ring of indole (fragment C). Nearly 27 excluded volume features are found to align the binding site. The hypothesis ADHH built on the class IV ligand has an excellent EF value with high sensitivity and selectivity.

Class V (6-substituted indolylquinolinones)

There are about 18 pharmacophoric features for the ligand 3-[5-(piperidin-1-yl)methyl]-1*H*-indol-2-yl-6-(1*H*-pyrazol-4-yl)quinolin-2(1*H*)-one, of which the four-feature hypothesis that matches the receptor–ligand interactions is AHHH. The best model among the six has A pointing to the carbonyl function of the quinolone nucleus (fragment B) and is oriented towards Cys87 in the hinge region of the receptor. The three hydrophobic points are located at the centroids of the quinolone ring (fragment B), the indole nucleus (fragment C), and the pyrrole ring of the indole nucleus (fragment C), which are surrounded by Leu15, Val23, Ala36, Val68, Leu84, and Leu137; also lining the active site are 25 excluded volumes. This hypothesis (ADHH) shows an excellent EF value (77%) with high sensitivity and selectivity.

Class VI (pyrazoloquinolinones)

In this case, unlike other classes, only one hypothesis model was built for the ligand (3-endo)-8-methyl-8-azabicyclo[3.2.1]oct-3-yl-1*H*-pyrrolo[2,3-*b*]pyridine-3-carboxylate. Of the 12 pharmacophore features for the ligand, only a single hypothesis could be formed with four features, namely, ADHP. The A feature is depicted by the nitrogen atom of the pyridine ring of the pyrrolopyridine nucleus of fragment B. This group forms a cohesive bond with the backbone NH of Ala36 and Tyr86. The D feature is based at the acidic proton NH^1 of the pyrrolopyridine nucleus, with Lys38/Glu85 amino acids as the acceptors. The third important feature, the hydrophobic site, is located at the pyridine ring of the pyrrolopyridine nucleus, which closely interacts with Val23. A positive ionizable feature is seen over the 8-azabicyclo[3.2.1]octane ring (fragment C), which is surrounded by Glu134, Asn135, and Lys136. Even though the hypothesis shows excellent overlay with the corresponding features in the ligands and the receptor, it has a poor EF value because of the absence of fragments A and D.

Common feature pharmacophore

The hypotheses were initially generated using the bound-state conformations of the ligands, which involved the overlay of the Chk1 inhibitors in rigid conformation only allowing a translation or rotation of the molecules to search for the overlap of a common feature among the inhibitors. Only three pharmacophoric features were found to be in agreement with the various models, namely, two Hs and one A. Of the 10 models, the best model had a good fit over the ligands 2HOG, 2HY0, 2AYP, and 2QHM. The 2E9O ligand did not fit the hypothesis, probably because of the rigidity seen in the tricyclic indazole ring. With a three-point pharmacophore model as a query, the chances of obtaining a "false positive" during virtual screen is higher compared with a four- or five-point pharmacophore hypothesis. As a result, the usefulness of the model was not considered for developing new pharmacophore models.

Alternative strategies were generated with a search for low-energy conformations of ligands that were then overlaid to develop other hypotheses. By this strategy, it was possible to develop models with four pharmacophoric features, namely, two Hs and two As. In this study, 10 hypotheses were generated, nine as four-point models and the 10th as a three-point model. Seven of the hypotheses had features that were identical to the models developed using the receptor–ligand strategy. The best four-point pharmacophore model possessed one hydrogen-bond donor, one hydrogen-bond acceptor, and two hydrophobe features (ADHH), with a good fit over all

Can. J. Chem. Downloaded from www.nrcresearchpress.com by Renmin University of China on 09/02/12
For personal use only.

the selected ligands (2AYP, 2E9O, 2HOG, 2HY0, and 2QHM). The common feature model, which was based on the sampling of multiple conformations for the molecules, has features and spatial distances similar to the best receptor-based hypothesis, except that the hydrogen-bond donor and acceptor features are swapped in fragment B. The EF statistics for this model are the same as that for the model built using the 2HOG crystal structure.

Comparison of pharmacophore models

The best pharmacophore model developed for Chk1 ligands using the ligand- and receptor-based hypotheses were clustered to assess similarity in the features and the interfeature distances. For the purpose of clustering seven hypotheses, five belonging to the receptor-based category and two to the ligand-based category were selected. Based on the RMSD between the matching features, a distance function (d_{ij}) was generated to cluster the hypotheses, which split the models into five bins (Fig. 10). The first cluster had the receptor-based hypotheses for both class I (DDHH, 3-ethylidene-1,3-dihydroindol-2-ones) and class IV (ADHH, 3-(indol-2-yl)indazoles) with $d_{ij} = 0.09$, as both have the features DHH in common. The second bin contained the lone receptor-based hypothesis developed on class V (ADHH, 6-substituted indolylquinolinones) with $d_{ij} = 0.13$, and the third bin covered the lone receptor-based hypothesis of class VI (ADHP, pyrazoloquinolinones) with $d_{ij} = 0.15$; the last bin shares the ADH features with cluster 1. Similarly, the hypotheses generated from theligand-based approach were clustered as a fourth group with $d_{ij} = 0.08$, with the ADH features in common with clusters 1, 2, and 3. The class III hypothesis (AHHH, 1,4-dihydroindeno[1,2-*c*]pyrazoles) stands in Ccluster 5 with $d_{ij} = 0.28$, indicating the distal relationship with other clusters.

The consensus from the pharmacophore models revealed that, for significant Chk1 inhibition, two hydrophobes, one hydrogen-bond donor, and one hydrogen-bond acceptor with interfeature distances as mentioned in Fig. 11 are vital.

Database screening

The receptor-based pharmacophore hypothesis was used to screen a database of 2.7 million druglike compounds. The molecules identified from this screen have druglike characteristics with respect to log *P*, molecular weight, and hydrogen-bond acceptor and donor groups. The structural cores that have been identified as hits are different from the training set molecules. Some of these molecules can be classified as quinolone analogs, isoquinoline analogs, *N*,*N*′-disubstituted urea analogs, coumarin analogs, phenyl hydrazine analogs, benziminopyran analogs ,and quinazolines analogs. The activities of these molecules were subsequently predicted by the 3D-QSAR models. The structures of these ligands, along with the predicted pIC_{50} values, are provided in Table 2. They are predicted to be potential inhibitors of Chk1 and are worthy of experimental investigation as judged by their predicted activities and ADME properties.

Conclusions

In conclusion, docking, 3D-QSAR (CoRIA, CoMFA, and CoMSIA), and pharmacophore studies delineated crucial site points on the Chk1 inhibitors, which can be modified to improve activity.

The docking analysis showed residues in the proximity of the ligands that are involved in ligand–receptor interactions, whereas CoRIA models were able to derive the magnitude of these interactions that impact the activity. The ligand-based 3D-QSAR methods (CoMFA and CoMSIA) highlight key areas on the molecules that are beneficial and (or) detrimental for activity. The docking studies and 3D-QSAR models are in excellent agreement in terms of binding-site interactions. Pharmacophore modeling with or without knowledge of the receptor provided hypotheses with comparable results. The statistical data with regards to sensitivity, selectivity, and RMSD scores for hypotheses generated by the receptor-based approach were better than the data obtained with the ligand-based approach. From the QSAR studies, we conclude that the absence of fragments A or D on these molecules results in a decrease in the activity. Although fragment D does not seem to have a significant role in the binding pocket, it is responsible for improving the overall lipophilicity of the molecule. From our 3D-QSAR studies and pharmacophore-modeling studies, it is clear that the best Chk1 inhibitor has hydrophobic features on fragment A that can interact with the amino acids Leu15, Val23, Ala36, Leu82, Leu84, and Tyr86. In addition, fragment B should interact with Leu62, Val67, Val68, Ile146, Phe149, and Leu137 through hydrophobic interactions. In addition, hydrogen-bond acceptor groups located on fragment A can interact with the ω-ammonium group of Lys38 and the backbone NH of Asp148. Similarly, the hydrogen-bond donor and (or) acceptor groups on fragment B can interact either with the backbone CO group of Glu85 or with the backbone NH of Cys87 in the hinge region of the Chk1 active site.

Finally, the active compounds predicted from the database screen of the pharmacophore models using the CoRIA, CoMFA, and CoMSIA approaches, coupled with in-silico ADME/toxicity profiles, are worthy of further experimental investigations.

Supplementary data

Supplementary data are available with the article through the journal Web site at http://nrcresearchpress.com/doi/suppl/10.1139/v2012-047.

Acknowledgements

The computational studies were possible because of grants to the Department of Pharmaceutical Chemistry from the Department of Science and Technology (DST, SR/FST/LSI-163/2003) through their FIST program, the Department of Biotechnology (DBT, file No. BT/PR11810/BRB/10/690/2009), and the Council for Scientific and Industrial Research (CSIR, file No. 01/2399/10/EMRII), New Delhi.

References

(1) Busby, E. C.; Leistritz, D. F.; Abraham, R. T.; Karnitz, L. M.; Sarkaria, J. N. *Cancer Res.* **2000**, *60*, 2108.

(2) Graves, P. R.; Yu, L.; Schwarz, J. K.; Gales, J.; Sausville, E. A.; O'Connor, P. M.; Piwnica-Worms, H. *J. Biol. Chem.* **2000**, *275* (8), 5600. doi:10.1074/jbc.275.8.5600.

Can. J. Chem. Downloaded from www.nrcresearchpress.com by Renmin University of China on 09/02/12
For personal use only.

(3) Jackson, J. R.; Gilmartin, A.; Imburgia, C.; Winkler, J. D.; Marshall, L. A.; Roshak, A. *Cancer Res.* **2000**, *60*, 566.
(4) Zhao, B.; Bower, M. J.; McDevitt, P. J.; Zhao, H.; Davis, S. T.; Johanson, K. O.; Green, S. M.; Concha, N. O.; Zhou, B. B. *J. Biol. Chem.* **2002**, *277* (48), 46609. doi:10.1074/jbc.M201233200.
(5) Messaoudi, S.; Anizon, F.; Peixoto, P.; David-Cordonnier, M. H.; Golsteyn, R. M.; Leonce, S.; Pfeiffer, B.; Prudhomme, M. *Bioorg. Med. Chem.* **2006**, *14* (22), 7551. doi:10.1016/j.bmc.2006.07.013.
(6) Lin, N. H.; Xia, P.; Kovar, P.; Park, C.; Chen, Z.; Zhang, H.; Rosenberg, S. H.; Sham, H. L. *Bioorg. Med. Chem. Lett.* **2006**, *16* (2), 421. doi:10.1016/j.bmcl.2005.09.064.
(7) Tong, Y.; Claiborne, A.; Stewart, K. D.; Park, C.; Kovar, P.; Chen, Z.; Credo, R. B.; Gu, W. Z.; Gwaltney, S. L. IIJudge, R. A.; Zhang, H.; Rosenberg, S. H.; Sham, H. L.; Sowin, T. J.; Lin, N. H. *Bioorg. Med. Chem.* **2007**, *15* (7), 2759. doi:10.1016/j.bmc.2007.01.012.
(8) Fraley, M. E.; Steen, J. T.; Brnardic, E. J.; Arrington, K. L.; Spencer, K. L.; Hanney, B. A.; Kim, Y.; Hartman, G. D.; Stirdivant, S. M.; Drakas, B. A.; Rickert, K.; Walsh, E. S.; Hamilton, K.; Buser, C. A.; Hardwick, J.; Tao, W.; Beck, S. C.; Mao, X.; Lobell, R. B.; Sepp-Lorenzino, L.; Yan, Y.; Ikuta, M.; Munshi, S. K.; Kuo, L. C.; Kreatsoulas, C. *Bioorg. Med. Chem. Lett.* **2006**, *16* (23), 6049. doi:10.1016/j.bmcl.2006.08.118.
(9) Converso, A.; Hartingh, T.; Garbaccio, R. M.; Tasber, E.; Rickert, K.; Fraley, M. E.; Yan, Y.; Kreatsoulas, C.; Stirdivant, S.; Drakas, B.; Walsh, E. S.; Hamilton, K.; Buser, C. A.; Mao, X.; Abrams, M. T.; Beck, S. C.; Tao, W.; Lobell, R.; Sepp-Lorenzino, L.; Zugay-Murphy, J.; Sardana, V.; Munshi, S. K.; Jezequel-Sur, S. M.; Zuck, P. D.; Hartman, G. D. *Bioorg. Med. Chem. Lett.* **2009**, *19* (4), 1240. doi:10.1016/j.bmcl.2008.12.076.
(10) Brnardic, E. J.; Garbaccio, R. M.; Fraley, M. E.; Tasber, E. S.; Steen, J. T.; Arrington, K. L.; Dudkin, V. Y.; Hartman, G. D.; Stirdivant, S. M.; Drakas, B. A.; Rickert, K.; Walsh, E. S.; Hamilton, K.; Buser, C. A.; Hardwick, J.; Tao, W.; Beck, S. C.; Mao, X.; Lobell, R. B.; Sepp-Lorenzino, L.; Yan, Y.; Ikuta, M.; Munshi, S. K.; Kuo, L. C.; Kreatsoulas, C. *Bioorg. Med. Chem. Lett.* **2007**, *17* (21), 5989. doi:10.1016/j.bmcl.2007.07.051.
(11) Huang, S.; Garbaccio, R. M.; Fraley, M. E.; Steen, J.; Kreatsoulas, C.; Hartman, G.; Stirdivant, S.; Drakas, B.; Rickert, K.; Walsh, E.; Hamilton, K.; Buser, C. A.; Hardwick, J.; Mao, X.; Abrams, M.; Beck, S.; Tao, W.; Lobell, R.; Sepp-Lorenzino, L.; Yan, Y.; Ikuta, M.; Murphy, J. Z.; Sardana, V.; Munshi, S.; Kuo, L.; Reilly, M.; Mahan, E. *Bioorg. Med. Chem. Lett.* **2006**, *16* (22), 5907. doi:10.1016/j.bmcl.2006.08.053.
(12) Foloppe, N.; Fisher, L. M.; Howes, R.; Kierstan, P.; Potter, A.; Robertson, A. G.; Surgenor, A. E. *J. Med. Chem.* **2005**, *48* (13), 4332. doi:10.1021/jm049022c.
(13) Du, J.; Xi, L.; Lei, B.; Lu, J.; Li, J.; Liu, H.; Yao, X. *J. Comput. Chem.* **2010**, *31* (15), 2783. doi:10.1002/jcc.21571.
(14) Schneider, G.; Fechner, U. *Nat. Rev. Drug Discov.* **2005**, *4* (8), 649. doi:10.1038/nrd1799.
(15) Deng, Y.; Roux, B. *J. Phys. Chem. B* **2009**, *113* (8), 2234. doi:10.1021/jp807701h.
(16) Lyne, P. D.; Kenny, P. W.; Cosgrove, D. A.; Deng, C.; Zabludoff, S.; Wendoloski, J. J.; Ashwell, S. *J. Med. Chem.* **2004**, *47* (8), 1962. doi:10.1021/jm030504i.
(17) Matthews, T. P.; Klair, S.; Burns, S.; Boxall, K.; Cherry, M.; Fisher, M.; Westwood, I. M.; Walton, M. I.; McHardy, T.; Cheung, K.-M. J.; Van Montfort, R.; Williams, D.; Aherne, G. W.; Garrett, M. D.; Reader, J.; Collins, I. *J. Med. Chem.* **2009**, *52* (15), 4810. doi:10.1021/jm900314j.
(18) Chen, J. J.; Liu, T. L.; Yang, L. J.; Li, L. L.; Wei, Y. Q.; Yang, S. Y. *Chem. Pharm. Bull. (Tokyo)* **2009**, *57* (7), 704. doi:10.1248/cpb.57.704.
(19) Chen, X. M.; Lu, T.; Lu, S.; Li, H. F.; Yuan, H. L.; Ran, T.; Liu, H. C.; Chen, Y. D. *J. Mol. Model.* **2010**, *16*, 1195. doi:10.1007/s00894-009-0630-y.
(20) Brown, S. P.; Muchmore, S. W. *J. Med. Chem.* **2009**, *52* (10), 3159. doi:10.1021/jm801444x.
(21) Foloppe, N.; Fisher, L. M.; Howes, R.; Potter, A.; Robertson, A. G.; Surgenor, A. E. *Bioorg. Med. Chem.* **2006**, *14* (14), 4792. doi:10.1016/j.bmc.2006.03.021.
(22) Datar, P. A.; Khedkar, S. A.; Malde, A. K.; Coutinho, E. C. *J. Comput. Aided Mol. Des.* **2006**, *20* (6), 343. doi:10.1007/s10822-006-9051-5.
(23) Dhaked, D. K.; Verma, J.; Saran, A.; Coutinho, E. C. *J. Mol. Model.* **2009**, *15* (3), 233. doi:10.1007/s00894-008-0399-4.
(24) Verma, J.; Khedkar, V. M.; Prabhu, A. S.; Khedkar, S. A.; Malde, A. K.; Coutinho, E. C. *J. Comput. Aided Mol. Des.* **2008**, *22* (2), 91. doi:10.1007/s10822-008-9172-0.
(25) Cramer, R. D., III; Patterson, D. E.; Bunce, J. D. *J. Am. Chem. Soc.* **1988**, *110* (18), 5959. doi:10.1021/ja00226a005.
(26) Klebe, G.; Abraham, U. *J. Comput. Aided Mol. Des.* **1999**, *13* (1), 1. doi:10.1023/A:1008047919606.
(27) Friesner, R. A.; Banks, J. L.; Murphy, R. B.; Halgren, T. A.; Klicic, J. J.; Mainz, D. T.; Repasky, M. P.; Knoll, E. H.; Shelley, M.; Perry, J. K.; Shaw, D. E.; Francis, P.; Shenkin, P. S. *J. Med. Chem.* **2004**, *47* (7), 1739. doi:10.1021/jm0306430.
(28) Friesner, R. A.; Murphy, R. B.; Repasky, M. P.; Frye, L. L.; Greenwood, J. R.; Halgren, T. A.; Sanschagrin, P. C.; Mainz, D. T. *J. Med. Chem.* **2006**, *49* (21), 6177. doi:10.1021/jm051256o.
(29) Halgren, T. A.; Murphy, R. B.; Friesner, R. A.; Beard, H. S.; Frye, L. L.; Pollard, W. T.; Banks, J. L. *J. Med. Chem.* **2004**, *47* (7), 1750. doi:10.1021/jm030644s.
(30) Cramer, R. D., III; Bunce, J. D.; Patterson, D. E.; Frank, I. E. *Quant. Struct. Act. Relat.* **1988**, *7*, 18.
(31) Dunn, W. J., III; Wold, S.; Edlund, U.; Hellberg, S.; Gasteiger, J. *Quant. Struct. Act. Relat.* **1984**, *3*, 131.
(32) Mitra, I.; Saha, A.; Roy, K. *Mol. Simul.* **2010**, *36* (13), 1067. doi:10.1080/08927022.2010.503326.
(33) Roy, P. P.; Paul, S.; Mitra, I.; Roy, K. *Molecules* **2009**, *14* (5), 1660. doi:10.3390/molecules14051660.
(34) Klebe, G. *J. Mol. Med.* **2000**, *78* (5), 269. doi:10.1007/s001090000084.
(35) Klebe, G. In *3D QSAR in Drug Design;* Springer: New York, 2002; p 87.
(36) Klebe, G.; Abraham, U.; Mietzner, T. *J. Med. Chem.* **1994**, *37* (24), 4130. doi:10.1021/jm00050a010.
(37) Wold, S.; Sjostrom, M.; Eriksson, L. *Chemom. Intell. Lab. Syst.* **2001**, *58* (2), 109. doi:10.1016/S0169-7439(01)00155-1.
(38) Bush, B. L.; Nachbar, R. B., Jr. *J. Comput. Aided Mol. Des.* **1993**, *7* (5), 587. doi:10.1007/BF00124364.
(39) Léger, C.; Politis, D. N.; Romano, J. P. *Technometrics* **1992**, *34*, 378.
(40) Pissurlenkar, R. R. S.; Shaikh, M. S.; Coutinho, E. C. *J. Mol. Model.* **2007**, *13* (10), 1047. doi:10.1007/s00894-007-0227-2.

Synthesis of heteroleptic pyrrolide/bipyridyl complexes of ruthenium(II)

Travis Lundrigan, Carla L.M. Jackson, Md. Imam Uddin, Lloyd A. Tucker, Adeeb Al-Sheikh Ali, Anthony Linden, T. Stanley Cameron, and Alison Thompson

Can. J. Chem. Downloaded from www.nrcresearchpress.com by Renmin University of China on 09/02/12
For personal use only.

Abstract: The synthesis and characterization of the first heteroleptic pyrrolide/2,2′-bipyridyl complexes of ruthenium(II) are reported. Pyrroles substituted at the 2-position with X = O functionality react with $Ru(bipy)_2Cl_2{\cdot}2H_2O$ to form complexes in which the pyrrolide ligands chelate to Ru(II). The library of pyrroles includes 2-formyl, 2-keto, 2-carboxylato, 2-sulfinyl, and 2-sulfonyl derivatives.

Key words: ruthenium complexation, formyl pyrrole, keto pyrrole, chelation.

Résumé : On a effectué la synthèse et caractérisé les premiers complexes hétéroleptiques pyrrolidure/2,2′-bipyridyle du ruthénium(II). Les pyrroles substitués en position 2 par une fonctionnalité X = O réagissent avec le $Ru(bipy)_2Cl_2{\cdot}2H_2O$ pour former des complexes dans lesquels les ligands pyrrolidures se chélatent au Ru(II). La bibliothèque de pyrroles comprend les dérivés 2-formyle, 2-céto, 2-carboxylato, 2-sulfinyle et 2-sulfonyle.

Mots-clés : complexation du ruthénium, formylpyrrole, cétopyrrole, chélation.

[Traduit par la Rédaction]

Introduction

The chemistry of the cyclopentadienyl unit as a ligand in transition metal chemistry is well-established.[1,2] However, the ability of isoelectronic and geometrically comparable pyrrolide ligands to coordinate to transition-metal centres is significantly underdeveloped.[3,4] It was frequently believed that pyrrolide–metal complexes were intrinsically unstable, based on attempts to prepare complexes of various transition metals using sodium pyrrolide that met only with disappointment.[5] Subsequently, π-cyclopentadieneyl-π-pyrrolyliron complexes (azaferrocenes) were discovered[5,6] following the synthesis of π-pyrrolide manganese tricarbonyl, apparently the first example of a pyrrolide–metal complex.[7] Numerous pyrrole-based metal complexes have since been reported, but the ligands are often cyclopyrrolic[8] (macrocycles containing pyrrole units), particularly tetrapyrrolic,[9] with limited examples of simple pyrrolic systems.

Pyrrolides may coordinate in several alternative modes: π coordination (η^5), involving the entire π system; an N-σ mode (η^1); and a C-σ mode (η^1). Most pyrrolide transition-metal complexes correspond to the N-σ η^1 mode. However, there are also examples of η^2 coordination to rhenium, tungsten, and osmium,[10,11] as well as examples of η^1 complexation to rhenium through the 2-position of pyrrole.[12,13]

Although pyrrolide complexes of transition metals such as rhenium[14,15] and molybdenum[16] have been reported, there are few examples reported with ruthenium(II).[17–20] For example,[18] a pyrrolide–ruthenium complex has been observed through the use of a bidentate α-substituted pyrrole, producing N,O-coordinated pyrrolide–ruthenium complexes as models for catalytic intermediates in the Murai coupling reaction (**A**, Fig. 1). These results lead us to postulate that there may be increased success with pyrrolide–metal complexation using bidentate α-substituted pyrroles. Furthermore, chelation facilitates the coordination of pyrrolyldipyrrinato ligands to tin(IV) complexes that feature a pyrrolide and a dipyrrinato unit.[21] Coordination of pyridylpyrrolides to K, Cu, Ag, Au, and Rh has recently been reported.[22] Bidentate coordination of pyrrole to ruthenium has also been accomplished through the reaction of TpRu(CO)(NCMe)(Me) with pyrrole, which results in the formation of product **B**.[19] The product contains an *N*-pyrrolide ligand with a coordinating pendant imine that arose from addition to the previously coordinated acetonitrile unit, presumably via metal-mediated N–H/C–H activation of the pyrrole, accompanied by the release of methane. Interestingly, lithium pyrrolide displaced triflate from TpRu(CO)(NCMe)(OTf) to give TpRu(*N*-pyrrolide)(CO)(NCMe), without C–H activation, akin to reactions previously reported for rhenium.[12,13] A similar approach has been utilized to prepare ruthenium complexes of azoferrocenes that, of course, feature a pyrrolide ligand.[18]

Within the context of dipyrrinato complexes,[23] dipyrrinato-

Received 25 April 2012. Accepted 4 June 2012. Published at www.nrcresearchpress.com/cjc on 2 August 2012.

T. Lundrigan, C.L.M. Jackson, M.I. Uddin, L.A. Tucker, T.S. Cameron, and A. Thompson. Department of Chemistry, Dalhousie University, PO BOX 15000, Halifax, NS B3H 4R2, Canada.
A.A.-S. Ali. Department of Chemistry, Dalhousie University, PO BOX 15000, Halifax, NS B3H 4R2, Canada; Chemistry Department, Taibah University, Almadinah Almunawarah, P.O. Box 30002, Saudi Arabia.
A. Linden. Institute of Organic Chemistry, University of Zurich, Winterthurerstrasse 190, CH-8057 Zurich, Switzerland.

Corresponding author: Alison Thompson (e-mail: alison.thompson@dal.ca).

Scheme 1. Synthetic route to 2-formyl and 2-keto pyrrolide – ruthenium(II) complexes.

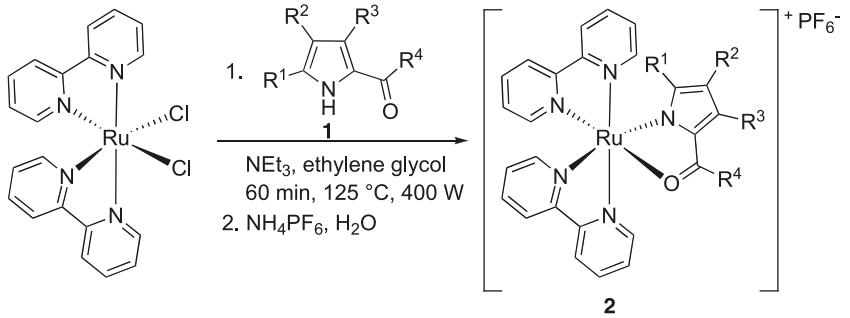
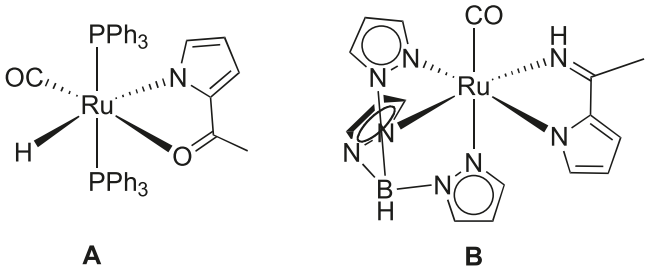


Fig. 1. Literature examples of bidentate pyrrolide–ruthenium(II) complexes.



bound ruthenium(II) complexes[24] have been reported recently, with two bipyridyl units further supporting the metal centre. Ruthenium complexes bearing bipyridyl ligands are very common, and are useful because of their photochemical and photophysical properties.[25] We herein report the synthesis and properties of the first heteroleptic pyrrolide 2,2′-bipyridyl (bipy) complexes of ruthenium(II).

Results and discussion

2-Formyl and 2-keto pyrroles

Cognisant of the dipyrrinato scaffold, whereby anionic pyrrolide and neutral azafulvene (imine) units act synergistically to chelate ruthenium(II) in bis(2,2′-bipy) complexes,[24] we first investigated 2-formyl and 2-keto pyrroles (Scheme 1) as potential sources of pyrrolide ligands. Pyrrole **1a**, fully substituted around the pyrrole ring and bearing a formal group in the 2-position, served as our first candidate. Following a modified literature procedure,[24] 1.1 equiv of the pyrrole were reacted with $[Ru(bipy)_2Cl_2]$ in ethylene glycol under microwave irradiation in the presence of triethyl amine. The resulting reaction mixture was then added to a solution of NH_4PF_6 so that the complex could be isolated as the PF_6^- salt via precipitation. Other counterions were employed, including triflate, tetraphenyl borate, and 3-TMS-1-propane sulfonate, but hexafluorophosphate provided complexes that precipitated the most readily.

Purification was achieved through the dissolution of the crude precipitate in dichloromethane (DCM), washing the solution with brine, and then drying the organic fraction over sodium sulfate. The solvent was removed in vacuo, and the resulting film was triturated with hexanes to give a solid that could be collected using a Millipore filter. Microwave irradiation was essential for the formation of these complexes, since conventional heating methods gave no complexation products. The temperature and time of reaction were both optimized for the microwave system (Table 1), using pyrrole **1a**. The literature procedure[24] suggests a reaction time of 35 min at 100 °C for complexation of dipyrrinato ligands to ruthenium(II), but optimum reaction conditions for the formation of pyrrolide–ruthenium(II) complexes were found to be 60 min at 125 °C.

Table 1. The optimization of time and temperature for the formation of complex **2a**.

Trial	Time (min)	Temp. (°C)	Isolated yield (%)
1	30	100	20
2	60	100	25
3	60	125	93
4	90	100	54
5	90	125	45

The optimized conditions were then applied to 2-formyl pyrroles (Table 2, entries 1–6) and 2-keto (Table 2, entries 7–9) pyrroles **1b**–**1i**, with high yields achieved throughout. Various alkyl groups were used as substituents around the pyrrole ring, with one example containing a halogen substituent. Fully substituted pyrroles (**1a**, **1b**, **1f**–**1g**, and **1i**) were tolerated well by the reaction, as were pyrroles featuring unsubstituted positions (**1c**–**1e** and **1h**). In most cases, small amounts of pyrrolic starting material remained after the reaction, but these were easily removed upon work-up and purification as described previously.

2-Carboxylate pyrroles

We then pursued complexation reactions with pyrroles containing a carboxylate functionality in the 2-position (Scheme 2), as the flanking chelating moiety appears to be the key to success. Initial attempts garnered little success (Table 3, entries 1 and 2), presumably via destabilization of the Ru–O bond courtesy of the presence of the OEt/OBn moiety; such instability has been previously reported in pyrrole–rhenium complexes.[14]

As such, we sought to use pyrroles that featured a halide substituent, especially as complex **2h** (Table 2, within the formyl series) had been prepared in essentially quantitative yield. Several 2-carboxylato-functionalized pyrroles of this genre were subsequently complexed to ruthenium(II) (Table 3, entries 3–5), albeit in yields lower than for the aldehydes and ketones.

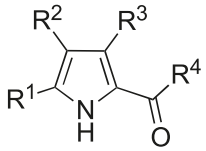
2-Sulfinyl and 2-sulfonyl pyrroles

The final set of ligands contained a sulfinyl moiety at the

Can. J. Chem. Downloaded from www.nrcresearchpress.com by Renmin University of China on 09/02/12
For personal use only.

Can. J. Chem. Downloaded from www.nrcresearchpress.com by Renmin University of China on 09/02/12
For personal use only.

Table 2. Isolated yields of 2-formyl and 2-keto pyrrolide ruthenium(II) complexes.



Entry		Complex	Isolated yield (%)
1	**1a**, R^1 = Me, R^2 = Et, R^3 = Me, R^4 = H	**2a**	93
2	**1b**, R^1 = Me, R^2 = Me, R^3 = Me, R^4 = H	**2b**	75
3	**1c**, R^1 = Me, R^2 = H, R^3 = Me, R^4 = H	**2c**	77
4	**1d**, R^1 = H, R^2 = H, R^3 = H, R^4 = H	**2d**	81
5	**1e**, R^1 = H, R^2 = Et, R^3 = Me, R^4 = H	**2e**	71
6	**1f**, R^1 = Me, R^2 = Heptyl, R^3 = Me, R^4 = H	**2f**	74
7	**1g**, R^1 = Me, R^2 = Et, R^3 = Me, R^4 = Ph	**2g**	80
8	**1h**, R^1 = Br, R^2 = H, R^3 = H, R^4 = Ph	**2h**	99
9	**1i**, R^1 = Me, R^2 = Heptyl, R^3 = Me, R^4 = Ph	**2i**	82

Scheme 2. Synthetic route to pyrrolide ester ruthenium(II) complexes.

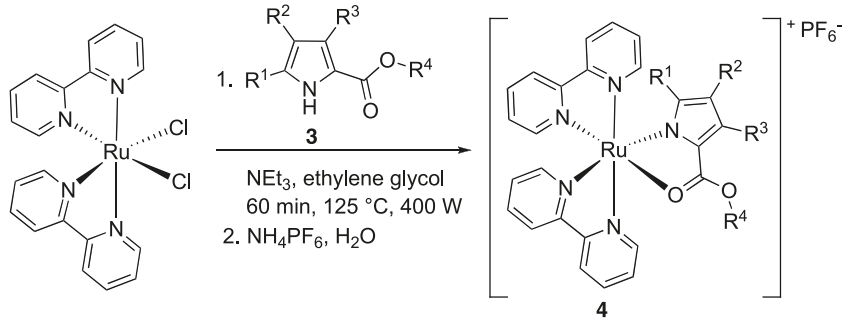
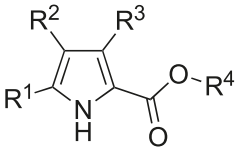


Table 3. Isolated yields of various pyrrolide ester ruthenium(II) complexes.



Entry		Complex	Isolated yield (%)
1	**3a**, R^1 = Me, R^2 = Et, R^3 = Me, R^4 = Et	**4a**	0
2	**3b**, R^1 = Me, R^2 = Et, R^3 = Me, R^4 = Bn	**4b**	0
3	**3c**, R^1 = H, R^2 = Br, R^3 = Me, R^4 = Et	**4c**	75
4	**3d**, R^1 = I, R^2 = Me, R^3 = Et, R^4 = Et	**4d**	70
5	**3e**, R^1 = I, R^2 = Me, R^3 = Me, R^4 = Et	**4e**	70

2-position (Scheme 3). These 2-(arylsulfinyl)pyrroles[26] are of special interest as they contain a chiral centre at the sulfoxide. Each ligand was synthesized as a racemate. Various aryl groups were substituted on the sulfur centre, with little substitution around the pyrrole ring, and these ligands were successfully complexed (Table 4, entries 1–3), although in yields generally lower than those for complexes containing pyrrolyl ligands bearing 2-carbonyl moieties. Diastereoselectivity within the complexation reaction was not observed.

For pyrroles **5d** and **5e** a formyl group was introduced at the 5-position to investigate binding competition between the two potential coordination sites (Table 4, entries 4 and 5). Comparing the carbonyl stretching frequencies of pyrrole **5d** to complex **6d** reveals that the frequency is red-shifted from 1670 cm^{-1} in the free ligand to 1545 cm^{-1} in the complex. A similar result is found when comparing the carbonyl stretching frequencies of pyrrole **1a** (1619 cm^{-1}) with that of complex **2a** (1578 cm^{-1}). As such, coordination must occur through the formyl group in each case, indicating that this coordination site is more favourable than the sulfinyl group.

Complexes **6f** and **6g** were synthesized using 2-(arylsulfenyl) and 2-(arylsulfonyl) pyrroles, respectively, to demonstrate that complexation can occur with pyrroles bearing 2-sulfur substituents at the sulfenyl, sulfinyl, and sulfonyl oxidation states (Table 4, entries 6 and 7).

All complexes **2**, **4**, and **6**, are air- and moisture-stable. They are deep red in the solid state and appear dark burgundy in solution, except complexes **6d**–**6f**, which are red-orange in solution. Each product was fully characterized using ^{1}H NMR, ^{13}C NMR, and UV–vis spectroscopy, as well as ESI-MS. Futhermore, several complexes were characterized using X-ray crystallography.

The absorption spectra of these complexes are characterized by intense $\pi \rightarrow \pi^*$ intraligand transitions in the UV range

Scheme 3. Synthetic route to pyrrolide sulfinyl ruthenium(II) complexes.

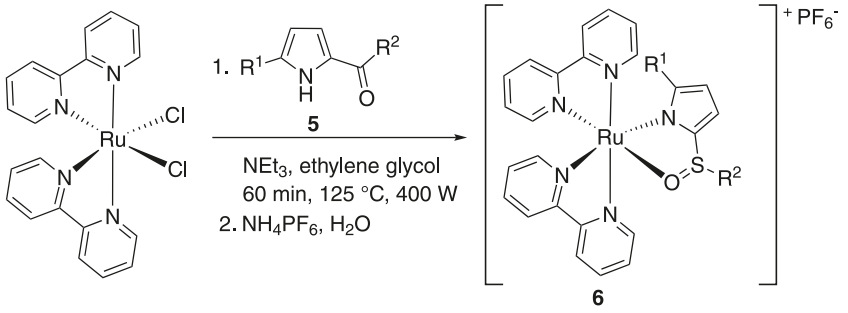


Table 4. Isolated yields of pyrrolide sulfinyl ruthenium(II) complexes.

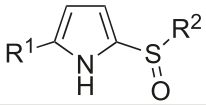
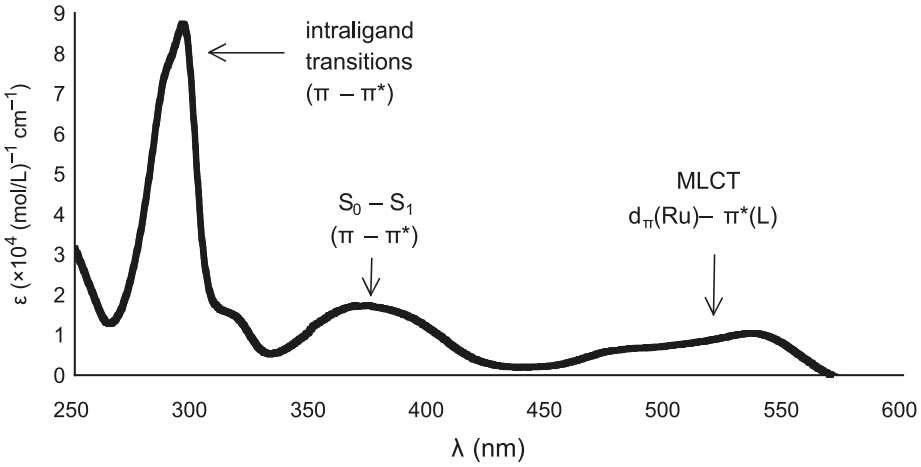
Entry		Complex	Isolated yield (%)
1	**5a**, R^1 = H, R^2 = Ph	**6a**	55
2	**5b**, R^1 = H, R^2 = *p*-tolyl	**6b**	60
3	**5c**, R^1 = H, R^2 = naphthyl	**6c**	70
4	**5d**, R^1 = CHO, R^2 = Ph	**6d**	70
5	**5e**, R^1 = CHO, R^2 = *p*-tolyl	**6e**	93
6	**5f**, R^1 = CHO, R^2 = Ph (sulfenyl)	**6f**	75
7	**5g**, R^1 = H, R^2 = Ph (sulfone)	**6g**	45

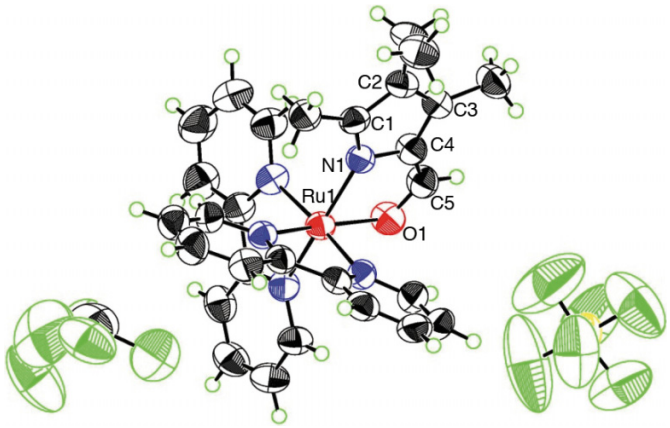
Fig. 2. UV–vis spectrum of **2a** in dichloromethane (DCM), with labeled transitions.



and metal-to-ligand charge transfer (MLCT) transitions, $d_\pi(Ru)\rightarrow\pi^*(L)$, in the visible region[27–29] (Fig. 2). The spectrum for complex **2a** shows the general trend of the absorption spectra for these complexes, consisting of the intense $\pi\rightarrow\pi^*$ bipy-localized transitions below 300 nm,[28] as well as lower energy bands ($S_o\rightarrow S_1$) between 300 and 400 nm. Each complex exhibits a broad MLCT transition containing a shoulder, explained by the overlapping $d_\pi(Ru)\rightarrow\pi^*$ absorptions from the bipyridyl and pyrrolide ligands, and these bands are located above 450 nm.

X-ray crystallographic data were collected for several of the new complexes (**2a**, **2b**, **2d**, **2g**, and **4e**), with structures being obtained for pyrrolide 2-formyl, 2-keto, and 2-carboxylate ruthenium(II) complexes. The structural details for **2b** and **2d** are included in the Supplementary data, as are those for **1a** and **1d**. Complex **2a** (2-formyl group) crystallizes in the

Fig. 3. Thermal ellipsoid diagram (50%) of **2a**·**CHCl$_3$**.



Can. J. Chem. Downloaded from www.nrcresearchpress.com by Renmin University of China on 09/02/12
For personal use only.

Can. J. Chem. Downloaded from www.nrcresearchpress.com by Renmin University of China on 09/02/12
For personal use only.

Fig. 4. Thermal ellipsoid diagrams (50%) showing bond lengths of the parent pyrrole (left, **1a**) and the corresponding coordinated pyrrolide (right, partial structure of **2a**); hydrogen atoms are omitted for clarity.

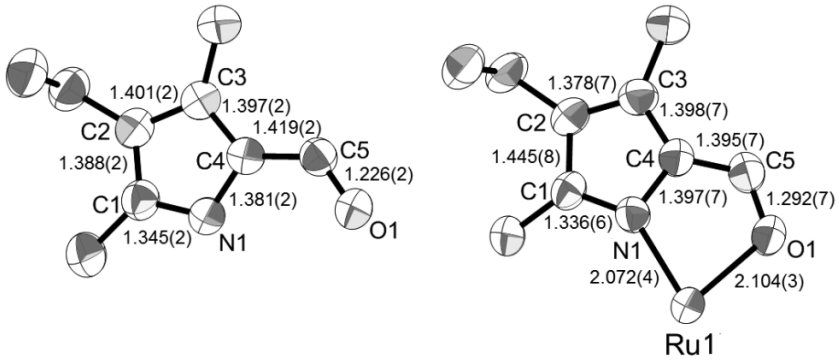
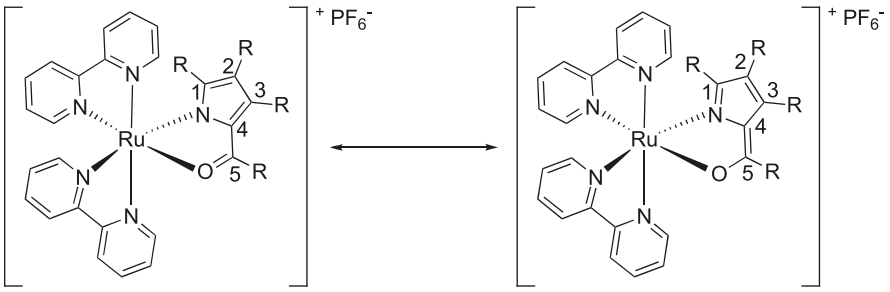


Fig. 5. Resonance structures of complexed pyrrolide (left, pyrrole; right, azafulvenium).



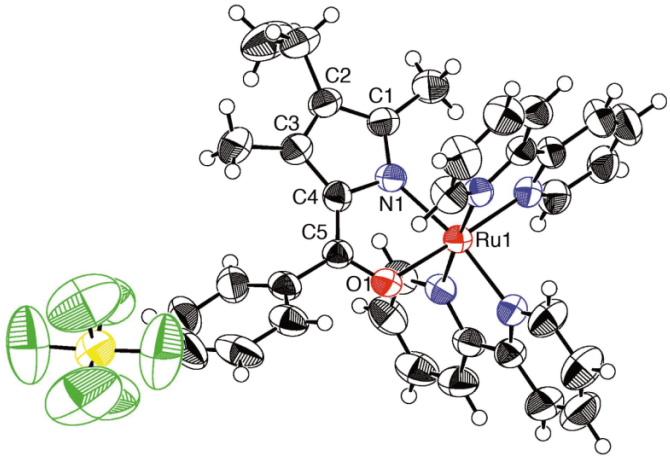
space group *P*-1, with one enantiomer of the complex occupying the asymmetric unit. The geometry of the ruthenium(II) centre was found to be distorted octahedral (Fig. 3).

The Ru–N_{bipy} bond lengths are in the range of 2.029(2)–2.065(1) Å and the Ru–$N_{pyrrole}$ bond length is 2.076(2) Å. The Ru–O bond length is longer at 2.097(2) Å. These Ru–O and Ru–N bond lengths are shorter than those found in similar pyrrole–ruthenium complexes.[18] To enable comparison of the structures of the uncoordinated pyrrole with the pyrrolide ligand within the complex, X-ray crystallographic data were obtained for the pyrrole **1a** (Fig. 4).

Analysis of the structures reveals that there is a lengthening of the C–O bond in the complex **2a** (1.292(7) Å) with respect to the C–O bond of the pyrrole **1a** (1.226(2) Å). Furthermore, the C4–C5 bond length (1.395(7) Å) in **2a**, which is formally a C–C single bond from the pyrrole to the carbonyl carbon atom, is shorter than in the corresponding bond in the parent pyrrole **1a** (1.419(2) Å). The formal C1–C2 C=C double bond of the pyrrole ring (1.445(8) Å) is longer in **2a** than the pyrrole **1a** (1.388(2) Å) (Fig. 4). It appears that all bonds have taken on double bond character, as is typical for an aromatic system. However, the increased C–O and C1–C2 bond lengths in **2a** suggest that the major resonance form of the pyrrolide ligand is the azafulvenium variant (Fig. 5).

Complex **2g** (2-keto group) crystallizes in the space group $P2_1/n$ with the geometry at the ruthenium(II) centre again being distorted octahedral (Fig. 6). The Ru–N_{bipy} bonds fall in the range of 2.035(2)–2.059(2) Å, and the Ru–$N_{pyrrole}$ and Ru–O bond lengths were both found to be 2.076(2) Å. The C–O bond length of pyrrole **1g**[22] (1.2434(9) Å) is shorter than the same bond in complex **2g** (1.284(3) Å). It appears that this ligand follows the same trend shown in complex **2a**. The C1–C2 and C4–C5 bond lengths in pyrrole **1g** (1.397(1) and 1.441(1) Å, respectively) undergo a similar increase and decrease upon complexation (1.423(5) and 1.399(4) Å, respectively, for complex **2g**).

Fig. 6. Thermal ellipsoid diagram (50%) of **2g**.



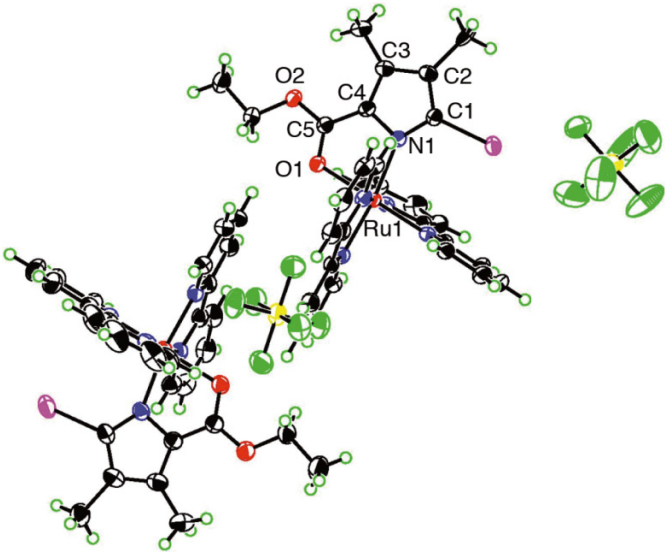
Complex **4e** (2-carboxylate) also crystallizes in the space group $P2_1/n$ with distorted octahedral geometry at the ruthenium(II) centre (Fig. 7). The Ru–N_{bipy} bond lengths are between 2.016(2) and 2.053(3) Å and the Ru–$N_{pyrrole}$ bond lengths are 2.087(2) and 2.088(3) Å. The Ru–O bond lengths are 2.1281(19) and 2.134(2) Å, which are much longer than those of the 2-formyl and 2-keto pyrrole–ruthenium complexes.

Conclusion

In summary, the first heteroleptic pyrrolyl 2,2′-bipyridine complexes of ruthenium(II) are reported, along with a reliable

Can. J. Chem. Downloaded from www.nrcresearchpress.com by Renmin University of China on 09/02/12
For personal use only.

Fig. 7. Thermal ellipsoid diagram (50%) of **4e**.



route for their high-yielding syntheses. A wide variety of pyrrolyl ligands containing numerous functionalities have been successfully coordinated to ruthenium(II) producing air- and moisture-stable complexes. The general synthetic method described should provide a route to pyrrolide–ruthenium complexes of various bidentate pyrroles and potentially a pathway to alternative pyrrolide-bound transition-metal complexes.

Experimental section

General experimental

All ^{1}H NMR (500 MHz) and ^{13}C NMR (125 MHz) spectra were recorded on a Bruker Avance AV-500 spectrometer. Chemical shifts are expressed in parts per million (ppm) using the solvent signals ($CDCl_3$, ^{1}H NMR 7.26 ppm; CD_2Cl_2, ^{1}H NMR 5.26 ppm, ^{13}C NMR 53.8 ppm; DMF-d_7, ^{1}H NMR 2.74 ppm, ^{13}C NMR 30.1 ppm) as an internal reference for ^{1}H and ^{13}C. Splitting patterns are indicated as follows: br, broad; s, singlet; d, doublet; t, triplet; q, quartet; m, multiplet; and app, apparent. All coupling constants (J) are reported in Hertz (Hz). Mass spectra were obtained using ion trap (ESI) instruments operating in positive mode. All microwave reactions were performed using a Biotage Initiator laboratory microwave apparatus. The following compounds were prepared according to literature procedures: **1a**,[30] **1b**,[30] **1c**,[2] **1d**,[30] **1e**,[31] **1g**,[32] **1h**,[33] **3c**,[34] **3d**,[35] **3e**,[36] and **5a**–**5g**.[26] Measurements were made on a Rigaku Raxis rapid-imaging plate area detector with graphite-monochromated Mo Kα radiation. The structures were solved by direct methods[37] and expanded using Fourier techniques.[38] The non-hydrogen atoms were refined anisotropically. Hydrogen atoms were refined using the riding model. Calculations were performed using the CrystalStructure[39,40] crystallographic software package.

General procedure for the synthesis of ruthenium complexes (GP1)

To a solution of the pyrrole (0.19 mmol) and $Ru(bipy)_2Cl_2{\cdot}2H_2O$ (0.17 mmol) in ethylene glycol (16 mL) was added triethylamine (0.5 mL). The resulting solution was reacted in a laboratory microwave at a controlled temperature of 125 °C for 60 min and then cooled to room temperature with a pressurized air supply. The cooled reaction mixture was added to a solution of NH_4PF_6 (3.1 mmol) in deionized water (100 mL). The suspension was stirred overnight and the resulting precipitate was then collected via suction filtration. Purification was achieved by dissolving the precipitate in DCM (80 mL), washing with brine (80 mL), and drying the organic fraction with sodium sulfate. After filtration, the solvent was removed in vacuo. The resulting film was triturated with hexanes and the resulting solid was collected using a Millipore filter.

Representative synthesis

*Bis(2,2′-bipyridyl)-(4-ethyl-2-formyl-3,5-dimethyl-*N*-pyrrolato)ruthenium(II) hexafluorophosphate (2a)*

Complex **2a** was synthesized using GP1 and pyrrole **1a** and was isolated as a microcrystalline dark burgundy solid (0.115 g, 93%). Crystals suitable for X-ray diffraction analysis were grown via the diffusion of hexane into a concentrated chloroform solution. UV–vis (DCM) λ_{max} (nm): 296 ε 115 000 L mol^{-1} cm^{-1}, 375 ε 40 000 L mol^{-1} cm^{-1}, 536 ε 20 000 L mol^{-1} cm^{-1}. δ_H (500 MHz, $CDCl_3$): 8.63 (1H, d, J = 4.9), 8.39 (1H, d, J = 8.0), 8.36 (1H, d, J = 8.2), 8.30 (1H, d, J = 8.2), 8.26 (1H, d, J = 8.1), 8.21 (1H, s), 7.99–7.95 (2H, m), 7.89 (1H, d, J = 5.7), 7.79–7.72 (3H, m), 7.54–7.51 (1H, m), 7.49 (1H, d, J = 5.6), 7.46–7.44 (1H, m), 7.18–7.16 (2H, m), 2.29–2.23 (5H, m, CH_2 + CH_3), 1.26 (3H, s), 0.95 (3H, t, J = 7.5). δ_C (125 MHz, DMF-d_7): 176.0, 160.0, 159.4, 158.8, 158.3, 153.9, 153.7, 152.5, 152.5, 151.3, 142.5, 136.9, 136.7, 136.1, 135.4, 133.2, 130.5, 127.6, 127.4, 127.4, 127.1, 124.5, 124.1, 124.1, 123.9, 18.1, 15.3, 12.3, 10.1. m/z [M – PF_6 + H$^+$]: 564.1. Crystal data for complex **2a**: $C_{30}H_{29}N_5OPF_6RuCl_3$, MM = 827.99 g/mol, dark-red needle crystal, 0.31 mm × 0.13 mm × 0.06 mm; primitive triclinic, space group P-1; a = 9.8219(4) Å; b = 13.6422(5) Å; c = 13.7188(3) Å; α = 73.941(8); β = 73.983(11); γ = 87.603(12)°; V = 1696.72(15) Å^3; Z = 2; ρ = 1.621 g/cm^3; μ(Mo Kα) = 0.8115 mm^{-1}; 22 241 reflections (11 932 unique, R_{int} = 0.052); $R(F)$ = 0.0596; $Rw(F)$ = 0.0713; GoF = 1.120.

*Bis(2,2′-bipyridyl)-(4-ethyl-3,5-dimethyl-2-benzoyl-*N*-pyrrolato)ruthenium(II) hexafluorophosphate (2g)*

Complex **2g** was synthesized using GP1 and pyrrole **1g** and was isolated as a microcrystalline dark burgundy solid (0.110 g, 80%). Crystals suitable for X-ray diffraction analysis were grown via the slow evaporation of solvent from a concentrated methanol solution. UV–vis (DCM) λ_{max} (nm): 296 ε 125 000 L mol^{-1} cm^{-1}, 330 ε 35 000 L mol^{-1} cm^{-1}, 540 ε 25 000 L mol^{-1} cm^{-1}. δ_H (500 MHz, DMF-d_7): 8.87 (1H, d, J = 8.0), 8.84 (1H, d, J = 8.1), 8.81 (1H, d, J = 8.2), 8.79–8.76 (2H, m), 8.21–8.18 (2H, m), 8.16–8.14 (1H, m), 8.09 (1H, d, J = 5.3), 8.00–7.98 (2H, m), 7.84–7.81 (1H, m), 7.78 (1H, d, J = 5.6), 7.73–7.70 (1H, m), 7.49–7.46 (1H, m), 7.44–7.40 (6H, m), 2.26 (2H, m, J = 7.1), 1.81 (3H, s), 1.39 (3H, s), 0.90 (3H, t, J = 7.5). δ_C (125 MHz, CD_2Cl_2): 186.2, 159.3, 158.8, 158.3, 157.8, 153.5, 152.9, 152.2, 151.6, 151.1, 138.6, 136.2, 136.0, 135.3, 134.6, 133.0,

132.0, 130.2, 128.5 (2C), 128.3 (2C), 127.0, 126.9, 126.7, 126.6, 123.6, 123.3, 123.2, 123.0, 18.2, 15.2, 12.6, 12.2, 1Ar-C signal missing. *m/z* $[M - PF_6 + H]^+$: 640.2. Crystal data for complex **2g**: $C_{35}H_{32}N_5OPF_6Ru$, MM = 784.70 g/mol, dark-red spear crystal, 0.36 mm × 0.14 mm × 0.09 mm; primitive monoclinic, space group $P2_1/n$; a = 11.7187(11) Å; b = 14.9960(12) Å; c = 19.2788(13) Å; V = 3366.0(5) Å^3; Z = 4; ρ = 1.548 g/cm^3; μ(Mo Kα) = 57.48 mm^{-1}; 24 900 reflections (6842 unique, R_{int} = 0.050); R = 0.0358, Rw = 0.0412; GoF = 1.080.

*Bis(2,2′-bipyridyl)-(ethyl 5-iodo-3,4-methylpyrrole-2-carboxylato-*N*-pyrrolato)ruthenium(II) hexafluorophosphate (4e)*

Complex **4e** was synthesized using GP1 and pyrrole **3e** was isolated as a microcrystalline dark burgundy solid (0.104 g, 70%). Crystals suitable for X-ray diffraction analysis were grown via the diffusion of diethyl ether into a concentrated DCM solution. UV–vis (DCM) λ_{max} (nm): 295 ε 80 000 L mol^{-1} cm^{-1}, 345 ε 15 000 L mol^{-1} cm^{-1}, 518 ε 10 000 L mol^{-1} cm^{-1}. δ_H (500 MHz, CD_2Cl_2): 8.65 (1H, dd, J = 5.6, 0.6), 8.35 (2H, dd, J =11.7, 8.1), 8.28 (1H, d, J = 8.1), 8.22 (1H, d, J = 8.0), 8.03–7.98 (3H, m), 7.84 (1H, td, J = 7.9, 1.3), 7.73–7.68 (2H, m), 7.59 (1H, ddd, J = 7.4, 5.8, 1.4), 7.53 (1H, dd, J = 5.6, 0.6), 7.50 (1H, ddd, J = 7.4, 5.8, 1.4), 7.19 (1H, ddd, J = 7.4, 5.8, 1.4), 7.07 (1H, ddd, J = 7.4, 5.9, 1.4), 4.27–4.24 (1H, m), 4.14–4.11 (1H, m), 2.24 (3H, s), 1.83 (3H, s), 1.19 (3H, t, J = 7.1). δ_C (125 MHz, CD_2Cl_2): 173.0, 160.1, 159.2, 158.3, 158.1, 154.3 (2C), 152.3, 150.6, 136.5, 136.4, 135.8, 135.0, 129.9, 129.4, 127.3, 127.1, 126.8, 126.7, 126.3, 123.7, 123.4, 123.2, 122.9, 97.6, 62.6, 14.5 (2C), 12.7. *m/z* $[M - PF_6 + H]^+$: 706.0. Crystal data for complex **4e**: $2(C_{29}H_{27}N_5OPF_6Ru)$ CH_2Cl_2 H_2O, MM = 1803.95 g/mol, deep-red block crystal, 0.28 mm × 0.17 mm × 0.09 mm; primitive monoclinic, space group $P2_1/n$; a = 23.1502(7) Å; b = 13.8523(3) Å; c = 23.3484(6) Å; β = 117.0574(10)°; V = 6668.0(3) Å^3; Z = 4; ρ = 1.797 g/cm^3; μ(Mo Kα) = 1.5965 mm^{-1}; 111 925 reflections (26 270 unique, R_{int} = 0.039); $R(F)$ = 0.0325; $Rw(F)$ = 0.0373; GoF = 1.058.

*Bis(2,2′-bipyridyl)-(2-(naphthylsulfinyl)-*N*-pyrrolato) ruthenium(II) hexafluorophosphate (6c)*

Complex **6c** was synthesized using GP1 and pyrrole **5c** was isolated as a microcrystalline dark burgundy solid (0.098 g, 70%). UV–vis (DCM) λ_{max} (nm): 297 ε 130 000 L mol^{-1} cm^{-1}, 341 ε 15 000 L mol^{-1} cm^{-1}, 530 ε 20 000 L mol^{-1} cm^{-1}. δ_H (500 MHz, CD_2Cl_2): 9.15 (1H, d, J = 5.2), 8.26 (1H, t, J = 6.7), 8.20–8.15 (2H, m), 8.04–8.01 (1H, m), 7.97–7.93 (1H, m), 7.77–7.75 (2H, m), 7.70 (1H, t, J = 7.9), 7.60–7.57 (3H, m), 7.51–7.47 (3H, m), 7.27–7.24 (1H, m), 7.22 (1H, d, J = 7.6), 7.17 (1H, ddd, J = 7.3, 5.8, 1.4), 7.11–7.08 (1H, m), 7.05–7.01 (1H, m), 6.94–6.90 (2H, m), 6.85 (1H, dd, J = 3.7, 1.3), 6.46–6.44 (1H, m), 6.22 (1H, dd, J = 3.7, 2.0), 6.05 (1H, t, J = 1.6). δ_C (125 MHz, CD_2Cl_2): 159.7, 157.9, 157.9, 153.4, 152.8, 152.7, 150.0, 136.1, 136.0, 135.1, 134.9, 134.7, 134.3, 133.9, 132.9, 129.3, 127.9, 127.5, 127.2, 126.6, 126.4, 126.3, 126.2, 126.1, 125.5, 125.2, 125.1, 124.6, 123.6, 123.0, 122.9, 121.6, 114.1, 112.2. *m/z* $[M - PF_6 + H]^+$: 654.1.

Supplementary data

Supplementary data are available with the article through the journal Web site at http://nrcresearchpress.com/doi/suppl/10.1139/v2012-045. CCDC 846489–846495 contain the X-ray data in CIF format for this manuscript. These data can be obtained, free of charge, via http://www.ccdc.cam.ac.uk/products/csd/request (Or from the Cambridge Crystallographic Data Centre, 12 Union Road, Cambridge CB2 1EZ, UK; fax: +44 1223 33603; or e-mail: deposit@ccdc.cam.ac.uk.

Acknowledgements

This work was supported by the Natural Sciences and Engineering Research Council of Canada (NSERC). The authors thank Beth Pearce, Dr. H. Martin Gillis, and Dr. Jose R. Garabatos-Perera (all previous members of the Thompson group at Dalhousie University) for the preparation of compounds **5d**, **5f**, and **5g**.

References

(1) Dias, A. R.; Veiros, L. F. *J. Organomet. Chem.* **2005**, *690* (7), 1840. doi:10.1016/j.jorganchem.2005.02.010.
(2) Kotora, M. *Top. Organomet. Chem.* **2005**, *8*, 57. doi:10.1007/b96002.
(3) Kowalski, K. *Coord. Chem. Rev.* **2010**, *254* (17–18), 1895. doi:10.1016/j.ccr.2010.01.004.
(4) Dias, A. R.; Ferreira, A. P.; Veiros, L. F. *C. R. Chim.* **2005**, *8* (9–10), 1444. doi:10.1016/j.crci.2004.07.005.
(5) King, R. B.; Bisnette, M. B. *Inorg. Chem.* **1964**, *3* (6), 796. doi:10.1021/ic50016a003.
(6) Joshi, K. K.; Pauson, P. L.; Qazi, A. R.; Stubbs, W. H. *J. Organomet. Chem.* **1964**, *1* (6), 471. doi:10.1016/S0022-328X(00)94482-6.
(7) Joshi, K. K.; Pauson, P. L. *Proc. Chem. Soc.* **1962**, 326.
(8) Melfi, P. J.; Kim, S. K.; Lee, J. T.; Bolze, F.; Seidel, D.; Lynch, V. M.; Veauthier, J. M.; Gaunt, A. J.; Neu, M. P.; Ou, Z.; Kadish, K. M.; Fukuzumi, S.; Ohkubo, K.; Sessler, J. L. *Inorg. Chem.* **2007**, *46* (13), 5143. doi:10.1021/ic700781t.
(9) Bröring, M.; Pfister, A.; Ilg, K. *Chem. Commun. (Camb.)* **2000**, (15), 1407. doi:10.1039/b003815f.
(10) Myers, W. H.; Welch, K. D.; Graham, P. M.; Keller, A.; Sabat, M.; Trindle, C. O.; Harman, W. D. *Organometallics* **2005**, *24* (22), 5267. doi:10.1021/om050393g.
(11) Cordone, R.; Harman, W. D.; Taube, H. *J. Am. Chem. Soc.* **1989**, *111* (15), 5969. doi:10.1021/ja00197a083.
(12) Johnson, T. J.; Alvey, L. J.; Brady, M.; Mayne, C. L.; Arif, A. M.; Gladysz, J. A. *Chem. Eur. J.* **1995**, *1* (5), 294. doi:10.1002/chem.19950010506.
(13) Johnson, T. J.; Arif, A. M.; Gladysz, J. A. *Organometallics* **1993**, *12* (12), 4728. doi:10.1021/om00036a006.
(14) Mirebeau, J.-H.; Le Bideau, F.; Marrot, J.; Jaouen, G. *Organometallics* **2008**, *27* (13), 2911. doi:10.1021/om800348a.
(15) Selivanova, S. V.; Dolphin, D.; van Lier, J. E.; Kudrevich, S. V. *Inorg. Chim. Acta* **2003**, *349*, 58. doi:10.1016/S0020-1693(03)00088-4.
(16) Zhu, G.; Tanski, J. M.; Churchill, D. G.; Janak, K. E.; Parkin, G. *J. Am. Chem. Soc.* **2002**, *124* (46), 13658. doi:10.1021/ja028512w.
(17) Foucault, H. M.; Bryce, D. L.; Fogg, D. E. *Inorg. Chem.* **2006**, *45* (25), 10293. doi:10.1021/ic061021i.
(18) Jazzar, R. F. R.; Varrone, M.; Burrows, A. D.; Macgregor, S. A.; Mahon, M. F.; Whittlesey, M. K. *Inorg. Chim. Acta* **2006**, *359* (3), 815. doi:10.1016/j.ica.2005.05.021.

Can. J. Chem. Downloaded from www.nrcresearchpress.com by Renmin University of China on 09/02/12
For personal use only.

(19) Pittard, K. A.; Cundari, T. R.; Gunnoe, T. B.; Day, C. S.; Petersen, J. L. *Organometallics* **2005**, *24* (21), 5015. doi:10.1021/om0506668.
(20) Rakowski DuBois, M.; Parker, K. G.; Ohman, C.; Noll, B. C. *Organometallics* **1997**, *16* (11), 2325. doi:10.1021/om9700268.
(21) Crawford, S. M.; Al-Sheikh Ali, A.; Cameron, T. S.; Thompson, A. *Inorg. Chem.* **2011**, *50*, 8207. doi:10-1021/ic200731t.
(22) Flores, J. A.; Andino, J. G.; Tsvetkov, N. P.; Pink, M.; Wolfe, R. J.; Head, A. R.; Lichtenberger, D. L.; Massa, J.; Caulton, K. G. *Inorg. Chem.* **2011**, *50*, 8121. doi:10.1021/ic2005503.
(23) Wood, T. E.; Thompson, A. *Chem. Rev.* **2007**, *107* (5), 1831. doi:10.1021/cr050052c.
(24) Smalley, S. J.; Waterland, M. R.; Telfer, S. G. *Inorg. Chem.* **2009**, *48* (1), 13. doi:10.1021/ic8016497.
(25) Gorman, B. A.; Francis, P. S.; Barnett, N. W. *Analyst (Lond.)* **2006**, *131* (5), 616. doi:10.1039/b518454a.
(26) Thompson, A.; Garabatos-Perera, J. R.; Gillis, H. M. *Can. J. Chem.* **2008**, *86* (7), 676. doi:10.1139/v08-054.
(27) Basu, A.; Kasar, T. G.; Sapre, N. Y. *Inorg. Chem.* **1988**, *27* (25), 4539. doi:10.1021/ic00298a008.
(28) Sullivan, B. P.; Salmon, D. J.; Meyer, T. J. *Inorg. Chem.* **1978**, *17* (12), 3334. doi:10.1021/ic50190a006.
(29) Yu, H.-J.; Huang, S.-M.; Li, L.-Y.; Jia, H.-N.; Chao, H.; Mao, Z.-W.; Liu, J.-Z.; Ji, L.-N. *Inorg. Biochem.* **2009**, *103* (6), 881. doi:10.1016/j.jinorgbio.2009.03.005.
(30) Kurti, L.; Czako, B. *Strategic Applications of Named Reactions in Organic Synthesis;* Elsevier: London, 2005.
(31) Coffin, A. R.; Roussell, M. A.; Tserlin, E.; Pelkey, E. T. *J. Org. Chem.* **2006**, *71* (17), 6678. doi:10.1021/jo061043m.
(32) Ali, A. A.; Cipot-Wechsler, J.; Crawford, S. M.; Selim, O.; Stoddard, R. L.; Cameron, T. S.; Thompson, A. *Can. J. Chem.* **2010**, *88* (8), 725. doi:10.1139/V09-180.
(33) Bray, B. L.; Mathies, P. H.; Naef, R.; Solas, D. R.; Tidwell, T. T.; Artis, D. R.; Muchowski, J. M. *J. Org. Chem.* **1990**, *55* (26), 6317. doi:10.1021/jo00313a019.
(34) Smith, K. M.; Bobe, F. W.; Minnetian, O. M.; Hope, H.; Yanuck, M. D. *J. Org. Chem.* **1985**, *50* (6), 790. doi:10.1021/jo00206a012.
(35) Sessler, J. L.; Cyr, M. J.; Lynch, V.; McGhee, E.; Ibers, J. A. *J. Am. Chem. Soc.* **1990**, *112* (7), 2810. doi:10.1021/ja00163a059.
(36) D'Auria, M.; De Luca, E.; Mauriello, G.; Racioppi, R.; Sleiter, G. *J. Chem. Soc., Perkin Trans. 1* **1997**, (16): 2369. doi:10.1039/a701674c.
(37) Sheldrick, G.M. *SHELX97;* University of Göttingen: Göttingen, Germany, 1997.
(38) Beurskens, P. T.; Admiraal, G.; Beurskens, G.; Bosman, W. P.; de Gelder, R.; Israel, R.; Smits, J. M. M. *The DIRDIF-99 Program System; Technical Report of the Crystallography Laboratory;* University of Nijmegen: The Netherlands, 1999.
(39) Carruthers, J. R.; Rollett, J. S.; Betteridge, P. W.; Kinna, D.; Pearce, L.; Larsen, A.; Gabe, E. *CRYSTALS, Issue 11;* Chemical Crystallography Laboratory, Oxford, UK, 1999.
(40) *CrystalStructure 3.8: Crystal Structure Analysis Package, 2000–2006;* Rigaku USA Inc.: The Woodlands, TX .

Can. J. Chem. Downloaded from www.nrcresearchpress.com by Renmin University of China on 09/02/12
For personal use only.

Sulfonated multiwalled carbon nanotubes (MWCNTs) as a new, efficient, and recyclable heterogeneous nanocatalyst for the synthesis of amines

M. M. Doroodmand, S. Sobhani, and A. Ashoori

Can. J. Chem. Downloaded from www.nrcresearchpress.com by Renmin University of China on 09/02/12
For personal use only.

Abstract: Sulfonated multiwalled carbon nanotubes (MWCNTs) were synthesized by chemical vapor deposition (CVD) as a new and facile one-pot method using acetylene (as the CNT precursor), thiophene (as the sulfur precursor), and ferrocene (for in situ liberation of metal nanoparticles as the CNT nanocatalyst). A low catalytic amount of the resulting sulfonated MWCNTs with a turnover number (TON) up to 980 and a turnover frequency (TOF) up to 11 160 h^{-1} was utilized as a new and recyclable heterogeneous nanocatalyst for the efficient one-pot synthesis of various amines (secondary and tertiary) by direct reductive amination of aldehydes and ketones using $NaBH_4$. The catalyst was easily isolated from the reaction mixture by simple filtration and reused at least five times without significant degradation in activity.

Key words: multiwalled carbon nanotubes, nanocatalyst, sulfonic acid, amine, reductive amination.

Résumé : On a réalisé la synthèse de nanotubes de carbone sulfonés à parois multiples (NTCPM) par une nouvelle méthode monotope simple de dépôt de vapeurs chimiques (DVC) implication l'acétylène comme précurseur des nanotubes de carbone, le thiophène comme précurseur du soufre et le ferrocène (pour la libération in situ des particules métalliques agissant comme nanocatalyseur dans la formation de nanotubes de carbones). On a utilisé une faible quantité catalytique des nanotubes de carbone sulfonés à parois multiples (NTCPM) ainsi obtenu, avec des nombres de renouvellement allant jusqu'à 980 et des fréquences de renouvellement allant jusqu'à 11 160 h^{-1}, comme nouveau catalyseur hétérogène recyclable pour la synthèse monotope efficace de diverses amines (secondaires et tertiaires) par amination réductrice directe d'aldéhydes et de cétones à l'aide de $NaBH_4$. On peut facilement isoler le catalyseur du mélange réactionnel, par simple filtration, et l'utiliser à nouveau au moins cinq fois sans dégradation significative de son activité.

Mots-clés : nanotubes de carbone sulfonés à parois multiples (NTCPM), nanocatalyseur, acide sulfonique, amination réductrice.

[Traduit par la Rédaction]

Introduction

Amines are of high importance in organic chemistry because of their presence in high quantities in biological and natural molecules, such as alkaloids, amino acids, nucleic acids, dyes, and fine chemicals.[1–4] Synthetic methodologies for amines vary depending on the location of the amine in the original source and the type of the amine. Often, there are multiple processes used for the synthesis of a particular amine or family of amines.[5–8] Among these processes, direct reductive amination is the most practical and convenient approach, since it allows the conversion of carbonyl functionality to structurally diverse secondary and tertiary amines.[9–12] This reaction offers compelling advantages over amine synthesis, including brevity, wide availability of commercial substrates, synthesis of an alkylated amine of higher order and generally mild reaction conditions. Several reagents, which affect reductive amination, have been recently developed.[13–18] However, most of the reagents may have one or more drawbacks such as hard reaction conditions, a tedious workup procedure, and the use of unrecyclable or unstable catalysts, which would eventually produce toxic waste. Therefore, the development of a new method to overcome these shortcomings remains an ongoing challenge for the synthesis of these significant scaffolds.

Heterogeneous catalysts for the synthesis of fine chemicals have attracted considerable attention from both the environmental and economical points of view because they offer several advantages in organic synthesis, e.g., simplification of reaction procedures, easy separation of products, long catalytic life, ease of catalyst recyclability, and thermal stability.[19]

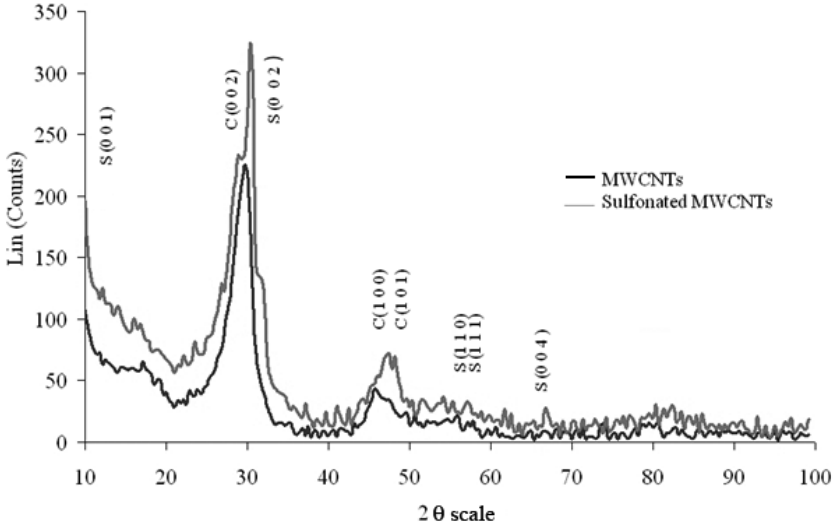
Carbon nanotubes (CNTs) appear to be one of the most promising nanomaterial supports for different functional

Received 26 October 2011. Accepted 8 June 2012. Published at www.nrcresearchpress.com/cjc on 2 August 2012.

M.M. Doroodmand. Department of Chemistry, College of Sciences, Shiraz University, Shiraz 71454, Iran; Nanotechnology Research Institute, Shiraz University, Shiraz 71454, Iran.
S. Sobhani and A. Ashoori. Department of Chemistry, College of Sciences, Birjand University, Birjand 414, Iran.

Corresponding author: S. Sobhani (e-mail: ssobhani@birjand.ac.ir and sobhanisara@yahoo.com).

Fig. 1. X-ray diffraction (XRD) spectra of sulfonated multiwalled carbon nanotubes (MWCNTs) (gray) and MWCNTs (black).



Can. J. Chem. Downloaded from www.nrcresearchpress.com by Renmin University of China on 09/02/12
For personal use only.

groups and nanocatalysts because of their properties such as their unique surface structure, small diameter, large active surface area, inherent size and hollow geometry, basal and edge plane sites, desirable chemical stability, high electric conductivity, and excellent mechanical and thermal properties.[20–23] On the other hand, the functionalization of CNTs decreases the hydrophobic character of the CNTs, caused by strong intertubular van der Waals forces, and modifies the physical and chemical properties of the CNTs. Sulfonic acid is one of the ideal grafting functional groups to the CNTs surface. Acid-assisted thermal decomposition and electrochemical modification and reduction are the typical synthetic routes for the preparation of sulfonated CNTs.[24] Generally, acid-assisted thermal decomposition involves refluxing the CNTs with concentrated acid under high temperatures. Such aggressive treatments may lead to severe damage to the CNTs backbone.[25] The electrochemical modification route allows mild operational conditions and its utility is only restricted to electrically contacted CNTs on the confined electrode surface.[26,27] In the case of aryl-functionalized CNTs, synthesized by conventional chemical reduction methods, the procedure is usually time-consuming because it involves especially complex processes or multiple steps.[28,29]

The most popular and widely used method for CNTs synthesis is chemical vapor deposition (CVD). It is because of its low setup cost, high production yield, ease of scale up, ability to harness plenty of hydrocarbons in each state (solid, liquid, or gas), ability to enable the use of various substrates, one-pot covalent functionalization, and ease of CNTs growth either in different forms (powder, thin or thick films, aligned or entangled, or straight or coiled nanotubes) or in a desired architecture of nanotubes on predefined sites of a patterned substrate.[30]

Because of the need for a clean and green recovery of the heterogeneous catalyst, especially acid catalysts, we wish to introduce a new method for the one-pot synthesis of sulfonated multiwalled carbon nanotubes (MWCNTs) by CVD using acetylene, thiophene, and ferrocene as C, S, and Fe precursors, respectively. We also studied the utility of the synthesized sulfonated MWCNTs as a new and recyclable heterogeneous catalyst for one-pot synthesis of different amines.

Results and discussion

For the synthesis of sulfonated MWCNTs, acetylene (as the CNT precursor), thiophene (as the sulfur precursor), and ferrocene (for in situ liberation of metal nanoparticles as the CNT nanocatalyst) were mixed with hydrogen and argon in a furnace at ~1300 °C. The sulfur-doped carbon nanostructure was produced and purified directly from any amorphous carbon via oxygen purging and the introduction of hydrogen peroxide into the setup. This process was carried out in a second furnace at ~500 °C. Oxygen converts sulfurous species and amorphous carbon to oxidized sulfurous compounds and carbon dioxide, respectively. During the purification process, sulfonated MWCNTs were produced in situ by further oxidation of sulfur-doped carbon nanostructures by a hydrogen peroxide aerosol. The oxidation process was followed by UV and MW irradiations. These irradiations simply provide the necessary energy to cleave the C–C bond, which leads to defect creation in the CNT matrix.

The synthesized sulfonated MWCNTs were then characterized by various methods including X-ray diffraction (XRD), Raman, scanning electron microscopy (SEM), transmission electron microscopy (TEM), and FT-IR. The amount of sulfonic acid loaded on the surface of the MWCNTs was determined by thermogravimetric analysis (TGA) and confirmed further by back titration.

XRD analysis

According to the XRD pattern (Fig. 1), the strong peaks positioned at $2\theta = 28°$, 42°, and 48° are related to C (002), C (100), and C (101), respectively. The peaks appearing at $2\theta = 12°$, 30°, 56°, 58°, and 66° belong to S (001), S (110), S (111), and S (004), respectively. The XRD pattern reveals the presence of sulfur atoms in the MWCNT matrix.

Raman spectra

A significant change in the defect of the Raman spectra of sulfonated MWCNTs compared with that of the MWCNTs,

Can. J. Chem. Downloaded from www.nrcresearchpress.com by Renmin University of China on 09/02/12
For personal use only.

Fig. 2. Raman spectra of sulfonated multiwalled carbon nanotubes (MWCNTs) (black) and MWCNTs (gray).

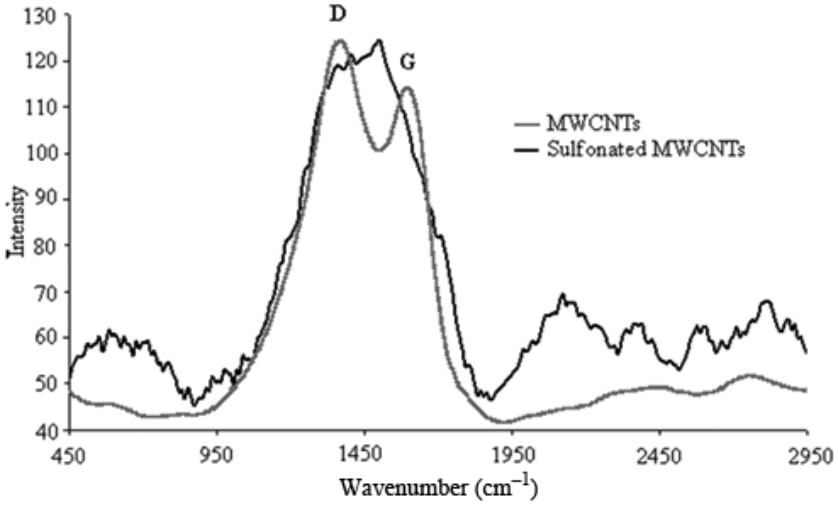
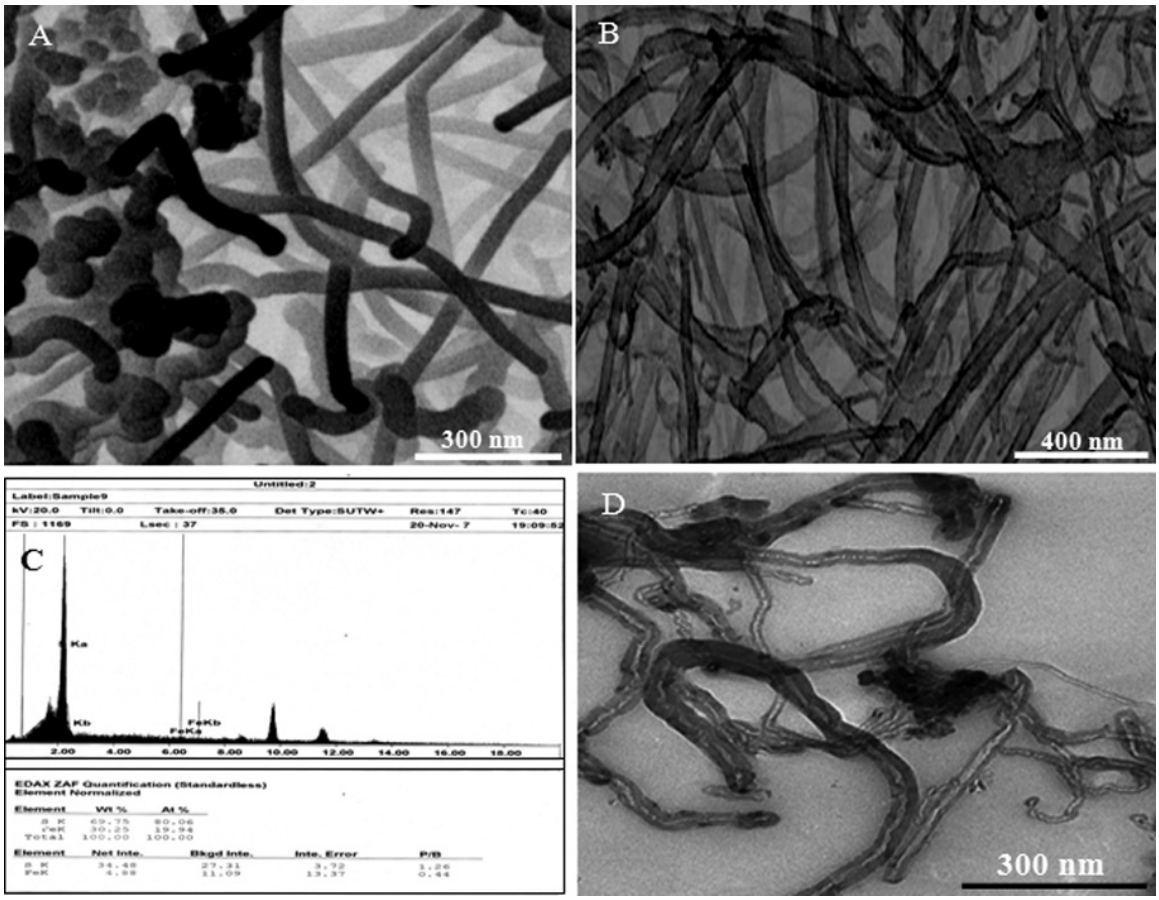


Fig. 3. Electronic microscopic images including (A) SEM, (B and D) TEM, and (C) EDX analysis of sulfonated MWCNTs.



shows the presence of sulfur atoms in the CNT matrix (Fig. 2).

SEM and TEM

The size and structure of the sulfonated MWCNTs were determined using SEM and TEM. According to the SEM (Fig. 3A) and TEM (Figs. 3B and 3D), it is clear that the synthesized sulfonated MWCNTs have a nanodimension ranging from ~10 to 30 nm.

FT-IR spectroscopy

The appearance of peaks at 1130 and 1531 cm^{-1} in the FT-IR spectrum of sulfonated MWCNTs (Fig. 4A) is ascertained to the C–S (in which carbon is available in the MWCNTs backbone) and S=O bonds, respectively. These two peaks are not observed in the spectrum of MWCNTs (Fig. 4B). This observation indicates the existence of C–SO_3H in the sulfonated MWCNTs. Two bands positioned at 3436 and 1635 cm^{-1} belong to the O–H stretching and bending

Can. J. Chem. Downloaded from www.nrcresearchpress.com by Renmin University of China on 09/02/12
For personal use only.

Fig. 4. FT-IR spectra of (A) sulfonated multiwalled carbon nanotubes (MWCNTs) and (B) MWCNTs.

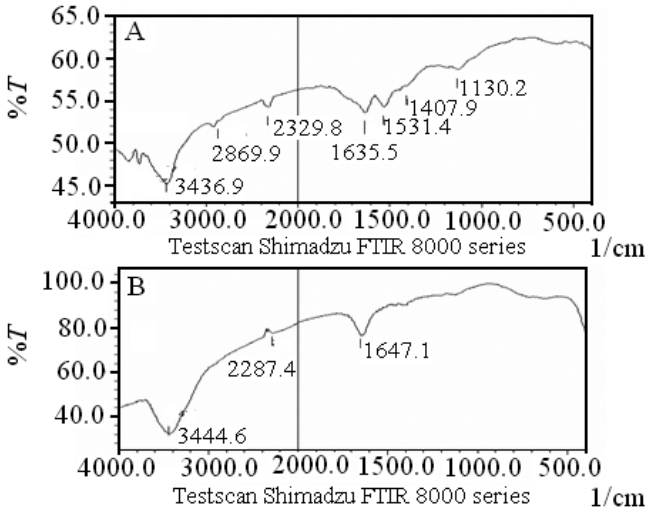
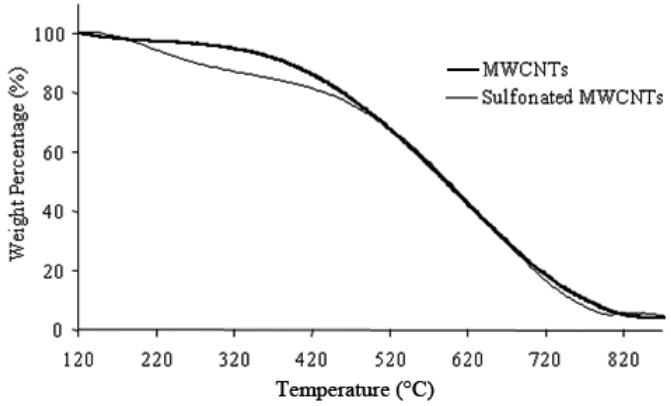


Fig. 5. Thermogram of sulfonated multiwalled carbon nanotubes (MWCNTs, gray) and MWCNTs (black).



vibrations, respectively. The OH group was produced during the activation of the MWCNTs and the formation of sulfonate functional groups.

TGA

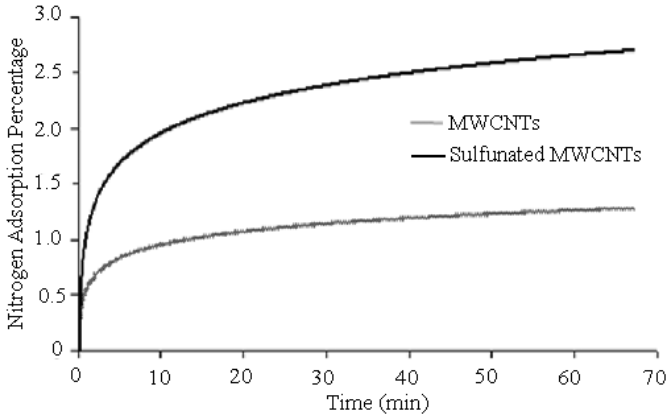
The thermal behavior of sulfonated MWCNTs and pure MWCNTs is shown in Fig. 5. A significant decrease in the weight percentage of the sulfonated MWCNTs at ~170 °C is related to the desorption of the sulfonate functional group from the catalyst surface. A sharp decrease in the weight percentage at ~620 °C is due to the decomposition of the MWCNTs. According to the thermogram, the amount of sulfonic acid functionalized on the MWCNTs is ~8.29% (*w*/*w*). This result is in agreement with back-titration analysis.

Nitrogen adsorption isotherm

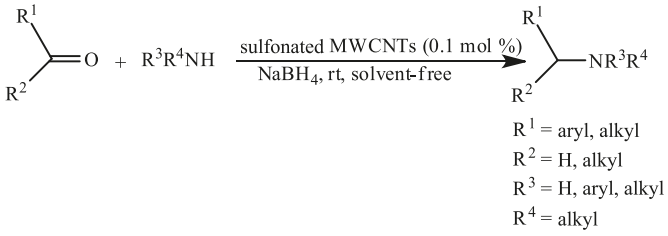
N_2 adsorption isotherms of the sulfonated MWCNTs and pure MWCNTs at 25 °C by using a homemade TGA system are shown in Fig. 6.

According to the N_2 adsorption isotherms, a significant increase (up to ~591 m^2 g^{-1}) in the active surface area of the MWCNTs was observed owing to the defects of the CNT matrix during the sulfonation process.

Fig. 6. Nitrogen adosorption isotherm of sulfonated multiwalled carbon nanotubes (MWCNTs, black) and MWCNTs (gray).



Scheme 1.



Catalytic activity of sulfonated MWCNTs in the one-pot synthesis of amines

As a part of our continuing research on the development of new applications of solid acids as heterogeneous catalysts in organic reactions,[31–34] we used sulfonated MWCNTs as a heterogeneous catalyst for the one-pot synthesis of amines by direct reductive amination of aldehydes and ketones (Scheme 1 and Table 1).

As shown in Table 1, substituted anilines or aliphatic (primary and secondary) amines underwent direct reductive amination with benzaldehyde and produced the corresponding secondary and tertiary amines in 75%–98% yields (Table 1, entries 1–8). In addition, the reaction of aniline with cyclopentanone and cyclohexanone gave high yields of the corresponding secondary amines (Table 1, entries 9 and 10).

In these transformations, turnover number (TON) and turnover frequency (TOF) were in the range of 750–980 and 830 – 11 160 h^{-1}, respectively, which demonstrates the high efficiency of sulfonated MWCNTs for the synthesis of a wide range of amines.

After performing the reductive amination of benzaldehyde with aniline under the conditions described in Table 1, EtOH was added to the reaction mixture and the catalyst was filtered off and reused for another reaction. This process was carried out for five runs without any noticeable reduction in the catalytic activity of the catalyst. The average isolated yield for at least five successive runs was 94.6%, which clearly demonstrates the practical reusability of the catalyst (Fig. 7).

Conclusion

In conclusion, sulfonated MWCNTs were synthesized via a new and facile one-pot method by CVD using acetylene (as

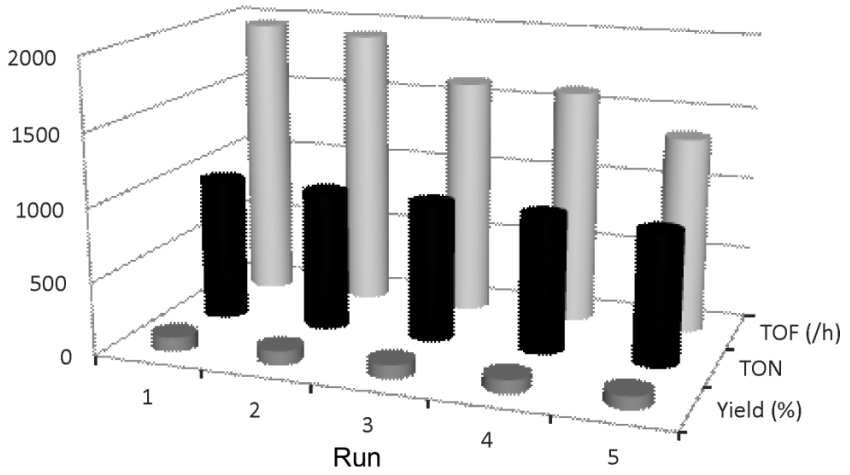
Can. J. Chem. Downloaded from www.nrcresearchpress.com by Renmin University of China on 09/02/12
For personal use only.

Table 1. Sulfonated multiwalled carbon nanotubes (MWCNTs) catalyzed direct reductive amination of aldehydes and ketones under solvent-free conditions at room temperature.

Entry	Amine	Carbonyl compound	Time (min)	Yield (%)[a]	TON[b]	TOF (h^{-1})[c]	δ_{C-H} (ppm)	δ_{C-H} (ppm) (ref.)
1	Aniline	Benzaldehyde	30	98	980	1960	4.57	4.30 (35)
2	3-Hydroxyaniline	Benzaldehyde	60	83	830	830	4.34	4.24 (36)
3	2-Methoxyaniline	Benzaldehyde	60	96	960	960	4.43	4.30 (35)
4	4-Methoxyaniline	Benzaldehyde	45	78	780	1040	4.34	4.22 (35)
5	4-Methylaniline	Benzaldehyde	15	95	950	3800	4.35	4.38 (37)
6	*n*-Butylamine	Benzaldehyde	5	93	930	11160	3.82	3.82 (38)
7	Dibutylamine	Benzaldehyde	15	94	940	3760	3.98	3.53 (35)
8	Piperidine	Benzaldehyde	5	75	750	9000	4.04	3.53 (38)
9	Aniline	Cyclopentanone	30	95	950	1900	3.70–3.83	3.72–3.81 (39)
10	Aniline	Cyclohexanone	30	94	940	1880	3.25–3.31	3.16–3.25 (39)

[a]Isolated yields. All of the products are known compounds and were identified by their physical and spectral data compared with reference samples.
[b]Turnover No. (TON) = mol product / mol catalyst.
[c]Turnover frequency (TOF) = TON/h.

Fig. 7. Recyclability of sulfonated multiwalled carbon nanotubes (MWCNTs) for the synthesis of benzyl phenylamine.



the CNT precursor), thiophene (as the sulfur precursor), and ferrocene (for in situ liberation of metal nanoparticles as the CNT nano catalyst). The synthesized sulfonated MWCNTs were applied as a new recyclable heterogeneous catalyst for the direct reductive amination of benzaldehyde and ketones with aromatic or aliphatic amines under solvent-free conditions at room temperature. Use of a small amount (0.1 mol %) of sulfonated MWCNTs as a water-tolerant and thermally stable catalyst, short reaction times, high yields, and recyclability of the catalyst without loss of reactivity for at least five reaction cycles are the remarkable properties of this work. Further investigations on the development of organic transformations using this new heterogeneous catalyst are ongoing in our laboratory.

Experimental section

Synthesis of sulfonated MWCNTs

Acetylene gas with a flow rate of ~50 mL min^{-1} was bubbled into a solution containing ferrocene (0.30 g) in benzene–thiophene (25 mL, volume ratio, 1:10). This solution was mixed with hydrogen and argon (flow rates = 0.5 and 800 mL min^{-1}, respectively). The resulting reaction mixture was introduced into a quartz tube and passed through a 80 cm tubing furnace with temperature of 1300 °C. The sulfur-doped carbon nanostructures were then directly purified from any amorphous carbon via oxygen purging and introducing hydrogen peroxide into the setup followed by online activation using UV and microwave (MW) irradiations.

General procedure for the reductive amination of aldehydes and ketones

An aldehyde or a ketone (5.0 mmol) was ground with a mixture of an amine (5.0 mmol) and sulfonated MWCNTs (0.1 mol %) in a mortar by a pestle at room temperature. $NaBH_4$ (5.5 mmol) was added to the resulting mixture, which was ground for an appropriate time (Table 1). EtOH (30 mL) was then added to the reaction mixture and the catalyst was filtered, washed by EtOH (2 × 20 mL), dried, and recycled for the similar reaction. The filtrate solvent was removed under reduced pressure and the resulting crude product was purified by column chromatography and eluted with *n*-hexane–EtOAc (20:1–2:1).

N-Benzylaniline

Yellow oil. ^1H NMR (400 MHz, $CDCl_3$, ppm) δ: 4.57 (s, 2H), 6.73–6.80 (m, 3H), 7.24–7.37 (m, 7H).

Can. J. Chem. Downloaded from www.nrcresearchpress.com by Renmin University of China on 09/02/12
For personal use only.

3-(Benzylamino)phenol

Brown oil. ^{1}H NMR (400 MHz, $CDCl_3$, ppm) δ: 4.34 (s, 2H), 6.15 (s, 1H), 6.22 (d, J = 7.6 Hz, 1H), 6.27 (d, J = 8.4 Hz, 1H), 7.053 (t, J = 8 Hz, 1H), 7.35–7.39 (m, 5H).

***N*-Benzyl-2-methoxyaniline**

Colorless oil. ^{1}H NMR (400 MHz, $CDCl_3$, ppm) δ: 3.92 (s, 3H), 4.43 (s, 2H), 4.71 (bs, 1H), 6.68 (d, J = 8 Hz, 1H), 6.77 (t, J = 7.6 Hz, 1H), 6.87 (d, J = 7.2 Hz, 1H), 6.92 (t, J = 7.6 Hz, 1H), 7.33–7.48 (m, 5H).

***N*-Benzyl-4-methoxyaniline**

Orange solid, mp 50–52 °C; crystallization solvent, *n*-hexane–EtOAc (20:1). ^{1}H NMR (400 MHz, $CDCl_3$, ppm) δ: 3.79 (s, 3H), 4.34 (s, 2H), 6.66 (d, J = 6.8 Hz, 2H), 6.84 (d, J = 6.8 Hz, 2H), 7.34 (d, J = 6.8 Hz, 1H), 7.39 (d, J = 7.6 Hz, 1H), 7.42–7.44 (m, 3H).

***N*-Benzyl-4-methylaniline**

Orange solid, mp 56–58 °C; crystallization solvent, *n*-hexane–EtOAc (20:1). ^{1}H NMR (400 MHz, $CDCl_3$, ppm) δ: 2.29 (s, 3H), 3.95 (bs, 1H), 4.35 (s, 2H), 6.61 (d, J = 8.0 Hz, 2H), 7.04 (d, J = 8.0 Hz, 2H), 7.31 (d, J = 7.2 Hz, 1H), 7.38 (d, J = 7.6 Hz, 1H), 7.40–7.43 (m, 3H).

***N*-Benzylbutan-1-amine**

Colorless oil. ^{1}H NMR (400 MHz, $CDCl_3$, ppm) δ: 0.94 (t, J = 7.2 Hz, 3H), 1.30–1.42 (m, 2H), 1.67–1.77 (m, 2H), 2.67–2.78 (m, 2H), 3.55 (bs, 1H), 3.82 (s, 2H), 7.31–7.35 (m, 2H), 7.39–7.45 (m, 3H).

***N*-Benzyl-di(*n*-butyl)amine**

Colorless oil. ^{1}H NMR (400 MHz, $CDCl_3$, ppm) δ: 0.99 (t, J = 7 Hz, 6H), 1.27–1.40 (m, 4H), 1.65–1.74 (m, 4H), 2.64 (t, J = 8.4 Hz, 4H), 3.98 (s, 2H), 7.28–7.44 (m, 5H).

***N*-Benzylpiperidine**

Yellow oil. ^{1}H NMR (400 MHz, $CDCl_3$, ppm) δ: 1.25–1.28 (m, 1H), 1.58–1.71 (m, 3H), 2.16–2.25 (m, 2H), 2.63–2.70 (m, 2H), 2.92–2.97 (m, 2H), 4.04 (s, 2H), 7.41–7.43 (m, 5H).

***N*-Cyclopentylaniline**

Yellow oil. ^{1}H NMR (400 MHz, $CDCl_3$, ppm) δ: 1.49–1.80 (m, 6H), 2.01–2.12 (m, 2H), 3.70–3.83 (m, 1H), 6.63 (d, J = 8.0 Hz, 2H), 6.70 (t, J = 6.4 Hz, 1H), 7.19 (t, J = 7.6 Hz, 2H).

***N*-Cyclohexylaniline**

Yellow oil. ^{1}H NMR (400 MHz, $CDCl_3$, ppm) δ: 1.17–1.43 (m, 5H), 1.66–1.70 (m, 1H), 1.77–1.82 (m, 2H), 2.07–2.10 (m, 2H), 3.25–3.31 (m, 1H), 6.62 (d, J = 7.6 Hz, 2H), 6.68 (t, J = 7.2 Hz, 1H), 7.18 (t, J = 7.6 Hz, 2H).

Acknowledgments

We are thankful to the Research Councils of the Shiraz and Birjand Universities for their support of this work.

References

(1) Lee, Y.; Ling, K. Q.; Lu, X.; Silverman, R. B.; Shepard, E. M.; Dooley, D. M.; Sayre, L. M. *J. Am. Chem. Soc.* **2002**, *124* (41), 12135. doi:10.1021/ja0205434.

(2) Gordon, E. M.; Barrett, R. W.; Dower, W. J.; Fodor, S. P. A.; Gallop, M. A. *J. Med. Chem.* **1994**, *37* (10), 1385. doi:10.1021/jm00036a001.

(3) Merla, B.; Risch, N. *Synthesis* **2002**, *2002* (10), 1365. doi:10.1055/s-2002-33121.

(4) Bradshaw, J. S.; Krakowiak, K. E.; Izatt, R. M. *Tetrahedron* **1992**, *48* (22), 4475. doi:10.1016/S0040-4020(01)81223-0.

(5) Lingaiah, N.; Babu, N. S.; Reddy, K. M.; Prasad, P. S. S.; Suryanarayana, I. *Chem. Commun.* **2007**, (3): 278. doi:10.1039/b613013e.

(6) Komeyama, K.; Morimoto, T.; Takaki, K. *Angew. Chem. Int. Ed.* **2006**, *45* (18), 2938. doi:10.1002/anie.200503789.

(7) Bae, J. W.; Cho, Y. J.; Lee, S. H.; Yoon, C.-O. M.; Yoon, C. M. *Chem. Commun.* **2000**, (19): 1857. doi:10.1039/b005194m.

(8) Gröger, H. *Chem. Rev.* **2003**, *103* (8), 2795. doi:10.1021/cr020038p.

(9) Borch, R. F.; Bernstein, M. D.; Durst, H. D. *J. Am. Chem. Soc.* **1971**, *93* (12), 2897. doi:10.1021/ja00741a013.

(10) Hutchins, R. O.; Markowitz, M. *J. Org. Chem.* **1981**, *46* (17), 3571. doi:10.1021/jo00330a048.

(11) Kim, S.; Oh, C. H.; Ko, J. S.; Ahn, K. H.; Kim, Y. J. *J. Org. Chem.* **1985**, *50* (11), 1927. doi:10.1021/jo00211a028.

(12) Mattson, R. J.; Pham, K. M.; Leuck, D. J.; Cowen, K. A. *J. Org. Chem.* **1990**, *55* (8), 2552. doi:10.1021/jo00295a060.

(13) Lee, O. Y.; Law, K. L.; Yang, D. *Org. Lett.* **2009**, *11* (15), 3302. doi:10.1021/ol901111g.

(14) Burkhardt, E. R.; Coleridge, B. M. *Tetrahedron Lett.* **2008**, *49* (35), 5152. doi:10.1016/j.tetlet.2008.06.095.

(15) Alinezhad, H.; Tajbakhsh, M.; Hamidi, N. *Chin. Chem. Lett.* **2010**, *21* (1), 47. doi:10.1016/j.cclet.2009.07.018.

(16) O'Connor, D.; Lauria, A.; Bondi, S. P.; Saba, S. H. *Tetrahedron Lett.* **2011**, *52* (1), 129. doi:10.1016/j.tetlet.2010.11.006.

(17) Zhang, M.; Yang, H.; Zhang, Y.; Zhu, C. H.; Li, W.; Cheng, Y.; Hu, H. *Chem. Commun. (Camb.)* **2011**, *47* (23), 6605. doi:10.1039/c1cc11201e.

(18) Gellerman, G.; Gaisin, V.; Brider, T. *Tetrahedron Lett.* **2010**, *51* (5), 836. doi:10.1016/j.tetlet.2009.12.020.

(19) Sheldon, R. A.; Van Bekkum, H. *Fine Chemicals through Heterogeneous Catalysis;* Wiley-VHC: Weinheim, Germany, 2001.

(20) Rajalakshmi, N.; Ryu, H.; Shaijumon, M. M.; Ramaprabhu, S. *J. Power Sources* **2005**, *140* (2), 250. doi:10.1016/j.jpowsour.2004.08.042.

(21) Liu, Z.; Gan, L. M.; Hong, L.; Chen, W.; Lee, J. Y. *J. Power Sources* **2005**, *139* (1–2), 73. doi:10.1016/j.jpowsour.2004.07.012.

(22) Xing, Y. *J. Phys. Chem. B* **2004**, *108* (50), 19255. doi:10.1021/jp046697i.

(23) Kim, H.; Subramanian, N. P.; Popov, B. N. *J. Power Sources* **2004**, *138* (1–2), 14. doi:10.1016/j.jpowsour.2004.06.012.

(24) Jiang, L.; Gao, L. *Carbon* **2003**, *41* (15), 2923. doi:10.1016/S0008-6223(03)00339-7.

(25) Peng, F.; Zhang, L.; Wang, H. J.; Lv, P.; Yu, H. *Carbon* **2005**, *43* (11), 2405. doi:10.1016/j.carbon.2005.04.004.

(26) Waje, M. M.; Wang, X.; Li, W.; Yan, Y. *Nanotechnology* **2005**, *16* (7), S395. doi:10.1088/0957-4484/16/7/013.

(27) Guo, D. J.; Li, H. L. *J. Electroanal. Chem.* **2004**, *573* (1), 197. doi:10.1016/S0022-0728(04)00369-9.

(28) Yang, S. D.; Zhang, X. G.; Mi, H. Y.; Ye, X. G. *J. Power Sources* **2008**, *175* (1), 26. doi:10.1016/j.jpowsour.2007.09.080.

(29) Du, C. Y.; Zhao, T. S.; Liang, Z. X. *J. Power Sources* **2008**, *176* (1), 9. doi:10.1016/j.jpowsour.2007.10.016.
(30) Kumar, M.; Ando, Y. *J. Nanosci. Nanotechnol.* **2010**, *10* (6), 3739. doi:10.1166/jnn.2010.2939.
(31) Sobhani, S.; Pakdin Parizi, Z.; Rezazadeh, S. *J. Organomet. Chem.* **2011**, *696* (3), 813. doi:10.1016/j.jorganchem.2010.10.015.
(32) Sobhani, S.; Rezazadeh, S. *J. Iran. Chem. Soc.* **2011**, *8* (1), 198.
(33) Sobhani, S.; Rezazadeh, S. *Synlett* **2010**, *2010* (10), 1485. doi:10.1055/s-0029-1220069.
(34) Sobhani, S.; Pakdin Parizi, Z.; Razavi, N. *Appl. Catal. A Gen.* **2011**, *409–410*, 162. doi:10.1016/j.apcata.2011.09.039.
(35) Cano, R.; Yus, M.; Ramón, D. J. *Tetrahedron* **2011**, *67* (42), 8079. doi:10.1016/j.tet.2011.08.063.
(36) Mittapelly, N.; Reguri, B. R.; Mukkanti, K. *Der Pharma Chemica* **2011**, *3* (4), 180.
(37) Tajbakhsh, M.; Hosseinzadeh, R.; Alinezhad, H.; Ghahari, S.; Heydari, A.; Khaksar, S. *Synthesis* **2011**, *2011* (3), 490. doi:10.1055/s-0030-1258384.
(38) Zhang, W.; Dong, X.; Zhao, W. *Org. Lett.* **2011**, *13* (19), 5386. doi:10.1021/ol202281h.
(39) Kawahara, R.; Fujita, K.; Yamaguchi, R. *Adv. Synth. Catal.* **2011**, *353* (7), 1161. doi:10.1002/adsc.201000962.

Can. J. Chem. Downloaded from www.nrcresearchpress.com by Renmin University of China on 09/02/12
For personal use only.

Theoretical study on the chemical formation mechanism of a β-myrcene ozonolysis reaction under atmospheric conditions

Yuyang Zhao, Jing Bai, Chenxi Zhang, Chen Gong, and Xiaomin Sun

Can. J. Chem. Downloaded from www.nrcresearchpress.com by Renmin University of China on 09/02/12
For personal use only.

Abstract: Density functional theory (DFT) was used to study the β-myrcene ozonolysis reaction. The reactants, intermediates, transition states, and products were optimized at the MPWB1K/6–31G(d,p) level. The single-point energies were performed at the MPWB1K/6–311+G(3df,2p) level. The profiles of the potential energy surfaces were constructed and the rate constants of the reaction steps were analyzed. The possible reaction mechanisms for the ozonolysis intermediates in real atmosphere are also discussed. Based on quantum chemistry information, the rate constants were calculated using Rice–Ramsperger–Kassel–Marcus (RRKM) theory and the canonical variational transition-state theory (CVT) with small curvature tunneling effect (SCT). Arrhenius equations of rate constants over the temperature range of 200–800 K are provided, and the lifetimes of the reaction species in the troposphere were estimated according to rate constants.

Key words: myrcene ozonolysis, DFT, RRKM theory, CVT/SCT, rate constant.

Résumé : On a fait appel à la théorie de la fonctionnelle de la densité (TFD) pour étudier la réaction d'ozonolyse du myrcène. On a optimisé les réactifs, les intermédiaires, les états de transition et les produits au niveau MPWB1K/6–31G(d,p) de la théorie. On a déterminé des énergies ponctuelles au niveau MPWB1K/6–311+G(3df,2p) de la théorie. On a construit les profils d'énergie potentielle et on a analyse des constantes de vitesse des diverses étapes réactionnelles. On discute aussi des mécanismes potentiels des intermédiaires d'ozonolyse dans un atmosphère réel. Sur la base des informations obtenues par la chimie quantique, on a calculé les constantes de vitesse à l'aide de la théorie de Rice–Ramsperger–Kassel–Marcus (RRKM) et de la théorie d'un état de transition variationnel et canonique (TVC) comportant un effet tunnel avec faible courbure (TFC). On a obtenu les équations d'Arrhenius des constantes de vitesse sur la plage de température allant de 200 à 800 K et on a évalué les temps de vie des espèces réactionnelles dans la troposphère à l'aide de ces constantes de vitesse.

Mots-clés : ozonolyse du myrcène, théorie de la fonctionnelle de la densité (TFD), théorie de RRKM, théorie d'un état de transition variationnel et canonique (TVC) comportant un effet tunnel avec faible courbure (TFC), constante de vitesse.

[Traduit par la Rédaction]

Introduction

β-Myrcene (7-methyl-3-methylene-1,6-octadiene) is an important member of the monoterpene family. Myrcene is produced by the mevalonic acid pathway of plants and emitted into the atmosphere through diffusion.[1]

Myrcene has three double bonds, including conjugated double bonds. It could easily react with O_3, OH, NO_3, and other species in the atmosphere and generate a series of oxidation products.[2] Ozonolysis of ethene, including the formation of primary and secondary ozonides, has been thoroughly researched with a theoretical method.[3–6] Several monoterpenes, including myrcene, reacted with ozone and hydroxyl radical to produce acetone at room temperature and 1 atm (1 atm = 101.325 kPa). The isobutenyl group of the monoterpenes might react with ozone to form acetone, which would account for the majority of the products in the first step of the reaction.[7,8] It has been reported that monoterpenes react more easily with O_3 than with the OH radical, and that the lifetime of myrcene is about 28 min under 50 ppb O_3.[9] The OH radicals, released from the gas-phase reactions of ozone with a series of monoterpenes, were scavenged by 2-butanol and reported to accelerate ozonolysis reactions to some extent.[10,11]

It was reported that three products, hydroxyacetone, formaldehyde, and acetone, were formed during the myrcene ozonolysis reaction.[12] Moreover, two kinds of mechanisms for the reaction between the Criegee intermediate and water were put forward.[13] The ozonolysis products of myrcene, such as 4-methylene-5-hexenal, were detected at room temperature.[14]

The gas-phase oxidation products and secondary organic aerosol yields from terpene reactions with ozone have been investigated experimentally. Wolkoff and co-workers[8,15–17] performed the experiment for the ozonolysis of monoterpenes and researched primary and secondary ozonides. The yield of

Received 21 March 2012. Accepted 9 May 2012. Published at www.nrcresearchpress.com/cjc on 8 August 2012.

Y. Zhao, J. Bai, C. Zhang, and C. Gong. Environment Research Institute, Shandong University, Jinan 250100, P.R. China.
X. Sun. Environment Research Institute, Shandong University, Jinan 250100, P.R. China; State Key Laboratory of Solid Lubrication, Lanzhou Institute of Chemical Physics, Chinese Academy of Science, Lanzhou 730000, P.R. China.

Corresponding author: Xiaomin Sun (e-mail: sxmwch@sdu.edu.cn).

Can. J. Chem. Downloaded from www.nrcresearchpress.com by Renmin University of China on 09/02/12
For personal use only.

aldehydes and ketones was reported and secondary organic aerosol yield (by mass, at 293 K) of the myrcene ozonolysis accounted for 11%. The ozonolysis aerosol yield of the terpenes with exocyclic double bonds, such as myrcene and linalool, was less than that of the one with endocyclic double bonds, such as limonene.[18] Up to now, no report has presented the calculation of the ozonolysis mechanisms of myrcene with the quantum chemistry method.

This paper is partially based on previous experimental data. A theoretical study was performed to reveal the reaction mechanisms of myrcene with ozone using the density functional theory (DFT) method. The thermodynamic parameters of the reaction steps, such as reaction barriers, enthalpies, and Gibbs free energies, were carefully analyzed. The rate constants were calculated using the Rice–Ramsperger–Kassel–Marcus (RRKM) theory and the canonical variational transition-state theory (CVT) with small curvature tunneling effect (SCT) (CVT/SCT) method, based on quantum chemistry information. Arrhenius equations of the rate constants with a temperature range of 200–800 K are given, and the lifetimes of the reaction species in the troposphere are estimated according to the rate constants.

Computational methods

Geometry optimization

DFT has become a powerful calculation tool because of its merits.[19,20] In this paper, the MPWB1K functional[21] and the 6–31G(d,p) basis set[22] were combined to optimize structures of stationary points and calculate vibrational frequencies. The single-point energies were determined at the MPWB1K/6–311+G(3df,2p) level. Each transition state was verified to connect the specific reactants with products by performing an intrinsic reaction coordinate (IRC) analysis. The profiles of potential energy surfaces were constructed. All work was carried out using the Gaussian 03 suite of programs.[23]

Kinetic calculation

Based on the geometry information from Gaussian output files, including coordinates, gradients, and force constants or Hessian matrix, the rate constants with the tunneling effects were calculated. The CVT/SCT effect correction is a useful method to calculate rate constants, which have been successfully applied to a great deal of research.[24–26] The RRKM method was used to calculate the rate constants of reactions that have no barrier or very low barriers. All kinetic calculations were carried out using the Polyrate 9.7 program[27] and the RRKM-TST program.[28]

In this paper, these methods were employed to study the rate constants of reaction steps over the range of 200–800 K and to discover the relationship between temperature and rate constants. It is obvious that most of the calculated rate constants can be fitted by Arrhenius equations, i.e., $k(T) = A \exp(-E_a/RT)$.

Results and discussion

The reactions of myrcene with O_3

The main possible channels of the myrcene ozonolysis reaction are provided in Fig. 1. Three main O_3 addition channels exist in myrcene ozonolysis reactions.

Reaction channel A of myrcene with O_3

The profile of the potential energy surface for myrcene ozonolysis channel A and subsequent reactions are provided in Fig. 2. In channel A, ozone is added to the C_1=C_2 double bond and forms a van der Waals complex (VdW) IM1, acting as a shallow well in the reaction. Then IM1 isomerizes to intermediate IM2 (primary ozonide, POZ) via transition state TS1 in rn. [1]; the reaction barrier and exothermic energy are 3.8 and 69.1 kcal mol^{-1} (1 cal = 4.184 J), respectively. In the subsequent reactions, two kinds of decomposition processes are identified from IM2. IM2 can decompose into IM3 and formaldehyde via transition state TS2 in rxn. [2]. Formaldehyde and its derivative formic acid have been detected in previous experiments.[18] The reaction barrier of this decomposition channel is 26.9 kcal mol^{-1}. Another reaction channel for IM2 exists, i.e., the decomposition of IM2 to P1 and CH_2O_2 via TS3 in rxn. [3]. The barrier is 28.1 kcal mol^{-1}, and 6.1 kcal mol^{-1} of energy was absorbed.

From the two competitive reactions, it can be concluded that rxn. [2] has a barrier 1.2 kcal mol^{-1} lower than that in rxn. [3]. The rate constant of rxn. [2] was calculated and proved to be larger than that of rxn. [3]. The geometry parameters are listed in Fig. 3.

Reaction channel B

The profile of the potential energy surface for myrcene ozonolysis channel B and subsequent reactions are provided in Fig. 4. The ozone addition channel B begins with the formation of IM4 (VdW), i.e., the association of O_3 and myrcene. Next, ozone is added to the C=C double bond in $>C_7$=$C_8(CH_3)_2$ via transition state TS4 and primary ozonide IM5 is formed in rxn. [4]. Channel B is similar to channel A. These two channels share two common traits, the formation of a five-membered ring adduct of myrcene with ozone and the carbonyl oxides, referring to Criegee intermediates (CH_2O_2, IM3, IM6, and $C_3H_6O_2$). The products consist of IM6 and acetone in rxn. [5] and P2 (4-methylene-5-hexenal) and $C_3H_6O_2$ in rxn. [6]. 4-Methylene-5-hexenal was reported by Reissell et al.[14] The geometry parameters are listed in Fig. 3, and the potential energy surface of channel B is provided in Fig. 4. The reaction channels are described in the following reactions (ΔE_b stands for barrier, and ΔE_r for reaction heat).

[1] $C_{10}H_{16} + O_3 \rightarrow IM4 \rightarrow TS4 \rightarrow IM5$
($\Delta E_b = 0.7$ kcal mol^{-1}, $\Delta E_r = -74.0$ kcal mol^{-1})

[2] $IM5 \rightarrow TS5 \rightarrow IM6 + C_3H_6O$
($\Delta E_b = 26.0$ kcal mol^{-1}, $\Delta E_r = -5.3$ kcal mol^{-1})

[3] $IM5 \rightarrow TS5 \rightarrow P2 + C_3H_6O_2$
($\Delta E_b = 24.8$ kcal mol^{-1}, $\Delta E_r = -8.6$ kcal mol^{-1})

Reaction channel C

The profile of the potential energy surface for myrcene ozonolysis channel C and subsequent reactions are provided in Fig. 5. The ozone addition channel C of myrcene is similar to channels A and B. After the barrierless association of myrcene and ozone to form IM7, the ozone is added to the

Fig. 1. The main possible reaction channels for the reaction of myrcene with O_3 and subsequent reactions.

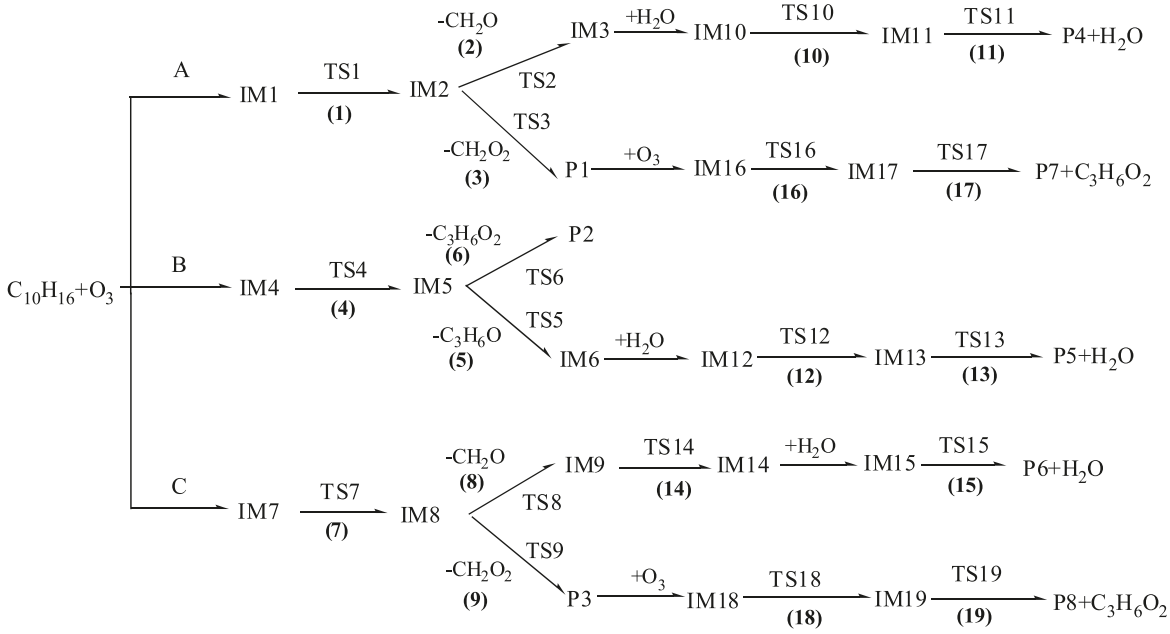
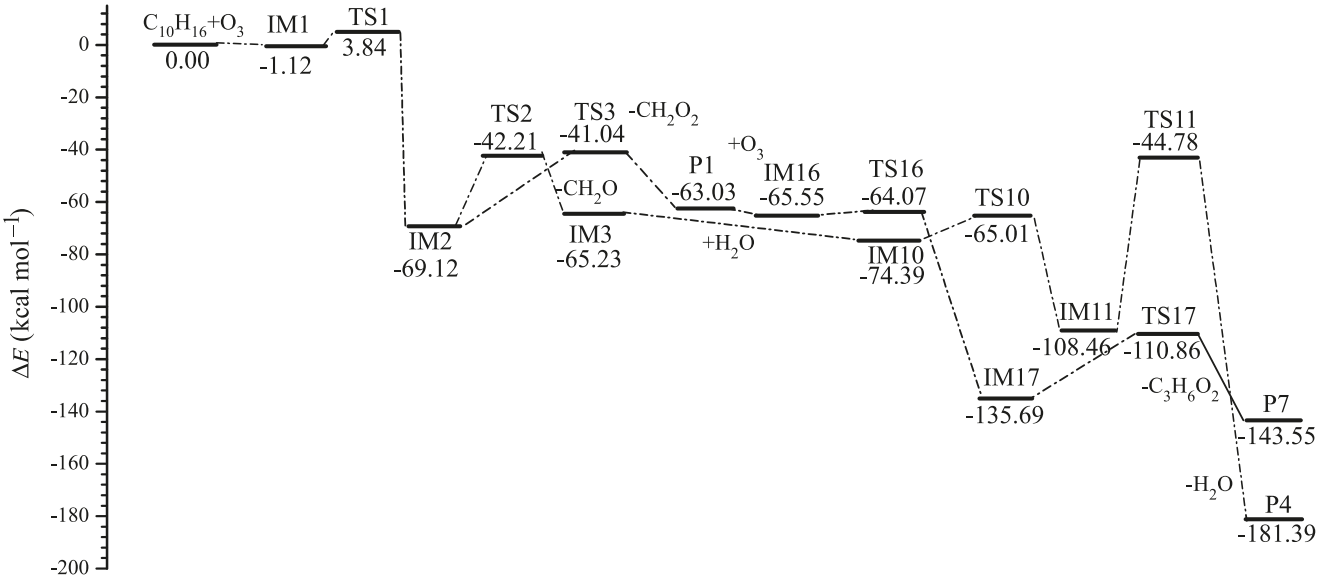


Fig. 2. The profile of the potential energy surface for myrcene ozonolysis channel A and subsequent reactions (energy unit, kcal mol^{-1}; 1 cal = 4.184 J).



C_3=C_4 double bond via transition state TS7 in rxn. [7], and primary ozonide IM8 was obtained. The subsequent competitive reactions produced IM9 (Criegee intermediate) and formaldehyde in rxn. [8] and P3 and CH_2O_2 in rxn. [9]. The geometry parameters are listed in Fig. 3. The reaction channels are given in the following reactions.

[4] $C_{10}H_{16} + O_3 \rightarrow IM7 \rightarrow TS7 \rightarrow IM5$
($\Delta E_b = 2.5$ kcal mol^{-1}, $\Delta E_r = -67.0$ kcal mol^{-1})

[5] $IM8 \rightarrow TS8 \rightarrow IM9 + CH_6O$
($\Delta E_b = 23.9$ kcal mol^{-1}, $\Delta E_r = -8.3$ kcal mol^{-1})

[6] $IM8 \rightarrow TS9 \rightarrow P3 + CH_2O_2$
($\Delta E_b = 29.7$ kcal mol^{-1}, $\Delta E_r = -0.4$ kcal mol^{-1})

Comparing reaction channels, we see that rxn. [8] has a lower barrier than rxn. [9]; therefore, rxn. [8] should have the larger rate constant at 298.13 K.

The subsequent reactions under atmospheric conditions

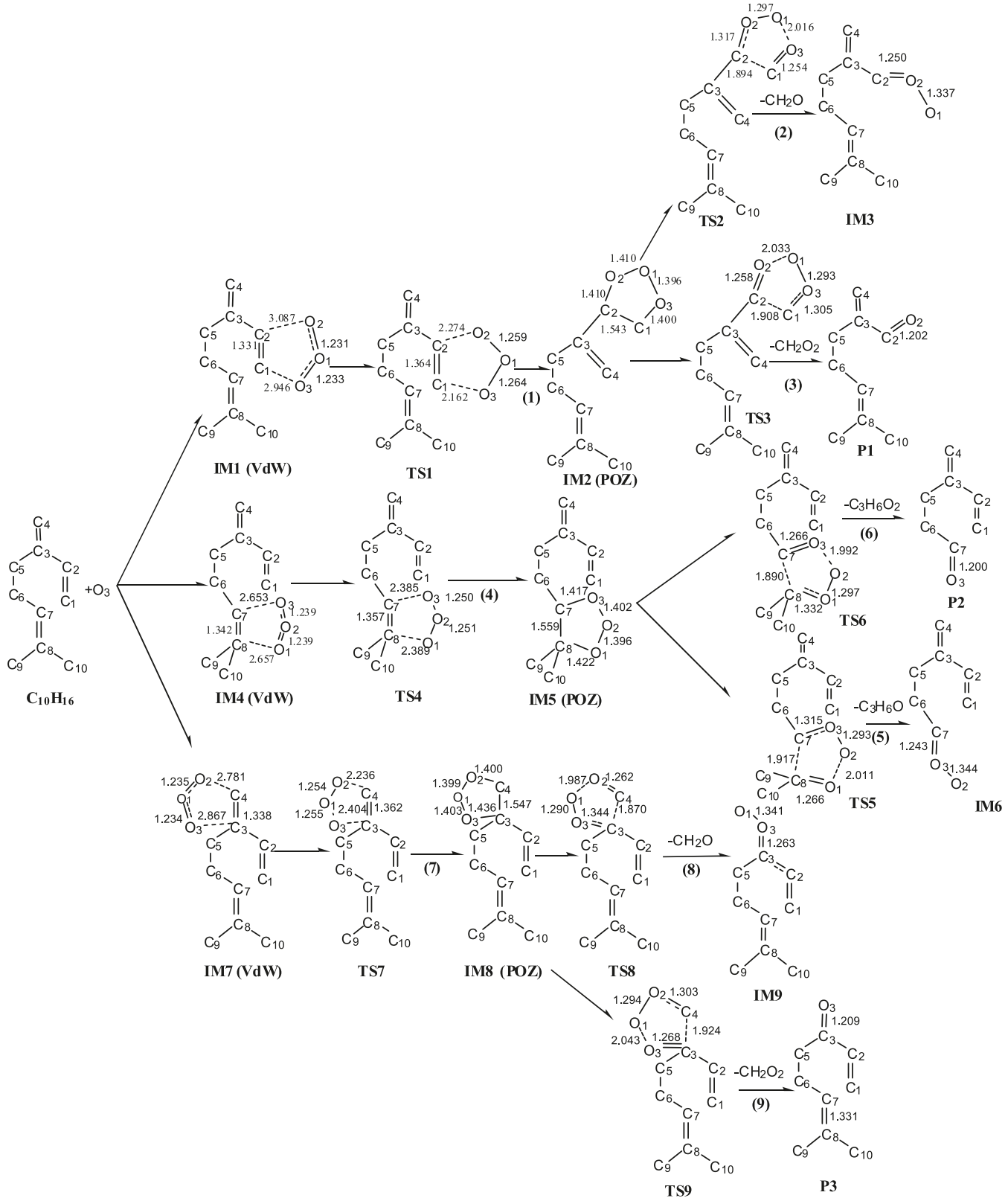
The reaction in the presence of H_2O

The H_2O molecule plays an important role in the secondary organic aerosol (SOA) formation.[29,30] The optimized geometries of the reactants, intermediates, transition states, and products for subsequent reactions of Criegee intermedi-

Can. J. Chem. Downloaded from www.nrcresearchpress.com by Renmin University of China on 09/02/12
For personal use only.

Can. J. Chem. Downloaded from www.nrcresearchpress.com by Renmin University of China on 09/02/12
For personal use only.

Fig. 3. The diagram of primary ozonide formation and subsequent decompositions.



ates with water are shown in Fig. 6. In channel A, the IM3 reacts with a H_2O molecule to form IM10 through a barrierless association, via transition state TS10 in rxn. [10]. An unstable hydroxyalkyl hydroperoxide (IM11) was formed (Fig. 6). Then, P4 was produced by removing an H_2O molecule from IM11 via transition state TS11 in rxn. [11]. This process includes the following details: after the rupture of the C_2–H_3 and O_2–O_1 bonds and the formation of the O_1–H_3

Fig. 4. The profile of the potential energy surface for myrcene ozonolysis channel B and subsequent reactions (energy unit, kcal mol^{-1}; 1 cal = 4.184 J).

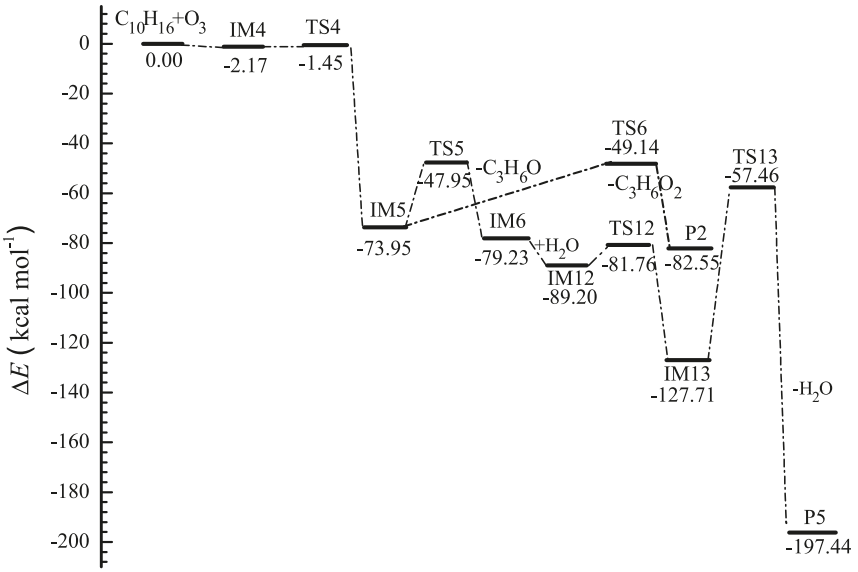
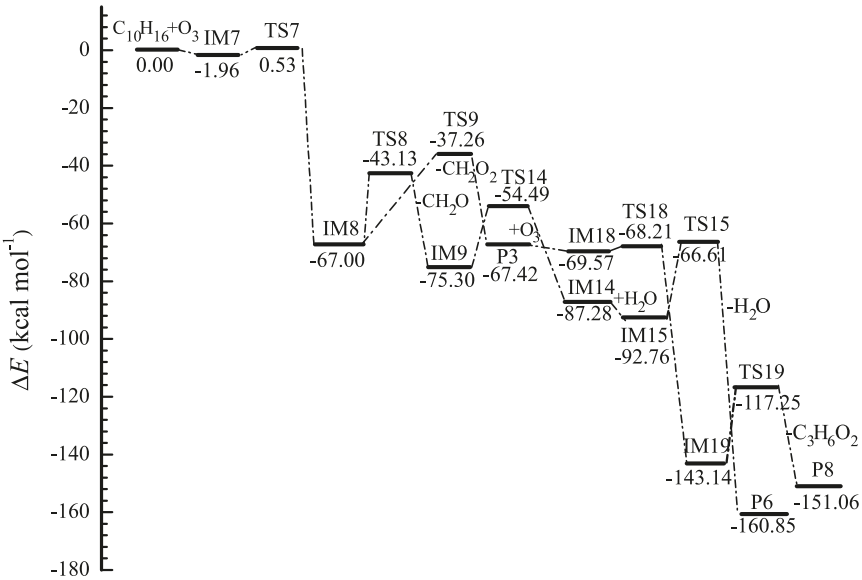


Fig. 5. The profile of the potential energy surface for myrcene ozonolysis channel C and subsequent reactions (energy unit, kcal mol^{-1}; 1 cal = 4.184 J).



bond, the O_1–H_1 hydroxyl group and the H_3 atom can form an H_2O molecule (Fig. 6). The result shows that the dehydration reaction has a higher reaction barrier than that of the H_2O addition reaction in rxn. [10]. It is implied that the dehydration reaction is the rate-determining reaction step. The profile of the potential energy surface is included in Fig. 2. The reaction channels are described in the following reactions.

[7] $\mathrm{IM3} + \mathrm{H_2O} \rightarrow \mathrm{IM10} \rightarrow \mathrm{TS10} \rightarrow \mathrm{IM11}$
($\Delta E_b = 9.4$ kcal mol^{-1}, $\Delta E_r = -34.1$ kcal mol^{-1})

[8] $\mathrm{IM11} \rightarrow \mathrm{TS11} \rightarrow \mathrm{P4} + \mathrm{H_2O}$
($\Delta E_b = 63.7$ kcal mol^{-1}, $\Delta E_r = -72.9$ kcal mol^{-1})

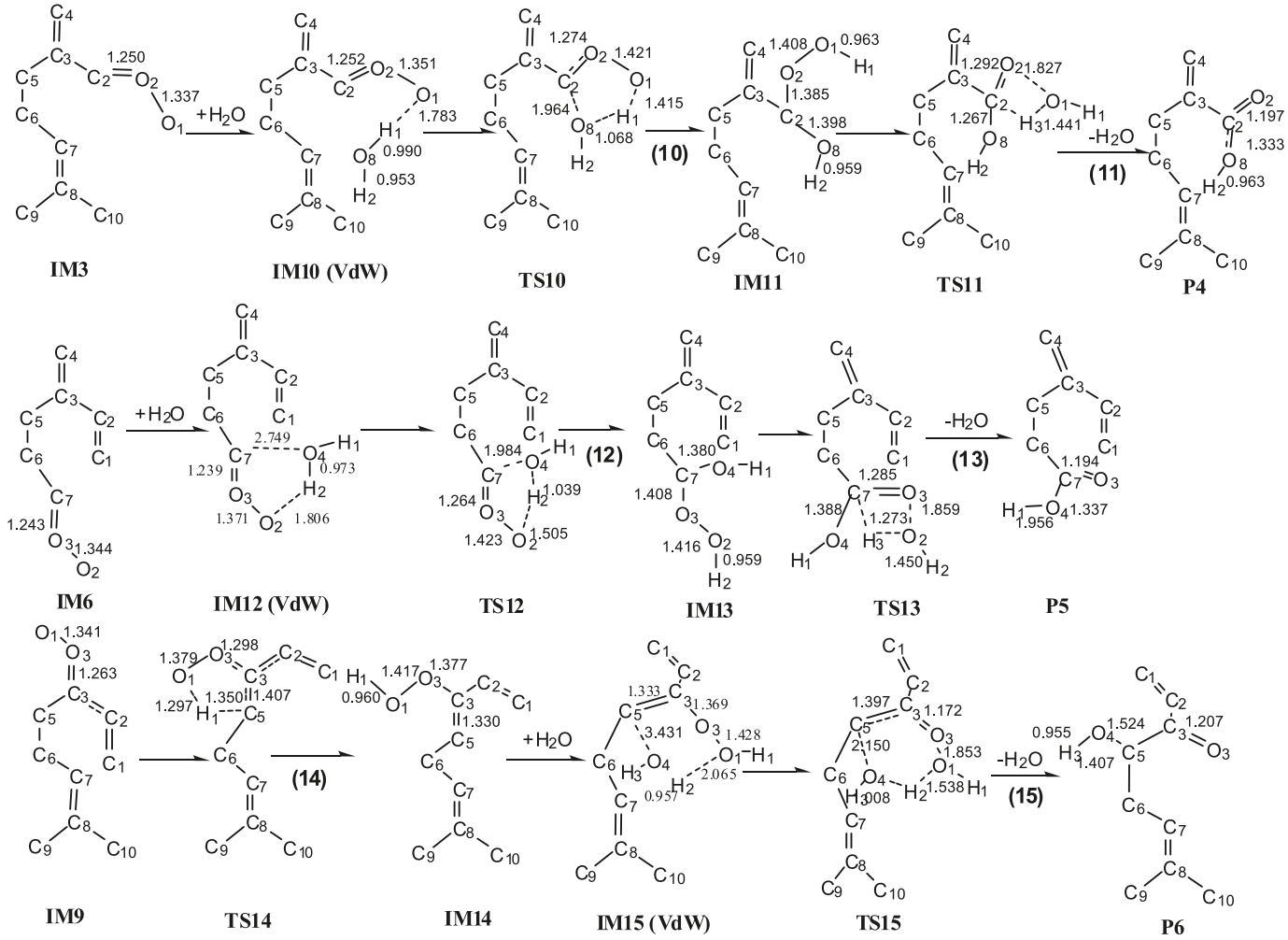
In channel B, IM6 can associate with a water to produce IM12 (VdW). In TS12, the O_4 atom of H_2O transfers to the C_7 atom and the H_2 atom of the H_2–O_4 tends to link to the O_2 atom. IM13 is obtained via TS12. Similarly, a H_2O is removed and P5 is obtained via TS13 in rxn. [13]. P5 is a carboxylic acid with two unsaturated double bonds (Fig. 6). The potential energy surface is shown in Fig. 4. The reaction channels are described by

[9] $\mathrm{IM6} + \mathrm{H_2O} \rightarrow \mathrm{IM12} \rightarrow \mathrm{TS12} \rightarrow \mathrm{IM13}$
($\Delta E_b = 7.4$ kcal mol^{-1}, $\Delta E_r = -38.5$ kcal mol^{-1})

[10] $\mathrm{IM13} \rightarrow \mathrm{TS13} \rightarrow \mathrm{P5} + \mathrm{H_2O}$
($\Delta E_b = 70.3$ kcal mol^{-1}, $\Delta E_r = -69.7$ kcal mol^{-1})

Can. J. Chem. Downloaded from www.nrcresearchpress.com by Renmin University of China on 09/02/12
For personal use only.

Fig. 6. The diagram of subsequent reactions of Criegee intermediates with water.



As for channel C, intramolecular hydrogen migration takes place in IM9, i.e., the H1 atom conjoined to the C_5 atom transfers to the O_1 atom via transition state TS14 in rxn. [14]. IM14 is associated with an H_2O, which forms IM15 (VdW), and then another H_2O and the product P6 are obtained via transition state TS15 in rxn. [15] (Fig. 6). The potential energy surface is shown in Fig. 5. The detailed reaction mechanism is represented by

[11] $\text{IM9} \rightarrow \text{TS14} \rightarrow \text{IM14}$
$(\Delta E_b = 20.8 \text{ kcal mol}^{-1},\ \Delta E_r = -12.0 \text{ kcal mol}^{-1})$

[12] $\text{IM14} + H_2O \rightarrow \text{IM15} \rightarrow \text{TS13} \rightarrow \text{P6} + H_2O$
$(\Delta E_b = 20.7 \text{ kcal mol}^{-1},\ \Delta E_r = -73.6 \text{ kcal mol}^{-1})$

The reaction in the presence of excessive O_3

The double bond in product P1 can also react with oxidizing species in the atmosphere. The reaction mechanism between ozone and P1 is presented in the following discussion. IM16, a VdW complex of ozone and P1, is used as the subsequent reactant. Next, an ozone molecule is added to the isobutenyl double bond, generating a primary ozonide IM17 via transition state TS16 in rxn. [16]. IM17 is ruptured via transition state TS17 and then P7 and $C_3H_6O_2$ are obtained. The profile of the potential energy surface is shown in Fig. 2. The reaction channels are represented by

[13] $\text{P1} + O_3 \rightarrow \text{IM16} \rightarrow \text{TS16} \rightarrow \text{IM17}$
$(\Delta E_b = 1.5 \text{ kcal mol}^{-1},\ \Delta E_r = -70.1 \text{ kcal mol}^{-1})$

[14] $\text{IM17} \rightarrow \text{TS17} \rightarrow \text{P7} + C_3H_6O_2$
$(\Delta E_b = 24.8 \text{ kcal mol}^{-1},\ \Delta E_r = -7.9 \text{ kcal mol}^{-1})$

To continue the reactions in channel C, another molecule of ozone can be added to the $>C_7{=}C_8(CH_3)_2$ double bond in P3. The profile of the potential energy surface is shown in Fig. 5. The subsequent reactions (rxns. [18] and [19]) are described by

[15] $\text{P3} + O_3 \rightarrow \text{IM18} \rightarrow \text{TS18} \rightarrow \text{IM19}$
$(\Delta E_b = 1.4 \text{ kcal mol}^{-1},\ \Delta E_r = -73.6 \text{ kcal mol}^{-1})$

[16] $\text{IM19} \rightarrow \text{TS19} \rightarrow \text{P8} + C_3H_6O_2$
$(\Delta E_b = 25.9 \text{ kcal mol}^{-1},\ \Delta E_r = -7.9 \text{ kcal mol}^{-1})$

The final products presented in the previous discussion can be categorized into four groups, including aldehydes (P1, P2,

Can. J. Chem. Downloaded from www.nrcresearchpress.com by Renmin University of China on 09/02/12
For personal use only.

Table 1. The rate constants of the rxns. [4]–[6], [12], and [13] for channel B with the canonical variational transition-state theory (CVT) with small curvature tunneling effect (SCT) (CVT/SCT) method at 200–800 K.

	Rate constant				
T (K)	rxn. [4] (cm^3 $molecule^{-1}$ s^{-1})	rxn. [5] (s^{-1})	rxn. [6] (s^{-1})	rxn. [12] (cm^3 $molecule^{-1}$ s^{-1})	rxn. [13] (s^{-1})
200	5.73×10^{-21}	1.01×10^{-14}	1.21×10^{-13}	2.95×10^{-14}	5.58×10^{-61}
220	1.73×10^{-20}	2.58×10^{-12}	2.39×10^{-11}	2.53×10^{-14}	2.27×10^{-54}
240	4.42×10^{-20}	2.66×10^{-10}	1.98×10^{-9}	2.22×10^{-14}	7.34×10^{-49}
260	9.90×10^{-20}	1.36×10^{-8}	8.39×10^{-8}	2.00×10^{-14}	3.39×10^{-44}
280	2.00×10^{-19}	3.99×10^{-7}	2.10×10^{-6}	1.82×10^{-14}	3.39×10^{-40}
298.15	3.51×10^{-19}	5.84×10^{-6}	2.70×10^{-5}	1.70×10^{-14}	4.99×10^{-37}
320	6.49×10^{-19}	9.92×10^{-5}	4.01×10^{-4}	1.58×10^{-14}	1.09×10^{-33}
340	1.07×10^{-18}	9.69×10^{-4}	3.51×10^{-3}	1.49×10^{-14}	5.22×10^{-31}
360	1.68×10^{-18}	7.37×10^{-3}	2.42×10^{-2}	1.42×10^{-14}	1.27×10^{-28}
380	2.54×10^{-18}	4.55×10^{-2}	1.31×10^{-1}	1.37×10^{-14}	1.73×10^{-26}
400	3.72×10^{-18}	1.84×10^{-1}	6.19×10^{-1}	1.10×10^{-14}	1.45×10^{-24}
450	8.52×10^{-18}	5.85×10	1.67×10^{-1}	1.04×10^{-14}	1.67×10^{-20}
500	1.71×10^{-17}	9.37×10^{1}	2.35×10^{2}	1.01×10^{-14}	3.01×10^{-17}
550	3.11×10^{-17}	9.20×10^{2}	2.06×10^{3}	9.94×10^{-15}	1.40×10^{-14}
600	5.23×10^{-17}	6.21×10^{3}	1.27×10^{4}	9.98×10^{-15}	2.34×10^{-12}
650	8.29×10^{-17}	3.13×10^{4}	5.90×10^{4}	1.02×10^{-14}	1.81×10^{-10}
700	1.25×10^{-16}	1.26×10^{5}	2.21×10^{5}	1.04×10^{-14}	7.57×10^{-9}
750	1.81×10^{-16}	4.19×10^{5}	6.98×10^{5}	1.08×10^{-14}	1.93×10^{-7}
800	2.54×10^{-16}	1.20×10^{6}	1.91×10^{6}	1.12×10^{-14}	3.31×10^{-6}

Note: Arrhenius equations for the reactions: rxn. [4], $k = 5.34 \times 10^{-15}$ exp(–2830.18/T) for this work and $k = 2.21 \times 10^{-15}$exp[–(520 ± 109)/T] in a previous experiment (ref. 31); rxn. [5], $k = 5.07 \times 10^{12}$ exp(–12312/T); rxn. [6], $k = 4.18 \times 10^{12}$ exp(–11788/T); rxn. [12], $k = 6.25 \times 10^{-15}$ exp(299.85/T); rxn. [13], $k = 4.96 \times 10^{12}$ exp(–33623/T).

and P7), ketones (P3), carboxylic acid (P4 and P5), ketone with a hydroxyl group (P6) and ketone with an aldehyde group (P8). P2 ($C_7H_{10}O$) (4-methylene-5-hexenal) has been detected in previous experiments[18] and proved to exist in the atmosphere. Further investigation into secondary ozonide (SOZ) formation is needed. The NO oxygen abstraction reaction with hydrocarbon peroxide is possible in urban areas with the NO_x pollutants from automobile exhaust.

Rate constants

The rate constant results achieved with the CVT/SCT method are reported for the five reaction steps in reaction channel B and listed in Table 1.

In this discussion, the barriers for all types of ozone addition reactions are low, but the rate constants of rxn. [4] are not high enough in contrast to the result from the experiments of Kim et al.[31] As one of the possible reasons, the energy released from the POZ formation was not considered for the subsequent decompositions in the Polyrate 9.7 and RRKM-TST programs. The magnitudes of the rate constants for decomposition rxns. [5] and [6] are 10^{-6} and 10^{-5}, respectively, at room temperature. It can be concluded that the rate constants of the IMb2 (POZ) rupture stay at a moderate level if calculated as an individual reaction.

The barrier for H_2O addition in rxn. [12] is low and the rate constant is 1.70×10^{-14} cm^3 $molecule^{-1}$ s^{-1} at room temperature. The rate constants of rxn. [13] are so low that it may take a long time for this dehydration reaction to complete. But this reaction can release a large amount of heat. Further research is still needed to get the dehydration mechanism to proceed in real conditions.

The equations for the rate constants are shown in the note for Table 1. The correlative coefficient R^2 is above 0.994. These equations are beneficial for the kinetic study of the ozonolysis of volatile terpenes. Based on experiment data, the Arrhenius equation for the gas-phase reaction of β-myrcene and ozone,[29] over the temperature range of 298∼318 K and 1 atm, was reported in previous research:[29]

$$k = (2.21^{+0.94}_{-0.66}) \times 10^{-15} \exp[-(520 \pm 109)/T]$$

where the rate constant k is in units of cm^3 $molecule^{-1}$ s^{-1} and the temperature T is in Kelvin.

The lifetimes of the reactants in rxns. [4]–[6], [12], and [13] were obtained over the range of 200–800 K and are listed in Table S3 of the Supplementary data.

Conclusions

1. The three reaction barriers in POZ formation for myrcene are different from each other. The reaction in the >C=C(CH_3)$_2$ site may take up a larger proportion than those in stable conjugated double bonds, which is also supported in the experiments.
2. The Criegee intermediates, such as CH_2O_2 and $C_3H_6O_2$, are formed in the myrcene ozonolysis mechanisms.
3. In the water addition reactions, H_2O acts as the catalyst of the OH migration and may promote the reactions to happen faster.
4. The barrier of ozone addition in POZ formation is low. However, the CVT/SCT rate constants are low. The barriers of the water addition to carbonyl oxides (Criegee intermediates) are low and the reactions tend to occur. However, the dehydration reaction of unstable hydroxyalkyl hydroperoxides formed by water addition has to overcome such a high barrier that the reaction occurs with difficulty. An alternative reaction channel for Criegee intermediates may exist, such as the formation of OH radicals to accelerate the reaction.

Can. J. Chem. Downloaded from www.nrcresearchpress.com by Renmin University of China on 09/02/12
For personal use only.

Can. J. Chem. Downloaded from www.nrcresearchpress.com by Renmin University of China on 09/02/12
For personal use only.

Supplementarydata

Supplementary data are available with the article through the journal Web site http://nrcresearchpress.com/doi/suppl/10.1139/v2012-050.

Acknowledgments

This work was supported financially by the National Nature Science Foundation of China (Grant Nos. 20977059 and 20903062), the National High Technology Research and Development Program 863 Project (2012AA06A301), the Independent Innovation Foundation of Shandong University (IIFSDU, 2010TS064), and the Open Project from the State Key Laboratory of Environmental Chemistry and Ecotoxicology, Research Center for Eco-Environmental Sciences, Chinese Academy of Sciences (No. KF2009-10).

References

(1) Lerdau, M.; Guenther, A.; Monson, R. *Bioscience* **1997**, *47* (6), 373. doi:10.2307/1313152.

(2) Atkinson, R.; Aschmann, S. M.; Winer, A. M.; Pitts, J. N. *Environ. Sci. Technol.* **1985**, *19* (2), 159. doi:10.1021/es00132a009.

(3) Anglada, J. M.; Crehuet, R.; Bofill, J. M. *Chem. Eur. J.* **1999**, *5* (6), 1809. doi:10.1002/(SICI)1521-3765(19990604)5:6<1809::AID-CHEM1809>3.0.CO;2-N.

(4) Ljubić, I.; Sabljić, A. *J. Phys. Chem. A* **2002**, *106* (18), 4745. doi:10.1021/jp025562e.

(5) Ljubić, I.; Sabljić, A. *Chem. Phys.* **2005**, *309* (2–3), 157. doi:10.1016/j.chemphys.2004.09.003.

(6) Ljubić, I.; Sabljić, A. *J. Phys. Chem. A* **2005**, *109* (10), 2381. doi:10.1021/jp044706h.

(7) Reissell, A.; Harry, C.; Aschmann, S. M.; Atkinson, R.; Arey, J. *J. Geophys. Res.* **1999**, *104* (D11), 13869. doi:10.1029/1999JD900198.

(8) Vibenholt, A.; Nørgaard, A. W.; Clausen, P. A.; Wolkoff, P. *Chemosphere* **2009**, *76* (4), 572. doi:10.1016/j.chemosphere.2009.02.060.

(9) Lee, A.; Schade, G.; Holzinger, R.; Goldstein, A. *Atmos. Chem. Phys.* **2005**, *5* (2), 505. doi:10.5194/acp-5-505-2005.

(10) Aschmann, S. M.; Arey, J.; Atkinson, R. *Atmos. Environ.* **2002**, *36* (27), 4347. doi:10.1016/S1352-2310(02)00355-2.

(11) Holzinger, R.; Lee, A.; Paw, K.; Goldstein, U. *Atmos. Chem. Phys.* **2005**, *5* (1), 67. doi:10.5194/acp-5-67-2005.

(12) Ruppert, L.; Plagens, H.; Becker, K. H.; Hjorth, J.; Jensen, N.; Virkkula, A.; vanDingenen, R.; Wirtz, K.; Horie, O.; Neeb, P.; Winterhalter, R. Product and Aerosol Formation from the Ozonolysis of Monoterpenes. In Workshop on Biogenic Hydrocarbons in the Atmospheric Boundary Layer, University of Virginia, 24–27 August 1997; Fuentes, J.D., Ed.; 1997; pp 127–130.

(13) Calogirou, A.; Larsen, B. R.; Kotzias, D. *Atmos. Environ.* **1999**, *33* (9), 1423. doi:10.1016/S1352-2310(98)00277-5.

(14) Reissell, A.; Aschmann, S. M.; Atkinson, R.; Arey, J. *J. Geophys. Res.* **2002**, *107* (D12), 4138. doi:10.1029/2001JD001234.

(15) Wolkoff, P.; Clausen, P. A.; Wilkins, C. K.; Nielsen, G. D. *Indoor Air* **2000**, *10* (2), 82. doi:10.1034/j.1600-0668.2000.010002082.x.

(16) Nørgaard, A. W.; Nøjgaard, J. K.; Larsen, K.; Sporring, S.; Wilkins, C. K.; Clausen, P. A.; Wolkoff, P. *Atmos. Environ.* **2006**, *40* (19), 3460. doi:10.1016/j.atmosenv.2006.02.007.

(17) Nøjgaard, J. K.; Nørgaard, A. W.; Wolkoff, P. *Atmos. Environ.* **2007**, *41* (37), 8345. doi:10.1016/j.atmosenv.2007.06.019.

(18) Lee, A.; Goldstein, A. H.; Keywood, M. D.; Gao, S.; Varutbangkul, V.; Bahreini, R.; Ng, N. L.; Flagan, R. C.; Seinfeld, J. H. *J. Geophys. Res.* **2006**, *111* (D7),o. D07302. doi:10.1029/2005JD006437.

(19) Kohn, W. Overview of Density Functional Ttheory. In *Density Functional Theory;* Gross, E. K. U., Dreizler, R. M., Eds.; Plenum Press: New York, 1995; pp 3–10.

(20) McDowell, S. A. C.; Amos, R. D.; Handy, N. C. *Chem. Phys. Lett.* **1995**, *235* (1–2), 1. doi:10.1016/0009-2614(95)00076-G.

(21) Zhao, Y.; Truhlar, D. G. *J. Phys. Chem. A* **2004**, *108* (33), 6908. doi:10.1021/jp048147q.

(22) Hariharan, P. C.; Pople, J. A. *Theor. Chim. Acta* **1973**, *28* (3), 213. doi:10.1007/BF00533485.

(23) Frisch, M. J.; Trucks, G. W.; Schlegel, H. B.; Scuseria, G. E.; Robb, M. A.; Cheeseman, J. R.; Montgomery, J. A., Jr.; Vreven, T.; Kudin, K. N.; Burant, J. C.; Millam, J. M.; Iyengar, S. S.; Tomasi, J.; Barone, V.; Mennucci, B.; Cossi, M.; Scalmani, G.; Rega, N.; Petersson, G. A.; Nakatsuji, H.; Hada, M.; Ehara, M.; Toyota, K.; Fukuda, R.; Hasegawa, J.; Ishida, M.; Nakajima, T.; Honda, Y.; Kitao, O.; Nakai, H.; Klene, M.; Li, X.; Knox, J. E.; Hratchian, H. P.; Cross, J. B.; Bakken, V.; Adamo, C.; Jaramillo, J.; Gomperts, R.; Stratmann, R. E.; Yazyev, O.; Austin, A. J.; Cammi, R.; Pomelli, C.; Ochterski, J. W.; Ayala, P. Y.; Morokuma, K.; Voth, G. A.; Salvador, P.; Dannenberg, J. J.; Zakrzewski, V. G.; Dapprich, S.; Daniels, A. D.; Strain, M. C.; Farkas, O.; Malick, D. K.; Rabuck, A. D.; Raghavachari, K.; Foresman, J. B.; Ortiz, J. V.; Cui, Q.; Baboul, A. G.; Clifford, S.; Cioslowski, J.; Stefanov, B. B.; Liu, G.; Liashenko, A.; Piskorz, P.; Komaromi, I.; Martin, R. L.; Fox, D. J.; Keith, T.; Al-Laham, M. A.; Peng, C. Y.; Nanayakkara, A.; Challacombe, M.; Gill, P. M. W.; Johnson, B.; Chen, W.; Wong, M. W.; Gonzalez, C.; Pople, J. A. *Gaussian 03,* Revision E.01; Gaussian, Inc.: Wallingford, CT, 2004.

(24) Miller, W. H. *J. Am. Chem. Soc.* **1979**, *101* (23), 6810. doi:10.1021/ja00517a004.

(25) Zhang, Q. Z.; Zhang, R. Q.; Chan, K. S.; Bello, I. *J. Phys. Chem. A* **2005**, *109* (40), 9112. doi:10.1021/jp0531661.

(26) Zhang, Q. Z.; Zhang, R. Q.; Gu, Y. S. *J. Phys. Chem. A* **2004**, *108* (6), 1064. doi:10.1021/jp036446u.

(27) Corchado, J. C.; Chuang, Y. Y.; Fast, P. L.; Hu, W. P.; Liu, Y. P.; Lynch, G. C.; Nguyen, K. A.; Jackels, C. F.; Fernandez Ramos, A.; Ellingson, B. A.; Lynch, B. J.; Zheng, J.; Melissas, V. S.; Villà, J.; Rossi, I.; Coitiño, E. L.; Pu, J.; Albu, T.; Steckler, R.; Garrett, B. C.; Isaacson, A. D.; Truhlar, D. G. *Polyrate,* vVersion 9.7; University of Minnesota: Minneapolis, MN, 2007.

(28) Hou, H.; Wang, B. *J. Phys. Chem. A* **2007**, *127*, 054306.

(29) Cocker, D. R., III; Clegg, S. L.; Flagan, R. C.; Seinfeld, J. H. *Atmos. Environ.* **2001**, *35* (35), 6049. doi:10.1016/S1352-2310(01)00404-6.

(30) Seinfeld, J. H.; Erdakos, G. B.; Asher, W. E.; Pankow, J. F. *Environ. Sci. Technol.* **2001**, *35* (9), 1806. doi:10.1021/es001765+.

(31) Kim, D.; Stevens, P. S.; Hites, R. A. *J. Phys. Chem. A* **2011**, *115* (4), 500. doi:10.1021/jp111173s.

Monte Carlo simulation of the radiolysis of the ceric sulfate dosimeter by low linear energy transfer radiation

Ianik Plante, Thititip Tippayamontri, Narongchai Autsavapromporn, Jintana Meesungnoen, and Jean-Paul Jay-Gerin

Can. J. Chem. Downloaded from www.nrcresearchpress.com by UNIVERSITAT DE VALENCIA on 10/20/12
For personal use only.

Abstract: The ceric sulfate dosimeter is based on the radio-induced reduction of Ce^{4+} in acidic medium. For low linear energy transfer (LET) radiation, the yield of Ce^{3+} is 2.4 molecules / 100 eV, regardless of the presence of oxygen. To investigate the reaction mechanisms of the ceric sulfate dosimeter, we simulated the chemical reaction kinetics curves and the evolution of $G(Ce^{3+})$, $G(O_2)$, and $G(H_2)$ in the ceric sulfate solution with and without oxygen. Studies of $G(Ce^{3+})$ as function of the initial concentration of Ce^{3+} and of the LET were also done. One important finding of this study is that $^{\bullet}OH$ radicals are scavenged by the reaction $^{\bullet}OH + HSO_4^- \rightarrow SO_4^{\bullet-} + H_2O$, rather than by the reaction $^{\bullet}OH + Ce^{3+} \rightarrow Ce^{4+} + OH^-$.

Key words: ceric sulfate dosimeter, radiolysis, free-radical and molecular yields, linear energy transfer (LET), Monte Carlo simulations.

Résumé : Le dosimètre cérique est basé sur la réduction radio-induite de Ce^{4+} en milieu acide. Pour les radiations de faible transfert d'énergie linéaire (TEL), le rendement de Ce^{3+} est 2,4 molécules / 100 eV, indépendamment de la présence d'oxygène. Pour étudier les mécanismes du dosimètre cérique, nous avons simulé l'évolution temporelle de $G(Ce^{3+})$, $G(O_2)$ et $G(H_2)$ dans une solution de sulfate cérique avec et sans oxygène. Des études des rendements en fonction de la concentration initiale de Ce^{3+} et du TEL ont également été réalisées. Une découverte importante de cette étude est que les radicaux $^{\bullet}OH$ sont captés par la réaction $^{\bullet}OH + HSO_4^- \rightarrow SO_4^{\bullet-} + H_2O$, plutôt que par la réaction $^{\bullet}OH + Ce^{3+} \rightarrow Ce^{4+} + OH^-$.

Mots-clés : dosimètre cérique, radiolyse, rendements radicalaires et moléculaires, transfert d'énergie linéaire (TEL), simulations Monte Carlo.

Introduction

The ceric sulfate dosimeter has been extensively studied and widely accepted. In fact, the International Commission on Radiological Units and Measurements rated this system as the next most useful to the ferrous sulfate dosimeter and recommended its use as a reference standard for radiation doses exceeding 500 Gy.[1] This dosimeter is based on the reduction of Ce^{4+} in acidic medium by the oxidizing species produced by the radiolysis of water. The yield (the number of molecules created or destroyed)[2] of Ce^{3+} for low linear energy transfer (LET) radiations is ~2.4 molec. / 100 eV of deposited energy, regardless of the presence or absence of oxygen.[3] The purpose of this work is to study the reaction mechanisms and kinetics occurring in the ceric sulfate dosimeter.

Experimentally, optimal results are obtained by using a solution of 0.4 mol/L H_2SO_4, 3×10^{-5} mol/L of Ce^{4+}, and 1×10^{-5} mol/L of Ce^{3+}.[3] The irradiation of the system leads to the production of radiolytic species such as $H^{\bullet}$, $^{\bullet}OH$, H_2, H_2O_2, e^-_{aq}, $HO_2^{\bullet}/O_2^{-\bullet}$.[4] Following their formation, these species chemically react with each other during the nonhomogeneous chemical phase, up to ~10^{-6} s after the track structure formation.[5,6] The contributions of these chemical reactions to radiolytic yields in neutral water has been previously discussed.[6] In the ceric dosimeter, there are reactions between radiolytic species, sulfuric acid, Ce^{3+}, and Ce^{4+}.[7]

The radiolytic species are scavenged in the ceric sulfate solution by the following mechanisms. As in the Fricke dosimeter, in acidic medium, the hydrated electrons react with protons to give $H^{\bullet}$ radicals. In the presence of oxygen, the following chemical reaction may happen:

[1] $\quad H^{\bullet} + O_2 \rightarrow HO_2^{\bullet}$

Received 29 April 2012. Accepted 18 June 2012. Published at www.nrcresearchpress.com/cjc on 22 August 2012.

I. Plante. Universities Space Research Association, NASA Johnson Space Center, 2101 NASA Parkway, Bldg 37, Mail Code SK, Houston, TX 77058, USA; Département de médecine nucléaire et radiobiologie, Faculté de médecine et des sciences de la santé, Université de Sherbrooke, Sherbrooke, QC J1H 5N4, Canada.
T. Tippayamontri, J. Meesungnoen, and J.-P. Jay-Gerin. Département de médecine nucléaire et radiobiologie, Faculté de médecine et des sciences de la santé, Université de Sherbrooke, Sherbrooke, QC J1H 5N4, Canada.
N. Autsavapromporn. Département de médecine nucléaire et radiobiologie, Faculté de médecine et des sciences de la santé, Université de Sherbrooke, Sherbrooke, QC J1H 5N4, Canada; International Open Laboratory, National Institute of Radiological Sciences, 4-9-1 Anagawa, Inage-ku, Chiba 263-8555, Japan.

Corresponding author: Ianik Plante (e-mail: Ianik.Plante-1@nasa.gov).

$HO_2^\bullet$ then reacts with Ce^{4+}:

[2] $$HO_2^\bullet + Ce^{4+} \rightarrow H^+ + Ce^{3+} + O_2$$

Similarly, $^\bullet OH$ radicals react with Ce^{3+} as follows:

[3] $$^\bullet OH + Ce^{3+} \rightarrow Ce^{4+} + OH^-$$

Hydrogen peroxide undergoes a Fenton-type reaction:

[4] $$H_2O_2 + Ce^{4+} \rightarrow Ce^{3+} + H^+ + HO_2^\bullet$$

Using rxns. [1]–[4], the material balance equation for the yields of Ce^{3+}, O_2, and H_2 is obtained.

[5] $$\begin{aligned} G(Ce^{3+}) &= 2G_{H_2O_2} - G_{^\bullet OH} + G_{H^\bullet} \\ G(O_2) &= G_{H_2O_2} \\ G(H_2) &= G_{H_2} \end{aligned}$$

where G_X is the primary yield[8] of species X. For ^{60}Co γ-irradiated 0.4 mol/L sulfuric acid aqueous solutions at room temperature (pH ~ 0.46), representative values of the primary free-radical and molecular product yields are[7]

[6] $$\begin{aligned} G_{e^-_{aq}+H^\bullet} &= 3.66 \\ G_{H_2O_2} &= 0.78 \\ G_{H_2} &= 0.40 \\ G_{^\bullet OH} &= 2.84 \\ G_{HO_2^\bullet} &= 0.02 \end{aligned}$$

Using material balance eq. [5] and the primary yields of the radiolytic species (eq. [6]), the values $G(Ce^{3+}) = 2.4$, $G(O_2) = 0.8$, and $G(H_2) = 0.4$ were obtained. These values are in good agreement with experimental data.[3,9]

It is known that the dose rate of the radiation may influence the yield values. At high dose rate, the chemical species formed in spurs are closer to those originating from different radiation tracks and may interact. This can change the radiation chemistry and, consequently, the radiolytic yields. Therefore, the highest dose rate used for the standard ceric dosimeter is usually ~10 Gy/s. In our calculations, since individual tracks are simulated, the dose is much smaller that 1 Gy, and the dose rate is much lower than 10 Gy/s.

In this work, Monte Carlo simulation of the irradiation of the ceric dosimeter by low-LET radiation was performed. The following studies were done: (*i*) the time evolution of the yields of Ce^{3+}, O_2, and H_2 for the ceric dosimeter with oxygen; (*ii*) the time evolution of the yields of Ce^{3+}, O_2, and H_2 for the ceric dosimeter without oxygen; (*iii*) the effect of the initial concentration of Ce^{3+} on the yields of Ce^{3+}; and (*iv*) the effect of the LET of the radiation on the yield of Ce^{3+}. In general, the results of the calculations are in good agreement with experimental data.

Materials and methods

Monte Carlo simulation techniques were used to model the complex succession of events that are generated in irradiated liquid water, sulfuric acid, and ceric sulfate solutions. To simulate the fast electrons or ^{60}Co γ-radiolysis, short (~100 μm) segments of 300 MeV proton tracks, over which the LET value obtained in simulation is nearly constant and equal to ~0.3 keV/μm were used. This approximation is adequate, since the spurs formed by low-LET protons and fast electrons are similar and in general are created too far from each other to influence the radiolytic yields before the end of spur expansion. The number of proton histories (~150) was chosen to ensure small statistical fluctuations of the results while keeping acceptable computer time limits.

Monte Carlo simulations of the ceric dosimeter

The detailed description and implementation of the Monte Carlo simulation codes that were used for this work were previously described.[5,6,10–12] Briefly, all stages of the track development (physical, $<10^{-15}$ s; physicochemical, 10^{-15}–10^{-12} s; nonhomogeneous chemical, 10^{-12}–10^{-6} s; and homogeneous chemical, $>10^{-6}$ s) were modeled on an event-by-event basis. The code IONLYS (which replaces the codes previously called TRACPRO and TRACELE) was used to simulate all events of the early physical and physicochemical stages in the track development. The description of the cross sections, transport models, and other relevant information has been published.[10] These codes have been modified and improved over the years,[13,14] notably to include the new electron cross-sections data by Michaud et al.[15] and the cross sections for multiple ionization (MI) of water molecules by ions.[14] In this study, the simulations were performed using short (10–100 μm) $^1H^+$ ion track segments of LET varying from ~0.3 to 65 keV/μm, for which the contribution of MI can be neglected.

The simulation of the chemistry was performed using the step-by-step (IONLYS-SBS) code.[5,11] The theory used for this code and the implementation of the IONLYS-SBS program has been discussed in previous work.[5,12] Briefly, the program simulates the Brownian motion of the chemical species and evaluates the probabilities of reactions of the particles during small time steps (~10^{-13} s). To avoid unnecessary long calculation times, the time steps were increased exponentially during the simulation. The possibility of occurrence of reactions for each pair of particles was evaluated at each time step by using their respective probabilities of reactions. Similarly, the particles were allowed to react with chemical species distributed in the bulk of the solution. Following chemical reactions, the reactants were removed from the list of particles and newly formed products were added. The diffusion-reaction process was repeated until the time corresponded to the end of the simulation. The parameters used by the IONLYS-SBS program, such as the diffusion coefficients of the particles and the reaction rate constants, are also given.[5] As is the case for the Fricke dosimeter, the full reaction kinetics for the ceric dosimeter was obtained by simulating the chemistry up to 50 s.[7]

Modeling the solution of the ceric sulfate dosimeter

The ceric sulfate dosimeter is a solution comprising Ce^{3+}, Ce^{4+}, and H_2SO_4, with or without oxygen. The concentrations of these compounds can be varied. The cerous ion concentration initially present affects the degree of linearity of the response of the dosimeter to radiation.[16] The higher the initial concentration, the more linear the response. However, unnecessarily high total cerium concentrations should be

Can. J. Chem. Downloaded from www.nrcresearchpress.com by UNIVERSITAT DE VALENCIA on 10/20/12
For personal use only.

Can. J. Chem. Downloaded from www.nrcresearchpress.com by UNIVERSITAT DE VALENCIA on 10/20/12
For personal use only.

Table 1. Reactions added to the acidic water reaction scheme to simulate the radiolysis of the ceric sulfate dosimeter at 25 °C.

No.	Reaction	k ((mol/L)$^{-1}$ s^{-1})	Scavenging power (s^{-1})	Reference
[R1]	$^{\bullet}OH + HSO_4^- \rightarrow SO_4^{\bullet-} + H_2O$	1.5×10^5	5.9×10^4	7
[R2]	$^{\bullet}OH + Ce^{3+} \rightarrow Ce^{4+} + OH^-$	3.0×10^8	3.0×10^3	16
[R3]	$H^{\bullet} + Ce^{4+} \rightarrow H^+ + Ce^{3+}$	3.6×10^7	1.1×10^3	21
[R4]	$HO_2^{\bullet} + Ce^{4+} \rightarrow H^+ + Ce^{3+} + O_2$	2.7×10^6	8.1×10^1	22
[R5]	$H_2O_2 + Ce^{4+} \rightarrow Ce^{3+} + H^+ + HO_2^{\bullet}$	5.2×10^4	1.6×10^0	*
[R6]	$SO_4^{\bullet-} + Ce^{3+} \rightarrow SO_4^{2-} + Ce^{4+}$	5.0×10^7	5.0×10^2	23

*The rate constant for this reaction was not found in existing databases. The value of the rate constant of the Fenton reaction ($H_2O_2 + Fe^{2+} \rightarrow {}^{\bullet}OH + Fe^{3+} + OH^-$) was used.[7]

avoided because of possible errors due to the build-up factor ratio when the ^{60}Co energy spectrum is degraded.[17] Consequently, a study was done as a function of the initial concentration of Ce^{3+} in the second part of this work.

Sulfuric acid (H_2SO_4) is a diprotic acid which dissociates according to

$$[7] \qquad H_2SO_4 \underset{pK_{a_1}}{\overset{H^+}{\rightleftarrows}} HSO_4^- \underset{pK_{a_2}}{\overset{H^+}{\rightleftarrows}} SO_4^{2-}$$

with $pK_{a_1} = -3$ and $pK_{a_2} = 1.987$ at 25 °C.[7] The pH of the solution was ~0.46; at this pH, ionic strength affects all reactions between ions, except the bimolecular self-recombination of hydrated electrons for which there is no evidence of such an effect.[18] Ionic strength effects were taken into account in the IONLYS-SBS program by using the equation obtained from the Brønsted–Bjerrum model of ionic reactions and the extended Debye–Hückel theory of ionic solutions. This equation is

$$[8] \qquad \log\left(\frac{k}{k_0}\right) = 1.02 Z_a Z_b \left(\frac{I^{1/2}}{1 + I^{1/2}}\right) - 2bI$$

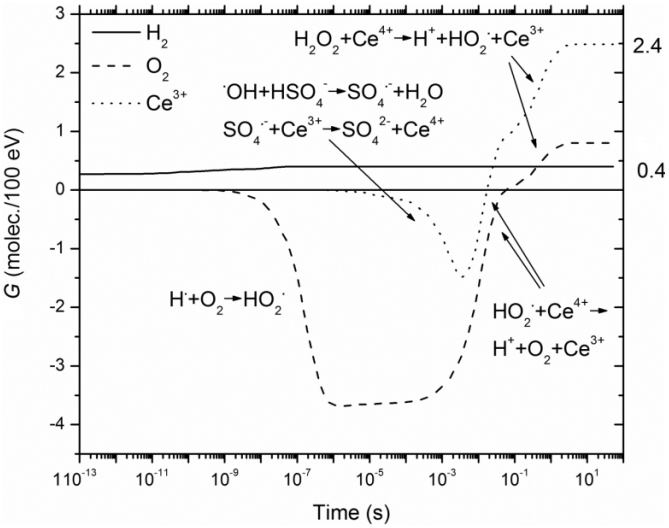
where k is the rate constant at ionic strength I, k_0 is the rate constant in the limit of zero ionic strength (i.e., infinite dilution), Z_a and Z_b are the algebraic numbers of the charges on the reactants, and b is a parameter taken as ($0.15\ Z_aZ_b$).[19] I is defined as

$$[9] \qquad I = \frac{1}{2}\sum_i Z_i^2 C_i$$

where Z_i is the charge number and C_i is the concentration of the ith ion.[19] The sum runs through all ions present in solution. The reactions added to the IONLYS-SBS code to simulate the ceric dosimeter, along with the rate constants and scavenging power, are presented in Table 1.

The reaction rate constants were obtained from several references and are known with some uncertainty. It is not uncommon for some reaction rate constants to have an uncertainty of up to an order of magnitude. The rate constants used in the simulations were taken from previous work.[12] The values of the rate constants are not expected to influence the stoichiometry of the reactions of the ceric dosimeter, but may alter the time profile of the calculated reaction kinetics.

Fig. 1. Time evolution of $G(Ce^{3+})$, $G(O_2)$, and $G(H_2)$ in the radiolysis of an air-saturated solution of 0.4 mol/L H_2SO_4, 3×10^{-5} mol/L of Ce^{4+}, and 1×10^{-5} mol/L of Ce^{3+} at 25 °C by 300 MeV protons. The concentration of dissolved oxygen is 2.5×10^{-4} mol/L. The values shown on the right are the experimental values of $G(Ce^{3+})$ and $G(H_2)$.



Results and discussion

The ceric dosimeter with oxygen

The simulation results are shown in Figs. 1 and 2 for the ceric dosimeter with $[O_2] = 2.5 \times 10^{-4}$ mol/L.

The most striking result in Fig. 1 is the time evolution of the yield of O_2. The $H^{\bullet}$ radicals are scavenged by oxygen through rxn. [1]; consequently, the yield of O_2 decreases to approximately –3.7, which is similar to the value of $G_{e^-_{aq}+H^{\bullet}} = 3.66$.[20] At ~$10^{-3}$ s, rxn. [2] will release an oxygen molecule for each $HO_2^{\bullet}$ molecule; hence, rxns. [1] and [2] have no net effect on oxygen production. On the other hand, rxn. [4] also starts approximately at this time, producing $HO_2^{\bullet}$, which will generate molecular oxygen through rxn. [2]. Therefore, $G(O_2)$ rises up to 0.8, corresponding to $G_{H_2O_2} = 0.78$. The most significant result of this study is the scavenging of the $^{\bullet}OH$ radicals, which is believed to occur through rxn. [3].[24] However, the curves depicted in Fig. 2 show that this reaction plays only a minor role, if any. In fact, the simulations indicate that $^{\bullet}OH$ is preferentially scavenged by rxn. [10].

Can. J. Chem. Downloaded from www.nrcresearchpress.com by UNIVERSITAT DE VALENCIA on 10/20/12
For personal use only.

Fig. 2. Time dependence of the extents ΔG (in molecules / 100 eV) of the main reactions involved in the formation (or decay) of Ce^{3+} and O_2, calculated from the simulations of the radiolysis of aerated ceric sulfate solution by ~300 MeV protons.

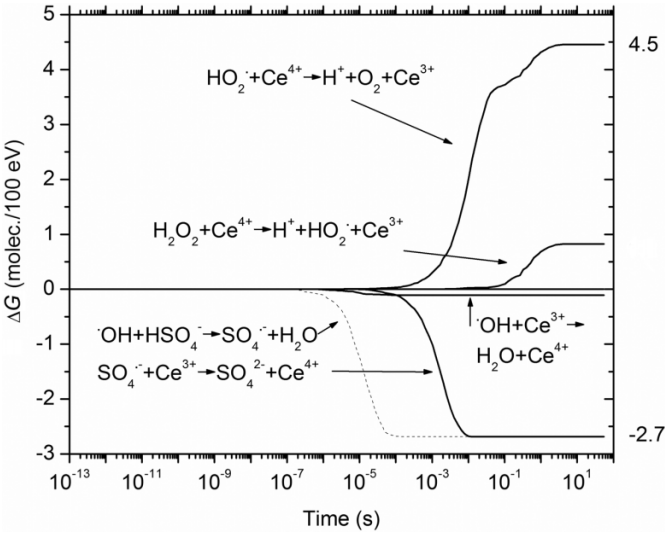
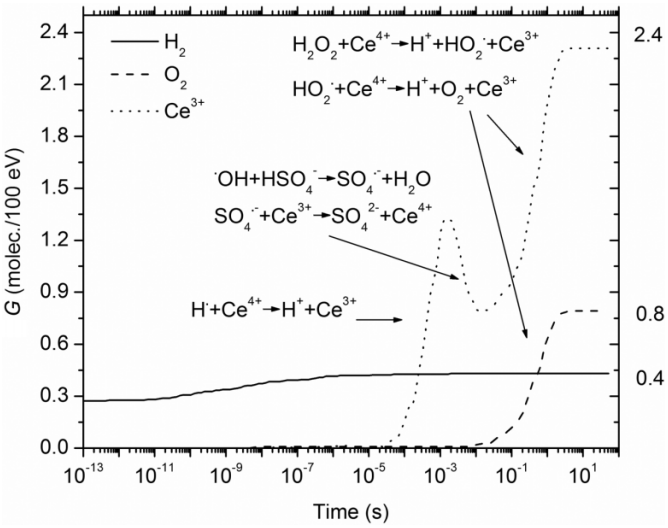


Fig. 3. Time evolution of $G(Ce^{3+})$, $G(O_2)$, and $G(H_2)$ (in molecules / 100 eV) in the radiolysis of deoxygenated solutions of 0.4 mol/L H_2SO_4, 3×10^{-5} mol/L of Ce^{4+}, and 1×10^{-5} mol/L of Ce^{3+} at 25 °C by 300 MeV protons. The values shown on the right are the experimental values of $G(Ce^{3+})$ and $G(H_2)$.



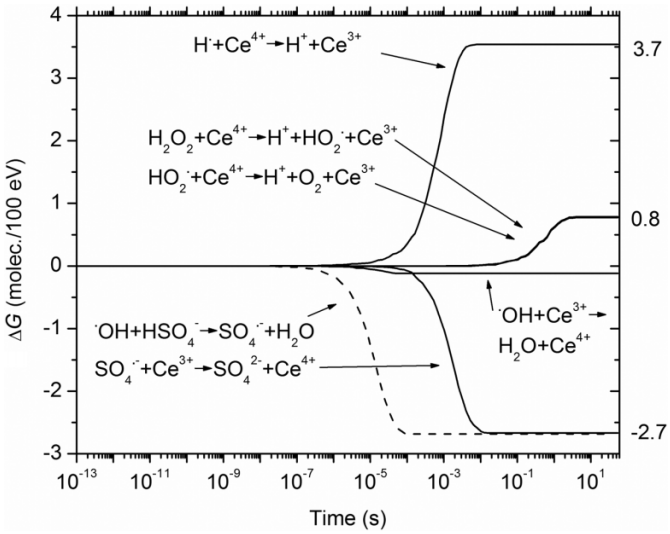
[10] $$^{\bullet}OH + HSO_4^- \rightarrow SO_4^{\bullet-} + H_2O$$

The rate constant of rxn. [3] is larger than the one of rxn. [10], but the concentration of H^+ in the ceric dosimeter is very high so the scavenging power of the latter is ~20 times higher (see Table 1). Following rxn. [10], the $SO_4^{\bullet-}$ radical oxidizes Ce^{3+} to Ce^{4+}.

[11] $$SO_4^{\bullet-} + Ce^{3+} \rightarrow SO_4^{2-} + Ce^{4+}$$

Actually, if rxn. [11] is not included in the IONLYS-SBS code, the calculated yields are not in agreement with the experimental results. The ΔG for this reaction is approximately –2.7, which shows that most of the $^{\bullet}OH$ radical follows this reaction scheme. The effect of this reaction is to reduce $G(Ce^{3+})$.

Fig. 4. Time dependence of the extents ΔG (in molecules / 100 eV) of the main reactions involved in the formation (or decay) of Ce^{3+} and O_2, calculated from the simulations of the radiolysis of deaerated solutions of 0.4 mol/L H_2SO_4, 3×10^{-5} mol/L of Ce^{4+}, and 1×10^{-5} mol/L of Ce^{3+} at 25 °C by 300 MeV protons.



Another consequence of this reaction for the simulation is that a background concentration of Ce^{3+} is necessary for this reaction to occur. If a simulation is attempted with diffusion-based chemistry programs such as IONLYS-IRT[6] or IONLYS-SBS[5,11] without Ce^{3+}, $SO_4^{\bullet-}$ is not scavenged, and therefore it is impossible to find adequate values of $G(Ce^{3+})$.

The ceric dosimeter without oxygen

The yields of Ce^{3+}, O_2, and H_2 are similar to those obtained in the ceric dosimeter with oxygen, but the kinetics curves are quite different (Figs. 3 and 4).

In this case, the yield of $HO_2^{\bullet}$ produced by the radiolysis of water is very small, therefore, rxn. [2] will only intervene for $HO_2^{\bullet}$ produced via rxn. [4]. The $H^{\bullet}$ radicals are directly scavenged by Ce^{4+}.

[12] $$H^{\bullet} + Ce^{4+} \rightarrow H^+ + Ce^{3+}$$

The major difference in the kinetics curves comes from rxn. [12], which intervenes much later than rxn. [1]. In this case, oxygen is produced from H_2O_2 via rxns. [2] and [4]. In both cases (with and without oxygen), molecular hydrogen does not react with the other chemical species; thus, $G(H_2) = G_{H_2} = 0.40$.

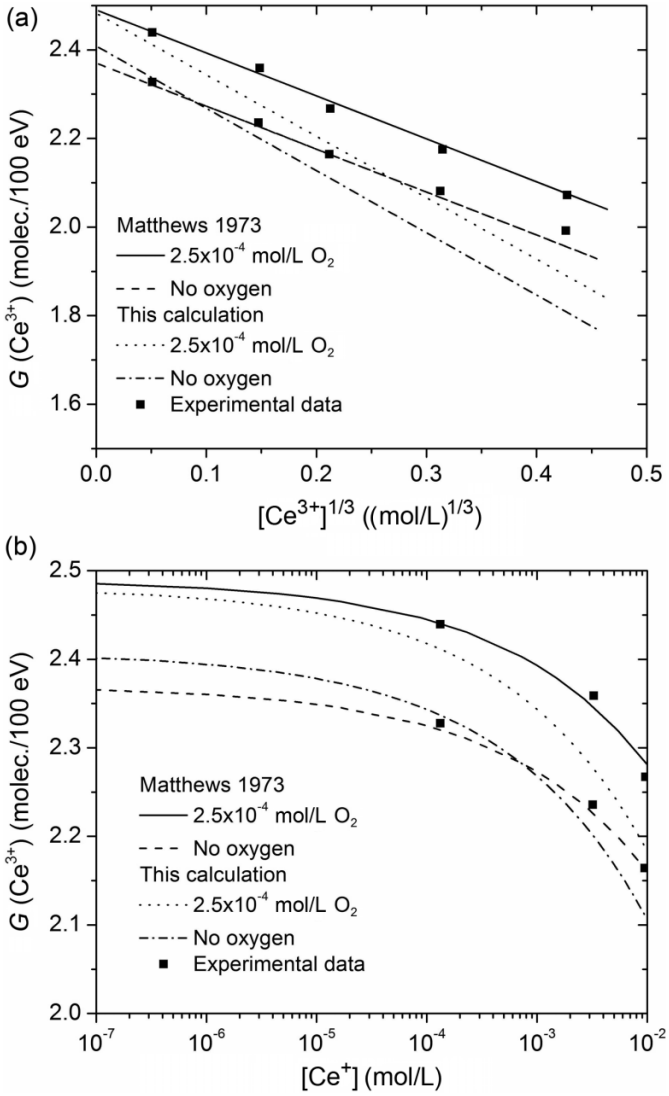
A difference in the yield of Ce^{3+} between aerated and deaerated solutions has been reported in the literature. Matthews[16] reported the following values:

[13] $$G(Ce^{3+})_{ox} = 2.49 - 0.97[Ce^{3+}]^{1/3}$$

[14] $$G(Ce^{3+})_{deox} = 2.37 - 0.87[Ce^{3+}]^{1/3}$$

Can. J. Chem. Downloaded from www.nrcresearchpress.com by UNIVERSITAT DE VALENCIA on 10/20/12
For personal use only.

Fig. 5. Effect of the initial ceric ion concentration on $G(Ce^{3+})$ in the radiolysis of a solution of 0.4 mol/L H_2SO_4 and 1×10^{-4} mol/L Ce^{4+}, with and without oxygen at 25 °C by 300 MeV protons. The results are compared with the reported values of Matthews.[25]



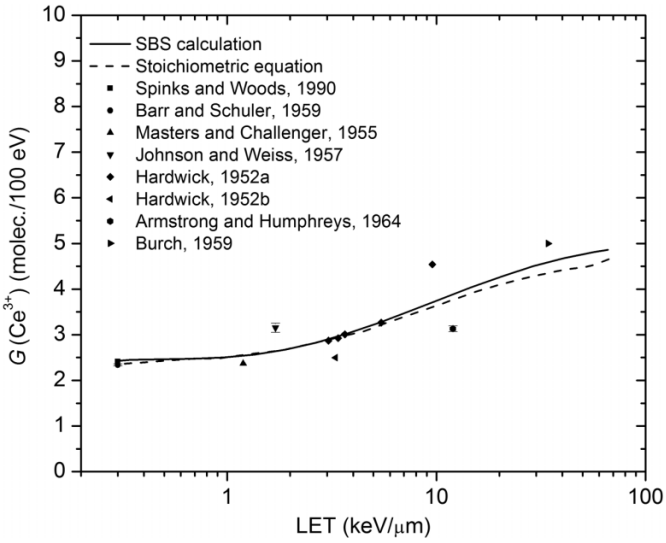
The values $G(Ce^{3+})_{ox} = 2.47$ and $G(Ce^{3+})_{deox} = 2.35$ are obtained by using $[Ce^{3+}] = 1 \times 10^{-5}$ mol/L. A small difference was also found in our calculated yields: $G(Ce^{3+})_{ox} = 2.48$ and $G(Ce^{3+})_{deox} = 2.31$. We try to explain this difference as follows. In the aerated system, the scavenging power of rxn. [1] is ~3×10^6 s^{-1}. There, the typical reaction time is ~3×10^{-7} s. Thus, rxn. [1] competes with rxns. [15] and [16] in the aerated system.

[15] $H^{\bullet} + {}^{\bullet}OH \rightarrow H_2O$

[16] $H^{\bullet} + H^{\bullet} \rightarrow H_2$

In fact, the ΔG values for rxns. [15] and [16] are 1.01 and 0.077 molec. / 100 eV in the oxygenated system and 1.13 and 0.11 molec. / 100 eV in the deoxygenated system. The net effect on the yield of Ce^{3+} by changing the ΔG of these reactions is not clear, since $H^{\bullet}$ and $^{\bullet}OH$ have opposite effects

Fig. 6. $G(Ce^{3+})$ (in molecules / 100 eV) for aerated 0.4 mol/L H_2SO_4 solutions, 3×10^{-5} mol/L of Ce^{4+}, and 1×10^{-5} mol/L of Ce^{3+} (ceric sulfate dosimeter), at 25 °C, with linear energy transfer (LET) in the range ~0.3–65 keV/μm.



on the yield of Ce^{3+}, and many reactions can be affected by this change. The difference in the ΔG of rxn. [16] between the oxygenated and deoxygenated systems is ~0.035 molec. / 100 eV, which would explain the difference of 0.07 molec. / 100 eV.

[17] $^{\bullet}OH + {}^{\bullet}OH \rightarrow H_2O_2$

It is very tempting to use rxn. [17] to explain the decrease of $G(Ce^{3+})$, because there is more $^{\bullet}OH$ available in the oxygenated system. However, the difference in ΔG between the oxygenated and deoxygenated solutions for this reaction is only ~0.01, which should contribute to a 0.04 rise in $G(Ce^{3+})$ in oxygenated solutions. Therefore, the decrease in $G(Ce^{3+})$ in deoxygenated solutions cannot be fully explained.

Effect of the concentration of Ce^{3+}

As reported in the previous section, $G(Ce^{3+})$ decreases with the concentration of Ce^{3+} as ~$[Ce^{3+}]^{1/3}$. A study was performed as a function of the concentration of Ce^{3+} to verify this assumption. The results are shown in Fig. 5*a*.

The trend is a linear decrease of $G(Ce^{3+})$ with $[Ce^{3+}]^{1/3}$, both in oxygenated and deoxygenated solutions, with slopes that are slightly different from those reported by Matthews.[25] However, because the abscissa is $[Ce^{3+}]^{1/3}$, the graphic can be misleading. The leftmost part of the graphic (up to 0.1 $(mol/L)^{1/3}$) covers concentrations of Ce^{3+} up to 10^{-3} mol/L. The agreement of our calculations with the data of Matthews[25] is better in this region. In fact, Hardwick[26] considered that the yield of cerous ion is independent of the ceric ion concentration over the range of 2×10^{-6} to ~10^{-2} mol/L. This is illustrated in Fig. 5*b*, where the abscissa is $[Ce^{3+}]$. There is some difference with the results of Matthews[25] at $[Ce^{3+}]$ higher than 10^{-3} mol/L. At these concentrations, the scavenging power of rxn. [3] is greater than 3×10^5 s^{-1}; therefore, the typical reaction time is less than ~3.3×10^{-6} s. At these time values, it is possible for rxn. [3] to compete

Can. J. Chem. Downloaded from www.nrcresearchpress.com by UNIVERSITAT DE VALENCIA on 10/20/12
For personal use only.

with $^{\bullet}OH + {}^{\bullet}OH \rightarrow H_2O_2$, leading to a decrease in the production of H_2O_2, which results in a decrease in $G(Ce^{3+})$.

Effect of LET on radiolytic yields

Most of the experimental work on the ceric sulfate system has been done with ^{60}Co γ-rays. Much less experimental data are available on this system for radiation of different LETs. As mentioned by Barr and Schuler,[27] $G(Ce^{3+})$ values increases with LET. This can be explained by noting that at a higher LET, more recombination of the radicals occurs, notably via the reaction $^{\bullet}OH + {}^{\bullet}OH \rightarrow H_2O_2$. Therefore, $G_{H_2O_2}$ increases and $G_{^{\bullet}OH}$ decreases with increasing LET, resulting in an increase in $G(Ce^{3+})$ as indicated by stoichiometric eq. [5]. For example, our previous calculations in acidic pH gave the values $G_{e^-_{aq}+H^{\bullet}} = 1.43$, $G_{H_2O_2} = 1.73$, and $G_{^{\bullet}OH} = 0.24$ at 65 keV/μm.[11] Using these values in eq. [5] yields $G(Ce^{3+}) = 4.64$.

To study the effect of LET on the yield of Ce^{3+}, simulations of the ceric dosimeter by proton tracks segments of energies from ~300 to 0.2 MeV, corresponding to LETs varying from ~0.3 to 65 keV/μm were performed. To ensure small statistical fluctuations on the results, 150 histories were simulated. The simulated $G(Ce^{3+})$ values were compared with the available experimental data from the literature and with calculations using the stoichiometric equation[28] (Fig. 6).

The simulation results show that $G(Ce^{3+})$ increases from ~2.45 molec. / 100 eV at 0.3 keV/μm to ~4.85 molec. / 100 eV at 65 keV/μm.[29] In general, the simulation results compare well with the experimental data, despite the relatively wide spread of measured G values and the scarcity of data for $G(Ce^{3+})$ in this LET range. However, it should be noted that different ions, such as $^4He^{2+}$ ions, were used in the experimental studies.[30]

Conclusion

Monte Carlo simulations of the ceric dosimeter with and without oxygen by low-LET radiation were performed. In both cases, the calculations are able to correctly reproduce the yields of Ce^{3+}, O_2, and H_2. The reaction kinetics curves indicate that $^{\bullet}OH$ radicals are scavenged mainly by HSO_4^-, yielding $SO_4^{\bullet-}$ radicals. The latter then oxidize a Ce^{3+} ion. The net effect on the yield of Ce^{3+} is the same as the direct reaction of $^{\bullet}OH$ with Ce^{3+}, but the reaction mechanism is different. These findings support an affirmation of Spinks and Woods,[24] which states that the mechanism of rxn. [3] has been simplified and reactions of the primary radicals with H_2SO_4 and its anions should not affect the stoichiometry of the reaction. Therefore, it may be useful to do an experiment to determine how $^{\bullet}OH$ radicals are scavenged in the ceric dosimeter. The good overall agreement between calculated and experimental yield values strongly supports the consistency and validity of the model used in this study.

Acknowledgements

The PhD studies of I.P. were supported by scholarships from the Natural Sciences and Engineering Research Council (NSERC) of Canada and the Canadian Space Agency. I.P. would also like to thank Dr. Francis A. Cucinotta (NASA) for useful discussions. The financial assistance provided by NSERC to J.-P.J.-G. is gratefully acknowledged.

References

(1) Matthews, R. *Int. J. Appl. Radiat. Isotopes* **1971**, *22* (3), 199. doi:10.1016/0020-708X(71)90124-4.
(2) In this paper, the values of the yield are expressed in units of molecules per 100 eV of absorbed energy (abbreviated as molec. / 100 eV). This can be converted into SI units (mol/J) by using 1 molec. / 100 eV = 0.103 64 μmol/J.
(3) Ferradini, C.; Pucheault, J. *Biologie de l'Action des Rayonnements Ionisants;* Masson: Paris, 1983.
(4) Ferradini, C.; Jay-Gerin, J.-P. *Can. J. Chem.* **1999**, *77* (9), 1542. doi:10.1139/v99-162.
(5) Plante, I. *Radiat. Environ. Biophys.* **2011**, *50* (3), 389. doi:10.1007/s00411-011-0367-8.
(6) Frongillo, Y.; Goulet, T.; Fraser, M.-J.; Cobut, V.; Patau, J. P.; Jay-Gerin, J.-P. *Radiat. Phys. Chem.* **1998**, *51* (3), 245. doi:10.1016/S0969-806X(97)00097-2.
(7) Autsavapromporn, N.; Meesungnoen, J.; Plante, I.; Jay-Gerin, J.-P. *Can. J. Chem.* **2007**, *85* (3), 214. doi:10.1139/v07-021.
(8) The primary yield refers to the yield after the spur expansion, i.e., at ~10^{-6} s. At ambient temperature, the spur expansion is essentially complete on the microsecond time scale after energy deposition. At this time, the species has diffusively escaped from spur or track reactions to become homogenously distributed in the bulk of the solution and available to react with added solutes (treated as spatially homogeneous) at moderate concentrations.
(9) Johnson, G. R. A.; Weiss, J. *Proc. Roy. Soc. A* **1957**, *240* (1221), 189. doi:10.1098/rspa.1957.0076.
(10) Cobut, V.; Frongillo, Y.; Patau, J. P.; Goulet, T.; Fraser, M.-J.; Jay-Gerin, J.-P. *Radiat. Phys. Chem.* **1998**, *51* (3), 229. doi:10.1016/S0969-806X(97)00096-0.
(11) Plante, I. *Radiat. Environ. Biophys.* **2011**, *50* (3), 405. doi:10.1007/s00411-011-0368-7.
(12) Plante, I. Ph.D. Thesis, University of Sherbrooke, Sherbrooke, Quebec, Canada, 2009.
(13) Muroya, Y.; Meesungnoen, J.; Jay-Gerin, J.-P.; Filali-Mouhim, A.; Goulet, T.; Katsumura, Y.; Mankhetkorn, S. *Can. J. Chem.* **2002**, *80* (10), 1367. doi:10.1139/v02-173.
(14) Meesungnoen, J.; Jay-Gerin, J.-P. *J. Phys. Chem. A* **2005**, *109* (29), 6406. doi:10.1021/jp058037z.
(15) Michaud, M.; Wen, A.; Sanche, L. *Radiat. Res.* **2003**, *159* (1), 3. doi:10.1667/0033-7587(2003)159[0003:CSFLEE]2.0.CO;2.
(16) Matthews, R. W. *Aust. J. Chem.* **1984**, *37* (3), 475. doi:10.1071/CH9840475.
(17) Brnjolfsson, A. A Significant Correction Factor in Gamma Ray Dosimetry. In *Radiation Chemistry;* Hart, E.J., Ed. Vol. 1, Advances in Chemistry Series No. 81, American Chemical Society: Washington, DC, 1968; pp 550–567.
(18) Schmidt, K. H.; Bartels, D. M. *Chem. Phys.* **1995**, *190* (1), 145. doi:10.1016/0301-0104(94)00332-5.
(19) Solomon, T. *J. Chem. Educ.* **2001**, *78* (12), 1691. doi:10.1021/ed078p1691.
(20) In a 0.4 mol/L H_2SO_4 solution, the hydrated electrons are scavenged in ~10^{-9} s by the reaction $H^+ + e^-_{aq} \rightarrow H^{\bullet} + H_2O$.[7] Therefore, we use $G_{e^-_{aq}+H^{\bullet}}$ instead of $G_{e^-_{aq}}$ and $G_{H^{\bullet}}$.
(21) Nichiporov, F. G.; Byakov, V. M. *High Energy Chem.* **1970**, *4*, 496. [Translated from Khim. Vys. Energ. *6*, 546].
(22) Czapski, G.; Bielski, B. H. J.; Sutin, N. *J. Phys. Chem.* **1963**, *67* (1), 201. doi:10.1021/j100795a503.
(23) Jiang, P.-Y.; Katsumura, Y.; Nagaishi, R.; Domae, M.; Ishikawa, K.; Ishigure, K.; Yoshida, Y. *J. Chem. Soc., Faraday Trans.* **1992**, *88* (12), 1653. doi:10.1039/ft9928801653.
(24) Spinks, J. W. T.; Woods, R. J. *An Introduction to Radiation Chemistry;* 3rd ed.; Wiley: New York, 1990.

(25) Matthews, R. W. *Radiat. Res.* **1973**, *55* (2), 242. doi:10.2307/3573680.
(26) Hardwick, T. J. *Can. J. Chem.* **1952**, *30* (1), 23. doi:10.1139/v52-004.
(27) Barr, N. F.; Schuler, R. H. *J. Phys. Chem.* **1959**, *63* (6), 808. doi:10.1021/j150576a008.
(28) Meesungnoen, J.; Benrahmoune, M.; Filali-Mouhim, A.; Mankhetkorn, S.; Jay-Gerin, J.-P. *Radiat. Res.* **2001**, *155* (2), 269. doi:10.1667/0033-7587(2001)155[0269:MCCOTP]2.0.CO;2.
(29) It is well-known that the yield of $HO_2^{\bullet}$ increases a little with the LET. However, the increase is at most 0.3 molec. / 100 eV for the values of the LET considered for this work.[14] Therefore, this contribution was neglected.
(30) Masters, B. J.; Challenger, G. E. *J. Phys. Chem.* **1955**, *59* (10), 1093. doi:10.1021/j150532a026.
(31) Johnson, G. R. A.; Weiss, J. *Proc. R. Soc. Lond. A Math. Phys. Sci.* **1957**, *240* (1221), 189. doi:10.1098/rspa.1957.0076.
(32) Armstrong, W. A.; Humphreys, W. G. *Can. J. Chem.* **1964**, *42* (5), 1092. doi:10.1139/v64-168.
(33) Burch, P. R. J. *Radiat. Res.* **1959**, *11* (4), 481. doi:10.2307/3570803.
(34) Hardwick, T. J. *Can. J. Chem.* **1952**, *30* (1), 39. doi:10.1139/v52-005.

Can. J. Chem. Downloaded from www.nrcresearchpress.com by UNIVERSITAT DE VALENCIA on 10/20/12
For personal use only.

Detailed mechanistic investigation into the S-nitrosation of cysteamine

Moshood K. Morakinyo, Itai Chipinda, Justin Hettick, Paul D. Siegel, Jonathan Abramson, Robert Strongin, Bice S. Martincigh, and Reuben H. Simoyi

Can. J. Chem. Downloaded from www.nrcresearchpress.com by UNIVERSITAT DE VALENCIA on 10/20/12
For personal use only.

Abstract: The nitrosation of cysteamine ($H_2NCH_2CH_2SH$) to produce cysteamine-*S*-nitrosothiol (CANO) was studied in slightly acidic medium by using nitrous acid prepared in situ. The stoichiometry of the reaction was $H_2NCH_2CH_2SH + HNO_2 \rightarrow H_2NCH_2CH_2SNO + H_2O$. On prolonged standing, the nitrosothiol decomposed quantitatively to yield the disulfide, cystamine: $2H_2NCH_2CH_2SNO \rightarrow H_2NCH_2CH_2S–SCH_2CH_2NH_2 + 2NO$. NO_2 and N_2O_3 are not the primary nitrosating agents, since their precursor (NO) was not detected during the nitrosation process. The reaction is first order in nitrous acid, thus implicating it as the major nitrosating agent in mildly acidic pH conditions. Acid catalyzes nitrosation after nitrous acid has saturated, implicating the protonated nitrous acid species, the nitrosonium cation (NO^+) as a contributing nitrosating species in highly acidic environments. The acid catalysis at constant nitrous acid concentrations suggests that the nitrosonium cation nitrosates at a much higher rate than nitrous acid. Bimolecular rate constants for the nitrosation of cysteamine by nitrous acid and by the nitrosonium cation were deduced to be 17.9 ± 1.5 $(mol/L)^{-1}$ s^{-1} and 6.7×10^4 $(mol/L)^{-1}$ s^{-1}, respectively. Both Cu(I) and Cu(II) ions were effective catalysts for the formation and decomposition of the cysteamine nitrosothiol. Cu(II) ions could catalyze the nitrosation of cysteamine in neutral conditions, whereas Cu(I) could only catalyze in acidic conditions. Transnitrosation kinetics of CANO with glutathione showed the formation of cystamine and the mixed disulfide with no formation of oxidized glutathione (GSSG). The nitrosation reaction was satisfactorily simulated by a simple reaction scheme involving eight reactions.

Key words: nitric oxide, nitrosation, thiols, cysteamine, kinetics.

Résumé : Opérant en milieu légèrement acide et utilisant de l'acide nitreux préparé in situ, on a étudié la réaction de nitrosation de la cystéamine ($H_2NCH_2CH_2SH$) conduisant à la cystéamine-*S*-nitrosothiol (CANO). La stoechiométrie de la réaction est $H_2NCH_2CH_2SH + HNO_2 \rightarrow H_2NCH_2CH_2SNO + H_2O$. Laissé longtemps au repos, le nitrosothiol se décompose quantitativement avec formation du disulfure, cystamine : $2H_2NCH_2CH_2SNO \rightarrow H_2NCH_2CH_2S–SCH_2CH_2NH_2 + 2NO$. Le NO_2 et le N_2O_3 ne sont pas les agents de nitrosation primaires puisque leur précurseur, le NO, n'a pas été détecté au cours du processus de nitrosation. La réaction est du premier ordre en acide nitreux, ce qui implique qu'il est l'agent de nitrosation majeur dans des conditions de pH légèrement acides. L'acide catalyse la nitrosation après une saturation par l'acide nitreux et ceci implique que, dans des environnements d'acidité élevée, le cation nitrosonium (NO^+) peut agir comme espèce nitrosante. La catalyse acide, à des concentrations constantes d'acide nitreux, suggère que le cation nitrosonium provoque la nitrosation avec une constante de vitesse beaucoup plus élevée que ce l'acide nitreux. On a déduit que les constantes de vitesse bimoléculaires pour la nitrosation de la cystéamine, par l'acide nitreux et par le cation nitrosonium, sont respectivement de $17{,}9 \pm 1{,}5$ $(mol/L)^{-1}$ s^{-1} et $6{,}7 \times 10^4$ $(mol/L)^{-1}$ s^{-1}. Les ions Cu(I) ainsi que Cu(II) sont tous les deux efficaces comme catalyseurs pour la formation et la décomposition du nitrosothiol de la cystéamine. Les ions Cu(II) catalysent la nitrosation de la cystéamine dans des conditions neutres alors que les ions Cu(I) ne la catalysent que dans des conditions acides. La transnitrosation du CANO avec du glutathion donne lieu à la formation de cystamine et du disulfure mixte, sans formation du produit doxydation du glutathion (GSSG). On peut simuler d'une façon satisfaisante la réaction de nitrosation par un schéma réactionnel simple impliquant huit réactions.

Mots-clés : oxyde nitrique, nitrosation, thiols, cystéamine, cinétique.

[Traduit par la Rédaction]

Received 2 February 2011. Accepted 16 April 2012. Published at www.nrcresearchpress.com/cjc on 22 August 2012.

M.K. Morakinyo and R. Strongin. Department of Chemistry, Portland State University, Portland, OR 97207-0751, USA.
I. Chipinda, J. Hettick, and P.D. Siegel. Allergy and Clinical Immunology Branch, Health Effects Laboratory Division, National Institute of Occupational Safety and Health, Centers for Disease Control and Prevention, 1095 Willowdale Road, Morgantown, WV 26505, USA.
J. Abramson. Department of Physics, Portland State University, Portland, OR 97207-0751, USA.
B.S. Martincigh. School of Chemistry, University of KwaZulu-Natal Westville Campus, Private Bag X54001, Durban 4000, Republic of South Africa.
R.H. Simoyi. Department of Chemistry, Portland State University, Portland, OR 97207-0751, USA; School of Chemistry, University of KwaZulu-Natal Westville Campus, Private Bag X54001, Durban 4000, Republic of South Africa.

Corresponding author: Moshood K. Morakinyo (e-mail: mkm2002ng@yahoo.com).

Can. J. Chem. Downloaded from www.nrcresearchpress.com by UNIVERSITAT DE VALENCIA on 10/20/12
For personal use only.

Introduction

Nitric oxide (NO) is a simple gaseous molecule with fascinating biological functions.[1] It is one of the most versatile bioactive molecules ever identified. Unlike other free radicals, it is relatively stable, but becomes unstable in biological systems due to its reaction with oxygen, superoxide anion ($O_2^{\bullet-}$), and haem proteins.[2] Nitrite (NO_2^-) is the major end product of its reaction with oxygen. Nitrite can also release NO on acidification and by the reductase activity of the enzyme, xanthine oxidoreductase, at pH conditions lower than 6.0.[3–5]

Nitric oxide has been the focus of many research groups in recent years, probably because of the realization that it is synthesized by mammalian cells and can act both as a physiological messenger and as a cytotoxic agent.[6] It is an essential physiological signaling molecule necessary for cell-to-cell communication and it is also involved in the regulation of gene expression and modification of sexual and aggressive behavior.[7,8] It is actively involved in smooth muscle relaxation due to its ability to activate guanosine 3′,5′-cyclic monophosphate (cGMP) in smooth muscle tissue.[9,10] The role of nitric oxide in the physiological system at any given time significantly depends on its concentration and its environment. It is known to perform most of its beneficial roles, such as vasorelaxation[11,12] and neurotransmission,[13,14] at low concentrations, on the order of 5–10 nmol/L.[15] At this concentration range it cannot effectively compete with superoxide dismutase (SOD) for $O_2^{\bullet-}$.

NO also readily reacts with $O_2^{\bullet-}$ to produce the highly damaging and genotoxic oxidant (peroxynitrite, $ONOO^-$):

$$[R1] \qquad NO + O_2^{\bullet-} \rightarrow ONOO^-$$

The bimolecular rate constant for rxn. [R1] is 6.7×10^9 $(mol/L)^{-1}$ s^{-1}.[15,16] Superoxide anion radical concentrations in the physiological environment are in the order of 4–10 μmol/L.[15] When NO concentrations are in the micromolar range, rxn. [R1], which produces the deleterious peroxynitrite, becomes competitive with the deactivating reaction that removes superoxide anion radical.

Excessive production of nitric oxide has thus been linked to so many cytotoxic activities such as septic shock and liver injury.[17,18] It is necessary to have processes that can reduce NO concentrations to beneficial levels in the physiological environment. Such processes would include its reaction with thiols to form *S*-nitrosothiols (RSNOs). For example, RSNOs have been shown to improve end-organ recovery in models of ischemia–reperfusion injury in the heart and liver.[19,20] Biological nitrosothiol formation is a post-translational modification of biological thiols that is subsequently linked to all those functions that are attributed to nitric oxide.[21] Possible roles of S-nitrosation include the regulation of apoptosis through glyceraldehyde-3-phosphate dehydrogenase modification[22] as well as involvement in the pathogenesis of Parkinson's disease.[23] There are several studies on nitrosothiol formation by Williams,[24–33] but these studies dwell on formations and characterizations and not so much on the mechanisms and kinetics. Despite the potential benefits of the relevance of the mechanistic basis of nitrosations (both S- and N-nitrosations),[34] very few studies have been directed at elucidating these mechanisms.

Cysteamine (2-aminoethanethiol) is a very important physiologically active β-aminothiol. It is produced in vivo by degradation of coenzyme A. Coenzyme A is a cofactor in many enzymatic pathways, which include fatty acid oxidation, heme synthesis, synthesis of the neurotransmitter acetylcholine, and amino acid catabolism.[35] Cysteamine is medically known as Cystagon and can be used as oral therapy for the prevention of hypothyroidism and as a growth enhancer in patients with nephropathic cystinosis.[36] Cysteamine and its disulfide (cystamine) can also be used in topical eye drops to dissolve corneal cystine crystals.[37,38] It has also been shown to be an effective molecule against hepatotoxicity caused by excessive production of nitric oxide.[17]

Although a series of studies have been performed on the metabolism of this thiol and its metabolites with respect to oxidation by reactive oxygen species,[39–41] nothing has been done on the elucidation of its mechanism of nitrosation by NO and (or) NO-derived metabolites (N_2O_3 and NO^+). Its nitrosation is well-known and has been reported in several manuscripts,[42,43] but the exact mechanistic details are still unknown. We report herein on the detailed kinetics and mechanism of the nitrosation of cysteamine. The nitrosating agent is produced in situ, by premixing H^+ and NO_2^- and utilizing a double-mixing stopped-flow spectrophotometer. This manuscript also reports on detailed product analysis as well as on transnitrosation kinetics. The most prevalent thiol-based antioxidant in the physiological environment is glutathione. It is envisaged that, in any discussion of S-nitrosation, glutathione would be a major player.

Experimental

Materials

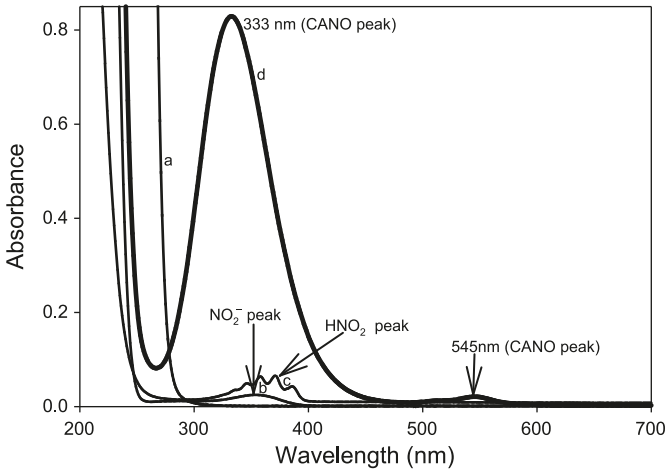
Cysteamine hydrochloride (CA, 2-aminoethanethiol hydrochloride) 98%, cystamine, cysteine (99+%), sodium perchlorate (Acros), glutathione, sodium nitrite, sodium chloride, perchloric acid (72%), ferrous sulfate (Fisher Scientific), cuprous chloride, and cupric chloride (GSF chemicals) were used as purchased. Stock solutions of CA and nitrite were prepared just before use. Reagent solutions were prepared with distilled and deionized water from a Barnstead Sybron Corporation water purification unit. Inductively coupled plasma mass spectrometry (ICP–MS) was used to show that our aqueous reaction medium did not contain enough transition-metal ions to affect the overall reaction kinetics and mechanism The highest metal ion concentration was cadmium at 1.5 ppb followed by lead at 0.43 ppb. Copper was virtually undetectable.

Methods

All experiments were carried out at 25.0 ± 0.1 °C and at a constant ionic strength of 1.0 mol/L ($NaClO_4$). The progress of the nitrosation reaction was monitored spectrophotometrically by following the absorbance of *S*-nitrosocysteamine (CANO) at its experimentally determined absorption peak of 545 nm, where an absorptivity coefficient of 16.0 ± 0.1 $(mol/L)^{-1}$ cm^{-1} was evaluated. Although CANO has a second absorption peak at 333 nm, with a much higher absorptivity coefficient of 536.0 $(mol/L)^{-1}$ cm^{-1}, its maximum absorption at 545 nm was used owing to the lack of interference

Can. J. Chem. Downloaded from www.nrcresearchpress.com by UNIVERSITAT DE VALENCIA on 10/20/12
For personal use only.

Fig. 1. UV–vis spectral scan of reactants 0.01 mol/L cysteamine hydrochloride (CA, a), 0.001 mol/L $NaNO_2^-$ (b), 0.001 mol/L HNO_2 (c), and product 0.001 mol/L *S*-nitrosocysteamine (CANO, d).



from the absorption peaks of nitrogen species (NO_2^-, NO^+, and HNO_2) at this absorption wavelength (see Fig. 1).

Product identification and verification was achieved by complementary techniques: UV–vis spectrophotometry, HPLC, quadrupole time-of-flight mass spectrometry (TOF-MS), and electron paramagnetic resonance (EPR) spectrometry. Kinetics measurements for fast reactions were performed on a Hi-Tech Scientific double-mixing SF61-DX2 stopped-flow spectrophotometer. For slower reactions, a PerkinElmer Lambda 25 UV–vis spectrophotometer was used.

Stoichiometric determinations were performed by mixing excess perchloric acid and nitrite with a fixed amount of CA such that CA was the limiting reagent. The reaction was allowed to proceed to completion while rapidly scanning the reacting solution between 200 and 700 nm. The concentration of CANO was deduced from its maximum absorption at 545 nm.

HPLC technique

The HPLC system utilized a Shimadzu Prominence (Columbia, Maryland) SPD-M10A VP diode array detector, dual LC 600 pumps, LPT-6B LC–PC interface controller, SIL-10AD auto injector, and Class-VP chromatography data system software. All samples were loaded on a reversed phase Discovery 5 μm C18 column (Supelco, Bellefonte, Pennsylvania). They were run isocractically at 0.15% trifluoroacetic acid (TFA) / H_2O to 10% methanol / H_2O, and CANO was detected at 545 nm (for selective scans) with maximum spectral scan mode employed to detect all eluents. A flow rate of 1 mL/min was maintained. All solutions for HPLC analysis were made with Milli-Q Millipore purified water and filtered with Whatman Polypropylene 0.45 μm pore-size filter devices before injection (10 μL) into the column using the auto injector. To curb the interaction of the protonated amines on the analytes with the silanol groups on the stationary phase (which was causing tailing of peaks), the sodium salt of 1-octanesulfonic acid (0.005 mol/L) was incorporated into the aqueous mobile phase as an HPLC ion-pairing agent. This was sufficient to neutralize the protonated amines and produce good resolution while eliminating peak tailing.

TOF-MS

Mass spectra were acquired on a Micromass QTOF-II (Waters Corporation, Millford, MA) quadrupole time-of-flight mass spectrometer. Analytes were dissolved in 50:50 acetonitrile / water – 1% formic acid mixture, and analyte ions were generated by positive-mode electrospray ionization (ESI) at a capillary voltage of 2.8 kV and a flow rate of 5 μL/min. The source block was maintained at 80 °C and the nitrogen desolvation gas was maintained at 150 °C and at a flow rate of 400 L/h. Data were visualized and analyzed with the Micromass MassLynx 4.0 software suite for Windows XP (Water Corporation, Millford, Massachusetts).

EPR Measurements

A Bruker e-scan EPR spectrometer (X-band) was used for the detection of radicals and to confirm the release of NO upon the decomposition of CANO. Detection of NO was through the use of the NO-specific spin trap, *aci*-nitroethane.[44] The following settings were used for a typical run: microwave power, 19.91 mW; modulation amplitude, 1.41 G; receiver gain, 448; time constant, 10.24 ms; sweep width, 100 G; and frequency, 9.78 GHz. All measurements were taken at room temperature.

Results

The major reaction studied was a simple nitrosation of cysteamine through in situ production of nitrous acid as the nitrosating agent. The yield of CANO varied, based on the order of mixing reagents. The highest yield, which gave quantitative formation of CANO, was obtained by premixing nitrite with acid and incubating the solution for approximately 1 s before subsequently reacting this nitrous acid with cysteamine in a third reagent stream of the double-mixing stopped-flow spectrophotometer. The value of the absorptivity coefficient of CANO at 545 nm adopted for this study of 16.0 mol/L^{-1} cm^{-1} was derived from this mixing order. Premixing CA with acid before the addition of nitrite gave a lower yield of CANO. The available protons are reduced by the protonation of CA.

$$[R2] \qquad H_2NCH_2CH_2SH + H^+ \leftrightarrow [H_3NCH_2CH_2SH]^+$$

This subsequently reduces the amount of the immediately available nitrosating agent, HNO_2.

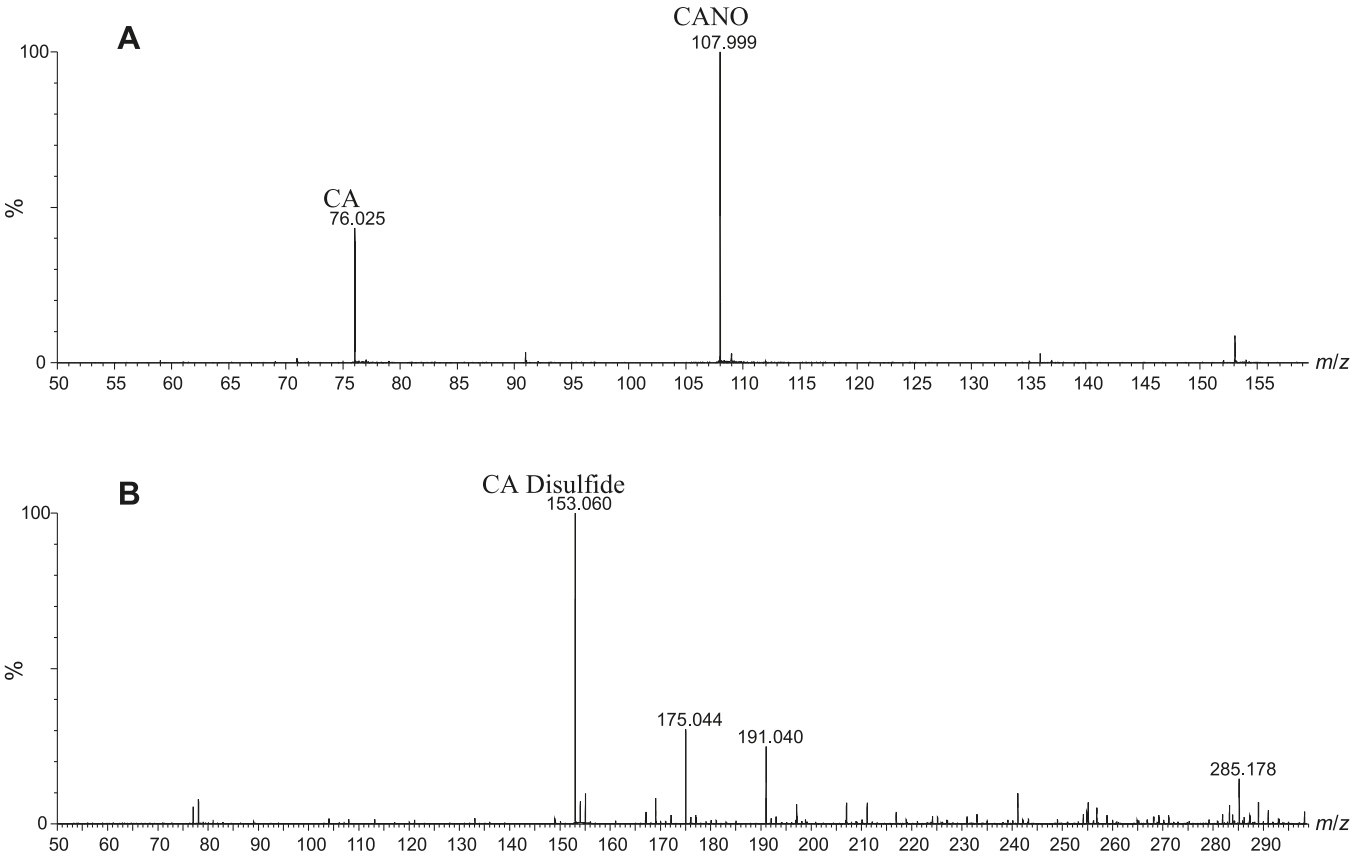
Stoichiometry and product analysis

The stoichiometry, in conditions of excess acid and nitrite over CA, was strictly 1:1.

$$[R3] \qquad H_2NCH_2CH_2SH + HNO_2 \rightarrow H_2NCH_2CH_2S-NO + H_2O$$

Stoichiometry rxn. [R3] is attained within a minute of mixing the reagents at high acid concentrations, and a little longer in lower acid concentrations. High acid concentrations rapidly form the product (CANO), which also rapidly decomposes. A resolvable mass spectrum is taken at low acid concentrations, and this generally will show both the reagent (CA) and the single product (CANO). This mass spectrum is shown in Fig. 2A. There are no other peaks that can be discerned from the reaction mixture, apart from those belonging to the reagent and the product. Incubation of the product of

Fig. 2. Mass spectrometry analysis of the product of nitrosation of cysteamine hydrochloride (CA) showing (A) formation of *S*-nitrosocysteamine (CANO), m/z = 107.9999; (B) product of decomposition of CANO after 24 h. Cystamine, a disulfide of CA was produced with a strong peak, m/z = 153.0608.



Can. J. Chem. Downloaded from www.nrcresearchpress.com by UNIVERSITAT DE VALENCIA on 10/20/12
For personal use only.

nitrosation overnight shows a final conversion of the CANO into the disulfide, cystamine ($H_2NCH_2CH_2S–SCH_2CH_2NH_2$, Fig. 2B).

$$[R4] \quad 2H_2NCH_2CH_2S-NO \rightarrow H_2NCH_2CH_2S-SCH_2CH_2NH_2 + 2NO$$

Nitric oxide can be trapped and observed by EPR techniques through the use of a nitroethane trap.[44] The aci-anion of this trap, formed in basic environments, generates a long-lived spin adduct with NO, which is detectable and quantifiable by its distinct EPR spectrum pattern and g value.

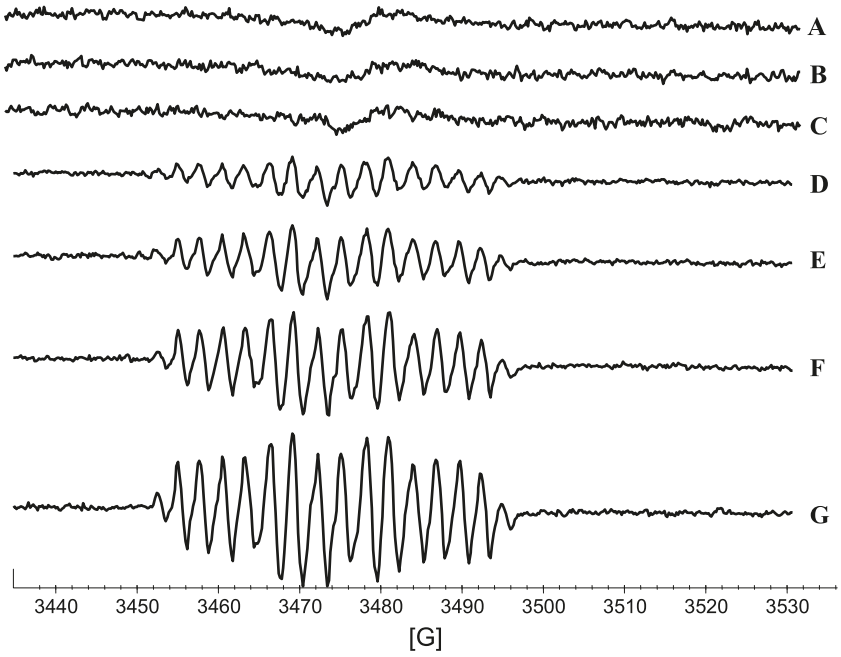
$$[R5] \quad CH_3CH=NO_2^- + {}^{\bullet}NO + OH^- \rightarrow [CH_3C(NO)(NO_2)]^{\bullet 2-} + H_2O$$

This adduct ($[CH_3C(NO)(NO_2)]^{\bullet 2-}$) is EPR-active. No peaks were obtained in the EPR spectrum when the nitroethane trap was utilized during the formation of CANO, indicating that NO is not released during the S-nitrosation and that it is not a major nitrosation agent in this mechanism. Upon use of the trap, however, during the decomposition of CANO, a strong EPR spectrum indicating the presence of NO was obtained, proving stoichiometry [R4]. Figure 3 shows a series of EPR spectra that proves the presence of NO in the decomposition of CANO. The first three spectra show that, on their own, nitroethane, CA, and NO_2^- cannot generate any active peaks that can be attributed to NO. In excess concentrations of the trapping reagent, heights of the spectral peaks can be used, after a standardization, as a quantitative measure of the available NO. NO has a very poor solubility in water, and so the technique is limited only to low NO concentrations.

Reaction kinetics

The reaction has a very simple dependence on cysteamine concentrations (see Figs. 4A and 4B). There is a linear first-order dependence on the rate of nitrosation with CA concentrations with an intercept kinetically indistinguishable from zero. The reaction kinetics are more reproducible in the format utilized in Fig. 4 in which concentrations of acid and nitrite are equal and in overwhelming excess over CA concentrations. The effect of nitrite is also simple and first-order (see Figs. 5) when nitrite concentrations do not exceed the initial acid concentrations. Effectively, under these conditions, all N(III) species in the reaction environment are in the form of protonated HNO_2. Acid effects are much more complex and are dependent on the ratio of initial acid to nitrite concentrations. The nitrosation response to acid differs, depending on whether initial proton (H_3O^+) concentrations exceed initial nitrite concentrations. The most important parameter affecting the rate of nitrosation is the concentration of HNO_2. A set of kinetics traces that encompass a proton concentration variation, which ranges from concentrations

Fig. 3. Electron paramagnetic resonance (EPR) spectra of the NO radical generated during the decomposition of *S*-nitrosocysteamine (CANO) using 0.5 mol/L nitroethane (NE) in 1.0 mol/L NaOH solution as the spin trap. (A) 0.5 mol/L NE, (B) 0.01 mol/L NO_2^-, (C) 0.04 mol/L cysteamine hydrochloride (CA), (D) [CANO] = 0.01 mol/L, (E) [CANO] = 0.02 mol/L, (F) [CANO] = 0.03 mol/L, and (G) [CANO] = 0.04 mol/L.



Can. J. Chem. Downloaded from www.nrcresearchpress.com by UNIVERSITAT DE VALENCIA on 10/20/12
For personal use only.

that are lower than nitrite to those that exceed, was performed. A simple plot of added acid to the rate of nitrosation shown in Fig. 6A clearly displays a discontinuity at the point where acid exceeds nitrite concentrations. By utilizing the dissociation constant of HNO_2, the final concentrations of H_3O^+, NO_2^-, and HNO_2 can be calculated for each set of initial concentrations. These data are shown in Table 1 for the input concentrations used for the set of kinetics experiments. Close examination of the data in Table 1 shows that the kinetics of the reaction are vastly different depending on whether initial acid concentrations exceed initial nitrite concentrations. When nitrite is in excess (the first four readings), there is a sharp nonlinear increase in the rate of nitrosation with nitrous acid concentrations (Fig. 6B), and a saturation in rate with respect to the actual proton concentrations despite the recalculation of the concentrations undertaken in Table 1. Figure 6B would strongly indicate second-order kinetics in nitrous acid, and a plot of nitrosation rate versus nitrous acid to the second power is linear (plot not shown). Table 1 shows that, in the series of data plotted for Fig. 6B, nitrous acid concentrations and excess proton concentrations increase while nitrite concentrations decrease, and the final observed rate of nitrosation is derived from these three species concentrations and not isolated to nitrous acid. At acid concentrations that exceed initial nitrite concentrations, there is a linear dependence in rate on acid concentrations (Fig. 6C). Note that a saturation would have been achieved in nitrous acid concentrations as would be expected in this format in which the nitrous acid saturates at 50 mmol/L. The increase in nitrosation rate with an increase in acid after saturation of HNO_2 indicates that other nitrosants apart from HNO_2 exist in the reaction environment.

Effect of copper

Copper has been implicated in many reactions involving organosulfur compounds.[45–47] Cu(I) is known to be much more active than Cu(II). It is easier to assay for Cu(II) and the addition of Cu(II) to organosulfur reactions involves its initial conversion to the more active Cu(I). Figure 7A shows that addition of Cu(II) rapidly increases the nitrosation reaction. Cu(II) ions, however, also catalyze the decomposition of CANO. A plot of the rate of nitrosation versus Cu(II) concentrations shows the sigmoidal rate increase followed by an abrupt saturation, which is typical of catalytic mechanisms (figure not shown). No nitrosation occurs in the presence of nitrite without acid (which is necessary to generate the HNO_2). Figure 7B, however, shows that, even in the absence of acid, Cu(II) ions can still effect the nitrosation of CA. Cu(I) ions, however, could not effect nitrosation in the absence of acid. Figure 7C shows the catalytic effect of Cu(II) ions on the decomposition of CANO. CANO was prepared in situ from two feed streams of the double-mixing stopped flow ensemble. Cu^{2+} ions derived from cupric chloride were next added from a third feed stream after complete production of CANO. All feed streams were buffered at pH 7.4. The two control experiments (traces a and b) show the slow decomposition expected from CANO solutions at pH 7.4. Trace b was treated with EDTA to sequester all metal ions in the reaction solution. This trace is identical to the one without EDTA (trace a), confirming the absence of metal ions in reagent solution, which can affect the decomposition kinetics. Addition of micromolar quantities of Cu(II) ions effects a big acceleration in the rate of decomposition. Higher Cu(II) concentrations give a strong autocatalytic decay of the nitrosothiol (trace f in Fig. 7C). The catalytic effect of Cu(II) ions on the decomposition can also be

Can. J. Chem. Downloaded from www.nrcresearchpress.com by UNIVERSITAT DE VALENCIA on 10/20/12
For personal use only.

Fig. 4. (A) Absorbance traces showing the effect of varying cysteamine hydrochloride (CA) concentrations. The reaction displays first-order kinetics in CA. $[NO_2^-]_0 = 0.10$ mol/L; $[H^+]_0 = 0.10$ mol/L; and (a) $[CA]_0 = 0.005$ mol/L; (b) $[CA]_0 = 0.006$ mol/L; (c) $[CA]_0 = 0.007$ mol/L; (d) $[CA]_0 = 0.008$ mol/L; (e) $[CA]_0 = 0.009$ mol/L; and (f) $[CA]_0 = 0.010$ mol/L. (B) Initial rate plot of the data in Fig. 4A. The plot shows the strong first-order dependence of the rate of formation of *S*-nitrosocysteamine (CANO) on CA, with an intercept kinetically indistinguishable from zero.

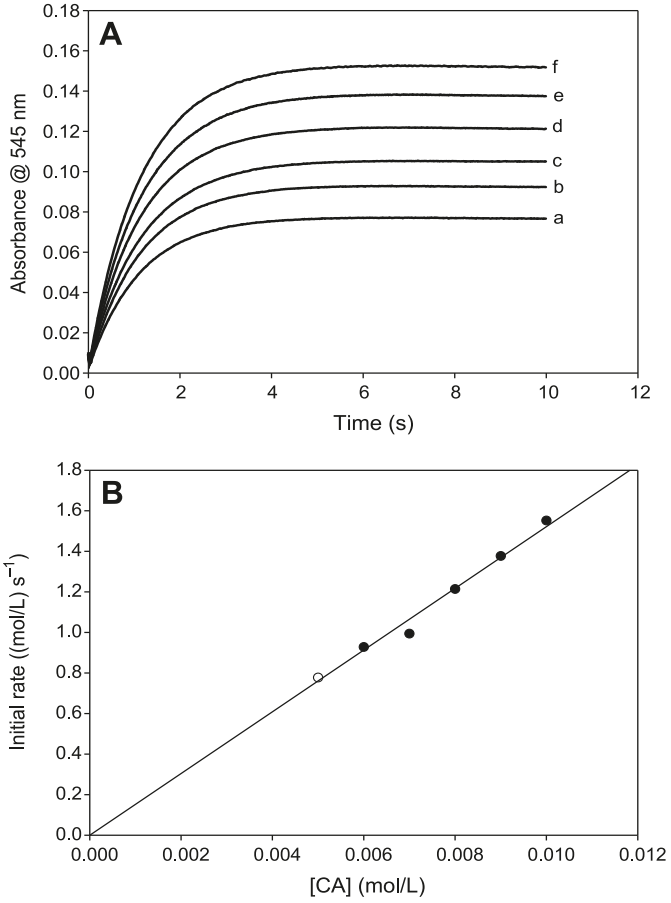
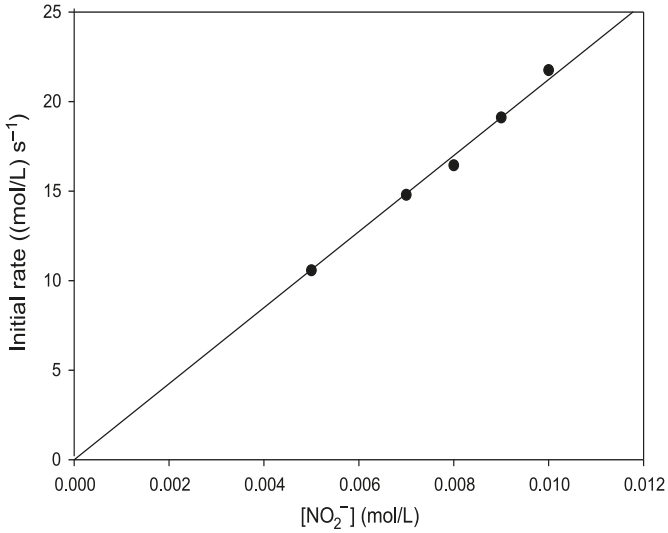


Fig. 5. Initial rate plot from the data derived from varying nitrite ion concentrations in excess acid over nitrite. $[CA]_0 = 0.10$ mol/L; $[H^+]_0 = 0.10$ mol/L; and $[NO_2^-]_0$ was varied from 0.005 to 0.010 mol/L. The plot shows strong first-order dependence on initial rate of formation of *S*-nitrosocysteamine (CANO) on nitrite. CA, cysteamine hydrochloride.



evaluated through the rate of production of nitric oxide, which is known to be the major product, together with the disulfide, of nitrosothiol decompositions. Figure 7D shows EPR spectra using the nitroethane trap, of the enhanced production of NO with addition of Cu(II) ions. All three spectra were taken after the same time lapse from CANO incubation, and thus the peak heights of the NO-induced spectra can be correlated with the extent of reaction.

Transnitrosation

The most abundant thiol in the physiological environment is glutathione (GSH). A pertinent reaction to study would be the interaction of any nitrosothiol formed in the physiological environment with glutathione. There is a crucial question about the lifetimes of the nitrosothiols formed. If thiols are carriers of NO from the point of production to the point of its usage, the nitrosothiols formed should be stable enough and have a long enough lifetime to enable them to perform this activity. Spectrophotometric study of transnitrosation is rendered complex by the fact that many nitrosothiols seem to absorb around the same wavelength and with similar absorptivity coefficients. Figure 8A shows a series of superimposed spectra of four well-known nitrosothiols, which show nearly identical spectra. Figure 8B shows the spectrophotometric characterization of possible transnitrosation in mixtures of CANO and GSH. GSNO has a higher absorptivity coefficient than CANO at the same wavelength,[48] and this explains the initial increase in absorbance on addition of GSH to CANO. LC–MS data have shown that the reaction mixture can transiently (before attainment of the equilibrium mixture) contain any of at least six components at varying times and concentrations: CANO, *S*-nitrosoglutathione (GSNO), GSH, CA–CA (cystamine), GSSG (oxidized glutathione), and CA–GS (mixed disulfide). The rate of transnitrosation will be difficult to evaluate owing to the presence of the mixed disulfide. Figure 8B shows that, relatively, CANO is more stable than GSNO because of the rapid rate of consumption of GSNO upon its formation as compared with the much slower CANO decomposition with or without EDTA. Figure 9 shows a GC–MS spectrum of mixtures of CANO and GSH. This involved a 3:5 ratio of CANO to GSH, which is also trace f in Fig. 8B. The remarkable aspect of this spectrum is the absence of the GSSG, whose precursor is GSNO. Thus, GSNO, when formed, rapidly decomposes by reacting with CA to form the mixed disulfide and releasing NO. The cystamine formed and observed in the spectrum is derived from the normal decomposition of CANO (see rxn. [R10], vide infra).

Mechanism

The overall rate of nitrosation is dependent on the rate of formation and accumulation of the nitrosating agents. A number of possibilities have been suggested, and these include HNO_2, NO, NO_2, N_2O_3, and the nitrosonium cation, ^+NO. Some nitrosants cannot exist under certain conditions; for

Can. J. Chem. Downloaded from www.nrcresearchpress.com by UNIVERSITAT DE VALENCIA on 10/20/12
For personal use only.

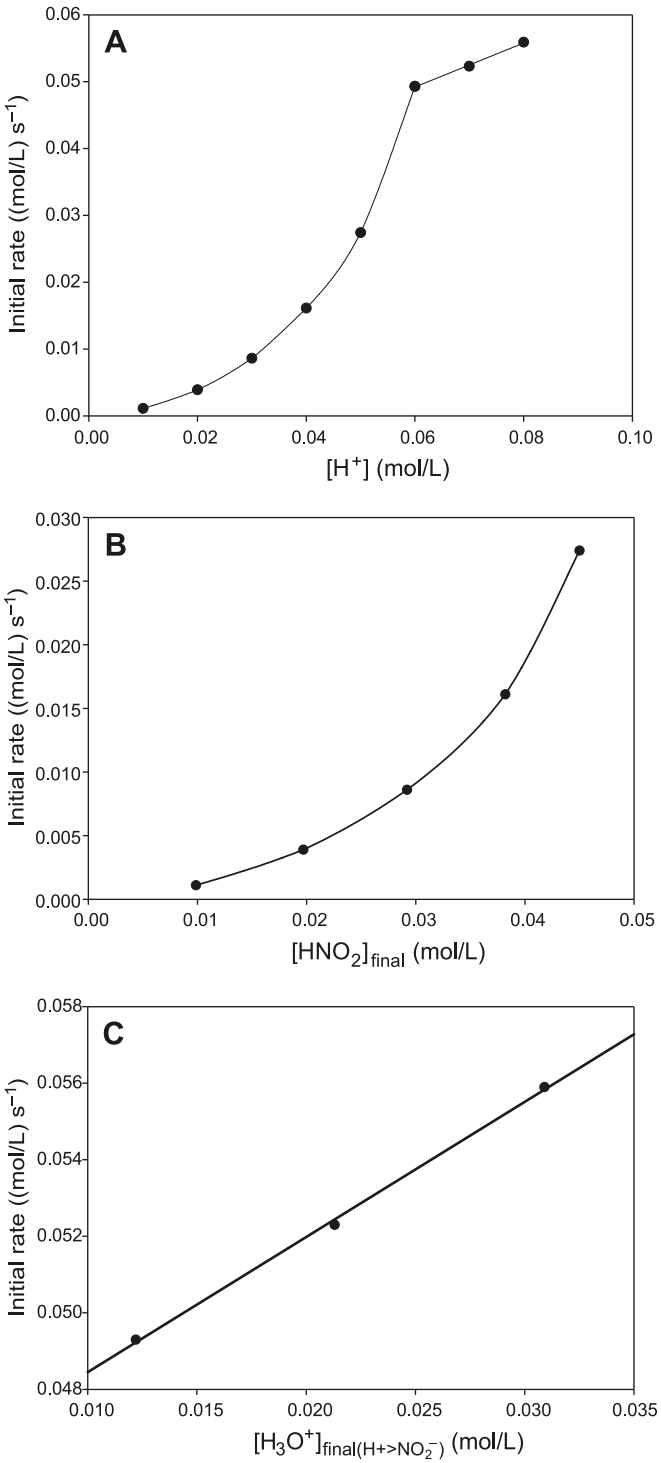


Fig. 6. (A) Plot of the raw kinetics data for the effect of added acid on the rate of nitrosation.$[CA]_0 = 0.05$ mol/L; $[NO_2^-]_0 = 0.05$ mol/L; and $[H^+]_0$ was varied between 0.01 and 0.08 mol/L. For the first four data points, $[NO_2^-]_0 > [H^+]_0$. The linear potion of the plot represents excess proton concentrations over nitrite. Acid concentrations plotted here are those experimentally added and not calculated. (B) Plot of initial rate versus nitrous acid concentrations of the experimental data in Fig. 6A and calculated in Table 1. This plot involves the region at which initial nitrite concentrations exceed acid concentrations. (C) Plot showing the linear dependence of the rate of formation of *S*-nitrosocysteamine (CANO) on $[H_3O^+]$ in high acid concentrations, where initial acid concentrations exceed nitrite concentrations. Nitrous acid concentrations are nearly constant in this range (see Table 1).

example, the ^+NO cannot exist at high pH[49] conditions and NO_2 cannot be produced in strictly anaerobic conditions. Figure 10 shows two nitrosation reactions at equivalent conditions except that one was run in solutions that had been degassed with argon and immediately capped. Aerobic environments can form NO_2 from NO and subsequently N_2O_3 will also be formed.[50]

[R6] $\quad NO + 1/2O_2 \rightarrow NO_2$

[R7] $\quad NO + NO_2 \rightarrow N_2O_3$

Both NO_2 and N_2O_3 are potent nitrosating agents.[29] There is a slightly higher rate of nitrosation in aerobic environments when compared with those in anaerobic environments. This is a reflection of the low dissolved oxygen concentrations available in aqueous solutions at approximately 2×10^{-4} mol/L. Thus, although formation for these nitrosants is favored, their viability is hampered by the low concentrations of oxygen as well as NO, which is only produced during the decomposition of the nitrosothiol. NO was not detected during the formation of CANO. In the aqueous environment utilized for these experiments, reaction of aqueous N_2O_3 to nitrous acid would be overwhelmingly dominant. This is a rapid equilibrium reaction that favors the weak acid, HNO_2.

[R8] $\quad N_2O_3(aq) + H_2O(l) \leftrightarrow 2HNO_2(aq); \quad K_H$

Early studies by Bunton and Steadman[51] had erroneously estimated a value for $K_H^{-1} = 0.20$ (mol/L)$^{-1}$, which would indicate appreciable amounts of N_2O_3(aq) over nitrous acid. A more accurate evaluation by Markovits et al.[52] gave a more realistic value of $K_H^{-1} = 3.03 \times 10^{-3}$ (SD 0.23×10^{-3}) (mol/L)$^{-1}$. According to Turney,[53] appreciable amounts of N_2O_3 can only exist in highly acidic environments, in the region of 5 mol/L perchloric acid. Such conditions are not applicable for the physiological environment. Most nitrosation studies in aerobic NO environments neglect the contribution to nitrosation by NO_2 and only concentrate on NO and N_2O_3. NO_2 concentration will always be negligibly low because of rxn. [R6], which is two orders of magnitude greater than the rate of nitrosation by NO_2 (1.1×10^9 (mol/L)$^{-1}$ s^{-1} vs 2.0×10^7 (mol/L)$^{-1}$ s^{-1}, respectively),[54,55] is hampered by the low concentrations of oxygen available. In the presence of NO, it is more unstable with respect to N_2O_3.

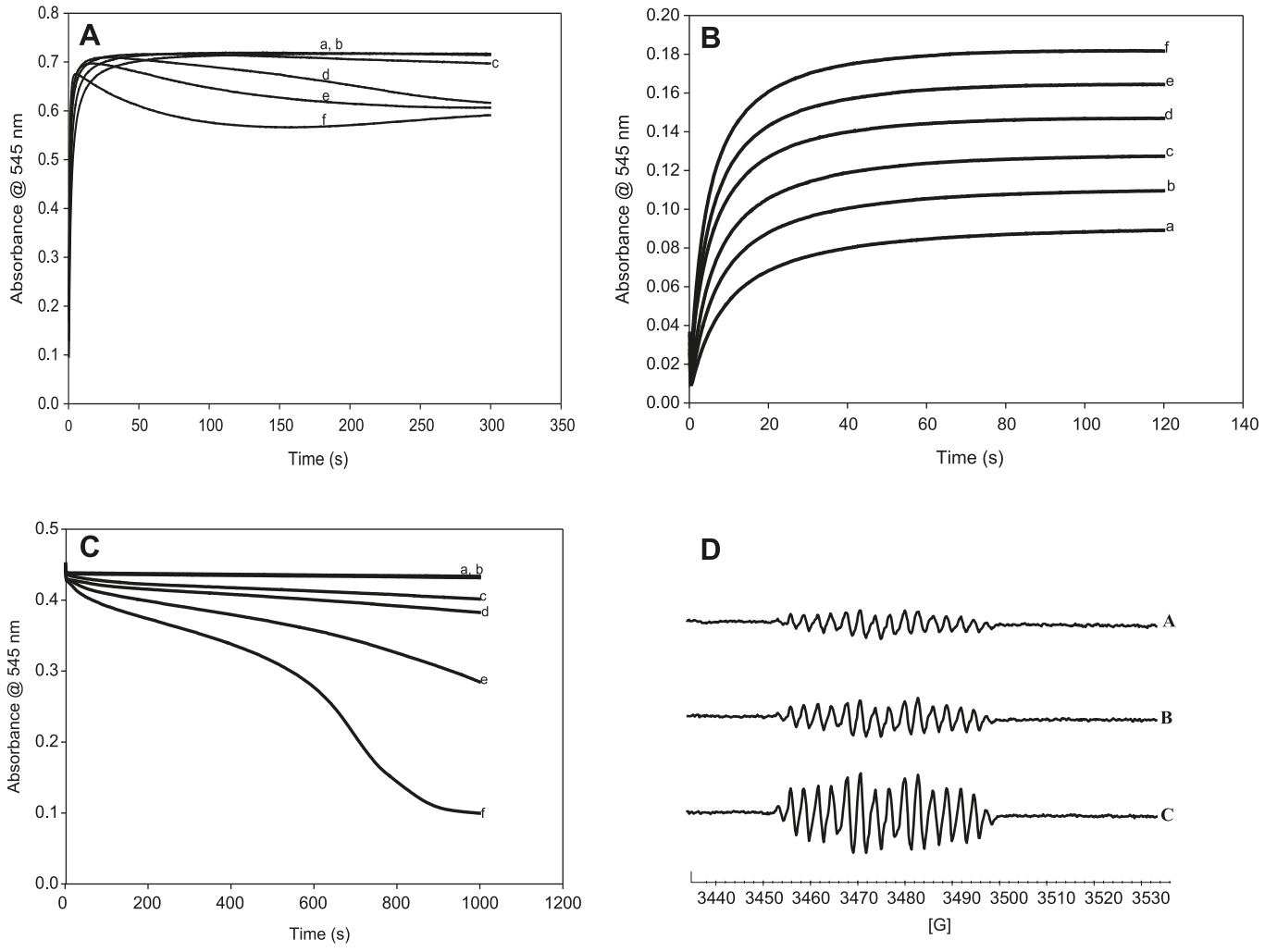
All nitrosation kinetics show first-order dependence in both thiol and nitrite with a complex dependence on acid. Data in Figs. 4 and 5 show this strong first-order dependence on CA and on nitrite. In conditions in which acid concentrations are less than initial nitrite concentrations, the effect of nitrite is more difficult to interpret, since a change in its concentrations concomitantly induces a change in both acid and HNO_2 concentrations, and thus its sole effect cannot be isolated. First-order kinetics in nitrite strongly suggest that the major nitrosant at the beginning of the reaction is HNO_2, since there is a direct correlation between nitrite concentrations and HNO_2, especially when there is consistently excess

Can. J. Chem. Downloaded from www.nrcresearchpress.com by UNIVERSITAT DE VALENCIA on 10/20/12
For personal use only.

Table 1. Input species concentrations and final reagent concentrations for acid dependence experiments (units of mol/L).

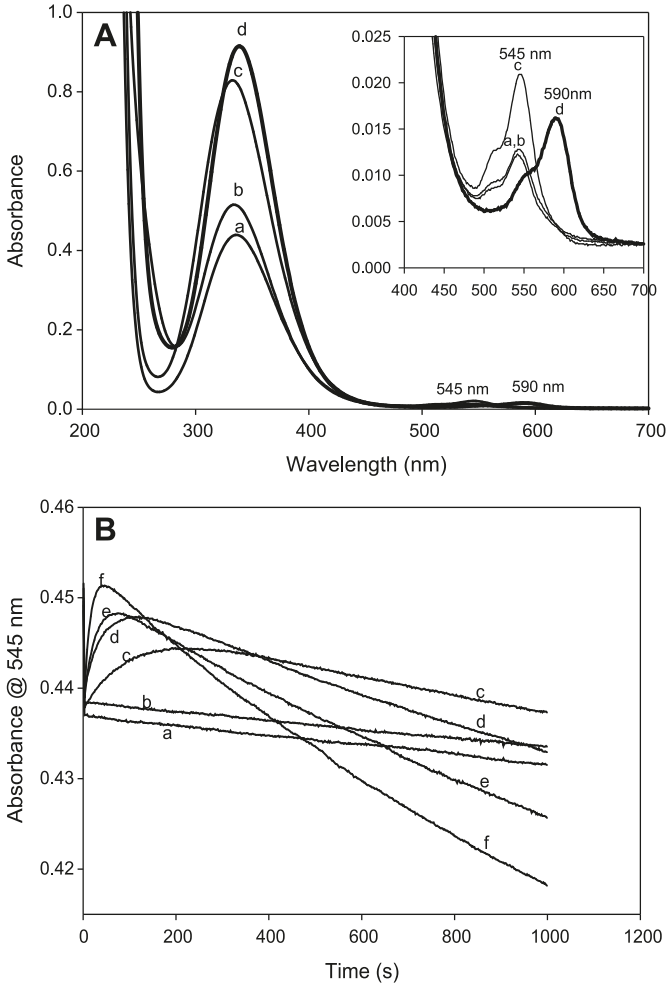
$[H^+]_{added}$	$[NO_2^-]_{added}$	$[HNO_2]_{initial}$	$[NO_2^-]_{final}$	$[HNO_2]_{final}$	$[H_3O^+]_{final}$
0.01	0.05	0.01	4.01×10^{-2}	9.86×10^{-3}	1.38×10^{-4}
0.02	0.05	0.02	3.04×10^{-2}	1.97×10^{-2}	3.63×10^{-4}
0.03	0.05	0.03	2.08×10^{-2}	2.92×10^{-2}	7.90×10^{-4}
0.04	0.05	0.04	1.18×10^{-2}	3.82×10^{-2}	1.82×10^{-3}
0.05	0.05	0.05	5.03×10^{-3}	4.50×10^{-2}	5.03×10^{-3}
0.06	0.05	0.05	2.22×10^{-3}	4.78×10^{-2}	1.22×10^{-2}
0.07	0.05	0.05	1.07×10^{-3}	4.89×10^{-2}	2.11×10^{-2}
0.08	0.05	0.05	8.93×10^{-4}	4.91×10^{-2}	3.09×10^{-2}

Fig. 7. (A) Absorbance traces showing the effect of varying Cu^{2+} concentrations on the rate of formation of CANO. There is a progressive increase in the rate of *S*-nitrosocysteamine (CANO) formation with an increase in Cu^{2+} concentration. $[CA]_0 = [NO_2^-]_0 = [H^+]_0 = 0.05$ mol/L; and (a) $[Cu^{2+}]_0 = 0.00$ mol/L, (b) $[Cu^{2+}]_0 = 5$ μmol/L, (c) $[Cu^{2+}]_0 = 15$ μmol/L, (d) $[Cu^{2+}]_0 = 100$ μmol/L, (e) $[Cu^{2+}]_0 = 1$ mmol/L, and (f) $[Cu^{2+}]_0 = 2.5$ mmol/L. CA, cysteamine hydrochloride. (B) Absorbance traces showing the formation of CANO via a reaction of CA, nitrite, and copper(II) without acid. The amount of CANO formed increases with an increase in Cu^{2+} concentration. No formation of CANO was observed with Cu^+. The result shows the catalytic effect of Cu^{2+} on the rate of formation of *S*-nitrosothiol (RSNO). $[CA]_0 = [NO_2^-]_0 = [H^+]_0 = 0.05$ mol/L; and (a) $[Cu^{2+}] = 0.0025$ mol/L, (b) $[Cu^{2+}] = 0.0030$ mol/L, (c) $[Cu^{2+}] = 0.0035$ mol/L, (d) $[Cu^{2+}] = 0.0040$ mol/L, (e) $[Cu^{2+}] = 0.0045$ mol/L, and (f) $[Cu^{2+}] = 0.0050$ mol/L. (C) Effect of Cu^{2+} on the stability of CANO in a pH 7.4 phosphate buffer. This reaction involves the reduction of Cu^{2+} to Cu^+, which causes the decomposition of CANO. $[CANO]_0 = 0.028$ mol/L; (a) $[Cu^{2+}]_0 = 0.00$ mol/L (pure CANO), (b) $[Cu^{2+}]_0 = 0.00$ mol/L (pure CANO in 0.00001 mol/L EDTA), (c) $[Cu^{2+}]_0 = 5$ μmol/L, (d) $[Cu^{2+}]_0 = 10$ μmol/L, (e) $[Cu^{2+}]_0 = 20$ μmol/L, and (f) $[Cu^{2+}]_0 = 30$ μmol/L. (D) Electron paramagnetic resonance (EPR) spectra of the NO radical showing the catalytic effect of Cu^{2+} on the rate of decomposition of CANO. The intensity of the spectra increases with an increase in Cu^{2+} concentration. $[CANO]_0 = 0.01$ mol/L; (a) $[Cu^{2+}]_0 = 0.00$, (b) $[Cu^{2+}]_0 = 1.0 \times 10^{-4}$ mol/L, and (c) $[Cu^{2+}]_0 = 2.0 \times 10^{-4}$ mol/L.



Can. J. Chem. Downloaded from www.nrcresearchpress.com by UNIVERSITAT DE VALENCIA on 10/20/12
For personal use only.

Fig. 8. (A) Superimposed spectra of four well-known nitrosothiols (a) CysNO, (b) *S*-nitrosocysteamine (CANO), (c) *S*-nitrosoglutathione (GSNO), and (d) nitrosothiol of penicillamine (SNAP). Three of them nearly have the same ε at 545 nm. The observed separation in the absorbances of these three at 545 nm is due to staggering of the time lag before acquiring the spectrum. (B) The effect of glutathione (GSH) on the stability of CANO in a pH 7.4 phosphate buffer. All experimental traces have $[CA]_0 = 0.03$ mol/L, $[NO_2^-]_0 = 0.03$ mol/L, and $[H^+]_0 = 0.05$ mol/L. (a) [GSH] = 0, (b) [GSH] = 0, (c) [GSH] = 0.01 mol/L, (d) [GSH] = 0.02 mol/L, (e) [GSH] = 0.03 mol/L, and (f) [GSH] = 0.05 mol/L. Traces a and b are controls. Trace a has no EDTA. Trace b is the same as trace a with 10 μmol/L of EDTA. There is no significant difference between traces a and b, indicating that the water used for preparing reagent solutions did not contain enough trace metal ions to affect the kinetics. Ten microlitres of EDTA was added to



acid over nitrite. After performing calculations for the relevant reactive species in the reaction medium (Table 1), the plot of the initial rate of nitrosation versus nitrous acid concentrations shows a parabolic dependence, which erroneously suggests second-order kinetics in HNO_2 (Fig. 6B) for the region in which initial nitrite concentrations exceed acid. As mentioned in the Results section, the data in Table 1 show that HNO_2 is not changing in isolation. Both nitrite and acid are also concomitantly changing, and so the effect observed in rate is not solely attributable to changes in HNO_2 concentrations. When acid is in excess over nitrite, the amount of HNO_2 saturates, but as can be seen in Fig. 6C, the rate keeps increasing linearly with an increase in acid, indicating the presence of multiple nitrosating agents apart from HNO_2. The simplest rate law that can explain this nitrosation rate involves ^+NO and HNO_2. ^+NO can be formed from the protonation of HNO_2:

[R9] $$HNO_2 + H_3O^+ \leftrightarrow H(OH)N{=}O^+ + H_2O; \quad K_b$$

($H(OH)N{=}O^+$ is a hydrated nitrosonium cation, $^+NO + H_2O$).

The overall rate of reaction, using these two nitrosants gives

[1] $$\text{Rate} = \left(\frac{[H^+][N(III)]_T}{[H^+] + K_a}\right)[CA](k_1 + k_2K_b[H^+])$$

where $[N(III)]_T$ is the total concentrations of nitrous acid and nitrite as calculated in Table 1 (columns 4 and 5) and $[H^+]$ is the calculated acid concentration in column 6 of Table 1. K_a is the acid dissociation constant of nitrous acid, K_b is the equilibrium for the protonation of nitrous acid (rxn. [R9]), k_1 is the bimolecular rate constant for the nitrosation of CA by HNO_2, and k_2 is the bimolecular rate constant for the nitrosation by ^+NO. K_a was taken as 5.62×10^{-4} $(mol/L)^{-1}$ and, thus, at high acid concentrations, a plot of Rate/$[N(III)]_T$ [CA] vs $[H^+]$ should give a straight line with slope k_2K_b and intercept k_1. This type of plot only applies to conditions of excess acid over nitrite (Fig. 6C). One can derive values for k_1 and product k_2K_b from these series of plots. A value of $k_1 = 17.9 \pm 1.5$ $(mol/L)^{-1}$ s^{-1} was derived from a series of several complementary experiments. k_2 was deduced as 6.70×10^4 $(mol/L)^{-1}$ s^{-1} after assuming a K_b value of 3.16×10^{-2} $(mol/L)^{-1}$.

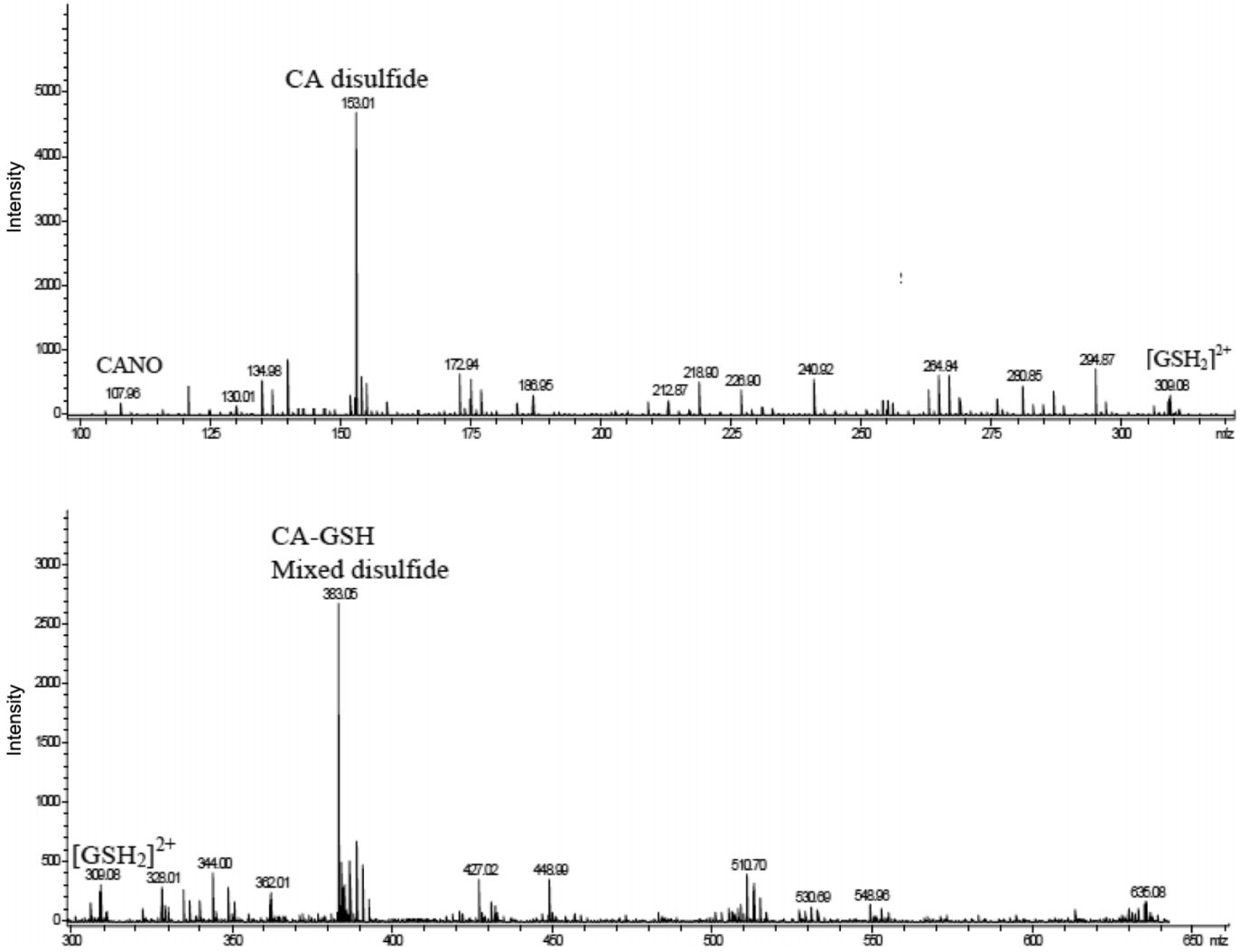
Decomposition of CANO

RSNOs differ greatly in their stabilities, and most of them have never been isolated in solid form. Homolysis of the S–N bond occurs both thermally and photochemically, but, generally, these processes are very slow at room temperature and in the absence of radiation of the appropriate wavelength. In vivo decomposition of RSNOs is likely to proceed through other pathways apart from these two. The presence of trace amounts of Cu(II) or Cu(I) can efficiently catalyze RSNOs to disulfide and nitric oxide (see Figs. 7A–7D).

[R10] $$2RSNO \rightarrow RSSR + 2NO$$

The characterization of the S–N bond is crucial in determining the stability of RSNOs, and, unfortunately, very little work has been performed in this area. The little crystallographic data available on isolable RSNOs indicate that the S–N bond is weak, sterically unhindered, elongated at between 0.17 and 0.189 nm,[56] and exists as either the cis (syn) or trans (anti) conformers. These conformers are nearly isoenergetic but separated by a relatively high activation barrier of ~11 kcal mol^{-1} (1 cal = 4.184 J). CANO is a primary *S*-nitrosothiol, with primary and secondary nitrosothiols known to be kinetically unstable to decomposition when compared with tertiary nitrosothiols.[57,58] *S*-Nitroso-*N*-acetylpenicillamine is the most well-known stable tertiary nitrosothiol.[59] The mechanism of decomposition of nitrosothiols was believed to

Fig. 9. A GC–MS spectrum of a 3:5 ratio of *S*-nitrosocysteamine (CANO) to glutathione (GSH); trace f in Fig. 8B. Final products were predominantly the mixed disulfide and cysteamine with no evidence of oxidized glutathione (GSSG). CA, cysteamine hydrochloride.

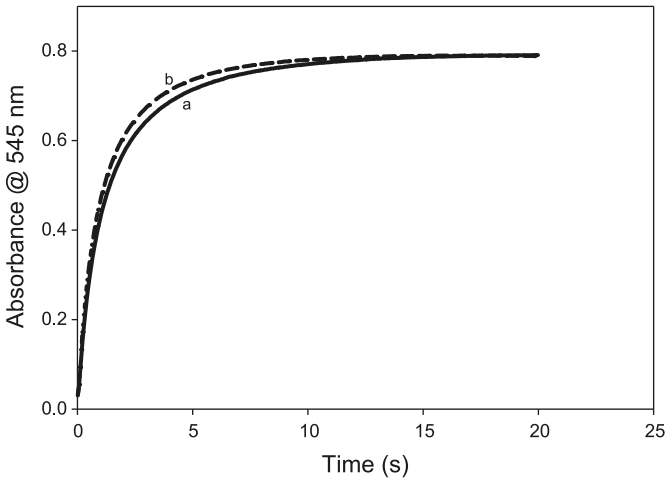


proceed through the homolytic cleavage of this weak S–N bond. Computed S–N bond dissociation energies for nitrosothiols show very little variation, however, between primary, secondary, and tertiary nitrosothiols, resulting in very similar homolysis rates of reaction at elevated temperatures for all nitrosothiols. The computed activation parameters for thermal homolysis to occur are prohibitively high for this to be a dominant pathway under normal biological conditions. For example, assuming an approximate S–N bond energy of 31 kcal,[58] a rough calculation will indicate that if decomposition was to proceed solely through homolysis, the half-life of a typical nitrosothiol would be in the region of years instead of the minutes to hours that are observed.[60] This analysis does not support the work reported by Roy et al.[61] in which they established homolysis as the major decomposition pathway. They also managed to trap the thiyl radical, RS·. Close examination of their reaction conditions show high trap concentrations (0.2 mol/L DMPO) and nitrosothiol (0.1 mol/L). Such conditions would catch even very low concentrations of thiyl radical, but would not necessarily indicate that this was the dominant pathway and whether it was derived solely from homolytic cleavage of the S–N bond. Nitrosothiol decomposition rates in the absence of metal ions are known to be mostly zero order[57] and this is inconsistent with an S–N bond homolysis-driven decomposition,[62] which would have been expected to be first order. In the presence of excess thiol, however, decomposition of nitrosothiols proceeds via a first-order decay process.[59] The absence of first-order decay kinetics in the decomposition of CANO also rules out homolysis as a dominant pathway. For a series of nitrosothiols, the homolysis-dependent decomposition rates are not dependent on the bulkiness of the substituent groups attached to the nitrosothiols, which seems to enhance the calculations that showed no discernible difference in the S–N bond energies irrespective of whether the nitrosothiol was primary, secondary, or tertiary.[63] In aerated solutions, the decay was autocatalytic, thus implicating N_2O_3 as the autocatalytic propagating species (see rxns. [R6] and [R7]). Nitrosothiol decompositions were much slower in solutions in which NO was not allowed to escape, implicating NO as a possible retardant of nitrosothiol decomposition.[25] This can be explained by the recombination of the thiyl radical with NO in the reaction cage after initial cleavage. Elimination of NO from the medium by bubbling air forces rxn. [R11] to the right.

Can. J. Chem. Downloaded from www.nrcresearchpress.com by UNIVERSITAT DE VALENCIA on 10/20/12
For personal use only.

Can. J. Chem. Downloaded from www.nrcresearchpress.com by UNIVERSITAT DE VALENCIA on 10/20/12
For personal use only.

Fig. 10. Evaluating the effect of oxygen on the rate of nitrosation of cysteamine. The solutions purged with argon (trace a) give a very slightly lower rate of nitrosation, indicating a small and insignifant contribution of nitrosation by N_2O_3. $[CA]_0 = 0.05$ mol/L; $[H^+]_0 = 0.08$ mol/L; and $[NO_2^-]_0 = 0.07$ mol/L. CA, cysteamine hydrochloride.



[R11] $\mathrm{RSNO} \leftrightarrow \mathrm{RS}^{\bullet} + \mathrm{NO}$

No mechanism has yet been proposed for the implication of N_2O_3 in the autocatalytic mechanism. One can assume that N_2O_3 should assist in the cleavage of the S–N bond, thus accelerating the rate of homolytic decomposition of RSNOs.

In aerated solutions, NO then undergoes rxns. [R6] and [R7] to yield N_2O_3.

[R12] $\mathrm{RSNO} + \mathrm{N_2O_3} \rightarrow \mathrm{RSN(NO_2)O}^{\bullet} + \mathrm{NO}$

The incorporation of the NO_2^- group in the nitrosothiol would weaken the S–N bond, leading to its easy cleavage and regeneration of the N_2O_3 molecule, which will further catalyze the decomposition.

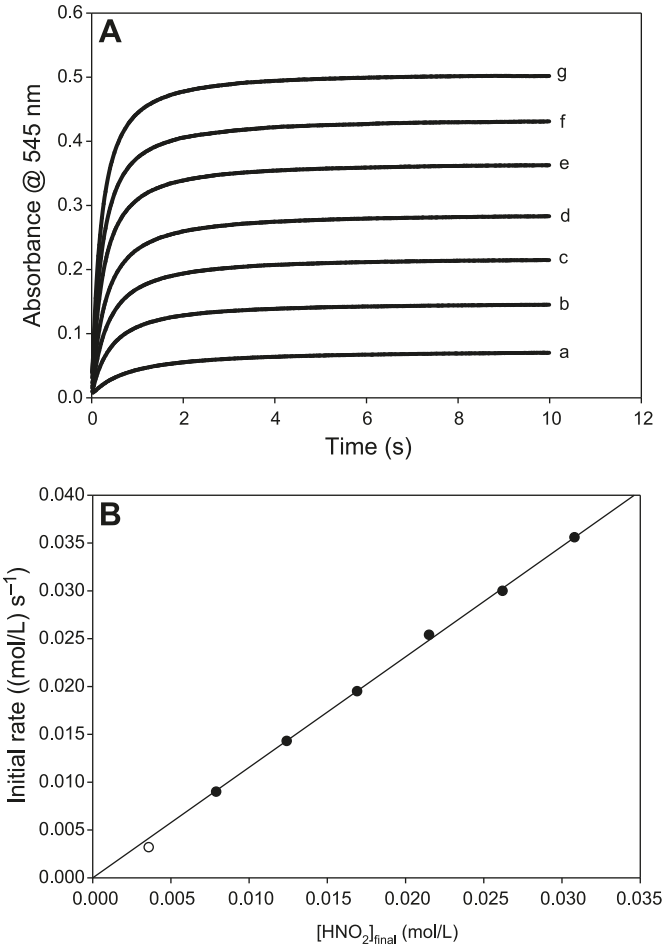
[R13] $\mathrm{RSN(NO_2)O}^{\bullet} \rightarrow \mathrm{RS}^{\bullet} + \mathrm{N_2O_3}$

The sequence of rxns. [R11]–[R13] will deliver autocatalysis in N_2O_3, since rxn. [R13] produces N_2O_3, which recycles back into rxn. [R12].

Recent results have suggested a novel pathway for the decomposition of nitrosothiols that involves an initial internal rearrangement to form an N-nitrosation product.[64] Typical nitrosothiol decomposition products after such an internal rearrangement would include thiiranes and 2-hydroxy-mercaptans. This mechanism has been used successfully to explain the production of a small but significant quantity of 2-hydroxy-3-mercaptopropionic acid (apart from the dominant product cystine) in the decomposition of *S*-nitrosocysteine. The GC–MS spectrum shown in Fig. 2, however, gives a dominant signal for dimeric cystamine, with very little evidence of any other significant products, indicating very little initial N-transnitrosation.

The copper-catalyzed decomposition of nitrosothiols has been well-documented.[65–67] The varying rates of nitrosothiol decompositions reported by different research groups can be traced possibly to adventitious metal ion catalysis from the water used in preparing reagent solutions. Even in our case, with the maximum metal ion concentrations of 0.43 ppb in Pb^{2+}, small differences can be observed in EDTA-laced reaction solutions and those that are not (see traces a and b in Fig. 7C). Nitrosothiol decompositions have also implicated other metal ions and not just specifically copper.[66] Although Cu(II) ions are used to catalyze nitrosothiol decomposition, the active reagent is Cu(I). In this catalytic mechanism, Cu redox cycles between the +2 and +1 oxidation states. Only trace amounts of Cu(I) are needed to effect the catalysis, and these can be generated from the reduction of Cu(II) ions from minute amounts of thiolate anions that exist in equilibrium with the nitrosothiol.

Fig. 11. (A) Evaluation of unambigous nitrous acid dependence by employing $[H^+]_0 = [NO_2^-]_0$ and varying both at the same equimolar concentrations. $[CA]_0$ fixed at 0.25 mol/L. (a) $[H^+]_0 = [NO_2^-]_0 = 0.005$ mol/L, (b) $[H^+]_0 = [NO_2^-]_0 = 0.010$ mol/L, (c) $[H^+]_0 = [NO_2^-]_0 = 0.015$ mol/L, (d) $[H^+]_0 = [NO_2^-]_0 = 0.020$ mol/L, (e) $[H^+]_0 = [NO_2^-]_0 = 0.025$ mol/L, (f) $[H^+]_0 = [NO_2^-]_0 = 0.030$ mol/L, and (g) $[H^+]_0 = [NO_2^-]_0 = 0.035$ mol/L. (B) Plot of initial rate of nitrosation versus initial nitrous acid concentrations as calculated in Table 2 and derived from the data in Fig. 11A. This plot is linear, as opposed to Fig. 6C.



[R14] $\mathrm{RSNO} \leftrightarrow \mathrm{RS^-} + \mathrm{NO^+}$

[R15] $2\mathrm{Cu^{2+}} + 2\mathrm{RS^-} \rightarrow \mathrm{RSSR} + 2\mathrm{Cu^+}$

[R16] $\mathrm{Cu^+} + \mathrm{RSNO} \rightarrow [\mathrm{RS(Cu)NO}]^+$

Can. J. Chem. Downloaded from www.nrcresearchpress.com by UNIVERSITAT DE VALENCIA on 10/20/12
For personal use only.

Table 2. Input species concentration and final reagent concentrations for nitrous acid dependence experiments with $[H^+]_0 = [NO_2^-]_0$.

$[H^+]_{added}$	$[NO_2^-]_{added}$	$[HNO_2]_{initial}$	$[H_3O^+]_{final}$	$[NO_2^-]_{final}$	$[HNO_2]_{final}$
5.00×10^{-3}	5.00×10^{-3}	5.00×10^{-3}	1.42×10^{-3}	1.42×10^{-3}	3.58×10^{-3}
1.00×10^{-2}	1.00×10^{-2}	1.00×10^{-2}	2.11×10^{-3}	2.11×10^{-3}	7.89×10^{-3}
1.50×10^{-2}	1.50×10^{-2}	1.50×10^{-2}	2.64×10^{-3}	2.64×10^{-3}	1.24×10^{-2}
2.00×10^{-2}	2.00×10^{-2}	2.00×10^{-2}	3.08×10^{-3}	3.08×10^{-3}	1.69×10^{-2}
2.50×10^{-2}	2.50×10^{-2}	2.50×10^{-2}	3.48×10^{-3}	3.48×10^{-3}	2.15×10^{-2}
3.00×10^{-2}	3.00×10^{-2}	3.00×10^{-2}	3.83×10^{-3}	3.83×10^{-3}	2.62×10^{-2}
3.50×10^{-2}	3.50×10^{-2}	3.50×10^{-2}	4.16×10^{-3}	4.16×10^{-3}	3.08×10^{-2}

Table 3. The set of reactions used for simulating the nitrosation of cysteamine. RSH, cysteamine.

Reaction No.	Reaction	k_f	k_r
M1	$H^+ + NO_2^- \rightleftharpoons HNO_2$	1.10×10^9	6.18×10^5
M2	$2HNO_2 \rightleftharpoons N_2O_3 + H_2O$	1.0×10^2	1.0×10^8
M3	$HNO_2 + H^+ \rightleftharpoons {}^+N{=}O + H_2O$	3.16×10^5	1.00×10^7
M4	$RSH + HNO_2 \rightarrow RSNO + H_2O$	17.9	~0
M5	$RSH + {}^+N{=}O \rightleftharpoons RSNO + H^+$	6.7×10^4	1.0×10^{-3}
M6	$N_2O_3 \rightleftharpoons NO + NO_2$	8.0×10^9	6.0×10^8
M7	$2RSNO \rightleftharpoons RSSR + 2NO$	4.0×10^{-3}	~0
M8	$RSH + N_2O_3 \rightarrow RSNO + HNO_2$	5.0×10^3	~0

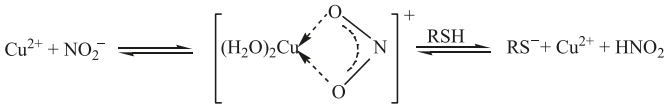
Note: k_f, forward rate constant; k_r, reverse rate constant.

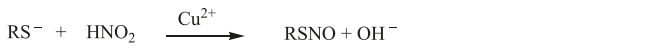
$$[R17] \qquad [RS(Cu)NO]^+ \rightarrow RS^- + NO + Cu^{2+}$$

The cascade of rxns. [R14]–[R17] continues until the nitrosothiol is depleted and converted to the disulfide. The complex formed in rxn. [R16] has been justified through density functional theory studies that report that Cu(I) binds more strongly to the S center than to the N center of the nitrosothiol.[65] This preferential binding weakens and lengthens the S–N bond, thus facilitating its cleavage. It is difficult to extrapolate this proposed mechanism into the physiological environment, but some experimental results have shown that protein-bound Cu^{2+} catalyzed nitric oxide generation from nitrosothiols, but not with the same efficiency as the free hydrated ion.[68] Further studies are needed to evaluate the efficiency of this catalysis, especially in copper-based enzymes.

Effect of Cu(II) on the nitrosation of cysteamine (Fig. 7B)

The fact that Cu(II) ions can assist in nitrosating CA from nitrite in the absence of acid while Cu(I) ions are unable to effect this can be explained by recognizing that nitrosation is an electrophilic process, where NO effectively attaches as the (formally) positive charge, while eliminating a positively charged proton. Cu(II), in this case, acts by complexing to the nitrite and forming a nitrosating species that will release the Cu(II) ions after nitrosation.



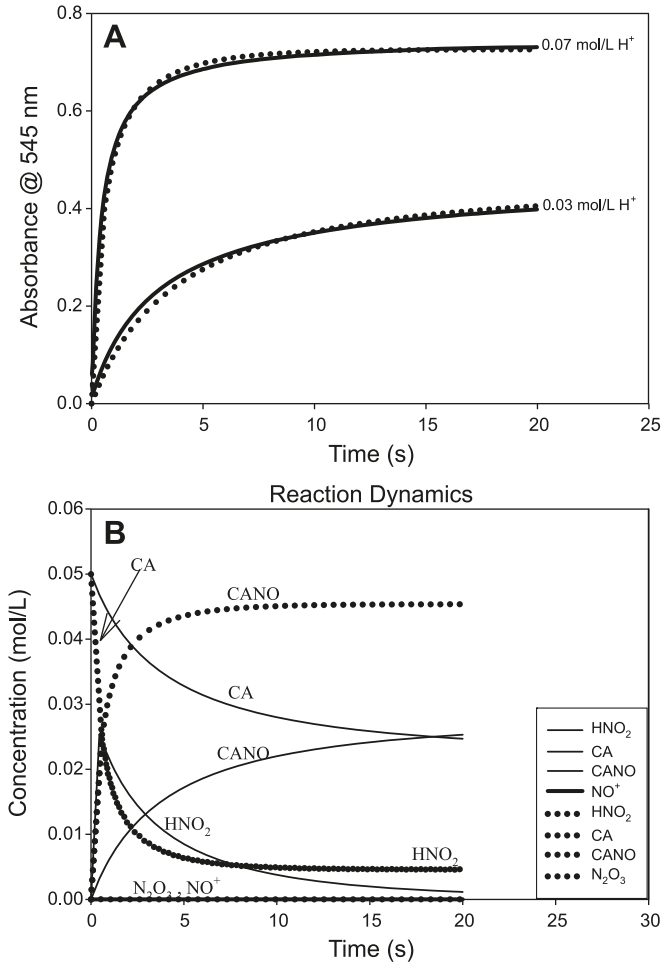


Further experiments on the effect of nitrous acid

Since nitrous acid is the major nitrosation species, another series of experiments were undertaken in which the effect of nitrous acid could be unambiguously determined. For the data shown in Fig. 11A, nitrite and acid were kept at equimolar concentrations and varied with that constraint. Final proton and nitrite concentrations after dissociation are also equal for electroneutrality (see Table 2). Thus, if our simple mechanism is plausible, a plot of nitrous acid versus initial nitrosation rate should be linear with the expected slight tailing at either extreme of the nitrous acid concentrations owing to nonlinear generation of the free acid derived from the quadratic equation. Using the same rate law as eq. [1], a value of k_1 can be derived and compared with values obtained from the Fig. 6C plot. Kinetics constants derived from the Fig. 11B plot are not expected to be as accurate as those from Fig. 6C, but should deliver values close to those from high acid environments. For the case of nitrous acid as the nitrosating agent (too low a concentration of excess H_3O^+ to effect equilibrium of rxn. [R9]), data derived from Fig. 11B delivered an upper limit rate constant for k_1 that was higher than that derived from Fig. 6C-type data, but well within the error expected for such a crude extrapolation. Other sets of kinetics data were derived in which CA concentrations were varied while keeping the nitrous acid concentrations constant. Varying nitrous acid concentrations were used and, for each, a CA dependence was plotted (data not shown). These were straight lines through the origin and with the slope determined by the concentration of nitrous acid and the free protons existing in solution after the dissociation of nitrous acid. For these kinetics data, eq. [1] had to be evaluated completely, since $K_a \approx [H_3O^+]$ and no valid approximation could be made. The values of k_1 and k_2K_b were utilized in eq. [1] to recalculate initial rates and slopes with respect to CA

Can. J. Chem. Downloaded from www.nrcresearchpress.com by UNIVERSITAT DE VALENCIA on 10/20/12
For personal use only.

Fig. 12. (A) Simulation of the short set of reactions shown in Table 3. Solid lines are experimental data and the symbols indicate simulations. The mechanism is dominated by the value of the bimolecular rate constant for the nitrosation of cysteamine hydrochloride (CA) by HNO_2 (k_1). $[CA]_0 = [NO_2^-]_0 = 0.05$ mol/L. (B) Results from the modeling that delivered simulations of the two traces shown in Fig. 12A. These simulations show the concentration variations of those species that could not be experimentally monitored. Neither N_2O_3 nor NO^+ rise to any significant concentration levels.



concentrations. These values were utilized to check the accuracy of the kinetics constants derived from high-acid-dependent experiments. It was noted that, within experimental error, these values checked and were generally robust.

Simulations

A small set of simple reactions was utilized to simulate the nitrosation kinetics. This set is shown in Table 3. At low acid concentrations, the nitrosation is dominated by HNO_2 as the nitrosant, and as acid concentrations are increased, both nitrous acid and the nitrosonium cation are involved in the nitrosation. Even though Table 3 includes nitrosation by N_2O_3, the lack of oxygen (approximately kept constant at 2.0×10^{-4} mol/L) and its most favored and rapid reaction to nitrous acid made the nitrosation by N_2O_3 insignificant. N_2O_3 is the dehydrated form of HNO_2 (rxn. [R8]), while reaction conditions were in an overwhelming excess of water. Its insignificant concentration ensured that the simulations were insensitive to value of the bimolecular nitrosation constant for N_2O_3 (k_{M8}). Figure 12B clearly shows that the concentration of N_2O_3 never rises to a level where it would be significant. The rate constants adopted for rxn. [M1] (Table 3) were not crucial for as long as they were fast (in both directions) and were connected by K_a. Increasing the forward and reverse rate constants while maintaining K_a only slowed the simulations, but did not alter the simulation results. Reaction [M2] (Table 3) was also a rapid hydration reaction that strongly favored HNO_2, thus rapidly depleting any N_2O_3 formed or merely keeping these concentrations depressed should the tandem rxns. [R6] + [R7] have been added to the mechanism. These were not utilized for this simulation because EPR experiments had not detected NO at the beginning of the reaction and had only detected NO during the decomposition of the nitrosothiol. There are no reliable thermodynamics parameters for rxn. [M3] (Table 3), since this would be heavily dependent on the pH of the medium. For the purposes of this simulation and some of our previous estimates, the equilibrium constant for rxn. [M3] was set at 3.16×10^{-2} $(mol/L)^{-1}$. Kinetics constants for rxns. [M4] and [M5] (Table 3) were derived from this study. In the absence of significant concentrations of N_2O_3, the simulations were insensitive to the kinetics constants utilized for rxns. [M6] and [M8] (Table 3). Reaction [M7] (Table 3) was assumed to be slow and, in the absence of Cu(II) ions or other adventitious ions, this is indeed so (see Figs. 7A and 7C). The simulations are shown in Fig. 12A, which gives a reasonably good fit from such a crude mechanism. Figure 12B is provided to show the concentration variation of some of the species that could not be experimentally determined. Of note is that N_2O_3 concentrations are depressed throughout the lifetime of the nitrosation. Even though ^+NO is also depressed in concentration, this can be explained by its high rate of nitrosation as soon as it is formed and an equilibrium that favors its hydration back to HNO_2 once the thiol is depleted.

Conclusion

This detailed kinetics study has shown that, even though there are several possible nitrosating agents in solution, in the physiological environment, with its slightly basic pH and low oxygen concentrations, the major nitrosant is HNO_2. Furthermore, the lifetime of CANO is not long enough to be able to be effectively used as a carrier of NO. GSH, which has been touted as a possible carrier of NO, appears to have a shorter lifetime than CANO. However, because of its overwhelming concentration in the physiological environment it might still be a major carrier of NO when it is compared with other thiols. Protein thiols, it appears, would be the best carriers by either intra- or inter-molecular transfer of NO through protein nitrosothionylation through exposed and accessible cysteine groups.[69]

Acknowledgements

This work was supported by Grant No. CHE 1053611 from the National Science Foundation (R.H.S.) and partly from Grant No. R01 EB2044 from the National Institutes of Health (R.S.).The findings and conclusions in this report are

those of the authors and do not necessarily represent the views of the National Institute for Occupational Safety and Health.

References

(1) Thomas, D. D.; Ridnour, L. A.; Isenberg, J. S.; Flores-Santana, W.; Switzer, C. H.; Donzelli, S.; Hussain, P.; Vecoli, C.; Paolocci, N.; Ambs, S.; Colton, C. A.; Harris, C. C.; Roberts, D. D.; Wink, D. A. *Free Radic. Biol. Med.* **2008**, *45* (1), 18. doi:10.1016/j.freeradbiomed.2008.03.020.

(2) Möller, M. N.; Li, Q.; Vitturi, D. A.; Robinson, J. M.; Lancaster, J. R., Jr; Denicola, A. *Chem. Res. Toxicol.* **2007**, *20* (4), 709. doi:10.1021/tx700010h.

(3) Li, H.; Samouilov, A.; Liu, X.; Zweier, J. L. *J. Biol. Chem.* **2001**, *276* (27), 24482. doi:10.1074/jbc.M011648200.

(4) Zweier, J. L.; Li, H.; Samouilov, A.; Liu, X. *Nitric Oxide* **2010**, *22* (2), 83. doi:10.1016/j.niox.2009.12.004.

(5) Godber, B. L.; Doel, J. J.; Sapkota, G. P.; Blake, D. R.; Stevens, C. R.; Eisenthal, R.; Harrison, R. *J. Biol. Chem.* **2000**, *275* (11), 7757. doi:10.1074/jbc.275.11.7757.

(6) Lincoln, J.; Hoyle, C. H. V.; Burnstock, G. *Nitric Oxide in Health and Disease;* Cambridge University Press: Cambridge, 1997.

(7) Williams, D. L. H. Nitric Oxide in Biological Systems. In *Nitrosation Reactions and the Chemistry of Nitric Oxide;* Elsevier: London, 2004; p 187.

(8) Priviero, F. B. M.; Leite, R.; Webb, R. C.; Teixeira, C. E. *Acta Pharmacol. Sin.* **2007**, *28* (6), 751. doi:10.1111/j.1745-7254.2007.00584.x.

(9) Nakane, M. *Clin. Chem. Lab. Med.* **2003**, *41* (7), 865. doi:10.1515/CCLM.2003.131.

(10) Stuart-Smith, K.; Warner, D. O.; Jones, K. A. *Eur. J. Pharmacol.* **1998**, *341* (2–3), 225. doi:10.1016/S0014-2999(97)01455-6.

(11) Newsholme, P.; Homem De Bittencourt, P. I.; O' Hagan, C.; De Vito, G.; Murphy, C.; Krause, M. S. *Clin. Sci. (Lond.)* **2010**, *118* (5), 341. doi:10.1042/CS20090433.

(12) Nahrevanian, H. *Braz. J. Infect. Dis.* **2009**, *13*, 440.

(13) Jadhav, V.; Jabre, A.; Chen, M.-F.; Lee, T.-J. *Stroke* **2009**, *40* (1), 261. doi:10.1161/STROKEAHA.108.516104.

(14) De Felice, M.; Porreca, F. *Cephalalgia* **2009**, *29* (12), 1277. doi:10.1111/j.1468-2982.2009.01873.x.

(15) Beckman, J. S.; Koppenol, W. H. *Am. J. Physiol. Cell Physiol.* **1996**, *40*, C1424.

(16) Huie, R. E.; Padmaja, S. *Free Radic. Res. Commun.* **1993**, *18* (4), 195. doi:10.3109/10715769309145868.

(17) Ozaki, T.; Kaibori, M.; Matsui, K.; Tokuhara, K.; Tanaka, H.; Kamiyama, Y.; Nishizawa, M.; Ito, S.; Okumura, T. *JPEN J. Parenter. Enteral Nutr.* **2007**, *31* (5), 366. doi:10.1177/0148607107031005366.

(18) Cauwels, A. *Kidney Int.* **2007**, *72* (5), 557. doi:10.1038/sj.ki.5002340.

(19) Glantzounis, G. K.; Rocks, S. A.; Sheth, H.; Knight, I.; Salacinski, H. J.; Davidson, B. R.; Winyard, P. G.; Seifalian, A. M. *Free Radic. Biol. Med.* **2007**, *42* (6), 882. doi:10.1016/j.freeradbiomed.2006.12.020.

(20) Chen, Y. Y.; Chu, H. M.; Pan, K. T.; Teng, C. H.; Wang, D. L.; Wang, A. H.; Khoo, K. H.; Meng, T. C. *J. Biol. Chem.* **2008**, *283* (50), 35265. doi:10.1074/jbc.M805287200.

(21) Wang, K.; Zhang, W.; Xian, M.; Hou, Y. C.; Chen, X. C.; Cheng, J. P.; Wang, P. G. *Curr. Med. Chem.* **2000**, *7*, 821.

(22) Hara, M. R.; Agrawal, N.; Kim, S. F.; Cascio, M. B.; Fujimuro, M.; Ozeki, Y.; Takahashi, M.; Cheah, J. H.; Tankou, S. K.; Hester, L. D.; Ferris, C. D.; Hayward, S. D.; Snyder, S. H.; Sawa, A. *Nat. Cell Biol.* **2005**, *7* (7), 665. doi:10.1038/ncb1268.

(23) Yao, D. D.; Gu, Z. Z.; Nakamura, T.; Shi, Z. Q.; Ma, Y. L.; Gaston, B.; Palmer, L. A.; Rockenstein, E. M.; Zhang, Z. H.; Masliah, E.; Uehara, T.; Lipton, S. A. *Proc. Natl. Acad. Sci. U. S.A.* **2004**, *101* (29), 10810. doi:10.1073/pnas.0404161101.

(24) Askew, S. C.; Barnett, D. J.; Mcaninly, J.; Williams, D. L. H. *J. Chem. Soc. Perkin Trans. 2* **1995**, 741.

(25) Beloso, P. H.; Williams, D. L. H. *Chem. Commun. (Camb.)* **1997**, (1), 89. doi:10.1039/a607228c.

(26) Dicks, A. P.; Li, E.; Munro, A. P.; Swift, H. R.; Williams, D. L. H. *Can. J. Chem.* **1998**, *76*, 789. doi:10.1139/v98-062.

(27) Dicks, A. P.; Beloso, P. H.; Williams, D. L. H. *J. Chem. Soc. Perkin Trans. 2* **1997**, 1429.

(28) Holmes, A. J.; Williams, D. L. H. *J. Chem. Soc. Perkin Trans. 2* **2000**, 1639.

(29) Noble, D. R.; Williams, D. L. H. *J. Chem. Soc. Perkin Trans. 2* **2002**, 1834.

(30) Williams, D. L. H. *Acc. Chem. Res.* **1999**, *32* (10), 869. doi:10.1021/ar9800439.

(31) Williams, D. L. H. *Nitric Oxide* **1997**, *1* (6), 522. doi:10.1006/niox.1997.0159.

(32) Williams, D. L. H. *Chem. Commun. (Camb.)* **1996**, (10), 1085. doi:10.1039/cc9960001085.

(33) Williams, D. L. H. *Transition Met. Chem.* **1996**, *21* (2), 189. doi:10.1007/BF00136555.

(34) Zamora, R.; Matthys, K. E.; Herman, A. G. *Eur. J. Pharmacol.* **1997**, *321* (1), 87. doi:10.1016/S0014-2999(96)00918-1.

(35) Kelly, G. S. *Altern. Med. Rev.* **1997**, *2*, 365.

(36) Gahl, W. A. *Eur. J. Pediatr.* **2003**, *162* (Suppl 1), S38. doi:10.1007/s00431-003-1349-x.

(37) Iwata, F.; Kuehl, E. M.; Reed, G. F.; Mccain, L. M.; Gahl, W. A.; Kaiser-Kupfer, M. I. *Mol. Genet. Metab.* **1998**, *64* (4), 237. doi:10.1006/mgme.1998.2725.

(38) Skovby, F.; Kleta, R.; Anikster, Y.; Christensen, R.; Gahl, W. A. *Am. J. Hum. Genet.* **2002**, *71*, 413.

(39) Chanakira, A.; Chikwana, E.; Peyton, D.; Simoyi, R. *Can. J. Chem.* **2006**, *84* (1), 49. doi:10.1139/v05-263.

(40) Martincigh, B. S.; Mundoma, C.; Simoyi, R. H. *J. Phys. Chem. A* **1998**, *102* (48), 9838. doi:10.1021/jp982575c.

(41) Simoyi, R. H.; Streete, K.; Mundoma, C.; Olojo, R. *South African J. Chem. (Suid-Africaanse Tydskrif Vir Chemie)* **2002**, *55*, 136.

(42) Liu, X.; Gillespie, J. S.; Martin, W. *Br. J. Pharmacol.* **1994**, *111*, 1287.

(43) Whiteside, W. M.; Sears, D. N.; Young, P. R.; Rubin, D. B. *Radiat. Res.* **2002**, *157* (5), 578. doi:10.1667/0033-7587(2002)157[0578:POSSNC]2.0.CO;2.

(44) Reszka, K. J.; Bilski, P.; Chignell, C. F. *Nitric Oxide* **2004**, *10* (2), 53. doi:10.1016/j.niox.2004.03.001.

(45) Choi, J. S.; Yoon, N. M. *J. Org. Chem.* **1995**, *60* (11), 3266. doi:10.1021/jo00116a001.

(46) Zhu, B. Z.; Antholine, W. E.; Frei, B. *Free Radic. Biol. Med.* **2002**, *32* (12), 1333. doi:10.1016/S0891-5849(02)00847-X.

(47) Reed, C. J.; Douglas, K. T. *Biochem. Biophys. Res. Commun.* **1989**, *162* (3), 1111. doi:10.1016/0006-291X(89)90788-2.

(48) Williams, D. L. H. Synthesis, Properties and Reactions of *S*-Nitrosothiols. In *Nitrosation Reactions and the Chemistry of Nitric Oxide;* Elsevier: London, 2004; p 137.

(49) Chipinda, I.; Simoyi, R. H. *J. Phys. Chem. B* **2006**, *110* (10), 5052. doi:10.1021/jp0531107.

(50) Jourd'heuil, D.; Jourd'heuil, F. L.; Feelisch, M. *J. Biol. Chem.* **2003**, *278* (18), 15720. doi:10.1074/jbc.M300203200.

Can. J. Chem. Downloaded from www.nrcresearchpress.com by UNIVERSITAT DE VALENCIA on 10/20/12
For personal use only.

(51) Bunton, C. A.; Stedman, G. *J. Chem. Soc.* **1958**, 2440. doi:10.1039/jr9580002440.
(52) Markovits, G. Y.; Schwartz, S. E.; Newman, L. *Inorg. Chem.* **1981**, *20* (2), 445. doi:10.1021/ic50216a025.
(53) Turney, T. A. *J. Chem. Soc.* **1960**, 4263. doi:10.1039/jr9600004263.
(54) Huie, R. E. *Toxicology* **1994**, *89* (3), 193. doi:10.1016/0300-483X(94)90098-1.
(55) Ford, E.; Hughes, M. N.; Wardman, P. *Free Radic. Biol. Med.* **2002**, *32* (12), 1314. doi:10.1016/S0891-5849(02)00850-X.
(56) Timerghazin, Q. K.; Peslherbe, G. H.; English, A. M. *Phys. Chem. Chem. Phys.* **2008**, *10* (11), 1532. doi:10.1039/b715025c.
(57) Stamler, J. S.; Toone, E. J. *Curr. Opin. Chem. Biol.* **2002**, *6* (6), 779. doi:10.1016/S1367-5931(02)00383-6.
(58) Grossi, L.; Montevecchi, P. C.; Strazzari, S. *J. Am. Chem. Soc.* **2001**, *123* (20), 4853. doi:10.1021/ja005761g.
(59) Bartberger, M. D.; Mannion, J. D.; Powell, S. C.; Stamler, J. S.; Houk, K. N.; Toone, E. J. *J. Am. Chem. Soc.* **2001**, *123* (36), 8868. doi:10.1021/ja0109390.
(60) Baciu, C.; Gauld, J. W. *J. Phys. Chem. A* **2003**, *107* (46), 9946. doi:10.1021/jp035205j.
(61) Roy, B.; du Moulinet d'Hardemare, A.; Fontecave, M. *J. Org. Chem.* **1994**, *59* (23), 7019. doi:10.1021/jo00102a028.
(62) Grossi, L.; Montevecchi, P. C. *J. Org. Chem.* **2002**, *67* (24), 8625. doi:10.1021/jo026154+.
(63) Field, L.; Dilts, R. V.; Ravichandran, R.; Lenhert, P. G.; Carnahan, G. E. *J. Chem. Soc. Chem. Commun.* **1978**, (6): 249. doi:10.1039/c39780000249.
(64) Peterson, L. A.; Wagener, T.; Sies, H.; Stahl, W. *Chem. Res. Toxicol.* **2007**, *20* (5), 721. doi:10.1021/tx700095u.
(65) Baciu, C.; Cho, K. B.; Gauld, J. W. *J. Phys. Chem. B* **2005**, *109* (4), 1334. doi:10.1021/jp0443759.
(66) McAninly, J.; Williams, D. L. H.; Askew, S. C.; Butler, A. R.; Russell, C. *J. Chem. Soc. Chem. Commun.* **1993**, (23): 1758. doi:10.1039/c39930001758.
(67) Singh, R. J.; Hogg, N.; Joseph, J.; Kalyanaraman, B. *J. Biol. Chem.* **1996**, *271* (31), 18596. doi:10.1074/jbc.271.31.18596.
(68) Dicks, A. P.; Williams, D. L. H. *Chem. Biol.* **1996**, *3* (8), 655. doi:10.1016/S1074-5521(96)90133-7.
(69) Foster, M. W.; Hess, D. T.; Stamler, J. S. *Trends Mol. Med.* **2009**, *15* (9), 391. doi:10.1016/j.molmed.2009.06.007.

Can. J. Chem. Downloaded from www.nrcresearchpress.com by UNIVERSITAT DE VALENCIA on 10/20/12
For personal use only.

Efficient one-pot syntheses of dibenzo[*a*,*i*] xanthene-diones and evaluation of their antioxidant activity

Jitender M. Khurana, Ankita Chaudhary, Anshika Lumb, and Bhaskara Nand

Can. J. Chem. Downloaded from www.nrcresearchpress.com by UNIVERSITAT DE VALENCIA on 10/20/12
For personal use only.

Abstract: Facile and convenient procedures for the synthesis of dibenzo[*a*,*i*]xanthene-diones have been described. The process employs one-pot condensation of aldehydes, 2-hydroxynaphthalene-1,4-dione, and 2-naphthol/2,7-dihydroxynaphthalene/2,6-dihydroxynaphthalene using catalytic sulfuric acid in water under reflux. Task-specific ionic liquid, 1-butyl-3-methylimidazolium hydrogen sulfate ([bmim]HSO_4), has also been found to be an effective catalyst for this transformation. The protocols defined herein prove to be efficient in terms of high yields, operational simplicity, easy workup, and short reaction time. Also, these compounds were screened for antioxidant activity by 2,2-diphenyl-1-picrylhydrazyl (DPPH) radical scavenging assay.

Key words: benzoxanthene, synthesis in water, task-specific ionic liquid, antioxidant activity, DPPH assay.

Résumé : On décrit une méthode simple et commode de synthèse des dibenzo[*a*,*i*]xanthènediones. Le procédé implique l'utilisation d'une condensation monotope d'aldéhydes, de 2-hydroxynaphtalène-1,4-dione et de 2-naphtol/2,7-dihydroxynaphtalène/2,6-dihydroxynaphtalène, en faisant appel à une catalyse par l'acide sulfurique dans l'eau, sous reflux. On a trouvé que le liquide ionique à tâche spécifique, le sulfate acide du 1-butyl-3-méthylimidazolium ([bmim]HSO_4) peut aussi être utilisé comme catalyseur efficace pour cette transformation. Les protocoles définis dans ce travail se sont avérés efficaces en termes de rendements élevés, simplicité d'opération, facilité d'extraction et de temps de réaction court. De plus, l'activité antioxydante de tous ces composés a été examinée par le biais de l'essai au piégeage du radical 2,2-diphényl-1-picrylhydrazyle (DPPH).

Mots-clés : benzoxanthène, synthèse en milieu aqueux, liquide ionique à tâche spécifique, activité antioxydante, essai au DPPH.

[Traduit par la Rédaction]

Introduction

Xanthenes and benzoxanthenes, being the structural motifs of a large number of naturally occurring as well as synthetic derivatives, hold a prominent position in medicinal chemistry.[1] Benzoxanthenes exhibit a broad spectrum of biological activities such as antiviral,[2] antibacterial,[3] anti-inflammatory, and [4] zoxazolamine antagonists,[5] as well as efficacy in photodynamic therapy.[6] These compounds can also be used as dyes,[7] pH-sensitive fluorescent materials for visualization of biomolecules,[8] and in laser technologies.[9] Moreover, natural and synthetic xanthenes and xanthones are also known for their antioxidant activity.[10] However, limited methods have been reported for the synthesis of dibenzo[*a*,*i*]xanthene-diones.[11] Development of improved and environmentally benign methodologies for the synthesis of xanthenes containing naphthoquinone fragments is an interesting challenge.

Multicomponent reactions (MCRs)[12] have emerged as an efficient and powerful tool for the synthesis of heterocyclic scaffolds and are useful for the construction of diverse chemical libraries of "druglike" molecules. The design of MCRs in nontoxic and nonvolatile media, such as ionic liquids, polyethylene glycol, and water, has gained significant impetus owing to environmental concerns. The advantages of conducting organic reactions in water include an enhancement in rate, ease of operation, and an improved safety profile.[13] Also, organic reactions in water exhibit unique reactivity and selectivity that is different from reactions in organic solvents.[14] In continuation of our studies on the development of new routes for the heterocyclic systems,[15] we have investigated the synthesis of dibenzo[*a*,*i*]xanthene-8,13-diones in aqueous medium and task-specific ionic liquid. Moreover, phenolic- and quinone-based compounds are known to show potent antioxidant activity that is attributed to their redox properties.[16] Therefore, we decided to screen the synthesized dibenzoxanthene-diones for their antioxidant activity by 2,2-diphenyl-1-picrylhydrazyl radical (DPPH) scavenging assay.

Results and discussion

We report herein an efficient synthetic route for the synthesis of 14-aryl-14*H*-dibenzo[*a*,*i*]xanthene-8,13-diones in aqueous media using H_2SO_4 as catalyst under reflux and also by utilizing the task-specific ionic liquid, 1-butyl-3-

Received 12 October 2011. Accepted 30 April 2012. Published at www.nrcresearchpress.com/cjc on 22 August 2012.

J.M. Khurana, A. Chaudhary, A. Lumb, and B. Nand. Department of Chemistry, University of Delhi, Delhi 110007, India.

Corresponding author: Jitender M. Khurana (e-mail: jmkhurana@chemistry.du.ac.in).

Can. J. Chem. Downloaded from www.nrcresearchpress.com by UNIVERSITAT DE VALENCIA on 10/20/12
For personal use only.

methylimidazolium hydrogen sulfate ([bmim]HSO_4), at 60 °C. Furthermore, the assessment of radical scavenging activity towards the DPPH radical was measured, and these compounds were found to scavenge the DPPH free radical efficiently.

The reaction conditions were optimized by the reactions of 4-methoxybenzaldehyde (1.0 mmol), 2-naphthol (1.0 mmol), and 2-hydroxynaphthalene-1,4-dione (1.0 mmol) in different media in the presence of acid catalysts like HCl, HNO_3, CH_3COOH, and H_2SO_4. The best result was obtained when the reaction was carried out in water in the presence of a catalytic amount of sulfuric acid (0.1 mmol) under reflux. The reaction underwent completion in 30 min yielding 92% of 14-(4-methoxyphenyl)-14*H*-dibenzo[*a,i*]xanthene-8,13-dione (**1a**) after a simple work up. In the absence of any catalyst, we did not observe any product formation even after 16 h of reflux. The synthesis of **1a** in different solvents such as EtOH, CH_2Cl_2, and CH_3CN under reflux using H_2SO_4 as catalyst yielded 85%, 40%,and 26% of 14-(4-methoxyphenyl)-14*H*-dibenzo[*a*,*i*]xanthene-8,13-dione (**1a**), respectively. Subsequently reactions of variously substituted aromatic aldehydes with 2-naphthol and 2-hydroxy-1,4-naphthoquinone were carried out in water using 10 mol % of H_2SO_4 as catalyst under reflux. The reactions proceeded efficiently, yielding the corresponding xanthene derivatives (**1a**–**1k**) in excellent yields (Scheme 1). The results have been summarized in Table 1 (method A, entries 1–11).

This cyclocondensation reaction was then investigated with different dihydroxynaphthalenes. The reaction of 4-methoxybenzaldehyde (1.0 mmol), 2,7-dihydroxynaphthalene (1.0 mmol), and 2-hydroxy-1,4-naphthoquinone (1.0 mmol) in water using H_2SO_4 as catalyst under reflux yielded 91% of 2-hydroxy-14-(4-methoxyphenyl)-14*H*-dibenzo[*a*,*i*]xanthene-8,13-dione (**2a**) after 30 min. Subsequently, reactions of other aldehydes also yielded the corresponding novel xanthene derivatives (**2a**–**2k**) (Table 1, method A, entries 12–22) in excellent yields. Replacement of 2,7-dihydroxynaphthalene with 2,6-dihydroxynaphthalene also led to the successful condensation under similar conditions to afford novel xanthene derivatives (**3a**–**3b**) in high yields (Table 1, method A, entries 23 and 24). None of the reactions of 2,7-dihydroxynaphthalene and 2,6-dihydroxynaphthalenes showed the formation of any bis-condensation product. Reactions using double molar concentrations of aldehydes and 2-hydroxy-1,4-naphthoquinone with 2,7-dihydroxynaphthalene and 2,6-dihydroxynaphthalenes did not show formation of bis-condensation products even after prolonged reaction times. Even reactions of initially formed **2** with aldehyde and 2-hydroxy-1,4-naphthoquinone to give bis-condensation products were unsuccessful. Reactions using 1,5-, 1,6-, and 1,7-dihydroxynaphthalenes led to the formation of 3,3′-(arylmethylene)bis(2-hydroxynaphthalene-1,4-dione) derivatives rather than desired xanthene-diones.

Reactions were then attempted using task-specific acidic ionic liquid [bmim]HSO_4. It was observed that the reaction of 4-methoxybenzaldehyde (1.0 mmol), β-naphthol (1.0 mmol), and 2-hydroxynaphthalene-1,4-dione (1.0 mmol) proceeded efficiently in [bmim]HSO_4 at 60 °C, yielding 91% of the corresponding xanthene derivative **1a** in 30 min without any other catalyst. The effect of the amount of ionic liquid on the reaction time and yields was also examined. A maximum yield of **1a** was obtained with 20 mol % of [bmim]HSO_4, which acted both as medium and catalyst. A further increase in the amount of [bmim]HSO_4 did not have any significant effect on product yield and reaction time. The condensation reactions of other diversely substituted aromatic aldehydes with 2-naphthol and 2-hydroxy-naphthalene-1,4-dione using 20 mol % of [bmim]HSO_4 under the standardized conditions gave excellent yields of the corresponding xanthene derivatives (Table 1, method B, entries 1–11). Also, on replacing 2-naphthol with 2,7- and 2,6-dihydroxynaphthalenes, the reactions underwent successful completion in [bmim]HSO_4 (Table 1, method B, entries 12–24). All attempts to achieve bis condensation under these conditions were unsuccessful.

We also examined the reusability of [bmim]HSO_4 by studying the catalytic activity of the recycled ionic liquid for the synthesis of **1a**. After separation of the product by filtration, the filtrate containing the ionic liquid was rinsed with ether and further vacuumed to dryness at 90 °C for 2 h to remove any moisture. The recovered [bmim]HSO_4 was reused directly for the next run. It was found that the ionic liquid can be used for the reactions for up to three runs without any appreciable loss of efficiency.

To survey the possible biological activities of these highly coloured 14-aryl-14*H*-dibenzo[*a*,*i*]xanthene-8,13-diones, these compounds (Table 1, entries 1–24) were subjected to a test of antioxidant activity. The antioxidant activity is represented by their capacities for scavenging the DPPH radical, and the results are summarized in Table 2 and Fig. 1.

Among the synthesized dibenzoxanthene-diones, compounds **2a**–**2k** and **3a** and **3b** showed potent DPPH radical-scavenging activity, comparable to that of the standard (butylated hydroxyl toluene, BHT) at higher concentrations of the tested compounds. Further, it was observed that the antioxidant property of dibenzoxanthene-diones was enhanced by introducing aldehydes having an electron-donating functionality.

Conclusion

In conclusion, we have devised efficient synthetic approaches for the synthesis of 14-aryl-14*H*-dibenzo[*a*,*i*]xanthene-8,13-dione derivatives. The three-component condensation has been proficiently performed in water as a "green" solvent using H_2SO_4 as catalyst. The ionic liquid, [bmim]HSO_4 also efficiently catalyses the cyclocondensation reaction. The antioxidant activity of these compounds was evaluated by DPPH free-radical scavenging assay, and we found them to be efficient DPPH free-radical scavengers.

Experimental

All the chemicals used were purchased from Sigma-Aldrich and used as received. Silica gel 60 F_{254} (precoated aluminium plates) from Merck was used to monitor reaction progress. The melting points were determined on a Tropical Labequip apparatus and are uncorrected. IR (KBr) spectra were recorded on PerkinElmer FTIR spectrophotometer and the values are expressed as ν_{max} (cm^{-1}). Absorbance measurements were made using an Analytikjena Specord 250 spectrophotometer. Elemental analysis was performed by a Vario EL III Elementar analyzer. Mass spectral data were recorded on a Jeol-Accutof JMS-T100 mass spectrometer having a DART

Scheme 1.

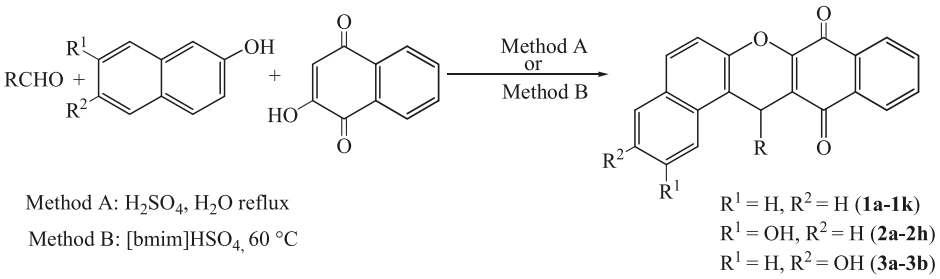


Table 1. Synthesis of dibenzo[*a*,*i*]xanthene-dione derivatives via a multicomponent condensation reaction.

					Method A		Method B			
Entry	RCHO	R^1	R^2	Product	Time (min)	Yield (%)	Time (min)	Yield (%)	mp (Obsd.)[a]	mp (lit.)
1	4-$CH_3OC_6H_4$	H	H	**1a**	30	92	30	91	279–281	278–280[11a]
2	C_6H_5	H	H	**1b**	45	91	40	89	>300	319–320[11a]
3	4-$CH_3C_6H_4$	H	H	**1c**	35	89	30	88	254–256	255–256[11a]
4	4-ClC_6H_4	H	H	**1d**	30	91	30	89	>300	305–306[11a]
5	4-$O_2NC_6H_4$	H	H	**1e**	25	90	25	90	>300	332–333[11a]
6	3-$O_2NC_6H_4$	H	H	**1f**	30	92	30	90	>300	304–305[11a]
7	2,4-$Cl_2C_6H_3$	H	H	**1g**	35	90	30	91	>300	301–302[11a]
8	2-ClC_6H_4	H	H	**1h**	45	90	35	89	280–282	281–282[11a]
9	4-FC_6H_4	H	H	**1i**	40	89	35	90	>300	—[b]
10	2-Naphthyl	H	H	**1j**	45	89	45	89	>300	—
11	4-BrC_6H_4	H	H	**1k**	35	88	35	87	284–295	294–298[11c]
12	4-$CH_3OC_6H_4$	OH	H	**2a**	30	92	30	91	>300	—
13	4-BrC_6H_4	OH	H	**2b**	45	91	40	89	>300	—
14	4-$CH_3C_6H_4$	OH	H	**2c**	35	89	30	88	>300	—
15	4-ClC_6H_4	OH	H	**2d**	30	91	30	89	>300	—
16	4-$O_2NC_6H_4$	OH	H	**2e**	25	90	25	90	>300	—
17	2-ClC_6H_4	OH	H	**2f**	30	92	30	90	>300	—
18	$(CH_3)_2CH$	OH	H	**2g**	35	90	30	91	>300	—
19	2-Thiophenyl	OH	H	**2h**	45	90	35	89	>300	—
20	3-BrC_6H_4	OH	H	**2i**	35	91	30	89	>300	—
21	C_6H_5	OH	H	**2j**	40	89	35	87	>300	—
22	2,4-$Cl_2C_6H_3$	OH	H	**2k**	30	88	30	86	>300	—
23	4-$CH_3OC_6H_4$	H	OH	**3a**	30	90	40	89	>300	—
24	4-BrC_6H_4	H	OH	**3b**	35	88	35	88	>300	—

Note: Method A: Reaction in water under reflux H_2SO_4 (0.1 mmol). Method B: Reaction in [bmim]HSO_4 at 60 °C.
[a]Ethanol was used for recrystallization.
[b]Known compound, but the mp is reported for the first time.

source. The ^1H and ^{13}C NMR spectra were recorded on a Bruker Spectrospin spectrometer and a Jeol JNM ECX-400P at 300 MHz and 400 MHz, respectively, using TMS as an internal standard. The chemical shift values are recorded on a δ scale, and the coupling constants (*J*) are in Hertz. [bmim]HSO_4 was prepared by the reported procedure.[17] The melting point, IR, ^1H NMR, and elemental analysis of all known compounds were found to be identical with those described in the literature.[11]

General procedure for the synthesis of 14-aryl-14*H*-dibenzo[*a*,*i*]xanthene-8,13-dione derivatives

Method A

A mixture of aldehyde (1.0 mmol), 2-naphthol (or 2,7-/2,6-dihydroxynaphthalene) (1.0 mmol), 2-hydroxynaphthalene-1,4-dione (1.0 mmol), H_2SO_4 (0.1 mmol), and 10 mL of water was stirred magnetically under reflux for the appropriate time as mentioned in Table 1. The progress of the reaction was monitored by TLC using petroleum ether – ethyl acetate (70:30, *v*/*v*) as eluent. After completion of the reaction, the reaction mixture was allowed to cool to room temperature. The precipitate formed was collected by filtration at pump, washed with cold dilute ethanol and recrystallized from ethanol to afford the pure xanthene derivative. The products were identified by spectral analysis.

Method B

A mixture of aldehyde (1.0 mmol), 2-naphthol (or 2,7-/2,6-dihydroxynaphthalene) (1.0 mmol), 2-hydroxynaphthalene-1,4-dione (1.0 mmol), and [bmim]HSO_4 (20 mol %) was stirred magnetically in an oil bath maintained at 60 °C for

Can. J. Chem. Downloaded from www.nrcresearchpress.com by UNIVERSITAT DE VALENCIA on 10/20/12
For personal use only.

Can. J. Chem. Downloaded from www.nrcresearchpress.com by UNIVERSITAT DE VALENCIA on 10/20/12
For personal use only.

Table 2. 2,2-Diphenyl-1-picrylhydrazyl (DPPH) radical scavenging activity (%) of 14-aryl-14*H*-dibenzo[*a*,*i*] xanthene-8,13-dione derivatives.

	Scavenging activity (%)	
Product	0.4 (μmol/L)/mL[a]	0.8 (μmol/L)/mL[a]
1a	60.23	79.88
1b	23.12	37.03
1c	54.03	71.43
1d	33.00	45.89
1e	10.43	14.69
1f	16.23	25.43
1g	43.12	70.00
1h	25.72	54.23
1i	8.14	15.26
1j	5.22	8.34
1k	17.62	28.38
2a	68.23	87.54
2b	55.14	74.59
2c	56.58	81.38
2d	63.61	71.38
2e	14.08	32.11
2f	53.44	69.03
2g	57.00	76.87
2h	47.57	66.55
2i	38.00	57.92
2j	45.94	48.86
2k	40.73	51.88
3a	79.00	89.88
3b	54.51	78.00
BHT[b]	87.43	89.01

Note: A 0.1 mmol/L methanolic solution of DPPH was used for all the experiments.

[a]The solutions of compounds were prepared in a mixture of methanol–acetone (1:1).

[b]Butylated hydroxyl toluene (BHT) was used as a reference compound.

an appropriate time as mentioned in Table 1. After completion of the reaction as monitored by TLC using petroleum ether – ethyl acetate (70:30, *v*/*v*) as eluent, the reaction mixture was allowed to cool to room temperature and then quenched with water (~5 mL). The precipitate formed was collected by filtration at the pump, washed with cold dilute ethanol, and recrystallized from ethanol to afford the pure xanthene derivative. The filtrate was rinsed with ether, concentrated under reduced pressure, and dried at 90 °C to recover the ionic liquid for subsequent reuse.

DPPH free-radical scavenging assay

A methanol solution of DPPH was used as a reagent for the spectrophotometric assay with modifications.[18] Solutions of different concentrations of dibenzoxanthene-diones (i.e., 0.8 and 0.4 (μmol/L)/mL) were prepared using a mixture of methanol–acetone (1:1). One millilitre of a 0.1 mmol/L methanolic solution of DPPH was added to 3 mL of the solution of the compounds and the mixture was shaken vigorously using a vortex mixer. Absorbance was read against a blank at 517 nm after incubation of the reaction mixtures for 60 min in the dark at room temperature. BHT was used as a reference compound. The radical-scavenging activities were expressed as an inhibition percentage and were calculated using the formula:

$$\text{Radical scavenging activity (\%)} = [(A_0 - A_1)/A_0 \times 100]$$

where A_0 is the absorbance of the control (blank, without compound) and A_1 is the absorbance of the compound. All the tests were carried out in triplicate and the results were averaged.

Spectral data

*14-(4-Methoxyphenyl)-14*H*-dibenzo[*a*,*i*]xanthene-8,13-dione (1a)*

Orange solid, mp 279–281 °C (lit.[11a] 278–280 °C). UV (4×10^{-5} mol/L solution in $CHCl_3$) λ_{max} (ε): 338 nm (1.26×10^4 L mol^{-1} cm^{-1}). IR (ν_{max}, cm^{-1}, KBr): 2963, 2919, 2853, 1718, 1702, 1685, 1590, 1508, 1366, 1211. ^{1}H NMR (300 MHz, $CDCl_3$) δ: 8.09–8.02 (m, 2H, Ar), 7.92 (d, J = 8.4 Hz, 1H, Ar), 7.81–7.67 (m, 3H, Ar), 7.52–7.33 (m, 4H, Ar), 7.31 (d, 2H, J = 8.7 Hz, Ar), 7.18 (s, 2H,Ar), 5.82 (s, 1H, CH), 3.60 (s, 3H, OCH_3). Anal. calcd for $C_{28}H_{18}O_4$: C 80.37, H 4.34; found: C 80.35, H 4.32.

*14-Phenyl-14*H*-dibenzo[*a*,*i*]xanthene-8,13-dione (1b)*

Orange solid, mp > 300 °C (lit.[11a] 319–320 °C). UV (4×10^{-5} mol/L solution in $CHCl_3$) λ_{max} (ε): 338 nm (2.26×10^4 L mol^{-1} cm^{-1}). IR (ν_{max} cm^{-1}) (KBr): 1224, 2854, 1612, 1630, 1589, 1363, 1282. ^{1}H NMR (300 MHz, $CDCl_3$) δ: 8.17–8.10 (m, 2H, Ar), 8.00 (d, J = 8.1 Hz, 1H, Ar), 7.90–7.75 (m, 3H, Ar), 7.60–7.39 (m, 6H, Ar), 7.20 (t, J = 14.7 Hz, 2H, Ar), 7.11–7.06 (m, 1H, Ar), 5.94 (s, 1H). Anal. calcd for $C_{27}H_{16}O_3$: C 83.49, H 4.15; found: C 83.47, H 4.13.

*14-(4-Methylphenyl)-14*H*-dibenzo[*a*,*i*]xanthene-8,13-dione (1c)*

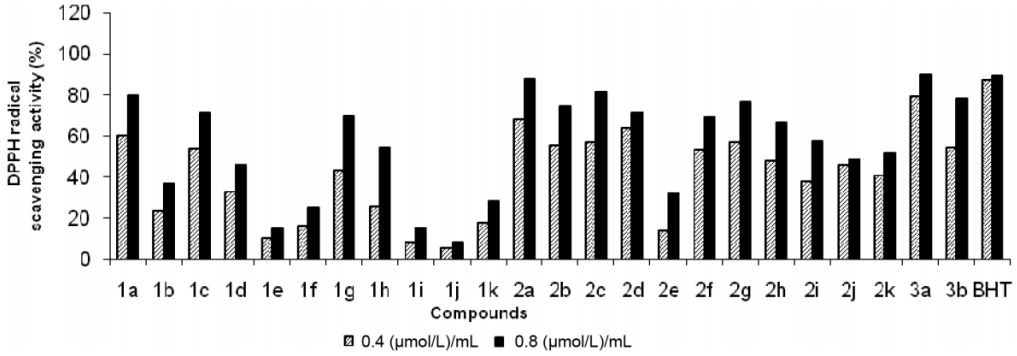
Orange solid, mp 254–256 °C (lit.[11a] 255–256 °C). UV (4×10^{-5} mol/L solution in $CHCl_3$) λ_{max} (ε): 333 nm (1.47×10^4 L mol^{-1} cm^{-1}). IR (ν_{max} cm^{-1}, KBr): 2920, 1665, 1637, 1591, 1577, 1364, 1286. ^{1}H NMR (400 MHz, $CDCl_3$) δ: 8.16 (d, J = 8.0 Hz, 1H, Ar), 8.11 (d, J = 7.6 Hz, 1H, Ar), 7.99 (d, J = 8.0 Hz, 1H, Ar), 7.89–7.76 (m, 3H, Ar), 7.60–7.42 (m, 4H, Ar), 7.29 (d, J = 8.0 Hz, 2H, Ar), 7.00 (d, J = 7.6 Hz, 2H, Ar), 5.90 (s, 1H, CH), 2.21 (s, 3H, CH_3). Anal. calcd for $C_{28}H_{18}O_3$: C 83.57, H 4.51; found: C 83.59, H 4.52.

*14-(4-Chlorophenyl)-14*H*-dibenzo[*a*,*i*]xanthene-8,13-dione (1d)*

Orange solid, mp > 300 °C (lit.[11a] 305–306 °C). UV (4×10^{-5} mol/L solution in $CHCl_3$) λ_{max} (ε): 336 nm (2.75×10^4 L mol^{-1} cm^{-1}). IR (ν_{max} cm^{-1}, KBr): 3046, 1667, 1637, 1591, 1577, 1367, 1286. ^{1}H NMR (400 MHz, $CDCl_3$) δ: 8.18 (d, 1H, J = 7.6 Hz, Ar), 8.14 (d, J = 7.6 Hz, 1H, Ar), 7.91–7.77 (m, 4H, Ar), 7.62–7.45 (m, 4H, Ar), 7.34 (d, J = 8.4 Hz, 2H, Ar), 7.15 (d, J = 8.4 Hz, 2H, Ar), 5.90 (s, 1H, CH). Anal. calcd for $C_{27}H_{15}ClO_3$: C 76.69, H 3.58; found: C 76.67, H 3.57.

Can. J. Chem. Downloaded from www.nrcresearchpress.com by UNIVERSITAT DE VALENCIA on 10/20/12
For personal use only.

Fig. 1. 2,2-Diphenyl-1-picrylhydrazyl (DPPH) radical scavenging activity (%) of 14-aryl-14*H*-dibenzo[*a*,*i*]xanthene-8,13-dione derivatives.



*14-(4-Nitrophenyl)-14*H*-dibenzo[a,i]xanthene-8,13-dione (1e)*

Orange solid, mp > 300 °C (lit.[11a] 332–333 °C). UV (4×10^{-5} mol/L solution in $CHCl_3$) λ_{max} (ε): 336 nm (2.43×10^4 L mol^{-1} cm^{-1}). IR (ν_{max} cm^{-1}, KBr): 2914, 1703, 1663, 1635, 1590, 1518, 1349, 1212. ^{1}H NMR (400 MHz, $CDCl_3$) δ: 8.20 (d, J = 7.6 Hz, 1H, Ar), 8.15 (d, J = 7.6 Hz, 1H, Ar), 8.05 (d, J = 8.8 Hz, 2H, Ar), 7.97–7.79 (m, 4H, Ar), 7.66–7.46 (m, 6H, Ar), 6.05 (s, 1H, CH). Anal. calcd for $C_{27}H_{15}NO_5$: C 74.82, H 3.49, N 3.23; found: C 74.84, H 3.51, N 3.24.

*14-(3-Nitrophenyl)-14*H*-dibenzo[a,i]xanthene-8,13-dione (1f)*

Orange solid, mp > 300 °C (lit.[11a] 304–305 °C). UV (4×10^{-5} mol/L solution in $CHCl_3$) λ_{max} (ε): 337 nm (2.50×10^4 L mol^{-1} cm^{-1}). IR (ν_{max} cm^{-1}, KBr): 2922, 1702, 1656, 1637, 1575, 1529, 1347, 1214. ^{1}H NMR (400 MHz, $CDCl_3$) δ: 8.21 (d, J = 8.0 Hz, 1H, Ar), 8.13 (d, J = 8.1 Hz, 1H, Ar), 8.10 (s, 1H, Ar), 8.00–7.82 (m, 6H, Ar), 7.66–7.61 (m, 2H, Ar), 7.52–7.41 (m, 3H, Ar), 6.06 (s, 1H, CH). Anal. calcd for $C_{27}H_{15}NO_5$: C 74.82, H 3.49, N 3.23; found: C 74.80, H 3.46 H 3.20.

*14-(2,4-Dichlorophenyl)-14*H*-dibenzo[a,i]xanthene-8,13-dione (1g)*

Orange solid, mp > 300 °C (lit.[11a] 301–302 °C). UV (4×10^{-5} mol/L solution in $CHCl_3$) λ_{max} (ε): 340 nm (2.75×10^4 L mol^{-1} cm^{-1}). IR (ν_{max} cm^{-1}, KBr): 3056, 1662, 1637, 1591, 1577, 1466, 1362, 1288. ^{1}H NMR (400 MHz, $CDCl_3$) δ: 8.20 (d, J = 7.8 Hz, 1H Ar), 8.15–8.11 (m, 2H, Ar), 7.89–7.79 (m, 3H, Ar), 7.65–7.43 (m, 4H, Ar), 7.32–7.26 (m, 2H, Ar), 7.10 –7.03(m, 1H, Ar), 6.15 (s, 1H, CH). Anal. calcd for $C_{27}H_{14}Cl_2O_3$: C 70.91, H 3.09; found: C 70.89, H 3.06.

*14-(2-Chlorophenyl)-14*H*-dibenzo[a,i]xanthene-8,13-dione (1h)*

Orange solid, mp 280–282 °C (lit.[11a] 281–282 °C). UV (4×10^{-5} mol/L solution in $CHCl_3$) λ_{max} (ε): 338 nm (2.51×10^4 L mol^{-1} cm^{-1}). IR (ν_{max} cm^{-1}, KBr): 3068, 1666, 1638, 1591, 1577, 1361, 1289. ^{1}H NMR (300 MHz, $CDCl_3$) δ: 8.23–8.12 (m, 2H, Ar), 8.14 (d, J = 7.5 Hz, 1H, Ar), 7.87–7.78 (m, 3H, Ar), 7.63–7.26 (m, 6H, Ar), 7.09–7.00 (m, 2H, Ar), 6.20 (s, 1H, CH). Anal. calcd for $C_{27}H_{15}ClO_3$: C 76.69, H 3.58; found: C 76.66, H, 3.56.

*14-(4-Fluorophenyl)-14*H*-dibenzo[a,i]xanthene-8,13-dione (1i)*

Orange solid, mp > 300 °C (decomp.). UV (4×10^{-5} mol/L solution in $CHCl_3$) λ_{max} (ε): 340 nm (2.52×10^4 L mol^{-1} cm^{-1}). IR (ν_{max} cm^{-1}, KBr): 2923, 2852, 2699, 1661, 1637, 1590, 1502, 1368, 1214. ^{1}H NMR (400 MHz, DMSO-d_6) δ: 7.93–7.83 (m, 3H, Ar), 7.80–7.75 (m, 1H, Ar), 7.60–7.42 (m, 4H, Ar), 7.37–7.33 (m, 2H, Ar), 7.29–7.18 (m, 4H, Ar), 5.91 (s, 1H, CH). Anal. calcd for $C_{27}H_{15}FO_3$: C 79.79, H 3.72; found: C 79.76, H 3.70.

*14-(2-Naphthyl)-14*H*-dibenzo[a,i]xanthene-8,13-dione (1j)*

Yellow solid, mp > 300 °C (decomp.). UV (4×10^{-5} mol/L solution in $CHCl_3$) λ_{max} (ε): 340 nm (2.25×10^4 L mol^{-1} cm^{-1}). IR (ν_{max} cm^{-1}, KBr): 2925, 1635, 1586, 1365, 1216. ^{1}H NMR (400 MHz, DMSO-d_6) δ: 8.23 (d, J = 7.56 Hz, 1H, Ar), 8.13 (d, J = 8.48 Hz, 1H, Ar), 8.016 (d, J = 9.20 Hz, 1H, Ar), 7.93–7.84 (m, 4H, Ar), 7.77–7.62 (m, 5H, Ar), 7.44–7.32 (m, 5H, Ar), 5.91 (s, 1H, CH). ^{13}C NMR (100 MHz, DMSO-d_6) δ: 178.28, 177.91, 156.70, 147.33, 141.58, 135.57, 133.18, 132.28, 131.97, 130.92, 130.86, 130.63, 130.26, 129.22, 128.98, 128.54, 128.26, 127.97, 127.82, 127.68, 127.23, 126.69, 126.41, 125.96, 125.02, 124.05, 117.92, 117.00, 115.88, 35.62. MS (ESI) m/z calcd for $C_{31}H_{18}O_3$: 438.13; found: 439.20 [M^+ + H]. Anal. calcd for $C_{31}H_{18}O_3$: C 84.92, H 4.14; found: C 84.90, H 4.12.

*14-(4-Bromophenyl)-14*H*-dibenzo[a,i]xanthene-8,13-dione (1k)*

Orange solid, mp 284–295 °C (lit.[11c] 294–298 °C). UV (4×10^{-5} mol/L solution in $CHCl_3$) λ_{max} (ε): 339 nm (2.25×10^4 L mol^{-1} cm^{-1}). IR (ν_{max} cm^{-1}, KBr): 3075, 1704, 1663. ^{1}H NMR (300 MHz, DMSO-d_6) δ: 8.18– 8.11 (m, 2H, Ar). 7.93–7.86 (m, 3H, Ar), 7.80 (t, J = 7.6 Hz, 1H, Ar), 7.62–7.50 (m, 2H, Ar), 7.45–7.40 (m, 2H, Ar). 7.34–7.26 (m, 4H, Ar), 5.87 (s, 1H, CH). Anal. calcd for $C_{27}H_{15}BrO_3$: C 69.39, H 3.24; found: C 69.37, H 3.22.

*2-Hydroxy-14-(4-methoxyphenyl)-14*H*-dibenzo[a,i]xanthene-8,13-dione (2a)*

Orange solid, mp > 300 °C (decomp.). UV (4×10^{-5} mol/L solution in $CHCl_3$) λ_{max} (ε): 357 nm (1.08×10^4 L mol^{-1} cm^{-1}). IR (ν_{max} cm^{-1}, KBr): 3297, 2924, 1700, 1650, 1627, 1591, 1377, 1210. ^{1}H NMR (400 MHz, DMSO-d_6) δ: 9.90 (s, 1H, OH), 8.18 (d, J = 7.56 Hz, 1H, Ar), 7.94 (d, J = 7.56 Hz, 1H, Ar), 7.86–7.62 (m, 4H, Ar), 7.44 (d, J =

Can. J. Chem. Downloaded from www.nrcresearchpress.com by UNIVERSITAT DE VALENCIA on 10/20/12
For personal use only.

8.96 Hz, 1H, Ar), 7.20–7.17 (m, 3H, Ar), 6.97–6.95 (m, 1H, Ar), 6.74 (d, J = 8.72 Hz, 2H, Ar), 5.45 (s, 1H, CH), 3.58 (s, 3H, OCH_3). ^{13}C NMR (100 MHz, DMSO-d_6) δ: 177.98, 177.78, 157.95, 156.70, 156.35, 147.42, 135.77, 135.35, 132.32, 131.57, 130.63, 130.34, 130.25, 129.57, 129.32, 128.66, 126.03, 124.56, 117.74, 116.14, 115.16, 113.88, 105.55, 55.10, 34.03. MS (ESI) m/z calcd for $C_{28}H_{18}O_5$: 434.12; found: 435.20 [M^+ + H].

2-Hydroxy-14-(4-bromophenyl)-14H-dibenzo[a,i]xanthene-8,13-dione (2b)

Orange solid, mp > 300 °C(decomp.). UV (4×10^{-5} mol/L solution in $CHCl_3$) λ_{max} (ε): 344 nm (1.62×10^4 L mol^{-1} cm^{-1}). IR (ν_{max} cm^{-1}, KBr): 3307, 2923, 1701, 1654, 1627, 1379, 1210; ^1H NMR (400 MHz, DMSO-d_6) δ: 9.93 (s, 1H, OH), 8.17 (d, J = 7.76 Hz, 1H, Ar), 7.95 (d, J = 7.80 Hz, 1H, Ar), 7.85–7.64 (m, 4H, Ar), 7.45 (d, J = 8.68 Hz, 1H, Ar), 7.39–7.16 (m, 5H, Ar), 6.99–6.96 (m, 1H, Ar), 5.50 (s, 1H, CH). ^{13}C NMR (100 MHz, DMSO-d_6) δ: 178.19, 177.93, 157.26, 157.84, 147.80, 143.26, 135.53, 132.61, 131.99, 131.74, 131.23, 131.00, 130.85, 130.54, 130.05, 128.95, 126.38, 124.94, 120.27, 118.20, 115.62, 114.65, 114.20, 105.77, 35.03. MS (ESI) m/z calcd for $C_{27}H_{15}BrO_4$: 482.02; found: 483.02 [M^+ + H], 485.02 [M^+ + H + 2].

2-Hydroxy-14-(4-methylphenyl)-14H-dibenzo[a,i]xanthene-8,13-dione (2c)

Orange solid, mp > 300 °C (decomp.). UV (4×10^{-5} mol/L solution in $CHCl_3$) λ_{max} (ε): 349 nm (1.19×10^4 L mol^{-1} cm^{-1}). IR (ν_{max} cm^{-1}, KBr): 3359, 2924, 1701, 1653, 1629, 1592, 1378, 1212. ^1H NMR (400 MHz, DMSO-d_6) δ: 9.94 (s, 1H, OH), 8.19 (d, J = 7.76 Hz, 1H, Ar), 7.96 (d, J = 7.76 Hz, 1H, Ar), 7.88–7.64 (m, 4H, Ar), 7.47 (d, J = 8.72 Hz, 1H, Ar), 7.23–7.19 (m, 3H, Ar), 7.00–6.98 (m, 3H, Ar), 5.48 (s, 1H, CH), 2.13 (s, 3H, CH_3). ^{13}C NMR (100 MHz, DMSO-d_6) δ: 178.25, 178.08, 157.07, 156.75, 141.09, 136.32, 135.66, 132.69, 131.93, 130.91, 130.65, 130.59, 129.70, 129.43, 129.00, 128.81, 126.37, 124.91, 118.09, 116.38, 115.41, 114.19, 105.99, 34.98, 20.98. MS (ESI) m/z calcd for $C_{28}H_{18}O_4$: 418.12; found: 419.12 [M^+ + H].

2-Hydroxy-14-(4-chlorophenyl)-14H-dibenzo[a,i]xanthene-8,13-dione (2d)

Orange solid, mp > 300 °C (decomp.). UV (4×10^{-5} mol/L solution in $CHCl_3$), λ_{max} (ε): 354 nm (1.76×10^4 L mol^{-1} cm^{-1}). IR (ν_{max} cm^{-1}, KBr): 3227, 1618, 1597, 1377, 1212. ^1H NMR (400 MHz, DMSO-d_6) δ: 9.93 (s, 1H, OH), 8.19 (d, J = 7.76 Hz, 1H, Ar), 7.95 (d, J = 7.80 Hz, 1H, Ar), 7.87–7.64 (m, 4H, Ar), 7.46 (d, J = 8.68 Hz, 1H, Ar), 7.31–7.17 (m, 5H, Ar), 6.99–6.97 (m, 1H, Ar), 5.52 (s, 1H, CH). ^{13}C NMR (100 MHz, DMSO-d_6) δ: 178.20, 177.94, 157.26, 156.85, 147.82, 142.84, 135.54, 132.62, 132.00, 131.73, 131.00, 130.85, 130.56, 130.04, 128.96, 128.82, 126.38, 124.95, 118.19, 115.70, 114.73, 114.21, 105.77, 34.94; MS (ESI) m/z calcd for $C_{27}H_{15}ClO_4$: 438.07; found: 439.10 [M^+ + H], 441.10 [M^+ + H + 2].

2-Hydroxy-14-(4-nitrophenyl)-14H-dibenzo[a,i]xanthene-8,13-dione (2e)

Orange solid, mp > 300 °C (decomp.). UV (4×10^{-5} mol/L solution in $CHCl_3$) λ_{max} (ε): 349 nm (2.25×10^4 L mol^{-1} cm^{-1}). IR (ν_{max} cm^{-1}, KBr): 3306, 2924, 1702, 1628, 1592, 1379, 1210. ^1H NMR (400 MHz, DMSO-d_6) δ: 9.99 (s, 1H, OH), 8.23 (d, J = 7.76 Hz, 1H, Ar), 8.10 (d, J = 8.68 Hz, 2H, Ar), 7.98–7.67 (m, 5H, Ar), 7.62 (d, 2H, J = 8.68 Hz, Ar), 7.52 (d, J = 8.72 Hz, 2H, Ar), 7.19 (s, 1H, Ar), 7.02–7.00 (m, 1H, Ar), 5.70 (s, 1H, CH). ^{13}C NMR (100 MHz, DMSO-d_6) δ: 177.56, 177.29, 156.88, 156.51, 150.62, 147.31, 146.12, 134.98, 132.07, 131.60, 130.54, 130.46, 129.91, 128.42, 125.87, 124.51, 123.54, 117.74, 114.38, 113.74, 113.47, 105.17, 35.1. MS (ESI) m/z calcd for $C_{27}H_{15}NO_6$: 449.09; found: 450.10 [M^+ + H].

2-Hydroxy-14-(2-chlorophenyl)-14H-dibenzo[a,i]xanthene-8,13-dione (2f)

Orange solid, mp > 300 °C (decomp.). UV (4×10^{-5} mol/L solution in $CHCl_3$) λ_{max} (ε): 358 nm (2.36×10^4 L mol^{-1} cm^{-1}). IR (ν_{max} cm^{-1}, KBr): 3298, 2924, 1700, 1623, 1591, 1375, 1210. ^1H NMR (400 MHz, DMSO-d_6) δ: 9.91 (s, 1H, OH), 8.22 (d, J = 7.8 Hz, 1H, Ar), 7.95 (d, J = 7.92 Hz, 1H, Ar), 7.88–7.64 (m, 4H, Ar), 7.43 (d, J = 8.72 Hz, 1H, Ar), 7.32–7.06 (m, 5H, Ar), 7.01–6.99 (m, 1H,Ar), 5.79 (s, 1H, CH). MS (ESI) m/z calcd for $C_{27}H_{15}ClO_4$: 438.07; found: 439.07 [M^+ + H], 441.07 [M^+ + H + 2].

2-Hydroxy-14-(isopropyl)-14H-dibenzo[a,i]xanthene-8,13-dione (2g)

Orange solid, mp > 300 °C (decomp.). UV (4×10^{-5} mol/L solution in $CHCl_3$) λ_{max} (ε): 355 nm (2.38×10^4 L mol^{-1} cm^{-1}). IR (ν_{max} cm^{-1}, KBr): 3354, 2966, 1702, 1625, 1591, 1570, 1398, 1211. ^1H NMR (400 MHz, DMSO-d_6) δ: 9.93 (s, 1H, OH), 8.09 (d, J = 7.36 Hz, 1H, Ar), 7.99 (d, J = 7.32 Hz, 1H, Ar), 7.83–7.76 (m, 3H, Ar), 7.67–7.63 (m, 1H, Ar), 7.34–7.28 (m, 2H, Ar), 7.05–7.02 (m, 1H, Ar), 4.51 (s, 1H, CH), 2.04 (m, 1H, $CH(CH_3)_2$), 0.86 (d, J = 6.88 Hz, 3H, CH_3), 0.63 (d, J = 6.88 Hz, 3H, CH_3). ^{13}C NMR (100 MHz, DMSO-d_6) δ: 178.84, 177.77, 159.38, 156.67, 148.64, 135.03, 132.33, 131.24, 130.47, 130.28, 130.20, 128.42, 125.88, 124.01, 117.65, 115.74, 113.63, 113.33, 104.77, 34.57, 33.39, 20.75, 17.71. MS (ESI) m/z calcd for $C_{24}H_{18}O_4$: 370.12; found: 371.17 [M^+ + H].

2-Hydroxy-14-(thienyl)-14H-dibenzo[a,i]xanthene-8,13-dione (2h)

Orange solid, mp > 300 °C (decomp.). UV (4×10^{-5} mol/L solution in $CHCl_3$) λ_{max} (ε): 347 nm (2.10×10^4 L mol^{-1} cm^{-1}). IR (ν_{max} cm^{-1}, KBr): 3295, 1698, 1658, 1624, 1589, 1381, 1213. ^1H NMR (400 MHz, DMSO-d_6) δ: 9.99 (s, 1H, OH), 8.18 (d, J = 7.76 Hz, 1H, Ar), 7.99 (d, J = 7.32 Hz, 1H, Ar), 7.89–7.87 (m, 2H, Ar), 7.82 (d, J = 8.72 Hz, 1H, Ar), 7.70–7.66 (m, 1H, Ar), 7.46 (d, J = 9.16 Hz, 1H, Ar), 7.27–7.22 (m, 2H, Ar), 7.05 (dd, $J^{1,2}$ = 2.28 Hz, $J^{1,3}$ = 8.72 Hz, 1H, Ar), 6.89–6.82 (m, 2H, Ar), 5.87 (s, 1H, CH). MS (ESI) m/z calcd for $C_{25}H_{14}O_4S$: 410.06; found: 411.06 [M^+ + H].

2-Hydroxy-14-(3-bromophenyl)-14H-dibenzo[a,i]xanthene-8,13-dione (2i)

Orange solid, mp > 300 °C (decomp.). UV (4×10^{-5} mol/L solution in $CHCl_3$) λ_{max} (ε): 340 nm (2.25×10^4 L mol^{-1} cm^{-1}). IR (ν_{max} cm^{-1}, KBr): 3329, 2926, 1700, 1626, 1569, 1592, 1376, 1208. ^1H NMR (400 MHz, DMSO-d_6) δ: 10.01 (s, 1H, OH), 8.20 (d, J = 7.36 Hz, 1H, Ar), 7.98 (d, J = 6.60 Hz, 1H, Ar), 7.93–7.75 (m, 3H, Ar), 7.70 (m, 1H, Ar),

Can. J. Chem. Downloaded from www.nrcresearchpress.com by UNIVERSITAT DE VALENCIA on 10/20/12
For personal use only.

7.50–7.48 (m, 2H, Ar), 7.32–7.15 (m, 4H, Ar), 7.03 (dd, $J^{1,2}$ = 2.20 Hz, $J^{1,3}$ = 8.80 Hz, 1H, Ar), 5.55 (s, 1H, CH). ^{13}C NMR (100 MHz, DMSO-d_6) δ: 177.67, 177.37, 156.81, 156.46, 147.41, 145.90, 134.97, 132.08, 131.49, 131.10, 130.60, 130.52, 130.43, 130.00, 129.63, 128.42, 127.61, 125.86, 124.47, 121.61, 117.73, 114.98, 113.96, 113.70, 105.19, 34.79. MS (ESI) *m/z* calcd for $C_{27}H_{15}BrO_4$: 482.02; found: 483.02 [M^+ + H], 485.02 [M^+ + H + 2].

2-Hydroxy-14-(phenyl)-14*H*-dibenzo[a,i]xanthene-8,13-dione (2j)

Orange solid, mp > 300 °C (decomp.). UV (4 × 10^{-5} mol/L solution in $CHCl_3$) λ_{max} (ε): 354 nm (1.96 × 10^4 L mol^{-1} cm^{-1}). IR (ν_{max} cm^{-1}, KBr): 3311, 2925, 1618, 1592, 1376, 1211. ^{1}H NMR (400 MHz, DMSO-d_6) δ: 9.95 (s, 1H, OH), 8.11 (d, J = 7.32 Hz, 1H, Ar), 7.94 (d, J = 6.60 Hz, 1H, Ar), 7.87–7.83 (m, 2H, Ar), 7.77 (d, J = 8.80 Hz, 1H, Ar), 7.66–7.62 (m, 1H, Ar), 7.46 (d, J = 8.80 Hz, 1H, Ar), 7.33 (d, J = 7.36 Hz, 2H, Ar), 7.24–7.18 (m, 3H, Ar), 7.09–7.06 (m, 1H, Ar), 7.00 (dd, $J^{1,2}$ = 2.20 Hz, $J^{1,3}$ = 8.76 Hz, 1H, Ar), 5.51 (s, 1H, CH). ^{13}C NMR (100 MHz, DMSO-d_6) δ: 177.70, 177.51, 156.65, 156.34, 147.29, 143.47, 135.07, 132.19, 131.40, 130.39, 130.18, 130.12, 129.27, 128.43, 128.37, 126.60, 125.86, 124.38, 117.61, 115.76, 114.77, 113.66, 105.33, 34.89. MS(ESI) *m/z* calcd for $C_{27}H_{16}O_4$: 404.10; found: 405.10[M^+ + H].

2-Hydroxy-14-(2,4-dichlorophenyl)-14*H*-dibenzo[a,i]xanthene-8,13-dione (2k)

Orange solid, mp > 300 °C (decomp.). UV (4 × 10^{-5} mol/L solution in $CHCl_3$) λ_{max} (ε): 350 nm (1.30 × 10^4 L mol^{-1} cm^{-1}). IR (ν_{max} cm^{-1}, KBr): 3338, 2926, 1702, 1627, 1593, 1572, 1466, 1450, 1378, 1213. ^{1}H NMR (400 MHz, DMSO-d_6) δ: 9.96 (s, 1H, OH), 8.23 (d, J = 7.72 Hz, 1H, Ar), 7.98 (d, J = 6.60 Hz, 1H, Ar), 7.90–7.84 (m, 2H, Ar), 7.79 (d, J = 8.76 Hz, 1H, Ar), 7.71–7.76 (m, 1H, Ar), 7.47–7.42 (m, 3H, Ar), 7.27–7.24 (m, 2H, Ar), 7.05 (dd, $J^{1,2}$ = 2.20 Hz, $J^{1,3}$ = 8.80 Hz, 1H, Ar), 5.79 (s, 1H, CH). ^{13}C NMR (100 MHz, DMSO-d_6) δ: 177.54, 177.35, 156.80, 156.51, 147.45, 139.61, 135.04, 133.53, 133.32, 132.47, 132.04, 131.55, 130.48, 130.37, 130.03, 129.79, 128.91, 128.39, 127.60, 125.77, 124.52, 117.61, 113.73, 105.48, 32.93. MS (ESI) *m/z* calcd for $C_{27}H_{14}Cl_2O_4$: 472.03; found: 473.03 [M^+ + H], 475.03 [M^+ + H + 2].

3-Hydroxy-14-(4-methoxyphenyl)-14*H*-dibenzo[a,i]xanthene-8,13-dione (3a)

Orange solid, mp > 300 °C (decomp.). UV (4 × 10^{-5} mol/L solution in $CHCl_3$) λ_{max} (ε): 355 nm (1.36 × 10^4 L mol^{-1} cm^{-1}). IR (ν_{max} cm^{-1}, KBr): 3386, 2926, 1624, 1516, 1371, 1290. ^{1}H NMR (400 MHz, DMSO-d_6) δ: 9.76 (s, 1H, OH), 8.16 (d, J = 7.80 Hz, 1H, Ar), 7.94–7.85 (m, 3H, Ar), 7.75 (d, J = 9.10 Hz, 1H, Ar), 7.66–7.57 (m, 2H, Ar), 7.23 (d, J = 8.72 Hz, 2H, Ar), 7.13 (d, J = 6.32 Hz, 1H, Ar), 7.06–7.03 (m, 1H, Ar), 6.73 (d, J = 9.64 Hz, 2H, Ar), 5.62 (s, 1H, CH), 3.57 (s, 3H, OCH_3). ^{13}C NMR (100 MHz, DMSO-d_6) δ: 178.78, 178.09, 158.26, 156.70, 155.51, 145.21, 136.57, 135.63, 133.72, 131.77, 130.87, 130.67, 129.93, 128.97, 128.09, 125.82, 124.89, 124.82, 120.04, 117.94, 117.57, 116.27, 114.22, 110.57, 55.43, 34.49. MS (ESI) *m/z* calcd for $C_{28}H_{18}O_5$: 434.12; found: 435.12 [M^+ + H].

3-Hydroxy-14-(4-bromophenyl)-14*H*-dibenzo[a,i]xanthene-8,13-dione (3b)

Orange solid, mp > 300 °C (decomp.). UV (4 × 10^{-5} mol/L solution in $CHCl_3$) λ_{max} (ε): 348 nm (1.48 × 10^4 L mol^{-1} cm^{-1}). IR (ν_{max} cm^{-1}, KBr): 3309, 2925, 1624, 1591, 1370, 1214. ^{1}H NMR (400 MHz, DMSO-d_6) δ: 9.78 (s, 1H, OH), 8.16 (d, J = 7.80 Hz, 1H, Ar), 7.93 (d, J = 7.76 Hz, 1H, Ar), 7.86–7.82 (m, 2H, Ar), 7.76 (d, J = 9.16 Hz, 1H, Ar), 7.66–7.56 (m, 2H, Ar), 7.35–7.26 (m, 4H, Ar), 7.14 (d, J = 6.32 Hz, 1H, Ar), 7.14 (dd, $J^{1,2}$ = 2.32 Hz, $J^{1,3}$ = 9.16 Hz, 1H, Ar), 5.66 (s, 1H, CH). ^{13}C NMR (100 MHz, DMSO-d_6) δ: 178.08, 177.94, 156.85, 156.59, 145.19, 143.64, 135.47, 133.73, 131.90, 131.67, 131.20, 130.75, 130.57, 128.88, 128.41, 125.54, 124.89, 124.66, 120.19, 117.91, 116.63, 115.37, 110.65, 34.92. MS (ESI) *m/z* calcd for $C_{27}H_{15}$ BrO_4: 482.02; found: 483.10 [M^+ + H], 485.10 [M^+ + H +2].

References

(1) (a) Robak, J.; Gryglewski, R. J. *Pol. J. Pharmacol.* **1996**, *48*, 55; (b) Wang, H. K.; Morris-Natschke, S. L.; Lee, K. H. *Med. Res. Rev.* **1997**, *17* (4), 367. doi:10.1002/(SICI)1098-1128(199707)17:4<367::AID-MED3>3.0.CO;2-U; (c) Rukavishnikov, A. V.; Smith, M. P.; Birrell, G. B.; Keana, J. F. W.; Griffith, O. H. *Tetrahedron Lett.* **1998**, *39* (37), 6637. doi:10.1016/S0040-4039(98)01429-4.

(2) Jamison, J. M.; Krabill, K.; Hatwalkar, A.; Jamison, E.; Tsai, C. *Cell Biol. Int. Rep.* **1990**, *14* (12), 1075. doi:10.1016/0309-1651(90)90015-Q.

(3) El-Brashy, A. M.; Metwally, M. E.; El-Sepai, F. A. *Farmaco* **2004**, *59* (10), 809. doi:10.1016/j.farmac.2004.07.001.

(4) Chibale, K.; Visser, M.; van Schalkwyk, D.; Smith, P. J.; Saravanamuthu, A. *Tetrahedron* **2003**, *59* (13), 2289. doi:10.1016/S0040-4020(03)00240-0.

(5) Saint-Ruf, G.; Hieu, H.-T.; Poupelin, J.-P. *Naturwissenschaften* **1975**, *62* (12), 584. doi:10.1007/BF01166986.

(6) Ion, R. M.; Frackowiak, D.; Wiktorowicz, K. *Acta Biochim. Pol.* **1998**, *45* (3), 833.

(7) Bhowmik, B. B.; Ganguly, P. *Spectrochim. Acta A Mol. Biomol. Spectrosc.* **2005**, *61* (9), 1997. doi:10.1016/j.saa.2004.07.031.

(8) Knight, C. G.; Stephens, T. *Biochem. J.* **1989**, *258*, 683.

(9) Ahmad, M.; King, T. A.; Ko, D.-K.; Cha, B. H.; Lee, J. *J. Phys. D Appl. Phys.* **2002**, *35* (13), 1473. doi:10.1088/0022-3727/35/13/303.

(10) (a) Nishiyama, T.; Sakita, K.; Fuchigami, T.; Fukui, T. *Polym. Degrad. Stabil.* **1998**, *62* (3), 529. doi:10.1016/S0141-3910(98)00038-X; (b) Lee, B. W.; Lee, J. H.; Lee, S.-T.; Lee, H. S.; Lee, W. S.; Jeong, T.-S.; Parka, K. H. *Bioorg. Med. Chem. Lett.* **2005**, *15* (24), 5548. doi:10.1016/j.bmcl.2005.08.099; (c) Suvarnakuta, P.; Chaweerungrat, C.; Devahastin, S. *Food Chem.* **2011**, *125* (1), 240. doi:10.1016/j.foodchem.2010.09.015.

(11) (a) Wu, L.; Zhang, J.; Fang, L.; Yang, C.; Yan, F. *Dyes Pigments* **2010**, *86* (1), 93. doi:10.1016/j.dyepig.2009.12.008; (b) Wu, L. Q.; Wu, Y. F.; Yang, C. G.; Yang, L. M.; Yang, L. J. *J. Braz. Chem. Soc.* **2010**, *21* (5), 941. doi:10.1590/S0103-50532010000500025; (c) Dabiri, M.; Tisseh, Z. N.; Bazgir, A. *J. Heterocycl. Chem.* **2010**, *47* (5), 1062. doi:10.1002/jhet.420.

(12) (a) Orru, R. V. A.; de Greef, M. *Synthesis* **2003**, *2003* (10), 1471. doi:10.1055/s-2003-40507; (b) Balme, G.; Bossharth, E.; Monteiro, N. *Eur. J. Org. Chem.* **2003**, *2003* (21), 4101. doi:10.1002/ejoc.200300378; (c) Brase, S.; Gil, C.; Knepper, K. *Bioorg. Med. Chem.* **2002**, *10* (8), 2415. doi:10.1016/

S0968-0896(02)00025-1; (d) Dömling, A.; Ugi, I. *Angew. Chem. Int. Ed.* **2000**, *39* (18), 3168. doi:10.1002/1521-3773(20000915)39:18<3168::AID-ANIE3168>3.0.CO;2-U; (e) Weber, L. *Drug Discov. Today* **2002**, *7*, 143; (f) Doöling, A. *Curr. Opin. Chem. Biol.* **2002**, *6* (3), 306. doi:10.1016/S1367-5931(02)00328-9.

(13) González-Cruz, D.; Tejedor, D.; De Armas, P.; García-Tellado, F. *Chem. Eur. J.* **2007**, *13* (17), 4823. doi:10.1002/chem.200700227.

(14) Herrerías, C. I.; Yao, X.; Li, Z.; Li, C. *Chem. Rev.* **2007**, *107* (6), 2546. doi:10.1021/cr050980b.

(15) (a) Khurana, J. M.; Kumar, S. *Tetrahedron Lett.* **2009**, *50* (28), 4125. doi:10.1016/j.tetlet.2009.04.125; (b) Khurana, J. M.; Magoo, D. *Tetrahedron Lett.* **2009**, *50* (33), 4777. doi:10.1016/j.tetlet.2009.06.029; (c) Khurana, J. M.; Magoo, D. *Tetrahedron Lett.* **2009**, *50* (52), 7300. doi:10.1016/j.tetlet.2009.10.032; (d) Khurana, J. M.; Nand, B.; Saluja, P. *Tetrahedron* **2010**, *66* (30), 5637. doi:10.1016/j.tet.2010.05.082.

(16) (a) Gaikwad, P.; Barik, A.; Priyadarsini, K. I.; Rao, B. S. M. *Res. Chem. Intermed.* **2010**, *36* (9), 1065. doi:10.1007/s11164-010-0220-8; (b) Kuwahara, R.; Hatate, H.; Yuki, T.; Murata, H.; Tanaka, R.; Hama, Y. *LWT-Food Sci. Technol.* **2009**, *42* (7), 1296. doi:10.1016/j.lwt.2009.02.020; (c) Nishiyama, T.; Sugimoto, T.; Miyamoto, N.; Uezono, M.; Nakajima, Y. *Polym. Degrad. Stabil.* **2000**, *70* (1), 103. doi:10.1016/S0141-3910(00)00096-3; (d) Vinothkumar, S. P.; Murali, K.; Gupta, J. K. *J. Pharm. Res.* **2010**, *3* (11), 2784.

(17) Wang, W.; Shao, L.; Cheng, W.; Yang, J.; He, M. *Catal. Commun.* **2008**, *9* (3), 337. doi:10.1016/j.catcom.2007.07.006.

(18) (a) Koleva, N.; van Beek, T. A.; Linssen, J. P. H.; De Groot, A.; Evastatieva, L. N. *Phytochem. Anal.* **2002**, *13* (1), 8. doi:10.1002/pca.611; (b) Miliauskas, G.; Venskutonis, P.; VanBeek, T. A. *Food Chem.* **2004**, *85* (2), 231. doi:10.1016/j.foodchem.2003.05.007.

Can. J. Chem. Downloaded from www.nrcresearchpress.com by UNIVERSITAT DE VALENCIA on 10/20/12
For personal use only.

$CuSO_4 \cdot 5H_2O$-catalyzed alkynylphosphonates formation — An efficient coupling reaction of terminal alkynes with *H*-phosphonates

Zhibo Qu, Xiaolan Chen, Jinwei Yuan, Lingbo Qu, Xu Li, Fujun Wang, Xiling Ding, and Yufen Zhao

Can. J. Chem. Downloaded from www.nrcresearchpress.com by UNIVERSITAT DE VALENCIA on 10/20/12
For personal use only.

Abstract: It was recently discovered that easily available $CuSO_4 \cdot 5H_2O$ could be employed as an efficient catalyst towards the coupling reactions of terminal alkynes with *H*-phosphonates, which finally led to the formation of a large variety of novel alkynylphosphates.

Key words: terminal alkynes, coupling, $CuSO_4 \cdot 5H_2O$, alkynylphosphonates.

Résumé : On a découvert récemment que le $CuSO_4 \cdot 5H_2O$, qui est facilement disponible, peut être utilisé comme catalyseur efficace pour les réactions d'alcynes vrais avec des *H*-phosphonates qui conduisent éventuellement à la formation d'une grande variété de nouveaux alcynylphosphates.

Mots-clés : alcynes vrais, couplage, $CuSO_4 \cdot 5H_2O$, alcynylphosphonates.

[Traduit par la Rédaction]

Introduction

The reactivity and versatility of alkynylphosphonates provide some biological activities,[1] but they also make them valuable precursors for other phosphonates,[2] and particularly for the synthesis of heterocycles by [2+2],[3] [3+2],[4] and [4+2][5] cycloaddition reactions. There are four traditional reaction categories useful for the preparation of alkynylphosphonates: the "apparent" Michaelis–Arbuzov[6] and Michaelis–Becker reactions,[7] the phosphite–allenylphosphonate rearrangement,[8] the carbanionic displacements at pentavalent phosphorus centers,[9] and conversions of vinyl- to alkynyl-phosphonates by addition–elimination reactions.[10] The increasing importance of phosphorus compounds in organic synthesis, materials science, and chemical biology always welcomes novel, efficient phosphorus involved bond-forming reactions for the construction of structurally sophisticated phosphorus compounds that are not readily available by classic methods. Metal-catalyzed cross-coupling reactions are among the most powerful reactions available for formation of carbon–heteroatom bonds, especially for that of the carbon–phosphorus bond. Metal-salt-catalyzed cross-coupling of *H*-phosphonates with carbon–carbon unsaturated compounds is one of the most straightforward ways of preparing phosphorus-containing compounds, which have wide applications in organic synthesis and industrial processes.[11] Lera and Hayes[12] demonstrated a method for the palladium-catalyzed synthesis of alkynylphosphonates from 1,1-dibromo-1-alkenes with H(O)$P(OR)_2$. Zhao and co-workers[13] disclosed a new methodology for catalytically constructing C–P bonds, an aerobic oxidative coupling of terminal alkynes with *H*-phosphonates that is catalyzed by Cu to generate alkynylphosphonates. Three easily oxidized copper(I) salts, including CuI, CuBr, and CuCl, and relatively expensive copper(II) salt – $Cu(OAc)_2 \cdot H_2O$ have been employed by Zhao's group to act as the catalysts for the C–P cross-coupling reaction of terminal alkynes with *H*-phosphonates. To the best of our knowledge, $CuSO_4 \cdot 5H_2O$, as a relatively benign and inexpensive reagent that can be stored and handled in the laboratory using normal laboratory methods, has not yet been employed as the catalyst for such air-induced C–P bond-forming reactions. Propargyl aryl ethers can react with a gold catalyst to furnish various allenes,[14] an important starting reactant leading to a variety of functionalized compounds, including important benzopyrans.[15] Herein, we wish to report an efficient method for the construction of alkynylphosphonates using $CuSO_4 \cdot 5H_2O$ as the catalyst of the reaction of terminal alkynes with *H*-phosphonates. By this method, we have synthesized a variety of novel alkynylphosphonates.

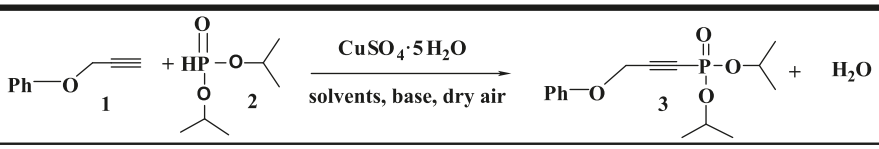
Received 25 October 2011. Accepted 1 April 2012. Published at www.nrcresearchpress.com/cjc on 30 August 2012.

Z. Qu, X. Chen, X. Li, F. Wang, and X. Ding. Department of Chemistry, Zhengzhou University, Key Laboratory of Chemistry Biology and Organic Chemistry, Zhengzhou 450052, P.R. China.
J. Yuan. School of Chemistry & Chemical Engineering, Henan University of Technology, Zhengzhou 450001, P.R. China.
L. Qu. Department of Chemistry, Zhengzhou University, Key Laboratory of Chemistry Biology and Organic Chemistry, Zhengzhou 450052, P.R. China; School of Chemistry & Chemical Engineering, Henan University of Technology, Zhengzhou 450001, P.R. China.
Y. Zhao. Department of Chemistry, Zhengzhou University, Key Laboratory of Chemistry Biology and Organic Chemistry, Zhengzhou 450052, P.R. China; Department of Chemistry, Xiamen University, Xiamen 361005, P.R. China.

Corresponding authors: Yufen Zhao (e-mail: yfzhao@xmu.edu.cn) and Xiaolan Chen (e-mail: chenxl@zzu.edu.cn).

Can. J. Chem. Downloaded from www.nrcresearchpress.com by UNIVERSITAT DE VALENCIA on 10/20/12
For personal use only.

Table 1. Selected screening results for $CuSO_4 \cdot 5H_2O$-mediated oxidative coupling of propargyl phenyl ether and diisopropyl phosphite.



Entry	Catalyst	Temp. (°C)	Base	Solvent	Yield (%)[a]
1	$CuSO_4 \cdot 5H_2O$ (10 mol %)	55	Et_3N	DMSO	47
2	$CuSO_4 \cdot 5H_2O$ (15 mo l%)	55	Et_3N	DMSO	58
3	$CuSO_4 \cdot 5H_2O$ (20 mol %)	55	Et_3N	DMSO	86
4	$CuSO_4 \cdot 5H_2O$ (25 mol %)	55	Et_3N	DMSO	85
5	$CuSO_4 \cdot 5H_2O$ (30 mol %)	55	Et_3N	DMSO	81
6[b]	$CuSO_4 \cdot 5H_2O$	55	Et_3N	DMF	82
7[b]	$CuSO_4 \cdot 5H_2O$	55	Et_3N	MeCN	Trace
8[b]	$CuSO_4 \cdot 5H_2O$	55	Et_3N	THF	Trace
9[b]	$CuSO_4 \cdot 5H_2O$	55	Et_3N	Toluene	Trace
10[b]	$CuSO_4 \cdot 5H_2O$	55	Et_3N	CH_2Cl_2	Trace
11[b]	$CuSO_4 \cdot 5H_2O$	55	Et_3N	$CHCl_3$	Trace
12[b]	$CuSO_4 \cdot 5H_2O$	55	$HNEt_2$	DMSO	83
13[b]	$CuSO_4 \cdot 5H_2O$	55	K_2CO_3	DMSO	46
14[b]	$CuSO_4 \cdot 5H_2O$	55	Tri-*n*-propylamine	DMSO	79
15[b]	$CuSO_4 \cdot 5H_2O$	55	Tri-*n*-butylamine	DMSO	85
16[b]	$CuSO_4 \cdot 5H_2O$	55	Cs_2CO_3	DMSO	81
17[b]	$CuSO_4 \cdot 5H_2O$	25	Et_3N	DMSO	Trace
18[b]	$CuSO_4 \cdot 5H_2O$	35	Et_3N	DMSO	24
19[b]	$CuSO_4 \cdot 5H_2O$	45	Et_3N	DMSO	58
20[b]	$CuSO_4 \cdot 5H_2O$	65	Et_3N	DMSO	51

Note: Reaction conditions: propargyl phenyl ether (0.6 mmol), diisopropyl phosphite (0.5 mmol), 20 mol% of catalyst, 1.5 mL of solvent, 55 °C, 28 h. Reactions were performed in dry air.

[a]Isolated yields.

[b]$CuSO_4 \cdot 5H_2O$ (20 mol %).

Results and discussion

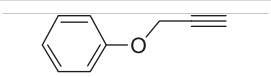
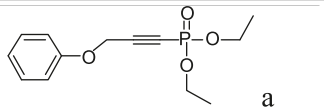
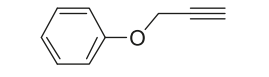
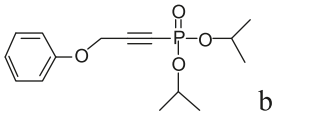
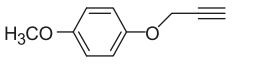
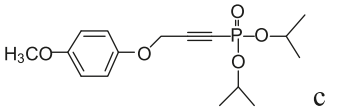
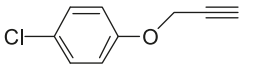
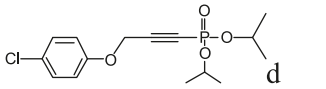
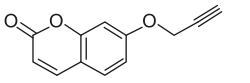
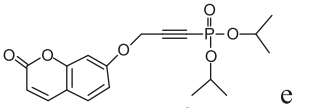
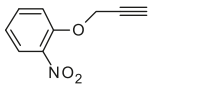
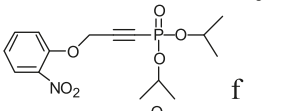
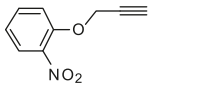
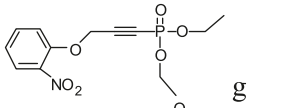
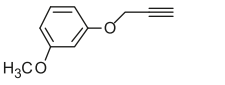
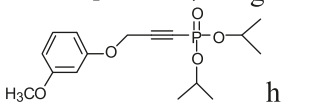
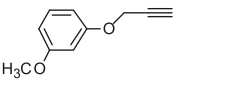
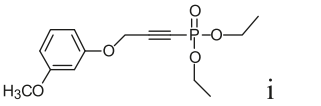
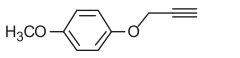
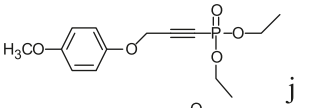
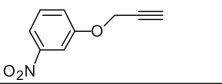
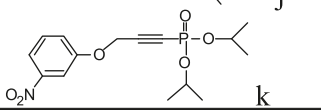
To find the optimal reaction conditions for this coupling reaction, we examined a variety of conditions for the reaction. The easily accessible terminal alkyne (propargyl phenyl ether) was chosen as a model substrate to determine the appropriate reaction conditions for this aerobic oxidative coupling. The principal results of this optimization study are complied in Table 1. We first focused our attention to the amount of the catalyst to be used. The optimum catalyst loading was found to be 20 mol % (based on Table 1, entry 3), whereas reducing it to 10 mol % (Table 1, entry 1) led to a significant drop in the yield of the product. At a 15 mol % catalyst loading (Table 1, entry 2) a slight decrease in the yield was obtained, but at 25 mol % (based on Table 1, entry 4) there was almost no change in the yield. At 30 mol % loading (Table 1, entry 5) a slight drop in the yield of the product was observed. After various solvents were examined, the polar aprotic solvents DMF (Table 1, entry 6) and DMSO gave the best value for the reaction and MeCN, THF, toluene, CH_2Cl_2, and $CHCl_3$ (Table 1, entries 7–11) produced only a trace amount of the product; therefore, DMSO was chosen as the solvent for this reaction. Bases, such as Et_3N, $HNEt_2$, K_2CO_3, tri-*n*-propylamine, tri-*n*-butylamine, and Cs_2CO_3 (Table 1, entries 3 and 12–16) were used in this study. Interestingly, using these bases gave the product in a good yield, except for K_2CO_3 (obtained in 46% yield). Comparing Table 1 entry 2 with entries 17–20, we found that using a reaction temperature of 55 °C produced better results than other temperatures.

After the optimization process for the loading amounts of catalyst, solvents, bases, and temperatures, we conclude that the optimal reaction conditions for this coupling reaction are as follows: a mixture of 0.6 mmol propargyl phenyl ether and 0.5 mmol diisopropyl phosphite in 1.5 mL of DMSO in the presence of 20 mol % $CuSO_4 \cdot 5H_2O$ and 30 mol % Et_3N, heated to 55 °C and stirred for 28 h in the dry air.

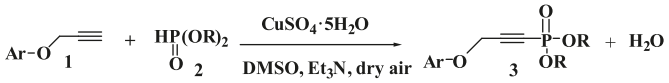
With the optimized conditions in hand, the scope of the reactants was then enlarged to use various terminal alkynes and two different *H*-phosphonates, as shown in Table 2. Generally, the coupling reaction proceeded well to afford the desired products in good yields, no matter which substituted propargyl aryl ethers, containing electron-rich groups (OCH_3 and $NHCOCH_3$) or electron-deficient groups (Cl and NO_2), were employed. Perhaps owing to the steric hindrance, there was a slightly observed decrease in yield when coumarin-containing propargyl aryl ethers (Table 2, entries 5, 13, and 16) instead of phenyl propargyl ethers were employed as the corresponding reactants. When the yields of these same propargyl aryl ethers reacted with two different *H*-phosphonates (Table 2, entries 1 and 2, 6 and 7, 8 and 9, 11 and 12, and 14 and 15), the isopropyl *H*-phosphonate always gave better yield than the ethyl *H*-phosphonate. A broader range of terminal alkynes, including phenyl acetylene (Table 2, entries 17 and 18), *p*-ethylphenylacetylene (Table 2, entry 19), 1-ethynyl-4-phenylbenzene (Table 2, entry 20), cyclopropyl

Can. J. Chem. Downloaded from www.nrcresearchpress.com by UNIVERSITAT DE VALENCIA on 10/20/12
For personal use only.

Table 2. $CuSO_4 \cdot 5H_2O$-catalyzed oxidative coupling of propargyl aryl ether with *H*-phosphonates.

Entry	Terminal alkyne	Product	Yield (%)[a]
1		 a	84
2		 b	86
3		 c	79
4		 d	71
5		 e	68
6		 f	83
7		 g	80
8		 h	76
9		 i	74
10		 j	73
11		 k	79

acetylene (Table 2, entry 21), and phenyl-diprop-2-ynylamine (Table 2, entry 22) were employed as the non-ether alkynes, which finally effectively led to a series of corresponding coupling products using inexpensive catalyst–$CuSO_4 \cdot 5H_2O$, demonstrating true versatility of the methodology.



A tentative mechanism for this coupling reaction, catalyzed by copper(II) salt – $CuSO_4 \cdot 5H_2O$, is proposed as shown in Scheme 1. The copper acetylide **4**, which was insoluble during the reaction procedure and disappeared completely at the end of the reaction, was formed by a reaction among propargyl aryl ether, $CuSO_4 \cdot 5H_2O$, and Et_3N. The trivalent phosphate **2′** (tautomer of the *H*-phosphonate **2**) then acted as a nucleophile to attack the copper(II) of **4**, forming intermediates **5**. The intermediate **6** was formed following an attack of alkynide anion (**5**) on the phosphorus cation (**5**). The product **3** was finally formed following the oxidation of **6** in dry air.

Conclusion

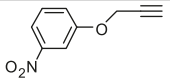
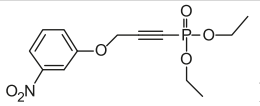
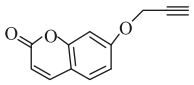
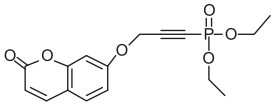
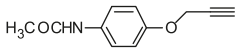
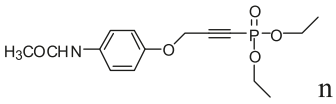
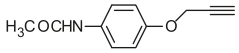
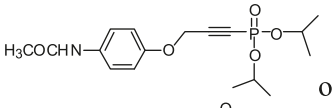
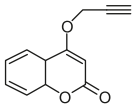
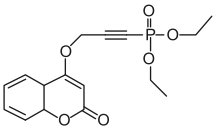
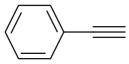
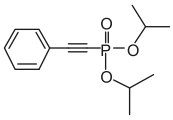
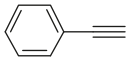
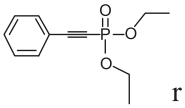
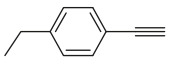
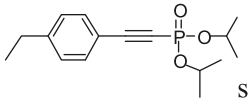
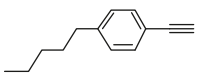
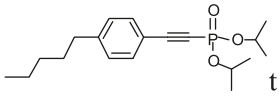
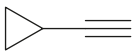
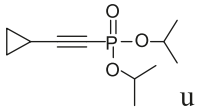
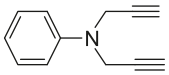
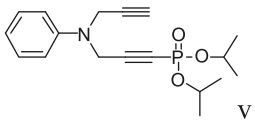
In summary, we have found an efficient and cheap catalytic system ($CuSO_4 \cdot 5H_2O$ / Et_3N / dry air) for the reaction of terminal alkynes with *H*-phosphonates. The method has the following advantages: (*i*) an inexpensive catalytic system, (*ii*) good functional group tolerance (bearing various substituents at the aryl positions), (*iii*) easy work-up procedure, and (*iv*) very mild reaction conditions (without exclusion of air and 55 °C). The method described in this paper can be used successfully for the straightforward synthesis of alkynylphosphonates.

Experimental section

General methods

All reactions were carried out at 55 °C with dry air. All

Table 2. *(concluded).*

Entry	Terminal alkyne	Product	Yield (%)[a]
12		 l	72
13		 m	65
14		 n	81
15		 o	82
16		 p	62
17		 q	86
18		 r	82
19		 s	83
20		 t	80
21		 u	76
22		 v	78

Note: Reaction conditions: 0.6 mmol terminal alkynes, 0.5 mmol *H*-phosphonates, 20 mol % $CuSO_4 \cdot 5H_2O$, 30 mol % Et_3N, 1.5 mL DMSO, 55 °C, 28 h.

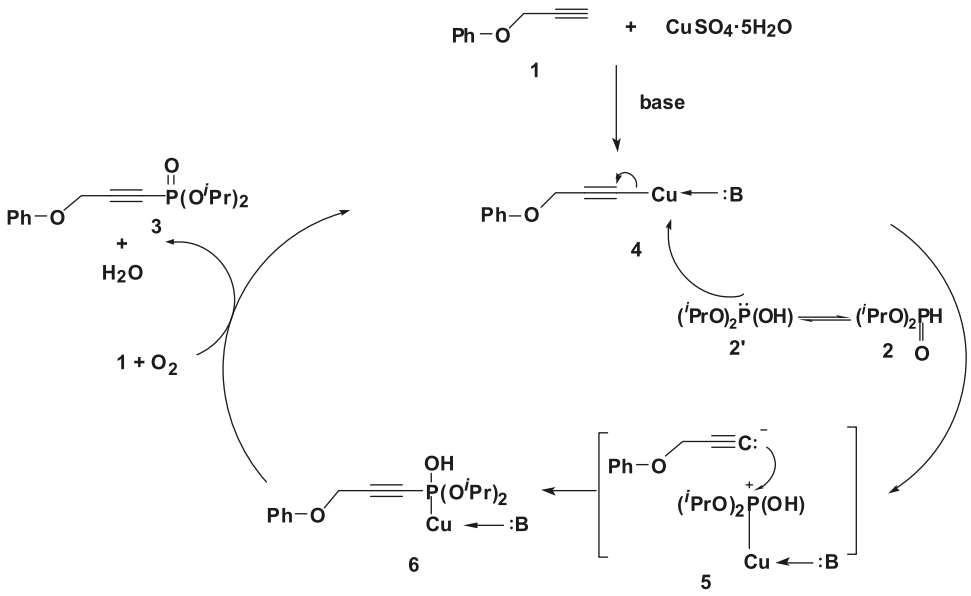
Can. J. Chem. Downloaded from www.nrcresearchpress.com by UNIVERSITAT DE VALENCIA on 10/20/12
For personal use only.

reagents were reagent grade, commercially available, and used without further purification. All reagents were weighed and handled in air at room temperature. Flash column chromatography was performed on silica gel (200–300 mesh), and thin layer chromatography (TLC) analyses were performed on silica gel plates (GF 254). ^1H and ^{13}C NMR spectra were recorded on a Bruker 400 MHz spectrometer with $CDCl_3$ as the solvent and TMS as an internal standard. ^{31}P NMR spectra were recorded on the same instrument with 85% H_3PO_4 as an external standard. ESI-MS spectra were recorded on a Bruker Esquire 3000. IR spectra were recorded on a Shimadazu IR-408. High-resolution mass spectra were performed on a Micromass Q-TOF MicroTM mass spectrometer with an ESI source (Waters, Manchester, UK).

Typical experimental procedure for the oxidative coupling of terminal propargyl aryl ethers with *H*-phosphonates

General procedure for the synthesis of compounds **a**–**v**: Terminal alkyne (0.6 mmol), $CuSO_4 \cdot 5H_2O$ (20 mmol%), *H*-phosphonate (0.5 mmol), triethylamine (30 mmol%), and

Scheme 1. Proposed reaction path.



DMSO (1.5 mL) were added to a round bottom flask (25 mL) at 55 °C under a dry-air atmosphere, immediately generating a yellow suspension. After stirring for about 28 h, the insoluble materials disappeared to produce a clear green solution in a short time, The resulting reaction solution was cooled down to room temperature, 20 mL of water was added, and then the target product was extracted with ethyl acetate. Following that, the organic layer was washed three times with saturated sodium chloride solution and then concentrated by a rotary evaporator. In the purification process, most of the liposoluble products were extracted in the organic layer and most of DMSO in water. In the end, the reaction solvent DMSO can be effectively washed away. The crude product was finally purified by column chromatography on silica gel by using petroleum ether/ethyl acetate as eluent to give the desired product. Spectroscopic data for these products are consistent with the proposed structures (spectra and characterization data can be found in the Supplementary data).

Supplementary data

Supplementary data are available with the article through the journal Web site http://nrcresearchpress.com/doi/suppl/10.1139/v2012-029.

Acknowledgements

We are grateful to the National Natural Science Foundation of China (Grant s 20972130 and 21072178), the Innovation Specialist Projects of Henan Province (Grant No. 114200510023), and the Technological Leading Projects of the Local Government of Zhengzhou (Grant No. 112PLJRC359) for their financial support of this research.

References

(1) (a) Mahajna, M.; Quistad, G. B.; Casida, J. E. *Chem. Res. Toxicol.* **1996**, *9*, 241. doi:10.1021/tx950127f; (b) Van derpoorten, K.; Migaud, M. E. *Org. Lett.* **2004**, *6*, 3461. doi:10.1021/ol0488993.

(2) (a) Sturtz, G.; Charrier, C.; Normant, H. *Bull. Soc. Chim. Fr.* **1966**, 1707 (b) Poss, A. J.; Belter, R. K. *J. Org. Chem.* **1987**, *52* (21), 4810. doi:10.1021/jo00230a034; (c) Corey, E. J.; Virgil, S. C. *J. Am. Chem. Soc.* **1990**, *112* (17), 6429. doi:10.1021/ja00173a059; (d) Guile, S. D.; Saxton, J. E.; Thornton-Pett, M. *J. Chem. Soc. Perkin Trans.* **1992**, *1* (14), 1763. doi:10.1039/p19920001763; (e) Christensen, B. G.; Leanza, W. J.; Alberts, S. G. *Chem. Abstr.* **1970**, *72*, 67109; (f) Rudinskas, A. J.; Hullar, T. L. *J. Org. Chem.* **1976**, *41* (14), 2411. doi:10.1021/jo00876a013; (g) Cristau, H. J.; Mbianda, X. Y.; Beziat, Y.; Gasc, M. B. *J. Organomet. Chem.* **1997**, *529* (1-2), 301. doi:10.1016/S0022-328X(96)06646-6; (h) Blackburn, G. M.; Forster, A. R.; Guo, M. J.; Taylor, G. E. *J. Chem. Soc. Perkin Trans.* **1991**, *1* (11), 2867. doi:10.1039/p19910002867; (i) Corey, E. J.; Virgil, S. C. *J. Am. Chem. Soc.* **1990**, *112* (17), 6429. doi:10.1021/ja00173a059; (j) Lecerclé, D.; Sawicki, M.; Taran, F. *Org. Lett.* **2006**, *8*, 4283. doi:10.1021/ol061589v.

(3) Ruder, S. M.; Norwood, B. K. *Tetrahedron Lett.* **1994**, *35* (21), 3473. doi:10.1016/S0040-4039(00)73213-8.

(4) (a) Saunders, B. C.; Simpson, P. *J. Chem. Soc.* **1963**, 3351. doi:10.1039/jr9630003351; (b) Tronchet, J. M. J.; Bonenfant, A. P.; Pallie, K. D.; Habashi, F. *Helv. Chim. Acta* **1979**, *62*, 1622. doi:10.1002/hlca.19790620528; (c) Shen, Y.; Zheng, J.; Xin, Y.; Lin, Y.; Qi, M. *J. Chem. Soc., Perkin Trans. 1* **1995**, *1995* (8), 997. doi:10.1039/p19950000997; (d) Palacios, F.; Ma Ochoa de Retana, A.; Pagalday, J. *Heterocycles* **1994**, *38* (1), 95. doi:10.3987/COM-93-6516.

(5) (a) Seyferth, D.; Paetsch, J. D. H. *J. Org. Chem.* **1969**, *34* (5), 1483. doi:10.1021/jo01257a070; (b) Acheson, R. M.; Ansell, P. J. *J. Chem. Soc., Perkin Trans. 1* **1987**, *1987*, 1275. doi:10.1039/p19870001275.

(6) (a) Ionin, B. I.; Petrov, A. A. *J. Gen. Chem. USSR* **1962**, *32*, 2355 (b) Ionin, B. I.; Petrov, A. A. *J. Gen. Chem. USSR* **1965**, *35*, 1910 (c) Simpson, P.; Burt, D. W. *Tetrahedron Lett.* **1970**, *11* (55), 4799. doi:10.1016/S0040-4039(00)89349-1; (d) Lodaya, J. S.; Koser, G. F. *J. Org. Chem.* **1990**, *55* (5), 1513. doi:10.1021/jo00292a026.

(7) (a) Meisters, A.; Swan, J. M. *Aust. J. Chem.* **1965**, *18* (2), 163. doi:10.1071/CH9650163; (b) Brestkin, A. P.; Vikhreva, L. A.; Godovikov, N. N.; Gorbatyuk, V. S.; Moralev, S. N.;

Can. J. Chem. Downloaded from www.nrcresearchpress.com by UNIVERSITAT DE VALENCIA on 10/20/12
For personal use only.

Kabachnik, M. I. *Bull. Acad. Sci. USSR* **1988**, *37* (9), 1900. doi:10.1007/BF00962510; (c) Suzuki, H.; Abe, H. *Tetrahedron Lett.* **1996**, *37* (21), 3717. doi:10.1016/0040-4039(96)00649-1; (d) Fletcher, M. D. *Organophosphorus Reagents;* Murphy, P.J. Ed.; University Press: Oxford, 2002; p 185.

(8) (a) Pudovik, A. N.; Aladzheva, I. M. *J. Gen. Chem. USSR* **1963**, *33*, 700; (b) Boisselle, A. P.; Meinhardt, N. A. *J. Org. Chem.* **1962**, *27* (5), 1828. doi:10.1021/jo01052a084; (c) Mark, V. *Tetrahedron Lett.* **1962**, *3* (7), 281. doi:10.1016/S0040-4039(00)70867-7.

(9) (a) Saunders, B. C.; Simpson, P. *J. Chem. Soc.* **1963**, 3351. doi:10.1039/jr9630003351; (b) Acheson, R. M.; Ansell, P. J.; Murray, J. R. *J. Chem. Res.* **1986**, *10*, 3001; (c) Aguiar, A. M.; Chattha, M. S. *J. Org. Chem.* **1971**, *36* (18), 2719. doi:10.1021/jo00817a034; (d) Rudinskas, A. J.; Hullar, T. L. *J. Med. Chem.* **1976**, *19* (12), 1367. doi:10.1021/jm00234a003; (e) Poss, A. J.; Belter, R. K. *J. Org. Chem.* **1987**, *52* (21), 4810. doi:10.1021/jo00230a034; (f) Ruder, S. M.; Norwood, B. K. *Tetrahedron Lett.* **1994**, *35* (21), 3473. doi:10.1016/S0040-4039(00)73213-8; (g) Gil, J. M.; Sung, J. W.; Park, C. P.; Oh, D. Y. *Synth. Commun.* **1997**, *27* (18), 3171. doi:10.1080/00397919708004175.

(10) (a) Craig, J. C.; Bergenthal, M. D.; Fleming, I.; Harley-Mason, J. *Angew. Chem. Int. Ed. Engl.* **1969**, *8* (6), 429. doi:10.1002/anie.196904291; (b) Negishi, E.; King, A. O.; Klima, W. L.; Patterson, W.; Silveira, J. A. *J. Org. Chem.* **1980**, *45* (12), 2526. doi:10.1021/jo01300a060; (c) Hall, R. G.; Trippett, S. *Tetrahedron Lett.* **1982**, *23* (25), 2603. doi:10.1016/S0040-4039(00)87407-9; (d) Shen, Y.; Lin, Y.; Xin, Y. *Tetrahedron Lett.* **1985**, *26*, 5137. doi:10.1016/S0040-4039(00)98884-1;; (e) Midura, W. H.; Mikolajczyk, M. *Tetrahedron Lett.* **1995**, *36* (16), 2871. doi:10.1016/0040-4039(95)00371-I; (f) Dizière, R.; Savignac, P. *Tetrahedron Lett.* **1996**, *37* (11), 1783. doi:10.1016/0040-4039(96)00131-1.

(11) Han, L. B.; Zhang, C.; Yazawa, H.; Shimada, S. *J. Am. Chem. Soc.* **2004**, *126* (16), 5080. doi:10.1021/ja0494297.

(12) Lera, M.; Hayes, C. J. *Org. Lett.* **2000**, *2* (24), 3873. doi:10.1021/ol0066173.

(13) Gao, Y. X.; Wang, G.; Chen, L.; Xu, P. X.; Zhao, Y. F.; Zhou, Y. B.; Han, L. B. *J. Am. Chem. Soc.* **2009**, *131* (23), 7956. doi:10.1021/ja9023397.

(14) Bolte, B.; Odabachian, Y.; Gagosz, F. *J. Am. Chem. Soc.* **2010**, *132*, 7294. doi:10.1021/ja1020469.

(15) Godoi, B.; Sperança, A.; Back, D. F.; Brandão, R.; Nogueira, C. W.; Zeni, G. *J. Org. Chem.* **2009**, *74*, 3469. doi:10.1021/jo900307k.

Can. J. Chem. Downloaded from www.nrcresearchpress.com by UNIVERSITAT DE VALENCIA on 10/20/12
For personal use only.

Flavonol glycosides from *Cardamine komarovii*

Seung Young Lee, Il Kyun Lee, and Kang Ro Lee

Abstract: Two new flavonol glycosides (**1** and **2**) were isolated from a MeOH extract of the aerial parts of *Cardamine komarovii* Nakai (Cruciferae) together with 13 known phenolic compounds (**3**–**15**). The structures of **1** and **2** were determined by spectroscopic methods including 1D and 2D NMR (COSY, HMQC, HMBC, NOESY, and TOCSY) and HR-FAB-MS data.

Key words: Cardamine komarovii, Cruciferae, flavonol glycosides.

Résumé : Les produits d'extractions des tiges de *Cardamine komarovii* Nakai, cruciféracée, par le méthanol ont permis d'isoler deux nouveaux glucosides (**1** et **2**) ainsi que 13 composés phénoliques connus (**3**–**15**). Les structures des **1** et **2** ont été déterminées par des méthodes spectroscopiques, dont la RMN 1D et 2D (« COSY », « HMQC », « HMBC », « NEOSY » et « TOSY ») et des données de spectrométrie de masse avec bombardement avec des atomes rapides et à haute résolution (SM-BAR-HR).

Mots-clés : Cardamine komarovii, cruciféracée, glucosides de flavonol.

[Traduit par la Rédaction]

Can. J. Chem. Downloaded from www.nrcresearchpress.com by UNIVERSITAT DE VALENCIA on 10/20/12
For personal use only.

Introduction

Cardamine komarovii Nakai (Cruciferae) is widely distributed throughout Asia.[1] The aerial parts of this plant have been used for the treatment of respiratory diseases and hemostasis in Chinese folk medicine.[2] In Korea, this indigenous herb is an edible wild vegetable and is also used as a folk medicine for the control of blood pressure.[2] As part of our continuing search for biologically active compounds from Korean medicinal plants, we investigated the constituents of the aerial parts of *C. komarovii* and reported their cytotoxic constituents, including megastigmane,[3] and flavonoids.[4] In our ongoing search on this source, we have further isolated two new flavonol glycosides (**1** and **2**) together with 13 known phenolic compounds (**3**–**15**).

Results and discussion

The 80% MeOH extract of the aerial parts of *C. komarovii* was subjected to repeated column chromatography on silica gel to afford **1** and **2** together with **3**–**15** (Fig. 1). The identification and structural elucidation of **1** and **2** were based on 1D- and 2D-NMR and HR-FAB-MS data.

Cardamoside A (**1**) was isolated as a yellowish gum with a molecular formula of $C_{48}H_{57}O_{27}$ on the basis of the $[M + H]^+$ peak at *m/z* 1065.3086 (calcd for $C_{48}H_{57}O_{27}$, 1065.3087) in the HR-FAB-MS. The IR spectrum of **1** indicated the presence of a hydroxyl group (3356 cm^{-1}), a carbonyl group (1657 cm^{-1}), and an aromatic ring (1451 cm^{-1}). The ^1H NMR spectrum of **1** showed an aglycone characterized by two doublet signals at δ 7.99 (d, J = 8.8 Hz, H-2′, 6′) and 6.89 (d, J = 8.8 Hz, H-3′, 5′), which were assigned to two aromatic protons of the B ring, with two meta-coupled doublets at δ_H 6.78 (d, J = 2.0 Hz, H-8) and 6.47 (d, J = 2.0 Hz, H-6) for the A ring. In the ^{13}C NMR spectrum, 15 carbon signals of an aglycone appeared at δ 161.0 (C-4′), 131.6 (C-2′, 6′), 115.9 (C-3′, 5′), and 121.2 (C-1′) of the B ring, as well as other signals at δ 178.2 (C-4), 163.3 (C-7), 161.6 (C-5), 158.2 (C-9), 156.8 (C-2), 134.2 (C-3), 106.5 (C-10), 100.2 (C-6), and 95.4 (C-8) of the A and C rings (Table 1). These spectral data implied that **1** was a kaempferol derivative.[5] In addition, the four anomeric protons appeared at δ 5.38, 4.15, 5.27, and 4.43 in the ^1H NMR spectrum, which showed correlations with anomeric carbons at δ 101.7, 104.2, 100.3, and 101.3 in the ^{13}C NMR spectrum by the HMQC, respectively. The characteristic coupling constant of anomeric protons at δ 5.38 (d, J = 7.8 Hz), 5.27 (d, J = 7.8 Hz) and 4.15 (d, J = 7.8 Hz) implied three β-D-glucopyranoses (Glc I, Glc II, and Glc III), and another anomeric proton at δ 4.43 (s) identified α-L-rhamnopyranose (Rha). The glycosidic position was established by an HMBC experiment, in which the long-range correlations were observed between the H-1″ (δ 5.38) of Glc I and the C-3 (δ 134.2) of aglycone, H-1‴ (δ 4.15) of Glc II and the C-4" (δ 80.9) of Glc I, H-1⁗ (δ 4.43) of Rha and the C-6″ (δ 66.7) of Glc I, and H-1⁗′ (δ 5.27) of Glc III and C-7 (δ 163.3) of aglycone (Fig. 1). The ^1H and ^{13}C NMR spectra of **1** also showed *trans-p*-coumaroyl unit signals[6] (δ 7.56 (d, J = 15.6 Hz, H-7⁗′), 7.55 (d, J = 8.8 Hz, H-2⁗′, 6″), 6.79 (d, J = 8.8 Hz, H-3⁗′, 5⁗′), and 6.43 (d, J = 15.6 Hz, H-8⁗′); δ 166.8 (C-9⁗′), 160.5 (C-4⁗′), 145.2 (C-7⁗′), 130.9 (C-2⁗′, 6⁗′), 125.9 (C-1⁗′), and 116.5 (C-3⁗′, 5⁗′)). The *trans-p*-

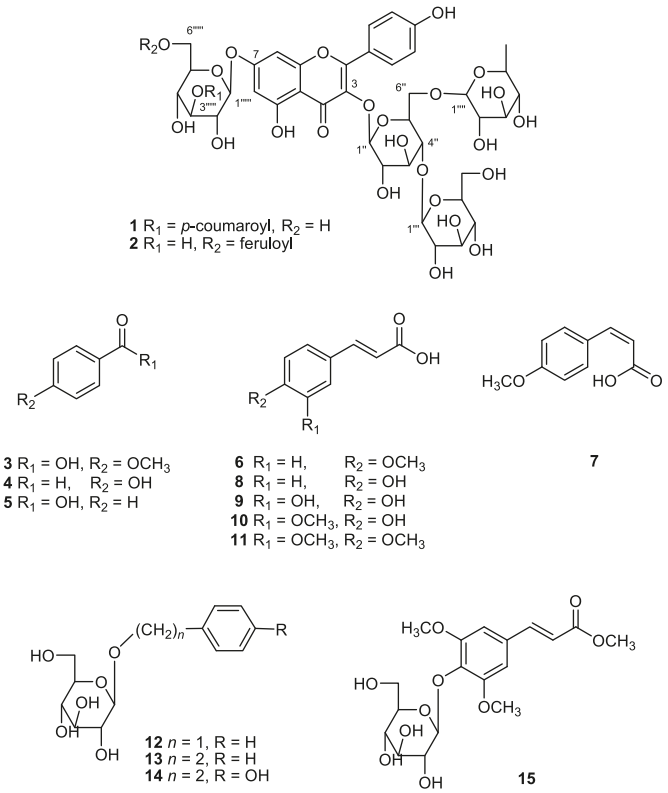
Received 15 May 2012. Accepted 28 June 2012. Published at www.nrcresearchpress.com/cjc on 30 August 2012.

S.Y. Lee, I.K. Lee, and K.R. Lee. Natural Products Laboratory, School of Pharmacy, Sungkyunkwan University, 300 Chonchon-dong, Jangan-ku, Suwon 440-746, Korea.

Corresponding author: Kang Ro Lee (e-mail: krlee@skku.ac.kr).

Can. J. Chem. Downloaded from www.nrcresearchpress.com by UNIVERSITAT DE VALENCIA on 10/20/12
For personal use only.

Fig. 1. Chemical structures of compounds **1**–**15**.



coumaroyl group linkage was confirmed by an HMBC experiment, in which a correlation was observed between the H-3′′′′′ (δ 5.03) of Glc III and the C-9′′′′′′ (δ 166.8) of the *trans*-*p*-coumaroyl group as shown in Fig. 2. The downfield shift of the signals at H-3′′′′′ (δ 5.03) and C-3′′′′′ (δ 77.9), as well as concomitant upfield shifts of the adjacent carbon signals at C-2′′′′′ (δ 71.9) and C-4′′′′′ (δ 68.2), suggested that the *trans*-*p*-coumaroyl group should be placed at C-3′′′′′ of **1**.[6] Alkaline hydrolysis of compound **1** afforded *trans*-*p*-coumaric acid,[6] together with kaempferol 3-*O*-β-D-glucopyranosyl-(1′′′→4′′)-[α-L-rhamnopyranosyl(1′′′′→6′′)]-β-D-glucopyranosyl-7-*O*-β-D-glucopyranoside (**1a**), which was confirmed by comparison of its ^{1}H NMR and FAB-MS data with literature values.[4] Acid hydrolysis of **1a** yielded kaempferol and sugar residues.[4] Kaempferol was confirmed by comparison of its ^{1}H NMR and FAB-MS data with literature values.[5] The sugar residues, D-glucopyranose and L-rhamnopyranose, were identified by co-TLC with authentic sugars ($CHCl_3$–MeOH–H_2O = 6:4:1; R_f value of D-glucopyranose, 0.31 and L-rhamnopyranose, 0.60) and by GC analysis of their corresponding trimethylsilylated L-cysteine adducts.[7] Thus, the structure of **1** was determined as kaempferol 3-*O*-β-D-glucopyranosyl-(1′′′→4′′)-[α-L-rhamnopyranosyl-(1′′′′→6")]-β-D-glucopyranosyl-7-*O*-(3′′′′-*O*-*trans*-coumaroyl)-β-D-glucopyranoside and it was named cardamoside A.

Cardamoside B (**2**) was isolated as a yellowish gum. Its molecular formula was determined as $C_{49}H_{58}NaO_{28}$ from the $[M + Na]^+$ peak at *m/z* 1117.3021 (calcd for $C_{49}H_{58}NaO_{28}$, 1117.3012) in the HR-FAB-MS spectrum. The IR, UV, and ^{1}H and ^{13}C NMR spectra of **2** were similar to those of **1**. The difference in NMR spectra was the acyl moiety, that is the *trans*-*p*-coumaroyl group in **1** was replaced with the *trans*-feruloyl group[8] (δ 7.50 (d, *J* = 15.9 Hz, H-7′′′′′′), 7.21 (d, *J* = 1.8 Hz, H-2′′′′′′), 7.01 (dd, *J* = 8.8, 1.8 Hz, H-6′′′′′′), 6.74 (d, *J* = 8.8 Hz, H-5′′′′′′), 6.40 (d, *J* = 15.9 Hz, H-8′′′′′′), 3.77 (s); δ 167.2, 150.1, 148.6, 145.9, 126.2, 123.9, 116.2, 114.8, 111.7, 56.3) in **2** (Table 1). The *trans*-feruloyl group linkage was confirmed by HMBC data, in which a correlation was observed between the H-6′′′′′ (δ 4.20, 4.45) of Glc III and the C-9′′′′′′ (δ 167.2) of the *trans*-feruloyl group as shown in Fig. 2. Moreover, the downfield shift of the signals at H-6′′′′′ (δ 4.20, 4.45) and C-6′′′′′′ (δ 63.8), as well as concomitant upfield shifts of the adjacent carbon signal at C-5′′′′′ (δ 73.9), suggested that the *trans*-feruloyl group should be placed at the C-6′′′′′ of **2**.[9] Alkaline hydrolysis of compound **2** afforded *trans*-ferulic acid[8] and kaempferol 3-*O*-β-D-glucopyranosyl-(1′′′→4′′)-[α-L-rhamnopyranosyl(1′′′′→6′′)]-β-D-glucopyranosyl-7-*O*-β-D-glucopyranoside (**2a**) (same as **1a**), which was confirmed by comparison of its ^{1}H NMR and FAB-MS data with literature values.[4] Acid hydrolysis of **2a** yielded kaempferol and a sugar residue. Kaempferol was confirmed by comparison of its ^{1}H NMR, and FAB-MS data with literature values, and D-glucopyranose and L-rhamnopyranose were identified by co-TLC with authentic sugars and by GC analysis of their corresponding trimethylsilylated L-cysteine adducts.[7] Thus, the structure of **2** was determined as kaempferol 3-*O*-β-D-glucopyranosyl-(1′′′→4′′)-[α-L-rhamnopyranosyl(1′′′′→6′′)]-β-D-glucopyranosyl-7-*O*-(6′′′′′-*O*-*trans*-feruloyl)-β-D-glucopyranoside and it was named cardamoside B.

Thirteen other known compounds obtained in this investigation were identified as *p*-anisic acid (**3**),[10] *p*-hydroxybenzaldehyde (**4**),[11] benzoic acid (**5**),[8] 4-methoxy-*trans*-cinnamic acid (**6**),[12] 4-methoxy-*cis*-cinnamic acid (**7**),[13] *p*-coumaric acid (**8**),[6] caffeic acid (**9**),[6] ferulic acid (**10**),[8] 3,4-dimethoxycinnamic acid (**11**),[14] benzyl glucopyranoside (**12**),[15] phenylethyl glucopyranoside (**13**),[15] *p*-hydroxy phenylethyl glucopyranoside (**14**),[15] and *p*-*trans*-sinaposyl glucopyranoside (**15**),[16] by comparing their spectroscopic data with those in the literature (Fig. 1). The known compounds **3**–**15** are reported from this plant source for the first time.

Experimental

General experimental procedures

IR spectra were recorded on a Bruker IFS-66/S FT-IR spectrometer. FAB and HR-FAB mass spectra were obtained on a JEOL JMS700 mass spectrometer. NMR spectra, including ^{1}H–^{1}H COSY, HSQC, HMBC, NOESY, and TOCSY experiments, were recorded on a Varian Unity Inova 500 NMR spectrometer operating at 500 MHz (^{1}H) and 125 MHz (^{13}C), with chemical shifts given in ppm (δ). Preparative HPLC was conducted using a Gilson 306 pump with a Shodex refractive index detector. Chromatographic separation was performed on an Apollo Silica 5 μm column (250 × 10 mm i.d.) or an Optimapak ODS-A (250 × 10 mm i.d.). Gas chromatography was carried out using a ZB-1MS capillary column (30 cm × 0.25 mm × 0.25 μm, Zebron); column temperature, 230 °C; injection temperature, 250 °C; and carrier gas, He. Silica gel 60 (Merck, 70–230 mesh and 230–400 mesh) and RP-C_{18} silica gel (Merck, 230–400 mesh) were used for column chromatography. The packing material for molecular sieve column chromatography was Sephadex LH-20 (Pharmacia Co.). Merck precoated silica gel F_{254} plates and RP-18 F_{254s}

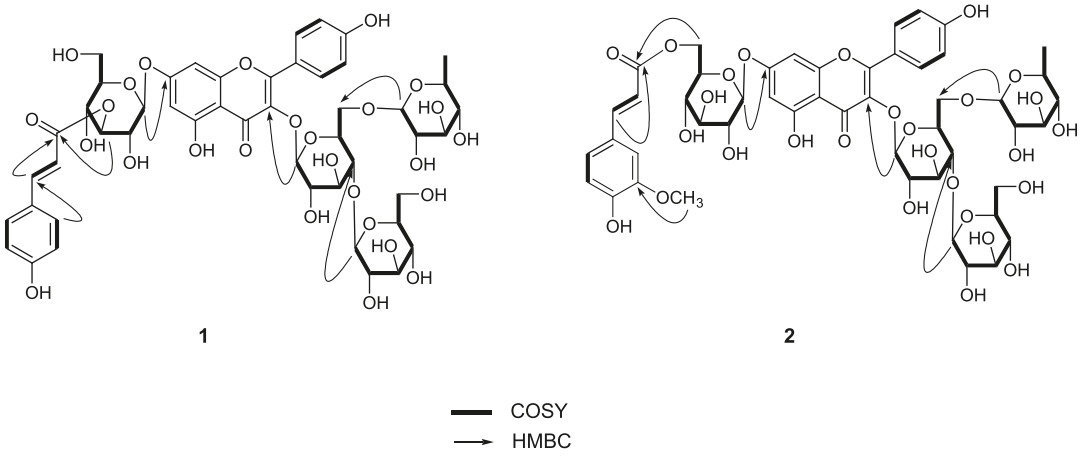
Can. J. Chem. Downloaded from www.nrcresearchpress.com by UNIVERSITAT DE VALENCIA on 10/20/12
For personal use only.

Table 1. ^{1}H and ^{13}C NMR spectral data of compounds **1** and **2** in DMSO-d_6.

	1		**2**	
Position	^{1}H (*J*)	^{13}C	^{1}H (*J*)	^{13}C
Flavonol				
2		156.8		156.6
3		134.2		134.1
4		178.2		178.2
5		161.6		161.8
6	6.47 d (2.0 Hz)	100.2	6.51 d (2.0 Hz)	99.7
7		163.3		163.4
8	6.78 d (2.0 Hz)	95.4	6.71 d (2.0 Hz)	95.7
9		158.2		158.4
10		106.5		106.4
1′		121.2		121.3
2′	7.99 d (8.8 Hz)	131.6	7.97 d (8.8 Hz)	131.6
3′	6.89 d (8.8 Hz)	115.9	6.86 d (8.8 Hz)	115.9
4′		161.0		161.0
5′	6.89 d (8.8 Hz)	115.9	6.86 d (8.8 Hz)	115.9
6′	7.99 d (8.8 Hz)	131.6	7.97 d (8.8 Hz)	131.6
Glc I				
1″	5.38 d (7.8 Hz)	101.7	5.38 d (7.8 Hz)	101.7
2″	3.24 m	74.6	3.21 m	74.5
3″	3.39 m	75.3	3.38 m	75.3
4″	3.34 m	80.9	3.34 m	80.9
5″	3.42 m	74.5	3.44 m	74.5
6″	3.77, 3.48 m	66.7	3.74, 3.45 m	66.7
Glc II				
1‴	4.15 d (7.8 Hz)	104.2	4.14 d (7.9 Hz)	104.2
2‴	2.96 m	73.9	2.95 m	73.8
3‴	3.12 m	77.1	3.12 m	77.2
4‴	3.06 m	70.7	3.06 m	70.7
5‴	3.17 m	77.5	3.17 m	77.5
6‴	3.70, 3.42 m	61.8	3.69, 3.41 m	61.8
Rha				
1⁗	4.43 s	101.3	4.40 s	101.3
2⁗	3.44 m	71.1	3.45 m	71.1
3⁗	3.32 m	71.4	3.30 m	71.4
4⁗	3.09 m	72.5	3.06 m	72.5
5⁗	3.38 m	68.9	3.24 m	68.9
6⁗	0.94 d (5.9 Hz)	18.4	0.91 d (6.1 Hz)	18.4
Glc III				
1′′′′′	5.27 d (7.8 Hz)	100.3	5.12 d (7.5 Hz)	100.1
2′′′′′	3.49 m	71.9	3.25 m	73.5
3′′′′′	5.03 d (9.0 Hz)	77.9	3.23m	77.3
4′′′′′	3,45 m	68.2	3,19 m	70.1
5′′′′′	3.59 m	77.6	3.70 m	73.9
6′′′′′	3.70, 3.52 m	61.0	4.20, 4.45 m	63.8
Acyl				
1′′′′′′		125.9		126.2
2′′′′′′	7.55 d (8.8 Hz)	130.9	7.21 d (1.8 Hz)	111.7
3′′′′′′	6.79 d (8.8 Hz)	116.5		148.6
4′′′′′′		160.5		150.1
5′′′′′′	6.79 d (8.8 Hz)	116.5	6.74 d (8.8 Hz)	116.2
6′′′′′′	7.55 d (8.8 Hz)	130.9	7.01 dd (8.8, 1.8 Hz)	123.9
7′′′′′′	7.56 d (15.6 Hz)	145.2	7.50 d (15.9 Hz)	145.9
8′′′′′′	6.43 d (15.6 Hz)	115.5	6.40 d (15.9 Hz)	114.8
9′′′′′′		166.8		167.2
OCH_3			3.77 s	56.3

Note: NMR data were obtained at 500 MHz for ^{1}H and 125 MHz for ^{13}C.

Fig. 2. Key ^{1}H–^{1}H COSY and HMBC correlations of **1** and **2**.



Can. J. Chem. Downloaded from www.nrcresearchpress.com by UNIVERSITAT DE VALENCIA on 10/20/12
For personal use only.

plates were used for TLC. Spots were detected on TLC under UV light or by heating after spraying with 10% H_2SO_4 in C_2H_5OH (*v*/*v*).

Plant material

The aerial parts of *C. komarovii* were collected at Goseung-gun in Gangwon-Do province, Korea, in August 2008, and the plants were identified by one of the authors (K.R.L.). A voucher specimen (SKKU 2008-11) has been deposited in the herbarium of the School of Pharmacy, Sungkyunkwan University, Suwon, Korea.

Extraction and Isolation

The aerial parts of *C. komarovii* (1.7 kg) were extracted using 80% aqueous MeOH at room temperature. The solvent was evaporated under reduced pressure to give a crude extract (120 g). The crude extract was dissolved in distilled water (800 mL) and successively extracted with *n*-hexane, $CHCl_3$, EtOAc, and *n*-BuOH to provide *n*-hexane (12 g), $CHCl_3$ (13 g), EtOAc (3 g), and *n*-BuOH (26 g) extracts. The $CHCl_3$-soluble fraction (13 g) was subjected to normal-phase column chromatography (CC) over a silica gel using $CHCl_3$/MeOH of increasing polarity (40:1 to 1:1) to give seven fractions (C1–C7). Fraction C3 (1.0 g) was isolated by Sephadex LH-20 chromatography (80% MeOH) and was purified with a silica gel preparatory HPLC with a solvent system of *n*-hexane/EtOAc (15:1) to yield **3** (5 mg). Fraction C3 (2.0 g) was isolated by Sephadex LH-20 chromatography (80% MeOH) and was subjected to reversed-phase CC over a RP-C_{18} silica gel using MeOH/H_2O (9:1) to provide four subfractions (C31–C34). Subfraction C32 (70 mg) was separated by preparative normal-phase HPLC using a solvent system of $CHCl_3$/MeOH (20:1) to obtain **4** (5 mg), **5** (4 mg), **6** (6 mg), and **7** (5 mg). Fraction C4 (2.5 g) was isolated by Sephadex LH-20 chromatography (80% MeOH) and was purified with a RP-C_{18} HPLC with a solvent system of MeOH/H_2O (1:1) to yield **8** (4 mg), **9** (4 mg), **10** (4 mg), and **11** (7 mg). The *n*-BuOH soluble fraction (26 g) was subjected to CC over HP-20 resin using 100% H_2O and 100% MeOH to give two fractions (B1 – 100% H_2O and B2 – 100% MeOH). Fraction B2 (9.7 g) was subjected to normal-phase CC over a silica gel using $CHCl_3$/MeOH/H_2O (10:4:0.5) to give 14 fractions (B21–B214). Fraction B22 (120 mg) was purified by preparative RP-C_{18} HPLC using a solvent system of MeOH/H_2O (2:3) to afford **15** (5 mg). Fraction B22 (500 mg) was isolated by Sephadex LH-20 chromatography (90% MeOH) and was purified over a silica gel CC using MeCN/H_2O (1:4) to yield **12** (3 mg), **13** (9 mg), and **14** (11 mg). Fraction B212 (500 mg) was isolated by Sephadex LH-20 chromatography (70% MeOH) and was purified over a silica gel CC using MeOH/H_2O (1:4) to yield **1** (13 mg), and **2** (15 mg).

Cardamoside A (1)

Yellowish gum. UV (MeOH) λ_{max} (log ε): 317 (4.1), 267 (3.8). IR (KBr, cm^{-1}) ν_{max}: 3356, 2941, 2832, 1657, 1602, 1451, 1167, 1032, 802, 670. ^{1}H NMR (DMSO-d_6, 500 MHz) and ^{13}C NMR (DMSO-d_6, 125 MHz): see Table 1. HR-FAB-MS *m*/*z*: 1065.3086 $[M + H]^+$ (calcd for $C_{48}H_{57}O_{27}$, 1065.3087).

Cardamoside B (2)

Yellowish gum. UV (MeOH) λ_{max} (log ε): 323 (4.0), 267 (3.9). IR (KBr, cm^{-1}) ν_{max}: 3355, 2947, 2832, 1452, 1032, 797, 670. ^{1}H NMR (DMSO-d_6, 500 MHz) and ^{13}C NMR (DMSO-d_6, 125 MHz): see Table 1. HR-FAB-MS *m*/*z*: 1117.3021 $[M + Na]^+$ (calcd for $C_{49}H_{58}NaO_{28}$, 1117.3012).

Alkaline hydrolysis of 1 and 2

Compounds **1** (10 mg) in 0.05 mol/L KOH (2 mL) was stirred at room temperature for 2 h. The hydrolysate was extracted with $CHCl_3$, and the $CHCl_3$ extract was evaporated in vacuo. The $CHCl_3$ extract was purified using HPLC (Optimapak ODS-A, 250 × 10 mm; mobile phase, 40% MeOH; detector, RI; and flow rate, 2.0 mL/min) to yield *trans-p*-coumaric acid (1.2 mg) and **1a** (7 mg). Compound **2** (10 mg) was treated using the same method to give **2a** (=**1a**) (6.5 mg) and *trans*-ferulic acid (1.3 mg).

1a (**2a**): yellowish gum. ^{1}H NMR (DMSO-d_6, 500 MHz) δ: 7.95 (d, J = 8.8 Hz, H-2′,6′), 6.87 (d, J = 8.8 Hz, H-3′,5′), 6.73 (d, J = 2.0 Hz, H-8), 6.44 (d, J = 2.0 Hz, H-6), 5.37 (d, J = 7.8 Hz, Glc I), 5.06 (d, J = 7.8 Hz, Glc III), 4.43 (s, Rha), 4.16 (d, J = 7.8 Hz, Glc II). FAB-MS *m*/*z*: 917 $[M - H]^-$.

Can. J. Chem. Downloaded from www.nrcresearchpress.com by UNIVERSITAT DE VALENCIA on 10/20/12
For personal use only.

Acid hydrolysis of 1a and 2a

Compounds **1a** (=**2a)** (5 mg) was heated in an ampoule with 1 mL of aq. 1.5 mol/L HCl at 80 °C for 2 h. After cooling, the reaction mixture was extracted with EtOAc. The EtOAc solvent was evaporated in vacuo, and the residue was purified by HPLC (Optimapak ODS-A, 250 × 10 mm; mobile phase, 50% MeOH; detector, RI; and flow rate, 2.0 mL/min) to yield kaempferol (1.5 mg). The structure was identified by ^{1}H NMR and MS spectral analysis.

Determination of the sugars of compounds 1 and 2

The sugar residues (each ~2.0 mg) obtained from the hydrolysis of **1** and **2** were dissolved in anhydrous pyridine (0.1 mL) and L-cysteine methyl ester hydrochloride (2 mg) was subsequently added. The mixture was stirred at 60 °C for 1.5 h. After the reaction mixture was dried in vacuo, the residue was trimethylsilylated with 1-trimethylsilylimidazole (0.1 mL) for 2 h. The mixture was partitioned between *n*-hexane and H_20 (0.3 mL each), and the organic layer (1 μL) was analyzed by GC–MS. Identification of D-glucopyranose, and L-rhamnopyranose for **1** and **2** were detected in each case by co-injection of the hydrolysate with standard silylated samples, giving single peaks at D-glucopyranose (10.11 min) and L-rhamnopyranose (5.54 min) for **1**, and at D-glucopyranose (10.19 min) and L-rhamnopyranose (5.49 min) for **2**. Retention times of authentic samples treated in the same way with 1-trimethylsilylimidazole in pyridine, were D-glucopyranose (10.14 min) and L-rhamnopyranose (5.51 min).

Acknowledgements

This research was supported by the Basic Science Research Program through the National Research Foundation of Korea (NRF) funded by the Ministry of Education, Science, and Technology (20110028285). We thank Dr. Do Kyun Kim, Dr. Eun Jung Bang, and Dr. Jung Ju Seo at the Korea Basic Science Institute, Daejeon, Korea, for their aid in obtaining the NMR and mass spectra.

References

(1) Lee T. B.; *Coloured Flora of Korea;* Hyang-Moon publishing Co.: Korea, 2003; p 433.
(2) Ahan, D. K.; *Illustrated Book of Korean Medicinal Herbs;* Koy-Hak Publishing Co.: Korea, 1998; p 400.
(3) Lee, I. K.; Kim, K. H.; Lee, S. Y.; Choi, S. U.; Lee, K. R. *Chem. Pharm. Bull. (Tokyo)* **2011**, *59* (6), 773. doi:10.1248/cpb.59.773.
(4) Lee, I. K.; Jeong, E.-K.; Choi, S. U.; Hong, J. K.; Lee, K. R. *Heterocycles* **2011**, *83* (11), 2615. doi:10.3987/COM-11-12330.
(5) Budzianowski, J. *Phytochemistry* **1991**, *30* (5), 1679. doi:10.1016/0031-9422(91)84233-I.
(6) Liu, H.; Orjala, J.; Sticher, O.; Rali, T. *J. Nat. Prod.* **1999**, *62* (1), 70. doi:10.1021/np980179f.
(7) Jiang, W.; Li, W.; Han, L.; Liu, L.; Zhang, Q.; Zhang, S.; Nikaido, T.; Koike, K. *J. Nat. Prod.* **2006**, *69* (11), 1577. doi:10.1021/np060195+.
(8) Young, H. S.; Kim, M. S.; Park, H. J.; Chung, H. Y.; Choi, J. S. *Arch. Pharm. Res.* **1992**, *15* (4), 322. doi:10.1007/BF02974106.
(9) Weckerle, B.; Michel, K.; Balazs, B.; Schreier, P.; Toth, G. *Phytochemistry* **2001**, *57* (4), 547. doi:10.1016/S0031-9422(01)00059-0.
(10) Sy, L. K.; Brown, G. D. *J. Nat. Prod.* **1998**, *61* (8), 987. doi:10.1021/np9800553.
(11) Bouaicha, N.; Amade, P.; Puel, D.; Roussakis, C. *J. Nat. Prod.* **1994**, *57* (10), 1455. doi:10.1021/np50112a019.
(12) Rahman, M. A. A.; Moon, S. S. *Arch. Pharm. Res.* **2007**, *30* (11), 1374. doi:10.1007/BF02977359.
(13) Lu, W.; Yamaoka, Y.; Taniguchi, Y.; Kitamura, T.; Takaki, K.; Fujiwara, Y. J. *Organomet. Chem.* **1999**, *580* (2), 290. doi:10.1016/S0022-328X(98)01160-7.
(14) Jung, W. Y.; Ma, E. S. *Yakhak Hoechi* **2003**, *47*, 1.
(15) Schwab, W.; Schreier, P. *Phytochemistry* **1988**, *27* (6), 1813. doi:10.1016/0031-9422(88)80450-3.
(16) Park, S. Y.; Kim, J. S.; Lee, S. Y.; Bae, K. H.; Kang, S. S. *Nat. Prod. Sci.* **2008**, *14*, 281.

A simple and straightforward approach toward selective C=C bond reduction by hydrazine

Hao Chen, Jianmin Wang, Xuechuan Hong, Hai-Bing Zhou, and Chune Dong

Can. J. Chem. Downloaded from www.nrcresearchpress.com by UNIVERSITAT DE VALENCIA on 10/20/12
For personal use only.

Abstract: A simple and straightforward method for reducing the C=C double bond with hydrazine is described. A number of representative C=C bonds in various steric and electronic environments were examined. Substituted alkenes can be selectively reduced in EtOH in the presence of hydrazine to give the corresponding products in up to 100% yields.

Key words: hydrazine, reduction, C=C double bond.

Résumé : On décrit une méthode simple et directe de réduire une double liaison C=C à l'aide d'hydrazine. On a appliqué la méthode à un certain nombre de doubles liaisons typiques, dans des environnements stériques et électroniques variés. Il est possible de réduire sélectivement des alcènes substitués dans l'éthanol, en présence d'hydrazine, pour conduire aux produits correspondants avec des rendements allant jusqu'à 100 %.

Mots-clés : hydrazine, réduction, double liaison C=C.

[Traduit par la Rédaction]

Introduction

The reduction of functionalized alkenes is one of the most fundamental reactions in organic chemistry.[1] In recent decades, various transition-metal catalysts such as Rh, Pt, and Pd were generally applied for the selective reduction of alkenes to the corresponding alkanes.[2,3] Despite the important progress in this field, these reported processes not only had harsh conditions and limited selectivity, but also produced significant amounts of inorganic and organic wastes that are of environmental concern. Thus, the development of more efficient, environmentally friendly, and economical nonmetal reagents for selective reduction of functionalized alkenes is of interest to the organic synthesis and medicinal chemistry communities as well.

In contrast, diimide reduction appears to offer an attractive solution, since NH=NH acts as a mild reducing agent for a variety of unsaturated bonds.[4,5] This reduction process has the potential to be environmentally benign, since nitrogen gas is the sole waste product. Imada et al.[6] reported the first green method for aerobic hydrogenation; the olefins can be reduced by treatment with hydrazine in the presence of $FLEt{\cdot}ClO_4$ under an O_2 atmosphere to give the product in excellent yields, with environmentally benign water and molecular nitrogen as the only waste products. *o*-Nitrobenzenesulfonylhydrazide (NBSH) is known to be another convenient precursor of diimide, since the *o*-nitrobenzene sulfinate is a good leaving group under mild conditions. In 2009, Marsh and Carbery[7] demonstrated NBSH forming the simple and efficient diimide alkene's reductions protocol. Meanwhile, it was also recognized that when the level of substitution of alkenes increases, the reaction becomes less efficient and low conversion is observed. Obviously, these methods provide improved results over traditional methods. However, the limitation of scope and the presence of organo or metal catalysts all preclude the straightforward approach to selective C=C double bond reduction.[8] Therefore, the development of more efficient, commercial available, and simple reducing agents is highly desirable.

To the best of our knowledge, there has not been a report on the facile reduction of the C=C double bond by hydrazine under mild conditions. Herein, we wish to report an unexpected reduction reaction of functionalized alkenes with commercially available hydrazine under simple thermal conditions that leads to a general and efficient method for selective C=C double bond reduction of substituted alkenes.

Results and discussion

Our studies were initiated by the reaction of 2-allylphenol **1a** with commercial hydrazine hydrate **2**. The reaction was carried out in air. To our delight, when 8 equiv of **2** was used, **1a** was fully converted to 2-propylphenol **3a** (Table 1, entry 7). As reasonably expected, no product was observed when the reaction was run under an argon atmosphere (Table 1, entry 10), which clearly indicates that diimide reduction occurred. After a brief survey of the reaction conditions, it was found that solvents and the amount of hydrazine were critical for the reaction efficiency (Table 1). 2-Allylphenol was treated with 2 equiv of hydrazine in EtOH at 80 °C, leading to trace amounts of the desired product after 14 h (Table 1, entry 9). Further study indicated that a 34% yield

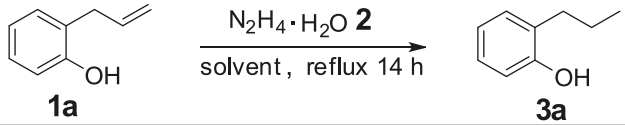
Received 27 June 2011. Accepted 6 July 2012. Published at www.nrcresearchpress.com/cjc on 30 August 2012.

H. Chen, J. Wang, X. Hong, H.-B. Zhou, and C. Dong. Key Laboratory of Combinatorial Biosynthesis and Drug Discovery (Wuhan University), Ministry of Education, State Key Laboratory of Virology, Wuhan University School of Pharmaceutical Science, Wuhan 430071, P.R. China.

Corresponding author: Chune Dong (e-mail: cdong@whu.edu.cn).

Can. J. Chem. Downloaded from www.nrcresearchpress.com by UNIVERSITAT DE VALENCIA on 10/20/12
For personal use only.

Table 1. Reduction of 2-allylphenol under various conditions.



1a **3a**

Entry	**2** (equiv)	Solvent	Conversion (%)[a]
1	8	MeOH	22
2	8	H_2O	35
3	8	CH_3CN	59
4	8	THF	9
5	8	DCM	2
6	8	Toluene	17
7	8	EtOH	100
8	4	EtOH	34
9	2	EtOH	1
10[b]	8	EtOH	No reaction

Note: Reaction conditions: 2-allylphenol (**1a**, 2 mmol), appropriate amount of hydrazine hydrate (**2**), solvent, reflux 14 h.

[a]Determined by ^{1}H NMR analysis of the crude reaction mixture.

[b]The reaction was run under an argon atmosphere.

of product was obtained when 4 equiv of **2** was employed (Table 1, entry 8). Additionally, among the tested solvents, ethanol was identified as the solvent of choice. Acetonitrile gave an inferior result, but dichloromethane, THF, and toluene were observed to be ineffective (Table 1, entries 1–6).

Having identified the optimal reaction conditions, we next explored the scope and limitations of this reduction reaction with hydrazine using various alkenes derivatives (**1b**–**1r**). The results are summarized in Table 2. Clearly, our reduction system proved rather effective for the selective reduction of a wide variety of substituted alkenes, providing the corresponding product in excellent yields. In addition to 2-allylphenol **1a**, terminal alkenes **1b** and **1c** also reacted smoothly with hydrazine giving the corresponding products in excellent yields (Table 2, entries 2 and 3). Additionally, a polarized alkene, such as **1d**, was efficiently reduced by hydrazine in 5.5 h, forming product **3d** in excellent yield (Table 2, entry 4). Aromatic alkenes with the phenyl ring substituted with an electron-donating or an electron-withdrawing group also performed well in this reduction (Table 2, entries 5–13). For example, *p*-methoxyl methyl cinnamate (**1i**) and *p*-trifluoromethyl cinnamic acid (**1l**) underwent smooth reduction (Table 2, entries 9 and 12). It can be clearly seen that when the level of th ealkene substitution increases, the reduction becomes less efficient. Tetra-substituted alkene **1r** remained inert under the same reaction conditions (Table 2, entry 18). Interestingly, in the case of styrene, a 16% yield of enthylbenzene was obtained (Table 2, entry 17), which indicates that, for mono-substituted alkenes, conjugation might play an important role in hydrazine-promoted reduction.

Clearly, this reduction system offers synthetic advantages with respect to metal-catalyzed hydrogenation and other reducing systems as well.

Conclusions

In conclusion, a simple, efficient, and highly selective C=C double bond reduction protocol has been developed. The hydrazine-mediated reducing system has been successfully applied to various substituted alkene reductions to form the desired products in excellent yields. We believe this reduction method, from a synthetic point of view, is a valuable alternative not only for the laboratory but also for industry.

Experimental section

General information

All reagents and solvents were obtained from commercial sources and were used without further purification. The hydrazine hydrate used in this study was 80% solution. Column chromatography was performed with silica gel (300–400 mesh). NMR spectroscopy was performed on a Bruker (400 MHz) spectrometer using TMS as the internal standard. Products were characterized by comparison of their ^{1}H NMR spectroscopic data with those reported in the literatures.

General procedure for reduction reactions with hydrazine hydrate

To 1 mmol of substrate **1** dissolved in 1.0 mL of solvent was added 8 mmol of hydrazine **2** and the mixture was heated to reflux for 5.5–24 h in air. After the reaction finished, the solvent was removed and the residue was extracted three times with ethyl acetate (3 × 5 mL) and dried over $MgSO_4$. The product was characterized by NMR.

Acknowledgments

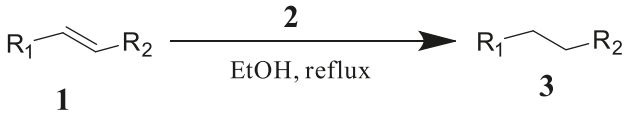
We are grateful to the Natural Science Foundation of China (Grant Nos. 20972121, 81172935, and 91017005), the Program for New Century Excellent Talents in University (NCET-10-0625), and the Research Fund for the Doctoral Program of Higher Education of China (20100141110021) and the Science Foundation of Ministry of Education for the New Teacher at the University of China (20090141120058) for support of this research.

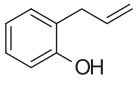
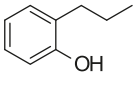
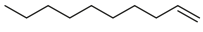
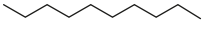
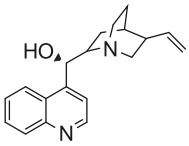
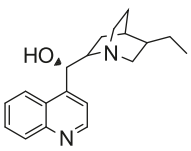
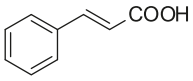
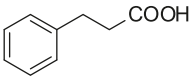
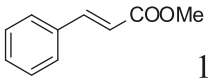
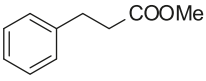
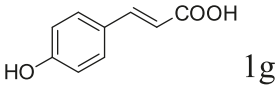
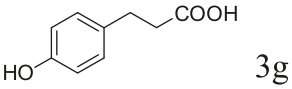
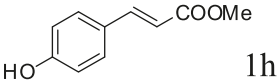
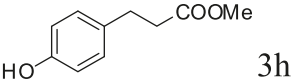
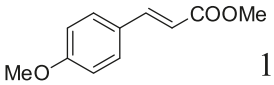
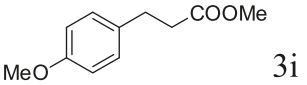
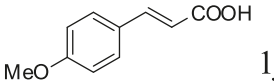
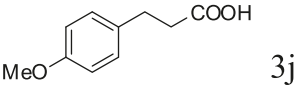
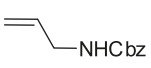
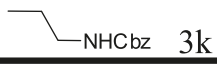
References

(1) (a) March, J. *Advanced Organic Chemistry: Reactions,*

Can. J. Chem. Downloaded from www.nrcresearchpress.com by UNIVERSITAT DE VALENCIA on 10/20/12
For personal use only.

Table 2. Scope of the reduction reactions promoted by hydrazine.



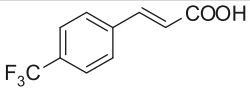
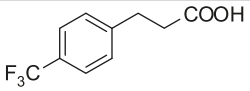
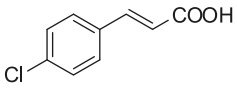
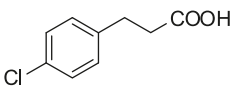
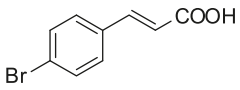
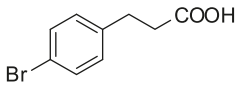
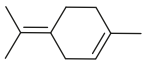
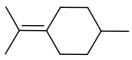
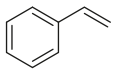
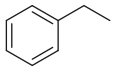
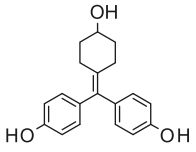
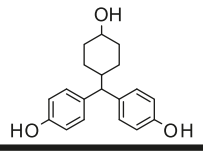
Entry	Substrate	Product	Yield (%)
1	 1a	 3a	100
2[a]	 1b	 3b	100
3[a]	 1c	 3c	100
4[b]	 1d	 3d	94
5[b]	 1e	 3e	96
6[b]	 1f	 3f	98
7[b]	 1g	 3g	96
8[b]	 1h	 3h	95
9[b]	 1i	 3i	98
10[b]	 1j	 3j	92
11[a]	 1k	 3k	100

Mechanism, and Structure; 4th ed.; John Wiley: Hoboken, NJ, 1992; (b) Larock, R. C. *Comprehensive Organic Transformation: A Guide to Functional Group Preparations;* Wiley-VCH: Hoboken, NJ, 1999.

(2) (a) Cui, X.; Burgess, K. *Chem. Rev.* **2005**, *105* (9), 3272. doi:10.1021/cr0500131; (b) Margathe, J. F.; Shipman, M.; Smith, S. C. *Org. Lett.* **2005**, *7* (22), 4987. doi:10.1021/ol051953a; (c) Di Bussolo, V.; Romano, M. R.; Favero, L.; Pineschi, M.; Crotti, P. *J. Org. Chem.* **2006**, *71* (4), 1696. doi:10.1021/jo051877p.

(3) (a) Mita, T.; Fukuda, N.; Roca, F. X.; Kanai, M.; Shibasaki, M. *Org. Lett.* **2007**, *9* (2), 259. doi:10.1021/ol062663c; (b) Åman, J.; Jarevång, T.; Somfai, P. *J. Org. Chem.* **1996**, *61* (23), 8148. doi:10.1021/jo9612638; (c) Raspolli Galletti, A. M.; Bonaccorsi, F.; Calvani, F.; Di Bugno, C. *Catal. Commun.* **2006**, *7*

Table 2. *(concluded).*

Entry	Substrate	Product	Yield (%)
12[b]	 1l	 3l	>99
13[b]	 1m	 3m	>99
14[b]	 1n	 3n	91
15[a]	 1o	 3o	42
16[a]	 1p	 3p	42
17[a]	 1q	 3q	16
18	 1r	 3r	—[c]

Note: Reaction conditions: **1** (5 mmol), hydrazine hydrate (**2**, 8 equiv), reflux in EtOH (5 mL), 14 h.

[a]Reaction time was 24 h.

[b]Reaction time was 5.5 h and the same result was observed in H_2O.

[c]No reaction.

(11), 896. doi:10.1016/j.catcom.2006.03.022; (d) Smit, C.; Fraaije, M. W.; Minnaard, A. J. *J. Org. Chem.* **2008**, *73* (23), 9482. doi:10.1021/jo801588d.

(4) (a) Hünig, S.; Müller, H. R.; Thier, W. *Angew. Chem. Int. Ed. Engl.* **1965**, *4* (4), 271. doi:10.1002/anie.196502711; (b) Pasto, D. J.; Taylor, R. T. *Organic Reactions;* Vol. 40; John Wiley & Sons: Hoboken, NJ, 1991, p 91; (c) Skouta, R.; Varma, R. S.; Li, C. J. *Green Chem.* **2005**, *7* (8), 571. doi:10.1039/b506881a.

(5) (a) Lee, B. K.; Sung, B. J.; Lee, W. K.; Yoon, D.-H.; Ha, H.-J. *Bull. Korean Chem. Soc.* **2009**, *30* (12), 3123. doi:10.5012/bkcs.2009.30.12.3123; (b) Zibinsky, M.; Stewart, T.; Prakash, G. K. S.; Kuznetsov, M. A. *Eur. J. Org. Chem.* **2009**, *2009* (21), 3635. doi:10.1002/ejoc.200900326; (c) Buszek, K. R.; Brown, N. *J. Org. Chem.* **2007**, *72* (8), 3125. doi:10.1021/jo0622173; (d) Komykhov, S. A.; Ostras, K. S.; Kobzar, K. M.; Musatov, V. I.; Desenko, S. M. *J. Heterocycl. Chem.* **2009**, *46* (6), 1413. doi:10.1002/jhet.218; (e) Haukaas, M. H.; O'Doherty, G. A. *Org. Lett.* **2002**, *4* (10), 1771. doi:10.1021/ol025844x.

(6) Imada, Y.; Iida, H.; Naota, T. *J. Am. Chem. Soc.* **2005**, *127* (42), 14544. doi:10.1021/ja053976q.

(7) Marsh, B. J.; Carbery, D. R. *J. Org. Chem.* **2009**, *74* (8), 3186. doi:10.1021/jo900237y.

(8) (a) Dhakshinamoorthy, A.; Alvaro, M.; Garcia, H. *Adv. Synth. Catal.* **2009**, *351* (14–15), 2271. doi:10.1002/adsc.200900362; (b) Lacombe, P.; Castagner, B.; Gareau, Y.; Ruel, R. *Tetrahedron Lett.* **1998**, *39* (38), 6785. doi:10.1016/S0040-4039(98)01490-7; (c) Myers, A. G.; Zheng, B. *J. Am. Chem. Soc.* **1996**, *118* (18), 4492. doi:10.1021/ja960443w; (d) Myers, A. G.; Zheng, B. *Tetrahedron Lett.* **1996**, *37* (28), 4841. doi:10.1016/0040-4039(96)00965-3.

Can. J. Chem. Downloaded from www.nrcresearchpress.com by UNIVERSITAT DE VALENCIA on 10/20/12
For personal use only.

Structural requirements of salicylaldehyde benzoylhydrazones and their Cu(II) complexes for anticancer activity

Shiow Jin Tan, Mahasin Alam Sk, Peter Peng Foo Lee, Yaw Kai Yan, and Kok Hwa Lim

Can. J. Chem. Downloaded from www.nrcresearchpress.com by UNIVERSITAT DE VALENCIA on 10/20/12
For personal use only.

Abstract: Salicylaldehyde benzoylhydrazone (H_2sb) has a variety of biological activities including anticancer activity. The Cu(II) complexes of H_2sbs possess enhanced anticancer activity as compared with their free ligands. A quantitative structure–activity relationship (QSAR) analysis was performed on a series of H_2sb ligands and their corresponding Cu(II) complexes to capture the structural requirements that are responsible for the bioactivity. The predictive QSAR models were developed using statistical techniques such as multiple linear regression (MLR) and principal component regression analysis (PCRA). We used different combinations of various descriptors such as a physicochemical descriptor, electrotopological state atom (ETSA) indices, and descriptors derived from density functional theory (DFT) calculations. The DFT-derived descriptors used for QSAR analysis are HOMO and LUMO energies, atomic charges, chemical potential, and hardness. Our developed models showed the importance of the lipophilicity index (ClogP), ETSA indices, and atomic charges for anticancer activities of the H_2sb analogs and their Cu(II) complexes. In addition, our MLR models revealed that, while the global lipophilicity index and hardness are important for anticancer activity of H_2sb ligands, chemical potential and HOMO energy are important for the anticancer activity of Cu(II) complexes.

Key words: salicylaldehyde benzoylhydrazone, copper(II) complexes, DFT, ETSA index, QSAR.

Résumé : La benzoylhydrazone du salicylaldéhyde (H_2sb) possède une grande variété d'activités biologiques, dont une activité anticancéreuse. Les complexes du Cu(II) avec la H_2sb possèdent une activité anticancéreuse amplifiée par rapport à celle des ligands non liés à un métal. On a effectué une analyse de relation structure–activité quantitative (RSAQ) sur une série de ligands dérivés de la H_2Sb ainsi que sur les complexes correspondants du Cu(II) afin de déterminer quelles caractéristiques structurales sont responsables de cette bioactivité. On a développé les modèles prédictifs de RSAQ en faisant appel à des techniques statistiques telles que l'analyse de la régression linéaire multiple (RLM) et l'analyse de la régression de la composante principale (ARCP). On a utilisé diverses combinaisons de descripteurs différents, tel un descripteur physicochimique, les indices électrotopologiques de l'état de l'atome (ETEA) et des descripteurs dérivés de calculs de la théorie de la fonctionnelle de la densité (TFD). Les descripteurs dérivés de la TFD qui ont été utilisés pour les analyses RSAQ sont l'énergie de l'orbitale moléculaire (OM) haute occupée (HO) ou basse vacante (BV), les charges atomiques, le potentiel chimique et la dureté. Les modèles qui ont été développés mettent en évidence l'importance de l'indice du caractère lipophile (ClogP), des indices électrotopologiques de l'état de l'atome (ETEA) et des charges atomiques sur les activités anticancéreuses des analogues de la H_2sb et de leurs complexes de Cu(II). De plus, nos modèles de régression linéaire multiple (RLM) démontrent l'importance de l'indice du caractère lipophile et de l'énergie de l'orbitale moléculaire HO sur l'activité anticancéreuse des complexes du Cu(II).

Mots-clés : benzoylhydrazone du salicylaldéhyde, complexes du cuivre, théorie de la fonctionnelle de la densité (TFD), indice électrotopologique de l'état de l'atome (ETEA), relation structure–activité quantitative (RSAQ).

[Traduit par la Rédaction]

Introduction

The biological activities of salicylaldehyde benzoylhydrazone (H_2sb) analogs have received great attention in the past years. H_2sb was first found to have promising bacteriostatic activity and later it was found that they are able to inhibit DNA synthesis and cell growth in a broad range of human and rodent cell lines.[1,2] In addition, H_2sb analogs have also been reported to have significant antitumor activities against a variety of cancer cell lines.[3,4] Interestingly, they also have been shown to be an effective copper chelator, and their Cu(II)

Received 2 May 2012. Accepted 25 June 2012. Published at www.nrcresearchpress.com/cjc on 30 August 2012.

S.J. Tan, M.A. Sk, and K.H. Lim. Division of Chemical and Biomolecular Engineering, School of Chemical and Biomedical Engineering, Nanyang Technological University, 62 Nanyang Drive, Singapore 637459.
P.P.F. Lee and Y.K. Yan. Natural Sciences and Science Education, National Institute of Education, Nanyang Technological University, 1 Nanyang Walk, Singapore 637616.

Corresponding author: Kok Hwa Lim (e-mail: kokhwa@ntu.edu.sg).

Can. J. Chem. Downloaded from www.nrcresearchpress.com by UNIVERSITAT DE VALENCIA on 10/20/12
For personal use only.

complexes possess enhanced antitumor activities when compared with the free H_2sb ligands.[3,4] Over the years, a significant amount of studies have been done on the Cu(II) complexes for their potential anticancer activity.[5,6] The main reason is that the Cu(II) complexes can serve as an alternative for the renowned platinum-based drugs (e.g., cisplatin and carboplatin), which have undesirable side effects and drug-resistance problems.[7] In 1998, Ainscough et al.[4] synthesized a series of H_2sb ligands and their Cu(II) complexes that showed promising antitumor activity against the human colon cancer cell line. To date, the mechanism for anticancer activity of H_2sb analogs and their Cu(II) complexes is still unclear. Thus, a detailed understanding on the properties of these compounds at the molecular level, such as steric and electronic properties, may provide important insights into the anticancer properties.[8] Among the diversified descriptors, the quantum chemical descriptors based on density functional theory (DFT) and semiempirical methods have been found useful in several quantitative structure–activity relationship (QSAR) studies conducted recently.[9–11] The net atomic charges, frontier molecular orbital energies (i.e., highest occupied molecular orbital (HOMO) and lowest unoccupied molecular orbital (LUMO)),[12] and DFT-based reactivity descriptors, such as global hardness, electronegativity, and chemical potential, have been demonstrated to correlate well with various biological activities. A preliminary QSAR study was performed by Ainscough et al.[4] on the H_2sb ligands using the octanol–water partition coefficient and the Hammett σ parameters for antitumor activity. However, they were unable to conduct QSAR analysis on the Cu(II) complexes because of the lack of accurate and transferable linear free energy relationship (LFER) parameters for the complexes. To the best of our knowledge no QSAR studies have been performed on Cu(II) complexes of H_2sb ligands. Moreover, very few QSAR studies on copper complexes for other bioactivities have been reported[5] owing to the lack of specific metal–ligand parameters in most of the common force fields, which generally do not predict the structure of metal complexes accurately.[13]

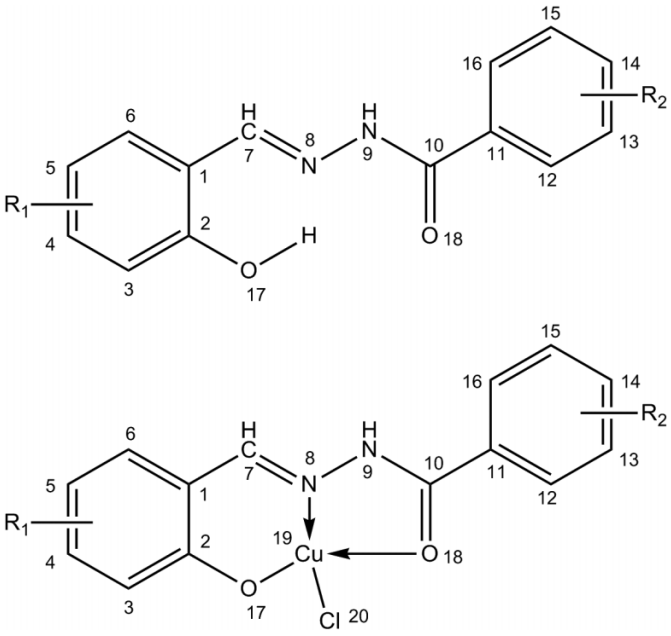
Thus, in the present study, we performed the QSAR analysis on the H_2sb analogs and their Cu(II) complexes to develop predictive QSAR models and to capture the structural changes that are responsible for the cancer inhibitory activity. We used the electrotopological state atom (ETSA) indices, physiochemical properties like the hydrophobicity index, DFT-derived descriptors such as E_{HOMO} and E_{LUMO}, chemical potential, global hardness, the global electrophilicity index, and atomic charges as descriptors for the QSAR studies. We performed multiple linear regression (MLR) analysis and principal component regression analysis (PCRA) to develop the QSAR models for the H_2sb analogs and their Cu(II) complexes.

Materials and methods

Molecular modelling

The general structures and arbitrary atom numberings for the H_2sb analogs and their Cu(II) complexes are illustrated in Fig. 1. All calculations were performed by the DFT[14,15] B3LYP (Becke's three-parameter hybrid function[16] with the nonlocal correlation of the Lee–Yang–Parr[17]) method with

Fig. 1. General structures of salicylaldehyde benzoylhydrazone ligands and their corresponding Cu(II) complexes with arbitrary numberings.



the 6–31G(d) basis set.[18] The calculations were carried out using the Gaussian 03 suite of programs.[19] Full geometry optimizations were performed on both the H_2sb ligands and their Cu(II) complexes at the B3LYP/6–31G(d) level (past studies[20–22] justified that the 6–31G(d) basis set is sufficient for current systems). Frequency analyses were performed on the optimized geometries to confirm that they are at minima (no imaginary frequency). The optimized stable structures of the H_2sb ligands and their Cu(II) complexes were used for the calculations of reactivity descriptors for the QSAR analysis. Natural population analysis (NPA)[23,24] was performed to obtain the natural atomic charges.

Data set and descriptor calculations

The anticancer activity data (IC_{50}, μmol) of H_2sb and their Cu(II) complexes were collected from the published work of Ainscough et al.[4] The IC_{50} (μmol) values taken from Ainscough et al. were first converted to IC_{50} (mol). The IC_{50} values were then converted to the logarithmic scale ($pIC_{50} = -\log IC_{50}$) and used as response variables to develop the QSAR models (see Table 1). The calculations of the *n*-octanol–water partition coefficient (ClogP), molar refractivity (MR), and geometrical parameters, such as Connolly accessible area (CAA), Connolly molecular area (CMA), and volume (*V*), were performed using the Chem 3D Ultra 11.0 software package.[25] ClogP and MR were calculated according to Ghose and Crippen's fragmentation method.[26] The ETSA index introduced by Kier and Hall and co-workers[27–29] was employed in the QSAR analysis for the exploration of atoms or regions of the compounds that modulate the activity comparatively to a greater extent. The ETSA index of a skeletal atom is defined as $S_i = I_i + \Delta I_i$, where I_i is the intrinsic electronic and topological character of an atom and ΔI_i is the perturbation effect of the molecular topological environment of each atom in the molecule. The I_i value of an atom is

Can. J. Chem. Downloaded from www.nrcresearchpress.com by UNIVERSITAT DE VALENCIA on 10/20/12
For personal use only.

Table 1. Structural features and experimental antitumor activities (pIC_{50}) of the 24 salicylaldehyde benzoylhydrazone (H_2sb) analogs and their corresponding Cu(II) complexes (cpx.).[4]

			Ligand	Cu(II) cpx.
No.	R_1[a]	R_2[a]	pIC_{50} (mol)	pIC_{50} (mol)
1	H	H	5.43	5.80
2	3-Me	H	5.59	5.82
3	3-OMe	H	5.43	5.82
4	5-Me	H	5.66	6.03
5	5-Cl	H	5.57	6.00
6	5-NO_2	H	4.84	5.40
7	H	2-Me	5.21	5.68
8	H	3-Me	5.60	5.85
9	H	4-Me	5.57	5.82
10	H	4-F	5.68	5.80
11	H	4-Cl	5.85	5.89
12	H	4-Br	5.77	5.80
13	H	4-NH_2	4.80	4.96
14	H	4-OMe	5.42	5.64
15	H	2-OH	5.74	5.96
16	H	4-OH	5.14	5.01
17	H	4-NO_2	5.77	5.82
18	H	4-*t*-Bu	5.89	6.22
19	H	4-SO_2Me	5.21	5.77
20	5-Me	4-Me	5.64	5.96
21	5-Me	4-Cl	5.74	6.01
22	5-Me	4-NH_2	5.16	5.16
23	5-Cl	4-Me	5.85	5.85
24	3,5-Cl	H	5.46	5.92

[a]See Fig. 1 for the definition.

defined as $I_i = [(2/N)^2\delta^v + 1]/\delta$, where N is the principal quantum number, δ^v and δ are the counts of the valence electrons and σ electrons, respectively, associated with the atom i in the hydrogen-suppressed graph. The general expression for the perturbation term is $\Delta I_i = \sum (I_i - I_j)/r_{ij}^2$, where I_i and I_j are the intrinsic state values for atoms i and j, respectively, and r_{ij} is the number of atoms through atom i to atom j, including the atoms i and j.

The energies of the highest occupied molecular orbital (E_{HOMO}) and lowest unoccupied molecular orbital (E_{LUMO}) are often used as quantum mechanical parameters to characterize the reactivity of molecules in many chemical reactions. Based on Koopmans' theorem,[30] ionization potential and electron affinity can be approximated as the $-E_{HOMO}$ and $-E_{LUMO}$, respectively. With the approximations according to Koopmans' theorem and the finite difference approach, the following set of DFT-based reactivity descriptors were derived and used in our QSAR study: (*i*) the global electrophilicity index ($\omega = \frac{\mu^2}{2\eta}$),[31] (*ii*) the chemical potential ($\mu = \frac{E_{LUMO}+E_{HOMO}}{2}$),[32] and (*iii*) the hardness $\eta = \frac{E_{LUMO}-E_{HOMO}}{2}$.[33]

Statistical analysis

Two statistical methods, MLR[34] and PCRA,[35] were employed to develop QSAR models. The leave-one-out (LOO) cross-validation method[36] was carried out to validate the predictive abilities of the MLR equations. The statistical qualities of the developed MLR equations were judged by using parameters such as square of the correlation coefficient (R^2), explained variance (R^2_a), variance ratio (F), probability factor related to the F ratio (p), the standard error of estimate (s), and predicted residual sums of squares (PRESS). All the statistical analyses were performed using MINITAB[37] software.

Results and discussion

MLR analysis

QSAR models for H_2sb ligands

The selected ETSA indices, natural atomic charges, lipophilicity indices, and quantum chemical descriptors derived from the DFT study for the H_2sb ligands and their Cu(II) complexes, used to deduce the QSAR models, are listed in Tables 2 and 3. All descriptors were subjected to correlation analysis, and highly intercorrelated descriptors were removed based on their correlation. MLR analysis was performed the on the H_2sb ligand's data set for anticancer activity. All possible combinations of the selected descriptors were taken into account during the model derivation. The QSAR models obtained from the MLR analysis for the H_2sb ligands were selected based on statistical measures such as R^2, the adjusted R^2 (R^2_a), the LOO cross-validated square of the correlation coefficient (Q^2), s, and the overall F statistics for the addition of each successive term (F) and are presented in Table 4. The QSAR models (eqs. [1]–[14]) obtained from the regression analysis for the H_2sb ligands are listed in Table 4.

The best QSAR model (Table 4, eq. [1]) developed with two parameters for the H_2sb ligand's data set shows the positive contribution of ClogP and the negative contribution of η towards the anticancer activity. Equation [1] (Table 4) explains 75.0% and predicts 62.1% of the variance of the activity. This indicates that the variations of lipophilicity and chemical hardness are induced becausee of ortho or para substitution at the salicylaldehyde ring or ortho, meta, or para substitution at the benzoylhydrazone's phenyl ring, which plays an important role in the interaction of the H_2sb compounds with cancer cells. This prompted us to further improve the models with the addition of other descriptors.

We developed four new equations with improved overall statistical qualities (Table 4, eqs. [2]–[5]) by introducing one additional descriptor in eq. [1] (Table 4) such as the electrotopological descriptors (S_{11} and S_{17}) and quantum chemical descriptors (q_1 and q_2). S_{11} and S_{17} are the ETSA indices of atoms 11 and 17, respectively, and q_1 and q_2 are the atomic charges on atoms 1 and 2, respectively. The similar statistical significance of these equations reveals that the descriptors S_{11}, S_{17}, q_1, and q_2 have comparable contributions towards the anticancer activity of H_2sb ligands. The negative coefficients of S_{11} (eq. [2], Table 4) and S_{17} (eq. [3], Table 4) also suggest that an increase in the values of these descriptors is detrimental to the anticancer activity of the H_2sb compounds. Moreover, the negative coefficient of q_1 (eq. [4], Table 4) and the positive coefficient of q_2 (eq. [5], Table 4) show that a decrease of atomic charge on atom 1 and an increase of atomic charge on atom 2 is favourable for the anticancer activity of H_2sb ligands. Equations [6] and [7] (Table 4) are the most statistically significant models constructed with three parameters, which explain 77.5% and 80.7% of the variance of activity,

Can. J. Chem. Downloaded from www.nrcresearchpress.com by UNIVERSITAT DE VALENCIA on 10/20/12
For personal use only.

Table 2. Calculated values of selected descriptors of salicylaldehyde benzoylhydrazone (H_2sb) ligands used in the quantitative structure–activity relationship (QSAR) analysis.

Complex	S_4	S_6	S_7	S_8	S_9	S_{10}	S_{11}	q_1	q_2	q_8	q_{18}	ClogP	E_{HOMO}	E_{LUMO}	μ	η	ω
1	1.717	1.701	1.397	3.793	2.393	–0.282	0.541	–0.188	0.378	–0.302	–0.584	3.189	–5.734	–1.630	–3.682	2.052	3.303
2	1.799	1.721	1.418	3.834	2.412	–0.281	0.543	–0.185	0.384	–0.304	–0.585	3.638	–5.655	–1.589	–3.622	2.033	3.226
3	1.633	1.661	1.358	3.813	2.389	–0.308	0.521	–0.185	0.350	–0.302	–0.584	3.011	–5.403	–1.548	–3.475	1.928	3.132
4	1.799	1.783	1.418	3.834	2.412	–0.281	0.543	–0.183	0.374	–0.303	–0.585	3.688	–5.582	–1.596	–3.589	1.993	3.231
5	1.565	1.548	1.334	3.775	2.369	–0.314	0.517	–0.174	0.374	–0.295	–0.581	4.006	–5.867	–1.846	–3.857	2.010	3.699
6	1.174	1.158	1.140	3.671	2.271	–0.412	0.436	–0.179	0.401	–0.293	–0.580	1.429	–6.435	–2.204	–4.320	2.115	4.410
7	1.720	1.706	1.407	3.834	2.433	–0.266	0.587	–0.188	0.378	–0.302	–0.584	3.348	–5.726	–1.567	–3.646	2.079	3.197
8	1.720	1.705	1.404	3.823	2.420	–0.275	0.558	–0.188	0.378	–0.301	–0.585	3.688	–5.706	–1.589	–3.648	2.059	3.231
9	1.719	1.704	1.403	3.815	2.412	–0.278	0.549	–0.188	0.378	–0.301	–0.586	3.688	–5.694	–1.571	–3.632	2.061	3.201
10	1.684	1.654	1.329	3.722	2.289	–0.445	0.309	–0.189	0.378	–0.302	–0.585	3.430	–5.788	–1.679	–3.734	2.055	3.392
11	1.707	1.686	1.377	3.782	2.369	–0.337	0.464	–0.189	0.379	–0.303	–0.582	4.000	–5.833	–1.810	–3.821	2.012	3.629
12	1.715	1.698	1.393	3.804	2.397	–0.299	0.519	–0.189	0.379	–0.303	–0.582	4.150	–5.829	–1.813	–3.821	2.008	3.635
13	1.707	1.687	1.378	3.784	2.371	–0.334	0.469	–0.186	0.376	–0.298	–0.593	2.217	–5.553	–1.379	–3.466	2.087	2.878
14	1.710	1.691	1.384	3.804	2.389	–0.327	0.480	–0.187	0.377	–0.300	–0.591	3.272	–5.643	–1.479	–3.561	2.082	3.046
15	1.687	1.656	1.325	3.723	2.273	–0.516	0.143	–0.187	0.377	–0.301	–0.562	3.769	–5.647	–1.441	–3.544	2.103	2.986
16	1.695	1.671	1.353	3.753	2.330	–0.389	0.389	–0.188	0.377	–0.300	–0.590	2.819	–5.672	–1.511	–3.591	2.080	3.100
17	1.668	1.634	1.303	3.717	2.271	–0.496	0.253	–0.191	0.380	–0.307	–0.576	1.429	–6.005	–2.912	–4.458	1.546	6.427
18	1.724	1.710	1.412	3.864	2.451	–0.278	0.551	–0.188	0.378	–0.301	–0.586	5.015	–5.686	–1.562	–3.624	2.062	3.184
19	1.674	1.643	1.316	3.746	2.301	–0.473	0.287	–0.190	0.380	–0.306	–0.578	1.887	–5.943	–2.144	–4.043	1.899	4.303
20	1.802	1.786	1.423	3.856	2.431	–0.277	0.550	–0.183	0.373	–0.302	–0.587	4.187	–5.543	–1.538	–3.540	2.003	3.129
21	1.789	1.769	1.397	3.823	2.388	–0.335	0.466	–0.184	0.374	–0.304	–0.583	4.499	–5.676	–1.777	–3.726	1.950	3.561
22	1.790	1.770	1.399	3.825	2.390	–0.332	0.470	–0.182	0.372	–0.299	–0.594	2.716	–5.419	–1.347	–3.383	2.036	2.810
23	1.567	1.552	1.339	3.798	2.388	–0.310	0.524	–0.173	0.374	–0.294	–0.583	4.505	–5.828	–1.790	–3.809	2.019	3.593
24	1.413	1.485	1.270	3.758	2.345	–0.345	0.492	–0.162	0.359	–0.291	–0.578	4.425	–6.061	–2.026	–4.043	2.017	4.051

Note: *S*, ETSA index; *q*, atomic charge; ClogP, *n*-octanol–water partition coefficient; E_{HOMO}, energy of the highest occupied molecular orbital; E_{LUMO}, energy of the lowest unoccupied molecular orbital; μ, chemical potential; η, hardness; and ω, global electrophilicity index.

Published by NRC Research Press

Can. J. Chem. Downloaded from www.nrcresearchpress.com by UNIVERSITAT DE VALENCIA on 10/20/12
For personal use only.

Table 3. Calculated values of selected descriptors of the Cu(II) complexes used in the quantitative structure–activity relationship (QSAR) analysis.

Complex[a]	S_1	S_6	S_8	S_{12}	S_{17}	S_{18}	S_{20}	q_1	q_{12}	q_{14}	q_{15}	q_{16}	q_{17}	q_{18}	ClogP	$E_{\beta\text{-LUMO}}$	μ_β
1	0.966	1.964	1.687	1.950	5.826	5.816	6.489	–0.211	–0.175	–0.204	–0.228	–0.212	–0.754	–0.686	2.089	–2.450	–4.042
2	0.982	1.984	1.701	1.955	5.957	5.871	6.561	–0.206	–0.175	–0.204	–0.228	–0.212	–0.759	–0.687	2.608	–2.411	–3.975
3	0.875	1.924	1.659	1.936	5.923	5.860	6.562	–0.209	–0.175	–0.205	–0.229	–0.212	–0.738	–0.686	1.823	–2.357	–3.809
4	0.982	2.046	1.701	1.954	5.881	5.846	6.529	–0.205	–0.175	–0.204	–0.229	–0.211	–0.754	–0.687	2.608	–2.410	–3.961
5	0.850	1.811	1.642	1.933	5.822	5.813	6.496	–0.201	–0.173	–0.202	–0.228	–0.210	–0.751	–0.685	2.612	–2.638	–4.198
6	0.556	1.421	1.496	1.871	5.738	5.760	6.457	–0.208	–0.171	–0.199	–0.227	–0.209	–0.739	–0.683	1.964	–2.963	–4.616
7	0.968	1.969	1.701	1.115	5.866	5.896	6.541	–0.211	0.028	–0.199	–0.236	–0.211	–0.755	–0.683	2.588	–2.382	–4.005
8	0.967	1.968	1.696	2.032	5.856	5.871	6.529	–0.211	–0.174	–0.200	–0.223	–0.219	–0.755	–0.687	2.588	–2.406	–4.005
9	0.967	1.967	1.694	1.986	5.850	5.856	6.520	–0.211	–0.168	0.001	–0.227	–0.203	–0.755	–0.687	2.588	–2.380	–3.984
10	0.907	1.917	1.600	1.611	5.776	5.733	6.446	–0.211	–0.161	0.449	–0.296	–0.197	–0.754	–0.686	2.232	–2.495	–4.088
11	0.946	1.949	1.661	1.855	5.824	5.812	6.494	–0.210	–0.163	–0.027	–0.241	–0.199	–0.753	–0.684	2.802	–2.609	–4.163
12	0.960	1.961	1.682	1.940	5.841	5.840	6.511	–0.210	–0.163	–0.095	–0.240	–0.199	–0.753	–0.684	2.952	–2.608	–4.160
13	0.947	1.950	1.663	1.861	5.825	5.815	6.495	–0.211	–0.153	0.202	–0.281	–0.187	–0.758	–0.698	0.994	–2.172	–3.804
14	0.949	1.954	1.671	1.893	5.846	5.848	6.523	–0.211	–0.151	0.352	–0.267	–0.197	–0.757	–0.694	0.725	–2.287	–3.908
15	0.905	1.919	1.589	0.115	5.784	5.736	6.460	–0.211	0.377	–0.191	–0.260	–0.200	–0.755	–0.663	1.422	–2.264	–3.902
16	0.927	1.934	1.632	1.736	5.801	5.774	6.471	–0.211	–0.154	0.357	–0.279	–0.192	–0.756	–0.693	1.422	–2.329	–3.946
17	0.879	1.897	1.571	1.586	5.780	5.746	6.462	–0.209	–0.173	0.075	–0.206	–0.210	–0.750	–0.678	1.964	–3.456	–4.674
18	0.966	1.973	1.706	2.033	5.904	5.941	6.593	–0.211	–0.204	0.009	–0.222	–0.227	–0.755	–0.688	3.915	–2.361	–3.968
19	0.887	1.906	1.588	1.654	5.808	5.792	6.497	–0.210	–0.172	–0.305	–0.210	–0.208	–0.751	–0.679	0.448	–2.888	–4.358
20	0.983	2.049	1.707	1.991	5.905	5.886	6.560	–0.205	–0.168	0.000	–0.227	–0.203	–0.755	–0.689	3.107	–2.341	–3.903
21	0.962	2.032	1.674	1.859	5.879	5.843	6.534	–0.205	–0.164	–0.027	–0.241	–0.200	–0.753	–0.686	3.321	–2.567	–4.080
22	0.963	2.033	1.676	1.866	5.880	5.845	6.535	–0.206	–0.154	0.202	–0.281	–0.187	–0.758	–0.699	1.493	–2.136	–3.726
23	0.851	1.815	1.649	1.969	5.846	5.853	6.527	–0.201	–0.166	0.003	–0.227	–0.201	–0.752	–0.688	3.111	–2.573	–4.142
24	0.734	1.748	1.596	1.912	5.821	5.809	6.509	–0.193	–0.172	–0.200	–0.228	–0.209	–0.741	–0.684	3.233	–2.789	–4.328

Note: *S*, ETSA index; *q*, atomic charge; ClogP, *n*-octanol–water partition coefficient; $E_{\beta\text{-LUMO}}$, energy of LUMO for the spin down configuration; μ_β, chemical potential for the spin down configuration.
[a]Refer to Table 1 for the detailed structures of the corresponding Cu(II) complexes for 1–24.

Table 4. Developed quantitative structure–activity relationship (QSAR) models with statistical parameters for 24 salicylaldehyde benzoylhydrazone (H_2sb) ligands.

No.	QSAR models[a]	R^2	R^2	Q^2	s	F
Two parameter						
[1]	pIC_{50} = 7.720 (±0.572) + 0.280 (±0.035) ClogP – 1.577 (±0.298) η	0.772	0.750	0.621	0.152	35.51
Three parameter						
[2]	pIC_{50} = 7.656 (±0.522) + 0.309 (±0.034) ClogP – 1.440 (±0.278) η – 0.676 (±0.293) S_{11}	0.820	0.793	0.698	0.138	30.32
[3]	pIC_{50} = 14.244 (±3.223) + 0.296 (±0.034) ClogP – 1.673 (±0.282) η – 0.668 (±0.325) S_{17}	0.812	0.783	0.710	0.141	28.71
[4]	pIC_{50} = 5.408 (±1.000) + 0.302 (±0.032) ClogP – 1.536 (±0.263) η – 11.655 (±4.361) q_1	0.832	0.807	0.672	0.133	32.98
[5]	pIC_{50} = 4.730 (±1.355) + 0.316 (±0.035) ClogP – 1.780 (±0.283) η + 8.700 (±3.648) q_2	0.822	0.796	0.716	0.137	30.85
[6]	pIC_{50} = 2.277 (±0.499) + 0.278 (±0.036) ClogP + 0.267 (±0.048) ω + 0.797 (±0.240)S_4	0.804	0.775	0.669	0.144	27.41
[7]	pIC_{50} = –4.952 (±2.167) + 0.302 (±0.033) ClogP + 0.203 (±0.042) ω – 28.973 (±7.195) q_8	0.832	0.807	0.671	0.133	33.09
Four parameter						
[8]	pIC_{50} = 5.133 (±0.889) + 0.361 (±0.036) ClogP – 1.697 (±0.240) η – 20.277 (±5.092) q_1 – 0.717 (±0.277) S_6	0.876	0.849	0.785	0.118	33.44
[9]	pIC_{50} = 5.817 (±0.868) + 0.375 (±0.037) ClogP – 1.571 (±0.225) η – 20.472 (±4.826) q_1 – 1.623 (±0.563) S_7	0.883	0.858	0.780	0.114	35.85
[10]	pIC_{50} = 12.291 (±2.174) + 0.374 (±0.033) ClogP – 1.549 (±0.212) η – 15.723 (±3.720) q_1 – 2.072 (±0.607) S_8	**0.896**	0.874	0.799	0.108	40.79
[11]	pIC_{50} = 8.586 (±1.320) + 0.362 (±0.033) ClogP – 1.441 (±0.222) η – 14.401 (±3.747) q_1 – 1.722 (±0.553) S_9	0.889	0.865	0.768	0.111	37.89
[12]	pIC_{50} = 4.660 (±0.953) + 0.338 (±0.032) ClogP – 1.399 (±0.243) η – 11.763 (±3.925) q_1 – 0.973 (±0.408) S_{10}	0.871	0.843	0.724	0.120	31.98
[13]	pIC_{50} = 3.553 (±1.345) + 0.326 (±0.033) ClogP – 1.699 (±0.261) η – 9.486 (±4.245) q_1 + 6.652 (±3.455) q_2	0.859	0.830	0.763	0.125	29.01
[14]	pIC_{50} = 11.093 (±2.307) + 0.297 (±0.028) ClogP – 1.368 (±0.239) η – 12.485 (±3.831) q_1 + 10.555 (±3.963) q_{18}	0.878	0.852	0.754	0.117	34.04

Note: S, ETSA index; q, atomic charge; ClogP, n-octanol–water partition coefficient; η, hardness; ω, global electrophilicity index; R^2, square of the correlation coefficient; R^2_a, explained variance; F, variance ratio; s, the standard error of estimate; and Q^2, leave-one-out cross-validated square of the correlation coefficient.

[a]The 95% confidence intervals for the regression coefficients are shown in parentheses.

Can. J. Chem. Downloaded from www.nrcresearchpress.com by UNIVERSITAT DE VALENCIA on 10/20/12
For personal use only.

respectively. Both equations show the importance of ω for predicting the cytotoxicity of the H_2sb ligands.

In addition, we derived four-parameter QSAR models (eqs. [8]–[14], Table 4) with improved overall statistical qualities (e.g., eq. [4], $R^2 = 0.832$ and $F = 32.98$; and eq. [10], $R^2 = 0.896$ and $F = 40.79$) by introducing an additional descriptor in eq. [4] (Table 4). The negative coefficient of S_8 (eq. [10], Table 4) suggests that an increase of the ETSA index of the imine N atom will decrease the anticancer activity. The calculated anticancer activity of H_2sb ligands from eq. [10] (Table 4) is plotted against the experimental activity (see Fig. 2*a*). Figure 2 shows the ability of our model to predict the anticancer activity of H_2sb ligands.

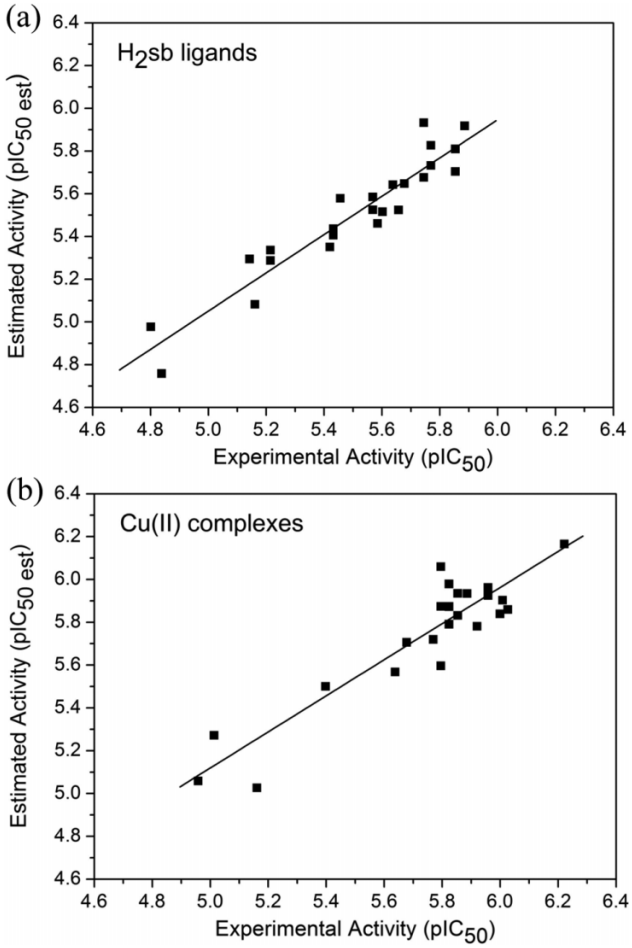
The similar statistical qualities of eqs. [8]–[12] (Table 4) reveal that the ETSA indices S_6, S_7, S_8, S_9, and S_{10} have similar contributions to the anticancer activity of H_2sb ligands (Table 4). Since the ETSA indices are derived from the availability of the valence electrons on the atoms plus the effects of the topology of neighbouring atoms, the values of S_2–S_8 are practically interdependent at these positions. The negative coefficients associated with the S_6–S_{10} indices suggest that the increase of the value of ETSA index of atoms 6–10 will decrease the anticancer activity of H_2sb. Moreover, atoms 7–10 are important atoms on the backbone of the H_2sb ligands, which are involved in the electronic conjugation along the H_2sb framework. Successful incorporation of ETSA indices of these atoms in the QSAR models suggests that these atoms may be crucial for the interaction between H_2sb ligands and the cancer cells. Equations [13] and [14] (Table 4) also suggest that the atomic charges on atoms 2 and 18 are important for the prediction of the anticancer activity of H_2sb ligands.

QSAR models for Cu(II) complexes

The QSAR models (eqs. [15]–[31]) for the Cu(II) complexes were developed in the same fashion as for the H_2sb ligands using the MLR technique and are listed in Tables 5 and 6. We used descriptors having low and moderate degrees of correlation based on Pearson's correlation coefficient. In general, if the Pearson's correlation coefficient is $r \in [-0.5, 0.5]$, there was a low degree of correlation between the two descriptors; if $r \in (0.5, 0.8)$ or $r \in (-0.8, -0.5)$, there was a moderate degree of correlation; and if $r \in [0.8, 1]$ or $r \in [-1, -0.8]$, there was a strong correlation between the descriptors.[38] Usually, the descriptors used to derive QSAR models have been selected based on lower correlation among the

Can. J. Chem. Downloaded from www.nrcresearchpress.com by UNIVERSITAT DE VALENCIA on 10/20/12
For personal use only.

Fig. 2. The estimated versus experimental activities of salicylaldehyde benzoylhydrazone (H_2sb) ligands and their Cu(II) complexes using the best equations. Ligands (eq. [10]): $n = 24$ and $R^2 = 0.896$; Cu (II) complexes (eq. [31]): $n = 24$ and $R^2 = 0.843$.



descriptors. However, we observed significant enhancement of the statistical qualities of the QSAR models developed for Cu(II) complexes by using the moderate intercorrelated descriptors. The descriptors having greater correlation with each other are found to have greater R^2 values with lower standard deviations and higher F values (see Tables 5 and 6). The best QSAR equation developed for the Cu(II) complexes contains descriptors S_9, S_{12}, q_{14}, and q_{18}. The descriptors S_{12} and q_{18} each have a correlation coefficient of 0.699. Since the two descriptors are of different types (one is an ETSA index and the other is atomic charge) and from different atoms, we could use them together to develop the QSAR models. Therefore, we developed the QSAR models for Cu (II) complexes using descriptors having low and moderate degrees of correlation.

The positive coefficients of ClogP, S_1, q_{15}, and q_{18} (Table 5, eq. [15]) indicate that the higher value of these parameters may be favourable for the higher anticancer activity of Cu(II) complexes. Equation [16] (Table 5) is built solely using ETSA indices and natural charges on selected atoms, i.e., S_8, q_1, q_{16}, and q_{18}, which explains 68.8% and predicts 55.2% of the variance of activity. The results suggest that the atoms 1, 8, 16, and 18 play an important role for the inhibition of cancer cells. Equations [15]–[18] (R^2_a and Q^2 ranged from 68.8% to 69.5% and 52.6% to 51.1%, respectively) and [19]–[22] (R^2_a and Q^2 ranged from 72.2% to 73.9% and 61.8% to 62.8%, respectively) exhibit comparable statistical qualities. Our results suggest that the electronic interactions of the benzoylhydrazone part to the copper are important for the cytotoxicity of the compounds. In particular, eqs. [21] and [22] (Table 5) show that the increase in the values of S_{18}, S_{20}, q_{10}, and q_{18} are favourable for the anticancer activity of the Cu(II) complexes.

We observe that most of the significant models presented in Table 6 are a combination of S_{12}, S_{18}, q_{12}, and q_{18} parameters, which indicates that atoms 12 and 18 are crucial for the prediction of the anticancer activity of the Cu(II) complexes. Our results also suggest that the substitution of an electron-withdrawing group to the benzoylhydrazone ring might be necessary for the biological activity of the Cu(II) complexes. Moreover, we show the capabilities of quantum chemical descriptors like chemical potential (μ_β) and HOMO energy for the spin down configuration ($E_{\beta\text{-HOMO}}$; eqs. [23] and [24], Table 6) for the prediction of the cytotoxicity of Cu(II) complexes. We also show the importance of S_5, S_8, q_1, q_5, q_7, and q_{14} for the anticancer activity of Cu(II) complexes (eqs. [25]–[29], Table 6).

The two best QSAR models developed for Cu(II) complexes, i.e., eqs. [30] and [31] (Table 6), show that the atoms 4, 9, 12, and 18 are crucial for the prediction of the anticancer activity of Cu(II) complexes. In comparison to the best equation derived for the ligands (Eqs. [10] and [11], Table 4), eqs. [30] and [31] are built solely on ETSA indices and atomic charges, whereas the models for the ligands are a combination of ClogP, η, ETSA indices, and atomic charges. Furthermore, these equations also illustrate the importance of the electronic interaction between atoms 12 and 18 in affecting the anticancer activity. We observe that eq. [31] (Table 6) is statistically better than eq. [30] (Table 6) because the former can predict a much higher variance of the activity than the latter (i.e., $Q^2_{\text{eq. [31]}} = 74.5\%$ and $Q^2_{\text{eq. [30]}} = 53.9\%$). The calculated anticancer activities of Cu(II) from eq. [31] (Table 6) are plotted as a function of experimental activity and are shown in Fig. 2*b*. Our present study shows that besides ClogP, the DFT-derived descriptors and electrotopological state atom index can successfully be used to develop the predictive QSAR models for anticancer activities of the H_2sb and their Cu(II) complexes.

Validation of the developed models

The predictive power of our developed models is validated both internally (using LOO cross validation) and externally (using training and test sets). The observed (Obs.), calculated (Calcd.), residual (Res.), predicted residual (Pres.), and LOO-predicted (Pred.) activities of the best QSAR model (eq. [10], Table 4) are listed in Table 7 (see the Supplementary data for the rest of the equations). We divided the data set of the 24 H_2sb ligands and 24 Cu(II) complexes into a training set (75% of the total data set) and a test set (remaining 25%) randomly for external validation. The compounds **3**, **5**, **11**, **13**, **21**,and **23** were selected as the test set

Can. J. Chem. Downloaded from www.nrcresearchpress.com by UNIVERSITAT DE VALENCIA on 10/20/12
For personal use only.

Table 5. Quantitative structure–activity relationship (QSAR) models derived using intercorrelated descriptors ($|r| < 0.5$) for 24 Cu(II) complexes of salicylaldehyde benzoylhydrazone (H_2sb) ligands.

No.	QSAR models[a]	R^2	R^2_a	Q^2	s	F
[15]	pIC_{50} = 19.745 (±3.841) + 0.840 (±0.400) S_1 + 3.786 (±1.813) q_{15} + 20.765 (±5.892) q_{18} + 0.173 (±0.046) ClogP	0.742	0.688	0.526	0.176	13.68
[16]	pIC_{50} = 21.663 (±5.040) + 2.740 (±0.819) S_8 + 20.035 (±8.382) q_1 – 12.971 (±4.345) q_{16} + 27.597 (±6.705) q_{18}	0.743	0.688	0.552	0.175	13.70
[17]	pIC_{50} = 19.198 (±3.802) + 0.593 (±0.275) S_4 + 3.805 (±1.804) q_{15} + 20.467 (±5.837) q_{18} + 0.176 (±0.046) ClogP	0.745	0.691	0.537	0.175	13.86
[18]	pIC_{50} = 19.313 (±3.779) + 1.418 (±0.637) S_7 + 3.487 (±1.777) q_{15} + 22.922 (±6.057) q_{18} + 0.159 (±0.047) ClogP	0.748	0.695	0.511	0.174	14.11
[19]	pIC_{50} = 24.935 (±7.293) + 2.105 (±0.800) S_{17} + 28.850 (±13.560) q_{10} + 28.608 (±5.478) q_{18} + 0.150 (±0.045) ClogP	0.770	0.722	0.618	0.166	15.94
[20]	pIC_{50} = 15.656 (±4.045) + 0.662 (±0.274) S_6 – 11.760 (±4.355) q_{16} + 20.312 (±5.419) q_{18} + 0.153 (±0.045) ClogP	0.778	0.731	0.624	0.163	16.60
[21]	pIC_{50} = 26.781 (±6.860) + 2.496 (±0.877) S_{18} + 34.400 (±13.490) q_{10} + 31.047 (±5.697) q_{18} + 0.118 (±0.049) ClogP	0.780	0.734	0.524	0.162	16.87
[22]	pIC_{50} = 17.454 (±8.281) + 3.244 (±1.108) S_{20} + 30.540 (±13.180) q_{10} + 29.471 (±5.369) q_{18} + 0.131 (±0.046) ClogP	0.784	0.739	0.628	0.161	17.25

Note: S, ETSA index; q, atomic charge; ClogP, n-octanol–water partition coefficient; R^2, square of the correlation coefficient; R^2_a, explained variance; F, variance ratio; s, the standard error of estimate; and Q^2, leave-one-out cross-validated square of the correlation coefficient.

[a]The 95% confidence intervals of the regression coefficients are shown in parentheses.

Table 6. Quantitative structure–activity relationship (QSAR) models derived using moderate degree correlated descriptors ($r < 0.8$) for 24 Cu(II) complexes of salicylaldehyde benzoylhydrazone (H_2sb) ligands.

No.	QSAR models[a]	R^2	R^2_a	Q^2	s	F
[23]	pIC_{50} = 44.403 (±7.276) + 0.574(±0.163) S_{12} + 55.090 (±10.090) q_{18} + 0.138 (±0.045) ClogP + 0.538 (±0.194) μ_β	0.787	0.742	0.536	0.160	17.55
[24]	pIC_{50} = 43.378 (±6.455) + 0.517 (±0.143) S_{12} + 51.734 (±8.678) q_{18} + 0.149 (±0.042) ClogP + 0.603 (±0.191) $E_{\beta\text{-HOMO}}$	0.804	0.762	0.633	0.153	19.45
[25]	pIC_{50} = 41.077 (±4.497) + 3.968 (±0.683) S_8 – 1.589 (±0.379) q_{12} + 56.029 (±6.940) q_{18} + 17.635 (±7.386) q_1	0.804	0.762	0.631	0.153	19.44
[26]	pIC_{50} = 39.243 (±4.335) + 4.284 (±0.707) S_8 –1.685 (±0.371) q_{12} + 59.234 (±6.964) q_{18} + 0.802 (±0.328) q_5	0.806	0.765	0.622	0.152	19.71
[27]	pIC_{50} = 44.651 (±9.690) + 0.675 (±0.142) S_{12} + 2.290 (±0.744) S_{18} – 62.220 (±22.990) q_7 + 68.702 (±9.011) q_{18}	0.808	0.767	0.678	0.152	19.93
[28]	pIC_{50} = 38.567 (±4.270) – 0.155 (±0.061) S_5 + 4.630 (±0.748) S_8 –1.649 (±0.368) q_{12} + 58.964 (±6.868) q_{18}	0.810	0.770	0.605	0.151	20.27
[29]	pIC_{50} = 30.371 (±5.946) + 0.605 (±0.126) S_{12} + 4.215 (±0.788) S_{18} + 73.226 (±9.881) q_{18} + 0.663 (±0.233) q_{14}	0.813	0.773	0.683	0.150	20.62
[30]	pIC_{50} = 40.650 (±5.057) + 5.105 (±0.759) S_9 – 1.891 (±0.365) q_{12} + 74.419 (±9.171) q_{18} + 0.574 (±0.210) q_{14}	0.835	0.800	0.539	0.141	23.99
[31]	pIC_{50} = 44.497 (±5.419) + 4.402 (±0.718) S_9 + 0.625 (±0.116) S_{12} + 78.065 (±9.346) q_{18} + 0.675 (±0.212) q_{14}	0.843	0.810	0.745	0.137	25.44

Note: S, ETSA index; q, atomic charge; ClogP, n-octanol–water partition coefficient; R^2, square of the correlation coefficient; R^2_a, explained variance; F, variance ratio; s, the standard error of estimate; and Q^2, leave-one-out cross-validated square of the correlation coefficient.

[a]The 95% confidence intervals of the regression coefficients are shown in parentheses.

and the remaining 18 compounds were treated as the training set. We developed the QSAR equations for the training set using the same descriptors that were used to develop the two best models eqs. [10] (Table 4) and [31] (Table 6).

$$[10tr]\quad pIC_{50}(\text{ligand}) = 10.784(\pm 2.131) + 0.349(\pm 0.037)\text{ClogP} - 1.486(\pm 0.208)\eta - 16.842(\pm 3.793)q_1 - 1.738(\pm 0.588)S_8$$

where n = 18, s = 0.096, R^2 = 0.908, R^2_a = 0.880, Q^2 = 0.537, and PRESS = 0.604.

$$[31tr]\quad pIC_{50}(\text{Cu cpx.}) = 41.685\,(\pm 6.938) + 4.247\,(\pm 0.831)S_9 + 0.564\,(\pm 0.141)S_{12} + 73.120\,(\pm 12.130)q_{18} + 0.665\,(\pm 0.251)q_{14}$$

where n = 18, s = 0.151, R^2 = 0.800, R^2_a = 0.739, Q^2 = 0.625, and PRESS = 0.555

Equations [10*tr*] and [31*tr*] have similar statistical qualities to eqs. [10] (Table 4) and [31] (Table 6), respectively. The Obs. and Pred. activities of the test set compounds using eqs. [10*tr*] and [31*tr*] are listed in Table 8. Our results show that the calculated values of compounds **3**, **5**, **11**, **13**, **21**, and

Can. J. Chem. Downloaded from www.nrcresearchpress.com by UNIVERSITAT DE VALENCIA on 10/20/12
For personal use only.

Table 7. Observed (Obs.), calculated (Calcd.), residual (Res.), leave-one-out-predicted (LOO-Pred.), and predicted residual (Pres.) activities of eq. [10] (Table 4).

Compound	Obs.	Calcd.	Res.	LOO-Pred.	Pres.
1	5.432	5.407	0.025	5.405	0.027
2	5.585	5.462	0.123	5.451	0.134
3	5.432	5.437	–0.005	5.438	–0.006
4	5.658	5.525	0.132	5.512	0.146
5	5.569	5.586	–0.018	5.590	–0.021
6	4.839	4.760	0.079	4.684	0.155
7	5.215	5.337	–0.123	5.355	–0.141
8	5.602	5.517	0.085	5.510	0.092
9	5.569	5.526	0.043	5.522	0.046
10	5.678	5.649	0.029	5.638	0.039
11	5.854	5.811	0.043	5.804	0.050
12	5.770	5.828	–0.058	5.836	–0.066
13	4.801	4.978	–0.177	5.023	–0.222
14	5.420	5.352	0.068	5.346	0.074
15	5.745	5.678	0.067	5.647	0.098
16	5.143	5.296	–0.153	5.315	–0.172
17	5.770	5.733	0.036	5.562	0.207
18	5.886	5.918	–0.032	5.927	–0.041
19	5.215	5.289	–0.074	5.305	–0.090
20	5.638	5.643	–0.005	5.644	–0.006
21	5.745	5.933	–0.189	5.965	–0.220
22	5.161	5.084	0.078	5.060	0.101
23	5.854	5.705	0.149	5.670	0.184
24	5.456	5.580	–0.124	5.743	–0.287

Table 8. Observed (Obs.), predicted (Pred.), and residual (Res.) values of test set compounds using eqs. [10*tr*] and [31*tr*] (training set).

	Equation [10*tr*]			Equation [31*tr*]		
Comp.	Obs.[a]	Pred.	Res.	Obs.[b]	Pred.	Res.
3	5.432	5.458	–0.026	5.824	5.771	0.053
5	5.569	5.563	0.006	6.000	5.814	0.186
11	5.854	5.807	0.047	5.886	5.911	–0.025
13	4.801	5.021	–0.220	4.959	5.098	–0.140
21	5.745	5.922	–0.177	6.009	5.884	0.125
23	5.854	5.677	0.177	5.854	5.816	0.038

[a] pIC_{50} values of H_2sb ligands.
[b] pIC_{50} values of Cu(II) complexes.

23 using eqs. [10] and [31] and the predicted values of these compounds (test set) using eqs. [10*tr*] and [31*tr*] are similar. This indicates the significant predictive power of our developed models.

Principal component regression analysis (PCRA)

Principal component analysis (PCA) was carried out on the H_2sb ligand and Cu(II) complex data sets to extract the factor loadings of different variables. The factor loadings (after VARIMAX rotation) of different variables for the data set of H_2sb ligands and Cu(II) complexes are presented in Tables 9 and 10, respectively. The nine factors were extracted from the PCA considering the eigenvalues greater than or equal to one. Factor loadings >0.70 are shown in boldface. The nine factors of H_2sb ligands and the copper complexes' descriptors account for 89.1% and 86.7% of the variance of the activity for the H_2sb ligands and Cu(II) complexes, respectively. When the factor scores are used as independent variables in MLR analysis, the following MLR equation is obtained for the H_2sb ligands:

$$[32] \quad pIC_{50}\ (\text{ligand}) = 5.501\ (\pm 0.025) + 0.100\ (\pm 0.026)F_1 - 0.107\ (\pm 0.026)F_3 + 0.239\ (\pm 0.026)F_7$$

where $n = 24$, $s = 0.123$, $R^2 = 0.856$, $R^2_a = 0.834$, $Q^2 = 0.641$, PRESS = 0.760

Equation [32] explains 83.4% and predicts 64.1% of the variance of the activity. The values mentioned in the parentheses are the 95% confidence intervals of the regression coefficients. All regression coefficients are significant at the 95% level as supported by their t and p values (see Table 11). All the factors contain the important information from a different combination of descriptors. The positive coefficients of

Can. J. Chem. Downloaded from www.nrcresearchpress.com by UNIVERSITAT DE VALENCIA on 10/20/12
For personal use only.

Table 9. Factor loadings of different variables of salicylaldehyde benzoylhydrazone (H_2sb) ligands after VARIMAX rotation.

Variable	F_1	F_2	F_3	F_4	F_5	F_6	F_7	F_8	F_9	Communality
pIC_{50}	0.329	0.026	–0.354	0.038	0.111	–0.146	**0.789**	–0.001	–0.022	0.892
S_1	**0.958**	0.098	0.068	–0.071	–0.035	0.037	0.130	–0.187	0.010	0.992
S_2	**0.905**	0.125	0.053	–0.305	–0.064	0.027	0.080	–0.174	–0.014	0.973
S_3	0.411	–0.127	0.120	**–0.807**	0.021	–0.014	0.057	–0.050	0.048	0.858
S_4	0.990	–0.020	0.029	–0.046	–0.002	0.001	0.062	–0.082	–0.023	0.995
S_5	0.615	–0.157	–0.018	0.021	–0.106	–0.095	–0.043	–0.746	0.024	0.983
S_6	**0.977**	0.007	0.056	0.059	0.023	0.021	0.108	–0.066	0.000	0.978
S_7	**0.914**	0.324	0.088	0.017	0.015	0.115	0.143	–0.105	0.013	0.994
S_8	0.690	0.597	0.073	0.135	0.289	0.201	0.094	0.049	0.019	0.992
S_9	0.529	0.746	0.089	0.080	0.202	0.286	0.107	–0.014	0.045	0.987
S_{10}	0.313	0.835	0.073	0.096	0.015	0.414	0.078	0.035	0.033	0.989
S_{11}	0.150	**0.829**	0.018	0.095	0.049	0.500	0.022	0.057	0.038	0.977
S_{12}	–0.006	0.297	–0.109	0.081	0.144	**0.901**	0.015	0.100	0.046	0.952
S_{13}	–0.029	**0.704**	0.070	0.125	0.207	0.085	0.049	0.146	–0.609	0.962
S_{14}	–0.185	**0.820**	–0.136	0.240	–0.134	–0.310	–0.090	0.158	0.196	0.969
S_{15}	0.032	**0.936**	0.097	0.087	0.185	–0.042	0.108	0.098	0.017	0.952
S_{16}	0.093	**0.949**	0.099	0.097	0.138	0.142	0.089	0.082	0.019	0.983
S_{17}	0.027	0.299	–0.131	**0.746**	0.247	0.072	–0.190	0.312	–0.117	0.877
S_{18}	0.179	0.221	–0.018	–0.092	**0.900**	–0.042	0.011	–0.170	0.111	0.943
q_1	–0.528	0.235	0.141	0.345	0.047	0.093	0.274	0.609	0.032	0.931
q_2	–0.265	–0.010	–0.119	–0.856	–0.061	–0.038	–0.227	–0.102	–0.067	0.890
q_3	–0.075	0.131	–0.119	**0.937**	–0.017	0.015	–0.181	–0.080	–0.066	0.958
q_4	0.097	–0.083	–0.022	–0.944	0.004	–0.021	–0.040	0.123	–0.034	0.926
q_5	–0.368	0.170	0.025	–0.030	0.144	0.110	–0.022	**0.874**	–0.055	0.965
q_6	0.003	–0.127	–0.053	–0.837	0.039	–0.051	–0.377	–0.054	–0.064	0.872
q_7	0.305	–0.355	**–0.801**	0.029	0.070	–0.005	–0.007	–0.227	–0.078	0.924
q_8	**–0.711**	0.285	0.467	0.072	–0.028	0.085	0.137	0.343	0.073	0.960
q_9	–0.535	0.475	0.345	0.034	–0.162	–0.492	0.156	0.142	0.164	0.972
q_{10}	–0.464	–0.008	–0.484	0.040	0.194	0.680	0.079	0.157	0.047	0.984
q_{11}	–0.073	0.045	–0.917	0.039	0.158	0.201	0.025	–0.090	0.156	0.949
q_{12}	0.045	–0.064	0.216	–0.063	–0.111	**–0.947**	0.046	–0.069	–0.025	0.973
q_{13}	–0.006	0.318	–0.502	–0.017	0.119	0.147	0.001	–0.017	**0.759**	0.965
q_{14}	0.173	–0.505	0.580	–0.172	–0.076	0.407	0.139	–0.124	–0.190	0.893
q_{15}	–0.154	0.342	**–0.807**	0.066	0.338	–0.042	0.042	0.038	0.152	0.938
q_{16}	0.204	–0.428	0.694	–0.192	0.037	0.040	0.029	–0.004	–0.416	0.921
q_{17}	**–0.867**	0.006	–0.135	0.336	0.074	0.030	–0.074	0.091	0.022	0.902
q_{18}	–0.317	–0.188	–0.410	0.026	–0.031	–0.792	0.228	0.013	0.021	0.986
ClogP	0.261	0.477	0.151	0.117	0.146	–0.079	**0.745**	0.113	–0.019	0.929
MR	–0.069	0.089	–0.129	0.042	**0.956**	0.121	0.106	0.085	–0.046	0.980
CAA	–0.041	0.014	–0.138	0.049	**0.971**	0.101	–0.005	0.120	–0.009	0.991
CMA	–0.043	0.025	–0.131	0.037	**0.977**	0.095	0.001	0.101	–0.014	0.995
V	–0.037	0.055	–0.113	0.027	**0.981**	0.070	0.043	0.029	–0.019	0.988
E_{HOMO}	**0.831**	0.114	0.385	0.338	–0.020	–0.026	–0.071	0.002	–0.001	0.971
E_{LUMO}	0.457	0.430	**0.727**	0.107	–0.121	–0.105	–0.067	–0.054	0.024	0.968
μ	0.644	0.326	0.631	0.211	–0.087	–0.079	–0.073	–0.034	0.015	0.984
η	–0.122	0.532	**0.713**	–0.168	–0.162	–0.132	–0.031	–0.083	0.037	0.887
ω	–0.393	–0.475	–0.714	–0.109	0.112	0.095	0.048	0.039	–0.024	0.927
Variance	0.207	0.133	0.141	0.113	0.094	0.088	0.036	0.050	0.029	0.891

Note: MR, molar refractivity; CAA, Connolly accessible area; CMA, Connolly molecular area; ClogP, *n*-octanol–water partition coefficient; *V*, volume; η, hardness; ω, global electrophilicity index; μ, chemical potential; E_{HOMO}, energy of the highest occupied molecular orbital; E_{LUMO}, energy of the lowest unoccupied molecular orbital; *S*, ETSA index; *q*, atomic charge.

F_1 and F_7 indicate that the higher the values of these parameters, the better the anticancer activity, whereas the negative coefficient of F_3 indicates an opposite effect. The factor score 1 shows the importance of the ETSA indices of atoms 1, 2, 6, 7,and 8, the atomic charges on atoms 8 and 17, and the energy of HOMO. Similarly, the factor score 3 signifies the importance of the atomic charges on atoms 7 and 15, the energy of LUMO, and the hardness. The factor score 7 indicates the importance of ClogP of the H_2sb ligands for anticancer activity.

The following MLR model was derived for the Cu(II) complexes using the factor scores as independent descriptors in MLR analysis.

Can. J. Chem. Downloaded from www.nrcresearchpress.com by UNIVERSITAT DE VALENCIA on 10/20/12
For personal use only.

Table 10. Factor loadings of different variables of Cu(II) complexes after VARIMAX rotation.

Variable	F_1	F_2	F_3	F_4	F_5	F_6	F_7	F_8	F_9	Communality
pIC_{50}	0.181	0.243	–0.630	0.095	–0.403	0.197	0.366	–0.030	0.040	0.835
S_1	**0.972**	0.176	0.092	–0.074	0.023	–0.043	–0.008	–0.036	0.031	0.994
S_2	**0.898**	0.246	0.080	–0.304	0.029	–0.075	–0.074	–0.029	–0.004	0.978
S_3	0.419	–0.103	0.121	**–0.800**	–0.006	0.003	–0.048	0.019	0.030	0.844
S_4	**0.982**	0.077	0.084	–0.056	0.021	0.019	0.006	0.062	–0.014	0.985
S_5	**0.727**	–0.141	–0.013	0.072	–0.096	–0.139	–0.485	–0.345	0.104	0.948
S_6	**0.973**	0.091	0.100	0.047	0.029	0.037	0.071	0.061	0.013	0.978
S_7	**0.898**	0.414	0.096	0.002	0.076	–0.004	0.050	–0.001	0.027	0.996
S_8	**0.733**	0.652	0.087	0.032	0.139	–0.001	0.071	–0.003	0.037	0.996
S_9	0.468	**0.837**	0.042	0.051	0.192	0.143	0.069	–0.003	0.051	0.989
S_{10}	0.252	**0.907**	0.014	0.045	0.309	–0.052	0.072	0.022	0.026	0.993
S_{11}	**0.079**	**0.898**	–0.050	0.059	0.395	–0.021	0.056	0.026	0.022	0.979
S_{12}	–0.048	0.390	–0.191	0.058	**0.855**	0.124	0.081	0.030	0.056	0.952
S_{13}	**–0.091**	0.716	0.055	0.095	–0.003	0.177	0.094	0.049	–0.609	0.945
S_{14}	–0.275	0.734	–0.123	0.232	–0.384	–0.170	–0.028	0.269	0.190	0.969
S_{15}	–0.049	**0.945**	0.059	0.060	–0.148	0.124	0.072	0.054	0.029	0.949
S_{16}	0.013	**0.982**	0.046	0.065	0.030	0.071	0.072	0.040	0.023	0.984
S_{17}	0.531	0.618	–0.012	0.355	0.105	0.288	0.003	0.130	–0.069	0.905
S_{18}	0.353	**0.814**	–0.012	0.085	0.129	0.401	–0.015	–0.044	0.062	0.979
S_{19}	0.671	0.637	0.115	–0.209	0.153	–0.229	0.045	–0.021	0.030	0.993
S_{20}	0.368	**0.701**	–0.017	0.270	0.092	0.514	0.008	0.044	0.003	0.975
q_1	–0.408	0.161	–0.064	0.280	0.091	0.108	**0.762**	0.189	–0.044	0.913
q_2	–0.240	–0.050	–0.214	**–0.786**	–0.026	–0.068	–0.347	0.006	–0.098	0.859
q_3	–0.092	0.137	–0.099	**0.934**	0.024	0.019	–0.180	0.058	–0.078	0.953
q_4	0.131	–0.094	0.012	–0.945	–0.005	–0.007	0.089	0.034	0.001	0.928
q_5	–0.521	0.175	0.046	–0.092	0.133	0.202	0.507	0.502	–0.149	0.902
q_6	–0.170	–0.135	0.020	–0.827	–0.007	0.016	–0.393	0.101	–0.024	0.897
q_7	**–0.752**	–0.088	–0.549	–0.077	–0.155	–0.054	–0.213	–0.067	–0.028	0.958
q_8	**–0.840**	0.205	0.383	–0.106	0.103	–0.034	0.216	–0.061	0.082	0.974
q_9	–0.630	0.409	0.078	–0.009	–0.554	–0.173	0.109	–0.024	0.169	0.948
q_{10}	0.031	–0.185	**–0.805**	0.086	0.497	0.156	0.095	0.047	–0.013	0.974
q_{11}	–0.033	0.023	**–0.951**	0.065	0.147	0.083	–0.045	0.037	0.096	0.951
q_{12}	0.054	–0.177	0.289	–0.041	**–0.909**	–0.142	–0.040	0.000	–0.030	0.969
q_{13}	–0.003	0.361	–0.530	–0.037	0.067	0.195	–0.035	–0.021	**0.714**	0.965
q_{14}	0.219	–0.378	0.547	–0.176	0.439	–0.050	0.084	–0.299	–0.141	0.833
q_{15}	–0.151	0.297	**–0.809**	0.070	–0.119	0.294	–0.017	0.105	0.113	0.896
q_{16}	0.096	–0.405	0.658	–0.111	0.232	–0.219	0.104	–0.001	–0.353	0.856
q_{17}	**–0.713**	–0.074	–0.316	0.512	0.016	0.094	–0.012	0.104	–0.041	0.898
q_{18}	–0.143	–0.288	–0.449	0.004	–0.823	–0.057	0.008	–0.028	0.005	0.986
q_{19}	–0.766	0.138	0.331	0.252	0.130	0.045	0.276	0.014	0.121	0.889
q_{20}	**–0.834**	–0.129	–0.480	0.001	–0.004	–0.001	0.195	–0.063	–0.022	0.985
ClogP	0.023	0.552	–0.382	–0.060	–0.027	0.106	0.539	–0.188	–0.015	0.793
CAA	–0.062	0.070	–0.150	0.004	0.108	**0.973**	0.052	0.020	0.010	0.993
CMA	–0.061	0.100	–0.154	0.008	0.093	**0.975**	0.046	–0.003	0.007	0.998
V	–0.016	0.129	–0.151	0.011	0.050	**0.966**	0.044	–0.055	0.023	0.980
$E_{\alpha\text{-HOMO}}$	0.240	0.127	–0.078	–0.046	0.011	–0.102	0.111	**0.828**	–0.005	0.789
$E_{\alpha\text{-LUMO}}$	0.381	0.434	**0.766**	0.086	–0.100	–0.094	–0.085	0.057	0.050	0.958
$E_{\beta\text{-HOMO}}$	**0.730**	0.206	0.480	0.394	0.013	0.031	–0.038	0.126	0.009	0.979
$E_{\beta\text{-LUMO}}$	0.420	0.442	**0.735**	0.097	–0.097	–0.095	–0.077	0.052	0.050	0.951
Variance	0.243	0.138	0.136	0.101	0.081	0.074	0.043	0.028	0.025	0.867

Note: MR, molar refractivity; CAA, Connolly accessible area; CMA, Connolly molecular area; ClogP, *n*-octanol–water partition coefficient; *V*, volume; η, hardness; ω, global electrophilicity index; μ, chemical potential; E_{HOMO}, energy of the highest occupied molecular orbital; E_{LUMO}, energy of the lowest unoccupied molecular orbital; *S*, ETSA index; *q*, atomic charge.

[33] $$pIC_{50}\ (\text{Cu cpx.}) = 5.750\ (\pm 0.035) + 0.076\ (\pm 0.036)F_2 - 0.198\ (\pm 0.036)F_3 - 0.127\ (\pm 0.036)F_5 + 0.115\ (\pm 0.036)F_7$$

where $n = 24$, $s = 0.172$, $R^2 = 0.752$, $R^2_a = 0.700$, $Q^2 = 0.611$, and PRESS = 0.885

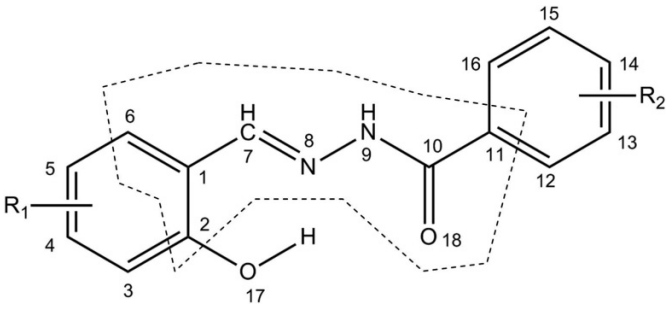
Equation [33] explains 70.0% and predicts 61.1% of the variance of the activity. The factor score 2 shows the importance of the ETSA indices of atoms 9, 10, 11, 15, 16, 18, and

Can. J. Chem. Downloaded from www.nrcresearchpress.com by UNIVERSITAT DE VALENCIA on 10/20/12
For personal use only.

Table 11. *t* Statistics and *p*values for the principal component regression analysis (PCRA) equations.

Eq. No.	Intercept/parameter	Coefficient	*t*	*p*
[32]	Intercept	5.50138	218.43	0.000
	F1	0.09985	3.88	0.001
	F3	–0.10746	–4.18	0.000
	F7	0.23922	9.30	0.000
[33]	Intercept	5.74955	163.53	0.000
	F2	0.07631	2.12	0.047
	F3	–0.19787	–5.51	0.000
	F5	–0.12663	–3.53	0.002
	F7	0.11499	3.20	0.005

Fig. 3. Structure of the salicylaldehyde benzoylhydrazone (H_2sb) ligand showing the fragment (atoms enclosed by the broken line) necessary for anticancer activities.



20 for the inhibitory activity of cancer cells. The factor score 3 indicates the importance of atomic charges on atoms 10, 11, and 15 and the energies of α-LUMO and β-LUMO, whereas the factor score 5 shows the importance of the ETSA index and atomic charge on atom 12. The factor score 7 signifies the importance of the atomic charge on atom 1. According to the PCRA results, we can divide the compound's structure into two parts (separated by atom 8), the salicylaldehyde part and the benzoylhydrazone part. We observe that upon copper coordination, the benzoylhydrazone part (especially atoms 9, 10, 11, 12, 15, 16, 18, and 20) becomes important for anticancer activity, whereas, for the ligands, the salicylaldehyde ring part (especially atoms 1, 2, 6, 7, and 17) is more interactive with the biomolecules. Since the factor scores are used as independent variables instead of the original variables in PCRA, the loss of information during the MLR analysis can be avoided and the quality of the developed equations can also be improved. This is because each factor score contains information from all of the original descriptors. For instance, factor scores shown in eq. [32] have included all the important descriptors that influenced the bioactivity of the H_2sb ligands, which was also found in the MLR analysis (Table 4). Furthermore, the PCRA analysis of H_2sb ligands pointed out the importance of the ETSA indices on atoms 1 and 2, which are not captured by MLR analysis. In summary, our present work shows that the cytotoxicity of substituted salicylaldehyde benzoylhydrazones and their Cu(II) complexes can be modelled successfully by using quantum chemical and topological descriptors. In addition, our developed QSAR models may be used for the prediction of anticancer activities of substituted salicylaldehyde benzoylhydrazones and their Cu(II) complexes, and may help to design new compounds with potentially higher cytotoxicities.

The QSAR models developed for 24 H_2sb ligands show the importance of the ETSA indices of atoms 6–11 and the atomic charges of atoms 1, 2, 8, and 18. This indicates that the benzoylhydrazone fragments (see Fig. 3) of the ligands are necessary for anticancer activities. Our QSAR results suggest that the strong correlation effect among the atoms on the benzoylhydrazone framework is consistent to our previous studies,[8] showing that there is strong conjugation along the molecular plane of the ligand. The strong conjugation effect along the benzoylhydrazone framework allows these atoms to have mutual effects toward each other when a different substitution group is added to the benzene ring. As a result, the ETSA indices of atoms 6–11 are mutually important for anticancer activity. Since the atomic charge on atom 2 is positive and negative on atom 1, our developed model shows that an increase in positive charge on atom 2 and in negative charge for atom 1 will increase the anticancer activities of H_2sb ligands. This indicates that the addition of electron-withdrawing groups near position 2 (e.g., position 3) and electron-donating groups near position 1 (e.g., position 5 and 6) is required for the anticancer activity of H_2sb ligands. Based on our QSAR study, more negative charge on atom 18 is favorable for the anticancer activities of H_2sb ligands. Thus, we need to modify the compounds in such a way that it will increase the negative charge on atom 18 and thus the anticancer activities. Since there is a local conjugation system between carbonyl oxygen atom 18 and the neighboring atoms (i.e., atoms 11 and 12), the addition of an electron-donating group to atom 12 will increase the charge density of atom 18 through the conjugation system and hence lead to improved activities. This can be further explained by the Cu(II) complexes of the H_2sb ligands. Atom 18 is the carbonyl oxygen involved in the complexation of H_2sb ligands with Cu to form their corresponding Cu(II) complexes. The calculated atomic charges of H_2sb ligands and their Cu(II) complexes show that atom 18 of the Cu(II) complexes has more negative charge than the one in their ligands (see Tables 2 and 3). According to our current QSAR analysis, the Cu(II) complexes will have enchanced anticancer activities, which is supported by the experimental finding that the Cu(II) complexes of H_2sb ligands have a better anticancer activity than their ligands.[4] Thus, the complexation of the ligands with Cu is essential for increasing the anticancer activity of the H_2sb ligands.

Can. J. Chem. Downloaded from www.nrcresearchpress.com by UNIVERSITAT DE VALENCIA on 10/20/12
For personal use only.

Conclusions

We have developed statistically significant QSAR models for the H_2sb ligands and their corresponding Cu(II) complexes for their anticancer activity using MLR and PCRA techniques. We used different combinations of various descriptors such as physicochemical and ETSA indices and molecular descriptors such as chemical hardness, chemical potential, and natural population (NPA) charges, derived from DFT calculations. Our developed models show the importance of ClogP, ETSA indices, and atomic charges for the anticancer activities of the H_2sb analogs and their Cu(II) complexes. In addition, our MLR models revealed the importance of the global lipophilicity index and hardness for the anticancer activity of H_2sb ligands, whereas our MLR models revealed the importance of chemical potential and HOMO energy for the spin down configuration for the anticancer activity of Cu(II) complexes. A positive coefficient for ClogP indicated that the increase in ClogP increases the anticancer activities of both the H_2sb ligands and their corresponding Cu(II) complexes. For the H_2sb ligands, we observed that an increase of hardness is detrimental to their anticancer properties, whereas an increase in chemical potential and HOMO energy for the spin down configurations of Cu(II) complexes are favorable for their anticancer activity. In conclusion, we have successfully developed QSAR models for Cu(II) complexes as well as for the ligands. The developed QSAR models may be used for the prediction of anticancer activities and to design new analogs of the H_2sb ligands and their corresponding Cu(II) complexes with potentially higher anticancer activities.

Supplementary data

Supplementary data are available with the article through the journal Web site http://nrcresearchpress.com/doi/suppl/10.1139/v2012-053.

Acknowledgements

S.J. Tan and M.A. Sk acknowledge scholarships from Nanyang Technological University (NTU), Singapore. This project is supported by AcRF RG73/10.

References

(1) Johnson, D. K.; Murphy, T. B.; Rose, N. J.; Goodwin, W. H.; Pickart, L. *Inorg. Chim. Acta* **1982**, *67*, 159. doi:10.1016/S0020-1693(00)85058-6.

(2) Pickart, L.; Goodwin, W. H.; Burgua, W.; Murphy, T. B.; Johnson, D. K. *Biochem. Pharmacol.* **1983**, *32* (24), 3868. doi:10.1016/0006-2952(83)90164-8.

(3) Fan, C. D.; Su, H.; Zhao, J.; Zhao, B. X.; Zhang, S. L.; Miao, J. Y. *Eur. J. Med. Chem.* **2010**, *45* (4), 1438. doi:10.1016/j.ejmech.2009.12.048.

(4) Ainscough, E. W.; Brodie, A. M.; Denny, W. A.; Finlay, G. J.; Gothe, S. A.; Ranford, J. D. *J. Inorg. Biochem.* **1999**, *77* (3–4), 125. doi:10.1016/S0162-0134(99)00131-2.

(5) Tan, S. J.; Lee, P. F.; Lim, K. H.; Yan, Y. K. *Future. Med. Chem.* **2010**, *2*, 1591.

(6) Ruiz-Azuara, L.; Bravo-Gomez, M. E. *Curr. Med. Chem.* **2010**, *17* (31), 3606. doi:10.2174/092986710793213751.

(7) Sedletska, Y.; Giraud-Panis, M.-J.; Malinge, J.-M. *Curr. Med. Chem. Anticancer Agents* **2005**, *5* (3), 251. doi:10.2174/1568011053765967.

(8) Tan, S. J.; Xi, H.-W.; Bedoura, S.; Lim, K. H. *Inorg. Chim. Acta* **2012**, *384*, 29. doi:10.1016/j.ica.2011.11.024.

(9) Sarmah, P.; Deka, R. C. *Int. J. Quantum Chem.* **2008**, *108* (8), 1400. doi:10.1002/qua.21635.

(10) Sarmah, P.; Deka, R. C. *J. Comput. Aided Mol. Des.* **2009**, *23* (6), 343. doi:10.1007/s10822-009-9265-4.

(11) Mladenović, M.; Mihailović, M.; Bogojević, D.; Matić, S.; Niciforović, N.; Mihailović, V.; Vuković, N.; Sukdolak, S.; Solujić, S. *Int. J. Mol. Sci.* **2011**, *12* (5), 2822. doi:10.3390/ijms12052822.

(12) Lee, W. Y.; Yan, Y. K.; Lee, P. P. F.; Tan, S. J.; Lim, K. H. *Metallomics* **2012**, *4* (2), 188. doi:10.1039/c1mt00147g.

(13) Wolohan, P.; Yoo, J.; Welch, M. J.; Reichert, D. E. *J. Med. Chem.* **2005**, *48* (17), 5561. doi:10.1021/jm0501376.

(14) Feller, D. *J. Chem. Phys.* **1990**, *93* (1), 579. doi:10.1063/1.459559.

(15) Hohenberg, P.; Kohn, W. *Phys. Rev. B* **1964**, *136* (3B), B864. doi:10.1103/PhysRev.136.B864.

(16) Becke, A. D. *J. Chem. Phys.* **1993**, *98* (7), 5648. doi:10.1063/1.464913.

(17) Lee, C. T.; Yang, W. T.; Parr, R. G. *Phys. Rev. B* **1988**, *37* (2), 785. doi:10.1103/PhysRevB.37.785.

(18) Hehre, W. J.; Radom, L.; Schleyer, P. V. R.; Pople, J. A. *Ab Initio Molecular Orbital Theory;* Wiley: New York, 1996.

(19) Frisch, M. J.; Trucks, G. W.; Schlegel, H. B.; Scuseria, G. E.; Robb, M. A.; Cheeseman, J. R.; Montgomery, J. A., Jr.; Vreven, T.; Kudin, K. N.; Burant, J. C.; Millam, J. M.; Iyengar, S. S.; Tomasi, J.; Barone, V.; Mennucci, B.; Cossi, M.; Scalmani, G.; Rega, N.; Petersson, G. A.; Nakatsuji, H.; Hada, M.; Ehara, M.; Toyota, K.; Fukuda, R.; Hasegawa, J.; Ishida, M.; Nakajima, T.; Honda, Y.; Kitao, O.; Nakai, H.; Klene, M.; Li, X.; Knox, J. E.; Hratchian, H. P.; Cross, J. B.; Bakken, V.; Adamo, C.; Jaramillo, J.; Gomperts, R.; Stratmann, R. E.; Yazyev, O.; Austin, A. J.; Cammi, R.; Pomelli, C.; Ochterski, J. W.; Ayala, P. Y.; Morokuma, K.; Voth, G. A.; Salvador, P.; Dannenberg, J. J.; Zakrzewski, V. G.; Dapprich, S.; Daniels, A. D.; Strain, M. C.; Farkas, O.; Malick, D. K.; Rabuck, A. D.; Raghavachari, K.; Foresman, J. B.; Ortiz, J. V.; Cui, Q.; Baboul, A. G.; Clifford, S.; Cioslowski, J.; Stefanov, B. B.; Liu, G.; Liashenko, A.; Piskorz, P.; Komaromi, I.; Martin, R. L.; Fox, D. J.; Keith, T.; Al-Laham, M. A.; Peng, C. Y.; Nanayakkara, A.; Challacombe, M.; Gill, P. M. W.; Johnson, B.; Chen, W.; Wong, M. W.; Gonzalez, C.; Pople, J. A. *GAUSSIAN 03,* Revision C.02; Gaussian, Inc.: Wallingford, CT, 2004.

(20) Karr, P. A.; Zandler, M. E.; Beck, M.; Jaeger, J. D.; McCarty, A. L.; Smith, P. M.; D'Souza, F. *Theochem-. J. Mol. Struct.* **2006**, *765* (1–3), 91.

(21) Liu, T.; Huang, M. B.; Yu, Z. Y.; Yan, D. Y. *Theochem-. J. Mol. Struct.* **2006**, *776* (1–3), 97.

(22) Xi, H.-W.; Judeh, Z. M. A.; Lim, K. H. *Theochem-. J. Mol. Struct.* **2009**, *897* (1–3), 22.

(23) Reed, A. E.; Weinhold, F. *J. Chem. Phys.* **1983**, *78* (6), 4066. doi:10.1063/1.445134.

(24) Reed, A. E.; Weinstock, R. B.; Weinhold, F. *J. Chem. Phys.* **1985**, *83* (2), 735. doi:10.1063/1.449486.

(25) Jin, L.; Wang, J. B.; Cao, G. Y.; Choy, W. C. H. *Phys. Lett. A* **2008**, *372* (25), 4622. doi:10.1016/j.physleta.2008.04.036.

(26) Ghose, A. K.; Crippen, G. M. *J. Chem. Inf. Comput. Sci.* **1987**, *27* (1), 21. doi:10.1021/ci00053a005.

(27) de Gregorio, C.; Kier, L. B.; Hall, L. H. *J. Comput. Aided Mol. Des.* **1998**, *12* (6), 557. doi:10.1023/A:1008048822117.

(28) Hall, L. H.; Mohney, B.; Kier, L. B. *Quant. Struct.–Act. Relat.* **1991**, *10* (1), 43. doi:10.1002/qsar.19910100108.
(29) Kier, L. B.; Hall, L. H.; Frazer, J. W. *J. Math. Chem.* **1991**, *7* (1), 229. doi:10.1007/BF01200825.
(30) Koopmans, T. *Physica* **1934**, *1* (1–6), 104. doi:10.1016/S0031-8914(34)90011-2.
(31) Parr, R. G.; Yang, W. T. *J. Am. Chem. Soc.* **1984**, *106* (14), 4049. doi:10.1021/ja00326a036.
(32) Iczkowski, R.; Margrave, J. L. *J. Am. Chem. Soc.* **1961**, *83* (17), 3547. doi:10.1021/ja01478a001.
(33) Parr, R. G.; Pearson, R. G. *J. Am. Chem. Soc.* **1983**, *105* (26), 7512. doi:10.1021/ja00364a005.
(34) Snedecor, G. W.; Cochran, W. G. *Statistical Methods;* 8th ed.; Iowa State University Press: Ames, IA, 1989; pp 333–366.
(35) Franke, R. *Theoretical Drug Design Methods;* Elsevier: Amsterdam, 1984; pp 184–195.
(36) Wold, S.; Eriksson, L. *Chemometric Methods in Molecular Design;* Waterbeemd, H. v. d., Ed.; Wiley-VCH: Weinheim, 1995; pp 312–317.
(37) *Minitab 15 Statistical Software.* Minitab, Inc.: State College, PA, 2006.
(38) Peck, R.; Olsen, C.; Devore, J. *Introduction to Statistics and Data Analysis;* 3rd ed.; Brooks/Cole Cengage Learning: Belmont, CA, 2008.

Can. J. Chem. Downloaded from www.nrcresearchpress.com by UNIVERSITAT DE VALENCIA on 10/20/12
For personal use only.

Hydrophilic gel composition effect on the molecular association and spectroscopic behavior of rhodamine B

M.S. Zakerhamidi and A. Karimi

Can. J. Chem. Downloaded from www.nrcresearchpress.com by UNIVERSITAT DE VALENCIA on 10/20/12
For personal use only.

Abstract: Electronic absorption spectra of rhodamine B dye in aqueous solutions and in a polyacrylamide hydrogel matrix with different structural compositions were studied at room temperature. The transport and the solute–solute interactions of rhodamine B in aqueous solutions across the hydrophilic gels were investigated via exploration of the spectral properties of the dye-loaded hydrogel. The nature of the dye pair interactions in these media was discussed using the Kasha exciton theory. In addition, the monomer–dimer equilibrium of rhodamine B molecules in hydrogels with different compositional percentages was studied by means of UV–vis spectroscopy and least-squares fitting methods.

Key words: rhodamine laser dye, polyacrylamide hydrogel, dye aggregation, Kasha exciton theory, guest–host interaction.

Résumé : Opérant à la température ambiante, on a étudié les spectres d'absorption électronique du colorant rhodamine B en solutions aqueuses ainsi que dans diverses matrices d'hydrogels de polyacrylamide de compositions structurales différentes. On a aussi étudié les propriétés de transport et les interactions soluté–soluté de la rhodamine B en solutions aqueuses à travers les gels hydrophiles en explorant les propriétés spectrales d'hydrogel imbibé du colorant. On discute de la nature des interactions de la paire de colorant dans ces milieux en faisant appel à la théorie de l'exciton de Kasha. Faisant appel à la spectroscopie UV–vis et les méthodes d'ajustements par les moindres carrés, on a de plus étudié l'équilibre monomère–dimère des molécules de rhodamine B dans les hydrogels de compositions différentes en pourcentage.

Mots-clés : colorant laser rhodamine, hydrogel de polyacrylamide, agréation de colorant, théorie de l'exciton de Kasha, interaction hôte–invité.

[Traduit par la Rédaction]

Introduction

Rhodamine dyes are an important class of xanthene dyes. They have great fluorescence quantum yields and large molar absorptions. They have been extensively studied because of their practical applications as the active agent in dye lasers and optical applications.[1–9] The most active rhodamine derivatives are obtained by substituting the hydrogen of the rhodamine skeleton by groups such as alkyls, amines, etc. This substitution changes the ground- and excited-state dipole moments of substituted rhodamine molecules,[10] as well as their other photophysical properties.

One of the appropriate laser dyes is the one that uses rhodamine B (RB) as a lasing agent, which is tunable around 610 nm. Rhodamine laser dyes such as RB can easily form aggregates[11,12] in solution that quench the dye fluorescence emission and, therefore, degrade the lasing ability of dye-laser systems. This quenching process is mainly due to the transfer of excitation energy between monomers and aggregate forms of the dye molecules,[13–16] which subsequently, decays nonradiatively.[17] This means that dye aggregations is extremely important in dye-laser applications.

The aggregation of the dye molecules leads to a strong coupling of the molecular transition dipoles. This electrostatic interaction between molecular transition dipoles of the chromophores splits energy levels of the excited states of the dye molecules. According to the Kasha exciton theory,[18] in an ideal system J- or H-aggregates can be formed depending on the angle between the transition dipoles and the monomer center-connected axis in aggregate form (Fig. 1).[12,19] For H-aggregates (Fig. 1*a*), the chromophores of the participating molecules are in parallel planes, whereas, in J-aggregates, they are in the same plane (Fig. 1*b*)). However, in reality, both cases of the dimer structures are idealistic, and the transition moments are neither parallel nor antiparallel exactly. Appearance of both H- and J-bands[12,18,19] in the dimer spectrum confirms that oblique orientation of the transition dipoles is more feasible (Fig. 1*c*).

In the oblique dimer form, the angle between the transition dipoles of aggregated molecules (α angle) express the J- or H-aggregate characteristic of the dimer structure. The α angle can take values between 0° and 180°, and the shift from J- to H-aggregate occurs at $\alpha = 70.6°$. In this case, the θ angle (the angle between the transition dipoles and the monomer center-connected axis) is 54.7° Fig. 2. An α angle greater than 70.6° is connected with the J-aggregate, whereas an α angle less than 70.6° belongs to the H-aggregate.

Received 19 May 2012. Accepted 4 July 2012. Published at www.nrcresearchpress.com/cjc on 30 August 2012.

M.S. Zakerhamidi and A. Karimi. Research Institute for Applied Physics and Astronomy, University of Tabriz, Tabriz, Iran.

Corresponding author: Mohammad Sadegh Zakerhamidi (e-mail: Zakerhamidi@tabrizu.ac.ir).

Can. J. Chem. Downloaded from www.nrcresearchpress.com by UNIVERSITAT DE VALENCIA on 10/20/12
For personal use only.

Fig. 1. Energy diagram and structure for monomer and dimer electronic energy levels (*a*) H-aggregate, (*b*) J-aggregate, and (*c*) oblique-aggregate.

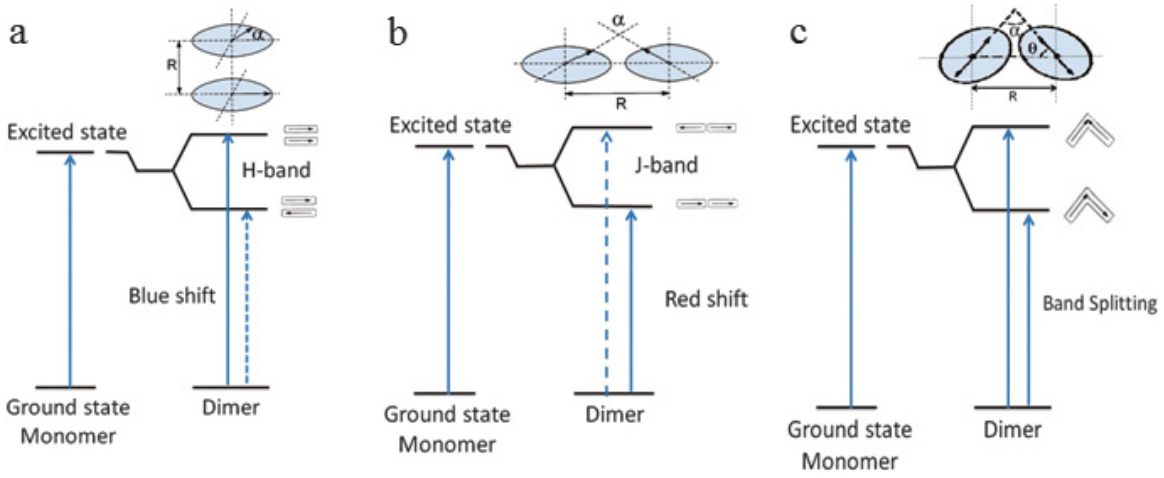
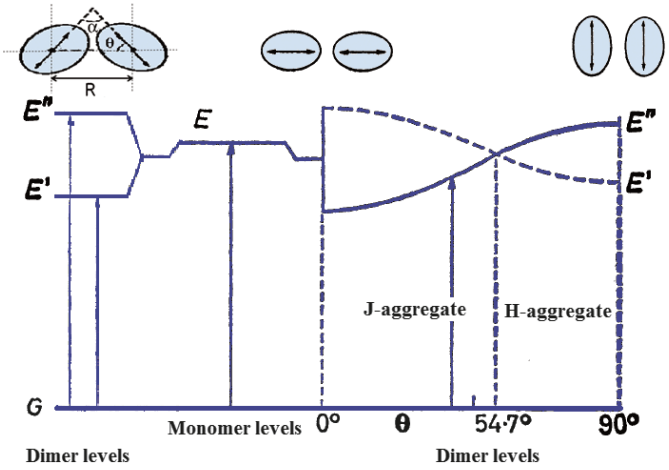


Fig. 2. Exciton band energy diagram for dimer aggregate molecules with transition dipoles inclined to the interconnected axis by angle θ.



Aggregation properties of the dyes can be controlled with different factors such as solvent media effect, concentration, temperature, and the presence of other solutes and cosolvents. We have ecently reported the influence of environment and concentration on the aggregative and photophysical properties of some oxazine, and thiazin dyes.[20–22] It was concluded that the host media affect the electronic absorption and aggregative characteristics of the ionic dyes.

Previously, the aggregation properties of some dyes in liquid solvent have been studied.[14,15,19] The solid-state media effects on the dye aggregation mechanism have been investigated recently.[23,24] All the research noted that the solvent matrix internal association and th einteraction of solvent molecules with the dye molecules are important parameters that determine the characteristics of the aggregate structures.

Polymer gels known as hydrogels, which have both solid- and liquid-like properties, are astonishing and fascinating materials. They are only composed of a cross-linked polymer network and interstitial fluid. These gels contain a great amount of water. The water uptake, the swelling process, is associated with a respective volume change.[20,21,25] Its structural framework is formed from three-dimensional networks of randomly cross-linked polymeric chains.

In this study, the aggregative properties of rhodamine B dye in polyacrylamide (PAAM) hydrogels with different compositional percentages of structural components were studied using optical spectroscopy. It would be interesting to understand the effect of the hydrogel host structure on the solute–solvent and solute–solute interactions and the monomer–dimer equilibrium of the aggregate dyes. This study is intended to provide the information about the effect of PAAM structural composition on guest–host interactions and the aggregative properties of RB in binary solvent systems by means of the exciton theory.

Experimental

Materials

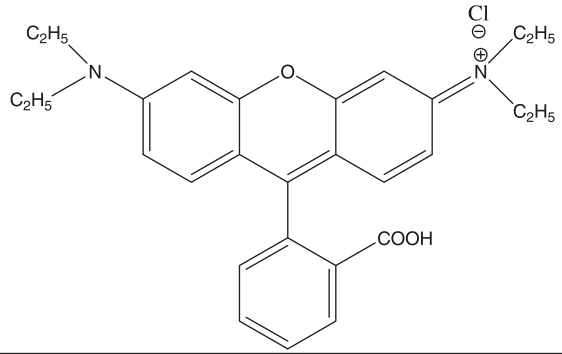
Acrylamide (97%), *N*,*N*-methylenebisacrylamide (≥98%), *N*,*N*,*N*,*N*-tetramethylethylenediamine (≥99%) (TEMED), and ammonium persulfate (≥98%) (APS) were used for synthesizing polyacrylamide gels with different compositional percentages (10%–40% PAAM/Water (*w*/*w*)).[20] All precursors were purchased from Sigma-Aldrich and used as received without any further purification. The laser-grade RB dye (Table 1) was procured from Exciton and used without further purification. Deionized water was used for all the dilutions and the polymerization reactions, as well as for the swelling and spectroscopic studies. Polyacrylamide gels were synthesized by the standard free radical copolymerization method.[26,27] The PAAM gels (with different compositions) were synthesized in cubic cells ($2 \times 2 \times 0.5$ cm^3) and, subsequent to polymerization, the prepared gels were taken out and used. The dye-loaded hydrogels were prepared by soaking the hydrogel hosts in aqueous solutions of RB dye with known concentrations for various durations of time (1 min to 10 h).

Absorption and emission spectroscopy

A double-beam Shimadzu UV-2450 Scan UV–vis spectrophotometer was used for recording the absorption spectra over a wavelength range of 300 to 800 nm, which was combined with a cell temperature controller. Emission spectra of the dye were studied with a JASCOFP-6200.

Can. J. Chem. Downloaded from www.nrcresearchpress.com by UNIVERSITAT DE VALENCIA on 10/20/12
For personal use only.

Table 1. Molecular structure of rhodamine B (RB).

Dye	Molecular structure
RB	

Results and discussion

Absorption spectra of rhodamine B in the hydrophilic gel matrix

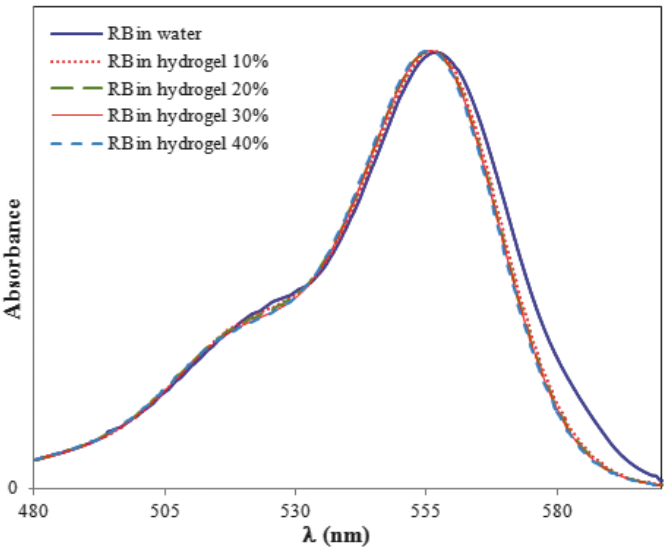
RB is a cationic dye and typically possesses doublet bands, i.e., a maximum (λ_{max}) and a shoulder ($\lambda_{shoulder}$).[12] The host nature can strongly influence the position and relative intensity of the doublet absorption bands. The shape variation of the dye optical spectrum might be controlled by distinct phenomena such as solvent–solute and solute–solute (ion pairing and dye aggregation) interactions.[28]

The visible spectra of the dye-loaded hydrogels were recorded at 22 °C. The aqueous solutions of the dye were prepared in a concentration range between 2×10^{-6} and 2×10^{-4} mol/L and the PAAM compositional percentage ranged from 10% to 40% *w*/*w*.

Absorption spectra of aqueous solutions of RB (5×10^{-5} mol/L) and hydrogel hosts (PAAM/water 10%–40% *w*/*w*) were investigated and are compared in Fig. 3. As can be seen from Fig. 3, the monomer absorption wavelengths of RB in aqueous solution is red-shifted as compared with those with different compositions of PAAM in hydrogels. The low absorption shifts of RB in different media means the dye senses same polarity in these media. Furthermore, the amount of the spectral shift for the higher compositional percentages of PAAM (30% and 40% *w*/*w*) as compared with the lower compositional percentages of PAAM (10% and 20% *w*/*w*) demonstrates the relationship between the size of pores in PAAM and the strength of dye–hydrogel interactions. In other words, the network structure and pore size play a key role in the diffusional behavior in hydrogels. The synthesized hydrogel showed a smaller pore size with an increase in concentration of the cross linker. The polymer chains of a higher compositional percentage of PAAM hydrogels are densely packed and provide strictly limited solute transport via the diffusion through free volumes. Therefore, RB dye molecules in the small pores of the hydrogel mostly interacted with active groups of the PAAM chains.

By increasing pore size, with lower compositional percentages of polyacrylamide, diffusion and transportation of RB occurs owing to a combination of molecular diffusion and convection in the water-filled pores. Finally, RB dye interacts with hydrogel water-filled pores in the same manner as the aqueous solution.

Fig. 3. Normalized visible absorption spectra of rhodamine B (RB, 5×10^{-5} mol/L) in aqueous solution and different percentages of polyacrylamide in hydrogels.



Determination of the dimer association constant of RB in hydrophilic gel matrix

Absorption UV–vis spectroscopy is one of the most suitable methods for the quantitative study of dye aggregation as a function of concentration, since, in the concentration range used (10^{-3}–10^{-6} mol/L), mainly monomer–dimer equilibrium can be detected.[19,29]

$$[1] \qquad 2[\mathrm{M}] \underset{K_{\mathrm{dissociation}}}{\overset{K_{\mathrm{association}}}{\rightleftharpoons}} [\mathrm{D}]$$

where [M] and [D] are the monomer and dimer concentrations, respectively. Therefore, the dimer formation equilibrium constant (K) can be calculated.

$$[2] \qquad K = \frac{[\mathrm{D}]}{[\mathrm{M}]^2}$$

At the point, one should consider two more equations based on mass balance and total absorption ($\mathrm{Abs}_{\mathrm{total}}$) in all samples.

$$[3] \qquad \text{Total analytical concentration} \equiv [\mathrm{C}] = [\mathrm{M}] + 2[\mathrm{D}]$$

$$[4] \qquad \begin{aligned} \mathrm{Abs}_{\mathrm{total}}(\lambda) &= \mathrm{Abs}_{\mathrm{monomer}}(\lambda) + \mathrm{Abs}_{\mathrm{dimer}}(\lambda) \\ &= \varepsilon_{\mathrm{m}}(\lambda)[\mathrm{M}]l + \varepsilon_{\mathrm{d}}(\lambda)[\mathrm{D}]l \end{aligned}$$

where $\varepsilon_{\mathrm{m}}(\lambda)$ and $\varepsilon_{\mathrm{d}}(\lambda)$ correspond to the molar absorption coefficients of the monomer and dimer at a given wavelength, respectively, and l is the optical path length. This equilibrium exists even in extremely dilute solutions and, consequently, the pure molar absorption coefficient of the monomer and dimer species at a particular wavelength and their concentrations, as well as the equilibrium constant, cannot be evaluated directly.

Fundamentally, three major routes including linear and nonlinear least-squares fitting and decomposition of the absorption spectra matrix into a product of target and projection matrices[30] have been used for evaluation of these unidentified parameters. In this paper we have used linear least-squares

Can. J. Chem. Downloaded from www.nrcresearchpress.com by UNIVERSITAT DE VALENCIA on 10/20/12
For personal use only.

fitting methods. In this method, dividing eq. [4] by [C]l and defining α as the fraction of dyes present as monomers gives

$$[5] \qquad \alpha = \frac{[M]}{[C]}$$

Combining this with eq. [2] gives

$$[6] \qquad K = \frac{(1-\alpha)[C]}{2\alpha^2[C]^2}$$

$$[7] \qquad \varepsilon_{total}(\lambda) = \varepsilon_m(\lambda)\alpha + \varepsilon_d(\lambda)\left(\frac{1-\alpha}{2}\right) = \left[\varepsilon_m(\lambda) - \frac{\varepsilon_d(\lambda)}{2}\right]\alpha + \frac{\varepsilon_d(\lambda)}{2}$$

Assuming that $\varepsilon_m(\lambda)$ and $\varepsilon_d(\lambda)$ are independent of concentration, variation of $\varepsilon_{total}(\lambda)$ vs α should yield a straight line with intercepts at $\varepsilon_m(\lambda)$ for $\alpha = 1$ and $\varepsilon_d(\lambda)/2$ for $\alpha = 0$ (Supplementary data). By systematic variation of K_d and analyzing the straight-line fitness in a series of wavelengths, one obtains the optimum dimerization constant as well as monomer and dimer spectra.[29]

The calculated dimerization constants for RB in water and in hydrogels with various percentages of constituents at different soaking times were obtained and are presented in Tables 2–5. These data show that dimerization constants for RB in different media and throughout different soaking times are different. In all hydrogels with various percentages of constituents, the dimeric constants are low at initial soaking times and increase with longer soaking times. In addition, the dimerization constants in hydrogels with a lower percentage of PAAM during the final soaking time show the approximate value of the dimerization constant in water. Furthermore, by increasing the percentage of PAAM in the hydrogel structure during the final soaking times, the dimerization constants decrease. These facts can be explained in terms of hydrogel firmness. In other words, in hydrogels with the higher percentage of polyacrylamidePAAM, pores sizes and the amount of free-water molecules in the polymer matrix decrease. It increases the quantity of freezing-water molecules in the pores of hydrogel and, therefore, increases strict hindrance and decreases the values of the dimeric association constants.

Aggregation of RB dye in hydrophilic gel matrix

Absorption spectra of aggregated dye molecules usually show large differences when compared with the individual molecules. By using Kasha exciton theory in its developed form the angle between the transition dipoles of chromophores can be obtained according to the following relationship[19]

$$[8] \qquad \alpha = 2\arctan\sqrt{\frac{\nu_H f_J}{\nu_J f_H}}$$

where ν is the position (in cm^{-1}) and f_i is the oscillator strength of the corresponding transition. The oscillator strengths (f_i) of the monomer and the dimer species were calculated using

$$[9] \qquad f_i = 4.32 \times 10^{-9} \int \varepsilon(\overline{\nu})\mathrm{d}\overline{\nu}$$

where ε is the value of the molar extinction coefficient and $\overline{\nu}$ is the position of the band in wavenumber. The term $\int \varepsilon_\nu \mathrm{d}\nu$ is the experimental value of the corresponding absorption integral. After subtracting the monomer absorption from the total visible spectrum, two Gaussian shaped bands for different forms of the dimeric species were obtained. The characteristics of these bands were used for calculation of the oscillator strengths and the angle between the transition dipoles of the chromophores.

The distance (R in Å) between the monomers in the dimer structure can be found by the following expression:[19]

$$[10] \qquad R = \sqrt[3]{\frac{2.14 \times 10^{10} \cos\alpha f_M}{\nu_M \Delta\nu}}, \qquad \Delta\nu = \nu_H - \nu_J$$

where f_M denotes the oscillator strength of the monomer transition. The difference in energy of the split levels depends on the interaction energy (U) between the dye molecules in the dimer species. The intermonomeric U of the dimer structure can be calculated by using the following relationship:[31]

$$[11] \qquad U = \frac{\nu_H - \nu_J}{2}$$

Moreover, the transition dipole (μ_i) of the monomeric, J- and H-bands (μ_i) can be obtained using the experimental value of the absorption integral according to the following equation

$$[12] \qquad |\mu_i|^2 = \left(\frac{3he^2 f_i}{8\pi^2 m_e \nu}\right)$$

where m_e and e are the mass and charge on the electron, respectively, h is Planck's constant, ν is the frequency at the corresponding band.

The spectral data and the excitonic parameters of the RB dye in aqueous solution and hydrogels (with the different compositional percentage of PAAM) were investigated and compared (Tables 2–5). The spectral properties and aggregation formation of the RB in the hydrogel host are dependent on soaking time. Although the water amount in the hydrogel structure is larger than the water amount in the polymer, the RB in aqueous solution and in the hydrogel matrix showed dissimilar behaviors.

RB in aqueous solution clearly shows H-aggregation and, in the final soaking time of hydrogel with different compositional percentages of PAAM, different values of excitonic parameters were obtained. In other words, the intermonomeric interaction energy of RB in aqueous solution is higher than in hydrogel media. In addition, the distance between the monomers that form the dimer and the α angle in aqueous solution are lower than in all percentages of hydrogel at final soaking time.

The excitonic parameters of RB in different percentages of hydrogels (Tables 2–5) show H-aggregate forms for all soaking times. In addition, an increase in soaking time increases the transition dipole of H-aggregation and the distance between the monomers and also decreases the intermonomeric interaction energy. Moreover, as the compositional percentage of the PAAM in the hydrogel increases, the change rate of aggregative parameters is reduced.

Can. J. Chem. Downloaded from www.nrcresearchpress.com by UNIVERSITAT DE VALENCIA on 10/20/12
For personal use only.

Table 2. Excitonic and spectroscopic parameters of rhodamine B (RB) in 10% *w/w* hydrogel and water.

Soaking time (min)	logK_d	ν_M (±3)	ν_H (±2)	ν_J (±3)	Oscillator strength (±0.001) Monomer	H-aggregate form	J-aggregate form	$\alpha°$ (±0.8)	R (±0.1)	μ_M (D) (±0.01)	μ_H (D) (±0.01)	μ_J (D) (±0.01)	$4\times U$ (cm^{-1}) (±0.5)
5	2.62±0.01	18147	19255	17227	0.172	0.067	0.016	52	3.9	4.48	2.71	1.40	4054.6
10	2.45±0.02	18159	19222	17231	0.301	0.184	0.034	54	4.9	5.93	4.51	2.06	3980.9
15	2.35±0.02	18166	19242	17291.5	0.399	0.330	0.087	57	5.1	6.83	6.03	3.28	3901.5
20	2.54±0.01	18170	19225	17362	0.467	0.248	0.080	62	5.2	7.39	5.24	3.14	3725.6
30	2.57±0.01	18174	19229	17393	0.581	0.351	0.129	61	5.4	8.24	6.23	3.97	3672.4
40	2.60±0.02	18176	19236	17384	0.636	0.397	0.118	60	5.9	8.62	6.62	3.80	3702.9
50	2.76±0.03	18177	19201	17305	0.724	0.323	0.073	61	6.5	9.20	5.98	3.00	3791.8
60	2.80±0.02	18177	19219	17347	0.770	0.374	0.114	60	6.2	9.49	6.43	3.73	3744.0
80	2.95±0.01	18180	19222	17384	0.850	0.314	0.105	62	6.3	9.97	5.89	3.58	3675.8
100	2.85±0.02	18179	19218	17348	0.864	0.423	0.135	60	6.4	10.05	6.84	4.06	3739.6
120	2.85±0.02	18179	19211	17383	0.896	0.473	0.134	58	6.7	10.23	7.24	4.05	3656.8
140	2.96±0.01	18179	19200	17371	0.914	0.383	0.092	61	7.0	10.34	6.51	3.35	3657.7
Water	3.00±0.01	18146	19616	17138	0.102	0.344	0.059	48	3.2	3.46	6.10	2.71	4956.4

Note: K_d, dimer formation equilibrium constant; ν, absorption frequency; α, angle between the transition dipoles of aggregated chromophores; R, distance between the monomers in the aggregated structure (Å); μ, transition dipole; U, interaction energy between the dye molecules in the aggregated form.

Table 3. Excitonic and spectroscopic parameters of rhodamine B (RB) in 20% *w/w* hydrogel and water.

Soaking time (min)	logK_d	ν_M (±3)	ν_H (±2)	ν_J (±3)	Oscillator strength Monomer	H-aggregate form	J-aggregate form	$\alpha°$ (±0.8)	R (±0.1)	μ_M (D) (±0.01)	μ_H (D) (±0.01)	μ_J (D) (±0.01)	$4\times U$ (cm^{-1}) (±0.5)
5	2.79±0.02	18123	19364	17265	0.177	0.019	0.004	52	3.9	4.56	1.44	0.70	4198.6
10	2.85±0.01	18139	19289	17236	0.282	0.075	0.019	53	4.5	5.75	2.87	1.52	4105.8
15	2.68±0.02	18145	19263	17236	0.361	0.120	0.029	55	5.0	6.50	3.64	1.88	4055.4
20	2.95±0.03	18147	19243	17223	0.468	0.228	0.059	55	5.3	7.41	5.02	2.70	4041.4
30	2.65±0.02	18149	19238	17224	0.567	0.272	0.051	53	6.0	8.15	5.48	2.51	4028.2
40	2.72±0.02	18152	19253	17238	0.650	0.289	0.059	51	6.2	8.72	5.65	2.70	4028.2
50	2.81±0.01	18153	19270	17268	0.739	0.305	0.070	54	6.4	9.30	5.80	2.93	4004.62
60	2.73±0.01	18156	19287	17308	0.776	0.398	0.105	57	6.3	9.53	6.62	3.59	3958.9
80	2.93±0.03	18159	19192	17385	0.892	0.291	0.084	59	6.7	10.22	5.67	3.21	3614.9
100	2.92±0.02	18157	19202	17358	0.937	0.391	0.111	58	6.8	10.47	6.58	3.68	3689.1
120	2.82±0.01	18157	19200	17392	0.946	0.552	0.142	58	7.0	10.52	7.82	4.17	3615.6
140	2.92±0.01	18158	19201	17389	0.991	0.490	0.124	58	7.1	10.77	7.37	3.90	3625.2
Water	3.00±0.01	18146	19616	17138	0.102	0.344	0.059	48	3.2	3.46	6.10	2.71	4956.4

Note: K_d, dimer formation equilibrium constant; ν, absorption frequency; α, angle between the transition dipoles of aggregated chromophores; R, distance between the monomers in the aggregated structure (Å); μ, transition dipole; U, interaction energy between the dye molecules in the aggregated form.

Can. J. Chem. Downloaded from www.nrcresearchpress.com by UNIVERSITAT DE VALENCIA on 10/20/12
For personal use only.

Table 4. Excitonic and spectroscopic parameters of rhodamine B (RB) in 30% *w*/*w* hydrogel and water.

Soaking time (min)	logK_d	ν_M (±3)	ν_H (±2)	ν_J (±3)	Oscillator strength			$\alpha°$ (±0.8)	R (±0.1)	μ_M (D) (±0.01)	μ_H (D) (±0.01)	μ_J (D) (±0.01)	$4\times U$ (cm^{-1}) (±0.5)
					Monomer	H-aggregate form	J-aggregate form						
5	2.80±0.03	18120	19183	17234	0.143	0.094	0.015	46	3.9	4.10	3.23	1.38	3898.2
10	2.85±0.03	18124	19174	17240	0.265	0.088	0.015	46	4.8	5.57	3.13	1.34	3868.3
15	2.88±0.02	18131	19185	17223.9	0.357	0.082	0.016	50	5.2	6.47	3.01	1.41	3921.8
20	2.94±0.02	18136	19259	17262	0.436	0.091	0.017	49	5.5	7.15	3.18	1.43	3993.8
30	2.86±0.01	18142	19272	17244	0.563	0.144	0.025	48	6.0	8.12	3.99	1.76	4056.4
40	2.75±0.01	18144	19286	17264	0.627	0.228	0.053	54	6.0	8.57	5.01	2.56	4045.6
50	2.61±0.01	18145	19287	17284	0.627	0.228	0.053	54	6.0	8.57	5.01	2.55	4007.6
60	2.59±0.02	18145	19321	17298	0.726	0.434	0.097	53	6.3	9.22	6.91	3.45	4047.8
80	2.75±0.01	18149	19254	17319	0.836	0.360	0.111	56	6.3	9.90	6.31	3.70	3871.0
100	2.91±0.01	18149	19217	17362	0.949	0.314	0.093	59	6.7	10.54	5.89	3.37	3709.8
120	2.94±0.01	18149	19196	17350	0.983	0.342	0.090	57	7.0	10.73	6.15	3.32	3691.8
140	2.94±0.01	18144	19197	17383	0.858	0.346	0.091	57	6.7	10.02	6.19	3.33	3627.4
Water	3.00±0.01	18146	19616	17138	0.102	0.344	0.059	48	3.2	3.46	6.10	2.71	4956.4

Note: K_d, dimer formation equilibrium constant; ν, absorption frequency; α, angle between the transition dipoles of aggregated chromophores; R, distance between the monomers in the aggregated structure (Å); μ, transition dipole; U, interaction energy between the dye molecules in the aggregated form.

Table 5. Excitonic and spectroscopic parameters of rhodamine B (RB) in 40% *w*/*w* hydrogel and water.

Soaking time (min)	logK_d	ν_M (±3)	ν_H (±2)	ν_J (±3)	Oscillator strength			$\alpha°$ (±0.8)	R (±0.1)	μ_M (D) (±0.01)	μ_H (D) (±0.01)	μ_J (D) (±0.01)	$4\times U$ (cm^{-1}) (±0.5)
					Monomer	H-aggregate form	J-aggregate form						
5	2.87±0.03	18106	19587	17110	0.135	0.053	0.014	57	3.3	3.98	2.39	1.30	4954.7
10	2.75±0.02	18117	19353	17255	0.237	0.078	0.020	57	4.2	5.27	2.92	1.58	4194.6
15	2.84±0.03	18123	19312	17293.7	0.325	0.059	0.017	59	4.6	6.18	2.55	1.44	4037.0
20	2.64±0.03	18125	19320	17161	0.383	0.152	0.038	56	4.9	6.70	4.09	2.17	4317.8
30	2.71±0.01	18130	19290	17234	0.481	0.149	0.039	57	5.3	7.51	4.06	2.18	4112.6
40	2.77±0.03	18131	19356	17175	0.570	0.187	0.051	58	5.5	8.17	4.53	2.52	4361.5
50	2.75±0.02	18134	19166	17437	0.795	0.034	0.010	59	6.5	9.65	1.94	1.11	3458.0
60	2.68±0.02	18134	19239	17281	0.880	0.047	0.014	60	6.4	10.15	2.28	1.32	3916.0
80	2.78±0.02	18136	19246	17281	0.971	0.056	0.016	59	6.7	10.67	2.48	1.39	3930.0
100	2.85±0.01	18140	19209	17290	1.021	0.152	0.045	60	6.8	10.94	4.10	2.36	3838.3
120	2.88±0.01	18137	19209	17290	1.058	0.152	0.045	60	6.9	11.13	4.10	2.36	3838.3
140	2.89±0.01	18137	19167	17391	1.048	0.141	0.044	61	7	11.05	3.96	2.31	3553.2
Water	3.00±0.01	18146	19616	17138	0.102	0.344	0.059	48	3.2	3.46	6.10	2.71	4956.4

Note: K_d, dimer formation equilibrium constant; ν, absorption frequency; α, angle between the transition dipoles of aggregated chromophores; R, distance between the monomers in the aggregated structure (Å); μ, transition dipole; U, interaction energy between the dye molecules in the aggregated form.

Published by NRC Research Press

Can. J. Chem. Downloaded from www.nrcresearchpress.com by UNIVERSITAT DE VALENCIA on 10/20/12
For personal use only.

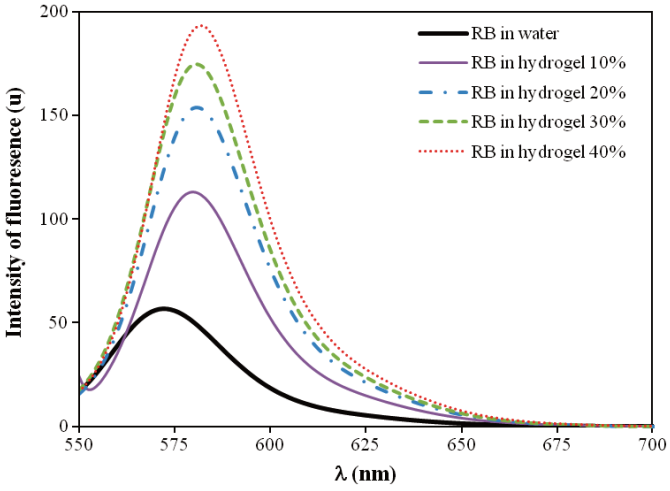
In the case of RB-loaded hydrogel, the degree of aggregation is clearly prevented by the swelling properties of the hydrogel host (K_d). It should be noted that, when hydrogels come in contact with water or an aqueous solution, the solution diffuses into the hydrogel and the hydrogel swells. The water in a hydrogel network exists in a continuum state between two extremes. The bound or freezing water is strongly associated with the hydrogel network through hydrogen bonds, whereas the free or nonfreezing water has a much greater mobility and is unaffected mainly by the hydrogel environment.[21] The free water molecules present in the relatively large pores of the hydrogel may be replaced by the guest dye molecules, whereas the bound water is strongly attached to the gel matrix and is not easily replaceable by the guest molecules. Moreover, the RB is more hydrophilic in nature and its interactions with free water and freezing-water regions in the hydrophilic gel are dissimilar. However, monitoring the time evolution of the replacement of the guest molecules confirms the presence of an equilibrium state between guest molecules preserved into both regions, i.e., if enough time is provided, because of the tendencies of the hydrogel functional groups, some of the guest molecules dissolved in the free water regions can diffuse into the bound water regions and interact with the hydrogel matrix.[20,21]

The obtained excitonic parameters suggest that, in the initial soaking time, the RB molecules interact with the free water of the hydrogel pores. By increasing this time, the RB molecules interact with the active functional groups of the hydrogel in the polymeric chain and freezing water molecules in the hydrogel pores. Furthermore, strict hindrance between hydrogel pores and the associated form of RB, as the soaking time increases, decreases the mobility, aggregation, and intermonomeric interaction energy of the dye molecules. Furthermore, increasing the compositional percentage of PAAM hydrogel (increasing the active sites in the polymer chains), increases the steric privation effect of the dye molecules (decreasing mobility) and, consequently, the aggregation parameters of RB in these media will vary largely as compared towith those in the hydrogels with lower compositional percentages of PAAM hydrogel.

Tables 2–5 demonstrate that the α and U values of dissolved RB in hydrogel hosts are dissimilar. It may be due to an existing dissimilar amount of active polymer sites, freezing water, and free water in various percentages of PAAM hydrogel. The values of U in all hydrogel media decrease with increasing percentages of PAAM. However, a decrease in U between the dye molecules of the dimer species confirms that the steric privation effect increases for the higher compositional percentages of the hydrogel. This confirms an increase in the distance between the monomers in the aggregate form of the dye.

Figure 4 shows the emission spectra of RB in different percentages of PAAM hydrogel and aqueous solution media. We used low concentrations of RB ($C = 2 \times 10^{-5}$ mol/L) for all percentages of PAAM with monomer excitation wavelengths and the standard method for detection of the fluorescence intensity for all the samples.We used these variations as a confirmation of microenvironment viscosity variation. This means that the dye acts as a viscosity sensitive probe in which its quantum yield increases as a result of microenvironment viscosity enhancement. In other words, by increasing the polymeric gel viscosity, RB molecules are protected from quenching and lead to fluorescence of a higher intensity.

Fig. 4. Emission spectra of rhodamine B (RB, 5×10^{-5} mol/L) in different compositional percentages of polyacrylamide with a monomer excitation wavelength.



This supports the decision that increasing the percentage of PAAM in the hydrogel matrix decreases the amount of free water in the hydrogel media and then decreases the ability of the media to solubilize the RB in dimer form and favors solubilization of RB into the hydrogel polymeric matrix in its monomeric form. Subsequently, an increase in the intensity of fluorescence can be observed.

Conclusions

Hydrogels with three-dimensional networks and randomly cross-linked polymeric chains contain active sites for interaction with guest molecules and contain structural water (freezing and free water). Freezing water molecules are strongly associated with the hydrogel network through hydrogen bonds, and free water molecules have a much greater mobility and are less influenced by the hydrogel environment. RB interactions with hydrogel active sites and freezing or free water molecules in polymer environments show different interactions as compared with the dye in aqueous solutions.

The dimerization constants of RB in low percentages of the hydrogel at the final soaking time show the approximate value of the dimeric constant of water. Moreover, as the compositional percentage of the hydrogel increases, the dimeric constants at the final soaking times show smaller values as compared witih those in hydrogels with lower percentages. Therefore, the degree of aggregation is clearly prevented by the pore size and swelling properties of the hydrogel host. The same behaviors were shown in the aggregation parameters. The angle between transition dipoles of aggregate molecules (α) and the transition dipole amount of the H-dimeric bands increase with an increase in soaking time. Furthermore, the values of U in all hydrogel media decrease with increasing percentages of PAAM and soaking times. In other words, a decrease in U between the dye molecules of dimer species confirms that the steric privation effect increases with increasing compositional percentages of hydrogel and the hydrogel swells (increases soaking time). By increasing soaking time and the compositional percentage of the hydrogel, the

steric privations in the hydrogel media increase the distance between the monomers in the aggregate form of the dye.

The obtained results confirm that, at shorter soaking times, RB molecules interact with free water in thr hydrogel pores. By increasing soaking time, RB interacts with the hydrogel interactive functional groups in the polymeric chain and freezing water molecules in the hydrogel pores.

Supplementary data

Supplementary data are available with the article through the journal Web site http://nrcresearchpress.com/doi/suppl/10.1139/v2012-055.

References

(1) Šašić, S.; Itoh, T.; Ozaki, Y. *J. Raman Spectrosc.* **2005**, *36* (6–7), 593. doi:10.1002/jrs.1329.

(2) Deshpande, A. V.; Namdas, E. B. *Chem. Phys. Lett.* **1996**, *263* (3–4), 449. doi:10.1016/S0009-2614(96)01247-X.

(3) Deshpande, A. V.; Namdas, E. B. *Appl. Phys. B* **1997**, *64* (4), 419. doi:10.1007/s003400050193.

(4) Michaels, A. M.; Nirmal, M.; Brus, L. E. *J. Am. Chem. Soc.* **1999**, *121* (43), 9932. doi:10.1021/ja992128q.

(5) Haugland, R. P. *Handbook of Fluorescent Probes and Research Products;* 9th ed.; Molecular Probes: Eugene, OR, 2002.

(6) Milijanić, S.; Cimerman, Z.; Frkanec, L.; Zinić, M. *Anal. Chim. Acta* **2002**, *468* (1), 13. doi:10.1016/S0003-2670(02)00627-X.

(7) Mohanty, J.; Nau, W. *Angew. Chem. Int. Ed.* **2005**, *44* (24), 3750. doi:10.1002/anie.200500502.

(8) Wang, X.; Song, M.; Long, Y. *J. Solid State Chem.* **2001**, *156* (2), 325. doi:10.1006/jssc.2000.9002.

(9) Saini, G. S. S.; Sharma, A.; Kaur, S.; Bindra, K. S.; Sathe, V.; Tripathi, S. K.; Mhahajan, C. G. *J. Mol. Struct.* **2009**, *931* (1–3), 10. doi:10.1016/j.molstruc.2009.05.015.

(10) Rauf, M. A.; Graham, J. P.; Bukallah, S. B.; Al-Saedi, M. A. S. *Spectrochim. Acta A Mol. Biomol. Spectrosc.* **2009**, *72* (1), 133. doi:10.1016/j.saa.2008.08.018.

(11) López Arbeloa, F.; Chaudhuri, R.; López Arbeloa, T.; López Arbeloa, I. *J. Colloid Interface Sci.* **2002**, *246* (2), 281. doi:10.1006/jcis.2001.8074.

(12) Tajalli, H.; Ghanadzadeh Gilani, A.; Zakerhamidi, M. S.; Moghadam, M. *Spectrochim. Acta [A]* **2009**, *72* (4), 697. doi:10.1016/j.saa.2008.09.033.

(13) El-Daly, S. A.; Gaber, M.; Al-Shihry, S. S.; El Sayed, Y. S. *J. Photochem. Photobiol. Chem.* **2008**, *195* (1), 89. doi:10.1016/j.jphotochem.2007.09.010.

(14) López Arbeloa, F.; Gonzalez, I. L.; Ruiz Ojeda, P.; López Arbeloa, I. *J. Chem. Soc. Faraday Trans.* **1982**, *78* (7), 989. doi:10.1039/f29827800989.

(15) López Arbeloa, F.; Ruiz Ojeda, P.; López Arbeloa, I. *J. Chem. Soc. Faraday Trans.* **1988**, *84* (12), 1903. doi:10.1039/f29888401903.

(16) Marmé, N.; Habl, G.; Knemeyer, J.-P. *Chem. Phys. Lett.* **2005**, *408* (4–6), 221. doi:10.1016/j.cplett.2005.04.008.

(17) Penzkofer, A.; Leupacher, W. *J. Lumin.* **1987**, *37* (2), 61. doi:10.1016/0022-2313(87)90167-0.

(18) Kasha, M.; Rawls, H. R.; Ashraf El-Bayoumi, M. *Pure Appl. Chem.* **1965**, *11* (3–4), 371. doi:10.1351/pac196511030371.

(19) Antonov, L.; Gergov, G.; Petrov, V.; Kubista, M.; Nygren, J. *Talanta* **1999**, *49* (1), 99. doi:10.1016/S0039-9140(98)00348-8.

(20) Zakerhamidi, M. S.; Tajalli, H.; Ghanadzadeh, A.; Milanchian, K.; Hosseini Nasab, N.; Moghadam, M. *J. Mol. Liq.* **2010**, *154* (1), 18. doi:10.1016/j.molliq.2010.03.003.

(21) Zakerhamidi, M. S.; Tajalli, H.; Ghanadzadeh, A.; Milanchian, K.; Hosseini Nasab, N.; Moghadam, M. *Spectrochim. Acta [A]* **2010**, *77* (1), 164. doi:10.1016/j.saa.2010.04.045.

(22) Ghanadzadeh Gilani, A.; Tajalli, H.; Zakerhamidi, M. S. *J. Mol. Liq.* **2008**, *143* (2–3), 81. doi:10.1016/j.molliq.2008.05.016.

(23) Meral, K.; Yílmaz, N.; Kaya, M.; Tabak, A.; Onganer, Y. *J. Lumin.* **2011**, *131* (10), 2121. doi:10.1016/j.jlumin.2011.05.023.

(24) Iyi, N.; Sasai, R.; Fujita, T.; Deguchi, T.; Sota, T.; López Arbeloa, F.; Kitamura, K. *Appl. Clay Sci.* **2002**, *22* (3), 125. doi:10.1016/S0169-1317(02)00144-8.

(25) Wu, S.; Li, H.; Chen, J. P. *J. Macromol. Sci. C.* **2004**, *44* (2), 113. doi:10.1081/MC-120034151.

(26) Osada, Y.; Gong, J. P.; Tanaka, Y. *J. Macromol. Sci. C.* **2004**, *44* (1), 87. doi:10.1081/MC-120027935.

(27) Bar-Cohen, Y. *Electroactive Polymer (EAP) Actuators as Artificial Muscles: Reality. Potential, and Challenges;* Vol. PM136; SPIE: Bellingham, WA, 2001.

(28) Oliveira, C. S.; Branco, K. P.; Baptista, M. S.; Indig, G. L. *Spectrochim. Acta [A]* **2002**, *58* (13), 2971. doi:10.1016/S1386-1425(02)00044-6.

(29) Ghanadzadeh Gilani, A.; Moghadam, M.; Zakerhamidi, M. S. *Comput. Methods Programs Biomed.* **2011**, *104* (2), 175. doi:10.1016/j.cmpb.2011.01.008.

(30) Scarminio, I.; Kubista, M. *Anal. Chem.* **1993**, *65* (4), 409. doi:10.1021/ac00052a017.

(31) Patil, K.; Pawar, R.; Talap, P. *Phys. Chem. Chem. Phys.* **2000**, *2* (19), 4313. doi:10.1039/b005370h.

Can. J. Chem. Downloaded from www.nrcresearchpress.com by UNIVERSITAT DE VALENCIA on 10/20/12
For personal use only.

Diphenylphosphinoethane-functionalized polystyrene resin-supported Pd(0) complex — A highly active and recyclable catalyst for the Stille reaction under aerobic conditions

Siavash Bahari, Babak Mohammadi-Aghdam, Rahim Molaei, and Zakiyeh Gharibi

Abstract: The polymer-supported palladium(II) diphenylphosphinoethane complex is a highly active catalyst that could be used for the Stille coupling reaction between aryl iodides and (or) chlorides and organostannanes at room temperature under aerobic conditions. This heterogeneous palladium catalyst is efficient, air-stable, and recyclable.

Key words: Stille coupling, supported palladium catalyst, aryl iodides, aryl chlorides, heterogeneous catalyst.

Résumé : Le complexe de diphényphoslphinoéthane palladium(II) déposé sur un polymère est un catalyseur très actif qui pourrait être utilisé pour la réaction de couplage de Stille entre des iodures ou chlorures d'aryles et des organostannanes, à la température ambiante, dans des conditions aérobiques. Ce catalyseur hétérogène du palladium est efficace, stable à l'air et il peut être recycler.

Mots-clés : couplage de Stille, catalyseur de palladium déposé sur un polymère, iodures d'aryles, chlorures d'aryles, catalyseur hétérogène.

[Traduit par la Rédaction]

Can. J. Chem. Downloaded from www.nrcresearchpress.com by UNIVERSITAT DE VALENCIA on 10/20/12
For personal use only.

Introduction

The Stille cross-coupling reaction of organohalides with organotin compounds has been proven to be a useful synthetic method for carbon–carbon bond formation in organic synthesis. Consequently, many effective palladium catalytic systems have been developed for the Stille cross-coupling reaction.[1–5] The yields of coupled products are often high, and the organotin reagents can be readily synthesized, purified, and stored. However, the reaction generally proceeds in the presence of a homogeneous palladium catalyst such as $Pd(PPh_3)_4$, $PdCl_2(PPh_3)_2$, or $PdCl_2(MeCN)_2$, which makes the recovery of the metal tedious if not impossible and might result in unacceptable palladium contamination of the product. The forcing conditions are typically at reflux in tetrahydrofuran (THF) or dioxane and the requirement for dry, oxygen-free environments is also a limitation of the Stille reaction. From the standpoint of green chemistry, the development of more environmentally benign conditions for the reaction, for example, the use of a heterogeneous palladium catalyst, would be desirable.[6]

In recent years there has been a tremendous upsurge of interest in various chemical transformations performed under heterogeneous catalysis.[7] Moreover, using inexpensive and noncorrosive heterogeneous catalysts, chemical transformations occur with better efficiency, higher purity of the products, and easier workup, with evident economic and ecological advantages, especially for industrial processes.

The use of heterogeneous catalysts for Stille coupling reactions leads to a reduction in waste. Polymer-supported transition-metal complexes having high activity have attracted significant interest because they can be easily recovered and reused.[6a] Although different methods are available for the Stille reaction, there is still a dearth of efficient processes for this reaction using polymer-supported palladium catalysts. Thus, the study of types of polymer-supported palladium catalysts that might be suitable for the Stille reaction has practical significance.

Resins are one class of polymeric supports originating from organic precursors that are widely employed as catalyst carriers and also in solid-phase organic synthesis. Resin-supported palladium complexes having high activity and selectivity are currently attracting a great interest because of their easy separation and recovery.[6b]

Polymer-supported palladium complex catalysts derived from chloromethyl polystyrene resin have been employed in both the Heck,[8] Suzuki,[9] and Sonogashira[10] reactions, and have shown lower leaching of palladium during cross-coupling. However, to the best of our knowledge, Stille reactions catalyzed by polymer-supported palladium complexes have received less attention.[11] Unfortunately, they have lower

Received 10 March 2012. Accepted 14 May 2012. Published at www.nrcresearchpress.com/cjc on 30 August 2012.

S. Bahari, B. Mohammadi-Aghdam, and Z. Gharibi. Department of Chemistry, Ahar Branch, Islamic Azad University, Ahar, Iran.
M. Molaei. Department of Chemistry, Ahar Branch, Islamic Azad University, Ahar, Iran; Department of Chemistry, Faculty of Science, Urmia University, Urmia, Iran.

Corresponding author: Babak Mohammadi-Aghdam (e-mail: b-mohammadi-a@iau-ahar.ac.ir and babak.mohammadi.a@gmail.com).

Can. J. Chem. Downloaded from www.nrcresearchpress.com by UNIVERSITAT DE VALENCIA on 10/20/12
For personal use only.

catalytic activity compared with their soluble counterparts in Stille reactions. In addition, the activity of the recycled catalysts gradually decreases because the palladium species leaches from the supporting polymer or silica gel. To overcome these limitations, a novel methodology for creating insoluble and highly active catalysts is needed. This encouraged us to investigate the diphenylphosphinoethane-functionalized polystyrene resin-supported Pd(0) complex,[10] PS-dpp-Pd(0), for the Stille reaction (Scheme 1). Our approach was guided by three imperatives: (*i*) the polymeric reagent should be easily accessible, (*ii*) start from readily available and cheap reagents, and (*iii*) the polymeric ligand should be air-stable, which should allow its storage in normal bottles with unlimited shelf life.

Kamali and co-workers[12] have already reported the use of an ethylenediamine-functionalized polystyrene resin-supported Pd(II) complex as an active and reusable catalyst in Sonogashira reactions.[13] Herein, we develop a mild protocol for the Stille coupling of aryl iodides and aryl chlorides with organostannanes under aerobic conditions with PS-dpp-Pd(0) as catalyst (Scheme 2).

Results and discussion

PS-dpp-Pd(0) was prepared according to the literature.[10]

We used known chloromethylated polystyrene cross-linked with 2% divinylbenzene as the support, as it allows grafting of metallic atoms via ligands, which are attached to the polymer beads. Reaction of polystyrene resin with diphenylphosphinoethane in dimethylformamide (DMF) at 100 °C, and then treatment of the phosphinated polystyrene with a solution of $[PdCl_2(PhCN)_2]$ in ethanol, and finally reduction with hydrazine monohydrate resulted in covalent attachment of the palladium complex to give the polymer-supported palladium(0) complex catalyst (Scheme 1).[10] This catalyst is safe, easy to handle, air-stable, and environmentally benign with fewer disposal problems.

Successful functionalization of the polymer was confirmed by elemental analysis. The P content of the resin was found to be 4.25% by inductively coupled plasma (ICP), which indicates that the resin had reacted with diphenylphosphinoethane. The metal loading of the polymer-supported palladium complex, determined by neutron activation analysis (NAA), was 5.42% (0.51 mmol/g).[10]

First, we optimized the amount of PS-dpp-Pd(0) catalyst required in the reaction between iodobenzene and 1-(tributylstannyl)-2-phenylethyne (Table 1). For optimization of the reaction conditions, we chose the reaction of 1-(tributylstannyl)-2-phenylethyne with iodobenzene as the model reaction, and the effects of the solvents, temperature, and catalyst were examined. Several solvents were screened for the reaction in the presence of a catalytic amount of PS-dpp-Pd(0). As shown in Table 1, the reaction was influenced significantly by the solvent employed. The reaction worked very well when organic solvents such as DMF and *N*-methylpyrrolidone (NMP) were used (Table 1, entries 4 and 7), with the best result obtained in the case of DMF (Table 1, entry 7). THF, PhH, and CH_3CN were not suitable solvents for this reaction. The optimum amount of PS-dpp-Pd(0) was found to be 2.0 mol % in the presence of iodobenzene (1 mmol) and 1-(tributylstannyl)-2-phenylethyne (1.2 mmol) in DMF (3 mL) at 65 °C under aerobic conditions. Increasing the amount of the palladium catalyst shortened the reaction time but did not increase the yield (Table 1, entry 10). A low palladium concentration prolonged the reaction time and led to a decreased yield (Table 1, entry 9).

To examine the scope of this coupling reaction, a variety of alkynylstannanes were coupled with various aryl iodides and aryl chlorides containing electron-withdrawing or electron-donating groups (Scheme 2). As shown in Table 2, the Stille coupling reactions proceeded smoothly under very mild conditions giving the corresponding products in excellent yields.

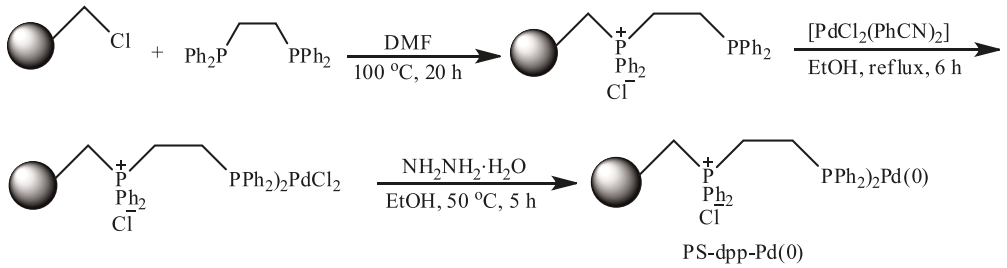
The optimized catalyst system was quite general and compatible with a wide range of functional groups, such as nitro, methoxy, carbonyl, and silyl, on either partner. We attempted to carry out the coupling reactions of heteroaryl iodides such as 3-iodopyridine with alkynylstannanes under the same reaction conditions, but this was unsuccessful; no desired coupled product was detected after 30 h of reaction time.

The developed methodology was also applicable for Stille coupling reactions of vinylstannanes with aryl iodides. The Stille coupling of aryl iodides with a variety of vinylstannanes was investigated (Scheme 3); the experimental results are summarized in Table 3. Stille coupling reactions of a variety of aryl iodides with (*Z*)- or (*E*)-vinylstannanes proceeded smoothly in the presence of a catalytic amount of PS-dpp-Pd(0) in DMF at 65 °C to afford the corresponding coupled products in high yields with retention of the configuration (Table 3, entries 1–6).

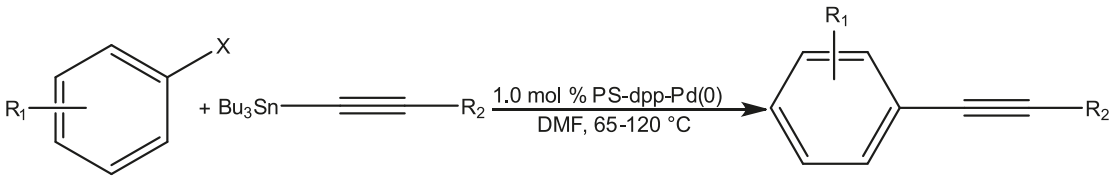
In a typical experiment, after the reaction was completed, PS-dpp-Pd(0) as a catalyst was isolated from the reaction mixture by simple filtration in the workup stage. The catalyst could be recycled by filtering it from the reaction mixture and then washing the solid reagent with water and acetonitrile, followed by drying in an oven. In every experiment, more than 98% of the PS-dpp-Pd(0) was easily recovered from the reaction mixture. Catalytic activity of the recovered catalyst was tested and showed the same activity as the PS-dpp-Pd(0) used for the first time. The nature of the recovered catalyst was traced by infrared (IR) spectroscopy. The results indicated that the catalyst showed no loss of activity as there was no change in its IR spectrum after being reused five times (Table 2, entry 1). The reusability of the catalyst is one of the most important benefits and makes it useful for commercial applications. The high catalytic activity, excellent reusability, and easy accessibility of PS-dpp-Pd(0) makes it a highly attractive supported palladium catalyst for the parallel solution-phase synthesis of diverse libraries of compounds.

In conclusion, we have developed PS-dpp-Pd(0) as a reusable catalyst for the heterogeneous Stille coupling reaction of alkynylstannane with aryl iodides and aryl chlorides under aerobic conditions. The advantages of our heterogeneous catalytic system over others are as follows: (*i*) the catalyst could be conveniently prepared from commercially available reagents; (*ii*) high yields, mild reaction conditions, and a simple workup procedure; and (*iii*) excellent performance and reusability of the catalyst. PS-dpp-Pd(0) as a catalyst is important from an environmental point of view and from the viewpoint of economic considerations because it produces little waste.

Scheme 1.



Scheme 2.



X = I, Cl

Table 1. Stille coupling of iodobenzene with 1-(tributylstannyl)-2-phenylethyne under various reaction conditions.

Entry	Solvent	PS-dpp-Pd(0) (mol %)	Temp. (°C)	Time (h)	Yield (%)[a]
1	THF	2.0	65	24	25
2	PhH	2.0	65	24	20
3	MeCN	2.0	65	24	33
4	NMP	2.0	65	7	80
5	DMF	2.0	25	24	33
6	DMF	2.0	40	24	58
7	DMF	2.0	65	7	85
8	DMF	2.0	80	6	77
9	DMF	1.0	65	10	73
10	DMF	2.5	65	5	80

Note: Reaction conditions: iodobenzene (1 mmol), 1-(tributylstannyl)-2-phenylethyne (1.2 mmol), solvent (3 mL), and aerobic conditions. PS-dpp-Pd(0), diphenylphosphinoethane-functionalized polystyrene resin-supported Pd(0) complex.

[a]Isolated yield.

Experimental

All reagents were purchased from Merck and Sigma-Aldrich and used without further purification. ^{1}H NMR spectra were recorded on Bruker Avance DRX 300 and 400 MHz instruments, using tetramethylsilane (TMS) as the internal standard. IR spectra were recorded on a Shimadzu 470 spectrophotometer. Melting points were taken in open capillary tubes with a Buchi 510 melting point apparatus and were uncorrected. Thin-layer chromatography (TLC) was performed on Merck precoated silica gel 60-F254 plates.

Typical procedure for the Stille coupling reaction

Aryl iodide or aryl chloride (1.0 mmol), PS-dpp-Pd(0) (1.0 mol %), and DMF (3 mL) were added to a flask, and the resulting mixture was stirred at room temperature for 15 min under aerobic conditions. To this suspension was added organostannane (1.2 mmol) and the reaction mixture was stirred at 65 °C for an appropriate time (TLC). The mixture was dissolved in Et_2O (30 mL). The PS-dpp-Pd(0) catalyst was separated from the reaction mixture by filtration after each experiment, washed with water and acetonitrile, and dried carefully before use in subsequent runs. The ethereal solution was treated with 20% aqueous KF (10 mL) for 30 min before being dried and concentrated. The solvent was removed under vacuum and the residue was purified by flash chromatography on silica gel using ethyl acetate / hexane as eluent to give the desired product.

The pure products were characterized by IR, ^{1}H NMR, and melting point. All the products are known compounds and the spectral data and melting points were identical to those reported in the literature.[14–27]

Diphenylacetylene (Table 2, entries 1 and 13)

mp 61–62 °C (lit.[17] mp 60–62 °C). ^{1}H NMR ($CDCl_3$, 300 MHz) δ: 7.55–7.50 (m, 4H), 7.34–7.30 (m, 6H).

(4-Methoxyphenyl)phenylacetylene (Table 2, entry 2)

mp 60–61 °C (lit.[18] mp 57–61 °C). ^{1}H NMR ($CDCl_3$,

Can. J. Chem. Downloaded from www.nrcresearchpress.com by UNIVERSITAT DE VALENCIA on 10/20/12
For personal use only.

Can. J. Chem. Downloaded from www.nrcresearchpress.com by UNIVERSITAT DE VALENCIA on 10/20/12
For personal use only.

Table 2. Stille coupling of aryl iodides and aryl chlorides with alkynylstannanes.

Entry	X	R_1	R_2	Temp. (°C)	Time (h)	Yield (%)[a]
1	I	H	Ph	65	7	85, 81[b]
2	I	4-OMe	Ph	65	7	84
3	I	4-Me	Ph	65	7	83
4	I	4-COMe	Ph	65	7	86
5	I	4-NO_2	Ph	65	7	86
6	I	3-NO_2	Ph	65	7	88
7	I	H	*n*-C_4H_9	65	7	87
8	I	4-Me	*n*-C_4H_9	65	9	86
9	I	4-NO_2	*n*-C_4H_9	65	7	87
10	I	4-OMe	*n*-C_4H_9	65	9	86
11	I	H	Me_3Si	65	9	85
12	I	4-NO_2	Me_3Si	65	8	84
13	Cl	H	Ph	120	11	75
14	Cl	4-Me	Ph	120	11	72
15	Cl	4-NO_2	Ph	120	13	71
16	Cl	H	*n*-C_4H_9	120	12	74
17	Cl	4-Me	*n*-C_4H_9	120	14	74
18	Cl	4-NO_2	*n*-C_4H_9	120	14	73

Note: Reaction conditions: iodobenzene or chlorobenzene (1 mmol), alkynylstannanes (1.2 mmol), diphenylphosphinoethane-functionalized polystyrene resin-supported Pd(0) complex (PS-dpp-Pd(0), 1.0 mol %), DMF (3 mL), and aerobic conditions.

[a]Isolated yield.

[b]Yield after the fifth cycle.

Scheme 3.

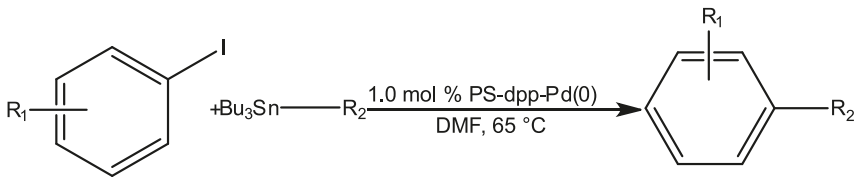


Table 3. Stille coupling of aryl iodides with vinylstannanes.

Entry	R_1	R_2	Time (h)	Yield (%)[a]
1	H	(*E*)-$MeOCH_2CH$=CH	7	88
2	4-OMe	(*E*)-PhCH=CH	9	89
3	4-Me	(*Z*)-PhCH=CH	9	85
4	4-OMe	(*E*)-BuCH=CH	7	87
5	4-NO_2	(*Z*)-PhCH=CH	7	87
6	4-NO_2	(*Z*)-BuCH=CH	7	87

Note: Reaction conditions: iodobenzene (1 mmol), vinylstannanes (1.2 mmol), diphenylphosphinoethane-functionalized polystyrene resin-supported Pd(0) complex (PS-dpp-Pd(0), 1.0 mol %), DMF (3 mL), aerobic conditions, and 65 °C.

[a]Isolated yield.

300 MHz) δ: 7.57–7.51 (m, 2H), 7.50 (d, J = 8.9 Hz, 2H), 7.40–7.35 (m, 3H), 6.91 (d, J = 8.9 Hz, 2H), 3.86 (s, 3H).

***Phenyl*-p-*tolyacetylene* (Table 2, entries 3 and 14)**

mp 70–72 °C (lit.[19] mp 72–73 °C). ^{1}H NMR ($CDCl_3$, 300 MHz) δ: 7.53–7.48 (m, 2H), 7.43 (d, J = 7.91 Hz, 2H), 7.30–7.25 (m, 3H), 7.10 (d, J = 7.91 Hz, 2H), 2.32 (s, 3H).

***(4-Acetylphenyl)phenylacetylene* (Table 2, entry 4)**

mp 95–97 °C (lit.[20] mp 94–96 °C). ^{1}H NMR ($CDCl_3$, 300 MHz) δ: 7.94 (d, J = 8.52 Hz, 2H), 7.60 (d, J = 8.52 Hz, 2H), 7.55–7.51 (m, 2H), 7.39–7.35 (m, 3H), 2.61 (s, 3H).

***(4-Nitrophenyl)phenylacetylene* (Table 2, entries 5 and 15)**

mp 121–122 °C (lit.[21] mp 120–121 °C). ^{1}H NMR ($CDCl_3$, 300 MHz) δ: 8.21 (d, J = 8.83 Hz, 2H), 7.66 (d, J = 8.73 Hz, 2H), 7.57–7.53 (m, 2H), 7.40–7.37 (m, 3H).

***(3-Nitrophenyl)phenylacetylene* (Table 2, entry 6)**

mp 68–70 °C (lit.[22] mp 68–70 °C). ^{1}H NMR ($CDCl_3$, 300 MHz) δ: 8.32 (s, 1H), 8.12 (d, J = 8.10 Hz, 1H), 7.77 (d, J = 7.81 Hz, 1H), 7.52–7.48 (m, 3H), 7.36–7.31 (m, 3H).

***1-Phenylhex-1-yne* (Table 2, entries 7 and 16)**

Oil.[23] ^{1}H NMR ($CDCl_3$, 300 MHz) δ: 7.44–7.41 (m, 2H), 7.30–7.25 (m, 3H), 2.43 (t, J = 7.4 Hz, 2H), 1.65–1.49 (m, 4H), 0.97 (t, J = 7.4 Hz, 3H).

***1-(1-Hexynyl)-4-methylbenzene* (Table 2, entries 8 and 17)**

Oil.[24] ^{1}H NMR ($CDCl_3$, 400 MHz) δ: 7.25 (d, J = 8.5 Hz, 2H), 7.05 (d, J = 8.5 Hz, 2H), 2.37 (t, J = 7.0 Hz, 2H), 2.30 (s, 3H), 1.61–1.42 (m, 4H), 0.92 (t, J = 7.4 Hz, 3H).

***1-(1-Hexynyl)-4-nitrobenzene* (Table 2, entries 9 and 18)**

Oil.[14] ^{1}H NMR ($CDCl_3$, 400 MHz) δ: 8.17 (d, J = 8.9 Hz, 2H), 7.53 (d, J = 8.9 Hz, 2H), 2.50 (t, J = 7.1 Hz, 2H),

Can. J. Chem. Downloaded from www.nrcresearchpress.com by UNIVERSITAT DE VALENCIA on 10/20/12
For personal use only.

1.65–1.58 (m, 2H), 1.53–1.48 (m, 2H), 0.98 (t, J = 7.1 Hz, 3H).

1-(1-Hexynyl)-4-methoxybenzene (Table 2, entry 10)

Oil.[25] ^{1}H NMR ($CDCl_3$, 300 MHz) δ: 7.34 (d, J = 8.8 Hz, 2H), 6.81 (d, J = 8.8 Hz, 2H), 3.82 (s, 3H), 2.91 (t, J = 7.1 Hz, 2H), 1.64–1.45 (m, 4H), 0.97 (t, J = 7.4 Hz, 3H).

Trimethyl(2-phenyl-1-ethynyl)silane (Table 2, entry 11)

Oil.[26] ^{1}H NMR ($CDCl_3$, 300 MHz) δ: 7.47–7.43 (m, 2H), 7.31–7.28 (m, 3H), 0.24 (m, 9H).

Trimethyl[(4-nitrophenyl)ethynyl]silane (Table 2, entry 12)

Oil.[10] ^{1}H NMR ($CDCl_3$, 300 MHz) δ: 8.16 (d, J = 8.7 Hz, 2H), 7.61 (d, J = 8.7 Hz, 2H), 0.18 (s, 9H).

(E)-1-(3-Methoxyprop-1-enyl)benzene (Table 3, entry 1)

Oil.[16] ^{1}H NMR ($CDCl_3$, 300 MHz) δ: 7.42–7.20 (m, 5H), 6.62 (d, J = 15.9 Hz, 1H), 6.27–6.30 (m, 1H), 4.04 (d, J = 6.1 Hz, 2H), 3.37 (s, 3H).

(E)-1-Methoxy-4-styrylbenzene (Table 3, entry 2)

mp 135–136 °C (lit.[16] mp 134–135 °C). ^{1}H NMR ($CDCl_3$, 400 MHz) δ: 7.52 (d, J = 7.5 Hz, 2H), 7.47 (d, J = 8.6 Hz, 2H), 7.35 (t, J = 7.5 Hz, 2H), 7.27–7.22 (m, 1H), 7.09 (d, J = 16.7 Hz, 1H), 7.00 (d, J = 16.7 Hz, 1H), 6.92 (d, J = 8.7 Hz, 2H), 3.85 (s, 3H).

(Z)-1-Methyl-4-styrylbenzene (Table 3, entry 3)

Oil.[16] ^{1}H NMR ($CDCl_3$, 400 MHz) δ: 7.30–7.20 (m, 5H), 7.17 (d, J = 8.0 Hz, 2H), 7.06 (d, J = 8.0 Hz, 2H), 6.60 (s, 2H), 2.34 (s, 3H).

(E)-1-(Hex-1-enyl)-4-methoxybenzene (Table 3, entry 4)

Oil.[16] ^{1}H NMR ($CDCl_3$, 400 MHz) δ: 7.25 (d, J = 8.5 Hz, 2H), 6.82 (d, J = 8.5 Hz, 2H), 6.29 (d, J = 15.4 Hz, 1H), 5.93 (dt, J = 15.4, 7.0 Hz, 1H), 3.82 (s, 3H), 2.20–2.15 (m, 2H), 1.45–1.33 (m, 4H), 0.91 (t, J = 7.0 Hz, 3H).

(Z)-1-Nitro-4-styrylbenzene (Table 3, entry 5)

mp 60–62 °C (lit.[16] mp 60.5–61.5 °C). ^{1}H NMR ($CDCl_3$, 400 MHz) δ: 8.10 (d, J = 8.7 Hz, 2H), 7.40 (d, J = 8.7 Hz, 2H), 7.25–7.18 (m, 5H), 6.80 (d, J = 12.5 Hz, 1H), 6.60 (d, J = 12.5 Hz, 1H).

(Z)-1-(Hex-1-enyl)-4-nitrobenzene (Table 3, entry 6)

Oil.[16] ^{1}H NMR ($CDCl_3$, 400 MHz) δ: 8.20 (d, J = 8.6 Hz, 2H), 7.40 (d, J = 8.6 Hz, 2H), 6.44 (d, J = 11.5 Hz, 1H), 5.84 (dt, J = 11.5, 7.0 Hz, 1H), 2.35–2.30 (m, 2H), 1.49–1.43 (m, 2H), 1.39–1.33 (m, 2H), 0.89 (t, J = 7.0 Hz, 3H).

Acknowledgement

We are thankful to the Islamic Azad University, Ahar Branch, for partial support of this research.

References

(1) (a) Stille, J. K. *Angew. Chem. Int. Ed. Engl.* **1986**, *25* (6), 508. doi:10.1002/anie.198605081; (b) Diederich, F.; Stang, P. J. *Metal-Catalyzed Cross-Coupling Reactions;* Wiley-VCH: Weinheim, 1998; (c) Shirakawa, E.; Hiyama, T. *J. Organomet. Chem.* **1999**, *576* (1–2), 169. doi:10.1016/S0022-328X(98)01056-0; (d) Miyaura, N. *Cross-Coupling Reactions;* Springer: Berlin, 2002; (e) Hegedus, L. S. In *Organometallics in Synthesis;* Schlosser, M., Ed.; Wiley: Chichester, 2002; p 1123; (f) Negishi, E., Ed.; *Handbook of Organopalladium Chemistry for Organic Synthesis;* Wiley-Interscience: New York, 2002; (g) Littke, A. F.; Fu, G. C. *Angew. Chem. Int. Ed.* **2002**, *41* (22), 4176. doi:10.1002/1521-3773(20021115)41:22<4176::AID-ANIE4176>3.0.CO;2-U.

(2) (a) Littke, A. F.; Schwarz, L.; Fu, G. C. *J. Am. Chem. Soc.* **2002**, *124* (22), 6343. and references cited therein. doi:10.1021/ja020012f; (b) Kim, Y. M.; Yu, S. *J. Am. Chem. Soc.* **2003**, *125* (7), 1696. doi:10.1021/ja028966t; (c) Menzel, K.; Fu, G. C. *J. Am. Chem. Soc.* **2003**, *125* (13), 3718. doi:10.1021/ja0344563; (d) Kim, W.-S.; Kim, H.-J.; Cho, C.-G. *J. Am. Chem. Soc.* **2003**, *125* (47), 14288. doi:10.1021/ja037043a; (e) Dubbaka, S. R.; Vogel, P. *J. Am. Chem. Soc.* **2003**, *125* (50), 15292. doi:10.1021/ja038328q; (f) Wolf, C.; Lerebours, R. *J. Org. Chem.* **2003**, *68* (18), 7077. doi:10.1021/jo034758n; (g) Wolf, C.; Lerebours, R. *J. Org. Chem.* **2003**, *68* (19), 7551. doi:10.1021/jo0347056; (h) Mazzola, R. D., Jr; Giese, S.; Benson, C.; West, F. G. *J. Org. Chem.* **2004**, *69* (1), 220. doi:10.1021/jo034788q; (i) Högenauer, K. *Synlett* **2001**, *2001* (6), 878. doi:10.1055/s-2001-14619; (j) Scrivanti, A.; Matteoli, U.; Beghetto, V.; Antonaroli, S.; Crociani, B. *Tetrahedron* **2002**, *58* (34), 6881. doi:10.1016/S0040-4020(02)00733-0; (k) Kim, N.; Kwon, M. S.; Park, C. M.; Park, J. *Tetrahedron Lett.* **2004**, *45* (38), 7057. doi:10.1016/j.tetlet.2004.07.126.

(3) (a) Herrmann, W. A.; Öfele, K.; von Preysing, D.; Schneider, S. K. *J. Organomet. Chem.* **2003**, *687* (2), 229. doi:10.1016/j.jorganchem.2003.07.028; (b) Hillier, A. C.; Grasa, G. A.; Viciu, M. S.; Lee, H. M.; Yang, C.; Nolan, S. P. *J. Organomet. Chem.* **2002**, *653* (1–2), 69. doi:10.1016/S0022-328X(02)01154-3.

(4) (a) Alonso, D. A.; Nájera, C.; Pacheco, M. C. *Org. Lett.* **2000**, *2* (13), 1823. doi:10.1021/ol0058644; (b) Choudary, B. M.; Madhi, S.; Chowdari, N. S.; Kantam, M. L.; Sreedhar, B. *J. Am. Chem. Soc.* **2002**, *124* (47), 14127. doi:10.1021/ja026975w; (c) Amatore, C.; Bahsoun, A. A.; Jutand, A.; Meyer, G.; Ntepe, A. N.; Ricard, L. *J. Am. Chem. Soc.* **2003**, *125* (14), 4212. doi:10.1021/ja0204978; (d) Minière, S.; Cintrat, J.-C. *J. Org. Chem.* **2001**, *66* (22), 7385. doi:10.1021/jo015824t.

(5) van Asselt, R.; Elsevier, C. J. *Tetrahedron* **1994**, *50* (2), 323. doi:10.1016/S0040-4020(01)80757-2.

(6) (a) Clapham, B.; Reger, T. S.; Janda, K. D. *Tetrahedron* **2001**, *57* (22), 4637. doi:10.1016/S0040-4020(01)00298-8; (b) Schwarz, J.; Bohm, V. P. W.; Gardiner, M. G.; Grosche, M.; Herrmann, W. A.; Hieringer, W.; Raudaschl-Sieber, G. *Chemistry* **2000**, *6* (10), 1773. doi:10.1002/(SICI)1521-3765(20000515)6:10<1773::AID-CHEM1773>3.0.CO;2-P.

(7) (a) Nasrollahzadeh, M.; Bayat, Y.; Habibi, D.; Moshaee, S. *Tetrahedron Lett.* **2009**, *50* (31), 4435. doi:10.1016/j.tetlet.2009.05.048; (b) Habibi, D.; Nasrollahzadeh, M. *Synth. Commun.* **2010**, *40* (21), 3159. doi:10.1080/00397910903370683; (c) Modarresi-Alam, A. R.; Nasrollahzadeh, M.; Khamooshi, F. *Arkivoc* **2007**, (xvi), 234; (d) Modarresi-Alam, A. R.; Khamooshi, F.; Nasrollahzadeh, M.; Amirazizi, H. A. *Tetrahedron* **2007**, *63* (36), 8723. doi:10.1016/j.tet.2007.06.048; (e) Mohammadi, B.; Hosseini Jamkarani, S. M.; Kamali, T. A.; Nasrollahzadeh, M.; Mohajeri, A. *Turk. J. Chem* **2010**, *34*, 613 doi:10.3906/kim-0906-28; (f) Nasrollahzadeh, M.; Habibi, D.; Shahkarami, Z.; Bayat, Y. *Tetrahedron* **2009**, *65* (51), 10715. doi:10.1016/j.tet.2009.10.029; (g) Habibi, D.; Nasrollahzadeh, M.; Bayat, Y. *Synth.*

Commun. **2011**, *41* (14), 2135. doi:10.1080/00397911.2010.497728; (h) Habibi, D.; Nasrollahzadeh, M.; Kamali, T. A. *Green Chem.* **2011**, *13* (12), 3499. doi:10.1039/c1gc15245a.

(8) Phan, N. T. S.; Brown, D. H.; Adams, H.; Spey, S. E.; Styring, P. *Dalton Trans.* **2004**, (9): 1348. doi:10.1039/b316553c.

(9) (a) Phan, N. T. S.; Brown, D. H.; Styring, P. *Tetrahedron Lett.* **2004**, *45* (42), 7915. doi:10.1016/j.tetlet.2004.08.153; (b) Byun, J. W.; Lee, Y. S. *Tetrahedron Lett.* **2004**, *45* (9), 1837. doi:10.1016/j.tetlet.2004.01.021; (c) Vassylyev, O.; Chen, J.; Panarello, A. P.; Khinast, J. G. *Tetrahedron Lett.* **2005**, *46* (40), 6865. doi:10.1016/j.tetlet.2005.08.029; (d) Shimizu, K.; Koizumi, S.; Hatamachi, T.; Yoshida, H.; Komai, S.; Kodama, T.; Kitayama, Y. *J. Catal.* **2004**, *228* (1), 141. doi:10.1016/j.jcat.2004.09.005.

(10) Bakherad, M.; Keivanloo, A.; Bahramian, B.; Mihanparast, S. *Tetrahedron Lett.* **2009**, *50* (46), 6418. doi:10.1016/j.tetlet.2009.05.118.

(11) (a) Dell'Anna, M. M.; Lofu, A.; Mastrorilli, P.; Mucciante, V.; Nobile, C. F. *J. Organomet. Chem.* **2006**, *691* (1-2), 131. doi:10.1016/j.jorganchem.2005.07.104; (b) Pathak, S.; Greci, M. T.; Kwong, R. C.; Mercado, K.; Prakash, G. K. S.; Olah, G. A.; Thompson, M. E. *Chem. Mater.* **2000**, *12* (7), 1985. doi:10.1021/cm0001556.

(12) Bakherad, M.; Keivanloo, A.; Bahramian, B.; Kamali, A. T. *J. Braz. Chem. Soc.* **2009**, *20* (5), 907. doi:10.1590/S0103-50532009000500015.

(13) (a) Kamali, A. T.; Bakherad, M.; Nasrollahzadeh, M.; Farhangi, S.; Habibi, D. *Tetrahedron Lett.* **2009**, *50* (39), 5459. doi:10.1016/j.tetlet.2009.07.017; (b) Kamali, T. A.; Habibi, D.; Nasrollahzadeh, M. *Synlett* **2009**, 2601; (c) Bakherad, M.; Keivanloo, A.; Tajbakhsh, M.; Kamali, A. T. *Synth. Commun.* **2009**, *40* (2), 173. doi:10.1080/00397910802573155.

(14) Liang, B.; Dai, M.; Chen, J.; Yang, Z. *J. Org. Chem.* **2005**, *70* (1), 391. doi:10.1021/jo048599z.

(15) Colvin, E. W.; Hamill, B. J. *J. Chem. Soc., Perkin Trans. 1* **1977**, (8): 869. doi:10.1039/p19770000869.

(16) Zhao, H.; Wang, Y.; Sha, J.; Sheng, S.; Cai, M. *Tetrahedron* **2008**, *64* (32), 7517. doi:10.1016/j.tet.2008.05.120.

(17) Carpino, L. A.; Chen, H.-W. *J. Am. Chem. Soc.* **1979**, *101* (2), 390. doi:10.1021/ja00496a019.

(18) Huggins, J. M.; Bergman, R. G. *J. Am. Chem. Soc.* **1981**, *103* (11), 3002. doi:10.1021/ja00401a016.

(19) Paquette, L. A.; Wittenbrook, L. S. *J. Am. Chem. Soc.* **1967**, *89* (17), 4483. doi:10.1021/ja00993a042.

(20) Arcadi, A.; Cacchi, S.; Fabrizi, G.; Marinelli, F.; Pace, P. *Eur. J. Org. Chem.* **1999**, *1999* (12), 3305. doi:10.1002/(SICI)1099-0690(199912)1999:12<3305::AID-EJOC3305>3.0.CO;2-O.

(21) Hunter, D. H.; Cram, D. J. *J. Am. Chem. Soc.* **1966**, *88* (24), 5765. doi:10.1021/ja00976a018.

(22) Chow, H.-F.; Wan, C.-W.; Low, K.-H.; Yeung, Y.-Y. *J. Org. Chem.* **2001**, *66* (5), 1910. doi:10.1021/jo001538q.

(23) Crisp, G. T.; Turner, P. D.; Stephens, K. A. *J. Organomet. Chem.* **1998**, *570* (2), 219. doi:10.1016/S0022-328X(98)00765-7.

(24) Katritzky, A. R.; Wang, J.; Karodia, N.; Li, J. *J. Org. Chem.* **1997**, *62* (12), 4142. doi:10.1021/jo962291t.

(25) Cheng, J.; Sun, Y.; Wang, F.; Guo, M.; Xu, J.-H.; Pan, Y.; Zhang, Z. *J. Org. Chem.* **2004**, *69* (16), 5428. doi:10.1021/jo049379o.

(26) Cai, M.; Zhou, Z.; Jiang, J. *Eur. J. Org. Chem.* **2006**, *2006* (6), 1400. doi:10.1002/ejoc.200501002.

(27) Cai, M.-Z.; Song, C.-S.; Huang, X. *Synthesis* **1997**, *1997* (5), 521. doi:10.1055/s-1997-1227.

Can. J. Chem. Downloaded from www.nrcresearchpress.com by UNIVERSITAT DE VALENCIA on 10/20/12
For personal use only.

MINIREVIEW / MINISYNTHÈSE

Three different mechanisms for azo-ether hydrolyses in aqueous acid[1]

Robin A. Cox and Erwin Buncel

Can. J. Chem. Downloaded from www.nrcresearchpress.com by MCGILL UNIVERSITY on 02/02/13
For personal use only.

Abstract: It has been shown recently that most ethers hydrolyze in aqueous acid media not by the traditional A1 or A2 process, but by a mechanism involving rate-determining proton transfer to the substrate, concerted with C–O bond cleavage. The reactions of azoethers are more complicated, because the azo group can be protonated in the acid reaction medium as well. This protonation has to be accounted for in the kinetic analysis. Often it simply ties up the substrate in an unreactive form; the hydrolysis reaction slows down as a result of the azo-protonated compound not being the reactant in the hydrolysis. However, there are other possibilities. If the ether group is suitably located in the substrate the azo-protonated compound can react with three water molecules (a "water wire") in a fast reaction, and the alkoxy group is lost as a result. Depending on the acidity, in this mechanism either the initial three-water attack, or the breakup of the resulting intermediate, can be rate-determining, and both of these were observed. A third possibility is that ring protonation of suitable substrates can occur, giving delocalized carbocations that can form a hydrolysis product in subsequent fast reactions. Thus, three different hydrolysis mechanisms for azoethers in acidic media can be observed. Six azoethers were studied, one of which contained two methoxy groups. Both of these hydrolyzed, but by different mechanisms.

Key words: azo compounds, ethers, hydrolysis, excess acidity, mechanism, acid media.

Résumé : Il a été démontré récemment que l'hydrolyse de la plupart des éthers dans des milieux aqueux ne se fait pas par le processus traditionnel A1 ou A2, mais que l'étape qui détermine la vitesse implique plutôt le transfert d'un proton vers le substrat, en concertation avec le clivage de la liaison C–O. Les réactions des azoéthers sont plus compliquées parce que le groupe azo peut aussi être protoné dans le milieu réactionnel acide. Il faut expliquer cette protonation dans l'analyse cinétique. Il arrive souvent qu'elle ne donne lieu qu'à une simple liaison avec le substrat sous une forme qui n'est pas réactive; il en résulte que la réaction d'hydrolyse s'en trouve ralentie en raison du fait que le composé azo protoné ne donne pas lieu à une hydrolyse. Toutefois, il existe d'autres possibilités. Si le groupe éther est bien situé dans le substrat, le composé azo protoné peut alors réagir avec trois molécules d'eau (une chaîne d'eau) dans une réaction rapide et il en résulte que le groupe alkoxy est ainsi perdu. Dans ce mécanisme, suivant l'acidité du milieu, l'étape déterminante de la vitesse de la réaction peut aussi bien être l'attaque initiale par trois molécules d'eau ou une rupture de l'intermédiaire qui en résulte et les deux cas ont pu être observés. Il existe une troisième possibilité, une protonation du cycle de substrats adéquats peut se produire conduisant à des carbocations délocalisés qui peuvent donner lieu à la formation d'un produit d'hydrolyse dans des réactions rapides subséquentes. Il est donc possible d'observer trois mécanismes différents d'hydrolyse pour les azoéthers en milieu acide. On a étudié six azoéthers, dont un qui contenait deux groupes méthoxy. Ces deux groupes ont été hydrolysés, mais par des mécanismes différents.

Mots-clés : composés azo, éthers, hydrolyse, acidité en excès, mécanisme, milieu acide.

[Traduit par la Rédaction]

In recent papers it has been shown that many ethers hydrolyze, not by a traditional A1 or A2 process, but in a concerted fashion as shown in Scheme 1.[3–5] (In Scheme 1 and subsequently, "aq" is meant to indicate the medium acting as a source or a sink for protons or water molecules; aq does not appear in the kinetic analysis.)[3–5] If the substrate is capable of forming a carbocation which has a long enough lifetime in the medium, it will do so, and the carbocation will then react with water (or presumably with another nucleophile if present), or rearrange and then react, and so on;[3] if the substrate cannot form a stable carbocation, reaction with a nucleophile in the medium (usually water) is concerted

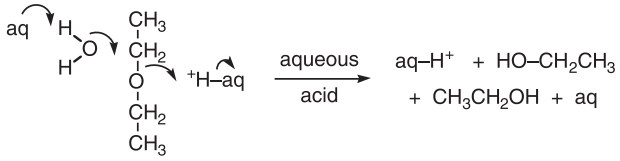
Received 28 February 2012. Accepted 24 July 2012. Published at www.nrcresearchpress.com/cjc on 5 November 2012.

R.A. Cox. 16 Guild Hall Drive, Scarborough, ON M1R 3Z8, Canada.
E. Buncel. Department of Chemistry, Queen's University, Kingston, ON K7L 3N6, Canada.

Corresponding authors: Robin A. Cox (e-mail: robin.a.cox@sympatico.ca) and Erwin Buncel (e-mail: buncele@chem.queensu.ca).

Dedicated to Professor Joe Bunnett, congratulating him on entering his ninth decade.

Scheme 1.



with the proton transfer, as shown in Scheme 1 for diethyl ether.[3–5]

The principle at work here was first enunciated by Jencks,[6] as an "enforced mechanism". If an intermediate does not have a long enough lifetime in the reaction medium (i.e., exist there for at least a couple of molecular vibrations, having, say, a lifetime of greater than about 10^{-13} s),[5] it cannot be involved in the reaction, and a mechanism without it is "enforced".[6] Oxygen-protonated intermediates in which the positive charge is localized on the oxygen and cannot be dispersed (usually by resonance) do not have long enough lifetimes to be reaction intermediates.[3–6] Nor do primary and most secondary carbocations.[5] Some carbonyl-protonated species, and some acylium ions, are unlikely to have long enough lifetimes to be reaction intermediates in dilute acid either.[5]

Specific protonated water species, such as H_3O^+, do not exist as such in water. If they had lifetimes long enough to be reaction intermediates they would have detectable IR or Raman spectra, but they do not; this has been discussed in some detail in recent reviews.[4,5] Thus, usually individual protonated water species are not involved in ether hydrolysis in aqueous acid media; the proton source is written as "H^+_{aq}".[3–5]

We have been interested in aromatic azo and azoxy compounds for over 50 years now;[7] most recently, we have looked at azoxypyridine rearrangements.[2] A number of these compounds have been aromatic azoethers,[7–11] and this paper concerns the several different hydrolysis mechanisms that we have found for these. The structures of the compounds dealt with here (**1**–**7**) are given in Scheme 2. (Compound **6** is formed as a result of the first hydrolysis of **5**.)[11] All of the azoethers **1**–**7** protonate on the azo group in relatively dilute acid; some contain a pyridine nitrogen that protonates in the pH region,[9,11] and so the substrates **3**–**6** in Scheme 2 are assumed to be already protonated there. The pK_{SH^+} values for the azo groups must be known before the kinetics can be analyzed. These and the related m^* values are listed in Table 1.

The values for **3**–**7**, determined using the excess acidity technique, are already in the literature;[10,11] no errors were given for **7**.[10] Those for **1** and **2**, which had not been determined that way, were found using eq. [1],[12] substituting eq. [2] into it, and, using the listed UV absorbance difference values (ΔA) as a function of acid concentration,[7] curve-fitting the result.[13]

$$[1] \qquad \log I - \log C_{H^+_{aq}} = m^* X + pK_{SH^+}$$

$$[2] \qquad I = C_{SH^+}/C_S = \frac{\Delta A - \Delta A_S}{\Delta A_{SH^+} - \Delta A} = \text{antilog}\,(m^* X + pK_{SH^+} + \log C_{H^+_{aq}})$$

Scheme 2.

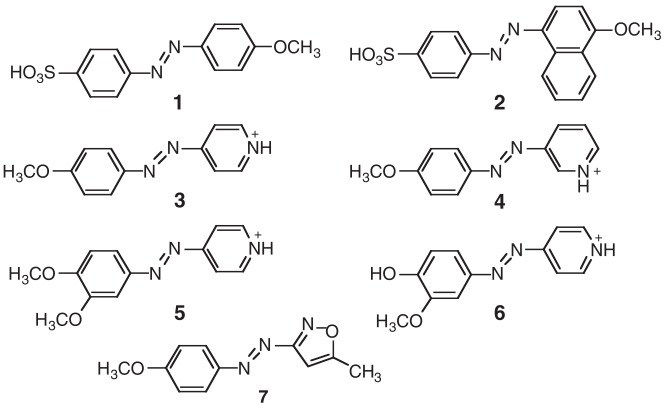


Table 1. Values of pK_{SH^+} and m^* for **1**–**7**.

Compound	pK_{SH^+}	m^*	Ref.
1	–2.133±0.026	1.542±0.025	This work
2	–0.959±0.027	1.472±0.048	This work
3	–2.66±0.24	0.80±0.10	11
4	–4.43±0.14	1.49±0.06	11
5	–3.66±0.32	0.80±0.10	11
6	–3.66±0.32	0.80±0.10	11
7	–5.50	1.1	10

Note: All compounds were measured at 25 °C in aqueous H_2SO_4 except for **2**, which was measured in aqueous HCl.

In these equations I is the ionization ratio defined in eq. [2], C is molar concentration, S and SH^+ are the substrate and the protonated substrate, respectively, and H^+_{aq} is the solvated proton; its concentration is basically the acid molarity for aqueous HCl and $HClO_4$. Values of these quantities, and of the excess acidity X, were obtained from the literature.[14] The pK_{SH^+} and m^* values obtained are given in Table 1. The slope parameter m^* essentially describes the type of substrate concerned, values being 1.0 for primary amines, 1.3 for tertiary amines, 0.8 for amides, and so on.[12] The pK_{SH^+} values determined at the time, –1.45 for **1** and –0.74 for **2**, are really the H_0 values at half-protonation,[7] and these were deemed not to be sufficiently accurate for this work. Both are insufficiently negative as they do not follow H_0 (which would imply an m^* value of 1.0),[12] and the measured values in this work are closer to 1.5 (Table 1).

The reaction rate data obtained for **1**–**7** are also analyzed using the excess acidity method.[14,15] We have found this to be a very useful technique for determining the mechanisms by which azo and azoxy compounds react in acid media,[2,11,16] and many other organic reactions have been studied as well.[3–5,14,17] Summarizing briefly, this method works as follows.[14,15]

$$[3] \qquad k_\psi C_S = k_0 a_S a_{H^+_{aq}}/f_\ddagger = k_0 C_S C_{H^+_{aq}} \frac{f_S f_{H^+_{aq}}}{f_\ddagger}$$

$$[4] \qquad \log \frac{f_S f_{H^+_{aq}}}{f_\ddagger} = m^\ddagger \log \frac{f_{B^*} f_{H^+_{aq}}}{f_{B^*H^+}} = m^\ddagger X$$

$$[5] \qquad \log k_\psi - \log C_{H^+_{aq}} = \log k_0 + m^\ddagger X$$

Can. J. Chem. Downloaded from www.nrcresearchpress.com by MCGILL UNIVERSITY on 02/02/13
For personal use only.

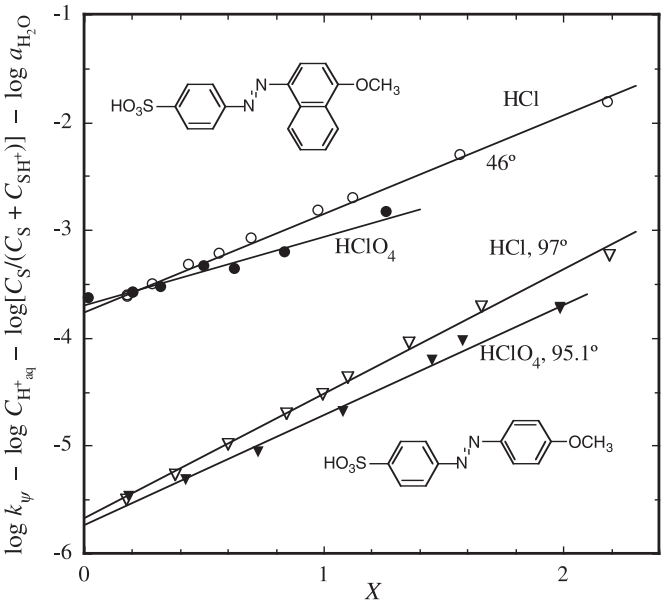
Can. J. Chem. Downloaded from www.nrcresearchpress.com by MCGILL UNIVERSITY on 02/02/13
For personal use only.

Table 2. All of the slopes, intercepts, and other kinetic correlation information obtained for **1**–**7**.

Compound[a]	Medium, temp. (°C)[b]	r[c]	N[d]	$\pm\sigma_y$[e]	$m^{\ddagger}$ slope	logk_0[b]
1	aq HCl, 97.0	0.998	9	0.052	1.155±0.029	–5.668±0.034
	aq $HClO_4$, 95.1	0.997	7	0.059	1.022±0.033	–5.732±0.044
2	aq HCl, 46	0.998	11	0.042	0.911±0.021	–3.754±0.021
	aq $HClO_4$, 46	0.982	7	0.056	0.643±0.055	–3.698±0.037
3	aq H_2SO_4, low acid	0.998	10	0.062	1.841±0.062	–3.390±0.038[f]
	aq H_2SO_4, high acid	0.998	13	0.047	1.029±0.026	–2.168±0.064[g]
4	aq H_2SO_4	0.9994	21	0.033	1.0268±0.0090	–6.400±0.018[h]
5	aq H_2SO_4, low acid	0.990	8	0.11	1.704±0.099	–2.046±0.067
	aq H_2SO_4, high acid	0.996	8(1)	0.090	0.849±0.033	–1.247±0.071
6	aq H_2SO_4	0.995	16(1)	0.040	0.2482±0.0074	–5.930±0.021
7	aq H_2SO_4, 30	0.999	9	0.14	1.786±0.034	–10.72±0.12
	aq H_2SO_4, 60	0.999	5	0.033	1.170±0.027	–7.269±0.068

[a]See Scheme 2.
[b]At 25 °C unless noted.
[c]Correlation coefficient.
[d]Number of points. Any rejected by the program used as not being part of the data set, to 95% confidence, are in parentheses.
[e]Root-mean-square deviation between experimental points and fitted line. All the other errors in the table are standard deviations.
[f]Activation enthalpy, 22.5 ± 1.0 kcal mol^{-1} (1 cal = 4.184 J); activation entropy, –22.3 ± 3.5 cal deg^{-1} mol^{-1}.
[g]Activation enthalpy, 17.20 ± 0.69 kcal mol^{-1}; activation entropy, –34.6 ± 2.3 cal deg^{-1} mol^{-1}.
[h]Activation enthalpy, 22.07 ± 0.40 kcal mol^{-1}; activation entropy, –21.7 ± 1.3 cal deg^{-1} mol^{-1}.

Fig. 1. Excess acidity plots of the left-hand side of eq. [6] against X, for **1** and **2**. The theoretical lines are drawn using the slope and intercept values given in Table 2.



Since a proton transfer is part of the rate-determining step in these reactions (Scheme 1), S and H^+_{aq} reacting in the slow step in the mechanism usually referred to by the term A-S_E2, the rate equation that applies is eq. [3], C_S canceling out on both sides.[14] Here, k_ψ are the experimentally observed pseudo-first-order rate constants, k_0 is the rate constant in the standard state (essentially infinite dilution in pure water),[14] a is molar activity, and f is the molar activity coefficient. The excess acidity method then makes the assumption of eq. [4], to which, after testing hundreds of examples, no exceptions have yet been found;[14] B* is a standard base. Taking logs of eq. [3], substituting eq. [4], and rearranging gives the excess acidity equation used in this work (eq. [5]).[3]

A plot of $\log k_\psi - \log C_{H^+_{aq}}$ against X will be linear if eq. [5] applies to the reaction directly. The slope parameter is given as $m^{\ddagger}$, since it refers to the transition state.[3,4] Examples of this behavior have been found for several ethers, ones capable of forming stable carbocations during hydrolysis under the reaction conditions used.[3] If the eq. [5] plot is not linear, it can be modified to see if any other species is involved in the reaction, along with the substrate and H^+_{aq} (e.g., a water molecule is involved in Scheme 1), by subtracting, for example, the molar water activity a_{H_2O} from the left-hand side. (Updated values of the water activity are listed.[14]) Many examples of this behavior were also found in the ether hydrolysis studies.[3–5]

Here, the azo substrates are also protonated on the azo group in an equilibrium sense, and the degree of protonation is dependent on the medium acidity. This too causes curvature in excess acidity plots, and it can also be accounted for by subtracting a protonation correction term, $\log[C_S/(C_S + C_{SH^+})]$, from the left-hand side of eq. [5].[14]

$$[6] \quad \log k_\psi - \log\frac{C_S}{C_S + C_{SH^+}} - \log C_{H^+_{aq}} - \log a_{H_2O} = \log k_0 + m^{\ddagger}X$$

These modifications produce eq. [6], which, except for the addition of the protonation correction term, is the same rate equation already found to apply to many ethers.[3–5] The protonation correction terms were calculated using eq. [1] and the pK_{SH^+} values given in Table 1. These values, measured at 25 °C, were corrected to the reaction temperature, if this was different, using the assumption that the free energy of protonation is temperature-independent, and the equation $\Delta G^\circ = 2.303\ RT\mathrm{p}K_{SH^+}$, as we have done before.[18] This seems to be a better assumption than assuming that pK_{SH^+} itself is temperature-independent, but there is little evidence either way.[19]

Scheme 3.

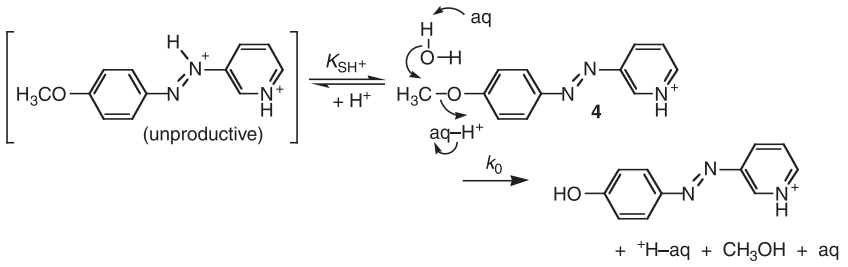
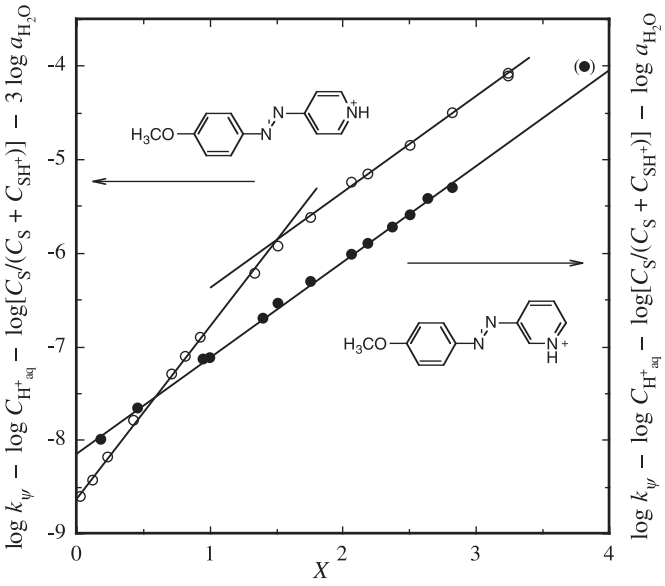


Fig. 2. Excess acidity plots against X, for the hydrolyses of **3** and **4** in aqueous H_2SO_4.



$$[7] \qquad \log k_0 = 10.31883 + \log T - \frac{\Delta G_\Theta^{\ddagger}}{R\Theta \ln 10} + \frac{\Delta H_\Theta^{\ddagger}}{R\Theta \ln 10} \cdot \frac{T - \Theta}{T}$$

If rate constants at only one reaction temperature are available, the quantity $\log k_0$ perforce refers to it. However, if data at several temperatures are available, it can be expanded according to the Clarke and Glew formulation[20] (better in practice than the Eyring equation[21]) as shown in eq. [7]. We find this formulation a more natural one to use, giving numbers with errors that are independent of one another.[20] Here, the absolute reaction temperature is T and Θ is the standard-state temperature of 298.15 K, 25 °C. The gas constant is R (1.98589 cal K^{-1} mol^{-1} here; 1 cal = 4.184 J) and the numerical term contains the Boltzmann and Planck constants required by the theory.[21] The entropy of activation $\Delta S_\Theta^{\ddagger}$ is readily obtained via $\Delta G_\Theta^{\ddagger} = \Delta H_\Theta^{\ddagger} - \Theta \Delta S_\Theta^{\ddagger}$; the subscript Θ means that these values are the standard-state 25 °C values.[20]

All of the rate constant data[7–11] for **1**–**7** were initially analyzed using eq. [6] (and eq. [7], if necessary). A simple linear regression of $\log k_\psi - \log C_{H^+_{aq}} - \log[C_S/(C_S + C_{SH^+})] - \log a_{H_2O}$ vs X was used if data at only one temperature were available; for data at several temperatures, a double linear regression of $\log k_\psi - \log C_{H^+_{aq}} - \log[C_S/(C_S + C_{SH^+})] - \log a_{H_2O} - \log T$ vs X and $(T - \Theta)/T$ was used. The programs used discarded data points that, to 95% confidence, were not part of the same data set as the rest;[22] here, this only happened twice. All of the derived quantities obtained in this work are given in Table 2. The results for **1** and **2** are illustrated in Fig. 1.

As can be seen from Fig. 1, compounds **1** and **2** follow eq. [6] exactly, with intercepts (k_0) that are, within experimental error, the same in both aqueous HCl and aqueous $HClO_4$ media (Table 2). If the protonation correction term is not included, the plots of rate constants against acidity curve downwards,[7,8] which shows that the azo-protonated form is not the reactant; protonation on the azo-group must deactivate the molecule. The slopes are different in the two different acid media, with the hydrolysis reaction being faster in aqueous HCl. This undoubtedly reflects the fact that there is an additional nucleophile present in that medium, chloride ion, which can participate in Scheme 1 too. It would probably be possible to obtain some idea of its catalytic effect by working on the difference between the two acid systems (ClO_4^- not being nucleophilic), but this was not done as the error would be quite high, and the measurement temperatures in the two acids were not quite the same for **1**.[7,8] It is sufficient to see that reaction is in fact faster in aqueous HCl. Amazingly, these are the only ether hydrolyses in the literature in which kinetic measurements in aqueous HCl media are reported.[3] There are none at all reported in aqueous HBr.[3]

Not all of the compounds obeyed eq. [6]. Compounds **1**, **2**, **4**, and **7** did; the excess acidity analyses given here for the Scheme 1 and (or) Scheme 3 mechanism being better than any of the previously reported mechanistic analyses for these compounds.[9,10] Compounds **3** and **5** followed an equation involving three water molecules rather than one (i.e., subtracting three times $\log a_{H_2O}$ rather than one in eq. [6] was required to achieve linearity), and compound **6** did not need the log water activity to be subtracted at all.

Figure 2 gives the excess acidity plots for **3** and **4**. Compound **4** (right-hand axis) also follows eq. [6] exactly; the reaction mechanism for **4** (and **1**, **2**, and **7**) is shown in Scheme 3. However, it is apparent from Fig. 2 that compound **3** follows a different mechanism, as we have found before,[11] one involving three water molecules. This is given here as Scheme 4.[11]

The protonated substrate reacts by adding water at the para position, which is activated by the presence of the positive charge on the azo group. Three water molecules are involved in a five-membered ring; the highly structured aqueous solvent does not need to reorganize first, as the structure is already there.[4] This behavior, involving cycles of two or three water molecules, is quite common;[4] a recent paper refers to this as a "water wire",[23] terminology that may well become more common. We have reported on this before;[11] the data

Can. J. Chem. Downloaded from www.nrcresearchpress.com by MCGILL UNIVERSITY on 02/02/13
For personal use only.

Scheme 4.

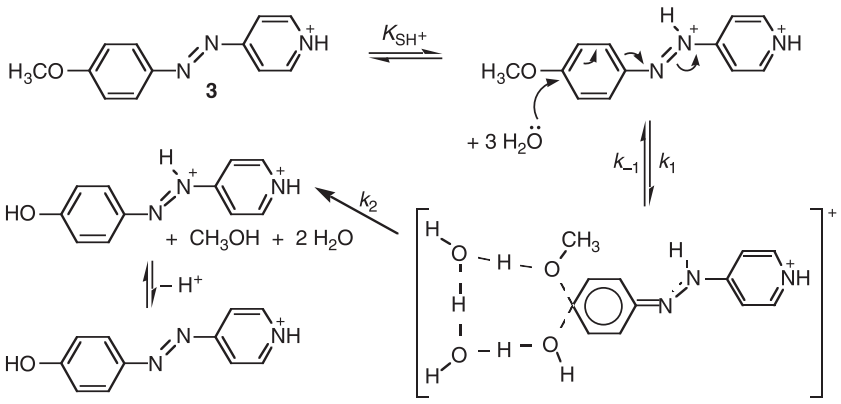
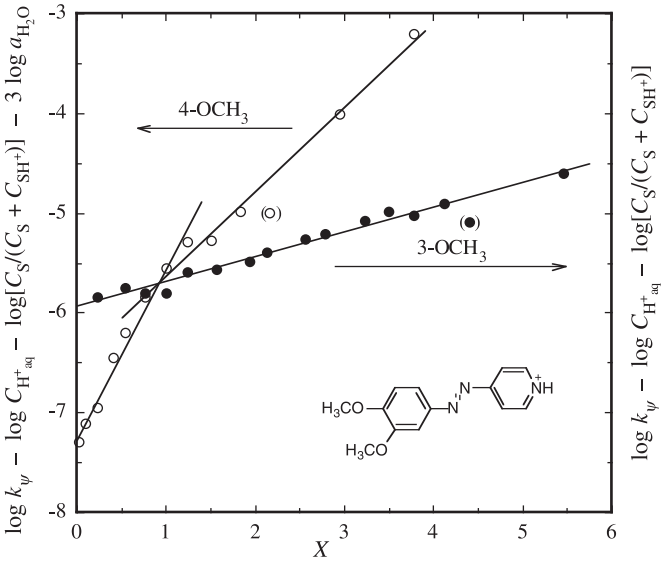


Fig. 3. Excess acidity plots against X for the hydrolyses of **5** (and **6**) in aqueous H_2SO_4.



have been reworked for this paper, as the water activities used previously were not the optimum ones.[14] Using the correct water activities does not change the mechanism at all; only the slope and intercept results, and the activation parameters, are marginally altered. Either k_1 or k_2 can be the rate-determining step, and it is evident from the break in Fig. 2 that both are, at different acidities.

Interestingly, the activation parameters for the k_1 and k_2 processes are not very similar; from the activation parameters in Table 2 one might guess the k_1 process to be the slow step initially, with a more negative entropy of activation, and the k_2 process at the higher ones, where there is less water present. The values given here in Table 1 for **3** and **4** (and **5** and **6**) supercede those given previously.[11]

Looking at compounds **5** (and **6**): as far as the 4-methoxy group is concerned, compound **5** reacts by way of exactly the same mechanism as does compound **3**, giving as a product compound **6**, as we have discussed previously.[11] Both of these reactions are quite fast in the standard state (Table 2), although **5** reacts more quickly than **3**. Presumably the 3-methoxy group in **5** activates the molecule somewhat. Subsequently, the 3-methoxy group in **6** also hydrolyzes, but much more slowly, and by a mechanism that does not involve the water activity. Both hydrolyses are illustrated in Fig. 3.

The mechanism by which the 3-methoxy group is lost involves protonation of one of the aromatic ring carbons as the rate-determining step. This is quite common for aromatic rings with several activating groups in acidic media,[24] and has been observed before for the hydrolysis of the methoxy group of 3,5-dihydroxyanisole.[25] This process has been analyzed,[3] and it was characterized by a shallow $m^{\ddagger}$ slope; the slope observed here (Table 2) is only 0.25. Slow carbon protonations do seem to have shallow $m^{\ddagger}$ slopes associated with them.[22]

The hydrolysis mechanism proposed for **6** is given in Scheme 5.[11] The proton is drawn as attacking the position para to the methoxy group. It is just as likely (perhaps more likely) that the proton attacks at either of the positions ortho to it. Without more experimental evidence (perhaps isotopic substitution studies)[11] it is not possible to say which one is predominantly attacked; in any case, the resulting product will be the same.

Compound **7** hydrolyzes normally, according to Scheme 3. The excess acidity plots at 30 and at 60 °C are given in Fig. 4. As can be seen, the 30 °C plot, covering a range of acidity of 40–80 wt % aqueous H_2SO_4, is accurately linear over an impressive nine orders of magnitude. The 60 °C plot is linear as well, but it is not parallel to the 30 °C one. The reason for this is unclear; this behavior has not been seen before in excess acidity plots, where the same $m^{\ddagger}$ slope usually applies at all temperatures.[14] For instance, the hydrolysis of isopropyl phenyl ether shows five accurately parallel excess acidity plots at 5, 15, 25, 35, and 45 °C.[3] It would be possible to obtain activation parameters in the standard state from the two intercepts, but this was not thought to be a good idea; the values would not be reliable without an understanding of the lack of parallelism.

In more general terms, looking at Table 2 it is apparent that the Scheme 3 process is quite slow, particularly in the case of **1**. Compound **2**, with its naphthyl ring, is more activated and reacts somewhat faster; it is also very easy to protonate on the azo group (Table 1) by comparison with the others. Compound **7** also reacts very slowly in the standard state. In contrast, the three-water-molecule process of Scheme 4 is quite fast. The entropy of activation for compound **4**, reacting via Scheme 3, is much more negative than those of other ethers that react this way, which mostly have

Can. J. Chem. Downloaded from www.nrcresearchpress.com by MCGILL UNIVERSITY on 02/02/13
For personal use only.

Scheme 5.

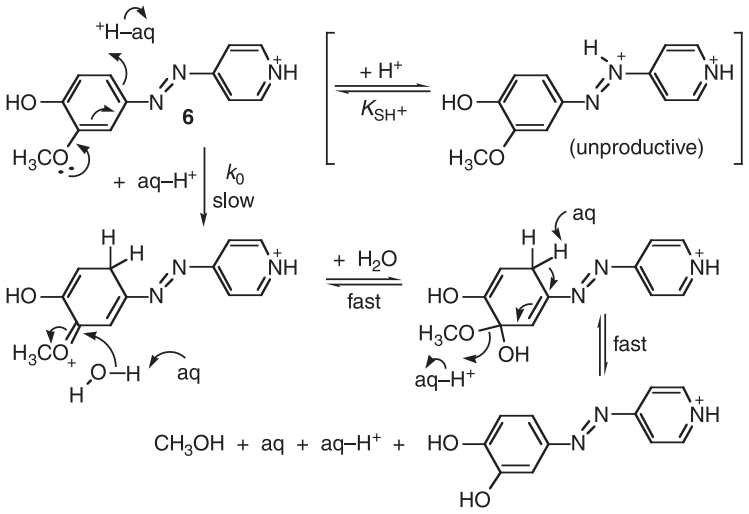
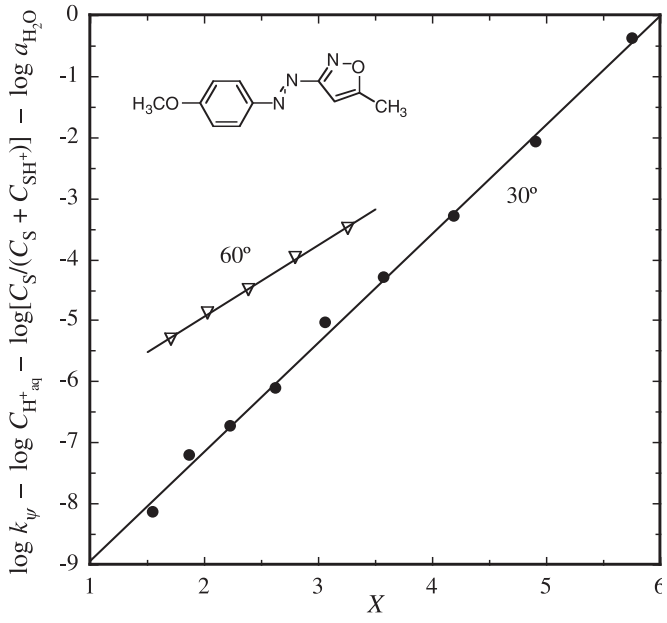


Fig. 4. Excess acidity plots for the hydrolysis of **7** in aqueous H_2SO_4. The theoretical lines are drawn using the slope and intercept values in Table 2.



values a few entropy units on either side of zero.[3] However, this is understandable as **4** contains one (or two) positive charges, and thus the solvent must be more electrostricted than is the case for the neutral ethers studied before.[3]

To summarize, these azoethers have quite interesting hydrolysis mechanisms, if suitably substituted, but many of them hydrolyze by the same Scheme 1 mechanism as do most ethers that cannot form stable carbocations in the medium used.[3,4]

Acknowledgments

Financial support by the Natural Sciences and Engineering Research Council of Canada (NSERC) is gratefully acknowledged by EB.

References

(1) Part 29 of the series "Studies of azo and azoxy dyestuffs" of which part 28 is ref. 2. Also part 33 of the series "Mechanistic studies in strong acids" of which part 32 is ref. 3.
(2) Buncel, E.; Keum, S.-R.; Rajagopal, S.; Cox, R. A. *Can. J. Chem.* **2009**, *87* (8), 1127. doi:10.1139/V09-080.
(3) Cox, R. A. *Can. J. Chem.* **2012**, *90*. In press.
(4) Cox, R. A. *Int. J. Mol. Sci. [Online]* **2011**, *12* (12), 8316. doi:10.3390/ijms12128316.
(5) Cox, R. A. *Adv. Phys. Org. Chem.* **2012**, *45*. In press.
(6) (a) Jencks, W. P. *Chem. Rev.* **1972**, *72* (6), 705. doi:10.1021/cr60280a004; (b) Jencks, W. P. *Acc. Chem. Res.* **1976**, *9* (12), 425. doi:10.1021/ar50108a001; (c) Jencks, W. P. *Acc. Chem. Res.* **1980**, *13* (6), 161. doi:10.1021/ar50150a001; (d) Jencks, W. P. *Chem. Soc. Rev.* **1981**, *10* (3), 345. doi:10.1039/cs9811000345.
(7) Bunnett, J. F.; Buncel, E. *J. Am. Chem. Soc.* **1961**, *83* (5), 1117. doi:10.1021/ja01466a028.
(8) Bunnett, J. F.; Buncel, E.; Nahabedian, K. V. *J. Am. Chem. Soc.* **1962**, *84* (21), 4136. doi:10.1021/ja00880a033.
(9) Buncel, E.; Onyido, I. *Can. J. Chem.* **1986**, *64* (11), 2115. doi:10.1139/v86-349.
(10) Onyido, I.; Opara, L. U. *J. Chem. Soc., Perkin Trans. 2* **1989**, (11), 1817. doi:10.1039/p29890001817.
(11) Cox, R. A.; Onyido, I.; Buncel, E. *J. Am. Chem. Soc.* **1992**, *114* (4), 1358. doi:10.1021/ja00030a034.
(12) Cox, R. A.; Yates, K. *J. Am. Chem. Soc.* **1978**, *100* (12), 3861. doi:10.1021/ja00480a033.
(13) Cox, R. A.; Yates, K. *Can. J. Chem.* **1981**, *59* (11), 1560. doi:10.1139/v81-230.
(14) Cox, R. A. *Adv. Phys. Org. Chem.* **2000**, *35*, 1. doi:10.1016/S0065-3160(00)35011-0.
(15) Cox, R. A. *Acc. Chem. Res.* **1987**, *20* (1), 27. doi:10.1021/ar00133a004.
(16) (a) Buncel, E.; Keum, S.-R.; Rajagopal, S.; Kiepek, E.; Cox, R. A. *Can. J. Chem.* **2008**, *86* (4), 298. doi:10.1139/v08-016; (b) Cox, R. A.; Fung, D. Y. K.; Csizmadia, I. G.; Buncel, E. *Can. J. Chem.* **2003**, *81* (6), 535. doi:10.1139/v03-049; (c) Cox, R. A.; Cheon, K.-S.; Keum, S.-R.; Buncel, E. *Can. J. Chem.* **1998**, *76* (6), 896 and many earlier papers. doi:10.1139/v98-082.
(17) (a) Cox, R. A. *Can. J. Chem.* **2008**, *86* (4), 290. doi:10.1139/v08-015; (b) Cox, R. A. *Can. J. Chem.* **1999**, *77* (5–6), 709.

Can. J. Chem. Downloaded from www.nrcresearchpress.com by MCGILL UNIVERSITY on 02/02/13
For personal use only.

doi:10.1139/v99-028; (c) Cox, R. A. *Can. J. Chem.* **1997**, *75* (8), 1093. doi:10.1139/v97-129; (d) Cox, R. A. *J. Chem. Soc., Perkin Trans. 2* **1997**, (9), 1743 and many earlier papers. doi:10.1039/a700949f.
(18) Cox, R. A.; Goldman, M. F.; Yates, K. *Can. J. Chem.* **1979**, *57* (22), 2960. doi:10.1139/v79-481.
(19) Cox, R. A.; Yates, K. *Can. J. Chem.* **1984**, *62* (11), 2155. doi:10.1139/v84-369.
(20) Clarke, E. C. W.; Glew, D. N. *Trans. Faraday Soc.* **1966**, *62*, 539. doi:10.1039/tf9666200539.
(21) For instance, see Laidler, K. J. *Theories of Chemical Reaction Rates;* McGraw–Hill, Inc.: New York. 1969. Chap. 3.
(22) Cox, R. A. *J. Phys. Org. Chem.* **1991**, *4* (4), 233. doi:10.1002/poc.610040406.
(23) Kwon, O.-H.; Mohammed, O. F. *Phys. Chem. Chem. Phys.* **2012**, *14* (25), 8974. doi:10.1039/c2cp23796b.
(24) Kresge, A. J.; Mylonakis, S. G.; Sato, Y.; Vitullo, V. P. *J. Am. Chem. Soc.* **1971**, *93* (23), 6181. doi:10.1021/ja00752a032.
(25) Schubert, W. M.; Quacchia, R. H. *J. Am. Chem. Soc.* **1963**, *85* (9), 1284. doi:10.1021/ja00892a015.

Can. J. Chem. Downloaded from www.nrcresearchpress.com by MCGILL UNIVERSITY on 02/02/13
For personal use only.

2-Hydroxyethylammonium acetate as a reusable and cost-effective ionic liquid for the efficient synthesis of bis(pyrazolyl)methanes and 2-pyrazolyl-1-nitroalkanes

Sara Sobhani, Razieh Nasseri, and Moones Honarmand

Can. J. Chem. Downloaded from www.nrcresearchpress.com by MCGILL UNIVERSITY on 02/02/13
For personal use only.

Abstract: A new and convenient method for the synthesis of bis(pyrazolyl)methanes by one-pot tandem Knoevenagel–Michael reaction of 3-methyl-1-phenyl-5-pyrazolone with aryl, heteroaryl, or alkyl aldehydes in the presence of 2-hydroxyethylammonium acetate (2-HEAA) as a task-specific ionic liquid is described. This method was also successfully applied for the synthesis of 2-pyrazolyl-1-nitroalkanes by Michael addition of 3-methyl-1-phenyl-5-pyrazolone with β-nitrostyrenes in short reaction times. The present protocol offers several advantages such as using a reusable and cost-effective ionic liquid, an environmentally benign reaction media, being amenable to scale-up and good to high yields of the products.

Key words: bis(pyrazolyl)methane, ionic liquid, aldehydes, β-nitrostyrene.

Résumé : On a développé une méthode nouvelle et simple de synthèse des bis(pyrazolyl)méthanes par une réaction monotope en tandem de Knoevenagel–Michael de la 3-méthyl-1-phényl-5-pyrazolone avec des aldéhydes d'aryles, d'hétéroaryles ou d'alkyles, en présence d'acétate de 2-hydroxyéthylammonium (acétate de 2-HEA) dans un liquide ionique spécifique pour cette réaction. On a appliqué cette méthode avec succès pour la synthèse de 2-pyrazolyl-1-nitroalcanes par le biais d'une addition de Michael de la 3-méthyl-1-phényl-5-pyrazolone sur le β-nitrostyrène avec un très court temps de réaction. Le présent protocole offre plusieurs avantages, tel l'usage d'un liquide ionique réutilisable et efficace, un milieu réactionnel écologique et la possibilité de pouvoir être amené à produit des grandes quantités de produits avec des rendements allant de bons à élevés.

Mots-clés : bis(pyrazolyl)méthane, liquide ionique, aldéhydes, β-nitrostyrène.

[Traduit par la Rédaction]

Introduction

Pyrazoles are an important class of bioactive drug targets in the pharmaceutical industry, as they are the core structure of numerous biologically active compounds.[1–3] Among the pyrazole derivatives, the synthesis of pyrazolone derivatives has attracted much attention from organic chemists because of their various biological activities, such as antitumor[4,5] and selective COX-2 inhibitory.[6] Pyrazolone derivatives are also used as cytokine inhibitors,[7] human telomerase inhibitors,[8] therapeutics for kinase-mediated inflamatory disorders,[9] and dyes.[10,11] For example, 2,4-dihydro-3*H*-pyrazol-3-one derivatives, including 4,4′-(arylmethylene)bis(3-methyl-1-phenyl-1*H*-pyrazol-5-ol)s, are being used as anti-inflammatory, antipyretic, gastric secretion stimulatory antidepressant, antibacterial, and antifilarial agents.[12–16] Moreover, the corresponding 4,4′-(arylmethylene)bis(1*H*-pyrazol-5-ol)s are applied as fungicides, pesticides, insecticides, dyestuffs, and chelating and extracting reagents for different metal ions.[17–20] The conventional chemical approach to 4,4′-(arylmethylene) bis(3-methyl-1-phenyl-1*H*-pyrazol-5-ol)s involves the successive Knoevenagel synthesis of the corresponding arylidene-pyrazolones and its base-promoted Michael reaction.[17,18,21] One-pot tandem Knoevenagel–Michael reaction of aldehydes with 2 equiv of 5-methyl-2-phenyl-2,4-dihydro-3*H*-pyrazol-3-one, which was performed under a variety of reaction conditions, is another approach for achieving these important scaffolds.[22–33] Even though, 4,4′-(arylmethylene)bis(3-methyl-1-phenyl-1*H*-pyrazol-5-ol)s could be synthesized by these methods, most of the methods suffer from limitations such as low yields, long reaction time, application of hazardous solvents, tedious work-up procedures and noncompliance with green chemistry protocols. On the other hand, a literature survey indicates that the methods for the synthesis of 4-substituted pyrazolones are mainly focused on the condensation reaction of 3-methyl-1-phenyl-5-pyrazolone with aldehydes.[22–33] It also shows that Michael addition of pyrazolone with Michael acceptors such as β-nitrostyrene as possibly the strongest and particularly versatile Michael acceptors has been less explored.[34,35] Therefore, it is necessary to develop an efficient and convenient method for the synthesis of 4-substituted pyrazolones such as bis(pyrazolyl)methanes and 2-pyrazolyl-1-nitroalkanes.

Received 14 April 2012. Accepted 17 July 2012. Published at www.nrcresearchpress.com/cjc on 19 September 2012.

S. Sobhani, R. Nasseri, and M. Honarmand. Department of Chemistry, College of Sciences, Birjand University, Birjand 414, Iran.

Corresponding author: Sara Sobhani (e-mail: ssobhani@birjand.ac.ir, sobhanisara@yahoo.com).

Can. J. Chem. Downloaded from www.nrcresearchpress.com by MCGILL UNIVERSITY on 02/02/13
For personal use only.

In recent years, room-temperature ionic liquids have received considerable attention as an alternative green reaction medium for numerous organic reactions because of their favorable properties, such as good solvating capability, wide liquid range, negligible vapor pressure, tunable polarity, high thermal stability, and ease of recyclability.[36,37] Ionic liquids, as catalysts, have also played a significant role in controlling these reactions.[38–40] The major concern in using ionic liquids as reaction media in industrial processes is the cost of the ionic liquid, which would be directly dependent on the price of the cations and anions that are used for their production.[41] The currently popular ionic liquids incorporate expensive cations, such as alkyl methyl imidazolium or dialkyl imidazolium, and expensive anions, such as tetrafluoroborate or hexafluorophosphate. Thus, introduction of cost-effective ionic liquids as reaction media should be a priority.

Having this point in mind, and as part of our continued interest in the development of new methods for the synthesis of pyrazolone derivatives,[30,31] herein, we wish to report a new method for environmentally benign synthesis of bis(pyrazolyl)methanes and 2-pyrazolyl-1-nitroalkanes in the presence of 2-hydroxyethylammonium acetate (2-HEAA)[42–44] as a cost-effective and reusable ionic liquid at room temperature.

Results and discussion

At first, to find the best solvent, the reaction of benzaldehyde (1 equiv) with 3-methyl-1-phenyl-5-pyrazolone (**1**, 2 equiv) was studied in EtOH, H_2O, CH_3CN, CH_2Cl_2, petroleum ether, and toluene in the presence of 2-HEAA (5 mol %) at room temperature (Table 1, entries 1–6). The results revealed that EtOH was the best solvent for this reaction (Table 1, entry 1). Low yield of the product was obtained in the absence of any solvent (Table 1, entry 7).

In the next step, to show the generality of this method, the reaction of different types of aldehydes with **1** in the presence of 2-HEAA (5 mol %) in EtOH at room temperature was investigated (Scheme 1). The results of these studies are summarized in Table 2.

As shown in Table 2, substituted benzaldehyde with electron-donating and electron-withdrawing groups underwent one-pot tandem Knoevenagel–Michael reaction with 2 equiv of **1** and gave the corresponding products in 74%–95% yields (entries 1–6). Both formyl groups in terphthaldehyde reacted with **1** to produce the desired product in 85% yield (Table 2, entry 7). The reaction of naphthalene-2-carbaldehyde as a polynuclear aromatic aldehyde gave the corresponding product in 40 min (Table 2, entry 8). Acid-sensitive aldehydes, such as thiophene-2-carbaldehyde, underwent smooth reactions without any decomposition or polymerization (Table 2, entry 9). This method is also applicable for the synthesis of bis(pyrazolyl)methanes (**2j** and **2k**) from the reaction of **1** with aliphatic aldehydes (Table 2, entries 10 and 11).

It was observed that the ionic liquid was reusable at least 15 times in multiple sequential condensations by the addition of new samples of benzaldehyde and **1** to the reaction mixture. This protocol was also easily amenable to scale-up. For example, the condensation of benzaldehyde with **1** in a semi scale-up procedure (20 times) was carried out successfully and produced the desired product in 85% yield.

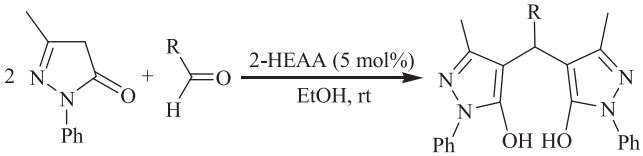
It is important to note that the reports for the condensation reaction of aldehydes with **1** in ionic liquid are rare in the literature.[45,46] In these reports, 4-[(5-hydroxy-3-methyl-1-phenyl-1*H*-pyrazol-4-yl)-phenyl-methyl]-5-methyl-2-phenyl-1,2-dihydropyrazol-3-ones (Fig. 1) were obtained instead of bis(pyrazolyl)methanes (**2**). Therefore, the present method is the first protocol for the synthesis of bis(pyrazolyl)methanes in the presence of an ionic liquid.

Table 1. Reaction of 3-methyl-1-phenyl-5-pyrazolone (**1**) with benzaldehyde under different reaction conditions.

Entry	Catalyst	Solvent	Time (min)	Yield (%)[a]
1	Ionic liquid	EtOH	15	90
2	Ionic liquid	H_2O	15	30
3	Ionic liquid	CH_3CN	60	70
4	Ionic liquid	CH_2Cl_2	60	65
5	Ionic liquid	Petroleum ether	60	60
6	Ionic liquid	Toluene	60	65
7	Ionic liquid	—	30	30

[a]Isolated yield; reaction conditions: benzaldehyde (1 mmol), 3-methyl-1-phenyl-5-pyrazolone (**1**, 2 mmol), catalyst (5 mol%), room temperature.

Scheme 1.



1 **2a-k**

R = aryl, alkyl, heteroaryl

To show the catalytic effect of 2-HEAA on the synthesis of bis(pyrazolyl)methanes **2**, the coupling reaction between benzaldehyde and **1** in the absence of ionic liquid at room temperature was considered. This reaction led to the formation of the desired product (**2a**) in low yield (40%) after 20 h (Table 3, entry 1). A similar reaction in the presence of $[CH_3CH_2NH_3^+][AcO^-]$ proceeded with a longer reaction time compared with 2-HEAA and produced the desired product in 81% yield (Table 3, entries 2 and 3). These results showed the role of the hydroxyl group of 2-HEAA in imparting the catalytic property and indicates that 2-HEAA can act as a functionalized or task-specific ionic liquid in this method. We have also found that lengthening of the alkyl chain in $[HO(CH_2)_nNH_3^+][AcO^-]$ has no influence on the efficiency of the ionic liquid (Table 3, entries 4 and 5).

We also suggest a plausible mechanism for the reaction of **1** and aldehydes in the presence of 2-HEAA (Scheme 2). The process represents a typical tandem reaction in which aldehydes first condensed with **1** to form the Knoevegel product followed by Michael addition with **1** to produce bis(pyrazolyl)methanes **2**. In this reaction, two spontaneous interactions between NH_3^+ and the OH of 2-HEAA with the carbonyl groups of aldehydes and the methylene group of **1** took place. These interactions activated the reactants and facilitated formation of the product.

Successful application of 2-HEAA as a reusable ionic liquid for the one-pot synthesis of bis(pyrazolyl)methanes encouraged us to study the applicability of this method for the synthesis of 2-pyrazolyl-1-nitroalkanes by the reaction of 3-

Can. J. Chem. Downloaded from www.nrcresearchpress.com by MCGILL UNIVERSITY on 02/02/13
For personal use only.

Table 2. Synthesis of bis(pyrazolyl)methanes **2a**–**2k** catalyzed by 2-hydroxyethylammonium acetate (2-HEAA).

Entry (Ref.)	Aldehyde	Product	Time (min)	Yield (%)[a]
1 (27)	3-Methylbenzaldehyde	**2a**	15	91
2 (30, 33)	4-Chlorobenzaldehyde	**2b**	15	92
3 (30)	4-Bromobenzaldehyde	**2c**	12	93
4 (30)	4-Nitrobenzaldehyde	**2d**	5	95
5 (27)	4-Cyanobenzaldehyde	**2e**	5	95
6 (30)	4-Hydroxybenzaldehyde	**2f**	30	74
7 (27)	Terephthaldehyde[b]	**2g**	40	85
8 (30)	Naphthalene-2-carbaldehyde	**2h**	40	81
9 (30)	Thiephene-2-carbaldehyde	**2i**	40	85
10 (30)	Isobutyraldehyde	**2j**	30	92
11 (30)	*n*-Butyraldehyde	**2k**	15	83

[a]Isolated yield; reaction conditions: 2-HEAA (5 mol %), EtOH, room temperature.
[b]Reaction conditions: terephthaldehyde (1 mmol), and 3-methyl-1-phenyl-5-pyrazolone (**1**, 4 mmol), 2-HEAA (5 mol %), EtOH (4 mL), room temperature.

Fig. 1. 4-[(5-Hydroxy-3-methyl-1-phenyl-1*H*-pyrazol-4-yl)-phenylmethyl]-5-methyl-2-phenyl-1,2-dihydropyrazol-3-ones.

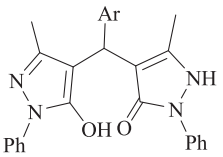


Table 3. The coupling reaction of benzaldehyde and 3-methyl-1-phenyl-5-pyrazolone (**1**) in the presence of different $[X(CH_2)_nNH_3^+][AcO^-]$.

Entry	$[X(CH_2)_nNH_3^+][AcO^-]$	Time	Yield (%)[a]
1	—	20 h	40
2	$n = 2$, X = H	1 h	81
3	$n = 2$, X = OH	20 min	90
4	$n = 3$, X = OH	20 min	90
5	$n = 5$, X = OH	15 min	92

[a]Isolated yield. Reaction conditions: benzaldehyde (1 mmol), 3-methyl-1-phenyl-5-pyrazolone (**1**, 2 mmol), ionic liquid (5 mol %), EtOH (4 mL), room temperature.

methyl-1-phenyl-5-pyrazolone with β-nitrostyrene (Scheme 3 and Table 4). As indicated in Table 4, Michael addition of 3-methyl-1-phenyl-5-pyrazolone with β-nitrostyrenes bearing electron-withdrawing or electron-releasing groups proceeded well to afford the corresponding 2-pyrazolyl-1-nitroalkanes in 83%–95% yields.

Conclusions

In conclusion, we have successfully developed a new and simple protocol for the synthesis of bis(pyrazolyl)methanes via a one-pot tandem Knoevenagel–Michael reaction in the presence of 2-HEAA as a task-specific ionic liquid. This simple procedure allows a series of bis(pyrazolyl)methanes to be synthesized in good to high yields from the reaction of aryl, heteroaryl, or alkyl aldehydes and 3-methyl-1-phenyl-5-pyrazolone at room temperature. The method was also applicable for the synthesis of 2-pyrazolyl-1-nitroalkanes via Michael addition reaction of 3-methyl-1-phenyl-5-pyrazolone with β-nitrostyrene in short reaction times. The present protocol offers several advantages such as using a reusable and cost-effective ionic liquid, an environmentally benign reaction media, being amenable to scale-up, and good to high yields of the products.

Experimental section

General procedures and materials

Chemicals were purchased from the Merck and Fluka Chemical Companies. Melting points were determined by a Buchi 510 apparatus and are uncorrected. IR spectra were run on a PerkinElmer 780 instrument. NMR spectra were recorded on a Bruker Avance DPX-250, 400, or 500. Mass spectra were recorded on a Shimadzu GC–MS QP5050A spectrometer operating at an ionization potential of 70 eV. Conductivities were measured by an Istek 915PDC apparatus at 25 °C. The electrochemical measurements were performed by a Solartron Electrochemical Interface model 1287 at 25 °C. The purity of the products and the progress of the reactions were accomplished by TLC on silica gel polygram SILG/UV_{254} plates. Elemental analysis for C, H, and N were obtained by using an Elementar Vario EL III.

A typical procedure for the synthesis of 2-HEAA

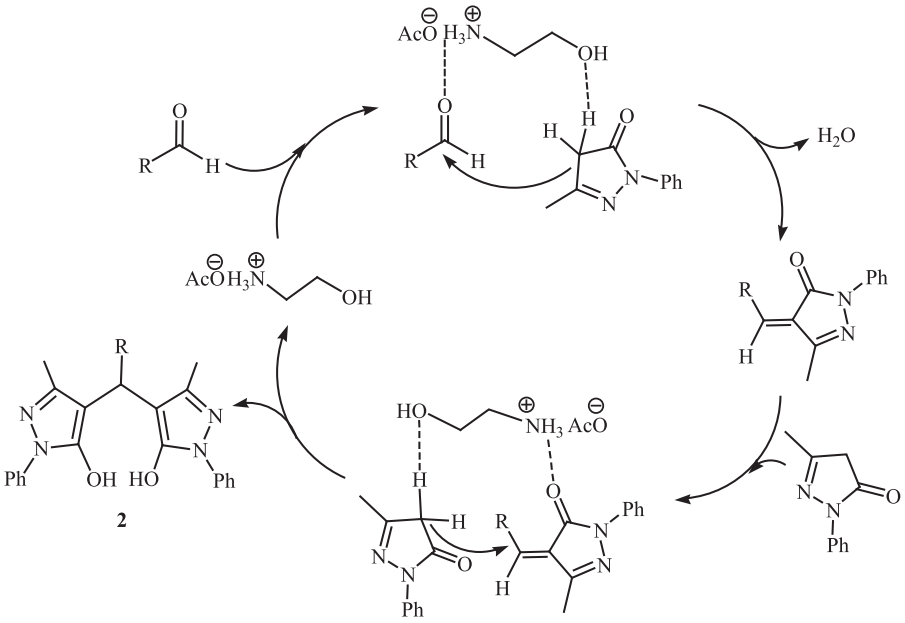
2-HEAA was prepared according to a previously reported procedure.[43] A solution of acetic acid (50 mmol, 3.00 g) in EtOH (1.5 mL) was added dropwise to a stirring solution of 2-aminoethanol (50 mmol, 3.05 g) in EtOH (1.5 mL) at room temperature within 1 h. The resultant solution was stirred at room temperature for another 20 h. EtOH was removed in vacuo, and the oil residue was dried in vacuo at 50 °C for 48 h to give 2-HEAA as a yellow viscous liquid (pH 7.96 at 25 °C, bp 191 °C, density = 1.11 g cm^{-3} at 25 °C, electrochemical stability between –0.6 and 0.7 V, relative viscosity = 9390.6 at 25 °C, conductivity = 263.3 μs cm^{-1}).

General procedure for the synthesis of bis(pyrazolyl) methanes (2)

2-HEAA (5 mol%) was added to a mixture of aldehyde (1 mmol) and **1** (2 mmol) in EtOH (4 mL) at room temperature. The mixture was stirred at room temperature for the

Can. J. Chem. Downloaded from www.nrcresearchpress.com by MCGILL UNIVERSITY on 02/02/13
For personal use only.

Scheme 2.



Scheme 3.

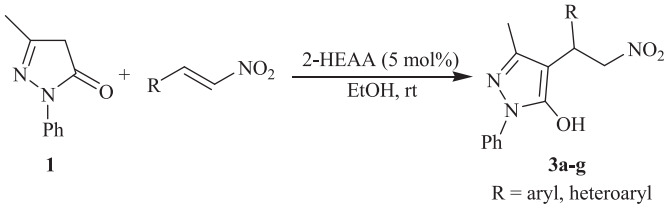


Table 4. Synthesis of 2-pyrazolyl-1-nitroalkanes **3a**–**3g** catalyzed by 2-hydroxyethylammonium acetate (2-HEAA).

Entry (Ref.)	R	Product	Time (min)	Yield (%)[a]
1 (35)	C_6H_5	**3a**	10	83
2 (34)	2-$CH_3OC_6H_4$	**3b**	8	91
3	4-$CH_3C_6H_4$	**3c**	8	84
4	4-ClC_6H_4	**3d**	5	95
5	4-$NO_2C_6H_4$	**3e**	5	95
6	4-BrC_6H_4	**3f**	8	95
7	2-Thienyl	**3g**	10	88

[a]Isolated yield. Reaction conditions: 3-methyl-1-phenyl-5-pyrazolone (**1**, 1 mmol), β-nitrostyrene (1 mmol), 2-HEAA (5 mol %), EtOH (4 mL), room temperature.

appropriate time (Table 2). After evaporation of the solvent, water (10 mL) was added to the reaction mixture and the resulting solid was filtered and washed three times with H_2O (5 mL). The pure product (**2**) was obtained from this solid by recrystallization in EtOH.

4,4′-[(3-Methylphenyl)methylene]bis(3-methyl-1-phenyl-pyrazol-5-ol) (2a)

White solid; yield: 91%, 0.41 g; mp 193–194 °C. IR (ν_{max}, cm^{-1}): 3023 (O–H). ^1H NMR (400 MHz, DMSO-d_6) δ_H: 2.25 (3H, s, CH_3), 2.31 (6H, s, CH_3), 4.91 (1H, s, CH), 6.98 (1H, d, $^3J_{HH}$ = 7.6 Hz, Ar), 7.06 (1H, s, Ar), 7.07 (1H, d, $^3J_{HH}$ = 6.8 Hz, Ar), 7.16 (1H, t, $^3J_{HH}$ = 7.2 Hz, Ar), 7.25 (2H, t, $^3J_{HH}$ = 7.2 Hz, Ar), 7.44 (4H, t, $^3J_{HH}$ = 7.6 Hz, Ar), 7.71 (4H, d, $^3J_{HH}$ = 7.6 Hz, Ar), 13.98 (2H, br s, OH). ^{13}C NMR (100 MHz, DMSO-d_6) δ_C: 12.1, 21.7, 33.6, 121.0, 124.8, 126.0, 127.1, 128.2, 128.5, 129.4, 137.5, 142.7, 146.7. MS *m/z* (%): 276 (28.4), 174 (21).

4,4′-[(4-Chlorophenyl)methylene]bis(3-methyl-1-phenyl-pyrazol-5-ol) (2b)

White solid; yield: 92%, 0.43 g; mp 212–214 °C. IR (ν_{max}, cm^{-1}): 3044 (O–H). ^1H NMR (500 MHz, DMSO-d_6) δ_H: 2.32 (6H, s, CH_3), 4.97 (1H, s, CH), 7.26 (4H, d, $^3J_{HH}$ = 8.2 Hz, Ar), 7.34 (2H, d, $^3J_{HH}$ = 8.0 Hz, Ar), 7.44 (4H, t, $^3J_{HH}$ = 7.14 Hz, Ar), 7.71 (4H, d, $^3J_{HH}$ = 7.6 Hz, Ar), 12.40 (1H, br s, OH), 13.87 (1H, br s, OH). ^{13}C NMR (125 MHz, DMSO-d_6) δ_C: 33.4, 40.1, 121.4, 126.4, 128.9, 129.8, 130.0, 131.4, 142.0, 147.1. MS *m/z* (%) 296 (6.3), 174 (14.0).

4,4′-[(4-Bromophenyl)methylene]bis(3-methyl-1-phenyl-pyrazol-5-ol) (2c)

White solid; yield: 93%, 0.48 g; mp 215–216 °C. ^1H NMR (400 MHz, DMSO-d_6) δ_H: 2.32 (6H, s, CH_3), 4.95 (1H, s, CH), 7.19 (2H, d, $^3J_{HH}$ = 8.0 Hz, Ar), 7.23–7.26 (2H, m, Ar), 7.42–7.48 (6H, m, Ar), 7.69 (4H, d, $^3J_{HH}$ = 7.6 Hz, Ar), 12.52 (1H, br s), 13.87 (2H, br s, OH). ^{13}C NMR (100 MHz, DMSO-d_6) δ_C: 12.1, 33.0, 119.5, 121.0, 126.1, 129.34, 130.0, 131.4, 142.1, 146.7.

4,4′-[(4-Nitrophenyl)methylene]bis(3-methyl-1-phenyl-pyrazol-5-ol) (2d)

Yellow solid; yield: 95%, 0.46 g; mp 229–231 °C. IR (ν_{max}, cm^{-1}): 3056 (O–H). ^1H NMR (500 MHz, DMSO-d_6) δ_H: 2.35 (6H, s, CH_3), 5.13 (1H, s, CH), 7.25–7.27 (2H, m, Ar), 7.44 (4 H, t, $^3J_{HH}$ = 7.0 Hz, Ar), 7.52 (2H, d, $^3J_{HH}$ = 8.1 Hz, Ar), 7.71 (4H, d, $^3J_{HH}$ = 7.6 Hz, Ar), 8.17 (2H, d, $^3J_{HH}$ = 8.2 Hz, Ar), 13.86 (2H, br s, OH). ^{13}C NMR (125 MHz, DMSO-d_6) δ_C: 34.1, 56.9, 121.5, 124.2, 126.6, 129.5, 129.8, 146.8, 147.2, 151.2. MS *m/z* (%): 307 (9.2), 174 (18.3).

Can. J. Chem. Downloaded from www.nrcresearchpress.com by MCGILL UNIVERSITY on 02/02/13
For personal use only.

4,4′-[(4-Cyanophenyl)methylene]bis(3-methyl-1-phenyl-pyrazol-5-ol) (2e)

White solid; yield: 95%, 0.44 g; mp 210–212 °C. IR (ν_{max}, cm^{-1}): 3090 (O–H). ^1H NMR (500 MHz, DMSO-d_6) δ_H: 2.33 (6H, s, CH_3), 5.07 (1H, s, CH), 7.25 (2H, t, $^3J_{HH}$ = 7.3 Hz, Ar), 7.42–7.46 (6H, m, Ar), 7.40 (4H, d, $^3J_{HH}$ = 7.8 Hz, Ar), 7.76 (2H, d, $^3J_{HH}$ = 8.3 Hz, Ar), 13.89 (2H, br s, OH). ^{13}C NMR (125 MHz, DMSO-d_6) δ_C: 18.5, 32.4, 114.8, 120.5, 125.5, 128.1, 128.9, 132.3, 137.4, 146.2, 155.5.

4,4′-[(4-Hydroxyphenyl)methylene]bis(3-methyl-1-phenyl-pyrazol-5-ol) (2f)

Yellow solid; yield: 74%, 0.33 g; mp 150–151 °C. IR (ν_{max}, cm^{-1}): 3420 (O–H). ^1H NMR (500 MHz, DMSO-d_6) δ_H: 2.31 (6H, s, CH_3), 4.86 (1H, s, CH), 6.67 (2H, d, $^3J_{HH}$ = 8.02 Hz, Ar), 7.06 (2H, d, $^3J_{HH}$ = 8.5 Hz, Ar), 7.24 (2H, t, $^3J_{HH}$ = 7.0 Hz, Ar), 7.44 (4H, t, $^3J_{HH}$ = 8.0 Hz, Ar), 7.72 (4H, d, $^3J_{HH}$ = 8.0 Hz, Ar), 9.16 (1H, br s, OH), 12.40 (1H, br s, OH), 13.95 (1H, br s, OH). ^{13}C NMR (125 MHz, DMSO-d_6) δ_C: 12.5, 33.2, 115.7, 121.4, 126.4, 128.9, 129.8, 133.2, 143.6, 147.0, 156.4. MS *m/z* (%): 279 (30.2), 174 (91.4).

1,4-Diphenylene-4,4′-(methylene)bis(3-methyl-1-phenyl-pyrazol-5-ol) (2g)

Yellow solid; yield: 85%, 0.67 g; mp 194–196 °C. ^1H NMR (500 MHz, DMSO-d_6) δ_H: 2.29 (12H, s, CH_3), 5.05 (2H, s, CH), 7.17 (4H, s, Ar), 7.22 (4H, t, $^3J_{HH}$ = 7.1 Hz, Ar), 7.41 (8H, t, $^3J_{HH}$ = 7.8 Hz, Ar), 7.69 (8H, d, $^3J_{HH}$ = 8.0 Hz, Ar), 12.41 (2H, br s, OH), 14.11 (2H, s, OH). ^{13}C NMR (125 MHz, DMSO-d_6) δ_C: 12.5, 33.7, 121.5, 127.8, 129.7, 140.9, 147.0, 155.0.

4,4′-[(2-Naphthyl)methylene]bis(3-methyl-1-phenyl-pyrazol-5-ol) (2h)

Pale yellow solid; yield: 81%, 0.39 g; mp (dec.) 194 °C. IR (ν_{max}, cm^{-1}): 3055 (O–H). ^1H NMR (400 MHz, DMSO-d_6) δ_H: 2.49 (6H, s, CH_3), 5.29 (1H, s, CH), 7.35 (2H, t, $^3J_{HH}$ = 7.2 Hz, Ar), 7.42 (1H, d, $^3J_{HH}$ = 8.4 Hz, Ar), 7.45–7.48 (2H, m, Ar), 7.50 (4H, t, $^3J_{HH}$ = 7.6 Hz, Ar), 7.73 (4H, d, $^3J_{HH}$ = 7.6 Hz, Ar), 7.76 (1H, s, Ar), 7.84–7.88 (3H, m, Ar). ^{13}C NMR (100 MHz, DMSO-d_6) δ_C: 11.4, 33.1, 105.5, 122.3, 125.5, 126.1, 126.5, 126.7, 127.5, 127.8, 128.3, 128.4, 129.6, 132.2, 133.3, 135.9, 139.1, 146.5.

4,4′-[(2-Thienyl)methylene]bis(3-methyl-1-phenyl-pyrazol-5-ol) (2i)

White solid; yield: 85%, 0.37 g; mp 190–192 °C. IR (ν_{max}, cm^{-1}): 3420 (O–H). ^1H NMR (500 MHz, DMSO-d_6) δ_H: 2.38 (6H, s, CH_3), 5.11 (1H, s, CH), 6.90 (2H, d, $^3J_{HH}$ = 8.5 Hz, Ar), 7.09–7.48 (7H, m, Ar), 7.77–7.85 (4H, m, Ar), 13.56 (2H, br s, OH). ^{13}C NMR (125 MHz, DMSO-d_6) δ_C: 12.5, 33.2, 121.3, 125.0, 125.1, 128.2, 128.6, 131.5, 131.9, 134.2, 139.8, 144.3, 154.9. MS *m/z* (%): 268 (100), 174 (71).

4,4′-[(isoPropyl)methylene]bis(3-methyl-1-phenyl-pyrazol-5-ol) (2j)

White solid; yield: 92%, 0.37 g; mp 210–212 °C. IR (ν_{max}, cm^{-1}): 3428 (O–H). ^1H NMR (500 MHz, DMSO-d_6) δ_H: 0.84 (6H, d, $^3J_{HH}$ = 7.9 Hz, CH_3), 2.21 (6H, s, CH_3), 2.55–2.69 (1H, m, CH), 2.97–3.08 (1H, m, CH), 7.25–7.28 (2H, m, Ar), 7.40–7.48 (4H, m, Ar), 7.71–7.43 (4H, m, Ar), 11.93 (1H, br s, OH), 13.64 (1H, br s, OH). MS *m/z* (%): 228 (21), 174 (33).

4,4′-[(n-Buthyl)methylene]bis(3-methyl-1-phenyl-pyrazol-5-ol) (2k)

White solid; yield: 83%, 0.34 g; mp 125–127 °C. IR (ν_{max}, cm^{-1}): 3420 (O–H). ^1H NMR (400 MHz, DMSO-d_6) δ_H: 0.85 (3H, t, $^3J_{HH}$ = 7.2 Hz, CH_3), 1.16–1.19 (2H, m, CH_2), 1.27–1.32 (2H, m, CH_2), 1.92–1.96 (2H, m, CH_2), 2.92 (6H, s, CH_3), 3.53 (1H, t, $^3J_{HH}$ = 8.0 Hz, CH), 4.00 (2H, br s, OH), 7.33 (2H, t, $^3J_{HH}$ = 7.2 Hz, Ar), 7.49 (4H, t, $^3J_{HH}$ = 8.0 Hz, Ar), 7.68 (4H, d, $^3J_{HH}$ = 8.0 Hz, Ar). ^{13}C NMR (100 MHz, DMSO-d_6) δ_C: 10.9, 14.3, 22.4, 28.28, 30.0, 31.7, 106.4, 122.6, 127.9, 129.7, 135.0, 145.7, 158.6. MS *m/z* (%): 243 (23.3), 174 (100).

General procedure for the synthesis of 2-pyrazolyl-1-nitroalkanes (3)

2-HEAA (5 mol %) was added to a mixture of β-nitrostyrene (1 mmol) and **1** (1 mmol) in EtOH (4 mL) at room temperature. The mixture was stirred at room temperature for the appropriate time (Table 4). After evaporation of the solvent, water (10 mL) was added to the reaction mixture, and the resulting solid was filtered and washed three times with H_2O (5 mL). The pure product (**3**) was obtained from this solid by recrystallization in EtOH.

3-Methyl-4-[2-nitro-1-(phenylethyl)ethyl]-1-phenyl-5-pyrazolone (3a)

White solid; yield: 83%, 0.32 g; mp 89–90 °C. IR (ν_{max}, cm^{-1}): 2901 (O–H). ^1H NMR (400 MHz, DMSO-d_6) δ_H: 2.51 (3H, s, CH_3), 4.58 (1H, t, $^3J_{HH}$ = 8.0 Hz, CH), 5.31 (1H, dd, $^3J_{HH}$ = 8.0 Hz, $^3J_{HH}$ = 7.6 Hz, CH_2), 5.37 (1H, dd, $^3J_{HH}$ = 8.8 Hz, $^3J_{HH}$ = 6.8 Hz, CH_2), 7.20 (1H, d, $^3J_{HH}$ = 7.2 Hz, Ar), 7.25 (1H, d, $^3J_{HH}$ = 7.2 Hz, Ar), 7.33 (2H, t, $^3J_{HH}$ = 7.6 Hz, Ar), 7.44 (2H, t, $^3J_{HH}$ = 8.0 Hz, Ar), 7.50 (2H, t, $^3J_{HH}$ = 7.6 Hz, Ar), 7.71 (2H, d, $^3J_{HH}$ = 8.0 Hz, Ar), 11.23 (1H, br s, OH).

3-Methyl-4-[2-nitro-1-(2-methoxyphenyl)ethyl]-1-phenyl-5-pyrazolone (3b)

White solid; yield: 91%, 0.32 g; mp 147–149 °C. IR (ν_{max}, cm^{-1}): 2955 (O–H). ^1H NMR (400 MHz, DMSO-d_6) δ_H: 2.16 (3H, s, CH_3), 3.85 (3H, s, OCH_3), 4.95 (1H, dd, $^3J_{HH}$ = 7.6 Hz, $^3J_{HH}$ = 6.8 Hz, CH), 5.15 (1H, dd, $^3J_{HH}$ = 14.2 Hz, $^3J_{HH}$ = 6.6 Hz, CH_2), 5.36 (1H, dd, $^3J_{HH}$ = 8.8 Hz, $^3J_{HH}$ = 6.6 Hz, CH_2), 6.91 (1H, t, $^3J_{HH}$ = 7.6 Hz, Ar), 7.01 (1H, d, $^3J_{HH}$ = 8.4 Hz, Ar), 7.19 (1H, t, $^3J_{HH}$ = 7.6 Hz, Ar), 7.24 (1H, t, $^3J_{HH}$ = 8.0 Hz, Ar), 7.43 (2H, t, $^3J_{HH}$ = 8.0 Hz, Ar), 7.51 (1H, d, $^3J_{HH}$ = 7.2 Hz, Ar), 7.70 (2H, d, $^3J_{HH}$ = 8.6 Hz, Ar). ^{13}C NMR (100 MHz, DMSO-d_6) δ_C: 11.7, 32.1, 56.0, 57.9, 76.1, 102.4, 111.3, 119.1, 120.7, 124.9, 127.5, 128.5, 128.6, 129.3, 137.8, 148.3, 156.5. MS *m/z* (%): 353 (3.6), 173 (30.8), 77 (100), 91 (64.8). Anal. calcd for $C_{19}H_{19}N_3O_4$ (353.14) (%): C 64.58, H 5.42, N, 11.89; found: C 64.64, H 5.48, N 11.91.

3-Methyl-4-[2-nitro-1-(4-methylphenyl)ethyl]-1-phenyl-5-pyrazolone (3c)

White solid; yield: 84%, 0.28 g; mp 80–81 °C. IR (ν_{max}, cm^{-1}): 2994 (O–H). ^1H NMR (400 MHz, $CDCl_3$) δ_H: 1.93

Can. J. Chem. Downloaded from www.nrcresearchpress.com by MCGILL UNIVERSITY on 02/02/13
For personal use only.

(3H, s, CH_3), 2.31 (3H, s, CH_3), 4.42 (1H, t, $^3J_{HH}$ = 8.0 Hz, CH), 4.81 (1H, dd, $^3J_{HH}$ = 12.8 Hz, $^3J_{HH}$ = 6.8 Hz, CH_2), 5.20 (1H, dd, $^3J_{HH}$ = 12.0 Hz, $^3J_{HH}$ = 9.6 Hz, CH_2), 7.06 (3H, d, $^3J_{HH}$ = 8.0 Hz, Ar), 7.13 (2H, t, $^3J_{HH}$ = 7.2 Hz, Ar), 7.20 (2H, d, $^3J_{HH}$ = 8.0 Hz, Ar), 7.30 (2H, d, $^3J_{HH}$ = 8 Hz, Ar), 10.9 (1H, br s, OH). ^{13}C NMR (100 MHz, $CDCl_3$) δ_C: 10.6, 21.0, 39.3, 76.8, 103.4, 120.7, 125.6, 127.4, 128.8, 129.5, 135.6, 136.2, 136.5, 137.1, 146.9. MS *m/z* (%): 337 (3.6), 118 (100), 42 (30.0); Anal. calcd for $C_{19}H_{19}N_3O_3$ (337.14) (%): C 67.64, H 5.68, N 12.46; found: C 67.54, H 5.71, N 12.39.

3-Methyl-4-[2-nitro-1-(4-chlorophenyl)ethyl]-1-phenyl-5-pyrazolone (3d)

White solid; yield: 95%, 0.34 g; mp 155–156 °C. IR (ν_{max}, cm^{-1}): 2900 (O–H). ^{1}H NMR (400 MHz, $CDCl_3$) δ_H: 1.91 (3H, s, CH_3), 4.39 (1H, t, $^3J_{HH}$ = 7.6 Hz, CH), 4.78 (1H, dd, $^3J_{HH}$ = 13.0 Hz, $^3J_{HH}$ = 6.8 Hz, CH_2), 5.12 (1H, dd, $^3J_{HH}$ = 12.6 Hz, $^3J_{HH}$ = 8.8 Hz, CH_2), 7.12 (1H, d, $^3J_{HH}$ = 8.0 Hz, Ar), 7.15 (3H, t, $^3J_{HH}$ = 6.8 Hz, Ar), 7.17–7.28 (5H, m, Ar), 11.10 (1H, br s, OH). ^{13}C NMR (100 MHz, $CDCl_3$) δ_C: 10.5, 14.2, 39.0, 76.5, 120.9, 126.3, 128.9, 129.0, 129.1, 129.3, 133.3, 136.9, 137.7, 146.7. MS *m/z* (%): 358 (3.3), 360 (1.1), 139 (3.3), 141 (1.1), 42 (CNO, 100). Anal. calcd for $C_{18}H_{16}ClN_3O_3$ (357.09) (%): C 60.42, H 4.51, N 11.74; found: C 60.51, H 4.55, N 11.81.

3-Methyl-4-[2-nitro-1-(4-nitrophenyl)ethyl]-1-phenyl-5-pyrazolone (3e)

White solid; yield: 94%, 0.34 g; mp 176–180 °C. IR (ν_{max}, cm^{-1}): 2832 (O–H). ^{1}H NMR (400 MHz, $CDCl_3$) δ_H: 2.24 (3H, s, CH_3), 4.65 (1H, t, $^3J_{HH}$ = 7.2 Hz, CH), 5.08 (1H, dd, $^3J_{HH}$ = 13.4 Hz, $^3J_{HH}$ = 7.2 Hz, CH_2), 5.41 (1H, dd, $^3J_{HH}$ = 13.2 Hz, $^3J_{HH}$ = 8.8 Hz, CH_2), 7.22 (1H, t, $^3J_{HH}$ = 7.2 Hz, Ar), 7.38 (2H, t, $^3J_{HH}$ = 7.6 Hz, Ar), 7.55 (2H, d, $^3J_{HH}$ = 7.6 Hz, Ar), 7.7 (2H, d, $^3J_{HH}$ = 8.8 Hz, Ar), 8.2 (2H, d, $^3J_{HH}$ = 8.4 Hz, Ar). ^{13}C NMR (100 MHz, $CDCl_3$) δ_C: 11.3, 39.7, 75.9, 120.0, 124.2, 124.4, 126.2, 128.8, 129.0, 129.3, 136.0, 146.2, 147.3, 148.4. MS *m/z*: 368 (1.2), 149 (2.9), 42 (100). Anal. calcd for $C_{18}H_{16}N_4O_5$ (368.11) (%): C 58.69, H 4.38, N 15.21; found: C 58.71, H 4.44, N 15.11.

3-Methyl-4-[2-nitro-1-(4-bromophenyl)ethyl]-1-phenyl-5-pyrazolone (3f)

White solid; yield: 95%, 0.38 g; mp 169–170 °C. IR (ν_{max}, cm^{-1}): 2703 (O–H). ^{1}H NMR (400 MHz, $CDCl_3$) δ_H: 2.18 (3H, s, CH_3), 4.62 (1H, dd, $^3J_{HH}$ = 8.8 Hz, $^3J_{HH}$ = 6.8 Hz, CH), 5.36 (2H, dd, $^3J_{HH}$ = 8.4 Hz, $^3J_{HH}$ = 6.8 Hz, CH_2), 7.22 (2H,d, $^3J_{HH}$ = 8.0 Hz, Ar), 7.45 (3H, t, $^3J_{HH}$ = 6.8 Hz, Ar), 7.53 (2H, d, $^3J_{HH}$ = 8.0 Hz, Ar), 7.70 (2H, d, $^3J_{HH}$ = 7.6 Hz, Ar), 11.33 (1H, br s, OH). ^{13}C NMR (100 MHz, $CDCl_3$) δ_C: 11.4, 38.6, 76.8, 103.2, 119.2, 120.7, 125.3, 129.4, 130.4, 131.9, 137.4, 139.9, 148.1. MS *m/z*: 401 (2.0), 403 (1.6), 226 (2.1), 228 (2.3), 173 (77.6), 76 (100). Anal. calcd for $C_{18}H_{16}BrN_3O_3$ (401.04) (%): C 53.75, H 4.01, N 10.45; found: C 53.85, H 4.21, N 10.38.

3-Methyl-4-[2-nitro-1-(thiophen-2-yl)ethyl]-1-phenyl-5-pyrazolone (3g)

White solid; yield: 88%, 0.29 g; mp 124–125 °C. IR (ν_{max}, cm^{-1}): 2802 (O–H). ^{1}H NMR (400 MHz, $CDCl_3$) δ_H: 2.13 (3H, s, CH_3), 4.91 (1H, t, $^3J_{HH}$ = 8.0 Hz, CH), 5.32 (2H, dd, $^3J_{HH}$ = 8.8 Hz, $^3J_{HH}$ = 6.8 Hz, CH_2), 6.97 (1H, dd, $^3J_{HH}$ = 6.6 Hz, $^3J_{HH}$ = 3.6 Hz, Ar), 7.11 (1H, d, $^3J_{HH}$ = 6.8 Hz, Ar), 7.22 (1H, t, $^3J_{HH}$ = 7.2 Hz, Ar), 7.39 (1H, d, $^3J_{HH}$ = 5.2 Hz, Ar), 7.45 (2H, t, $^3J_{HH}$ = 8.0 Hz, Ar), 7.71 (2H, d, $^3J_{HH}$ = 8.2 Hz, Ar), 11.35 (1H, br s, OH). ^{13}C NMR (100 MHz, $CDCl_3$) δ_C: 11.1, 34.3, 77.3, 103.8, 119.0, 121.2, 125.4, 127.4, 129.4, 137.3, 143.0, 148.2, 162.4. Anal. calcd for $C_{16}H_{15}N_3O_3$ S (329.08) (%): C 58.34, H 4.59, N 12.76; found: C 58.25, H 4.50, N 12.69.

Acknowledgments

We are thankful to Birjand University Research Council for their support of this work.

References

(1) McDonald, E.; Jones, K.; Brough, P. A.; Drysdale, M. J.; Workman, P. *Curr. Top. Med. Chem.* **2006**, *6* (11), 1193. doi:10.2174/156802606777812086.

(2) Elguero, J. In *Comprehensive Heterocyclic Chemistry II;* Katritzky, A. R.; Rees, C. W.; Scriven, E. F. V., Eds.; Pergamon: Oxford, 1996; Vol. 5.

(3) Elguero, J.; Goya, P.; Jagerovic, N.; Silva, A. M. S. Pyrazoles as Drugs: Facts and Fantasies. In *Targets in Heterocyclic Systems;* Attanasi, O. A.; Spinelli, D., Eds.; Italian Society of Chemistry: Roma, 2002; Vol. 6, pp 52–98.

(4) Park, H.-J.; Lee, K.; Park, S.-J.; Ahn, B.; Lee, J.-C.; Cho, H. Y.; Lee, K.-I. *Bioorg. Med. Chem. Lett.* **2005**, *15* (13), 3307. doi:10.1016/j.bmcl.2005.03.082.

(5) Clark, M. P.; Laughlin, S. K.; Laufersweiler, M. J.; Bookland, R. G.; Brugel, T. A.; Golebiowski, A.; Sabat, M. P.; Townes, J. A.; Vanrens, J. C.; Djung, J. F.; Natchus, M. G.; De, B.; Hsieh, L. C.; Xu, S. C.; Walter, R. L.; Mekel, M. J.; Heitmeyer, S. A.; Brown, K. K.; Juergens, K.; Taiwo, Y. O.; Janusz, J. M. *J. Med. Chem.* **2004**, *47* (11), 2724. doi:10.1021/jm049968m.

(6) Cho, I. H.; Noh, J. Y.; Park, S. W.; Ryu, H. C.; Lim, J. W.; Kim, J. H.; Chae, M. Y.; Kim, D. H.; Jung, H. S.; Park, H. J.; Kim, Y. H.; Min, I. K. US Patent 2,004,002, 2004; p 532.

(7) Clark, M. P.; Laughlin, S. K.; Golebiowski, A.; Brugel, T. A.; Sabat, M. WO Patent 2005047, 2005; p 287.

(8) Kakiuchi, Y.; Sasaki, N.; Satoh-Masuoka, M.; Murofushi, H.; Murakami-Murofushi, K. *Biochem. Biophys. Res. Commun.* **2004**, *320* (4), 1351. doi:10.1016/j.bbrc.2004.06.094.

(9) Clark, M. P.; Bookland, R. G. *Expert Opin. Ther. Pat.* **2005**, *15* (11), 1617. doi:10.1517/13543776.15.11.1617.

(10) Ishida, M. WO Patent 2006212, 2006.

(11) Speckbacher, M.; Braun, H.-J. WO Patent 2006012, 2006; p 934.

(12) Sugiura, S.; Ohno, S.; Ohtani, O.; Izumi, K.; Kitamikado, T.; Asai, H.; Kato, K.; Hori, M.; Fujimura, H. *J. Med. Chem.* **1977**, *20* (1), 80. doi:10.1021/jm00211a016.

(13) Behr, L. C.; Fusco, R.; Jarboe, C. H. In *The Chemistry of Heterocyclic Compounds, Pyrazoles, Pyrazolines, Pyrazolidines, Indazoles and Condensed Rings;* Weissberger, A., Ed.; Interscience Publishers: New York, 1967.

(14) Rosiere, C. E.; Grossman, M. I. *Science* **1951**, *113* (2945), 651. doi:10.1126/science.113.2945.651.

(15) Bailey, D. M.; Hansen, P. E.; Hlavac, A. G.; Baizman, E. R.; Pearl, J.; Defelice, A. F.; Feigenson, M. E. *J. Med. Chem.* **1985**, *28* (2), 256. doi:10.1021/jm00380a020.

(16) Mahajan, R. N.; Havaldar, F. H.; Fernandes, P. S. *J. Indian Chem. Soc.* **1991**, *68* (4), 245.

(17) Singh, D.; Singh, D. *J. Indian Chem. Soc.* **1991**, *68* (3), 165.
(18) Londershausen, M. *Pestic. Sci.* **1996**, *48* (4), 269. doi:10.1002/(SICI)1096-9063(199612)48:4<269::AID-PS478>3.0.CO;2-B.
(19) Lube, H. A. *The Chemistry of Synthetic Dyes and Pigments;* American Chemical Society: Washington, DC, 1970.
(20) Garnovskii, A. D.; Uraev, A. I.; Minkin, V. I. *ARKIVOC* **2004**, *2004* (iii), 29.
(21) Singh, D.; Singh, D. *J. Chem. Eng. Data* **1984**, *29* (3), 355. doi:10.1021/je00037a040.
(22) Pavlov, P. T.; Goleneva, A. F.; Lesnov, A. E.; Prokhorova, T. S. *Pharm. Chem. J.* **1998**, *32* (7), 370. doi:10.1007/BF02645994.
(23) Buzykin, B. I.; Lonshchakova, T. I. *Bull. Acad. Sci. USSR, Div. Chem. Sci.* **1971**, *20* (10), 2224. doi:10.1007/BF00851295.
(24) Wang, W.; Wang, S.-X.; Qin, X.-Y.; Li, J.-T. *Synth. Commun.* **2005**, *35* (9), 1263. doi:10.1081/SCC-200054854.
(25) Elinson, M. N.; Dorofeev, A. S.; Nasybullin, R. F.; Nikishin, G. I. *Synthesis* **2008**, *2008* (12), 1933. doi:10.1055/s-2008-1067079.
(26) Sujatha, K.; Shanthi, G.; Selvam, N. P.; Manoharan, S.; Perumal, P. T.; Rajendran, M. *Bioorg. Med. Chem. Lett.* **2009**, *19* (15), 4501. doi:10.1016/j.bmcl.2009.02.113.
(27) Niknam, K.; Saberi, D.; Sadegheyan, M.; Deris, A. *Tetrahedron Lett.* **2010**, *51* (4), 692. doi:10.1016/j.tetlet.2009.11.114.
(28) Hasaninejad, A.; Shekouhy, M.; Zare, A.; Hoseini Ghattali, S. M. S.; Golzar, N. *J. Iran. Chem. Soc.* **2011**, *8* (2), 411.
(29) Niknam, K.; Mirzaee, S. *Synth. Commun.* **2011**, *41* (16), 2403. doi:10.1080/00397911.2010.502999.
(30) Sobhani, S.; Hasaninejad, A.-R.; Maleki, M. F.; Parizi, Z. P. *Synth. Commun.* **2012**, *42* (15), 2245. doi:10.1080/00397911.2011.555589.
(31) Sobhani, S.; Safaei, E.; Hasaninejad, A. R.; Rezazadeh, S. *J. Organomet. Chem.* **2009**, *694* (18), 3027. doi:10.1016/j.jorganchem.2009.05.004.
(32) Hasaninejad, A. R.; Zare, A.; Shekouhy, M.; Golzar, N. *Org. Prep. Proced. Int.* **2011**, *43* (1), 131. doi:10.1080/00304948.2010.526827.
(33) Mosaddegh, E.; Hassankhani, A.; Baghizadeh, A. *J. Chil. Chem. Soc.* **2010**, *55* (4), 419. doi:10.4067/S0717-97072010000400001.
(34) Mustafa, A.; Fleifel, A. M.; Ali, M. I.; Hassan, N. M. *Justus Liebigs Ann. Chem.* **1970**, *739* (1), 75. doi:10.1002/jlac.19707390111.
(35) Perkalin, V. V.; Sopava, A. S. *Uch. Zap. Leninger. Gos. Ped. Inst.* **1959**, *160*, 45.
(36) Welton, T. *Chem. Rev.* **1999**, *99* (8), 2071. doi:10.1021/cr980032t.
(37) Wasserscheid, P.; Keim, W. *Angew. Chem. Int. Ed.* **2000**, *39* (21), 3772.
(38) Mi, X.; Luo, S.; Cheng, J. P. *J. Org. Chem.* **2005**, *70* (6), 2338. doi:10.1021/jo048391d.
(39) Hangarge, R. V.; Jarikote, D. V.; Shingare, M. S. *Green Chem.* **2002**, *4* (3), 266. doi:10.1039/b111634g.
(40) Singh, V.; Kaur, S.; Sapehiyia, V.; Singh, J.; Kad, G. L. *Catal. Commun.* **2005**, *6* (1), 57. doi:10.1016/j.catcom.2004.10.011.
(41) Wasserscheid, P.; Welton, T. *Ionic Liquid in Synthesis;* Wiley-VCH: Weinheim, 2004.
(42) Zhang, S. J.; Yuan, X. L.; Chen, Y. H.; Zhang, Y. Q. Chin. Patent 10069408.5, 2005.
(43) Yue, C.; Mao, A.; Wei, Y.; Lü, M. *Catal. Commun.* **2008**, *9* (7), 1571. doi:10.1016/j.catcom.2008.01.002.
(44) Shaterian, H. R.; Honarmand, M. *Synth. Commun.* **2011**, *41* (23), 3573. doi:10.1080/00397911.2010.519594.
(45) Zang, H.; Su, Q.; Mo, Y.; Cheng, B. *Ultrason. Sonochem.* **2011**, *18* (1), 68. doi:10.1016/j.ultsonch.2010.08.001.
(46) Zang, H.; Su, Q.; Guo, S.; Mo, Y.; Cheng, B. *Chin. J. Chem.* **2011**, *29* (10), 2202. doi:10.1002/cjoc.201180381.

Can. J. Chem. Downloaded from www.nrcresearchpress.com by MCGILL UNIVERSITY on 02/02/13
For personal use only.

Separation of bitumen from oil sands using a switchable hydrophilicity solvent

Amy Holland, Dominik Wechsler, Anjali Patel, Brian M. Molloy, Alaina R. Boyd, and Philip G. Jessop

Can. J. Chem. Downloaded from www.nrcresearchpress.com by MCGILL UNIVERSITY on 02/02/13
For personal use only.

Abstract: Separation of bitumen from oil sands is far more efficient with an organic solvent than with the conventional hot water (Clark) process, but the removal of the organic solvent from the bitumen requires distillation. Distillation is problematic because of the energy cost and the need for a volatile solvent (which is therefore likely to be flammable and smog-forming). A switchable hydrophilicity solvent (SHS) is a solvent that is water-miscible in the presence of an atmosphere of CO_2 but separates from water when CO_2 is absent. Extraction of bitumen from low-grade high-fines oil sands using a SHS ($CyNMe_2$) is efficient, removing 94%–97% of the bitumen. The resulting solids (sand and clay) are dry, free-flowing, and contaminated with only 0.4 wt % of bitumen and as little as 102 ppm of the solvent. No distillation step was required to recover the solvent from the bitumen. Instead, carbonated water extraction removed the solvent from the oil. Losses of the $CyNMe_2$ solvent were, for the best method, 0.06 grams of solvent per gram of bitumen recovered. The method recovers more oil than the Clark process, produces cleaner solids, works with low-grade high-fines oil sands, and requires neither distillation nor a volatile solvent.

Key words: oil sands, solvent, carbon dioxide, extraction, bitumen.

Résumé : La séparation du bitume à partir des sables bitumineux est beaucoup plus efficace avec un solvant organique que par le procédé conventionnel de Clark avec de l'eau chaude; toutefois, la séparation du bitume et du solvant organique nécessite une distillation. La distillation est problématique en raison du coût de l'énergie et de la nécessité d'utiliser un solvant volatil (qui est selon toute vraisemblance plus inflammable et plus susceptible de former du smog). Un solvant dont le caractère hydrophile peut être commutable (SCC) est un solvant qui est miscible dans l'eau en présence d'une atmosphère de CO_2, mais qui se sépare de l'eau quand le CO_2 est absent. L'utilisation d'un SCC ($CyNMe_2$) pour l'extraction du bitume à partir des sables bitumineux extra fins de faible qualité est efficace, enlevant de 94 % à 97 % du bitume. Les solides qui en résultent (sable et argile) sont secs, d'une grande fluidité et ne sont contaminés que par 0,4 % en poids de bitume et aussi peu que 102 ppm de solvant. Aucune étape de distillation n'est nécessaire pour récupérer le solvant du bitume. Il faut plutôt utiliser de l'eau pétillante pour enlever le solvant de l'huile. On a établi que les pertes du solvant $CyNMe_2$ s'élèvent, pour la meilleure méthode, à 0,06 grammes de solvant par gramme de bitume récupéré. La méthode permet de récupérer plus d'huile que le procédé de Clark, elle permet de produire des solides plus propres, elle peut être utilisée pour des sables bitumineux extra fins de faible qualité et elle ne nécessite aucune distillation et aucun solvant volatil.

Mots-clés : sables bitumineux, solvant, dioxyde de carbone, extraction, bitume.

[Traduit par la Rédaction]

Introduction

Separation of the bitumen from bituminous sand (popularly known as "oil sands") is currently performed as a flotation process using large quantities of hot and alkaline water. The resulting separation is incomplete, leaving sand and clay particles suspended in water and contaminated with bitumen (10% or more of the original amount).[1] The suspension is then left in a tailings pond to settle over years. Wildfowl landing in the tailings ponds have been killed by exposure to the bitumen. The current flotation method is also limited because it is incapable of separating "oil-wet" bituminous sand (meaning that the oil and the solid materials (sand and clay) are in direct contact rather than having an intervening layer of water). About 20% of Canada's geologically accessible deposits and much of those in the US are oil-wet. For these reasons, alternative extraction processes have been sought for many years.

A much cleaner separation of bitumen from sand and clay could be achieved with an organic solvent extraction, but the conventional method of removing organic solvent from product is distillation. Examples of organic solvent-based processes include the Nevtah LES process (using hydrocarbon

Received 26 April 2012. Accepted 4 July 2012. Published at www.nrcresearchpress.com/cjc on 3 October 2012.

A. Holland, D. Wechsler, and B.M. Molloy. GreenCentre Canada, 945 Princess Street, Kingston, ON K7L 3N6, Canada.
A. Patel and A.R. Boyd. Department of Chemistry, Queen's University, Kingston, ON K7L 3N6, Canada.
P.G. Jessop. Department of Chemistry, Queen's University, Kingston, ON K7L 3N6, Canada; GreenCentre Canada, 945 Princess Street, Kingston, ON K7L 3N6, Canada.

Corresponding author: P.G. Jessop (e-mail: jessop@chem.queensu.ca).

Can. J. Chem. Downloaded from www.nrcresearchpress.com by MCGILL UNIVERSITY on 02/02/13
For personal use only.

solvents),[2] the Dravo Process (heptane/cyclohexane/ethanol mixture),[3,4] the Dow–Kellog process (CH_2Cl_2),[5,6] and the SESA process (naphtha or kerosene).[7,8] In every case, extraction of the bitumen is followed by a distillation step to remove the solvent, which is problematic because it requires both significant energy input and the use of a volatile solvent. Volatile solvents are flammable, contribute to smog, and cause inhalation risks to workers; they can be toxic, carcinogenic, neurotoxic, mutagenic, or narcotic, all by inhalation. In contrast, nonvolatile or low-volatility solvents do not pose these problems, or pose them to a lesser degree, but such solvents are usually avoided because they cannot be removed by distillation. If a nondistillative method for removal of solvent from bitumen could be identified, then organic solvent extraction could be a viable method for the separation of bituminous sand.

In earlier publications, we described several switchable hydrophilicity solvents (SHS),[9,10] including cyclohexyldimethylamine ($CyNMe_2$). An SHS is a solvent that can readily interconvert between two forms; one form is hydrophobic and forms a biphasic mixture when mixed with water (this is the normal behaviour for $CyNMe_2$). The other form is hydrophilic and completely miscible with water. The trigger for the change to hydrophilic is the addition of CO_2 at 1 bar (1 bar = 100 kPa) (which converts $CyNMe_2$ into water-soluble $[CyNHMe_2][HCO_3]$), whereas the trigger for the return to hydrophobic is the removal of the CO_2. These solvents can be used, in the absence of CO_2, for applications that would normally require a hydrophobic solvent, such as the extraction of oil from an oily solid. The SHS can then be washed out of the oil with carbonated water, leaving pure oil product. The separation of the SHS from the carbonated water is triggered by the removal of the CO_2. Thus, product and solvent can be separated from each other without distillation and without requiring a volatile solvent. We have reported this process for the extraction of soybean oil from soybeans[9] and algae lipids from microalgae.[11] Whether this process can be applied to the separation of bitumen from oil sands is the subject of this paper.

Results and discussion

In all experiments described in this report, low-grade, high-fines, water-wet oil sands were used.

The ability of $CyNMe_2$ to dissolve bitumen from oil sands

First, the ability of $CyNMe_2$ to dissolve bitumen was established. A sample of bitumen was obtained by toluene extraction from oil sands, followed by a Büchner funnel filtration to remove the solids. After removal of the toluene from the bitumen by evaporation, $CyNMe_2$ was added to dissolve the bitumen. The bitumen entirely dissolved, demonstrating that $CyNMe_2$ is able to dissolve all of the toluene-soluble bitumen.

To determine whether the SHS can dissolve asphaltenes, $CyNMe_2$ was used to extract bitumen from oil sands. $CyNMe_2$ was removed by extraction with carbonated water and the bitumen was then mixed with *n*-pentane. A large amount of bitumen remained undissolved. The insoluble solid material was isolated and then heated, causing it to melt into a black tar, showing that the solids were asphaltenes rather than mineral fines. This demonstrates that $CyNMe_2$ is capable of dissolving bitumen containing a substantial amount of asphaltenes.

The time required to extract bitumen from oil sands using an organic solvent depends on the solvent choice. Mixing a lump of oil sand (30–50 g) with solvent (a ratio of 5:1.5 oil sands/solvent by mass) visually demonstrated the effect of solvent choice (see Figs. 1–4 in the Supplementary data). Using hot water, after 15 min without stirring, the oil sands chunk remained intact and no dissolution was observed visually. After stirring, the solid chunk was observed to slowly break up and the water became discoloured. With hexanes, a small amount of dissolution was observed with or without stirring, and again breakup of the solid material was slow. With toluene, good extraction was observed in 15 min but breakup required stirring. With $CyNMe_2$, good extraction was observed in 5 min; the oil sands chunk broke up with minimal stirring, showing that the $CyNMe_2$ was much more efficient at dissolving the bitumen from the oil sands.

Separation of solvent from bitumen

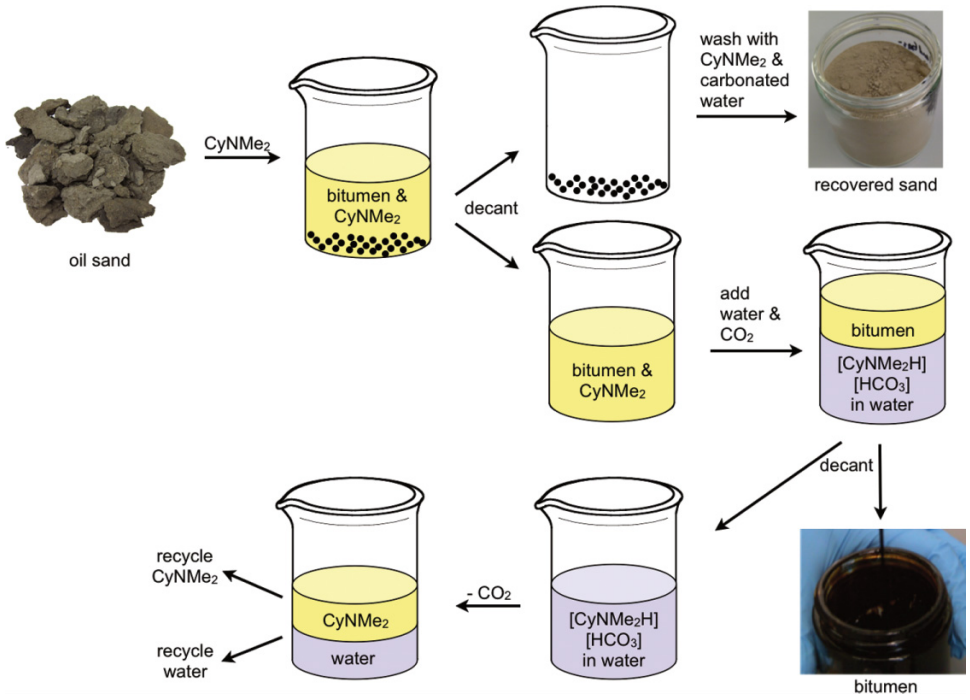
The proposed oil sands separations process (Fig. 1) starts with a conventional extraction of the bitumen from the sand and clay using an SHS ($CyNMe_2$) in its hydrophobic form. After filtration or decantation, the solids are separated from the bitumen/solvent mixture. The solids are washed with fresh solvent and then carbonated water. The bitumen/solvent mixture is then treated with carbonated water to extract the $CyNMe_2$ by converting it to the water-soluble bicarbonate salt $[CyNMe_2H][HCO_3]$. The washed bitumen is then removed by decantation, and the bicarbonate salt solution is heated and treated with either N_2 or air to remove the CO_2. The $CyNMe_2$ solvent separates from the water. Both the amine and the water can be reused.

Because the bitumen content of oil sands varies from sample to sample, tests of the extraction method were performed on six samples and the results averaged. These small-scale tests, using 25 g samples of oil sands, showed that the average mass of bitumen recovered by this process was 1.9 g, although 0.23 g of that material was residual $CyNMe_2$ remaining in the bitumen (12 wt % contamination of the bitumen) and 0.14 g was water (average 7% water content). Thus, the actual mass of bitumen, not including residual solvent and water, was 1.5 g (6% of the original mass of the oil sands sample). The amount of water in the bitumen was insufficient to have carried with it much $CyNMe_2$ or its salt, so the residual $CyNMe_2$ in the bitumen is believed to be dissolved in the oil phase rather than in entrained or emulsified water. The wt % solids in the bitumen was zero, within experimental error. Because of the high viscosity of the bitumen, some losses of bitumen to the sides of the glassware were unavoidable.

The recovered sand/clay mixture was dry and free flowing (mass 22.5 g or 90% of the original mass). Toluene washing of the solids showed that, on average, they contained 0.096 g of residual bitumen (0.4 wt % of the mass of solids). Thus, the removal of bitumen from the oil sand was at least 94% complete. Keeping in mind that some bitumen was lost to the sides of the glassware, the extraction of bitumen was likely somewhat more than 94% complete. A second extraction would presumably greatly increase this value. Simply rinsing the solids with $CyNMe_2$ multiple times while still on the filter,

Can. J. Chem. Downloaded from www.nrcresearchpress.com by MCGILL UNIVERSITY on 02/02/13
For personal use only.

Fig. 1. The proposed process for separating bitumen from oil sands.



rather than doing a second extraction, increases the bitumen removal to over 97% complete.

The total recovery of solids and bitumen is 24 g, which is 96% of the original mass of the oil sands sample. Most of the remaining 4% is likely the water content of the oil sands.

The process required a total of 45 mL (53 g) of $CyNMe_2$ to wash the 25 g of oil sands, corresponding to 2.1 grams of solvent per gram of oil sands. Of the 53 g of solvent, 0.23 g (0.4%) was lost to the bitumen and 0.007 g to the sand/clay solid product.

Two large-scale tests, using 500 g samples of oil sands, were performed. To economize on the amount of solvent, these tests were performed with only 213 g of $CyNMe_2$, or 0.42 grams of solvent per gram of oil sands. Nevertheless, the results were similar. The recovered bitumen fraction was 52 g and contained 12 wt % SHS and 14% water; the amount of pure bitumen was therefore 38.5 g (7.7% of the original mass). The recovered sand/clay solid product was 455 g (91% of the original mass).

The mixing method during the treatment of the bitumen/$CyNMe_2$ mixture with carbonated water was merely the agitation caused by the CO_2 bubbling. Tests were also performed with an overhead stirrer at 2500 rpm to see whether better mixing could help lower the concentration of residual amine in the bitumen. Using this method, the average amount of amine remaining in the bitumen was 8 wt %. After the mixture was allowed to settle for 16 h, the amine content was reduced to 5%. This represents a significant improvement, cutting the losses of amine to bitumen by more than half. This blending treatment did not significantly affect the water content of the bitumen, which was still 7%. Thus, the actual bitumen content of this fraction was 88%, and the loss of $CyNMe_2$ was 0.06 grams per gram of recovered bitumen (i.e., 5 grams of solvent per 88 grams of bitumen).

Table 1. Residual solvent content of sand/clay solids after repeated washes with carbonated water.

	$CyNMe_2$ on solids (ppm)	
No. of washings	After 5 min	After 30 min
1	892	646
2	575	314
3	158	—
4	102	—

Note: A 75–80 g sample of contaminated sand/clay mixture containing 6.4 wt % $CyNMe_2$, washed with 100 mL of carbonated water for the times indicated.

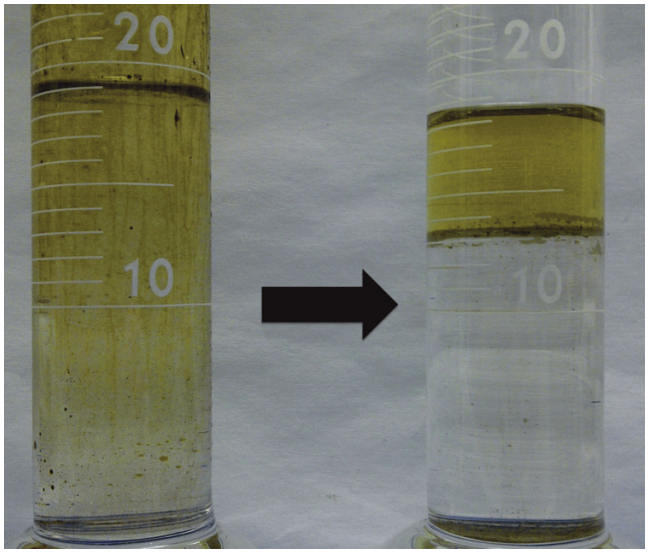
Tests were also performed with a blender, which stirs at >15 800 rpm: bitumen contaminated with 12 wt % $CyNMe_2$ was mixed with carbonated water using this blender for 1 min periods followed by 1 min of CO_2 bubbling without mixing. After 15 such cycles, the contamination of the bitumen had dropped to 8 wt %.

Separation of solvent from the sand/clay solids

The solids liberated from the bitumen should have a low amine content (ideally <300 ppm) so that it can be returned to the environment. The solids, immediately after being washed with $CyNMe_2$, contained 6.4 wt % amine (64 000 ppm). Washing a 75 g sample of these contaminated solids with 100 mL normal water (uncarbonated) lowered the contamination to 1.7%. Four such washes brought the contamination down to 480 ppm. Washing with carbonated water is more efficient (Table 1), bringing the amine content to the desired level of ~300 ppm after only two washes. Note that samples below 1500 ppm have no odor.

Can. J. Chem. Downloaded from www.nrcresearchpress.com by MCGILL UNIVERSITY on 02/02/13
For personal use only.

Fig. 2. The mixture of carbonated water and $CyNMe_2$ after the bitumen has been decanted (left) and the same mixture after the CO_2 has been removed (right). The organic layer is coloured because of residual bitumen.



Separation of solvent from carbonated water

The recovery of $CyNMe_2$ from the carbonated aqueous layer requires the effective removal of the CO_2 from the aqueous phase. Heating the water/$CyNMe_2$/CO_2 mixture to 70 °C for 1 h with continuous bubbling of nitrogen through the liquid, via a gas dispersion tube, caused the amine to form a second liquid phase (Fig. 2). The composition of the aqueous phase was 16 wt % amine. The aqueous phase was reused repeatedly, carrying a constant 16 wt % amine every cycle after the first.

No solids are visible in the aqueous phase before or after amine removal. The wt % solids in the aqueous phase after one use was found gravimetrically to be the same as that in the fresh water supply, within experimental error.

Performing the CO_2 removal with slightly reduced pressure (750 mbar) rather than nitrogen bubbling was not as effective. While an amine phase did appear, the aqueous phase still contained 31 wt % amine.

For the SHS process to be industrially viable, the reuse of solvent is necessary. To determine if the solvent changed at all after multiple uses, $CyNMe_2$ was cycled through the process four times and was studied spectroscopically after each cycle (^{1}H NMR, GC, and IR are shown in the Supplementary data). Overall, no change in the $CyNMe_2$ was observed. Because the solvent is being purified by the treatment with carbonated water and because there is no high-temperature step, there should be no significant degradation of the solvent; the solvent should only need to be topped up with fresh solvent because of losses to the bitumen and the sand/clay solids.

Conclusion

Separation of bitumen from low-grade high-fines oil sands was achieved by using $CyNMe_2$ as a switchable hydrophilicity solvent, as shown in Fig. 1. This solvent dissolves bitumen from the oil sands more readily than toluene or hexanes. The resulting sand/clay solids were dry, free-flowing, and contaminated with only 0.4 wt % of bitumen. The removal of bitumen from the oil sands was 94%–97% complete. Subsequent removal of the solvent from the sand/clay solids by carbonated water rinses brought the solvent content of the solids down as low as 102 ppm. The used carbonated water could then be reused for solids washing or for solvent recovery from the bitumen.

Although $CyNMe_2$ is an oil-miscible organic solvent, no distillation step was required to recover the solvent from the bitumen. Instead, carbonated water extraction removed the solvent from the oil. The isolated bitumen did not contain a detectable quantity of solids but did contain some residual solvent. When the best method was used, losses of the $CyNMe_2$ solvent were 0.06 grams of solvent per gram of solvent-free bitumen recovered.

Further research is being performed to reduce the amount of solvent remaining in the bitumen.

Table 2. Composition and properties of the low-grade high-fines oil sands ore.

Parameter	Value
Bitumen	7.5%
Fines	37%
D50	75 μm
MBI	3.8
Na	200 ppm
K	4.3 ppm
Ca	1.0 ppm
Mg	0.4 ppm

Experimental methods

Equipment and materials

The oil sands samples were low-grade ore having a high fines content, received from the Horizon site of Canadian Natural Resource Ltd., Fort McMurray, Alberta, Canada. The samples were stored in a sealed container in a freezer at –15 °C until needed. Characterization of the oil sands from that part of the formation is given in Table 2. $CyNMe_2$was purchased from Acros Organics and used without further purification. The CO_2 was 99.8% purity or greater. Carbonated water was prepared by bubbling CO_2 via a gas dispersion tube into tap water at 1 atm (1 atm = 101.325 kPa).

After separations, the amount of solvent remaining in the bitumen was determined by ^{1}H NMR spectroscopy. The amount of water remaining in the bitumen was determined with a Karl-Fisher coulometer. The amount of solid matter remaining in the bitumen was determined by thermogravimetric analysis.

NMR and IR spectroscopy and gas chromatography were performed with a Varian 400 MHz NMR spectrometer, a Varian 660 FT-IR in ATR mode, and a Varian 450 GC-FID.

Small-scale extractions

Oil sands (25 g), a magnetic stir bar, and then $CyNMe_2$ (20 mL) were placed in a 150 mL glass beaker and stirred magnetically at 125 rpm for 10 min. The resulting slurry was split between two 125 mL centrifuge bottles with an additional 5 mL of $CyNMe_2$ added to wash any remaining solids in the beaker into the bottles. The sample was centrifuged at 1500 rpm for 30 min followed by decantation of the supernatant, although some fine

Can. J. Chem. Downloaded from www.nrcresearchpress.com by MCGILL UNIVERSITY on 02/02/13
For personal use only.

particles remained in the supernatant. To wash the liberated sand/clay solids, fresh $CyNMe_2$ (10 mL) was added to the solids and the mixture was centrifuged at 1500 rpm for 30 min and decanted; this washing procedure was then performed once more. The solids were washed with 30 mL of carbonated water and centrifuged at 1500 rpm for 30 min. The water (containing some solvent and fine particles) was removed by decantation and the solids were allowed to air dry. The combined organic supernatants had a total volume of approximately 45 mL.

The combined organic supernatant layers were filtered using a Büchner funnel with No. 1 filter paper to remove fine particles (Table 1). The filtrate was added to a 250 mL glass graduated cylinder containing 90 mL of precarbonated water. Additional carbon dioxide was bubbled into the aqueous layer via a gas dispersion tube for 90 min at atmospheric pressure. When the solvent switch was complete, the bitumen became very viscous and started to clump together. The bitumen was removed by decantation. The amount of solvent, water, and solid matter remaining in the bitumen was determined.

The extraction was performed six times and the results averaged.

Large-scale extractions

Standard method

Oil sands (500 g) and then $CyNMe_2$ (150 mL, 127 g) were placed in a 2 L glass beaker and stirred using an overhead stirrer impeller at 800 rpm for 10 min. The resulting slurry was transferred to a Büchner funnel with No. 1 filter paper using 50 mL (43 g) of solvent. The beaker was rinsed with an additional 50 mL (43 g) of $CyNMe_2$, which was then passed through the filter, thereby rinsing the sand/clay solids in the filter. The organic filtrate (300 mL) was removed from the apparatus and split into two aliquots. The solids on the filter paper were rinsed with 400 mL of carbonated water.

At this point, the organic filtrate was split in half and the two halves processed differently. The results described previously were obtained with the following method. Half of the organic filtrate (150 mL) was added to 300 mL of carbonated water in a 600 mL PTFE beaker. Carbon dioxide at atmospheric pressure was bubbled through the mixture via a glass gas-dispersion tube until the bitumen layer was clumping together, which took 2–4 h. The bitumen was removed by decantation. The amounts of solvent, water, and solid matter remaining in the bitumen were determined and corrected to represent the entire sample rather than just the half.

The experiment was performed twice and the results averaged.

High shear variation

A portion of the organic filtrate (100 mL) obtained using the standard method was added to 200 mL of carbonated water in a 600 mL PTFE beaker equipped with an overhead stirrer and a gas dispersion tube for carbon dioxide introduction. The solution was mechanically stirred at 2500 rpm and continuously bubbled with carbon dioxide for 2 h. Bitumen samples were taken immediately after bubbling and stirring was stopped and again after the mixture was allowed to sit for 16 h. Samples were analyzed for solvent and water content only.

Using a blender to help remove residual $CyNMe_2$ from the bitumen

Previously isolated bitumen (398 g) was transferred to a blender (Waring model LBC15) and homogenized for several seconds. A small sample was removed and analysed by ^{1}H NMR spectroscopy, which showed the presence of 12.6 wt % $CyNMe_2$. Carbonated water (500 mL), containing 16 wt % $CyNMe_2$ (because it had been used already to remove $CyNMe_2$), was added to the blender and sank below the bitumen. CO_2 was bubbled through the mixture via a gas dispersion tube placed so that the gas would be delivered to the aqueous phase. The bitumen/water mixture was blended at 15 800 rpm for fifteen 1 min intervals with 1 min of rest between each blending cycle, with CO_2 bubbling continued throughout. After the 15 cycles, a sample of the bitumen was removed for analysis by ^{1}H NMR spectroscopy. The bitumen was allowed to settle overnight, after which samples of bitumen were taken for ^{1}H NMR spectroscopy from the cover, wall of the blender, the layer of the bitumen on top of the aqueous phase, and the frit that was used to deliver CO_2.

Observing asphaltene content in recovered bitumen

Testing $CyNMe_2$-extracted bitumen with n*-pentane and toluene*

Bitumen that had been extracted with $CyNMe_2$ (the majority of which was then removed by carbonated water) was weighed into three separate beakers.

In one beaker, 25 mL of *n*-pentane was added to 2.3 g of the bitumen and swirled. A spatula was used to aid in the dissolution by mixing and (or) stirring the bitumen, but some solid material never dissolved. The liquid portion was filtered using a Büchner funnel and an additional 40 mL of pentane was added to the beaker. Even with more stirring, the residual solids did not dissolve in the additional pentane. The material in the beaker was filtered using the Büchner funnel. The residual solids weighed 0.63 g. To confirm that these solids were organic rather than sand or clay, the solids were placed on a watch glass and heated with a heat gun until they melted into a black tar.

Similar experiments were performed with toluene (25 mL of toluene dissolving 2.0 g of bitumen) and with $CyNMe_2$ (25 mL of $CyNMe_2$ dissolving 2.0 g of bitumen) instead of pentane; in both cases, dissolution was complete and no solids were observed visually.

Dissolving toluene-extracted bitumen with $CyNMe_2$

In a beaker, 34 g of oil sands was extracted twice with 10 mL of toluene, using a Büchner funnel to filter the liquids each time. The combined filtrate was transferred to a round-bottom flask and the solvent was removed by rotary evaporation followed by addition of methanol and evaporation of the methanol/toluene azeotrope. $CyNMe_2$ (20 mL) was then added to the resulting bitumen. Dissolution was complete and no solids were observed.

Removal of residual $CyNMe_2$ from the recovered sand/clay solids

Preparation of the sand/clay solids sample

Oil sands were washed with $CyNMe_2$, after which the slightly wet filtered solids were stored in a sealed jar. Small samples were placed into three 4 dram vials and ~2 mL of $CDCl_3$ was added to each vial, followed by 10 μL of ethyl acetate as an internal standard. The samples were shaken vigorously to remove any $CyNMe_2$ from the solids. The supernatant was removed and filtered into an NMR tube.

Can. J. Chem. Downloaded from www.nrcresearchpress.com by MCGILL UNIVERSITY on 02/02/13
For personal use only.

Analysis of the liquid by NMR spectroscopy showed that the solids contained an average of 6.4 wt % $CyNMe_2$.

Washing the recovered solids with carbonated water

A 75–80 g sample of the slightly $CyNMe_2$-wet solids was placed into a 600 mL PTFE beaker with 100 mL of tap water. The mixture was stirred at 2400 rpm using an overhead stirrer equipped with a four-blade, 5 cm propeller, for the desired time, with or without CO_2 bubbling during the stirring. If CO_2 was used, it was added to the solution by bubbling through a gas dispersion tube at 1 atm. After the desired time, the solids were filtered using a Büchner funnel and No. 2 filter paper. If additional washes were required, the solids were scraped back into the beaker and a fresh 100 mL of tap water was added. The stirring and bubbling with CO_2 was repeated if necessary. After the final wash, the solids were filtered with the Büchner funnel and an additional 100 mL of tap water was poured over top to push through any residual carbonated water. The solids were scraped into a jar to be kept for analysis of $CyNMe_2$ content. Three samples of the solids were taken for NMR analysis. The samples were made by weighing an amount of the solids into a preweighed 1 dram vial, adding ~1 mL of $CDCl_3$ and 10 μL of EtOAc as an internal standard. The sample was shaken vigorously and the supernatant was filtered into an NMR tube. The wt % of $CyNMe_2$ on the solids was determined from an average of the three samples.

Comparing $CyNMe_2$ with other conventional solvents

Each sample of oil sand (30–50 g) was combined with solvent (1.5 grams of solvent per 5 grams of oil sands and either hexanes, hot water, toluene, or $CyNMe_2$) and visual observations were made every 5 min.

Recovery of solvent from carbonated water

All experiments were repeated at least twice to verify results, unless otherwise stated.

Using vacuum to recover the amine from the aqueous layer

A 32.3 wt % solution of $CyNMe_2$ (in its protonated form) in carbonated water was obtained as the aqueous fraction from an oil sands extraction performed as shown in Fig. 1. A 25 mL sample of this mixture was measured into a 500 mL round-bottom flask. The round-bottom flask was attached to a water condenser that was chilled to 5 °C, using an ethylene glycol/water chiller. A fractionation column was attached on top of the condenser to help with the evaporation problem and then a vacuum adaptor was attached to the top of the fractionation column. Using a diaphragm pump and vacuum controller the vacuum was set to the desired pressure. The round-bottom flask assembly was placed in a preheated oil bath set to the desired temperature. After the desired time, the solution was cooled and the pressure was released. The solution was decanted into a 50 mL graduated cylinder and the volumes of the layers were recorded. The concentration of DMCA in the aqueous layer was measured by removing an aliquot for analysis by NMR (using ethyl acetate as the internal standard and d_3-acetonitrile as the solvent).

Using nitrogen as a purge to recover $CyNMe_2$ from the aqueous layer

A 25 mL sample of the 32.3 wt % solution of $CyNMe_2$ in carbonated water was measured into a 500 mL two-neck round-bottom flask. One neck of the round-bottom flask was attached to a water condenser that was chilled to 5 °C, using an ethylene glycol / water chiller. A fractionation column was attached on top of the condenser, to further inhibit evaporative losses, and left open to the atmosphere. The second neck of the round-bottom flask was attached to a gas dispersion tube to deliver nitrogen at atmospheric pressure. The round-bottom flask was placed in a preheated oil bath set to the desired temperature. After the desired time, the solution was cooled and decanted into a 50 mL graduated cylinder to allow measurement of the volumes of the layers recovered. The concentration of $CyNMe_2$ in the aqueous layer was measured by removing an aliquot for analysis by ^1H NMR (using ethyl acetate as the internal standard and d_3-acetonitrile as the solvent).

Supplementary data

Supplementary data are available with the article through the journal Web site http://nrcresearchpress.com/doi/suppl/10.1139/v2012-061.

Acknowledgements

We gratefully acknowledge the donation of oil sands samples and the characterization of that ore by Canadian Natural Resources Ltd. and funding from the Natural Sciences and Engineering Research Council of Canada (NSERC), the Walter C. Sumner Foundation, and the Canada Research Chairs program. P.G.J. thanks the Killam Trusts/Canada Council for the Arts for a fellowship. Switchable Solutions Inc. is thanked for supporting and commercializing the switchable hydrophilicity solvent technology.

References

(1) *Oil Sands;* Government of Alberta Web site. http://www.energy.alberta.ca/OilSands/1715.asp (accessed January 2012).
(2) *The Joint Venture Partner's Proven Technology;* Nevtah Capital Management Corp. Web site. http://www.nevtahoilsands.com/index.html (accessed Jan. 2012).
(3) Williams, B. *Oil Gas J.* **1982**, *80* (3), 66.
(4) Tis, D. J.; Culbertson, R. W.; Kelley, M. N. *Energy Progress* **1984**, *4* (1), 56.
(5) Haschke, E. M.; Gimber, G. A.; Groves, K. O. U.S. Patent, 4532024 A 19850730, 1985.
(6) Ayasse, C.; Cover, A. E. *Advances in Petroleum Recovery and Upgrading Technology Conference, 6th Conference;* Alberta Oil Sands Technology and Research Authority: Edmonton, Alberta, 1985.
(7) Meadus, F. W.; Bassaw, B. P.; Sparks, B. D. *Fuel Process. Technol.* **1982**, *6* (3), 289. doi:10.1016/0378-3820(82)90008-X.
(8) Meadus, F. W.; Chevrier, P. J.; Sparks, B. D. *Fuel Process. Technol.* **1982**, *6* (3), 277. doi:10.1016/0378-3820(82)90007-8.
(9) Jessop, P. G.; Phan, L.; Carrier, A.; Robinson, S.; Dürr, C. J.; Harjani, J. R. *Green Chem.* **2010**, *12* (5), 809. doi:10.1039/b926885e.
(10) Jessop, P. G.; Kozycz, L.; Rahami, Z. G.; Schoenmakers, D.; Boyd, A. R.; Wechsler, D.; Holland, A. M. *Green Chem.* **2011**, *13* (3), 619. doi:10.1039/c0gc00806k.
(11) Boyd, A. R.; Champagne, P.; McGinn, P. J.; MacDougall, K. M.; Melanson, J. E.; Jessop, P. G. *Bioresour. Technol.* **2012**, *118,* 628. doi:10.1016/j.biortech.2012.05.084.

Revised mechanism for the hydrolysis of ethers in aqueous acid[1]

Robin A. Cox

Can. J. Chem. Downloaded from www.nrcresearchpress.com by MCGILL UNIVERSITY on 02/02/13
For personal use only.

Abstract: It has been shown recently that many supposed reaction intermediates in aqueous media do not have lifetimes long enough for them to serve this purpose. Among these are oxygen-protonated species where the positive charge is not delocalized, primary and secondary carbocations, and the commonly written species H_3O^+ and HO^-. This means that the mechanisms for many of the organic reactions that take place in aqueous media are in need of revision. This paper concerns the acid hydrolysis of simple ethers, many of which cannot form carbocations stable enough to exist in water. Rather than an A1 process in which an oxygen-protonated species dissociates into an alcohol and a carbocation, which is then quenched by water, or an A2 process in which a water molecule or another nucleophilic species assists in this, the mechanism for most ethers is a general-acid-catalyzed process in which proton transfer to oxygen is concerted with C–O bond cleavage in cases where a stable carbocation can exist, or additionally concerted with nucleophilic attack for those cases in which stable carbocation formation is not possible. All of the cases for which rate constant data could be found in the literature are analyzed and discussed in this paper, with the exception of the hydrolyses of several azoethers, where additional hydrolysis mechanisms are possible. These will be discussed in a subsequent paper.

Key words: ethers, hydrolysis, excess acidity, mechanism, acid media.

Résumé : Il a été démontré récemment que plusieurs intermédiaires réactionnels potentiels pour des réactions dans des milieux aqueux n'ont pas de temps de vie suffisants pour servir à ces fins. Parmi ceux-ci, les espèces contenant un oxygène protoné dans lesquelles la charge positive n'est pas délocalisée, les carbocations primaires et secondaires et les espèces communément représentées pas les formules H_3O^+ et HO^-. Cette observation implique qu'il faut réviser plusieurs mécanismes de réactions organiques se produisant dans des milieux aqueux. Dans ce travail, on examine particulièrement le cas des catalyses acides d'éthers simples pour lesquels plusieurs ne peuvent pas former de carbocations suffisamment stables pour exister dans l'eau. Plutôt q'un processus A1 dans lequel une espèce contenant un oxygène protoné se dissocie en un alcool et un carbocation qui est ensuite piégé par une molécule d'eau ou un processus A2 dans lequel une molécule d'eau ou une autre espèce nucléophile catalyse ce processus, le mécanisme pour la plupart des éthers est un processus de catalyse acide générale dans lequel le transfert de proton vers l'oxygène est concerté avec la rupture de la liaison C–O dans les cas où un carbocation peut exister ou, dans les cas où la formation d'une carbocation stable n'est pas possible, un processus dans lequel une concertation additionnelle d'une attaque nucléophile se fait sentir. On a analysé et on discute de tous les cas pour lesquels on peut trouver des données relatives à la constante de vitesse dans la littérature, à l'exception des hydrolyses de plusieurs azoéthers pour lesquels des mécanismes d'hydrolyse additionnels sont possibles. Ceux-ci seront discutés dans un travail ultérieur.

Mots-clés : éthers, hydrolyse, excès d'acidité, mécanisme, milieu acide.

[Traduit par la Rédaction]

Introduction

The excess acidity method has been shown to be the best method to use for the analysis of rate constant results obtained in aqueous acid media.[2–5] Recently, it has been found that the very commonly assumed species H_3O^+ does not have a long enough lifetime to act as a reaction intermediate in aqueous solution. This has been discussed at some length in a recent review,[2] and the excess acidity method showed itself to be very amenable to the analysis of rate data in this new situation, being applied to the hydrolyses of trioxane and diethyl ether there.[2]

The current paper amplifies this by covering all of the rate data for ether hydrolyses that could be found in the literature,[6–19] mostly by Lajunen and his group in Finland,[9–18] who used the excess acidity method themselves. Exceptions are some azoethers,[20–22] which are sufficiently different to require a separate paper. In fact, there is amazingly little rate data available; only one study uses aqueous HCl as a hydrolysis medium,[20] and none at all use HBr. Most of the studies were carried out using aqueous $HClO_4$,[6,7,9–20] which only has H_2O as an available nucleophile. The structures of the ethers dealt with in this paper are given as **1**–**19** in Scheme 1.

Received 16 March 2012. Accepted 6 July 2012. Published at www.nrcresearchpress.com/cjc on 22 October 2012.

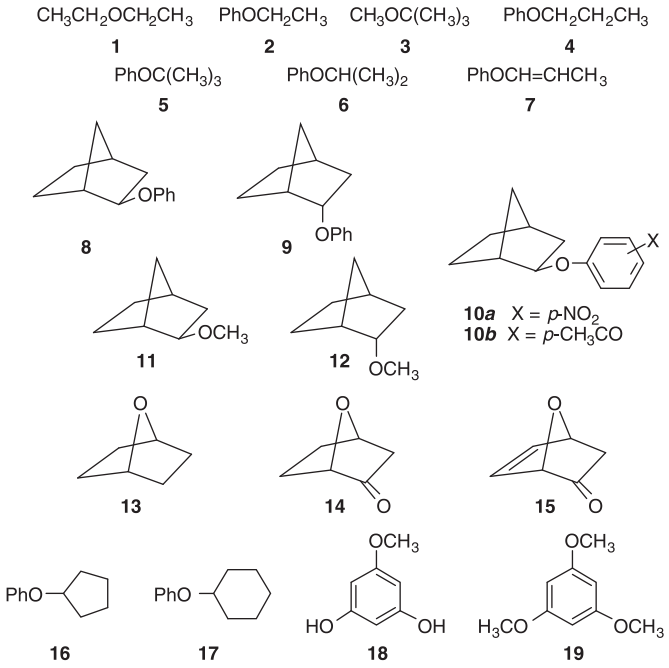
R.A. Cox. 16 Guild Hall Drive, Scarborough, ON M1R 3Z8, Canada.

E-mail for correspondence: robin.a.cox@sympatico.ca.

Dedicated to the memory of Jerry Kresge, good friend, excellent chemist; a sad loss to us all.

Can. J. Chem. Downloaded from www.nrcresearchpress.com by MCGILL UNIVERSITY on 02/02/13
For personal use only.

Scheme 1.

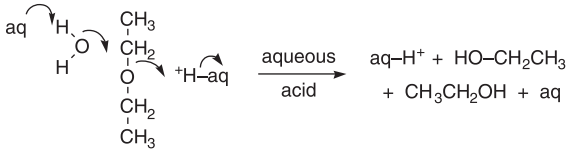


It is anticipated that a series of future papers dealing with other reaction mechanisms in need of modification will be required. The principle at work was first enunciated by Jencks[23] in terms of an "enforced mechanism". If an intermediate does not have a long enough lifetime in the reaction medium (i.e., existing there for at least a couple of molecular vibrations, say a lifetime of more than about 10^{-13} s),[24] it cannot be involved in the reaction, and a mechanism without it is "enforced".[23] Only the very latest fast IR technology can detect any kind of structure in protonated water, given as $H_{13}O_6^+$,[25] but even that only accounts for maybe 30% of the solvated protons, the IR spectrum degenerating to a continuum absorption.[26] This structure is by no means undisputed, theoretical calculations in particular suggesting a different one,[27] but the theoreticians agree that the positive charge in a proton cluster cannot be localized,[27,28] it is simply on the cluster as a whole. In terms of reaction mechanism, the actual structure of the solvated proton is unimportant, since all of the possibilities have exceedingly short lifetimes.

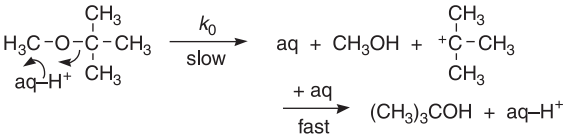
As far as ether hydrolysis is concerned, oxygen-protonated species in which the positive charge is not dispersed in some way (usually by resonance) also have lifetimes that are much too short to be reaction intermediates.[2,23] (This is not terribly surprising, one would have thought; $^+NR_4$ species are common enough in water, but $^+OR_3$ species, which are known, cannot exist in water, and $^+FR_2$ ones are not known at all.) This has the interesting consequence that, since the oxygen-protonated species cannot be a reaction intermediate, the pK_{BH^+} value for the site is of lesser importance, since it does not enter into the kinetic analysis.[2] Also, neither primary nor secondary carbocations in which the positive charge is not delocalized can exist in nonacidic aqueous media,[2,29] so they will probably not be reaction intermediates either.

The mechanism found for the hydrolysis of diethyl ether **1** is given in Scheme 2,[2] and Scheme 3 contains the likely mechanism for **3**, where the tertiary *tert*-butyl cation will probably be stable.

Scheme 2.



Scheme 3.



Experimental

$$[1] \qquad k_\psi C_S = k_0 a_S a_{H^+_{aq}} a_{H_2O} / f_\ddagger = k_0 C_S C_{H^+_{aq}} a_{H_2O} \frac{f_S f_{H^+_{aq}}}{f_\ddagger}$$

$$[2] \qquad \log k_\psi - \log C_{H^+} - \log a_{H_2O} = \log k_0 + m^\ddagger X$$

The excess acidity rate equation[5] that applies to Scheme 2 is eq. [1].[2] Here, the observed pseudo-first-order reaction rate constants as a function of acid concentration, and in many cases temperature, are k_ψ; values for **1**–**19** were taken from the literature.[6–19] The substrate concentration (C_S) cancels out on both sides; molar concentration, C; molar activity, a; and molar activity coefficient, f. The solvated proton concentration is $C_{H^+_{aq}}$, the molar water activity is a_{H_2O}, and the excess acidity is X; the published values for all of these in aqueous $HClO_4$, HCl, and H_2SO_4 media were taken from the literature[5] and corrected to the reaction temperature as before.[5] The logarithms of all activity coefficient ratios, such as the one in eq. [1], were assumed to be linear functions of X, no exceptions to this assumption having been found to date,[2,5] and so taking the logarithms of eq. [1] and rearranging results in eq. [2]. The slope parameter is given as $m^\ddagger$, since it refers to the transition state.[5] Since the protonated substrate is not an intermediate, it does not appear in the reaction schemes, and its pK_{BH^+} and m^* values[5] do not apply.

If the reaction in question follows Scheme 3, then the rate equation that is obeyed is eq. [3], which is simply eq. [2] without the water activity.

$$[3] \qquad \log k_\psi - \log C_{H^+} = \log k_0 + m^\ddagger X$$

$$[4] \qquad \log k_0 = 10.31883 + \log T - \frac{\Delta G_\Theta^\ddagger}{R\Theta \ln 10} + \frac{\Delta H_\Theta^\ddagger}{R\Theta \ln 10} \cdot \frac{T - \Theta}{T}$$

The rate constant for the reaction in the standard state, essentially water at 25 °C,[5] is k_0. If rate constants at different temperatures are not available, this quantity, perforce, refers to the reaction temperature. However, if they are available, $\log k_0$ can be expanded according to the Clarke and Glew formulation[30] (performs better in practice than the Eyring equation[31]) as shown in eq. [4]. This formulation has been found to be a more natural one to use, giving better numbers with errors that are independent of one another.[30] Here, the

Can. J. Chem. Downloaded from www.nrcresearchpress.com by MCGILL UNIVERSITY on 02/02/13
For personal use only.

absolute reaction temperature is T and Θ is the standard-state temperature of 298.15 K, 25 °C. The gas constant is R (1.98589 cal K^{-1} mol^{-1} here; 1 cal = 4.184 J) and the numerical term contains the Boltzmann and Planck constants required by the theory.[31] The entropy of activation $\Delta S_{\Theta}^{\ddagger}$ is easily obtained via $\Delta G_{\Theta}^{\ddagger} = \Delta H_{\Theta}^{\ddagger} - \Theta\Delta S_{\Theta}^{\ddagger}$.

All of the rate constant data[6–19] for **1**–**19** were analyzed according to Schemes 2 and 3, and the actual mechanism followed for the compound under analysis was indicated by the higher correlation coefficients and lower errors on the derived quantities. Data at only one temperature were analyzed by a simple linear regression of $\log k_{\psi} - \log C_{H^+_{aq}}(-\log a_{H_2O})$ vs X, and those at several temperatures by a double linear regression of $\log k_{\psi} - \log C_{H^+_{aq}}(-\log a_{H_2O}) - \log T$ vs X and $(T - \Theta)/T$. The programs used for the correlations will discard data points that, to 95% confidence, were not part of the same data set as the rest;[32] in this work this only happened twice.

Results

All of the statistical information obtained for **1**–**19**, analyzed according to both Schemes 2 and 3, is given in Table 1. This was used to decide on the mechanism followed by each compound, since in many cases plots according to both schemes were linear by eye. If the correlation coefficient was higher, and all of the errors listed in Table 1 (root-mean square deviation between experimental points and fitted line, error on the slope, error on the intercept, and errors on the enthalpy and entropy of activation) were lower, for one scheme over the other, that scheme was chosen as the mechanism which that compound followed. (For the double linear regressions, the F test was also provided by the program used, but since this is calculated using the same information as is used for the correlation coefficient, and thus gives the same result, it is not listed in Table 1.) For some of the simpler ethers (**2**, **3**, **4**, and **7**), there was simply not enough experimental data for this decision to be made, so it was based on likelihood, and the observed similarity in behavior to other compounds in the group. In the case of compounds **16** and **17**, it was not possible to decide between either scheme on any basis.

The experimental results calculated for each compound according to the chosen scheme, slopes, intercepts, and activation parameters, are given in Table 2 (both schemes for **16** and **17**). Also given are the solvent isotope effects found for many of the compounds; since these were all derived from only one measurement obtained in deuterated media,[6–19] the errors on them could not be obtained.

The results obtained for one of the simple ethers studied, isopropyl phenyl ether **6**,[11,12] are illustrated in Fig. 1. Two sets of results obtained by different people at different times were combined, and the agreement between them was excellent, it not being possible to distinguish points obtained in the different studies in the figure. It was found that **6** followed Scheme 3 rather than Scheme 2, so the quantity plotted against X in Fig. 1 is $\log k_{\psi} - \log C_{H^+_{aq}}$.

In Fig. 2, concerning both **10a** and **10b**,[14] plots according to both Scheme 2 (left axis) and Scheme 3 (right axis) are shown, and it can be clearly seen that these ethers follow Scheme 2 (linear) and not Scheme 3 (curves) (see Table 1).

In Fig. 3, for compounds **11** and **12**, plots according to both schemes are also shown, and it is again clear that both of these ethers hydrolyze according to Scheme 2. This is fairly obvious for **12**, but is not nearly so obvious for **11**, just by eyeballing the figure. Lajunen et al., who also used excess acidity plots, also saw this,[9–18] and often could not really decide between the A1 and A2 mechanisms, which at the time were thought to be the only possibilities available. However, the data are quite reliable enough to make the Scheme 2 decision (see Table 1).

Discussion

The simple ethers **1** and **2** clearly hydrolyze according to Scheme 2, a concerted process with a water molecule involved; none of the possible cationic intermediates would be stable under the reaction conditions. The excess acidity method is quite capable of deciding how many water molecules are involved in the reaction; in many cases, where water adds to a carbonyl group (ester hydrolyses,[33] amide hydrolyses,[34] or benzimidate hydrolyses[33]), two water molecules have been found to be involved. Here, however, it is only one. In the acidity region covered by the first set of results in Table 2, 60–90 wt % aqueous H_2SO_4,[6] the water activity is changing rapidly, but the proton concentration is not.[35] Assuming no water involvement leads to strong downward curvature in the excess acidity analysis (Table 1), and assuming two leads to curvature that is just as strong in the upward direction. Only one water molecule leads to the observed perfectly straight line.[2] In Table 2 there are two kinetic studies of the hydrolysis of **1**,[6,7] but they are not strictly comparable, since one of them was performed at 120.1 °C and high pressure,[7] whereas the other, already discussed,[2] was performed at normal pressure and at temperatures of 80–100 °C.[6] It probably would be possible to use the activation parameters in Table 2 to obtain a volume of activation for **1**, but this was not done as there was no way to estimate the error involved, which would probably be considerable. However, the $m^{\ddagger}$ slopes for both of the studies of **1** in Table 2 are, within experimental error, the same.

The other simple ethers (**3**–**7**) do form free carbocations. This is not surprising for **3** and **5**, which can give stable *tert*-butyl cations under the reaction conditions, and **7** gives a variety of reaction products derived from the Claisen rearrangement,[9] which does not require the formation of a detached carbocation.[9] However, **4** gives a wide variety of products derived from the isopropyl cation;[9] presumably, as the *n*-propyl group begins to detach and acquire positive charge it will rearrange to the isopropyl cation, which then attacks the substrate and the other reaction products.[9] The products were not given in the major kinetic study of **6**,[11] but in the other study of **6** various isopropylphenols were identified as reaction products.[12] The conclusion must be that the secondary isopropyl cation is indeed stable enough to be a reaction intermediate under the reaction conditions, which were really quite acidic, 9–10 mol/L aqueous $HClO_4$.[9,11,12] However, it is not formed nearly as readily as is the tertiary *tert*-butyl cation; according to the $\log k_0$ values in Table 1 **4** and **6** react much more slowly than do **3** and **5** (and **7**). Compounds **1** and **2** react much more slowly still and by a different mechanism.

Can. J. Chem. Downloaded from www.nrcresearchpress.com by MCGILL UNIVERSITY on 02/02/13
For personal use only.

Table 1. All of the statistical information obtained for all of the compounds in the study, used to determine which mechanism applies.

Compound[a]	r^b	N^c	$\pm\sigma_y{}^d$	Slope[e]	Intercept[f]	$\Delta H_\Theta^{\ddagger g}$	$\Delta S_\Theta^{\ddagger h}$	Ref.
1 (2)*	0.9993	10(1)	0.036	0.015	0.21	1.4	4.6	2, 6[i]
1 (3)	0.978	10(1)	0.088	0.036	0.52	3.3	11.0	2, 6[i]
1 (2)*	0.997	6	0.048	0.036	0.031	—	—	7
1 (3)	0.994	6	0.042	0.031	0.027	—	—	7
2 (2)*	0.9986	10	0.050	0.034	0.15	—	—	9
2 (3)	0.9981	10	0.039	0.026	0.12	—	—	9
3 (2)	0.9998	7	0.020	0.014	0.0214	—	—	8
3 (3)*	0.9997	7	0.020	0.014	0.0216	—	—	8
4 (2)	0.9993	11	0.042	0.027	0.12	—	—	9
4 (3)*	0.9990	11	0.035	0.022	0.10	—	—	9
5 (2)	0.998181	15	0.040	0.028	0.017	0.52	1.7	10
5 (3)*	0.998184	15	0.037	0.026	0.015	0.48	1.6	10
6 (2)	0.9991	51(2)	0.058	0.012	0.055	0.31	1.1	11, 12
6 (3)*	0.9992	51(2)	0.043	0.0090	0.041	0.24	0.81	11, 12
7 (2)	0.9994	9	0.039	0.025	0.078	—	—	9
7 (3)*	0.9993	9	0.031	0.020	0.062	—	—	9
8 (2)	0.9996	16	0.027	0.012	0.029	0.62	2.1	13
8 (3)*	0.9997	16	0.020	0.0089	0.022	0.46	1.5	13
9 (2)*	0.9997	13	0.037	0.017	0.066	0.52	1.8	13
9 (3)	0.9994	13	0.043	0.020	0.075	0.59	2.0	13
10a (2)*	0.9989	18(1)	0.040	0.024	0.057	0.66	2.2	14
10a (3)	0.9978	18(1)	0.047	0.028	0.068	0.77	2.6	14
10b (2)*	0.999	11	0.047	0.025	0.069	1.2	3.9	14
10b (3)	0.997	11	0.069	0.037	0.103	1.7	5.8	14
11 (2)*	0.9998	10	0.017	0.011	0.035	0.33	1.1	15
11 (3)	0.9994	10	0.027	0.018	0.056	0.52	1.8	15
12 (2)*	0.999	15	0.055	0.022	0.13	0.71	2.4	15
12 (3)	0.995	15	0.074	0.030	0.17	0.94	3.3	15
13 (2)*	0.9995	10	0.030	0.024	0.069	0.55	1.9	16
13 (3)	0.9989	10	0.037	0.030	0.085	0.68	2.3	16
14 (2)*	0.9998	11	0.016	0.010	0.048	0.34	1.2	17
14 (3)	0.9994	11	0.022	0.014	0.068	0.49	1.7	17
15 (2)	0.99759	13	0.060	0.031	0.16	1.3	4.5	18
15 (3)*	0.99761	13	0.045	0.023	0.12	1.0	3.4	18
16 (2)	0.9976	13	0.093	0.050	0.20	0.97	3.4	12
16 (3)*	0.9970	13	0.084	0.046	0.18	0.89	3.1	12
17 (2)	0.9974	13	0.085	0.048	0.20	0.91	3.2	12
17 (3)*	0.9970	13	0.077	0.043	0.18	0.83	2.9	12
18 (2)* [j]	0.9997	15	0.015	0.0072	0.038	0.26	0.89	19
18 (3)	0.998	15	0.024	0.011	0.059	0.41	1.4	19
19 (2)* [j]	0.9983	9	0.042	0.037	0.19	0.84	3.0	19
19 (3)	0.996	9	0.048	0.043	0.22	0.97	3.4	19

[a]See Scheme 1. The mechanistic scheme assumed (Scheme 2 or 3) is in parentheses. The one best suited, or chosen, is indicated by a star.

[b]Multiple correlation coefficient if activation parameters could be calculated; otherwise a linear correlation coefficient.

[c]Number of points. Any rejected by the program used as not being part of the data set, to 95% confidence, are in parentheses.

[d]Root-mean-square error between experimental points and the fitted line. All the other errors in the table are standard deviations.

[e]±Error in the slope.

[f]±Error in the intercept.

[g]±Error in the enthalpy of activation (kcal mol^{-1}).

[h]±Error in the entropy of activation (cal deg^{-1} mol^{-1}).

[i]The original data are from ref. 6 and the analysis is from ref. 2.

[j]See text. The actual mechanism does involve a water molecule (see Scheme 4).

Compounds **8** and **9**, *exo*- and *endo*-2-phenoxynorbornane, respectively, were studied to see if the 2-norbornyl cation would be formed under the reaction conditions.[13] Table 2 shows that **8**, unlike **9**, reacts without the involvement of water and that it reacts some 4.5 orders of magnitude faster in the standard state due to the reaction having a much lower enthalpy of activation. Thus, the 2-norbornyl cation is evidently stable in the 4–7 mol/L aqueous perchloric acid reac-

Can. J. Chem. Downloaded from www.nrcresearchpress.com by MCGILL UNIVERSITY on 02/02/13
For personal use only.

Table 2. Excess acidity slopes and intercepts, solvent isotope effects, and activation parameters, if obtainable, and the most likely mechanism followed, for all of the compounds in the study.

Compound	Mechanism	Slope[a]	log $k_0^{25°}$ [b]	$\Delta H_\Theta^{\ddagger}$[c]	$\Delta S_\Theta^{\ddagger}$[d]	k_H/k_D	Ref.
1	Scheme 2	0.949	–12.23	32.8	–12.3	—	2, 6[e]
1	Scheme 2	0.924	–6.493	(at 120.1 °C and 50 atm; 1 atm = 101.325 kPa)			7
2	Scheme 2	1.778	–12.94	(at 75 °C)			9
3	Scheme 3	1.244	–5.918	—	—	—	8
4	Scheme 3	1.507	–11.24	(at 75 °C)			9
5	Scheme 3	1.257	–3.317	25.88	+13.1	—	10
6	Scheme 3	1.4589	–11.096	33.48	+3.05	0.55	11, 12
7	Scheme 3	1.447	–8.617	(at 45 °C)		0.61	9
8	Scheme 3	1.3083	–7.186	28.29	+3.5	0.43	13
9	Scheme 2	1.975	–11.764	35.70	–0.5	0.48	13
10a	Scheme 2	1.684	–8.082	26.60	–14.2	—	14
10b	Scheme 2	1.557	–7.642	28.8	–4.9	0.57	14
11	Scheme 2	1.683	–8.133	31.79	+3.0	—	15
12	Scheme 2	1.517	–11.36	36.85	+5.2	—	15
13	Scheme 2	1.610	–8.435	29.94	–4.6	0.63	16
14	Scheme 2	1.395	–10.286	32.64	–4.0	0.52	17
15	Scheme 3	0.871	–10.22	29.7	–5.7	0.34	18
16	Scheme 2[f]	2.273	–11.42	35.10	–0.9	0.32	12
16	Scheme 3[f]	1.801	–10.85	33.22	+3.3	0.34	12
17	Scheme 2[f]	2.088	–11.43	34.93	–1.6	0.52	12
17	Scheme 3[f]	1.593	–10.76	32.85	+2.5	0.56	12
18	Scheme 4	0.9616	–7.645	23.24	–23.48	—	19
19	Scheme 4	1.535	–10.40	27.35	–22.3	—	19

[a]Value of $m^{\ddagger}$.
[b]At 25 °C unless otherwise noted.
[c]Enthalpy of activation (kcal mol^{-1}) at the standard temperature Θ of 25 °C, 298.15 K.
[d]Entropy of activation (cal deg^{-1} mol^{-1}), at the standard temperature Θ of 25 °C, 298.15 K.
[e]The original data are from ref. 6 and the analysis is from ref. 2.
[f]Impossible to decide between schemes on the basis of the statistical information in Table 1.

tion media,[13] but it can only be formed from the exo compound, presumably via anchimeric assistance by the suitably located C–C bonds. The endo isomer reacts with water according to Scheme 2. (The structure of the 2-norbornyl cation, which used to be described as nonclassical, was the subject of much argument in the literature before 1999, when Werstiuk and Muchall showed that it was T-shaped and that it was a π complex rather than being σ-bridged.)[36]

However, addition of electron-withdrawing groups to the phenyl ring of **8**, as in **10a** and **10b** (Fig. 2), is enough to change the mechanism from Scheme 3 back to Scheme 2; a free carbocation is not formed. Table 2 shows that the reaction is slower for **10a** and **10b** than it is for **8**. Compound **10a** also has a fairly negative entropy of activation in comparison with most of the other table entries. It may be that electron-donating substituents would change the situation, but experimental problems prevented a reliable study of any of these.[14]

Compounds **11** and **12**, norbornanes with methoxy rather than phenoxy substituents (Fig. 3), on the other hand, do not form free carbocations from either the exo- or endo-position. Compound **11** reacts more slowly than does **8**, and has a higher enthalpy of activation, and again the endo compound **12** reacts much more slowly than does the exo-**11**.

Of the five-member ring ethers **13**, **14**, and **15**, only **15** is in a position to give a stable carbocation, delocalized because of the double bond in the ring, and indeed this is how it reacts according to the statistical evaluation in Table 1, although there is not a lot of difference between the three according to the numbers in Table 2. Compound **15** is different from the other two in having a smaller $m^{\ddagger}$ slope and a smaller k_H/k_D value, but what, if anything, this means is not clear without having more information about other compounds to go on.

Compounds **16** and **17**, cyclopentyl and cyclohexyl phenyl ether, would probably be expected to react via Scheme 2, but the experimental data[12] did not permit a decision between Schemes 2 and 3 to be made (Table 1). Both react very slowly owing to a high enthalpy of activation (Table 2) and give phenol and the corresponding alcohols as the major products.[12]

Compounds **18** and **19** are different, not reacting according to Schemes 2 or 3, but preferring to ring-protonate,[19] which may be a good indication of the instability of oxygen-protonated species; these molecules would sooner lose their aromaticity than form undelocalized oxygen-protonated species. However, water is still involved in the slow step (see Table 1), and one possible mechanism for the reaction of these two compounds is given as Scheme 4. There is nothing wrong with protonated alkoxybenzenes as reaction intermediates,[37] but, since a water molecule is clearly involved in this reaction (Table 1), the intermediate in Scheme 4 is written as being

Can. J. Chem. Downloaded from www.nrcresearchpress.com by MCGILL UNIVERSITY on 02/02/13
For personal use only.

Fig. 1. Excess acidity plot according to Scheme 3 for the kinetics of the hydrolysis of isopropyl phenyl ether (**6**) at several different temperatures. (For clarity, single measurements at 55 and 65 °C[12] are not included in the figure.)

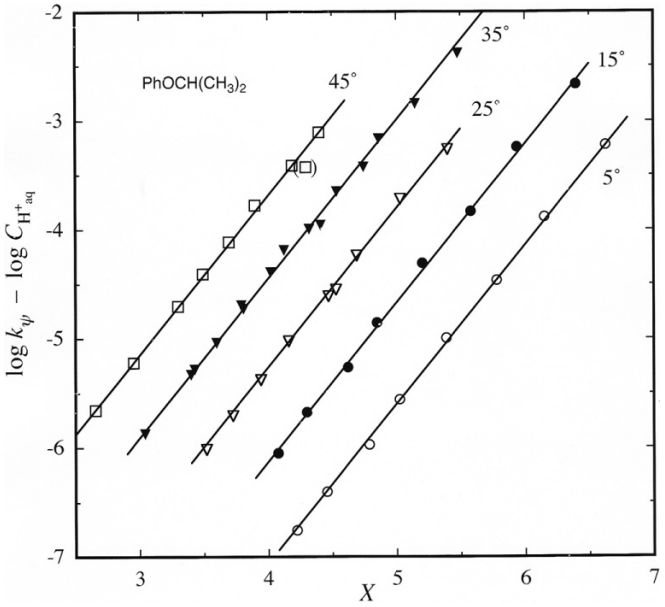


Fig. 2. Excess acidity plots according to Scheme 2 (linear, left axis) and Scheme 3 (curved, right axis) of the kinetics of the hydrolysis of compounds **10a** and **10b**.

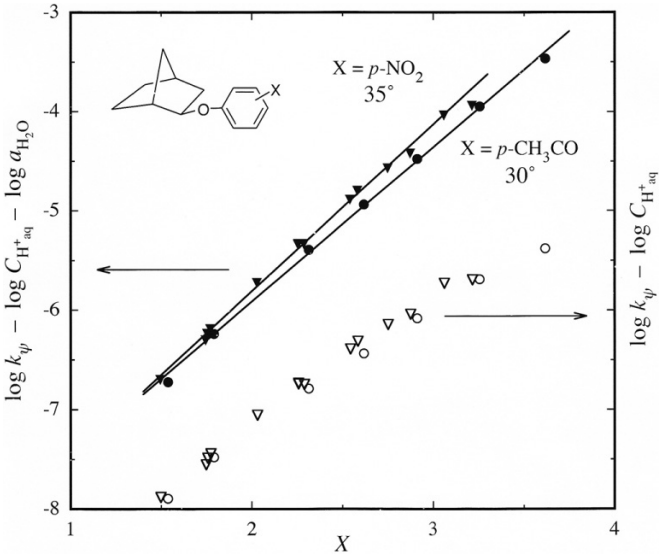
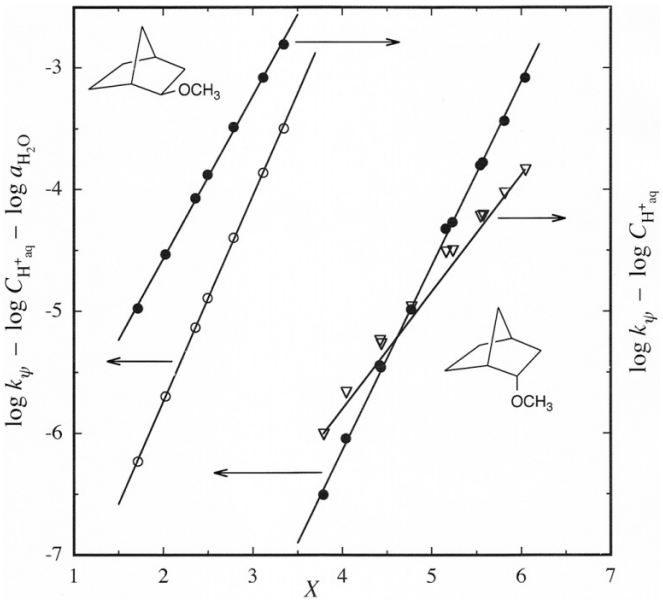


Fig. 3. Excess acidity plots according to Scheme 2 (left axis) and Scheme 3 (right axis) of the kinetics of the hydrolysis of compounds **11** and **12**.



neutral. Compound **18** has an $m^{\ddagger}$ slope value of less than one, and both **18** and **19** have low activation enthalpies and large negative entropies of activation. For both compounds, the bond between the oxygen and the phenyl ring is the one cleaved, according to isotope exchange studies.[19]

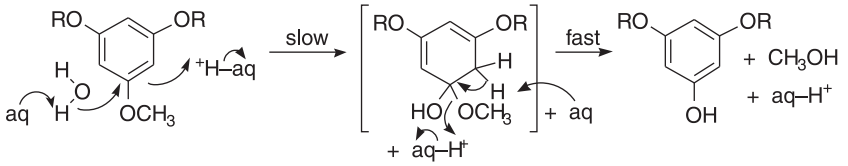
All of the reported k_H/k_D values in Table 1 are around 0.5. Two competing effects are at work here. Acids are stronger in D_2O than they are in H_2O, which leads to k_H/k_D values of usually around 0.3 for reactions that are specific-acid-catalyzed (equilibrium protonation).[38] However, for the general acid catalysis seen here, this number would probably be greater than 0.5. D is heavier than H, which would lead to slower reaction in D_2O than in H_2O if proton transfer is involved in the slow step,[38] as it is in Scheme 2. It seems that the stronger acid effect wins out here. The k_H/k_D values for the Scheme 3 mechanism in Table 2, not involving proton transfer, do seem to be smaller than the others.

The slope values in Table 2, referred to as $m^{\ddagger}$, are really all over the place, ranging from a low of 0.9 to nearly 2.3. It was originally hoped[39] that these values would have a useful meaning in interpreting the mechanisms of reactions in acidic media, but it seems that this may not be the case, unlike the m^* slopes referring to equilibrium protonation, which do indeed seem to describe the behavior of different types of base in acidic media.[5,40] It is probably going to be necessary to collect a lot of these $m^{\ddagger}$ slopes for different reactions, particularly with the new interpretation of reaction mechanisms in aqueous media described before[2] and in this paper, and stare at the numbers before deciding whether or not they do in fact have any meaning and, if so, what it is.

In more general terms, Scheme 2 seems improbable on the face of it, since it seems to require several molecules to come together at the transition state. However, this is somewhat illusory. As has been pointed out before,[2] in a highly structured medium such as water,[41] with everything hydrogen-bonded together, all the water molecules and protons needed do not really have to be bought into position first. For instance, the ether oxygen is bound to be hydrogen-bonded to the solvent. The entropies of activation for all of the compounds for which they could be obtained in Table 2 are, with some exceptions, positive, or at least only slightly negative. The only process really contributing to the entropy change is the formation of two species from one, resulting in the small positive entropy of activation observed in most cases.

Reactions are known where solvent reorganization can be important; these often involve very short-lived intermediates.

Scheme 4.



One example is found in the addition of thiol anions to acetaldehyde in acidic media.[42] Here, the trapping by acid of an initially formed anionic addition intermediate with a very short lifetime is thought to be kinetically significant.[42] Another example is found in the hydrations of *cis*- and *trans*-cyclooctene in dilute aqueous acid. These give the cyclooctyl cation with an estimated lifetime of 5×10^{-12} s,[43] short enough not to be solvationally equilibrated. These may have to react by preassociation mechanisms; the cis-isomer is thought to react this way but not the trans.[43] This is not thought to be the case for any of the substrates involved in the work in this paper, but it is certainly a factor to be borne in mind.

In Eigen's[44] famous review the reaction rate constants for proton transfer reactions are given as being of the order of 10^{10} $(mol/L)^{-1}$ s^{-1} (see Table 4 of his review).[44] This implies a lifetime for protonated water species, whatever their structure, of some 10^{-10} s. However, this cannot be the case; if it were, the various individual protonated water species would give rise to identifiable IR or Raman spectra, which they do not.[25,26] On a more careful reading of the review, it becomes apparent that the measured rate constants for proton movement along hydrogen bonds, in ice and in water, actually result in lifetimes of the order 10^{-13} s for individual protonated water species.[44] This is exactly the same as the lifetimes implied by the modern fast IR measurements[25,26] discussed in the Introduction, and consistent with the Grotthuss chain-transfer process[45] for the movement of protons along hydrogen bonds.

The reactions under consideration here are all very slow. Solvent reorganization and proton transfer probably contribute maybe a kilocalorie or two, or the equivalent in entropy terms, to the overall activation energy in each case, but the enthalpy of activation values found in this work (Table 2) are very much higher than that. It is a simplification, of course, but probably the easiest way of thinking about the mechanisms of slow reactions in mainly aqueous media is that the protons and water molecules required by the reaction are pretty much already there. In Schemes 2–4, the frequently used term "aq" is simply meant to imply sources or sinks for protons and water molecules; they are not kinetically involved.

Together with the previous review,[2] the work described in this paper shows quite clearly that many commonly accepted reaction mechanisms in aqueous media are going to have to be revised. Also, it is probably best to write H^+_{aq} or aq–H^+, rather than H^+ or H_3O^+ in reaction schemes. H_3O^+ does not exist in water.[46]

Acknowledgments

Valuable correspondence with Professors Evgenii Stoyanov, Chris Reed, and Dan Singleton is gratefully acknowledged. I also thank the referees for their invaluable comments, which have contributed to making this a far better paper.

References

(1) Part 32 of the series *Mechanistic Studies in Strong Acids*, of which part 31 is ref. 2, and parts 29 and 30 are refs. 3 and 4.
(2) Cox, R. A. *Int. J. Mol. Sci.* [Online] **2011**, *12* (12), 8316. doi:10.3390/ijms12128316.
(3) Buncel, E.; Keum, S.-R.; Rajagopal, S.; Kiepek, E.; Cox, R. A. *Can. J. Chem.* **2008**, *86* (4), 298. doi:10.1139/v08-016.
(4) Buncel, E.; Keum, S.-R.; Rajagopal, S.; Cox, R. A. *Can. J. Chem.* **2009**, *87* (8), 1127. doi:10.1139/V09-080.
(5) Cox, R. A. *Adv. Phys. Org. Chem.* **2000**, *35*, 1. doi:10.1016/S0065-3160(00)35011-0.
(6) Jaques, D.; Leisten, J. A. *J. Chem. Soc.* **1964**, 2683. doi:10.1039/jr9640002683.
(7) Koskikallio, J.; Whalley, E. *Can. J. Chem.* **1959**, *37* (4), 788. doi:10.1139/v59-106.
(8) Modena, G.; Rivetti, F.; Scorrano, G.; Tonellato, U. *J. Am. Chem. Soc.* **1977**, *99* (10), 3392. doi:10.1021/ja00452a034.
(9) Lajunen, M.; Laine, R.; Aaltonen, M. *Acta Chem. Scand.* **1997**, *51*, 1155. doi:10.3891/acta.chem.scand.51-1155.
(10) Lajunen, M.; Tanskanen-Lehti, K. *Acta Chem. Scand.* **1994**, *48*, 861. doi:10.3891/acta.chem.scand.48-0861.
(11) Lajunen, M.; Setälä, J. *Acta Chem. Scand.* **1997**, *51*, 334. doi:10.3891/acta.chem.scand.51-0334.
(12) Lajunen, M.; Kähkönen, M. *Acta Chem. Scand.* **1992**, *46*, 726. doi:10.3891/acta.chem.scand.46-0726.
(13) Lajunen, M.; Himottu, M. *Acta Chem. Scand.* **1989**, *43*, 957. doi:10.3891/acta.chem.scand.43-0957.
(14) Lajunen, M.; Himottu, M.; Tanskanen-Lehti, K. *Acta Chem. Scand.* **1997**, *51*, 515. doi:10.3891/acta.chem.scand.51-0515.
(15) Lajunen, M.; Jantunen, J.; Telkki, T.; Toukoniitty, E. *Acta Chem. Scand.* **1999**, *53*, 348. doi:10.3891/acta.chem.scand.53-0348.
(16) Lajunen, M.; Uotila, R. *Acta Chem. Scand.* **1992**, *46*, 968. doi:10.3891/acta.chem.scand.46-0968.
(17) Lajunen, M.; Kaitaranta, E.; Dahlqvist, M. *Acta Chem. Scand.* **1994**, *48*, 399. doi:10.3891/acta.chem.scand.48-0399.
(18) Lajunen, M.; Mäki, E. *Acta Chem. Scand.* **1991**, *45*, 578. doi:10.3891/acta.chem.scand.45-0578.
(19) Schubert, W. M.; Quacchia, R. H. *J. Am. Chem. Soc.* **1963**, *85* (9), 1284. doi:10.1021/ja00892a015.
(20) (a) Bunnett, J. F.; Buncel, E. *J. Am. Chem. Soc.* **1961**, *83* (5), 1117. doi:10.1021/ja01466a028; (b) Bunnett, J. F.; Buncel, E.; Nahabedian, K. V. *J. Am. Chem. Soc.* **1962**, *84* (21), 4136. doi:10.1021/ja00880a033.
(21) (a) Buncel, E.; Onyido, I. *Can. J. Chem.* **1986**, *64* (11), 2115. doi:10.1139/v86-349; (b) Cox, R. A.; Onyido, I.; Buncel, E. *J. Am. Chem. Soc.* **1992**, *114* (4), 1358. doi:10.1021/ja00030a034.
(22) Onyido, I.; Opara, L. U. *J. Chem. Soc., Perkin Trans. 2* **1989**, (11): 1817. doi:10.1039/p29890001817.
(23) (a) Jencks, W. P. *Chem. Rev.* **1972**, *72* (6), 705. doi:10.1021/cr60280a004; (b) Jencks, W. P. *Acc. Chem. Res.* **1976**, *9* (12), 425. doi:10.1021/ar50108a001; (c) Jencks, W. P. *Acc. Chem. Res.* **1980**, *13* (6), 161. doi:10.1021/ar50150a001; (d) Jencks, W. P. *Chem. Soc. Rev.* **1981**, *10* (3), 345. doi:10.1039/cs9811000345.

Can. J. Chem. Downloaded from www.nrcresearchpress.com by MCGILL UNIVERSITY on 02/02/13
For personal use only.

(24) For instance, see the summary in Whalen, D. L. *Adv. Phys. Org. Chem.* **2005**, *40*, 247. doi:10.1016/S0065-3160(05)40006-4.
(25) Stoyanov, E. S.; Stoyanova, I. V.; Reed, C. A. *Chem. Sci.* **2011**, *2* (3), 462. doi:10.1039/c0sc00415d.
(26) Stoyanov, E. S.; Reed, C. A. Personal communication, 2011.
(27) Knight, C.; Voth, G. A. *Acc. Chem. Res.* **2012**, *45* (1), 101. and earlier papers by Voth. doi:10.1021/ar200140h.
(28) For instance, Shevkunov, S. V. *Russ. J. Gen. Chem.* **2004**, *74* (10), 1471. doi:10.1007/s11176-005-0039-y.
(29) (a) Murphy, T. J. *J. Chem. Educ.* **2009**, *86* (4), 519. doi:10.1021/ed086p519; (b) Bentley, T. W.; Schleyer, P. R. *J. Am. Chem. Soc.* **1976**, *98* (24), 7658. doi:10.1021/ja00440a036.
(30) Clarke, E. C. W.; Glew, D. N. *Trans. Faraday Soc.* **1966**, *62*, 539. doi:10.1039/tf9666200539.
(31) For instance, see Laidler, K. J. *Theories of Chemical Reaction Rates;* McGraw–Hill, Inc.: New York, 1969; Chap. 3.
(32) Cox, R. A. *J. Phys. Org. Chem.* **1991**, *4* (4), 233. doi:10.1002/poc.610040406.
(33) Cox, R. A. *Can. J. Chem.* **2005**, *83* (9), 1391. doi:10.1139/v05-142.
(34) Cox, R. A. *Can. J. Chem.* **2008**, *86* (4), 290. doi:10.1139/v08-015.
(35) Cox, R. A. *J. Am. Chem. Soc.* **1974**, *96* (4), 1059. doi:10.1021/ja00811a018.
(36) (a) Werstiuk, N. H.; Muchall, H. M. *J. Mol. Struct. THEOCHEM* **1999**, *463* (3), 225. doi:10.1016/S0166-1280(98)00625-3; (b) Werstiuk, N. H.; Muchall, H. M. *J. Phys. Chem. A* **2000**, *104* (10), 2054. doi:10.1021/jp992043b.
(37) Kresge, A. J.; Chiang, Y.; Hakka, L. E. *J. Am. Chem. Soc.* **1971**, *93* (23), 6167. doi:10.1021/ja00752a030.
(38) For instance, see Ruff, F.; Csizmadia, I. G. *Organic Reactions: Equilibria, Kinetics and Mechanism;* Elsevier: Amsterdam, 1994; pp 215 and 222.
(39) Cox, R. A. *Acc. Chem. Res.* **1987**, *20* (1), 27. doi:10.1021/ar00133a004.
(40) Bagno, A.; Scorrano, G.; More O'Ferrall, R. A. *Res. Chem. Intermed.* **1987**, *7* (4), 313. doi:10.1007/BF03155656.
(41) Marcus, Y. *Chem. Rev.* **2009**, *109* (3), 1346 and references cited therein. doi:10.1021/cr8003828.
(42) Gilbert, H. F.; Jencks, W. P. *J. Am. Chem. Soc.* **1977**, *99* (24), 7931. doi:10.1021/ja00466a029.
(43) Chiang, Y.; Kresge, A. J. *J. Am. Chem. Soc.* **1985**, *107* (22), 6363. doi:10.1021/ja00308a033.
(44) Eigen, M. *Angew. Chem. Int. Ed. Engl.* **1964**, *3* (1), 1. doi:10.1002/anie.196400011.
(45) Grotthuss, C. J. T. *Ann. Chim.* **1806**, *LVIII*, 54.
(46) (a) Silverstein, T. P. *J. Chem. Educ.* **2011**, *88* (7), 875. doi:10.1021/ed1010213; (b) Ault, A. *J. Chem. Educ.* **2010**, *87* (9), 937. doi:10.1021/ed100345k.

Can. J. Chem. Downloaded from www.nrcresearchpress.com by MCGILL UNIVERSITY on 02/02/13
For personal use only.

Symmetry-adapted perturbation theory study for some magnesium complexes

Mehdi D. Esrafili and Sirous Yourdkhani

Can. J. Chem. Downloaded from www.nrcresearchpress.com by MCGILL UNIVERSITY on 02/02/13
For personal use only.

Abstract: A systematic theoretical study on Mg–ligand interactions has been carried out employing both ab initio correlated wave function and density functional methods. The interactions of the $Mg(CH_3N_2)_2$ moiety with BF, CO, N_2, NH_3, and H_2O ligands have been investigated by performing calculations at the B3LYP, MP2, MP4, and CCSD(T)/6–311++G(3df,3pd) levels of theory. Results indicate that the interaction energies of the $Mg(CH_3N_2)_2$–L complexes increase in the order $NH_3 > H_2O > BF > CO > N_2$. Symmetry-adapted perturbation theory (SAPT) analysis has been carried out to understand the nature of the forces involved in the bonding. The SAPT results indicate that the stabilities of the Mg–L interactions are attributed mainly to electrostatic effects, while induction and dispersion forces also play a significant role. The evaluated SAPT interaction energies for the $Mg(CH_3N_2)_2$–L complexes are generally in good agreement with those obtained using the supermolecule CCSD(T) methods, suggesting that SAPT is a proper method to study the intermolecular interactions in these complexes. The results also suggest an explanation for the unique role of Mg^{2+} as a carrier of water molecules that mediate enzymatic hydrolysis reactions.

Key words: Mg–ligand interaction, SAPT analysis, ab initio, EDA.

Résumé : On a réalisé une étude théorique systématique des interactions Mg–ligand en faisant appel à des méthodes de fonction d'onde ab initio corrélée et fonctionnelle de la densité. Les interactions de la portion $Mg(CH_2H_2)_2$ avec les ligands BF, CO, N_2, NH_3 et H_2O ont été étudiés en faisant des calculs aux niveaux B3LYP, MP2, MP4 et CCSD(T)/6–0311++G(3df,3pd) de la théorie. Les résultats indiquent que les énergies d'interaction des complexes $Mg(CH_2H_2)_2$–L augmentent dans l'ordre $NH_3 > H_2O > BF > CO > N_2$. On a effectué une analyse selon la théorie de la perturbation adaptée à la symétrie (TPAS) dans le but de comprendre la nature des forces impliquées dans les liaisons. Les résultats de la TPAS indiquent que les stabilités des interactions Mg–L peuvent être attribuées principalement aux effets électrostatiques, alors que les forces d'induction et de dispersion jouent aussi un rôle important. Les énergies d'interactions telles qu'évaluées par la TPAS pour les complexes $Mg(CH_2H_2)_2$–L sont généralement en bon accord avec celles obtenues à l'aide des méthodes de la supermolécule, CCSD(T); ces résultats suggèrent que la méthode TPAS est une méthode qui peut très bien s'appliquer à l'étude des interactions intermoléculaires dans ces complexes. Les résultats suggèrent aussi une explication pour le rôle unique du Mg^{2+} comme porteur de molécules d'eau pour catalyseur les réactions d'hydrolyse enzymatiques.

Mots-clés : interaction Mg–ligand, analyse par la théorie de la perturbation adaptée à la symétrie (TPAS), ab initio, « EDA ».

[Traduit par la Rédaction]

Introduction

It is widely known that metal–ligand interactions are very important for the structures and stabilities of a broad range of biological complexes and crystals.[1–5] Magnesium (Mg) plays a prominent role in many structural and reactive biochemical processes. Over 300 enzymes require Mg ions for their catalytic activity, including all enzymes utilizing or synthesizing adenosine triphosphate (ATP),[6–8] or those that use other nucleotides to synthesize DNA and RNA.[9–11] ATP exists in cells normally as a chelate of ATP and a Mg ion. As the Mg ion has only one valence state, +2, it cannot play a direct role in any redox-mediated enzymatic reactions. The general mode of action of Mg cations in such enzymes appears to be to bind portions of the active site. Mg plays a central role in plants and is necessary for synthesis of chlorophyll and photosynthesis.[12] A combination of different factors, rather flexible coordination geometry and the relatively high charge density, makes divalent Mg, Mg(II), capable of satisfactorily coordinating with the broad spectrum of "hard" and "soft" ligands present in metalloenzymes. Thus, an accurate and well-balanced theoretical description of the ligand binding ability and hydration of Mg(II) ions is required to increase our understanding of Mg enzymology using the tools of computational quantum chemistry.

In principle, the supermolecular ab initio calculations have become very popular tools for the investigation of intermolecular interactions. However, this method does not provide

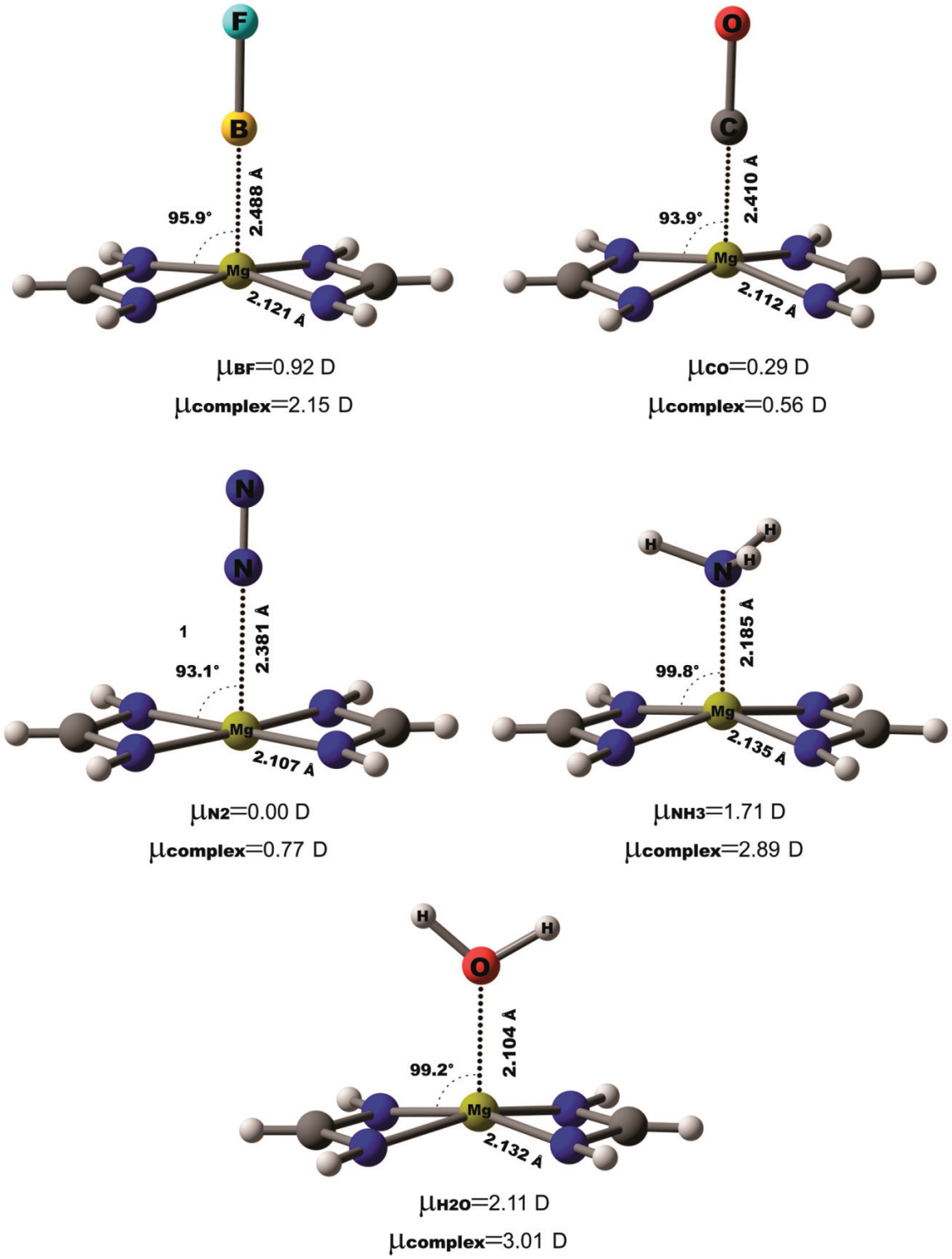
Received 4 April 2012. Accepted 19 July 2012. Published at www.nrcresearchpress.com/cjc on 22 October 2012.

M.D. Esrafili. Laboratory of Theoretical Chemistry, Department of Chemistry, University of Maragheh, Maragheh, Iran.
S. Yourdkhani. Department of Chemistry, Tarbiat Modares University, Tehran, Iran.

Corresponding author: Mehdi D. Esrafili (e-mail: esrafili@maragheh.ac.ir).

Can. J. Chem. Downloaded from www.nrcresearchpress.com by MCGILL UNIVERSITY on 02/02/13
For personal use only.

Fig. 1. Optimized structures and calculated dipole moments of $Mg(CH_3N_2)_2$–L complexes at the MP2/6–311++G(3df,3pd) level of theory, L = BF, CO, N_2, NH_3, and H_2O.



information on the character of these interactions. To get more insight into the physical nature of the interaction one can use the Kitaura–Morokuma (KM) interaction energy decomposition scheme[13] or the perturbation scheme known as the symmetry-adapted perturbation theory (SAPT) method.[14–16] The first step in such an investigation is to find the optimal structure on the intermolecular potential energy surface by a supermolecular method, while the second stage is to perform the SAPT calculations for the minimal configuration. In particular, SAPT provides not only a conceptual basis for understanding intermolecular interactions, but also an efficient computational framework for accurate predictions of interaction energies. In SAPT, the interaction energy is calculated as the sum of terms of distinct physical origin (i.e., the

Can. J. Chem. Downloaded from www.nrcresearchpress.com by MCGILL UNIVERSITY on 02/02/13
For personal use only.

first-order electrostatic and the second-order induction and dispersion energies) each of these terms being accompanied by a corresponding exchange correction due to the simultaneous exchange of electrons between the monomers. In the many-body version of SAPT the interacting monomers are described through Møller–Plesset or even coupled cluster theory, depending on the accuracy required for each individual interaction term. The quality of the total interaction energies compares with that obtained from the CCSD(T) method.[17,18]

Several computational studies on Mg–ligand interactions have been published[19–26] in which the application of various density functional theories (DFT) or second-order Møller–Plesset (MP2) perturbation theory was assessed by performing ab initio calculations on small Mg complexes. Among these are Mg–aqua complexes,[19–21] clusters containing one or two formates,[22] and complexes with a single neutral ligand, such as cytosine or a guanine–cytosine base pair.[23,24] In addition, earlier investigations indicated that chlorophyll interacts with nucleophilic ligands and forms stable monosolvates with nucleophiles, such as water, alcohols, amines, ketones, and ethers.[27–30] It was also known that Mg in chlorophyll with coordination number 4 is coordinately unsaturated. It is the coordination unsaturation of the Mg that leads to chlorophyll–nucleophile interactions, and in the absence of extraneous nucleophiles, to self-interactions to form dimers.[31] Thus, in nonpolar solvents, the coordination unsaturation of the Mg is relieved by coordination of the ketone oxygen function of one chlorophyll molecule with the Mg atom of a second chlorophyll molecule to form a dimer. Krauss and Stevens[32] have evaluated the binding energies for a series of hexacoordinated Mg complexes containing one formate and varying numbers of water and formamide ligands. In most cases only the binding energy[20,22–26] or enthalpy[20,21] was calculated, and no systematic high-level study on the nature of ligand to metal binding appears to have been performed to date.

The first goal of this investigation is to provide reliable high-level ab initio results for a set of 1:1 complexes to improve the energetic, structural, and electronic description of the ligand binding ability of a simplified chlorophyll model (Fig. 1). In the model, the combination of the two amidine ligands, $CH_3N_2^-$, has the same charge and bonding geometry as the full porphyrin ring. We hereby investigate the intrinsic properties for binding of L = BF, CO, N_2, H_2O, and NH_3 ligands to the $Mg(CH_3N_2)_2$ complex. A second goal of this study is the analysis of the nature of the metal–ligand bond in the Mg(II) complexes by means of an energy decomposition method. This provides information on the relative importance of the electrostatic, induction, and dispersive contributions to the interaction energy. Altogether our results could be particularly useful for the refinement of molecular mechanics force fields as well as comparison with other partitioning schemes used for the calibration of some molecular mechanics potentials.

Computational details

Ab initio and DFT calculations

All ab initio and DFT calculations were performed using the Gaussian 03 package.[33] The geometry of the investigated $Mg(CH_3N_2)_2L$ complexes was optimized at the MP2 level employing the 6–311++G(3df,3pd) basis set. Then corresponding frequency calculations were carried out at the same level to ensure that the optimized structures are true minima. The interaction energy for each complex was calculated at the HF, MP2, MP4, CCSD(T), and B3LYP levels of theory by using the supermolecule method,[34] which defines it as the difference between the energy of the cluster and those of the individual molecules in isolation

$$[1] \qquad E_{\text{int}} = E_n - \sum_i^n E_i$$

where E_n is the total energy of the cluster of size n, and E_i is the energy of the individual monomers in the cluster geometry. The results of eq. [1] are subject to the basis superposition error (BSSE) as each molecule uses the basis set of the others in the cluster, decreasing the energy and resulting in overestimated interaction energies. Hence, BSSE was corrected by using the Boys and Bernardi counterpoise (CP) method.[35]

Energy decomposition analysis

For SAPT energy decomposition analysis, molecular integrals were first obtained with the DALTON 2.0 package;[36] SAPT partitioning was then performed using the SAPT2008 program.[37] The SAPT interaction energy is represented as a double perturbation expansion of various polarization and exchange contributions.[38]

$$[2] \qquad E_{\text{int}} = \sum_{n=1}^{\infty}\sum_{j=0}^{\infty}\left(E_{\text{pol}}^{(nj)} + E_{\text{exch}}^{(nj)}\right)$$

The polarization corrections of the first order in intermolecular interaction, $E_{\text{elst}}^{(1j)}$, describe the classical electrostatic interaction and are denoted $E_{\text{pol}}^{(1j)}$. The $E_{\text{exch}}^{(1j)}$ is the repulsive first-order exchange component resulting from the antisymmetrization (symmetry adaption) of the wave function. The second-order corrections can be decomposed into the induction and dispersion parts.

$$[3] \qquad E_{\text{pol}}^{(2j)} = E_{\text{ind}}^{(2j)} + E_{\text{disp}}^{(2j)} \quad \text{and} \quad E_{\text{exch}}^{(2j)} = E_{\text{exch-ind}}^{(2j)} + E_{\text{exch-disp}}^{(2j)}$$

The induction component is the energy of interaction of the permanent multipole moments of one monomer and the induced multipole moments on the other, whereas the dispersion part comes from the correlation of electron motions on one monomer with those on the other monomer.

In this study, two different levels of SAPT calculations were used

$$[4] \qquad \text{SAPT0} = E_{\text{elst}}^{(10)} + E_{\text{exch}}^{(10)} + E_{\text{ind,resp}}^{(20)} + E_{\text{exch-ind,resp}}^{(20)} + E_{\text{disp}}^{(20)} + E_{\text{exch-disp}}^{(20)} + \delta E_{\text{int,resp}}^{(\text{HF})}$$

$$[5] \qquad \text{SAPT} = \text{SAPT0} + E_{\text{elst,resp}}^{(12)} + E_{\text{elst,resp}}^{(13)} + {}^tE_{\text{ind}}^{(22)} + {}^tE_{\text{exch-ind}}^{(22)} + \varepsilon_{\text{exch}}^{(1)}(\text{CCSD}) + \varepsilon_{\text{disp}}^{(2)}(2)$$

where $\varepsilon_{\text{exch}}^{(1)}(\text{CCSD}) = E_{\text{exch}}^{(1)}(\text{CCSD}) - E_{\text{exch}}^{(10)}$, and $\varepsilon_{\text{disp}}^{(2)}(2) = E_{\text{disp}}^{(21)} + E_{\text{disp}}^{(22)}$. The subscript "resp" indicates that the induc-

Can. J. Chem. Downloaded from www.nrcresearchpress.com by MCGILL UNIVERSITY on 02/02/13
For personal use only.

tion and exchange–induction contributions include the coupled–perturbed HF response.[38] $\delta E_{int,resp}^{(HF)}$ contains the third- and higher-order HF induction and exchange induction contributions. The ${}^{t}E_{ind}^{(22)}$ represents the part of $E_{ind}^{(22)}$ that is not included in $E_{ind,resp}^{(20)}$.

We also performed energy decomposition analysis based on KM method[13]

$$[6] \quad E_{int}(\mathrm{RHF}) = E_{elst} + E_{exch} + E_{CTPLX(Mg\rightarrow L)} + E_{CTPLX(L\rightarrow Mg)} + R$$

where E_{elst} and E_{exch} are electrostatic and exchange, respectively; E_{CTPLX} refers to the charge-transfer and polarization coupled term; and R is the coupling term. All KM analyses were performed using the GAMESS program.[39]

Results and discussion

Geometries and binding energies

Figure 1 shows the optimized structures for the complexes formed between $Mg(CH_3N_2)_2$ moiety and the neutral ligands (L = BF, CO, N_2, NH_3, and H_2O). All the structures were characterized as energy minima on the MP2/6–311++G(3df,3pd) potential energy surface with C_S symmetry. For each complex shown in Fig. 1, the equilibrium Mg–L distance involving the Mg atom and the donor atom of the ligand, Mg–N_A lengths and the optimized $\angle N_A$–Mg–L bond angle are also reported (N_A refers to the amidine nitrogen). The individual distances and angles correspond to fully optimized dimer structures, that is, with both inter- and intra-molecular degrees of freedom relaxed. From Fig. 1, it is apparent that the estimated Mg–L distances are in a range 2.104–2.488 Å, which is much smaller than the sum of van der Waals radii of corresponding counterparts. The binding distance is calculated to be 2.104 Å in the $Mg(CH_3N_2)_2$–H_2O complex that is about 0.4 Å shorter than the $Mg(CH_3N_2)_2$–BF one. More specifically, the optimized Mg–H_2O bond distance is slightly longer than the Mg–O(H_2O) distances in the $[Mg(H_2O)_{6-n}(CH_3OH)_n]^{2+}$ (n = 1–6) complexes[40] and the crystalline structure of $Mg[H_2O]_6^{2+}$[41]. In the $Mg(CH_3N_2)_2$, the Mg atom is in the plane of the amidine ligands. However, the binding of L ligands to Mg lead to very different $\angle N_A$–Mg–L values. It is expected that the $Mg(CH_3N_2)_2$–L complex formation is associated with a dipole moment enhancement due to the charge transfer and electron polarization of the molecules involved in the interaction. Dipole moments (μ) of the free ligands and the $Mg(CH_3N_2)_2$–L complexes are shown in Fig. 1. For all the complexes studied here, the largest dipole moment component is directed along the Mg–L bond. The estimated dipole moments for the $Mg(CH_3N_2)_2$–L complexes are 3.01 D (H_2O), 2.89 D (NH_3), 2.15 D (BF), 0.77 D (N_2), and 0.56 D (CO). One possible explanation for the small dipole moment of the $Mg(CH_3N_2)_2$–CO system may be the unfavorable orientation of individual C=O and $Mg(CH_3N_2)_2$ dipoles in the complex.

Table 1 lists the CP-corrected interaction energies obtained at the HF, MP2, MP4, CCSD(T), B3LYP, SAPT0, and SAPT methods. From a more quantitative point of view, the first important finding is that values of the interaction energies depend appreciably on the method used and (or) the dimer considered. First, it is evident that E_{int}^{HF} is always smaller in magnitude than others. It is clear from Table 1 that the interaction energies of these complexes increase in the order $NH_3 > H_2O > BF > CO > N_2$. A more detailed analysis of these results shows that, in general, the SAPT0 and MP2 methods provide larger stabilization energies than the others. Considering the MP2 results, it is evident that the inclusion of correlation reproduces a stabilization of the complexes as high as 0.8–11.7 kJ/mol. Higher order perturbation (MP4) exhibits only minor variation on the ligand binding energies. As can be seen, the HF method greatly underestimates the interaction energies of the complexes and, in the cases of N_2 ligand, predicts a small binding energy of –0.80 kJ/mol. This indicates that dispersion must play a large role in the stabilization of the $Mg(CH_3N_2)_2$–N_2 complex. The fact that HF interaction energies for the $Mg(CH_3N_2)_2$–NH_3 and $Mg(CH_3N_2)_2$–H_2O are more negative suggests that these interactions may depend more on electrostatic effects than those occurring between the $Mg(CH_3N_2)_2$ and L = BF, CO, and N_2. Previous publications[42,43] demonstrated that the difference between the MP2 and HF energies is mainly assigned to the effects of high-order electrostatic interaction. Consequently, owing to the significant gain of the attraction by electron correlation (0.8–11.7 kJ/mol at the MP2 level), dispersion force plays a considerable role in the stability of the complexes. Focusing on the CCSD(T) results, which are available for each type of system considered, it can be seen that the NH_3 is bound about –53 kJ/mol more strongly than N_2. It should also be noted that the MP2 binding energies are all slightly higher than those of CCSD(T) and that the difference between MP2 and CCSD(T) binding energies increases in the order $N_2 > CO > NH_3 > H_2O > BF$.

Table 1. Calculated binding energies of $Mg(CH_3N_2)_2$–L (L = BF, CO, N_2, NH_3, and H_2O) complexes with different levels of theory using 6–311++G(3df,3pd) basis set.

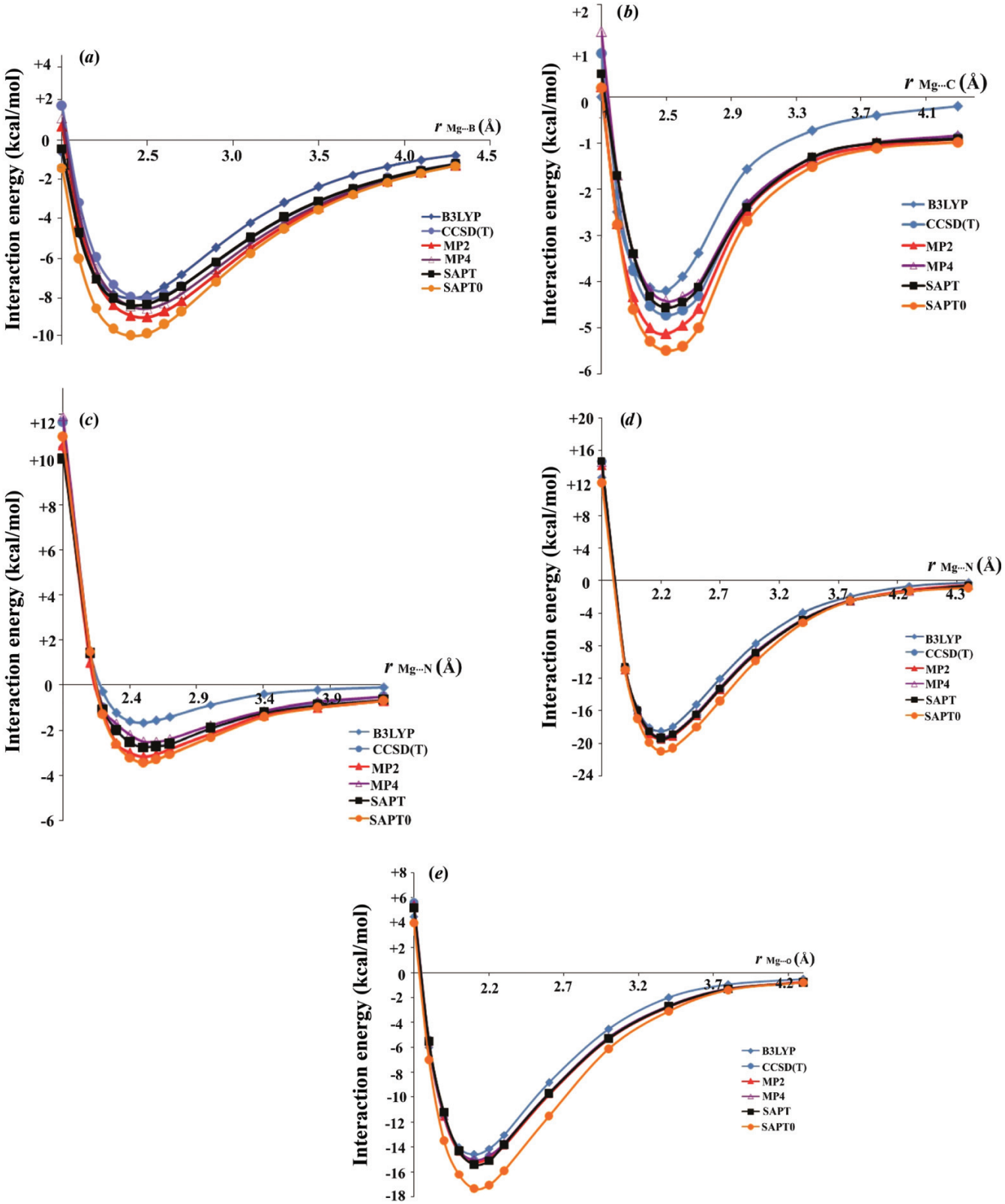
Method	BF	CO	N_2	NH_3	H_2O
HF	–22.2	–9.21	–0.80	–77.96	–63.01
MP2	–33.9	–21.1	–12.5	–81.73	–63.85
MP4	–35.1	–17.8	–9.29	–80.43	–63.01
CCSD(T)	–33.8	–19.2	–10.3	–80.85	–63.14
B3LYP	–33.7	–16.8	–6.49	–77.54	–61.21
SAPT0	–42.12	–23.0	–14.1	–94.71	–73.52
SAPT	–34.8	–18.5	–11.6	–80.97	–64.43

Note: All interaction energies in –kJ/mol.

Prior to examining the individual contributions to the intermolecular energy, we shall discuss the accuracy of the SAPT0 and SAPT results. From Table 1, it is evident that the SAPT0 binding energies are all slightly higher than those of MP2 as computed using the 6–311++G(3df,3pd) basis set and that the difference between MP2 and SAPT0 energies increases as the interaction between the Mg and ligand becomes more negative. Similar as in supermolecular results, the $Mg(CH_3N_2)_2$–NH_3 is the most stable complex (–94.71 kJ/mol at the SAPT0 level). Table 1 also indicates that the SAPT interaction energies for the title complexes are generally in good agreement with those obtained using the supermolecule MP4 and CCSD(T) methods, suggesting that SAPT is a proper method to study the intermolecular interactions in these studied complexes. The calculated SAPT binding energy for the $Mg(CH_3N_2)_2$–NH_3 complex

Can. J. Chem. Downloaded from www.nrcresearchpress.com by MCGILL UNIVERSITY on 02/02/13
For personal use only.

Fig. 2. Potential energy curves of Mg–L interactions in $Mg(CH_3N_2)_2$–L complexes using different theoretical methods. (*a*) L = BF, (*b*) L = CO, (*c*) L = N_2, (*d*) L = NH_3, and (*e*) L = H_2O.



is –80.97 kJ/mol, which overestimates CCSD(T) and MP4 energies by about 0.13 and 0.54 kJ/mol, respectively. It is interesting to note that, in the case of the BF ligand, SAPT binding energies are underestimated in relation to MP4.

Figure 2 presents the variation of the interaction energies with the separation distance, $r_{Mg–L}$, for the $Mg(CH_3N_2)_2$–L complexes using different correlated methods. In each case, a distinct minimum is observed; however, for the L = N_2,

Can. J. Chem. Downloaded from www.nrcresearchpress.com by MCGILL UNIVERSITY on 02/02/13
For personal use only.

Table 2. Calculated symmetry-adapted perturbation theory (SAPT) and Kitaura–Morokuma (KM) energy components for $Mg(CH_3N_2)_2$–L (L = BF, CO, N_2, NH_3, and H_2O) complexes.

Energy term	BF	CO	N_2	NH_3	H_2O
SAPT analysis					
$E_{elst}^{(10)}$	–99.35	–54.97	–30.3	–156.3	–104.9
$E_{exch}^{(10)}$	103.0	59.12	35.7	100.7	63.2
$E_{ind,resp}^{(20)}$	–33.3	–13.3	–11.4	–33.6	–23.2
$E_{exch-ind,resp}^{(20)}$	14	5.28	1.51	6.49	2.05
$\delta E_{int,resp}^{(HF)}$	–12	–5.32	4.02	4.86	–0.08
$E_{disp}^{(20)}$	–15.4	–15.0	–15.1	–18.9	–12.6
$E_{exch-disp}^{(20)}$	0.88	1.3	1.51	2.18	2.1
$E_{elst,resp}^{(12)}$	–1.09	–1.3	–0.38	–0.46	–0.54
$E_{elst,resp}^{(13)}$	3.48	1.47	1.80	3.68	1.63
$^tE_{ind}^{(22)}$	–0.96	–0.92	–1.55	–0.8	–0.75
$^tE_{exch-ind}^{(22)}$	0.63	0.54	0.29	0.63	8.16
$\varepsilon_{exch}^{(1)}(CCSD)$	6.62	5.78	4.02	11.3	8.16
$\varepsilon_{disp}^{(2)}(2)$	–0.88	–1.13	–1.63	–0.63	–1.17
KM analysis					
E_{elst}	–99.35	–54.97	–30.3	–156.3	–104.9
E_{exch}	101.9	61.63	36.5	102.5	64.35
$E_{CTPLX}(Mg \rightarrow L)$	–26.2	–9.71	–6.53	–12.9	–7.91
$E_{CTPLX}(L \rightarrow Mg)$	–6.20	–7.75	–4.40	–15.2	–15.6
R	7.62	1.59	3.94	–3.94	1.09

Note: All interaction energies terms in kJ/mol.

the minimum observed is slightly shallow in nature. If one compares the potential energy curves (PECs) obtained with more accurate and sophisticated CCSD(T) results, a close agreement of the CCSD(T) distance with SAPT results is found. On the contrary, the SAPT0 method fails to produce the CCSD(T) results. The MP2 and MP4 methods quite satisfactorily produce the PECs and are in good agreement with the CCSD(T) and SAPT results. A close inspection of Fig. 2 reveals an interesting observation. Because the Mg–CO and Mg–N_2 interactions are dominated by electrostatic and dispersion interactions, the DFT/B3LYP was found unable to yield satisfactory PECs because about 40% of the short-range dispersion energy is neglected by the B3LYP functional.[44] From Fig. 2, we also see that the difference between SAPT0 and SAPT is largest at short distances and dies off to zero at large distances. This suggests that intramolecular correlation effects are significant at short binding distances.

Interaction energies partitioning

To better understand the nature and the extent of different forces contributing to the intermolecular attraction in the $Mg(CH_3N_2)_2$–L complexes, individual energy components of the total interaction energy were obtained using the SAPT. The electrostatic component of the interaction energy is represented here by the sum of $E_{elst}^{(10)}$, $E_{elst,resp}^{(12)}$, and $E_{elst,resp}^{(13)}$. From Table 2, it is evident that the electrostatic energies dramatically increase as we progress from N_2 to NH_3. The electrostatic interaction pulls the two monomers close to each other, which results in large values of all other energy components. For L = N_2, CO, and BF, the exchange energy becomes even larger than the absolute value of the electrostatic energy, but the large attractive induction and dispersion energies lead to a stabilizing interaction. From Table 2, it is found that all contributions of the electrostatic, induction, and dispersion terms have a stabilizing effect. Of course, the major contribution is the electrostatic interaction energy, which presents between 49% and 74% of the total stabilization energy. Considering the SAPT results, it is also found that first-order electrostatic effects ($E_{elst}^{(10)}$) account for about 75% of the overall attraction in the Mg–NH_3 complex. By comparison, the induction component of this interaction represents about 17% of the total attractive forces, whereas dispersion contributes 8% to the stability of this complex. Thus, it can be said that BF, CO, NH_3, and H_2O interactions are remarkably dependent on both electrostatic and induction forces, with electrostatic playing the largest role in their stability. Based on our SAPT results, the electrostatic contribution to the overall attraction energies of L = BF, CO, N_2, NH_3, and H_2O are 66%, 64%, 49%, 74%, and 73%, respectively. The first-order electrostatic effect can be interpreted mainly as the dipole–dipole interaction, which is why $E_{elst}^{(10)}$ is larger for the NH_3 ligand than for N_2. It is clear in the light of the values of the dipole moments of the two molecules (0.00 (N_2) and 1.71 D (NH_3)).

The total first- and second-order exchange contributions (including both induction and dispersion contributions) reduce the stabilizing effect of the terms just discussed. As expected, the major exchange contribution results from the first-order exchange term, which represents 85%–90% of the total exchange contribution at intermediate distances, whereas the second-order induction and dispersion components represented 3%–8% and 1%–3% of the total exchange, respectively. Regarding the total exchange energy, we obtained the

Can. J. Chem. Downloaded from www.nrcresearchpress.com by MCGILL UNIVERSITY on 02/02/13
For personal use only.

Fig. 3. Correlation between Kitaura–Morokuma (KM) total CTPLX energies and (*a*) $E^{(20)}_{ind,resp}$ and (*b*) $E^{(20)}_{ind,resp} + E^{(20)}_{exch-ind,resp} + \delta E^{HF}_{int}$.

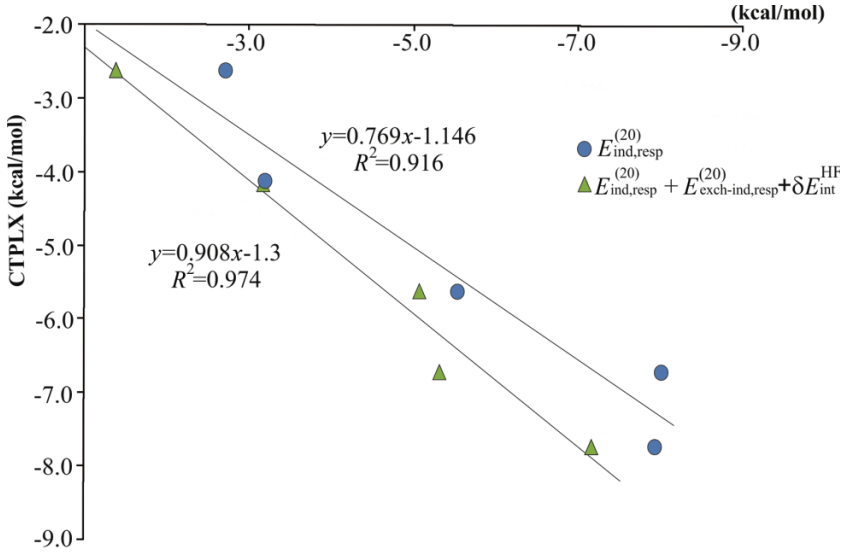


Table 3. Calculated complementary exchange energy for some representative Mg–L distances of $Mg(CH_3N_2)_2$–L complexes (L = BF, CO, N_2, NH_3, and H_2O).

Distance	Term	BF	CO	N_2	NH_3	H_2O
2.2	$E^{(10)}_{exch}$	215.9	117.1	68.71	95.75	43.75
	E_{exch}	217.1	119.9	69.54	97.64	44.84
	$\varepsilon_{compl\text{-}exch}$	**1.21**	**2.7**	**0.84**	**1.9**	**1.1**
2.6	$E^{(10)}_{exch}$	75.95	34.7	19.8	22.8	10.9
	E_{exch}	76.95	36.5	20.4	23.7	11.5
	$\varepsilon_{compl\text{-}exch}$	**1.0**	**1.8**	**0.54**	**0.92**	**0.59**
3.0	$E^{(10)}_{exch}$	25.8	8.04	6.41	6.3	3.3
	E_{exch}	26.5	8.88	6.74	6.74	3.6
	$\varepsilon_{compl\text{-}exch}$	**0.67**	**0.84**	**0.3**	**0.46**	**0.3**
3.4	$E^{(10)}_{exch}$	8.67	3.3	2.1	1.9	1.0
	E_{exch}	8.88	3.8	2.2	2.1	1.2
	$\varepsilon_{compl\text{-}exch}$	**0.2**	**0.50**	**0.1**	**0.2**	**0.2**
3.8	$E^{(10)}_{exch}$	2.93	1.3	0.71	0.63	0.4
	E_{exch}	2.97	1.4	0.71	0.67	0.4
	$\varepsilon_{compl\text{-}exch}$	**0.04**	**0.1**	**0.00**	**0.04**	**0.00**

Note: All interaction energies terms in kJ/mol.

following order: BF > NH_3 > H_2O > CO > N_2. For L = BF, CO, and N_2, the exchange repulsion is more than three times the total energy (in absolute value), and it overcompensates the attractive electrostatic term, thus, the first-order energy is repulsive.

The induction contribution to the interaction energy is mainly contained in $E^{(20)}_{ind,resp}$. This is a second-order energy correction that results from the distortion of the charge distribution of one monomer by the electrostatic charge distribution of another monomer, and vice versa. This mutual polarization of the monomer by the static electric field of the other is the polarizabilities of the monomers. Consequently, in the traditional X–Y···Z complex the effect would be larger the more polar the X–Y bond becomes. The leading intramonomer correlation contribution is included in $^tE^{(22)}_{ind}$ and accounts for only 0.5%–3% of the induction energy. The attractive part of the induction energy is substantially quenched by the repulsive exchange-induction energy (represented by $E^{(20)}_{exch-ind,resp}$ and $^tE^{(22)}_{exch-ind}$). It is interesting to note that, although these types of interactions are largely dependent on electrostatic forces, the induction interaction between the $Mg(CH_3N_2)_2$ moiety and L seems to play a significant role in determining the geometric structures and stabilities of these complexes. For the H_2O, NH_3, and CO ligands, the estimated induction energy contribution to the total stabilization energy is about 17%. This contribution is even larger for the L = BF and N_2 complexes. This is probably due to the larger polarizability of N_2 and BF compared with the others.

The other attraction effect comes from dispersion and this term is significantly greater in absolute value for the Mg–NH_3 complex than for others. The ratios of the $E^{(20)}_{disp}$ term to the total SAPT energy are evaluated to be 144% (N_2), 87% (CO), 50% (BF), 24% (NH_3), and 21% (H_2O). In the molecule–molecule interaction involving closed-shell species, the interplay between the induction and dispersion effects may be well-characterized by analyzing the ratio of these two contributions, $E^{(20)}_{exch-disp}/E^{(20)}_{exch-disp,resp}$.[45] The greatest ratio should indicate the system particularly favored by the dispersion ef-

Can. J. Chem. Downloaded from www.nrcresearchpress.com by MCGILL UNIVERSITY on 02/02/13
For personal use only.

fect. The ratios are 1.02, 1.00, 0.34, 0.24, and 0.06 for H_2O, N_2, NH_3, CO, and BF, respectively.

Additionally, for comparison of the two decomposition schemes SAPT and KM, we also performed KM decomposition for the title systems. It may be noted that SAPT contributions are closely related to KM's three-component decomposition of a Hartree–Fock interaction energy into Coulomb, Heitler–London, and CTPLX terms. For a quantitative comparison of SAPT and KM results, all calculations have to be made in the same "Gaussian" basis sets. According to Table 2, the first-order polarization contribution in SAPT exactly equals the E_{elst} term in the KM scheme, as they are defined in the same way. When we compare the relative metal-to-ligand energy for the different Mg–L complexes, we get the following order: BF > NH_3 > CO > N_2 > H_2O. Table 2 also indicates that, for the L = BF, CO, N_2, NH_3, and H_2O ligands, the ligand-to-metal term yields about 5%, 11%, 11%, 8%, and 12% of the total attractive forces, respectively. Therefore, the Mg–L bonds in $Mg(CH_3N_2)_2$–L complexes have more electrostatic than covalent character, especially in the $Mg(CH_3N_2)_2NH_3$ complex. The induction energy can be described as resulting from the interaction between the highest occupied molecular orbital and the lowest unoccupied molecular orbital. The inductive type of molecular orbital interaction can also be correlated to the extent of charge transfer. It would be interesting to examine if the extent of charge transfer can be correlated to the total induction energy. From Fig. 3, it is clear that the total CTPLX term correlates significantly with $E_{ind}^{(20)}$. However, a much better correlation may be found if one considers the $E_{ind,resp}^{(20)} + E_{exch-ind,resp}^{(20)} + \delta E_{int}^{HF}$ term instead of $E_{ind}^{(20)}$. It suggests that the both charge-transfer and polarization effects are important, and their magnitudes depend on the Mg–L interaction under study.

Within the single-exchange approximation, the uncorrelated Hartree–Fock limit leads to a strict coincidence between first-order exchange-repulsion ($E_{exch}^{(10)}$) and the Heitler–London exchange.[46] With approximate Hartree–Fock wave functions for the monomers, a "complementary exchange energy" may be added: $E_{exch}(KM) = E_{exch}^{(10)} + \varepsilon_{compl\text{-}exch}$. The complementary exchange disappears in the full-exchange series beyond the single-exchange approximation, if and only if the monomer ground-state wave functions used in perturbation treatment are the correlated ground-state wave functions. It is also a very useful quantity to evaluate the quality of a given finite basis set for computing intermolecular interactions. Because the exact and single-exchange complementary exchange energies are almost identical for larger intermolecular distances, $\varepsilon_{compl\text{-}exch}$ is a good indicator of how far an approximate SCF wave function built from some given basis set is from the Hartree–Fock limit. In Table 3, we present the values obtained for $\varepsilon_{compl\text{-}exch}$ at a few representative intermolecular distances for the treated different dimers. We also report the values of the Heitler–London exchange energy for comparison. The values obtained for $\varepsilon_{compl\text{-}exch}$ were found to be in good agreement with typical values reported for hydrogen-bonded clusters.[47] This illustrates the good quality of the basis sets used in this work.

Concluding remarks

In summary, we have systematically investigated the interaction of small ligands BF, CO, N2, H_2O, and NH_3 with $Mg(CH_3N_2)_2$. We also focused on the decomposition of the interaction energy into physically meaningful terms and on the basis of the parameters of molecular properties characterized and described the intermolecular interaction. Our results can be summarized as follows:

1. Our results indicated that the interaction energies of the $Mg(CH_3N_2)_2$–L complexes increase in the order NH_3 > H_2O > BF > CO > N_2. A more detailed analysis of these results shows that, in general, the SAPT0 and MP2 methods provide larger stabilization energy than the others. Furthermore, the SAPT interaction energies for the title complexes are generally in good agreement with those obtained using the supermolecule MP4 and CCSD(T) methods, suggesting that SAPT is a proper method to study the intermolecular interactions in these studied complexes.
2. It is evident that the electrostatic energies dramatically increase as we progress from N_2 to NH_3. For L = N_2, CO, and BF, the exchange energy becomes even larger than the absolute value of the electrostatic energy, but the large attractive induction and dispersion energies lead to a stabilizing interaction.
3. The major exchange contribution results from the first-order exchange term, which represents 85%–90% of the total exchange contribution at intermediate distances, whereas the second-order induction and dispersion components represent 3%–8% and 1%–3% of the total exchange, respectively.
4. We found a reasonable correlation between the total KM CTPLX term and the SAPT induction energy. It suggests that the both charge-transfer and polarization effects are important, and their magnitudes depend on the Mg–L interaction under study.
5. The values obtained for $\varepsilon_{compl\text{-}exch}$ were found to be rather small when compared with typical values. This illustrates the good quality of the basis sets used in this work.

Acknowledgments

MDE wishes to thank Professor K. Morokuma, (Fukui Institute for Fundamental Chemistry, Kyoto University, Japan) for many stimulating and helpful discussions as well as technical support.

References

(1) Lipscomb, W. N.; Sträter, N. *Chem. Rev.* **1996**, *96* (7), 2375. doi:10.1021/cr950042j.
(2) Strickland, N.; Harvey, J. N. *J. Phys. Chem. B* **2007**, *111* (4), 841. doi:10.1021/jp064091j.
(3) Feixas, F.; Solà, M.; Swart, M. *Can. J. Chem.* **2009**, *87* (7), 1063. doi:10.1139/V09-037.
(4) Gholivand, K.; Mahzouni, H. R.; Esrafili, M. D. *Theor. Chem. Acc.* **2010**, *127* (5–6), 539. doi:10.1007/s00214-010-0743-5.
(5) Tsai, A.-L.; Berka, V.; Martin, E.; Olson, J. S. *Biochemistry* **2012**, *51* (1), 172. doi:10.1021/bi2015629.
(6) Carrell, H. L.; Glusker, J. P.; Burger, V.; Manfre, F.; Tritsch, D. *Proc. Natl. Acad. Sci. U.S.A.* **1989**, *86* (12), 4440. doi:10.1073/pnas.86.12.4440.
(7) Yamashita, M. M.; Almassy, R. J.; Janson, C. A.; Cascio, D.; Eisenberg, D. *J. Biol. Chem.* **1989**, *264*, 17681.
(8) Davis, J. F.; Hostomaka, Z.; Hostomsky, Z.; Jordan, S. R.;

Can. J. Chem. Downloaded from www.nrcresearchpress.com by MCGILL UNIVERSITY on 02/02/13
For personal use only.

Matthews, D. A. *Science* **1991**, *252*, 88. doi:10.1126/science.1707186 .
(9) Draper, D. E. *Biophys. J.* **2008**, *95*, 5489. doi:10.1529/biophysj.108.131813.
(10) Hsiao, C.; Williams, L. D. *Nucleic Acids Res.* **2009**, *37* (10), 3134. doi:10.1093/nar/gkp119.
(11) Hsiao, C.; Tannenbaum, M.; VanDeusen, H.; Hershkovitz, E.; Perng, G.; Tannenbaum, A.; Williams, L. D. Complexes of Nucleic Acids with Group I and II Cations. In *Nucleic Acid Metal Ion Interactions;* The Royal Society of Chemistry: London, 2008; pp 1–35.
(12) Robert, E. *Molecular Mechanisms of Photosynthesis;* Blackwell Science: Oxford, UK, 2002.
(13) Kitaura, K.; Morokuma, K. *Int. J. Quantum Chem.* **1976**, *10* (2), 325. doi:10.1002/qua.560100211.
(14) Jeziorska, M.; Cencek, W.; Patkowski, K.; Jeziorski, B.; Szalewicz, K. *J. Chem. Phys.* **2007**, *127* (12), 124303. doi:10.1063/1.2770721.
(15) Misquitta, A. J.; Podeszwa, R.; Jeziorski, B.; Szalewicz, K. *J. Chem. Phys.* **2005**, *123* (21), 214103. doi:10.1063/1.2135288.
(16) Misquitta, A. J.; Szalewicz, K. *J. Chem. Phys.* **2005**, *122* (21), 214109. doi:10.1063/1.1924593.
(17) Riley, K. E.; Hobza, P. *J. Chem. Theory Comput.* **2008**, *4* (2), 232. doi:10.1021/ct700216w.
(18) Esrafili, M. D.; Beheshtian, J.; Hadipour, N. L. *Int. J. Quantum Chem.* **2011**, *111* (12), 3184. doi:10.1002/qua.22628.
(19) Markham, G. D.; Glusker, J. P.; Bock, C. L.; Trachtman, M.; Bock, C. W. *J. Phys. Chem.* **1996**, *100* (9), 3488. doi:10.1021/jp952531t.
(20) Glendening, E. D.; Feller, D. *J. Phys. Chem.* **1996**, *100* (12), 4790. doi:10.1021/jp952546r.
(21) Dudev, T.; Cowan, J. A.; Lim, C. *J. Am. Chem. Soc.* **1999**, *121* (33), 7665. doi:10.1021/ja984470t.
(22) Yliniemela, A.; Uchimaru, T.; Hirose, T.; Baldwin, B. W.; Tanabe, K. *J. Mol. Struct. THEOCHEM* **1996**, *369*(1–3), 9. doi:10.1016/S0166-1280(96)04641-6.
(23) Prado, M. A. S.; Garcia, E.; Martins, J. B. L. *Chem. Phys. Lett.* **2006**, *418* (1–3), 264. doi:10.1016/j.cplett.2005.10.142.
(24) Zhang, Y.; Huang, K. *J. Mol. Struct. THEOCHEM* **2007**, *812* (1–3), 51. doi:10.1016/j.theochem.2007.02.009.
(25) Gomes, J. R. B.; Ribeiro Da Silva, M. D. M. C.; Freitas, V. L. S.; Ribeiro Da Silva, M. A. V. *J. Phys. Chem. A* **2007**, *111* (30), 7237. doi:10.1021/jp0729009.
(26) Da Costa, L. M.; De Mesquita Carneiro, J. W.; Paes, L. W. C. *J. Mol. Model.* **2011**, *17* (8), 2061. doi:10.1007/s00894-010-0909-z.
(27) Katz, J. J.; Strain, H. H.; Leussing, D. L.; Dougherty, R. C. *J. Am. Chem. Soc.* **1968**, *90* (3), 784. doi:10.1021/ja01005a041.
(28) Livingston, R.; Weil, S. *Nature* **1952**, *170* (4331), 750. doi:10.1038/170750b0.
(29) Fiedor, L. *Biochemistry* **2006**, *45* (6), 1910. doi:10.1021/bi0514055.
(30) Karki, K.; Roccatano, D. *J. Chem. Theory Comput.* **2011**, *7* (4), 1131. doi:10.1021/ct1004627.
(31) Katz, J. J.; Dougherty, R. C.; Boucher, L. J. *The Chlorophylls;* Vernon, L. P., Seely, G. R., Eds.; Academic Press Inc.: New York, 1966.
(32) Krauss, M.; Stevens, W. J. *J. Am. Chem. Soc.* **1990**, *112* (4), 1460. doi:10.1021/ja00160a025.
(33) Frisch, M. J.; Trucks, G. W.; Schlegel, H. B.; Scuseria, G. E.; Robb, M. A.; Cheeseman, J. R.; Montgomery, J. A., Jr.; Vreven, T.; Kudin, K. N.; Burant, J. C.; Millam, J. M.; Iyengar, S. S.; Tomasi, J.; Barone, V.; Mennucci, B.; Cossi, M.; Scalmani, G.; Rega, N.; Petersson, G. A.; Nakatsuji, H.; Hada, M.; Ehara, M.; Toyota, K.; Fukuda, R.; Hasegawa, J.; Ishida, M.; Nakajima, T.; Honda, Y.; Kitao, O.; Nakai, H.; Klene, M.; Li, X.; Knox, J. E.; Hratchian, H. P.; Cross, J. B.; Adamo, C.; Jaramillo, J.; Gomperts, R.; Stratmann, R. E.; Yazyev, O.; Austin, A. J.; Cammi, R.; Pomelli, C.; Ochterski, J. W.; Ayala, P. Y.; Morokuma, K.; Voth, G. A.; Salvador, P.; Dannenberg, J. J.; Zakrzewski, V. G.; Dapprich, S.; Daniels, A. D.; Strain, M. C.; Farkas, O.; Malick, D. K.; Rabuck, A. D.; Raghavachari, K.; Foresman, J. B.; Ortiz, J. V.; Cui, Q.; Baboul, A. G.; Clifford, S.; Cioslowski, J.; Stefanov, B. B.; Liu, G.; Liashenko, A.; Piskorz, P.; Komaromi, I.; Martin, R. L.; Fox, D. J.; Keith, T.; Al-Laham, M. A.; Peng, C. Y.; Nanayakkara, A.; Challacombe, M.; Gill, P. M. W.; Johnson, B.; Chen, W.; Wong, M. W.; Gonzalez, C.; Pople, J. A. *Gaussian 03;* Gaussian, Inc.: Pittsburgh, PA, 2003.
(34) Hobza, P.; Zahradnik, R. *Chem. Rev.* **1988**, *88* (6), 871. doi:10.1021/cr00088a004.
(35) Boys, S. F.; Bernardi, F. *Mol. Phys.* **1970**, *19* (4), 553. doi:10.1080/00268977000101561.
(36) *Dalton, a Molecular Electronic Structure Program,* Release 2005. http://www.kjemi.uio.no/software/dalton/dalton.html..
(37) Bukowski, R.; Cencek, W.; Jankowski, P.; Jeziorski, B.; Jeziorska, M.; Kucharski, S. A.; Lotrich, V. F.; Misquitta, A. J.; Moszynski, R.; Patkowski, K.; Podeszwa, R.; Rybak, S.; Szalewicz, K.; Williams, H. L.; Wheatley, R. J.; Wormer, P. E. S.; Żuchowski, P. S. *SAPT2008: "An Ab Initio Program for Many-Body Symmetry-Adapted Perturbation Theory Calculations of Intermolecular Interaction Energies" by Sequential and Parallel Versions;* University of Delaware and University of Warsaw, 2008.http://www.physics.udel.edu/_szalewic/SAPT/SAPT.html.
(38) Jeziorski, B.; Moszynski, R.; Szalewicz, K. *Chem. Rev.* **1994**, *94* (7), 1887. doi:10.1021/cr00031a008.
(39) Schmidt, M. W.; Baldridge, K. K.; Boatz, J. A.; Elbert, S. T.; Gordon, M. S.; Jensen, J. H.; Koseki, S.; Matsunaga, N.; Nguyen, K. A.; Su, S. J.; Windus, T. L.; Dupuis, M.; Montgomery, J. A. *J. Comput. Chem.* **1993**, *14* (11), 1347. doi:10.1002/jcc.540141112.
(40) Dudev, T.; Cowan, J. A.; Lim, C. *J. Am. Chem. Soc.* **1999**, *121* (33), 7665. doi:10.1021/ja984470t.
(41) Bock, C. W.; Kaufman, A.; Glusker, J. C. *Inorg. Chem.* **1994**, *33* (3), 419. doi:10.1021/ic00081a007.
(42) Jaffe, R. L.; Smith, G. D. *J. Chem. Phys.* **1996**, *105* (7), 2780. doi:10.1063/1.472140.
(43) Esrafili, M. D. *J. Mol. Model.* **2012**, *18* (5), 2003. doi:10.1007/s00894-011-1221-2.
(44) Song, H.-J.; Xiao, H.-M.; Dong, H.-S. *J. Chem. Phys.* **2006**, *124* (7), 074317. doi:10.1063/1.2170079.
(45) Cukras, J.; Sadlej, J. *Chem. Phys. Lett.* **2008**, *459* (1–6), 44. doi:10.1016/j.cplett.2008.05.019.
(46) Arrighini, P. Intermolecular Forces and Their Evaluation by Perturbation Theory. In *Lectures Notes in Chemistry;* Springer-Verlag: Berlin, 1981.
(47) Langlet, J.; Caillet, J.; Caffarel, M. *J. Chem. Phys.* **1995**, *103* (18), 8043. doi:10.1063/1.470170.

Theoretical prediction of gas adsorption kinetics based on equilibrium data

Krzysztof Nieszporek and Tomasz Banach

Abstract: Based on the equilibrium adsorption isotherms, new expressions describing the rate of adsorption were developed. The theoretical model takes into account the influence of diffusional effects on the rate of adsorption. Other nonideal effects such as surface energetic heterogeneity or intermolecular interactions can be taken into account by using the adequate equilibrium isotherm. The accuracy of the presented rate equations was verified using real adsorption systems.

Key words: adsorption, kinetics, equilibria, isotherm, thermodynamics.

Résumé : En se basant sur les isothermes d'absorption d'équilibre, on a développé de nouvelles expressions pour décrire la vitesse d'adsorption. Le modèle théorie tient compte de l'influence des effets de diffusion sur la vitesse d'adsorption. L'utilisation de l'isotherme d'équilibre adéquate permet aussi de tenir compte d'autres effets de non-idéalité, telle l'hétérogénéité énergétique de la surface ou les interactions intermoléculaires. On a vérifié le degré d'exactitude des équations de vitesse présentées en faisant appel à des systèmes d'adsorption réels.

Mots-clés : adsorption, cinétique, équilibre, isotherme, thermodynamique.

[Traduit par la Rédaction]

Can. J. Chem. Downloaded from www.nrcresearchpress.com by MCGILL UNIVERSITY on 02/02/13
For personal use only.

Introduction

Over the last few decades, the wide application of adsorption phenomena in the chemical, environmental, and biotechnology industries can be observed. Purification and separation using adsorption processes is environmentally friendly and more economical than traditional methods. As the software-controlling apparatus should quickly respond to the changing process conditions, there is a need for analytical expressions describing equilibrium and rate of adsorption.

There are several models for adsorption equilibrium isotherms. The most basic of them is the still being developed Langmuir model.[1] It assumes the lattice of identical adsorption centers on a flat surface, a single adsorption layer, and a lack of interactions between adsorbed molecules. Modifications of the Langmuir isotherm have been carried out in two directions. The first takes into account the interactions between adsorbed molecules. For example, by using the Bragg–Williams approximation, the new Fowler–Guggenheim isotherm was proposed.[2] The other modifications of the Langmuir isotherm deal with surface nonideal effects called energetic heterogeneity. By applying the integral equation approach it has been shown that, for example, the Temkin, Freundlich, and Dubinin–Radushkevich isotherms are the extensions of the Langmuir isotherm for energetically heterogeneous surfaces.[3]

It is well-known that the rate of adsorption can be controlled by two factors: the diffusion effects and the speed of surface reaction depending on the interaction energy of the adsorbed molecules with the surface and neighbouring particles. There are many papers dealing with the theoretical description of the experimental kinetic isotherms,[4] but, in most cases, the authors use old well-known expressions; for example, Lagergren,[5] the pseudo-second-order equation,[6] etc. Although these expressions are based on the surface-reaction model, it is well-known that the transport of substance from the bulk phase to the surface occurs in several steps. Thus, the overall process of adsorption may be controlled by film (or external) diffusion, pore diffusion and adsorption on the surface, or combination of more than one step. The main goal of the present paper is the theoretical description of a kinetics experiment considering the combined mechanism of the adsorption rate. We show a new theoretical model describing the kinetics of gas adsorption by using the equilibrium isotherms. Therefore, to have a thorough representation of adsorption kinetics, it is necessary to use a suitable equilibrium isotherm equation. The proposed expressions are the alternative to those developed by using the statistical rate theory (SRT) of interfacial transport.[7–9]

Our theoretical studies were examined based on the literature experimental adsorption data.[10] They included alkane adsorption data on activated carbons.

Theory

It has been shown that the correct description of adsorption kinetics should take into account the effect of the pressure or concentration gradient in the near-surface region.[11,12] It can be assumed that there exists a subsurface region located close to the surface of adsorbing molecules. In this region the ad-

Received 25 May 2012. Accepted 26 July 2012. Published at www.nrcresearchpress.com/cjc on 18 October 2012.

K. Nieszporek and T. Banach. Department of Theoretical Chemistry, Maria Curie-Sklodowska University, Pl. M. Curie-Sklodowskiej 3, 20-031 Lublin, Poland.

Corresponding author: Krzysztof Nieszporek (e-mail: krzysn@hektor.umcs.lublin.pl).

Can. J. Chem. Downloaded from www.nrcresearchpress.com by MCGILL UNIVERSITY on 02/02/13
For personal use only.

sorbate pressure (p) differs from that in the bulk phase (p^0), i.e., from the bulk pressure monitored during a kinetics experiment. Pańczyk,[11] then later Nieszporek,[12] described such a model of an adsorption system with different pressure regions of a kinetics experiment. Therefore, the pressure change in the near-surface region can be described by the following equation[12]

$$[1] \qquad \frac{\mathrm{d}p}{\mathrm{d}t} = \alpha(p^0 - p) - \beta\frac{\mathrm{d}\theta}{\mathrm{d}t}$$

where α and β are expressed as follows:

$$[2] \qquad \alpha = \frac{1}{h}\sqrt{\frac{kT}{2\pi m}}, \qquad \beta = N_0\frac{S_A kT}{S_G h}$$

where S_G, S_A, h, and N_0 are the quantities characterizing the properties of the surface of the adsorbing phase. S_G is the area of the interface between the near-surface region and the bulk gas phase, h is the distance between S_G and the area of the adsorbing surface S_A, N_0 is the number of adsorption centers per unit of surface area, and m is the mass of the adsorbing molecule.

Recently, Plazinski[13] studied the applicability of the film-diffusion model for description of the adsorption kinetics at the solid/solution interfaces. By assuming a free molecular flow between the bulk phase and the near-surface region, the diffusion of adsorbing species across the subsurface film can be expressed in terms of Fick's law

$$[3] \qquad \frac{\mathrm{d}c}{\mathrm{d}t} = k_s(c - c_s) - \frac{m}{V_s M}\frac{\mathrm{d}\theta}{\mathrm{d}t}$$

where k_s is the mass-transfer coefficient, V_s is the volume of the subsurface region, M is the maximum adsorbed amount, and c and c_s are the concentrations of sorbate in the bulk and subsurface regions, respectively. It can be seen that by substituting c and c_s with p and p^0, eqs. [1] and [3] become mathematically identical.

In our recent papers,[9,12] we combined eq. [2] with the SRT of interfacial transport[7,8] to describe the rate of pure and mixed-gas adsorption. In the present paper we show another application of eq. [1] to describe the rate of gas (or liquid) adsorption by using any model of adsorption equilibria.

Let us consider the adsorption system in which the overall rate of adsorption is governed only by the rate of the gas particle diffusion in the subsurface region expressed by eq. [1]. This assumption corresponds to the single-resistance model.[14] Because a local equilibrium exists between the adsorbate in the subsurface region and those adsorbed onto the solid, the kinetics of adsorption is influenced by the adsorption isotherm equation linking the surface coverage fraction with the bulk-phase pressure. This assumption is similar to that accepted in the statistical theory approach,[7,8] which links the rate of transport between two phases with different chemical potentials of the molecules in these phases. Thus, the rate of adsorption $\mathrm{d}\theta/\mathrm{d}t$ can be written as follows:

$$[4] \qquad \frac{\mathrm{d}\theta}{\mathrm{d}t} = \frac{\mathrm{d}\theta}{\mathrm{d}p}\frac{\mathrm{d}p}{\mathrm{d}t}$$

For our needs, eq. [4] is a general expression helpful in the theoretical description of adsorption kinetics. It makes it possible to use any model of adsorption equilibria and then can take into account the nonideal effects in the adsorbed phase.

It is interesting to note that, by applying eqs. [3] and [4], Plazinski[13] showed a theoretical interpretation of the empirical Lagergren equation. Considering the region of very low adsorbate pressures, the adsorption system is well-represented by Henry's law

$$[5] \qquad \theta = K_H p$$

where K_H is a constant, because

$$[6] \qquad \frac{\mathrm{d}\theta}{\mathrm{d}p} = K_H$$

Equation [4] combined with eqs. [1] and [6] leads to the following expression

$$[7] \qquad \frac{\mathrm{d}\theta}{\mathrm{d}t} = K_H\frac{\mathrm{d}p}{\mathrm{d}t} = K_H\alpha(p^0 - p) - K_H\beta\frac{\mathrm{d}\theta}{\mathrm{d}t}$$

and then

$$[8] \qquad \frac{\mathrm{d}\theta}{\mathrm{d}t} = \frac{K_H\alpha}{1 + K_H\beta}(p - p^0)$$

Assuming that during the kinetic experiment the adsorbate pressure above the surface does not vary significantly (the amount of adsorbate in the bulk phase is considerably predominant over the adsorbed amount), p and p^0 can be expressed by Henry's equation and then we arrive at the Lagergren pseudo-first-order equation.

It is well-known that, in real adsorption systems, both surface energetic heterogeneity and interactions between adsorbed molecules exist. One of the most popular theoretical isotherms offering a satisfactory description of the equilibrium of adsorption is the generalized Langmuir–Freundlich (GLF) equation

$$[9] \qquad \theta = \frac{N^{(e)}}{M} = \frac{\left(Kp\ \exp\left\{\frac{\varepsilon^0}{kT}\right\}\right)^{kT/c}\ \exp\left\{\frac{\omega\theta}{c}\right\}}{1 + \left(Kp\ \exp\left\{\frac{\varepsilon^0}{kT}\right\}\right)^{kT/c}\ \exp\left\{\frac{\omega\theta}{c}\right\}}$$

where θ is the partial surface coverage, $K\ \exp\{\varepsilon^0/kT\}$ is the adsorption constant (ε^0 is the most probable energy of adsorption), kT/c is the surface energetic heterogeneity parameter, ω is the product of the interaction energy between two molecules adsorbed on two adjacent sites on a lattice and the coordination number of that lattice, and $N^{(e)}$ is the equilibrium coverage at pressure p. For the mathematical purposes, it is convenient to rewrite eq. [4] as follows:

$$[10] \qquad \frac{\mathrm{d}\theta}{\mathrm{d}t} = \frac{\mathrm{d}\theta}{\mathrm{d}\ln p}\frac{\mathrm{d}\ln p}{\mathrm{d}t} = \frac{1}{p}\frac{\mathrm{d}\theta}{\mathrm{d}\ln p}\frac{\mathrm{d}p}{\mathrm{d}t}$$

Rearranging eq. [9] we have

$$[11] \qquad p = \frac{1}{K}\left(\frac{\theta}{1 - \theta}\right)^{c/kT}\ \exp\left\{\frac{\omega\theta}{kT}\right\}$$

and then

$$[12] \qquad \frac{\mathrm{d}\ln p}{\mathrm{d}\theta} = \frac{c}{kT}\frac{1}{\theta(1 - \theta)} + \frac{\omega}{kT}$$

Can. J. Chem. Downloaded from www.nrcresearchpress.com by MCGILL UNIVERSITY on 02/02/13
For personal use only.

Combining eq. [10] with eq. [12] we arrive at the following adsorption rate equation

$$[13] \qquad \frac{d\theta}{dt} = \frac{1}{p}\left[\frac{c}{kT}\frac{1}{\theta(1-\theta)} + \frac{\omega}{kT}\right]^{-1}\left[\alpha(p-p^0) + \beta\frac{d\theta}{dt}\right]$$

which can be simplified as follows:

$$[14] \qquad \frac{d\theta}{dt} = \frac{\alpha(p-p^0)}{p\left[\frac{c}{kT}\frac{1}{\theta(1-\theta)} + \frac{\omega}{kT}\right] - \beta}$$

Equation 14 describes the rate of gas adsorption on energetically heterogeneous surfaces when the interactions between adsorbed molecules are described by the mean field approximation. An unquestionable advantage of eq. [14] is its simple mathematical form and the possibility of simulating (in some range) diffusional effects. This is due to the fact that eq. [14] has been developed by using eq. [1], which directly results from Fick's law. On the other hand, the important disadvantage of eq. [14] is its limited applicability. Namely, GLF (eq. [9]) was obtained by using the condensation approximation (CA), which assumes clear energetic nonideality of molecule–surface interactions. When adsorption occurs such as that on an energetically homogeneous surface ($kT/c \rightarrow 1$), the error connected with CA increases. This inaccurate property of GLF is clearly visible when eq. [9] is used to describe the enthalpic effects accompanying gas adsorption. In that case, the corresponding isosteric heat of adsorption (q^{st}) has the following form

$$[15] \qquad q^{st} = q^{st0} - c\ln\frac{\theta}{1-\theta} + \omega\theta$$

where q^{st0} is the nonconfigurational isosteric heat of adsorption. While assuming a lack of interactions ($\omega/kT = 0$), q^{st} is coverage-dependent even if the surface is energetically homogeneous. Since the adsorption occurs as if it was an energetically homogeneous surface at low adsorbate pressures, eq. [15] should be applied with caution.

Recently, we demonstrated a new isotherm corresponding to the uniform adsorption energy distribution[9]

$$[16] \qquad \theta = \frac{kT}{\Delta\varepsilon}\ln\left(\frac{1 + pK_L^m \exp\left\{\frac{\omega\theta}{kT}\right\}}{1 + pK_L^l \exp\left\{\frac{\omega\theta}{kT}\right\}}\right)$$

where K_L^m and K_L^l are the adsorption constants, and

$$[17] \qquad \Delta\varepsilon = kT\ln\frac{K_L^m}{K_L^l}$$

For our purposes we called it the generalized uniform Langmuir (GUL) isotherm. Equation [16] is the exact solution of the integral equation approach and we do not have to deal with CA error. It means that the GUL isotherm can be used even if the surface is quite energetically homogeneous.

To determine the corresponding kinetic equation, it is convenient to rewrite eq. [16] as follows:

$$[18] \qquad p = \frac{1 - \exp\left\{\frac{\Delta\varepsilon\theta}{kT}\right\}}{\exp\left\{\frac{\omega\theta}{kT}\right\}}\left(K_L^l \exp\left\{\frac{\Delta\varepsilon\theta}{kT}\right\} - K_L^m\right)$$

and, finally, by applying eq. [4] we arrive at the following kinetic expression

$$[19] \qquad \frac{d\theta}{dt} = \frac{\alpha\left(K_L^l \exp\left\{\frac{\Delta\varepsilon\theta}{kT}\right\} - K_L^m\right)\left(\exp\left\{\frac{\Delta\varepsilon\theta}{kT}\right\} + \exp\left\{\frac{\theta(\Delta\varepsilon+\omega)}{kT}\right\}K_L^l p_0 - \exp\left\{\frac{\omega\theta}{kT}\right\}K_L^m p_0 - 1\right)}{\beta\exp\left\{\frac{\omega\theta}{kT}\right\}\left(K_L^m - \exp\left\{\frac{\Delta\varepsilon\theta}{kT}\right\}K_L^l\right)^2 - \frac{\Delta\varepsilon}{kT}\exp\left\{\frac{\Delta\varepsilon\theta}{kT}\right\}(K_L^l - K_L^m)}$$

Summing up, we have shown two new theoretical kinetic isotherms (eqs. [14] and [19]) that can be used to describe the single-gas adsorption rate on energetically heterogeneous surfaces. These new expressions take into account the interactions between adsorbed molecules. Having at our disposal the equilibrium experimental isotherms, most of the parameters in eqs. [14] and [19] can be determined by using eqs. [9] and [16]. Hence, the calculations of the rate of adsorption need only to adjust two best-fit parameters, α and β. The adsorbate pressure (p) can be calculated by using the corresponding equilibrium isotherms (eqs. [9] and [16]) for actual surface coverage.

Results and discussion

To analyze the applicability of the derived kinetics eqs. [14] and [19], we used the experimental data reported by Qiao and Hu.[10] The authors report both equilibrium and kinetics isotherms of simple gases on activated carbon. These data satisfy our requirements: the analysis of experimental equilibrium isotherms gives the values of the best-fit parameters, which then can be used to calculate the adsorption rate.

The practical calculations of the rate of adsorption were done by using Mathematica 7.0 software. For the calculations, we assumed the following boundary conditions: $\theta(t = 0) = 0$ and $p(t = 0) = p^0$. The values of α and β characterizing the geometric properties of the solid phase were calculated by applying the random walk Monte Carlo procedure with 10^6 steps. At each step the values of α and β were generated randomly to find the best agreement of the theoretical curve with the experimental data. Each calculation was repeated a few times with a gradual decrease of the search limits of each parameter. The quality of the adjustment of theoretical kinetics isotherm was characterized by the following error function

$$[20] \qquad AAD\% = \frac{1}{n}\sum_{i=1}^{n}\frac{|N_t^{exp} - N_t^{calcd}|}{N_t^{exp}}100$$

The average absolute deviation (AAD%) has a significant property — the greatest impacts on the value of the error function have deviations at low adsorbate pressures or short times of adsorption. As most of the empirical rate equations show large relative errors for the predicted adsorbed amount at the initial times of adsorption, the AAD% function makes

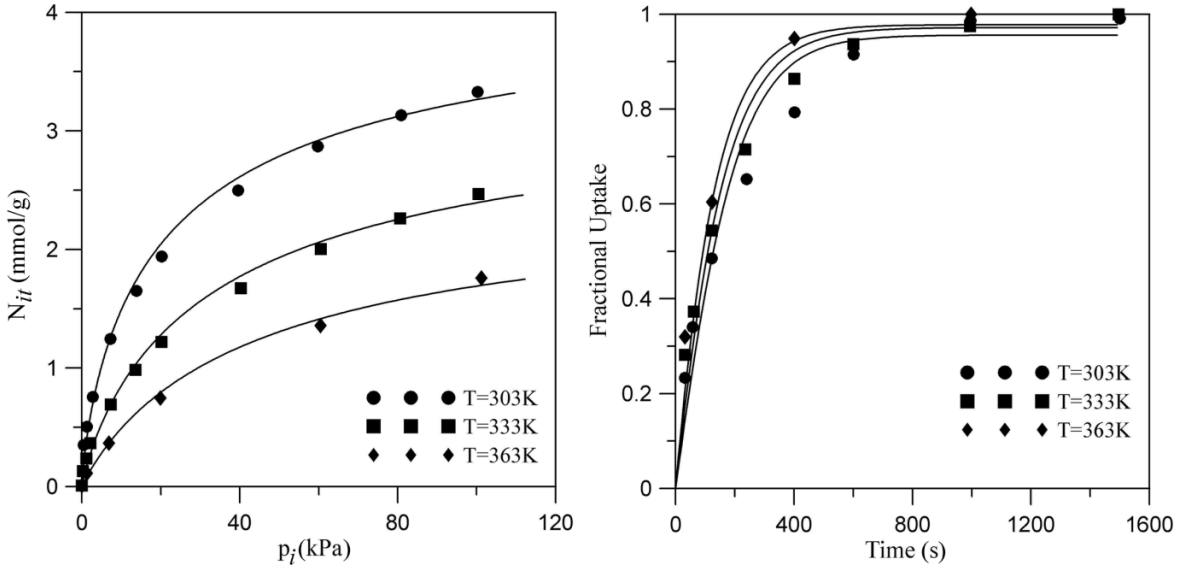
Can. J. Chem. Downloaded from www.nrcresearchpress.com by MCGILL UNIVERSITY on 02/02/13
For personal use only.

Table 1. Values of the best-fit parameters occurring in generalized Langmuir–Freundlich (GLF) eq. [9] and kinetics isotherm [14] obtained by fitting the experimentally measured equilibrium and kinetics isotherms of ethane and propane at Norit AC.[10] The last two columns include the values of average absolute deviation (AAD%) corresponding to equilibrium (eq.) and kinetics (kin.) isotherms adjustment.

T (K)	M (mmol/g)	$K_i \exp\{\varepsilon_i^0/kT\}$ (kPa^{-1})	ω/k (T)	c/k (T)	α	β	AAD% (eq.)	AAD% (kin.)
C_2H_6								
303	4.31	4.7×10^{-2}	41.28	382.97	2.24×10^{9}	9.64×10^{12}	9.11	7.90
333	3.55	2.6×10^{-2}			3.36×10^{5}	1.93×10^{8}	8.21	4.77
363	2.52	2.2×10^{-2}			9.12×10^{7}	5.55×10^{11}	9.10	3.17
C_3H_8								
303	4.19	2.0×10^{-1}			4.77×10^{6}	1.77×10^{10}	16.27	7.89
333	3.67	1.0×10^{-1}	46.80	369.86	2.42×10^{2}	1.13×10^{6}	10.10	5.05
363	3.03	7.2×10^{-2}			2.85×10^{2}	1.33×10^{6}	13.60	4.84

Note: T, temperature; k, Boltzmann constant; M, maximum adsorbed amount; K_i, adsorption constant; ε_i^0, most probable adsorption energy; ω, interaction parameter; c, energetic heterogeneity parameter; α and β, parameters defined in eq. [2].

Fig. 1. Equilibrium and kinetics adsorption isotherms of C_2H_6 on Norit AC at different temperatures[10] fitted by using generalized Langmuir–Freundlich (GLF) equilibrium (eq. [9]) and kinetics isotherms (eq. [14]), respectively.



it possible to assess the applicability of the proposed kinetic equations.

Qiao and Hu[10] reported equilibrium C_2H_6 and C_3H_8 isotherms measured at three temperatures: 303, 333, and 363 K. For the calculations, we mainly assumed that the parameters c/k and ω/k are temperature-independent and are common for all isotherms of a given system. Thus, a few isotherms measured at different temperatures can be adjusted simultaneously. Although this type of assumption makes the calculations significantly more difficult and decreases the quality of the fit, it eliminates the correlations between the values of the best-fit parameters.

During the theoretical analysis of experimental isotherms using the expressions based on the Langmuir model, M should be temperature-independent. However, taking the typical behaviour of experimental isotherms into account, we can see that, with the increasing temperature, adsorption isotherms reach a plateau at lower surface coverage. Hence, M is usually accepted as temperature-dependent to increase the agreement between the theoretical curves and the experimental data.

The results for the calculations of equilibrium and kinetics isotherms for C_2H_6 and C_3H_8 adsorbed at Norit AC by using GLF eqs. [9] and [14] are shown in Table 1 and Figs. 1 and 2.

Figures 1 and 2 confirm the well-known applicability of GLF eq. [9]. Although some deviations of the theoretically calculated isotherms from the experimental data exist, the values of the best-fit parameters M, $K \exp\{\varepsilon^0/kT\}$, c/k, and ω/k seem to be correctly determined. The heterogeneity parameters (c/k) for both gases are similar because ethane and propane have similar chemical properties. It is worth noting that energetic heterogeneity is the property of the entire adsorption system, but not only of the surface, it also reflects the nonideality of adsorbent–adsorbate interaction energy. The interaction parameters (ω/k) have similar values for ethane and propane (the value of ω/k for propane is slightly larger).

While considering the results of the calculations of the rate of alkane adsorption, we should explain the meaning of "fractional uptake" used by Qiao and Hu.[10] The authors defined it as the uptake at any time divided by its value at final equilibrium, i.e., when $t \rightarrow \infty$. Then the values of $\partial\theta/\partial t$

Can. J. Chem. Downloaded from www.nrcresearchpress.com by MCGILL UNIVERSITY on 02/02/13
For personal use only.

Fig. 2. Equilibrium and kinetic adsorption isotherms of C_3H_8 on Norit AC at different temperatures[10] fitted by using generalized Langmuir–Freundlich (GLF) eq. [9] and corresponding kinetics isotherm [14].

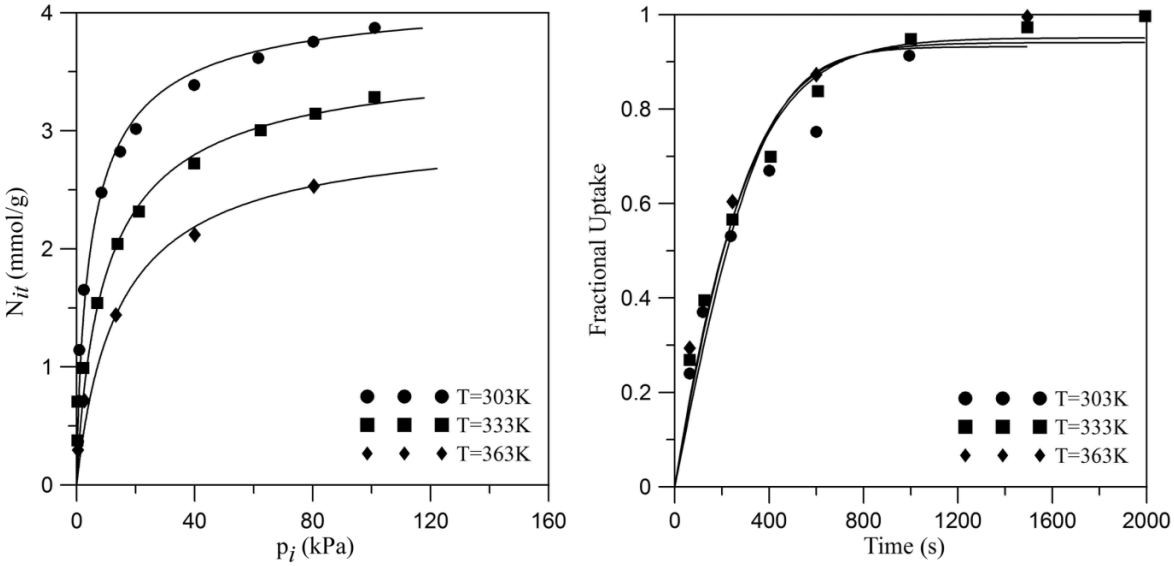


Table 2. Values of the best-fit parameters occurring in generalized uniform Langmuir (GUL) eq. [16] and kinetics isotherm [19] (corresponding to the uniform energy distribution) obtained by fitting experimentally measured equilibrium (eq.) and kinetics (kin.) isotherms of ethane and propane on Norit AC.[10]

T (K)	M (mmol/g)	K_L^l (kPa^{-1})	ω/k (T)	$\Delta\varepsilon/k$ (T)	α	β	AAD% (eq.)	AAD% (kin.)
C_2H_6								
303	9.44	2.32×10^{-6}	469.22	3651	5.65×10^{6}	7.57×10^{10}	1.33	4.01
333	8.73	2.42×10^{-6}			2.11×10^{7}	3.39×10^{11}	3.84	5.21
363	7.17	3.28×10^{-6}			8.56×10^{5}	1.74×10^{10}	3.41	2.86
C_3H_8								
303	10.53	1.05×10^{-8}	634.27	6232	2.17×10^{9}	2.87×10^{12}	1.89	6.10
333	10.39	1.49×10^{-8}			1.59×10^{5}	2.68×10^{9}	1.03	3.56
363	9.58	2.54×10^{-8}			5.68×10^{7}	9.44×10^{11}	1.42	5.77

Note: T, temperature; k, Boltzmann constant; M, maximum adsorbed amount; K_L^l, adsorption constant; ω, interaction parameter; $\Delta\varepsilon$, energetic heterogeneity parameter; α and β, parameters defined in eq. [2]; AAD%, average absolute deviation.

should be multiplied by $M/N^{(e)}$, where $N^{(e)}$ can be calculated by using GLF eq. [9].

Generally, the quality of fit of the kinetic data is quite good. However, the theoretical kinetic isotherm (eq. [14]) is derived from the GLF isotherm (eq. [9]) and then it inherits its limitations. For that reason GLF should not be used for almost energetically homogeneous adsorption systems (i.e., when $kT/c \rightarrow 1$). Table 1 shows that this situation occurs in our case. On the other hand, the experimental data reported by Qiao and Hu[10] were determined in the region of very low adsorbate pressures. It is known that under such pressure conditions, the adsorption occurs as it does on an energetically homogeneous surface.

In the next step of calculations, we used GUL eqs. [16] and [19], corresponding to the uniform energy distribution. The results are shown in Table 2 and Figs. 3 and 4.

It can be stated that GUL eq. [16] describes the equilibrium of adsorption better than GLF eq. [9]. Table 2 shows that all GUL fits are characterized by lower values of AAD %. The application of GUL isotherm eq. [16] indicates evidently stronger interactions between adsorbed alkanes. As eq. [16] is the exact solution of the integral equation approach it has nothing to do with CA error. The analysis of isotherms were performed simultaneously, and the parameters $\Delta\varepsilon/k$ and ω/k characterize the adsorption system.

The results of the calculations for the rate of adsorption by eq. [19] are only just a little bit better than before — the values of AAD% (kin.) are similar for both theoretical models (see Tables 1 and 2).

These calculations were done by assuming the temperature independence of the energetic heterogeneity and interaction energy between adsorbed molecules. Undoubtedly, it seems that the theoretical analysis of single isotherms separately should lead to lower AAD% values. Thus, we finally follow this line and show the agreement between the proposed theoretical models and the experimental data obtained by assuming some temperature dependences of the surface energetic heterogeneity and the interactions between adsorbed molecules. It means that, during the theoretical analysis of equilibrium adsorption, all best-fit parameters are adjusted separately for each experimental isotherm. Tables 3 and 4 show the values of the best-fit parameters determined by ad-

Fig. 3. Equilibrium and kinetic adsorption isotherms of C_2H_6 on Norit AC at different temperatures[10] fitted by using generalized uniform Langmuir (GUL) eq. [16] and corresponding kinetics isotherm [19].

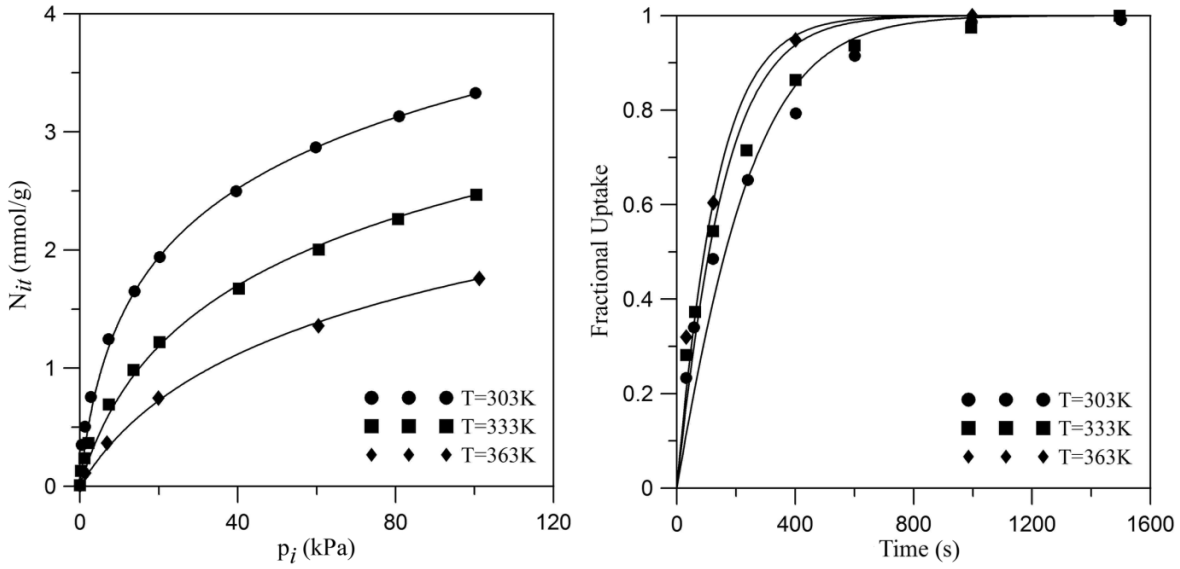


Fig. 4. Equilibrium and kinetic adsorption isotherms of C_2H_6 on Norit AC at different temperatures[10] fitted by using generalized uniform Langmuir (GUL) eq. [16] and corresponding kinetics isotherm [19].

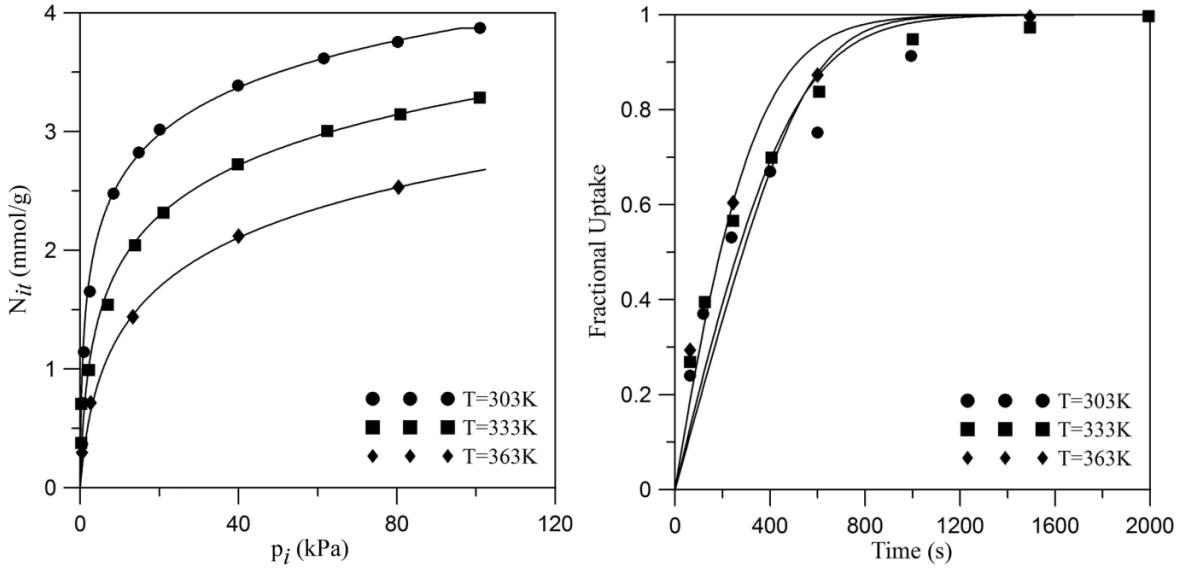


Table 3. Values of the best-fit parameters occurring in generalized Langmuir–Freundlich (GLF) eq. [9] and corresponding kinetics isotherm [14] obtained by fitting the experimentally measured equilibrium (eq.) and kinetics (kin.) isotherms of ethane and propane on Norit AC[10] at 333 K.

T (K)	M (mmol/g)	$K_i \exp\{\varepsilon_i^0/kT\}$ (kPa^{-1})	ω/k (T)	c/k (T)	α	β	AAD% (eq.)	AAD% (kin.)
C_2H_6								
333	3.57	2.64×10^{-2}	74.08	376.50	2.53×10^{5}	1.45×10^{9}	8.24	4.60
C_3H_8								
333	3.68	1.02×10^{-1}	34.34	380.17	1.10×10^{6}	1.88×10^{10}	9.72	4.85

Note: T, temperature; k, Boltzmann constant; M, maximum adsorbed amount; K_i, adsorption constant; ε_i^0, most probable adsorption energy; ω, interaction parameter; $\Delta\varepsilon$, energetic heterogeneity parameter; α and β, parameters defined in eq. [2]; AAD%, average absolute deviation.

justing equilibrium and kinetic isotherms of C_2H_6 and C_3H_8 on Norit AC at 333 K. The results for the calculations are shown graphically in Figs. 5 and 6.

A comparison of the results of the calculations determined by using the GLF model (shown in Tables 1 and 3) shows similar agreement between the theoretical isotherms and the

Can. J. Chem. Downloaded from www.nrcresearchpress.com by MCGILL UNIVERSITY on 02/02/13
For personal use only.

Table 4. Values of the best-fit parameters occurring in generalized uniform Langmuir (GUL) eq. [16] and corresponding kinetics isotherm [19] obtained by fitting the experimentally measured equilibrium (eq.) and kinetics (kin.) isotherms of ethane and propane on Norit AC[10] at 333 K.

T (K)	M (mmol/g)	K_L^l (kPa^{-1})	ω/k (T)	$\Delta\varepsilon/k$ (T)	α	β	AAD% (eq.)	AAD% (kin.)
C_2H_6								
333	7.15	2.42×10^{-6}	809.59	3766	5.61×10^{-3}	6.37×10^{-8}	2.56	3.05
C_3H_8								
333	10.24	1.49×10^{-8}	743.69	6220	2.30×10^{-3}	10.46	0.86	0.98

Note: T, temperature; k, Boltzmann constant; M, maximum adsorbed amount; K_L^l, adsorption constant; ω, interaction parameter; $\Delta\varepsilon$, energetic heterogeneity parameter; α and β, parameters defined in eq. [2]; AAD%, average absolute deviation.

Fig. 5. Equilibrium and kinetics adsorption isotherms of C_2H_6 on Norit AC at 333 K[10] fitted by using generalized Langmuir–Freundlich (GLF) eq. [9] and corresponding kinetics isotherm [14]. During the calculations we assumed that c/k and ω/k are temperature-dependent (see Table 3).

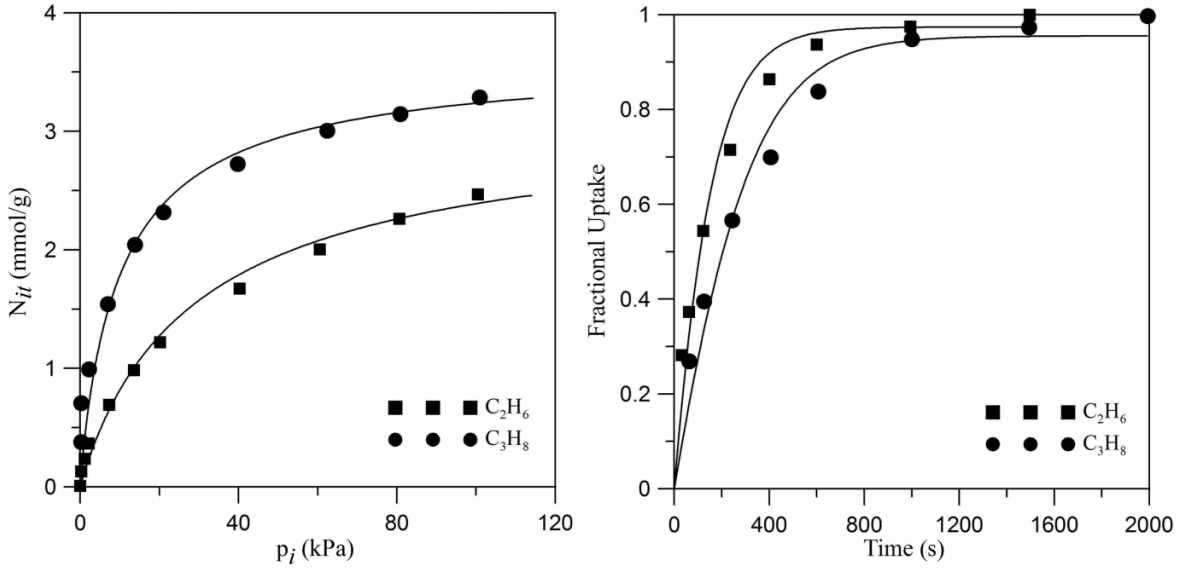
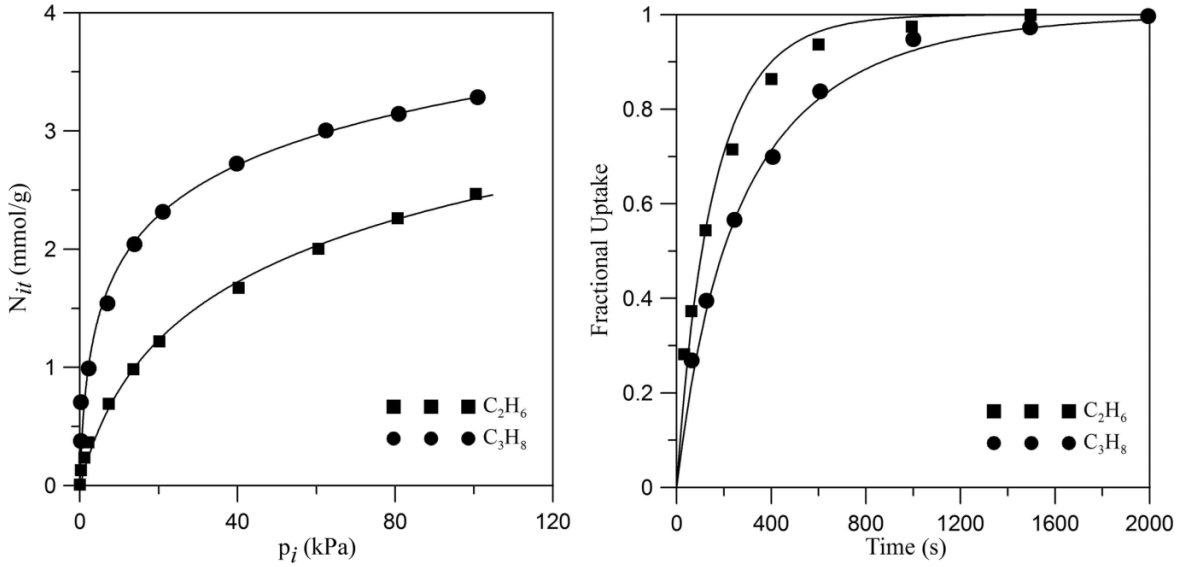


Fig. 6. Equilibrium and kinetics adsorption isotherms of C_2H_6 on Norit AC at 333 K[10] fitted by using generalized uniform Langmuir (GUL) eq. [16] and corresponding kinetics isotherm [19]. During the calculations we assumed that $\Delta\varepsilon/k$ and ω/k were temperature-dependent (see Table 4).



experimental data. Allowing for the temperature dependence of c/k and ω/k results in only a slightly better agreement between the experimental and theoretical kinetics isotherms.

As far as the GUL isotherms (eqs. [16] and [19]) are concerned, we obtained evidently better results. Release of the best-fit parameters $\Delta\varepsilon/k$ and ω/k leads to much better agree-

Can. J. Chem. Downloaded from www.nrcresearchpress.com by MCGILL UNIVERSITY on 02/02/13
For personal use only.

Can. J. Chem. Downloaded from www.nrcresearchpress.com by MCGILL UNIVERSITY on 02/02/13
For personal use only.

ment between the theoretically calculated and experimentally measured isotherms. For example, when $\Delta\varepsilon/k$ and ω/k were assumed as temperature-independent and determined during simultaneous adjustment of all equilibrium isotherms, AAD% (eq.) for ethane and propane at 333 K were equal to 3.84 and 1.03, respectively (see Table 2), whereas adjusting for only single isotherms at 333 K, the AAD% (eq.) were equal to 2.56 and 0.86, respectively. An even greater difference between both models of calculations exists in the case of kinetics isotherms. Namely, AAD% (kin.) (determined when $\Delta\varepsilon/k$ and ω/k were temperature-independent) for ethane and propane were equal to 5.21 and 3.56, respectively (Table 2). When these parameters were temperature-dependent, the AAD% (kin.) were equal to 3.05 and 0.98, respectively (Table 4).

Summing up, we have shown two ways for calculations of the theoretical equilibrium and kinetics isotherms differentiated by considering the temperature dependence of some best-fit parameters. It is difficult to state which calculation procedure is recommended. Undoubtedly, simultaneous adjustment of all equilibrium isotherms is more correct. However, the most practical applications of theoretical equilibrium isotherms are characterized by allowing temperature dependence of the adsorption capacity. To get better agreement of theoretical equilibrium and kinetics isotherms with the experimental data, other best-fit parameters in the theoretical isotherms can be released. Unfortunately, in such a case the values of the best-fit parameters are frequently correlated and difficult to interpret.

Conclusions

We proposed a new theoretical description of the rate of gas adsorption. By differentiating a theoretical equilibrium isotherm, it can be easy to determine the corresponding kinetic equation. Plazinski[13] confirmed the correctness of this method by obtaining the theoretical interpretation of the Lagergren pseudo-first-order equation.

By using equilibrium isotherms (eqs. [9] and [16]) we obtained two new theoretical kinetics eqs. [14] and [19]. They have a relatively simple mathematical form and lead to good agreement with the experimentally measured data. The calculations take into account both the surface energetic heterogeneity and the interactions between adsorbed molecules.

Most of the parameters appearing in kinetics isotherms can be obtained from the theoretical analysis of equilibrium data. During calculations of the rate of adsorption, only two best-fit parameters (α and β) must be adjusted. Compared with the corresponding SRT kinetics isotherms,[9,12] this is an unquestionable advantage, because, in the case of the SRT equations, besides α and β an additional two best-fit parameters must be adjusted during the analysis of kinetics experiment.

Undoubtedly, better results have been determined in the case of isotherm eq. [14], especially when each equilibrium isotherm was adjusted separately. It is due to the fact that GLF eq. [9] has been obtained by using the condensation approximation. On the other hand, the GUL isotherm eq. [16] corresponding to the uniform energy distribution is free of such error connected with CA application.

The application of the new rate equations for adsorption from the liquid phase is a separate issue. This is because the adsorption from solutions is a more complicated process than gas adsorption. A solution is typically a system of more than one component, and there are at least two substances that can adsorb. Thus, it is essentially an exchange process and, hence, molecules adsorb not only because they are attracted by solids but also because the solution may reject them. In the case of dilute solutions, it is commonly assumed that all the equations derived from monolayer gas adsorption remain valid after replacing pressure by concentration and modifying the dimensions of some parameters. After such modifications, the new rate eqs. [14] and [19] can be applied to adsorption from liquids.

Kinetics equations determined by eq. [4] can be applied to the adsorption systems when the rate of adsorption is controlled by the surface reaction mechanism. It seems that even when the intraparticle diffusion is the rate-determining step, eq. [4] can still successfully describe the adsorption rate. It is due to the fact that its solution takes into account the variance of pressure in the near-surface region by applying Fick's law.

References

(1) Langmuir, I. *J. Am. Chem. Soc.* **1918**, *40* (9), 1361. doi:10.1021/ja02242a004.
(2) Fowler, R. H.; Guggenheim, E. A. *Statistical Thermodynamics;* Cambridge University Press: Cambridge, 1938.
(3) Rudzinski, W.; Nieszporek, K.; Moon, H.; Rhee, H.-K. *Heterog. Chem. Rev.* **1994**, *1*, 275.
(4) Azizian, S. *J. Colloid Interface Sci.* **2004**, *276* (1), 47. doi:10.1016/j.jcis.2004.03.048.
(5) Lagergren, S.; Sven, K. *Vetenskapsakad. Handl.* **1898**, *24*, 1.
(6) Ho, Y. S.; McKay, G. *Water Res.* **2000**, *34* (3), 735. doi:10.1016/S0043-1354(99)00232-8.
(7) Ward, C. A. *J. Chem. Phys.* **1977**, *67* (1), 229. doi:10.1063/1.434547.
(8) Ward, C. A.; Findlay, R. D.; Rizk, M. *J. Chem. Phys.* **1982**, *76* (11), 5599. doi:10.1063/1.442865.
(9) Nieszporek, K.; Banach, T. *Ind. Eng. Chem. Res.* **2011**, *50* (6), 3078. doi:10.1021/ie101340z.
(10) Qiao, S.; Hu, X. *Chem. Eng. Sci.* **2000**, *55* (9), 1533. doi:10.1016/S0009-2509(99)00427-3.
(11) Panczyk, T. *Phys. Chem. Chem. Phys.* **2006**, *8* (32), 3782. doi:10.1039/b602360f.
(12) Nieszporek, K. *Appl. Surf. Sci.* **2009**, *255* (8), 4627. doi:10.1016/j.apsusc.2008.11.087.
(13) Plazinski, W. *Appl. Surf. Sci.* **2010**, *256* (17), 5157. doi:10.1016/j.apsusc.2009.12.083.
(14) Ho, Y. S.; Ng, J. C. Y.; McKay, G. *Separ. Purif. Methods* **2000**, *29* (2), 189. doi:10.1081/SPM-100100009.

Formal transfer potentials of strontium and uranyl ions at water|1,2-dichloroethane interfaces

Tom J. Stockmann, Anne-Marie Montgomery, and Zhifeng Ding

Can. J. Chem. Downloaded from www.nrcresearchpress.com by MCGILL UNIVERSITY on 02/02/13
For personal use only.

Abstract: The extraction of dioxouranium (UO_2^{2+}), or uranyl, and strontium (Sr^{2+}) ions from spent nuclear fuel (SNF), often through a biphasic (aqueous / organic solvent) ligand assisted process, is critical for the implementation of a closed-loop nuclear fuel cycle whereby SNF is diverted from permanent geological disposal and the life of the nuclear industry is extended. Deeper understanding of the biphasic extraction process can be achieved through facile electrochemical experiments at a liquid|liquid interface. Of primary importance to developing a quantitative analysis of the ligand assisted or facilitated ion transfer (FIT) (i.e., transfer through interfacial complexation) case is to first quantify the free or simple metal IT; that is the amount of applied potential required to "push" ions across the water|organic interface. This value is, in fact, a constant referred to as the formal transfer potential ($\Delta_o^w\phi^{o'}$), which is unique to each metal ion in the biphasic system. Because of their hydrophilicity they often limit the polarizable potential window. Values for $\Delta_o^w\phi^{o'}$, for the most part, have only been estimated. With a microinterface housed at the tip of a 25 μm capillary it is possible to reduce the Faradaic current to observe their transfer. Herein is described the quantification of $\Delta_o^w\phi^{o'}_{UO_2^{2+}}$ and $\Delta_o^w\phi^{o'}_{Sr^{2+}}$ or the formal transfer potentials for dioxouranium and strontium ions, respectively.

Key words: liquid|liquid electrochemistry, simple ion transfer, formal transfer potential, strontium ion, dioxouranium, uranyl, micropipette.

Résumé : L'extraction des ions dioxouranium (UO_2^{2+}) ou uranyles ou strontium (Sr^{2+}) des combustibles nucléaires irradiés (CNI), souvent par le biais d'un processus en deux phases (aqueuse/solvant organique) assisté par un ligand, est souvent une étape critique dans l'implantation d'un cycle fermé de combustible nucléaire dans lequel le CNI n'est pas immédiatement envoyé à l'élimination géologique définitive en faveur d'une extension de sa vie dans l'industrie nucléaire. On peut obtenir une compréhension profonde du processus d'extraction biphasique par le biais d'expériences électrochimiques simples à une interface liquide|liquide. Dans le développement d'une méthode d'analyse quantitative du transfert d'ion assisté ou facilité (TIF) par un ligand, c'est-à-dire un transfert par le biais d'une complexation interfaciale, il est important de commencer par quantifier le transfert d'un ion (TI) libre ou d'un ion métallique simple; ceci correspond à la quantité de potentiel appliquée requise pour « pousser » les ions à traverser l'interface eau|interface organique. En fait, cette valeur est une constante souvent désignée comme le potentiel de transfert formel ($\Delta_o^w\phi^{o'}$) qui, dans un système biphasique, est unique pour chaque ion métallique. En raison de leur caractère hydrophile, ils limitent souvent la fenêtre du potentiel polarisable. Jusqu'à maintenant, les valeurs de $\Delta_o^w\phi^{o'}$ n'ont pour la plupart qu'été évaluées. Avec une micro-interface montée à la pointe d'un capillaire de 25 μm, il est possible de réduire de courant faradique afin de pouvoir observer le transfert. Dans ce travail, on décrit la quantification des potentiels de transfert formel des ions dixouranium et strontium, respectivement $\Delta_o^w\phi^{o'}_{UO_2^{2+}}$ et $\Delta_o^w\phi^{o'}_{Sr^{2+}}$.

Mots-clés : électrochimie liquide|liquide, transfert d'ion simple, potentiel de transfert formel, ion strontium, dioxouranium, uranyle, micropipette.

[Traduit par la Rédaction]

Introduction

With the imminent depletion of the world's fossil fuel supply and the long-recognized environmental issues surrounding anthropogenic CO_2 emission,[1] alternative energy sources are being sought; front runners include solar and nuclear power generation. Nuclear power plants, unlike solar, are not an intermittent energy source[1] and, therefore, are considered more reliable. Implementing a closed-loop fuel cycle, whereby spent nuclear fuel (SNF) is recycled instead of — as in the present model — prepared for permanent geologic disposal, could extend the life of the nuclear industry for hundreds of years.[1]

Indeed, the majority of SNF, approximately 95%, is UO_2 suitable for energy production; the other 5% is fission decay products (e.g., ^{90}Sr and ^{137}Cs) that can behave as neutron absorbers, disrupting the fission process and lowering the fuel rod's efficiency.[2] Crucially, these other metals have isotopes

Received 14 June 2012. Accepted 7 August 2012. Published at www.nrcresearchpress.com/cjc on 26 October 2012.

T.J. Stockmann, A.-M. Montgomery, and Z. Ding. Department of Chemistry, The University of Western Ontario, 1151 Richmond Street, London, ON N6A 5B7, Canada.

Corresponding author: Zhifeng Ding (e-mail: zfding@uwo.ca).

Can. J. Chem. Downloaded from www.nrcresearchpress.com by MCGILL UNIVERSITY on 02/02/13
For personal use only.

that are valuable in and of themselves for use in nuclear medicine or radioimmunotherapy (RIT).[3–7] ^{90}Y, combined with monoclonal antibodies (mAb), has found some success in targeting and treating cancer.[3,4,6,7] Similarly, ^{82}Rb is used for myocardial perfusion imaging, a diagnostic technique examining the heart and circulatory system.[8] The advantage of ^{90}Y and ^{82}Rb is that they are short-lived isotopes ($t_{1/2}$ = 64 h and 76 s, respectively), which is useful because it means less radiolytic toxicity to patients, but also means that, for these isotopes to be effective, on-site clinical generators are required.[7,9–11] These in-house generators use a parent/daughter strategy and, from the preceding examples, take the form of ^{90}Sr/^{90}Y and ^{82}Sr/^{82}Rb.[7,9–11] Interestingly, strontium is a major component of SNF[2] and, thus, could be a source for parent isotopes.

SNF should not be viewed simply as waste, but as a potential resource. This begs the question as to how to selectively and effectively isolate these materials. ^{90}Sr has been separated from the nuclear waste stream almost since the inception of the civilian nuclear industry because of its use in other applications.[12] However, its recent incorporation into the medicinal field has sparked interest towards improving the purity of ^{90}Sr extraction.

Contemporary methods of metal ion separation involve the use of aqueous/organic biphasic systems with processes like plutonium/uranium extraction (PUREX) and transuranic extraction (TRUEX).[13–15] In either case, a ligand, dissolved in the organic phase, coordinates to the metal center causing it to partition into the organic phase.

Ion partitioning or ion transfer (IT) of metals has been analyzed through a facile electrochemical technique at the interface between two immiscible electrolytic solutions (ITIES), often between water and 1,2-dichloroethane (w|DCE)[16–21] or water and nitrobenzene (w|NB).[22,23] In this method ions are pushed or pulled across the ITIES by an applied potential. Should a potential be administered to either phase, a potential drop or difference would develop across the ITIES, such that $\Delta_o^w\phi = \phi_w - \phi_o$, where ϕ is the potential in phase w (aqueous) or o (organic). A positive potential, administered to the aqueous phase, will repel cations prompting them to cross the interface while attracting anions from the organic phase. If applied to free metal species, this is termed simple IT and shown in eq. [1]

$$[1] \qquad i_w^{z_i} \rightleftharpoons i_o^{z_i}$$

where species i with charge z transfers from w to o. However, if a ligand (L) is dissolved in the organic phase and used to assist IT, the mechanism is called facilitated ion transfer (FIT) and eq. [2] is used.

$$[2] \qquad i_w^{z_i} + nL_o^w \rightleftharpoons iL_o^{z_i}$$

Just as in conventional electrochemistry at a solid electrode where $\Delta G = -zFE^{o'}$, the Gibbs free energy can be related to the potential difference developed across the ITIES in the same manner, $\Delta G = -zF\Delta_o^w\phi^{o'}$. Where $E^{o'}$ is the formal redox potential at a solid electrode, $\Delta_o^w\phi^{o'}$ is the formal transfer potential at an aqueous|organic solvent interface, z is the charge, and F is Faraday's constant.

The theory of FIT at a w|o interface, using cyclic voltammetry (CV), has been developed thoroughly.[18,19,24,25] Equation [3] forms the basis of a diagnostic method for evaluating various ligands and biphasic systems, if we assume that diffusion processes are equal in both phases.

$$[3] \qquad -\frac{zF}{RT}\left(\Delta_o^w\phi_{iL_n^{z+}}^{o'} - \Delta_o^w\phi_{i^{z+}}^{o'}\right) = n\ \ln c_o^* + \ln\beta$$

Equation [3] differentiates between the formal transfer potential of the metal–ligand complex, $\Delta_o^w\phi_{iL_n^{z+}}^{o'}$, and that of the free metal species, $\Delta_o^w\phi_{i^{z+}}^{o'}$; where the latter is a constant and behaves like a point of reference, whereby, with increasing initial ligand concentration, c_o^*, the metal ions transfer more easily. Thus, the formal transfer potential of the metal–ligand complex is linearly dependent on the ligand concentration. The n and β terms are the overall stoichiometry of the interfacial complexation reaction (eq. [2]) and its associated overall complexation constant, respectively. In this way, by varying the ligand concentration in the organic phase and measuring $\Delta_o^w\phi_{iL_n^{z+}}^{o'}$ through CV experiments, n and β can be determined and used as a quantitative measure towards the fitness of various ligand and solvent combinations.

Unfortunately, this is complicated by the fact that most free metal ionic species transfer outside the polarized potential window (PPW) and their formal transfer potential constants are difficult to determine because of their high hydrophilicity. At first, Girault and co-workers,[26,27] working at a large (centimetre scale) ITIES, used the ratio between the current at the edge of scan and the return peak current (I_{eos}/I_{rp}), along with working curves generated through numerical calculations, to estimate the transfer of alkali and other multiply charged metals. Similarly, Samec and co-workers[28,29] implemented sophisticated numerical calculations compared with the profile of the PPW edge to estimate the formal transfer potential.

Later, with improvements towards the micro-ITIES apparatus, a microhole interface was utilized.[30–32] This technique was based on the principle of minimal supporting electrolyte first developed for solid ultramicroelectrodes by Oldham,[33] but later extended to the micro liquid|liquid interface by Wilke.[32] Girault and co-workers[30] examined several cations and anions through direct curve fitting of the experimentally acquired CVs. However, this micro-ITIES is typically supported at a hole formed in a polyamide sheet (25 μm thick) via UV photoablation. It is difficult to ensure a consistent microhole size and geometry while, additionally, the polyamide film can become deformed by absorption of the organic solvent, limiting the number of times it can be used. This approach focused on reducing the interfacial size and the amount of electrolyte in solution to limit the Faradaic current in the hopes of observing simple IT at higher potentials.

Herein, we describe the facile observation of IT of metal species at a micro-ITIES, housed at the tip of a 25 μm diameter silanized borosilicate glass capillary, with the formal transfer potential being obtained directly from differential pulse voltammograms (DPVs). This is made possible by the use of a custom-modified micropipette holder intended for physiological applications, which is equipped with a syringe greatly stabilizing the ITIES at the capillary tip. This apparatus was used to observe the IT of Sr^{2+} and UO_2^{2+} directly, at conventional concentrations, for the first time; in this way determining their formal transfer potential. Additionally, a glass

Can. J. Chem. Downloaded from www.nrcresearchpress.com by MCGILL UNIVERSITY on 02/02/13
For personal use only.

capillary can be used almost indefinitely and our fabrication method ensures a consistent micro-ITIES size of 25 μm in diameter.

Experimental

Chemicals

All chemicals were of reagent grade and utilized without further purification. Uranium nitrate hexahydrate ($UO_2(NO_3)_2{\cdot}6H_2O$) and strontium nitrate ($Sr(NO_3)_2$) were purchased from Fisher Scientific (ThermoFisher Scientific, Ottawa, Ontario) and Sigma-Aldrich (Sigma-Aldrich Canada Ltd., Mississauga, Ontario), respectively. Trihexyltetradecylphosphonium chloride ($P_{66614}Cl$) and potassium tetrakis(pentafluorophenyl)borate (KTB) were obtained from Strem (Strem Chemicals Inc., Newburyport, Massachusetts) and Boulder Scientific (Boulder Scientific Company, Longmont, Colorado), respectively. Aqueous solutions were made up using ultrapure Milli-Q water (18.2 MΩ). The organic phase supporting electrolyte $P_{66614}TB$ was prepared through a simple metathesis reaction between the $P_{66614}Cl$ and KTB salts in dichloromethane using a procedure described elsewhere.[34]

Micropipette

A few recent publications describe the micropipette fabrication,[20,21,34,35] however, a brief outline follows. First, a borosilicate glass capillary (1.0 mm internal and 2.0 mm external diameters, Sutter Instrument Co., Novato, California) was pulled near its center using a Narishige electric puller (model No. PP-83, Japan), which results in two capillaries with tapered ends; these ends were flame annealed using a Bunsen burner so that the small tapered tip was closed. A 1.0–1.5 cm length of Pt wire (25 μm in diameter, Goodfellow Cambridge Ltd., Huntingdon, UK) was then inserted into the top or open end of the capillary and pushed down into the tapered tip. The wire was fixed in place by annealing it, under vacuum, using the electric puller; in this way the wire was encased in approximately 1–2 mm of glass. The sealed end was subsequently polished using a series of grinding and polishing pads (Buehler Canada, Markham, Ontario) until the surface of the glass was smooth and a cross section of the Pt wire was exposed; the quality of the capillary surface was routinely checked using an optical microscope. Polishing was complete when the surface was free of defects and the R_g, that is the ratio of external (r_g) to internal (a) diameter ($R_g = r_g/a$), was greater than 50. The next step was removal of the Pt wire via etching through immersion in aqua regia (3:1 solution of HCl–HNO_3). The capillary tip was silanized using trimethylchlorosilane; in this process Ar gas is bubbled through the capillary in the silane solvent for 5 min and, afterwards, the capillary is dried and baked overnight in an oven at 100 °C.

Instrumentation

The Modulab System (Ametek Advanced Measurement Technology, Farnborough, New Hampshire, UK) equipped with a femto ammeter was utilized for all electrochemical experiments. Owing to the reduced current required at a micro-ITIES, a two-electrode system was employed with the working electrode (WE) lead attached to a BNC connector that was subsequently fixed to the micropipette holder. The holder is designed with an incorporated internal silver wire that is sealed with the aqueous phase; the BNC connector provides the external contact. The counter electrode (CE) and reference electrode (RE) leads were coupled together with a standard alligator clip on the end gripping another silver wire immersed in the organic phase. Figure 1 illustrates the disassembled micropipette holder highlighting its components. The following electrochemical cell was used

$$\mathrm{Ag}\,|\,\mathrm{AgNO_3}\,|\,\underset{(aq)}{3\ \mathrm{mM\ X(NO_3)_2}}\,\|\,\underset{(DCE)}{5\ \mathrm{mM\ P_{66614}TB}}\,|\,\mathrm{AgTB}\,|\,\mathrm{Ag}\qquad \text{Cell 1}$$

A CCD camera (Motic Inc., Richmond, British Columbia) fixed to a variable 12× magnification lens assembly (Navitar, Rochester, New York) was used to continuously monitor the ITIES, ensuring it did not fluctuate during experimentation.

Curve fitting was performed using Igor Pro 6.22a (Wavemetric Inc., Portland, Oregon) on an Acer Aspire laptop (Acer America Corporation (Canada), Mississauga, Ontario) with a 1.66 GHz Intel Core 2 Duo processor and 2 GB of DDR2 RAM.

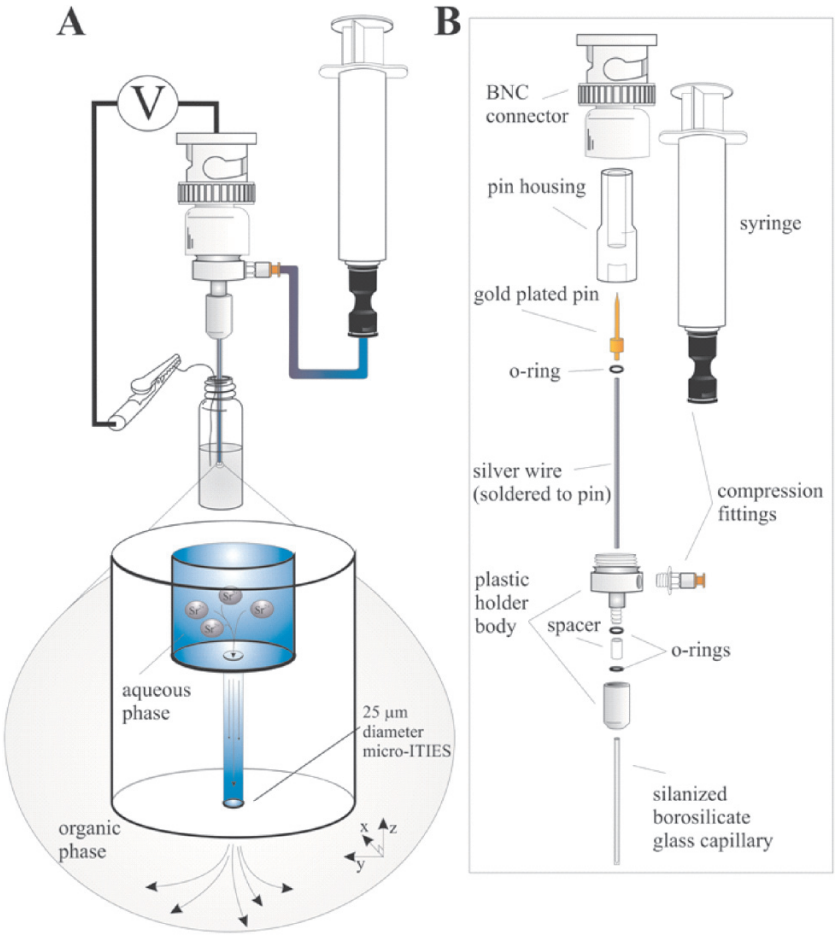
Results and discussion

Figure 2A shows the CV obtained with cell 1 and X equal to Sr^{2+}; the trace was acquired utilizing an initial potential of 0.210 V and scanning in the forward direction to a final potential of approximately 1.200 V, at which point the CV was scanned in the reverse direction towards negative potentials. During this first segment a peak-shaped wave can be seen at roughly 0.786 V. Subsequently, the potential was swept in the reverse direction towards more negative potentials; a sigmoidal-shaped wave can be observed at approximately 0.780 V. The sigmoidal wave is difficult to discern, however, an inflection in the current–potential response of the return sweep at ~0.9 V was deemed to coincide with the limiting or steady-state current (i_l) for the return transfer of Sr^{2+}; thus, the half-wave potential was evaluated by graphing $\ln[(i_l - i)/i]$ vs E and determining the potential at the x-intercept, as described in Bard and Faulkner.[36] These two curve features were attributed to the IT of Sr^{2+} from w to o and back, displaying peak- and sigmoidal-shaped waves, respectively. The asymmetry of IT is a direct result of the pipette geometry.[37,38] Using Sr^{2+} IT as an example, during the forward scan ions in the pipette transfer from w to o, however, the volume of material near the interface is small and rapidly consumed; the current–potential response rises exponentially, but is then followed by an exponential decay as ions must diffuse towards the ITIES from higher up in the microchannel. The voltammogram shows peak-shaped waves. During the reverse scan, material that has crossed the ITIES occupies a relatively large (compared with the volume within the microchannel) hemispherical volume surrounding the micro-ITIES; thus, mass transfer of material towards the interface appears to be faster than its rate of consumption, generating a rise in current followed by a plateau or steady state.

The asymmetric shape of the forward and reverse curves is in good agreement with simple IT of a cation across a w|o interface as described in the literature for a micro-ITIES housed at the tip of a micropipette.[37,38] By convention, the

Can. J. Chem. Downloaded from www.nrcresearchpress.com by MCGILL UNIVERSITY on 02/02/13
For personal use only.

Fig. 1. (A) Micropipette plus holder with perspective view of micro-ITIES. (B) Component diagram of the micropipette holder.



transfer of a cation from w to o elicits a positive current response.

The scan was continued to the second switching potential of approximately –0.590 V and another peak-shaped curve feature can be observed in this segment at –0.400 V; this has been attributed to the IT of nitrate from w to o. The scan direction was subsequently changed towards increasing potential and progressed until 0.210 V was reached, completing one cycle by returning to the initial potential. For this final portion, a sigmoidal wave can be observed with a half-wave potential of –0.307 V. This observation concerning peak and sigmoidal waves is expected based on diffusion regimes for simple IT at a micropipette.[37,38] Nitrate IT was used to calibrate the polarized potential window (PPW), operating as an internal standard or reference; based on the TATB assumption,[39] or scale, the formal transfer potential of nitrate, $\Delta_o^w\phi^{o'}_{NO_3^-}$, was taken to be –0.380 V.[40] The TATB assumption[39] leads to eq. [4].

$$[4] \qquad \Delta_o^w\phi^{o'}_{X^+} - \Delta_o^w\phi_{1/2,X^+} = \Delta_o^w\phi^{o'}_{NO_3^-} - \Delta_o^w\phi_{1/2,NO_3^-}$$

where the half-wave potentials were obtained from the CV using the peak potentials and eq. [5] from Bard and Faulkner.[36]

$$[5] \qquad \Delta_o^w\phi_{1/2} = \Delta_o^w\phi_p - \frac{0.028\ \text{V}}{z_i}$$

where p denotes the peak potential. It is critical to reiterate that the ITIES was monitored continuously throughout each experiment for any change in its shape or position; none was observed microscopically.

Additionally, the theoretical peak current can be described by the diffusion coefficients obtained from the literature for nitrate[41] and strontium[42] of 1.4 and 1.2 × 10^{-5} cm^2 s^{-1}, respectively, and using the following equation[36]

$$[6] \qquad i_p = 0.4463\left(\frac{F^3}{RT}\right)^{1/2} z_i^{3/2} D^{1/2} c_w^* A v^{1/2}$$

where A is the interfacial surface area, v is the scan rate, and c_w^* is the initial concentration of the ion in the aqueous phase. The expected peak current values for nitrate and strontium were calculated to be 4.2 and 5.1 nA; the nitrate peak at 4.5 nA demonstrates good agreement with the calculated value, however, the strontium peak current was measured to be 17.3 nA, which is higher than the theoretical expectation. This may be due to ion-pair formation at the interface between strontium and TB^- to accelerate the IT.

Interestingly, the simple IT of metal species typically limits the PPW generating a "linear ramp" in the current–potential response. The ability to observe the Sr^{2+} IT of these metals in this case is attributed to the great reduction in the interfacial size to 25 μm, significant improvement surrounding the experimental setup by means of a syringe to backfill the

Can. J. Chem. Downloaded from www.nrcresearchpress.com by MCGILL UNIVERSITY on 02/02/13
For personal use only.

Fig. 2. Using cell 1 with X equal to Sr^{2+}: (A) cyclic voltammogram (CV) obtained with an initial/final potential of 0.210 V, a potential range from approximately –0.590 to 1.200 V, and a scan rate of 0.020 V s^{-1}; and (B) differential pulse voltammogram (DPV) acquired with a potential from –0.590 to 1.200 V; and a step, pulse amplitude, period, and pulse width of 4 mV, 50 mV, 0.1 s, and 0.05 s, respectively.

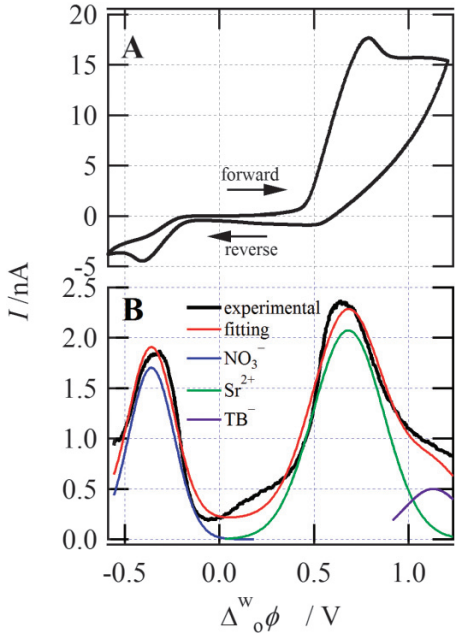
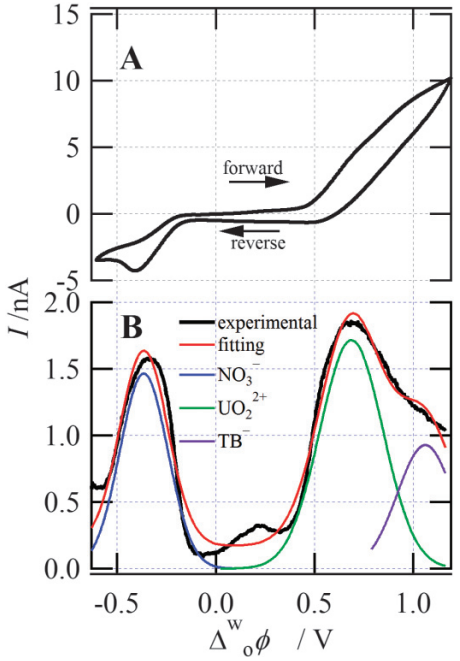


Fig. 3. Using cell 1 with X equal to UO_2^{2+}: (A) cyclic voltammogram (CV) obtained with an initial/final potential of –0.100 V, a potential from approximately –0.600 to 1.200 V, and a scan rate of 0.020 V s^{-1}; (B) differential pulse voltammogram (DPV) acquired with a potential from –0.600 to 1.200 V; and a step, pulse amplitude, period, and pulse width of 4 mV, 50 mV, 0.1 s, and 0.05 s, respectively.



capillary, along with silanization of the outside of the capillary tip, all of which contribute to a highly stable ITIES. From the calibrated CV, the formal transfer potential of Sr^{2+} was estimated to be 0.768 V.

Similarly, dioxouranium was also studied using cell 1 (X = UO_2^{2+}) as shown in Fig. 3A; however, during the forward scan, a familiar exponential increase in current is observed and is typical of metals limiting the PPW. Examining the UO_2^{2+} CV closely, an inflection can be discerned at 0.820 V separating two possible curve features; considering the first to be UO_2^{2+} IT was a peak potential of 0.757 V, $\Delta^w_o\phi^{o'}_{UO_2^{2+}}$ was estimated to be 0.743 V.

Alkali and other metal ion formal transfer potentials limiting the PPW were estimated by Girault and co-workers.[26,27] using a large (centimetre scale) w|DCE interface along with the ratio of the current at the edge of scan to the return peak current (I_{eos}/I_{rp}), which they compared with a working curve derived through numerical calculations. It is important to note that, with the exception of Cs, Girault and co-workers.[26,27] did not strictly observe the IT of these metals. Later, using a microhole apparatus with minimal supporting electrolyte in either phase and a curve-fitting technique,[32,33] IT of Li^+ and Cs^+ were observed,[30] along with UO_2^{2+};[31] $\Delta^w_o\phi^{o'}_{UO_2^{2+}}$ was estimated to be 0.865 V.

The present CV results are similar to those shown previously for alkali metals and dioxouranium,[26,30,31] and both are complicated by the possible simultaneous transfer of the anionic component of the supporting electrolyte in the organic phase, in this case TB^-. Further to this is the question of sufficient electrolyte concentration, since the metal species behaves as both supporting electrolyte and analyte. In the microhole experiment,[30–33] the lack of supporting electrolyte leads to a predictable distortion of the current–potential response, which can mean up to a threefold increase in the observed steady-state current; in the present case, higher electrolyte concentrations are thought to mitigate this phenomenon, however, some uncompensated i_R-drop may still be present.

To confirm the formal transfer potentials obtained using CV, DPVs were also implemented, as illustrated in Figs. 2B and 3B for cell 1 with X equal to Sr^{2+} and UO_2^{2+}, respectively. The instrument parameters included initial and final potentials of approximately –0.590 and 1.250 V, respectively, along with a step, pulse amplitude, pulse period, and pulse width of 4 mV, 50 mV, 0.1 s, and 0.05 s, respectively. Examining the DPVs in Fig. 2B and 3B, only two peaks are observed in each curve. Moving in the forward direction, the first peak, at –0.398 V, is associated with simple nitrate IT, whilst the second peak, at approximately 0.582 and 631 V (for Sr^{2+} and UO_2^{2+}, respectively), is the metal and (or) TB^- IT. Nitrate IT was again employed to calibrate the potential scale, using eq. [1] along with eq. [7] from Girault's book[43]

$$[7] \qquad \Delta^w_o\phi_{max} = \Delta^w_o\phi^{o'} + \frac{RT}{zF}\ln\sqrt{\frac{D_w}{D_o}} - \frac{\Delta E}{2}$$

where ΔE is the pulse amplitude and $\Delta^w_o\phi_{max}$ is the potential at maximum current response (i.e., peak potential); R, T, z, and F are the gas constant, temperature in Kelvin, charge, and Faraday's constant, respectively; and D_w and D_o are the diffusion coefficients in the aqueous and organic phases

Can. J. Chem. Downloaded from www.nrcresearchpress.com by MCGILL UNIVERSITY on 02/02/13
For personal use only.

respectively, these were taken to be equal and, thus, eq. [3] reduces to a simple relation.

In the positive potential region, a transfer peak and a shoulder were observed for both DPVs with $Sr(NO_3)_2$ and $UO_2(NO_3)_2$ in the aqueous phase, respectively (Figs. 2B and 3B). Especially, it is plausible that the shoulder is at the same Galvani potential difference in these figures. Whereas the peak potential values are very close to those for the transfer of the two ions obtained from the CVs in Figs. 2A and 3A, the shoulder was proposed as the TB^- transfer from o to w. To elucidate between strontium/dioxouranium and TB^- IT, a multipeak Gaussian curve fitting was applied directly to the DPVs for each ion; nitrate (blue), metal ion (green), TB^- (purple), and a composite of the three (red). From the curve fitting the formal transfer potential for the strontium and dioxouranium cations was found to be 0.654 and 0.699 V, respectively. The respective $\Delta^{w}_{o}\phi^{o'}_{TB^-}$ for cell 1 with X equal to Sr^{2+} and $UO_2{}^{2+}$ was found to be 1.161 and 1.131 V. The formal transfer potentials for TB^- found here are in good agreement with each other and agree with our recent data using alkali metal ions in place of Sr^{2+} and $UO_2{}^{2+}$.[40]

The difference in formal transfer potentials observed between the two methods is thought to arise from uncompensated i_R-drop present in the CV case, which is mitigated through the DPV experiment. The two cations have a charge of 2+ that might bring more experimental error in determining the formal transfer potential. Especially in the case of Sr^{2+}, the IT is closer to the PPW edge. Therefore, the values obtained from the DPVs are considered to be better estimates.

The formal transfer potential discovered using DPV for Sr^{2+} (0.654) is similar to that shown recently for Rb^+ of 0.562 V.[40] It has been shown, through the alkali metal ions, that with increasing atomic radius down through the periodic table, there is a decrease in the formal transfer potential.[40] Strontium has a van der Waals radius of 2.49 Å compared with that for rubidium of 3.03 Å,[44] however, the increased formal transfer potential is a consequence of increased charge density (1+ versus 2+ on the metal center). Additionally, these two metals should possess similar hydration spheres, since Rb^+ and Cs^+ are proposed to both have eight water molecules coordinated to them in solution; therefore, when comparing Sr^{2+} and Rb^+, this should not play a significant role. Additionally, when Mähler and Persson[45] examined the hydration spheres of the alkali metals using large angle X-ray scattering and double difference IR, they showed that rubidium and cesium were only weakly coordinated; by extension, strontium should also be weakly coordinated.

Conclusion

To the best of our knowledge, the simple ITs of strontium and uranium, which typically limits the PPW, were observed for the first time utilizing a microinterface hosted by a 25 μm diameter micropipette. The determination of the formal transfer potentials for these free metal ions were characterized through the facile use of DPV and CV. $\Delta^{w}_{o}\phi^{o'}_{Sr^{2+}}$ and $\Delta^{w}_{o}\phi^{o'}_{UO_2{}^{2+}}$ were determined to be 0.768 and 0.743 V, respectively, using CV, and 0.654 and 0.699 V, respectively, from DPV, which were resolved from TB^- transfer using a Gaussian multipeak curve-fitting approach.

The observation of simple IT of these heavy metal ions was made possible by the reduction of the micropipette diameter to 25 μm along with our significant improvement on experimental setup, such as the unique design of the micropipette holder and capillary fabrication. This setup offers a facile approach to micropipette fabrication, which generates a consistent, uniform microinterface that can be used repeatedly. The philosophy behind this approach, analogous to the microhole technique,[30] is to decrease the amount of Faradaic current by reducing the interfacial surface area and thus allowing simple IT of metals limiting the PPW to be observed. Interestingly, however, owing to the improved interfacial stability, conventional electrolyte concentrations can be used.

Acknowledgements

We would like to extend our eternal gratitude to J.C. Wren, J. Noël, D.W. Shoesmith, P.J. Ragogna, J. Dube, K. Swanick, J. Zhang, D. Vaccerello, S. McPhee, and M. Hart for their helpful discussions and technical support. A special thanks to J. Vanstone, J. Aukima, and J. Smith at the Electronic Shop of The University of Western Ontario Chemistry Department for the fabrication and modification of the micropipette holder. T.J.S. is grateful for a Queen Elizabeth II Graduate Scholarship in Science and Technology. This work was supported by the Ontario Research Fund, the Natural Sciences and Engineering Research Council of Canada Foundation for Innovation, the Ontario Innovation Trust, the Premier's Research Excellence Award, and The University of Western Ontario.

References

(1) Hoffert, M. I.; Caldeira, K.; Benford, G.; Criswell, D. R.; Green, C.; Herzog, H.; Jain, A. K.; Kheshgi, H. S.; Lackner, K. S.; Lewis, J. S.; Lightfoot, H. D.; Manheimer, W.; Mankins, J. C.; Mauel, M. E.; Perkins, L. J.; Schlesinger, M. E.; Volk, T.; Wigley, T. M. L. *Science*, **2002**, *298* (5595), 981. doi:10.1126/science.1072357.

(2) Bruno, J.; Ewing, R. C. *Elements* **2006**, *2* (6), 343. doi:10.2113/gselements.2.6.343.

(3) Chinn, P.; Braslawsky, G.; White, C.; Hanna, N. *Cancer Immunol. Immunother.* **2003**, *52* (5), 257.

(4) Goldenberg, D. M. *Cancer Immunol. Immunother.* **2003**, *52* (5), 281.

(5) Hudson, P. J.; Souriau, C. *Nat. Med.* **2003**, *9* (1), 129. doi:10.1038/nm0103-129.

(6) Wester, D. W.; Steele, R. T.; Rinehart, D. E.; DesChane, J. R.; Carson, K. J.; Rapko, B. M.; Tenforde, T. S. *Appl. Radiat. Isot.* **2003**, *59* (1), 35. doi:10.1016/S0969-8043(03)00151-9.

(7) Bonardi, M. L.; Martano, L.; Groppi, F.; Chinol, M. *Appl. Radiat. Isot.* **2009**, *67* (10), 1874. doi:10.1016/j.apradiso.2009.06.005.

(8) Dhar, R.; Ananthasubramaniam, K. *Cardiol. Rev.* **2011**, *19* (5), 255. doi:10.1097/CRD.0b013e318224253e.

(9) Alvarez-Diez, T. M.; deKemp, R.; Beanlands, R.; Vincent, J. *Appl. Radiat. Isot.* **1999**, *50* (6), 1015. doi:10.1016/S0969-8043(98)00170-5.

(10) Yoshinaga, K.; Klein, R.; Tamaki, N. *J. Cardiol.* **2010**, *55* (2), 163. doi:10.1016/j.jjcc.2010.01.001.

(11) O'Hara, M. J.; Rapko, B. M.; Edwards, M. K.; Wester, D. W. Medicinal Isotope Generators. Battelle Memorial Institute, Columbus, OH. 2008, p 26. WO2008130881A1.

(12) Samanta, S. K. Recovery, Purification, and Quality Evaluation

of ^{90}Sr. In *IAEA Radioisotopes and Radiopharmaceuticals*; Series No. 2; IAEA: Vienna, Austria, 2010, p 49–78.
(13) Paiva, A. P.; Malik, P. *J. Radioanal. Nucl. Chem.* **2004**, *261* (2), 485. doi:10.1023/B:JRNC.0000034890.23325.b5.
(14) Fujii, T.; Aoki, K.; Yamana, H. *Solvent Extr. Ion Exch.* **2006**, *24* (3), 347. doi:10.1080/07366290600647002.
(15) Antony, M. P.; Kumaresan, R.; Suneesh, A. S.; Rajeswari, S.; Robertselvan, B.; Sukumaran, V.; Manivannan, R.; Syamala, K. V.; Venkatesan, K. A.; Srinivasan, T. G.; Vasudeva Rao, P. R. *Radiochim. Acta* **2011**, *99* (4), 207. doi:10.1524/ract.2011.1815.
(16) Shao, Y.; Girault, H. H. *J. Electroanal. Chem.* **1992**, *334* (1–2), 203.
(17) Beattie, P. D.; Delay, A.; Girault, H. H. *J. Electroanal. Chem.* **1995**, *380* (1–2), 167.
(18) Reymond, F.; Carrupt, P.-A.; Girault, H. H. *J. Electroanal. Chem.* **1998**, *449* (1–2), 49.
(19) Reymond, F.; Lagger, G.; Carrupt, P.-A.; Girault, H. H. *J. Electroanal. Chem.* **1998**, *451* (1–2), 59.
(20) Stockmann, T. J.; Ding, Z. *Anal. Chem.* **2011**, *83* (19), 7542. doi:10.1021/ac2018684.
(21) Stockmann, T. J.; Lu, Y.; Zhang, J.; Girault, H. H.; Ding, Z. *Chem. Eur. J.* **2011**, *17* (47), 13206. doi:10.1002/chem.201102491.
(22) Koryta, J. *Electrochim. Acta* **1979**, *24* (3), 293. doi:10.1016/0013-4686(79)85048-3.
(23) Homolka, D.; Wendt, H. *Ber. Bunsenges. Phys. Chem* **1985**, *89* (10), 1075. doi:10.1002/bbpc.19850891012.
(24) Samec, Z.; Homolka, D.; Marecek, V. *J. Electroanal. Chem. Interfacial Electrochem.* **1982**, *135* (2), 265. doi:10.1016/0368-1874(82)85125-3.
(25) Kakiuchi, T.; Senda, M. *J. Electroanal. Chem.* **1991**, *300* (1–2), 431.
(26) Shao, Y.; Stewart, A. A.; Girault, H. H. *J. Chem. Soc., Faraday Trans.* **1991**, *87* (16), 2593. doi:10.1039/ft9918702593.
(27) Lagger, G.; Tomaszewski, L.; Osborne, M. D.; Seddon, B. J.; Girault, H. H. *J. Electroanal. Chem.* **1998**, *451* (1–2), 29.
(28) Samec, Z.; Mareèek, V.; Colombini, M. P. *J. Electroanal. Chem. Interfacial Electrochem.* **1988**, *257* (1–2), 147.
(29) Sabela, A.; Mareèek, V.; Samec, Z.; Fuoco, R. *Electrochim. Acta* **1992**, *37* (2), 231. doi:10.1016/0013-4686(92)85008-9.
(30) Olaya, A. J.; Méndez, M. A.; Cortes-Salazar, F.; Girault, H. H. *J. Electroanal. Chem.* **2010**, *644* (1), 60. doi:10.1016/j.jelechem.2010.03.030.
(31) Stockmann, T. J.; Olaya, A. J.; Méndez, M. A.; Girault, H. H.; Ding, Z. *Electroanalysis* **2011**, *23* (11), 2677. doi:10.1002/elan.201100401.
(32) Wilke, S. *J. Electroanal. Chem.* **2001**, *504* (2), 184. doi:10.1016/S0022-0728(01)00433-8.
(33) Oldham, K. B. *J. Electroanal. Chem.* **1992**, *337* (1–2), 91.
(34) Stockmann, T. J.; Zhang, J.; Wren, J. C.; Ding, Z. *Electrochim. Acta* **2012**, *62* (0), 8. doi:10.1016/j.electacta.2011.10.087.
(35) Stockmann, T. J.; Ding, Z. *J. Electroanal. Chem.* **2010**, *649* (1–2), 23.
(36) Bard, A. J.; Faulkner, L. R. *Electrochemical Methods: Fundamentals and Applications;* 2nd ed.; John Wiley: New York. 2001.
(37) Taylor, G.; Girault, H. H. J. *J. Electroanal. Chem. Interfacial Electrochem.* **1986**, *208* (1), 179. doi:10.1016/0022-0728(86)90307-4.
(38) Campbell, J. A.; Girault, H. H. *J. Electroanal. Chem. Interfacial Electrochem.* **1989**, *266* (2), 465. doi:10.1016/0022-0728(89)85091-0.
(39) Parker, A. J. *Electrochim. Acta* **1976**, *21* (9), 671. doi:10.1016/0013-4686(76)85035-9.
(40) Stockmann, T. J.; Montgomery, A.-M.; Ding, Z. F. *J. Electroanal. Chem.* **2012**, *684*, 6. doi:10.1016/j.jelechem.2012.08.013.
(41) Valente, A. J. M.; Ribeiro, A. C. F.; Lobo, V. M. M.; Jiménez, A. *J. Mol. Liq.* **2004**, *111* (1–3), 33. doi:10.1016/j.molliq.2003.06.007.
(42) Harned, H. S.; Polestra, F. M. *J. Am. Chem. Soc.* **1953**, *75* (17), 4168. doi:10.1021/ja01113a011.
(43) Girault, H. *Analytical and Physical Electrochemistry;* 1st ed.; EPFL Press, Lausanne, Switzerland, 2004.
(44) Mantina, M.; Valero, R.; Cramer, C. J.; Truhlar, D. G. In *CRC Handbook of Chemistry and Physics;* Haynes, W.M., Ed. CRC Press/Taylor, Boca Raton, FL, 2012; Vol. 92, p 9–49.
(45) Mähler, J.; Persson, I. *Inorg. Chem.* **2012**, *51* (1), 425. doi:10.1021/ic2018693.

Can. J. Chem. Downloaded from www.nrcresearchpress.com by MCGILL UNIVERSITY on 02/02/13
For personal use only.

Preparation of graphite by thermal annealing of polyacrylamide precursor for adsorption of Cs(I) and Co(II) ions from aqueous solutions

H.S. Hassan and Elsayed K. Elmaghraby

Can. J. Chem. Downloaded from www.nrcresearchpress.com by MCGILL UNIVERSITY on 02/02/13
For personal use only.

Abstract: In the present work, graphite nanostructures are prepared by thermolysis of a prepared polyacrylamide gel. The gel was prepared by radical chain polymerization and the synthesis of the nanostructures was done by step annealing at different temperatures. The structural of the prepared materials was studied by X-ray diffraction (XRD). The presence of carboxylic and phenolic functional groups on the graphite surface was confirmed by FT-IR analysis. Batch adsorption experiments were conducted to study the effect of equilibration time, initial metal cation concentration, and solution pH for the removal of Cs(I) and Co(II) from aqueous solutions. Kinetic data of Cs(I) adsorption was found to be well fitted with a pseudo-first-order kinetic model. The obtained isotherm data were correlated with the Langumir and Freundlich isotherm models. The effect of temperature on the equilibrium distribution values was utilized to evaluate the change in the standard thermodynamic quantities of enthalpy ($\Delta H°$), entropy ($\Delta S°$), and Gibbs free energy ($\Delta G°$).

Key words: adsorption, Cs(I), Co(II), graphite, aqueous solution.

Résumé : Dans ce travail, on a préparé des nanostructures de graphite par thermolyse d'une préparation de gel de polyacrylamide. Le gel a été préparé par la technique de la polymérisation radicalaire en chaîne alors que la synthèse des nanostructures a été réalisée par la technique de recuisson à diverses températures. Les caractéristiques structurales des matériaux obtenus ont été étudiées par diffraction des rayons-X (DRX). La présence des groupes fonctionnels carboxyliques et phénoliques sur la surface de graphite a été confirmée par analyse infrarouge par transformation de Fourier (IR-TF). On a fait appel à des expériences d'adsorption globale pour étudier l'effet du temps d'équilibre, de la concentration initiale du cation métallique et du pH de la solution pour l'élimination des ions Cs(I) et Co(II) à partir de solutions aqueuses. On a trouvé que les données cinétiques d'adsorption du Cs(I) s'ajustent bien avec un modèle cinétique de pseudo-premier ordre. On a pu établir une corrélation entre les données d'isothermes et les modèles isothermes de Langmuir et Freundlich. On a utilisé l'effet de la température sur les valeurs de distribution d'équilibre pour évaluer le changement des quantités thermodynamiques standard d'enthalpie ($\Delta H°$), d'entropie ($\Delta S°$) et l'énergie libre de Gibbs ($\Delta G°$).

Mots-clés : adsorption, Cs(I), Co(II), graphite, solution aqueuse.

[Traduit par la Rédaction]

Introduction

The toxicity and the biological effects of hazardous materials, which are dangerous to public health and the environment, are attracting progressively more attention. The most hazardous pollutants identified in liquids waste and radioactive liquid waste of low and intermediate levels are Co(II), Cs(I), and Sr(II).[1] These pollutants are routinely and (or) accidentally released. Radioactive cesium has a relatively long half-life of about 30 years; as well, its stable isotope is hazardous to the environment.[2] Stable and radioactive cobalt isotopes are used in nuclear medicine, enamels, semiconductors, grinding wheels, and painting on glass. Acute cobalt poisoning in humans causes damage to the thyroid and liver and may cause mutations (genetic changes) in living cells.[3,4]

The techniques of chemical precipitation, ion exchange, membrane filteration, and reverse osmosis are usually used for the removal of pollutants from wastewaters.[5,6] In special situations, these methods fail to meet the Environmental Protection Agency's requirements;[7] or budget.[8] Among the most promising techniques, adsorption takes the attention because of its efficiency and low-cost operation.

Porous carbons with their large surface area, microporous character, and chemical nature are potential adsorbents for the removal of heavy metals from wastewater.[9] However, applications of porous carbon-based adsorbents with a large fraction of micropores (<2 nm) occupying most of the pore volume can be limited by slow diffusion kinetics.[10,11] Carbon nanostructures have found their place as an alternative for the porous carbon. Their physical properties, combined with their chemical inertness, make them potentially useful for technological applications for removal of hazardous materials.[12–14]

In the present work, graphite nanostructures are prepared

Received 4 April 2012. Accepted 8 July 2012. Published at www.nrcresearchpress.com/cjc on 22 October 2012.

H.S. Hassan. Hot Laboratory Center, Atomic Energy Authority, P.O. 13759 Cairo, Egypt.
E.K. Elmaghraby. Experimental Nuclear Physics Department, Nuclear Research Center, Atomic Energy Authority, Cairo 13759, Egypt.

Corresponding author: H.S. Hassan (e-mail: hisoliman2000@yahoo.com).

by thermolysis of a polyacrylamide gel. The adsorption behavior of Cs(I) and Co(II) were studied extensively.

Experimental

Chemicals and reagents

All reagents used in this work were AR grade chemicals and were used without further purification.

Instrumentation

Differential thermal analysis (DTA) was carried out by using a TA50 thermal analyzer (Shimadzu, Japan). The temperature was swapped at a constant rate of 5 °C/min from room temperature to 550 °C under atmospheric conditions. Infrared spectra (FT-IR) for prepared samples were determined using a Bomen Miclson FT-IR spectrophotometer, model MB157 (Canada). Investigation of the crystalline structure was performed using X-ray diffraction (XRD) with a JEOL X-ray diffractometer using Ni-filtered Cu Kα radiation ($\lambda_{K\alpha}$ = 0.154 184 nm). Continuous scanning was applied with a slow scanning speed and a small time constant. Adsorption and uptake of metals were determined by the metal concentration in the sample and solution using an atomic absorption spectrophotometer (Buck Scientific, VGP 210).

Preparation of the gel

Pure acrylamide (AA) powder and ammonium persulfate (APS) were used in the preparation of the organosulfonic acids. Each 56.9 g (0.8 mol) of AA monomer was dissolved in double-distilled water up to 200 mL. A hot plate stirrer was used to dissolve the monomer in water at room temperature at a low frequency. The stirrer was adjusted to heat the solution within the reaction flask to a temperature of 80 °C. The initiator was dissolved in water so that 0.1 mol/L of APS was heated to 80 °C. Mixing of the APS solution and the AA monomer solution took place at 80 °C. The blend was stirred heating for 10 min to ensure complete mixing. In the present work, 1 mL (0.001 mol) of APS solution was added to 20 mL (0.08 mol) of AA solution, i.e., to have a molecular monomer to initiator ratio of 80:1. Only 20 mL of the monomer was used in the preparation of the gel to avoid the overheating that occurs during the exothermic polymerization reaction. Using large amounts of monomer solution would require special attention and the use of a heat sink setup.

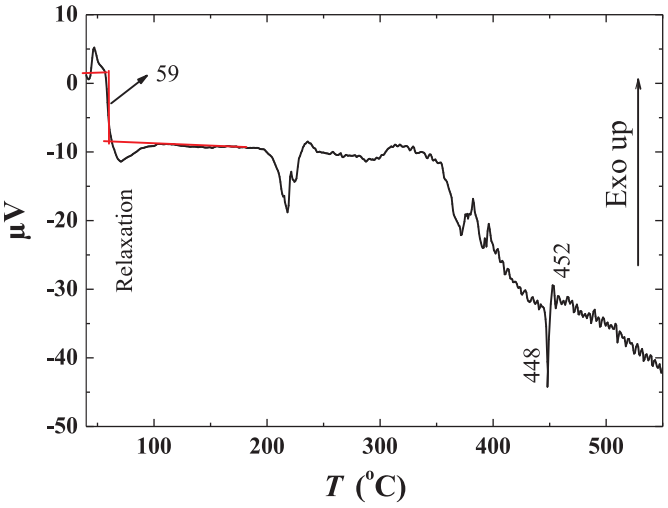
Polymerization occurs with complete consumption of the monomer to form the polymers, i.e., there are no effective termination reactions. After the preparation of the gel, the reaction process continued for a long time to degrade the properties of the prepared samples. After preparation of the gel, samples were left to dry at 60 °C for 5 days to ensure the full consumption of the monomer and solidification of the gel.

Differential thermal analysis

The thermal properties were deduced from the DTA curve. Figure 1 shows a discontinuity at 59 °C that represents the glass transition temperature. The enthalpic relaxation peak appearing at about 70 °C resulted from the slow quenching of the samples during the casting process.[15]

Several endothermic peaks were observed between 211 and 391 °C and are associated with the decomposition of the

Fig. 1. Differential thermal analysis curve of the solidified gel sample. The arrow points to the direction of the exothermic processes.



gel into sulfur trioxide, water, carbon monoxide, and carbon dioxide, in addition to a formation of complex organic compounds and direct subsequent volatilization of components such as acrylonitrile, hydrogen cyanide, acrylamide, and diones. The most important is an endothermic peak at 448 °C followed by an exothermic peak at 452 °C, which implies the formation and subsequent crystallization of a material.

Syntheses of graphite

According to the results of the thermal analysis, samples were treated thermally at 250 °C for 3 h at ambient temperature. After annealing, samples were left overnight to complete thermolytic reaction at room temperature. Then the samples were smashed and annealed at 350 °C for an extra 3 h and with extra annealing at 460 °C for 3 h to stimulate the formation of graphite structures. The last two steps were done inside an isolated Pyrex glass bottle to isolate the sample from the ambient atmosphere and then left to cool gradually to room temperature. The maximum uncertainties of the annealing temperature in the oven were 5% according to the position inside the cavity of the oven.

Adsorption experiments

Stock solutions of the metal ions to be examined were prepared by dissolving a known quantity of both cesium and cobalt chloride in double-distilled water. The pH of each solution was adjusted with liquid 1 mol/L NaOH and 1 mol/L HCl solution.

In all experiments, The kinetic behavior of Cs(I) and Co (II) ions on prepared powder was followed up by application of batch technique. The adsorbent (0.1 g) and 10 mL of the desired solution were placed in a horizontal shaker, at room temperature (25 ± 1 °C), for a specified period of contact time. Then a fixed volume (1 mL) of the clear solution was pipetted out for determination of the amount of unsorbed metal ion; the metal concentration retained in the solid phase (mmol/kg) was calculated by using the following equation:

$$[1] \qquad q_t = [(C_0 - C_t)]\frac{V}{m}$$

Can. J. Chem. Downloaded from www.nrcresearchpress.com by MCGILL UNIVERSITY on 02/02/13
For personal use only.

Can. J. Chem. Downloaded from www.nrcresearchpress.com by MCGILL UNIVERSITY on 02/02/13
For personal use only.

Fig. 2. IR spectra of the prepared material.

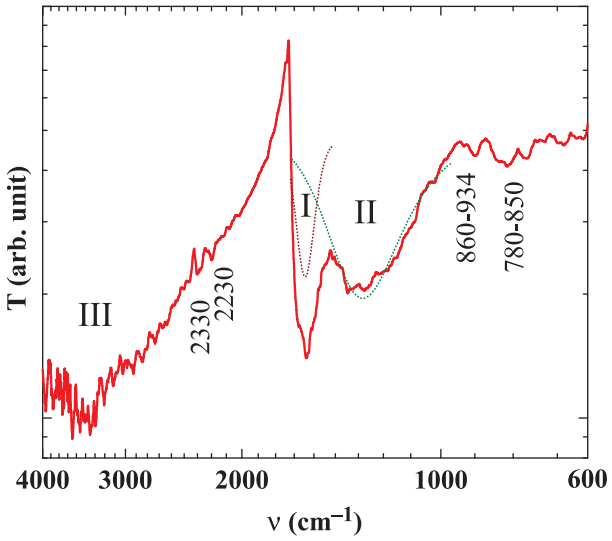
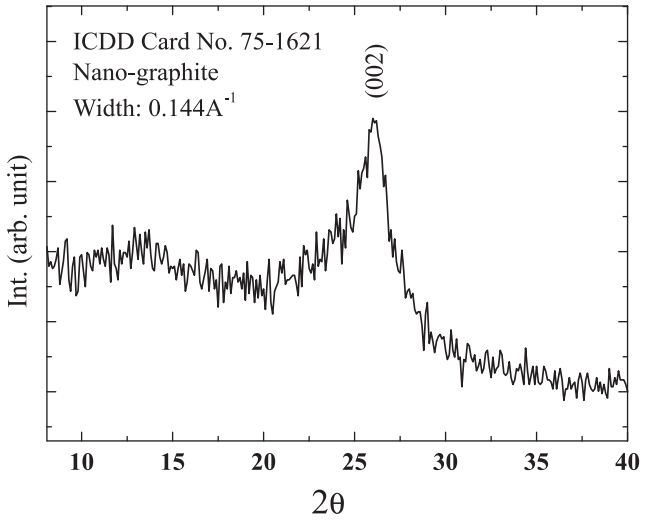


Fig. 3. X-ray diffractogram showing the broad reflection of graphite nanostructure.



where C_0 and C_t are the initial and time interval concentrations (mmol/L) of metal ion in solution, respectively, V is the volume of the solution in litres, and m is the weight of the adsorbent in grams.

Adsorption isotherms

Batch adsorption studies of Cs(I) and Co(II) ions were performed at different temperatures (25, 40, and 60 °C) to obtain the equilibrium isotherms. The adsorption processes of Cs(I) and Co(II) ions on the prepared powder adsorbent were tested with Langmuir and Freundlich isotherm models. The two empirical adsorption models, Freundlich and Langmuir, which are correspondent to heterogeneous and homogeneous adsorbent surfaces, respectively, were investigated in this study.

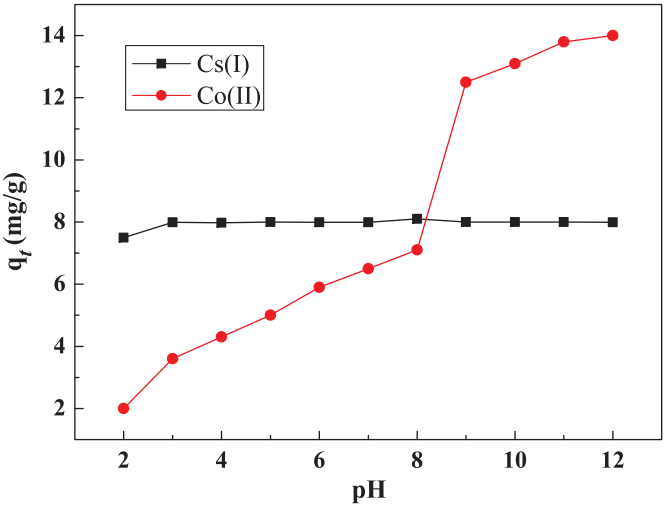
Results and discussion

Characterization of the material

IR spectroscopy of the prepared material was carried out in the range 400–4000 cm^{-1} as shown in Fig. 2. There is a strong absorption region between 1500 and 1700 cm^{-1}, labeled region I. The absorption in that region is attributed to four origins. The first is centered on 1650 cm^{-1} and indicates the presence of a C=O stretching vibration that is associated with an amide. The second source is a medium absorption around 1600 cm^{-1}, which is associated with C–C in the presence of C=O, which is usually found in dienes. The third source of absorption is C=N usually appearing between 1615 and 1700 cm^{-1}, which may be shifted to a lower wavenumber because of a conjunction with C=O. The last source of absorption is the N=O stretching vibration that appeared between 1500 and 1600 cm^{-1}. This type of absorption is accompanied by absorption between 1300 and 1400 cm^{-1} of the bending vibration, which exists in the spectrum.

There is a second broad absorption peak (region II), which consists of complicated absorptions. The first contributing functional group is the N=O bending by absorption between 1300 and 1400 cm^{-1}. The main contributing absorption is the S=O stretching of sulfoxides (1030–1060 cm^{-1}), stretching in sulfonic acids (1345 cm^{-1}), and stretching in sulfates (1350–1450 cm^{-1}). The absorption at 880–995 cm^{-1} is attributed to R=C–H and R=CH_2 stretching vibrations that are shifted to a lower frequency because of a conjunction with a heavy radical, while the absorption at 780–850 cm^{-1} is attributed to its out-of-plane bending of these stretching vibrations.

Fig. 4. Effect of pH value on Cs(I) and Co(II) adsorption.

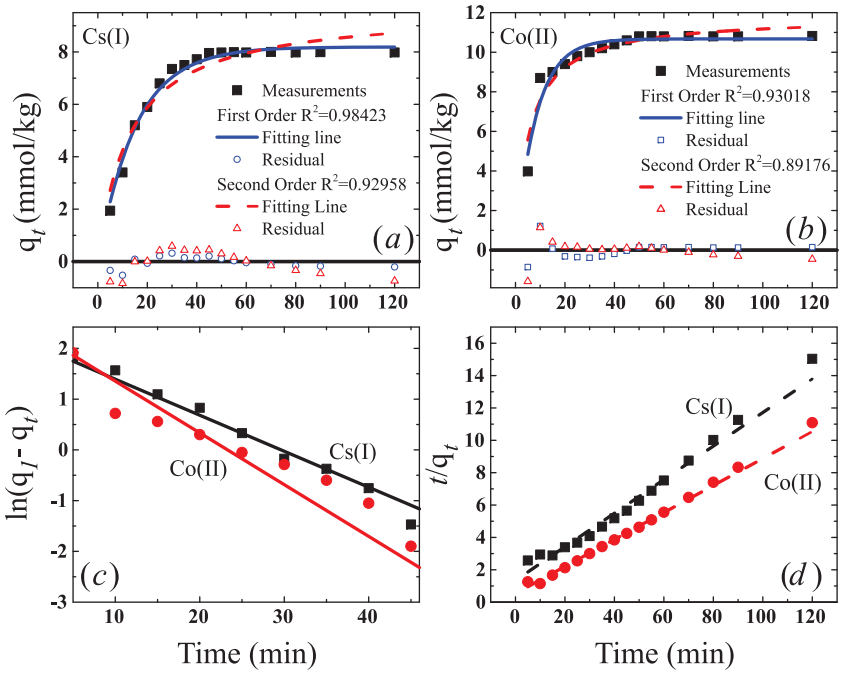


In region III, the broad absorption band in the range 3290–2750 cm^{-1} is attributed to O–H stretching vibrations of phenolic or alcoholic functional groups. The sharp medium peak at 2230 cm^{-1} is attributed to a conjugated C≡N (nitrile) stretching vibration. The 2330 cm^{-1} absorption is attributed to entrapped CO_2 gas within one or more structures of carbon.[16,17] The CO_2 gas was produced during the thermolysis process.

The hydroxyl, phenol, nitriles, and amides that are formed with the carbon nanostructure, on the surface, provide hydrophilic sites on the hydrophobic surface of the as-produced carbon nanostructures,[18] causing them to be dispersed in aqueous solution.

The synthesized powder was also characterized using XRD as shown in Fig. 3. After annealing at 460 °C, a broad XRD

Fig. 5. Effect of contact time on adsorption of (*a*) Cs(I) and (*b*) Co(II) ions on the prepared carbon at pH 5. Continuous lines represent model approximation (solid line, first-order kinetics; broken line, second-order kinetics). The residuals are represented by open symbols (see text).



reflection was observed that corresponds to the formation of a nonocrystalline graphite structure (tubes, pellets, particles, etc.), see Fig. 3. The average size of the crystallites can be obtained directly from the width of the peak, that is 4 ± 1 nm. Hence, it is possible to perform mass production of the graphite nanostructure using the polyacryloamidic route.

The effect of pH

The value of pH is the key factor that controls the adsorption processes because it controls the electrostatic interactions between the adsorbent and the adsorbate. To investigate the dependence of the maximum removal efficiency of cesium and cobalt on the value of pH, experiments were conducted in the pH range 2–12 (see Fig. 4). The uptake of Co(II) and Cs(I) ions was inhibited in acidic medium (pH < 2.0), which is attributed to the competition between hydrogen ion and the studied ions for adsorption onto the prepared powder.

The uptake of Cs(I) remained almost constant because cesium does not tend to hydrolyze or form complexes readily; hence, over a wide pH range it is present as the Cs ion. However, the exchange properties of the material depend on the pH of the system, not because of any effect on cesium speciation.[19] At pH 2–3, the reduced adsorption is caused by the different solubilities of the constituents of graphite and H^+ competitive adsorption.

The removal of Co(II) from the solution was low at low pH, but increased remarkably with increasing pH. There are many cobalt species that could be present depending on the pH value,[20] such as Co^{2+}, $Co(OH)^+$, $Co(OH)_2$, and $Co(OH)^{3-}$. At low pH, the main species was Co^{2+}. As the pH of an aqueous suspension increases, the surface charge of the powder becomes more negative and thus results in binding the positively charged Co^{2+} ions more strongly. In the present results, up to pH 8, cobalt exists primarily as unhydrolyzed Co(II) ion, but, at pH > 8, it strongly hydrolyzes and starts to precipitate in the form of the insoluble hydroxide, $Co(OH)_2$. All future sorption studies were carried out at pH 5.

The results indicate that cobalt adsorption is favorable with lower ionic strength, higher pH, and lower initial concentration. The mechanisms of heavy-metal ion adsorption on carbon are very complicated and appear attributable to physical adsorption, electrostatic attraction, precipitation, and chemical interaction between the metal ions and surface functional groups.

Kinetic studies

Effect of contact time and temperature

Figure 5 shows the plots of the amount sorbed of Cs(I) and Co(II) ions from aqueous solution onto graphite powders as a function of contact time and at a fixed pH (pH 5) and at room temperature (25 ± 1 °C). The figure shows a high initial rate of removal within the first 30 min of contact (60%–70% removed), followed by a slower subsequent removal rate that gradually approached an equilibrium condition in about 2 h. The rapid uptake of the studied ions by graphite may be due to adsorption and (or) exchange of the ions with some ions on the surface of the graphite.

Adsorption kinetics modeling

In this model, the study of adsorption describes the solute uptake rate and, evidently, this rate controls the residence time of adsorbate uptake at the solid–solution interface. In this part of the study, the kinetics of Cs(I) and Co(II) ion adsorption onto a prepared sample powder were analyzed using pseudo-first-order[21] and pseudo-second-order[22] kinetic models, respectively. The conformity between experimental data and each of the model-predicted values is expressed by the correlation coefficient (R^2). Relatively high R^2 values indicate

Can. J. Chem. Downloaded from www.nrcresearchpress.com by MCGILL UNIVERSITY on 02/02/13
For personal use only.

Table 1. The calculated parameters of the pseudo-first- and the pseudo-second-order kinetic models.

	First-order kinetics parameter			Second-order kinetics parameter				
Ion	k_1 (min^{-1})	q_1 calcd (mmol/kg)	R^2	k_2 (kg/mmol min^{-1})	q_2 calcd (mmol/kg)	h (mmol/kg min^{-1})	R^2	q_e exp. (mmol/kg)
Cs(I)	0.065	8.19	0.984	0.008	9.64	0.743	0.929	7.98
Co(II)	0.102	10.75	0.980	0.013	11.99	1.868	0.932	10.8

Note: k_1, pseudo-first-order rate constant; q_1, amount of metal ion adsorbed onto the prepared powder at equilibrium; k_2, pseudo-second-order rate constant; q_2, amount of metal ion adsorbed onto the prepared powder at equilibrium by applying second-order kinetics; h, initial adsorption rate;

that the model successfully describes the kinetics of metal ion adsorption.

In the pseudo-first-order model (Lagergren equation),[21] the adsorption kinetics of metal ions from liquid to solid is considered as a reversible reaction with an equilibrium state being established between two phases. A simple pseudo-first-order model[21] was therefore used to correlate the rates of reaction and is expressed as follows:

$$[2] \qquad \frac{dq_t}{dt} = k_1(q_1 - q_t)$$

where q_1 and q_t are the amounts of metal ion adsorbed onto the prepared powder at equilibrium and after time t (in mmol/kg), respectively, and k_1 is the pseudo-first-order rate constant (min^{-1}). After integration and by applying the boundary conditions $t = 0$ to $t = t$ and $q_t = 0$ to $q_t = q_t$, respectively, the integrated form of this equation becomes

$$[3] \qquad \ln(q_1 - q_t) = \ln q_1 - k_1 t$$

The values of $\ln(q_1 - q_t)$ are linearly correlated with t. Therefore, the plot of $\ln(q_1 - q_t)$ vs t should give a linear relationship, from which k_1 and q_1 can be determined by iteration analysis. It is worth mentioning that the direct determination of the equilibrium capacity by experimental procedure can lead to incorrect and (or) misleading results. Instead, by rearranging eq. [3]

$$[4] \qquad q_t = q_1[1 - \exp(-k_1 t)]$$

and by using least-squares fitting to reduce the sum of squares of the deviation from experimentally measured capacities, the values of the amounts of metal ions adsorbed at equilibrium (q_e) and k_1 can be determined.

For the pseudo-second-order model of adsorption, the kinetic rate equation is expressed as

$$[5] \qquad \frac{dq_t}{dt} = k_2(q_2 - q_t)^2$$

where k_2 (kg mmol^{-1} min^{-1}) is the rate constant of the pseudo-second-order equation. For the boundary conditions $t = 0$ to $t = t$ and $q_t = 0$ to $q_t = q_t$, the integrated form of eq. [5] becomes

$$[6] \qquad \frac{1}{(q_2 - q_t)} = \frac{1}{q_2} + k_2 t$$

Equation [5] can be rearranged to obtain a linear form equation

$$[7] \qquad q_t = q_2\left(1 - \frac{1}{1 + q_2 k_2 t}\right)$$

Fig. 6. Adsorption isotherms of (*a*) Co(II) and (*b*) Cs(I) ions from aqueous solution onto prepared graphite.

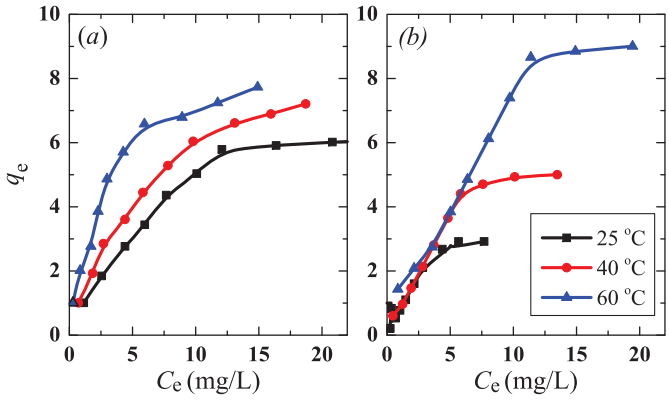
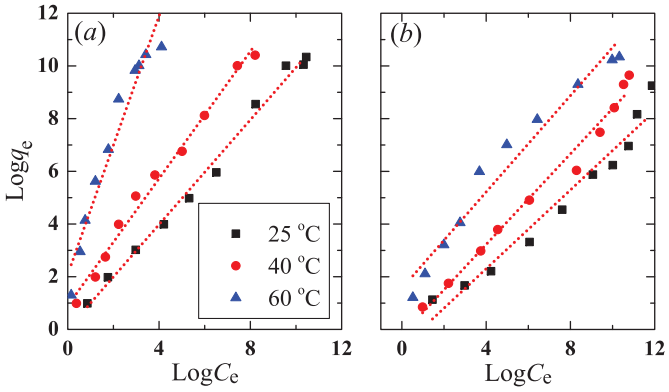


Fig. 7. Freundlich isotherm plots for adsorption of (*a*) Cs(I) and (*b*) Co(II) ions from aqueous solution onto prepared graphite.



$$[8] \qquad \frac{t}{q_t} = \frac{1}{k_2 q_2^2} + \frac{t}{q_2}$$

The plot of (t/q_t) and of t should give a linear relationship from which q_2 and k_2 can be determined or, alternatively, by the technique mentioned before.

Comparisons of the the experimental results with the model fitting for the material capacity (q_t) for both Cs(I) and Co(II) are shown in Fig. 5. The results show that the adsorption capacity of Cs(I) increased rapidly with an increase in contact time until about 40 min, and then the increasing rate slowed down gradually until the material was saturated. The model fitting shows that the pseudo-first-order model is suitable for sorption of Cs(I) on the prepared material. This observation suggests a fast monolayer adsorption onto the nanostructure material. The first-order reaction is associated mainly with diffusion through the organic foam that holds

Can. J. Chem. Downloaded from www.nrcresearchpress.com by MCGILL UNIVERSITY on 02/02/13
For personal use only.

Can. J. Chem. Downloaded from www.nrcresearchpress.com by MCGILL UNIVERSITY on 02/02/13
For personal use only.

Table 2. Langmuir and Freundlich isotherm parameters for the adsorption of Cs(I) and Co(II) ions onto prepared graphite at different temperatures.

		Langmuir model parameter			Freundlich model parameter		
Ions	Temp. (°C)	$Q°$ (mmol/kg)	$b\times10^{-3}$ (l/mol)	R^2	$1/n$	K_f (mmol/kg)	R^2
Cs(I)		67.3	35.7	0.9966	0.991	1.22	0.991
	40	72.2	48.7	0.9956	0.542	4.01	0.986
	60	86.5	97.1	0.9830	0.263	7.90	0.973
Co(II)	25	114.4	25.4	0.9981	0.914	4.87	0.995
	40	205.5	49.9	0.9939	0.859	11.62	0.986
	60	226.5	171.8	0.9969	0.748	36.39	0.985

Note: $Q°$, Langmuir constant representing maximum monolayer capacity; b, Langmuir constant related to energy of adsorption; n, Freundlich constant related to intensity of adsorption; K_f, Freundlich constant related to adsorption capacity.

the carbon nanostructures; the foam is an organic substance that is associated with the synthesis of the carbon nanostructures. The rate constant of the prepared nanostructure carbon is very high and reached 0.0652 min^{-1} in comparison with porous activated carbon.[23]

In the case of cobalt at pH 5, pseudo-first-order model fitting shows a reasonable value of R^2 as compared with the pseudo-second-order model (Fig. 5*b*). The kinetics of the mechanism may be more complicated. A kinetic model with a correlation coefficient (R^2) closer to one would be more desirable. However, the greater weight of first-order fitting is after 40 min; therefore, and as shown in Fig. 5*c*, the fitting is not appreciable for the first 40 min. That suggests a strong contribution of second-order and higher kinetics to the ion-exchange processes rather than pseudo-first-order kinetics at the beginning of the adsorption process. In Table 1, the product $k_2q_2^2$ is the initial adsorption rate represented as $h = k_2q_2^2$. Furthermore, the theoretical and experimental q_e values are in good accordance with each other.

Adsorption isotherms

The equilibrium isotherm is important for describing how solutes interact with the adsorbent and, therefore, is critical in optimizing the use of the adsorbent. In this respect, the adsorption isotherms for the removal of Cs(I) and Co(II) ions from aqueous solution onto prepared graphite at three different temperatures were determined and are shown in Fig. 6. The amount of Cs(I) and Co(II) ions adsorbed per unit mass of the graphite increased with the initial metal concentration until the plateau values, representing saturation of the active groups that are available for interaction with Cs(I) and Co(II) ions on the material, were reached. Two commonly used empirical adsorption models, Freundlich and Langmuir models, which correspond to heterogeneous and homogeneous adsorbent surfaces, respectively, were employed in this study.

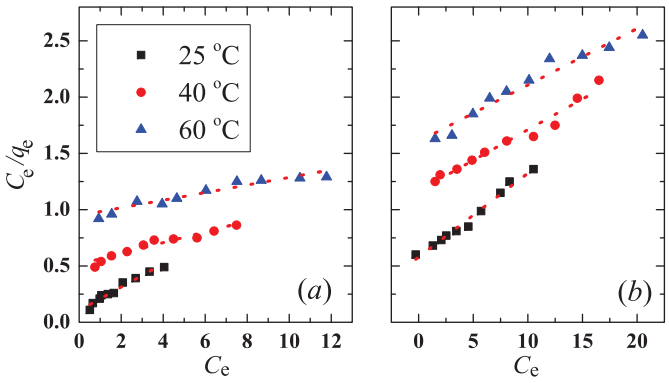
Freundlich isotherm model

The Freundlich equation was derived to model the multilayer sorption and for sorption onto heterogeneous surfaces. The logarithmic form of the Freundlich equation may be written as

$$[9] \qquad \log q_e = \log K_f + (1/n)\log C_e$$

where C_e is the remaining concentration in the aqueous phase, and K_f and n are the Freundlich constants related to adsorption capacity and intensity of adsorption, respectively. The plot of $\log q_e$ vs $\log C_e$ is shown in Fig. 7, which suggests that adsorption of Cs(I) and Co(II) ions onto graphite obeys the Freundlich isotherm over the entire range of adsorption concentration. The numerical values of the constants $1/n$ and K_f were computed from the slope and intercepts using the linear least-squares fitting method and are given in Table 2. The $1/n$ value is usually dependent on the nature and strength of the adsorption process as well as on the distribution of active sites. The numerical values of K_f represent the adsorption capacities of Cs(I) and Co(II) ions onto graphite.

Fig. 8. Langmuir isotherm plots for adsorption of (*a*) Cs(I) ions and (*b*) Co(II) ions from aqueous solution onto prepared graphite.



Langmuir isotherm model

The Langmuir isotherm model assumes maximum adsorption occurs when the surface is covered by the adsorbate. The linear form of the Langmuir equation is given by the following formula

$$[10] \qquad \frac{C_e}{q_e} = \left(\frac{1}{Q°b}\right) + \left(\frac{1}{Q°}\right)C_e$$

where q_e (mmol/kg) is the amount adsorbed at equilibrium concentration (C_e, mmol/L), $Q°$ (mmol/kg) is the Langmuir constant representing maximum monolayer capacity, and b is the Langmuir constant that is related to energy of the adsorption. The isotherm data has been fitted to a linear relationship using the Langmuir equation and is shown in Fig. 8. The regression constants are tabulated in Table 2. The Langmuir constants $Q°$ and b increased with temperature, showing that the sorption capacity and intensity of adsorption are en-

Can. J. Chem. Downloaded from www.nrcresearchpress.com by MCGILL UNIVERSITY on 02/02/13
For personal use only.

Fig. 9. Plot of $\ln K_c$ vs $1/T$ for adsorption of Cs(I) and Co(II) ions onto prepared graphite.

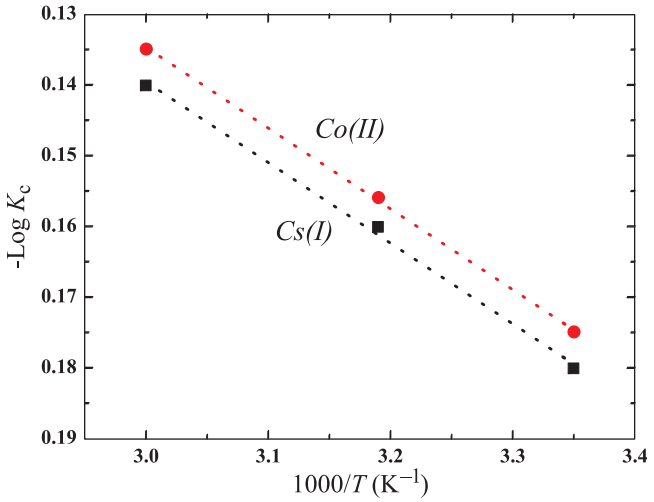


Table 3. Thermodynamic parameters of Cs(I) and Co(II) on prepared graphite.

Metal	$\Delta H°$ (kJ/mol)	$\Delta S°$ (J/mol K^{-1})	$-\Delta G°$ (KJ/mol) At 25 °C	At 40 °C	At 60 °C
Cs(I)			2.9	6.8	15.5
Co(II)	40.7	98.6	9.7	12.5	14.6

hanced at higher temperatures. This increase in adsorption capacity with temperature suggests that the active surfaces available for adsorption have increased with increasing temperature.[24]

Effect of temperature

The effects of temperature on the adsorption behavior of Cs(I) and Co(II) onto graphite powder were studied using van't Hoff's equations, which take the form

$$[11] \quad \log K_c = -\frac{\Delta H^\circ}{2.303RT} + \frac{\Delta S^\circ}{2.303R}$$

$$[12] \quad \Delta G^\circ = -RT \ln K_c$$

where K_c is the adsorption equilibrium constant, R is the gas constant, and T is the absolute temperature in Kelvin. The values of K_c at the different studied temperatures were determined from the product of the Langmuir equation parameters $Q°$ and b.[24] The plot of $\log K_c$ vs $1/T$ is a straight line as shown in Fig. 9 The values of $\Delta H°$, $\Delta S°$, and $\Delta G°$ are evaluated and tabulated in Table 3. The values of free energy decrease (from –2.9 to –15.5 kJ/mol for Cs(I) and from –9.7 to –14.6 kJ/mol for Co(II)) with an increase in temperature, indicating that the process is favorable at higher temperatures. The negative value of $\Delta G°$ indicates that the adsorption behavior of Cs(I) and Co(II) ions is spontaneous, with a high preference of metal ion adsorption in prepared graphite. The changes of energy for physical adsorption are up to –1.123 kJ/mol and those for chemical adsorption are up to –22.71 kJ/mol.[25] From Table 3, the magnitude of adsorption $\Delta G°$, ranging from –2.9 to –15.5 kJ/mol for Cs(I) and from –9.7 to –14.6 kJ/mol for Co(II), suggests that the adsorption can be considered as a chemical adsorption. However, the positive values of $\Delta H°$ and $\Delta S°$ indicate that the adsorption is spontaneous and endothermic.

Conclusions

On the thermal annealing of polyacrylamide gel, nanostructured carbon particles were synthesed. The structure and composition were investigated by XRD and FT-IR, which confirmed the existence of functional groups on the nanostructured graphite surfaces. The prepared material has promising applications in the treatment of the aqueous environment for heavy metals such as Cs(I) and Co(II) because of its low cost, high capacity, ease of production, and rapid uptake rate. The adsorption of Cs(I) and Co(II) on the prepared powder was investigated by batch technique. For the pH range 2–12, the adsorption of Cs(I) remains almost constant, whereas the adsorption of Co(II) is low at low pH and increases rapidly at pH > 8 as it hydrolyzes and starts to precipitate. Equilibrium isotherms were studied using the Freundlich and Langmuir isotherm models to assess the maximum adsorption capacities of both metal ions and the equilibrium adsorptions. The maximum adsorption capacity of Cs (I) was found to be greater than that of Co(II).

References

(1) Smičiklas, I.; Dimović, S.; Plećaš, I. *Appl. Clay Sci.* **2007**, *35* (1–2), 139. doi:10.1016/j.clay.2006.08.004.
(2) Khan, S. *J. Radioanal. Nucl. Chem.* **2003**, *258* (1), 3. doi:10.1023/A:1026217020215.
(3) Rengaraj, S.; Moon, S.-H. *Water Res.* **2002**, *36* (7), 1783. doi:10.1016/S0043-1354(01)00380-3.
(4) Netzer, A.; Hughes, D. *Water Res.* **1984**, *18* (8), 927. doi:10.1016/0043-1354(84)90241-0.
(5) Chen, J.; Wang, X. *Separ. Purif. Tech.* **2000**, *19* (3), 157. doi:10.1016/S1383-5866(99)00069-6.
(6) Gupta, V. K.; Ali, I. *Separ. Purif. Tech.* **2000**, *18* (2), 131. doi:10.1016/S1383-5866(99)00058-1.
(7) Borba, C. E.; da Silva, E. A.; Fagundes-Klen, M. R.; Kroumov, A. D.; Guirardello, R. *J. Hazard. Mater.* **2008**, *152* (1), 366. doi:10.1016/j.jhazmat.2007.07.005.
(8) Malkoc, E.; Nuhoglu, Y.; Dundar, M. *J. Hazard. Mater.* **2006**, *138* (1), 142. doi:10.1016/j.jhazmat.2006.05.051.
(9) Demirbas, E.; Kobya, M.; Senturk, E.; Ozkan, T. *Water SA* **2004**, *30* (4), 533.
(10) Pattanayak, J.; Mondal, K.; Mathew, S.; Lalvani, S. *Carbon* **2000**, *38* (4), 589. doi:10.1016/S0008-6223(99)00144-X.
(11) Pelekani, C.; Snoeyink, V. *Water Res.* **1999**, *33* (5), 1209. doi:10.1016/S0043-1354(98)00329-7.
(12) Iijima, S. *Nature* **1991**, *354* (6348), 56. doi:10.1038/354056a0.
(13) Hussain, T.; Iqbal, M. *J. Anal. Appl. Pyrolysis* **2011**, *90* (2), 106. doi:10.1016/j.jaap.2010.10.012.
(14) Chai, S.-P.; Lee, K.-Y.; Ichikawa, S.; Mohamed, A. R. *Appl. Catal. A Gen.* **2011**, *396* (1–2), 52. doi:10.1016/j.apcata.2011.01.038.
(15) Gabbott, P. A Practical Introduction to Differential Scanning Calorimetry. In *Principles and Applications of Thermal Analysis;* Blackwell Publishing Ltd.; Oxford, UK, 2008; pp 1–50.
(16) Matranga, C.; Chen, L.; Smith, M.; Bittner, E.; Johnson, J. K.;

Bockrath, B. *J. Phys. Chem. B* **2003**, *107* (47), 12930. doi:10.1021/jp0364654.
(17) Ramesh, P.; Sampath, S. *Analyst (Lond.)* **2001**, *126* (11), 1872. doi:10.1039/b106199m.
(18) Yavari, R.; Huang, Y. D.; Ahmadi, S. J. *J. Radioanal. Nucl. Chem.* **2011**, *287* (2), 393. doi:10.1007/s10967-010-0909-6.
(19) Cornell, R. M. *J. Radioanal. Nucl. Chem.* **1993**, *171* (2), 483. doi:10.1007/BF02219872.
(20) Wang, Q.; Li, J.; Chen, C.; Ren, X.; Hu, J.; Wang, X. *Chem. Eng. J.* **2011**, *174* (1), 126. doi:10.1016/j.cej.2011.08.059.
(21) Lagergren, S. *K. Sven. Vetenskapsakad Handl.* **1898**, *24*, 1.
(22) Ho, Y. S.; McKay, G.; Wase, D. A. J.; Forster, C. F. *Adsorpt. Sci. Technol.* **2000**, *18* (7), 639. doi:10.1260/0263617001493693.
(23) Wang, L.; Feng, M.; Liu, C.; Zhao, Y.; Li, S.; Wang, H.; Yan, L.; Tian, G.; Li, S. *Sep. Sci. Technol.* **2009**, *44* (16), 4023. doi:10.1080/01496390903183253.
(24) Xiangke, W.; Wenming, D.; Yingchun, G.; Changhui, W.; Zuyi, T. *J. Radioanal. Nucl. Chem.* **2001**, *250* (2), 267. doi:10.1023/A:1017922924421.
(25) Jaycok, M.; Partt, G. *Chemistry of Interfaces;* Ellis Horwood: New York, 1981.

Can. J. Chem. Downloaded from www.nrcresearchpress.com by MCGILL UNIVERSITY on 02/02/13
For personal use only.

Complexations of the hydrophilic and hydrophobic moieties of benzethonium chloride by cucurbit[7]uril in aqueous solution

Brendan C. MacGillivray and Donal H. Macartney

Can. J. Chem. Downloaded from www.nrcresearchpress.com by MCGILL UNIVERSITY on 02/02/13
For personal use only.

Abstract: The sequential complexations of the hydrophilic and hydrophobic end groups of benzethonium chloride by cucurbit[7]uril (CB[7]) in aqueous solution have been investigated using ^{1}H NMR spectroscopy and electrospray ionization mass spectrometry. The initial binding is to the benzyldimethylammonium group, with a stability constant of $(8.7 \pm 3.1) \times 10^7$ $(mol/L)^{-1}$. This binding constant and the complexation-induced upfield shifts of the benzyl guest protons are similar to those values observed with other cationic guests containing benzyl moieties. This equilibrium is followed by the binding of a second equivalent of the host to the hydrophobic 2-(2,4,4-trimethylpentyl) group, with a stability constant of $(4.0 \pm 1.9) \times 10^3$ $(mol/L)^{-1}$. The relatively strong binding of this uncharged hydrophobic end of the guest molecule is consistent with the inclusion of eight heavy (nonhydrogen) atoms within the inner cavity of CB[7], with its low polarizability. The packing coefficient for the 2-(2,4,4-trimethylpentyl) group with the inner cavity is calculated to be 61%, close to Rebek's ideal value of 55%.

Key words: cucurbit[7]uril (CB[7]), benzethonium, host–guest complex, hydrophobic, hydrophilic.

Résumé : Faisant appel à la spectroscopie RMN du ^{1}H et à la spectrométrie de masse avec ionisation par électronébulisation, on a étudié les complexations séquentielles des groupes terminaux hydrophiles et hydrophobes du chlorure de benzéthonium par une solution aqueuse de cucurbit[7]urile. La fixation initiale se fait au niveau du groupe benzyldiméthylammonium, avec une constante de stabilité de $(8{,}7 \pm 3{,}1) \times 10^7$ $(mol/L)^{-1}$. Ces constantes de fixation ainsi que les déplacements chimiques vers les hauts champs, induits par la complexation, des protons benzyles invités sont semblables aux valeurs qui ont été observées avec d'autres invités cationiques contenant des portions benzyliques. Cet équilibre est suivi par la fixation d'un deuxième équivalent de l'invité par le groupe hydrophobe 2-(2,4,4-triméthylpentyl), avec une constante de stabilité de $(4{,}0 \pm 1{,}9) \times 10^3$ $(mol/L)^{-1}$. Cette fixation relativement forte de la portion hydrophobe non chargée de la molécule hôte est en accord avec l'inclusion de huit atomes lourds (qui ne sont pas des atomes d'hydrogène) dans la cavité intérieure du CB[7] de faible polarisabilité. On a calculé que le coefficient de compactage du groupe 2-(2,4,4-triméthylpentyle) à l'intérieur de la cavité est de 61 %, très près de la valeur idéale de 55 % de Rebek.

Mots-clés : cucurbit[7]urile, benzéthonium, complexe hôte–invité, hydrophobe, hydrophile.

[Traduit par la Rédaction]

Introduction

The cucurbit[*n*]urils (CB[*n*], $n = 5–8, 10$) are a family of macrocyclic host molecules comprised of *n* glycoluril units bridged by 2*n* methylene groups.[1–4] While the CB[6] member was first prepared over 100 years ago,[5] it has been in the last decade, since the methods for preparing the other members of the family were first reported,[6,7] that investigations into the applications of CB[*n*] as host molecules have significantly increased.[4] Guest molecules may bind to the CB[*n*] hosts by means of ion–dipole, dipole–dipole, and dipole–quadrupole interactions, as well as the hydrophobic effect. The largest stability constants have been observed between CB[7] (Fig. 1), the most soluble member of the family, and cationic guests based on ferrocene,[8–11] adamantyl,[12,13] or bicyclo[2.2.2] octane groups.[12,13] These ultrahigh affinity guests form CB[7] complexes with stabilities that rival that of the avidin–biotin complex in nature, and this feature has been applied to the binding of ultrahigh affinity labeled proteins to CB[*n*]-coated beads.[14] The cucurbiturils have been found to be relatively nontoxic,[15–18] and there have been a diverse set of guests of biological and medicinal interest investigated with CB[7], including proteins,[19] anticancer agents,[20,21] vitamins,[22] and fungicides.[23] The ability to solubilize more hydrophobic guests in aqueous solution,[24] as well as to significantly modulate the pK_a values of acidic guests,[25,26] have led to the applications of CB[7] in drug delivery,[24,26] stability,[27,28] and controlled release.[29]

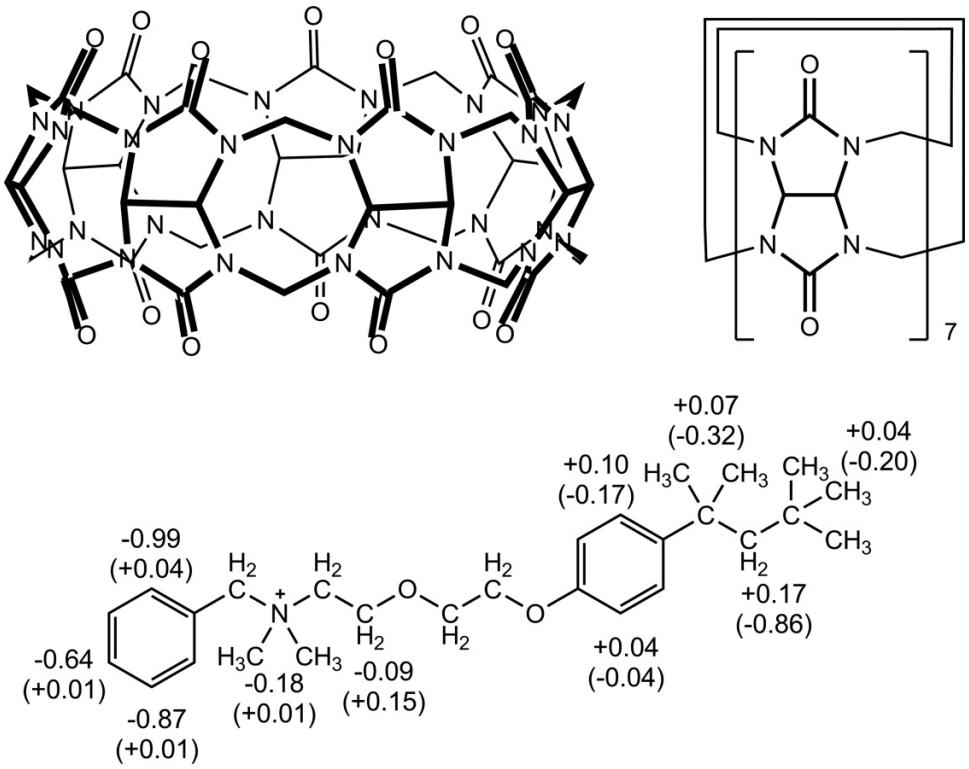
Benzethonium chloride (Fig. 1) is a synthetic quaternary ammonium compound used primarily as an antifungal preservative.[30] It also has moderate antiseptic and anti-infective properties, making it useful as a disinfectant and a viable

Received 4 June 2012. Accepted 27 July 2012. Published at www.nrcresearchpress.com/cjc on 22 October 2012.

B.C. MacGillivray and D.H. Macartney. Department of Chemistry, Queen's University, 90 Bader Lane, Kingston, ON K7L 3N6, Canada.

Corresponding author: Donal H. Macartney (e-mail: donal@chem.queensu.ca).

Fig. 1. Structure of cucurbit[7]uril (CB[7], top) and the benzethonium cation (bottom). The ^{1}H NMR limiting chemical shift change, $\Delta\delta_{lim}$, values are shown for the guest proton resonances upon formation of the host–guest complex between the benzethonium cation and CB[7]. The top numbers represent the shifts associated with the first host binding event and the bottom numbers in brackets represent shifts associated with the second binding event. The shifts of some of the guest protons were obscured by the proton resonances of CB[7] and the solvent, and therefore could not be measured.



Can. J. Chem. Downloaded from www.nrcresearchpress.com by MCGILL UNIVERSITY on 02/02/13
For personal use only.

alternative to alcohol-based hand sanitizers. It was recently determined in a cell-based small molecule screen that benzethonium is selectively toxic to human pharyngeal cancer cells, but not to normal human or mouse cells.[31] When it is desirable to isolate organisms from solutions containing antimicrobial agents, such as benzethonium chloride, nonionic detergents, or phospholipids, which trap the antimicrobial agents within micelles, are commonly employed. These molecules, however, can also be lethal to the microorganisms. Macrocyclic host molecules, such as β-cyclodextrin, have been shown to be effective as an alternative to detergents for neutralizing quaternary ammonium compounds such as benzethonium chloride.[32] The cyclodextrins generally bind to cationic guests with binding constants considerably smaller than determined for the cucurbiturils, owing to weaker ion–dipole interactions between the positive charge(s) on the guest and the portal functional groups (hydroxyls on cyclodextrins versus ureido carbonyls on cucurbiturils). A recent example is the superior binding of CB[7] to a series of local anaesthetics[33] compared with β-cyclodextrin or the *p*-sulfonated calix[4]arene.[34] The CB[7] host, therefore, should be more efficient at neutralizing the antimicrobial effects of the benzethonium cation than either β-cyclodextrin or nonionic detergents.

The benzethonium cation possesses a hydrophilic cationic benzyldimethylammonium fragment on one end and a hydrophobic 2-(2,4,4-trimethylpentyl)-substituted phenyl group on the other end, with a diethyleneglycol unit in the centre. This would allow for the binding of two cucurbit[7]uril host molecules using different noncovalent interactions to stabilize the host–guest interactions. We have observed a similar phenomenon with coenzyme B_{12}, where the first CB[7] bound to the protonated α-axial 5,6-dimethylbenzimidazole base, which had dissociated from the Co(III) centre ($K_{CB[7]}$ = (3.02 ± 0.35) × 10^6 (mol/L)$^{-1}$).[22] This was followed by a second weaker binding to the neutral β-axial 5′-deoxyadenosyl ligand ($K_{CB[7]}$ = (1.1 ± 0.2) × 10^3 (mol/L)$^{-1}$) without its detachment from the Co(III) centre. The three orders of magnitude difference in the binding constants allowed for the two processes to be observed separately in the ^{1}H NMR spectrum.

While the cationic benzylammonium fragment is known to bind strongly to CB[7],[35,36] there have been few studies of the binding of branched hydrocarbon groups to this host molecule. Florea and Nau[37] recently reported that CB[6] is capable of binding a range of hydrocarbons in aqueous solution, with host–guest stability constants of up to 10^6 (mol/L)$^{-1}$ (isobutene and cyclopentane). The binding of the hydrocarbons to CB[7] was investigated using a competitive fluorescent dye displacement technique, as the low solubility of CB[6] in pure water prevents the use of NMR spectroscopy. Nau et al.[38] also carried out a detailed analysis of the role of the hydrophobic effect in the complexation of neutral molecules to CB[*n*] hosts, and this has shown that CB[6] and CB[7] possess cavity sizes (inner cavity volumes of 142 and 242 Å^3, respectively) that allow for the inclusion of guests with up to seven and 12 heavy atoms,

Can. J. Chem. Downloaded from www.nrcresearchpress.com by MCGILL UNIVERSITY on 02/02/13
For personal use only.

respectively. The largest binding constants for CB[7] with both neutral and cationic guests are observed with those containing adamantyl (nine heavy atoms) or ferrocenyl (11 heavy atom) groups. Nau and co-workers[37,38] have shown that these findings are in line with the empirical determination of Mecozzi and Rebek[39] that the optimal host–guest stability is found when the guest occupies 55% ± 9% of the interior cavity volume of the host.

The 2-(2,4,4,-trimethylpentyl) group on the benzethonium cation has eight heavy atoms and would be therefore expected to displace the 7–8 waters located in the CB[7] cavity and bind reasonably strongly using the hydrophobic effect. In this study, we used electrospray ionization mass spectrometry (ESI-MS) and ^{1}H NMR spectroscopy to investigate the relative complexations of the CB[7] host molecule to the hydrophilic and hydrophobic ends of the benzethonium cation in aqueous solution.

Experimental section

Materials

Cucurbit[7]uril was prepared and characterized by the method of Day et al.[7] Benzethonium chloride and benzyltrimethylammonium bromide (Sigma-Aldrich) were used as received.

Methods

The ESI mass spectrum was recorded on a QStar XL TOF instrument and the ^{1}H NMR spectra were obtained using Bruker Avance AM 400 and 500 MHz instruments. The 1:1 host–guest stability constant ($K^1_{CB[7]}$) was determined by a ^{1}H NMR competitive binding experiment in D_2O (50 mmol/L NaOAc buffer, pD 4.7), using the protocol of Isaacs and co-workers,[40] with the benzyltrimethylammonium cation as the competitor guest ($K_{CB[7]} = (2.5 \pm 0.6) \times 10^8$ (mol/L)$^{-1}$).[36] The 2:1 host–guest binding constant ($K^2_{CB[7]}$) was determined by a ^{1}H NMR titration in which the ratio of the bound to total guest (determined by integrations of proton resonances) as a function of [CB[7]] was fit to a 1:1 binding isotherm. Molecular modelling of the structures of the host–guest complex was performed using Chem3D software (CambridgeSoft) with MM2 energy minimizations.

Results and discussion

Host–guest complexation

ESI-MS measurements

The high-resolution electrospray ionization mass spectrum (ESI-MS) of an aqueous solution of the benzethonium cation in the presence of a fivefold excess of CB[7] reveals peaks with m/z = 1574.6675 and 1380.0013. The former peak corresponds to the 1:1 [CB[7]·benzethonium]$^+$ complex (calculated m/z = 1574.6645 for $C_{69}H_{84}N_{29}O_{16}^+$) and the second peak corresponds to the 2:1 [CB[7]·benzethonium·CB[7]·Na]$^{2+}$ complex (calculated m/z = 1379.9987 for $C_{111}H_{126}N_{57}O_{30}Na^{2+}$).

NMR measurements

^{1}H NMR spectroscopy has proven to be a very useful method for determining the portion(s) of guest molecules that are located within the hydrophobic cavity as opposed to being positioned adjacent to the polar carbony-lined portals of the cucurbiturils. An upfield shift in a resonance of the guest proton upon complexation by CB[7] ($\Delta\delta_{lim} = \delta_{bound} - \delta_{free}$) is indicative of its position within the cavity, whereas a downfield shift indicates that the guest proton is located outside, near one of the portals. A ^{1}H NMR titration of the benzethonium cation by CB[7] is shown in Fig. 2. The complexation-induced chemical shift changes for the guest proton resonances indicate two sequential binding processes by CB[7] host molecules. The first process is the binding of the more hydrophilic end of the molecule, over the benzyldimethylammonium group (protons H_j, H_k, H_l, and H_m; Fig. 2). This is followed by the complexation of the more hydrophobic end, containing the 2-(2,4,4-trimethylpentyl) substituent on the aromatic ring (protons H_a, H_b, and H_c; Fig. 2). The slight downfield shifts in the H_f, H_g, and H_h protons of the central linker indicate that this portion of the molecule is not complexed by the CB[7] host. The limiting chemical shift changes ($\Delta\delta_{lim}$) are given in Fig. 1 for the two binding processes. A gas-phase energy minimization calculation (MM2) for the structure of the 2:1 host–guest complex between CB[7] and the benzethonium cation, which is consistent with the complexation-induced chemical shift changes, is shown in Fig. 3.

Binding of the hydrophilic moiety

The addition of 1 equiv of CB[7] to a solution of the benzethonium guest results in the complexation of the benzyldimethylammonium end of the molecule bearing the positive charge. The limiting chemical shift changes for the aromatic and methylene protons are upfield and are of comparable magnitude to other cationic guest molecules with benzyl end groups, such as the benzylammonium,[41] benzyltrimethylammonium,[36] benzylcholine,[42] and *N*-benzyl-1-(1-naphthyl)ethylammonium[35] cations (Fig. 4). The magnitudes of the $\Delta\delta_{lim}$ values suggest that the complexation places the benzyl group within the cavity with the quaternary nitrogen centre placed near the oxygens of the ureido carbonyl groups on the portals.

Complexation at the first binding site is mainly driven by ion–dipole interactions between the cationic ammonium group of the benzethonium cation and the polar portals of CB[7]. This binding site is also stabilized by the hydrophobic effect, which results from the terminal phenyl group of benzethonium being encapsulated by the hydrophobic cavity of CB[7]. As a result of these two effects working in tandem, CB[7] is able to form a very stable complex with the benzethonium cation. In the case of tightly bound host–guest complexes ($K_{CB[7]} > 10^4$ (mol/L)$^{-1}$), the binding constant cannot be determined by fitting a binding curve from a ^{1}H NMR titration with host and guest concentration in the millimolar range. The plot of $\Delta\delta_{obs}$ for the aromatic proton resonances as a function of [CB[7]]/[benzethonium] is linear until a 1:1 ratio (Fig. 5), and as such it was not possible to accurately determine the first binding constant by fitting this data. Instead, the binding constant was determined by a competition study with a known competitor, using the protocol of Isaacs and co-workers.[40] The host–guest stability constant for the CB[7] complex with the benzethonium cation was determined to be $K^1_{CB[7]} = (8.7 \pm 3.1) \times 10^7$ (mol/L)$^{-1}$ using the benzyltrimethylammonium cation (Fig. 4*b*, $K_{CB[7]} = (2.5 \pm 0.6) \times 10^8$ (mol/L)$^{-1}$)[36] as the competititor guest.

The stability constant for the 1:1 host–guest complex between CB[7] and the benzethonium cation may be compared with other cationic guests containing benzylammonium moieties (Fig. 4).

Fig. 2. ^{1}H NMR (400 MHz) titration of the benzethonium cation (1.00 mmol/L) by cucurbit[7]uril (CB[7], *) in D_2O: (*a*) 0.00 equiv CB[7], (*b*) 0.42 equiv CB[7], (*c*) 0.99 equiv CB[7], (*d*) 1.39 equiv CB[7], (*e*) 1.61 equiv CB[7], (*f*) 2.10 equiv CB[7], and (*g*) 3.52 equiv CB[7].

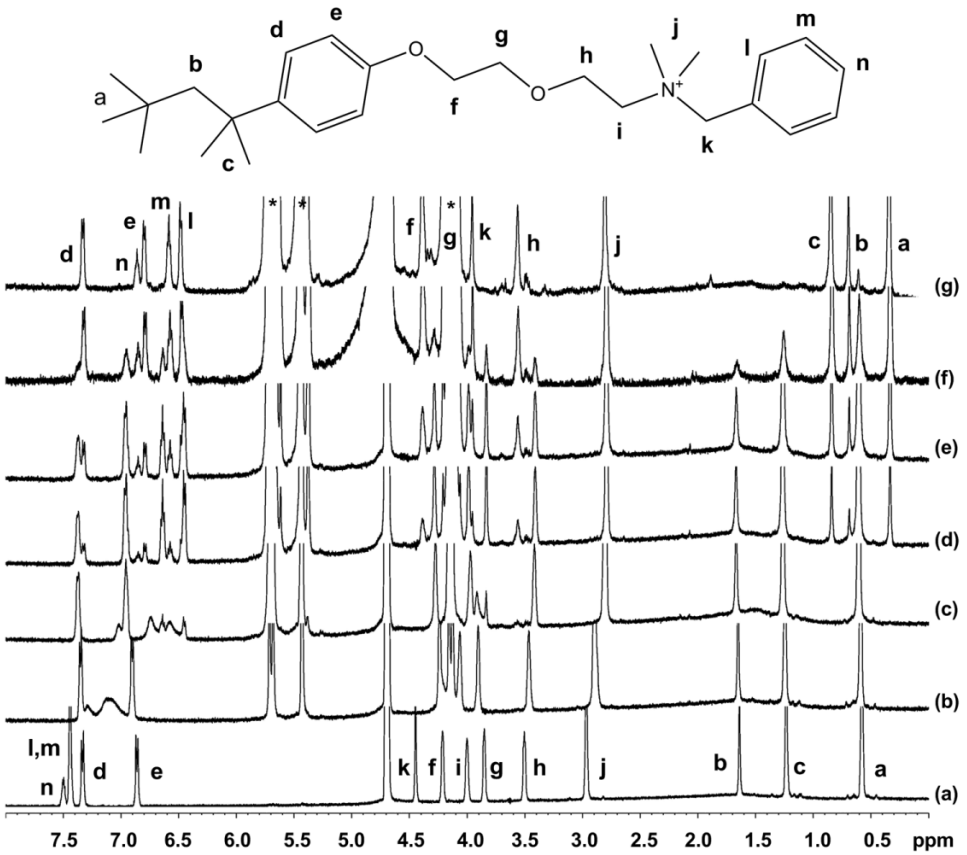
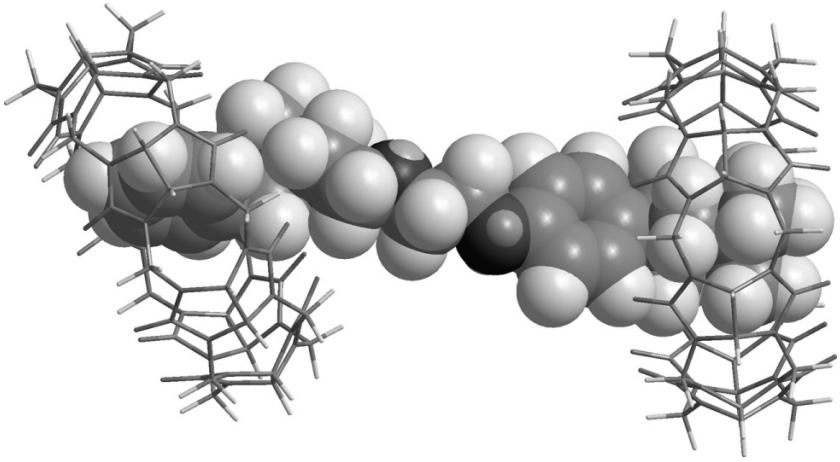


Fig. 3. A gas-phase energy-minimization (MM2) calculation of the structure of the 2:1 host–guest [CB[7]·benzethonium·CB[7]]$^+$ complex. CB[7], cucurbit[7]uril.



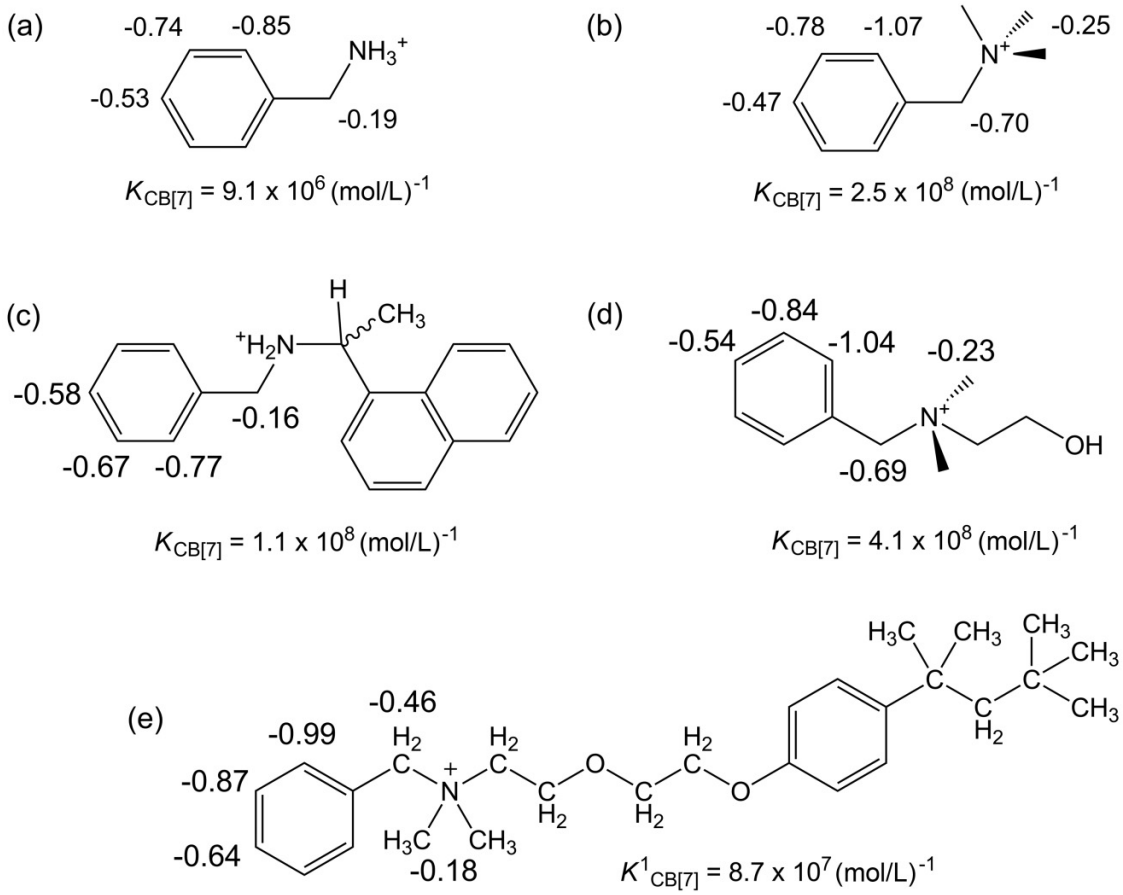
The value for benzethonium is within the range of 10^7–10^8 (mol/L)$^{-1}$ reported for this series of guests.[35,36,41,42] The more hydrophobic benzyltrialkylammonium cations tend to form a more stable complex with CB[7] than the benzylammonium cations. In addition, the values of $\Delta\delta_{lim}$ (Fig. 4) suggest a deeper inclusion of the benzyltrialkylammonium cations compared with the benzylammonium cations.

Binding of the hydrophobic moiety

The addition of further cucurbit[7]uril beyond 1 equiv to the benzethonium guest results in a second weaker binding interaction with the more hydrophobic end of the molecule, the 2-(2,4,4-trimethylpentyl) substituent on the phenyl ring. The most notable changes in the ^{1}H NMR spectra of the host–guest mixtures (Fig. 2) are the upfield shifts of the alkyl protons of

Can. J. Chem. Downloaded from www.nrcresearchpress.com by MCGILL UNIVERSITY on 02/02/13
For personal use only.

Fig. 4. The cucurbit[7]uril (CB[7]) complexation-induced limiting chemical shift changes ($\Delta\delta_{lim}$, ppm) for cationic guests containing benzylammonium and related binding sites: (*a*) benzylammonium,[41] (*b*) benzyltrimethylammonium,[36] (*c*) *N*-benzyl-1-(1-naphthyl) ethylammonium,[35] (*d*) benzylcholine,[42] and (*e*) benzethonium. The stability constants ($K_{CB[7]}$) for the 1:1 host–guest complexes with CB[7] are indicated below the guest.

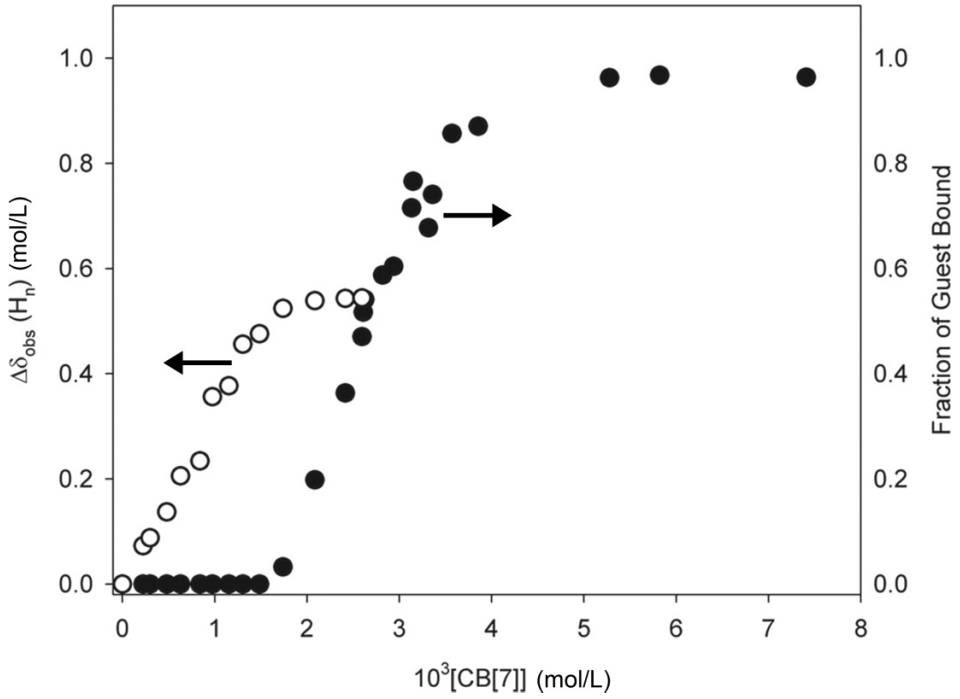


this substituent, with slow exchange behaviour (separate resonances for the free and bound guest protons) on the NMR timescale. The largest shift is found for the methylene protons (H_b), with $\Delta\delta_{lim} = -0.86$ ppm, while the methyl protons shift upfield to a smaller extent (−0.20 and −0.32 ppm for methyl protons, H_a and H_c, respectively). The stability constant for the binding of the second CB[7] to this hydrophobic region was determined to be $K^2_{CB[7]} = (4.0 \pm 1.9) \times 10^3$ (mol/L)$^{-1}$ by integrating the methyl proton resonances associated with the free and bound benzethonium cations. Recently, Yu et al.[43] reported that the benzyl(dimethyl)hexadecylammonium cation formed both 1:1 (encapsulating the benzyl group) and 2:1 (second CB[7] complexes the hexadecyl chain) host–guest complexes with CB[7], with stability constants of 1.88×10^8 and 4.8×10^4 (mol/L)$^{-1}$, respectively.

The value for complexing the hydrophobic 2-(2,4,4-trimethylpentyl) portion of the benzethonium cation, with eight heavy atoms, is comparable in magnitude to those we determined previously for butan-2-one (3.1×10^3 (mol/L)$^{-1}$)[44] and 3,3-dimethylbutan-2-one (6.74×10^3 (mol/L)$^{-1}$),[44] which have five and nine heavy atoms, respectively. Nau et al.[38] recently analyzed the properties of the inner cavity of cucurbiturils and determined that the cavity of cucurbiturils, including CB[7], have a very low polarizability and are capable of tightly binding hydrophobic groups of a certain size, specified by either the number of heavy (nonhydrogen) atoms or by the molar volume. In the case of CB[7], the highest reported affinities for neutral guests are adamantylcarboxylic acid (3.2×10^5 (mol/L)$^{-1}$)[40] and hydroxymethylferrocene (3.2×10^6 (mol/L)$^{-1}$),[8] which have 9 and 11 heavy atoms, respectively, in the adamantyl and ferrocenyl fragments. The capacity of the CB[7] cavity appears to be 12 heavy atoms, as we have reported that the 2-aminopyridinium cation, bound to CB[7] in a 1:2 host–guest complex, can undergo a photodimerization[45] to yield a product whose volume is 151 Å^3 (the packing coefficient (PC) = 62%),[37] with all of the guest but the two amino substituents within the inner cavity. Mecozzi and Rebek,[39] based on host–guest binding in capsules, calculated that the optimum PC, obtained by dividing the volume of the guest by the volume of the cavity of the host, is 55% ± 9%, with the remaining void space necessary to retain some vibrational, rotational, and translational degrees of freedom of the guest, along with vibrational degrees of freedom for the host, to maximize entropy. Host–guest complexes with lower or higher PC values were associated with lower stability constants in solution. Nau et al.[38] considered Mecozzi and Rebek's[39] principle of 55% packing coefficient ideal in host–guest complexes. The "expanded" cavity volume of CB[7], which includes the "bond dipole regions" near the

Can. J. Chem. Downloaded from www.nrcresearchpress.com by MCGILL UNIVERSITY on 02/02/13
For personal use only.

Fig. 5. Plots of $\Delta\delta_{obs}$ for H_n (○, left ordinate) and the fraction of guest bound by a second cucurbit[7]uril (CB[7]; ●, right ordinate) against the total CB[7] concentration, from the ^{1}H NMR titration (see Fig. 2 for partial data) of the benzethonium cation (1.5 mmol/L) with CB[7] in D_2O.



Can. J. Chem. Downloaded from www.nrcresearchpress.com by MCGILL UNIVERSITY on 02/02/13
For personal use only.

portals, was calculated to be 279 Å^3, compared with the "inner" cavity volume of 242 Å^3.[37] The latter is considered to be the more appropriate cavity volume when it comes to binding hydrophobic guests.

With the benzethonium guest, the uncharged hydrophobic 2-(2,4,4-trimethylpentyl) substituent has eight heavy atoms and the upfield shifts of all of the protons within this substituent suggests that the inner cavity can accommodate them. The molar volume of 2,2,4-trimethylpentane was calculated to be 147 Å^3,[46] and using the inner cavity volume of CB[7], results in a packing coefficient of 61%, close to Mecozzi and Rebek's[39] ideal value of 55%. This accounts for the relatively strong binding of this neutral moiety on the benzethonium guest.

The demonstration that the neutral 2-(2,4,4-trimethyl)pentyl moiety of the benzethonium cation forms a stable host–guest interaction with CB[7], by virtue of hydrophobic effect, may be applied to other hydrophobic guests of biological and medicinal interest, to increase their aqueous solubility and contribute to controlled release applications. We are presently investigating the binding of CB[7] to other guests bearing hydrophobic groups of similar molar volumes (e.g., the antimicrobial and potential antitumour agent alexidine) to evaluate the relationship between the nature of the guest binding sites and the stability and properties of the host–guest complexes. The observance of slow exchange behaviour in the ^{1}H NMR spectra of the benzethonium cation in the presence of CB[7] suggests that the kinetics of dissociation of the CB[7] from both the hydrophilic and hydrophobic ends of the cation should be investigated in view of potential controlled release applications.

At present, quaternary ammonium antimicrobial agents, such as benzethonium chloride, may be removed or have their activity neutralized by the applications of nonionic micelle-forming detergents or complexing agents, such as cyclodextrins. The CB[7] is an attractive alternative as it forms very stable host–guest complexes at lower host to benzethonium ratios than used with cyclodextrins or detergents, by virtue of stronger ion–dipole interactions between the guest (benzylammonium group) and the polar portals. In addition, CB[7] has been demonstrated to be relatively nontoxic to cells and bacteria,[15–18] which is a problem with some neutralizing detergents. The complexations of quaternary ammonium biocides by cyclodextrins have been shown to have a wide range of effects on their antimicrobial activity, from total inhibition or a reduction in activity to a significant increase in activity, depending on the nature of the cyclodextrins and the biocides, and their relative concentrations.[47] Further investigations of the effects of CB[7] and other cucurbit[*n*]urils on the antimicrobial activity of these quaternary ammonium agents, including benzethonium chloride, as well as the kinetics of the controlled release of these guests will be necessary to adjudicate their applicability as inactivating or activating hosts.

Conclusion

The benzethonium cation is capable of forming sequential 1:1 and 2:1 host–guest complexes with CB[7] in aqueous solution. The initial binding of the benzyldimethylammonium end of the guest is facilitated by ion–dipole interactions with the polar portals, as well as hydrophobic interactions of the aromatic ring in the CB[7] cavity. The second, weaker binding process involves the complexation of the other end of the host, which involves encapsulation of the hydrophobic 2-(2,4,4-trimethylpentyl) group in the host cavity. A calculation of the packing coefficient, using the inner cavity volume of CB[7] gives a value of 61%, and

accounts for the reasonable binding stability, given that the only driving force for the host–guest complexation on this end of the guest molecule is the hydrophobic effect.

Acknowledgments

The authors gratefully acknowledge the financial support of this work by the Natural Sciences and Engineering Research Council of Canada (NSERC) in the form of a Discovery Grant.

References

(1) Lagona, J.; Mukhopadhyay, P.; Chakrabarti, S.; Isaacs, L. Angew. Chem. Int. Ed. **2005**, *44* (31), 4844. doi:10.1002/anie.200460675.

(2) Kim, K.; Selvapalam, N.; Ko, Y. H.; Park, K. M.; Kim, D.; Kim, J. *Chem. Soc. Rev.* **2007**, *36* (2), 267. doi:10.1039/b603088m.

(3) Isaacs, L. *Chem. Commun. (Camb.)* **2009**, (6): 619. doi:10.1039/b814897j.

(4) Masson, E.; Ling, X.; Joseph, R.; Kyeremeh-Mensah, L.; Lu, X. *RSC Adv.* **2012**, *2* (4), 1213. doi:10.1039/c1ra00768h.

(5) Behrend, R.; Meyer, E.; Rusche, F. *Liebigs Ann. Chem.* **1905**, *339* (1), 1. doi:10.1002/jlac.19053390102.

(6) Kim, J.; Jung, I. S.; Kim, S. Y.; Lee, E.; Kang, J. K.; Sakamoto, S.; Yamaguchi, K.; Kim, K. *J. Am. Chem. Soc.* **2000**, *122* (3), 540. doi:10.1021/ja993376p.

(7) Day, A.; Arnold, A. P.; Blanch, R. J.; Snushall, B. *J. Org. Chem.* **2001**, *66* (24), 8094. doi:10.1021/jo015897c.

(8) Jeon, W. S.; Moon, K.; Park, S. H.; Chun, H.; Ko, Y. H.; Lee, J. Y.; Lee, E. S.; Samal, S.; Selvapalam, N.; Rekharsky, M. V.; Sindelar, V.; Sobransingh, D.; Inoue, Y.; Kaifer, A. E.; Kim, K. *J. Am. Chem. Soc.* **2005**, *127* (37), 12984. doi:10.1021/ja052912c.

(9) Rekharsky, M. V.; Mori, T.; Yang, C.; Ko, Y. K.; Selvapalam, N.; Kim, H.; Sobransingh, D.; Kaifer, A. E.; Liu, S.; Isaacs, L.; Chen, W.; Moghaddam, S.; Gilson, M. K.; Kim, K.; Inoue, Y. *Proc. Natl. Acad. Sci. U.S.A.* **2007**, *104* (52), 20737. doi:10.1073/pnas.0706407105.

(10) Wang, R.; Yuan, L.; Macartney, D. H. *Organometallics* **2006**, *25* (7), 1820. doi:10.1021/om051054q.

(11) Yuan, L.; Macartney, D. H. *J. Phys. Chem. B* **2007**, *111* (24), 6949. doi:10.1021/jp0701284.

(12) Moghaddam, S.; Yang, C.; Rekharsky, M.; Ko, Y. H.; Kim, K.; Inoue, Y.; Gilson, M. K. *J. Am. Chem. Soc.* **2011**, *133* (10), 3570. doi:10.1021/ja109904u.

(13) Ko, Y. H.; Hwang, I.; Lee, D.-W.; Kim, K. *Isr. J. Chem.* **2011**, *51* (5–6), 506. doi:10.1002/ijch.201100041.

(14) Lee, D.-W.; Park, K. M.; Banerjee, M.; Ha, S. H.; Lee, T.; Suh, K.; Paul, S.; Jung, H.; Kim, J.; Selvapalam, N.; Ryu, S. H.; Kim, K. *Nat. Chem.* **2011**, *3* (2), 154. doi:10.1038/nchem.928.

(15) Jeon, Y. J.; Kim, S. Y.; Ko, Y. H.; Sakamoto, S.; Yamaguchi, K.; Kim, K. *Org. Biomol. Chem.* **2005**, *3,* 2122. doi:10.1039/b504487a.

(16) Wheate, N. J.; Buck, D. P.; Day, A. I.; Collins, J. G. *Dalton Trans.* **2006**, (3): 451. doi:10.1039/b513197a.

(17) Uzunova, V. D.; Cullinane, C.; Brix, K.; Nau, W. M.; Day, A. I. *Org. Biomol. Chem.* **2010**, *8* (9), 2037. doi:10.1039/b925555a.

(18) Hettiarachchi, G.; Nguyen, D.; Wu, J.; Lucas, D.; Ma, D.; Isaacs, L.; Briken, V. *PLoS ONE* **2010**, *5* (5), e10514. doi:10.1371/journal.pone.0010514.

(19) Urbach, A. R.; Ramalingam, V. *Isr. J. Chem.* **2011**, *51* (5–6), 664. doi:10.1002/ijch.201100035.

(20) Wheate, N. J. *J. Inorg. Biochem.* **2008**, *102* (12), 2060. doi:10.1016/j.jinorgbio.2008.06.005.

(21) Plumb, J. A.; Venugopal, B.; Oun, R.; Gomez-Roman, N.; Kawazoe, Y.; Venkataramanan, N. S.; Wheate, N. J. *Metallomics* **2012**, *4,* 561. doi:10.1039/C2MT20054F.

(22) Wang, R.; MacGillivray, B. C.; Macartney, D. H. *Dalton Trans.* **2009**, (18): 3584. doi:10.1039/b904028e.

(23) Koner, A. L.; Ghosh, I.; Saleh, N.; Nau, W. M. *Can. J. Chem.* **2011**, *89* (2), 139. doi:10.1139/V10-079.

(24) Walker, S.; Oun, R.; McInnes, F. J.; Wheate, N. J. *Isr. J. Chem.* **2011**, *51* (5–6), 616. doi:10.1002/ijch.201100033.

(25) Macartney, D. H. *Isr. J. Chem.* **2011**, *51* (5–6), 600. doi:10.1002/ijch.201100040.

(26) Ghosh, L.; Nau, W. M. *Adv. Drug Deliv. Rev.* **2012**, *64* (9), 764. doi:10.1016/j.addr.2012.01.015.

(27) Wang, R.; Macartney, D. H. *Org. Biomol. Chem.* **2008**, *6* (11), 1955. doi:10.1039/b801591k.

(28) McInnes, F. J.; Anthony, N. G.; Kennedy, A. R.; Wheate, N. J. *Org. Biomol. Chem.* **2010**, *8* (4), 765. doi:10.1039/b918372h.

(29) Liu, J.; Du, X. J. *Mater. Chem.* **2010**, *20* (18), 3642. doi:10.1039/b915510d.

(30) McDonnell, G.; Russell, A. D. *Clin. Microbiol. Rev.* **1999**, *12,* 147. PMID:9880479.

(31) Yip, K. W.; Mao, X.; Au, P. Y. B.; Hedley, D. W.; Chow, S.; Dalili, S.; Mocanu, J. D.; Bastianutto, C.; Schimmer, A.; Liu, F. F. *Clin. Cancer Res.* **2006**, *12* (18), 5557. doi:10.1158/1078-0432.CCR-06-0536.

(32) Simpson, W. J. *FEMS Microbiol. Lett.* **1992**, *90* (2), 197. doi:10.1111/j.1574-6968.1992.tb05151.x.

(33) Wyman, I. W.; Macartney, D. H. *Org. Biomol. Chem.* **2010**, *8* (1), 247. doi:10.1039/b915694a.

(34) Li, Q.; Guo, D.-S.; Qian, H.; Liu, Y. *Eur. J. Org. Chem.* **2012**, *2012* (21), 3962. doi:10.1002/ejoc.201200515.

(35) Yuan, L.; Wang, R.; Macartney, D. H. *Tetrahedron Asymmetry* **2007**, *18* (4), 483. doi:10.1016/j.tetasy.2007.02.009.

(36) St-Jacques, A. D.; Wyman, I. W.; Macartney, D. H. *Chem. Commun. (Camb.)* **2008**, (40): 4936. doi:10.1039/b811823j.

(37) Florea, M.; Nau, W.M. *Angew. Chem. Int. Ed.* **2011**, *50* (40), 9338. doi:10.1002/anie.201104119.

(38) Nau, W. M.; Florea, M.; Assaf, K. I. *Isr. J. Chem.* **2011**, *51* (5–6), 559. doi:10.1002/ijch.201100044.

(39) Mecozzi, S.; and Rebek, J., Jr. *Chem. Eur. J.* **1998**, *4* (6), 1016. doi:10.1002/(SICI)1521-3765(19980615)4:6<1016::AID-CHEM1016>3.0.CO;2-B.

(40) Liu, S. M.; Ruspic, C.; Mukhopadhyay, P.; Chakrabarti, S.; Zavalij, P. Y.; Isaacs, L. *J. Am. Chem. Soc.* **2005**, *127* (45), 15959. doi:10.1021/ja055013x.

(41) Hettiarachchi, D. S. N.; Macartney, D. H. Unpublished work.

(42) Wyman, I. W.; Macartney, D. H. *Org. Biomol. Chem.* **2010**, *8* (1), 253. doi:10.1039/b917610a.

(43) Yu, J.-S.; Wu, F.-G.; Zhou, Y.; Zheng, Y.-Z.; Yu, Z.-W. *Phys. Chem. Chem. Phys.* **2012**, *14* (24), 8506. doi:10.1039/c2cp40629b.

(44) Wyman, I. W.; Macartney, D. H. *Org. Biomol. Chem.* **2008**, *6* (10), 1796. doi:10.1039/b801650j.

(45) Wang, R.; Yuan, L.; Macartney, D. H. *J. Org. Chem.* **2006**, *71* (3), 1237. doi:10.1021/jo052136r.

(46) Huibers, P. D. T.; Katritzky, A. R. *J. Chem. Inf. Comput. Sci.* **1998**, *38* (2), 283. doi:10.1021/ci9700438.

(47) Leclercq, L.; Nardello-Rataj, V.; Rauwel, G.; Aubry, J.-M. Eur. J. Pharm. Sci. **2010**, *41* (2), 265. doi:10.1016/j.ejps.2010.06.017.

Can. J. Chem. Downloaded from www.nrcresearchpress.com by MCGILL UNIVERSITY on 02/02/13
For personal use only.

Photochemical conversion of AgCl nanocubes to hybrid AgCl–Ag nanoparticles with high activity and long-term stability towards photocatalytic degradation of organic dyes

Jizhuang Wang, Changhua An, Meiyu Zhang, Chuan Qin, Xijuan Ming, and Qinhui Zhang

Can. J. Chem. Downloaded from www.nrcresearchpress.com by MCGILL UNIVERSITY on 02/02/13
For personal use only.

Abstract: The performance of a photocatalytic reaction is mainly determined by the quality of the photocatalyst. For real applications, significantly enhancing the stability and activity of the photocatalysts still remains a challenge for materials scientists and chemists. In this paper, we have achieved a highly efficient plasmonic AgCl–Ag nanophotocatalyst via photochemical conversion of AgCl nanocubes. Compared with reported photocatalysts, the as-achieved nanophotocatalyst exhibits superior activity, long-term stability, and wide applicability in the decomposition of organic dye pollutants. For example, only 30 s is needed to bleach methyl orange molecules assisted by AgCl–Ag nanoparticles. Furthermore, the catalyst can be reused up to 50 times without significant loss of activity. A possible mechanism was discussed and the specified photocatalytic reactions verified that both $O_2^{\bullet-}$ and $OH^{\bullet}$ radicals were the main active species in decomposing pollutants. The excellent performance of the present photocatalyst suggests promising applications in environmental remediation, clean energy creation, and solar cells.

Key words: pasmonic photocatalyst, silver chloride, visible light photocatalysis, organic pollutant.

Résumé : La performance d'une réaction photocatalytique est déterminée principalement par la qualité du photocatalyseur. Pour des applications réelles, l'augmentation significative de la stabilité et de l'activité du photocatalyseur reste le défi à surmonter pour les scientifiques et les chimistes. Dans ce travail, on a préparé un nanophotocatalyseur AgCl–Ag plasmonique très efficace en procédant à une conversion photochimique de nanocubes de AgCl. Par comparaison avec les photocatalyseurs rapportés antérieurement, le nanophotocatalyseur tel que préparé présente une activité supérieure, une stabilité à long terme et une large plage de domaines d'application dans la décomposition des colorants organiques polluants. Par exemple, à l'aide de nanoparticules de AgCl–Ag, il suffit de 30 s pour blanchir des molécules de méthylorange. De plus, le catalyseur peut être réutilisé jusqu'à 50 fois sans perte significative d'activité. On discute d'un mécanisme potentiel pour cette réaction et, faisant appel à des radicaux $O_2^{\bullet-}$ et $OH^{\bullet}$, il a été possible de vérifier que les réactions photocatalytiques spécifiées sont bien les espèces catalytiques principales dans la décomposition des polluants. L'excellente performance de ce photocatalyseur suggère qu'il devrait posséder des applications prometteuses dans la dépollution environnementale, la création d'énergie propre et dans les cellules solaires.

Mots-clés : photocatalyseur plasmonique, chlorure d'argent, photocatalyseur à la lumière visible, polluant organique.

[Traduit par la Rédaction]

Introduction

Since the discovery of photocatalytic splitting of water to produce hydrogen on TiO_2 electrodes,[1] photocatalysis has attracted much attention as a promising green approach for utilizing solar energy to solve energy and environmental issues. Great progress has been made in the fields of new energy generation,[2–4] conversion of carbon dioxide into valuable chemicals,[5–7] environmental purification,[8,9] solar cells,[10] and water disinfection.[11,12] Nowadays, the development of visible light driven photocatalysts has become one of the most important topics in this area. The strategies to create visible-light response photocatalysts can be classified into two categories. One is to narrow the band gap of TiO_2 by doping external elements, i.e., metals or nonmetals,[13–16] and engineering microstructures of titanate.[17] The other is to explore complex oxide visible photocatalysts, such as Ag_3PO_4,[18] $InTaO_4$,[2] $BiFeO_3$,[19,20] Bi_2WO_6,[21,22] and $PbBi_2Nb_2O_9$.[23] For real

Received 25 May 2012. Accepted 13 August 2012. Published at www.nrcresearchpress.com/cjc on 12 November 2012.

J. Wang, C. An, M. Zhang, C. Qin, and X. Ming. State Key Laboratory of Heavy Oil Processing and College of Science, China University of Petroleum, Qingdao, Shandong 266555, P.R. China.
Q. Zhang. State Key Laboratory of Heavy Oil Processing, College of Chemical Engineering, China University of Petroleum, Qingdao, Shandong 266555, P.R. China.

Corresponding author: Changhua An (e-mail: anchh@upc.edu.cn).

Can. J. Chem. Downloaded from www.nrcresearchpress.com by MCGILL UNIVERSITY on 02/02/13
For personal use only.

applications, significantly enhancing the stability and activity of the photocatalysts still remains a challenge to materials scientists and chemists.

Nanoparticles of noble metals, i.e., Au and Ag with surface plasmon resonance (SPR) effects, exhibit high absorption efficiency in the visible region, making them an ideal class of light absorber materials in the photocatalysis field.[24,25] Doping TiO_2 with Au (or Ag) has been demonstrated to greatly enhance the photoactivity of TiO_2 by reducing the recombination rate of the photogenerated charge carriers.[24,26–28] The absorption edges of TiO_2 were only extended to approximately 420 nm, leading to most of the solar spectrum being unable to drive these photocatalysts.

Silver halides decorated with Ag or Au represent a class of promising plasmonic photocatalysts because they not only exhibit high absorption coefficients in the visible region owing to the contribution of SPR, but also show enhanced photocatalytic performance.[29–31] For example, Ag@AgCl (or AgBr) photocatalysts have been prepared[29,32] through ion-exchange reactions followed by the UV conversion of some Ag^+ to Ag^0 on the surfaces of the parent crystallites. The microscale and irregular shapes of the obtained catalysts result in reduced surface areas, unclear interfaces, and thus reduced catalytic performance compared with nanoparticles. Therefore, creating photocatalysts with high activity, long-term stability, and wide applicability is of paramount importance and highly desirable.

Herein, we have developed a simple photochemical conversion of AgCl nanocubes to fabricate a class of long-term stable hybrid plasmonic AgCl–Ag nanoparticles with superior activity towards the decomposition of organic pollutants, i.e., methyl orange (MO), rhodamine B (RhB), methylene blue (MB), malachite green (MG), crystal violet (CV), alizarin red (AR), and methyl red (MR). MO molecules can be rapidly decomposed within 30 s under visible light irradiation with the assistance of the AgCl–Ag nanoparticles. The catalyst can be recycled up to 50 times without losing activity. These features mean the as-achieved nanophotocatalysts have good prospects in water disinfection and environmental remediation.

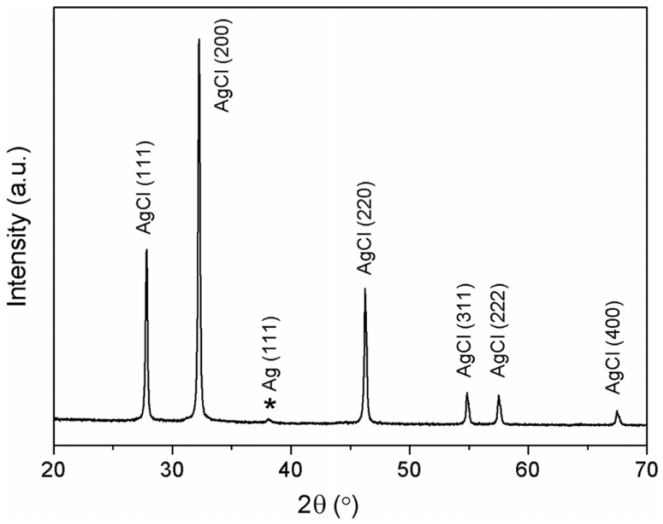
Experimental

Preparation of catalysts

AgCl nanocubes were synthesized by a simple polyol precipitation process.[30] In a typical procedure, 10 mL of ethylene glycol (EG, Sinopharm Chemical Reagent Co., Ltd) was placed in a 50 mL flask and heated at 60 °C under magnetic stirring at 350 rpm. Then poly(vinyl pyrrolidone) (PVP, 54 mg, Sinopharm Chemical Reagent Co., Ltd) and NaCl (22 mg, AR, Sinopharm Chemical Reagent Co., Ltd) were added. After they were dissolved completely, a 1 mL EG solution of $AgNO_3$ (52 mg/mL, Sinopharm Chemical Reagent Co., Ltd) was rapidly injected to this mixture. The mixture was maintained at 60 °C for 30 min, resulting in a milky dispersion containing AgCl nanoparticles. The sample was rinsed with deionized water several times and collected via centrifugation.

The as-prepared AgCl nanoparticles can be easily dispersed in 10 mL deionized water. The water dispersion of AgCl was irradiated with a 300 W Xe arc lamp equipped with an UV cutoff filter for different times, i.e., 0, 20, 40, and 60 min (corresponding samples were denoted as AgCl, AgCl–Ag-20, AgCl–Ag-40, AgCl–Ag-60, respectively). The color of the resulting dispersion changed from milky to grayish purple, indicating metallic silver nanoparticles were produced on the surfaces of AgCl. The synthesis of the referred catalyst (AgCl–Ag-ref) is described in the Supplementary data.

Fig. 1. X-ray diffraction (XRD) pattern of the as-prepared AgCl–Ag nanoparticles.



Characterization

The crystalline phases of the products were analyzed by X-ray diffraction (XRD, Philips X'Pert with Cu Kα radiation (λ = 0.154 18 nm). The morphology and size of the AgCl–Ag nanoparticles were observed by an S-4800 field emission scanning electron microscope (SEM; Hitachi, Japan). The optical absorption spectra were measured on a UV–vis spectrometer (Specord 205, Analytik Jena) over a range of 200 to 900 nm.

Evaluation of photocatalytic performance

In a typical reaction, a 10 mL water dispersion of the as-prepared AgCl–Ag nanoparticles was transferred to an aqueous solution of MO (10 mL, 10 mg L^{-1}). The mixture was stored in the dark for 60 min with magnetic stirring to reach the adsorption–desorption equilibrium of MO molecules on the surface of the nanoparticles. The reaction was then started under a 300 W Xe arc lamp (PLS-SXE300/300UV) equipped with a UV cutoff filter as the visible light source (λ ≥ 400 nm). The degradation rate of MO was measured by UV–vis spectroscopy at different times. After the reaction was completed, centrifuging the solution enables the AgCl–Ag nanoparticles to be collected to catalyze new reactions.

For the degradation of RhB, MB, MG, CV, and alAR, the conditions were kept identical to that of MO except that half the amount of the as-prepared AgCl–Ag nanoparticles was used. The decomposition of MR was performed in ethanol solution because of its insolublity in water.

Results and discussion

Characterization of the AgCl–Ag photocatalyst

Figure 1 presents an XRD pattern of the as-prepared AgCl–Ag nanoparticles. It clearly shows that the sample is composed of cubic AgCl (JCPDS card No. 31-1238) and metallic Ag (JCPDS card No. 87-0717). The diffraction peaks at 27.28°, 32.23°, 46.24°, 54.82°, 57.49°, and 67.46° can be

Can. J. Chem. Downloaded from www.nrcresearchpress.com by MCGILL UNIVERSITY on 02/02/13
For personal use only.

Fig. 2. X-ray photoelectron spectroscopy (XPS) spectra of the as-prepared AgCl–Ag. (A) survey, (B) Ag 3d, and (C) Cl 2p.

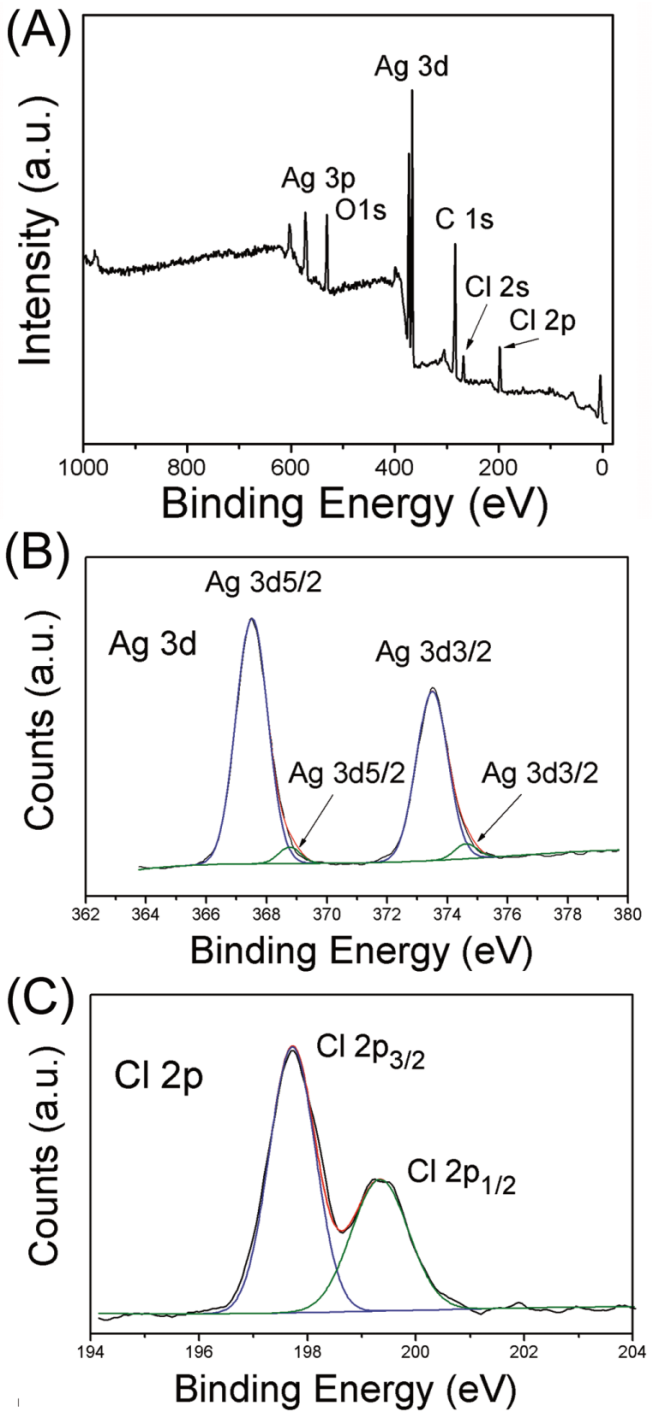
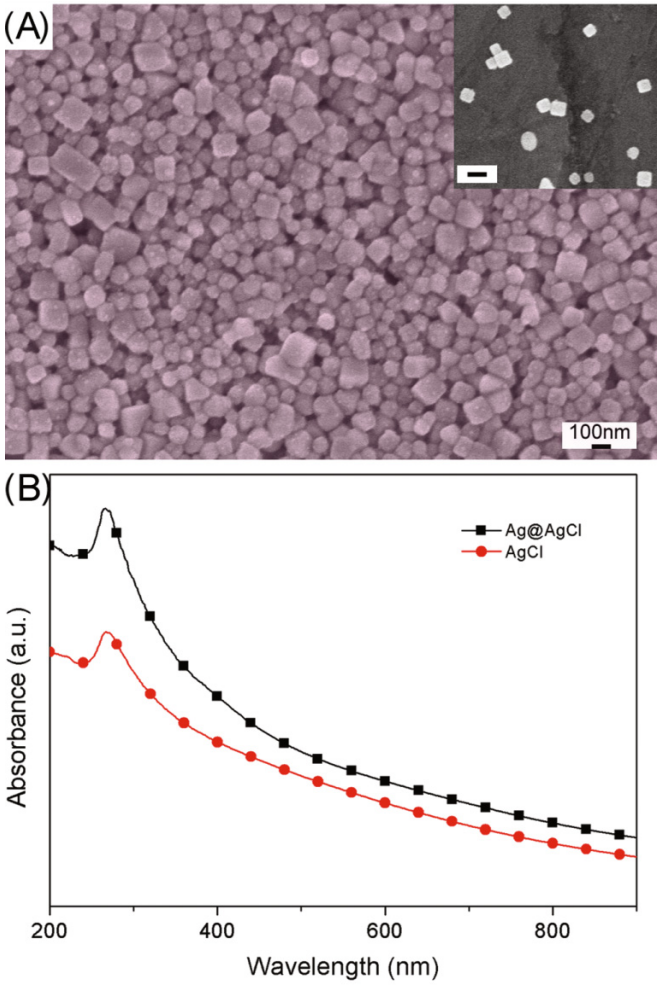


Fig. 3. (A) SEM images of AgCl–Ag. The inset at the top right corner shows the AgCl nanoparticles (scale bar is the same as for AgCl–Ag). (B) UV–vis absorbance spectra of AgCl and AgCl–Ag.



assigned to the (111), (200), (220), (311), (222), and (400) planes, respectively, of the AgCl nanoparticles. The peak at 38.07° is attributed to the diffraction of the (111) plane of metallic Ag. The elemental composition and silver content of the AgCl–Ag were further confirmed by X-ray photoelectron spectroscopy (XPS). Figure 2A reveals that Ag and Cl are the main components, and trace amounts of C and O are the adventitious hydrocarbon from the XPS instrument. As shown in Fig. 2B, the peaks at 367.5 and 373.5 eV may be assigned to the binding energy of Ag 3d 5/2 and Ag 3d 3/2 of Ag^+ in AgCl, respectively, and the peaks at 368.8 and 374.6 eV may be attributed to metallic Ag^0. The results confirmed the existence of Ag^0, and the surface ratio of metallic Ag^0 and Ag^+ is approximately 1:13. For Cl 2p, two peaks are observed at the binding energies of 197.7 and 199.3 eV.

Figure 3A shows the SEM images of as-prepared AgCl (inset) and AgCl–Ag nanoparticles. The smooth AgCl nanoparticles exhibit a cubic shape with an average edge length of 90 nm. After photochemical reduction, Ag nanoparticles are assembled on the surfaces of the parent AgCl nanocubes. The AgCl–Ag hybrid nanoparticles display convex a cubic and near-spherical shape. The UV–vis absorption spectra (Fig. 3B) of the parent AgCl and AgCl–Ag nanoparticles exhibit a similar shape, indicating that tiny Ag nanoparticles are distributed evenly on the surfaces of AgCl nanocubes. For AgCl, there is little absorption in the visible region due to its large band gaps, i.e., a direct band gap of 5.15 eV (241 nm) and an indirect band gap of 3.25 eV (382 nm).[33] The AgCl–Ag

Can. J. Chem. Downloaded from www.nrcresearchpress.com by MCGILL UNIVERSITY on 02/02/13
For personal use only.

Fig. 4. (A) The change in UV–vis spectra for the methyl orange (MO) solution with reaction time. (B) The normalized concentration of the MO as a function of reaction time in both linear (–■–) and logarithmic (–●–) scale. C_0 is the concentration of MO before irradiation; C is the concentration of MO at reaction time t.

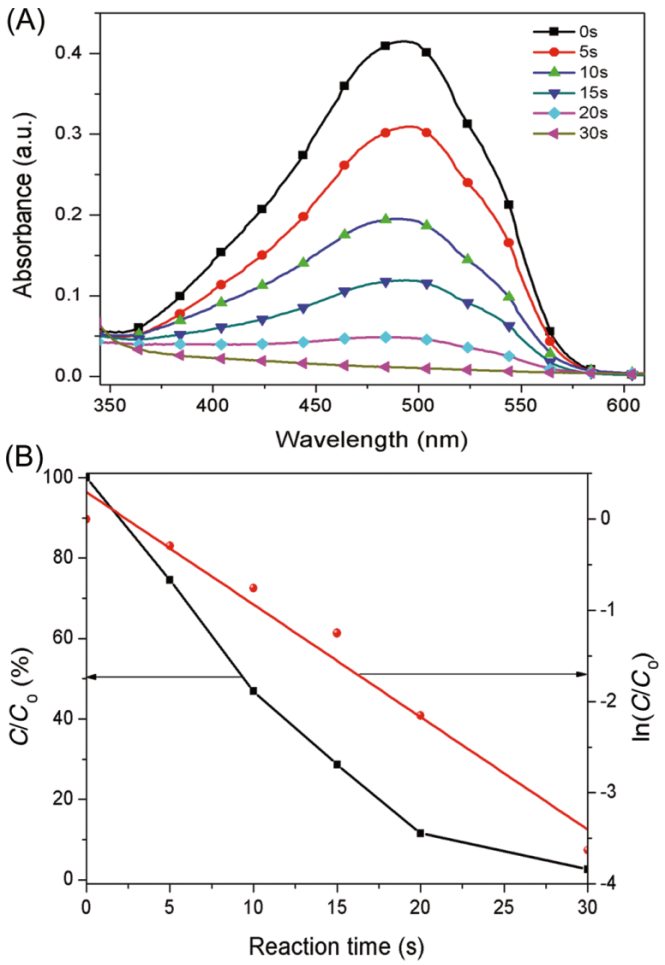


Fig. 5. Photocatalytic degradation of methyl orange (MO) for different samples under visible light irradiation, showing that AgCl–Ag-20 nanoparticles exhibits the highest performance. AgCl–Ag-20, AgCl irradiated with a 300 W Xe arc lamp for 20 min.

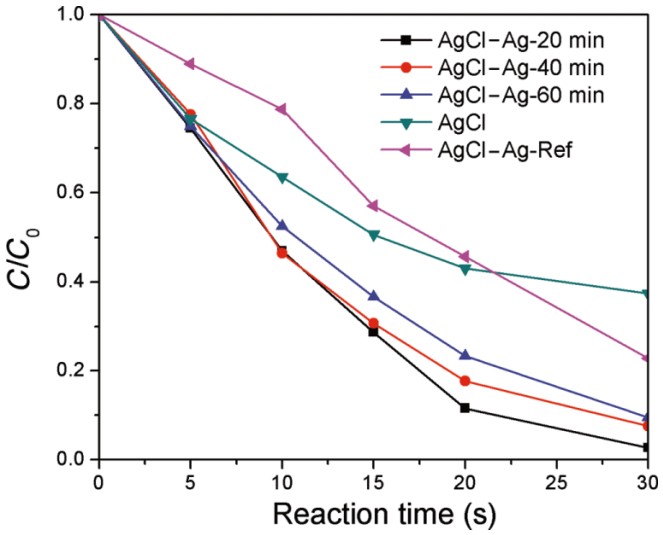
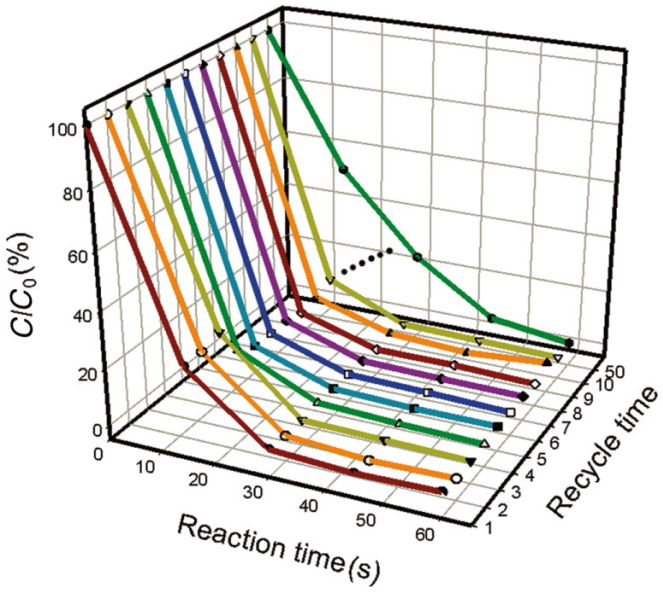


Fig. 6. The degradation curve of methyl orange (MO) solution for 50 successive reactions catalyzed with the same batch of AgCl–Ag-20 nanoparticles (as shown in Fig. 1) under visible light irradiation. AgCl–Ag-20, AgCl irradiated with a 300 W Xe arc lamp for 20 min.

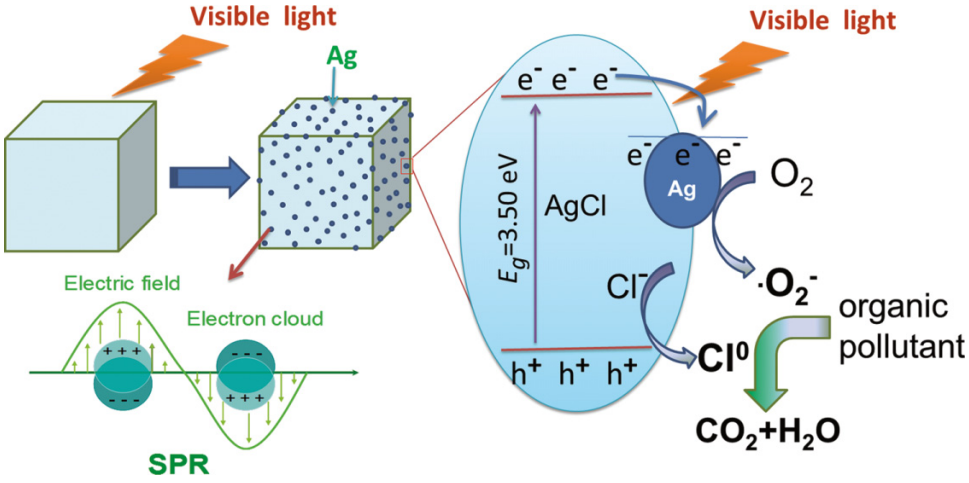


nanoparticles show a stronger absorption in the visible region than the parent AgCl owing to the SPR of the Ag species.

Photocatalytic performance of AgCl–Ag

The photocatalytic performance of the as-prepared AgCl–Ag nanoparticles was evaluated by degradation of MO (5 mg L^{-1}) molecules under visible light irradiation. Figure 5A shows the evolution of the absorption spectra of methyl orange (MO) with reaction time over the AgCl–Ag-20 nanophotocatalyst. The color of the MO solution gradually changes from orange to transparent as the reaction proceeds (Supplementary data, Fig. S1), and the MO molecules rapidly decomposed within 30 s under visible light irradiation with the assistance of the AgCl–Ag nanoparticles. The blank tests in the dark with AgCl, AgCl–Ag, and under visible light without catalyst were carried out. The color of the MO solution remained unchanged, demonstrating that the AgCl–Ag nanoparticles are crucial for the degradation of the dye. Meanwhile, the effects of Ag on the photocatalytic activity were also investigated by a series of controlled experiments. As shown in Fig. 5, AgCl–Ag-20 shows the best photocatalytic performance compared with the other samples. However, AgCl–Ag-20 also shows higher activity than pure AgCl, which only degrades 63% of MO within the same time frame. The enhanced activity of AgCl–Ag may account for the synergy between the SPRs of Ag nanograins on the surface of AgCl and the polarization field from AgCl. Furthermore, the Brunauer–Emmett–Teller (BET) nitrogen adsorption analysis reveals that the specific surface area was 33.2 m^2 g^{-1}, further suggesting that the enhanced activity is not caused merely by its surface property. While excessive Ag may increase the probability of hole capture by the negative

Fig. 7. Schematic illustration of the photocatalytic reaction pathway of AgCl–Ag nanoparticles under visible light.



charge on the Ag nanoparticles, and destroy the structure of the as-achieved catalyst, this may lead to the decreased activity of the catalysts containing a high content of Ag. The function of $\ln(C/C_0)$ versus reaction time (t; Fig. 4B) exhibits a linear relationship, indicating the reaction follows pseudo-first-order kinetics. The rate constant was determined to be 0.123 s^{-1}.

In consideration of practical applications, we also tested the stability and applicability of the present hybrid nanophotocatalyst. Figure 6 shows the recycled reactions using the same batch of catalysts. The used nanophotocatalyst can still maintain high efficiency even after 50 reactions. Note that if the dye concentration was increased to 10 mg L^{-1}, the catalyst can still be reused 35 times without much decrease in activity (Supplementary data Figs. S2 and S3). Inspired by the superior stability and activity of the photocatalysts, other typical organic pollutants, such as RhB, MB, MB, CV, AR, and MR, were also selected to trigger the degradation reactions. The results demonstrate that these dyes can also be bleached steadily (Supplementary data Fig. S4), confirming the broad applicability of the as-prepared AgCl–Ag nanophotocatalysts.

Photocatalytic mechanism

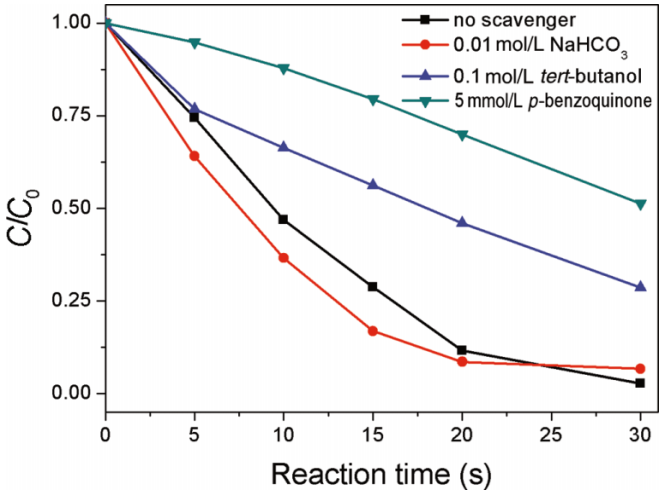
Usually, semiconductor photocatalysts, e.g., TiO_2, have wide band gaps, which make them stable against corrosion in surrounding environments.[34,35] The band gap of the as-prepared AgCl nanocubes was determined to be 3.50 eV on the basis of UV–vis absorption spectrum (Supplementary data Fig. S5), which makes it a class of alternative stable photocatalysts, although visible-light excitation is difficult. The position of the conduction band (E_{CB}) of the AgCl nanocubes can be determined by the equation $E_{CB} = X - E_C - 0.5E_g$,[36] where E_C represents the energy of the free electrons on the hydrogen scale (4.5 eV), X is the electronegativity of the semiconductor, and E_g represents the band gap of the semiconductor. Thus, the E_{CB} and the position of the valence band (E_{VB}) were calculated to be −0.341 and 3.159 eV, respectively. As presented in Fig. 7A, a possible mechanism is proposed. Here, well-defined interfaces in hybrid AgCl–Ag nanoparticles may provide proper environments for enhancement of their photocatalytic performance. Ag nanoparticles can act as a sinker for photoinduced charge carriers, promoting charge separation to enhance the overall photocatalytic efficiency in contact with the parent semiconductor.[37,38] As reported by Huang and co-workers[29] and our group,[30] the interactions between the SPR of the Ag nanoparticles and the polarization field provided by the AgCl determine the photocatalytic efficiency. In the present system, photoillumination of uniform parent AgCl nanocubes results in an even distribution of Ag nanoparticles on their surfaces, and thus leads to more even charge distributions of the free electrons in Ag nanoparticles more evenly than previously reported.[29–32] In other words, regions of negative and positive charges in the Ag nanoparticles have been separated effectively, which are far from and close to the AgCl–Ag interface, respectively. The migration of photoexcited electrons away from the AgCl–Ag interfaces also prevents photoreduction of AgCl to Ag, leading to a high stability of the hybrid nanoparticles. Therefore, there is synergy between the enhanced absorption of visible light by the SPR of the Ag nanoparticles and the polarization field provided by the AgCl facilitates electron–hole separation and interfacial charge transfer. That is to say, electron and hole were delivered into the two distinct regions (Ag and AgCl region). In the Ag/solution region, photogenerated electrons can be scavenged by O_2 in the solution to form $O_2^{\bullet-}$ and other reactive oxygen species.[38–41] To confirm the roles of oxidizing species, radical and hole trapping tests weren designed to further elucidate the photocatalytic mechanism. As shown in Fig. 8, the $NaHCO_3$ scavenger for holes (h^+) and adsorbed $OH^{\bullet}$ have no significant effects on the activity of the catalyst. However, if 0.1 mol/L of *tert*-butyl alcohol for $OH^{\bullet}$ was introduced, the MO degradation rate was decreased (i.e., after reacting for 20 s, 46% MO was left in the solution.). With the addition of $O_2^{\bullet-}$ scavenger (*p*-benzoquinone), the rate of bleaching MO was depressed significantly. These results indicate that the surface-adsorbed $O_2^{\bullet-}$ and $OH^{\bullet}$ are active species in the reaction. Due to the longer life time of active e^- compared with h^+,[39] the $O_2^{\bullet-}$ and $OH^{\bullet}$ generation can be produced by the following reactions

$$O_2 + e^- \rightarrow O_2^{\bullet-}$$

Can. J. Chem. Downloaded from www.nrcresearchpress.com by MCGILL UNIVERSITY on 02/02/13
For personal use only.

Can. J. Chem. Downloaded from www.nrcresearchpress.com by MCGILL UNIVERSITY on 02/02/13
For personal use only.

Fig. 8. Photodegradation kinetics of methyl orange (MO) in AgCl–Ag water dispersion under visible light irradiation with different scavengers.



$$O_2^{\bullet -} + h^+ \rightarrow OOH^{\bullet}$$

$$OOH^{\bullet} + H^+ + e^- \rightarrow H_2O_2$$

$$H_2O_2 + e^- \rightarrow OH^{\bullet} + OH$$

Therefore, $O_2^{\bullet -}$ and $OH^{\bullet}$ radicals come from photoexcited electrons and accumulate on the silver surfaces, which is in accord with the previous discussion. Holes (h^+) play a minor role in the present reactions. The mechanism can be understood as a plasmon-induced photocatalytic reaction. Of course, further studies are still necessary to provide insight into the unraveling of the process of charge generation, transport, and the photocatalytic reaction mechanism.

Conclusion

In summary, photochemical conversion of AgCl nanocubes has been demonstrated to be a facile strategy for the preparation of highly efficient plasmonic AgCl–Ag nanophotocatalysts with strong activity, stability, and wide applicability towards the decomposition of various organic dye pollutants. MO molecules can be decomposed completely within 30 s in the presence of the as-achieved nanophotocatalyst. Furthermore, it can be reused approximately 50 times without losing activity. The possible photocatalytic reaction mechanism indicates that Ag nanoparticles play an important role in enhancing the absorption of visible light, separating electron–hole pairs and generating oxidizing species. The excellent efficiency of the plasmonic nanophotocatalyst has promise for applications in environmental remediation, clean energy creation, and solar cells.

Supplementary data

Supplementary data are available with the article throught the journal Web site at http://nrcresearchpress.com/doi/suppl/10.1139/v2012-079.

Acknowledgement

This work was financially supported by the National Natural Science Foundation of China (Grant No. 21001116).

References

(1) Fujishima, A.; Honda, K. *Nature* **1972**, *238* (5358), 37. doi:10.1038/238037a0.
(2) Zou, Z.; Ye, J.; Sayama, K.; Arakawa, H. *Nature* **2001**, *414* (6864), 625. doi:10.1038/414625a.
(3) Maeda, K.; Xiong, A.; Yoshinaga, T.; Ikeda, T.; Sakamoto, N.; Hisatomi, T.; Takashima, M.; Lu, D.; Kanehara, M.; Setoyama, T.; Teranishi, T.; Domen, K. *Angew. Chem. Int. Ed.* **2010**, *49* (24), 4096. doi:10.1002/anie.201001259.
(4) Ingram, D. B.; Linic, S. *J. Am. Chem. Soc.* **2011**, *133* (14), 5202. doi:10.1021/ja200086g.
(5) Liu, Q.; Zhou, Y.; Kou, J.; Chen, X.; Tian, Z.; Gao, J.; Yan, S.; Zou, Z. *J. Am. Chem. Soc.* **2010**, *132* (41), 14385. doi:10.1021/ja1068596.
(6) Roy, S. C.; Varghese, O. K.; Paulose, M.; Grimes, C. A. *ACS Nano* **2010**, *4* (3), 1259. doi:10.1021/nn9015423.
(7) Yokoi, N.; Miura, Y.; Huang, C.-Y.; Takatani, N.; Inaba, H.; Koshiyama, T.; Kanamaru, S.; Arisaka, F.; Watanabe, Y.; Kitagawa, S.; Ueno, T. *Chem. Commun. (Camb.)* **2011**, *47* (7), 2074. doi:10.1039/c0cc03015e.
(8) Chen, C.; Ma, W.; Zhao, J. *Chem. Soc. Rev.* **2010**, *39* (11), 4206. doi:10.1039/b921692h.
(9) Takahashi, D.; Hirono, S.; Hayashi, C.; Igarashi, M.; Nishimura, Y.; Toshima, K. *Angew. Chem. Int. Ed.* **2010**, *49* (52), 10096. doi:10.1002/anie.201005161.
(10) Kang, T. S.; Smith, A. P.; Taylor, B. E.; Durstock, M. F. *Nano Lett.* **2009**, *9* (2), 601. doi:10.1021/nl802818d.
(11) Chorianopoulos, N. G.; Tsoukleris, D. S.; Panagou, E. Z.; Falaras, P.; Nychas, G.-J. E. *Int. J. Food Microbiol.* **2011**, *28* (1), 164. doi:10.1016/j.fm.2010.07.025.
(12) Zhang, L.; Wong, K.-H.; Yip, H.-Y.; Hu, C.; Yu, J. C.; Chan, C.-Y.; Wong, P.-K. *Environ. Sci. Technol.* **2010**, *44* (4), 1392. doi:10.1021/es903087w.
(13) Kaden, W. E.; Wu, T.; Kunkel, W. A.; Anderson, S. L. *Science* **2009**, *326* (5954), 826. doi:10.1126/science.1180297.
(14) Jaimy, K. B.; Ghosh, S.; Sankar, S.; Warrier, K. G. K. *Mater. Res. Bull.* **2011**, *46* (6), 914. doi:10.1016/j.materresbull.2011.02.030.
(15) Khan, S. U. M. *Science* **2002**, *297* (5590), 2243. doi:10.1126/science.1075035.
(16) Chen, X.; Burda, C. *J. Am. Chem. Soc.* **2008**, *130* (15), 5018. doi:10.1021/ja711023z.
(17) Chen, X.; Liu, L.; Yu, P. Y.; Mao, S. S. *Science* **2011**, *331* (6018), 746. doi:10.1126/science.1200448.
(18) Yi, Z.; Ye, J.; Kikugawa, N.; Kako, T.; Ouyang, S.; Stuart-Williams, H.; Yang, H.; Cao, J.; Luo, W.; Li, Z.; Liu, Y.; Withers, R. L. *Nat. Mater.* **2010**, *9* (7), 559. doi:10.1038/nmat2780.
(19) Luo, J.; Maggard, P. A. *Adv. Mater. (Deerfield Beach Fla.)* **2006**, *18* (4), 514. doi:10.1002/adma.200500109.
(20) Gao, F.; Chen, X. Y.; Yin, K. B.; Dong, S.; Ren, Z. F.; Yuan, F.; Yu, T.; Zou, Z. G.; Liu, J.-M. *Adv. Mater. (Deerfield Beach Fla.)* **2007**, *19* (19), 2889. doi:10.1002/adma.200602377.
(21) Zhang, L. W.; Wang, Y.-J.; Cheng, H.-Y.; Yao, W.-Q.; Zhu, Y.-F. *Adv. Mater. (Deerfield Beach Fla.)* **2009**, *21* (12), 1286. doi:10.1002/adma.200801354.

(22) Fu, H.; Pan, C.; Zhang, L.; Zhu, Y. *Mater. Res. Bull.* **2007**, *42* (4), 696. doi:10.1016/j.materresbull.2006.07.017.
(23) Kim, H. G.; Hwang, D. W.; Lee, J. S. *J. Am. Chem. Soc.* **2004**, *126* (29), 8912. doi:10.1021/ja049676a.
(24) Awazu, K.; Fujimaki, M.; Rockstuhl, C.; Tominaga, J.; Murakami, H.; Ohki, Y.; Yoshida, N.; Watanabe, T. *J. Am. Chem. Soc.* **2008**, *130* (5), 1676. doi:10.1021/ja076503n.
(25) Zhang, Q.; Ge, J.; Pham, T.; Goebl, J.; Hu, Y.; Lu, Z.; Yin, Y. *Angew. Chem. Int. Ed.* **2009**, *48* (19), 3516. doi:10.1002/anie.200900545.
(26) Tian, Y.; Tatsuma, T. *J. Am. Chem. Soc.* **2005**, *127* (20), 7632. doi:10.1021/ja042192u.
(27) Subramanian, V.; Wolf, E. E.; Kamat, P. V. *J. Am. Chem. Soc.* **2004**, *126* (15), 4943. doi:10.1021/ja0315199.
(28) Hou, W.; Liu, Z.; Pavaskar, P.; Hung, W. H.; Cronin, S. B. *J. Catal.* **2011**, *277* (2), 149. doi:10.1016/j.jcat.2010.11.001.
(29) Wang, P.; Huang, B.; Qin, X.; Zhang, X.; Dai, Y.; Wei, J.; Whangbo, M.-H. *Angew. Chem. Int. Ed.* **2008**, *47* (41), 7931. doi:10.1002/anie.200802483.
(30) An, C.; Peng, S.; Sun, Y. *Adv. Mater. (Deerfield Beach Fla.)* **2010**, *22* (23), 2570. doi:10.1002/adma.200904116.
(31) Hu, C.; Peng, T.; Hu, X.; Nie, Y.; Zhou, X.; Qu, J.; He, H. *J. Am. Chem. Soc.* **2010**, *132* (2), 857. doi:10.1021/ja907792d.
(32) Wang, P.; Huang, B.; Zhang, X.; Qin, X.; Jin, H.; Dai, Y.; Wang, Z.; Wei, J.; Zhan, J.; Wang, S.; Wang, J.; Whangbo, M.-H. *Chem. Eur. J.* **2009**, *15* (8), 1821. doi:10.1002/chem.200802327.
(33) Glaus, S.; Calzaferri, G. *Photochem. Photobiol.* **2003**, *2* (4), 398. doi:10.1039/b211678b.
(34) Albu, S. P.; Ghicov, A.; Macak, J. M.; Hahn, R.; Schmuki, P. *Nano Lett.* **2007**, *7* (5), 1286. doi:10.1021/nl070264k.
(35) Varghese, O. K.; Gong, D.; Paulose, M.; Ong, K. G.; Dickey, E. C.; Grimes, C. A. *Adv. Mater. (Deerfield Beach Fla.)* **2003**, *15* (78), 624. doi:10.1002/adma.200304586.
(36) Liu, Q.; Zhou, Y.; Kou, J.; Chen, X.; Tian, Z.; Gao, J.; Yan, S.; Zou, Z. *J. Am. Chem. Soc.* **2010**, *132* (41), 14385. doi:10.1021/ja1068596.
(37) Hirakawa, T.; Kamat, P. V. *J. Am. Chem. Soc.* **2005**, *127* (11), 3928. doi:10.1021/ja042925a.
(38) Choi, M.; Shin, K.-H.; Jang, J. *J. Colloid Interface Sci.* **2010**, *341* (1), 83. doi:10.1016/j.jcis.2009.09.037.
(39) Hoffmann, M. R.; Martin, S. T.; Choi, W.; Bahnemann, D. W. *Chem. Rev.* **1995**, *95* (1), 69. doi:10.1021/cr00033a004.
(40) Houas, A. *Appl. Catal. B* **2001**, *31* (2), 145. doi:10.1016/S0926-3373(00)00276-9.
(41) Soni, S. S.; Henderson, M. J.; Bardeau, J.-F.; Gibaud, A. *Adv. Mater. (Deerfield Beach Fla.)* **2008**, *20* (8), 1493. doi:10.1002/adma.200701066.

Can. J. Chem. Downloaded from www.nrcresearchpress.com by MCGILL UNIVERSITY on 02/02/13
For personal use only.

In silico search for an endogenous anti-Alzheimer's molecule — Screening amino acid metabolic pathways

Autumn R. Meek, Gordon A. Simms, and Donald F. Weaver

Can. J. Chem. Downloaded from www.nrcresearchpress.com by MCGILL UNIVERSITY on 02/02/13
For personal use only.

Abstract: Alzheimer's disease (AD) is a neurodegenerative disorder arising from abnormal aggregation of β-amyloid (Aβ) and progressing at different rates from person to person. There may exist endogenous compounds within the brain that play a role in inhibiting aggregation. We have devised a unique in silico screening strategy of endogenous molecules within the human brain, with special emphasis on amino acid metabolic pathways, to identify compounds with the potential to inhibit Aβ aggregation. Metabolites of tryptophan were computationally identified through this screening as potential therapeutics and were optimized via molecular modelling to determine their capacity to bind to Aβ. The most successful molecule identified was 3-hydroxyanthranilic acid (3-HAA). This endogenous molecule was then computationally explored to design novel analogues of 3-HAA with the goal of improving Aβ antiaggregant activity. These combined in silico methods of screening, identifying, and successfully "analoguing" an endogenous molecule of the brain as an AD therapeutic has yielded positive results and a novel approach to computer-aided drug design.

Key words: Alzheimer's disease, binary quantitative structure–activity relationship (QSAR), 3-hydroxyanthranilic acid (3-HAA).

Résumé : La maladie d'Alzheimer est une maladie neurodégénerative qui se pose à partir de l'agrégation anormale de la protéine β-amyloïde (Aβ) et progresse à des rythmes différent d'une personne à personne. Il peut exister des composés endogènes dans le cerveau qui peuvent jouer un rôle dans inhiber l'agrégation. Nous avons développé une stratégie de dépistage unique in silico des molécules endogènes dans le cerveau humain, avec un accent particulier sur les voies métaboliques des acides amines,d'identifier des composés ayant un potential d'inhiber l'agrégation.Les métabolites du tryptophane ont été identifiés par ce calcul de dépistage en tant qu'agents thérapeutiques potentiels et ont été optimisés par modélisation moléculaire afin déterminer leur capacité à se lier à la protéine Aβ. La molécule la plus couronnée de succès identifiés était l'acide 3-hydroxyanthranilique (3-HAA). Cette molécule endogène a ensuite été exploré de calcul pour la conception de nouveaux analogues de 3-HAA dans le but d'améliorer l'activité antiagrégant. Ces méthodes combinées de dépistage in silico, l'identification et succès en « l'analoguement » d'une molécule endogène du cerveau comme une thérapeutique d'AD a donné des résultats positive et une approche nouvelle pour la conception des médicaments assistée par ordinateur.

Mots-clés : maladie d'Alzheimer, relation quantitative structure activité (RQSA) binaire, acide 3-hydroxyanthranilique (3-HAA).

[Traduit par la Rédaction]

Introduction

Alzheimer's disease (AD) is a progressive degenerative neurological disorder in which individuals exhibit decline in cognitive awareness; currently, there is no curative or disease-modifying agent available for the treatment of AD.[1–3] Pathologically, AD is defined by the presence in the brain of two distinct misfolded protein aggregates: neurotoxic β-amyloid (Aβ) plaques and tau neurofibrillary tangles.[1] Thus, AD is thought to arise from the misfolding of Aβ, a 39–43 amino acid protein that normally occurs in a nontoxic unaggregated α-helical or random coil conformation.[4,5] The misfolding is initiated when a positively charged tetrapeptide motif within Aβ (L-histidyl-L-histidyl-L-glutamyl-L-lysine; $H_{13}HQK_{16}$ or simply HHQK) interacts with negatively charged glycosaminoglycans on the neuronal membrane surface; this begins a nucleation process whereby one misfolded Aβ triggers additional misfolding with subsequent aggregation into neurotoxic oligomers that destroy adjacent neurons.[6,7]

Although AD is a leading cause of death and disability, there are no curative drugs available for its treatment. Moreover, there is no proven molecular platform around which

Received 11 June 2012. Accepted 13 August 2012. Published at www.nrcresearchpress.com/cjc on 7 November 2012.

A.R. Meek and G.A. Simms. Department of Chemistry, Dalhousie University, 6274 Coburg Road, P.O. Box 15000, Halifax, NS B3H 4R2, Canada.
D.F. Weaver. Department of Chemistry, Dalhousie University, 6274 Coburg Road, P.O. Box 15000, Halifax, NS B3H 4R2, Canada; Department of Medicine (Neurology), Dalhousie University, 6274 Coburg Road, P.O. Box 15000, Halifax, NS B3H 4R2, Canada.

Corresponding author: Donald F. Weaver (e-mail: donald.weaver@dal.ca).

Can. J. Chem. Downloaded from www.nrcresearchpress.com by MCGILL UNIVERSITY on 02/02/13
For personal use only.

drugs can be designed for the treatment of AD. Since the clinical course of AD is highly variable from person to person, we are proposing the existence of one or more endogenous molecules in the human brain that might inhibit the pathological Aβ aggregation process (i.e., an "endogenous anti-Alzheimer molecule"; EAM). For instance, if a small molecule endogenous to the human brain were to bind to the HHQK region of Aβ, it could, in principle, prevent misfolding by maintaining the protein in its nontoxic monomeric form; furthermore, such a molecule could be the starting point in the design of future therapeutics. To this end, we are proposing the novel approach of an in silico screening of molecules endogenous to the human brain to identify species that have the potential to interact with the HHQK region of Aβ. Furthermore, we wish to use the identified EAM as a platform from which to develop novel analogues to increase antiaggregant efficacy.

Conceptual approach

The human brain contains many molecules; a full in silico screening of all the molecules in the human brain would be inefficient. Accordingly, we initially sought a conceptual approach to enable a more efficient screening of endogenous brain molecules. To achieve this, we sought to identify other neurodegenerative disorders, similar to AD, whose neurochemical bases are understood and for which therapeutics are already available.

Parkinson's disease (PD) is another protein misfolding disorder; fibrils of misfolded α-synuclein are found in the Lewy bodies that are the characteristic hallmarks of the disease.[8,9] Similar to Aβ, α-synuclein normally exists in an unfolded state, but becomes toxic when it begins fibrillization and takes on the form of oligomers and protofibrils.[10] There is evidence that dopamine and its precursor, levodopa, may act to stabilize α-synuclein protofibrils, and dopamine can also inhibit fibrillization of the protein.[9] While dopamine cannot be administered directly to patients due to its inability to penetrate the blood–brain barrier, levodopa can be administered as it is capable of being transported into the brain.[8] Levodopa is metabolized into dopamine, and this will allow for dopaminergic levels to be increased using an endogenous molecule for treatment.[8] This treatment of PD involves targeting metabolites of dopamine. Therefore, an endogenous amino acid pathway provides therapeutic opportunities for the treatment of PD.

Similar to PD, AD is also a protein misfolding disorder wherein Aβ forms β-sheets in a nucleation dependent process similar to α-synuclein.[5,10] If dopamine and its metabolites may inhibit α-synuclein fibrillization, this generates the interesting hypothesis that some other amino acid based endogenous molecule may be able to act similarly in the course of AD. Consequently, we decided to selectively screen amino acid metabolic pathways in our pursuit of an endogenous anti-Alzheimer's agent; these metabolites are assumed to be able to cross the blood–brain barrier via the large neutral amino acid transporter. This in silico approach to identifying an EAM, and then developing it as a platform for "analoguing", is an approach to drug design that is both novel and cost-effective.

Computational methods

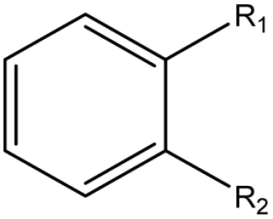
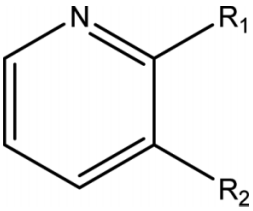
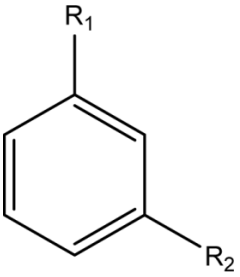
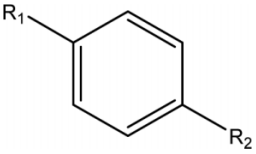
In silico methods

An endogenous library of 1451 compounds (with molecular weights less than 600) in database form was screened for potential EAMS targeting the HHQK region of Aβ; in particular, we focussed on amino acid metabolites found in the human brain. The most promising results of the in silico screen that could potentially bind to the HHQK region of Aβ were selected for gas- and solution-phase optimizations using the Chemistry at Harvard Macromolecular Mechanics (CHARMM) force field in the Molecular Operating Environment (MOE).[11,12] Optimization in MOE uses three sequential algorithms of steepest descent, conjugate gradient, and truncated Newton to find a minimum on the potential energy surface.[12] These optimizations were performed to determine the capacity of each molecule to bind to the HHQK region on different conformations of Aβ; both binding energies and number of interactions formed were considered in selecting the molecule with the most potential. The endogenous molecule that demonstrated the best capacity to bind to Aβ was selected for analoguing, with 50 analogues (Tables 1 and 2) being synthesized and tested for in vitro activity with the half maximal inhibitory concentration (IC_{50}) being calculated to perform a quantitative structure–activity relationship (QSAR) study using binary methods. The analogues were designed through the use of diverse bioisosteric substitutions, where bioisosteres are functional groups, which, although not identical, have similar physical or chemical properties that produce broadly similar biological activities for a given chemical compound.[13] In altering specific properties by these substitutions, we can evaluate the impact on biological activity, and what groups are favoured to increase activity or improve the stability of the molecule.[13,14]

For the binary QSAR, the training set was composed of 34 molecules, and the pIC_{50} (the –log of the IC_{50} value) was calculated for each compound. The molecules in the training set were selected to represent the different types of substituted compounds found in the initial 50 analogues, and covered a range of both active and inactive species (in terms of inhibiting Aβ aggregation). The binary threshold was set at –2.0 for the model, thus any compound with a pIC_{50} greater than –2.0 was considered inactive. All available descriptors in MOE were calculated initially (330+, composed of both two- and three-dimensional descriptors related to physicochemical, electronic, topologic, and geometric properties), and removed one by one to improve the predictive capacity of the model. Descriptors were removed based on their relative importance, as calculated by the software, and based on redundancy (several different descriptors described identical properties, and thus only one of each type would be necessary). The final model was composed of nine descriptors covering a variety of two- and three-dimensional properties. The descriptors used are PM3_HF (the heat of formation calculated using the PM3 Hamiltonian), SlogP_VSA5 (the log *P* (partition coefficient) in octanol–water calculated based on the accessible surface area of the molecule), SMR_VSA0, SMR_VSA1, SMR_VSA4, and SMR_VSA5 (these descriptors look at the contributions to molar refractivity based on the accessible van der Waals surface area falling within a specific range), vdw_vol (the

Can. J. Chem. Downloaded from www.nrcresearchpress.com by MCGILL UNIVERSITY on 02/02/13
For personal use only.

Table 1. First series of analogues of 3-hydroxyanthranilic acid: disubstituted molecules.

Structure	Compound ID	R_1	R_2
	GS-1002	$-NH_2$	–OH
	GS-1004	–COOH	$-NH_2$
	GS-1005	$-NH_2$	$-OCH_3$
	GS-1006	$-NH_2$	$-OCH_2CH_3$
	GS-1007	$-NH_2$	$-OC_6H_5$
	GS-1008	$-NH_2$	–Cl
	GS-1009	$-NH_2$	–Br
	GS-1010	$-NH_2$	$-CH_2CH_3$
	GS-1014	–COOH	–OH
	GS-1016	$-NO_2$	–OH
	GS-1017	$-NH_2$	$-CH_2OH$
	GS-1018	$-NH_2$	$-CH_2CH_2OH$
	GS-1019	–OH	$-CH_2NH_2$
	GS-1022	–OH	–OH
	GS-1025	$-NH_2$	$-NH_2$
	GS-1031	–OH	$-OCH_3$
	GS-1032	$-OCH_3$	$-OCH_3$
	GS-1033	–OH	$-OCH_2C_6H_5$
	GS-1034	$-OCH_2C_6H_5$	$-OCH_2C_6H_5$
	GS-1035	$-OCH_3$	$-OCH_2C_6H_5$
	GS-1036	$-NHCH_3$	$-OCH_3$
	GS-1037	$-N(CH_3)_2$	$-OCH_3$
	GS-1038	$-NHCH_2C_6H_5$	$-OCH_3$
	GS-1039	$-N(CH_2C_6H_5)_2$	$-OCH_3$
	GS-1044	–NHCHO	–OH
	GS-1045	$-NHC_6H_5$	–OH
	GS-1046	$-NHC_6H_5$	$-OCH_3$
	GS-1047	$-NHCH_3$	–OH
	GS-1048	$-N(CH_3)_2$	–OH
	GS-1049	$-NHCH_2C_6H_5$	–OH
	GS-1015	–COOH	–OH
	GS-1003	–COOH	–OH
	GS-1020	$-NH_2$	–OH
	GS-1023	–OH	–OH
	GS-1026	$-NH_2$	$-NH_2$
	GS-1040	$-NHCH_3$	$-OCH_3$
	GS-1041	$-N(CH_3)_2$	$-OCH_3$
	GS-1042	$-NHCH_2C_6H_5$	$-OCH_3$
	GS-1043	$-N(CH_2C_6H_5)_2$	$-OCH_3$
	GS-1021	$-NH_2$	–OH
	GS-1024	–OH	–OH
	GS-1027	$-NH_2$	$-NH_2$
	GS-1050	$-NHCH_3$	–OH

Can. J. Chem. Downloaded from www.nrcresearchpress.com by MCGILL UNIVERSITY on 02/02/13
For personal use only.

Table 2. First series of analogues of 3-hydroxyanthranilic acid: trisubstituted molecules.

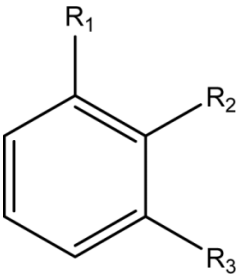
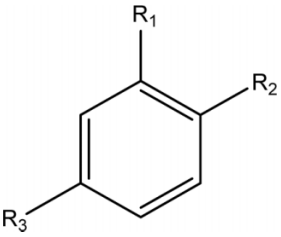
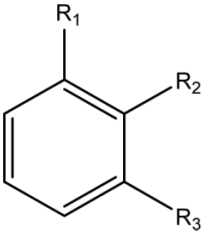
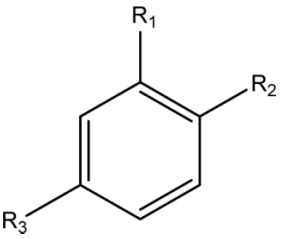
Structure	Compound ID	R_1	R_2	R_3
	GS-1001	–COOH	$–NH_2$	–OH
	GS-1011	–COOH	$–NH_2$	$–NH_2$
	GS-1028	$–CH_3$	$–NH_2$	–OH
	GS-1012	–OH	–COOH	$–NH_2$
	GS-1013	–COOH	–OH	$–NH_2$
	GS-1029	$–NH_2$	–OH	$–CH_3$
	GS-1030	–OH	$–NH_2$	$–CH_3$

Table 3. Second series of analogues of 3-hydroxyanthranilic acid: trisubstituted molecules.

Structure	Compound ID	R_1	R_2	R_3
	GS-1051	$–COOCH_3$	$–NH_2$	–OH
	GS-1052	–COOH	$–NH_2$	$–NH_2$
	GS-1053	–OH	$–NH_2$	$–NH_2$
	GS-1054	$–CH_3$	$–NHCH_2C_6H_5$	–OH
	GS-1068	–COOH	$–CH_3$	$–NH_2$
	GS-1069	–COOH	$–CH_3$	–OH
	GS-1070	–COOH	–OH	–OH
	GS-1071	–COOH	$–NH_2$	–Cl
	GS-1072	–COOH	$–NH_2$	$–NO_2$
	GS-1073	–COOH	$–NH_2$	$–CH_3$
	GS-1076	–COOH	$–NH_2$	$–NHSO_2CH_3$
	GS-1055	$–NHCH_2C_6H_5$	–OH	$–CH_3$
	GS-1056	–OH	$–NHCH_2C_6H_5$	$–CH_3$

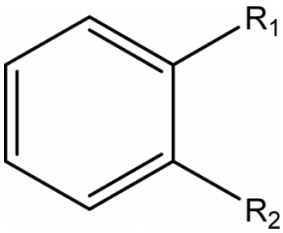
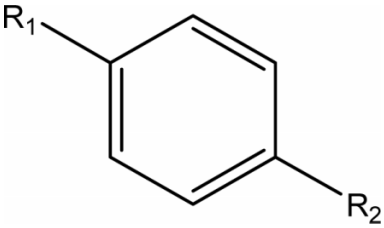
van der Waals volume of the molecule), vsa_don (the sum of the van der Waals surface area of the pure hydrogen bond donors), and vsurf_W2 (the hydrophilic volume of the molecule).[12] Upon statistical validation of the training set, the model was applied to the validation set of 16 molecules. As the model performed acceptably for the validation set, it was then applied to a series of 86 novel analogues developed from the original series of 50 molecules, again making use of bioisosteric substitution. Twenty-six of these analogues were synthesized to determine the accuracy of the model in predicting activity (Tables 3 and 4).

Statistical methods

The QSAR concept involves the assumption that the physical properties of a compound and its biological efficacy are related; therefore, related compounds will have similar properties.[15] QSARs involve quantitative models that are first used to relate and then predict a particular property for a series of compounds.[15] Various descriptors are calculated, and then statistical tools are applied to determine which of the descriptors are relevant to the desired property.[15] For the purposes of this study, the desired property is the IC_{50} of the compound in question is the inhibition of Aβ aggregation. The measured

Can. J. Chem. Downloaded from www.nrcresearchpress.com by MCGILL UNIVERSITY on 02/02/13
For personal use only.

Table 4. Second series of analogues of 3-hydroxyanthranilic acid: disubstituted molecules.

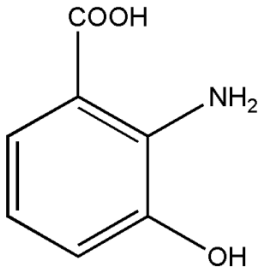
Structure	Compound ID	R_1	R_2
	GS-1057	$-NHCOOC(CH_3)_3$	–OH
	GS-1058	$-NHCOOC(CH_3)_3$	–OH
	GS-1059	$-NHCH_3$	$-NO_2$
	GS-1060	$-N(CH_3)_2$	$-NO_2$
	GS-1061	$-NHCH_3$	$-NH_2$
	GS-1062	$-N(CH_3)_2$	$-NH_2$
	GS-1063	$-NHCOOC(CH_3)_3$	$-NH_2$
	GS-1064	$-NHCOOC(CH_3)_3$	$-NHCOOC(CH_3)_3$
	GS-1065	$-NHCOCH_3$	$-NH_2$
	GS-1066	$-NHCOCH_3$	$-NHCOCH_3$
	GS-1067	$-NHCOCH_3$	$-NHCOOC(CH_3)_3$
	GS-1074	$-NHCH_2C_6H_5$	–OH
	GS-1075	$-NHC_6H_5$	–OH

IC_{50}s of the analogues used for this QSAR were all either highly active or inactive and this precluded the use of conventional QSAR methodologies; therefore, a binary QSAR was performed. Binary QSARs are nonlinear and involve the use of probability distributions to predict activity, with relative importance of descriptors being ranked by the MOE program on how well they can predict both activity and inactivity.[12,16] The goal of a binary QSAR remains the same as other methods (to use the minimum amount of descriptors to accurately predict the activity of compounds). If too many descriptors are used, there is a risk of "overfitting" the data and losing the predictive capacity of the QSAR. A binary QSAR can only provide information on whether or not a compound is active; it cannot predict relative IC_{50} values.

With a binary QSAR, the sensitivity and selectivity of the model can be evaluated. The sensitivity is the measure of the number of correctly predicted active compounds divided by the number of compounds observed to be active. Similarly, the selectivity is the measure of the number of correctly predicted inactive compounds divided by the number of observed inactive compounds. A further statistical measure can be obtained from these results; Cohen's kappa can be used to assess the accuracy of the model, and takes into account the role of chance in accurate predictions.[17] The ideal value for Cohen's kappa is close to 1 for the best model possible.[17]

Statistical evaluations of the QSAR model were performed for the training set, validation set, and novel analogues. The total accuracy as well as the sensitivity, selectivity, and Cohen's kappa were used to determine the relevance and accuracy of the model. MOE's cross validation function was also applied to the training set model. The sensitivity, specificity, and Cohen's kappa were also calculated for the validation set and the series of novel analogues.

Fig. 1. 3-Hydroxyanthranilic acid.



Synthetic and biological methods

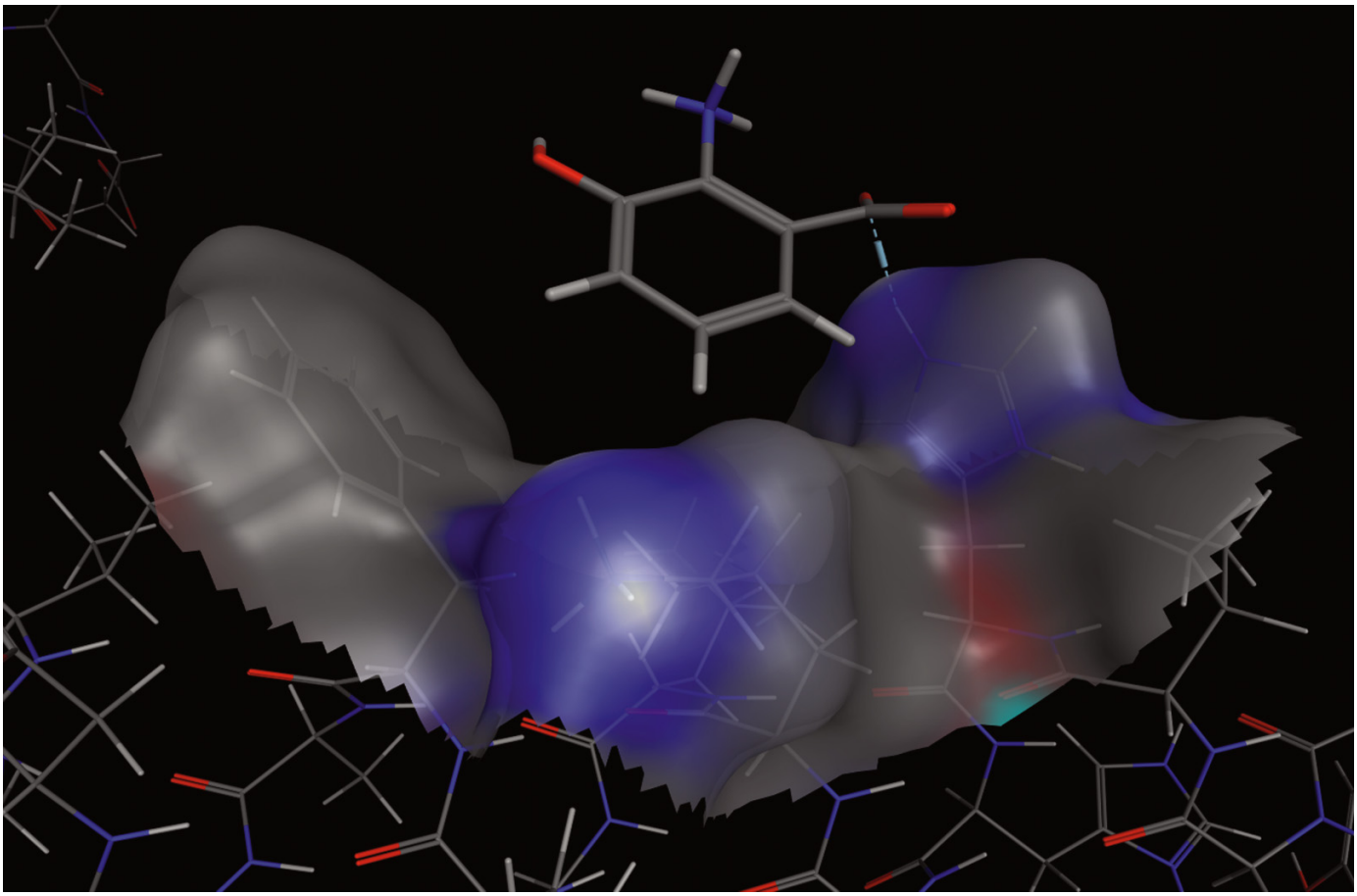
Chemical syntheses

All glassware was flame-dried and stored in an oven overnight at 120 °C; before use, glassware was purged with argon and allowed to cool to room temperature. All reactions were carried out under atmosphere or argon gas, and were monitored by thin-layer chromatography (TLC) analysis. Dried solvents were purchased from EMD (Canada) and all other chemicals were used as received from Sigma-Aldrich (Canada) and VWR (Canada). Flash chromatography was carried out on 44–63 μm silica gel (230–325 mesh). High-resolution mass spectrometry (HR-MS) was conducted on a BrukermicroTOF Focus orthogonal electrospray ionization time-of-flight mass spectrometer. The ^1H NMR spectra were recorded at 500 MHz.

Aβ aggregation inhibition assays

Aβ40 (>95%) was purchased from AnaSpec (USA) and was stored at −80 °C until used. Hexafluoroisopropanol (HFIP), 3-HAA, and materials for the tris(hydroxymethyl)aminomethane (Tris) buffers were obtained from Sigma-Aldrich

Fig. 2. Interaction between 3-hydroxyanthranilic acid (3-HAA) and the L-histidyl-L-histidyl-L-glutamyl-L-lysine (HHQK) region of β-amyloid (Aβ). The aromatic ring is interacting with Lys16, while the carboxylate group has formed a hydrogen bond with His13.



Can. J. Chem. Downloaded from www.nrcresearchpress.com by MCGILL UNIVERSITY on 02/02/13
For personal use only.

(USA) and were of the highest grade. All water used in the in vitro studies was micropore filtered and deionized. Aβ40 (1.0 mg) was pretreated in a 1.5 mL microfuge tube with 1 mL of HFIP and sonicated for 10 min to disassemble any preformed Aβ aggregates. The HFIP was removed with a stream of argon and the Aβ dissolved in Tris base (5.8 mL, 20 mmol/L, pH ~10). The pH was adjusted to 7.4 with concentrated HCl (~10 μL) and the solution filtered using a syringe filter (0.2 μm) before being used.

Thioflavin T aggregation assay

A thioflavin T (ThT) aggregation assay was used to quantify the attenuation of β-amyloid aggregation by small molecule antiaggregants. Aβ, in its monomeric form, is soluble in aqueous solution at physiological temperature and pH, and has an α-helical/random coil structure; during aggregation, soluble monomers undergo a structural transformation to a β-sheet conformation, thereby resulting in insoluble aggregates, or plaques, high in β-sheet content. ThT, a benzothiazole dye, has a high affinity for protein with high β-sheet content, and as such may be used to visualize Aβ aggregates. Unbound ThT has fluorescence excitation (λ_{ex}) and emission (λ_{em}) wavelengths at 430 and 342 nm, respectively; upon binding to amyloid fibrils, ThT undergoes a characteristic spectral shift (λ_{ex} = 442 nm, λ_{em} = 482 nm), which can be used to differentiate bound and unbound ThT.

Pretreated Aβ40 (40 μmol/L in 20 mmol/L Tris, pH 7.4) was diluted with an equal volume of 8 μmol/L ThT in Tris (20 mmol/L, pH 7.4, 300 mmol/L NaCl). Aliquots of Aβ/ThT (200 μL) were added to wells of a black polystyrene 96 well plate, followed by 2 μL of a compound in dimethyl sulfoxide (DMSO) (of variable concentration) or DMSO alone (controls). Incubations were performed in triplicate and contained 20 μmol/L Aβ and various concentrations of the compound in 20 mmol/L Tris, pH 7.4, 150 mmol/L NaCl, and 1% DMSO. Plates were covered with clear polystyrene lids and incubated at 37 °C in a Tecan GENios microplate reader. Fluorescence readings (λ_{ex} = 450 nm, λ_{em} = 480 nm) were taken every 15 min, after the sample was shaken at high intensity for 15 s and then allowed to settle for 10 s before each reading. Active compounds attenuated the increase in fluorescence over time that occurred in the controls.

Results and discussion

Identifying an EAM

The in silico screen of endogenous small molecules of the brain led to the successful identification of several small molecules of the tryptophan metabolic pathway as potential therapeutics capable of targeting the HHQK region of Aβ. These molecules all contained features that would allow for interactions with the positively charged amino acids in the

Can. J. Chem. Downloaded from www.nrcresearchpress.com by MCGILL UNIVERSITY on 02/02/13
For personal use only.

HHQK region of Aβ: either through cation–π, ion–ion, ion–dipole, or even π–π stacking interactions (in the case of the histidine residues). In silico simulations were performed in both gas- and solution-phase environments for D- and L-tryptophan, tryptamine, and 3-hydroxyanthranilic acid (3-HAA) to determine their suitability for binding to Aβ to prevent aggregation. Of these species, 3-HAA (see Fig. 1) demonstrated favourable results for binding to the HHQK region of Aβ: This was further supported by in vitro data. Figure 2 shows one such successful binding interaction between 3-HAA and Aβ. The success of 3-HAA inhibiting Aβ aggregation in vitro relative to a compound with known activity (NCE-0217, proprietary to the Weaver group) and a compound with known inactivity (β-alanine) is demonstrated in Fig. 3.

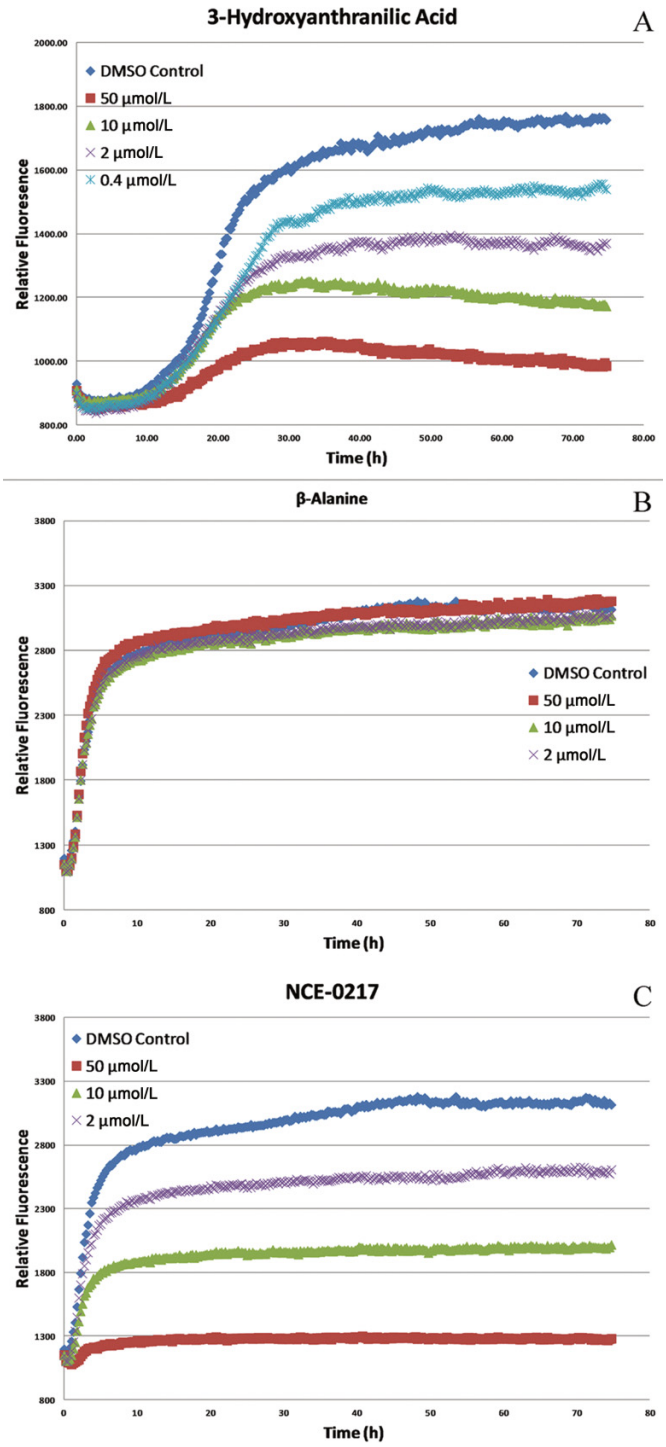
Given the success of 3-HAA in binding to Aβ in silico, its endogenous nature, and its small size, 3-HAA presented itself as an ideal platform from which to develop novel analogues.

Expanding 3-HAA as an endogenous molecular platform

Given the successful identification of 3-HAA as an EAM, it was selected as a platform for the development of novel analogues in an attempt to improve its antiaggregant activity. Thus, 50 analogues were then prepared and tested for their IC_{50} values in inhibiting Aβ aggregation. The measured IC_{50} values were used to perform a binary QSAR study to allow for the prediction of new analogues with improved activities. Furthermore, binary QSAR methods were used for a very small data set in an approach usually reserved for high throughput screening data.

The results of the predictions of the QSAR model for the training and validation sets are given in Table 5. The final model of nine descriptors demonstrated statistical results for the training set. The total accuracy of the model when applied to the training set was 0.97, with a sensitivity of 0.92 and a selectivity of 1.00. Cross-validation of the model resulted in a total accuracy of 0.91, with 0.83 for the sensitivity and 0.95 for the specificity; these numbers indicate that the current model for the training set is valid. The Cohen's kappa value for the model is 0.93. Given the positive predictions from the model applied to the training set, it was then applied to the validation set, which was slightly less successful. For the validation set, one compound was incorrectly predicted inactive and four compounds were incorrectly predicted active, with one of them being on the borderline. Given that the model assigns values to the compounds on a scale of 0 to 1, with 0 being inactive, and 1 being active, 0.5 was selected as the point from which activity was determined: if the value was >0.5 it was active, and if the value was <0.5 it was inactive. Of the compounds incorrectly predicted active, the QSAR model assigned a value of 0.5012 to one of them, thus it is difficult to truly assign activity to this compound. Using the original activity assignments, the Cohen's kappa for the validation set was calculated as 0.23, with a sensitivity of 0.67 and a specificity of 0.77; however, if the borderline compound was assumed to be predicted inactive, Cohen's kappa jumped to 0.35. The value of Cohen's kappa is fair, but not nearly as good as that calculated for the training set. Despite somewhat of a loss in predictivity when applied to the training set, the model was used to determine the activities of 86 additional novel analogues as a better model was unlikely to be developed with the limited data available. Of the 86 new compounds, 39 were predicted to be active. To determine the efficacy of the QSAR prediction, a selection of 26 of the 86

Fig. 3. The thioflavin T (ThT) binding assays of (A) 3-hydroxyanthranilic acid (3-HAA), (B) β-alanine, and (C) NCE-0217 as measured at varying concentrations over a three-day period. Lower curves indicate more significant inhibition of β-amyloid (Aβ) aggregation.



Can. J. Chem. Downloaded from www.nrcresearchpress.com by MCGILL UNIVERSITY on 02/02/13
For personal use only.

Table 5. Results of the binary quantitative structure–activity relationship (QSAR) model applied to the training and validation data sets.

Training set			Validation set		
Compound ID	IC_{50} (μmol/L)	Predicted activity[a]	Compound ID	IC_{50} (μmol/L)	Predicted activity[a]
GS-1001	5.05	Active	GS-1007	297.95	Inactive
GS-1002	4.545	Active	GS-1008	300	Inactive
GS-1003	300	Inactive	GS-1013	9.999	Active
GS-1004	300	Inactive	GS-1016	300	**Active**
GS-1005	300	Inactive	GS-1017	300	Inactive
GS-1006	300	Inactive	GS-1019	300	**Active**
GS-1009	300	Inactive	GS-1021	2.323	Active
GS-1010	300	Inactive	GS-1023	300	**Active**
GS-1011	300	Inactive	GS-1032	300	Inactive
GS-1012	300	Inactive	GS-1034	300	Inactive
GS-1014	300	Inactive	GS-1037	300	Inactive
GS-1015	300	Inactive	GS-1038	300	Inactive
GS-1018	300	Inactive	GS-1040	300	Inactive
GS-1020	300	Inactive	GS-1042	300	**Active**
GS-1022	8.2315	Active	GS-1046	300	Inactive
GS-1024	12.8775	Active	GS-1048	8.888	**Inactive**
GS-1025	300	Inactive			
GS-1026	300	Inactive			
GS-1027	1.818	**Inactive**			
GS-1028	2.424	Active			
GS-1029	21.816	Active			
GS-1030	14.3925	Active			
GS-1031	300	Inactive			
GS-1033	300	Inactive			
GS-1035	300	Inactive			
GS-1036	300	Inactive			
GS-1039	300	Inactive			
GS-1041	300	Inactive			
GS-1043	300	Inactive			
GS-1044	262.6	Inactive			
GS-1045	2.727	Active			
GS-1047	6.9185	Active			
GS-1049	1.616	Active			
GS-1050	2.02	Active			

[a]Errors in prediction are indicated in bold font.

analogues were synthesized and tested for their ability to inhibit Aβ aggregation. A mixture of active and inactive compounds were selected for the synthesis, and the results indicate that the QSAR model performed better than indicated by the validation set, but not quite as good as it performed for the training set. Of the 26 compounds, 21 had activities correctly predicted by the QSAR model (see Table 6). The sensitivity and selectivity were therefore measured as 0.75 and 0.83, respectively, with a Cohen's kappa value of 0.56. The majority of the compounds that were not correctly predicted were those with functional groups not implicated in the original 50 3-HAA analogues, which may explain the model's difficulty in predicting the activity. Overall, the binary QSAR performed quite well for predicting the activity of novel 3-HAA analogues.

Table 6. Results of the quantitative structure–activity relationship (QSAR) model applied to 26 novel 3-hydroxyanthranilic acid (3-HAA) analogues.

Compound ID	Predicted activity[a]	Biological activity
GS-1051	**Inactive**	Active
GS-1052	Inactive	Inactive
GS-1053	Active	Active
GS-1054	Active	Active
GS-1055	Active	Active
GS-1056	Active	Active
GS-1057	Active	Active
GS-1058	Active	Active
GS-1059	Active	Active
GS-1060	Active	Active
GS-1061	Active	Active
GS-1062	Active	Active
GS-1063	Active	Active
GS-1064	**Active**	Inactive
GS-1065	**Inactive**	Active
GS-1066	**Active**	Inactive
GS-1067	**Active**	Inactive
GS-1068	Inactive	Inactive
GS-1069	Inactive	Inactive
GS-1070	Inactive	Inactive
GS-1071	Inactive	Inactive
GS-1072	Active	Active
GS-1073	Inactive	Inactive
GS-1074	Active	Active
GS-1075	Active	Active
GS-1076	Active	Active

[a]Errors in prediction are indicated in bold font.

Conclusions

The in silico screen of endogenous molecules of the human brain has led to the successful identification of metabolites of tryptophan as potential therapeutics for treating Alzheimer's disease. 3-HAA was the most successful in in silico simulations for binding to the HHQK region of Aβ, and thus was successfully analogued to improve binding efficacy. Furthermore, binary QSARs can be used to effectively predict compound activities for small data sets when there is a lack of range of biological activity. Despite the fact that a binary QSAR can only predict whether a compound will be active or inactive, it has still proved to be a useful tool in the development of novel analogues based on 3-HAA. The results of the QSAR also indicate that using an endogenous molecule like 3-HAA as a starting point has proved to be a viable option in the development of Aβ antiaggregants. The binary QSAR model proved itself both useful and accurate in identifying the activity of novel analogues, allowing for a more streamlined and cost-effective approach to molecular synthesis: synthesis can be focussed on molecules deemed active, and materials and time are not wasted pursuing unviable compounds. Once an adequate number of the newest series of novel analogues have been synthesized and tested for Aβ aggregation inhibition, a new QSAR model will be applied that will incorporate the newest data to improve predictivity and further aid in the

identification of molecules with antiaggregation properties that may help in treating AD in a more effective manner. In silico methods can be successfully used in an effective manner in both the identification of an EAM as a potential therapeutic and its development as a platform from which to develop novel analogues with improved activity. This methodology has not been pursued previously and represents a new, cost-effective, and convenient approach to drug design.

Acknowledgements

Funding for research was provided by the Nova Scotia Health Research Foundation, the Gunn Family Studentship in Alzheimer's Research (studentship to AM), the Alzheimer's Society of Canada, and the Canadian Institutes of Health Research (operating grant to DFW and studentship to GS).

References

(1) Parihar, M.; Hemnani, T. *J. Clin. Neurosci.* **2004**, *11* (5), 456. doi:10.1016/j.jocn.2003.12.007.

(2) Grossberg, G. T. *J. Clin. Psychiatry* **2003**, *64* (suppl 9), 3.

(3) Brookmeyer, R.; Johnson, E.; Ziegler-Graham, K.; Arrighi, H. M. Alzheimers Dement. **2007**, *3* (3), 186. doi:10.1016/j.jalz.2007.04.381.

(4) Lahiri, D. K.; Greig, N. H. *Neurobiol. Aging* **2004**, *25* (5), 581. doi:10.1016/j.neurobiolaging.2004.02.002.

(5) Walsh, D. M.; Selkoe, D. J. *J. Neurochem.* **2007**, *101* (5), 1172. doi:10.1111/j.1471-4159.2006.04426.x.

(6) Giulian, D.; Haverkamp, L. J.; Yu, J.; Karshin, W.; Tom, D.; Li, J.; Kazanskaia, A.; Kirkpatrick, J.; Roher, A. E. *J. Biol. Chem.* **1998**, *273,* 29719. doi:10.1074/jbc.273.45.29719.

(7) Yoda, M.; Miura, T.; Takeuchi, H. *Biochem. Biophys. Res. Commun.* **2008**, *376* (1), 56. doi:10.1016/j.bbrc.2008.08.093.

(8) Kadieva, M. G.; Oganesyan, E. T.; Mutsueva, S. Kh. *Pharm. Chem. J.* **2005**, *39,* 453. doi:10.1007/s11094-006-0001-2.

(9) Agorogiannis, E. I.; Agorogiannis, G. I.; Papadimitriou, A.; Hadjigeorgiou, G. M. *Neuropathol. Appl. Neurobiol.* **2004**, *30* (3), 215. doi:10.1111/j.1365-2990.2004.00558.x.

(10) Lotharius, J.; Brundin, P. *Nat. Rev. Neurosci.* **2002**, *3* (12), 932. doi:10.1038/nrn983.

(11) Brooks, B. R.; Bruccoleri, R. E.; Olafson, B. D.; Sates, D. J.; Swaminathan, S.; Karplus, M. *J. Comput. Chem.* **1983**, *4* (2), 187. doi:10.1002/jcc.540040211.

(12) *Molecular Operating Environment,* version 2010.10; Chemical Computing Group Inc.: Montreal, QC, 2010.

(13) Patani, G. A.; LaVoie, E. J. *Chem. Rev.* **1996**, *96* (8), 3147. doi:10.1021/cr950066q.

(14) Lima, L. M.; Barreiro, E. J. *Curr. Med. Chem.* **2005**, *12,* 23.

(15) Carbó-Dorca, R.; Robert, D.; Amat, L.; Gironés, X.; Besalú, E. *Molecular Quantum Similarity in QSAR and Drug Design;* Springer-Verlag: Berlin, 2000.

(16) Labute, P. Binary QSAR: A New Method for the Determination of Quantitative Structure–Acitivty Relationships. In *Proceedings of the 4th Pacific Symposium on Biocomputing (PSB'99),* The Orchid and Mauna Lani, Big Island of Hawaii, 4–9 January 1999, p 444.

(17) Cohen, J. *Educ. Psychol. Meas.* **1960**, *20* (1), 37. doi:10.1177/001316446002000104.

Can. J. Chem. Downloaded from www.nrcresearchpress.com by MCGILL UNIVERSITY on 02/02/13
For personal use only.

Application of the high-speed self-reversal background corrector to the determination of cadmium by chemical vapor generation atomic absorption spectrometry

Christophe Waterlot, Aurélie Pelfrêne, and Francis Douay

Can. J. Chem. Downloaded from www.nrcresearchpress.com by MCGILL UNIVERSITY on 02/02/13
For personal use only.

Abstract: Concentrations of cadmium (Cd) in extracting solutions (neutral salts) from contaminated soils are often too low to be determined by conventional flame atomic absorption spectrometry. For this reason, determination of Cd requires sensitive analytical methods free from interference problems generated by samples. In this context, vapor generation atomic absorption spectrometry (HGAAS) was combined with a high-speed self-reversal background corrector. This new approach was successfully applied after optimization of the analytical parameters to obtain a maximal absorbance signal of the volatile Cd species. The optimum condition was achieved with a 3% (*m*/*v*) $NaBH_4$ in 1.5% (*m*/*v*) NaOH reducing solution and a solution containing 0.3 mol/L HNO_3. The detection limit was 1 ng mL^{-1} under the previous conditions and the relative standard deviation was up to 5% for 10 replicate analyses of Cd at 0.2 and 1 ng mL^{-1}, reflecting a very highly sensitive and reproducible method. Moreover, the results showed that the proposed combination was an efficient method to overcome the interference problems caused by different coexisting cations, As, Al, Ca, Cu, Fe, Mg, Mn, Ni, Pb, Se and Zn, up to 10 μg mL^{-1}. The method was validated with analyses of two standard reference materials and was used for Cd determination in 0.01 mol/L $CaCl_2$ extracts from contaminated kitchen garden soils. The data were compared with those obtained by two other more conventional methods, electrothermal atomic absorption spectrometry (ETAAS) and flame atomic absorption spectrometry (FAAS). The analytical results obtained by the ETAAS and HGAAS were in a good agreement, suggesting the suitability of the method for Cd determination in 0.01 mol/L $CaCl_2$ extracting solution.

Key words: cadmium, absorption atomic spectrometry, vapor generation, high-speed self-reversal method, interference.

Résumé : Les concentrations en cadmium (Cd) dans les solutions d'extraction (sels neutres) de sols contaminés sont souvent trop faibles pour pouvoir être déterminées par spectrométrie d'absorption atomique en utilisant une simple flamme pour atomiser les éléments. La quantification de Cd à l'état de traces requière donc des méthodes d'analyses sensibles mais aussi exemptes d'interférences. Dans ce contexte, le dosage de Cd a été réalisé au moyen d'un spectromètre d'absorption atomique couplé à un générateur d'hydrure en mode continu et combiné à une méthode de correction du bruit de fond par renversement de spectre. Les conditions optimales d'utilisation de la technique ont été déterminées de manière à obtenir une sensibilité maximale. Pour des concentrations de 2,5 et 5 ng mL^{-1}, les absorbances maximales de Cd ont été obtenues en préparant une solution de $NaBH_4$ à 3 % dans une solution de soude à 1,5 % et en analysant des solutions dont la concentration en HNO_3 a été de 0,3 mol/L. Dans ces conditions, la limite de détection a été de 1 ng mL^{-1} et un coefficient de variation de 5 % a été trouvé en analysant à 10 reprises des solutions de Cd à 0,2 et 1 ng mL^{-1}, montrant ainsi une bonne sensibilité et reproductibilité de la méthode. De plus, la méthode analytique proposée s'est avérée être une méthode efficace permettant de minimiser les interférences causées par les cations As, Al, Ca, Fe, Mn, Ni, Pb, Se et Zn jusqu'à 10 μg mL^{-1}. La méthode a été validée par la détermination des concentrations en Cd dans les solutions d'extraction au $CaCl_2$ 0,01 mol/L de sols certifiés et de sols contaminés. Les données acquises avec la méthode proposées ont été comparées à celles obtenues en utilisant des méthodes d'analyses plus conventionnelles, spectrométrie absorption atomique avec atomisation électrothermique et flamme. L'ensemble des résultats obtenus a montré que la méthode proposée était sensible, reproductible et permettait de s'affranchir de certaines interférences.

Mots-clés : cadmium, spectrométrie d'absorption atomique, générateur d'hydrure, méthode par renversement de spectre, interférence.

Received 7 March 2012. Accepted 27 August 2012. Published at www.nrcresearchpress.com/cjc on 7 November 2012.

C. Waterlot, A. Pelfrêne, and F. Douay. Université Lille Nord de France, 1bis rue Georges Lefèvre, 59044 Lille CEDEX, France; Groupe ISA, Equipe Sols et Environnement, Laboratoire Génie Civil et géo-Environnement (LGCgE) Lille Nord de France (EA 4515), 48 boulevard Vauban, 59046 Lille CEDEX, France.

Corresponding author: Christophe Waterlot (e-mail: christophe.waterlot@isa-lille.fr).

Can. J. Chem. Downloaded from www.nrcresearchpress.com by MCGILL UNIVERSITY on 02/02/13
For personal use only.

Introduction

The human health risk of cadmium (Cd) exposure comes mainly through the environment from industry, mining, and motor vehicles. One of the particularities of this element is that it stays in the body for a long time when taken up by food, animals, and humans, even at low concentrations. Therefore, Cd is one of the most hazardous elements for human health and is of interest as a toxic pollutant even at trace levels.[1–7] For this reason, the determination of Cd at trace levels in environmental samples has been the subject of a number of recent publications.[8–12]

Interferences and matrix effects are often problematic, especially when Cd is determined using electrothermal absorption atomic spectrometry (ETAAS).[10,13–15] Consequently, new methods have been developed to minimize these interferences[10,14,16–18] and today, some of them, such as the use of a flow injection system with an on-line separation and preconcentration system combined with flame atomic absorption spectrometry (FAAS), are less prone to these interference problems.[17–19]

Less current methods that offer many advantages (speciation potentialities and no sample pretreatment before analysis) compared with ETAAS[20] consist of measuring Cd by AAS using the chemical vapor generation (CVG) technique. Cold vapor generation (CV)[21–24] and hydride generation (HG)[25–29] are the two methods used in the determination of Cd by CVGAAS. The fact that these techniques are able to form volatile hydrides offers several important advantages such as separation of the analyte from the matrix resulting in reducing matrix related interferences in comparison with ETAAS. However, the CVG technique is not totally free from interference. Indeed, strong interferences in Cd determination (such as Cu) were reported by Tsalev.[20] Even if compounds such as thiourea and L-cysteine are used to improve the tolerance of interferences, the suppression effects of the Cd signal in the presence of As, Cu, Fe, Pb, Mn, Ni, Se, Sn, and Zn concentrations in the range 0.1–10 μg mL^{-1} were highlighted.[22] Bujdoš et al.[27] observed a substantial decrease in the integrated absorbance signals in the presence of As, Cu, Fe, Ni, Sb and Pb for concentration levels ranging from 0.1 to 2 μg mL^{-1}. We therefore attempted to combine hydride generation - flame atomic absorption spectrometry (HGAAS), fitted with a 3-channel peristaltic pump, with the high-speed self-reversal (HSSR) background corrector to study the effect of potential interferents (PI) from common cations in soil solutions and other hydride-forming elements on the formation of CdH_2 and the determination of Cd. Based on the first approach of the Smith and Hieftje method,[30] this background correction system was described as an universal technique, properly working in flame and graphite furnace atomization over the entire wavelength range from 190 to 900 nm and is based on the broadening, which occurs in the resonance lines when a hollow cathode lamp is operated in a pulsed mode with a high frequency (100 Hz) at high current, up to a maximum of 600 mA.[31,32]

In the current study, the Cd lamp was operated with two different discharges, a low current value (10 mA) and then, a high current value (300 mA) to increase the emission intensity and was pulsed with a frequency of 100 Hz (HSSR-BGC). Because the high current mode measures only the background absorption, the difference between the absorption of both types of light provides accurate background compensation and measurement of the atomic absorption of the studied element.

Analytical characteristics of the proposed method (HGAAS-HSSR) were studied after the determination of the best experimental conditions and were compared with those obtained by flame atomic absorption spectrometry (FAAS) and ETAAS. This method was then applied to determine Cd in 0.01 mol/L $CaCl_2$ extracts from two reference materials (CRM BCR-483 and SRM 2710a) and contaminated kitchen garden soil samples.

Materials and methods

Instrumentation

An atomic absorption spectrometer (AA-6800, Shimadzu, Tokyo, Japan) with an ASC-6100 autosampler (Shimadzu, Tokyo, Japan) was fitted with an HVG-1 hydride vapor generator (Shimadzu, Tokyo, Japan). This continuous reagent flow system was combined with a continuous sample flow to obtain a constant output signal as soon as equilibrium was reached. A flame-in-tube quartz T-tube (170 mm length and 5 mm inner diameter) was placed in the optical axis directly over a conventional air/acetylene flame burner head equipped with T-cell tube holder and was heated. The instrumental conditions used for the determination of Cd by HGAAS in continuous flow mode were the following: pre-spray time, 60 s; integration time, 5 s; post-reaction purge time, 25 s; burner height, 14 mm; and carrier gas, argon (70 mL min^{-1} flow rate), used for stripping the solution for efficient separation of volatile species from the liquid phase. The background correction was conducted using a pulsed Cd hollow cathode lamp (Hamamatsu, Iwata, Japan) with a frequency of 100 Hz and lamp currents ranging from 8 to 100 mA and a bandwidth of 1.0 nm.

The same optical parameters were used for Cd determination by traditional FAAS. In contrast, slight modifications about the instrumental conditions were made for optimization: pre-spray time, 5 s; integration time, 3 s; post-reaction purge time, 10 s; and burner height, 7 mm.

For electrothermal atomization, the high-sensitivity GFA-EX7 (Shimadzu, Tokyo, Japan) and high-density graphite tube were used in combination with the ASC-6100 autosampler and the ASK-6100 autodiluter (Shimadzu, Tokyo, Japan). Cadmium was determined in soil extracts at 228.802 nm using a pulsed Cd hollow cathode lamp (Hamamatsu) operated in the range 8−100 mA with a bandwidth of 1.0 nm in combination with the HSSR corrector. A mixture of palladium (30 mg) and magnesium nitrate (20 mg) in 5 mL of 1.4 mol/L nitric acid was used as a chemical modifier to minimize the chloride interferences[13] produced by the extracting solutions (e.g., acid digestion and calcium chloride). The temperature program used throughout this paper is presented in Table 1.

All solutions were prepared from analytical grade reagents unless specified otherwise.

Soil sampling and pretreatment

Seven kitchen garden soils (KG1–KG7) were sampled with a hand auger up to a depth of 25 cm in a contaminated area located in the North of France. A composite sample of the ploughed layer of the soils was made starting from 5 to 10 subsamples taken randomly from the garden area. The topsoil samples were first oven-dried at 40 °C and gently crushed to pass through a 2 mm sieve and then sieved with an ultra-

Can. J. Chem. Downloaded from www.nrcresearchpress.com by MCGILL UNIVERSITY on 02/02/13
For personal use only.

Table 1. Instrumental parameters for electrothermal absorption atomic spectrometry (ETAAS) determination.

Furnace program step	Temp. (°C)	Hold time (s)	Ramp rate (°C s^{-1})	Argon gas flow rate (L min^{-1})
Dry-1	150	5	24	1
Dry-2	150	5	26	1
Pyrolysis-1	800	5	10	1
Pyrolysis-2	800	3[a]	0	0
Atomization	2200	6[a]	3400	0
Cleaning	2400	3	3400	1

[a]The high-sensitivity mode was applied and the argon flow was stopped.

centrifugal mill less than 250 μm (Retsch type ZM 200, Hann, Germany). Cadmium concentrations in the seven kitchen garden topsoil samples were in the 8.8–30.9 mg kg^{-1} dry weight (DW) range. The contamination of these garden soils was explained by the atmospheric fallout discharged by two PbZn smelters. Compared with the agricultural soils located in the same area,[33] it is important to note that the high Cd levels in kitchen garden samples can be explained by the various anthropogenic activities such as vehicular traffic, the addition of coal-burning waste or slag to improve soil texture, and the use of pesticide and fertilizers.[34]

Reagents and glassware

All solutions used throughout the study were prepared from analytical grade reagents unless specified otherwise. Double-distilled water (Carlo Erba, Val de Reuil, France) with a specific conductivity of 0.1 μS cm^{-1} was used to prepare all aqueous solutions and dilutions. Calcium chloride was analytical reagent grade from Acrōs Organics (Noisy-le-Grand, France). Standard solutions of aluminum, arsenic, cadmium, calcium, copper, iron, magnesium, manganese, lead, and zinc were prepared by dilution of 1000 μg mL^{-1} certified standard solutions in 2% HNO_3 (Chemical Products for Analysis, Association Corporation Standard Distribution called C.P.A. groupe A.C.S.D., Voisins le Bretonneux, France) and nickel and selenium solutions were prepared from standard solutions containing 1000 μg mL^{-1} of metal in 1 mol/L HNO_3 (Reagecon, Shannon, Ireland). The solution of sodium tetrahydroborate ($NaBH_4$) was prepared by dissolving the powder (Alfa Aesar, Karlsruhe, Germany) in NaOH solution (Sigma-Aldrich, Saint Quentin Fallavier, France) to obtain a 3% (*m*/*v*) $NaBH_4$ in 1.5% (*m*/*v*) NaOH reducing solution.[27] This solution was prepared daily just before use. All glassware and polypropylene material used was previously treated for 1 day in 0.5 mol/L nitric acid (J.T. Baker for metal trace analysis; Deventer, Netherlands) to leach trace elements, rinsed with double-distilled water, and stored in closed plastic bags.

Cadmium extraction procedure

Triplicate samples of each soil sample (3 g) and seven replicate samples of CRM BCR-483 (certified reference material composed of sewage–sludge-amended soil from Great Billings Sewage Farm, Northampton, UK) and SRM 2710a (standard reference material (soil) from Montana, USA) were weighed in a polypropylene tube and 30 mL of 0.01 mol/L $CaCl_2$ was added. The suspensions were shaken using a rotor disc (10 rpm) for 2 h. The extract was separated from the solid residue by centrifugation at 4530 rpm (Rotanta 460 Hettich, Tuttingen, Germany) for 20 min at room temperature. Afterwards, the solution was filtered over an acetate Millipore membrane (Millipore, 0.45 μm porosity, Minisart) and was transferred to a polypropylene container. The Cd concentrations measured in the 0.01 mol/L $CaCl_2$ extract were expressed as μg kg^{-1} DW after drying topsoil samples at 105 °C in an oven (Binder, Tuttlingen, Germany) until it reached a constant mass according to the NF ISO 11465 standard.

Statistical analyses

The Cd concentrations in 0.01 mol/L $CaCl_2$ extracts from soil samples are presented as the arithmetic mean in μg kg^{-1} with the standard deviation. The statistical significance of these mean concentrations obtained by ETAAS, FAAS, and HGAAS was determined by applying Student's *t* test. All statistical tests were performed using Statistica 6.0 (Statsoft, Tulsa, Oklahoma), and the level of significance was set at $p < 0.05$.

Results and discussion

Optimization of acid concentration for Cd determination by HGAAS-HSSR

Cadmium can be included in the hydride-forming elements, since it is converted to volatile species when reacted with sodium tetrahydroborate ($NaBH_4$), the most widely used compound to generate cadmium dihydride (CdH_2) using the vapor generation technique,[35] although the species are not stable.[36] Optimal conditions to produce in situ CdH_2 may be achieved using an alkaline solution containing 3% $NaBH_4$ (*m*/*v*) and 0.5% or 1.5% NaOH (*m*/*v*).[21,26] In our experiments, the best conditions were obtained with a reducing solution of $NaBH_4$ in 1.5% NaOH (Fig. 1*a*). One of the most important parameters, governing the formation of CdH_2, is the concentration of HNO_3 in the sample solution.[27,36,37] Indeed, the chemical mechanism of cadmium dihydride generation, called "nascent hydrogen," was considered by Sanz-Medel et al.[36] as the following equations:

$$Cd + 2H_3O^+ \rightarrow Cd^{2+} + 2H_2O + 2H^*$$

$$BH_4^- + 3H_2O + H^+ \rightarrow H_3BO_3 + 8H^*$$

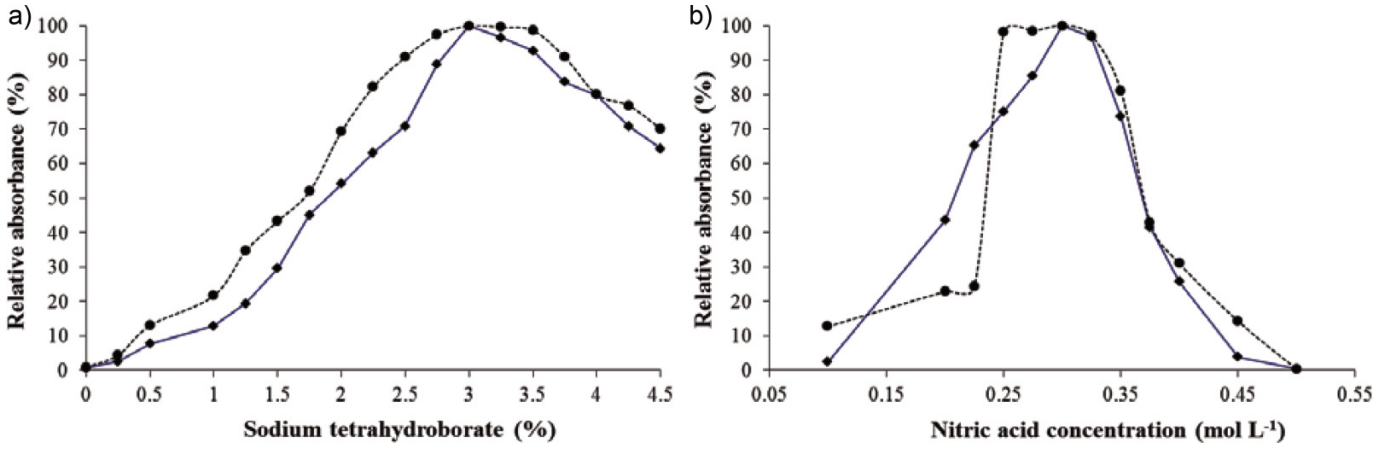
$$8H^* + Cd^{2+} \rightarrow CdH_2 + 2H_2 + 2H^+$$

However, this mechanism was criticized by Laborda et al.[38] for Zn because neither tetrahydroborate ($E°(H_3BO_3/BH_4^-) = -0.482$ V) nor zinc ($E°(Zn^{2+}/Zn) = -0.716$ V) can reduce protons to atomic hydrogen ($E°(H^+/H) = -2.106$ V) with regard to their standard potential. The same holds true for Cd because of its lower standard potential ($E°(Cd^{2+}/Cd) = -0.403$ V). The generation of hydride can be explained by considering the hydrogenation process. Hydrides could be generated by the direct action of borane complexes or indirect action through the formation of hydroboron intermediates, which are stable in strongly acidic conditions.[39]

In this study, volumes of 70% HNO_3 ranging from 63 to 326 μL were added to 2.5 and 5 ng mL^{-1} Cd solutions. In both experiments, the maximal integrated absorbance signal was achieved with a solution containing 0.3 mol L^{-1} HNO_3

Can. J. Chem. Downloaded from www.nrcresearchpress.com by MCGILL UNIVERSITY on 02/02/13
For personal use only.

Fig. 1. Effect of HNO_3 concentration on the signal of (*a*) 2.5 (broken line) and (*b*) 5 ng mL^{-1} (solid line) sample solutions ($n = 3$).



(Fig. 1*b*). Even if the absorption signal of 2.5 ng mL^{-1} Cd reached a plateau at 0.25–0.352 mol L^{-1} concentrations, the results demonstrate that the concentration of HNO_3 strongly affects the amount of hydrogen gas generated from $NaBH_4$ and thus the formation of Cd volatile species such as CdH_2. At higher HNO_3 concentrations (>0.35 mol L^{-1}), the integrated absorbance signals decreased dramatically because of the dilution of the analyte vapour, reflecting the high production of hydrogen in these experimental concentrations. In our experiments, it is worth noting that the absorbance signals depended on the ratio BH_4^-/H^+, where H^+ was the proton in the solution after neutralization of a significant part of HNO_3 by NaOH contained in the $NaBH_4$ solution. For optimal CdH_2 formation, this ratio must be kept in very narrow range between 1.3 and 1.45. Therefore, as observed in a previous study,[27] the strong influence of the ratio BH_4^-/H^+ on the absorbance signal of CdH_2 explains the strong influence of the HNO_3 concentration to generate Cd volatile species.

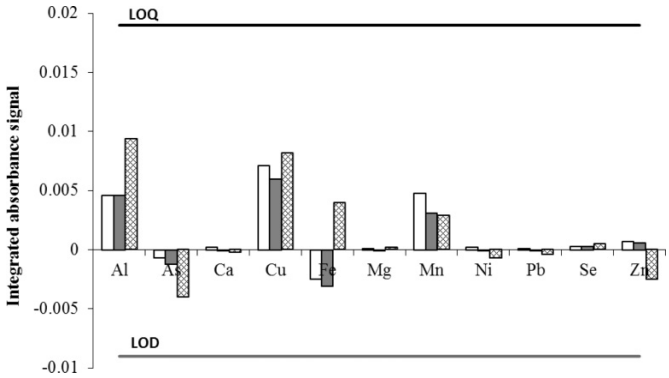
Analytical performance

Under the optimal conditions described previously and using the HSSR method for background correction, absorbance (*A*) was a linear function of the Cd concentration in the range of 0.5–5 ng mL^{-1}. The correlation coefficient of the calibration curve is $r = 0.9994$ and the regression equation is $A = 0.101C - 0.021$, where *C* the concentration of Cd in ng mL^{-1}. The detection (LOD) and quantification (LOQ) limits are given by $LOD = 3\sigma/k$ and $LOQ = 10\sigma/k$, respectively, where σ is the standard deviation of 10 measurements of a reagent blank containing 0.3 mol L^{-1} HNO_3 and *k* is the slope of the calibration curve. The detection limit, found to be 1 ng mL^{-1}, is much lower than that found by FAAS (10-fold) and much higher than that obtained using ETAAS (17-fold) under similar conditions.[40] The LOQ was 3.33 ng mL^{-1}. Accordingly, it was found that the LOQ was 33.3 μg kg^{-1} with respect to the liquid:solid ratio used in the soil extraction procedure. The precision (relative standard deviation of 10 replicate analyses) was up to 5% at the 1 ng mL^{-1} Cd concentration level.

Interference studies

Under the optimized conditions, the effect of 11 coexisting cations on the generation of CdH_2 was investigated. Potential interferents (PI) included Al, As, Ca, Cu, Fe, Mg, Mn, Ni, Pb, Se, and Zn at concentrations of 1, 5, and 10 μg mL^{-1} and were first investigated without Cd in solutions and then with a 5 ng mL^{-1} Cd standard to obtain a Cd solution at a 2.5 ng mL^{-1} concentration.

Fig. 2. Integrated absorbance signal of potential interferents at 1 (white), 5 (grey), and 10 μg mL^{-1} (cross-hatched) in a solution without Cd ($n = 3$).



The integrated absorbance signals of each solution containing one PI in absence of Cd are shown in Fig. 2. Taking into consideration the regression equation, no effects from As, Ca, Mg, Ni, Pb, Se, Zn, and Fe at 1 and 5 μg mL^{-1} were observed on the integrated absorbance signal of Cd. Small effects were reported for Al, Cu, and Mn for the three concentrations (1, 5, and 10 μg mL^{-1}) and Fe at 10 μg mL^{-1}. Nevertheless, the Cd concentrations related to the integrated absorbance signal were in the LOD–LOQ range in all cases.

The effect of each of these 11 interfering cations in a Cd solution at a 2.5-ng mL^{-1} concentration level was evaluated using the optimized method. For this, we expressed the results in terms of relative absorbance, defined as the ratio of the absorbance between the solution with Cd at 2.5 ng mL^{-1} and cations and without them (Table 2). The integrated absorbance signal of this solution without any interfering cations was 0.231 (100%). The relative absorbances were in the 96%–129% range. No suppression of the integrated absorbance signal of Cd was observed from the interfering cations, as in other studies.[22,28] However, among the hydride-forming elements, we can note

Table 2. Effect of interfering cations on the relative absorbance of 2.5 ng mL^{-1} Cd.

Ion	Relative absorbance (%) [PI][a] = 1 μg mL^{-1}	[PI][a] = 5 μg mL^{-1}	[PI][a] = 10 μg mL^{-1}
Aluminum	107	104	114
Arsenic	99	98	94
Calcium	110	109	112
Copper	85	64	37
Iron	96	96	129
Manganese	107	104	104
Magnesium	100	100	99
Nickel	100	100	99
Lead	100	100	99
Selenium	100	100	101
Zinc	101	101	96

Note: Means, minimums, maximums, and standard deviations (SDs) are given.

[a]Potential interferent (PI) concentration.

Table 3. Cadmium concentrations depending on the analytical methods used.

Soil sample	HGAAS-HSSR (μg kg^{-1})	ETAAS (μg kg^{-1})	FAAS (μg kg^{-1})
CRM BCR-483[a]	473±26	473±19	474±15
SRM 2710a[b]	4075±78	3885±51	4643±280
KG1	115±13	114±9	143±1
KG2	65±2	65±8	ND
KG3	124±4	126±9	135±5
KG4	149±6	145±4	131±10
KG5	31±3	32±1	ND
KG6	74±4	75±1	81±5
KG7	38±4	38±3	ND

Note: ND, not determined because of the low concentrations; HGAAS, hydride generation - flame atomic absorption spectrometry; ETAAS, electrothermal absorption atomic spectrometry; FAAS, flame atomic absorption spectrometry; HSSR, high-speed self-reversal background corrector. Results are expressed in mg kg^{-1} dry weight.

[a]Indicative value is 450 ± 50 μg kg^{-1} from Quevauviller et al.[43] and 480 ± 10 μg kg^{-1} from Pueyo et al.[44]

[b]No indicative value.

Can. J. Chem. Downloaded from www.nrcresearchpress.com by MCGILL UNIVERSITY on 02/02/13
For personal use only.

that a slight underestimation of the integrated absorbance signal of Cd was obtained from As only at a high concentration (10 μg mL^{-1}). At this concentration level, competition between As and Cd with BH_4^- to form the corresponding hydride should represent a condensed-phase interference. However, regarding the results obtained in previous studies,[28,41] we cannot exclude interferences between As hydride and Cd hydride in the atomization process. Pohl and Zyrnicki[41] reported the presence of spectral interferences between As (λ = 228.812 nm) and Cd (λ = 228.802 nm) in spite of gas–liquid phase separation in the hydride generation technique. No effect of As on Cd absorbance was observed for the Cd:As concentration ratio below 2000. The improvement of the Cd absorbance in the presence of As can be explained by the background correction technique used in this study. Indeed, it was already shown that the HSSR method was a suitable method for the correction of spectral interferences between As and Cd in FAAS and ETAAS.[40] In contrast, the suppressions of the Cd signal absorbance (15%, 36%, and 63%) were observed in the presence of Cu at the three concentrations (1, 5, and 10 μg mL^{-1}, respectively). As far as we know, the cause of the signal changes has not been clearly attributed. Even at low concentration levels, Cu seems to interfere in the hydride generation reaction of Cd with $NaBH_4$. This can be explained by the formation of Cu hydride as reported by Sturgeon et al.[42] Finally, a concentration of 3.15 ng Cd mL^{-1} was measured in the mixture of Cd at 2.5 ng mL^{-1} and Fe at 10 μg mL^{-1}, reflecting a slight overestimation of the value.

Application

The proposed method was applied to the determination of Cd concentration in $CaCl_2$ extracts from two reference materials and seven contaminated soil samples. Therefore, 193 μL of HNO_3 (70%) was added to 10 mL of each $CaCl_2$ extract and the Cd values were compared with the values obtained with more conventional analytical techniques, ETAAS and FAAS (when it was possible owing to Cd concentrations lower than the detection limit, $LOD_1 = 3\sigma = 54$ μg kg^{-1} and $LOD_2 = 3\sigma/k = 301$ μg kg^{-1} in 0.01 mol/L $CaCl_2$). The results are given in Table 3.

According to the statistical tests, no significant differences were observed between the data obtained using the HGAAS and ETAAS methods. Some differences were obtained between the Cd concentrations with these two methods and those obtained with the FAAS measurements (e.g., KG1, KG3, KG4, and KG6; Table 2), reflecting that the FAAS method is not already a suitable method for the determination of Cd in 0.01 mol/L $CaCl_2$ extracting solution mainly because of the low Cd concentrations. Regarding the results obtained using ETAAS, the reliability of the proposed method is evident. On the other hand, the analytical results of the CRM BCR-483 from HGAAS and ETAAS were very close to that of the indicative value (recovery = 105%). In comparison with the results obtained by Pueyo et al.[44] using ICP–MS, better recovery was obtained (98.5%). All results showed the efficiency of the continuous sample flow combined with the continuous reagent flow system to minimize interferences. However, interference of Cu on the Cd signal absorbance was reported. Moreover, it appeared that the HSSR method was able to reduce As interference in the atomization step of its hydride up to 10 μg mL^{-1}.

Conclusion

Cadmium determination was optimized by combining vapor hydride generation atomic absorption spectrometry and high-speed self-reversal methods (HGAAS-HSSR) in terms of the concentration of NaOH in the reducing solution, gas flow rate, and concentration of HNO_3 in sample solutions. For the best conditions, the detection limit was 1 ng mL^{-1} and the relative standard deviation was up to 5% at 0.2 and 1 ng mL^{-1} Cd concentration levels, reflecting the high sensitivity and precision of this method. Furthermore, the results of Cd determination in $CaCl_2$ extracts from soil samples measured by ETAAS were in agreement with those obtained using the chemical vapor hydride generator atomic absorption spectrom-

etry combined with the high-speed self-reversal background corrector, reflecting that the HGAAS-HSSR method was suitable for low Cd concentrations in $CaCl_2$ soil extracts without any need for sample pretreatment.

References

(1) Das, P.; Samantaray, S.; Rout, G. R. *Environ. Pollut.* **1997**, *98* (1), 29. doi:10.1016/S0269-7491(97)00110-3.

(2) Satarug, S.; Baker, J. R.; Urbenjapol, S.; Haswell-Elkins, M.; Reilly, P. E. B.; Williams, D. J.; Moore, M. R. *Toxicol. Lett.* **2003**, *137* (1–2), 65. doi:10.1016/S0378-4274(02)00381-8.

(3) Vig, K.; Megharaj, M.; Sethunathan, N.; Naidu, R. *Adv. Environ. Res.* **2003**, *8* (1), 121. doi:10.1016/S1093-0191(02)00135-1.

(4) Satarug, S.; Moore, M. R. *Environ. Health Perspect.* **2004**, *112* (10), 1099. doi:10.1289/ehp.6751.

(5) Lalor, G. C. *Sci. Total Environ.* **2008**, *400* (1–3), 162. doi:10.1016/j.scitotenv.2008.07.011.

(6) Fowler, B. A. *Toxicol. Appl. Pharmacol.* **2009**, *238* (3), 294. doi:10.1016/j.taap.2009.05.004.

(7) Satarug, S.; Garrett, S. H.; Sens, M. A.; Sens, D. A. *Environ. Health Perspect.* **2010**, *118* (2), 182. doi:10.1289/ehp.0901234.

(8) Pereira, L. A.; de Amorim, I. G.; da Silva, J. B. B. *Talanta* **2004**, *64* (2), 395. doi:10.1016/j.talanta.2004.02.026.

(9) Afridi, H. I.; Kazi, T. G.; Jamali, M. K.; Kazi, G. H.; Arain, M. B.; Jalbani, N.; Shar, G. Q. *Spectrosc. Lett.* **2006**, *39* (2), 203. doi:10.1080/00387010500531266.

(10) Ferreira, S. L. C.; de Andrade, J. B.; Korn, M. G. A.; Pereira, M. G.; Lemos, V. A.; dos Santos, W. N. L.; de Medeiros Rodrigues, F.; Souza, A. S.; Ferreira, H. S.; da Silva, E. G. P. *J. Hazard. Mater.* **2007**, *145* (3), 358. doi:10.1016/j.jhazmat.2007.03.077.

(11) Parham, H.; Pourreza, N.; Rahbar, N. *J. Hazard. Mater.* **2009**, *163* (2–3), 588. doi:10.1016/j.jhazmat.2008.07.007.

(12) Shabani, A. M. H.; Dadfarnia, S.; Motavaselian, F.; Ahmadi, S. H. *J. Hazard. Mater.* **2009**, *162* (1), 373. doi:10.1016/j.jhazmat.2008.05.049.

(13) Creed, J.; Martin, T.; Lobring, L.; O'Dell, J. *Environ. Sci. Technol.* **1992**, *26* (1), 102. doi:10.1021/es00025a010.

(14) Duarte, A. T.; Dessuy, M. B.; Silva, M. M.; Vale, M. G. R.; Welz, B. *Microchem. J.* **2010**, *96* (1), 102. doi:10.1016/j.microc.2010.02.008.

(15) Viñas, P.; Aguinaga, N.; López-García, I.; Hernández-Córdoba, M. *J. AOAC Int.* **2002**, *82,* 736.

(16) Chamjangali, M. A.; Farooji, S. T.; Bahramian, B. *J. Hazard. Mater.* **2010**, *174* (1–3), 843. doi:10.1016/j.jhazmat.2009.09.130.

(17) Fraser, S. M.; Ure, A. M.; Mitchell, M. C.; West, T. S. *J. Anal. At. Spectrom.* **1986**, *1* (1), 19. doi:10.1039/ja9860100019.

(18) Gawin, M.; Konefal, J.; Trzewik, B.; Walas, S.; Tobiasz, A.; Mrowiec, H.; Witek, E. *Talanta* **2010**, *80* (3), 1305. doi:10.1016/j.talanta.2009.09.021.

(19) Stafilov, T.; Zendelovska, D.; Pavlovska, G.; Čundeva, K. *Spectrochim. Acta B* **2002**, *57,* 907. doi:10.1016/S0584-8547(02)00017-4.

(20) Tsalev, D. L. *Spectrochim. Acta B* **2000**, *55,* 917. doi:10.1016/S0584-8547(00)00202-0.

(21) Garrido, M. L.; Muñoz-olivas, R.; Cámara, C. *J. Anal. At. Spectrom.* **1998**, *13* (4), 295. doi:10.1039/a707419k.

(22) Chuachuad, W.; Tyson, J. F. *Can. J. Anal. Sci. Spectrosc.* **2004**, *49,* 362.

(23) Chuachuad, W.; Tyson, J. F. *J. Anal. At. Spectrom.* **2005**, *20* (4), 273. doi:10.1039/b416355a.

(24) Pourreza, N.; Ghanemi, K. *J. Hazard. Mater.* **2010**, *178* (1–3), 566. doi:10.1016/j.jhazmat.2010.01.122.

(25) Matusiewicz, H. *Spectrochim. Acta B* **1997**, *52,* 1711. doi:10.1016/S0584-8547(97)00089-X.

(26) Matusiewicz, H.; Kopras, M.; Sturgeon, E. *Analyst (Lond.)* **1997**, *122* (4), 331. doi:10.1039/a606747f.

(27) Bujdoš, M.; Streško, V.; Medved, J.; Kubová, J. *Fresen. Environ. Bull.* **2002**, *11,* 686.

(28) Bujdoš, M.; Streško, V.; Medved, J.; Kubová, J. *Chem. Pap.* **2003**, *57,* 201.

(29) Vargas-Razo, C.; Tyson, J. F. *Fresenius J. Anal. Chem.* **2000**, *366* (2), 182. doi:10.1007/s002160050036.

(30) Smith, S. B., Jr; Hieftje, G. M. *Appl. Spectrosc.* **1983**, *37* (5), 419. doi:10.1366/0003702834634893.

(31) Oppermann, U.; Schram, J.; Felkel, D. *Spectrochim. Acta B* **2003**, *58,* 1567. doi:10.1016/S0584-8547(03)00034-X.

(32) Waterlot, C.; Douay, F. *Talanta* **2009**, *80* (2), 716. doi:10.1016/j.talanta.2009.07.053.

(33) Sterckeman, T.; Douay, F.; Proix, N.; Fourrier, H.; Perdrix, E. *Water Air Soil Pollut.* **2002**, *135* (1–4), 173. doi:10.1023/A:1014758811194.

(34) Douay, F.; Pruvot, C.; Roussel, H.; Ciesielski, H.; Fourrier, H.; Proix, N.; Waterlot, C. *Water Air Soil Pollut.* **2008**, *188* (1–4), 247. doi:10.1007/s11270-007-9541-7.

(35) Cacho, J.; Beltrán, I.; Nerin, C. *J. Anal. At. Spectrom.* **1989**, *4* (7), 661. doi:10.1039/ja9890400661.

(36) Sanz-Medel, A.; Valdés-Hevia y Temprano, M. C.; Bordel Garcia, N.; Fernández de la Campa, M. R. *Anal. Chem.* **1995**, *67* (13), 2216. doi:10.1021/ac00109a048.

(37) Liva, M.; Muñoz-Olivas, R.; Cámara, C. *Talanta* **2000**, *51* (2), 381. doi:10.1016/S0039-9140(99)00292-1.

(38) Laborda, F.; Bolea, M. T.; Baranguan, J. R.; Castillo, J. R. *Spectrochim. Acta B* **2002**, *57,* 797. doi:10.1016/S0584-8547(02)00010-1.

(39) D'Ulivo, A.; Onor, M.; Pitzalis, E. *Anal. Chem.* **2004**, *76* (21), 6342. doi:10.1021/ac040078o.

(40) Waterlot, C.; Douay, F. *Can. J. Civ. Eng.* **2010**, *37* (2), 346. doi:10.1139/L09-156.

(41) Pohl, P.; Zyrnicki, W. *Anal. Chim. Acta* **2001**, *429* (1), 135. doi:10.1016/S0003-2670(00)01257-5.

(42) Sturgeon, R. E.; Liu, J.; Boyko, V. J.; Luong, V. T. *Anal. Chem.* **1996**, *68* (11), 1883. doi:10.1021/ac951259g.

(43) Quevauviller, Ph.; Rauret, G.; Ure, A.; Bacon, J.; Muntau, H. Report EUR 17127 EN; European Commission, 1997.

(44) Pueyo, M.; López-Sánchez, J. F.; Rauret, G. *Anal. Chim. Acta* **2004**, *504* (2), 217. doi:10.1016/j.aca.2003.10.047.

Can. J. Chem. Downloaded from www.nrcresearchpress.com by MCGILL UNIVERSITY on 02/02/13
For personal use only.

Polyethersulfone polymers and oligomers — Morphology and crystallization

Abdelkader Benhalima, François Hudon, Finda Koulibaly, Christian Tessier, and Josée Brisson

Can. J. Chem. Downloaded from www.nrcresearchpress.com by MCGILL UNIVERSITY on 02/02/13
For personal use only.

Abstract: Crystal forms of polyethersulfones (PES) were investigated by using a model compound and a low molecular weight oligomer. These are amorphous as-synthesized, and can undergo solvent-induced crystallization under the appropriate conditions. The model compound, 4,4′-bis(*p*-methoxyphenoxy)diphenyl sulfone, yielded monocrystals, and its structure was solved using X-ray diffraction. Conformational disorder is present, two conformers cohabiting in 55:45 proportions. This model compound, combined to previous structural studies published in the literature, served as a basis for conformational studies of polyethersulfone. Low molecular weight polymers submitted to solvent-induced crystallization resulted in a PES crystal form different from that previously published in the literature, as shown by powder X-ray diffraction.

Key words: polyethersulfone, solvent-induced crystallization, crystal structure, polymorphism, X-ray diffraction.

Résumé : On a étudié les formes cristallines de sulfones de polyéthers (SPE) en se basant sur un composé modèle et un oligomère de faible poids moléculaire. Ces sont des produits amorphes obtenus par une synthèse-as et, dans des conditions appropriées, ils peuvent donner lieu à une cristallisation induite par un solvant. Le composé modèle, le sulfone de 4,4′-bis(*p*-méthoxyphénoxy)diphényle, peut être isolé sous la forme de monocristaux et on a déterminé sa structure par diffraction des rayons-X. On a décelé un désordre conformationnel alors que deux conformères coexistent dans des proportions de 55 : 45. Les données relatives au composé modèle combinées aux études publiées antérieurement sur les structures ont servi de base pour les études conformationnelles des sulfones de polyéthers. Les polymères de faibles poids moléculaires soumis à une cristallisation induite par un solvant ont conduit à la formation de SPE dont la forme cristalline, d'après la diffraction des rayons-X, serait différente de celles rapportées antérieurement dans la littérature.

Mots-clés : sulfone de polyéther, cristallisation induite par un solvant, structure cristalline, polymorphie, diffraction des rayons X.

[Traduit par la Rédaction]

Introduction

Polyethersulfones, abbreviated PES, stand out among other high-performance thermoplastic polymers because of their thermal stability, amorphous morphology, and good solubility in low polarity solvents (ketones and chlorinated aromatic hydrocarbons). They are finding increasing use as membranes for a variety of applications, such as hemodialysis, water filtration, and gas separation, and are serious candidates for fuel cell membranes.

A regular polymer such as PES is rarely entirely amorphous. Blackadder et al.[1] showed that PES can undergo solvent-induced crystallization in dichloromethane under specific conditions. Upon crystallization, PES solubility markedly decreases because of the increase in interchain interactions that must be weakened before dissolution occurs.

Improving crystallization of PES could yield a better range of properties and therefore applications. On the other hand, solvent-induced crystallization has been identified as a cause for the increase in brittleness in PES upon contact with chlorinated solvents, and techniques to inhibit this crystallization could, in turn, be useful for specific applications where this crystallization issue causes problems.[2] For this, a better knowledge of the crystal phase of PES and conditions that favour its growth is needed.

The limited crystallization of regular PES and its oligomers is an exception in the world of rigid polymers. For example, polyetheretherketones (PEEKs) have a similar rigidity, but nevertheless crystallize extremely well, as reported in the literature.[3] Polythioethersulfones (PTES) and polyparaphenylenesulfone (PPS), which are also similar in chemical repeat unit and rigidity, also crystallize readily.[3] Atwood et al.[4] suggested that the combined effect of a T_g higher than that of PEEK, and a difference in the valence angle of C–S–C diarylsulfone versus C–C–C diarylketone links may explain the low PES crystallinity, whereas other authors mention the limited difference between glass transition temperature and melt temperature as the cause for the limited crystallinity observed.[5] However, this behaviour may also be related in part to the adopted crystal phase conformation. Polyethylene te-

Received 6 June 2012. Accepted 19 July 2012. Published at www.nrcresearchpress.com/cjc on 23 October 2012.

A. Benhalima, F. Hudon, F. Koulibaly, C. Tessier, and J. Brisson. Centre de recherche sur les matériaux avancés (CERMA) and Département de chimie, Faculté des sciences et de génie, Université Laval, Québec, QC G1V 0A6, Canada.

Corresponding author: Josée Brisson (e-mail: josee.brisson@chm.ulaval.ca).

Can. J. Chem. Downloaded from www.nrcresearchpress.com by MCGILL UNIVERSITY on 02/02/13
For personal use only.

rephtalate is usually obtained in an amorphous form, which does not crystallize easily unless submitted to annealing, stretching, or solvent-induced crystallization. It has been proposed that the key in its amorphous phase stability lies in the fact that the lowest energy conformation is not the all-trans conformation found in the crystal form and favoured by packing interactions, but a gauche conformation.[6–8] A similar origin for the limited crystallization may exist for PES.

With limited data on the PES crystalline form itself, crystal structures of model compounds become of utmost interest. Few have been studied in the literature, and the present work testifies to the difficulty in crystallizing model compounds composed of a little as two repeat units. A four-ring oligomer bearing amine terminal groups was studied by Bocelli and Rizzoli.[9] Cyclic ethersulfone oligomer crystal structures were reported by the group of Colquhoum and Williams,[3] as these yield high-quality single crystals. However, packing of these cyclic analogues is incompatible with that of polymer chains, and ring constraints may favour conformations different from those adopted in long polymeric chains. From the study of these cyclic oligomers, it was observed that face-to-face π-stacking and C–H···π interactions provided the main stabilization mechanism for crystallization.[3] Whether such interactions are at play in PES is unknown.

In recent years, our group has focussed on the design of rigid–flexible copolymers with rigid block lengths close to the thickness of a single crystalline lamellae.[10] These rigid blocks adopt the same crystal structure as the homopolymers and, because of their lower molecular weights, crystallize more readily. Furthermore, during the course of the synthesis, various low molecular weight model compounds were synthesized and attempts to crystallize them were made. The present article therefore reports the crystal structure of a new model compound, X-ray diffraction of an oligomer as well as conformational analysis, in the aim of shedding light on the crystallization of polyethersulfones for future applications.

Experimental

Synthesis and crystallization of 4,4′-bis(*p*-methoxyphenoxy)diphenyl sulfone (MPDS)

4,4′-Bis(*p*-methoxyphenoxy)diphenyl sulfone, abbreviated MDPS, was synthesized by reacting 5.085 g (20.0 mmol) of 4,4′-difluorodiphenyl sulfone, 4.967 g (40.0 mmol) of 4-methoxyphenol, and 6.08 g (44.0 mmol) of potassium carbonate in a round-bottomed flask. Thirty millilitres of dimethylacetamide (DMAc) was added to this mixture and the resulting solution was heated to 160 °C overnight under argon atmosphere. The reaction mixture was diluted with dichloromethane and washed with saturated NaCl water three times to remove DMAc and potassium carbonate. The organic layer was washed three times with distilled water and dried over MgSO4, filtered, evaporated, and dried in vacuo at 60 °C to give a white solid (MDPS). The MDPS was crystallized by solvent evaporation of the toluene/methanol solutions (3:1).

Synthesis and characterization of polyethersulfone oligomers

PPS oligomers were synthesized by chain-growth polymerization of 4-fluoro-4′-hydroxydiphenylsulfone, following the work of Yokozawa et al.,[11] which was end-capped by the addition of 4-methoxy phenol in dimethylacetamide. Methoxy end groups were deprotected by the addition of BBr_3 in CH_2Cl_2. Molecular weights of ethersulfones oligomers were determined by MALDI-TOF mass spectroscopy in positive linear mode, using a Bruker Autoflex mass spectrometer equipped with an UV laser (λ = 337 nm, 3 ns second pulse). NaCl was used as a cationizating agent in a dithranol matrix. M_n was found to be 1600 g mol^{-1} and the polydispersity index was 1.15. Oligomer crystallization was performed following the work of Blackadder et al.[1] by first dissolving the PES copolymer in dichloromethane and then lowering the temperature of the 20 wt % solutions to 5 °C for 24 h. The resulting powder was dried in air until the powder did not feel sticky any more, then introduced into a 1 mm diameter glass capillary (Charles Supper Company), and sealed using a match. X-ray diffraction diagrams were registered right away on a Bruker diffractometer equipped with a Kristalloflex 760 generator, a three-circle goniometer, and a Hi-Star area detector. The generator produced a graphite-monochromatized copper radiation (Cu Kα = 1.5418 Å) at 40 kV and 40 mA. For the MPDS model compound, the X-ray powder pattern was also calculated from the *x*, *y*, and *z* coordinates fo the resolved crystal structure using the Mercury 2.3[12] program (Cambridge Crystallographic Data Centre) and imposing a constant full-width at a half-height of 0.4°.

Single crystal determination of MPDS

A yellow crystal of MDPS having approximate dimensions of 0.16 mm × 0.15 mm × 0.07 mm was mounted on a glass fiber using Paratone N hydrocarbon oil. Measurements were made at 200(2) K on a Bruker APEX II area detector diffractometer equipped with graphite-monochromated Mo Kα radiation. Frames corresponding to an arbitrary hemisphere of data were collected using ω scans of 0.5° counted for a total of 30 seconds per frame. An orientation matrix corresponding to the cell constants listed in Table 1, along with additional details on data acquisition, was obtained from a least-squares refinement using the measured positions of 3181 centered reflections in the range $2.23° < \theta < 18.44°$. The APEX 2 program was used for cell parameter retrieval and data collection.[13]

Data were integrated using the SAINT program.[14] The data were corrected for Lorentz and polarization effects. A multiscan absorption correction was performed using the SADABS program.[15] The structure was solved and refined using SHELXS-97 and SHELXL-97.[16] All non-H atoms were refined anisotropically. Hydrogen atoms were placed at idealized positions. Neutral atom scattering factors were taken from the *International Tables for X-ray Crystallography*.[17] All calculations and drawings for this crystal structure were performed using the SHELXTL package.[18] The final model was checked either for missed symmetry or voids in the crystal structure using the PLATON software.[19,20] None was found. The crystal structure gives a satisfactory chekcif report (available in the Supplementary data).

Results and discussion

Polyethersulfone crystallinity

Experimental data on PES crystallization present in the literature is limited, to the best of our knowledge, to mainly two publications, which report X-ray diffraction of a sample crystallized at low temperature in the presence of a solvent[1] and spherulite-like structures.[21] The same crystallization

Can. J. Chem. Downloaded from www.nrcresearchpress.com by MCGILL UNIVERSITY on 02/02/13
For personal use only.

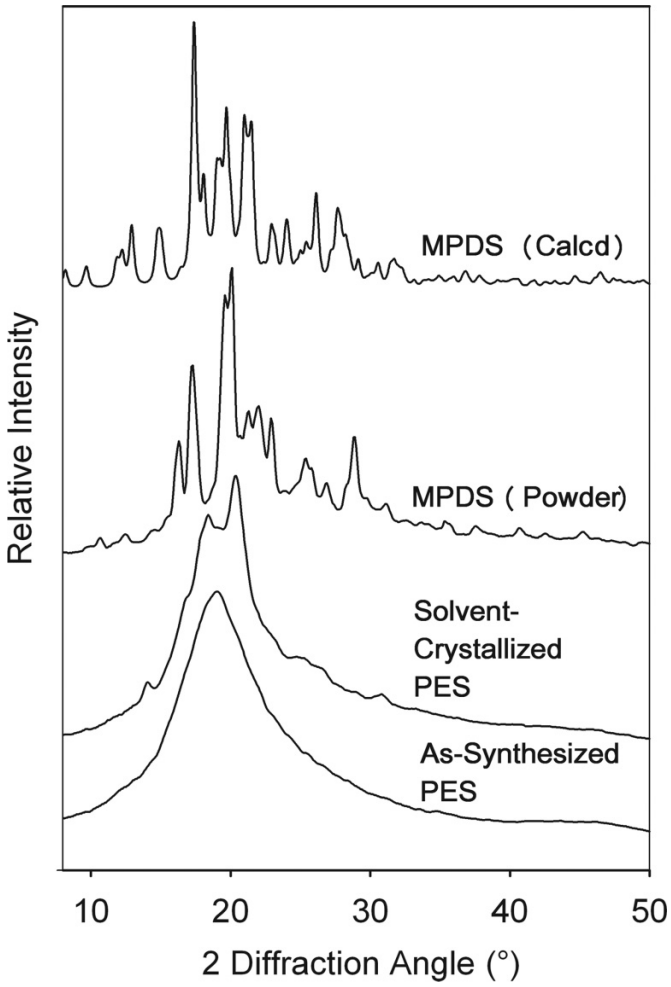
Table 1. Crystal data and structure refinement for 4,4′-bis(*p*-methoxyphenoxy)diphenyl sulfone.

Empirical formula	$C_{26}H_{22}O_6S$
Formula weight	462.50
Temperature (K)	200 (2)
Wavelength (Å)	0.71073
Crystal system	Orthorhombic
Space group	*P*2(1)2(1)2(1)
Unit cell dimension	
a (Å)	10.069(4)
b (Å)	10.350(4)
c (Å)	21.607(9)
α (°)	90
β (°)	90
γ (°)	90
Volume (Å^3)	2251.7(16) Å^3
Z	4
Density (calcd) (Mg/m^3)	1.364
Absorption coefficient (mm^{-1})	0.185
F(000)	968
Crystal size (mm^3)	0.16×0.15×0.07
θ range for data collection (°)	1.88–25.00
Index range	$-11 \le h \le 11$, $-12 \le k \le 12$, $-25 \le l \le 25$
Reflections collected	22624
Independent reflections	3955 (R(int) = 0.0560)
Observed reflections	2838 ($I > 2\sigma(I)$)
Completeness to θ = 25.00° (%)	100.0
Absorption correction	Semi-empirical from equivalents
Max and min transmission	0.9872 and 0.9610
Refinement method	Full-matrix least-squares on F^2
Data/restraints/parameters	3955/193/352
Goodness-of-fit on F^2	1.238
Final *R* indices ($I > 2\sigma(I)$)	$R1$ = 0.0450, $wR2$ = 0.0790
R indices (all data)	$R1$ = 0.0727, $wR2$ = 0.0871
Absolute structure parameter	0.10(9) (Flack x), 0.07(5) (Hooft, Straver and Spek y)
Largest diff. peak and hole (e Å^{-3})	0.229 and –0.165

procedure was applied to the low molecular weight PES blocks available in our lab, and the results are reported in Fig. 1, along with diffraction of the initial polymer as-synthesized and of the only oligomer studied from which we were able to obtain single crystals, MPDS. Whereas, as synthesized, PES oligomer samples showed only a broad peak due to scattering of the amorphous phase, small narrow peaks began to be observed after solvent treatment, although the amorphous halo was still predominant. These, however, disappeared if the sample was dried too much, indicating that solvent molecules may be included as an adduct in the crystal form, as previously proposed in the literature.[1,21]

Observed diffraction peak positions are reported in Table 2, along with those previously reported for PES by Blackadder et al,[1] and those of similar rigid–flexible polymers.[22–27] The diagram observed in the present work presents two intense diffraction spots at approximately 4.9 Å (18°) and 4.2 Å (21°). This does not match the previous report by Blackadder et al.,[1] in which the two most intense spots were positioned at 4.50 Å (19.7°) and 3.32 Å (26.9°), as reported in Table 2.

Fig. 1. X-ray diffraction powder diagrams of polyethersulfone (PES) and of a model compound, 4,4′-bis(*p*-methoxyphenoxy)diphenyl sulfone (MPDS), experimental powder spectrum (Powder) and as calculated from single crystal structure (Calcd.).



The experimental powder X-ray diffraction diagram of the MPDS model compound, as well as the diagram calculated from the single crystal structure of this compound (which is discussed in the following section) are shown in Fig. 1. As observed in the figure, experimental and calculated MPDS spectra do not match, indicating that this compound is polymorphic. The main difference lies in the relative intensity of the peak at 17.3°, the most intense for MPDS as calculated from the crystal structure, which is of much lower relative intensity in the observed spectrum, although many of the smaller intensity peaks also change in intensity below at higher diffraction angles. The main diffraction peak positions remain unchanged, within experimental error.

The strongest peaks are at similar 2θ positions for PES from this work and for MPDS, although smaller intensity peaks

Table 2. X-ray powder diffraction data for the main peaks of various rigid copolymer structures (polyetheretherketone (PEEK) peak positions calculated using unit cell dimensions proposed by Ho and Cheng[22,23]).

		PES		PEEK				PTEK					
		Form I[1]	This work	Form I[22,23]		Form II[22,23]		Form I[25]		Form II[24]		PPS[26,27]	
2θ (°)	*d* (Å)	I	I	hkl	I	hkl	I	hkl	I	hkl	I	hkl	I
14.0	6.3	—	w	—	—	—	—	—	—	—	—	—	—
15.6	5.7	—	—	—	—	020	**s**	—	—	020	**s**	—	—
16.4	5.4	—	sh	—	—	—	—	011	vs	—	—	200	**vs**
18.0	4.9	w	m	—	—	021	m	—	—	021	**s**	—	—
18.7	4.8	—	—	110	**vs**	—	—	110	vs	—	—	—	—
19.7	4.5	**s**	—	—	—	—	—	—	—	—	—	—	—
20.7	4.3	—	s	111	**s**	—	—	—	—	—	—	—	—
21.1	4.2	—	—	—	—	100	**vs**	—	—	—	—	111	**s**
22.8	3.9	m	—	200	**vs**	110	—	200	vs	110, 022	**vs**	—	—
24.5	3.6	m	w	—	—	—	—	—	—	111	m	—	—
26.5	3.3	**s**	w	—	—	—	—	—	—	—	—	112	**s**
27.8	3.2	—	—	—	—	102	m	—	—	121	m	—	—
28.9	3.1	—	vw	211	**s**	—	—	21-1	s	—	—	—	—
29.5	3.0	w	—	—	—	—	—	—	—	—	—	310	w
31.6	2.8	—	—	—	—	040	w	—	—	040	w	311, 114	w

Note: PES, polyethersulfone; PTEK, polythioetherketone; PPS, polyparaphenylenesulfone.

Can. J. Chem. Downloaded from www.nrcresearchpress.com by MCGILL UNIVERSITY on 02/02/13
For personal use only.

differ. This indicates that a similarity in structural features may occur between PES and this model compound.

Crystal structure of the MPDS model compound

The crystal structure of the MPDS model compound is reported in the present work. Atomic positions are given in Table 3, and Table 4 lists anisotropic displacement parameters. This structure is different from any of the ethersulfone model compounds reported in the literature. As depicted in Fig. 2, which also shows the numbering of the atoms, the chain exhibits conformational disorder, two different conformations appearing in the crystal packing with 55% and 45% occupancy factors at the site of a phenoxy group. This disorder is located at one of the phenyl ether groups, the rest of the structure remaining well-ordered, as if multiple conformations were possible at this specific position. Further, these two conformations are well-defined in the crystal state, as illustrated by the occurrence of similar temperature factors for the ordered and disordered parts of the molecules, as reported in Table 4. This highly unusual phenomenon points to a large conformational flexibility, and already gives insights on the possible cause for a low crystallinity of the parent PES polymer.

Geometry of the sulfonic group is comparable to that of various previously determined sulfone structures, which have been the object of a review:[28] S=O distances are short, (1.435(2) and 1.446(2) Å), corresponding to strong double bonds; the large O–S–O bond angle of 120.10(13)° is comparable to values of 116.9(8)° to 120.61(8)° for previously reported sulfones; and the C–S–C of 104.11(13)° is small for a tetrahedral angle, again as observed for other sulfones (104.11(13)°), which has been attributed to the effect of lone-pair repulsion on the sulfone group oxygen atoms.[28] Ether groups have normal geometries, with distances varying from 1.380(3) to 1.419(11) Å, with one exception, at 1.431(7) Å in one of the two disordered conformations. This may, however, be related to a slightly incorrect position of the C4 carbon atom common to both disordered conformations, as the temperature factor is larger perpendicular to the ring plane for this atom, and as an abnormally low valence C–O–C angle of 113.5(10)° is also observed, significantly lower than the average 120°–121° diaryl ether bond angle.[3,4] However, two distinct positions of this carbon atom could not be resolved, the two positions being most probably too close.

Conformational features of this structure can be described either by the dihedral angle between the two aromatic ring planes or by the two successive torsion angles C–X–C–C and C–C–X–C related to the two C–X bonds of the sulfone or ether groups. For the sulfone group, the dihedral angle is 81.0° and the torsion angles (C–S–C–C) are 87.4(3)° and 91.5(2)°, in agreement with the 90° value predicted by Koch and Moffitt[29] for maximum conjugation between aromatic rings and a sulfone group, and are also in agreement with a recent X-ray study of sulfones in which the dihedral angle between the ring plane and the sulfone plane varied from 75.3° to 86.6°.[28] A few values were found to depart from this optimal value in the literature: a value of −67°[9] and one of −102.3°[30] were observed for hydrogen-bond-forming NH_2-terminated aryl ether sulfones and an ortho-substituted nitro compound that showed steric hindrance exhibited a value of 61.2°.[28] The SO_2 plane, therefore, generally lies between the two phenyl planes in an "open-book" conformation. This conformation is also the one proposed by Tabor et al.[31] for PPS, and no evidence suggests that it should be any different for PES.

Phenoxy groups show a much larger variability in conformation than sulfone groups do. The number of aryl ethersulfone crystal structures is limited, but variations are large even within this selected group, with two main conformations having been observed: the first is analogous to the open-book conformation, although dihedral angles between aromatic rings are closer to 70° than to 90°, with successive torsion angles of 87.3° and −61.6°;[9] in the second conformation

Can. J. Chem. Downloaded from www.nrcresearchpress.com by MCGILL UNIVERSITY on 02/02/13
For personal use only.

Table 3. Atomic coordinates ($\times 10^4$), occupancy factors (Occ.), and equivalent isotropic displacement parameters (Å^2 $\times$ 10^3) for 4,4′-bis(*p*-methoxyphenoxy)diphenyl sulfone. *U*(eq) is defined as one third of the trace of the orthogonalized $\mathbf{U^{ij}}$ tensor.

Atom	Occ.	*x*	*y*	*z*	*U*(eq)
S(1)	1	2060 (1)	2303 (1)	7667 (1)	61 (1)
O(1)	1	5086 (2)	–1573 (2)	6265 (1)	70 (1)
O(2)	1	6921 (2)	–720 (2)	3894 (1)	74 (1)
O(5)	1	1780 (2)	1781 (2)	8269 (1)	74 (1)
O(6)	1	2681 (2)	3556 (2)	7609 (1)	69 (1)
C(1)	1	575 (3)	2348 (3)	7250 (1)	52 (1)
C(2)	1	–488 (3)	1539 (3)	7397 (1)	66 (1)
C(3)	1	–1631 (3)	1571 (3)	7055 (2)	74 (1)
C(4)	1	–1723 (3)	2398 (4)	6563 (1)	74 (1)
C(5)	1	–685 (3)	3200 (3)	6406 (1)	66 (1)
C(6)	1	451 (3)	3185 (3)	6753 (1)	59 (1)
C(7)	1	3040 (3)	1186 (3)	7265 (1)	55 (1)
C(8)	1	2980 (4)	–110 (3)	7416 (2)	84 (1)
C(9)	1	3703 (4)	–1006 (4)	7086 (2)	86 (1)
C(10)	1	4436 (3)	–611 (3)	6587 (2)	59 (1)
C(11)	1	4506 (3)	672 (3)	6432 (2)	71 (1)
C(12)	1	3818 (3)	1564 (3)	6780 (2)	71 (1)
C(13)	1	5572 (3)	–1292 (3)	5671 (2)	57 (1)
C(14)	1	6912 (3)	–1170 (3)	5586 (1)	59 (1)
C(15)	1	7394 (3)	–980 (3)	4990 (1)	59 (1)
C(16)	1	6538 (3)	–910 (3)	4499 (1)	58 (1)
C(17)	1	5183 (3)	–1047 (3)	4593 (2)	64 (1)
C(18)	1	4711 (3)	–1220 (3)	5182 (2)	63 (1)
C(19)	1	8291 (4)	–508 (4)	3776 (2)	89 (1)
O(3A)	0.55	–2791 (6)	2146 (5)	6164 (3)	69 (2)
C(20A)	0.55	–3180 (17)	3087 (11)	5724 (4)	56 (2)
C(21A)	0.55	–3328 (13)	4375 (10)	5888 (5)	73 (3)
C(22A)	0.55	–3593 (8)	5288 (8)	5457 (3)	65 (2)
C(23A)	0.55	–3806 (15)	4935 (11)	4850 (4)	82 (2)
C(24A)	0.55	–3699 (10)	3669 (7)	4695 (4)	69 (2)
C(25A)	0.55	–3391 (8)	2727 (9)	5132 (3)	75 (2)
O(4A)	0.55	–4146 (5)	5910 (4)	4456 (2)	81 (1)
C(26A)	0.55	–4447 (19)	5587 (15)	3844 (7)	81 (3)
O(3B)	0.45	–3036 (7)	2692 (6)	6353 (3)	64 (2)
C(20B)	0.45	–3070 (20)	3297 (13)	5763 (5)	56 (2)
C(21B)	0.45	–2838 (10)	2520 (11)	5253 (4)	75 (2)
C(22B)	0.45	–3058 (9)	3038 (7)	4687 (4)	82 (2)
C(23B)	0.45	–3523 (13)	4265 (8)	4587 (5)	69 (2)
C(24B)	0.45	–3765 (10)	5015 (10)	5096 (4)	51 (3)
C(25B)	0.45	–3461 (18)	4556 (13)	5689 (5)	71 (4)
O(4B)	0.45	–3723 (6)	4659 (5)	4003 (2)	86 (2)
C(26B)	0.45	–4220 (20)	5907 (18)	3889 (9)	81 (3)

adopted, a first ring is close to the C–O–C bridge plane and the other is almost perpendicular to this plane, with torsion angle values of 6.0° and 76.7°, 19.8° and 66.7°, or 64° and 2°.[25,32] In the crystal structure of the MPDS reported here, disorder occurs at this position, and three different sets of torsion angles were observed. None fit the open-book conformation and only one fits the second conformation previously observed, with torsion angle values of –16.1(4)° and –75.8(4)° in the nondisordered section of the molecule. In the disordered section of the molecule, the conformation adopted is either planar, with torsions angles of –0.6(9)° and 1.8(19)°, or corresponds to a new conformation with torsion angles of –28.8(9)° and –46.5(15)°. The variety of possible conformations, and the disorder observed, are in part due to a large flexibility of the phenoxy conformation, which has been established by theoretical calculations of diphenyl ether derivatives using ab initio[33,34] and semi-empirical DFT calculations.[35] An energy rotation barrier around the ether C–O bond of approximately 8 kcal/mol (1 cal = 4.184 J) was found, with a global minimum at approximately 35°, associated with a large, flat minimum

Can. J. Chem. Downloaded from www.nrcresearchpress.com by MCGILL UNIVERSITY on 02/02/13
For personal use only.

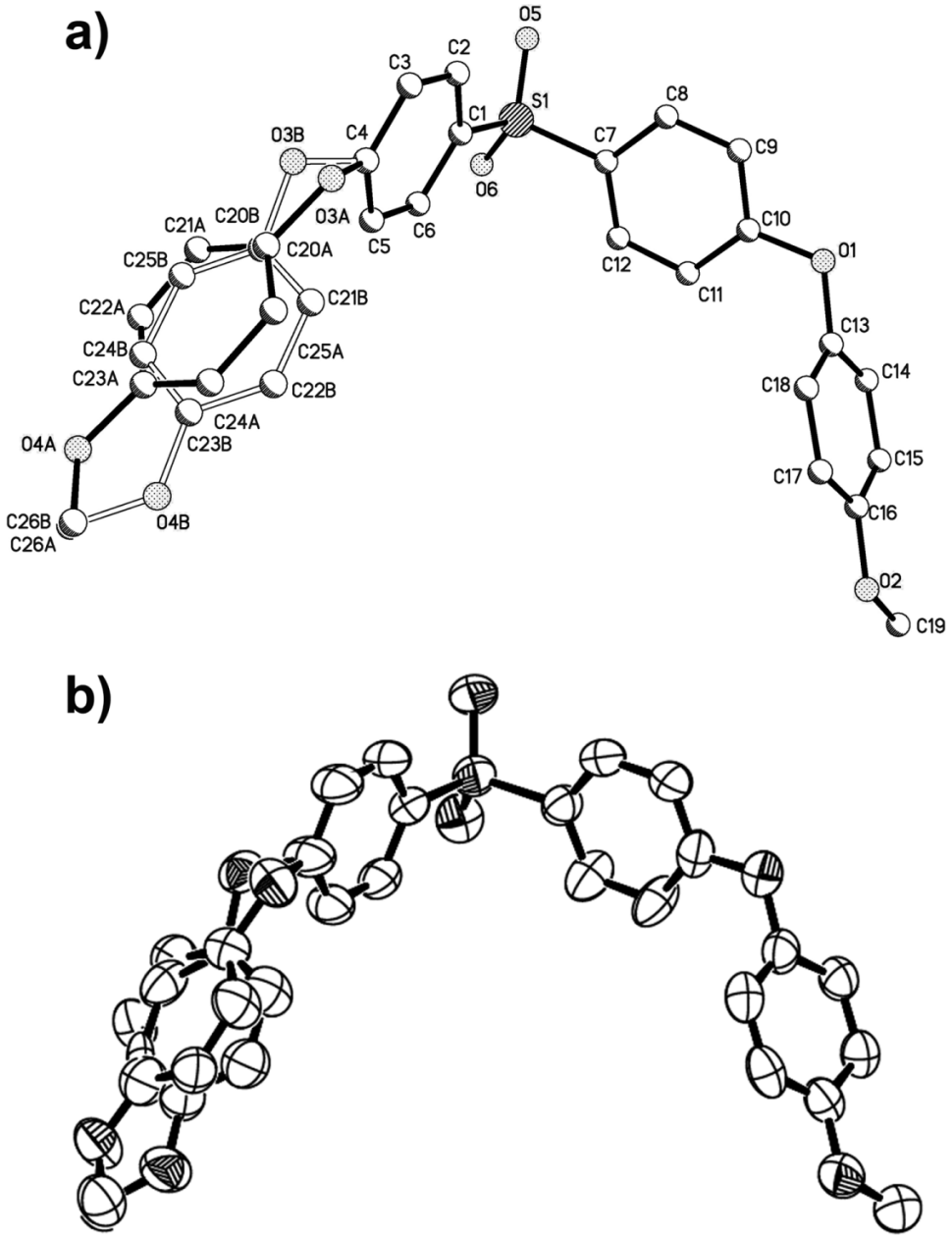
Table 4. Anisotropic displacement parameters ($Å^2 \times 10^3$) for 4,4′-bis(*p*-methoxyphenoxy) diphenyl sulfone. The anisotropic displacement factor exponent takes the form $-2\pi^2[h^2a^{*2}U^{11} + \cdots + 2hka^*b^*U^{12}]$.

Atom	U^{11}	U^{22}	U^{33}	U^{23}	U^{13}	U^{12}
S(1)	67 (1)	69 (1)	46 (1)	–5 (1)	1 (1)	8 (1)
O(1)	69 (2)	69 (1)	72 (2)	3 (1)	12 (1)	15 (1)
O(2)	79 (2)	85 (2)	58 (1)	2 (1)	–5 (1)	15 (1)
O(5)	93 (2)	89 (2)	40 (1)	–1 (1)	5 (1)	16 (1)
O(6)	75 (1)	65 (1)	69 (1)	–11 (1)	–5 (1)	–3 (1)
C(1)	55 (2)	58 (2)	44 (2)	–1 (2)	8 (1)	2 (2)
C(2)	76 (2)	66 (2)	54 (2)	14 (2)	11 (2)	–1 (2)
C(3)	58 (2)	91 (3)	71 (2)	25 (2)	7 (2)	–16 (2)
C(4)	55 (2)	98 (3)	67 (2)	24 (2)	–2 (2)	–16 (2)
C(5)	49 (2)	83 (2)	67 (2)	23 (2)	–2 (2)	–10 (2)
C(6)	49 (2)	67 (2)	61 (2)	5 (2)	11 (2)	–6 (2)
C(7)	54 (2)	63 (2)	48 (2)	–3 (2)	3 (2)	3 (2)
C(8)	106 (3)	86 (3)	60 (2)	24 (2)	30 (2)	31 (2)
C(9)	112 (3)	75 (2)	70 (2)	24 (2)	31 (2)	38 (2)
C(10)	48 (2)	66 (2)	64 (2)	–10 (2)	0 (2)	10 (2)
C(11)	63 (2)	60 (2)	90 (3)	–17 (2)	32 (2)	–14 (2)
C(12)	69 (2)	56 (2)	88 (2)	–15 (2)	24 (2)	–16 (2)
C(13)	58 (2)	54 (2)	59 (2)	–6 (2)	2 (2)	12 (2)
C(14)	52 (2)	68 (2)	57 (2)	1 (2)	–7 (2)	9 (2)
C(15)	50 (2)	61 (2)	66 (2)	–5 (2)	–7 (2)	7 (2)
C(16)	68 (2)	52 (2)	54 (2)	–6 (2)	–14 (2)	12 (2)
C(17)	61 (2)	55 (2)	76 (3)	–7 (2)	–26 (2)	11 (2)
C(18)	49 (2)	56 (2)	82 (3)	–4 (2)	–3 (2)	5 (2)
C(19)	85 (3)	111 (3)	70 (2)	9 (2)	6 (2)	23 (2)
O(3A)	56 (3)	62 (4)	89 (4)	14 (3)	–8 (3)	–10 (3)
C(20A)	50 (3)	56 (4)	62 (2)	4 (2)	–4 (2)	–16 (3)
C(21A)	84 (6)	68 (6)	67 (5)	–7 (4)	2 (5)	7 (5)
C(22A)	67 (4)	59 (5)	69 (5)	–13 (4)	–21 (4)	5 (4)
C(23A)	103 (5)	73 (4)	70 (4)	–8 (3)	10 (4)	16 (4)
C(24A)	68 (4)	82 (6)	57 (3)	–5 (4)	–3 (3)	9 (5)
C(25A)	98 (6)	52 (3)	74 (3)	–7 (3)	–6 (4)	6 (4)
O(4A)	96 (3)	67 (3)	78 (3)	6 (3)	–16 (3)	16 (2)
C(26A)	82 (6)	82 (7)	80 (4)	2 (4)	–13 (3)	11 (5)
O(3B)	50 (4)	78 (5)	63 (4)	5 (3)	10 (3)	–6 (4)
C(20B)	50 (3)	56 (4)	62 (2)	4 (2)	–4 (2)	–16 (3)
C(21B)	98 (6)	52 (3)	74 (3)	–7 (3)	–6 (4)	6 (4)
C(22B)	103 (5)	73 (4)	70 (4)	–8 (3)	10 (4)	16 (4)
C(23B)	68 (4)	82 (6)	57 (3)	–5 (4)	–3 (3)	9 (5)
C(24B)	25 (4)	49 (5)	78 (7)	–2 (5)	2 (6)	11 (4)
C(25B)	78 (7)	68 (7)	68 (8)	–14 (6)	23 (6)	–1 (6)
O(4B)	127 (5)	65 (3)	67 (3)	5 (3)	8 (3)	21 (3)
C(26B)	82 (6)	82 (7)	80 (4)	2 (4)	–13 (3)	11 (5)

region between 30° and 95°.[33] This feature of the potential energy surface explains why, in the absence of stabilizing contacts, two different conformations are adopted with almost equal probabilities in MPDS.

The packing adopted by this molecule is presented in Fig. 3, and is clearly incompatible with that of an extended chain polymer. In the present MPDS ethersulfone model compound, as in polysulfones and poly(ethersulfones), there are no hydrogen atoms on polar atoms, and therefore no classical hydrogen bonds can form. Nevertheless, as observed previously,[28,36] soft hydrogen bonds can form between aromatic hydrogen atoms and sulfone oxygen atoms. In the present case, two short contacts are observed between the oxygen atoms of the sulfone group and the hydrogen atoms of the aromatic rings, with distances of 2.634 Å for O6···H3 and 2.651 Å for O5···H17. It is worth noting that the two S=O bond distances are significantly different, with values of 1.435(2)Å for S1–O5 and 1.446(2) Å for S1–O6, the longer distance corresponding to the weakest O···H contact. This difference in S=O bonds is therefore proposed to be the effect

Fig. 2. Single molecule of 4,4′-bis(*p*-methoxyphenoxy)diphenyl sulfone in its two observed conformers (labelled A and B), present in a 55:45 ratio. Hydrogen atoms are omitted for clarity. (*a*) Numbering of atoms. (*b*) ORTEP view with 50% probability.



of a weakening of the S=O bond due to a soft hydrogen bond interaction.

As shown in Fig. 4, for MPDS, one soft hydrogen bond is formed between the sulfonic group and a hydrogen atom of an aromatic ring bonded to both the sulfonic and the ether group, whereas a second bond is formed between the sulfonic group and a ring bonded to the ether and a methoxy end group. Although only one of the two disordered conformers is depicted in the figure for clarity, interestingly, the disordered ring is the one not interacting with the sulfone group; neither of the two disordered conformations observed showed such interactions. Therefore, it is proposed that sulfone – aromatic ring interactions are important and play a role in either stabilizing the crystal phase, if such interactions can exist in a regular close packing of polyethersulfones or, alternatively, stabilizing the amorphous phase, thereby contributing to a high energy barrier for crystallization and to a decrease in resulting crystallinity. The absence of such interactions may lead to disorder, and may therefore inhibit crystallization.

Comparison with similar rigid polymer structures

It is also interesting to compare the X-ray diffraction patterns and crystal structures of related rigid polymers, as strong similarities exist between some of these rigid polymers. Figure 5 illustrates conformations adopted in the crystal phase by a few representative rigid polymers. In poly(etherketone) (PEK) and PEEK, the aromatic ether and ketone linkages are crystallo-

Can. J. Chem. Downloaded from www.nrcresearchpress.com by MCGILL UNIVERSITY on 02/02/13
For personal use only.

Fig. 3. Packing of the major conformation (55%) of 4,4′-bis(*p*-methoxyphenoxy)diphenyl sulfone (*ac* plane). Hydrogen atoms are omitted for clarity.

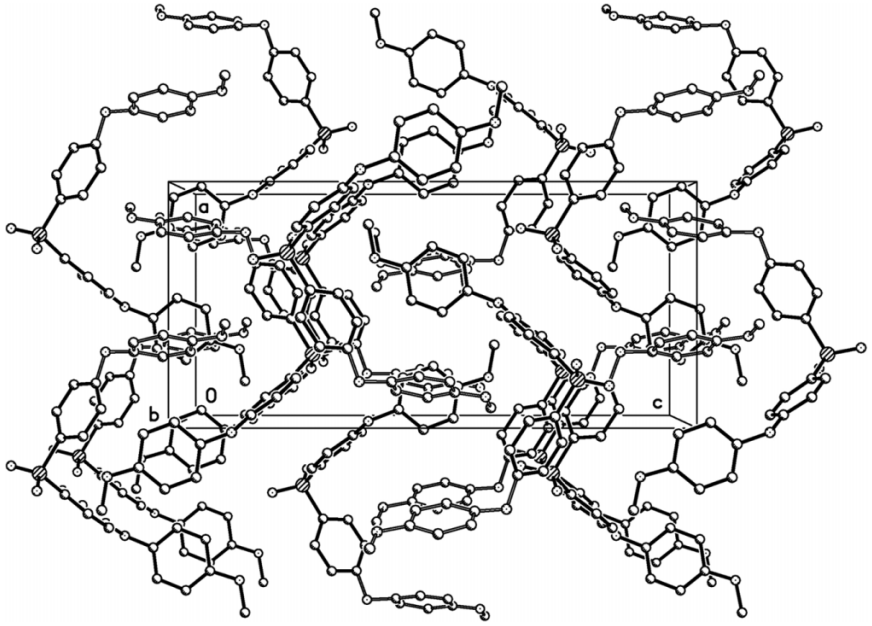


Fig. 4. Soft hydrogen bonds between the SO_2 group and the aromatic hydrogen atoms of 4,4′-bis(*p*-methoxyphenoxy)diphenyl sulfone.

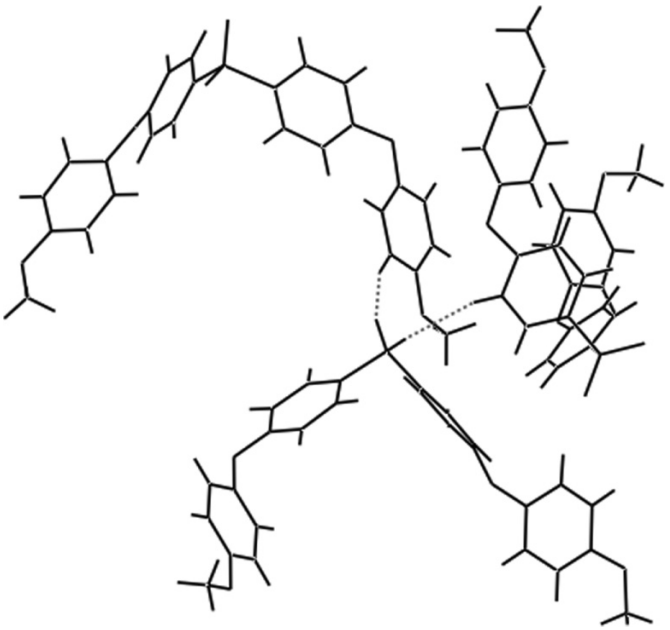
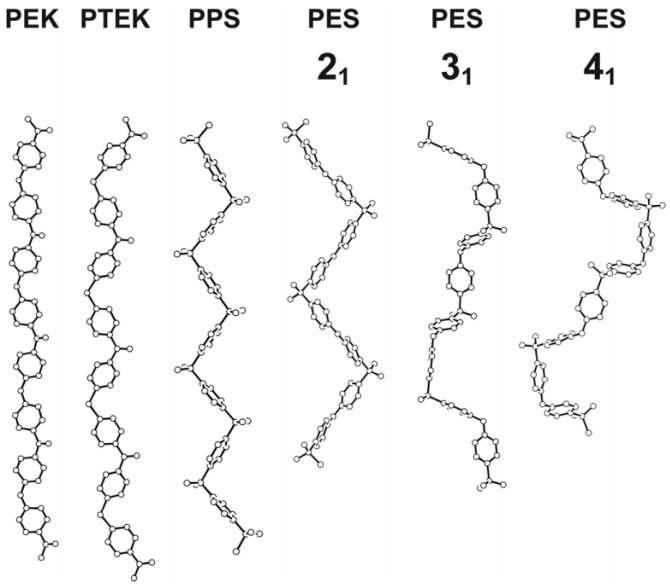


Fig. 5. Comparison between crystal structure conformations of rigid polymers. From left to right: polyetherketone (PEK), polythioetherketone (PTEK), polyparaphenylenesulfone (PPS), and possible conformations for polyethersulfone (PES).



graphically interchangeable, only slight variations in unit cell dimensions and relative intensity of the diffraction spots being observed.[37] These polymers are highly crystalline, surprisingly so for aromatic polymers, which are often low in crystallinity.[3] This has been attributed to the geometrical equivalence of aromatic ether and carbonyl linkages, which allows the chain to remain in a linear geometry favourable to crystallization.[37] Two crystal polymorphs are known, each having the same planar conformation and differing by the packing mode. Form I, obtained by crystallization from the melt, exhibits diffraction peaks at 3.8 and 4.8 Å and has been proposed to be monoclinic, with one chain at the center of the unit cell and another at the corner of the cell.[38] Its packing has been described as an edge-to-face phenyl packing.[39] Form II, obtained from the solution of cold crystallization, has an intense peak at 4.2 Å. Two different structures have been proposed for this form, a two-chain orthorhombic structure, also with one chain at the center and the other at the corner, but with slightly different chain organization,[38] and a one-chain or-

Can. J. Chem. Downloaded from www.nrcresearchpress.com by MCGILL UNIVERSITY on 02/02/13
For personal use only.

Table 5. Torsion angles and helix pitch of polyethersulfone (PES) models.

	Torsion angle (°)				
PES	C–C–S–C	C–S–C–C	C–C–O–C	C–O–C–C	Helix pitch (Å)
Model compound (ref. 9)	96.2	–67.0	87.3	–62.0	—
MDPS conformation I	91.5 (2)	87.4 (3)	–16.1 (4)	–75.8 (4)	—
MDPS conformation IIa	91.5 (2)	87.4 (3)	–28.8 (9)	–46.5 (15)	—
MDPD conformation IIb	91.5 (2)	87.4 (3)	33.1 (7)	75.5 (16)	—
2_1 Helix	90	78	20	–30	15.7
3_1 Helix	90	90	–30	90	25.0
4_1 Helix	90	78	20	60	26.2

Note: MPDS, 4,4′-bis(*p*-methoxyphenoxy)diphenyl sulfone.

Can. J. Chem. Downloaded from www.nrcresearchpress.com by MCGILL UNIVERSITY on 02/02/13
For personal use only.

thorhombic structure.[39] Random etherketone copolymers are even more crystalline than regular polymers, which further illustrates the crystallographic equivalence of ether and ketone groups in this class of rigid polymers.[40]

Polythioetherketone (PTEK), in which the ether group of PEK is replaced by a thioether group, also crystallizes well, in spite of the fact that thioether bond lengths and C–S–C bond angles are different from those of the ketone group.[3] Deformations occur on carbon atoms adjacent to the thioether bridge, opening up the thioether bond angle. This allows the polymer and related oligomers to remain essentially linear, and the conformation is very similar to that of PEK. This polymer is known to crystallize as two different polymorphs. Comparison of peak positions for the most intense reflections, as reported in Table 2, show strong similarity with PEK form I. Strong similarities in peak positions and relative intensities are also found between PEK form II and PTEK form II.[24,41] Form I is a body-centered monoclinic structure, whereas chains are at the corner and middle of the unit cell in the orthorhombic form II.

A third rigid polymer for which the crystal structure is known is presented in Table 2, PPS, in which the only linker between aromatic rings is a sulfone group.[27,42] Data on oligomers of PPS and proposed crystal structure show that the favoured conformation is not planar but of the open-book type, where rings are orthogonal (or nearly so) to the C–S–C plane,[42,43] as depicted in Fig. 5. This leads to a completely different chain packing and unit cell dimensions than in the case of PEK, PEEK, and PTEK. Two crystal polymorphs are also observed in this case, with peak positions bearing little similarity to those of PEK or PTEK, which can be attributed to the different chain conformation adopted.

In contrast to these rigid polymers, the crystal structure of PES has never been solved, and its repeat distance is also unknown, this polymer usually being amorphous as synthesized or even after annealing at higher temperatures in spite of its regularity, which is highly unusual. Further, when a low crystallinity is observed as synthesized, it disappears upon heating above the melt ing point.

The conformation adopted by the MPDS molecule is not all-trans nor reminiscent of a conformation leading to extended chains, as in the zig-zag conformation adopted in forms I and II of PEK and PTEK. It is also different from that of the crystal phase of PPS, which is an open-book zig-zag conformation, as shown in Fig. 5. The most interesting feature of this conformation is the fact that the open-book conformation is adopted for the sulfone group, but not for the ether groups.

As can be seen in Table 2, the diffraction diagrams of PEK, PTEK, and PPS do not match that observed in the present work for PES, the closest one being that of PPS, which exhibits three intense diffraction peaks at 16.4°, 21.1°, and 26.5°, as compared with two intense peaks at 18.0° and 21.1° for PES. PES is therefore proposed to exhibit a different crystal packing and possibly different conformation than that of related previously studied rigid polymers. Changing the carbonyl group by a sulfone group, therefore, has a more profound effect on the crystal form that by changing an ether group to a thioether group, which leads one to suspect that the change is not merely related to packing but may also relate to the conformation adopted by the chains.

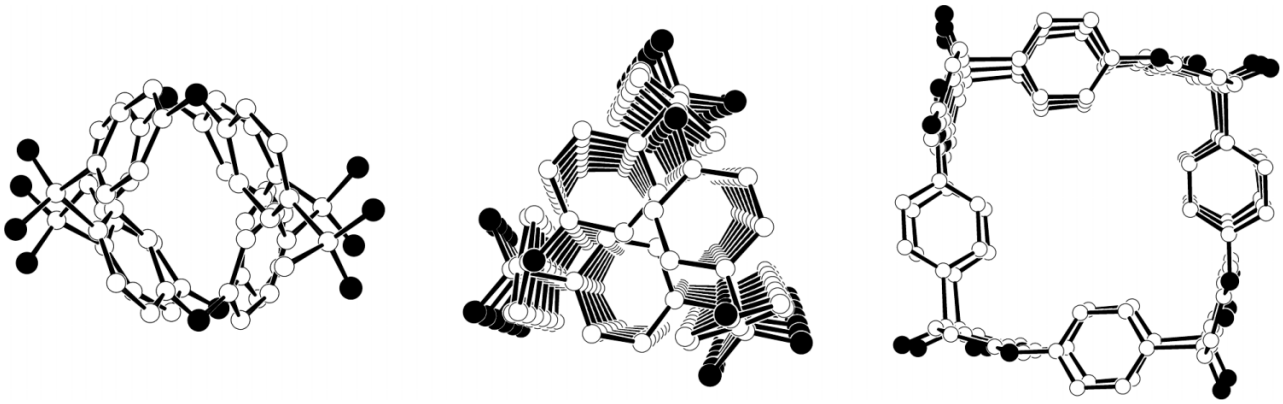
Investigation of possible conformations of PES

In the absence of a repeat distance value, it is very difficult to determine without ambiguity the conformation adopted by PES in its crystal forms. In the present study, a few low-energy conformations were built and compared. These are reported at the right in Fig. 5. In all cases, helices were investigated, although pseudohelical forms cannot be excluded.

The 2_1 helix is the simplest form, conformationwise. It is similar to that of PPS, combining open-book around the sulfone group and parallel ring arrangements around the ether linkage. As reported in Table 5, torsion angles around the sulfone groups have values of 90° and 78°, and are both close to the minimum energy conformation of 90°. The ether group shows torsion angle values of 20° and –30°, close to those observed for MDPS conformation IIa (although in this conformation successive torsion angles were of the same sign, which is not the case for the 2_1 helix). This yields a zig-zag conformation reminiscent of the PPS conformation, but with bends occurring every two aromatic cycles. The chain "bends" at each sulfone group, whereas the ether groups remain in the same plane at the aromatic cycles to which they are linked. A packing similar to that of PPS would be possible with this conformation.

Various helices could be built using slight variations in the torsion angles of one of the conformations of MDPS. For example, the 3_1 helix shown in Fig. 5 is relatively compact, and its conformation angles are 90° around the sulfone group, as in the case of most crystal structures. Around the ether group, a first torsion angle of –30° is found, which is close to one value observed for MDPS conformations I and IIa However, the second torsion angle is 90°, which deviates signifi-

Fig. 6. Top view of three possible conformations of polyethersulfone (PES): 2_1, 3_1, and 4_1 helices.



cantly from values observed for model compounds, a value close to the one observed by Bocelli et al.[9] for a PES model compound, although the two successive torsion angles were not the same. The 4_1 helix was obtained from slight deviations from the torsion angles adopted by the MPDS conformation IIb and is a more "open" helix, exhibiting a void at the center. It is also close, but with opposite signs, to MDPS conformation I. This similarity, and the previously noted similarity in powder diffraction diagrams, indicates this could be the conformation adopted by the crystal structure of PES that was observed in the present work.

A top view of each of these three helices is presented in Fig. 6. The 2_1 and 3_1 helices are relatively compact, whereas a void is present at the center of the 4_1 helix. In all cases, the oxygen atoms (shown in black in this figure) lie on the outer surface of the helix. If soft hydrogen bonds between the helix and solvent molecules stabilize this crystal form, solvent molecules would be present between helices. On the other hand, as can be seen in Fig. 5, some solvent molecules could also be trapped at the middle of a 4_1 helix.

The presence of solvent molecules in the crystal structure, stabilizing the helical conformation, is in agreement with observations by Blackadder and Ghavamikia[21] that birefringent spherulitic structures and crystal-like globules can be observed in chloroform of dichloromethane, and that structures loose their birefringence and crystallinity upon drying.

Conclusion

A new crystal form for PES was observed from solvent-induced crystallization of low molecular weight PES. X-ray diffraction shows a strong similarity with X-ray diffraction patterns of the small molecule model MPDS. The crystal structure of MPDS is disordered, illustrating the relative flexibility for rotation around ether linkages, as compared with relatively more rigid sulfone bonds. For this reason, it is proposed that ether and sulfone bonds are not crystallographically interchangeable, thus destabilizing the crystal form of this polymer as compared with that of other rigid polymers, where all aryl bonding groups are crystallographically interchangeable.

Various low-energy helical forms exist for PES, and all have oxygen atoms at their outer surface with which solvent molecules can form soft hydrogen bonds to stabilize the conformation. Further, a 4_1 helix PES model built using torsion angles close to those of a MPDS conformation presents a void at the center and can therefore accommodate additional solvent molecules. Upon drying, evaporation of the solvent increases the free volume, allowing the chain to adopt other conformations and resulting in a loss of short-range order and crystallinity. It is proposed as a possible conformation for the new PES crystal form reported in the present work.

Supplementary data

Supplementary data are available with the article through the journal Web site at http://nrcresearchpress.com/doi/suppl/10.1139/v2012-066. CCDC 871798 contains the X-ray data in CIF format for this manuscript. These data can be obtained, free of charge, via http://www.ccdc.cam.ac.uk/products/csd/request (or from the Cambridge Crystallographic Data Centre, 12 Union Road, Cambridge CB2 1EZ, UK; fax: 44 1223 336033; or e-mail:deposit@ccdc.cam.ac.uk.

Acknowledgements

The authors wish to acknowledge the financial support of the Natural Sciences and Engineering Council of Canada (NSERC). The assistance of R. Plesu, of CERMA, Université Laval, for X-ray diffraction, and of A. Furtos, of Université de Montréal, for MALDI-TOF, is gratefully acknowledged.

References

(1) Blackadder, D. A.; Ghavamikia, H.; Windle, A. H. *Polymer (Guildf.)* **1979**, *20* (6), 781. doi:10.1016/0032-3861(79)90257-X.

(2) Arzak, A.; Eguiazábal, J. I.; Nazábal, J. *J. Macromol. Sci. Phys.* **1994**, *B33* (2), 261.

(3) Colquhoun, H. M.; Williams, D. J. *Acc. Chem. Res.* **2000**, *33* (3), 189. doi:10.1021/ar980123c.

(4) Attwood, T. E.; King, T.; Leslie, V. J.; Rose, J. B. *Polymer (Guildf.)* **1977**, *18* (4), 369. doi:10.1016/0032-3861(77)90085-4.

(5) McGrath, J. E.; Ward, T. C.; Viswanathan, R.; Webster, D. C. Society for the Advancement of Material and Process Engineering (SAMPE) 12th National Conference, Seattle, Washington, Oct. 7–9 1980, p 305.

(6) Clagett, D. C. In *Encyclopedia of Polymer Science and Engineering*; H. F. Mark, N. M. Bikales, C. G. Overberger, G. Menges and J. I. Kroschwitz, Eds.; Wiley: New York, 1989; Vol. 6, pp 114–115.

Can. J. Chem. Downloaded from www.nrcresearchpress.com by MCGILL UNIVERSITY on 02/02/13
For personal use only.

Can. J. Chem. Downloaded from www.nrcresearchpress.com by MCGILL UNIVERSITY on 02/02/13
For personal use only.

(7) Jadhav, J. Y.; Kantor, S. W. In *Encyclopedia of Polymer Science and Engineering*; H. F. Mark, N. M. Bikales, C. G. Overberger, G. Menges and J. I. Kroschwitz, Eds.; Wiley, New York, 1989; Vol. 12, p 219.
(8) Schmidt-Rohr, K.; Hu, W.; Zumbulyadis, N. *Science* **1998**, *280* (5364), 714. doi:10.1126/science.280.5364.714.
(9) Bocelli, G.; Rizzoli, C. *Acta Crystallogr.* **1990**, *C46* (11), 2259. doi:10.1107/S0108270190005005.
(10) Manet, S.; Tibirna, C.; Boivin, J.; Delabroye, C.; Brisson, J. *Macromolecules* **2006**, *39* (3), 1093. doi:10.1021/ma052248k.
(11) Yokozawa, T.; Taniguchi, T.; Suzuki, Y.; Yokoyama, A. *J. Polym. Sci. A Polym. Chem.* **2002**, *40* (20), 3460. doi:10.1002/pola.10429.
(12) Macrae, C. F.; Bruno, I. J.; Chisholm, J. A.; Edgington, P. R.; McCabe, P.; Pidcock, E.; Rodriguez-Monge, L.; Taylor, R.; van de Streek, J.; Wood, P. A. *J. Appl. Cryst.* **2008**, *41* (2), 466. doi:10.1107/S0021889807067908.
(13) *APEX 2,* version 2.0.2; Bruker AXS Inc.: Madison, WI, 2005b.
(14) *SAINT,* version 7.07a; Bruker AXS Inc.: Madison, WI, 2003.
(15) Sheldrick, G. M. *SADABS,* version 2004/1; Bruker AXS Inc.: Madison, WI, 2004.
(16) Sheldrick, G. M. *SHELXS-97 and SHELXL-97,* Programs for the refinement of crystal structures; University of Gottingen: Gottingen, Germany, 1997.
(17) *International Tables for Crystallography*. Wilson, A. J. C., Ed.; Kluwer Academic Publishers: Dordecht, 1992; Vol. C, Tables 4.2.6.8 (pp 219–222) and 6.1.1.4 (pp 500–502).
(18) *SHELXTL,* version 6.12; Bruker AXS Inc.: Madison, WI, 2001.
(19) Spek, A. L. *Acta Crystallogr.* **1990**, *A46,* C-34.
(20) Spek, A. L. *PLATON, A Multipurpose Crystallographic Tool;* University of Utrecht, Utrecht, the Netherlands, 2005.
(21) Blackadder, D. A.; Ghavamikia, H. *Polymer (Guildf.)* **1979**, *20* (11), 1433. doi:10.1016/0032-3861(79)90285-4.
(22) Ho, R.-M.; Cheng, S. Z. D.; Hsiao, B. S.; Gardner, K. H. *Macromolecules* **1994**, *27* (8), 2136. doi:10.1021/ma00086a023.
(23) Cheng, S. Z. D.; Ho, R.-M.; Hsiao, B. S.; Gardner, K. H. *Macromol. Chem. Phys.* **1996**, *197* (1), 185. doi:10.1002/macp.1996.021970115.
(24) Colquhoun, J. M.; Lewis, D. F.; Williams, D. J. *Polymer (Guildf.)* **1999**, *40* (19), 5415. doi:10.1016/S0032-3861(98)00740-X.
(25) Colquhoun, H. M.; Lewis, D. F.; Williams, D. J. *Macromolecules* **1999**, *32* (10), 3384. doi:10.1021/ma9819586.
(26) Robello, D. R.; Ulman, A.; Urankar, E. N. *Macromolecules* **1993**, *26* (25), 6718. doi:10.1021/ma00077a004.
(27) Colquhoun, H. M. *Polymer (Guildf.)* **1997**, *38* (4), 991. doi:10.1016/S0032-3861(96)00779-3.
(28) Rudolph, F. A. M.; Fuller, A. L.; Slawin, A. M. Z.; Bühl, M.; Aitken, R. A.; Woolins, J. D. *J. Chem. Cryst.* **2010**, *40* (3), 253. doi:10.1007/s10870-009-9643-8.
(29) Koch, H. P.; Moffitt, W. E. *Trans. Faraday Soc.* **1951**, *47,* 7. doi:10.1039/tf9514700007.
(30) Bocelli, G.; Cantoni, A. *Acta Crystallogr.* **1990**, *C46* (2), 2257. doi:10.1107/S0108270190004991.
(31) Tabor, J.; Magré, E. P.; Boon, J. *Eur. Polym. J.* **1971**, *7* (8), 1127. doi:10.1016/0014-3057(71)90145-5.
(32) Colquhoun, H. M.; Williams, D. J. *Macromolecules* **1996**, *29* (9), 3311. doi:10.1021/ma951628a.
(33) Kendrick, J.; Robson, E.; Weaver, M. *J. Chem. Soc., Faraday Trans.* **1995**, *91* (16), 2609. doi:10.1039/ft9959102609.
(34) Feigel, M. *J. Mol. Struct. THEOCHEM* **1996**, *366* (1–2), 83. doi:10.1016/0166-1280(96)04512-5.
(35) Straßner, T. *Can. J. Chem.* **1997**, *75* (7), 1011. doi:10.1139/v97-121.
(36) Glidewell, C.; Harrison, W. T. A.; Low, J. N.; Sime, J. G.; Wardell, J. L. *Acta Crystallogr.* **2001**, *B57* (2), 190. doi:10.1107/S0108768100015494.
(37) Dawson, P. C.; Blundell, D. J. *Polymer (Guildf.)* **1980**, *21* (5), 577. doi:10.1016/0032-3861(80)90228-1.
(38) Blundell, D. J.; Newton, A. B. *Polymer (Guildf.)* **1991**, *32* (2), 308. doi:10.1016/0032-3861(91)90019-F.
(39) Gardner, K. H.; Hsiao, B. S.; Matheson, R. S.; Wood, B. A. *Polymer (Guildf.)* **1992**, *33* (12), 2483. doi:10.1016/0032-3861(92)91128-O.
(40) Colquhoun, H. M.; Dudman, C. C.; Blundell, D. J.; Bunn, A.; Mackenzie, P. D.; McGrail, P. T.; Nield, E.; Rose, J. B.; Williams, D. J. *Macromolecules* **1993**, *26* (1), 107. doi:10.1021/ma00053a016.
(41) Takahashi, T.; Hii, S.-H.; Sakurai, K. *J. Macromol. Sci. B Phys.* **1998**, *37* (1), 59. doi:10.1080/00222349808220455.
(42) Colquhoun, H. M.; Aldred, O. K.; Kohnke, F. H.; Herbertson, P. H.; Baxter, I.; Williams, D. J. *Macromolecules* **2002**, *35* (5), 1685. doi:10.1021/ma011597l.
(43) Hamerton, I.; Heald, C. R.; Howlin, B. J. *Macromol. Theory Simul.* **1996**, *5* (2), 305. doi:10.1002/mats.1996.040050211.

A solid-state NMR investigation of the colossal expansion material, $Ag_3Co(CN)_6$

Brett C. Feland, Guy M. Bernard, and Roderick E. Wasylishen

Can. J. Chem. Downloaded from www.nrcresearchpress.com by MCGILL UNIVERSITY on 02/02/13
For personal use only.

Abstract: Presented here is a solid-state NMR investigation of the so-called "colossal expansion" material, $Ag_3Co(CN)_6$, a compound that exhibits some of the largest positive and negative thermal expansion properties reported. This study explores the ^{13}C, ^{15}N, and ^{59}Co NMR properties of this material at room temperature and at variable temperatures with the goal of probing the effects of this colossal expansion behaviour on these properties. We found that the flexible nature of the crystal framework leads to a distribution of electric field gradients, and that, oddly enough, no strong correlation is observed between the NMR parameters of $Ag_3Co(CN)_6$ and its colossal expansion nature. The ^{59}Co isotropic chemical shift increased and the ^{59}Co nuclear quadrupolar coupling constant decreased with increasing temperature, but neither of these relationships were extraordinary when compared to other octahedral Co(III) complexes. The link between the colossal expansion and the NMR properties of $Ag_3Co(CN)_6$ may be the distribution of lattice parameters and hence unusually broad features in the ^{59}Co NMR spectra. The high order of symmetry at the cobalt site resulted in a small quadrupolar coupling constant less than 1 MHz in magnitude. We also observed a $|^1J(^{107/109}Ag,^{15}N)|$ value of 96 Hz, the largest $^{107/109}Ag–^{15}N$ coupling constant reported to date.

Key words: colossal expansion material, solid-state NMR, Co-59 NMR, C-13 NMR, N-15 NMR.

Résumé : Dans ce travail, on rapporte les résultats d'une étude RMN à l'état solide du matériau dit d' « expansion colossale », $Ag_3CO(CN)_6$, un composé qui possède des propriétés d'expansion thermique positives et négatives parmi les plus grandes. Cette étude examine les propriétés RMN du ^{13}C, du ^{15}N et du ^{59}Co, à la température ambiante ainsi qu'à des températures variables, dans le but d'étudier les effets de ce comportement d'expansion colossale sur ces propriétés. On a trouvé que la nature flexible du réseau cristallin conduit à une distribution des gradients des champs électriques et que, d'une façon surprenante, il n'existe aucune corrélation forte entre les paramètres RMN du $Ag_3CO(CN)_6$ et sa nature d'expansion colossale. Le déplacement chimique isotrope du ^{59}Co augmente alors que la constante de couplage quadripolaire nucléaire du ^{59}Co diminue avec une augmentation de la température; aucune de ces relations n'est toutefois extraordinaire quand on les compare avec celles d'autres complexes octaédriques du Co(III). Le lien entre l'expansion colossale et les propriétés RMN du $Ag_3CO(CN)_6$ pourrait provenir de la distribution des paramètres de réseaux et, en conséquence, de caractéristiques anormalement larges dans les spectres RMN du ^{59}Co. Le degré de symétrie élevé au niveau du site du cobalt conduit à une constante de couplage quadripolaire faible, dont l'amplitude est inférieure à 1 Mhz. On a aussi observé une valeur $|^1J(^{107/109}Ag,^{15}N)|$ de 96 Hz, la constante de couplage la plus grande observée jusqu'à maintenant pour $^{107/109}Ag,^{15}N$.

Mots-clés : matériau d'expansion colossale, RMN à l'état solide, RMN du Co-59, RMN du C-13, RMN du N-15.

[Traduit par la Rédaction]

Introduction

In 2008, Goodwin et al.[1] reported that silver hexacyanocobaltate(III), $Ag_3Co(CN)_6$, exhibits the highest known relative positive and negative thermal crystal framework expansion. The structure of this material has been known since 1968; it arranges itself in a trigonal lattice (Fig. 1) and is comprised of alternating layers of Ag^+ and $[Co(CN)_6]^{3-}$ ions.[1,2] It crystallizes in the $P\bar{3}1m$ space group (No. 162) with (hexagonal setting) unit cell parameters $a = b = 7.030\,66(9)$ Å and $c = 7.117\,48(17)$ Å at 300 K.[1] Using variable temperature X-ray and neutron powder diffraction techniques, Goodwin et al. discovered that, with regards to the crystal unit cell, positive thermal expansion (PTE) occurs in the *a–b* plane parallel to the ion layers (i.e., $da/dT > 0$), and negative thermal expansion (NTE) occurs along the *c* axis, perpendicular to these layers (i.e., $dc/dT < 0$). The space group does not change over the temperature range studied by diffraction techniques (16–500 K), and the material decomposes at 500 K.[1] In addition to NTE, $Ag_3Co(CN)_6$ exhibits large negative linear compressibility,[3] in which the unit cell expands along the *c* axis with increasing hydrostatic pressure. Such compounds[4] that display both PTE and NTE properties simultaneously do not vary greatly in unit cell volume over broad temperature ranges, and powders of these solids could potentially be used to develop materials that resist compression in extreme

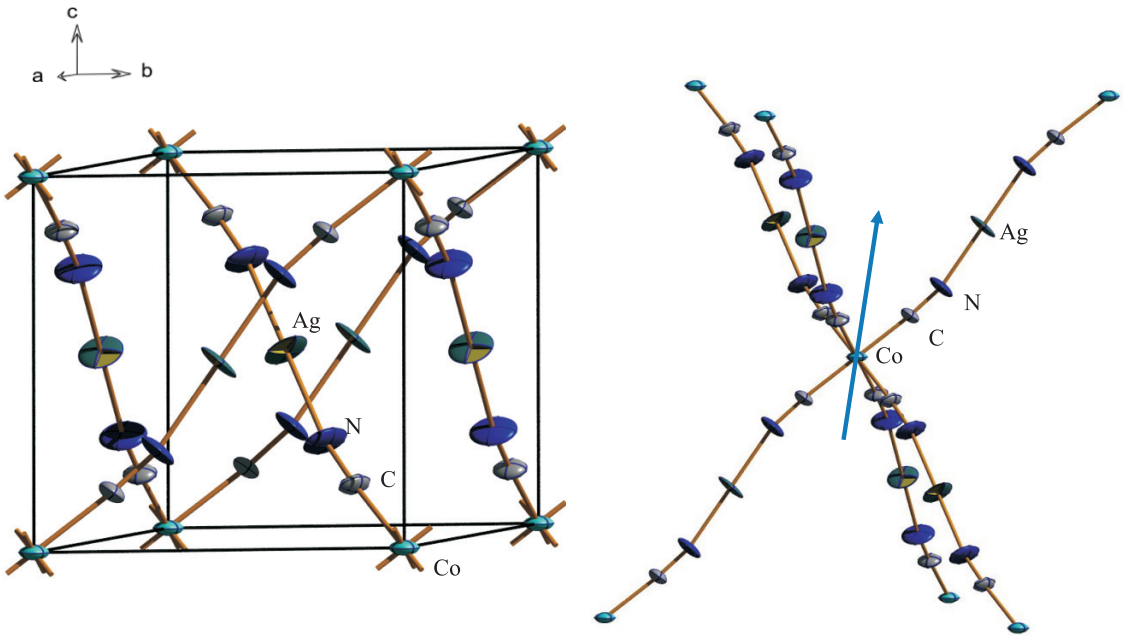
Received 14 June 2012. Accepted 3 August 2012. Published at www.nrcresearchpress.com/cjc on 20 November 2012.

B.C. Feland, G.M. Bernard, and R.E. Wasylishen. Department of Chemistry, University of Alberta, 11227 SK Drive N.W., Edmonton, AB T6G 2G2, Canada.

Corresponding author: Roderick E. Wasylishen (e-mail: roderick.wasylishen@ualberta.ca).

Can. J. Chem. Downloaded from www.nrcresearchpress.com by MCGILL UNIVERSITY on 02/02/13
For personal use only.

Fig. 1. Unit cell of $Ag_3Co(CN)_6$ (left), and a cobalt-centred view (right) highlighting the rotational axis of symmetry. The image was generated using previously reported diffraction data from Goodwin et al.[1] Thermal ellipsoids represent 50% electron density.



temperature and pressure conditions. However, ordered layers of such materials may also potentially be useful in highly sensitive pressure detectors.[1,3]

The diffraction studies of Goodwin et al.[1] and others,[3,5,6] including neutron total scattering and reverse Monte Carlo analyses,[6] indicate that bond flexing in the Co–CN–Ag–NC–Co chains occurs during thermal expansion/contraction of the material, and that the octahedral orientation around each Co^{3+} remains largely unaffected by temperature. The PTE/NTE in $Ag_3Co(CN)_6$ has been compared to the flexing of a piece of lattice fencing,[1] and the source of this colossal expansion behaviour has been attributed to argentophillic interactions.[7] The relative NTE coefficients were nearly a full order of magnitude larger than any previously reported values (although other NTE coefficients nearly as large have since been reported),[4] whereas the PTE coefficients are of the same order as the largest known.

Cobalt-59 NMR parameters are known to be very sensitive to slight changes in structure.[8] Isotropic ^{59}Co chemical shifts fall over a range greater than 17 000 ppm, and ^{59}Co nuclear quadrupolar coupling constants can be greater than 170 MHz.[8–10] Therefore, in this study we chose to examine the temperature dependence of the solid-state ^{59}Co NMR parameters of $Ag_3Co(CN)_6$ and determine if any correlation can be made between this PTE/NTE behaviour and the magnetic shielding and electric field gradient (EFG) tensors at the ^{59}Co site. We also studied the ^{13}C and ^{15}N NMR properties of this material to further investigate the claim that the cyanide groups are entirely C-bound to the cobalt[1] and to investigate possible dynamics of the cyanide ligand.

Background and theory

For the sake of simplicity, rather than discussing magnetic shielding, we shall focus on chemical shift (CS), which is related to magnetic shielding by[11]

$$[1] \qquad \delta_{ii} = \frac{\sigma_{ref} - \sigma_{ii}}{1 - \sigma_{ref}} \approx \sigma_{ref} - \sigma_{ii}$$

$$[2] \qquad \delta_{ii} = \frac{\nu_{ii} - \nu_{ref}}{\nu_{ref}}$$

Here, σ_{ii} denotes absolute magnetic shielding tensor principal component values relative to a bare nucleus, δ_{ii} denotes chemical shift tensor principal components (typically expressed in ppm) referenced to a chosen standard, ν_{ii} is the resonant frequency of each principal component, and ν_{ref} is the isotropic resonant frequency of the reference compound. The CS interaction is typically described by a second-rank tensor in its principal axis system (PAS) and takes the form

$$[3] \qquad \begin{bmatrix} \delta_{11} & 0 & 0 \\ 0 & \delta_{22} & 0 \\ 0 & 0 & \delta_{33} \end{bmatrix}$$

where δ_{11}, δ_{22}, and δ_{33} are the principal components of the CS tensor defined such that $\delta_{11} \geq \delta_{22} \geq \delta_{33}$.[11] These principal components are, for spin $I = 1/2$ nuclei, observed at the points of discontinuity in the solid-state NMR "powder pattern" spectrum of a simple, one-site stationary powder sample in the absence of any effects other than CS anisotropy (CSA). If the crystal structure of the material is such that a threefold (or greater) axis of rotational symmetry passes through the nucleus of interest, two of the CS tensor principal components will be equivalent and oriented perpendicular to the symmetry axis, while the third component will be oriented parallel to the axis. We designate these components $\delta_\perp$ and $\delta_\parallel$, respectively. In such cases the isotropic chemical shift (δ_{iso}) is defined as $\delta_{iso} = (2\delta_\perp + \delta_\parallel)/3$ and the span is defined as $\Omega = |\delta_\perp - \delta_\parallel|$.

For nuclei with spin $I > 1/2$, the nuclear quadrupolar interaction

Can. J. Chem. Downloaded from www.nrcresearchpress.com by MCGILL UNIVERSITY on 02/02/13
For personal use only.

also affects the NMR powder pattern. The nuclear quadrupolar interaction is dependent on the EFG tensor at the quadrupolar nucleus, in this case ^{59}Co (I = 7/2). The EFG about a specific nucleus is characterized by a symmetric, traceless tensor, whose three principal components in the PAS (eq_{ii}) follow[12,13]

$$[4] \qquad |eq_{zz}| \geq |eq_{yy}| \geq |eq_{xx}|$$

Since the sum of the three principal components is zero, only two parameters are required to describe them. Typically, we consider the nuclear quadrupolar coupling constant (C_Q) and quadrupolar asymmetry parameter (η_Q), which are related to the EFG by[12,13]

$$[5] \qquad C_Q = \frac{e^2 Q q_{zz}}{h}$$

$$[6] \qquad \eta_Q = \frac{q_{xx} - q_{yy}}{q_{zz}}$$

Here, e is the elementary charge, Q is the nuclear quadrupole moment of the nucleus, and h is Planck's constant.

The full frequency width (W) of the solid-state NMR spectrum of a noninteger spin quadrupolar nucleus (I = 3/2, 5/2, 7/2, or 9/2) is related to the quadrupolar frequency ν_Q and to C_Q by[12]

$$[7] \qquad \nu_Q = \frac{3C_Q}{2I(2I-1)}$$

$$[8] \qquad W = (2I-1)\nu_Q$$

including all transitions (i.e., for I = 7/2, $m_I = +7/2 \leftrightarrow +5/2$, $m_I = +5/2 \leftrightarrow +3/2$, …, $m_I = -5/2 \leftrightarrow -7/2$, and W simplifies to $W = 6\nu_Q = (3/7)C_Q$). Generally, the span expressed in frequency units (Hz) is less than C_Q, and as such W is independent of the CSA interaction for nearly all cases, including the one studied here. If C_Q is large, it is typical to focus on the central $m_I = +1/2 \leftrightarrow -1/2$ transition, as the full width of the powder pattern, including all satellite transitions, may be too broad to observe on most NMR spectrometers.[12,14] However, if C_Q is small enough that the entire spectrum can be observed (W typically on the order of 2 MHz or less), C_Q is often obtained by measuring the full frequency width of the spectrum.

As with the CS tensor, when a threefold or greater axis of symmetry passes through the site under investigation, certain restrictions are placed on the orientation of the EFG tensor.[15–19] The largest component of the tensor (eq_{zz}) lies along the axis of symmetry, whereas the other components are equivalent and oriented perpendicular to the axis, which makes $\eta_Q = 0$. Note that if a nucleus is located in a site of perfect three-dimensional long-range tetrahedral or octahedral (or higher) symmetry, then $C_Q = 0$. Also, EFGs tend to be more sensitive to the long-range environment (within a simple point charge model, the EFG at a nucleus is inversely proportional to r^3, where r is the distance from the nucleus to the point charge), whereas CS tensors tend to be mainly sensitive to the short-range environment.[13]

Results and discussion

^{13}C and ^{15}N solid-state NMR spectroscopy

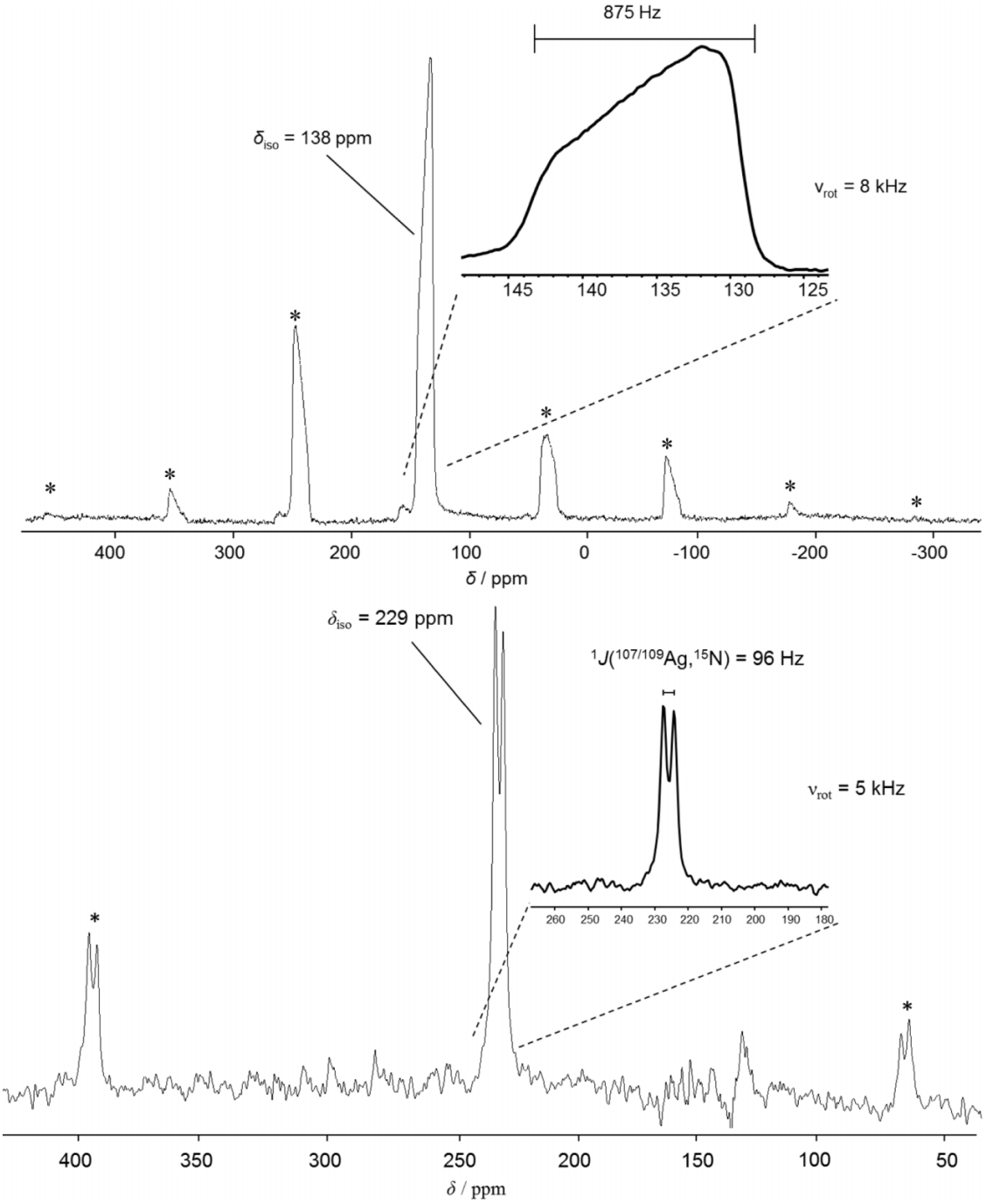
Figure 2 shows the solid-state ^{13}C and ^{15}N NMR spectra of 33% $^{13}C^{15}N$-labelled $Ag_3Co(CN)_6$ acquired with magic angle spinning (MAS) at 7.05 T. A 96 Hz splitting observed in the ^{15}N NMR spectrum is attributed to $^1J(^{107/109}Ag,^{15}N)$. ^{13}C NMR spectra demonstrate that this splitting is not due to $^1J(^{13}C,^{15}N)$ coupling (vide infra). ^{107}Ag and ^{109}Ag are both spin I = 1/2 nuclei with similar natural abundances (51.84% and 48.16%, respectively) and magnetogyric ratios (-1.089×10^7 and -1.252×10^7 rad s^{-1} T^{-1}, respectively).[20] As a result, our experimental line widths were too broad to resolve coupling to the two isotopes of silver. Thus, the observed $^1J(^{107/109}Ag,^{15}N)$ coupling is an average of the two. Nevertheless, 96 Hz is the largest value of $|^1J(^{107/109}Ag,^{15}N)|$ that has been reported to date for any material. This indicates that nitrogen is directly bonded to silver in $Ag_3Co(CN)_6$. There was no indication of splitting due to $J(^{59}Co,^{15}N)$ in the ^{15}N NMR spectrum (vide infra).

Splittings due to ^{59}Co–^{13}C spin-spin coupling were observed in the ^{13}C NMR spectra acquired with MAS, however, individual peaks were broad and poorly resolved. Nevertheless, the MAS isotropic and spinning side band line widths of ~875 Hz (see Fig. 2) and peak shapes do allow us to place an upper limit on $|^1J(^{59}Co,^{13}C)|$ of 130 Hz ($|^1J(^{59}Co,^{13}C)|$ = (875 Hz / 7) + ~10% error). This is in good agreement with the value of $^1J(^{59}Co,^{13}C)$ reported for $K_3Co(CN)_6$ dissolved in water, 126.0 Hz.[21,22] If all MAS side bands in the ^{13}C NMR spectrum are added together, the resulting line shape is symmetric (eight overlapping peaks of equal intensity). The asymmetry in each individual side band is due to the orientation dependence of the carbon-13 shielding tensor and the ^{59}Co–^{13}C spin-spin coupling tensors.[23–25] There was no indication of $J(^{107/109}Ag,^{13}C)$ coupling, which is expected to be small as it is a two-bond indirect spin-spin coupling constant. The weak-intensity peaks observed in the ^{13}C NMR spectrum (Fig. 2) are attributed to trace amounts of unreacted $K_3Co(^{13}C^{15}N)_6$. It should be noted that the spectral line widths in both the ^{15}N and ^{13}C NMR spectra were too broad to resolve $^1J(^{13}C,^{15}N)$, which is expected to be on the order of 10 Hz based on the $^1J(^{13}C,^{15}N)$ coupling within the free cyanide ion in solution as well as in several transition-metal complexes.[26,27] The observed spin-spin coupling in the spectra confirm the conclusion made by Goodwin et al.[1] based on neutron scattering data that the CN^- ions are entirely C-bound to the Co and N-bound to the Ag.[28] Furthermore, we observe no evidence of dynamic disorder of the cyanide ligand. Such disorder would result in decoupling of indirect spin-spin coupling interactions.

Room-temperature (RT) ^{59}Co NMR spectroscopy

Cobalt-59 NMR spectra were acquired at different magnetic field strengths (B_0 = 4.70, 7.05, 11.75, and 21.14 T), and as outlined as follows, the results were consistent. Stationary sample spectra were simulated using the program WSolids1.[29] Baseline corrections were applied to all MAS sample spectra. A typical ^{59}Co NMR spectrum of natural abundance $Ag_3Co(CN)_6$ obtained at 11.75 T with MAS is shown in Fig. 3. Because the cobalt nucleus is located at a site of nearly perfect octahedral symmetry, W is small

Fig. 2. Solid-state ^{13}C (top) and ^{15}N (bottom) NMR spectra of $Ag_3Co(CN)_6$ (33% $^{13}C^{15}N$ labelled) at 7.05 T with magic angle spinning (MAS). *Denotes spinning side bands.



Can. J. Chem. Downloaded from www.nrcresearchpress.com by MCGILL UNIVERSITY on 02/02/13
For personal use only.

(264 kHz), a consequence of $C_Q \approx 616$ kHz. Analysis indicates that the line shapes of solid-state ^{59}Co NMR spectra are determined primarily by the magnetic shielding and first-order quadrupolar interactions. The effects of any indirect spin-spin or dipolar coupling interactions are small and not observed in the ^{59}Co NMR spectra. We also discovered that the C_Q for ^{59}Co is, in this case, small enough that we can observe the entire ^{59}Co NMR spectrum including central and satellite transitions, but large enough that W is independent of the CSA. Figure 4 highlights this conclusion. It shows the full ^{59}Co NMR spectrum for $Ag_3Co(CN)_6$ at two different magnetic field strengths with 5 kHz MAS plotted in the frequency domain. Broken lines indicate the edges of the spinning sideband manifold and that the spectral width is unaffected by field strength. By measuring the full width of the ^{59}Co NMR spectrum of $Ag_3Co(CN)_6$ at RT and 11.75 T with MAS (Fig. 3), including the satellite transitions, we are able to use eqs. [7] and [8] to obtain C_Q, which is 616 ± 37 kHz. We verified that the observed W was not an artifact of the excitation profile by stepping the transmitter offset

Fig. 3. Solid-state ^{59}Co NMR spectrum of $Ag_3Co(CN)_6$ obtained at 11.75 T (118.6 MHz) with 8 kHz MAS. Isotropic peak indicated; all others are spinning side bands. Spectrum is the result of signal averaging 54 000 transients.

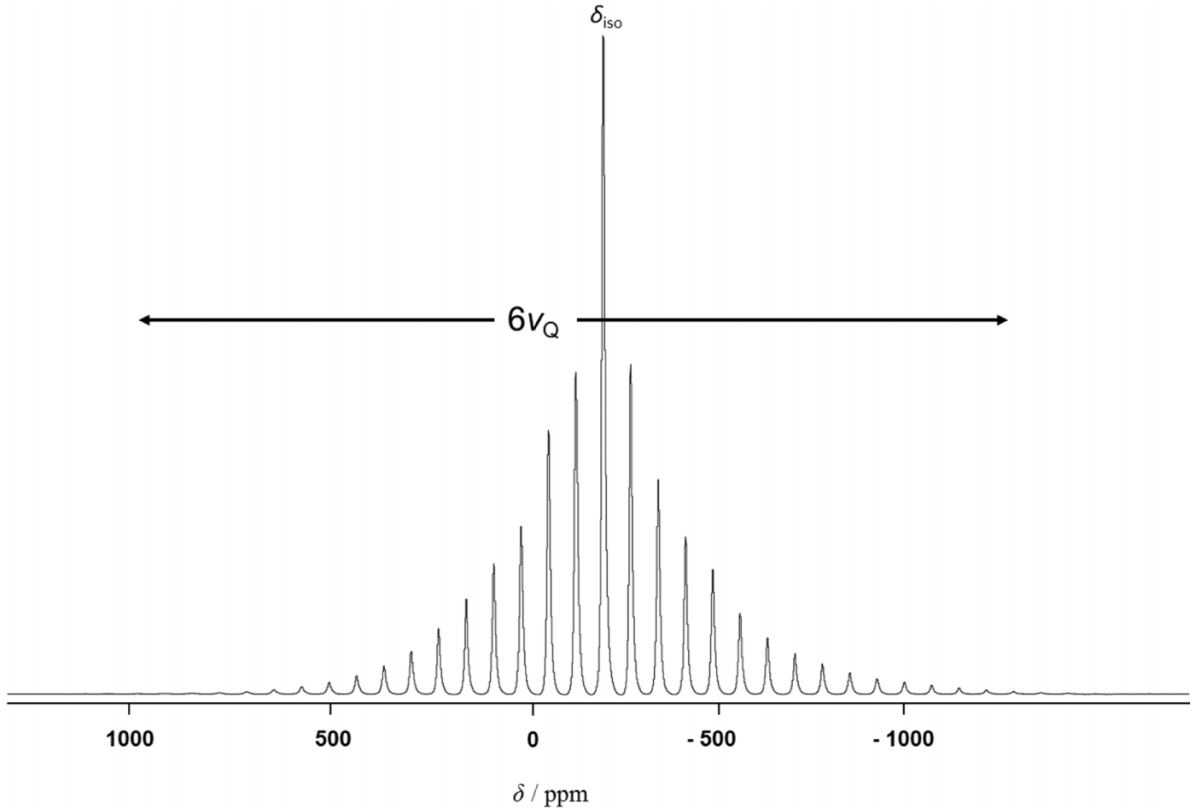
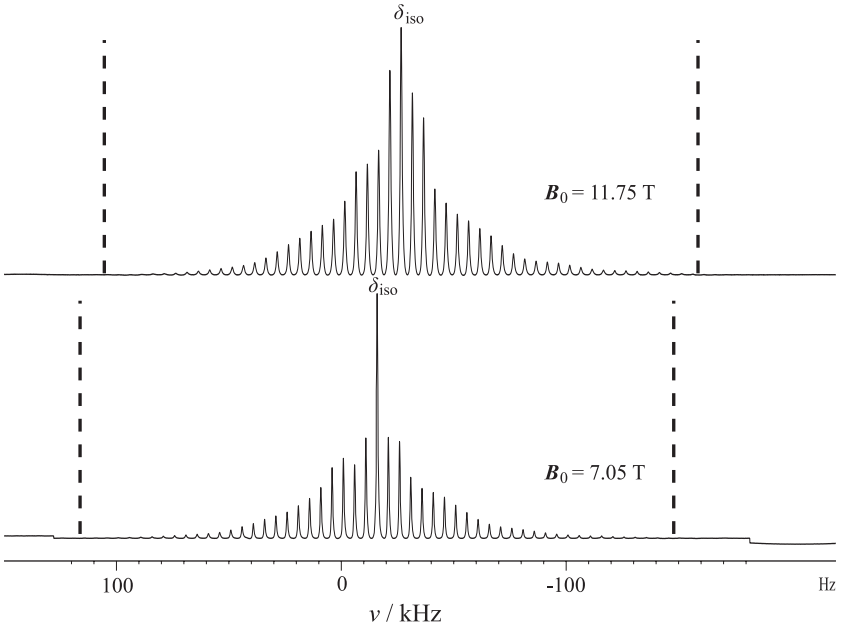


Fig. 4. Solid-state ^{59}Co NMR spectra of $Ag_3Co(CN)_6$ acquired at two different field strengths with 5 kHz MAS. Spectra are shown on the same frequency shift (Hz) scale. Full-spectrum width is indicated with broken lines in both spectra.



(vide infra). The error in C_Q was estimated on the basis of observing the entire spectrum ± one spinning sideband on each edge of the spectrum.

The measured ^{59}Co isotropic chemical shift of $Ag_3Co(CN)_6$ is –224 ± 1 ppm when spun at 8 kHz MAS (measured at 11.75 T). Note that sample heating caused by friction due to spinning causes a small increase in this value when compared with stationary spectra. See the variable-temperature (VT) NMR results for more details.

To first order, the central NMR transition ($m_I = +1/2 \leftrightarrow -1/2$) of noninteger spin quadrupolar nuclei is not perturbed by the quadrupolar interaction, and thus its line shape depends

Can. J. Chem. Downloaded from www.nrcresearchpress.com by MCGILL UNIVERSITY on 02/02/13
For personal use only.

Fig. 5. Solid-state ^{59}Co NMR spectra of stationary room-temperature $Ag_3Co(CN)_6$ acquired at three different field strengths. Spectra are shown on the same chemical shift (ppm) scale. The CS tensor principal components, $\delta_\perp$ (left) and $\delta_\parallel$ (right), have been indicated with broken lines.

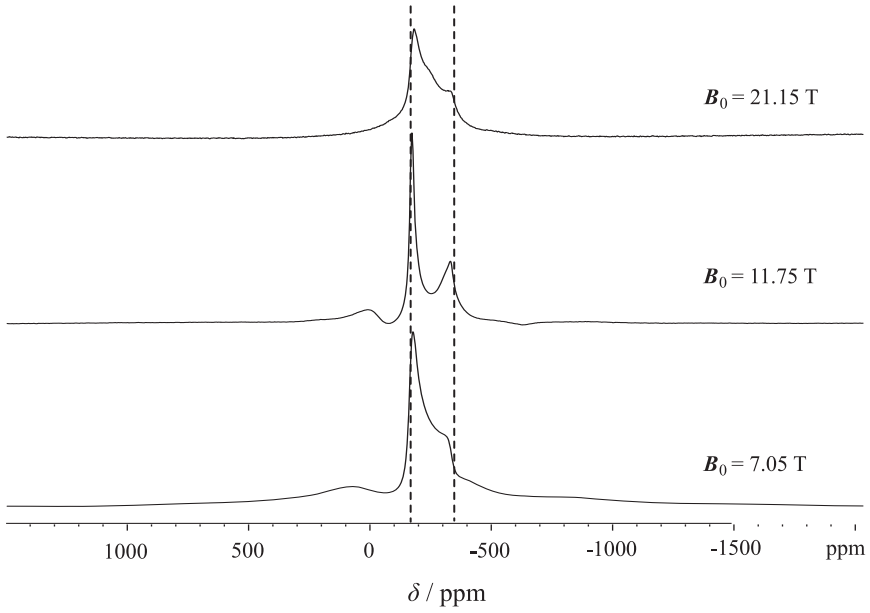
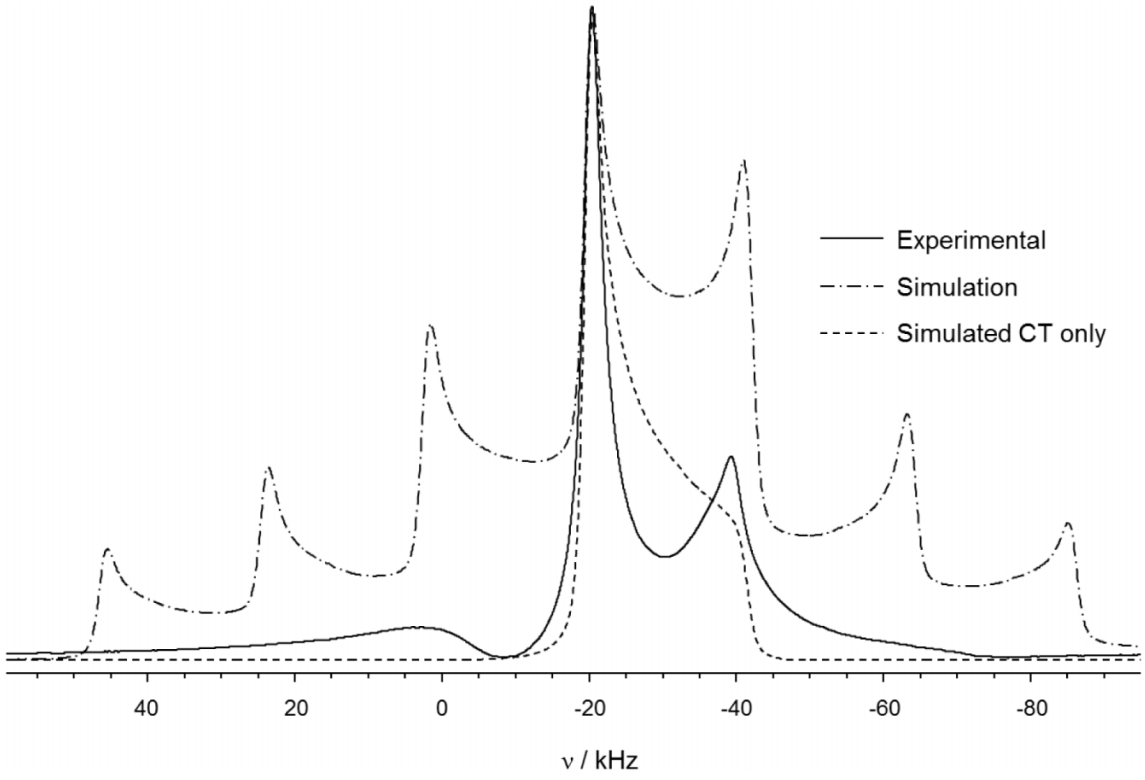


Fig. 6. Solid-state ^{59}Co NMR spectrum of stationary $Ag_3Co(CN)_6$ obtained at 11.75 T (118.6 MHz). A simulated spectrum was calculated using WSolids1 with C_Q = 616 kHz, $\delta_\perp$ = –167 ppm, and $\delta_\parallel$ = –350 ppm. The simulated central transition (CT) and full simulated spectrum have been shown separately to highlight the overlap between central and satellite transitions.



solely (in the absence of spin-spin coupling) on the magnetic shielding interaction.[12] Since C_Q is small in our case, one can ignore the second-order quadrupolar interaction when analyzing the central ^{59}Co NMR transition. Figure 5 highlights this observation and validates this assumption by showing the solid-state ^{59}Co NMR spectra of stationary $Ag_3Co(CN)_6$ at three different field strengths. The broken lines in this figure indicate the location of the two unique

Can. J. Chem. Downloaded from www.nrcresearchpress.com by MCGILL UNIVERSITY on 02/02/13
For personal use only.

Can. J. Chem. Downloaded from www.nrcresearchpress.com by MCGILL UNIVERSITY on 02/02/13
For personal use only.

components to the CS tensor, $\delta_\perp$ and $\delta_\parallel$. One can see that the width of the central transition (in ppm) is independent of the magnetic field strength, thus proving that this transition is unaffected by the EFG interaction. From an analysis of the central transition of the ^{59}Co NMR spectrum of $Ag_3Co(CN)_6$ at 11.75 T and RT (shown in Fig. 6), it was determined that $\delta_\perp = -167 \pm 8$ ppm and $\delta_\parallel = -350 \pm 20$ ppm. Simulated spectra were calculated using the previously obtained value for C_Q of 616 kHz. Errors in CSA parameters were estimated based on this and other analyses of spectra at different field strengths. In Fig. 6, the central-transition-only simulation is shown to highlight the analysis of the cobalt CSA parameters. The full simulated spectrum is also shown; however, the experimental satellite transitions (ST) are much broader than the central transition (CT), and as such the calculated STs are not reflected in the experimental spectrum. Notice that the error in $\delta_\parallel$ is much greater than that of $\delta_\perp$. Inspection of this and other spectra at different field strengths (Figs. 5 and 6) reveals that the STs often overlap with the CT in such a way that the CT and first-order satellite transitions (ST1, $m_I = +3/2 \leftrightarrow +1/2$ and $m_I = -3/2 \leftrightarrow -1/2$) are of the same order of magnitude. This makes it particularly difficult to determine the CSA parameters accurately, as one of the ST1 transitions and the CT $\delta_\parallel$ feature are essentially coincident. The spectral line shape and broad satellite transitions will be discussed further later in this paper.

It should be noted that the pulse width and transmitter frequency used in the ^{59}Co NMR experiments had no significant effect on the observed spectra. For example, we attempted to move the transmitter to the high- and low-frequency edges of the MAS spectrum to ensure that excitation profile limitations were not causing spectral distortions. In addition, we tried shortening the pulse width (pulse power optimized for a 4 μs 90° pulse on a solution setup sample) to widen the excitation profile. Neither of these changes affected our observed spectra. Also, to ensure that we observed the entire spectrum and did not fail to observe any of the outermost side bands due to noise, 54 000 transients were signal-averaged to generate the spectrum at 11.75 T shown in Fig. 3. So, we can be confident that we have observed the entirety of the ^{59}Co NMR spectrum in all of our experiments.

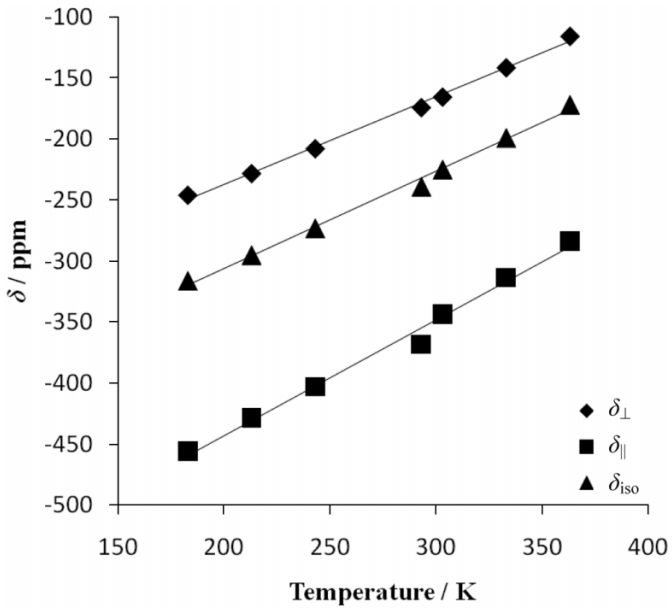
^{109}Ag NMR spectroscopy

Silver-109 NMR experiments were attempted for solid $Ag_3Co(CN)_6$ using a 7 mm rotor at 11.75 T with 5 kHz MAS. However, despite several attempts of 8–10 h each (see the Experimental section), no resonances (peaks) were observed. This is probably because the ^{109}Ag nuclei have extremely long spin-lattice relaxation times.

Variable-temperature (VT) ^{59}Co NMR spectroscopy

VT data were acquired for MAS and stationary samples at 4.70 T at temperatures ranging from 183–363 K; the results are summarized in Fig. 7. Data were also acquired at 11.75 T for stationary samples from 293–435 K. VT stationary sample spectra are presented in Fig. 8. Examination of these spectra, as well as the stationary sample spectrum shown in Fig. 6, highlights the key challenge of these ^{59}Co NMR experiments. We observe significant overlap between the CT powder pattern (which arises due to CSA) and the STs,

Fig. 7. Summary of solid-state variable-temperature (VT) ^{59}Co NMR data obtained for $Ag_3Co(CN)_6$ at 4.70 T (47.5 MHz).

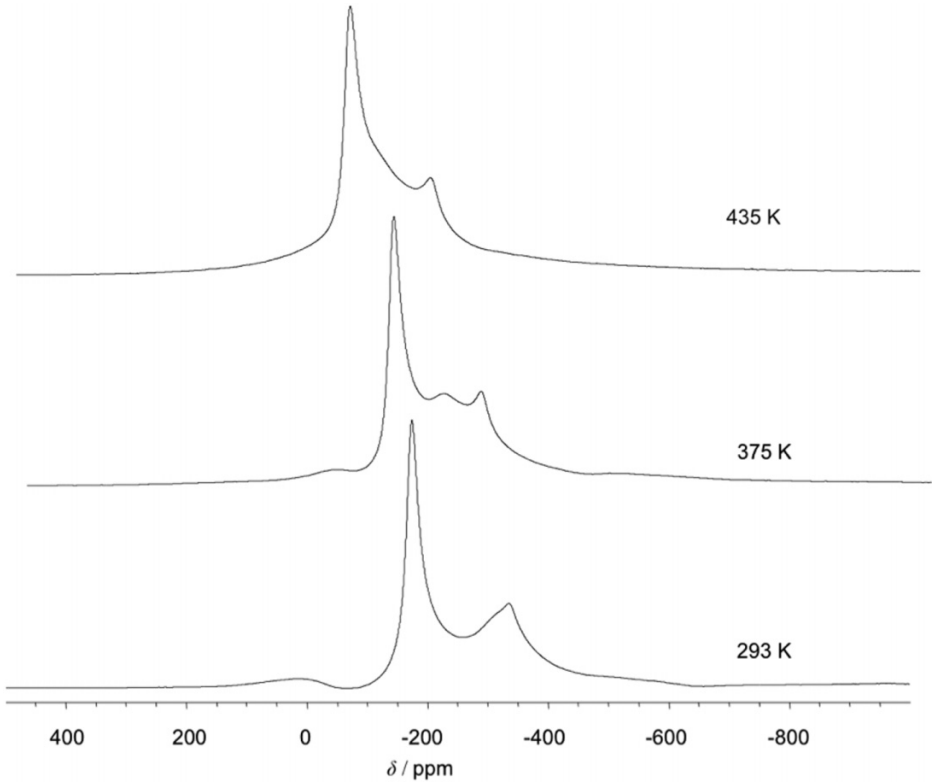


which accounts for the odd shape of the CSA powder pattern. However, features in the powder patterns for the satellite transitions are very poorly defined, and we are unable to completely resolve individual sets of transitions (ST1 $m_I = +3/2 \leftrightarrow +1/2$ and $m_I = -3/2 \leftrightarrow -1/2$, ST2 $m_I = +5/2 \leftrightarrow +3/2$ and $m_I = -5/2 \leftrightarrow -3/2$, etc.). Nonetheless, the satellite transition "horns" appear to narrow for the higher-temperature spectra in Fig. 8. This is evident when one observes that the shoulder in the middle of the CT, which is in fact an ST1 horn, shifts closer to the isotropic shift at higher temperatures, as do the features at the higher-frequency end of the spectrum, which eventually are lost within the CT. This suggests that C_Q decreases slightly at higher temperatures, although the broad features prevent quantification of this decrease.

The ill-defined nature of the features in the powder pattern suggests that there is a distribution of EFG and shielding tensor parameters about the cobalt nucleus.[30] In addition, the line widths of the spectra observed for samples undergoing MAS increased with increasing magnetic field strength, with values of approximately 0.9, 1.1, and 3.0 kHz for spectra obtained at 4.70, 11.75, and 21.14 T, respectively. This suggests a distribution of ^{59}Co NMR chemical shifts as well. Both of these observations are likely a result of the material adopting a range of unit cell *a* and *c* parameters at any given temperature. This distribution in lattice parameters has been previously suggested by Goodwin et al.[1] on the basis of neutron powder diffraction results and DFT calculations, and the lattice for this material has been described as "atypically soft".[1] That is to say, there is very little difference in lattice enthalpy between unit cells of different conformations for certain *a*:*c* ratios that lie along the so-called "low enthalpy valley".[1] It is interesting to note that while this lattice parameter distribution severely broadens the solid-state ^{59}Co NMR satellite transitions, which depend on the EFG and the CS tensors, the CS tensor principal components can still be resolved from the CT line shape. Though the CT features are by no

Can. J. Chem. Downloaded from www.nrcresearchpress.com by MCGILL UNIVERSITY on 02/02/13
For personal use only.

Fig. 8. Selected solid-state variable-temperature (VT) ^{59}Co NMR spectra obtained for $Ag_3Co(CN)_6$ at 11.75 T (118.6 MHz).



means sharp, the CS tensor is still less affected by this distribution than the EFG tensor. This is reasonable given that the satellite transitions fall over a much wider frequency range than the central transition and thus any distribution that might broaden the CT will broaden the STs even more so. In other words, the satellite transitions are more sensitive to slight changes in structure than the central transition.

Although we are only able to qualitatively describe the decrease in C_Q for ^{59}Co with increasing temperature, we can quantify the temperature dependence of the chemical shift tensor components. Figure 7 reveals that these increase (i.e., shielding decreases) linearly with temperature. From a linear regression analysis of the data, the isotropic shift increases by +0.79 ± 0.03 ppm/K, whereas $\delta_\perp$ varies by +0.72 ± 0.02 ppm/K and $\delta_\parallel$ varies by +0.95 ± 0.04 ppm/K. These results seem typical for cobalt nuclei. For example, the isotropic ^{59}Co NMR shift of solid $K_3Co(CN)_6$ increases by 0.97 ppm/K,[31] and dC_Q/dT = –0.15810 kHz/K.[31–33] If the temperature dependence of the ^{59}Co quadrupolar coupling constant for $Ag_3Co(CN)_6$ is of a similar order of magnitude as the potassium salt of this anion, we are unlikely to be able to quantify it given the large error in our measurements of C_Q, caused by the poorly defined STs. Table 1 shows, for comparison, the ^{59}Co nuclear quadrupolar coupling constants for various octahedral solid materials.[31,34–36]

Some CASTEP[37–39] calculations of the ^{59}Co NMR parameters of $Ag_3Co(CN)_6$ were performed using the unit cell parameters reported in the supplementary information section of the Goodwin et al. paper.[1] Over the temperature range 183 to 363 K, calculations suggest that the isotropic ^{59}Co NMR chemical shift increases linearly with temperature by ~1.0 ppm/K while the span decreases linearly by ~1.0 ppm/K and ranges from about 320 to 150 ppm. Experimentally $d\delta_{iso}/dT$ = +0.79 ± 0.03 ppm/K and $d\Omega/dT$ = –0.23 ppm/K, with Ω ranging from 210 to 168 ppm. Qualitatively, the experimental results are reproduced by the CASTEP calculations; however, the decrease in the span with increasing temperature is overestimated. The calculated C_Q values range from ~+6 to –6 MHz from 183 to 363 K and decrease linearly with an increase in temperature, with a value of approximately –2 MHz at room temperature. While the calculated values of C_Q do not agree with experimental values, the calculations correctly indicate that the EFG at the cobalt site is decreasing with increasing temperature. The discrepancy between calculated and experimental results may at least in part be due to the neglect of thermal vibrations. Also, the calculations of C_Q may be falling short because we are dealing with a very small EFG; in this case, C_Q is less than 1 MHz, whereas values in excess of 170 MHz are known.[8–10]

Table 1. Cobalt-59 nuclear quadrupolar coupling constants for various octahedral Co compounds with errors (where reported).

Compound	C_Q (MHz)	Reference
$Ag_3Co(CN)_6$	0.616±0.037	This work
$LaCo(CN)_6$	1.08	34
$Co(acac)_3$	5.53±0.07	35
$K_3Co(CN)_6$	6.18±0.05	31
$Na_3Co(NO_2)_6$	8.2±0.1	36
NaCo(edta)	35±2	36

Can. J. Chem. Downloaded from www.nrcresearchpress.com by MCGILL UNIVERSITY on 02/02/13
For personal use only.

Conclusion

The observed $Ag_3Co(CN)_6$ ^{13}C and ^{15}N NMR spectra and *J*-coupling features confirm the Co–CN–Ag–NC–Co structure previously reported.[1,2] The $^1J(^{107/109}Ag,^{15}N)$ coupling of 96 Hz is the largest $^{107/109}Ag–^{15}N$ spin-spin coupling constant reported to date. The relatively small C_Q of 616 ± 37 kHz observed from the ^{59}Co NMR spectra of $Ag_3Co(CN)_6$ suggests a near-perfect octahedral environment about ^{59}Co, which also agrees with the reported structure.[1–3,7]

The ^{59}Co NMR spectra (or more specifically, the broad poorly resolved nature of the observed satellite transitions) clearly indicate the EFG at the Co nucleus is more sensitive to variations or distributions in lattice parameters than the CS parameters (expressed in Hz). This is easily justifiable given that ^{59}Co has a large nuclear quadrupole moment (Q), and any variations in eq_{zz} caused by variations in structure are magnified and reflected in C_Q.[8] Also, EFGs depend on long-range order, and CS interactions depend mainly on local environment,[13] so this suggests, as expected, that crystal structure variations that occur during colossal positive/negative expansion are not the result of severe distortions of the local $[Co(CN)_6]^{3-}$ octahedra.[1,3,5–7] The broad distribution of lattice parameters precludes an accurate characterization of C_Q as a function of temperature. Most likely, $^{107/109}Ag$ NMR parameters would be more sensitive to the colossal expansion; however, because of the low receptivity and expected long T_1 relaxation times of the silver nuclei, such experiments are not feasible.

Lastly, we conclude that while the ^{59}Co NMR parameters of $Ag_3Co(CN)_6$ vary with temperature, these variations, $d\delta_{iso}/dT = +0.79 \pm 0.03$ ppm/K, $d\delta_{\perp}/dT = +0.72 \pm 0.02$ ppm/K, $d\delta_{\parallel}/dT = +0.95 \pm 0.04$ ppm/K, and the fact that C_Q appears to decrease slightly with increasing temperature, do not seem anomalous or significantly different from the temperature dependence of the ^{59}Co NMR parameters of $K_3Co(CN)_6$.[31] Thus, we do not observe a strong correlation between the temperature dependence of these solid-state NMR parameters and the colossal expansion nature of this material. Perhaps it is the distribution of lattice parameters and resulting broad, almost featureless ^{59}Co NMR powder patterns that distinguish $Ag_3Co(CN)_6$ from other octahedral Co(III) salts and reflect its colossal expansion behaviour.

Experimental

Synthesis

All natural abundance reagents were purchased from the Sigma-Aldrich Co. Isotopically labelled $K^{13}C^{15}N$ (98%) was obtained from Cambridge Isotope Laboratories, Inc. $Ag_3Co(CN)_6$ was synthesized according to the method outlined in the literature[1,2,40] by dissolving equimolar amounts of silver nitrate and potassium hexacyanocobaltate(III) in water, boiling and mixing the resulting solutions, and filtering the resulting precipitate. This material was prepared several times. In a typical synthesis, 1.033 g of $K_3Co(CN)_6$ and 1.567 g of $AgNO_3$ were each dissolved in 15 mL of distilled water. The two solutions were mixed, and the resulting mixture was boiled and stirred for ~1 h. $Ag_3Co(CN)_6$ was obtained as a white precipitate, rinsed with cold water, and dried at about 60 °C for 17 h (yield = 1.415 g, 85%). The product was identified using X-ray powder diffraction[1] and IR spectroscopy in addition to solid-state NMR measurements.[41–43] A sample of $Ag_3Co(CN)_6$ kindly provided by Professor J. Evans[1,6,7] was also studied, and yielded identical results.

Labelled $Ag_3Co(CN)_6$ (33% $^{13}C^{15}N$) was prepared by first synthesizing $K_3Co(CN)_6$ using the methods described by Poskozim[44] and then reacting it with $AgNO_3$ as described previously. To generate the labelled compound, 33% $^{13}C^{15}N$-labelled KCN was reacted with $CoCl_2$. $K^{13}C^{15}N$ (0.284 g) and 0.561 g of natural abundance KCN were dissolved in 20 mL of distilled water and added dropwise to a 20 mL solution of 0.485 g $CoCl_2$ in distilled water. The resulting mixture was stirred while boiling for 1.5 h. Yellow $K_3Co(CN)_6$ crystals (yield = 0.661 g, 99%) were obtained and washed with 10 mL of cold ethanol. Then, 0.526 g of the labelled product and 0.788 g of silver nitrate were each dissolved in 15 mL of water. The two solutions were mixed and boiled with stirring for 1 h. A light grey precipitate was obtained and dried in an oven at about 100 °C for about 3 days (yield = 0.713 g, 86%). The products were both identified using X-ray powder diffraction[1] and IR spectroscopy in addition to solid-state NMR measurements.[41–43]

Solid-state NMR spectroscopy

Room-temperature NMR spectra were obtained at the University of Alberta, Edmonton, Alberta, at 4.70 T on a CMX Infinity 200 spectrometer, at 7.05 T on a Bruker Avance 300 spectrometer, and at 11.75 T on a Bruker Avance 500 spectrometer. Variable-temperature experiments were performed on the CMX 200 and Bruker Avance 500 systems. Experiments at 21.14 T were carried out on a Bruker Avance II 900 spectrometer at the National Ultrahigh-Field NMR Facility for Solids in Ottawa, Ontario. For nearly all ^{59}Co NMR spectra, simple one-pulse experiments were performed with pulse widths typically ranging from 2–4 μs (pulse power optimized for a 4 μs 90° pulse on a 1.0 mol/L aqueous solution of $K_3Co(CN)_6$). No differences in spectral line shapes were observed for experiments performed with different pulse widths (i.e., selective versus nonselective pulses). The T_1 relaxation time of ^{59}Co was qualitatively determined to be on the order of 100 ms, and as such recycle delays of about 0.5 s were typically used.

Room-temperature experiments including ^{13}C, ^{15}N, and ^{59}Co NMR, and VT ^{59}Co NMR studies were performed. ^{109}Ag NMR experiments were attempted for $Ag_3Co(CN)_6$ using a 7 mm rotor at 11.75 T with 5 kHz MAS. Pulse delays ranged from 1 min to 2 h; however, no ^{109}Ag NMR signal was observed. This is probably due to very long T_1 relaxation times for the silver nuclei. T_1 times for ^{13}C and ^{15}N were not determined; however, recycle delays of 10 min were necessary to observe any signal. Powder samples were subjected to both stationary and MAS conditions at rotor frequencies ranging from 4 to 15 kHz. Various rotor frequencies were used to determine the isotropic peak of each ^{13}C and ^{15}N spectrum.

^{59}Co NMR spectra were externally referenced to a 1.0 mol/L aqueous solution of $K_3Co(CN)_6$ ($\delta = 0.00$ ppm) at RT.[31] The same solution was used as a setup sample to find appropriate power levels for 90° pulses. ^{13}C NMR spectra were externally referenced to TMS by using powdered

Can. J. Chem. Downloaded from www.nrcresearchpress.com by MCGILL UNIVERSITY on 02/02/13
For personal use only.

adamantane as a secondary reference. The $^{13}CH_2$ group isotropic peak was set to 38.56 ppm,[45] and the adamantane sample was used for the experimental setup. ^{15}N NMR spectra were referenced to the isotropic shift of neat liquid ammonia using powdered ammonium nitrate (99% ^{15}N enriched) as a secondary reference and setup sample. The $^{15}NH_4^+$ isotropic peak was set to 23.8 ppm.[46]

Errors in chemical shift measurements in spectra with MAS were estimated based on experimental line widths. Errors in CS tensor components were estimated based on the range of parameters used to calculate simulated spectra that still provided a visually acceptable fit of the experimental data. Errors in C_Q for ^{59}Co NMR spectra with MAS were estimated based on the assumption that the total width of the spectrum was observed within ± 1 spinning side bands on either edge of the spectrum.

Probe temperature calibration was attempted for the 4.70 T VT experiments using lead(II) nitrate as a standard;[47,48] however, we were unable to complete the calibration procedure. Nonetheless, a linear relationship between the ^{59}Co chemical shift parameters of $Ag_3Co(CN)_6$ was observed, and it is highly unlikely that a lack of calibration would significantly affect the slope of this curve. Rather, it is the intercept that would probably be most significantly affected, which we have not reported. Solid-state NMR spectra were simulated using WSolids1[29] version 1.20.15, a program developed by K. Eichele at the Universität Tübingen and originally created in the Wasylishen research group, that calculates spectral line shapes based on NMR parameters.

Acknowledgements

The authors wish to thank the Natural Sciences and Engineering Research Council of Canada (NSERC) and the University of Alberta for funding. Access to the 900 MHz NMR spectrometer was provided by the National Ultrahigh-Field NMR Facility for Solids in Ottawa, Ontario, a national research facility funded by the Canada Foundation for Innovation, the Ontario Innovation Trust, Recherche Québec, the National Research Council of Canada, and Bruker BioSpin and managed by the University of Ottawa (www.nmr900.ca). NSERC is acknowledged for a Major Resources Support grant. In particular, the authors wish to thank V. Terskikh at the National Ultrahigh-field NMR Facility for Solids for the acquisition of ^{59}Co NMR spectra at 21.14 T, helpful discussions, and CASTEP calculations. The authors are very grateful to Professor J. Evans[1,6,7] of the University of Durham for supplying a sample of $Ag_3Co(CN)_6$ and for helpful discussions about the lattice parameter distribution in the material. In addition, the authors thank the spectral services department at the University of Alberta, as well as T. Nakashima and the rest of R.E.W.'s Solid-State NMR research group. R.E.W. holds a Canada Research Chair in physical chemistry at the University of Alberta.

References

(1) Goodwin, A. L.; Calleja, M.; Conterio, M. J.; Dove, M. T.; Evans, J. S. O.; Keen, D. A.; Peters, L.; Tucker, M. G. *Science* **2008**, *319* (5864), 794. doi:10.1126/science.1151442.

(2) Pauling, L.; Pauling, P. *Proc. Natl. Acad. Sci. U.S.A.* **1968**, *60* (2), 362. doi:10.1073/pnas.60.2.362.

(3) Goodwin, A. L.; Keen, D. A.; Tucker, M. G. *Proc. Natl. Acad. Sci. U.S.A.* **2008**, *105* (48), 18708. doi:10.1073/pnas.0804789105.

(4) Korcok, J. L.; Katz, M. J.; Leznoff, D. B. *J. Am. Chem. Soc.* **2009**, *131* (13), 4866. doi:10.1021/ja809631r.

(5) Calleja, M.; Goodwin, A. L.; Dove, M. T. *J. Phys. Condens. Matter* **2008**, *20* (25), 255226. doi:10.1088/0953-8984/20/25/255226.

(6) Conterio, M. J.; Goodwin, A. L.; Tucker, M. G.; Keen, D. A.; Dove, M. T.; Peters, L.; Evans, J. S. O. *J. Phys. Condens. Matter* **2008**, *20* (25), 255225. doi:10.1088/0953-8984/20/25/255225.

(7) Goodwin, A. L.; Keen, D. A.; Tucker, M. G.; Dove, M. T.; Peters, L.; Evans, J. S. O. *J. Am. Chem. Soc.* **2008**, *130* (30), 9660. doi:10.1021/ja803623u.

(8) Chan, J. C. C.; Au-Yeung, S. C. F. *Annu. Rep. NMR Spectrosc.* **2000**, *41*, 1. doi:10.1016/S0066-4103(00)41008-2.

(9) Ooms, K. J.; Terskikh, V. V.; Wasylishen, R. E. *J. Am. Chem. Soc.* **2007**, *129* (21), 6704. doi:10.1021/ja0710095.

(10) Freeman, R.; Murray, G. R.; Richards, R. E. *Proc. R. Soc. Lond. A Math. Phys. Sci.* **1957**, *242* (1231), 455. doi:10.1098/rspa.1957.0188.

(11) Harris, R. K.; Becker, E. D.; Cabral de Menezes, S. M.; Granger, P.; Hoffman, R. E.; Zilm, K. W. *Pure Appl. Chem.* **2008**, *80* (1), 59. doi:10.1351/pac200880010059.

(12) Wasylishen, R. E.; Bernard, G. M. In *Comprehensive Organometalic Chemistry;* Mingos, D. M. P., Crabtree, R. H., Eds. Elsevier: Oxford, 2007; Vol. I, p 451–482.

(13) Slichter, C. P. *Principles of Magnetic Resonance,* 2nd ed.; Springer: New York, 1978.

(14) Duer, M. J. *Introduction to Solid-State NMR Spectroscopy;* Blackwell Science: Oxford, 2002.

(15) Akitt, J. W.; Mann, B. E. *NMR and Chemistry: An Introduction to Modern NMR Spectroscopy,* 4th ed.; Stanley Thornes: Cheltenham, UK, 2000.

(16) Power, W. P.; Wasylishen, R. E.; Mooibroek, S.; Pettitt, B. A.; Danchura, W. *J. Phys. Chem.* **1990**, *94* (2), 591. doi:10.1021/j100365a019.

(17) Power, W. P.; Mooibroek, S.; Wasylishen, R. E.; Cameron, T. S. *J. Phys. Chem.* **1994**, *98* (6), 1552. doi:10.1021/j100057a005.

(18) Akitt, J. W.; Mcdonald, W. S. *J. Magn. Reson.* **1984**, *58*, 401.

(19) Jeffrey, K. R.; Penner, G. H. Structural Phase Transitions. In *NMR Crystallography;* Harris, R. K.; Wasylishen, R. E.; Duer, M. J., Eds.; John Wiley & Sons Ltd.: Chichester, 2009; p 387–413.

(20) Harris, R. K.; Becker, E. D.; De Menezes, S. M. C.; Goodfellow, R.; Granger, P. *Pure Appl. Chem.* **2001**, *73* (11), 1795. doi:10.1351/pac200173111795.

(21) Lauterbur, P. C. *J. Chem. Phys.* **1965**, *42* (2), 799. doi:10.1063/1.1696017.

(22) Dykes, D.; Huckerby, T. N.; Oldham, C. *Inorg. Nucl. Chem. Lett.* **1977**, *13* (1), 63. doi:10.1016/0020-1650(77)80014-7.

(23) Harris, R. K.; Olivieri, A. C. Spinning Sideband Analysis for Spin-1/2 Nuclei. In *Encyclopedia of Nuclear Magnetic Resonance;* Grant, D. M., Harris, R. K., Eds.; John Wiley and Sons Ltd.: Chichester, 2002; Vol. 9, p 141–150.

(24) Bryce, D. L. Tensor Interplay. In *NMR Crystallography;* Harris, R. K.; Wasylishen, R. E.; Duer, M. J., Eds.; John Wiley & Sons Ltd.: Chichester, 2009; p 289–301.

(25) Bryce, D. L.; Wasylishen, R. E. Quadrupolar Nuclei in Solids: Influence of Different Interactions on Spectra. In *NMR of Quadrupolar Nuclei in Solid Materials;* Wasylishen, R. E.; Ashbrook, S. E.; Wimperis, S., Eds.; John Wiley & Sons Ltd.: Chichester, 2012; Chapter 4. In press.

(26) Friesen, K. J.; Wasylishen, R. E. *J. Magn. Reson.* **1982**, *48*, 152.
(27) Wasylishen, R. E.; Muldrew, D. H.; Friesen, K. J. *J. Magn. Reson.* **1980**, *41*, 341.
(28) Geiser, U.; Schlueter, J. A. *Acta Crystallogr. C* **2003**, *59* (3), i21. doi:10.1107/S0108270103001264.
(29) Eichele, K. *WSolids1,* version 1.20.15; Universität Tübingen: Tübingen, Germany, 2011.
(30) Kemp, T. F.; Smith, M. E. *Solid State Nucl. Magn. Reson.* **2009**, *35* (4), 243. doi:10.1016/j.ssnmr.2008.12.003.
(31) Nielsen, U. G.; Jakobsen, H. J.; Skibsted, J. *Solid State Nucl. Magn. Reson.* **2001**, *20* (1-2), 23. doi:10.1006/snmr.2001.0027.
(32) Lourens, J. A. J.; Reynhardt, E. C. *Phys. Status Solidi A* **1972**, *11* (2), 739. doi:10.1002/pssa.2210110238.
(33) Lourens, J. A. J.; Reynhardt, E. C. *Phys. Status Solidi A* **1972**, *12* (1), 215. doi:10.1002/pssa.2210120123.
(34) Ganguly, P.; Venkatraman, T. N.; Rajamohanan, P. R.; Ganapathy, S. *J. Phys. Chem. B* **1997**, *101* (51), 11099. doi:10.1021/jp9729775.
(35) Eichele, K.; Chan, J. C. C.; Wasylishen, R. E.; Britten, J. F. *J. Phys. Chem. A* **1997**, *101* (30), 5423. doi:10.1021/jp970370i.
(36) Kirby, C. W.; Power, W. P. *Can. J. Chem.* **2001**, *79* (3), 296. doi:10.1139/cjc-79-3-296.
(37) Clark, S. J.; Segall, M. D.; Pickard, C. J.; Hasnip, P. J.; Probert, M. J.; Refson, K.; Payne, M. C. *Z. Kristallogr.* **2005**, *220* (5-6-2005), 567. doi:10.1524/zkri.220.5.567.65075.
(38) Pickard, C. J.; Mauri, F. *Phys. Rev. B* **2001**, *63* (24), 245101. doi:10.1103/PhysRevB.63.245101.
(39) Charpentier, T. *Solid State Nucl. Magn. Reson.* **2011**, *40* (1), 1. doi:10.1016/j.ssnmr.2011.04.006.
(40) Ludi, A.; Güdel, H. U.; Dvořák, V. *Helv. Chim. Acta* **1967**, *50*, 2035. doi:10.1002/hlca.19670500737.
(41) Kettle, S. F. A.; Aschero, G. L.; Diana, E.; Rossetti, R.; Stanghellini, P. L. *Inorg. Chem.* **2006**, *45* (13), 4928. doi:10.1021/ic0514041.
(42) Reguera, E.; Quintana, G.; Fernandez-Bertran, J. *Transition Met. Chem.* **1997**, *22* (5), 527. doi:10.1023/A:1018536018533.
(43) Dunsmuir, J. T.; Lane, A. P. *J. Chem. Soc. A* **1971**, 776. doi:10.1039/j19710000776.
(44) Poskozim, P. S. *J. Chem. Educ.* **1969**, *46* (6), 384. doi:10.1021/ed046p384.
(45) Earl, W. L.; VanderHart, D. L. *J. Magn. Reson.* **1982**, *48*, 35.
(46) Penner, G. H.; Bernard, G. M.; Wasylishen, R. E.; Barrett, A.; Curtis, R. D. *J. Org. Chem.* **2003**, *68* (11), 4258. doi:10.1021/jo0207372.
(47) Bielecki, A.; Burum, D. P. *J. Magn. Reson. A* **1995**, *116* (2), 215. doi:10.1006/jmra.1995.0010.
(48) Beckmann, P. A.; Dybowski, C. *J. Magn. Reson.* **2000**, *146* (2), 379. doi:10.1006/jmre.2000.2171.

Can. J. Chem. Downloaded from www.nrcresearchpress.com by MCGILL UNIVERSITY on 02/02/13
For personal use only.

Density functional theory study on the structural, reactivity, and electronic properties of all mono-, di-, tri-, tetra-, and penta-fluoroanilines as monomers for conducting polymers

Hossein Shirani Il Beigi

Can. J. Chem. Downloaded from www.nrcresearchpress.com by MCGILL UNIVERSITY on 02/02/13
For personal use only.

Abstract: Electrical and structural properties of mono-, di-, tri-, tetra-, and penta-fluoroanilines as candidate monomers for new conducting polymers have been investigated using hybrid density functional theory (B3LYP/6–311+G**) based methods. The effects of the number and position of the fluorine atoms on the electrical and structural properties of fluoroanilines and their radical cations have also been investigated. The values of the vibrational frequencies, charge and spin-density distributions, ionization potentials, dipole moments, electric polarizabilities, HOMO-LUMO gaps, and the NICS values of these compounds have been calculated and analyzed as well. The results showed that the double bonds in 2-fluoroaniline and 2,5-difluoroaniline are more delocalized compared with other fluoroanilines; therefore, these molecules have the most aptitude for the electropolymerization reactions. The frequency analysis showed that the electrochemical stability of 2-fluoroaniline is greater than the other fluoroanilines. Also, this molecule possesses the largest NICS value compared to the other fluoroanilines. Consequently, 2-fluoroaniline has the largest ring current and the highest conductivity among all other monomers. Based on the results obtained, 2-fluoroaniline and 2,5-difluoroaniline are the best candidate monomers among all fluoroanilines for the synthesis of corresponding conducting polymers.

Key words: fluoroanilines, conducting polymers, PANI, DFT-B3LYP.

Résumé : Faisant appel à une méthode basée sur une théorie hybride de la fonctionnelle de la densité (B3LYP/6–311+G**), on a étudié les propriétés électriques et structurales de mono-, di-, tri-, tétra- et pentafluoroanilines (PANI) comme monomères candidats pour la préparation de nouveaux polymères conducteurs. On a aussi examiné les effets du nombre et de la position des atomes de fluor sur les propriétés électriques et structurales des fluoroanilines et de leurs cations radicaux. On a calculé les valeurs des fréquences de vibration, des distributions de charge et de densité de spin, des potentiels d'ionisation, des moments dipolaires, des polarisabilités électriques et des écarts des orbitales moléculaires (OM) hautes occupes (HO) et basses vacantes (BV) et on a aussi calculé et analysé les valeurs des déplacements chimiques indépendants du noyau (DCIN) de ces composés. Les résultats montrent que les doubles liaisons de la 2-fluoroaniline et de la 2,5-difluoroaniline sont plus délocalisées que celles des autres fluoroanilines; ces molécules sont donc plus susceptibles de donner des réactions d'électropolarisation. L'analyse des fréquences a montré que la stabilité électrochimique de la
2-fluoroaniline est plus grande que celles des autres fluoroanilines. Cette molécule, par comparaison avec les autres fluoroaniline, possède aussi la valeur la plus élevée pour le déplacement chimique indépendant du noyau. En conséquence, par rapport à tous les autres monomères, la 2-fluoroaniline possède le courant de cycle le plus grand et la conductivité la plus élevée. Sur la base des résultats obtenus, parmi toutes les fluoroanilines, la 2-fluoroaniline et la 2,5-difluoroanile sont les meilleurs candidats comme monomères pour la synthèse des polymères conducteurs correspondants.

Mots-clés : fluoroanilines, polymères conducteurs (PANI), théorie de la fonctionnelle de la densité B3LYP.

[Traduit par la Rédaction]

Introduction

Electrochemical synthesis of electrically conducting organic polymers, first described in detail for polyaniline (PANI), has proven to have an important role in developing new polymeric materials with electrical properties similar to metals.[1] Electrically conducting polymers as advanced materials and the new class of "synthetic metals" have drawn great attention in the last years.[2] The reversibility of charging–discharging processes and high specific capacitance of the polymers in their oxidized states have stimulated suggestions for a variety of applications, such as rechargeable batteries, super-capacitors, electro-chromic devices, etc.[3] Also, the 2000 Nobel Prize in Chemistry recognized the discovery of conducting poly-

Received 7 July 2012. Accepted 10 July 2012. Published at www.nrcresearchpress.com/cjc on 8 November 2012.

H. Shirani Il Beigi. Young Researchers Club, Toyserkan Branch, Islamic Azad University, Toyserkan, Iran.

E-mail for correspondence: Hossein Shirani Il Beigi (e-mail: shiranihossein@gmail.com).

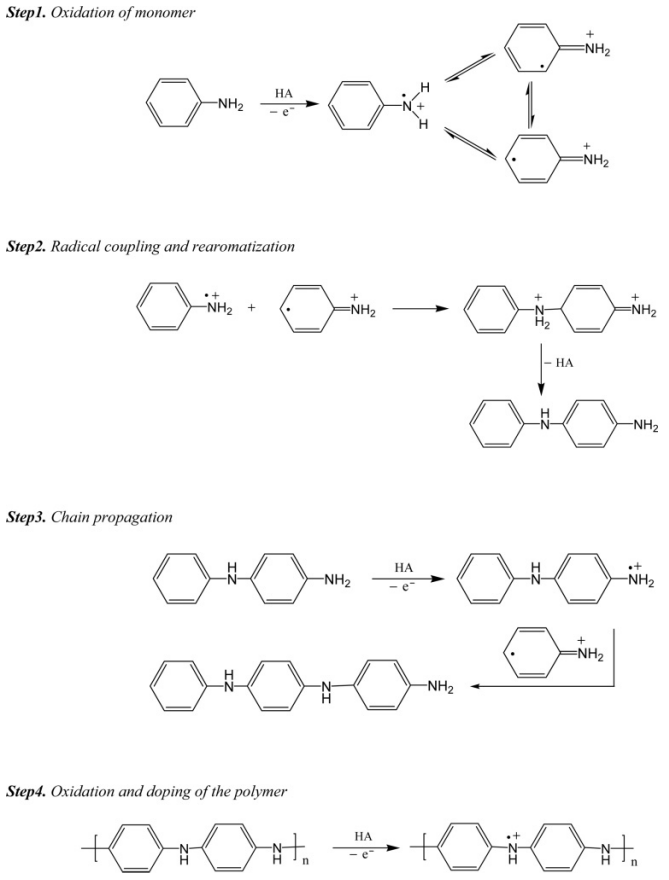
Can. J. Chem. Downloaded from www.nrcresearchpress.com by MCGILL UNIVERSITY on 02/02/13
For personal use only.

mers.[4,5] Conducting polymers are the most probable systems for nano-electronic applications because of the change in their optical and electrical properties in nanometric dimensions.[6–8] Polyanilines (PANIs) can produce one-dimensional morphologies, such as nano-structure polymers (nano-tube, -wire, -fiber, -filament, -rod, -composite, and -particle), and much research has been conducted on them.[9–11] Conductive polymers are materials that play important roles in nano-materials.[12] Most scientists have been interested in nano-materials because of the many applications of nano-technology in different sciences such as medicine, petrochemicals, materials, electronics, quantum computers, etc.[13–17] Nano-fibers with diameters of tens of nanometers appear to be intrinsic morphological units that were found, "naturally" formed, in the early stage of the chemical oxidative polymerization of aniline.[18] It has been known from the early years of polymer research that PANI fibrils of ~100 nm diameter can form "naturally" during electrochemical polymerization on the surface of electrodes.[19,20] Some recent research indicates that uniform PANI nano-fibers can be obtained without the need of a template, simply by controlling the electrochemical polymerization kinetics.[21–23] Conducting filaments of PANI have been prepared in the 3 nm wide hexagonal channel systems of the aluminosilicate.[24] PANIs have spectacular optical and chromic properties, which can be distinguished from other conducting electro-active polymers.[25]

Among intrinsic conducting polymers with conjugated double bonds, PANIs and their related derivatives are especially promising for commercial applications because of their easy synthesis, higher conductivity, and good environmental stability.[26,27] PANIs have been used as biosensors, gas sensors, micro actuators, data storages, polymer batteries, electronic devices, and functional membranes.[28–31] In PANIs, the mechanism of polymerization involves the formation of radical cations that react with another monomer to develop a polymeric structure (Fig. 1).[32]

PANIs have an electronic conducting mechanism that seems to be unique among other conducting polymers when doped by protonation as well as undergoing p-type doping.[33–41] PANIs may exist in a range of oxidation states; the one that can be doped to a high conducting state is called emeraldine.[42] An emeraldine salt has amine (-NH-) and imine (=N-) sites in equal proportions. The imine sites can be protonated to the bipolaron (dication) emeraldine salt form.[42] However, this form undergoes further rearrangement to form the delocalized polaron lattice, which is considered a polysemiquinone radical cation salt.[43] The structures of each stage of this process are shown in Fig. 2.[43] The conductivity of PANIs in emeraldine salt form depends on temperature as well as humidity.[44,45] In addition, the conductivity and preparation conditions[46,47] of PANIs relate to the formation of structural defects and the polymer morphology.[48] It has been reported that the conductivity of PANIs is dependent on solvent.[49] The solvent causes a change in the polymer conformation, which results in increased conductivity.[50] A recent study reports PANI salts possessing unprecedentedly high electrical conductivities of up to 1300 S/cm.[51] Although theoretical calculations have predicted that the bipolaron state is energetically more favored than that of polaron, it is widely accepted that polarons are the charge carriers that are responsible for high conductivity.[52] It has been proposed that the presence of coulombic interactions, dielectric screening, and local disorder in the PANI lattice act to stabilize the delocalized polaron state.[53,54] The proposed orthorhombic structure is shown in Fig. 3.[55–70]

Fig. 1. Mechanism of electrochemical polymerization.[42]



Computational procedures

The structures of mono-, di-, tri, and tetra-fluoroanilines and their radical cations were optimized using B3LYP/6–311+G**and UB3LYP/6–311+G** levels of theory[71,72] with the GAUSSIAN 98 package of programs.[73–75] Atomic charges were calculated using the NBO method.[76,77] The nuclear independent chemical shift (NICS)[78] and magnetic susceptibility values were calculated using GIAO/B3LYP/6–311+G** and CSGT/B3LYP/6–311+G** methods, respectively.

Results and discussion

Structural analysis of fluoroanilines

The optimized structural parameters obtained at the B3LYP/6–311+G** level of theory for all fluoroanilines (as shown in Fig. 4) and UB3LYP/6–311+G** level of theory for all radical cations have been calculated and listed in Tables 1 and 2. To predict the extent of the π-conjugation character of these monomers, the *f* coefficient has been used, which is defined in eq. [1] for each aniline ring,

$$[1] \qquad f = 2R23/(R12 + R34)$$

where R23 is the length of the C_2–C_3 bond and [(R12 + R34)/2) is the average length of the C_1–C_2 and C_3–C_4 bonds in the

Fig. 2. The doping of emeraldine base with protons to form the conducting emeraldine salt form of polyaniline (a polaron lattice).[44]

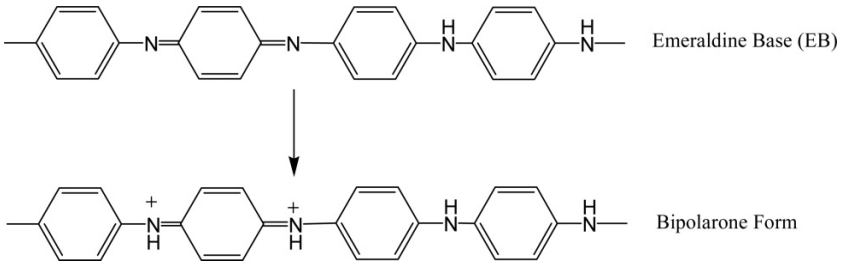
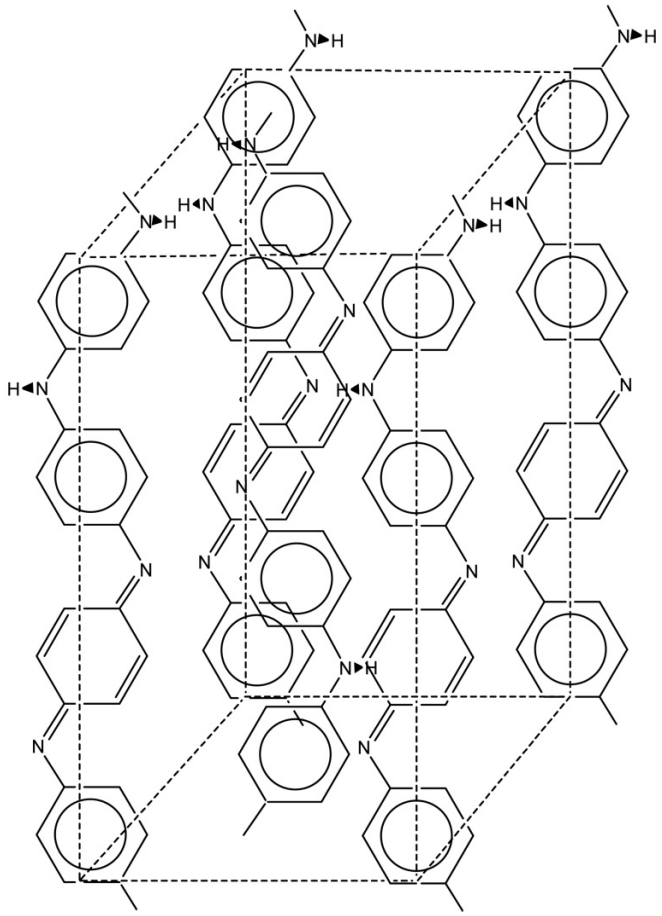


Fig. 3. Proposed EB-II orthorhombic crystal structure for the emeraldine base.



aniline ring. The value of the *f* coefficient gives a measure of the relative importance of the aromatic character (see Fig. 5, which is a polysemiquinone structure of the propagating radical cation polymer chain).

f coefficients for all fluoroanilines and their radical cations are presented in Table 1. As shown in the table, the *f* coefficient has the following trend for all neutral molecules,

$$G < B < H < P = O = J < L < I < F < C < Q < S = N = K = E < T = \text{Aniline} < R < D < M$$

As shown in the table, 2,5-difluoroaniline (G) and 2-fluoroaniline (B) have the smallest values for the *f* coefficient. Therefore, it can be suggested that the double bonds in 2,5-difluoroaniline and 2-fluoroaniline are more delocalized. Also as shown in Table 1, the radical cation monomers have smaller values of the *f* coefficient compared with other neutral monomers. Therefore, it can be suggested that the double bonds in radical cation forms are more delocalized compared with other neutral species.

Charge and spin-density distribution analysis

The electropolymerization process for each molecular radical cation is obtained from (N-C_6) linkages,[42] so it can be said that in a compound, the electropolymerization rate will be higher with greater atomic positive charge in position N . It can also be said that in a compound, the electropolymerization rate will be higher with greater atomic negative charge in position C_6. The NBO atomic charge distribution over the ring atoms of fluoroanilines and their radical cations have been calculated and presented in Table 3. As shown in this table, monomer G has the maximal negative charge on positions C_6 and the minimal negative charge on position N. This means that the electropolymerization rate of 2,5-difluoroaniline (G) can be higher compared with other molecules, in fact the initiation step of the polymerization is faster for this monomer, but the length of polymer chain may be shorter because of the large substituent effects.

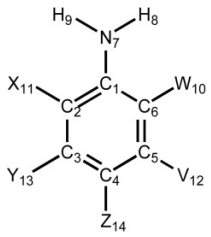
From an electric charge distribution point of view, there is no significant preference for the tacticity of the fluoroaniline polymer chains, as the distributed electric charges are identical for a couple and are only slightly different for other fluoroaniline radical cations. Therefore, electric charges cannot account for any possible preferences (if any) in the tacticity of the fluoroanilines polymer chains that might be observed experimentally. The atomic charge distributions in the neutral fluoroanilines show, more or less, the same behavior as found for their radical cations. Also, it can be said that in a compound, the electropolymerization rate will be higher with greater spin density in position C_6. The spin-density distribution (Fig. 6) over the ring atoms of fluoroaniline radical cations has been calculated and presented in Table 4. As shown in this table, it is obvious that monomer G has the maximal spin density on position C_6, and it has the minimal spin density on position N as well. This means that the electropolymerization rate of 2,5-difluoroaniline can be higher compared with other molecules.

Electric dipole moments

The orientations of the polymer chains in the condensed phases are the most important parameters affecting the electric charge transport properties of polymers, so that the electrical

Can. J. Chem. Downloaded from www.nrcresearchpress.com by MCGILL UNIVERSITY on 02/02/13
For personal use only.

Fig. 4. All possible mono-, di-, tri-, tetra-, and penta-fluoroaniline isomers.



A: X=Y=W=V=H aniline
B: X=F, Y=Z=V=W=H 2-fluorobenzenamine
C: Y=F, X=Z=V=W=H 3-fluorobenzenamine
D: Z=F, X=Y=V=W=H 4-fluorobenzenamine
E: X=Y=F, Z=V=W=H 2,3-difluorobenzenamine
F: X=Z=F, Y=V=W=H 2,4-difluorobenzenamine
G: X=V=F, Y=Z=W=H 2,5-difluorobenzenamine
H: X=W=F, Y=Z=V=H 2,6-difluorobenzenamine
I: Y=Z=F, X=V=W=H 3,4-difluorobenzenamine
J: Y=V=F, X=Z=W=H 3,5-difluorobenzenamine
K: X=Y=Z=F, V=W=H 2,3,4-trifluorobenzenamine
L: X=Y=V=F, Z=W=H 2,3,5-trifluorobenzenamine
M: X=Y=W=F, Z=V=H 2,3,6-trifluorobenzenamine
N: X=Z=W=F, V=Y=H 2,4,6-trifluorobenzenamine
O: Y=Z=V=F, X=W=H 3,4,5-trifluorobenzenamine
P: X=Z=V=F, Y=W=H 2,4,5-trifluorobenzenamine
Q: X=Y=Z=V=F, W=H 2,3,4,5-tetrafluorobenzenamine
R: X=Y=Z=W=F, V=H 2,3,4,6-tetrafluorobenzenamine
S: X=Y=V=W=F, Z=H 2,3,5,6-tetrafluorobenzenamine
T: X=Y=Z=V=W=F 2,3,4,5,6-pentafluorobenzenamine

Can. J. Chem. Downloaded from www.nrcresearchpress.com by MCGILL UNIVERSITY on 02/02/13
For personal use only.

conductivity of a polymer chain is altered when its orientation and consequently its symmetry and non-isotropic interactions are changed. These overall interactions can be well expressed in terms of interactions between local dipole moments of monomers. The local alignment of dipole moments of monomers in solution, with respect to the orientation of the polymer chain, determines the electrochemical properties of the polymer formed on electrode surface. In addition, the orientation of monomers in the double layer of the solution in an electropolymerization cell depends on both the size and direction of the dipole moment vectors of both monomers and polymer chains.

It is necessary to study the dipole moments of these fluoroanilines to be able to predict their electropolymerization properties. The size of the dipole moment vector and its components calculated for fluoroanilines in this study are presented in Table 5. Analysis of calculated dipole moments shows that the orientation of the dipole moment vector is pointed toward the nitrogen atom for all fluoroanilines. The size and direction of the dipole moment vector depends more on the position (symmetry) of the substituent than its number.

It can also be seen in Table 5 that the dipole moments for all compounds have the following trend,

$$O > I > Q > K > J > T > P > D > E > L > C > R > F > S > G > N > M > \text{Aniline} > B > H$$

The size of the dipole moment vector for monomers O and I are greater than other compounds. Therefore, compounds O and I have a high solubility in polar solvents. These characteristics increase the efficiency of electrochemical polymerization processes of these monomers.

Ionization potentials

The first step in the electropolymerization of conducting polymers is the formation of intermediate radical cations from monomers, which can be considered as an ionization reaction[37],

$$[2] \qquad M \rightarrow M^{\cdot +} + \bar{e}$$

where M and $M^{\cdot +}$ denote monomer and its radical cation, respectively. One can see that the stability of intermediate radical cations has an important role in the electropolymerization process. Therefore, it is useful to calculate the electronic energy difference between the neutral monomer (as the initial species) and positively charged monomer (as the intermediate one). This energy difference is proportional to the ionization ootential (IP) of the monomer. Calculated values of IP for fluoroanilines based on eq. [2] are presented in Table 5. The trend of electrochemical stability of these monomers is,

$$\text{Aniline} < B < D < F < C = I < H < G < P < N < E < K < O < J < M < R < Q < L < T < S$$

Since ionization potential energies are directly proportional to the electrochemical oxidation potentials of the compounds, it can be stated that the electrochemical stability of 2-fluoroaniline (B) is greater than other fluoroanilines.

Electric polarizabilities

Values of polarizabilities of compounds containing halogen are used to interpret light scattering and intensities of vibrational Raman spectra.[5] Values for exact electrical polarizabilities as well as average polarizabilities (α_{ave}) for aniline and all fluoroanilines have been calculated and listed in Table 5. Based on this table, it can be claimed that the polarization values of these monomers are dependent on positions of fluorine atoms.

Vibrational spectra

The vibrational frequencies for all fluoroanilines were calculated using optimized structures at the B3LYP/6–311+G** level of theory. Calculated IR absorption frequencies and intensities for all fluoroanilines are presented in Table 6. To facilitate the comparison, the frequencies are divided into low-frequency (<1000 cm^{-1}) and high-frequency groups (>1000 cm^{-1}). Analysis of the frequencies listed in Table 6 suggests that thermal decomposition has the following trend,

$$G > \text{Aniline} > C > J > B > M > H > E > D = K > F > I > L > N > O = T > S > R > Q > P$$

Can. J. Chem. Downloaded from www.nrcresearchpress.com by MCGILL UNIVERSITY on 02/02/13
For personal use only.

Table 1. B3LYP/6–311+G** optimized values of (a) bond lengths (Å) and the *f* coefficient for fluoroanilines.

Molecule	C1-C2	C2-C3	C3-C4	C4-C5	C5-C6	C6-C1	C1-N7	*f*
Aniline	1.405	1.391	1.395	1.395	1.391	1.405	1.381	0.994
	1.435	*1.371*	*1.413*	*1.413*	*1.371*	*1.434*	*1.335*	*0.963*
B	1.401	1.379	1.397	1.394	1.392	1.404	1.375	**0.986**
	1.440	*1.370*	*1.401*	*1.420*	*1.368*	*1.430*	*1.331*	*0.964*
C	1.405	1.383	1.386	1.395	1.390	1.407	1.378	0.991
	1.426	*1.366*	*1.417*	*1.405*	*1.374*	*1.441*	*1.334*	*0.961*
D	1.405	1.392	1.385	1.385	1.392	1.405	1.383	0.998
	1.434	*1.368*	*1.409*	*1.409*	*1.368*	*1.434*	*1.336*	*0.962*
E	1.400	1.384	1.387	1.394	1.390	1.405	1.373	0.993
	1.434	*1.375*	*1.403*	*1.415*	*1.369*	*1.435*	*1.331*	*0.966*
F	1.401	1.381	1.387	1.384	1.394	1.402	1.377	0.991
	1.439	*1.366*	*1.402*	*1.415*	*1.367*	*1.430*	*1.332*	*0.962*
G	1.403	1.378	1.397	1.385	1.385	1.403	1.372	**0.984**
	1.447	*1.376*	*1.391*	*1.425*	*1.366*	*1.419*	*1.331*	*0.970*
H	1.400	1.381	1.395	1.395	1.381	1.400	1.370	0.988
	1.436	*1.366*	*1.410*	*1.410*	*1.366*	*1.436*	*1.327*	*0.960*
I	1.404	1.384	1.388	1.384	1.391	1.405	1.380	0.991
	1.427	*1.364*	*1.425*	*1.403*	*1.370*	*1.438*	*1.335*	*0.956*
J	1.406	1.382	1.387	1.387	1.382	1.406	1.375	0.990
	1.432	*1.368*	*1.411*	*1.411*	*1.369*	*1.432*	*1.330*	*0.962*
K	1.400	1.386	1.390	1.384	1.392	1.403	1.375	0.993
	1.433	*1.371*	*1.416*	*1.410*	*1.368*	*1.433*	*1.332*	*0.962*
L	1.402	1.383	1.388	1.386	1.384	1.405	1.370	0.991
	1.443	*1.383*	*1.390*	*1.423*	*1.366*	*1.422*	*1.330*	*0.976*
M	1.392	1.387	1.385	1.396	1.379	1.401	1.368	0.999
	1.427	*1.371*	*1.414*	*1.401*	*1.370*	*1.443*	*1.327*	*0.965*
N	1.399	1.383	1.386	1.386	1.383	1.399	1.372	0.993
	1.435	*1.364*	*1.408*	*1.408*	*1.364*	*1.435*	*1.329*	*0.959*
O	1.405	1.383	1.389	1.389	1.383	1.405	1.377	0.990
	1.432	*1.365*	*1.420*	*1.420*	*1.365*	*1.431*	*1.334*	*0.957*
P	1.401	1.380	1.387	1.387	1.386	1.402	1.374	0.990
	1.444	*1.370*	*1.394*	*1.431*	*1.364*	*1.422*	*1.332*	*0.965*
Q	1.400	1.385	1.391	1.388	1.384	1.403	1.372	0.992
	1.438	*1.375*	*1.407*	*1.428*	*1.364*	*1.425*	*1.331*	*0.970*
R	1.399	1.388	1.389	1.387	1.382	1.392	1.370	0.996
	1.428	*1.370*	*1.423*	*1.401*	*1.367*	*1.439*	*1.328*	*0.961*
S	1.401	1.384	1.387	1.387	1.384	1.401	1.366	0.993
	1.434	*1.373*	*1.406*	*1.406*	*1.373*	*1.434*	*1.326*	*0.967*
T	1.399	1.386	1.390	1.390	1.386	1.399	1.368	0.994
	1.433	*1.371*	*1.417*	*1.417*	*1.371*	*1.433*	*1.328*	*0.962*

Published by NRC Research Press

Can. J. Chem. Downloaded from www.nrcresearchpress.com by MCGILL UNIVERSITY on 02/02/13
For personal use only.

Table 2. B3LYP/6–311+G** optimized values of bond angles (°) for fluoroanilines.

Molecule	C6-C1-C2	C6-C1-N7	C2-C1-N7	C1-C6-W	C1-C2-X	C5-C4-C3	C3-C4-Z	C5-C4-Z
Aniline	118.4	120.8	120.8	119.5	119.5	118.7	120.6	120.6
	120.1	*120.0*	*120.0*	*119.5*	*119.5*	*120.8*	*119.6*	*119.6*
B	116.6	123.2	120.3	118.9	116.9	119.2	120.1	120.8
	118.4	*122.6*	*119.1*	*119.1*	*116.2*	*121.4*	*119.2*	*119.4*
C	118.7	120.9	120.4	119.6	121.5	117.0	120.5	122.6
	120.5	*119.3*	*120.2*	*119.3*	*121.6*	*119.4*	*118.9*	*121.6*
D	118.3	120.9	120.8	119.7	119.7	121.4	119.3	119.3
	119.9	*120.0*	*120.0*	*119.6*	*119.6*	*122.9*	*118.5*	*118.5*
E	117.3	123.1	119.6	119.3	118.4	117.9	119.6	122.6
	119.2	*122.1*	*118.8*	*119.1*	*117.9*	*120.4*	*118.3*	*121.3*
F	116.4	123.2	120.3	119.1	117.2	121.7	118.7	119.6
	118.3	*122.5*	*119.2*	*119.2*	*116.4*	*123.3*	*118.4*	*118.3*
G	116.9	122.9	120.3	120.9	116.9	117.4	122.0	120.6
	118.6	*122.9*	*118.6*	*121.3*	*116.3*	*119.8*	*121.4*	*118.8*
H	115.0	122.5	122.5	116.4	116.4	119.8	120.1	120.1
	117.1	*121.4*	*121.4*	*115.8*	*115.8*	*122.3*	*118.9*	*118.9*
I	118.5	120.9	120.5	119.8	121.5	119.3	119.9	120.8
	120.3	*119.5*	*120.2*	*119.4*	*121.5*	*121.2*	*118.4*	*120.4*
J	119.1	120.4	120.4	121.6	121.6	115.5	122.2	122.2
	121	*119.5*	*119.5*	*121.4*	*121.4*	*118.3*	*120.9*	*120.9*
K	117.0	123.2	119.7	119.2	118.6	120.0	119.0	121.0
	119.0	*122.1*	*118.9*	*119.1*	*118.0*	*122.0*	*118.0*	*120.1*
L	117.7	122.7	119.6	121.0	118.5	116.4	121.4	122.2
	119.4	*122.6*	*118.0*	*121.3*	*117.8*	*119.1*	*120.6*	*120.4*
M	115.7	122.4	121.9	116.5	117.9	118.5	119.7	121.8
	117.8	*121.0*	*121.2*	*115.8*	*117.5*	*121.2*	*118.0*	*120.8*
N	114.9	122.6	122.6	116.7	116.7	122.1	118.9	118.9
	116.9	*121.6*	*121.6*	*115.9*	*115.9*	*124*	*118.0*	*118.0*
O	118.9	120.5	120.5	121.6	121.6	117.5	121.2	121.2
	120.9	*119.6*	*119.6*	*121.4*	*121.4*	*119.8*	*120.1*	*120.1*
P	116.7	122.9	120.4	120.9	117.3	119.6	120.2	120.1
	118.6	*122.7*	*118.8*	*121.2*	*116.4*	*121.5*	*120.3*	*118.2*
Q	117.5	122.8	119.7	121.0	118.7	118.2	120.3	121.4
	119.5	*122.2*	*118.3*	*121.1*	*117.9*	*120.4*	*119.8*	*119.7*
R	115.5	122.6	122.6	116.8	118.1	120.4	119.2	120.4
	117.7	*121.1*	*121.2*	*115.9*	*117.6*	*122.6*	*117.6*	*119.9*
S	116.6	121.7	121.7	117.9	117.9	117.5	121.3	121.3
	118.7	*120.6*	*120.6*	*117.5*	*117.5*	*120.5*	*119.8*	*119.8*
T	116.3	121.8	121.8	118.1	118.1	119.0	120.5	120.5
	118.6	*120.7*	*120.7*	*117.5*	*117.5*	*121.5*	*119.3*	*119.3*

Note: Corresponding values for the related radical cations are given in the lower row in italic font. See Fig. 1 for definitions of bond lengths and angles.

Published by NRC Research Press

Fig. 5. Polysemiquinone structure of the propagating radical cation polymer chain[44].

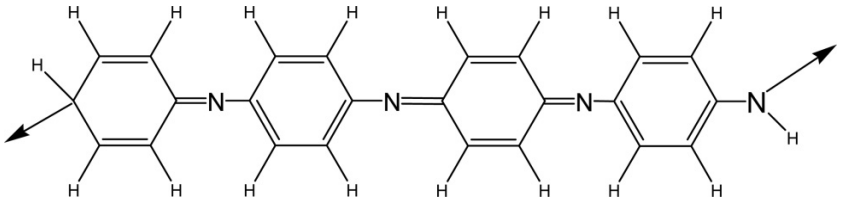
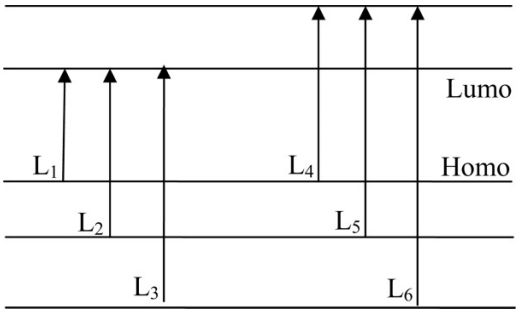


Table 3. Natural bond orbital (NBO) charge distribution on nitrogen and carbon atoms in the B3LYP/6–311+G** optimized structures of aniline and fluoroanilines (and their radical cations).

Molecule	$-\delta_N$	δ_{C1}	δ_{C2}	δ_{C3}	δ_{C4}	δ_{C5}	δ_{C6}
Aniline	0.801 (0.262)	0.169 (–0.014)	–0.263 (0.034)	-0.182 (–0.182)	–0.257 (0.005)	–0.182 (–0.182)	–0.263 (0.034)
B	0.797 (0.572)	0.113 (0.189)	0.360 (0.467)	–0.251 (–0.257)	–0.238 (–0.040)	–0.196 (–0.164)	–0.250 (–0.179)
C	0.797 (0.573)	0.187 (0.246)	–0.329 (–0.264)	0.436 (0.450)	–0.321 (–0.091)	–0.164 (–0.180)	–0.277 (–0.142)
D	0.806 (0.582)	0.156 (0.227)	–0.242 (–0.158)	–0.246 (–0.221)	0.369 (0.533)	–0.246 (–0.221)	–0.242 (–0.158)
E	0.795 (0.565)	0.127 (0.196)	0.301 (0.387)	0.373 (0.368)	–0.306 (0.095)	–0.179 (–0.167)	–0.264 (–0.169)
F	0.801 (0.581)	0.099 (0.180)	0.380 (0.465)	–0.313 (–0.302)	0.386 (0.537)	–0.261 (–0.215)	–0.231 (–0.167)
G	**0.790 (0.322)**	0.131 (0.375)	0.347 (–0.327)	–0.233 (0.186)	–0.303 (0.145)	0.422 (–0.160)	**–0.316** (0.077)
H	0.794 (0.565)	0.057 (0.141)	0.373 (0.455)	–0.265 (–0.255)	–0.220 (–0.031)	–0.265 (–0.255)	0.373 (0.455)
I	0.798 (0.585)	0.171 (0.239)	–0.314 (–0.259)	0.376 (0.410)	0.310 (0.488)	–0.232 (–0.229)	–0.257 (–0.145)
J	0.791 (0.565)	0.202 (0.256)	–0.344 (–0.245)	0.451 (0.443)	–0.382 (–0.140)	0.451 (0.443)	–0.344 (–0.245)
K	0.798 (0.576)	0.113 (0.184)	0.316 (0.381)	0.316 (0.330)	0.325 (0.488)	–0.248 (–0.220)	–0.247 (–0.162)
L	0.874 (0.574)	0.207 (0.207)	0.418 (0.418)	0.365 (0.365)	–0.159 (–0.159)	0.468 (0.468)	–0.284 (–0.284)
M	0.791 (0.569)	0.072 (0.147)	0.314 (0.366)	0.361 (0.380)	–0.288 (–0.089)	–0.248 (–0.257)	0.360 (0.472)
N	0.808 (0.571)	0.321 (0.128)	–0.225 (0.460)	0.314 (–0.303)	–0.204 (0.548)	0.314 (–0.303)	–0.225 (0.460)
O	0.791 (0.582)	0.187 (0.253)	–0.329 (–0.249)	0.389 (0.402)	0.253 (0.443)	0.389 (0.402)	–0.309 (–0.249)
P	0.797 (0.587)	0.117 (0.190)	0.365 (0.472)	–0.299 (–0.307)	0.328 (0.493)	0.363 (0.417)	–0.299 (–0.267)
Q	0.792 (0.582)	0.129 (0.199)	0.301 (0.395)	0.329 (0.327)	0.268 (0.439)	0.376 (0.415)	-0.311 (–0.266)
R	0.793 (0.577)	0.057 (0.136)	0.327 (0.369)	0.302 (0.338)	0.341 (0.500)	–0.315 (–0.308)	0.377 (0.467)
S	0.858 (0.558)	0.151 (0.151)	0.381 (0.381)	0.374 (0.374)	–0.149 (–0.149)	0.374 (0.374)	0.381 (0.381)
T	0.791 (0.573)	0.071 (0.147)	0.313 (0.379)	0.315 (0.331)	0.280 (0.444)	0.315 (0.331)	0.313 (0.379)

Fig. 6. The schemes of HLG and spine-density distribution of aniline, monomer B and monomer G.



2,5-Difluoroaniline has the highest low-frequency values among all of these monomers; this means that 2,5-difluoroaniline has the largest force constant for its bending modes of vibration. Higher values of low frequencies obtained for this monomer can be regarded as a higher protection from thermal decomposition for this molecule. Also, the analysis of zero-point energy (ZPE) values for aniline and fluoroanilines shows that ZPE of 2,5-difluoroaniline is greater than for other monomers; as a result, the relative thermal stability of 2,5-difluoroaniline is higher than other monomers.

Displacements of the C_4 and H_{14} atoms (see Fig. 4) with the highest intensity vibrations in the IR spectrum of fluoroanilines have been compared in Table 7. It can be seen in this table that the displacement of the C_4 atom of monomer G is greater than for other monomers. It is important to note that the displacements are given based on the respective standard Cartesian coordinates of the molecules, which may be evidently different from each other. The displacement of the H_{14} atom of monomer G is greater than for other compounds. Furthermore, the force constant of the C_4–H_{14} bond in monomer G is greater than for other monomers. On the basis of the vibrational analysis carried out in this study, it can be predicted that the electropolymerization of the fluoroanilines can be enhanced, or even controlled, by the use of appropriate IR radiation.

Electronic properties

The energy gap between the highest occupied and the lowest unoccupied molecular orbital (HOMO and LUMO, respectively), known as the HOMO–LUMO gap or simply HLG, is a critical parameter determining molecular electrical transport properties and electric admittance (being charged under ap-

Can. J. Chem. Downloaded from www.nrcresearchpress.com by MCGILL UNIVERSITY on 02/02/13
For personal use only.

Can. J. Chem. Downloaded from www.nrcresearchpress.com by MCGILL UNIVERSITY on 02/02/13
For personal use only.

Table 4. Distribution of spin density over nitrogen and carbon atoms in the B3LYP/6–311+G** optimized structures of aniline and fluoroaniline radical cations.

Molecule	N	C1	C2	C3	C4	C5	C6
Aniline	0.356	0.092	0.199	–0.106	0.433	–0.106	0.199
B	0.363	0.074	0.266	–0.148	0.399	–0.057	0.129
C	0.343	0.074	0.111	–0.067	0.449	–0.143	0.299
D	0.342	0.108	0.168	–0.077	0.362	–0.077	0.168
E	0.367	0.078	0.191	–0.111	0.418	–0.088	0.186
F	0.355	0.089	0.223	–0.122	0.339	–0.039	0.121
G	**0.323**	0.064	0.350	–0.165	0.395	–0.005	**0.303**
H	0.389	0.033	0.222	–0.123	0.390	–0.123	0.222
I	0.328	0.100	0.082	–0.027	0.361	–0.098	0.238
J	0.347	0.059	0.205	–0.108	0.477	–0.108	0.205
K	0.351	0.091	0.146	–0.077	0.344	–0.063	0.176
L	0.340	0.073	0.299	–0.133	0.400	–0.022	0.058
M	0.371	0.034	0.129	–0.075	0.405	–0.153	0.289
N	0.379	0.058	0.181	–0.095	0.322	–0.094	0.199
O	0.325	0.098	0.146	–0.042	0.351	–0.042	0.149
P	0.328	0.083	0.278	–0.142	0.337	–0.016	0.038
Q	0.333	0.099	0.207	–0.077	0.324	0.006	0.056
R	0.363	0.048	0.119	–0.055	0.340	–0.131	0.252
S	0.376	0.052	0.184	–0.107	0.420	–0.101	0.189
T	0.360	0.066	0.151	–0.064	0.334	–0.063	0.157

Table 5. Electric dipole moments, polarizability tensor elements, and ionization potentials calculated at the B3LYP/6–311+G** level of theory for the optimized structures of aniline and fluoroanilines.

	Electric dipole moment (D)			Polarizabilities (Å)				
Molecule	μ_x	μ_y	μ_{tot}	α_{xx}	α_{yy}	α_{zz}	α_{ave}	IP (ev)
Aniline	–0.0001	1.8209	1.8209	84.048	102.591	47.618	78.086	7.51
B	1.1609	–1.3461	1.7776	102.097	84.409	46.527	77.678	7.70
C	3.1923	–0.0168	3.1924	99.816	87.279	46.321	77.805	7.78
D	3.1233	1.7211	3.5662	97.990	87.867	46.035	77.297	7.71
E	3.1085	–1.5723	3.4835	98.961	88.753	45.468	77.727	7.98
F	3.1096	0.0758	3.1105	97.109	89.360	45.011	77.160	7.74
G	–0.1224	2.0236	2.0730	84.612	102.956	45.062	77.543	7.93
H	0.0000	0.2497	0.2497	85.057	102.281	45.373	77.570	7.92
I	–4.6266	–0.5062	4.6542	102.750	87.537	45.301	78.529	7.78
J	3.2010	–1.9367	3.7413	98.169	90.233	45.214	77.872	8.07
K	4.5197	0.5890	4.5579	94.206	93.980	44.299	77.495	7.99
L	3.2150	0.2640	3.2258	98.319	90.640	44.309	77.756	8.22
M	–1.8544	0.2502	1.8712	91.816	96.638	44.467	77.640	8.16
N	–1.9654	0.0000	1.9654	102.701	84.847	44.622	77.390	7.96
O	0.0000	–5.2633	5.2633	85.504	103.362	44.366	77.744	8.03
P	3.1524	1.8046	3.6324	96.835	91.252	44.029	77.372	7.95
Q	–3.4041	–3.1693	4.6510	101.405	88.643	43.485	77.844	8.21
R	3.1290	0.1896	3.1347	100.606	88.948	43.401	77.652	8.17
S	–0.0001	2.1387	2.1387	86.905	103.190	43.595	77.897	8.43
T	3.1905	1.7988	3.6626	100.266	91.330	43.013	78.203	8.41

Note: The values of α_{ave} have been calculated using $\alpha_{ave} = (1/3)(\alpha_{xx}+\alpha_{yy}+\alpha_{zz})$.

plied electric filed), because it is a measure of the electron density hardness. A reasonable estimate of HLG values can be obtained from both HF and DFT calculations.[23,24] The HLG values determine the voltage produced in a photovoltaic cell as well as the electromotive force (EMF) of an electrochemical cell.[22] An increase in the chain length of a conductive polymer (or the length of the π-conjugated system) decreases the HLG values of the polymer. Therefore, it seems that HLG values of a polymer cannot be determined exactly from their monomers.[5] However, the study of HLG values of monomers may

Table 6. B3LYP/6–311+G** calculated IR absorption frequencies in cm^{-1} (intensities in km/mol) for aniline and fluoroanilines.

Molecule	Low-frequency range	High-frequency range
Aniline	217(4.1) 338(0.0) 379(2.1) 417(0.0) 511(25.5) 539(0.26) 635(0.38) 700(34.3) 759(50.7) 819(0.0) 834(9) 877(5.1) 964(0.0) 984(0.12)	1006.1(6.55) 1021(0.03) 1046(3.66) 1119(8.9) 1179(2.9) 1200(15.59) 1315(91.9) 1342(8.66) 1364(1.06) 1496(0.31) 1530(8.2) 1619(7.76) 1638(0.77) 1655(271) 3151(20.8) 3152(4.71) 3169(3.37) 3173(36.7) 3192 (12.8) 3637(59.1) 3556(33.7)
B	185 (4.80) 286(1.62) 296(4.82) 388(3.11) 438(2.75) 451(6.14) 539(0.57) 567(2.52) 587(2.02) 719(0.15) 749(84.2) 772(19.68) 842(0.12) 861(14.7) 929(3.84) 969(0.0)	1020(1.07) 1058(8.12) 1140(27.95) 1179(7) 120.5(99.23) 1296(18.94) 1339(62.49) 1358(21.05) 1492(9.11) 1542(167.5) 1618(9.2) 1631(34.16) 1667(182) 3160(10) 3178(7.69) 3189(10.61) 3202(5.26) 3639(81.28) 3762(50.78)
C	216(4.55) 235(0.33) 316(1.4) 358(0.0) 460(9.59) 462(2.65) 521(6.34) 542(2.5) 685(25.1) 753(5.44) 765(38.92) 841(32.51) 854(5.16) 964(32.78) 969(0.0)	1009(12.22) 1046(11.18) 1105(3.91) 1163(120.1) 1192(15.88) 1305(28.97) 1341(28.33) 1354(29.47) 1497(12.68) 1525(99.22) 1622(91.88) 1645(7.64) 1664(366.61) 3164(9.9) 3181(15.25) 3187(2.43) 3213(0.971) 3636(68.73) 3755(37.45)
D	151(0.72) 322(0.03) 328(0.14) 358(2.33) 427(0.0) 435(3.45) 465(3.48) 513(32) 654(0.1) 703(0.95) 758(57.4) 804)0.02) 832(64.82) 859(3.37) 927(1.68) 940(0.02)	10022(0.35) 1029(0.0) 1132(17.38) 1175(2.72) 1234(155) 1317(50.77) 1320(0.8) 1340(8.2) 1463(1.18) 1543(271)1632(0.0) 1642(61.48) 1663(92.25) 3163(12.97) 3164(16.67) 3198(3.99) 3198(2.04) 3639(61.24) 3758(35.27)
E	153(2.4) 242(2.9) 287(1.61) 295(0.51) 298(2.41) 396(4.6) 491(1.6) 508(1.88) 541(1.04) 567(2.18) 593(0.3) 697(21.67) 718(32.24) 775(45.79) 827(7.56) 853(0.03) 960(0.23) 995(30.84)	1070(60.13) 1117(54.88) 1186(5.96) 1225(74.85) 1276(49.97) 1352(26.78) 1364(55.96) 1511(86.54) 1547(159) 1626(16.93) 1635(25.32) 1671(282.12) 3170(7.96) 3188(9.31) 3212(0.3) 3637(89.54) 3759(53.42)
F	149(1.41) 234(0.62) 294(4.96) 329(0.9) 351(0.0)381(6.24) 454.49(5.27) 454.50(4.86) 506(4.45) 573(1.94) 596(11.39) 701(0.57) 728(19.08) 808(33.25) 811(21.94) 860(43.67) 928(0.09) 963(49.79)	1034(4.78) 1120(93.37) 1160(27.14) 1237(70.6) 1282(47.92) 1335(42.82) 1360(11.36) 1466(10.56) 1547(339) 1630(81.93) 1637(51.63) 1675(44.39) 3171(9.83) 3205(1.47) 3215(0.38) 3641(81.59) 3763(51.68)
G	221(3.87) 293(3.72) 341(3.99) 366(0.52) 403(2.98) 446(0.08) 454(6.71) 507(3.28) 588(1.05) 620(3.85) 699(0.1) 730(39.78) 779(11.11) 796(22.86) 839(50.42) 924(2.69) 982(29.88)	1047(10.93) 1122(10.66) 1177(81.87) 1204(172) 1280(0.24) 1338(32.18) 1358(22.48) 1476(17.35) 1545(266.64) 1628(13.62) 1636(41.12) 1676(253) 3139(2.18) 3199(1.52) 3219(0.14) 3638(91.61) 3760(54.93)
H	155(8.28) 261(0.0) 282(5.69) 292(2.86) 317(4.45) 409(0.0) 486(1.6) 501(4.54) 558(1.27) 562(0.0) 571(1.09) 699(7.86) 705(16.96) 764(59.53) 853(9.01) 888(0.0) 925(55.51) 945(1.45)	1078(13.46) 1120(129) 1176(52.31) 1243(19.67) 1265(5.65) 1327(74.17) 1362(5.22) 1509(61.87) 1542(193) 1621(63.21) 1626(54.78) 1674(118.77) 3191(1.41) 3202(3.07) 3211(1.59) 3641(101) 3765(68.44)
I	146(0.66) 230(0.88) 284(0.19) 323(0.87) 329(0.05) 355(1.54) 448(0.78) 460(7.76) 512(1.23) 590(9.43) 628(14.95) 688(0.53) 748(8.4) 785(61.38) 808(24.24) 837(33.94) 933(3.44) 965(17.23)	1050(2.56) 1134(47.43) 1184(32.07) 1234(143) 1284(45) 1336(16.64) 1358(37.43) 1481(11.22) 1549(335) 1635(60.28) 1646(68.94) 1673(123) 3174(11.04) 3186(2.38) 3198(1.29) 3639(71.2) 3758(38.59)
J	204(2.24) 233(2.32) 247(0.0) 313(1.19) 326(2.33) 366(0.06) 511(8.37) 514(5.49) 543(3.92) 591(2.13)609(0.14) 610(0.0) 673(25.72) 804(7.88) 825(63.05) 830(12.98) 986(56.19)	1004(0.01) 1031(34.69) 1070(27.74) 1123(113) 1181(142) 1258(0.23) 1358(15.79) 1382(0.084) 1506(57.79) 1509(71.72) 1628(213) 1650(20.43) 1673(499) 3195(2.02) 31896(1.56) 3230(2.32) 3230(2.32) 3636(76.78) 3755(41.05)
K	151(1.32) 159(0.87) 278(0.04) 289(0.0) 290(4.13) 312(0.27) 345(0.32) 381(4.44) 468(2) 496(0.58) 536(0.46) 592(0.82) 618(13.69) 678(24.63) 730(0.31) 759(13.5) 805(39.02) 922(0.54) 987(105)	1005(58.43) 1118(74.61) 1190(29.44) 1243(23.2) 1283(86.35) 1343(24.13) 1375(33.55) 1531(160) 1545(293) 1634(94.77) 1640(6.6) 1679(97) 3178(7.39) 3204(0.41) 3640(89.61) 3761(54.54)
L	141(3.68) 203(0.44) 246(2.89) 285(1.5) 300(1.92) 333(3.01) 356(0.44) 412(3.78) 451(1.22) 516(5.25) 583(0.12) 592(3.12) 619(6.48) 623(1.2) 723(2.59) 769(48.4) 803(21.94) 825(42.89)	1052(39.09) 1106(117) 1140(78.36) 1219(57.54) 1236(100.74) 1355(11.41) 1405(0.83) 1488(66.27) 1551(267) 1636(68.06) 1640(39.39) 1681(381) 3198(0.68) 3229(3.82) 3635(98.67) 3757(57.91)
M	157(0.0) 159(10.9) 281(1.78) 282(5.07) 287(0.49) 329(4.13) 375(0.0) 428(0.0) 460(0.03) 495(0.99) 548(1.67) 596(5.64) 605(6.09) 695(8.6) 737 (0.4) 744(24) 791(49.44) 913(53.96) 913(0.63)	1058(71.86) 1135(129) 1169(52.49) 1249(68.2) 1261(14.03) 1342(27.28) 1362(14.13) 1533(231) 1538(167) 1626(53.23) 1363(3.77) 1680(182) 3203(0.95) 3218(0.4) 3637(109) 3761(71.58)
N	140(4.1) 209(1.35) 263(0.0) 281(6.21) 317(3.41) 322(0.91) 359(3.39) 382(0.0) 455(6.26) 516(8.43) 559(0.0) 567(1.4) 598(11.83) 625(0.28) 405(0.05) 815(41.28) 843(56.77) 846(0.0) 951(44.74)	1003(66.25) 1118(87.01) 1133(185) 1207(3.43) 1273(22.3) 1356(10.71) 1376(1) 1480(41.47) 1549(372) 1623(1381) 1642(104) 1685(16.98) 3221(0.26) 3221(2.05) 3643(102) 3767(68.97)

Can. J. Chem. Downloaded from www.nrcresearchpress.com by MCGILL UNIVERSITY on 02/02/13
For personal use only.

Table 6 (*concluded*).

Molecule	Low-frequency range	High-frequency range
O	135(0.68) 203(0.71) 253(0.0) 273(0.05) 306(0.91) 310(1.24) 329(0.0) 342(1.56) 455(0.04) 512(2.26) 582(0.0) 589(4.34) 631(17.8) 630(6.99) 699(0.21) 790(60.28) 815(51.76) 827(0.0)	1013(13.41) 1027(66.83) 1080(102) 1180(62.13) 1233(17.95) 1248(137) 1339(29.02) 1415(2.3) 1495(43.3) 1555(379) 1636(146) 1650(72.33) 1684(182) 3195(0.71) 3195(1.02) 3638(79.10) 3757(42.35)
P	128(2.65) 193(0.02) 279(1.38) 288(3.3) 299(3.02) 339(2.2) 368(1.86) 410(2.83) 428(1.11) 458(5.18) 499(2.37) 620(0.6) 669(0.17) 695(0.69) 695(28.92) 763(4.83) 824(4.4) 866(104) 869(51.59)	1052(6.33) 1119(32.48) 1185(143) 1236(104) 1244(70) 1339(23.97) 1399(5.02) 1463(31.25) 1558(467.23) 1636(65.26) 1643(43.12) 1685(68.58) 31.93(0.61) 3215(1.3) 3639(91.92) 3761(55.57)
Q	130(2.94) 159(0.5) 203(0.12) 272(0.54) 281(1.09) 301(2.49) 317(2.14) 323(1.37) 352(0.12) 396(2.78) 445(0.21) 479(0.46) 574(4.32) 590(4.22) 498 997(0.49) 675(1.05) 710(0.28) 712(26.03) 822(28.74) 957(175)	1033(32.68) 1103(114) 1160(19.96) 1229(135) 1269(28.67) 1339(19.3) 1441(2.19) 1525(170) 1555(401) 1639(73.14) 1644(53.6) 1689(140.97) 3200(0.18) 3638(99.12) 3759(58.91)
R	133(3.48) 159(1.87) 209(2.25) 272(2.24) 280(3.55) 305(0.93) 318(1.51) 326(2.29) 383(0.7) 400(0.0) 441(1.61) 485(2.99) 548(4.16) 569(1.21) 660(0.42) 675(2.7) 691(0.17) 731(22.48) 845(29.35) 914(94.3)	1015(136) 1129(47.17) 1148(168) 1207(34.12) 1287(8.56) 1348(16.84) 1412(2.97) 1526(162) 1550(419) 1625(125) 1649(15.48) 1689(43.33) 3220(0.052) 3639(110) 3739(72.16)
S	134(0.0) 160(11) 202(0.17) 279(0.16) 282(4.83) 300(0.0) 312(0.54) 334(4.29) 386(0.0) 435(0.0) 442(0.93) 476(0.17) 574(2.16) 595(2.74) 658(0.0) 676(5.96) 680(0.0) 715(12.84) 800(38.44)	1104(70.27) 1109(152) 1157(45) 1183(112) 1271(34.08) 1358(5.39) 1413(10.92) 1536(150) 1546(347) 1630(48.36) 1646(20.02) 1686(259) 3228(6.63) 3634(118) 3758(75.26)
T	135(4.9) 137(0.0) 188(3.05) 210(1.82) 269(1.84) 273(0.15) 282(3.35) 308(0.86) 321(2.76) 343(1.41) 369(0.02) 415(0.02) 449(0.02) 451(0.66) 562(3.18) 602(1.11) 646(0.00) 658(0.88) 703(0.05) 756(0.02) 939(141)	1031(240) 1118(101) 1161(80.46) 1173(0.19) 1311(3.14) 1340(12.76) 1501(15.84) 1538(302) 1545(374) 1629(104) 1653(4.4) 1694(86.66) 3636(118) 3760(75.43)

Note: The vibrational frequencies as well as their IR intensities are calculated with scale factors $f = 1.0100$ for low-frequency vibrations (<1000 cm^{-1}) and $f = 0.9679$ for high-frequency vibrations (>1000 cm^{-1}). Some specific vibrational modes may not be active in IR for certain compounds because of the selection rules arising from symmetrical characteristics.

Table 7. Analysis of C_4–H_{14} displacement (Å) for the most intense vibrational mode of fluoroanilines in the IR spectrum.

	C_4			H_{14}		
Molecule	Δx	Δy	Δr	Δx	Δy	Δr
Aniline	0.00	0.06	0.060	0.00	0.06	0.060
B	0.09	–0.05	0.103	0.08	0.08	0.113
C	0.07	0.06	0.092	0.10	0.03	0.104
E	0.10	0.02	0.102	0.07	0.11	0.130
G	–0.09	–0.10	0.134	0.36	–0.11	0.376
H	0.00	0.13	0.130	0.00	0.15	0.150
J	–0.11	0.07	0.130	–0.13	0.08	0.155

Note: z displacements for C_4 and H_{14} are zero for all compounds. The values of Δr have been calculated using $(\Delta r)^2 = (\Delta x)^2+(\Delta y)^2+(\Delta z)^2$.

be used to predict the comparative band gap behavior of the corresponding polymers.

The HLG values of fluoroanilines defined in Fig. 7 are calculated and listed in Table 8. It can be seen that HOMO–LUMO gap has the following trend,

$$S < D < F < P < I < \text{Aniline} = N < T < K < B < G < O < R < C < Q < H < M = E < L < J$$

where HLG values of S and D are smaller than other compounds. It can also be seen in Table 8 that the HLG value of monomer B is smaller than that of monomer G (Fig. 6); this shows that the conductivity of monomer B is greater than for monomer G. It should be noted here that HLG values are not the only parameters that determine the electric conductivity of a polymer film, the orientation and alignment of the monomers in the polymer chain are two characteristics that play an important role in the electric conductivity as well.

Nuclear independent chemical shift (NICS) analysis

The nuclear independent chemical shift (NICS) at the GIAO/B3LYP/6–311+G** and magnetic susceptibilities at the CSGT/B3LYP/6–311+G** levels of theory[78] for all fluoroanilines were calculated and are listed in Table 9. The negative values of NICS represent the magnetic shielding and electric current in cyclic compounds. NICS results showed that monomer B has the highest NICS value; this compound has the largest electrical current and the highest conductivity among all of other monomers. Based on this table, it can be claimed that the magnetic susceptibilities of these molecules increase with the number of the fluorine atoms.

Conclusion

Hybrid density functional theory (B3LYP/6–311+G**) basis set calculations have been carried out to study the structural, electric, electrochemical, and spectroscopic properties of all fluoroanilines as candidate monomers for new conducting

Can. J. Chem. Downloaded from www.nrcresearchpress.com by MCGILL UNIVERSITY on 02/02/13
For personal use only.

Fig. 7. Molecular orbital energy spacing, including HOMO–LUMO gap (HLG), for aniline and fluoroanilines.

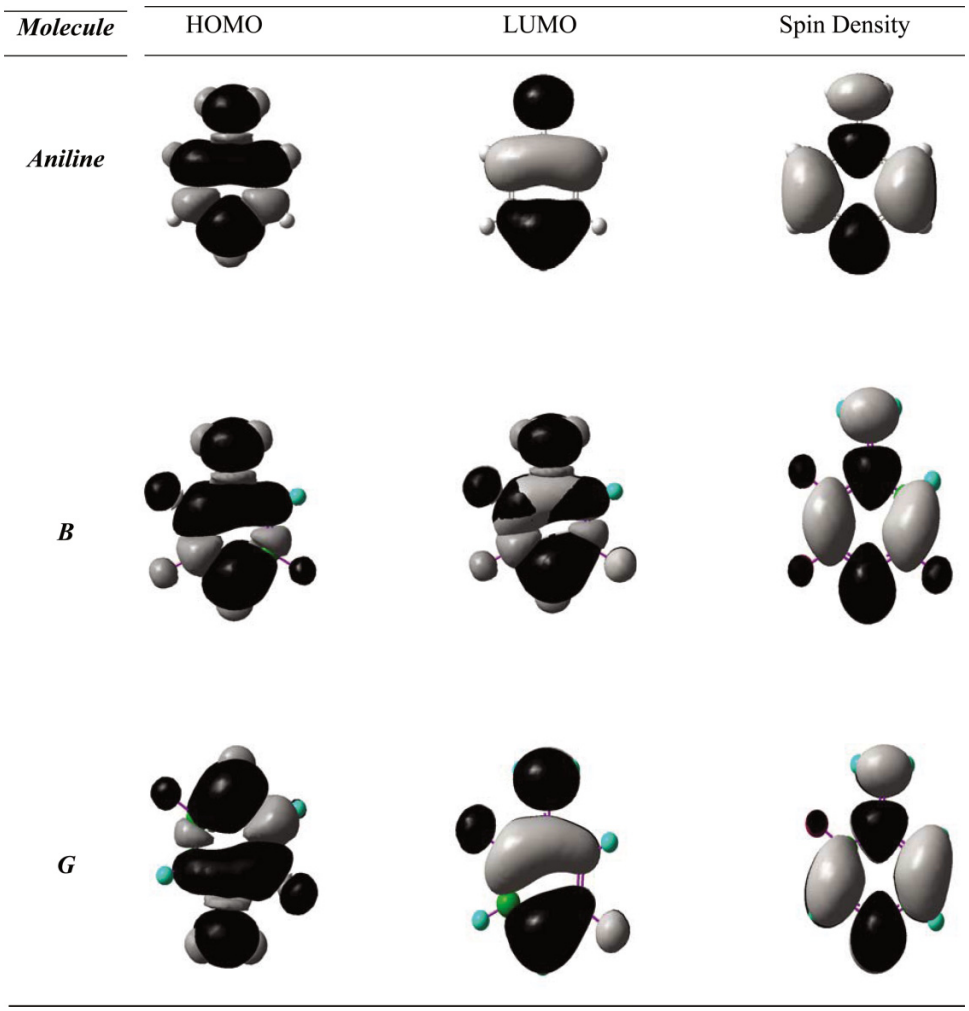


Table 8. The B3LYP/6–311+G** calculated values of energy gaps Li (defined in Fig. 7) including HOMO–LUMO gap (HLG) L_1 for aniline and fluoroanilines (in kcal/mol, 1 cal = 4.184 J)

Molecule	L_1	L_2	L_3	L_4	L_5	L_6
Aniline	4.49	5.28	7.1	4.68	5.78	7.20
B	4.54	5.54	7.12	4.85	5.84	7.43
C	4.60	5.52	7.00	4.82	5.73	7.11
D	4.25	5.58	6.70	4.65	5.99	7.11
E	4.77	5.56	7.21	4.92	5.70	7.35
F	4.33	5.56	6.83	4.81	6.04	7.31
G	4.55	5.41	7.03	4.95	5.81	7.43
H	4.73	5.62	7.63	4.87	5.76	7.50
I	4.37	5.53	6.74	4.77	5.92	7.13
J	4.83	5.58	7.05	4.96	5.71	7.17
K	4.52	5.54	6.91	4.80	5.82	7.19
L	4.81	5.48	7.08	4.50	5.67	7.27
M	4.77	5.48	7.82	4.92	5.63	7.42
N	4.49	5.61	7.03	4.83	5.95	7.73
O	4.57	5.57	6.78	4.89	5.89	7.10
P	4.36	5.45	6.79	4.89	5.98	7.32
Q	4.62	5.51	6.87	4.77	5.67	7.02
R	4.59	5.53	7.80	4.72	5.67	7.15
S	4.19	5.45	7.22	4.94	5.49	7.26
T	4.51	5.28	6.78	4.81	5.58	7.09

Table 9. Calculated NICS values at GIAO/ B3LYP/6–311+G** and magnetic Susceptibilities at CSGT/B3LYP/6–311+G**.

Molecule	NICS(0)	NICS(0.5)	NICS(1)	χ
Aniline	–7.71	–8.92	–8.82	–58.19
B	**–15.51**	**–15.89**	**–11.16**	–64.26
C	–9.31	–9.72	–8.73	–62.81
D	–9.70	–10.19	–9.18	–63.67
E	–11.56	–11.41	–9.56	–68.51
F	–12.11	–11.88	–9.86	–69.39
G	–11.12	–11.28	–9.37	–68.75
H	–12.38	–12.20	–10.15	–69.66
I	–11.23	–11.04	–9.23	–68.26
J	–10.91	–10.56	–8.71	–67.72
K	–13.57	–12.81	–10.12	–73.96
L	–13.00	–12.08	–9.40	–73.14
M	–13.94	–13.09	–10.26	–74.49
N	–14.15	–13.27	–10.35	–74.63
O	–12.59	–11.75	–9.21	–72.68
P	–13.58	–12.72	–9.94	–74.12
Q	–14.99	–13.63	–10.21	–78.64
R	–15.49	–14.32	–10.74	–79.47
S	–15.41	–13.94	–10.36	–79.08
T	–15.09	–15.09	–10.09	—

Can. J. Chem. Downloaded from www.nrcresearchpress.com by MCGILL UNIVERSITY on 02/02/13
For personal use only.

Can. J. Chem. Downloaded from www.nrcresearchpress.com by MCGILL UNIVERSITY on 02/02/13
For personal use only.

polymers. The values of NBO atomic charges, spin density distributions, dipole moments, ionization potentials (IPs), vibrational frequencies, NICS values, and HOMO–LUMO gaps (HLGs) have been calculated and analyzed. The results show that double bonds in 2-fluoroaniline and 2,5-difluoroaniline are more delocalized compared with other fluoroanilines. The analysis of charge and spin-density distributions showed that the electropolymerization rate of 2,5-difluoroaniline can be higher compared to other molecules. The analysis of dipole moments shows that the size and direction of the dipole moment vector is more dependent on the position of the substituent than its number. Electrochemical stability of 2-fluoroaniline is greater than other fluoroanilines. The HLG value of 2-fluoroaniline is smaller than for 2,5-difluoroaniline; this shows that probably the conductivity of 2-fluoroaniline is greater than 2,5-difluoroaniline. 2-Fluoroaniline possesses the largest NICS value; therefore this compound has the largest electrical current and most conductivity among all other monomers. Results of the present study show that 2-fluoroaniline (B) and 2,5-difluoroaniline (G) are the best candidate monomers among all fluoroanilines for the synthesis of corresponding conducting polymers. Furthermore, the synthesis feasibility and experimental measurement of these monomers are interesting subjects for study.

Acknowledgements

This research was supported by the Islamic Azad University, Toyserkan Branch, Toyserkan, Iran.

References

(1) Shirani, H. I. B.; Jameh-Bozorghi, S. *Chemistry Central Journal* **2011**, *5*:13. doi:doi:10.1186/1752-153X-5-13.
(2) Wallace, G. G.; Spinks, G. M.; Kane-Maguire, L. A. P.; Teasda, P. R. In *Conductive electroactive polymers: intelligent polymer systems*; CRC Press, Queensland, 2009; pp. 50–85.
(3) Jameh-Bozorghi, S.; Shirani, H. I. B. *J. Fluor. Chem.* **2011**, *132* (3), 190. doi:10.1016/j.jfluchem.2011.01.002.
(4) MacDiarmid, A. G. *Angew. Chem. Int. Ed.* **2001**, *40* (14), 2581. doi:10.1002/1521-3773(20010716)40:14<2581::AID-ANIE2581>3.0.CO;2-2.
(5) Sabzyan, H.; Nikoofard, H. *J. Chem. Phys.* **2004**, *306,* 105.
(6) Heeger, A. J. *J. Phys. Chem. B* **2001**, *105* (36), 8475. doi:10.1021/jp011611w.
(7) Niu, L.; Li, Q.; Wei, F.; Chen, X.; Wang, H. *Synth. Met.* **2003**, *139* (2), 271. doi:10.1016/S0379-6779(03)00170-X.
(8) Smit, M. A.; Ocampo, A. L.; Espinosa-Medina, M. A.; Sebastian, P. J. *J. Power Sources* **2003**, *124* (1), 59. doi:10.1016/S0378-7753(03)00730-4.
(9) Neves, S.; Gazotti, W. A.; De Paoli, M. A. In *Encyclopedia of Nanoscience and Nanotechnology*; Nalwa, H. S., Ed.; American Scientific Publishers, Los Angeles, Vol. 2, 2004; pp. 133–152.
(10) Gangopadhyay, R. In *Encyclopedia of Nanoscience and Nanotechnology*; Nalwa, H. S., Ed.; American Scientific Publishers, Los Angeles, Vol. 2, 2004; pp. 105–131.
(11) Wallace, G. G.; Innis, P. C.; Kane-Maguire, L. A. P. In *Encyclopedia of Nanoscience and Nanotechnology*; Nalwa, H. S., Ed.; American Scientific Publishers, LosAngeles, Vol. 4, 2004; pp. 113–130.
(12) Epstein, A. J. In *Organic Electronic Materials: Conjugated Polymers and Low Molecular Weight Organic Solids*; Farchioni, R., Grosso, G., Eds.; Springer, Amsterdam, Vol. 41, 2001.
(13) Zhang, X.; Manohar, S. K. *Chem. Commun. (Camb.)* **2004**, *20* (20), 2360. doi:10.1039/b409309g.
(14) Yu, L.; Lee, J. I.; Shin, K. W.; Park, C. E.; Holze, R. *J. Appl. Polym. Sci.* **2003**, *88* (6), 1550. doi:10.1002/app.12127.
(15) Michaelson, J. C.; McEvoy, A. J. *Chem. Commun.* **1994**, 79.
(16) Li, G. C.; Zhang, Z. K. *Macromolecules* **2004**, *37* (8), 2683. doi:10.1021/ma035891k.
(17) Zhang, X.; Goux, W. J.; Manohar, S. K. *J. Am. Chem. Soc.* **2004**, *126* (14), 4502. doi:10.1021/ja031867a.
(18) Huang, J. *Pure Appl. Chem.* **2006**, *78* (1), 15. doi:10.1351/pac200678010015.
(19) Mantovani, J. G.; Warmack, R. J.; Annis, B. K.; Macdiarmid, A. G.; Scherr, E. *J. Appl. Polym. Sci.* **1990**, *40* (910), 1693. doi:10.1002/app.1990.070400923.
(20) Wei, Y.; Sun, Y.; Jang, G. W.; Tang, X. *J. Polym. Sci. Part C: Polym. Lett.* **1990**, *28,* 81.
(21) Choi, S.-J.; Park, S.-M. *J. Electrochem. Soc.* **2002**, *149* (2), E26. doi:10.1149/1.1432675.
(22) Li, W. G.; Wang, H. L. *J. Am. Chem. Soc.* **2004**, *126* (8), 2278. doi:10.1021/ja039672q.
(23) Liang, L.; Liu, J.; Windisch, C. F., Jr; Exarhos, G. J.; Lin, Y. H. *Angew. Chem. Int. Ed.* **2002**, *41* (19), 3665. doi:10.1002/1521-3773(20021004)41:19<3665::AID-ANIE3665>3.0.CO;2-B.
(24) Wu, C.-G.; Bein, T. *Science* **1994**, *1757,* 264.
(25) Huang, L. M.; Wang, Z. B.; Wang, H. T.; Cheng, X. L.; Mitra, A.; Yan, Y. *J. Mater. Chem.* **2002**, *12* (2), 388. doi:10.1039/b107499g.
(26) Croissant, M. J.; Napporn, T.; Leger, J.-M.; Lamy, C. *Electrochim. Acta* **1998**, *43* (16–17), 2447. doi:10.1016/S0013-4686(97)10157-8.
(27) Niu, L.; Li, Q.; Wei, F.; Chen, X.; Wang, H. *J. Electroanal. Chem.* **2003**, *544,* 121. doi:10.1016/S0022-0728(03)00085-8.
(28) Vidal, J. C.; Garcia, E.; Castillo, J. R. *Anal. Chim. Acta* **1999**, *385* (1–3), 213. doi:10.1016/S0003-2670(98)00838-1.
(29) Campbell, T. E.; Hodgson, A. J.; Wallace, G. G. *Electroanalysis* **1999**, *11* (4), 215. doi:10.1002/(SICI)1521-4109(199904)11:4<215::AID-ELAN215>3.0.CO;2-#.
(30) Kincal, D.; Kumar, A.; Child, A. D.; Reynolds, J. R. *J. Synth. Met.* **1998**, *92* (1), 53. doi:10.1016/S0379-6779(98)80022-2.
(31) Kemp, N. T.; Flanagan, G. U.; Kaiser, A. B.; Trodahl, H. J.; Chapman, B.; Partridge, A. C.; Buckley, R. G. *Synth. Met.* **1999**, *101* (1–3), 434. doi:10.1016/S0379-6779(98)01118-7.
(32) Genies, E. M.; Syed, A. A.; Tsintavis, C. *Mol. Cryst. Liq. Cryst. (Phila. Pa.)* **1985**, *121* (1–4), 181. doi:10.1080/00268948508074858.
(33) Liu, J. M.; Yang, S. C. *Chem. Commun.* **1991**, 1529.
(34) Bredas, J. L.; Chance, R. R.; Silbey, R. *Phys. Rev. B* **1982**, *5843,* 26. doi:10.1103/PhysRevB.26.5843.
(35) Wei, Z. X.; Wan, M. X. *J. Appl. Polym. Sci.* **2003**, *87* (8), 1297. doi:10.1002/app.11541.
(36) Wei, Z. X.; Zhang, Z. M.; Wan, M. X. *Langmuir* **2002**, *18* (3), 917. doi:10.1021/la0155799.
(37) Wan, M. X. In *Encyclopedia of Nanoscience and Nanotechnology*; Nalwa, H. S., Ed.; American Scientific Publishers, Los Angeles, Vol. 2, 2004; pp. 153–169.
(38) Qiu, H. J.; Wan, M. X. *J. Polym. Sci. A Polym. Chem.* **2001**, *39* (20), 3485. doi:10.1002/pola.10002.
(39) Skotheim, T. A. *Handbook of Conducting Polymers*; Marcel Dekker, New York, Vol. 15, 1986.

Can. J. Chem. Downloaded from www.nrcresearchpress.com by MCGILL UNIVERSITY on 02/02/13
For personal use only.

(40) Skothiem, T. A.; Elsenbaumer, R.; Reynolds, J. *Handbook of Conducting Polymers*; Marcel Dekker, New York, 1998.
(41) Qiu, H. J.; Wan, M. X.; Matthews, B.; Dai, L. M. *Macromolecules* **2001**, *34* (4), 675. doi:10.1021/ma001525e.
(42) Wei, Y.; Sun, Y.; Patel, S.; Tang, X. *Polymer Prepr.* **1989**, *30,* 228.
(43) Focke, W. W.; Wnek, G. E.; Wei, Y. *J. Phys. Chem.* **1987**, *91* (22), 5813. doi:10.1021/j100306a059.
(44) Ray, M.; MacDiarmid, A.; Epstein, A. G. *J. Synth. Met.* **1987**, *21,* 23.
(45) Wei, Y.; Hariharan, R.; Patel, S. A. *Macromolecules* **1990**, *23,* 758. doi:10.1021/ma00205a01110.1021/ma00205a011.
(46) Fosong, W.; Jinsong, T.; Lixiang, W.; Hongfang, Z.; Zhishen, M. *Mol. Cryst. Liq. Cryst. (Phila. Pa.)* **1988**, *175,* 160.
(47) Pron, A.; Genoud, F.; Menardo, C.; Nechschein, M. *Synth. Met.* **1988**, *193,* 24.
(48) Schacklette, L. W.; Baughman, R. H. *Mol. Cryst. Liq. Cryst. (Phila. Pa.)* **1990**, *193,* 189.
(49) Lu, Y.; Li, J.; Wu, W. *Synth. Met.* **1989**, *87,* 30.
(50) MacDiarmid, A. J.; Epstein, J. *Synth. Met.* **1995**, *69,* 85. doi:10.1016/0379-6779(94)02374-8.
(51) Lee, K.; Cho, S.; Park, S. H.; Heeger, A. J.; Lee, C.-W.; Lee, S.-H. *Nature* **2006**, *65,* 441.
(52) Brédas, J. L.; Chance, R. R.; Silbey, R. *Phys. Rev. B* **1982**, *26* (10), 5843. doi:10.1103/PhysRevB.26.5843.
(53) Angelopolos, M.; Asturias, G. E.; Ermer, S. P.; Scherr, E. M.; MacDiarmid, A. G.; Akhtar, M.; Kiss, Z.; Epstein, A. *J. Mol. Cryst. Liq. Cryst. (Phila. Pa.)* **1988**, *160,* 151.
(54) Epstein, A. J.; Ginder, J. M.; Zuo, F.; Bigelow, R. W.; Woo, H.-S.; Tanner, D. B.; Richter, A. F.; Huang, W.-S.; MacDiarmid, A. G. *Synth. Met.* **1987**, *18* (1–3), 303. doi:10.1016/0379-6779(87)90896-4.
(55) Ou, R.; Samuels, R. *J. Polym. Sci., B, Polym. Phys.* **1999**, *37* (24), 3473. doi:10.1002/(SICI)1099-0488(19991215)37:24<3473::AID-POLB8>3.0.CO;2-X.
(56) Nakajima, T.; Kawagoe, T. *Synth. Met.* **1989**, *28* (1–2), C629. doi:10.1016/0379-6779(89)90583-3.
(57) Watanabe, A.; Mori, K.; Mikuni, M.; Nakamura, Y.; Matsuda, M. *Macromolecules* **1989**, *22* (8), 3323. doi:10.1021/ma00198a022.
(58) Zhang, D.; Hwang, J. H.; Yang, S. C. Mat. Res. Soc. Symp. Proc. 173, 1990; pp. 305–308.
(59) Bonnell, D. A.; Angelopoulos, M. *Synth. Met.* **1989**, *33* (3), 301. doi:10.1016/0379-6779(89)90476-1.
(60) Javadi, H. H. S.; Cromack, K. R.; MacDiarmid, A. G.; Epstein, A. J. *Phys. Rev. B.* **1989**, *39* (6), 3579. doi:10.1103/PhysRevB.39.3579.
(61) Angelopoulos, M.; Ray, A.; MacDiarmid, A. G.; Epstein, A. J. *Synth. Met.* **1987**, *21* (1–3), 21. doi:10.1016/0379-6779(87)90062-2.
(62) Wei, Y.; Hariharan, R.; Patel, S. A. *Macromolecules* **1990**, *23* (3), 758. doi:10.1021/ma00205a011.
(63) Fosong, W.; Jinsong, T.; Lixiang, W.; Hongfang, Z.; Zhishen, M. *Mol. Cryst. Liq. Cryst. (Phila. Pa.)* **1988**, *160,* 175.
(64) Pron, A.; Genoud, F.; Menardo, C.; Nechtschein, M. *Synth. Met.* **1988**, *24* (3), 193. doi:10.1016/0379-6779(88)90257-3.
(65) Thyssen, A.; Borgerding, A.; Schiltze, J. W. Makromol. Chem. Macromol. Symp. 8 1987; pp. 1423–1425.
(66) Schacklette, L. W.; Baughman, R. H. *Mol. Cryst. Liq. Cryst. (Phila. Pa.)* **1990**, *189,* 193.
(67) Lu, Y.; Li, J.; Wu, W. *Synth. Met.* **1989**, *30* (1), 87. doi:10.1016/0379-6779(89)90644-9.
(68) Shirani, H. I. B.; Bozorghi, S. J. *J. Iran. Chem. Res.* **2010**, *3,* 17.
(69) Omrani, A.; Sabzyan, H. *J. Phys. Chem. A* **2005**, *109* (39), 8874. doi:10.1021/jp0518310.
(70) Zora, M.; Ozaka, I. *J. Mol. Struct. THEOCHEM* **2003**, *638* (1–3), 157. doi:10.1016/S0166-1280(03)00562-1.
(71) Gross, E. K.; Dreiz, R. M. *Density Functional Theory*; Plenum Press, New York, 1995.
(72) Sundaraganesan, N.; Umamaheswari, H.; Joshua, B. D.; Meganathan, C.; Ramalingam, M. *J. Mol. Struct. THEOCHEM* **2008**, *850* (1–3), 84. doi:10.1016/j.theochem.2007.10.031.
(73) Frisch, M. J.; Trucks, G. W.; Schlegel, H. B.; Scuseria, G. E.; Robb, M. A.; Cheeseman, J. R.; V.G. Zakrazewski Montgomery, J. A., Jr.; Startmann, R. E.; Burant, J. C.; Dapprich, S.; Millam, J. M.; Daniels, A. D.; Kudin, K. N.; Strain, M. C.; Farkas, O.; Tomasi, J.; Barone, V.; Cossi, M.; Cammi, R.; Mennucci, B.; Adamo, C.; Clifford, S.; Ochterski, J.; Petersson, G. A.; Ayala, P. Y.; Cui, Q.; Morokuma, K.; Malik, D. K.; Rabuck, A. D.; Raghavachar, K.; Foresman, J. B.; Cioslowski, J.; Ortiz, J. V.; Stefanov, B. B.; Liu, G.; Liashenko, A.; Piskorz, P.; Komaromi, I.; Gomperts, R.; Martin, R. L.; Fox, D. J.; Keith, T.; Al-Laham, M. A.; Peng, C. Y.; Nanyakkara, A.; Gonzalez, C.; Challacombe, M.; Gill, M. W.; Johnson, B.; Chen, W.; Wong, M. W.; Andres, J. L.; Head-Gordon, M.; Replogle, E. S.; Pople, J. A. *GAUSSIAN 98 (Revision A3)*; Gaussian Inc, Pittsburgh, PA, 1998.
(74) Alkorta, I.; Elguero, J. *J. Struct. Chem.* **2005**, *16* (1), 77. doi:10.1007/s11224-005-1089-9.
(75) Andersson, M. P.; Uvdal, P. *J. Phys. Chem. A* **2005**, *109* (12), 2937. doi:10.1021/jp045733a.
(76) E. D. Glendening, A. E. Reed, J. E. Carpener, F. Weinhold, *NBO Version3.1*.
(77) (a) Foster, J. P.; Weinhold, F. *J. Am. Chem. Soc.* **1980**, *102* (24), 7211. doi:10.1021/ja00544a007; (b) Reed, A. E.; Curtiss, L. A.; Weinhold, F. *Chem. Rev.* **1988**, *88* (6), 899. doi:10.1021/cr00088a005; (c) Weinhold, F. *Natural bond orbital methods*; In *Encyclopedia of Computational Chemistry*; Schleyer, P. R.; Allinger, N. L.; Clark, T.; Gasteiger, J.; Kollman, P. A., Eds.; Wiley, Chichester, UK, Vol. 3, 1998; pp. 1792–1811.
(78) Stanger, A. , *J. Org. Chem.* **2006**, *71* (3), 883. doi:10.1021/jo051746o.

DFT/B3LYP Study of the Substituent Effects on the Reaction Enthalpies of the Antioxidant Mechanisms of Sesamol Derivatives in the Gas phase and water

Meysam Najafi, Mohammad Najafi, and Houshang Najafi

Can. J. Chem. Downloaded from www.nrcresearchpress.com by MCGILL UNIVERSITY on 02/02/13
For personal use only.

Abstract: In this paper, the study of various ortho and meta–substituted Sesamol derivatives is presented. The reaction enthalpies related to three antioxidant action mechanisms HAT, SET–PT, and SPLET for substituted Sesamols, have been calculated using the DFT/B3LYP method in gas phase and water. Calculated results show that electron-withdrawing substituents increase the bond dissociation enthalpy (BDE), ionization potential (IP), and electron transfer enthalpy (ETE), while electron-donating ones cause a rise in the proton dissociation enthalpy (PDE) and proton affinity (PA). In the ortho position, substituents show a larger effect on reaction enthalpies than in the meta position. In comparison with the gas phase, water attenuates the substituent effect on all reaction enthalpies. In the gas phase, BDEs are lower than PAs and IPs, i.e., HAT represents the thermodynamically preferred pathway. On the other hand, the SPLET mechanism represents the thermodynamically favored process in water. Results show that calculated enthalpies can be successfully correlated with Hammett constants (σ_m) of the substituted Sesamols. Furthermore, calculated IP and PA values for substituted Sesamols show linear dependence on the energy of the highest occupied molecular orbital (E_{HOMO}).

Key words: antioxidant, Sesamol, solvent effect, substituent effect, DFT, E_{HOMO}.

Résumé : Dans ce travail, on présente une étude de divers dérivés du Sesamol substitués dans les positions ortho et méta. Faisant appel à des calculs théoriques de la fonctionnelle de la densité au niveau B3LYP de la théorie, on a calculé les enthalpies de réactions, en phase gazeuse et en solution dans l'eau, de trois mécanismes d'action antioxydante, le transfert d'un atome d'hydrogène (TAH), le transfert d'un seul électron suivi d'un transfert de proton (TSE-TP) et une perte d'un proton suivie d'un transfert électron (PPSTE), des Sesamols substitués. Les résultats des calculs montrent que les substituants électroaffinitaires augmentent l'enthalpie de dissociation de la liaison (EDL), le potentiel d'ionisation (PI) et l'enthalpie de transfert d'électron (ETE) alors que les groupes électrodonneurs provoquent une augmentation de l'enthalpie de dissociation de la liaison (EDL) et une augmentation de l'affinité pour le proton (AP). Les effets des substituants sur les enthalpies de réaction sont plus pour les dérivés substitués en position ortho que pour ceux substitués en position méta. En phase gazeuse, les enthalpies de dissociation de la liaison (EDL) sont plus faibles que les augmentations de l'affinité pour le proton (AP) ou les potentiels d'ionisation (PI), c'est-à-dire que le transfert d'un atome d'hydrogène (TAH) correspond à la voie favorisée d'un point de vue thermodynamique. Toutefois, dans l'eau, la perte d'un proton suivie d'un transfert électron (PPSTE) est le mécanisme thermodynamiquement favorisé. Les résultats montrent qu'il est possible d'établir une corrélation entre les enthalpies calculées et les constantes d'Hammett (σ_m) des Sésamols substitués. De plus, il existe une corrélation linéaire entre les valeurs calculées des potentiels d'ionisation (PI) et des affinités pour le proton (AP) et l'énergie de l'orbitale moléculaire haute occupée (E_{OMHO}).

Mots-clés : antioxydant, Sésamol, effet de solvant, effet de substituant, théorie de la fonctionnelle de la densité, énergie de l'orbitale moléculaire haute occupée (E_{OMHO}).

[Traduit par la Rédaction]

Received 3 August 2012. Accepted 11 September 2012. Published at www.nrcresearchpress.com/cjc on 22 November 2012.

Abbreviations: DFT, density functional theory; BDE, bond dissociation enthalpy; IP, ionization potential; PDE, proton dissociation enthalpy; PA, proton affinity; ETE, electron transfer enthalpy; SET–PT, single electron transfer followed by proton transfer; SPLET, sequential proton loss electron transfer; HAT, hydrogen atom transfer; PCM, polarized continuum model; EDG–substituent, electron-donating group; EWG–substituent, electron-withdrawing group.

M. Najafi, M. Najafi, and H. Najafi. Department of Physiology, Faculty of Medicine, Kermanshah University of Medical Sciences, Kermanshah, Iran.

Corresponding author: Meysam Najafi (e-mail: meysamnajafi2012@yahoo.com).

Can. J. Chem. Downloaded from www.nrcresearchpress.com by MCGILL UNIVERSITY on 02/02/13
For personal use only.

Introduction

In recent years, the border between chemistry and biochemistry has become even more diffuse. The role of antioxidant has lately received much attention because they can avoid or at least significantly reduce the peroxidation of lipids by free radicals, which are related to a variety of disorders and diseases.[1–3] Antioxidants are generally supposed to protect cells against oxidative damage, resulting in health benefits, because the compounds prevent oxidation of biological molecules.[4] Sesamol is a natural organic compound that has antioxidant properties due to phenolic and benzodioxole groups in its structure.[5–10] The propagation and initiation of free radical chain reactions can be delayed or minimized by the donation of hydrogen, electron, or proton from the antioxidants. The polyphenols are more likely to scavenge free radicals at the initiation stage of lipid peroxidation and to a lesser extent at the propagation stage. Antioxidants free radicals can also react with lipid free radicals to form a stable complex compound, thereby preventing some damage. The phenolic antioxidants (ArOH) inhibit oxidation by transferring their phenolic H atom to a chain–carrying peroxyl radical ($ROO^{\bullet}$) at a rate much faster than that of chain propagation.[11] This yields an aryloxyl radical ($ArO^{\bullet}$) that it propagate peroxidation, because it is stabilized by resonance.

[1.1] $ArOH \rightarrow ArO^{\bullet} + H^{\bullet}$

[1.2] $ROO^{\bullet} + H^{\bullet} \rightarrow ROOH$

It is proposed that chain-breaking antioxidants can play their protective role via two major mechanisms.[11–13] In the first, H atom transfer (HAT) mechanism, the phenolic H atom is transferred in one step, as shown in eq. [1.1]). In the HAT mechanism, the bond dissociation enthalpy (BDE) of the phenolic O–H bond is one of the important parameters in evaluating the antioxidant action; the lower the BDE, the easier the dissociation of the phenolic O–H bond. The second mechanism, single electron transfer followed by proton transfer (SET–PT), takes place in two steps:

[2.1] $ROO^{\bullet} + ArOH \rightarrow ROO^{-} + ArOH^{+\bullet}$

[2.2] $ArOH^{+\bullet} \rightarrow ArO^{\bullet} + H^{+}$

In the first step, a cation radical is formed (eq. [2.1]). In the second step, deprotonation of $ArOH^{+\bullet}$ occurs (eq. [2.2]), followed by the protonation of ROO^{-},

[2.3] $ROO^{-} + H^{+} \rightarrow ROOH$

Ionization potential (IP) and proton dissociation enthalpy (PDE) represent enthalpies of the SET–PT process.[14,15] In the SET–PT mechanism, the IP is the most significant parameter; the lower the IP value, the easier the electron extraction. However, low IP values favour raising electron–transfer reactivity, because they enhance the chance of generating a superoxide anion radical through the transfer of the electron directly to surrounding O_2.[11,16,17] The PDE parameter is not a limiting step in the free radical scavenging action.

Another mechanism has been discoveredthat was named sequential proton loss electron transfer (SPLET), taking place in two steps (eqs. [3.1] and [3.2]):[18–21]

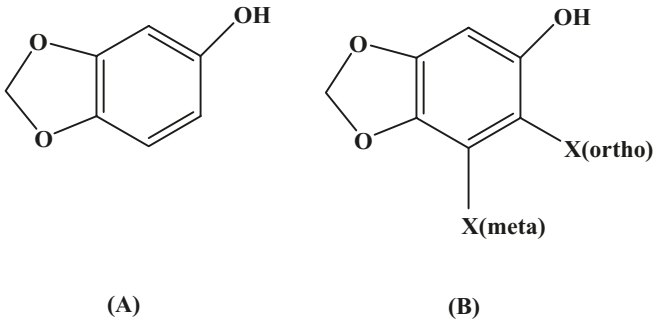
[3.1] $ArOH \rightarrow ArO^{-} + H^{+}$

[3.2] $ArO^{-} + ROO^{\bullet} \rightarrow ArO^{\bullet} + ROO^{-}$

[3.3] $ROO^{-} + H^{+} \rightarrow ROOH$

The reaction enthalpy of the first step (eq. [3.1]) corresponds to the proton affinity (PA) of the phenoxide anion (ArO^{-}).[22–24] In the second step (eq. [3.2]), electron transfer from phenoxide anion to $ROO^{\bullet}$ occurs, and the phenoxy radical is formed. The reaction enthalpy of this step is denoted as electron transfer enthalpy (ETE). The second step of SPLET is the limiting step (ETE), and therefore PA is far from the best indicator to rationalize the SPLET–like free radical scavenging. From the antioxidant action viewpoint, the net result of SPLET is the same as in the two previously mentioned mechanisms, the transfer of the hydrogen atom to the free radicals. The BDE actually correlates with the global thermodynamics of the three processes. Although, reaction enthalpies (BDE, IP, PA) related to three mechanisms are of importance in evaluating the antioxidant action, other criteria, including solubility, bioavailability, and nontoxicity, must also be considered when designing an effective and safe antioxidant.[25] The biological implications and the great potential of Sesamols as antioxidant aroused our interest in elucidating its antioxidant activity by means of DFT/B3LYP calculations, which have been successfully used for a variety of antioxidants in previous studies.[26–30] Because in chemistry one often needs to compare a group of reactions differing only in the substitution, it is also important to study the effect of substituents on the reaction enthalpy. The substituent effects are among the most important concepts of structural effects influencing the chemical, physicochemical, and biochemical properties of chemical species.[31–36] In recent years, many previous experimental[22–24,37–42] and theoretical[12,22,33,43–50] investigations have been carried out on phenols and mono-substituted phenols in gas and solvent environments. Theoretical studies of the substituent effect can be utilized in the synthesis of substances with enhanced antioxidant properties. In the present paper, we investigate the effect of various substituents on reaction enthalpies related to HAT, SPLET, and SPT–ET mechanisms of Sesamol derivations. Understanding the role of different structural features and preparation of new compounds with enhanced antioxidant property is of great interest. In this paper Sesamol (Fig. 1A) is the basic structure (non–substituent), and the various substituents such as electron–withdrawing groups (EWG) and electron–donating groups (EDG) were located in ortho and meta positions on the aromatic ring of Sesamol (Fig. 1B). For Sesamol, the energy of the antioxidant action has not been studied yet. No systematic study of solvent and substituent effects on BDE, IP, and PA of substituted Sesamols have been published yet. Indeed, there are actually only a few new insights from the polyphenol–calculation community. Therefore, we have systematically investigated the substituent effect on reaction enthalpies of homolytic (HAT mechanism) and heterolytic two–step (SPLET and SET–PT) mechanisms of O–H bond cleavage for mono–substituted Sesamols in gas phase and

Fig. 1. (A) Structure of Sesamol. (B) Studied Sesamols: X=Br, Ethyl, CH=CH_2, CCH, CF_3, Me, Cl, CN, COMe, COH, COOH, F, NMe_2, NHMe, NH_2, NO_2, OMe, OH, Ph, t–Bu.



water. Correlations of calculated enthalpies with Hammett constants of substituents were investigated. So far as we know, no attempt to find a relationship between structural parameters and reaction enthalpies related to HAT, SPLET, and SET–PT mechanisms in the case of Sesamols has been made previously. This work also shows linear dependence between calculated enthalpies and the energy of the highest occupied molecular orbital (E_{HOMO}) of studied molecules in the two environments. Because SET–PT and SPLET mechanisms are of importance in solvated media, it is interesting to explore how the solvent alters the reaction enthalpies of individual steps of the two mechanisms.[18–21,33,41,70] Because Sesamol is a powerful water–soluble antioxidant, water as the main cell environment was chosen to assess the substituent effect on above mentioned enthalpies in solution phase. To shed light on the solvent effect, PCM (polarized continuum model) calculations have been performed for the molecules in water.

Computational details

The geometries of the molecules and respective radicals, radical cations, and anions were optimized using the DFT method with B3LYP functional[71–73] and the 6–31G (d, p) basis set[71,72] in the gas phase and solution phase. Single point calculations were performed using the 6–311++G (2d, 2p) basis set.[74,75] The ground–state geometries of molecules were optimized at the restricted B3LYP level, and the geometry of the radicals, radical cations, anions were optimized at the restricted B3LYP open shell (half electron) level. We estimated the change in the ROB3LYP energies of phenoxyl radicals, radical cations, and anions when the geometries were optimized at the UB3LYP and ROB3LYP levels. It was observed that the two energies differ by less than 0.09 kcal mol^{-1} (1 cal = 4.182 J). Thus, the ROB3LYP method was used for the geometry optimization of all the substituted phenoxyl radicals, radical cations, and anions. The optimized structures were confirmed to be real minima by frequency calculation. For the species having more conformers, all conformers were investigated. The conformer with the lowest electronic energy was used in this work. All reported enthalpies were zero–point (ZPE) corrected with unscaled frequencies. On the basis of the DFT optimized geometries, the partial charges were obtained using 6–31(d,p) basis set.[71,72] Solvent contribution to the total enthalpies was computed employing the PCM method.[76,77] All calculations were performed using the Gaussian 98 program package.[78] All enthalpies were calculated for 298.15 K and 1.0 atmosphere pressure (101.325 kPa).

Results and discussion

Total enthalpies of the studied species X, H(X) at temperature T are usually estimated from the expression (4),[14,42]

$$[4] \quad H(\mathrm{X}) = E_0 + \mathrm{ZPE} + \Delta H_{trans} + \Delta H_{rot} + \Delta H_{vib} + RT$$

where E_0 is the calculated total electronic energy, ZPE stands for zero–point energy, ΔH_{trans}, ΔH_{rot}, and ΔH_{vib} are the translational, rotational, and vibrational contributions to the enthalpy, respectively. Finally, RT represents PV work term and is added to convert the energy to enthalpy. From the calculated total enthalpies we have determined following quantities:

$$[5] \quad \mathrm{BDE} = H(\mathrm{ArO}^{\bullet}) + H(\mathrm{H}^{\bullet}) - H(\mathrm{ArOH})$$

$$[6] \quad \mathrm{IP} = H(\mathrm{ArOH}^{+\bullet}) + H(\mathrm{e}^{-}) - H(\mathrm{ArOH})$$

$$[7] \quad \mathrm{PDE} = H(\mathrm{ArO}^{\bullet}) + H(\mathrm{H}^{+}) - H(\mathrm{ArOH}^{+\bullet})$$

$$[8] \quad \mathrm{PA} = H(\mathrm{ArO}^{-}) + H(\mathrm{H}^{+}) - H(\mathrm{ArOH})$$

$$[9] \quad \mathrm{ETE} = H(\mathrm{ArO}^{\bullet}) + H(\mathrm{e}^{-}) - H(\mathrm{ArO}^{-})$$

The calculated gas phase enthalpy of the proton, $H(H^+)$, and electron, $H(e^-)$, is 6.197 and 3.145 kJ mol^{-1}, respectively.[79] Obtained results reveal that water causes considerable changes in the total enthalpies of molecule, radical, anion, and the radical cation of studied compounds. The enthalpy of H^+ hydration is –1090 kJ mol^{-1}.[80] It severely affects PAs and PDEs. Since the enthalpy of electron hydratation, $\Delta_{hydr}H(e^-)$, could not be found in the literature, electron hydration enthalpy computed using B3LYP/6–311++G**, $\Delta_{hydr}H(e^-)$ = –105 kJ mol^{-1}, was employed.[81] In a previous paper, Rimarèík et al. calculated H^+ and e^- solvation enthalpies in organic solvents, which were not available in the literature using PCM DFT/B3LYP/6–311++G** method as the enthalpy change in the process,[81]

$$[10] \quad \mathrm{solvent(l)} + \mathrm{H}^{+}(\mathrm{g}) \rightarrow \mathrm{solvent}^{+}(\mathrm{solv})$$

or

$$[11] \quad \mathrm{solvent(l)} + \mathrm{e}^{-}(\mathrm{g}) \rightarrow \mathrm{solvent}^{-}(\mathrm{solv})$$

where they employed the following model: a proton or electron was "attached" to one molecule of solvent. Obtained species were optimized using the PCM approach in the same solvent.[81] Potential inaccuracies related to computed solvation enthalpies will be canceled when the substituent effect is studied, as the difference in the reaction enthalpies of substituted and nonsubstituted Sesamols, i.e., in terms of ΔBDE, ΔPA, ΔETE, ΔIP, and Δ. On the other hand, BDE, PA, and IP values allow the determination of the preferred reaction pathway in the studied solvents.

Can. J. Chem. Downloaded from www.nrcresearchpress.com by MCGILL UNIVERSITY on 02/02/13
For personal use only.

Can. J. Chem. Downloaded from www.nrcresearchpress.com by MCGILL UNIVERSITY on 02/02/13
For personal use only.

Table 1. Calculated BDEs and ΔBDEs in (kJ mol^{-1}) of ortho- and meta-substituted Sesamols in gas phase and water, and Hammett constants of substituents σ_m.[36]

	Gas				Water				
	Ortho		Meta		Ortho		Meta		
Substituent	BDE	ΔBDE	BDE	ΔBDE	BDE	ΔBDE	BDE	ΔBDE	σ_m
EDG									
NMe_2	336.9	–43.1	366.9	–14.1	333.0	–27.6	353.2	–7.4	–0.24
NHMe	334.3	–45.7	368.0	–13.0	319.4	–41.2	355.1	–5.5	–0.24
NH_2	340.6	–39.4	368.4	–12.6	328.0	–32.6	353.1	–7.5	–0.16
t-Bu	363.9	–16.1	379.0	–2.0	334.6	–26.0	357.7	–2.9	–0.10
Ethyl	363.2	–16.8	378.6	–2.4	352.4	–8.2	358.3	–2.3	–0.07
Me	368.9	–11.1	377.9	–3.1	354.3	–6.3	357.8	–2.8	–0.07
Ph	372.5	–7.5	383.6	2.6	355.5	–5.1	364.0	3.4	0.06
$CH{=}CH_2$	372.4	–7.6	384.2	3.2	356.0	–4.6	364.0	3.4	0.06
OH	352.2	–27.8	375.4	–5.6	355.1	–5.5	358.3	–2.3	0.12
OMe	356.9	–23.1	375.4	–5.6	358.7	–1.9	357.6	–3.0	0.12
EWG									
CCH	386.3	6.3	384.3	3.3	360.0	–0.6	368.2	7.6	0.21
F	396.8	16.8	384.0	3.0	382.4	21.8	364.4	3.8	0.34
COH	399.6	19.6	389.5	8.5	387.4	26.8	369.7	9.1	0.35
COOH	400.0	20.0	386.5	5.5	383.9	23.3	371.5	10.9	0.37
Cl	399.3	19.3	384.5	3.5	391.1	30.5	366.6	6.0	0.37
COMe	395.8	15.8	385.3	4.3	396.8	36.2	368.0	7.4	0.38
Br	401.0	21.0	384.6	3.6	396.2	35.6	366.5	5.9	0.39
CF_3	421.4	41.4	391.9	10.9	392.3	31.7	371.2	10.6	0.43
CN	425.7	45.7	394.5	13.5	397.4	36.8	376.5	15.9	0.56
NO_2	433.0	53.0	393.3	12.3	399.8	39.2	377.8	17.2	0.71

Bond dissociation enthalpies of ortho- and meta-substituted Sesamols

In gas phase

Knowledge of BDE has been accumulating substantially for the past 15–20 years owing to the development of both experimental and theoretical (quantum chemical) techniques.[38,39,41,45,47,69,70,82–94] In previous studies the solvent and substituent effects on O–H BDE values, substituted phenols have been investigated using the PCM method.[41,45,47,70,91] Fu et al.[86] and Guerra et al.[87] determined the solvation effect of water on the ΔBDE values of para-substituted phenols via PCM method, and in these studies reaction enthalpies were calculated using B3LYP method and the 6–31G* basis set. Russo et al.[57] have investigated the solvent effect on the BDE value of several phenolic antioxidants using the PCM method. Klein et al.[70] indicated that the PCM method could describe the substituent effect in very good agreement with experimental data for O–H BDE values of substituted phenols in water.[40] In this study, all conformers have been optimized, and the conformer with higher stability was used in each case. The calculated BDE for the basic structure, Sesamol, in gas phase reached 380 kJ mol^{-1}. The computed gas phase BDE and ΔBDE values, where ΔBDE = BDE(X–ArOH) – BDE(ArOH), for substituents placed in ortho and meta positions (Fig. 1B) are reported in Table 1. The O–H BDE value of the structure with NO_2 substituent in ortho and meta position were higher compared with the BDE value of Sesamol. For ortho-substituted Sesamols with NMe_2, NH_2, and NHMe the BDE values are lower compared with the Sesamol. For ortho-substituted Sesamols with halogens, the BDE values are higher than for Sesamol. For ortho-substituted Sesamols with COH, COOH, and COMe, the BDE values are higher than the BDE value of Sesamol. The O–H BDE of structure with OH substituent in ortho and meta position was lower cmopared with the BDE value of Sesamol. For meta-substituted Sesamols with NMe_2, NH_2, and NHMe, the BDE values are lower than for Sesamol. For ortho- and meta-substituted Sesamols with OMe, the BDE values are lower than the BDE value of Sesamol. The difference between the highest and lowest BDE values for ortho- and meta-substituent Sesamols were 91.4 and 32.6 kJ mol^{-1}, respectively. The obtained results can be interpreted knowing that electron–withdrawing groups in the ortho and the meta position stabilize the parent molecule and destabilize the radical; hence, they increase the O–H BDE. However, electron–donating groups in the ortho and meta positions have an opposite effect, and therefore their presence leads to a decrease in the O–H BDE.

In water

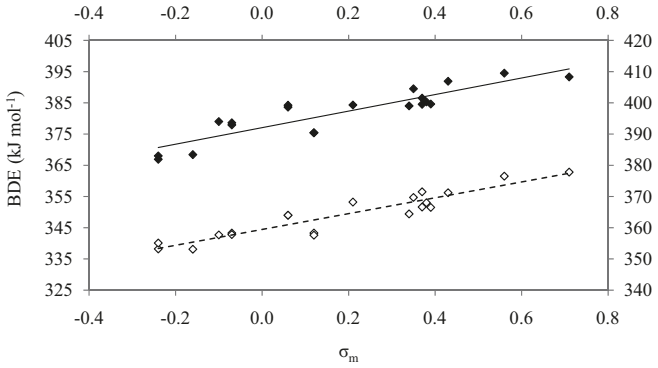
The calculated BDE for Sesamol is 360.6 kJ mol^{-1} in water phase, and that is lower than in gas phase BDE by 20 kJ mol^{-1}. The computed BDEs and ΔBDEs in water for ortho- and meta–substituted Sesamols are reported in Table 1. For ortho-substituted Sesamols with NMe_2, NH_2, and NHMe, the BDE values are 27.6, 32.6, and 41.2 kJ mol^{-1} lower than for Sesamol, respectively. For ortho-substituted Sesamols with

Can. J. Chem. Downloaded from www.nrcresearchpress.com by MCGILL UNIVERSITY on 02/02/13
For personal use only.

halogens, the BDE values are 13 kJ mol^{-1} higher ythan for Sesamol. For meta-substituted Sesamols with halogens, the BDE values are 4.5 kJ mol^{-1} higher than the BDE value of Sesamol. For ortho- and meta-substituted Sesamols with COH, COOH, and COMe, the BDE values are ca. 25 and 9 kJ mol^{-1} higher than the BDE value of Sesamol, respectively. An inspection of the O–H BDE values appearing in Table 1 shows that in water, calculated BDE values were lower than those calculated for the gas phase. Water causes considerable changes in the enthalpies of molecules and corresponding radicals of the studied structures, but overall results reveal a weak dependence of BDE values on the solvent polarity because the enthalpy changes are similar for both thes molecule and the radical structures. In water, electron–donating substituents decrease BDE values, whereas electron–withdrawing groups increase BDE values, similar to the results found for the gas phase. The difference between the highest and lowest BDE values in the water for the ortho and meta positions were 80 and 23.5 kJ mol^{-1}, respectively. In comparison with the gas phase, the effects of various substituents, including EDG and EWG, the BDE values in the ortho and meta positions were decreased in the water phase. Therefore, we can conclude that in comparison with the gas phase, the effect of EDG–substituents and EWG–substituents on BDE in the ortho and meta positions decreases in water. Since water causes unequal stabilization–destabilization of the parent molecule and the respective radical, this could be a fundamental reason for the obtained results. Therefore, a decrease in BDEs (negative ΔBDEs) for EDG–substituted Sesamols is the combined result of the radical stabilization and the parent molecule destabilization. However, increased BDEs (positive ΔBDEs) for EWG–substituted Sesamols seem to be due to the combination of both the parent and the radical destabilization. The overall results of the calculations of O–H BDE can be summarized by the fact that EWG–substituted Sesamols with higher BDEs may exhibit weaker antioxidant activity compared with EDG-substituted Sesamols in gas phase and water. In the present study, computed results for substituted Sesamols show that substituents in ortho positions exert significantly stronger influence on O–H BDE than substituents in the meta position in gas phase and water. These results are in agreement with previous studies in the meta and ortho substituted phenols and chromans.[11,41,49,63,69]

The Hammett equation (and its extended forms) has been one of the most widely used means for the study and interpretation of organic reactions and their mechanisms. Hammett constants σ_m (for substituents in the meta position) and σ_p (for substituents in the para position) obtained from the ionization of organic acids in solutions can frequently successfully predict equilibrium and rate constants for a variety of families of reactions.[35,36] Hammett constants correlate very well with the changes in BDE in the case of anilines, phenols, or thiophenols.[39,42,83,93] DiLabio et al. found that BDE and ΔBDE values of para substituted phenols, 6-substituted-3-pyridinols, 2-substituted-5-pyrimidinols, and anilines are linearly dependent on Hammett constants σ_p.[16,88,95] Klein et al. found that BDE and ΔBDE values of para substituted and meta substituted phenols are linearly dependent on Hammett constants σ_p and σ_m.[37,48] Klein et al. have shown that BDE values of meta substituted chromans are linearly dependent on Hammett constants σ_m in the gas phase and water. BDE values

Fig. 2. Dependence of BDE on σ_m for meta-substituted Sesamols in gas phase (solid squares, solid line, bottom x-axis, left y-axis) and water (open squares, dashed line, top x-axis, right y-axis).



computed for the meta-substituted Sesamols in the gas phase and water are plotted against Hammett constants in Fig. 2.[69] The correlation coefficients in gas and water reached 0.92 and 0.93, respectively. Equations obtained from the linear regression are as follows:

$$[12] \quad \mathrm{BDE(kJmol^{-1})} = 26.5 \times \sigma_m + 380.1(\mathrm{gas})$$

$$[13] \quad \mathrm{BDE(kJmol^{-1})} = 25.4 \times \sigma_m + 360.6(\mathrm{water})$$

Linear regressions show that the DFT method describes the expected linear BDE vs. Hammett constant dependence satisfactorily. This is very important because this can be utilized in the synthesis of novel Sesamol derivatives with enhanced antioxidant properties.

Ionization potentials of ortho- and meta-substituted Sesamols

In gas phase

This paper represents the first theoretical systematic study of substituted Sesamol IP values. In previous studies the substituent effect on IPs of para- and meta-substituted phenols have been investigated in the gas phase employing the B3LYP approach.[41,47] Chandra et al. calculated IP values for substituted pyridinethiols in the gas phase.[82] In this paper, the calculated IP for the Sesamol in gas phase reached 730.5 kJ mol^{-1}. The computed gas phase IPs and ΔIP = IP(X–ArOH) – IP(ArOH) for substituents in the ortho and meta positions are reported in Table 2. In the ortho and meta positions, the highest IP values were found for strong EWG substituents (NO_2, CF_3, and CN); the lowest IPs were obtained for strong EDG substituents (NMe_2, NH_2, and NHMe). For halogens in ortho positions, the IP values are higher than for Sesamol. For ortho- and meta–substituted Sesamols with strong EDGs (NMe_2, NH_2, and NHMe) IP values are lower than for Sesamol. The decrease in IP of the molecules with the OH group in ortho and meta positions are ca. 26 and 18 kJ mol^{-1}, respectively. For ortho- and meta-substituted Sesamols with OMe, the decrease in IP reached 24 and 22 kJ mol^{-1}, respectively. The halogens in the ortho and meta positions induce 19 and 15 kJ mol^{-1} increase in IP, respectively. For ortho- and meta-substituted Sesamols with COH,

Can. J. Chem. Downloaded from www.nrcresearchpress.com by MCGILL UNIVERSITY on 02/02/13
For personal use only.

Table 2. Calculated IPs and ΔIPs in (kJ mol^{-1}) of ortho- and meta-substituted Sesamols in gas phase and water.

	Gas				Water			
	Ortho		Meta		Ortho		Meta	
Substituent	IP	ΔIP	IP	ΔIP	IP	ΔIP	IP	ΔIP
NMe_2	675.0	–55.5	658.2	–72.3	235.0	–49.4	230.4	–54.1
NHMe	675.3	–55.2	661.3	–69.2	233.8	–50.6	229.2	–55.3
NH_2	682.1	–48.4	677.1	–53.4	241.8	–42.6	239.5	–45.0
t–Bu	710.4	–20.1	707.7	–22.8	274.6	–9.8	272.7	–11.8
Ethyl	714.7	–15.8	713.2	–17.3	276.1	–8.3	274.7	–9.8
Me	716.2	–14.3	714.7	–15.8	275.7	–8.7	274.1	–10.4
Ph	705.8	–24.7	706.5	–24.0	281.6	–2.8	281.8	–2.7
$CH{=}CH_2$	720.3	–10.2	714.9	–15.6	280.0	–4.4	281.0	–3.5
OH	704.2	–26.3	711.6	–18.9	263.6	–20.8	272.6	–11.9
OMe	706.0	–24.5	708.5	–22.0	265.9	–18.5	271.1	–13.4
CCH	734.0	3.5	725.2	–5.3	297.4	13.0	295.5	11.0
F	749.6	19.1	747.9	17.4	299.5	15.1	297.8	13.3
COH	758.2	27.7	758.4	27.9	310.2	25.8	309.8	25.3
COOH	756.4	25.9	748.2	17.7	306.2	21.8	307.2	22.7
Cl	747.5	17.0	744.1	13.6	301.3	16.9	299.5	15.0
COMe	742.2	11.7	742.4	11.9	300.6	16.2	299.2	14.7
Br	745.2	14.7	742.7	12.2	301.1	16.7	299.6	15.1
CF_3	767.9	37.4	766.2	35.7	316.6	32.2	321.0	36.5
CN	783.4	52.9	780.4	49.9	324.5	40.1	322.9	38.4
NO_2	789.9	59.4	787.9	57.4	330.8	46.4	332.1	47.6

COOH, and COMe, IP values are higher than the IP value of Sesamol. The IP values of Sesamols with the strongest electron–withdrawing NO_2 group in ortho and meta positions were higher by ca. 60 and 40 kJ mol^{-1} compared with non-substituted Sesamol, respectively. The difference between the highest and lowest IP values for the ortho and meta positions was 130 and 96 kJ mol^{-1}, respectively. As is known in organic chemistry, the EWG substituents stabilize the parent molecule and destabilize the radical and radical cation. This results in an increase in IP. However, EDG subsitutents have an opposite effect. Therefore, their presence in the molecule leads to a decrease in IP. The decrease in IP values (negative ΔIPs) of EDG–substituted Sesamols has the combined result of cation radical stabilization and parent molecule destabilization. However, the increased IP values (positive ΔIPs) of EWG–substituted Sesamols may result from the combination of both the parent and the cation radical destabilization. These results are in accordance with data published for substituent phenols.[41,47,82–85]

In water

The computed IPs using the above-mentioned calculated $\Delta_{hydr}H(e^-)$ value[81] in the water for molecules substituted in the meta and ortho positions are reported in Table 2. Table 2 also summarizes ΔIP values. Water causes considerable changes in the enthalpies of the molecule and cation radical of studied Sesamols. The calculated IP for Sesamol in water is lower than that in the gas phase by 284.5 kJ mol^{-1}. IP is significantly lower than that in the gas phase because of the negative enthalpy of electron hydration in water. For strong EDGs, i.e., NMe_2, NH_2, and NHMe, in ortho and meta positions, we found decreases in IP values of 50 and 40 kJ mol^{-1}, respectively. For the OH group in ortho and meta positions, the decrease in IP reached ca. 20 and 11 kJ mol^{-1}, respectively. For halogens in ortho and meta positions, the increase in IP reached 15 and 13 kJ mol^{-1}, respectively. For ortho- and meta-substituted Sesamols with strong electron–withdrawing NO_2 group, the increase in IP value was ca. 46 and 35 kJ mol^{-1}, respectively. In water, substituent-induced changes are lower than those observed in the gas phase. The EWG–substituents stabilize the parent molecule and destabilize the radical cation. On the other hand, EDG–substituents have an opposite effect. Water causes ca. 15 kJ mol^{-1} attenuation of substituent effects in terms of the narrower ΔIP range. Again, substituents in ortho positions exert stronger influence upon IP than the same substituents in meta positions. Values in Table 3 also reveal that IP values in water are considerably lower than corresponding gas phase values.

Klein et al. confirmed that there are linear relations between IPs of substituted phenols and Hammett constants σ_p and σ_m in the gas phase.[41] THe IP values computed for the meta-substituted Sesamols in the gas phase and water are plotted against Hammett constants in Fig. 3. The correlation coefficients in gas phase and water reached 0.95 and 0.94, respectively. Equations obtained from the linear regression are as follows:

$$[14] \quad IP(kJmol^{-1}) = 125.1 \times \sigma_m + 730.5(gas)$$

$$[15] \quad IP(kJmol^{-1}) = 100.1 \times \sigma_m + 284.5(water)$$

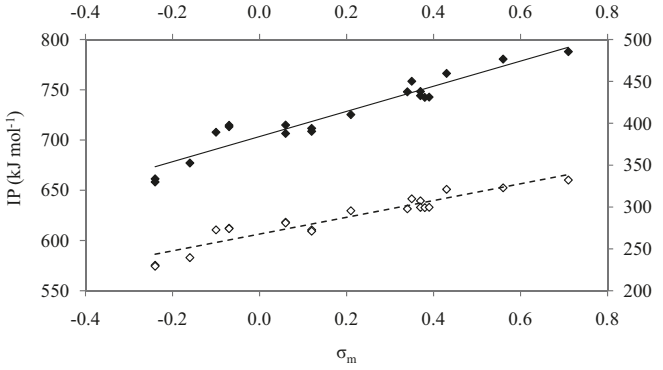
We can conclude that the DFT method describes the expected linear IP vs. Hammett constant dependence satisfactorily.

Can. J. Chem. Downloaded from www.nrcresearchpress.com by MCGILL UNIVERSITY on 02/02/13
For personal use only.

Table 3. Calculated E_{HOMO} in (eV) of ortho- and meta-substituted Sesamols in gas phase and water.

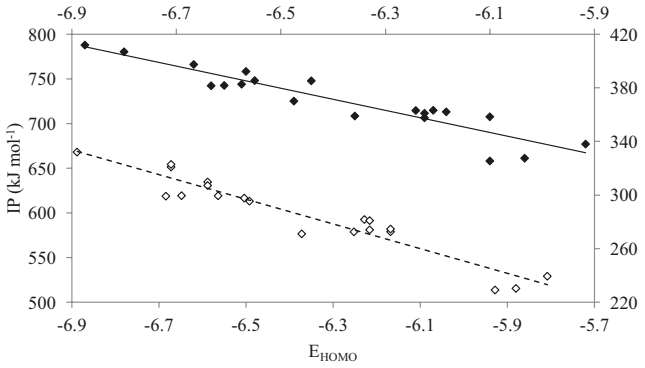
	Gas		Water	
Substituent	Ortho	Meta	Ortho	Meta
NMe_2	–5.90	–5.94	–6.14	–6.05
NHMe	–5.92	–5.86	–6.16	–6.09
NH_2	–5.85	–5.72	–6.07	–5.99
t–Bu	–5.94	–5.94	–6.23	–6.29
Ethyl	–5.90	–6.04	–6.21	–6.29
Me	–6.09	–6.11	–6.37	–6.33
Ph	–6.08	–6.09	–6.36	–6.34
$CH=CH_2$	–6.08	–6.07	–6.36	–6.33
OH	–6.13	–6.09	–6.51	–6.36
OMe	–6.12	–6.25	–6.40	–6.46
CCH	–6.25	–6.39	–6.49	–6.56
F	–6.25	–6.35	–6.52	–6.57
COH	–6.38	–6.50	–6.60	–6.64
COOH	–6.38	–6.48	–6.59	–6.64
Cl	–6.57	–6.51	–6.75	–6.62
COMe	–6.47	–6.58	–6.70	–6.72
Br	–6.45	–6.55	–6.67	–6.69
CF_3	–6.55	–6.62	–6.71	–6.71
CN	–6.72	–6.78	–6.81	–6.71
NO_2	–6.87	–6.87	–6.98	–6.89

Fig. 3. Dependence of IP on σ_m for meta–substituted Sesamols in gas phase (solid squares, solid line, bottom x-axis, left y-axis) and water (open squares, dashed line, top x-axis, right y-axis).



To accelerate the discovery of novel antioxidants, considerable effort has been devoted to investigating the structure–activity relationships (SARs) for antioxidants. Furthermore, rational design strategies for antioxidants have been proposed and applied in research. It was shown that IPs determined using the DFT computational approach are sufficiently accurate to characterize the electron-donating ability of antioxidants.[96,97] The energy of the highest occupied molecular orbital (E_{HOMO}) represents an alternative parameter to assess the electron-donating ability of antioxidants. This is widely used in the antioxidant study because of the simple calculation procedure in which only the calculation for the parent molecule is required.[98,99] The E_{HOMO} is derived from DFT by employing Janak's theorem.[100] Janak's theorem states that the derivative of the total DFT energy with respect to the occupation of a given orbital is equal to the corresponding orbital energy. According to Janak's theorem, E_{HOMO} must be exactly equal to the ionization potential. Therefore, HOMO energy represents an applicable parameter for prediction of antioxidant activity[101,102] and oxidant scavenging ability[103] via SET–PT mechanism. Our results for E_{HOMO} for Sesamol in the gas phase and water are –6.15 and –6.28 eV, respectively. As a general rule, the higher the E_{HOMO}, the more active the compound is as an antioxidant.[103,104] The computed E_{HOMO} values of Sesamols in the gas phase and water are summarized in Table 3. These reveal that in the case of EWG-substituents, E_{HOMO} values become more negative, while the presence of EDG-substituents results in less negative E_{HOMO} values. Therefore, Sesamols with strong electron-donating groups are better electron donors. A previous study showed that the B3LYP/6–311+G(2d,2p) method significantly underestimates vertical gas phase ionization potentials obtained from E_{HOMO} for mono-substituted anilines, phenols, and thiophenols.[93] However, the trends in ionization potentials, in terms of ΔIPs, are described reliably. Therefore, we decided to find expected linear dependence between calculated IPs and corresponding E_{HOMO} values (Fig. 4). For meta-substituted Sesamols, correlation coefficients in gas phase and water reached 0.95 and 0.96, respectively. The obtained equations are as follows:

Fig. 4. Dependence of IP on E_{HOMO} for meta-substituted Sesamols in gas phase (solid squares, solid line, bottom x-axis, left y-axis) and water (open squares, dashed line, top x-axis, right y-axis).



[16] $$IP(kJmol^{-1}) = -103.2 \times E_{HOMO}(eV) + 77.1(gas)$$

[17] $$IP(kJmol^{-1}) = -110.4 \times E_{HOMO}(eV) - 428(water)$$

The equations enable fast IP estimations for mono-substituted Sesamols from the computed E_{HOMO} values. This can be useful in the selection of suitable candidates for the synthesis of novel Sesamol derivatives with enhanced antioxidant properties.

Proton affinities of ortho and meta substituted Sesamols

In gas phase

PA represents the reaction enthalpy of the first step in the SPLET mechanism (eq. [3.1]). PAs of substituted Sesamols have not been obtained by theoretical calculations previously.

Can. J. Chem. Downloaded from www.nrcresearchpress.com by MCGILL UNIVERSITY on 02/02/13
For personal use only.

Table 4. Calculated PAs and ΔPAs in (kJ mol^{-1}) of ortho- and meta-substituted Sesamols in gas phase and water.

	Gas				Water			
	Ortho		Meta		Ortho		Meta	
Substituent	PA	ΔPA	PA	ΔPA	PA	ΔPA	PA	ΔPA
NMe_2	1517.2	15.9	1509.3	8.0	68.1	11.4	60.8	4.3
NHMe	1514.5	13.2	1508.8	7.5	69.8	13.1	61.1	4.6
NH_2	1516.4	15.1	1508.1	6.8	66.1	9.4	61.6	5.1
t–Bu	1508.1	6.8	1503.8	2.5	65.0	8.3	59.7	3.2
Ethyl	1508.7	7.4	1503.4	2.1	63.8	7.1	59.5	3.0
Me	1505.1	3.8	1502.3	1.0	61.3	4.6	59.3	2.8
Ph	1506.1	4.8	1492.7	–8.6	60.4	3.7	58.6	2.1
$CH{=}CH_2$	1505.3	4.0	1493.6	–7.7	59.9	3.2	55.9	–0.6
OH	1510.9	9.6	1504.8	3.5	64.0	7.3	55.0	–1.5
OMe	1506.8	5.5	1504.5	3.2	61.9	5.2	55.2	–1.3
CCH	1505.7	4.4	1486.7	–14.6	60.3	3.6	55.4	–1.1
F	1490.7	–10.6	1486.7	–14.6	44.1	–12.6	45.2	–11.3
COH	1464.6	–36.7	1481.2	–20.1	45.3	–11.4	42.7	–13.8
COOH	1454.6	–46.7	1483.6	–17.7	41.1	–15.6	46.4	–10.1
Cl	1482.8	–18.5	1483.4	–17.9	41.7	–15.0	43.9	–12.6
COMe	1466.3	–35.0	1474.2	–27.1	43.0	–13.7	47.9	–8.6
Br	1478.5	–22.8	1486.2	–15.1	41.0	–15.7	45.3	–11.2
CF_3	1454.6	–46.7	1463.6	–37.7	28.3	–28.4	40.6	–15.9
CN	1444.2	–57.1	1462.4	–38.9	15.7	–41.0	37.4	–19.1
NO_2	1437.2	–64.1	1456.7	–44.6	19.0	–37.7	34.6	–21.9

In previous studies, the substituent effect on PAs of para- and meta-substituted phenols have been investigated by DFT using B3LYP functional in the gas phase.[22–24,41,42] Chandra et al. also calculated PA values for substituted pyridinethiols in the gas phase.[82] Calculated gas phase PA for Sesamol reached 1501.3 kJ mol^{-1}. The computed PAs and ΔPAs for the various substituents in ortho and meta positions in the gas phase are reported in Table 4. The highest values of PA for ortho and meta positions were found for NMe_2, NH_2, and NHMe groups. The lowest PA values for these positions were found for NO_2, CF_3, and CN groups. Compared with nonsubstituted Sesamol, for Sesamols with NMe_2, NH_2, and NHMe groups in ortho and meta positions, PA values are higher compared with the PA value of Sesamol. The halogens in ortho and meta positions cause a decrease in PA value. For ortho- and meta–substituted Sesamols with COH, COOH, and COMe, PAs are lower than for Sesamol. For strong electron–withdrawing NO_2 substituent in ortho and meta positions, the drops in PA reached largest values compared with the PA value of Sesamol. The differences between the highest and lowest gas phase PA values for ortho and meta substituents were 80 and 53 kJ mol^{-1}, respectively. In agreement with previous studies on substituted phenols, it can be concluded that EDG substituents increase PA, whereas EWG ones decrease PA.[22–24,42] It is known that a charged molecule is more sensitive to the effect of substituent than its neutral counterpart. EWG substituents stabilize ArO^- but destabilize the parent phenol. Electron donating groups have an opposite effect.[15,39,84,85]

In water

The present calculated PA for the Sesamol reached 56.5 kJ mol^{-1} in water. For Sesamols substituted in meta and ortho positions, computed PAs and ΔPAs in water are reported in Table 4. Water causes considerable changes in the enthalpies of anions. Calculated PA for Sesamol in water is lower than for the gas phase by 1445.5 kJ mol^{-1}. Because of the large negative enthalpy of H^+ hydration, PAs in water are significantly lower than gas phase values. Again, EWG substituents decrease PAs, whereas EDG groups increase PAs, in agreement with results for substituted phenols in water.[70] Again, strong electron–donating NMe_2, NH_2, and NHMe cause an increase in PA. For ortho- and meta–substituted Sesamols, PA values are higher in comparison with the Sesamol. The presence of OH group in ortho and meta positions results in 7 and 2.5 kJ mol^{-1} PA growth, respectively. For halogens in ortho and meta positions, the drops in PAs reached 15 and 12 kJ mol^{-1}, respectively. The largest decrease in PA occurs for Sesamol with a NO_2 group in ortho and meta positions. Differences between the highest and lowest PA values for the 3 studied positions were 50 (ortho) and 27 kJ mol^{-1} (meta). It confirms that water attenuates substituent induced changes. Klein et al. found a linear dependence between PAs of substituted phenols and Hammett constants in gas phase and water.[41,70] There is also a linear relation between PAs of substituted pyridinethiols with Hammett constants.[82] For the meta-substituted Sesamols in gas phase and water, computed PAs are plotted against Hammett constants in Fig. 5. The correlation coefficients in gas phase and water reached 0.94 and 0.95, respectively. Equations obtained from the linear regression are as follows:

$$[18] \quad PA(kJmol^{-1}) = -55.6 \times \sigma_m + 1501(gas)$$

$$[19] \quad PA(kJmol^{-1}) = -30.8 \times \sigma_m + 56.5(water)$$

Can. J. Chem. Downloaded from www.nrcresearchpress.com by MCGILL UNIVERSITY on 02/02/13
For personal use only.

Fig. 5. Dependence of PA on σ_m for meta-substituted Sesamols in gas phase (solid squares, solid line, bottom x-axis, left y-axis) and water (open squares, dashed line, top x-axis, right y-axis).

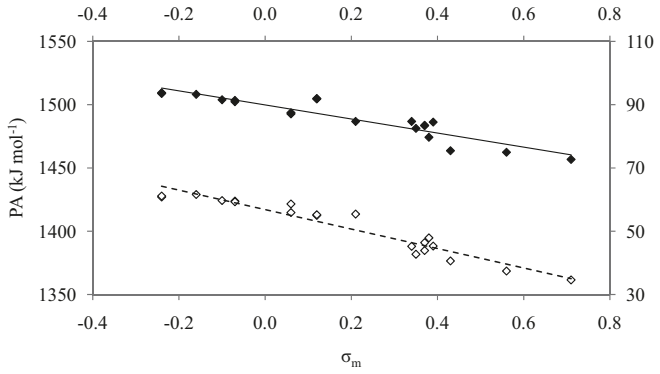
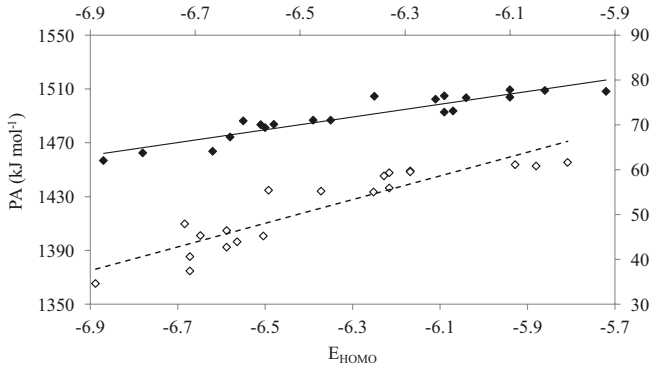


Fig. 6. Dependence of PA on E_{HOMO} for meta-substituted Sesamols in gas phase (solid squares, solid line, bottom x-axis, left y-axis) and water (open squares, dashed line, top x-axis, right y-axis).



These results show good linearity for the PA = $f(\sigma_m)$ dependences. We have also performed linear correlation of PA values with E_{HOMO} in the two environments. We also searched for expected linear dependence between calculated PAs and corresponding $-E_{HOMO}$ values (Fig. 5). Obtained dependences for substituents in meta position are shown in Fig. 6. Correlation coefficients reached 0.95 (gas phase) and 0.94 (water). The following regression linar relations were obtained:

$$[20] \quad PA(kJmol^{-1}) = 47.3 \times E_{HOMO}(eV) + 1787(gas)$$

$$[21] \quad PA(kJmol^{-1}) = 31.7 \times E_{HOMO}(eV) + 256(water)$$

The positive line slopes reflect the fact that the EDG–substituents increase PA, as well as the absolute value of E_{HOMO}. On the other hand, EWG–substituents cause a decrease in PAs and absolute E_{HOMO} values. Obtained equations may be used to predict PAs for meta–substituted Sesamols from their E_{HOMO}. We can conclude that E_{HOMO} can be employed for fast estimations of reaction enthalpies for the first step of both investigated SET–PT and SPLET mechanisms.

Proton dissociation enthalpies and electron transfer enthalpies in gas phase and water

PDE and ETE represent the reaction enthalpies of the second steps in SET–PT and SPLET mechanisms, respectively. To obtain the whole SET–PT and SPLET energetics picture, it is also important to study PDEs and ETEs and to investigate the solvent and substituent effects on these reaction enthalpies. In previous papers the substituent effect on PDEs for substituted phenols have been theoretically investigated by DFT using B3LYP functional.[12,15,41,69,105] In recent papers, the PDE and ETE values of ortho- and meta-substituted chromans have been calculated in gas and water.[69,105] There are no experimental PDEs available yet. Calculated PDEs for the Sesamol reached 1045.2 kJ mol^{-1} in the gas phase and 150.1 kJ mol^{-1} in water. The PDE of Sesamol in water is lower by 895 kJ mol^{-1}. Because of the large enthalpy of proton hydration, PDEs in water are significantly lower than gas phase values. Water also causes considerable changes in the enthalpies of radicals and radical cations of the studied structures. Computed PDE values for the substituents in ortho and meta position in the gas phase and water are reported in Table 5. The highest PDEs were found for strong EDG substituents (NMe_2, NH_2, and NHMe), whereas lowest PDEs were obtained for strong EWG substituents (NO_2, CF_3, and CN). This trend is opposite to that observed for PAs. It is known that electron–donating groups stabilize $ArOH^{+\bullet}$ but destabilize the parent structure, while electron–withdrawing groups have an opposite effect.[15,39,94] These results are in agreement with previous papers on substituted phenols and chromans.[12,15,41,44,69,105] For substituted Sesamol, ETEs were not studied previously. In the literature, only DFT/B3LYP ETEs of substituted phenols and chromans are available.[41,69,33,105] Calculated ETE values for Sesamol reached 248.3 kJ mol^{-1} in the gas phase and 330.5 kJ mol^{-1} in water. The computed ETEs values for Sesamol with substituents in ortho and meta position are compiled in Table 5. In gas phase and water, highest ETEs were found for strong EWG substituents (NO_2, CF_3, and CN). Lowest ETEs were found in the case of strong EDG substituents (NMe_2, NH_2, NHMe). This trend corroborates with that observed for BDEs and IPs. It is known that electron-withdrawing groups are favorable to stabilize ArO^-. Electron-donating groups have an opposite effect. Therefore, electron-withdrawing groups increase ETE values, while electron-donating groups decrease ETEs.[15,39,85,94,106]

Conclusions

In this article, the reaction enthalpies of the individual steps of three antioxidant action mechanisms, HAT, SET–PT, and SPLET, for various ortho- and meta-substituted Sesamols were calculated in gas phase and in water. The obtained results indicate that electron–withdrawing substituents increase the bond dissociation enthalpy (BDE), ionization potential (IP), and electron transfer enthalpy (ETE), while electron–donating substituents cause a rise in the proton dissociation enthalpy (PDE) and proton affinity (PA). Water attenuates the substituent effect on all reaction enthalpies. In the gas phase, BDEs are lower than PAs and IPs, i.e., HAT represents the thermodynamically preferred pathway. On the other hand, SPLET mechanism represents the thermodynamically favored process in water. The results show that calculated enthalpies can be successfully correlated with Hammett constants (σ_m) of the

Table 5. Calculated PDEs and ETEs in (kJ mol^{-1}) of ortho- and meta-substituted Sesamols in gas phase and water.

	Gas				Water			
	Ortho		Meta		Ortho		Meta	
Substituent	PDE	ETE	PDE	ETE	PDE	ETE	PDE	ETE
NMe_2	1080.6	225.1	1113.6	243.0	175.0	300.3	196.7	318.8
NHMe	1070.8	222.8	1111.6	241.9	170.7	299.6	199.9	320.4
NH_2	1068.2	221.9	1104.2	238.1	166.2	299.5	187.9	317.9
t–Bu	1055.3	245.6	1067.4	246.5	154.7	316.7	159.2	322.4
Ethyl	1054.5	247.2	1062.3	246.1	154.9	319.6	159.7	324.3
Me	1053.0	243.6	1060.1	246.4	154.8	321.6	162.7	323.9
Ph	1059.9	265.0	1061.0	262.8	154.0	329.5	156.2	331.8
$CH{=}CH_2$	1048.6	265.5	1062.6	261.7	150.1	334.4	157.0	334.4
OH	1057.0	232.8	1059.7	251.5	162.2	311.0	169.7	329.7
OMe	1054.0	237.0	1063.7	243.7	158.5	314.0	168.5	324.2
CCH	1054.5	277.6	1050.8	272.3	143.0	350.0	146.6	346.1
F	1033.4	266.1	1031.0	271.1	135.5	347.4	132.6	345.6
COH	1033.9	287.3	1026.0	282.2	155.9	363.2	136.8	356.4
COOH	1038.1	291.8	1033.2	281.7	139.1	366.1	136.2	351.5
Cl	1038.8	277.5	1033.3	278.9	137.1	349.1	131.0	349.2
COMe	1038.5	281.8	1037.7	279.9	145.6	359.6	132.8	346.5
Br	1041.6	282.2	1031.8	282.2	137.9	350.4	130.9	349.6
CF_3	1026.2	303.4	1016.6	309.0	128.8	369.4	120.2	359.1
CN	1009.1	322.1	1006.0	309.9	119.8	377.1	114.5	365.5
NO_2	1006.7	324.4	1000.3	315.4	126.1	387.3	112.6	371.6

Can. J. Chem. Downloaded from www.nrcresearchpress.com by MCGILL UNIVERSITY on 02/02/13
For personal use only.

substituted Sesamols. It has been also found that PA and IP values for substituted Sesamols can be estimated from their E_{HOMO} values. This fact may be useful for the development of new Sesamol based antioxidants.

Acknowledgement

I would like to thank my colleagues for their valuable discussions on the computational matters.

References

(1) Pryor, W. A. *Free Radic. Biol. Med.* **2000**, *28* (1), 141. doi:10.1016/S0891-5849(99)00224-5.
(2) Niki, E. *Free Radic. Res.* **2000**, *33* (6), 693. doi:10.1080/10715760000301221.
(3) Wang, X.; Quinn, P. J.; Prog, J. *Lipid Res.* **1999**, *38* (4), 309. doi:10.1016/S0163-7827(99)00008-9.
(4) Hou, Y. C.; Tsai, S. Y.; Liu, I. L.; Yu, C. P.; Chao, P. D. L. *J. Agric. Food Chem.* **2008**, *56* (20), 9636. doi:10.1021/jf801453f.
(5) Tadolini, B.; Juliano, C.; Piu, L.; Franconi, F.; Cabrini, L. *Free Radic. Res.* **2000**, *33* (1), 105. doi:10.1080/10715760000300661.
(6) Burton, G. W.; Ingold, K. U. *Acc. Chem. Res.* **1986**, *19* (7), 194. doi:10.1021/ar00127a001.
(7) Joseph, G. S.; Jayaprakasha, G. K.; Selvi, A. T.; Jena, B. S.; Sakariah, K. K. *Int. J. Food Microbiol.* **2005**, *101* (2), 153. doi:10.1016/j.ijfoodmicro.2004.11.001.
(8) Wynn, J. P.; Kendrick, A.; Ratledge, C. *Lipids* **1997**, *32* (6), 605. doi:10.1007/s11745-997-0077-1.
(9) Shively, M. L.; Thompson, D. C. *Int. J. Pharm.* **1995**, *117* (1), 119. doi:10.1016/0378-5173(94)00331-X.
(10) Santinho, A. J. P.; Pereira, N. L.; De Freitas, O.; Collett, J. H. *Int. J. Pharm.* **1999**, *186* (2), 191. doi:10.1016/S0378-5173(99)00171-4.
(11) Wright, J. S.; Johnson, E. R.; Dilabio, G. A. *J. Am. Chem. Soc.* **2001**, *123* (6), 1173. doi:10.1021/ja002455u.
(12) Vafiadis, A. P.; Bakalbassis, E. G. *Chem. Phys.* **2005**, *316* (1–3), 195. doi:10.1016/j.chemphys.2005.05.015.
(13) Musialik, M.; Litwinienko, G. *Org. Lett.* **2005**, *7* (22), 4951. doi:10.1021/ol051962j.
(14) Zhang, H. Y.; Ji, H. F. *J. Mol. Struct.: (THEOCHEM)* **2003**, *663* (1–3), 167. doi:10.1016/j.theochem.2003.08.124.
(15) Zhang, H. Y.; Sun, Y. M.; Wang, X. L. *J. Org. Chem.* **2002**, *67* (8), 2709. doi:10.1021/jo016234y.
(16) Pratt, D. A.; Dilabio, G. A.; Brigati, G.; Pedulli, G. F.; Valgimigli, L. *J. Am. Chem. Soc.* **2001**, *123* (19), 4625. doi:10.1021/ja005679l.
(17) Burton, G. W.; Doba, T.; Gabe, E. J.; Hughes, L.; Lee, F. L.; Prasad, L.; Ingold, K. U. *J. Am. Chem. Soc.* **1985**, *107* (24), 7053. doi:10.1021/ja00310a049.
(18) Litwinienko, G.; Ingold, K. U. *J. Org. Chem.* **2003**, *68* (9), 3433. doi:10.1021/jo026917t.
(19) Litwinienko, G.; Ingold, K. U. *J. Org. Chem.* **2004**, *69* (18), 5888. doi:10.1021/jo049254j.
(20) Foti, M. C.; Daquino, C.; Geraci, C. *J. Org. Chem.* **2004**, *69* (7), 2309. doi:10.1021/jo035758q.
(21) Litwinienko, G.; Ingold, K. U. *J. Org. Chem.* **2005**, *70* (22), 8982. doi:10.1021/jo051474p.
(22) Vianello, R.; Maksic, Z. B. *Tetrahedron* **2006**, *62* (14), 3402. doi:10.1016/j.tet.2006.01.049.
(23) Fujio, M.; McIver, R. T., Jr; Taft, R. W. *J. Am. Chem. Soc.* **1981**, *103* (14), 4017. doi:10.1021/ja00404a008.

Can. J. Chem. Downloaded from www.nrcresearchpress.com by MCGILL UNIVERSITY on 02/02/13
For personal use only.

(24) McMahon, T. B.; Kebarle, P. *J. Am. Chem. Soc.* **1977**, *99* (7), 2222. doi:10.1021/ja00449a032.
(25) Mulder, P.; Korth, H. G.; Ingold, K. U. *Helv. Chim. Acta* **2005**, *88* (2), 370. doi:10.1002/hlca.200590021.
(26) Wang, L. F.; Zhang, H. Y. *Bioorg. Chem.* **2005**, *33* (2), 108. doi:10.1016/j.bioorg.2005.01.002.
(27) Navarrete, M.; Rangel, C.; Corchado, J. C.; Espinosa–Garcia, J. *J. Phys. Chem. A* **2005**, *109* (21), 4777. doi:10.1021/jp050717e.
(28) Navarrete, M.; Rangel, C.; Espinosa-García, J.; Corchado, J. C. *J. Chem. Theory Comput.* **2005**, *1* (2), 337. doi:10.1021/ct0498932.
(29) Wayner, D. D. M.; Lusztyk, E.; Ingold, K. U.; Mulder, P. *J. Org. Chem.* **1996**, *61* (18), 6430. doi:10.1021/jo952167u.
(30) Nikolic, M. K. *J. Mol. Struct.: (THEOCHEM)* **2007**, *818,* 141. doi:10.1016/j.theochem.2007.05.011.
(31) Chen, W.; Song, J.; Guo, P.; Cao, W.; Bian, J. *Bioorg. Med. Chem. Lett.* **2006**, *16* (22), 5874. doi:10.1016/j.bmcl.2006.08.063.
(32) Lucarini, M.; Pedrielli, P.; Pedulli, G. F.; Cabiddu, S.; Fattuoni, C. *J. Org. Chem.* **1996**, *61* (26), 9259. doi:10.1021/jo961039i.
(33) Klein, E.; Lukes, V.; Ilcin, M. *Chem. Phys.* **2007**, *336* (1), 51. doi:10.1016/j.chemphys.2007.05.007.
(34) Mohajeri, A.; Asemani, S. S. *J. Mol. Struct.: (THEOCHEM)* **2009**, *930,* 15. doi:10.1016/j.molstruc.2009.04.031.
(35) Krygowski, T. M.; Steupien, B. T. *Chem. Rev.* **2005**, *105* (10), 3482. doi:10.1021/cr030081s.
(36) Hansch, C.; Leo, A.; Taft, R. W. *Chem. Rev.* **1991**, *91* (2), 165. doi:10.1021/cr00002a004.
(37) Zhu, Q.; Zhang, X. M.; Fry, A. J. *Polym. Degrad. Stabil.* **1997**, *57* (1), 43. doi:10.1016/S0141-3910(96)00224-8.
(38) Denisov, E. T. *Polym. Degrad. Stabil.* **1995**, *49* (1), 71. doi:10.1016/0141-3910(95)00037-M.
(39) Bordwell, F. G.; Cheng, J. P. *J. Am. Chem. Soc.* **1991**, *113* (5), 1736. doi:10.1021/ja00005a042.
(40) Lind, J.; Shen, X.; Eriksen, T. E.; Merenyi, G. *J. Am. Chem. Soc.* **1990**, *112* (2), 479. doi:10.1021/ja00158a002.
(41) Klein, E.; Lukes, V. *J. Phys. Chem. A* **2006**, *110* (44), 12312. doi:10.1021/jp063468i.
(42) Chandra, A. K.; Uchimaru, T. *Int. J. Mol. Sci.* **2002**, *3* (4), 407. doi:10.3390/i3040407.
(43) Zhu, Q.; Zhang, X. M.; Fry, A. J. *Polym. Degrad. Stabil.* **1997**, *57* (1), 43. doi:10.1016/S0141-3910(96)00224-8.
(44) Klein, E.; Lukes, V. *J. Mol. Struct.: (THEOCHEM)* **2007**, *805* (1–3), 153. doi:10.1016/j.theochem.2006.11.002.
(45) Bakalbassis, E. G.; Lithoxoidou, A. T.; Vafiadis, A. P. *J. Phys. Chem. A* **2003**, *107* (41), 8594. doi:10.1021/jp034400v.
(46) Korth, H. G.; De Heer, M. I.; Mulder, P. *J. Phys. Chem. A* **2002**, *106* (37), 8779. doi:10.1021/jp025713d.
(47) Bakalbassis, E. G.; Lithoxoidou, A. T.; Vafiadis, A. P. *J. Phys. Chem. A* **2006**, *110* (38), 11151. doi:10.1021/jp061718p.
(48) Klein, E.; Lukes, V. *Chem. Phys.* **2006**, *330* (3), 515. doi:10.1016/j.chemphys.2006.09.026.
(49) Bosque, R.; Sales, J. *J. Chem. Inf. Comput. Sci.* **2003**, *43* (2), 637. doi:10.1021/ci025632e.
(50) Mulder, P.; Korth, H. G.; Pratt, D. A.; Dilabio, G. A.; Valgimigli, L.; Pedulli, G. F.; Ingold, K. U. *J. Phys. Chem. A* **2005**, *109* (11), 2647. doi:10.1021/jp047148f.
(51) Jackson, R. A.; Hosseini, K. M. *J. Chem. Soc. Chem. Commun.* **1992**, *13* (13), 967. doi:10.1039/c39920000967.
(52) Patel, A.; Netscher, T.; Gille, L.; Mereiter, K.; Rosenau, T. *Tetrahedron* **2007**, *63* (24), 5312. doi:10.1016/j.tet.2007.03.114.
(53) Tafazoli, S.; Wright, J. S.; O'Brien, P. J. *Chem. Res. Toxicol.* **2005**, *18* (10), 1567. doi:10.1021/tx0500575.
(54) Lee, S. B.; Lin, C. Y.; Gill, P. M. W.; Webster, R. D. *J. Org. Chem.* **2005**, *70* (25), 10466. doi:10.1021/jo0517951.
(55) Wilson, G. J.; Lin, C. Y.; Webster, R. D. *J. Phys. Chem. B* **2006**, *110* (23), 11540. doi:10.1021/jp0604802.
(56) Yamauchi, R.; Kato, K.; Ueno, Y. *J. Agric. Food Chem.* **1995**, *43* (6), 1455. doi:10.1021/jf00054a008.
(57) Leopoldini, M.; Marino, T.; Russo, N.; Toscano, M. *J. Phys. Chem. A* **2004**, *108* (22), 4916. doi:10.1021/jp037247d.
(58) Espinosa-García, J. *Chem. Phys. Lett.* **2004**, *388* (4–6), 274. doi:10.1016/j.cplett.2004.03.023.
(59) Guo, Y.; Zhu, Y.; Xue, Y.; Xie, D. *Spectrochimica Acta Part A* **2007**, *68* (5), 1287. doi:10.1016/j.saa.2007.02.005.
(60) Zhang, H. Y.; Ji, H. F. *New J. Chem.* **2006**, *30* (4), 503. doi:10.1039/b600025h.
(61) Povalishev, V. N.; Polozov, G. I.; Shadyro, O. I. *Bioorg. Med. Chem. Lett.* **2006**, *16* (5), 1236. doi:10.1016/j.bmcl.2005.11.078.
(62) Singh, N. K.; O'Malley, P. J.; Popelier, P. L. A. *J. Mol. Struct.: (THEOCHEM)* **2007**, *811* (1–3), 249. doi:10.1016/j.theochem.2007.01.034.
(63) Wright, J. S.; Carpenter, D. J.; McKay, D. J.; Ingold, K. U. *J. Am. Chem. Soc.* **1997**, *119* (18), 4245. doi:10.1021/ja963378z.
(64) Setiadi, D. H.; Chass, G. A.; Torday, L. L.; Varro, A.; Papp, J. G. *J. Mol. Struct.: (THEOCHEM)* **2003**, *637* (1–3), 11. doi:10.1016/S0166-1280(02)00597-3.
(65) Wieser, H.; Vecchi, M.; Schlachter, M. *Int. J. Vitam. Nutr. Res.* **1986**, *56,* 45.
(66) van Acker, S. A. B. E.; Koymans, L. M. H.; Bast, A. *Free Radic. Biol. Med.* **1993**, *15* (3), 311. doi:10.1016/0891-5849(93)90078-9.
(67) Mukai, K.; Yokoyama, S.; Fukuda, K.; Uemoto, Y. *Bull. Chem. Soc. Jpn.* **1987**, *60* (6), 2163. doi:10.1246/bcsj.60.2163.
(68) Burton, G. W.; Le Page, Y.; Gabe, E. J.; Ingold, K. U. *J. Am. Chem. Soc.* **1980**, *102* (26), 7791. doi:10.1021/ja00546a032.
(69) Najafi, M.; Nazarparvar, E.; Haghighi Mood, K.; Zahedi, M.; Klein, E. *Comput. Theoret. Chem.* **2011**, *965* (1), 114. doi:10.1016/j.comptc.2011.01.035.
(70) Klein, E.; Rimarcik, J.; Lukes, V. *Acta Chim. Slov.* **2009**, *2,* 37.
(71) Becke, A. D. *J. Chem. Phys.* **1993**, *98* (7), 5648. doi:10.1063/1.464913.
(72) Becke, A. D. *Phys. Rev. A* **1988**, *38* (6), 3098. doi:10.1103/PhysRevA.38.3098.
(73) Lee, C.; Yang, W.; Parr, R. G. *Phys. Rev. B* **1988**, *37* (2), 785. doi:10.1103/PhysRevB.37.785.
(74) Davidson, E. R.; Feller, D. *Chem. Rev.* **1986**, *86* (4), 681. doi:10.1021/cr00074a002.
(75) Hehre, W. J.; Radom, L.; Schleyer, P. V. R.; Pople, J. A. *Ab Initio Molecular Orbital Theory*; Wiley, New York, 1986.
(76) Miertus, S.; Scrocco, E; Tomasi, J. **1981**, *J Chem Phys 55*: 117–129.
(77) Cossi, M.; Rega, N.; Scalmani, G.; Barone, V. *J. Comput. Chem.* **2003**, *24* (6), 669. doi:10.1002/jcc.10189.
(78) Frisch, M. J.; Trucks, G. W.; Schlegel, H. B.; Scuseria, G. E.; Robb, M. A.; Cheeseman, J. R.; Zakrzewski, V. G.; Montgomery, J. A., Jr.; Stratmann, R. E.; Burant, J. C.; Dapprich, S.; Millam, J. M.; Daniels, A. D.; Kudin, K. N.; Strain, M. C.;

Can. J. Chem. Downloaded from www.nrcresearchpress.com by MCGILL UNIVERSITY on 02/02/13
For personal use only.

Farkas, O.; Tomasi, J.; Barone, V.; Cossi, M.; Cammi, R.; Mennucci, B.; Pomelli, C.; Adamo, C.; Clifford, S.; Ochterski, J.; Petersson, G. A.; Ayala, P. Y.; Cui, Q.; Morokuma, K.; Malick, D. K.; Rabuck, A. D.; Raghavachari, K.; Foresman, J. B.; Cioslowsk, J.; Ortiz, J. V.; Stefanov, B. B.; Liu, G.; Liashenko, A.; Piskorz, P.; Komaroni, I.; Gomperts, R.; Martin, R. L.; Fox, D. J.; Keith, T.; Al–Laham, M. A.; Peng, C. Y.; Nanayakkara, A.; Gonzales, C.; Challacombe, M.; Gill, P. M. W.; Johnson, B. G.; Chen, W.; Wong, M. W.; Andres, J. L.; Head–Gordon, M. R. E. S.; Pople, J. A. *Gaussian 98*; Gaussian, Inc, Pittsburgh, PA, 1998.

(79) Bizarro, M. M.; Cabral, B. J. C.; dos Santos, R. M. B.; Simons, J. A. M. *Pure Appl. Chem.* **1999**, *71,* 1249.

(80) Bartmess, J. E. *J. Phys. Chem.* **1994**, *98* (25), 6420. doi:10.1021/j100076a029.

(81) Rimarcik, J.; Lukes, V.; Klein, E.; Ilcin, M. *J. Mol. Struct.: (THEOCHEM)* **2010**, *952* (1–3), 25. doi:10.1016/j.theochem.2010.04.002.

(82) Nam, P. C.; Nguyen, M. T.; Chandra, A. K. *J. Phys. Chem. A* **2006**, *110* (37), 10904. doi:10.1021/jp0630020.

(83) Bordwell, F. G.; Zhang, X. M.; Satish, A. V.; Cheng, J. P. *J. Am. Chem. Soc.* **1994**, *116* (15), 6605. doi:10.1021/ja00094a015.

(84) Brinck, T.; Haeberlein, M.; Jonsson, M. *J. Am. Chem. Soc.* **1997**, *119* (18), 4239. doi:10.1021/ja962931+.

(85) de Heer, M. I.; Korth, H.-G.; Mulder, P. *J. Org. Chem.* **1999**, *64* (19), 6969. doi:10.1021/jo9901485.

(86) Fu, Y.; Liu, R.; Liu, L.; Guo, Q. X. *J. Phys. Org. Chem.* **2004**, *17* (4), 282. doi:10.1002/poc.725.

(87) Guerra, M.; Amorati, R.; Pedulli, G. F. *J. Org. Chem.* **2004**, *69* (16), 5460. doi:10.1021/jo0495236.

(88) Pratt, D. A.; Dilabio, G. A.; Mulder, P.; Ingold, K. U. *Acc. Chem. Res.* **2004**, *37* (5), 334. doi:10.1021/ar010010k.

(89) Zhu, Q.; Zhang, X. M.; Fry, A. J. *Polym. Degrad. Stabil.* **1997**, *57* (1), 43. doi:10.1016/S0141-3910(96)00224-8.

(90) Berry, R. J.; Wilson, A. L.; Schwartz, M. *J. Mol. Struct.: (THEOCHEM)* **2000**, *496* (1–3), 121. doi:10.1016/S0166-1280(99)00181-5.

(91) Leopoldini, M.; Pitarch, I. P.; Russo, N.; Toscano, M. *J. Phys. Chem. A* **2004**, *108* (1), 92. doi:10.1021/jp035901j.

(92) Najafi, M.; Zahedi, M.; Klein, E. *Comput. Theoret. Chem.* **2011**, *978* (1–3), 16. doi:10.1016/j.comptc.2011.09.014.

(93) Klein, E.; Lukes, V.; Cibulkova, Z.; Polovkova, J. *J. Mol. Struct.: (THEOCHEM)* **2006**, *758* (2-3), 149. doi:10.1016/j.theochem.2005.10.015.

(94) Brinck, T.; Haeberlein, M.; Jonsson, M. *J. Am. Chem. Soc.* **1997**, *119* (18), 4239. doi:10.1021/ja962931+.

(95) DiLabio, G. A.; Pratt, D. A.; Lofaro, A. D.; Wright, J. S. *J. Phys. Chem. A* **1999**, *103* (11), 1653. doi:10.1021/jp984369a.

(96) DiLabio, G. A.; Pratt, D. A.; Wright, J. S. *Chem. Phys. Lett.* **1999**, *311* (3–4), 215. doi:10.1016/S0009-2614(99)00786-1.

(97) DiLabio, G. A.; Pratt, D. A.; Wright, J. S. *J. Org. Chem.* **2000**, *65* (7), 2195. doi:10.1021/jo991833e.

(98) Migliavacca, E.; Carrupt, P. A.; Testa, B. *Helv. Chim. Acta* **1997**, *80* (5), 1613. doi:10.1002/hlca.19970800519.

(99) Zhang, H. Y. *J. Am. Oil Chem. Soc.* **1998**, *75* (12), 1705. doi:10.1007/s11746-998-0320-4.

(100) Janak, J. F. *Phys. Rev. B* **1978**, *18* (12), 7165. doi:10.1103/PhysRevB.18.7165.

(101) Zhang, H. Y. *J. Am. Oil Chem. Soc.* **1999**, *76,* 1109.

(102) Kancheva, V. D.; Saso, L.; Boranova, P. V.; Khan, A.; Saroj, M. K.; Pandey, M. K.; Malhotra, S.; Nechev, J. Z.; Sharma, S. K.; Prasad, A. K.; Georgieva, M. B.; Joseph, C.; DePass, A. L.; Rastogi, R. C.; Parmar, V. S. *Biochimie* **2010**, *92* (9), 1089. doi:10.1016/j.biochi.2010.06.012.

(103) Lavarda, F. C. *Int. J. Quantum Chem.* **2003**, *95* (3), 219. doi:10.1002/qua.10692.

(104) Bi, W.; Bi, Y.; Xue, P.; Zhang, Y.; Gao, X.; Wang, Z.; Li, M.; Baudy–Floch, M.; Ngerebara, N.; Gibson, K. M.; Bi, L. *J. Med. Chem.* **2010**, *53* (18), 6763. doi:10.1021/jm100529e.

(105) Najafi, M.; Haghighi Mood, K.; Zahedi, M.; Klein, E. *Comput. Theoret. Chem.* **2011**, *969* (1–3), 1. doi:10.1016/j.comptc.2011.05.006.

(106) Rimarcik, J.; Lukes, V.; Klein, E.; Rottmannova, L. *Comput. Theoret. Chem.* **2011**, *967* (2–3), 273. doi:10.1016/j.comptc.2011.04.029.

A short formal total synthesis of (±)-hirsutic acid

Guillaume Revol, Christian Fuchs, and Samir Z. Zard

Abstract: A short formal total synthesis of (±)-hirsutic acid is described using a Claisen rearrangement and a radical cascade as the key steps. The radical sequence involves an intermolecular addition of a radical derived from a xanthate followed by a cyclization and transfer of the xanthate group.

Key words: hirsutic acid, complicatic acid, triquinanes, Claisen rearrangement, radical cyclization, xanthates.

Résumé : Une synthèse totale formelle courte de l'acide (±)-hirsutique est décrite, employant comme étapes-clés un réarrangement de Claisen et une cascade radicalaire. La séquence radicalaire implique une addition intermoléculaire d'un radical issu d'un xanthate, suivie d'une cyclisation, puis du transfert du groupe xanthate.

Mots-clés : acide hirsutique, acide complicatique, triquinanes, réarrangement de Claisen, cyclisation radicalaire, xanthates.

Can. J. Chem. Downloaded from www.nrcresearchpress.com by MCGILL UNIVERSITY on 02/02/13
For personal use only.

Introduction

(+)-Hirsutic acid **1** (Fig. 1) was isolated in 1947 from a fungus (*Stereum hirsutum*), but its structure was only determined 20 years later.[1,2] It belongs to the family of linear triquinanes and is closely related to (+)-complicatic acid **2**, a secondary metabolite from the fungus *Stereum complicatum*, which also produces hirsutic acid.[3] The biogenetic precursor for both compounds is presumably (+)-hirsutene (**3**), a linear triquinane isolated from a basidiomycete, *Coriolis consors*.[4] While a few of these natural products exhibit interesting biological acivities, it is mostly the intricate structure of hirsutic acid and its congeners that has attracted the attention of synthetic organic chemists over four decades. Thus, no less than nine total and formal syntheses of hirsutic acid have been reported so far.[5–13]

Apart from constructing the triquinane skeleton of hirsutic acid **1**, there is the challenge of controlling the stereochemistry of seven chiral centers, including the tertiary carboxylic acid at C-11. This complicates significantly the synthetic planning in comparison with hirsutene **3** where this carbon is not chiral and simply bears a *geminal* dimethyl group. In contemplating simpler routes to hirsutic acid, we envisaged the possibility of using the chirality at C-11 to install the remaining six chiral centers. Our retrosynthetic analysis is outlined in Scheme 1.

Intermediate tricyclic enone **4** is a key precursor in several of the published syntheses. It can be converted into complicatic acid in four steps and into hirsutic acid in five steps as was initially demonstrated by Matsumoto and co-workers[6] in 1971. We envisaged obtaining this compound by a radical addition–cyclization of *S*-acetyl xanthate **6** on monocyclic enone **5**. This enone could, in principle, be obtained through a Claisen rearrangement starting from allylic alcohol **7**, itself derived from the simple and commercially available ketoester **8**.

Indeed, allylic alcohol **7** had already been prepared by Kato et al.,[14] both as racemate and as optically pure material. The synthesis of the racemic modification is displayed in Scheme 2. Treatment of ketoester **8** with methyl iodide and potassium carbonate accomplished the desired methylation to give compound **9** in near quantitative yield. The unsaturation could be introduced using Saegusa's conditions[15] applied on the corresponding enol silyl ether **10**. Unfortunately, enone **11** was obtained in a variable overall yield ranging from 12% to 51%. Nevertheless, this was sufficient to confirm the selectivity of the reduction step leading to allylic alcohol **7**.

Using Luche conditions,[16] the reduction at –40 °C furnished an 80:20 mixture of allylic alcohol **7** and completely reduced alcohol **12**, respectively, in 65% combined yield. Both the yield and the selectivity could be increased by lowering the reaction temperature to –78 °C (Scheme 2). Furthermore, we later found that enone **11** could be obtained more reliably and in much better yield by oxidation of ketone **9** with an excess of 2-iodoxybenzoic acid (IBX), according to the procedure described by Nicolaou et al.[17]

The conversion of alcohol **7** into enone intermediate **5** relied on a Claisen rearrangement.[18] After a number of mostly unsuccessful attempts, we finally found that heating a mixture of alcohol **7**, *n*-butyl vinyl ether, and a catalytic amount of mercuric acetate to 200 °C in a microwave oven for 2 h furnished the desired aldehyde **14** in 48%–60% yield.[19] This compound was rapidly treated with isopropenylmagnesium bromide in THF at 0 °C to furnish carbinol **15** in a yield ranging between 52% and 70%. Oxidation with manganese dioxide in refluxing dichloroethane (DCE) afforded enone **5**, whereas acetylation gave acetate **16** in 58% and 63% yield, respectively (Scheme 3).

Received 3 April 2012. Accepted 30 April 2012. Published at www.nrcresearchpress.com/cjc on 15 June 2012.

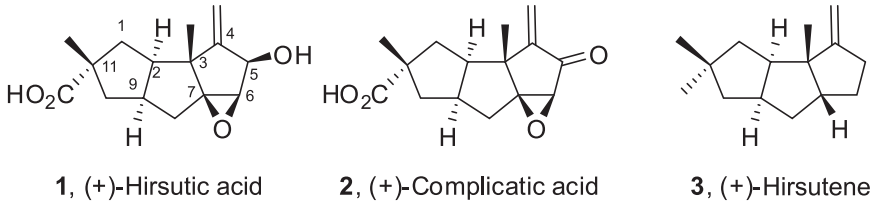
G. Revol, C. Fuchs, and S.Z. Zard. Laboratoire de Synthèse Organique, CNRS UMR 7652, École Polytechnique, 91128, Palaiseau, France.

Corresponding author: Samir Z. Zard (e-mail: Samir.Zard@polytechnique.edu).

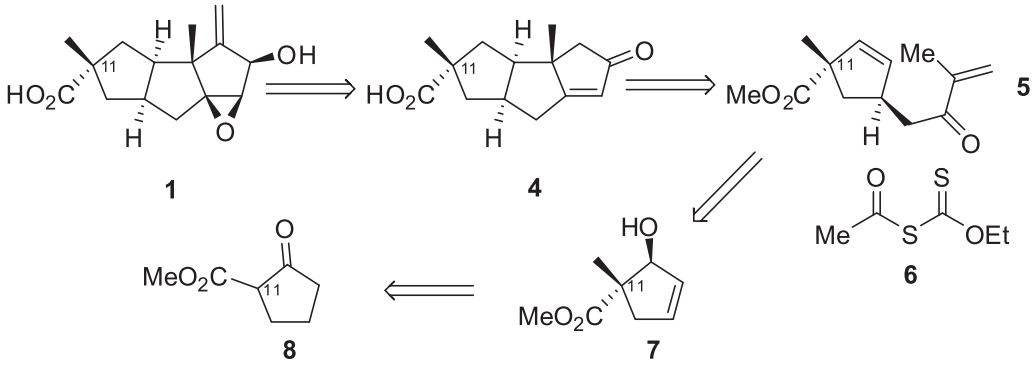
This article is part of a Special Issue dedictated to Professor Derrick Clive. This paper is dedicated with respect and admiration to Professor Derrick Clive.

Can. J. Chem. Downloaded from www.nrcresearchpress.com by MCGILL UNIVERSITY on 02/02/13
For personal use only.

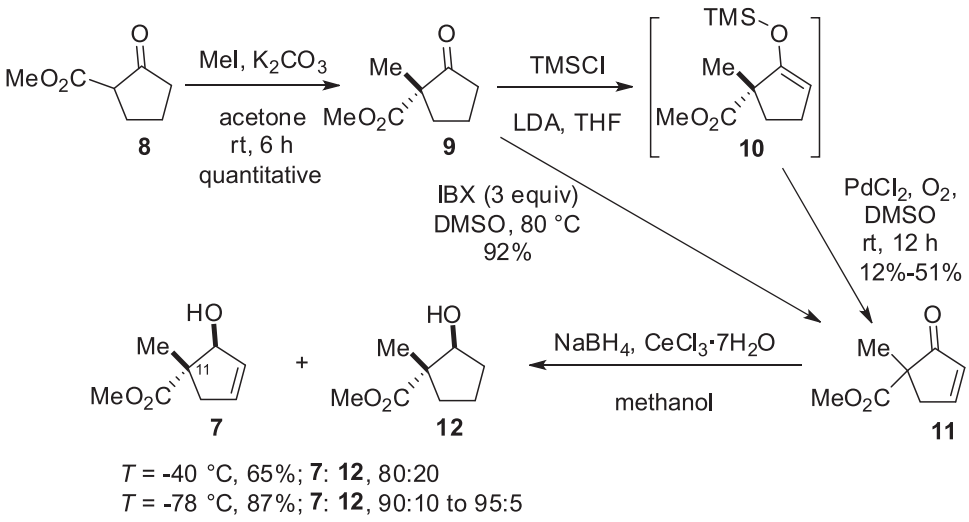
Fig. 1. (+)-Hirsutic acid and congeners.



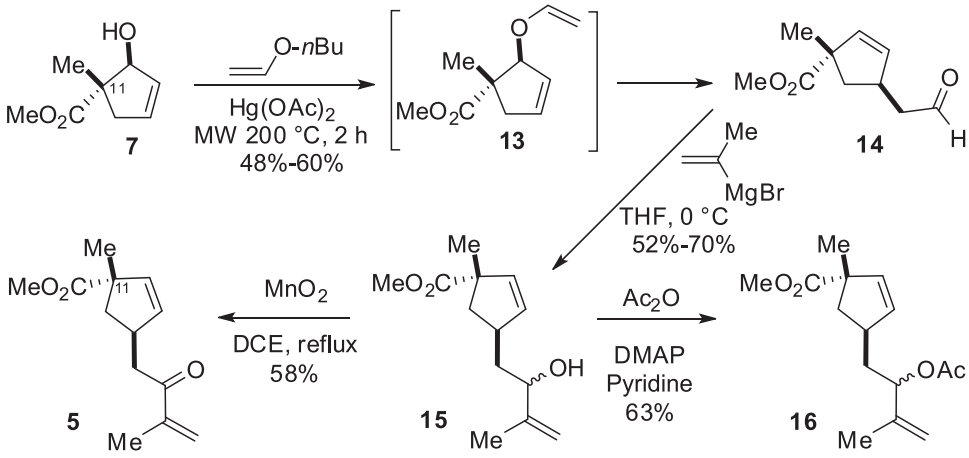
Scheme 1. Retrosynthetic analysis for hirsutic acid.



Scheme 2. Synthesis of allylic alcohol **7a**.

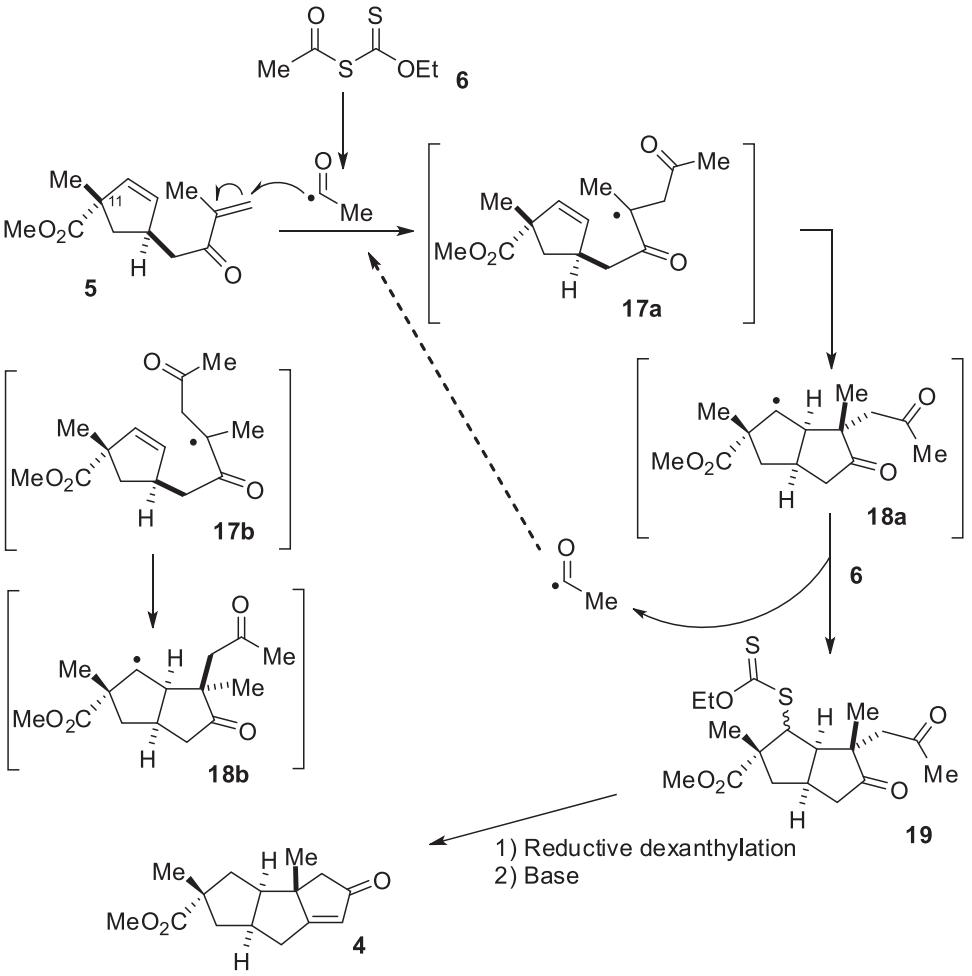


Scheme 3. Synthesis of enone intermediate **5**.



Can. J. Chem. Downloaded from www.nrcresearchpress.com by MCGILL UNIVERSITY on 02/02/13
For personal use only.

Scheme 4. Key radical cascade.



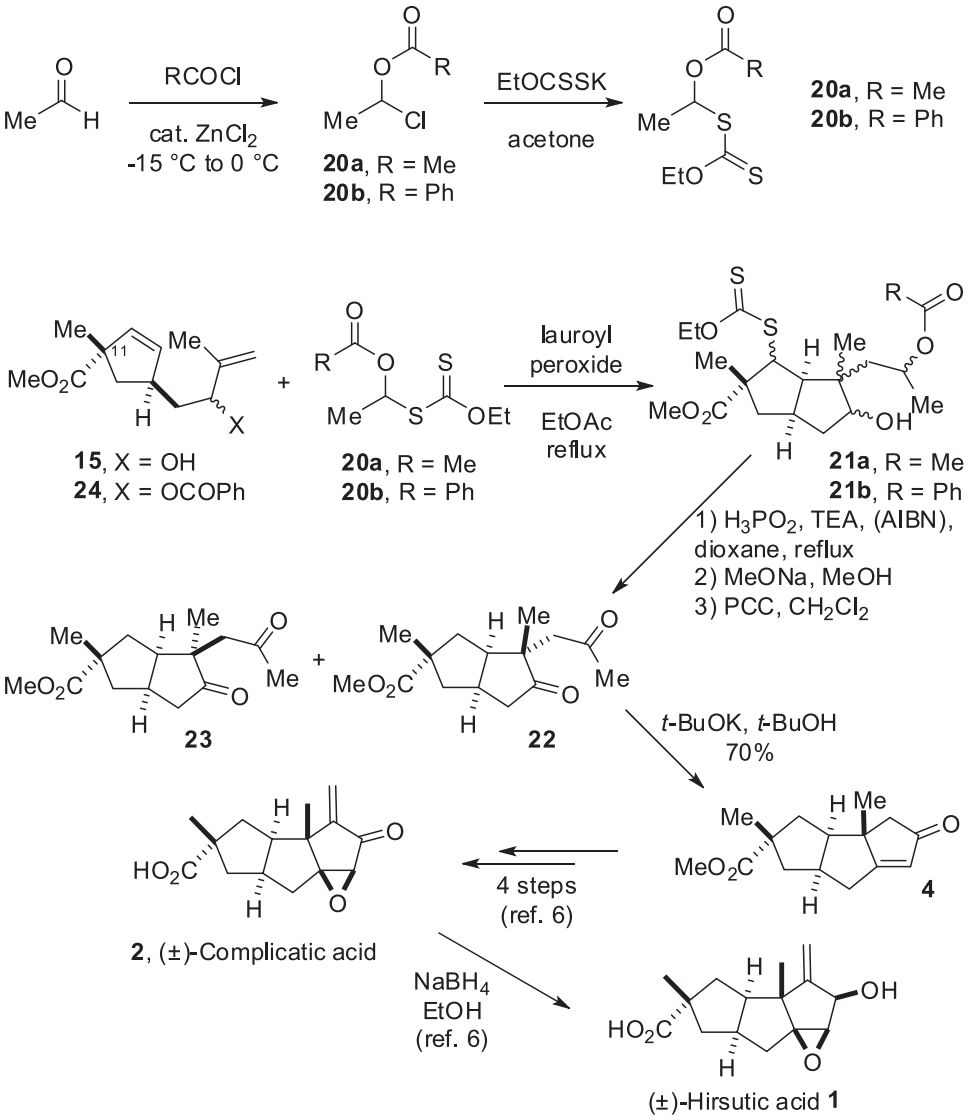
We were now in a position to examine the key radical cascade based on xanthate chemistry.[20] The anticipated sequence of intermolecular radical addition – cyclization is outlined in Scheme 4. In analogy with previous work,[21] the acetyl radical generated from *S*-acetyl xanthate **6** should add to the enone in **5**, and the resulting adduct radical **17a** should undergo ring closure and transfer of the xanthate group to finally give bicyclic structure **19** via intermediate radical **18a**. We hoped that the smaller methyl group would occupy the more congested endo face, resulting in the correct relative stereochemistry found in hirsutic acid, in preference to the alternative conformation shown as **17b**, which would lead to the epimeric cyclized radical **18b**. Reductive removal of the xanthate group and base-induced Robinson-type annelation would deliver ultimately tricyclic enone **4**, thus completing the formal synthesis of both complicatic and hirsutic acids.

Unfortunately, our attempts to add *S*-acetyl xanthate **6** to enone **5** met with failure. This contrasts with the successful addition of *S*-butanoyl xanthate to an enone we achieved a few years ago.[21] We also failed to accomplish an addition of *S*-acetyl xanthate **6** to allyl acetate **16**. *S*-Acyl xanthates are rather labile substances: a small quantity of a nucleophilic impurity can cause complete decomposition by an ionic chain process.[20a] This lability is more pronounced in the smaller members of the family.

Faced with these unexpected setbacks, we slightly modified our approach by replacing the *S*-acetyl xanthate **6** with acetoxy xanthate **20a**. This xanthate is readily prepared by displacement of chloride from 1-acetoxy-1-chloroethane, a known compound[22] obtained by reaction of acetaldehyde with acetyl chloride in the presence of catalytic zinc chloride (Scheme 5). However, the addition of xanthate **20a** to enone **5** again surprisingly gave a complex mixture from which the desired bicyclic structure could not be isolated. In contrast, the reaction with allylic alcohol **15** proceeded as expected to furnish bicyclic derivative **21**, as a complex mixture of diastereoisomers **21a**, which were not further purified. Reductive elimination of the xanthate with triethylammonium hypophosphite,[23] saponification of the acetate group with sodium methylate, and oxidation of both alcohol groups with pyridinium chlorochromate (PCC) gave a 1:4 mixture of two epimeric diketones (**22** and **23**) in 42% overall yield from alcohol **15**. Unfortunately, the major epimer had the wrong relative stereochemistry. The ratio of the two epimers **22** and **23** could be improved to 1:2 by using xanthate **20b**, where the acetate group was replaced with the bulkier benzoate. The overall yield of the epimeric mixture of **22** and **23** for the four steps from allylic alcohol **15** remained roughly the same (24%–41%).

Both bicyclic diketones are known compounds, and the correct epimer **22** has indeed been converted into hirsutic acid by base-induced cyclisation into Matsumoto's intermediate

Scheme 5. Final steps in the formal synthesis of (±)-hirsutic acid.



4.[6] This completes a short, formal total synthesis of both (±)-complicatic acid and (±)-hirsutic acid. While the key radical cascade finally succeeded, it is still very far from perfect. The crude model for the ring closure displayed in Scheme 4 clearly does not reflect reality. The cyclization leads to what appears as the slightly more congested and unwanted isomer. More effort is therefore needed to establish the best combination of xanthate and allylic alcohol **15** or a derivative thereof that ultimately leads to the greatest ratio in favour of the desired epimer **22**. Some progress was made using benzoate **20b**, and this could perhaps be improved further. Placing a bulky group on the allylic alcohol in **15** could also be used to modify the stereoselectivity. Indeed, a preliminary small-scale experiment using benzoate **24** in combination with xanthate **20b** resulted in an approximately 2:3 ratio of the desired[22] over the undesired, [23] but this has to be confirmed on a larger scale, and this would also provide a reliable value for the yield. Nevertheless, despite these various shortcomings, the present route to hirsutic acid is significantly shorter than most of the earlier syntheses. More generally, it illustrates the potential of xanthate chemistry for the construction of polyquinanes through the combination of the radical process with the powerful Claisen rearrangement. Finally, this synthesis could be easily made enantioselective since allylic alcohol **7** has already been prepared in enantiopure form by Kato et al.[14] The methylation of ketoester **8** could also be performed in an enantioselective manner by the use of a chiral base or through the use of chiral imines or hydrazones, allowing the control of the absolute stereochemistry at the very beginning of the synthesis.

Acknowledgement

C.F. and G.R. would like to thank Ecole Polytechnique, Palaiseau, France, for a scholarship.

References

(1) Heatley, N. G.; Jennings, M. A.; Florey, H. W. *Br. J. Exp. Pathol.* **1947**, *28*, 35.

(2) (a) Comer, F. W.; McCapra, F.; Qureshi, I. H.; Trotter, J.; Scott, A. I. *J. Chem. Soc. Chem. Commun.* **1965**, 310; (b) Comer, F. W.; McCapra, F.; Qureshi, I. H.; Scott, A. I.

Can. J. Chem. Downloaded from www.nrcresearchpress.com by MCGILL UNIVERSITY on 02/02/13
For personal use only.

Can. J. Chem. Downloaded from www.nrcresearchpress.com by MCGILL UNIVERSITY on 02/02/13
For personal use only.

Tetrahedron **1967**, *23* (12), 4761. doi:10.1016/S0040-4020(01)92573-6; (c) Comer, F. W.; Trotter, J. *J. Chem. Soc. Chem. Commun.* **1966**, 11; (d) Walker, D. C. *J. Chem. Soc. Chem. Commun.* **1967**, 1050.

(3) Mellows, G.; Mantle, P. G.; Feline, T. C.; Williams, D. J. *Phytochemistry* **1973**, *12* (11), 2717. doi:10.1016/0031-9422(73)85086-1.

(4) Nozoe, S.; Furukawa, J.; Sankawa, U.; Shibata, S. *Tetrahedron Lett.* **1976**, *17* (3), 195. doi:10.1016/0040-4039(76)80013-5.

(5) (a) Lansbury, P. T.; Wang, N. Y.; Rhodes, J. E. *Tetrahedron Lett.* **1971**, *12* (21), 1829. doi:10.1016/S0040-4039(01)87473-6; (b) Lansbury, P. T.; Wang, N. Y.; Rhodes, J. E. *Tetrahedron Lett.* **1972**, *13* (20), 2053. doi:10.1016/S0040-4039(01)85038-3.

(6) (a) Sakan, F.; Hashimoto, H.; Ichihara, A.; Shirahama, H.; Matsumoto, T. *Tetrahedron Lett.* **1971**, *12* (40), 3703. doi:10.1016/0040-4039(71)80007-2; (b) Hashimoto, H.; Tsuzuki, K.; Sakan, F.; Shirahama, H.; Matsumoto, T. *Tetrahedron Lett.* **1974**, *15* (43), 3745. doi:10.1016/S0040-4039(01)91998-7; (c) Hayano, K.; Ohfune, Y.; Shirahama, H.; Matsumoto, T. *Tetrahedron Lett.* **1978**, *19* (23), 1991. doi:10.1016/S0040-4039(01)94729-X.

(7) Trost, B. M.; Shuey, C. D.; DiNinno, F., Jr. *J. Am. Chem. Soc.* **1979**, *101* (5), 1284. doi:10.1021/ja00499a043.

(8) (a) Yamazaki, M.; Shibasaki, M.; Ikegami, S. *Chem. Lett.* **1981**, *10* (9), 1245. doi:10.1246/cl.1981.1245; (b) Yamazaki, M.; Shibasaki, M.; Ikegami, S. *J. Org. Chem.* **1983**, *48* (23), 4402. doi:10.1021/jo00171a054; (c) Shibasaki, M.; Yamazaki, M.; Iseki, K.; Ikegami, S. *Tetrahedron Lett.* **1982**, *23* (50), 5311. doi:10.1016/S0040-4039(00)85826-8; (d) Nishida, M.; Iseki, K.; Shibasaki, M.; Ikegami, S. *Chem. Pharm. Bull. (Tokyo)* **1990**, *38* (12), 3230. doi:10.1248/cpb.38.3230.

(9) (a) Greene, A. E.; Luche, M.-J.; Deprès, J.-P. *J. Am. Chem. Soc.* **1983**, *105* (8), 2435. doi:10.1021/ja00346a054; (b) Greene, A. E.; Luche, M.-J.; Serra, A. A. *J. Org. Chem.* **1985**, *50* (21), 3957. doi:10.1021/jo00221a001.

(10) Magnus, P.; Exon, C.; Albaugh-Robertson, P. *Tetrahedron* **1985**, *41* (24), 5861. doi:10.1016/S0040-4020(01)91425-5.

(11) Schuda, P. F.; Phillips, J. L.; Morgan, T. M. *J. Org. Chem.* **1986**, *51* (14), 2742. doi:10.1021/jo00364a023.

(12) Singh, V.; Tosh, D. K.; Mobin, S. M. *Tetrahedron Lett.* **2004**, *45* (8), 1729. doi:10.1016/j.tetlet.2003.12.095.

(13) Banwell, M. G.; Austin, K. A. B.; Willis, A. C. *Tetrahedron* **2007**, *63* (28), 6388. doi:10.1016/j.tet.2007.03.073.

(14) (a) Kato, K.; Suzuki, H.; Tanaka, H.; Miyasaka, T. *Tetrahedron Asymmetry* **1998**, *9* (6), 911. doi:10.1016/S0957-4166(98)00065-2; (b) Kato, K.; Suzuki, H.; Tanaka, H.; Miyasaka, T.; Baba, M.; Yamaguchi, K.; Akita, H. *Chem. Pharm. Bull. (Tokyo)* **1999**, *47* (9), 1256. doi:10.1248/cpb.47.1256.

(15) Ito, Y.; Hirao, T.; Saegusa, T. *J. Org. Chem.* **1978**, *43* (5), 1011. doi:10.1021/jo00399a052.

(16) (a) Luche, J.-L. *J. Am. Chem. Soc.* **1978**, *100* (7), 2226. doi:10.1021/ja00475a040; (b) Gemal, A. L.; Luche, J.-L. *J. Am. Chem. Soc.* **1981**, *103* (18), 5454. doi:10.1021/ja00408a029.

(17) Nicolaou, K. C.; Zhong, Y.-L.; Baran, P. S. *J. Am. Chem. Soc.* **2000**, *122* (31), 7596. doi:10.1021/ja001825b.

(18) Martín Castro, A. M. *Chem. Rev.* **2004**, *104* (6), 2939. doi:10.1021/cr020703u.

(19) Huber, R. S.; Jones, G. B. *J. Org. Chem.* **1992**, *57* (21), 5778. doi:10.1021/jo00047a041.

(20) (a) For reviews on the xanthate radical addition – transfer process see Zard, S. Z. *Angew. Chem. Int. Ed. Engl.* **1997**, *36* (7), 672. doi:10.1002/anie.199706721; (b) Quiclet-Sire, B.; Zard, S. Z. *Chemistry* **2006**, *12* (23), 6002. doi:10.1002/chem.200600510; (c) Quiclet-Sire, B.; Zard, S. Z. *Top. Curr. Chem.* **2006**, *264*, 201. doi:10.1007/128_029; (d) Zard, S. Z. *Aust. J. Chem.* **2006**, *59* (10), 663. doi:10.1071/CH06263; (e) Zard, S. Z. *Org. Biomol. Chem.* **2007**, *5* (2), 205. doi:10.1039/b615592h; (f) Quiclet-Sire, B.; Zard, S. Z. *Pure Appl. Chem.* **2011**, *83* (3), 519. doi:10.1351/PAC-CON-10-08-07.

(21) Briggs, M. E.; El Qacemi, M.; Kalaï, C.; Zard, S. Z. *Chem. Commun. (Camb.)* **2004**, *45*, 6017.

(22) (a) Ulich, L. H.; Adams, R. *J. Am. Chem. Soc.* **1921**, *43* (3), 660. doi:10.1021/ja01436a036; (b) Luk'yanov, S. M.; Borodaev, S. V.; Borodaeva, S. V. *J. Org. Chem. USSR* **1983**, *19*, 1872; (c) Bagal, S.; Tournier, L.; Zard, S. Z. *Synlett* **2006**, 1485. doi:10.1002/chin.200643058.

(23) (a) Barton, D. H. R.; Jang, D. O.; Jaszberenyi, J. C. *Tetrahedron Lett.* **1992**, *33* (39), 5709. doi:10.1016/0040-4039(92)89012-2; (b) Boivin, J.; Jrad, R.; Juge, S.; Nguyen, V. T. *Org. Lett.* **2003**, *5* (10), 1645. doi:10.1021/ol0342610.

Unnatural C-1 homologues of pancratistatin — Synthesis and promising biological activities

Sergey Vshyvenko, Jon Scattolon, Tomas Hudlicky, Anntherese E. Romero, Alexander Kornienko, Dennis Ma, Ian Tuffley, and Siyaram Pandey

Can. J. Chem. Downloaded from www.nrcresearchpress.com by MCGILL UNIVERSITY on 02/02/13
For personal use only.

Abstract: Several C-1 homologues of pancratistatin and 7-deoxypancratistatin were synthesized by a phenanthrene–phenathridone oxidative recyclization strategy. The key steps involved the enzymatic dihydroxylation of bromobenzene, addition of an aryl alane to an epoxyaziridine, an intramolecular aziridine opening on silica gel in solid phase, and the above-mentioned recylization strategy. Experimental and spectral data are reported for all new compounds. All synthesized C-1 homologues of pancratistatin and 7-deoxypancratistatin were evaluated for antiproliferative activity in a panel of human cancer cell lines. As expected, the 7-hydroxy compounds were found to be more potent and the activity of the C-1 benzoxymethyl analogue exceeded that of narciclasine, which was used as a positive control.

Key words: C-1 homologues of pancratistatin, amaryllidaceae alkaloids, anticancer activities, intramolecular aziridine opening, solid-phase silica catalysis.

Résumé : On a réalisé la synthèse de plusieurs homologues en C-1 de la pancratistatine et de la 7-désoxypencratistatine en faisant appel à une stratégie de recyclisation oxydante phenantrène–phénathridone. Les étapes clés impliquent la dihydroxylation du bromobenzène, l'addition d'une arylalane à une époxyaziridine, une ouverture intramoléculaire d'aziridine sur gel de silice en phase solide et la stratégie de recyclisation mentionnée plus haut. Les données expérimentales et spectrales sont rapportées pour tous les nouveaux produits. Tous les homologues en C-1 de la pancratistatine et de la 7-désoxypencratistatine ont été évalués pour leur activité à contrer la prolifération dans un éventail de lignées de cellules cancéreuses humaines. Tel que prévu, les composés 7-hydroxy sont les plus puissants alors que l'activité de l'analogue C-1 benzoxyméthyle est supérieure à celle de la narciclasine qui a été utilisée comme contrôle positif.

Mots-clés : analogues en C-1 de la pancratistatine, alcaloïdes des amaryllidacées, activité anticancéreuse, ouverture intramoléculaire d'aziridine, catalyse par le gel de silice en phase solide.

[Traduit par la Rédaction]

Introduction

Pancratistatin (**1**), narciclasine (**2**), and other Amaryllidaceae constituents, Fig. 1, continue to attract attention on account of their promising anticancer properties. Since the isolation of pancratistatin in 1984 by Pettit et al.[1] and its preliminary evaluation as a potent antitumor agent, many creative syntheses of **1** and its congeners have been reported.[2] The activity concerning the total synthesis of these constituents continues unabated to the present day.[3] More recently, however, the studies of these natural products have shifted toward the investigation of unnatural derivatives that would offer the potential of better bioavailability than the rather insoluble natural products. In the last two decades, many reports have appeared describing the synthesis and evaluation of truncated derivatives from the groups of Pettit,[4] McNulty,[5] Kornienko,[6] Chapleur,[7] Alonso,[8] Marion,[9] Banwell,[10] and Gonzalez.[11] Truncated derivatives of the core of these constituents as well as various heteroatom analogues have been reported and some of these compounds displayed various levels of biological activity, usually of lower potency than the natural products. The only exceptions were compounds that contained a large lipophilic fragment in position C-1. The first example of such an analogue was the benzoate ester of the C-1 hydroxyl of pancratistatin, prepared and tested by Pettit et al.,[4c] which displayed nanomolar activity. Later, a library of C-1 nitrogenated derivatives prepared by Marion et al.[9] showed the highest activity with substituents such as benzamide.

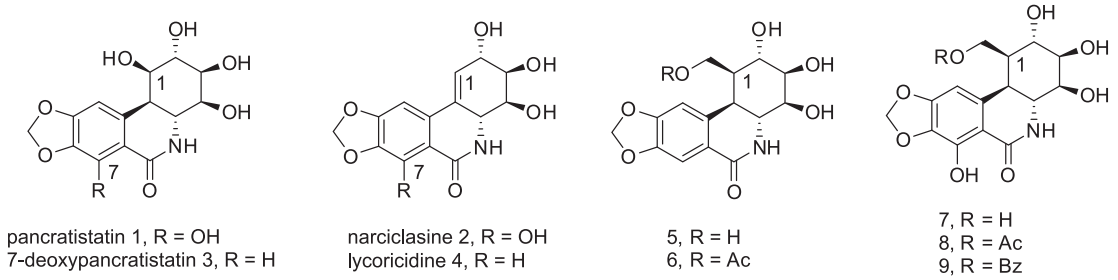
Received 3 August 2012. Accepted 8 August 2012. Published at www.nrcresearchpress.com/cjc on 19 September 2012.

S. Vshyvenko, J. Scattolon, and T. Hudlicky. Chemistry Department and Centre for Biotechnology, Brock University, 500 Glenridge Avenue, St. Catharines, ON L2S 3A1, Canada.
A.E. Romero and A. Kornienko. Chemistry Department, New Mexico Institute of Mining and Technology, 801 Leroy Place, Socorro, NM 87801, USA.
D. Ma, I. Tuffley, and S. Pandey. Department of Chemistry and Biochemistry, University of Windsor, 401 Sunset Avenue, Windsor, ON N9B 3P4, Canada.

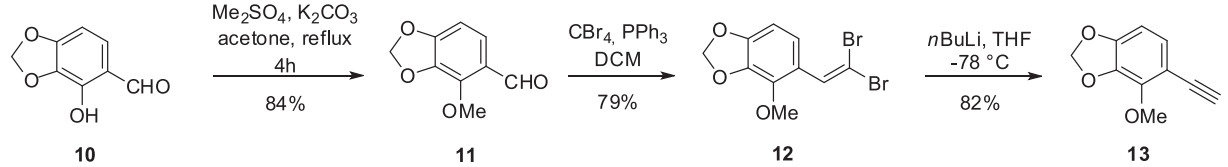
Corresponding author: Tomas Hudlicky (e-mail: thudlicky@brocku.ca).

Dedicated to Professor Derrick Clive in recognition of his outstanding contributions to the art and craft of organic synthesis.

Fig. 1. Pancratistatin, other Amaryllidaceae congeners, and C-1 homologues.



Scheme 1.



In our group, we have been investigating various truncated derivatives of pancratistatin, and 7-deoxypancratistatin,[12] as well as derivatives with variations of functionality at the aromatic core,[13] including an indole mimic of 7-deoxypancratistatin.[14] More recently, and inspired by Pettit's report of the C-1 benzoate ester,[4c] we investigated carbon homologues of 7-deoxypancratistatin at position C-1 and found that the hydroxymethyl and acetoxymethyl derivatives (**5** and **6**, respectively) were reasonably active.[3a] 7-Deoxypancratistatin is far less active than pancratistatin as it lacks the 7-OH functionality and we reasoned that the C-1 homologues of **1** might approach the activity of the natural products. Indeed, this was shown to be the case and homologues **7** and **8** showed nanomolar activities in preliminary screening.[15] In this paper, we report the full details of the synthesis of these compounds, the synthesis of the C-1 benzoxymethyl analogue, as well as the complete details of the biological evaluation in several cell lines.

Results and discussion

The strategy for the synthesis of C-1 homologues followed the previously disclosed approach in which a C-1 aldehyde possessing the full pancratistatin core is generated by the oxidative cleavage–recyclization in a phenanthrene–phenanthridol transformation.[16] To adjust this protocol to the synthesis of the pancratistatin core, the hydroxy aldehyde **10**, prepared from piperonal by a known method,[17] was chosen as the starting material.

As shown in Scheme 1, compound **10** was methylated to **11**[18] and converted via the Corey–Fuchs reaction to acetylene **13**.

The alane generated from **13** was reacted with epoxyaziridine **14**,[19] which was prepared in five steps from bromobenzene via enzymatic dihydroxylation, the Yamada aziridination protocol, dehalogenation, and epoxidation. Addition of the epoxyaziridine **14** to the alane gave acetylene **15**, which was subjected to reduction conditions. The best results for selective alkyne–alkene reduction were obtained using a short time for the hydrogenation (1–1.5 h) under Lindlar's conditions with 1 atm (1 atm = 101.325 kPa) of hydrogen to provide the *cis*-olefin **16**. Different catalysts and conditions led to significant over-reduction of **15**. The intramolecular aziridine opening was accomplished by heating the *tert*-butyldimethylsilyl triflate (TBS)-protected ether **17** adsorbed on silica gel according to a solid-phase protocol developed in our laboratory for an aziridine opening of this type.[14–16] It is worth mentioning that the addition of 10% *w*/*w* quinoline to the substrate during the solid-phase cyclization helps to suppress the decomposition of material and improves the yield of this reaction from 45% to 74%, probably because of the decreased acidity of the silica gel.

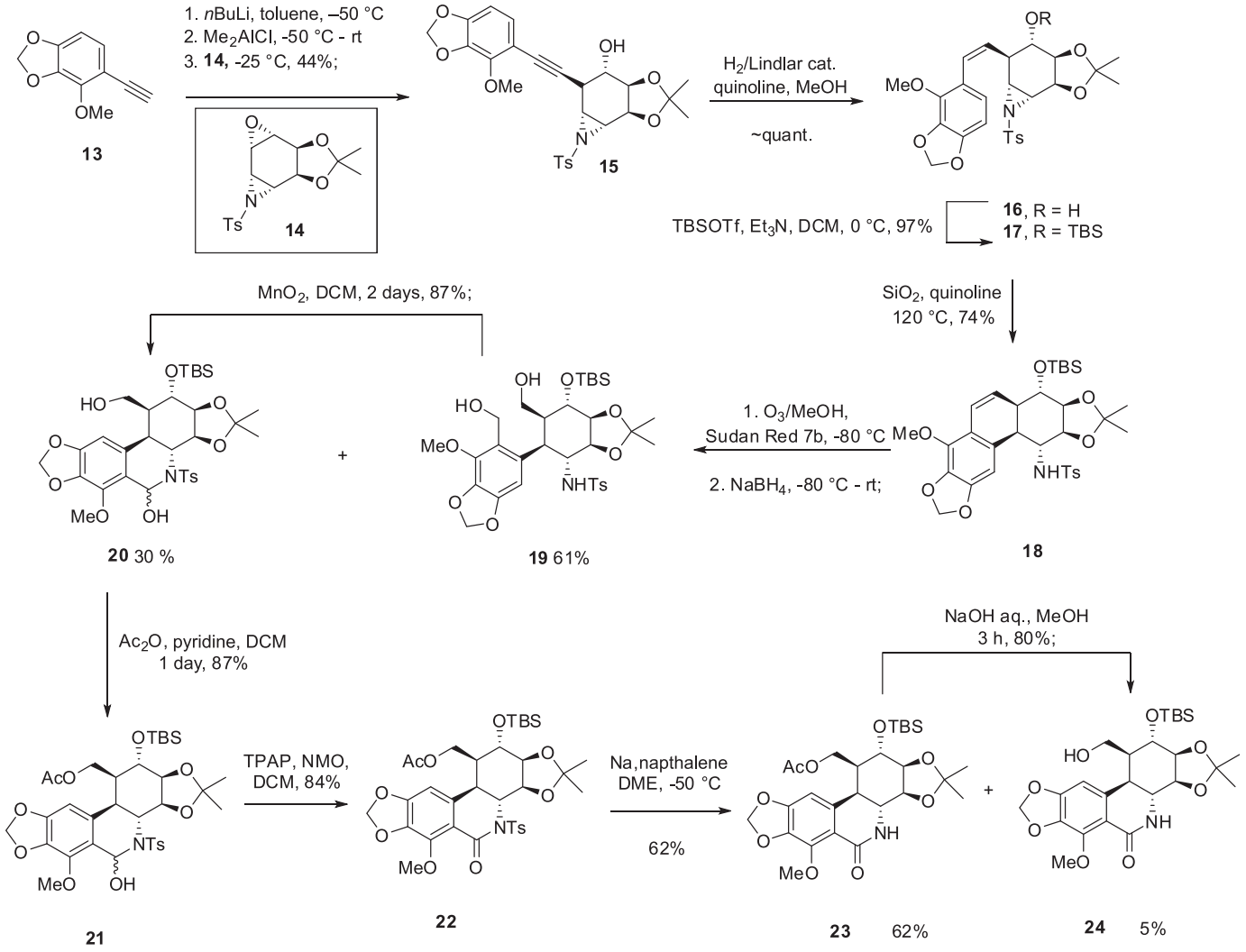
The product of the silica-catalyzed cyclization, phenanthrene **18**, was subjected to several different sets of oxidative protocols. The originally disclosed conditions,[16] which included OsO_4/$NaIO_4$-promoted oxidation–recyclization, did not lead to the desired product. This was probably the result of an increased steric hindrance by the methoxy group in the environment of the double bond (this interaction was absent in the cyclization of the precursor to 7-deoxypancratistatin). Instead, a different protocol was developed, which included selective ozonolysis of the double bond in the presence of azo dye Sudan Red 7B to help prevent oxidation of the electron-rich aromatic ring. Reductive workup of the ozonide with sodium borohydride led to a mixture of diol **19** and hemiaminal **20**. The former compound was subjected to selective oxidation of the benzylic alcohol by MnO_2, generating the intermediate aldehyde, which, after in situ cyclization, produced compound **20**.

The primary alcohol in **20** was selectively acetylated by stirring with acetic anhydride in pyridine–dichloromethane. Several different oxidation conditions were attempted to transform the hemiaminal moiety to the phenathridone amide, including pyridinium dichromate (PDC), pyridinium chlorochromate (PCC), *o*-iodoxybenzoic acid (IBX), Dess–Martin, and tetrapropylammonium perruthenate / *N*-methylmorpholine-*N*-oxide (TPAP/NMO). Of these, only the latter conditions led to the desired product; all other conditions led to the decomposition of the starting material. Detosylation with Na/naphthalene in 1,2-dimethoxyethane (DME) provided compound **23** with traces of alcohol **24** (Scheme 2).

The O-demethylation of **23** was performed by freshly fused LiCl in dry dimethylformamide (DMF).[20] Alternative

Can. J. Chem. Downloaded from www.nrcresearchpress.com by MCGILL UNIVERSITY on 02/02/13
For personal use only.

Scheme 2.



protocols of demethylation such as BBr_3[21] or sodium dodecathiolate[22] did not lead to product. In the first case, overdeprotection of the acetonide and the methylenedioxo groups was observed. In the second case, the reaction did not proceed at all. Desilylation led to compound **25**, which can be selectively deprotected to provide either acetoxymethyl derivative **8** or hydroxymethyl analogue **7** (Scheme 3).

To provide access to the benzoate derivative **9**, a point of diversion in synthesis was chosen to be compound **23**, which possesses all the required functionality and is prone to basic hydrolysis. Benzoylation of alcohol **24** provided access to compound **27**, which was subjected to the deprotection protocol to furnish the C-1 benzoxymethyl derivative **9** (Scheme 4).

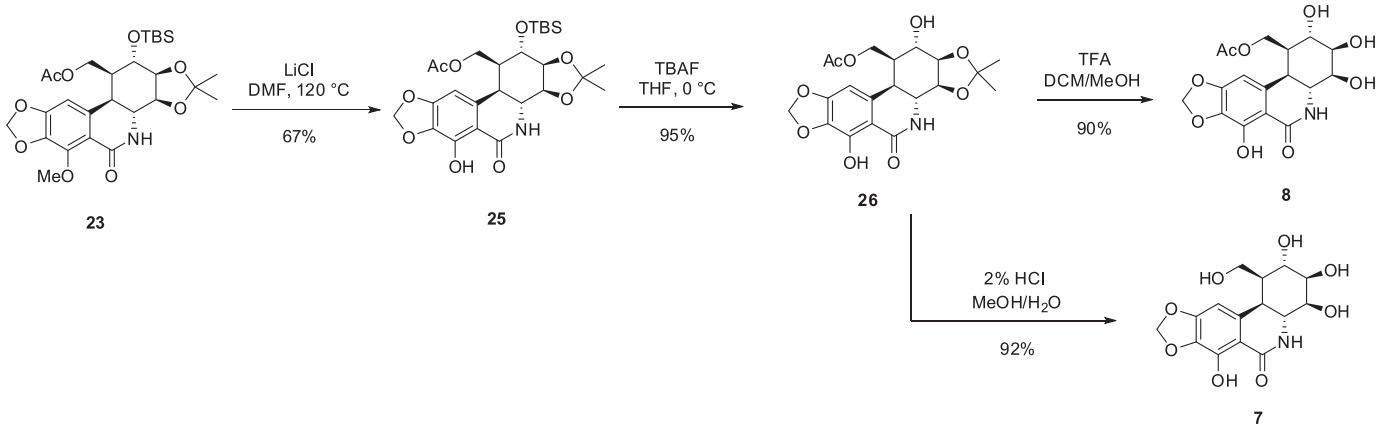
Evaluation of biological activities

The hydroxymethyl, acetoxymethyl, and benzoxymethyl analogues (**7**, **8**, and **9**, respectively), together with their 7-deoxy counterparts (**5** and **6**), were evaluated in a small panel of cancer cell lines diversely representing several types of human malignancy (Table 1). As expected, the 7-hydroxy compounds were found to be more potent, again underscoring the beneficial effect of the 7-hydroxy substituent. For example, both **7** and **8** were about 10 times more potent than their 7-deoxy analogues (**5** and **6**) against the prostate DU-145 cells, and this 10-fold difference in activity is similar to that between **1** and **3**.[2a,13b] In addition, the double-digit nanomolar potency of the acetoxymethyl analogue (**8**) is noteworthy and it approaches that of narciclasine, which was used as a reference compound. The most encouraging activity was found, however, with the benzoxymethyl compound (**9**). It is three to five times more potent than narciclasine against the pancreatic BXPC-3 and prostate DU-145 cancer cells, while showing a similar magnitude of effect toward the other two cell lines used. This finding is consistent with the previous observations of the beneficial effects imparted by large hydrophobic C-1 substituents as was reported by Pettit et al.[4c] for the C1-benzoate derivative of pancratistatin. The benzoate moiety could be part of the cytotoxic pharmacophore or it could merely assist the parent hydroxyl compound in cell penetration and then undergo intracellular hydrolytic removal to its hydroxy analogue (**7**). Further studies are required to provide a satisfactory answer to this important question.

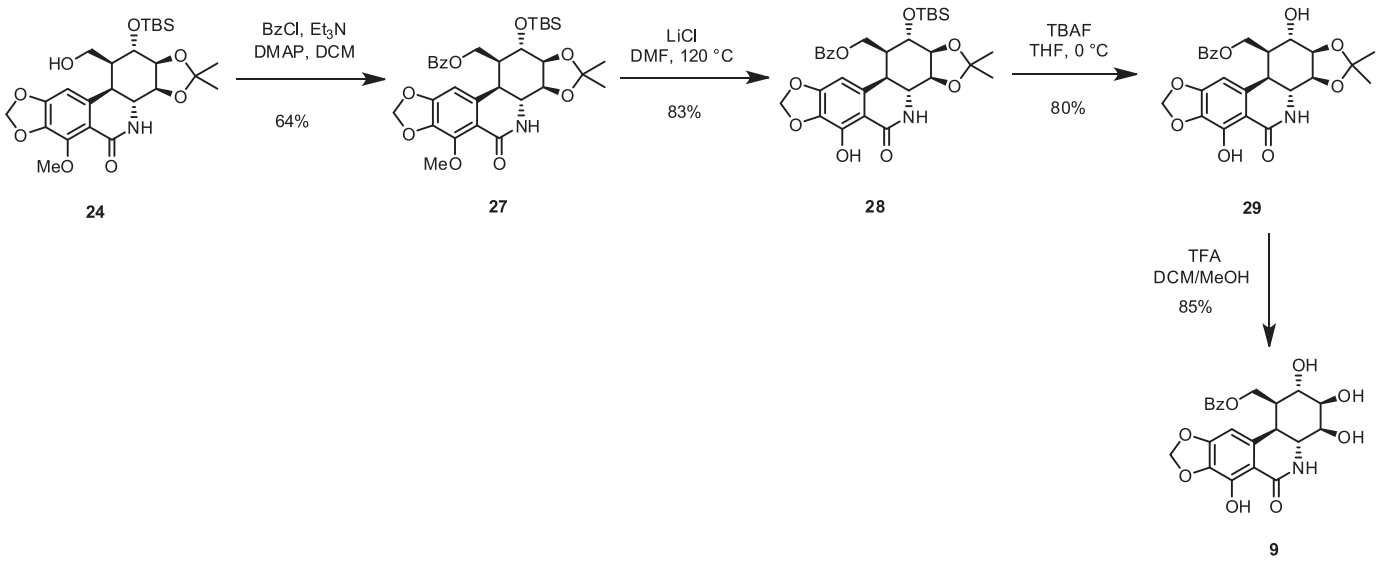
Can. J. Chem. Downloaded from www.nrcresearchpress.com by MCGILL UNIVERSITY on 02/02/13
For personal use only.

Can. J. Chem. Downloaded from www.nrcresearchpress.com by MCGILL UNIVERSITY on 02/02/13
For personal use only.

Scheme 3.



Scheme 4.



As pancratistatin was previously found to be effective in selectively producing cytotoxicity in an array of cancers, we additionally evaluated the activity of **5**–**9** in the colorectal cancer cell line HCT 116 and in the osteosarcoma cell line Saos-2 with the water soluble tetrazolium salt (WST-1)-based colorimetric assay for cell viability. After 48 h of treatment, all of these pancratistatin analogues decreased cell viability in a dose-dependent manner. The benzoate ester analogue (**9**) demonstrated the greatest anticancer activity at lower concentrations and had half-maximal inhibitory concentration (IC_{50}) values below 0.05 μmol/L after 48 h in both HCT 116 and Saos-2 cells (Figs. 2A and 2B, respectively); however, its effectiveness plateaus at 0.1 μmol/L, after which **7** becomes more effective against HCT 116 cells and **8** becomes more effective against Saos-2 cells.

The effect of pancratistatin analogues on cellular viability of colorectal cancer and osteosarcoma cells was determined by the WST-1-based colorimetric assay. HCT 116 and Saos-2 cells (Figs. 2A and 2B, respectively) were treated with pancratistatin analogues for 48 h and the WST-1 reagent was used to quantify cell viability. Absorbance was read at 450 nm and expressed as a percentage of the control (Me_2SO). Values are expressed as the mean ± SD from quadruplicates of three independent experiments.

Conclusions

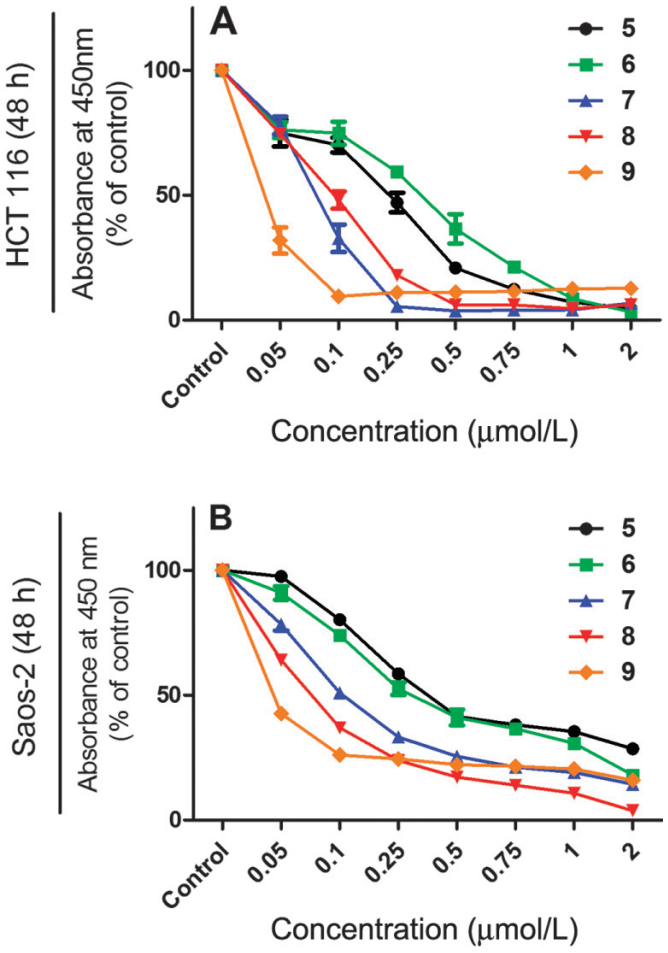
Three new C-1 homologues of pancratistatin have been synthesized and tested in various cancer cell lines. The results were compared with the two previously tested C-1 homologues of 7-deoxypancratistatin. The newly synthesized C-1 homologues manifested nanomolar antiproliferative activities against a panel of human cancer cell lines similar to the parent natural products. The benzoxymethyl compound (**9**), however, exhibited the most encouraging activity, which was three to five times more potent than that of narciclasine against the pancreatic BXPC-3 and prostate DU-145 cancer cells. The various C-1 analogues screened in this study have very high cytoxicity at low concentrations in a variety of aggressive cancer cells. We observed remarkable enhancement of cytotoxicity in compounds containing the hydroxyl group at C-7 and the benzoate ester at C-1 in human colorectal cancer and osteosarcoma. These novel analogues may hold the potential to be very effective anticancer therapeutic agents.

Table 1. Activity of C-1 analogues with narciclasine as a standard (IC_{50}, μmol/L).

Cancer type	Cell line	Structure narciclasine **2**	**5**	**6**	**7**	**8**	**9**
Pancreatic	BxPC-3	0.05±0.01	0.77±0.01	0.34±0.05	0.22±0.01	0.07±0.01	0.01±0.00
Prostate	DU-145	0.03±0.01	1.10±0.20	0.72±0.27	0.09±0.01	0.06±0.01	0.01±0.00
Lung	NCI-H460	0.05±0.03	0.40±0.01	0.53±0.01	0.09±0.01	0.07±0.01	0.03±0.01
Breast	MCF-7	0.06±0.03	0.86±0.06	1.81±1.20	0.24±0.10	0.52±0.47	0.08±0.01

Note: The half-maximal inhibitory concentration (IC_{50}) is the concentration required to reduce the viability of cells by 50%, after 48 h of treatment with indicated compounds, relative to the dimethyl sulfoxide (DMSO) control; ±standard deviation (SD) from two independent experiments, each performed in four replicates, determined by the 3-(4,5-dimethylthiazol-2-yl)-2,5-diphenyltetrazolium bromide (MTT) assay.

Fig. 2. Pancratistatin analogues cause cytotoxicity in cancer cells in a dose-dependent manner.



Experimental section

General

Reactions were carried out under inert atmosphere in oven-dried glassware unless stated otherwise. LiCl was fused under vacuum immediately before use. Solvents were distilled: CH_2Cl_2, DMF, *i*-Pr_2NEt, and pyridine from CaH_2, MeOH from magnesium methoxide, tetrahydrofuran (THF) and DME from Na/benzophenone, toluene from Na, and quinoline from Zn. Qualitative thin-layer chromatography (TLC) was done with precoated silica gel aluminum sheets (EMD silica gel 60 F_{254}) with detection by UV or by spraying with a cerium ammonium molybdate (CAM) solution (5 g of $(NH_4)_6Mo_7O_{24}{\cdot}4H_2O$, 1 g of $Ce(SO_4)_2$, and 100 mL of 10% H_2SO_4) or a 0.5% aqueous $KMnO_4$ solution followed by heating. Melting points are uncorrected. Flash chromatography was performed using silica gel SiliaFlash P60 from Silicycle (40–66 μm). Optical rotation was measured in a 1 dm cell at 20–25 °C and 589 nm with a concentration (*c*) in g/100 mL. IR spectra were recorded in KBr pellets or as a thin film. ^1H and ^{13}C NMR spectra were recorded at 300 or 600 MHz and 75 or 150 MHz, respectively, and were calibrated on the solvent residual peak or tetramethylsilane (TMS) signal ($CDCl_3$, 7.28 ppm; DMSO-d_6, 2.51 ppm); the chemical shifts are reported in ppm. Copies of ^1H and ^{13}C NMR spectra for compounds **7**–**9**, **12**, **13**, and **15**–**29**) are available in the Supplementary data.

4-Methoxy-1,3-benzodioxole-5-carbaldehyde (11)

Dimethyl sulfate (22.7 mL, 240 mmol) was added to a mixture of K_2CO_3 (55.2 g, 400 mmol) and phenol **10** (made from piperonal by literature procedure;[17] 33.2 g, 200 mmol) in acetone (260 mL). The reaction was stirred under reflux until consumption of the starting material was observed (TLC, approximately 4 h). Then the reaction mixture was cooled and inorganic salts were removed by filtration and rinsed with acetone (2 × 100 mL). The solution was evaporated, redissolved in CH_2Cl_2, and washed sequentially with a 10% solution of NaOH, water, and saturated solution of NaCl. The organic solution was then dried over anhydrous Na_2SO_4 and evaporated to obtain compound **11** (30.2 g, 84%) as pale brown crystals, which was used without further purification; mp 102–104 °C (EtOH) (lit.[18] mp 103–105 °C (EtOH)). R_f = 0.65 (hexanes/EtOAc, 9:1). ^1H NMR ($CDCl_3$, 300 MHz) δ: 10.24 (s, 1H), 7.49 (d, *J* = 8.3 Hz, 1H), 6.62 (d, *J* = 8.3 Hz, 1H), 6.05 (s, 2H), 4.14 (s, 3H).

5-(2,2-Dibromovinyl)-4-methoxy-1,3-benzodioxole (12)

Triphenylphosphine (64.0 g, 244 mmol) in CH_2Cl_2 (100 mL) was added dropwise to a stirring solution of CBr_4 (40.5 g, 122 mmol) in CH_2Cl_2 (150 mL) at 0 °C (ice bath). After 15 min of stirring, a solution of aldehyde (**11**; 11.0 g,

Can. J. Chem. Downloaded from www.nrcresearchpress.com by MCGILL UNIVERSITY on 02/02/13
For personal use only.

Can. J. Chem. Downloaded from www.nrcresearchpress.com by MCGILL UNIVERSITY on 02/02/13
For personal use only.

61.0 mmol) in CH_2Cl_2 (50 mL) was added dropwise. Upon completion, the reaction was reduced in volume to 100 mL and slowly poured into vigorously stirred hexanes (1400 mL). The mixture was then filtered through a short plug of silica, washed with a mixture of hexanes/EtOAc (10:1, 200 mL), and evaporated. Subjection of this material to flash column chromatography (eluent hexanes/EtOAc, 9:1) and concentration of the relevant fractions gave **12** (16.11 g, 78.6%) as a white solid; mp 38–40 °C (pentane). R_f = 0.9 (hexanes/EtOAc, 9:1). IR (KBr, cm^{-1}) ν: 3448, 2981, 2948, 2934, 2900, 2876, 2838, 2770, 1625, 1605, 1471, 1427, 1384, 1350, 1265, 1213, 1126, 1072, 1045, 979, 960, 939, 929, 848, 829, 788, 767, 729, 644. ^{1}H NMR ($CDCl_3$, 300 MHz) δ: 7.49 (s, 1H), 7.24 (d, J = 8.3 Hz, 1H), 6.57 (d, J = 8.3 Hz, 1H), 5.96 (s, 2H), 4.02 (s, 3H). ^{13}C NMR ($CDCl_3$, 75 MHz) δ: 149.7, 141.1, 136.1, 132.3, 122.5, 121.4, 102.3, 101.2, 89.0, 59.9. MS (+EI) m/z (%): 338 ([^{81}Br + ^{81}Br, M]$^+$, 49), 336 ([^{81}Br + ^{79}Br, M]$^+$, 100), 334 ([^{79}Br + ^{79}Br, M$^+$], 51), 242 (55), 240 (57), 176 (53), 175 (42), 131 (29). HR-MS (+EI) calcd for $C_{10}H_8Br_2O_3$: 333.8820; found: 333.8845. Anal. calcd for $C_{10}H_8Br_2O_3$: C 35.75, H 2.40; found: C 35.99, H 2.41.

5-Ethynyl-4-methoxy-1,3-benzodioxole (13)

To a solution of **12** (19.38 g, 57.68 mmol) in THF (350 mL) was added a solution of *n*-BuLi (52.9 mL, 2.5 mol/L, and 130 mmol) at –78 °C. After 20 min of stirring at –78 °C, the reaction mixture was warmed to room temperature over a period of 2 h. A saturated solution of NH_4Cl (40 mL) was poured into the reaction mixture, which was later extracted by CH_2Cl_2 (3 × 50 mL). The combined organic phases were dried over Na_2SO_4, filtered, and evaporated. The crude compound was purified by flash chromatography (hexanes/EtOAc 2:1) and white crystals of acetylene **13** were obtained (8.5 g, 81.7%); mp 77–78 °C (pentane). R_f = 0.9 (hexanes/EtOAc, 2:1). IR (KBr, cm^{-1}) ν: 3278, 3254, 3000, 2945, 2901, 2846, 2794, 2097 (weak), 1620, 1600, 1469, 1433, 1336, 1267, 1229, 1077, 1043, 979, 950, 930, 797. ^{1}H NMR ($CDCl_3$, 300 MHz) δ: 7.01 (d, J = 7.9 Hz, 1H), 6.50 (d, J = 8.29 Hz, 1H), 5.98 (s, 2H), 4.11 (s, 3H), 3.20 (s, 1H). ^{13}C NMR ($CDCl_3$, 75 MHz) δ: 150.1, 144.8, 136.2, 128.0, 108.1, 102.9, 101.3, 79.9, 79.4, 60.0. MS (+EI) m/z (%): 176 ([M]$^+$, 100), 175 (29), 131 (16), 53 (18). HR-MS (+EI) calcd for $C_{10}H_8O_3$: 176.0473; found: 176.0475. Anal. calcd for $C_{10}H_8O_3$: C 68.18, H 4.58; found: C 68.27, H 4.55.

(3a*S*,4*R*,5*R*,6*R*,7*S*,7a*R*)-6-[(4-Methoxy-1,3-benzodioxol-5-yl)ethynyl]-2,2-dimethyl-8-[(4-methylphenyl)sulfonyl] hexahydro-4,5-epimino-1,3-benzodioxol-7-ol (15)

To a solution of alkyne **13** (1.580 g, 8.95 mmol) in toluene (30 mL) at –50 °C, *n*-BuLi (3.80 mL, 2.35 mol/L, and 8.95 mmol) was added dropwise. After 15 min of stirring, Me_2AlCl (9.0 mL, 1.0 mol/L, and 8.95 mmol) was added dropwise. The reaction mixture was warmed to 0 °C within 1 h and stirred for an additional 40 min at 0 °C. The reaction mixture was allowed to warm to room temperature and stirred for 40 min. The reaction mixture was cooled to –30 °C and a solution of epoxide **14** (1.510 g, 4.47 mmol) in toluene (20 mL) was added dropwise. The reaction mixture was stirred for 1 h and was allowed to warm to room temperature overnight. The reaction mixture was cooled to 0 °C by ice bath and quenched with 1 N HCl (1 mL), followed by ice-cold water (1 mL) and 1 N HCl (2 mL). The reaction mixture was filtered through a plug of Celite and extracted with EtOAc (3 × 20 mL). The combined organic phases were dried over Na_2SO_4, filtered, and evaporated. The crude product was purified by column chromatography (gradient hexanes/EtOAc 5:1 to 3:1) to give the product as colourless oil (1.02 g, 44%). Repetition of this procedure on a 4.12 g scale of **13** provided **15** in a 38% yield. $[\alpha]_D^{24}$ +78.4 (*c* 1.0, $CHCl_3$). R_f = 0.3 (hexanes/EtOAc, 2:1). IR (film, cm^{-1}) ν: 3482, 3093, 2986, 2935, 2900, 1620, 1599, 1470, 1434, 1404, 1383, 1332, 1307, 1260, 1225, 1186, 1183, 1071, 985. ^{1}H NMR ($CDCl_3$, 300 MHz) δ: 7.83 (d, J = 8.3 Hz, 2H), 7.39 (d, J = 8.3 Hz, 2H), 6.88 (d, J = 8.1 Hz, 1H), 6.47 (d, J = 8.3 Hz, 1H), 5.96 (s, 2H), 4.48 (d, J = 6.2 Hz, 1H), 4.19 (t, J = 5.7 Hz, 1H), 4.06 (s, 3H), 3.98–3.95 (m, 1H), 3.44–3.41 (m, 1H), 3.26 (d, J = 6.8 Hz, 1H), 3.24 (dd, J = 5.0, 2.1 Hz, 1H), 3.08 (d, J = 8.7 Hz, 1H), 2.48 (s, 3H), 1.51 (s, 3H), 1.34 (s, 3H). ^{13}C NMR ($CDCl_3$, 75 MHz) δ: 149.7, 145.4, 144.4, 136.3, 134.1, 130.1, 127.9, 127.2, 110.1, 108.8, 102.8, 101.3, 87.6, 80.5, 75.5, 70.3, 69.0, 60.0, 42.3, 40.2, 31.9, 27.3, 25.1, 21.7. MS (+FAB) m/z (%): 514 ([M + H]$^+$, 24), 513 ([M]$^+$, 13), 258 (12), 238 (11), 230 (14), 179 (26), 155 (28), 149 (23), 43 (100). HR-MS (+FAB) calcd. for $C_{26}H_{28}NO_8S^+$ [M + 1]$^+$: 514.1457; found: 514.1502.

(3a*S*,4*R*,5*R*,6*R*,7*S*,7a*R*)-6-[(*Z*)-2-(4-Methoxy-1,3-benzodioxol-5-yl)vinyl]-2,2-dimethyl-8-[(4-methylphenyl) sulfonyl]hexahydro-4,5-epimino-1,3-benzodioxol-7-ol (16)

To a solution of compound **15** (427 mg, 0.83 mmol) in MeOH (20 mL) was added quinoline (11 mg, 0.09 mmol). The solution was charged with a Lindlar catalyst (5%, 100 mg) and allowed to stir under H_2 (1 atm) for 45 min. After consumption of the starting material was observed (NMR), the reaction mixture was filtered through a pad of Celite, washed with CH_3OH (3 × 30 mL), evaporated, and used without further purification. An analytical sample was purified by column chromatography (hexanes/EtOAc, 3:1) to provide **16** as a waxy solid. $[\alpha]_D^{20}$ +2.7 (*c* 1.78, $CHCl_3$). R_f = 0.4 (hexanes/ EtOAc, 2:1). IR (film, cm^{-1}) ν: 3482, 2987, 2934, 2900, 1621, 1598, 1470, 1434, 1404, 1382, 1332, 1260, 1218, 1162, 1070, 1043. ^{1}H NMR ($CDCl_3$, 300 MHz) δ: 7.74 (d, J = 8.3 Hz, 2H), 7.32 (d, J = 8.3 Hz, 2H), 6.60 (d, J = 11.4 Hz, 1H), 6.55 (d, J = 8.1 Hz, 1H), 6.46 (d, J = 8.0 Hz, 1H), 5.98 (d, J = 1.2 Hz, 1H), 5.96 (d, J = 1.2 Hz, 1H), 5.73 (t, J = 11.2 Hz, 1H), 4.43 (d, J = 6.2 Hz, 1H), 4.16–4.13 (m, 1H), 3.96 (s, 3H), 3.72–3.68 (m, 1H), 3.18 (d, J = 6.4 Hz, 1H), 3.15–3.10 (m, 1H), 3.08 (d, J = 6.4 Hz, 1H), 2.84 (d, J = 9.2 Hz, 2H), 2.43 (s, 3H), 1.49 (s, 3H), 1.30 (s, 3H). ^{13}C NMR ($CDCl_3$, 75 MHz) δ: 148.9, 145.2, 141.3, 136.6, 134.3, 130.0, 128.1, 127.9, 127.8, 122.5, 122.2, 109.7, 102.6, 101.0, 75.8, 70.1, 69.3, 59.7, 43.1, 40.5, 37.8, 27.1, 24.7, 21.7. MS (+FAB) m/z (%) [M]$^+$: 517 (16), 516 (42), 515 (29), 514 (15), 386 (25), 285 (14), 284 (15), 269 (15), 203 (30), 165 (61), 91 (100). HR-MS

Can. J. Chem. Downloaded from www.nrcresearchpress.com by MCGILL UNIVERSITY on 02/02/13
For personal use only.

(+FAB) calcd for $C_{26}H_{31}NO_8S$ [M + 1]$^+$: 516.1692; found: 516.1666. Anal. calcd for $C_{26}H_{29}NO_8S$: C 60.57, H 5.67; found: C 60.33, H 5.55.

(3a*S*,4*R*,5*R*,6*R*,7*S*,7a*R*)-7-{*Tert*-butyl[dimethylsylil]oxy}-6-[(*Z*)-2-(4-methoxy-1,3-benzodioxol-5-yl)vinyl]-2,2-dimethyl-8-[(4-methylphenyl)sulfonyl]hexahydro-4,5-epimino-1,3-benzodioxol (17)

To a solution of alcohol **16** (1.07 g, 2.07 mmol) in 30 mL of CH_2Cl_2 was added Et_3N (0.58 mL, 4.15 mmol) at 0 °C and *tert*-butyldimethylsilyl triflate (0.53 mL, 2.29 mmol) was added dropwise. After the complete consumption of the starting material was observed (TLC), the reaction mixture was quenched by water (10.0 mL) and extracted with CH_2Cl_2 (3 × 20 mL). The combined organic phases were washed with 10% citric acid (5 mL), brine (5 mL), dried over Na_2SO_4, and concentrated to afford **17** as pale yellow oil (1.26 g, 97%). The compound was used without further purification. An analytical sample was purified by silica gel chromatography (hexanes/EtOAc, 4:1). $[\alpha]_D^{24}$ –18.5 (*c* 2.0, $CHCl_3$). R_f = 0.85 (hexanes/EtOAc, 2:1). IR (KBr, cm^{-1}) ν: 3446, 2986, 2954, 2931, 2887, 2856, 1622, 1600, 1470, 1435, 1382, 1332, 1257, 1218, 1163, 1071, 1043. ^{1}H NMR ($CDCl_3$, 300 MHz) δ: 7.78 (d, *J* = 8.2 Hz, 2H), 7.30 (d, *J* = 8.2 Hz, 2H), 6.67 (d, *J* = 8.0 Hz, 1H), 6.60 (d, *J* = 11.5 Hz, 1H), 6.39 (d, *J* = 8.0 Hz, 1H), 5.96–5.93 (m, 2H), 5.65 (t, *J* = 11.5 Hz, 1H), 4.39 (d, *J* = 5.9 Hz, 1H), 3.98 (s, 3H), 3.89 (t, *J* = 6.03 Hz, 1H), 3.67 (t, *J* = 6.3 Hz, 1H), 3.12 (d, *J* = 6.6 Hz, 1H), 2.98–2.91 (m, 2H), 2.45 (s, 3H), 1.52 (s, 3H), 1.34 (s, 3H), 0.78 (s, 9H), 0.00 (s, 3H), –0.08 (s, 3H). ^{13}C NMR ($CDCl_3$, 75 MHz) δ: 148.7, 144.4, 141.4, 136.3, 135.0, 129.7, 129.6, 127.8, 127.6, 122.9, 122.4, 109.3, 102.3, 100.8, 71.8, 71.4, 59.6, 43.4, 39.7, 39.2, 27.7, 25.7, 25.5, 21.6, 18.0, –4.6, –4.8. MS (+FAB) *m*/*z* (%) [M]$^+$: 628 (8), 514 (13), 343 (17), 256 (10), 228 (10), 215 (19), 165 (36), 73(100). HR-MS (+FAB) calcd for $C_{32}H_{44}NO_8SSi$ [M + 1]$^+$: 630.2557; found: 630.2492. Anal. calcd for $C_{32}H_{43}NO_8SSi$: C 61.02, H 6.88; found: C 61.28, H 7.02.

***N*-((1*R*,2*S*,3*S*,4*S*,4a*R*,11b*R*)-4-{[*Tert*-butyl(dimethyl)silyl]oxy}-3,3-dimethoxy-7-methoxy-1,2,3,4,4a,11b-hexahydrophenanthro[2,3-*d*][1,3]dioxol-1-yl) benzenesulfonamide (18)**

Olefin **17** (100 mg, 0.561 mmol), quinoline (15 mg, 0.12 mmol), and silica gel (500 mg), which has been activated in advance by heating under vacuum for 24 h at 150 °C, were suspended in CH_2Cl_2 (10 mL). The solvent was removed in vacuo and the flask containing silica gel supporting the absorbed reactants was heated at 120 °C under a nitrogen atmosphere and stirred for 36 h. The reaction mixture was then separated by column chromatography (hexanes/EtOAc, 4:1) to give 74 mg (74%) of olefin **18** as a clear and colourless oil. $[\alpha]_D^{24}$ –25.1 (*c* 1.0, $CHCl_3$). R_f = 0.45 (hexanes/EtOAc, 2:1). IR (KBr, cm^{-1}) ν: 3275, 2983, 2953, 2932, 2889, 2857, 1633, 1614, 1599, 1479, 1384, 1361, 1331, 1221, 1158, 1092, 841. ^{1}H NMR ($CDCl_3$, 300 MHz) δ: 7.43 (d, *J* = 8.1 Hz, 2H), 7.13 (d, *J* = 8.1 Hz, 2H), 6.65 (dd, *J* = 9.8, 3.4 Hz, 1H), 6.22 (s, 1H), 5.92 (d, *J* = 1.5 Hz, 1H), 5.82 (d, *J* = 1.5 Hz, 1H), 5.74 (dd, *J* = 9.8, 1.5 Hz, 1H), 4.59 (d, *J* = 8.8 Hz, 1H), 4.28 (m, 1H), 4.11 (s, 1H), 4.02–3.99 (m, 1H), 3.97 (s, 3H), 3.80–3.70 (m, 1H), 2.79–2.78 (m, 1H), 2.61–2.56 (m, 1H), 2.41 (s, 3H), 1.73 (s, 1H), 1.45 (s, 3H), 1.34 (s, 3H), 0.88 (s, 9H), 0.10 (s, 3H), 0.05 (s, 3H). ^{13}C NMR ($CDCl_3$, 75 MHz) δ: 147.5, 142.1, 139.5, 138.6, 135.5, 129.4, 129.8, 126.8, 125.3,120.5, 119.7,109.2,104.8,100.7,79.1,78.3,70.3,59.7,53.7,42.4,39.1, 27.8,26.3,25.7,21.5,18.0,–5.03,–5.056. MS (+FAB) *m*/*z* (%) [M]$^+$: 629 (3), 129 (13), 111 (12), 99 (13), 57 (100). HR-MS (+FAB) calcd for $C_{32}H_{43}NO_8SSi$ [M]$^+$: 629.2479; found: 629.2472.

***N*-[(3a*S*,4*R*,5*R*,6*S*,7*S*,7a*S*)-7-{[*Tert*-butyl(dimethyl)silyl]oxy}-6,6′-bis(hydroxymethyl)-7′-methoxy-2,2-dimethyl-3,4,5,6,7,7a-hexahydro-5,5′-bi-1,3-benzodioxol-4-yl]-4-methylbenzenesulfonamide (19)**

To a solution of **18** (254 mg, 0.404 mmol) in MeOH (50 mL) was added a few crystals of Sudan Red 7B. The solution was cooled down to –80 °C and a oxygen–ozone mixture was bubbled through until the disappearance of the pink color. The consumption of the starting material was also checked by TLC. A stream of nitrogen was bubbled through the reaction mixture for 5 min. $NaBH_4$ (250 mg, 6.67 mmol) was slowly added and reaction mixture was gradually warmed from –80 °C to room temperature. The solvent was removed in vacuo and the residue was redissolved in CH_2Cl_2 (50 mL), neutralized by 10% citric acid, and washed with water (50 mL). The organic phase was separated, dried over Na_2SO_4, filtered, and evaporated. The crude product was subjected to column chromatography (hexanes/EtOAc, 1:1) to give **19** as a white crystalline solid (164.3 mg, 61%) and **20** as a mixture of anomers (80 mg, 30%); mp 121–123 °C ($CHCl_3$). $[\alpha]_D^{20}$ –30.8 (*c* 1.09, $CHCl_3$). R_f = 0.45 (hexanes/EtOAc, 1:1). IR (KBr, cm^{-1}) ν: 3472, 3386, 3172, 2927, 2855, 1622, 1482, 1385, 1332, 1255, 1220, 1158, 1095, 1057, 837. ^{1}H NMR ($CDCl_3$, 600 MHz) δ: 7.51 (d, *J* = 7.8 Hz, 2H), 7.13 (d, *J* = 7.8 Hz, 2H), 6.57 (s, 1H), 5.96 (s, 1H), 5.90 (s, 1H), 5.44 (d, *J* = 7.0 Hz, 1H), 4.77 (d, *J* = 11.8 Hz, 1H), 4.42 (d, *J* = 11.9 Hz, 1H), 4.27–4.24 (m, 1H), 4.17–4.10 (m, 2H), 4.00 (s, 3H), 3.95–3.86 (m, 1H), 3.70 (dd, *J* = 11.9, 6.1 Hz, 1H), 3.59 (dd, *J* = 11.8, 6.3 Hz, 1H), 3.37 (dd, *J* = 11.8, 3.9 Hz, 1H), 2.92 (br s, 2H), 2.39 (s, 3H), 2.00–1.96 (m, 1H), 1.56 (s, 3H), 1.32 (s, 3H), 0.92 (s, 9H), 0.14 (s, 3H), 0.11 (s, 3H). ^{13}C NMR ($CDCl_3$, 150 MHz) δ: 149.1, 142.1, 141.6, 139.2, 135.1, 132.4, 128.8, 126.8, 124.6, 109.7, 103.5, 101.0, 79.9, 79.0, 71.5, 61.3, 60.0, 57.0, 55.2, 47.3, 38.2, 27.4, 25.9, 25.8, 21.5, 18.0, 21.6, 21.0, 18.0, –4.8, –5.0. MS (+FAB) *m*/*z* (%): 664 ([M – H]$^+$, 6), 648 (7), 372 (11), 302 (11), 254 (21), 248 (12), 73 (100). HR-MS (+EI) calcd for $C_{32}H_{47}NO_{10}SSi$ [M]$^+$: 665.2690; found: 665.2803. Anal. calcd for $C_{32}H_{47}NO_{10}SSi$: C 57.72, H 7.11; found: C 57.76, H 6.99.

(3a*S*,3b*R*,10b*R*,11*S*,12*S*,12a*S*)-12-{[*Tert*-butyl(dimethyl)silyl]oxy}-11-(hydroxymethyl)-6-methoxy-2,2-dimethyl-4-[(4-methylphenyl)sulfonyl]-3,3b,4,5,10b,11,12,12a-octahydrobis[1,3]dioxolo[4,5-*c*:4′,5′-*j*]phenanthridin-5-ol (20)

To a solution of alcohol **19** (100 mg, 0.15 mmol) in CH_2Cl_2 (100 mL) was added MnO_2 (268 mg, 3 mmol). The reaction mixture was vigorously stirred until total consump-

Can. J. Chem. Downloaded from www.nrcresearchpress.com by MCGILL UNIVERSITY on 02/02/13
For personal use only.

tion of the starting material was observed (TLC). The reaction mixture was filtered through a plug of Celite® and washed with CH_2Cl_2 (3 × 100 mL). The solvent was removed in vacuo, affording **20** as a white solid compound (87 mg, 87%, mixture of anomers); mp 106–116 °C ($CHCl_3$). R_f = 0.5 and 0.65 (hexanes/EtOAc, 1:1). IR (KBr, cm^{-1}) ν: 3452, 2985, 2954, 2931, 2894, 2857, 1624, 1483, 1384, 1341, 1251, 1163, 1077, 839. NMR of the major anomer: ^1H NMR ($CDCl_3$, 300 MHz) δ: 7.55 (d, J = 8.1 Hz, 2H), 7.03 (d, J = 8.1 Hz, 2H), 6.65 (s, 1H), 6.08 (s, 1H), 5.92–5.91 (m, 2H), 5.26 (dd, J = 9.9, 5.4 Hz, 1H), 4.38 (t, J = 3.0 Hz, 1H) 4.25–4.21 (m, 2H), 4.11 (s, 3H), 3.74 (dd, J = 11.0, 7.9 Hz, 1H), 3.37 (dd, J = 11.0, 3.6 Hz, 1H), 2.87 (dd, J = 12.9, 5.1 Hz, 1H), 2.33 (s, 3H), 2.16 (br s, 1H), 2.15 (br s, 1H), 2.06 (s, 1H), 1.44 (s, 3H), 1.37 (s, 3H), 0.92 (s, 9H), 0.15 (s, 3H), 0.10 (s, 3H). ^{13}C NMR ($CDCl_3$, 150 MHz) δ: 150.0, 142.9, 140.5, 138.3, 134.0, 130.0, 128.9, 127.2, 121.3, 109.4, 101.0, 100.2, 78.9, 76.4, 73.5, 68.1, 59.9, 59.3, 53.1, 48.1, 34.4, 27.9, 26.2, 25.7, 21.4, 17.9, –4.8, –5.1. MS (+EI) *m/z* (%) $[M - Ts - H_2O]^+$: 491 (15), 432 (13), 302 (22.2), 302 (10.5), 247 (31.1), 246 (19.9), 43 (100). HR-MS (+EI) calcd for $C_{32}H_{45}NO_{10}SSi$ $[M]^+$: 663.2533; found: 663.2549. Anal. calcd for $C_{32}H_{45}NO_{10}SSi$: C 57.90, H 6.83; found: C 58.02, H 7.03.

{(3a*S*,3b*R*,10b*R*,11*S*,12*S*,12a*S*)-12-{[*Tert*-butyl(dimethyl) silyl]oxy}-5-hydroxy-6-methoxy-2,2-dimethyl-4-[(4-methylphenyl)sulfonyl]-3,3b,4,5,10b,11,12,12a-octahydrobis[1,3]dioxolo[4,5-*c*:4′,5′-*j*]phenanthridin-11-yl} methyl acetate (21)

Pyridine (50 mg, 0.63 mmol) was added to a solution of hemiaminal **20** (48 mg, 0.072 mmol) in CH_2Cl_2 (3 mL), followed by the addition of acetic anhydride (29.5 mg, 0.29 mmol). The reaction mixture was stirred until consumption of the starting material was observed (TLC). The reaction mixture was quenched with water (5 mL) and extracted by CH_2Cl_2 (3 × 4 mL). The combined organic phases were dried over Na_2SO_4, filtered, and evaporated. The crude product was subjected to column chromatography (eluent hexanes/EtOAc, 4:1) affording **21** as a colourless oil (43 mg, 87% mixture of anomers). R_f = 0.9 and 0.8 (hexanes/EtOAc, 1:1). IR (KBr, cm^{-1}) ν: 3462, 2984, 2953, 2931, 2896, 2857, 1743, 1624, 1481, 1371, 1342, 1330, 1250, 1222, 1164, 1077, 840. NMR of the major anomer: ^1H NMR ($CDCl_3$, 600 MHz) δ: 7.56 (d, J = 8.2 Hz, 2H), 7.08 (d, J = 8.0 Hz, 2H), 6.66 (s, 1H), 6.012 (s, 1H), 5.94 (m, 2H), 5.31 (dd, J = 10.0, 5.1 Hz, 1H), 4.37 (m, 1H) 4.22–4.21 (m, 1H), 4.08 (s, 3H), 3.96 (s, 1H), 3.91 (dd, J = 11.4, 4.4 Hz, 1H), 3.05 (s, 1H), 2.91 (dd, J = 13.2, 4.5 Hz, 1H), 2.35 (s, 3H), 2.15 (s, 1H), 1.93 (s, 3H), 1.47 (s, 3H), 1.38 (s, 3H), 0.93 (s, 9H), 0.15 (s, 3H), 0.11 (s, 3H). ^{13}C NMR ($CDCl_3$, 150 MHz) δ: 170.8, 150.0, 143.0, 140.6, 138.5, 134.1, 129.8, 128.9, 127.2, 121.3, 109.3, 101.0, 100.1, 78.9, 76.3, 73.3, 67.2, 61.2, 59.9, 53.2, 45.6, 33.8, 29.7, 26.3, 25.7, 25.5, 21.4, 20.8, 17.9, –5.0, –5.2. MS (+FAB) *m/z* (%) $[M - H_2O]^+$: 688 (47), 230 (12), 117 (17), 302 (11), 247 (31), 117 (17), 73 (100). HR-MS (+FAB) calcd for $C_{34}H_{46}NO_{10}SSi$ $[M - H_2O]^+$: 688.2612; found: 688.2642. Anal. calcd for $C_{34}H_{47}NO_{11}SSi$: C 57.85, H 6.71; found: C 57.80, H 6.67.

{(3a*S*,3b*R*,10b*R*,11*S*,12*S*,12a*S*)-12-{[*Tert*-butyl(dimethyl) silyl]oxy}-6-methoxy-2,2-dimethyl-4-[(4-methylphenyl) sulfonyl]-5-oxo-3a,3b,4,5,10b,11,12,12a-octahydrobis[1,3] dioxolo[4,5-*c*:4′,5′-*j*]phenanthridin-11-yl}methyl acetate (22)

A predried (by $MgSO_4$) solution of *N*-methylmorpholine-*N*-oxide (100 mg, 0.85 mmol) in CH_2Cl_2 (20 mL) was added to hemiaminal **21** (30 mg, 0.042 mmol) in CH_2Cl_2 (10 mL), followed by activated crushed molecular sieves (0.5 g, 4 Å). After stirring for 15 min, a few crystals of tetrapropylammonium perruthenate were added and the reaction was stirred until consumption of the starting material was observed (TLC). The reaction mixture was filtered through a plug of Celite and washed with CH_2Cl_2 (3 × 50 mL). The combined organic phases were evaporated and subjected to column chromatography (hexanes/EtOAc, 2:1) affording **22** as a colourless oil (25 mg, 84%). $[\alpha]_D^{24}$ +41.4 (*c* 0.9, $CHCl_3$). R_f = 0.65 (eluent hexanes/EtOAc, 1:1). IR (KBr, cm^{-1}) ν: 3450, 2984, 2953, 2930, 2857, 1742, 1710, 1614, 1484, 1360, 1253, 1169, 1090, 1021, 839. ^1H NMR ($CDCl_3$, 300 MHz) δ: 8.20 (d, J = 8.3 Hz, 2H), 7.29 (d, J = 8.3 Hz, 2H), 6.73 (s, 1H), 6.06 (s, 1H), 6.02 (s, 1H), 4.83 (dd, J = 7.9, 5.5 Hz, 1H), 4.46 (s, 1H), 4.26 (t, J = 11.1 Hz, 1H), 4.17–4.13 (m, 1H), 4.12–4.08 (m, 1H), 4.04 (s, 3H), 4.00–3.95 (m, 1H), 3.47 (dd, J = 13.1, 3.3 Hz, 1H), 2.66–2.63 (m, 1H), 2.43 (s, 3H), 2.08 (s, 1H), 1.48 (s, 3H), 1.33 (s, 3H), 0.89 (s, 9H), 0.15 (s, 3H), 0.13 (s, 3H). ^{13}C NMR ($CDCl_3$, 150 MHz) δ: 170.8, 163.7, 153.4, 144.8, 143.4, 138.8, 136.7, 136.1, 128.9, 128.7, 126.8, 117.8, 109.1, 102.0, 100.1, 79.0, 76.3, 66.9, 60.9, 60.7, 60.4, 59.7, 43.4, 36.5, 27.9, 26.1, 25.7, 21.6, 20.9, 18.0, –4.9, –5.1. MS (+EI) *m/z* (%): 639 (3.1), 549 (6.6), 492 (3.4), 434 (2.9), 374 (3.9), 43 (100). HR-MS (+EI) calcd for $C_{33}H_{42}NO_{11}SSi^+$ $[M - CH_3]^+$: 688.2248; found: 688.2436.

((3a*S*,3b*R*,10b*R*,11*S*,12*S*,12a*S*)-12-{[*Tert*-butyl(dimethyl) silyl]oxy}-6-methoxy-2,2-dimethyl-5-oxo-3,3b,4,5,10b,11,12,12a-octahydrobis[1,3]dioxolo[4,5-*c*:4′,5′-*j*]phenanthridin-11-yl)methyl acetate (23)

To a solution of **22** (64 mg, 0.09 mmol) in dry DME (7 mL) at –50 °C was added a solution of Na/naphthalene in DME (0.5 mol/L) dropwise until a light green colour persisted and total consumption of the starting material was observed (TLC). The solution was stirred for 10 min before the reaction was quenched with a saturated solution of NH_4Cl (aq, 1 mL). The reaction was warmed to room temperature and extracted with CH_2Cl_2 (6 × 15 mL). The combined organic phases were dried over Na_2SO_4, filtered, and concentrated. The products **23** and **24** were isolated by column chromatography (gradient hexanes / EtOAc, 2:1 to 1:1) as a clear and colourless oil for **23** (30 mg, 62%) and a white crystalline solid for **24** (2 mg; 5%). Repetition of this procedure on a 1.01 g gram scale provided **23** in a 48% and **24** in a 10% yield. $[\alpha]_D^{20}$ +32.4 (*c* 1.0, $CHCl_3$). R_f = 0.28 (hexanes/EtOAc, 1:1). IR (KBr, cm^{-1}) ν: 3417, 3228, 3109, 2987, 2953, 2932, 2897, 2858, 1743, 1676, 1617, 1481, 1385, 1366, 1339, 1250, 1222, 1169, 1088, 1071, 1057, 1033, 840. ^1H NMR ($CDCl_3$, 600 MHz) δ: 6.69 (s, 1H), 6.06 (s,

Can. J. Chem. Downloaded from www.nrcresearchpress.com by MCGILL UNIVERSITY on 02/02/13
For personal use only.

1 H), 6.01 (s, 1H), 5.92 (s, 1H), 4.57 (s, 1H), 4.23 (d, J = 7.5 Hz, 1H), 4.19–4.18 (m, 1H), 4.16–4.14 (m, 1H), 4.07 (s, 3H), 3.42 (dd, J = 13.8, 8.3 Hz, 1H), 3.31 (dd, J = 13.8, 3.6 Hz, 1H), 2.66–2.65 (m, 1H), 2.11 (s, 3H), 1.45 (s, 3H), 1.39 (s, 3H), 0.91 (s, 9H), 0.16 (s, 3H), 0.15 (s, 3H). ^{13}C NMR ($CDCl_3$, 150 MHz) δ: 170.9, 163.5, 152.4, 145.4, 137.5, 135.5, 116.2, 109.9, 101.8, 99.9, 78.3, 77.8, 67.0, 61.1, 60.9, 52.5, 41.9, 35.1, 28.2, 26.1, 25.69, 25.65, 20.9, 18.0, –5.0, –5.1. MS (+FAB) *m/z* (%): 552 (12), 551 (36), 550 ([M + 1]$^+$, 100), 246 (10), 220 (11), 117 (101). HR-MS (+FAB) calcd for $C_{27}H_{40}NO_9Si$ [M + 1]$^+$: 550.2472; found: 550.2459.

((3a*S*,3b*R*,10b*R*,11*S*,12*S*,12a*S*)-12-{[*Tert*-butyl(dimethyl) silyl]oxy}-6-hydroxy-2,2-dimethyl-5-oxo-3,3b,4,5,10b,11,12,12a-octahydrobis[1,3]dioxolo[4,5-*c*:4′,5′-*j*]phenanthridin-11-yl)methyl acetate (25)

To a solution of **23** (39 mg, 0.071 mmol) in DMF (5 mL) was added LiCl (50 mg, 1.2 mmol) followed by three cycles of freeze–pump–thaw. The reaction mixture was heated to 120 °C for 2.5 h. The reaction mixture was cooled to room temperature, diluted with water (100 mL), and extracted with diethyl ether (10 × 15 mL). The combined organic phases were dried over Na_2SO_4, filtered, and concentrated. The product was isolated by column chromatography (hexanes/EtOAc, 3:1) as a clear and colourless oil that solidifies after drying (25.7 mg, 68%). Repetition of this procedure on a 0.296 g gram scale provided **25** in a 67% yield; mp 68–69 °C ($CHCl_3$). $[\alpha]_D^{20}$ –35.2 (*c* 1.0, $CHCl_3$). R_f = 0.8 (hexanes/EtOAc, 1:1). IR (KBr, cm^{-1}) *v*: 3402, 3348, 3285, 3212, 3087, 2987, 2953, 2933, 2899, 2859, 2795, 1743, 1627, 1601, 1464, 1389, 1366, 1353, 1341, 1301, 1250, 1226, 1171, 1081, 1032, 940, 838, 778. ^{1}H NMR ($CDCl_3$, 600 MHz) δ: 12.68 (s, 1H), 6.53 (s, 1H), 6.26 (s, 1H), 6.07 (s, 2H), 4.57 (s, 1H), 4.30 (dd, J = 11.1, 3.3 Hz, 1H), 4.22 (t, J = 11.0 Hz, 1H), 4.21–4.18 (m, 2H), 3.50 (dd, J = 14.4, 7.8 Hz, 1H), 3.36 (dd, J = 14.4, 3.7 Hz, 1H), 2.70–2.69 (m, 1H), 2.11 (s, 3H), 1.49 (s, 3H), 1.41 (s, 3H), 0.91 (s, 9H), 0.17 (s, 3H), 0.16 (s, 3H). ^{13}C NMR ($CDCl_3$, 150 MHz) δ: 170.8, 169.9, 153.1, 146.9, 133.9, 133.0, 110.0, 107.3, 102.3, 97.3, 78.4, 77.6, 67.0, 61.10, 53.2, 41.7, 33.9, 28.3, 26.0, 25.7, 20.9, 18.0, –5.0, –5.1. MS (+EI) *m/z* (%): 536 ([M + 1]$^+$, 9), 535 (25), 360 (17), 256 (11), 231 (10), 218 (19), 205 (21), 149 (25), 43 (100). HR-MS (+EI) calcd for $C_{26}H_{37}NO_9Si$ [M]$^+$: 535.2238; found: 535.2248.

[(3a*S*,3b*R*,10b*R*,11*S*,12*S*,12a*R*)-6,12-Dihydroxy-2,2-dimethyl-5-oxo-3,3b,4,5,10b,11,12,12a-octahydrobis[1,3] dioxolo[4,5-*c*:4′,5′-*j*]phenanthridin-11-yl]methylacetate(26)

Compound **25** (52 mg, 0.097 mmol) was taken up in THF (2.5 mL) and cooled to 0 °C. A solution of tetrabutylammonium fluoride (TBAF) in THF (1 mol/L, 0.107 mL, 0.107 mmol) was added dropwise over 1 min. The reaction mixture was stirred until total consumption of the starting material was observed (TLC). The reaction mixture was quenched with water (5 mL) and extracted with CH_2Cl_2 (6 × 15 mL). The combined organic phases were dried over Na_2SO_4, filtered, and evaporated. The final product was isolated by column chromatography (hexanes/EtOAc, 1:1) to give **26** as a white crystalline solid (38 mg, 95%); mp > 200 °C (CH_2Cl_2–CH_3OH). $[\alpha]_D^{24}$ +6.2 (*c* 0.48, DMSO). R_f = 0.3 (hexanes / ethyl acetate, 1:1). IR (KBr, cm^{-1}) *v*: 3449, 3270, 2988, 2911, 1743, 1672, 1625, 1600, 1466, 1443, 1357, 1307, 1245, 1231, 1166, 1087, 1071, 1032, 844. ^{1}H NMR (DMSO-d_6, 600 MHz) δ: 13.35 (s, 1H), 8.55 (s, 1H), 6.61 (s, 1H), 6.08 (s, 1H), 6.06 (s, 1H), 5.50 (d, J = 3.6 Hz, 1H), 4.34 (br s, 1H), 4.25 (d, J = 4.8 Hz, 1H), 4.20 (dd, J = 11.4, 3.6 Hz, 1H), 4.16–4.15 (m, 1H), 4.13 (d, J = 11.4 Hz, 1H), 3.51 (dd, J = 15.0, 8.4 Hz, 1H), 3.19 (dd, J = 14.4, 3.6 Hz, 1H), 2.03 (s, 3H), 1.41 (s, 3H), 1.31 (s, 3H). ^{13}C NMR (DMSO-d_6, 150 MHz) δ: 170.9, 169.8, 152.7, 146.3, 135.0, 132.6, 109.0, 107.7, 102.4, 97.6, 77.9, 76.9, 65.2, 61.2, 53.4, 34.3, 28.3, 26.4, 21.2. MS (+EI) *m/z* (%): 422 ([M + 1], 24), 421 ([M$^+$], 100), 248 (34), 247 (60), 232 (27), 231 (32), 218 (11), 206 (17), 145 (14). HR-MS calcd for $C_{20}H_{23}NO_9$ [M]$^+$: 421.13728; found: 421.13792. Anal. calcd for $C_{20}H_{23}NO_9$: C 57.00, H 5.50; found: C 57.18, H 5.48.

[(1*S*,2*S*,3*R*,4*S*,4a*R*,11b*R*)-2,3,4,7-Tetrahydroxy-6-oxo-1,2,3,4,4a,5,6,11b-octahydro[1,3]dioxolo[4,5-*j*] phenanthridin-1-yl]methyl acetate (8)

Compound **26** (38 mg, 0.09 mmol) was taken up in a CH_2Cl_2–CH_3OH mixture (1:1, 4 mL) and cooled to 0 °C. Trifluoroacetic acid (2 mL) was added dropwise and the reaction mixture was stirred until consumption of the starting material was observed (TLC). The reaction mixture was dried in vacuo, triturated with CH_2Cl_2 (3 × 15 mL) and finally dried under high vacuum. The final product was isolated by column chromatography on silica gel (deactivated by 10% *w/w* of water, eluent CH_2Cl_2–CH_3OH, 10:1) to give **8** as a white crystalline compound (31 mg, 90%); mp > 200 °C (CH_2Cl_2–CH_3OH). $[\alpha]_D^{24}$ +36.8 (*c* 0.2, THF). R_f = 0.3 (CH_2Cl_2–CH_3OH 10:1). IR (KBr, cm^{-1}) *v*: 3459, 3287, 3214, 2991, 2923, 1750, 1709, 1670, 1628, 1595, 1466, 1436, 1384, 1342, 1264, 1227, 1196, 1090, 1070, 1034. ^{1}H NMR (DMSO-d_6, 600 MHz) δ: 13.26 (s, 1H), 7.40 (s, 1H), 6.59 (s, 1H), 6.08 (s, 1H), 6.06 (s, 1H), 5.17 (m, 1H), 5.10–5.09 (m, 2H), 4.40 (m, 1H), 4.16 (dd, J = 10.9, 3.5 Hz, 1H), 4.11 (s, 1H), 3.84 (m, 1H), 3.71 (m, 1H), 3.52 (dd, J = 13.6, 9.8 Hz, 1 H), 3.26 (m, 1H), 2.66 (m, 1H), 2.03 (s, 3H). ^{13}C NMR (DMSO-d_6, 150 MHz) δ: 171.0, 169.9, 152.8, 146.3, 135.7, 132.5, 107.5, 102.4, 97.8, 73.1, 71.2, 68.9, 61.8, 51.6, 40.5, 36.5, 21.3. MS (+EI) *m/z* (%): 381 ([M]$^+$, 12), 321 (16), 279 (12), 277 (99), 276 (11), 256 (12), 247 (11), 205 (13), 201 (16), 199 (12), 185 (13), 183 (11), 179 (21), 167 (14), 149 (37), 129 (12), 123 (11), 69 (100). HR-MS (+EI) calcd for $C_{17}H_{19}NO_9$: 381.1060; found: 381.1055.

(1*S*,2*S*,3*R*,4*S*,4a*R*,11b*R*)-2,3,4,7-Tetrahydroxy-1-(hydroxymethyl)-1,3,4,4a,5,11b-hexahydro[1,3]dioxolo[4,5-*j*]phenanthridin-6(2*H*)-one (7)

Compound **26** (48 mg, 0.11 mmol) was taken up in a CH_2Cl_2–CH_3OH mixture (1:1, 4 mL) and two drops of concentrated HCl were added. The reaction was stirred until total consumption of the starting material was observed (TLC). The reaction mixture was neutralized by the dropwise addition of a saturated solution of $NaHCO_3$ and evaporated to dryness. The final product was isolated by column chromatography on silica gel (deactivated by 10% *w/w* of water, eluent CH_2Cl_2–CH_3OH, 5:1) to give **7** as a white crystalline compound (36 mg, 92%); mp > 200 °C (CH_2Cl_2–CH_3OH).

Can. J. Chem. Downloaded from www.nrcresearchpress.com by MCGILL UNIVERSITY on 02/02/13
For personal use only.

$[\alpha]_D^{20}$ +48.0 (*c* 0.5, abs DMSO). R_f = 0.4 (CH_2Cl_2–CH_3OH 5:1). IR (KBr, cm^{-1}) ν: 3386, 2917, 1670, 1638, 1598, 1466, 1439, 1384, 1352, 1304, 1228, 1089, 1077, 1064, 1032. ^1H NMR (DMSO-d_6, 300 MHz) δ: 13.25 (s, 1H), 7.31 (s, 1H), 6.55 (s, 1H), 6.07 (s, 1H), 6.06 (s, 1H), 5.02 (m, 3H), 4.47 (dd, *J* = 6.4, 4.0 Hz, 1H), 4.18 (m, 1H), 3.91 (m, 1H), 3.82 (m, 1H), 3.67 (m, 1H), 3.43 (m, 1H), 3.14 (m, 1H), 2.37 (br. s, 1H). ^{13}C NMR (DMSO-d_6, 150 MHz) δ: 169.9, 152.8, 146.1, 136.7, 132.2, 107.4, 102.4, 97.9, 73.2, 71.4, 69.5, 57.7, 51.8, 44.3, 36.9. MS (+EI) *m*/*z* (%): 339 $[M]^+$: (0.4), 85 (39), 84 (80), 83 (57), 68 (13), 66 (100). HR-MS (+EI) calcd for $C_{15}H_{17}NO_8$: 339.0954; found: 339.0925.

(3a*S*,3b*R*,10b*R*,11*S*,12*S*,12a*S*)-12-{[*Tert*-butyl(dimethyl) silyl]oxy}-11-(hydroxymethyl)-6-methoxy-2,2-dimethyl-3b,4,10b,11,12,12a-hexahydrobis[1,3]dioxolo[4,5-*c*:4′,5′-*j*] phenanthridin-5(3a*H*)-one (24)

To a solution of **23** (170 mg, 0.309 mmol) in methanol (5 mL) was added NaOH (aq 40%, 0.5 mL) and stirred until total consumption of the starting material was observed (TLC). The reaction was quenched with a saturated solution of NH_4Cl (1 mL). The mixture was evaporated and the residue was extracted with CH_2Cl_2 (6 × 15 mL). The combined organic phases were dried over Na_2SO_4, filtered, and concentrated. The final product was isolated by column chromatography (gradient hexanes / EtOAc, 2:1 to 1:1) to give **24** as a white crystalline solid (125 mg; 80%); mp 148–149 °C ($CHCl_3$). $[\alpha]_D^{20}$ +32.6 (*c* 0.63, $CHCl_3$). R_f = 0.2 (hexanes/EtOAc, 1:1). IR (KBr, cm^{-1}) ν: 3416, 2987, 2952, 2932, 2893, 2857, 1660, 1618, 1501, 1481, 1439, 1384, 1350, 1295, 1250, 1220, 1169, 1083, 1056, 841. ^1H NMR ($CDCl_3$, 600 MHz) δ: 6.61 (s, 1H), 6.05 (s, 1H), 6.00 (s, 1H), 5.86 (s, 1H), 4.68(s, 1H), 4.20 (d, *J* = 4.5 Hz, 1H), 4.14 (dd, *J* = 8.2, 5.0 Hz, 1H), 4.08 (s, 3H), 3.95 (dt, *J* = 10.1, 6.0 Hz, 1H), 3.67–3.66 (m, 1H), 3.49 (dd, *J* = 13.8, 8.4 Hz, 1H), 3.28 (dd, *J* = 13.8, 3.7 Hz, 1H), 2.53–2.52 (m, 1H), 1.91 (s, 1H), 1.46 (s, 3H), 1.40 (s, 3H), 0.91 (s, 9H), 0.18 (s, 6H). ^{13}C NMR ($CDCl_3$, 150 MHz) δ: 163.6, 152.2, 145.4, 137.3, 136.3, 116.3, 101.7, 99.8, 78.3, 78.0, 67.4, 60.9, 58.8, 52.7, 45.2, 35.3, 28.1, 26.2, 25.7, 17.9, –4.92, –4.94. MS (+FAB) *m*/*z* (%): 508 ([M + 1], 14), 507 ([M^+], 37), 450 (16), 449 (10), 434 (17), 433 (16), 392 (22), 374 (12), 345 (12), 261 (100). HR-MS (+FAB) calcd for $C_{25}H_{37}NO_8Si$ $[M]^+$: 507.2289; found: 507.2287.

((3a*S*,3b*R*,10b*R*,11*S*,12*S*,12a*S*)-12-{[*Tert*-butyl(dimethyl) silyl]oxy}-6-methoxy-2,2-dimethyl-5-oxo-3a,3b,4,5,10b,11,12,12a-octahydrobis[1,3]dioxolo[4,5-*c*:4′,5′-*j*]phenanthridin-11-yl)methyl benzoate (27)

To a solution of **24** (121 mg, 0.24 mmol) in CH_2Cl_2 (25 mL) was added triethylamine (0.04 mL, 0.48 mmol) at 0 °C followed by benzoyl chloride (0.03 mL, 0.26 mmol) and crystals of 4-dimethylaminopyridine (DMAP). The reaction mixture was stirred at 0 °C until total consumption of the starting material was observed (TLC). The reaction mixture was quenched with distilled water (10 mL) and extracted with CH_2Cl_2 (3 × 15 mL). The combined organic phases were washed with a solution of citric acid (10%, 10 mL), dried over sodium sulfate, filtered, and concentrated. The final product was isolated by column chromatography (gradient hexanes/EtOAc 2:1 to 1:1) to give **27** as a white crystalline powder (94 mg, 64%); mp 90–92 °C ($CHCl_3$). $[\alpha]_D^{20}$ –15.1 (*c* 1, $CHCl_3$). R_f = 0.4 (hexanes/EtOAc, 1:1). IR (KBr, cm^{-1}) ν: 3467, 3416, 3387, 3069, 2986, 2952, 2932, 2896, 2857, 1722, 1674, 1616, 1502, 1481, 1453, 1385, 1339, 1273, 1221, 1093, 1071, 1028, 838. ^1H NMR ($CDCl_3$, 300 MHz) δ: 8.06 (d, *J* = 7.2 Hz, 2H), 7.63–7.58 (m, 1H), 7.48 (t, *J* = 7.5 Hz, 2H), 6.74 (s, 1H), 6.01–6.02 (m, 3H), 4.68 (s, 1H), 4.53–4.45 (m, 2H), 4.20–4.16 (m, 2H), 4.07 (s, 3H), 3.53 (dd, *J* = 13.8, 7.5 Hz, 1H), 3.40–3.35 (m, 1H), 2.86–2.83 (m, 1H), 1.50 (s, 3H), 1.40 (s, 3H), 0.90 (s, 9H), 0.18 (s, 6H). ^{13}C NMR ($CDCl_3$, 75 MHz) δ: 166.4, 163.6, 152.4, 145.4, 135.6, 133.2, 129.8, 129.6, 128.4, 116.1, 110.0, 101.7, 99.9, 78.3, 77.9, 67.2, 61.6, 60.9, 52.5, 42.1, 35.2, 28.2, 26.1, 25.6, 17.9, –4.9, –5.0. MS (+FAB) *m*/*z* (%): 614 ([M + 2]$^+$, 12), 613 (36), 612 (89), 179 (12), 105 (100). HR-MS calcd for $C_{32}H_{42}NO_9Si^+$ $[M]^+$: 612.2251; found: 612.2653.

((3a*S*,3b*R*,10b*R*,11*S*,12*S*,12a*S*)-12-{[*Tert*-butyl(dimethyl) silyl]oxy}-6-hydroxy-2,2-dimethyl-5-oxo-3a,3b,4,5,10b,11,12,12a-octahydrobis[1,3]dioxolo[4,5-*c*:4′,5′-*j*]phenanthridin-11-yl)methyl benzoate (28)

To a solution of **27** (74.3 mg, 0.122 mmol) in dry DMF (5 mL) was added LiCl (50 mg, 1.2 mmol) followed by three cycles of freeze–pump–thaw. The reaction mixture was heated to 120 °C for 3.5 h. The reaction was then cooled to room temperature, diluted with distilled water (50 mL), and extracted with diethyl ether (6 × 15 mL). The combined organic phases were dried over Na_2SO_4, filtered, and concentrated. The product was isolated by column chromatography (hexanes/EtOAc, 2:1) to give **28** as a white crystalline solid (60 mg, 83%); mp 141–145 °C ($CHCl_3$). R_f = 0.8 (hexanes/EtOAc, 1:1). $[\alpha]_D^{20}$ –63.0 (*c* 1.0, $CHCl_3$). IR (KBr, cm^{-1}) ν: 3449, 2953, 2931, 2901, 2858, 1721, 1674, 1655, 1637, 1627, 1603, 1461, 1385, 1351, 1341, 1304, 1271, 1219, 1113, 1081, 837. ^1H NMR ($CDCl_3$, 600 MHz) δ: 12.70 (s, 1H), 8.07 (d, *J* = 8.0 Hz, 2H), 7.62–7.60 (m, 1H), 7.49–7.47 (m, 2H), 6.59 (s, 1H), 6.11 (s, 1H), 6.06 (s, 1H), 6.02 (s, 1H), 4.68 (s, 1H), 4.55–4.54 (m, 2H), 4.23–4.21 (m, 2H), 3.63–3.59 (m, 1H), 3.43 (dd, *J* = 14.4, 3.5 Hz, 1H), 2.89 (s br, 1H), 1.53 (s, 3H), 1.42 (s, 3H), 0.91 (s, 9H), 0.16–0.15 (m, 6H). ^{13}C NMR ($CDCl_3$, 150 MHz) δ: 170.0, 166.4, 153.2, 146.9, 134.0, 133.2, 133.1, 129.8, 129.6, 129.4, 110.1, 107.3, 102.3, 97.3, 78.4, 77.7, 67.2, 61.6, 53.2, 41.8, 34.0, 30.3, 28.4, 26.1, 25.7, 17.9, –4.9, –5.0. MS (+FAB) *m*/*z* (%): 599 ([M + 2]$^+$, 11), 598 (29), 597 (8), 596 (4), 179 (11), 73 (100). HR-MS (+FAB) calcd for $C_{31}H_{40}N_1O_9Si^+$ [M + 1]$^+$: 598.2472; found: 598.2446.

[(3a*S*,3b*R*,10b*R*,11*S*,12*S*,12a*R*)-6,12-Dihydroxy-2,2-dimethyl-5-oxo-3a,3b,4,5,10b,11,12,12a-octahydrobis[1,3] dioxolo[4,5-*c*:4′,5′-*j*]phenanthridin-11-yl]methyl benzoate (29)

Compound **28** (42 mg, 0.07 mmol) was dissolved in THF (2.5 mL) and cooled to 0 °C. A 1 mol/L solution of TBAF in THF (0.077 mL, 0.077 mmol) was added dropwise and the reaction mixture was stirred until total consumption of the starting material was observed (TLC). The reaction mixture was quenched by distilled water (5 mL) and extracted with CH_2Cl_2 (6 × 15 mL). The combined organic phases were dried over Na_2SO_4, filtered, and evaporated. The final product was isolated by column chromatography (hexanes/EtOAc,

Can. J. Chem. Downloaded from www.nrcresearchpress.com by MCGILL UNIVERSITY on 02/02/13
For personal use only.

1:1) to give **29** as a white crystalline solid (27.2 mg, 80%); mp > 200 °C (THF). $[\alpha]_D^{21}$ –40.1 (*c* 1.0, THF). R_f = 0.3 (hexanes/EtOAc, 1:1). IR (KBr, cm^{-1}) *v*: 3446, 3255, 2986, 2930, 2905, 2854, 1720, 1672, 1626, 1601, 1466, 1384, 1356, 1343, 1311, 1222, 1166, 1088, 1071, 1027, 713. ^1H NMR (DMSO-d_6, 600 MHz) δ: 13.36 (s, 1H), 8.57 (s, 1H), 7.97–7.96 (m, 2H), 7.69–7.67 (m, 1H), 7.56–7.53 (m, 2H), 6.74 (s, 1H), 6.07 (s, 1H), 5.99 (s, 1H), 5.56 (dd, *J* = 4.3 Hz, 1H), 4.53 (dd, *J* = 11.3, 4.3 Hz, 1H), 4.46–4.45 (m, 1H), 4.43–4.39 (m, 1H), 4.29 (d, *J* = 5.0 Hz, 1H), 4.19 (dd, *J* = 8.3, 5.3 Hz, 1H), 3.63 (dd, *J* = 14.4, 8.4 Hz, 1H), 3.26 (dd, *J* = 14.4, 3.6 Hz, 1H), 2.97–2.95 (m, 1H), 1.45 (s, 3H), 1.33 (s, 3H). ^{13}C NMR (DMSO-d_6, 150 MHz) δ: 169.9, 166.1, 152.7, 146.3, 135.0, 133.9, 132.5, 130.0, 129.7, 129.2, 109.0, 107.7, 102.3, 97.9, 78.0, 77.1, 65.5, 62.0, 53.4, 34.3, 30.3, 28.3, 26.4. MS (+FAB) *m*/*z* (%): 484 ([M + 1]$^+$, 4), 483 ([M]$^+$, 26), 248 (13), 247 (59), 232 (13), 231 (28), 205 (11), 122 (16), 105 (100). HR-MS (+FAB) calcd for $C_{25}H_{25}NO_9$ [M]$^+$: 483.1529; found: 483.1532.

[(1*S*,2*S*,3*R*,4*S*,4a*R*,11b*R*)-2,3,4,7-Tetrahydroxy-6-oxo-1,2,3,4,4a,5,6,11b-octahydro[1,3]dioxolo[4,5-*j*] phenanthridin-1-yl]methyl benzoate (9)

Compound **29** (32 mg, 0.066 mmol) was dissolved in a mixture of CH_2Cl_2–CH_3OH (1:1, 4 mL) and cooled to 0 °C. Trifluoroacetic acid (1 mL) was added dropwise and the reaction was stirred until total consumption of the starting material was observed (TLC). The reaction mixture was dried in vacuo, triturated with CH_2Cl_2 (3 × 15 mL), and finally dried under high vacuum. The final product was isolated by column chromatography on silica gel (deactivated by 10% *w*/*w* of water, gradient CH_2Cl_2–CH_2Cl_2/CH_3OH (50:1) to CH_2Cl_2/CH_3OH (25:1)) to give **9** as a white crystalline compound (25 mg, 85%); mp > 200 °C (CH_2Cl_2). R_f = 0.6 (CH_2Cl_2/CH_3OH 10:1). $[\alpha]_D^{20}$ –24.9 (*c* 1, THF). IR (KBr, cm^{-1}) *v*: 3423, 3386, 2956, 2921, 2852, 1716, 1672, 1627, 1600, 1466, 1384, 1363, 1340, 1278, 1095, 1072, 1038, 711. ^1H NMR (DMSO-d_6, 600 MHz) δ: 13.27 (s, 1H), 8.00 (d, *J* = 7.7 Hz, 2H), 7.68 (t, *J* = 7.6 Hz, 1H), 7.57–7.54 (m, 2H), 7.43 (s, 1H), 6.72 (s, 1H), 6.07 (s, 1H), 6.01 (s, 1H), 5.19 (m, 2H), 5.13 (m, 1H), 4.66 (t, *J* = 10.7 Hz, 1H), 4.48 (dd, *J* = 10.9, 4.0 Hz, 1H), 4.24–4.23 (m, 1H), 3.88–3.87 (m, 1H), 3.75–3.73 (m, 1H), 3.62 (dd, *J* = 13.6, 9.9 Hz, 1H), 3.31 (dd, *J* = 13.8, 4.2 Hz, 1H), 2.85–2.84 (m, 1H). ^{13}C NMR (DMSO-d_6, 150 MHz) δ: 170.0, 166.3, 152.8, 146.3, 135.8, 133.8, 132.5, 130.3, 129.7, 129.2, 107.5, 102.4, 98.0, 73.1, 71.2, 69.2, 62.5, 51.6, 36.6. MS (+FAB) *m*/*z* (%): 444 ([M + 1]$^+$, 4), 219 (12), 136 (11), 121 (11), 109 (15), 107 (17), 105 (23), 97 (18), 95 (29), 55 (100). HR-MS (+FAB) calcd for $C_{22}H_{22}NO_9$ [M + 1]$^+$: 444.1295; found: 444.1262.

Cell culture

The human non-small cell lung cancer line, NCI-H460 (American Type Culture Collection (ATCC) No. HTB-177), and human pancreatic adenocarcinoma cancer cell line, BxPC-3 (ATCC No. CRL-1687,) were cultured in RPMI-1640 medium supplemented with 10% fetal bovine serum (FBS) (GIBCO BRL Carlsbad, California), 100 mg/L penicillin G, and 100 mg/L streptomycin (Cellgro, Manassas, Virginia). Human prostate carcinoma cells, DU-145 (ATCC No. HTB-81), were cultured in Dulbecco's modified Eagle's medium (Cellgro) supplemented with 10% FBS, 100 mg/L penicillin G, and 100 mg/L streptomycin. Human mammary carcinoma cells, MCF-7 (ATCC No. HTB-22), were cultured using Dulbecco's modified Eagle's medium supplemented with 10% FBS, 100 mg/L penicillin G, 100 mg/L streptomycin, 1.0 mmol/L GlutaMAX, and 1.0 mmol/L sodium pyruvate (Gibco).

MTT assay

To evaluate the cytotoxic effects of the C-1 homologues of pancratistatin, mitochondrial dehydrogenase activities were measured. Briefly, BxPC-3, NCI-H460, DU-145, and MCF-7 lines were assessed by seeding 4×10^3 cells/well into microplates. The cells were grown for 24 h before treatment at concentrations ranging from 0.001 to 10 μmol/L and incubated for 48 h. MTT reagent (5 mg/mL, MP Biomedical, Solon, Ohio) was added to each well and incubated further for 2 h. The resulting formazan crystals were dissolved in DMSO and the optical density (OD) was determined at a wavelength of 490 nm. The experiments were repeated at least twice for each compound per cell line. Cells treated with 0.1% DMSO and narciclasine were used as negative and positive controls, respectively.

Cell culture

The human colorectal cancer cell line HCT 116 (ATCC, Cat. No. CCL-247, Manassas, Virginia) was grown and cultured with McCoy's mMedium 5a (Gibco BRL, VWR, Mississauga, Ontario) supplemented with 2 mmol/L L-glutamine, 10% FBS, and 10 mg/mL gentamicin (Gibco BRL, VWR). A human osterosarcoma cell line, Saos-2 (ATCC, Cat. No. HTB-85, Manassas, Virginia), was grown in McCoy's 5A mMedium Modified (Sigma-Aldrich Canada, Mississauga, Ontario) supplemented with 15% (*v*/*v*) FBS (Thermo Scientific, Waltham, Massachusetts) and 10 mg/mL gentamicin (Gibco BRL, VWR). All cells were grown at 37 °C and 5% CO_2.

WST-1 assay for cell viability

The WST-1-based colorimetric assay was conducted as per the manufacturer's protocol (Roche Applied Science, Indianapolis, Indiana) to determine cell viability as a function of active cell metabolism. Ninty-six well, clear bottom tissue culture plates were seeded with approximately 2.0×10^3 HCT 116 cells/well or 6.0×10^3 Saos-2 cells/well, and treated with various compounds at the indicated concentrations and durations. Following treatment, the WST-1 reagent was added to each well and incubated for 4 h at 37 °C. Absorbance readings were taken at 450 nm on a Wallac Victor^3 1420 multilabel counter (PerkinElmer, Woodbridge, Ontario) and were expressed as percentages of the solvent control group (Me_2SO).

Supplementary data

Supplementary data (copies of ^1H and ^{13}C NMR spectra for compounds **7**–**9**, **12**, **13**, and **15**–**29**) are available with the article through the journal Web site at http://nrcresearchpress.com/doi/suppl/10.1139/v2012-073.

Can. J. Chem. Downloaded from www.nrcresearchpress.com by MCGILL UNIVERSITY on 02/02/13
For personal use only.

Acknowledgements

The authors are grateful to the following agencies for financial support of this work: Natural Sciences and Engineering Research Council of Canada (NSERC) (Idea to Innovation and Discovery Grants), Canada Research Chair Program, Canada Foundation for Innovation (CFI), TDC Research, Inc., TDC Research Foundation, and Brock University. A.E.R. and A.K. are thankful for the support of the National Center for Research Resources (5P20RR016480-12) and the National Institute of General Medical Sciences (8 P20 GM103451-12). S.P. thanks the Knights of Columbus Chapter 9671 (Windsor, Ontario). The Canadian Institutes of Health Research (CIHR) Canada Graduate Scholarship awarded to D.M. is gratefully acknowledged.

References

(1) Pettit, G. R.; Gaddamidi, V.; Cragg, G. M.; Herald, D. L.; Sagawa, Y. *J. Chem. Soc. Chem. Commun.* **1984**, (24): 1693. doi:10.1039/c39840001693.

(2) (a) For reviews see Kornienko, A.; Evidente, A. *Chem. Rev.* **2008**, *108* (6), 1982. doi:10.1021/cr078198u; (b) Manpadi, M.; Kornienko, A. *Org. Prep. Proced. Int.* **2008**, *40* (2), 107. doi:10.1080/00304940809458083; (c) Chapleur, Y.; Chrétien, F.; Ahmed, S. I.; Khaldi, M. *Curr. Org. Synth.* **2006**, *3* (3), 341. doi:10.2174/157017906777934872; (d) Rinner, U.; Hudlicky, T. *Synlett* **2005**, 365; (e) Bridges, A. *Chemtracts: Organic Chemistry* **1996**, *9*, 101.

(3) (a) For a recent compilation of total syntheses of Amaryllidaceae constituents see Collins, J.; Rinner, U.; Moser, M.; Hudlicky, T.; Ghiviriga, I.; Romero, A. E.; Kornienko, A.; Ma, D.; Griffin, C.; Pandey, S. *J. Org. Chem.* **2010**, *75* (9), 3069. doi:10.1021/jo1003136; (b) For syntheses published after 2009 see Yadav, J. S.; Satheesh, G.; Murthy, C. V. S. R. *Org. Lett.* **2010**, *12* (11), 2544. doi:10.1021/ol100755v; (c) Dam, J. H.; Madsen, R. *Eur. J. Org. Chem.* **2009**, *2009* (27), 4666. doi:10.1002/ejoc.200900719.

(4) (a) Pettit, G. R.; Melody, N.; O'Sullivan, M.; Thompson, M. A.; Herald, D. L.; Coates, B. *J. Chem. Soc. Chem. Commun.* **1994**, 2725. doi:10.1039/c39940002725; (b) Pettit, G. R.; Freeman, S.; Simpson, M. J.; Thompson, M. A.; Boyd, M. R.; Williams, M. D.; Pettit, G. R., III; Doubek, D. L. *Anticancer Drug Des.* **1995**, *10*, 243; (c) Pettit, G. R.; Melody, N.; Herald, D. L. *J. Org. Chem.* **2001**, *66* (8), 2583. doi:10.1021/jo000710n; (d) Pettit, G. R.; Melody, N.; Herald, D. L.; Knight, J. C.; Chapuis, J.-C. *J. Nat. Prod.* **2007**, *70* (3), 417. doi:10.1021/np068046e; (e) Pettit, G. R.; Ducki, S.; Eastham, S. A.; Melody, N. *J. Nat. Prod.* **2009**, *72* (7), 1279. doi:10.1021/np9001948; (f) Pettit, G. R.; Tan, R.; Bao, G.-H.; Melody, N.; Doubek, D. L.; Gao, S.; Chapuis, J.-C.; Williams, L. *J. Nat. Prod.* **2012**, *75* (4), 771. doi:10.1021/np200862y.

(5) (a) McNulty, J.; Mao, J.; Gibe, R.; Mo, R.; Wolf, S.; Pettit, G. R.; Herald, D. L.; Boyd, M. R. *Bioorg. Med. Chem. Lett.* **2001**, *11* (2), 169. doi:10.1016/S0960-894X(00)00614-4; (b) McNulty, J.; Larichev, V.; Pandey, S. *Bioorg. Med. Chem. Lett.* **2005**, *15* (23), 5315. doi:10.1016/j.bmcl.2005.08.024; (c) McNulty, J.; Nair, J. J.; Griffin, C.; Pandey, S. *J. Nat. Prod.* **2008**, *71* (3), 357. doi:10.1021/np0705460; (d) McNulty, J.; Nair, J. J.; Little, J. R. L.; Brennan, J. D.; Bastida, J. *Bioorg. Med. Chem. Lett.* **2010**, *20* (17), 5290. doi:10.1016/j.bmcl.2010.06.130; (e) McNulty, J.; Nair, J. J.; Singh, M.; Crankshaw, D. J.; Holloway, A. C. *Bioorg. Med. Chem. Lett.* **2010**, *20* (7), 2335. doi:10.1016/j.bmcl.2010.01.157.

(6) (a) Manpadi, M.; Kireev, A. S.; Magedov, I. V.; Altig, J.; Tongwa, P.; Antipin, M. Y.; Evidente, A.; van Otterlo, W. A. L.; Kornienko, A. *J. Org. Chem.* **2009**, *74* (18), 7122. doi:10.1021/jo901494r; (b) Kireev, A. S.; Nadein, O. N.; Agustin, V. J.; Bush, N. E.; Evidente, A.; Manpadi, M.; Ogasawara, M. A.; Rastogi, S. K.; Rogelj, S.; Shors, S. T.; Kornienko, A. *J. Org. Chem.* **2006**, *71* (15), 5694. doi:10.1021/jo0607562.

(7) Ibn-Ahmed, S.; Khaldi, M.; Chrétien, F.; Chapleur, Y. *J. Org. Chem.* **2004**, *69* (20), 6722. doi:10.1021/jo049153l.

(8) (a) Oritz, J. C.; Ozores, L.; Cagide-Fagin, F.; Alonso, R. *Chem. Commun. (Camb.)* **2006**, 4239. doi:10.1039/B606277F; (b) Nieto-García, O.; Lago-Santomé, H.; Cagide-Fagín, F.; Ortiz-Lara, J. C.; Alonso, R. *Org. Biomol. Chem.* **2012**, *10* (4), 825. doi:10.1039/c1ob06374j.

(9) Marion F.; Annereau, J.-P.; Fahy, J. WO 2010012714 (A1), 4 February 2010.

(10) (a) Banwell, M. G.; Cowden, C. J.; Gable, R. W. *J. Chem. Soc., Perkin Trans. 1* **1994**, (24): 3515. doi:10.1039/p19940003515; (b) Matveenko, M.; Banwell, M. G.; Joffe, M.; Wan, S.; Fantino, E. *Chem. Biodivers.* **2009**, *6* (5), 685. doi:10.1002/cbdv.200800319.

(11) de la Sovera, V.; Bellomo, A.; Gonzalez, D. *Tetrahedron Lett.* **2011**, *52* (3), 430. doi:10.1016/j.tetlet.2010.11.084.

(12) (a) Rinner, U.; Siengalewicz, P.; Hudlicky, T. *Org. Lett.* **2002**, *4* (1), 115. doi:10.1021/ol0169877; (b) Hudlicky, T.; Rinner, U.; Gonzalez, D.; Akgun, H.; Schilling, S.; Siengalewicz, P.; Martinot, T. A.; Pettit, G. R. *J. Org. Chem.* **2002**, *67* (25), 8726. doi:10.1021/jo020129m; (c) Rinner, U.; Hillebrenner, H. L.; Adams, D. R.; Hudlicky, T.; Pettit, G. R. *Bioorg. Med. Chem. Lett.* **2004**, *14* (11), 2911. doi:10.1016/j.bmcl.2004.03.032.

(13) (a) Moser, M.; Sun, X.; Hudlicky, T. *Org. Lett.* **2005**, *7* (25), 5669. doi:10.1021/ol052372o; (b) Hudlicky, T.; Moser, M.; Banfield, S. C.; Rinner, U.; Chapuis, J.-C.; Pettit, G. R. *Can. J. Chem.* **2006**, *84* (10), 1313. doi:10.1139/v06-078.

(14) (a) Rinner, U.; Hudlicky, T.; Gordon, H.; Pettit, G. R. *Angew. Chem. Int. Ed.* **2004**, *43* (40), 5342. doi:10.1002/anie.200460218; (b) Hudlicky, T.; Rinner, U.; Finn, K. J.; Ghiviriga, I. *J. Org. Chem.* **2005**, *70* (9), 3490. doi:10.1021/jo040292c.

(15) Vshyvenko, S.; Scattolon, J.; Hudlicky, T.; Romero, A. E.; Kornienko, A. *Bioorg. Med. Chem. Lett.* **2011**, *21* (16), 4750. doi:10.1016/j.bmcl.2011.06.068.

(16) Collins, J.; Drouin, M.; Sun, X.; Rinner, U.; Hudlicky, T. *Org. Lett.* **2008**, *10* (3), 361. doi:10.1021/ol702440f.

(17) Garcia, A.; Castedo, L.; Domínguez, D. *Tetrahedron* **1995**, *51* (31), 8585. doi:10.1016/0040-4020(95)00473-L.

(18) Loriot, M.; Robin, J.-P.; Brown, E. *Tetrahedron* **1984**, *40* (13), 2529. doi:10.1016/S0040-4020(01)83505-5.

(19) Schilling, S.; Rinner, U.; Chan, C.; Ghiviriga, I.; Hudlicky, T. *Can. J. Chem.* **2001**, *79* (11), 1659. doi:10.1139/v01-139.

(20) Trost, B. M.; Pulley, S. R. *J. Am. Chem. Soc.* **1995**, *117* (40), 10143. doi:10.1021/ja00145a038.

(21) (a) Jana, C. K.; Studer, A. *Chemistry* **2008**, *14* (21), 6326. doi:10.1002/chem.200800903; (b) Cho, Y.-S.; Cho, C.-G. *Tetrahedron* **2008**, *64* (9), 2172. doi:10.1016/j.tet.2007.12.031.

(22) Werner, L.; Machara, A.; Adams, D. R.; Cox, D. P.; Hudlicky, T. *J. Org. Chem.* **2011**, *76* (11), 4628. doi:10.1021/jo200567n.

2-(Selenocyanatomethyl)-2-propenol — A convenient synthon for ligation via the deselenative allylic rearrangement of allyl selenosulfides: preparation, functional group compatibility, and application

David Lachkar, Caroline Boudet, Xavier Guinchard, and David Crich

Abstract: The preparation and reactions of 2-(selenocyanatomethyl)-2-propenol are described and reveal the compatibility of the allylic selenocyanate group with a range of mild oxidizing and Lewis acidic conditions. 2-(Selenocyanatomethyl)-2-propenol and its derivatives are employed in the functionalization of simple and amino acid derived thiols in methanolic solution at room temperature to give 2-(hydroxymethyl)allyl sulfides in good to excellent yield.

Key words: selenocyanates, selenosulfides, selenosulfoxides, ligation.

Résumé : Nous décrivons la préparation et les réactions de dérivatisation du 2-(sélénocyanatométhyl)-prop-2-énol, montrant ainsi la compatibilité fonctionnelle du groupement sélénocyanate allylique envers les réactions en conditions oxydantes et en présence d'acides de Lewis. Cet alcool et ses dérivés fonctionnalisés ont été engagés dans des réactions de fonctionnalisation de thiols à température ambiante dans des conditions douces pour conduire à des sulfures de 2-(hydroxyméthyl)allyle avec de bons rendements.

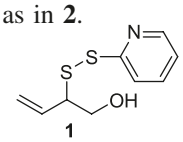
Mots-clés : sélénocyanates, sélénosulfures, sélénosulfoxydes, ligature.

Can. J. Chem. Downloaded from www.nrcresearchpress.com by MCGILL UNIVERSITY on 02/02/13
For personal use only.

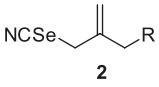
Introduction

Organoselenium chemistry is a major component of the organic chemist's toolbox,[1] and the organoselenocyanates are some of the most readily available and versatile of the chalcogenide-based reagents. For our part, we have developed the use of allylic seleno Bunte salts and allylic selenocyanates as convenient precursors to the allyl selenosulfides, substrates for dechalcogenative rearrangement to allyl alkyl sulfides (Scheme 1),[2] and as our contribution to the burgeoning field[3] of chemical ligation. In continuation of this program we required a minimal hydroxyl-substituted allylic selenocyanate to serve as a handle for introduction of the allylic selenocyanate group into a range substrates. We report here on the synthesis of 2-(selenocyanatomethyl)allyl alcohol for this purpose, on functional group compatibility of the selenocyanate moiety, and on its incorporation into various substrates.

In earlier work on the desulfurative allylic rearrangement of allyl alkyl disulfides, we developed 2-(2-pyridyldithio)-3-propenol (**1**) or its analogs as precursors to the necessary allyl alkyl disulfides,[2b,4] but were foiled in many of our attempts to derivatize the hydroxyl group by the relative sensitivity of the allylic disulfide functionality.[5] For this reason, we turned to the allylic selenocyanates[6] with the expectation of greater stability to a number of derivatization reactions.[2b] To avoid possible problems arising from facile 1,3-sigmatropic rearrangement of disymmetric allylic selenocyanates, we targeted systems in which such rearrangements would have a degenerate nature, namely, those based on methallyl selenocyanate substituted at the 2 postion as in **2**.



1



2

We focused on 2-(selenocyanatomethyl)-3-propenol (**6**), as the smallest possible alcohol derived from methallyl selenocyanate. To this end, *p*-methoxybenzyl alcohol was alkylated with methallyl chloride to give the ether[7] **3**, which was converted with sulfuryl chloride into the known[8] methallyl chloride **4** in 29% yield (Scheme 2). Reaction with potassium

Received 13 January 2012. Accepted 3 July 2012. Published at www.nrcresearchpress.com/cjc on 22 October 2012.

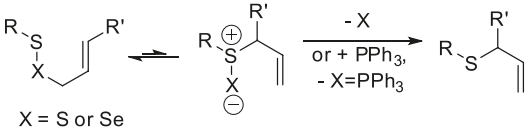
D. Lachkar, C. Boudet, and X. Guinchard. Centre de Recherche de Gif, Institut de Chimie des Substances Naturelles, CNRS, 1 Avenue de la Terrasse, 91190 Gif-sur-Yvette, France.
D. Crich. Centre de Recherche de Gif, Institut de Chimie des Substances Naturelles, CNRS, 1 Avenue de la Terrasse, 91190 Gif-sur-Yvette, France; Department of Chemistry, Wayne State University, 5101 Cass Avenue, Detroit, MI 48202, USA.

Corresponding author: David Crich (e-mail: dcrich@chem.wayne.edu).

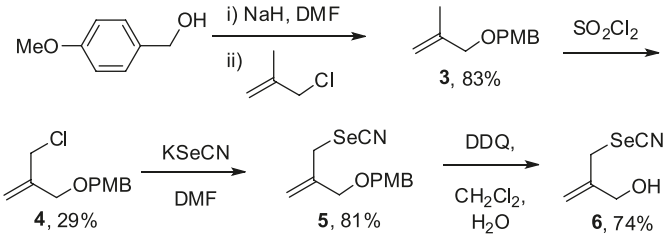
This article is part of a Special Issue dedicated to Professor Derrick Clive. We dedicate this paper to Professor Derrick L. J. Clive, a pioneer in the application of organoselenium chemistry to organic synthesis, and in honor of his many seminal contributions to organic chemistry.

Can. J. Chem. Downloaded from www.nrcresearchpress.com by MCGILL UNIVERSITY on 02/02/13
For personal use only.

Scheme 1. Dechalcogenative allylic selenosulfide and disulfide rearrangements.



Scheme 2. Preparation of 2-(selenocyanatomethyl)-3-propenol.



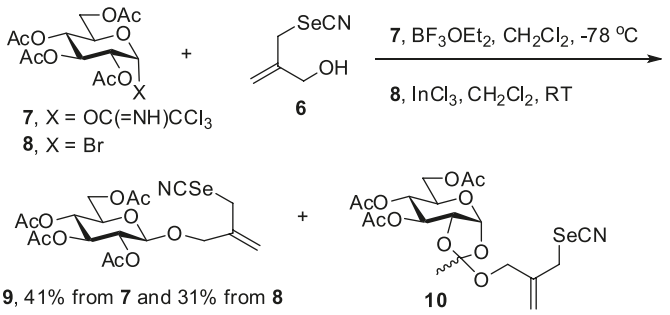
selenocyanate in DMF then afforded the selenocyanate **5** in 81% yield. Exposure to 2,3-dichloro-5,6-dicyano-1,4-benzoquinone (DDQ) in wet dichloromethane finally gave the desired alcohol **6** in 74% yield and demonstrated the stability of the allylic selenocyanate functionality to the mild oxidative conditions used for removal of the *p*-methoxybenzyl ether (Scheme 2).

With **6** in hand we turned to its application as a glycosyl acceptor. Activation of tetraacetyl-α-glucopyranosyl trichloroacetimidate[9] (**7**) in the presence of **6** with BF_3 etherate afforded the desired β-glycoside **9** in 41% yield (Scheme 3) typically accompanied by the orthoester products **10**. Orthoesters of this general type are typical byproducts in neighboring group participation directed glycosylation reactions and are particularly problematic when the acceptor is a primary alcohol.[10] When acetobromoglucose **8** was employed as donor and indium trichloride[11] as promotor the glycoside **9** was obtained in 31% yield, but attempts at activation of **8** with more typical silver-based reagents resulted only in the formation of decomposition products. While the yields from these glycosylations are only moderate, they are nevertheless instructive as they demonstrate the stability of the allylic selenocyanate functionality toward selected Lewis acidic conditions.

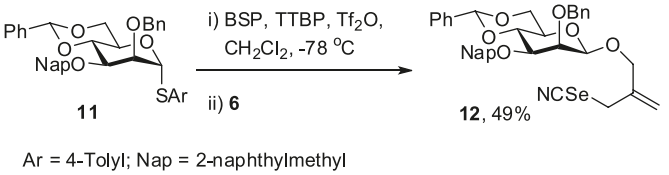
In a second glycosylation reaction, donor **11** was coupled to **6** using the 1-benzenesulfinylpiperidine (BSP) / trifluoromethanesulfonic anhydride conditions[12] in the presence of the hindered base 2,4,6-tri-*tert*-butylpyrimidine (TTBP)[13] (Scheme 4). Glycoside **12** was obtained as a single isomer in 49% yield.

Encouraged by these results, we investigated the compatibility of **6** with typical conditions for phosphitylation such as would be necessary for incorporation into nucleotides.[14] Thus, **6** was allowed to react with dibenzyl *N*,*N*-di(isopropyl)phosphoramidite in the presence of tetrazole as promoter, to give a presumed intermediate phosphite **13**, followed by exposure to *m*-CPBA as oxidant (Scheme 5). Unfortunately, complex reaction mixtures were obtained under all reaction conditions investigated from which the anticipated phosphate **14** could only be isolated in modest yield. A cyclic byproduct **16** was obtained in varying quantities from all reaction mixtures and affords a possible explanation for the complexity: Arbuzov-type reaction initiated by intramolecular attack of the first formed phosphite on the electron-deficient selenocyanate.

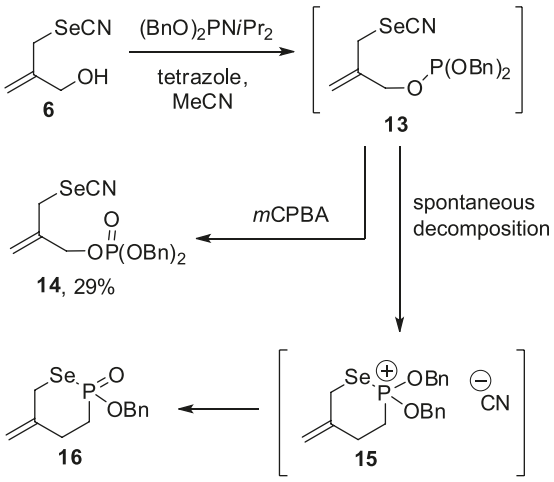
Scheme 3. Formation of 2-(selenocyanatomethyl)allyl tetraacetyl-α-D-glucopyranoside (**9**).



Scheme 4. Formation of 2-(selenocyanatomethyl)allyl β-D-mannopyranoside (**12**).



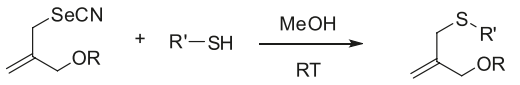
Scheme 5. Reaction of **6** with a phosphoramidite.

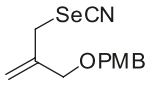
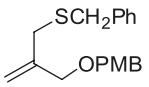
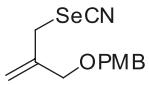
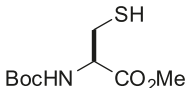
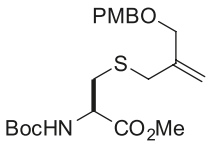
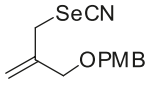
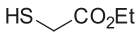
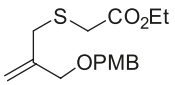
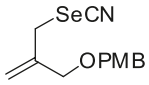
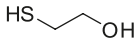
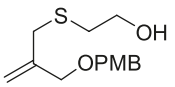
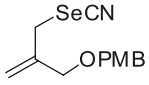
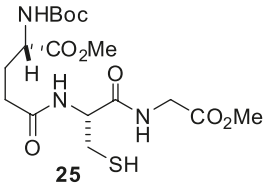
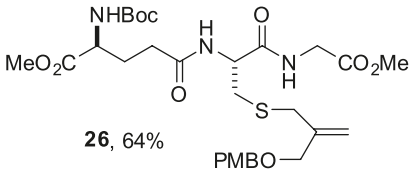
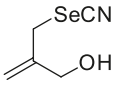
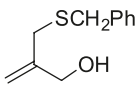
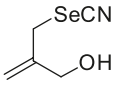
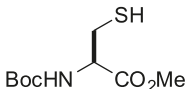
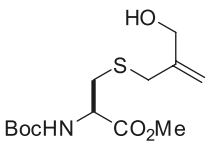
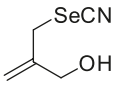
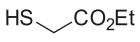
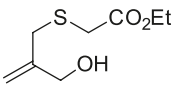
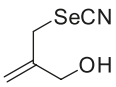
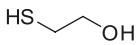
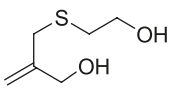


Finally, attention was turned to the ligation reaction. Thus, selenocyanates **5**, **6**, **9**, and **12** were allowed to react with a variety of aliphatic thiols in methanol at room temperature under an argon atmosphere. After stirring overnight, and filtration to remove precipitated selenium, chromatography on silica gel afforded the coupled products with the yields set out in Table 1.

In an attempt to probe the mechanism of the ligation reaction, we monitored the reaction of selenocyanate **6** with benzylmercaptan in deuteriomethanol at room temperature by ^1H and ^{77}Se NMR spectroscopy (Figs. 1 and 2). In the ^1H NMR spectrum a slight upfield shift of the signals attributed to **6** is observed on addition of the thiol, followed by the formation of a set of new signals assigned to the intermediate selenosulfide. This substance is then transformed rapidly and cleanly into the final product (**18**). The kinetics of the reaction are such

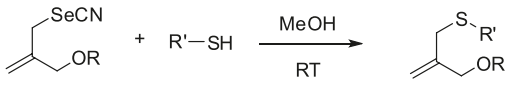
Table 1. Ligation of **6** and its derivatives with assorted thiols.

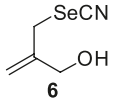
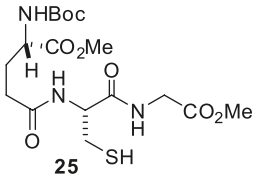
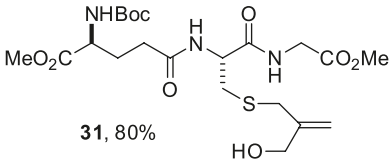
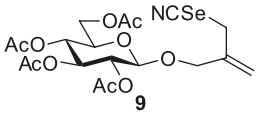
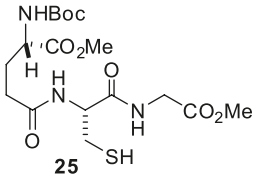
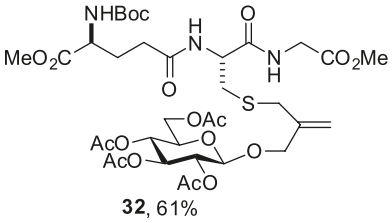
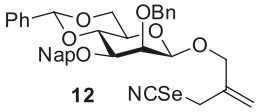
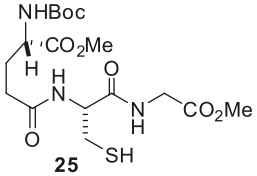
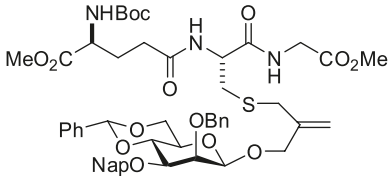
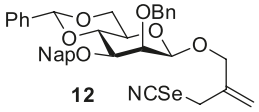
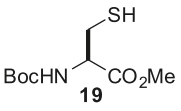
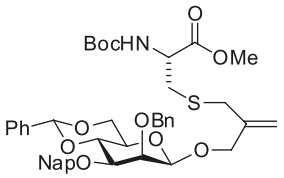


Entry	Substrate	Thiol	Product, yield
1	 **5**	$PhCH_2SH$ **17**	 **18**, 76%
2	 **5**	 **19**	 **20**, 83%
3	 **5**	 **21**	 **22**, 92%
4	 **5**	 **23**	 **24**, 57%
5	 **5**	 **25**	 **26**, 64%
6	 **6**	$PhCH_2SH$ **17**	 **27**, 86%
7	 **6**	 **19**	 **28**, 52%
8	 **6**	 **21**	 **29**, 57%
9	 **6**	 **23**	 **30**, 91%

Can. J. Chem. Downloaded from www.nrcresearchpress.com by MCGILL UNIVERSITY on 02/02/13
For personal use only.

Table 1 (*concluded*).



Entry	Substrate	Thiol	Product, yield
10	 **6**	 **25**	 **31**, 80%
11	 **9**	 **25**	 **32**, 61%
12	 **12**	 **25**	 **33**, 63%
13	 **12**	 **19**	 **34**, 57%

that the onset of the formation of **18** is seen before the complete conversion of **6** to the selenosulfide intermediate. A set of minor signals attributable neither to the selenosulfide nor to the final product, and which are lost by the end of the reaction, may represent the selenosulfoxide intermediate, a functional group that to date has not been described in the literature. To probe this possibility further, we turned to ^{77}Se NMR spectroscopy. The rapid transformation of **6** to the selenosulfide is clearly seen, with its disappearance later as the reaction proceeds to completion. A minor unidentified signal is formed over the course of the reaction at δ 500 but, as this signal persists at the end of the reaction, it cannot be the selenosulfoxide intermediate and must represent a minor selenium-containing byproduct. Unfortunately, selenosulfoxides, like their thiosulfoxide cousins,[2] must retain their status as hypothetical reaction intermediates for the present.

In conclusion, 2-(selenocyanatomethyl)-3-propenol (**6**) is a readily prepared functionalized allylic selenocyanate whose alcohol moiety may be derivatized by glycosylation under standard conditions without detriment to the selenium functionality. Attempted derivation of **6** as a phosphite ester was, however, mostly unsatisfactory because of the apparent incompatibility of the selenocyanate group with a strong intramolecular nucleophile. Alcohol **6** itself and its derivatives react with a variety of thiols in methanolic solution at room temperature to give the corresponding mixed dialkyl sulfides with the corresponding loss of selenium. Finally, compatibility of the selenocyanate functionality with oxidative removal of a *p*-methoxybenzyl ether and Lewis and (or) Brønsted acidic conditions of glycosylation reactions has been demonstrated.

Experimental

^{1}H NMR (300 or 500 MHz), ^{13}C NMR (75 MHz), and ^{77}Se NMR (95 MHz) spectra were recorded on Bruker spectrometers. ^{1}H and ^{13}C NMR chemical shifts are given in ppm with respect to tetramethylsilane, following referencing to the in-

Can. J. Chem. Downloaded from www.nrcresearchpress.com by MCGILL UNIVERSITY on 02/02/13
For personal use only.

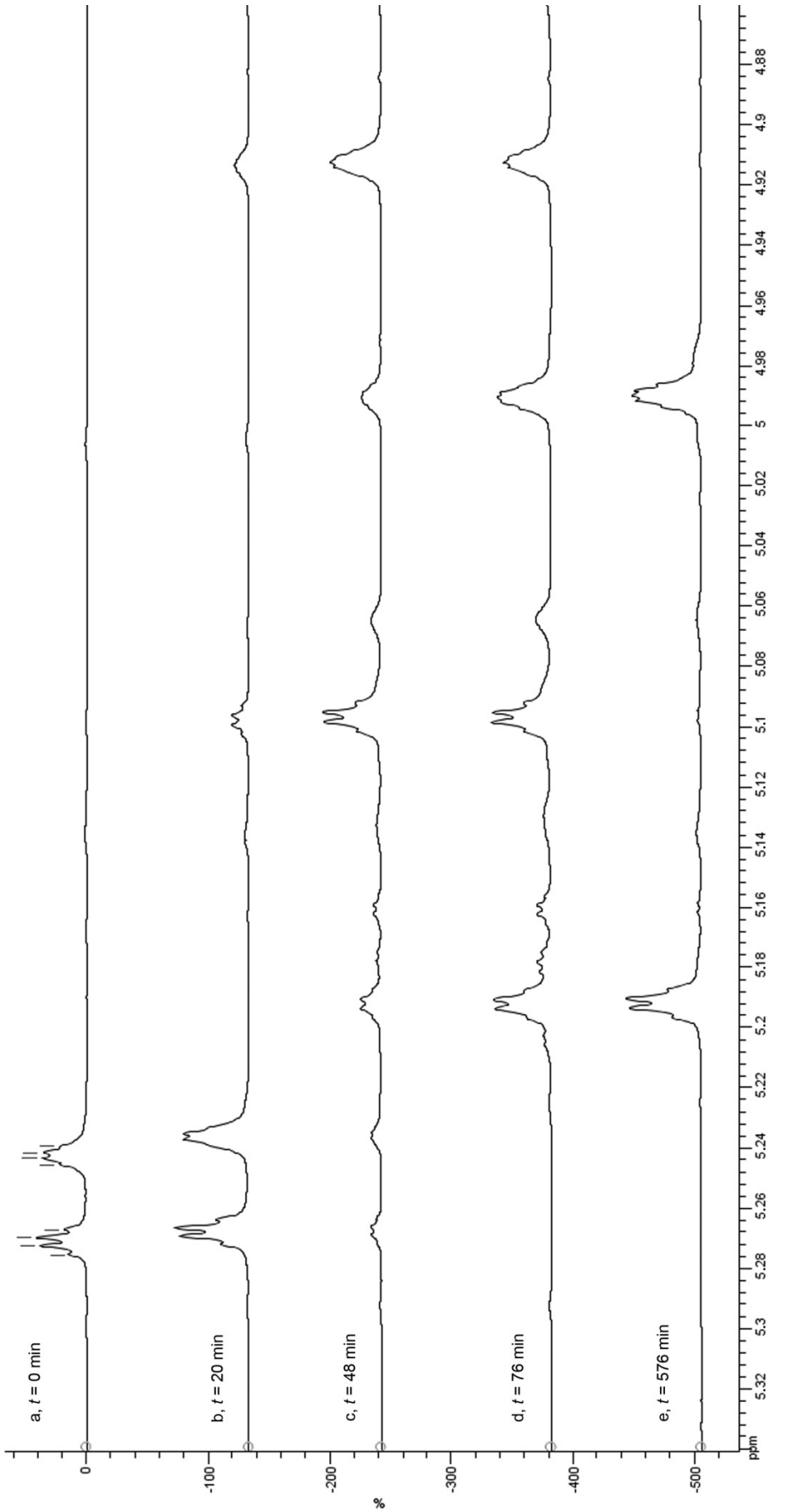


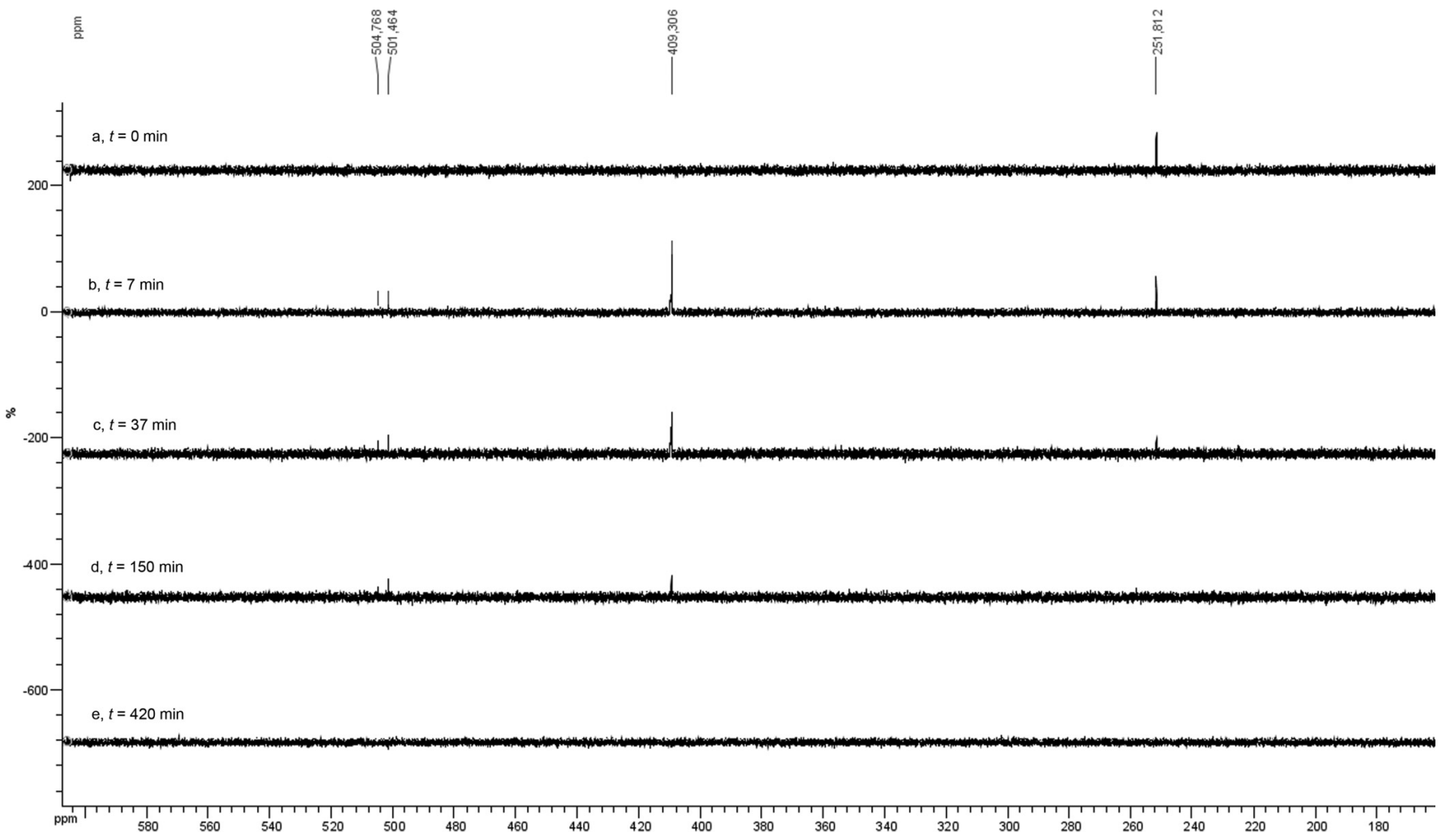
Fig. 1. Vinylic proton region of the ^{1}H NMR spectra for the reaction of **6** with benzyl mercaptan. (*a*) **6**; (*b*) **6** + benzylmercaptan; (*c*) after 48 min with formation of selenosulfide; (*d*) after 76 min; and (*e*) after 576 min.

Published by NRC Research Press

Can. J. Chem. Downloaded from www.nrcresearchpress.com by MCGILL UNIVERSITY on 02/02/13
For personal use only.

Can. J. Chem. Downloaded from www.nrcresearchpress.com by MCGILL UNIVERSITY on 02/02/13
For personal use only.

Fig. 2. ^{77}Se NMR spectra of the reaction of **6** with benzyl mercaptan. (*a*) **6**; (*b*) **6** + benzylmercaptan; (*c*) after 37 min with formation of selenosulfide; (*d*) after 150 min; and (*e*) after 420 min.



Can. J. Chem. Downloaded from www.nrcresearchpress.com by MCGILL UNIVERSITY on 02/02/13
For personal use only.

ternal solvent signal. ^{77}Se NMR chemical shifts are given in ppm with respect to dimethylselenide with the aid of referencing to the internal solvent signal. Multiplicities are given as follows: s (singlet), br s (broad singlet), d (doublet), t (triplet), q (quadruplet), dd (doublet of doublet), dt (doublet of triplet), and m (multiplet). Coupling constants (*J*) are given in Hz. Infrared spectra were recorded on a PerkinElmer FT-IR instrument and the data are reported in reciprocal centimetres (cm^{-1}). Mass spectra were recorded on a Micromass LCT (ESI). Reactions were performed using oven-dried $MgSO_4$ glassware under an atmosphere of dry argon. TLC plates (Merck 60 F_{254} aluminum sheets) were visualized by UV and (or) spraying with vanillin (1%) + sulfuric acid (5%) in EtOH followed by heating. THF and CH_2Cl_2 were dried by standing over molecular sieves under argon. Unless otherwise noted, all reagent-grade chemicals and solvents were obtained from commercial suppliers and were used as received. Specific rotations are expressed in deg cm^3 g^{-1} dm^{-1} and *c* is expressed in g/100 cm^3.

2-(Chloromethyl)allyl *p*-methoxybenzyl ether (4)

p-Methoxybenzyl methallyl ether (**3**)[7] (9.2 mmol, 1.77 g) in CH_2Cl_2 (100 mL) was treated with $LiClO_4$ (1.8 mmol, 0.2 g) and pyridine (11. mmol, 0.89 mL) and cooled to –78 °C before SO_2Cl_2 (11.0 mmol, 0.89 mL) was added. After 1 h at 0 °C, the reaction mixture was quenched with saturated aqueous $NaHCO_3$, extracted with CH_2Cl_2, and washed with brine. The combined organic layers were dried over $MgSO_4$, filtered, and evaporated in vacuo. The crude product was purified by chromatography over silica gel (eluent, MTBE/Hept 5:95) to give **4** (0.60 g, 29%) whose spectral data correspond to those reported in the literature.[8]

2-(Selenocyanatomethyl)allyl *p*-methoxybenzyl ether (5)

KSeCN (11.8 mmol, 1.7 g) was added to a solution of **4** (5.9 mmol, 1.34 g) in DMF (24 mL) and the solution was stirred at 40 °C for 3 h. Water was added and the solution was extracted twice with MTBE. The combined organic layers were dried over $MgSO_4$, filtered and evaporated in vacuo. The crude product was purified by chromatography on silica gel (eluent, AcOEt/Hept 1:3) to give **5** (1.41 g, 81%) as a yellow oil. IR (neat, cm^{-1}): 817, 921, 1031, 1077, 1174, 1246, 1302, 1514, 1610, 2148, 2836. ^{1}H NMR (500 MHz, $CDCl_3$) δ: 3.78 (s, 2H), 3.83 (s, 3H), 4.12 (s, 2H), 4.46 (s, 2H), 5.27 (s, 1H), 5.33 (s, 1H), 6.91 (d, J = 8.2 Hz, 2H), 7.28 (d, J = 7.9 Hz, 2H). ^{13}C NMR (75.5 MHz, $CDCl_3$) δ: 31.9 (CH_2), 55.4 (CH_3), 70.8 (CH_2), 72.3 (CH_2), 102.4 (CN), 114.1 (2 CH), 118.6 (CH_2),[3] 129.7 (2 CH), 129.8 (Cq), 140.5 (Cq), 159.6 (Cq). HRMS (ESI) calcd for $C_{13}H_{19}N_2O_2Se$: 315.0606; found: 315.0634 $[M + NH_4]^+$.

2-(Selenocyanatomethyl)prop-2-en-1-ol (6)

Water (330 μL) and DDQ (1.1 mmol, 230 mg) were added to a solution of **10** (0.68 mmol, 200 mg) in CH_2Cl_2 (6.6 mL) and the resulting solution was stirred for 3 h. It was quenched with an aqueous saturated solution of $NaHCO_3$, extracted with CH_2Cl_2, and washed with brine. The combined organic layers were dried over $MgSO_4$, filtered, and evaporated in vacuo. The crude product was purified by chromatography on silica gel (eluent, AcOEt/Hept 1:1) to give **6** (87.6 mg, 74%) as a yellow oil. IR (neat, cm^{-1}): 727, 915, 1022, 1054, 1197, 1366, 1426, 1646, 1738, 2150, 2923, 3394. ^{1}H NMR (500 MHz, $CDCl_3$) δ: 2.6–2.8 (br s, OH), 3.79 (s, 2H), 4.25 (s, 2H), 5.26 (s, 1H), 5.27 (s, 1H). ^{13}C NMR (75.5 MHz, $CDCl_3$) δ: 31.5 (CH_2), 63.9 (CH_2), 102.6 (CN), 117.1 (CH_2), 142.8 (Cq). ^{77}Se NMR (95.4 MHz, $CDCl_3$) δ: 251.8. HRMS (ESI) calcd for C_5H_6NOSe: 176.9693; found: 175.9606 $[M - H]^-$.

2-(Selenocyanatomethyl)allyl 2,3,4,6-tetra-*O*-acetyl-β-D-glucopyranoside (9)

***From trichloroacetimidate* 7**

A solution of **6** (0.28 mmol, 50 mg) in CH_2Cl_2 (1 mL) and 4 Å molecular sieves was stirred 30 min at room temperature and then cooled at –78 °C. $BF_3.OEt_2$ (0.16 mmol, 20 μL) and **7** (0.71 mmol, 350 mg) were added and the solution was stirred at 0 °C for 2 h 30 min. The reaction mixture was then quenched with NEt_3, filtered, and evaporated in vacuo. The crude product was purified by chromatography on silica gel (eluent, AcOEt/Hept 1:1) to give **9** (58.3 mg, 41%) as a colorless oil.

***From bromide* 8**

Compound **6** (0.28 mmol, 50 mg) was added to CH_2Cl_2 (2 mL) and 4 Å molecular sieves. The solution was stirred for 30 min at room temperature and the donor **8** was added (0.381 mmol, 140 mg). $InCl_3$ (0.14 mmol, 31.4 mg) was then added and the solution was stirred for 3 days at room temperature. The reaction mixture was diluted in CH_2Cl_2 and filtered through a Celite pad. The filtrate was evaporated in vacuo and the crude product was purified by chromatography on silica gel (eluent, AcOEt/Hept 1:1) to give **14** (45.1 mg, 31%) as a colorless oil. $[\alpha]_D^{25}$ –15.4 (*c* 0.54, $CHCl_3$). IR (neat, cm^{-1}): 697, 907, 1367, 1431, 1744, 2153, 2940. ^{1}H NMR (500 MHz, $CDCl_3$) δ: 1.98 (s, 3H), 2.00 (s, 3H), 2.03 (s, 3H), 2.07 (s, 3H), 3.64–3.77 (m, 3H), 4.13–4.23 (m, 3H), 4.41 (d, J = 12.3 Hz, 1H), 4.53 (d, J = 7.9 Hz), 4.98 (dd, J = 7.9, 9.7 Hz, 1H), 5.06 (t, J = 9.7 Hz, 1H), 5.18 (t, J = 9.5 Hz, 1H), 5.23 (s, 1H), 5.29 (s, 1H). ^{13}C NMR (75.5 MHz, $CDCl_3$) δ: 20.6 (2 CH_3), 20.7 (CH_3), 20.8 (CH_3), 31.3 (CH_2), 61.8 (CH_2), 68.3 (CH), 71.2 (CH), 72.0 (CH), 72.7 (CH), 69.9 (CH_2), 100.0 (CH), 101.6 (CN), 119.1 (CH_2), 139.3 (Cq), 169.3 (CO), 169.4 (CO), 170.2 (CO), 170.6 (CO). ^{77}Se NMR (95.4 MHz, $CDCl_3$) δ: 248.0. HRMS (ESI) calcd for $C_{19}H_{29}N_2O_{10}Se$: 525.0982; found: 525.1033 $[M + NH_4]^+$.

4-Methylphenyl 2-*O*-benzyl-4,6-*O*-benzylidene-3-*O*-(2-naphthalenylmethyl)-α-D-thiomannopyranoside (11)

A mixture of (4-methylphenyl) 4,6-*O*-benzylidene-β-D-thiomannopyranoside (2.4 mmol, 900 mg) and *n*-Bu_2SnO (2.9 mmol, 722 mg), in dry toluene (25 mL), was refluxed overnight. The resulting solution was cooled at room temperature and then concentrated under reduced pressure. The residue was dissolved in dry DMF (10 mL) and then CsF (4.8 mmol, 730 mg) and NAPBr (3.6 mmol, 780 mg) were added. The resulting mixture was stirred 6 h at room temperature, diluted with CH_2Cl_2, and filtered through Celite. The filtrate was concentrated under reduced pressure. The residue was dissolved in dry DMF (10 mL), cooled at 0 °C, and NaH (4.8 mmol, 231 mg) was added. After 10 min of stirring, BnBr (4.8 mmol, 570 μL) was added. The resulting mixture was stirred overnight at room temperature, quenched with an aqueous saturated $NaHCO_3$ solution, and extracted twice with CH_2Cl_2. The combined organic layer was brine, dried ($MgSO_4$), and concentrated under reduced pressure. The crude product was purified by chromatography on silica gel (eluent, 10% *t*-BuOMe

Can. J. Chem. Downloaded from www.nrcresearchpress.com by MCGILL UNIVERSITY on 02/02/13
For personal use only.

in heptane) to give 4-methylphenyl 2-*O*-benzyl-4,6-*O*-benzylidene-3-*O*-(2-naphthalenylmethyl)-α-D-thiomannopyranoside (**11**, 1.32 g, 91%) as a clear viscous oil. $[\alpha]^{22}_D$ +102.2 (*c* 1.0, $CHCl_3$). ^1H NMR (500 MHz, $CDCl_3$) δ: 2.32 (s, 3H), 3.89 (t, *J* = 10.0 Hz, 1H), 4.02–4.07 (m, 2H), 4.23 (dd, *J* = 10.0 Hz, *J* = 4.5 Hz, 1H), 4.26–4.37 (m, 2H), 4.72 (d, *J* = 13.5 Hz, 1H), 4.75 (d, *J* = 13.5 Hz, 1H), 4.81 (d, *J* = 12.5 Hz, 1H), 4.94 (d, *J* = 12.5 Hz, 1H), 5.44 (s, 1H), 5.64 (s, 1H), 7.08 (d, *J* = 7.5 Hz, 2H), 7.29–7.48 (m, 10H), 7.52–7.55 (m, 2H), 7.70–7.73 (m, 1H), 7.78–7.83 (m, 3H). ^{13}C NMR (75 MHz, $CDCl_3$) δ: 65.4, 68.5, 72.9, 73.0, 76.2, 77.8, 79.0, 87.3, 101.5, 125.6, 125.8, 126.0, 126.1, 126.1, 126.2, 127.6, 127.8, 127.9, 128.0, 128.1, 128.4, 128.8, 129.8, 129.9, 132.2, 132.9, 133.6, 135.8, 137.6, 137.7, 137.9. HRMS (ESI) calcd for $C_{38}H_{36}O_5S$: 622.2627; found: 622.2641 $[M + NH_4]^+$.

2-(Selenocyanatomethyl)allyl 2-*O*-benzyl-4,6-*O*-benzylidene-3-*O*-(2-naphthylmethyl)-β-D-mannopyranoside (12)

A stirred solution of thioglycoside **11** (0.54 mmol, 330 mg), TTBP (1.0 mmol, 248 mg), BSP (0.6 mmol, 119 mg) in CH_2Cl_2 (10 mL) was cooled to –78 °C and treated with Tf_2O (0.6 mmol, 96 μL). The resulting solution was stirred for 1 h before addition of a solution of **6** (0.63 mmol, 110 mg) in CH_2Cl_2 (2 mL). After stirring for 1 h at –78 °C, the reaction mixture was quenched with saturated aqueous $NaHCO_3$, warmed to room temperature and extracted twice with CH_2Cl_2. The combined organic layers were dried over $MgSO_4$, filtered, and evaporated in vacuo and the residue was purified by chromatography on silica gel (eluent, XXXX 1:4) to give **12** (172 mg, 49%) as a colorless oil. $[\alpha]_D^{23}$ –31.2 (*c* 0.92, $CHCl_3$). IR (neat, cm^{-1}): 1086, 1377, 1454, 2149, 2874, 3047. ^1H NMR (500 MHz, $CDCl_3$) δ: 3.34–3.42 (m, 1H), 3.60–3.75 (m, 3H), 3.94–4.02 (m, 2H), 4.2 (d, *J* = 12.5 Hz, 1H), 4.29 (t, *J* = 9.6 Hz, 1H), 4.34–4.38 (m, 1H), 4.51 (s, 2H), 4.81–4.86 (m, 1H), 4.90–5.02 (m, 3H), 5.28 (s, 1H), 5.33 (s, 1H), 5.69 (s, 1H), 7.31–7.90 (m, 17H). ^{13}C NMR (75.5 MHz, $CDCl_3$) δ: 31.7, 67.9, 68.7, 70.3, 72.8, 75.1, 76.2, 78.1, 78.8, 101.4, 101.8, 119.2, 125.8, 126.1, 126.3, 126.6, 127.9, 128.1, 128.3, 128.4, 128.8, 129.1, 133.2, 133.4, 135.9, 137.7, 138.5, 139.8. ^{77}Se NMR (95.4 MHz, $CDCl_3$) δ: 247.4. HRMS (ESI) calcd for $C_{36}H_{39}N_2O_6Se$: 675.1968; found: 675.1996 $[M + NH_4]^+$.

Dibenzyl 2-(selenocyanatomethyl)allyl phosphate (14)

A stirred solution of **6** (0.28 mmol, 50 mg) in CH_3CN (2.64 mL) was cooled to 0 °C and treated with 1*H*-tetrazole (0.77 mmol, 53.6 mg). Dibenzyl-*N*,*N*-diisopropyl phosphoramidite (0.57 mmol, 187 μL) was then added and the resulting solution was stirred for 1 h. *m*-CPBA (0.99 mmol, 171 mg) was then added and, after 10 min, the reaction mixture was quenched with water. The solution was extracted with CH_2Cl_2 and the combined organic layers were dried over $MgSO_4$, filtered, and evaporated in vacuo. The crude product was purified by chromatography on silica gel (eluent, AcOEt/Hept 1:1) to give **14** (35.5 mg, 29%) as a colorless oil. ^1H NMR (500 MHz, $CDCl_3$) δ: 3.56 (s, 2H), 4.52 (s, 1H), 4.53 (s, 1H), 4.99–5.09 (m, 4H), 5.20 (s, 1H), 5.27 (s, 1H), 7.32–7.35 (m, 8H). ^{13}C NMR (75.5 MHz, $CDCl_3$) δ: 31.1, 67.7, 67.8, 69.8, 69.9, 120.5, 128.3, 128.9, 129.0, 129.7. ^{31}P NMR (75.5 MHz, $CDCl_3$) δ: –0.43. HRMS (ESI) calcd for $C_{19}H_{24}N_2O_4P^{77}Se$: 455.0633; Found: 455.0643 $[M + NH_4]^+$.

2-(Benzyloxy)-5-methylene-1,3,2-oxaselenaphosphinane 2-oxide (16)

This compound, a colorless oil, was obtained in varying amounts from different preparations of **14**. IR (neat, cm^{-1}): 672, 697, 741, 789, 976, 1008, 1261, 1456. ^1H NMR (500 MHz, $CDCl_3$) δ: 3.30–3.38 (m, 1H), 3.54–3.60 (m, 1H), 4.68–4.78 (m, 2H), 5.11–5.22 (m, 4H), 7.32–7.44 (m, 5H). ^{13}C NMR (75.5 MHz, $CDCl_3$) δ: 24.9, 68.9, 74.6, 74.7, 117.8, 128.4, 128.9, 135.5, 136.9. ^{31}P NMR (75.5 MHz, $CDCl_3$) δ: 8.07. ^{77}Se NMR (95.4 MHz, $CDCl_3$) δ: 208.8; 213.7. HRMS (ESI) calcd for $C_{11}H_{14}O_3PSe$: 304.9846; found: 304.9933 $[M + H]^+$.

General procedure for ligation

To freshly prepared selenocyanate **5** or **6** (1 mmol) in degassed MeOH (10 mL) under an argon atmosphere was added a solution of thiol (1.2 mmol) in MeOH (5 mL). The reaction mixture was stirred at room temperature overnight and filtered through a Celite pad, which was further rinsed with MeOH. The solvent was evaporated to dryness and the residue was purified by column chromatography.

2-(Benzylthiomethyl)allyl *p*-methoxybenzyl ether (18)

Prepared according to the general procedure, by reaction of **5** (1.01 mmol, 300 mg) with benzylmercaptan **17** (1.21 mmol, 143 μL), affording **18** (241 mg, 76%) as a colorless oil. IR (neat, cm^{-1}): 702, 819, 910, 1034, 1087, 1302, 1453, 1512, 1612, 2835. ^1H NMR (500 MHz, $CDCl_3$) δ: 3.11 (s, 2H), 3.63 (s, 2H), 3.80 (s, 3H), 4.07 (s, 2H), 4.43 (s, 2H), 5.05 (s, 1H), 5.19 (s, 1H), 6.86–6.90 (m, 2H), 7.24–7.30 (m, 7H). ^{13}C NMR (75.5 MHz, $CDCl_3$) δ: 34.3 (CH_2), 35.6 (CH_2), 55.5 (CH_3), 71.1 (CH_2), 72.1 (CH_2), 114.0 (2 CH), 115.1 (CH_2), 127.1, 128.7, 129.3 (5 CH), 129.5, 129.6 (2 CH), 130.5 (Cq), 138.4 (Cq), 141.9 (Cq), 159.4 (Cq). HRMS (ESI) calcd for $C_{19}H_{26}NO_2S$: 332.1679; found: 332.1670 $[M + NH_4]^+$.

N-(*tert*-Butoxycarbonyl) *S*-(*p*-methoxybenzyloxymethyl)allyl L-cysteine methyl ester (20)

Prepared according to the general procedure, by reaction of **5** (1.01 mmol, 300 mg) with the L-cysteine derivative **19** (1.26 mmol, 209 μL), affording **20** (356 mg, 83%) as a colorless oil. $[\alpha]_D^{25}$ +8.5 (*c* 0.66, $CHCl_3$). IR (neat, cm^{-1}): 819, 915, 1034, 1246, 1366, 1513, 1613, 1713, 1746, 2976, 3359. ^1H NMR (500 MHz, $CDCl_3$) δ: 1.45 (s, 9H), 2.78–2.93 (m, 2H), 3.16–3.26 (m, 2H), 3.75 (3H, CH_3), 3.80 (3H, CH_3), 4.05 (s, 2H), 4.44 (s, 2H, CH_2), 4.51–4.54 (br s, 1H), 5.08 (s, 1H), 5.18 (s, 1H), 5.29–5.34 (br s, 1H), 6.88 (d, *J* = 8.5 Hz, 2H), 7.26 (d, *J* = 8.7 Hz, 2H). ^{13}C NMR (75.5 MHz, $CDCl_3$) δ: 14.2 (CH_3), 28.5 (3 CH_3), 33.6 (CH_2), 35.4 (CH_2), 52.7 (CH), 55.5 (CH_3), 70.6 (CH_2), 72.1 (CH_2), 114.0 (2 CH), 115.9 (CH_2), 129.6 (2 CH), 130.4 (Cq), 141.6 (Cq), 159.4 (Cq), 171.8 (CO). HRMS (ESI) calcd for $C_{21}H_{34}N_2O_6S$: 425.1872; found: 426.1928 $[M + NH_4]^+$.

Ethyl 2-(*p*-methoxybenzyloxymethyl)allylthioacetate (22)

Prepared according to the general procedure, by reaction of **5** (0.17 mmol, 50 mg) with ethyl thioglycolate (**21**, 0.20 mmol, 24.4 mg), affording **22** (48.3 mg, 92%) as a colorless oil. IR (neat, cm^{-1}): 818, 911, 1034, 1090, 1171, 1246, 1512, 1609, 1724, 2936. ^1H NMR (500 MHz, $CDCl_3$) δ: 1.30 (t, *J* = 7.0 Hz, 3H), 3.15 (s, 2H), 3.35 (s, 2H), 3.83 (s, 3H), 4.09 (s, 2H), 4.20 (q, *J* = 7.1 Hz, 2H), 4.46 (s, 2H), 5.13 (s, 1H), 5.23 (s, 1H), 6.90 (d, *J* = 8.6 Hz, 2H), 7.29 (d, *J* = 8.2 Hz, 2H). ^{13}C NMR (75.5 MHz,

Can. J. Chem. Downloaded from www.nrcresearchpress.com by MCGILL UNIVERSITY on 02/02/13
For personal use only.

$CDCl_3$) δ: = 32.2, 34.9, 41.5, 55.3, 61.3, 61.7, 71.9, 113.8, 115.9, 129.1, 129.4, 130.3, 140.8, 159.2, 170.4. HRMS (ESI) calcd for $C_{16}H_{26}NO_4S$: 328.1577; found: 328.1557 $[M + NH_4]^+$.

_p_-Methoxybenzyl 2-(2-hydroxyethyl)thiomethyl ether (24)

Prepared according to the general procedure, by reaction of **5** (0.14 mmol, 40 mg) with 2-mercaptoethanol (**23**, 0.16 mmol, 13.0 mg), affording **24** (23.1 mg, 57%) as a colorless oil. IR (neat, cm^{-1}): 712, 760, 818, 915, 1033, 1066, 1173, 1301, 1511, 1612, 1647, 2835, 2912, 3399. ^1H NMR (500 MHz, $CDCl_3$) δ: 2.68 (t, J = 5.8 Hz, 2H), 3.25 (s, 2H), 3.72 (t, J = 5.8 Hz, 2H), 3.83 (s, 3H), 4.10 (s, 2H), 4.47 (s, 2H), 5.01 (s, 1H), 5.13 (s, 1H), 6.91 (d, J = 8.5 Hz, 2H), 7.29 (d, J = 8.2 Hz, 2H). ^{13}C NMR (75.5 MHz, $CDCl_3$) δ: 34.2, 34.3, 35.3, 60.1, 70.6, 71.9, 113.8, 115.4, 129.4, 144.8, 156.3. HRMS (ESI) calcd for $C_{14}H_{20}O_3S$: 268.1133; found: 269.1215 $[M + H]^+$.

_N_-(*tert*-Butoxycarbonyl) _S_-(_p_-methoxybenzyloxymethyl)allyl glutathione dimethyl ester (26)

Prepared according to the general procedure, by reaction of **5** (0.10 mmol, 30 mg) with the glutathione derivative **25** (0.12 mmol, 59.7 mg), affording **26** (40.6 mg, 64%) as a colorless oil. $[\alpha]_D^{25}$ +0.5 (_c_ 0.98, $CHCl_3$). IR (neat, cm^{-1}): 735, 1031, 1169, 1207, 1246, 1512, 1646, 1706, 1742, 2952, 3301. ^1H NMR (500 MHz, $CDCl_3$) δ: 1.45 (s, 9H), 1.98 (m, 1H), 2.15 (m, 1H), 2.87 (m, 2H), 3.29 (s, 2H), 3.75 (s, 3H), 3.76 (s, 3H), 3.82 (s, 3H), 4.07 (s, 2H), 4.14 (s, 2H), 4.45 (s, 1H), 5.21 (m, 1H), 5.37 (m, 1H), 6.89 (d, J = 8.5 Hz, 2H), 7.28 (d, J = 8.5 Hz, 2H). ^{13}C NMR (75.5 MHz, $CDCl_3$) δ: 28.3 (3 CH_3), 28.7 (CH_2), 32.9 (CH_2), 34.9 (CH_2), 41.3 (CH_2), 52.4, 55.3, 70.7 (CH_2), 71.9 (CH_2), 113.8, 116.2 (2 CH), 129.5 (2 CH), 141.5 (Cq), 154.2 (Cq), 155.5 (Cq), 170.1 (Cq), 172.2 (Cq), 173.0 (Cq). HRMS (ESI) calcd for $C_{29}H_{44}N_3O_{10}S$: 626.2669; found: 626.2769 $[M + H]^+$.

2-(Benzylthiomethyl)prop-2-en-1-ol (27)

Prepared according to the general procedure, by reaction of **6** (0.57 mmol, 100 mg) with benzyl mercaptan **17** (0.68 mmol, 80 μL), affording **27** (94.5 mg, 86%) as a colorless oil. IR (neat, cm^{-1}): 756, 907, 1028, 1232, 1453, 1494, 2916, 3347. ^1H NMR (500 MHz, $CDCl_3$) δ: 3.06 (s, 2H), 3.58 (s, 2H), 4.15 (s, 2H), 4.92 (s, 1H), 5.12 (s, 1H), 7.17–7.27 (m, 5H). ^{13}C NMR (75.5 MHz, $CDCl_3$) δ: 34.2 (CH_2), 35.4 (CH_2), 64.6 (CH_2), 113.7 (CH_2), 127.1, 128.6, 129.2 (5 CH), 138.1 (Cq), 144.2 (Cq). HRMS (ESI) calcd for $C_{11}H_{18}NOS$: 212.1104; found: 211.0785 $[M + NH_4]^+$.

_N_-(*tert*-Butoxycarbonyl) _S_-(hydroxymethyl)allyl L-cysteine methyl ester (28)

Prepared according to the general procedure, by reaction of **6** (0.57 mmol, 100 mg) with the L-cysteine derivative **19** (0.68 mmol, 160.4 mg), affording **28** (90.3 mg, 52%) as a colorless oil. $[\alpha]_D^{26}$ +8.5 (_c_ 0.55, $CHCl_3$). IR (neat, cm^{-1}): 913, 1055, 1217, 1367, 1437, 1513, 1698, 2978, 3374. ^1H NMR (500 MHz, $CDCl_3$) δ: 1.42 (s, 9H), 2.00 (s, 2H), 3.20 (s, 2H), 3.73 (s, 3H), 4.11–4.22 (m, 2H), 4.49–4.54 (br s, 1H), 5.01 (s, 1H), 5.16 (s, 1H) 5.26–5.31 (br s, 1H). ^{13}C NMR (75.5 MHz, $CDCl_3$) δ: 14.3 (CH_3), 28.5 (3 CH_3), 34.1(CH_2), 35.4 (CH_2), 52.8 (CH), 64.1 (CH_2), 114.2 (CH_2), 144.3 (Cq), 171.8 (CO). HRMS (ESI) calcd for $C_{13}H_{27}N_2O_5S$: 328.1635; found: 328.1184 $[M + NH_4]^+$.

Ethyl 2-(hydroxybenzyloxymethyl)allylthioacetate (29)

Prepared according to the general procedure, by reaction of **6** (0.57 mmol, 100 mg) with ethyl thioglycolate **21** (0.68 mmol, 75 μL), affording **29** (61.8 mg, 57%) as a colorless oil. IR (neat, cm^{-1}): 757, 908, 1125, 1155, 1271, 1367, 1410, 1650, 1725, 2982, 3428. ^1H NMR (500 MHz, $CDCl_3$) δ: 1.24 (t, J = 7.1 Hz, 3H), 2.16 (br s, 1H), 3.11(s, 2H), 3.28 (s, 2H), 4.05–4.17 (m, 4H), 5.10 (s, 1H), 5.16 (s, 1H). ^{13}C NMR (75.5 MHz, $CDCl_3$) δ: 14.3, 21.2, 32.4, 35.1, 60.6, 61.6, 64.2, 114.6, 143.5, 170.7. HRMS (ESI) calcd for $C_8H_{18}NO_3S$: 208.1002; found: 213.0549 $[M + NH_4]^+$.

2-(2-Hydroxyethylthiomethyl)prop-2-en-1-ol (30)

Prepared according to the general procedure, by reaction of **6** (0.13 mmol, 22 mg) with 2-mercaptoethanol **23** (0.14 mmol, 10.7 mg), affording **30** (16.8 mg, 91%) as a colorless oil. IR (neat, cm^{-1}): 695, 820, 1062, 1104, 1254, 1314, 1520, 1605, 3420. ^1H NMR (500 MHz, MeOD) δ: 2.70 (t, J = 6.0 Hz, 2H), 3.27 (s, 2H), 3.75 (t, J = 5.9 Hz, 2H), 4.26 (s, 2H), 5.07 (s, 1H), 5.18 (s, 1H). ^{13}C NMR (75.5 MHz, $CDCl_3$) δ: 34.1, 34.3, 60.3, 64.3, 114.1, 145.6.

_N_-(*tert*-Butoxycarbonyl) _S_-(hydroxymethyl)allyl glutathione dimethyl ester (31)

Prepared according to the general procedure, by reaction of **6** (0.28 mmol, 50 mg) with the glutathione derivative **25** (0.35 mmol, 154.7 mg), affording **31** (115.1 mg, 80%) as a colorless oil. $[\alpha]_D^{24}$ +2.4 (_c_ 0.92, $CHCl_3$). IR (neat, cm^{-1}): 733, 1028, 1052, 1207, 1365, 1435, 1516, 1645, 1688, 1742, 2980, 3293. ^1H NMR (500 MHz, $CDCl_3$) δ: 1.44 (s, 9H), 1.98 (m, 1H), 2.18 (m, 1H), 2.38 (m, 2H), 2.88 (m, 1H), 2.93 (m, 2H), 3.33 (dd, J = 13.7 Hz, J = 20.2 Hz, 2H), 3.76 (s, 6H), 4.23 (s, 2H), 4.40 (s large, 1H), 4.68 (q, J = 6.9 Hz, 1H), 5.15 (s, 1H), 5.22 (s, 1H). ^{13}C NMR (75.5 MHz, $CDCl_3$) δ: 25.6 (CH_2), 28.5 (3 CH_3), 32.3 (CH_2), 34.4 (CH_2), 41.3 (CH_2), 52.4 (2 CH_3), 53.0 (CH), 64.0 (CH), 68.0 (CH_2), 80.3 (Cq), 114.3 (CH_2), 144.40 (Cq), 155.70 (NH–C=O), 169.95 ((C=O)O–Me), 170.13 ((C=O)NH), 172.47 (C=O), 172.93 (C=O). HRMS (ESI) calcd for $C_{21}H_{36}N_3O_9S$: 506.2094; found: 506.2159 $[M + H]^+$.

_N_-(*tert*-Butoxycarbonyl) _S_-[(2,3,4,6-tetra-_O_-acetyl-β-D-glucopyranosyl)methyl]allyl glutathione dimethyl ester (32)

Prepared according to the general procedure, by reaction of the glucose derivative **9** (0.04 mmol, 21.7 mg) with the glutathione derivative **25** (0.05 mmol, 23.3 mg) in CH_3CN, affording **32** (21.9 mg, 61%) as a colorless oil. $[\alpha]_D^{25}$ –5.6 (_c_ 0.82, $CHCl_3$). IR (neat, cm^{-1}): 910, 1040, 1167, 1367, 1437, 1518, 1660, 1747, 2932, 2953, 3313. ^1H NMR (500 MHz, $CDCl_3$) δ: 1.43 (s, 9H), 2.00 (s, 3H), 2.03 (s, 3H), 2.05 (s, 3H), 2.10 (s, 3H), 2.31–2.41 (m, 2H), 2.75–2.89 (m, 2H), 3.22 (s, 2H), 3.75 (s, 3H), 3.76 (s, 3H), 4.05 (m, 2H), 4.17–4.19 (m, 1H), 4.21–4.26 (m, 1H), 4.33–4.42 (m, 2H), 4.54–4.63 (m, 2H), 4.98–5.14 (m, 2H), 5.14–5.26 (m, 3H), 5.29–5.36 (m, 1H), 6.72–6.82 (br s, 1H), 7.01–7.08 (br s, 1H). ^{13}C NMR (75.5 MHz, $CDCl_3$) δ: 20.8, 20.9, 21.0, 28.5, 29.9, 32.3, 32.8, 34.8, 41.5, 52.5, 52.6, 52.7, 52.9, 62.1, 68.7, 70.2, 71.5, 72.0, 73.0, 100.1, 116.8, 140.3, 169.6, 170.1, 170.5, 170.7, 172.3, 173.0. HRMS (ESI) calcd for $C_{35}H_{57}N_4O_{18}S$: 853.3383; found: 853.3362 $[M + NH_4]^+$.

Can. J. Chem. Downloaded from www.nrcresearchpress.com by MCGILL UNIVERSITY on 02/02/13
For personal use only.

_N_-(*tert*-Butoxycarbonyl) _S_-[(2-_O_-benzyl-4,6-_O_-benzylidene-3-_O_-(2-naphthylmethyl)-β-D-mannopyranosyl)methyl]allyl glutathione dimethyl ester (33)

Prepared according to the general procedure, by reaction of the mannose derivative **12** (0.18 mmol, 120 mg) with the glutathione derivative **25** (0.24 mmol, 105 mg), affording **33** (113 mg, 63%) as a colorless oil. $[\alpha]_D^{26}$ –13.4 (*c* 1.40, $CHCl_3$). ^{1}H NMR (500 MHz, $CDCl_3$) δ: 1.43 (s, 9H), 1.86–2.00 (br s, 1H), 2.04 (s, 2H), 2.10–2.25 (br s, 1H), 2.28–2.38 (m, 1H), 2.76–2.92 (m, 2H), 3.23 (s, 1H), 3.63–3.68 (m, 1H), 3.72 (s, 6H), 3.88–4.03 (m, 4H), 4.06–4.17 (m, 2H), 4.24 (t, J = 9.6 Hz, 1H), 4.28–4.43 (m, 2H), 4.44–4.65 (m, 3H), 4.76–4.82 (m, 2H), 4.89–5.00 (m, 1H), 4.83–5.05 (m, 1H), 5.15–5.21 (m, 2H), 5.27–5.34 (br s, 1H), 5.65 (s, 1H), 6.69–6.81(br s, 1H), 6.97–7.07 (br s, 1H), 7.21–7.93 (m, 17H). ^{13}C NMR (75.5 MHz, $CDCl_3$) δ: 14.4, 28.5, 32.4, 35.0, 41.5, 52.6, 60.6, 67.9, 68.7, 70.5, 72.5, 75.1, 76.0, 78.0, 78.8, 101.7, 116.4, 125.8, 126.0, 126.2, 126.3, 126.5, 127.9, 128.1, 128.3, 128.4, 128.9, 129.1, 133.1, 133.4, 135.9, 137.9, 138.5, 140.6, 170.1, 170.8, 172.3, 173.0.

_N_-(*tert*-Butoxycarbonyl) _S_-[(2-_O_-benzyl-4,6-_O_-benzylidene-3-_O_-(2-naphthylmethyl)-β-D-mannopyranosyl)methyl]allyl L-cysteine methyl ester (34)

Prepared according to the general procedure, by reaction of the mannose derivative **12** (0.18 mmol, 127 mg) with the L-cysteine derivative **19** (0.23 mmol, 51.3 mg), affording **34** (79.6 mg, 57%) as a colorless oil. $[\alpha]_D^{20}$ –20.1 (*c* 0.45, $CHCl_3$). IR (neat, cm^{-1}): 698, 730, 817, 857, 908, 1049, 1165, 1368, 1453, 1496, 1602, 1709, 2872, 2924. ^{1}H NMR (500 MHz, $CDCl_3$) δ: 1.44 (s, 9H), 2.76–2.92 (m, 2H), 3.17 (s, 1H), 3.26–3.37 (m, 1H), 3.60–3.65 (m, 1H), 3.92–3.95 (m, 2H), 4.03–4.12 (m, 1H), 4.18–4.34 (m, 2H), 4.39–4.51 (m, 2H), 4.68–4.84 (q, J = 10.5 Hz, 2H), 4.87 (d, J = 12.3 Hz, 1H), 4.99 (d, J = 12. 3 Hz, 1H), 5.08 (s, 1H), 5.16 (s, 1H), 5.39 (br s, 1H), 5.63 (s, 1H), 7.24–7.81 (m, 17H). ^{13}C NMR (75.5 MHz, $CDCl_3$) δ: 28.5, 29.9, 33.2, 35.2, 67.8, 68.8, 70.3, 72.5, 75.0, 75.9, 78.0, 78.8, 101.5, 101.7, 116.2, 125.8, 126.0, 126.2, 126.3, 126.4, 127.8, 128.1, 128.2, 128.4, 128.8, 129.1, 133.1, 133.4, 135.9, 137.8, 138.5, 140.5. HRMS (ESI) calcd for $C_{43}H_{53}N_2O_{10}S$: 789.3415; found: 789.3381 $[M + NH_4]^+$.

Monitoring of the reaction of 6 with benzylmercaptan by ^{1}H and ^{77}Se NMR spectroscopy

The reaction of **6** (0.23 mmol, 40 mg) with benzyl mercaptan (0.27 mmol, 34 mg) in CD_3OD (1 mL) was monitored by NMR spectroscopy through an iterative sequence of ^{1}H spectra (64 scans, 500 MHz, 300 K), ^{77}Se NMR spectra (64 scans, 95 MHz, 300 K), and DEPT ^{77}Se spectra (32 scans, 95 MHz, 300 K). Acquisition parameters for F1: size, 32 768 points; spectral width, 47 619 Hz).

Acknowledgments

We thank J.-F. Gallard and S. Picard, Institut de Chimie des Substances Naturelles (ICSN), for help with the recording of ^{77}Se NMR spectra and for the gift of **11**, respectively.

References

(1) (a) Clive, D. L. J. *Tetrahedron* **1978**, *34* (8), 1049. doi:10.1016/0040-4020(78)80135-5; (b) Paulmier, C. *Selenium Reagents and Intermediates in Organic Synthesis;* Pergamon Press: Oxford, 1986; (c) *Organoselenium Chemistry;* Liotta, D., Ed.; Wiley: New York, 1987; (d) Reich, H. J. *Acc. Chem. Res.* **1979**, *12* (1), 22. doi:10.1021/ar50133a004; (e) Liotta, D. *Acc. Chem. Res.* **1984**, *17* (1), 28. doi:10.1021/ar00097a005; (f) Krief, A.; Hevesi, L. *Organoselenium Chemistry;* Springer-Verlag: New York, 1988; (g) Sharpless, K. B.; Gordon, K. M.; Lauer, R. F.; Patrick, D. W.; Singer, S. P.; Young, M. W. *Chem. Scr.* **1975**, *8A,* 9; (h) *Organic Selenium Compounds. Their Chemistry and Biology;* Klaymann, D. L.; Gunther, W. H. H., Eds.; Wiley: New York, 1973; (i) Santi, C.; Santoro, S.; Battistelli, B. *Curr. Org. Chem.* **2010**, *14* (20), 2442. doi:10.2174/138527210793358231; (j) Wirth, T. *Tetrahedron* **1999**, *55* (1), 1. doi:10.1016/S0040-4020(98)00946-6; (k) Freudendahl, D. M.; Shahzad, S. A.; Wirth, T. *Eur. J. Org. Chem.* **2009**, *2009* (11), 1649. doi:10.1002/ejoc.200801171; (l) *Organoselenium Chemistry: A Practical Approach;* Back, T. G., Ed.; Oxford University Press: Oxford, 1999; (m) Crich, D.; Grant, D.; Krishnamurthy, V.; Patel, M. *Acc. Chem. Res.* **2007**, *40* (6), 453. doi:10.1021/ar600020v; (n) Guillemin, J.-C. *Curr. Org. Chem.* **2011**, *15,* 1670.

(2) (a) Crich, D.; Krishnamurthy, V.; Hutton, T. K. *J. Am. Chem. Soc.* **2006**, *128* (8), 2544. doi:10.1021/ja057521c; (b) Crich, D.; Krishnamurthy, V.; Brebion, F.; Karatholuvhu, M.; Subramanian, V.; Hutton, T. K. *J. Am. Chem. Soc.* **2007**, *129* (33), 10282. doi:10.1021/ja072969u.

(3) Hackenberger, C. P. R.; Schwarzer, D. *Angew. Chem. Int. Ed.* **2008**, *47* (52), 10030. doi:10.1002/anie.200801313.

(4) Crich, D.; Subramanian, V.; Karatholuvhu, M. *J. Org. Chem.* **2009**, *74* (24), 9422. doi:10.1021/jo902012m.

(5) (a) Crich, D.; Yang, F. *J. Org. Chem.* **2008**, *73* (18), 7017. doi:10.1021/jo8015314; (b) Subramanian, V.; Moumé-Pymbock, M.; Hu, T.; Crich, D. *J. Org. Chem.* **2011**, *76* (10), 3691. doi:10.1021/jo102411j.

(6) Riague, E. H.; Guillemin, J.-C. *Organometallics* **2002**, *21* (1), 68. doi:10.1021/om010453s.

(7) Wallace, G. A.; Scott, R. W.; Heathcock, C. H. *J. Org. Chem.* **2000**, *65* (13), 4145. doi:10.1021/jo0002801.

(8) Kałuża, Z.; Kazimierski, A.; Lewandowski, K.; Suwińska, K.; Szczęsna, B.; Chmielewski, M. *Tetrahedron* **2003**, *59* (31), 5893. doi:10.1016/S0040-4020(03)00939-6.

(9) Schmidt, R. R.; Jung, K.-H. In *Carbohydrates in Chemistry and Biology;* Ernst, B., Hart, G. W., Sinaÿ, P., Eds.; Wiley-VCH: Weinheim, 2000; Vol. 1, p 5.

(10) (a) Garegg, P. J.; Konradsson, P.; Kvarnström, I.; Norberg, T.; Svensson, S. C. T.; Wigiliu, B. *Acta Chem. Scand. A* **1985**, *39b,* 569. doi:10.3891/acta.chem.scand.39b-0569; (b) Banoub, J.; Bundle, D. R. *Can. J. Chem.* **1979**, *57* (16), 2091. doi:10.1139/v79-335; (c) Crich, D.; Dai, Z.; Gastaldi, S. *J. Org. Chem.* **1999**, *64* (14), 5224. doi:10.1021/jo990424f; (d) Fraser-Reid, B.; Grimme, S.; Piacenza, M.; Mach, M.; Schlueter, U. *Chemistry* **2003**, *9* (19), 4687. doi:10.1002/chem.200304856; (e) Nukada, T.; Berces, A.; Zgierski, M. Z.; Whitfield, D. M. *J. Am. Chem. Soc.* **1998**, *120* (51), 13291. doi:10.1021/ja981041m.

(11) Mukherjee, D.; Ray, P. K.; Chowdhury, U. S. *Tetrahedron* **2001**, *57* (36), 7701. doi:10.1016/S0040-4020(01)00699-8.

(12) Crich, D.; Smith, M. *J. Am. Chem. Soc.* **2001**, *123* (37), 9015. doi:10.1021/ja0111481.

(13) Crich, D.; Smith, M.; Yao, Q.; Picione, J. *Synthesis* **2001**, *2001* (2), 323. doi:10.1055/s-2001-10798.

(14) Beaucage, S. L.; Iyer, R. P. *Tetrahedron* **1992**, *48* (12), 2223. doi:10.1016/S0040-4020(01)88752-4.

A versatile method for the synthesis of γ-pyrones

Garrison E. Beye, Athanasios Karagiannis, Alieh Kazemeini, and Dale E. Ward

Abstract: A versatile three-step procedure to annulate a γ-pyrone onto a methylene ketone was developed involving (*i*) aldol reaction with a dithiolane-protected β-ketoaldehyde, (*ii*) oxidation of the aldol adduct to a β-diketone, and (*iii*) treatment of the resulting dithiolane-protected 1,3,5-trione with 2-iodoxybenzoic acid (IBX) and trifluoromethanesulfonic acid (triflic acid; TfOH) in acetonitrile at ambient temperature to give the corresponding γ-pyrone. Cyclization proceeded with IBX alone, but significantly improved yields were obtained with added acid, particularly triflic acid. A dithiolane was more effective than a dithiane or acyclic dithioacetal protecting group. The method was amenable to the preparation of a variety of substituted γ-pyrones simply by altering the initial aldol reactants. Overall yields of 50%–60% were obtained in six examples. The method was applied to prepare a key fragment for the total synthesis of baconipyrones A and C and siphonarin B.

Key words: γ-pyrone synthesis, 2-iodoxybenzoic acid (IBX), 1,3-dione, dithiolane, siphonariid polypropionates.

Résumé : On a développé une méthode versatile, en trois étapes, qui permet de réaliser l'annellation d'une γ-pyrone sur une méthylène cétone et qui implique les étapes suivantes : (*i*) une réaction aldolique impliquant un β-cétoaldéhyde protégé par un dithiolane; (*ii*) l'oxydation de l'adduit aldolique en β-dicétone et (*iii*) le traitement de la 1,3,5-trione protégée par un groupe dithiolane qui en résulte par de l'acide 2-iodoxybenzoïque (IBX) et de l'acide trifluorométhanesulfonique (acide triflique, TfOH), dans de l'acétonitrile, à la température ambiante, pour conduire à la formation de la γ-pyrone correspondante. La cyclisation se produit même si on utilise l'acide IBX seul, mais les rendements sont de beaucoup améliorés en présence d'un acide additionnel, tel l'acide triflique. Le groupe dithiolane est beaucoup plus efficace qu'un dithiane ou un dithioacétal acyclique comme groupe protecteur. La méthode peut être utilisée pour la préparation d'une variété de γ-pyrones substituées; il suffit de modifier les réactifs aldoliques utilisés. On a obtenu des rendements allant de 50 % à 60 % dans les six exemples étudiés. La méthode a été appliquée à la préparation de fragments clés dans la synthèse totale des baconipyrones A et C et de la siphonarine B.

Mots-clés : synthèse de γ-pyrone, acide 2-iodoxybenzoïque (IBX), 1,3-dione, dithiolane, polypropionates de siphonariides.

[Traduit par la Rédaction]

Can. J. Chem. Downloaded from www.nrcresearchpress.com by MCGILL UNIVERSITY on 02/02/13
For personal use only.

Introduction

A γ-pyrone motif in polypropionate natural products imbues these privileged structures with a range of biological properties.[1] In recent years, there has been a resurgence of interest in the synthesis of γ-pyrone-containing natural products and in the formation of the γ-pyrone moiety.[2,3] The synthesis of γ-pyrones can be accomplished through a variety of methods, but many of these methods lack generality.[4,5] The most common approach involves dehydrative cyclization of 1,3,5-triketones, classically achieved by treatment with strong protic acids.[4] Such harsh conditions are generally not appropriate for the synthesis of complex natural products, and in recent years a variety of alternative reagents to achieve this transformation have been reported, including PPh_3/CCl_4,[6] dimethyl sulfoxide (DMSO)/$(COCl)_2$ (Swern reagent),[6] Amberlyst with P_2O_5 on Celite,[7] sterically hindered diarylammonium sulfonates,[8] and $C_6F_5SO_3H$/heptane.[9] Although the most popular of these methods, PPh_3/CCl_4,[6] has been featured in several natural product syntheses,[3,10] failed applications have also been reported.[7] Cyclizations of masked derivatives of 1,3,5-triketones (e.g., ethylene ketals,[11] enol ethers,[12] silyl enol ethers,[13] enamines,[14] and 5-hydroxy-1,3-cyclohexanediones[15]) to produce γ-pyrones also have been reported. Despite the work thus far, the scope and limitations of the available methods have not been systematically investigated especially with respect to the nature and number of substituents. To the best of our knowledge, there are no methods capable of annulating a γ-pyrone onto a ketone that allows flexibility in the substitution pattern. Herein, we report the synthesis and cyclization of dithiolane-protected 1,3,5-triketones to afford γ-pyrones with a high degree of synthetic versatility.

Results and discussion

In the context of our synthetic studies on the polypropionates from *Siphonaria zelandica*,[16,17] we envisioned the synthesis of the key γ-pyrone fragment (**2**) by functional group

Received 22 July 2012. Accepted 31 July 2012. Published at www.nrcresearchpress.com/cjc on 25 November 2012.

G.E. Beye*, A. Karagiannis, A. Kazemeini, and D.E. Ward. Department of Chemistry, University of Saskatchewan, 110 Science Place, Saskatoon, SK S7N 5C9, Canada.

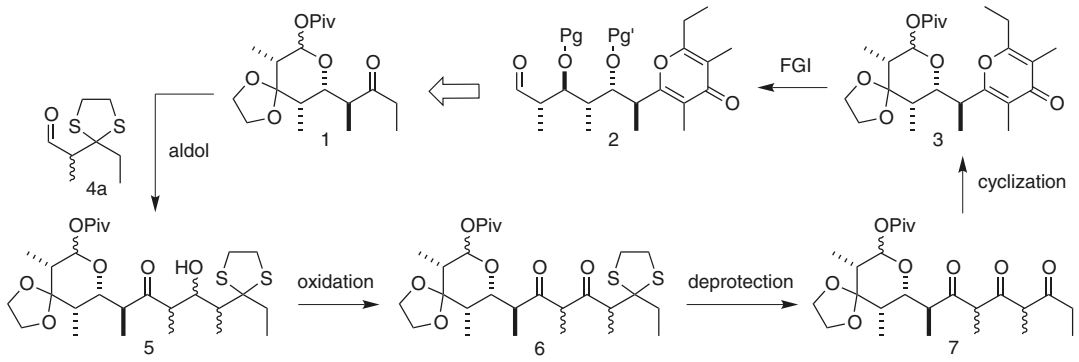
Corresponding author: Dale E. Ward (e-mail: dale.ward@usask.ca).

*Present address: Bayer Healthcare LLC, 800 Dwight Way, Berkeley, CA.

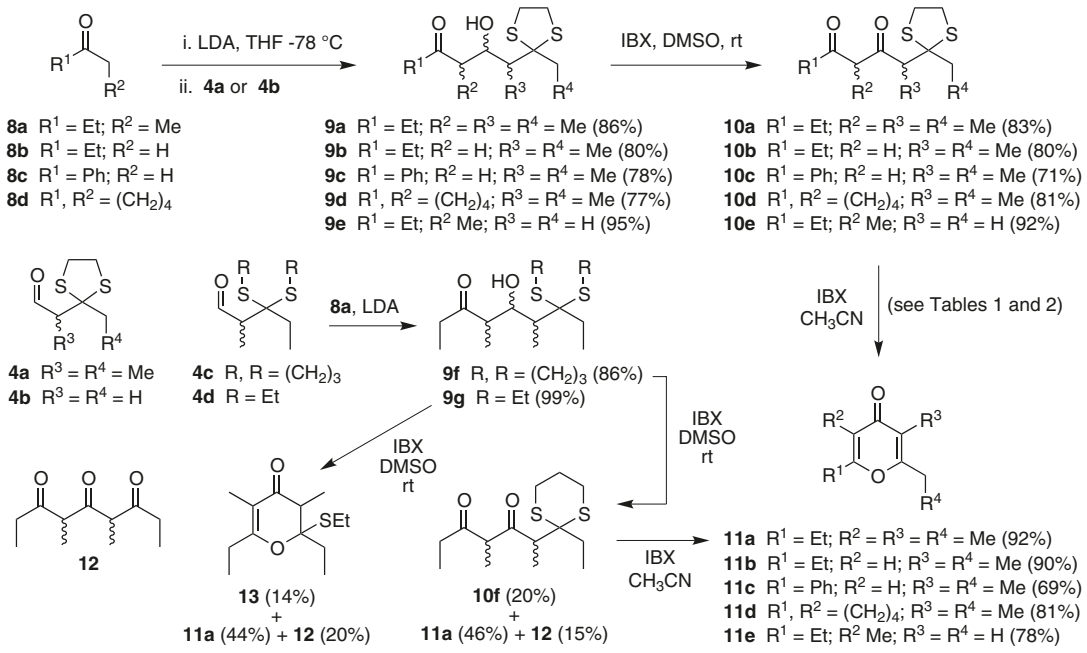
This article is part of a Special Issue dedicated to Professor Derrick Clive.

Can. J. Chem. Downloaded from www.nrcresearchpress.com by MCGILL UNIVERSITY on 02/02/13
For personal use only.

Scheme 1. Synthetic strategy for γ-pyrone synthesis.



Scheme 2. Synthesis of γ-pyrones.



manipulation on **3**, obtained via cyclization of the 1,3,5-triketone intermediate **7** (Scheme 1). The latter would be accessed from readily available ethyl ketone **1**[16,18] through a simple three-step procedure: aldol reaction with dithioacetal aldehyde **4a**[16] followed by oxidation of the resulting adduct **5** to dione **6** and then hydrolysis of the dithioacetal protecting group. This strategy would provide significant flexibility in terms of the timing of installation of the γ-pyrone as the sequence might be delayed or interrupted in response to unforeseen synthetic challenges.

The planned sequence for introduction of the γ-pyrone was tested using 3-pentanone (**8a**) as a model ketone (Scheme 2). Addition of aldehyde **4a**[16] to the lithium diisopropylamide (LDA)-generated lithium enolate of **8a** gave a mixture of aldol diastereomers **9a** in 86% yield. Surprisingly, treatment of **9a** with 2-iodoxybenzoic acid (IBX)[19] in hot (80 °C) acetonitrile according to More and Finney's[20] procedure gave the known[6,21] γ-pyrone **11a** as the only isolable compound in ~30% yield. Despite extensive experimentation, the yield of this process could not be improved; *retro*-aldol was suspected as a significant decomposition pathway. Considering that oxidation of the alcohol in **9a** must occur prior to cyclization, an alternative oxidation protocol (i.e., IBX in DMSO at room temperature) was employed to arrive at diketone **10a**. Subjecting **10a** to IBX oxidation in hot acetonitrile gave a dramatically improved yield of **11a** (Table 1, entry 1) compared with the reaction of **9a** under the same conditions.

A series of experiments was performed to further optimize the formation of **11a** from **10a** (Table 1). Increasing the amount of IBX to 1.5 equiv gave a moderate improvement in the yield that was unchanged using 2 equiv (Table 1, entries 2 and 3). Changing the solvent[20] proved deleterious (Table 1, entries 4 and 5). The addition of water to facilitate hydrolysis of the dithioacetal attenuated the reaction significantly (Table 1, entry 6). The dithiane **9f** and diethyl thioacetal **9g** were prepared by aldol reactions of **8a** with aldehydes **4c** and **4d**, respectively. Oxidation of **9f** with IBX in DMSO under the same conditions that proved successful with **9a**, gave pyrone **11a** (46%), trione **12**[6,22] (15%), and dione **10f** (20%). Despite extensive experimentation, the yield of **11a** from the oxidation

Can. J. Chem. Downloaded from www.nrcresearchpress.com by MCGILL UNIVERSITY on 02/02/13
For personal use only.

Table 1. Initial optimization of γ-pyrone formation by 2-iodoxybenzoic acid (IBX) oxidation of diketones.

Entry	Diketone	Solvent	IBX (equiv)	Pyrone	Yield (%)[a]
1	**10a**	MeCN	1	**11a**	63
2	**10a**	MeCN	1.5	**11a**	77
3	**10a**	MeCN	2	**11a**	77
4	**10a**	EtOAc	2		NR[b]
5	**10a**	DMSO	2	**11a**	Decomp.
6	**10a**	aq MeCN[c]	2	**11a**	<40[d]
7	**10f**	MeCN	2	**11a**	38
8	**10b**	MeCN	2	**11b**	29
9	**10c**	MeCN	2	**11c**	27
10	**10d**	MeCN	2	**11d**	31

Note: Reaction of diketone (~0.2 mmol, 0.04 mol/L) for 24 h at 80 °C.
[a]Isolated yield of pyrone.
[b]No reaction.
[c]H_2O (5% v/v).
[d]Yield estimated by ^{1}H NMR spectroscopy using an internal standard.

Table 2. Optimization of γ-pyrone formation by 2-iodoxybenzoic acid (IBX) oxidation of diketones **10** in the presence of acid additives.

Entry	Diketone	Acid (equiv)	Temp. (°C)	Time (h)	Pyrone	Yield (%)[a]
1	**10a**	*p*-TsOH (0.1)	80	24	**11a**	83
2	**10a**	*p*-TsOH (1)	80	24	**11a**	>95[b]
3[c]	**10a**	*p*-TsOH (2)	80	24		NR[d]
4	**10f**	*p*-TsOH (1)	80	24	**11a**	90
5	**10b**	*p*-TsOH (1)	80	24	**11b**	50
6	**10d**	*p*-TsOH (1)	80	24	**11b**	64
7	**10d**	CH_3COOH (1)	80	24	**11d**	41
8	**10d**	CF_3COOH (1)	80	24	**11d**	51
9	**10d**	CF_3SO_3H (1)	80	24	**11d**	83
10	**10d**	CF_3SO_3H (0.1)	80	24	**11d**	50[b]
11	**10d**	CF_3SO_3H (0.5)	80	24	**11d**	70[b]
12	**10d**	CF_3SO_3H (2)	80	24	**11d**	80[b]
13[c]	**10d**	CF_3SO_3H (1)	80	24	**11d**	<15[b]
14	**10d**	CF_3SO_3H (1)	rt[e]	1	**11d**	65[b]
15	**10d**	CF_3SO_3H (1)	rt[e]	3	**11d**	75[b]
16	**10d**	CF_3SO_3H (1)	rt[e]	13	**11d**	80[b]
17	**10d**	CF_3SO_3H (1)	rt[e]	24	**11d**	80[b]
18	**10a**	CF_3SO_3H (1)	rt[e]	18	**11a**	92
19	**10b**	CF_3SO_3H (1)	rt[e]	16	**11b**	88
20	**10c**	CF_3SO_3H (1)	rt[e]	2	**11c**	69
21	**10d**	CF_3SO_3H (1)	rt[e]	16	**11d**	81
22	**10e**	CF_3SO_3H (1)	rt[e]	16	**11e**	78

Note: Reaction of diketone (~0.2 mmol, 0.04 mol/L) and IBX (2 equiv) in acetonitrile.
[a]Isolated yield of pyrone.
[b]Yield estimated by ^{1}H NMR spectroscopy using an internal standard.
[c]Reaction without IBX.
[d]No reaction.
[e]Room temperature (rt, ~21 °C).

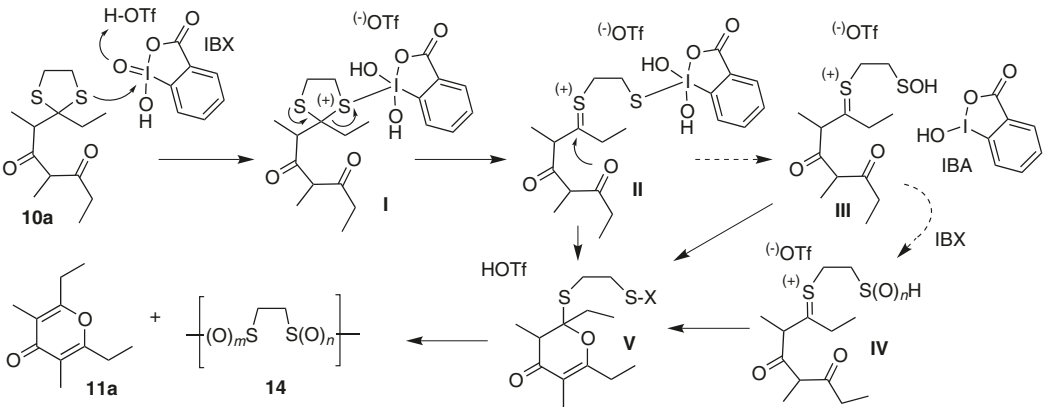
of **9f** could not be significantly improved. It is noteworthy that subjecting triketone **12** to IBX gave little, if any, pyrone **11a**. However, subjecting **10f** to IBX in hot acetonitrile gave **11a**, albeit in poor yield (Table 1, entry 7). Treatment of **9g** with IBX in DMSO at room temperature also produced **11a** (44%) and **12** (20%), along with the dihydropyran **13** (14%) but without evidence of the desired diketone. Having established conditions for the transformation of **10a** into pyrone **11a** in reasonable yield (Table 1, entries 2 and 3), oxidations of diones **10b**–**10d**, prepared analogously to **10a**, were attempted (Table 1, entries 7–10). Unfortunately, only modest yields of the corresponding pyrones **11b**–**11d** were obtained; thus, additional optimization studies were conducted.

The hydrolysis of dithioacetals by treatment with IBX in DMSO is well-known, with dithianes and acyclic dithioacetals being much more susceptible than dithiolanes.[23,24] The fate of the dithiane moiety under these oxidative conditions is likely 1,2-dithiolan-1,1-dioxide[25] and we could identify this compound in the ^{1}H NMR spectra of the crude products from IBX oxidations of **9f** in DMSO and of **10f** in hot acetonitrile. However, the byproduct(s) of oxidative hydrolysis of dithiolanes and in IBX-mediated formation of **11a** from **10a** (or **9a**) is (are) uncertain. Speculating that acidic byproducts were plausible (vide infra), the effect of an added acid on the reaction of **10a** with IBX was investigated (Table 2). A small improvement in yield of **11a** was observed on addition of a catalytic amount of *p*-TsOH·H_2O (Table 2, entry 1), but near quantitative conversion was observed with stoichiometric amounts (Table 2, entry 2). Reaction of **10a** with *p*-TsOH in the absence of IBX returned starting material (Table 2, entry 3), confirming the crucial role of IBX in the transformation. Reaction of **10f** with IBX gave a markedly higher yield of **11a** in the presence of *p*-TsOH (1 equiv) (Table 2, entry 4; cf. Table 1, entry 7); however, these conditions gave more modest improvements with **10b** and **10d** (Table 2, entries 5 and 6; cf. Table 1, entries 8 and 10).

The effect of acid additives was further explored with the recalcitrant **10d** (Table 2, entries 6–17). The yield of pyrone **11d** increased with increasing acidity of the additive (Table 2, entries 6–9) and the highest conversion was obtained with trifluoromethanesulfonic acid (triflic acid; TfOH) (1 equiv; Table 2, entry 9). Conversions improved with increasing amounts of triflic acid up to 1 equiv (Table 2, entries 10–12), but there was little reaction in the absence of IBX (Table 2, entry 13). Although pyrone formation does not occur at room temperature with IBX alone (heterogeneous mixture), the conversion of **10d** to **11d** was complete within ~13 h with added triflic acid (homogeneous mixture) (Table 2, entries 14–17). Subjecting diketones **10a**–**10e** to these optimized conditions and monitoring the reaction progress by thin layer chromatography (TLC) gave the corresponding pyrones **11a**–**11e** in good to excellent yields (Table 2, entries 18–22).

A plausible mechanism for the formation of pyrone **11a** from diketone **10a** is illustrated in Scheme 3. In analogy with previous proposals,[23,24] we suggest that one of the dithiolane sulfur atoms becomes associated with IBX (i.e., **I**), a process that would be facilitated by acid, and assistance from the neighboring sulfur atom leads to the fragmented sulfonium ion **II**. In the case of dithianes, it was proposed that the analogous sulfonium ion is attacked by the iodoxy oxygen ultimately leading to deprotected ketone.[23] With the much less reactive dithiolanes and in the presence of acid (i.e., giving a less nucleophilic OH versus $O^{(-)}$ on IBX), we suggest that **II** might rearrange to **III** (and iodosobenzoic acid (IBA)) that could be

Scheme 3. Plausible mechanism for γ-pyrone formation.



Scheme 4.

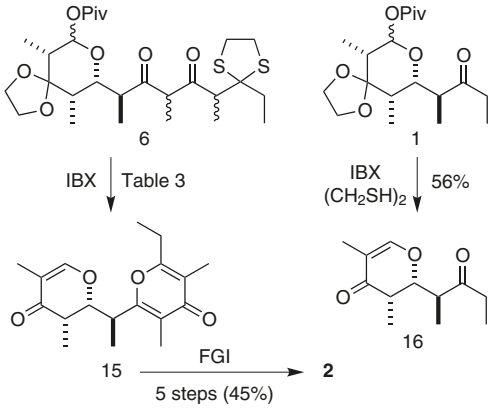


Table 3. Optimization of 2-iodoxybenzoic acid (IBX)-mediated transformation of **6** to γ-pyrone **15**.

Entry	Acid (equiv)	Temp. (°C)	Time (h)	Yield (%)[a]
1	None	80	24	41
2[b]	None	80	24	48
3	*p*-TsOH (1)	80	24	60[c]
4	*p*-TsOH (1)	rt[d]	72	63
5	CF_3SO_3H (1)	rt[d]	16	81

Note: Reaction of **6** (~0.1–0.2 mmol, 0.04 mol/L) with IBX (2 equiv) in acetonitrile.
[a]Isolated yield of **15**.
[b]IBX added portionwise.
[c]Including 20% of an unidentified diastereomer of **15**.
[d]Room temperature (rt, ~21 °C).

further oxidized by IBX (e.g., to **IV**). In any event, the sulfonium ions **II**–**IV** are poised to cyclize by attack of the δ-carbonyl group, ultimately leading to the pyrone **11a** after elimination of the sulfide group. Presumably, the cyclization occurs via the keto tautomers of the diketones **10** as the intramolecular hydrogen bond in the enol tautomers would prevent ring closure. Thus, another possible beneficial effect of added acid is accelerated keto–enol tautomerism. Interestingly, **10a**, the diketone easiest to cyclize, is predominantly in the keto form, whereas **10b**–**10e** are almost exclusively in the enol form (by ^{1}H NMR in $CDCl_3$). Because we were unable to detect signals in the ^{1}H NMR spectra of the crude product (or by monitoring reactions conducted in CD_3CN) that would correspond to the methylene groups originating from the dithiolane, the formation of a polymeric material is suggested (e.g., **14**).

Towards the total synthesis of siphonariid polypropionates, this methodology was applied to the synthesis of the key γ-pyrone fragment (**2**; Scheme 1).[16] Aldol reaction of the readily available ketone **1** with aldehyde **4a** followed by oxidation of the resulting adducts **5** gave diketone **6** in excellent yield.[16] Reactions of **6** with IBX under a variety of conditions were investigated (Scheme 4 and Table 3). Using the method initially successful with **10a** (cf. Table 1, entry 3) resulted in the formation of **15**[16] as the only isolable pyrone-containing product in moderate yield (Table 3, entry 1). The yield of **15** could not be improved by modifying the procedure (i.e., with variations in reaction time, temperature, stoichiometry, IBX addition rate, concentration, etc.). Although these conditions resulted in the formation of the desired pyrone, elimination of the pivaloate and hydrolysis of the ketal in **6** occurred concomitantly. The latter transformations were presumed to be acid-mediated and the acidity of IBX was suspected.[26] However, ketone **1** was inert to IBX (and its reduced congeners IBA and *o*-iodobenzoic acid) under these reaction conditions. Interestingly, the addition of ethanedithiol (0.1 equiv) to a reaction of **1** and IBX (1 equiv) in acetonitrile at 80 °C gave the dihydropyrone **16** in 56% yield. This result suggested that IBX-mediated cyclization of diketones **10** might produce acidic compounds by oxidation of the dithiolane byproducts and prompted a study of the effect of acid additives on the reaction (Table 2). Indeed, the addition of *p*-TsOH·H_2O (1 equiv) to the reaction of **6** with IBX at 80 °C improved the yield of **15** but also produced ~20% of an unwanted diastereomer (Table 3, entry 3); however, prolonged reaction at room temperature suppressed the isomerization (Table 3, entry 4). Finally, the reaction of **6** with IBX and triflic acid at room temperature gave **15** in excellent yield (Table 3, entry 5). Straightforward functional group transformations on **15** produced **2**, a key fragment in the total syntheses of baconipyrones A and C and siphonarin B.[16]

Conclusion

A simple three-step procedure to annulate a γ-pyrone onto a methylene ketone was developed involving (*i*) aldol reaction with

Can. J. Chem. Downloaded from www.nrcresearchpress.com by MCGILL UNIVERSITY on 02/02/13
For personal use only.

Can. J. Chem. Downloaded from www.nrcresearchpress.com by MCGILL UNIVERSITY on 02/02/13
For personal use only.

a dithiolane-protected β-ketoaldehyde, (*ii*) oxidation of the aldol adduct to a β-diketone, and (*iii*) treatment of the resulting dithiolane-protected 1,3,5-trione with 2-iodoxybenzoic acid (IBX) and triflic acid in acetonitrile at ambient temperature. Despite the lower reactivity of dithiolanes towards IBX, cyclization of the dithiolane-protected 1,3,5-trione was much more effective than the corresponding dithiane or *S*,*S*-diethyl acetal protecting groups. In contrast to other approaches, the method provides easy access to a variety of substituted γ-pyrones simply by changing the ketone and (or) aldehyde components. Dithiolane-protected β-ketoaldehydes are readily prepared on gram scale from commerically available β-ketoesters. The synthetic utility of the method was demonstrated through the synthesis of a key intermediate used in the total synthesis of several natural products.

Experimental

General methods

Anhydrous solvents were distilled under argon atmosphere as follows: tetrahydrofuran (THF) from benzophenone sodium ketyl and DMSO from CaH_2 at reduced pressure (stored over 4 Å molecular sieves). All experiments involving air- and (or) moisture-sensitive compounds were conducted in an oven-dried round-bottom flask capped with a rubber septum, and attached via a needle and connecting tubing to an argon manifold equipped with a mercury bubbler (~5 mm positive pressure of argon). Low-temperature baths were ice/water (0 °C) and CO_2(s)/acetone (–78 °C). Unless otherwise noted, reaction temperatures refer to that of the bath. Concentration refers to the removal of volatiles at water aspirator pressure on a rotary evaporator. Preparative TLC (PTLC) was carried out on glass plates (20 × 20 cm^2) precoated (0.25 mm) with silica gel 60 F_{254}. Materials were detected by visualization under an UV lamp (254 nm) and (or) by treating a 1 cm vertical strip removed from the plate with a solution of phosphomolybdic acid (5%) containing a trace of ceric sulfate in aqueous sulfuric acid (5% v/v) followed by charring on a hot plate. Flash column chromatography (FCC) was performed according to Still et al.[27] with silica gel 60 (40–63 μm). All mixed solvent eluents are reported as v/v solutions. Unless otherwise noted, all reported compounds were homogeneous by TLC and by ^{1}H NMR.

Spectral data

High-resolution mass spectra (HR-MS) and low-resolution mass spectra (LR-MS) were obtained on a double-focusing high-resolution spectrometer; only partial data are reported. Electron impact (EI) ionization was accomplished at 70 eV. IR spectra were recorded on a Fourier transform interferometer using a diffuse reflectance cell (i.e., diffuse reflectance infrared Fourier transform (DRIFT) spectroscopy); only diagnostic and (or) intense peaks are reported. Unless otherwise noted, NMR spectra were measured in $CDCl_3$ solution at 500 MHz for ^{1}H and 125 MHz for ^{13}C. Signals due to the solvent (^{13}C NMR) or residual protonated solvent (^{1}H NMR) served as the internal standard: $CDCl_3$ (7.26 δ_H, 77.23 δ_C); C_6D_6 (7.16 δ_H, 128.39 δ_C); and $(CD_3)_2SO$ (2.50 δ_H, 39.52 δ_C). The ^{1}H NMR chemical shifts and coupling constants were determined assuming first-order behavior. Multiplicity is indicated by one or more of the following: s (singlet), d (doublet), t (triplet), q (quartet), m (multiplet), br (broad), and ap (apparent); lists of coupling constants (*J*) correspond to the order of the multiplicity assignment. Coupling constants (*J*) are reported to the nearest 0.5 Hz (i.e., ±0.25 Hz as consistent with the digital resolution ~0.2 Hz/point). The ^{1}H NMR assignments were made based on chemical shift and multiplicity and were confirmed by homonuclear decoupling and (or) two-dimensional correlation experiments (gradient correlation spectroscopy (gCOSY), gradient heteronuclear single quantum coherence (gHSQC), and gradient heteronuclear multiple bond coherence (gHMBC)).[28] The ^{13}C NMR assignments were made on the basis of chemical shift and multiplicity[29] (as determined by ^{13}C-DEPT (distortionless enhancement by polarization transfer) or gHSQC) and were confirmed by two-dimensional ^{1}H/^{13}C correlation experiments (gHSQC and (or) gHMBC).[28] ^{1}H and ^{13}C NMR spectra for all reported compounds can be found in the Supplementary data.

Materials

The following compounds and reagents were prepared as described previously: **1**, **4a**, **6**, and **15**;[16] IBX[30]; and ethyl 2-methyl-3-oxopentanoate.[31] Aldehyde **4b** was prepared from ethyl acetoacetate according to Rama Rao et al.[32] except IBX (88% yield) was used in the final step instead of pyridinium dichromate (PDC; 65% yield). *i*-Pr_2NH was freshly distilled under argon atmosphere from CaH_2. All other reagents were commercially available and, unless otherwise noted, were used as received.

General procedure for $LiAlH_4$ reduction of esters

A solution of ester (typically 40–60 mmol) in THF (~0.5 mol/L) was added dropwise via syringe to a stirred suspension of lithium aluminum hydride (1.2 equiv) in THF (~0.5 mol/L) at 0 °C under Ar. The mixture was allowed to warm to ambient temperature and the reaction progress was monitored by TLC until the ester was consumed (~1–2 h). The mixture was cooled to 0 °C and water (*n* mL for *n* g of lithium aluminum hydride) was added slowly. (Caution: H_2 evolution.) To the vigorously stirred suspension, 15% aq NaOH (*n* mL) and water (3*n* mL) were added dropwise sequentially. The initially gray suspension turned white over 1 h. The mixture was filtered through Celite washing with ethyl acetate. The combined filtrate and washings were dried over Na_2SO_4 and concentrated to give the product.

General procedure for IBX oxidation of primary alcohols

IBX (1.5 equiv) was added to a stirred solution of alcohol (typically 20–30 mmol) in anhydrous DMSO (~0.5 mol/L) at room temperature. When TLC analysis indicated complete consumption of alcohol (~2 h), the mixture was diluted with ethyl acetate and washed sequentially with saturated aq $NaHCO_3$, water, and brine, dried over Na_2SO_4, and concentrated to give the crude aldehyde.

*2-(2-Methyl-1,3-dithiolan-2-yl)acetaldehyde (***4b***)*

IBX oxidation of 2-(2-methyl-1,3-dithiolan-2-yl)ethanol[32] (3.69 g, 22.5 mmol) according to the general procedure followed by fractionation of the crude product by FCC (10% ethyl acetate in hexane) gave the title compound (3.21 g, 88%). IR ν_{max} (cm^{-1}): 1721. ^{1}H NMR (500 MHz, $CDCl_3$) δ: 9.78 (1H, br s, HC-1), 3.46–3.32 (4H, m, H_2C-4, H_2C-5′),

Can. J. Chem. Downloaded from www.nrcresearchpress.com by MCGILL UNIVERSITY on 02/02/13
For personal use only.

2.97 (2H, br s, HC-3), 1.85 (3H, s, H_3C-1″). ^{13}C NMR (125 MHz, $CDCl_3$) δ: 200.7 (d, C-1), 61.3 (s, C-2), 56.7 (t, C-2), 40.6 (t × 2, C-4, C-5′), 33.7 (q, C-1″). LR-MS (EI) *m*/*z* (relative intensity): 162 ($[M]^+$, 77), 146 (6), 134 (12), 119 (100), 87 (11), 74 (45), 58 (95). HR-MS *m*/*z* calcd for $C_6H1_0OS_2$: 162.0173; found: 162.0169 (EI). Spectral data were in accord with those previously reported.[32]

Preparation of aldehyde 4c from ethyl 2-methyl-3-oxopentanoate

Ethyl 2-(2-ethyl-1,3-dithian-2-yl)propanoate

$F_3B{\cdot}OEt_2$ (6.2 mL, 6.9 g, 49 mmol) was added to a stirred solution of ethyl 2-methyl-3-oxopentanoate (7.0 g, 45 mmol) and 1,2-dithioethane (4.8 mL, 5.4 g, 47 mmol) in CH_2Cl_2 (64 mL) at room temperature under Ar. After 30 min (reaction complete by TLC analysis), the mixture was diluted with diethyl ether (300 mL) and saturated aq $NaHCO_3$ (200 mL) was added with vigorous stirring. (Caution: effervescence.) After 30 min, the organic layer was washed sequentially with water and brine, dried over Na_2SO_4, concentrated, and fractionated by FCC (15% ethyl acetate in hexane) to give the title compound as a pale yellow oil (9.5 g, 86%). IR ν_{max} (cm^{-1}): 1734. ^1H NMR (500 MHz, $CDCl_3$) δ: 4.22–4.09 (2H, m, H_2CO), 3.40 (1H, q, *J* = 7 Hz, HC-2), 3.12 (1H, ddd, *J* = 3, 11.5, 14.5 Hz, HC-4), 2.93 (1H, ddd, *J* = 3, 11.5, 14.5 Hz, HC-6), 2.71–2.66 (2H, m, HC-4, HC-6), 2.19 (1H, dq, *J* = 7.5, 15 Hz, HC-1″), 2.05–1.99 (1H, m, HC-5′), 1.89–1.78 (2H, m, HC-1″, HC-5′), 1.31 (3H, d, *J* = 7 Hz, H_3C-3), 1.27 (3H, t, *J* = 7 Hz, H_3CCH_2), 1.10 (3H, t, *J* = 7.5 Hz, H_3C-2″). ^{13}C NMR (125 MHz, $CDCl_3$) δ: 173.5 (s, C-1), 60.6 (t, CH_2O), 55.6 (s, C-2), 46.3 (d, C-2), 27.9 (t, C-1″), 26.2 (t, C-4), 26.1 (t, C-6), 24.8 (t, C-5′), 14.4 (q, H_3CCH_2), 13.7 (q, C-3), 9.4 (q, C-2″). LR-MS (EI) *m*/*z* (relative intensity): 248 ($[M]^+$, 20), 219 (13), 147 (100), 128 (20), 100 (7), 68 (10). HR-MS *m*/*z* calcd for $C_{11}H_{20}O_2S_2$: 248.0905; found: 248.0904 (EI).

2-(2-Ethyl-1,3-dithian-2-yl)propan-1-ol

$LiAlH_4$ reduction of the above ethyl 2-(2-ethyl-1,3-dithian-2-yl)propanoate (5.5 g, 22 mmol) according to the general procedure followed by fractionation of the crude product by FCC (20% ethyl acetate in hexane) to give the title compound (4.0 g, 89%). IR ν_{max} (cm^{-1}): 3419. ^1H NMR (500 MHz, $CDCl_3$) δ: 3.96 (1H, ddd, *J* = 5.5, 6,11.5 Hz, HC-1), 3.73 (1H, ddd, *J* = 5.5, 6.5, 11.5 Hz, HC-1), 2.89–2.72 (4H, m, H_2C-4, H_2C-6), 2.40 (1H, dd, *J* = 6, 6.5 Hz, HO), 2.25–2/17 (1H, m, HC-2), 2.11 (1H, dq, *J* = 7.5, 15 Hz, HC-1″), 1.97–1.87 (3H, m, HC-1″, H_2C-5′), 1.11 (3H, d, *J* = 7 Hz, H_3C-3), 1.03 (3H, t, *J* = 7.5 Hz, H_3C-2″). ^{13}C NMR (125 MHz, $CDCl_3$) δ: 65.5 (t, C-1), 57.8 (s, C-2), 41.1 (d, C-2), 28.8 (t, C-1″), 25.9 (t, C-4), 25.8 (t, C-6), 25.3 (t, C-5′), 12.8 (q, C-3), 9.4 (q, C-2″). LR-MS (EI) *m*/*z* (relative intensity): 206 ($[M]^+$, 13), 177 (10), 147 (100), 99 (10), 73 (17). HR-MS *m*/*z* calcd for $C_9H_{18}OS_2$: 206.0790; found: 206.0792 (EI).

*2-(2-Ethyl-1,3-dithian-2-yl)propanal (***4c***)*

IBX oxidation of the above 2-(2-ethyl-1,3-dithian-2-yl) propan-1-ol (1.52 g, 7.4 mmol) according to the general procedure followed by fractionation of the crude product by FCC (10% ethyl acetate in hexane) gave the title compound (1.24 g, 83%). IR ν_{max} (cm^{-1}): 1716, 2830, 2733. ^1H NMR (500 MHz, $CDCl_3$) δ: 9.96 (1H, d, *J* = 2.5 Hz, HC-1), 2.86–2.79 (5H, m, HC-2, H_2C-4, H_2C-6), 2.12 (1H, dq, *J* = 7.5, 15 Hz, HC-1″), 2.01–1.89 (2H, m, HC-1″, H_2C-5′), 1.18 (3H, d, *J* = 7 Hz, H_3C-3), 1.03 (3H, t, *J* = 7.5 Hz, H_3C-2″). ^{13}C NMR (125 MHz, $CDCl_3$) δ: 202.5 (s, C-1), 54.5 (s, C-2), 50.8 (d, C-2), 29.4 (t, C-1″), 26.1 (t, C-4), 25.5 (t, C-6), 24.9 (t, C-5′), 9.7 (q, C-3), 9.4 (q, C-2″). LR-MS (EI) *m*/*z* (relative intensity): 204 ($[M]^+$, 23), 175 (9), 147 (100), 107 (16), 102 (20), 87 (7), 73 (28). HR-MS *m*/*z* calcd for $C_9H_{16}OS_2$: 204.0643; found: 204.0650 (EI).

Preparation of aldehyde 4d from ethyl acetoacetate

Ethyl 3,3-bis(ethylthio)-2-methylpentanoate

Freshly distilled $TiCl_4$ (0.90 mL, 8.2 mmol) was added via syringe to a stirred solution of ethyl acetoacetate (1.30 g, 8.2 mmol) and ethanethiol (1.6 mL, 21 mmol) at 0 °C under Ar. After 1 h, the ice bath was removed and, after 24 h, the reaction was quenched by the addition of ice cold saturated aq $NaHCO_3$. The mixture was diluted with diethyl ether, washed sequentially with ice cold sat aq $NaHCO_3$ and brine, dried over Na_2SO_4, concentrated, and fractionated by FCC (5% ethyl acetate in hexane) to give the title compound (440 mg, 20%). IR ν_{max} (cm^{-1}): 1735. ^1H NMR (500 MHz, $CDCl_3$) δ: 4.14–4.03 (2H, m, H_2CO), 2.90 (1H, q, *J* = 7 Hz, HC-2), 2.72–2.48 (4H, m, H_2CS × 2), 2.00–1.83 (2H, m, H_2C-4), 1.26 (3H, d, *J* = 7 Hz, H_3CC-2), 1.22 (3H, t, *J* = 7 Hz, H_3CCO), 1.15 (3H, t, *J* = 7.5 Hz, H_3CCS), 1.14 (3H, t, *J* = 7.5 Hz, H_3CCS), 1.01 (3H, t, *J* = 7.5 Hz, H_3C-5). ^{13}C NMR (125 MHz, $CDCl_3$) δ: 173.4 (s, C-1), 65.9 (s, C-3), 60.5 (t, CH_2O), 48.3 (d, C-2), 30.5 (t, C-4), 23.83 (t, CH_2S), 23.77 (q, CH_2S), 14.3 (q, CH_3CO), 14.2 (q, CH_3C-2), 13.9 (q, CH_3CS), 13.7 (q, CH_3CS), 9.8. LR-MS (EI) *m*/*z* (relative intensity): 264 ($[M]^+$, 1), 203 (53), 157 (33), 129 (100), 101 (8), 67 (17). HR-MS *m*/*z* calcd for $C_{12}H_{24}O_2S_2$: 264.1218; found: 264.1216 (EI).

3,3-Bis(ethylthio)-2-methylpentan-1-ol

$LiAlH_4$ reduction of the ethyl 3,3-bis(ethylthio)-2-methylpentanoate (454 mg, 1.70 mmol) according to the general procedure followed by fractionation of the crude product by FCC (20% ethyl acetate in hexane) gave the title compound (367 mg, 97%). IR ν_{max} (cm^{-1}): 3356. ^1H NMR (500 MHz, $CDCl_3$) δ: 3.88 (1H, br d, *J* = 11 Hz, HC-1), 3.68 (1H, br d, *J* = 11 Hz, HC-1), 2.67–2.60 (4H, m, H_2CS × 2), 2.40 (1H, br s, HO), 2.10–2.03 (1H, m, HC-2), 1.89–1.77 (2H, m, H_2C-4), 1.22 (3H, t, *J* = 7.5 Hz, H_3CCS), 1.21 (3H, t, *J* = 7.5 Hz, H_3CCS), 1.14 (3H, d, *J* = 7 Hz, H_3CC-2), 1.02 (3H, t, *J* = 7.5 Hz, H_3C-5). ^{13}C NMR (125 MHz, $CDCl_3$) δ: 67.8 (s, C-3), 65.7 (t, C-1), 43.8 (d, C-2), 30.6 (t, C-4), 24.1 (t, CH_2S), 24.0 (t, CH_2S), 14.7 (q, CH_3CS), 14.4 (q, CH_3CS), 13.7 (q, CH_3C-2), 9.6 (q, C-5). LR-MS (EI) *m*/*z* (relative intensity): 222 ($[M]^+$, 1), 163 (5), 161 (100), 131 (38), 103 (31). HR-MS *m*/*z* calcd for $C_{10}H_{22}OS_2$: 222.1112; found: 222.1120 (EI).

*3,3-Bis(ethylthio)-2-methylpentanal (***4d***)*

IBX oxidation of the 3,3-bis(ethylthio)-2-methylpentan-1-ol (1.52 g, 7.4 mmol) according to the general procedure followed by fractionation of the crude product by FCC (10% ethyl acetate in hexane) gave the title compound (1.24 g, 83%). IR ν_{max} (cm^{-1}): 1720. ^1H NMR (500 MHz, $CDCl_3$) δ: 9.97 (1H, d, *J* = 2 Hz, HC-1), 2.70–2.60 (5H, m, HC-2, H_2CS × 2), 1.90–1.80 (2H, m, H_2C-4), 1.23 (3H, t, *J* = 7.5 Hz, H_3CCS), 1.22 (3H, d, *J* = 7 Hz, H_3CC-2,), 1.21 (3H, t, *J* = 7.5 Hz, H_3CCS), 1.03 (3H, t, *J* = 7.5 Hz, H_3C-5).

Can. J. Chem. Downloaded from www.nrcresearchpress.com by MCGILL UNIVERSITY on 02/02/13
For personal use only.

^{13}C NMR (125 MHz, $CDCl_3$) δ: 203.3 (d, C-1), 65.4 (s, C-3), 54.0 (d, C-2), 30.8 (t, C-4), 23.7 (t, CH_2S), 23.5 (t, CH_2S), 14.05 (q, CH_3CS), 14.03 (q, CH_3CS), 10.6 (q, CH_3C-2), 9.6 (q, C-5). LR-MS (EI) *m/z* (relative intensity): 220 ($[M]^+$, 3), 159 (100), 131 (83), 101 (30), 84 (24), 69 (60). HR-MS *m/z* calcd for $C_{10}H_{20}OS_2$: 220.0956; found: 220.0953 (EI).

General procedure for aldol reaction

A solution of *n*-BuLi in hexane (1.2 equiv) was added dropwise via syringe to a stirred solution of freshly distilled diisopropylamine (1.25 equiv) in THF (~0.2 mol/L) at 0 °C under argon. After 15 min, the mixture was cooled to –78 °C and the ketone (1.2 equiv) was added dropwise via syringe. After 30 min, a solution of aldehyde (typically 2–10 mmol) in THF (~0.3 mol/L, 1.0 equiv) was added via syringe. After 15 min, the reaction was quenched by the addition of saturated aq $NaHCO_3$. The reaction mixture was diluted with ethyl acetate, washed sequentially with saturated aq $NaHCO_3$ and brine, dried over Na_2SO_4, and concentrated to give the crude aldol product.

***6-(2-Ethyl-1,3-dithiolan-2-yl)-5-hydroxy-4-methylheptan-3-one* (9a)**

Following the general procedure, aldol reaction of 3-pentanone (0.17 g, 2.0 mmol) with **4a** (316 mg, 1.66 mmol) and fractionation of the crude product by FCC (30% ethyl acetate in hexane) gave the title compound as a 48:42:10 mixture of diastereomers (393 mg, 86%). IR ν_{max} (cm^{-1}): 3480, 1707. ^{1}H NMR (500 MHz, $CDCl_3$) δ: 4.50–4.42 (0.9H, m, HC-5), 4.26 (0.1H, br d, J = 8.5 Hz, HC-5), 3.86 (0.1H, br s, HO), 3.27 (4H, br s, H_2C-4, H_2C-5′), 3.19 (0.48H, br s, HO), 3.16 (0.42H, br s, HO), 2.77–2.65 (1H, m, HC-4), 2.60–2.40 (2H, m, H_2C-2), 2.22–1.80 (3H, m, H_2C-1″, HC-6), 1.20 (1.5H, d, J = 7 Hz, H_3CC-4), 1.14 (0.3H, d, J = 7 Hz, H_3CC-4), 1.13–0.99 (6H, m, H_3C-2″, H_3C-7), 0.97 (1.3H, d, J = 7 Hz, H_3CC-4). ^{13}C NMR (125 MHz, $CDCl_3$; two major isomers only) δ: 215.4 (s), 214.6 (s), 77.9 (s), 77.6 (s), 74.5 (d), 72.8 (d), 51.6 (d), 49.7 (d), 43.4 (d), 41.9 (d), 40.24 (t), 40.19 (t), 39.75 (t), 39.67 (t), 37.0 (t), 36.8 (t), 36.6 (t), 35.2 (t), 14.1 (q), 13.9 (q), 11.6 (q), 11.1 (q), 10.9 (q), 10.8 (q), 7.9 (q), 7.7 (q). LR-MS (EI) *m/z* (relative intensity): 276 ($[M]^+$, 1), 229 (1), 190 (1), 161 (2), 133 (100). HR-MS *m/z* calcd for $C_{13}H_{24}O_2S_2$: 276.1208; found: 276.1218 (EI).

***6-(2-Ethyl-1,3-dithiolan-2-yl)-5-hydroxyheptan-3-one* (9b)**

Following the general procedure, aldol reaction of butanone (1.2 mL, 0.99 g, 14 mmol) with **4a** (2.00 g, 10.5 mmol) and fractionation of the crude product by FCC (25% ethyl acetate in hexane) gave the title compound as a 7:1 mixture of diastereomers (2.05 g, 80%). IR ν_{max} (cm^{-1}): 3477, 1710. ^{1}H NMR (500 MHz, $CDCl_3$; major isomer only) δ: 4.78 (1H, m, HC-5), 3.25 (1H, d, J = 2 Hz, HO), 3.24–3.19 (4H, m, H_2C-4, H_2C-5′), 2.67 (1H, dd, J = 9, 16 Hz, HC-4), 2.51–2.42 (2H, m, H_2C-1), 2.32 (1H, dd, J = 4, 16 Hz, HC-4), 2.05–1.95 (2H, m, H_2C-1″), 1.98 (1H, br q, J = 7 Hz, HC-6), 1.05 (3H, d, J = 7 Hz, H_3C-7), 1.01 (6H, ap t, J = 7 Hz, H_3C-1, H_3C-2″). ^{13}C NMR (125 MHz, $CDCl_3$;) δ: 210.9 (s, C-3), 77.6 (d, C-2), 68.4 (s, C-5), 48.6 (t, C-4), 45.7 (d, C-6), 40.1 (t, C-4), 39.6 (t, C-5′), 36.8 (t, C-1″ or C-2), 36.1 (t, C-1″ or C-2), 11.0 (q, C-2″ or C-7), 10.7 (q, C-2″ or C-7), 7.7 (q, C-1). HR-MS *m/z* calcd for $C_{12}H_{22}O_2S_2$: 262.1053; found: 262.1056 (EI).

***4-(2-Ethyl-1,3-dithiolan-2-yl)-3-hydroxy-1-phenylpentan-1-one* (9c)**

Following the general procedure, aldol reaction of acetophenone (0.24 g, 2.0 mmol) with **4a** (317 mg, 1.67 mmol) and fractionation of the crude product by FCC (50% ethyl acetate in hexane) gave the title compound as a >10:1 mixture of diastereomers (401 mg, 78%). IR ν_{max} (cm^{-1}): 3497, 3059, 1677. ^{1}H NMR (500 MHz, $CDCl_3$) δ: 7.98 (2H, ap d, J = 7 Hz, Ph), 7.57 (1H, t, J = 7 Hz, Ph), 7.47 (2H, ap t, J = 8 Hz, Ph), 4.99 (1H, dd, HC-3), 3.38 (1H, d, J = 2 Hz, HO), 3.29 (1H, dd, J = 8, 16 Hz, HC2), 3.30–3.23 (4H, m, H_2C-4, H_2C-5′), 2.98 (1H, dd, J = 4.5, 16.5 Hz, HC-2), 2.07 (3H, ap q, J = 7 Hz, H_2C-1″, HC-4), 1.19 (3H, d, J = 7 Hz), 1.08 (3H, t, J = 7 Hz). ^{13}C NMR (125 MHz, $CDCl_3$) δ: 199.6 (s, C-1), 137.3 (s, Ph), 133.5 (d, Ph), 128.8 (d × 2, Ph), 128.4 (d × 2, Ph), 77.8 (q, C-2), 68.8 (t, C-3), 46.1 (d, C-5), 44.9 (t, C-2), 40.3 (t, C-4), 39.8 (t, C-5′), 36.3 (t, C-1″), 11.3 (q, C-5), 10.9 (q, C-2″). LR-MS (EI) *m/z* (relative intensity): 310 ($[M]^+$, 1), 263 (1), 217 (2), 190 (2), 161 (3), 133 (100), 105 (30), 77 (18). HR-MS *m/z* calcd for $C_{16}H_{22}O_2S_2$: 310.1061; found: 310.1067 (EI).

***2-(1-Hydroxy-2-(2-ethyl-1,3-dithiolan-2-yl)-propyl) cyclohexanone* (9d)**

Following the general procedure, aldol reaction of cyclohexanone (0.62 g, 6.5 mmol) with **4a** (1.01 g, 5.32 mmol) and fractionation of the crude product by FCC (30% ethyl acetate in hexane) gave the title compound as a 12:1 mixture of diastereomers (1.18 g, 77%). IR ν_{max} (cm^{-1}): 3469, 1707. ^{1}H NMR (500 MHz, $CDCl_3$) δ: 4.38 (1H, br d, J = 9 Hz, HC-1), 3.49 (1H, d, J = 2.5 Hz, HO), 3.27–3.15 (4H, m, H_2C-4″, H_2C-5′), 2.47–2.41 (2H, m, HC-2, HC-6), 2.33 (1H, ddd, J = 5, 11, 13 Hz, HC-6), 2.18–1.93 (5H, m, H2, C-1″, HC-3, HC-5, HC-2), 1.94–1.87 (1H, m, HC-4), 1.79–1.56 (2H, m, HC-4, HC-5), 1.49–1.42 (1H, m, HC-3), 1.12 (3H, d, J = 7 Hz, H_3C-3′), 1.07 (3H, t, J = 7 Hz, H_3C-2″). ^{13}C NMR (125 MHz, $CDCl_3$) δ: 215.3 (s, C-1), 78.3 (s, C-2″), 71.1 (d, C-1), 55.0 (d, C-2), 43.3 (d, C-2), 42.6 (t, C-6), 40.4 (t, C-4″), 39.7 (t, C-5′), 35.2 (t, C-1″), 30.4 (t, C-3), 28.1 (t, C-5), 24.4 (t, C-4), 10.84 (q, C-2″ or C-3′), 10.80 (q, C-2″ or C-3′). LR-MS (EI) *m/z* (relative intensity): 288 ($[M]^+$, 1), 241 (1), 195 (1), 161 (1), 133 (100), 81 (6), 73 (6). HR-MS *m/z* calcd for $C_{14}H_{24}O_2S_2$: 288.1218; found: 288.1216 (EI).

***6-(2-Ethyl-1,3-dithiolan-2-yl)-5-hydroxyheptan-3-one* (9e)**

Following the general procedure, aldol reaction of 3-pentanone (0.18 mL, 0.15 g, 1.7 mmol) with **4b** (317 mg, 1.55 mmol) and fractionation of the crude product by FCC (20% ethyl acetate in hexane) gave the title compound as 1.5:1 mixture of diastereomers (386 mg, 86%). IR ν_{max} (cm^{-1}): 3503, 1710. ^{1}H NMR (500 MHz, $CDCl_3$) δ: 4.60 (0.4H, ddd, J = 1, 3.5, 8 Hz, HC-5), 4.56 (0.6H, ddd, J = 1, 3.5, 9.5 Hz, HC-5), 3.00–2.84 (2H, m, HC-4, HC-6), 2.76-.240 (6H, m, H_2C-2, HC-4, HC-4, HC-6, HO), 2.31–2.17 (1H, m, HC-1″), 2.11–1.95 (2H, m, HC-1″, HC-5′), 1.92–1.72 (2H, m, HC-5′, HC-6), 1.20 (1.2H, d, J = 7 Hz, H_3CC-4), 1.07 (2.4H, d, J = 7 Hz), 1.05 (1.2H, d, J = 7 Hz), 1.04 (2.4H, t, J = 7 Hz), 1.03 (1.2H, t, J = 7 Hz), 0.98 (2.4H, d, J = 7 Hz, H_3CC-4), 0.97 (2.4H, t, J = 7 Hz), 0.95 (1.2H, t, J = 7.5 Hz). ^{13}C NMR (125 MHz, $CDCl_3$; *major isomer) δ: 215.3* (s, C-3), 214.6 (s, C-3), 73.6* (d, C-5), 71.7 (d, C-5), 59.6 (s, C-2), 59.2* (s, C-2), 51.4 (d, C-4), 49.7* (d, C-4), 41.6 (d, C-6), 40.2* (d,

Can. J. Chem. Downloaded from www.nrcresearchpress.com by MCGILL UNIVERSITY on 02/02/13
For personal use only.

C-6), 36.6* (t, C-2), 35.3 (t, C-2), 29.4 (t, C-1″), 29.3 (t, C-1″), 26.03 (t, C-4), 25.99* (t, C-4), 25.97* (t, C-6), 25.88 (t, C-6), 25.36 (t, C-5′), 25.35* (t, C-5′), 14.1* (q × 2, CH_3C-4), 9.6* (q, C-2″), 9.5 (q, C-2″), 7.9* (q × 2), 7.7 (q), 7.3* (q). LR-MS (EI) *m/z* (relative intensity): 290 ([M]$^+$, 4), 204 (4), 183 (1), 175 (6), 147 (100). HR-MS *m/z* calcd for $C_{14}H_{26}O_2S_2$: 290.1374; found: 290.1384 (EI).

*5-Hydroxy-4-methyl-6-(2-methyl-1,3-dithiolan-2-yl)hexan-3-one (***9f***)*

Following the general procedure, aldol reaction of 3-pentanone (0.42 g, 4.9 mmol) with **4c** (650 mg, 4.01 mmol) and fractionation of the crude product by FCC (30% ethyl acetate in hexane) gave the title compound as a 2.5:1 mixture of diastereomers (955 mg, 95%). IR ν_{max} (cm^{-1}): 3476, 1706. ^{1}H NMR (500 MHz, $CDCl_3$) δ: 4.24 (0.7H, dddd, J = 2, 2.5, 4, 8.5 Hz, HC-5), 4.09 (0.3H, dddd, J = 2, 4, 7, 9 Hz, HC-5), 3.51 (0.3H, d, J = 4, Hz, HO), 3.46 (0.7H, d, J = 2.5, Hz, HO), 3.41–3.32 (4H, m, H_2C-4, H_2C-5′), 2.72–2.62 (1H, m, HC-4), 2.58–2.50 (2H, m, H_2C-2), 2.13–1.94 (2H, m, H_2C-6), 1.83 (2.1H, s, H_3C-1), 1.82 (0.9H, s, H_3C-1), 1.14 (2.1H, d, J = 7 Hz, H_3CC-4), 1.10 (0.9H, d, J = 7 Hz, H_3CC-4), 1.05 (3H, ap t, H_3C-1). ^{13}C NMR (125 MHz, $CDCl_3$; *major isomer) δ: 215.34 (s, C-3), 215.29* (s, C-3), 72.3 (d, C-5), 70.7* (d, C-5), 65.7* (s, C-2), 65.5 (s, C-2), 51.7 (d, C-4), 51.4* (d, C-4), 48.61* (t, C-6), 48.59 (t, C-6), 40.3 (t, C-4), 40.22* (t, C-4), 40.18* (t × 2, C-5′), 36.3 (t, C-2), 35.6* (t, C-2), 34.0 (t, C-1″), 33.8* (t, C-1″), 13.5 (q, CH_3C-4), 11.4* (q, CH_3C-4), 7.8* (q, C-1), 7.7 (q, C-1). LR-MS (EI) *m/z* (relative intensity): 248 ([M]$^+$, 39), 187 (7), 171 (14), 155 (21), 133 (56), 121 (36), 101 (23), 74 (37), 57 (100). HR-MS *m/z* calcd for $C_{11}H_{20}O_2S_2$: 248.0905; found: 248.0912 (EI).

*7,7-Bis(ethylthio)-5-hydroxy-4,6-dimethylnonan-3-one (***9g***)*

Following the general procedure, aldol reaction of 3-pentanone (0.12 mL, 0.10 g, 1.1 mmol) with **4d** (192 mg, 0.871 mmol) and fractionation of the crude product by FCC (20% ethyl acetate in hexane) gave the title compound as a 3:1 mixture of diastereomers (265 mg, 99%). IR ν_{max} (cm^{-1}): 3436, 1715. ^{1}H NMR (500 MHz, C_6D_6) δ: 4.50 (0.75H, br d, J = 9 Hz, HC-5), 4.45 (0.25H, dd, J = 1.5, 9.5 Hz, HC-5), 3.70 (0.25H, d, J = 2 Hz, HO), 3.66 (0.75H, d, J = 2 Hz, HO), 2.72–2.50 (4H, m, HC-2, HC-4, HCS × 2), 2.41–2.12 (3H, m, HC-2, HCS × 2), 2.10–1.95 (1H, m, HC-6), 1.85–1.64 (2H, m, H_2C-8), 1.23 (0.75H, d, J = 7 Hz), 1.18 (0.75H, d, J = 7 Hz), 1.10* (2.25H, d, J = 7 Hz), 1.09 (2.25H, t, J = 7 Hz), 1.04 (0.75H, t, J = 7 Hz), 1.02–0.88 (6H, m), 0.82 (2.25H, d, J = 7 Hz). ^{13}C NMR (125 MHz, C_6D_6; *major isomer) δ: 213.4* (s, C-3), 213.2 (s, C-3), 74.1* (d, C-5), 72.2 (d, C-5), 69.5 (d, C-7), 69.1* (s, C-7), 51.5 (d, C-4), 49.6* (d, C-4), 43.7 (d, C-6), 42.0* (d, C-6), 37.4* (t, C-2), 35.9 (t, C-2), 30.6* (t × 2, C-8), 25.1* (t, CH_2S), 23.7* (t, CH_2S), 15.1 (q, CH_3C-4), 14.5 (q, CH_3CS), 14.4* (q, CH_3CS), 14.23* (q, CH_3CS), 14.20 (q, CH_3CS), 13.9* (q, CH_3C-4), 10.09 (q), 9.51* (q), 9.48 (q), 9.37* (q), 8.16* (q), 8.13 (q). LR-MS (EI) *m/z* (relative intensity): 306 (1), 245 (10), 227 (13), 159 (10), 131 (100), 115 (20), 73 (10). HR-MS *m/z* calcd for $C_{15}H_{30}O_2S_2$: 306.1687; found: 306.1692 (EI).

General procedure for IBX oxidation of aldol adducts

IBX (2 equiv) was added to a stirred solution of the aldol (typically 0.2–0.5 mmol) in DMSO (~0.04 mol/L at ambient temperature. When TLC analysis indicated the consumption of aldol (~24 h), the mixture diluted with ethyl acetate, washed sequentially with saturated $NaHCO_3$, water and brine, dried over Na_2SO_4, and concentrated to give the crude product.

*2-(2-Ethyl-1,3-dithiolan-2-yl)-4-methylheptane-3,5-dione (***10a***)*

Following the general procedure, IBX oxidation of **9a** (393 mg, 1.42 mmol) and fractionation of the crude product by FCC (20% ethyl acetate in hexane) gave the title compound (326 mg, 83%). IR ν_{max} (cm^{-1}): 3400, 1722, 1699, 1574. ^{1}H NMR (500 MHz, $CDCl_3$; a 30:35:35 mixture of enol and two keto (a and b) tautomers, respectively) δ: 16.84 (0.3H, s, HO enol), 3.96 (0.35H, q, J = 7 Hz, HC-4 keto a), 3.88 (0.35H, q, J = 7 Hz, HC-4 keto b), 3.39 (0.35H, q, HC-2 keto a or b), 3.35 (0.35H, q, HC-2 keto a or b), 3.30 (0.3H, q, HC-2 enol), 3.25–3.10 (4H, m, H_2C-4, H_2C-5′), 2.58–2.40 (2H, m, H_2C-6), 2.11–1.83 (2H, m, H_2C-1″), 1.86 (0.9H, s, H_3CC-4 enol), 1.38 (0.9H, d, J = 7 Hz, H_3C-1 enol), 1.33–1.27 (4.2H, m, H_3C-1, H_3CC-4 keto), 1.15–0.97 (6H, m, H_3C-2″, H_3C-7 enol and keto). ^{13}C NMR (125 MHz, $CDCl_3$) δ: 208.9 (s), 208.7 (s), 208.1 (s), 207.5 (s), 196.4 (s), 192.8 (s), 103.9 (s), 75.4 (s), 74.0 (s), 62.4 (d), 61.5 (d), 56.7 (d), 56.5 (d), 47.5 (d), 41.0 (t), 40.40 (t), 40.38 (t), 40.23 (t), 40.21 (t), 40.13 (t), 39.69 (t), 35.6 (t), 34.7 (t), 34.2 (t), 32.5 (t), 32.4 (t), 30.0 (t), 15.8, 15.6 (q), 15.4 (q), 13.2 (q × 2), 12.4 (q), 10.7 (q), 10.31 (q), 10.29 (q), 9.3 (q), 7.8 (q), 7.7 (q). LR-MS (EI) *m/z* (relative intensity): 274 ([M]$^+$, 3), 245 (2), 189 (1), 159 (10), 133 (100), 113 (6), 57 (26). HR-MS *m/z* calcd for $C_{13}H_{22}O_2S_2$: 274.1061; found: 274.1060 (EI).

*6-(2-Ethyl-1,3-dithiolan-2-yl)heptane-3,5-dione (***10b***)*

Distilled DMSO (0.069 mL, 76 mg, 0.97 mmol) was added to a stirred solution of oxalyl chloride (0.050 mL, 74 mg, 0.58 mmol) in CH_2Cl_2 (5.8 mL) at –78 °C under Ar. After 15 min, a solution of **9b** (101 mg, 0.386 mmol) in CH_2Cl_2 (1 mL) was added dropwise via syringe over 10 min. After 1 h, *i*-Pr_2EtN (0.54 mL, 3.1 mmol) was added to the reaction mixture and the reaction was allowed to warm to 0 °C. The mixture was diluted with ethyl acetate and washed sequentially with saturated aq NH_4Cl, saturated aq $NaHCO_3$ and brine, dried over Na_2SO_4, concentrated, and fractionated by FCC (25% ethyl acetate in hexane) to give the title compound (80 mg, 80%). IR ν_{max} (cm^{-1}): 3408, 1718, 1699, 1599. ^{1}H NMR (500 MHz, $CDCl_3$; >10:1 enol form) δ: 15.49 (1H, s, OH), 5.62 (1H, s, HC-4), 3.20–2.90 (4H, m, H_2C-4, H_2C-5′), 2.87 (1H, q, J = 7 Hz, HC-2), 2.32 (2H, ap q, J = 7.5 Hz, H_2C-6), 2.10 (1H, dq, J = 7, 15 Hz, HC-1″), 1.94 (1H, dq, J = 7, 15 Hz, HC-1″), 1.42 (3H, d, J = 7 Hz, H_3C-1), 1.13 (3H, t, J = 7.5 Hz, H_3C-7), 1.10 (3H, t, J = 7 Hz, H_3C-2″). ^{13}C NMR (125 MHz, $CDCl_3$; >10:1 enol form) δ: 196.7 (s, C-3), 194.4 (s, C-5), 99.3 (d, C-4), 74.8 (s, C-2), 53.3 (d, C-2), 41.0 (d, C-4), 40.1 (d, C-5′), 35.9 (d, C-1″), 31.3 (s, C-6), 16.4 (d, C-1), 10.8 (d, C-2″), 9.9 (d, C-7). HR-MS *m/z* calcd for $C_{12}H_{20}O_2S_2$; 260.0905; found: 260.0905 (EI).

Can. J. Chem. Downloaded from www.nrcresearchpress.com by MCGILL UNIVERSITY on 02/02/13
For personal use only.

4-(2-Ethyl-1,3-dithiolan-2-yl)-1-phenylpentane-1,3-dione (10c)

Following the general procedure, IBX oxidation of **9c** (347 mg, 1.12 mmol) and fractionation of the crude product by FCC (50% ethyl acetate in hexane) gave the title compound (246 mg, 71%). IR ν_{max} (cm^{-1}): 3058, 1601, 1570. ^1H NMR (500 MHz, $CDCl_3$; >10:1 enol form) δ: 16.12 (1H, s, HO enol), 7.88 (2H, ap d, J = 7 Hz, Ph), 7.52 (1H, t, J = 7.5 Hz, Ph), 7.45 (2H, ap t, J = 7.5 Hz, Ph), 6.35 (1H, s, HC-2), 3.30–3.20 (4H, m, H_2C-4, H_2C-5′), 3.04 (1H, q, J = 7 Hz, HC-4), 2.13–1.97 (2H, m, H_2C-1″), 1.50 (3H, d, J = 7 Hz, H_3C-4), 1.14 (3H, t, J = 7 Hz, H_3C-2″). ^{13}C NMR (125 MHz, $CDCl_3$; >10:1 enol form) δ: 199.5 (s, C-1), 182.4 (s, C-3), 134.9 (s, Ph), 132.5 (d, Ph), 128.8 (d × 2, Ph), 127.2 (d × 2, Ph), 97.1 (d, C-2), 74.9 (s, C-2), 54.1 (d, C-4), 41.0 (t, C-4), 40.2 (t, C-5′), 36.1 (t, C-1″), 16.4 (q, C-5), 10.9 (q, C-2″). LR-MS (EI) m/z (relative intensity): 308 ($[M]^+$, 2), 279 (2), 215 (2), 189 (3), 159 (6), 147 (34), 133 (100), 105 (46), 77 (37). HR-MS m/z calcd for $C_{16}H_{20}O_2S_2$: 308.0905; found: 308.0898 (EI).

2-[2-(2-Ethyl-1,3-dithiolan-2-yl)-1-oxopropyl]cyclohexanone (10d)

Following the general procedure, IBX oxidation of **9d** (297 mg, 1.03 mmol) and fractionation of the crude product by FCC (20% ethyl acetate in hexane) gave the title compound (239 mg, 81%). IR ν_{max} (cm^{-1}): 3454, 1714, 1587, 1579. ^1H NMR (500 MHz, $CDCl_3$; >10:1 enol form) δ: 16.15 (1H, s, HO enol), 3.33 (1H, q, J = 7 Hz, HC-2), 3.24–3.12 (4H, m, H_2C-4, H_2C-5′), 2.45–2.20 (4H, m, H_2C-3, H_2C-6), 2.15–1.87 (2H, m, H_2C-1″), 1.75–1.62 (4H, m, H_2C-4, H_2C-5), 1.36 (3H, d, J = 7 Hz, H_3C-3′), 1.06 (3H, t, J = 7 Hz, H_3C-2″). ^{13}C NMR (125 MHz, $CDCl_3$; >10:1 enol form) δ: 203.2 (s, C-1), 183.5 (s, C-1), 106.7 (s, C-2), 75.1 (s, C-2″), 48.1 (d, C-2), 40.9 (t, C-4″), 39.6 (t, C-5′), 35.7 (t, C-1″), 31.6 (t, C-6), 24.3 (t, C-3), 23.1 (t, C-4 or C-5), 21.7 (t, C-4 or C-5), 15.7 (q, C-3′), 10.8 (q, C-2″). LR-MS (EI) m/z (relative intensity): 286 ($[M]^+$, 2), 257 (1), 225 (1), 193 (5), 159 (7), 133 (100). HR-MS m/z calcd for $C_{14}H_{24}O_2S_2$: 286.1061; found: 286.1058 (EI).

3-Methyl-1-(2-methyl-1,3-dithiolan-2-yl)hexane-2,4-dione (10e)

Following the general procedure, IBX oxidation of **9e** (955 mg, 3.85 mmol) and fractionation of the crude product by FCC (25% ethyl acetate in hexane) gave the title compound (880 mg, 92%). IR ν_{max} (cm^{-1}): 3404, 1726, 1699. ^1H NMR (500 MHz, $CDCl_3$; 2.7:1 mixture of keto and enol tautomers) δ: 16.38 (1H, s, HO enol), 3.71 (1H, q, J = 7 Hz, HC-4 keto), 3.39–3.24 (4H, m, H_2C-4, H_2C-5′ keto/enol), 3.25 (1H, d, J = 17 Hz, HC-6 keto), 3.19 (1H, d, J = 17 Hz, HC-6 keto), 3.16 (1H, s, HC-6 enol), 2.61–2.42 (2H, m, H_2C-2 keto/enol), 1.91 (3H, s, H_3C-1″ enol), 1.860 (3H, s, H_3CC-4 enol), 1.856 (3H, s, H_3C-1″ keto), 1.32 (3H, d, J = 7 Hz, H_3CC-4 keto), 1.14 (3H, t, J = 7.5 Hz, H_3C-1 enol), 1.05 (3H, t, J = 7.5 Hz, H_3C-1 keto). ^{13}C NMR (500 MHz, $CDCl_3$) δ: 207.7 (s, C-3 keto), 204.3 (s, C-5 keto), 195.0 (s, C-3 enol), 188.4 (s, C-5 enol), 105.1 (s, C-4 enol), 64.0 (s, C-2 enol), 62.0 (s, C-2 keto), 61.4 (t, C-4 keto), 56.4 (d, C-6 keto), 50.6 (d, C-6 enol), 39.88 (t, C-4 enol), 39.86 (t, C-4 keto), 39.7 (t × 2, C-5′ keto/enol), 35.0 (t, C-2 keto), 32.7 (q, C-1″ enol), 32.0 (q, C-1″ keto), 29.7 (t, C-2 enol), 12.8 (q, C-4 keto), 12.7 (q, C-4 enol), 9.4 (q, C-1 enol), 7.8 (q, C-1 keto). LR-MS (EI) m/z (relative intensity): 246 ($[M]^+$, 13), 145 (6), 133 (11), 119 (100), 101 (7), 57 (37). HR-MS m/z calcd for $C_{11}H_{18}O_2S_2$: 246.0748; found: 246.0710 (EI).

6-(2-Ethyl-1,3-dithian-2-yl)-4-methylheptane-3,5-dione (10f)

Following the general procedure, IBX oxidation of **9f** (96 mg, 0.33 mmol) and fractionation of the crude product by FCC (50% ethyl acetate in hexane) gave **11a** (27 mg, 46%), **12**[6,22] (10 mg, 15%), and the title diketone (19 mg, 20%). IR ν_{max} (cm^{-1}): 3394, 1724, 1696, 1625. ^1H NMR (500 MHz, $(CD_3)_2SO$; a 1.3:1 mixture of diastereomers along with ~5% of the enol form) δ: 17.03 (0.05H, s, HO enol), 4.17–4.09 (1H, m, HC-4), 3.87 (0.41H, q, J = 7 Hz, HC-6), 3.72 (0.54H, q, J = 7 Hz, HC-6), 3.16–2.40 (6H, m, H_2C-4, H_2C-5′, H_2C-6), 2.06–1.62 (4H, m, H_2C-2, H_2C-1″), 1.23 (1.25H, d, J = 7 Hz), 1.17 (1.65H, d, J = 7 Hz), 1.12 (1.25H, d, J = 7 Hz), 1.10 (1.65H, d, J = 7 Hz), 1.01 (1.25H, t, J = 7 Hz), 0.99 (1.65H, t, J = 7 Hz), 0.94 (1.65H, t, J = 7 Hz), 0.90 (1.25H, t, J = 7 Hz). ^{13}C NMR (125 MHz, $CDCl_3$) δ: 210.6, 210.2, 209.2, 209.0, 64.9, 62.7, 56.1, 56.0, 50.45, 50.39, 34.5, 33.9, 28.5, 28.3, 27.0, 26.9, 26.3, 24.90, 24.86, 14.4, 14.2, 13.7, 12.9, 9.5, 9.4, 7.93, 7.86. LR-MS (EI) m/z (relative intensity): 288 ($[M]^+$, 21), 213 (1), 181 (9), 175 (41), 149 (10), 147 (100). HR-MS m/z calcd for $C_{14}H_{24}O_2S_2$: 288.1218; found: 288.1224 (EI).

General procedure for pyrone formation

IBX (2 equiv) was added to a stirred solution of diketone (~0.2 mmol) in acetonitrile (5 mL, ~0.04 mol/L) at ambient temperature. CF_3SO_3H (1 equiv) or p-TsOH·H_2O (1 equiv) (or no acid) was added. The mixture was heated at the temperature indicated in Tables 1–3. After the indicated time, the mixture was diluted with ethyl acetate, washed with saturated aq $NaHCO_3$ and brine, dried over Na_2SO_4, concentrated, and fractionated by FCC (60%–80% ethyl acetate in hexane) to give the product.

2,6-Diethyl-3,5-dimethyl-4H-pyran-4-one (11a)

^1H NMR (500 MHz, $CDCl_3$) δ: 2.57 (4H, q, J = 7.5 Hz, H_2C × 2), 1.92 (6H, s, H_3CC × 2), 1.19 (6H, t, J = 7.5 Hz, H_3CCH_2 × 2). ^{13}C NMR (125 MHz, $CDCl_3$) δ: 180.1 (s, C-4), 164.5 (s × 2, C-2, C-6), 118.0 (s × 2, C-3, C-5), 25.0 (t × 2, CH_2), 11.5 (q × 2, CH_3CH_2), 9.6 (q × 2, CH_3C). LR-MS (EI) m/z (relative intensity): 180 ($[M]^+$, 72), 179 (100), 171 (12), 151 (11), 149 (46). HR-MS m/z calcd for $C_{11}H_{16}O_2$: 180.1150; found: 180.1144 (EI). Spectral data were in accord with those previously reported.[6,21]

2,6-Diethyl-3-methyl-4H-pyran-4-one (11b)

IR ν_{max} (cm^{-1}): 1664, 1625, 1601. ^1H NMR (500 MHz, $CDCl_3$) δ: 6.1 (1H, s, HC-5), 2.61 (2H, q, J = 7.5 Hz, H_2CC-2), 2.51 (2H, q, J = 7.5 Hz, H_2CC-6), 1.90 (3H, s, H_3CC-3), 1.23 (3H, t, J = 7.5 Hz, H_3CCC-2 or H_3CCC-6), 1.22 (3H, t, J = 7.5 Hz, H_3CCC-2 or H_3CCC-6). ^{13}C NMR (125 MHz, $CDCl_3$) δ: 180.6 (s, C-4), 169.3 (s, C-6), 166.0 (s, C-2), 119.7 (s, C-3), 110.9 (d, C-5), 26.9 (t, H_2CC-6), 25.0 (t, H_2CC-2), 11.6 (q, H_3CCC-2 or H_3CCC-6), 11.1 (q, H_3CCC-2 or H_3CCC-6), 9.4 (q, CH_3C-3). LR-MS (EI) m/z (relative intensity): 166 ($[M]^+$, 79), 165 (100), 151 (9), 123 (9), 99 (25), 83 (9). HR-MS m/z calcd for $C_{10}H_{14}O_2$: 166.0994; found: 166.0993 (EI).

Can. J. Chem. Downloaded from www.nrcresearchpress.com by MCGILL UNIVERSITY on 02/02/13
For personal use only.

***6-Ethyl-3-methyl-6-phenyl-4H-pyran-4-one* (11c)**

IR ν_{max} (cm^{-1}): 1651, 1618. ^1H NMR (500 MHz, $CDCl_3$) δ: 7.77–7.74 (2H, m, Ph), 7.49–7.46 (3H, m, Ph), 6.73 (1H, s, HC-5), 2.75 (2H, q, J = 7.5 Hz, H_2CC-2), 2.01 (3H, s, H_3CC-3), 1.34 (3H, t, J = 7.5 Hz, H_3CC-1). ^{13}C NMR (125 MHz, $CDCl_3$) δ: 180.4 (s, C-4), 165.5 (s, C-2), 162.6 (s, C-6), 132.0 (s, Ph), 131.2 (d, Ph), 129.2 (d × 2, Ph), 125.8 (d × 2, Ph), 120.6 (s, C-3), 109.6 (d, C-5), 25.2 (t, C-1″), 11.7 (q, CH_3CC-2), 9.6 (q, CH_3C-3). LR-MS (EI) *m/z* (relative intensity): 214 ($[M]^+$, 100), 199 (7), 171 (15), 147 (10), 105 (18), 77 (17). HR-MS *m/z* calcd for $C_{14}H_{14}O_2$: 214.0994; found: 214.0993 (EI). Spectral data were in accord with those previously reported.[33]

***2-Ethyl-3-methyl-5,6,7,8-tetrahydro-4H-chromen-4-one* (11d)**

IR ν_{max} (cm^{-1}): 1705, 1660, 1612. ^1H NMR (500 MHz, $CDCl_3$) δ: 2.56 (2H, q, J = 7.5 Hz, H_2CC-2), 2.50–2.47 (2H, m, H_2C-8), 2.44–2.41 (2H, m, H_2C-5), 1.93 (3H, s, H_3CC-3), 1.81–1.75 (2H, m, H_2C-7), 1.71–1.65 (2H, m, H_2C-6), 1.20 (3H, t, J = 7.5 Hz, H_3CCC-2). ^{13}C NMR (125 MHz, $CDCl_3$) δ: 179.6 (s, C-4), 164.6 (s, C-2), 162.4 (s, C-8a), 120.2 (s, C-4a), 118.4 (s, C-3), 27.5 (t, C-8), 25.0 (t, CH_2C-2), 22.1 (t, C-7), 21.8 (t, C-6), 21.1 (t, C-5), 11.7 (q, CH_3CC-2), 9.5 (q, CH_3C-3). LR-MS (EI) *m/z* (relative intensity): 192 ($[M]^+$, 79), 191 (100), 177 (18), 125 (6). HR-MS *m/z* calcd for $C_{12}H_{16}O_2$: 192.1150; found: 192.1147 (EI).

***2-Ethyl-3,6-dimethyl-4H-pyran-4-one* (11e)**

IR ν_{max} (cm^{-1}): 1661, 1603, 1585. ^1H NMR (500 MHz, $CDCl_3$) δ: 6.05 (1H, s, HC-5), 2.58 (2H, q, J = 7.5 Hz, H_2CC-2), 2.21 (3H, s, H_3CC-6), 1.92 (3H, s, H_3CC-3), 1.21 (3H, t, J = 7.5 Hz, H_3CCC-2). ^{13}C NMR (125 MHz, $CDCl_3$) δ: 180.3 (s, C-4), 165.7 (s, C-2), 164.6 (s, C-5), 119.6 (s, C-3), 112.6 (d, C-5), 25.0 (t, CH_2C-2), 19.8 (q, CH_3C-6), 11.6 (q, CH_3C-3), 9.4 (q, CH_3CC-2). LR-MS (chemical ionization (CI)) *m/z* (relative intensity): 152 ($[M]^+$, 85), 151 (100), 137 (9), 108 (17), 85 (37), 67 (7). HR-MS *m/z* calcd for $C_9H_{12}O_2$: 152.0837; found: 152.0834 (EI).

***4,6-Dimethylnonane-3,5,7-trione* (12)[6,22]**

IR ν_{max} (cm^{-1}): 3364, 1711, 1668, 1616. ^1H NMR (500 MHz, $CDCl_3$; an approximately 4:1:1 mixture of enol and two keto (a and b) diastereomers, respectively) δ: 16.55 (1H, s, HO; enol), 3.85 (0.5H, q, J = 7 Hz, HC-4, HC-6; keto a), 3.84 (0.5H, q, J = 7 Hz, HC-4, HC-6; keto b), 3.71 (1H, q, J = 7 Hz, HC-4; enol), 2.60–2.30 (6H, m, H_2C-2, H_2C-8; keto and enol), 1.89 (3H, s, H_3CC-6; enol), 1.74 (1H, s, H_3C-1, H_3C-9; dienol?), 1.34 (3H, d, J = 7 Hz, H_3CC-4; keto), 1.32 (1.5H, d, J = 7 Hz, H_3CC-4, H_3CC-6; keto a or b), 1.31 (1.5H, d, J = 7 Hz, H_3CC-4, H_3CC-6; keto a or b), 1.16 (3H, t, J = 7 Hz, H_3C-9; enol), 1.12 (1H, t, J = 7 Hz, H_3C-1, H_3C-9; dienol?), 1.08–1.02 (6H, m, H_3C-1 (enol) and H_3C-1, H_3C-9 (keto a and b)). ^{13}C NMR (125 MHz, $CDCl_3$; approximately a 4:1:1 mixture of enol and two keto (a and b) diastereomers, respectively)) δ: 206.6, 206.0, 205.8, 204.4, 201.8, 196.5, 184.6, 106.0, 102.7, 57.5, 57.3, 50.2, 33.7, 32.7, 32.0, 28.4, 11.28, 11.27, 11.2, 10.2, 7.0, 6.0, 5.81, 5.76. LR-MS (EI) *m/z* (relative intensity): 198 ($[M]^+$, 1), 169 (20), 142 (18), 113 (62), 84 (40), 66 (43), 57 (100). HR-MS *m/z* calcd for $C_{11}H_{18}O_3$: 198.1256; found: 198.1267 (EI).

***2,6-Diethyl-2-(ethylthio)-3,5-dimethyl-2H-pyran-4(3H)-one* (13)**

Following the general procedure, IBX oxidation of aldol **9g** (93 mg, 0.30 mmol) and fractionation of the crude product by FCC (5% ethyl acetate in hexane) gave **11a** (24 mg, 44%), **12**[6,22] (12 mg, 20%), and the title compound (10 mg, 14%). IR ν_{max} (cm^{-1}): 1721, 1665, 1622. ^1H NMR (500 MHz, $CDCl_3$) δ: 2.58 (1H, dq, J = 12, 7.5 Hz, HCS), 2.49–2.45 (1H, m, J = 12, 7.5 Hz, HCS), 2.4 (1H, q, J = 7 Hz, HC-3), 2.32 (2H, ap q, J = 7.5 Hz, H_2CC-6), 2.05–1.85 (2H, m, H_2CC-2), 1.76 (3H, s, H_3CC-5), 1.19 (3H, t, J = 7.5 Hz, H_3CCS), 1.13 (3H, t, J = 7.6 Hz, H_3CCC-6), 1.06 (3H, d, J = 7.2 Hz, H_3CC-3), 0.99 (3H, t, J = 7.46 Hz, H_3CCC-2). ^{13}C NMR (125 MHz, $CDCl_3$) δ: 195.8 (s, C-4), 167.5 (s, C-6), 108.4 (s, C-5), 95.4 (s, C-2), 46.0 (s, C-3), 27.5 (s, CH_2C-2), 25.6 (s, CH_2C-6), 22.4 (s, CH_2S), 14.5 (q, CH_3CS), 12.7 (q, CH_3C-3), 11.2 (q, CH_3CC-6), 9.4 (q, CH_3C-5), 8.4 (q, CH_3CC-2). LR-MS (EI) *m/z* (relative intensity): 242 ($[M]^+$, 5), 181 (100), 149 (9), 130 (50), 113 (40), 101 (38), 83 (30), 69 (15). HR-MS *m/z* calcd for $C_{13}H_{22}O_2S$: 242.1341; found: 242.1339 (EI).

***(2R,3S)-3,5-dimethyl-2-((S)-3-oxopentan-2-yl)-2H-pyran-4(3H)-one* (16)**

IBX (24 mg, 0.086 mmol) and ethanedithiol (6 μL, 6 mg, 0.07 mmol) were added to a stirred solution of **6** (an approximately 1:1 mixture of anomers; 24 mg, 0.7 mmol) in acetonitrile (4 mL) at 80 °C. After 1 day, the solution was diluted with ethyl acetate and washed with saturated aq $NaHCO_3$ and brine, dried over Na_2SO_4, concentrated, and fractionated by PTLC (50% ethyl acetate in hexanes) to give the title compound (8 mg, 56%, unoptimized). IR ν_{max} (cm^{-1}): 1718, 1672, 1623. ^1H NMR (500 MHz, $CDCl_3$): δ 7.12 (1H, s, HC-6), 4.49 (1H, dd, J = 3, 10.5 Hz, HC-2), 3.03 (1H, dq, J = 10.5, 7 Hz, HC-2), 2.64–2.49 (2H, m, H_2C-4), 2.40 (1H, dq, J = 3, 7.5 Hz, HC-3), 1.64 (3H, s, H_3CC-5), 1.08 (3H, t, J = 7 Hz, H_3C-5′), 1.07 (3H, d, J = 7.5 Hz, H_3CC-3), 0.99 (3H, d, J = 7 Hz, H_3C-1). ^{13}C NMR (125 MHz, $CDCl_3$) δ: 212.4 (s, C-3′), 197.2 (s, C-4), 159.0 (d, C-6), 112.8 (s, C-5), 83.2 (d, C-2), 56.0 (d, C-2), 41.0 (d, C-3′), 36.8 (t, C-4), 12.6 (q, C-1), 10.7 (q, CH_3C-5), 9.7 (q, CH_3C-3), 7.6 (q, C-5′). LR-MS *m/z* (relative intensity): 210 ($[M]^+$, 15), 195 (12), 153 (12), 141 (9), 125 (19), 85 (52), 69 (13), 57 (100) (EI). HR-MS *m/z* calcd for $C_{12}H_{18}O_3$: 210.1256; found: 210.1248 (EI).

Supplementary data

Supplementary data are available with the article through the journal Web site http://nrcresearchpress.com/doi/suppl/10.1139/v2012-067.

Acknowledgements

Financial support from the Natural Sciences and Engineering Research Council of Canada (NSERC) and the University of Saskatchewan is gratefully acknowledged.

References

(1) Wilk, W.; Waldmann, H.; Kaiser, M. *Bioorg. Med. Chem.* **2009**, *17* (6), 2304. doi:10.1016/j.bmc.2008.11.001.

(2) Sharma, P.; Powell, K. J.; Burnley, J.; Awaad, A. S.; Moses, J. E. *Synthesis* **2011**, 2865. doi:10.1055/s-0030-1260168.

(3) Yamamura, S.; Nishiyama, S. *Bull. Chem. Soc. Jpn.* **1997**, *70* (9), 2025. doi:10.1246/bcsj.70.2025.

Can. J. Chem. Downloaded from www.nrcresearchpress.com by MCGILL UNIVERSITY on 02/02/13
For personal use only.

(4) Afarinkia, K.; Vinader, V. In *Science of Synthesis;* Thomas, E. J., Ed.; Georg Thieme Verlag: Stuttgart, New York, 2003; Vol. 14, pp 275–346.
(5) Brimble, M. A.; Gibson, J. S.; Sperry, J. In *Comprehensive Heterocyclic Chemistry III;* Black, D., Ed. Elsevier: Oxford, 2008; Vol. 7, pp 419–699.
(6) Arimoto, H.; Nishiyama, S.; Yamamura, S. *Tetrahedron Lett.* **1990**, *31* (39), 5619. doi:10.1016/S0040-4039(00)97913-9.
(7) Lister, T.; Perkins, M. V. *Angew. Chem. Int. Ed.* **2006**, *45* (16), 2560. doi:10.1002/anie.200504573.
(8) Sakakura, A.; Watanabe, H.; Nakagawa, S.; Ishihara, K. *Chem. Asian J.* **2007**, *2* (4), 477. doi:10.1002/asia.200600380.
(9) Sakakura, A.; Watanabe, H.; Ishihara, K. *Org. Lett.* **2008**, *10* (12), 2569. doi:10.1021/ol800860p.
(10) (a) Paterson, I.; Chen, D. Y.-K.; Acena, J. L.; Franklin, A. S. *Org. Lett.* **2000**, *2* (11), 1513. doi:10.1021/ol000027n; (b) Paterson, I.; Chen, D. Y.-K.; Franklin, A. S. *Org. Lett.* **2002**, *4* (3), 391. doi:10.1021/ol017082w; (c) Yadav, J. S.; Sathaiah, K.; Srinivas, R. *Tetrahedron* **2009**, *65* (17), 3545. doi:10.1016/j.tet.2008.12.049.
(11) Dorman, L. C. *J. Org. Chem.* **1967**, *32* (12), 4105. doi:10.1021/jo01287a101.
(12) Koreeda, M.; Akagi, H. *Tetrahedron Lett.* **1980**, *21* (13), 1197. doi:10.1016/S0040-4039(00)71369-4.
(13) (a) Gillingham, D. G.; Hoveyda, A. H. *Angew. Chem. Int. Ed.* **2007**, *46* (21), 3860. doi:10.1002/anie.200700501; (b) Jung, M. E.; Salehi-Rad, R. *Angew. Chem. Int. Ed.* **2009**, *48* (46), 8766. doi:10.1002/anie.200904607.
(14) McCombie, S. W.; Metz, W. A.; Nazareno, D.; Shankar, B. B.; Tagat, J. *J. Org. Chem.* **1991**, *56* (16), 4963. doi:10.1021/jo00016a028.
(15) Mizuno, A.; Kusama, H.; Iwasawa, N. *Chem. Eur. J.* **2010**, *16* (28), 8248. doi:10.1002/chem.201001068.
(16) Beye, G. E.; Ward, D. E. *J. Am. Chem. Soc.* **2010**, *132* (20), 7210. doi:10.1021/ja102356j.
(17) Becerril-Jiménez, F.; Ward, D. E. *Org. Lett.* **2012**, *14* (6), 1648. doi:10.1021/ol300432y.
(18) Ward, D. E.; Jheengut, V.; Akinnusi, O. T. *Org. Lett.* **2005**, *7* (6), 1181. doi:10.1021/ol050195l.
(19) Duschek, A.; Kirsch, S. F. *Angew. Chem. Int. Ed.* **2011**, *50* (7), 1524. doi:10.1002/anie.201000873.
(20) More, J. D.; Finney, N. S. *Org. Lett.* **2002**, *4* (17), 3001. doi:10.1021/ol026427n.
(21) Mullock, E. B.; Suschitzky, H. *J. Chem. Soc. C* **1967**, 828. doi:10.1039/j39670000828.
(22) (a) Sakakibara, M.; Mori, K. *Tetrahedron Lett.* **1979**, *20* (26), 2401. doi:10.1016/S0040-4039(01)86303-6; (b) Ansell, J. M.; Hassner, A.; Burkholder, W. E. *Tetrahedron Lett.* **1979**, *20* (27), 2497. doi:10.1016/S0040-4039(01)86330-9; (c) Mori, K.; Ebata, T.; Sakakibara, M. *Tetrahedron* **1981**, *37* (4), 709. doi:10.1016/S0040-4020(01)97687-2.
(23) Nicolaou, K. C.; Mathison, C. J. N.; Montagnon, T. *J. Am. Chem. Soc.* **2004**, *126* (16), 5192. doi:10.1021/ja0400382.
(24) (a) Wu, Y. K.; Shen, X.; Huang, J. H.; Tang, C. J.; Liu, H. H.; Hu, Q. *Tetrahedron Lett.* **2002**, *43* (36), 6443. doi:10.1016/S0040-4039(02)01346-1; (b) Shukla, V. G.; Salgaonkar, P. D.; Akamanchi, K. G. *Synlett* **2005**, 1483. doi:10.1055/s-2005-868496.
(25) (a) Luiken, S.; Kirschning, A. *J. Org. Chem.* **2008**, *73* (5), 2018. doi:10.1021/jo7025146; (b) Field, L.; Barbee, R. B. *J. Org. Chem.* **1969**, *34* (1), 36. doi:10.1021/jo00838a010.
(26) Gallen, M. J.; Goumont, R.; Clark, T.; Terrier, F.; Williams, C. M. *Angew. Chem. Int. Ed.* **2006**, *45* (18), 2929. doi:10.1002/anie.200504156.
(27) Still, W. C.; Kahn, M.; Mitra, A. *J. Org. Chem.* **1978**, *43* (14), 2923. doi:10.1021/jo00408a041.
(28) Reynolds, W. F.; Enríquez, R. G. *J. Nat. Prod.* **2002**, *65* (2), 221. doi:10.1021/np010444o.
(29) The multiplicity of ^{13}C NMR signals refers to the number of attached Hs (i.e., s = C, d = CH, t = CH_2, q = CH_3).
(30) Frigerio, M.; Santagostino, M.; Sputore, S. *J. Org. Chem.* **1999**, *64* (12), 4537. doi:10.1021/jo9824596.
(31) Brown, C. A. *Synthesis* **1975**, *1975* (05), 326. doi:10.1055/s-1975-23746.
(32) Rama Rao, A. V.; Venkatswamy, G.; Javeed M., S. M.; Deshpande, V. H.; Ramamohan Rao, B. *J. Org. Chem.* **1983**, *48* (9), 1552. doi:10.1021/jo00157a039.
(33) Wittek, P. J.; Hindley, K. B.; Harris, T. M. *J. Org. Chem.* **1973**, *38* (5), 896. doi:10.1021/jo00945a010.

Enantioselective synthesis of (*R*)-tolterodine using lithiation/borylation–protodeboronation methodology

Stefan Roesner and Varinder K. Aggarwal

Can. J. Chem. Downloaded from www.nrcresearchpress.com by MCGILL UNIVERSITY on 02/02/13
For personal use only.

Abstract: The synthesis of the pharmaceutical (*R*)-tolterodine is reported using lithiation/borylation–protodeboronation of a homoallyl carbamate as the key step. This step was tested with two permutations: an electron-neutral aryl Li-carbamate reacting with an electron-rich boronic ester and an electron-rich aryl Li-carbamate reacting with an electron-neutral boronic ester. It was found that the latter arrangement was considerably better than the former. Further improvements were achieved using magnesium bromide in methanol leading to a process that gave high yield and high enantioselectivity in the lithiation/borylation reaction. The key step was used in an efficient synthesis of (*R*)-tolterodine in a total of eight steps in a 30% overall yield and 90% ee.

Key words: asymmetric synthesis, boronic esters, *gem*-diarylalkyl, lithiation/borylation reaction, tolterodine.

Résumé : La synthèse du médicament : la (*R*)-toltérodine a été réalisé suivant une étape clé de lithiation/borylation-protodéboronation d'un carbamate homoallilyque. Deux permutations ont été évalué. Premièrement un carbamate d'aryle et de lithuim éléctronqiuement neutre réagissant sur un estre boronique riche en électron et deuxièmement un carbamate d'aryle et de lithium riche en électron réagissant sur un ester boronique électroniquement neutre. Cette dernière s'est révélée être la meilleure. D'autres améliorations ont été obtenues : notament en utilisant le bromure de magnésium en solution dans le méthanol. Cette méthodologie donne un rendement et une énantiosélectivité élevé pour la réaction de lithiation/borylation. L'étape clé permet de réaliser une synthèse éfficace de la (*R*)-toltérodine en huit étapes avec un rendement global de 30% et un ee de 90%.

Mots-clés : synthèse asymétrique, esters boroniques, *gem*-diarylalkyle, réaction de lithiation/borylation, toltérodine.

Introduction

The enantioselective synthesis of pharmaceuticals and biologically active natural products is a major theme for synthetic chemists. In particular, the formation of chiral *gem*-diarylalkyl compounds, a motif that is present in many therapeutically important molecules, is especially challenging owing to the lack of nearby functional groups that might be enlisted to enable the formation of C–C bonds.[1] Examples of these compounds include (*R*)-tolterodine (**1**, Detrol), (+)-sertraline (**2**, Zoloft), and (+)-indatraline (**3**) (Fig. 1).

(*R*)-Tolterodine (**1**) is a potent competitive muscarine receptor antagonist for the treatment of urinary incontinence and other symptoms related to an overactive bladder,[2] a compound that has achieved blockbuster status ($1.21 billion in sales in 2008[3]). Because of its importance and challenging *gem*-diarylalkyl stereocenter, it has become a popular target for asymmetric synthesis. Whereas the original route relied on optical resolution to separate (*R*)-tolterodine from the racemate,[4] initial asymmetric routes used chiral auxiliaries[5] or asymmetric Me-CBS (Corey–Bakshi–Shibata) reduction[6] to introduce the stereogenic center. More recently, asymmetric strategies have utilized transition-metal-catalyzed processes including hydrogenation,[7] hydroformylation,[8] or arylboration.[9]

Recently, we reported the highly enantioselective syntheses of (+)-sertraline (**2**) and (+)-indatraline (**3**) using a lithiation/borylation[10]–protodeboronation[11] strategy (Scheme 1). (+)-Sertraline (**2**), a potent competitive selective serotonin reuptake inhibitor (SSRI), is a commonly prescribed therapeutic for the treatment of depression and other anxiety-related disorders and has also achieved blockbuster status[12] ($3.36 billion in sales in 2004[13]). The related molecule, (+)-indatraline (**3**), is a potent psychoactive compound that acts as a monoamine reuptake inhibitor[14] and has the potential to be used in maintenance therapy to treat cocaine abuse.[15] A lithiation/borylation reaction and subsequent protodeboronation gave access to both **2** and **3** in high yield and excellent enantioselectivity. In contrast with other substrates devoid of the alkene function, for homoallylic carbamate **4** it was found necessary to add a crown ether or to carry out a solvent exchange to $CHCl_3$ to achieve 1,2-metalate rearrangement of the intermediate ate complex.[11b] The requirement for such unusual conditions has made us probe this type of rearrangement further with a view to applying it in the asymmetric synthesis of (*R*)-tolterodine. Once again, we found that modifications of

Received 25 June 2012. Accepted 30 July 2012. Published at www.nrcresearchpress.com/cjc on 29 November 2012.

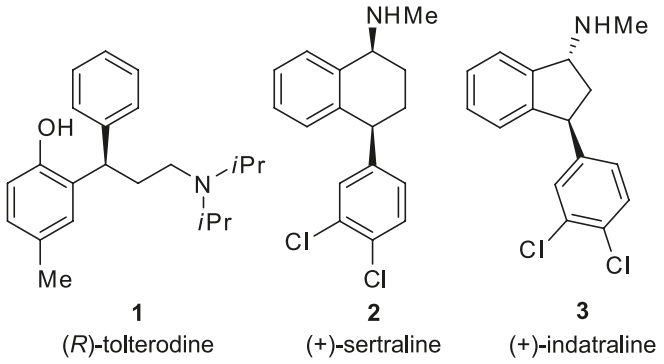
S. Roesner and V.K. Aggarwal. School of Chemistry, University of Bristol, Cantock's Close, Bristol, BS8 1TS, UK.

Corresponding author: Varinder K. Aggarwal (e-mail: V.Aggarwal@bristol.ac.uk).

This paper is part of a Special Issue dedicated to Professor Derrick Clive and is for his many creative contributions to synthetic chemistry.

Can. J. Chem. Downloaded from www.nrcresearchpress.com by MCGILL UNIVERSITY on 02/02/13
For personal use only.

Fig. 1. Pharmaceutically important molecules containing the *gem*-diaryl substructure.



1 (*R*)-tolterodine **2** (+)-sertraline **3** (+)-indatraline

the improved conditions for this class of substrates were required to promote 1,2-metallate rearrangement, but this did ultimately enable us to complete a successful synthesis of (*R*)-tolterodine using our lithiation/borylation–protodeboronation strategy.

Results and discussion

Encouraged by the results for the synthesis of (+)-sertraline and (+)-indatraline, we applied a similar strategy for the synthesis of (*R*)-tolterodine (**1**). The retrosynthetic analysis for **1** (Scheme 2) involves, as a key step, the lithiation/borylation of benzylic carbamate **4** with boronic ester **7** to form **8**. Subsequent protodeboronation of tertiary boronic ester **8** would lead to olefin **9**. Both the lithiation/borylation[10] and protodeboronation[11] have been found to be highly stereoselective, occurring with retention of the stereochemistry. Functional group manipulation of the key intermediate **9** would then provide (*R*)-tolterodine (**1**).

However, attempts to realize this in practice were not straightforward: when we carried out the lithiation/borylation of carbamate **4** with boronic ester **7**, using 12-crown-4, trimethylsilyl chloride (TMSCl), and H_2O as additives, no product was formed (Scheme 3). A solvent switch after ate complex formation from diethyl ether to $CHCl_3$ gave only trace amounts of tertiary boronic ester **8**. Both sets of conditions had been successfully employed in the synthesis of sertraline; the only difference here was the use of 2-methoxy-5-methylphenyl boronic ester in place of 3,4-dichlorophenyl boronic ester. Monitoring the reaction by ^{11}B NMR revealed that an intermediate boron–ate complex (**A**) formed (~5 ppm), but instead of a 1,2-migration to the product, ate complex **A** decomposed over time returning some starting material.

Previous experiments in the syntheses of **2** and **3** revealed that the double bond can interfere in the lithiation/borylation process, presumably by formation of a Li–π complex, as the saturated compound underwent smooth lithiation/borylation under standard conditions (either (*i*) no additives were required, simply warming to room temperature (RT) or (*ii*) the addition of $MgBr_2$/MeOH prior to warming to RT).[11b] To determine whether the problem was related to the double bond, propylcarbamate **10** was tested in the lithiation/borylation reaction with pinacol boronic ester **7** (Scheme 4). The formation of a boron–ate complex was confirmed by ^{11}B NMR, but again no product could be isolated. We believed that the extra steric hindrance of the aryl boronic ester (bearing an ortho substituent) was perhaps responsible for the low reactivity. We therefore investigated the use of the less-hindered neopentyl boronic ester **12**, instead of the pinacol boronic ester **7**, under the same reaction conditions. Utilizing carbamate **10** and neopentyl boronic ester **12** in the lithiation/borylation reaction gave tertiary boronic ester **13** in 62% isolated yield after column chromatography. To our delight, lithiation/borylation of homoallylic carbamate **4** (99% enantiomeric excess (ee)) and neopentyl boronic ester **12** gave tertiary boronic ester **14** in good yield and high enantioselectivity (Table 1, entry 1). This showed that the presence of the double bond was not interfering in the reaction. However, attempts to improve both yield and enantioselectivity by the addition of additives after ate complex formation were not successful (Table 1, entries 2–8).

We therefore considered an alternative protocol. Instead of using carbamate **4** with 2-methoxy-5-methylphenyl boronic ester we decided to switch the two aryl groups. In other words, we considered the possibility of the reaction of homoallylic carbamate **18** with phenyl boronic ester in a lithiation/borylation reaction. Although the two ate complexes have similar steric properties, we believed that the presence of the *ortho*-methoxy group might assist in the expulsion of the carbamate, thereby promoting the 1,2-metallate rearrangement.

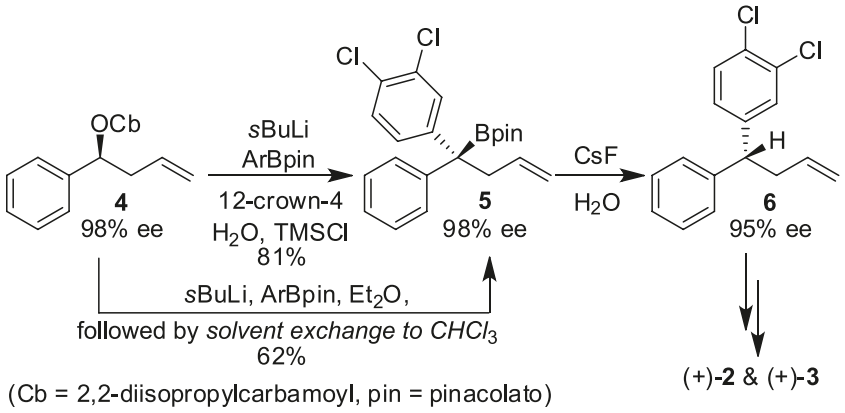
Homoallylic carbamate **18** was synthesized in a three-step sequence starting from the commercially available aldehyde **15** (Scheme 5). The phenolic hydroxyl group was protected as the methyl ether to give aldehyde **16**. Subsequent, Brown-mediated asymmetric allylation using (+)-B-allyl (diisopinocampheyl)borane ((+)-Ipc_2Ball) gave alcohol **17** in 92% ee,[16] which was followed by carbamoylation furnishing the desired carbamate in 97% yield and 92% ee.

The lithiation/borylation reaction between racemic homoallylic carbamate **18** and phenyl pinacol boronic ester **19** now proceeded well to give tertiary boronic ester **8** in 40% yield (Table 2, entry 1). In contrast with our earlier work, the reaction gave only a poor yield when neopentyl boronic ester **20** was used (Table 2, entry 2). Therefore, an optimization of the lithiation/borylation reaction of carbamate **18** with phenyl pinacol boronic ester **19** was carried out. Better results were obtained with the Lewis acidic additives TMSCl or $MgBr_2$ in anhydrous MeOH (Table 2, entries 6 and 8). The optimum conditions/additives of the lithiation/borylation reaction ($MgBr_2$/MeOH; Table 2, entry 8) were applied to the enantioenriched carbamate **18** and we were pleased to find that the reaction proceeded with 98% es (Scheme 6). Hence, we used these optimized conditions to complete the synthesis of (*R*)-tolterodine.

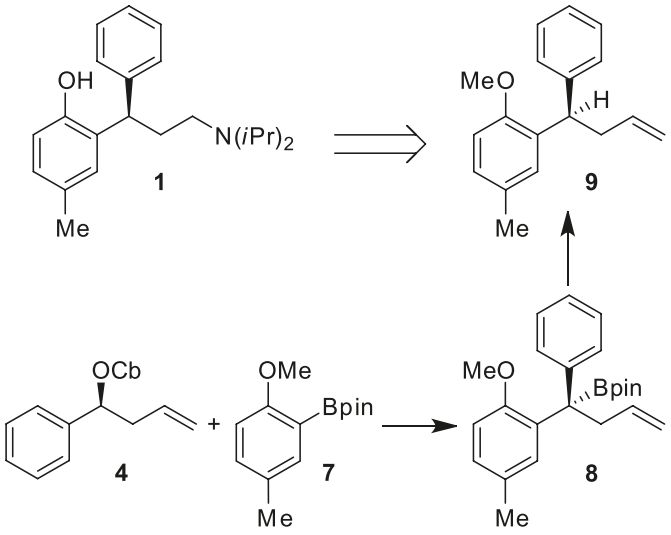
Interestingly, when we reinvestigated the lithiation/borylation reaction as applied in the synthesis of sertraline, the reaction with an electron-rich aryl group associated with carbamate **4** and an electron-deficient aryl group (3,4-$Cl_2C_6H_4$) on boronic ester **21** worked much better than having an electron-deficient aryl group associated with carbamate **22** and an electron-rich aryl group on boronic ester **19** (Scheme 7). This suggests that this arrangement of electronic substitution of the aryl rings is likely to be general.

With the lithiation/borylation problem solved, we focused on the next step: protodeboronation of tertiary boronic ester **8**.

Scheme 1. Enantioselective syntheses of (+)-sertraline (**2**) and (+)-indatraline (**3**) using a lithiation/borylation–protodeboronation strategy.



Scheme 2. Retrosynthetic scheme for the synthesis of (*R*)-tolterodine (**1**).



Unfortunately, our standard procedure for the protodeboronation of diarylalkyl boronic esters (1.5 equiv CsF, 2.5 equiv H_2O, 1,4-dioxane)[11] proceeded very sluggishly and it took 48 h at 80 °C until full conversion of **8** was achieved. This is probably due to the electron-rich aryl ring, which makes deboronation more difficult. In the case of protodeboronation of aryldialkyl boronic esters, we also found that CsF/H_2O was very slow, but that tetrabutylammonium fluoride trihydrate (TBAF·3H2O) was considerably superior.[11a] Using these previously reported conditions (1.5 equiv TBAF·3H_2O, toluene), tertiary boronic ester **8** was smoothly protodeboronated at ambient temperature within 90 min in excellent yield and enantioselectivity to give key intermediate **9** (Scheme 6).

The remaining synthesis was completed in a three-step sequence (Scheme 6). The double bond in olefin **9** was successfully cleaved by a Lemieux–Johnson oxidation,[17] with in situ generated osmium tetroxide, to the corresponding aldehyde **23**. Subsequent reductive amination with diisopropylamine and sodium triacetoxyborohydride gave the protected tolterodine precursor **24** in a good yield. Finally, removal of the methyl group by acidic hydrolysis resulted in the formation of (*R*)-tolterodine (**1**) in an excellent yield. The *R* configuration was confirmed by comparison of the optical rotations, $[\alpha]_D^{20}$ +28.0 (*c* 0.50, MeOH) for **1** with that reported in the literature ($[\alpha]_D^{20}$ +32.5 (*c* 0.89, MeOH)).[7e] Thus, using our lithiation/borylation–protodeboronation methodology as a key step, (*R*)-tolterodine was synthesized through an eight-step sequence in an overall yield of 30%.

Conclusion

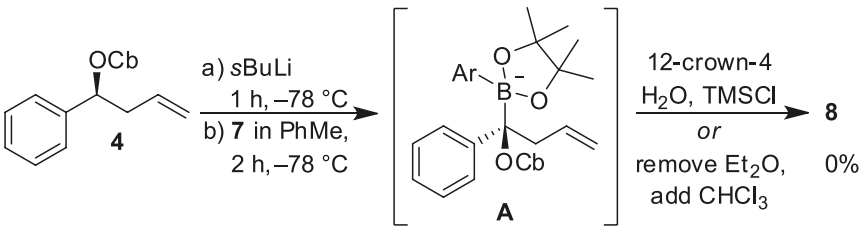
In conclusion, lithiation/borylation and subsequent protodeboronation has been used in the generation of *gem*-diarylalkyl stereocenters in both high yield and high enantioselectivity. More importantly, we have found that the optimum arrangement of groups is to have an electron-rich aryl group associated with the carbamate to promote the 1,2-metallate rearrangement, otherwise, reversion to starting materials tends to dominate. This methodology has been applied to a highly enantioselective synthesis of (*R*)-tolterodine.

Experimental

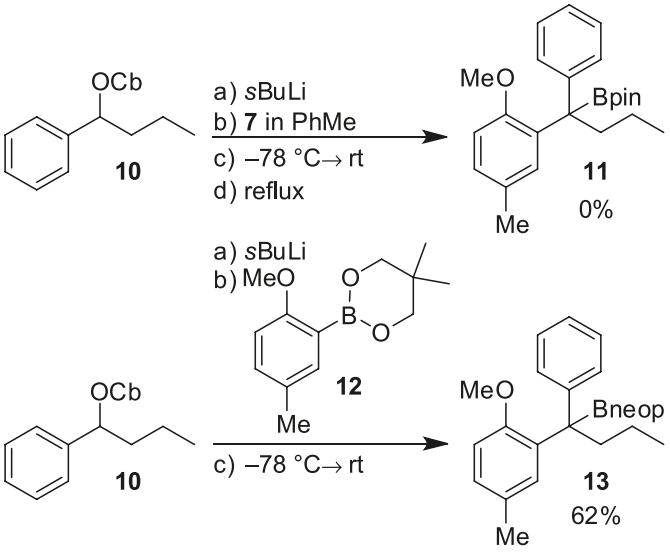
Reaction mixtures were stirred magnetically. Air- and moisture-sensitive reactions were carried out in flame-dried glassware under argon atmosphere using standard Schlenk manifold technique. All required fine chemicals were purchased from Acros Organics, Alfa Aesar, Inochem-Frontier Scientific, or Sigma-Aldrich and used as received unless otherwise mentioned. Anhydrous solvents were prepared using anhydrous solvent drying columns.[18] Microwave reactions were carried out in a Biotage Initiator EXP EU microwave synthesizer. Analytical thinlayer chromatography (TLC) was performed on aluminum-backed silica plates (Merck, silica gel 60 F_{254}, 0.25 mm). Compounds were visualized by exposure to UV light or by staining the plates with a 5% solution of phosphomolybdic acid ($H_3PMo_{12}O_{40}$) in EtOH followed by heating. Flash column chromatography was performed on silica gel (Sigma-Aldrich, silica gel 60, 40–63 μm). ^{1}H NMR spectra were recorded in $CDCl_3$ at 400 or 500 MHz on a Joel ECP 400, a Varian 400, or a Varian 500 Fourier transform (FT) spectrometer. Chemical shifts (δ_H) are quoted in parts per million (ppm) and referred to $CHCl_3$ (7.27 ppm). ^{1}H NMR coupling constants are reported in hertz and refer to apparent multiplicities. Data are reported as follows: chemical shift, multiplicity (s = singlet, br s = broad singlet, d = doublet,

Can. J. Chem. Downloaded from www.nrcresearchpress.com by MCGILL UNIVERSITY on 02/02/13
For personal use only.

Scheme 3. Lithiation/borylation of carbamate **4** and boronic ester **7**.

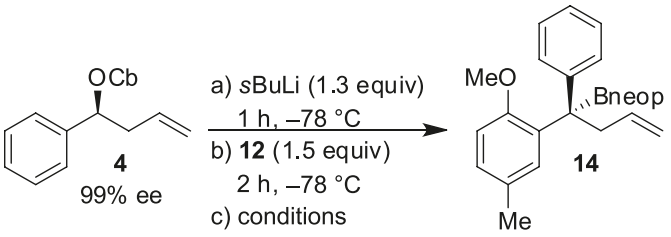


Scheme 4. Lithiation/borylation of carbamate **10**, pinacol boronic ester **7**, and neopentyl boronic ester **12**.



t = triplet, m = multiplet, dd = doublet of doublet, etc.), coupling constant, integration, and assignment. ^{13}C NMR spectra were recorded at 101 or 126 MHz on a Jeol ECP 400, a Varian 400, or a Varian 500 instrument. Chemical shifts (δ_C) are quoted in ppm and referenced to $CHCl_3$ (77.0 ppm). ^{11}B NMR spectra were measured using quartz NMR tubes at 96 or 128 MHz on a Jeol Lambda 300, a Joel ECP (Eclipse) 300, or a Varian 400 with complete proton decoupling using $BF_3{\cdot}Et_2O$ (0.0 ppm) as an external standard. Mass spectra were recorded by the University of Bristol, School of Chemistry departmental mass spectrometry service using chemical ionization (CI) or electrospray ionization (ESI) techniques for low- and high-resolution mass spectra (LR-MS and HR-MS, respectively). All IR spectra were recorded on the neat compounds using a PerkinElmer Spectrum One FT-IR spectrometer. Optical rotations were obtained using a Bellingham + Stanley Ltd. ADP220 polarimeter. Melting points were measured with a Reichert hot stage apparatus and are uncorrected. Chiral HPLC separations were performed on an Agilent 1100 Series HPLC unit equipped with a UV–vis diode array detector using a Daicel Chiralpak IB column (4.6 × 250 mm^2, 5 μm) fitted with a guard (4 × 10 mm^2). (Chiral HPLC traces and ^1H and ^{13}C NMR spectra can be found in the Supplementary data).

Table 1. Optimization of the lithiation/borylation reaction conditions for carbamate **4**.

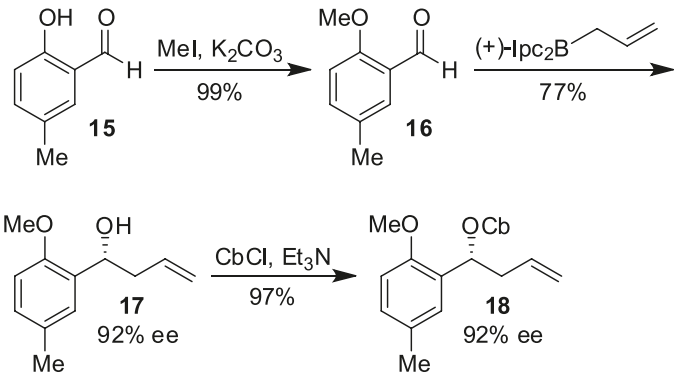


Entry	Conditions	Yield (%)	es (%)[a]
1	No additives	52	94
2	Solvent exchange to $CHCl_3$	10	90
3	Reaction in toluene	19	45
4	12-Crown-4	32	53
5	TMSCl	8	93
6	12-Crown-4, TMSCl	1	93
7	$MgBr_2$/MeOH	1	96
8	$MgBr_2{\cdot}Et_2O$	50	13

Note: es, enantiospecifity. Reaction conditions: **4** (0.3 mol/L in diethyl ether), *s*-BuLi (1.3 mol/L in cyclohexane/hexane, 98:2), **12** (0.9 mol/L in diethyl ether). Where applicable, 1.2 equiv of additive were used. The enantiomeric excess (ee) was determined after oxidation of an aliquot of the tertiary boronic ester by chiral HPLC.

[a]es = (product ee/starting material ee) × 100.

Scheme 5. Synthesis of carbamate **18**.

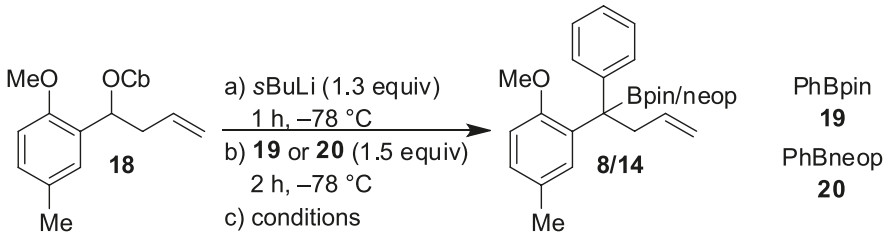


2-(2-Methoxy-5-methylphenyl)-4,4,5,5-tetramethyl-1,3,2-dioxaborolane (7)

This compound was synthesized following a literature procedure performed on a different substrate.[19] Boronic ester **7** (2.02 g, 8.14 mmol, >99%) was obtained as a white solid, which was used without further purification; mp 75–76 °C

Can. J. Chem. Downloaded from www.nrcresearchpress.com by MCGILL UNIVERSITY on 02/02/13
For personal use only.

Table 2. Optimization of the lithiation/borylation reaction conditions for carbamate **18**.



Entry	Boronic ester	Conditions	Yield (%)
1	**19**	No additives	40
2	**20**	No additives	13
3	**19**	Solvent exchange to $CHCl_3$	44
4	**19**	Reaction in toluene	16
5	**19**	12-Crown-4	33
6	**19**	TMSCl	51
7	**19**	12-Crown-4, TMSCl	17
8	**19**	$MgBr_2$/MeOH	74
9	**19**	$MgBr_2{\cdot}Et_2O$	15

Note: Reaction conditions: **18** (0.3 mol/L in diethyl ether), *s*-BuLi (1.3 mol/L in cyclohexane/hexane, 98:2), **19** or **20** (0.9 mol/L in diethyl ether). Where applicable, 1.2 equiv of additive were used.

Can. J. Chem. Downloaded from www.nrcresearchpress.com by MCGILL UNIVERSITY on 02/02/13
For personal use only.

(diethyl ether). IR (neat, cm^{-1}) ν_{max}: 2981, 1605, 1585, 1243. ^1H NMR (400 MHz, $CDCl_3$, ppm) δ_H: 7.49 (d, J = 2.3 Hz, 1H, H_{Ar}), 7.20 (dd, J = 8.4, 2.3 Hz, 1H, H_{Ar}), 6.77 (d, J = 8.4 Hz, 1H, H_{Ar}), 3.81 (s, 3H, OCH_3), 2.29 (s, 3H, $C_{Ar}CH_3$), 1.36 (s, 12H, CH_3). ^{13}C NMR (101 MHz, $CDCl_3$, ppm) δ_C: 162.2 ($COCH_3$), 137.1 (CH), 132.9 (CH), 129.2 (C), 110.5 (CH), 83.4 ($OC(CH_3)_2$), 56.0 (OCH_3), 24.8 (CH_3), 20.2 ($C_{Ar}CH_3$). ^{11}B NMR (96 MHz, $CDCl_3$, ppm) δ_B: 30.0 (br s). MS *m/z* (%) (CI^+): 249 ($[M + H]^+$, 100), 248 ($[M]^+$, 60), 247 (18), 145 (15), 123 ($[Ar + H]^+$, 15), 101 (24). HR-MS (CI^+) calcd for $C_{14}H_{22}O_3{}^{11}B$ $[M + H]^+$: 249.1662; found: 249.1664.

2-(2-Methoxy-5-methylphenyl)-5,5-dimethyl-1,3,2-dioxaborinane (12)

This compound was synthesized following a literature procedure performed on a different substrate.[19] Boronic ester **12** (3.51 g, 14.4 mmol, 96%) was obtained as a white solid, which required no further purification; mp 59–61 °C (diethyl ether). IR (neat, cm^{-1}) ν_{max}: 2936, 1603, 1584, 1241. ^1H NMR (400 MHz, $CDCl_3$, ppm) δ_H: 7.47 (d, J = 2.2 Hz, 1H, H_{Ar}), 7.17 (dd, J = 8.4, 2.2 Hz, 1H, H_{Ar}), 6.78 (d, J = 8.4 Hz, 1H, H_{Ar}), 3.82 (s, 3H, OCH_3), 3.80 (s, 4H, OCH_2), 2.29 (s, 3H, $C_{Ar}CH_3$), 1.05 (s, 6H, CH_3). ^{13}C NMR (101 MHz, $CDCl_3$, ppm) δ_C: 161.7 ($COCH_3$), 136.2 (CH), 132.0 (CH), 129.1 (C), 110.4 (CH), 72.4 (OCH_2), 55.9 (OCH_3), 31.7 ($C(CH_3)_2$), 21.9 (CH_3), 20.3 ($C_{Ar}CH_3$). ^{11}B NMR (96 MHz, $CDCl_3$, ppm) δ_B: 26.3 (br s). MS *m/z* (%) (CI^+): 235 ($[M + H]^+$, 100), 234 ($[M]^+$, 53), 233 (19), 123 ($[Ar + H]^+$, 31), 75 (53). HR-MS (CI^+) calcd. for $C_{13}H_{20}O_3{}^{11}B$ $[M + H]^+$: 235.1506; found: 235.1500.

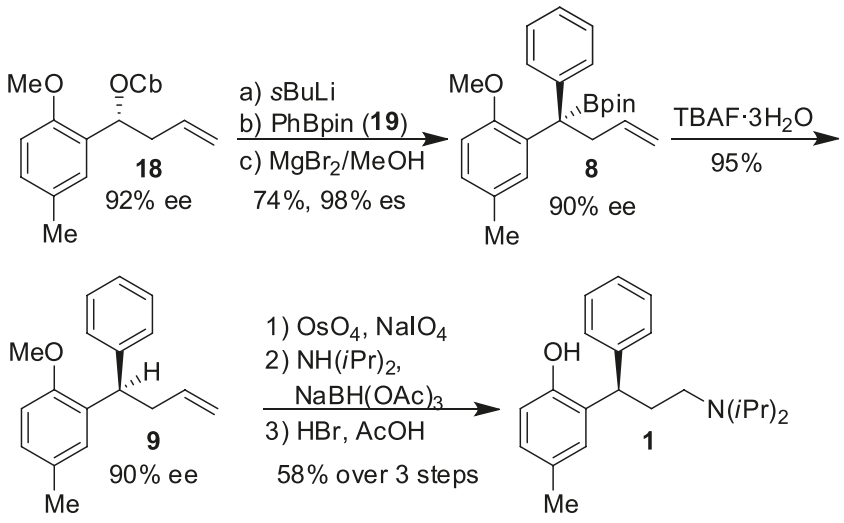
1-Phenylbutyl diisopropylcarbamate (10)

To a suspension of sodium hydride (60% dispersion in mineral oil, 300 mg, 7.50 mmol, 1.5 equiv) in anhydrous tetrahydrofuran (THF; 20 mL), 1-phenylbutan-1-ol (751 mg, 5.00 mmol, 1.0 equiv) was added dropwise and the mixture was stirred for 75 min at RT. A solution of *N*,*N*-diisopropylcarbamoyl chloride (982 mg, 6.00 mmol, 1.2 equiv) in anhydrous THF (5.0 mL) was added and the reaction mixture was heated under reflux for 44 h. The solvent was removed in vacuo and the residue was portioned between water and diethyl ether. The phases were separated and the aqueous layer was re-extracted with diethyl ether. The combined organic layers were dried over anhydrous $MgSO_4$, filtered, and concentrated under reduced pressure. The residue was subjected to flash chromatography (SiO_2, pentane/EtOAc, 6:1) to obtain carbamate **10** (1.13 g, 4.07 mmol, 81%) as a colourless oil. TLC (pentane/EtOAc, 6:1): 0.46. IR (neat, cm^{-1}) ν_{max}: 2962, 1687. ^1H NMR (400 MHz, $CDCl_3$, ppm) δ_H: 7.37–7.29 (m, 4H, H_{Ar}), 7.29–7.23 (m, 1H, H_{Ar}), 5.71 (t, J = 6.9 Hz, 1H, CHOCb), 4.04 (br m, 1H, $CH(CH_3)_2$), 3.84 (br m, 1H, $CH(CH_3)_2$), 1.94 (m, 1H, $CHHCHO$), 1.76 (m, 1H, $CHHCHO$), 1.44–1.27 (m, 2H, CH_2CH_3), 1.22 (br m, 12H, $CH(CH_3)_2$), 0.92 (t, J = 7.4 Hz, 3H, CH_2CH_3). ^{13}C NMR (101 MHz, $CDCl_3$, ppm) δ_C: 155.1 (NCO), 141.8 (C), 128.2 (CH), 127.3 (CH), 126.5 (CH), 76.4 (CHOCb), 46.1 (br, $CH(CH_3)_2$), 39.0 (CH_2CHO), 21.4 (br, $CH(CH_3)_2$), 18.9 (CH_2CH_3), 13.9 (CH_2CH_3). MS *m/z* (%) (CI^+): 278 ($[M + H]^+$, 77), 236 (11), 218 (10), 146 ($[CbOH + H]^+$, 100), 133 ($[Ph(CH_2)_4]^+$, 57), 128 (16), 102 (12), 91 ($[PhCH_2]^+$, 30). HR-MS (CI^+) calcd for $C_{17}H_{28}NO_2$ $[M + H]^+$: 278.2120; found: 278.2116.

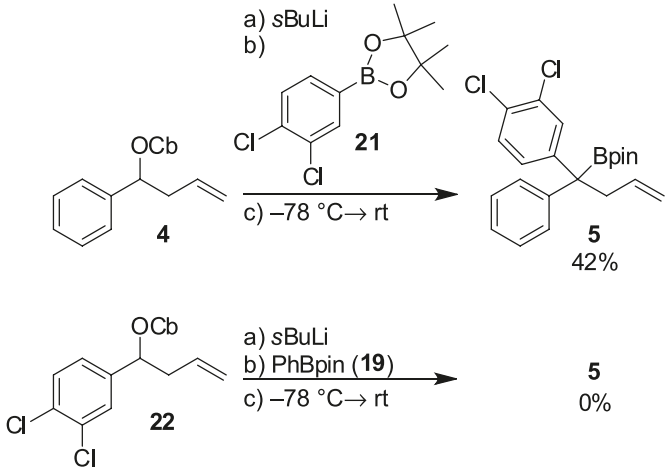
2-(1-(2-Methoxy-5-methylphenyl)-1-phenylbutyl)-5,5-dimethyl-1,3,2-dioxaborinane (13)

1-Phenylbutyl diisopropylcarbamate (**10**; 139 mg, 0.50 mmol, 1.0 equiv) was dissolved in anhydrous diethyl ether (1.5 mL) and chilled to −78 °C. *s*-BuLi (500 μL, 1.3 mol/L solution in cyclohexane/hexane, 98:2, 0.65 mmol, 1.3 equiv) was added dropwise and the mixture was stirred at this temperature for 1 h. A solution of neopentyl ester **12** (176 mg, 0.75 mmol, 1.5 equiv) in anhydrous diethyl ether (0.5 mL)

Scheme 6. Synthesis of (*R*)-tolterodine (**1**).



Scheme 7. Lithiation/borylation of carbamates **4** and **22**.



was added dropwise and the mixture was stirred for 2 h at −78 °C. The cooling bath was removed and stirring was continued at RT overnight (15 h). The reaction mixture was cooled to 0 °C and 1 mol/L KH_2PO_4(aq) (2.0 mL) was added slowly. After stirring for 10 min at RT, the phases were separated and the aqueous phase was extracted with diethyl ether. The combined organic phases were dried over anhydrous $MgSO_4$, filtered, and the solvent was removed in vacuo. The crude product was purified by column chromatography (SiO_2, pentane/EtOAc, 30:1) to give tertiary boronic ester **13** (114 mg, 0.31 mmol, 62% or 92% based on recovered starting material (BRSM)) as a colourless oil, which crystallized upon standing to white cubes; mp 86–87 °C (pentane/EtOAc). TLC (pentane/EtOAc, 30:1): 0.22. IR (neat, cm^{-1}) ν_{max}: 2955, 2873, 1494, 1244. ^1H NMR (400 MHz, $CDCl_3$, ppm) δ_H: 7.42–7.38 (m, 2H, H_{Ar}), 7.28–7.23 (m, 2H, H_{Ar}), 7.16–7.11 (m, 1H, H_{Ar}), 6.97 (ddd, J = 8.2, 2.2, 0.6 Hz, 1H, H_{Ar}), 6.82–6.79 (m, 2H, H_{Ar}), 3.85 (s, 3H, OCH_3), 3.53 (s, 4H, OCH_2), 2.25–2.17 (m, 1H, C*H*HCH_2), 2.19 (s, 3H, $C_{Ar}CH_3$), 2.02–1.93 (m, 1H, CH*H*CH_2), 1.31–1.21 (m, 1H, C*H*HCH_3), 0.87–0.78 (m, 4H, CH_2CH_3, CH*H*CH_3), 0.65 (s, 6H, CH_3). ^{13}C NMR (101 MHz, $CDCl_3$, ppm) δ_C: 154.9 (C), 144.0 (C), 136.3 (C), 130.9 (CH), 129.4 (CH), 129.3 (C), 127.2 (CH), 126.7 (CH), 124.5 (CH), 110.4 (CH), 72.3 (OCH_2), 56.1 (OCH_3), 34.8 (CH_2CH_2), 31.6 ($C(CH_3)_2$), 21.5 (CH_3), 20.8 ($C_{Ar}CH_3$), 17.9 (CH_2CH_3), 14.8 (CH_2CH_3). ^{11}B NMR (96 MHz, $CDCl_3$, ppm) δ_B: 27.9 (br s). MS *m*/*z* (%) (CI^+): 367 ($[M + H]^+$, 16), 366 ($[M]^+$, 30), 351 ($[M – Me]^+$, 14), 323 ($[M – n\text{-}Pr]^+$, 5), 289 ($[M – Ph]^+$, 30), 253 ($[M – Bneop]^+$, 7), 245 ($[M – Ar]^+$, 100), 203 (28), 177 (16), 149 (12), 131 (34), 123 (46), 105 (15), 93 (99). HR-MS (CI^+) calcd for $C_{23}H_{32}O_3{}^{11}B$ $[M + H]^+$: 367.2445; found: 367.2457.

2-(1-(2-Methoxy-5-methylphenyl)-1-phenylbut-3-enyl)-5,5-dimethyl-1,3,2-dioxaborinane (14)

Following the experimental procedure for tertiary boronic ester **13**, 1-phenylbut-3-enyl diisopropylcarbamate (**4**) (139 mg, 0.50 mmol, 1.0 equiv) in anhydrous diethyl ether (1.5 mL), *s*-BuLi (570 μL, 1.14 mol/L solution in cyclohexane/hexane, 98:2, 0.65 mmol, 1.3 equiv), and neopentyl ester **12** (176 mg, 0.75 mmol, 1.0 equiv) in anhydrous diethyl ether (0.75 mL) gave, after purification by column chromatography (SiO_2, pentane/EtOAc, 30:1), tertiary boronic ester **14** (94 mg, 0.26 mmol, 52% or 97% BRSM) as a colourless oil. TLC (pentane/EtOAc, 30:1): 0.12. IR (neat, cm^{-1}) ν_{max}: 2928, 1495, 1245. ^1H NMR (400 MHz, $CDCl_3$, ppm) δ_H: 7.49–7.42 (m, 2H, H_{Ar}), 7.30–7.23 (m, 2H, H_{Ar}), 7.18–7.13 (m, 1H, H_{Ar}), 6.98 (ddd, J = 8.1, 2.2, 0.6 Hz, 1H, H_{Ar}), 6.85–6.78 (m, 2H, H_{Ar}), 5.68 (dddd, J = 17.3, 10.2, 7.4, 6.2 Hz, 1H, C*H*CH_2), 4.97–4.84 (m, 2H, CHC*H*$_2$), 3.86 (s, 3H, OCH_3), 3.56 (s, 4H, OCH_2), 3.13 (ddt, J = 15.4, 7.4, 1.2 Hz, 1H, C*H*H), 2.84 (ddt, J = 15.4, 6.2, 1.6 Hz, 1H, CH*H*), 2.20 (s, 3H, $C_{Ar}CH_3$), 0.71 (s, 6H, CH_3). ^{13}C NMR (101 MHz, $CDCl_3$, ppm) δ_C: 154.8 (C), 143.7 (C), 137.1 (*C*HCH$_2$), 135.8 (C), 130.7 (CH), 129.6 (CH), 129.4 (C), 127.3 (CH), 126.9 (CH), 124.8 (CH), 115.6 (CH*C*H$_2$), 110.4 (CH), 72.3 (OCH_2), 56.1 (OCH_3), 37.5 (CH_2), 31.6 ($C(CH_3)_2$), 21.6 (CH_3), 20.8 ($C_{Ar}CH_3$). ^{11}B NMR (96 MHz, $CDCl_3$, ppm) δ_B: 28.1 (br s). MS *m*/*z* (%) (CI^+): 365 ($[M + H]^+$, 89), 364 ($[M]^+$, 75), 349 ($[M – Me]^+$, 49), 323 ($[M – allyl]^+$, 49), 287 ($[M – Ph]^+$, 32), 243 ($[M – Ar]^+$, 100), 203 (12), 149 (36), 131 (33), 123 (19), 105

Can. J. Chem. Downloaded from www.nrcresearchpress.com by MCGILL UNIVERSITY on 02/02/13
For personal use only.

Can. J. Chem. Downloaded from www.nrcresearchpress.com by MCGILL UNIVERSITY on 02/02/13
For personal use only.

(24), 93 (77). HR-MS (CI^+) calcd for $C_{23}H_{30}O_3{}^{11}B$ $[M + H]^+$: 365.2288; found: 365.2278.

2-Methoxy-5-methylbenzaldehyde (16)

This compound was synthesized following a literature procedure[20] and yielded a pale yellow oil (4.44 g, 29.6 mmol, 99%), which was used without further purification. IR (neat, cm^{-1}) ν_{max}: 2863, 1676, 1494, 1250. ^1H NMR (400 MHz, $CDCl_3$, ppm) δ_H: 10.45 (s, 1H, CHO), 7.64 (d, J = 2.5 Hz, 1H, H_{Ar}), 7.36 (dd, J = 8.6, 2.5 Hz, 1H, H_{Ar}), 6.90 (d, J = 8.6 Hz, 1H, H_{Ar}), 3.91 (s, 3H, OCH_3), 2.32 (s, 3H, CH_3). ^{13}C NMR (101 MHz, $CDCl_3$, ppm) δ_C: 190.0 (CHO), 160.0 (C), 136.6 (CH), 130.0 (C), 128.6 (CH), 124.5 (C), 111.6 (CH), 55.7 (OCH_3), 20.2 (CH_3). MS *m/z* (%) (CI^+): 151 ($[M + H]^+$, 100), 123 ($[Ar + H]^+$, 26), 89 (68). HR-MS (CI^+) calcd for $C_9H_{11}O_2$ $[M + H]^+$: 151.0759; found: 151.0756.

(*R*)-1-(2-Methoxy-5-methylphenyl)but-3-en-1-ol (17)

This compound was synthesized following a literature procedure performed on a different substrate.[16] Flash chromatography (SiO_2, pentane/diethyl ether, 9:1) gave alcohol **17** (74 mg, 0.38 mmol, 77%) as white needles; mp 44–45 °C (pentane/diethyl ether). $[\alpha]_D^{20}$ +56.3 (*c* 1.79, $CHCl_3$, for 98% ee). TLC (pentane/diethyl ether, 9:1): 0.08. IR (neat, cm^{-1}) ν_{max}: 3361, 2922, 1498, 1243. ^1H NMR (400 MHz, $CDCl_3$, ppm) δ_H: 7.16 (d, J = 2.0 Hz, 1H, H_{Ar}), 7.05 (dd, J = 8.2, 2.0 Hz, 1H, H_{Ar}), 6.79 (d, J = 8.2 Hz, 1H, H_{Ar}), 5.93–5.81 (ddt, J = 16.9, 10.3, 6.9 Hz, 1H, C*H*CH_2), 5.19–5.10 (m, 2H, CHC*H*$_2$), 4.93 (dt, J = 8.1, 5.3 Hz, 1H, C*H*OH), 3.84 (s, 3H, OCH_3), 2.62–2.47 (m, 3H, CH_2, OH), 2.31 (s, 3H, CH_3). ^{13}C NMR (101 MHz, $CDCl_3$, ppm) δ_C: 154.3 (C), 135.3 (*C*HCH_2), 131.4 (C), 129.9 (C), 128.5 (CH), 127.5 (CH), 117.5 (CH*C*H_2), 110.4 (CH), 69.8 (CHOH), 55.4 (OCH_3), 42.0 (CH_2), 20.6 (CH_3). MS *m/z* (%) (ESI^+): 215 ($[M + Na]^+$, 100), 175 ($[M – allyl + Na]^+$, 10), 107 ($[Ar – Me]^+$, 5). HR-MS (ESI^+) calcd. for $C_{12}H_{16}O_2Na$ $[M + Na]^+$: 215.1043; found: 215.1038. HPLC: Chiralpak IB, 20 °C, 0.5% *i*-PrOH in hexane, 0.7 mL/min, UV detection at 210.8 nm, retention times: (*S*)-1-(2-methoxy-5-methylphenyl)but-3-en-1-ol, 27.6 min; (*R*)-1-(2-methoxy-5-methylphenyl)but-3-en-1-ol, 30.1 min; 92% ee.

(*R*)-1-(2-Methoxy-5-methylphenyl)but-3-enyl diisopropylcarbamate (18)

Alcohol **17** (1.32 g, 6.84 mmol, 1.0 equiv), *N*,*N*-diisopropylcarbamoyl chloride (1.34 g, 8.21 mmol, 1.2 equiv), and Et_3N (1.23 mL, 8.89 mmol, 1.3 equiv) were dissolved in anhydrous toluene (7.0 mL) in a microwave vial. The vial was sealed and heated for 2 h at 150 °C. After cooling to ambient temperature, the salts were removed by filtration through a plug of silica and the solids were thoroughly washed with diethyl ether. The solvent was removed in vacuo and the residue was subjected to flash chromatography (SiO_2, pentane/EtOAc, 9:1) to obtain 2.11 g (*R*)-carbamate **18** (6.6 mmol, 97%) as a pale yellow oil. $[\alpha]_D^{21}$ −1.0 (*c* 1.00, $CHCl_3$). TLC (pentane/EtOAc, 9:1): 0.27. IR (neat, cm^{-1}) ν_{max}: 2969, 1686, 1249. ^1H NMR (400 MHz, $CDCl_3$, ppm) δ_H: 7.09 (d, J = 2.2 Hz, 1H, H_{Ar}), 7.02 (dd, J = 8.2, 2.2 Hz, 1H, H_{Ar}), 6.76 (d, J = 8.2 Hz, 1H, H_{Ar}), 6.15 (dd, J = 7.1, 5.3 Hz, 1H, CHOCb), 5.80 (ddt, J = 17.1, 10.1, 7.0 Hz, 1H, C*H*CH_2), 5.08–4.99 (m, 2H, CHC*H*$_2$), 4.01 (br m, 1H, C*H*$(CH_3)_2$), 3.90 (br m, 1H, C*H*$(CH_3)_2$), 3.81 (s, 3H, OCH_3), 2.65–2.53 (m, 2H, CH_2), 2.28 (s, 3H, $C_{Ar}CH_3$), 1.24 (br m, 12H, CH_3). ^{13}C NMR (101 MHz, $CDCl_3$, ppm) δ_C: 154.9 (NCO), 154.0 (C), 134.7 (*C*HCH_2), 129.6 (C), 129.3 (C), 128.5 (CH), 127.3 (CH), 116.9 (CH*C*H_2), 110.5 (CH), 70.8 (CHOCb), 55.5 (OCH_3), 45.7 (br, *C*$H(CH_3)_2$), 40.1 (CH_2), 21.1 (br, CH_3), 20.7 ($C_{Ar}CH_3$). MS *m/z* (%) (ESI^+): 342 ($[M + Na]^+$, 100), 220 ($[M – Ar + Na]^+$, 4), 175 ($[M – OCb]^+$, 7), 114 (4). HR-MS (ESI^+) calcd for $C_{19}H_{29}O_3NaN$ $[M + Na]^+$: 342.2040; found: 342.2033. HPLC: Chiralpak IB, 0 °C, 0.2% *i*-PrOH in hexane, 0.5 mL/min, UV detection at 210.8 nm, retention times: (*S*)-1-(2-methoxy-5-methylphenyl)but-3-enyl diisopropylcarbamate, 36.3 min; (*R*)-1-(2-methoxy-5-methylphenyl)but-3-enyl diisopropylcarbamate, 40.9 min; 92% ee.

(*R*)-2-(1-(2-Methoxy-5-methylphenyl)-1-phenylbut-3-enyl)-4,4,5,5-tetramethyl-1,3,2-dioxaborolane (8)

(*R*)-Carbamate **18** (515 mg, 1.61 mmol, 1.0 equiv) was dissolved in anhydrous diethyl ether (5.0 mL) and chilled to −78 °C. *s*-BuLi (1.41 mL, 1.49 mol/L solution in cyclohexane/hexane, 98:2, 2.10 mmol, 1.3 equiv) was added dropwise and the reaction mixture was stirred at this temperature for 1 h. A solution of PhBpin (4,4,5,5-tetramethyl-2-phenyl-1,3,2-dioxaborolane, 490 mg, 2.42 mmol, 1.5 equiv) in anhydrous diethyl ether (2.5 mL) was added dropwise and the mixture was stirred for 2 h at −78 °C. Afterwards, a 1.0 mol/L solution of $MgBr_2$ in anhydrous MeOH[10b] (1.93 mL, 1.93 mmol, 1.2 equiv) was added slowly. After 5 min, the cooling bath was removed and stirring was continued at RT overnight (16 h). Then, the reaction mixture was cooled to 0 °C and 1 mol/L KH_2PO_4(aq) (2.0 mL) was added slowly. After stirring for 10 min at RT, the phases were separated and the aqueous phase was extracted with diethyl ether. The combined organic phases were dried over anhydrous $MgSO_4$, filtered, and the solvent was removed in vacuo. The crude product was purified by column chromatography (SiO_2, pentane/EtOAc, 30:1) to give tertiary boronic ester **8** (449 mg, 1.19 mmol, 74%) as a white solid; mp 134–136 °C (pentane/EtOAc). $[\alpha]_D^{21}$ −88.0 (*c* 1.00, $CHCl_3$, for 90% ee). TLC (pentane/EtOAc, 30:1): 0.10. IR (neat, cm^{-1}) ν_{max}: 2974, 1497, 1240. ^1H NMR (400 MHz, $CDCl_3$, ppm) δ_H: 7.46 (d, J = 7.8 Hz, 2H, H_{Ar}), 7.26 (t, J = 7.8 Hz, 2H, H_{Ar}), 7.15 (t, J = 7.8 Hz, 1H, H_{Ar}), 6.96 (dd, J = 8.2, 1.7 Hz, 1H, H_{Ar}), 6.81 (d, J = 1.7 Hz, 1H, H_{Ar}), 6.76 (d, J = 8.2 Hz, 1H, H_{Ar}), 5.65 (ddt, J = 17.1, 10.2, 6.8 Hz, 1H, C*H*CH_2), 4.95 (dd, J = 17.1, 1.4 Hz, 1H, CHCH_{trans}H), 4.87 (dd, J = 10.2, 1.4 Hz, 1H, CHCH_{cis}H), 3.77 (s, 3H, OCH_3), 3.10 (dd, J = 15.2, 6.8 Hz, 1H, C*H*H), 2.94 (dd, J = 15.2, 6.8 Hz, 1H, CH*H*), 2.19 (s, 3H, $C_{Ar}CH_3$), 1.11 (s, 6H, CH_3), 1.10 (s, 6H, CH_3). ^{13}C NMR (101 MHz, $CDCl_3$, ppm) δ_C: 154.8 (C), 143.0 (C), 136.7 (*C*HCH_2), 134.4 (C), 130.4 (CH), 129.9 (CH), 129.2 (C), 127.3 (CH), 127.1 (CH), 125.1 (CH), 115.7 (CH*C*H_2), 110.1 (CH), 83.0 (C), 55.1 (OCH_3), 38.8 (br, CB), 37.8 (CH_2), 24.6 (CH_3), 24.4 (CH_3), 20.8 ($C_{Ar}CH_3$). ^{11}B NMR (96 MHz, $CDCl_3$, ppm) δ_B: 30.2 (br s). MS *m/z* (%) (ESI^+): 401 ($[M + Na]^+$, 100), 279 (9), 223 (4), 134 (5). HR-MS (ESI^+) calcd for $C_{24}H_{31}O_3Na{}^{11}B$ $[M + Na]^+$: 401.2258; found: 401.2245. The enantiomeric excess of the chiral boronic ester was determined by HPLC analysis of an aliquot oxidized to **25**.

Can. J. Chem. Downloaded from www.nrcresearchpress.com by MCGILL UNIVERSITY on 02/02/13
For personal use only.

(*S*)-1-(2-Methoxy-5-methylphenyl)-1-phenylbut-3-en-1-ol (25)

A solution of tertiary boronic ester **8** (38 mg, 0.10 mmol, 1.0 equiv) in THF (5.0 mL) was cooled to 0 °C and a mixture of 2 mol/L NaOH(aq) (2.0 mL) and 30% H_2O_2 (1.0 mL) was added slowly under vigorous stirring. The reaction mixture was stirred at RT for 2 h. The solvent was removed under reduced pressure and the residue was portioned between water and diethyl ether. The phases were separated and the aqueous layer was extracted with diethyl ether. The combined organic layers were washed with brine, dried over anhydrous $MgSO_4$, filtered, and the solvent was removed in vacuo. The residue was purified by flash chromatography (SiO_2, pentane/EtOAc, 9:1) to give tertiary alcohol **25** (21 mg, 79 μmol, 79%) as a colourless oil, which crystallized on standing to form a white solid; mp 52–53 °C (pentane/EtOAc). $[\alpha]_D^{24}$ +100.2 (*c* 1.57, $CHCl_3$, for 94% ee). TLC (pentane/EtOAc, 9:1): 0.32. IR (neat, cm^{-1}) ν_{max}: 3517, 2923, 1497, 1237. ^1H NMR (400 MHz, $CDCl_3$, ppm) δ_H: 7.35–7.31 (m, 2H, H_{Ar}), 7.30–7.24 (m, 3H, H_{Ar}), 7.22–7.17 (m, 1H, H_{Ar}), 7.08 (ddd, J = 8.2, 2.2, 0.6 Hz, 1H, H_{Ar}), 6.78 (d, J = 8.2 Hz, 1H, H_{Ar}), 5.86 (ddt, J = 17.2, 10.3, 6.8 Hz, 1H, C*H*CH_2), 5.15–5.05 (m, 2H, CHC*H*$_2$), 4.64 (br s, 1H, OH), 3.56 (s, 3H, OCH_3), 3.14 (ddd, J = 14.5, 6.8, 1.1 Hz, 1H, C*H*H), 2.89 (ddd, J = 14.5, 6.8, 1.1 Hz, 1H, CH*H*), 2.35 (s, 3H, CH_3). ^{13}C NMR (101 MHz, $CDCl_3$, ppm) δ_C: 155.0 (C), 147.7 (C), 134.5 (*C*HCH_2), 134.0 (C), 129.9 (C), 128.8 (CH), 128.1 (CH), 127.5 (CH), 126.3 (CH), 125.6 (CH), 117.6 (CH*C*H_2), 112.5 (CH), 77.5 (COH), 55.8 (OCH_3), 45.8 (CH_2), 20.9 (CH_3). MS *m*/*z* (%) (CI^+): 269 ($[M + H]^+$, 4), 251 ($[M – OH]^+$, 100), 227 ($[M – allyl]^+$, 85), 149 ($[M – Ar + H]^+$, 30), 135 (20), 105 (34). HR-MS (CI^+) calcd for $C_{18}H_{21}O_2$ $[M + H]^+$: 269.1542; found: 269.1545. HPLC: Chiralpak IB, 20 °C, 3.0% *i*-PrOH in hexane, 0.7 mL/min, UV detection at 210.8 nm, retention times: (*R*)-1-(2-methoxy-5-methylphenyl)-1-phenylbut-3-en-1-ol, 8.6 min; (*S*)-1-(2-methoxy-5-methylphenyl)-1-phenylbut-3-en-1-ol, 9.7 min; 90% ee.

(*R*)-1-Methoxy-4-methyl-2-(1-phenylbut-3-enyl)benzene (9)

A solution of tertiary boronic ester **8** (328 mg, 0.87 mmol, 1.0 equiv) and TBAF·$3H_2O$ (411 mg, 1.30 mmol, 1.5 equiv) in anhydrous toluene (9.0 mL) was stirred for 1.5 h at RT. Afterwards, the reaction mixture was washed with 0.5 mol/L NaOH(aq), water, and brine. The organic phase was dried over anhydrous $MgSO_4$, filtered, and the solvent was removed under reduced pressure to give olefin **9** (207 mg, 0.82 mmol, 95%) as a colourless oil, which required no purification. $[\alpha]_D^{20}$ –10.0 (*c* 1.00, $CHCl_3$, for 90% ee). IR (neat, cm^{-1}) ν_{max}: 2922, 1498, 1240. ^1H NMR (400 MHz, $CDCl_3$, ppm) δ_H: 7.30–7.25 (m, 4H, H_{Ar}), 7.19–7.12 (m, 1H, H_{Ar}), 7.02 (d, J = 2.2 Hz, 1H, H_{Ar}), 6.96 (dd, J = 8.3, 2.2 Hz, 1H, H_{Ar}), 6.74 (d, J = 8.3 Hz, 1H, H_{Ar}), 5.75 (ddt, J = 17.1, 10.2, 6.8 Hz, 1H, C*H*CH_2), 5.03 (ddt, J = 17.1, 2.8, 1.3 Hz, 1H, CHC*H*$_{trans}$H), 4.93 (ddt, J = 10.2, 2.8, 1.3 Hz, 1H, CHC*H*$_{cis}$H), 4.47 (t, J = 7.9 Hz, 1H, CH), 3.75 (s, 3H, OCH_3), 2.78 (ddt, J = 7.9, 6.8, 1.3 Hz, 2H, CH_2), 2.27 (s, 3H, CH_3). ^{13}C NMR (101 MHz, $CDCl_3$, ppm) δ_C: 154.9 (C), 144.5 (C), 137.3 (*C*HCH_2), 132.8 (C), 129.5 (C), 128.5 (CH), 128.2 (CH), 128.1 (CH), 127.4 (CH), 125.8 (CH), 115.8 (CH*C*H_2), 110.8 (CH), 55.6 (OCH_3), 43.3 (CH), 39.1 (CH_2), 20.7 (CH_3). MS *m*/*z* (%) (ESI^+): 275 ($[M + Na]^+$, 100), 270 ($[M + NH_4]^+$, 18), 211 ($[M – allyl]^+$, 22). HR-MS (ESI^+) calcd for $C_{18}H_{20}ONa$ $[M + Na]^+$: 275.1406; found: 275.1413. The enantiomeric excess of the chiral olefin was determined by HPLC analysis of an aliquot, which has been hydroborated and oxidized to **26**.

(*R*)-4-(2-Methoxy-5-methylphenyl)-4-phenylbutan-1-ol (26)

A solution of 9-borabicyclo[3.3.1]nonane (9-BBN; 390 μL, 0.5 mol/L in THF, 0.20 mmol, 1.75 equiv) was added to a solution of olefin **9** (29 mg, 0.11 mmol, 1.0 equiv) in anhydrous THF (1.0 mL) and stirred for 2 h at ambient temperature. The reaction mixture was cooled to 0 °C and a mixture of 2 mol/L NaOH(aq) (1.0 mL) and 30% H_2O_2 (0.5 mL) was added slowly. The reaction mixture was stirred vigorously for 2 h at RT. The solution was diluted with water and extracted with diethyl ether. The combined organic layers were dried over anhydrous $MgSO_4$, filtered, concentrated under reduced pressure, and the residue was purified by column chromatography (SiO_2, pentane/EtOAc, 4:1) to give alcohol **26** (23 mg, 85 μmol, 75%) as a colourless oil. $[\alpha]_D^{21}$ +6.5 (*c* 0.62, $CHCl_3$, for 90% ee). TLC (pentane/EtOAc, 4:1): 0.10. IR (neat, cm^{-1}) ν_{max}: 3334, 2937, 1498, 1243. ^1H NMR (400 MHz, $CDCl_3$, ppm) δ_H: 7.31–7.24 (m, 4H, H_{Ar}), 7.19–7.12 (m, 1H, H_{Ar}), 7.03–7.00 (m, 1H, H_{Ar}), 6.96 (dd, J = 8.2, 2.2 Hz, 1H, H_{Ar}), 6.74 (d, J = 8.2 Hz, 1H, H_{Ar}), 4.39 (t, J = 7.8 Hz, 1H, CH), 3.76 (s, 3H, OCH_3), 3.67 (t, J = 6.6 Hz, 2H, CH_2OH), 2.27 (s, 3H, CH_3), 2.14–2.00 (m, 2H, CH_2CH), 1.60–1.51 (dq, J = 8.1, 6.6 Hz, 2H, C$H_2$$CH_2$OH), 1.35 (br s, 1H, OH). ^{13}C NMR (101 MHz, $CDCl_3$, ppm) δ_C: 154.8 (C), 144.8 (C), 133.2 (C), 129.6 (C), 128.3 (CH), 128.1 (CH), 128.1 (CH), 127.3 (CH), 125.8 (CH), 110.7 (CH), 62.9 (CH_2OH), 55.7 (OCH_3), 42.7 (CH), 31.1 (CH_2), 31.0 (CH_2), 20.7 (CH_3). MS *m*/*z* (%) (ESI^+): 293 ($[M + Na]^+$, 100), 290 (13), 282 (2), 211 ($[M – ($$CH_2$$)_3$OH)]$^+$, 2). HR-MS ($ESI^+$) calcd for $C_{18}H_{22}ONa$ $[M + Na]^+$: 293.1512; found: 293.1517. HPLC: Chiralpak IB, 20 °C, 1.5% *i*-PrOH in hexane, 0.7 mL/min, UV detection at 210.8 nm, retention times: (*S*)-1-(2-methoxy-5-methylphenyl)-1-phenylbut-3-en-1-ol, 48.8 min; (*R*)-4-(2-methoxy-5-methylphenyl)-4-phenylbutan-1-ol, 50.2 min; 90% ee.

(*R*)-3-(2-Methoxy-5-methylphenyl)-3-phenylpropanal (23)

This compound was synthesized following a literature procedure performed on a different substrate.[17] The crude material was filtered through a plug of silica (pentane/EtOAc, 1:1), and the solvent was removed in vacuo to afford aldehyde **23** (163 mg, 0.64 mmol, 97%) as a pale yellow oil, which required no further purification. $[\alpha]_D^{22}$ +14.0 (*c* 1.00, $CHCl_3$) (lit.[21] value $[\alpha]_D^{20}$ –16.2 (*c* 1.4, $CHCl_3$, for 99% ee of the (*S*)-isomer)). IR (neat, cm^{-1}) ν_{max}: 2919, 1721, 1498, 1241. ^1H NMR (400 MHz, $CDCl_3$, ppm) δ_H: 9.70 (t, J = 2.2 Hz, 1H, CHO), 7.32–7.23 (m, 4H, H_{Ar}), 7.22–7.16 (m, 1H, H_{Ar}), 6.98 (dd, J = 8.3, 2.0 Hz, 1H, H_{Ar}), 6.87 (d, J = 2.0 Hz, 1H, H_{Ar}), 6.75 (d, J = 8.3 Hz, 1H, H_{Ar}), 5.00 (t, J = 7.8 Hz, 1H, CH), 3.77 (s, 3H, OCH_3), 3.09 (dd, J = 7.8, 2.2 Hz, 2H, CH_2), 2.23 (s, 3H, CH_3). ^{13}C NMR (126 MHz, $CDCl_3$, ppm) δ_C: 201.9 (CHO), 154.5 (C), 142.9 (C), 131.3 (C), 129.8 (C), 128.8 (CH), 128.4 (CH), 128.0 (CH), 128.0 (CH), 126.3 (CH), 110.8 (CH), 55.5 (OCH_3), 48.5 (CH_2), 38.3 (CH), 20.6 (CH_3). MS *m*/*z* (%) (ESI^+): 277 ($[M + Na]^+$, 38), 237 (11), 211 ($[M – CH_2CHO]$, 100). HR-MS (ESI^+) calcd for $C_{17}H_{18}O_2Na$ $[M + Na]^+$: 277.1199; found: 277.1204. HPLC: Chiralpak IB, 0 °C, 2.0% *i*-PrOH in hexane, 0.5 mL/min, UV detection at 210.8 nm, retention times: (*S*)-3-(2-methoxy-5-methylphenyl)-3-

Can. J. Chem. Downloaded from www.nrcresearchpress.com by MCGILL UNIVERSITY on 02/02/13
For personal use only.

phenylpropanal, 24.7 min; (*R*)-3-(2-methoxy-5-methylphenyl)-3-phenylpropanal, 27.6 min; 90% ee.

(*R*)-*N*,*N*-Diisopropyl-3-(2-methoxy-5-methylphenyl)-3-phenylpropan-1-amine (24)

A mixture of aldehyde **23** (25 mg, 98 μmol, 1.0 equiv), diisopropylamine (28 μL, 0.20 mmol, 2.0 equiv), and $NaBH(OAc)_3$ (42 mg, 0.20 mmol, 2.0 equiv) in anhydrous THF (1.0 mL) was stirred for 18 h at ambient temperature. Then, saturated $NaHCO_3$(aq) solution (0.5 mL) was added, the phases were separated, and the aqueous layer was extracted with EtOAc. The combined organic layers were washed with 3.0 mol/L HCl(aq) and brine, dried over anhydrous Na_2SO_4, filtered, and the solvent was removed under reduced pressure. Purification of the residue by column chromatography (SiO_2, pentane/EtOAc/Et_3N, 75:24:1) afforded tertiary amine **24** (23 mg, 68 μmol, 69%) as a pale yellow oil. $[\alpha]_D^{20}$ −11.0 (*c* 1.00, $CHCl_3$) (lit.[22] value $[\alpha]_D$ −6.14 (*c* 0.95, $CHCl_3$, for 81% ee). TLC (pentane/EtOAc/Et_3N, 75:24:1): 0.16. IR (neat, cm^{-1}) ν_{max}: 2962, 1497, 1239. ^1H NMR (400 MHz, $CDCl_3$, ppm) δ_H: 7.31–7.22 (m, 4H, H_{Ar}), 7.16–7.12 (m, 1H, H_{Ar}), 7.07 (d, *J* = 2.2 Hz, 1H, H_{Ar}), 6.94 (dd, *J* = 8.2, 2.2 Hz, 1H, H_{Ar}), 6.72 (d, *J* = 8.2 Hz, 1H, H_{Ar}), 4.35 (t, *J* = 7.7 Hz, 1H, CH), 3.75 (s, 3 H, OCH_3), 2.98 (sept, *J* = 6.5 Hz, 2H, C*H*(CH_3)$_2$), 2.37–2.30 (m, 2H, C*H*HN + C*H*HCH), 2.26 (s, 3H, $C_{Ar}CH_3$), 2.16–2.09 (m, 2H, CH*H*N + CH*H*CH), 0.94 (d, *J* = 6.5 Hz, 6H, CH_3), 0.93 (d, *J* = 6.5 Hz, 6H, CH_3). ^{13}C NMR (126 MHz, $CDCl_3$, ppm) δ_C: 154.9 (C), 145.1 (C), 133.5 (C), 129.5 (C), 128.3 (CH), 128.2 (CH), 128.0 (CH), 127.1 (CH), 125.6 (CH), 110.6 (CH), 55.6 (OCH_3), 48.7 (*C*H(CH_3)$_2$), 44.1 (CH_2N), 41.3 ($C_{Ar}CH$), 37.0 (*C*H_2CH), 20.7 (CH_3), 20.5 ($C_{Ar}CH_3$). MS *m*/*z* (%) (ESI^+): 340 ($[M + H]^+$, 100), 298 ($[M - i\text{-}Pr]^+$, 15), 211 ($[M - (CH_2)_2N(i\text{-}Pr)_2]^+$, 7), 113 (4). HR-MS ($ESI^+$) calcd for $C_{23}H_{34}ON$ $[M + H]^+$: 340.2635; found: 340.2625.

(*R*)-Tolterodine (1)

This compound was synthesized following a literature procedure performed on a different substrate.[7e] Flash chromatography (SiO_2, pentane/EtOAc, 70:30, 2% Et_3N) yielded a pale yellow oil, which crystallized upon standing. (*R*)-tolterodine (**1**; 91 mg, 0.28 mmol, 87%) was obtained as an off-white solid; mp 78–79 °C (pentane/EtOAc/Et_3N). $[\alpha]_D^{20}$ +28.0 (*c* 0.50, MeOH) (lit.[7e] value $[\alpha]_D$ +32.5 (*c* 0.89, MeOH, for 99% ee). TLC (pentane/EtOAc, 70:30, 2% Et_3N): 0.18. IR (neat, cm^{-1}) ν_{max}: 3249, 2971, 2927, 1493. ^1H NMR (500 MHz, $CDCl_3$, ppm) δ_H: 10.27 (br s, 1H, $C_{Ar}OH$), 7.36–7.32 (m, 4H, H_{Ar}), 7.26–7.22 (m, 1H, H_{Ar}), 6.87 (dd, *J* = 8.2, 2.0 Hz, 1H, H_{Ar}), 6.82 (dd, *J* = 8.2, 1.5 Hz, 1H, H_{Ar}), 6.57 (s, 1H, H_{Ar}), 4.50 (dd, *J* = 10.8, 3.2 Hz, 1H, CH), 3.25 (sept, *J* = 6.7 Hz, 2H, C*H*(CH_3)), 2.79–2.70 (m, 1H, C*H*HN), 2.46–2.33 (m, 2H, CH*H*N + C*H*HCH), 2.14 (s, 3H, $C_{Ar}CH_3$), 2.13–2.04 (m, 1H, CH*H*CH), 1.15 (d, *J* = 6.7 Hz, 6H, CH_3), 1.10 (d, *J* = 6.7 Hz, 6H, CH_3). ^{13}C NMR (126 MHz, $CDCl_3$, ppm) δ_C: 153.2 (C), 144.7 (C), 132.3 (C), 129.3 (C), 128.6 (CH), 128.5 (CH), 128.3 (CH), 127.7 (CH), 126.1 (CH), 118.1 (CH), 48.0 (*C*H(CH_3)$_2$), 42.1 (CH_2N), 39.4 ($C_{Ar}CH$), 33.2 (*C*H_2CH), 20.7 ($C_{Ar}CH_3$), 19.9 (CH_3), 19.5 (CH_3). MS *m*/*z* (%) (ESI^+): 348 ($[M + Na]^+$, 1), 326 ($[M + H]^+$, 100), 284 ($[M - i\text{-}Pr + H]^+$, 2), 197 ($[M - (CH_2)_2N(i\text{-}Pr)_2]^+$, 1), 109 ($[Ar]^+$, 5). HR-MS ($ESI^+$) calcd for $C_{22}H_{32}ON$ $[M + H]^+$: 326.2478; found: 326.2466.

Supplementary data

Supplementary data are available with the article through the journal Web site http://nrcresearchpress.com/doi/supp/10.1139/v2012-069.

Acknowledgements

We wish to thank the Engineering and Physical Sciences Research Council (EPSRC) and the European Research Council (ERC: FP7/2007–2013, ERC grant No. 246785) for financial support. V.K.A. thanks the Royal Society for a Wolfson Research Merit Award and EPSRC for a Senior Research Fellowship. We thank Inochem-Frontier Scientific for the generous donation of boronic acids and boronic esters.

References

(1) (a) Prat, L.; Mojovic, L.; Levacher, V.; Dupas, G.; Quéguiner, G.; Bourguignon, J. *Tetrahedron Asymmetry* **1998**, *9* (14), 2509. doi:10.1016/S0957-4166(98)00228-6; (b) Selim, K. B.; Matsumoto, Y.; Yamada, K.; Tomioka, K. *Angew. Chem. Int. Ed.* **2009**, *48* (46), 8733 and references therein. doi:10.1002/anie.200904676.

(2) (a) Nilvebrant, L.; Andersson, K.-E.; Gillberg, P.-G.; Stahl, M.; Sparf, B. *Eur. J. Pharmacol.* **1997**, *327* (2–3), 195. doi:10.1016/S0014-2999(97)89661-6; (b) Hills, C. J.; Winter, S. A.; Balfour, J. A. *Drugs* **1998**, *55* (6), 813. doi:10.2165/00003495-199855060-00008.

(3) *Pfizer Annual Report to Shareholders*, **2008**.

(4) Jönsson, N. A.; Sparf, B. A.; Mikiver, L.; Moses, P.; Nilvebrant, L.; Glas, G. EP 0325571, A1, **1989**.

(5) Andersson, P. G.; Schink, H. E.; Österlund, K. *J. Org. Chem.* **1998**, *63* (22), 8067. doi:10.1021/jo981259r.

(6) Hedberg, C.; Andersson, P. G. *Adv. Synth. Catal.* **2005**, *347* (5), 662. doi:10.1002/adsc.200404234.

(7) (a) Ulgheri, F.; Marchetti, M.; Piccolo, O. *J. Org. Chem.* **2007**, *72* (16), 6056. doi:10.1021/jo0705667; (b) Jagdale, A. R.; Sudalai, A. Tetrahedron Lett. 2008, *49* (23), 3790. doi:10.1016/j.tetlet.2008.04.007; (c) Gallagher, B. D.; Taft, B. R.; Lipshutz, B. H. *Org. Lett.* **2009**, *11* (23), 5374. doi:10.1021/ol9020404; (d) Yoo, K.; Kim, H.; Yun, J. *J. Org. Chem.* **2009**, *74* (11), 4232. doi:10.1021/jo900530s; (e) Wang, X.; Guram, A.; Caille, S.; Hu, J.; Preston, J. P.; Ronk, M.; Walker, S. *Org. Lett.* **2011**, *13* (7), 1881. doi:10.1021/ol200422p.

(8) Botteghi, C.; Corrias, T.; Marchetti, M.; Paganelli, S.; Piccolo, O. *Org. Process Res. Dev.* **2002**, *6* (4), 379. doi:10.1021/op020014k.

(9) (a) Chen, G.; Tokunaga, N.; Hayashi, T. *Org. Lett.* **2005**, *7* (11), 2285. doi:10.1021/ol0507367; (b) Sörgel, S.; Tokunaga, N.; Sasaki, K.; Okamoto, K.; Hayashi, T. *Org. Lett.* **2008**, *10* (4), 589. doi:10.1021/ol702879u; (c) Kobayashi, K.; Nishikata, T.; Yamamoto, Y.; Miyaura, N. *Bull. Chem. Soc. Jpn.* **2008**, *81* (8), 1019. doi:10.1246/bcsj.81.1019.

(10) (a) Stymiest, J. L.; Bagutski, V.; French, R. M.; Aggarwal, V. K. *Nature* **2008**, *456* (7223), 778. doi:10.1038/nature07592.; (b) Bagutski, V.; French, R. M.; Aggarwal, V. K. *Angew. Chem. Int. Ed.* **2010**, *49* (30), 5142. doi:10.1002/anie.201001371.; (c) These reactions are based on the seminal studies by Hoppe on the lithiation and trapping of secondary benzylic carbamates. See Hoppe, D.; Carstens, A.; Krämer, T. Angew. Chem. Int. Ed. Engl. **1990**, *29* (12), 1424. doi:10.1002/anie.199014241.;

(d) Carstens, A.; Hoppe, D. *Tetrahedron* **1994**, *50* (20), 6097. doi:10.1016/S0040-4020(01)90461-2.

(11) (a) Nave, S.; Sonawane, R. P.; Elford, T. G.; Aggarwal, V. K. *J. Am. Chem. Soc.* **2010**, *132* (48), 17096. doi:10.1021/ja1084207; (b) Roesner, S.; Casatejada, J. M.; Elford, T. G.; Sonawane, R. P.; Aggarwal, V. K. *Org. Lett.* **2011**, *13* (21), 5740. doi:10.1021/ol202251p; (c) Elford, T. G.; Nave, S.; Sonawane, R. P.; Aggarwal, V. K. *J. Am. Chem. Soc.* **2011**, *133* (42), 16798. doi:10.1021/ja207869f; (d) Aggarwal, V. K.; Ball, L. T.; Carobene, S.; Connelly, R. L.; Hesse, M. J.; Partridge, B. M.; Roth, P.; Thomas, S. P.; Webster, M. P. *Chem. Commun.* **2012**, *48,* 9230. doi:10.1039/C2CC32176A.

(12) (a) Koe, B. K.; Weissman, A.; Welch, W. M.; Browne, R. G. *J. Pharmacol. Exp. Ther.* **1983**, *226,* 686; (b) Welch, W. M.; Kraska, A. R.; Sarges, R.; Koe, B. K. *J. Med. Chem.* **1984**, *27* (11), 1508. doi:10.1021/jm00377a021.

(13) Maggon, K. *Drug Discov. Today* **2005**, *10* (11), 739. doi:10.1016/S1359-6446(05)03468-9.

(14) (a) Bøgesø, K. P.; Christensen, A. V.; Hyttel, J.; Liljefors, T. *J. Med. Chem.* **1985**, *28* (12), 1817. doi:10.1021/jm00150a012; (b) Hyttel, J.; Larsen, J. J. *J. Neurochem.* **1985**, *44* (5), 1615. doi:10.1111/j.1471-4159.1985.tb08803.x.

(15) Negus, S. S.; Brandt, M. R.; Mello, N. K. *J. Pharmacol. Exp. Ther.* **1999**, *291,* 60.

(16) Jadhav, P. K.; Bhat, K. S.; Perumal, P. T.; Brown, H. C. *J. Org. Chem.* **1986**, *51* (4), 432. doi:10.1021/jo00354a003.

(17) Yu, W.; Mei, Y.; Kang, Y.; Hua, Z.; Jin, Z. *Org. Lett.* **2004**, *6* (19), 3217. doi:10.1021/ol0400342.

(18) Pangborn, A. B.; Giardello, M. A.; Grubbs, R. H.; Rosen, R. K.; Timmers, F. J. *Organometallics* **1996**, *15* (5), 1518. doi:10.1021/om9503712.

(19) Roush, W. R.; Walts, A. E.; Hoong, L. K. *J. Am. Chem. Soc.* **1985**, *107* (26), 8186. doi:10.1021/ja00312a062.

(20) Kahnberg, P.; Lager, E.; Rosenberg, C.; Schougaard, J.; Camet, L.; Sterner, O.; Nielsen, E. Ø.; Nielsen, M.; Liljefors, T. *J. Med. Chem.* **2002**, *45* (19), 4188. doi:10.1021/jm020839k.

(21) Tokunaga, N.; Hayashi, T. *Tetrahedron Asymmetry* **2006**, *17* (4), 607. doi:10.1016/j.tetasy.2006.01.036.

(22) Paras, N. A.; Simmons, B.; MacMillan, D. W. C. *Tetrahedron* **2009**, *65* (16), 3232. doi:10.1016/j.tet.2008.12.054.

Can. J. Chem. Downloaded from www.nrcresearchpress.com by MCGILL UNIVERSITY on 02/02/13
For personal use only.

Synthesis of 6-substituted salicylates via biomimetic aromatization utilizing the cross metathesis of a vinyl dioxinone with homoallylic alcohols

Peter S. Blencowe and Anthony G.M. Barrett

Can. J. Chem. Downloaded from www.nrcresearchpress.com by MCGILL UNIVERSITY on 02/02/13
For personal use only.

Abstract: We herein report biomimetic syntheses of 6-substituted salicylates from the cross metathesis of 2,2-dimethyl-6-vinyl-1,3-dioxin-4-one with homoallylic alcohols, oxidation, and aromatization of the intermediate enone–dioxinones. Of particular note is the use of the catalyst 1,4-diazabicyclo[2.2.2]octane in the microwave thermolytic ketene generation and trapping, cyclization, and dehydration reaction sequence.

Key words: salicylates, biomimetic synthesis, dioxinone, polyketide synthesis.

Résumé : Dans ce travail, on rapporte les synthèses biomimétiques de salicylates substitués en position-6, par le biais d'une réaction de métathèse croisée de la 2,2-diméthyl-6-vinyl-1,3-dioxin-4-one avec des alcools homoallyliques, suivie d'une oxydation et d'une aromatisation de l'intermédiaire énone–dixoinones. Il est important de noter l'utilisation du 1,4-diazabicyclo[2.2.2]octane comme catalyseur dans la génération thermolytique du cétène, de son piégeage, de sa cyclisation et de sa déshydrogénation dans la séquence réactionnelle.

Mots-clés : salicylates, synthèse biomimétique, dioxinone, synthèse d'un polycétide.

[Traduit par la Rédaction]

Introduction

Salicylates have long been applied in medicine, fragrances, flavorings, and cosmetics. Simple examples include acetyl salicylic acid and methyl salicylate (oil of wintergreen).[1] 6-Substituted salicylates also occur widely in natural products, which show a wide variety of activities. These include macrocyclic salicylates such as salicylihalamide A and B;[2] apicularen A;[3] and marinomycins A–D,[4] which show anticancer activity (the latter class also displaying antibacterial activity); the fungal metabolite CJ-12 950,[5] which has the potential to treat hypercholesterolemia and hyperlipidemia; long-chain salicylic acids such as anacardic acid and derivatives that are antibiotics and antioxidants;[6] and the diacetylenic natural product frutescin.[7]

The most common syntheses of salicylates are via modification of salicylic acid (itself available from the Kolbe–Schmitt reaction)[8] by esterification or through modification via classical aromatic chemistry. De novo syntheses of these systems are less common but include methods such as oxidative cyclization,[9,10] cycloaromatization of conjugated polyenynes,[11] Diels–Alder reactions,[12] titanium(IV) chloride mediated [3 + 3] additions,[13] and domino "Michael–retro-Michael–Wittig" reactions.[14]

Previously reported biomimetic syntheses of salicylates have involved the synthesis of polycarbonyl precursors via partially reduced pyrones **2**[15] or by addition reactions to β-ketoaldehydes **4** (Scheme 1).[16] In the first case, substrates were limited to those that could be selectively reduced (i.e., not 6-phenacyl-4-hydroxy-2-pyrone), and in the second case a *tert*-butyl ester was necessary to prevent self-condensation of sodioformylacetone.

Inspired by the polyketide biosynthesis for aromatic natural products and the related biomimetic synthesis studies by Harris and Harris,[17] we sought to extend our work on the synthesis of resorcylates from diketodioxinones,[18] to the synthesis of 6-substituted salicylates. We reasoned that salicylates **7** would be available by intramolecular aldol condensation of diketo esters **8**, synthesized by ketene generation and trapping from dioxinone **9**, itself available through cross metathesis of dioxinone **10** and enone **11** (Scheme 2).

Herein, we report the concise synthesis of 6-substituted salicylates using dioxinones as stable precursors without the requirement for protecting groups or harsh reaction conditions.

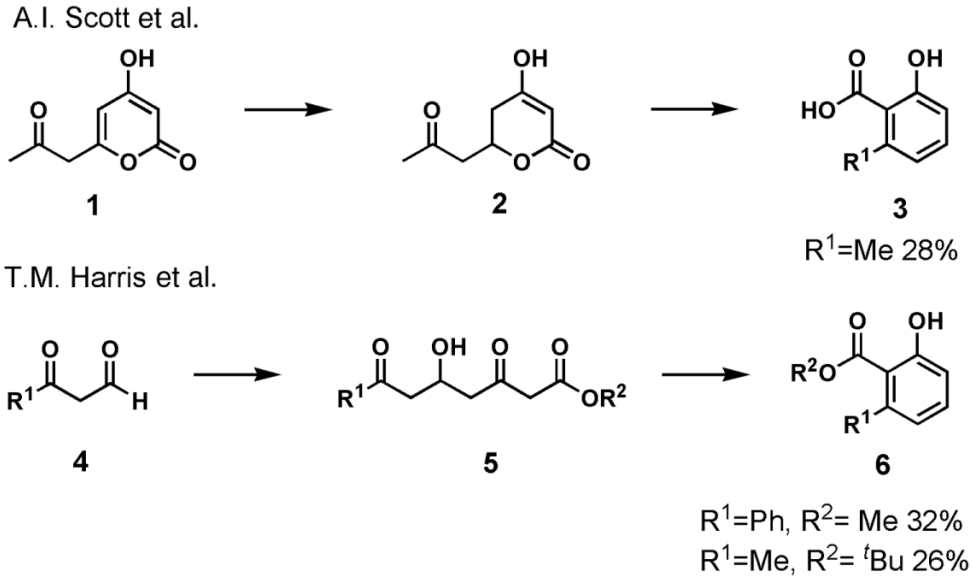
Received 26 June 2012. Accepted 31 July 2012. Published at www.nrcresearchpress.com/cjc on 29 November 2012.

P.S. Blencowe and A.G.M. Barrett. Department of Chemistry, Imperial College, London, SW7 2AZ, UK.

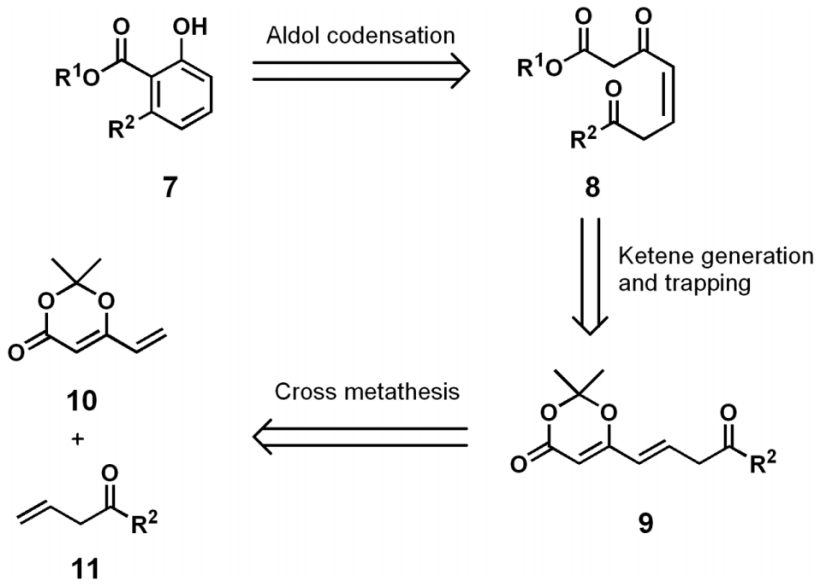
Corresponding author: Anthony G.M. Barrett (e-mail: agm.barrett@imperial.ac.uk).

This article is part of a Special Issue dedicated to Professor Derrick Clive. Dedicated to Derrick Clive in recognition of his scholarship and original elegant contributions to synthetic organic chemistry.

Scheme 1. Previous biomimetic routes to 6-substituted salicylic acid derivatives.



Scheme 2. Retrosynthesis of salicylates from dioxinone precursor **10**.



Results and discussion

Vinyl dioxinone **10** was prepared by the procedure of Gebauer and Blechert[19] from *tert*-butyl 5-chloro-3-oxopentanoate[20] in a 72% yield over two steps. The homoallylic alcohols **14a**–**14k** were synthesized in 82%–94% yields by reaction of allylmagnesium bromide with the corresponding aldehydes.[21] Oxidation of homoallylic alcohol **14a** with pyridinium chlorochromate (PCC)[22] gave the enone **11** in a 64% yield, but attempted cross metathesis of **11** with vinyl dioxinone **10** using the Grubbs–Hoveyda II catalyst **12** was unsuccessful and only gave rise to the enedione **13** in a poor yield. In contrast, cross metathesis of homoallylic alcohol **14a** with vinyl dioxinone **10** gave dioxinone **15a** in an 81% yield (Scheme 3).[23]

Subsequently, we examined the oxidation of the cross metathesis product **15a** to give enone–dioxinone **16a** (Table 1). Our initial attempts involving pyridinium chlorochromate and manganese dioxide were unsuccessful with unreacted starting material being recovered (Table 1, entries 1 and 2). Modified Oppenauer oxidation[24] was of limited use owing to contamination of the product with the hydrogen acceptor 2,4-dinitrobenzaldehyde. Swern conditions gave an intractable mixture of products possibly because of chlorination as has been observed for aryl vinyl ketones.[25]

In contrast to these failures, oxidations with hypervalent iodine reagents were more useful. While oxidation with iodoxybenzoic acid (IBX) in dimethyl sulfoxide (DMSO)[26] resulted in overoxidation, reaction in ethyl acetate[27] gave

Can. J. Chem. Downloaded from www.nrcresearchpress.com by MCGILL UNIVERSITY on 02/02/13
For personal use only.

Can. J. Chem. Downloaded from www.nrcresearchpress.com by MCGILL UNIVERSITY on 02/02/13
For personal use only.

Scheme 3. Cross metathesis reactions of vinyl dioxinone **10**.

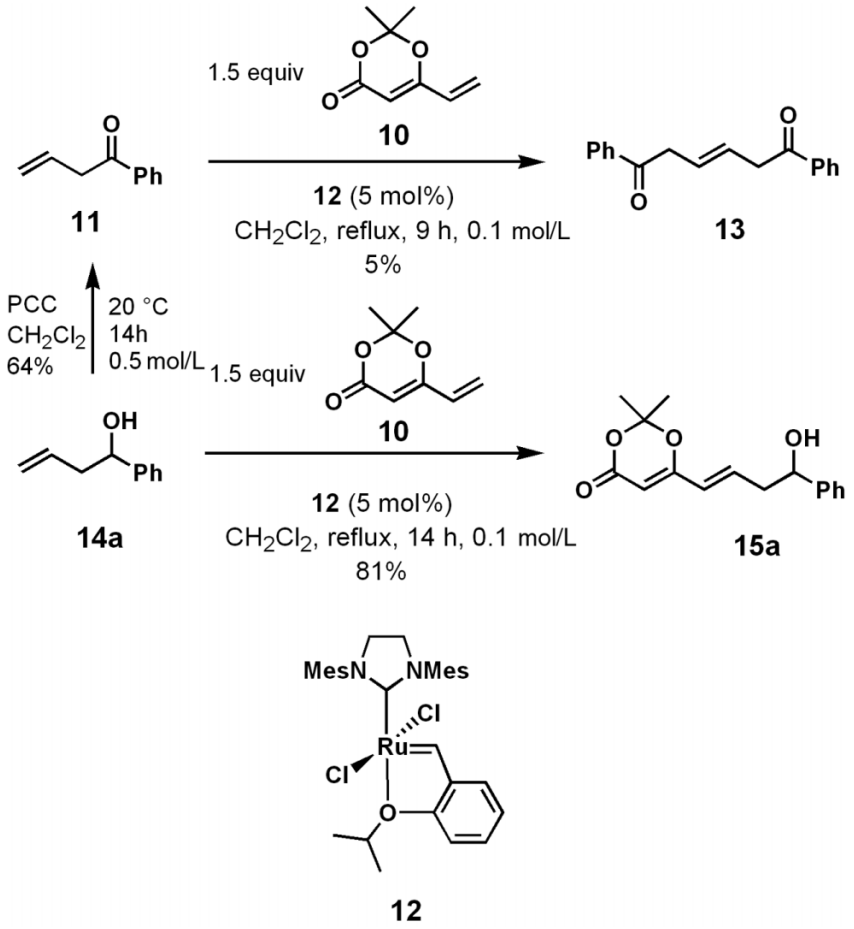
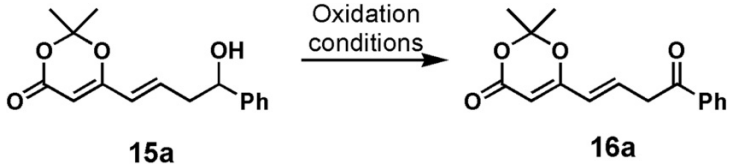


Table 1. Conditions for the oxidation of **15a**.



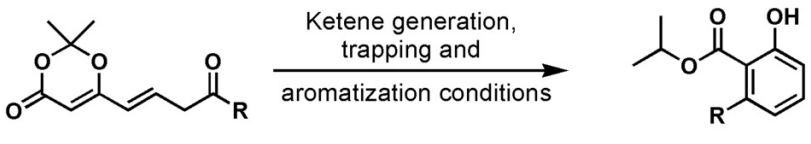
Entry	Oxidation conditions	Yield of **16a** (%)
1	PCC, CH_2Cl_2, 20 °C	0
2	MnO_2, CH_2Cl_2, 20 °C	0
3	IBX, EtOAc, 80 °C	67
4	DMP, CH_2Cl_2, 20 °C	40
5	DMP, CH_2Cl_2, 0 °C	77

Note: PCC, pyridinium chlorochromate; IBX, iodoxybenzoic acid; DMP, Dess–Martin periodinane.

enone–dioxinone **16a** in a 67% yield (Table 1, entry 3). Dess–Martin periodinane (DMP)[28] was found to be most efficient and oxidation at 0 °C gave enone **16a** in a 77% yield (Table 1, entries 4 and 5).

Reflux of a toluene solution of dioxinone **16a** and in situ trapping of the resultant ketene with 2-propanol gave the salicylate **17a** in a 53% yield (Table 2, entry 1). When heating of **16a** was carried out under microwave conditions, ketene generation and trapping was complete within 45 min (as observed by ^{1}H NMR spectroscopy), and heating of the intermediate for a further 8 h to effect aromatization gave salicylate **17a** in a 14% yield (Table 2, entry 2).[29] It was found that the microwave reaction of **16a** in the presence of 1,4-diazabicyclo [2.2.2]octane (DABCO) was more rapid and gave salicylate **17a** in a 55% yield after 1.5 h (Table 2, entry 3). Excess DABCO was not required for the acceleration (Table 2, entry

Table 2. Optimization of ketene generation, trapping by isopropanol, and aromatization.

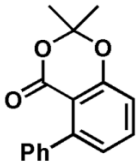


16a **17a**

Entry	Additive (equiv)	Temperature (°C)[a]	Solvent[b]	Time (h)	Yield of **17a** (%)
1	—	Reflux[c]	PhMe	26	53
2	—	120	EtOAc	8	14
3	DABCO (10)	120	EtOAc	1.5	55
4	DABCO (1)	120	EtOAc	2	47
5	DABCO (1)	120	EtOAc	8	51

[a]Microwave heating.
[b]*i*-PrOH (40 equiv.) was added as the trapping agent.
[c]Conventional heating.

Fig. 1. Possible benzodioxinone product.



18

4) and prolonged heating failed to give any further conversion (Table 2, entry 5). The mechanism of rate enhancing action by DABCO is yet to be determined, though alkene (trans to cis) isomerization is a possibility.[30]

As has been shown previously, reaction of diketodioxinones with triethylamine smoothly gave the corresponding benzodioxinones.[31] In contrast, we have now found that the reaction of enone–dioxinone **16a** with triethylamine, Hünig's base, 5 mol/L hydrochloric acid, or ammonium acetate resulted only in decomposition and the arene **18** was not formed. No reaction was observed with acetic acid (Fig. 1).

The optimized reaction conditions for the cross metathesis, oxidation, and aromatization were applied to synthesize a range of salicylates **17a**–**17i** in good yields (Scheme 4). Efficient cross metathesis in some cases required the use of an increased amount (10 mol %) of catalyst **12** to achieve an acceptable yield. In these cases, some self-metathesis of vinyl dioxinone **10** was observed (<10%). The homoallylic alcohol **15k** failed to undergo cross metathesis, presumably because of coordination of the pyridine nitrogen to ruthenium, resulting in catalyst deactivation.

In all cases, aromatization proceeded in good yield except in one instance (**16j** → **17j**). In this example, steric hindrance presumably suppressed the initial intramolecular aldol reaction. Notably, the nature of the para substituent on the aryl unit (R) had little effect with both electron-donating groups (**16e**) and electron-withdrawing groups (**16b**) undergoing aromatization with comparable efficiency.

Conclusion

A range of isopropyl 6-aryl and 6-alkyl salicylate esters were prepared from the vinyl dioxinone **10** by cross metathesis with the homoallylic alcohols **14a**–**14i**, Dess–Martin periodinane (DMP) oxidation, and aromatization via generation and trapping of enedione–ketenes. The methodology is a mild and convenient process for the preparation of salicylates with these substitution patterns. Further aspects of this methodology will be reported in due course. ^{1}H and ^{13}C NMR spectra for all new compounds can be found in the Supplementary data.

Experimental

General methods

All reactions were carried out in oven-dried glassware under N_2, using commercially supplied solvents and reagents unless otherwise stated. CH_2Cl_2 was redistilled from CaH_2. Flash chromatography was carried out on silica gel (eluents are given in parentheses). Analytical TLC was performed on precoated silica gel F_{254} aluminum plates with visualization under UV light and by staining with acidic vanillin or acidic potassium permanganate solutions. Melting points were determined using a hot-stage microscope and are uncorrected. ^{1}H and ^{13}C NMR spectra were, respectively, recorded at 400 and 101 MHz with the solvent used in each case specified and spectra referenced to residual solvent peaks. Elemental analysis was carried out by the London Metropolitan elemental analysis service.

With the exception of commercially available pent-4-en-2ol (**14g**) the homoallylic alcohols **14a**,[32] **14b**,[33] **14c**,[34] **14d**,[34] **14e**,[32] **14f**,[32] **14h**,[35] **14i**,[35] **14j**,[32] and **14k**,[36] were prepared as described in the literature from the corresponding aldehydes by reaction with allylmagnesium bromide.[21]

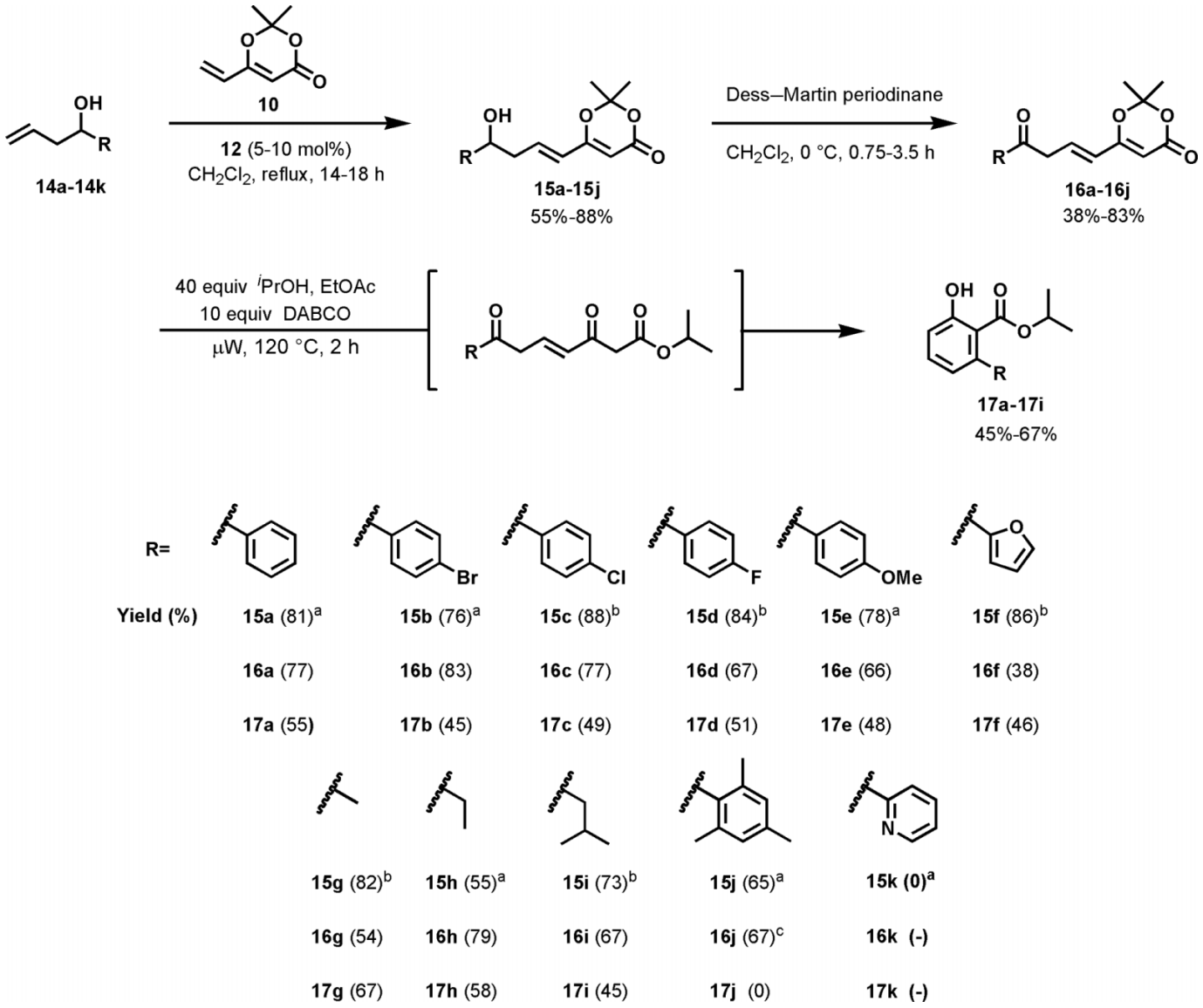
General procedure A for cross metathesis of homoallylic alcohols 14a–14k

Catalyst **12** (5–10 mol %) was added with stirring to vinyl dioxinone **10** (1.5–2 equiv) and homoallylic alcohol (**14a**–**14k**, 0.1 mol/L) in CH_2Cl_2 at reflux and heating was continued for

Can. J. Chem. Downloaded from www.nrcresearchpress.com by MCGILL UNIVERSITY on 02/02/13
For personal use only.

Can. J. Chem. Downloaded from www.nrcresearchpress.com by MCGILL UNIVERSITY on 02/02/13
For personal use only.

Scheme 4. Synthesis of 6-aryl and 6-alkyl salicylates.



14–18 h. The mixture was rotary evaporated and chromatographed to give the corresponding dioxinone (**15a**–**15j**).

General procedure B for oxidation of dioxinones 15a–15j

DMP (1.4 equiv) was added with stirring to dioxinone (**15a**–**15j**, 0.1 mol/L) in CH_2Cl_2 at 0 °C and stirring continued at this temperature for 0.75–3.5 h. The mixture was chromatographed eluting with Et_2O, and the fractions containing product were rotary evaporated. Chromatography of the residue gave the enone–dioxinone (**16a**–**16j**).

General procedure C for aromatization of enone–dioxinones 16a–16j

Molecular sieves (100 mg per 0.1 mmol **16a**–**16j**), DABCO (10 equiv), *i*-PrOH (40 equiv), and enone-dioxinone (**16a**–**16j**) in EtOAc (0.02 mol/L) were placed in a 10 mL microwave vial and microwave heated at 120 °C for 2 h. The resulting mixture was filtered and rotary evaporated. The residue was taken up in EtOAc (10 mL) and washed with 1 mol/L aqueous HCl. The aqueous layer was extracted further with EtOAc (2 × 10 mL), and the combined organic layers were dried ($MgSO_4$), rotary evaporated, and chromatographed to give the salicylates **17a**–**17i**.

*(***E***)-6-(4-Hydroxy-4-phenylbut-1-enyl)-2,2-dimethyl-4*H*-1,3-dioxin-4-one (*15a*)*

According to general procedure A, reaction of alcohol **14a** (210 mg, 1.42 mmol) and dioxinone **10** (328 mg, 2.13 mmol) with catalyst **12** (45 mg, 0.071 mmol) for 14 h and chromatography (hexanes–Et_2O, 7:3 to 1:1) gave dioxinone **15a** (315 mg, 81%) as a brown oil. IR (thin film, cm^{-1}): 3422, 1703, 1649, 1589, 1389, 1373, 1273, 1252, 1200, 1018, 967, 903, 757, 700. ^{1}H NMR (400 MHz, $CDCl_3$, ppm) δ: 7.40–7.32 (m, 5H), 6.64–6.55 (m, 1H), 6.02–5.95 (m, 1H), 5.25 (s, 1H), 4.84 (dd, J = 7.8, 4.9 Hz, 1H), 2.70–2.60 (m, 2H), 2.27 (br s, 1H), 1.70 (s, 6H). ^{13}C NMR (101 MHz, $CDCl_3$, ppm) δ: 162.9,

Can. J. Chem. Downloaded from www.nrcresearchpress.com by MCGILL UNIVERSITY on 02/02/13
For personal use only.

162.0, 143.5, 137.9, 128.6, 128.0, 125.6, 125.0, 106.4, 93.9, 73.3, 42.3, 25.0. MS (EI) *m/z*: 275 $[M + H]^+$. HR-MS (EI) *m/z* calcd for $C_{16}H_{19}O_4$: 275.1283 $[M + H]^+$; found: 275.1288. Anal. calcd for $C_{16}H_{18}O_4$: C 70.06, H 6.61; found: C 70.15, H 6.71.

***(E)-6-(4-(4-Bromophenyl)-4-hydroxybut-1-enyl)-2,2-dimethyl-4H-1,3-dioxin-4-one* (15b)**

According to general procedure A, reaction of alcohol **14b** (491 mg, 2.16 mmol) and dioxinone **10** (500 mg, 3.25 mmol) with catalyst **12** (68 mg, 0.11 mmol) for 16 h and chromatography (hexanes–Et_2O, 7:3 to 1:3) gave dioxinone **15b** (577 mg, 76%) as a brown solid; mp 85–90 °C (Et_2O–pentane). IR (thin film, cm^{-1}): 3451, 1689, 1651, 1590, 1391, 1375, 1275, 1201, 1010, 971, 820, 600. ^1H NMR (400 MHz, $CDCl_3$, ppm) δ: 7.49 (d, J = 8.3 Hz, 2H), 7.23 (d, J = 8.3 Hz, 2H), 6.56 (dt, J = 15.6, 7.8 Hz, 1H), 5.97 (d, J = 15.6 Hz, 1H), 5.24 (s, 1H), 4.81 (t, J = 6.1 Hz, 1H), 2.64–2.56 (m, 2H), 2.31 (br s, 1H), 1.70 (s, 6H). ^{13}C NMR (101 MHz, $CDCl_3$, ppm) δ: 162.8, 162.0, 142.5, 137.3, 131.7, 127.4, 125.3, 121.7, 106.4, 94.0, 72.6, 42.3, 25.0. MS (ESI) *m/z*: 355 $[M(^{81}Br) + H]^+$, 353 $[M(^{79}Br) + H]^+$. HR-MS (ESI) *m/z* calcd for $C_{16}H_{18}BrO_4$: 353.0388 $[M + H]^+$; found: 353.0389. Anal. calcd for $C_{16}H_{17}BrO_4$: C 54.41, H 4.85; found: C 54.25, H 4.73.

***(E)-6-(4-(4-Chlorophenyl)-4-hydroxybut-1-enyl)-2,2-dimethyl-4H-1,3-dioxin-4-one* (15c)**

According to general procedure A, reaction of alcohol **14c** (183 mg, 1 mmol) and dioxinone **10** (308 mg, 2 mmol) with catalyst **12** (63 mg, 0.1 mmol) for 18 h and chromatography (hexanes–Et_2O, 3:2 to 2:3) gave dioxinone **15c** (271 mg, 88%) as a brown solid; mp 76–80 °C (Et_2O–pentane). IR (thin film, cm^{-1}): 3457, 1690, 1652, 1591, 1394, 1376, 1279, 1203, 1087, 1021, 971, 830. ^1H NMR (400 MHz, $CDCl_3$, ppm) δ: 7.36–7.26 (m, 4H), 6.55 (dt, J = 15.7, 7.8 Hz, 1H), 5.97 (d, J = 15.6 Hz, 1H), 5.24 (s, 1H), 4.85–4.77 (m, 1H), 2.66–2.56 (m, 2H), 2.14 (d, J = 3.4 Hz, 1H), 1.70 (s, 6H). ^{13}C NMR (101 MHz, $CDCl_3$, ppm) δ: 162.7, 161.9, 141.9, 137.2, 133.6, 128.8, 127.0, 125.4, 106.4, 94.1, 72.6, 42.4, 25.0. MS (ESI) *m/z*: 311 $[M(^{37}Cl) + H]^+$, 309 $[M(^{35}Cl) + H]^+$. HR-MS (ESI) *m/z* calcd for $C_{16}H_{18}ClO_4$: 309.0894 $[M + H]^+$; found: 309.0887. Anal. calcd for $C_{16}H_{17}ClO_4$: C 62.24, H 5.55; found: C 62.18, H 5.43.

***(E)-6-(4-(4-Fluorophenyl)-4-hydroxybut-1-enyl)-2,2-dimethyl-4H-1,3-dioxin-4-one* (15d)**

According to general procedure A, reaction of alcohol **14d** (166 mg, 1 mmol) and dioxinone **10** (308 mg, 2 mmol) with catalyst **12** (63 mg, 0.1 mmol) for 18 h and chromatography (hexanes–Et_2O, 3:2 to 2:3) gave dioxinone **15d** (244 mg, 84%) as a brown gum. IR (thin film, cm^{-1}): 3429, 1701, 1650, 1603, 1508, 1390, 1375, 1274, 1202, 1156, 1018, 835. ^1H NMR (400 MHz, $CDCl_3$, ppm) δ: 7.35–7.30 (m, 2H), 7.08–7.03 (m, 2H), 6.56 (dt, J = 15.2, 7.8 Hz, 1H), 5.98 (d, J = 15.6 Hz, 1H), 5.25 (s, 1H), 4.83 (dd, J = 7.8, 4.9 Hz, 1H), 2.70–2.55 (m, 2H), 2.21 (br s, 1H), 1.70 (s, 6H). ^{13}C NMR (101 MHz, $CDCl_3$, ppm) δ: 162.8, 162.0, 162.3 (d, J = 245.7 Hz), 139.3, 137.5, 127.3 (d, J = 8 Hz), 125.2, 115.4 (d, J = 22.5 Hz), 106.4, 94.0, 72.6, 42.4, 25.0. MS (ESI) *m/z*: 293 $[M + H]^+$. HR-MS (ESI) *m/z* calcd for $C_{16}H_{18}FO_4$: 293.1189 $[M + H]^+$; found: 293.1177. Anal. calcd for $C_{16}H_{17}FO_4$: C 65.74, H 5.86; found: C 65.90, H 5.90.

***(E)-6-(4-Hydroxy-4-(4-methoxyphenyl)but-1-enyl)-2,2-dimethyl-4H-1,3-dioxin-4-one* (15e)**

According to general procedure A, reaction of alcohol **14e** (120 mg, 0.67 mmol) and dioxinone **10** (156 mg, 1.01 mmol) with catalyst **12** (21 mg, 0.034 mmol) for 18 h and chromatography (hexanes–Et_2O, 3:2 to 2:3) gave dioxinone **15e** (158 mg, 78%) as a brown oil. IR (thin film, cm^{-1}): 3424, 1702, 1650, 1512, 1389, 1374, 1245, 1018, 831. ^1H NMR (400 MHz, $CDCl_3$, ppm) δ: 7.30–7.27 (m, 2H), 6.92–6.89 (m, 2H), 6.59 (dt, J = 15.7, 7.8 Hz, 1H), 5.99 (d, J = 15.6 Hz, 1H), 5.26 (s, 1H), 4.79 (dd, J = 7.8, 4.9 Hz, 1H), 3.82 (s, 3H), 2.73–2.54 (m, 2H), 1.90 (br s, 1H), 1.71 (s, 6H). ^{13}C NMR (101 MHz, $CDCl_3$, ppm) δ: 162.9, 162.0, 159.3, 138.0, 135.6, 126.9, 125.0, 114.0, 106.4, 93.9, 73.0, 55.3, 42.3, 25.0. MS (ESI) *m/z*: 305 $[M + H]^+$. HR-MS (ESI) *m/z* calcd for $C_{17}H_{21}O_5$: 305.1389 $[M + H]^+$; found: 305.1382. Anal. calcd for $C_{17}H_{20}O_5$: C 67.09, H 6.62; found: C 66.96, H 6.55.

***(E)-6-(4-(Furan-2-yl)-4-hydroxybut-1-enyl)-2,2-dimethyl-4H-1,3-dioxin-4-one* (15f)**

According to general procedure A, reaction of alcohol **14f** (138 mg, 1 mmol) and dioxinone **10** (308 mg, 2 mmol) with catalyst **12** (63 mg, 0.1 mmol) for 18 h and chromatography (hexanes–Et_2O, 3:2 to 1:1) gave dioxinone **15f** (228 mg, 86%) as a brown gum. IR (thin film, cm^{-1}): 3400, 1689, 1654, 1590, 1379, 1280, 1197, 1017, 1003, 973, 728, 596. ^1H NMR (400 MHz, $CDCl_3$, ppm) δ: 7.41–7.38 (m, 1H), 6.58 (dt, J = 16.1, 7.8 Hz, 1H), 6.36 (dd, J = 2.9, 2.0 Hz, 1H), 6.27 (d, J = 3.4 Hz, 1H), 6.02 (d, J = 15.6 Hz, 1H), 5.27 (s, 1H), 4.89–4.80 (m, 1H), 2.80–2.72 (m, 2H), 2.19 (d, J = 4.4 Hz, 1H), 1.70 (s, 6H). ^{13}C NMR (101 MHz, $CDCl_3$, ppm) δ: 162.8, 162.0, 155.5, 142.2, 137.0, 125.2, 110.3, 106.4, 106.3, 94.0, 66.6, 38.8, 25.0. MS (ESI) *m/z*: 265 $[M + H]^+$. HR-MS (ESI) *m/z* calcd for $C_{14}H_{17}O_5$: 265.1076 $[M + H]^+$; found: 265.1075. Anal. calcd for $C_{14}H_{16}O_5$: C 63.63, H 6.10; found: C 63.53, H 6.05.

***(E)-6-(4-Hydroxypent-1-enyl)-2,2-dimethyl-4H-1,3-dioxin-4-one* (15g)**

According to general procedure A, reaction of alcohol **14g** (103 μL, 1.00 mmol) and dioxinone **10** (308 mg, 2.00 mmol) with catalyst **12** (63 mg, 0.10 mmol) for 18 h and chromatography (pentane–Et_2O, 55:45 to 1:3) gave dioxinone **15g** (173 mg, 82%) as a brown oil. IR (thin film, cm^{-1}): 3435, 1702, 1650, 1590, 1389, 1374, 1273, 1253, 1201, 1123, 1017, 971, 903, 816, 796, 603. ^1H NMR (400 MHz, $CDCl_3$, ppm) δ: 6.60 (dt, J = 15.4, 7.5 Hz, 1H), 6.01 (dt, J = 15.6, 1.0 Hz, 1H), 5.28 (s, 1H), 3.99 (m, 1H), 2.35–2.42 (m, 2H), 1.72–1.75 (m, 7H), 1.26 (d, J = 6.4 Hz, 3H). ^{13}C NMR (101 MHz, $CDCl_3$, ppm) δ: 163.0, 162.1, 138.2, 124.9, 106.4, 93.8, 67.0, 42.3, 25.1, 25.0, 23.4. MS (ESI) *m/z*: 213 $[M + H]^+$. HR-MS (ESI) *m/z* calcd for $C_{11}H_{17}O_4$: 213.1127 $[M + H]^+$; found: 213.1123. Anal. calcd for $C_{11}H_{16}O_4$: C 62.25, H 7.60; found: C 62.12, H 7.48.

***(E)-6-(4-Hydroxyhex-1-enyl)-2,2-dimethyl-4H-1,3-dioxin-4-one* (15h)**

According to general procedure A, reaction of alcohol **14h** (300 mg, 3.00 mmol) and dioxinone **10** (693 mg, 4.80 mmol) with catalyst **12** (94 mg, 0.15 mmol) for 18 h and chromatography (hexanes–Et_2O, 1:1 to 2:3) gave dioxinone **15h** (372 mg, 55%) as a brown oil. IR (thin film, cm^{-1}): 3427,

Can. J. Chem. Downloaded from www.nrcresearchpress.com by MCGILL UNIVERSITY on 02/02/13
For personal use only.

1707, 1650, 1591, 1340, 1375, 1274, 1254, 1203, 1019, 971, 904, 801, 603. ^{1}H NMR (400 MHz, $CDCl_3$, ppm) δ: 6.60 (dt, J = 15.4, 7.5 Hz, 1H), 5.99 (dt, J = 15.7, 1.5 Hz, 1H), 5.26 (s, 1H), 3.63–3.74 (m, 1H), 2.37–2.47 (m, 1H), 2.28–2.37 (m, 1H), 1.70 (s, 7H), 1.45–1.57 (m, 2H), 0.97 (t, J = 7.6 Hz, 3H). ^{13}C NMR (101 MHz, $CDCl_3$, ppm) δ: 162.9, 162.0, 138.5, 124.7, 106.3, 93.7, 72.1, 40.1, 30.0, 25.0, 9.8. MS (ESI) *m/z*: 227 $[M + H]^+$. HR-MS (ESI) *m/z* calcd for $C_{12}H_{19}O_4$: 227.1283 $[M + H]^+$; found: 227.1283. Anal. calcd for $C_{12}H_{18}O_4$: C 63.70, H 8.02; found: C 63.75, H 8.13.

(E)-6-(4-Hydroxy-6-methylhept-1-enyl)-2,2-dimethyl-4H-1,3-dioxin-4-one (15i)

According to general procedure A, reaction of alcohol **14i** (128 mg, 1.00 mmol) and dioxinone **10** (308 mg, 2.00 mmol) with catalyst **12** (63 mg, 0.10 mmol) for 18 h and chromatography (hexanes–Et_2O, 55:45 to 45:55) gave dioxinone **15i** (185 mg, 73%) as a brown gum. IR (thin film, cm^{-1}): 3421, 1703,1650, 1590, 1389, 1374, 1273, 1253, 1202, 1017, 969, 903. ^{1}H NMR (400 MHz, $CDCl_3$, ppm) δ: 6.63 (dt, J = 15.4, 7.5 Hz, 1H), 6.01 (dt, J = 15.6, 1.5 Hz, 1H), 5.28 (s, 1H), 3.81–3.91 (m, 1H), 2.38–2.48 (m, 1H), 2.26–2.37 (m, 1H), 1.77–1.84 (m, 1H), 1.73 (s, 6H), 1.65 (d, J = 4.4 Hz, 1H), 1.43–1.50 (m, 1H), 1.24–1.32 (m, 1H), 0.93–0.97 (m, 6H). ^{13}C NMR (101 MHz, $CDCl_3$, ppm) δ: 163.0, 162.0, 138.5, 124.9, 106.4, 93.8, 68.8, 46.5, 41.2, 25.1, 25.0, 24.6, 23.4, 22.0. MS (ESI) *m/z*: 277 $[M + Na]^+$, 255 $[M + H]^+$. Anal. calcd for $C_{14}H_{22}O_4$: C 66.12, H 8.72; found: C 66.10, H 8.65.

(E)-6-(4-Hydroxy-4-mesitylbut-1-enyl)-2,2-dimethyl-4H-1,3-dioxin-4-one (15j)

According to general procedure A, reaction of alcohol **14j** (350 mg, 1.84 mmol) and dioxinone **10** (426 mg, 2.76 mmol) with catalyst **12** (58 mg, 0.09 mmol) for 16 h and chromatography (hexanes–Et_2O, 4:1 to 1:1) gave dioxinone **15j** (377 mg, 65%) as a brown gum. IR (thin film, cm^{-1}): 3442, 2951, 1702, 1650, 1591, 1389, 1373, 1273, 1202, 1017, 967, 851, 801. ^{1}H NMR (400 MHz, $CDCl_3$, ppm) δ: 6.84 (s, 2H), 6.64 (dt, J = 15.7, 7.8 Hz, 1H), 6.02 (d, J = 15.6 Hz, 1H), 5.29–5.22 (m, 2H), 2.97–2.85 (m, 1H), 2.63–2.49 (m, 1H), 2.41 (s, 6H), 2.26 (s, 3H), 2.00 (d, J = 2.4 Hz, 1H), 1.71 (s, 6H). ^{13}C NMR (101 MHz, $CDCl_3$, ppm) δ: 163.0, 162.0, 138.8, 137.0, 135.8, 135.6, 130.3, 124.6, 106.3, 93.8, 70.5, 39.0, 25.0, 24.9, 20.7. MS (ESI) *m/z*: 317 $[M + H]^+$. HR-MS (ESI) *m/z* calcd for $C_{19}H_{25}O_4$: 317.1753 $[M + H]^+$; found: 317.1753. Anal. calcd for $C_{19}H_{24}O_4$: C 72.13, H 7.65; found: C 71.97, H 7.59.

(E)-2,2-Dimethyl-6-(4-oxo-4-phenylbut-1-enyl)-4H-1,3-dioxin-4-one (16a)

According to general procedure B, oxidation of dioxinone **15a** (329 mg, 1.21 mmol) for 3.5 h and chromatography (hexanes–Et_2O, 7:3 to 1:1) gave enone–dioxinone **16a** (255 mg, 77%) as a yellow solid; mp 58–61 °C (Et_2O–pentane). IR (thin film, cm^{-1}): 1714, 1687, 1655, 1597, 1392, 1369, 1278, 1204, 1019, 991, 905, 816. ^{1}H NMR (400 MHz, $CDCl_3$, ppm) δ: 8.04–7.91 (m, 2H), 7.74–7.56 (m, 1H), 7.56–7.36 (m, 2H), 6.85 (dt, J = 15.7, 7.1 Hz, 1H), 6.08 (d, J = 15.6 Hz, 1H), 5.31 (s, 1H), 3.93 (dd, J = 7.1, 1.2 Hz, 2H), 1.73 (s, 6H). ^{13}C NMR (101 MHz, $CDCl_3$, ppm) δ: 196.3, 162.4, 161.6, 136.2, 133.7, 133.7, 128.8, 128.2, 125.7, 106.6, 94.6, 41.7, 25.0. MS (ESI) *m/z*: 273 $[M + H]^+$. HR-MS (EI) *m/z* calcd for $C_{16}H_{17}O_4$: 273.1127 $[M + H]^+$; found: 273.1121. Anal. calcd for $C_{16}H_{16}O_4$: C 70.58, H 5.92; found: C 70.53, H 5.85.

(E)-6-(4-(4-Bromophenyl)-4-oxobut-1-enyl)-2,2-dimethyl-4H-1,3-dioxin-4-one (16b)

According to general procedure B, oxidation of dioxinone **15b** (23 mg, 0.065 mmol) for 2 h and chromatography (hexanes–Et_2O, 1:1) gave enone–dioxinone **16b** (19 mg, 83%) as a yellow solid; mp 68–72 °C (Et_2O–pentane). IR (thin film, cm^{-1}): 1713, 1693, 1659, 1586, 1391, 1374, 1273, 1199, 1011, 991, 970, 800. ^{1}H NMR (400 MHz, $CDCl_3$, ppm) δ: 7.85–7.80 (m, 2H), 7.67–7.62 (m, 2H), 6.81 (dt, J = 15.5, 6.9 Hz, 1H), 6.07 (d, J = 15.6 Hz, 1H), 5.30 (s, 1H), 3.89 (dd, J = 7.1, 1.2 Hz, 2H), 1.72 (s, 6H). ^{13}C NMR (101 MHz, $CDCl_3$, ppm) δ: 187.9, 160.9, 141.9, 134.9, 133.5, 132.2, 132.0, 130.2, 129.1, 128.1, 128.0, 107.2, 100.8, 25.1. MS (CI) *m/z*: 370 $[M(^{81}Br) + H_2O]^+$, 368 $[M(^{79}Br) + H_2O]^+$. Anal. calcd for $C_{16}H_{15}BrO_4$: C 54.72, H 4.31; found: C 54.63, H 4.21.

(E)-6-(4-(4-Chlorophenyl)-4-oxobut-1-enyl)-2,2-dimethyl-4H-1,3-dioxin-4-one (16c)

According to general procedure B, oxidation of dioxinone **15c** (82 mg, 0.266 mmol) for 2 h and chromatography (hexanes–Et_2O, 7:3 to 1:1) gave enone–dioxinone **16c** (63 mg, 77%) as an orange oil. IR (thin film, cm^{-1}): 1711, 1689, 1587, 1376, 1391, 1270, 1200, 1089, 1022, 985, 839, 784. ^{1}H NMR (400 MHz, $CDCl_3$, ppm) δ: 7.93–7.88 (m, 2H), 7.50–7.45 (m, 2H), 6.81 (dt, J = 15.7, 7.1 Hz, 1H), 6.07 (dt, J = 15.7, 1.5 Hz, 1H), 5.31 (s, 1H), 3.90 (dd, J = 6.8, 1.5 Hz, 2H), 1.72 (s, 6H). ^{13}C NMR (101 MHz, $CDCl_3$, ppm) δ: 195.0, 162.3, 161.7, 140.2, 134.4, 133.2, 129.6, 129.2, 125.9, 106.6, 94.7, 41.6, 25.0. MS (ESI) *m/z*: 309 $[M(^{37}Cl) + H]^+$, 307 $[M(^{35}Cl) + H]^+$. HR-MS (ESI) *m/z* calcd for $C_{16}H_{16}ClO_4$: 307.0737 $[M + H]^+$; found: 307.0732. Anal. calcd for $C_{16}H_{15}ClO_4$: C 62.65, H 4.93; found: C 62.77, H 4.84.

(E)-6-(4-(4-Fluorophenyl)-4-oxobut-1-enyl)-2,2-dimethyl-4H-1,3-dioxin-4-one (16d)

According to general procedure B, oxidation of dioxinone **15d** (226 mg, 0.774 mmol) for 3 h and chromatography (hexanes–Et_2O, 7:3 to 1:1) gave enone–dioxinone **16d** (143 mg, 67%) as an orange oil. IR (thin film, cm^{-1}): 1710, 1692, 1597, 1379, 1275, 1200, 1158, 1021, 846, 793. ^{1}H NMR (400 MHz, $CDCl_3$, ppm) δ: 8.02–7.97 (m, 2H), 7.20–7.14 (m, 2H), 6.82 (dt, J = 15.5, 6.9 Hz, 1H), 6.07 (d, J = 16.1 Hz, 1H), 5.30 (s, 1H), 3.90 (dd, J = 1.2, 7.1 Hz, 2H), 1.72 (s, 6H). ^{13}C NMR (101 MHz, $CDCl_3$, ppm) δ: 194.7, 167.3, 163.5 (d, J = 239.3 Hz), 161.7, 133.4, 132.5, 130.9 (d, J = 9.6 Hz), 125.8, 116.0 (d, J = 20.9 Hz), 106.6, 94.6, 41.6, 25.0. HR-MS (CI) *m/z* calcd for $C_{16}H_{19}NO_4F$: 308.1298 $[M + NH_4]^+$; found: 308.1301. Anal. calcd for $C_{16}H_{15}FO_4$: C 66.20, H 5.21; found: C 66.15, H 5.14.

(E)-6-(4-(4-Methoxyphenyl)-4-oxobut-1-enyl)-2,2-dimethyl-4H-1,3-dioxin-4-one (16e)

According to general procedure B, oxidation of dioxinone **15e** (150 mg, 0.493 mmol) for 0.75 h and chromatography (hexanes–Et_2O, 7:3 to 3.5:10) gave enone–dioxinone **16e** (98 mg, 66%) as a yellow solid; mp 89–92 °C (Et_2O–pentane). IR (thin film, cm^{-1}): 1710, 1674, 1655, 1573, 1374, 1255, 1204, 1182, 1020, 984, 967, 844, 790, 597. ^{1}H NMR (400 MHz, $CDCl_3$, ppm) δ: 7.97–7.92 (m, 2H), 6.99–6.94 (m,

Can. J. Chem. Downloaded from www.nrcresearchpress.com by MCGILL UNIVERSITY on 02/02/13
For personal use only.

2H), 6.84 (dt, J = 15.4, 7.0 Hz, 1H), 6.06 (d, J = 15.7 Hz, 1H), 5.30 (s, 1H), 3.89 (s, 3H), 3.87 (dd, J = 7.3, 1.5 Hz, 2H), 1.72 (s, 6H). ^{13}C NMR (101 MHz, $CDCl_3$, ppm) δ: 194.8, 163.9, 162.5, 161.8, 134.3, 130.6, 129.2, 125.5, 114.0, 106.5, 94.4, 55.5, 41.5, 25.0. MS (ESI) *m/z*: 303 $[M + H]^+$. HR-MS (ESI) *m/z* calcd for $C_{17}H_{19}O_5$: 303.1232 $[M + H]^+$; found: 303.1226. Anal. calcd for $C_{17}H_{18}O_5$: C 67.54, H 6.00; found: C 67.43, H 6.05.

***(E)-6-(4-(Furan-2-yl)-4-oxobut-1-enyl)-2,2-dimethyl-4H-1,3-dioxin-4-one* (16f)**

According to general procedure B, oxidation of dioxinone **15f** (94 mg, 0.356 mmol) for 2 h and chromatography (hexanes–Et_2O, 7:3 to 1:1) gave enone–dioxinone **16f** (35 mg, 38%) as a yellow oil. IR (thin film, cm^{-1}): 1721, 1675, 1655, 1466, 1392, 1376, 1275, 1204, 1019. ^{1}H NMR (400 MHz, $CDCl_3$, ppm) δ: 7.63 (d, J = 1.0 Hz, 1H), 7.28–7.25 (m, 1H), 6.76 (dt, J = 15.6, 7.3 Hz, 1H), 6.58 (dd, J = 3.4, 1.5 Hz, 1H), 6.12–6.04 (m, 1H), 5.30 (s, 1H), 3.78 (dd, J = 7.3, 1.5 Hz, 2H), 1.71 (s, 6H). ^{13}C NMR (101 MHz, $CDCl_3$, ppm) δ: 185.1, 162.4, 161.8, 152.0, 146.9, 132.9, 125.9, 117.9, 112.6, 106.6, 94.6, 41.6, 25.0. MS (ESI) *m/z*: 263 $[M + H]^+$. HR-MS (ESI) *m/z* calcd for $C_{14}H_{15}O_5$: 263.0919 [M + H]; found: 263.0912. Anal. calcd for $C_{14}H_{14}O_5$: C 64.12, H 5.38; found: C 60.65, H 5.34.

***(E)-2,2-Dimethyl-6-(4-oxopent-1-enyl)-4H-1,3-dioxin-4-one* (16g)**

According to general procedure B, oxidation of dioxinone **15g** (145 mg, 0.684 mmol) for 1.25 h and chromatography (pentane–Et_2O, 1:1 to 2:3) gave enone–dioxinone **16g** (78 mg, 54%) as a yellow oil. IR (thin film, cm^{-1}): 1711, 1654, 1593, 1390, 1274, 1273, 1251, 1200, 1158, 1016, 968, 903, 859, 808. ^{1}H NMR (400 MHz, $CDCl_3$, ppm) δ: 6.67 (dt, J = 15.7, 7.3 Hz, 1H), 6.00 (dt, J = 15.6, 1.5 Hz, 1H), 5.32 (s, 1H), 3.39 (dd, J = 7.3, 1.0 Hz, 2H), 2.24 (s, 3H), 1.74 (s, 6H). ^{13}C NMR (101 MHz, $CDCl_3$, ppm) δ: 204.5, 162.4, 161.8, 132.9, 125.8, 106.6, 94.7, 46.7, 30.1, 25.0. MS (ESI) *m/z*: 233 $[M + Na]^+$, 211 $[M + H]^+$. HR-MS (ESI) *m/z* calcd for $C_{11}H_{15}O_4$: 211.0965 $[M + H]^+$; found: 211.0966.

***(E)-2,2-Dimethyl-6-(4-oxohex-1-enyl)-4H-1,3-dioxin-4-one* (16h)**

According to general procedure B, oxidation of dioxinone **15h** (60 mg, 0.265 mmol) for 0.75 h and chromatography (hexanes–Et_2O, 1:1) gave enone–dioxinone **16h** (47 mg, 79%) as a yellow oil. IR (thin film, cm^{-1}): 1711, 1630, 1586, 1460, 1391, 1376, 1276, 1252, 1200, 1096, 1017, 973, 903, 812. ^{1}H NMR (400 MHz, $CDCl_3$, ppm) δ: 6.66 (dt, J = 15.6, 6.8 Hz, 1H), 5.98 (dt, J = 15.7, 1.5 Hz, 1H), 5.29 (s, 1H), 3.34 (dd, J = 7.3, 1.5 Hz, 2H), 2.50 (q, J = 7.3 Hz, 2H), 1.71 (s, 6H), 1.08 (t, J = 7.3 Hz, 3H). ^{13}C NMR (101 MHz, $CDCl_3$, ppm) δ: 207.3, 162.4, 161.7, 133.3, 125.6, 106.5, 94.5, 45.5, 36.1, 25.0, 7.6. MS (ESI) *m/z*: 247 $[M + Na]^+$, 225 $[M + H]^+$.

***(E)-2,2-Dimethyl-6-(6-methyl-4-oxohept-1-enyl)-4H-1,3-dioxin-4-one* (16i)**

According to general procedure B, oxidation dioxinone **15i** (151 mg, 0.594 mmol) for 1.25 h and chromatography (pentane–Et_2O, 7:3 to 1:1) gave enone–dioxinone **16i** (101 mg, 67%) as a yellow oil. IR (thin film, cm^{-1}): 1707, 1655, 1594, 1451, 1392, 1373, 1277, 1204, 1105, 1019, 979, 906, 864, 849, 812. ^{1}H NMR (400 MHz, $CDCl_3$, ppm) δ: 6.68 (dt, J = 15.7, 7.3 Hz, 1H), 6.00 (dt, J = 15.7, 1.5 Hz, 1H), 5.31 (s, 1H), 3.34 (dd, J = 7.3, 1.0 Hz, 2H), 2.37 (d, J = 7.3 Hz, 2H), 2.10–2.25 (m, 1H), 1.74 (s, 6H), 0.96 (d, J = 6.4 Hz, 6H). ^{13}C NMR (101 MHz, $CDCl_3$, ppm) δ: 206.6, 162.4, 161.8, 133.3, 125.6, 106.5, 94.5, 51.9, 46.3, 25.0, 24.5, 22.5. MS (ESI) *m/z*: 275 $[M + Na]^+$, 253 $[M + H]^+$. Anal. calcd for $C_{14}H_{20}O_4$: C 66.65, H 7.99; found: C 66.74, H 7.90.

***(E)-6-(4-Mesityl-4-oxobut-1-enyl)-2,2-dimethyl-4H-1,3-dioxin-4-one* (16j)**

2-Iodoxybenzoic acid (842 mg, 2.94 mmol) was added with stirring to dioxinone **15j** (310 mg, 0.981 mmol) in EtOAc (7 mL) open to the air at 80 °C for 2 h. The mixture was filtered through Celite and rotary evaporated. Chromatography (hexanes–Et_2O, 4:1 to 1:1) of the residue gave enone–dioxinone **16j** as a 2:1 mixture of the β,δ-enone: α,β-enone (207 mg, 67%) as a yellow oil. IR (thin film, cm^{-1}): 1713, 1698, 1603, 1373, 1268, 1200, 1148, 1017, 978, 852, 802, 602. β,δ-Enone: ^{1}H NMR (400 MHz, $CDCl_3$, ppm) δ: 6.87 (s, 2H), 6.78 (dt, J = 15.6, 7.8 Hz, 1H), 6.04 (d, J = 15.7 Hz, 1H), 5.31 (s, 1H), 3.63 (dd, J = 7.1, 1.2 Hz, 2H), 2.30 (s, 3H), 2.21 (s, 6H), 1.73 (s, 6H). ^{13}C NMR (101 MHz, $CDCl_3$, ppm) δ: 206.5, 162.4, 161.8, 138.7, 133.8, 132.8, 132.5, 128.6, 125.8, 106.6, 94.7, 47.8, 25.0, 21.1, 19.2. α,β-Enone: ^{1}H NMR (400 MHz, $CDCl_3$, ppm) δ: 6.87 (s, 2H), 6.47–6.29 (m, 2H), 5.22 (s, 1H), 3.16 (d, J = 6.4 Hz, 2H), 2.30 (s, 3H) 2.14 (s, 6H), 1.66 (s, 6H). ^{13}C NMR (101 MHz, $CDCl_3$, ppm) δ: 206.5, 162.4, 161.8, 141.6, 138.7, 136.1, 133.8, 132.5, 128.4, 106.6, 94.5, 36.3 25.0, 21.1, 19.2. MS (CI) *m/z*: 332 $[M + H_2O]^+$, 315 $[M + H]^+$. Anal. calcd for $C_{19}H_{22}O_4$: C 72.59, H 7.05; found: C 72.44, H 6.95.

***Isopropyl 3-hydroxybiphenyl-2-carboxylate* (17a)**

According to general procedure C, aromatization of enone–dioxinone **16a** (50 mg, 0.184 mmol) and chromatography (hexanes–Et_2O, 100:0 to 19:1) gave salicylate **17a** (26 mg, 55%) as a colorless solid; mp 53–55 °C (Et_2O–pentane). IR (thin film, cm^{-1}): 1650, 1606, 1597, 1441, 1370, 1278, 1225, 1178, 1097, 922, 897, 814. ^{1}H NMR (400 MHz, $CDCl_3$, ppm) δ: 10.96 (s, 1H), 7.48–7.30 (m, 4H), 7.30–7.12 (m, 2H), 7.01 (dd, J = 8.3, 1.0 Hz, 1H), 6.78 (dd, J = 7.3, 1.0 Hz, 1H), 5.05–4.85 (m, 1H), 0.86 (d, J = 6.4 Hz, 6H). ^{13}C NMR (101 MHz, $CDCl_3$, ppm) δ: 170.4, 161.5, 145.0, 143.2, 133.3, 128.3, 127.6, 126.6, 122.4, 116.6, 112.6, 69.1, 20.9. HR-MS (EI) *m/z* calcd for $C_{16}H_{17}O_3$: 257.1178 $[M + H]^+$; found: 257.1168. Anal. calcd for $C_{16}H_{16}O_3$: C 74.98, H 6.29; found: C 74.90, H 6.37.

***Isopropyl 4′-bromo-3-hydroxybiphenyl-2-carboxylate* (17b)**

According to general procedure C, aromatization of enone–dioxinone **16b** (100 mg, 0.29 mmol) and chromatography (hexanes–Et_2O, 100:0 to 9:1) gave salicylate **17b** (43 mg, 45%) as a colorless solid; mp 79–83 °C (Et_2O–pentane). IR (thin film, cm^{-1}): 1663, 1600, 1575, 1492, 1444, 1363, 1314, 1273, 1209, 1173, 1100, 1066, 918, 807. ^{1}H NMR (400 MHz, $CDCl_3$, ppm) δ: 11.04 (s, 1H), 7.54–7.46 (m, 2H), 7.40 (t, J = 8.1 Hz, 1H), 7.14–7.06 (m, 2H), 7.02 (dd, J = 8.3, 1.0 Hz, 1H), 6.73 (dd, J = 7.3, 1.0 Hz, 1H), 4.98 (spt, J = 6.2 Hz, 1H), 0.91 (d, J = 6.4 Hz, 6H). ^{13}C NMR (101 MHz, $CDCl_3$, ppm) δ: 170.1, 161.8, 143.6, 142.2, 133.5, 130.6, 130.0, 122.2, 120.7, 117.1, 112.2, 69.5, 21.0. MS (CI) *m/z*: 354 $[M(^{81}Br) + H_2O]^+$, 352 $[M(^{79}Br) + H_2O]^+$, 337 $[M(^{81}Br) + H]^+$, 335

Can. J. Chem. Downloaded from www.nrcresearchpress.com by MCGILL UNIVERSITY on 02/02/13
For personal use only.

[M(^{79}Br) + H]$^+$. HR-MS (CI) *m/z* calcd for $C_{16}H_{16}BrO_3$: 335.0283 [M + H]$^+$; found: 335.0274. Anal. calcd for $C_{16}H_{15}BrO_3$: C 57.33, H 4.51; found: C 57.25, H 4.56.

***Isopropyl 4′-chloro-3-hydroxybiphenyl-2-carboxylate* (17c)**

According to general procedure C, aromatization of enone-dioxinone **16c** (69 mg, 0.23 mmol) and chromatography (hexanes–Et_2O, 100:0 to 97:3) gave salicylate **17c** (32 mg, 49%) as a colorless solid; mp 73–76 °C ($CHCl_3$). IR (thin film, cm^{-1}): 1665, 1601, 1576, 1492, 1444, 1363, 1314, 1272, 1172, 1101, 807. ^{1}H NMR (400 MHz, $CDCl_3$, ppm) δ: 11.04 (s, 1H), 7.40 (t, *J* = 7.8 Hz, 1H), 7.37–7.30 (m, 2H), 7.20–7.12 (m, 2H), 7.02 (dd, *J* = 8.6, 1.2 Hz, 1H), 6.73 (dd, *J* = 7.6, 1.2 Hz, 1H), 4.98 (spt, *J* = 6.3 Hz, 1H), 0.91 (d, *J* = 6.4 Hz, 6H). ^{13}C NMR (101 MHz, $CDCl_3$, ppm) δ: 170.1, 161.8, 143.6, 141.7, 133.5, 132.7, 129.6, 127.7, 122.3, 117.1, 112.3, 69.4, 21.0. MS (CI) *m/z*: 310 [M(^{37}Cl) + H_2O]$^+$, 308 [M(^{35}Cl) + H_2O]$^+$, 293 [M(^{37}Cl) + H]$^+$, 291 [M(^{35}Cl) + H]$^+$. HR-MS (CI) *m/z* calcd for $C_{16}H_{16}ClO_3$: 291.0788 [M + H]$^+$; found: 291.0786. Anal. calcd for $C_{16}H_{15}ClO_3$: C 66.10, H 5.20; found: C 65.98, H 5.24.

***Isopropyl 4′-fluoro-3-hydroxybiphenyl-2-carboxylate* (17d)**

According to general procedure C, aromatization of enone–dioxinone **16d** (35 mg, 0.21 mmol) and chromatography (hexanes–Et_2O, 19:1) gave salicylate **17d** (17 mg, 51%) as a colorless solid; mp 85–87 °C (Et_2O–pentane). IR (thin film, cm^{-1}): 1650, 1606, 1513, 1445, 1367, 1280, 1227, 1213, 1177, 1093, 842, 815. ^{1}H NMR (400 MHz, $CDCl_3$, ppm) δ: 11.01 (s, 1H), 7.40 (t, *J* = 7.8 Hz, 1H), 7.22–7.16 (m, 2H), 7.10–7.03 (m, 2H), 7.01 (dd, *J* = 8.3, 1.5 Hz, 1H), 6.74 (dd, *J* = 7.6, 1.2 Hz, 1H), 4.98 (spt, *J* = 6.3 Hz, 1H), 0.91 (d, *J* = 6.4 Hz, 6H). ^{13}C NMR (101 MHz, $CDCl_3$, ppm) δ: 170.3, 161.7, 143.8, 139.2 133.4, 129.8, 122.5, 116.9, 114.5, 114.3, 112.5, 69.3, 21.0. MS (CI) *m/z*: 275 [M + H]$^+$. HR-MS (CI) *m/z* calcd for $C_{16}H_{16}FO_3$: 275.1083 [M + H]$^+$; found: 275.1081. Anal. calcd for $C_{16}H_{15}FO_3$: C 70.06, H 5.51; found: C 70.00, H 5.60.

***Isopropyl 3-hydroxy-4′-methoxybiphenyl-2-carboxylate* (17e)**

According to general procedure C, aromatization of enone–dioxinone **16e** (37 mg, 0.12 mmol) and chromatography (hexanes–Et_2O, 100:0 to 19:1) gave salicylate **17e** (17 mg, 48%) as a yellow solid; mp 42–45 °C (Et_2O). IR (thin film, cm^{-1}): 1655, 1602, 1515, 1446, 1369, 1271, 1243, 1218, 1175, 1094, 1034, 807. ^{1}H NMR (400 MHz, $CDCl_3$, ppm) δ: 10.86 (s, 1H), 7.38 (t, *J* = 7.8 Hz, 1H), 7.18–7.11 (m, 2H), 6.98 (dd, *J* = 8.3, 1.0 Hz, 1H), 6.94–6.87 (m, 2H), 6.77 (dd, *J* = 7.3, 1.0 Hz, 1H), 4.97 (spt, *J* = 6.3 Hz, 1H), 3.86 (s, 3H), 0.91 (d, *J* = 6.4 Hz, 6H). ^{13}C NMR (101 MHz, $CDCl_3$, ppm) δ: 170.5, 161.4, 158.7, 144.6, 135.7, 133.3, 129.4, 122.6, 116.3, 113.0, 112.8, 69.1, 55.4, 21.1. MS (CI) *m/z*: 304 [M + H_2O]$^+$, 287 [M + H]$^+$. HR-MS (CI) *m/z* calcd for $C_{17}H_{19}O_4$: 287.1283 [M + H]$^+$; found: 287.1275. Anal. calcd for $C_{17}H_{18}O_4$: C 71.31, H 6.34; found: C 68.02, H 6.55.

***Isopropyl 2-(furan-2-yl)-6-hydroxybenzoate* (17f)**

According to general procedure C, aromatization of enone–dioxinone **16f** (30 mg, 0.12 mmol) and chromatography (hexanes–Et_2O, 100:0 to 19:1) gave salicylate **17f** (13 mg, 46%) as a colorless oil. IR (thin film, cm^{-1}): 1664, 1606, 1572, 1453, 1374, 1275, 1222, 1178, 1103. ^{1}H NMR (400 MHz, $CDCl_3$, ppm) δ: 10.67 (s, 1H), 7.47 (d, *J* = 1.0 Hz, 1H), 7.40 (t, *J* = 7.8 Hz, 1H), 7.03 (dd, *J* = 8.3, 1.0 Hz, 1H), 6.95 (dd, *J* = 7.3, 1.0 Hz, 1H), 6.47 (dd, *J* = 3.4, 2.0 Hz, 1H), 6.40 (d, *J* = 2.9 Hz, 1H), 5.13 (spt, *J* = 6.3 Hz, 1H), 1.12 (d, *J* = 6.4 Hz, 6H). ^{13}C NMR (101 MHz, $CDCl_3$, ppm) δ: 170.0, 161.2, 154.2, 141.7, 133.5, 132.8, 122.3, 118.0, 112.7, 111.1, 107.1, 69.3, 21.5. MS (CI) *m/z*: 247 [M + H]$^+$. HR-MS (CI) *m/z* calcd for $C_{14}H_{15}O_4$: 247.0970 [M + H]$^+$; found: 247.0972.

***Isopropyl 2-hydroxy-6-methylbenzoate* (17g)**

According to general procedure C, aromatization of enone–dioxinone **16g** (73 mg, 0.348 mmol) and chromatography (pentane–Et_2O, 100:0 to 98:2) gave salicylate **17g** (45 mg, 67%) as a colorless oil. IR (thin film, cm^{-1}): 1727, 1650, 1606, 1580, 1459, 1439, 1365, 1291, 1251, 1212, 1165, 1100, 1078, 1034, 965, 911, 863, 806, 756, 702. ^{1}H NMR (400 MHz, $CDCl_3$, ppm) δ: 11.43 (s, 1H), 7.27 (t, *J* = 7.8 Hz, 1H), 6.84 (d, *J* = 8.3 Hz, 1H), 6.71 (d, *J* = 7.3 Hz, 1H), 5.34 (spt, *J* = 6.2 Hz, 1H), 2.56 (s, 3H), 1.43 (d, *J* = 6.4 Hz, 6H). ^{13}C NMR (101 MHz, $CDCl_3$, ppm) δ: 171.2, 162.8, 141.3, 133.9, 122.9, 115.6, 112.7, 69.7, 24.2, 22.0. MS (ESI) *m/z*: 212 [M + H_2O]$^+$, 195 [M + H]$^+$. Anal. calcd for $C_{11}H_{14}O_3$: C 68.02, H 7.27; found: C 67.87, H 7.21.

***Isopropyl 2-hydroxy-6-ethylbenzoate* (17h)**

According to general procedure C, aromatization of enone-dioxinone **16h** (76 mg, 0.339 mmol) and chromatography (pentane–Et_2O, 100:0 to 19:1) gave salicylate **17h** (41 mg, 58%) as a colorless oil. IR (thin film, cm^{-1}): 1727, 1654, 1606, 1577, 1447, 1363, 1308, 1295, 1245, 1207, 1167, 1102, 931, 908, 816. ^{1}H NMR (400 MHz, $CDCl_3$, ppm) δ: 11.33 (s, 1H), 7.30 (t, *J* = 8.1 Hz, 1H), 6.85 (dd, *J* = 8.3, 1.5 Hz, 1H), 6.74 (d, *J* = 7.3 Hz, 1H), 5.36 (spt, *J* = 6.3 Hz, 1H), 2.96 (q, *J* = 7.3 Hz, 2H), 1.43 (d, *J* = 6.4 Hz, 6H), 1.23 (t, *J* = 7.3 Hz, 3H). ^{13}C NMR (101 MHz, $CDCl_3$, ppm) δ: 171.0, 162.6, 147.4, 134.1, 121.7, 115.6, 112.2, 69.7, 29.6, 21.8, 16.5. MS (ESI) *m/z*: 231 [M + Na]$^+$, 209 [M + H]$^+$. Anal. calcd for $C_{12}H_{16}O_3$: C 69.21, H 7.74; found: C 69.18, H 7.64.

***Isopropyl 2-hydroxy-6-isobutylbenzoate* (17i)**

According to general procedure C, aromatization of enone–dioxinone **16i** (78 mg, 0.310 mmol) and chromatography (pentane–Et_2O, 100:0 to 19:1) gave salicylate **17i** (31 mg, 45%) as a colorless oil. IR (thin film, cm^{-1}): 1651, 1606, 1577, 1478, 1363, 1308, 1294, 1250, 1229, 1202, 1164, 1097, 1062, 911, 833, 803, 763, 709. ^{1}H NMR (400 MHz, $CDCl_3$, ppm) δ: 11.35 (s, 1H), 7.28 (t, *J* = 7.8 Hz, 1H), 6.86 (dd, *J* = 8.3, 1.5 Hz, 1H), 6.66 (dd, *J* = 7.6, 1.2 Hz, 1H), 5.37 (spt, *J* = 6.3 Hz, 1H), 2.82 (d, *J* = 7.3 Hz, 2H), 1.76–1.91 (m, 1H), 1.43 (d, *J* = 6.4 Hz, 6H), 0.89 (d, *J* = 6.4 Hz, 6H). ^{13}C NMR (101 MHz, $CDCl_3$, ppm) δ: 171.2, 162.8, 144.5, 133.5, 123.7, 115.8, 112.5, 69.6, 45.5, 30.0, 22.5, 21.8. MS (ESI) *m/z*: 259 [M + Na]$^+$, 237 [M + H]$^+$. Anal. calcd for $C_{14}H_{20}O_3$: C 71.16, H 8.53; found: C 71.08, H 8.45.

Supplementary data

Supplementary data are available with the article through the journal Web site http://nrcresearchpress.com/doi/suppl/10.1139/v2012-071.

Acknowledgements

We would like to thank GlaxoSmithKline for the generous endowment (to A.G.M.B.) and the Thorpe Bequest (Imperial

College) for studentship support (to P.S.B.). We also thank P.R. Haycock and R.N. Sheppard for NMR spectroscopy services and J. Barton for mass spectra.

References

(1) Ekinci, D.; Şentürk, M.; Küfrevioğlu, O. I. *Expert Opin. Ther. Pat.* **2011**, *21* (12), 1831. doi:10.1517/13543776.2011.636354.

(2) Erickson, K. L.; Beutler, J. A.; Cardellina, J. H., II; Boyd, M. R. *J. Org. Chem.* **1997**, *62* (23), 8188. doi:10.1021/jo971556g.

(3) Jansen, R.; Kunze, B.; Reichenbach, H.; Höfle, G. *Eur. J. Org. Chem.* **2000**, *2000* (6), 913. doi:10.1002/(SICI)1099-0690(200003)2000:6<913::AID-EJOC913>3.0.CO;2-L.

(4) Kwon, H. K.; Kauffman, C. A.; Jensen, P. R.; Fenical, W. *J. Am. Chem. Soc.* **2006**, *128* (5), 1622. doi:10.1021/ja0558948.

(5) Dekker, K. A.; Aiello, R. J.; Hirai, H.; Inagaki, T.; Sakakibara, T.; Suzuki, Y.; Thompson, J. F.; Yamauchi, Y.; Kojima, N. *J. Antibiot.* **1998**, *51* (1), 14. doi:10.7164/antibiotics.51.14.

(6) Tyman, J. H. P. *Chem. Soc. Rev.* **1979**, *8* (4), 499. doi:10.1039/cs9790800499.

(7) Bohlmann, F.; Tsankova, E.; Jakupovic, J. *Phytochemistry* **1984**, *23* (5), 1103. doi:10.1016/S0031-9422(00)82618-7.

(8) Lindsey, A. S.; Jeskey, H. *Chem. Rev.* **1957**, *57* (4), 583. doi:10.1021/cr50016a001.

(9) Mohan, R.; Kates, S. A.; Dombroski, M. A.; Snider, B. B. *Tetrahedron Lett.* **1987**, *28* (8), 845. doi:10.1016/S0040-4039(01)81004-2.

(10) Langer, P.; Köhler, V. *Chem. Commun. (Camb.)* **2000**, (17): 1653. doi:10.1039/b004387g.

(11) García-García, P.; Fernández-Rodríguez, M. A.; Aguilar, E. *Angew. Chem. Int. Ed.* **2009**, *48* (30), 5534. doi:10.1002/anie.200901269.

(12) Danishefsky, S.; Singh, R. K.; Gammill, R. B. *J. Org. Chem.* **1978**, *43* (2), 379. doi:10.1021/jo00396a060.

(13) (a) Chan, T.-H.; Brownbridge, P. *J. Am. Chem. Soc.* **1980**, *102* (10), 3534. doi:10.1021/ja00530a038; (b) Langer, P.; Bose, G. *Angew. Chem. Int. Ed.* **2003**, *42* (34), 4033. doi:10.1002/anie.200351263; (c) Brownbridge, P.; Chan, T. H.; Brook, M. A.; Kang, G. J. *Can. J. Chem.* **1983**, *61* (4), 688. doi:10.1139/v83-127.

(14) Holtz, E.; Albrecht, U.; Langer, P. *Tetrahedron* **2007**, *63* (16), 3293. doi:10.1016/j.tet.2007.02.062.

(15) Scott, A. I.; Guilford, H.; Ryan, J. J.; Skingle, D. *Tetrahedron* **1971**, *27* (14), 3025. doi:10.1016/S0040-4020(01)98096-2.

(16) Harris, T. M.; Murray, T. P.; Harris, C. M.; Gumulka, M. *J. Chem. Soc. Chem. Commun.* **1974**, *10* (10), 362. doi:10.1039/c39740000362.

(17) Harris, T. M.; Harris, C. M. *Tetrahedron* **1977**, *33* (17), 2159. doi:10.1016/0040-4020(77)80001-X.

(18) Navarro, I.; Basset, J.-F.; Hebbe, S.; Major, S. M.; Werner, T.; Howsham, C.; Bräckow, J.; Barrett, A. G. M. *J. Am. Chem. Soc.* **2008**, *130* (31), 10293. doi:10.1021/ja803445u.

(19) Gebauer, J.; Blechert, S. *J. Org. Chem.* **2006**, *71* (5), 2021. doi:10.1021/jo052421a.

(20) Hoffman, R. V.; Kim, H.; Wilson, A. L. *J. Org. Chem.* **1990**, *55* (9), 2820. doi:10.1021/jo00296a047.

(21) Hathaway, S. J.; Paquette, L. A. *J. Org. Chem.* **1983**, *48* (19), 3351. doi:10.1021/jo00167a047.

(22) Wasylenko, W. A.; Kebede, N.; Showalter, B. M.; Matsunaga, N.; Miceli, A. P.; Liu, Y.; Ryzhkov, L. R.; Hadad, C. M.; Toscano, J. P. *J. Am. Chem. Soc.* **2006**, *128* (40), 13142. doi:10.1021/ja062712g.

(23) Homoallylic alcohols such as **14a** have been shown to have rate-increasing effects due to hydrogen bonding with ruthenium cross metathesis catalysts; see Hoveyda, A. H.; Lombardi, P. J.; O'Brien, R. V.; Zhugralin, A. R. *J. Am. Chem. Soc.* **2009**, *131* (24), 8378. doi:10.1021/ja9030903.

(24) Graves, C. R.; Zeng, B. S.; Nguyen, S. B. T. *J. Am. Chem. Soc.* **2006**, *128* (39), 12596. doi:10.1021/ja063842s.

(25) Yin, J.; Gallis, C. E.; Chisholm, D. *J. Org. Chem.* **2007**, *72* (18), 7054. doi:10.1021/jo0711992.

(26) Frigerio, M.; Santagostino, M. *Tetrahedron Lett.* **1994**, *35* (43), 8019. doi:10.1016/0040-4039(94)80038-3.

(27) More, J. D.; Finney, N. S. *Org. Lett.* **2002**, *4* (17), 3001. doi:10.1021/ol026427n.

(28) Dess, D. B.; Martin, J. C. *J. Org. Chem.* **1983**, *48* (22), 4155. doi:10.1021/jo00170a070.

(29) Attempts to isolate the ene–dione ester intermediate by silica gel chromatography resulted in decomposition.

(30) Harris, C. M.; Harris, T. M. *J. Org. Chem.* **1971**, *36* (15), 2181. doi:10.1021/jo00814a032.

(31) Basset, J.-F.; Leslie, C.; Hamprecht, D.; White, A. J. P.; Barrett, A. G. M. *Tetrahedron Lett.* **2010**, *51* (5), 783. doi:10.1016/j.tetlet.2009.11.134.

(32) Denmark, S. E.; Nguyen, S. T. *Org. Lett.* **2009**, *11* (3), 781. doi:10.1021/ol8028725.

(33) Thadani, A. N.; Batey, R. A. *Org. Lett.* **2002**, *4* (22), 3827. doi:10.1021/ol026619i.

(34) Li, G.-L.; Zhao, G. *J. Org. Chem.* **2005**, *70* (11), 4272. doi:10.1021/jo050186q.

(35) Tan, X.-H.; Shen, B.; Deng, W.; Zhao, H.; Liu, L.; Guo, Q.-X. *Org. Lett.* **2003**, *5* (11), 1833. doi:10.1021/ol034267p.

(36) Singh, S.; Kumar, S.; Chimni, S. S. *Tetrahedron Asymmetry* **2002**, *13* (24), 2679. doi:10.1016/S0957-4166(02)00743-7.

Can. J. Chem. Downloaded from www.nrcresearchpress.com by MCGILL UNIVERSITY on 02/02/13
For personal use only.

Synthesis of hydrazine and azapeptide derivatives by alkylation of carbazates and semicarbazones

Yesica Garcia-Ramos, Caroline Proulx, and William D. Lubell

Abstract: Hydrazine and azapeptide analogs were synthesized effectively by alkylation of alkylidene carbazates and semicarbazones. In comparisons of benzylidene, benzhydrylidene, and fluorenylidene *tert*-butyl carbazates in alkylations using bases of different pK_b character, superior conversion was obtained using the fluorenone derivative. Mild alkylation conditions were found employing Et_4NOH as base and used to convert fluorenylidene *tert*-butyl carbazate into 13 different protected hydrazines. Moreover, racemization was avoided during alkylation of fluorenylidene semicarbazide in the synthesis of aza-propargylglycinylphenylalanine *tert*-butyl ester, the protecting groups from which could be selectively removed.

Key words: carbazate, tetraethylammonium hydroxide, semicarbazone, alkylation, fluorenone hydrazine.

Résumé : L'alkylation de carbazates et de semicarbazones d'alkylidène permet de réaliser efficacement la synthèse d'analogues hydrazino- et aza- de peptides. Des comparaisons des réactions d'alkylation des *tert*-butyl carbazates de benzylidène, de benzhydrylidène et de fluorénylidène en présence de bases de pK_b divers ont permis de montrer que les meilleures conversions sont obtenues avec le dérivé de la fluorénone. Des conditions d'alkylation douces, faisant appel à Et_4NOH comme base, ont été utilisées pour transformer le *tert*-butyl carbazate de fluorénylidène en 13 hydrazines protégées différentes. De plus, il a été possible d'éviter la racémisation au cours de l'alkylation du fluorénylidènesemicarbazide dans la synthèse de l'ester *tert*-butylique de l'aza-propargylglycinylphénylalanine à partir duquel les groupes protecteurs peuvent être enlevés d'une façon sélective.

Mots-clés : carbazate, hydroxyde de tétraéthylammonium, semicarbazone, alkylation, hydrazone de la fluorénone.

[Traduit par la Rédaction]

Can. J. Chem. Downloaded from www.nrcresearchpress.com by MCGILL UNIVERSITY on 02/02/13
For personal use only.

Introduction

Hydrazine derivatives are employed as pesticides and drugs for treating depression, Parkinson disease, and tuberculosis.[1,2] Substituted hydrazine analogs have also been used as building blocks for heterocycle and azapeptide synthesis.[3,4] The latter peptidomimetics have evoked particular interest for studying biologically active peptides because of their potential for rigidifying conformation, increasing metabolic stability, and improving bioavailability.[5,6]

Hydrazine synthesis has, however, remained a challenge owing to the inherent difficulty in differentiating the adjacent nitrogen atoms. Different ways have been described for functionalizing hydrazine selectively. For example, monoalkylation of hydrazine, usually in excess, has been achieved using different alkyl halides, albeit mixtures may ensue from multiple alkylation.[7,8] Alternatively, alkyl hydrazines have been synthesized by hydrogenation and by hydride reduction of their corresponding hydrazones.[9–11] Issues of overalkylation have been addressed by employing carbazates in reductive amination protocols,[4] as well as by reactions with reactive alkyl halides; however, *N*′,*N*′-dialkylcarbazate has been observed as a side product from the latter process and removed by chromatography.[12,13] Combinations of protecting groups have also been employed in attempts to enhance reactivity and selectivity in the alkylation of hydrazine. For example, *N*-*tert*-butyloxycarbonyl- and *N*-benzyloxycarbonyl-aminophthalimides were shown to be sufficiently reactive acid partners in protocols featuring alkylations with alcohols using the Mitsunobu reaction.[14] Although a variety of alkylations of such carbamatophthalimides were successful, attempts to employ ureidophthalimides in similar Mitsunobu conditions as well as in reactions with alkyl halides and potassium *tert*-butoxide as base returned mostly starting material.[15] Considering alkylation of such aza-glycine amide derivatives is a key step for the diversity-oriented synthesis of azapeptide and azadiketopiperazine derivatives, semicarbazones were subsequently explored and shown to undergo alkylation effectively using alkyl halides and relatively strong bases.[15,16] Conditions have also been developed for the alkylation of *tert*-butylisopropylidene carbazate;[17] in particular, 77%–93% yields were obtained in reactions with a set of six primary alkyl bromides using potassium hydroxide under phase-transfer conditions, albeit at 80 °C.[18] In addition, a set of five *tert*-butyl arylidene and cyclohexylidene carba-

Received 20 June 2012. Accepted 8 August 2012. Published at www.nrcresearchpress.com/cjc on 30 November 2012.

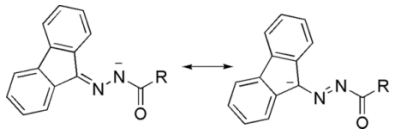
Y. Garcia-Ramos, C. Proulx, and W.D. Lubell. Département de Chimie, Université de Montréal, C.P. 6128, Succursale Centre-Ville, Montreal, QC H3C 3J7, Canada.

Corresponding author: William D. Lubell (e-mail: william.lubell@umontreal.ca).

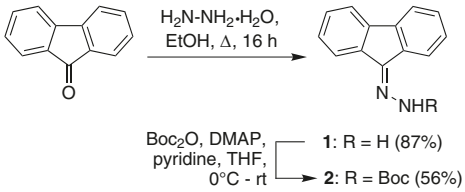
This article is part of a Special Issue dedicated to Professor Derrick Clive.

Can. J. Chem. Downloaded from www.nrcresearchpress.com by MCGILL UNIVERSITY on 02/02/13
For personal use only.

Fig. 1. Resonance stabilization of the fluorenylidene hydrazone anion.



Scheme 1. Synthesis of fluorenylidene *tert*-butyl carbazate (**2**).



zates were alkylated with allyl and benzyl bromides, respectively, in a >85% yield using cesium carbonate in the absence of solvent with ball milling at 30 Hz.[19]

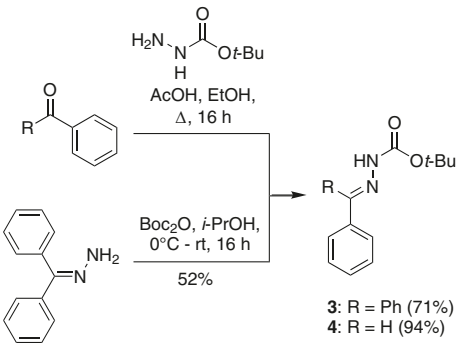
The introduction, alkylation, and deprotection of semicarbazone-protected aza-glycine residues has given rise to the submonomer synthesis of azapeptides.[16] For the key alkylation reaction, aza-glycine has been protected with benzylidene and diphenylmethylidene hydrazones, respectively, on solid support and in solution, to achieve chemoselective deprotonation employing KO-*t*-Bu and *tert*-butyliminotri (pyrrolidino)-phosphorane (BTPP) as base.[15] In the alkylation of the azadipeptide ester, aza-Gly-Phe-O-*t*-Bu, racemization was, however, detected owing to the competitive removal of the ester α proton. The influence of the hydrazone structure in the alkylation of aza-glycine analogs has thus been examined in pursuit of a means for avoiding racemization without sacrificing yield by employment of milder basic conditions. In early studies, electron-withdrawing groups were considered for favoring deprotonation by anion stabilization; however, their inductive effects had modest influence at best during alkylation. Inspired by the application of fluorenyl imines in the alkylation of glycine esters,[20] the resonance stabilization of the 14 π-electron fluorenyl anion (Fig. 1) has now been explored for favoring deprotonation of the semicarbazone and compared with reactions of the benzylidene and diphenylmethylidene counterparts. The application of this strategy has led to effective means for selective hydrazine alkylation under mild conditions and ambient temperature, as well as a racemization-free method for assembling azadipeptide building blocks for azapeptide synthesis.

Results and discussion

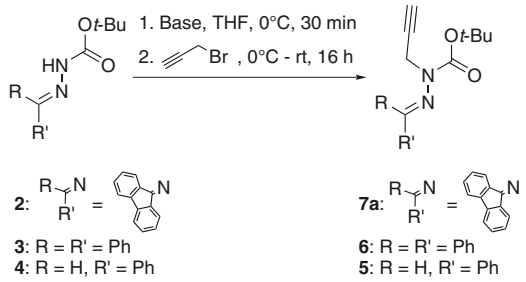
Fluorenylidene *tert*-butyl carbazate (**2**) was made by acylation of fluorenone hydrazone (**1**),[21] using di-*tert*-butyl dicarbonate (Scheme 1). On the other hand, diphenylmethylidene and benzylidene carbazates (**3** and **4**) were synthesized effectively from the condensation of benzophenone and benzaldehyde, respectively, with *tert*-butyl carbazate in ethanol (Scheme 2).[22]

With carbazates **2**–**4** in hand, alkylation was studied using propargyl bromide (150 mol %) and different bases (150 mol %), with the pK_a of the conjugate acids varying from 19 to 10.7

Scheme 2. Synthesis of carbazates **3** and **4**.



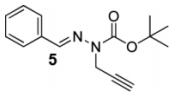
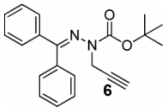
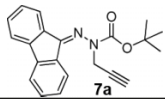
Scheme 3. Propargylation of alkylidene carbazates **2**–**4**.



(Scheme 3 and Table 1).[23–28] Conversion was analyzed by ^{1}H NMR spectroscopy. Complete alkylation was consistently observed using all three carbazates and *tert*-butoxide as strong base, and no reaction occurred with triethylamine as the weakest base. Significant differences in reactivity were observed employing 2-*tert*-butyl-1,1,3,3-tetramethylguanidine and hydroxide ion as base. Using such bases, fluorenylidene *tert*-butyl carbazate (**2**) gave superior conversion in comparison with carbazates **3** and **4**. In particular, complete conversion was achieved in the alkylation of **2** employing the 10% tetraethylammonium hydroxide in H_2O (Table 1, entry 5). For comparison, 10% sodium hydroxide in H_2O was also employed in the alkylations of carbazates **2**–**4** with propargyl bromide (150 mol%). Although a slight improvement in conversion to diphenylketamine carbazate (**6**) was observed using **3** and aqueous NaOH, yields of carbazates **5**–**7** were superior with aqueous tetraethylammonium hydroxide, albeit nearly identical in the alkylation of **2** with both forms of the aqueous hydroxide ion. The scope of the alkylation of **2** was thus examined employing aqueous tetraethylammonium hydroxide.

To examine the scope of the alkylation reaction employing Et_4NOH (150 mol %) as base, **2** (100 mol %) was treated with different alkylating agents (150 mol %) in tetrahydrofuran (THF) at 0 °C and the reactions were allowed to warm to room temperature over 16 h (Table 2). Yields varied with the electronic and steric natures of the electrophile. For example, reactive alkyl halides (Table 2, entries 1–9) gave 62%–89% yields of isolated carbazates **7a**–**7i**. On the other hand, the reaction with bulky alkyl halides isopropyliodide and 1-bromoethylbenzene required microwave irradiation (50–60 °C) to give alkyl branched carbazates **7j** and **7k** in 55% and 61% yields, respectively. Relative to the ethyl and butyl counterparts, the longer alkyl chain of 1-iodooctane

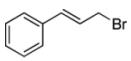
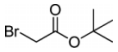
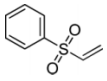
Table 1. Conversions from alkylation of carbazates **2**–**4** (100 mol %) with propargyl bromide (150 mol %) in tetrahydrofuran (THF).

Entry	Base (150 mol %)	pK_a (conjugate acid)[a]	 5	 6	 7a
1	KO-*t*-Bu	32.2 (DMSO[b])[24]	100	100	100
2	EtONa	29.8 (DMSO[b])[24] 15.9 (H_2O)[24]	100	100	100
3	MeONa	29.0 (DMSO[b])[24] 15.5 (H_2O)[24]	100	69	57
4	NaOH	31.4 (DMSO[b])[24] 15.75 (H_2O)[24]	50	Trace[c]	90
5	Et_4NOH[d]	31.4 (DMSO[b])[24] 15.75 (H_2O)[24]	84	50	100
6	2-*tert*-Butyl-TMG[e]	13.2 (DMSO[b])[25] 13.6 (H_2O)[25] 23.3 (MeCN)[27]	33	Trace[c]	100
7	DBU[f]	23.9 (MeCN)[26,27]	SM[g]	SM[g]	30
8	Et_3N	9.0 (DMSO[b])[28] 10.7 (H_2O)[28] 18.5 (MeCN)[25]	SM[g]	SM[g]	SM[g]

Note: After stirring with base at 0 °C for 30 min, the alkyl halide was added and the reaction was allowed to warm to room temperature for 16 h, before conversion (%) was ascertained by NMR spectroscopy.

[a]Literature for pK_a values are cited in refs. 21–25.
[b]DMSO, dimethyl sulfoxide.
[c]Trace product was detected.
[d]Aqueous solution (10%).
[e]TMG, 1,1,3,3-tetramethylguanidine.
[f]DBU, 1,8-diazabicyclo[5.4.0]undec-7-ene.
[g]Starting material (SM) was only detected.

Table 2. Alkylation of fluorenylidene *tert*-butyl carbazate (**2**) using Et_4NOH.

Entry	RX	Product	Yield (%)
1		**7a**	87
2	CH_3I	**7b**	85
3	CH_3CH_2I	**7c**	82
4	$CH_3CH_2CH_2CH_2I$	**7d**	62
5		**7e**	89
6		**7f**	77
7	$CH_2{=}CHCH_2I$	**7g**	83
8	$N{\equiv}CCH_2I$	**7h**	71
9		**7i**	73
10	$(CH_3)_2CHI$	**7j**	55
11		**7k**	61
12	$CH_3(CH_2)_7I$	**7l**	60
13		**7m**	56

reduced the yield of carbazate **7l** to a 60% yield. Attempts to perform Michael reactions using *tert*-butyl acrylate, acrylamide, and dimethylvinyl phosphonate provided only recovered starting material, perhaps because of competitive retro-Michael reactions. On the contrary, phenylvinylsulfone reacted with **2** to furnish carbazate **7m** in a 56% yield.

The synthesis and alkylation of aza-Gly-Phe-O-*t*-Bu dipeptides **8** and **11** were subsequently explored using propargyl bromide and tetraethylammonium hydroxide to examine effects on yield and racemization. Benzhydrylidene **8** was synthesized by activation of benzophenone hydrazone with *p*-nitrophenyl chloroformate and coupling to L-phenylalanine *tert*-butyl ester (Scheme 4).[29] From the alkylation of **8** with propargyl bromide using KO-*t*-Bu (130 mol %) as base, aza-propargylglycine **9** was produced as a racemic mixture, as ascertained by supercritical fluid chromatography (SFC) analysis on a Chiralpak AD-H column. Removal of the Phe α proton was considered to compete with semicarbazone deprotonation during alkylation of **8** using KO-*t*-Bu as a relatively strong base. Alkylation of **8** was next performed with the weaker base Et_4NOH and gave **9** without racemization, albeit in a 43% yield.

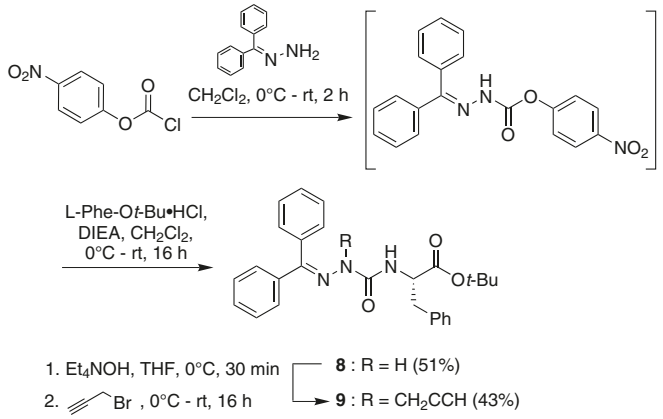
Fluorenylidene aza-glycinyl-phenylalanine *tert*-butyl ester (**11**) was synthesized by treatment of L- and D,L-phenylalanine *tert*-butyl ester with phosgene to prepare the corresponding isocyanate, which was reacted with fluorenone hydrazone (**1**, Scheme 5).[30] Azadipeptide **11** was alkylated as described above using Et_4NOH and furnished aza-propargylglycine **12** without racemization in a 92% yield.

After alkylation, fluorenylidene aza-propargylglycinyl-D,L-phenylalanine *tert*-butyl ester (D,L-**12**) was selectively converted to amino ester **13** and semicarbazone acid **14** by respective treatments with $NH_2OH{\cdot}HCl$ in pyridine at 60 °C

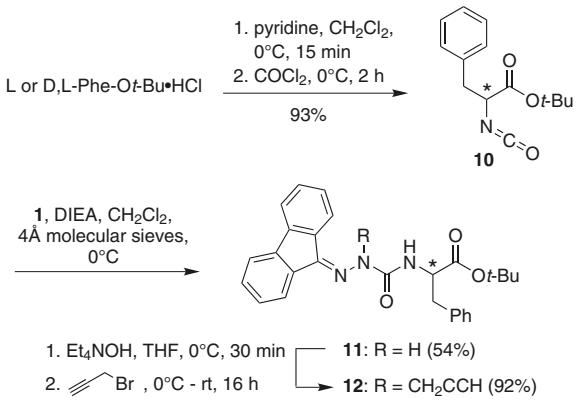
Can. J. Chem. Downloaded from www.nrcresearchpress.com by MCGILL UNIVERSITY on 02/02/13
For personal use only.

Can. J. Chem. Downloaded from www.nrcresearchpress.com by MCGILL UNIVERSITY on 02/02/13
For personal use only.

Scheme 4. Synthesis and alkylation of benzhydrylidene aza-Gly-Phe-O-*t*-Bu (**8**).



Scheme 5. Synthesis and alkylation of fluorenylidene aza-Gly-Phe-O-*t*-Bu (**11**).



for 12 h, and anhydrous acid. In the latter reaction, *tert*-butyl ester removal was accomplished more efficiently with HCl gas in CH_2Cl_2 than 1:1 TFA/CH_2Cl_2 (Scheme 6).

In summary, milder conditions for the alkylation of semicarbazones have been achieved by employing fluorenone derivatives. Tetraethylammonium hydroxide proved an efficient base for the alkylation of fluorenylidene carbazate **2** with diverse alkyl halides at ambient temperature. Moreover, racemization was avoided and a high yield was achieved in the alkylation of the fluorenylidene azadipeptide **11**. In addition, the orthogonal semicarbazone and carboxylate functions of aza-propargylglycine **12** were selectively removed. In light of the potential for subsequent employment of the alkyl derivatives in the synthesis of hydrazines, heterocycles, and longer azapeptide sequences, this method may find valuable applications in medicinal chemistry and peptide science.

Experimental section

General method

Unless specified otherwise, fluorenone hydrazone (**1**), *tert*-butyl 3-diphenylmethylene carbazate (**3**), and *tert*-butyl 3-benzylidene carbazate (**4**) were prepared according to the literature protocols.[21,22] Alkyl halides were purchased from Sigma-Aldrich and filtered through a small plug of silica gel prior to use. Anhydrous solvents (THF and dichloromethane (DCM)) were obtained by passage through a solvent filtration system (GlassContour, Irvine, California). Flash chromatography[31] was on 230–400 mesh silica gel, and thin-layer chromatography was performed on silica gel 60 F_{254} plates from Merck. Melting points were determined on a Gallankamp apparatus. Specific rotations ($[\alpha]_D$ values) were calculated from optical rotations measured at 20 °C in $CHCl_3$ at the specified concentrations (*c* in g/100 mL) using a 1 dm cell (*l*) on a PerkinElmer Polarimeter 341, using the general formula $[\alpha]_D^{20} = (100\alpha)/(lc\alpha)$. Accurate mass measurements were performed on an (LC–MS) instrument from Agilent technologies in positive electrospray ionization (ESI) mode at the Université de Montréal Mass Spectrometry facility. Sodium adducts, $[M + Na]^+$, were used for empirical formula confirmation. ^1H and ^{13}C NMR spectra were measured in $CDCl_3$ (7.26 and 77.36 ppm, respectively), coupling constant (*J*) values were measured in hertz (Hz), and chemical shift values in parts per million (ppm). IR spectra were recorded neat on an ATR Bruker apparatus.

^1H and ^{13}C NMR spectra for compounds **2**, **5**, **6**, **7a**–**7n**, and **8**–**12** and SFC traces for compounds **9** and **12** can be found in the Supplementary data.

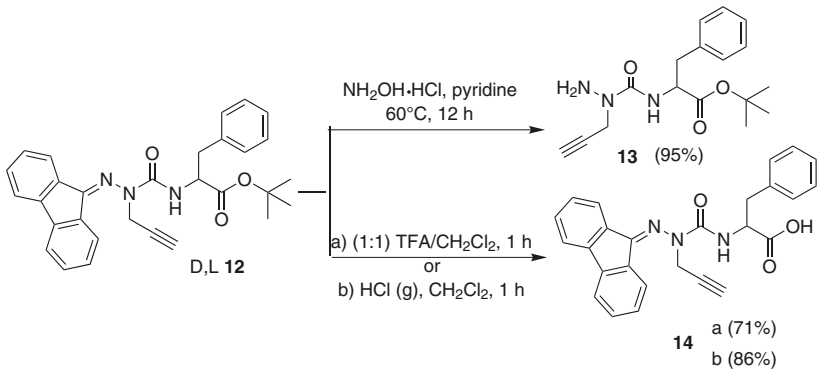
tert-*Butyl 3-fluorenylidene carbazate (2)*

A solution of fluorenone hydrazone (250 mg, 1.28 mmol, 1 equiv) in THF (10 mL) was treated with pyridine (103 μL, 1.28 mmol, 1 equiv) and 4-dimethylaminopyridine (DMAP; 16 mg, 0.13 mmol, 0.2 equiv), cooled with an ice bath, and treated slowly with di-*tert*-butyl dicarbonate (419 mg, 1.92 mmol, 1.5 equiv). The ice bath was removed and the reaction mixture was allowed to warm to room temperature. After 16 h, CH_2Cl_2 (50 mL) was added to the mixture, which was extracted three times with H_2O, dried with $MgSO_4$, filtered, and evaporated under vacuum. The residue was purified by silica gel flash chromatography (100% CH_2Cl_2). Evaporation of the collected fractions gave a yellow solid (193.7 mg, 51% yield); mp 109.8–111 °C. R_f 0.32 (8:2 hexane/EtOAc). IR (neat, cm^{-1}) ν_{max}: 2997, 2968, 1729, 1707, 1507, 1230, 1150, 768. ^1H NMR (400 MHz, $CDCl_3$) δ: 8.85 (s, 1H), 7.94 (d, J = 7.5 Hz, 1H), 7.79 (dt, J = 7.7, 0.9 Hz, 1H), 7.74 (dt, J = 7.5, 0.9 Hz, 1H), 7.61 (dt, J = 7.4, 0.9 Hz, 1H), 7.47 (td, J = 7.6, 1.0 Hz, 1H), 7.37 (hd, J = 3.9, 1.2 Hz, 2H), 7.31 (td, J = 7.5, 1.1 Hz, 1H), 1.61 (s, 9H). ^{13}C NMR (300 MHz, $CDCl_3$) δ: 153.1, 142.7, 139.4, 137.4, 131.3, 130.2, 130.1, 128.6, 128.2, 125.6, 122.7, 121.2, 119.9, 82.7, 28.6. HR-MS (LC-ESI) *m*/*z* calcd for $C_{18}H_{18}N_2O_2Na$ $(M + Na)^+$: 317.1261; found: 317.1254.

tert-*Butyl* N-*(propargyl)benzylidene carbazate (5)*

tert-Butyl 3-benzylidene carbazate (**4**; 52.9 mg, 0.24 mmol, 1 equiv) was dissolved in 1 mL of anhydrous THF at 0 °C, treated with potassium *tert*-butoxide (39 mg, 0.34 mmol, 1.5 equiv) for 30 min, followed by propargyl bromide (51 μL, 0.34 mmol, 1.5 equiv). The ice bath was removed and the mixture was allowed to warm to room temperature. After stirring for 16 h, CH_2Cl_2 was added to the mixture, which was then extracted twice with H_2O, dried with $MgSO_4$, and evaporated. The residue was purified by flash chromatography using 1:9 EtOAc/hexane as the solvent system. Evaporation of the collected fractions gave carbazate **5** as an oil (27.1 mg, 44% yield). R_f 0.42 (8:2 hexane/EtOAc). IR (neat, cm^{-1}) ν_{max}:

Scheme 6. Orthogonal deprotection of fluorenylidene aza-propargylglycinyl-D,L-phenylalanine *tert*-butyl ester (D,L-**12**).



3292, 3262, 2978, 2931, 1699, 1409, 1348, 1147, 755, 693. ^{1}H NMR (400 MHz, $CDCl_3$) δ: 7.94 (s, 1H), 7.73 (dd, J = 7.8, 1.4 Hz, 2H), 7.38 (m, 3H), 4.67 (d, J = 2.0 Hz, 2H), 2.27 (t, J = 2.4 Hz, 1H), 1.59 (s, 9H). ^{13}C NMR (300 MHz, $CDCl_3$) δ: 152.9, 141.7, 135.2, 129.9, 128.9, 127.6, 82.8, 77.5, 73.3, 34.3, 28.6. HR-MS (LC-ESI) m/z calcd for $C_{15}H_{18}N_2O_2Na$ $(M + Na)^+$: 281.1260; found: 281.1260.

tert-*Butyl* N-*(propargyl)benzhydrylidene carbazate (6)*

Employing the procedure used to make carbazate **5**, *tert*-butyl 3-diphenylmethylene carbazate (**3**; 54.7 mg, 0.18 mmol, 1 equiv) was reacted with potassium *tert*-butoxide (28.4 mg, 0.26 mmol, 1.5 equiv) and propargyl bromide (38 μL, 0.26 mmol, 1.5 equiv.), and the product was purified by flash chromatography using 5:95 EtOAc/hexane as the solvent system to afford carbazate **6** as an oil (35.9 mg, 63% yield). R_f 0.64 (8:2 hexane/EtOAc). IR (thin film, cm^{-1}) ν: 3290, 3059, 2976, 1693, 1366, 1237, 1150, 694. ^{1}H NMR (400 MHz, $CDCl_3$) δ: 7.61 (m, 2H), 7.44 (m, 3H), 7.37 (m, 5H), 4.40 (d, J = 1.9 Hz, 2H, CH_2), 2.28 (t, J = 2.5 Hz, 1H), 1.25 (s, 9H). ^{13}C NMR (300 MHz, $CDCl_3$) δ: 173.3, 152.0, 138.2, 135.9, 131.0, 129.6, 129.4, 129.1, 128.4, 128.2, 81.6, 79.6, 72.5, 40.8, 28.3. HR-MS (LC-ESI) m/z calcd for $C_{21}H_{22}N_2O_2Na$ $(M + Na)^+$: 357.1574; found: 357.1562.

tert-*Butyl* N-*(propargyl)fluorenylidene carbazate (7a)*

tert-Butyl 3-fluorenylidene carbazate (**2**; 51.4 mg, 0.17 mmol, 1 equiv) was dissolved in 1 mL of anhydrous THF at 0 °C, treated with 10% tetraethylammonium hydroxide in H_2O (384 μL, 0.27 mmol, 1.5 equiv), stirred for 30 min, and treated with propargyl bromide (39 μL, 0.27 mmol, 1.5 equiv). The ice bath was removed, and the mixture was allowed to warm to room temperature, stirred for 16 h, treated with CH_2Cl_2, extracted twice with H_2O, dried with $MgSO_4$, filtered, and evaporated. The residue was purified by flash chromatography using 5:95 EtOAc/hexane as the solvent system. Evaporation of the collected fractions gave carbazate **7a** as a yellow solid (50.2 mg, 87% yield); mp 139.7–140.0 °C. R_f 0.61 (8:2 hexane/EtOAc). IR (thin film, cm^{-1}) ν: 3314, 1685, 1357, 1339, 1243, 1153, 1140, 738. ^{1}H NMR (400 MHz, $CDCl_3$) δ: 7.93 (m, 2H), 7.60 (dd, J = 12.8, 7.5 Hz, 2H), 7.44 (t, J = 7.5 Hz, 2H), 7.29 (dt, J = 17.2, 7.5 Hz, 2H), 4.59 (d, J = 2.2, 2H), 2.24 (t, J = 2.2 Hz, 1H), 1.39 (s, 9H). ^{13}C NMR (300 MHz, $CDCl_3$) δ: 166.9, 152.6, 143.1, 141.6, 136.8, 132.4, 131.9, 131.8, 128.6, 128.5, 128.3, 123.7, 120.3, 120.0, 82.6, 79.7, 72.1, 41.6, 28.4. HR-MS (LC-ESI) m/z calcd for $C_{21}H_{20}N_2O_2Na$ $(M + Na)^+$: 355.1417; found: 355.1399.

tert-*Butyl* N-*(methyl)fluorenylidene carbazate (7b)*

Employing the procedure to make carbazate **7a**, carbazate **2** (52.6 mg, 0.18 mmol, 1 equiv) was reacted with 10% tetraethylammonium hydroxide in H_2O (395 μL, 0.27 mmol, 1.5 equiv) and iodomethane (17 μL, 0.27 mmol, 1.5 equiv), and the product was purified by flash chromatography using 5:95 EtOAc/hexane as the solvent system. Carbazate **7b** was obtained as a yellow solid (46.6 mg, 85% yield); mp 66–67.8 °C. R_f 0.61 (8:2 hexane/EtOAc). IR (thin film, cm^{-1}) ν: 2998, 2970, 1685, 1366, 1130, 736. ^{1}H NMR (400 MHz, $CDCl_3$) δ: 7.91 (d, J = 7.3 Hz, 1H), 7.87 (d, J = 7.4, 1H), 7.61 (dd, J = 14.2, 7.4 Hz, 2H), 7.44 (tq, J = 7.5, 1.2 Hz, 2H), 7.30 (m, 2H), 3.42 (s, 3H), 1.41 (s, 9H). ^{13}C NMR (300 MHz, $CDCl_3$) δ: 165.4, 153.5, 142.6, 141.2, 136.6, 132.0, 131.4, 131.1, 128.3, 128.2, 127.8, 123.1, 120.0, 119.7, 81.4, 38.4, 28.2. HR-MS (LC-ESI) m/z calcd. for $C_{19}H_{20}N_2O_2Na$ $(M + Na)^+$: 331.1417; found: 331.1408.

tert-*Butyl* N-*(ethyl)fluorenylidene carbazate (7c)*

Employing the procedure to make carbazate **7a**, carbazate **2** (52.9 mg, 0.18 mmol, 1 equiv) was reacted with 10% tetraethylammonium hydroxide in H_2O (397 μL, 0.27 mmol, 1.5 equiv) and iodoethane (22 μL, 0.27 mmol, 1.5 equiv), and the product was purified by flash chromatography using 5:95 EtOAc/hexane as the solvent system. Carbazate **7c** was obtained as a yellow solid (47.6 mg, 82% yield); mp 150.8–153.7 °C. R_f 0.57 (8:2 hexane/EtOAc). IR (thin film, cm^{-1}) ν: 2972, 2925, 1681, 1448, 1363, 1276, 1164, 738. ^{1}H NMR (400 MHz, $CDCl_3$) δ: 7.92 (d, J = 7.5 Hz, 1H), 7.88 (d, J = 7.3, 1H), 7.61 (dd, J = 13, 7.4 Hz, 2H), 7.43 (t, J = 7.4 Hz, 2H), 7.33–7.25 (m, 2H), 3.9 (q, J = 7.1 Hz, 2H), 1.38 (s, 9H), 1.3 (t, J = 7.1 Hz, 3H). ^{13}C NMR (300 MHz, $CDCl_3$) δ: 152.7, 142.9, 141.4, 137.0, 132.1, 131.7, 131.6, 128.5, 128.4, 128.0, 123.3, 120.2, 119.9, 81.5, 46.5, 28.5, 13.8. HR-MS (LC-ESI) m/z calcd for $C_{20}H_{23}N_2O_2$ $(M + H)^+$: 323.1754; found: 323.1764.

tert-*Butyl* N-(n-*butyl)fluorenylidene carbazate (7d)*

Employing the procedure to make carbazate **7a**, **2** (60.6 mg, 0.21 mmol, 1 equiv) was reacted with 10% tetraethylammonium hydroxide in H_2O (455 μL, 0.31 mmol, 1.5 equiv) and 1-iodobutane (35 μL, 0.31 mmol, 1.5 equiv), and the product was purified by flash chromatography using 1:9 EtOAc/hexane

Can. J. Chem. Downloaded from www.nrcresearchpress.com by MCGILL UNIVERSITY on 02/02/13
For personal use only.

Can. J. Chem. Downloaded from www.nrcresearchpress.com by MCGILL UNIVERSITY on 02/02/13
For personal use only.

as the solvent system. Carbazate **7d** was obtained as a yellow solid (45.7 mg, 62% yield); mp 80–82 °C. R_f 0.6 (8:2 hexane/EtOAc). IR (thin film, cm^{-1}) ν: 2921, 2876, 1682, 1446, 1364, 1245, 1145, 736. ^{1}H NMR (400 MHz, $CDCl_3$) δ: 7.90 (m, 2H), 7.61 (dd, J = 13.3, 7.4 Hz, 2H), 7.43 (t, J = 7.3 Hz, 2H), 7.33–7.26 (m, 2H), 3.87 (t, J = 7.3 Hz, 2H), 1.69 (m, 2H), 1.43–1.38 (m, 11H), 0.94 (td, J = 7.3, 2 Hz, 3H). ^{13}C NMR (300 MHz, $CDCl_3$) δ: 165.9, 152.9, 142.9, 141.4, 137.1, 132.1, 131.8, 131.6, 128.5, 128.0, 123.4, 120.2, 119.9, 81.6, 51.8, 31.1, 28.5, 20.5, 14.1. HR-MS (LC-ESI) *m/z* calcd for $C_{22}H_{27}N_2O_2$ $(M + H)^+$: 351.2067; found: 351.2077.

tert-*Butyl* N-*(benzyl)fluorenylidene carbazate (7e)*

Employing the procedure to make carbazate **7a**, **2** (200 mg, 0.68 mmol, 1 equiv) was reacted with 10% tetraethylammonium hydroxide in H_2O (1.5 mL, 1.02 mmol, 1.5 equiv) and benzyl bromide (122 μL, 1.02 mmol, 1.5 equiv), and the product was purified by flash chromatography using 1:9 EtOAc/hexane as the solvent system. Carbazate **7e** was obtained as a yellow solid (232.3 mg, 89% yield); mp 106.7–109.1 °C. R_f 0.47 (8:2 hexane/EtOAc). IR (thin film, cm^{-1}) ν: 2980, 2918, 1685, 1321, 1242, 1148, 730. ^{1}H NMR (400 MHz, $CDCl_3$) δ: 7.90 (d, J = 7 Hz, 1H), 7.79 (d, J = 7.1, 1H), 7.59 (dd, J = 10.9, 7.7 Hz, 2H), 7.42 (m, 4H), 7.30 (t, J = 7.3, 3H), 7.23 (m, 2H), 5.05 (s, 2H), 1.37 (s, 9H). ^{13}C NMR (300 MHz, $CDCl_3$) δ: 165.4, 152.9, 142.9, 141.4, 138.5, 137.1, 132.1, 131.8, 131.6, 128.6, 128.48, 128.46, 128.45, 128.1, 127.5, 123.4, 120.2, 119.9, 82.1, 56.3, 28.5. HR-MS (LC-ESI) *m/z* calcd for $C_{25}H_{24}N_2O_2Na$ $(M + Na)^+$: 407.173; found: 407.1725.

tert-*Butyl* N-*(cinnamyl)fluorenylidene carbazate (7f)*

Employing the procedure to make carbazate **7a**, carbazate **2** (50 mg, 0.17 mmol, 1 equiv) was reacted with 10% tetraethylammonium hydroxide in H_2O (376 μL, 0.26 mmol, 1.5 equiv) and cinnamyl bromide (52 mg, 0.26 mmol, 1.5 equiv), and the product was purified by flash chromatography using 1:9 EtOAc/hexane as the solvent system. Carbazate **7f** was obtained as an oil (53.4 mg, 77% yield). R_f 0.4 (8:2 hexane/EtOAc). IR (thin film, cm^{-1}) ν: 2973, 2928, 1687, 1448, 1366, 1226, 1142, 729. ^{1}H NMR (400 MHz, $CDCl_3$) δ: 7.90 (m, 2H), 7.60 (dd, J = 15.8, 7.5 Hz, 2H), 7.42 (hd, J = 3.8, 1 Hz, 2H), 7.37–7.2 (m, 7H), 6.64 (d, J = 15.8 Hz, 1H), 6.40 (dt, J = 15.8, 6.4 Hz, 1H), 4.61 (dd, J = 6.3, 1 Hz, 2H), 1.40 (s, 9H). ^{13}C NMR (300 MHz, $CDCl_3$) δ: 165.4, 152.4, 142.4, 140.9, 136.6, 136.4, 132.4, 131.7, 131.2, 131.1, 128.2, 128.0, 127.9, 127.6, 127.2, 126.2, 124.8, 122.9, 119.7, 119.4, 81.4, 53.8, 28.0. HR-MS (LC-ESI) *m/z* calcd for $C_{27}H_{26}N_2O_2Na$ $(M + Na)^+$: 433.1886; found: 433.1885.

tert-*Butyl* N-*(allyl)fluorenylidene carbazate (7g)*

Employing the procedure to make carbazate **7a**, carbazate **2** (50 mg, 0.17 mmol, 1 equiv) was reacted with 10% tetraethylammonium hydroxide in H_2O (376 μL, 0.25 mmol, 1.5 equiv) and allyl iodide (24 μL, 0.25 mmol, 1.5 equiv), and the product was purified by flash chromatography using 1:9 EtOAc/hexane as the solvent system. Carbazate **7g** was obtained as a yellow solid (47.3 mg, 83% yield); mp 109.2–111.4 °C. R_f 0.47 (8:2 hexane/EtOAc). IR (thin film, cm^{-1}) ν: 2956, 2921, 2852, 1676, 1374, 1251, 1142, 738. ^{1}H NMR (400 MHz, $CDCl_3$) δ: 7.90 (d, J = 7.6 Hz, 1H), 7.88 (d, 1H), 7.61 (dd, J = 14.9, 7.5 Hz, 2H), 7.43 (td, J = 7.5, 1.0 Hz, 2H), 7.29 (m, 2H), 6.01 (m, 1H), 5.30 (dq, J = 17.1, 1.5 Hz, 1H), 5.16 (dq, J = 10.3, 1.2 Hz, 1H), 4.46 (d, J = 6 Hz, 2H), 1.39 (s, 9H). ^{13}C NMR (300 MHz, $CDCl_3$) δ: 165.4, 152.9, 142.9, 141.4, 138.5, 137.1, 132.1, 131.8, 131.6, 128.6, 128.5, 128.1, 127.5, 123.4, 120.2, 119.9, 82.1, 56.3, 28.5. HR-MS (LC-ESI) *m/z* calcd for $C_{21}H_{22}N_2O_2Na$ $(M + Na)^+$: 357.1573; found: 357.1558.

tert-*Butyl* N-*(cyanomethyl)fluorenylidene carbazate (7h)*

Employing the procedure to make carbazate **7a**, **2** (52.8 mg, 0.18 mmol, 1 equiv) was reacted with 10% tetraethylammonium hydroxide in H_2O (396 μL, 0.27 mmol, 1.5 equiv) and iodoacetonitrile (20 μL, 0.27 mmol, 1.5 equiv), and the product was purified by flash chromatography using 1:9 EtOAc/hexane as the solvent system. Carbazate **7h** was obtained as a yellow solid (42.7 mg, 71% yield); mp 165–168 °C. R_f 0.32 (8:2 hexane/EtOAc). IR (thin film, cm^{-1}) ν: 2980, 2187, 1715, 1595, 1345, 1313, 1235, 1144, 726. ^{1}H NMR (400 MHz, $CDCl_3$) δ: 7.88 (m, 1H), 7.81 (m, 1H), 7.60 (m, 2H), 7.46 (m, 2H), 7.30 (m, 2H), 4.67 (m, 2H), 1.40 (s, 9H). ^{13}C NMR (300 MHz, $CDCl_3$) δ: 167.4, 152.3, 143.3, 141.6, 136.4, 132.9, 132.3, 131.7, 128.7, 128.6, 128.2, 123.8, 120.5, 120.1, 116.0, 84.2, 40.4, 28.3. HR-MS (LC-ESI) *m/z* calcd for $C_{20}H_{20}N_3O_2$ $(M + H)^+$: 334.1550; found: 334.1566.

tert-*Butyl* N-*(tert-butylacetyl)fluorenylidene carbazate (7i)*

Employing the procedure to make carbazate **7a**, carbazate **2** (50 mg, 0.17 mmol, 1 equiv) was reacted with 10% tetraethylammonium hydroxide in H_2O (368 μL, 0.25 mmol, 1.5 equiv) and *tert*-butyl bromoacetate (38 μL, 0.25 mmol, 1.5 equiv), and the product was purified by flash chromatography using 1:9 EtOAc/hexane as the solvent system. Carbazate **7i** was obtained as a yellow solid (50.6 mg, 73% yield); mp 135.5–136.7 °C. R_f 0.39 (8:2 hexane/EtOAc). IR (thin film, cm^{-1}) ν: 2978, 2929, 1745, 1692, 1365, 1224, 1147, 752. ^{1}H NMR (400 MHz, $CDCl_3$) δ: 7.86 (d, J = 7.5 Hz, 2H), 7.61 (d, J = 7.5 Hz, 1H), 7.58 (d, J = 7.6 Hz, 1H), 7.42 (td, J = 7.6 Hz, 2H), 7.28 (m, 2H), 4.46 (s, 2H), 1.47 (s, 18H). ^{13}C NMR (300 MHz, $CDCl_3$) δ: 168.8, 153.0, 142.9, 141.5, 137.1, 132.1, 131.9, 131.6, 128.8, 128.4, 128.3, 123.5, 120.1, 119.9, 82.4, 82.0, 54.7, 28.4. HR-MS (LC-ESI) *m/z* calcd for $C_{24}H_{29}N_2O_4$ $(M + H)^+$: 409.2122; found: 409.2104.

tert-*Butyl* N-*(isopropyl)fluorenylidene carbazate (7j)*

Employing the procedure to make carbazate **7a**, carbazate **2** (51.9 mg, 0.18 mmol, 1 equiv) was reacted with 10% tetraethylammonium hydroxide in H_2O (383 μL, 0.26 mmol, 1.5 equiv) and isopropyl iodide (26 μL, 0.26 mmol, 1.5 equiv), and stirred at 50 °C under microwave irradiation in a 300 MW Biotage apparatus on the high absorption level with automated temperature monitoring for 12 h. The product was purified by flash chromatography using 5:95 EtOAc/hexane as the solvent system. Carbazate **7j** was obtained as a yellow solid (32.4 mg, 55% yield); mp 119.7–120.8 °C. R_f 0.75 (8:2 hexane/EtOAc). IR (thin film, cm^{-1}) ν: 2965, 2919, 2850, 1683, 1302, 1088, 737. ^{1}H NMR (400 MHz, $CDCl_3$) δ: 7.92 (d, J = 7.5 Hz, 1H), 7.87 (d, J = 7.5, 1H), 7.60 (dd, J = 12.6, 7.5 Hz, 2H), 7.41 (m, 2H), 7.30 (t, J = 7.5 Hz, 1H), 7.24 (t, J = 7.3 Hz, 1H), 4.71 (q, J = 6.6 Hz, 1H), 1.34 (s, 15H). ^{13}C NMR (300 MHz, $CDCl_3$) δ: 166.5, 152.2, 143.0, 141.4, 137.2, 132.0, 131.9, 131.5, 128.5, 128.4, 128.0, 123.4, 120.2, 119.9, 81.4, 51.5,

Can. J. Chem. Downloaded from www.nrcresearchpress.com by MCGILL UNIVERSITY on 02/02/13
For personal use only.

28.5, 20.3. HR-MS (LC-ESI) *m/z* calcd for $C_{21}H_{24}N_2O_2Na$ (M + Na)$^+$: 359.173; found: 359.1727.

tert-*Butyl* N-*(1-(*R,S)-*ethylbenzyl)fluorenylidene carbazate (7k)*

Employing the procedure to make carbazate **7a**, carbazate **2** (57.6 mg, 0.2 mmol, 1 equiv) was reacted with 10% tetraethylammonium hydroxide in H_2O (432 μL, 0.29 mmol, 1.5 equiv) and 1-bromoethylbenzene (40 μL, 0.29 mmol, 1.5 equiv), and stirred at 60 °C under microwave irradiation in a 300 MW Biotage apparatus on the high absorption level with automated temperature monitoring for 12 h. The product was purified by flash chromatography using 1:9 diethyl ether/petroleum ether as the solvent system. Carbazate **7k** was obtained as a yellow oil (47 mg, 61% yield). R_f 0.57 (8:2 hexane/EtOAc). IR (thin film, cm^{-1}) ν: 2973, 2939, 1682, 1448, 1366, 1290, 1154, 729. ^{1}H NMR (400 MHz, $CDCl_3$) δ: 7.91 (d, J = 7.5 Hz, 1H), 7.83 (m, 1H), 7.62–7.55 (m, 4H), 7.44–7.40 (m, 2H), 7.33–7.23 (m, 5H), 5.71 (m, 1H), 1.73 (s, 3H), 1.32 (s, 9H). ^{13}C NMR (300 MHz, $CDCl_3$) δ: 165.7, 152.4, 142.9, 142.6, 141.3, 137.3, 132.0, 131.9, 131.4, 128.5, 128.45, 128.44, 128.4, 127.9, 127.8, 127.4, 123.4, 120.2, 119.9, 81.8, 59.0, 28.5. HR-MS (LC-ESI) *m/z* calcd for $C_{26}H_{27}N_2O_2$ (M + H)$^+$: 399.2067; found: 399.2059.

tert-*Butyl* N-*(octanyl)fluorenylidene carbazate (7l)*

Employing the procedure to make carbazate **7a**, **2** (54.3 mg, 0.18 mmol, 1 equiv) was reacted with 10% tetraethylammonium hydroxide in H_2O (407 μL, 0.28 mmol, 1.5 equiv) and 1-iodooctane (51 μL, 0.28 mmol, 1.5 equiv), and the product was purified by flash chromatography using 1:9 EtOAc/hexane as the solvent system. Carbazate **7l** was obtained as a yellow oil (45.2 mg, 60% yield). R_f 0.39 (8:2 hexane/EtOAc). IR (thin film, cm^{-1}) ν: 2924, 2853, 1689, 1449, 1365, 1142, 731. ^{1}H NMR (400 MHz, $CDCl_3$) δ: 7.91 (d, J = 7.5 Hz, 1H), 7.85 (m, 1H), 7.61 (dd, J = 13.4, 7.5 Hz, 2H), 7.43 (t, J = 7.5 Hz, 2H), 7.33–7.25 (m, 2H), 3.86 (t, J = 7.4 Hz, 2H), 1.71 (m, 2H), 1.38 (s, 9H), 1.32–1.24 (m, 10H), 0.87 (m, 3H). ^{13}C NMR (300 MHz, $CDCl_3$) δ: 165.8, 152.9, 142.9, 141.4, 137.1, 132.1, 131.8, 131.6, 128.5, 128.1, 123.4, 120.2, 119.9, 81.6, 52.1, 32.1, 29.6, 29.5, 28.9, 28.5, 27.2. HR-MS (LC-ESI) *m/z* calcd for $C_{26}H_{34}N_2O_2Na$ (M + Na)$^+$: 429.2512; found: 429.2498.

tert-*Butyl* N-*(phenylethylsulfone)fluorenylidene carbazate (7m)*

Employing the procedure to make carbazate **7a**, carbazate **2** (51.4 mg, 0.17 mmol, 1 equiv) was reacted with 10% tetraethylammonium hydroxide in H_2O (386 μL, 0.26 mmol, 1.5 equiv) and phenyl vinyl sulfone (44 mg, 0.26 mmol, 1.5 equiv), and the product was purified by flash chromatography using 1:9 EtOAc/hexane as the solvent system. Carbazate **7m** was obtained as a yellow oil (45.4 mg, 56% yield). R_f 0.18 (8:2 hexane/EtOAc). IR (thin film, cm^{-1}) ν: 2974, 2923, 1693, 1446, 1307, 1279, 1141, 728. ^{1}H NMR (400 MHz, $CDCl_3$) δ: 7.96 (d, J = 7.7 Hz, 2H), 7.80 (d, J = 7.3 Hz, 1H), 7.67–7.54 (m, 6H), 7.43 (m, 2H), 7.30 (m, 1H), 7.23 (t, J = 7.5 Hz, 1H), 4.18 (t, J = 7.5 Hz, 2H), 3.61 (t, J = 7.4 Hz, 2H), 1.34 (s, 9H). ^{13}C NMR (300 MHz, $CDCl_3$) δ: 166.1, 152.1, 142.8, 141.1, 139.0, 136.3, 133.9, 132.2, 131.7, 131.2, 129.4, 128.3, 128.2, 128.1, 127.8, 123.2, 120.1, 119.7, 82.5, 54.0, 45.6, 28.0. HR-MS (LC-ESI) *m/z* calcd for $C_{26}H_{26}N_2O_4SNa$ (M + Na)$^+$: 485.1505; found: 485.1518.

Benzhydrylidene aza-glycinyl-L-phenylalanine* tert-*butyl ester (8)

In a flame-dried round-bottom flask, at 0 °C, a solution of 4-nitrophenylchloroformate (1.12 g, 5.58 mmol, 1.1 equiv) in dry CH_2Cl_2 (40 mL) was treated dropwise by cannula with a 0 °C solution of benzophenone hydrazone (1 g, 5.07 mmol, 1 equiv) in dry CH_2Cl_2 (40 mL). The ice bath was removed and the reaction mixture was allowed to warm to room temperature. After stirring for 1 h, the mixture was cooled to 0 °C, and treated dropwise by cannula with a premixed 0 °C solution of L-Phe-O-*t*-Bu·HCl (1.44 g, 5.60 mmol, 1.1 equiv) and *N*, *N*-diisopropylethylamine (DIEA; 1.80 mL, 10.14 mmol, 2 equiv) in CH_2Cl_2 (13 mL). The ice bath was removed. The reaction mixture was allowed to warm to room temperature and stirred for 16 h. The volatiles were evaporated and the residue was purified on a column of silica gel using flash chromatography with 30% diethyl ether in petroleum ether as the solvent system. Ester **8** was obtained as an oil (1.15 g, 51% yield). $[\alpha]_D^{20}$ 14.2 (*c* 1.02, $CHCl_3$). R_f 0.21 (8:2 hexane/EtOAc). IR (thin film, cm^{-1}) ν: 2974, 2931, 1662, 1590, 1515, 1333, 1109, 692. ^{1}H NMR (400 MHz, $CDCl_3$) δ: 8.08 (d, J = 9.2 Hz, 1H), 7.24–7.67 (m, 15H), 6.80–6.91 (m, 1H), 4.77–4.82 (m, 1H), 3.17–3.30 (m, 2H), 1.48 (s, 9H). ^{13}C NMR (300 MHz, $CDCl_3$) δ: 170.5, 162.9, 154.7, 148.4, 136.4, 135.8, 131.2, 129.5, 129.4, 129.2, 128.2, 128.0, 127.0, 126.9, 126.7, 125.7, 115.2, 81.9, 53.6, 38.3, 27.6. HR-MS (LC-ESI) *m/z* calcd for $C_{27}H_{29}N_3O_3Na$ (M + Na)$^+$: 466.2101; found: 466.2082.

Benzhydrylidene aza-propargylglycinyl-L-phenylalanine* tert-*butyl ester (9)

Employing the procedure to make carbazate **7a**, **8** (50 mg, 0.11 mmol, 1 equiv) was reacted with 10% tetraethylammonium hydroxide in H_2O (243 μL, 0.16 mmol, 1.5 equiv) and propargyl bromide (25 μL, 0.16 mmol, 1.5 equiv), and the product was purified by flash chromatography eluting with 1:9 EtOAc/hexane. Ester **9** was obtained as a white oil (21.1 mg, 43% yield). $[\alpha]_D^{20}$ −1.8 (*c* 1.24, $CHCl_3$). R_f 0.33 (8:2 hexane/EtOAc). IR (thin film, cm^{-1}) ν: 3227, 2967, 2920, 1734, 1671, 1505, 1150, 694. ^{1}H NMR (400 MHz, $CDCl_3$) δ: 7.45 (m, 6H), 7.36 (m, 4H), 7.27 (m, 5H), 7.08 (d, J = 8.2 Hz, 1H), 4.77 (m, 1H), 4.21 (dd, J = 17.9, 2.4 Hz, 1H), 3.91 (dd, J = 17.9, 2.4 Hz, 1H), 3.20 (d, J = 5.9 Hz, 2H), 2.08 (t, J = 2.4 Hz, 1H), 1.43 (s, 9H). ^{13}C NMR (300 MHz, $CDCl_3$) δ: 171.1, 158.3, 158.0, 138.8, 136.8, 135.8, 130.3, 130.0, 129.5, 129.0, 128.9, 128.7, 128.4, 127.1, 82.2, 79.0, 72.2, 55.3, 38.8, 35.4, 28.3. HR-MS (LC-ESI) *m/z* calcd for $C_{30}H_{31}N_3O_3Na$ (M + Na)$^+$: 504.2258; found: 504.2234. The degree of racemization (enantiomeric excess, 98.9%) was determined by SFC analysis on a chiral stationary phase (Chiralcel AD-H 25 cm, 15% *i*-PrOH, 3 mL/min, 35 °C, 150 bar (1 bar = 100 kPa), t_r (major): 3.33 min, t_r (minor): 5.29 min).

Fluorenylidene aza-glycinyl-L-phenylalanine* tert-*butyl ester (11)

In a flame-dried flask under N_2, L-Phe-O-*t*-Bu·HCl (500 mg, 1.95 mmol, 1 equiv) was suspended in CH_2Cl_2 (8 mL), treated with pyridine (629 μL, 7.8 mmol, 4 equiv), cooled to 0 °C for 15 min, and treated with a 20% solution of phosgene in toluene (1.45 mL, 2.93 mmol, 1.5 equiv). (Caution: Phosgene is extremely toxic and should be employed in a well-ventilated hood.) After stirring for 2 h at 0 °C, the mixture was washed twice with ice cold 0.5 mol/L HCl. The combined aqueous

Can. J. Chem. Downloaded from www.nrcresearchpress.com by MCGILL UNIVERSITY on 02/02/13
For personal use only.

fractions were extracted with cold CH_2Cl_2. The combined organic phases were washed with ice cold NaCl, dried with $MgSO_4$, filtered, and evaporated. The resulting isocyanate **10** was obtained as an oil (375.7 mg, 74% yield), which was used directly in the next reaction without further purification. ^{1}H NMR (400 MHz, $CDCl_3$) δ: 7.33 (m, 3H), 7.26 (m, 2H), 4.16 (dd, J = 5.0, 7.5 Hz, 1H), 3.14 (dd, J = 4.8, 13.8 Hz, 1H), 3.04 (dd, J = 7.5, 13.7 Hz, 1H), 1.50 (s, 9H). Under inert atmosphere, to fluorenone hydrazone (195 mg, 1 mmol, 1 equiv) in CH_2Cl_2 (8 mL) containing molecular sieves at 0 °C, DIEA (174 μL, 1 mmol, 1 equiv) was added. The mixture was stirred for 15 min and treated with a solution of isocyanate **10** (375.7 mg, 1.5 mmol, 1.5 equiv) in CH_2Cl_2 (2 mL). The ice bath was removed. The reaction was allowed to warm to room temperature, stirred for 16 h, and evaporated. The residue was purified by flash chromatography eluting with 2:8 EtOAc/hexane. Azadipeptide **11** was isolated as a yellow solid (261.5 mg, 54% yield); mp 65.6–67.6 °C. R_f 0.18 (8:2 hexane/EtOAc). $[\alpha]_D^{20}$ 25.9 (c 1.04, $CHCl_3$). IR (thin film, cm^{-1}) ν: 2966, 2919, 1673, 1508, 1149, 1115, 1077, 727. ^{1}H NMR (400 MHz, $CDCl_3$) δ: 8.73 (s, 1H), 7.87 (d, J = 7.7 Hz, 1H), 7.76 (d, J = 7.5 Hz, 1H), 7.67 (dd, J = 17.0, 7.5 Hz, 2H), 7.49 (td, J = 7.5, 0.7 Hz, 1H), 7.40 (m, 2H), 7.36–7.28 (m, 6H), 7.03 (d, J = 8.2 Hz, 1H), 4.85 (m, 1H), 3.25 (m, 2H), 1.47 (s, 9H). ^{13}C NMR (300 MHz, $CDCl_3$) δ: 171.0, 155.4, 143.7, 142.5, 139.5, 137.2, 136.6, 131.2, 130.2, 130.1, 130.0, 128.8, 128.4, 128.3, 127.3, 125.7, 121.8, 121.2, 120.0, 82.6, 54.4, 39.1, 28.3. HR-MS (LC-ESI) m/z calcd for $C_{27}H_{27}N_3O_3Na$ $(M + Na)^+$: 464.1945; found: 464.1943.

Fluorenylidene aza-glycinyl-D,L-phenylalanine tert-*butyl ester (D,L-11)*

D,L-**11** was synthesized employing the same procedure described for **11** using D,L-Phe-O-*t*-Bu·HCl and was obtained as a yellow solid (236.2 mg, 54% yield).

Fluorenylidene aza-propargylglycinyl-L-phenylalanine tert-*butyl ester (12)*

Using the procedure to make carbazate **7a**, ester **11** (50 mg, 0.11 mmol, 1 equiv) was reacted with 10% tetraethylammonium hydroxide in H_2O (250 μL, 0.17 mmol, 1.5 equiv) and propargyl bromide (33 μL, 0.22 mmol, 1.5 equiv), and the product was purified by flash chromatography eluting with 1:9 EtOAc/hexane. Ester **12** was obtained as a yellow solid (42 mg, 83% yield); mp 82.5–85.4 °C. $[\alpha]_D^{20}$ –50.8 (c 1.04, $CHCl_3$). R_f 0.3 (8:2 hexane/EtOAc). IR (thin film, cm^{-1}) ν: 3208, 2958, 2921, 2854, 1750, 1742, 1674, 1497, 1217, 1144, 736. ^{1}H NMR (400 MHz, $CDCl_3$) δ: 7.93 (d, J = 7.6 Hz, 1H), 7.83 (d, J = 7.5 Hz, 1H), 7.65 (d, J = 7.4 Hz, 1H), 7.60 (d, J = 7.5 Hz, 1H), 7.47 (m, 2H), 7.31 (m, 2H), 7.21 (s, 5H), 6.54 (d, J = 7.9 Hz, 1H), 4.80 (m, 1H), 4.68 (dd, J = 17.4, 2.3 Hz, 1H), 4.54 (dd, J = 17.4, 2.3 Hz, 1H), 3.18 (m, 2H), 2.21 (t, J = 2.3 Hz, 1H), 1.40 (s, 9H). ^{13}C NMR (300 MHz, $CDCl_3$) δ: 170.8, 164.2, 158.4, 143.6, 141.6, 136.8, 136.6, 133.0, 132.1, 130.1, 129.8, 129.0, 128.8, 128.6, 127.1, 123.6, 120.7, 120.2, 82.3, 79.1, 72.6, 55.1, 40.5, 38.9, 28.3. HR-MS (LC-ESI) m/z calcd for $C_{30}H_{29}N_3O_3Na$ $(M + Na)^+$: 502.2101; found: 502.2079. The degree of racemization (enantiomeric excess, 99.8%) was determined by SFC analysis on a chiral stationary phase (Chiralcel AD-H 25 cm, 15% *i*-PrOH, 3 mL/min, 35 °C, 150 bar, t_r (major): 8.26 min, t_r (minor): 21.32 min).

Aza-propargylglycinyl-D,L-phenylalanine tert-*butyl ester (13)*

Fluorenylidene aza-propargylglycinyl-D,L-phenylalanine *tert*-butyl ester (D,L-**12**; 54.4 mg, 0.11 mmol, 1 equiv) was treated with a solution of NH_2OH·HCl (28 mg, 0.44 mmol, 4 equiv) in pyridine (12 mL) at 60 °C for 12 h. The volatiles were evaporated and the residue was purified by flash chromatography eluting with 4:6 EtOAc/hexane. Ester **13** was obtained as a white oil (34.3 mg, 95% yield). R_f 0.1 (8:2 hexane/EtOAc). IR (thin film, cm^{-1}) ν: 3285, 2982, 2936, 1726, 1658, 1498, 1368, 1152. ^{1}H NMR (400 MHz, $CDCl_3$) δ: 7.31–7.20 (m, 5H), 6.91 (d, J = 8.3 Hz, 1H), 4.64 (m, 1H), 4.40 (dd, J = 2.4, 17.5 Hz, 1H), 4.31 (dd, J = 2.4, 17.5 Hz, 1H), 3.72 (s, 2H), 3.09 (m, 2H), 2.30 (t, J = 2.4 Hz, 1H), 1.41 (s, 9H). ^{13}C NMR (300 MHz, $CDCl_3$) δ: 170.7, 157.1, 136.0, 128.9, 127.6, 126.1, 81.1, 77.3, 72.7, 53.9, 39.0, 38.0, 27.3. HR-MS (LC-ESI) m/z calcd for $C_{17}H_{23}N_3O_3Na$ $(M + Na)^+$: 340.1632; found: 340.1620.

Fluorenylidene aza-propargylglycinyl-D,L-phenylalanine acid (14)

tert-Butyl ester D,L-**12** (48.6 mg, 0.1 mmol, 1 equiv) in dry CH_2Cl_2 (10 mL) was treated with bubbles of HCl for 1 h. The volatiles were evaporated and the residue was purified by flash chromatography eluting with 1:20 MeOH/CH_2Cl_2. Acid **14** was obtained as a yellow solid (37 mg, 86% yield): decomposition was observed after 98.1 °C. R_f 0.2 (9:1 CH_2Cl_2/MeOH). IR (thin film, cm^{-1}) ν: 3265, 1709, 1663, 1506, 1447, 1314, 1230, 1154, 1083, 931, 730. ^{1}H NMR (400 MHz, $CDCl_3$) δ: 10.49 (s, 1H), 7.85 (d, J = 7.6 Hz, 1H), 7.75 (d, J = 6.9 Hz, 1H), 7.59 (dd, J = 7.4, 13.1 Hz, 2H), 7.44 (t, J = 6.7 Hz, 2H), 7.27 (m, 2H), 7.16 (m, 5H), 6.45 (d, J = 5.6 Hz, 1H), 4.83 (m, 1H), 4.55 (m, 2H), 3.22 (m, 2H), 2.19 (m, 1H). ^{13}C NMR (300 MHz, $CDCl_3$) δ: 163.8, 158.1, 142.6, 140.6, 135.5, 135.2, 132.1, 131.3, 128.8, 128.6, 128.1, 127.9, 127.8, 127.6, 126.3, 122.7, 119.7, 119.2, 77.8, 71.9, 39.6, 36.8. HR-MS (LC-ESI) m/z calcd for $C_{26}H_{21}N_3O_3Na$ $(M + Na)^+$: 446.1475; found: 446.1481.

Supplementary data

Supplementary data are available with the article through the journal Web site http://nrcresearchpress.com/doi/suppl/10.1139/v2012-070.

Acknowledgments

This research was supported by the Natural Sciences and Engineering Research Council of Canada (NSERC) and the Canadian Institutes of Health Research (CIHR; grant No. TGC-114046). C.P. is grateful to NSERC and Boehringer Ingelheim for graduate student fellowships. The authors thank Dr. A. Fürtös, K. Venne, and M.-C. Tang for assistance with mass spectrometry as well as V.N.G. Lindsay and C. Camy for SFC analyses.

References

(1) Alizadeh, A.; Babaki, M.; Zohreh, N. *Synthesis* **2008**, (20), 3295. doi:10.1055/s-0028-1083142.

(2) Ragnarsson, U. *Chem. Soc. Rev.* **2001**, *30* (4), 205. doi:10.1039/b010091a.

(3) Melendez, R. E.; Lubell, W. D. *J. Am. Chem. Soc.* **2004**, *126* (21), 6759. doi:10.1021/ja039643f.

Can. J. Chem. Downloaded from www.nrcresearchpress.com by MCGILL UNIVERSITY on 02/02/13
For personal use only.

(4) Boeglin, D.; Lubell, W. D. *J. Comb. Chem.* **2005**, *7* (6), 864. doi:10.1021/cc050043h.
(5) Gante, J. *Synthesis* **1989**, (6), 405. doi:10.1055/s-1989-27269.
(6) Proulx, C.; Sabatino, D.; Hopewell, R.; Jochen, S.; Garcia-Ramos, Y.; Lubell, W. D. *Future Med. Chem.* **2011**, *3,* 1139. doi:10.4155/fmc.11.74.
(7) Biel, J. H.; Drukker, A. E.; Mitchell, T. F.; Sprengeler, E. P.; Nuhfer, P. A.; Conway, A. C.; Horita, A. *J. Am. Chem. Soc.* **1959**, *81* (11), 2805. doi:10.1021/ja01520a048.
(8) Han, H.; Janda, K. D. *J. Am. Chem. Soc.* **1996**, *118* (11), 2539. doi:10.1021/ja9535470.
(9) Kline, G. B.; Cox, S. H. *J. Org. Chem.* **1961**, *26* (6), 1854. doi:10.1021/jo01065a040.
(10) Braden, T. M.; Coffey, D. S.; Doecke, C. W.; LeTourneau, M. E.; Martinelli, M. J.; Meyer, C. L.; Miller, R. D.; Pawlak, J. M.; Pedersen, S. W.; Schmid, C. R.; Shaw, B. W.; Staszak, M. A.; Vicenzi, J. T. *Org. Process Res. Dev.* **2007**, *11* (3), 431. doi:10.1021/op700040v.
(11) Licandro, E.; Perdicchia, D. *Eur. J. Org. Chem.* **2004**, (4), 665. doi:10.1002/ejoc.200300416.
(12) Bonnet, D.; Margathe, J.-F.; Radford, S.; Pflimlin, E.; Riche, S.; Doman, P.; Hibert, M.; Ganesan, A. *ACS Comb. Sci.* **2012**, *14* (5), 323. doi:10.1021/co300015k.
(13) Spiegel, J.; Mas-Moruno, C.; Kessler, H.; Lubell, W. D. *J. Org. Chem.* **2012**, *77* (12), 5271.
(14) Brosse, N.; Pinto, M. F.; Bodiguel, J.; Jamart-Gregoire, B. *J. Org. Chem.* **2001**, *66* (8), 2869. doi:10.1021/jo005696t.
(15) Bourguet, C. B.; Proulx, C.; Klocek, S.; Sabatino, D.; Lubell, W. D. *J. Pept. Sci.* **2010**, *16* (6), 284. doi:10.1002/psc.1235.
(16) Sabatino, D.; Proulx, C.; Klocek, S.; Bourguet, C. B.; Boeglin, D.; Ong, H.; Lubell, W. D. *Org. Lett.* **2009**, *11* (16), 3650. doi:10.1021/ol901423c.
(17) Zawadzki, S.; Zwierzak, A. *Pol. J. Chem.* **2003**, *77,* 315.
(18) Meyer, K. G. *Synlett* **2004**, *13* (13), 2355. doi:10.1055/s-2004-831336.
(19) Nun, P.; Martin, C.; Martinez, J.; Lamaty, F. *Tetrahedron* **2011**, *67* (42), 8187. doi:10.1016/j.tet.2011.07.056.
(20) Kobayashi, S.; Yazaki, R.; Seki, K.; Yamashita, Y. *Angew. Chem. Int. Ed.* **2008**, *47* (30), 5613. doi:10.1002/anie.200801322.
(21) Minabe, M.; Takabayashi, Y.; Setta, Y.; Nakamura, H.; Kimura, T.; Tsubota, M. *Bull. Chem. Soc. Jpn.* **1996**, *69* (12), 3633. doi:10.1246/bcsj.69.3633.
(22) Lawton, G.; Moody, C. J.; Pearson, C. J.; Williams, D. J. *J. Chem. Soc. Perkin Trans. 1* **1987**, 885. doi:10.1039/p19870000885.
(23) McEwen, W. K. *J. Am. Chem. Soc.* **1936**, *58* (7), 1124. doi:10.1021/ja01298a017.
(24) Olmstead, W. L.; Margolin, Z.; Bordwell, F. G. *J. Org. Chem.* **1980**, *45* (16), 3295. doi:10.1021/jo01304a032.
(25) Kolthoff, I. M.; Chantooni, M. K.; Bhowmik, S. *J. Am. Chem. Soc.* **1968**, *90* (1), 23. doi:10.1021/ja01003a005.
(26) Galezowski, W.; Jarczewski, A.; Stanczyk, M.; Brzezinski, B.; Bartl, F.; Zundel, G. *J. Chem. Soc., Faraday Trans.* **1997**, *93* (15), 2515. doi:10.1039/a700668c.
(27) Leffek, K.T.; Pruszynski, P.; Thanapaalasingham, K. *Can. J. Chem.* **1989**, *67* (4), 590. doi:10.1139/v89-089.
(28) Crampton, M. R.; Robotham, I. A. *J. Chem. Res. (S)* **1997**, 22. doi:10.1039/a606020j.
(29) Bourguet, C. B.; Sabatino, D.; Lubell, W. D. *Pept. Sci.* **2008**, *90* (6), 824. doi:10.1002/bip.21103.
(30) Nowick, J. S.; Powell, N. A.; Nguyen, T. M.; Noronha, G. *J. Org. Chem.* **1992**, *57* (26), 7364. doi:10.1021/jo00052a069.
(31) Still, W. C.; Kahn, M.; Mitra, A. *J. Org. Chem.* **1978**, *43* (14), 2923. doi:10.1021/jo00408a041.

Synthesis, characterization, and solid-state polymerization of cross-conjugated octatetraynes

Yuming Zhao, Thanh Luu, Guy M. Bernard, Tyler Taerum, Robert McDonald, Roderick E. Wasylishen, and Rik R. Tykwinski

Can. J. Chem. Downloaded from www.nrcresearchpress.com by MCGILL UNIVERSITY on 02/02/13
For personal use only.

Abstract: Two series of cross-conjugated 1,3,5,7-octatetraynes (**1a**–**1l** and **6a**–**6d**) have been synthesized. UV–vis spectroscopic analysis shows that pendent groups connected to the cross-conjugated skeleton have little effect on the λ_{max} energies, irrespective of whether the groups are electron withdrawing or donating. A number of the isolated products readily give crystals suitable for X-ray crystallography, and the solid-state structural properties of five derivatives (**1k**, **1l**, **6a**, **6c**, and **6d**) have been examined by X-ray crystallographic analysis. Parallel packing of the polyynes in the solid state indicates that four of the five samples are potentially suitable for topochemical polymerization, based on solid-state packing parameters θ, *R*, and *d*. Attempts to effect a solid-state reaction have been explored through UV–vis and γ-ray irradiation as well as thermal heating. The course of these reactions was monitored by differential scanning calorimetry (DSC) analysis, as well as UV–vis and solid-state ^{13}C NMR spectroscopy (for **1d**, **1j**, **1k**, and **6d**), which offered evidence of polymer formation from these reactions. Structural determination of the product(s), however, remains elusive.

Key words: polytriacetylenes, polyynes, solid-state NMR spectroscopy, tetraynes, topochemical polymerization.

Résumé : On a réalisé la synthèse de deux séries de 1,3,5,7-octatétraynes à conjugaisons croisées (**1a**–**1l** et **6a**–**6d**). L'analyse de leurs spectres UV–visible montre que les groupes pendants attachés au squelette à conjugaison croisée n'ont que peu d'effet sur les énergies des λ_{max}, que les groupes attachés soient électroaffinitaires ou électrorépulsifs. Un certain nombre de produits isolés fournissent des cristaux susceptibles d'être soumis à une diffraction par des rayons-X; on a ainsi pu déterminer les propriétés structurales de cinq dérivés (**1k**, **1l**, **6a**, **6c** et **6d**) par une analyse des données cristallographiques par cette méthode. L'entassement parallèle des polyynes à l'état solide indique que quatre des cinq échantillons pourraient éventuellement être susceptibles de donner lieu à une polymérisation topochimique si on se base sur leurs paramètres d'empilement θ, *R* et *d*. On a exploré la possibilité de réaliser des réactions à l'état solide par des irradiations UV–visible et par des rayons γ ainsi que par un chauffage thermique. On a suivi le cours de ces réactions par le biais d'une analyse par calorimétrie à balayage différentiel (CBD) ainsi que par les spectroscopies UV–visible et RMN du ^{13}C à l'état solide (pour les composés **1d**, **1j**, **1k** et **6d**) qui fournissent des données suggérant qu'il y a formation de polymères au cours de ces réactions. La détermination des structures de ces produits demeure toutefois incertaine.

Mots-clés : polytriacétylènes, polyynes, spectroscopie RMN à l'état solide, tétraynes, polymérisation topochimique.

[Traduit par la Rédaction]

Introduction

During the past couple of decades, solid-state polymerization of polyynes has been the subject of considerable exploration in the quest for conjugated organic materials with qualities suitable for applications in nanoscience, nonlinear optics, organic electronics, supramolecular chemistry, and sensing.[1–8] Solid-state polymerization of polyynes is an attractive route to such materials because it can provide large and nearly defect-free polymer crystals, as well as materials with unique solution-state properties.[9–11] The topochemical polymerization of a "diacetylene" (diyne) monomer into a polydiacetylene polymer was first reported by Wegner[12] in 1969. In the intervening years, the breadth of this general process has been studied and expanded. These investigations have documented quite clearly that the solid-state packing of the polyyne precursor in the crystalline state is crucial to formation of the desired polymer.[13–16] In polyyne crystals, molecules must move cooperatively during the reaction process to arrive at the ordered structure of the polymeric product

Received 17 February 2012. Accepted 28 June 2012. Published at www.nrcresearchpress.com/cjc on 30 November 2012.

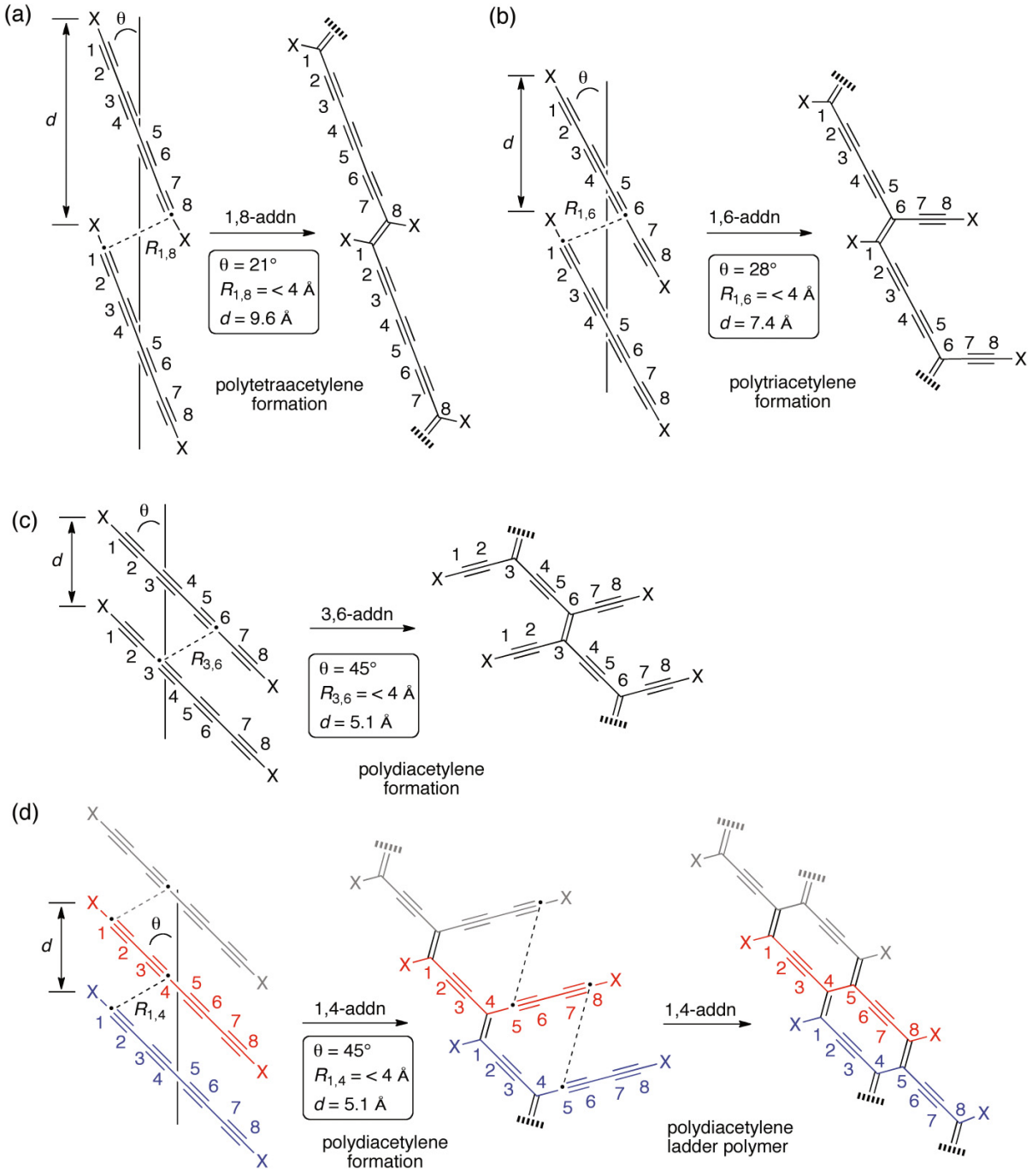
Y. Zhao. Department of Chemistry Memorial University of Newfoundland, St. John's, NL A1B 3X7, Canada.
T. Luu, G.M. Bernard, T. Taerum, and R.E. Wasylishen. Department of Chemistry, University of Alberta, Edmonton, AB T6G 2G2, Canada.
R. McDonald. X-ray Crystallography Laboratory, Department of Chemistry, University of Alberta, Edmonton, AB T6G 2G2, Canada.
R.R. Tykwinski. Department of Chemistry and Pharmacy & Interdisciplinary Center of Molecular Materials (ICMM), University of Erlangen-Nuremberg, Henkestrasse 42, 91054 Erlangen, Germany.

Corresponding author: Rik R. Tykwinski (e-mail: rik.tykwinski@chemie.uni-erlangen.de).

Dedicated to Professor Derrick Clive in recognition of a lifetime of contributions to organic synthesis.

Can. J. Chem. Downloaded from www.nrcresearchpress.com by MCGILL UNIVERSITY on 02/02/13
For personal use only.

Fig. 1. Schematic crystal packing for several modes of octatetrayne polymerization, and optimal parameters θ, *R*, and *d* for each addition pattern. (*a*) Polytetraacetylene formation via 1,8-addition. (*b*) Polytriacetylene formation via 1,6-addition. (*c*) Polydiacetylene formation via 3,6-addition. (*d*) Ladder polymer formation via two sequential 1,4-additions.

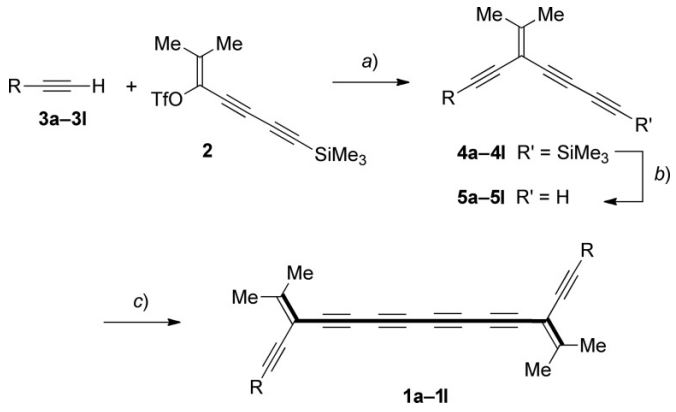


(i.e., a phase transition). When the solid-state arrangement of the polyyne precursors offers a reaction pathway with minimal translational energy, a topochemical reaction is possible when initiated by, for example, heat, UV light, pressure, or γ-ray radiation. Such reactions are common for diynes and selectively form the polydiacetylene product. For longer polyyne precursors, however, multiple reaction possibilities exist, as schematically shown in Fig. 1 for tetraynes. Thus, while polyyne precursors offer a tantalizing opportunity to form highly conjugated polymer products,[15,17,18] the various modes of reactivity present a number of challenges, including the realization of the single crystals with optimal packing parameters, dictating one particular reaction pathway to the exclusion of another, and characterization of the often insoluble reaction product(s).

Efforts to effect polymerization of polyynes beyond the length of a diyne have been relatively rare, although several examples are described for the polymerization of triynes,[19]

Can. J. Chem. Downloaded from www.nrcresearchpress.com by MCGILL UNIVERSITY on 02/02/13
For personal use only.

Scheme 1. Synthesis of tetraynes **1a**–**1l**. Reagents and conditions: (*a*) $PdCl_2(PPh_3)_2$, CuI, *i*-Pr_2NH, THF, rt; (*b*) K_2CO_3, MeOH, THF; (*c*) CuCl, TMEDA, acetone or acetone/CH_2Cl_2 (1:1), O_2 (air), rt. The longest linearly conjugated segment is highlighted in bold. THF, tetrahydrofuran; TMEDA, tetramethylethylenediamine.



pentaynes,[20] and hexaynes.[21] There has been slightly more work done in the area of tetraynes,[22] likely because of the fact that tetraynes are both easy to synthesize and relatively stable under ambient conditions.[23] In considering the topochemical polymerization of tetraynes, several pathways must be considered, as outlined in Fig. 1. In each case, packing parameters based on the orientation of neighbouring molecules stacked parallel in the solid state govern reactivity patterns that might be energetically accessible. The packing parameters are defined as (*i*) the stacking or translational distance of the monomers in the parallel stack (*d*), (*ii*) the angle formed between the polyyne and the stacking axis (the "tilt angle"; θ), and (*iii*) the distance between the reacting carbon atoms in neighbouring molecules of the stack (*R*).[13,15] For example, 1,8-addition for a tetrayne gives a polytetraacetylene product (Fig. 1*a*), whereas 1,6-addition forms a polytriacetylene[24] product (Fig. 1*b*). A variety of reaction pathways are possible that would result in polydiacetylene formation via a formal 1,4-addition pattern, such as those in Figs. 1*c* and 1*d*, which afford interesting cross-conjugated polymers.[25] It is noteworthy that topochemical polymerization can also lead to polydiacetylene "ladder polymers" through two sequential 1,4-polymerization events (Fig. 1*d*).[17b] As part of an ongoing interest in the structural and electronic properties of cross-conjugated enyne systems,[25a,26] we serendipitously discovered that a large number of cross-conjugated tetrayne products crystallize with the polyynes stacked in parallel, with packing parameters potentially suitable for topochemical polymerization. Thus, we report herein on the synthesis and study of two series of tetraynes, the spectroscopic characterization of these compounds, our efforts to polymerize these polyynes, and difficulties encountered in the characterization of the product(s) of these solid-state reactions.

Synthesis

Notably, the synthesis of the cross-conjugated tetrayne series **1a**–**1l** is achieved in three efficient steps, as described in Scheme 1 and summarized in Table 1.[27] First, Pd-catalyzed Sonogashira cross coupling[28] of the known vinyl triflate **2**[29] with various terminal acetylenes (**3a**–**3l**) gave enynes **4a**–**4l**. These reactions generally proceeded smoothly at room temperature (rt) and were complete within 2 h. Isolated yields of triynes **4a**–**4l** were good to excellent, and, with the exception of **4a** (an oil), triynes **4** are isolated as stable solids. Protodesilylation of **4a**–**4l** then provided the terminal alkynes **5a**–**5l**, which were carried on directly, following workup, to the oxidative homocoupling step using Cu-mediated Hay conditions.[30] The homocoupling reactions were typically complete in ~0.5 h at rt using either acetone or a mixture of acetone/CH_2Cl_2 (1:1) as solvent. Isolated yields for **1a**–**1l** ranged from excellent to poor, depending primarily on the stability of the resulting product. Nitroaryl functionalized tetraynes **1e**–**1g** had particularly poor stability, even at low temperature and in solution. This resulted in drastically reduced isolated yields for **1e** and **1f**, whereas **1g** was insufficiently stable for isolation. While *n*-butyl- and cyano-substituted tetraynes **1a** and **1h**, respectively, were also relatively unstable at room temperature, yields were nevertheless reasonable and the products could be handled without significant decomposition if kept in solution.

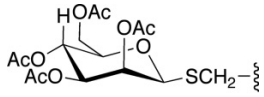
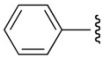
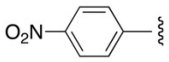
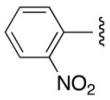
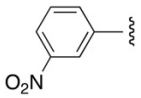
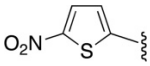
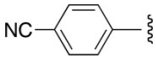
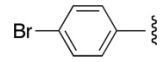
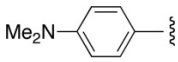
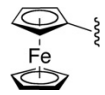
Next, our investigations of α,ω-polyynes[31] led to the formation of the dibromoolefinic analog of tetrayne **1c**, namely **6a** (Scheme 2). Compound **6a** was isolated as a crystalline solid with interesting solid-state packing based on X-ray analysis (vide infra). This suggested a second class of octatetraynes that might be explored for their solid-state behaviour. Tetraynes **6a**–**6d** were easily synthesized starting from commercially available acid chlorides **7a**–**7d** as shown in Scheme 2 and summarized in Table 2. In the first step, a Friedel–Crafts acylation reaction of **7a**–**7d** with 1,4-bis-trimethylsilyl-1,3-butadiyne (**8**) in the presence of $AlCl_3$ afforded the intermediate ketones **9a**–**9d**, after quenching of the reaction and aqueous workup.[32] The crude ketones were then converted directly to dibromoolefins **10a**–**10d** via the Ramirez olefination reaction.[33] Isolated yields were good to excellent over the two steps, and **10a**–**10d** were obtained as stable crystalline solids. With diyne precursors **10a**–**10d** in hand, desilylation using K_2CO_3/MeOH gave the terminal alkynes, which were carried on directly to Hay[30] homocoupling in CH_2Cl_2. The desired products (**6a**–**6d**) were isolated pure in good to moderate yields by either column chromatography or recrystallization from hexanes.

^{13}C-labelling of compound 6d

It is well-established that solid-state ^{13}C NMR spectroscopy can provide invaluable structural information concerning the products of topochemical polymerization reactions.[34] With this in mind, the synthesis of tetrayne **6d** enriched with ^{13}C atoms was undertaken (Scheme 3). The synthesis began with the known dibromoolefin **11**,[35] which incorporated ~34% ^{13}C at position C(1) (indicated with an *). The reaction of the dibromoolefin **11** with excess lithium diisopropylamide (LDA) at low temperature effected elimination, and the resulting lithiated diyne product was trapped via the reaction with Me_3SiCl to give differentially silylated diyne **12**.[36] Following a similar reaction sequence as outlined in Scheme 2, diyne **12** was then converted into ketone **13** via a Friedel–Crafts acylation with **7d**, and the ketone was carried on directly to a standard dibromoolefination reaction affording dibromoolefin **14** in a reasonable yield (35%) over the two steps. The presence of the triisopropylsilyl group in **14** necessitated the use of

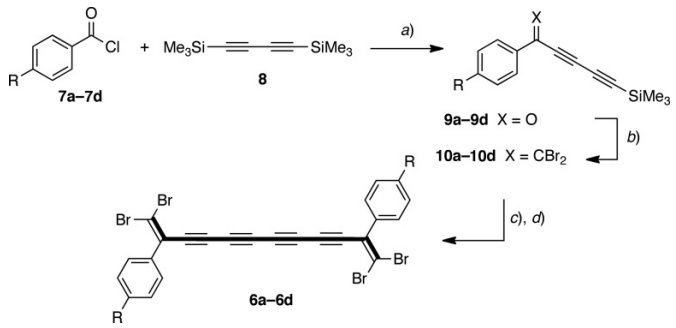
Can. J. Chem. Downloaded from www.nrcresearchpress.com by MCGILL UNIVERSITY on 02/02/13
For personal use only.

Table 1. Synthetic details and selective physical properties of enetriyne precursors **4a**–**4l** and tetraynes **1a**–**1l**.

		4		**1**		
Entry	R	Yield (%)	Description (mp, °C)[a]	Yield (%)	Description (mp, °C)[a]	DSC, dp (T_{onset}/T_{max}; °C)
a	*n*-Butyl	98	Unstable oil	94	Unstable oil	—
b		65	Colourless solid (54–57)	91	Brown solid (57–62)	—
c		96	Colourless solid (71–72)	66	Yellow, waxy solid	—
d		90	Yellow solid (94–95)	95	Yellow solid	172/193
e		87	Yellow solid (93–94)	27	Unstable, yellow semisolid	—
f		91	Yellow solid (77–78)	39	Unstable, yellow semisolid	—
g		36	Yellow solid (68–69)	0	—	—
h		80	Yellow solid (60–62)	74	Unstable, yellow solid	—
i		79	Colourless, waxy solid	85	Yellow solid	123/131
j		83	Yellow solid (82–83)	76	Yellow solid	157/165
k		56	Yellow solid (84–85)	75	Orange solid	160/187
l[b]	*i*-Pr_3Si	93	Colourless solid (30–31)	96	Yellow solid (103–104)	145

Note: mp: melting point, DSC: differential scanning calorimetry, dp: decomposition, *T*: temperature.
[a]Measured in an open capillary tube.
[b]Synthesized as reported in ref. 27.

Scheme 2. Synthesis of tetraynes **6a**–**6d**. Reagents and conditions: (*a*) $AlCl_3$, CH_2Cl_2, –20 °C; (*b*) CBr_4, PPh_3, CH_2Cl_2; (*c*) K_2CO_3, MeOH/THF; (*d*) CuCl, TMEDA, CH_2Cl_2, O_2 (air), rt. The longest linearly conjugated segment is highlighted in bold. THF, tetrahydrofuran; TMEDA, tetramethylethylenediamine.



tetrabutylammonium fluoride (TBAF) to effect desilylation, and the thus formed terminal diyne was then subjected to oxidative homocoupling under Hay conditions. As a result of the partial labelling, three isotopomers were formed from the homocoupling reaction, including compound **6d** (no labelled carbon), **6d*** (one labelled carbon), and **6d**** (two labelled carbons). As expected, however, the ^{13}C NMR spectrum of this mixture is identical to that of the unlabelled compound **6d**, except for the enhanced signal of the C(1) carbon of the octayne chain and the associated ^{13}C–^{13}C coupling (vide infra).

Solution-state ^{13}C NMR spectroscopic characterization

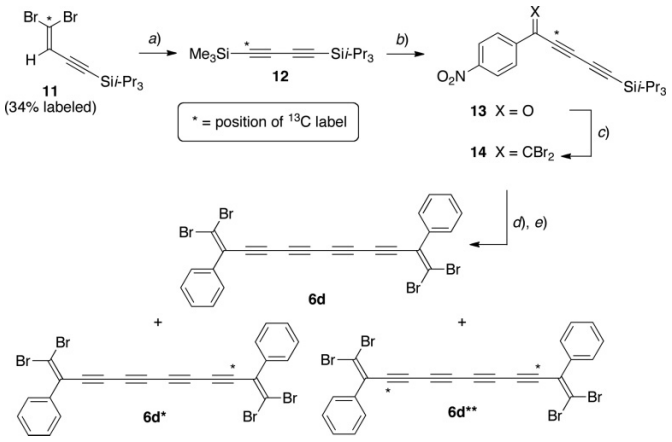
Solution-state ^{13}C NMR spectroscopy of compounds **1a**–**1l** shows that the α carbons of the isopropylidene backbone (Me_2C=C<) are easily identified because they are quite deshielded, resonating in the range of 160–165 ppm.[37] Electron-withdrawing aryl groups result in a downfield shift of this signal, such that the resonances of **1d** (4-NO_2–C_6H_4–), **1e** (2-NO_2–C_6H_4–), **1f** (3-NO_2–C_6H_4–), and **1h** (4-NC–C_6H_4–) are found at 163.9, 165.0, 163.4, and 163.6 ppm, respectively. Conversely, electron-donating groups result in a slight upfield shift of this carbon resonance, as with derivatives **1j** (4-NMe_2–

Table 2. Synthetic details and selective physical properties of diyne monomers **10a**–**10d** and tetraynes **6a**–**6d**.

		10		**6**		
Entry	R	Yield (%)	Description (mp, °C) [a]	Yield (%)	Description (dp, °C)[a]	DSC: mp/dp (°C); T_{onset} /T_{max} (°C)
a	H	77	Colourless solid (85–87)	75	Yellow solid (185)	—; 191/192 (dp)
b	OMe	90	Off-white solid (72–74)	46	Yellow-green solid (168–170)	176 (mp); 176/179 (dp)
c	*t*-Bu	65	Yellow solid (96–98)	80	Yellow solid (168–179)[b]	190;[c] 230/233 (dp)
d	NO_2	51	Off-white solid (80–83)	51	Yellow solid (~190)	—; 189/191 (dp)

Note: mp: melting point, dp: decomposition, DSC: differential scanning calorimetry, *T*: temperature.
[a]Measured in an open capillary tube.
[b]Apparent melting point.
[c]Weak exotherm.

Scheme 3. Synthesis of isotopomers **6d/6d*/6d****. Reagents and conditions: (*a*) LDA, THF, –78 °C, then Me_3SiCl, 67%; (*b*) **7d**, $AlCl_3$, CH_2Cl_2, –20 °C; (*c*) CBr_4, PPh_3, CH_2Cl_2, 0 °C, 35% (from **12**); (*d*) TBAF, THF, rt; (*e*) CuCl, TMEDA, CH_2Cl_2, O_2, rt, 42% (from **14**). LDA, lithium diisopropylamide; THF, tetrahydrofuran; TBAF, tetra-*n*-butylammonium fluoride; TMEDA, tetramethylethylenediamine.



C_6H_4–) and **1k** (ferrocenyl) at 159.5 and 159.9 ppm, respectively. The analogous carbons for tetraynes **6a**–**6d**, terminated with a dibromovinyl group (Br_2C=C<), are found at much lower chemical shift values, a result of the heavy atom effect, typically in the range of ~100 ppm based on published studies using ^{13}C labelling.[38] This places the resonance in the region of the alkyne carbon signals and complicates unambiguous assignment for **6a**–**6d**. Empirically, however, signals observed for **6a**–**6d** (and **10a**–**10d**) in the range of 102–108 ppm are consistent with this assignment. Conversely, the β-alkylidene carbons (Me_2C=C<) for isopropylidene compounds such **1a**–**1l** are typically found in the range of 99–100 ppm,[37] and thus they are also difficult to conclusively discern from the alkyne carbon resonances. For compounds **6d** and **14**, the β-alkylidene carbon (Br_2C=C<) can be identified at 127.6 and 128.3 ppm, respectively, as a result of the large one-bond coupling ($^1J(^{13}C, ^{13}C)$ = 98 Hz) in each case to the ^{13}C-labelled carbon at C(1). This compares to one-bond $^1J(^{13}C, ^{13}C)$ values of 34.6, 67.6, and 171.5 Hz for ethane, ethylene, and acetylene, respectively.[39]

Generally, the resonances of carbons C(3) and C(4) of an octatetrayne moiety (–C(1)≡C(2)–C(3)≡C(4)–C≡C–C≡C–) are found upfield relative to those of C(1) and C(2).[35,40,41] In the case of **1a**–**1l**, this places C(3) and C(4) at either ~64 or 68 ppm, regardless of the substitution pattern. The adjacent carbons C(1) and C(2), on the other hand, resonate in the range of 74–77 ppm. A similar pattern is found for **6a**–**6d**, where labelling of **6d*/6d**** provides an opportunity to identify each specific carbon within this tetrayne series. The labelled carbon C(1) for **6d*/6d**** is observed at 75.6 ppm, and the large coupling with C(2) at δ 82.7 ($^1J(^{13}C, ^{13}C)$ = 187 Hz) sets this carbon resonance. Coupling between C(1) and C(3) at 71.4 ppm is also clearly observed with $^2J(^{13}C, ^{13}C)$ = 32 Hz, and C(4) is thus identified as the remaining resonance at 64.9 ppm.

Solution-state UV–vis spectroscopic characterization

Highest occupied and lowest unoccupied molecular orbital (HOMO–LUMO) transitions for **1a**–**1l** and **6a**–**6d** should result from the longest linearly conjugated segment of these molecules (the ene–tetrayne–ene group highlighted in bold, Schemes 1 and 2).[27] In **1a**–**1l**, there is a progression of three absorptions at approximately 350, 375, and 405 nm (Fig. 2*a*). The various pendent functional groups have a negligible effect on the energy of these transitions as a result of the cross-conjugated framework.[25–27,42] The most distinguishing effect based on structure is observed for derivatives with strong electron withdrawing and donating substituents, **1d** and **1j**, respectively, where an enhancement in molar absorptivity is observed in comparison with other derivatives. For the organometallic member of the series (**1k**), a weak, broad peak at 450 nm is attributed to the absorption characteristic of the ferrocenyl groups.

All members of the second series of tetraynes **6a**–**6d** also display three peaks in the low-energy region of the spectra at ~359, 387, and 419 nm (Fig. 2*b*). In addition, all four compounds have similar molar absorptivity values (ε). Thus, for **6a**–**6d**, as observed for **1a**–**1l**, varying the pendent substituents does not appreciably influence the wavelength of maximum absorption (λ_{max}) values.

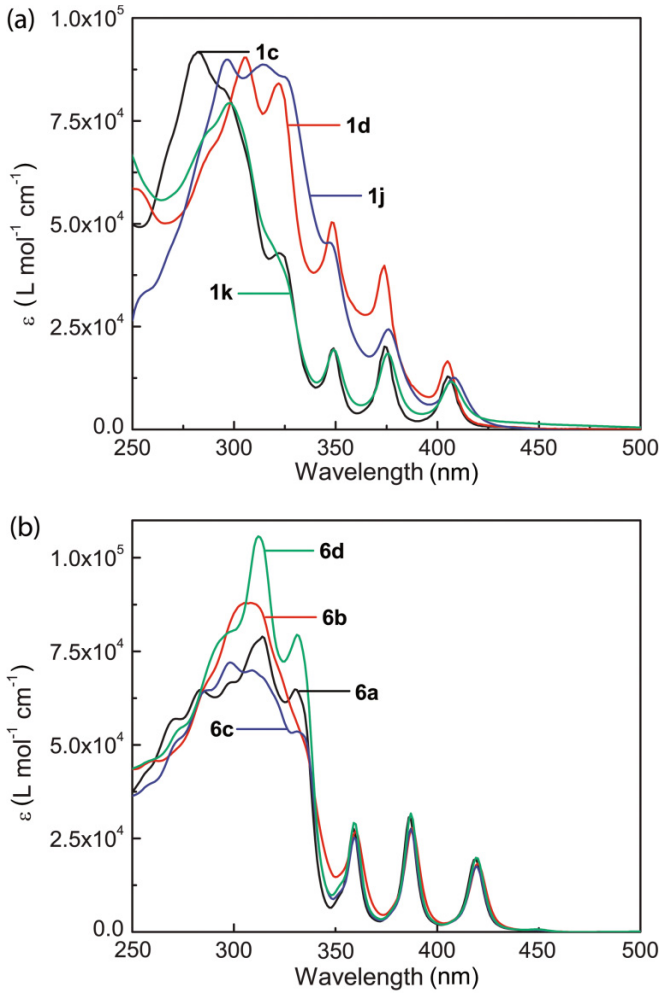
Solid-state properties and attempted topochemical polymerization

Looking at the kinetic and thermal stability of cross-conjugated tetraynes **1a**–**1l** and **6a**–**6d**, derivatives with 4-nitrophenyl (**1d**), 4-*N*,*N*-dimethylaminophenyl (**1j**), ferrocenyl (**1k**), and triisopropylsilyl (**1l**) substituents show sufficient stability for detailed study, as do all four compounds **6a**–**6d**. As described in the following sections, our studies to date

Can. J. Chem. Downloaded from www.nrcresearchpress.com by MCGILL UNIVERSITY on 02/02/13
For personal use only.

Can. J. Chem. Downloaded from www.nrcresearchpress.com by MCGILL UNIVERSITY on 02/02/13
For personal use only.

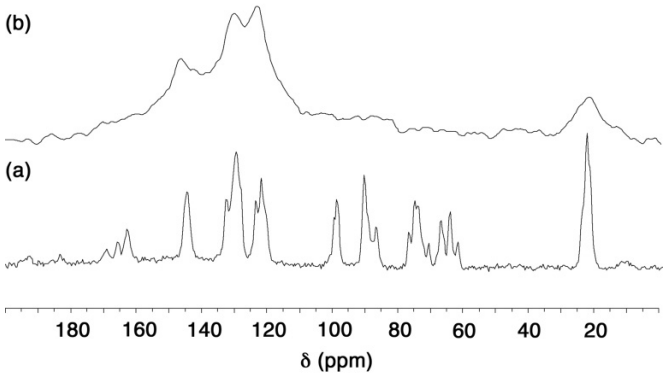
Fig. 2. Electronic absorption spectra (ε, L mol^{-1} cm^{-1}) for (*a*) **1c**, **1d**, **1j**, and **1k** in $CHCl_3$ and (*b*) **6a**–**6d** in THF.



include differential scanning calorimetry (DSC) analysis for all eight of these compounds, X-ray crystallographic analysis of **1k**, **1l**, **6a**, **6c**, and **6d**, and solid-state ^{13}C NMR spectroscopic analysis of **1d**, **1j**, **1k**, and **6d** during attempts to effect topochemical polymerization.

Last but not least, it is useful to point out several common threads from this study, as a prelude to the specific discussions that follow. Many reports for the solid-state reaction of polyynes have underscored the fact that the most important criteria for effective topochemical polymerization are the solid-state packing parameters θ, *R*, and *d* as summarized in Fig. 1. Supplemented with DSC analysis, this information offers, a priori, a guide for the selection of crystalline candidates for further study. It will become clear in the following sections, however, that a combination of suitable packing parameters and "sharp" DSC traces are only a part of the story for polymerization of tetraynes. As the solid-state ^{13}C NMR spectroscopic studies eventually demonstrate, each "promising prospect" for thermal polymerization to a defined product results in only ambiguous evidence of the nature of the product, regardless of how "optimal" the packing parameters.

Fig. 3. Solid-state ^{13}C NMR spectra for **1d** recorded (*a*) before heating and (*b*) after heating at 120 °C for 2 h and then 160 °C for 1 h.



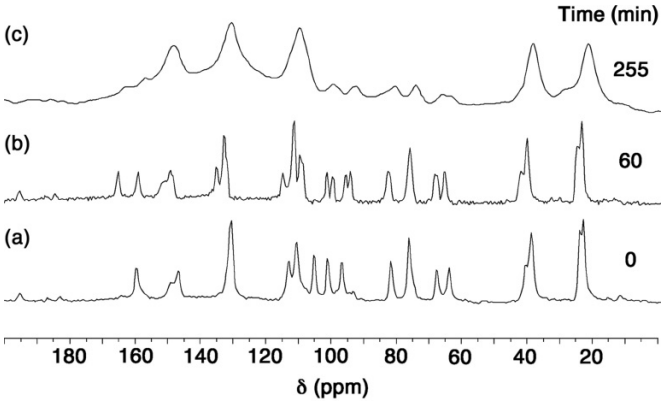
Tetrayne 1d

The DSC profile of **1d** shows a relatively broad and featureless Gaussian-shaped peak at 193 °C (see the Supplementary data), which suggests that the polymerization probably occurs in a random, nonregioselective manner. This premise has been examined by solid-state ^{13}C NMR spectroscopy. The spectrum of pristine **1d** (Fig. 3*a*) shows moderate resolution, and major signals for the sp and sp^2 carbons in the region of 64–100 ppm are reasonably consistent with solution-state ^{13}C NMR data. In addition to the expected resonances, however, several unidentified peaks are observed, likely the result of nonequivalent carbon atoms in the solid state (from a structure where C_2 symmetry has been lost). The same is true for the resonance of the external vinylidene carbon (Me_2C=C), which is observed at 164 ppm in addition to two additional signals at a similar chemical shift. After heating the sample of **1d** at 120 °C for 2 h, the resulting ^{13}C NMR spectrum is identical to that of the original, indicating that polymerization had not occurred at this temperature. Subsequent heating at 160 °C for 1 h, on the other hand, gives a black solid. The spectrum of this product shows that the characteristic resonances for interior tetrayne carbons at 64–67 ppm are completely gone after heating (Fig. 3*b*). While in agreement with a polymerized product, the loss of acetylenic signals coincides with the appearance of several broadened resonances in the region of 100–160 ppm, presumably the result of sp^2 carbons of olefinic and aryl moieties. In addition, the resonances of the methyl groups are also broadened significantly to a range of 15–30 ppm. The transition to broad featureless resonances, along with the absence of signals from sp carbon atoms, suggests that a random and nonregioselective polymerization occurs for this sample upon heating.

Tetrayne 1j

The DSC trace of **1j** shows a sharp exotherm at 165 °C (see the Supplementary data), suggesting that a solid-state reaction may be more regioselective than that observed for **1d**. In the absence of crystallographic data, the reaction has been explored by solid-state ^{13}C NMR spectroscopy. The spectrum of **1j** at room temperature (Fig. 4*a*) shows reasonable resolution when compared to the solution-state ^{13}C NMR spectrum. All eight unique sp and sp^2 carbons of the cross-conjugated enyne skeleton are clearly observed at 65, 68, 77, 82, 98, 102, 106,

Fig. 4. Solid-state ^{13}C NMR spectra for **1j** recorded (*a*) before heating (time = 0), (*b*) after heating at 100 °C for 60 min, and (*c*) after heating at 100 °C for 255 min.



and 160 ppm, while the two methyl carbons of the isopropylidene moiety are also distinct at 23 and 25 ppm. Finally, the *N*,*N*-dimethylanilino carbons are observed at 40 ppm. After heating at 100 °C for 1 h, the crystalline sample turns dark brown, and the ^{13}C NMR spectrum shows several distinct differences with fair resolution (Fig. 4*b*). The most significant changes upon heating are (*i*) the emergence of two nonequivalent vinylidene peaks at 159 and 165 ppm, (*ii*) splitting of the signal at 130 ppm, and (*iii*) several additional resonances in the range of 90–110 ppm. The characteristic resonances of the carbons of the polyyne fragment have approximately the same chemical shift values (in the region of 60–85 ppm), but they are broadened. Additional heating at 100 °C for ~3 h yields a black solid, the spectrum of which shows severely broadened signals, centred at 20, 40, 110, 130, and 150 ppm (Fig. 4*c*), although many of the major features observed in the initial spectrum after 60 min (Fig. 4*b*) are still distinguishable. In combination, these spectra suggest that polymerization may proceed in a regioselective manner, since distinct chemical shifts are still observed for the product (i.e., Fig. 4*c*). Several points deserve further discussion. If the reaction occurs via 1,6-addition, C_2 symmetry of the starting tetrayne would be destroyed while generating a polytriacetylene (PTA) product. The upfield signals at 60–70 ppm are not, however, consistent with the presence of a diyne group of a PTA. Alternatively, reaction via 1,8-addition would afford a polytetraacetylene product (Fig. 1*a*), and resonances in the ranges of 60–70 ppm could be consistent with the formation of an unsymmetrical triyne moiety.[43] Unfortunately, without crystallographic data of the starting material or product, more definitive conclusions are difficult to draw.

Tetrayne 1k

For ferrocenyl-substituted **1k**, an exotherm is found at ~187 °C in the DSC analysis, and a shoulder peak is also noticeable at slightly lower temperature (165 °C; see the Supplementary data). Compound **1k** is remarkably crystalline, and orange-brown translucent needle-shaped crystals of **1k** suitable for X-ray crystallography are obtained easily by diffusion of methanol into an Et_2O solution at –4 °C. The solid-state structure shows that the 16-carbon C_{2v} symmetrical enyne skeleton is virtually planar with a maximum deviation of 0.056(3) Å from a least-squares plane (Fig. 5). All triple bonds are comparable to other reported tetraynes (Table 3).[13] The carbons of the tetrayne framework show a gradual curvature with bond angles deviating from 180° by less than 4° in all cases (Table 4). The plane of the cyclopentadienyl ligand for the ferrocene group is, nevertheless, twisted out of the enyne plane by an angle of ~31°.

The most notable feature of the solid-state structure of **1k** is the parallel stacking of tetrayne moieties, suggesting the possibility of a topochemical polymerization. In the solid-state packing of **1k**, molecules show a tilt angle (θ) of 30° and the translational distance (*d*) is 7.4 Å. There are two potential modes for 1,6-polymerization, with $R_{1,6} = R_{3,8} = 3.7$ Å. Thus, these features correspond quite well with the optimal parameters of θ = 28°, $R_{1,6} < 4$ Å, and $d = 7.4$ Å for topochemical polymerization in a 1,6-addition manner.

With a viable crystal seemingly in hand for effecting 1,6-polymerization, several approaches have been explored. Polymerization via UV irradiation (monochromic 280 nm for 12 h) fails to induce polymerization, and crystals show a diffraction pattern identical to the original tetrayne sample. Likewise, γ-ray irradiation (^{60}Co, 54 ± 3 krad/h for 2 weeks) also fails to initiate polymerization. Attempts to induce a thermal reaction show that when heated to 150 °C for 30 min, crystals of **1k** transform into a black solid, suggesting that topochemical polymerization of **1k** can be effected through heating. The resulting solid is, however, amorphous rather than crystalline, as established by X-ray crystallographic analysis.

UV–vis spectroscopy was used to analyze the thermal polymerization of **1k** in a solid film cast onto a quartz plate. Three characteristic absorptions are observed for **1k** at 354, 381, and 414 nm, and these absorptions are redshifted by 5–7 nm for **1k** versus those measured in $CHCl_3$ (Fig. 6). After heating the sample open to air at 150 °C for 5 min, the UV–vis spectrum clearly shows loss of the low-energy absorptions ascribed to the ene–tetrayne–ene moiety, and these signals are replaced by a broad featureless peak at 400–550 nm. Disappointingly, the lack of specific fine structure in the spectrum of the product offers little hint as to the structure(s) resulting from polymerization.

Following the results of the UV–vis study, thermally initiated polymerization of a crystalline sample of **1k** was explored by heating to 150 °C under air. Attempts to analyze the polymerization product by solution-state ^1H and ^{13}C NMR spectroscopy did not, however, afford meaningful spectra because the sample is not soluble in typical organic solvents. Finally, the thermal polymerization for **1k** was monitored by solid-state ^{13}C NMR spectroscopy, while the sample was heated at 150 °C, and spectra were acquired over a period of 5 h (Fig. 7). The solid-state spectrum of the pristine tetrayne **1k** shows excellent resolution in comparison with the solution-state spectrum, and all unique sp and sp^2 carbons of the conjugated skeleton are clearly identified. As the sample is heated, the spectra show gradual peak broadening that increases with heating time. After heating the sample for 300 min, the spectrum is dominated by three broad signals centered at approximately 30, 75, and 142 ppm. The most intense, at δ 75 ppm, seemingly derives from the carbons of the ferrocenyl group (the isotropic ^{13}C chemical shift for solid ferrocene is 70 ppm[44]), and this broad signal engulfs the

Can. J. Chem. Downloaded from www.nrcresearchpress.com by MCGILL UNIVERSITY on 02/02/13
For personal use only.

Can. J. Chem. Downloaded from www.nrcresearchpress.com by MCGILL UNIVERSITY on 02/02/13
For personal use only.

Fig. 5. ORTEP) drawing (50% probability level) of **1k** showing a segment of crystal packing. Geometry parameters: θ = 30°, $R_{1,6}$ = 3.7 Å, $R_{3,8}$ = 3.7 Å, and d = 7.4 Å. (Note: The numbering of the carbon chain corresponds to the structural characterization listed in Tables 3 and 4, whereas the numbering for $R_{1,6}$ and $R_{3,8}$ refers to reactivity patterns from Fig. 1.)

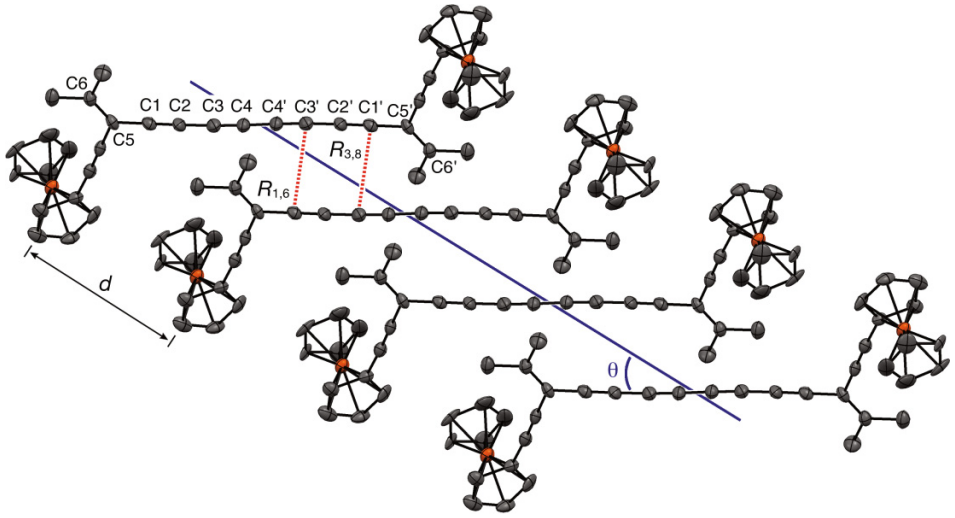


Table 3. Selected bond lengths for tetraynes **1k**, **1l**, **6a**, **6c**, and **6d**.

	Bond length (Å)						
Product	C(1)–C(2)	C(2)–C(3)	C(3)–C(4)	C(4)–C(5)	C(5)–C(6)	C(6)–C(7)	C(7)–C(8)
1k	1.185(5)	1.383(6)	1.211(5)	1.355(8)[a]			
1l	1.200(3)	1.369(3)	1.209(3)	1.365(3)	1.203(3)	1.373(3)	1.200(3)
6a	1.207(4)	1.364(4)	1.199(4)	1.361(5)	1.211(4)	1.357(4)	1.207(4)
6c	1.207(4)	1.365(4)	1.203(4)	1.371(6)[a]			
6d	1.204(4)	1.363(4)	1.204(5)	1.357(7)[a]			

[a]C(4)—C(4′).

Table 4. Selected bond angles for tetraynes **1k**, **1l**, **6a**, **6c**, and **6d**.

	Bond angle (°)									
Product	C(10)–C(9)–C(1)	C(9)–C(1)–C(2)	C(1)–C(2)–C(3)	C(2)–C(3)–C(4)	C(3)–C(4)–C(5)	C(4)–C(5)–C(6)	C(5)–C(6)–C(7)	C(6)–C(7)–C(8)	C(7)–C(8)–C(11)	C(8)–C(11)–C(12)
1k	121.3(4)[a]	178.9(5)[b]	176.6(5)	177.1(5)	177.5(6)[c]					
1l	121.95(18)	179.1(2)	177.8(2)	177.5(2)	179.4(2)	179.5(3)	178.1(2)	177.1(2)	178.2(2)	121.22(18)
6a	119.5(3)	177.4(4)	179.0(4)	179.4(4)	179.3(4)	179.8(4)	179.7(4)	177.8(4)	176.8(4)	118.3(3)
6c	120.9(3)[a]	175.9(3)[b]	178.3(3)	178.5(3)	179.6(4)[c]					
6d	120.2(3)[a]	174.3(4)[b]	179.1(4)	177.1(4)	179.8(6)[c]					

[a]C(6)–C(5)–C(1).
[b]C(5)–C(1)–C(2).
[c]C(3)–C(4)–C(4′).

region where polyyne signals are expected, making any particular assignments impossible. The signal at the highest chemical shift is very broad, spanning from 120–160 ppm, and probably results from sp^2 carbons of the vinylidene carbons and olefinic carbons formed during polymerization, or both. A background signal from the probe is also expected to contribute signal to this region. Thus, in comparison with **1j**, there is little clear evidence that **1k** polymerizes through a regioselective process, i.e., 1,6-addition, as suggested by its crystallographic analysis.

Tetrayne 1l

DSC analysis of crystalline **1l** shows a well-defined melting point at 103–104 °C, which is then followed by decomposition of the sample at 145 °C (see the Supplementary data). Yellow single crystals of tetrayne **1l** are obtained by diffusion of MeOH into a CH_2Cl_2 solution at –20 °C. Surprisingly, two different polymorphs of **1l** could be obtained from seemingly identical crystallization conditions. In addition, there appears to be no way to direct which polymorph will result for a given crystallization attempt. Both solid-state structures adopt geo-

Can. J. Chem. Downloaded from www.nrcresearchpress.com by MCGILL UNIVERSITY on 02/02/13
For personal use only.

Fig. 6. Solid-state UV–vis spectra for **1k** before and after heating the thin-film sample to 150 °C for 5 min.

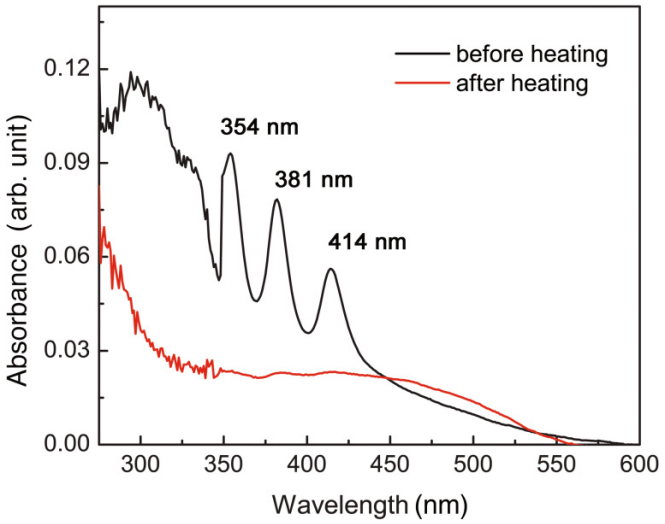
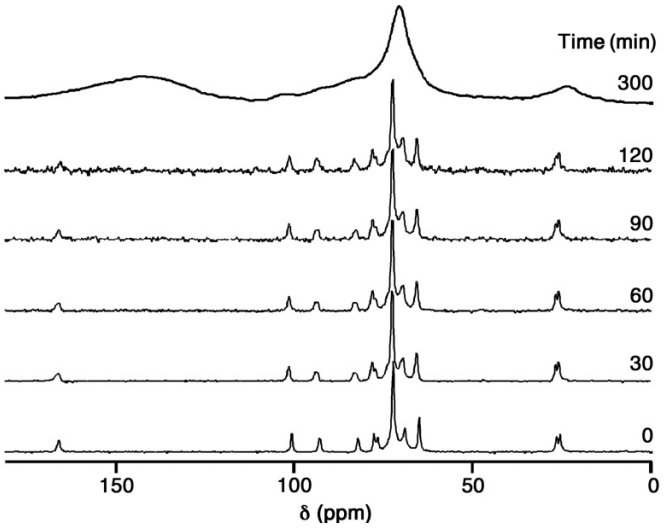


Fig. 7. Solid-state ^{13}C NMR spectra for **1k** recorded before and after heating at 150 °C for the times shown.



metrically similar s-trans orientations with respect to the octatetrayndiyl moiety (as shown in Fig. 8).[27] For one structure, molecules are aligned in parallel stacks, such that topochemical polymerization might be possible (this structure is shown in Fig. 8). The π framework of **1l** in this polymorph is virtually planar, with a maximum deviation of 0.02 Å from a least-squares plane for the 16 carbons of the conjugated skeletons. Triple bonds are unremarkable and comparable to other reported polyynes of this length (Table 3).[13,45] The eight tetrayne carbons show only a slight curvature with bond angles deviating from linear by less than 3° in all cases (Table 4).

Crystal packing analysis of tetrayne **1l** shows that the individual molecules are aligned in a parallel fashion that is predicted to favour the 1,6-addition polymerization (Fig. 8). The packing parameters of θ = 28° and d = 7.7 Å correspond quite well to those required for 1,6-polymerization, while two close contacts are also in a favourable range, $R_{1,6}$ = 3.7 Å and $R_{3,8}$ = 3.6 Å.

In spite of the favourable packing parameters observed for **1l**, all efforts to effect the thermal polymerization of single crystals for this tetrayne have been unsuccessful. Heating a sample of **1l** at 90 °C (i.e., just below the melting point) for 8 h gives a sample that is slightly darkened to yield an opaque solid that is no longer crystalline as documented by the absence of an X-ray diffraction pattern. Other methods to initiate the polymerization have also been explored, including monochromatic UV irradiation (280 nm for 24 h) and γ-irradiation (54 ± 3 krad/h for 2 weeks). In both cases, darkened yellow-orange single crystals are produced. X-ray analysis of these crystals, however, reveals exactly the same diffraction pattern as found for pristine **1l**, and there appears to be little change in the solid beyond a possible reaction at the outer surface of the crystal. Thus, there is so far no efficient way to trigger a solid-state polymerization in single crystals of **1l**.

Tetrayne 6a

DSC analysis of tetrayne derivative **6a** shows a sharp, narrow exotherm at 192 °C, which is consistent with the possibility of a reasonably well-defined topochemical polymerization (see the Supplementary data). Compound **6a** affords crystals for X-ray crystallography from a mixture of hexanes and CH_2Cl_2. The solid-state structure (Fig. 9 and Tables 3 and 4) shows that neighbouring molecules align in stacks as centrosymmetric dimeric pairs, thus giving an alternating A–B–A–B pattern. This is most easily identified in Fig. 9 by the different twist angles of the phenyl rings, which rotate out of the planar enyne framework by ~56° and 43°. The C–C≡C angles of **6a** deviate slightly from linearity, but by no more than about 3° (Table 4), whereas the torsion angle generated from vinyl groups (C10–C9···C11–C12) is ~3°.

Analysis of the solid-state packing parameters shows that the tetrayne groups of neighbouring molecules are aligned with θ = 42°, $R_{1,4}$ = $R_{3,6}$ = $R_{5,8}$ = 3.4 Å, and d = 5.1 Å. Thus, whereas 1,6-polymerization is not possible ($R_{1,6}$ = 4.3 Å), the observed packing values are quite close to the optimal values for 1,4-polymerization (θ = 45°, $R_{1,4}$ < 4 Å, and d = 5.1 Å). Combined with the intense and sharp exotherm in the DSC measurement, it seems possible that compound **6a** might undergo a 1,4-topochemical polymerization reaction. Because of our focus on 1,6-polymerization processes, however, further studies on **6a** have not yet been conducted.

Tetrayne 6b

The DSC spectrum of tetrayne **6b** shows a sharp endotherm at ~176 °C, immediately followed by a broad exotherm at 179 °C (see the Supplementary data). No melting point is, however, observed in a capillary melting point analysis. Thus, it is not clear if the initial endotherm observed by DSC is a phase transition or a true melting point. In any case, this behaviour suggests that product analysis from a thermal solid-state reaction would not be straightforward, so no further analysis of this compound has been pursued.

Tetrayne 6c

Compound **6c** shows an apparent melting point of 168–170 °C in a capillary melting point analysis, and the sample slowly darkens as the temperature is increased. DSC analysis,

Fig. 8. ORTEP drawing (50% probability level) of **1l** showing a segment of crystal packing. Geometry parameters: θ = 28°, $R_{1,6}$ = 3.7 Å, $R_{3,8}$ = 3.6 Å, and d = 7.7 Å. (Note: The numbering of the carbon chain corresponds to the structural characterization listed in Tables 3 and 4, whereas the numbering for $R_{1,6}$ and $R_{3,8}$ refers to reactivity patterns from Fig. 1.)

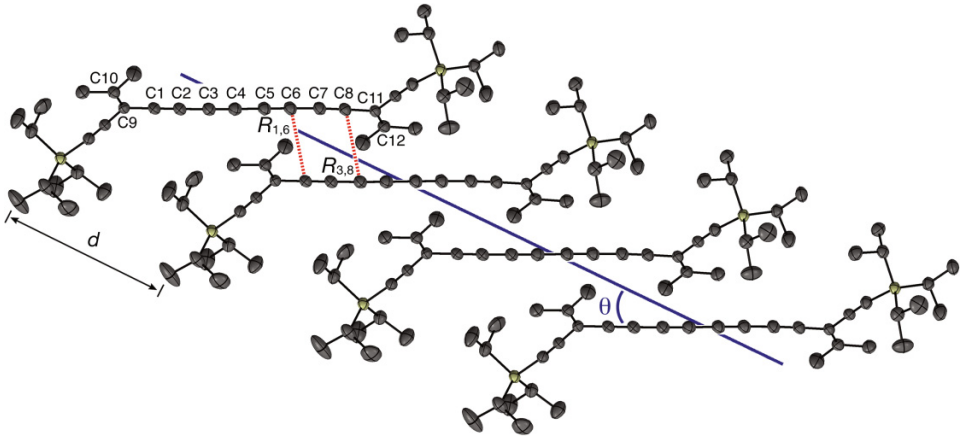
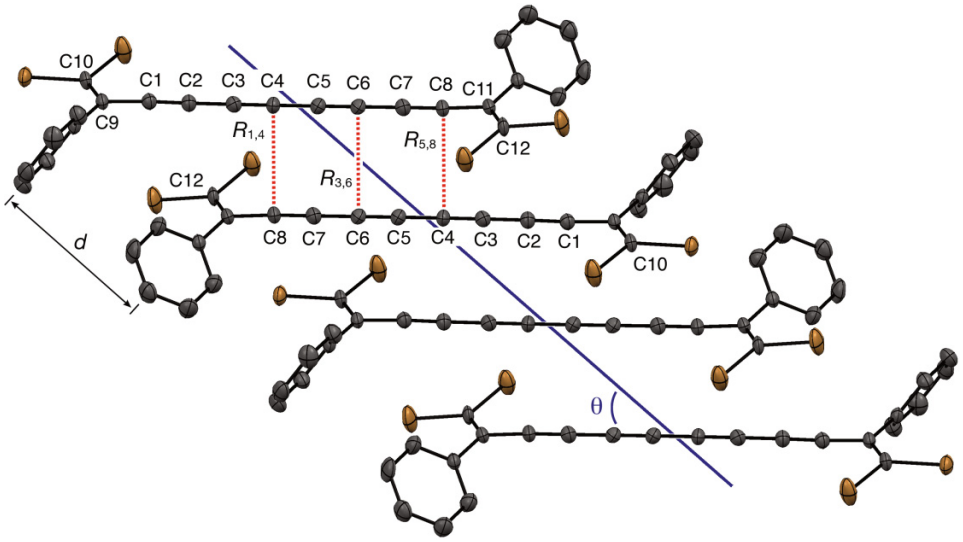


Fig. 9. ORTEP drawing (50% probability level) of **6a** showing a segment of the crystal packing. Geometry parameters: θ = 42°, $R_{1,4}$ = 3.4 Å, $R_{3,6}$ = 3.4 Å, $R_{5,8}$ = 3.4 Å, and d = 5.1 Å. (Note: The numbering of the carbon chain corresponds to the structural characterization listed in Tables 3 and 4, whereas the numbering for $R_{1,4}$, $R_{3,6}$, and $R_{5,8}$ refers to reactivity patterns from Fig. 1.)



on the other hand, shows an initial broad, weak exotherm with an onset at about 190 °C, and a second, sharp exotherm that initiates at about 230 °C, with a maximum at 233 °C (see the Supplementary data).

X-ray quality crystals of **6c** were obtained via the diffusion of hexanes into a solution of **6c** in hexanes/CH_2Cl_2 at –4 °C. The solid-state structure of **6c** (Fig. 10 and Tables 3 and 4) reveals that the terminal acetylene angles C(5)–C(1)–C(2) are the most distorted at 175.9(3)°. The enyne framework of the centrosymmetric structure is completely planar, whereas the aryl rings twist significantly from this plane by 65°. Analysis of the crystal packing shows that neighbouring molecules of compound **6c** are aligned in a parallel fashion, and the packing parameters for **6c** are similar to that observed for **6a**, with θ = 38°, $R_{1,4}$ = 3.8 Å, $R_{3,6}$ = 3.7 Å, $R_{5,8}$ = 3.8 Å, and d = 5.9 Å. Thus, packing parameters are suboptimal for either 1,4- or 1,6-polymerization, and thermal analysis of this compound has not been further explored.

Tetrayne 6d

DSC analysis of the nitro-derivative **6d** shows a very sharp exotherm at 191 °C (T_{onset} = 189 °C and T_{max} = 191 °C, see the Supplementary data). **Warning:** An explosion occurred at approximately 190 °C when heating a small quantity of compound **6d** (60 mg) in a capped tightly packed solid-state NMR rotor. When handling any polyyne, one should always take the appropriate safety precautions when the sample is heated above room temperature. This is particularly true if the sample is a terminal polyyne, where precautions should be taken at all temperatures.

Single crystals of **6d** for analysis by X-ray crystallography were obtained via the evaporation of a $CDCl_3$ or $CHCl_3$

Can. J. Chem. Downloaded from www.nrcresearchpress.com by MCGILL UNIVERSITY on 02/02/13
For personal use only.

Fig. 10. ORTEP drawing (50% probability level) of **6c** showing a segment of the crystal packing. Geometry parameters: θ = 38°, $R_{1,4}$ = 3.8 Å, $R_{3,6}$ = 3.7 Å, $R_{5,8}$ = 3.8 Å, and d = 5.9 Å. (Note: The numbering of the carbon chain corresponds to the structural characterization listed in Tables 3 and 4, whereas the numbering for $R_{1,4}$, $R_{3,6}$, and $R_{5,8}$ refers to reactivity patterns from Fig. 1.)

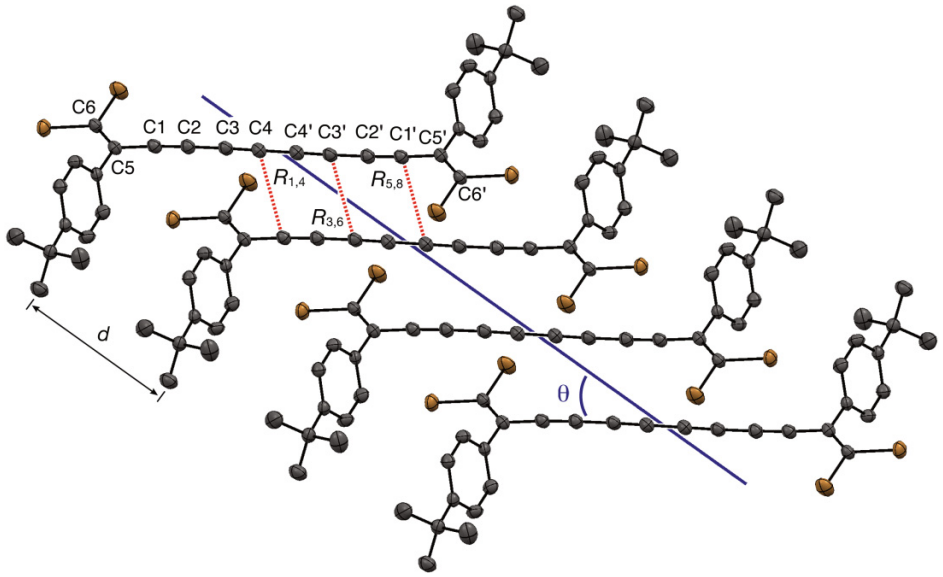
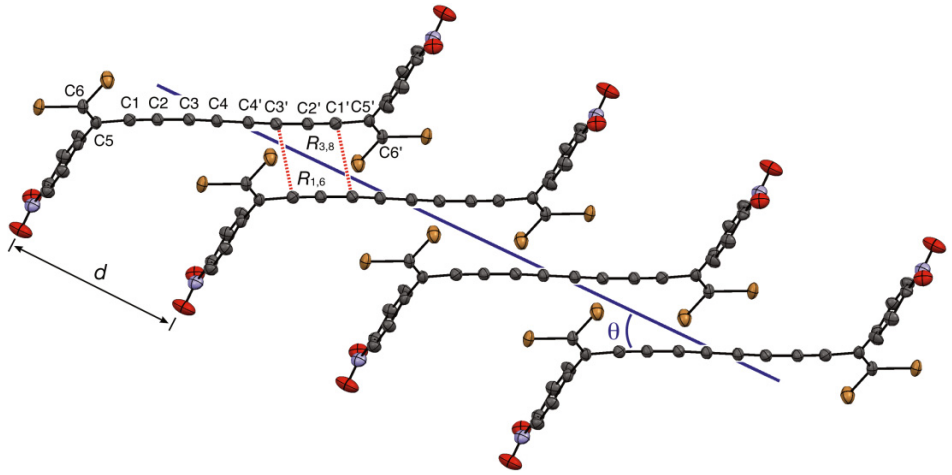


Fig. 11. ORTEP drawing (50% probability level) of **6d** showing a segment of crystal packing. Geometry parameters: θ = 29°, $R_{1,6}$ = 3.5 Å, $R_{3,8}$ = 3.5 Å, and d = 7.5 Å. (Note: The numbering of the carbon chain corresponds to the structural characterization listed in Tables 3 and 4, whereas the numbering for $R_{1,6}$ and $R_{3,8}$ refers to reactivity patterns from Fig. 1.)



solution at −4 °C (Fig. 11). As with **6a** and **6c** (Table 4), the terminal C(5)–C(1)–C(2) bond angle of **6d** is the most distorted from linearity at 174.3(4)°, and the centrosymmetric enyne framework is planar. Molecules of compound **6d** are packed in parallel stacks, and the distance separating reactive atoms of adjacent molecules is $R_{1,6}$ = $R_{3,8}$ = 3.5 Å. The translational distance (d) is 7.5 Å, with a packing angle (θ) of 29°. These values are thus ideal for a 1,6-topochemical polymerization.

The UV–vis absorption spectrum of compound **6d** has been measured in the solid state (Fig. 12) for a thin film produced by casting a solution of compound **6d** in CH_2Cl_2 onto a quartz slide and allowing the solvent to evaporate. The UV–vis spectrum of the film shows absorbance values of 368, 400, and 434 nm, which are somewhat red-shifted from those for the sample in solution (359, 384, and 419 nm in THF). As the thin film is then heated at 170 °C under an argon atmosphere for 17 h, UV–vis absorption spectra have been examined at various time intervals (Fig. 12). After heating for 1 h, the intensity of the three low-energy absorbances decreases, and λ_{max} values are slightly blue-shifted to 365, 397, and 430 nm. After heating for 5 h, only two distinct signals remain in the low-energy region at ~393 and 424 nm, and these two signals finally merge into one broad signal after heating for a total of 17 h. Rather surprisingly, this analysis implies that the conjugated ene–tetrayne–ene framework is transformed into a *less conjugated* product, rather than one with extended conjugation as would be expected upon formation of a polytriacetylene product (Fig. 13).

Can. J. Chem. Downloaded from www.nrcresearchpress.com by MCGILL UNIVERSITY on 02/02/13
For personal use only.

Can. J. Chem. Downloaded from www.nrcresearchpress.com by MCGILL UNIVERSITY on 02/02/13
For personal use only.

Fig. 12. Solid-state UV–vis spectra for compound **6d** before and after heating at 170 °C for the times given.

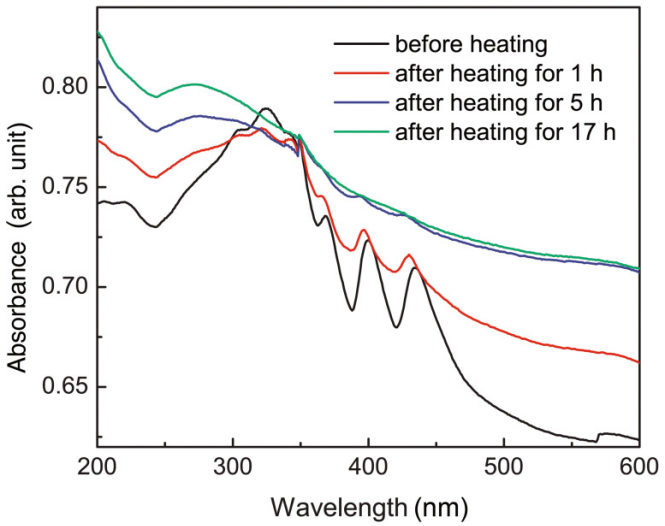
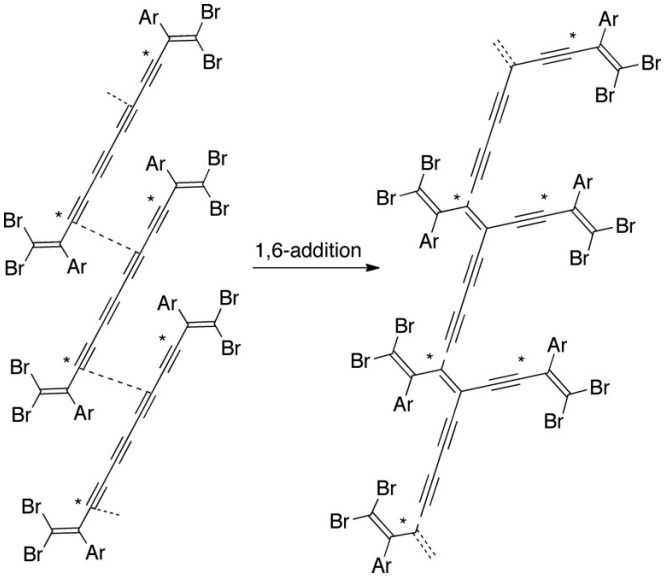
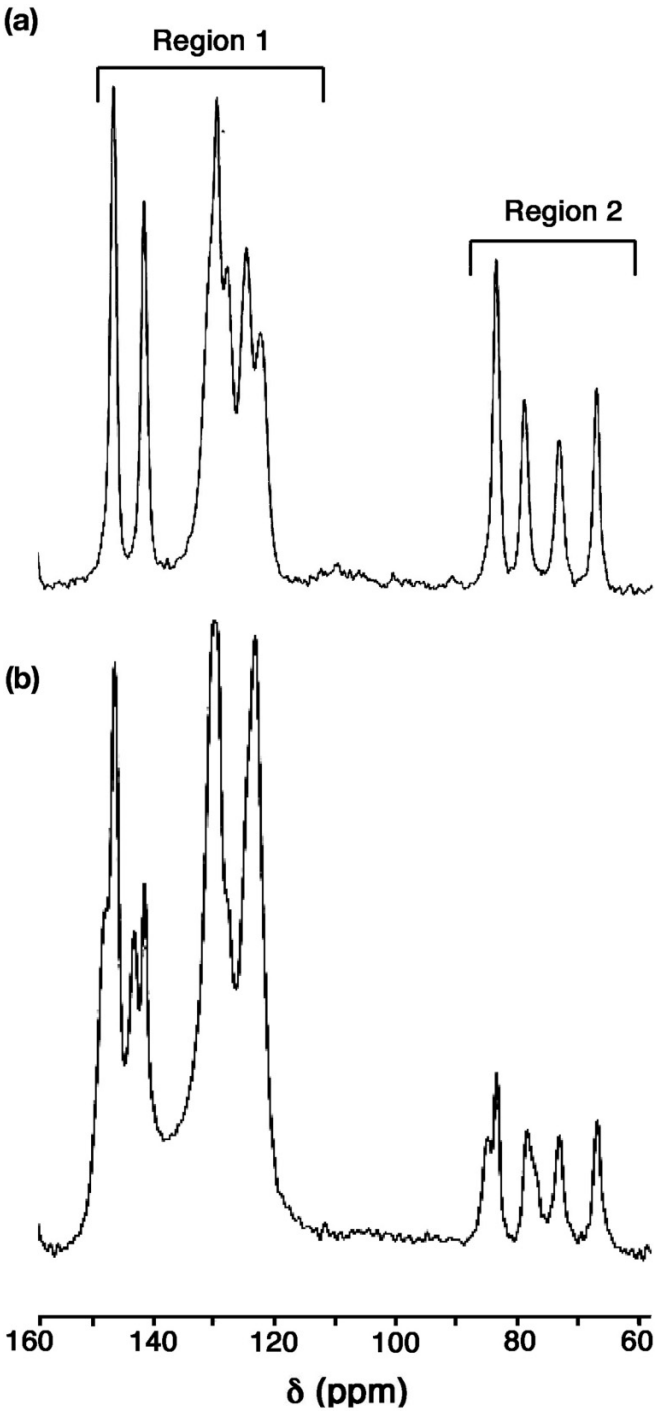


Fig. 13. Idealized structure resulting from 1,6-polymerization of **6d** or labelled **6d/6d*/6d**** (* indicates ^{13}C atoms).



Thermal polymerization of **6d** has been explored by heating a crystalline sample to 170 °C under argon (see the previous warning for compound **6d**). Attempts to analyze the resulting sample by solution-state ^{1}H and ^{13}C NMR spectroscopy show that the resulting polymer is insoluble, and useful spectra could not be obtained. Solid-state ^{13}C NMR spectroscopy has therefore been used to explore the thermal transformation of **6d** (Fig. 14). In the pristine sample, four aromatic and two alkenyl signals are observed in region 1 (Fig. 14, 120–150 ppm). These resonances are found at similar chemical shifts as in solution, except for the α-vinyl signal ($Br_2C{=}C<$), which appears downfield from its solution value of 107.5 ppm. The alkynyl peaks appear in region 2 (Fig. 14, 60–90 ppm), and chemical shifts for the four distinct signals (67, 73, 79, and 84 ppm) correlate well with those found in the solution-state

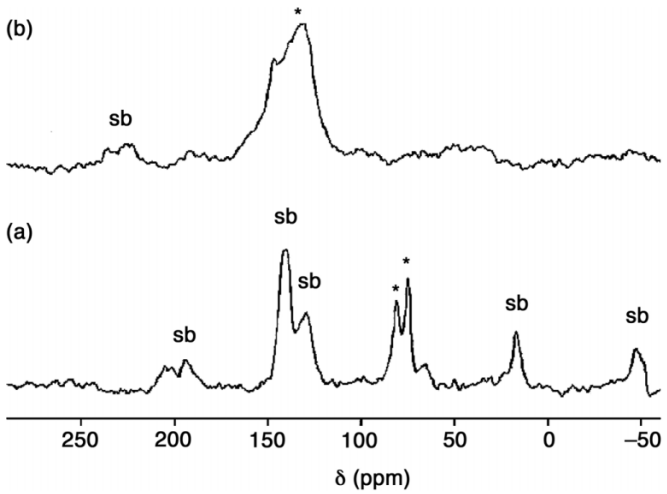
Fig. 14. Solid-state ^{13}C NMR spectra of compound **6d** (*a*) before heating and (*b*) after heating at 170 °C for 6 h under argon.



spectrum at 64.8, 71.2, 75.9, and 82.6 ppm. After heating the solid at 170 °C under an Ar atmosphere for 6 h, both downfield signals in region 1 (Fig. 14, 142 and 147 ppm) appear to split into two signals, while the remaining two signals in region 1 broaden somewhat. Signals in region 2 follow a similar pattern, where two signals (79 and 84 ppm) seemingly split and those at 67 and 73 ppm broaden slightly. Furthermore, the intensity of all alkyne signals in region 2 decreases noticeably

Can. J. Chem. Downloaded from www.nrcresearchpress.com by MCGILL UNIVERSITY on 02/02/13
For personal use only.

Fig. 15. Solid-state ^{13}C NMR spectra for compound **6d/6d*/6d****. (*a*) Before heating. (*b*) After heating (sb, spinning side band; *, labelled ^{13}C signal). Spectra were acquired at 11.75 T (125 MHz for ^{13}C) using CP/MAS and a spinning frequency of 8 kHz. Spectra acquired at various spinning frequencies (not shown) confirmed that the peaks in the 100–150 ppm region in (*a*) arise primarily from spinning sidebands.



relative to those in region 1. The spectral changes in regions 1 and 2 for the spectrum acquired after heating suggest a loss of molecular symmetry, which is evidence for polymerization as shown for the idealized transformation outlined in Fig. 13. Unfortunately, it is once again not clear if the reaction proceeds via a 1,6-addition process as suggested by X-ray crystallographic analysis or via an alternative pathway.

Crystals of partially labelled tetrayne sample **6d/6d*/6d**** could be obtained, but unfortunately only on a small scale, giving a total sample amount of ~1 mg. X-ray crystallography has established that the solid-state geometric packing of this sample is identical to that of unlabelled **6d**. A solid-state ^{13}C NMR spectrum of **6d/6d*/6d**** was acquired at 11.75 T (125 MHz for ^{13}C) using cross-polarization/magic-angle spinning (CP/MAS) and a spinning frequency of 8 kHz (Fig. 15). In the pristine sample, two strong signals are observed at 75.4 and 81.5 ppm owing to the presence of ^{13}C labelling. This is surprising given that the solid-state structure of **6d** is expected to be centrosymmetric based on the crystallographic analysis, and only a single resonance for the labelled carbon is observed in solution (75.6 ppm; see the Supplementary data). The origin of the second signal is, at present, unexplained. Unfortunately, spinning side bands are also quite intense. After heating the sample holder containing compound **6d/6d*/6d**** at 170 °C under Ar for 3 days, the resulting spectrum shows the enhanced ^{13}C signals at ~130 and 142 ppm, characteristic of sp^2-hybridized carbon atoms. At first sight, this result is inconsistent with the analysis of unlabelled **6d** for which alkyne signals are still observed after heating (Fig. 14). It is likely, however, that the extended heating time for **6d/6d*/6d**** at 170 °C (3 days) versus that of **6d** (6 h) results in additional and nonselective reactions, ultimately giving a material composed primarily of sp^2-hybridized carbon. Thus, compound **6d/6d*/6d**** may undergo a 1,6-topochemical polymerization, but the structure of the final product, frustratingly, remains unsolved.

Conclusions

We have described the synthesis of functionalized, cross-conjugated tetraynes. UV–vis spectroscopic analysis shows that the electronic characteristics of the tetrayne moiety dominate the lower energy absorption region, and the side groups, either electron-donating or electron-withdrawing, have only a marginal influence on the absorption energy of the central tetrayne chromophore. The solid-state structural properties of five derivatives have been examined by X-ray crystallographic analysis. Examination of the crystal structures with an eye toward inducing solid-state reactions shows that the packing parameters (θ, *R*, and *d*) for all but **6c** fall within a range suitable for topochemical polymerization, and the values for three (**1k**, **1l**, and **6d**) are quite close to the values ideal for a 1,6-polymerization. To our knowledge, this is the first series of structurally similar tetraynes that shows a consistent packing motif conducive to topochemical polymerization. In addition to X-ray crystallography, DSC analysis also supports the prospect of a viable polymerization reaction toward a defined product in many cases. Thus, the polymerization of tetraynes has been explored using thermal, photochemical, and (or) γ-irradiation for initiation. Furthermore, the thermally induced solid-state reaction of **1d**, **1j**, **1k**, and **6d** has been studied in more detail via solid-state ^{13}C NMR spectroscopy. In all cases, however, it has been frustratingly difficult to ascertain the structure of the product, often owing to broadening of the observed resonances in the ^{13}C spectra, presumably because of a regiorandom polymerization reaction.

Our inability to effect clean polymerization of these crystallized samples is the most significant outcome of this study. A survey of reports for topochemical polymerization of diynes shows that there is typically a good correlation between packing parameters and successful polymerization to a polydiacetylene product. Combined with reports of successful polymerization of polyynes as described in the Introduction, this leads to the naïve assumption that the controlled polymerization of polyynes might also be predicted based on solid-state packing. But the story is not so simple, and it is now quite obvious to conclude that the successful polymerization of tetraynes is far more complex than a simple analysis of solid-state packing parameters θ, *R*, and *d*.

Experimental section

Irradiation with ^{60}Co

Single crystals of either **4k** or **4l** were placed into a glass vial and subjected to the irradiation from a ^{60}Co source (~54 ± 3 krad/h, previously located at the Chemistry Department, University of Alberta, Edmonton, Alberta) for 2 weeks at room temperature. After irradiation, the colours of the crystals became slightly darker and the crystals were re-examined by X-ray single crystal diffraction analysis.

X-ray crystallographic data

Data for 1k

Single crystals of **1k** were obtained via the diffusion of methanol into an Et_2O solution at –4 °C. Formula $C_{40}H_{30}Fe_2$, fw = 622.34; monoclinic crystal system, space group $P2_1/c$ (No. 14); a = 18.075(3) Å, b = 7.4082(11) Å, c = 11.7293(16) Å; β = 103.751(3)°; V = 1525.6(4) Å^3; Z = 2; $\rho_{(calcd.)}$ = 1.355 g cm^{-3}; $2\theta_{max}$ = 52.80°; μ = 0.978 mm^{-1};

Can. J. Chem. Downloaded from www.nrcresearchpress.com by MCGILL UNIVERSITY on 02/02/13
For personal use only.

$T = -80$ °C; total data collected = 7305. Final $R_1(F) = 0.0562$ (1455 observed reflections with $F_o^2 \geq 2\sigma(F_o^2)$); $wR_2(F^2) = 0.0901$ for 212 variables, 3133 unique reflections, and 0 restraints; residual electron density = 0.326 and −0.327 e Å^{-3}. CCDC 862755.

Data for 1l

Single crystals of **1l** were obtained via the diffusion of MeOH into a CH_2Cl_2 solution at –20 °C (as reported in ref. 27). Formula $C_{38}H_{54}Si_2$, fw = 566.99; monoclinic crystal system, space group $P2_1/c$ (No. 14); a = 13.5571(8) Å, b = 7.7132(5) Å, c = 35.616(2) Å; β = 96.5990(10)°; V = 3699.7(4) Å^3; Z = 4; $\rho_{(calcd.)}$ = 1.018 g cm^{-3}; $2\theta_{max}$ = 51.50°; μ = 0.118 mm^{-1}; $T = -80$ °C; total data collected = 19122. Final $R_1(F) = 0.0472$ (4842 observed reflections with $F_o^2 \geq 2\sigma(F_o^2)$); $wR_2(F^2) = 0.1366$ for 365 variables, 7039 unique reflections, and 0 restraints; residual electron density = 0.389 and −0.235 e Å^{-3}. CCDC HOZSAQ.

Data for 6a

Single crystals of **6a** were obtained via the diffusion of hexanes into a solution of hexanes/CH_2Cl_2 at −4 °C. Formula $C_{24}H_{10}Br_4$, fw = 617.96; triclinic crystal system, space group $P\bar{1}$ (No. 2); a = 9.4512(7) Å, b = 10.1187(7) Å, c = 11.6133(8) Å; α = 96.0941(13)°, β = 92.5663(13)°, γ = 103.4569(13)°; V = 1071.25(13) Å^3; Z = 2; $\rho_{(calcd.)}$ = 1.916 g cm^{-3}; $2\theta_{max}$ = 52.76°; μ = 7.521 mm^{-1}; $T = -80$ °C; total data collected = 7878. R_1 = 0.0368 (3413 observed reflections with $F_o^2 \geq 2\sigma(F_o^2)$); wR_2 = 0.0930 for 253 variables, 4356 unique reflections, and 0 restraints; residual electron density = 1.164 and −0.586 e Å^{-3}. CCDC 862756.

Data for 6c

Single crystals of **6c** were obtained via the diffusion of hexanes into a solution of hexanes/CH_2Cl_2 at −4 °C. Formula $C_{32}H_{26}Br_4$, fw = 730.17; triclinic crystal system, space group $P\bar{1}$ (No. 2); a = 5.8968(7) Å, b = 11.1037(14) Å, c = 11.9247(15) Å; α = 69.2510(17)°, β = 78.1507(18)°, γ = 86.0880(19)°; V = 714.58(15) Å^3; Z = 1; $\rho_{(calcd.)}$ = 1.697 g cm^{-3}; $2\theta_{max}$ = 52.74°; μ = 5.651 mm^{-1}; $T = -80$ °C; total data collected = 5606. R_1 = 0.0342 (2418 observed reflections with $F_o^2 \geq 2\sigma(F_o^2)$); wR_2 = 0.0905 for 163 variables, 2911 unique reflections, and 0 restraints; residual electron density = 0.618 and −0.492 e Å^{-3}. CCDC 862758.

Data for 6d

Single crystals of **6c** were obtained via the evaporation of a $CDCl_3$ solution at −4 °C. Formula $C_{24}H_8Br_4N_2O_4$, fw = 707.96; orthorhombic crystal system, space group *Pbcn* (No. 60); a = 7.5156(7) Å, b = 14.8934(14) Å, c = 21.328(2) Å; V = 2387.3(4) Å^3; Z = 4; $\rho_{(calcd.)}$ = 1.970 g cm^{-3}; $2\theta_{max}$ = 52.82°; μ = 6.777 mm^{-1}; $T = -80$ °C; total data collected = 14313. R_1 = 0.0322 (1968 observed reflections with $F_o^2 \geq 2\sigma(F_o^2)$); wR_2 = 0.0825 for 154 variables, 2461 unique reflections, and 0 restraints; residual electron density = 1.129 and −0.406 e Å^{-3}. CCDC 862757.

Synthetic and spectroscopic details

General experimental details

Column chromatography: silica gel 60 (230–400 mesh) from General Intermediates of Canada. Thin-layer chromatography (TLC): aluminium sheet coated with silica gel F_{254} from Whatman; visualization by UV light or $KMnO_4$ stain. Melting point: Fisher-Johns or Gallenkamp apparatus; uncorrected. UV–vis spectra: Varian Cary 400 at rt; λ in nm (ε in L mol^{-1} cm^{-1}). IR spectra (cm^{-1}): Nicolet Magna-IR 750 (neat) or Nic-Plan IR microscope (solids). ^{1}H and ^{13}C solution-state NMR: Varian 300, 400, 500, or 600 and Bruker AM-300 instruments, at rt in $CDCl_3$; solvent peaks (7.24 ppm for ^{1}H and 77.0 ppm for ^{13}C) as reference. For simplicity, the coupling constants of the aryl protons have been reported as pseudo-first-order, even though they are AA′BB′ second-order spin systems; coupling constants are reported as observed. ^{13}C solid-state NMR: CMX Infinity 200 as well as Bruker Avance 300 and 500 spectrometers operating at 50, 75, and 125 MHz, respectively, for ^{13}C. Samples were packed in 4 mm outside diameter (o.d.) MAS rotors spinning at frequencies ranging from 5 to 12 kHz. All spectra were acquired with cross polarization using contact times of 1.0–6.0 ms, ^{1}H 90° pulses of 2.5–4.0 μs, and recycle delays of 3.0–10.0 s. To improve decoupling efficiency, the two-pulse phase modulated (TPPM) sequence of Griffin and co-workers[46] was used. Spectra were referenced to tetramethylsilane (TMS; δ = 0) by setting the high-frequency peak of adamantine to 38.56 ppm.[47] EI-MS (*m*/*z*): Kratos MS 50 instrument. ESI-MS (*m*/*z*): Micromass Zabspec oaTOF or PE Biosystems Mariner TOF instruments. Elemental analyses were performed by the Microanalytical Service, Department of Chemistry, University of Alberta.

General methods

Reagents and solvents were purchased reagent grade and used without further purification. Compounds **2**,[29] **3b**,[48] **3g**,[49] **3k**,[50] **10a**–**10c**,[31] and **11**[35] were prepared based on literature precedent. Anhydrous $MgSO_4$ was used as the drying agent after aqueous workup. Evaporation and concentration in vacuo was done at H_2O-aspirator pressure. All reactions were performed in standard glassware under an inert atmosphere of Ar or N_2. A positive pressure of Ar or N_2 was essential to the success of all Pd-catalyzed reactions. Deoxygenation of solvents was accomplished by vigorously bubbling Ar or N_2 through the solution at rt for ~30 min. Brine refers to a saturated aqueous solution of NaCl. Flash chromatography was conducted on silica gel using the eluent system defined in the individual experimental procedures.

For mass spectrometric analyses, low-resolution data are provided in cases when M^+ is not the base peak; otherwise, only high-resolution data are provided. The samples for ESI mass spectrometry were typically dissolved in $ClCH_2CH_2Cl$ and made use of a 3:1 MeOH/toluene mixture as the carrier solvent.

DSC measurements were measured on a PerkinElmer Pyris 1 DSC instrument. Melting points from DSC analysis are reported as the peak maxima, and in cases when the sample decomposed, the onset temperature of the decomposition exothermic peak is reported, as well as the exothermic maxima corresponding to the decomposition.

Formation of the Hay catalyst was conducted as follows: CuI (50 mg) and tetramethylethylenediamine (TMEDA, 75 mg) were added to CH_2Cl_2 (2 mL) and stirred until homogeneous; this solution was prepared fresh for each reaction. Wet THF/MeOH refers to the use of THF and MeOH that have not been previously dried by distillation, i.e., the solvent is

Can. J. Chem. Downloaded from www.nrcresearchpress.com by MCGILL UNIVERSITY on 02/02/13
For personal use only.

used "straight out of the bottle" and is assumed to contain a small amount of water.

General procedure A — Desilylation procedure

To the appropriate trimethylsilyl polyyne in wet THF/MeOH (1:1, 20 mL) was added K_2CO_3 (~20 mg), and the resulting mixture was stirred at rt until TLC indicated the starting material had been consumed (~2 h). Ether (50 mL) and saturated aq NH_4Cl (50 mL) were added, the organic phase separated, washed with saturated aq NH_4Cl (2 × 50 mL), dried over $MgSO_4$, and filtered. The solvent was then reduced to ~1 mL via rotary evaporation, taking care to ensure that the product remained in solution during the concentration process. The resulting solution was carried on to the next step.

General procedure B — Palladium-catalyzed cross-coupling procedure

The appropriate alkyne **3** was added to a solution of vinyl triflate **2** in THF (20 mL) and the resulting mixture deoxygenated. $PdCl_2(PPh_3)_2$ (~0.05 equiv) and *i*-Pr_2NH were sequentially added, the solution was stirred for 5 min, CuI (~0.15 equiv) was added, and the solution was stirred under conditions described in the individual procedures, typically until TLC analysis no longer showed the presence of either **2** or **3**. Ether (40 mL) and H_2O (30 mL) were then added, the organic phase separated, washed with saturated aq NH_4Cl (2 × 50 mL), dried over $MgSO_4$, filtered, and the filtrate concentrated in vacuo. Flash column chromatography and (or) precipitation from MeOH gave the desired enyne oligomer.

General procedure C — Copper-catalyzed oxidative acetylenic-coupling procedure

The terminal acetylene from general procedure A was added to acetone (10 mL), acetone/CH_2Cl_2 (1:1, 10 mL), or CH_2Cl_2 (60 mL). A solution of Hay catalyst mixture (1 mL) was then added. The mixture was stirred at rt under air until TLC analysis no longer showed the deprotected polyyne (generally less than 0.5 h). The reaction solution was concentrated in vacuo to ~5 mL and diethyl ether (50 mL) was added. The ethereal solution was consecutively washed with a 10% HCl solution (25 mL), saturated aq $NaHCO_3$ (25 mL), and brine (25 mL), dried, and the solvent removed. Flash column chromatography and (or) precipitation from MeOH gave the product **1** or **6**.

Compound **1a**

Compound **4a** (66 mg, 0.26 mmol) was desilylated with K_2CO_3 in MeOH/THF (1:1) as described in general procedure A, and homocoupled in acetone (10 mL) in the presence of Hay catalyst (1 mL) and air for 1 h as described in general procedure C. Flash chromatography (hexane/CH_2Cl_2, 2:1) afforded **1a** (45 mg, 94%) as a brown oil that slowly decomposed over a period of hours to days when stored neat. R_f = 0.78 (hexane/CH_2Cl_2, 2:1). UV–vis ($CHCl_3$) λ_{max} (ε): 302 (57 800), 320 (41 700), 348 (17 100), 374 (18 800), 405 (11 800). IR ($CHCl_3$, cast, cm^{-1}): 2958, 2932, 2872, 2193, 2125, 1959, 1587. ^1H NMR (300 MHz, $CDCl_3$) δ: 2.33 (t, J = 6.6 Hz, 4H), 2.02 (s, 6H), 2.01 (s, 6H), 1.54–1.36 (m, 8H), 0.90 (t, J = 7.2 Hz, 6H). ^{13}C NMR (75 MHz, $CDCl_3$, APT) δ: 159.7, 100.5, 94.2, 75.7, 75.8, 75.5, 67.7, 64.0, 30.8, 23.1, 23.0, 22.0, 19.2, 13.6. EI HR-MS calcd for $C_{28}H_{30}$ (M^+): 366.2347; found: 366.2349.

Compound **1b**

Compound **4b** (20 mg, 0.035 mmol) was desilylated with K_2CO_3 in MeOH/THF (1:1) as described in general procedure A, and homocoupled in acetone (10 mL) in the presence of Hay catalyst (1 mL) and air for 0.5 h as described in general procedure C. Flash chromatography (hexane / ethyl acetate, 1:5) afforded **1b** (16 mg, 91%) as a brown solid; mp 57–62 °C. R_f = 0.62 (hexane / ethyl acetate, 1:5). IR (CH_2Cl_2, cast, cm^{-1}): 2934, 2193, 1750, 1587, 1433. ^1H NMR (600 MHz, $CDCl_3$) δ: 5.51 (d, J = 3.5 Hz, 2H), 5.28 (t, J = 10.1 Hz, 2H), 5.09 (dd, J = 10.1 Hz, J = 3.5 Hz, 2H), 5.02 (s, 2H), 4.29 (dd, J = 12.3 Hz, J = 5.7 Hz, 2H), 4.13 (dd, J = 12.3 Hz, J = 2.4 Hz, 2H), 3.73 (d, J = 17.0 Hz, 4H), 3.71 (m, 2H), 3.43 (d, J = 17.0 Hz, 4H), 2.16 (s, 6H), 2.07 (s, 12 H), 2.04 (s, 12H), 1.97 (s, 6H). ^{13}C NMR (75 MHz, $CDCl_3$, APT) δ: 170.7, 170.1, 170.0, 169.7, 162.3, 99.7, 87.6, 80.9, 76.9, 76.4, 75.1, 72.1, 70.2, 69.6, 68.1, 65.8, 62.6, 31.8, 29.3, 23.4, 23.2, 20.80, 20.75, 20.66, 20.6. ESI-MS m/z (MeOH): 1029.3 ([M + Na]$^+$).

Compound **1c**

Compound **4c** (68 mg, 0.24 mmol) was desilylated with K_2CO_3 in MeOH/THF (1:1) as described in general procedure A, and homocoupled in acetone (10 mL) in the presence of Hay catalyst (1 mL) and air for 0.5 h as described in general procedure C. Flash chromatography (hexane/CH_2Cl_2, 2:1) afforded **1c** (32 mg, 66%) as a yellow waxy solid. R_f = 0.61 (hexane/CH_2Cl_2, 2:1). UV–vis ($CHCl_3$) λ_{max} (ε): 282 (91 200), 296 (82 100), 322 (41 900), 349 (18 600), 374 (19 900), 405 (11 800). IR (μscope, cm^{-1}): 3057, 2930, 2906, 2194, 2127, 1598, 1583, 1490, 1443. ^1H NMR (300 MHz, $CDCl_3$) δ: 7.46–7.42 (m, 4H), 7.32–7.28 (m, 6H), 2.13 (s, 6H), 2.12 (s, 6H). ^{13}C NMR (75 MHz, $CDCl_3$, APT) δ: 161.5, 131.5, 128.5, 128.4, 122.9, 100.4, 92.9, 84.4, 76.4, 75.0, 67.9, 64.1, 23.4, 23.3. EI HR-MS calcd for $C_{32}H_{22}$ (M^+): 406.1722; found: 406.1728.

Compound **1d**

Compound **4d** (88 mg, 0.27 mmol) was desilylated with K_2CO_3 in MeOH/THF (1:1) as described in general procedure A, and homocoupled in acetone (10 mL) in the presence of Hay catalyst (1 mL) and air for 0.5 h as described in general procedure C. Flash chromatography (hexane/CH_2Cl_2, 2:1) afforded **1d** (64 mg, 95%) as a yellow solid; mp > 115 °C (dec). R_f = 0.57 (hexane/CH_2Cl_2, 2:1). UV–vis ($CHCl_3$) λ_{max} (ε): 287 (66 700), 306 (90 400), 323 (83 700), 349 (50 200), 374 (39 800), 405 (15 900). IR (μscope, cm^{-1}): 3104, 2932, 2847, 2198, 2128, 1594, 1520, 1491, 1432, 1343. ^1H NMR (400 MHz, $CDCl_3$) δ: 8.17 (d, J = 8.8 Hz, 4H), 7.57 (d, J = 8.8 Hz, 4H), 2.149 (s, 6H), 2.146 (s, 6H). ^{13}C NMR (100 MHz, $CDCl_3$, APT) δ: 163.9, 147.1, 132.1, 129.7, 123.6, 99.9, 90.8, 89.5, 76.7, 74.2, 68.1, 63.9, 23.54, 23.47. EI HR-MS calcd for $C_{32}H_{20}N_2O_4$ (M^+): 496.1423; found: 496.1425. DSC: decomposition 172 °C (onset), 193 °C (peak).

Compound **1e**

Compound **4e** (53 mg, 0.16 mmol) was desilylated with K_2CO_3 in MeOH/THF (1:1) as described in general procedure A, and homocoupled in acetone (10 mL) in the presence of Hay catalyst (1 mL) and air for 2 h as described in general procedure C. Flash chromatography (hexane/CH_2Cl_2, 2:1) afforded **1e** (11 mg, 27%) as a yellow waxy semisolid that

Can. J. Chem. Downloaded from www.nrcresearchpress.com by MCGILL UNIVERSITY on 02/02/13
For personal use only.

slowly decomposed over a period of hours to days. R_f = 0.28 (hexane/CH_2Cl_2, 2:1). UV–vis ($CHCl_3$) λ_{max} (ε): 283 (72 300), 304 (63 000), 323 (52 600), 349 (28 500), 374 (27 000), 405 (14 700). IR (μscope, cm^{-1}): 2927, 2200, 1608, 1567, 1528, 1479, 1438, 1336. ^1H NMR (400 MHz, $CDCl_3$) δ: 8.06 (dd, J = 8.0, 1.2 Hz, 2H), 7.66 (dd, J = 8.0, 1.6 Hz, 2H), 7.57 (td, J = 8.0, 1.2 Hz, 2H), 7.44 (td, J = 8.0, 1.6 Hz, 2H), 2.22 (s, 6H), 2.15 (s, 6H). ^{13}C NMR (100 MHz, $CDCl_3$, APT) δ: 165.0, 149.0, 134.7, 132.9, 128.7, 124.7, 118.5, 100.1, 92.2, 88.0, 76.6, 74.3, 68.0, 64.0, 23.6, 23.5. EI HR-MS calcd for $C_{32}H_{20}N_2O_4$ (M^+): 496.1423; found: 496.1419.

***Compound* 1f**

Compound **4f** (77 mg, 0.24 mmol) was desilylated with K_2CO_3 in MeOH/THF (1:1) as described in general procedure A, and homocoupled in acetone (10 mL) in the presence of Hay catalyst (1 mL) and air for 0.5 h as described in general procedure C. Flash chromatography (hexane/CH_2Cl_2, 2:1) afforded **1f** (23 mg, 39%) as a yellow waxy semisolid that slowly decomposed over a period of hours to days. R_f = 0.4 (hexane/CH_2Cl_2, 2:1). UV–vis ($CHCl_3$) λ_{max} (ε): 280 (98 100), 299 (87 500), 320 (54 200), 348 (20 100), 374 (21 400), 405 (13 300). IR (CH_2Cl_2, cast, cm^{-1}): 3087, 2197, 1536, 1346. ^1H NMR (300 MHz, $CDCl_3$) δ: 8.28–8.27 (m, 2H), 8.17–8.13 (m, 2H), 7.75–7.72 (m, 2H), 7.49 (t, J = 8.1 Hz, 2H), 2.152 (s, 6H), 2.146 (s, 6H). ^{13}C NMR (75 MHz, $CDCl_3$, APT) δ: 163.4, 148.2, 137.1, 129.4, 126.3, 124.8, 123.1, 99.9, 90.2, 86.9, 74.3, 68.1, 64.0, 23.6, 23.5 (one coincident peak not observed). EI HR-MS calcd for $C_{32}H_{20}N_2O_4$ (M^+): 496.1423; found: 496.1409.

***Compound* 1h**

Compound **4h** (40 mg, 0.13 mmol) was desilylated with K_2CO_3 in MeOH/THF (1:1) as described in general procedure A, and homocoupled in acetone (10 mL) in the presence of Hay catalyst (1 mL) and air for 0.5 h as described in general procedure C. Flash chromatography (hexane/CH_2Cl_2, 2:1) afforded **1h** (22 mg, 74%) as a yellow waxy semisolid that slowly decomposed over a period of hours to days when stored neat. R_f = 0.63 (hexane/CH_2Cl_2, 2:1). UV–vis ($CHCl_3$) λ_{max} (ε): 300 (104 400), 323 (69 600), 348 (17 600), 374 (17 700), 405 (9 700). IR (CH_2Cl_2, cast, cm^{-1}): 2228, 2194, 2126, 1959, 1603, 1450, 1432. ^1H NMR (300 MHz, $CDCl_3$) δ: 7.59 (d, J = 8.4 Hz, 4H), 7.51 (d, J = 8.4 Hz, 4H), 2.14 (s, 12H). ^{13}C NMR (75 MHz, $CDCl_3$, APT) δ: 163.6, 132.1, 132.0, 127.8, 118.5, 111.8, 100.0, 91.1, 88.7, 76.7, 74.3, 68.1, 64.0, 23.6, 23.5. EI HR-MS calcd for $C_{34}H_{20}N_2$ (M^+): 456.1627; found: 456.1629.

***Compound* 1i**

Compound **4i** (93 mg, 0.26 mmol) was desilylated with K_2CO_3 in MeOH/THF (1:1) as described in general procedure A, and homocoupled in acetone/CH_2Cl_2 (1:1; 10 mL) in the presence of Hay catalyst (1 mL) and air for 0.5 h as described in general procedure C. Flash chromatography (hexane/CH_2Cl_2, 2:1) afforded **1i** (63 mg, 85%) as a yellow solid; mp > 110 °C (dec). R_f = 0.21 (hexane/CH_2Cl_2, 2:1). UV–vis ($CHCl_3$) λ_{max} (ε): 288 (104 300), 322 (49 000), 349 (17 600), 375 (20 100), 406 (12 200). IR (CH_2Cl_2, cast, cm^{-1}): 2198, 1589, 1485, 1425. ^1H NMR (400 MHz, $CDCl_3$) δ: 7.43 (d, J = 8.8 Hz, 4H), 7.29 (d, J = 8.8 Hz, 4H), 2.11 (s, 12H). ^{13}C NMR (100 MHz, $CDCl_3$, APT) δ: 162.0, 132.8, 131.6, 122.7, 121.8, 100.2, 91.7, 85.4, 76.4, 74.7, 67.9, 64.0, 23.4, 23.3. ESI HR-MS (MeOH/toluene, 1:1) calcd for $C_{32}H_{20}{}^{79}Br_2$ (M^+): 561.9926; found: 561.9928. DSC: decomposition 123 °C (onset), 131 °C (peak).

***Compound* 1j**

Compound **4j** (73 mg, 0.23 mmol) was desilylated with K_2CO_3 in MeOH/THF (1:1) as described in general procedure A, and homocoupled in acetone/CH_2Cl_2 (1:1; 10 mL) in the presence of Hay catalyst (1 mL) and air for 20 min as described in general procedure C. Flash chromatography (hexane/CH_2Cl_2, 2:1) afforded **1j** (43 mg, 76%) as a yellow solid; mp > 115 °C (dec). R_f = 0.52 (hexane/CH_2Cl_2, 2:1). UV–vis ($CHCl_3$) λ_{max} (ε): 296 (94 600), 314 (92 000), 347 (46 900), 376 (24 000), 408 (12 800). IR ($CHCl_3$, cast, cm^{-1}): 2902, 2194, 2122, 1958, 1608, 1520, 1480, 1444. ^1H NMR (400 MHz, $CDCl_3$) δ: 7.31 (d, J = 9.2 Hz, 4H), 6.61 (d, J = 9.2 Hz, 4H), 2.96 (s, 12H), 2.10 (s, 6H), 2.09 (s, 6H). ^{13}C NMR (100 MHz, $CDCl_3$, APT) δ: 159.5, 150.2, 132.6, 111.7, 109.6, 100.7, 94.1, 82.3, 75.9, 75.5, 67.8, 64.1, 40.1, 23.2, 23.1. ESI HR-MS (MeOH/toluene, 1:1) calcd for $C_{36}H_{32}N_2$ (M^+): 492.2565; found: 492.2560. DSC: decomposition 157 °C (onset), 165 °C (peak).

***Compound* 1k**

Compound **4k** (70 mg, 0.18 mmol) was desilylated with K_2CO_3 in MeOH/THF (1:1) as described in general procedure A, and homocoupled in acetone/CH_2Cl_2 (1:1; 10 mL) in the presence of Hay catalyst (1 mL) and air for 0.5 h as described in general procedure C. Flash chromatography (hexane/CH_2Cl_2, 2:1) afforded **1k** (42 mg, 75%) as an orange solid; mp > 120 °C (dec). R_f = 0.4 (hexane/CH_2Cl_2, 2:1). UV–vis ($CHCl_3$) λ_{max} (ε): 298 (78 800), 349 (19 400), 376 (18 400), 407 (11 500). IR (μscope, cm^{-1}): 3098, 2987, 2932, 2904, 2214, 2191, 1577, 1424. ^1H NMR (500 MHz, $CDCl_3$) δ: 4.42 (m, 4H), 4.20 (m, 14H), 2.08 (s, 6H), 2.07 (s, 6H). ^{13}C NMR (125 MHz, $CDCl_3$, APT) δ: 159.9, 100.7, 91.9, 80.5, 76.0, 75.3, 71.4, 69.9, 68.9, 67.8, 64.8, 64.1, 23.4, 23.2. ESI HR-MS (MeOH/toluene, 3:1) calcd for $C_{40}H_{30}Fe_2$ (M^+): 622.1046; found: 622.1043. DSC: decomposition 160 °C (onset), 187 °C (peak).

***Compound* 4a**

Triflate **2** (108 mg, 0.333 mmol) was cross-coupled with 1-hexayne (30 mg, 0.36 mmol) in degassed THF (20 mL) in the presence of $PdCl_2(PPh_3)_2$ (12 mg, 0.017 mmol), diisopropylamine (2 mL), and CuI (6 mg, 0.03 mmol) for 3 h as described in general procedure B. Flash chromatography (hexane/CH_2Cl_2, 2:1) afforded **4a** (84 mg, 98%) as a colourless oil that slowly turned brown. R_f = 0.75 (hexane/CH_2Cl_2, 2:1). IR (CH_2Cl_2, cast, cm^{-1}): 2959, 2933, 2873, 2198, 2097. ^1H NMR (300 MHz, $CDCl_3$) δ: 2.32 (t, J = 7.2 Hz, 2H), 2.00 (s, 3H), 1.98 (s, 3H), 1.56–1.36 (m, 4H), 0.90 (t, J = 6.9 Hz, 3H), 0.18 (s, 9H). ^{13}C NMR (125 MHz, $CDCl_3$, APT) δ: 157.0, 100.5, 93.3, 90.5, 88.1, 76.1, 75.4, 74.6, 30.8, 22.8, 22.7, 22.0, 19.1, 13.6, –0.4. EI-MS *m*/*z* (rel. intensity): 256 (M^+, 100), 241 ([M – Me]$^+$, 88). EI HR-MS calcd for $C_{17}H_{24}Si$ (M^+): 256.1647; found: 256.1642.

***Compound* 4b**

Triflate **2** (32 mg, 0.099 mmol) was cross-coupled with 2-propynl 2,3,4,6-*O*-acetyl-1-thio-β-D-mannopyranoside (40 mg, 0.099 mmol) in degassed THF (20 mL) in the pres-

Can. J. Chem. Downloaded from www.nrcresearchpress.com by MCGILL UNIVERSITY on 02/02/13
For personal use only.

ence of $PdCl_2(PPh_3)_2$ (3 mg, 0.004 mmol), diisopropylamine (2 mL), and CuI (1.5 mg, 0.0079 mmol) for 1 h as described in general procedure B. Flash chromatography (hexane / ethyl acetate, 3:1) afforded **4b** (37 mg, 65%) as a colourless solid vide infra; mp 54–57 °C. R_f = 0.33 (hexane / ethyl acetate, 3:1). IR (μscope, cm^{-1}): 2961, 2916, 2849, 2199, 2098, 1744, 1592, 1433. ^1H NMR (600 MHz, $CDCl_3$) δ: 5.51 (d, J = 3.5 Hz, 1H), 5.28 (t, J = 10.0 Hz, 1H), 5.09 (dd, J = 10.0 Hz, J = 3.6 Hz, 1H), 5.02 (s, 1H), 4.29 (dd, J = 10.0 Hz, J = 0.6 Hz, 1H), 4.13 (dd, J = 10.0 Hz, J = 0.2 Hz, 1H), 3.72 (d, J = 16.7 Hz, 1H), 3.70 (m, 1H), 3.42 (d, J = 16.7 Hz, 1H), 2.16 (s, 3H), 2.07 (s, 3H), 2.05 (s, 3H), 2.023 (s, 3H), 2.020 (s, 3H), 1.96 (s, 3H), 0.18 (s, 9H). ^{13}C NMR (75 MHz, CD_2Cl_2, APT) δ: 170.8, 170.4, 170.2, 169.9, 160.4, 99.9, 91.6, 87.8, 87.5, 81.3, 79.8, 77.1, 76.3, 74.0, 72.3, 70.5, 66.0, 62.7, 30.1, 23.2, 23.0, 20.9, 20.7, 19.6, −0.4 (one coincident peak not observed). ESI HR-MS calcd for $C_{28}H_{36}O_9NaSSi$ ($[M + Na]^+$): 599.1742; found: 599.1740.

***Compound* 4c**

Trimethylphenylethynylsilane (60 mg, 0.34 mmol) was desilylated with K_2CO_3 in THF/MeOH (1:1) as per general procedure A to give **3c**, which was cross-coupled with triflate **2** (109 mg, 0.336 mmol) in degassed THF (20 mL) in the presence of $PdCl_2(PPh_3)_2$ (12 mg, 0.017 mmol), diisopropylamine (2 mL), and CuI (6 mg, 0.03 mmol) for 50 min as described in general procedure B. Flash chromatography (hexane/CH_2Cl_2, 2:1) afforded **4c** (90 mg, 96%) as a colourless solid; mp 71–72 °C. R_f = 0.63 (hexane/CH_2Cl_2, 2:1). IR (CH_2Cl_2, cast, cm^{-1}): 2960, 2904, 2199, 2094, 1594, 1489. ^1H NMR (400 MHz, $CDCl_3$) δ: 7.45–7.42 (m, 2H), 7.31–7.27 (m, 3H), 2.10 (s, 3H), 2.09 (s, 3H), 0.20 (s, 9H). ^{13}C NMR (100 MHz, $CDCl_3$, APT) δ: 158.8, 131.4, 128.25, 128.19, 123.1, 100.5, 92.1, 90.9, 88.0, 85.0, 76.0, 73.8, 23.00, 23.06, −0.4. EI MS m/z (rel. intensity): 276.1 (M^+, 100), 261.1 ($[M - Me]^+$, 88). EI HR-MS calcd for $C_{19}H_{20}Si$ (M^+): 276.1334; found: 276.1334.

***Compound* 4d**

Trimethyl(4-nitrophenylethynyl)silane (75 mg, 0.34 mmol) was desilylated with K_2CO_3 in THF/MeOH (1:1) as described in general procedure A to give **3d**, which was cross-coupled with triflate **2** (109 mg, 0.336 mmol) in degassed THF (20 mL) in the presence of $PdCl_2(PPh_3)_2$ (12 mg, 0.017 mmol), diisopropylamine (2 mL), and CuI (6 mg, 0.03 mmol) for 50 min as described in general procedure B. Flash chromatography (hexane/CH_2Cl_2, 1:1) afforded **4d** (97 mg, 90%) as a yellow solid; mp 94–95 °C. R_f = 0.40 (hexane/CH_2Cl_2, 1:1). IR ($CHCl_3$, cast, cm^{-1}): 2960, 2199, 2095, 1595, 1519, 1491, 1433, 1342. ^1H NMR (400 MHz, $CDCl_3$) δ: 8.15 (d, J = 8.9 Hz, 2H), 7.54 (d, J = 8.9 Hz, 2H), 2.11 (s, 6H), 0.19 (s, 9H). ^{13}C NMR (100 MHz, $CDCl_3$, APT) δ: 161.2, 146.9, 132.0, 129.9, 123.5, 100.1, 91.5, 90.3, 90.2, 87.6, 76.6, 72.8, 23.22, 23.19, −0.5. EI MS m/z (rel. intensity): 321.1 (M^+, 100), 306.1 ($[M - Me]^+$, 58). EI HR-MS calcd for $C_{19}H_{19}NO_2Si$ (M^+): 321.1185; found: 321.1180. Anal. calcd for $C_{19}H_{19}NO_2Si$: C 70.99, H 5.96; found: C 70.88, H 5.96.

***Compound* 4e**

Trimethyl(2-nitrophenylethynyl)silane (75 mg, 0.34 mmol) was desilylated with K_2CO_3 in THF/MeOH (1:1) as described in general procedure A to give **3e**, which was cross-coupled with triflate **2** (109 mg, 0.336 mmol) in degassed THF (20 mL) in the presence of $PdCl_2(PPh_3)_2$ (12 mg, 0.017 mmol), diisopropylamine (2 mL), and CuI (6 mg, 0.032 mmol) for 2 h as described in general procedure B. Flash chromatography (hexane/CH_2Cl_2, 1:1) afforded **4e** (95 mg, 87%) as a yellow solid; mp 93–94 °C. R_f = 0.45 (hexane/CH_2Cl_2, 1:1). IR (CH_2Cl_2, cast, cm^{-1}): 2960, 2199, 2094, 1607, 1526, 1480, 1438, 1343. ^1H NMR (400 MHz, $CDCl_3$) δ: 8.02 (dd, J = 8.3, 1.2 Hz, 1H), 7.62 (dd, J = 7.8, 1.5 Hz, 1H), 7.54 (dt, J = 7.5, 1.3 Hz, 1H), 7.41 (dt, J = 8.3, 1.5 Hz, 1H), 2.17 (s, 3H), 2.11 (s, 3H), 0.19 (s, 9H). ^{13}C NMR (100 MHz, $CDCl_3$, APT) δ: 162.4, 148.9, 134.6, 132.8, 128.5, 124.6, 118.6, 100.2, 93.0, 91.2, 87.9, 87.3, 76.3, 73.1, 23.3, 23.2, −0.4. EI MS m/z (rel. intensity): 321.1 (M^+, 35), 73.0 (Me_3Si^+, 100). EI HR-MS calcd for $C_{19}H_{19}NO_2Si$ (M^+): 321.1185; found: 321.1182. Anal. calcd for $C_{19}H_{19}NO_2Si$: C 70.99, H 5.96, N 4.36; found: C 71.10, H 5.95, N 4.29.

***Compound* 4f**

Trimethyl(3-nitrophenylethynyl)silane (75 mg, 0.34 mmol) was desilylated with K_2CO_3 in THF/MeOH (1:1) as described in general procedure A to give **3f**, which was cross-coupled with triflate **2** (109 mg, 0.336 mol) in degassed THF (20 mL) in the presence of $PdCl_2(PPh_3)_2$ (12 mg, 0.017 mmol), diisopropylamine (2 mL), and CuI (6 mg, 0.032 mmol) for 10 min as described in general procedure B. Flash chromatography (hexane/CH_2Cl_2, 1:1) afforded **4f** (98 mg, 91%) as a yellow solid; mp 77–78 °C. R_f = 0.49 (hexane/CH_2Cl_2, 1:1). IR (CH_2Cl_2, cast, cm^{-1}): 3084, 2960, 2904, 2200, 2095, 1572, 1532, 1477, 1433, 1351. ^1H NMR (400 MHz, $CDCl_3$) δ: 8.27–8.25 (m, 1H), 8.15–8.11 (m, 1H), 7.72 (dt, J = 7.5, 1.1 Hz, 1H), 7.48 (t, J = 7.9 Hz, 1H), 2.12 (s, 3H), 2.11 (s, 3H), 0.19 (s, 9H). ^{13}C NMR (75 MHz, $CDCl_3$, APT) δ: 160.7, 148.2, 137.1, 129.4, 126.2, 125.0, 122.9, 100.1, 91.5, 89.6, 87.8, 87.7, 73.1, 23.3, 23.2, −0.4 (one signal coincident or not observed). EI MS m/z (rel. intensity): 321.1 (M^+, 100), 306.1 ($[M - Me]^+$, 48). EI HR-MS calcd for $C_{19}H_{19}NO_2Si$ (M^+): 321.1185; found: 321.1176.

***Compound* 4g**

Trimethyl(5-nitrothienyl-2-ylethynyl)silane (76 mg, 0.34 mmol) was desilylated with K_2CO_3 in THF/MeOH (1:1) as described in general procedure A to give **3g**, which was cross-coupled with triflate **2** (109 mg, 0.336 mmol) in degassed THF (20 mL) in the presence of $PdCl_2(PPh_3)_2$ (12 mg, 0.017 mmol), diisopropylamine (2 mL), and CuI (6 mg, 0.03 mmol) for 1 h as described in general procedure B. Flash chromatography (hexane/CH_2Cl_2, 2:1) afforded **4g** (40 mg, 36%) as a yellow solid; mp 68–69 °C. R_f = 0.18 (hexane/CH_2Cl_2, 1:1). IR (CH_2Cl_2, cast, cm^{-1}): 3108, 2960, 2196, 2097, 1587, 1531, 1503, 1430, 1332. ^1H NMR (400 MHz, $CDCl_3$) δ: 7.77 (d, J = 4.4 Hz, 1H), 7.06 (d, J = 4.4 Hz, 1H), 2.11 (s, 3H), 2.09 (s, 3H), 0.20 (s, 9H). ^{13}C NMR (100 MHz, $CDCl_3$, APT) δ: 162.4, 150.8, 130.8, 130.6, 128.5, 99.8, 93.8, 91.9, 87.5, 83.6, 77.0, 72.1, 23.4, 23.3, −0.5. EI HR-MS calcd for $C_{17}H_{17}NO_2SSi$ (M^+): 327.0749; found: 327.0749.

***Compound* 4h**

4-Trimethylsilylethynylbenzonitrile (43 mg, 0.22 mmol) was desilylated with K_2CO_3 in THF/MeOH (1:1) as described in general procedure A to give **3h**, which was cross-coupled with triflate **2** (70 mg, 0.22 mmol) in degassed THF (20 mL) in the presence of $PdCl_2(PPh_3)_2$ (6 mg, 0.009 mmol), diiso-

Can. J. Chem. Downloaded from www.nrcresearchpress.com by MCGILL UNIVERSITY on 02/02/13
For personal use only.

propylamine (2 mL), and CuI (3 mg, 0.02 mmol) for 1.5 h as described in general procedure B. Flash chromatography (hexane/CH_2Cl_2, 1:1) afforded **4h** (52 mg, 80%) as a yellow solid; mp 60–62 °C. R_f = 0.48 (hexane/CH_2Cl_2, 1:1). IR (CH_2Cl_2, cast, cm^{-1}): 2960, 2904, 2229, 2199, 2095, 1604, 1499, 1433. ^1H NMR (400 MHz, $CDCl_3$) δ: 7.59 (d, J = 8.6 Hz, 2H), 7.50 (d, J = 8.6 Hz, 2H), 2.11 (s, 6H), 0.20 (s, 9H). ^{13}C NMR (75 MHz, $CDCl_3$, APT) δ: 160.9, 132.0, 131.9, 128.1, 118.5, 111.6, 100.2, 91.5, 90.4, 89.5, 87.7, 73.0, 23.3, –0.4 (two coincident peaks not observed). EI MS *m/z* (rel. intensity): 301.1 (M^+, 93), 286.1 ([M – Me]$^+$, 100). EI HR-MS calcd for $C_{20}H_{19}NSi$ (M^+): 301.1287; found: 301.1292.

Compound 4i

(4-Bromophenylethynyl)trimethylsilane (101 mg, 0.399 mmol) was desilylated with K_2CO_3 in THF/MeOH (1:1) as described in general procedure A to give **3i**, which was cross-coupled with triflate **2** (130 mg, 0.401 mmol) in degassed THF (20 mL) in the presence of $PdCl_2(PPh_3)_2$ (14 mg, 0.020 mmol), diisopropylamine (2 mL), and CuI (7 mg, 0.04 mmol) for 2 h as described in general procedure B. Flash chromatography (hexane/CH_2Cl_2, 1:1) afforded **4i** (112 mg, 79%) as a colourless waxy solid. R_f = 0.80 (hexane/CH_2Cl_2, 1:1). IR ($CHCl_3$, cast, cm^{-1}): 2959, 2198, 2094, 1484, 1421. ^1H NMR (400 MHz, $CDCl_3$) δ: 7.42 (d, J = 8.4 Hz, 2H), 7.28 (d, J = 8.4 Hz, 2H), 2.08 (s, 6H), 0.20 (s, 9H). ^{13}C NMR (75 MHz, $CDCl_3$, APT) δ: 159.3, 132.8, 131.5, 122.5, 122.0, 100.4, 91.1, 91.0, 87.9, 86.2, 76.2, 73.5, 23.1, 23.0, –0.4. EI HR-MS calcd for $C_{19}H_{19}{}^{81}BrSi$ (M^+): 356.0419; found: 356.0419.

Compound 4j

N,*N*-Dimethyl(4-trimethylsilylethynylphenyl)amine (109 mg, 0.501 mmol) was desilylated with K_2CO_3 in THF/MeOH (1:1) as described in general procedure A to give **3j**, which was cross-coupled with triflate **2** (162 mg, 0.501 mmol) in degassed THF (20 mL) in the presence of $PdCl_2(PPh_3)_2$ (18 mg, 0.026 mmol), diisopropylamine (2 mL), and CuI (9 mg, 0.05 mmol) for 1.5 h as described in general procedure B. Flash chromatography (hexane/CH_2Cl_2, 2:1) afforded **4j** (133 mg, 83%) as a yellow solid; mp 82–83 °C. R_f = 0.50 (hexane/CH_2Cl_2, 2:1). IR ($CHCl_3$, cast, cm^{-1}): 2959, 2902, 2200, 2094, 1609, 1521, 1481, 1445. ^1H NMR (400 MHz, $CDCl_3$) δ: 7.30 (d, J = 8.8 Hz, 2H), 6.60 (d, J = 8.8 Hz, 2H), 2.96 (s, 6H), 2.09 (s, 3H), 2.07 (s, 3H), 0.22 (s, 9H). ^{13}C NMR (100 MHz, $CDCl_3$, APT) δ: 156.9, 150.0, 132.5, 111.7, 109.8, 100.9, 93.3, 90.5, 88.2, 82.9, 75.6, 74.4, 40.1, 22.9, 22.8, –0.4. EI HR-MS calcd for $C_{21}H_{25}NSi$ (M^+): 319.1756; found: 319.1750. Anal. calcd for $C_{21}H_{25}NSi$: C 78.94, H 7.89, N 4.38; found: C 78.70, H 8.04, N 4.47.

Compound 4k

Ethynylferrocene **3k** (76 mg, 0.36 mmol) was cross-coupled with triflate **2** (117 mg, 0.362 mmol) in degassed THF (20 mL) in the presence of $PdCl_2(PPh_3)_2$ (13 mg, 0.018 mmol), diisopropylamine (2 mL), and CuI (7 mg, 0.04 mmol) for 2 h as described in general procedure B. Flash chromatography (hexane/CH_2Cl_2, 2:1) afforded **4k** (78 mg, 56%) as a yellow solid; mp 84–85 °C. R_f = 0.82 (hexane/CH_2Cl_2, 2:1). IR (μscope, cm^{-1}): 3099, 2964, 2908, 2214, 2191, 2091, 1593, 1426, 1410. ^1H NMR (600 MHz, $CDCl_3$) δ: 4.42 (t, J = 1.8 Hz, 2H), 4.21 (s, 5H), 4.19 (t, J = 1.8 Hz, 2H), 2.06 (s, 3H), 2.05 (s, 3H), 0.19 (s, 9H). ^{13}C NMR (75 MHz, $CDCl_3$, APT) δ: 157.6, 100.9, 91.1, 90.7, 88.1, 81.2, 74.2, 71.4, 70.0, 68.8, 65.1, 23.1, 22.9, –0.3 (one coincident peak not observed). EI HR-MS calcd for $C_{23}H_{24}FeSi$ (M^+): 384.0997; found: 384.1001.

Compound 6a

Compound **10a** (62.5 mg, 0.164 mmol) was desilylated with K_2CO_3 in MeOH/THF (1:1) as described in general procedure A, and the resulting product was subjected to a homocoupling reaction in CH_2Cl_2 (60 mL) in the presence of Hay catalyst (1 mL) and air as described in general procedure C. Flash chromatography (hexanes/CH_2Cl_2, 7:1) gave **6a** (38.0 mg, 75%) as a yellow crystalline solid; mp 185 °C (dec). R_f = 0.46 (hexanes/CH_2Cl_2, 7:1). UV–vis (THF) λ_{max} (ε): 299 (66 600), 314 (78 600), 330 (64 700), 359 (27 600), 386 (30 600), 419 (19 500). IR ($CHCl_3$, cast, cm^{-1}): 3010, 2192, 1524, 1488. ^1H NMR (500 MHz, $CDCl_3$) δ: 7.36 (s). ^{13}C NMR (100 MHz, $CDCl_3$) δ: 136.6, 129.5, 129.1, 128.7, 128.5, 105.3, 81.9, 76.5, 70.9, 64.9. EI MS *m/z* (rel. intensity): 617.7 (M^+, 80), 298.1 ([M – 4Br]$^+$, 100). HR-MS calcd for $C_{24}H_{10}{}^{79}Br_2{}^{81}Br_2$ (M^+): 617.7475; found: 617.7488. Anal. calcd for $C_{24}H_{10}Br_4$: C 46.66, H 1.63; found: C 46.35, H 1.46. DSC: decomposition 191 °C (onset), 192 °C (peak).

Compound 6b

Compound **10b** (582 mg, 1.42 mmol) was desilylated with K_2CO_3 in MeOH/THF (1:1) as described in general procedure A, and the resulting product was subjected to a homocoupling reaction in CH_2Cl_2 (60 mL) in the presence of Hay catalyst (1 mL) and air as described in general procedure C. Flash chromatography (hexanes/CH_2Cl_2, 3:1) gave **6b** (223 mg, 46%) as a yellow-green solid; mp 168–170 °C. R_f = 0.41 (hexanes/CH_2Cl_2, 3:1). UV–vis (THF) λ_{max} (ε): 296 (80 200, sh), 308 (93 100), 331 (59 200, sh), 360 (26 900), 388 (27 800), 420 (18 300). IR ($CHCl_3$, cast, cm^{-1}): 2924, 2190, 1605, 1505, 1252. ^1H NMR (300 MHz, $CDCl_3$) δ: 7.32 (d, J = 9.0 Hz, 4H), 6.88 (d, J = 9.0 Hz, 4H), 3.81 (s, 6H). ^{13}C NMR (100 MHz, $CDCl_3$, APT) δ: 156.0, 123.0, 129.1, 128.8, 114.0, 104.2, 81.7, 70.9, 65.0, 55.3 (one signal coincident or not observed). EI HR-MS calcd for $C_{26}H_{14}{}^{79}Br_2{}^{81}Br_2O_2$ (M^+): 677.7686; found: 677.7697. Anal. calcd for $C_{26}H_{14}Br_4O_2$: C 46.06, H 2.08; found: C 45.87, H 1.93. DSC: mp 176 °C; decomposition 176 °C (onset), 179 °C (peak).

Compound 6c

Compound **10c** (401 mg, 0.914 mmol) was desilylated with K_2CO_3 in MeOH/THF (1:1) as described in general procedure A, and the resulting product was subjected to a homocoupling reaction in CH_2Cl_2 (60 mL) in the presence of Hay catalyst (1 mL) and air as described in general procedure C. Flash chromatography (hexanes/CH_2Cl_2, 7:1) gave **6c** (265 mg, 80%) as a yellow crystalline solid; mp 168–179 °C (dec). R_f = 0.52 (hexanes/CH_2Cl_2, 7:1). UV–vis (THF) λ_{max} (ε): 299 (72 100), 309 (70 500), 331 (55 100), 359 (25 200), 387 (27 600), 419 (17 500). IR ($CHCl_3$, cast, cm^{-1}): 2963, 2182, 1531. ^1H NMR (300 MHz, $CDCl_3$) δ: 7.38 (d, J = 8.7 Hz, 4H), 8.7 (d, J = 8.7 Hz, 4H), 1.30 (s, 18H). ^{13}C NMR (100 MHz, $CDCl_3$) δ: 152.3, 133.5, 129.4, 128.2, 125.6, 104.6, 81.8, 77.3, 70.9, 65.0, 34.9, 31.3. EI HR-MS calcd for $C_{32}H_{26}{}^{79}Br_2{}^{81}Br_2$ (M^+): 729.8727; found: 729.8750. DSC: decomposition initial onset ~200 °C; 229 °C (onset), 233 °C (peak).

Can. J. Chem. Downloaded from www.nrcresearchpress.com by MCGILL UNIVERSITY on 02/02/13
For personal use only.

***Compound* 6d**

Compound **10d** (1.10 g, 2.58 mmol) was desilylated with K_2CO_3 in MeOH/THF (1:1) as described in general procedure A, and the resulting product was subjected to a homocoupling reaction in CH_2Cl_2 (60 mL) in the presence of Hay catalyst (1 mL) and air as described in general procedure C. Flash chromatography (hexanes/CH_2Cl_2, 1:1) gave **6d** (469 mg, 51%) as a yellow crystalline solid; mp > 190 °C (dec). R_f = 0.4 (hexanes/CH_2Cl_2, 1:1). UV–vis (THF) λ_{max} (ε): 296 (80 200), 312 (106 200), 331 (80 000), 359 (29 200), 387 (31 700), 419 (19 900). IR ($CHCl_3$, cast, cm^{-1}): 3104, 2188, 2114, 1517, 1346. ^1H NMR (400 MHz, $CDCl_3$) δ: 8.24 (d, J = 9.2 Hz, 4H), 7.57 (d, J = 9.2 Hz, 4H). ^{13}C NMR (100 MHz, $CDCl_3$) δ: 147.8, 142.5, 129.6, 127.4, 123.8, 107.5, 82.6, 75.4, 71.2, 64.8. EI MS *m/z* (rel. intensity): 707.7 (M^+, 23), 388.0 ([M – 4Br]$^+$, 6). HR-MS calcd for $C_{24}H_8{}^{79}Br_2{}^{81}Br_2N_2O_4$: 707.7177 ($M^+$); found: 707.7217. Anal. calcd for $C_{24}H_8Br_4N_2O_4$: C 40.72, H 1.14, N 3.96; found: C 40.94, H 1.10, N 3.80. DSC: decomposition 189 °C (onset), 191 °C (peak).

***Compound* 10d**

Under an inert atmosphere of nitrogen, 4-nitrobenzoyl chloride (2.45 g, 13.2 mmol) and bis(trimethylsilyl)butadiyne (**8**; 2.30 g, 11.8 mmol) were dissolved in CH_2Cl_2 (100 mL) and the temperature of the solution lowered to –20 °C. $AlCl_3$ (2.4 g, 18.0 mmol) was added slowly over ~1 min, the cooling bath removed, and the reaction mixture allowed to warm to rt over ~3 h. The reaction was carefully quenched by the addition of the reaction mixture to 10% HCl (50 mL) in ice (50 mL). (Caution: This step is exothermic and can cause the CH_2Cl_2 to boil!) Et_2O (70 mL) was added, the organic layer separated, washed with saturated aq $NaHCO_3$ (2 × 20 mL) and brine (2 × 20 mL), dried over $MgSO_4$, and the solvent removed in vacuo. The resulting product **9d** was carried on to the next step without further purification.

CBr_4 (3.15 g, 9.50 mmol) and PPh_3 (5.00 g, 19.1 mmol) were added to CH_2Cl_2 (100 mL) at 0 °C and the solution stirred for ~5 min at rt until the mixture turned orange. The ketone **9d**, dissolved in CH_2Cl_2 (~5 mL), was added in one portion. The reaction was allowed to warm to rt and monitored by TLC analysis until the ketone was no longer observed (~1 h). When the reaction was judged complete, the solvent was reduced to ~5 mL, hexanes (50 mL) were added, the inhomogeneous mixture filtered through a plug of Celite layered on top of silica gel, and the resulting filtrate was concentrated in vacuo. This process can be repeated a second time if necessary to remove phosphine/phosphonium byproducts. Column chromatography (silica gel, hexanes/CH_2Cl_2, 1:1) gave **10d** (2.54 g, 51%) as a cream-coloured powder; mp 80–83 °C. R_f = 0.60 (hexanes/CH_2Cl_2, 1:1). IR ($CHCl_3$, cast film, cm^{-1}): 2960, 2096, 1595, 1523. ^1H NMR (300 MHz, $CDCl_3$) δ: 8.22 (d, J = 8.7 Hz, 2H), 7.58 (d, J = 8.7 Hz, 2H), 0.19 (s, 9H). ^{13}C NMR (125 MHz, $CDCl_3$, APT) δ: 147.7, 143.4, 129.7, 128.1, 123.8, 104.8, 96.7, 86.8, 83.2, 73.8, –0.6. EI MS *m/z* (rel. intensity): 426.9 (M^+, 28), 411.9 ([M – CH_3]$^+$, 100). HR-MS calcd for $C_{15}H_{13}NO_2Si^{79}Br^{81}Br$ (M^+): 426.9062; found: 426.9064. Anal. calcd for $C_{15}H_{13}NO_2SiBr_2$: C 42.18, H 3.07, N 3.28; found: C 42.30, H 2.81, N 3.16.

***Compound* 11**

$^{13}CBr_4$ (287 mg, 0.865 mmol), CBr_4 (431 mg, 1.30 mmol), and PPh_3 (1.14 g, 4.33 mmol) were added to CH_2Cl_2 (15 mL) at 0 °C and the solution stirred for ~5 min at rt until the mixture turned bright orange. Triisopropylsilylpropargylaldehyde (501 mg, 2.38 mmol) dissolved in CH_2Cl_2 (~2 mL) was added in one portion. The reaction was allowed to warm to rt and monitored by TLC analysis until the ketone was no longer observed (~1 h). When the reaction was judged complete, the solvent was reduced to ~5 mL, hexanes (25 mL) were added, the inhomogeneous mixture filtered through a plug of Celite layered on top of silica gel, and the resulting filtrate concentrated in vacuo. This process can be repeated a second time if necessary to remove phosphine/phosphonium byproducts. Column chromatography gave **11** (638 mg, 73%) with ~34% labelling. Spectral data are consistent with those previously reported, see ref. 35. ^1H NMR (500 MHz, $CDCl_3$) δ: 6.59 (d, J = 1.5 Hz, 1H), 1.08 (s, 21H). ^{13}C NMR (125 MHz, $CDCl_3$) δ: 120.0 (d, ^1J = 360 Hz), 102.9 (C*, s and d, ^1J = 360 Hz), 102.5 (s), 100.8 (d, ^3J = 25 Hz), 18.6, 11.1.

***Compound* 12**

To a solution of compound **11** (638 mg, 1.74 mmol) in Et_2O (2 mL) at –78 °C was added via cannula a solution of LDA (formed from BuLi (2.5 mol/L in hexanes, 2.1 mL, 5.3 mmol) and diisopropylamine (0.73 mL, 0.53 mg, 5.23 mmol) in Et_2O (17 mL)) at –78 °C, and the resulting solution was stirred for 2 h at –78 °C. To this mixture was added dropwise Me_3SiCl (0.33 mL, 0.28 mg, 2.61 mmol). The reaction was allowed to warm to rt and stirred overnight. Et_2O (10 mL) and saturated aq NH_4Cl (10 mL) were added. The organic phase was separated, washed with brine (2 × 10 mL), and dried over $MgSO_4$. Solvent removal and purification by column chromatography (silica gel, hexanes) afforded **12** (325 mg, 67%) as a colourless oil. R_f = 0.67 (hexanes), which was carried on to the next step without further purification.

***Compound* 14**

Under an inert atmosphere of nitrogen, 4-nitrobenzoyl chloride (239 mg, 1.29 mmol) and compound **12** (321 mg, 1.15 mmol) were dissolved in CH_2Cl_2 (12 mL) and the temperature of the solution lowered to –20 °C. $AlCl_3$ (230 mg, 1.72 mmol) was added slowly over ~1 min, the cooling bath removed, and the reaction mixture allowed to warm to rt over ~3 h. The reaction was carefully quenched by the addition of the reaction mixture to 10% HCl (25 mL) in ice (25 mL). (Caution: This step is exothermic and can cause the CH_2Cl_2 to boil!) Et_2O (50 mL) was added, the organic layer separated, washed with saturated aq $NaHCO_3$ (2 × 20 mL) and brine (2 × 20 mL), dried over $MgSO_4$, and the solvent removed in vacuo to give ketone **13** as a colourless oil. The ketone **13** was carried on to the next step without further purification.

CBr_4 (764 mg, 2.30 mmol) and PPh_3 (1.21 g, 4.61 mmol) were added to CH_2Cl_2 (12 mL) at 0 °C and the solution stirred for ~5 min at rt until the mixture turned bright orange. Ketone **13**, dissolved in CH_2Cl_2 (~2 mL), was added in one portion. The reaction was allowed to warm to rt and monitored by TLC analysis until the ketone was no longer observed (~1 h). When the reaction was judged complete, the solvent was reduced to ~5 mL, hexanes (50 mL) were added, and the inhomogeneous mixture filtered through a plug of Celite layered on top of silica gel. The resulting filtrate was concentrated in vacuo to give compound **14** (206 mg, 35%) as a colourless oil.

Can. J. Chem. Downloaded from www.nrcresearchpress.com by MCGILL UNIVERSITY on 02/02/13
For personal use only.

^{13}C NMR (125 MHz, $CDCl_3$) δ: 147.7, 143.5, 129.7, 128.3 (d, J = 98 Hz), 123.8, 104.5, 94.3, 88.5 (d, J = 18 Hz), 83.6 (d, J = 202 Hz), 72.7 (C*, m), 18.5, 11.2.

Compounds* 6d/6d*/6d*

To compound **14** (206 mg, 0.403 mmol) in THF (6 mL) was added TBAF (1.0 mol/L in THF, 0.52 mL, 0.52 mmol). The solution was stirred at rt until TLC analysis showed complete conversion to the terminal alkyne. Et_2O and saturated aq NH_4Cl were added, the organic phase was separated, washed with saturated aq NH_4Cl (2 × 10 mL) and brine (10 mL), and then dried over $MgSO_4$. The solution was concentrated to 1–2 mL via rotary evaporation and diluted with CH_2Cl_2 (6 mL). Hay catalyst (1 mL) was added and the reaction continued as described in general procedure C to give a mixture of isotopomers **6d/6d*/6d**** (59.7 mg, 42%). Spectral data were consistent with those of **6d**. ^{13}C NMR (125 MHz, $CDCl_3$) δ: 147.9, 142.7, 129.7, 127.6 (d, J = 98 Hz), 124.0, 107.6, 82.7 (d, J = 187 Hz), 75.6 (C*, m), 71.4 (d, J = 32 Hz), 64.9.

Supplementary data

Supplementary data are available with the article through the journal Web site at http://nrcresearchpress.com/doi/suppl/10.1139/v2012-075). CCDC HOZSAQ and 862755–862758 contain the X-ray data in CIF format for this manuscript. These data can be obtained, free of charge, via http://www.ccdc.cam.ac.uk/products/csd/request (or from the Cambridge Crystallographic Data Centre, 12 Union Road, Cambridge CB2 1EZ, UK; fax: 44 1223 336033; or e-mail: deposit@ccdc.cam.ac.uk).

Acknowledgments

We are grateful for financial support for this work as provided by the University of Alberta, the Alberta Ingenuity Fund, the Natural Sciences and Engineering Research Council of Canada (NSERC), and Petro Canada (Young Innovator Award to R.R.T.). R.E.W. is a Canada Research Chair in Physical Chemistry at the University of Alberta.

References

(1) Hoheisel, T. N.; Schrettl, S.; Szilluweit, R.; Frauenrath, H. *Angew. Chem. Int. Ed.* **2010**, *49* (37), 6496. doi:10.1002/anie.200907180.

(2) Yoon, B.; Lee, S.; Kim, J. M. *Chem. Soc. Rev.* **2009**, *38* (7), 1958. doi:10.1039/b819539k.

(3) Sun, X. M.; Chen, T.; Huang, S. Q.; Li, L.; Peng, H. S. *Chem. Soc. Rev.* **2010**, *39* (11), 4244. doi:10.1039/c001151g.

(4) Reppy, M. A.; Pindzola, B. A. *Chem. Commun. (Camb.)* **2007**, (42): 4317. doi:10.1039/b703691d.

(5) Carpick, R. W.; Sasaki, D. Y.; Marcus, M. S.; Eriksson, M. A.; Burns, A. R. *J. Phys. Condens. Matter* **2004**, *16* (23), R679. doi:10.1088/0953-8984/16/23/R01.

(6) Materny, A.; Chen, T.; Vierheilig, A.; Kiefer, W. *J. Raman Spectrosc.* **2001**, *32* (6–7), 425. doi:10.1002/jrs.716.

(7) Zhou, W. D.; Li, Y. L.; Zhu, D. B. *Chem. Asian J.* **2007**, *2* (2), 222. doi:10.1002/asia.200600218.

(8) Ahn, D. J.; Kim, J. M. *Acc. Chem. Res.* **2008**, *41* (7), 805. doi:10.1021/ar7002489.

(9) Bässler, H. *Adv. Polym. Sci.* **1984**, *63,* 1. doi:10.1007/BFb0017650.

(10) Baughman, R. H. *J. Polym. Sci., Polym. Phys. Ed.* **1974**, *12* (8), 1511. doi:10.1002/pol.1974.180120801.

(11) Bloor, D.; Chance, R. R., Eds. *Polydiacetylenes;* Martinus Nijhoff: Dordrecht, 1985.

(12) Wegner, G. *Z. Naturforsch.* **1969**, *24b,* 824.

(13) Szafert, S.; Gladysz, J. A. *Chem. Rev.* **2006**, *106* (11), PR1. doi:10.1021/cr068016g.

(14) Enkelmann, V. *Adv. Polym. Sci.* **1984**, *63,* 91. doi:10.1007/BFb0017652.

(15) Baughman, R. H.; Yee, K. C. *J. Polym. Sci.: Macromol. Rev.* **1978**, *13* (1), 219. doi:10.1002/pol.1978.230130104.

(16) Paley, M. S.; Frazier, D. O.; Abeledeyem, H.; McManus, S. P.; Zutaut, S. E. *J. Am. Chem. Soc.* **1992**, *114* (9), 3247. doi:10.1021/ja00035a013.

(17) For reviews see: (a) Lauher, J. W.; Fowler, F. W.; Goroff, N. S. *Acc. Chem. Res.* **2008**, *41* (9), 1215. doi:10.1021/ar8001427; (b) Sarkar, A.; Okada, S.; Matsuzawa, H.; Matsuda, H.; Nakanishi, H. *J. Mater. Chem.* **2000**, *10* (4), 819. doi:10.1039/a907438d; (c) Fowler, F. W.; Lauher, J. W. *J. Phys. Org. Chem.* **2000**, *13* (12), 850. doi:10.1002/1099-1395(200012)13:12<850::AID-POC316>3.0.CO;2-L.

(18) For theoretical predictions see Yang, S.; Kertesz, M. *Macromolecules* **2007**, *40* (18), 6740. doi:10.1021/ma0708040.

(19) For examples see: (a) Xu, R.; Schweizer, W. B.; Frauenrath, H. *Chemistry* **2009**, *15* (36), 9105. doi:10.1002/chem.200900985; (b) Mizukoshi, K.; Okada, S.; Kimura, T.; Shimada, S.; Matsuda, H. *Bull. Chem. Soc. Jpn.* **2008**, *81* (8), 1028. doi:10.1246/bcsj.81.1028; (c) Xiao, J.; Yang, M.; Lauher, J. W.; Fowler, F. W. *Angew. Chem. Int. Ed.* **2000**, *39* (12), 2132. doi:10.1002/1521-3773(20000616)39:12<2132::AID-ANIE2132>3.0.CO;2-8; (d) Hlavatý, J.; Kavan, L.; Kasahara, N.; Oya, A. *Chem. Commun. (Camb.)* **2000**, (9): 737. doi:10.1039/b000895h; (e) Enkelmann, V. *Chem. Mater.* **1994**, *6* (8), 1337. doi:10.1021/cm00044a035; (f) Okada, S.; Hayamizu, K.; Matsuda, H.; Masaki, A.; Nakanishi, H. *Bull. Chem. Soc. Jpn.* **1991**, *64* (3), 857. doi:10.1246/bcsj.64.857; (g) Kiji, J.; Kaiser, J.; Wegner, G.; Schulz, R. C. *Polymer (Guildf.)* **1973**, *14* (9), 433. doi:10.1016/0032-3861(73)90009-8.

(20) (a) Rubin, Y.; Lin, S. S.; Knobler, C. B.; Anthony, J.; Boldi, A. M.; Diederich, F. *J. Am. Chem. Soc.* **1991**, *113* (18), 6943. doi:10.1021/ja00018a035; (b) Okada, S.; Nakanishi, H.; Matsuzawa, H.; Katagi, H.; Oshikiri, T.; Kasai, H.; Sarkar, A.; Oikawa, H.; Rangel-Rojo, R.; Fukuda, T.; Matsuda, H. *SPIE* **1999**, *3796,* 76. doi:10.1117/12.368302.

(21) For examples see: (a) Inayama, S.; Tatewaki, Y.; Okada, S. *Polym. J.* **2010**, *42* (3), 201. doi:10.1038/pj.2009.326; (b) Okada, S.; Hayamizu, K.; Matsuda, H.; Masaki, A.; Minami, N.; Nakanishi, H. *Macromolecules* **1994**, *27* (22), 6259. doi:10.1021/ma00100a005.

(22) For examples see: (a) Chen, G. A.; Mahmud, I.; Dawe, L. N.; Daniels, L. M.; Zhao, Y. *J. Org. Chem.* **2011**, *76* (8), 2701. doi:10.1021/jo2000447; (b) Ding, L. H.; Olesik, S. V. *Chem. Mater.* **2005**, *17* (9), 2353. doi:10.1021/cm048781g; (c) Li, T. S.; Okada, S.; Nakanishi, H. *Polym. Bull.* **2003**, *51* (2), 103. doi:10.1007/s00289-003-0199-z; (d) Sarkar, A.; Okada, S.; Komatsu, K.; Nakanishi, H.; Matsuda, H. *Macromolecules* **1998**, *31* (17), 5624. doi:10.1021/ma9803077; (e) Hayamizu, K.; Okada, S.; Doi, T.; Kawanami, H.; Kikuchi, N.; Matsuda, H.; Nakanishi, H. *Bull. Chem. Soc. Jpn.* **1995**, *68* (3), 791. doi:10.1246/bcsj.68.791.

Can. J. Chem. Downloaded from www.nrcresearchpress.com by MCGILL UNIVERSITY on 02/02/13
For personal use only.

(23) (a) Jahnke, E.; Tykwinski, R. R. *Chem. Commun. (Camb.)* **2010**, *46* (19), 3235. doi:10.1039/c003170d; (b) Chalifoux, W. A.; Tykwinski, R. R. *C. R. Chim.* **2009**, *12* (3-4), 341. doi:10.1016/j.crci.2008.10.004.

(24) For the stepwise formation of polytriacetylenes see Martin, R. E.; Gunter, P.; Bosshard, C.; Gubler, U.; Gramlich, V.; Gross, M.; Boudon, C.; Gisselbrecht, J. P.; Diederich, F. *Chem. Eur. J.* **1997**, *3* (9), 1505 and references therein. doi:10.1002/chem.19970030919.

(25) For reviews of cross-conjugated systems see: (a) Gholami, M.; Tykwinski, R. R. *Chem. Rev.* **2006**, *106* (12), 4997. doi:10.1021/cr0505573; (b) Nielsen, M. B.; Diederich, F. *Chem. Rev.* **2005**, *105* (5), 1837. doi:10.1021/cr9903353; (c) Hopf, H. *Angew. Chem. Int. Ed. Engl.* **1984**, *23* (12), 948. doi:10.1002/anie.198409481.

(26) Tykwinski, R. R.; Zhao, Y. *Synlett* **2002**, (12): 1939. doi:10.1055/s-2002-35578.

(27) The synthesis of **1l** and **4l** has been reported; see: (a) Zhao, Y.; McDonald, R.; Tykwinski, R. R. *J. Org. Chem.* **2002**, *67* (9), 2805. doi:10.1021/jo015995y; (b) Zhao, Y.; McDonald, R.; Tykwinski, R. R. *Chem. Commun. (Camb.)* **2000**, (1): 77. doi:10.1039/a906900c.

(28) (a) Chinchilla, R.; Najera, C. *Chem. Rev.* **2007**, *107* (3), 874. doi:10.1021/cr050992x; (b) Tykwinski, R. R. *Angew. Chem. Int. Ed.* **2003**, *42* (14), 1566. doi:10.1002/anie.200201617; (c) Sonogashira, K.; Tohda, Y.; Hagihara, N. *Tetrahedron Lett.* **1975**, *16* (50), 4467. doi:10.1016/S0040-4039(00)91094-3.

(29) Stang, P. J.; Ladika, M. *Synthesis* **1981**, (1), 29. doi:10.1055/s-1981-29318.

(30) Hay, A. S. *J. Org. Chem.* **1962**, *27* (9), 3320. doi:10.1021/jo01056a511.

(31) Luu, T.; Elliott, E.; Slepkov, A. D.; Eisler, S.; McDonald, R.; Hegmann, F. A.; Tykwinski, R. R. *Org. Lett.* **2005**, *7* (1), 51. doi:10.1021/ol047931q.

(32) Walton, D. R. M.; Waugh, F. *J. Organomet. Chem.* **1972**, *37* (1), 45. doi:10.1016/S0022-328X(00)89260-8.

(33) Desai, N. B.; McKelvie, N.; Ramirez, F. *J. Am. Chem. Soc.* **1962**, *84* (9), 1745. doi:10.1021/ja00868a057.

(34) For representative examples see refs. 19a, 19b, 19f, 21a, 21b, 22d, and 22e.

(35) Eisler, S.; Slepkov, A. D.; Elliott, E.; Luu, T.; McDonald, R.; Hegmann, F. A.; Tykwinski, R. R. *J. Am. Chem. Soc.* **2005**, *127* (8), 2666. doi:10.1021/ja044526l.

(36) Luu, T.; Medos, B. J.; Graham, E. R.; Vallee, D. M.; McDonald, R.; Ferguson, M. J.; Tykwinski, R. R. *J. Org. Chem.* **2010**, *75* (24), 8498. doi:10.1021/jo101870y.

(37) Eisler, S.; McDonald, R.; Loppnow, G. R.; Tykwinski, R. R. *J. Am. Chem. Soc.* **2000**, *122* (29), 6917. doi:10.1021/ja000617g.

(38) Bichler, P.; Chalifoux, W. A.; Eisler, S.; Shi Shun, A. L. K.; Chernick, E. T.; Tykwinski, R. R. *Org. Lett.* **2009**, *11* (3), 519. doi:10.1021/ol8023665.

(39) Wasylishen, R. E. *Annu. Rep. Nucl. Magn, Reson. Spectrosc.* **1977**, *7,* 245

(40) Bohlmann, F.; Brehm, M. *Chem. Ber.* **1979**, *112* (3), 1071. doi:10.1002/cber.19791120330.

(41) Wakabayashi, T.; Tabata, H.; Doi, T.; Nagayama, H.; Okuda, K.; Umeda, R.; Hisaki, I.; Sonoda, M.; Tobe, Y.; Minematsu, T.; Hashimoto, K.; Hayashi, S. *Chem. Phys. Lett.* **2007**, *433* (4–6), 296. doi:10.1016/j.cplett.2006.11.077.

(42) (a) Burri, E.; Diederich, F.; Nielsen, M. B. *Helv. Chim. Acta* **2001**, *85* (7), 2169. doi:10.1002/1522-2675(200207)85:7<2169::AID-HLCA2169>3.0.CO;2-Z; (b) Zhao, Y.; Campbell, K.; Tykwinski, R. R. *J. Org. Chem.* **2002**, *67* (2), 336. doi:10.1021/jo015810n; (c) Zhao, Y. M.; Zhou, N. Z.; Slepkov, A. D.; Ciulei, S. C.; McDonald, R.; Hegmann, F. A.; Tykwinski, R. R. *Helv. Chim. Acta* **2007**, *90* (5), 909. doi:10.1002/hlca.200790092; (d) Zhao, Y. M.; Slepkov, A. D.; Akoto, C. O.; McDonald, R.; Hegmann, F. A.; Tykwinski, R. R. *Chem. Eur. J.* **2004**, *11* (1), 321. doi:10.1002/chem.200400822.

(43) (a) Eisler, S.; Chahal, N.; McDonald, R.; Tykwinski, R. R. *Chem. Eur. J.* **2003**, *9* (11), 2542. doi:10.1002/chem.200204584; (b) Shi Shun, A. L. K.; Chernick, E. T.; Eisler, S.; Tykwinski, R. R. *J. Org. Chem.* **2003**, *68* (4), 1339. doi:10.1021/jo026481h.

(44) Orendt, A. M.; Facelli, J. C.; Jiang, Y. J.; Grant, D. M. *J. Phys. Chem. A* **1998**, *102* (39), 7692. doi:10.1021/jp981079l.

(45) Chalifoux, W. A.; McDonald, R.; Ferguson, M. J.; Tykwinski, R. R. *Angew. Chem. Int. Ed.* **2009**, *48* (42), 7915. doi:10.1002/anie.200902760.

(46) Bennett, A. E.; Rienstra, C. M.; Auger, M.; Lakshmi, K. V.; Griffin, R. G. *J. Chem. Phys.* **1995**, *103* (16), 6951. doi:10.1063/1.470372.

(47) Earl, W. L.; VanderHart, D. L. *J. Magn. Reson.* **1982**, *48,* 35.

(48) Gan, Z.; Roy, R. *Tetrahedron Lett.* **2000**, *41* (8), 1155. doi:10.1016/S0040-4039(99)02285-6.

(49) Müller, T. J. J.; Robert, J. P.; Schmälzlin, E.; Bräuchle, C.; Meerholz, K. *Org. Lett.* **2000**, *2* (16), 2419. doi:10.1021/ol006048z.

(50) Doisneau, G.; Balavoine, G.; Fillebeen-Khan, T. *J. Organomet. Chem.* **1992**, *425* (1–2), 113. doi:10.1016/0022-328X(92)80026-T.

MINIREVIEW / MINISYNTHÈSE

Mesoporous silica and organosilica materials — Review of their synthesis and organic functionalization

Tewodros Asefa and Zhimin Tao

Abstract: Mesoporous silica and organosilica materials are a class of nanostructured materials that have porous structures with tunable nanometer pores, large surface areas, high pore volumes, and, in some cases, well-ordered mesostructures. Furthermore, in the case of mesoporous organosilicas, the materials possess various types of organic functional groups. This review highlights the different synthetic methods developed for mesoporous silica and organosilica nanomaterials. The review also discusses the various synthetic strategies used to functionalize the surfaces of mesoporous silica materials and produce highly functionalized mesoporous materials. Rational design and synthetic methods developed to place judiciously chosen one or more than one type of functional group(s) on the surfaces of mesoporous silica materials and generate monofunctional and multifunctional mesoporous silica materials are also introduced. These organic functionalization methods have made possible the synthesis of organically functionalized mesoporous silicas and mesoporous organosilicas with various interesting properties and many potential applications in different areas, ranging from catalysis to drug delivery and biosensing.

Key words: mesoporous silica, mesoporous organosilica, nanoporous material, organic functionalization, nanomaterial.

Résumé : Les silices mésoporeuses et les matériaux organosiliciés forment une classe de matériaux nanostructurés possédant des structures poreuses dont les pores de l'ordre du nanomètre sont ajustables, volumes élevés de pores et, dans certains cas, des nanostructures bien organisées. De plus, dans le cas des produits organosiliciés mésoporeux, les matériaux peuvent porter divers types de groupes fonctionnels organiques. Cette revue permet de mettre en relief les diverses méthodes de synthèse développées pour les silices mésoporeuses et pour les nanomatériaux organosiliciés. Cette revue discute aussi des diverses stratégies de synthèse utilisées pour fonctionnaliser les surfaces des matériaux siliciés mésoporeux et pour produire des matériaux mésoporeux hautement fonctionnalisés. On introduit aussi des méthodes de conception et de synthèse rationnelles développées pour introduire à des endroits choisis d'une façon judicieuse un ou plusieurs types de groupes fonctionnels sur les surfaces de matériaux siliciés mésoporeux et pour générer des matériaux siliciés mésoporeux monofonctionnels et multifonctionnels. Ces méthodes de fonctionnalisation organiques rendent possibles les synthèses de silices et de matériaux organosiliciés mésoporeux organiquement fonctionnalisées possédant diverses propriétés intéressantes et plusieurs possibilités d'applications dans divers domaines, allant de la catalyse à l'administration de médicaments et à la biodétection.

Mots-clés : silice mésoporeuse, organosilice mésoporeuse, matériau nanoporeux, fonctionnalisation organique, nanomatériel.

[Traduit par la Rédaction]

Introduction

Over the last two decades, a variety of nanomaterials with unique physical and chemical properties has been reported.[1–6] This includes mesoporous silica materials, which are a class of nanoporous materials with uniform cylindrical mesochannel and tunable nanosize pores, large surface areas per unit mass, and sometimes controllable particle sizes and shapes. Because of the extensive research advances made in materials chemistry in the last two decades,[7–9] mesoporous silica materials that possess not only a diverse range of structural features but also different functional groups on their easily

Received 10 July 2012. Accepted 24 August 2012. Published at www.nrcresearchpress.com/cjc on 3 December 2012.

T. Asefa. Department of Chemistry and Chemical Biology, Rutgers, The State University of New Jersey, 610 Taylor Road, Piscataway, NJ 08854, USA; Department of Chemical and Biochemical Engineering, Rutgers, The State University of New Jersey, Piscataway, NJ 08854, USA; The Institute for Advanced Materials, Devices and Nanotechnology (IAMDN), Rutgers, The State University of New Jersey, 607 Taylor Road, Piscataway, NJ 08854, USA.
Z. Tao. Department of Physics, Tsinghua University, Beijing 100084, China.

Corresponding authors: Tewodros Asefa (e-mail: tasefa@rci.rutgers.edu) and Zhimin Tao (ztao@tsinghua.edu.cn).

This article is part of a Special Issue dedicated to Professor Geoffrey Ozin.

Can. J. Chem. Downloaded from www.nrcresearchpress.com by MCGILL UNIVERSITY on 02/02/13
For personal use only.

Can. J. Chem. Downloaded from www.nrcresearchpress.com by MCGILL UNIVERSITY on 02/02/13
For personal use only.

modifiable external or internal surfaces can now be easily synthesized.[10,11] The fact that mesoporous silica materials can be synthesized with different particle sizes, morphology, and mesoporosity, as well as different functional groups, allows these materials to have different tunable physical and chemical properties. This, in turn, enables mesoporous silica materials to have many potential applications, such as delivery vehicles for pharmaceutical and biological molecules, host materials for bioimaging or biocatalytic agents, and platform materials for sensory or catalytic moieties.[12–17] At the same time, the possible toxicities of these engineered nanoparticles on humans and the environment have become a concern; thus, many toxicity studies of different nanomaterials are being broadly assessed by many researchers.[18–21] Considering the promising applications of mesoporous silica materials in a variety of areas such as nanomedicine or catalysis, it has also become essential to obtain as much information as possible regarding their structure–property relationships so that they may be well utilized for catalysis and biological, medical, and other applications. Such studies are being conducted in different laboratories worldwide.

In this review, we first briefly highlight the history of the various synthetic methods developed for mesoporous silica and organic-functionalized mesoporous silica materials. The different synthetic mechanisms proposed for mesoporous silica materials by different research groups are then summarized. These mechanisms help our understanding of how various mesoporous silica materials with different structural features form and how their particle sizes, shapes, and pore structures can be controlled. Finally, chemical routes utilized for surface modification of mesoporous silica materials or to produce a diverse range of multifunctional mesoporous silica nanomaterials are discussed.

Syntheses and structural properties of various mesoporous silica materials

Synthetic mechanism

According to the International Union of Pure and Applied Chemistry (IUPAC), mesopores are defined as pores with sizes in the range of 2–50 nm. The first report on the synthesis of mesoporous materials, e.g., MCM-41 (Mobil Crystalline Materials), in the early 1990s was a milestone in materials chemistry.[22,23] These materials have significantly larger pores than molecular sieves and zeolites. Their smaller pore sizes are actually what causes the latter to have limited applications. Thus, these new reports on the syntheses of mesoporous materials with larger pores than molecular sieves and zeolites invigorated a wave of research interest on the synthesis of other mesoporous materials with different ordered structures and pore sizes.

The general approach to synthesis of mesoporous silica materials involves "soft-templating", which is actually the same as the method used to make traditional molecular sieve and zeolite materials. However, there are some key differences between the two, i.e., between the synthetic methods used for making the two classes of porous materials (mesoporous silicas versus molecular sieves and (or) zeolites). Traditional molecular sieve and zeolite materials are typically synthesized through hydrothermal reactions between aluminosilicate gels and quaternary organic compounds having short alkyl chains, such as tetrapropylammonium or tetrabutylammonium ions.[24–26] While these organic groups serve as templating agents, they only allow the formation of micropores, i.e., pores with diameters < 2 nm according to IUPAC.

In one of the first groundbreaking works in the early 1990s, Kato and co-workers[28] developed a convenient method for synthesizing mesoporous silicas by using polysilicate kanemite ($NaHSi_2O_5{\cdot}3H_2O$) as the silica precursor and alkyltrimethylammonium chlorides, which have a much bigger size than tetrapropylammonium or tetrabutylammonium ions, as the structure-directing or templating agents. Moreover, by changing the length of the alkyl chains, the authors showed that the layered kanemite could be intercalated with different guest molecules and, most importantly, could be made to have tunable pore sizes ranging from 2 to 4 nm in diameter. Although this demonstrated one of the first syntheses of mesoporous materials with tunable pore sizes, the experiment did not result in materials with an extensive array of ordered mesoporous structures. This was the case until the reports on the synthesis of MCM-41 by Kresge and co-workers.[22,23]

In major groundbreaking works, also in the early 1990s, Kresge and co-workers[22,23] reported the synthesis of MCM-41 and the concomitant syntheses of MCM-48 and -50 mesoporous silicas (the M41S family of mesoporous materials). These were among the first series of mesoporous materials with not only mesoscopic pores but also well-ordered mesoporous structures to be documented in the literature. These reports also paved a new avenue to a vast number of the other ordered mesoporous materials reported subsequently. The M41S family of mesoporous materials was synthesized from the hydrolysis and condensation of silica precursors around ordered arrays of surfactant micelle templates, followed by the removal of the templates by calcination or solvent extraction. The synthetic method, sometimes called soft-templating, allowed the formation of different types of mesoporous silica materials having regular arrays of uniform cylindrical channel pores as a result of the spontaneous self-assembly of surfactant species, such as the cationic surfactant cetyltrimethylammonium ion (i.e., $C_{16}H_{33}(CH_3)_3N^+$), in aqueous solution into a regular array of cylindrical micelle aggregates or templates. Furthermore, the synthesis enabled mesoporous silica materials with different pore sizes to form simply by using surfactants with different alkyl chain lengths or by adding auxiliary hydrocarbons (e.g., alkylated benzene) into the reaction mixture to swell the micelles. Furthermore, the shapes of the regular arrays of surfactant micelles as well as the resulting mesoprous silica materials were easily changed from hexagonal to cubic by increasing the molar ratio of surfactant-to-silica precursor in the solutions.

To explain how the highly ordered structures in the M41S family of mesoporous materials formed, Kresge and co-workers[22,23] proposed a mechanism known as liquid crystal templating (LCT) (Fig. 1*a*). Acoording to the authors, the process involves the following four steps: (1) surfactant micelles form in the aqueous solution and assemble into cylindrical micelles; (2) the cylindrical micelles are stacked into a regular array of liquid crystalline structures; (3) anionic silicates form in the solution from the silica sources such as tetraethyl orthosilicate (TEOS) and then adsorb onto the

Can. J. Chem. Downloaded from www.nrcresearchpress.com by MCGILL UNIVERSITY on 02/02/13
For personal use only.

positively charged surfaces of liquid crystalline surfactant micelles; and (4) the removal of the surfactant templates either by calcination or by solvent extraction results in the mesoporous silicas. In an alternative pathway described by the same authors, step 3 was considered to take place at the same time as steps 1 and 2.[22,23] As the steps in this LCT process vary upon changing reaction conditions, such as by changing the ionic strength in the solution, the anionic charges on the silicate species and the surfactant concentrations in the solution, or by adding co-surfactants, the structures of the final mesoporous materials can also change accordingly.[22,23]

Interestingly, mesoporous silicas were also shown to form at very low concentrations of silicate and surfactant in strongly basic solutions, conditions under which liquid crystalline phases should not form according to the surfactant–water phase diagrams.[29] Thus, based on these observations, Davis and co-workers[31] proposed an alternative mechanism called cooperative self-assembly for the synthesis of MCM-41. This consisted of the following three synthetic steps: (1) the surfactant micelles form in such a way that the cationic head groups of the surfactant would be in contact with the surrounding solvent molecules; (2) negatively charged silicates, which form from silica precursors under basic conditions, aggregate on the periphery of surfactant micelles via Coulombic attraction, producing a layer of silicate species; and (3) the silicate–surfactant complexes spontaneously form hexagonally ordered mesostructures as the condensation of silicates with the surfactant molecules takes place. This model suggested that charge matching between cationic surfactants and anionic silicates could play an important role for the self-assembly of silicate–surfactant complexes into ordered arrays.[32] However, this proposition was still not able to explain why the ordered packing structures of surfactant–silicate complexes changed as the surfactant-to-silicate ratio was altered.

Using ^{14}N nuclear magnetic resonance (NMR) spectroscopy, Steel et al.[33] investigated surfactant mesophases during the formation of highly ordered mesostructured materials and proposed a so-called "puckering layer" model, in which silicate species were first formed and then directed by surfactant templates into layered structures. These layered structures were further wrinkled into hexagonal channels as the silicate species aggregated around the surfactant micelle templates. Around the same time as this proposition was made, Stucky and co-workers[29] reported the synthesis of MCM-41 materials at different temperatures and with different reaction times. The authors investigated the structures and compositions of the mesoporous materials using X-ray diffraction and ^{29}Si magic-angle spinning (MAS) solid-state NMR spectroscopy. Based on the results, they provided an explanation for how the ordered mesoporous structures in the mesoporous silicas were formed, which is illustrated in Fig. 1*b*. Their proposed model included the following processes: (1) oligomeric silica polyanions (denoted as I^-) outcompete monovalent silicates to bind with cationic head groups of surfactants (denoted as S^+); (2) charge density matching at the interface between the silicate anions and the surfactant cations takes place, forming surfactant–silicate complexes (S^+I^-), which lead to thermodynamically favored lamellar configurations in the early stages of the reaction; (3) as polymerization of the silicates continues, two oppositely facing lamellar layers with the same charge, which tend to repel apart, result in the reduction of charge density of the anionic silicates while, at the same time, augmenting the head group area of the surfactant assembly; and (4) to match the reduced charge density and keep the silicate-to-surfactant ratio constant, the hexagonal mesophases shape up. This cooperative mechanism provided a good explanation for the precipitated mesophases from dilute surfactant and silicate solutions, and also predicted the possible formation of cubic mesostructures under some specific reaction conditions.

Huo et al.[34,35] extended the model proposed by Stucky and co-workers[29] so that it would be generic enough to explain the formation of various other mesostructured nanomaterials (besides mesoporous silica), those having inorganic–organic interfaces, and those synthesized from reactants containing different charges. For instance, this model managed to explain the formation of a variety of mesostructured metal oxides at low pH from inorganic compounds that are more acidic than silicic acid. Furthermore, the model was applied to different mesophases, where S^-I^+-type assembly was possible by simply varying the $[H^+]$ in solutions and where the charge density between the cationic inorganic species (I^+) and the anionic surfactant templates (S^-) was matched. Furthermore, the model could also be applied to systems containing positively charged surfactant S^+ and inorganic moieties I^+ (or negatively charged S^- and I^-).[34,35] In this case, the formation of the mesophases and their structures could be controlled as long as the mediated counterions X^- (or X^+ in the case of S^- and I^-) were properly chosen. In cases where a cationic surfactant and an inorganic compound were used, X^- (X^- = halide ions, e.g., Cl^- or Br^- ions) first bound to the cationic head groups of surfactants and formed (X^-S^+)-type double layers.[34,35] This left the outer negatively charged surface to bind to the positively charged inorganic species (I^+); the resulting aggregate generated a sandwich-like triple-layered ($I^+X^-S^+$) structure. Likewise, ($I^-X^+S^-$) self-assembly was formulated for reactions containing I^-, S^-, and X^+ (X^+ = alkali metal ions, e.g., Na^+ or K^+).[34,35] Both $I^+X^-S^+$- and $I^-X^+S^-$-type self-assembled structures were found to be stable, versatile, and lead to a diverse range of mesophases as well as self-assembled surfactant-templated mesostructured materials. The removal of the surfactant templates from these as-made mesostructured materials by calcination or solvent extraction then resulted in different types of mesoporous materials. Thus, this model provided a theoretical foundation and an experimental guidance for phase-controlled synthesis of a variety of mesoporous silica materials.

Shortly after this proposal, the Pinnavaia group[36,37] demonstrated a synthetic route to mesoporous silicas using neutral surfactants (S^0) (e.g., primary amines and polyethylene oxides, PEO) as templates with inorganic silica precursors (I^0) (e.g., TEOS). In this case, the surfactant monomers first formed rod- or worm-like neutral micelles in aqueous solution, which were bound to hydrolyzed silica sources via hydrogen bonding (S^0I^0). This was followed by the condensation of silanol groups of the hydrolyzed silicate species and their assembly with the surfactant micelles into the hexagonal mesostructured materials. With the addition of a co-solvent (for example, ethanol or methanol) in the reaction solutions to enhance the solubility of the neutral surfactant molecules,

Fig. 1. (*a*) Proposed liquid crystal templating (LCT) mechanism for MCM-41 formation via two possible pathways (indicated as 1 and 2) as stated in the text.[22,23] (From Beck et al. 1992, reproduced (adapted) with permission of J. Am. Chem. Soc., Vol. 114, p 10834, © 1992 American Chemical Society). (*b*) Illustration to demonstrate the phase shift of surfactant–silicate aggregates from lamellar to hexagonal form.[29] (From Monnier et al. 1993, reproduced (adapted) with permission of Science, Vol. 261, p 1299, © 1993 The American Association for the Advancement of Science). (*c*) Silicatropic liquid crystal (SLC) model proposed to explain the cooperative formation of surfactant micelle–silicate species mesophases.[41] (From Firouzi et al. 1995, reproduced (adapted) with permission of Science, Vol. 267, p 1138, © 1995 The American Association for the Advancement of Science).

Can. J. Chem. Downloaded from www.nrcresearchpress.com by MCGILL UNIVERSITY on 02/02/13
For personal use only.

nonionic molecules also self-assembled into hexagonal-type mesoporous silicas, denoted as the HMS or MSU series.[36,37] These materials had larger pores and thicker pore walls, but short-range-ordered hexagonal structures compared with that of MCM-41. This is because a much weaker interaction, i.e., hydrogen bonding between the neutral surfactant molecules and the silica precursors, is involved in HMS or MSU synthesis, whereas stronger interaction, i.e., electrostatic forces between charged ion pairs, is involved in MCM-41 synthesis.[36,37] Moreover, the residual alcohols, either used as a co-solvent or produced in the reaction when the TEOS underwent hydrolysis, were believed to destruct the liquid crystalline structures originally formed when the nonionic surfactants were added, thereby leading to a less-ordered mesostructure.[36]

With these research reports on nonionic surfactant template synthesis of mesoporous materials in place, the LCT mechanism proposed previously was revisited by the Goltner group[38–40] to describe the synthesis of mesoporous silicas (pore diameter = 3 nm) in reactions where neutral surfactants in relatively high concentrations were used. The formation of a homogenous lyotropic liquid crystal (LLC) phase was detected even before the addition of silica precursors. These ordered liquid crystalline mesophases were believed to then serve as templates for directing the condensation of inorganic silicates. The big similarity between the phase diagrams of the surfactant / silica precursor / water system at high surfactant concentration and the surfactant/water system without silica precursors further supported the formation of organic mesophases independent of the inorganic silicate species.[38–40]

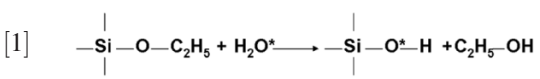
By incorporating the "ion exchange" concept adopted in the work reported by Inagaki et al.,[41] Chmelka and co-workers[30,42] proposed a silicatropic liquid crystal (SLC) model to further explain how mesoporous silicas were formed under low concentrations of ion pairs of organic and inorganic species. Based on neutron scattering data and various NMR spectra, the authors explained how mesophases with ordered arrays were self-assembled as follows: (1) An equilibrated solution of organic surfactant contained the individual molecules as well as various micelles with different geometries, whereas silicates in extremely basic condition were oligomerized to form polyanionic charged species. (2) Immediately after the silica precursors and surfactants were mixed, ion exchange took place between surfactant anions and negatively charged silicates to form organic–inorganic complexes in which the double-four-ring silicate oligomers (cubic octamer) were preferentially formed. (3) The silicate species in diluted surfactant solutions were coordinated with the isotropic micelles, forming an ordered surfactant–silicate array, shaping an SLC mesophase.[30,42] This model underscored the existence of micelle aggregates with certain geometries in solutions containing surfactant and silica precursors and the presence of cooperative organization of surfactant–silicate moieties into ordered arrays of mesostructures. This proposed mechanism was also what has finally become the generally accepted mechanism for the direct synthesis of mesoporous silica materials with different pore sizes and shapes.

Synthetic condition and structural determination

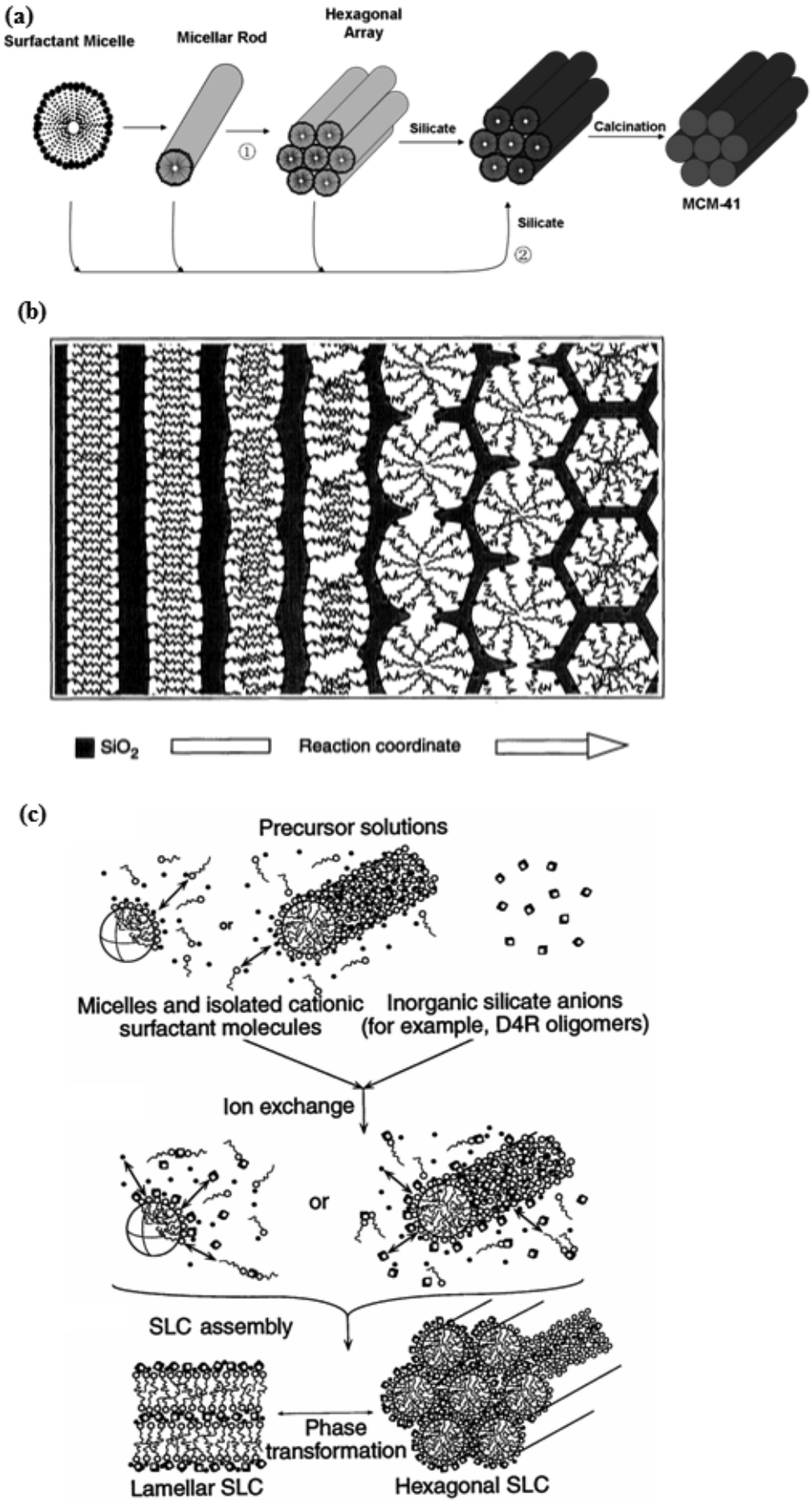
The combination of the "sol-gel" process and supramolecular self-assembly under hydrothermal conditions is what has been widely adopted as the synthetic method towards various mesoporous silica materials. In the process, silica precursors such as TEOS are dissolved into an aqueous solution containing surfactant. The silica precursors then undergo hydrolysis and condensation to form a solution called *sol*, which contains oligomeric and polymeric silicate species. In the presence of surfactant and their aggregates (or micelles), the hydrolysis and condensation reactions of silica precursors lead to the formation of organic–inorganic (i.e., surfactant–silicate) species that become increasingly polymerized and form a *gel* as the reactions proceed. The self-assembled surfactant–silicate material (or the *gel*) ultimately precipitates out of the solution. The solution is then filtered, and the solid materials are washed and treated by calcination or solvent extraction to remove the surfactant-templating agents and to produce the mesoporous silica materials.

The experimental variables, such as pH, reaction temperature, type of surfactant or silica source, etc., employed during the supramolecular self-assembly of the mesostructured materials can affect how the sol-gel reactions and self-assembly processes take place, and thereby what structural features of the final mesoporous silica materials will have.[7–9] Thus, the selection of an appropriate silica precursor and surfactant is vital for mesoporous silicas with the desired structural features to form. Furthermore, as temperature and pH affect the rates of hydrolysis and condensation of silica precursors and the dynamic self-assembly process in which the silica precursors aggregate with the surfactant micelles, these variables should be optimized to obtain mesoporous silicas with suitable or optimized structures for various applications. For example, TEOS, which is one of the most commonly used silica precursors, undergoes hydrolysis and polymerization as illustrated in eqs. [1]–[3] with variable reaction rates in solutions at different pHs.

Hydrolysis

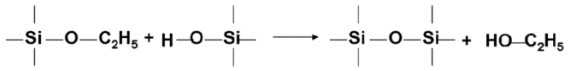


Can. J. Chem. Downloaded from www.nrcresearchpress.com by MCGILL UNIVERSITY on 02/02/13
For personal use only.

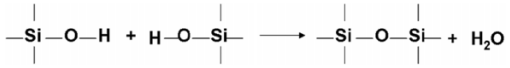


Can. J. Chem. Downloaded from www.nrcresearchpress.com by MCGILL UNIVERSITY on 02/02/13
For personal use only.

Condensation

[2] 

or

[3] 

Brinker and Scherer[43,44] suggested that the hydrolysis of silica precursors and silicate intermediates occurs with the oxygen atoms from water molecules (asterisked in eq. [1] initiating nucleophilic attack on silicon atoms of the silica precursors or intermediates, regardless of what the pH of the solution is. Subsequently, the condensation reaction, which produces alcohol (eq. [2]) or water (eq. [3]) as the byproduct, takes place to produce dimers, linear or cyclic silicate trimers, and tetramers that grow into a cross-linked network of silicate structures.[43,44] The rate of the hydrolysis reaction decreases as the length of the silicate species increases,[9] since the alkyloxide groups on longer silicate chains are worse leaving groups owing to their reduced ability to donate electrons as well as their increased steric hindrance for nucleophilic attack.[43,44]

The rate of hydrolysis or condensation of silica precursors during the synthesis of mesoporous materials strongly depends on the pH of the solution. For example, under basic conditions, hydrolysis of silica precursors is accelerated, since OH^-, which is a good electron-providing group with a small size, can attack effectively the silicon atoms of the silica precursors. However, when pH > 8, the condensation rate decreases and even becomes reversible. As a result, penta- or hexa-coordinated silicate intermediates are transiently produced or, conversely, highly cross-linked silicates are unable to form in such strongly alkaline solution.[7,43] Under acidic conditions, the silanol groups on the silica oligomers are easily protonated, making the silicon atoms become more electrophilic. Simultaneously, the counterions (X^-), such as F^-, Cl^-, or Br^-, from the acidic catalysts or surfactant act as the nucleophiles to attack the silicon atoms.[43,44] This results in the rapture of Si–O bonds and the formation of Si–X bonds that can be more easily hydrolyzed. The silicate species with protonated silanols then fuse together or with other silicate species having neutral silanols, leading to polymerization.[43] In this process, the stronger X^--bonded surfactants catalyze the condensation reaction and often result in faster polymerization.[45] At pH < 2, the rate of condensation becomes higher at lower pH; whereas at 2 < pH < 8, condensation becomes quicker at higher pH.[7] At pH 2 (i.e., the isoelectronic point or pI of silica), the rate of condensation becomes the slowest because of the zero net charge carried by silicon atoms. Under this condition, silicates undergo the slowest hydrolysis because of the limited amount of available protons or hydroxyl ions on them. However, once hydrolyzed, the silica precursors produce either positively and negatively charged silicate species that lead to faster condensation. For this reason, neutral solutions were once thought inappropriate for synthesis of mesoporous silicas with ordered structures.[9]

As mentioned previously, the synthesis of MCM-41[22,23] is possible with surfactants at concentrations below the critical micelle concentration (CMC). However, it is well-known that surfactants at such low concentrations cannot form micelles or mesophases. Furthermore, the hydrolysis and condensation of silica precursors such as TEOS without surfactants only lead to the formation of amorphous silica. Thus, combining these facts and observations, it was concluded that the surfactant-directed condensation of silica at the micelle–silicate interface must be responsible for the formation of mesostructured or mesoporous silica materials.[46]

To explain this further, a packing parameter (p) of an effective surfactant ion pair, first defined by Israelachvili,[47] was introduced by Stucky and co-workers[29,48] as a structural variable to analyze the geometry of surfactant–silicate mesophases and the phase transformation of mesostructures under various conditions. The packing parameter is given by the equation $p = v/a_0 l_c$, where v is the molecular volume, a_0 is the head-group area with minimum energy at the hydrophobic–hydrophilic interface, and l_c is the maximum length of the hydrophobic chain. As the value of p increases, the ordered mesostructures change from hexagonal, cubic, and lamellar aggregates to their reverse counterparts because of the changes in the physicochemical properties of the solutions; i.e., changes in either the surfactant (changes in its v, a_0, or l_c) or the reaction conditions (e.g., pH, temperature, and type of solvent used in the reaction).[49]

Surfactants employed in the synthesis of mesoporous silica materials can be cationic, nonionic, and to a lesser extent, anionic. Regardless of the type of surfactant used for the synthesis of mesoporous silicas, once the concentration of surfactant reaches the surfactant's CMC value, the surfactant molecules in aqueous media assemble into micelles with centripetal (hydrophobic) tails and centrifugal (hydrophilic) heads, forming a system with the lowest interfacial energy. Surfactants with low CMC values were generally found to be suitable for the synthesis of mesoporous silicas with highly ordered structures.[50] Similarly, for a given surfactant, any reaction variable including pH, temperature, a co-solvent, or an electrolyte that can lower the surfactant's CMC often lead to mesoporous silicas with well-ordered structures. Given the fact that the pI of silica is 2.0, silica is negatively charged under most pH values. Thus, cationic surfactants, which were originally used in mesoporous silica materials syntheses,[22,23,29,31,33–35] especially those with quaternary ammonium head groups and long alkyl chains, are more suitable for synthesis of mesoporous silicas because of their stable positively charged head groups independent of the pH of the solution and their comparatively low CMC values.

Huo et al.[48] reported the formation of different types of mesophases and mesoporous silica materials when cationic surfactants with different sizes were used in the synthesis. Under similar alkaline solutions containing a mixture of TEOS and different alkyltrimethylammonium ($C_nH_{2n+1}(CH_3)_3N^+$) surfactants, the authors described the formation of hexagonal MCM-41 when n = 10–18, but lamellar MCM-50 when $n \geq 20$. Given $p = v/a_0 l_c$ and the fixed a_0 value of the surfactant, the ratio between v and l_c remained nearly unchanged for $C_nH_{2n+1}(CH_3)_3N^+$ when n = 10–18. This ratio further increased as the value of v was kept constant and the value of l_c became smaller owing to the coiled hydrocarbon chain when $n \geq 20$.[48] The change in mesophase and the structure of the materials from MCM-50 to MCM-41 was also demonstrated

Can. J. Chem. Downloaded from www.nrcresearchpress.com by MCGILL UNIVERSITY on 02/02/13
For personal use only.

by inserting hydroxyl groups into the surfactant molecules. The hydroxyl groups enhanced the hydrophilicity of the head groups of the surfactant, and thereby reduced their effective head group area a_0 and their p values.[48] Furthermore, upon changing the methyl groups of the cationic surfactant (i.e., $C_nH_{2n+1}(C_2H_5)_3N^+$) to ethyl groups or upon changing the solution from basic to acidic, the value of p generally became smaller. This can be accompanied by the formation of cubic SBA-1 (Santa-Barbara Amorphous-1) material for $n \leq 18$ and hexagonal SBA-3 for $n \geq 20$.

Gemini surfactants, a class of amphiphilic molecules encompassing two traditional surfactants connected by a spacer via covalent bonds (e.g., $[C_nH_{2n+1}(CH_3)_2N^+–(CH_2)_s–N^+(CH_3)_2C_mH_{2m+1}]\cdot 2Br^-$ or $C_{n–s–m}$, in a simplified notation), were also employed as templating agents for the synthesis of mesoporous silicas.[51,52] Gemini surfactants generally have lower CMC values and higher surface activity compared with either one of the single-chain surfactants in them. If the length of the spacer (s) in the gemini surfactant remains unchanged while either one of the two alkyl chains gets longer (i.e., either n or m increases), the the $C_{n–s–m}$ gemini surfactant becomes more like a mono-quaternary ammonium surfactant and, most importantly, its CMC value decreases exponentially. Furthermore, for gemini surfactants with $n = m = 12$ or 16, the CMC value of the surfactant gradually reaches the highest value as the value of s is increased from 1 to 5, but then the CMC value dramatically declines when $s = 6–16$.[53] The spacer between the two head groups of the individual surfactant chains was also found to play an important role on the shape of the micelles and the rate of their formation.[54–56] For example, the shorter spacers resulted in the formation of aggregates with less curvature and a faster rate of formation of the micelles. Thus, by changing n and m as well as s of the gemini surfactants, not only different micelles can be prepared but also mesoporous silicas with different structures and tunable pore sizes can be synthesized. For instance, when $C_{16–s–16}$-type surfactants with $s = 2$ or 3, $s = 8$, and $s = 12$ were used as templating agents, lamellar-type MCM-50, hexagonal MCM-41, and cubic MCM-48 mesoporous silicas, respectively, were obtained.[51,52] When $C_{n–s–1}$ was used as the surfactant, SBA-2 mesoporous silica with a three-dimensional hexagonal cage structure formed.[48,51,52]

As briefly mentioned, neutral surfactants were also employed as templating agents to synthesize mesoporous silicas. In particular, the work by the Pinnavaia group[36,37] on the synthesis of various mesoporous silica materials at neutral pH using different neutral surfactants is worth mentioning. Specifically, primary amines or PEO-based surfactants were used and self-assembled with TEOS via hydrogen bonding at ambient temperatures, producing ordered mesoporous silicas. When the neutral surfactants were composed of $C_8–C_{18}$ alkyl chains containing primary amines, hexagonal mesoporous silicas with correspondingly increasing micro- or mesopore sizes (1.6–3.1 nm) depending on the size of the alkyl chains were obtained.[36] Interestingly, the mesoporous silicas produced with these neutral surfactant-templating agents had smaller pores and thicker pore walls compared with those synthesized using cationic surfactants with similar alkyl chain lengths as templates.[36] When alkyl chains containing PEO groups, $C_nH_{2n+1}O(CH_2CH_2O)_iH$, with $n = 11–15$ and $i = 9–30$, were used as templating agents, various mesoporous silica materials called the MSU series were formed. When the value of i changed from 9 to 30, the materials' pore sizes generally increased from 2.5 to 4.8 nm and their surface areas decreased from 1010 to 525 m^2/g.[37] Furthermore, substituting the C_6H_{13} with a phenyl group (that is, using alkyl chains with shorter lengths but with the same total number of carbon atoms) led to the formation of a material called MSU-2 mesoporous silica having a reduced pore size and surface area.

The other most commonly and successfully utilized neutral surfactants for the synthesis of mesoporous silica materials are a class of block copolymers called Pluronics. A Pluronic surfactant composed of polyethylene oxide – polypropylene oxide (PEO–PPO) block copolymers was among the first of these types of surfactants to have been used for the synthesis of mesoporous silica, specifically mesoporous silica called MSU-3 having large pores (5.8 nm) and high surface area (1190 m^2/g).[37] However, although these MSU-type mesoporous silicas had mesoporous structures and high surface areas, their mesoporous structures were not well-ordered, as evidenced by their disordered pore structures in their TEM images and the broad peaks in their X-ray diffraction (XRD) patterns. By optimizing the reaction temperatures to 25–65 °C,[57] by switching to gemini-type or sorbitan ester derivatives,[58,59] or by replacing the inorganic silica precursors with water-soluble silicates,[60] some improvements in their structures were made and MSU-X mesoporous silicas with worm-hole mesostructures and, most importantly, some short-range-ordered structures were obtained.[58,61] It is also worth mentioning that these MSU-X mesoporous silicas exhibited high (hydro)thermal stability owing to the high degree of silica cross-linkages in their structures.[58,61]

In a groundbreaking work, Zhao et al.[62,63] demonstrated the use of Pluronics multiblock copolymers of high molecular weights as templating agents in aqueous acidic solutions (pH < 1) to produce SBA-type mesoporous silicas with highly ordered mesostructures and tunable large pores. In their syntheses, different poly(alkylene oxide) (PAO) triblock copolymers, also known as Pluronic triblock copolymers, (e.g., poly(ethylene oxide)–poly(propylene oxide)–poly(ethylene oxide), i.e., PEO–PPO–PEO, or $EO_n–PO_l–EO_m$), were mixed with TEOS at low temperatures of 35–80 °C and aged for a few days.[62] By changing the synthetic conditions, SBA-type mesoporous silicas with various pore sizes and wall thicknesses were produced. When the surfactant had a low EO:PO ratio, the as-made mesoporous materials had hexagonally ordered mesoporous structures, which were named SBA mesoporous silica materials. The most notable member of this family of materials is hexagonally ordered SBA-15 mesoporous silica, which has typical pore sizes in the range of 3–10 nm depending on the specific synthetic conditions used to make it. It is worth noting that the pore sizes, as well as wall thicknesses, of SBA-15 are bigger than those of hexagonally ordered MCM-41. Increasing the surfactant-to-TEOS ratio in the reaction mixture resulted in the formation of lamellar structure, whereas increasing the EO:PO ratio led to the formation of cubic-shaped mesoporous silica called SBA-16.[62]

When triblock copolymers were replaced by star-shaped diblock copolymers, the synthesis led to the formation of cubic-

Can. J. Chem. Downloaded from www.nrcresearchpress.com by MCGILL UNIVERSITY on 02/02/13
For personal use only.

ordered mesostructures, usually having a higher surface area (>1000 m^2/g) and a smaller pore size (3.0–4.5 nm) compared with those obtained with Pluronics.[63] Furthermore, whereas shorter EO segments on the Pluronics surfactants favored the formation of lamellar-shaped aggregates, the longer ones led to the formation of cubic-ordered mesostructured materials called SBA-11. The cubic-ordered mesostructured materials were also produced when neutral surfactants with shorter alkyl chains such as $C_{16}H_{33}$ were used as templating agents. Their longer alkyl chain counterparts such as $C_{18}H_{37}$, however, favored the formation of a 3D hexagonally ordered mesoporous silica material called SBA-12.[63]

During the formation of SBA-X type mesoporous silicas with these nonionic PAO surfactants under acidic solutions (with pH < 2), electrostatic- and hydrogen-bonding interactions were suggested to be the prominent types of interactions occurring between the nonionic PAOs and the silica precursors in solutions. During the self-assembly process, the counterions X^- (e.g., halide, NO_3^-, or SO_4^{2-}) from the acid added into the solution to lower the pH bound to the positively charged silicate species in the periphery, and they subsequently attracted the protonated PEO sections of the surfactant molecules.[64–66] This then led to the formation of $(S^0H^+)(X^-I^+)$-type self-assembled structures, and ultimately materials such as SBA-15 mesoporous silica.

This proposed mechanism for formation of mesoporous silica using nonionic Pluronic surfactants was supported by solid-state NMR spectroscopy and XRD data. Besides the well-ordered mesoporous structures, gas adsorption measurement of the SBA-type material further revealed that there were some small disordered pores (diameter < 3.4 nm) between the large pores.[67] The formations of these complementary micro- and (or) meso-pores were suggested to be formed as a result of the insertion of the hydrophilic PEO chains into the silicate network during the very early stage of the supramolecular self-assembly of the material.[65,67] These sidewall pores exhibited a high thermal stability and also contributed to the total surface area of the material,[67] potentially serving as a host for guest molecules and some catalytic groups.

Later, by using various neutral triblock copolymers in acidic media, the Zhao group synthesized many new types of mesoporous silicas with a variety of shapes, named FDU-type mesoporous silicas.[9] The list includes caged cubic-ordered mesoporous silicas with large pore sizes (up to 12 nm) called FDU-1,[68] 3D bicontinuous gyroid-shaped mesoporous silicas with narrow pore size distributions (4.5–9.5 nm in pore diameter) called FDU-5,[69] and cagelike face-centered cubic-ordered mesoporous materials with large pore mouths (4–9 nm in pore diameter) called FDU-12.[70]

The fact that $(S^+X^-I^+)$, (S^+I^-), and $(S^0H^+)(X^-I^+)$ types of interactions between cationic or neutral surfactants and inorganic silica sources led to mesoporous silicas made researchers become curious about whether anionic surfactants could also be utilized as templating agents for the synthesis of mesoporous silicas via (S^-I^+) or $(S^-X^+I^-)$ types of interaction. Common anionic surfactants include those containing long hydrocarbon chains with terminal sulfate, sulfonate, phosphate, and carboxylate groups and whose pK_a values are generally >2 (or the pI of silica).

To examine the feasibility of the use of anionic surfactants in supramolecular self-assembly of mesostructured materials, it is essential to understand the possible interactions in the system used for the synthesis. On the one hand, for reaction media where pH << pK_a of the anionic surfactant, the anionic surfactants remain barely dissociated and barely soluble in aqueous solutions, making the interactions owing to charge matching between surfactants and silica precursors almost impossible. Therefore, acidic conditions are not usually suitable for the preparation of mesoporous silicas with anionic surfactants via the (S^-I^+) route. On the other hand, under basic conditions with pH ≥ pK_a of the anionic surfactant, condensation of silica precursors leads to negatively charged silicate networks that repel the anionic surfactants. Thus, a counterion X^+ has to be involved for an $(S^-X^+I^-)$ type of interaction to occur and for mesoporous silica to form under basic conditions.

These hypotheses were first tested by the Dai group,[71,72] which successfully synthesized bridged inorganic–organic nanocomposite materials using anionic sodium dodecyl sulfate (SDS) as the surfactant and 3-aminopropyltriethoxysilane (APTES) as the silica precursor in the presence of coordination compounds containing the metal cations Cd^{2+}, Zn^{2+}, or Ni^{2+}. The Coulombic force between the anionic surfactant and the cationic metal compounds and the strong coordination bonds formed between the metal ions and the amine groups in APTES led to the self-assembly of such a system into different types of mesophases, depending on the type of metal used and the mole ratio of the substances used for the synthesis.[72] Similarly, the Tatsumi group[73,74] reported the synthesis of mesoporous silicas using anionic surfactants as templating agents. Specifically, the authors used 3-aminopropyltrimethoxysilane (APS) or *N*-trimethoxysilylpropyl-*N*,*N*,*N*-trimethylammonium chloride (TMAPS) as the co-structure-directing agent (CSDA) to form $S^-X^+I^-$ types of self-assembled structures or anionic-surfactant-templated mesoporous silicas (AMSs). During the synthesis, the alkoxysilyl portion of APS or TMAPS was integrated with the alkoxysilyl portion of a typical silica source (e.g., TEOS) to produce the silica network. The protonated amino groups of APS (i.e., protonated $X(H)^+$ species, which were produced when their $pK_b \geq 14 - pH$) or when the positively charged quaternary ammonium ions of TMAPS made electrostatic interactions between the silicate ions and the anionic surfactants (e.g., *N*-acyl amino acids or long alkylsulfates) possible. This finally led to the formation of as-synthesized AMS materials. Furthermore, by changing the type of anionic surfactant and its mole composition, AMS materials with different mesostructures, ranging from hexagonal- and cubic-ordered 3D materials called AMS-1 and AMS-2, respectively, to double-diamond-shaped bicontinuous cubic-ordered AMSs called AMS-10 were produced.[74–77] It is worth noting that, compared with mesoporous silicas synthesized by using cationic or neutral surfactants, AMS generally possessed smaller surface areas (typically in the range of 387–963 m^2/g).

Neutral chiral molecules (e.g., *N*-acyl-L-alanine or *N*-acyl-D-alanine) can also be used as templating agents for making mesoporous silicas. Interestingly, such templating agents form mesoporous materials that are chiral. Che et al.[78] synthesized chiral mesoporous silicas with helically twisted rod-like morphologies of 130–180 nm in diameter and 1–6 μm in length. The material had uniform hexagonally ordered

Can. J. Chem. Downloaded from www.nrcresearchpress.com by MCGILL UNIVERSITY on 02/02/13
For personal use only.

mesochannels with an average pore diameter of 2.2 nm.[78] Moreover, by using APS as the CSDA, instead of TMAPS, the ratio of left-handed to right-handed structures in the resulting material was altered from 65:35 to 75:25. These novel mesoporous silica materials with a chiral mesoporous structure were further used successfully to direct the growth of chiral metal nanowires inside their channel pores.[78] Thus, besides their interesting structures, the resulting chiral mesostructured materials may also find potential applications in chiral catalysis and enantioseparation.[79]

Efforts towards the synthesis of mesoporous silicas by using unconventional molecules or nonsurfactant systems as templating agents were made by Wei and co-workers.[80–84] The authors attempted and successfully synthesized various mesoporous silica materials by using carbohydrates, such as glucose or maltose, or hydroxyl carboxylates, such as citric acid or tartaric acid, as pore-forming agents.[80–84] In their typical synthetic procedure, they mixed the organic SDAs to interact with the inorganic silica precursors at ambient temperatures and under mild pH (~6 or slightly higher).[80–84] After extraction of the organic groups from the final solid materials, they obtained MCM-41-like materials with tubular mesopores, high surface areas (~1000 m^2/g), and large pore volumes (~1.0 cm^3/g). Furthermore, they showed that the pore sizes in the materials were reasonably monodisperse (2–6 nm in diameter) and tunable by changing the concentration of the organic templates[80–84] or, to a lesser extent, by changing the type and molecular size of the templates.[80]

The mechanism leading to the formation of the mesophases and mesoporous silica materials with nonsurfactant templates was proposed to be similar to those obtained with surfactant (nonionic) templates.[36,37] Hydrogen-bonding interactions between the nonsurfactant molecules and the silica precursors were again considered to play significant roles in their self-assembly into mesostructured materials.[80,83] Other interactions were also considered to be possible depending on the composition of the reaction mixture. For instance, when TEOS and tartaric acid were used with metal chlorides such as NaCl, $MgCl_2$, and $AlCl_3$, the metal ions were coordinated with the carboxylate groups in tartaric acid, forming metal-modified structure-templating complexes. These complexes then interacted with the inorganic silica species and underwent self-assembly.[84] In this process, the larger metal ions were found to promote the formation of enlarged aggregates, in the order of $Al^{3+} > Mg^{2+} > Na^{+}$.[84]

It is worth noting at this point that the synthesis of porous silicas using nonsurfactant templates was actually attempted in 1997, when Mann and co-workers[85] reported the synthesis of macroporous MCM-41 fibers (~500 nm pore width) with an extended length scale porous structure using a thread of multicellular filaments from soil bacteria as templates. In the synthesis, bacterial filaments were used not only as the templating agents but also as an alignment axis for silica growth as well as as pore-swelling agents.

It is important to mention here that all these nonsurfactant self-assembly routes to mesoporous silicas are considered to be more environmentally friendly compared with traditional surfactant self-assembly syntheses, as the former utilize greener organic or natural and (or) biological molecules as templates. However, although they have large surface areas and pore sizes, the mesoporous silica materials resulting from nonsurfactant self-assembly routes do not have highly tunable porous structures because of the limitation of the templating agents.

The other unconventional materials or molecules that have been successfully used as structure-directing agents or templates for the synthesis of mesoporous silica materials include ionic liquids. Room-temperature ionic liquids (RTILs) are a group of organic salts that remain liquid over a wide range of temperatures and that possess negligible vapor pressures and high ionic strengths. With regard to the use of ionic liquids as templates, the first report can be dated back to as early as the year 2000, where the Dai group[86] reported the synthesis of porous silica aerogels using RTILs as SDAs for silicate species produced by hydrolysis and condensation. In the report by Dai et al.,[86] formic acid, tetramethylorthosilicate (TMOS) and 1-ethyl-3-methylimidazolium bis[(trifluoromethyl)sulfonyl]amide were mixed and self-assembled under mild conditions. The removal of the RTILs from the materials with acetonitrile under reflux resulted in a homogeneous silica aerogel, without further supercritical drying. Later on, alkylated imidazolium-based ionic liquids were employed as templates to synthesize MCM-41-like hexagonal mesoporous silicas and organic–inorganic hybrid mesoporous nanocomposite materials.[87,88] This approach offered a new avenue for the synthesis of mesoporous silicas with highly ordered structures by using RTILs as SDAs.

The low volatility and high thermal stability of RTILs renders the RTILs' unique properties and advantageous features as templating agents for the synthesis of mesoporous silicas compared with other organic SDAs. For example, at 40 °C, the long-chain RTIL,1-alkyl-3-methylimidazolium chloride (i.e., $[C_n\text{min}]^+Cl^-$, where n = No. of carbon atoms in the alkyl chain; for example, $n = 16$), interacted with TMOS in the presence of acidic catalysts and produced ordered lamellar supermicroporous silica, with an interlayer spacing of ~2.7 nm and a slit pore diameter of ~1.3 nm.[89] However, unlike conventional surfactant templates, changing the alkyl chain length of the RTIL from $n = 14$ to $n = 18$ did not result in any change in the microstructures of the materials, leaving the pore diameters to vary only between 1.2 and 1.5 nm. Despite this drawback, at an elevated reaction temperature of 90 °C (40 °C < melting point of $[C_n\text{min}]^+Cl^-$, $n = 14–18 < 90$ °C), the pore structure became wormhole-like with a bigger pore size of ~2.7 nm.[90] Moreover, the synthesis using short-chain $[C_4\text{min}]^+BF_4^-$ or 1-butyl-3-methylimidazolium-tetrafluoroborate led to the formation of highly ordered mesoporous silicas that had bicontinuous wormhole-like mesopores of ~2.5 nm in diameter and ~2.5–3.1 nm in wall thickness.[91]

The self-assembly mechanism for $[C_n\text{min}]^+X^-$-templated synthesis of mesoporous silicas (here X^- stands for generic counterion, usually containing atoms of high electronegativity) involves interactions between X^- with silanol groups of silica precursors via hydrogen bonding on one side and π–π stacking between neighboring imidazole rings on the other side.[91] By using this mechanism, the effect of temperature on the structures of the mesoporous silica materials formed using the RTIL as the SDA can be explained. At elevated temperatures (or temperatures higher than the melting point of the RTIL), the fluidity of the RTIL molecules increases,

Can. J. Chem. Downloaded from www.nrcresearchpress.com by MCGILL UNIVERSITY on 02/02/13
For personal use only.

promoting molecular movement and altering their spatial aggregation to different micro- or meso-structures.

Besides acidic solutions, RTILs were also successfully used in basic solutions to produce mesoporous silicas. The Lin group used basic solutions for the self-assembly of $[C_n\text{min}]^+Br^-$ (n = 14, 16, or 18) with TEOS at 80 °C.[92] They obtained mesoporous silicas with pore sizes of 2.7–3.3 nm and with various morphologies ranging from spherical/ellipsoid to rodlike as the carbon number in the RTILs' alkyl chains increased and the intermolecular stacking between $[C_n\text{min}]^+$s subsequently strengthened.

The advantages of employing RTILs as templating agents to synthesize mesoporous silicas include their application as SDAs over a broad range of reaction temperatures as many of them remain liquid and stable under wide temperature ranges. It was also shown that some RTILs in the resulting mesostructured materials could render the materials with interesting properties, including inherent germicidal and antibacterial properties.[92]

Molecules such as folic acid have also been successfully used as templating agents for synthesis of mesoporous silica materials. For example, the self-assembly of folic acids and TEOS was recently shown to produce hexagonally ordered mesoporous materials with pore sizes of 2.5–3.0 nm, very large surface areas of up to 1155 m^2/g, and chiral mesostructures.[88] The materials were also shown to load many benzyl ring-containing anticancer drugs (e.g., doxorubicin) through π–π stacking between the drug and the mesoporous materials (specifically because of the pterin moiety of their folic acid groups).[93] Furthermore, because of their chiral properties, these mesoporous materials can be expected to find potential applications in chiral separation or asymmetric catalysis. Similar chiral-mesostructured silica materials were also obtained by using small chiral amino acid molecules, such as *N*-acyl-L-alanine or *N*-acyl-D-alanine, as templating agents, as indicated in the previous sections.[78]

Despite the different synthetic mechanisms proposed for mesoporous materials and the various synthetic routes used to make them, it is generally accepted that the interactions between templating agents and silica precursors play an essential role in the formation of highly ordered mesoporous silicas. Furthermore, the reaction times and temperatures influence how the organic templates aggregate and assemble with silicate species. This, in turn, determines the types of mesoporous silica materials the synthesis ultimately results in. For example, in surfactant-templated synthesis of mesoporous silicas, the addition of co-solvent could affect the shape and size of surfactant micelles and thus the dimension of the mesopores, depending on the polarity of the additives and the ionic strength of the solution. In general, in aqueous media, polar additives tend to fill up the gaps between the hydrophilic tails of the micelles, which leads to increased micelle volume but decreased micelle curvature. Nonpolar co-solvents, on the other hand, occupy the hydrophobic center and enlarge the sizes of the micelles.[9,51,62,63] For example, 1,3,5-trimethylbenzene has been commonly used as a swelling agent in the synthesis of SBA-type mesoporous silicas with bigger pores.[62,63] Besides increasing the pore diameters of the mesoporous materials, such additives can also affect the formation of the mesostructured silica materials. Generally, additives that induce more surfactant–silicate interactions tend to form more stable and organized silicate structures, and vice versa. In addition, elegant synthetic methods, sometimes called morphosynthesis, which were applied first by the Ozin group and a few other research groups, allowed fine tuning of the morphologies of mesoporous silica materials or produced mesoporous silicas with interesting structures and shapes, akin to the silica-based materials synthesized by organisms.[1,3]

Irrespective of the synthetic methods and the types of SDAs used, after the synthesis of the as-made mesostructured silica materials, all the surfactant templates have to be removed to generate the pores within the materials. This is typically performed either by solvent extraction or by high-temperature calcination.

The solvent-extraction method involves stirring the self-assembled silica–surfactant material in a solvent to wash off the surfactant, organic molecules, or ions from the material. As such, this method does not degrade the surfactant or the organic templates. Therefore, the extracted surfactant or templating agents can be recycled and reused, if necessary. Furthermore, this method results in mesoporous silicas with large densities of the surface hydroxyl groups, which can assist the materials during its functionalization with various guest molecules (see next section for more detail). However, this method has some disadvantages as well. Most notably, this method often results in incomplete removal of the organic templates, which sometimes causes detrimental effects, especially when the mesoporous silicas are applied in biological systems.

The second method, i.e., calcination, involves heating the as-made surfactant containing mesostructured silica material at high temperature (typically above 350 °C) in air or oxygen to remove the surfactant templates in the form of CO_2 and H_2O. This method enables the complete removal of the organic templates from the materials; therefore, this method is highly recommended, especially when as-synthesized mesostructured materials possess strong interactions between their surfactant templates and silica networks or when the final mesoporous silica materials are required to be completely free of organic templates, for example, for biological applications. However, compared with solvent extraction, calcination of mesostructured materials renders some disadvantages as well. In particular, calcination results in mesoporous silicas with lower densities of the surface silanol groups. Furthermore, calcination sometimes results in the partial collapse of the ordered structures or the mesochannel pores in the mesoporous silicas. By optimizing the calcination conditions, such as by using relatively low heating temperatures and short calcination times, some of these problems could be minimized.

Functionalization of mesoporous silicas

Functionalization strategies

Generally, functionalization of nanomaterials often enables the materials to obtain applications in many different areas. For instance, organic functionalization of nanomaterials allows the nanomaterials to have increased adsorption capacity and improved release profiles to guest (drug) molecules. Functional groups on nanomaterials can also serve as ligands to strongly bind to organometallic complexes and to catalytic

Can. J. Chem. Downloaded from www.nrcresearchpress.com by MCGILL UNIVERSITY on 02/02/13
For personal use only.

groups and then form nanomaterial-supported heterogeneous nanocatalysts.

The functionalization of mesoporous silicas typically involves the introduction of organic functional groups into the materials by using organosilanes. The process results in functional groups on the external, internal, or both surfaces of the mesoporous silica material. In some cases, the functional groups can also be within the framework of the mesoporous silica materials. To achieve organic functionalization of mesoporous silica materials, three basic synthetic strategies can be employed generally: (*i*) stepwise (post-grafting) synthesis, (*ii*) one-pot (co-condensation) synthesis, and (*iii*) self-assembly synthesis with bridging organosilanes into periodic mesoporous organosilica (PMO)-type materials.

Post-grafting synthetic method for functionalized mesoporous silicas

The post-grafting synthetic method to functionalized mesoporous silicas is comprised generally of two steps, i.e., synthesis of as-made mesostructured silica materials, followed by a post-synthetic modification of their surfaces with organosilanes. For example, Liu and co-workers[94] synthesized mercaptopropyl-functionalized MCM-41 mesoporous silica by treating calcined MCM-41 mesoporous silica, with a surface area of 900 m^2/g and an average mesopore size of ~5.5 nm, with tris(methoxy)mercaptopropylsilane (TMMPS) in chloroform. The mesoporous structure of the material was found to remain intact after surface modification of the MCM-41 by the mercaptopropyl groups. Because of its mercaptopropyl groups, this surface-modified material showed significantly improved binding affinity and higher adsorption capacity towards heavy metal ions such as Hg^{2+}.[94] This clearly exemplifies the benefits of the functionalization of mesoporous silicas with organic functional groups.

The post-grafting synthetic method for functionalized mesoporous silica materials has advantages and disadvantages. Its advantages include (*i*) it enables the introduction of functional groups to as-made mesoporous silica without causing the mesostructure and mesoporosity of the material to degrade; (*ii*) it can be used for selective functionalization of the inner or outer surface of the mesoporous silica by sequential organosilane grafting procedures, i.e., grafting the outer surface of the surfactant-containing mesostructured silica with one type of organic group, followed by extraction of the surfactant templates to empty the pores, and finally grafting the second functional group onto the inner pore surfaces of the mesoporous silica; and (*iii*) it involves a simple procedure to effectively functionalize the surfaces of mesoporous silicas with organic or other functional groups. Among its disadvantages, its inability to produce homogeneous distribution of the functional groups throughout the channel pores of the mesoporous materials is the most notable one.

The degree of functionalization of mesoporous silica can be affected by how the parent mesoporous silica is synthesized. For example, if the as-made mesoporous silica is prepared by calcination rather than solvent extraction, the material will have less silanol groups and thus lower ability to react with organosilanes (such as 3-mercaptopropyltriethoxysilane), resulting in less density of the organic functional groups (e.g., mercaptopropyl groups) in the mesoporous material.[94] The conditions and reagents employed during the grafting of the organosilanes onto the mesoporous silica, such as pH, temperature, reaction time, and the organosilane and the solvent used, can also affect the density of the grafted organic groups in the final material. Our group,[95] for example, found that the density of grafted organic groups on mesoporous silica can vary depending on the type of solvent (e.g., ethanol versus toluene) and the reaction time employed during the grafting synthesis. While the grafting of 3-aminopropyltrimethoxysilane onto mesoporous silicas in toluene produced higher densities of the organoamine groups in the materials, the corresponding grafting in ethanol led to significantly less density of the organoamine groups that were spatially distributed in the materials. Interestingly, the two materials exhibited different properties in catalysis, i.e., the material with less density of the organoamine (or basic catalytic) groups catalyzed the Henry reaction much more efficiently than the one with more organoamine (or basic catalytic) groups.[95] This result shows that the polarity and relative permittivity of the solvents can play important roles during the grafting of organic groups on mesoprous silicas and affect the distribution of the grafted organic groups and the physicochemical properties of the resulting organic-functionalized mesoporous silicas.[96] Similarly, temperature or ionic strength can affect the rates of reactions between the organosilanes and the silanol groups on the mesoporous silica and, consequently, some of the properties of the resulting organic-functionalized mesoporous silicas.

It is worth mentioning that the density and distribution of the functional groups formed on mesoporous silica can also rely on the physical properties of the as-made mesoporous silica, such as its morphology, pore size, and surface area. For instance, the surface coverage of organoammonium groups on the SBA-15-type mesoporous silica was found to be about three times denser than that on MCM-41-type mesoporous silica after the two parent materials were stirred with the quaternary ammonium-containing organosilanes under the same conditions and for the same period of time.[18]

In another interesting novel approach, the Jaroniec group[97] reported the post-synthetic functionalization of template-containing materials directly, which allowed the substitution of the surfactant templates in the as-synthesized mesostructured silicas with organic functional groups from the organosilanes. In this method, the reactive organosilanes with desired functional ligands replaced the surfactant templates in as-synthesized materials, producing stable surface-functionalized mesoporous silicas with surface areas up to 800 m^2/g and pore widths up to 4.9 nm in a relatively short reaction time (8–10 h).[97] Besides allowing the functionalization of mesoporous silicas with organic functional groups, this method removes the surfactant templates without the need of additional calcination or solvent-extraction steps. Furthermore, this method does not compromise the mesostructures of the material. Moreover, it does not degrade the surfactant, making it potentially recycleable and reuseable, as necessary.

Co-condensation synthetic method for functionalized mesoporous silicas

The co-condensation or one-pot synthetic method for functionalized mesoporous silicas involves the co-assembly of the

Fig. 2. (*a*) Organic functionalization of mesoporous silicas by hydrophilic (R_1) or hydrophobic (R_2) organic groups, where R represents a normal alkyl chain.[10] (From Trewyn et al. 2007, reproduced (adapted) with permission of Acc. Chem. Res., Vol. 40, p 846, © 2007 American Chemical Society. (*b*) Synthetic procedure of periodic mesoporous organosilicas (PMOs) under basic conditions, with some common organic bridging groups used to prepare the PMOs.[109] (From Hatton et al. 2005, reproduced (adapted) with permission of Acc. Chem. Res., Vol. 38, p 305, © 2005 American Chemical Society.

Can. J. Chem. Downloaded from www.nrcresearchpress.com by MCGILL UNIVERSITY on 02/02/13
For personal use only.

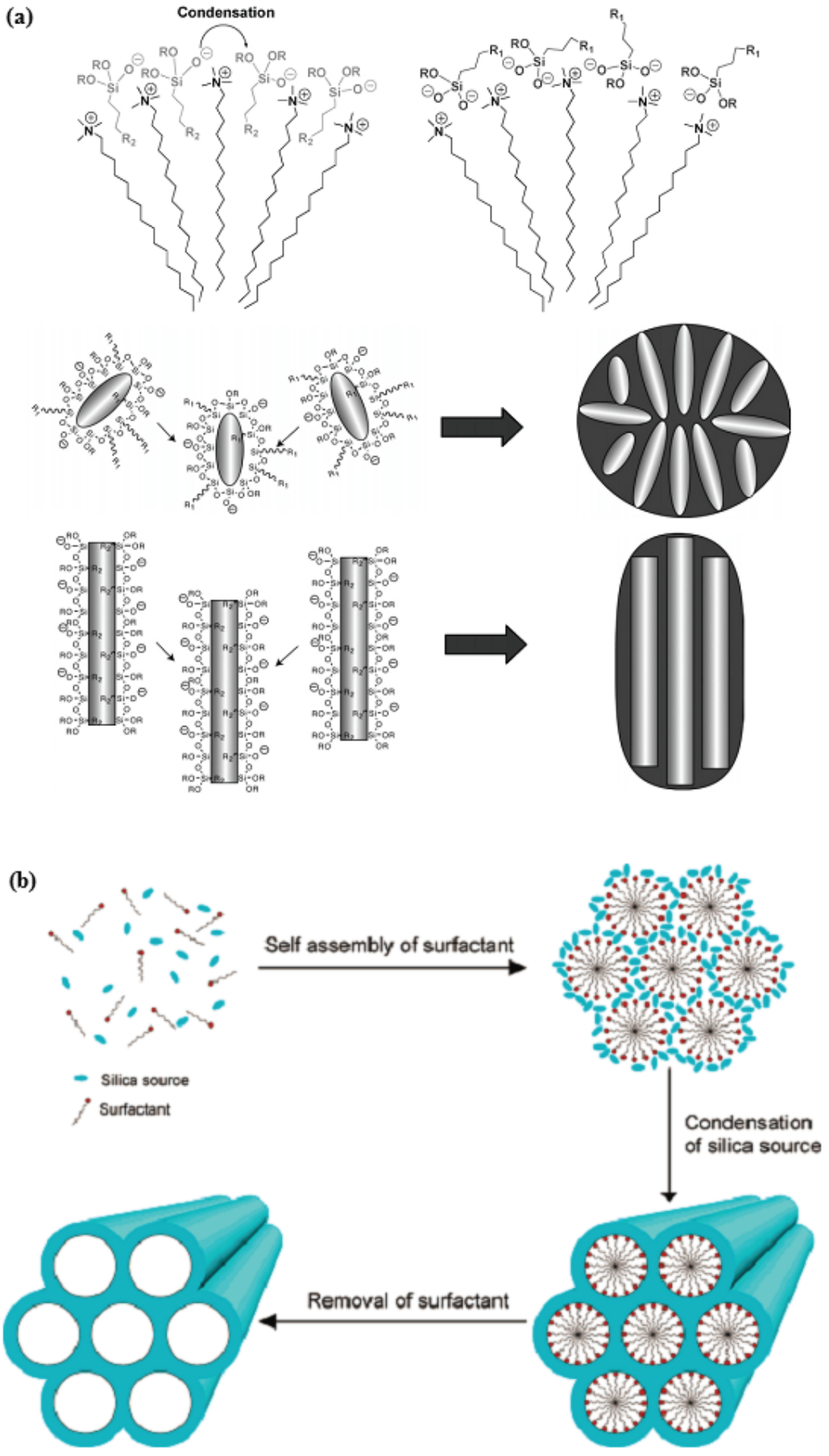
silica precursors (including organosilanes) with the SDAs in one pot. As a result, the organic-functionalized mesoporous silicas are produced directly in one step, and the organic functional groups are incorporated into the mesoporous material while the mesostructured material forms. Using this synthetic method, for example, mesoporous silicas functionalized with alkyl, aryl, allyl, vinyl, amino, and epoxy groups were successfully synthesized.[98–101]

During co-condensation synthesis, the kind of organosilanes added to undergo co-assembly with the silica precursor (e.g., TEOS) and the kind of templating agents used in the reaction can determine what types of mesophases, template–silicate aggregates, and organic-functionalized mesoporous silica materials form. For instance, the Lin group[102–104] reported the synthesis of organic-functionalized mesoporous silicas with controlled morphology simply by varying the mole proportion of the organoalkoxysilane used in the reaction mixture during the co-condensation synthesis. The authors specifically demonstrated the synthesis of monofunctional mesoporous silicas by using organosilanes containing 3-[2-(aminoethylamino)ethylamino]propyl (AEP) or 3-cyanopropyl (CP) groups.[102] The authors also showed that the syntheses could yield bifunctional mesoporous silicas by co-condensation of the two organosilanes in the same reaction mixture, along with the silica precursor and the surfactant-templating agent. Interestingly, as the mole ratio of the two organosilanes was varied, the structures of the resulting organic-functionalized mesoporous silicas changed. For example, as the relative amount of organosilane containing AEP over that containing CP was increased, the shape of the bifunctionalized mesoporous silicas changed from rod- to sphere-shaped. Furthermore, an increase in the composition of AEP augmented the pore size of the final mesoporous material, possibly because of the hydrophilic nature of the AEP groups.[102]

The type of organic groups in the organosilanes can also affect the rate of the co-condensation reaction and the density of the organic groups in the final organic-functionalized mesoporous silica material. This was demonstrated, for example, with co-condensation synthesis of organic-functionalized mesoporous materials using TEOS and a variety of organoalkoxysilanes containing amine, isocyanate, nitrile, or vinyl groups in the presence of cetyltrimethylammonium bromide (CTAB) surfactant.[103] The syntheses resulted in various functionalized mesoporous silicas, which were found to have some differences in the surface coverage of the organic groups.[103] In comparison with the organoalkoxysilanes with a hydrophilic moiety (e.g., primary amines), those with hydrophobic functional groups (e.g., isocyanate, nitrile, or vinyl groups) were more effectively condensed and incorporated in the functionalized materials in higher density. On the other hand, organosilanes containing more hydrophilic organic groups produced bigger organic-functionalized mesoporous silicas in a nanoarray geometry with increased curvature. These differences were explained by the authors as follows. Having a similar size of siloxane head group, the organoalkoxysilanes encompassing hydrophobic tails gave rise to reduced curvature in the self-assembled micelles and thus significantly smaller particle size of the organic-functionalized mesoporous silica compared with a pristine MCM-41 material synthesized from TEOS under the same conditions. Nonetheless, regardless of being hydrophilic or hydrophobic, when the organic groups in the organosilanes were longer, the organic-functionalized mesoporous silicas had bigger mesopore diameters.[103]

The density of the functional groups in organic-functionalized mesoporous silicas obtained by the co-condensation synthetic method was also found to depend on how strongly the terminal groups in the organosilanes interacted with the cationic surfactant ions and their counterions. Thus, the organosilanes used in co-condensation should be more carefully chosen in order not to compromise the self-assembly process, and thereby the structures of the organic-functionalized mesoporous materials. Organosilanes containing thiolate, carboxylate, or sulfonate groups exchange with the Br^- ions of CTAB, and thus interact with surfactant ions forming the micelle–silica aggregates. However, the strength of these interactions varied, causing a decrease in the degree of interaction and stability of the corresponding micelle–silica aggregates in the order of sulfonate > carboxylate > thiolate.[104] This, in turn, led to organic-functionalized mesoporous silicas with different densities of the organic functional groups. Based on these results, the following mechanism was proposed to explain how the organosilanes affected the degree of functionalization of the mesoporous materials during co-condensation (Fig. 2*a*).[10,103,104] In an aqueous basic solution containing cationic surfactant and silica precursors, the organosilanes interacted with the micelle–silicate complexes through two possible processes: (*i*) electrostatic interaction between negatively charged silicate moieties and positively charged head groups of the cationic surfactant and (*ii*) condensation or co-condensation between the hydrolyzed organosilicate or silicate species that were derived from the organosilanes or silica sources (such as TEOS), respectively. During these processes, organosilanes with hydrophobic tail groups exhibited a tendency to insert their functional groups into the gaps between surfactant micelles. As a result of this, hydrophobic organosilanes stabilized the mesophases better, accelerated their condensation with any silica precursor present, and produced organic-functionalized mesoporous silicas with more ordered and intact structural features. In contrast, organosilanes with hydrophilic tail groups exhibited a tendency to weaken the micelle–silica aggregates, underwent less condensation with silica precursors, and undermined the structural integrity of the resulting materials. In either case (i.e., organosilanes with hydrophobic or hydrophilic tails), at the end of the synthesis and solvent extraction of the templating agents, functionalized

Can. J. Chem. Downloaded from www.nrcresearchpress.com by MCGILL UNIVERSITY on 02/02/13
For personal use only.



Can. J. Chem. Downloaded from www.nrcresearchpress.com by MCGILL UNIVERSITY on 02/02/13
For personal use only.

mesoporous silicas with organic functional groups exposed on the inner and outer surfaces of the mesoporous material were formed.

Generally, compared with the post-grafting synthetic method, co-condensation synthesis offers a more convenient route for the modification of mesoporous silicas with rather homogenous distribution of functional groups. It is also worth including that, apart from their roles as functional surface modifiers, organosilanes adopted in co-condensation synthesis can influence the physical properties of the organic-functionalized mesoporous materials, such as their size, morphology, and mesoporosity.

Self-assembly of bridging organosilanes to periodic mesoporous organosilicas

Another more popular synthetic route to organic-functionalized mesoporous silicas employs a different class of organosilanes rather than the ones mentioned previously. These organosilanes, which are called bridging organoalkoxysilanes, have a general formula of $(RO)_3Si–R'–Si(OR)_3$ (where R = alkyl and R′ = alkyl or alkenyl). The method of their self-assembly into mesoporous materials was independently and almost simultaneously developed by three research groups, led by Ozin, Inagaki, and Stein.[105–107] In a typical synthesis, these organosilanes by themselves or in combination with silica precursors self-assemble in the presence of surfactant templates and generate the organic-functionalized mesoporous materials, called PMOs.[105–107] Specifically, the bridging organosilane and cationic surfactant are mixed into slightly alkaline solutions, stirred, and aged for hours or days. The solution is then filtered, and the surfactant templates from the recovered solid material are subsequently removed by solvent extraction to produce the PMO material.[105–107] The resulting materials (i.e., PMOs) constitute a new class of organic–inorganic hybrid mesoporous silicas with highly ordered mesoporous structures, and most importantly, with organic functional groups (R′) covalently bonded via non-hydrolyzable Si–C bonds among two or more than two siloxane groups on the walls of the mesoporous materials (Fig. 2*b*).[108–110] It is worth emphasizing that the R′ functional moieties introduced into the framework of mesoporous materials with these organosilanes become a part of the framework of the final functionalized mesoporous material.

Like the structures of organic-functionalized mesoporous silica synthesized from the co-condensation of terminal organosilanes, those of the PMOs depend on the synthetic conditions as well as the types of surfactant and SDAs employed during their synthesis. For instance, when 1,2-bis(trimethoxysilyl)ethane (BTME, $(H_3CO)_3Si–CH_2–CH_2–Si(OCH_3)_3$) was self-assembled with octadecyltrimethylammonium chloride (ODTMA, $C_{18}H_{37}N(CH_3)_3Cl$) surfactant, 2D-hexagonal PMOs containing bridging ethane groups with a surface area of ~750 m^2/g and a pore size of ~3.1 nm were formed.[106] Increasing the concentration of surfactant and the alkalinity of the solution during the synthesis resulted in 3D-hexagonal PMOs, possessing a surface area of ~1170 m^2/g and a pore size of ~2.7 nm.[106] The presence of the bridging organic groups (ethane groups in this case) and their density in the PMO materials can be reliably determined by using solid-state ^{13}C and ^{29}Si NMR spectroscopy.[105,106] For PMOs containing reactive groups such as ethylene (–Si–CH=CH–Si–), the presence of the functional groups (ethylene) can also be verified by using specific reactions, in which the bridging organic groups can undergo the reactions. For example, the bromination reaction can be applied to ethylene–PMO as bromination of the ethylene groups converts the sp^2-hybridized carbon atoms of the ethylene–PMO into sp^3-hybridized carbon atoms. This can easily be probed by methods such as ^{13}C solid-state NMR spectroscopy, indirectly allowing the determination of the presence of ethylene groups in the original PMO.[105]

Besides hexagonal-ordered mesostructures, PMOs with other structures can also be made by following other procedures that were employed to synthesize different types of mesoporous silicas and terminal-organic-functionalized mesoporous materials. In addition to 2-D and 3-D hexagonally ordered mesoporous silicas, the self-assembly of $(C_2H_5CO)_3Si–R'–Si(OC_2H_5)_3$, in which R′ = $–CH_2–CH_2–$ or –CH=CH–, with CTAB can produce wormlike PMOs with uniform mesochannels (pore size = 2.2–2.4 nm and surface area > 1200 m^2/g) and thicker pore walls compared with the synthesized MCM-41.[107]

Recently, a new strategy to synthesize PMOs using the self-assembly of organosilanes and block copolymers in the presence of reactive organic precursors was reported by the Jaroniec group.[111] In a typical synthesis, reactive precursors (e.g., *N*-hydroxyurea) were added into the solution containing PEO–PPO–PEO as the soft template, followed by addition of bridged organosilane (1,2-bis(triethoxysilyl)ethane or BTES). Acidic ethanol solution was used to extract the templates in as-prepared samples, producing PMOs with an ethane–silica framework with reactive organic functionalities in the hydrophilic realm of the well-orderd mesostructure.[111]

Owing to the presence of organic groups in their framework, PMOs exhibit improved hydrothermal stability and enhanced hydrophobicity, compared with regular mesoporous silicas.[107] PMOs are also unique compared with terminal-functionalized mesoporous silicas that can be produced by either postsynthetic grafting or co-condensation method. The most important difference between the two types of materials is that the organic functional groups in PMOs are part and parcel of the material's framework compared with those of the latter. This can, in turn, result in a different electron density and chemical microenvironment in the framework of the mesoporous materials, rendering PMOs distinct physicochemical properties. Furthermore, unlike those in terminal-organic-functionalized mesoporous silicas, the R′ groups are part of the mesoporous framework in PMOs; thus, changes in the type of the organic groups can significantly modify the physical as well as the mechanical properties, besides the chemical properties, of the materials.

Conclusion

Mesoporous silica and organosilica materials can be synthesized with different structures and physiochemical properties such as high surface areas, pore volumes and tunable nanosize pores. In this review, the various methods used to synthesize different types of mesoporous silica and organosilica materials are described. The synthetic methods developed for introducing organic functional groups into mesoporous

Can. J. Chem. Downloaded from www.nrcresearchpress.com by MCGILL UNIVERSITY on 02/02/13
For personal use only.

silicas to further tune the materials' properties have also been included. The different mechanisms to illustrate how mesostructured materials form have been summarized. The advantages and disadvantages of the different types of organic functionalization methods have been discussed. Their organically modifiable surfaces allow mesoporous materials to be versatile for various applications. Their unique properties, such as high surface area, nanometer pores, and easily modifiable surfaces, lead to many different potential applications for these materials in many areas, including catalysis, drug delivery, molecular adsorption, and organic separations. Typical examples where these functionalized mesoporous materials have been successfully utilized in catalysis, drug delivery, or chiral separation have been mentioned in different sections.

Acknowledgement

Z.T. thanks Tsinghua Research Fund No. 100401007 and Chinese Postdoctoral Science Foundation No. 20100480314 for financial support. T.A. gratefully acknowledges the partial financial assistance to his research group by the US National Science Foundation (NSF) under Grant Nos. CAREER CHE-1004218, NSF DMR-0968937, NSF NanoEHS-1134289, NSF-ACIF for 2010, and NSF Special Creativity grant in 2011.

References

(1) Yang, H.; Coombs, N.; Ozin, G. A. *Nature* **1997**, *386* (6626), 692. doi:10.1038/386692a0.
(2) Stark, W. J. *Angew. Chem. Int. Ed. Engl.* **2011**, *50* (6), 1242. doi:10.1002/anie.200906684.
(3) Yang, H.; Kuperman, A.; Coombs, N.; Mamiche-Afara, S.; Ozin, G. A. *Nature* **1996**, *379* (6567), 703. doi:10.1038/379703a0.
(4) Paulo, C. S.; Pires das Neves, R.; Ferreira, L. S. *Nanotechnology* **2011**, *22* (49), 494002. doi:10.1088/0957-4484/22/49/494002.
(5) Jokerst, J. V.; Gambhir, S. S. *Acc. Chem. Res.* **2011**, *44* (10), 1050. doi:10.1021/ar200106e.
(6) Ambrogio, M. W.; Thomas, C. R.; Zhao, Y. L.; Zink, J. I.; Stoddart, J. F. *Acc. Chem. Res.* **2011**, *44* (10), 903. doi:10.1021/ar200018x.
(7) Lin, H.-P.; Mou, C.-Y. *Acc. Chem. Res.* **2002**, *35* (11), 927. doi:10.1021/ar000074f.
(8) Soler-Illia, G. J.; Sanchez, C.; Lebeau, B.; Patarin, J. *Chem. Rev.* **2002**, *102* (11), 4093. doi:10.1021/cr0200062.
(9) Wan, Y.; Zhao, D. *Chem. Rev.* **2007**, *107* (7), 2821. doi:10.1021/cr068020s.
(10) Trewyn, B. G.; Slowing, I. I.; Giri, S.; Chen, H. T.; Lin, V. S. *Acc. Chem. Res.* **2007**, *40* (9), 846. doi:10.1021/ar600032u.
(11) Lin, Y.-S.; Haynes, C. H. *Chem. Mater.* **2009**, *21* (17), 3979. doi:10.1021/cm901259n.
(12) Giri, S.; Trewyn, B. G.; Lin, V. S. *Nanomedicine* **2007**, *2* (1), 99. doi:10.2217/17435889.2.1.99.
(13) Trewyn, B. G.; Giri, S.; Slowing, I. I.; Lin, V. S.-Y. *Chem. Commun. (Camb.)* **2007**, (31): 3236. doi:10.1039/b701744h.
(14) Slowing, I. I.; Vivero-Escoto, J. L.; Wu, C. W.; Lin, V. S. *Adv. Drug Deliv. Rev.* **2008**, *60* (11), 1278. doi:10.1016/j.addr.2008.03.012.
(15) Manzano, M.; Colilla, M.; Vallet-Regí, M. *Expert Opin. Drug Deliv.* **2009**, *6* (12), 1383. doi:10.1517/17425240903304024.
(16) Vivero-Escoto, J. L.; Slowing, I. I.; Trewyn, B. G.; Lin, V. S. *Small* **2010**, *6* (18), 1952. doi:10.1002/smll.200901789.
(17) Lee, J. E.; Lee, N.; Kim, T.; Kim, J.; Hyeon, T. *Acc. Chem. Res.* **2011**, *44* (10), 893. doi:10.1021/ar2000259.
(18) Tao, Z.; Toms, B. B.; Goodisman, J.; Asefa, T. *Chem. Res. Toxicol.* **2009**, *22* (11), 1869. doi:10.1021/tx900276u.
(19) Fadeel, B.; Garcia-Bennett, A. E. *Adv. Drug Deliv. Rev.* **2010**, *62* (3), 362. doi:10.1016/j.addr.2009.11.008.
(20) Kunzmann, A.; Andersson, B.; Thurnherr, T.; Krug, H.; Scheynius, A.; Fadeel, B. *Biochim. Biophys. Acta* **2011**, *1810* (3), 361. doi:10.1016/j.bbagen.2010.04.007.
(21) Garcia-Bennett, A. E. *Nanomedicine* **2011**, *6* (5), 867. doi:10.2217/nnm.11.82.
(22) Kresge, C. T.; Leonowicz, M. E.; Roth, W. J.; Vartuli, J. C.; Beck, J. S. *Nature* **1992**, *359* (6397), 710. doi:10.1038/359710a0.
(23) Beck, J. S.; Vartuli, J. C.; Roth, W. J.; Leonowicz, M. E.; Kresge, C. T.; Schmitt, K. D.; Chu, C. T. W.; Olson, D. H.; Sheppard, E. W.; McCullen, S. B.; Higgins, J. B.; Schlenker, J. L. *J. Am. Chem. Soc.* **1992**, *114* (27), 10834. doi:10.1021/ja00053a020.
(24) Kokotailo, G. T.; Lawton, S. L.; Olson, D. H.; Meier, W. M. *Nature* **1978**, *272* (5652), 437. doi:10.1038/272437a0.
(25) Kokotailo, G. T.; Chu, P.; Lawton, S. L.; Meier, W. M. *Nature* **1978**, *275* (5676), 119. doi:10.1038/275119a0.
(26) Davis, M. E.; Lobo, R. F. *Chem. Mater.* **1992**, *4* (4), 756. doi:10.1021/cm00022a005.
(27) Manton, M. R. S.; Davidtz, J. C. *J. Catal.* **1979**, *60* (1), 156. doi:10.1016/0021-9517(79)90078-2.
(28) Yanagisawa, T.; Shimizu, T.; Kuroda, K.; Kato, C. *Bull. Chem. Soc. Jpn.* **1990**, *63* (4), 988. doi:10.1246/bcsj.63.988.
(29) Monnier, A.; Schüth, F.; Huo, Q.; Kumar, D.; Margolese, D.; Maxwell, R. S.; Stucky, G. D.; Krishnamurty, M.; Petroff, P.; Firouzi, A.; Janicke, M.; Chmelka, B. F. *Science* **1993**, *261* (5126), 1299. doi:10.1126/science.261.5126.1299.
(30) Firouzi, A.; Kumar, D.; Bull, L. M.; Besier, T.; Sieger, P.; Huo, Q.; Walker, S. A.; Zasadzinski, J. A.; Glinka, C.; Nicol, J.; Margolese, D.; Stucky, G. D.; Chmelka, B. F. *Science* **1995**, *267* (5201), 1138. doi:10.1126/science.7855591.
(31) Chen, C.-Y.; Li, H.-X.; Davis, M. E. *Microporous Mater.* **1993**, *2* (1), 17. doi:10.1016/0927-6513(93)80058-3.
(32) Davis, M. E. *Nature* **2002**, *417* (6891), 813. doi:10.1038/nature00785.
(33) Steel, A.; Carr, S. W.; Anderson, M. W. *J. Chem. Soc. Chem. Commun.* **1994**, (13): 1571. doi:10.1039/c39940001571.
(34) Huo, Q.; Margolese, D. I.; Ciesla, U.; Feng, P.; Gier, T. E.; Sieger, P.; Leon, R.; Petroff, P. M.; Schüth, F.; Stucky, G. D. *Nature* **1994**, *368* (6469), 317. doi:10.1038/368317a0.
(35) Huo, Q.; Margolese, D. I.; Ciesla, U.; Demuth, D. G.; Feng, P.; Gier, T. E.; Sieger, P.; Firouzi, A.; Chmelka, B. F.; Schüth, F.; Stucky, G. D. *Chem. Mater.* **1994**, *6* (8), 1176. doi:10.1021/cm00044a016.
(36) Tanev, P. T.; Pinnavaia, T. J. *Science* **1995**, *267* (5199), 865. doi:10.1126/science.267.5199.865.
(37) Bagshaw, S. A.; Prouzet, E.; Pinnavaia, T. J. *Science* **1995**, *269* (5228), 1242. doi:10.1126/science.269.5228.1242.
(38) Liquid-crystalline phases as templates for the synthesis of mesoporous silica. Attard, G. S.; Glyde, J. C.; Goltner, C. G. *Nature* **1995**, *378* (6555), 366. doi:10.1038/378366a0.
(39) Attard, G. S.; Corker, J. M.; Göltner, C. G.; Henke, S.; Templer, R. H. *Angew. Chem. Int. Ed. Engl.* **1997**, *36* (12), 1315. doi:10.1002/anie.199713151.
(40) Göltner, C. G.; Henke, S.; Weissenberger, M. C.; Antonietti, M. *Angew. Chem. Int. Ed.* **1998**, *37* (5), 613. doi:10.1002/

Can. J. Chem. Downloaded from www.nrcresearchpress.com by MCGILL UNIVERSITY on 02/02/13
For personal use only.

(SICI)1521-3773(19980316)37:5<613::AID-ANIE613>3.0.CO;2-G.
(41) Inagaki, S.; Fukushima, Y.; Kuroda, K. *J. Chem. Soc. Chem. Commun.* **1993**, *77* (8), 680. doi:10.1039/c39930000680.
(42) Firouzi, A.; Atef, F.; Oertli, A. G.; Stucky, G. D.; Chmelka, B. F. *J. Am. Chem. Soc.* **1997**, *119* (15), 3596. doi:10.1021/ja963007i.
(43) Brinker, C. J. *J. Non-Cryst. Solids* **1988**, *100* (1–3), 31. doi:10.1016/0022-3093(88)90005-1.
(44) Brinker, C. J.; Scherer, G. W. *Sol-Gel Science: The Physics and Chemistry of Sol-Gel Processing;* Academic Press: London, 1990.
(45) Lin, H.-P.; Kao, C.-P.; Mou, C.-Y. *Microporous Mesoporous Mater.* **2001**, *48* (1–3), 135. doi:10.1016/S1387-1811(01)00336-5.
(46) Cheng, C. F.; Luan, Z. H.; Klinowski, J. *Langmuir* **1995**, *11* (7), 2815. doi:10.1021/la00007a075.
(47) Israelachvili, J. N. *Intermolecular and Surface Forces;* Academic Press: London, 1992.
(48) Huo, Q.; Margolese, D. I.; Stucky, G. D. *Chem. Mater.* **1996**, *8* (5), 1147. doi:10.1021/cm960137h.
(49) Israelachvili, J. N.; Ladyzhinski, I. *NATO Sci. Ser.* **2005**, *160*, 1. doi:10.1007/1-4020-2340-5_1.
(50) Yu, C. Z.; Fan, J.; Tian, B. Z.; Stucky, G. D.; Zhao, D. Y. *J. Phys. Chem. B* **2003**, *107* (48), 13368. doi:10.1021/jp027046u.
(51) Huo, Q.; Leon, R.; Petroff, P. M.; Stucky, G. D. *Science* **1995**, *268* (5215), 1324. doi:10.1126/science.268.5215.1324.
(52) Van Der Voort, P.; Mathieu, M.; Mees, F.; Vansant, E. F. *J. Phys. Chem. B* **1998**, *102* (44), 8847. doi:10.1021/jp982653w.
(53) Zana, R.; Benrraou, M.; Rueff, R. *Langmuir* **1991**, *7* (6), 1072. doi:10.1021/la00054a008.
(54) Danino, D.; Talmon, Y.; Zana, R. *Langmuir* **1995**, *11* (5), 1448. doi:10.1021/la00005a008.
(55) Zana, R.; Talmon, Y. *Nature* **1993**, *362* (6417), 228. doi:10.1038/362228a0.
(56) Alami, E.; Beinert, G.; Marie, P.; Zana, R. *Langmuir* **1993**, *9* (6), 1465. doi:10.1021/la00030a006.
(57) Prouzet, E.; Pinnavaia, T. J. *Angew. Chem. Int. Ed. Engl.* **1997**, *36* (5), 516. doi:10.1002/anie.199705161.
(58) Kim, S. S.; Zhang, W.; Pinnavaia, T. J. *Science* **1998**, *282* (5392), 1302. doi:10.1126/science.282.5392.1302.
(59) Prouzet, E.; Cot, F.; Nabias, G.; Larbot, A.; Kooyman, P.; Pinnavaia, T. J. *Chem. Mater.* **1999**, *11* (6), 1498. doi:10.1021/cm9810281.
(60) Kim, S.-S.; Pauly, T. R.; Pinnavaia, T. J. *Chem. Commun. (Camb.)* **2000**, (17): 1661. doi:10.1039/b002856h.
(61) Tanev, P. T.; Pinnavaia, T. J. *Chem. Mater.* **1996**, *8* (8), 2068. doi:10.1021/cm950549a.
(62) Zhao, D. Y.; Feng, J. L.; Huo, Q. S.; Melosh, N.; Fredrickson, G. H.; Chmelka, B. F.; Stucky, G. D. *Science* **1998**, *279* (5350), 548. doi:10.1126/science.279.5350.548.
(63) Zhao, D.; Huo, Q.; Feng, J.; Chmelka, B. F.; Stucky, G. D. *J. Am. Chem. Soc.* **1998**, *120* (24), 6024. doi:10.1021/ja974025i.
(64) Ruthstein, S.; Frydman, V.; Kababya, S.; Landau, M.; Goldfarb, D. *J. Phys. Chem. B* **2003**, *107* (8), 1739. doi:10.1021/jp021964a.
(65) Flodström, K.; Wennerström, H.; Alfredsson, V. *Langmuir* **2004**, *20* (3), 680. doi:10.1021/la030173c.
(66) Flodström, K.; Teixeira, C. V.; Amenitsch, H.; Alfredsson, V.; Lindén, M. *Langmuir* **2004**, *20* (12), 4885. doi:10.1021/la049637c.
(67) Ryoo, R.; Ko, C. H.; Kruk, M.; Antochshuk, V.; Jaroniec, M. *J. Phys. Chem. B* **2000**, *104* (48), 11465. doi:10.1021/jp002597a.
(68) Yu, C.; Yu, Y.; Zhao, D. *Chem. Commun. (Camb.)* **2000**, (7): 575. doi:10.1039/b000603n.
(69) Liu, X.; Tian, B.; Yu, C.; Gao, F.; Xie, S.; Tu, B.; Che, R.; Peng, L. M.; Zhao, D. *Angew. Chem. Int. Ed.* **2002**, *41* (20), 3876. doi:10.1002/1521-3773(20021018)41:20<3876::AID-ANIE3876>3.0.CO;2-R.
(70) Fan, J.; Yu, C.; Gao, F.; Lei, J.; Tian, B.; Wang, L.; Luo, Q.; Tu, B.; Zhou, W.; Zhao, D. *Angew. Chem. Int. Ed.* **2003**, *42* (27), 3146. doi:10.1002/anie.200351027.
(71) Dai, S.; Burleigh, M. C.; Ju, Y. H.; Gao, H. J.; Lin, J. S.; Pennycook, S. J.; Barnes, C. E.; Xue, Z. L. *J. Am. Chem. Soc.* **2000**, *122* (5), 992. doi:10.1021/ja993168x.
(72) Zhang, Z.; Dai, S. *J. Am. Chem. Soc.* **2001**, *123* (37), 9204. doi:10.1021/ja0158556.
(73) Yokoi, T.; Yoshitake, H.; Tatsumi, T. *Chem. Mater.* **2003**, *15* (24), 4536. doi:10.1021/cm034499i.
(74) Che, S.; Garcia-Bennett, A. E.; Yokoi, T.; Sakamoto, K.; Kunieda, H.; Terasaki, O.; Tatsumi, T. *Nat. Mater.* **2003**, *2* (12), 801. doi:10.1038/nmat1022.
(75) Gao, C.; Sakamoto, Y.; Sakamoto, K.; Terasaki, O.; Che, S. *Angew. Chem. Int. Ed.* **2006**, *45* (26), 4295. doi:10.1002/anie.200504114.
(76) Gao, C.; Qiu, H.; Zeng, W.; Sakamoto, Y.; Terasaki, O.; Sakamoto, K.; Chen, Q.; Che, S. *Chem. Mater.* **2006**, *18* (16), 3904. doi:10.1021/cm061107+.
(77) Gao, C.; Sakamoto, Y.; Terasaki, O.; Sakamoto, K.; Che, S. *J. Mater. Chem.* **2007**, *17* (34), 3591. doi:10.1039/b704398h.
(78) Che, S.; Liu, Z.; Ohsuna, T.; Sakamoto, K.; Terasaki, O.; Tatsumi, T. *Nature* **2004**, *429* (6989), 281. doi:10.1038/nature02529.
(79) Qiu, H.; Che, S. *Chem. Soc. Rev.* **2011**, *40* (3), 1259. doi:10.1039/c0cs00002g.
(80) Wei, Y.; Jin, D. L.; Ding, T. Z.; Shih, W. H.; Liu, X. H.; Cheng, S. Z. D.; Fu, Q. *Adv. Mater. (Deerfield Beach Fla.)* **1998**, *10* (4), 313. doi:10.1002/(SICI)1521-4095(199803)10:4<313::AID-ADMA313>3.0.CO;2-M.
(81) Wei, Y.; Xu, J.; Dong, H.; Dong, J. H.; Qiu, K.; Jansen-Varnum, S. A. *Chem. Mater.* **1999**, *11* (8), 2023. doi:10.1021/cm981004u.
(82) Pang, J.-B.; Qiu, K.-Y.; Wei, Y.; Lei, X.-J.; Liu, Z.-F. *Chem. Commun. (Camb.)* **2000**, (6): 477. doi:10.1039/a909420b.
(83) Pang, J.; Qiu, K. Y.; Wei, Y. *J. Non-Cryst. Solids* **2001**, *283* (1–3), 101. doi:10.1016/S0022-3093(01)00343-X.
(84) Pang, J. B.; Qiu, K. Y.; Wei, Y. *Chem. Mater.* **2001**, *13* (7), 2361. doi:10.1021/cm000925d.
(85) Davis, S. A.; Burkett, S. L.; Mendelson, N. H.; Mann, S. *Nature* **1997**, *385* (6615), 420. doi:10.1038/385420a0.
(86) Dai, S.; Ju, Y. H.; Gao, H. J.; Lin, J. S.; Pennycook, S. J.; Barnes, C. E. *Chem. Commun. (Camb.)* **2000**, (3): 243. doi:10.1039/a907147d.
(87) Lee, B.; Luo, H.; Yuan, C. Y.; Lin, J. S.; Dai, S. *Chem. Commun. (Camb.)* **2004**, (2): 240. doi:10.1039/b312178j.
(88) Ma, Z.; Yu, J.; Dai, S. *Adv. Mater. (Deerfield Beach Fla.)* **2010**, *22* (2), 261. doi:10.1002/adma.200900603.
(89) Zhou, Y.; Antonietti, M. *Adv. Mater. (Deerfield Beach Fla.)* **2003**, *15* (17), 1452. doi:10.1002/adma.200305265.
(90) Zhou, Y.; Antonietti, M. *Chem. Mater.* **2004**, *16* (3), 544. doi:10.1021/cm034442w.

(91) Zhou, Y.; Schattka, J. H.; Antonietti, M. *Nano Lett.* **2004**, *4* (3), 477. doi:10.1021/nl025861f.
(92) Trewyn, B. G.; Whitman, C. M.; Lin, V. S. Y. *Nano Lett.* **2004**, *4* (11), 2139. doi:10.1021/nl048774r.
(93) Atluri, R.; Hedin, N.; Garcia-Bennett, A. E. *J. Am. Chem. Soc.* **2009**, *131* (9), 3189. doi:10.1021/ja8096477.
(94) Feng, X.; Fryxell, G. E.; Wang, L. Q.; Kim, A. Y.; Liu, J.; Kemner, K. M. *Science* **1997**, *276* (5314), 923. doi:10.1126/science.276.5314.923.
(95) Sharma, K. K.; Asefa, T. *Angew. Chem. Int. Ed.* **2007**, *46* (16), 2879. doi:10.1002/anie.200604570.
(96) Sharma, K. K.; Anan, A.; Buckley, R. P.; Ouellette, W.; Asefa, T. *J. Am. Chem. Soc.* **2008**, *130* (1), 218. doi:10.1021/ja074128t.
(97) Antochshuk, V.; Jaroniec, M. *Chem. Mater.* **2000**, *12* (8), 2496. doi:10.1021/cm000268p.
(98) Burkett, S. L.; Sims, S. D.; Mann, S. *Chem. Commun. (Camb.)* **1996**, (11): 1367. doi:10.1039/cc9960001367.
(99) Fowler, C. E.; Burkett, S. L.; Mann, S. *Chem. Commun. (Camb.)* **1997**, (18): 1769. doi:10.1039/a704644h.
(100) Lim, M. H.; Blanford, C. F.; Stein, A. *J. Am. Chem. Soc.* **1997**, *119* (17), 4090. doi:10.1021/ja9638824.
(101) Fowler, C. E.; Mann, S.; Lebeau, B. *Chem. Commun. (Camb.)* **1998**, (17): 1825. doi:10.1039/a803736a.
(102) Huh, S.; Wiench, J. W.; Trewyn, B. G.; Song, S.; Pruski, M.; Lin, V. S. *Chem. Commun. (Camb.)* **2003**, (18): 2364. doi:10.1039/b306255d.
(103) Huh, S.; Wiench, J. W.; Yoo, J. C.; Pruski, M.; Lin, V. S. *Chem. Mater.* **2003**, *15* (22), 4247. doi:10.1021/cm0210041.
(104) Radu, D. R.; Lai, C. Y.; Huang, J.; Shu, X.; Lin, V. S. *Chem. Commun. (Camb.)* **2005**, (10): 1264. doi:10.1039/b412618a.
(105) Asefa, T.; MacLachlan, M. J.; Coombs, N.; Ozin, G. A. *Nature* **1999**, *402* (6764), 867. doi:10.1038/47229.
(106) Inagaki, S.; Guan, S.; Fukushima, Y.; Ohsuna, T.; Terasaki, O. *J. Am. Chem. Soc.* **1999**, *121* (41), 9611. doi:10.1021/ja9916658.
(107) Melde, B. J.; Holland, B. T.; Blanford, C. F.; Stein, A. *Chem. Mater.* **1999**, *11* (11), 3302. doi:10.1021/cm9903935.
(108) Asefa, T.; Yoshina-Ishii, C.; MacLachlan, M. J.; Ozin, G. A. *J. Mater. Chem.* **2000**, *10* (8), 1751. doi:10.1039/b000950o.
(109) Hatton, B.; Landskron, K.; Whitnall, W.; Perovic, D.; Ozin, G. A. *Acc. Chem. Res.* **2005**, *38* (4), 305. doi:10.1021/ar040164a.
(110) Hunks, W. J.; Ozin, G. A. *J. Mater. Chem.* **2005**, *15* (35–36), 3716. doi:10.1039/b504511h.
(111) Gu, S.; Jaroniec, M. *J. Mater. Chem.* **2011**, *21* (17), 6389. doi:10.1039/c1jm10322a.

Can. J. Chem. Downloaded from www.nrcresearchpress.com by MCGILL UNIVERSITY on 02/02/13
For personal use only.

REVIEW / SYNTHÈSE

Recent advances in the synthesis of colloidal nanowires

Anton Repko and Ludovico Cademartiri

Abstract: We review critically the advances in the synthesis of colloidal nanowires that have occurred over the past three years, with a focus on those that produced very thin (or "ultrathin") nanowires (~2–3 nm in diameter or less). We discuss the importance of these ultrathin nanowires, especially in light of the emerging evidence of their topological properties and their potential similarities with polymers.

Key words: nanowires, ultrathin, polymers, topology, synthesis, colloidal.

Résumé : On fait une revue critique des améliorations aux méthodes de synthèse des nanofils colloïdaux qui ont été proposées au cours des trois dernières années, en particuliers pour celles qui conduisent à la production de nanofils très fins (ou ultrafins) (de diamètres d'environ 2 à 3 nm de diamètre ou moins). On discute de l'importance de ces nanofils ultrafins, particulièrement à la lumière de données qui émergent relativement à leurs propriétés topologiques et leurs similarités potentielles avec les polymères.

Mots-clés : nanofils, ultrafin, polymères, topologie, synthèse, colloïdal.

[Traduit par la Rédaction]

Can. J. Chem. Downloaded from www.nrcresearchpress.com by MCGILL UNIVERSITY on 02/02/13
For personal use only.

Why should we care about nanowires?

Nanowires can be defined summarily as solids the size of whose atomic lattice is in the nanoscale along two out of three dimensions.[3–12] They can be made in a variety of phases and compositions: ceramics,[13] semiconductors,[14] metals,[15–17] polymers,[18] and glasses.[19] They can be crystalline[13] or amorphous.[19] They can be colloidally stable[15–17] or supported on surfaces.[13]

There is no widespread consensus on what range of aspect ratios characterize a nanowire. Typically, the properties of nanowires depend very weakly on their aspect ratio: most of the physical properties arising from the extension of the atomic lattice along one axis (e.g., polarization of photoluminescence[20]) are already evident at relatively small aspect ratios (~2–10). Large aspect ratios (e.g., 10^2 or more) are desired for interconnects (the length of a nanowire determines how far two places (e.g., electrodes) can be connected by it), or for the integration at a higher density of devices (i.e., a higher level of integration can be envisioned if multiple devices could be embedded on one nanowire).[21] On the other hand, nanowires with very large aspect ratios are difficult to make, integrate in planar devices (they tend to flex), and keep dispersed in solution (they are very prone to bundling).

Why should we care then about nanowires? Their morphology is attractive, for example, for any application that requires

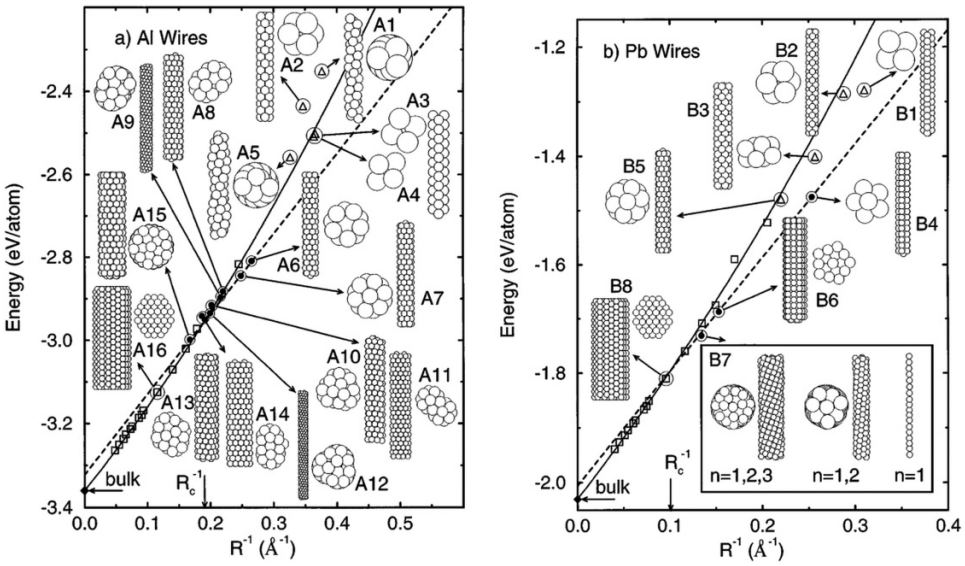
Received 1 June 2012. Accepted 19 July 2012. Published at www.nrcresearchpress.com/cjc on 7 November 2012.

A. Repko. Department of Materials Science & Engineering, Iowa State University of Science and Technology, 2240J Hoover Hall, Ames, IA 50011, USA; Department of Inorganic Chemistry, Faculty of Science, Charles University in Prague, Hlavova 2030, 128 40 Prague 2, Czech Republic.
L. Cademartiri. Department of Materials Science & Engineering, Iowa State University of Science and Technology, 2240J Hoover Hall, Ames, IA 50011, USA.

Corresponding author: Ludovico Cademartiri (e-mail: lcademar@iastate.edu).

This article is part of a Special Issue dedicated to Professor Geoffrey Ozin. Reactions capable of producing very thin (2–3 nm or less) and colloidally stable filaments of inorganic materials are, as we will argue in the following pages, one of the most interesting developments in the field of nanochemistry over the past few years. I was directly involved with the discovery of one of these syntheses while in the Ozin lab.[1] Since I had the privilege of being invited to contribute this manuscript to this Festschrift for Geoff Ozin's 70th birthday, I feel it is appropriate to dedicate this contribution to Geoff in light of his contributions to chemistry but also of his invaluable mentorship. Geoff was a demanding advisor, an unfailing supporter, a tireless teacher, and an inexhaustible (and sometimes exhausting) source of enthusiasm, drive, and inspiration. I have always felt, as his student, that being overwhelmed was a much better fate than being underwhelmed. As Ph.D. programs suffer from the epidemic lack of enthusiasm that is so convincingly demonstrated by the popularity of Ph.D. Comics,[2] one realizes that there really is no substitute for the kind of energy Geoff provides. Happy Birthday Geoff, and may you keep inspiring young scientists for many more years. I'll never cease to be amazed! Mazel tov! L.C.

Fig. 1. "Weird" wires: Results of a simulation of the structures of Al and Pb wires of decreasing diameter. As illustrated, noncrystalline structures dominated by the surface effects emerge as the diameter is reduced. (From Gülseren et al. 1998, reproduced (adapted) with permission of Phys. Rev. Lett., Vol. 80, p 3776, © 1998 American Physical Society.)



both large surface areas and contiguity of the atomic lattice (characteristics they share with mesoporous materials, their structural "negative"). In the case of batteries,[22–24] the one-dimensional geometry allows nanowires to have a large surface area in contact with the electrolyte and to accommodate the large volume swings associated with Li intercalation.[23] In the case of solar cells, the shape of nanowires can be harnessed to improve the absorption of light into the material.[13,25,26] In the case of piezoelectric transducers, the one-dimensional geometry allows for more efficient transduction.[27,28] In all these applications, nanowires are grown from flat substrates to preserve a solid connection with what is typically a planar device.

The case for the importance of colloidal nanowires would seem less clear. Their integration on planar devices requires their placement with nanoscale precision and their precisely controlled bonding to the substrate, both of which are challenges to this day.[29] Their directed self-assembly in controlled architectures, while interesting from a biomimetic perspective, is more troublesome than for nanostructures with smaller aspect ratios,[30,31] e.g., high aspect ratio nanowires are difficult to stabilize as colloids.

Nonetheless, we argue that there are at least two arguments that can justify an interest in colloidal nanowires.

1. The potential utility of nanowires is typically assessed by first considering the intrinsic physical properties (e.g., electrical conductivity) of the phase they are made of (e.g., Si, GaAs, or ZnO), and then how a one-dimensional morphology can affect the characteristics (e.g., quantum confinement) and applicability of those properties. A different perspective is to first consider their morphology and the properties that it bestows on the nanowires: one-dimensional morphologies are capable, in principle, of unique topological properties (e.g., entanglement and reptation) that elude bulk and approximately isotropic inorganic crystals. Many of the functions of polymers are based on their topological properties (e.g., glues and rubbers). The application of these functions has always been constrained by the physical and chemical limitations of the typically organic composition of polymers. From this perspective, it is plausible to speculate that bringing topological properties to the inorganic world of crystalline nanowires could introduce new capabilities of technological significance.
2. Recent years have seen the development of reliable synthetic strategies for the synthesis of colloidally stable spherical clusters, especially of metals.[32–40] These structures are monodisperse and possess atomic structures that are often quite different from those shown by the bulk phase with the same composition. There is convincing theoretical and experimental evidence that metal nanowires could also show (when reduced to diameters of only a few atoms) atomic structures that are quite different from those of the bulk phase (Fig. 1) and possessing different properties.[41–53] These properties could be studied more easily and made to be much more applicable if these wires could be made on a larger scale and in a colloidally stable state.

Both of these arguments require the synthesis of especially thin nanowires. In an attempt to classify this search for ever thinner nanowires, the vague term "ultrathin" is commonly applied to nanowires that are ~2–3 nm in diameter or less.[7]

Topological properties in nanowires

Two aspects that determine the topological properties of one-dimensional objects are (*i*) the ratio between their contour length (*L*), i.e., the length of the object along the path of their "backbone", and their persistence length (*p*) and (*ii*) the dynamics of the conformation of the object or, in other words, the extent by which the persistence length is determined by dynamic fluctuations in the conformation.[54] The persistence length[55] is the minimum distance that separates two points on

Can. J. Chem. Downloaded from www.nrcresearchpress.com by MCGILL UNIVERSITY on 02/02/13
For personal use only.

Can. J. Chem. Downloaded from www.nrcresearchpress.com by MCGILL UNIVERSITY on 02/02/13
For personal use only.

a path whose tangents to the path are, on a time average over thermal fluctuations, uncorrelated with each other. Linear polymers are straight molecules with a coiled conformation in solution. They coil because the C–C bonds that form their backbone can rotate around their axis owing to Brownian motion at room temperature. Therefore, the conformation of polymers is typically dynamic: its persistence length is almost entirely determined by its variations in time. When searching for topological properties in other objects (e.g., nanowires), one should look for large *L*/*p* ratios and spontaneous deformations at room temperature. In the case of nanowires, these requirements translate, to a first approximation, into long lengths and very small diameters. The persistence length of a solid cylinder can be estimated from its diameter (*d*) and from the Young's modulus (*Y*) of its atomic structure by using the formula

$$[1] \qquad p = \frac{\pi d^4 Y}{64 k_B T}$$

where k_B is Boltzmann's constant and T is the absolute temperature. (The formula can be derived by noticing that $p = B/k_BT$, where B is the bending stiffness, which is expressed as $B = IY$, where I is the moment of inertia of the cross section of the object. In the case of a cylindrical rod, $I = \pi d^4/64$. For details, see the treatment by Landau and Lifshitz,[55] by Harris and Hearst,[56] and the summary of Hatami-Marbini and Mofrad.[57]) If we take this formula at face value, any solid of respectable strength (e.g., 10 GPa, the modulus of wood) would need to be extraordinarily thin (<17 Å) to exhibit a persistence length of less than a micrometer, and its length would have to be of millimetres or centimetres to obtain the kind of *L*/*p* ratios that would lead to noticeable topological properties. However, this equation should be applied with caution to solids of near-molecular dimensions, since their deformation might occur by mechanisms that can be substantially different (e.g., not elastic) from those found in bulk solids.

Recent reports of topological properties and transformations in nanowires

Equation [1] seems to suggest that the topological properties of polymers should never be exhibited by crystalline solids. Nonetheless, recent work by the Ozin and Winnik laboratories[58] demonstrates that ultrathin nanowires of a crystalline material (Bi_2S_3) can show a wormlike conformation (analogous to that of semiflexible polymers) and *L*/*p* ratios of ~10^4 (analogous to those of the longest synthetic polymers). The data reported was from static light scattering and electron microscopy, and it was therefore impossible to conclude from them that the persistence length of those wires originated exclusively from thermal fluctuations of their conformation. Nonetheless, there are strong hints that at least part of the observed persistence length is a result of dynamic changes in the conformation: (*i*) the nanowires conformed over distances much larger than the persistence length to flat surfaces without breaking, (*ii*) the changes in direction of the nanowires observed under transmission electron microscopy (TEM) were smooth and not sharp as twinning would predict, and (*iii*) a dilute solution of nanowires injected in a dilute (micromolar) solution of cross-linker (a molecule bearing two amine groups) would lead to the formation of flexible and dense microfibers composed of cross-linked nanowires.[59]

Recently, the groups of B. Xing and H. Chen[60] demonstrated how 2 nm thick Au nanowires can be forced to coil into tight springs (radius of ~25–50 nm) by encapsulation in block copolymer micelles (Fig. 2).[60] Remarkably, the nanowires coiled without snapping or breaking and without penetrating the soft interface of the micelle. In another remarkable topological transformation in nanowires, Chen's group[61] showed how straight ultrathin Ag–Au alloy nanowires would coil into double helices as a third metal was deposited on their surface (Fig. 2).

Therefore, much work needs to be done to understand (*i*) the extent by which inorganic crystals can replicate the properties of polymers and (*ii*) if and how this combination of properties would be of technological interest. But the results are encouraging!

The scope of this review

Early work on the synthesis of ultrathin nanowires was covered to a good extent in a previous review.[7] This review will attempt to identify and elucidate emergent patterns in the syntheses of colloidal ultrathin nanowires by focusing on developments over the past three years that we consider to be conceptually novel. Despite the fairly large number of new reports of ultrathin nanowires, most of the experimental work in this area of research is still phenomenological: mechanisms are often postulated, but they are rarely supported by sufficient evidence. Therefore, we found it very difficult to discern patterns.

In these few pages, (*i*) we critically review the recent literature, (*ii*) we attempt to find heuristic guidelines for the synthesis of ultrathin nanowires, and (*iii*) we highlight the new strategies that have been developed. Please note that some of the approaches that we discuss do not report nanowires, but they are based on concepts that we believe could be used to make ultrathin nanowires.

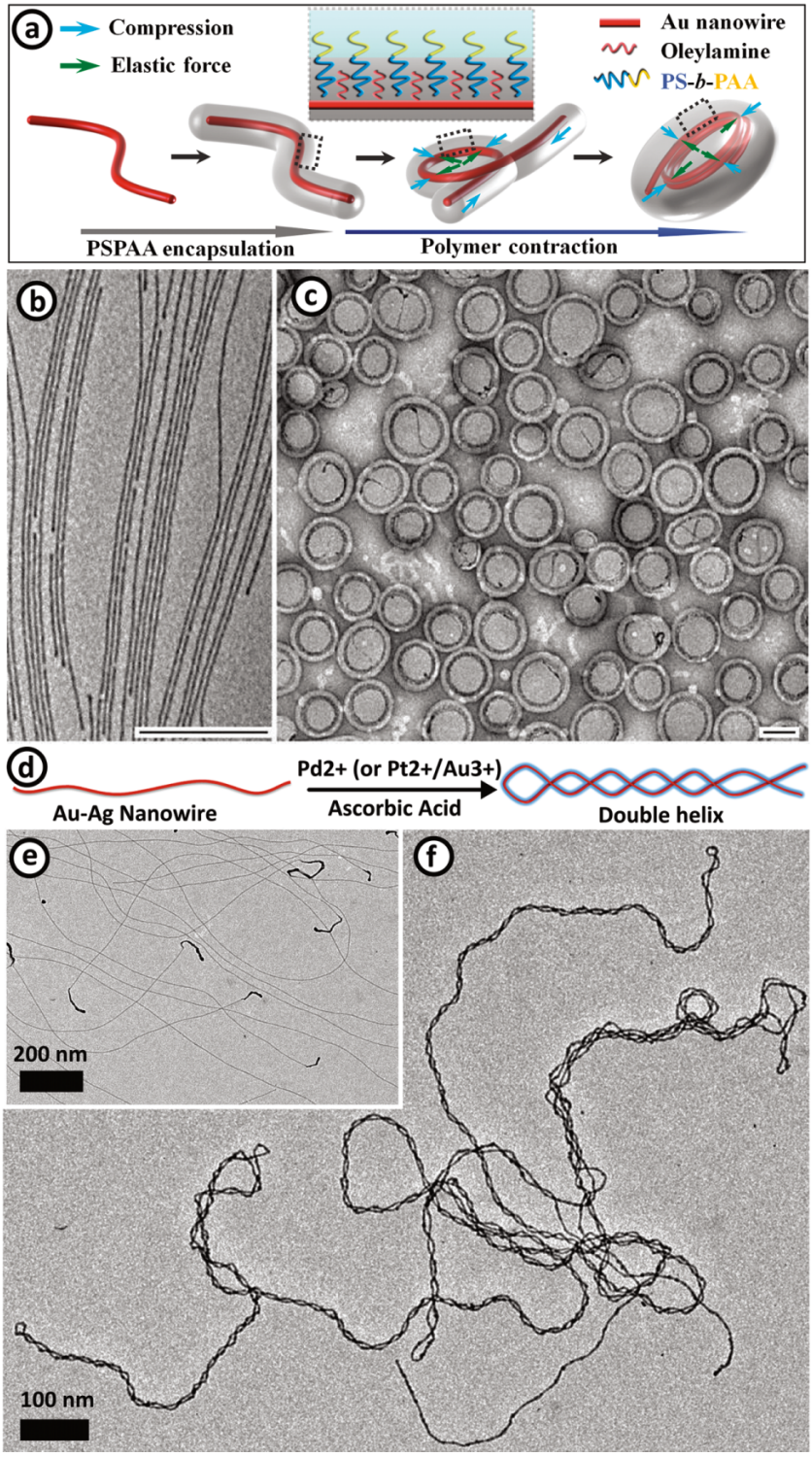
General strategies for the synthesis of colloidal nanowires

The strategies for the synthesis of nanowires have not changed substantially and are distinguished by the approach they use to break the symmetry of the growth process (Fig. 3).

Controlling the spatial distribution of precursors

When a crystal grows in solution, from gas, and from melt, the precursors are uniformly distributed and will collide with its facets in a way that is typically proportional to their surface area. Therefore, crystal growth is usually approximately isotropic and the growth rates of different crystal facets are largely dependent on their chemical potential. The crystal habit can be controlled by managing the spatial distribution of the precursor or, in often equivalent terms, the exposure of the crystal to the precursor. At a macroscopic scale, this approach is the essential principle of operation of Czochralski crystallization, in which the crystal is slowly pulled out of the melt, and of Bridgman crystallization, in which the crystal gradually fills the container it occupies (Fig. 3).[62] At the nanoscale, the exposure of the crystal to the precursor is often controlled by templates that can be either "hard" or "soft". Nanowires (or

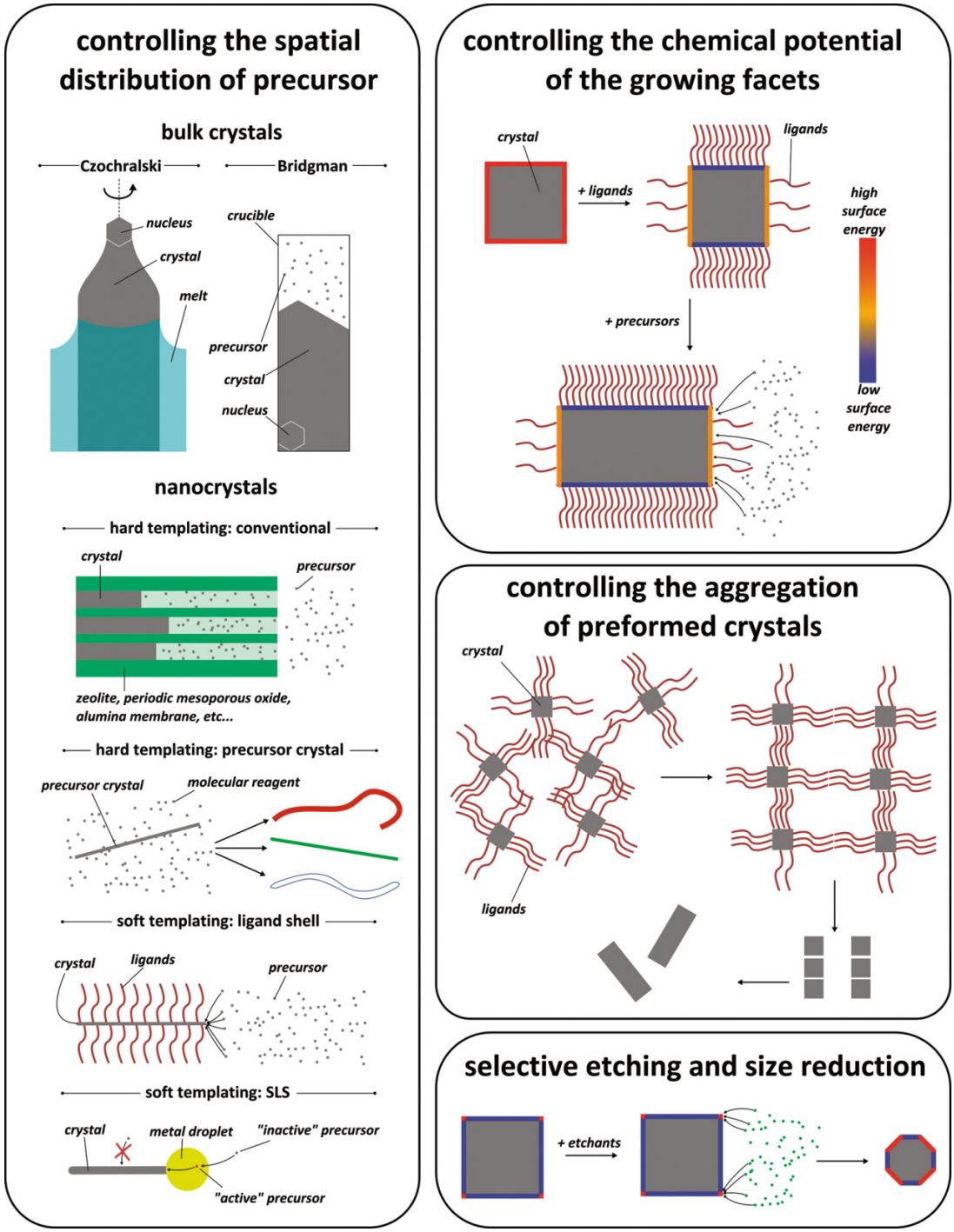
Fig. 2. Topological transformations in ultrathin nanowires:[60,61] (*a*) schematic of the encapsulation and coiling of Au nanowires within PS_{154}–*b*-PAA_{49} micelles, (*b*) TEM micrograph of ultrathin Au nanowires before encapsulation, (*c*) TEM micrograph of ultrathin Au nanowires coiled into individual micelles, (*d*) schematic of the coiling of Au–Ag ultrathin nanowires induced by deposition of a third metal, (*e*) TEM micrograph of the as-synthesized Au–Ag nanowires, and (*f*) TEM micrograph of a coiled (Au–Ag) Pd double helix nanowire. (From Xu et al. 2010, reproduced (adapted) with permission of J. Am. Chem. Soc., Vol. 132, p 11920, © 2010 American Chemical Society and from Wang et al. 2011, reproduced (adapted) with permission of J. Am. Chem. Soc., Vol. 133, p 20060, © 2011 American Chemical Society.)



Can. J. Chem. Downloaded from www.nrcresearchpress.com by MCGILL UNIVERSITY on 02/02/13
For personal use only.

Can. J. Chem. Downloaded from www.nrcresearchpress.com by MCGILL UNIVERSITY on 02/02/13
For personal use only.

Fig. 3. General strategies for the synthesis of anisotropic shapes.



other shaped crystals) can be nucleated and grown a la Bridgman in a hard template that provides a rigidly confined anisotropic environment (e.g., zeolites,[63–67] alumina membranes,[68] periodic mesoporous materials,[69–71] and carbon nanotubes[72]): as the facets of the nanostructure contact the hard surface of the template, they become inaccessible to the precursor and they stop growing (Fig. 3). The nanoscale dimensions of nanowires enable new approaches to templating that are fundamentally distinct from those employed in bulk crystallization: nanowires can be formed by using a hard template in the form of a "precursor" crystal (Fig. 3). A molecular reagent reacts with the precursor crystal and, through a chemical process (e.g., galvanic replacement,[73–75] ion exchange,[76,77] oxidation and diffusion,[78] or hydrolysis and condensation[19,79]), transforms its composition and often its shape; the composition and the shape of the precursor crystal is a determining factor in the composition and the shape of the product. In the case of soft templates, the exposure to the precursor is typically controlled

Can. J. Chem. Downloaded from www.nrcresearchpress.com by MCGILL UNIVERSITY on 02/02/13
For personal use only.

by steric hindrance. Nanowires are typically grown in solution in the presence of ligands that bind to their surface.[1,80–94] The ligands modulate the surface energy of the growing facets, but might also modulate the accessibility of the facets to incoming precursors (Fig. 3). Another form of soft templating is provided by nanoscale liquid droplets (typically of a low melting metal, e.g., Bi).[89,95,96] These droplets act as localized "nanoreactors" in which the "active" precursor that adds to the crystal is formed.[97] These metal droplets can be patterned on surfaces to create nanowire arrays or can spontaneously form in solution and attach to the growing ends of nanorods and nanowires (Fig. 3). The attachment of these droplets can break the symmetry of highly symmetric atomic lattices (e.g., it has allowed the formation of colloidal nanorods from cubic phases like PbSe).[98] This approach can be used for growing ultrathin nanowires, as recently demonstrated for 4 nm thick In_2O_3 nanowires.[99]

Controlling the chemical potential of the growing facets

The natural habit of a crystal is largely determined by the chemical potential of its facets (see, for example, the work of Gibbs,[100] Wulff,[101] Cerf,[102] and von Laue[103]). In principle, any control over the chemical potential of the facets would offer some control over the shape and the crystallographic orientation of the crystal. The chemical potential of a growing surface is typically controlled by binding a labile ligand to it. As the ligand binds, the chemical potential of the surface is reduced. (Chemical etching works in a similar way by removing parts of the surface that have a higher chemical potential.) This approach is especially suitable for the specific conditions that are used in the synthesis of colloidal nanomaterials. In these syntheses, the nuclei are typically formed in large quantities and are entirely immersed in a solution that is homogeneously populated by precursor. Therefore, a ligand dissolved in the solution can control equally the growth of all particles growing in it. The binding of ligands to surfaces can reduce their rate of growth by sterically impeding the adsorption of precursor to them (as discussed previously) and (or) by reducing their chemical potential (Fig. 3). Therefore, ligands can limit (but almost never halt) the natural tendency of the lattice to grow along a specific crystallographic direction. For example, we are not aware of Bi_2S_3 nanowires that are elongated along an axis different from [001][83,104–107] (Bi_2S_3 has a strongly anisotropic unit cell consisting of Bi_2S_3 "ribbons" stretching along the *c* axis of the unit cell). This incomplete control on the crystal orientation is a distinctive limitation of current wet chemistry approaches to the growth of nanowires or nanorods. It seems to indicate that the effect of ligands on the surface energy of the crystals is not sufficiently strong and that their binding is not sufficiently selective of specific crystal facets. Nonetheless, ligands that form strong bonds with the surface of crystals are typically considered inefficient in the growth of nanocrystals as they can prevent them from forming (e.g., this hypothesis is consistent with our experience in trying to grow PbS nanocrystals from a trioctylphosphine sulfide precursor).

Controlling the aggregation of preformed crystals

"Classical" crystallization is defined by the time-averaged addition of molecular, ionic, or atomic species to the growing surface of a nucleus or a crystal. In the classical approaches to crystallization (e.g., Czochralski or Bridgman), only one nucleus (i.e., the "seed") is provided, nucleation is eliminated, and the growth proceeds from the melt or from atomic or molecular precursors in the vapour phase. Colloid science deals instead with the simultaneous nucleation and growth of large ensembles of crystals.[108] In these conditions, crystals display the tendency to grow also (and sometimes exclusively) by processes of aggregation.[109] These processes typically lead to polycrystalline solids but can also be controlled to form large single crystals by the crystallographically oriented coupling of separate crystals (Fig. 3).[110–114] Aggregation that is not crystallographically oriented can still result in the formation of a single crystal if the size of the crystal is sufficiently small that a structural rearrangement is energetically favourable.[115] It is interesting to note that aggregation processes can be quite different from the adsorption, surface diffusion, and desorption processes involved in the addition of molecular, atomic, or ionic precursors. For example, the process of aggregation between nanoscale seeds can be guided at a long range and facilitated by the presence of electric or magnetic dipoles.[94,116] (In ionic solids like NaCl, the electrostatic interaction typically plays a role only at a very short range. The most stable facets of NaCl are (100), which appear to be electrically neutral at all distances much larger than the Na–Cl bond length. In nanocrystals, however, the whole solid can possess a dipole that can act, compatibly with screening, at much larger distances.)

Selective etching and size reduction

Another approach to the control of shape in crystals focuses on establishing selective dissolution, rather than selective deposition. In some instances, the dissolution occurs in a post-processing step (as commonly done to etch trenches in silicon wafers), whereas, in other cases, it occurs at the same time as the growth process (Fig. 3). This approach is especially well-developed for metallic structures, where controlled etching has been used to form highly controlled and monodisperse prismatic structures.[117,118]

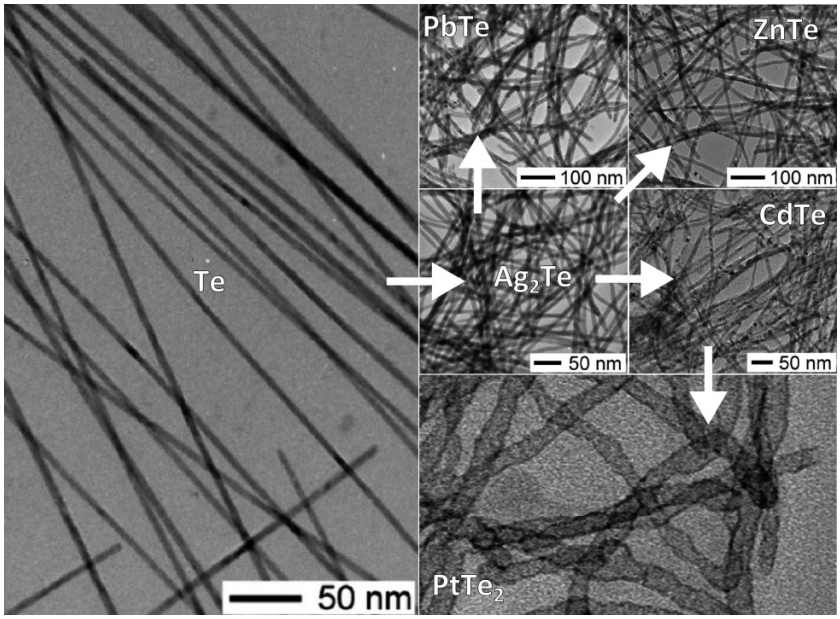
Advances in the recent literature

Interesting new approaches to these strategies have been demonstrated in the past three years. We categorize these works in terms of the strategy that they developed or introduced.

Chemical transformations of nanowire "precursors"

The chemical transformation of precursor or template nanostructures by ion-exchange or galvanic replacement can serve not only as means to obtain nanostructures with different compositions. In the case of ion exchange, the transformation of the atomic structure can lead to changes in the shape and size of the nanostructures. In many cases, especially for very thin and long nanostructures, the structural strains can be so large that the objects are broken apart in smaller isotropic objects.[119] Nonetheless, the ion exchange can induce topotactic structural transformations that minimize the strain to the existing atomic structure. For example, amine-coated 1.4 nm $CdCl_2$ lamelles could be smoothly converted into CdSe lamelles.[120]

Fig. 4. Chemical transformations of Te nanowires. The transformation of Te to Ag_2Te occurs via topotactic transformation and preserves the nanostructure morphology. Conversions to CdTe, ZnTe, and PbTe also preserve the one-dimensional morphology. Conversion of CdTe nanowires to $PtTe_2$ is instead accompanied by a large volume change, which is accommodated by the nanostructure by changing its morphology to that of a nanotube. (From Moon et al. 2010, reproduced (adapted) with permission of ACS Nano, Vol. 4, pp 2309–2319, © 2010 American Chemical Society.)



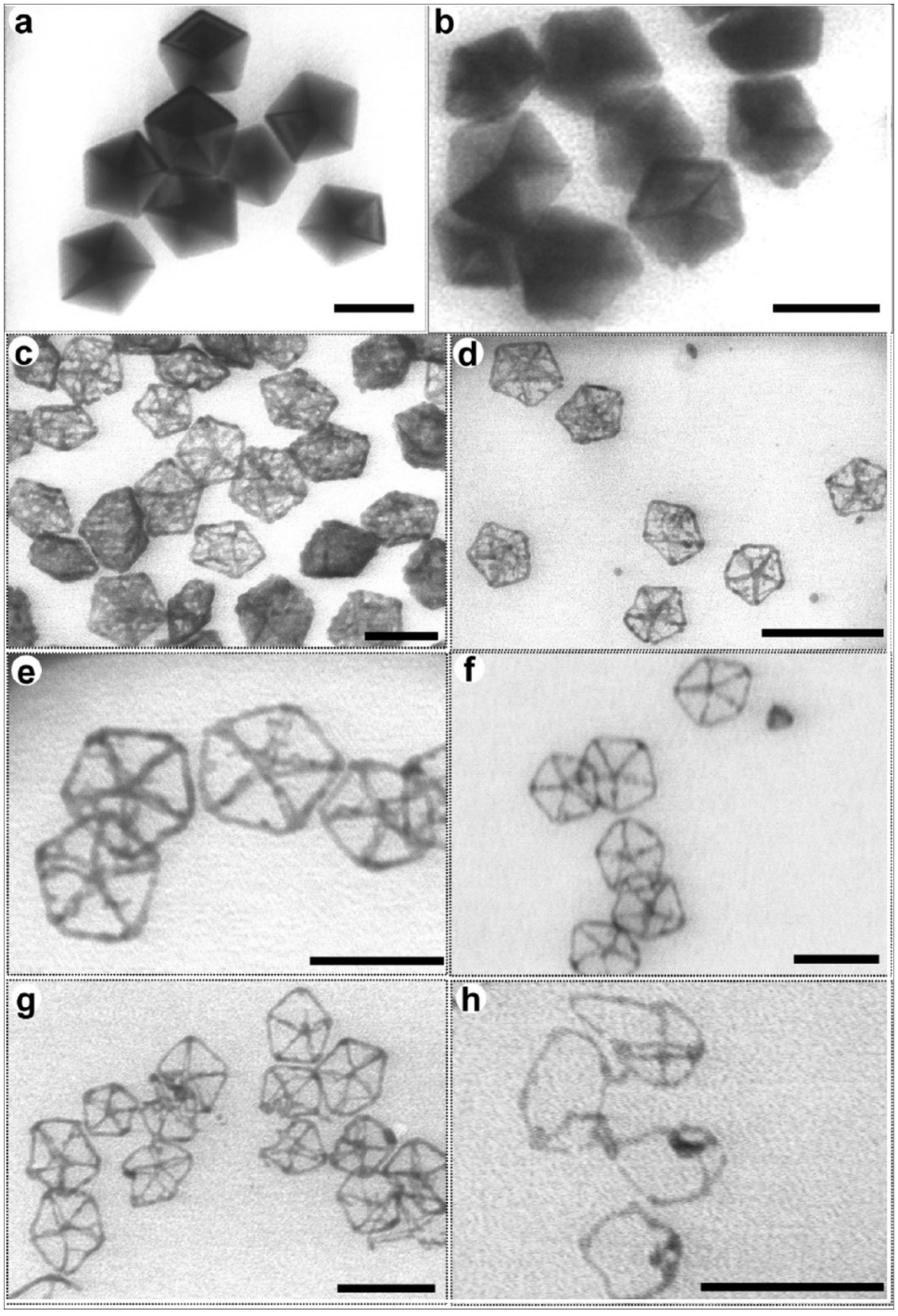
Can. J. Chem. Downloaded from www.nrcresearchpress.com by MCGILL UNIVERSITY on 02/02/13
For personal use only.

In the case of galvanic replacement, however, dissolution and deposition occur in different places. This spatial separation can lead to predictable and useful changes in the shape of the template structure[73] or to a collapse of the structure. For example, the surface of cubic Ag nanoparticles (50 nm) can be partially doped with Au and subsequently etched by $Fe(NO_3)_3$. Dealloying leads to the migration of Au atoms and to the formation of nanoframes with 10 nm thick edges.[121] Alternatively, Ag nanocubes with truncated corners (80 nm) separated the Ag dissolution on (111) from Au deposition on (100), so that the subsequent etching of Ag led to nanoboxes with holes at the corners. Therefore, while the dealloying approach avoids the spatial separation of dissolution and deposition, it still transforms the morphology of the template structure. Selenium and tellurium nanowires appear to be promising candidates and can be prepared, for example, by hydrothermal reduction in the presence of poly(vinylpyrrolidone) (PVP).[122,123] Tellurium nanowires, especially, have been used recently as templates for the preparation of Pd, Pt,[123] PdPt, PdAu,[124] and tellurides of Ag, Cd, Zn, Pb, Pt,[77] and Bi.[125] Oxide nanowires can also undergo ion exchange; for example, $Cd(OH)_2$ (4 nm) to CdSe[126] and $K_2Ti_8O_{17}$ (7 nm) to (Sr, Ba, and Pb)TiO_3.[127]

Complete galvanic transformation of Te nanowires (7 nm) into Pd or Pt nanowires or nanotubes can be achieved in ethylene glycol at 50 °C (2 h).[123] $PdCl_2$ (10 mmol/L), H_2PtCl_6 (5 mmol/L), or $[PtCl_2(NH_3)_2]$ were used in twofold excess to the Te in the nanowires (2.5 mmol/L). The authors state that the increased viscosity of ethylene glycol reduced the reaction rate, which, in turn, prevented the formation of large nanoparticles. Pd^{2+} or Pt^{2+} precursors led to a relatively small contraction in volume and preserved the continuous nanowire morphology. However, Pt^{4+} yielded a larger volume contraction, which, in turn, led to a morphological change of nanowires into nanotubes with 2 nm walls and 5.2 nm diameter. This work shows how the valence of the precursor can be used to reduce the size of a nanostructure, without necessarily compromising its dimensionality.

The reaction of Te nanowires with $AgNO_3$ led to Ag_2Te nanowires and subsequent ion exchanges were used to transform them into CdTe, ZnTe, PbTe, and $PtTe_2$ nanostructures (Fig. 4).[77] While the first step (Te → Ag_2Te) was associated with a large (twofold) volume increase, the conversion of the Te lattice into the Ag_2Te lattice was topotactic despite the large change in symmetry (from trigonal to monoclinic) and helped to retain the crystal habit and the single-crystalline nature of the nanostructure. To achieve further ion exchange against otherwise unfavourable thermodynamic conditions (i.e., Ag_2Te is expected to have a very low solubility product, since $K_{SP}(Ag_2Se) = 10^{-54}$),[128] the authors used tributylphoshine as a selective complexing reagent for silver. The transition from the Ag_2Te lattice to the (Cd, Zn, and Pb)Te lattices did not involve a large volume change (<20%), so the single-crystalline structure was retained. Further transformation to $PtTe_2$ was instead accompanied by a 46% volume contraction and led to polycrystalline nanotubes with 1–2 nm wall thickness. Thus, in a similar way as electrochemical potentials are used for the thermodynamic description of galvanic replacement, the viability of ion exchange in inorganic nanomaterials can be estimated from the corresponding solubility products. Still, an otherwise thermodynamically unfavourable reaction can be made favourable by selectively solvating specific ions by ligation.

Fig. 5. TEM micrographs of defect templating on Ag decahedra: (*a*) as-synthesized Ag decahedra, (*b*) Ag decahedra after the deposition of Au, and (*c*)–(*h*) the effect of the etching of Ag on the morphology of the particles. The ratio of Au:Ag in the samples is 0.2, 0.15, 0.07, 0.05, 0.03, and 0.01 respectively. Scale bars are 50 nm. (From McEachran et al. 2011, reproduced (adapted) with permission of J. Am. Chem. Soc., Vol. 133, p 8067, © 2011 American Chemical Society.)

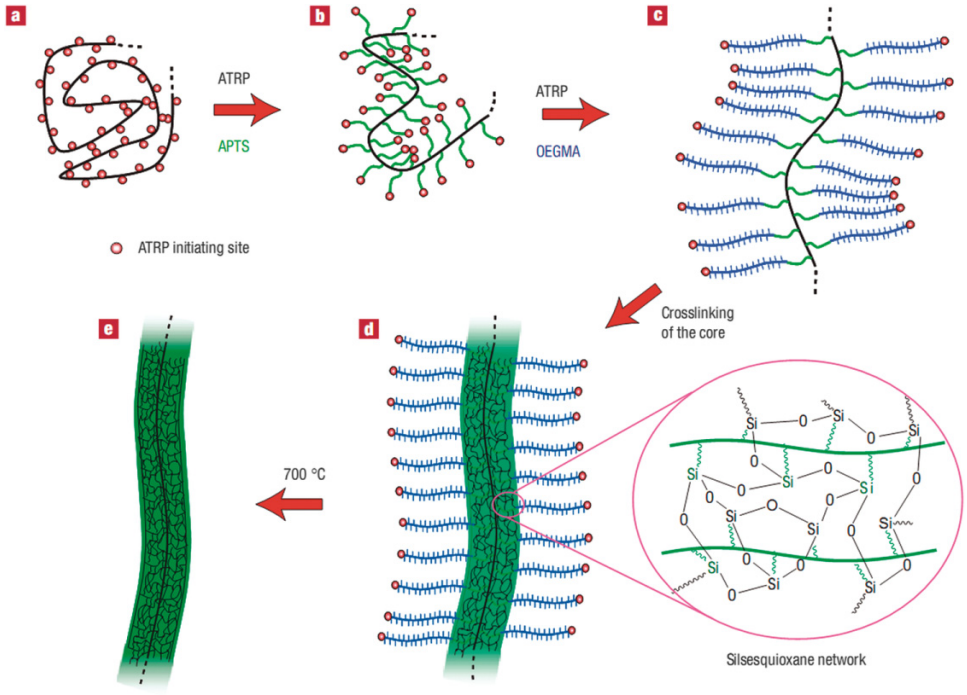


Can. J. Chem. Downloaded from www.nrcresearchpress.com by MCGILL UNIVERSITY on 02/02/13
For personal use only.

"Defect" templating

Another "style" of templating, with great potential for the reduction of feature sizes, uses defects as nucleation centers (Fig. 5). This approach is based on one of the most common aspects of heterogeneous nucleation and crystal growth (i.e., crystal defects) that was previously used and controlled to yield nanostructures on flat surfaces.[129] Colloidal nanostructures can display well-defined defects in their atomic structure.[3,117] These predictable defects can emerge on the surface of the colloid, where they will exhibit a higher chemical potential than the surrounding surface. This localized increase in chemical potential can act as a "template" that directs the

Fig. 6. Schematic of polymer-based templating of ultrathin silica and organosilica nanowires: (*a*) and (*b*) the polymer backbone undergoes atom transfer radical polymerization (ATRP) to form a polymer brush whose brushes are populated by silanes, (*b*) and (*c*) further polymerization allows the growth of a hydrophilic outer shell, (*c*) and (*d*) hydrolysis and condensation of the silane inner shell produces a water-dispersible organosilica nanowire, and (*d*) and (*e*) calcination at 700 °C leads to ultrathin pure silica nanowires. (From Yuan et al. 2008, reproduced with permission of Nat. Mater, Vol. 7, p 719, © 2008 Nature Publishing Group.)



nucleation and deposition of another material. The underlying colloid can then be dissolved to yield ultrathin nanostructures.

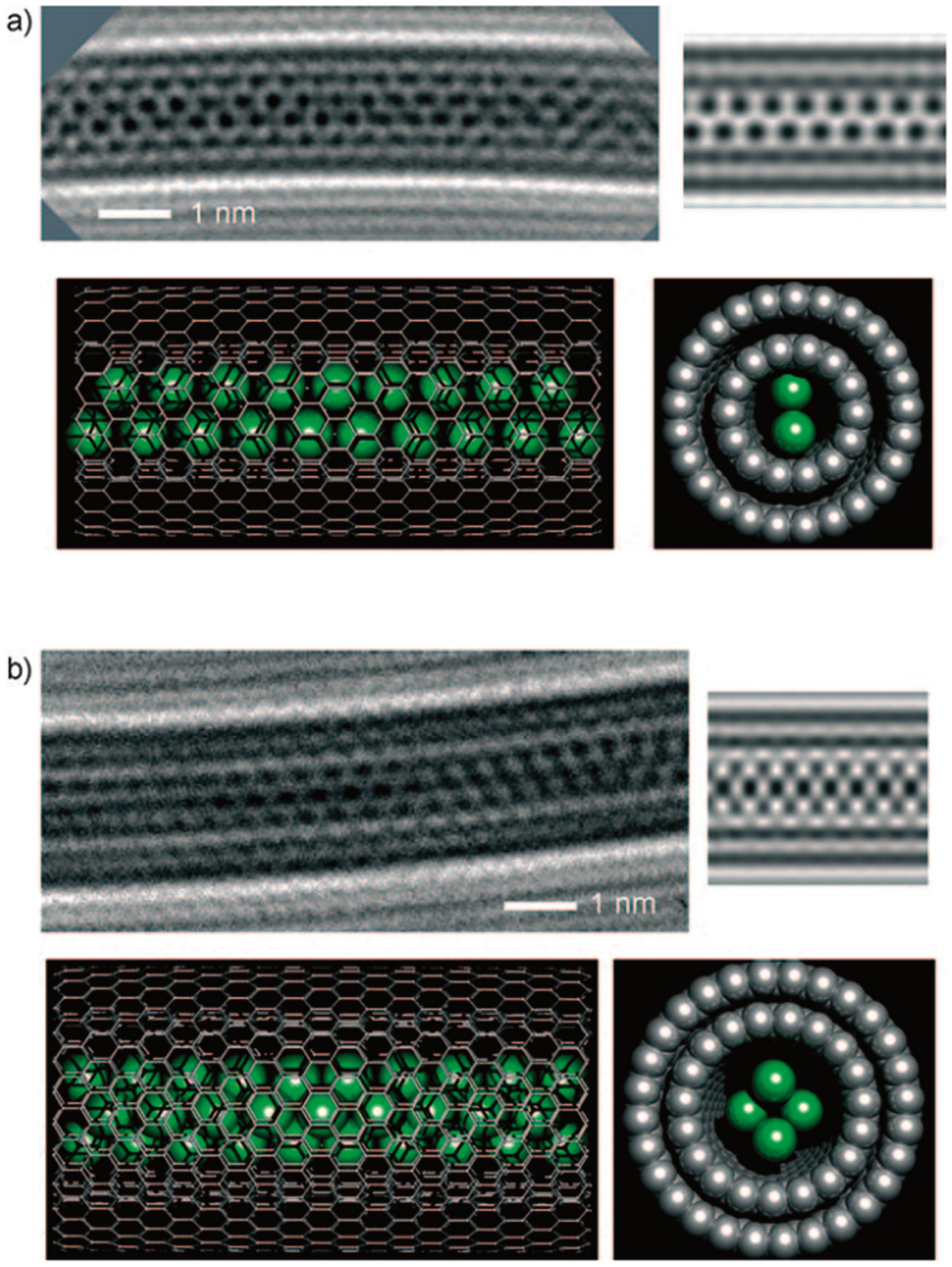
Ag decahedrons (size = 50 nm) entirely delimited by (111) facets joined by twinning boundaries at the edges were used as templates for deposition of Au. The Au deposited preferentially on the twin boundaries. Subsequent etching of silver resulted in nanoframes of 3 nm thickness.[75] Au deposition was obtained by reducing $HAuCl_4$ with ascorbic acid, whereas the galvanic replacement was suppressed by maintaining a high pH (8–9). (Higher pH led to a coverage of the (111) facets.) The thickness of the beams composing the frames (3–4.5 nm) and their overall size (40–50 nm) could be somewhat tuned by the amount of Au (Au:Ag = 3%–10%): a reduction of the thickness of the edges to 1.6 nm (at 1% Au) led to a loss of the integrity of the frames. While the reaction required a certain fine-tuning of the reaction conditions and the choice of an unusual template, we believe that this work illustrates a concept that could be explored for the fabrication of other ultrathin nanostructures, such as nanowires. The higher chemical potential of defects can, in principle, be employed for the deposition of most crystals.

Polymer templating

Müller and co-workers[19] at the University of Bayreuth demonstrated a very elegant example of bottom-up nanowire design (Fig. 6). They took a polymer backbone as a template and grewside chains decorated by silanes on it (by atom transfer radical polymerization (ATRP)). The side chains were further extended with hydrophilic monomers. The hydrolysis and condensation of the silanes within the inner shell formed an organosilica network in the shape of a nanowire. The hydrophilic outer shell provided these hybrid nanowires with dispersibility in water. The hybrid nanowires exhibited a glass transition at $T < -45$ °C and they decomposed above 200 °C. Above 530 °C they yielded pure silica nanowires, following a weight loss of 96.5%. A calcination of the nanowires at 700 °C produced dense silica nanowires.[19] This bottom-up approach could precisely control the thickness (9–21 nm) and length (140–300 nm) of the nanowires by driving polymerizations to a designed degree. Müller and co-workers[79] extended this work by demonstrating the formation of silica nanotubes by incorporating a nonhydrolyzable innermost shell in the polymer brush. This method could be quite broadly applicable to sol–gel precursors and should be amenable to the fabrication of ultrathin structures. However, it is limited by the underlying polymer chemistry (e.g., the length of the nanowire and their polydispersity will depend on how large and monodisperse a polymer can be polymerized) and its compatibility with the sol–gel chemistry. Additional challenges could be found in maintaining the structural integrity of the nanowires upon the large mass loss occurring during calcination. Nonetheless, the possibility of translating the control of structure given by polymer chemistry to the design and synthesis of ultrathin inorganic structures is tantalizing. Furthermore, it is conceivable that the oxide nanowires obtained with this method could be further transformed into a multitude of other compositions by appropriate chemical transformations (e.g., reduction and sulfidation).[130]

Can. J. Chem. Downloaded from www.nrcresearchpress.com by MCGILL UNIVERSITY on 02/02/13
For personal use only.

Fig. 7. Characterization and simulation of two- and four-atom thick Eu nanowires within double-walled carbon nanotubes (CNTs): (*a*) two-atom thick nanowires and (*b*) four-atom thick nanowires. (From Kitaura et al. 2009, reproduced (adapted) with permission of Angew. Chem, Int. Ed. Engl., Vol. 48, p 8299, © 2009 John Wiley and Sons.)



Can. J. Chem. Downloaded from www.nrcresearchpress.com by MCGILL UNIVERSITY on 02/02/13
For personal use only.

Other ultrathin nanowires might grow by polymer templating. For example, the successful synthesis of 1.8 nm Au nanowires capped by oleylamine reported by the Xia group[17] and others,[15,16,131] appears to be templated by the formation, reduction, and assembly of a one-dimensional AuCl–oleylamine complex.[17]

Carbon nanotube templating

Hard templating in zeolites[63–67] or periodic mesoporous oxides[69–71] is a proven method for producing nanowires of precise diameters. However, it is difficult to extract, isolate, and colloidally stabilize the nanowires embedded in them. Furthermore, these approaches do not lend themselves well to scale-up. These issues might not be so severe if carbon nanotubes (CNTs) are chosen as templates. CNTs can be produced in fairly large quantities and are somewhat dispersible in a few solvents. They can encapsulate the nanowire within them, providing it with protection against degradation and agglomeration.

Deposition of Eu (under 10^{-6} Torr (1 Torr = 133.3224 Pa) and 500–600 °C) into double-walled CNTs led to ultrathin (one to four atoms across) metal nanowires that were resistant to oxidation and ultrasonication (Fig. 7).[72] Eu–Eu spacing was larger than in bulk metal by 7%–18%. The authors claim that

Can. J. Chem. Downloaded from www.nrcresearchpress.com by MCGILL UNIVERSITY on 02/02/13
For personal use only.

a similar procedure also worked for producing analogous nanowires from Sm, Sr, and Yb. While CNT templating seems to be a promising way to obtain nanowires of reactive metals and to enable fundamental studies on the physics of ultrathin nanowires, it might remain severely limited as a synthetic approach by the relatively limited colloidal stability of CNTs.

Ligand-controlled growth of atomically thin nanowires

Some of the most remarkable findings of the past three years in the formation of ultrathin nanowires demonstrated the formation of colloidally stable one-dimensional structures held together by single bonds.

The Ritter group[132] at Harvard University obtained colloidally stable and atomically thin nanowires of Pd^{3+} and $Pd^{2.5+}$ by a clever use of molecular inorganic chemistry. The nanowires were fairly long (~0.5 μm) and showed semiconducting (Pd^{3+}) or metallic ($Pd^{2.5+}$) conductivity. The nanowires were dispersible in CH_2Cl_2 and coordinated by acetate (or hexanoate) and benzo[*h*]quinolinyl and accompanied by F^- or BF_4^- anions. However, their crystals were not stable above –35 °C. (These Pd nanowires remind us of the AuCl–oleylamine polymer used to form Au nanowires.[17]) While the approach by the Ritter group[132] is elegant and apparently effective, it might not be widely applicable to other metals.

In a procedurally simpler, but mechanistically mysterious example, Liu and Yang[133] grew atomically thin (0.4 nm) anatase (TiO_2) nanowires from $Ti(OBu)_4$ in the presence of oleic acid and oleylamine at 180 °C. While the nanowires did not exceed 25 nm in length, this work is remarkable in that it displays the possibility of creating nanowires with a truly monodisperse section by fairly traditional ligand-based approaches and without the use of a hard template. We and others have previously argued on several occasions about the importance of pursuing the synthesis of perfectly monodisperse colloids.[29,134–138] We have attempted to achieve this objective in our research and not quite succeeded yet. These colloidal nanowires do represent one of the very few cases where this objective has been accomplished successfully with nanowires, with ceramics, and by using a fairly conventional strategy.

Much longer (~μm) but somewhat thicker (1.8 nm) nanowires of EuOF were obtained instead by decomposition of $Eu(CF_3COO)_3$ in the presence of oleic acid and oleylamine at 310 °C.[139] ZnS ultrathin (~2.0 nm) nanowires were obtained by decomposing a single source precursor ($Zn(S_2CN\text{-}n\text{-}Bu_2)_2$) in the presence of dodecylamine and triphenylphosphine.[87] In a previous example, ultrathin ZnS nanowires (1.2 nm in diameter) were obtained by reacting a *S*-oleylamine solution with a Zn^{2+}–oleylamine precursor in the presence of dodecanethiol.[86]

Growth in aqueous solutions

Interesting cases have also been reported in which well-known chemistry, investigated in a novel way, has led to ultrathin nanowires.

For example, the slow evaporation of ammonia at 60 °C from an aqueous $[Cd(NH_3)_4]^{2+}$ solution led to the growth of $Cd(OH)_2$ nanowires (4 nm × ~100 nm) on SiO_2 spheres (300 nm)[126] from which they can be detached later by exposure to ultrasounds. The authors postulated that the colloids of silica provided a large and negatively charged surface area that would promote the growth of nanowires of the positively charged cadmium hydroxide. This approach does not use organic ligands; presumably, the nanowires are stabilized by electrostatic repulsion. Somewhat similarly, ultrathin $W_{18}O_{49}$ nanowires were obtained when WCl_6 was dissolved in ethanol and treated in an autoclave at 180 °C. During this process, the chloride undergoes hydrolysis and forms bundles of <2 nm nanowires.[140] The hydrothermal treatment of molybdenic acid in water–dodecanethiol at neutral pH led to single-walled MoO_3 nanotubes with diameters of 6 nm.[141] The authors indicate that the reduction by dodecanethiol could be responsible for straining the individual MoO_3 layers (α-MoO_3 is known for its layered orthorombic structure) into tubes. It is possible that nanowires of other materials can be prepared by analogous approaches, but they have so far escaped our attention.

Oriented attachment

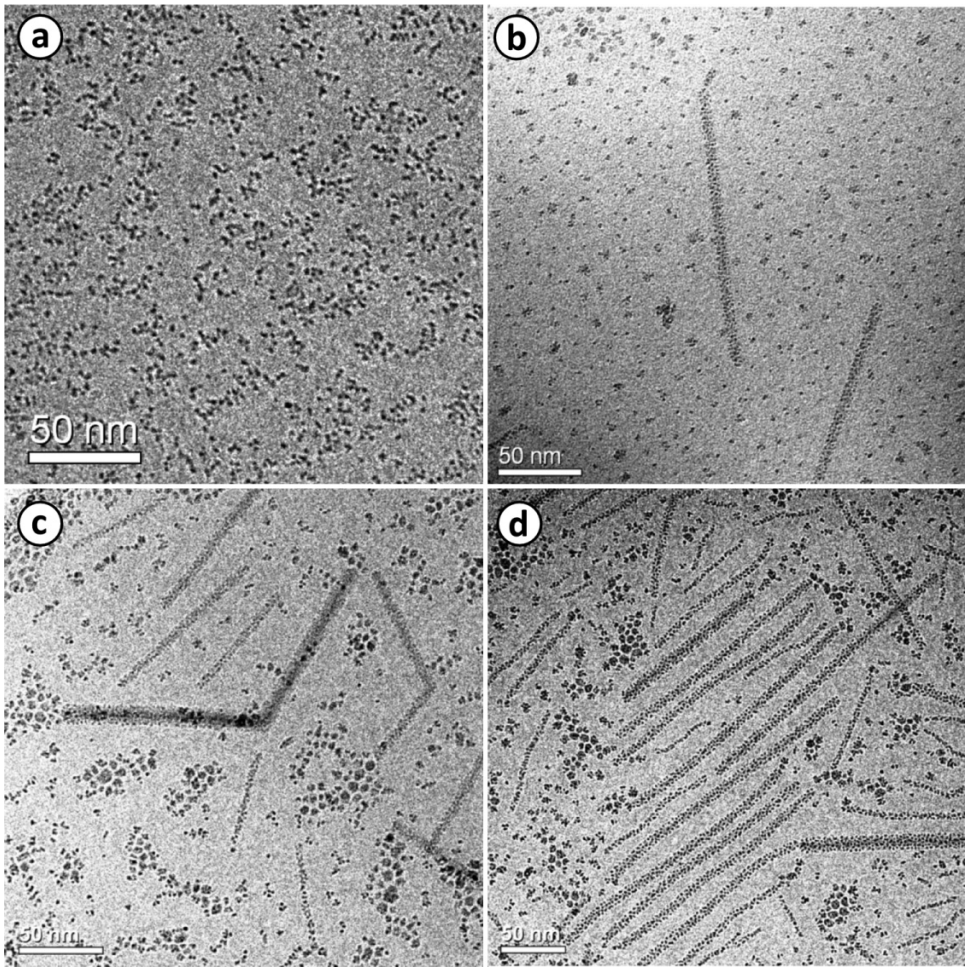
Oriented attachment is usually proposed when there is a transformation of nanocrystals into nanowires. "Oriented" typically implies that two identical facets (e.g., (111)) on two separate crystals attach, leading to the seamless welding of the two crystals. Temporary electric dipoles (quite often present in growing ionic crystals, depending on the composition of a facet[94]) are often invoked to justify the occurrence of this phenomenon, which is otherwise thought to be exceedingly rare owing to the geometric requirements of the collision. However, in some cases, we should be careful at suggesting electric dipoles for at least two reasons: (*i*) magic-sized clusters[142] (CdSe) typically possess high symmetries that are often not compatible with electric dipoles (fluctuating adhesion or dissociation of atoms could, nonetheless, lead to temporary dipoles by temporarily breaking this symmetry) or (*ii*) metallic particles, e.g., 2–3 nm Au, Pd, and Pt,[143] which cannot create permanent dipoles (this limitation is valid if the particle is indeed metallic and has conduction or freely moving electrons (Au clusters can be semiconducting)). Nonetheless, the ligands attached to the particles could bear charge and form dipoles and control aggregation.[116,144,145]

Furthermore, it is interesting to note how the size of the particles involved in the attachment can somewhat relieve the requirements of orientation. As shown in recent in situ high-resolution (HR)-TEM studies by the Alivisatos group,[115] the nonoriented attachment of small nuclei can result in a structural rearrangement to form a single crystal.

Cryo-TEM was quite remarkably and convincingly put to use to show the prearrangement of nanoparticles prior to fusion. The self-assembly and fusion of goethite (iron oxide) nanoparticles was demonstrated during aging in water at 80 °C for several days (Fig. 8).[112] The rodlike aggregates had a shape similar to that of the final goethite nanorods (even twinned rods were present). This observation, together with the aligned fringes in cryo-HR-TEM, suggested a crystallographic alignment of nanoparticles in rodlike aggregates before their final fusion occurred.

The recent work of the Ozin laboratory[58] further demonstrated that end-to-end attachment can be an effective mechanism in producing nanowires with large aspect ratios. Bi_2S_3 nanowires (1.6 nm wide) were grown in solution by reacting a slurry of bismuth citrate in oleylamine with a sulfur–oleylamine solution at 100 °C.[1] The nanowires can grow for hours without changing diameter and yet would elongate in the same time frame from a few nanometers to hundreds of micrometers. Static

Fig. 8. Cryo-TEM investigation of the formation of mesocrystals from goethite nanocrystals: (*a*) the as-prepared and purified goethite nanocrystals before aging and (*b*)–(*d*) the goethite nanocrystal dispersion after 5, 10, and 24 days of aging, respectively. (From Yuwono et al. 2010, reproduced (adapted) with permission of J. Am. Chem. Soc., Vol. 132, 2163–2164, © 2010 American Chemical Society.)



Can. J. Chem. Downloaded from www.nrcresearchpress.com by MCGILL UNIVERSITY on 02/02/13
For personal use only.

light scattering determined that their conformation was worm-like (analogous to that of many semiflexible polymers) and characterized by a persistence length of 17.5 nm. The knowledge of these structural parameters allowed for the development of a kinetic model for the growth of these nanowires that explained how, while the yield of the reaction increased logarithmically with time, the number of nanowires in the solution decreased by two orders of magnitude over 2 h of growth. The model included a process of epitaxial addition to the ends of the nanowires and an end-to-end coupling of separate nanowires. The coupling process had a rate constant comparable to that of the chain coupling observed in many step-growth polymerizations. Nonetheless, the nanowires appear to be polycrystalline by X-ray diffraction.

Conclusion

In the past three years, the efforts in the synthesis and characterization of ultrathin colloidal nanowires have (*i*) yielded a multitude of new compositions, especially for metals, (*ii*) progressed our understanding of their growth, and (*iii*) produced some remarkable observations of their properties.[132,146–148] We could summarize the take away messages as follows.

Ultrathin colloidal nanowires can be produced by a number of approaches

Ligand-controlled precipitation or reduction, hydrothermal synthesis, condensation of polymer brushes, vapour–liquid–solid growth, solution–liquid–solid growth, oriented attachment, chemical transformation, and size reduction of precursor nanostructures are all viable approaches that are, in different measures, displaying flexibility in terms of the compositions they can obtain. Despite the number of approaches that are available, none of them display chemical flexibility, clear potential for scalability, and atomic-level control of the structure. Much work remains to be done.

Amine-terminated ligands are featured in a majority of the syntheses

Is this just a result of the popularity of oleylamine in academic nanochemistry laboratories or is there some more substantial aspect to it? Is the impurity of the commercially available oleylamine to be credited for these results? It would not be the first time that impurities in a ligand obtained with "technical" purity have determined the role of the ligand in nanocrystal synthesis.[149–152]

Can. J. Chem. Downloaded from www.nrcresearchpress.com by MCGILL UNIVERSITY on 02/02/13
For personal use only.

In-depth studies of the kinetics and thermodynamics of crystal nucleation and growth are sorely needed in this area

Much of the development of syntheses of these systems, especially for ligand-based approaches, still depends on serendipity and (or) screening of a broad spectrum of conditions and reagents. To this day, we have a lack of predictive power in this area (a trait that is shared to an extent with the wider field of nanocrystal synthesis). This issue seems to be dictated, among other things (e.g., purity of reagents, as discussed previously), by a substantial lack of experimental data (e.g., surface energies, binding constants, dissociation energies, and solubility constants) on which to build a quantitative and predictive framework for nanowire synthesis. When theoretical predictions exist, they are often difficult to validate quantitatively.[153] The exquisite control that crystal growers have achieved on the growth of single crystal silicon resulted from an equally exquisite knowledge of the thermodynamic variables involved in the process. Unless a similar quantitative framework is established, we believe that this area of nanochemistry is bound to be stunted in its development and in its ability to translate into real world application. A partial solution for this problem, at least for ultrathin morphologies, might be offered by approaches such as those demonstrated, for example, by Müller and co-workers[19,79] and Ritter and coworkers,[132] that build the nanowire from the bottom up as a molecular construct. In these approaches, the morphology of the structure is "hard-wired" in the molecular structure that acts as a precursor.

Topological properties are starting to emerge as a powerfully distinctive aspect of ultrathin nanowires

The increasing availability of ultrathin nanowires is resulting in the first observations of topological transformations.[59–61] The increasing quality of the materials is permitting sophisticated studies on the structure and conformation of these wires in solution.[58] The next few years should give the first definitive answers to the fundamental questions that we mentioned in the introduction (Why should we care about nanowires?): Can the topological properties of polymers be observed (and used) in colloidal inorganic crystals of near molecular dimensions? Can colloidal nanowires be produced with the atomic structures predicted by theory at near-molecular dimensions? More pragmatically, what are we going to do with these extremely interesting materials between crystals and polymers?

Acknowledgments

We thank Iowa State University for start-up funding. A.R. acknowledges the support of the Grant Agency of the Czech Republic under project No. P108/10/1250 and the Long-Term Research Plan MSM0021620857 of the Ministry of Education of the Czech Republic.

References

(1) Cademartiri, L.; Malakooti, R.; O'Brien, P. G.; Migliori, A.; Petrov, S.; Kherani, N. P.; Ozin, G. A. *Angew. Chem. Int. Ed. Engl.* **2008**, *47* (20), 3814. doi:10.1002/anie.200705034.

(2) Cham, J. *Piled Higher and Deeper.* http://www.phdcomics.com/comics.php.

(3) Cademartiri, L.; Ozin, G. A. *Concepts of Nanochemistry*; Wiley-VCH: Weinheim, 2009.

(4) Ozin, G. A.; Arsenault, A. C.; Cademartiri, L. *Nanochemistry: A Chemical Approach to Nanomaterials;* 2nd ed.; Royal Society of Chemistry: Cambridge, UK, 2009.

(5) Hu, J. T.; Odom, T. W.; Lieber, C. M. *Acc. Chem. Res.* **1999**, *32* (5), 435. doi:10.1021/ar9700365.

(6) Xia, Y. N.; Yang, P. D.; Sun, Y. G.; Wu, Y. Y.; Mayers, B.; Gates, B.; Yin, Y. D.; Kim, F.; Yan, Y. Q. *Adv. Mater. (Deerfield Beach Fla.)* **2003**, *15* (5), 353. doi:10.1002/adma.200390087.

(7) Cademartiri, L.; Ozin, G. A. *Adv. Mater. (Deerfield Beach Fla.)* **2009**, *21* (9), 1013. doi:10.1002/adma.200801836.

(8) Duan, X.; Huang, Y.; Cui, Y.; Wang, J.; Lieber, C. M. *Nature* **2001**, *409* (6816), 66. doi:10.1038/35051047.

(9) Huang, M. H.; Mao, S.; Feick, H.; Yan, H. Q.; Wu, Y. Y.; Kind, H.; Weber, E.; Russo, R.; Yang, P. D. *Science* **2001**, *292* (5523), 1897. doi:10.1126/science.1060367.

(10) Duan, X. F.; Huang, Y.; Cui, Y.; Wang, J. F.; Lieber, C. M. *Nature* **2001**, *409* (6816), 66. doi:10.1038/35051047.

(11) Huang, Y.; Duan, X. F.; Cui, Y.; Lauhon, L. J.; Kim, K. H.; Lieber, C. M. *Science* **2001**, *294* (5545), 1313. doi:10.1126/science.1066192.

(12) Huang, Y.; Duan, X. F.; Wei, Q. Q.; Lieber, C. M. *Science* **2001**, *291* (5504), 630. doi:10.1126/science.291.5504.630.

(13) Law, M.; Greene, L. E.; Johnson, J. C.; Saykally, R.; Yang, P. D. *Nat. Mater.* **2005**, *4* (6), 455. doi:10.1038/nmat1387.

(14) Holmes, J. D.; Johnston, K. P.; Doty, R. C.; Korgel, B. A. *Science* **2000**, *287* (5457), 1471. doi:10.1126/science.287.5457.1471.

(15) Huo, Z.; Tsung, C.-k.; Huang, W.; Zhang, X.; Yang, P. *Nano Lett.* **2008**, *8* (7), 2041. doi:10.1021/nl8013549.

(16) Wang, C.; Hu, Y.; Lieber, C. M.; Sun, S. *J. Am. Chem. Soc.* **2008**, *130* (28), 8902. doi:10.1021/ja803408f.

(17) Lu, X.; Yavuz, M. S.; Tuan, H.-Y.; Korgel, B. A.; Xia, Y. *J. Am. Chem. Soc.* **2008**, *130* (28), 8900. doi:10.1021/ja803343m.

(18) Gilroy, J. B.; Gadt, T.; Whittell, G. R.; Chabanne, L.; Mitchels, J. M.; Richardson, R. M.; Winnik, M. A.; Manners, I. *Nat. Chem.* **2010**, *2* (7), 566. doi:10.1038/nchem.664.

(19) Yuan, J. Y.; Xu, Y. Y.; Walther, A.; Bolisetty, S.; Schumacher, M.; Schmalz, H.; Ballauff, M.; Müller, A. H. E. *Nat. Mater.* **2008**, *7* (9), 718. doi:10.1038/nmat2232.

(20) Hu, J.; Li, L.-s.; Yang, W.; Manna, L.; Wang, L.-w.; Alivisatos, A. P. *Science* **2001**, *292* (5524), 2060. doi:10.1126/science.1060810.

(21) Park, W. I.; Zheng, G.; Jiang, X.; Tian, B.; Lieber, C. M. *Nano Lett.* **2008**, *8* (9), 3004. doi:10.1021/nl802063q.

(22) Hu, L. B.; Wu, H.; Hong, S. S.; Cui, L. F.; McDonough, J. R.; Bohy, S.; Cui, Y. *Chem. Commun. (Camb.)* **2011**, *47* (1), 367. doi:10.1039/c0cc02078h.

(23) Lee, H. W.; Muralidharan, P.; Ruffo, R.; Mari, C. M.; Cui, Y.; Kim, D. K. *Nano Lett.* **2010**, *10* (10), 3852. doi:10.1021/nl101047f.

(24) Rolison, D. R.; Nazar, L. F. *MRS Bull.* **2011**, *36* (07), 486. doi:10.1557/mrs.2011.136.

(25) Garnett, E.; Yang, P. D. *Nano Lett.* **2010**, *10* (3), 1082. doi:10.1021/nl100161z.

(26) Law, M.; Greene, L. E.; Radenovic, A.; Kuykendall, T.; Liphardt, J.; Yang, P. D. *J. Phys. Chem. B* **2006**, *110* (45), 22652. doi:10.1021/jp0648644.

Can. J. Chem. Downloaded from www.nrcresearchpress.com by MCGILL UNIVERSITY on 02/02/13
For personal use only.

(27) Wang, X. D.; Song, J. H.; Liu, J.; Wang, Z. L. *Science* **2007**, *316* (5821), 102. doi:10.1126/science.1139366.
(28) Wang, Z. L.; Song, J. H. *Science* **2006**, *312* (5771), 242. doi:10.1126/science.1124005.
(29) Cademartiri, L.; Kitaev, V. *Nanoscale* **2011**, *3* (9), 3435. doi:10.1039/c1nr10365b.
(30) Liu, J. W.; Zhu, J. H.; Zhang, C. L.; Liang, H. W.; Yu, S. H. *J. Am. Chem. Soc.* **2010**, *132* (26), 8945. doi:10.1021/ja910871s.
(31) Nie, Z.; Petukhova, A.; Kumacheva, E. *Nat. Nanotechnol.* **2010**, *5* (1), 15. doi:10.1038/nnano.2009.453.
(32) Akola, J.; Walter, M.; Whetten, R. L.; Hakkinen, H.; Gronbeck, H. *J. Am. Chem. Soc.* **2008**, *130* (12), 3756. doi:10.1021/ja800594p.
(33) Lopez-Acevedo, O.; Akola, J.; Whetten, R. L.; Gronbeck, H.; Hakkinen, H. *J. Phys. Chem. C* **2009**, *113* (13), 5035. doi:10.1021/jp8115098.
(34) Qian, H. F.; Jin, R. C. *Nano Lett.* **2009**, *9* (12), 4083. doi:10.1021/nl902300y.
(35) Jin, R. C.; Qian, H. F.; Wu, Z. K.; Zhu, Y.; Zhu, M. Z.; Mohanty, A.; Garg, N. *J. Phys. Chem. Lett.* **2010**, *1* (19), 2903. doi:10.1021/jz100944k.
(36) Parker, J. F.; Fields-Zinna, C. A.; Murray, R. W. *Acc. Chem. Res.* **2010**, *43* (9), 1289. doi:10.1021/ar100048c.
(37) Jadzinsky, P. D.; Calero, G.; Ackerson, C. J.; Bushnell, D. A.; Kornberg, R. D. *Science* **2007**, *318* (5849), 430. doi:10.1126/science.1148624.
(38) Cathcart, N.; Mistry, P.; Makra, C.; Pietrobon, B.; Coombs, N.; Jelokhani-Niaraki, M.; Kitaev, V. *Langmuir* **2009**, *25* (10), 5840. doi:10.1021/la9005967.
(39) Bakr, O. M.; Amendola, V.; Aikens, C. M.; Wenseleers, W.; Li, R.; Dal Negro, L.; Schatz, G. C.; Stellacci, F. *Angew. Chem., Int. Ed. Engl.* **2009**, *48* (32), 5921. doi:10.1002/anie.200900298.
(40) Cathcart, N.; Kitaev, V. *J. Phys. Chem. C* **2010**, *114* (38), 16010. doi:10.1021/jp101764q.
(41) Gülseren, O.; Ercolessi, F.; Tosatti, E. *Phys. Rev. Lett.* **1998**, *80* (17), 3775. doi:10.1103/PhysRevLett.80.3775.
(42) Agrawal, B. K.; Singh, V.; Srivastava, R.; Agrawal, S. *Phys. Rev. B* **2006**, *74* (24), 245405. doi:10.1103/PhysRevB.74.245405.
(43) Agrawal, B. K.; Singh, V.; Srivastava, R.; Agrawal, S. *Nanotechnology* **2006**, *17* (9), 2340. doi:10.1088/0957-4484/17/9/044.
(44) Menon, M.; Srivastava, D.; Ponomareva, I.; Chernozatonskii, L. A. *Phys. Rev. B* **2004**, *70* (12), 125313. doi:10.1103/PhysRevB.70.125313.
(45) Ponomareva, I.; Menon, M.; Srivastava, D.; Andriotis, A. N. *Phys. Rev. Lett.* **2005**, *95* (26), 265502. doi:10.1103/PhysRevLett.95.265502.
(46) Cao, J. X.; Gong, X. G.; Zhong, J. X.; Wu, R. Q. Phys. Rev. Lett. **2006**, *97* (13), 136105. doi:10.1103/PhysRevLett.97.136105.
(47) Wang, B. L.; Wang, G. H.; Ren, Y.; Sun, H. Q.; Chen, X. S.; Zhao, J. J. *J. Phys. Condens. Matter* **2003**, *15* (14), 2327. doi:10.1088/0953-8984/15/14/308.
(48) Zhao, J. J.; Buia, C. L.; Han, J.; Lu, J. P. *Nanotechnology* **2003**, *14* (5), 501. doi:10.1088/0957-4484/14/5/304.
(49) Kang, J. W.; Seo, J. J.; Byun, K. R.; Hwang, H. J. *Phys. Rev. B* **2002**, *66,* 8.
(50) Kang, J. W.; Seo, J. J.; Hwang, H. J. *J. Phys. Condens. Matter* **2002**, *14* (39), 8997. doi:10.1088/0953-8984/14/39/309.
(51) Ju, S. P.; Lin, J. S.; Lee, W. J. *Nanotechnology* **2004**, *15* (9), 1221. doi:10.1088/0957-4484/15/9/019.
(52) Wang, J. L.; Chen, X. S.; Wang, G. H.; Wang, B. L.; Lu, W.; Zhao, J. J. *Phys. Rev. B* **2002**, *66,* 5. doi:10.1103/PhysRevB.66.085408.
(53) Lagos, M. J.; Sato, F.; Bettini, J.; Rodrigues, V.; Galvao, D. S.; Ugarte, D. *Nat. Nanotechnol.* **2009**, *4* (3), 149. doi:10.1038/nnano.2008.414.
(54) Rubinstein, M.; Colby, R. H. *Polymer Physics;* Oxford University Press, 2003.
(55) Landau, L. D.; Lifshitz, E. M. *Statistical Physics;* Butterworth-Heinemann, 1980.
(56) Harris, R. A.; Hearst, J. E. *J. Chem. Phys.* **1966**, *44* (7), 2595. doi:10.1063/1.1727098.
(57) Hatami-Marbini, H.; Mofrad, M. R. K. In *Cellular and Biomolecular Mechanics and Mechanobiology;* Gefen, A., Ed.; Springer: New York, 2011; p 569.
(58) Cademartiri, L.; Guerin, G.; Bishop, K. J. M.; Winnik, M. A.; Ozin, G. A. *J. Am. Chem. Soc.* **2012**, *134* (22), 9327. doi:10.1021/ja301855z.
(59) Cademartiri, L.; Scotognella, F.; O'Brien, P. G.; Lotsch, B. V.; Thomson, J.; Petrov, S.; Kherani, N. P.; Ozin, G. A. *Nano Lett.* **2009**, *9* (4), 1482. doi:10.1021/nl803417v.
(60) Xu, J.; Wang, H.; Liu, C. C.; Yang, Y. M.; Chen, T.; Wang, Y. W.; Wang, F.; Liu, X. G.; Xing, B. G.; Chen, H. Y. *J. Am. Chem. Soc.* **2010**, *132* (34), 11920. doi:10.1021/ja105433d.
(61) Wang, Y.; Wang, Q. X.; Sun, H.; Zhang, W. Q.; Chen, G.; Wang, Y. W.; Shen, X. S.; Han, Y.; Lu, X. M.; Chen, H. Y. *J. Am. Chem. Soc.* **2011**, *133* (50), 20060. doi:10.1021/ja208121c.
(62) Scheel, H. J.; Capper, P. *Crystal Growth Technology: From Fundamentals and Simulation to Large-scale Production;* Wiley-VCH: Weinheim, Germany, 2008.
(63) Romanov, S. *J. Phys. Condens. Matter* **1993**, *5* (8), 1081. doi:10.1088/0953-8984/5/8/009.
(64) Coleman, N. R. B.; Morris, M. A.; Spalding, T. R.; Holmes, J. D. *J. Am. Chem. Soc.* **2001**, *123* (1), 187. doi:10.1021/ja005598p.
(65) Coleman, N. R. B.; O'Sullivan, N.; Ryan, K. M.; Crowley, T. A.; Morris, M. A.; Spalding, T. R.; Steytler, D. C.; Holmes, J. D. *J. Am. Chem. Soc.* **2001**, *123* (29), 7010. doi:10.1021/ja015833j.
(66) Crowley, T. A.; Ziegler, K. J.; Lyons, D. M.; Erts, D.; Olin, H.; Morris, M. A.; Holmes, J. D. *Chem. Mater.* **2003**, *15* (18), 3518. doi:10.1021/cm034139v.
(67) Ziegler, K. J.; Polyakov, B.; Kulkarni, J. S.; Crowley, T. A.; Ryan, K. M.; Morris, M. A.; Erts, D.; Holmes, J. D. *J. Mater. Chem.* **2004**, *14* (4), 585. doi:10.1039/b311585b.
(68) Paxton, W. F.; Kistler, K. C.; Olmeda, C. C.; Sen, A.; St. Angelo, S. K.; Cao, Y. Y.; Mallouk, T. E.; Lammert, P. E.; Crespi, V. H. *J. Am. Chem. Soc.* **2004**, *126* (41), 13424. doi:10.1021/ja047697z.
(69) Ko, C. H.; Ryoo, R. *Chem. Commun.* **1996**, 2467. doi:10.1039/cc9960002467.
(70) Liu, Z.; Sakamoto, Y.; Ohsuna, T.; Hiraga, K.; Terasaki, O.; Ko, C. H.; Shin, H. J.; Ryoo, R. *Angew. Chem., Int. Ed. Engl.* **2000**, *39* (17), 3107. doi:10.1002/1521-3773(20000901)39:17<3107::AID-ANIE3107>3.0.CO;2-J.
(71) Fukuoka, A.; Sakamoto, Y.; Guan, S.; Inagaki, S.; Sugimoto, N.; Fukushima, Y.; Hirahara, K.; Iijima, S.; Ichikawa, M. *J. Am. Chem. Soc.* **2001**, *123* (14), 3373. doi:10.1021/ja004067y.

Can. J. Chem. Downloaded from www.nrcresearchpress.com by MCGILL UNIVERSITY on 02/02/13
For personal use only.

(72) Kitaura, R.; Nakanishi, R.; Saito, T.; Yoshikawa, H.; Awaga, K.; Shinohara, H. *Angew. Chem., Int. Ed. Engl.* **2009**, *48* (44), 8298. doi:10.1002/anie.200902615.
(73) Chen, J. Y.; McLellan, J. M.; Siekkinen, A.; Xiong, Y. J.; Li, Z. Y.; Xia, Y. N. *J. Am. Chem. Soc.* **2006**, *128* (46), 14776. doi:10.1021/ja066023g.
(74) Skrabalak, S. E.; Chen, J.; Sun, Y.; Lu, X.; Au, L.; Cobley, C. M.; Xia, Y. *Acc. Chem. Res.* **2008**, *41* (12), 1587. doi:10.1021/ar800018v.
(75) McEachran, M.; Keogh, D.; Pietrobon, B.; Cathcart, N.; Gourevich, I.; Coombs, N.; Kitaev, V. *J. Am. Chem. Soc.* **2011**, *133* (21), 8066. doi:10.1021/ja111642d.
(76) Vasquez, Y.; Henkes, A. E.; Bauer, J. C.; Schaak, R. E. *J. Solid State Chem.* **2008**, *181* (7), 1509. doi:10.1016/j.jssc.2008.04.007.
(77) Moon, G. D.; Ko, S.; Xia, Y. N.; Jeong, U. *ACS Nano* **2010**, *4* (4), 2307. doi:10.1021/nn9018575.
(78) Yin, Y. D.; Rioux, R. M.; Erdonmez, C. K.; Hughes, S.; Somorjai, G. A.; Alivisatos, A. P. *Science* **2004**, *304* (5671), 711. doi:10.1126/science.1096566.
(79) Müllner, M.; Yuan, J. Y.; Weiss, S.; Walther, A.; Förtsch, M.; Drechsler, M.; Müller, A. H. E. *J. Am. Chem. Soc.* **2010**, *132* (46), 16587. doi:10.1021/ja107132j.
(80) Grebinski, J. W.; Hull, K. L.; Zhang, J.; Kosel, T. H.; Kuno, M. *Chem. Mater.* **2004**, *16* (25), 5260. doi:10.1021/cm048498h.
(81) Pradhan, N.; Xu, H. F.; Peng, X. G. *Nano Lett.* **2006**, *6* (4), 720. doi:10.1021/nl052497m.
(82) Malakooti, R.; Cademartiri, L.; Migliori, A.; Ozin, G. A. *J. Mater. Chem.* **2008**, *18* (1), 66. doi:10.1039/b713383a.
(83) Sigman, M. B., Jr; Korgel, B. A. *Chem. Mater.* **2005**, *17* (7), 1655. doi:10.1021/cm0478733.
(84) Liu, Z. P.; Xu, D.; Liang, J. B.; Shen, J. M.; Zhang, S. Y.; Qian, Y. T. *J. Phys. Chem. B* **2005**, *109* (21), 10699. doi:10.1021/jp050332w.
(85) Yu, T. Y.; Joo, J.; Park, Y. I.; Hyeon, T. *Angew. Chem., Int. Ed. Engl.* **2005**, *44* (45), 7411. doi:10.1002/anie.200500992.
(86) Deng, Z. T.; Yan, H.; Liu, Y. *Angew. Chem., Int. Ed. Engl.* **2010**, *49* (46), 8695. doi:10.1002/anie.201003952.
(87) Zhu, G. X.; Zhang, S. G.; Xu, Z.; Ma, J.; Shen, X. P. *J. Am. Chem. Soc.* **2011**, *133* (39), 15605. doi:10.1021/ja2049258.
(88) Sun, Y. G.; Yin, Y. D.; Mayers, B. T.; Herricks, T.; Xia, Y. N. *Chem. Mater.* **2002**, *14* (11), 4736. doi:10.1021/cm020587b.
(89) Hanrath, T.; Korgel, B. A. *Adv. Mater. (Deerfield Beach Fla.)* **2003**, *15* (5), 437. doi:10.1002/adma.200390101.
(90) Lifshitz, E.; Bashouti, M.; Kloper, V.; Kigel, A.; Eisen, M. S.; Berger, S. *Nano Lett.* **2003**, *3* (6), 857. doi:10.1021/nl0342085.
(91) Kuno, M.; Ahmad, O.; Protasenko, V.; Bacinello, D.; Kosel, T. H. *Chem. Mater.* **2006**, *18* (24), 5722. doi:10.1021/cm061559m.
(92) Talapin, D. V.; Yu, H.; Shevchenko, E. V.; Lobo, A.; Murray, C. B. *J. Phys. Chem. C* **2007**, *111* (38), 14049. doi:10.1021/jp074319i.
(93) Kuno, M. *Phys. Chem. Chem. Phys.* **2008**, *10* (5), 620. doi:10.1039/b708296g.
(94) Cho, K. S.; Talapin, D. V.; Gaschler, W.; Murray, C. B. *J. Am. Chem. Soc.* **2005**, *127* (19), 7140. doi:10.1021/ja050107s.
(95) Puthussery, J.; Kosel, T. H.; Kuno, M. *Small* **2009**, *5* (10), 1112. doi:10.1002/smll.200801838.
(96) Lee, S. K. C.; Yu, Y.; Perez, O.; Puscas, S.; Kosel, T. H.; Kuno, M. *Chem. Mater.* **2010**, *22* (1), 77. doi:10.1021/cm902049p.
(97) Stach, E. A.; Pauzauskie, P. J.; Kuykendall, T.; Goldberger, J.; He, R. R.; Yang, P. D. *Nano Lett.* **2003**, *3* (6), 867. doi:10.1021/nl034222h.
(98) Yong, K. T.; Sahoo, Y.; Choudhury, K. R.; Swihart, M. T.; Minter, J. R.; Prasad, P. N. *Nano Lett.* **2006**, *6* (4), 709. doi:10.1021/nl052472n.
(99) Shen, G. Z.; Liang, B.; Wang, X. F.; Huang, H. T.; Chen, D.; Wang, Z. L. *ACS Nano* **2011**, *5* (8), 6148. doi:10.1021/nn2014722.
(100) Gibbs, J. W. *The Collected Works of J. Willard Gibbs;* Longmans, Green and Co., London, 1902.
(101) Wulff, G. *Z. Krystallogr. Mineral.* **1901**, *34,* 449.
(102) Cerf, R. *The Wulff Crystal in Ising and Percolation Models;* Springer: New York, 2006; Vol. Ecole d'Eté de Probabilités de Saint-Flour XXXIV.
(103) von Laue, M. *Z. Kristallogr.* **1943**, *105,* 124.
(104) Yang, X. H.; Wang, X.; Zhang, Z. D. *Mater. Chem. Phys.* **2006**, *95* (1), 154. doi:10.1016/j.matchemphys.2005.05.035.
(105) Malakooti, R.; Cademartiri, L.; Akcakir, Y.; Petrov, S.; Migliori, A.; Ozin, G. A. *Adv. Mater. (Deerfield Beach Fla.)* **2006**, *18* (16), 2189. doi:10.1002/adma.200600460.
(106) Tang, J.; Alivisatos, A. P. *Nano Lett.* **2006**, *6* (12), 2701. doi:10.1021/nl0615930.
(107) Schricker, A. D.; Sigman, M. B., Jr.; Korgel, B. A. *Nanotechnology* **2005**, *16* (7), S508. doi:10.1088/0957-4484/16/7/027.
(108) Matijevic, E. *Chem. Mater.* **1993**, *5* (4), 412. doi:10.1021/cm00028a004.
(109) Matijević, E. *Colloid J.* **2007**, *69* (1), 29. doi:10.1134/S1061933X0701005X.
(110) Niederberger, M.; Cölfen, H. *Phys. Chem. Chem. Phys.* **2006**, *8* (28), 3271. doi:10.1039/b604589h.
(111) Cölfen, H.; Antonietti, M. *Angew. Chem., Int. Ed. Engl.* **2005**, *44* (35), 5576. doi:10.1002/anie.200500496.
(112) Yuwono, V. M.; Burrows, N. D.; Soltis, J. A.; Penn, R. L. *J. Am. Chem. Soc.* **2010**, *132* (7), 2163. doi:10.1021/ja909769a.
(113) Burrows, N. D.; Yuwono, V. M.; Penn, R. L. *MRS Bull.* **2010**, *35* (2), 133. doi:10.1557/mrs2010.633.
(114) Banfield, J. F.; Welch, S. A.; Zhang, H. Z.; Ebert, T. T.; Penn, R. L. *Science* **2000**, *289* (5480), 751. doi:10.1126/science.289.5480.751.
(115) Yuk, J. M.; Park, J.; Ercius, P.; Kim, K.; Hellebusch, D. J.; Crommie, M. F.; Lee, J. Y.; Zettl, A.; Alivisatos, A. P. *Science* **2012**, *336* (6077), 61. doi:10.1126/science.1217654.
(116) Bishop, K. J. M.; Wilmer, C. E.; Soh, S.; Grzybowski, B. A. *Small* **2009**, *5* (14), 1600. doi:10.1002/smll.200900358.
(117) Pietrobon, B.; McEachran, M.; Kitaev, V. *ACS Nano* **2009**, *3* (1), 21. doi:10.1021/nn800591y.
(118) Jin, R. C.; Cao, Y. W.; Mirkin, C. A.; Kelly, K. L.; Schatz, G. C.; Zheng, J. G. *Science* **2001**, *294* (5548), 1901. doi:10.1126/science.1066541.
(119) Son, D. H.; Hughes, S. M.; Yin, Y.; Alivisatos, A. P. *Science* **2004**, *306* (5698), 1009. doi:10.1126/science.1103755.
(120) Son, J. S.; Wen, X. D.; Joo, J.; Chae, J.; Baek, S. I.; Park, K.; Kim, J. H.; An, K.; Yu, J. H.; Kwon, S. G.; Choi, S.-H.; Wang, Z.; Kim, Y.-W.; Kuk, Y.; Hoffmann, R.; Hyeon, T. *Angew. Chem., Int. Ed. Engl.* **2009**, *48* (37), 6861. doi:10.1002/anie.200902791.
(121) Lu, X. M.; Au, L.; McLellan, J.; Li, Z. Y.; Marquez, M.; Xia, Y. N. *Nano Lett.* **2007**, *7* (6), 1764. doi:10.1021/nl070838l.

Can. J. Chem. Downloaded from www.nrcresearchpress.com by MCGILL UNIVERSITY on 02/02/13
For personal use only.

(122) Gates, B.; Wu, Y. Y.; Yin, Y. D.; Yang, P. D.; Xia, Y. N. *J. Am. Chem. Soc.* **2001**, *123* (46), 11500. doi:10.1021/ja0166895.

(123) Liang, H. W.; Liu, S.; Gong, J. Y.; Wang, S. B.; Wang, L.; Yu, S. H. *Adv. Mater. (Deerfield Beach Fla.)* **2009**, *21* (18), 1850. doi:10.1002/adma.200802286.

(124) Zhu, C. Z.; Guo, S. J.; Dong, S. J. *Adv. Mater. (Deerfield Beach Fla.)* **2012**, *24* (17), 2326. doi:10.1002/adma.201104951.

(125) Zhang, G. Q.; Kirk, B.; Jauregui, L. A.; Yang, H. R.; Xu, X. F.; Chen, Y. P.; Wu, Y. *Nano Lett.* **2012**, *12* (1), 56. doi:10.1021/nl202935k.

(126) Ko, S.; Kim, J. W.; Moon, G. D.; Shim, H. S.; Kim, W. B.; Jeong, U. *Langmuir* **2010**, *26* (6), 4377. doi:10.1021/la903415n.

(127) Yadav, G. G.; Zhang, G. Q.; Qiu, B.; Susoreny, J. A.; Ruan, X. L.; Wu, Y. *Nanoscale* **2011**, *3* (10), 4078. doi:10.1039/c1nr10624d.

(128) *CRC Handbook of Chemistry and Physics,* 92nd ed.; Haynes, W. M., Ed.; CRC Press, Boca Raton, FL, 2011.

(129) Nolph, C. A.; Liu, H.; Reinke, P. *Surf. Sci.* **2011**, *605* (13–14), L29. doi:10.1016/j.susc.2011.04.017.

(130) Juárez, B. H.; Ibisate, M.; Palacios, J. M.; López, C. *Adv. Mater. (Deerfield Beach Fla.)* **2003**, *15* (4), 319. doi:10.1002/adma.200390078.

(131) Pazos-Pérez, N.; Baranov, D.; Irsen, S.; Hilgendorff, M.; Liz-Marzán, L. M.; Giersig, M. *Langmuir* **2008**, *24* (17), 9855. doi:10.1021/la801675d.

(132) Campbell, M. G.; Powers, D. C.; Raynaud, J.; Graham, M. J.; Xie, P.; Lee, E.; Ritter, T. *Nat. Chem.* **2011**, *3* (12), 949. doi:10.1038/nchem.1197.

(133) Liu, C. M.; Yang, S. H. *ACS Nano* **2009**, *3* (4), 1025. doi:10.1021/nn900157r.

(134) Whetten, R. L.; Khoury, J. T.; Alvarez, M. M.; Murthy, S.; Vezmar, I.; Wang, Z. L.; Stephens, P. W.; Cleveland, C. L.; Luedtke, W. D.; Landman, U. *Adv. Mater. (Deerfield Beach Fla.)* **1996**, *8* (5), 428. doi:10.1002/adma.19960080513.

(135) Cademartiri, L.; Bishop, K. J. M.; Snyder, P. W.; Ozin, G. A. *Philos. T. Roy. Soc. A* **2012**, *370* (1969), 2824. doi:10.1098/rsta.2011.0254.

(136) Ozin, G. A.; Hou, K.; Lotsch, B. V.; Cademartiri, L.; Puzzo, D. P.; Scotognella, F.; Ghadimi, A.; Thomson, J. *Mater. Today* **2009**, *12* (5), 12. doi:10.1016/S1369-7021(09)70156-7.

(137) Cademartiri, L.; Ozin, G. A. *Philos. T. Roy. Soc. A* **2010**, *368* (1927), 4229. doi:10.1098/rsta.2010.0126.

(138) Qian, H.; Zhu, M.; Wu, Z.; Jin, R. *Acc. Chem. Res.* **2012**, *45* (9), 1470. doi:10.1021/ar200331z.

(139) Du, Y. P.; Zhang, Y. W.; Yan, Z. G.; Sun, L. D.; Yan, C. H. *J. Am. Chem. Soc.* **2009**, *131* (45), 16364. doi:10.1021/ja9080088.

(140) Xi, G. C.; Ouyang, S. X.; Li, P.; Ye, J. H.; Ma, Q.; Su, N.; Bai, H.; Wang, C. *Angew. Chem., Int. Ed. Engl.* **2012**, *51* (10), 2395. doi:10.1002/anie.201107681.

(141) Hu, S.; Ling, X.; Lan, T.; Wang, X. *Chem. Eur. J.* **2010**, *16* (6), 1889. doi:10.1002/chem.200902113.

(142) Riehle, F. S.; Bienert, R.; Thomann, R.; Urban, G. A.; Krüger, M. *Nano Lett.* **2009**, *9* (2), 514. doi:10.1021/nl080150o.

(143) Liu, R.; Liu, J. F.; Jiang, G. B. *Chem. Commun. (Camb.)* **2010**, *46* (37), 7010. doi:10.1039/c0cc02466j.

(144) Kalsin, A. M.; Fialkowski, M.; Paszewski, M.; Smoukov, S. K.; Bishop, K. J. M.; Grzybowski, B. A. *Science* **2006**, *312* (5772), 420. doi:10.1126/science.1125124.

(145) Walker, D. A.; Wilmer, C. E.; Kowalczyk, B.; Bishop, K. J. M.; Grzybowski, B. A. *Nano Lett.* **2010**, *10* (6), 2275. doi:10.1021/nl1012079.

(146) Thomson, J. W.; Lawson, G.; O'Brien, P.; Klenkler, R.; Helander, M. G.; Petrov, S.; Lu, Z. H.; Kherani, N. P.; Adronov, A.; Ozin, G. *Adv. Mater. (Deerfield Beach Fla.)* **2010**, *22* (39), 4395. doi:10.1002/adma.201001349.

(147) Lu, Y.; Huang, J. Y.; Wang, C.; Sun, S. H.; Lou, J. *Nat. Nanotechnol.* **2010**, *5* (3), 218. doi:10.1038/nnano.2010.4.

(148) Lu, Y.; Song, J.; Huang, J. Y.; Lou, J. *Adv. Funct. Mater.* **2011**, *21* (20), 3982. doi:10.1002/adfm.201101224.

(149) Peng, X..; Manna, L.; Yang, W.; Wickham, J.; Scher, E.; Kadavanich, A.; Alivisatos, A. P. *Nature* **2000**, *404* (6773), 59. doi:10.1038/35003535.

(150) Joo, J.; Pietryga, J. M.; McGuire, J. A.; Jeon, S. H.; Williams, D. J.; Wang, H. L.; Klimov, V. I. *J. Am. Chem. Soc.* **2009**, *131* (30), 10620. doi:10.1021/ja903445f.

(151) Wang, F. D.; Buhro, W. E. *J. Am. Chem. Soc.* **2012**, *134* (11), 5369. doi:10.1021/ja300135c.

(152) Evans, C. M.; Evans, M. E.; Krauss, T. D. *J. Am. Chem. Soc.* **2010**, *132* (32), 10973. doi:10.1021/ja103805s.

(153) Talapin, D. V.; Rogach, A. L.; Haase, M.; Weller, H. *J. Phys. Chem. B* **2001**, *105* (49), 12278. doi:10.1021/jp012229m.

Solid-state dye-sensitized solar cells from polymer-templated TiO_2 bilayer thin films

Honghan Fei, Xiaojuan Fan, David L. Rogow, and Scott R.J. Oliver

Can. J. Chem. Downloaded from www.nrcresearchpress.com by MCGILL UNIVERSITY on 02/02/13
For personal use only.

Abstract: We report an inexpensive method using solvent-swollen poly(methyl methacrylate) as a sacrificial template for mesoporous titanium oxide thin films with tunable meso/nano morphology. The conversion efficiency reaches 4.2% despite using a solid-state electrolyte, which circumvents the longevity issues of liquid electrolytes. The cells show a large short-circuit photocurrent density of 7.98 mA, open-circuit voltage of 0.78 V, and maximum conversion efficiency of 4.2% under air-mass 1.5 global illumination. At higher titania precursor ratios, nanodisk particles are formed that increase light scattering and double the efficiency over our previous reports. The tunability of the semiconductor morphology and all solid-state nature of the cells makes the method a viable alternative to existing solar cell technology.

Key words: polymer templating, TiO_2 thin film, dye-sensitized solar cell, poly(methylmethacrylate), nanodisk.

Résumé : On a mis au point une méthode peu coûteuse de préparation de films minces d'oxyde de titane mésoporeux avec une morphologie ajustable méso/nano qui fait appel à l'utilisation de poly(méthacrylate de méthyle) gonflé par un solvant comme matrice sacrifiée. L'efficacité de la conversion atteint 4,2 % même si on utilise un électrolyte à l'état solide pour contourner les problèmes de longévité des électrolytes liquides. Les cellules permettent de déceler une densité élevée (7,98 mA) de photocourant de court-circuit, un voltage de circuit ouvert de 0,78 V et une efficacité de conversion de 4,2 % sous une illumination globale de 1,5 de la masse d'air. À des rapports plus élevés de blanc de titane, il se forme des particules nanodisques qui augmentent la diffusion de la lumière et dont l'efficacité est égale au double de ce qui avait été rapporté antérieurement. La possibilité de modifier la morphologie du semiconducteur et la nature d'état complètement solide des cellules fait que cette méthode est une alternative viable à la technologie des cellules solaires existantes.

Mots-clés : matrice de polymère, film mince d'oxyde de titane, cellule solaire sensibilité par un colorant, poly(méthacrylate de méthyle), nanodisque.

[Traduit par la Rédaction]

Introduction

Since O'Regan and Gratzel's[1–5] significant breakthrough in 1991, extensive studies have been devoted to the development of dye-sensitized solar cells (DSSCs). The cells have the potential to replace conventional silicon-based solar cells due to their lower cost. They also employ, however, liquid electrolyte usually in the form of an I^-/I_3^- redox couple dissolved in an organic solvent such as acetonitrile. This configuration causes long-term practical problems including flammability, reduced stability, and evaporation and (or) leakage of electrolyte. Recent efforts have led to the development of solid-state electrolytes using room-temperature ionic liquids or iodide-containing polymers to achieve photovoltaic performance comparable to the record of 11% for liquid-electrolyte-based DSSCs.[6–8]

TiO_2 semiconductor thin-film anodes serve as the electron carrier and require sensitization by an adsorbed dye that can be excited in the visible region. While most research has focused on the nature of the dye,[9–11] electrolyte, and redox couple,[12–14] it is becoming evident that the TiO_2 morphology is equally important to determining cell properties.[15–18] Unlike the high-vacuum chemical vapor deposition (CVD) or solvothermal method,[9,19,20] the polymer templating of inorganic materials approach is facile, inexpensive, and not substrate-specific.[21–23] There have been several reports where the TiO_2 thin-film anode of DSSCs was prepared by polymer templating.[16,24,25] Caruso and co-workers[16] reported the synthesis of mesoporous TiO_2 beads with hexadecylamine as a template to achieve high-performance DSSCs of 7.20% with liquid electrolyte. Wang et al.[24] developed a method based on octadecylamine as a structure directing agent for a single-layer TiO_2 nanostructure. Their maximum conversion efficiency was 1.5%, comparatively low with respect to DSSCs but a solid-state electrolyte was used.

Although polymer swelling by organic solvents is a common phenomenon, combining this swelling with templating

Received 30 May 2012. Accepted 24 July 2012. Published at www.nrcresearchpress.com/cjc on 6 November 2012.

H. Fei, D.L. Rogow, and S.R.J. Oliver. University of California, Santa Cruz, Department of Chemistry and Biochemistry, 1156 High Street, Santa Cruz, CA 95064, USA.
X. Fan. University of California, Santa Cruz, Department of Chemistry and Biochemistry, 1156 High Street, Santa Cruz, CA 95064, USA; Marshall University, Department of Physics and Physical Science, Huntington, WV 25755, USA.

Corresponding author: Scott R.J. Oliver (e-mail: soliver@ucsc.edu).

This article is part of a Special Issue dedicated to Professor Geoffrey Ozin.

Can. J. Chem. Downloaded from www.nrcresearchpress.com by MCGILL UNIVERSITY on 02/02/13
For personal use only.

effects has occurred only in recent years.[18,23,26–29] Caruso's group[27] first reported the use of agarose gels to template high-crystalline macroporous metal oxide monoliths.[28] Our group had independently been employing polymer templates to achieve a variety of titania morphologies including monoliths,[27,28] networks,[29] beads,[16,17] and thin films.[18,23] The advantage of this method is that the resultant morphology can, to some degree, be controlled through the choice of polymer, its concentration, degree of swelling, and (or) cross-linking. Studies on optimizing the swollen polymer templating method for DSSCs, however, are limited. Indeed, the detailed mechanisms were not investigated regarding the synthetic procedures and conditions.

The photoanode of DSSCs is the side from which light enters the cell, where the light traverses from the conductive working electrode towards the sensitized semiconductor layer. Multilayer TiO_2 thin films with increasing particle size and porosity from the bottom layer to the top layer leads to ~23%–48% higher conversion efficiency than the typical nonporous single layers of nanoparticles.[25,30–32] Stathatos et al.[32] reported the synergistic effect with two distinct nanoparticle layers that increased the efficiency from 4.8% to 6.9%.[29] In theory, the enhancement is due to light scattering (i.e., Mie, Rayleigh, and Raman scattering) by the top layer, which enhances the absorption of red light by the surface layer and, in turn, light harvesting.[31] Previous studies have created a DSSC multilayer photoanode with a submicrometer size Al_2O_3 and SiO_2 top layer to light scatter and facilitate light energy capture by the 400 nm particle size TiO_2 bottom layer.[31] Cao and co-workers[33–35] developed hierarchically structured ZnO aggregates 100–400 nm in size to provide both large surface area and efficient light scattering. They achieved an impressive enhancement of DSSC conversion efficiency from 2.4% to 5.4% compared with conventional ZnO nanoparticle thin films.[33–35] These light-scattering layers based on TiO_2 and ZnO lead to higher open-circuit voltage (V_{oc}),[30,32] short-circuit current density (J_{sc}),[15,25] or both.[33–36]

Herein, we describe an inexpensive one-step method to synthesize a double-layer porous anatase thin film using methyl ethyl ketone (MEK) swollen poly(methyl methacrylate) (PMMA) as a sacrificial structure directing agent. The ratio of nanodisks to nanospheres in the composite film scales with titanium precursor concentration. The nanodisks, coupled with an improved solid-state electrolyte and sensitizing dye, lead to a much higher J_{sc} and conversion efficiency over our previous reports.

Experimental

Materials

Titanium *n*-butoxide (Alfa Aesar) and PMMA (MW 350 000, Sigma-Aldrich) were used as-purchased. MEK (Acros Organics) was used as solvent. 4,4′-Dicarboxylate-2.2′-dipyridyl (98%, Alfa-Aesar), ruthenium(III) chloride hydrate (35%–40% Ru, Acros), and ammonium thiocyanate (≥98%, Fisher Scientific) were used as received to synthesize the N3 dye according to literature methods.[37] The polymer electrolyte components were also used as-purchased without further modification: LiI (MP Biomedicals), I_2 (>99.9%, Alfa-Aesar), poly(ethylene oxide) (PEO, MW 5 000 000, Polysciences, Inc.).

Preparation of TiO_2 thin film

PMMA was first stirred in 20 mL MEK at a concentration of 10% (*w*/*v*). After stirring at 40 °C for 4–8 h, the PMMA was completely dissolved and a clear transparent solution was formed. Titanium *n*-butoxide (4%, 6%, or 8% (*w*/*v*)) was then introduced quickly and the solution sealed with parafilm and stirred at room temperature for 2–4 h. The yellow transparent solution was spin-coated on F-doped SnO_2 (FTO) glass (Hartford Glass Co.) that had been first cleaned with ethanol and deionized water and sonicated and dried under an N_2 stream. The thin film was heated in a tube furnace to 450 °C at a rate of 1 °C/min, then annealed for 2 h. Annealing removed the PMMA and resulted in the final double-layer pure-phase anatase thin-film anode. Sonication of the thin film in deionized water removed the top layer, leaving only the transparent bottom layer on the substrate.

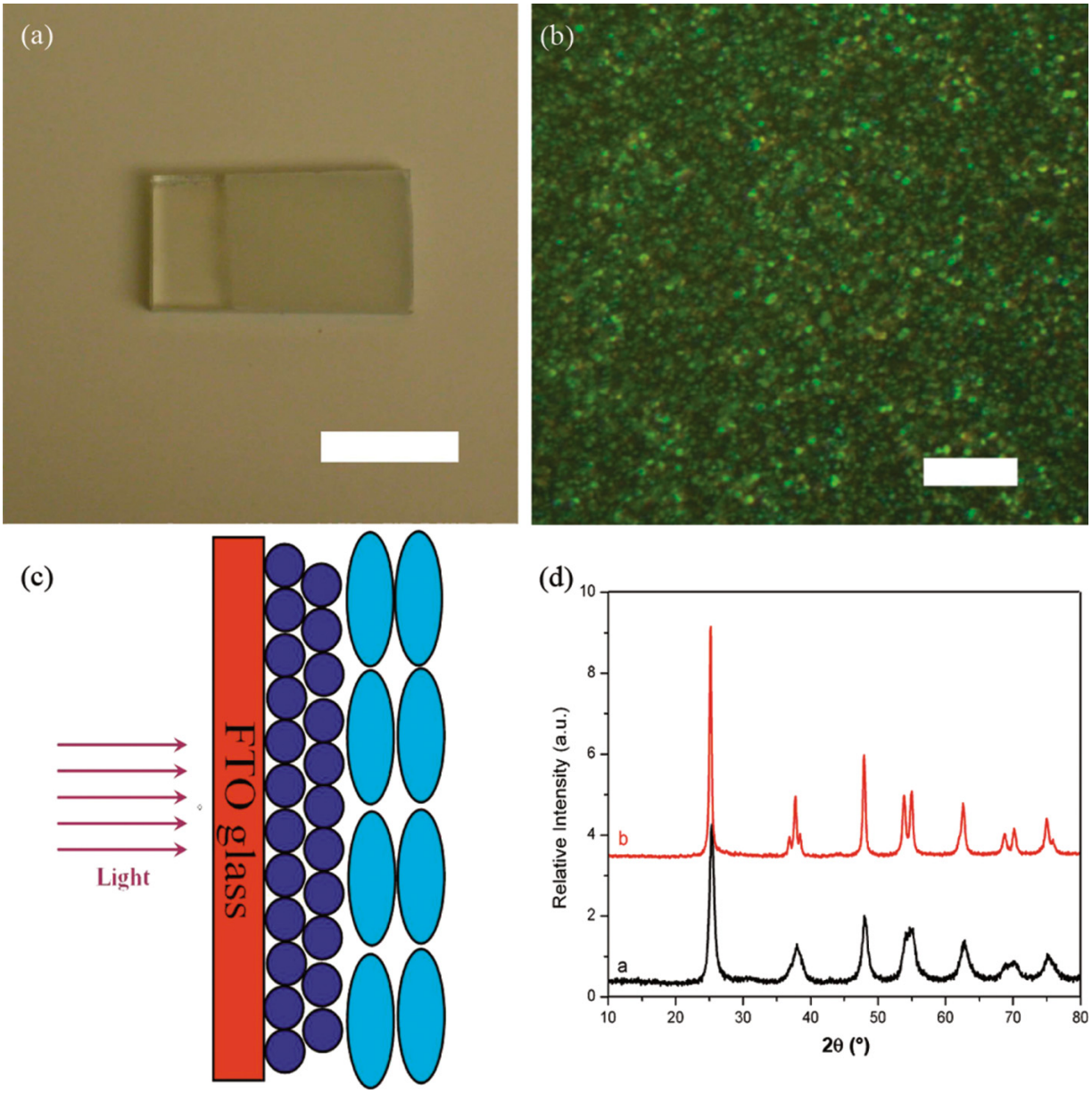
Fabrication of solar cells

The N3 dye was used to sensitize the TiO_2 electrode by immersing the created thin film in a 0.5 mmol/L dye solution in absolute ethanol for at least 48 h. The film was then rinsed with ethanol and dried thoroughly. The electrolyte solution was prepared using reported methods[38] with slight modification: 0.01 mol/L LiI, 1 mmol/L I_2, 6 mmol/L PEO, and 0.011 mmol/L (0.0220 g) TiO_2 (Degussa P25) dissolved in 25 mL acetonitrile. The electrolyte solution was cast dropwise on the film at a temperature of 70 °C using a hot plate. The electrolyte deposition was repeated several times and the thin film became dark red in color. Finally, another FTO glass plate sputter-coated with gold was placed on top of the surface with no applied pressure. This sandwich configuration was compressed with alligator clips to facilitate penetration of the electrolyte into the TiO_2 nanostructure. The edge area of the solar cell was then sealed with epoxy to avoid contact of the electrolyte with air, thus ensuring long-term stability. Photovoltaic performance and characterization were carried out 6 h after preparation of the cell.

Instrumentation

Scanning electron micrographs (SEMs) were collected on a Hitachi S-2700 SEM. Samples for powder X-ray diffraction (PXRD) were obtained by manually removing material from the FTO glass using a razor blade. A Rigaku Americas Miniflex Plus diffractometer was scanned from 10° to 80° (2θ) at a scan rate of 2° (2θ) per minute and with a 0.04° step size, under Cu Kα radiation (λ = 1.5418 Å). The solid-state DSSCs (SDSSCs) were illuminated using a calibrated Xe lamp (660 W, Leviton Manufacturing Co.). Current–voltage (*I*–*V*) measurements were carried out with a CHI 440 electrochemical workstation. UV–vis spectroscopic studies were performed with a Hewlett-Packard Model 8452A spectrophotometer. Tapping-mode atomic force microscope (AFM) images were collected with a PicoLE SPM instrument (Molecular Imaging Inc.) to acquire the bottom layer morphology. Thermogravimetric analysis (TGA) was performed using a TA Instruments 2050 TGA by heating from 25 to 800 °C in air at a rate of 15 °C/min. Fourier transform infrared (FTIR) spectroscopy of the materials was collected on a PerkinElmer Spectrum One spectrophotometer with KBr pellets. ^{1}H NMR spectra were collected with a Varian Oxford 600 MHz

Fig. 1. (*a*) Optical image of the as-synthesized TiO_2 thin film on F-doped SnO_2 (FTO) glass (scale bar, 1 cm). (*b*) Top-view optical micrograph of the TiO_2 thin film (scale bar, 10 μm). (*c*) Schematic of the as-synthesized bilayer TiO_2 thin film on FTO glass. (*d*) Powder X-ray diffraction (PXRD) pattern of the TiO_2 product calcination (red, top layer; black, bottom layer; see the Web version of this article for colour).



Can. J. Chem. Downloaded from www.nrcresearchpress.com by MCGILL UNIVERSITY on 02/02/13
For personal use only.

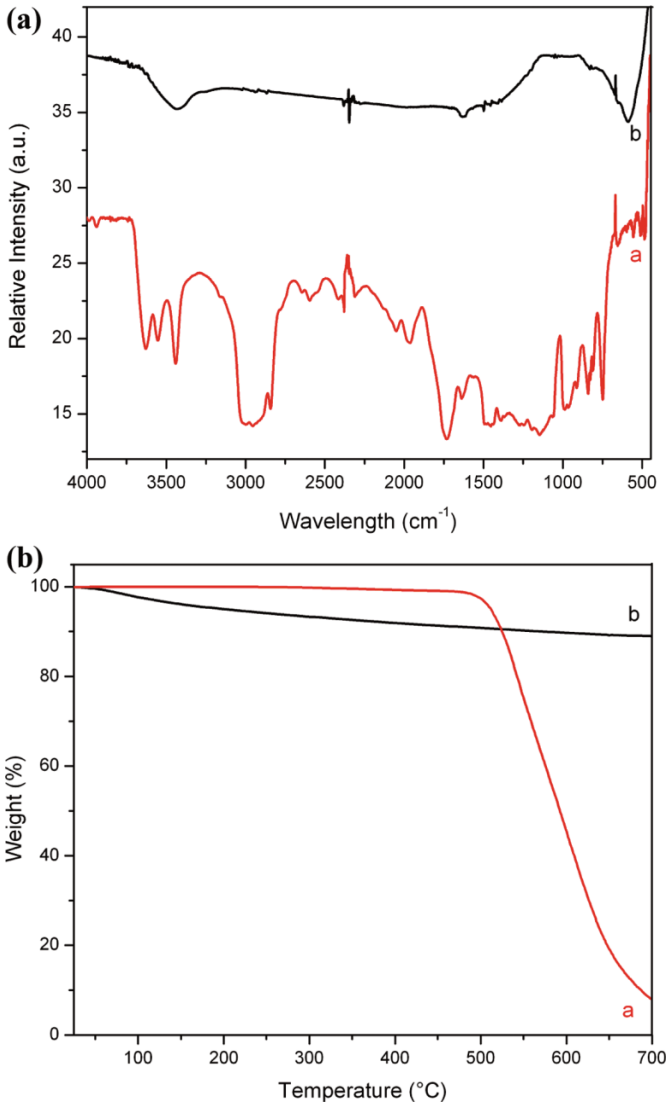
spectrometer by dissolving the sample in 700 μL of deuterated chloroform with tetramethylsilane as internal standard.

Results and discussion

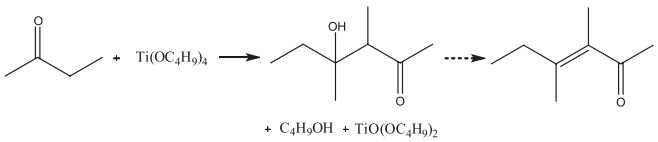
The optimum concentration of PMMA in MEK was determined to be 10% (*w*/*v*). Lower ratios did not give rise to a nanodisk morphology, which facilitates light scattering (vide infra). Ratios higher than 15% resulted in overly viscous mixtures and inhomogeneous films after spin coating as well as cracks after annealing. The PXRD pattern of both top and bottom-layer thin films after annealing at 450 °C for 2 h indicated pure-phase anatase (Fig. 1*d*). This form of titania has been shown to have better photoelectrochemical properties than rutile.[4] The FTIR and TGA traces of the titania before dye sensitization and pure PMMA clearly demonstrate that the annealing removed almost all of the original polymer (Figs. 2*a* and 2*b*). The ~10% decrease in mass in the TGA of the calcined sample is likely due to physisorbed water up to 100 °C and the remainder is trace amounts of PMMA in the porous thin film. The FTIR of titania after calcination further indicates only a negligible amount of organics in the calcined thin film, with the disapearence of bands at ~3000 and ~1750 cm^{-1}, characteristic of C–H and C=O bands, respectively. Two weak broad bands located at 3500 and 700 cm^{-1} are possibly due to O–H from physisorbed water and Ti–O stretching, respectively.[39]

Can. J. Chem. Downloaded from www.nrcresearchpress.com by MCGILL UNIVERSITY on 02/02/13
For personal use only.

Fig. 2. FTIR (top) and TGA curves (bottom) in the range of 25 to 800 °C for (*a*) pure PMMA powder and (*b*) powder removed from a thin film prepared from 8% (*m*/*v*) titanium precursor and 10% (*w*/*v*) poly(methyl methacrylate) (PMMA) in methyl ethyl ketone (MEK) followed by annealing at 450 °C for 2 h.



Scheme 1. Self-condensation of 2-butanone via titanium *n*-butoxide into 5-methyl-4-hepten-3-one, 1-butanol, and titanoxane.



A possible mode of formation of the pure anatase phase thin film is self-condensation of 2-butanone (Scheme 1). Yatluk et al.[40] reacted titanium alkoxide with carbonyl compounds to form titanoxane, while MEK self-condensed into 3,4-dimethyl-3-hexene-2-one. Titanoxane is known to crystallize into anatase or rutile by annealing under air.[41,42] This pathway would explain the observed colour change of solution, from colourless to yellow after introducing the titanium precursor into 2-butanone, with the intensity increasing with stirring time. ^{1}H NMR (Supplementary data Figs. S1–S3) of neat titanium *n*-butoxide and MEK solution after introduction of the titanium precursor also support an aldol condensation reaction. Although the products provided small intergrated peak areas due to the MEK solvent as well as ketone precursor, the bands (δ 0.82, m, 2H; δ 1.10, m, 2H; δ 2.25, m, 3H; and δ 2.47, m, 3H) are characteristic of the self-condensed product of either β-hydroxycarbonyl or dehydrated self-condensed ketone. The pure titanium precursor (δ 0.92, m, 3H; δ 1.22, m, 2H; δ 1.39, m, 2H; and δ 1.52, m, 2H) have no replicate peaks in the condensation product but provide comparable intergrated area, indicating the completeness of the reaction. In addition, spin coating neat titanium precursor in an attempt to obtain a TiO_2 thin film was unsuccessful; instead amorphous organic residues were present after calcination.

Optical images and micrographs of the thin film after sintering (Figs. 1*a* and 1*b*) indicate that the surface is homogeneous and crack-free over the long range (2 cm × 1 cm). Most calcined nanoparticle TiO_2 thin films in the literature lack such long-range homogeneity and often have cracks.[43] The as-synthesized TiO_2 thin films consist of a bilayer structure (Fig. 1*c*), with the top layer characterized by SEM and the bottom layer by tapping mode AFM after sonication. SEM images of porous thin films made from 10% (*w*/*v*) PMMA and 4%, 6%, 8% (*w*/*v*) titania precursor are shown in Fig. 3. The top layer is composed of nanosphere particles and is likely responsible for enhancing the light scattering effect. The films from all percentages of titanium *n*-butoxide have the identical underlayer. A cross-sectional SEM image indicates that the thickness of thin film is ~7 μm. Though slightly thinner than the conventional P25 deposition method, this thickness is within the optimized range shown for liquid-based DSSCs cells.[1,37]

A nanodisk morphology is observed for the samples using higher concentrations of titania precursor (6%, Fig. 3*b*; and 8%, Fig. 3*c*). This new morphology not observed before for DSSCs is in a higher concentration for the 8% sample. The nanodisks all show a similar thickness of ~50 nm and a round shape with an average diameter of ~500 nm. The nanosphere morphology, however, is still present and mixed with the nanodisks. Although the percentage of nanodisks increases with Ti *n*-butoxide concentration, the nanosphere particle size shows little change, with an average size of ~150 nm. One possible explanation for this new type of nanodisk morphology is that our system uses swollen PMMA with limited interior channels or pores for the growth of the metal oxide. Higher concentrations of titania precursor lead to a more complete filling and replica of the original channel space of the swollen PMMA. This pathway would also account for the lack of nanodisk formation in our previously reported experiments with 2%–8% PMMA, which gave only nanospheres because of the larger swollen volume.

The nanodisks likely possess distinct optical properties from typical nanospheres. Specifically, increased light scattering is possible, which would lead to enhanced photoelectrochemical performance.[31,32] UV–vis spectra of the three mentioned calcined TiO_2 thin films before dye loading are shown in Fig. 4. The energy difference between the TiO_2 valence and conduction bands is well-known to lie between 3.0 and 3.3 eV,

Fig. 3. SEM images of the top TiO_2 layer synthesized by 10% (*w*/*v*) poly(methyl methacrylate) (PMMA) and (*a*) 4% (*w*/*v*) titanium *n*-butoxide, (*b*) 6% (*w*/*v*) titanium *n*-butoxide, (*c*) 8% (*w*/*v*) titanium *n*-butoxide in methyl ethyl ketone (MEK; scale bar: 1 μm). The inset of (*c*) is a closer side image of a nanodisk (scale bar, 500 nm).

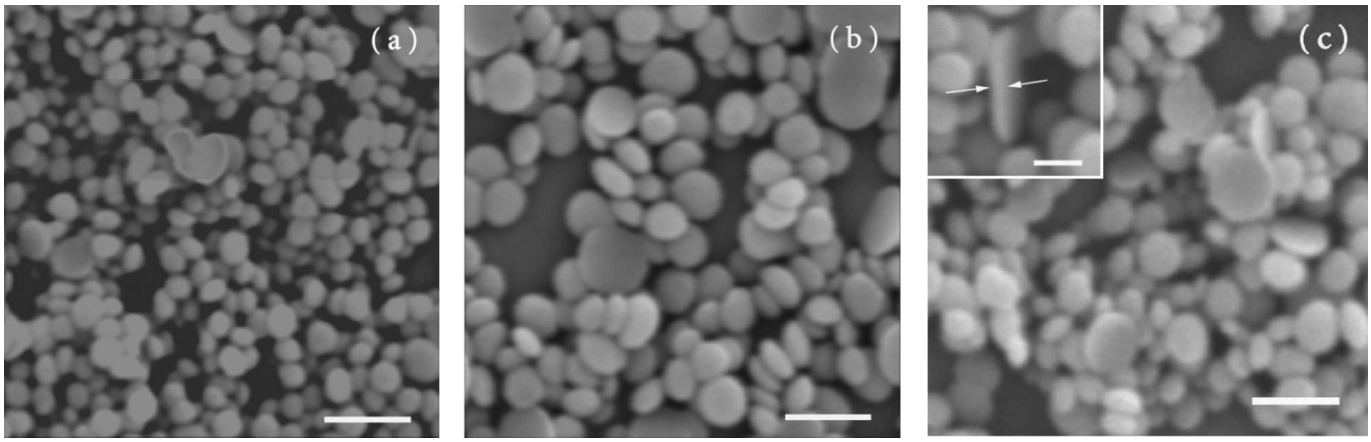


Fig. 4. UV–vis spectra of TiO_2 thin films synthesized by 10% (*w*/*v*) poly(methyl methacrylate) (PMMA) and the shown percentage (*w*/*v*) of titanium *n*-butoxide in methyl ethyl ketone (MEK). The spectrum for bare glass is shown for comparison.

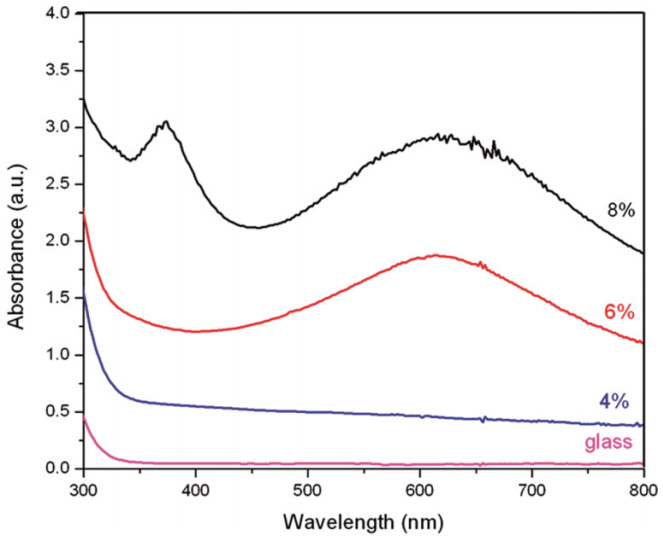
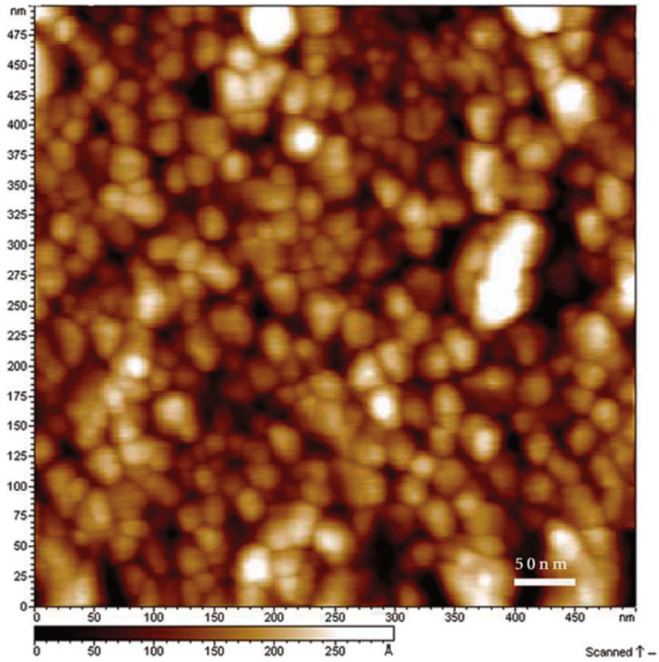


Fig. 5. Tapping-mode atomic force microscope (AFM) image of the bottom layer of the porous TiO_2 thin film from 8% Ti-butoxide (scale bar, 50 nm).



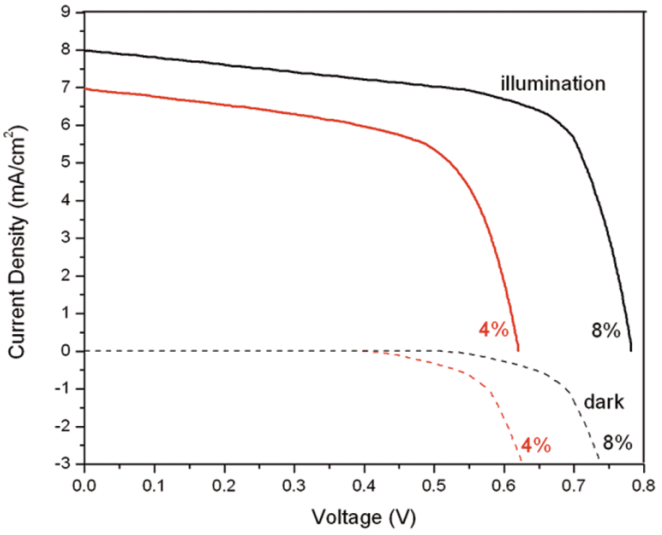
corresponding to a wavelength range of 375–400 nm. Therefore, no absorption occurs in the visible region above 400 nm and dye sensitization is required. Increased absorption is observed in the 500–750 nm wavelength range as the titanium *n*-butoxide concentration is increased. Ferber and Luther used Mie theory to account for the light-scattering ability of the top layer of bilayer DSSCs.[43] The surface particles enhance the photon scattering mainly in the 500–750 nm region. Nanodisk scattering increases the light path length within the top layer, thus enhancing light adsorption and contributing to the higher photocurrent density.[43] The stronger light-scattering effect of nanodisks has already been studied for WO_3, where the absorption profile from 400 to 500 nm is enhanced over that of a WO_3 nanosphere thin film. Moreover, ultrathin WO_3 nanodisks extend the absorption to the near-IR region of 500–780 nm.[44,45] Therefore, it is reasonable to ascribe our increased TiO_2 thin film red light absorption to the presence of the nanodisk morphology and its scattering effect. The absorption band occurring from 350 to 400 nm at 8% Ti *n*-butoxide is due to an interband transition, as discussed earlier.[46]

The bottom nanostructure layer was analyzed by tapping-mode AFM (Fig. 5). The top layer was first removed by sonication in deionized water, leaving only the transparent bottom layer on the substrate. The bottom layer image indicates an average nanoparticle size of ~20 nm. The average sizes of the nanoparticles in the top and bottom layers as determined by the Scherrer eq. ($0.9\lambda/(\beta \cos \theta)$, where λ is the X-ray wavelength, β is the peak width at half height, and θ is the Bragg angle) of the strongest PXRD peak (Fig. 1*d*, red and

Can. J. Chem. Downloaded from www.nrcresearchpress.com by MCGILL UNIVERSITY on 02/02/13
For personal use only.

Can. J. Chem. Downloaded from www.nrcresearchpress.com by MCGILL UNIVERSITY on 02/02/13
For personal use only.

Fig. 6. Photocurrent density–voltage curves for the TiO_2 thin film (solid lines) prepared from 4% (*w*/*v*) and 8% (*w*/*v*) Ti *n*-butoxide, sensitized by N3 dye and coated with a polymer electrolyte composed of poly(ethylene oxide) (PEO), TiO_2 (Degussa P25), LiI, and I_2 under 100 W/cm^2 (AM 1.5 illumination). Dark conditions (broken lines) are also shown for comparison.



black, respectively) were 145.2 and 22.0 nm, respectively. Both the top and bottom layers are therefore crystalline, with the calculated particle size matching well with the observed particle size (Figs. 3 and 5). The nanocrystalline TiO_2 bottom layer with ~20 nm particle size increases the surface area up to 1000-fold over that of the top layer, for greater adsorption of dye.[4,43] The more compact array of the underlayer serves to also minimize contact of the electrolyte with the anode conductive glass. This separation likely retards the back transfer of electrons, which is known to be the main pathway for electron–hole recombination and low conversion efficiency of DSSCs.[14,47,48]

Considering the higher ratio of nanodisks and increased homogeneity, the optimized sample from 10% PMMA and 8% titanium *n*-butoxide was tested for *I*–*V* measurements and a sample with 4% titanium *n*-butoxide was tested for comparison (Fig. 6). Under an illumination of AM 1.5 (100 mW/cm^2), the nanodisk cell from 8% titanium precursor exhibits V_{oc} = 0.78 V, J_{sc} = 7.98 mA/cm^2, a fill factor of 67.2%, and the overall light-to-electricity efficiency reaches 4.2%. The corresponding cell from 4% titania, however, reaches V_{oc} = 0.62 V, J_{sc} = 6.99 mA/cm^2, a fill factor of 61.9%, and an overall conversion efficiency of only 2.7%. The cell with the higher ratio titanium precusor exhibits 25% higher open-circuit voltage performance, likely because of the longer electron residence time in the larger distinct particle sizes, further increasing the Fermi level of the photoelectrode semiconductor. The higher V_{oc} is also likely due to the larger particle size and higher crystallinity, which are known to limit electron–hole recombination. Usually, electron trapping would also occur and lower the current density. It seems the better light-harvesting ability of our nanodisk morphology overcomes this disadvantage, for a slightly enhanced current. The improved current density might be also ascribed to the higher adsorption of dye owing to a more homogeneous structure and pore space versus that of the thin film made from 4% titanium precursor.

Our previous report used a lower ratio of 8% PMMA and 6% Ti *n*-butoxide, a *meso*-tetra(4-carboxyphenyl)porphyrin dye and electrolyte containing polyethylene glycol, KI, and I_2 without P25 inorganic nanoparticle filler (Table 1).[18] The *I*–*V* curve for the present report shows an increase in J_{sc} from 3.02 to 7.98 mA/cm^2, but a decrease of V_{oc} from 1.18 to 0.78 V. The increase in current density is likely due to several factors (*i*) the nanodisk morphology leads to more effective light scattering, thereby enhancing light harvesting and limiting the back transfer of electrons; (*ii*) the P25 TiO_2 nanoparticles reduce the crystallinity of the PEO electrolyte for a more effective charge transport;[38] (*iii*) the N3 dye has a stronger absorption ability in the 350–650 nm region, with absorbance greater than 0.5 in 0.5 mmol/L ethanol solution. The latter two points are also backed up by the current improvement from 4% titanium precursor compared with our previous cells. Our previous *meso*-tetra(4-carboxyphenyl)porphyrin dye has weaker absorption from 350 to 500 nm. Therefore, the N3 dye also contributes to this effective optimization for light-harvesting efficiency by an SDSSC.[30,37,48]

The open-circuit voltage arises from the difference between the Fermi level of the TiO_2 semiconductor and the electrolyte redox potential. The lower V_{oc} for the current data is likely due to the smaller particle size of the top layer, which is ~150 nm compared with ~500 nm in our earlier report.[18] The closer match of the two layers for the current report likely increases the lifetime of charge carriers and raises the Fermi level.[32] Despite the relatively slight decrease in V_{oc}, J_{sc} significantly increases from 3.02 to 7.98 mA/cm^2. This enhancement was achieved by the optimization of the film morphology, particle size, and improvement in the dye and electrolyte, greatly increasing light-to-electricity conversion efficiency.

Conclusion

A simple swollen polymer method has been developed to fabricate an inexpensive large-area SDSSC with a new record efficiency of 4.2%. This test was carried out under a large sensitizing area (2 cm^2) and only requires the commercially available solid-state polymer PEO to achieve efficient photovoltaic performance. The rare nanodisk morphology of the TiO_2 thin films contributes to high scattering of low-energy visible light for enhancing light absorption and photovoltaic performance. The fabrication method is low cost and far more reliable and tunable than the conventional P25 backblading method. We are currently working on further optimizing the porosity and thus performance of the thin films through the choice and concentration of both inorganic precursor and polymer.

Supplementary data

Supplementary data are available with the article through the journal Web site at http://nrcresearchpress.com/doi/suppl/10.1139/v2012-065.

Acknowledgements

The authors wish to acknowledge Professor Yat Li at UC Santa Cruz, Department of Chemistry and Biochemistry, for assistance with SEM data collection. We also thank Professor

Table 1. Comparison of sample composition and photovoltaic performance between our previous[18] and current studies.

		Previous study[18]	Current study
Sample composition	Photoanode	Nanoparticle bilayer	Nanodisk bilayer
	Dye	*meso*-Tetra(4-carboxyphenyl)porphyrin	*cis*-Bis(isothiocyanato)bis(2,2′-bipyridyl-4,4′-dicarboxylato)ruthenium(II)
	Electrolyte	Polyethylene glycol, KI, and I_2	PEO, LiI, I_2, and P25 TiO_2
Photovoltaic performance	V_{oc} (V)	1.18	0.78
	J_{sc} (mA/cm^2)	3.02	7.98
	Efficiency (%)	2.0	4.2

Note: V_{oc}, open-circuit voltage; J_{sc}, short-circuit current density; PEO, poly(ethylene oxide).

Can. J. Chem. Downloaded from www.nrcresearchpress.com by MCGILL UNIVERSITY on 02/02/13
For personal use only.

Shaowei Chen at UC Santa Cruz, Department of Chemistry and Biochemistry, for help with *I–V* testing and AFM.

References

(1) O'Regan, B.; Grätzel, M. *Nature* **1991**, *353* (6346), 737. doi:10.1038/353737a0.
(2) Bach, U.; Lupo, D.; Comte, P.; Moser, J. E.; Weissörtel, F.; Salbeck, J.; Spreitzer, H.; Grätzel, M. *Nature* **1998**, *395* (6702), 583. doi:10.1038/26936.
(3) Hagfeldt, A.; Gratzel, M. *Acc. Chem. Res.* **2000**, *33* (5), 269. doi:10.1021/ar980112j.
(4) Grätzel, M. *Inorg. Chem.* **2005**, *44* (20), 6841. doi:10.1021/ic0508371.
(5) Grätzel, M. *Nature* **2001**, *414* (6861), 338. doi:10.1038/35104607.
(6) Bai, Y.; Cao, Y. M.; Zhang, J.; Wang, M.; Li, R. Z.; Wang, P.; Zakeeruddin, S. M.; Gratzel, M. *Nat. Mater.* **2008**, *7* (8), 626. doi:10.1038/nmat2224.
(7) Bai, Y.; He, G.-j.; Zhao, Y.-j.; Duan, C.-y.; Dang, D.-b.; Meng, Q.-j. *Chem. Commun. (Camb.)* **2006**, (14): 1530. doi:10.1039/b517002h.
(8) Wu, J. H.; Hao, S.; Lan, Z.; Lin, J.; Huang, M.; Huang, Y.; Li, P.; Yin, S.; Satot, T. *J. Am. Chem. Soc.* **2008**, *130* (35), 11568. doi:10.1021/ja802158q.
(9) Yum, J. H.; Chen, P.; Gratzel, M.; Nazeeruddin, M. K. *ChemSusChem* **2008**, *1* (8–9), 699. doi:10.1002/cssc.200800084.
(10) Hardin, B. E.; Hoke, E. T. A.; Armstrong, P. B.; Yum, J.-H.; Comte, P.; Torres, T.; Fréchet, J. M. J.; Nazeeruddin, M. K.; Grätzel, M.; McGehee, M. D. *Nat. Photonics* **2009**, *3* (7), 406. doi:10.1038/nphoton.2009.96.
(11) Bessho, T.; Yoneda, E. Y.; Yum, J.-H.; Guglielmi, M.; Tavernelli, I.; Imai, H.; Rothlisberger, U.; Nazeeruddin, M. K.; Grätzel, M. *J. Am. Chem. Soc.* **2009**, *131* (16), 5930. doi:10.1021/ja9002684.
(12) Li, T. C. S.; Spokoyny, A. M.; She, C.; Farha, O. K.; Mirkin, C. A.; Marks, T. J.; Hupp, J. T. *J. Am. Chem. Soc.* **2010**, *132* (13), 4580. doi:10.1021/ja100396n.
(13) Cameron, P. J.; Peter, L. M. Z.; Zakeeruddin, S. M.; Grätzel, M. *Coord. Chem. Rev.* **2004**, *248* (13–14), 1447. doi:10.1016/j.ccr.2004.02.010.
(14) Nakade, S.; Saito, Y.; Kubo, W.; Kitamura, T.; Wada, Y.; Yanagida, S. *J. Phys. Chem. B* **2003**, *107* (33), 8607. doi:10.1021/jp034773w.
(15) Palomares, E.; Clifford, J. N.; Haque, S. A.; Lutz, T.; Durrant, J. R. *J. Am. Chem. Soc.* **2003**, *125* (2), 475. doi:10.1021/ja027945w.
(16) Chen, D. H.; Huang, F.; Cheng, Y.-B.; Caruso, R. A. *Adv. Mater. (Deerfield Beach Fla.)* **2009**, *21* (21), 2206. doi:10.1002/adma.200802603.
(17) Chen, D. C.; Cao, L.; Huang, F.; Imperia, P.; Cheng, Y.-B.; Caruso, R. A. *J. Am. Chem. Soc.* **2010**, *132* (12), 4438. doi:10.1021/ja100040p.
(18) Fan, X.; Demaree, D. P.; St. John, J. M.; Tripathi, A.; Oliver, S. R. J. *Appl. Phys. Lett.* **2008**, *92* (19), 193108. doi:10.1063/1.2924277.
(19) Feng, X. J.; Shankar, K.; Varghese, O. K.; Paulose, M.; Latempa, T. J.; Grimes, C. A. *Nano Lett.* **2008**, *8* (11), 3781. doi:10.1021/nl802096a.
(20) Boyd, D. A.; Greengard, L. B.; Brongersma, M.; El-Naggar, M. Y.; Goodwin, D. G. *Nano Lett.* **2006**, *6* (11), 2592. doi:10.1021/nl062061m.
(21) Zhao, D.; Feng, J. H. *Science* **1998**, *279* (5350), 548. doi:10.1126/science.279.5350.548.
(22) Hu, L. H.; Dai, S. Y.; Weng, J.; Xiao, S. F.; Sui, Y. F.; Huang, Y.; Chen, S. H.; Kong, F. T.; Pan, X.; Liang, L. Y.; Wang, K. J. *J. Phys. Chem. B* **2007**, *111* (2), 358. doi:10.1021/jp065541a.
(23) Fei, H.; Yang, Y. ; Rogow, D. L.; Fan, X.; Oliver, S. R. J. *ACS Appl. Mater. Interfaces* **2010**, *2,* (4), 974. doi:10.1021/am100087b.
(24) Wang, Y. Q.; Chen, S. G.; Tang, X. H.; Palchik, O.; Zaban, A.; Koltypin, Y.; Gedanken, A. *J. Mater. Chem.* **2001**, *11* (2), 521. doi:10.1039/b006070o.
(25) Tian, Z. P.; Tian, H. M.; Wang, X. Y.; Yuan, S. K.; Zhang, J. Y.; Zhang, X. B.; Yu, T.; Zou, Z. G. *Appl. Phys. Lett.* **2009**, *94* (3), 031905. doi:10.1063/1.3073834.
(26) Deshpande, A. S.; Shchukin, D. G. U.; Ustinovich, E.; Antonietti, M.; Caruso, R. A. *Adv. Funct. Mater.* **2005**, *15* (2), 239. doi:10.1002/adfm.200400220.
(27) Zhou, J. F.; Zhou, M. F.; Caruso, R. A. *Langmuir* **2006**, *22* (7), 3332. doi:10.1021/la052771s.
(28) Fan, X.; Fei, H.; Demaree, D. H.; Brennan, D. P.; St. John, J. M.; Oliver, S. R. J. *Langmuir* **2009**, *25* (10), 5835. doi:10.1021/la8029837.
(29) Brennan, D. P.; Dobley, A.; Sideris, P. J.; Oliver, S. R. J. *Langmuir* **2005**, *21* (25), 11994. doi:10.1021/la051468o.
(30) Xue, M.; Zhu, G. Z.; Zhang, Y.; Fang, Q.; Hewitt, I. J.; Qiu, S. *Cryst. Growth Des.* **2008**, *8* (2), 427. doi:10.1021/cg0701022.

(31) Wang, M.-S.; Guo, G.-C.; Chen, W.; Xu, G.; Zhou, W. W.; Wu, K.; Huang, J.-S. *Angew. Chem. Int. Ed.* **2007**, *46* (21), 3909. doi:10.1002/anie.200604946.
(32) Stathatos, E.; Lianos, P. *Adv. Mater. (Deerfield Beach Fla.)* **2007**, *19* (20), 3338. doi:10.1002/adma.200602535.
(33) Zhang, Q. F. C.; Chou, T. P.; Russo, B.; Jenekhe, S. A.; Cao, G. *Angew. Chem. Int. Ed.* **2008**, *47* (13), 2402. doi:10.1002/anie.200704919.
(34) Zhang, Q. F.; Chou, T. P. R.; Russo, B.; Jenekhe, S. A.; Cao, G. *Adv. Funct. Mater.* **2008**, *18* (11), 1654. doi:10.1002/adfm.200701073.
(35) Zhang, Q.; Dandeneau, C. S.; Zhou, X.; Cao, G. *Adv. Mater. (Deerfield Beach Fla.)* **2009**, *21* (41), 4087. doi:10.1002/adma.200803827.
(36) Wang, L.-S.; Zhang, J.-F.; Yang, S.-P. *Acta Crystallogr. Sect. E Struct. Rep. Online* **2004**, *E60* (10), m1484. doi:10.1107/S1600536804023141.
(37) Nazeeruddin, M. K.; Kay, A.; Rodicio, I.; Humphry-Baker, R.; Mueller, E.; Liska, P.; Vlachopoulos, N.; Graetzel, M. *J. Am. Chem. Soc.* **1993**, *115* (14), 6382. doi:10.1021/ja00067a063.
(38) Stergiopoulos, T.; Arabatzis, I. M.; Katsaros, G.; Falaras, P. *Nano Lett.* **2002**, *2* (11), 1259. doi:10.1021/nl025798u.
(39) Peng, G.-W.; Chen, S.-K.; Liu, H.-S. *Appl. Spectrosc.* **1995**, *49* (11), 1545. doi:10.1366/0003702953965786.
(40) Yatluk, Y. G.; Sosnovskikh, V. Y.; Suvorov, A. L. *Russ. J. Org. Chem.* **2004**, *40* (6), 763. doi:10.1023/B:RUJO.0000044535.29531.0d.
(41) Haoudi, A.; Dhamelincourt, P.; Mazzah, A.; Drache, M.; Conflant, P.; Lazraq, M. *J. Mater. Chem.* **2000**, *10* (4), 1001. doi:10.1039/a909346j.
(42) Gunji, T.; Nagao, Y.; Misono, T.; Abe, Y. *J. Non-Cryst. Solids* **1989**, *107* (2–3), 149. doi:10.1016/0022-3093(89)90455-9.
(43) Ferber, J.; Luther, J. *Sol. Energy Mater. Sol. Cells* **1998**, *54* (1–4), 265. doi:10.1016/S0927-0248(98)00078-6.
(44) Wolcott, A.; Kuykendall, T. R.; Chen, W.; Chen, S. W.; Zhang, J. Z. *J. Phys. Chem. B* **2006**, *110* (50), 25288. doi:10.1021/jp064777b.
(45) Gu, B. X.; Wang, L. M.; Ewing, R. C. *J. Nucl. Mater.* **2000**, *278* (1), 64. doi:10.1016/S0022-3115(99)00224-X.
(46) Yoon, M.; Seo, M.; Jeong, C.; Jang, J. H.; Jeon, K. S. *Chem. Mater.* **2005**, *17* (24), 6069. doi:10.1021/cm0515855.
(47) Huang, S. Y.; Schlichthorl, G.; Nozik, A. J.; Gratzel, M.; Frank, A. J. *J. Phys. Chem. B* **1997**, *101* (14), 2576. doi:10.1021/jp962377q.
(48) Khairutdinov, R. F.; Hurst, J. K. *J. Phys. Chem. B* **1999**, *103* (18), 3682. doi:10.1021/jp984701i.

Can. J. Chem. Downloaded from www.nrcresearchpress.com by MCGILL UNIVERSITY on 02/02/13
For personal use only.

Unexpected lyotropic liquid crystals from ion-induced columnar assembly of Schiff-base macrocycles

Joseph K.-H. Hui, Jian Jiang, and Mark J. MacLachlan

Can. J. Chem. Downloaded from www.nrcresearchpress.com by MCGILL UNIVERSITY on 02/02/13
For personal use only.

Abstract: Schiff-base macrocycles **1**, which have a crown ether-like interior, form ionic nematic lyotropic liquid crystals in various organic solvents when functionalized with long alkoxy substituents and complexed to diverse ammonium and alkali metal salts. From X-ray diffraction and transmission electron microscopy studies, and by comparison with the organization of macrocycles functionalized with shorter chains, these macrocycles assemble into lyotropic liquid crystals where the macrocycles are stacked and the cation is included in their interiors.

Key words: macrocycle, supramolecular, liquid crystal, Schiff base, lyotropic.

Résumé : Les macrocycles **1**, formés à partir de bases de Schiff, qui comportent une partie intérieure semblable à un éther couronne et qui ont été fonctionnalisés avec des substituants à longues chaînes alkoxy, forment des cristaux liquides lyotropes nématiques et ioniques dans divers solvants organiques et ils se complexent à divers sels d'ammonium et de métaux alcalins. Sur la base d'études par diffraction des rayons-X et de microscopie de transmission d'électron ainsi que par comparaisons avec l'organisation de macrocycles fonctionnalisés avec des chaînes plus courtes, on a pu observer que ces macrocycles s'assemblent en cristaux liquides lyotropes dans lesquels les macrocycles sont empilés et le cation est inclus à l'intérieur.

Mots-clés : macrocycle, supramoléculaire, cristal liquide, base de Schiff, lyotrope.

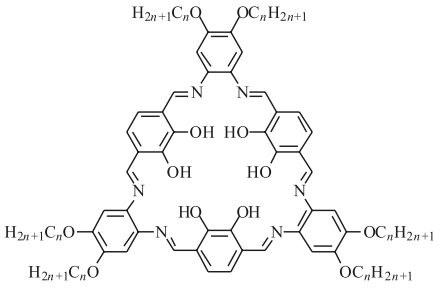
[Traduit par la Rédaction]

Introduction

Liquid crystals (LCs) play an important role in a variety of applications, notably temperature sensors[1–4] and displays.[5–8] These applications utilize thermotropic LCs, which form a temperature-dependent liquid crystalline phase between the crystalline state and the isotropic melt. A large number of organic and inorganic substances have been investigated that exhibit thermotropic liquid crystallinity.[9–13]

Lyotropic LCs, on the other hand, form liquid crystalline phases in solution where the molecules organize into micelles, nematic LCs, hexagonal LCs, and other phases.[14] Typically, lyotropic LCs can be prepared in water with amphiphilic molecules (surfactants) that have a polar headgroup and a hydrophobic tail.[15–19] Soaps, for example, form lyotropic LCs in water. Numerous compounds that exhibit lyotropic mesomorphism have been found to have good anisotropic ionic conductivities.[20] G-quartets are known to assemble into rigid rods in aqueous solution that organize into lyotropic LC phases.[21] However, lyotropic LCs detected in organic solvents are rare, but are promising as an organizational method for constructing supramolecular materials.[22–25]

Here we report novel lyotropic LCs formed by complexes between macrocycles **1c–1e** (and mixtures) and various ammonium or alkali metal salts. These species form LCs in chloroform, toluene, and chlorobenzene. Based on an amphiphilic ionic columnar structure, these mesogens represent an unusual motif for observing liquid crystallinity. These new LC phases may serve as templates for constructing ion-conducting lyotropic phases or new mesoporous materials formed in non-aqueous solvent.



1a $n = 4$
1b $n = 6$
1c $n = 8$
1d $n = 10$
1e $n = 12$

Received 7 June 2012. Accepted 23 July 2012. Published at www.nrcresearchpress.com/cjc on 7 November 2012.

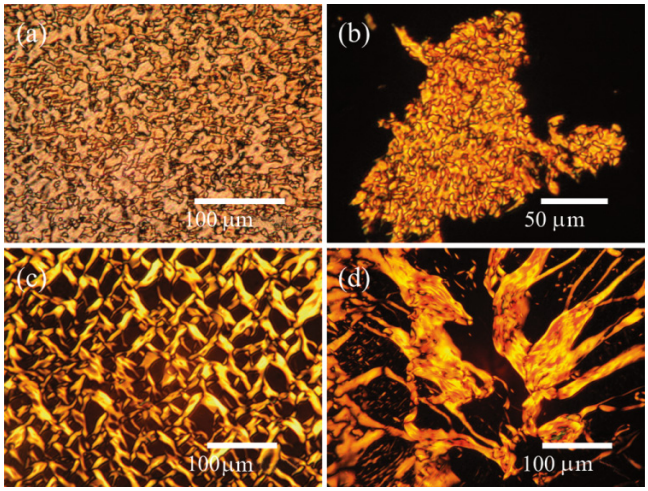
J.K.-H. Hui, J. Jiang, and M.J. MacLachlan. Department of Chemistry, University of British Columbia, 2036 Main Mall, Vancouver, BC V6T 1Z1, Canada.

Corresponding author: Mark J. MacLachlan (e-mail: mmaclach@chem.ubc.ca).

This article is part of a Special Issue dedicated to Professor Geoffrey Ozin on the occasion of his 70th birthday, and in recognition of his outstanding contributions to the fields of materials science and nanochemistry.

Can. J. Chem. Downloaded from www.nrcresearchpress.com by MCGILL UNIVERSITY on 02/02/13
For personal use only.

Fig. 1. Polarized optical micrographs of chloroform solutions of NH_4BF_4 with macrocycles (*a*) **1e**, (*b*) **1d**, and (*c* and *d*) **1c** (1:1 ratio of **1**–NH_4^+) show typical textures observed for the liquid crystal (LC) samples under crossed polarizers. Samples were viewed at room temperature between a slide and a cover slip as the solvent evaporated from samples that were approximately 10 wt % macrocycle **1**.



Experimental

General procedures

All reagents were used as received unless otherwise stated. Ammonium tetrafluoroborate, lithium tetrafluoroborate, sodium tetrafluorobroate, and sodium tetraphenylborate were obtained from Sigma-Aldrich. Chlorobenzene, HPLC grade chloroform, and toluene were obtained from Fisher Scientific. The syntheses of Schiff base macrocycles **1c**–**1e** were carried out according to literature procedures.[26]

Equipment

Polarizing optical microscopy (POM) studies were performed with an Olympus BX41 microscope equipped with a digital camera. The textures were identified by comparison with literature references and the book *Textures of liquid crystals*.[27] We have not been able to find a good example of the "mesh" texture as shown in Figs. 1*c* and 1*d*, but we believe it is also from the nematic phase. X-ray diffraction (XRD) data of the solution samples were obtained on a D8 Discover X-ray diffractometer equipped with GADDS, in which chloroform solutions at a concentration of approximately 40 wt % macrocycle were contained in sealed 0.2 mm thin-walled special glass capillary tubes manufactured by Charles Supper. Powder X-ray diffraction (PXRD) data were recorded on a D8 Advance powder X-ray diffractometer by drop-casting the sample solutions onto silicon plates. IR spectra were obtained neat with a Thermo Nicolet 6700 FT-IR equipped with ATR.

General sample preparation of lyotropic LCs for POM imaging

The Schiff base macrocycle (i.e., **1c**–**1e**) (1.5 mg) was dissolved in chloroform (1 mL) and was mixed with an excess amount of ammonium or alkali metal salt (50 mg) for ~5 s to give a dark red solution. The solution was allowed to stand for 5 min before the removal of the excess salts by filtration through a short pad (5–10 mm) of cellulose (Kimwipe). The dark red solution was then concentrated through evaporation before drop-casting onto the microscope glass slides for viewing under POM to observe the liquid crystalline textures. We observed lyotropic liquid crystallinity at about 15 wt % macrocycle in samples that were prepared on a larger scale. The optical micrographs obtained under crossed polarizers were persistent over a broad concentration range.

Results and discussion

Ion-induced lyotropic liquid crystallinity from Schiff base macrocycles 1c–1e

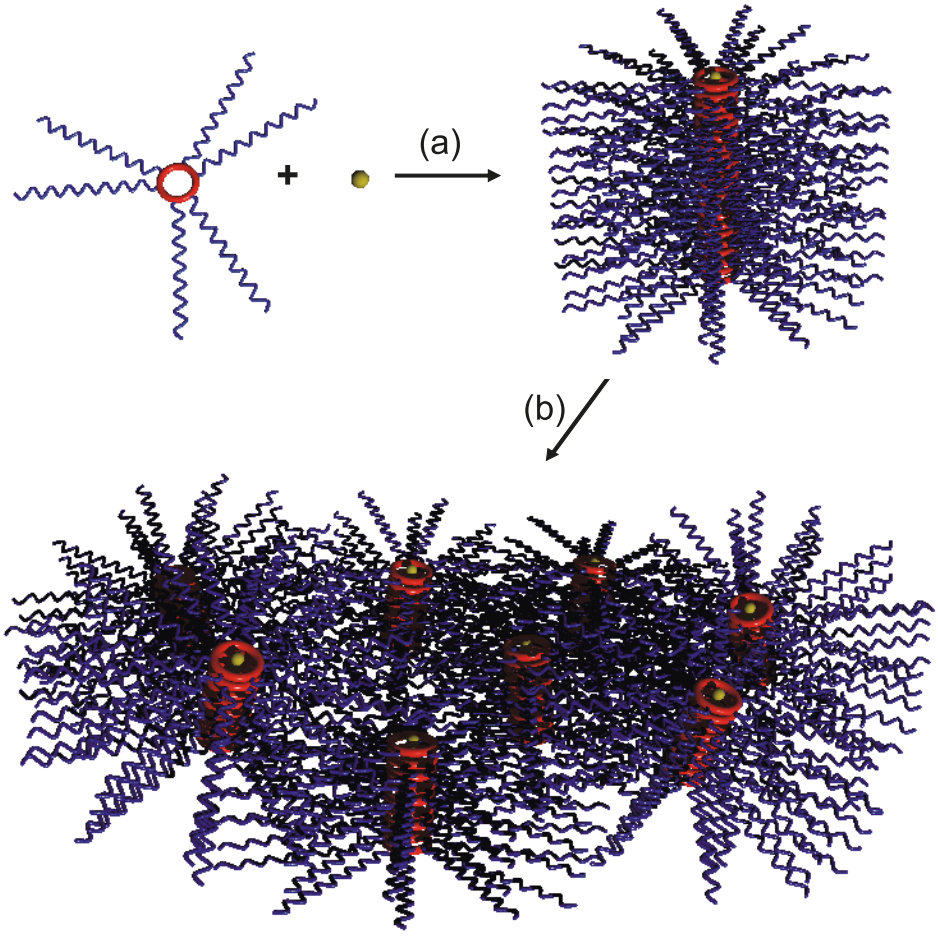
We previously reported a series of conjugated triangular [3+3] Schiff base macrocycles (**1**) having two peripheral alkoxy substituents on each phenylenediimine unit.[26] The macrocycles with butyloxy and hexyloxy side chains (macrocycles **1a** and **1b**) self-assemble into hierarchically organized nanofibers upon the addition of alkali metal or ammonium salts,[28] with the cations situated in the center of a column of macrocycles. This polycationic macrocycle assembly is charge balanced by counteranions located outside of the columnar aggregates.

As macrocycles **1a**–**1e** have the same symmetry (D_{3h}) as the well-known family of thermotropic mesogens, hexaalkoxytriphenylenes,[29,30] we explored whether macrocycles **1** could form thermotropic liquid crystalline phases. Our attempts to impart liquid crystallinity upon macrocycles **1** simply by introducing long alkyl chains led to substances with reduced melting points, but no liquid crystallinity.[26]

Chloroform solutions of macrocycle **1e** failed to show any birefringence, even when concentrated. However, when chloroform solutions of macrocycle **1e** with NH_4BF_4 (1:1) were viewed under crossed polarizers with a POM, to our surprise, we observed a texture characteristic of a nematic LC (Fig. 1*a*). The lyotropic mesomorphism was apparent at a concentration of approximately 10 wt % and higher. In the LC phase, the samples were relatively viscous but fluid.

Based on our results with the shorter chain analogues (macrocycles **1a** and **1b**),[31] we postulate that upon the addition of NH_4BF_4, macrocycle **1e** stacks and binds the cation in its interior, forming a polyelectrolyte. This is supported by ^{1}H NMR data; when NH_4BF_4 was added to macrocycle **1e**, we observed substantial line broadening and shifting as observed with macrocycle **1b**.[32–34] Electrospray ionization mass spectrometry (ESI-MS) of macrocycle **1e** with NH_4BF_4 showed the molecular ion as the dominant peak, but also displayed peaks corresponding to oligomers (dimers and trimers). In addition, elemental analysis of the aggregates indicated that their composition was about three macrocycles to four ammonium salts (a ratio of 1:1.3 macrocycle **1e**–NH_4BF_4). In the case of macrocycles **1a** and **1b**, the assemblies subsequently organize into insoluble fibers through electrostatic interactions.[28] With longer chains present in macrocycle **1e**, however, the macrocycles are more soluble and instead form a lyotropic LC in solution. Unlike macrocycles **1a** and **1b** with shorter alkoxy chains that allow the columnar aggregates to pack into nanofibers, long dodecyloxy chains on macrocycle **1e** render the columnar aggregates more soluble (Fig. 2). The macrocycles retain the one-dimensional ion-induced columnar assembly and organize with some long-range orientational order in terms of the alignment of the columns.

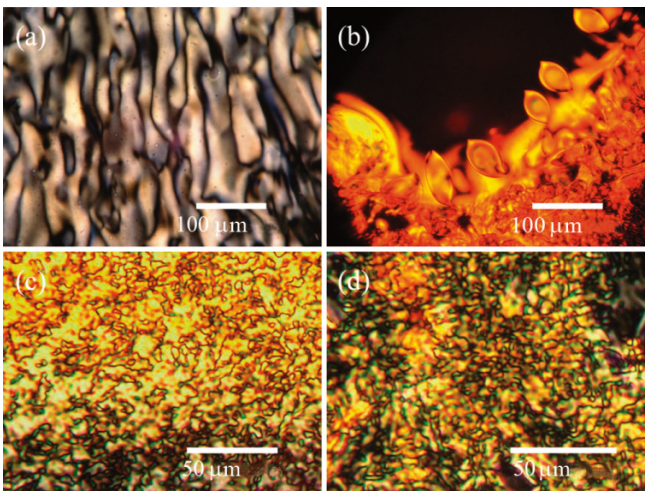
Fig. 2. Model for the ion-induced assembly leading to the formation of lyotropic liquid crystals (LCs). (*a*) In solvent, macrocycles **1c**–**1e** combine with cations (yellow spheres) to form a 1-D polymeric structure where the macrocycles are bridged by the cations. (*b*) Upon concentration, these 1-D assemblies organize into a nematic LC phase where they retain orientational order. The counteranions have been omitted for clarity.



Addition of NH_4BF_4 to macrocycles **1c** and **1d**, having octyloxy and decyloxy chains, respectively, also gave birefringent chloroform solutions. The optical micrograph of macrocycle **1d** with NH_4BF_4 displays a texture (Fig. 1*b*) that is similar to that observed for macrocycle **1e** and characteristic of a nematic mesophase. Macrocycle **1c**, however, showed textures in chloroform possibly corresponding to both smectic and nematic mesophases, as shown in Figs. 1*c* and 1*d*. One texture, which may be of a smectic phase, was observed around the outer area of the sample droplet, whereas the nematic phase occurred at the center (it is possible that both textures correspond to the nematic phase). The columnar aggregates formed from macrocycles **1** appended with octyloxy substituents (i.e., macrocycle **1c**) appear to retain higher orientational and positional order than those of macrocycles **1d** and **1e**, represented by the smectic mesogenic texture. From these experiments, the transition between nanofibers and LCs occurs between hexyloxy and octyloxy substituents for the macrocycles.

To investigate the scope of mesophase formation in this system, we varied the ions and the solvent. When macrocycle **1e** was combined with $LiBF_4$ or $NaBF_4$ in chloroform, nematic mesophases were identified by POM (Figs. 3*a* and 3*b*). In

Fig. 3. Polarized optical micrographs of macrocycle **1e** observed under crossed polarizers at room temperature. (*a*) $LiBF_4$ in chloroform, (*b*) $NaBF_4$ in chloroform, (*c*) NH_4BF_4 in toluene, and (*d*) NH_4BF_4 in chlorobenzene.



Can. J. Chem. Downloaded from www.nrcresearchpress.com by MCGILL UNIVERSITY on 02/02/13
For personal use only.

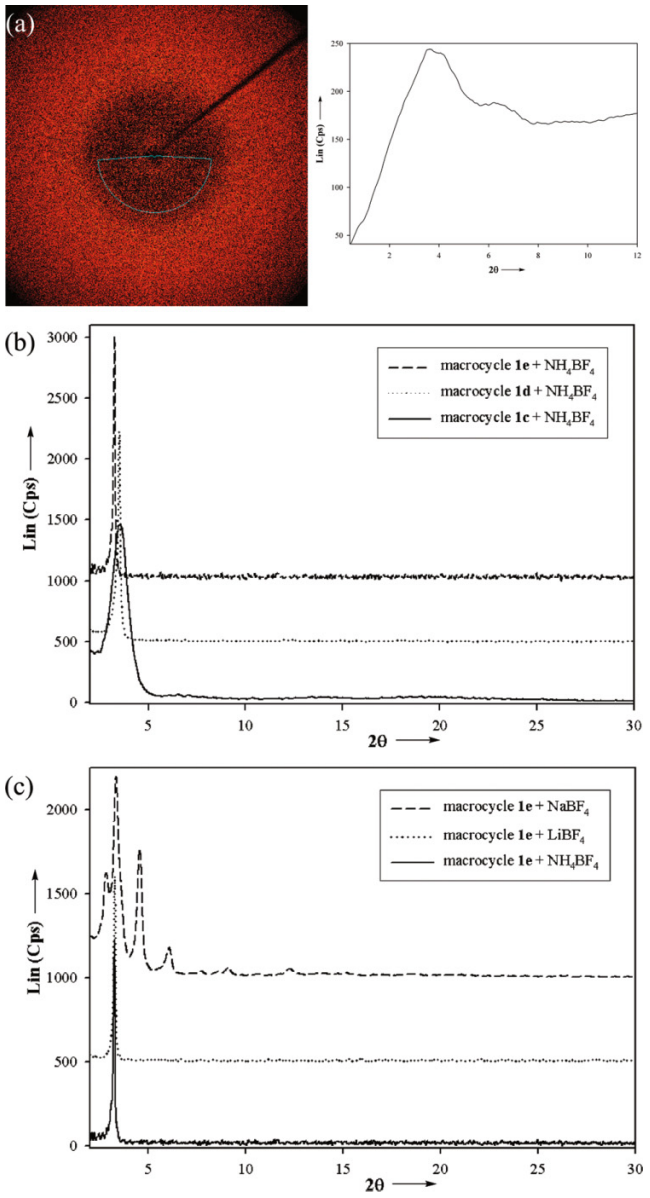
Can. J. Chem. Downloaded from www.nrcresearchpress.com by MCGILL UNIVERSITY on 02/02/13
For personal use only.

addition, macrocycle **1e** was mixed with NH_4BPh_4 to observe the effect of counteranions on the morphology of the LC phase. Surprisingly, even with the bulky BPh_4^- anion, liquid crystallinity was observed. Furthermore, we prepared macrocycle **1e** with NH_4BF_4 in different solvents, namely toluene and chlorobenzene (Figs. 3*c* and 3*d*). Once again, nematic mesophases were imaged by POM and the textures are similar to the one prepared in chloroform. These results show that the lyotropic mesomorphism is robust and can be observed with diverse cations, anions, and organic solvents.

Whereas XRD is a crucial method for phase identification of thermotropic LCs, it is much more problematic with lyotropic LCs, where the low concentration and greater disorder leads to very weak X-ray scattering. Efforts to obtain XRD from solutions of NH_4^+ complexes of macrocycles **1c**–**1e** in chloroform (where they are liquid crystalline) have been a challenge owing to insufficient diffraction. However, after numerous attempts of varying the concentration of the chloroform solution of macrocycle **1c** with NH_4BF_4, a diffraction pattern with sufficient signal intensity was obtained at a concentration of approximately 40 wt % macrocycle **1c** (Fig. 4*a*). The integration of the XRD pattern shows a broad diffraction peak centered near 3.7° 2θ. To obtain diffraction patterns with higher intensity, we undertook XRD studies of the films prepared from the dried LC samples.[35] Although these are not the lyotropic LCs themselves, XRD of the films should give an indication of the order present in the sample prior to drying. XRD patterns of dried samples of macrocycles **1c**–**1e** with NH_4BF_4 all displayed one intense broad diffraction peak with d spacing of approximately 24.8, 25.4, and 26.9 Å, respectively (Fig. 4*b*). Since the dried film of macrocycle **1c** with NH_4BF_4 has a diffraction peak with 2θ very close to that of the liquid sample, we believe that the films have a similar structure to the lyotropic LC from which they were formed. From rough modelling of a hypothetical columnar assembly (Supplementary data Fig. S1), this diffraction peak corresponds quite well to the expected interstack separation rather than intermolecular separation within the stack. As well, the increase in the d spacing with increasing chain length agrees with this interpretation. The absence of additional diffraction peaks is also consistent with a poorly organized structure, as expected for a nematic LC. XRD of films prepared from the LC phases of macrocycle **1e** with $LiBF_4$ and $NaBF_4$ in chloroform was also measured for comparison with the diffraction pattern of the NH_4BF_4 sample. All three XRD patterns have a diffraction peak at 26.9 Å d spacing (Fig. 4*c*), supporting the assignment of this peak as owing to interstack organization, since this is not expected to show a metal dependence. The patterns for the $LiBF_4$ and NH_4BF_4 show only one peak and are virtually identical. Interestingly, additional peaks are observed in the XRD pattern of the $NaBF_4$ sample, indicating that the columnar aggregates are more ordered with the incorporation of Na^+. Quite possibly, the additional ordering is only present upon solidification. We have no explanation for this discrepancy, but perhaps the Na^+ interacts with the interior of the macrocycles in a different way that facilitates improved order.

As the ESI-MS and NMR data suggested that the macrocycles aggregate in solution with the presence of salts, we investigated their supramolecular assembly in the solid state by transmission electron microscopy (TEM). Figure 5 shows the morphology of a dried sample of macrocycle **1c** with

Fig. 4. (*a*) Left: X-ray diffraction (XRD) pattern of macrocycle **1c** with NH_4BF_4 in chloroform (approximately 40 wt %). Right: Integration of the outlined area. Dried XRD patterns of (*b*) macrocycles **1c**–**1e** with NH_4BF_4 and (*c*) macrocycle **1e** with NH_4BF_4, LiBF4, and $NaBF_4$.



NH_4BF_4. Fibers with diameters of approximately 25 nm and lengths of hundreds of nanometers were observed. This phenomenon is attributed to the macrocycles forming one-dimensional polyelectrolytes with the cations binding to the interior and the counteranions of the salts surrounding on the outside, which further organize into nanofibers through electrostatic interactions. This self-assembly is identical to that of the shorter chain analogues (macrocycles **1a** and **1b**),[28] despite the formation of lyotropic LCs for macrocycles **1c**–**1e**. However, the fibers of macrocycle **1c** with NH_4BF_4 are narrower and shorter than those prepared from the shorter chain analogues (macrocycles **1a** and **1b**).

Can. J. Chem. Downloaded from www.nrcresearchpress.com by MCGILL UNIVERSITY on 02/02/13
For personal use only.

Fig. 5. (*a* and *b*) Transmission electron microscopy (TEM) images of macrocycle **1c** with NH_4BF_4. The sample was prepared by drop-casting the chloroform solution onto carbon-coated grids and dried at ambient conditions.

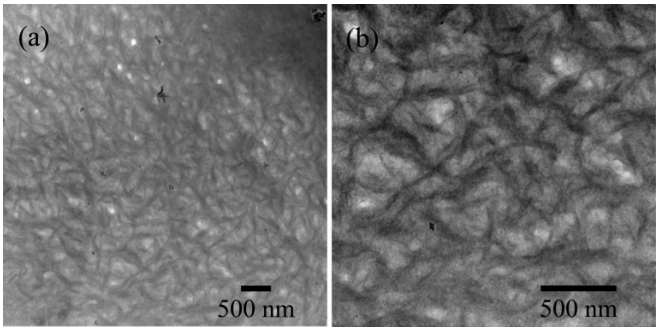


Fig. 6. Polarized optical micrographs of mixtures of (*a* and *b*) macrocycles **1b/1c** and (*c* and *d*) macrocycles **1b/1e** with NH_4BF_4 in chloroform. All images were taken with crossed polarizers at room temperature.

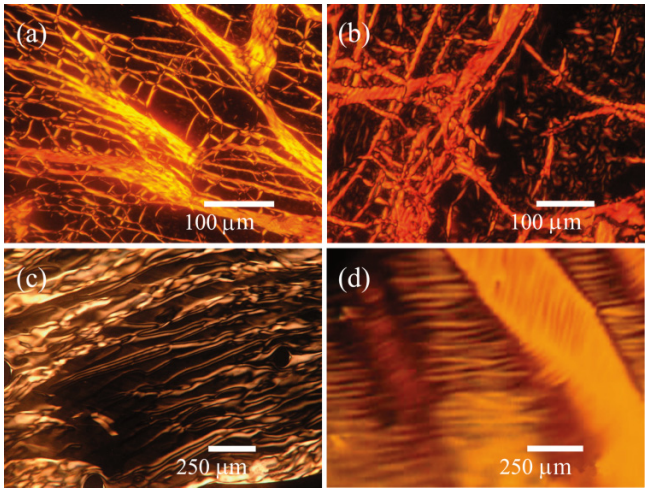
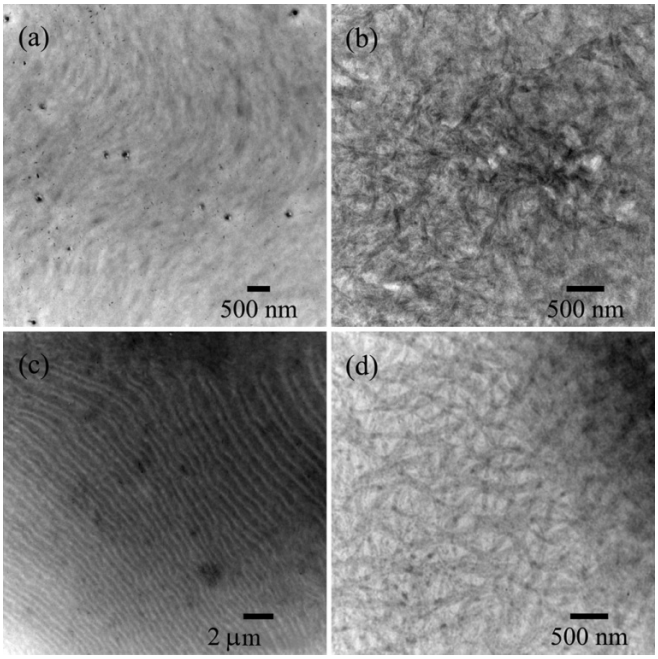


Fig. 7. Transmission electron microscopy (TEM) images of mixtures of (*a* and *b*) macrocycles **1b/1c** and (*c* and *d*) macrocycles **1b/1e** with NH_4BF_4. The samples were prepared by drop-casting the chloroform solution onto carbon-coated grids and dried at ambient conditions.



Ion-induced lyotropic liquid crystallinity from the mixtures of Schiff base macrocycles 1b/1c and 1b/1e

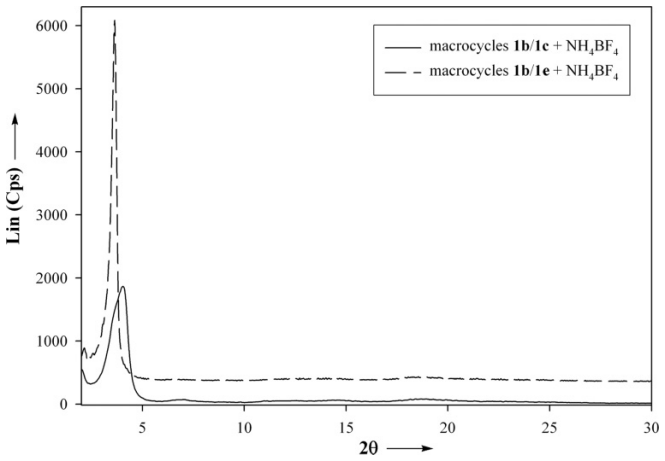
As noted, addition of alkali metal or ammonium salts to macrocycle **1** functionalized with short and long alkoxy substituents leads to the formation of nanofibers and lyotropic LCs, respectively. We were interested to know what would happen if the two types of macrocycles were combined in the presence of salts in solution. We performed the investigation by observing a chloroform solution of macrocycles **1b** and **1c** (1:1 mixture) that was combined with excess NH_4BF_4.[36] The solution sample displayed an oily streak LC texture when viewed by POM as shown in Fig. 6*a*. The texture observed for the mixture is different than that obtained from macrocycle **1c** alone with the ammonium salt. It is noteworthy that a helical texture was observed in segments of the LC (Fig. 6*b*). The occurrence of these textures was unexpected, and the difference in texture suggests that the incorporation of macrocycle **1b** led to different packing behavior among the polyelectrolytes when compared with that of macrocycle **1c** alone with NH_4BF_4. Moreover, the optical micrographs of the chloroform solution containing a 1:1 mixture of macrocycles **1b** and **1e** with NH_4BF_4 (Figs. 6*c* and 6*d*) also display different textures than the solution sample with macrocycle **1e** alone. Surprisingly, a fingerprintlike texture (Fig. 6*d*) could be seen in the early stage of the observation after transferring the chloroform sample onto the microscope glass slide, but the lines slowly merged together and eventually disappeared because of the flow of the LC.

We further examined the dried samples of the NH_4^+ complexed mixtures by TEM. The images (Figs. 7*a* and 7*b*) reveal that the morphology of macrocycles **1b** and **1c** with NH_4BF_4 resemble the morphology observed for the sample with macrocycle **1c** alone (Fig. 5). On the other hand, for the sample of the NH_4^+ complex of macrocycles **1b** and **1e**, two textures, fingerprintlike and nanofibrous, could be seen under TEM (Figs. 7*c* and 7*d*). As illustrated in Fig. 7*c*, the spacing between the black lines of the fingerprintlike region is 207 ± 42 nm (based on a count of 75). Figure 7*d* shows that the fibers have diameters of approximately 90 nm and lengths of hundreds of nanometers. The morphological studies of the dried mixtures support the formation of columnar assemblies from the addition of NH_4BF_4 to a mixture of two macrocycles.

The mixture of macrocycles **1b** and **1c** with NH_4BF_4 was further analyzed by ESI-MS. A mass-to-charge ratio corresponding to one macrocycle **1b** and one macrocycle **1c** with NH_4^+ was detected, along with the signals of the NH_4^+-complexed homodimers of the respective macrocycles. The same ESI-MS features were observed from the sample of macrocycles **1b** and **1e** combined with NH_4BF_4. This data supports co-aggregation of the two macrocycles in the electrostatic assembly rather than phase separation.

Can. J. Chem. Downloaded from www.nrcresearchpress.com by MCGILL UNIVERSITY on 02/02/13
For personal use only.

Fig. 8. X-ray diffraction (XRD) patterns of the dried mixtures of macrocycles **1b/1c** and macrocycles **1b/1e** with NH_4BF_4.



XRD investigations were undertaken on the chloroform solutions of the NH_4^+ complexed mixtures. Despite repeated efforts, we were unable to obtain satisfactory data on the solutions, even when concentrated. Instead, we performed the XRD analyses on dried samples of the mixtures to gain stronger diffraction signals (Fig. 8). The XRD patterns of both dried mixtures only show one intense peak at low angle with d spacing of approximately 21.9 and 24.4 Å for the NH_4^+ complexes of macrocycles **1b** with **1c** and **1e**, respectively. The d spacing of each mixture, which reflects the distance of the interstack separation, is expected to be larger than that of the macrocycle with shorter substituents and smaller than that of the longer alkoxy chain component because each mixture originates from macrocycles **1b** with **1c** or **1e**. The PXRD data agree with this postulation, in which the values of the mixtures lie between the measured d spacing of macrocycles **1b** (20.2 Å), **1c** (24.8 Å), or **1e** (26.9 Å) alone with NH_4BF_4.

Conclusion

In summary, we have discovered unusual lyotropic LCs that form in nonpolar organic solvents such as chloroform, toluene, and chlorobenzene. We postulate that these mesogens are formed by ion-induced columnar assemblies of a Schiff base macrocycle–cation complex, where they have a charged interior surrounded by hydrophobic alkyl substituents. The polyelectrolytic columns retain a degree of orientational ordering in solution, leading to lyotropic mesomorphism. This ion-induced assembly is reminiscent of the organization observed in self-assembled G quartets with alkali metals,[22] but, to the best of our knowledge, is unprecedented in macrocycle chemistry. Electrostatic self-assembly of macrocycles into lyotropic mesogens may be a useful design principle for constructing organized materials that can function as ion-conducting materials or as templates for nanostructures (for example, after cross-linking of polymerizable substituents on the macrocycles). We are now pursuing these directions.

Supplementary data

Supplementary data are available with the article through the journal Web site at http://nrcresearchpress.com/doi/suppl/10.1139/v2012-063.

Acknowledgements

We are grateful to the Natural Sciences and Engineering Research Council of Canada (NSERC) and the University of British Columbia (UBC) for funding this work. We also thank A. Lam of the UBC Chemistry Department's Structural Chemistry Facility for help in collecting XRD diffractions for the liquid samples.

References

(1) Stasiek, J. A.; Kowalewski, T. A. *Opto-Electron. Rev.* **2002**, *10* (1), 1.
(2) Vejrazka, J.; Marty, P. *Heat Transfer Eng.* **2007**, *28* (2), 154. doi:10.1080/01457630601023641.
(3) Stasiek, J.; Stasiek, A.; Jewartowski, M.; Collins, M. W. *Opt. Laser Technol.* **2006**, *38* (4–6), 243. doi:10.1016/j.optlastec.2005.06.028.
(4) Iles, A.; Fortt, R.; de Mello, A. J. *Lab Chip* **2005**, *5* (5), 540. doi:10.1039/b419081e.
(5) Hird, M. *Chem. Soc. Rev.* **2007**, *36* (12), 2070. doi:10.1039/b610738a.
(6) Kawamoto, H. *Proc. IEEE* **2002**, *90* (4), 460. doi:10.1109/JPROC.2002.1002521.
(7) Gray, G. W.; Kelly, S. M. *J. Mater. Chem.* **1999**, *9* (9), 2037. doi:10.1039/a902682g.
(8) Toyooka, T.; Yoda, E.; Yamanashi, T.; Kobori, Y. *Displays* **1999**, *20* (5), 221. doi:10.1016/S0141-9382(99)00026-8.
(9) Wicklein, A.; Lang, A.; Muth, M.; Thelakkat, M. *J. Am. Chem. Soc.* **2009**, *131* (40), 14442. doi:10.1021/ja905260c.
(10) Cardinaels, T.; Ramaekers, J.; Driesen, K.; Nockemann, P.; Van Hecke, K.; Van Meervelt, L.; Goderis, B.; Binnemans, K. *Inorg. Chem.* **2009**, *48* (6), 2490. doi:10.1021/ic801772q.
(11) Driscoll, J. A.; Keyes, P. H.; Heeg, M. J.; Heiney, P. A.; Verani, C. N. *Inorg. Chem.* **2008**, *47* (16), 7225. doi:10.1021/ic8005162.
(12) Chen, L.; Hu, T.-H.; Xie, H.-L.; Zhang, H.-L. *J. Polym. Sci. A Polym. Chem.* **2010**, *48* (13), 2838. doi:10.1002/pola.24060.
(13) Ma, K.; Lee, K.-M.; Minkova, L.; Weiss, R. G. *J. Org. Chem.* **2009**, *74* (5), 2088. doi:10.1021/jo802605k.
(14) Hegmann, T.; Qi, H.; Marx, V. M. *J. Inorg. Organomet. Polym. Mater.* **2007**, *17* (3), 483. doi:10.1007/s10904-007-9140-5.
(15) Hulvat, J. F.; Sofos, M.; Tajima, K.; Stupp, S. I. *J. Am. Chem. Soc.* **2005**, *127* (1), 366. doi:10.1021/ja047210m.
(16) Tschierske, C. *J. Mater. Chem.* **1998**, *8* (7), 1485. doi:10.1039/a800946e.
(17) Coppola, L.; Gianferri, R.; Nicotera, I.; Oliviero, C.; Ranieri, G. A. *Phys. Chem. Chem. Phys.* **2004**, *6* (9), 2364. doi:10.1039/b316621j.
(18) Nesrullajev, A.; Kazancı, N.; Yıldız, T. *Mater. Chem. Phys.* **2003**, *80* (3), 710. doi:10.1016/S0254-0584(03)00079-8.
(19) Tracey, A. S.; Radley, K. *Langmuir* **1990**, *6* (7), 1221. doi:10.1021/la00097a004.
(20) Gin, D. L.; Pecinovsky, C. S.; Bara, J. E.; Kerr, R. L. *Struct. Bond.* **2008**, *128,* 181. doi:10.1007/430_2007_064.
(21) Davis, J. T.; Spada, G. P. *Chem. Soc. Rev.* **2007**, *36* (2), 296. doi:10.1039/b600282j.
(22) Pieraccini, S.; Gottarelli, G.; Mariani, P.; Masiero, S.; Saturni, L.; Spada, G. P. *Chirality* **2001**, *13* (1), 7. doi:10.1002/1520-636X(2001)13:1<7::AID-CHIR3>3.0.CO;2-M.
(23) Giorgi, T.; Grepioni, F.; Manet, I.; Mariani, P.; Masiero, S.; Mezzina, E.; Pieraccini, S.; Saturni, L.; Spada, G. P.; Gottarelli,

G. *Chem. Eur. J.* **2002**, *8* (9), 2143. doi:10.1002/1521-3765(20020503)8:9<2143::AID-CHEM2143>3.0.CO;2-G.
(24) Kuang, G.-C.; Ji, Y.; Jia, X.-R.; Li, Y.; Chen, E.-Q.; Wei, Y. *Chem. Mater.* **2008**, *20* (13), 4173. doi:10.1021/cm8006952.
(25) Li, X.-Q.; Zhang, X.; Ghosh, S.; Würthner, F. *Chem. Eur. J.* **2008**, *14* (27), 8074. doi:10.1002/chem.200800915.
(26) Gallant, A. J.; Hui, J. K.-H.; Zahariev, F. E.; Wang, Y. A.; MacLachlan, M. J. *J. Org. Chem.* **2005**, *70* (20), 7936. doi:10.1021/jo050742g.
(27) Dierking, I. *Textures of Liquid Crystals;* Wiley-VCH: Weinheim, Germany, 2003.
(28) Hui, J. K.-H.; Frischmann, P. D.; Tso, C.-H.; Michal, C. A.; MacLachlan, M. J. *Chem. Eur. J.* **2010**, *16* (8), 2453. doi:10.1002/chem.200902712.
(29) Stackhouse, P. J.; Hird, M. *Liq. Cryst.* **2008**, *35* (5), 597. doi:10.1080/02678290802040026.
(30) Destrade, C.; Mondon, M. C.; Malthete, J. *J. Phys.* **1979**, *40* (C3), 17.
(31) Gallant, A. J.; MacLachlan, M. J. *Angew. Chem. Int. Ed.* **2003**, *42* (43), 5307. doi:10.1002/anie.200352395.
(32) Ishi-i, T.; Hirashima, R.; Tsutsumi, N.; Amemori, S.; Matsuki, S.; Teshima, Y.; Kuwahara, R.; Mataka, S. *J. Org. Chem.* **2010**, *75* (20), 6858. doi:10.1021/jo101212d.
(33) Petitjean, A.; Cuccia, L. A.; Schmutz, M.; Lehn, J.-M. *J. Org. Chem.* **2008**, *73* (7), 2481. doi:10.1021/jo702495u.
(34) Liang, Y.; Jasbi, S. Z.; Haftchenary, S.; Morin, S.; Wilson, D. J. *Biophys. Chem.* **2009**, *144* (1–2), 1. doi:10.1016/j.bpc.2009.05.007.
(35) IR spectra of the thin films were nearly identical and verified the structural integrity of the macrocycle. Notably, the C=N stretching mode observed at 1609 cm^{-1} in the free macrocycle is present at 1618 cm^{-1} in all of the metal and ammonium tetrafluoroborate complexes.
(36) The sample was prepared by first dissolving macrocycles **1b** and **1c** (1:1 ratio) with chloroform in the same vial, and the resulting red solution was left at ambient conditions for 5 min. Excess NH_4BF_4 was then added to the mixture of macrocycles and the dark red solution was allowed to stand for 5 min before removing the excess salts by filtration through a short pad (~5–10 mm) of cellulose.

Can. J. Chem. Downloaded from www.nrcresearchpress.com by MCGILL UNIVERSITY on 02/02/13
For personal use only.

Secrets revealed — Spatially selective wetting of plasma-patterned periodic mesoporous organosilica

Wendong Wang, Ian B. Burgess, Benjamin D. Hatton, Jack Alvarenga, and Joanna Aizenberg

Can. J. Chem. Downloaded from www.nrcresearchpress.com by MCGILL UNIVERSITY on 02/02/13
For personal use only.

Abstract: We report a simple method to pattern wetting properties on thin films of periodic mesoporous organosilica (PMO). A hydrophobic methane PMO thin film was covered by masks and exposed to oxygen plasma to make the unmasked area hydrophilic. The wettability patterns could be revealed only when the films were immersed in water or exposed to moisture. We expect that our method would extend the utility of PMO to such areas as sensing and information security.

Key words: wetting, plasma, mesoporous materials, thin film.

Résumé : On a mis au point une méthode simple de déterminer les propriétés de mouillage de films minces d'organosilice mésoporeux périodique (OMP). Un film mince d'OMP de méthane hydrophobe a été recouvert de masques et exposé à un plasma d'oxygène pour produire des surfaces hydrophiles non masquées. Les patrons de mouillage ne peuvent être mis en évidence que lorsque les films sont immergés dans l'eau ou exposés à de l'humidité. On a bon espoir que cette méthode permettra d'étendre la plage d'utilité des OMP aux domaines de la détection et de la sécurité de l'information.

Mots-clés : capacité de mouillage, plasma, matériaux mésoporeux, film mince.

[Traduit par la Rédaction]

Introduction

Spatially patterned porous materials combine the characteristics of a pattern, such as shape and dimensions, with the characteristics of a porous material, such as high surface area and large pore volume, to deliver functions that promise applications in sensors, catalysis, photonics, displays, microfluidics, and electronics.[1–6] Patterns of ordered mesoporous materials have been produced using self-assembled monolayers (SAMs),[2,7,8] photolithography,[4] micromolding in capillary,[1,6] direct writing,[5] ink-jet printing,[5] and scanning electrochemical microscopy.[9] These patterns are produced either by selectively generating materials in the patterned area or by selectively removing materials from the nonpatterned area. In other words, they are distinguished by the physical presence or absence of materials. Here, we report a method to create patterns of different wettability on thin films of mesoporous organosilica. This method creates patterns of properties, in contrast to patterns of materials. These patterns only reveal themselves when the films are immersed in water or exposed to moisture. We expect our method could lead to applications in sensing and information security and also could provide a convenient platform for fundamental studies in wetting dynamics and nanofluidics.

Experimental

Materials

Bis(triethoxysilyl)methane was purchased from Gelest. Cetyltrimethylammonium chloride (CTACl) 25 wt % solution in water was purchased from Sigma-Aldrich. Reagents were used as received.

Synthesis of methane periodic mesoporous organosilica (PMO) thin films

The synthesis was performed according to a previous report.[10] Briefly, bis(triethoxysilyl)methane was added into a solution of CTACl, HCl, water, and ethanol with moderate stirring. The molar ratio of the reactants was

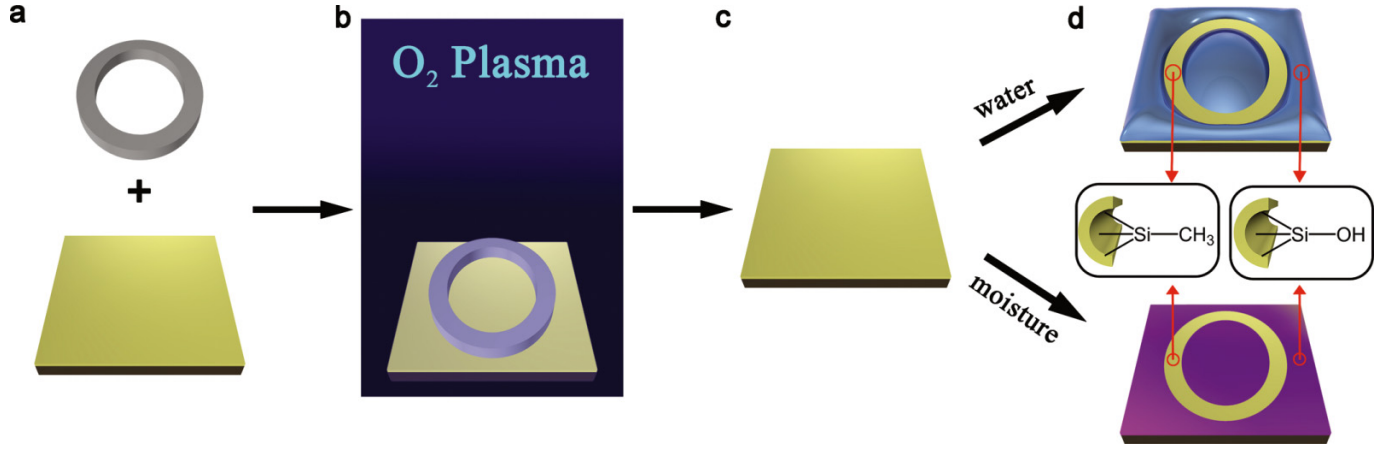
Received 3 June 2012. Accepted 16 September 2012. Published at www.nrcresearchpress.com/cjc on 21 November 2012.

W. Wang, I.B. Burgess, and B.D. Hatton. Wyss Institute for Biologically Inspired Engineering, Harvard University, Cambridge, MA 02138, USA; School of Engineering and Applied Sciences, Harvard University, Cambridge, MA 02138, USA.
J. Alvarenga. Wyss Institute for Biologically Inspired Engineering, Harvard University, Cambridge, MA 02138, USA.
J. Aizenberg. Wyss Institute for Biologically Inspired Engineering, Harvard University, Cambridge, MA 02138, USA; School of Engineering and Applied Sciences, Harvard University, Cambridge, MA 02138, USA; Department of Chemistry and Chemical Biology, Harvard University, Cambridge, MA 02138, USA; Kavli Institute for Bionano Science & Technology, Harvard University, Cambridge, MA 02138, USA.

Corresponding author: Joanna Aizenberg (e-mail: jaiz@seas.harvard.edu).

This article is part of a Special Issue dedicated to Professor Geoffrey Ozin.

Fig. 1. Scheme of the patterning experiments. (*a*) Methane periodic mesoporous organosilica thin film and an O-shaped mask. (*b*) Plasma treatment. (*c*) The resulting patterned thin film after plasma treatment is optically indistinguishable from the original film. (*d*) The pattern revealed by adding water droplets on the film or by exposing the film to water vapor.



Si/CTACl/HCl/H_2O/EtOH = 1:0.15:0.0002:19.1:15. The solution was aged for 70–90 min. These as-deposited thin films were heated at 150 °C for 2 h (ramping 1 °C / min) and then at 500 °C for 2 h (ramping 1 °C / min) under continuous nitrogen flow.

Patterning by plasma treatment

Stencil masks were cut out of 90 μm thick plastic films (PET) using a VersaLaser cutting system. Metallic letters were ordered from Gemini Sign Letters. Stencil masks or metallic letters were placed directly on top of the thin film as masks. Plasma exposure was performed under oxygen atmosphere for 20–40 s on a FEMTO plasma system from Diener Electronics.

Characterizations

Low-angle X-ray diffraction (XRD) was performed on a Scintag XDS2000 diffractometer using Cu Kα radiation operated at 40 kV and 30 mA. Transmission electron microscopy (TEM) was performed on JEOL 2100 TEM with an accelerating voltage of 200 kV. Ellipsometry data were collected on a Woollam spectroscopic ellipsometer over a wavelength range of 500–900 nm. Photos and videos were taken on a Canon EOS Rebel T2i model.

Results and discussion

The material we choose is methane periodic mesoporous organosilica (PMO). PMO, invented in 1999, is a class of mesoporous materials with organosiliceous pore walls that have one organic bridging group covalently bonded to two or more silicon atoms.[11–13] These bridging organic groups impart unique chemical, biological, optical, and dielectric properties to PMO and distinguish PMO from its pure siliceous counterpart.[14,15] We use methane PMO, with a –CH_2– bridge, as an archetype to demonstrate our patterning technique because, at a temperature higher than 400 °C, the transformation of bridging –CH_2– groups into terminal –CH_3 groups hydrophobizes the surface of the pore wall[10,16,17] and exposes the terminal methyl groups for subsequent plasma treatment. Another PMO that can be similarly hydrophobized is three-ring PMO; in contrast, ethane and ethene PMO do not possess this ability.[10]

We chose plasma treatment as the way to generate patterns. Plasma treatment with the aid of a preformed mask was shown to be a fast (on the order of minutes) and clean (liquid-free) method to create patterns of SAMs on a flat surface at length scales from sub-100 nm to centimetres.[18] We have previously extended this technique to three-dimensional (3D) porous siliceous inverse-opal structures by iterating silanization and shadow-masked oxygen plasma to produce spatial patterns of surface chemistry within the pores.[19,20] The slow propagation of plasma oxidation fronts in porous structures enables patterning by masking only the top surfaces of the structures.[18–20] In this report, we use oxygen plasma to convert terminal methyl groups into silanol groups in thermally treated methane PMO. This conversion switches the hydrophobic pore wall to a hydrophilic one, and enables us to create patterns of different wettability in one single material (Fig. 1).

We produced thin films of methane PMO by spin-coating, followed by thermal treatment at 500 °C to remove surfactants and to initiate self-hydrophobization.[10,17] The mesostructure of methane PMO was confirmed by low-angle XRD and TEM (Figs. 2 and 3). The decrease in d spacing (from 4.2 to 3.2 nm) and the increase in diffraction intensity after thermal treatment are due to anisotropic shrinkage in the out-of-plane direction[21] and increased electron density contrast.[22] Both wormlike[23] and two-dimensional (2D) hexagonally ordered porous channels were observed in TEM.

We then patterned thin films in oxygen plasma treatment with preformed masks placed directly on their top surfaces. Masks were made out of metal, plastic, or glass. A flat smooth surface is required to provide a conformal contact with the underlying thin films. The plasma treatment did not alter the visible appearance of methane PMO thin films (Fig. 4). As a specific example, the O-shaped pattern was revealed when a water droplet was placed on the surface of the film or when the film was exposed to water vapor. The refractive index of the thermally treated thin film was 1.26 ± 0.01 at 633 nm (repeated wetting by water could increase the refractive index up to 1.30 ± 0.02 at 633 nm). Vapor condensation inside mesopores was studied previously in the context of the application of PMOs as low-dielectric constant materials in semiconductor microproces-

Can. J. Chem. Downloaded from www.nrcresearchpress.com by MCGILL UNIVERSITY on 02/02/13
For personal use only.

Fig. 2. Low-angle X-ray diffraction (XRD) diffractograms of methane periodic mesoporous organosilica thin films (*a*) before and (*b*) after thermal treatment at 500 °C. The d spacings calculated from the main peaks are 4.2 and 3.2 nm for (*a*) and (*b*), respectively.

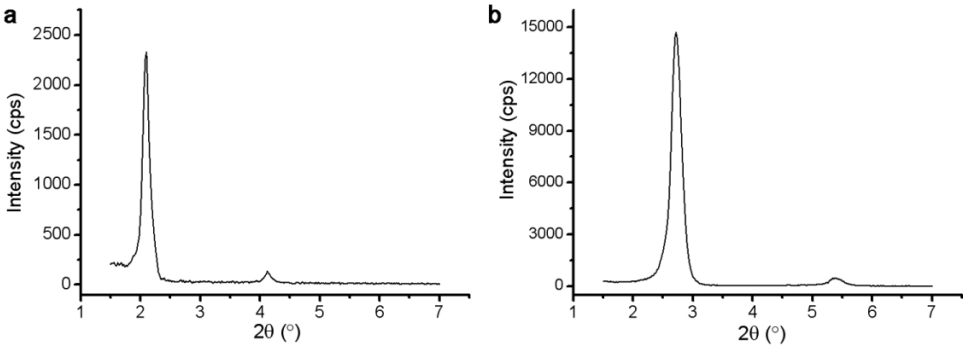
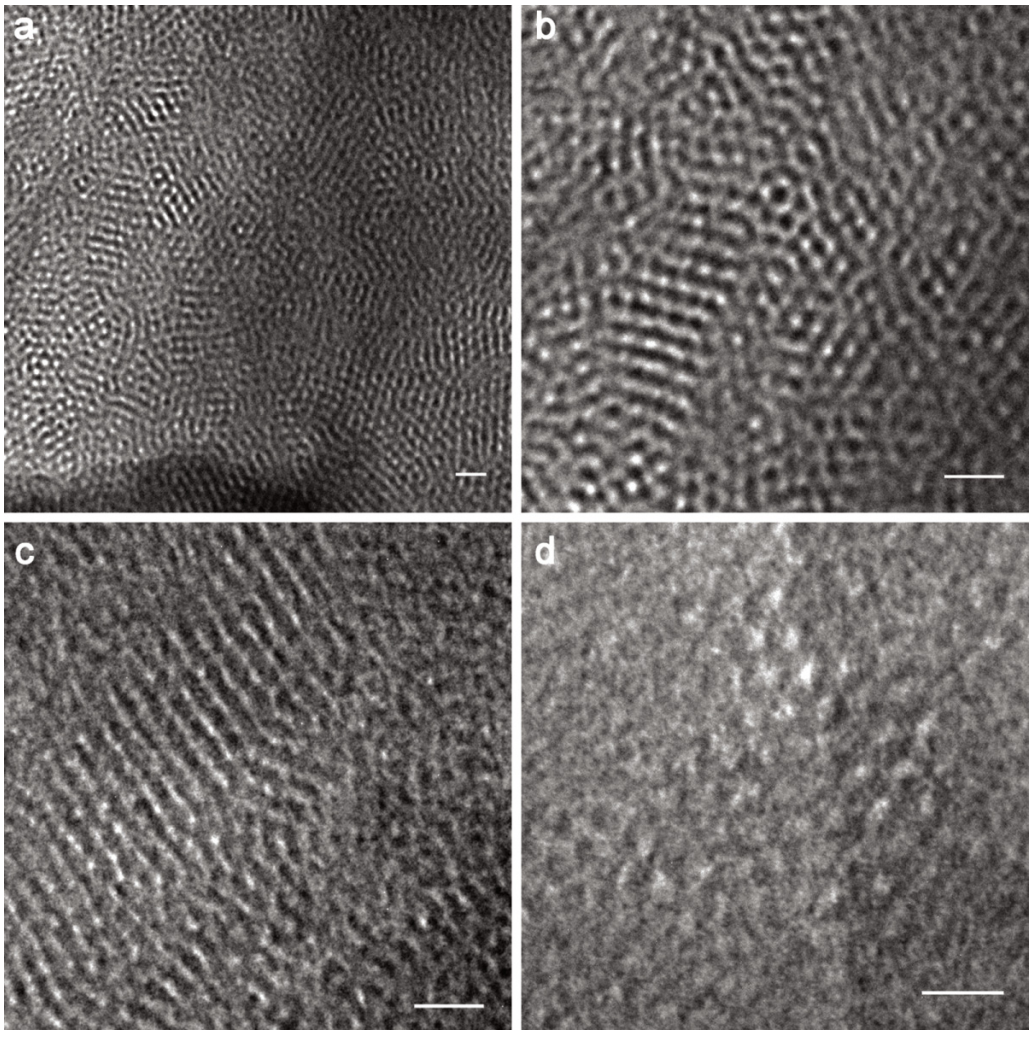


Fig. 3. (*a*)–(*d*) Representative transmission electron microscopy (TEM) images of methane periodic mesoporous organosilica (PMO) after thermal treatment. The scale bar is 10 nm.

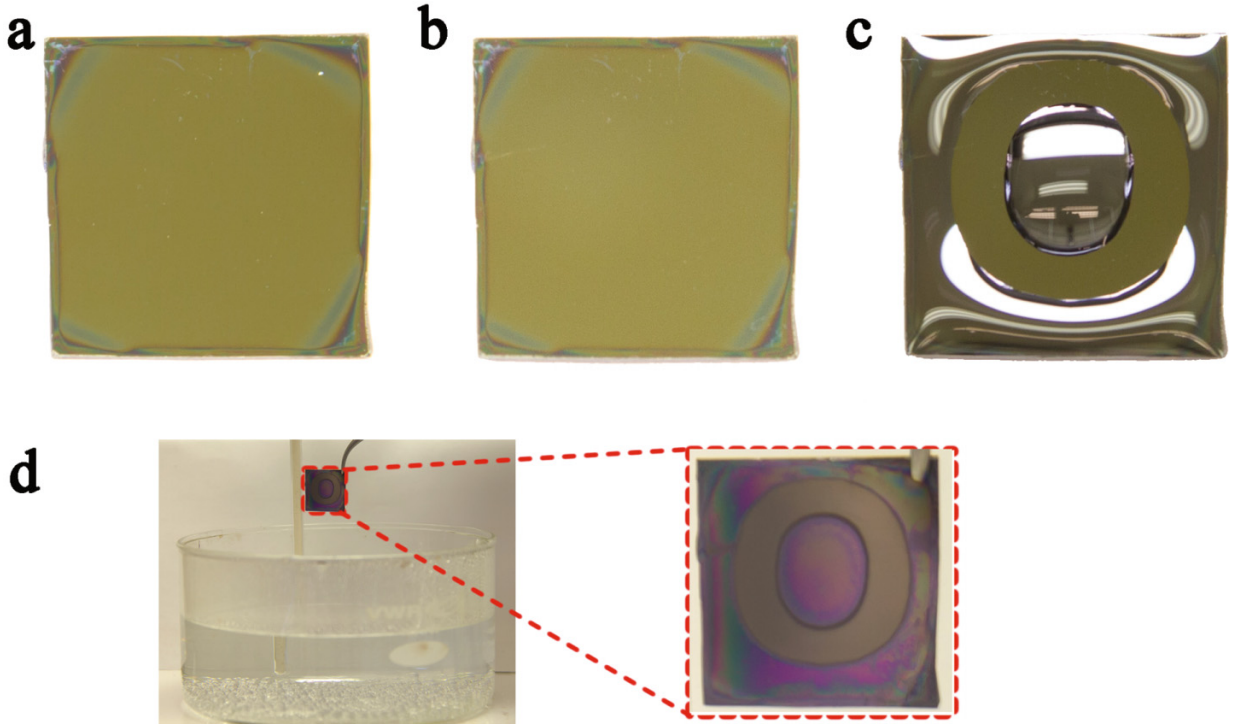


sors.[10] This vapor condensation increased the effective refractive index of the hydrophilic regions of the pores to the range of 1.4–1.5,[10] providing enough contrast in refractive indices to make the pattern visible to the naked eye. The principle behind this vapor-phase response is different from most of the current sensing methods that exploit properties imparted by the physisorbed molecules on the porous surface[23] and could lead to further design of novel vapor sensors.

The versatility of our technique is illustrated in the gallery of wetting patterns (Fig. 5). The top two rows show that

Can. J. Chem. Downloaded from www.nrcresearchpress.com by MCGILL UNIVERSITY on 02/02/13
For personal use only.

Fig. 4. Photos of thin films (*a*) before and (*b*) after the plasma-patterning treatment, and O-shaped pattern revealed (*c*) by wetting the thin film with water or (*d*) by exposing the thin film to the vapor above an 80 °C water bath.



Can. J. Chem. Downloaded from www.nrcresearchpress.com by MCGILL UNIVERSITY on 02/02/13
For personal use only.

successive addition of water gradually diminished the unwetted area and changed the shape of the pattern from a star to a circle as the result of a balance of surface tensions (glass substrates are used for optimum visual effect). The first image on the third row shows that the star-shaped pattern was visible when the whole thin film was covered with water (silicon wafer as the substrate). This visual contrast under water demonstrates that liquid water did not fill the mesopores in the hydrophobic regions. The star-shaped pattern and the letters "GAO" were made from positive masks (metallic letters), whereas the smiley face and the Canadian flag were made from negative masks (plastic sheets with patterned areas removed by laser cutting).

We also observed that an increase in the duration of plasma treatment increased the wettability of a pattern (Supplementary data, movies 1–3). The vertical line and the horizontal line in movies 1–3 (Supplementary data) were exposed to plasma for 20 and 40 s, respectively. Placing a droplet at the area where the two lines cross revealed that water wet the horizontal lines (more hydrophilic) faster than the vertical lines (less hydrophilic) (Supplementary data, movie 1). Excess water was removed by the capillary action from the tip of a glass pipette (inside diameter ~1 mm) (Supplementary data, movie 2). Water added at the end of the lines spontaneously transferred to the center because the curvature of a water droplet at the center was larger than the curvature of a water droplet at the end and, consequently, the Laplace pressure was smaller at the center than that at the end (Supplementary data, movie 3). The transportation of water seems to occur inside the mesoporous thin films rather than along the surface of the thin film because no visible bulge exists along the line of water transportation. We further used these wetting phenomena in an interesting demonstration of hiding and revealing the pattern of a smiley face (Supplementary data, movie 4). Detailed analysis in quantifying the hydrophilicity after plasma treatment and further exploration on liquid transport phenomena are ongoing in our lab.

Conclusion

In conclusion, we have demonstrated that plasma treatment of thermally processed thin films of methane PMO is a fast and clean method to create patterns of wettability. These patterns can only be revealed when exposed to water or moisture. We also demonstrated a few interesting phenomena of wetting dynamics. Our technique may provide a way to study some fundamental aspects of wetting dynamics, such as fluid transport in the presence of a gradient of wettability and the complex geometry of wettability patterns, as well as some applications of this selective wetting phenomenon, such as hiding, revealing, and transforming shapes (and hence information), in sensing and information security.

Supplementary data

Supplementary data are available with the article through the journal Web site (http://nrcresearchpress.com/doi/suppl/10.1139/v2012-092).

Acknowledgements

Ellipsometry measurements and TEM imaging were performed at the Center for Nanoscale Systems (CNS), a member of the National Nanotechnology Infrastructure Network (NNIN), which is supported by the National Science Founda-

Fig. 5. Gallery of wetting patterns.



Can. J. Chem. Downloaded from www.nrcresearchpress.com by MCGILL UNIVERSITY on 02/02/13
For personal use only.

tion (NSF) under award No. ECS-0335765. CNS is part of Harvard University. This work was supported by the Air Force Office of Scientific Research (AFOSR), award No. FA9550-09-1-0669-DOD35CAP. IBB acknowledges support from the Natural Sciences and Engineering Research Council of Canada (NSERC) through the Postgraduate Scholarship - Doctoral (PGS-D) program.

References

(1) Trau, M.; Yao, N.; Kim, E.; Xia, Y.; Whitesides, G. M.; Aksay, I. A. *Nature* **1997**, *390,* 674. doi:10.1038/37764.

(2) Yang, H.; Coombs, N.; Ozin, G. A. *Adv. Mater. (Deerfield Beach Fla.)* **1997**, *9* (10), 811. doi:10.1002/adma.19970091010.

(3) Yang, P.; Deng, T.; Zhao, D.; Feng, P.; Pine, D.; Chmelka, B. F.; Whitesides, G. M.; Stucky, G. D. *Science* **1998**, *282* (5397), 2244. doi:10.1126/science.282.5397.2244.

(4) Doshi, D. A.; Huesing, N. K.; Lu, M.; Fan, H.; Lu, Y.; Simmons-Potter, K.; Potter, B. G., Jr.; Hurd, A. J.; Brinker, C. J. *Science* **2000**, *290* (5489), 107. doi:10.1126/science.290.5489.107.

(5) Fan, H.; Lu, Y.; Stump, A.; Reed, S. T.; Baer, T.; Schunk, R.; Perez-Luna, V.; López, G. P.; Brinker, C. J. *Nature* **2000**, *405* (6782), 56. doi:10.1038/35011026.

(6) Yang, P.; Wirnsberger, G.; Huang, H. C.; Cordero, S. R.; McGehee, M. D.; Scott, B.; Deng, T.; Whitesides, G. M.; Chmelka, B. F.; Buratto, S. K.; Stucky, G. D. *Science* **2000**, *287* (5452), 465. doi:10.1126/science.287.5452.465.

(7) Hozumi, A.; Kojima, S.; Nagano, S.; Seki, T.; Shirahata, N.; Kameyama, T. *Langmuir* **2007**, *23* (6), 3265. doi:10.1021/la061405l.

(8) Costacurta, S.; Falcaro, P.; Malfatti, L.; Marongiu, D.; Marmiroli, B.; Cacho-Nerin, F.; Amenitsch, H.; Kirkby, N.; Innocenzi, P. *Langmuir* **2011**, *27* (7), 3898. doi:10.1021/la103863d.

(9) Guillemin, Y.; Etienne, M.; Sibottier, E.; Walcarius, A. *Chem. Mater.* **2011**, *23* (24), 5313. doi:10.1021/cm202668t.

(10) Wang, W.; Grozea, D.; Kohli, S.; Perovic, D. D.; Ozin, G. A. *ACS Nano* **2011**, *5* (2), 1267. doi:10.1021/nn102929t.

(11) Inagaki, S.; Guan, S.; Fukushima, Y.; Ohsuna, T.; Terasaki, O. *J. Am. Chem. Soc.* **1999**, *121* (41), 9611. doi:10.1021/ja9916658.

(12) Melde, B. J.; Holland, B. T.; Blanford, C. F.; Stein, A. *Chem. Mater.* **1999**, *11* (11), 3302. doi:10.1021/cm9903935.

(13) Asefa, T.; MacLachlan, M. J.; Coombs, N.; Ozin, G. A. *Nature* **1999**, *402,* 867. doi:10.1038/47229.

(14) Hoffmann, F.; Cornelius, M.; Morell, J.; Froba, M. *Angew. Chem. Int. Ed.* **2006**, *45* (20), 3216. doi:10.1002/anie.200503075.

(15) Wang, W.; Lofgreen, J. E.; Ozin, G. A. *Small* **2010**, *6* (23), 2634. doi:10.1002/smll.201000617.
(16) Asefa, T.; MacLachlan, M. J.; Grondey, H.; Coombs, N.; Ozin, G. A. *Angew. Chem. Int. Ed.* **2000**, *39* (10), 1808. doi:10.1002/(SICI)1521-3773(20000515)39:10<1808::AID-ANIE1808>3.0.CO;2-G.
(17) Hatton, B. D.; Landskron, K.; Whitnall, W.; Perovic, D. D.; Ozin, G. A. *Adv. Funct. Mater.* **2005**, *15* (5), 823. doi:10.1002/adfm.200400221.
(18) Lin, M.-H.; Chen, C.-F.; Shiu, H.-W.; Chen, C.-H.; Gwo, S. *J. Am. Chem. Soc.* **2009**, *131* (31), 10984. doi:10.1021/ja901619h.
(19) Burgess, I. B.; Mishchenko, L.; Hatton, B. D.; Kolle, M.; Lončar, M.; Aizenberg, J. *J. Am. Chem. Soc.* **2011**, *133* (32), 12430. doi:10.1021/ja2053013.
(20) Burgess, I. B.; Koay, N.; Raymond, K. P.; Kolle, M.; Lončar, M.; Aizenberg, J. *ACS Nano* **2012**, *6* (2), 1427. doi:10.1021/nn204220c.
(21) Wang, W. D.; Grozea, D.; Kim, A.; Perovic, D. D.; Ozin, G. A. *Adv. Mater. (Deerfield Beach Fla.)* **2010**, *22* (1), 99. doi:10.1002/adma.200901498.
(22) Gibaud, A.; Dourdain, S.; Vignaud, G. *Appl. Surf. Sci.* **2006**, *253* (1), 3. doi:10.1016/j.apsusc.2006.05.121.
(23) Sanchez, C.; Boissière, C.; Grosso, D.; Laberty, C.; Nicole, L. *Chem. Mater.* **2008**, *20* (3), 682. doi:10.1021/cm702100t.

Can. J. Chem. Downloaded from www.nrcresearchpress.com by MCGILL UNIVERSITY on 02/02/13
For personal use only.

Nanomorphology tuning of the thermal response of TiO_2/SiO_2 Bragg stacks

Ida Pavlichenko, Armin T. Exner, Gennady Logvenov, Giuseppe Scarpa, Paolo Lugli, and Bettina V. Lotsch

Can. J. Chem. Downloaded from www.nrcresearchpress.com by MCGILL UNIVERSITY on 02/02/13
For personal use only.

Abstract: Herein, we present a comparative study of thermo- and environmentally responsive TiO_2/SiO_2 one-dimensional photonic crystals (Bragg stacks) fabricated by different deposition methods and fabrication schemes, featuring various multilayer nanomorphologies. These include dense multilayer systems processed by physical vapor deposition and wet-chemistry protocols, as well as porous systems, namely, nanoparticle-based optical filters exhibiting textural porosity, and evaporation-induced self-assembled mesoporous Bragg stacks exhibiting predominantly structural porosity, as well as hybrid structures comprising both dense and porous layers. We investigate the spectral shift of the photonic stop band for the different Bragg stack nanomorphologies induced by the humidity-enhanced thermo-optic effect in a temperature range from 15 to 60 °C. We also demonstrate the response and recovery kinetics of the multilayer systems during external changes in ambient humidity. Notably, the choice of fabrication method plays a significant role in the thermal and humidity response of the system. Taking advantage of different material nanomorphologies we can tune the thermal shift of the photonic stop band in the range 0.2–32.9 nm for the Bragg stacks at ambient relative humidity. In addition, we can design dense multilayer systems nonresponsive to humidity and achieve time responses of the porous systems to external changes in humidity ranging from about 1 to 3 s.

Key words: thermoresponsive photonic crystal, Bragg stack, thermo-optic effect, humidity.

Résumé : Dans ce travail, on rapporte les résultats d'une étude comparative de cristaux photoniques monodimensionnels (empilements de Bragg) de TiO_2/SiO_2 à réponses thermiques et environnementales préparés par diverses méthodes de déposition et de schémas de fabrications caractérisées par diverses nanomorphologies multicouches. Celles-ci incluent des systèmes multicouches denses obtenus par des dépôts de vapeurs physiques et des protocoles de chimiques humides ainsi que des systèmes poreux, particulièrement, des filtres optiques à base de nanoparticules présentant une texture poreuse des empilements de Bragg mésoporeux auto-assemblés par évaporation induite comportant principalement une structure poreuse ainsi que des structures hybrides comportant des couches denses et d'autres poreuses. On a étudié le déplacement spectral du filtre coupe bande photonique des nanomorphologies des différents empilements de Bragg induit par l'effet thermo-optique rehaussé par l'humidité sur la plage de température allant de 15 à 60 °C. On a déterminé les cinétiques de réponse et de récupération des systèmes multicouches lors de changements externes dans l'humidité ambiante. On a particulièrement noté que la méthode de choix pour la fabrication joue un rôle significatif dans la réponse du système à la chaleur et à l'humidité. Tirant avantage des nanomorphologies des divers matériaux, il est possible d'ajuster le déplacement thermique du filtre coupe bande photonique pour la plage allant de 0,2 à 32,9 nm des empilements de Bragg dans l'humidité relative ambiante. De plus, il est possible de développer des systèmes multicouches qui ne réagissent pas à l'humidité et qui peuvent atteindre des temps de réponse allant de 1 à 3 s pour des systèmes poreux soumis à un changement d'humidité.

Mots-clés : cristal photonique à réponse thermique, empilement de Bragg, effet thermo-optique, humidité.

[Traduit par la Rédaction]

Received 17 June 2012. Accepted 13 August 2012. Published at www.nrcresearchpress.com/cjc on 21 November 2012.

I. Pavlichenko* and B.V. Lotsch. Max Planck Institute for Solid State Research, Heisenbergstrasse 1, D-70569 Stuttgart, Germany; Department of Chemistry, Ludwig Maximilian University of Munich, Butenandtstrasse 5-13 (D), D-81377 Munich, Germany.
A.T. Exner*, G. Scarpa, and P. Lugli. Institute for Nanoelectronics, Technical University of Munich, Arcisstrasse 21, D-80333 Munich, Germany.
G. Logvenov. Max Planck Institute for Solid State Research, Heisenbergstrasse 1, D-70569 Stuttgart, Germany.

Corresponding author: Bettina V. Lotsch (e-mail: b.lotsch@fkf.mpg.de).

*I. Pavlichenko and A. T. Exner contributed equally to this work.
This article is part of a Special Issue dedicated to Professor Geoffrey Ozin.
The manuscript was written through contributions of all authors. All authors have given approval to the final version of the manuscript.

Can. J. Chem. Downloaded from www.nrcresearchpress.com by MCGILL UNIVERSITY on 02/02/13
For personal use only.

Introduction

The development of periodic dielectric nanostructures, i.e., photonic crystals (PCs), with tailored optical and built-in chemical properties has recently been brought to fruition by the materials science and photonics communities.[1,2] The photonic stop band, a characteristic region of high reflectivity in the optical spectrum manifesting itself in "structural color", provides ample possibilities for the design of tunable optical systems.[3] A variety of stop-band tuning mechanisms along with promising synthetic routes towards the fabrication of stimuli-responsive PCs have been reported.[4] Widespread interest in the production of tunable photonic nanostructures is due to potential applications in fields as diverse as sensor design,[5] micro-optics,[6] optofluidics,[7] medical diagnostics,[8] color displays,[9] food and water quality control,[10] and many others. One of the proposed photonic stop-band tuning scenarios employs materials featuring responsiveness to an external *temperature* change, such as hydrogels,[11,12] microgels,[13] polyglycidol – polystyrene core – shell particles,[14] magnetic fluids,[15] liquid-crystal elastomers,[16] or $BaTiO_3$[17] through the thermo-optic effect (TOE).[18] The principle of thermo-optic spectral tuning is based on the thermo-optic coefficient (TOC), namely, the dependence of the refractive index (n) on temperature (T) and, hence, dn/dT, owing to both changes of the dielectric function and thermal expansion/contraction. Thermo-optic photonic stop-band tuning has already been successfully demonstrated in microring resonators,[19] thermo-optic switches,[18] and wavelength-division multiplexing.[20,21] Substantial interest has arisen from the thermo-optic tuning realized with one-dimensional systems, i.e., periodic multilayer structures with a modulation of the dielectric constant in one direction, such as thermally tunable multilayer optical filters,[22] and monolithic microcavities[23] deposited by complex physical vapor deposition (PVD) methods. Interestingly, owing to the recent progress in synthetic chemistry, sputtered and evaporated PCs may be complemented by lower cost and easier to fabricate analogues (sol–gel processed one-dimensional PCs, also called Bragg stacks (BSs)) without a significant loss in the optical quality.[24,25] Although one of the main problems in the fabrication of sol–gel coatings in general and of multilayers in particular is the stress induced during heat treatment of the layers leading to defects and cracks in the films, an ample amount of recent publications successfully dealt with the optimization of the fabrication routes to achieve better optical and mechanical quality films and BSs.[26] In contrast to the PVD-deposited PCs, synthetic BSs offer a plethora of modification possibilities towards enhancing or modifying their environmental response, for example, by varying the nanomorphology (denoted further as "morphology") of the individual layers, i.e., the texture, porosity, curvature, size, and shape of the particles or monoliths constituting the layers.[27,28] While the influence of the BSs' morphology on the stop-band tuning of wet-chemistry synthesized TiO_2/SiO_2 BSs induced by chemical stimuli has already been examined,[29–33] a comprehensive study of the interrelation between morphology and shift in *thermoresponsive* sol–gel processed BSs has not yet been performed.

Recently, we demonstrated the thermal tunability of nanoparticle-based TiO_2/SiO_2 BSs fabricated by a spin-coating method.[34] It was shown that the shift of the stop band due to the thermo-optic effect in the constituent materials in such systems is amplified in the presence of ambient humidity: The observed enhancement of the shift is due to adsorption of water molecules into the interparticle voids in the layers, causing an increase in the effective refractive index (RI) of the layers. Therefore, one can introduce an *effective* thermo-optic effect including both thermal and humidity influences on the effective RI. Furthermore, we simulated the influence of the layer thickness, refractive index, and thermo-optic coefficient on the thermal response of various BS architectures to work out design criteria for optimizing the thermal tuning performance of the BSs.[35]

The general goal of our present study is to rationally design photonic crystals that are tunable by both the inherent thermo-optic effect of the constitutent materials and by concurrent temperature-dependent adsorption of humidity into the multilayer system. As the latter is highly sensitive to the porosity of the layers, this aspect of the layer morphology will be central to our experimental focus. In this manuscript, we demonstrate the influence of the morphology of the constituent layers on the thermal tuning properties of various one-dimensional TiO_2/SiO_2 BSs. We show that the layer morphology is one of the key factors to be taken into account when designing tailor-made thermally tunable BSs. Towards this end, the BSs were fabricated by different sol–gel synthesis schemes, ranging from nonporous wet-chemistry-processed nanostructures to porous systems, that is, nanoparticle-based optical filters exhibiting textural porosity, and evaporation-induced self-assembled mesoporous Bragg stacks exhibiting predominantly structural porosity, as well as hybrid structures comprising both dense and porous layers. The thermo-optic response of these systems is interpreted and rationalized by comparison with the thermal response of a nonporous, PVD-derived optical filter. We also present a comparative study of the response and recovery times of the proposed structures and demonstrate that the fabrication method can serve as a design criterion for producing tailor-made photonic crystals with desired thermal response under ambient conditions.

Experimental

Materials

Tetraethyl orthotitanate (TEOT, 99%) and tetraethyl orthosilicate (TEOS, 99%) were purchased from Merck (Darmstadt, Germany); ethanol (99%), *n*-butanol (99%), colloidal silica LUDOX SM-30 (30 wt % in H_2O), and Pluronic F127 and P123 were purchased from Sigma-Aldrich (Dorset, UK); HNO_3 (0.1 mol/L) was purchased from Acros Organics (Geel, Belgium); and HCl (0.1 mol/L, 2 mol/L, 37%) was obtained from Biesterfeld (Hamburg, Germany).

Titania nanoparticle (NP) suspension was prepared as described elsewhere.[34] Particle size distribution of the precursor TiO_2 and SiO_2 suspensions was analyzed using dynamic light-scattering photocorrelation spectroscopy (Malvern Nano ZS Zetasizer) at 20 °C. Silica sol for TiO_2-NP/SiO_2-sol and TiO_2-sol/SiO_2-sol BSs was prepared by mixing TEOS, ethanol, and HCl in a ratio of 1:10:1 and 2:10:2, respectively, and subsequent ageing for 12 h. Titania sol (0.1 mol/L) for TiO_2-sol/SiO_2-sol BSs was prepared by mixing TEOT (0.228 g) in ethanol (10 mL) with subsequent ageing until the desired optical quality of spin-coated thin films was reached. To synthesize the mesoporous silica sol (meso-SiO_2), TEOS

Can. J. Chem. Downloaded from www.nrcresearchpress.com by MCGILL UNIVERSITY on 02/02/13
For personal use only.

(3.12 g) was diluted in ethanol (19 mL) with the subsequent addition of surfactant Pluronic F127 (1.5 g), HCl (0.15 g, 2 mol/L), and H_2O (1.35 mL). The mixture was stirred for 5 min until it became translucent and was subsequently aged for 1 h. To prepare the mesoporous titania sol (meso-TiO_2), TEOT (2.1 g) was diluted in *n*-butanol (7.4 mL) with Pluronic P123 (0.65 g) and HCl (1.35 mL, 37%). The solution was stirred vigorously for 5 min and afterwards aged for at least 1 h. All suspensions were filtered prior to use (Acrodisc, GHP, 13 mm, 0.2 μm). The anatase modification of the TiO_2 powder calcined at 350 °C for 1 h was confirmed by X-ray diffraction (Bruker D8 Discover).

Bragg stack fabrication

Evaporated dense TiO_2/SiO_2 BSs

The dense TiO_{2-x}/SiO_{2-x} multilayers were deposited in a Pfeiffer Vacuum Classic 500 evaporation system in vacuum ($<2 \times 10^{-6}$ mbar; 1 bar = 100 kPa) onto soda-lime glass substrates at room temperature starting from the TiO_{2-x} layer. The TiO_{2-x} layers were evaporated by using an electron gun. The SiO_{2-x} layers were evaporated by using resistive heating of SiO_2 contained in a molybdenum boat. The deposition rate for both materials was approximately 0.2 nm s^{-1}, which was monitored, as well as the layer thicknesses, in situ by a quartz crystal microbalance (QCM). The alternation of the layers was achieved by shuttering the flux of the corresponding layer. The oxygen content in the multilayers was reduced because of deposition in vacuum; therefore, further annealing in an oxygen atmosphere for 1 h at 450 °C was performed to recover the stoichiometry and optical properties of the multilayers.

TiO_2/SiO_2 BSs based on sol–gel fabrication methods

We obtained TiO_2-sol/SiO_2-sol BSs by sequential spin-coating of silica sol (3000 rpm, 1500 rpm s^{-1}) and titania sol without calcination. For the titania sol (0.1 mol/L), we performed triple spin-coating (4000 rpm, 2000 rpm s^{-1}) until the necessary film thickness was achieved. Nanoparticle-based (NP-based) BSs were prepared by spin-coating as described elsewhere.[34] TiO_2-NP/SiO_2-sol BSs were prepared by sequential spin-coating of a titania NP suspension (3000 rpm, 1500 rpm s^{-1}) and silica sol (3000 rpm, 1500 rpm s^{-1}) with subsequent calcination of the films at 200 °C for 15 min. Similarly, TiO_2-sol/meso-SiO_2 BSs were fabricated by spin-coating mesoporous silica (2500 rpm, 2000 rpm s^{-1}) and titania sol (0.05 mol/L, 3000 rpm, 2000 rpm s^{-1}). Mesoporosity was generally achieved by taking advantage of the evaporation-induced self-assembly (EISA) method and through subsequently removing the surfactant via calcination of the films at 400 °C for 15 min. Meso-TiO_2 /meso-SiO_2 were obtained by spin-coating mesoporous titania (5000 rpm, 2000 rpm s^{-1}) and mesoporous silica (5000 rpm, 2000 rpm s^{-1}). The single thin film thickness and refractive index were characterized by spectroscopic ellipsometry, performed on a Woollam M200D variable angle ellipsometer in the entire spectral range of 190–1000 nm at angles of incidence of 65°, 70°, and 75°. To calculate the porosity of the layers the Lorentz–Lorenz equation was used, for which the RIs of the single films were measured first with void pores and then with the pores filled with toluene. Scanning electron microscopy (SEM, JEOL JSM-6500F operating at an accelerating voltage of 2–5 kV) was used to examine the morphology of the BSs' cross sections and flat surfaces.

Thermo-optic and humidity response characterization

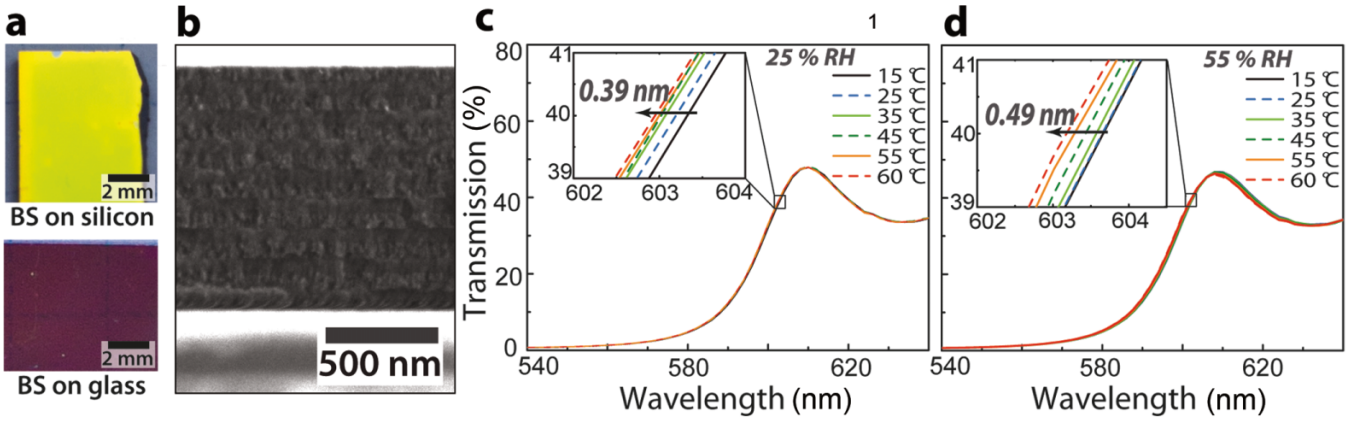
To obtain transmission spectra of the BSs in the range of 400–800 nm we used a monochromator (Cornerstone260 1/4 m) with a high-pressure arc lamp as a light source and a 10×10 mm^2 calibrated silicon detector connected to a digital lock-in amplifier (Merlin).[34] The temperature of the BS was varied by two Peltier elements and the PT100 temperature sensor was attached to the other side of the BS above the optical axis. Peltier elements and the temperature sensor were connected to a remote-controlled source meter (Keithley). The heating and cooling of the Peltier elements were regulated by a proportional integral derivative (PID) controller. The measured deviation of the temperature during the measurement was less than 0.1 °C. For each temperature the sample was equilibrated for 60 s. The measurements in N_2 atmosphere (to mimic 0% relative humidity) were performed in a cryostat with two windows, in which the samples of interest were kept for 24 h prior to the measurements.

For the response and recovery time characterization we changed the relative humidity (RH) of the environment (20%) by introducing water vapor onto the sample surface. The tubing with the nitrogen stream carrying the water vapor was mounted above the surface of the BS. The measured RH of the vapor was 65%. Additionally, the valve located on the tubing allowed the instant turning off of the vapor stream. In a typical experiment, the BS was fixed under an optical microscope such that the measurement spot could be constantly monitored. Time-dependent spectroscopy was performed with a fiber optic spectrometer (Ocean Optics USB2000+) integrated with an optical light microscope (Leica DM2500 M).

Results and discussion

Photonic multilayer systems fabricated by PVD feature inherently dense oxide layers (Fig. 1) and can therefore be taken as a nonporous reference system for our comparative study of the thermo-optic tuning behavior. Evaporated TiO_2/SiO_2 multilayers have been extensively examined as all-dielectric optical filters for passive optical elements[36,37] and therefore represent an excellent "classical" platform for the comparison with BSs obtained by wet-chemistry methods. Photographs of the evaporated BS samples, deposited under the same conditions, are shown in Fig. 1*a*: The top image presents a BS on a Si wafer, captured at an angle of ≈45° with respect to the normal to the BS's surface, and the bottom image shows a BS on a glass substrate, captured normal to the BS's surface. As can be seen in Fig. 1*a*, such BSs are almost defectless, however, their optical properties, including RI and absorption properties, are highly dependent on the deposition method and annealing conditions.[38] The cross-sectional SEM image in Fig. 1*b* depicts a BS composed of 8.5 bilayers (BLs) of 60 nm TiO_2 ($n \approx 2.41$) and 90 nm SiO_2 ($n \approx 1.55$). The maximum transmission of the BS annealed in air at 450 °C for 1 h to annihilate oxygen vacancies is around 50%. It is known that films deposited by PVD show a columnar microstructure with intercolumnar voids leading to inhomogeneities and roughness.[36,39] Nevertheless, the high RIs obtained for electron beam (e-beam) evaporated TiO_2 and thermally evaporated SiO_2 by spectroscopic ellipsometry are testament to their overall low porosity. Note, however, that the RI of SiO_2 may likewise be rationalized by the presence of residual substoichiometric oxide species (SiO_{2-x}) in the film. The impact of

Fig. 1. (*a*) Photographs of the electron beam (e-beam) evaporated TiO_2 (60 nm) and thermally evaporated SiO_2 (90 nm) 8.5 bilayer (BL) Bragg stack (BS) (starting from the first TiO_2 layer) deposited on a Si wafer (top image: captured at an angle) and on a glass substrate (bottom image: captured normal to the BS surface). The scale bar is 2 mm. (*b*) The cross-sectional SEM image of the evaporated BS from 1*a* (bottom). The scale bar is 500 nm. (*c*) Transmission spectra of the BS shown in 1*a* (bottom) featuring a blue shift of the stop band of ≈0.39 nm in a temperature range of 15 to 60 °C at 25% relative humidity (RH). (*d*) Transmission spectra of the same BS as in 1*c* demonstrating a slightly larger blue shift of the stop band (≈0.49 nm) in a temperature range of 15 to 60 °C at 55% RH.



textural porosity on the thermo-optic response of the BS can be derived from the dependence of the optical shift on the environmental humidity as seen in Figs. 1*c* and 1*d*. Clearly, the magnitude of the thermal shift at 55% RH (0.49 nm) is higher than at 25% RH (0.39 nm) upon an increase in temperature from 15 to 60 °C, which can be rationalized by the effective TOC enhanced by the penetration of ambient humidity into the textural pores of the BS.

To put the humidity-enhanced thermo-optic response of the PVD-derived BS into perspective, we compare it with the response of solution-processed, spin-coated BSs with the same average layer thicknesses (the thickness of spin-coated BSs can deviate about 10%–20% on average) and number of bilayers (8.5), but composed of TiO_2 and SiO_2 NP layers. An intrinsic property of the NP-based BSs is textural porosity (porosity arising from interparticle voids in the film). With the measured NP size distributions (6–10 nm for SiO_2 and 8–20 nm for TiO_2 NPs) one can obtain films with 10% and 25% porosity for SiO_2 and TiO_2, respectively.[34] First, we investigated the thermo-optic response of the PVD-derived and porous NP-based BSs decoupled from the influence of ambient humidity. Consequently, in this experiment one can derive the shift of the stop band caused solely by the impact of the TOE. Figures 2*a* and 2*b* highlight the thermo-optic response of the samples kept in a nitrogen atmosphere for 24 h prior to the experiment. Clearly, the evaporated BS shows a small shift of 0.2 nm upon heating from 15 to 60 °C, whereas the NP-based BS shows a fairly linear thermo-optic response of 1.0 nm, which is in agreement with the theoretical value of the thermo-optic shift in this temperature range based on the TOCs reported for titania and silica, respectively.[34] We assume that the smaller shift observed for the evaporated BS is due to the TOCs of the layer materials being slightly different from the literature values for TiO_2[40] (1.77×10^{-4} K^{-1}) and SiO_2[41] (1×10^{-5} K^{-1}) owing to the presence of substoichiometric oxide species (TiO_{2-x} and SiO_{2-x}) in the multilayer.

To demonstrate the humidity-enhanced thermal tunability of the NP-based BS, we performed similar measurements in ambient humidity (25% RH). One can discern a humidity-amplified blue shift of 4.4 nm owing to the effective TOE, which is about four times larger than in N_2 atmosphere (Fig. 2*c*). This observation suggests a significant difference in the porosity of the solution-processed and thermally evaporated BSs. Specifically, the higher textural porosity of the NP-based BS renders it more accessible to water, thus leading to a more pronounced humidity enhancement of the thermal shift.

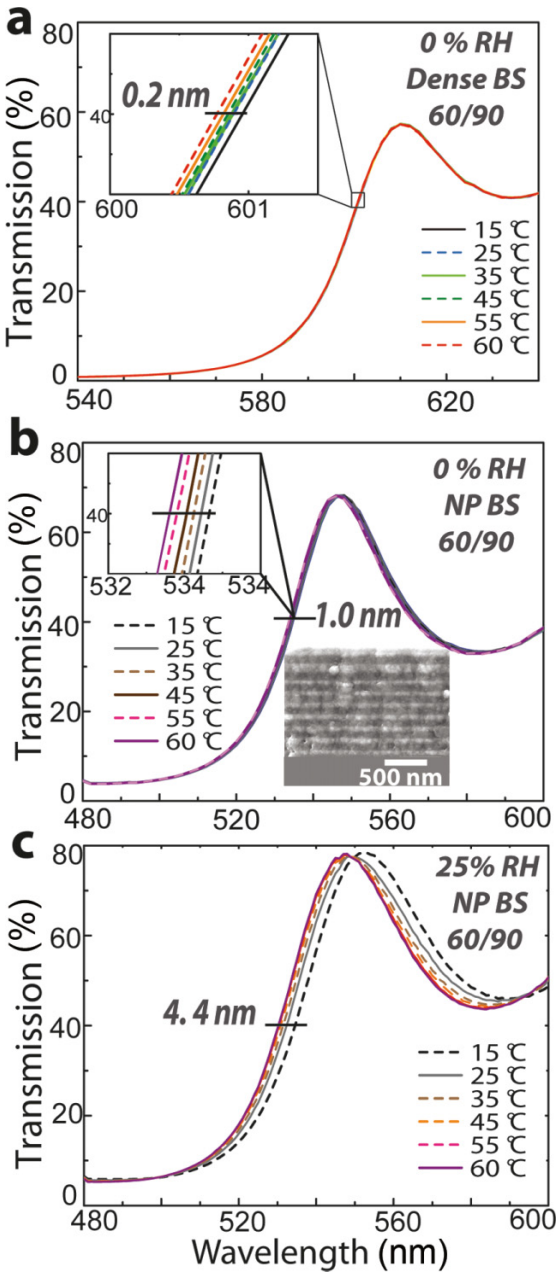
Having discussed two model systems with different porosities and, hence, thermal response behavior, it is instructive to explore alternative, yet solution-based routes to low-porosity BS architectures that can "mimic" the low-response thermo-optic behavior of evaporated BSs. In Figs. 3*a*, 3*d*, and 3*g*, we demonstrate the tuning properties of a BS fabricated by alternate spin-coating of titania and silica sols. As can be inferred from the SEM image (Fig. 3*a*), the 4 BL TiO_2-sol/SiO_2-sol BS apparently has a rather dense morphology. Low porosity of the layers is also confirmed by the thermal tuning behavior presented in Fig. 3*d* at ambient humidity. Notably, the shift of the stop band is only 0.8 nm upon heating from 15 to 60 °C. Evidently, the magnitude of the effective thermal shift of the TiO_2-sol/SiO_2-sol BS is only slightly larger than the one of the PVD-derived BS at 25% RH (0.39 nm, Fig. 1*c*). The low RI and at the same time the low response to temperature changes may be in part due to organic residues within the sol–gel based structure rendering the BS more hydrophobic, as no calcination was done after film deposition (see the Experimental section).

In contrast, a much higher thermal response is observed for hybrid systems in which one of the layers is kept dense, while the other possesses textural or structural porosity, as is the case for NP-based and mesoporous layers, respectively (Figs. 3*b* and 3*c*, respectively). As can be seen from Figs. 3*e* and 3*f*, both systems exhibit a significant response to heating under ambient conditions. The blue shift of a TiO_2-NP/SiO_2-sol is 8.9 nm for the blue and 20.0 nm for the red edge of the stop band, and the responses of TiO_2-sol/meso-SiO_2 BSs are 32.0 and

Can. J. Chem. Downloaded from www.nrcresearchpress.com by MCGILL UNIVERSITY on 02/02/13
For personal use only.

Can. J. Chem. Downloaded from www.nrcresearchpress.com by MCGILL UNIVERSITY on 02/02/13
For personal use only.

Fig. 2. (*a*) Transmission spectra of the evaporated Bragg stack (BS) shown in Fig. 1*a* (bottom) demonstrating a small blue shift of the stop band of ≈0.2 nm upon heating from 15 to 60 °C in N_2 atmosphere. (*b*) Transmission spectra of the nanoparticle (NP)-based TiO_2/SiO_2 8.5 bilayer (BL) BS featuring a blue shift of the stop band of ≈1.0 nm upon heating from 15 to 60 °C in N_2 atmosphere. The inset shows the cross-sectional SEM image of the corresponding BS. The scale bar is 500 nm. (*c*) Transmission spectra of the BS from Fig. 2*b* recorded under ambient conditions (25% RH) in the *T* range of 15 to 60 °C. (From Pavlichenko et al.[34] 2012, reproduced with permission of J. Phys. Chem. C, Vol. 116, pp 298–305, © 2012 American Chemical Society. RH, relative humidity.

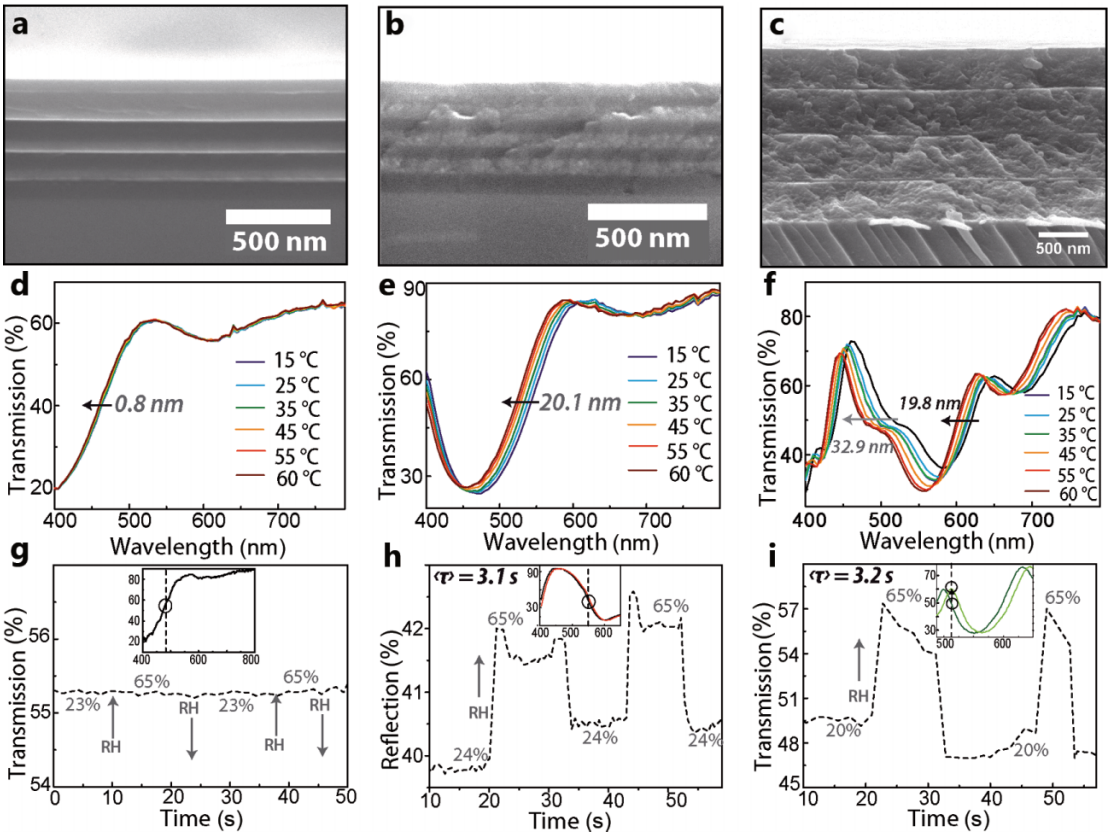


19.8 nm for the blue and red edges of the stop band, respectively. The shifting behavior of both systems is in good agreement with previous predictions relating the relative changes of the blue and red edges of the stop band to the RI changes taking place primarily in one type of layer in the bilayer system:[27,35] (*i*) The larger magnitude of the shift for the red edge of the stop band in the TiO_2-NP/SiO_2-sol system suggests that the high RI material TiO_2 undergoes the dominant RI changes; hence, we conclude that the water mainly adsorbs in the porous TiO_2–NP layers rather than in the dense SiO_2-sol ones. (*ii*) The transmission of the stop band is higher at higher *T*, indicative of a gradual lowering of the RI contrast of the layers with increasing *T*, suggesting that upon heating water desorbs mainly from the TiO_2 layers, thus reducing their RI and, hence, the overall RI contrast. These phenomena illustrate the predominant influence of TiO_2 on the thermal response. On the contrary, the change of the stop band for the TiO_2-sol/meso-SiO_2 BS is larger at the red edge and the transmission is lower at higher temperatures, highlighting the dominant influence of porous SiO_2 rather than dense TiO_2, as water seems to condense primarily into the silica layers.

Next, we compared the tuning properties of the porous hybrid systems with their nonhybrid analogues, in which both layers are comprised of either NPs or mesoporous materials, namely, with the TiO_2-NP/SiO_2-NP BS (Fig. 2*c*) and a meso-TiO_2/meso-SiO_2 3 BL BS (Fig. 4*a*). The thermal shift (20.1 nm for the red edge of the stop band) of the hybrid TiO_2-NP/SiO_2-sol BS in the *T* range between 15 and 60 °C at 30% RH is larger than for the nonhybrid TiO_2-NP/SiO_2-NP system (4.4 nm at 25% RH and 16.4 nm at 45% RH). The higher response of the hybrid system compared with the TiO_2-NP/SiO_2-NP stack may be due to more restricted moisture diffusion into the latter owing to the larger number of BLs, rendering the multilayer system more compact and less accessible to moisture. Along similar lines, for the TiO_2-sol/meso-SiO_2 BS the thermal shifts between 15 and 60 °C (32.0 and 19.8 nm for the blue and red edges, respectively) are larger than the 20.9 nm (blue edge) and 13.1 nm (red edge) shifts for the meso-TiO_2/meso-SiO_2 BS shown in Fig. 4*b*. The observed behavior may be rationalized by the differences in layer thicknesses and hence the relative impact of the more porous layers on the adsorption behavior: higher porosity films of SiO_2 were obtained with the triblock copolymer F127 used as a template (Fig. 5*a*), resulting in nanometer-sized channels (~10 nm) organized into two-dimensional (2D) hexagonal domains parallel to the substrate, as also observed previously.[42] In contrast, P123-templated TiO_2 (Fig. 5*b*) forms pores with an average size of 5 nm,[43] which is about half the size of the SiO_2 pores. Therefore, the larger porosity of SiO_2 together with the larger layer thickness of the SiO_2 layers in the sol–meso BS compared to the meso–meso BS is the most likely rationale for the larger thermal response observed for the sol–meso BS. Other factors may be fluctuations in ambient humidity, the mutual influence of adjacent layers (of higher and lower porosity) and their pore sizes and texture on the confinement and transport of moisture within the multilayer,[26,28] as well as other phenomena such as pore blocking at the interfaces and capillary and surface wettability effects that are naturally augmented in complex nanomorphologies.

To analyze the kinetics of the environmental response (i.e., separated from the pure thermo-optic response) and the possible impact of the layer morphology on the response time, we investigated the behavior of the multilayer systems with respect to changes in ambient humidity, while keeping the temperature constant. Time-resolved measurements were car-

Fig. 3. Cross-sectional SEM images of (*a*) TiO_2-sol (55 nm, RI = 1.92)/SiO_2-sol (90 nm, RI = 1.46) 4 BL BS, (*b*) hybrid TiO_2-NP (60 nm, RI = 1.90)/SiO_2-sol (80 nm, 1.46) 4 BL BS, and (*c*) hybrid TiO_2-sol (55 nm, RI = 1.92)/meso-SiO_2 (450 nm, RI = 1.16) BL BS. The scale bar is 500 nm. (*d*)–(*f*) Transmission spectra corresponding to (*a*)–(*c*), demonstrating various magnitudes of the thermal shift of the stop band in a temperature range of 15 to 60 °C at 25% RH. (*g*) and (*i*) Time-resolved transmission and (*h*) reflection changes in response to the change in RH from ≈20% to 65%; $<\tau>$ is the response time. The inset graphs show the reflection and transmission spectra of the BS demonstrating the change in transmission at (*g*) 480 nm and (*i*) 512 nm, and reflection at (*h*) 550 nm corresponding to the RH change from ≈20% to 65%. RI, refractive index; BL, bilayer; BS, Bragg stack; NP, nanoparticle; meso, mesoporous; RH, relative humidity.

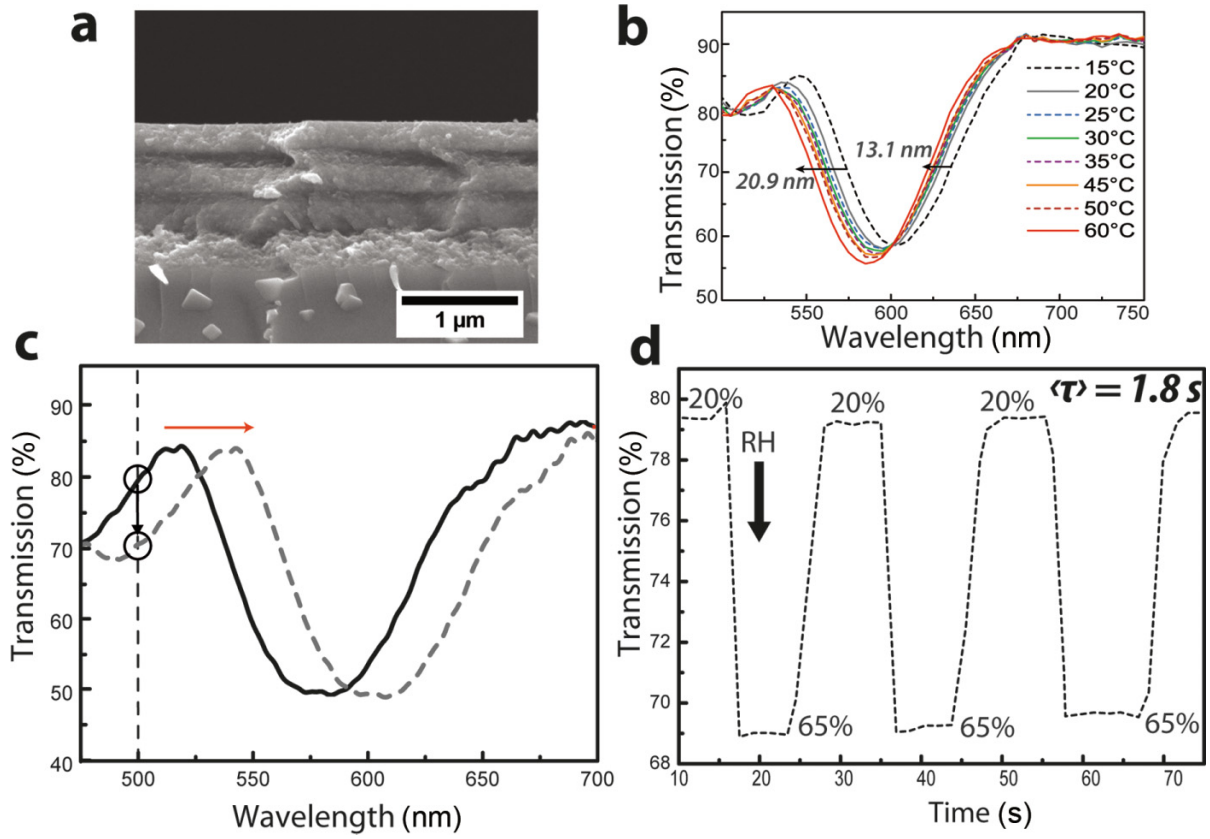


ried out by detecting changes in the reflection/transmission spectrum occurring during the instantaneous change in RH of the environment, from ≈20% to 65%. The change in reflection/transmission was monitored at fixed wavelengths. Note that only the initial shifts right after the RH increase or decrease were recorded, while subsequent slower processes, e.g., owing to diffusion of humidity within the multilayer stacks, were neglected. Therefore, the response times only reflect the principal accessibility of the outer surfaces of the multilayer system.

Comparison of the response times (given as $<\tau>$) to humidity changes for the two dense systems (TiO_2-sol/SiO_2-sol and PVD-derived BS) shows a peculiar difference: The dense sol-based BS shows a complete lack of response to humidity change (Fig. 3*g*), whereas the response of its classical evaporated counterpart occurs promptly (1.3 s), albeit being associated with only a minor shift of 0.5 nm. The absence of response to the transient humidity changes for the sol–sol BS may be due to the larger hydrophobicity of the noncalcined layers and concomitant slow diffusion of water within the multilayer system. The porous systems with similar layer morphologies show rather fast response times, $<\tau>$, which are around 1.5–2 s for the NP–NP BS as reported earlier[35] and ≈1.8 s for the meso–meso BS (Figs. 4*c* and 4*d*). The response times of the hybrid BSs are somewhat larger than those of the NP–NP, meso–meso, and dense PVD-BSs: The $<\tau>$ are around 3 s for both multilayer systems (Figs. 3*h* and 3*i*). Although there is no clear trend discernible, fast response times may be triggered by (*i*) low accessibility of the layers to ambient humidity as seen for the PVD-BS, presumably resulting in surface rather than bulk condensation of water, and (*ii*) fast percolation of water within the porous layers as in the meso–meso BS. The *overall* shifts induced right after the humidity change are a testament to both the porosity and the connectivity of the water percolation pathways within the multilayer systems: The magnitude of the red shift increases in the order dense/sol (≈0 nm) < dense/PVD (≈0.5 nm) < sol–NP (≈5 nm) < NP–NP (≈8 nm) < sol–meso (≈12 nm) < meso–meso (≈25 nm), thus reflecting the increasingly porous and interconnected layer morphologies along this series, which is consistent with the observations made previously. The somewhat lower and more sluggish humidity-induced shifts observed for the hybrid

Can. J. Chem. Downloaded from www.nrcresearchpress.com by MCGILL UNIVERSITY on 02/02/13
For personal use only.

Fig. 4. (*a*) Cross-sectional SEM images of the meso-TiO_2 (220 nm, RI = 1.59)/meso-SiO_2 (140 nm, RI = 1.16) 4 BL BS. The scale bar is 1 μm. (*b*) Transmission spectra of a BS shown in (*a*) showing a blue shift of the left stop band edge of ≈20.9 nm and of the right stop band edge of ≈13.1 nm in the temperature range between 15 and 60 °C at 30% RH. (*c*) Transmission spectra of the BS in (*a*) demonstrating the change in transmission at 500 nm corresponding to the relative humidity change from 20% to 65%. (*d*) Time-resolved transmission change in response to the change in RH from 20% to 65%; $<\tau>$ is the response time. RI, refractive index; BL, bilayer; BS, Bragg stack; meso, mesoporous; RH, relative humidity.



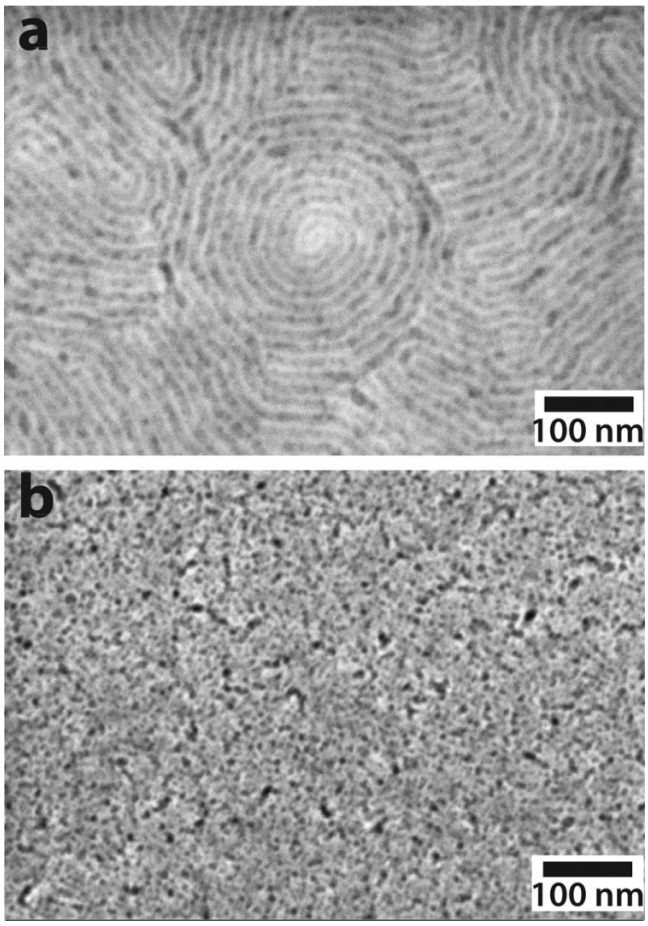
systems compared with their thermal response can be rationalized by the fact that the dense layer is mediating the humidity response of the system, thus preventing fast penetration of moisture into the multilayer. In terms of BS design criteria, an optimally fast and strong effective thermo-optic response can be seen in porous multilayer systems with the same morphologies, such as fully NP-based or meso BSs.

Conclusion

We have studied the influence of the nanomorphology on the effective, i.e., humidity-enhanced thermo-optic response of different TiO_2/SiO_2 BSs: PVD-derived and sol–gel BSs both show relatively small blue shifts of 0.39 and 0.80 nm, respectively, upon heating of the system from 15 to 60 °C at ambient relative humidity. This similarity in the optical response suggests low textural porosity in both systems, thus rendering the solution-processed sol–gel multilayer an excellent substitute for the classical low-response optical filters deposited by PVD. Alternatively, we have shown that a low thermo-optic response (1 nm as compared with 4.4 nm at 25% RH) even for porous architectures can be realized by excluding ambient humidity, equivalent to encapsulation of the system. Analysis of the effective thermo-optic response of hybrid systems composed of both dense and porous layers as well as that of an all-meso BS reveals large optical shifts attributable to a higher degree of textural porosity and accessibility of the system compared with the dense PVD and sol-based counterparts. Furthermore, the impact of morphology on the response and recovery times of the proposed systems to abrupt changes in humidity from ≈20% to 65% was studied. The fastest kinetics were observed for systems with the same layer morphologies (1.3 s for the evaporated, 1.5–2.0 s for the nanoparticle-based and 1.8 s for the meso BS), whereas the response of the hybrid sol–NP (3.1 s) and sol–meso (3.2 s) systems takes somewhat longer. Low or even complete insensitivity towards humidity was observed for PVD- and sol-derived BSs owing to their low degree of textural porosity, combined with larger hydrophobicity of the noncalcined layers in the sol–sol configuration. These observations point to a substantial tunability of the overall thermo-optic response as well as the response kinetics through the choice of the fabrication method and, thus, the resulting morphology of the layers. As a perspective, the multilayers presented in this study lend themselves well as general model systems with precisely controlled porosities and types of curvatures, which can translate the adsorption of arbitrary fluids under ambient conditions into a visibly perceptible optical readout.

Can. J. Chem. Downloaded from www.nrcresearchpress.com by MCGILL UNIVERSITY on 02/02/13
For personal use only.

Fig. 5. Top-view SEM images of mesoporous (*a*) silica and (*b*) titania films.



Can. J. Chem. Downloaded from www.nrcresearchpress.com by MCGILL UNIVERSITY on 02/02/13
For personal use only.

Acknowledgment

This work was supported by the Nanosystems Initiative Munich (NIM) Cluster of Excellence as well as the Center for NanoScience (CeNS). The doctoral scholarships for I. Pavlichenko, granted by the Elite Network of Bavaria, and for A. Exner, granted by the Institute for Advanced Study (IAS) and the International Graduate School of Science and Engineering (IGSSE), are gratefully acknowledged. We thank V. Duppel, M. Konuma, A. Folger, and P. Zehetmaier for their experimental assistance and fruitful discussions.

References

(1) Bonifacio, L. D.; Lotsch, B. V.; Puzzo, D. P.; Scotognella, F.; Ozin, G. A. *Adv. Mater. (Deerfield Beach Fla.)* **2009**, *21* (16), 1641. doi:10.1002/adma.200802348.

(2) Aguirre, C. I.; Reguera, E.; Stein, A. *Adv. Funct. Mater.* **2010**, *20* (16), 2565. doi:10.1002/adfm.201000143.

(3) Joannopoulos, J. D.; Villeneuve, P. R.; Fan, S. *Nature* **1997**, *386* (6621), 143. doi:10.1038/386143a0.

(4) Ge, J.; Yin, Y. *Angew. Chem. Int. Ed.* **2011**, *50* (7), 1492. doi:10.1002/anie.200907091.

(5) Nair, R. V.; Vijaya, R. *Prog. Quantum Electron.* **2010**, *34* (3), 89. doi:10.1016/j.pquantelec.2010.01.001.

(6) Friese, C.; Werber, A.; Krogmann, F.; Mönch, W.; Zappe, H. *IEEJ T. Electr. Electr.* **2007**, *2* (3), 232. doi:10.1002/tee.20138.

(7) Hoi, S.-K.; Chen, X.; Kumar, V. S.; Homhuan, S.; Sow, C.-H.; Bettiol, A. A. *Adv. Funct. Mater.* **2011**, *21* (15), 2847. doi:10.1002/adfm.201002632.

(8) Mano, J. F. *Adv. Eng. Mater.* **2008**, *10* (6), 515. doi:10.1002/adem.200700355.

(9) Wang, H.; Kerins, F.; Kamp, U.; Bonifacio, L.; Arsenault, A. C.; Ozin, G. A. Photonic Crystal Display Materials. *Inform. Display* **2011**, *7–8*, 1.

(10) Bonifacio, L. D.; Ozin, G. A.; Arsenault, A. C. *Small* **2011**, *7* (22), 3153. doi:10.1002/smll.201101074.

(11) Kang, J.-H.; Moon, J. H.; Lee, S.-K.; Park, S.-G.; Jang, S. G.; Yang, S.; Yang, S.-M. *Adv. Mater. (Deerfield Beach Fla.)* **2008**, *20* (16), 3061. doi:10.1002/adma.200800141.

(12) Debord, J. D.; Lyon, L. A. *J. Phys. Chem. B* **2000**, *104* (27), 6327. doi:10.1021/jp001238c.

(13) Li, G.; Pandya, P. D.; Seo, S. S. *Int. J. Polym. Anal. Characterization* **2009**, *14* (4), 351. doi:10.1080/10236660902875208.

(14) Griffete, N.; Dybkowska, M.; Glebocki, B.; Basinska, T.; Connan, C.; Maître, A.; Chehimi, M. M.; Slomkowski, S.; Mangeney, C. *Langmuir* **2010**, *26* (13), 11550. doi:10.1021/la100537v.

(15) Pu, S.; Bai, X.; Wang, L. *J. Magn. Magn. Mater.* **2011**, *323* (22), 2866. doi:10.1016/j.jmmm.2011.06.040.

(16) Wu, G.; Jiang, Y.; Xu, D.; Tang, H.; Liang, X.; Li, G. *Langmuir* **2011**, *27* (4), 1505. doi:10.1021/la1037124.

(17) Soten, B. I.; Miguez, H.; Yang, S. M.; Petrov, S.; Coombs, N.; Tetreault, N.; Matsuura, N.; Ruda, H. E.; Ozin, G. A. *Adv. Funct. Mater.* **2002**, *12* (1), 71. doi:10.1002/1616-3028(20020101)12:1<71::AID-ADFM71>3.0.CO;2-I.

(18) Coppola, G.; Sirleto, L.; Rendina, I.; Iodice, M. *Opt. Eng.* **2011**, *50* (7), 071112. doi:10.1117/1.3574378.

(19) Shen, X.; Han, K.; Liu, H.; Li, H.; Tang, G. Proceedings of the International Workshop on Metamaterials, Nanjing, China, 9–12 November, 2008; IEEE, 2008; pp 149–152.

(20) Hohlfeld, D.; Epmeier, M.; Zappe, H. *Sens. Actuators* **2003**, *103* (1–2), 93. doi:10.1016/S0924-4247(02)00320-5.

(21) Domash, L. H.; Ma, E.; Lourie, M.; Sharfin, W.; Wagner, M. *SPIE Proc.* **2003**, *4989,* 161. doi:10.1117/12.479819.

(22) Hohlfeld, D.; Zappe, H. *J. Opt. A, Pure Appl. Opt.* **2004**, *6* (6), 504. doi:10.1088/1464-4258/6/6/002.

(23) Regoliosi, P.; Guehl, M.; Scarpa, G.; Lugli, P.; Persano, L.; Del Carro, P.; Camposeo, A.; Cingolani, R.; Pisignano, D.; Bietti, S.; Grilli, E.; Guzzi, M. *Appl. Phys. Lett.* **2008**, *92* (25), 253310. doi:10.1063/1.2953069.

(24) Calvo, M. E.; Colodrero, S.; Hidalgo, N.; Lozano, G.; López-López, C.; Sánchez-Sobrado, O.; Míguez, H. *Energy Environ. Sci.* **2011**, *4* (12), 4800. doi:10.1039/c1ee02081a.

(25) Klein, L. C. *Annu. Rev. Mater. Sci.* **1993**, *23* (1), 437. doi:10.1146/annurev.ms.23.080193.002253.

(26) Barhoum, M.; Morrill, J. M.; Riassetto, D.; Bartl, M. H. *Chem. Mater.* **2011**, *23* (23), 5177. doi:10.1021/cm202019b.

(27) Fuertes, M. C.; Colodrero, S.; Lozano, G.; Gonzalez-Elipe, A. R.; Grosso, D.; Boissiere, C.; Sanchez, C.; Soler-Illia, G. J. A. A.; Míguez, H. *J. Phys. Chem. C* **2008**, *112* (9), 3157. doi:10.1021/jp710612y.

(28) Illia, G. S.; Fuertes, M. C.; Angelomé, P. C.; Marchi, M. C.; Troiani, H.; Luca, V.; Míguez, H. *J. Phys. Chem.* **2007**, *4*.

(29) Hidalgo, N.; Calvo, M. E.; Míguez, H. *Small* **2009**, *5* (20), 2309. doi:10.1002/smll.200900411.

(30) López-López, C.; Colodrero, S.; Raga, S. R.; Lindström, H.; Fabregat-Santiago, F.; Bisquert, J.; Míguez, H. *J. Mater. Chem.* **2012**, *22* (5), 1751. doi:10.1039/c1jm15202e.
(31) Hidalgo, N.; Calvo, M. E.; Bellino, M. G.; Soler-Illia, G. J. A. A.; Míguez, H. *Adv. Funct. Mater.* **2011**, *21* (13), 2534. doi:10.1002/adfm.201002486.
(32) Choi, S. Y.; Mamak, M.; von Freymann, G.; Chopra, N.; Ozin, G. A. *Nano Lett.* **2006**, *6* (11), 2456. doi:10.1021/nl061580m.
(33) Colodrero, S.; Ocaña, M.; González-Elipe, A. R.; Míguez, H. *Langmuir* **2008**, *24* (16), 9135. doi:10.1021/la801210q.
(34) Pavlichenko, I.; Exner, A. T.; Guehl, M.; Lugli, P.; Scarpa, G.; Lotsch, B. V. *J. Phys. Chem. C* **2012**, *116* (1), 298. doi:10.1021/jp208733t.
(35) Pavlichenko, I.; Exner, A. T.; Lugli, P.; Scarpa, G.; Lotsch, B. V. J. Intell. Mater. Struct. **2012**. doi:10.1177/1045389X12453970.
(36) Sagdeo, P. R.; Shinde, D. D.; Misal, J. S.; Kamble, N. M.; Tokas, R. B.; Biswas, A.; Poswal, A. K.; Thakur, S.; Bhattacharyya, D.; Sahoo, N. K.; Sabharwal, S. C. *J. Appl. Phys. D, Appl.Phys.* **2010**, *43* (4), 045302. doi:10.1088/0022-3727/43/4/045302.
(37) Macleod, H. A. *Thin-Film Optical Filters;* 4th ed.; CRC Press: Boca Raton, FL, 2010.
(38) Duyar, Ö.; Placido, F.; Zafer Durusoy, H. *J. Phys. D Appl. Phys.* **2008**, *41* (9), 095307. doi:10.1088/0022-3727/41/9/095307.
(39) Tien, C.-L. *Appl. Surf. Sci.* **2009**, *256* (3), 870. doi:10.1016/j.apsusc.2009.08.077.
(40) Gülşen, G.; Naci Inci, M. *Opt. Mater.* **2002**, *18* (4), 373. doi:10.1016/S0925-3467(01)00176-8.
(41) Ghosh, G. *J. Non-Cryst. Solids* **1995**, *189* (1–2), 191. doi:10.1016/0022-3093(95)00247-2.
(42) Naik, S. P.; Yamakita, S.; Ogura, M.; Okubo, T. Microporous Mesoporous Mater. **2004**, *75* (1-2), 51. doi:10.1016/j.micromeso.2004.06.028.
(43) Tao, J.; Shen, Y.; Gu, F.; Zhu, J.; Zhang, J. *J. Mater. Sci. Technol.* **2007**, *23,* 513.

Can. J. Chem. Downloaded from www.nrcresearchpress.com by MCGILL UNIVERSITY on 02/02/13
For personal use only.

A DFT study of reversed isotope shifts in H/D substitution of free-base porphyrin and related free-base tetrapyrroles

Christopher Henchy, Ciaran Murray, Claudine Crépin, and John G. McCaffrey

Can. J. Chem. Downloaded from www.nrcresearchpress.com by MCGILL UNIVERSITY on 02/02/13
For personal use only.

Abstract: DFT/B3LYP calculations are used to analyse the occurrence of reverse isotope shift ratios (ISR) in H/D substitution of the free-base tetrapyrroles, in situations where the frequency ratio ν_H/ν_D is less than 1. The reverse ISR effect is found to be most evident in the out-of-plane bending modes (b_{2g} and b_{3u} symmetry) involving some N–H motion for the four molecules studied, viz., porphine (H_2P), tetraaza-porphine (H_2TAP), tetrabenzo-porphine (H_2TBP), and phthalocyanine (H_2Pc). It was analysed by following the evolution of the normal mode frequencies with incremental variation of the H atom masses from 1 to 2 amu. This method allows direct, unambiguous mode correlations to be established between the light and the heavy isotopologues. When the NH(D) motion is predominant, the H to D frequency evolution decreases in a continuous manner for a particular normal mode. In the case of two modes of the same symmetry and whose frequencies are similar, their frequency evolutions could cross, depending on the extent of NH(D) motion involved in them. The evolution diagrams may show avoided crossings of various extents, which thereby reflects the degree of the NH(D) motion in the modes. The reverse ISR effect is directly correlated to these avoided crossings. Because the isotope shifts are quite small (<10 cm^{-1}) and occur in the congested 1500–500 cm^{-1} spectral region, high-resolution methods yielding narrow line transitions are required for experimental analysis. The matrix isolation technique is particularly well suited for this work and is proposed for use in a search for this effect.

Key words: vibrational spectroscopy, porphyrins, DFT calculations, matrix-isolation.

Résumé : Des calculs DFT basés sur la fonctionnelle B3LYP ont été menés sur des molécules tétrapyrroliques afin d'analyser le cas de rapports de déplacements isotopiques (RDI) inverses reliés à la substitution H/D dans les bases libres, c'est-à-dire le cas de rapports de fréquences ν_H/ν_D inférieurs à 1. Ces rapports RDI inverses apparaissent clairement dans les modes de pliage hors plan (symétries b_{2g} et b_{3u}) impliquant un mouvement N–H pour les quatre molécules étudiées : porphine (H_2P), tétraazaporphine (H_2TAP), tétrabenzoporphine (H_2TBP) et phthalocyanine (H_2Pc). Les RDI inverses ont été analysés en suivant l'évolution des fréquences des modes normaux lors d'une augmentation continue de 1 à 2 amu de la masse de l'atome d'hydrogène. Cette méthode permet d'établir de façon directe et non ambiguë les corrélations entre les fréquences des deux isotopologues. Lorsque le mouvement N-H(D) est prédominant dans un mode donné, l'évolution de la fréquence de H à D diminue continûment. Lorsque deux modes de même symétrie ont des fréquences voisines, leurs évolutions en fréquence de H à D peuvent se croiser, selon le degré d'implication du mouvement N-H(D) dans les deux modes considérés. Les diagrammes d'évolutions correspondants peuvent alors montrer des croisements évités plus ou moins prononcés, reflétant ainsi le poids du mouvement N-H(D) dans les modes impliqués. L'effet de RDI inversé est directement corrélé à ces croisements évités. Les déplacements isotopiques sont assez faibles (<10 cm^{-1}) et ont lieu dans une région spectrale très dense (1500–500 cm^{-1}). C'est pourquoi, il est nécessaire d'utiliser des méthodes spectroscopiques à haute résolution permettant l'observation de transitions en bandes fines pour une analyse expérimentale. La technique d'isolation en matrice est particulièrement bien adaptée et elle est proposée pour la recherche expérimentale de cet effet.

Mots-clés : spectroscopie vibrationnelle, porphyrines, calculs DFT, isolation en matrice.

Received 11 July 2012. Accepted 10 September 2012. Published at www.nrcresearchpress.com/cjc on 27 November 2012.

C. Henchy, C. Murray*, and J.G. McCaffrey. Department of Chemistry, National University of Ireland, Maynooth, Co. Kildare, Ireland.
C. Crépin. Institut des Sciences Moléculaires d'Orsay - UMR 8214 (ISMO), Bâtiment 210, Université Paris-Sud, 91405 Orsay CEDEX, France.

Corresponding author: John G. McCaffrey (e-mail: john.mccaffrey@nuim.ie).

*Present address: Tyndall National Institute, Lee Maltings, University College, Cork, Ireland.

The time one of us (JMcC) spent as a graduate student in Geff Ozin's group was the beginning of an enriching, life-long career in research and education. In particular, the use of group theoretical quantum chemistry and the matrix-isolation techniques, all of which are used in this contribution, were first encountered in the Ozin lab. Accordingly, it is with pleasure and gratitude that the present article is dedicated to Geff.

Can. J. Chem. Downloaded from www.nrcresearchpress.com by MCGILL UNIVERSITY on 02/02/13
For personal use only.

Introduction

The tautomerism exhibited by the free-base tetrapyrroles, in which the two inner hydrogen atoms migrate between opposite pairs of the four central nitrogen atoms, has been studied with a wide variety of both experimental[1] and theoretical[2] means. Of the methods applied, vibrational spectroscopy is a direct means of probing the mechanism underlying the tautomerism, since the N–H stretch and in-plane bending modes have been proposed to be involved. In spectroscopic work, isotope substitution[3] is a well-known tool in achieving a reliable vibrational analysis, with substitution of hydrogen (H) by deuterium (D) by far the most utilized method, as it produces the largest frequency shifts[4] because of the approximate factor of two[5] difference in the masses of the isotopes. Arising from the inverse relationship between the mode frequency, ν, and the mass of the H-atom isotope, m, given by the expression,

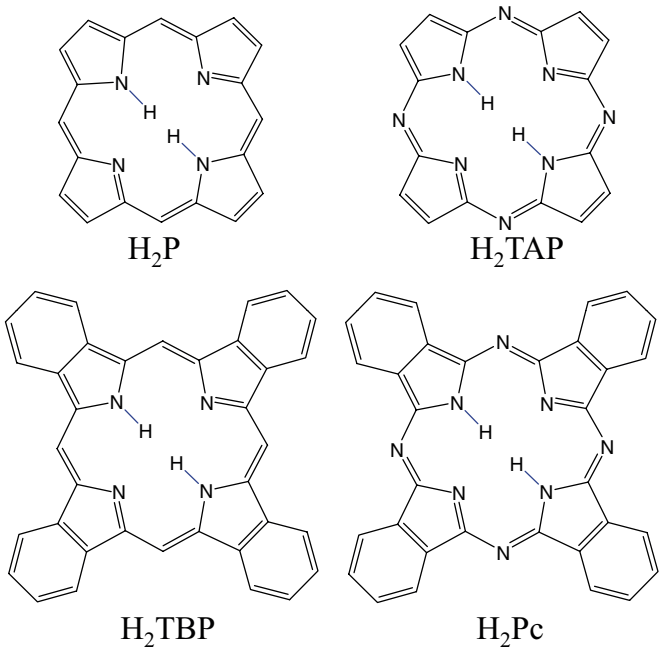
$$[1] \qquad \nu = \frac{1}{2\pi}\sqrt{\frac{k}{m}}$$

in which k is the force constant, the heavier isotope is thereby expected to occur at lower values. This behaviour assists greatly in making mode assignments in experimental spectra. Moreover, for the free-base tetrapyrroles, H/D substitution of the two inner hydrogens is particularly appealing as the D_{2h} molecular symmetry is conserved, allowing direct comparisons between the two isotopologues.

However, in a recent combined IR/Raman and high-level density functional theory (DFT) study[6] of free-base phthalocyanine (H_2Pc), we observed quite peculiar behaviour upon H/D substitution, whereby the frequency of one particular mode of the deuterium isotopologue was found to be higher than that of hydrogen. The mode in question is the IR-active out-of-plane bending vibration observed in Ar matrices at 722.7 cm^{-1} for H_2Pc, but which shifts up to 729.9 cm^{-1} in D_2Pc. The observed isotope shift ratio (ISR) of 0.990, determined as the ν_H/ν_D ratio, was very well reproduced in the theoretical DFT results. To probe whether this unusual reversed ISR (<1) effect is a peculiarity of Pc, we have extended the theoretical work in the present study to cover the 3 most closely related free-base tetrapyrroles, namely porphine (P), tetraaza-porphine (TAP), and tetrabenzo-porphine (TBP). The structures of all four molecules are provided in Fig. 1, revealing the strong similarities of these very important materials, often called the "colours of life".[7]

A theoretical prediction of the occurrence of a reversed isotope shift ratio (ISR < 1) was made several years ago by Li and Zgierski in their work on developing a local mode description of the vibrations in the porphines for both free-base and metallo-porphines.[8] Their vibrational analysis was based on a valence force field and conducted with the Wilson-GF matrix method.[9] However, as will be shown later, the upward shifts in the heavier isotope were much larger than what we have seen with the force fields generated in the present quantum chemical method. The earlier work[8] only considered in-plane vibrations, i.e., the N–H stretches and in-plane bending modes, but as we have found experimentally[6], the most easily identifiable instance of the reversed ISR effect in the phthalocyanines involved an out-of-plane N–H bending

Fig. 1. Structures of the 4 closely related free-base tetrapyrrole molecules, namely porphine (H_2P), tetraaza-porphine (H_2TAP), tetrabenzo-porphine (H_2TBP) and phthalocyanine (H_2Pc), whose vibrational frequency shifts upon H/D isotope substitution have been studied by the DFT method. The bond lengths and bond angles found in the DFT/B3LYP geometry optimisations are provided in Table 2 for the four molecules. With the present method, all are found to have high (D_{2h}) symmetry.



motion. A more recent DFT calculation of free-base phthalocyanine by Liu et al. also found a reverse ISR.[10] While these authors did not present an analysis of the origins of this effect, they did comment that for the mode concerned, the direction of the H atom motions was opposite to that of the D atoms.

A group theoretical analysis of the four free-base tetrapyrroles, all belonging to the D_{2h} point group, provides the symmetry types and numbers of the normal vibrational modes of the molecules being studied. The results of such an analysis, in which the z-axis is aligned with the two central N–H bonds, are collected in Table 1.[11] As expected, the numbers of modes in the two tetra-aryl molecules (tetrabenzo-porphine and phthalocyanine) are much larger because of the increase in the number of atoms, N. For the purposes of illustration, the material presented herein will concentrate on the smaller parent molecules porphine and tetraaza-porphine. However, in all four molecules the symmetry types of the 6 modes involving N–H motion are the same and can be compared with the complete normal vibrational modes in Table 1.

The main goal then is to establish the correlations between similar NH and ND modes and to rationalize the observed and calculated frequency shifts. Calculating normal mode frequencies with incremental (artificial) variation of the masses of H from 1 to 2 allows these correlations to be established. When the NH(D) motion is predominant, the H to D evolution in the normal mode frequency will decrease in a continuous manner. In the case of two modes of the same symmetry and whose

Can. J. Chem. Downloaded from www.nrcresearchpress.com by MCGILL UNIVERSITY on 02/02/13
For personal use only.

Table 1. A summary of a group theoretical analysis of the normal modes of vibration for the tetra-pyrrole molecules examined in the present work.

D_{2h}	Species				N–H vibrational modes		
Sym.	H_2P (38)	H_2TAP (34)	H_2TBP (62)	H_2Pc (58)	STR	IPB	OPB
a_g	19	17	31	29	✓		
b_{1g}	8	7	14	13			
b_{2g}	9	8	15	14			✓
b_{3g}	18	16	30	28		✓	
a_u	8	7	14	13			
b_{1u}	18	16	30	28	✓		
b_{2u}	18	16	30	28		✓	
b_{3u}	10	9	16	15			✓
#Modes	108	96	180	168			

Note: The values in parenthesis are the numbers of atoms in each of the molecules. On the right-hand side, the symmetries of the six possible N–H motions are provided for an analysis conducted with the *z*-axis co-linear with the two central N–H bonds. The abbreviations STR, IPB, and OPB represent the N–H stretching, in-plane bending, and out-of-plane bending modes, respectively.

frequencies are similar, their frequency evolutions could cross, depending on the extent of NH(D) motion involved in them. The evolution diagrams will thus show avoided crossings of various extents, which thereby reveal the degree of the NH(D) motion in the modes. If both normal modes involve similar atomic motions, including the NH(D) one, they will be distorted around the mass of H corresponding to the crossing, to avoid it. This is similar to the well-known characteristic of avoided crossing found in potential energy surfaces for electronic states with the same spatial symmetry.[12] It allows an analysis of the underlying mode interactions. In the present paper, the instances of ISR < 1 are especially focussed on.

Methods

DFT was utilized with the 6–311G++(2d,2p) basis set for both geometry optimization and the calculation of the vibrational frequencies. The B3LYP functional is currently the most effective for calculating ground-state molecular vibrational frequencies, and when used with a large basis set, generates accurate IR intensities. Moreover, as demonstrated in our previous study of both zinc and free-base phthalocyanine, the Raman intensities are also reliable.[6] Another advantage of this method is that it runs efficiently on multiprocessor computers. The present calculations were conducted with the Gaussian-03 suite of programmes[13] running, as described elsewhere[6], on a Linux workstation with two quad-core processors. All the calculated vibrational frequencies presented in this work are, unless stated otherwise, unscaled values obtained within the harmonic approximation.

Because of the un-intuitive nature of the effect being analysed, the approach taken in calculating the vibrational frequencies involves increasing the masses between H and D incrementally, in steps of 0.05 amu, so that the evolution of the modes from the light to the heavy isotopologue can be followed in a near-continuous manner. This is the approach we utilized in our previous phthalocyanine work.[6] Recently, this method has been applied successfully by Wright and coworkers in their work on re-numbering the vibrational modes of benzene and its monosubstituted derivatives.[14] The task in the present analysis is to track the mass dependence of the normal modes to see where they cross, but more importantly, it is to identify where curve-avoidance occurs and analyse the underlying mode coupling that produce ISR values less than 1. In doing this, we exploit the high symmetries found in the optimized geometries of the free-base tetrapyrroles. Accordingly, this analysis is done on normal modes of a given symmetry type with a particular focus on those modes involving the N–H vibrations. As mentioned earlier, there are only 3 types of N–H motions, but 6 distinct symmetries are involved. Thus, the reducible representation (Γ) for motion involving ONLY the two inner H-atoms (iH) can be shown to be $\Gamma_{iH} =$ 6 –2 0 0 0 0 2 2. Application of the reduction formula to Γ_{iH} gives the symmetries of the N–H vibrations as $1a_g$, $1b_{2g}$, $1b_{3g}$, $1b_{1u}$, $1b_{2u}$, and $1b_{3u}$. These 6 modes as listed in Table 1 for the 4 free-base molecules considered.

To analyse details of the atomic motions producing the reverse isotope substitution ratios (ISR < 1), we have extracted the contributions of the internal coordinates to the normal modes. The internal mode contributions to a specific normal mode are expressed as percentages, which were generated directly in the Gaussian-03 package.[15] The calculation of the "% Internal modes" involves a projection of the normal modes onto the displacement vectors that define the redundant internal coordinates. Only the most important terms are given, with the default being all modes greater than 0.1, with the cut-off being reduced until the total of 0.9 is reached. This is implemented with the "freq=internal" command in the input file.

Results

The optimized geometries obtained with the DFT/B3LYP method and the 6–311G++(2d,2p) basis set for the 4 free-base tetrapyrrole molecules studied are shown in Fig. 1. Complete listings of the geometric parameters for the free-base tetrapyrroles, porphine (H_2P), tetraaza-porphine (H_2TAP), tetrabenzo-porphine (H_2TBP), and phthalocyanine (H_2Pc) are provided in Table 2. In all cases, high (D_{2h}) symmetry was preserved in the geometry optimisations, and no imaginary

Can. J. Chem. Downloaded from www.nrcresearchpress.com by MCGILL UNIVERSITY on 02/02/13
For personal use only.

Table 2. A summary of the geometric parameters obtained with the DFT/B3LYP optimization conducted in the present work on the 4 free-base tetrapyrrole molecules, porphine (H_2P), tetraaza-porphine (H_2TAP), tetrabenzo-porphine (H_2TBP), and phthalocyanine (H_2Pc).

Length (Å)	P	TAP	TBP	Pc
N–H	1.0104	1.0076	1.0112	1.009
N–C_α	1.3692	1.3701	1.3709	1.375
C_α–C_m	1.3900	—	1.3839	—
C_α–N_m	—	1.3195	—	1.313
C_α–C_β	1.4316	1.4436	1.4448	1.45
C_β–C_β	1.368	1.3616	1.413	1.409
C_β–H_1	1.0768	1.0759	—	—
C_β–C_γ	—	—	1.3985	1.394
C_γ–C_δ	—	—	1.3828	1.386
C_δ–C_δ	—	—	1.4073	1.406
C_γ–H_1	—	—	1.0812	1.08
C_δ–H_2	—	—	1.0812	1.081
N′–$C_{\alpha'}$	1.3600	1.3593	1.3598	1.362
$C_{\alpha'}$–C_m	1.3961	—	1.3949	—
$C_{\alpha'}$–N_m	—	1.3338	—	1.332
C_m–H_m	1.0812	—	1.0806	—
$C_{\alpha'}$–$C_{\beta'}$	1.457	1.4657	1.4632	1.465
$C_{\beta'}$–$C_{\beta'}$	1.3521	1.3466	1.404	1.4
$C_{\beta'}$–$H_{1'}$	1.078	1.0766	—	—
$C_{\beta'}$–$C_{\gamma'}$	—	—	1.3931	1.389
$C_{\gamma'}$– $C_{\delta'}$	—	—	1.3894	1.392
$C_{\delta'}$–$C_{\delta'}$	—	—	1.4014	1.401
$C_{\gamma'}$–$H_{1'}$	—	—	1.0818	1.081
$C_{\delta'}$–$H_{2'}$	—	—	1.0814	1.081
Angle (°)				
H-N-C_α	124.5724	124.5932	123.6462	123.736
N-C_α-C_m	125.652	—	126.1288	—
N-C_α-N_m	—	127.7457	—	128.100
C_α-N-C_α	110.8552	110.8136	112.7076	112.527
N-C_α-C_β	106.5301	106.5535	106.1348	106.135
C_α-C_β-C_β	108.0423	108.0397	107.5114	107.601
C_α-C_β-H_1	124.3741	123.3376	—	—
C_β-C_β-H_1	127.5835	128.6226	—	—
C_β-C_β-C_γ	—	—	120.5013	120.960
C_β-C_γ-C_δ	—	—	118.4767	117.829
C_γ-C_δ-C_δ	—	—	121.022	121.211
C_β-C_γ-H_1	—	—	121.1432	120.586
C_γ-C_δ-H_2	—	—	119.696	119.622
C_α-C_m-H_m	115.9102	—	115.3433	—
$C_{\alpha'}$-C_m-H_m	116.9554	—	116.3284	—
N′-$C_{\alpha'}$-C_m	125.5188	—	125.6994	—
N′-$C_{\alpha'}$- N_m	—	127.5626	—	121.688
$C_{\alpha'}$-N′-$C_{\alpha'}$	105.7553	105.5281	107.6054	107.226
N′-$C_{\alpha'}$-$C_{\alpha'}$	110.8457	111.0377	110.5212	110.697
$C_{\alpha'}$-$C_{\beta'}$-$C_{\beta'}$	106.2767	106.1983	105.6761	105.690
$C_{\beta'}$-$C_{\beta'}$-H_1	125.4496	124.2356	—	—
$C_{\beta'}$-$C_{\beta'}$-H_2	128.2737	129.5661	—	—
$C_{\beta'}$-$C_{\beta'}$-$C_{\gamma'}$	—	—	120.7253	121.223
$C_{\beta'}$-$C_{\gamma'}$-$C_{\delta'}$	—	—	118.3937	117.670
$C_{\gamma'}$-$C_{\delta'}$-$C_{\delta'}$	—	—	120.8811	121.107
$C_{\beta'}$-$C_{\gamma'}$-$H_{1'}$	—	—	121.4854	120.925
$C_{\gamma'}$-$C_{\delta'}$-$H_{2'}$	—	—	119.7205	119.636

Note: The atom labelling follows standard notation used in our previous work on H_2Pc.[6]

low frequencies were found. These results indicate that the planar geometry is the most stable in all 4 cases.

In the present H/D isotope substitution study, we focus on the vibrations involving N–H motion of which there are 3 types. As indicated in Table 1, the N–H stretching (STR) modes are the a_g and b_{1u} symmetries corresponding to the Raman-active symmetric and IR-active asymmetric vibrations, respectively. The N–H in-plane bending (IPB) modes are of b_{3g} and b_{2u} symmetry, arising from the in-phase and out-of-phase bending motions, which are Raman-active and IR-active, respectively. The N–H out-of-plane bending (OPB) modes are of b_{2g} and b_{3u} symmetry, the Raman-active in-phase and IR-active out-of-phase modes, respectively. The behaviour of each of these 3 N–H modes will now be analysed on the basis of the 6 possible symmetries that they possess.

From the summary of the group theory results presented in Table 1, one might expect that the H/D isotope dependence of the N–H OPB motion would be the easiest to follow. For instance, in H_2TAP the OPB mode is 1 of only 8 (b_{2g}) normal modes, while the N–H stretch should be the most difficult, being 1 of 17 (a_g) modes. In H_2TBP, this stretching mode is 1 of 31 modes. However, as we have found experimentally for H_2Pc, identifying the OP bending in H/D substitution is far from obvious when the frequency of some modes *increase* in D_2Pc![6] The contrasting behaviour of these modes arises, as will be elaborated later, for two reasons. The first is that the N–H stretch modes occur at high frequencies, energetically distinct from all other modes except for the C-H stretching modes, while the IPB and OPB modes occur in congested regions where multiple mode crossings occur. The second reason is that the internal N–H stretching modes are very well localized on the N–H bonds. In contrast, avoided crossings occur in the IP and OP bending motions, rendering mode attributions in the deuterium isotopologue difficult.

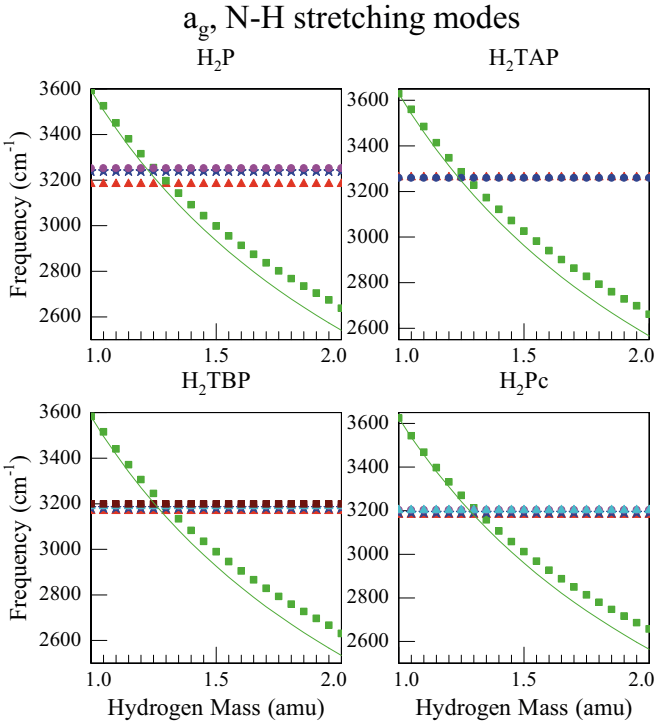
N–H stretching (a_g and b_{1u}) modes

The frequencies of the N–H stretching modes are shown in Figs. 2 and 3 for the 4 free-base tetrapyrrole molecules studied, as a function of incrementally increasing the H-atom mass from 1 to 2 amu. Taking porphine (H_2P) as an example, shown on the upper left in Fig. 2, the Raman-active (but weak) a_g N–H stretching mode crosses directly over three C-H stretching modes and continues to decrease monotonically from 3593.5 cm^{-1} in H_2P to 2638.3 cm^{-1} in D_2P. This corresponds to a shift of 955.2 cm^{-1} and a ν_H/ν_D (ISR) ratio of 1.362. This is close to the expected value of approximately $\sqrt{2}$ for H/D isotopic substitution of a normal mode involving nearly pure N–H motion.[16] The solid curve in Fig. 2 shows the theoretical mass dependence ($1/\sqrt{m_H}$) given by eq. [1]. It is evident that the agreement between the DFT predicted data and this theoretical dependence is good.

The mass dependence of the (strong) IR-active b_{1u} mode, shown on the upper left in Fig. 3, exhibits a similar pattern with the N–H stretch at 3552.3 cm^{-1} in H_2P, crossing over three C-H stretches as the masses of the central hydrogens are increased. The N-D mode has a frequency of 2611.9 cm^{-1}, which gives a ν_H/ν_D ratio of 1.360. As illustrated in Fig. 3, this pattern is observed for the 3 other molecules studied. H_2TAP is the simplest system having the least amount of C-H modes, just 2 in number. In contrast, the tetra-aryl molecules, H_2TBP and H_2Pc, have numerous C-H modes. However in all cases,

Can. J. Chem. Downloaded from www.nrcresearchpress.com by MCGILL UNIVERSITY on 02/02/13
For personal use only.

Fig. 2. Dependence of the vibrational frequencies of the Raman-active N–H stretch (a_g symmetry) normal modes of the 4 (D_{2h}) free-base tetrapyrrole molecules with H/D isotope substitution of the two inner hydrogens. The values shown are harmonic results calculated by increasing the H mass from 1 to 2 in increments of 0.05 amu. The solid trace provides the predicted inverse dependence of the frequency on the square root of the mass, indicating close agreement with the calculated values. The frequencies of the C-H stretching modes are completely unaffected by the H/D isotope substitution of the two inner hydrogens.

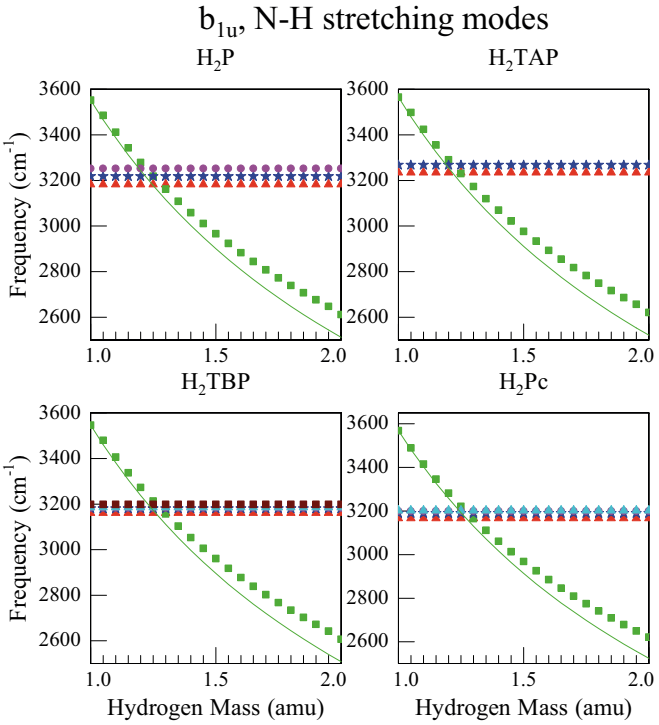


direct crossings of the normal modes occur indicating the absence of coupling between N–H(D) stretching modes and C-H stretching modes.

The frequencies of the N–H stretching modes of H_2P, H_2TAP, H_2TBP, and H_2Pc are collected in the upper section of Table 3 for the light and heavy isotopologues. The ISR (ν_H/ν_D) values calculated from these frequencies are listed for the two (a_g and b_{1u}) symmetries involved. From the values provided in Table 3, it is clear that the ISR values span a small range, from 1.364 for the a_g mode of phthalocyanine (Pc) to 1.360 for the b_{1u} mode of porphine (P). It is evident that for both symmetries, presented in Figs. 2 and 3, respectively, the N–H stretching mode passes directly through the C-H stretching modes in all four molecules without any interaction amongst these high-frequency modes. An examination of the C-H stretching modes reveals that the changes in their frequencies, after being crossed by the N–H modes, are extremely small. In all cases, except TBP where it is 0.04 cm^{-1}, these changes are in the third decimal place. With this small magnitude, these shifts are less than the uncertainty of the method and are not considered significant.

An analysis of the internal modes reveals the small deviation of the calculated ISR values (1.36) from $\sqrt{2}$ arises from the involvement of the pyrrole ring deformation that accompanies the N–H stretching motion for kinematic reasons. No other internal motions are involved in these nearly pure NH(D) stretching modes. See the upper panels of Tables 4 and 5 for details of the % internal N–H motions of these modes in the smaller tetrapyrroles, TAP and porphine, respectively.

Fig. 3. Similar to Fig. 2 except for the IR-active b_{1u} symmetry normal modes.



OPB (b_{3u} and b_{2g}) modes

b_{3u} N–H bending modes

The mass dependences of the b_{3u} OPB modes of P, TAP, TBP, and Pc are shown in the 4 panels of Fig. 4. In the frequency range 800–550 cm^{-1} presented in these plots, all 4 molecules show the same number of normal modes, and the mass dependence is clearly not simple in any of them.[17] Most conspicuous is the pronounced avoided crossing that occurs between two modes in the central section of the P and TAP plots. In both cases a normal mode that starts out strongly mass dependent, and is an N–H OPB motion, becomes mass independent and evolves into a mode that involves large amplitude C-H OPBs. This is clearly not a correct mode attribution of the light to the heavy isotopologues. To help analyse the complex behaviour exhibited, the theoretical mass dependence given by eq. [1] is overlaid as a solid trace in Fig. 4. This curve, in contrast with the previous ones generated for the a_g and b_{1u} modes, was calculated from the lowest frequency D_2 mode, because the N–H OPB motion is manifested more strongly in the heavier isotopologues of these molecules than in the lighter ones (corresponding to a less congested spectral region for b_{3u} modes). The internal mode analysis provided in Table 4 for TAP shows the contribution in D_2TAP as 72%, while it is only 53% in H_2TAP. Table 5 reveals a similar pattern for the b_{3u} mode of porphine.

Table 3. H/D isotope shifts for the 6 internal N–H modes of the 4 tetrapyrrole molecules studied.

Motion	Molecule	ν_{H_2}	ν_{D_2}	Shift	ν_H/ν_D	ν_{H_2}	ν_{D_2}	Shift	ν_H/ν_D
N–H stretch		b_{1u}				a_g			
	P	3552.34	2611.88	940.46	1.3601	3593.47	2638.31	955.16	1.3620
	TAP	3565.39	2621.13	944.25	1.3602	3629.13	2661.83	967.30	1.3634
	TBP	3546.71	2606.78	939.93	1.3606	3583.25	2630.36	952.89	1.3623
	Pc	3569.08	2621.36	947.73	1.3615	3625.17	2657.21	967.96	1.3643
N–H OP Bend		b_{3u}				b_{2g}			
	P	739.89	541.8	198.09	1.3656	631.22	473.78	157.44	1.3323
		651.38	657.91	–6.53	**0.9901**	*NC*	*NC*		
	TAP	760.83	547.66	213.17	1.3892	641.4	479.74	161.66	1.3370
		656.65	664.47	–7.82	**0.9882**	*NC*	*NC*		
	TBP	766.76	560.41	206.35	1.3682	711.65	520.08	191.57	1.3683
		713.22	720.33	–7.11	**0.9901**	689.24	695.66	–6.42	**0.9908**
		684.58	684.84	–0.26	0.9996	637.72	638.56	–0.84	0.9987
	Pc	778.36	566.31	212.05	1.3744	680.33	495.23	185.1	1.3738
		740.49	746.78	–6.29	**0.9916**	657.47	659.1	–1.63	0.9975
		704.03	704.28	–0.25	0.9996	505.86	511.42	–5.56	**0.9891**
N–H IP Bend		b_{2u}				b_{3g}			
	P	1003.52	882.82	120.7	1.1367	1264.1	1184.6	79.5	1.0671
		967.16	967.43	–0.27	0.9997	1213.11	1214.33	–1.22	0.9990
	TAP	970.33	851.43	118.9	1.1396	1250.89	1240.82	10.07	*1.008**
		957.24	957.49	–0.25	0.9997	1216.82	1202.66	14.16	*1.012**
	TBP	1067.7	989.03	78.67	1.0795	1253.59	1181.6	71.99	1.0609
		1038.52	1038.81	–0.29	0.9997	1217.56	1218.7	–1.14	0.9991
	Pc	1068.39	981.15	87.24	1.0889	1223.56	1191.4	32.16	1.0270
		1029.31	1029.37	–0.06	0.9999	1211.42	1211.42	0	1.0000

Note: All frequencies are unscaled DFT results given in cm^{-1}. The isotope shift ratios (ISR) are calculated as $\nu H/\nu D$, i.e., the hydrogen frequency divided by the deuterium value. ISR values significantly less than one are highlighted as they are indicative of strongly avoided crossings.

*No curve crossings occur between these two modes in TAP. The values chosen for inclusion were selected on the basis of the similarities of their motion with the three other tetrapyrrole molecules.

Can. J. Chem. Downloaded from www.nrcresearchpress.com by MCGILL UNIVERSITY on 02/02/13
For personal use only.

From the match shown for P in the upper left panel of Fig. 4, between the calculated data and the simple $1/\sqrt{m_H}$ mass-dependence, it is clear that the frequency of the "pure" N–H OP mode decreases from 739.9 cm^{-1} in H_2P to 541.8 cm^{-1} in D_2P. The resulting ν_H/ν_Dratio is 1.366, quite close to the expected value of $\sqrt{2}$. This mode crosses a pure C-H OPB with a frequency of 709.5 cm^{-1}, which is H-atom mass-independent and is thereby not affected by the N–H isotopic substitution. In contrast, it produces an avoided crossing with another C-H OPB mode, which has an initial value of 651.4 cm^{-1} in H_2P but increases to 657.9 cm^{-1} in D_2P. A clear consequence of the avoided crossing is that this mode shifts up in frequency by 6.53 cm^{-1} and produces an ISR value (ν_H/ν_D ratio) considerably less than unity — the value is 0.9901. As indicted in Table 3, similar behaviour is exhibited by this mode in all 4 molecules. The most extreme situation is found for TAP, which has an ISR value of 0.9882.

Figure 5 shows a vector diagram for the atomic motions involved in the modes of TAP that exhibits the most pronounced reversed ISR effect. From the motions presented, the association of the 760.8 cm^{-1} mode with the 547.7 cm^{-1} mode is unquestionable. Thus as illustrated, the vector diagrams for the N–H OPB motions of H_2TAP and D_2TAP are indistinguishable for these two frequencies. However, a consequence of these mode assignments is that the mode at 656.7 cm^{-1} must be correlated with that at 664.5 cm^{-1}, an upward shift of 7.82 cm^{-1} in D_2TAP. This correlation is supported by the very similar C-H OPB motions illustrated for both isotopologues on the bottom of Fig. 5. However, on closer scrutiny of these two diagrams it can be seen that the direction of the N–H bending motion with respect to the molecule is reversed in the N-D mode. This change in the motion of the light and heavy isotopologues is found to be a characteristic of all the modes exhibiting the large reverse ISR, which involve strongly avoided mode crossings.

Reverse ISRs are observed to be larger in cases with more pronounced avoided crossings, i.e., with stronger coupling, W, between the modes. The reversal of the directions of the H-atom motions in the light and heavy species can be seen as a direct consequence of perturbation theory in first order. In the simplified case of two coupled modes, one mode, ν_H, involving large H motion and the other, ν_N, involving little H motion as is the case for when the H→D progression is very flat except in the region of the crossing, the result of perturbation theory will give new modes ν'_N with $|\nu'_N\rangle = |\nu_N\rangle + W/(E_{nN} - E_{nH})|\nu_H\rangle$. The reason for the reversed directions can be understood as follows. Since the sign of the matrix element W ($= \langle\nu_H|W|\nu_N\rangle$) does not change from H to D, but it does change for the energy term, i.e., $(E_{nN} - E_{nH}) < 0$ for H, whereas $(E_{nN} - E_{nH}) > 0$ for D, this means that the motion of $H(|m_H\rangle)$ appears with opposite signs in the description of $|\nu_N\rangle$ in the hydrogenated and the deuterated species, i.e., reversal of directions. This "reversal" is larger and more obvious when the coupling W strength is greater.

Table 4. Contributions of the N–H internal modes to the normal modes involving crossings, or avoided crossings of TAP.

	H_2TAP			D_2TAP			ISR
Sym.	Mode#	Frequency	% Int. Mode	Mode#	Frequency	% Int. Mode	νH/νD
a_g							
	96	3629.13	68% N–H stretch	88	2661.83	61.6% N-D stretch	1.3634
b_{1u}							
	95	3565.38	68% N–H stretch	87	2621.13	62.4% N-D stretch	1.3602
b_{2g}							
	23	641.4	54.8% N–H OPB	22	479.73	68.4% N-D OPB	1.3370
b_{3u}							
	36	760.82	52.8% N–H OPB	24	547.66	72% N-D OPB	1.3892
	24	656.65	22.4% N–H OPB	25	664.46	7.6% N-D OPB	**0.9882**
b_{2u}							
	67	1266.18	21.2% N–H IPB	66	1242.04	7.6% N-D IPB	1.0194
	63	1198.73	18.8% N–H IPB	62	1116.18	18% N-D IPB	1.0740
	52	970.32	19.2% N–H IPB	46	851.42	24% N-D IPB	1.1396
	51	957.23	4% N–H IPB	52	957.49	0% N-D IPB	0.9997
	38	776.51	10.8% N–H IPB	33	726.39	23.2% N-D IPB	1.0690
	33	748.85	2% N–H IPB	36	754.00	9.6% N-D IPB	**0.9932**
b_{3g}							
	62	1164.35	20.4% N–H IPB	61	1108.93	17.2% N-D IPB	1.0500
	65	1250.89	15.6% N–H IPB	65	1240.82	6% N-D IPB	1.0081
	64	1216.82	11.2% N–H IPB	65	1202.66	4.8% N-D IPB	1.0118
	49	950.62	26.4% N–H IPB	45	849.92	16.8% N-D IPB	1.1185
	39	778.95	14% N–H IPB	29	711.09	30% N-D IPB	1.0954

Note: Avoided crossings are easily identified when the ISR values are less than 1. Instances with particularly strong coupling, producing large avoided crossings, are highlighted in boldface.

Table 5. Contributions of the N–H internal modes to the normal modes involving crossings, or avoided crossings of porphine.

	H_2P			D_2P			ISR
Sym	Mode	Frequency	% Int. Mode	Mode	Frequency	% Int. Mode	νH/νD
a_g							
	108	3593.47	77.8% N–H stretch	96	2638.31	61.2% N-D stretch	1.3620
b_{1u}							
	107	3552.34	77.8% N–H stretch	95	2611.88	61.4% N-D stretch	1.3601
b_{2g}							
	23	631.22	50.8% N–H OPB	22	473.78	65.2% N-D OPB	1.3323
b_{3u}							
	35	739.89	32% N–H OPB	24	541.81	70.4% N-D OPB	1.3656
	24	651.38	21.2% N–H OPB	25	657.91	8.4% N-D OPB	**0.9901**
b_{2u}							
	71	1260.59	26% N–H IPB	65	1120.28	16.4% N-D IPB	1.1252
	67	1179.31	7.6% N–H IPB	69	1195.31	8% N-D IPB	**0.9866**
	57	1003.52	14.8% N–H IPB	50	882.81	27.2% N-D IPB	1.1367
	53	967.16	1.6% N–H IPB	55	967.44	0% N-D IPB	0.9997
	41	796.36	8% N–H IPB	38	759.71	18% N-D IPB	1.0482
b_{3g}							
	72	1264.10	26.4% N–H IPB	68	1184.59	10.8% N-D IPB	1.0671
	69	1213.11	4% N–H IPB	72	1214.33	0% N-D IPB	0.9990
	56	992.92	16.8% N–H IPB	49	881.53	20.0% N-D IPB	1.1264
	43	800.34	8.8% N–H IPB	36	752.31	24.4% N-D IPB	1.0638

Note: Avoided crossings are identified by ISR $<$ 1.

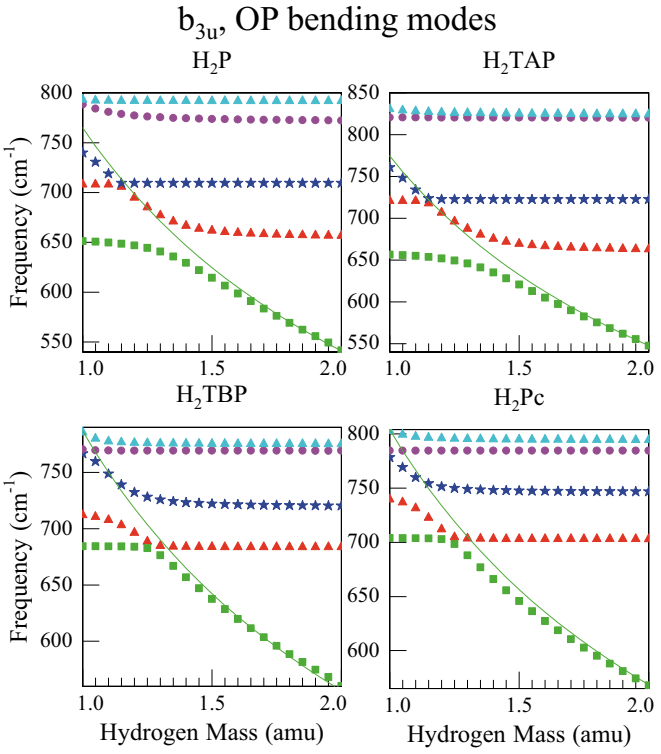
b_{2g} N–H bending modes

The H/D isotope dependences of the Raman-active b_{2g} N–H OPB modes of porphine and TAP are, as shown in the upper panels of Fig. 6, relatively straightforward, exhibiting a continuous mode evolution from the light to the heavy isotopologue. As indicated in Table 3, they exhibit an ISR of 1.33 and follow the simple mass dependence shown by the smooth curve in Fig. 6. In contrast, TBP and Pc are both complicated by the existence of an additional mode that is crossed by the N–H b_{2g} OPB mode at different locations.

Can. J. Chem. Downloaded from www.nrcresearchpress.com by MCGILL UNIVERSITY on 02/02/13
For personal use only.

Can. J. Chem. Downloaded from www.nrcresearchpress.com by MCGILL UNIVERSITY on 02/02/13
For personal use only.

Fig. 4. Mass dependence of the IR-active b_{3u} symmetry normal modes for the OPB vibrations. In contrast to the high frequency modes, strong coupling occurs between the N–H OPB modes and especially the C-H OPB modes. This is indicated by the large avoided crossing that is clearly evident in the top two panels where P and TAP results are shown. A strong correlation exists between the N–H OPB modes of the light and heavy isotopologues, as indicated by the theoretical mass dependence of the frequency. However, the frequency of the C-H OPB mode "crossed" by the N–H mode *increases* in the deuterated molecule, leading to reversed isotope shift ratios (ISR < 1).



Again, the mass dependence curve is very instructive in identifying the correct mode evolution. As listed in Table 3, the 711.7 cm^{-1} mode of H_2TBP correlates with the 520.1 cm^{-1} mode of D_2TBP, giving an ISR value of 1.368; a similar value is present for phthalocyanine. However, the curve avoidance that is now present produces ISR values significantly less than 1 in both cases for the modes crossed. Table 3 lists these as 0.991 and 0.989 for TBP and Pc, respectively.

IPB (b_{2u} and b_{3g}) modes

Summaries of the isotope dependences of the b_{2u} and b_{3g} N–H IPB modes are provided in Figs. 7 and 8, respectively. The mass dependences of these modes are evidently not simple but are quite similar for all 4 molecules. It is clear that these IPB modes do not show a mass dependence that is as strong as ($m_H^{-1/2}$), shown by the smooth line. Instead, several modes appear to have a weak, near-linear dependence on mass. The slope of the ($m_H^{-1/2}$) law is never approached, whatever the isotopologue. This effect is due to an extreme dilution of NH IP motions in many modes of the same symmetry. Modes exhibiting the highest absolute slope at $m_H = 1$ or 2 correspond in fact to the modes involving the highest % of NH or ND IP motion, respectively. This is verified in Tables 4 and 5, where the b_{2u} and b_{3g} modes exhibiting the highest % are reported for TAP and P, respectively.

b_{2u} N–H bending modes

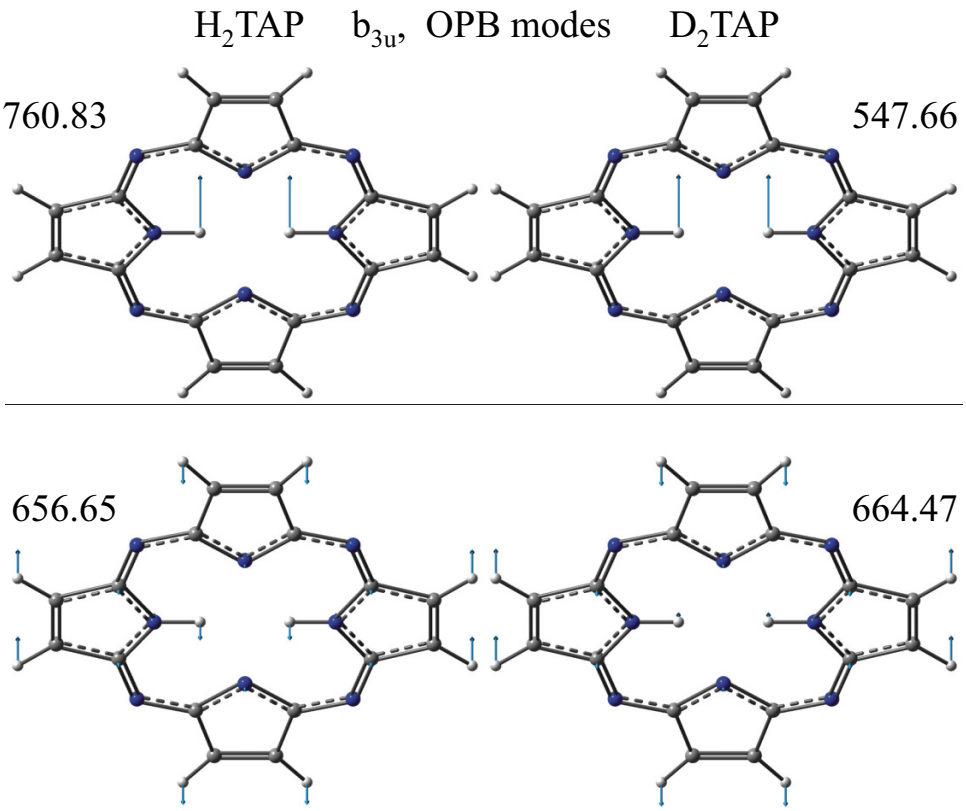
Some mode crossings do occur for the b_{2u} N–H IPB motion, and because of the similarity of the behaviour in the mid-frequency region for all 4 molecules, the modes in the 850–1070 cm^{-1} range have been chosen for inclusion in Table 3.

The IR-active b_{2u} modes of porphine and TAP are quite similar, showing a diluted effect upon isotopic substitution of the inner hydrogens. As listed in Table 3, the mode at 1003.5 cm^{-1} in H_2P, involving an N–H IPB, drops down to 882.8 cm^{-1} in D_2P. This shift corresponds to a ν_H/ν_D ratio of only 1.137, a value much less than $\sqrt{2}$. This mode shows a weak avoided crossing with the one at 967.2 cm^{-1}, a pyrrole ring stretching mode. This avoided crossing has the effect of increasing the frequency of the pyrrole ring stretching mode in D_2P by a small amount to 967.4 cm^{-1} and generating a ν_H/ν_D ratio of 0.9997. While the 0.27 cm^{-1} shift in frequency for the pyrrole mode is small, similar values are exhibited by all the tetrapyrroles, except Pc where it is yet smaller, 0.06 cm^{-1}. The significance of these ISR values is hard to ascertain because while they are consistently less than 1, they are very close to it. It is worth noting however that for the pure C-H stretching a_g and b_{1u} modes crossed over by the N–H(D) mode (see Figs. 2 and 3), the ISR values are much closer to 1. In the present IPB b_{2u} mode, vector diagrams indicate that there is some N–H character in the pyrrole ring stretch, so the small ISR values are deemed significant.

While not included in the global ISR summary provided in Table 3, it is evident in Fig. 7 that mode crossings do occur in the lower frequency range, but the crossing regions vary from molecule to molecule. Thus direct crossings are exhibited by P and Pc, while avoided crossings are present in TAP and TBP. Information on the avoided crossing in the former is provided in Table 4, where the 776.5 cm^{-1} mode of H_2TAP decreases to 726.4 cm^{-1} for D_2TAP with a small ISR value of 1.069. However, this then produces a frequency increase in the interacting mode at 748.9 cm^{-1} that moves up to 754.0 cm^{-1} in D_2TAP and has an ISR significantly less than 1, with a value of 0.9932. Porphine does not exhibit this behaviour, so a corresponding value is not given in Table 5.

In the higher frequency region, only P and TBP exhibit avoided crossings and detailed information on the behaviour of porphine is presented in Table 5. It is evident there that a reverse ISR is present with an upward frequency shift of 16 cm^{-1}, producing an ISR value of 0.9866. Thus the highest frequency N–H IPB mode at 1260.6 cm^{-1} correlates with the 1120.3 cm^{-1} mode of D_2P, yielding a diminished ISR of 1.125. A consequence of this attribution is that the H_2P mode at 1179.3 cm^{-1} must be associated with the 1195.3 cm^{-1} mode of D_2P. An upward shift of 108 cm^{-1} was previously highlighted by Li et al. for a b_{2u} symmetry asymmetric deformation, δ_{as}(NH), mode.[8] However, this earlier correlation involved modes at 986 and 1094 cm^{-1}, which do not correspond to the present ones at 1179 and 1195 cm^{-1}.

Fig. 5. Vector diagrams showing the very similar atomic motions involved in the pure N–H OPB motion of TAP for the hydrogenated and deuterated molecules, top left and right, respectively. In the bottom, the motions in the C-H mode involved in the avoided crossing with the N–H OPB are shown. The 656/664 cm^{-1} mode correlations of the two istopomers are clearly correct. However, on closer scrutiny it is evident that the direction of the small N–H motion, which this mode possesses, is reversed in the H and D molecules. This behavior is exhibited in all the modes involved in the avoided crossings.



Can. J. Chem. Downloaded from www.nrcresearchpress.com by MCGILL UNIVERSITY on 02/02/13
For personal use only.

b_{3g} IPB N–H modes

The Raman-active b_{3g} modes presented in Fig. 8 exhibit similar behaviour to the IR-active b_{2u} modes, but the mass dependence is even more diluted. This dilution effect is extreme in the case of the larger molecules TBP and Pc, where every mode, except one at 1140 cm^{-1}, shows a slight mass dependence. As a result, most of the modes are parallel, which mitigates against curve crossings. In contrast, the behaviour in P and TAP is more well-defined with two modes at around 810 and 1020 cm^{-1}, clearly mass independent, while the remainder all show some mass dependence.

Taking porphine as an example, the most "pure" N–H IPB mode (listed in Table 5 as 26.4%) has a frequency of 1264.1 cm^{-1}, a value that decreases to 1184.6 cm^{-1} as the mass is increased from 1 to 2 amu. As quoted in Table 3, this correlation produces a ν_H/ν_D ratio of 1.067, and the aforementioned mode exhibits an avoided crossing with the one at 1213.1 cm^{-1} involving C-H IPBs. It thereby generates a small increase in the frequency in the heavy isotopologue. This increase is listed in Table 3 as 1.22 cm^{-1}, and when compared with TBP, consistent ISR values of 0.999 are obtained. No curve crossings occur between these two modes in TAP. The TAP values chosen for inclusion in Table 3 were selected on the basis of the similarities of their motion with the 3 other tetrapyrrole molecules.

Discussion

To examine the occurrence of the reversed ISRs, the so-called product rule presented by Wilson et al. on isotope shifts in high-symmetry molecules will now be considered.[9] The general form of the product rule for isotopic substitution is given (Ref. 9, p. 248) as:

$$[2]\qquad \frac{\omega_1'\omega_2'\ldots\omega_n'}{\omega_1\omega_2\ldots\omega_n} = \left[\left(\frac{\mu_\alpha'}{\mu_\alpha}\right)^a\left(\frac{\mu_\beta'}{\mu_\beta}\right)^b\ldots\left(\frac{M'}{M}\right)^t\left(\frac{I_x'}{I_x}\right)^{r_x}\left(\frac{I_y'}{I_y}\right)^{r_y}\left(\frac{I_z'}{I_z}\right)^{r_z}\right]^{1/2}$$

Equation [2] pertains to all the vibrational frequencies $\omega_1\omega_2\ldots\omega_n$ of a single symmetry species for the light molecule, while $\omega_1'\omega_2'\ldots\omega_n'$ are the corresponding values of the heavy isotopologue. In eq. [2] the exponents *a, b,*. . . relate to the atoms being substituted, while the values of *t*, r_x, r_y, and r_z are the translation and rotation representations, respectively. μ, *M*, and *I* are the reduced mass, the total molecular mass, and the moments of inertia, respectively. Appendix A presents the equations specific to the 6 vibrational modes sensitive to H/D substitution of the two inner H-atoms for D_{2h} symmetry. A comparison of the numerical values arising from the DFT calculations done on H_2TAP/D_2TAP with the theoretical values predicted by the specific equations in Appendix A is provided in Table 6.

Can. J. Chem. Downloaded from www.nrcresearchpress.com by MCGILL UNIVERSITY on 02/02/13
For personal use only.

Fig. 6. Similar to Fig. 4 except for the Raman-active b_{2g} symmetry N–H OPB modes. Particularly simple behaviour is exhibited in the smaller molecules P and TAP, as indicated by the close agreement with the solid curve showing the theoretical mass dependence.

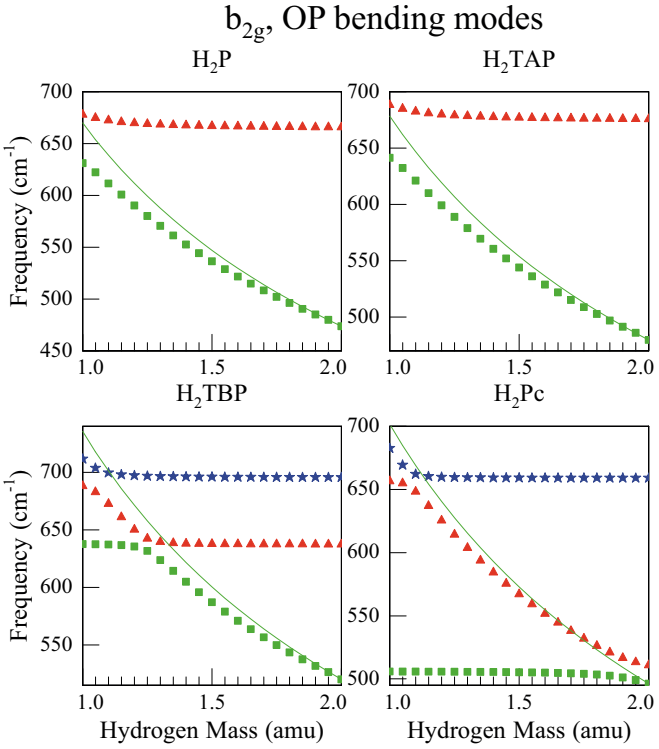
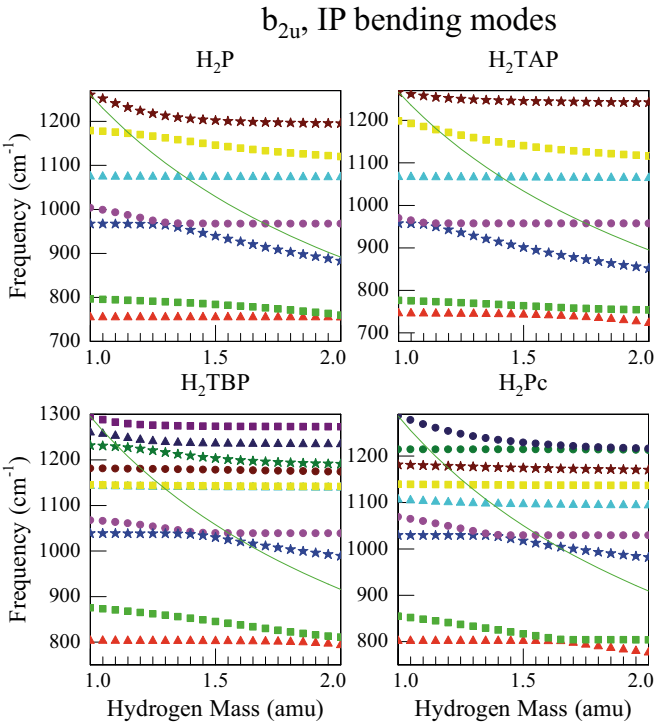


Fig. 7. Mass dependence of the IR-active b_{2u} symmetry for the N–H IPB modes. Particularly evident is the large number of modes and the fact that they nearly all show a dependence on mass. This reveals immediately that the N–H bending vibration is diluted over many modes, none of which can show the expected mass dependence of a pure mode indicated by the smooth curve.



As indicated by the values given in Table 6, the product rule unfortunately does not reveal the reversed ISR effect very clearly. However, the deviations between the calculated DFT values and those predicted by eq. [2] are largest for the IPB and OPB modes. These deviations, shown on the right-hand column in Table 6, are greater than the N–H stretch (STR) modes and the two modes where no H/D dependence is (correctly) predicted. The reason for this inability to highlight the reversed ISR is because eq. [2] involves *all* the modes of the same symmetry. This means that the normal modes with avoided crossings (reversed ISRs) are "compensated" by other regular modes. Despite this shortcoming, the product rule indicates the accuracy of the DFT results, as the deviations between calculation and theory are very small indeed.

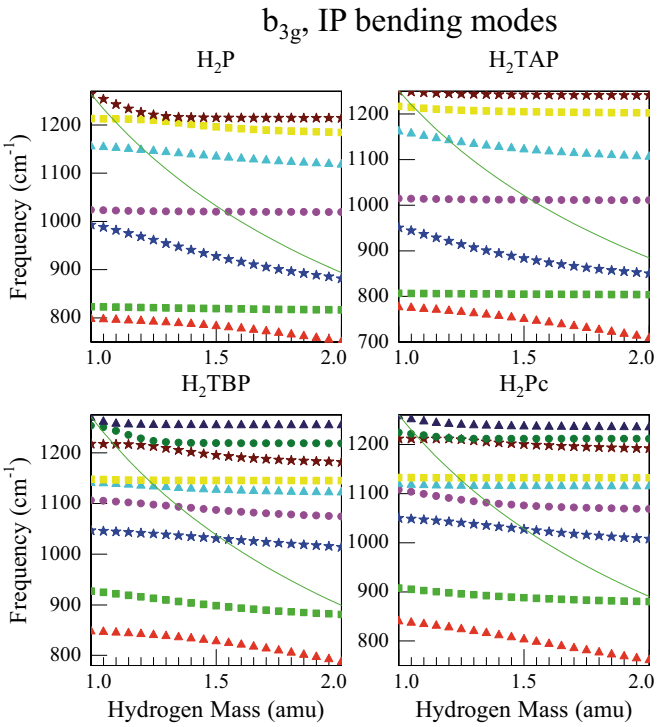
Comparison with other calculations

In the detailed theoretical study carried out by Li and Zgierski on developing a force field for free-base porphine, upward frequency shifts were proposed for the b_{1g} and b_{2u} IPB modes upon deuteration.[8] However, the previous study dealt only with the in-plane vibrations, namely the N–H stretching and IPB modes. Because of the use of a different axis system (see Note 11) in the current and previous works, b_{1g} symmetry of Li et al.[8] corresponds to our b_{3g} mode, while the b_{2u} modes are the same in both studies. In Scheme I of Ref. 8, these workers proposed a large increase in the frequency of two modes upon H/D isotopic substitution, both of which involved IPB. Specifically, they proposed that the b_{1g} N–H IPB mode crosses with the a pyrrole half-ring stretch mode, which had the effect of shifting the frequency of the pyrrole mode up by 56 cm^{-1}, from 976 cm^{-1} in H_2P to 1032 cm^{-1} in D_2P. The other mode that showed this effect was a b_{2u} mode, in which the asymmetric N–H IPB vibrations and the pyrrole ring stretch cross. This caused the pyrrole stretch to shift up in energy by 108 cm^{-1}, from 986 cm^{-1} to 1094 cm^{-1}. It is not evident why the OPB modes were not analysed for this effect in the earlier study; it may have been due to their interest in the role of the N–H stretch and IPB vibrations in the tautomerism of free-base porphine.[8]

As indicated in the upper left panels in Figs. 7 and 8, reverse isotope shifts of this magnitude are not exhibited by porphine in the b_{3g} and b_{2u} IPB modes, respectively. Evidently there are significant differences between Li's results[8] and the findings of the present DFT method. The earlier work identified only two instances of this increased frequency, both of which are much larger than what we find. These differences may arise for a number of reasons. Their calculations were carried out with the GF matrix method and a valence force field. While their method was paramaterised to give a good match with experimental data, it is likely the valence force field is not capable of accounting for all the interactions present in molecules of this size. Complete sets of force constants are of course available from quantum chemical calculations, and the use of high level DFT calculations are currently the most powerful for predicting the ground-state vibrational frequencies of large polyatomic molecules. Based on the favourable findings of our previous DFT results on ZnPc and H_2Pc and the matrix-IR spectra[6] of these

Can. J. Chem. Downloaded from www.nrcresearchpress.com by MCGILL UNIVERSITY on 02/02/13
For personal use only.

Fig. 8. Similar to Fig. 7 except for the Raman-active b_{3g} symmetry N–H IPB modes.



molecules, we are confident that the present results are a more accurate reflection of the extent of the up-shifted frequencies.

Li et al. identified the NH(D) IPB b_{2u} modes at 1223 (825) cm^{-1}, corresponding to 1261 (883) cm^{-1} in our calculations.[8] These modes exhibit, as listed in Table 5, the highest % of NH(D) IPB motion. A mode which also involves non-negligible NH bending motions was identified at 986 cm^{-1} (ν_{44a}) in the previous work and corresponds to the mode at 1003 cm^{-1} in the present work (14.8% N–H IPB in Table 5). This mode is found to correlate with the mode at 883 cm^{-1} in the deuterated species, i.e., the mode involving the highest % N-D IPB motion. In the discussed case, the entries in Table 5 show that modes at 1261 and 1003 cm^{-1} in the H species correlate with modes at 1120 and 883 cm^{-1}, with a decrease of the N-"H" IPB % in the higher frequency mode and an increase of the N-"H" IPB % in the lower frequency one, explaining the earlier result. It must be mentioned that the b_{2u} mode at 1094 cm^{-1} highlighted by Li et al.[8] in the correlations for the D species, corresponds to a mode at 1076 cm^{-1} in our calculation; this mode does not involve N-D IPB motion. The discrepancies between the earlier results from Li et al. and the present results on b_{3g} modes of porphine are similarly explained. The curves of Fig. 7 and 8 show clearly the correlations between H and D species and are summarized in Table 5. Because of a strong mixing of various atomic motions in the b_{3g} and b_{2u} modes for the frequency range of interest, a slightly different description of normal modes can have important consequences in their assignments, as highlighted by the example in this last discussion.

Comparison with experiments

The results of the current calculations can be compared with experimental isotope substitution work, but because the mass-related shifts are quite small in the congested 1500–500 cm^{-1} spectral range, high-resolution methods yielding narrow line transitions are required for analysis. The matrix-isolation technique is particularly well suited for this work. Currently however, only a very limited number of tetrapyrroles have been examined in this way. One system that has been examined already is our recent work on the phthalocyanines, from which the current investigation has emerged.[6] The other is the earlier study of Radziszewski et al., who used matrix-IR spectroscopy to look at deuteration effects in free-base porphine.[18] To compare the present theoretical results on porphine with the experimental matrix work,[19] the simulated DFT IR absorption spectra of H_2P and D_2P are shown scaled by a factor of 0.98 in Fig. 9 on the same spectral range as shown in Fig. 12 of the Radziszewski et al.[18] paper. The agreement between the two studies is very good, which testifies to the strength of the current method in predicting not only the IR absorption frequencies of the tetrapyrroles but also their intensities.

In agreement with Radziszewski et al.[18], the mode of H_2P, which was observed at 731 cm^{-1} and attributed to OPB, is predicted at 739.9 cm^{-1} (scaled by 0.98, 725.1 cm^{-1}) in the present calculations. However, their comment that this motion will be distributed over several fundamental modes of D_2P is not borne out by our calculations. As Fig. 10 shows (and listed in Table 3), the N-D OPB mode is well defined and is located at 541.8 cm^{-1} (scaled by 0.98, 530.9 cm^{-1}) in a sparse region of the IR spectrum. Moreover, it is actually much stronger than the corresponding H_2P OPB, so it should be easily identified. While Radziszewski et al. did not present any spectra for this lower frequency region in this early work[18], they did show a strong band around 540 cm^{-1} in Fig. 1 for D_2P in a more recent work.[20] Confusingly, this band is not listed under the D_2P (d_2) column in their Table 1 of Ref. 20, but instead a strong band at 540 cm^{-1} is listed for H_2P in the (d_0) column. From the actual H_2P (d_0) and D_2P (d_2) spectra shown in Fig. 1 of Ref. 20, we conclude that the 540 cm^{-1} band is the OPB of D_2P. Contrary to the expectation of Radziszewski et al.,[18] the frequency of this mode is indicative of an ISR value of a "pure" N–H vibration. This result is entirely consistent with the results of the current DFT calculations. Clearly, it is not a diluted motion, distributed over many bands as Radziszewski et al. stated in their 1989 paper.[18]

The reason this OPB vibration is not diluted over several modes is evident in Fig. 4. As indicated in that plot, its mass dependence is limited to just two modes, both of which exhibit the inverse dependence on the root of mass. This simple behaviour is entirely attributable to the small number (10) of b_{3u} symmetry modes listed in Table 1 for the OPB of free-base porphine. Essentially identical behaviour is predicted for TAP, while Fig. 4 predicts the OPB will only be slightly more complex in H_2TBP and H_2Pc because of the crossing of a single, lower frequency mode.

A key aspect of the current work is the upward shift in the frequencies of specific modes (highlighted in Table 3) in the heavier isotopologue upon H/D substitution. As indicated in that table, the most pronounced instance of this effect in free-base porphine is expected in the OPB mode, where the 651.4 cm^{-1} mode shifts up to 657.9 cm^{-1}. This region is highlighted in Fig. 10 on an expanded intensity scale. This region was presented in the more recent paper by Radziszewski

Can. J. Chem. Downloaded from www.nrcresearchpress.com by MCGILL UNIVERSITY on 02/02/13
For personal use only.

Table 6. A comparison of the numerical values arising from the DFT calculations done on the normal modes of H_2TAP/D_2TAP with the theoretical values predicted by the product rule for isotope shifts as given by eq. [2].

Symmetry (No.) Desc.	D_2TAP $\omega'_1 \ldots \omega'_n$	H_2TAP $\omega_1 \ldots \omega_n$	DFT Freq.Ratios $\omega'_1 \ldots \omega'_n/\omega_1 \ldots \omega_n$	Product rule (eq. [2])	$\Delta =$
a_g (17) STR	1.06216E+52	1.50154E+52	**0.707378629**	**0.707378522**	1.07126E-07
b_{1g} (7) *No H/D dep*	4.89979E+18	4.89978E+18	1.000000804	1	8.03673E-07
b_{2g} (8) OPB	1.59631E+21	2.25506E+21	**0.707879423**	**0.707760485**	0.000118938
b_{3g} (16) IPB	9.26087E+47	1.30883E+48	**0.707570706**	**0.707557622**	1.30842E-05
a_u (7) *No H/D dep*	5.81598E+18	5.81597E+18	1.000001708	1	1.70809E-06
b_{1u} (16) STR	1.38722E+49	1.95482E+49	**0.709641213**	**0.709641106**	1.06391E-07
b_{2u} (16) IBP	5.74105E+48	8.09008E+48	**0.70964135**	**0.709641106**	2.43709E-07
b_{3u} (9) OPB	5.8226E+22	8.20495E+22	**0.709644992**	**0.709641106**	3.88552E-06

Note: All the normal modes are given even those (b_{1g} and a_u symmetries) where no isotope (H/D) dependence is expected upon substitution of the two inner H-atoms (see Table 1).

Fig. 9. Low-resolution (fwhm = 4 cm^{-1}) plots of the IR absorption spectra generated by the DFT/B3LYP method for the vibrational modes of H_2P and D_2P. The spectral range and format has been selected for direct comparison with the matrix-IR absorption data published by Radziszewski et al.[18] As indicated, the predicted values are scaled by a factor of 0.98 throughout.

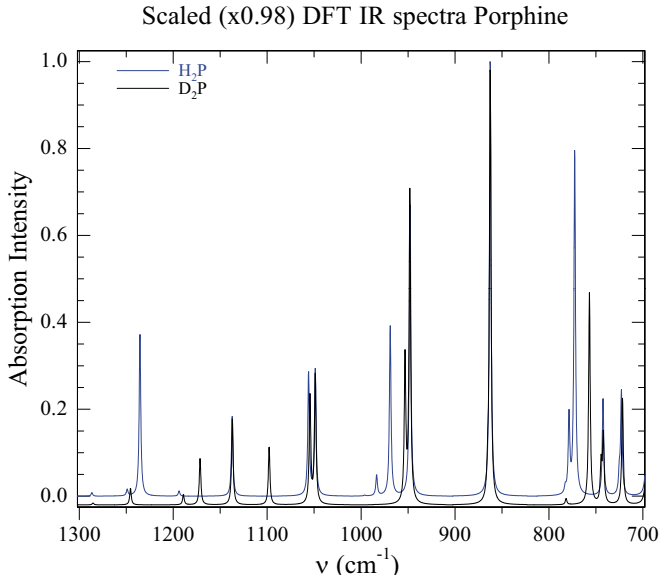
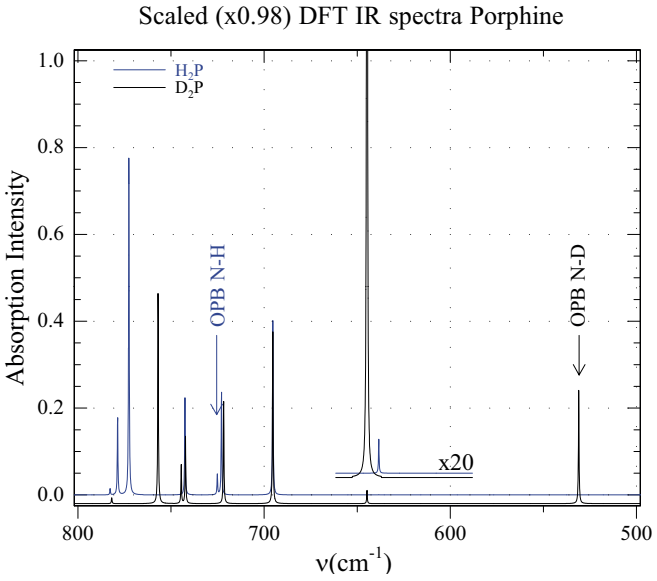


Fig. 10. High-resolution (fwhm = 0.2 cm^{-1}) plots of the IR absorption spectra generated by the DFT/B3LYP method for H_2P and D_2P. The spectral range presented is the region where the large isotope shift on the OPB is predicted. This range was presented in the latest matrix-IR absorption data published by Radziszewski et al.[20], but the band at 540 cm^{-1} in the D_2P spectrum was not attributed to the OPB mode of D_2P.



et al. but was not analysed or discussed in the text of the article.[20] In any case, the ISR effect will not be immediately evident in the recorded spectra, because while the D_2P mode at 657.9 cm^{-1} has significant intensity (4.3 km/mol), that of the related H_2P mode at 651.34 $cm^{-1}$is very weak (0.08 km/mol). In the experimental spectrum of the heavier isotope, this ISR effect will present an "unknown" peak in the spectrum not easily connected with H_2P. However, using the matrix-isolation technique, which has high sensitivity, it should be possible to observe the ISR effect in porphine as already done in phthalocyanine.[6]

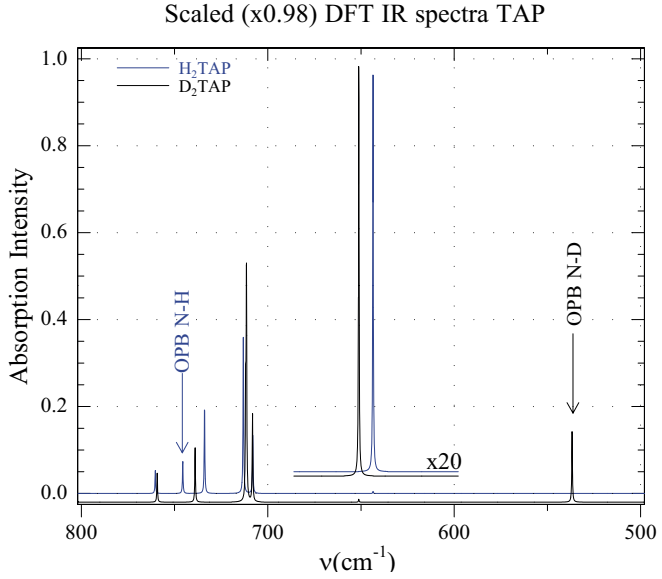
Future work on the reverse ISR effect

While the reverse ISR effect will not be immediately evident in porphine, the situation is much more favourable for its identification in TAP. Figure 11 presents the low-frequency spectral region of interest. Once again the OPB of this molecule shows the expected mass dependence of the N–H OPBs, as indicated by the labelled arrows. Fortuitously, in this case the intensities of the reversed ISR (0.988) modes are of comparable magnitude in the two isotopologues. These two bands are shown with expanded intensities in the centre of Fig. 11. On the basis of the present DFT calculations, TAP is the system of choice for a matrix-isolation study of this reverse ISR effect, because it produces the largest effect, the H_2TAP and D_2TAP modes are equally strong and they occur in a sparse region of the IR spectrum. To the best of our knowledge this study has not yet been attempted.

Conclusions

The results of the present DFT calculations of H/D substitution on the free-base tetrapyrroles can be summarized as follows. The

Fig. 11. High-resolution (fwhm = 0.2 cm^{-1}) plots of the IR absorption spectra generated by the DFT/B3LYP method for H_2TAP and D_2TAP. The spectra range and format has been selected for examination of the region where the large isotope shift on the OPB mode is predicted to occur.



high-frequency, N—H bond stretching modes are well localized and direct crossings occur with the C-H stretching modes. As these internal modes involve very different motions that are localized on specific bonds, no intermode coupling occurs, yielding the expected values for the isotope shift ratios.

The lower-frequency N–H OPB motions are not distributed over several normal modes principally because the b_{2g} and b_{3u} modes are not numerous. As a result, these modes involve well-defined OPB motions in both the N–H and the N–D bonds. For the smaller tetrapyrroles (P and TAP) no crossings occur for the b_{2g} symmetry Raman-active modes. In the larger molecules, crossings occur but the b_{2g} modes of Pc and TBP still involve localized N–H motions, as illustrated by the similarity with the simple mass-dependence curves. Due to a single mode crossing that occurs in both Pc and TBP, frequency increases do occur in the heavier isotopologue, but because of the involvement of only two modes, instances of reversed ISR can be easily identified in the mass-dependent calculations.

The IR-active b_{3u} OPB modes are slightly more numerous than their b_{2g} Raman counterparts and exhibit more complex behaviour. For all 4 molecules, the N–H OPB mode is crossed by two modes. Clear differences exist between the crossings of these two modes. One is not (or is only very weakly) coupled with the N–H OP bend and passes directly through, while the other mode is strongly coupled and produces a large avoided crossing. A consequence of the strong coupling in the latter case is that the frequency in the heavier isotopologue increases significantly yielding reversed ISR values.

More complicated behaviour is observed for the N–H IPB modes than the OPB modes just described because of the larger number of modes with b_{2u} and b_{3g} symmetries. As a result, the N–H motions are dispersed over many normal modes. Accordingly, the decrease in the NH frequencies is much less than the $m_H^{-1/2}$ mass dependence due to the dilution of this motion over several modes. No normal mode can be identified as "the" NH or ND IPB mode, since the percentages of NH(D) motion are always below 30%. Another consequence of this is that most of the modes are nearly parallel, which reduces the extent of modes crossings. Crossings appear in a congested spectral region, where a mode exists involving no NH(D) motion. This is the case in the region 1000 cm^{-1} in all molecules. In all instances, the crossing is direct and the modes are clearly not strongly coupled. For the b_{3g} modes couplings occur for some molecules in the high-frequency (1200 cm^{-1}) range but produce only weak avoided crossings. The best examples of this are present in porphine and TBP. This coupling does not occur in TAP and only weakly in Pc.

The b_{3u} and b_{2g} OPB modes provide the most clear-cut examples of the effect of avoided crossings. Thus, some of these modes have no effect on each other showing simple, direct crossing without intermode coupling, whereas large avoided crossings are observed in other cases, implying mode frequencies in the same spectral range. Reverse ISR values are obtained in these last cases of large avoided crossings, i.e., crossing between strongly coupled modes involving same atomic motions. This leads to a mixture of these motions, which depend very strongly on minor molecular effects such as the mass of the H atom on the vibration. In all the situations of reverse ISR effect, the vector diagrams of the atomic motions reveal a reversal of the directions of the N–H and N-D movements between the light and heavy isotopologue, explaining how ISR < 1 can arise.

Based on predictions made in the present work and the previously identified instance in which an ISR has already been observed in matrix-IR spectra[6] of the phthalocyanines, it would appear that TAP is the ideal system to make a definitive experimental study of this effect through observation of OPB modes.

Acknowledgement

This work was supported by the Ulysses France-Ireland research exchange grant 2010–2012 (PHC program Ulysses No. 25709VA).

References

(1) Braun, J.; Limbach, H.-H.; Williams, P. G.; Morimoto, H.; Wemmer, D. E. *J. Am. Chem. Soc.* **1996**, *118* (30), 7231. doi:10.1021/ja954146n.

(2) Baker, J.; Kozlowski, P. M.; Jarzecki, A. J.; Pulay, P. *Theor. Chem. Acc.* **1997**, *97* (1–4), 59. doi:10.1007/s002140050237.

(3) Mielke, Z.; Sobczyk, L. *Vibrational Isotope Effects in Hydrogen Bonds*, Chapter 10; In *Isotope Effects in Chemistry and Biology*; Kohen, A.; Limbach, H.-H., Eds.; CRC Press, Boca Raton, 2006; ISBN 0–8247–2449–6.

(4) An ISR effect of 2.9736, more than two times larger than the ν_H/ν_D ISR of 1.41, would occur in a substitution of muonium (Mu, mass 0.1139775 amu) by the H atom (1.0078250 amu), but because of the short lifetime of the former "atom", this is generally not a viable experimental proposal.

(5) Herzberg, G. *Molecular Spectra and Molecular Structure: Infrared and Raman of Polyatomic Molecules*; Krieger Pub Co., 1991.

(6) Murray, C.; Dozova, N.; McCaffrey, J. G.; FitzGerald, S.; Shafizadeh, N.; Crépin, C. *Phys. Chem. Chem. Phys.* **2010**, *12* (35), 10406. doi:10.1039/c0cp00055h.

(7) Milgrom, L. R. *The colours of life. An introduction to the chemistry of porphyrins and related compounds*; Oxford University Press, Oxford, 1997; ISBN 019–855380–3.

Can. J. Chem. Downloaded from www.nrcresearchpress.com by MCGILL UNIVERSITY on 02/02/13
For personal use only.

Can. J. Chem. Downloaded from www.nrcresearchpress.com by MCGILL UNIVERSITY on 02/02/13
For personal use only.

(8) Li, X.; Zgierski, M. Z. *J. Phys. Chem.* **1991**, *95* (11), 4268. doi:10.1021/j100164a020.
(9) Wilson, E. B.; Decius, J. C.; Cross, P. C. *Molecular Vibrations*; McGraw-Hill, New York, 1955, Reprinted, Dover, 1980.
(10) (a) Liu, J.; Zhang, X.; Zhang, Y.; Jiang, J. *Spectrochim. Acta [A]* **2007**, *67* (5), 1232. doi:10.1016/j.saa.2006.10.013; (b) Zhang, X.; Zhang, Y.; Jiang, J. *Vib. Spectrosc.* **2003**, *33* (1–2), 153. doi:10.1016/j.vibspec.2003.08.001.
(11) In our previous vibrational analysis of the phthalocyanines (Ref. 4) the *z*-axis was chosen perpendicular to the plane of the molecules H_2Pc and D_2Pc. This was done to allow the modes of these D_{2h} species to be directly correlated with those of D_{4h}, ZnPc. Use, in the present work, of the axes system in which the *z*-axis is aligned with the two N–H bonds has the effect of interchanging the 1 and 3 subscripts of the irreducible representations.
(12) Longuet-Higgins, H. C. *Proc. R. Soc. Lond. A Math. Phys. Sci.* **1975**, *344* (1637), 147. doi:10.1098/rspa.1975.0095.
(13) Frisch, M. J.; Trucks, G. W.; Schlegel, H. B.; Scuseria, G. E.; Robb, M. A.; Cheeseman, J. R.; Montgomery, J. A., Jr.; Vreven, T.; Kudin, K. N.; Burant, J. C.; Millam, J. M.; Iyengar, S. S.; Tomasi, J.; Barone, V.; Mennucci, B.; Cossi, M.; Scalmani, G.; Rega, N.; Petersson, G. A.; Nakatsuji, H.; Hada, M.; Ehara, M.; Toyota, K.; Fukuda, R.; Hasegawa, J.; Ishida, M.; Nakajima, T.; Honda, Y.; Kitao, O.; Nakai, H.; Klene, M.; Li, X.; Knox, J. E.; Hratchian, H. P.; Cross, J. B.; Bakken, V.; Adamo, C.; Jaramillo, J.; Gomperts, R.; Stratmann, R. E.; Yazyev, O.; Austin, A. J.; Cammi, R.; Pomelli, C.; Ochterski, J. W.; Ayala, P. Y.; Morokuma, K.; Voth, G. A.; Salvador, P.; Dannenberg, J. J.; Zakrzewski, V. G.; Dapprich, S.; Daniels, A. D.; Strain, M. C.; Farkas, O.; Malick, D. K.; Rabuck, A. D.; Raghavachari, K.; Foresman, J. B.; Ortiz, J. V.; Cui, Q.; Baboul, A. G.; Clifford, S.; Cioslowski, J.; Stefanov, B. B.; Liu, G.; Liashenko, A.; Piskorz, P.; Komaromi, I.; Martin, R. L.; Fox, D. J.; Keith, T.; Al-Laham, M. A.; Peng, C. Y.; Nanayakkara, A.; Challacombe, M.; Gill, P. M. W.; Johnson, B.; Chen, W.; Wong, M. W.; Gonzalez, C.; Pople, J. A. *Gaussian 03, Revision E.01*; Gaussian Inc., Wallingford, CT, 2004.
(14) Gardner, A. M.; Wright, T. G. *J. Chem. Phys.* **2011**, *135* (11), 114305. doi:10.1063/1.3638266.
(15) Groner, P. *Normal coordinate analysis*; In *Handbook of Vibrational Spectroscopy*; Vol. 3; Chalmers, J. M.; Griffiths, P. R.; Wiley, NY.; p. 1992, 2002.
(16) The theoretically predicted ν_H/ν_D ratio depends on the reduced mass of the normal mode under consideration. It will be close to, but slightly less than $\sqrt{2}$ in the case of a pure X-H(D) vibration, where X is the mass of the entire molecule minus 1(2). Since the mass of the H-atom is 1.0078250 amu and the D atom is 2.0141018 amu, the limiting (with X of infinite mass) predicted ν_H/ν_D ratio is $\sqrt{1.9985} = 1.41367$.
(17) This finding may seem inconsistent with the group theory analysis presented in Table 1, but the additional modes of TBP and Pc are located at frequencies both above and below the range shown in the figure. The least number of modes are indeed present in the smaller molecules P and TAP.
(18) Radziszewski, J. G.; Waluk, J.; Michl, J. *Chem. Phys.* **1989**, *136* (2), 165. doi:10.1016/0301-0104(89)80044-8.
(19) Radziszewski, J. G.; Waluk, J.; Nepras, M.; Michl, J. *J. Phys. Chem.* **1991**, *95* (5), 1963. doi:10.1021/j100158a015.
(20) Radziszewski, J. G.; Nepras, M.; Balaji, V.; Waluk, J.; Vogel, E.; Michl, J. *J. Phys. Chem.* **1995**, *99* (39), 14254. doi:10.1021/j100039a011.

Appendix A

The values of the numbers *t*, r_x, r_y, and r_z in eq. [2] can be read directly from the character table of the point group, while the exponents *a, b*. . . must be determined by group theoretical methods for the atoms concerned. For the D_{2h} molecule free-base tetraazaporphine (H_2TAP) H/D substitution will produce the reducible representation (Γ_{iH}) for the motion involving ONLY the two inner H-atoms

$$\Gamma_{iH} = 6 \quad -2 \quad 0 \quad 0 \quad 0 \quad 0 \quad 2 \quad 2$$

which gives $1a_g$, $1b_{2g}$, $1b_{3g}$, $1b_{1u}$, $1b_{2u}$, and $1b_{3u}$. Thus, the value for exponent *a* is 1 in the case of H/D substitution for all six symmetries. Moreover, as *only* H-atoms are being substituted, the reduced mass term μ'_α/μ_α in eq. [2] becomes m_H/m_D.

Substitution of these values in eq. [2] thereby provides the following expressions for the isotopic shifts of the 6 modes affected by substitution of the two inner hydrogen atoms.

a_g [17]:
$$\frac{\omega'_8\omega'_{17}\ldots\omega'_{69}\omega'_{72}}{\omega_8\omega_{17}\ldots\omega_{69}\omega_{72}} = \left[\left(\frac{m_H}{m_D}\right)^1\right]^{1/2}$$

b_{2g} [8]:
$$\frac{\omega'_5\omega'_{11}\ldots\omega'_{31}\omega'_{39}}{\omega_5\omega_{13}\ldots\omega_{32}\omega_{35}} = \left[\left(\frac{m_H}{m_D}\right)^1\left(\frac{I_Y^{D2}}{I_Y^{H2}}\right)^1\right]^{1/2}$$

b_{3g} [16]:
$$\frac{\omega'_9\omega'_{13}\ldots\omega'_{64}\omega'_{68}}{\omega_9\omega_{12}\ldots\omega_{64}\omega_{68}} = \left[\left(\frac{m_H}{m_D}\right)^1\left(\frac{I_x^{D2}}{I_x^{H2}}\right)^1\right]^{1/2}$$

b_{1u} [16]:
$$\frac{\omega'_{14}\omega'_{23}\ldots\omega'_{66}\omega'_{71}}{\omega_{11}\omega_{19}\ldots\omega_{66}\omega_{71}} = \left[\left(\frac{m_H}{m_D}\right)^1\left(\frac{M^{D2}}{M^{H2}}\right)^1\right]^{1/2}$$

b_{2u} [16]:
$$\frac{\omega'_9\omega'_{13}\ldots\omega'_{64}\omega'_{68}}{\omega_9\omega_{12}\ldots\omega_{64}\omega_{68}} = \left[\left(\frac{m_H}{m_D}\right)^1\left(\frac{M^{D2}}{M^{H2}}\right)^1\right]^{1/2}$$

b_{3u} [9]:
$$\frac{\omega'_1\omega'_3\ldots\omega'_{27}\omega'_{33}}{\omega_1\omega_3\ldots\omega_{26}\omega_{34}} = \left[\left(\frac{m_H}{m_D}\right)^1\left(\frac{M^{D2}}{M^{H2}}\right)^1\right]^{1/2}$$

In these equations the mode numbering, ω_n, is that generated by the DFT calculation, which also provides the moments of inertia for the two isotopologues. m_H and m_D are the atomic masses of hydrogen and deuterium, respectively, while M^{D2} and M^{H2} are the molecular masses of D_2TAP and H_2TAP, respectively. The outcome of this analysis is compared with DFT results in Table 6.

TRIBUTE

Can. J. Chem. Downloaded from www.nrcresearchpress.com by Renmin University of China on 09/02/12
For personal use only.

Tak-Hang (Bill) Chan was born on 28 June 1941 in Hong Kong. He developed an interest in chemistry during his high school years very much because of the inspiring teaching of his chemistry teacher, K.T. Cheung, of Pui Ching Middle School in Hong Kong. After finishing high school, he applied to Canadian universities and was admitted to the University of Ottawa. Even though his family did not have the financial resources to support his education in Canada, they scraped up enough money to get him the airfare to Canada in 1958. In his first year of study, he worked as a dishwasher on the weekends to pay for his tuition and living expenses. In the summer of 1959, he started his first summer job as a gardener. The work was short-lived, but his employer gave him the nickname Bill, which he has continued to use.

He transferred to the University of Toronto (U of T) where he completed his undergraduate education while continuing to work part time. At U of T, he came under the influence of George Wright (organometallic chemistry) and Adrian Brook (organosilicon chemistry), leading to a later research interest in those areas. In the summers of 1961 and 1962, he worked as a summer research student in the laboratory of Morris Kates with the National Research Council of Canada (NRC) in Ottawa, Ontario. At that time, chemistry at U of T was very much physical science (mathematics, physics, and chemistry) in emphasis. The work in the Kates' lab exposed him to biochemistry and, together, they published two papers on lipid chemistry. After completion of his undergraduate degree in 1962, he was accepted into the graduate program at Princeton University, Princeton, New Jersey. However, before he went to the United States, he applied for and was granted landed immigrant status in Canada.

At Princeton University, Bill did his Ph.D. thesis under the supervision of Richard Hill, a true scholar/teacher. The thesis research allowed him to appreciate the wonderful world of natural products and the challenge of stereochemistry. By 1965, he was ready to finish his Ph.D. thesis. This was also the year that Robert Woodward, together with Roald Hoffmann, electrified the chemical world with the publication of a series of papers on the role of orbital symmetry on chemical reactions. In spite of other tempting offers, he decided to work for a year as a postdoctoral fellow in Woodward's laboratory on the total synthesis of vitamin B_{12}. It was a tremendous experience, not only in learning from the great master, but also to meet other bright young chemists, especially the contingent from Canada, including Pierre Deslongchamps, Larry Weiler, Chiu Ming Wong, and David Dolphin.

Bill Chan joined the chemistry department of McGill University, Montreal, Quebec, in 1966 and began his independent research career. During his McGill career, Bill served as Chair of the Chemistry Department (1985–1991), Dean of Science (1991–1999), and Vice Principal (Academic) (1994–1999). In 2000, he was named the Tomlinson Professor of Chemistry, a chair that he held until his retirement in 2005. Bill now serves the Department in the well-deserved capacity of Professor Emeritus. In 1979, he was the first Western scientist to bring modern chemistry to China in the post-Cultural Revolution era, and had an enormous impact on Chinese chemistry.

In the first phase of his research, Chan made pioneering contributions to the use of organosilicon reagents for organic synthesis. He and his co-workers developed the use of β-functionalized silanes for alkene synthesis (T.H. Chan. *Acc. Chem. Res.* 1977, **10**: 442–448). This led to a general synthesis of allenes, allene oxides, and bridgehead alkenes. Following that, he examined the regioselectivity and stereochemistry of electrophilic substitution of vinylsilanes. Together with Ian Fleming of the University of Cambridge, Cambridge, UK, he published an important review (T.H. Chan and I. Fleming. *Synthesis*. 1979. 761–786), which has served as the key review in the use of organosilicon compounds for organic synthesis. Chan then developed the use of enol silyl ethers for synthesis. An important contribution was the use of 1,3-bis(trimethylsiloxy)-1-methoxy-1,3-butadiene as a dianion equivalent of methyl acetoacetate. This synthon is often referred to in the chemical literature as "Chan's diene" and is used in many synthetic applications including a novel cycloaromatization reaction (P. Brownbridge, T.H. Chan, M. Brook, and G.J. Kang. *Can. J. Chem.* 1983. **61**: 688). In the course of his study on enol silyl ether chemistry, a new rearrangement reaction was discovered (S.D. Lee, T.H. Chan, and K.S. Kwon. *Tetrahedron Lett*. 1984. **25**: 3399) and is now known as the Chan Rearrangement. The reaction has been used in the syntheses of several complex natural products including boromycin, taxol, and diazonamide A. Another focus of his in organosilicon chemistry involved the study of α-silylcarbanions, which have been used for enantioselective (T.H. Chan and P. Pellon. *J. Am. Chem. Soc.* 1989. **111**: 8737–8738) and regioselective synthesis (T.H. Chan, K. Koumaglo, R. Horvath, D. Wang, Z.Y. Wei, G.L. Yi, and J.S. Li. 1988. *Silicon chemistry*. Ellis Horwood Ltd., New York. Chapter 5).

From 1990 onward, Chan began the second phase of his research career. He has played a leadership role in the development of green chemistry research in Canada. Green chemistry is the effort to develop new chemical reactions and processes that are benign to the environment. The field is relatively young and the term "green chemistry" was first coined in the 1990s. In 1991, he published his first research paper on a new organometallic reaction in aqueous media together with his graduate student, C.J. Li (C.J. Li and T.H. Chan. *Tetrahedron Lett.* 1991. **32**: 7017–7020). Before this study, organometallic-type reactions were usually carried out in organic solvent under anhydrous conditions. Chan was able to demonstrate that a number of organometallic-type reactions can be carried out in aqueous media (T.H. Chan, C.J. Li, M.C. Lee, and Z.Y. Wei. *Can. J. Chem.* 1994. **72**: 1181–1192). In particular, the indium-mediated reaction has found extensive applications in organic synthesis, especially for carbohydrates, as this eliminates the need for protecting group chemistry.

Chan has also contributed to the understanding of the mechanisms of these reactions in aqueous media (T.H. Chan and Y. Yang. *J. Am. Chem. Soc.* 1999*.* 141: 3228–3229; W. Miao, L.W. Chung, Y.-D. Wu, and T.H. Chan. *J. Am. Chem. Soc.* 2004. **126**: 13326–13334). Chan then followed the study in aqueous media to the investigation of organometallic reactions in ionic liquids, including the use of indium, tin, zinc, and magnesium (M.C. Law, K.Y. Wong, T.H. Chan. *Chem. Commun.* 2006. 2457–2459).

As a result of the study on ionic liquids, he and his group proposed a novel liquid-phase strategy for organic synthesis by using ionic tags as a soluble support (W. Miao and T.H. Chan. *Acc. Chem. Res.* 2006. **39**: 897–908). The homogeneous reaction is usually carried out in a relatively polar solvent. After the reaction, the ion-tagged species is easily separated from

Can. J. Chem. Downloaded from www.nrcresearchpress.com by Renmin University of China on 09/02/12
For personal use only.

the other reagents by precipitation with a less polar solvent. The ion-tagged species can function in the role of a catalyst, as a reagent, or as the substrate in the synthesis of small molecules or bio-oligomers. He demonstrated the success of this approach in the synthesis of peptides, oligosaccharides, and nucleotides in collaboration with Masad Damha of McGill University (R.A. Donga, M. Hassler, T.H. Chan, and M.J. Damha. *Nucleosides, Nucleotides and Nucleic Acids.* 2007. **26**(10–12): 1287–1293).

In 1997, Chan and Li published the monograph *Organic Reactions in Aqueous Media*, and this was the first book on the subject and was recognized as the definitive reference in the field. In 2007, a second edition, *Comprehensive Organic Reactions in Aqueous Media*, was published to bring up-to-date the development in this important and rapidly expanding area of research.

In addition to his research contributions, Chan is also dedicated to the teaching of green chemistry to students. In 2000, he developed and taught the first undergraduate course on green chemistry offered in a Canadian university. He has championed green chemistry teaching by sharing his experience in teaching this course with colleagues in Canada and internationally. A number of Canadian universities now offer green chemistry as part of their curriculum. In 2002, Chan became the founding coordinator of the Canadian Green Chemistry Network, linking more than 50 researchers from over 20 Canadian universities and research institutes with the mission to promote green chemistry research and education in Canada, as well as to foster international collaboration. This network serves as part of the international networks affiliated with the Green Chemistry Institute of the American Chemical Society. Green chemistry is now a thriving area of research in several Canadian universities including Queen's University, Kingston, Ontario, Saint Mary's University, Halifax, Nova Scotia, University of Ottawa, McGill University, and Université de Montréal. Bill Chan has been cited as "le «père» de la chimie verte au Canada" (see *Le magazine de l'Université de Sherbrooke.* Vol. 1, No. 1).

Chan has contributed to research in medicinal/pharmaceutical chemistry. This had started as an interest in natural products chemistry with a synthesis of specionin, which may be of interest in controlling the spruce budworm problem in Canada (A.K. Mohammad-Ali, T.H. Chan, A.W. Thomas, B. Jewett, and G.M. Strunz. *Can. J. Chem.* 1994. **72**: 2137–2143). This was followed by the enantioselective synthesis of epigallocatechin-3-gallate (EGCG), the active polyphenol component from green tea (L. Li and T.H. Chan. *Org. Lett.* 2001. **3**: 739–741). In collaboration with Q.P. Dou of the Karmanos Cancer Center of Wayne State University, Detroit, Michigan, an extensive program on the development of green tea polyphenols and analogs as anticancer agents has been developed. This has led to a novel pro-drug of the green tea polyphenol (–)-epigallocatechin-3-gallate as a potential anticancer agent. (K.R. Landis-Piwowar, C. Huo, D. Chen, V. Milacic, G. Shi, T.H. Chan, and Q.P. Dou. *Cancer Res.* 2007. **67**: 4303–4310). The compound was found to be active in animal models against breast cancer and androgen-independent prostate cancer. Several patents on green tea polyphenols have been filed worldwide and some have been granted.

Another ongoing project is in collaboration with Larry M.C. Chow of the Hong Kong Polytechnic University to discover novel flavonoid dimers for overcoming multidrug resistance in cancer chemotherapy. Treatment of cancer patients with chemotherapeutic drugs often leads to the emergence of tumors with a multidrug-resistant (MDR) phenotype, which constitutes a major obstacle for cancer chemotherapy. Three major ATP-binding cassette (ABC) family members, ABCB1, ABCC1, and BCRP, are responsible for the majority of efflux-based MDR. Chan and his collaborators have developed potent modulators for all three types of transporters with safety and selectivity (K.F. Chan, Y. Zhao, B.A. Burkett, I.L. Wong, L.M. Chow, and T.H. Chan. *J. Med. Chem.* 2006. **49**: 6742–6759; I.L. Wong, K.F. Chan, K.H. Tsang, C.Y. Lam, Y. Zhao, T.H. Chan, L.M. Chow. *J. Med. Chem.* 2009. **52**: 5311–5322; K.F. Chan, I.L.K. Wong, B.A. Burkett, Y. Zhao, C.S.W. Yan, J.W.Y. Kan, K.H. Tsang, C.Y. Lam, T. Chow, T.H. Chan, and L.M.C. Chow. *Prog. Nutr.* 2010. **12**: 51–57). Several patents on these novel flavonoid dimers have been filed and development is expected to continue.

Bill Chan has received numerous awards including the Merck Sharpe & Dohme Award (1982), the Canada Council's Senior Killam Fellowship (1983–1985), and the R.U. Lemieux Award of the Canadian Society of Chemistry (1993). He was also named Fellow of the Royal Society of Canada in 1993. Now we are privileged to have this special issue of the *Canadian Journal of Chemistry* dedicated to him, to celebrate his outstanding contributions to scientific research, to science education, and his service to the broad scientific community in Canada and worldwide.

Chao-Jun Li
McGill University, Montreal, Quebec

Michael A. Brook
McMaster University, Hamilton, Ontario

HOMMAGE

Can. J. Chem. Downloaded from www.nrcresearchpress.com by Renmin University of China on 09/02/12
For personal use only.

Tak-Hang (Bill) Chan est né le 28 juin 1941 à Hong Kong. Il manifeste de l'intérêt pour la chimie au cours de ses études secondaires, en grande partie grâce aux talents d'enseignement de son professeur de chimie, K.T. Cheung, à l'école intermédiaire Pui Ching (Hong Kong). À la fin de ses études secondaires, il fait des demandes auprès d'universités canadiennes et est admis à l'Université d'Ottawa. Même si sa famille ne dispose pas des ressources financières nécessaires pour soutenir son éducation au Canada, elle rassemble à grand-peine suffisamment d'argent pour payer son billet d'avion, en 1958. Au cours de sa première année d'études, il travaille la fin de semaine comme plongeur de vaisselle pour payer ses frais de scolarité et de subsistance. Au cours de l'été 1959, il obtient son premier emploi d'été comme jardinier. Ce travail est de courte durée, mais son employeur le surnomme Bill, surnom qu'il utilise encore aujourd'hui.

Il quitte l'Université d'Ottawa pour l'Université de Toronto où il termine ses études de premier cycle tout en occupant un emploi à temps partiel. Là-bas, il se retrouve sous l'influence de George Wright (chimie organométallique) et d'Adrian Brook (chimie des composés d'organosilicium), ce qui le mènera plus tard à s'intéresser à ces deux domaines de recherche. Au cours des étés 1961 et 1962, il travaille comme étudiant d'été au laboratoire de Morris Kates pour le Conseil national de recherches du Canada (CNRC) à Ottawa (Ontario). À cette époque, on considère la chimie surtout comme une science physique (mathématiques, physique et chimie) à l'Université de Toronto. Les travaux effectués au laboratoire de Kates l'exposent à la biochimie et ensemble, ils publient deux articles sur la lipochimie. Après l'obtention de son diplôme de premier cycle en 1962, il est accepté au programme d'études supérieures à l'Université de Princeton au New Jersey. Toutefois, avant de se rendre aux États-Unis, il fait une demande de statut d'immigrant admis au Canada, qu'il obtient.

À l'Université de Princeton, Bill rédige sa thèse de doctorat sous la direction de Richard Hill, un véritable professeur érudit. Cette thèse de recherche lui permet de comprendre le monde merveilleux des produits naturels et le défi que représente la stéréochimie. En 1965, il termine sa thèse de doctorat. C'est également l'année où Robert Woodward et Roald Hoffmann exaltent le monde de la chimie par la publication d'une série d'articles sur le rôle de la symétrie orbitale dans les réactions chimiques. Malgré d'autres offres alléchantes, Bill décide de travailler pendant un an à titre de boursier postdoctoral au laboratoire de Robert Woodward sur la synthèse totale de la vitamine B_{12}. Cette expérience est extraordinaire, non seulement pour apprendre au contact du grand maître, mais aussi pour faire la rencontre d'autres jeunes chimistes brillants, en particulier le contingent canadien composé notamment de Pierre Deslongchamps, de Larry Weiler, de Chiu Ming Wong et de David Dolphin.

Bill Chan se joint au Département de chimie de l'Université McGill de Montréal (Québec) en 1966 et commence sa carrière de chercheur indépendant. Au cours de sa carrière à McGill, il s'acquitte des fonctions de directeur du Département de chimie (1985–1991), de doyen des sciences (1991–1999) et de vice-recteur à l'enseignement (1994–1999). En 2000, il est nommé Professeur Tomlinson de chimie, une chaire qu'il dirige jusqu'au moment de sa retraite, en 2005. Maintenant, Bill offre ses services au Département à titre de professeur émérite, titre qu'il a bien mérité. En 1979, il est le premier scientifique occidental à introduire la chimie moderne en Chine dans l'ère de l'après-révolution culturelle, et il a une influence énorme sur la chimie en Chine.

Dans la première phase de ses travaux de recherche, Bill apporte des contributions d'avant-garde à l'utilisation de réactifs d'organosilicium dans la synthèse organique. Avec ses collègues, il intègre l'utilisation de silanes β-fonctionnalisés dans la synthèse des alcènes (T.H. Chan. *Acc. Chem. Res.* 1977, **10**: 442–448). Cette intégration conduit à une synthèse générale d'allènes, d'oxydes d'allène et d'alcènes en tête de pont. Par la suite, il examine la régiosélectivité et la stéréochimie de la substitution électrophile des vinylsilanes. En collaboration avec Ian Fleming de l'Université de Cambridge (Royaume-Uni), il publie un article de synthèse important (T.H. Chan et I. Fleming. *Synthesis*. 1979. 761–786) qui sert de synthèse clé dans l'utilisation de composés d'organosilicium pour la synthèse organique. Bill met ensuite au point l'utilisation des éthers d'énols silylés pour la synthèse. L'une de ses contributions importantes est l'utilisation du 1,3-bis(triméthylsiloxy)-1-méthoxy-1,3-butadiène comme équivalent dianion de l'acétoacétate de méthyle. Dans la documentation relative à la chimie, on appelle souvent ce synthon le « diène de Chan », que l'on utilise dans de nombreuses applications synthétiques, dont une réaction de cycloaromatisation originale (P. Brownbridge, T.H. Chan, M. Brook et G.J. Kang. *Can. J. Chem.* 1983. **61**: 688). Au cours de ses travaux sur la chimie des éthers d'énols silylés, il découvre une nouvelle réaction de réarrangement (S.D. Lee, T.H. Chan et K.S. Kwon. *Tetrahedron Lett.* 1984. **25**: 3399) que l'on nomme désormais le réarrangement de Chan. Cette réaction est utilisée dans la synthèse de plusieurs produits naturels complexes, dont celle de la boromycine, du paclitaxel et du diazonamide A. Un autre volet de ses travaux en chimie des organosiliciums est l'étude des α-silylcarbanions, utilisés dans la synthèse énantiosélective (T.H. Chan et P. Pellon. *J. Am. Chem. Soc.* 1989. **111**: 8737–8738) et régiosélective (T.H. Chan, K. Koumaglo, R. Horvath, D. Wang, Z.Y. Wei, G.L. Yi et J.S. Li. 1988. *Silicon chemistry*. Ellis Horwood Ltd., New York. Chapitre 5).

À partir de 1990, Bill Chan amorce la seconde phase de sa carrière de chercheur. Il joue un rôle de chef de file dans le développement de la recherche en chimie verte au Canada. La chimie verte consiste à s'efforcer de mettre au point des réactions et des procédés chimiques originaux qui ne nuisent pas à l'environnement. Ce domaine est relativement jeune et l'expression « chimie verte » a été inventée dans les années 1990. En 1991, il publie avec C.J. Li, son étudiant diplômé, son premier article sur une nouvelle réaction organométallique en milieu aqueux (C.J. Li et T.H. Chan. *Tetrahedron Lett.* 1991. **32**: 7017–7020). Avant la réalisation de ces travaux, on effectuait généralement les réactions de type organométallique dans un solvant organique, sous des conditions anhydres. Bill parvient à démontrer que plusieurs réactions de type organométallique peuvent se produire en milieu aqueux (T.H. Chan, C.J. Li, M.C. Lee et Z.Y. Wei. *Can. J. Chem.* 1994. **72**: 1181–1192). Notamment, on découvre de vastes applications de la réaction médiée par l'indium en synthèse organique, surtout pour les hydrates de carbone, car elle permet d'éliminer le recours à des groupes protecteurs.

Bill Chan contribue également à la compréhension des mécanismes de ces réactions en milieu aqueux (T.H. Chan et Y. Yang. *J. Am. Chem. Soc.* 1999. 141: 3228–3229; W. Miao,

Can. J. Chem. Downloaded from www.nrcresearchpress.com by Renmin University of China on 09/02/12
For personal use only.

L.W. Chung, Y.-D. Wu et T.H. Chan. *J. Am. Chem. Soc.* 2004. **126**: 13326–13334). Par la suite, il se sert de ses travaux en milieu aqueux pour étudier les réactions organométalliques dans des liquides ioniques, en utilisant notamment l'indium, l'étain, le zinc et le magnésium (M.C. Law, K.Y. Wong, T.H. Chan. *Chem. Commun.* 2006. 2457–2459).

Les travaux menés sur les liquides ioniques donnent lieu à la proposition, par Bill et son équipe de recherche, d'une stratégie en phase liquide originale pour la synthèse organique en utilisant des étiquettes ioniques (*ionic tags*) comme support soluble (W. Miao et T.H. Chan. *Acc. Chem. Res.* 2006. **39**: 897–908). La réaction homogène s'effectue habituellement dans un solvant relativement polaire. Après la réaction, l'espèce marquée d'un ion (*ion-tagged species*) est facilement séparée des autres réactifs par précipitation avec un solvant moins polaire. Elle peut jouer le rôle de catalyseur, de réactif, ou de substrat dans la synthèse de petites molécules ou de bio-oligomères. Bill met en évidence le succès de cette méthode en synthétisant des peptides, des oligosaccharides et des nucléotides, en collaboration avec Masad Damha de l'Université McGill (R.A. Donga, M. Hassler, T.H. Chan et M.J. Damha. Nucleosides, Nucleotides and Nucleic Acids. 2007. **26**(10–12): 1287–1293).

En 1997, Bill et C. J. Li publient la monographie *Organic Reactions in Aqueous Media*. Il s'agit du premier ouvrage abordant ce sujet et on le reconnaît comme étant « la » référence du domaine. En 2007, une deuxième édition de l'ouvrage *Comprehensive Organic Reactions in Aqueous Media* est publiée pour mettre à jour les découvertes qui se font dans ce domaine de recherche important et qui connaît une expansion fulgurante.

Outre ses contributions à la recherche, Bill se consacre également à l'enseignement de la chimie verte. En 2000, il met sur pied et donne le premier cours de premier cycle de chimie verte offert dans une université canadienne. Il se fait le défenseur de l'enseignement de la chimie verte en partageant son expérience en enseignement de ce cours avec des collègues au Canada et à l'échelle internationale. Plusieurs universités canadiennes offrent maintenant la chimie verte dans leur programme d'études. En 2002, Bill devient le coordonnateur fondateur du Réseau canadien de chimie verte, qui réunit plus de 50 chercheurs provenant d'une vingtaine d'universités et d'instituts de recherche canadiens, et dont la mission est de promouvoir la recherche et l'éducation en chimie verte au Canada et d'encourager la collaboration internationale. Ce réseau fait partie des réseaux internationaux affiliés au Green Chemistry Institute de l'American Chemical Society. La chimie verte est maintenant un domaine de recherche florissant au sein de plusieurs universités canadiennes dont l'Université Queen's à Kingston (Ontario), l'Université Saint Mary's à Halifax (Nouvelle-Écosse), l'Université d'Ottawa, l'Université McGill et l'Université de Montréal. Bill Chan est cité comme étant « le "père" de la chimie verte au Canada » (voir le magazine de l'Université de Sherbrooke *UdeS*, vol. 1, no 1).

Bill Chan contribue également à la recherche en chimie pharmaceutique. Le point de départ est un intérêt pour la chimie des produits naturels et la synthèse de la spécionine, une molécule qui pourrait s'avérer intéressante dans la lutte contre le problème de la tordeuse des bourgeons de l'épinette au Canada (A.K. Mohammad-Ali, T.H. Chan, A.W. Thomas, B. Jewett et G.M. Strunz. *Can. J. Chem.* 1994. **72**: 2137–2143). Par la suite, il met au point la synthèse énantiosélective de l'épigallocatéchine-3-gallate (EGCG), le polyphénol actif présent dans le thé vert (L. Li et T.H. Chan. *Org. Lett.* 2001. **3**: 739–741). En collaboration avec Q.P. Dou du Karmanos Cancer Center de l'Université d'État Wayne à Détroit (Michigan), il met sur pied un vaste programme sur la mise au point d'agents anticancéreux en utilisant des polyphénols du thé vert et des analogues. Ce programme mène à la création du promédicament polyphénol (–)-épigallocatéchine-3-gallate du thé vert comme agent anticancéreux potentiel (K.R. Landis-Piwowar, C. Huo, D. Chen, V. Milacic, G. Shi, T.H. Chan et Q.P. Dou. *Cancer Res.* 2007. **67**: 4303–4310). Chez les modèles animaux, ce composé se révèle actif contre le cancer du sein et celui de la prostate androgéno-indépendant. Plusieurs demandes de brevets relatifs aux polyphénols de thé vert ont été déposées dans le monde entier et certains ont été accordés.

Un autre projet en cours, en collaboration avec Larry M.C. Chow de l'Université polytechnique de Hong Kong, consiste à trouver de nouveaux dimères de flavonoïdes pour vaincre la multirésistance aux médicaments en chimiothérapie anticancéreuse. Le traitement des patients cancéreux par des produits chimiothérapeutiques mène souvent à l'apparition de tumeurs qui présentent un phénotype de multirésistance aux médicaments (MRM), ce qui constitue un obstacle majeur à la chimiothérapie anticancéreuse. Trois principaux membres de la famille des cassettes de liaison à l'ATP (ABC, pour *ATP-binding cassette*), à savoir ABCB1, ABCC1 et BCRP, sont responsables de la majorité des MRM par efflux. Chan et ses collaborateurs mettent au point des modulateurs puissants pour ces trois types de transporteurs qui sont sûrs et sélectifs (K.F. Chan, Y. Zhao, B.A. Burkett, I.L. Wong, L.M. Chow et T.H. Chan. *J. Med. Chem.* 2006. **49**: 6742–6759; I.L. Wong, K.F. Chan, K.H. Tsang, C.Y. Lam, Y. Zhao, T.H. Chan et L.M. Chow. *J. Med. Chem.* 2009. **52**: 5311–5322; K.F. Chan, I.L.K. Wong, B.A. Burkett, Y. Zhao, C.S.W. Yan, J.W.Y. Kan, K.H. Tsang, C.Y. Lam, T. Chow, T.H. Chan et L.M.C. Chow. *Prog. Nutr.* 2010. **12**: 51–57). Plusieurs brevets sur ces dimères de flavonoïdes sont déposés et des développements en ce sens devraient se poursuivre.

Bill Chan reçoit de nombreuses récompenses dont le prix Merck Sharpe & Dohme (1982), la bourse de perfectionnement en recherche Killam du Conseil des Arts du Canada (1983–1985) et le prix R.U. Lemieux de la Société canadienne de chimie (1993). Il est également nommé membre de la Société royale du Canada en 1993. Nous avons maintenant le privilège de lui consacrer ce numéro spécial de la *Revue canadienne de chimie* pour célébrer ses contributions remarquables à la recherche et à l'éducation scientifiques et son dévouement à l'ensemble de la communauté scientifique au Canada et dans le monde entier.

Chao-Jun Li
Université McGill, Montréal (Québec)

Michael A. Brook
Université McMaster, Hamilton (Ontario)